Russian Journal of Applied Chemistry, Vol. 74, No. 1, 2001, pp. 1–6. Translated from Zhurnal Prikladnoi Khimii, Vol. 74, No. 1, 2001, pp. 3–7.

INORGANIC SYNTHESIS AND INDUSTRIAL INORGANIC CHEMISTRY

Hydrothermal Synthesis of Chromium Dioxide

M. G. Osmolovskii, I. I. Kozhina, L. Yu. Ivanova, and O. L. Baidakova

St. Petersburg State University, St. Petersburg, Russia

Received August 4, 2000

Abstract—Two procedures for hydrothermal synthesis of chromium dioxide are compared: from chromium(VI) oxide and from chromium(VI) and chromium(III) oxides. The reaction products obtained in the presence of modifying agents such as antimony, iron, tellurium, and tin compounds are described in relation to the synthesis temperature.

Chromium dioxide, known as one of "intermediate" chromium oxides, has a rutile structure. The ferromagnetic properties of the compound distinguish CrO_2 from all other oxides of *d* elements. The quadruple-charged state of chromium, demonstrated by neutron diffraction analysis [1], is one more distinctive feature of the compound.

First syntheses of pure chromium dioxide were done by thermal decomposition of dry chromium(VI) oxide in oxygen under elevated pressure [2, 3]. The T–p_{O_2} diagram of phase transformations in the series CrO_3–$CrO_{2.67}$ (β-oxide)–$CrO_{2.44}$ (γ-oxide)–CrO_2–Cr_2O_3 was described in [4]. CrO_2 is stable in oxygen under a pressure of 10 MPa in the interval 255–280°C. At lower oxygen pressure, the limits of the narrowing range have not been determined precisely. Later investigations of ways to synthesize chromium dioxide [5–12] were aimed at obtaining powders suitable for use in magnetic recording media. These were hydrothermal syntheses in the presence of modifying additives. A distinctive feature of the powders is that their particles are small and needle-shaped. The coercive force of such a powder depends on the needle thickness.

Two main methods of hydrothermal synthesis are known: from a $CrO_3 + H_2O$ mixture (procedure A) [5–7, 11] and from $CrO_3 + Cr_2O_3 + H_2O$ mixture (procedure B) [8–10, 12]. The molar ratio Cr/H_2O is commonly within the range 0.9–1.5 in procedures A and B. The chemical aspect of these processes has been described incompletely. It is known that α-CrOOH and only trace amounts of CrO_2 are formed at 300–325°C from a dilute chromic acid solution (molar ratio $CrO_3/H_2O < 0.06$) [14]. According to [15], the hydrothermal decomposition of CrO_3 to chromium dioxide under a pressure of 50–200 MPa is preceded by stepwise formation of β and γ chromium oxides, and fast decomposition to CrO_2 occurs at above 360°C. However, at temperatures below 320°C CrO_2 is insufficiently stable in aqueous medium, chromium dioxide may decompose to give β-CrOOH even under elevated pressure of oxygen [16]. This temperature lies near the thermal stability limit of CrO_2 [4]. The common temperature of hydrothermal synthesis of CrO_2 is 350–400°C [5–11].

The hydrothermal process A is commonly described by the equation $CrO_3 \rightarrow CrO_2 + 1/2O_2$. Processes of the type B were described by the equations $Cr_2O_3 + CrO_3 \rightarrow \rightarrow 3CrO_2$ and $Cr_2O_3 + 3CrO_3 \rightarrow 5CrO_2 + O_2$ in [17], $Cr_2O_3 \cdot 3CrO_3 \cdot H_2O \rightarrow 5CrO_2 + O_2 + H_2O$ in monograph [18]; the occurrence of the process in two stages: $Cr_2O_3 + 2CrO_3 \rightarrow 3CrO_2 + CrO_3$ (250°C, nucleation) and $CrO_3 \rightarrow CrO_2 + 1/2O_2$ (75°C, growth of CrO_2 at nuclei) is reported in [10]. Apparently, the proposed schemes are tentative and contradict some facts, e.g., the good solubility of chromium(VI) oxide [19]. As modifying additives serve compounds of Sb, Te, Sb + Fe, Te + Fe, Sn + Te, and Sn + Te + Fe. Their amounts per 100 mol of chromium are in the range from 0.05 to 2.0 mol and more in the case of iron(III). A solid solution $(Cr, Fe)O_2$ and phases with the rutile structure such as $CrSbO_4$, Cr_2TeO_6, $FeSbO_4$, etc., and solid solutions on their base, e.g., $(Cr, Fe)SbO_4$, are formed in the course of the reaction [6, 20]. Already in [6], an assumption was made that these compounds can serve as nuclei in chromium dioxide formation; however, no experimental evidence in favor was presented. The proposed model of three-stage heteroepitaxial formation of CrO_2 in the presence of Sn + Te compounds [21] was based on a comparison of the finite sizes of chromium dioxide crystals with the surface area of the

1070-4272/01/7401-0001$25.00

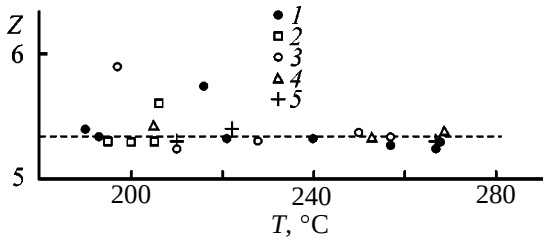

Fig. 1. Average oxidation state of chromium, *Z*, in solution vs. the synthesis temperature *T*. Synthesis procedure: (*1*–*4*) A and (*5*) B; the same for Fig. 2. (*1*, *5*) $SnO_2 \cdot nH_2O$ + $H_2TeO_4 \cdot 2H_2O$, (*2*) Sb_2O_3 + γ-Fe_2O_3, (*3*) Sb_2O_3, and (*4*) no additives; the same for Fig. 2.

modifier-matrix (hydrated tin dioxide) and the amount of the second modifier, tellurium compound. In the same communication a pathway of the hydrothermal reaction A via formation of a chromium chromate solution was reported. As noticed previously [22], this pathway is rather similar to that of reaction B. In this work, reaction A is analyzed in more detail and a reaction by pathway B is described for the first time. The obtained additional data make possible a more thorough description of the process mechanisms, including detailed description of the mechanism of modifying action of additives, and consideration of methods for control over size and composition of nanoparticles.

All experiments were performed in a 0.5-l Cr17Ni13Mo2Ti steel autoclave in which a quartz test tube with a mixture to be decomposed was placed. The experiments by procedure A were performed with the molar ratio Cr/H_2O = 0.9, and those by procedure B, with Cr(VI) : Cr(III) : H_2O = 0.41 : 0.27 : 1.0. The modifying additives were introduced in preparing the paste. In all cases the ratio of the total amount of chromium compounds to the autoclave volume (with correction for the test tube material volume) was 0.5 mol l^{-1}. The reaction product was washed out of the test tube with subsequent centrifugation in synthesizing a viscous paste or was extracted from the tube by breaking it into pieces, with subsequent grinding and drying at 110°C. The rate of mixture heating in the autoclave was 100–150 deg min^{-1}.

Table 1. Chromium oxides isolated from products of CrO_3 hydrothermal decomposition performed without modifying additives (*n* is number of moles of chromium)

Synthesis no.	*T*, °C	τ, h	Solid products	n_s/n_{in}
628	205	6.0	Not formed	0
633	253	6.8	Chromium γ-oxide	0.35
630	269	7.5	Chromium γ-oxide, CrO_2	0.45

The onset of oxygen evolution in heating of mixture A was recorded at 145–165°C in all the performed 500 runs. As a result, a chromium chromate solution with a Cr(VI) : Cr(III) ratio close to 7 : 2 (or with average oxidation state of chromium of 5.33) is formed. Apparently, this is the same Cr(VI) : Cr(III) ratio as in β chromium oxide $CrO_{2.67}$, well soluble in water [23]. An X-ray phase analysis (XPA) demonstrated the absence of β-oxide in the reaction products. In performing the reaction by procedure B, CrO_3, Cr_2O_3, and H_2O start to react in the stage of component mixing, and the mixture heats-up. At temperatures below 200°C such a mixture does not evolve oxygen (to within the experimental error). The Cr(VI) : Cr(III) ratio in the soluble part of the product is the same as in synthesis by procedure A.

Figure 1 presents the average oxidation states of chromium in centrifugates, determined for a number syntheses of types A and B at 190–270°C. The results are independent of the presence of additives or, as shown below, of whether or not CrO_2, CrO_3, or γ chromium oxide are contained in the reaction products. The mixture of products obtained at 300–400°C is a pumice-like solid mass. According to XPA, this mass is practically pure chromium dioxide. Some products of this kind were subjected to dry milling, wet grinding, and multiple washing with centrifuging. The starting portion of a powder was about 200 g; washing was terminated at a chromium content of 10 mg l^{-1} in the centrifugate. The total amount of washing water was varied within 5–8 l, and the total content of chromium in the centrifugate was in the range from 0.2 to 6.0 g. The average oxidation state of chromium in washing water varied between 5.23 and 5.44.

Thus, there exists a mother liquor from which chromium dioxide is formed. The initial concentration of chromium in the solution is as high as 10 M. This solution is the same for synthesis procedures A and B, the Cr(VI) : Cr(III) ratio in the solution is close to 7 : 2.

Data on solid products obtained by hydrothermal decomposition of pure chromium(VI) oxide (procedure A, no modifiers) are presented in Table 1. At 263°C, 35% of the initial amount of CrO_3 is converted into γ chromium oxide. This conclusion is made on the basis of gravimetric analysis and XPA of a dried precipitate. With the temperature increasing to 269°C, 45% of the starting CrO_3 is converted into oxides to give a mixture of chromium γ-oxide and

dioxide. The content of CrO_2, evaluated on the basis of the specific magnetization of the precipitate, was about 10% of the total mass of oxides (Table 1, run no. 630). The final pressure in run no. 630 was as high as 10 ± 1 MPa, and the partial pressure of oxygen, ca. 8 MPa. The latter was evaluated independently by two methods: from the residual pressure at room temperature and from the amount of gas passing through the gas meter in relieving the pressure. The obtained temperatures of formation of γ-oxide and CrO_2 under hydrothermal conditions are in good agreement with the "non-hydrothermal" phase diagram of chromium oxides [4]. Since in the synthesis procedure A oxygen starts to be evolved at about 150°C irrespective of the presence of modifiers, reduction of Cr(VI) to Cr(III) may favor formation of mixed oxides $Cr(III)Sb(V)O_4$ and $Cr(III)_2Te(VI)O_6$ already at this temperature. Indeed, the use of $H_2TeO_4 \cdot 2H_2O$ allowed isolation of Cr_2TeO_6 from the product of a reaction carried out at 150°C.

With antimony(III) oxides used as modifiers (in procedure A), mixed oxide $CrSbO_4$ is formed at a higher temperature than that observed for orthotelluric acid. This process is limited by two factors: dissolution of Sb_2O_3 and oxidation Sb(III) → Sb(V). For example, at a molar ratio Sb : Cr = 2 : 98 (with senarmontite as modifier), a precipitate was isolated after synthesis at 197°C, composed of only spindle-shaped monodisperse $CrSbO_4$ particles; the weight of the precipitate was less than 1/10 of that expected on the basis of the reaction. The rest of antimony(III) or antimony(V) was not isolated in centrifugation, but was separated from a centrifugate allowed to stand for a year in the form of an Sb_6O_{13} precipitate (ASTM 21-51). Consequently, despite the dissolution of senarmontite at 197°C, complete oxidation Sb(III) → Sb(V) did not occur. Raising the synthesis temperature to 228°C allowed complete conversion of antimony into spindle-like monodisperse $CrSbO_4$ particles. However, centrifugation was also done in two stages: immediately upon dissolving the product and a year after. The dimensions of spindles synthesized at 197 and 228°C were the same within experimental error: length 86 and 91 nm, respectively; maximum thickness (diameter) 31 nm.

XPA demonstrated a slight increase in interplanar spacings of the $CrSbO_4$ phase, compared with the data of [24]. This made necessary the refining of unit cell parameters for $CrSbO_4$ and $FeSbO_4$, for which purpose preparations synthesized by the ceramic technology were used. XPA data for the purposefully synthesized phases [20] coincided with published evidence. Simultaneously, it was found that the parameters of a $Cr_{1-x}Fe_xSbO_4$ solid solution at $x \le 0.4$ coincide with the parameters of $CrSbO_4$ [20]. The XPS spectra of a $CrSbO_4$ phase synthesized by procedure A at 197°C demonstrated the absence of iron in the compounds, which conclusively excluded from consideration the possibility that the lattice parameters of $CrSbO_4$ increase because of the iron(III) impurity in chromium(VI) oxide. XPS also revealed that the entire amount of antimony is present in the form of Sb(V), with molar ratios Cr(III)/Cr(VI) = 2.8 and Sb/Cr = 2.3. These results indicate that the surface of the $CrSbO_4$ phase is enriched with antimony atoms, presumably through their sorption from the mother liquor, and also with Cr(III) atoms. There were no thermal effects in the derivatogram of the sample. Continuous mass loss (7%) was recorded in the interval 200–800°C, presumably resulting mainly from dehydration of a preparation obtained under hydrothermal conditions. The complexity of the chemical composition of the oxide surface and the presence of water in it can serve as an additional reason for the distortion of the X-ray characteristics of the preparation, with the main reason being, presumably, the ultradispersity of the $CrSbO_4$ phase.

Table 2. Solid compounds isolated from products of CrO_3 hydrothermal decomposition performed in the presence of antimony oxides and γ-Fe_2O_3. Designations: S, Sb_2O_3, senarmontite; V, Sb_2O_3, valentinite; and G, γ-Fe_2O_3

Synthesis no.	Sb : Fe : Cr molar ratio	Type of Sb_2O_3	T, °C	Solid products
705	0.5 : 1.5 : 98	S	195	G + S + (Fe, Cr)SbO_4
704	2 : 6 : 92	S	206	G + (Fe, Cr)SbO_4
703	0.5 : 1.5 : 98	V	200	Not determined*
702	2 : 6 : 92	V	205	V + (Fe, Cr)SbO_4

* The precipitate mass was less than 2 wt % relative to modifiers, which is insufficient for XPA.

The presence of iron(III) oxide as a second additive hinders the dissolution of antimony oxides (Table 2). Synthesis by procedure A at a temperature close to 200°C is also accompanied by a structural transformation in γ-Fe_2O_3. The relative intensities of lines in the X-ray diffraction patterns of the starting γ-Fe_2O_3 were in full agreement with those in the ASTM file 25-1402, being different, and described by ASTM file 13-458, for its undissolved part. Also, a phase was formed with much larger, compared with $CrSbO_4$, unit cell parameters. In all probability, the obtained phase is a solid solution (Fe, Cr)SbO_4 whose composition cannot be interpreted using X-ray analysis

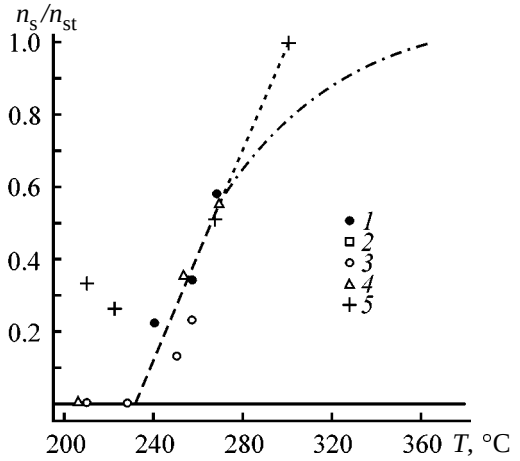

Fig. 2. Mole fraction of chromium in the oxides Cr_2O_3, $CrO_{2.44}$, and CrO_2, n_s/n_{st}, vs. temperature T of hydrothermal synthesis. (n_{st}) Number of moles of chromium in the starting compounds and (n_s) number of chromium moles in solid reaction products. Correction is made for the interaction of the starting chromium compounds with modifiers.

[20]. According to electron microscopy, the particles of the isolated precipitate had a complex star-like shape.

CrO_2 is not formed yet in the course of reaction A in the presence of senarmontite at 228°C, but at 250°C its amount is rather high. As in the case of $SnO_2 \cdot nH_2O$ + $H_2TeO_4 \cdot 2H_2O$ additives, chromium γ-oxide $CrO_{2.44}$ is not formed in the presence of antimony compounds. The temperature dependence of the degree of conversion of the starting chromium compound (CrO_3 in the given case) into oxides, n_s/n_{st}, is presented in Fig. 2. The onset temperature of the conversion is estimated to be 230–235°C.

For syntheses by procedure B, $SnO_2 \cdot nH_2O$ and $H_2TeO_4 \cdot 2H_2O$ additives were taken at a molar ratio Sn : Te : Cr = 0.2 : 0.2 : 99.4. The only solid compound found after synthesis at 210°C is chromium(III) oxide. Minor additions of tin and tellurium compounds were not detected on the background of chromium(III) oxide. The product synthesized at 222°C was CrO_2 in a mixture with Cr_2O_3. Chromium γ-oxide was not formed in this case, as also in procedure A with modifiers. Pressure buildup in the autoclave was only recorded after CrO_2 appeared.

The temperature at which the formation of chromium dioxide by pathway A was complete was determined from the coincidence of pressures in continuous heating of the autoclave at a rate of 150 deg h^{-1} to 400°C and in subsequent cooling. The poor precision of gas gages gave no way of performing the measurements with sufficient accuracy, and only an approximate value of 360 ± 10°C was determined. As indicated by experimental data, the completion temperature of the process is related to the partial pressure of oxygen and the Cr : H_2O ratio in solution. For example, in decomposition of the mixture by procedure B with additives the formation of CrO_2 is practically complete at 300°C, but in this case the partial pressure of oxygen is approximately two times lower than that in procedure A. The partial pressure release from the autoclave in procedure A also leads to completion of CrO_2 formation at 300°C: Soluble chromium compounds found in washing the product constitute only 2% of the initial amount of CrO_3.

To the point of completion of crystallization, a considerable part of water is contained in chromium chromate. For example, the partial pressure of water vapor for procedure A at 300°C was estimated to be 0.6–0.8 MPa, even though the amount of water in the autoclave was twice that necessary for reaching the equilibrium vapor density and pressure of pure water [25]: 46.2 g l^{-1} and 8.59 MPa. The final concentrations of water vapor in the autoclave for procedures A and B at complete evaporation of water are 109.6 and 133.2 g l^{-1}, respectively, which enables complete evaporation of water at 348 and 357°C [25]. Since in the latter case the formation of CrO_2 is complete at 300°C, the partial pressure of oxygen governs the reaction course.

Thus, both procedures of synthesis involve crystallization of chromium dioxide from a chromium chromate solution.

The majority of n_s/n_{st} values in Fig. 2 were determined by weighing the CrO_2 precipitate with correction made for the mass of the mixed oxide $CrSbO_4$. The strong deviation of three n_s/n_{st} values from the zero line in procedure B at 210–222°C is due to incomplete dissolution of Cr_2O_3. For the case of decomposition by procedure A without additives, calculation was based on the results of gravimetric analysis of chromium γ-oxide and its mixture with CrO_2. Apparently, the partial pressure of oxygen will be somewhat lower in obtaining chromium γ-oxide, compared with CrO_2 formation. However, the observed shift of the two indicated points does not disturb the apparent overall tendency for the partial pressure of oxygen to grow in proportion to the increasing degree of conversion and temperature. Consequently, there exists a relationship between the concentration, pressure, and temperature. As final temperatures of the process in Fig. 2 are indicated 300°C and the interval 350–370°C. In the range 240–270°C the temperature de-

pendence of the degree of conversion is nearly linear. Lowering the partial pressure of oxygen (synthesis by procedure A) leads to an increase in the amount of the solid phase in the attainment of chemical equilibrium, i.e., in fact, to complete conversion at $300 \le T \le 350$°C. In synthesis by procedure B, the occurrence of the second reaction, partial dissolution of the excess amount of chromium(III) oxide, is possible in parallel with CrO_2 crystallization, which restores the Cr(VI) : Cr(III) ratio in the solution; however, the extent of this reaction is low. Even though XPA failed to show chromium(III) oxide impurity in the product obtained at 300°C by procedure B, its presence was revealed by electron microscopy and, indirectly, by magnetic methods.

Thus, both processes, A and B, occur by the same mechanism. A more detailed study of how crystals of modifying phases and chromium dioxide itself grow can be more conveniently performed with process A in which there is no constant background of unreacted chromium(III) oxide.

As starting reagents in the syntheses served analytically pure CrO_3, Cr_2O_3 obtained by decomposition of analytically pure ammonium dichromate and having a specific surface area $S_{sp} = 27$ m^2 g^{-1}, Sb_2O_3 in the form of senarmontite ($S_{sp} = 5.7$ m^2 g^{-1}) and valentinite ($S_{sp} = 2.9$ m^2 g^{-1}), iron γ-oxide of "for ferrites" grade ($S_{sp} = 5$ m^2 g^{-1}), $H_2TeO_4 \cdot 2H_2O$ of pure grade, and hydrated tin(IV) oxide ($S_{sp} = 204$ m^2 g^{-1} in terms of anhydrous substance) obtained by treatment of tin with nitric acid. The temperature in the autoclave was measured with a Chromel–Copel thermocouple, which was inserted in a well protected from reagents by a quartz test tube 8 mm in diameter. The temperature was recorded by a KSP-4 self-recorder with an accuracy of ±5°C and maintained constant within the same limits. X-ray phase analysis was performed on DRF and DRON-3M instruments with copper- and chromium-filtered radiation. Electron micrographs were taken on a Tesla BS 613B electron microscope (100 000 magnification). Chemical analysis of solutions for the content of Cr(VI) was done by the volumetric method; the sum Cr(VI) + Cr(III) was determined upon oxidation of Cr(III) with ammonium peroxodisulfate. Minor amounts of chromium (in washing water) were determined by photocolorimetry. The error of titrimetric measurements of the average state of chromium oxidation was not greater than 0.2. Gravimetric analysis was performed by calcining chromium oxides to constant weight at 850°C.

CONCLUSIONS

(1) Hydrothermal decomposition of CrO_3 and $CrO_3 + Cr_2O_3$ mixture to give CrO_2 passes through a stage producing a chromium chromate solution with Cr(VI) : Cr(III) = 7 : 2.

(2) Crystallization of chromium oxides is governed by an unambiguous relationship between the partial pressure of oxygen and the concentration and temperature of the chromium chromate solution. Formation of $CrO_{2.44}$ in the presence of modifying additives is ruled out by the lowered temperature of CrO_2 formation.

(3) The process of CrO_2 formation ends before complete evaporation of water from the solution, below the critical point of water.

(4) Complete conversion of the modifying additive [antimony(III) compound] into the $CrSbO_4$ phase occurs at a temperature lower than the CrO_2 crystallization temperature. The isolated $CrSbO_4$ phase is composed of monodisperse nanospindles.

REFERENCES

1. Burdett, J.K., Miller, G.J., Richardson, J.W., and Smith, J.V., *J. Am. Chem. Soc*., 1988, vol. 110, no. 24, pp. 8064–8071.
2. Schwarts, R.S., Fankuchen, I., and Ward, R., *J. Am. Chem. Soc*., 1952, vol. 74, no. 7, pp. 1676–1677.
3. Ariya, S.M., Shchukarev, S.A., and Glushkova, V.B., *Zh. Obshch. Khim*., 1953, vol. 23, no. 8, pp. 1241–1245.
4. Wilhelmi, K.-A., *Acta Chem. Scand*., 1968, vol. 22B, pp. 2565–2572.
5. Swoboda, T.J., Arthur, P., Cox, N.L., *et al*., *J. Appl. Phys*., 1961, vol. 32, pp. 374s–375s.
6. Mihara, T., Kawamoto, T., Terada, Y., and Hirota, E., *Ferrites: Proc. Int. Conf. (July 1970, Kyoto, Japan)*, Baltimore, 1971, pp. 476–479.
7. Ariya, S.M., Vasilevskii, Yu.A., Volodina, A.P., *et al*., in *Issledovaniya v oblasti neorganicheskoi tekhnologii. Soli, okisly, kisloty* (Investigations in Inorganic Technology: Salts, Oxides, and Acids), Leningrad: Nauka, 1972, pp. 332–334.
8. Chen, H.Y., Hiller, D.M., Hudson, J.E., and Westenbroek, C.J.A., *IEEE Trans. Magn*., 1984, vol. 20, no. 1, pp. 24–26.
9. Grandall, T.G., Chen, H.-Y., Cole, G.R., *et al*., *IEEE Trans. Magn*., 1987, vol. 23, no. 1, pp. 36–38.
10. Auweter, H., Feser, R., Jakusch, H., *et al*., *IEEE Trans. Magn*., 1990, vol. 26, no. 1, pp. 66–68.

11. Schuster, K. and Stopperka, K., J. *Signal AM*, 1978, vol. 6, no. 2, pp. 141–143.
12. RF Patent 2 022 718.
13. Osmolovskii, M.G., Zvereva, I.A., Ivanova, L.Yu., and Petrov, A.E., *Vestn. Leningr. Gos. Univ., Ser. 4*, 1991, no. 1, pp. 114–115.
14. Thamer, B.J., Douglass, R.M., and Staritzky, E., *J. Am. Chem. Soc.*, 1957, vol. 79, no. 3, pp. 547–550.
15. Hestermans, P., *High Temp.-High Press.*, 1974, vol. 6, no. 4, pp. 615–618.
16. Shibasaki, Y., *Mater. Res. Bull.*, 1972, vol. 7, no. 10, pp. 1125–1133.
17. Hibst, H., *J. Magn. Mater.*, 1988, vol. 74, no. 1, pp. 193–202.
18. Braginskii, G.I. and Timofeev, E.N., *Tekhnologiya magnitnykh lent* (Technology of Magnetic Tapes), Leningrad: Khimiya, 1987.
19. *Spravochnik khimika* (Chemist's Handbook), Nikol'skii, B.P., Ed., Moscow: Khimiya, 1964, vol. 3.
20. Osmolovskii, M.G., *Vestn. Sankt-Peterb. Gos. Univ., Ser. 4*, 1997, no. 3, pp. 113–115.
21. Osmolovskii, M.G. and Otkupshchikov, A.Yu., in *Problemy sovremennoi khimii koordinatsionnykh soedinenii* (Problems of the Modern Chemistry of Coordination Compounds), Leningrad: Leningr. Gos. Univ., 1983, no. 7, pp. 5–29.
22. Osmolovskii, M.G., Ivanova, L.Yu., and Dunaev, A.I., in *Sbornik trudov 8-i konferentsii sotsialisticheskikh stran "Magnitnye nakopiteli", Bekhine, ChSSR, 10–15 sentyabrya 1989 g.* (Proc. 8th Conf. of Socialist Countries "Magnetic Storage Devices," Behine, CSSR, September 10–15, 1989), Prague: VUZORT, 1990, vol. 1, pp. 167–173.
23. Kubota, B., *J. Am. Ceram. Soc.*, 1961, vol. 44, no. 5, pp. 239–248.
24. Brandt, K., *Arkiv Kemi, Miner. Geol.*, 1943, vol. 17A, no. 15, pp. 1–8.
25. *Spravochnik khimika* (Chemist's Handbook), Nikol'skii, B.P., Ed., Moscow: Khimiya, 1962, vol. 1.

Russian Journal of Applied Chemistry, Vol. 74, No. 1, 2001, pp. 7–11. Translated from Zhurnal Prikladnoi Khimii, Vol. 74, No. 1, 2001, pp. 8–12.

INORGANIC SYNTHESIS AND INDUSTRIAL INORGANIC CHEMISTRY

Nature of Contamination and Preparation of Pure Precipitates of Rh(III) and Ir(III) Ammonium Sodium Hexanitrites

S. V. Korenev, A. B. Venediktov, V. A. Nadolinnyi, and A. V. Belyaev

Institute of Inorganic Chemistry, Siberian Division, Russian Academy of Sciences, Novosibirsk, Russia

Received May 12, 2000

Abstract—Various spectroscopic methods and X-ray phase analysis were applied to study the distribution of copper(II) and lead(II) between the solution and the precipitate of $(NH_4)_2Na[Rh(NO_2)_6]$. Promising methods are proposed for fine purification of ammonium sodium hexanitrites of rhodium(III) and iridium(III) to remove contaminants, irrespective of the mechanism of their ingress into crystalline phases.

Precipitation of poorly soluble ammonium sodium hexanitrites (ASHs) $(NH_4)_2Na[M(NO_2)_6]$ (M = Rh, Ir) [1] from nitrite solutions is among methods for separating platinum metals [2], which has long been used in their refining [3, 4]. Owing to the complex elemental composition of the solutions from which ASHs are isolated in practice, these precipitates are commonly contaminated with both noble and base metals [4, 5]. The fundamental aspects of coprecipitation of impurity elements with matrices of crystalline ASHs have not been known.

The aim of this study was to obtain quantitative physicochemical data characterizing the ingress of impurities into the ASH phases of rhodium(III), to reveal on this basis the possible mechanisms of these processes, and to find ways to obtain salts with as low degree of contamination as possible. The choice of lead(II) and copper(II) as models is due to the fact that these elements are characterized by high level of coprecipitation and ASH precipitates free of Cu(II) and Pb(II) impurities can only be obtained by an exceedingly labor-consuming procedure [4, 5].

Solutions of chloride complexes of rhodium in 0.1 M HCl were prepared from reagent-grade rhodium(III) chloride. The solution concentrations were determined spectrophotometrically, by reaction with tin(II) chloride [6]. The absorption spectra were taken on a Specord M 40 instrument.

Working solutions of $Na_3[Rh(NO_2)_6]$ were prepared by treatment of standard chloride solutions with sodium nitrite of ultrapure grade at heating on a water bath for 1 h and then transferred into volumetric flasks. The starting acid solutions of rhodium(III) were partly neutralized by preliminary treatment with sodium carbonate. The nitrite : rhodium molar ratio was 10 : 1. Nitrite solutions of copper(II) and lead(II) were prepared in a similar manner.

Lead(II) nitrate of ultrapure grade and chemically pure grade copper(II) were used in the study. The concentrations of the starting Cu(II) and Pb(II) solutions were determined by EDTA titration [7]. The other reagents used were of no less than chemically pure grade.

The distribution of impurity components between the solution and the solid phase of rhodium(III) ASH was studied at 22–23°C as follows. Nitrite solutions of rhodium(III) and impurity were mixed, and a calculated amount of ammonium chloride was added to make the ammonium/rhodium ratio close to 20. The formed ASH precipitates were kept in the mother liquor for a prescribed time, separated, washed with 1% NH_4Cl and a minimum possible amount of cold water, dried in air to constant weight, and weighed. The yield of ASH in the solid phase was no less than 99% in all cases. A study of the granulometric composition of rhodium(III) ASH demonstrated that after keeping the crystals under mother liquor for 7 h the average particle size becomes ca. 21 μm and does not change further, with a normal size distribution of particles.

The impurity content in solid phases was determined by an appropriate analytical method. The amount of impurity was expressed in weight percent impurity component in the ASH phase.

Treatment with sodium nitrite of solutions containing copper(II) gave emerald-green precipitates of basic copper(II) chlorides of variable composition whose nature was studied in detail in [8]. For this reason,

1070-4272/01/7401-0007$25.00

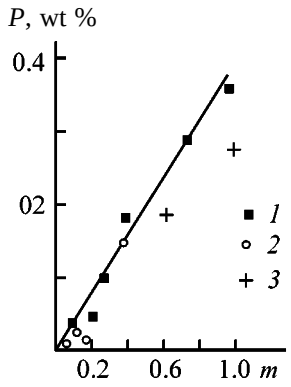

Fig. 1. Copper(II) distribution between rhodium(III) ASH precipitate and nitrite solution. (*P*) Copper content in the ASH phase and (*m*) Cu/Rh molar ratio in solution. (*1*) Set A and (*2*) set B. Time of keeping the system before precipitate isolation (h): (*1, 2*) 24 and (*3*) 12.

solutions containing copper(II) were always prepared separately. The precipitates formed were separated and the obtained copper(II) solutions were used, after determining their concentration, in sorption experiments. The content of copper in ASH phases was determined by the ESR. The ESR spectra were recorded on a Varian E-109 instrument in the X frequency range. The concentration of paramagnetic centers in ASH precipitates was determined using $CuSO_4 \cdot 5H_2O$ as reference with an accuracy of ±2%.

There is no published evidence concerning the mechanisms of impurity coprecipitation on such specific supports as ASHs of rhodium(III) and iridium(III). Previously, it has been shown that salts $(NH_4)_2Na[M(NO_2)_6]$ (M = Rh, Ir) crystallize to give an fcc unit cell with the lattice constant a = 10.517(1) (M = Rh) and 10.512(2) Å (M = Ir) [9]. In addition, it was found in [10] that rhodium(III) and indium(III) salts form a continuous series of solid solutions. As a result, all patterns obtained in studying the ASH of rhodium(III) are to the full extent applicable to its iridium analog. Moreover, the solubilities of rhodium(III) and iridium(III) salts at room temperature are the same and equal to ca. 4.0×10^{-3} M.

One of the main stages of the study consisted in obtaining quantitative data on impurity sorption on ASH precipitates. In this study, by the term "sorption" is meant the characteristic of impurity distribution between the solution and the crystalline phase, irrespective of the distribution mechanism.

In studying the sorption of copper(II), several sets of experiments were performed with varied concentrations of copper(II) and rhodium(III). Set A was carried out at $C_{Rh} = 9.66 \times 10^{-3}$ and equilibrium copper(II) concentrations of (0.95–9.5) $\times 10^{-3}$ M. The content of copper(II) in the ASH precipitates was 0.035–0.36%. Set B was performed for solutions with rhodium(III) concentration of 2.63×10^{-2} M with the equilibrium Cu(II) concentration varied within 3.1×10^{-4}–1.0×10^{-2} M, with the content of copper(II) in the precipitates equal to 0.080–0.154%. In these two sets, the ASH precipitates were separated from the mother liquor after being kept in it for 24 h. The isolated ASH precipitates had color in the range from nearly white to light green. According to X-ray diffraction analysis, all the precipitates were single-phase, with the identical unit cell parameters of salts contaminated with copper(II) and pure ASHs. In both sets the content of copper(II) in the precipitates depended linearly on its equilibrium concentration in solution. In set A, the contaminated precipitates were washed with electrolyte (2 M Na_2SO_4, 1 M HCl) solutions to desorb copper(II) impurities. However, these attempts failed. This indicates indirectly that the contamination mechanism does not have purely adsorption nature.

It can be seen from the presented data that raising the rhodium(III) concentration in a solution leads to lower content of copper(II) in the support. Two experiments performed at lowered initial concentration of rhodium(III) ($C_{Rh} = 5.50 \times 10^{-3}$ M) confirmed that precipitates obtained from solutions concentrated with respect to rhodium(III) are more pure than those in the case of dilute solutions. This effect cannot indicate a change in the sorption mechanism since the same data plotted in the coordinates Cu content in the precipitate (%)–Cu/Rh molar ratio fall on the common linear dependence shown in Fig. 1.

The fact that adsorption does not give any significant contribution to contamination of crystals with copper(II) is mainly determined by the support properties. The solubility of ASH has a narrow supersaturation region, and, therefore, a great number of crystal nuclei with approximately the same sorption capacity are formed in any precipitation technique. Shortening the precipitate aging time from 24 to 12 h (Fig. 1) makes the copper(II) content in ASH somewhat lower, and not higher, which also points to a minor contribution of occlusion to the mechanism of ASH precipitate contamination by copper(II).

Figure 2 shows a typical ESR spectrum of copper(II), observed in the ASH matrix. The spectrum is due to the Cu^{2+} ion and is described by the spin Hamiltonian

$$H = g_{xx}\beta H_x S_x + g_{yy}\beta H_y S_y + g_{zz}\beta H_z S_z + A_{xx} S_x J_x + A_{yy} S_y J_y + A_{zz} S_z J_z$$

with the following parameters: $g_{zz} = g_{\|} = 2.2218$, $g_{xx} = g_{yy} = g_{\perp} = 2.0097$, and $A_{zz} = A_{\|} = 170$ G.

The observed parameters of the ESR signal from copper(II) ions are characteristic of distorted octahedral environment of these ions formed by nitrogen atoms [11]. The resolved hyperfine structure of the signal from copper ions indicates the absence of exchange interaction between the neighboring copper ions. Thus, Cu^{2+} ions in the ASH matrix are at large distances from one another and form no isolated clusters. These data suggest that copper(II) impurity atoms are isolated and uniformly distributed over the volume of the ASH crystalline phase.

The low content of copper(II) in ASH and the lattice constant of the crystalline salt, remaining constant, give no way of confirming experimentally the formation of solid solutions in the system under consideration by methods of crystallography. Nevertheless, there exists a possibility of confirming this fact by changing the chemical form of Cu(II) in the starting solution.

For this purpose, ASH precipitation from nitrite solutions in the presence of copper(II) was effected by 2 M NH_4NO_3 + 2 M $NH_3 \cdot H_2O$ buffer solution at rhodium(III) concentration of 1.10×10^{-2} M in the range of equilibrium copper(II) concentrations 5.28×10^{-3}–1.14×10^{-2} M. The precipitate was separated from the mother liquor 2 h after the precipitation to preclude decomposition of hexanitrorhodate(III) ions in the alkaline medium. The amount of copper(II) in the precipitates was found to be much lower (0.01–0.02%) than that in sets A and B. The ASH yield varied within 99.0–99.5%. The ESR spectra of the obtained crystalline phases indicated only slight changes in the nearest environment of Cu^{2+} ions, compared with the data for sets A and B.

The pronounced decrease in the copper(II) content in the ASH phase on changing its chemical form in solution indirectly points to the mechanism by which solid solutions are formed between the main component and the impurity. The essence of the process consists in isomorphic substitution of octahedral $[Rh(NO_2)_6]^{3-}$ anions at ASH crystal lattice sites by distorted octahedral $[Cu(NO_2)_6]^{4-}$ ions. The possibility of such substitution is indicated by the closeness of the lattice constants of $K_2Pb[Cu(NO_2)_6]$ (a = 10.65 Å [12]) and $(NH_4)_2Na[Rh(NO_2)_6]$ (a = 10.52 Å).

Such a comparison is justified since the crystal lattices of the above salts are constituted by bulky complex anions, while the cations occupy tetrahedral and octahedral voids in these structures. It should also

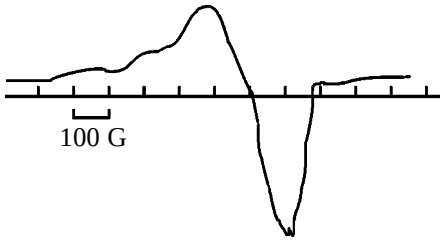

Fig. 2. Typical ESR spectrum of copper(II) in the ASH matrix.

be noted that the hexanitrocuprate(III) ion exists in aqueous solutions in very low concentrations. According to [13], copper(II) forms complexes with one and two nitro groups at 25°C in aqueous solutions, with the step instability constants pK_1 1.25 and pK_2 0.30. Presumably, copper(II) ions with one or two nitro groups in the inner sphere are adsorbed onto an ASH crystal in its formation, and in the course of crystal growth the environment of the copper ion is completed to become octahedral.

The proposed mechanism is in agreement with the entire body of experimental data and gives insight into the main reason for contamination of ASH precipitates with copper(II). With account of this mechanism and the linear isotherms of adsorption, it can be stated that if the above-mentioned solid phases of basic copper salts were not formed in the system, rhodium(III)–copper(II) solid solutions with any Cu(II) content could be obtained.

The fact of lead(II) ingress into the ASH phases in their crystallization from solutions containing Pb(II) and the complications in purification of salts to remove this impurity were noticed as far back as the early 1930s [4]. The understanding of ways of contamination by lead(II) was only gained after a detailed study of the properties of lead salts of Rh(III) and Ir(III) hexanitro complexes [14]. It was shown in [14] that treatment of solutions of complex ions $[M(NO_2)_6]^{3-}$ (M = Rh, Ir) with lead(II) salts leads to the formation of precipitates with formula $Pb_3[M \cdot (NO_2)_6]_2 \cdot 12H_2O$. The precipitates are single-phase and have a cubic lattice with lattice constants a = 10.567(3) for rhodium(III) and a = 10.604(3) Å for iridium(III). Drying the salts at 120°C leads to complete removal of crystallization water, accompanied by a practically linear decrease in the lattice constants a to 10.446(3) (M = Rh) and 10.478(3) Å (M = Ir). The solubility of lead(II) salts in water at room temperature is 1.2×10^{-4} (M = Rh) and 5.0×10^{-5} M (M = Ir).

Thus, the poorly soluble lead salts with the anions

$[M(NO_2)_6]^{3-}$ crystallize to form a cubic lattice with lattice constants close to those for ammonium sodium salts. As indicated by the presented data, the lattice constant a varies between the salts of this series by ca. 0.15 Å. Hence follows that the salts under consideration are isomorphic and form solid solutions in the entire range of concentrations, with any of these salts acting as collector for another if the latter is present in solution in a much lower concentration. Indeed, mixing of nitrite solutions of rhodium(III) and lead(II) in any proportion always gives crystalline phases with lattice constant $a \approx 10.57$ Å. However, at high concentrations of sodium nitrite in solution the forming precipitates are always colored yellow, which is due to sorption of nitrite complexes of lead on the crystals. According to [13], lead(II) forms poorly stable complexes with nitrite ions (at 25°C and ionic strength of 1 M $\log K_1 = 1.87$).

In ASH formation from chloride solutions (in agreement with actual practice) the concentration of lead(II) is determined by the equilibrium concentration of chloride ions, which is as high as 4 M. In this case, with account of the $PbCl_2$ solubility product equal to 1.6×10^{-5} [15], the concentration of lead(II) in solutions will be at the level of 1×10^{-6} M. As a result, no independent phase of lead salts with $[M(NO_2)_6]^{3-}$ can be formed and the crystallizing ASHs act as collector for microscopic amounts of lead(II). Thus, the ASH phases will be always contaminated with lead(II) if Pb(II) ions are not removed from a solution prior to ASH precipitation.

A search for ways to obtain purer ASH precipitates was carried out in several directions. It follows from the presented sorption data that lowering the concentration of copper(II) in solutions prior to ASH precipitation must decrease the contamination of the precipitate. Indeed, the ASH precipitate obtained by the standard procedure from a solution modeling, as regards the composition, an industrial solution contained 0.38% copper(II) at its concentration prior to precipitation of 9.60×10^{-3} M. Pretreatment of the solution with sodium carbonate gives an ASH containing 0.11% copper(II). To make lower the contamination with lead(II), it is advisable to treat the solution with minor amounts of salts containing, e.g., sulfate, carbonate, or phosphate anions forming poorly soluble salts with lead(II) [15]. Fundamentally different is the binding of copper(II) into stable complexes that cannot form solid solutions with ASH. As shown above, copper(II) ammines may be such complexes. It should, however, be taken into account that introduction of ammonia may lead to formation of ammine complexes of platinum, which is undesirable from the practical standpoint [16].

With account of the fact that the mechanism of contamination with copper(II) and lead(II) is associated with isomorphic crystallization, fine purification of the ASHs of rhodium(III) and iridium(III) by the above methods may be rather labor-consuming. In this study, a method was developed making it possible to obtain special-purity salts, which has little sensitivity to the mechanism of impurity ingress. On introducing a weighed portion of ASH into a sodium nitrite solution somewhat acidified with nitric acid, the salt dissolves by the reaction

$$NH_4^+ + NO_2^- \rightarrow N_2 + H_2O,$$

with the complex anions $[M(NO_2)_6]^{3-}$ (M = Rh, Ir) not involved. The optimal dissolution regimes were determined, making it possible to minimize the time and temperature of the reactions performed and to prevent loss of platinum metals in repeated precipitations of ASH. For example, in a precipitate of rhodium(III) ASH, originally containing 0.30% copper(II), the concentration of copper(II) impurity after double precipitation by the proposed technique was on the order of 0.001%. This method can be compared with the procedures proposed in [5]. One of these is the preliminary purification of nitrite solutions to remove base metals prior to ASH precipitation; however, in this case the concentration of the most difficultly separable impurities [Pb(II), Cu(II), Ni(II)] decreases only 3–5-fold. In [5], low efficiency of nitrite solution purification to remove base metals by extraction and ion exchange was revealed and salting-out of $Na_3[Rh(NO_2)_6]$ under the action of an excess of sodium nitrite after preliminary purification by a procedure mentioned above was proposed as the most suitable method for rhodium(III) recovery. In this case, 30–70% of impurity ions (Cu, Pb, Sn, Fe, Zn, etc.) remains in mother liquors. Comparison of the proposed procedures and their quantitative characteristics concerning the purification of ASH precipitates readily shows the advantages of the proposed technique.

CONCLUSIONS

(1) Quantitative data on contamination of precipitated ammonium sodium rhodium(III) hexanitrites with copper(II) and lead(II) ions were obtained and the mechanism of impurity ingress was established. The fact that the properties of ammonium sodium hexanitrites of Rh(III) and Ir(III) are close allows the

revealed relationships to be applied to the case of contamination of $(NH_4)_2Na[Ir(NO_2)_6]$.

(2) Various methods were compared and a new efficient procedure for obtaining pure $(NH_4)_2Na \cdot [M(NO_2)_6]$ (M = Rh, Ir) was developed.

ACKNOWLEDGMENTS

The authors are deeply grateful to S.A. Gromilov for X-ray phase analysis of the samples studied.

REFERENCES

1. Lebedinskii, V.V. and Shenderetskaya, E.V., *Izv. Sekt. Platiny*, 1955, no. 29, pp. 61–65.
2. Muraveiskaya, G.S., Chernyaev, I.I., and Sorokina, V.F., *Zh. Neorg. Khim.*, 1963, vol. 8, no. 3, pp. 578–582.
3. Leidie, E., *C. R. Acad. Sci. Paris*, 1890, vol. 111, pp. 106–115.
4. Wichers, E., Gilchrist, R., and Swendger, Wm.H., *Purification of the Six Platinum Metals, Technical Publication of the American Inst. of Mining and Metals Engineering*, March, 1928, no. 87.
5. Mamonov, S.N., Sorkinova, G.A., and Ryumin, A.I., Abstracts of Papers, *XV Chernyaevskoe soveshchanie po khimii, analizu i tekhnologii platinovykh metallov* (XV Chernyaev Meet. on Chemistry, Analysis, and Technology of Platinum Metals), Moscow, 1993, p. 311.
6. Venediktov, A.B., Gomboeva, Ts.N., and Belyaev, A.V., *Koord. Khim.*, 1985, vol. 11, no. 3, pp. 346–351.
7. Schwarzenbach, G. und Flaschka, H., *Die Komplexometrische Titration*, Stuttgart: Ferdinand Enke, 1965.
8. Venediktov, A.B. and Korenev, S.V., *Sib. Khim. Zh.*, 1991, no. 6, pp. 48–52.
9. Gromilov, S.A., Baidina, I.A., Alekseev, V.I., *et al.*, *Zh. Neorg. Khim.*, 1990, vol. 35, no. 3, pp. 682–684.
10. Gromilov, S.A., Khranenko, S.P., Belyaev, A.V., *et al.*, Abstracts of Papers, *VI Vsesoyuznyi simpozium po izomorfizmu* (VI All-Union Symp. on Isomorphism), Zvenigorod, 1988, p. 61.
11. Abragam, A. and Bleaney, B., *Electron Paramagnetic Resonance of Transition Ions*, Oxford: Clarendon, 1970.
12. Cavalca, L., Nardelli, M., and Grazioli, D., *Gazz. Chim. Ital.*, 1956, vol. 86, no. 11, pp. 1041–1047.
13. Sillen, L.G. and Martell, A.E., *Stability Constants of Metal–Ion Complexes*. London: Chem. Soc., Burlington House, 1967.
14. Korenev, S.V., Gromilov, S.A., and Venediktov, A.B., *Zh. Strukt. Khim.*, 1994, vol. 35, no. 1, pp. 141–145.
15. Lur'e, Yu.Yu., *Spravochnik po analiticheskoi khimii* (Handbook of Analytical Chemistry), Moscow: Khimiya, 1967.
16. Venediktov, A.B., Tkachev, S.V., and Korenev, S.V., *Koord. Khim.*, 1997, vol. 23, no. 9, pp. 690–700.

Russian Journal of Applied Chemistry, Vol. 74, No. 1, 2001, pp. 12–17. Translated from Zhurnal Prikladnoi Khimii, Vol. 74, No. 1, 2001, pp. 12–18.

INORGANIC SYNTHESIS AND INDUSTRIAL INORGANIC CHEMISTRY

Thermolysis of Coprecipitated Copper(II)–Nickel(II) Hydroxides

M. N. Kopylovich, A. M. Kirillov, and A. K. Baev

Lisbon Technical University, Lisbon, Portugal
Belarussian State Technological University, Minsk, Belarus

Received May 4, 2000

Abstract—Coprecipitated copper(II)–nickel(II) hydroxides and mechanical mixtures of these were obtained at varied metal ion ratio and time of mother liquor aging and studied by potentiometric titration, chemical and differential thermal analyses, IR spectroscopy, and X-ray phase analysis.

Hydroxide–oxide compounds are widely used as materials in various fields of science and technology, in particular, as rather inexpensive and stable catalysts [1]. For example, it has been shown that systems containing aqua and hydroxo complexes of copper(II) and nickel(II) are promising catalysts for selective oxidation of alkanes [2–5]. It is also known that some industrial processes of basic organic and petrochemical syntheses are performed with copper- and nickel-containing catalysts, including those of the oxide–hydroxide type [6–8]. Catalysts of this kind are mainly obtained by mixing of the appropriate oxides followed by thermal treatment [9, 10]. However, this method fails to always yield complex materials with sufficient reproducibility. Moreover, the ceramic synthesis technology employs high temperatures, which leads to energy losses and frequently impairs the catalytic activity of the synthesized materials. Therefore, coprecipitation of hydroxides is in some cases a more promising route to mixed copper–nickel systems containing hydroxo and oxo groups [9].

The results of previous studies established the formation of unstable heteronuclear hydroxo complexes of copper–nickel in aqueous solutions [11, 12]. It has been proposed to rely upon this fact in developing a new synthesis method based on formation in solution of unstable hydroxo complexes involving metal ions, passing subsequently into a solid phase which acts as a precursor for the target materials [13].

Apparently, to implement this idea, it is necessary to study in detail the conditions under which hydroxide precipitates can be obtained, the processes of their thermal decomposition, and products formed in these processes by various analytical methods, and just this was the purpose of the present study.

Potentiometric titration was performed with temperature control (±0.1°C) on a pH-150 pH-meter-millivoltmeter. Glass electrode of the ESL-15-11 type and silver chloride electrode of the EVL-1M4 type served as measuring and reference electrodes, respectively; the pH measurement error was ±0.02 pH units. The titration was done as follows: 1 M NaOH solution was added from a burette with scale division value of 0.02 ml to the starting mixture of 1 M Cu(II) and Ni(II) nitrates. To obtained comparable results and simplify the interpretation of the titration curves, the added NaOH volume was converted to the molar ratio $[OH^-]/[M^{2+}]$.

With account of the potentiometric titration data, solid phases were isolated by gradually adding to the starting mixture of 1 M Cu(II) and Ni(II) nitrates, with continuous stirring, 1 M NaOH solution in a stoichiometric ratio of 1 : 2, respectively. The obtained solid phases were homogenized for 5 min and filtered off under a vacuum, washed 3 or 4 times with water and then *i*-C_3H_7OH to negative reaction for NO_3^- ions [14], dried at 30–40°C in an oven, and analyzed. For comparison purposes, mechanical mixtures of Cu(II) and Ni(II) hydroxides (MMHs) were obtained under identical conditions at the same Cu(II) : Ni(II) ratios and studied in a similar way. To reveal the effect of the time of aging of the hydroxide precipitates on their properties, samples were also synthesized at Cu : Ni ratio of 1 : 1 and aging time of 24 and 72 h.

In making chemical analysis, a weighed portion of a hydroxide was dissolved in concentrated HNO_3 and analyzed. The total content of copper(II) and nickel(II) was found complexometrically with murexide; that of nickel(II), by direct titration with Na_2EDTA in ammonia buffer with murexide after masking Cu^{2+} with

1070-4272/01/7401-0012$25.00

thiosulfate ions [15, 16]; and that of copper(II), as the difference of the first two quantities. Differential thermal analysis was done on an MOM derivatograph (Hungary) at a heating rate of 10 deg min^{-1} and sensitivity of DTA and DTG galvanometers of 1/10; 0.500-g samples were heated from room temperature to 1000°C, with calcined aluminum oxide used as reference. The IR spectra (KBr pellets) were taken on a Specord 75-IR spectrophotometer in the range 4000–400 cm^{-1}. X-ray diffraction patterns of the samples were taken on a DRON-3 diffractometer with CuK_α radiation and Ni filter at a scanning rate of 2 deg min^{-1}.

Figure 1 shows the curves of titration with NaOH solution of aqueous Cu(II), Ni(II), and Cu(II)–Ni(II) nitrate solutions with varied ratio of metal ions. The titration curve of a nitrate solution of copper(II) shows two equivalence points (curve *1*). The jump in the pH range 4.3–4.9 at $[OH^-]/[M^{2+}]$ = 1.5–1.8, with the equivalence point at pH 7.0, $[OH^-]/[M^{2+}]$ = 1.7, corresponds to complete precipitation of polynuclear hydroxo complexes of copper(II) [17]. Addition of alkali to the system at pH 9.45 and $[OH^-]/[M^{2+}]$ = 1.8–2.3 does not lead to any increase in pH and corresponds to conversion of polynuclear hydroxo complexes into mononuclear hydroxides. On further introduction of OH groups into the system, the hydroxide suffers no changes, and the steep increase in pH (second jump) is presumably associated with coordination saturation of metal ions with hydroxide ligands and appearance of an excess of free OH groups in solution. In potentiometric titration of nickel nitrate (curve *2*) in the pH range 6.1–7.6 at $[OH^-]/[M^{2+}]$ = 0.0–1.5, mononuclear hydroxides are formed with minor precipitation. Intense precipitation of Ni(II) ions coincides with the onset of the jump at pH 7.6, with the equivalence point (pH 9.6, $[OH^-]/[M^{2+}] \cong$ 2.0) corresponding to complete precipitation of nickel(II) in the form of polynuclear compounds [12, 15].

The titration curves of a mixture of Cu(II) and Ni(II) nitrate solutions (Fig. 1, curves *3*–*5*) show three jumps. The first of these corresponds to precipitation of polynuclear copper(II) compounds, which is confirmed by the close pH values of the equivalence points of binary solutions and a Cu(II) nitrate solution. The second jump corresponds to precipitation of polynuclear nickel(II) compounds, and the third, presumably, to precipitation of a heteronuclear hydroxide. It can be seen that despite the similarity of the titration curves for individual and binary systems, the latter cannot be considered additive. This fact also confirms the possibility of formation, together with

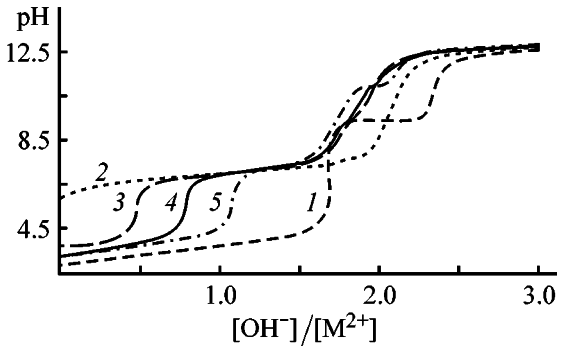

Fig. 1. Potentiometric titration curves of aqueous solutions of nitrates of (*1*) copper(II), (*2*) nickel(II), and (*3*–*5*) mixtures of these with varied content of Cu(II). Content of copper(II) (wt %): (*3*) 30, (*4*) 50, and (*5*) 70.

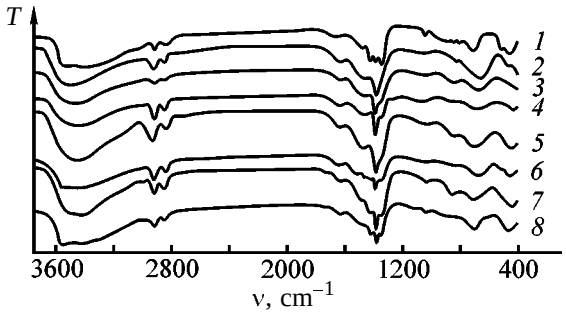

Fig. 2. IR spectra of hydroxides. (*T*) Transmission and (*ν*) wave number. Hydroxide (wt %): (*1*) 100 Cu; (*2*) 100 Ni; (*3*, *4*) 30 Cu, 70 Ni; (*5*, *6*) 50 Cu, 50 Ni; and (*7*, *8*) 70 Cu, 30 Ni. (*3*, *4*, *5*) CPH and (*4*, *6*, *8*) MMH.

two fractions of homopolymers, of a certain amount of a heteropolynuclear hydroxide precipitate [11, 12].

The results of IR spectral studies of coprecipitated hydroxides (CPHs) and MMHs (Fig. 2) indicate the presence in them of various kinds of water. The presence of a broad band of stretching vibrations of H_2O at 3650–3100 cm^{-1} points to stronger hydrogen bonds between OH^- groups. These bands are more intense and shifted to longer wavelengths in the case of CPHs (spectra *3*, *5*, *7*), which indicates an additional stability of CPHs ensured by the formation of intramolecular hydrogen bonds between aqua and hydroxo ligands [18]. Bending (1630–1625 cm^{-1}) and rocking (845–830 cm^{-1}) vibrations of H_2O indicate the presence of coordination-bound water in the compound. As shown by the IR spectra of nickel(II) and copper(II) hydroxides (Fig. 2, spectra *1*, *2*), and also by published data [19, 20], the bands peaked at 1387–1350 cm^{-1} can be attributed to bending vibrations of OH groups bonded to copper(II) and nickel(II) atoms. The absorption peaks at 1060–1035 and 700–500 cm^{-1} may belong to bending vibrations of the bridging M–O–M bonds (M = Cu or Ni), and the bands at 400–500 cm^{-1} cor-

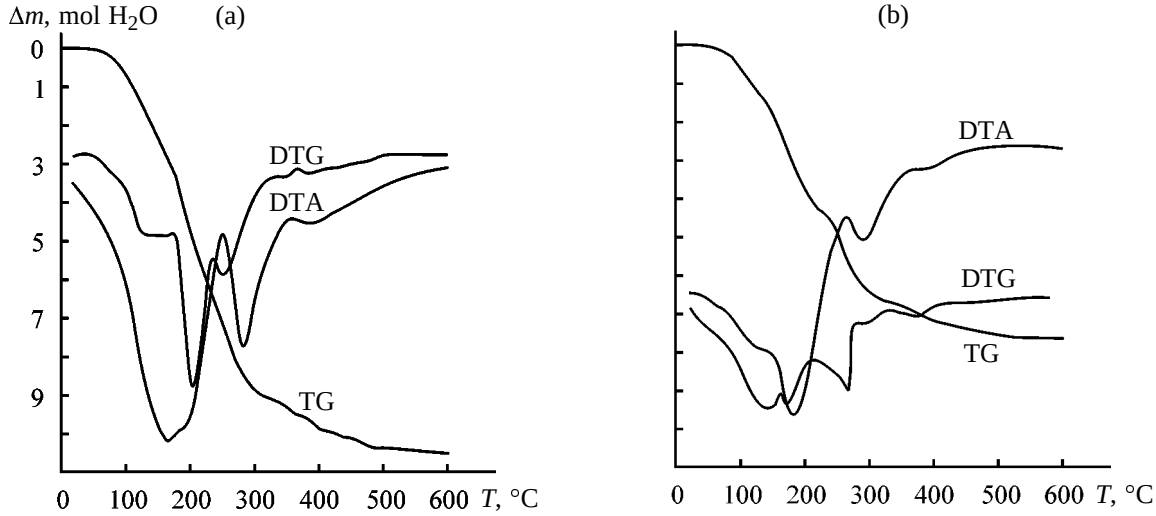

Fig. 3. Thermogravigrams of (a) CPH and (b) MMH of composition 30% Cu(II) + 70% Ni(II). (Δ*m*) Weight loss and (*T*) temperature.

respond to stretching vibrations of M–O bonds. It should be noted that the IR spectra of MMHs are more complex than those of CPHs because of the splitting of the ν(H–OH) and δ(H–OH) bands into doublets and triplets (spectra *4*, *6*, *8*). In addition, in CPHs with the Cu(II) content[1] of 30 and 50% (spectra *3*, *5*), bands of some characteristic vibrations are shifted by 10–30 cm^{-1} to smaller wave numbers, which may be due to formation of heteronuclear structures in the hydroxide precipitate [12].

Table 1. XPA data for products formed in decomposition of hydroxides of composition 30% Cu(II) + 70% Ni(II) at 1000°C

d_{exp}	I/I_0, %	d_{ref}	*hkl*	Phase
Coprecipitated hydroxides				
2.426	100	2.426	101, 031	Ni_2CuO_3
2.181	3	2.168	002	″
2.098	68	2.093	200	$Cu_{0.2}Ni_{0.8}O$
1.482	42	1.479	220	″
1.453	3	1.463	200, 060	Ni_2CuO_3
1.284	2	1.296	103	″
1.262	11	1.262	311	$Cu_{0.2}Ni_{0.8}O$
1.198	17	1.212	202, 062	Ni_2CuO_3
Mechanical mixture of hydroxides				
2.755	2	2.751	110	CuO
2.531	9	2.530	002	″
2.422	87	2.416	111	$Cu_{0.2}Ni_{0.8}O$
2.332	9	2.323	111	CuO
2.099	100	2.093	200	$Cu_{0.2}Ni_{0.8}O$
1.855	3	1.866	202	CuO
1.483	54	1.479	220	$Cu_{0.2}Ni_{0.8}O$
1.400	2	1.410	311	CuO
1.379	2	1.375	220	″
1.315	1	1.304	311	″
1.262	18	1.262	311	$Cu_{0.2}Ni_{0.8}O$
1.209	16	1.208	222	″

To confirm this assumption and determine the content of water, the obtained CPH and MMH were subjected to thermal analysis. The weight loss curve (Fig. 3) was recalculated to moles of H_2O, which furnishes an opportunity to directly analyze the obtained thermogravigrams of decomposition of the hydroxide precipitate in terms of stoichiometry. The DTA curve of CPH of the composition 30% Cu(II) + 70% Ni(II) (Fig. 3a) shows three endothermic peaks in the intervals 40–240, 240–360, and 360–480°C. The first endothermic effect corresponds to deaquation with the loss of 7.23 mol of crystallization water, and the second and third, to liberation of 3.33 mol of bound water, equivalent to loss of 6.66 mol of OH^- groups, with a mixed oxide formed. An X-ray phase analysis of this oxide (Table 1) demonstrated the presence of approximately equal amounts of two complex oxide phases: Ni_2CuO_3 (orthorhombic crystal system, a = 2.925, b = 8.775, c = 4.336 Å) and $Cu_{0.2}Ni_{0.8}O$ (cubic crystal system, a = 4.217 Å).

A chemical analysis of the obtained hydroxides, both freshly precipitated and aged for 1 and 3 days (Table 2), demonstrated that the molar ratios of Cu(II) and Ni(II) ions in the starting solutions and the hydroxides coincide, which points to complete precipita-

[1] Here and hereinafter, molar percents.

Table 2. Data of thermogravimetric and chemical analyses of copper(II)–nickel(II) hydroxides

Composition, %	Temperature of endothermic effect, °C				Weight loss, wt %					$CuO : NiO : H_2O$ molar ratio
	I	II	III	IV	I	II	III	IV	Σ	
30 Cu(II)–70 Ni(II):										
CPH	40–240 (165)*		240–360 (280)	360–480 (380)	27.0 (6.66)**		11.4 (2.81)	3.6 (0.89)	42.8	1 : 2.33 : 10.56
MMH	40–160 (140)	160–260 (180)	260–360 (285)	360–510	10.0 (2.18)	14.6 (3.17)	6.8 (1.48)	3.3 (0.74)	35.2	1 : 2.33 : 7.66
50 Cu(II)–50 Ni(II):										
CPH	40–190 (130)	190–250	250–350 (280)	350–520	12.0 (1.53)	9.5 (1.22)	8.29 (1.05)	3.8 (0.45)	33.0	1 : 1 : 4.25
MMH	40–140	140–250 (170)	250–340 (280)	340–520	7.0 (0.90)	14.8 (2.25)	7.8 (0.66)	3.0 (0.38)	32.8	1 : 1 : 4.23
50 Cu(II)–50 Ni(II), 1 day:										
CPH	40–160 (140)	160–220 (180)	220–330 (265)	330–500	11.0 (1.42)	9.2 (1.18)	10.1 (1.3)	2.7 (0.35)	33.4	1 : 1 : 4.3
MMH	40–160	160–250 (175)	250–350 (290)	350–500 (385)	10.0 (1.30)	12.0 (1.56)	6.7 (0.87)	3.3 (0.43)	32.0	1 : 1 : 4.16
50 Cu(II)–50 Ni(II), 3 days:										
CPH	40–240 (140)		240–400 (290)	400–500	18.0 (2.37)		15.2 (2.09)	1.8 (0.24)	35.0	1 : 1 : 4.61
70 Cu(II)–30 Ni(II):										
CPH	40–155	155–235 (180)	235–380 (260)	380–500	8.1 (1.72)	12.6 (2.77)	9.3 (1.87)	1.8 (0.38)	31.8	2.33 : 1 : 6.74
MMH	40–140 (110)	140–240 (155)	240–330 (260)	330–520	8.0 (1.69)	16.2 (3.41)	4.4 (0.93)	2.8 (0.59)	31.4	2.33 : 1 : 6.62
100 Cu(II)	40–140	140–320 (160)		320–460	6.0 (0.37)	20.8 (1.28)		7.6 (0.47)	28.4	1 : 0 : 1.75
100 Ni(II)	40–240		240–360 (275)	360–500 (385)	24.8 (1.72)		11.2 (0.75)	4.0 (0.3)	40.0	0 : 1 : 2.77

* Peak temperature.
** Mole of H_2O.

tion of metal ions with the initial component ratio preserved in the precipitate. In this case, the following scheme of dehydration of the obtained CPH composed of 30% Cu(II) + 70% Ni(II) can be proposed:

$$CuNi_{2.33}(OH)_{6.66}\cdot 7.23H_2O \xrightarrow[-7.23H_2O]{} CuNi_{2.33}(OH)_{6.66}$$

$$\xrightarrow[-3.33H_2O]{} \sim 0.8(Ni_2CuO_3 + Cu_{0.2}Ni_{0.8}O).$$

Thermal decomposition of MMH composed of 30% Cu(II) + 70% Ni(II) (Fig. 3b) occurs in a different way. The splitting of the endothermic peak at 40–260°C in two: at 40–160°C with a peak at 140°C and at 160–260°C with a peak at 180°C, points to a more complicated nature of deaquation of a mixture of copper(II) and nickel(II) hydroxides. No similarity in amounts of removed water is observed between CPH and MMH, although the endothermic effects occur in virtually the same temperature intervals (Fig. 3). Moreover, the total loss of water is 7.66 mol, which is 2.9 mol less than in the case of CPH of the same composition. Thus, the hydroxides, the processes of their thermal decomposition, and the resulting products exhibit specific features depending on the preparation procedure (coprecipitation or mechanical mixing). An X-ray phase analysis of the products of decomposition of MMH containing 30% Cu(II) and 70% Ni(II) (Table 2) demonstrated the presence of a $Cu_{0.2}Ni_{0.8}O$ phase with minor CuO admixtures (up to 10%), with the $Cu_{0.2}Ni_{0.8}O$ phase probably formed via sintering of CuO and NiO oxides.

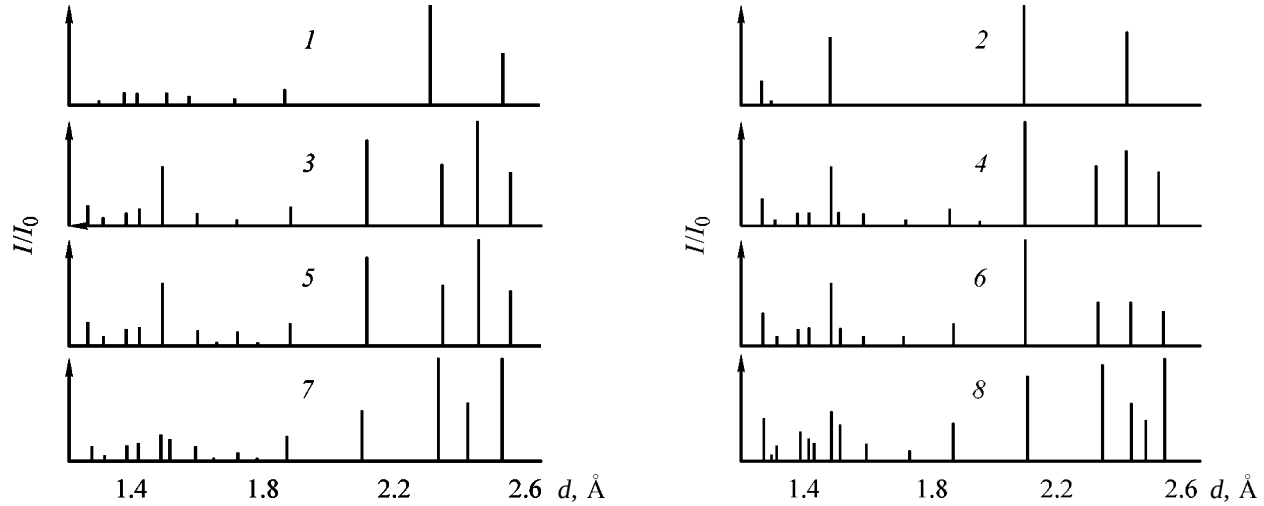

Fig. 4. X-ray diffraction patterns of the products of decomposition (T = 1000°C) of (*1*) copper(II) and (*2*) nickel(II) hydroxides, (*3*, *5*–*7*) copper(II)–nickel(II) CPHs, and (*4*, *8*) MMHs. (I/I_0) Relative intensity and (*d*) interplanar spacing. Initial content of copper(II) (wt %): (*3*–*6*) 50 and (*7*, *8*) 70; aging time (days): (*5*) 1 and (*6*) 3.

Thermogravimetric analysis of CPH and MMH containing 50% Cu(II) and 50% Ni(II) also revealed differences in their dehydration. Despite the close temperature intervals of the main endothermic effects, they differ in the amount of removed water. The total amount of water in CPH somewhat exceeds that in the corresponding MMH, increasing on passing from an unaged sample to a hydroxide isolated after 3 days of aging under mother liquor. This may be due to decomposition, in the course of precipitate aging, of a part of heteronuclear copper(II)–nickel(II) hydroxide, accompanied by disintegration of hydroxo bridges and subsequent aquation of metal ions. Thus, the longer the time of CPH aging, the smaller the amount of heteronuclear hydroxide it contains. An additional argument in favor is the amount of double oxide indicated by X-ray diffraction patterns of the products of complete decomposition (T = 1000°C) of mixed hydroxides (Fig. 4). The products of decomposition of CPH containing 50% Cu(II) and 50% Ni(II) (patterns *3*, *5*, *6*) contain phases of CuO (interplanar spacings 2.530, 2.323, 1.886, and 1.418 Å), NiO (2.088, 1.476, 1.259 Å), and $NiCuO_2$ (tetragonal crystal system, a = 4.121, c = 4.355 Å) with the main reflections at 2.427, 1.500, 1.302, 1.251, and 1.213 Å. With increasing time of aging of the initial CPH, the intensities of CuO and NiO reflections grow and the signals from $NiCuO_2$ become weaker (2.427, 1.213 Å); the reflections at 1.500, 1.302, and 1.251 Å totally disappear from the X-ray diffraction patterns of the decomposition products of CPH, subjected to aging for 1 and 3 days (Fig. 4, patterns *5*, *6*). A correlation is observed between the increasing time of CPH aging and the decreasing intensity of signals from $NiCuO_2$ in the products of its decomposition. For example, an X-ray diffraction pattern of a product of CPH decomposition (3 days of aging) shows only a single $NiCuO_2$ band (2.427 Å) with intensity of 49% (pattern *6*). It should be noted that the X-ray diffraction patterns of decomposition products of MMH containing 50% Cu(II) and 50% Ni(II) show no double oxide phase, with only the CuO and NiO phases present, which also confirms the occurrence of a chemical interaction between Cu and Ni atoms in CPH formation, just in the stage of coprecipitation, rather than in that of thermal treatment.

An X-ray phase analysis of decomposition products of CPH and MMH containing 30% Cu(II) and 70% Ni(II) (Fig. 4, patterns *7*, *8*) demonstrated the presence of only copper(II) and nickel(II) oxide phases. However, the thermal behavior of the given CPH and MMH is not additive with respect to the temperature intervals of endothermic effects and weight loss (Table 1), and the total weight loss is practically the same (31.8 and 31.4%, respectively). This can be accounted for by the different physical properties (density, porosity, specific surface area) of the hydroxides obtained by coprecipitation and mechanical mixing [21].

Thus, a technique is proposed on the basis of the investigation performed for obtaining copper(II)–nickel(II) CPH whose thermal treatment can yield new inorganic materials and, in particular, catalytic systems applicable in organic and petrochemical syntheses. The temperature intervals in which various kinds of water are removed were determined and differences were revealed between the thermal properties

of CPH and MMH whose dehydration occurs under milder conditions because of the absence of Cu–OH–Ni bridge bonds and is accompanied by liberation of a lesser amount of water. The phase composition of the products of CPH and MMH decomposition at T = 1000°C was determined; it was shown that complex oxide compounds Ni_2CuO_3, $Cu_{0.2}Ni_{0.8}O$, and $NiCuO_2$ are present together with the CuO and NiO phases. The optimal hydroxide composition [30% Cu(II) + Ni(II)] was determined at which the yield of double oxides reaches 100% (Table 1), and the efficiency of preparing these compounds from unaged CPH was confirmed.

CONCLUSIONS

(1) A procedure was developed for synthesizing coprecipitated copper(II) and nickel(II) hydroxides, ensuring formation of complex oxide catalysts with molecular distribution of the components.

(2) The optimal composition [30% Cu(II) + 70% Ni(II)] of hydroxide whose thermal decomposition gives double oxides in up to 100% yields was determined.

REFERENCES

1. Dzis'ko, V.A., Karnaukhov, A.P., and Tarasova, D.V., *Fizikokhimicheskie osnovy sinteza okisnykh katalizatorov* (Physicochemical Principles of Synthesis of Oxide Catalysts), Novosibirsk: Nauka, 1978.
2. Barton, D.H.R., Csuhai, E., Doller, D., and Geletii, Y.V., *Tetrahedron*, 1991, vol. 47, no. 33, pp. 6561–6570.
3. Koksharova, T.V., Seifullina, I.I., and Levandovskaia, T.Yu., Abstracts of Papers, *XXXIII Int. Conf. on Coordination Chemistry*, Florence (Italy), August 30–September 4, 1998, p. 598.
4. Ivanova, E.A., Bogomolova, O.P., Filippova, T.Yu., *et al*., *Vestn. Mosk. Gos. Univ., Ser. 2: Khim.*, 1991, vol. 32, no. 2, pp. 203–205.
5. Karahanov, E.A., Narin, S.Yu., and Dedov, A.G., *Catal. Lett.*, 1989, vol. 3, p. 31.
6. Tolman, W.B., Lam, B., Berreau, L.M., *et al*., Abstracts of Papers, *XXXIII Int. Conf. on Coordination Chemistry*, Florence (Italy), August 30–September 4, 1998, p. 128.
7. Shilov, A.E. and Shul'pin, G.B., *Aktivatsiya i katalitycheskie reaktsii uglevodorodov* (Activation and Catalytic Reactions of Hydrocarbons), Moscow: Nauka, 1995.
8. Berezin, N.V., Denisov, E.T., and Emanuel', N.M., *Okislenie tsiklogeksana* (Oxidation of Cyclohexane), Moscow: Mosk. Gos. Univ., 1962.
9. Schwarz, J.A., *Chem. Rev*., 1995, vol. 95, no. 3, pp. 477–510.
10. Dzis'ko, V.A., *Osnovy metodov prigotovleniya katalizatorov* (Principles of Methods for Catalyst Preparation), Novosibirsk: Nauka, 1983.
11. Kopylovich, M.N., Baev, A.K., and Chernik, A.A., *Zh. Neorg. Khim*., 1996, vol. 41, no. 10, pp. 1751–1756.
12. Chernik, E.O., Kirillov, A.M., Kopylovich, M.N., and Baev, A.K., Abstracts of Papers, *XIX Vserossiiskoe Chugaevskoe soveshchanie po khimii kompleksnykh soedinenii* (XIX All-Russia Tschugaeff Meet. on Chemistry of Complex Compounds), Ivanovo, June 21–25, 1999, p. 244.
13. Kopylovich, M.N. and Baev, A.K., Abstracts of Papers, *Mezhdunarodnaya nauchnaya konferentsiya "Zhidkofaznye sistemy i nelineinye protsessy v khimii i khimicheskoi tekhnologii"* (Int. Scientific Conf. "Liquid-Phase Systems and Nonlinear Processes in Chemistry and Chemical Technology"), Ivanovo, September 13–15, 1999, p. 31.
14. Alekseev, V.N., *Kurs kachestvennogo khimicheskogo polumikroanaliza* (A Course of Qualitative Chemical Semimicroanalysis), Moscow: Khimiya, 1973.
15. Lur'e, Yu.Yu., *Spravochnik po analiticheskoi khimii* (Handbook of Analytical Chemistry), Moscow: Khimiya, 1989.
16. Schwarzenbach, G. und Flaschka, H., *Die Komplexometrische Titration*, Stuttgart: Ferdinand Enke, 1965.
17. Kopylovich, M.N., Radion, E.V., and Baev, A.K., *Koord. Khim*., 1995, vol. 21, no. 1, pp. 66–71.
18. Pimentel, G.C., *The Hydrogen Bond*, McClellan, A.L. and Pauling, L., Eds., San Francisco: Freeman, 1960.
19. Nakamoto, K., *Infrared Spectra of Inorganic and Coordination Compounds*, New York: Wiley, 1963.
20. Yurchenko, E.N., Kustova, G.N., and Batsanov, S.S., *Kolebatel'nye spektry neorganicheskikh soedinenii* (Vibration Spectra of Inorganic Compounds), Novosibirsk: Nauka, 1981.
21. Komarov, V.S., *Adsorbenty: Voprosy teorii, sinteza i struktury* (Adsorbents: Problems of Theory, Synthesis, and Structure), Minsk: Belaruskaya Navuka, 1997.

Russian Journal of Applied Chemistry, Vol. 74, No. 1, 2001, pp. 18–20. Translated from Zhurnal Prikladnoi Khimii, Vol. 74, No. 1, 2001, pp. 18–21.

INORGANIC SYNTHESIS AND INDUSTRIAL INORGANIC CHEMISTRY

Physicochemical Study of Ta_2O_5 and SiO_2–Ta_2O_5 Film Formation from Film-Forming Solutions

R. V. Gryaznov, L. P. Borilo, V. V. Kozik, and A. G. Mal'chik

Tomsk State University, Tomsk, Russia

Received March 23, 2000; in final form, July 2000

Abstract—In order to study physicochemical processes of formation of Ta_2O_5 and SiO_2–Ta_2O_5 films from film-forming solutions, the properties of these solutions, and also the thermal-oxidative breakdown and the properties of the obtained films, were studied.

At present, particular attention is given to physicochemical properties of thin films, since the development of new fields of modern technology assigned a prominent place to the application of various materials in the thin-film state. The broadest application in various fields of electronics is characteristic of dielectric films based on complex oxides [1]. For thin-film materials to be successfully used, a relationship should be established between their physicochemical and service properties, composition, and preparation conditions.

EXPERIMENTAL

Film-forming solutions (FFSs) were prepared from tetraethoxysilane (TEOS), ethanol, and tantalum pentachloride. The viscosity was measured with a VPZh-2 or VPZh-4 glass capillary viscometer. The decomposition of deposits obtained from FFSs was studied on a Q-1500 derivatograph. The films were formed on glass or single-crystal silicon substrates with the surface area of 1–1.5 cm^2 by centrifugation and drawing, at a speed of centrifuge rotation of 1000–5000 rpm and drawing velocity of 1–5 mm s^{-1}. The uniformity of the films formed across their thickness was monitored by determining the optical thickness at 6–8 points for each sample. The film adhesion to the substrate was determined sclerometrically, and the refractive index and thickness, with an LEF-3M laser ellipsometer. Films 120–140 nm thick were obtained and studied. IR transmission spectra of the films were recorded in the 4000–400 cm^{-1} range on IR-75, M-40, and SF-20 instruments. As known, the film-forming ability is exhibited by the substances that can form macromolecules or associates in solution, which are attached to the surface when the solution is applied to a substrate and decompose to oxides upon solvent evaporation at elevated temperature [2]. The temporal stability of film-forming solutions is a factor important in technological regard, and, therefore, the relationship between the viscosity of solutions, their storage time, and the possibility of their use to obtain films was studied experimentally. When $TaCl_5$ is dissolved in ethanol, alkoxy derivatives are formed [3]:

$$TaCl_5 + 3C_2H_5OH \rightarrow TaCl_2(OC_2H_5)_3 + 3HCl.$$

A study of the film-forming ability of alcoholic $TaCl_5$ solutions demonstrated that the obtained solutions possess a viscosity (Fig. 1, curve *1*) sufficient for obtaining films, and the film-forming ability is preserved for a long time since the chloride ion, being a ligand of π-donor type, forms cluster compounds with tantalum. With account taken of published data on cluster compounds of tantalum [3], it may be assumed that chloride ions serve as bridges in the formation of stable polynuclear structures of tantalum alkoxy derivatives

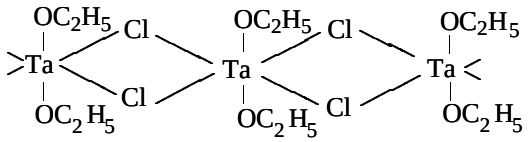

Thus, the film-forming ability of an alcoholic solu-

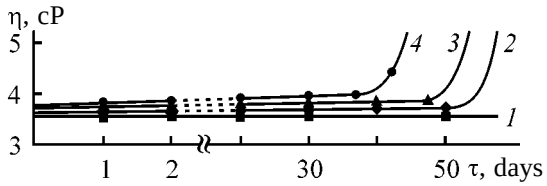

Fig. 1. Variation of the viscosity η of $TaCl_5$-containing FFS with time τ.

1070-4272/01/7401-0018$25.00

Table 1. Assignment of bands in the IR spectra of powders at different temperatures

FFS	*T*, K	Vibration frequency, cm^{-1}					
		H–OH stretching	$–OC_2H_5$ stretching	H–O–H bending	$–OC_2H_5$ bending	Si–O–Si	O–Si–O–Ta–O
$TaCl_5$	373	3600	–	1640	–	–	400
	773	–	–	–	–	–	400
	848	–	–	–	–	–	400
	900	–	–	–	–	–	400
$TaCl_5$ + TEOS	373	3560	–	1640	1100	600–800	460–400
	600	3600	2900	1640	1100	600	460–400
	633	–	2900	–	1100	600	460–400
TEOS	373	3660	2935	1640	1095	600–800	460
	473	3680	2935	1640	1100	800	460
	773	–	–	–	1100	800	460

tion of tantalum pentachloride is not limited to the stages of its ripening and aging.

To study the properties of film-forming solutions in the system TEOS–$TaCl_5$–C_2H_5OH, kinetic curves describing the variation of the solution viscosity were taken at different salt concentrations (Fig. 1, curves *2*–*4*). More complex processes are observed in these solutions. The solutions have no ripening range, which is probably associated with processes of tantalum pentachloride dissolution in ethanol. However, after 2 days the viscosity starts to grow steadily because of the simultaneously occurring processes of hydrolytic polycondensation of TEOS and alkoxy derivatives of tantalum:

$$Si(OC_2H_5)_3OH + TaCl_2(OC_2H_5)_3 \rightarrow C_2H_5OH$$

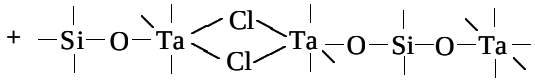

etc.

Therefore, the time during which stable film-forming properties are preserved decreases to 30 days. On lowering the SiO_2 concentration in a film to 10–20%, the time of FFS serviceability is again extended to 48 days. This probably occurs because the forming cluster compounds of tantalum hinder the hydrolytic polycondensation of tetraethoxysilane.

The oxide film formation consists in that the chemical composition of the starting film-forming compounds undergoes changes first in solution, then at the instant of film formation on the substrate surface, and, finally, during thermal treatment [4]. To determine the conditions of film synthesis, the main stages of formation of pure oxides and complex oxides on their base were studied. On heating a powder obtained by drying at 333 K an alcoholic solution of $TaCl_5$, the following processes occur according to thermal analysis data (Fig. 2): partial evaporation of physically adsorbed water and alcohol, reaction of $TaCl_5$ with atmospheric oxygen, and, finally, combustion of oxochlorides and alkoxy derivatives of tantalum to form the oxide.

The IR data (Table 1) confirm the presence of ethoxy groups at the oxide formation temperature of 800–840 K. At higher temperatures there are no stretching or bending vibrations of ethoxy groups.

Complex oxides SiO_2–Ta_2O_5 are formed in four stages (Fig. 3). The activation energy was calculated for all the processes involved by the Horowitz–Metzger method (Table 2) [5].

In stage I, physically adsorbed water and alcohol are removed, which is accompanied by an endothermic effect at 393 K. The second endothermic peak

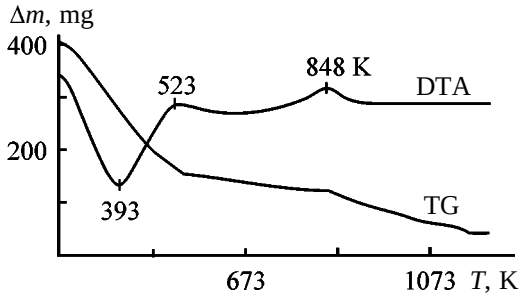

Fig. 2. Derivatograms of alcoholic $TaCl_5$ solution dried at 333 K. (Δ*m*) Weight loss and (*T*) temperature; the same for Fig. 3.

Table 2. Kinetic parameters of SiO_2, Ta_2O_5, and SiO_2–Ta_2O_5 film formation

Formation stage	SiO_2			Ta_2O_5			SiO_2–Ta_2O_5		
	T, K	conversion, %	E_a, kJ mol^{-1}	*T*, K	conversion, %	E_a, kJ mol^{-1}	*T*, K	conversion, %	E_a, kJ mol^{-1}
I	298–473	33.0	41.4	298–473	51.7	44.1	298–473	50.0	40.5
II	473–623	29.0	51.8	473–573	15.0	32.1	473–623	34.5	32.6
III	823–973	37.5	68.5	573–923	33.3	107.8	623–763	3.4	60.9
IV	–	–	–	–	–	–	763–973	12.0	117.4

Table 3. Physicochemical properties of SiO_2–Ta_2O_5 films

Parameter	Parameter value at indicated Ta_2O_5 content in film, %								
	10	20	30	40	50	60	70	80	90
Refractive index	1.51	1.61	1.63	1.66	1.69	1.72	1.75	1.83	1.91
Dielectric constant	4.6	5.1	7.4	9.2	11.0	12.5	14.3	15.1	16.5
Adhesion, kg mm^{-2}	0.93	0.95	0.91	0.96	0.97	0.94	0.96	0.94	0.95

(734 K) is due to evaporation of water released upon condensation of silanol groups. The activation energy calculated for this stage (Table 2) is in agreement with the value characteristic of the condensation of hydroxyl-containing organosilicon compounds [6]. In the final stage of the process (exothermic peak at 848 K) the ethoxy groups contained in the products of FFS solvation and hydrolysis are oxidized, and the formation of the SiO_2–Ta_2O_5 film is complete. The activation energy of this stage is typical of a chemical reaction.

The firmness of film attachment to the surface, and the optical and electrical properties of films, determine the possibilities of their practical use. The optical and electrophysical properties, adhesion, and porosity were studied for SiO_2–Ta_2O_5 films (120–140 nm, silicon substrate) (Table 3). It was found that the obtained films exhibit good adhesion to various substrates and contain no micropores.

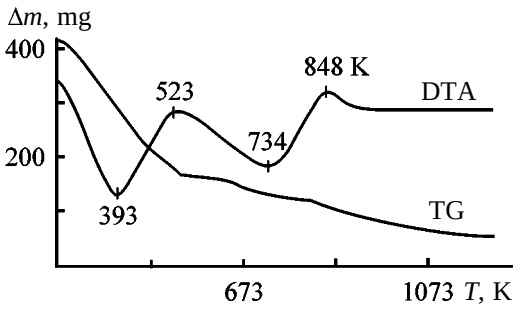

Fig. 3. Derivatogram of film formation from FFS with $TaCl_5$ and $Si(OC_2H_5)_4$.

CONCLUSION

An alcoholic solution of tantalum pentachloride possesses film-forming ability, with unlimited durability of stable film-forming properties. Gravimetry and IR spectroscopy were applied to establish the sequence of main stages of Ta_2O_5 and SiO_2–Ta_2O_5 formation from film-forming solutions. The properties of the obtained films were studied.

REFERENCES

1. Borisenko, A.I., Novikov, V.V., Prikhod'ko, N.E., *et al.*, *Tonkie neorganicheskie plenki v mikroelektronike* (Thin Inorganic Films in Microelectronics), Leningrad: Nauka, 1972.
2. Mal'chik, A.G., Borilo, L.P., and Kozik, V.V., *Zh. Prikl. Khim.*, 1996, vol. 69, no. 2, pp. 224–227.
3. Fairbrother, F., *The Chemistry of Niobium and Tantalum*, Amsterdam: Elsevier, 1967.
4. Tochitskii, E.I., *Kristallizatsiya i termoobrabotka tonkikh plenok* (Crystallization and Thermal Treatment of Thin Films), Minsk: Nauka i Tekhnika, 1976.
5. Fialko, M.B., *Neizotermicheskaya kinetika v termicheskom analize* (Nonisothermal Kinetics in Thermal Analysis), Tomsk: Tomsk. Gos. Univ., 1981.
6. Voronkov, M.G., Mileshkevich, V.P., and Yuzhelevskii, Yu.A., *Siloksanovaya svyaz'* (Siloxane Bond), Novosibirsk: Nauka, 1976.

Russian Journal of Applied Chemistry, Vol. 74, No. 1, 2001, pp. 21–23. Translated from Zhurnal Prikladnoi Khimii, Vol. 74, No. 1, 2001, pp. 22–24.

SORPTION AND ION-EXCHANGE PROCESSES

Sorption of Precious Metals with Carbon Sorbents

Yu. E. Golodkov, V. V. Elshin, V. I. Dudarev, and L. M. Oznobikhin

Irkutsk Higher School of Ministry of Internal Affairs, Irkutsk, Russia
Irkutsk State Technical University, Irkutsk, Russia

Received July 5, 1997; in final form, September 2000

Abstract—Sorption of gold and silver cyanide complexes with carbon sorbents based on composite polymeric materials and its thermodynamic characteristics were studied.

Hydrometallurgy based on carbon sorbents is one of the most efficient processes for recovery of precious metals from ores and concentrates. Such technology has advantages in the selectivity of gold and silver recovery [1–4]. The main factors hampering a wide use of this technology in the Russian gold mining industry are low mechanical resistance to wear of the industrial carbon sorbents and their short supply [5, 6]. "Carbon-in-pulp" processes are widely used in other countries in industrial production of gold [3, 7].

In this work, we studied sorption with carbon polymeric sorbents of gold and silver leached with cyanides from ores of complex composition by carbon polymeric sorbents. Data on the synthesis of wear-resistant carbon sorbents were reported in [8]. IPI-T sorbent prepared in industrial quantities from phenol–formaldehyde resins and their waste is of industrial importance. Physicochemical characteristics of IPI-T sorbent and certain known materials are compared in Table 1.

Up to now, both the mechanism of sorption of precious metals from solutions and pulps and problems of the directed synthesis of sorbents are the matter of discussions [8–10].

EXPERIMENTAL

We obtained the isotherms and kinetic curves of gold and silver sorption on IPI-T using a temperature-controlled device. To obtain sorption isotherms, variable samples of the sorbent and constant volumes of solutions with fixed initial concentrations of gold and silver cyanide complexes were used. The solutions were obtained by cyanide leaching of ores of the Kuranakh mining field. Mixers provided vigorous agitation of the sorbent in the solution. The concentrations of precious and nonferrous metals (determined by atomic absorption method) and anions were monitored.

Figure 1 shows the isotherms of gold and silver sorption from cyanide solutions with IPI-T sorbent in comparison with IGI-65, Norit, and Futamura carbon. As seen, the highest sorption power is characteristic for Norit activated carbon, while IPI-T sorbent has a slightly lower sorption power than imported carbons. Isotherms are described by the Freundlich equation

$$a = kC^{1/n}, \quad (1)$$

Table 1. Physicochemical characteristics of carbon sorbents

Sorbent	Main fraction, mm	Bulk density, g dm^{-3}	Pore volume, cm^3 g^{-1}			Specific surface area, m^2 g^{-1}	Wear resistance,* %
			macro- V_{ma}	meso- V_{me}	micro- V_{mi}		
IGI-65	0.5–1.5	490	0.57	0.08	0.34	540	83
Taiko CW 612 B (Futamura)	1.2–2.5	530	0.18	0.21	0.36	600	91
R 2515 (Norit)	2.0–2.2	450	0.10	0.16	0.43	600	93
IPI-T	2.0–5.0	460	0.26	0.20	0.15	516	85

* Wear resistance according to GOST (State Standard) 16188–70.

1070-4272/01/7401-0021$25.00

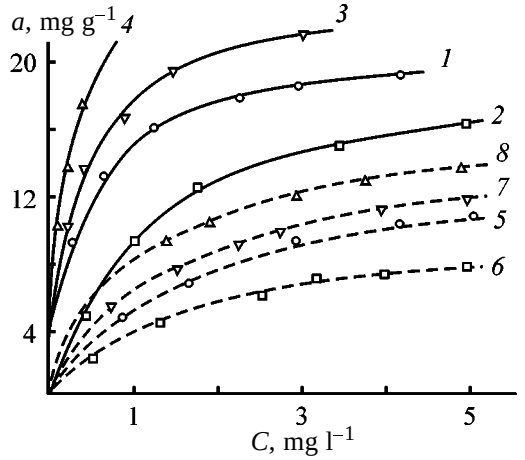

Fig. 1. Isotherms of (*1–4*) gold and (*5–8*) silver sorption from cyanide solutions: (*a*) equilibrium concentration of metal ions in the sorbent and (*C*) equilibrium concentration of metal ions in the solution. Sorbent: (*1, 5*) IPI-T, (*2, 6*) IGI-65, (*3, 7*) Futamura, and (*4, 8*) Norit.

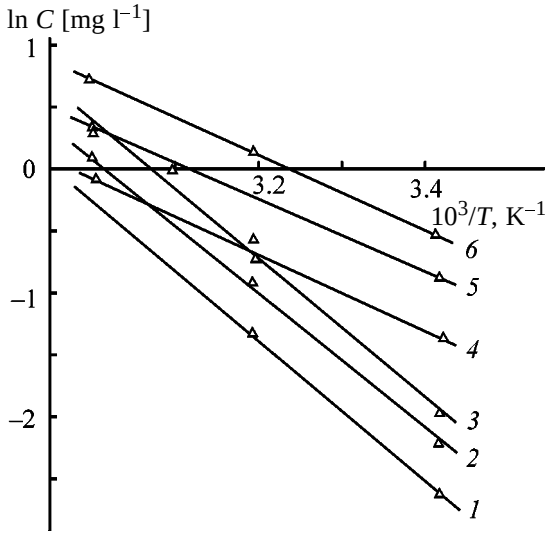

Fig. 2. Temperature dependence of (*1–3*) gold and (*4–6*) silver sorption with IPI-T sorbent from cyanide solutions: (*C*) equilibrium concentration of metal ions in the solution. Metal sorption (mg g^{-1}): (*1*) 3.0, (*2*) 4.0, (*3*) 5.0, (*4*) 1.0, (*5*) 1.5, and (*6*) 2.0.

Table 2. Sorption constants

Sorbent	$[Au(CN)_2]^-$		$[Ag(CN)_2]^-$	
	k	*n*	*k*	*n*
IGI-65	9.2	1.8	2.4	1.5
IPI-T	15.0	3.2	3.5	1.7
Taiko CW 61 B (Futamura)	18.0	3.5	4.3	2.2
R 2515 (Norit)	22.5	3.7	6.0	2.3

Table 3. Heat of gold and silver sorption by IPI-T

Sorbent capacity, mg g^{-1}	Heat of sorption, kJ mol^{-1}	
	$[Au(CN)_2]^-$	$[Ag(CN)_2]^-$
1.0	–	25.76
1.5	–	24.51
2.0	–	24.30
3.0	48.29	–
4.0	47.05	–
5.0	46.31	–

Table 4. Constants *K* and activation energies *E* of sorption

Complex	$K \times 10^{-4}$, s^{-1}, at indicated *T*, °C			*E*, kJ mol^{-1}
	20	40	60	
$[Au(CN)_2]^-$	1.172	1.508	1.886	9.62
$[Ag(CN)_2]^-$	0.753	0.967	1.250	10.19

where *a* is the equilibrium concentration of metal ion in the carbon (mg g^{-1}), *C* is the equilibrium concentration of metal ion in the solution (mg l^{-1}), and *k* and *n* are constants. Calculated *k* and *n* are listed in Table 2. The temperature dependences of *C* for IPI-T sorbent at the fixed *a* measured within the 20–60°C range are shown in Fig. 2. The differential heats of sorption of metal ions were calculated by the isosteric method [11] from linear slopes (Table 3).

The sorption kinetics was studied within the 20–60°C range (Fig. 3). The rate constant *K* of the sorption was calculated from the slope of the $\log C$–*t* straight line in accordance with the equation

$$\log C = \log C_0 - 0.434\,tK, \qquad (2)$$

where C_0 is the initial metal concentration in the solution (mg l^{-1}), *C* is the actual concentration (mg l^{-1}), and *t* is time (s).

The activation energy of sorption was calculated by the equation

$$E = -2.303R\frac{d\log K}{dT^{-1}}, \qquad (3)$$

where *T* is temperature (K). The results are listed in Table 4.

The temperature dependence of the sorption rate constant and the values of the sorption activation

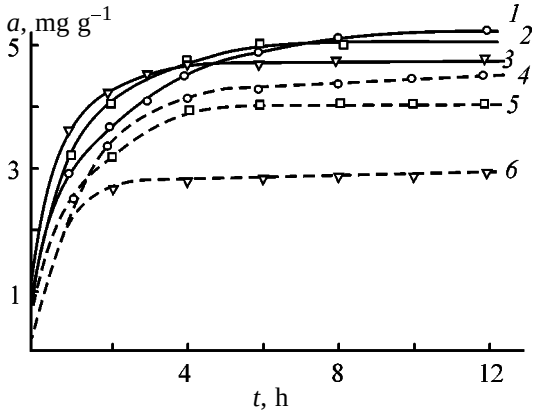

Fig. 3. Kinetics of (*1–3*) gold and (*4–6*) silver sorption from cyanide solutions with IPI-T sorbent: (*a*) equilibrium concentration of metal ions in the sorbent and (*t*) time. Temperature (°C): (*1*, *4*) 20, (*2*, *5*) 40, and (*3*, *6*) 60.

energy show that in this case the internal-diffusion model of the gold and silver sorption with IPI-T sorbent is the most probable.

CONCLUSION

The efficient sorption recovery of gold and silver from cyanide solutions with the IPI-T carbon sorbent with a high wear resistance was demonstrated. This sorbent is characterized by only slightly lower sorption power with respect to these metals as compared to imported carbons. The internal-diffusion sorption is the most probable mechanism of gold and silver sorption with IPI-T.

REFERENCES

1. Gross, J. and Scott, W., *Precipitation of Gold and Silver from Cyanide Solutions on Charcoal*, Washington: Government, 1927.
2. Kuz'minykh, V.M. and Tyurin, N.G., *Izv. Vyssh. Uchebn. Zaved., Tsvetn. Metall.*, 1968, no. 4, pp. 65–70.
3. Telegina, L.E. and Kofman, V.Ya., *Tsvetn. Metall. Byull.*, 1982, no. 17, pp. 15–17.
4. Elshin, V.V., Golodkov, Yu.E., and Voiloshnikov, G.I., in *Obogashchenie rud: Mezhvuzovskii sbornik* (Ore Concentration: Intercollegiate Coll.), Irkutsk, 1989, pp. 69–75.
5. Kostomarova, M.A., Peredii, M.A., and Surinova, S.I., *Khim. Tverd. Topl.*, 1976, no. 2, pp. 5–15.
6. Chernov, V.K. and Voiloshnikov, G.I., Abstracts of Papers, *Vsesoyuznaya konferentsiya "Osnovnye napravleniya i mery po uskoreniyu progressa v zolotoi almazodobyvayushchei promyshlennosti na period do 2000 goda"* (All-Union Conf. "Main Directions and Measures To Accelerate Progress in Gold and Dia mond Extraction up to 2000"), Moscow, 1985, part 2, pp. 31–32.
7. *Carbon-in-Pulp Technology for the Extraction of Gold, Incorporating Papers Presented at the Murdoch Univ. Symp. on Carbon-in-Pulp Technology*, Australia, 1982.
8. *Sovremennye dostizheniya v ugol'no-sorbtsionnykh protsessakh, Materialy Mezhdunarodnoi nauchno-tekhnicheskoi konferentsii*, (Proc. Int. Scientific Technical Conf. "Recent Achievements in Carbon-Sorption Technology"), Irkutsk, 1996.
9. Abstracts of Papers, *Konferentsiya "Sovremennoe sostoyanie i perspectivy razvitiya ugol'no-sorbtsionnykh protsessov (v gidrometallurgii blagorodnykh metallov)"* (Conf. "Modern State and Prospects of Carbon-Sorption Technology (in Hydrometallurgy of Precious Metals)"), Irkutsk, 1990.
10. Dudarenko, V.V. and Kazdobin, K.A., *Ukr. Khim. Zh.*, 1987, vol. 53, no. 1, pp. 42–47.
11. Dubinin, M.M., in *Prirodnye sorbenty* (Natural Sorbents), Moscow: Nauka, 1967, pp. 5–24.

Russian Journal of Applied Chemistry, Vol. 74, No. 1, 2001, pp. 24–27. Translated from Zhurnal Prikladnoi Khimii, Vol. 74, No. 1, 2001, pp. 25–28.

SORPTION AND ION-EXCHANGE PROCESSES

Sorption of Chromium(VI) from Aqueous Solutions on AM-2b Anion Exchanger

L. A. Voropanova and E. Yu. Getoeva

North-Caucasus State Technological University, Vladikavkaz, North Ossetia, Russia

Received June 25, 1999; in final form, March 2000

Abstract—Sorption of chromium(VI) from a solution with the initial concentration of CrO_3 of up to 30 mg dm^{-3} on a commercial macroporous AM-2b anion exchanger pretreated by various methods was studied. The optimal conditions for efficient sorption were found.

Sorption of metal ions on a number of sorbents is largely influenced by the solution acidity. Sorption of Cr(VI) from solutions with various pH was studied in [1, 2]. It was shown that sorption is governed by the state of ions in the solutions, which, in turn, depends on pH. For example, at pH < 7 chromium(VI) solutions contain the $Cr_2O_7^{2-}$, $HCrO_4^-$, and CrO_4^{2-} ions, whereas at pH > 7 they contain the $HCrO_4^-$ and CrO_4^{2-} ions. In 0.5–2.0 N solutions of H_2SO_4 the $Cr_3O_{10}^{2-}$ and $Cr_4O_{13}^{2-}$ anions are formed. Polycondensation of CrO_4^{2-} anion in acidified aqueous solutions yields chromium(VI) isopolyanions:

$$nCrO_4^{2-} + 2(n - a)H^+ = Cr_nO_{3n+a}^{2a-} + (n - a)H_2O. \quad (1)$$

The final polycondensation products are hydrated polymeric oxides with the composition $(CrO_3)_n \cdot mH_2O$. All intermediates containing polyanions have some oxygen excess in comparison with the trioxide. The composition of these intermediates can be presented by the general formula $Cr_nO_{3n+a}^{2a-}$, where n is the number of chromium(VI) atoms in the anion and a is the excess of oxygen atoms in the polyanion relative to the trioxide [3]. At the same time, CrO_2^{2+} cations are known, for which $a < 0$. It was found [3] that a and n are integer quantities varying from –4 to 1 and from zero to infinity, respectively.

For studying chromium(VI) sorption, we used macroporous bifunctional AM-2b anion exchanger containing benzyldimethylamine and benzyldimethylammonium functional groups [4].

Sorption was carried out under static conditions with continuous stirring at a constant pH as in [5, 6]. The sorbent was saturated with 0.1 N solutions of H_2SO_4 or NaOH (SO_4^{2-} and OH^- forms) for 1 h or kept in distilled water (Cl^- form).

Data on sorption from solutions with the initial concentration C_{init} = 3000, 1500, and 1500 mg dm^{-3} recalculated on CrO_3 are given in Figs. 1a–1c for the AM-2b sorbent (weight 2 g) in the SO_4^{2-}, OH^-, and Cl^- forms, respectively.

For the anion exchanger in the SO_4^{2-} form in the range pH 2–12 the dependence of the residual concentration on solution pH passes through four minima: at pH 2, 4, 6, and 9. In this case, the exchange sorption capacity (ESC) in 20 min is 160, 170, 150, and 130 mg of sorbate per gram of sorbent, respectively.

For the anion exchanger in the OH^- form in the range pH 1–11 the dependence has three minima: at pH 1, 3, and 6 (Fig. 1b). The ESC is 130, 127, and 110 mg g^{-1}, respectively.

For the anion exchanger kept in water (Cl^- form) at pH 1–11 the best results were obtained at pH 2–6 and 9 (Fig. 1c). The ESC is 144 and 90 mg g^{-1}, respectively.

As seen from Fig. 1, the sorption depends on both pH and conditions of sorbent pretreatment, because it is determined by the state of chromium(VI) ions in the solution and the state of functional groups of the anion exchanger [1]. Probably, the sorption maximum at pH ≤ 4 is due to the formation of isopolychromates and to the increased degree of protonation of the amine groups of the anion exchanger [1]. The sorption at pH < 7 is governed by the formation of $Cr_2O_7^{2-}$ ions being the product of polymerization of monomers in the solution. The sorption maximum at pH 9 results from the ion exchange with CrO_4^{2-} anions and from complexation in the resin phase. The

1070-4272/01/7401-0024$25.00

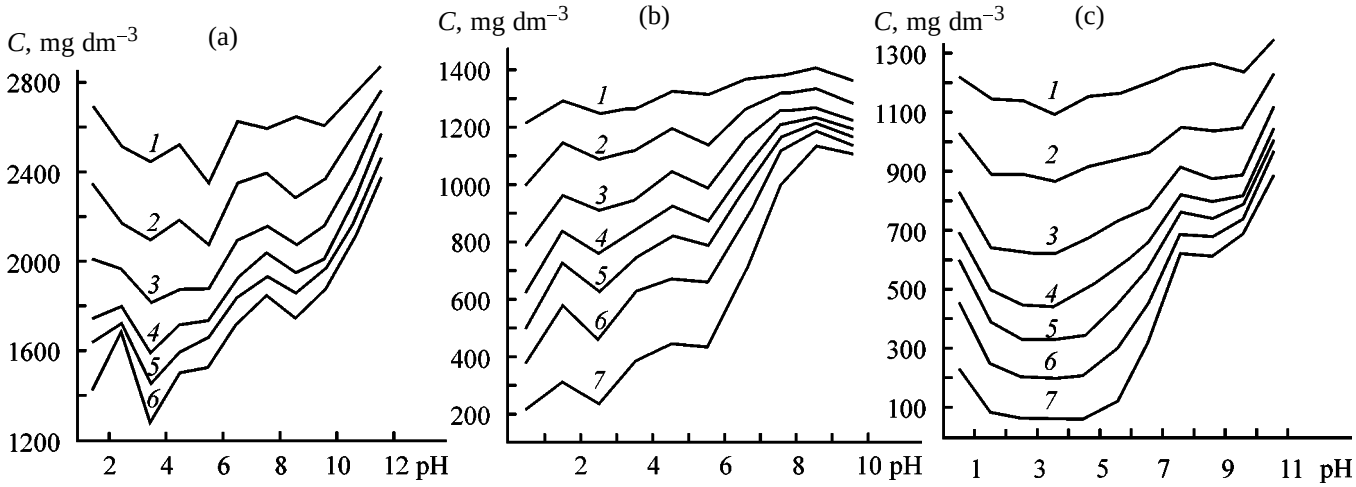

Fig. 1. Residual concentration of Cr(VI) ions C vs. solution pH at various times of sorption on AM-2b anion exchanger. Sorption time (min): (*1*) 2, (*2*) 5, (*3*) 10, (*4*) 15, (*5*) 20, (*6*) 30, and (*7*) 60. (a) SO_4^{2-} form, (b) OH^- form, and (c) preliminary treatment in water.

shift of the third maximum toward more acidic region (Fig. 1b) may be due to the fact that the low-basic groups of the AM-2b anion exchanger in the OH^- form loss virtually completely the exchange capability at pH $\geq$ 9.

The kinetic curves of Cr(VI) sorption on AM-2b anion exchanger kept in water at pH 4 are shown in Fig. 2.

Figure 3 demonstrates the isotherms of chromium(VI) sorption for the sorption time of 60 and 80 min, constructed from the data in Fig. 2.

As seen from Figs. 2 and 3, sorption increases with increasing time and initial solution concentration, which is due to polymerization.

By kinetic analysis of sorption using the substitution and graphical procedures [6], we determined the order n of the process with respect to the sorbate (n = 2):

$$-dC/d\tau = kC^n,$$

where C is the residual concentration of the sorbate in the solution, τ is the sorption time, and k is a constant.

The second order of the process suggests that the sorption process is kinetically controlled and is limited by chromium complex formation on the sorbent surface [6].

The sorption rate limited by complex formation is also governed by pH of the medium. Chromium(VI)-containing ions polymerize by polycondensation reaction (1) involving protons or hydroxide ions.

In the systems studied, the composition and struc-

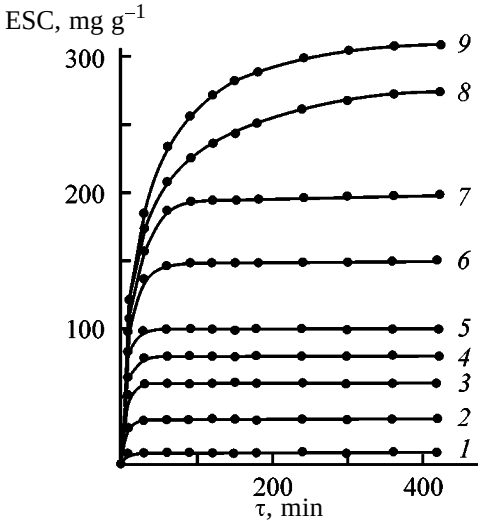

Fig. 2. Kinetic curves of Cr(VI) sorption on AM-2b anion exchanger kept in water at pH 4. (ESC) exchange sorption capacity. Initial concentration of CrO_3, mg dm^{-3}: (*1*) 100, (*2*) 340, (*3*) 600, (*4*) 800, (*5*) 1000, (*6*) 1500, (*7*) 2000, (*8*) 3000, and (*9*) 4000. The same for Fig. 3.

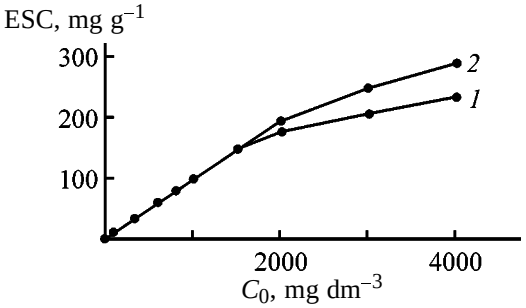

Fig. 3. Isotherms of chromium(VI) sorption for sorption times (*1*) 60 and (*2*) 180 min. (C_0) initial concentration of CrO_3.

Table 1. Kinetic analysis of chromium(VI) sorption at pH 4, performed by kinetic equations for gel and film using data of Fig. 2

C_0, mg dm^{-3}	Film kinetics		Gel kinetics	
	$K \times 10^2$	r*	$B \times 10^3$	r
340	21.18	0.9993	2.41	0.9952
600	21.32	0.9983	2.39	0.9969
800	15.28	0.9998	1.85	0.9987
1000	15.72	0.9943	2.05	0.9983
1500	8.29	0.9920	1.01	0.9967
2000	5.94	0.9969	0.63	0.9988
3000	2.31	0.9567	0.22	0.9852
4000	1.76	0.9618	0.16	0.9852

* (r) Correlation coefficient.

ture of chromium(VI) isopolyanion of the composition Cr_nO_{3n+1} are governed by pH of the initial solution. However, reaction (1) is not in equilibrium but continues in the course of the ion-exchange process, which is confirmed experimentally by pH variations in the course of sorption.

Sorption can proceed by the reactions [7]

$$2RCl + CrO_4^{2-} = R_2CrO_4 + 2Cl^-,$$

$$mR_2CrO_4 + (n - m)CrO_4^{2-} + (n - 1)H^+ = R_{2m}Cr_nO_{3n+1}(OH)_{n-1},$$

$$2RCl + HCrO_4^- = R_2OHO_3Cr^+ + 2Cl^-, \text{ etc.}$$

Table 2. Diffusion coefficient D at various times of contact τ of AM-2b anion exchanger with Cr(VI) solution at pH_{sorp} 4 as calculated from data of Fig. 2

τ, min	$B\tau$	$D \times 10^6$, cm^2 s^{-1}	τ, min	$B\tau$	$D \times 10^6$, cm^2 s^{-1}	τ, min	$B\tau$	$D \times 10^6$, cm^2 s^{-1}	τ, min	$B\tau$	$D \times 10^6$, cm^2 s^{-1}
C_0^* = 340 mg dm^{-3}			C_0 = 600 mg dm^{-3}			C_0 = 800 mg dm^{-3}			C_0 = 1000 mg dm^{-3}		
1	0.00097	1.2	1	0.00087	1.1	1	0.00034	0.4	1	0.000005	0.1
2	0.00128	1.6	2	0.00133	1.7	2	0.00056	0.7	2	0.000008	0.1
3	0.00154	1.9	3	0.00179	2.3	3	0.00075	1.0	3	0.00132	1.7
4	0.00171	2.2	4	0.00206	2.6	4	0.00101	1.3	4	0.00173	2.2
5	0.00188	2.4	5	0.00216	2.7	5	0.00125	1.6	5	0.00203	2.6
7	0.00236	3.2	7	0.00241	3.0	7	0.00167	2.1	6	0.00193	2.4
10	0.00283	3.3	10	0.00246	3.1	10	0.00186	2.3	7	0.00211	2.7
15	0.00294	3.7	15	0.00286	3.6	15	0.00199	2.5	8	0.00207	2.6
						20	0.00208	2.6	9	0.00219	2.8
						25	0.00216	2.7	10	0.00223	2.8
									15	0.00216	2.7
									20	0.00208	2.6
									25	0.00216	2.7
C_0 = 1500 mg dm^{-3}			C_0 = 2000 mg dm^{-3}			C_0 = 3000 mg dm^{-3}			C_0 = 4000 mg dm^{-3}		
1	0.00038	0.5	1	0.00045	0.6	1	0.00032	0.4	1	0.00013	0.2
2	0.00052	0.7	2	0.00053	0.7	2	0.00038	0.5	2	0.00027	0.3
3	0.00059	0.7	3	0.00052	0.7	3	0.00041	0.5	3	0.00026	0.3
4	0.00070	0.9	4	0.00054	0.7	4	0.00039	0.5	4	0.00026	0.3
5	0.00079	1.0	5	0.00054	0.7	5	0.00039	0.5	5	0.00025	0.3
6	0.00086	1.1	6	0.00056	0.7	6	0.00038	0.5	6	0.00024	0.3
7	0.00094	1.2	7	0.00058	0.7	7	0.00036	0.5	7	0.00023	0.3
8	0.00100	1.3	8	0.00058	0.7	8	0.00036	0.5	8	0.00022	0.3
9	0.00101	1.3	9	0.00061	0.8	9	0.00035	0.4	9	0.00023	0.3
10	0.00101	1.3	10	0.00062	0.8	10	0.00034	0.4	10	0.00022	0.3
15	0.00099	1.3	15	0.00061	0.8	15	0.00032	0.4	15	0.00020	0.3
20	0.00101	1.3	20	0.00058	0.7	20	0.00032	0.4	20	0.00019	0.2
25	0.00108	1.4	25	0.00060	0.8	25	0.00030	0.4	25	0.00019	0.2
30	0.00110	1.4	30	0.00059	0.8	30	0.00028	0.4	30	0.00020	0.3
40	0.00111	1.4	40	0.00062	0.8	40	0.00026	0.3	40	0.00019	0.2
50	0.00100	1.3	50	0.00064	0.8	50	0.00025	0.3	50	0.00019	0.2
60	0.00097	1.3	60	0.00065	0.8	60	0.00023	0.3	60	0.00018	0.2

* (C_0) Initial concentration of CrO_3 solution.

where R is the fixed polycation of the anion exchanger.

Further complexation may be associated with redox reactions, e.g.,

$$Cr^{6+} + 3e \rightarrow Cr^{3+} \text{ etc.}$$

The kinetic analysis of sorption was performed by kinetic equations for gel and film [8]. Table 1 shows that at a Cr(VI) concentration from 340 to 800 mg dm^{-3} the sorption is described by a kinetic equation for film, whereas at concentrations from 1000 to 4000 mg dm^{-3} it is described by a kinetic equation for gel.

The results of calculation of the diffusion coefficients D ($cm^2\ s^{-1}$) are given in Table 2 in relation to the time of contact of the anion exchanger with the solution containing different initial concentrations of Cr(VI) ions. The diffusion coefficient D is calculated by the equation

$$D = Br^2/\pi^2,$$

where r is the sorbent grain radius and B, the coefficient calculated from the tabulated data [9].

As seen from Table 2, the diffusion coefficient D decreases as the concentration C_0 of the initial solution grows. At $C_0 \geq 1000$ mg dm^{-3} D is approximately constant, irrespective of contact time.

From the equation

$$\log C_{sorb} = p\log C_s + \log(K/K_p)$$

where p is the polymerization factor, $C_{sorb} = ESC \cdot M^{-1} V_{sp}^{-1}$ is the ion concentration in the sorbent (mol dm^{-3}), V_{sp} is the specific swelling of the sorbent ($cm^3\ g^{-1}$), C_s is the ion concentration in solution (mg dm^{-3}), K is the equilibrium constant, and K_p is the polymerization constant, we determined the polymerization factors p using the procedure described in [9].

C_{init}, mg dm^{-3}	p
800–1500	0.27
1925–4200	0.14

The difference in the values of the polymerization factor p indicates that over the initial concentration range studied the chromium(VI) complexes of various compositions are sorbed. With growing initial solution concentration the degree of polymerization of the complexes increases according to Eq. (1).

CONCLUSION

(1) The calculations of the diffusion coefficient and polymerization factor, along with the kinetic analysis, indicate that at higher concentrations of the sorbate the sorption process is kinetically controlled and is limited by chromium(VI) complex formation on the sorbent surface and by chromium(VI) polymerization in the solution and on the sorbent surface.

(2) Sorption of chromium(VI) from aqueous solution is optimal at acid treatment of the sorbent and pH 4: ESC 350 mg CrO_3 per gram of sorbent at the initial solution concentration $C_{init} \leq 4000$ mg CrO_3 dm^{-3}.

REFERENCES

1. Gutsanu, V.L. and Muntyan, S.A., *Zh. Prikl. Khim.*, 1985, vol. 58, no. 9, pp. 1981–1983.
2. Umarakhunov, M.Kh., Nikitina, L.V., and Rshchaev, N.U., *Zh. Fiz. Khim.*, 1996, vol. 70, no. 10, pp. 1854–1856.
3. Voropanova, L.A., in *Trudy VI regional'noi konferentsii "Problemy khimii i khimicheskoi tekhnologii"* (Proc. VI Regional Conf. "Problems of Chemistry and Chemical Technology"), Voronezh, 1998.
4. *Ionnoobmennye materialy dlya protsessov gidrometallurgii, ochistki stochnykh vod i vodopodgotovki: Spravochnik* (Ion-Exchange Materials for Hydrometallurgy, Wastewater Purification, and Water Treatment: Handbook), Moscow: Vses. Nauchno-Issled. Inst. Khim. Tekhnol., Gos. Komitet po Ispol'z. Atomnoi Energii SSSR, 1983.
5. RF Patent 2091317.
6. Voropanova, L.A., Rubanovskaya, S.G., and Getoeva, E.Yu., *Zh. Prikl. Khim.*, 1998, vol. 71, no. 9, pp. 1439–1444.
7. Helfferich, F., *Ionenaustauscher. Grundlagen der Struktur-Herstellung-Theorie*, Weinheim: Chemie, 1959, vol. 1.
8. Zelikman, A.N., Vol'dman, G.N., and Belyavskaya, L.V., *Teoriya gidrometallurgicheskikh protsessov* (Theory of Hydrometallurgical Processes), Moscow: Metallurgiya, 1975.
9. Kislinskaya, G.E., Ermolenko, V.I., and Sheka, I.A., *Zh. Neorg. Khim.*, 1977, vol. 12, no. 9.

Russian Journal of Applied Chemistry, Vol. 74, No. 1, 2001, pp. 28–30. Translated from Zhurnal Prikladnoi Khimii, Vol. 74, No. 1, 2001, pp. 29–31.

SORPTION AND ION-EXCHANGE PROCESSES

The Chemical Resistance of Chabazite from Transbaikal Region

E. L. Zonkhoeva

Geological Institute, Siberian Division, Russian Academy of Sciences, Ulan-Ude, Buryatia, Russia

Received March 3, 2000

Abstract—The chemical resistance of natural chabazite of Margintui volcanic field (Transbaikal Region) in 0.01, 0.1, 1.0, and 3.0 N HCl at was studied in relation to the treatment time. The order, degree, and relative rate of cation extraction from the chabazite phase were determined.

Studying the chemical resistance of zeolites is important for understanding the mechanism of their crystallization under natural and artificial conditions. Acid treatment can be used for preparing zeolitic sorbents and catalysts with controllable properties, which significantly extends the possibilities of their application.

At treatment of zeolites with dilute acid solutions the proton of the acid first interacts with the molecules of zeolite water to form hydroxonium ions participating in cation-exchange reactions [1]. At higher concentrations of the acid the proton interacts with the oxygen of the aluminosilicate skeleton with formation of hydroxide groups. As a result, the Al–O–Si bonds break and aluminum(III) passes into the solution. In this stage, decationization and dealuminization occur simultaneously.

A majority of works is devoted to chemical resistance of zeolites, especially of mordenites. At the same time, the resistance of chabazite is studied insufficiently. For example, dealumination and amorphization of chabazite boiled in 0.12 M solution of HCl has been reported in [2]. In 2 M HCl solution the chabazite crystal structure degrades completely. Chabazite is unstable to the action of HCl vapor at 200°C [3].

The acid resistance of natural chabazite was studied by Piguzova [4]. It was found that up to 12–17% aluminum(III) is extracted from chabazite on treatment with 0.006 N HCl. As a result, the maximal pore volume increases by a factor of approximately 3 compared to the initial sample. In 3 N HCl solution, the ratio SiO_2/Al_2O_3 reaches 15, but the mineral structure remains unchanged.

Bogdanova and Belitskii [5] studied the resistance of 25 zeolite samples, including chabazite samples, to treatment for 1 h with 1 N HCl on a boiling water bath. Among the four groups, chabazite is classed with the third group of zeolites, weakly reactive with respect to dissolution. Treatment of chabazite with the concentrated acid resulted in the extraction of 97% of aluminum and total removal of Ca(II), Mg(II), and Ba(II) ions. After treatment, the residual chabazite retained the shape of the crystals.

Thus, no data are available on the chemical resistance of chabazite in relation to the treatment time.

In this work, the chemical resistance of chabazite from the Margintui volcanic field (Transbaikal Region) of the composition $Ca_{0.85}Na_{0.1}K_{0.08}Mg_{0.03} \cdot (Al_{1.7}Si_{4.2}O_{12}) \cdot H_2O$ in acid solutions of various concentrations was studied as a function of the contact time. The grain size of the mineral was 1–2 mm. Weighed portions of chabazite were placed in 0.01, 0.1, 1.0, or 3.0 N HCl for 1, 3, and 24 h at the solid-to-liquid ratio of 1 : 30. After separating the phases, chabazite was studied by X-ray phase analysis (DRON-2.0 diffractometer, CuK_α radiation) and by chemical analysis for Si, Al, K, Na, Ca, and Mg. The Al and Si concentrations were determined on an SF-46 spectrophotometer and the K, Na, Ca, and Mg concentrations, on a Saturn atomic absorption spectrophotometer (table, Fig. 1).

The samples treated with 0.01, 0.1, 1.0, and 3 M acid solutions are denoted as A, B, C, and D, respectively. The figures 1, 3, and 24 denote the treatment time (h). The degree of extraction of exchangeable cations and aluminum(III) is recalculated on oxides (Fig. 1). The rate v of passing of the ions into the solution was determined from the formula $m = vt$, and the relative rate per gram of zeolite, by the formula $\alpha = v/M$ (h^{-1}), where m is the weight (g) of the cation passed into the solution in time t (h), and M is the weighed portion of chabazite (g) [6].

The X-ray diffraction patterns of the initial sample

1070-4272/01/7401-0028$25.00

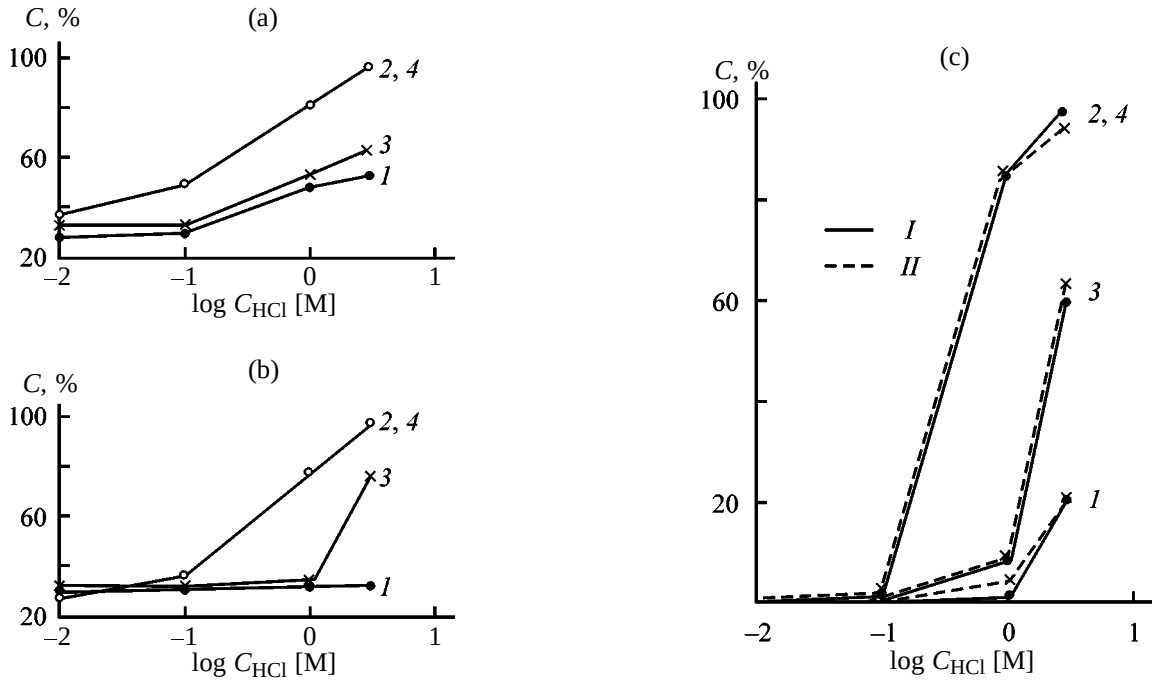

Fig. 1. Degree of extraction *C* from chabazite of (a) sodium, (b) potassium, and (c) calcium and aluminum as a function of acid concentration C_{HCl}. Treatment time (h): (*1*) 1, (*2*, *4*) 24, and (*3*) 3. Ion: (*I*) calcium and (*II*) aluminum.

agree with the reference data [7]. The crystal structure of chabazite, when treated with 1 N HCl solution for 24 h (sample C-24) and with 3 N HCl solution for 3 and 24 h (samples D-3 and D-24, respectively), degrades. The most intense reflections d_{101}, d_{211}, d_{401}, and d_{214} were retained in the diffraction pattern of the C-24 sample, but in that of the D-24 sample all reflections were absent. All other conditions of acid treatment did not affect the chabazite crystal structure.

According to chemical analysis, Na and K are the predominant exchangeable cations extracted from the chabazite solid phase into 0.01 and 0.1 N HCl (table; Figs. 1a, 1b). Upon 24-h treatment with 0.1 N HCl, only 1.11% of aluminum(III) and 2.43% of calcium(II) are extracted (table, Fig. 1c).

Magnesium(II), present in chabazite in a small amount (0.31%), is extracted to 45% as the mineral is rendered amorphous by treatment with 3 N HCl. No extraction of silicon from the chabazite occurs.

Because calcium ions in the chabazite exchangeable complex are predominant, their behavior in the systems studied is of a special interest. Figure 1c shows that on treatment of chabazite with 0.1 N HCl (sample B-24) calcium is extracted simultaneously with the start of washing-out of aluminum, but the relative extraction rate of aluminum is higher than that of calcium and other exchangeable cations (see table).

With growing acid concentration the relative rate of passing of calcium into the solution increases considerably.

The distribution and coordination of various cat-

Relative rate α of washing-out of the cations from the chabazite phase

Sample	Relative rate, α, h^{-1}				
	Al(III)	Ca(II)	Mg(II)	Na(I)	K(I)
A-1	–	–	–	0.0014	0.0022
A-3	–	–	–	0.0006	0.0008
A-24	–	–	–	0.0001	0.0001
B-1	–	–	–	0.0015	0.0023
B-3	–	–	–	0.0005	0.0008
B-24	0.0950	0.0001	–	0.0001	0.0001
C-1	0.0950	0.0030	–	0.0024	0.0023
C-3	0.0030	0.0015	–	0.0009	0.0008
C-24	0.0030	0.0021	–	0.0002	0.0002
D-1	0.0200	0.0123	–	0.0026	0.0024
D-3	0.0190	0.0124	–	0.0011	0.0018
D-24	0.0040	0.0023	0.0007	0.0002	0.0003

Note: The dash stands for the absence of ion extraction from the chabazite phase.

ions in the chabazite have been studied in a number of works [3, 8–11]. Within the large chabazite cavity calcium ions occupy three different positions: near a six-membered ring outside the hexagonal prism, in an eight-membered ring, and inside the dihedral angle formed by the four-membered rings. The calcium coordination sphere contains water molecules separating calcium ions from the walls of the aluminosilicate skeleton and the oxygen atoms of the skeleton. Evidently, an acid proton breaks the Al–O and Ca–O bonds, which destabilizes the chabazite crystal structure and facilitates simultaneous passing of aluminum and calcium into the solution. The table clearly shows that the interaction of chabazite with an acid is a two-stage process involving ion-exchange recovery of alkali metal ions as the first stage and the dealumination combined with decalcination as the second stage.

The extent of dealumination and decationization of chabazite largely depends on the time of acid treatment. The effect produced by the treatment time on the metal ion recovery is more pronounced for sodium than for potassium (Figs. 1a and 1b, respectively). The increase in the amount of the potassium ions is due to dissolution of chabazite at treatment (1 N acid solution, 24 h and 3 N solution, 3 and 24 h). The relative rate of passing of the ions into the acid solution increases with growing acid concentration and decreases with increasing treatment time.

CONCLUSION

The study of chemical resistance of natural chabazite treated with 0.01–3 N HCl for different times showed that treatment with 0.01 and 0.1 N solutions results in the extraction of sodium and potassium ions. In 1.0 and 3.0 N acid solutions, calcium and aluminum ions are extracted along with alkali metal ions. Such a sequence of the extraction of exchangeable cations implies that calcium ions are stronger bound in the chabazite structure than alkali metal ions. Removal of aluminum(III) ion from the tetrahedral position does not affect the chabazite crystal structure, except for the case when treatment results in mineral degradation (1.0 N acid solution, 24 h and 3 N solution, 3 and 24 h). The degree of dealumination and decationization depends on the time of contact of chabazite with the acid.

REFERENCES

1. Chelishchev, N.F., Berenshtein, B.G., and Volodin, V.F., *Tseolity – novyi tip mineral'nogo syr'ya* (Zeolites: A Novel Type of Mineral Raw Materials), Moscow: Nedra, 1987.
2. Tsitsishvili, G.V., Andronikashvili, T.G., Kirov, G.N., and Filizova, L.D., *Prirodnye tseolity* (Natural Zeolites), Moscow: Khimiya, 1985.
3. Breck, D.W., *Zeolite Molecular Sieves: Structure, Chemistry and Use*, New York: Wiley, 1974.
4. Piguzova, L.I., in *Prirodnye sorbenty* (Natural Sorbents), Moscow: Nauka, 1967, pp. 166–188.
5. Bogdanova, V.I. and Belitskii, I.A., *Geol. Geofiz.*, 1968, no. 4, pp. 44–53.
6. Yuminov, A.V., Makurin, Yu.N., and Berezyuk, V.G., *Zh. Prikl. Khim.*, 1997, vol. 70, no. 3, pp. 406–409.
7. Semushin, V.N., *Rentgenograficheskii opredelitel' tseolitov* (Index of X-ray Diffraction Data for Zeolite Identification), Novosibirsk: Nauka, 1986, p. 53, card 104.
8. Mortier, W.J., Pluth, J.J., and Smith, J.V., *Mater. Res. Bull.*, 1977, vol. 12, no. 3, p. 241.
9. Calligaris, M., Nardin, G., and Randaccio, L., *Zeolites*, 1984, vol. 4, no. 4, p. 251.
10. Calligaris, M., Nardin, G., and Randaccio, L., *Zeolites*, 1986, vol. 6, no. 2, p. 137.
11. Butikova, I.K., Shepelev, Yu.F., and Smolin, Yu.I., *Kristallografiya*, 1993, vol. 38, no. 4, pp. 68–72.

Russian Journal of Applied Chemistry, Vol. 74, No. 1, 2001, pp. 31–35. Translated from Zhurnal Prikladnoi Khimii, Vol. 74, No. 1, 2001, pp. 32–36.

SORPTION AND ION-EXCHANGE PROCESSES

Deoxygenation of Aqueous Solutions by Cathodically Polarized Copper-Containing Redox Cation Exchanger

T. A. Kravchenko, N. V. Sotskaya, and O. V. Sleptsova

Voronezh State University, Voronezh, Russia

Received June 7, 1999; in final form, January 2000

Abstract—Oxygen reduction in aqueous solutions by cathodically polarized copper-containing redox resins was studied. To provide reagent-free, continuous, and exhaustive deoxygenation, the rate of surface electroless oxidation with oxygen should be equal to the rate of electrochemical reduction (regeneration) of the redox centers.

The modern industry imposes stringent requirements on deoxygenation of water and aqueous solutions of electrolytes. There are various procedures for removing oxygen from liquid media [1]; however, copper-containing redox resins (electron and ion exchangers) are the most efficient for exhaustive deoxygenation [2, 3]. When deoxygenation is performed by reducing sorption of oxygen on a copper-containing redox cation exchanger, oxygen reacts with dispersed copper to form copper oxides or copper ions fixed as counterions in the ion-exchange matrix. The redox resins are unique substances since they have high redox capacity and developed porous structure and can be reduced or oxidized without liberation of the products of their own conversion. In addition, copper-containing redox resins have sufficient electrical conductivity and stability to electric current [4] which allows reducing sorption of oxygen on these materials under conditions of cathodic polarization [5–7], i.e., oxygen electrosorption. Previously [8, 9] we determined two consecutive and parallel pathways of electrosorption. The first occurs via redox transformations of the surface of the redox resin grains and heterogeneous chemical reactions to form chemisorbed copper–oxygen complex. The electric current regenerates the surface reaction centers of the redox resin, thus providing fast and continuous deoxygenation. The rate-determining step is heterogeneous chemical reaction (1). The subsequent electrochemical reduction of copper–oxygen compounds (2) is relatively fast:

$$\mathrm{R \cdot Cu} \xrightarrow[(1)]{\mathrm{O_2}} \mathrm{R \cdot [Cu \ldots O]} \underset{(2)}{\overset{\mathrm{e}}{\rightleftarrows}} \mathrm{R \cdot Cu},$$

where R is the polymeric matrix of the redox cation exchanger.

The second pathway is sorption and reduction of oxygen with copper of the redox resin in the depth of its grains, where the reaction centers are not affected even by the maximal cathodic polarization. At polarizing currents insufficient for regeneration of all redox centers, this pathway also provides exhaustive removal of oxygen from the solution. However, in this case the deoxygenation is slow and requires intermittent regeneration of the redox filter.

The aim of this work was to determine conditions providing constantly high rate of oxygen electrosorption from aqueous solutions on copper-containing redox resin, i.e., conditions providing continuous regeneration of the reaction surface.

We studied oxygen electrosorption on EI-21 SNU copper-containing redox resin [2] prepared from KU-23 macroporous sulfonic cation exchanger. The redox centers of this redox cation exchnager are clusters of copper atoms located around the ion groups of the resin. The diameter of resin grains is 0.5–1.0 mm. The redox capacity of the sorbent ε (the content of dispersed copper) ranged from 6.5×10^3 to 12.0×10^3 g-equiv m^{-3} of the resin. Deoxygenation with both reduced and oxidized form of the resin was studied. The degree of oxidation of the resin α was determined by microscopic examination of the concentric ring of Cu_2O clearly seen on a section of a resin grain. The oxidized form of the resin was reduced either with alkali solution of sodium dithionite $Na_2S_2O_4$ (electroless reduction) or electrochemically at $i = 0.1$ A m^{-2} and cathodic polarization $E = -0.9$ V in the absence of solution flow. Oxygen electrosorption was studied in a flow three-cell reactor of the filter-press type. The reactor consists of cathodic and two anodic cells separated by MA-40 anion-exchange

1070-4272/01/7401-0031$25.00

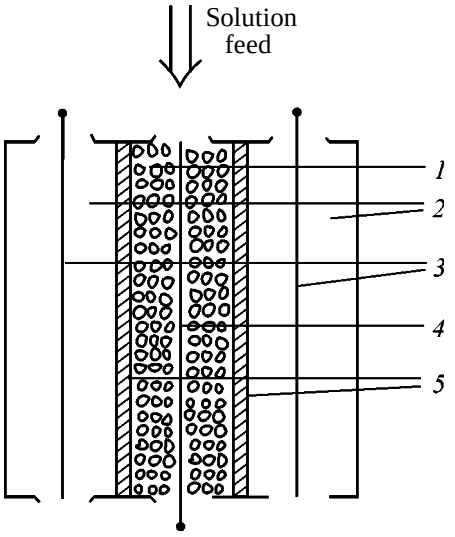

Fig. 1. Scheme of electrosorption reactor: (*1*) cathodic cell packed with the redox resin, (*2*) anodic cells, (*3*) platinum anodes, (*4*) copper cathode, and (*5*) anion-exchange membranes.

membranes (Fig. 1). The vertical electrodes were fixed along the longitudinal axis of the cells. A bed of granulated redox resin was arranged around the vertical copper wire cathode in the working cell with 1–6 cm height (h) and 1.2 cm^2 cross section. A Luggin capillary of a silver chloride reference electrode was fixed in the immediate vicinity of the cathode. A working 0.04 M solution of sodium sulfate was fed from the top with a flow velocity form 0.1 to 0.7 cm s^{-1}. The electrosorption reactor was polarized under galvanostatic conditions. The potentials were measured vs. a standard hydrogen electrode.

The rate of oxygen electrosorption $i(\Delta c)$ (A m^{-2}) was estimated from a decrease in its concentration and expressed in the units of current density:

$$i(\Delta c) = zFu\,\Delta c/s,$$

where z is the number of electrons involved in the reaction ($z = 4$); F is the Faraday number (26.8 A h mol^{-1}; u is flow rate of the oxidizing agent (l h^{-1}); Δc is difference in the oxidizing agent concentration at the inlet (c_0) and outlet (c) of the reactor, determined with the aid of a KL-215 oxygen meter (M); and s is the geometrical surface area of grains (m^2).

Table 1. Rate of oxygen electrosorption $i(\Delta c)$ and limiting current density i_{lim} for the reduced and oxidized forms of the redox resin; $\varepsilon = 10.5 \times 10^3$ g-equiv m^{-3}, c_0 = 8.6 mg l^{-1}, u = 0.46 cm s^{-1}, at i = 0.086 A m^{-2}

α, %	$i(\Delta c)$	i_{lim}	$-E$, V
	A m^{-2}		
0	1.31 ± 0.11	1.06 ± 0.07	0.2
50	0.84 ± 0.04	0.34 ± 0.03	0.9

The rate of electrochemical process was estimated from the limiting current density of the polarization curves I_{lim}, which is the limiting current of preceding chemical reaction and is described by the equation [8, 9]

$$I_{lim} = i_{react} = -zF\omega_0/\nu,$$

where ω_0 is rate of reduction of dissolved oxygen with the redox resin in the absence of the polarization, and ν is the stoichiometric number.

Let us consider the rate of oxygen electrosorption as influenced by the reactivity of the redox resin. For this purpose we studied both the reduced and oxidized forms of the resin (Table 1). The rate of oxygen electrosorption $i(\Delta c)$ and the limiting current density of polarization curves i_{lim} considerably decrease with accumulation of copper oxides in the depth of resin grains (i.e., at high oxidation degrees of the resin α). The oxidized form has a lower electrical conductivity, and hence the oxygen electrosorption on this form occurs at higher overvoltage as compared to the reduced form. Thus, the oxygen reduction on the redox resin with highly reactive reducing centers is the fastest.

The reactivity of the redox resin is determined by not only the presence of copper oxides but also the amount of reactive copper (the redox capacity of the resin ε). As seen from Fig. 2, the rate of electrosorption on the redox resins with a low content of dispersed copper is considerably higher than the limiting current density. These parameters become close starting from $\varepsilon = 10.5 \times 10^3$ g-equiv m^{-3}. The fact that $i(\Delta c)$ is higher than i_{lim} indicates that oxygen is reduced not only by the surface but also by internal reaction centers of a grain. This can decrease the reactivity of the redox resin and decelerate oxygen reduction (Table 1).

To maintain constantly high rate of the process, the rate of electroless oxidation of the redox centers with oxygen $i(\Delta c)$ should be equal to the rate of the electrochemical reduction i_{lim}. In addition, polarization currents higher than the limiting value are undesirable because of hydrogen evolution. Commercial EI-21-75 redox resin with relatively high capacity (ca. $10.5 \times$

10^3 m^{-3}) meets the indicated requirements. This sorbent can be used for oxygen electrosorption.

The redox resin after sorption or electrosorption of O_2 can be regenerated by treatment with chemical reducing agents or by cathodic polarization in a stationary solution. The regeneration procedure (chemical or electrochemical) affects the limiting current (Table 2) and does not affect the rate of oxygen sorption.

The limiting current density i_{lim} for the redox resin regenerated by chemical reduction is somewhat lower as compared to the resin regenerated by the electrochemical procedure. The constancy of the electrosorption rate indicates that the number of the reaction centers remains the same. However, the state of these centers can change owing to sorption of the reducing agent and its oxidation products, which, in turn, should affect the rate of heterogeneous chemical oxidation of these centers and hence the limiting current of their reduction. Cathodic activation of the redox centers of the resin regenerated by the chemical procedure increases the limiting current density to the value observed for the electrochemicaly regenerated redox resin. When the cathodically activated redox resin is treated with the reducing agent, the resin is converted into the initial state characterized by a low limiting current. Thus, deoxygenation on the redox resin preliminarily activated by cathodic polarization will occur via oxidation and reduction of its surface with the maximal limiting current density. In the case of the chemically regenerated redox resin the process will mainly occur via formation and accumulation of copper oxides in the depth of a grain, which will deactivate the resin, thus decelerating the O_2 electrosorption. The activity of cathodically activated redox resin and hence the rate of oxygen electrosorption of this resin remain constantly high.

Thus, the copper-containing redox resin suitable for deoxygenation of aqueous solutions should be in the reduced form, have high redox capacity, and be activated by cathodic polarization. Only in this case the rate of oxygen electrosorption at polarization with the limiting current is equal to the limiting current density of the polarization $i(\Delta c) = i_{lim}$ and the process occurs via consecutive oxidation and reduction of the surface of the resin grains, thus providing continuous regeneration of the redox centers. This can be the case only for the redox resin with definite properties and under definite conditions. Among them are, first of all, polarizing current and concentration and feeding rate of dissolved oxygen. Let us consider each of this parameters.

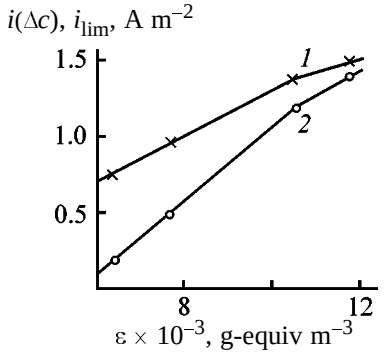

Fig. 2. (*1*) Rate of oxygen electrosorption $i(\Delta c)$ and (*2*) limiting current density i_{lim} at oxygen concentration in the solution of c_0 = 8.6 mg l^{-1}, flow velocity of the solution u = 0.46 cm s^{-1}, and height of the resin bed h = 6 cm as functions of the copper content in the redox resin ε.

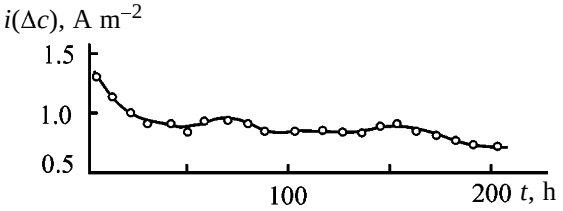

Fig. 3. Rate of oxygen electrosorption $i(\Delta c)$ by EI-21-75 redox resin at polarizing current density i = 0.86 A m^{-2}, $\varepsilon = 10.5 \times 10^3$ g-equiv m^{-3}, c_0 = 8.6 mg l^{-1}, u = 0.46 cm s^{-1}, and h = 6 cm as a function of time.

Deoxygenation with required rate can be maintained for a long time by polarization of the cathodically activated redox resin with the maximum possible current (which should depend on the limiting current) at which no hydrogen is liberated. This is indeed the case in oxygen reduction on EI-21-75 industrial copper-containing redox resin with $\varepsilon = 10.5 \times 10^3$ g-equiv m^{-3} at the equilibrium concentration c_0 = 8.6 mg l^{-1}, the flow velocity of the solution u = 0.46 cm s^{-1}, and the polarizing current density i = 0.86 A m^{-2} (Fig. 3). Negligible decrease in the reactivity of the resin in 200 h under these conditions can

Table 2. Change of the O_2 content in the solution Δc, electrosorption rate $i(\Delta c)$, and limiting current density i_{lim} for the redox resin regenerated by (I) chemical and (II) electrochemical procedure. $\varepsilon = 10.5 \times 10^3$ g-equiv m^{-3}, c_0 = 8.6 mg l^{-1}, u = 0.46 cm s^{-1}

Regeneration procedure	Δc, mg l^{-1}	$i(\Delta c)$	i_{lim}
		A m^{-2}	
I	4.08 ± 0.32	0.78 ± 0.04	0.91 ± 0.11
II*	3.92 ± 0.15	0.75 ± 0.06	0.20 ± 0.03

* With sodium dithionite.

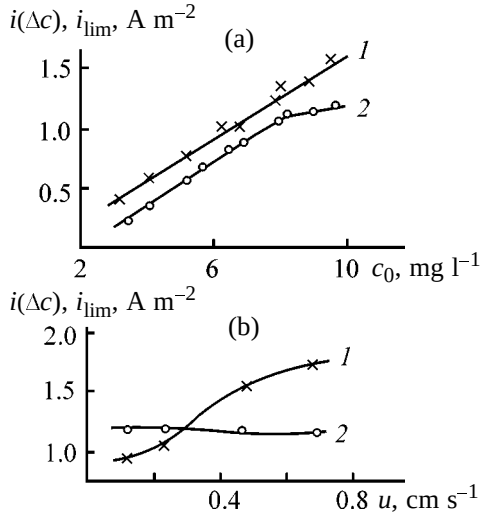

Fig. 4. (*1*) Rate of oxygen electrosorption $i(\Delta c)$ and (*2*) limiting current density i_{lim} as functions of (a) oxygen concentration in the solution c_0 ($\varepsilon = 10.5 \times 10^3$ g-equiv m^{-3}, $u = 0.46$ cm s^{-1}, and $h = 6$ cm) and (b) flow velocity of the solution u (cm s^{-1}) ($c_0 = 8.6$ mg l^{-1} and $h = 1$ cm).

be due to reducing sorption of oxygen by not only the first but also the second pathway with accumulation of Cu_2O inside a resin grain. Clearly the rate of electroless oxidation with oxygen slightly differs form that of electrochemical reduction of the resin. The equality can be attained only when the polarizing current and the rate of electroless reduction of oxygen on the resin $i(\Delta c)$ are the same. Since the polarizing current is restricted by the limiting current, the rate of oxygen reduction $i(\Delta c)$, the limiting current of the polarization curves i_{lim}, and the external polarizing current should be equal: $i = i(\Delta c) = i_{lim}$.

When the cathodically activated resin with high capacity (ε ca. 12×10^3 g-equiv m^{-3}, Fig. 2) is used, the rate of oxygen reduction $i(\Delta c)$ and the limiting current coincide at the equilibrium concentration $c_0 = 8.6$ mg l^{-1} and flow velocity of the solution $u = 0.46$ cm s^{-1}. In the case of the most frequently used industrial redox resin with $\varepsilon = 10.5 \times 10^3$ g-equiv m^{-3} these parameters slightly differ. In this connection let us consider $i(\Delta c)$ and i_{lim} for this redox resin as influenced by the oxygen concentration c_0 and flow velocity of the solution u. The electrosorption rate and the limiting current density regularly increase with increasing O_2 content in the solution (Fig. 4). At the O_2 concentration higher than 7.5 mg l^{-1} $i(\Delta c)$ exceeds the limiting current i_{lim}, suggesting oxidation of the reaction centers in the depth of a grain. The ratio of these parameters is similar at high flow rate of the solution and lower height of the resin bed (Fig. 4b).

Oxygen electrosorption on the industrial redox resin with $\varepsilon = 10.5 \times 10^3$ g-equiv m^{-3} should be performed at the flow velocity of the solution $u \le 0.23$ cm s^{-1} and the oxygen concentration $c_0 \le 7.5$ mg l^{-1}. In addition, since copper deposition on the cation exchanger involves treatment of the redox resin with a reducing agent (sodium dithionite), the sorbent should be electrochemically regenerated to increase i_{lim}.

Since in practice all parameters of the process are nonuniform throughout the resin bed of arbitrary height at large gradients of oxygen concentration in the bed, the reduction by the second pathway will occur in all cases [9]. Hence, to reach exhaustive deoxygenation, the process should be successively performed in several electrosorption reactors at the polarizing current corresponding to the rate of oxygen reduction.

Thus, continuous oxygen electrosorption on the copper-containing redox resin is provided mainly by maintaining constantly high reactivity of the resin by cathodic polarization at equal rates of electroless oxidation and electrochemical reduction of the redox centers. This is possible at definite internal and external parameters of the process (redox capacity of the resin, its oxidation degree, polarizing current density, flow velocity of the solution, and oxygen content in the solution).

CONCLUSIONS

Based on the results of this work we propose the following principles of oxygen electrosorption on the copper-containing redox resin, which provide continuous and exhaustive deoxygenation.

(1) Highly reactive cathodically activated redox resin in the reduced form with a high redox capacity should be used.

(2) To maintain high reactivity of the resin, the rate of electroless oxidation with oxygen should be equal to the rate of electrochemical reduction of the resin, which is the case when the limiting polarizing current density is equal to the rate of oxygen reduction. In the case of EI-21-75 redox resin this balance is attained at the O_2 concentrations lower than 7.5 mg l^{-1} and the flow velocity of the solution less than 0.3 cm s^{-1}.

ACKNOWLEDGMENTS

This work was financially supported by the Competitive Center of Basic Natural Science (project no. 97-0-9.3-44).

REFERENCES

1. *Spravochnik po svoistvam, metodam analiza i ochistke vody* (Handbook on Properties of Water and Methods of Its Analysis and Purification), Kul'skii, L.A., Goronovskii, I.G., Koganovskii, A.M., *et al*., Eds., Kiev: Naukova Dumka, 1980.
2. Kozhevnikov, A.V., *Elektronoionoobmenniki* (Electron and Ion Exchangers), Leningrad: Khimiya, 1972.
3. Polipanov, I.S. and Sazonov, A.M., *Zh. Prikl. Khim*., 1979, vol. 52, no. 2, pp. 335–338.
4. Kravchenko, T.A., Sotskaya, N.V., Aristov, I.V., and Berezina, N.P., *Elektrokhimiya*, 1996, vol. 32, no. 2, pp. 204–206.
5. Kravchenko, T.A., Krivneva, G.G., Kuznetsova, N.V., and Shatalov, A.Ya., *Zh. Prikl. Khim*., 1980, vol. 53, no. 2, pp. 334–338.
6. Kravchenko, T.A., Krivneva, G.G., Kuznetsova, N.V., and Shatalov, A.Ya., *Zh. Prikl. Khim*., 1980, vol. 53, no. 3, pp. 681–684.
7. Kuznetsova, N.V., Kravchenko, T.A., and Shatalov, A.Ya., *Zh. Prikl. Khim*., 1980, vol. 53, no. 4, pp. 840–843.
8. Sleptsova, O.V., Sotskaya, N.V., and Kravchenko, T.A., *Zh. Fiz. Khim*., 1996, vol. 70, no. 9, pp. 1657–1660.
9. Sleptsova, O.V., Sotskaya, N.V., and Kravchenko, T.A., *Zh. Fiz. Khim*., 1997, vol. 71, no. 10, pp. 1899–1901.

Russian Journal of Applied Chemistry, Vol. 74, No. 1, 2001, pp. 36–38. Translated from Zhurnal Prikladnoi Khimii, Vol. 74, No. 1, 2001, pp. 36–38.

SORPTION AND ION-EXCHANGE PROCESSES

Synthesis and Physicochemical Study of Polyfunctional Ion Exchangers Based on Dextramine Waste from Levomycetin Production

E. E. Ergozhin, G. A. Menayakova, and R. B. Atshabarova

Bekturov Institute for Chemical Research, Ministry of Education and Science of Kazakhstan Republic, Almaty, Kazakhstan

Received March 14, 2000; in final form, August 2000

Abstract—New polyfunctional anion exchangers are synthesized from dextramine (waste from levomycetin production) by condensation of its glycidyl ethers with certain polyamines. The polycondensation conditions are optimized, and physicochemical properties of the resulting ion exchangers are studied.

Ion-exchange materials are widely used in solving various environmental problems, in complex processing of raw materials, development of closed processes, water treatment, hydrometallurgy, and food industry [1–8]. Therefore, development of methods for synthesis of such materials from cheap and available components is an urgent problem [9–12].

EXPERIMENTAL

In this work the subject matter was *L*-1-(*p*-nitrophenyl)-2-aminopropane-1,3-diol (waste from levomycetin production)

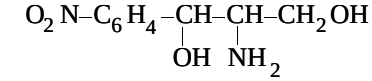

and also its reduced form *L*-1-(*p*-aminophenyl)-2-aminopropane-1,3-diol

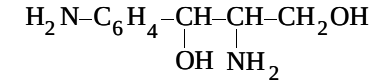

L-1-(*p*-Nitrophenyl)-2-aminopropane-1,3-diol diglycidyl ether (DGED) was synthesized at a molar

Table. 1. Effect of reagent mass ratio on properties of the resins*

GE : amine	EC, mg-equiv g^{-1}	*W*, %	GE : amine	EC, mg-equiv g^{-1}	*W*, %
DGED : PEI			TGED : PEI		
1 : 1.0	8.3	9.5	1 : 0.5	8.7	9.8
1 : 1.5	8.8	9.2	1 : 1.0	9.9	9.8
1 : 2.0	9.6	9.7	1 : 2.0	10.5	9.9
1 : 2.5	9.7	9.6	1 : 3.0	11.7	9.9
DGED : PEPA			TGED : PEPA		
1 : 0.5	6.8	9.2	1 : 0.5	7.9	9.5
1 : 1	6.9	9.1	1 : 1.0	9.2	9.7
1 : 1.5	7.3	9.1	1 : 2.0	10.6	9.6
1 : 2	7.2	9.3	1 : 3.0	Strong swelling	
DGED : PMVP			TGED : PMVP		
1 : 1	4.2	8.9	1 : 0.5	6.8	9.3
1 : 1.5	4.7	9.0	1 : 1.0	7.5	9.5
1 : 2	5.6	9.1	1 : 2.0	8.2	9.5
1 : 2.5	5.5	8.9	1 : 3.0	8.8	9.4

*(EC) Exchange capacity in 0.1 N HCl and (*W*) moisture content.

1070-4272/01/7401-0036$25.00 © 2001 MAIK "Nauka/Interperiodica"

Table 2. Physicochemical characteristics of the resins

Parameter	Resin based on indicated components					
	DGED			TGED		
	PEI	PEPA	PMVP	PEI	PEPA	PMVP
Moisture content, %	9.7	9.1	9.1	9.9	9.6	9.4
Specific volume, ml g^{-1}	4.2	4.9	3.6	4.7	5.2	3.9
EC in 0.1 N HCl, mg-equiv g^{-1}	9.6	7.3	5.6	11.7	10.6	8.8
EC loss (%) after treatment with:						
5 N H_2SO_4, 100°C, 30 min	2.0	0.7	0.5	0.5	0.4	0
5 N NaOH, 100°C, 30 min	2.8	1.1	0.7	0.1	0	0
10% H_2O_2, 25°C, 24 h	7.2	0.7	2.2	2.4	3.8	1.0
EC loss (%) after thermal treatment at 100°C	12	9.0	3.0	8.0	10	3.0

ratio monomer : epichlorohydrin (ECH) : NaOH = 1 : 6 : 3 [14]. As a result we obtained 311 g of a red viscous liquid (yield 96%). The epoxy group content in the product was 22% (83% of the theoretical value).

L-1-(*p*-Aminophenyl)-2-aminopropane-1,3-diol tetraglycidyl ether (TGED) was synthesized at a molar ratio monomer : ECH : NaOH = 1 : 12 : 6. 397 g of a yellow viscous liquid was obtained (yield 98%). The epoxy group content in the product, determined as in [15], was 40.3% (95.3% of the theoretical value).

The required amounts of the amine and ECH was loaded in a round-bottomed flask equipped with a reflux condenser, a drop funnel, a thermometer, and a stirrer. One mole of water was added. The reaction mixture was heated to 80°C, and 50% NaOH was gradually added over a period of 30 min. Hot water (80°C) was added until salts were dissolved. The organic phase was separated, washed with water, and volatile products were removed in a vacuum.

Found (%): C 56, H 6.3, N 8.4;
$C_{15}H_{20}N_2O_4$.
Calculated (%): C 55.5, H 6.1, N 8.6.

Found (%): C 61.5, H 7.6, N 6.4;
$C_{21}H_{30}N_2O_6$.
Calculated (%): C 62, H 7.3, N 6.8.

Polycondensation of the glycidyl ethers (GEs) with polyamines was performed at various component ratios at 80°C for 30 min, with subsequent heating at 100°C for 10 h. The polyamines were polyethylenimine (PEI), polyethylenepolyamine (PEPA), and poly-2-methyl-5-vinylpyridine (PMVP). PEI was used as a 50% aqueous solution (intrinsic viscosity 0.14, $M = 10 \times 10^3$, titrable nitrogen in an anhydrous sample 29.3%). PEPA [M = 290 (determined by cryoscopy), total nitrogen 22.6%, titrable nitrogen 19.8%] was allowed to stand over granulated KOH for 6 days. PMVP: $M = 10 \times 10^3$, 8.6% titrable nitrogen.

Solid resins were ground, converted into the OH form with 5% NaOH, and characterized as follows. Infrared spectra were registered on a UR-20 spectrophotometer using KBr technique. The potentiometric titration was carried out with an EV-74 ionometer. The thermal and chemical resistance was determined according to the GOST (State Standard) 10899–64.

Results on the effect of the reagent ratio on the ion-exchange characteristics of the resins are given in Table 1.

Study of the exchange capacity (EC), thermal and chemical resistance, and the yield of the ion exchangers allowed optimization of synthesis of the resins. The optimal proportions (mass ratio) of the components are as follows. DGED : PEI = 1 : 2, DGED : PEPA = 1 : 1.5, DGED : PMVP = 1 : 2, TGED : PEI = 1 : 3, TGED : PEPA = 1 : 2, and TGED : PMVP = 1 : 3. The resins obtained under the optimal conditions show sufficiently high thermal and chemical resistance (Table 2).

In Table 3 are summarized data on the sorption of Cu^{2+}, Ni^{2+}, and Co^{2+} from 0.05 N solutions with the resins obtained. For comparison are given data on EDE-10P commercial ion-exchange resin.

CONCLUSIONS

(1) New polyfunctional ion exchangers are synthesized by polycondensation of glycidyl ethers derived from *L*-1-(*p*-nitrophenyl)-2-aminopropane-1,3-diol or its reduced form with certain polyamines.

Table 3. Sorption characteristics of the resins

Resin	EC, mg-equiv g^{-1}, for indicated ions		
	Cu^{2+}	Ni^{2+}	Co^{2+}
DGED : PEI	5.8	4.5	4.1
DGED : PEPA	4.8	4.2	3.7
TGED : PEI	6.2	4.8	4.6
TGED : PEPA	5.3	4.6	4.2
EDE-10P	1.0	1.2	0.8

(2) The resins obtained show sufficiently high thermal and chemical resistance and sorption capacity for copper, nickel, and cobalt.

REFERENCES

1. Ergozhin, E.E. and Menligaziev, E.Zh., *Polifunktsional'nye ionoobmenniki* (Polyfunctional Ion Exchangers), Alma-Ata: Nauka, 1986.
2. Polovinkina, G.M., Salazkin, S.N., Malofeeva, G.I., *et al*., *Zh. Prikl. Khim*., 1989, vol. 62, no. 2, pp. 337–341.
3. Alekperov, E.P., *Plast. Massy*, 1991, no. 7, pp. 56–57.
4. Kim Dae Su, Han Mi Jeong, and Lee Jae Rock, *Polym. Eng. Sci*., 1995, vol. 35, no. 17, pp. 1353–1358.
5. Tao, Z., Du, J., and Chu, T., *React. Funct. Polym*., 1996, vol. 31, no. 1, pp. 17–24.
6. Alexandratos, S.D., Shelley, S.A., Horwitz, E.P., and Chiarizia, R., *Solvent Extr. Ion Exch*., 1998, vol. 16, no. 4, pp. 951–966.
7. Smirnov, Yu.N. and Dzhavadyan, E.A., *Vysokomol. Soedin., Ser. B*, 1998, vol. 40, no. 6, pp. 1031–1035.
8. Zakordonskii, V.P., Gnatyshin, M.N., and Soltys, M.N., *Zh. Prikl. Khim*., 1998, vol. 71, no. 9, pp. 1524–1528.
9. Imanbekov, K.I., Nusipova, A.M., and Erkasov, R.Sh., *Izv. Vyssh. Uchebn. Zaved., Ser. Khim. Khim. Tekhnol*., 1998, vol. 41, no. 2, pp. 122–124.
10. Vasil'ev, E.P., Bagrov, F.V., and Kol'tsov, N.I., *Plast. Massy*, 1999, no. 9, pp. 3–6.
11. Tadzhikhodzhaev, Z.A., *Zh. Prikl. Khim*., 1999, vol. 72, no. 2, pp. 336–339.
12. Vishnevskaya, G.P. and Frolova, E.N., *Plast. Massy*, 1999, no. 1, pp. 39–40.
13. Ergozhin, E.E., Menayakova, G.A., Atshabarova, R.B., *et al*., *Izv. Min. Nauki Vyssh. Obrazov. Resp. Kazakhstan, Ser. Khim*., 1999, no. 2, pp. 81–86.
14. US Patent 2 951 822.
15. Paquin, A.M., *Epoxyverbindungen und Epoxydharze*, Berlin: Springer, 1958.

Russian Journal of Applied Chemistry, Vol. 74, No. 1, 2001, pp. 39–43. Translated from Zhurnal Prikladnoi Khimii, Vol. 74, No. 1, 2001, pp. 39–43.

SORPTION AND ION-EXCHANGE PROCESSES

New Polymeric Sorbents Based on *N*-(Vinyloxyethyl)dithiocarbamoylethylcarbonitrile

S. V. Amosova, L. I. Antsiferova, L. P. Shaulina, N. P. Golentovskaya, D.-S. D. Toryashinova, and S. A. Kustova

Irkutsk Institute of Chemistry, Siberian Division, Russian Academy of Sciences, Irkutsk, Russia
Irkutsk State University, Irkutsk, Russia

Received February 23, 1999; in final form, March 2000

Abstract—Homo- and copolymers based on *N*-(vinyloxyethyl)dithiocarbamoylethylcarbonitrile actively sorbing silver, gold, and mercury were prepared.

Proceeding with systematic investigations of the polymerization ability of derivatives of *N*-(2-vinyloxyethyl)dithiocarbamic acid [1, 2], we studied in this work the properties of a new monomer, *N*-(vinyloxyethyl)dithiocarbamoylethylcarbonitrile (VC):

CH_2=CH–O–CH_2–CH_2–NH–C(S)S–CH_2–CH_2–C≡N.

The synthesis of this compound was described elsewhere [3]. Bright yellow powdered polymer was prepared in a high yield by cationic homopolymerization (Table 1).

Cationic polymerization involves the vinyloxy group, whereas the dithiocarbamate group is preserved. The IR spectra of VC homopolymer contain the bands at 1400, 1490, 1580, and 3310–3400 cm^{-1} [–C(S)–NH–] and at 2250 cm^{-1} (C≡N). The bands at 244 and 364 nm in the UV spectra indicate the presence of the C=S group in the polymer. The molecular weight (weight-average) *M* is 5800–6100. Spectral data and elemental analysis confirm the linear structure of the polymer. The polymer is soluble in acetone, dioxane, and DMSO.

The VC homopolymer with maleic anhydride (MA) gives the copolymers with alternating comonomer units. The weight-average molecular weight reaches 5200–5500. The IR spectra exhibit the bands at 1850 and 1775 cm^{-1} belonging to the stretching vibrations of the MA carbonyl groups; the VC units are characterized by the main bands at 1400, 1490, 1580, 2250, and 3200–3400 cm^{-1}. The results of elemental analysis (Table 2) and spectral data suggest that, irrespective of the initial composition, copolymers are formed through the double bonds of VC and MA monomers. The copolymerization constants calculated using the Fineman–Ross procedure (r_1 = 0.05 + 0.01, r_2 = 0.09 + 0.01) suggest characteristic alternation of the units in the polymer, i.e., cross-coupling is the decisive process in the chain growth.

The VC–MA copolymers are yellow powders soluble in DMSO, DMF, chloroform, and in hot water. The radical copolymerization of MA and VC gives the copolymers with alternating comonomer units, whereas polymerization of VC and vinyl acetate (VA) yields the polymer products containing nearly 12 VA units per VC unit, irrespective of the composition of the initial reaction mixture (Table 3). The IR spectra of copolymers prepared at different initial ratios of VC and VA are similar. There are no bands of the stretching vibrations of the VA double bond and

Table 1. Homopolymerization of VC; [VC] = 0.46 M, chloroform solvent, $SnCl_4$ catalyst, 20°C

$SnCl_4$, wt %	τ, min	Yield, %	Conversion, %	*M*	Elemental analysis			
					C	H	N	S
0.2	30	98.4	99.0	5800	45.98	5.01	11.07	29.67
0.3	20	98.9	99.2	6100	46.02	5.00	11.19	29.64
0.5	18	98.7	98.9	5900	45.97	4.99	11.18	29.70

1070-4272/01/7401-0039$25.00

Table 2. Bulk copolymerization of VC and MA; [AIBN] = 0.3%, 60°C, τ = 24 h

Content of VC in monomer mixture, mol %	Maximal rate $A \times 10^{-3}$, mol l^{-1} s^{-1}	Maximal conversion	Yield	Elemental analysis, %		Content of VC in copolymer, mol %
		%		N	S	
16.67	0.07	13.7	13.1	8.82	20.07	49.34
25.00	0.19	28.9	27.9	8.87	20.02	49.42
33.33	0.39	47.6	46.2	8.87	20.33	49.75
50.00	0.45	64.8	63.2	8.89	20.35	49.88
50.00*	0.63	76.9	75.7	8.85	20.32	49.73
66.67	0.24	35.2	34.5	8.82	20.34	49.67
75.00	0.13	22.5	21.3	8.83	20.30	49.65

* At 70°C.

Table 3. Copolymerization of VC and VA; [AIBN] = 0.3%, 70°C, τ = 24 h

Content of VC in monomer mixture, mol %	Conversion	Yield	Elemental analysis, %				Content of VC in copolymer, mol %
	%		C	H	N	S	
20.00	58.2	56.8	56.90	7.07	2.73	6.31	18.79
33.33	69.4	68.1	56.74	6.99	2.90	6.28	19.26
50.00	73.3	70.9	57.00	6.97	2.94	6.40	19.58
20.00*	64.2	62.7	56.97	7.05	2.80	6.42	19.14

* At 80°C.

Table 4. Copolymerization of VC and ST; [AIBN] = 0.3%, 70°C, τ = 24 h

Content of VC in monomer mixture, mol %	Solvent	Conversion	Yield	Elemental analysis, %			Content of VC in copolymer, mol %
		%		C	N	S	
5.00	–	86.3	85.1	89.44	0.74	1.72	5.59
9.09	–	87.6	87.0	87.94	1.28	2.99	9.49
16.67	–	88.2	86.9	84.99	5.25	9.39	30.34
25.00	Benzene	82.7	81.8	72.76	6.17	11.52	35.27
25.00	Chloroform	83.9	82.7	73.55	5.54	11.34	33.46
33.33	–	84.6	82.4	74.83	5.45	12.38	34.43
66.67	Chloroform	78.3	76.8	64.10	6.77	5.49	41.11

VC vinyloxy group; the bands at 1720 and 1235 cm^{-1} belong to the –OCOCH group and that at 2250 cm^{-1}, to the nitrile groups. The UV bands at 244 and 364 nm indicate the presence of the C=S groups in the VC–VA copolymer. These copolymers (molecular weight ~4700) are yellow powders soluble in acetone, ethyl acetate, and chloroform.

The data on copolymerization of VC with styrene (ST) indicate that the composition of the resulting copolymers depends on the composition of the initial monomer mixture only at a low content of VC (5–9 mol%).

The reactivity of VC in copolymerization with ST and VA (Tables 3, 4) differs from that exhibited in copolymerization of ST and VC with simple vinyl ethers [4]. This is probably due to the fact that VC can initiate homopolymerization of ST and VA [5] under the copolymerization conditions (AIBN, 60°C). The VC–ST copolymers can be obtained as white powders or white soft fibers in the case of at least two-fold excess of VC. The resulting copolymers are soluble in DMSO, DMF, benzene, toluene, acetone, chloroform; they are well wettable with water.

It is known [6] that polymers containing the dithio-

carbamate fragment exhibit the sorption activity with respect to coordination-active metal ions. In contrast to VC–MA and VC–VA copolymers, the VC and VC–ST copolymers are rather stable in solutions of hydrochloric, sulfuric, and nitric acids at concentrations higher than 1 M, which allowed us to study the sorption properties of VC and VC–ST polymers with respect to ions of silver (in HNO_3, H_2SO_4), gold (in HCl, H_2SO_4), and mercury (in HCl, HNO_3, H_2SO_4).

The dependences of the metal recovery on the concentration and nature of the mineral acid are shown in Fig. 1. It should be noted that for the homopolymer the recovery of mercury ions from the solutions of nitric and sulfuric acid remains almost constant with increasing acid concentration from 1 to 7 M. In the case of gold and silver the recovery of metals decreases with increasing acid concentration in the above range. Such run of the recovery curves is probably due to the predominantly donor–acceptor interaction of metal ions with the active centers of the polymer. For gold occurring in a solution of hydrochloric acid as tetrachloride complex the ion-exchange interaction through the protonated nitrogen atoms is also possible. The effect of hydrochloric acid on the sorption recovery of mercury can be explained by formation of chloride complexes [7].

The data on the sorption kinetics in 1 M acid solutions indicate that both polymers recover silver with a high rate: the equilibrium is attained in 10 min. In the case of mercury the equilibrium is attained in 10 min and 2 h for VC and VC–ST copolymers, respectively. In the case of gold chloride complex the equilibrium is attained in 30 min, whereas the main fraction of the metal is recovered in 10 min.

The sorption capacity of polymers was determined from the curves of equilibrium distribution of metal ions between the solid phase and solution (Fig. 2, Table 5). As seen from Table 5, the VC homopolymer (PVC) is an efficient sorbent with respect to all three metal ions, whereas the VC copolymer is efficient with respect to mercury and gold ions. The sorption capacity of the copolymer with respect to silver and mercury ions decreases (approximately by half) with decreasing content of the active nitrogen and sulfur atoms, whereas for gold the sorption capacity increases. This is probably due to the steric factors related to the distribution of the active centers in the polymer and to the structure of the gold tetrachloride complex.

To elucidate the interaction mechanism, we studied the IR spectra of the VC copolymer and its concentrate (polymer with sorbed metal).

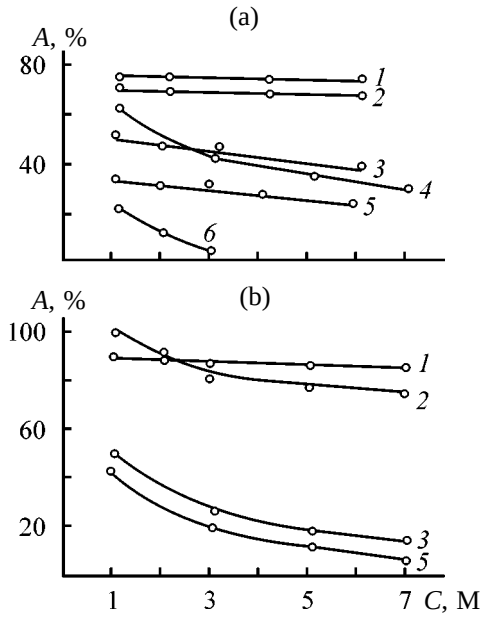

Fig. 1. Recovery A of (a) mercury and (b) silver on the (*1*, *2*, *4*) VC and (*3*, *5*, *6*) VC–ST polymers as influenced by the nature and concentration of acid C. Sorbent weight m = 10 mg, V = 20 ml, τ = 2 h. VC: m_{Hg} = 1.0, m_{Ag} = 8.0 mg; VC–ST: m_{Hg} = 3.6, m_{Ag} = 1.0 mg. Acid: (*1*, *5*) HNO_3, (*2*, *3*) H_2SO_4, and (*4*, *6*) HCl.

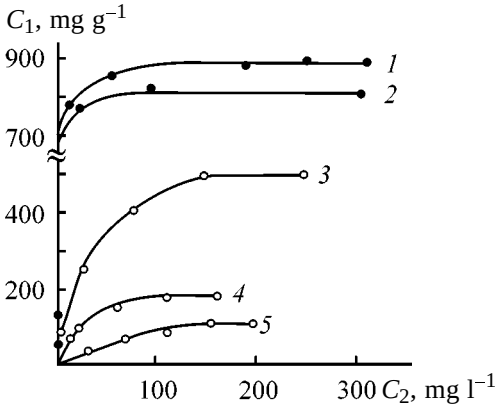

Fig. 2. Equilibrium distribution of (*1*, *2*) silver and (*3*–*5*) mercury in 1 M solutions of (*1*) nitric, (*2*–*4*) sulfuric, and (*5*) hydrochloric acids; (*1*–*3*, *5*) PVC and (*4*) VC–ST Sorbent weight m = 10 mg, V = 20 ml. Metal content (C_1) in the solid phase and (C_2) in solution.

Shift of the bands and variation of their intensity in the 1000–1250 cm^{-1} range for the concentrate indicates participation of the thioamide fragment in the coordination. Disappearance of the stretching vibration band at 1070 cm^{-1} suggests possible coordination through the C=S group. Moreover, certain changes are also observed in the 550–640 cm^{-1} range corresponding to the stretching vibrations of the C–S group. At the same time the band at 2250 cm^{-1} in the co-

Table 5. Sorption capacity (SC) of the polymers and distribution coefficients *D* of metals in 1 M acid solutions

Parameter	PVC			VC–ST copolymer		
	HCl	H_2SO_4	HNO_3	HCl	H_2SO_4	HNO_3
			M = Hg			
SC, mg g^{-1}	120	500	180	60	240	180
D	1.0×10^3	1.0×10^4	6.0×10^3	7.4×10^2	2.0×10^4	6.9×10^4
			M = Ag			
SC, mg g^{-1}	–	790	900	–	166	103
D	–	3.3×10^5	1.8×10^5	–	7.2×10^4	2.7×10^4
			M = Au			
SC, mg g^{-1}	218	300	–	560	490	–
D	8.9×10^4	4.6×10^4	–	4.0×10^4	1.9×10^4	–

polymer spectra remains unchanged, which rules out participation of the C≡N group in the metal coordination. Thus, the above results allow us to propose the following structures of complexes formed in the sorbent phase:

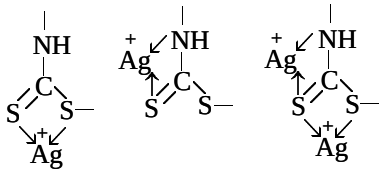

1 **2** **3**

In this case, high sorption capacity of the VC homopolymer with respect to mercury and silver ions may be due to the ability of the active centers to form strong complexes with several metal ions (structure **3**).

It should be noted that the polymers in question recover mercury from 1 M hydrochloric acid solutions.

The sorption isotherms for silver (PVC), gold (PVC, VC–ST copolymer), and mercury (PVC, 1 M H_2SO_4; VC–ST copolymer, 1 M H_2SO_4, HNO_3) exhibit a large slope. The distribution coefficients of the metal ions calculated from these isotherms are very high (Table 5). These results suggest that these polymers can recover metal ions from dilute solutions.

As seen from Fig. 1, the VC–ST copolymer does not noticeable recover mercury from hydrochloric acid of concentration higher than 3 M, and this property can be used for desorption. It was found that 6 M HCl almost completely removes mercury from VC and VC–ST polymers in 1 h. The regenerated polymer can be used in further sorption–desorption cycles. The noble metals can be eluted with a 3% solution of thiourea in 1 M HCl: 10 ml of this solution completely recovers 59 μg of gold in 30 min. At 50°C the desorption period decreases to 10 min, but in this case the sorption activity of the regenerated sorbent decreases.

The sorption properties of the polymers in question were evaluated by studying sorption of iron, copper, nickel, and cobalt (C_m = 1 mg ml^{-1}) under the conditions used for recovery of noble metals.

After calcination of the polymer with the sorbed metal and dissolution of the residue the content of the metal was determined by atomic absorption spectroscopy. No sorption was observed and the content of metal in the initial solution reached 95–97%. These data show that noble metals are selectively recovered from 1 M solution of mineral acids.

The PVC sorbent and its concentrate with sorbed silver dissolve in DMF, which allows atomic absorption analysis of silver in DMF solutions after preliminary concentration. For example, a weighed portion of PVC sorbent was placed into a 1 M HNO_3 solution containing certain amounts of silver and non-noble metal ($C_{Ag} : C_M$ = 1 : 40). The concentrate was recovered and treated with DMF (10 ml). The content of silver was determined from the calibration curve plotted using the standard solutions of silver in DMF containing sorbent in the amounts required for sorption. It was found by atomic absorption spectroscopy of DMF solutions that 95–97% of silver is recovered at its initial concentration of 1.0–2.5 μg ml^{-1}. Dissolution of the concentrate in an organic solvent significantly simplifies the sample preparation.

EXPERIMENTAL

The colorless crystalline VC monomer (mp 61°C, soluble in organic solvents) was prepared in a yield of 85% by the procedure given in [3]. Maleic anhydride (mp 52.8°C) was twice recrystallized from chloroform and vacuum-sublimed over P_2O_5. ST, VA, AIBN, and solvents were purified using common procedures [8]. The IR spectra were registered on an IFS-25 spectrophotometer (KBr pellets). The radical polymerization was performed in the ampules using a high-vacuum setup, the process was controlled with an MKDP-2 isothermal microcalorimeter. Under the conditions of radical polymerization (70–90°C, 0.03% AIBN concentration) the VC homopolymerization does not proceed to a noticeable extent (yield lower than 1% at 1.3% conversion). The molecular weight of the polymer products was determined in THF on a Waters liquid chromatograph equipped with a Data Modul-730 integrator by gel-permeation chromatography. The columns were packed with ultra silica gel (10^4, 10^5, and 10^6 Å pore size). The polymer compositions were evaluated from the content of nitrogen and sulfur [9].

The sorption properties were determined under the steady-state conditions upon the contact of the required polymer sample with a solution of mineral acid of certain concentration containing required amount of metal. The residual concentration of silver and gold was determined by the atomic absorption method [10], whereas the content of mercury was determined spectrophotometrically using dithizone [11]. The content of metal in the solid phase was evaluated as the difference between the initial and residual concentrations of metal in the solution.

The solutions of silver and mercury nitrates (1.00 and 3.6 mg ml^{-1}) and hydrochloric acid solution of gold (1.62 mg ml^{-1}) were used as initial references.

CONCLUSIONS

(1) Linear homopolymer of *N*-(vinyloxyethyl)-dithiocarbamoylethylcarbonitrile (molecular weight 5200–5500) and its copolymers with maleic anhydride, vinyl acetate, and styrene were prepared by cationic polymerization. The polymer compositions are almost independent of the monomer ratio in the initial reaction mixture.

(2) Homopolymer of *N*-(vinyloxyethyl)dithiocarbamoylethylcarbonitrile and its copolymer with styrene are stable in 1–6 M solutions of hydrochloric, sulfuric, and nitric acids and effectively recover silver, gold, and mercury from multicomponent solutions in 10–30 min. The sorption–atomic absorption procedure to determine silver using DMF solutions of the concentrate was proposed.

REFERENCES

1. Antsiferova, L.I., Amosova, S.V., Kositsyna, E.I., *et al*., *Sib. Khim. Zh.*, 1991, no. 6, pp. 72–76.
2. Antsiferova, L.I., Amosova, S.V., Kruglova, V.A., *et al*., *Sib. Khim. Zh.*, 1992, no. 2, pp. 77–80.
3. Amosova, S.V., Ivanova, N.I., Khamidulina, S.A., *et al*., *Zh. Org. Khim.*, 1994, vol. 30, no. 1, pp. 77–80.
4. *Copolymerization*, Ham, G.E., Ed., New York: Interscience, 1964.
5. Antsiferova, L. I., Amosova, S.V., Toryashinova, D.-S.D., *et al*., *Vysokomol. Soedin., Ser. A*, 1988, vol. 40, no. 1, pp. 24–30.
6. Basargin, N.N., Rogovskii, Yu.G., and Zharova, V.M., *Organicheskie reagenty i khelatnye sorbenty v analize mineral'nykh ob"ektov* (Organic Reagents and Chelate Sorbents in Analysis of Mineral Objects), Moscow: Nauka, 1980.
7. Gladyshev, V.P., Levitskaya, S.A., and Filipova, L.M., *Analiticheskaya khimiya rtuti* (Analytical Chemistry of Mercury), Moscow: Nauka, 1974.
8. Weissberger, A. and Proskauer, E.S., *Organic Solvents. Physical Properties and Methods of Purification*, Riddick, J.A. and Toops, E.E., Eds., New York: Interscience, 1955.
9. Toroptseva, A.M., Belogorodskaya, K.V., and Bondarenko, V.M., *Laboratornyi praktikum po khimii i tekhnologii vysokomolekulyarnykh soedinenii* (Laboratory Course on Chemistry and Technology of Macromolecular Compounds), Leningrad: Khimiya, 1972.
10. Britske, M.E., *Atomno-absorbtsionnyi spektrokhimicheskii analiz* (Atomic Absorption Spectrochemical Analysis), Moscow: Khimiya, 1982.
11. Marczenko, Z., *Kolorymetryczne oznaczanie pierwiastkow*, Warsaw: Naukowa-techniczne, 1968.

Russian Journal of Applied Chemistry, Vol. 74, No. 1, 2001, pp. 44–47. Translated from Zhurnal Prikladnoi Khimii, Vol. 74, No. 1, 2001, pp. 44–47.

APPLIED ELECTROCHEMISTRY AND CORROSION PROTECTION OF METALS

Modeling of Gaseous Chlorine Production in a Static Electrolyzer

G. S. Zenin and A. M. Sazonov

St. Petersburg Northwest Polytechnic Institute, St. Petersburg, Russia

Received March 20, 2000

Abstract—Transfer of hydroxide and hydroxonium ions in bulk of sodium chloride solution in the course of gaseous chlorine production in a static electrolyzer was considered and a relationship was derived to determine the characteristics of a chlorinator. Principles of selecting electrolyzer currents to obtain gaseous chlorine in a static chlorinator were recommended.

Sodium hypochlorite produced by electrolysis of sodium chloride solutions is used in water treatment [1–3]. Since the resulting solutions also contain sodium chloride, it is fed into water being treated together with the hypochlorite solution, which results in increased consumption of the salt and excessive mineralization of water.

There are some data [4, 5] on the electrochemical production of gaseous chlorine for water decontamination in reactors similar in design to those used in the chlorine industry [6]. However, the implementation of this process in water-treatment stations requires complicated process schemes.

In the early stage of development of the chlorine industry, gaseous chlorine was produced in static electrolyzers, for which a qualitative theory of the electrolysis process was developed [7–9], and semiempirical relationships concerning interelectrode transfer of hydroxide and hydroxonium ions were obtained. These ions, generated in the course of electrolysis, determine the current efficiency with respect to gaseous chlorine [10]. The publications on the production of gaseous chlorine in static electrolyzers practically do not consider the effects of design characteristics of reactors on the current efficiency with respect to gaseous chlorine and on the electrolyte service life as a function of the electrolysis current.

To determine the ratio between the volumes of anodic and cathodic zones and to substantiate the optimum electrolysis conditions, we simulated in this work the operation of a chlorinator.

The relationships in gaseous chlorine formation in static electrolyzers are determined, along with the electrode current density, by the anolyte acidity, which depends on the conditions of the transfer of hydroxide ions generated on the cathode and of hydroxonium ions generated on the anode at simultaneous formation of oxygen and chlorine, and also on secondary reactions in solution involving dissolved chlorine [6]. During the electrolysis, simultaneously with the transfer of sodium ions and chlorine, hydroxide ions are transferred to the anode and hydroxonium ions, to the cathode. The ions form in the interelectrode space a neutral boundary whose width and position depend on the migration and diffusion flows in the bulk of solution:

$$j_a = j_-^m + j_-^d, \qquad j_c = j_+^m + j_+^d. \tag{1}$$

Here j_-^m, j_+^m, j_-^d, and j_+^d are the flows of the negative and positive ions driving under the action of migration and diffusion, respectively.

As the current efficiency with respect to gaseous chlorine at a constant current density is determined by the anolyte pH [11], we will consider a model of transfer of hydroxonium and hydroxide ions at a constant sodium chloride concentration (Fig. 1). Taking into consideration the condition of solution electro-

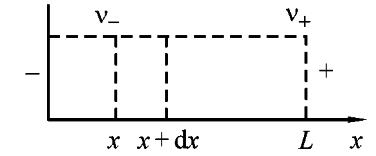

Fig. 1. Directions of ion flows in the electrolysis in a chlorinator with an immobile solution: (ν_-, ν_+) rates of the motion of hydroxide and hydroxonium ions from the cathode and anode, respectively; (L) chlorinator length; (x, $x + dx$) unit thickness of a solution layer.

1070-4272/01/7401-0044$25.00 © 2001 MAIK "Nauka/Interperiodica"

neutrality, we can write the following expressions for hydroxide ions (c_-):

$$S\,dx\frac{dc}{d\tau} = Q_-^m + Q_-^d. \quad (2)$$

Here S is the area through which the amounts Q_-^m and Q_-^d of hydroxide ions are transferred in unit time $d\tau$ by migration and concentration diffusion, respectively;

$$Q_-^m = S\nu_- c_-(x) - S\nu_- c_-(x + dx),$$
$$Q_-^d = SD\,\partial c_-(x)/\partial x - SD\,\partial c_-(x + dx)/\partial x, \quad (3)$$

ν and D_- are the mobility and diffusion coefficient of hydroxide ions.

Substitution of Eq. (3) into (2) gives expression (4):

$$S\,dx\frac{\partial c_-}{\partial\tau} = S\nu_-[c_-(x + dx) - c_-(x)] - SD[\partial c_-(x + dx)/\partial x - \partial c_-(x)/\partial x], \quad (4)$$

or

$$\frac{\partial c_-}{\partial\tau} = \nu\,\partial c_-/\partial x - D_-\partial^2 c_-/\partial x^2. \quad (5)$$

For hydroxonium ions

$$\frac{\partial c_+}{\partial\tau} = -\nu\,\partial c_+/\partial x - D_+\partial^2 c_+/\partial x^2. \quad (6)$$

The right sides of Eqs. (5) and (6) represent changes in the ion flows due to migration and diffusion:

$$\frac{\partial c_\pm}{\partial\tau} = -\frac{\partial}{\partial x}(j_{a,c}), \quad (7)$$

The ion flows due to migration and diffusion in an anolyte and a catholyte, respectively, are [12]

$$j_a = \nu\,\partial c_- + D_-\partial c_-/\partial x, \qquad j_c = \nu\,\partial c_+ + D_+\partial c_+/\partial x. \quad (8)$$

Gaseous chlorine is formed with a sufficiently high current efficiency if a solution in the anodic zone is acidic or neutral [11], i.e., as long as a neutral boundary determined by condition (9) exists in solution:

$$j_a = j_c. \quad (9)$$

Expressions (7) and (8) give

$$\frac{\partial}{\partial\tau}(c_- - c_+) = 0.$$

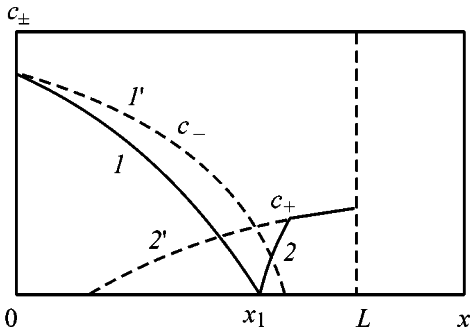

Fig. 2. Variation of the concentration of (*1, 1'*) hydroxide and (*2, 2'*) hydroxonium ions in the interelectrode space of a chlorinator (*1', 2'*) without and (*1, 2*) with the occurrence of recombination of hydroxide and hydroxonium ions.

or

$$c_- - c_+ = A. \quad (10)$$

The distribution of the concentrations in relation to the interelectrode distance is schematically presented in Fig. 2 for a hypothetical case when the chemical reactions on the boundary x_1 between the hydroxide and hydroxonium ions (curves *1'*, *2'*) are absent. The plot is based on the assumption that, because of the formation of gaseous chlorine, the current efficiency with respect to hydroxide ions is greater than the efficiency with respect to hydroxonium ions ($\eta_- > \eta_+$). Thus, for τ = const

$$c_-(x) > c_+(x), \qquad 0 < x < x_1,$$
$$c_+(x) > c_-(x), \qquad x_1 < x < L. \quad (11)$$

Actually the dependence of the concentrations of the hydroxide and hydroxonium ions on the interelectrode distance (Fig. 2) corresponds to curves *1* and *2*, which lie below curves *1* and *2* because of reduction in the concentrations of hydroxide and hydroxonium ions owing to a reaction between them, the parameter A being zero in the point x. As the migration component of the flows in Eqs. (1) is much greater than the concentration diffusion [12], we can neglect the latter in the first approximation. Then the dependence of the concentrations of the hydroxide and hydroxonium ions on the interelectrode distance and electrolysis time can be presented as

$$c_\pm = \frac{I\tau\eta_\pm}{FV_\pm} - \frac{(I_\pm l/E_\pm)_{\tau,x}}{FS\nu_\pm^0}. \quad (12)$$

Here $V_\pm$ is the volume of the alkaline or acidic zone of solution in a chlorinator; $\nu_\pm^0$ is the limiting mobility;

$\eta_\pm$ is the current efficiency with respect to hydroxide or hydroxonium ions in the electrolysis; I_+ is the fraction of current transferred by hydroxide or hydroxonium ions; $E_\pm/l$ is the electric field strength at the instant of time τ at the distance x from the electrode.

According to the data of [13],

$$(I_\pm)_{\tau,x} = I(T_\pm)_{\tau,x}, \quad (E_\pm/l)_{\tau,x} = I/S(\chi_\pm)_{\tau,x},$$

$$F\nu_\pm^0 = \lambda_\pm^0, \tag{13}$$

where $\chi_\pm$ and $\lambda_\pm^0$ are the specific and limiting equivalent conductivities of the hydroxide or hydroxonium ions, and $T_\pm$ is the transfer number of the ions.

Substituting expressions (13) in (12) and (12) in (10), in view of the relationship $A = 0$ valid under real electrolysis conditions, we obtain

$$\frac{I\tau\eta_-}{FV_-} - \frac{(T_-\chi_-)_{\tau,x}}{\lambda_-^0} - \frac{I\tau\eta_+}{FV_+} - \frac{(T_+\chi_+)_{\tau,x}}{\lambda_+^0} = 0. \tag{14}$$

Rearranging terms responsible for migration to the right side of Eq. (14), we obtain the equation describing the displacement of the neutral zone in a chlorinator in the course of electrolysis:

$$\frac{I\tau(\eta_-/V_- - \eta_+/V_+)}{F} = \frac{(T_-\chi_-)_{\tau,x}}{\lambda_-^0} - \frac{(T_+\chi_+)_{\tau,x}}{\lambda_+^0}. \tag{15}$$

Designating the chlorinator volume as V, we can express the volume of the anodic (acid) zone of a chlorinator as

$$V_+ = V - V_-. \tag{16}$$

In view of (16) we can bring expression (15) to the form

$$[\eta_-/V_- - \eta_+/(V - V_-)] = K, \tag{17}$$

$$K = \frac{F}{I\tau}\frac{(T_-\chi_-)_{\tau,x}}{\lambda_-^0} - \frac{(T_+\chi_+)_{\tau,x}}{\lambda_+^0}.$$

Equation (17) allows us to estimate the time of continuous operation of a chlorinator at a specified current.

According to Hittorf's law, it follows for the electrode balance with the neutralization of hydroxide and hydroxonium ions formed in the interelectrode space [14] that

$$\Delta c_- T_- = \Delta c_+ T_+, \tag{18}$$

where Δc_- and Δc_+ are the decreases in the concentration of hydroxide and hydroxonium ions in the catholyte and anolyte, respectively, due to their transfer to the neutral boundary where their recombination occurs.

In view of Eq. (18) and also of the expressions

$$(\chi_-)_{\tau,x}/\lambda_-^0 = \Delta c_- \text{ and } (\chi_+)_{\tau,x}/\lambda_+^0 = \Delta c_+,$$

it is evident that at $K = 0$ decreases in the concentrations of hydroxide and hydroxonium ions are in balance. Therefore, for stable operation of a chlorinator its volume should be related to the volume of its cathode zone by expression (19), which can be used to determine the design characteristics of the chlorinator.

$$V_- = V\frac{\eta_-}{\eta_- + \eta_+}. \tag{19}$$

Expression (19) is valid provided that the concentration of sodium chloride near the neutral boundary is constant, otherwise it is necessary to include in Eq. (15) additional terms responsible for the transfer of chloride and sodium ions. In practice, to maintain a constant concentration of sodium chloride in solution, it is appropriate to fill the interelectrode space with crystalline sodium chloride and to carry out the electrolysis at currents ensuring a slower decrease in the concentration of chloride ions in solution, compared to its growth due to sodium chloride dissolution. Furthermore, sodium chloride crystals, being a porous filling material, considerably reduce solution stirring [15]. As mixed solutions of sodium chloride and hydroxide have a greater density than a pure solution of sodium chloride [16], it is necessary to place the anode above the cathode, which will reduce gravitational convection of solution in a chlorinator.

The resulting relationship was used in designing and manufacturing ship plants for sewage treatment and disinfection [17], and the exploitation of the serial plants confirmed the results of our calculations [18].

CONCLUSION

A mathematical model of a chlorinator for the production of gaseous chlorine in a static electrolyzer was developed, which made it possible to deduce an expression for the calculation of design characteristics of the chlorinator.

REFERENCES

1. Kul'skii, L. A. and Goronovskii, I. G., *Gipokhloritnye ustanovki KG-12, KG-13 i KG-14 dlya elektrokhimicheskogo khlorirovaniya vody na vodoprovodakh* (Hypochlorite Installations KG-12, KG-13, and KG-14 for Electrochemical Water Chlorination in Water Pipes), Kiev: Akad. Nauk Ukr. SSR, 1946.
2. Perlina, A.M., Razumovskii, E.S., Medrish, G.A., and Terekhov, A.A., *Ustanovki maloi proizvoditel'nosti dlya ochistki i obezzarazhivaniya pit'evoi i stochnykh vod* (Small-Capacity Installations for Purification and Disinfection of Potable Water and Sewage), Moscow: Stroiizdat, 1974.
3. Razumovskii, E.S., Medrish, G.A., and Kazaryan, V.A., *Ochistka i obezzarazhivanie stochnykh vod malykh naselennykh punktov* (Purification and Disinfection of Sewage of Small Settlements), Moscow: Stroiizdat, 1986.
4. US Patent 4136005.
5. FR Patent Pending 2455566.
6. Yakimenko, L.M., *Elektrolizery s tverdym katodom* (Electrolyzers with Solid Cathode), Moscow: Khimiya, 1966.
7. Billiter, J., *Die technische Elektrolyse der Nichtmetalle*, Wien: Springer, 1954.
8. Angel, G., *Die Alkalichloridelektrolyse in Diaphragmazellen. Eine theoretische und experimentelle Untersuchung*, Berlin: Chemie, 1933.
9. Khomyakov, K.G., Mashovets, V.P., and Kuz'min, L.L., *Tekhnologiya elektrokhimicheskikh proizvodstz* (Technology of Electrochemical Productions), Moscow: Goskhimizdat, 1949.
10. Briner, K., *J. Chem. Phys.*, 1907, no. 5, pp. 398–409.
11. Angel G., *Die Alkalichloridelektrolyse in Diaphragmazellen*, Stockholm: Beckman, 1933.
12. Erdey-Gruz, T., *Transport Phenomena in Aqueons Solutions*, Budapest: Akad. Kiado, 1974.
13. Antropov, L.I., *Teoreticheskaya elektrokhimiya* (Theoretical Electrochemistry), Moscow: Vysshaya Shkola, 1975.
14. Levin, A.I., *Teoreticheskie osnovy elektrokhimii* (Theoretical Foundations of Electrochemistry), Moscow: Metallurgiya, 1972.
15. Varshavskaya, N.L., Electrochemical Properties of Ions in Concentrated Solutions of Electrolytes and Mixtures of Electrolytes, *Cand. Sci. Dissertation*, Leningrad, 1966.
16. *Spravochnik po elektrokhimii* (Reference Book on Electrochemistry), Sukhotin, A.M., Ed., Leningrad: Khimiya, 1981.
17. *TU* (Technical Specifications) *5.498-3102–86, 1986: Automated Installation for the Purification and Disinfection of Waste and Household Waters on Ships.*
18. Zenin, G.S. and Medvedev, V.A., Abstracts of Papers, *Vsesoyuznaya nauchno-tekhnicheskaya konferentsiya "voprosy obespecheniya okhrany okruzhayushchei sredy pri ekspluatatsii sudov i rekuperatsii vtorichnykh resursov na predpriaytiyakh otrasli"* (All-Union Scientific and Technical Conf. "Problems of Ensuring Environmental Protection at Exploitation of Ships and Recuperation of Secondary Resources at Plants on Shipping Industry"), Krylov Central Scientific and Technical Association, Leningrad: Sudostroenie, 1986, pp. 17–19.

Russian Journal of Applied Chemistry, Vol. 74, No. 1, 2001, pp. 48–50. Translated from Zhurnal Prikladnoi Khimii, Vol. 74, No. 1, 2001, pp. 47–49.

APPLIED ELECTROCHEMISTRY AND CORROSION PROTECTION OF METALS

Anodic Dissolution of NiS in Sulfite Electrolytes

M. I. Natorkhin

St. Petersburg State Technical University, St. Petersburg, Russia

Received November 19, 1999; in final form, October 2000

Abstract—Electrochemical behavior of nickel sulfide in weakly acidic and ammonia electrolytes containing sulfite ions and also in copper sulfite electrolyte stabilized by EDTA was studied.

Since hydrometallurgical processing of copper–nickel ores is used at the majority of modern plants [1], the corresponding chemical reactions must be studied in more detail.

Laboratory modeling of complex multicomponent processes on separate samples under special conditions is regarded as promising [2, 3].

Autoclave decomposition of sulfides in aqueous medium by sulfur dioxide has been described in the literature [4]:

$$MS + 2SO_2 = MSO_4 + 2S,$$

This technique has several drawbacks. Sulfur is known [5] to dissolve readily in the presence of sulfite ion:

$$SO_3^{2-} + S = S_2O_3^{2-},$$

The SO_3^{2-} and $S_2O_3^{2-}$ ions are efficient complex-forming agents for copper [6, 7], which catalyzes the dissolution of nickel sulfide [8].

The aim of this work was to study in more detail the electrochemical behavior of pure nickel β-sulfide in sulfite-containing electrolytes.

To model the industrial process, nickel sulfide with a nickel content of 50% was synthesized from N0-grade nickel and analytically pure grade sulfur by the known procedure [9]. The working electrode was made from a nickel sulfide sample soldered to a copper current lead. The idle surface was insulated with a nitro lacquer. The operating surface (area 1 cm^2) was smoothed with emery paper no. 0 and washed with alcohol and distilled water. Cyclic voltammograms (CVA) and stationary voltammograms were recorded on a PI-50-1.1 potentiostat equipped with a PDP4-002 plane-table recorder. The experiments were carried out in a standard YaES-2 electrochemical cell (glass electrode cell). Its temperature was maintained at 90 ± 0.5°C with a UTU 2/77 thermostat. We used a three-electrode cell with nickel sulfide under study as an anode, a platinum cathode, and a saturated silver chloride auxiliary electrode (AgCl / Ag). The electrode potentials are given vs. normal hydrogen electrode. The electrolytes were prepared from analytically pure and chemically pure grade reagents.

It should be noted that the addition of Na_2SO_3 to copper sulfate in the cold results in an insignificant reduction of Cu^{2+} ions to Cu^+ ions and in formation of green complex compounds. With excess of Na_2SO_3 or on heating, brick-red Chevreul's salt is precipitated [10]:

$$3CuSO_4 + 3Na_2SO_3 + 3H_2O = CuSO_3 \cdot Cu_2SO_3 \cdot 2H_2O\downarrow + 3Na_2SO_4 + H_2SO_4.$$

Hence, simultaneous presence of $CuSO_4$ and Na_2SO_3 at 90°C is impossible. However, if a strong complexing agent L stabilizing Cu(II) ions is added to the electrolyte, Chevreul's salt is not formed and $[CuL_n]^{2+}$, a quantity of $[CuL_n]^+$, and Cu_2SO_3 (stability constant $\log\beta = 7.58$) will be present in the solution. As NiS is further dissolved at the anode and sulfur passes into the anolyte, more stable Cu(I) thiosulfate complexes $[Cu(S_2O_3)]^-$, $[Cu(S_2O_3)_2]^{3-}$, and $[Cu_2(S_2O_3)_3]^{4-}$ (stability constant $\log\beta = 10.35$) can be formed [11]. Disodium dihydrogen ethylenediaminetetraacetate (Na_2EDTA) was used as such a stabilizing agent [for Cu(II) $\log\beta = 18.86$].

The solubility of sodium sulfite decreases with increasing temperature, being 260 g l^{-1} at 90°C. However, the solubility of sodium thiosulfate, which can be formed, is approximately ten times higher. The CVA curves for nickel sulfide in Na_2SO_3 solutions

1070-4272/01/7401-0048$25.00

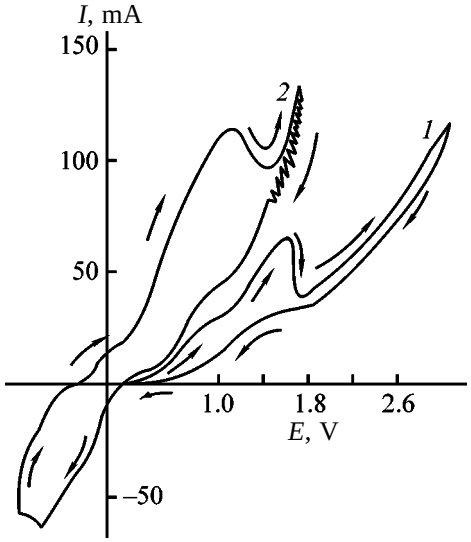

Fig. 1. Cyclic voltammograms of NiS in solutions containing (*1*) 100 and (*2*) 250 g l^{-1} Na_2SO_3. Potential sweep rate –100 mV s^{-1}, temperature 90 ± 0.5°C; the same for Figs. 2–4. (*I*) Current asnd (*E*) potential; the same for Figs. 2–4.

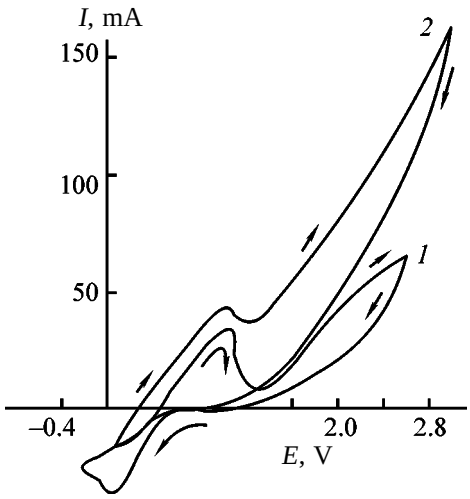

Fig. 2. Cyclic voltammograms of NiS in solutions of (*1*) 0.5 M $CuSO_4$ and (*2*) 0.5 M $CuSO_4$ + 20 g l^{-1} EDTA + 0.1 g l^{-1} Na_2SO_3.

of various concentrations (from 100 up to nearly saturated, 250 g l^{-1}) are shown in Fig. 1. An increase in the Na_2SO_3 concentration leads to a rise in the anodic current. In saturated Na_2SO_3 solution NiS actively dissolves to give loose bright green nickel hydroxide, which is precipitated on the cell bottom. A backward run of curve *2* in the potential range 1.8–1.4 V is accompanied by periodic current oscillations, which proves the presence of a semiconducting film on the electrode surface [12, 13] (possibly $NiSO_3$). The film causes a salt-type passivation.

An addition of significant amounts of Na_2SO_3 to a $CuSO_4$ solution at 90°C makes no sense because the Chevreul's salt is formed even in the presence of EDTA. A stable electrolyte containing 0.5 M $CuSO_4$, 20 g l^{-1} EDTA, and 0.1 g l^{-1} Na_2SO_3 was prepared in this work. Even such a minor addition of Na_2SO_3 results in significant changes in the electrolyte parameters. The solution becomes dark green. The CVA curves of nickel sulfide in a 0.5 M $CuSO_4$ solution and in a 0.5 M $CuSO_4$ solution containing 20 g l^{-1} Na_2EDTA and 0.1 g l^{-1} Na_2SO_3 are shown in Fig. 2.

In potentiostatic experiments at the potentials of NiS in the range 0.64–1.57 V, we observed a fast current drop (within 10–15 s) followed by current stabilization. This fact suggests formation of a film on the electrode surface which does not retard nickel sulfide dissolution (Fig. 3). In this case sulfur is deposited on the NiS surface. The intensity of green coloration of copper complexes remains almost unchanged even on a long-term electroleaching.

Oxidative leaching of sulfide raw materials with aqueous ammonia is widely used in industry [14]. At anodic polarization NiS does not dissolve in pure NH_4OH. The process course is significantly changed when sulfite ions are introduced. Two CVA curves for nickel sulfide in a solution containing 200 g l^{-1} Na_2SO_3 and 2% NH_4OH and in a solution containing 100 g l^{-1} Na_2SO_3 and 20% NH_4OH are shown in Fig. 4. In the anodic branch of curve *1* an area of insignificant electrode passivation is observed, which seems to be of a salt type.

In the case of the system containing 20% NH_4OH (curve *2*) NiS is actively dissolved without passivation. Blue-violet concentration flows of $[Ni(NH_3)_n]^{2+}$ are formed while the surface of nickel sulfide remains golden yellow. In the backward run of curve *2*, ran-

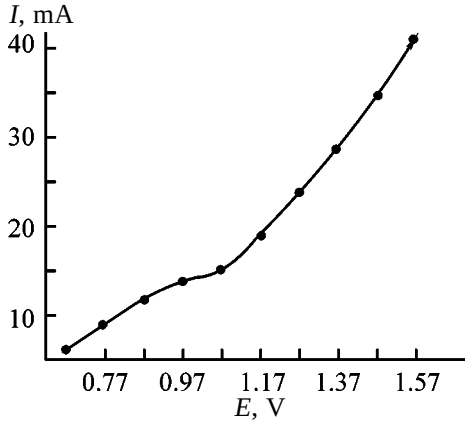

Fig. 3. Stationary polarization curve of NiS in 0.5 M $CuSO_4$ containing 20 g l^{-1} EDTA and 0.1 g l^{-1} Na_2SO_3.

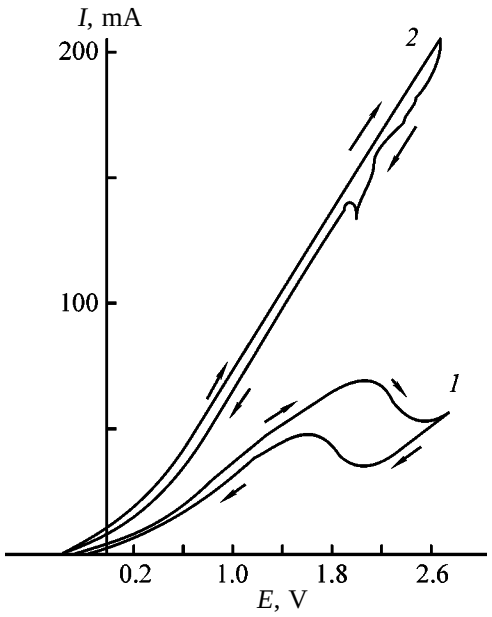

Fig. 4. Cyclic voltammograms of NiS in the solutions containing (*1*) 200 g l^{-1} Na_2SO_3 with 2% NH_4OH and (*2*) 100 g l^{-1} Na_2SO_3 with 20% NH_4OH.

dom current oscillations are observed, which seem to have the same origin as in the case of Fig. 1.

CONCLUSIONS

(1) In a pure Na_2SO_3 solution NiS actively dissolves with simultaneous formation of insoluble Ni^{2+} hydroxo compounds with a pH-dependent composition.

(2) It is possible to use Na_2SO_3 as a depolarizing addition to $CuSO_4$ in the presence of Na_2EDTA as a stabilizing complexone.

(3) Simultaneous action of NH_4OH and Na_2SO_3 results in active dissolution of NiS and formation of $[Ni(NH_3)_n]^{2+}$ complexes.

REFERENCES

1. Sinel'shchikova, N.V. and Makarova, S.N., *Gidrometallurgiya medi i nikelya* (Hydrometallurgy of Copper and Nickel), Moscow: Tsvetmetinformatsiya, 1976.
2. Belyakov, E.A. and Kasikov, A.G., *Zh. Prikl. Khim.*, 1983, vol. 56, no. 6, pp. 1257–1261.
3. Simanova, S.A., Bashmakov, V.I., and Troshina, O.N., *Zh. Prikl. Khim.*, 1993, vol. 66, no. 1, pp. 27–30.
4. Sobol', S.I. and Frash, G.M., *Tsvetn. Met.*, 1974, no. 2, pp. 14–21.
5. Karapet'yants, M.Kh. and Drakin, S.I., *Obshchaya i neorganicheskaya khimiya* (General and Inorganic Chemistry), Moscow: Khimiya, 1981.
6. Shul'man, V.M., Savel'ev, Z.A., and Novoselov, R.I., *Izv. Sib. Otd. Akad. Nauk SSSR, Ser. Khim. Nauk*, 1972, issue 2, pp. 55–58.
7. Onstott, E.I. and Laitinen, H.A., *J. Am. Chem. Soc.*, 1950, vol. 72, pp. 4724–4728.
8. Borbat, V.F. and Voronov, A.B., *Avtoklavnaya tekhnologiya pererabotki nikel'-pirrotinovykh kontsentratov* (Autoclave Processing of Nickel Pyrrhotine Concentrates), Moscow: Metallurgiya, 1980.
9. *Handbuch der präparativen anorganischen Chemie*, Brauer, G., Huber, F., *et al.*, Eds., Stuttgart: Ferdinand Enke, 1978, vol. 2.
10. Yampol'skii, A.M., *Mednenie i nikelirovanie* (Copper and Nickel Plating), Moscow: Mashgiz, 1958.
11. Babich, V.A. and Gorelov, I.P., *Zh. Anal. Khim.*, 1971, vol. 26, pp. 1943–1946.
12. Gurel, D. and Gurel, O., *Oscillations in Chemical Reactions*, Berlin: Akademie, 1984.
13. Khobotova, E.B. and Larin, V.N., *Zh. Prikl. Khim.*, 1995, vol. 68, no. 3, pp. 416–420.
14. Borbat, V.F. and Leshch, I.Yu., *Novye protsessy v metallurgii nikelya i kobal'ta* (New Processes in Nickel and Cobalt Metallurgy), Moscow: Metallurgiya, 1976.

Russian Journal of Applied Chemistry, Vol. 74, No. 1, 2001, pp. 51–54. Translated from Zhurnal Prikladnoi Khimii, Vol. 74, No. 1, 2001, pp. 50–53.

APPLIED ELECTROCHEMISTRY AND CORROSION PROTECTION OF METALS

Anodic Dissolution of Nickel Sulfide in Acidic Cu(II) Electrolytes

M. I. Natorkhin

St. Petersburg State Technical University, St. Petersburg, Russia

Received November 19, 1999; in final form, September 2000

Abstract—The effect of ligands on the anodic dissolution of NiS in copper-containing acidic electrolytes was studied.

Hydrometallurgical processing of non-ferrous metals is being actively developed at modern enterprises [1, 2]. It is known [3] that copper ions present in pressure leaching solutions have a significant catalytic effect on nickel sulfide dissolution. However, simultaneous presence of copper and sulfate ions results in passivation of the sulfide surface and, consequently, exerts an adverse effect on the process parameters.

The aim of this work was to study the effects of electrolyte anion composition and depassivating additions to sulfate electrolytes on the electrochemical behavior of nickel sulfide in copper-containing electrolytes. The origin of the catalytic action of copper ions is not fully understood. Pure copper is considered to be able to deposit at a sulfide surface [3] to form microgalvanic couples, which increase the anodic potential at certain parts of the surface. At the same time, Cu^{2+} ions in acid solutions can act as an additional oxidizing agent [4] capable of oxidizing sulfur in sulfides to the elemental form.

$$Cu^{2+} + 2e = Cu,\ E^0 = 0.334\ V;$$

$$Cu^{2+} + Cl^- + e = CuCl,\ E^0 = 0.538\ V;$$

$$Cu^{+} + e = Cu,\ E^0 = 0.521\ V.$$

It is copper which is likely to hinder further oxidation of elemental sulfur to sulfate ions, which is extremely convenient, as sulfide sulfur is removed from the process in the elemental form. We used β-NiS with a nickel content of 50 at. % as a subject of the study, because, according to [5], in the course of the oxidative dissolution of nickel sulfides Ni_3S_2 and Ni_7S_6, which occurs by the electrochemical mechanism [6], the surface is gradually enriched in a sulfide with a higher Ni content, up to NiS [7].

Nickel sulfide NiS (50 at. %) was synthesized by the known procedure [8] from equimolar amounts of cathodic N0-grade nickel and analytically pure grade sulfur in an evacuated quartz ampule. The working electrode was made from a nickel sulfide sample soldered to a copper holder. Its idle surface was insulated with a nitro lacquer. Before experiments the NiS surface under study (area 1 cm^2) was smoothed with emery paper no. 0 and washed with alcohol and distilled water. Experiments with fluorine-containing electrolytes were carried out in a fluoroplastic cell with a temperature-controlled water jacket. In the other cases a YaES-2 glass cell (glass electrode cell) temperature-controlled with a UTU 2/77 thermostat was used. Electrochemical experiments were carried out on a PI-50-1.1 potentiostat equipped with a PDP4-002 plane-table recorder. We used a three-electrode cell with nickel sulfide under study as a working electrode, a platinum auxiliary electrode, and a saturated silver chloride reference electrode (electrode potentials are given vs. normal hydrogen electrode). Electrolytes were prepared from chemically pure, ultrapure, and analytically pure grade reagents.

The following processes of oxidative dissolution of nickel sulfide in copper chloride and copper sulfate solutions were studied.

$$2CuCl_2 + NiS = NiCl_2 + 2CuCl\downarrow + S\downarrow, \quad (1)$$

$$2CuSO_4 + 2NiS = 2NiSO_4 + Cu_2S\downarrow + S\downarrow. \quad (2)$$

The processes have both advantages and drawbacks: process (1) involves high concentrations of chlorides hampering further electrolyte treatment, and process (2) requires high temperatures and pressures and also involves passivation of the NiS surface due to Cu_2S deposition. The accelerating effect of copper

1070-4272/01/7401-0051$25.00

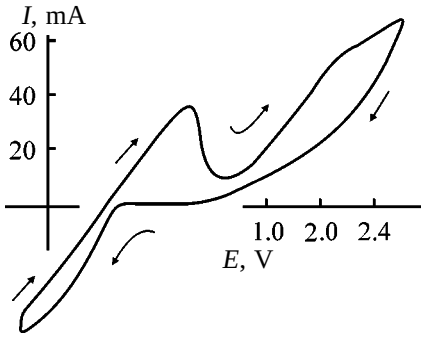

Fig. 1. Cyclic voltammogram of NiS in 0.5 M $CuSO_4$ at 90 ± 0.5°C: (*I*) current and (*E*) potential; the same for Figs. 3–5. Rate of potential scanning 100 mV s^{-1}; the same for Figs. 4 and 5.

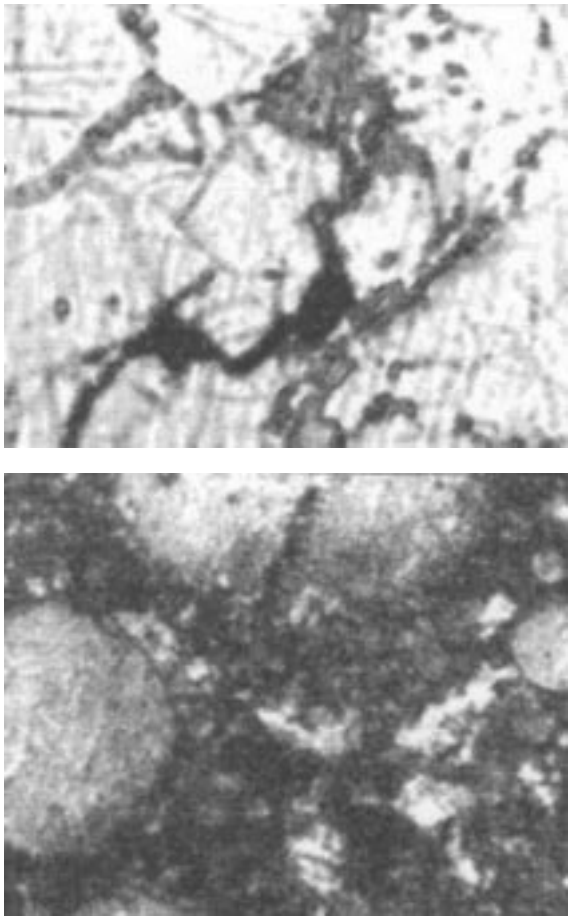

Fig. 2. Photomicrographs of NiS etched for 2 min at a potential of 1 V in (a) 0.5 M $CuSO_4$ at 20°C and (b) 0.5 M $Cu(NO_3)_2$ + 200 g l^{-1} KBr at 90°C. Magnification: (a) 800 and (b) 10.

activators on the anodic dissolution of NiS is due to the possibility of removing insoluble copper products from the nickel sulfide surface owing to the formation of copper(I) complex ions under certain conditions [9].

Sulfate ions do not form complexes with copper(I) ions under common conditions [9]; therefore, the steady-state currents of NiS dissolution are insignificant. As chloride ions form sufficiently stable complexes with Cu(I) ions, copper contained in a Cu_2S passivating film can partially pass into solution in the form of $[CuCl_2]^-$ ions, which is observed in the experiments. An increase in the concentration of chloride ions (addition of NaCl) can result in a rise of the NiS dissolution currents.

The cyclic voltammogram (CVA) obtained on NiS in 0.5 M $CuSO_4$ (pH 2.2) at 90°C is shown in Fig. 1. The anodic peak in the forward branch seems to be due to the dissolution of both NiS and copper deposited in the course of cathodic polarization.

The electroetching of an NiS sample in 0.5 M $CuSO_4$ for 2 min at a potential of 1 V results in the formation of a new phase on the nickel sulfide surface. A photomicrograph of the etched part is shown in Fig. 2a. The light-colored phase is the starting nickel sulfide. The composition of the dark-colored phase is (mol %) S 54.6–52.8 and Ni 45.4–47.3. This phase probably corresponds to Ni_3S_4 in the Ni–S phase diagram [10].

Anodic dissolution of NiS in $CuCl_2$ occurs according to Eq. (1), whereas in excess NaCl it is described by the equation

$$CuCl_2 + NiS + 2NaCl = 2NaCuCl_2 + NiCl_2 + S\downarrow. \quad (3)$$

The behavior of NiS in 0.5 M $CuCl_2$ at various rates of potential scanning is shown in Fig. 3. As known [11], in the case of diffusion control the peak current (I_p) is proportional to $V_s^{1/2}$ (V_s is the rate of potential scanning). The peak current I_p and passivation current I_{pas} as functions of potential sweep rate are given below:

V_r, mV s^{-1}	I_p, mA	I_{pas}, mA
10	32	10
100	65	20
200	91	37

Applying the linear regression approach to these data, we obtained the formula

$$I_p = 14.3 + 5.3\ V_s^{1/2}. \quad (4)$$

The effect of NaCl addition in amounts of 50–200 g l^{-1} to 0.5 M $CuCl_2$ on the forward branches of CVA is shown in Fig. 4. The anodic peak observed in the region of 0.1 V is shifted to the cathodic region,

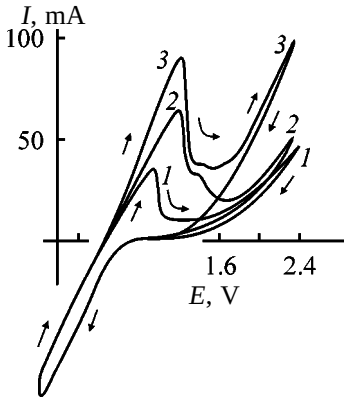

Fig. 3. Cyclic voltammogram of NiS in 0.5 M $CuCl_2$ at 90 ± 0.5°C. Potential scanning rate ($mV\ s^{-1}$): (*1*) 10, (*2*) 100, and (*3*) 200.

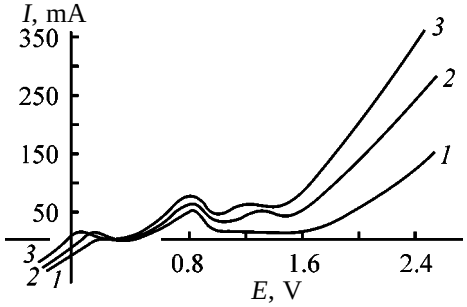

Fig. 4. Voltammograms of NiS in 0.5 M $CuCl_2$ with NaCl additions at 90 ± 0.5°C. NaCl ($g\ l^{-1}$): (*1*) 50, (*2*) 100, and (*3*) 200.

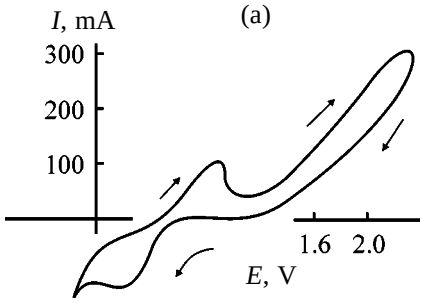

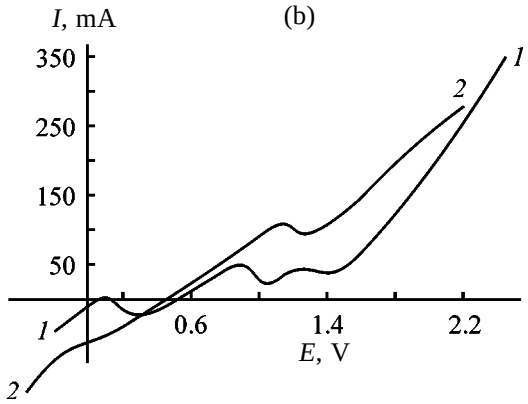

Fig. 5. Voltammograms of NiS (a) in 0.5 M $Cu(NO_3)_2$ at 90 ± 0.5°C and (b) in (*1*) 0.5 M $CuCl_2$ + 200 $g\ l^{-1}$ NaCl and (*2*) 0.5 M $Cu(NO_3)_2$ + 200 $g\ l^{-1}$ KBr.

whereas the peak current in the region of 0.8 V increases by 30–40% as the concentration of chloride ions increases. A significant increase (from 10 to 70 mA) of the current corresponding to the passivation plateau points to partial dissolution of the passivation film due to formation of $[CuCl_2]^-$ [12, 13].

The cyclic voltammetric curves of NiS dissolution in 0.5 M $Cu(NO_3)_2$ solution and in 0.5 M $Cu(NO_3)_2$ solution with addition of 200 $g\ l^{-1}$ KBr are shown in Figs. 5a and 5b, respectively.

Comparison of the anodic branches of the NiS CVAs in 0.5 M $Cu(NO_3)_2$ with addition of 200 $g\ l^{-1}$ KBr and NaCl (Fig. 5b) showed that in the case of chlorides (curve *1*) dissolution of the passivating film (convex section) occurs in the potential range 1.1–1.4 V, and in the case of nitrates (curve *2*) it occurs at 2–3 times greater passivation currents. Furthermore, the passivating film is displaced from the electrode surface by molten sulfur (Fig. 2b). At high anode potentials in the nitrate–bromide system the passivating film is absent from the electrode surface, and only the bright golden NiS surface and molten sulfur are observed. The passivating surface film is formed at low anode potentials (0.6–0.8 V) and is dissolved as the potential is increased to 1.0–1.2 V. In the course of the dissolution molten sulfur is formed (light circular parts), which tightly adheres to the sulfide surface and gradually displaces the passivating film. With 10 $g\ l^{-1}$ of KBr added to $Cu(NO_3)_2$, the rates of NiS dissolution are greater than in the case of addition of 200 $g\ l^{-1}$ NaCl to $CuCl_2$. Therefore, KBr additions are more efficient and more suitable for further processing of nickel-containing solutions.

CONCLUSIONS

(1) Anions capable of complex formation with both Cu(II) and Cu(I) ions accelerate anodic dissolution of NiS in copper-containing electrolytes.

(2) The rates of anodic dissolution are the highest in the nitrate–bromide system, as the Cu_2S film formed at low potentials is dissolved by copper bromide complexes and thus is completely displaced by molten sulfur formed on the NiS surface.

(3) A new surface phase, probably Ni_3S_4, is initially formed upon anodic dissolution of NiS in $CuSO_4$.

ACKNOWLEDGMENTS

The authors thank Prof. A.A. Kazakov for assistance in preparation of photomicrographs and L.N. Ertseva for electron-microscopic examination of the etched NiS surface.

REFERENCES

1. Sinel'shchikova, N.V. and Makarova, S.N., *Gidrometallurgiya medi i nikelya* (Hydrometallurgy of Copper and Nickel), Moscow: Tsvetmetinformatsiya, 1976.
2. *Tsvetnaya metallurgiya Finlyandii* (Non-Ferrous Metallurgy of Finland), Moscow: Tsvetmetinformatsiya, 1971.
3. Borbat, V.F. and Voronov, A.B., *Avtoklavnaya tekhnologiya pererabotki nikel'-pirrotinovykh kontsentratov* (Autoclave Processing of Nickel–Pyrrhotine Concentrates), Moscow: Metallurgiya, 1980.
4. Lilich, L.S. and Khripun, M.K., *Rastvory v neorganicheskoi khimii* (Solutions in Inorganic Chemistry), Leningrad: Leningr. Gos. Univ., 1984.
5. Muravchik, B.L. and Kipnis, A.Ya., *Zh. Prikl. Khim.*, 1982, vol. 55, no. 12, pp. 2650–2654.
6. *Gidrometallurgiya: Sbornik perevodov* (Hydrometallurgy: Coll. of Translations), Laskorin, B.N., Ed., Moscow: Metallurgiya, 1978.
7. Belyakov, E.A. and Kasikov, A.G., *Zh. Prikl. Khim.*, 1983, vol. 56, no. 6, pp. 1257–1261.
8. *Handbuch der präparativen anorganischen Chemie*, Brauer, G., Huber, F., *et al.*, Eds., Stuttgart: Ferdinand Enke, 1978.
9. *Kratkii spravochnik po khimii* (Concise Handbook on Chemistry), Goronovskii, I.T., Nazarenko, Yu.P., and Nekryach, E.F., Eds., Kiev: Naukova Dumka, 1987.
10. Elliott, R. P., *Constitution of Binary Alloys*, New York: McGraw-Hill, 1965.
11. *Organic Electrochemistry. An Introduction and a Guide*, Baizer, M.M. and Lund, H., Eds., New York: Marcel Dekker, 1983.
12. Chernobaev, I.P. and Kasatkin, L.A., *Zh. Prikl. Khim.*, 1975, vol. 48, no. 2, pp. 345–349.
13. Dzhusulov, E.A., Pozin, M.Yu., and Tikhonov, K.I., *Zh. Prikl. Khim.*, 1979, vol. 52, no. 8, pp. 1692–1696.

Russian Journal of Applied Chemistry, Vol. 74, No. 1, 2001, pp. 55–57. Translated from Zhurnal Prikladnoi Khimii, Vol. 74, No. 1, 2001, pp. 53–55.

APPLIED ELECTROCHEMISTRY AND CORROSION PROTECTION OF METALS

Discharge Characteristics of an $LaAl/C_8CrO_3$ Lithium Battery with Organic Electrolyte

L. N. Ol'shanskaya, S. S. Popova, A. G. Nichvolodin, and A. A. Ol'shanskaya

Technological Institute, Saratov State Technical University, Engels, Russia

Received December 7, 1999; in final form, March 2000

Abstract—Applicability of Paykert's equation, which relates the battery capacity to the discharge current, to prototypes of $LiAl/C_8CrO_3$ lithium batteries with an organic electrolyte (1 M $LiClO_4$ in a 1 : 1 mixture of propylene carbonate and dimethoxyethane) was examined. Pressed and rolled samples with and without modification of the C_8CrO_3 electrode with manganese dioxide were tested in the 0–50°C range.

Lithium batteries find a wide and steady demand in the market of chemical current sources. Their undoubted advantages over traditional chemical current sources are high specific energy (150–300 W h kg^{-1} and higher), wide operating temperature range (–30 to +60°C), high discharge voltage (3.0–3.5 V), hermetically sealed design, possibility of using in any position in space, tolerance for magnetic field and X-ray radiation, and the use of available and environmentally clean raw materials [1–3]. However, their high fire and explosion hazared, as well as the absence of reliable theories describing behavior of various types of batteries under such conditions, make difficult their large-scale application.

The aim of this work was to study the discharge characteristics of $LiAl/C_8CrO_3$ batteries of pressed and rolled designs with a nonaqueous organic electrolyte [1 M $LiClO_4$ in a mixture of propylene carbonate (PC) and dimethoxyethane (DME) taken in a 1 : 1 volume ratio] within the 0–50°C range and to find out whether the dependence of the capacity of such batteries on the discharge current can be described by the Paykert's equation $I^{n-1}C = K$.

On the basis of the experimental time dependences of the discharge voltage at various discharge currents [4, 5] we have simulated the discharge process and examined the relations between the battery capacity and the discharge current. It was shown that a number of internal (weight of active substances, their physicochemical properties, and design features of chemical current sources) and external (discharge current, temperature, humidity, etc.) factors affect the battery capacity, which is one of its most important electric characteristics.

Repeated efforts [4–9] were made to find a quantitative correlation between the discharge current of batteries and their actual discharge capacity, the Paykert's empirical equation being accepted as the most suitable:

$$I^n\tau = K, \tag{1}$$

whence

$$I^{n-1}C = K,$$

where n is a constant independent of capacity, which characterizes the battery type; K is a constant increasing with the weight of the active materials in the battery; C is the battery capacity (A h or mA h).

For the first time the Paykert's equation was suggested for lead batteries, but it can also be applied to chemical current sources based on the other systems [3, 4, 6, 10]. The constants n and K for a battery can be found from the experimental parameters of its operation in two different modes [10]. If the discharge time is τ_1 at the discharge current I_1, and τ_2 at I_2, then, according to Eq. (1),

$$I_1^n\tau_1 = I_2^n\tau_2 = K. \tag{2}$$

This equation in the logarithmic form for n is

$$n = \frac{\log\tau_2 - \log\tau_1}{\log I_1 - \log I_2}. \tag{3}$$

Hence, for the battery capacity C we have

$$C = KI^{1-n}. \tag{4}$$

1070-4272/01/7401-0055$25.00

Time τ, discharge capacity *C*, and constants *n* and *K* of various batteries. Discharge current 1 and 10 mA

T, °C	τ_1, h	τ_{10}, h	*K*	*n*	C_1, mA h	C_{10}, mA h
			$LiAl/C_8CrO_3$ Rolled batteries			
0	310	27	310	1.06	310	270
5	395	31	395	1.08	395	310
10	473	36	473	1.12	473	360
15	544	47	544	1.06	544	470
20	591	55	591	1.03	591	550
25	634	57	634	1.05	634	570
30	681	62	681	1.04	681	620
35	719	66	719	1.03	719	660
40	766	70	766	1.04	766	700
45	865	82	865	1.02	865	820
50	874	77	874	1.06	874	770
			Pressed batteries			
20	471	35	471	1.13	471	350
			$LiAl/C_8CrO_3$ (30 wt % MnO_2) Pressed batteries			
20	480	42.5	480	1.05	480	425

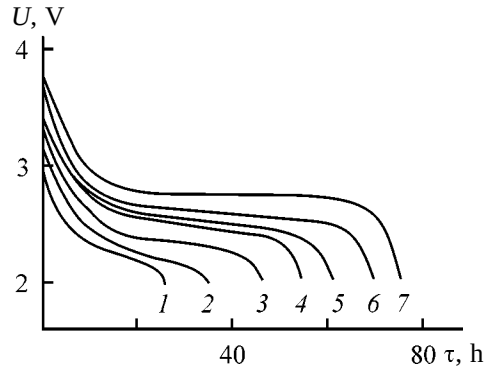

Fig. 1. Discharge curves *U*–τ (I_2 = 10 mA) of pressed and rolled lithium batteries $LiAl/LiClO_4$ + PC + DME/C_8CrO_3 at various temperatures. Temperature (°C): (*1*) 0, (*2*) 10, (*3*) 15, (*4*) 20, (*5*) 30, (*6*) 40, and (*7*) 50.

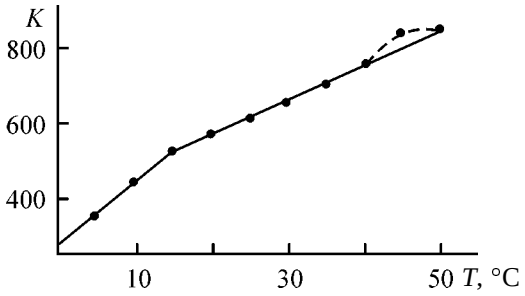

Fig. 2. Constant *K* of the Paykert's equation as a function of temperature *T* (°C).

An examination of the discharge characteristics (Fig. 1) and the determination of the constants *n* and *K* for the developed prototypes of pressed and rolled $LiAl/C_8CrO_3$ batteries of the *R*6 (316) dimension type (see table) showed that *n* varies in the range 1.02–1.13 and is almost independent of temperature, battery design, and composition of active masses of the electrodes. On the contrary, the constant *K* is a linear function of temperature, the temperature coefficient $\Delta K/\Delta T$ decreasing on passing from the 0–15°C to 15–50°C range (Fig. 2). The presence of two temperature ranges with different $\Delta K/\Delta T$ values may be due to specific features of lithium intercalation–deintercalation in active masses of the electrodes of the $LiAl/C_8CrO_3$ chemical current sources under development [11]. In the case of lead batteries the constant *K* linearly depends on temperature in the range from –20 to +20°C, and *n* varies from 1.35 to 1.72 [4, 12, 13].

Examination of the data in the table for the prototypes of $LiAl/C_8CrO_3$ lithium batteries shows that the constant *K* for the rolled batteries is higher by approximately 25% than for the pressed batteries.

Thus, the analytical dependences obtained show that the Paykert's equation can be applied to find a quantitative correlation between the actual discharge capacity of an $LiAl/C_8CrO_3$ battery and its discharge current in the I_{50}–I_{500} discharge mode (or from 0.02

to 0.002 C_{nom}) within the 0–50°C range. It follows from a formal comparison that the constants n and K calculated for lithium batteries are lower than the published characteristics of lead batteries [4, 12, 13], which can result from the fact that the discharge parameters of these systems differ by a factor of tens or even hundreds.

REFERENCES

1. Kedrinskii, I.A., Dmitrienko, V.E., and Grudyanov, I.I., *Litievye istochniki toka* (Lithium Current Sources), Moscow: Energoatomizdat, 1992.
2. Crompton, T.R., *Small Batteries*, vol. 2: *Primary Cells*, London: Basingstoke, 1982.
3. Varypaev, V.N., Dasoyan, M.A., and Nikol'skii, V.A., *Khimicheskie istochniki toka* (Chemical Current Sources), Moscow: Vysshaya Shkola, 1990.
4. Galushkin, N.E., *Modelirovanie raboty khimicheskikh istochnikov toka* (Modeling of Operation of Chemical Current Sources), Shakhty: Donskaya Gos. Akad. Servisa, 1998.
5. Galushkin, N.E. and Kudryavtsev, Yu.D., *Elektrokhimiya*, 1997, vol. 33, no. 5, pp. 605–606.
6. Morozov, G.P. and Gantman, S.A., *Khimicheskie istochniki toka dlya pitaniya sredstv svyazi* (Chemical Current Sources for Communication Devices), Moscow: Voenizdat, 1949.
7. Landfors, J. and Simonsson, D., *J. Electrochem. Soc.*, 1992, vol. 129, no. 10, pp. 2768–2772.
8. Belyaev, B.V., *Elektrotekhnika*, 1968, no. 3, pp. 35–40.
9. Rudenko, M.G., *Zh. Fiz. Khim.*, 1993, vol. 67, no. 9, pp. 1873–1879.
10. Fedot'ev, N.P., Alabyshev, A.F., Rotinyan, A.L., *et al.*, *Prikladnaya elektrokhimiya* (Applied Electrochemistry), Leningrad: Khimiya, 1967.
11. Russian Inventor's Certificate no. 1 238 662.
12. Dasoyan, M.A., Novoderezhkin, V.V., and Tomashevskii, B.E., *Proizvodstvo elektricheskikh akkumulyatorov* (Production of Electric Batteries), Moscow: Vysshaya Shkola, 1977.
13. Dasoyan, M.A. and Aguf, I.A., *Osnovy rascheta, konstruirovaniya i tekhnologii proizvodstva svintsovykh akkumulyatorov* (Principles of Calculation, Design, and Production of Lead Batteries), Leningrad: Energiya, 1978.

Russian Journal of Applied Chemistry, Vol. 74, No. 1, 2001, pp. 58–62. Translated from Zhurnal Prikladnoi Khimii, Vol. 74, No. 1, 2001, pp. 56–60.

CATALYSIS

Oxidation of I^- and S^{2-} Anions by Oxygen in Aqueous Suspensions of Silica Gel

V. N. Pak, C. D. Hanson, and S. R. Coon

Herzen Russian State Pedagogic Institute, St. Petersburg, Russia
University of Northern Iowa, Cedar Falls, Iowa, the United States

Received September 19, 2000

Abstract—Oxidation of I^- and S^{2-} anions on the silica gel surface by atmospheric oxygen was studied at room temperature. The possibility and rate of oxidation processes are determined by the content of silica gel and oxygen in the systems. Tentative interpretation of the results is based on the assumption that a highly reactive singlet $^1O_2$ species is formed in the oxygen ensemble on the silica surface.

Molecular oxygen can be transferred into an electronically excited singlet $^1\Delta_g$ state in a number of ways, including dye-sensitized photoexcitation in solutions [1–9] and zeolites [10, 11], decomposition of unstable oxygen-containing substances [1, 2, 12], laser evaporation of metal oxides [13, 14], and microwave discharge [2, 15]. The relatively long lifetime (10^{-3}–10^{-6} s in solutions), moderately high excitation energy (22.54 kcal mol^{-1}), and high chemical activity of the singlet form $^1\Delta_g$ of oxygen allow it to be considered as actual oxidizing agent in various processes, including those practically important [1–15].

It is a common knowledge that the solid substance most widely occurring in the nature, silicon dioxide, does not possess under standard conditions any redox properties, at least at the temperature of ambient air. At the same time, it cannot be positively stated that molecules with enhanced reactivity in electronically excited singlet state cannot be present in the oxygen ensemble even at room temperature under conditions of dynamic equilibrium between the SiO_2 surface and the gas phase. The excess amount and the nonuniform distribution of the surface energy may be a reason for conversion of some (presumably only a minor) part of paramagnetic $^3O_2$ molecules into the paired-spin state $^1O_2$. The energy necessary for this to occur is relatively low and, presumably, can be provided by fluctuations of the SiO_2 surface energy.

This hypothesis was the reason for undertaking the present investigation. In choosing a means of verification of the hypothesis, it was necessary to keep in mind not only the low concentration of excited oxygen molecules, but also the high probability of their impact deactivation, drastically impairing the possibility of their direct detection. In this connection, it seemed the most appropriate to assess experimentally the possibility of oxidation of a number of substances at room temperature directly on the silica surface with the aim of ensuring the involvement in the process of a finite fraction of singlet oxygen present on the surface.

Below are presented the results obtained in studying two heterogeneous reactions involving atmospheric oxygen. The first of these is oxidation of the iodide ion to molecular iodine. The choice of this reaction is governed by the reliably established fact that I^- is oxidized at room temperature neither by atmospheric nor by pure oxygen, whereas under the action of ozone [16] or singlet oxygen [17] this process occurs. The second reaction, oxidation of the sulfide ion on silica gel, is of particular interest in view of the possibility of occurrence of successive oxidative transformations and the wide variety of the involved charge states of sulfur.

EXPERIMENTAL

The study was performed on ultrapure silica gel S-157 (Fisher) with a specific surface area of 700 $m^2 g^{-1}$, giving reason to expect that analytically detectable content of oxidation products can be reached. All experiments were carried out at 25°C using a 0.1-mm sieved fraction of silica gel particles.

The rate of I^- oxidation in an aqueous suspension of a silica gel of a given type at a constant temperature is determined by the I^- and O_2 concentrations. An excess of I^- in the working solution can be used, in fact ensuring $[I^-]$ = const. The concentration of oxy-

1070-4272/01/7401-0058$25.00

gen is determined by the conditions of its supply into the system, i.e., by the intensity of bubbling and stirring. With the number of variable parameters deliberately restricted, the aim was to reveal the very possibility of oxidation and determine the fundamental conditions for its occurrence. For example, in a set of experiments, 50 ml of an aqueous KI solution was added to variable weighed portions of silica gel and stirred with a magnetic stirrer in open vessels in air, with the resulting suspension sampled at regular intervals of time, centrifuged, and analyzed for the content of molecular iodine. In order to ensure additional enrichment of the suspensions with oxygen, air was bubbled at a rate of 30 and 50 $cm^3\ min^{-1}$. In some experiments, oxidation of the iodide ion, unhindered by oxygen diffusion, was studied. For this purpose, 0.5-g portions of silica gel were impregnated with 2 ml of 1 M KI solution and exposed to air. After a prescribed time elapsed, the same solution was added to the weighed portions, with the solution volume brought to 50 ml, the suspensions were thoroughly stirred, and samples were taken for analysis.

The appearance and accumulation of molecular iodine in solution was recorded photometrically on a Shimadzu UV-2401 PC automated spectrometer in quartz cells with optical thickness of 1 cm. The enhanced solubility of iodine in solutions containing an excess of I^- ions is due to the formation of stable associates $I_2 \cdot I^-$ [17]. The electronic spectrum of I_3^- contains no broad band characteristic of an aqueous solution of iodine, whereas two peaks in the UV are close and furnish an opportunity for direct photometric determination of molecular iodine (Fig. 1). A calibration procedure demonstrated that the Bouguer–Beer law is observed at λ_{max} = 351 nm with a molar extinction coefficient $\varepsilon = 1.851 \times 10^4\ l\ mol^{-1}\ cm^{-1}$ in the concentration range 0.01–0.1 mM I_2 in a 1 M solution of KI, which well matched the goal of analytical measurements in the experiments.

The extent of oxidation of the sulfide ion on the silica gel surface and the possibility of formation, in the process, of sulfur oxides SO_2 and SO_3 were determined by Fourier ion-cyclotron resonance mass spectrometry on an IonSpec OMEGA 50 instrument. A glass ampule containing ca. 4 g of silica gel impregnated with a 1 M aqueous solution of $(NH_4)_2S$ and then kept in air was connected to the input for taking gas samples, and all components desorbed into the analyzer chamber by evacuation at room temperature were recorded. In experiments on S^{2-} oxidation in aqueous suspensions, 50 ml of 1 M $(NH_4)_2S$ solution was added to weighed portions of silica gel, and the

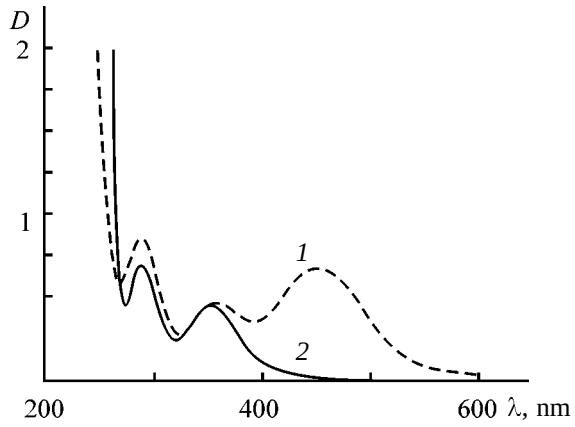

Fig. 1. Electronic spectra of iodine in (*1*) water and (*2*) 1 M solution of potassium iodide. (*D*) Optical density and (λ) wavelength; the same for Fig. 2.

mixture was stirred with a magnetic stirrer in open vessels in air.

Suspension samples taken at certain intervals of time were centrifuged and analyzed on a Dionex DX-100 liquid ion chromatograph equipped with an electrical conductivity detector and a 250-mm-long column packed with an anion-exchange resin containing bound ammonium groups. Preliminary calibration experiments demonstrated that sulfide ions are partially sorbed and/or smeared over the column in analyzing aqueous solutions containing mixtures of S^{2-}, SO_3^{2-}, and SO_4^{2-} anions in concentrations of the order of tens of ppm and, therefore, are not recorded, whereas sulfite and sulfate ions are determined together, without being separated, and are eluted as a single peak with a retention time of 3.7–3.8 min.

Formation of molecular iodine can be reliably established already during the first minutes after placing a weighed portion of silica gel in a starch-containing KI solution by the appearance of a characteristic light blue coloration. The oxidation of the iodide ion can also be observed visually in the absence of starch owing to the fast appearance of yellow coloration, particularly noticeable on the surface of silica particles and passing into solution on stirring. A typical set of spectra illustrating the accumulation of the $I_2 \cdot I^-$ form of molecular iodine are shown in Fig. 2; they completely coincide with the spectra of iodine in 1 M KI solution, taken in the course of calibration (Fig. 1). Thus, the fact of iodide ion oxidation on the silica gel surface is beyond doubt.

The essential role of the rate of oxygen supply to the silica gel surface in the course of oxidation is clearly demonstrated by the dependence in Fig. 3. The noticeable production of molecular oxygen in the ini-

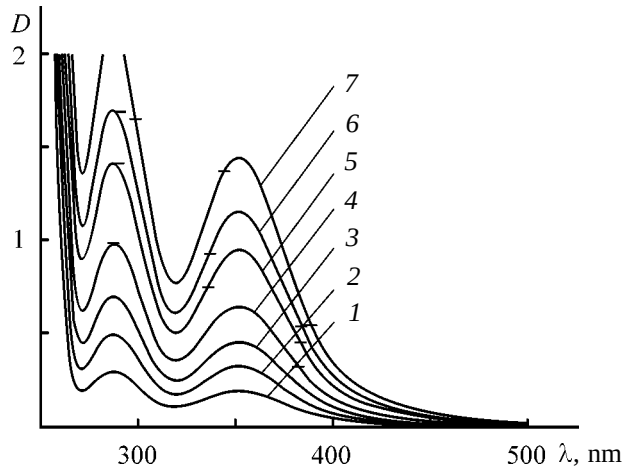

Fig. 2. Electronic spectra characterizing the accumulation of I_3^- in 50 ml of 1 M aqueous KI solution containing 1 g of suspended silica gel. Air bubbling at a rate of 30 $cm^3\ min^{-1}$. Time of oxidation (h): (*1*) 0.2, (*2*) 0.4, (*3*) 0.6, (*4*) 1.0, (*5*) 1.5, (*6*) 2.5, and (*7*) 3.5.

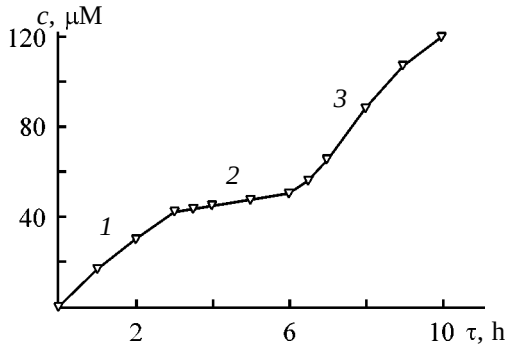

Fig. 3. Iodine concentration *c* vs. time τ of oxidation in 50 ml of 1 M KI solution containing 0.5 g of suspended silica gel. (*1*) Stirring with magnetic stirrer (150 rpm), (*2*) no stirring, and (*3*) stirring with additional bubbling of air (50 $cm^3\ min^{-1}$).

tial stage is largely ensured by the amount of oxygen present in silica gel pores and by gas supply into the system, enhanced by stirring. Switching-off the stirrer (portion *2*) lowers the content of oxygen, decelerating the oxidation. In portion *3* of the curve, the process is intensified by bubbling air through the system at a rate of 50 $cm^3\ min^{-1}$.

The kinetic curves presented in Fig. 4 furnish additional evidence in favor of the oxygen activation on the silica gel surface. The increase in silica gel mass under conditions of continuous stirring is accompanied by nearly proportional acceleration of molecular iodine formation (curves *1–3*). Air bubbling largely lifts the diffusion limitation on oxygen supply, markedly intensifying the oxidation (curves *4*, *5*). The process is accelerated to an even greater extent in the case of direct access of air to the surface of silica gel impregnated with 1 M KI solution (curve *6*).

In the aggregate, the obtained results suggest that an electronically excited $^1O_2$ species is present in the ensemble of oxygen molecules adsorbed onto the silica gel surface, ensuring the occurrence of the reaction

$$4I^- + {}^1O_2 + 2H_2O \rightarrow 2I_2 + 4OH^-, \quad (1)$$

$$2I_2 + I^- = I_3^-. \quad (2)$$

The involvement of just singlet oxygen in I^- oxidation seems to be the most likely, since formation of ozone and, the more so, of atomic oxygen requires gross energy expenditure. Appearance of charged oxygen species on the silica surface under so mild conditions is also hardly possible.

It should be emphasized that the oxidation rate is extremely low and the process can only be recorded because of the high specific surface area of silica gel. The maximum amount of molecular iodine, obtained in 12 h of experiment, is mere 10^{11}–10^{12} molecules per 1 cm^2 of SiO_2 surface, i.e., a vanishingly small fraction of a conventional monolayer.

Quantitative monitoring of the oxidation of the sulfide ion on the silica gel surface is hindered by the wide variety of products obtained, reversibility of transformations, and partial removal of gaseous substances from the reaction zone. However, even the results of preliminary qualitative experiments allow rather important conclusions. It is known that solutions containing the sulfide ion gradually become turbid in air because of the liberation of elemental sulfur; however, this process is slow and its consequences can only be observed after a long time. For example, 1 M H_2SO_4 solution remains transparent for many hours. At the same time, placing in this solution a weighed portion of silica gel causes visually observable formation of elemental sulfur on the surface of SiO_2 particles. Such a drastic acceleration of oxidation probably indicates that an active oxygen species is involved in the process:

$$2S^{2-} + {}^1O_2 + 2H_2O \rightarrow 2S + 4OH^-. \quad (3)$$

However, the oxidation in the system containing S^{2-}, O_2, H_2O, and solid SiO_2 does not terminate at this point and proceeds further with higher oxidation states of sulfur reached. Correspondingly, the mass spectrum of silica gel impregnated with 1 M solution of $(NH_4)_2S$ shows, together with the reliably recorded

components: N_2, O_2, H_2O, and H_2S, also stable weak signals with masses of 64 and 80, undoubtedly belonging to ionized oxides SO_2 and SO_3 (Fig. 5). It is possible, in principle, that SO_2 formation is a result of direct oxidation of sulfide ions by singlet oxygen on the silica gel surface:

$$2S^{2-} + 3^1O_2 + 2H_2O \rightarrow 2SO_2 + 4OH^-. \quad (4)$$

However, even in the case when oxidation proceeds in two successive stages, the occurrence of the reaction (following the liberation of elementary sulfur)

$$S + {}^1O_2 \rightarrow SO_2 \quad (5)$$

at room temperature seems to be rather uncommon and illustrative. The final stage of oxidation

$$2SO_2 + {}^1O_2 \rightarrow 2SO_3 \quad (6)$$

again indicates that highly reactive singlet oxygen is present on the silica gel surface. In all probability, along with the above reactions in the suspension, there occur equilibria and transformations typical of charged sulfur species, e.g.:

$$SO_2 + H_2O \rightleftarrows H_2SO_3 \rightleftarrows H^+ + HSO_3^- \rightleftarrows 2H^+ + SO_3^{2-}, \quad (7)$$

$$2SO_3^{2-} + {}^1O_2 \rightarrow 2SO_4^{2-}, \quad (8)$$

$$SO_2 + 2H_2S \rightarrow 3S + 2H_2O, \quad (9)$$

$$2SO_3 + S \rightarrow 3SO_2, \quad (10)$$

and also some others, including those involving unstable polythionic acids. The wide variety of possible reactions, and also partial removal of gaseous products from the system, may give rise to fluctuations in the content of sulfite and sulfate ions being formed. Indeed, these latter can be detected in the suspension soon after the onset of oxidation (Fig. 6), and their concentration changes, on the general background of growth, in a clearly nonmonotonic manner.

Thus, the above examples indirectly confirm the presence of singlet oxygen on the silica surface under standard conditions. It is the chemical activity of singlet oxygen that is presumably responsible for the oxidation on the SiO_2 surface of substances quite stable at the temperature of the ambient air. The large specific surface area of silica gel makes it possible to record oxidative transformations limited by low content of active oxygen under laboratory conditions. Consequently, there is good reason to believe that the

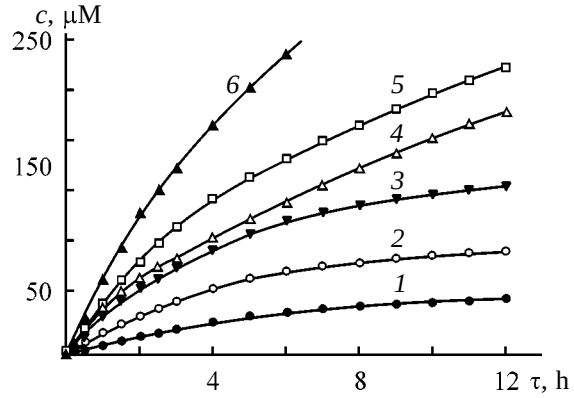

Fig. 4. Kinetic curves describing iodide ion oxidation under varied experimental conditions. (*c*) Concentration of iodine and (τ) time. (*1–3*) 0.25, 0.5, and 1 g of silica gel, respectively, in 50 ml of 1 M aqueous KI solution (stirring rate 100 rpm); (*4, 5*) the same as (*3*), but with additional bubbling of air at a rate of 30 and 50 cm^3 min^{-1}, respectively; (*6*) 0.5 g of silica gel impregnated with 2 ml of 1 M KI solution in oxidation in air.

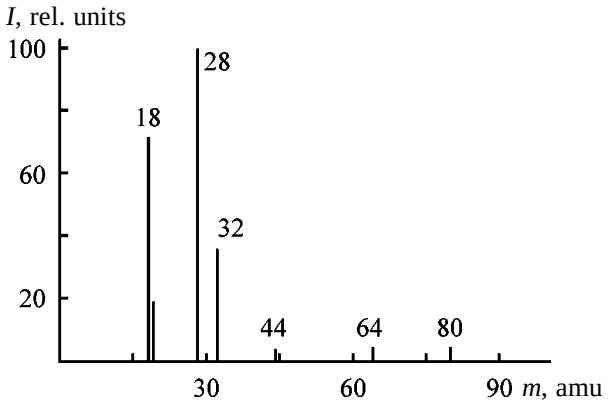

Fig. 5. Mass spectra of desorption products from the surface of silica gel impregnated with 1 M solution of $(NH_4)_2S$ and then kept in air for 20 min. (*I*) Relative signal intensity and (*m*) mass of singly ionized particles.

investigated, and many similar (which is not improbable) processes are of fundamental importance in the nature in view of the overwhelming predominance of silica on the Earth's surface and also in water basins, in suspended and precipitated states.

Finally, it should be noted that the alternative hypothetical reason for "cold" oxidative catalysis on SiO_2, based on the concepts (extensively developed in the 1970–1980s [18, 19]) assuming that coordination-unsaturated electron-acceptor centers are present on the surface of amorphous varieties of silica, is rather unlikely. It is difficult to admit of the possibility of firm adsorption and strong polarization of reagents, necessary for lowering the activation barriers of oxi-

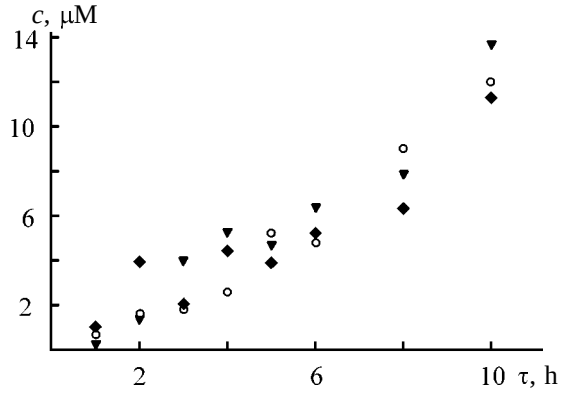

Fig. 6. Total concentration c of sulfite and sulfate ions vs. time τ of oxidation in a suspension of 1 g of SiO_2 in 50 ml of 1 M $(NH_4)_2S$ solution at a stirring rate of 100 rpm (three sets of experiments are represented).

dation processes. Moreover, the probability of reactions (1), (3), and (4) at coordination centers of silica gel is strongly limited by the action of the topochemical factor consisting in the necessity for attachment of several particles of the probable reactants in close proximity to ensure their interaction.

CONCLUSIONS

(1) The iodide ion is oxidized with oxygen at room temperature in suspensions of silica gel in aqueous KI solution to give I_3^- species.

(2) Stepwise oxidation of the sulfide ion with oxygen in suspensions of silica gel in aqueous solution of $(NH_4)_2S$, also proceeding at room temperature, gives elemental sulfur, SO_2, SO_3, and the anions SO_3^{2-} and SO_4^{2-}.

(3) The obtained results suggest that the electronically excited singlet species $^1O_2$ is involved in the oxidation reactions and serve as indirect evidence in favor of the hypothesis that oxygen can be activated on the silica surface.

ACKNOWLEDGMENT

The authors are grateful to the College of Natural Sciences, University of Northern Iowa, for the financial support of the study.

REFERENCES

1. March, J., *Advanced Organic Chemistry*, New York: Wiley, 1985.
2. Wasserman, H.H. and Ives, J.L., *Tetrahedron*, 1981, vol. 37, pp. 1825–1852.
3. Shen, H.R., Spikes, J.D., Smith, C.J., and Kopecek, J., *J. Photochem. Photobiol. A: Chem.*, 2000, vol. 130, pp. 1–6.
4. Lledias, F. and Hansberg, W., *Photochem. Photobiol.*, 1999, vol. 70, pp. 887–892.
5. Solterman, A.T., Luiz, M., Biasutty, M.A., *et al.*, *J. Photochem. Photobiol. A: Chem.*, 1999, vol. 129, pp. 25–32.
6. Toutchkine, A. and Clennan, E.L., *J. Am. Chem. Soc.*, 2000, vol. 122, pp. 1834–1835.
7. Figueiredo, T.L.C., Johnstone, R.A.W., Sorensen, A.P.M., *et al.*, *Photochem. Photobiol.*, 1999, vol. 69, pp. 517–528.
8. Waiblinger, F., Keck, J., Fluegge, A.P., *et al.*, *J. Photochem. Photobiol. A: Chem.*, 1999, vol. 126, pp. 43–49.
9. Tung, C.H., Wang, H., and Ying, Yu.M., *J. Am. Chem. Soc.*, 1998, vol. 120, pp. 5179–5186.
10. Clennan, E.L. and Sram, J.P., *Tetrahedron Lett.*, 1999, vol. 40, pp. 5275–5278.
11. Zhou, W. and Clennan, E.L., *Org. Lett.*, 2000, vol. 2, pp. 437–440.
12. Nardello, V., Aubry, J.M., and Linker, T., *Photochem. Photobiol.*, 1999, vol. 70, pp. 524–530.
13. Aubriet, F., Maunit, B., Courrier, B., and Muller, J.F., *Rapid Commun. Mass Spectrom.*, 1997, vol. 11, pp. 1596–1601.
14. Maunit, B., Hachimi, A., Manuelly, P., *et al.*, *Int. J. Mass Spectrom. Ion Processes*, 1996, vol. 156, pp. 173–187.
15. Herron, J.T. and Huie, R.E., *Ann. N.Y. Acad. Sci.*, 1970, vol. 171, pp. 229–238.
16. Radel, S.R. and Navidi, M.H., *Chemistry*, New York: West, 1990.
17. Kepka, A.G. and Grossweiner, L.I., *Photochem. Photobiol.*, 1973, vol. 18, pp. 49–61.
18. Kiselev, V.F., *Poverkhnostnye yavleniya v poluprovodnikakh i dielektrikakh* (Surface Phenomena in Semiconductors and Insulators), Moscow: Nauka, 1970.
19. Chuiko, A.A., *Teor. Eksp. Khim.*, 1987, vol. 23, no. 5, pp. 597–618.

Russian Journal of Applied Chemistry, Vol. 74, No. 1, 2001, pp. 63–65. Translated from Zhurnal Prikladnoi Khimii, Vol. 74, No. 1, 2001, pp. 61–63.

CATALYSIS

Heterogeneous-Catalytic Dimerization of Methanol

L. N. Kurina, A. K. Golovko, S. I. Galanov, E. Yu. Voronov, O. I. Sidorova, and S. S. Novikov

Tomsk State University, Tomsk, Russia
Institute of Petroleum Chemistry, Siberian Division, Russian Academy of Sciences, Tomsk, Russia

Received August 1, 2000

Abstract—Oxide systems supported by α-Al_2O_3 and MgO were studied in oxidative dimerization of methanol. The highest selectivity is exhibited by tin oxide promoted with Na_2O and La_2O_3 supported by magnesium oxide. Reactions of partial oxidation and etherification of methanol and ethylene glycol proceed on this system to the same extent as dimerization of methanol to ethylene glycol.

Ethylene glycol, one of the most important products of petrochemical synthesis, is commonly obtained from ethylene raw materials whose price is steadily rising. A search for new routes to ethylene glycol without using ethylene is of practical interest. The most promising are techniques using as raw material directly synthesis gas or products of its processing (formaldehyde, methanol) [1, 2]. The already proposed procedures of ethylene glycol synthesis are multistage, endothermic, and economically unfeasible. A possibility was demonstrated [3, 4] of homogeneous oxidative pyrolysis of methanol to give ethylene glycol in up to 8% yield. In [5], it was proposed to synthesize dimethyl ethylene glycol ether by oxidation of dimethyl ether and to isolate ethylene glycol by subsequent hydrolysis. Heterogeneous catalytic dimerization of methanol into ethylene glycol in a flow-through reactor in a single stage may show more promise than the already proposed variations of synthesis. In addition to being practically important, this process is interesting in theoretical regard. The reactions of oxidative dimerization of methane and hydrocarbons in which a hydrogen atom in methane is replaced by an alkyl or aryl group (propylene, toluene) are well understood [6]. At the same time, reactions of dimerization of heterosubstituted methanes, e.g., CH_3OH, are little studied.

EXPERIMENTAL

Oxide supported catalysts were obtained by impregnation of α-Al_2O_3 and MgO supports with salt solutions and subsequent drying at 150°C for 4 h and calcination at 800°C for 6 h.

Experiments were done in a flow-through installation with a fixed catalyst bed. The ratio $CH_3OH : O_2 : N_2 = 4 : 1 : 4$, the time of contact was varied between 1 and 0.5 s. The reaction products were analyzed chromatographically. The reaction gases were analyzed for the content of CO_2, CO, O_2, N_2, and H_2 on an LKhM-80 chromatograph by a procedure described in [7]. The condensate was analyzed on a Khrom-5 chromatograph with a flame-ionization detector and 2.4-m-long column packed with Separon-SDA sorbent. Analysis conditions: column temperature 100°C; time 10 min, with subsequent programmed heating to 205°C at a rate of 10 deg min^{-1}; flow rate of carrier-gas helium 1.8×10^{-3} m^3 h^{-1}. The selectivity with respect to dimerization products was calculated as a total for ethylene glycol and its conversion products: glycolaldehyde, glyoxal, and di- and monomethyl ethers.

The phase composition of samples was determined on a DRON-3M diffractometer with CuK_α radiation. The specific surface area of the samples was measured chromatographically on the basis of low-temperature adsorption of argon.

The catalysts under study and their properties are characterized in Table 1. The key factor in choosing the catalytic systems was high selectivity in dimerization of methane (sample nos. 1–3, 5, 6) [6, 8, 9], toluene (sample no. 3) [6], and dimethyl ether (sample no. 4) [5].

Catalytic system nos. 1–4 promote nonselective oxidation of methanol to carbon oxides or its partial oxidation to formaldehyde, with products of dimerization found in the condensate in trace amounts. A study of the process of methanol dimerization in the batch mode on the lead–tin system, performed by

1070-4272/01/7401-0063$25.00

Table 1. Characteristics of catalysts

Sample no.	Catalyst	Composition, wt %	Phase composition	S_{sp}, $m^2\ g^{-1}$
1	$BaO/\alpha\text{-}Al_2O_3$	20 BaO	BaO, $\alpha\text{-}Al_2O_3$	1.1
2	$MgO/\alpha\text{-}Al_2O_3$	20 MgO	MgO, $\alpha\text{-}Al_2O_3$	0.9
3	$PbO–SnO_2/\alpha\text{-}Al_2O_3$	16 PbO, 4 SnO_2	SnO_2, $PbO_{rhombic}$, PbO_{tetr}, Pb_2SnO_4, $\alpha\text{-}Al_2O_3$	2.2
4	$Na_2O–SnO_2/MgO$	5 Na_2O, 5 SnO_2	Na_2SnO_3, MgO	9.5
5	$Na_2O–SnO_2/MgO$	10 Na_2O, 10 SnO_2	Na_2SnO_3, $MgSnO_3$, MgO	6.5
6	La_2O_3/MgO	5 La_2O_3	La_2O_3, MgO	9.7

Table 2. Effect of temperature on the ratio of methanol dimerization products in the condensate

Product	Content of products, mol %, at indicated temperature, °C			
	500	550	570	600
Catalyst 5% Na_2O–5% SnO_2/MgO				
Ethylene glycol	80 ± 0.5	66 ± 0.5	22 ± 0.5	24 ± 0.5
Glyoxal	9 ± 1	15 ± 1	18 ± 1	16 ± 1
Glycolaldehyde	5 ± 1	12 ± 1	26 ± 1	30 ± 1
Ethylene glycol methyl ether	4 ± 0.5	6 ± 0.5	14 ± 0.5	15 ± 0.5
Ethylene glycol dimethyl ether	1 ± 0.5	1 ± 0.5	17 ± 0.5	12 ± 0.5
Catalyst 10% Na_2O–10% SnO_2/MgO				
Ethylene glycol	88 ± 0.5	76 ± 0.5	16 ± 0.5	8 ± 0.5
Glyoxal	2 ± 1	4 ± 1	17 ± 1	24 ± 1
Glycolaldehyde	–	3 ± 1	26 ± 1	16 ± 1
Ethylene glycol methyl ether	10 ± 0.5	11 ± 0.5	22 ± 0.5	34 ± 0.5
Ethylene glycol dimethyl ether	–	4 ± 0.5	18 ± 0.5	18 ± 0.5

analogy with toluene dimerization [6] by alternately passing through the catalyst the oxidative mixture and methanol, also failed to give positive results since lead oxide was reduced to metal in the catalyst reduction cycle, and methanol underwent catalytic cracking with carbonization of the catalyst surface.

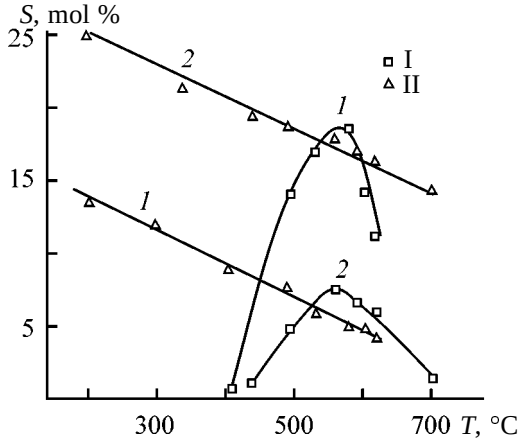

Selectivity *S* with respect to products of (I) dimerization and (II) partial oxidation of methanol vs. reaction temperature *T*. Catalyst: (*1*) 10% Na_2O–10% SnO_2/MgO and (*2–5*) 5% Na_2O–5% SnO_2/MgO.

It was found in studying the $Na_2O–SnO_2/MgO$ systems at reaction temperatures of up to 350°C that the main reactions also include partial oxidation of methanol to formaldehyde and its deep oxidation to CO_x (with mainly formaldehyde and methylal present among reaction products). The methanol conversion is about 25%. Trace amounts of ethylene glycol are detected in the condensate. Raising the temperature of the reaction on $Na_2O–SnO_2/MgO$ catalysts (nos. 4, 5) not only led to higher conversion, but also improved the selectivity with respect to the dimerization products (see figure). It should be noted that adiabatic heating-up of the catalyst bed within 30–40°C from the preset temperature was observed at temperatures of 400°C and higher.

The distribution of methane dimerization products in the condensate for magnesium–tin systems is presented in Table 2 in relation to temperature. The overall selectivity with respect to products of partial oxi-

dation and dimerization is not higher than 50% over the entire range of temperatures studied. Raising the reaction temperature to above 550°C leads to higher share of the reactions of nonselective oxidation and thermal decomposition of methanol and its conversion products to CO_x. Close temperature dependences of methanol conversion, selectivity, and distribution of dimerization products were obtained for the La_2O_3/MgO catalyst. The yield of dimerization products also increases beginning with 300°C, with the maximum yield observed at a reaction temperature of 550°C (Table 3).

According to the obtained data, the following scheme of oxidative transformations of methanol on magnesium–tin and lanthanum–magnesium systems can be suggested in the form of a set of successive and parallel reactions: dimerization (pathway *1*), partial oxidation of methanol to formaldehyde and formic acid (pathway *2*), partial oxidation of dimerization products (pathway *2*), etherification and esterification (pathway *3*), acetalization (pathway *4*), and deep oxidation and thermal decomposition of products to give CO and CO_2:

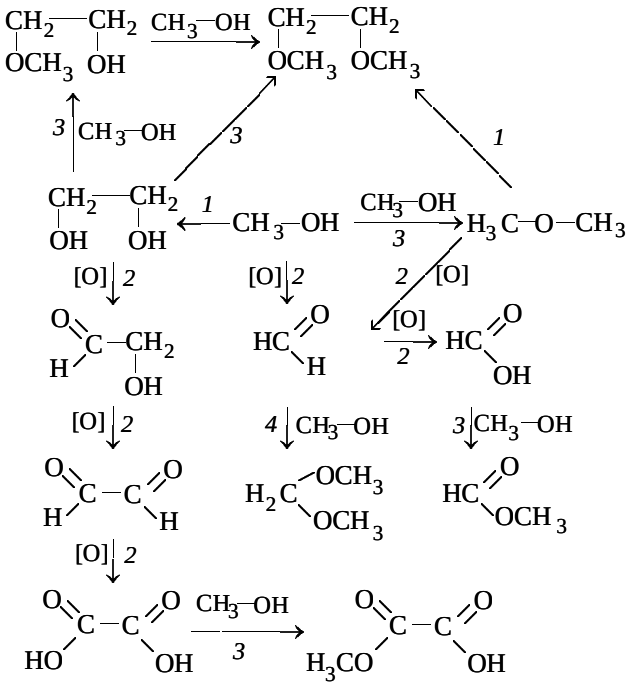

At longer time of contact and high conversion of methanol its major part is consumed for CO_x formation. The efficiency of the process can be raised by making the time of contact shorter and the methanol conversion lower; in this case, the share of undesirable reactions of partial ethylene glycol oxidation and etherification decreases. Owing to the large difference in evaporation temperature between methanol and ethylene glycol, recycling of the starting raw materials can be readily implemented.

Table 3. Effect of temperature on the yield of methanol conversion products. Catalyst La_2O_3/MgO

T, °C	Methanol conversion, %	Yield of products, mol %	
		partial oxidation	dimerization
200	6.1	2.1	–
250	7.3	2.4	–
350	12.0	4.0	–
450	24.1	15.3	14.2
500	32.4	15.5	16.7
570	42.2	16.2	28.4
580	63.0	16.4	21.5
600	74.2	15.8	24.2

REFERENCES

1. Sheldon, R.A., *Chemicals from Synthesis Gas: Catalytic Reactions of CO and H_2*, Dordrecht: Reidel, 1983.
2. Korneeva, G.A. and Loktev, S.M., *Usp. Khim.*, 1989, vol. 58, no. 1, pp. 118–137.
3. GDR Patent 268 684.
4. Sprangenberg, H.-J., Lachmann, J., Borger, I., *et al.*, *Z. Phys. Chem.*, 1990, vol. 271, no. 1, pp. 5–16.
5. JPN Appl. 63-27 445.
6. Mamedov, E.A. and Sokolovskii, V.D., *Okislitel'naya degidrodimerizatsiya uglevodorodov* (Oxidative Dehydrodimerization of Hydrocarbons), Novosibirsk: Nauka, 1992.
7. Vigdergauz, M.S., *Gazovaya khromatografiya kak metod issledovaniya nefti* (Gas Chromatography as Method for Studying Oil), Moscow: Nauka, 1973.
8. Kurzina, I.A., Galanov, S.I., Kurina, L.N., and Belousova, V.N., *Zh. Prikl. Khim.*, 1999, vol. 72, no. 2, pp. 242–245.
9. Galanov, A.I., Physicochemical Study of Oxidative Dehydrodimerization of Methane on Oxide Catalysts, *Cand. Sci. Dissertation*, Tomsk, 1998.

Russian Journal of Applied Chemistry, Vol. 74, No. 1, 2001, pp. 66–70. Translated from Zhurnal Prikladnoi Khimii, Vol. 74, No. 1, 2001, pp. 64–68.

CATALYSIS

Effect of Pore Structure of Al–Co–Mo Catalyst on Its Efficiency in Hydrodesulfurization of Black Oil

M. A. Lur'e, L. P. Milova, V. V. Chenets, I. Z. Kurets, L. N. Storozheva, and F. K. Shmidt

Irkutsk State University, Irkutsk, Russia

Received August 1, 2000

Abstract—The effect of the volume of macropores (>100 nm) and pores 10–100 nm in radius in the Al–Co–Mn catalyst on its activity in hydrodesulfurization of black oil produced from West-Siberian oil was studied at varied process parameters.

The steadily growing demand for environmentally clean motor fuels can be satisfied by implementing cracking processing of heavy cuts of oil, from which heteroatoms, and in the first place sulfur, should be removed preliminarily. The growing share of sulfurous and sour oils in petroleum production [1] makes this problem even more acute. A thorough-going method for obtaining high-quality raw materials for manufacture of motor fuels satisfying modern requirements is hydrodesulfurization of petroleum residues with the use of heterogeneous catalysts. However, implementation of such a process is a rather difficult task, primarily due to the nature of heavy oil cuts, which are a complex heterogeneous system whose components are characterized by various elemental compositions, structures, and physicochemical properties. The petroleum residues constitute a colloid system of organic compounds in which asphaltenes (disperse component) are dispersed in mutually soluble oil tars and hydrocarbons.

With the fraction composition of petroleum products becoming heavier, the type of sulfurous compounds changes from thiols to sulfides and thiophenes, the degree of their aromaticity grows, and the reactivity decreases. For example, only structures containing thiophene and 2, 3, or more benzene rings are present in the narrow 425–455°C fraction [2]. About 60–80% of the entire amount of sulfur is contained in residues after oil distillation at atmospheric pressure [3], and about 20% in tars and asphaltenes [4].

The low diffusion rate of high-molecular-weight components of heavy petroleum raw material in the liquid phase and catalyst pores hinders the access of hydrogen and sulfurous compounds to the internal surface of the catalyst, making slower the rate of hydrodesulfurization. Therefore, one of the main requirements to a catalyst is that it should contain a zone of coarse pores, partly obviating the diffusion hindrance and increasing the coverage of the catalyst surface. The available relevant evidence is contradictory. The possible reason is the wide variety of raw materials used in investigations. The pore structure and physicochemical properties of catalysts should be optimized for each particular raw material and required product quality, as it was done in developing a catalyst for hydrodesulfurization of deasphalted vacuum residue produced from West-Siberian oil [5].

Previously, the advantage has been demonstrated of using coarsely porous catalysts for hydrorefining of the residue formed in distillation of products obtained in thermal cracking of vacuum residue [6]. As regards the process of black oil hydrorefining, the effect of the number of macropores (more than 100 nm in diameter) on the efficiency of the Al–Co–Mo catalyst has been studied in 24-h tests at 380°C and 10 MPa [7]. Here we report on the estimated efficiencies of heteroporous Al–Co–Mo catalysts in hydrorefining of black oil at various process parameters and during a longer time (100 and 500 h).

EXPERIMENTAL

In addition to a commercial Al–Co–Mo catalyst, test samples of varied pore structure were used. The γ-Al_2O_3 support for the test catalyst samples was synthesized by the nitrate method, with its pore structure controlled by introducing varied amounts of a 25% $NH_3 \cdot H_2O$ solution into the aluminum hydroxide paste being formed. The catalysts were prepared by successive impregnation of a support, extruded and

1070-4272/01/7401-0066$25.00

Table 1. Pore structure of catalysts

Sample	Distribution of pores, $cm^3\ g^{-1}$, with respect to radius, nm				S_{sp}, $m^2\ g^{-1}$
	>5	5–10	10–100	>100	
A	0.62	0.14	0.45	0.03	140
B	0.42	0.10	0.07	0.25	190
C	0.96	0.06	0.50	0.40	110
Commercial	0.48	0.19	0.23	0.06	200

Table 2. Efficiency of heteroporous catalysts in desulfurization of black oil (420°C, 10 MPa)

Sample	W_s, mg sulfur g^{-1} cat. h^{-1}		$W_s^{in} : W_s^f$	Amount of sulfur removed in 100 h	
	initial	final		g sulfur g^{-1} cat.	g sulfur g^{-1} CP
A	92	25	3.7	3.6	9.8
B	115	21	5.5	3.1	8.2
C	124	38	3.3	5.1	10.8
Commercial	61	14	4.4	2.2	6.7

calcined at 550°C, with solutions of ammonium paramolybdate $(NH_4)_6Mo_7O_{24}$ and cobalt nitrate. The obtained catalyst mass was dried in air for 24 h, at 60–70°C for 2–3 h under an IR lamp with intermittent stirring, and in an oven at 120°C for 4 h. The dried samples were calcined in air at 500°C for 6 h. The concentrations of Mo(VI) and Co(II) in oxide samples were 8.5 ± 0.5 and 3.0 ± 0.2 wt %, respectively. The pore structure was studied by mercury porosimetry. The specific surface area S_{sp} was determined dynamically from thermal desorption of nitrogen. The characteristics of the prepared heteroporous samples and the commercial catalyst are listed in Table 1.

The catalysts were tested for activity in a flow-through installation with a 200-ml reactor without recirculation at hydrogen consumption of 1000 nl l^{-1}. Prior to testing, the catalysts were sulfidized at 400°C, with diesel fraction used as sulfidizing agent. Special-purpose experiments revealed that there is no external-diffusion hindrance of the process of black oil hydrodesulfurization under the adopted conditions.

To evaluate the desulfurizing activity and its dynamics in the tests, the content of sulfur in the starting black oil and periodically taken samples of the hydrogenizate was determined by the method of burning [8]. The catalyst activity was evaluated on the basis of the average apparent rate W and extent α of the process.

The starting black oil contained sulfur, asphaltenes, tars, V, and Ni in amounts of 1.7, 2.0, 2.5 wt %, 27 and 18 ppm, respectively.

Table 2 presents the estimated desulfurization efficiencies of catalysts in the course of 100-h tests at 420°C, pressure of 10 MPa, and initial degrees of desulfurization of 40–50%. The space velocities of black oil supply at a given desulfurization level were in the range from 1 to 3 h^{-1}, depending on the catalyst activity. The amount of condensation products (CPs) deposited on the catalyst surface in the course of operation was determined by the burning method, with a cooled spent catalyst preliminarily washed with diesel fraction and vacuum-treated at 100°C and 2–3 mm Hg.

As seen from Table 2, test samples surpass the commercial catalyst in every respect, which apparently indicates that there is no significant contribution of pores less than 10 nm in radius to the catalyst activity and 10–100-nm pores and macropores play an important role. According to increasing initial desulfurization rate, the test samples form the same sequence (A < B < C) as those arranged in the order of increasing macropore volume (Tables 1, 2). However, according to the retention of activity, final desulfurization rate, and amount of sulfur removed in 100 h, the catalysts are arranged in the order of increasing total volume of 10–100-nm pores and macropores (C > A > B). In the same order the catalysts are arranged according to increasing amount of removed sulfur per unit mass of formed CP. This parameter characterizes the stability of desulfurizing ability with respect to surface coking. Thus, the efficient prolonged operation of a catalyst requires the presence of a sufficient

Table 3. Results obtained in tests with coarsely porous and commercial catalysts (10 MPa)

Sample	*T*, °C	Amount of sulfur removed in 500 h		
		g/100 ml cat.	g l^{-1} cat.	g g^{-1} Mo
C	380	470	9.4	105
Commercial		422	6.4	72
C	420	720	13.3	150
Commercial		515	7.8	87

number of pores 10–100 nm in diameter and macropores. Apparently, with the surface of macropores, which are the most accessible to raw material components, primarily coked and deactivated, the increasing amount of pores 10–100 nm in radius is involved in the process, and it is this fact that ensures the stability of catalyst operation at a sufficient amount of pores of both types.

The results of more prolonged tests with the most efficient sample B and a commercial sample are presented in Fig. 1 and Table 3.

Industrial hydrodesulfurization is performed at elevated temperature, which is associated with the decrease in the desulfurizing activity with time and the necessity for preservation of a prescribed content of sulfur in the product. In this connection, it was of interest to compare the efficiencies of the coarsely porous and commercial samples at temperatures of 380 and 420°C, approximately corresponding to the lower and upper temperature limits of hydrorefining of heavy oil stock. The hydrogen pressure was 10 MPa; space velocity, 2 h^{-1}; catalyst grain size, 3 mm.

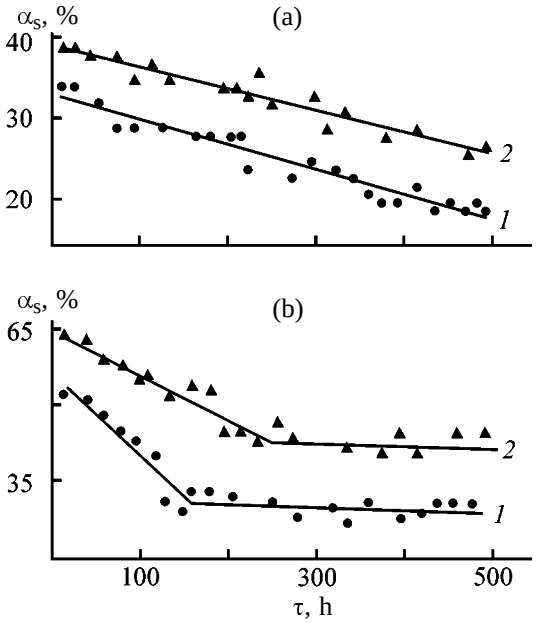

Fig. 1. Extent of black oil hydrodesulfurization, α_s, vs. the time of catalyst operation, τ. P = 10 MPa, V_s = 2 h^{-1}. Catalyst: (*1*) commercial and (*2*) coarsely porous. Temperature (°C): (a) 380 and (b) 420.

Both in the "mild" and "rigorous" temperature regimes, the coarsely porous sample surpasses the commercial catalyst in the extent of desulfurizing, output capacity of unit reactive volume and mass, and efficiency of utilization of the active component during the entire period of testing (Fig. 1, Table 3). With increasing process temperature, the above parameters grow to a greater degree for the coarsely porous sample, compared with the commercial catalyst. The fact that the difference between the catalyst efficiencies grows as the temperature is elevated can be attributed to the increasing diffusion hindrance, this being more pronounced in the case of a narrow-pore commercial sample.

At low process temperature, the activity, on the whole, changes monotonically (Fig. 1a). At high temperature, the deactivation proceeds in the initial part of a run faster than in the final stage (Fig. 1b).

The significant advantage of the coarsely porous sample in the output capacity per unit mass, compared with the value per unit reaction volume (Table 3), is due to the lower (approximately 1.4-fold) bulk density of the given catalyst.

In addition to evaluating the rate of desulfurizing, it seems appropriate to determine the effect exerted by the process parameters on the decomposition rate of asphaltenes contained in the raw material, with account of the fact that the asphaltenes contain ca. 20% sulfur and may strongly affect the course of the hydrorefining as a whole. The amount of asphaltenes in the starting black oil and hydrogenizates was determined by their precipitation in petroleum ether [8]. To solve the problem in hand, the method of mathematical experiment design was employed [9, 10]. The 2^3 design matrix of the trifactorial experiment in coded and natural values and the response functions (the rates of desulfurizing W_s and asphaltene decomposition W_a) are presented in Table 4. The duration of each test was 24 h at an extent of desulfurization in the range 20–30%. The given desulfurization level was ensured at varied temperature, pressure, and catalyst grain size by varying the space velocity of the raw material. It should also be noted that at a grain size of 0.4 mm the black oil desulfurization proceeds in a mode close to kinetic control [7].

Table 4. Experiment matrix in natural and calculated values of factors and quantities

T, °C, x_1	P, MPa, x_2	Grain size, mm, x_3	W_s, mg sulfur g^{-1} cat. h^{-1}				W_a, mg asphaltene g^{-1} cat. h^{-1}			
			commercial catalyst		sample C		commercial catalyst		sample C	
			y_1	$\hat{y}_1$	y_2	$\hat{y}_2$	y_3	$\hat{y}_3$	y_4	$\hat{y}_4$
–380	–2.5	0.4	3.1	3.3	3.7	3.8	–	4.0	0.0	0.0
+400	–2.5	0.4	4.2	4.3	5.9	5.9	5.6	3.4	1.3	1.3
–380	+10.0	0.4	4.1	4.1	4.6	4.8	4.2	4.0	3.3	3.9
+400	+10.0	0.4	5.2	5.1	7.1	7.0	–	4.6	7.5	6.9
–380	–2.5	3	1.4	1.1	2.9	2.8	0.9	0.8	0.0	0.0
+400	–2.5	3	1.9	2.1	3.5	3.8	0.1	0.2	1.8	2.5
–380	+10.0	3	1.8	1.9	3.1	3.0	1.0	0.8	2.0	1.9
+400	+10.0	3	2.9	2.9	6.0	6.0	1.3	1.4	3.2	3.3

The processing of the obtained experimental data gave the following equations.

For the commercial catalyst:

rate of hydrodesulfurization

$$y_1 = 3.1 + 0.5x_1 + 0.4x_2 - 1.1x_3, \quad S\{y\} = 0.17, \; S\{b_i\} = 0.06; \tag{1}$$

rate of cracking hydrogenation of asphaltenes

$$y_3 = 2.4 + 0.3x_2 - 1.6x_3 + 0.3x_1x_2, \quad S\{y\} = 0.20, \; S\{b_i\} = 0.1. \tag{2}$$

For the coarsely porous catalyst:

rate of hydrodesulfurization

$$y_2 = 4.6 + 1.0x_1 + 0.6x_2 - 0.7x_3 + 0.3x_1x_2 + 0.2x_1x_2x_3, \tag{3}$$

$$S\{y\} = 0.24, \; S\{b_i\} = 0.1;$$

rate of cracking hydrogenation of asphaltenes

$$y_4 = 2.4 + 1.1x_1 + 1.6x_2 - 0.6x_3 - 0.8x_2x_3 - 0.4x_1x_2x_3, \tag{4}$$

$$S\{y\} = 0.38, \; S\{b_i\} = 0.15.$$

All the coefficients in Eqs. (1)–(4) are significant (verified using Student's criterion at significance level of 0.05) and describe adequately the investigated range of factor variation ($F_{calc} < F_{f_1 f_2}^{0.05}$).

Analysis of Eqs. (1)–(4) suggests, in the first place, that the coarsely porous catalyst shows higher rate of black oil desulfurization both at the "zero" point (390°C, 6.25 MPa) and under "extreme" conditions (400°C, 10 MPa). The activity (rate of desulfurization) of the coarsely porous sample exceeds that of the commercial catalyst by 50 and 40 rel. %, respectively. Moreover, the sensitivity of the coarsely porous catalyst to the process conditions, i.e., the effect of the factors, much exceeds that for the industrial catalyst. This enables a more accurate adjustment of the conditions for performing the hydrodesulfurization.

The same considerations apply to the process of cracking hydrogenation of asphaltenes. In this case, the effect of the factors is even more pronounced. For example, the W_a value is practically the same for the industrial and coarsely porous catalysts at the zero point (390°C, 6.25 MPa), whereas under more severe process conditions (400°C, 10 MPa) the rate of cracking hydrogenation of asphaltenes is more than 1.8 times higher for the latter.

It is of interest to consider the kinetic aspect of the hydrorefining process. Studying the diffusion kinetics is a rather difficult task. In the given case, the complications are in the first place due to difficulties in experimental determination of the diffusion parameters for the system catalyst–raw material. The hydrorefining of the heavy oil cut consists in the interaction of two disperse systems (catalyst and raw material). All the reactions constituting the process occur on the surface of the polydisperse catalyst under conditions of its continuous deactivation. An in-depth kinetic analysis was beyond the scope of this study. Therefore, we restricted ourselves to a simplified formal approach on the assumption that models relying upon the formal kinetics can be used to find the necessary regime, e.g., to determine the flow rate of

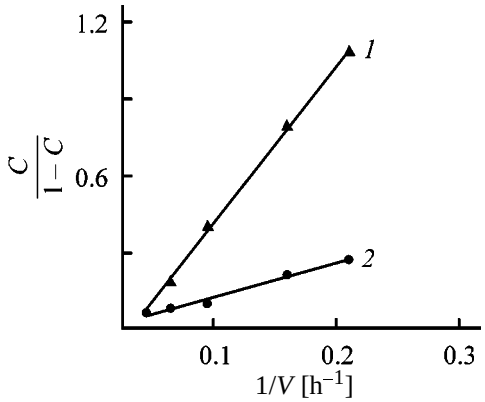

Fig. 2. (*1*) Hydrodesulfurization and (*2*) deasphalting as second-order reactions. Coarse-porous sample, T = 420°C, P = 10 MPa. (*C*) Conversion and (*V*) space velocity of the raw material.

the raw material that would ensure the necessary extent of the process.

Processing of the results of 24-h tests with heteroporous catalysts at 420°C, 10 MPa, and varied time of contact (feed rate 5–30 h^{-1}) demonstrated that, irrespective of the pore structure and grain size of a catalyst, the processes of desulfurization and asphaltene cracking are described by a second-order equation

$$\frac{C}{1-C} = k\omega\frac{1}{V}, \quad (5)$$

where C is the 24-h-average conversion (fraction units), k is the reaction rate constant, ω is the content of a component in the raw material, and V is the raw material space velocity (h^{-1}).

Figure 2 shows, as an example, data obtained for a coarsely porous sample. In all cases the correlation factors were in the range 0.96–0.99.

The revealed second order is obviously only apparent and can be accounted for by differences in reactivity between separate components. Commonly, hydrogenolysis of individual sulfurous compounds is a reaction having true or pseudo-first order with respect to sulfur concentration. Consequently, the rate constant of black oil desulfurizing is bound to decrease steadily as the most reactive compounds are converted. A similar reasoning is valid for reactions of cracking of asphalt–tar components. It is also not improbable that the observed second order is due, to some extent, to the catalyst deactivation inevitably occurring in the course of the process.

CONCLUSION

The highest efficiency in black oil desulfurization is exhibited by the catalyst whose pore structure is characterized by the presence of macropores (>100 nm) and pores 10–100 nm in radius in approximately equal amounts (0.40 ± 0.05 cm^3 g^{-1} each).

The advantage of a catalyst with the pore structure of this kind over a commercial Al–Co–Mo sample is retained at various process parameters. The process of black oil desulfurization is satisfactorily described by a second-order equation.

REFERENCES

1. Sweeney, B.N.C., *Oil Gas J.*, 1993, vol. 91, no. 29, pp. 30–42.
2. Kalechits, I.V., *Sovremennye tendentsii razrabotki protsessov polucheniya malosernistykh kotel'nykh topliv* (Modern Trends in Development of Processes for Obtaining Low-Sulfur Fuel Oils), Moscow: TsNIITEneftekhim, 1969.
3. Eigenson, A.S., Ezhov, B.M., Berg, G.A., *et al.*, *Khim. Tekhnol. Topl. Masel*, 1977, no. 7, pp. 21–26.
4. Kosugi, M., *J. Jpn. Petrol. Inst.*, 1978, vol. 21, no. 5, pp. 302–311.
5. Berg, G.A. and Khabibullin, S.G., *Kataliticheskoe gidrooblagorazhivanie neftyanykh ostatkov* (Catalytic Hydrorefining of Oil Residues), Leningrad: Khimiya, 1986.
6. Lur'e, M.A., Kurets, I.Z., Storozheva, L.N., *et al.*, *Kinet. Katal.*, 1991, vol. 32, no. 6, pp. 1399–1405.
7. Milova, L.P., Lur'e, M.A., Zaidman, N.M., *et al.*, *Kinet. Katal.*, 1983, vol. 24, no. 5, pp. 1115–1120.
8. Zhestkov, D.K., in *Metody analiza organicheskikh soedinenii nefti, ikh smesei i proizvodnykh* (Methods for Analysis of Organic Petroleum Compounds, Their Mixtures, and Derivatives), Moscow: Nauka, 1969, coll. 2, pp. 21–27.
9. Adler, Yu.P., *Planirovanie eksperimenta pri poiske optimal'nykh uslovii* (Experiment Design in a Search for Optimal Conditions), Moscow: Nauka, 1976.
10. Radchenko, E.D., Popov, A.A., Khots, M.S., *et al.*, *Khim. Tekhnol. Topl. Masel*, 1981, no. 3, pp. 31–34.

Russian Journal of Applied Chemistry, Vol. 74, No. 1, 2001, pp. 71–73. Translated from Zhurnal Prikladnoi Khimii, Vol. 74, No. 1, 2001, pp. 69–71.

CATALYSIS

Activity of Polymeric and Zeolite-Containing Catalysts in Production of Methyl *tert*-Butyl Ether

L. M. Koval', A. M. Bazhina, S. S. Safronova, S. A. Perevezentsev, V. A. Kosukhin, V. I. Erofeev, and Yu. V. Ryabov

Tomsk State University, Tomsk, Russia
Department of Scientific and Technical Development, Tomsk Petrochemical Concern, Joint-Stock Company, Tomsk, Russia

Received March 23, 2000; in final form, August 2000

Abstract—The effect of structural and acid characteristics of catalysts of various nature (sulfonic cation exchangers of the KU-23 type and high-silica zeolite of the ZSM-5 type) on their activity and selectivity in production of methyl *tert*-butyl ether from isobutylene and methanol was studied.

A decrease in the toxicity of motor transport exhaust is one of the urgent environmental problems. Significant advances in this field can be reached by using environmentally safe fuel additives. In recent years, various oxygen-containing compounds, lower alcohols and ethers, found a wide use as high-octane components for production of commercial gasolines. They have high octane numbers (>100) and do not form toxic substances in combustion [1]. In addition, the use of oxygen-containing components reduces petroleum expenditure for production of the required amount of commercial gasoline.

Methyl *tert*-butyl ether (MTBE) is the component which most efficiently increases the octane number of unleaded gasolines [2]. The main raw materials for MTBE production are methanol and isobutylene. Isobutylene is the component of the butylene–butadiene fraction (BBF) of petroleum pyrolysis; its content in BBF is 16–18 wt %. Ion-exchange resins are highly efficient and selective catalysts for synthesis of MTBE. However, their use is limited owing to relatively narrow interval of operating temperatures; therefore, selection of the optimal and thermostable catalyst for this process is an urgent problem despite the existence of large-tonnage industrial equipment for MTBE production in advanced countries [3, 4].

In this connection the aim of this work was to study the effect of physicochemical characteristics of KU-23 cation exchangers on the selectivity of MTBE formation from BBF and methanol. We also studied this process in the presence of ZSM-5 zeolite catalyst having a wide range of operating temperatures.

EXPERIMENTAL

The KU-23-16/60 and KU-23-30/100 sulfonic cation exchangers and high-silica zeolite of the ZSM-5 type in H form (H-HSZ) with the silicate ratio SiO_2/Al_2O_3 = 50 were used as catalysts for synthesis of MTBE from methanol and isobutylene. The catalytic activity of the samples was determined on a laboratory flow-type setup with a fixed bed of the catalyst in the temperature range 50–120°C for sulfonic cation exchangers and 80–250°C for H-HSZ at a pressure of 1 MPa; the molar ratio methanol : isobutylene was 1 : 1. Liquid reaction products were analyzed chromatographically on a column packed with 15 wt % PEG 1500 on S-22. Gaseous reaction products were analyzed on a column packed with Al_2O_3.

The pore structure of the samples was studied on a vacuum setup equipped with a McBain quartz balance. Benzene was used as an adsorbate. The pore-volume distribution was evaluated from the isotherms of benzene desorption at 20°C with the use of the Thompson–Kelvin formula. The acidity of the samples was determined spectrophotometrically in aqueous medium with the series of Hammett indicators with pH of transition from 0.8 to 6.4 by the procedure described in [5].

The comparative characteristics of the catalytic activity of the KU-23 and HSZ cation exchangers under the same conditions of synthesis of MTBE from BBF and methanol are presented in Table 1. With selected process parameters [temperature 80°C, pressure 1 MPa, space velocity of raw materials (isobutylene of BBF) 1 h^{-1}, and molar ratio of isobutylene and meth-

1070-4272/01/7401-0071$25.00

Table 1. Results of synthesis of MTBE from BBF isobutylene and methanol. T = 80°C, P = 1 MPa, and w = 1 h^{-1}

Catalyst	Selectivity, wt %			Conversion of isobutylene, wt %
	MTBE	DB*	TB*	
KU-23-16/60	96	0.2	3.8	84
KU-23-30/100	85	13	2	61
H-HSZ-50	68	–	32	17

* (DB) Diisobutylene and (TB) *tert*-butanol.

Table 2. Optimal conditions for synthesis of MTBE from BBF isobutylene and methanol. Space velocity of raw materials 1 h^{-1}

Catalyst	T, °C	P, MPa	S*	K*
			wt %	
KU-23-16/60	80	1	96	84
KU-23-30/100	100	1.5	98	85
H-HSZ-50	150	1	83	25

* (S) Selectivity with respect to MTBE and (C) conversion.

anol 1 : 1], the degree of conversion of isobutylene does not exceed 84% and the maximal selectivity with respect to MTBE reaches 96%. The degree of conversion and the selectivity of formation of MTBE on high-silica zeolite are 17 and 70%, respectively. As a by-product only *tert*-butanol, formed owing to the presence of moisture in raw materials, was detected. At a low metanol : isobutylene ratio and higher temperature isobutylene dimerizes. With increasing temperature, at a certain concentration of reactants, intermolecular dehydration of methanol, hydration of isobutylene, and formation of methyl *sec*-butyl and metabutylene ethers take place.

The dependences of the selectivity and degree of conversion of raw materials (isobutylene of BBF) on the temperature and pressure pass through maxima. The optimal parameters of synthesis ensuring the maximal catalytic activity and selectivity of the studied samples are presented in Table 2. For the KU-23-30/100 sample, the pressure has a positive effect on the selectivity (increase from 85 to 98%) and catalytic activity (the degree of conversion of isobutylene increases from 60 to 85%). For the KU-23-16/60 sample, the similar results are observed under mild conditions of synthesis (P = 1 MPa and T = 80°C). The reaction of methanol with isobutylene on H-HSZ proceeds at 150°C and is characterized by low conversion of isobutylene.

As was shown previously [6] and in this work, the catalyst activity depends on many factors, in particular, on its structural characteristics. The studied sulfonic cation exchangers are wide-porous (16/60) and narrow-porous (30/100). The equivalent pore diameters dominating in the samples are presented in Table 3. The experimental data show that the sample of cation exchanger with wider pores, KU-23-16/60 (d > 15 nm), exhibits the highest activity in production of MTBE from BBF and methanol under the same conditions. For the narrow-porous sample, KU-23-30/100 (d = 1 mn), a significant increase in the yield of product and conversion of isobutylene is observed with increase in pressure by a factor of 1.5. Under the selected conditions of MTBE synthesis, the H-HSZ narrow-porous sample of the ZSM-5 type exhibits low catalytic activity as well. It is evident that in the case of sulfonic cation exchanger KU-23-16/60 the system of wide transition pores facilitates mass transfer in the catalyst granules, which, in turn, increases the yield of the target product and the degree of conversion of isobutylene.

The difference in the catalytic activity of the samples is also related to their acid–base characteristics caused by the acidic groups $-SO_2-OH$ in the styrene–divinylbenzene matrix of ion-exchange resins or Lewis or Brønsted acid centers in the case of H-HSZ. The measurement of the total acidity of the samples and differentiation of acid centers with respect to their strength (Table 3) showed that on the surface of the samples there are several types of acid centers different in the strength and that the strong acid centers corresponding to the pK of the indicator transition 2.5 prevail. The KU-23-16/60 sample with increased concentration of acid centers (151.7×10^{-7} mol m^{-2}) exhibits a high catalytic activity, and for low-efficient catalyst in synthesis of MTBE (KU-23-30/100 sample) the concentration of acid groups is two orders of magnitute lower (1.7×10^{-7} mol m^{-2}). The feature of distribution of acid centers on the surface of the zeolite catalyst with respect to strength is the same as in the case of sulfonic cation exchanger 30/100, and their concentration is approximately 0.4×10^{-7} mol m^{-2}. The difference in the catalytic characteristics of these two samples can be apparently caused by severe diffusion deceleration in the H-HSZ sample, which makes difficult mass transfer along the narrow zeolite pores.

CONCLUSIONS

(1) The KU-23 sulfonic cation exchanger with coarse pores and maximal concentration of acid cen-

Table 3. Acid characteristics and pore diameters *d* of the catalyst samples

Catalyst	Concentration of acid centers $C \times 10^7$, mol m^{-2}								*d*, nm
	at indicated pH of indicator transition							total	
	0.8	1.3	2.5	3.5	4.1	4.9	6.4		
KU-23-16/60	6.0	31.6	77.0	14.0	3.0	4.7	15.0	151.7	3.37 17.3 25.5
KU-23-30/100	0.1	0.4	0.9	0.07	0.06	0.01	0.1	1.7	1
H-HSZ-50	0.01	0.04	0.3	0.04	0.01	0.00	0.04	0.4	0.93

ters on the surface exhibits the highest activity in catalytic synthesis of methyl *tert*-butyl ether.

(2) Synthesis on the narrow-porous catalysts is also possible at increased pressure, which makes promising the use of microporous high-silica zeolites, exhibiting specific acid characteristics and high heat resistance, as catalysts for synthesis of methyl *tert*-butyl ether.

REFERENCES

1. Chaplits, D.N., Stryakhileva, M.N., Pavlova, I.N., *et al.*, *Vydelenie izobutilena i izoamilenov iz uglevodorodnykh fraktsii: Tematicheskii obzor* (Recovery of Isobutylene and Isoamylenes from Hydrocarbon Fractions: A Topical Review), Moscow: TsNIITEneftekhim, 1981.
2. Anichkin, A.I., Gorshkov, V.A., Kolobrodov, V.P., and Pavlov, S.Yu., *Khim. Tekhnol. Topl. Masel*, 1998, no. 2, p. 42.
3. Girolamo, M.D. and Tagliabue, L., *Catal. Today*, 1999, no. 52, pp. 307–319.
4. Stryakhileva, M.N., Krymova, G.N., Chaplits, D.N., *et al.*, *Proizvodstvo metil-tret-alkilovykh efirov – vysokooktanovykh komponentov benzinov: Tematicheskii obzor* (Production of Methyl *tert*-Alkyl Ethers, High-Octane Components of Gasolines: Topical Review), Moscow: TsNIITEneftekhim, 1988.
5. Nechiporenko, A.P., Burenina, T.A., and Kol'tsov, S.I., *Zh. Obshch. Khim.*, 1985, vol. 55, no. 9, pp. 1907–1912.
6. Cherches, B.Kh., Shunkevich, A.A., Belotserkovskaya, T.N., and Elizarov, Yu.G., *Zh. Prikl. Khim.*, 1999, vol. 72, no. 4, pp. 623–627.

Russian Journal of Applied Chemistry, Vol. 74, No. 1, 2001, pp. 74–76. Translated from Zhurnal Prikladnoi Khimii, Vol. 74, No. 1, 2001, pp. 71–73.

CATALYSIS

Kinetics of Phase-Transfer Formation of Potassium Carbazolate, Catalyzed with 18-Crown-6

I. B. Frolova and O. I. Kachurin

Litvinenko Institute of Physical Organic Chemistry and Coal Chemistry, Ukrainian National Academy of Sciences, Donetsk, Ukraine

Received April 4, 1998; in final form, June 2000

Abstract—Kinetics of formation of potassium carbazolate in the system liquid–solid, catalyzed with 18-crown-6, was studied. Applicability of the previously proposed macrokinetic model to this process was demonstrated.

Previously [1] we showed that in the absence of catalysts the phase-transfer formation of potassium carbazolate

$$(C_{12}H_8NH)_{sol} + KOH_{solid} \underset{k_-}{\overset{k}{\rightleftarrows}} (C_{12}H_8NK)_{solid} + (H_2O)_{liq}$$

follows zero-order kinetics with respect to concentration of carbazole in the toluene solution. Based on this fact, we proposed the adequate mathematic model considering the transport of hydroxide ion to the phase boundary organic phase–aqueous interphase as the stage limiting the reaction kinetics:

$$\frac{dx}{d\tau} = k\frac{m_b^{2/3}}{w} - k_- xw, \quad (1)$$

where x and m_b are the current amounts of carbazolate and KOH (mmol), respectively, and w is the amount of "free" water given by the equilibrium

$$KOH + H_2O \underset{}{\overset{K}{\rightleftarrows}} KOH \cdot H_2O. \quad (2)$$

In this work we studied the effect on this process of 18-crown-6 (18-C-6), the commonly used phase-transfer catalyst able to transport KOH into the toluene medium [2].

The procedure was similar to that described previously [1]. The process was carried out in refluxing toluene (110°C) with powdered KOH (grain size 20 ± 10 μm) in a device equipped with a stirrer and a reflux condenser. In all runs the same amount of KOH (1.5 mmol) of the same dispersity was used and the amount of carbazole was varied from 1 to 3 mmol, which corresponded to variation of its concentration in the solution from 16.8 to 50 mM. The concentration of 18-C-6 was varied from 3 to 10 mM.

The dependence of the initial rate of the process on the catalyst concentration is presented in Table 1 and Fig. 1. This dependence is an ascending curve with saturation. In the initial portion of the curve (up to [18-C-6] ≈ 5 mM) the initial rate (mmol min^{-1}) increases approximately linearly with increasing concentration of the catalyst:

$$V_{init} \times 10^2 = (0.9 \pm 0.5) + (0.91 \pm 0.14)[18\text{-Cr-6}],$$

$$R = 0.977, \; S = 0.53.$$

It is likely that at given charges (1.5 mmol of KOH and 1 mmol of carbazole in 60 ml of toluene) the maximal catalytic effect is reached at [18-C-6] ≈ 6 mM and corresponds to the initial rate of 0.06 mmol min^{-1}.

Table 1. Initial rate of formation of potassium carbazolate V_{init} and kinetic coefficients of Eq. (1) at various concentrations of 18-crown-6*

C, mM	$V_{init} \times 10^2$, mmol min^{-1}	$k \times 10^2$, $mmol^{4/3}$ min^{-1}	$k_- \times 10^2$, $mmol^{-1}$ min^{-1}
0 [1]	0.9	1.1 ± 0.3	2.3 ± 0.5
3.0	3.2 ± 0.6	4.2 ± 0.7	2.2 ± 0.4
4.0	5.1**		
5.0	5.2 ± 0.3	6.7 ± 0.4	2.4 ± 0.3
7.5	6.4 ± 0.2	8.5 ± 0.3	2.1 ± 0.4
10.0	6.0 ± 0.1	8.0 ± 0.1	4.3 ± 0.9

* Charge (±0.05 mmol): carbazole 1.00, KOH 1.50, H_2O 1.69, and toluene 60 ml; 110°C.

** Data of single run.

1070-4272/01/7401-0074$25.00 © 2001 MAIK "Nauka/Interperiodica"

As seen from data listed in Table 2, an increase in the carbazole concentration in the solution by a factor of 3 at a constant amount of KOH does not substantially affect the initial rate of the process; this is true for the state of the maximal catalysis efficiency reached with the given catalyst ([18-C-6] = 7.5 mM). Thus, as in the case of the noncatalyzed process, under catalysis with crown ether the process rate is limited by the transport of the reagent to the phase boundary aqueous interphase–organic phase; the reaction proceeds not in the bulk of the organic phase but at the phase boundary or in the vicinity of the phase boundary. It is well known that aqueous interphase at the surface of solid salts or alkalis (ω-phase) efficiently sorbs the phase-transfer catalyst from the organic phase [3]. It is likely that the phase-transfer catalyst dissolved in the ω-phase facilitates the reagent transport in the bulk of this phase between the solid | liquid and liquid | liquid phase boundaries. This mechanism can easily explain the saturability of the catalytic effect of the phase-transfer catalyst.

Since, as mentioned above, potassium carbazolate is formed (and also hydrolyzed) at the liquid | liquid phase boundary, the process rate, if only in view of mathematical formalism, should be described by macrokinetic model (1). This suggestion was verified by the mathematical simulation [1]. This procedure is based on simultaneous solution of differential kinetic equation (1) and algebraic equation corresponding to equilibrium (2). The calculation was carried out by numerical integration by the second-order Runge–Kutta procedure. As seen from Fig. 2, the dynamics of accumulation of carbazolate during the experiment is adequately described by this mathematical model with appropriate values of kinetic coefficients k, k_-, and K. The averages of k, k_-, and $V_{init} = k(m_b)_0^{2/3}/w_0$ (from 3–4 similar runs) are listed in Table 1. It should be noted that the numerical values of k_- and $K = 0.02$ are almost the same as in the case of the noncatalyzed process [1], which additionally suggests the identity of the mechanisms of both processes.

EXPERIMENTAL

The experimental procedure differed from that described in [1] only in the method of monitoring the course of the reaction. Potassium carbazolate formed in the catalyzed process occurs partially in the form of the complex with crown ether, slowly crystallizing from the filtered toluene solution. Therefore, the amount of unchanged carbazole was determined as the difference between the total content of carbazole in the toluene sample treated with water (spectrophotometrically, as described in [1]) and the amount of potassium ions in the aqueous extract of this sample. The content of potassium ions was determined using a pH-673m device equipped with an EM-K-01 ion-selective electrode. The potentiometric data were processed using the calibration plots.

Experiments were repeated no less than three times. The results of calculations given in this work are the averages with their root-mean-square deviations.

The initial content of water in the reaction mixtures was evaluated as the sum of the amounts of water added with alkali (~15%) and toluene (~0.03%).

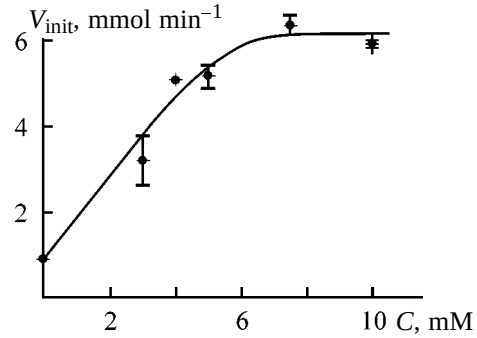

Fig. 1. Initial rate of formation of potassium carbazolate V_{init} as a function of concentration of 18-crown-6 C.

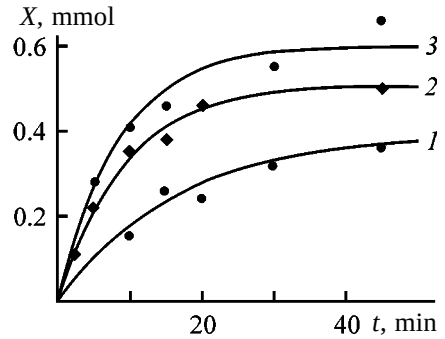

Fig. 2. Calculated (curves) and experimental (points) dynamics of accumulation of potassium carbazolate (X). (t) Reaction time. 18-C-6 concentration (mM): (*1*) 3.0, (*2*) 5.0, and (*3*) 7.5.

Table 2. Initial rates of formation of potassium carbazolate V_{init} at various concentrations of carbazole C_c^*

Carbazole amount, mmol	C_c, mM	$V_{init} \times 10^2$, mmol min^{-1}	Number of runs
1.0	16.8	6.4 ± 0.2	3
2.0	33.3	8.4 ± 0.6	3
3.0	50.0	7.7 ± 0.5	4

* Toluene volume 60 ml; KOH and H_2O amounts 1.50 and 1.69 mmol, respectively; [18-C-6] 7.5 mM; 110°C.

18-Crown-6 was added to the reaction mixtures in the form of solution with given concentration, which was prepared by dissolution in toluene of the sample recrystallized from acetonitrile.

CONCLUSIONS

(1) 18-Crown-6 catalyzes the phase-transfer formation of potassium carbazolate in the system solid KOH–toluene at 110°C, providing the maximal sixfold increase in the initial rate of the process.

(2) Under conditions of the maximal efficiency of phase-transfer catalysis with 18-crown-6, formation of potassium carabazolate follows the zero-order kinetics with respect to carbazole concentration in the toluene solution.

(3) The kinetics of the catalyzed formation of potassium carbazolate is adequately described by the macrokinetic model proposed previously for the similar noncatalyzed process, which suggests the identity of the mechanisms of these processes.

REFERENCES

1. Frolova, I.B., Okhrimenko, Z.A., and Kachurin, O.I., *Zh. Prikl. Khim.*, 1998, vol. 71, no. 9, pp. 1478–1482.
2. Kachurin, O.I., Frolova, I.B., and Okhrimenko, Z.A., *Ukr. Khim. Zh.*, 1989, vol. 55, no. 7, pp. 749–752.
3. Liotta, S.L., Burgess, I.M., Ray, S.S., *et al*., *Phase-Transfer Catalysis. New Chemistry, Catalysts, and Applications*, Startks, Ch.M., Ed., Washington, DC: Am. Chem. Soc., 1987. Translated under the title *Mezhfaznyi kataliz: Khimiya, katalizatory i primenenie*, Moscow: Khimiya, 1995, pp. 20–25.

Russian Journal of Applied Chemistry, Vol. 74, No. 1, 2001, pp. 77–81. Translated from Zhurnal Prikladnoi Khimii, Vol. 74, No. 1, 2001, pp. 74–78.

PRODUCTION AND USE OF NEW MATERIALS

Silicon Dioxide Modified with Fluorine

E. I. Mel'nichenko, M. D. Koryakova, V. M. Nikitin, G. F. Krysenko, and N. V. Speshneva

Institute of Chemistry, Far East Division, Russian Academy of Sciences, Vladivostok, Russia

Received June 3, 1999; in final form, June 2000

Abstract—IR spectroscopy and X-ray phase and chemical analyses were used to study the physicochemical properties of fluoride-containing amorphous silicon dioxide obtained by hydrolysis of $(NH_4)_2SiF_6$, and its previously unknown biocide properties were discovered. Results of biotesting are presented.

Alkaline hydrolysis of $(NH_4)_2SiF_6$ gives an amorphous porous mass with hydrated surface, which is an active silica filler and is known as "white black" [1].

A distinctive feature of silica gel obtained by hydrolysis of the SiF_6^{2-} ion (or SiF_4) is the presence of fluoride ions in it [2, 3]. The surface of the silicon dioxide prepared by this procedure is hydrophobic rather than hydrophilic [4]. However, the presence of residual fluorine in silicon dioxide has not been related to any specific physicochemical properties of silica gel and, therefore, such silicon dioxide was not classed with fluoride materials.

With account of the fact that ammonium hexafluorosilicate occupies a prominent place in developing practically all flowsheets for processing of mineral raw materials based on ammonium hydrofluoride and is involved in reagent circulation, the SiO_2 by-product is supposed to be produced in large amounts. This requires closer analysis of the effect exerted by residual fluoride ions on some properties of silicon dioxide and a search for new fields of its application.

The aim of this work was to study the chemical composition and biocide properties of hydrolytic silicon dioxide containing fluoride ions.

EXPERIMENTAL

Fluoride-containing silicon dioxide was isolated by precipitation with ammonia from saturated solution of sublimed $(NH_4)_2SiF_6$. The precipitate was washed with double-distilled water and dried at 90–105°C. Analysis for fluoride ions was made by steam distillation and titration of the distillate with a $Th(NO_3)_4$ solution. A sample obtained upon single washing of the precipitate contained 6.9% fluoride ions, and that furnished by triple washing, 3.2%. Further increase in the number of washings (to 6 or 7) lowered the residual content of fluoride ions to 0.7–0.8%.

The presence of the NH_4^+ ion was judged from the IR spectra. A conventional spectrum did not contain the characteristic bands of the ammonium ion. Only a spectrum taken in a thick layer, at the band intensities of the main substance of 200%, demonstrated the presence of ammonium in hydrolytic silicon dioxide. Chemical analysis for the ammonium ion was done by the Kjeldahl method involving evaporation with a 20% NaOH solution. The empirical formula of hydrolytic silicon dioxide containing fluoride ions and ammonium ions was established by chemical analysis:

Found, %: NH_4^+ 1.8, F^- 6.9.
$(NH_4)_{0.065}SiO_{1.915}F_{0.235}$.
Calculated, %: NH_4^+ 1.82, F^- 6.95.

The biocide activity was evaluated by standard procedures [5]. The Czapek–Dox medium was inoculated with an aqueous suspension of mold spores taken from a building wall infested by fungi. Glass tubes 1 cm high, filled with a substance under study, were placed at the center of a Petri dish inoculated with fungi, and the culture was grown for 2 days in a thermostat. The fungicide activity was determined as the radius of the zone uninfected by fungi.

The algicide activity was evaluated from the action on larvae of *Balanus* barnacles, the most common fouling organisms at the Peter the Great Bay (Sea of Japan). Fluoride ions were leached with seawater (1 l) from 1 g of hydrolytic SiO_2 in the course of 1 and 7 days, with subsequent 2-, 10-, and 100-fold dilution of the leaching solution. Larvae (100–150 specimens) were introduced into the prepared solutions, and the

1070-4272/01/7401-0077$25.00

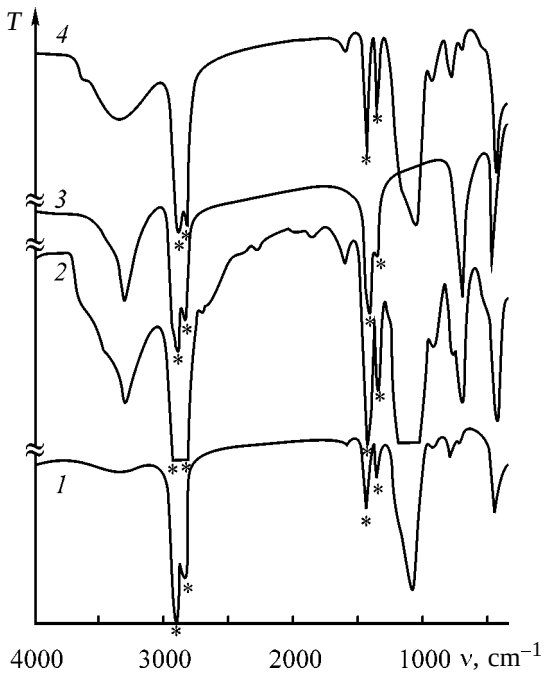

Fig. 1. IR spectra of (*1*–*3*) amorphous SiO_2 with varied content of fluoride ions prepared from $(NH_4)_2SiF_6$ and (*4*) $(NH_4)_2SiF_6$. (*T*) Transmission and (*ν*) wave number. Content of fluoride ions (%): (*1*, *2*) 6.9 and (*3*) 3.

deceased larvae were counted under a binocular microscope in a Bogorov chamber.

The chemistry of silicon dioxide was considered in detail in the biological respect, including its toxicity, in the monograph by Iler [4]. However, no attention was given to the behavior of various kinds of inclusions in SiO_2, especially in its amorphous forms. Depending on the preparation method and nature of inclusions, the SiO_2 properties may vary widely. For example, silicon dioxide obtained from SiF_4 has an extremely low bulk density (0.0248 g cm^{-3}) and can flow like water [4]. To evaluate the effect of fluoride ions on the properties of hydrolytic SiO_2 and determine in what form ammonium ions are incorporated, a highly sensitive method of biotesting was used together with the conventional physicochemical techniques.

According to chemical analysis data, the sample contained 1.8% ammonium ions, whereas the IR spectrum contained no corresponding bands (Fig. 1, spectrum *1*). That is why other conditions were chosen for taking an IR spectrum, which made it possible to confirm the presence of ammonium ions in the sample (Fig. 1, spectrum *2*). In addition to the main Si–O band (1100 cm^{-1}) and bands associated with the ammonium ion (3330 and 1400 cm^{-1}) and water (3400–3600 and 1630 cm^{-1}), four absorption bands were observed at 470, 720, 800, and 945 cm^{-1}. The first two of these completely coincided, as also did the absorption bands related to ammonium ion vibrations, with the spectrum of $(NH_4)_2SiF_6$ (Fig. 1, spectrum *2*) and indicated the presence of this compound in SiO_2. The band at 800 cm^{-1} was assigned to vibrations of the Si–F bond, characteristic of the $[SiX_4]$ structural unit, and the band at 945 cm^{-1} was attributed, using IR spectral tables, to vibrations of the Si–F bond in $[SiF_2]$ and $[SiF_3]$ [6].

Thus, fluoride ions contained in hydrolytic SiO_2 obtained from $(NH_4)_2SiF_6$ are present in the form of coprecipitated $(NH_4)_2SiF_6$ and, according to published data, are bound to surface silicon atoms.

Figure 2a shows a thermogram of this product. It is seen that the sample loses weight mainly in two stages: at 100 and 240°C. The total weight loss is more than 20% [$(NH_4)_2SiF_6$ 8.9% and water the rest].

The gas phase composition was determined on heating a sample in a quartz tube. It was found that only water is lost below 140°C, then, up to 230°C, water and ammonia, and above this temperature $(NH_4)_2SiF_6$ is evaporated. The release of ammonia and the temperature regime correspond to the established thermal behavior of pure $(NH_4)_2SiF_6$.

A comparison of sample spectra before and after annealing in the temperature interval 300–700°C demonstrated that, upon heating, the intensities of the bands at 800 and 945 cm^{-1} (vibrations of the Si–F bond) remained practically unchanged. Therefore, it can be stated that fluoride ions bound to surface silicon atoms are retained up to 700°C. After annealing at this temperature, the sample could absorb 6.5% moisture (Fig. 2b). In contrast to fluoride ions, ammonia was absent in the sample already upon heating to 300°C.

Since SiO_2 gel occludes $(NH_4)_2SiF_6$, it would be expected that this kind of silicon dioxide exhibits biocide activity characteristic of salts of hexafluorosilicic acid.

Biotesting for resistance to fouling organisms (larvae of *Balanus improvisus*) was performed. Table 1 lists data on larval loss in leaching solutions obtained from SiO_2 samples containing 3.2 and 6.9% fluoride ions. In contrast to copper sulfate solutions (1 g per liter of seawater), the loss of larvae was observed in 100% of cases even at 1 : 1 dilution. At stronger dilution, 15–35% of larvae died in leaching solutions, and only 5–8%, in a copper sulfate solution diluted to the

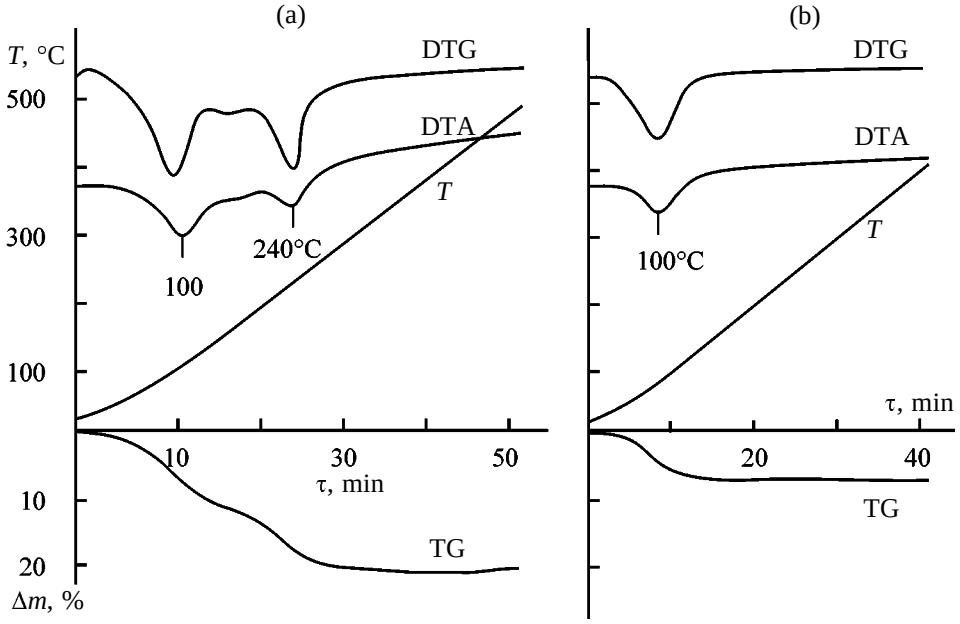

Fig. 2. Thermograms of amorphous SiO_2 precipitated from $(NH_4)_2SiF_6$. (*T*) Temperature, (τ) time, and (Δ*m*) weight loss. SiO_2: (a) freshly precipitated and (b) annealed at 700°C.

same extent, indicating the high biocide properties of SiO_2 precipitated from an $(NH_4)_2SiF_6$ solution.

It was found that, even in a multiply diluted leaching solution, the survived larvae (about 90%) lost their response to light and oxygen and did not restore these functions on being placed in pure seawater.

For comparative evaluation of the toxic properties of silicon dioxide modified with fluorine with respect to *Penicillium*, *Aspergillus*, *Mucor*, and *Cladosporium* mold fungi, biotesting was also performed for $(NH_4)_2SiF_6$, CaF_2, and fluoride-free SiO_2 obtained from rice husk. As a control substance was used copper sulfate distinguished by its fungicide and bactericide properties. Below is given the toxicity series of the substances studied, constructed on the basis of the no-fungus-growth zone radius: $(NH_4)_2SiF_6 \approx SiO_2$ (6.9% F) > $CuSO_4$ > SiO_2 (3.2% F).

Silicon dioxide obtained from rice husk and CaF_2 exhibited zero fungicide activity.

The practically equal toxicities of $(NH_4)_2SiF_6$ and SiO_2 (6.9% F) were a surprising result, as amorphous silicon dioxide is an insoluble and nonaggressive substance, and the content of fluoride ion in its sample was by a factor of 10 lower than in ammonium hexafluorosilicate. This result is very interesting and can be of practical significance.

These data were confirmed by full-scale tests. Inspection of a fungus-infected building wall treated with a lime solution with addition of $(NH_4)_2SiF_6$ (1 : 3 molar ratio) revealed a biocide effect. Table 2 lists the number of fungi at certain intervals of time after the surface treatment.

It can be seen that ammonium hexafluorosilicate, combined with calcium hydroxide, ensures a practically complete elimination of fungi and further protection of the treated surface from infestation with fungi. These data disprove the argument [2] that fluorosilicates are incompatible with CaO or $CaCO_3$ because of the formation of inactive CaF_2. The silica gel formation in the process has been disregarded.

The hydrolysis of $(NH_4)_2SiF_6$ can be described by the equations

$$(NH_4)_2SiF_6 + 4NH_3 + 2H_2O = SiO_2 + 6NH_4F,$$

$$(NH_4)_2SiF_6 + 3Ca(OH)_2 = SiO_2 + 3CaF_2 + 2NH_3 + 4H_2O.$$

Table 1. Behavior of larvae in leaching solutions of fluoride-containing silicon dioxide

Content of fluoride ions in sample	Dilution	Number of larvae dead in 24 h, %
3.2	–	28
6.9	–	100
6.9	1 : 1	100
6.9	1 : 10	35

Table 2. Number of fungi on infested surface

Surface sample	Surface infestation	
	cells m^{-2}	%
Before treatment	520 000	100
After treatment:		
in 1 day	17 000	3.3
in 3 months	5000	1.0
in 6 months	3000	0.6
in 9 months	2500	0.5

Table 3. $(NH_4)_2SiF_6$ leaching from SiO_2. Sample weight 10 g, s : l = 1 : 10

Duration of leaching, weeks	Mass of dry product, mg	Content of fluoride ion in residue, %
1	93.7	6.3
2	187.4	5.7
3	281.1	5.1
4	359.1	4.6
5	437.2	4.1
6	515.3	3.6
7	577.7	3.2
15	870.0	1.3

Reaction of $(NH_4)_2SiF_6$ with calcium hydroxide gives no $CaSiF_6$. The SiO_2 gel precipitating from fluoride solutions occludes $(NH_4)_2SiF_6$. The assumption that the action of SiO_2 on biological objects is due to liberation of $(NH_4)_2SiF_6$ contained in its pores required experimental verification. Therefore, SiO_2 leaching with water was performed, with subsequent chemical and X-ray phase analysis of the leaching product and IR spectral study of SiO_2 after treatment.

Indeed, only $(NH_4)_2SiF_6$ was found in solution. Table 3 illustrates the dynamics of its leaching from a sample with solid to liquid phase ratio of 1 : 10.

It can be seen that only after 15 weeks $(NH_4)_2SiF_6$ completely passed into solution, which indicates low mobility of $(NH_4)_2SiF_6$ molecules entrapped in pores, associated with the structuring of the molecules [7].

On sample treatment with water, all vibration bands characteristic of the starting substance were preserved in the IR spectra of residues for 24 h. However, the intensity of the band at 720 cm^{-1}, associated with the SiF_6^{2-} ion, decreased approximately threefold in a week. This confirmed, with account of the X-ray diffraction pattern of the dry residue, the conclusion that fluoride ions are present in hydrolytic SiO_2 in two forms: as occluded mother liquor [8] and hydroxide groups on the surface, substituted by fluoride ions.

Upon prolonged contact of a sample with water, bands at 3650 cm^{-1} appeared in the SiO_2 spectrum, associated with OH groups in pores (Fig. 1, spectrum *4*). Their appearance was probably due to $(NH_4)_2SiF_6$ removal from pores.

The slow leaching of $(NH_4)_2SiF_6$ from SiO_2 ensures prolonged biocide action of a lime solution with addition of $(NH_4)_2SiF_6$, applied to a surface infested by fungi. The hydrophobic properties of SiO_2 gel, in their turn, do not favor the vital functions of fungal colonies. The antimycotic effect is also enhanced by calcium fluoride filling the pores of the treated surface, which is unfavorable for aerobic fungi.

The obtained data allow hydrolytic silicon dioxide to be regarded as silicon oxyfluoride. With account of the structure of common silica gels $SiO_2 \cdot nH_2O$ and the results of studies of residues and leaching products by chemical, X-ray phase, and IR spectral analyses, additionally confirmed by biotesting, the empirical formula $(NH_4)_{0.065}SiO_{1.915}F_{0.235}$ is more adequately represented as $SiO_{1.98}F_{0.04} \cdot n(NH_4)_2SiF_6$ with $SiO_{1.98}F_{0.04}$ matrix. The matrix formula was found from the mass of ammonium hexafluoride passed into solution. Its amount (8.7% relative to weighed portion and 5.6% in terms of fluoride ions in the starting sample) corresponded to about 1.26% firmly bound fluoride ions belonging to the SiO_2 matrix.

The fraction of surface fluoride ions can be decreased or increased only slightly, which is due to the strictly defined number of OH groups on the surface, of which no more than a half can be replaced by fluoride ions without disruption of the SiO_2 structure [4]. The content of fluoride ions in a sample can only be changed via $(NH_4)_2SiF_6$ absorption.

CONCLUSIONS

(1) IR spectral and chemical analyses demonstrated that amorphous silicon dioxide obtained by hydrolysis of $(NH_4)_2SiF_6$ contains fluoride ions imparting to it biocide properties characteristic of salts of hexafluorosilicic acid.

(2) It is shown that a part of fluoride ions are present in SiO_2 in the form of $(NH_4)_2SiF_6$ occluded in the course of precipitation, with the other part replacing the surface OH^- groups and being preserved upon heating to 700°C. In accordance with the content of

firmly bound fluoride ions (~1.26%), hydrolytic silicon dioxide is regarded as silicon oxyfluoride $SiO_{1.98} \cdot F_{0.04}$ containing up to 8.9% $(NH_4)_2SiF_6$.

REFERENCES

1. Opalovskii, A.A. and Fedotova, T.D., *Gidroftoridy* (Hydrofluorides), Novosibirsk: Nauka, 1973.
2. Ryss, I.G., *Khimiya ftora i ego neorganicheskikh soedinenii* (Chemistry of Fluorine and Its Inorganic Compounds), Moscow: Gos. Nauchno-Tekh. Izd. Khimicheskoi Literatury, 1956.
3. Rakov, E.G. and Teslenko, V.V., *Pirogidroliz neorganicheskikh ftoridov* (Pyrohydrolysis of Inorganic Fluorides), Moscow: Energoatomizdat, 1987.
4. Iler, R.K., *The Chemistry of Silica*, New York: Wiley–Interscience, 1979.
5. *Biopovrezhdeniya* (Biodamage), Il'ichev, V.D., Ed., Moscow: Vysshaya Shkola, 1987.
6. Gordon, A.J. and Ford, R.A., *The Chemist's Companion. A Handbook of Practical Data, Techniques and References*, New York: Wiley–Interscience, 1972.
7. Strelko, V.V., Mitsyuk, B.M., and Vysotskii, Z.Z., *Teor. Eksp. Khim.*, 1967, vol. 3, no. 2, pp. 263–266.
8. Egorov, Yu.V., *Statika sorbtsii mikrokomponentov oksigidratami* (Statics of Microcomponent Sorption by Oxyhydrates), Moscow: Atomizdat, 1975.

Russian Journal of Applied Chemistry, Vol. 74, No. 1, 2001, pp. 82–85. Translated from Zhurnal Prikladnoi Khimii, Vol. 74, No. 1, 2001, pp. 79–82.

ENVIRONMENTAL PROBLEMS OF CHEMISTRY AND TECHNOLOGY

Features of Cr(III) Cation-Exchange Recovery from Wash Water of Standard Chrome Plating

S. V. Plokhov, N. A. Barinova, and M. G. Mikhalenko

Nizhni Novgorod State Technical University, Nizhni Novgorod, Russia

Received October 25, 1999; in final form April, 2000

Abstract—Features of treatment of the standard chrome plating wash water to remove Cr(III) with KU-1 cation exchanger in the H form were considered. The optimal conditions of Cr(III) recovery and ion exchanger regeneration were determined.

In [1, 2], a two-stage scheme of recovery and utilization of the main components of the standard chrome plating wash water was proposed. The scheme is based on the ion exchange followed by electrochemical treatment of chromium-containing eluates. The model and real wash waters with variable content of metal ions (g l^{-1}) were used: chromium(VI) (in the form of CrO_4^{2-} and $Cr_2O_7^{2-}$) up to 2.0, copper(II) up to 0.01, nickel(II) up to 0.01, and iron(III) up to 0.015. Along with chromium(VI) and the above foreign metal ions, wash water of standard chrome plating contains Cr(III). The chromium(VI) recovery from wash water by ion exchange was studied in [3, 4].

In this work we studied the features of Cr(III) ion-exchange recovery from wash water of standard chrome plating and determined its optimal parameters.

To recover Cr(III), we used a KU-1 cation exchanger in the H form, which was loaded into a column of 160 mm height and 18 mm inner diameter. The ratio of the cation exchanger bed height and column diameter was 9 : 1. The average diameter of ion exchanger grain was 2.5×10^{-3} m. Ion exchange was studied by both dynamic (with the concentration control at the ion-exchange column outlet) and static methods. The chromium(III) content was determined spectrophotometrically and by atomic absorption with SF-26 and S-115 spectrophotometers, respectively. The error of the above methods was 1.5–2.0%.

Ion exchange involves a series of successive stages of mass transfer over the interface controlled by hydrodynamic regime of the movement of the liquid phase [5]. Therefore, the efficiency of ion exchange should depend on the linear velocity of the flow of chromium-containing wash water. This is confirmed by ion-exchange output curves at various flow velocities (Fig. 1a) and ion-exchange characteristics (dynamic exchange capacity DEC and capacity up to breakthrough CB). DEC is the maximal mass of chromium(III) ions retained by 1 kg of swollen ion exchanger under the taken dynamic conditions of water flow. CB is the maximal mass of Cr(III) ions retained by 1 kg of ion exchanger up to appearance of Cr(III) in the eluate. The velocity of wash water flow U 3.25 m h^{-1} corresponds to the absence of CB and insignificant decrease in DEC. At this and higher flow rate, CB cannot be determined quantitatively by the above method of analysis. Hence, only linear flow velocities lower than 3.25 m h^{-1} are of practical interest. DEC and CB (Fig. 1b) are nonlinear functions of U: CB has a maximum at the flow velocity of 2.0 m h^{-1}, and DEC decreases with increasing U. The flow velocity of 2.0 m $^{-1}$ is optimal, as it corresponds to high DEC value and maximal CB (31.6 and 10.6 g per kg of the resin, respectively).

The analysis of the ion-exchange kinetics with equations of diffusion kinetics suggests existence of the limiting stage of ion exchange. It is known [5] that at the metal concentration from 0.003 to 0.1 M ion exchange proceeds under conditions of mixed kinetics. The contribution of the internal diffusion constituent increases with increasing metal concentration. Since for these conditions the theory is not developed completely, to determine the limiting stage we used equations of internal diffusion kinetics for the case of simplest models (sphere, cylinder, plate) [6], which are as follows:

$$-\ln(1 - F) = Bt - \ln A, \quad (1)$$

where A and B are coefficients depending on the

1070-4272/01/7401-0082$25.00

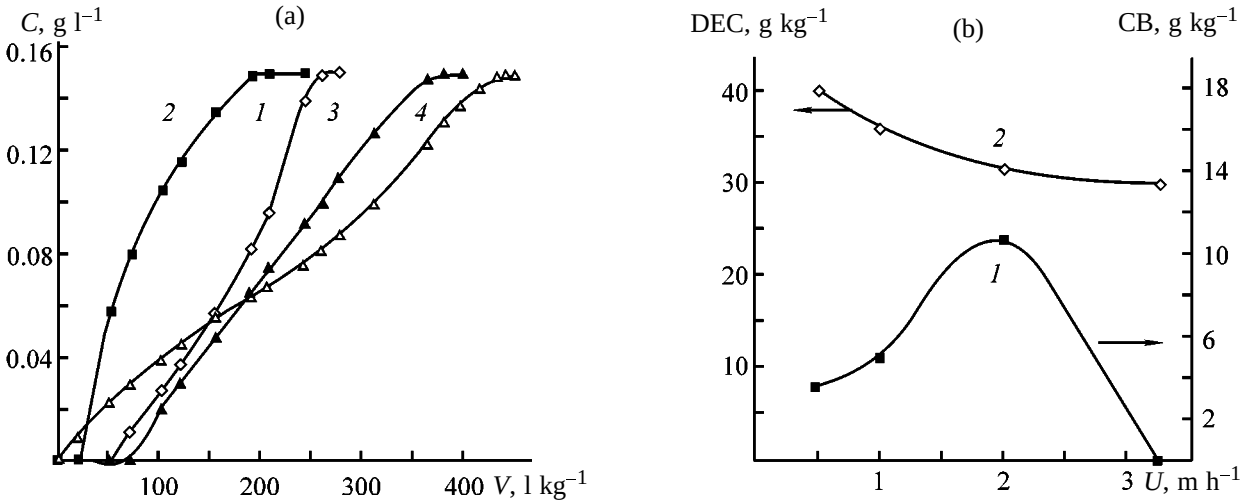

Fig. 1. Effect of (a) volume V and (b) flow velocity U of wash water on (a) the outlet concentration of Cr(III) C and (b) (*1*) CB and (*2*) DEC. Chromium(III) concentration 0.15 g l^{-1}; the same for Fig. 2. (a) Wash water flow velocity U (m h^{-1}): (*1*) 0.5, (*2*) 1.0, (*3*) 2.0, and (*4*) 3.25.

model taken, F is the exchange degree, and t is the exchange time.

The use of Eq. (1) is advisable at $F > 0.7$, because at high exchange degree the contribution of the internal diffusion constituent is very large. Coefficient A is the criterion of adequacy of the model taken and is 0.61, 0.69, and 0.81 for sphere, cylinder, and plate, respectively. In this case, the sphere model is the most acceptable. At high F, coefficient B can be determined from the slope of the $-\ln(1 - F)$–t dependences. Then, the apparent diffusion coefficient D can be calculated:

$$B = D\pi^2 / R^2, \quad (2)$$

where R is the ion exchanger grain radius.

The value of D is 1.5×10^{-8} cm^2 s^{-1}. This value corresponds to the prevalence of the internal diffusion constituent and small contribution of the external diffusion. This allows explanation of the dependence of DEC on the velocity of wash water flow (Fig. 1b, curve *2*). At increased velocity, the contact time in the ion exchanger grain–liquid phase system becomes shorter, and hence, DEC decreases (especially strongly at the velocities higher than 3.25 m h^{-1}).

The effect of chromium(III) concentration in the wash water on the ion exchange dynamics was found at the wash water flow velocity of 2.0 m h^{-1} (Fig. 3a). With increasing metal ion concentration from 0.1 to 0.3 g l^{-1}, CB and DEC change (Fig. 3b), and their maxima are observed at a Cr(III) concentration of 0.15 g l^{-1}. Probably, such dependences are due to Cr(III) complexation in sulfate solutions. At the Cr(III) concentration increased to 0.15 g l^{-1} transfer of metal ion from the solution to the surface of the ion exchanger grain accelerates, and DEC and CB increase. At Cr(III) concentration higher than 0.15 g l^{-1}, the internal diffusion constituent becomes prevailing, and DEC and CB decrease. The apparent diffusion coefficient D was 3.5×10^{-8} $cm^2 s^{-1}$. The effect of Cr(III) concentration was studied also for other velocities of wash water flow within the 0.1–6.25 m h^{-1} range. It was found that the shape of the DEC and CB dependences and the location of curve maxima are independent of the chromium(III) concentration. This is caused by a fairly narrow range in variation of the Cr(III) concentrations studied.

The above data on chromium(III) recovery show that fairly high wash water volume to breakthrough, maximal capacity to breakthrough (it amounts to 7.3, 10.6, 2.1, and 1.0 g per kg of the resin for concentra-

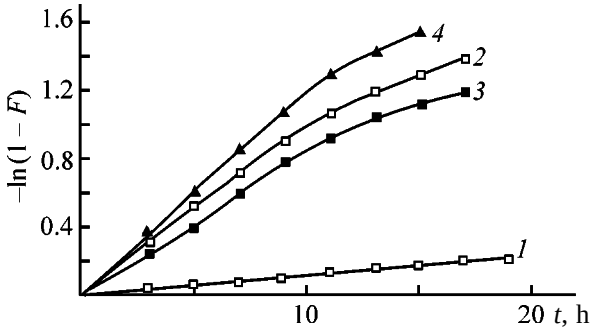

Fig. 2. Kinetics of Cr(III) sorption with KU-1 cation exchanger in the H form: (F) exchange degree and (t) time. Wash water flow rate U (m h^{-1}): (*1*) 0.5, (*2*) 1.0, (*3*) 2.0, and (*4*) 3.25.

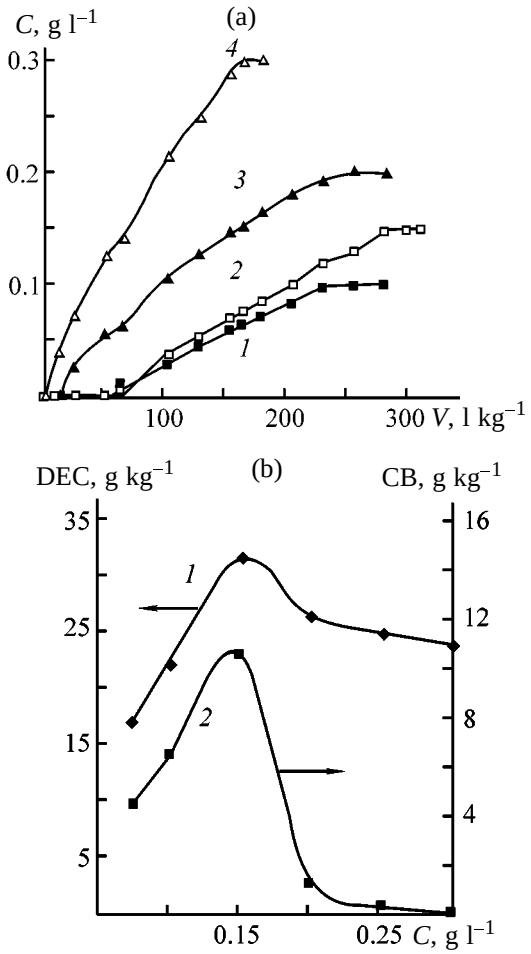

Fig. 3. Influence of wash water volume V and Cr(III) concentration C on (a) the outlet concentration of Cr(III) C and (b) (*1*) DEC and (*2*) CB. Wash water flow velocity 2.0 m h^{-1}. (a) Cr(III) concentration (g l^{-1}): (*1*) 0.1, (*2*) 0.15, (*3*) 0.2, and (*4*) 0.3.

tions of 0.1, 0.15, 0.2, and 0.3 g l^{-1}, respectively), and maximal DEC (31.6 g kg^{-1}) correspond to the Cr(III) concentration of 0.15 g l^{-1}.

Ion exchanger regeneration was performed with sulfuric acid solutions. We considered the effect of acid concentration and flow velocity of the solution on this process. The effect of acid concentration was studied by the static method. Cation exchanger was saturated with Cr(III) ions under the optimal conditions (0.15 g l^{-1}, 2 m h^{-1}) and then washed up to absence of trace amounts of Cr(III) in the eluate. Then, the resin was dried to the constant weight. The samples of solutions containing the same amount of H_2SO_4 and various amounts of water were added to the equal samples of the ion exchanger (4.0 g). The ratio of the cation exchanger to H_2SO_4 was 1 : 6.25 (by weight). The amount of Cr(III) recovered was determined by chemical analysis as a function of the time of cation exchanger contact with the solution. The data obtained are listed in the table.

Amount of chromium(III) recovered in regeneration

H_2SO_4, g l^{-1}	Amount of Cr(III), g, in indicated time, h				
	1	3	22	24	47
25.0	0.015	0.023	0.052	0.067	0.084
50.0	0.031	0.049	0.080	0.104	0.116
100.0	0.027	0.034	0.066	0.083	0.099
150.0	0.022	0.031	0.062	0.080	0.102
200.0	0.021	0.032	0.063	0.083	0.104
250.0	0.022	0.033	0.064	0.083	0.105

As seen, the best recovery is reached with 50.0 g l^{-1} H_2SO_4, which was used in the subsequent experiments.

We found that the maximal amount of the metal recovered corresponds to the flow velocity of sulfuric acid of 1.0 m h^{-1} (Fig. 4). This follows from comparison of the areas under the corresponding curves. At any volume of the sulfuric acid solution, the velocity of 1.0 m h^{-1} corresponds to the maximal amount of Cr(III) in the eluate, which is important for the further processing of the eluates into the commercial product. This result can be explained as follows. At the flow velocity of the H_2SO_4 solution below 1.0 m h^{-1}, the regeneration of the resin is controlled by mixed kinetics and at higher velocities, it is controlled by internal diffusion kinetics, which decreases the amount of recovered Cr(III).

The dependences of the recovery degree on the amount of sulfuric acid solution show that the maximal recovery is reached at a flow velocity of 1.0 m h^{-1} (98%), while for the velocities of 0.25, 0.5, and 2.0 m h^{-1} it was 64.4, 80.1, and 78.3%, respectively.

The volume of the acid solution required for complete regeneration was 43.12 l per kg of the resin [98% of chromium(III) recovery]. The 80% recovery of Cr(III) is reached on passing 7.2 l per kg of the resin. It is reasonable to maintain this level of the resin regeneration, because the additional volume of the acid required to reach the 98% recovery is unduly large. On the other hand, the incomplete regeneration degree should lower DEC and CB in the further use of the ion exchanger, which should be taken into consideration when designing the equipment for treatment of industrial wastewater.

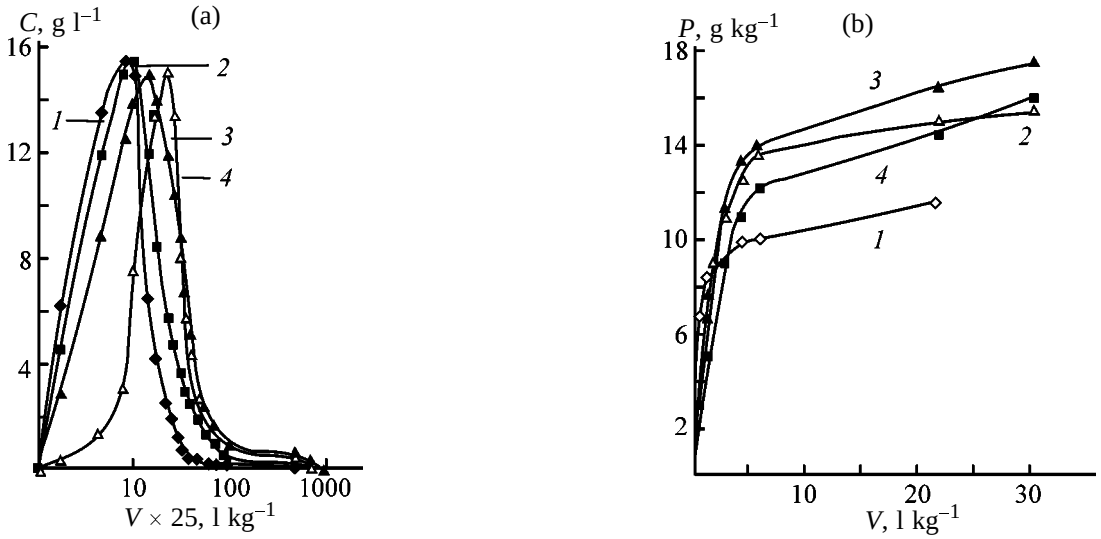

Fig. 4. Effect of the volume of the regenerating solution V on (a) the outlet concentration of Cr(III) C and (b) the amount of Cr(III) recovered P. Concentration of H_2SO_4 50 g l^{-1}. H_2SO_4 flow velocity (m h^{-1}): (*1*) 0.25, (*2*) 0.5, (*3*) 1.0, and (*4*) 2.0.

CONCLUSIONS

(1) Optimal parameters of Cr(III) cation exchange recovery from wash water of the standard chrome plating were determined: Cr(III) content in wash water 0.15 g l^{-1} and wash water flow velocity 2.0 m h^{-1}. Under these conditions, the dynamic exchange capacity and the cation exchanger capacity to breakthrough were 31.6 and 10.6 g per kg of the resin, respectively.

(2) It is advisable to regenerate the ion exchanger with 50 g l^{-1} sulfuric acid at the flow velocity of 1.0 m h^{-1} to recovery degree of 80%.

REFERENCES

1. Barinova, N.A., Ershov, D.A., and Plokhov, S.V., Abstracts of Papers, *III Respublikanskaya nauchno-tekhnicheskaya konferentsiya molodykh uchenykh i spetsialistov* (III Republican Scientific and Technical Conf. of Young Scientists and Specialists), Kazan, October 10–11, 1997, p. 50.
2. Barinova, N.A., Plokhov, S.V., and Gol'denberg, G.L., Abstracts of Papers, *Mezhdunarodnaya nauchno-prakticheskaya konferentsiya "Ekologiya i zhizn'"* (Int. Scientific and Practical Conf. "Ecology and Life"), Penza, February 6–7, 1999, pp. 120–122.
3. Barinova, N.A., Plokhov, S.V., and Gol'denberg, G.L., Abstracts of Papers, *Mezhdunarodnaya konferentsiya "Progressivnaya tekhnologiya i voprosy ekologii v gal'vanotekhnike i proizvodstve pechatnykh plat"* (Int. Conf. "Advanced Technology and Ecology in Electroplating and Production of Printed-Circuit Boards"), Penza, May 26–27, 1998, pp. 56–58.
4. Barinova, N.A., Plokhov, S.V., and Gol'denberg, G.L., Abstracts of Papers, *Mezhdunarodnaya nauchno-prakticheskaya konferentsiya "Pochva, otkhody proizvodstva i potrebleniya: problemy okhrany i kontrolya"* (Int. Scientific and Practical Conf. "Soils, Waste of Production and Consumption: Problems of Conservation and Control"), Penza, June 3–4, 1998, pp. 91–92.
5. Ashirov, A., *Ionoobmennaya ochistka stochnykh vod, rastvorov i gazov* (Ion-Exchange Treatment of Wastewater, Solutions, and Gases), Leningrad: Khimiya, 1983.
6. Kokotov, Yu.A. and Pasechnik, V.A., *Ravnovesie i kinetika ionnogo obmena* (Equilibrium and Kinetics of Ion Exchange), Leningrad: Khimiya, 1970.

Russian Journal of Applied Chemistry, Vol. 74, No. 1, 2001, pp. 86–89. Translated from Zhurnal Prikladnoi Khimii, Vol. 74, No. 1, 2001, pp. 83–86.

ENVIRONMENTAL PROBLEMS OF CHEMISTRY AND TECHNOLOGY

Color Removal from Aqueous Solutions of Humic Substances in the Presence of Praestol and Aluminum Sulfate

V. F. Kurenkov, S. V. Snigirev, and L. S. Kogdanina

Kazan State Technological University, Kazan, Tatarstan, Russia

Received September 5, 2000

Abstract—Color removal from aqueous solutions of humic substances by introducing Praestol (cationic coagulant) in combination with aluminum sulfate (flocculant) was studied as a function of the coagulant and flocculant concentrations, chemical composition of flocculant, its molecular weight, macromolecule conformation in solutions, pH, and the order and time of coagulant and flocculant introduction.

Numerous problems of the natural and wastewater decontamination can be successfully solved by the use of flocculant (F) in combination with coagulant (C) [1, 2]. The promising approach to solution of these problems is based on the use of macromolecular flocculants Praestols[1] of cationic type belonging to widely used polyacrylamide flocculants. These compounds are copolymers of acrylamide (AA) and dimethylaminopropylacrylamide methylene chloride (DMAPA MC). It was found previously that cationic Praestols in combination with aluminum sulfate as a coagulant can be used for color removal from water [3]. It was shown also that the mixtures of cationic and anionic Praestols promote sedimentation of kaolin–water suspensions [4]. For efficient use of Praestols for color removal from water, data are required on the influence of molecular characteristics of flocculants and features of dispersed systems on flocculation. This matter is poorly studied by now. In this work we studied the effect of chemical composition, molecular weight, and conformation in solution of cationic Praestol on color removal from model solutions of humic substances. This process was studied also as influenced by pH of the medium and the order and time of the flocculant and coagulant $[Al_2(SO_4]_3$ introduction.

EXPERIMENTAL

The characteristics of the cationic Praestol samples used in our experiments are listed in the table. The Praestol samples A, B, C, and D were prepared at the Moscow–Stockhausen–Perm Russian–German Private Company; F, G, H and I samples were prepared by chemical degradation of Praestol C. Aluminum sulfate $Al_2(SO_4)_3 \cdot 18H_2O$, pure grade [GOST (State Standard) 3758–65], and distilled water were used. Other reagents were of chemically pure grade.

The content of the DMAPA MC ionic units in the Praestol macromolecules was evaluated from the content of chloride anions determined mercurimetrically [5].

The molecular weight of Praestol M was evaluated by measuring the intrinsic viscosity of its aqueous

Characteristics of Praestol flocculants of cationic type

Sample*	Brand	[η], $cm^3\ g^{-1}$	Unit content, mol %	
			AA	DMAPA MC
A	611	920	91	9
B	650	690	80	20
C	644	620	73	27
E	655	555	67	33
F	–	370	73	27
G	–	270	73	27
H	–	175	73	27
I	–	100	73	27

* Structural formula of macromolecule:

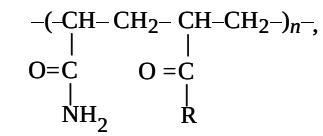

where R = $NH–(CH_2)_3–\overset{\displaystyle CH_3}{\overset{|}{N^+}}(Cl^-)–CH_3$.

[1] Moscow–Stockhausen–Perm Russian–German Private Company.

1070-4272/01/7401-0086$25.00 © 2001 MAIK "Nauka/Interperiodica"

solutions [η], since according to Mark–Kuhn–Houwink equation, $M \sim [\eta]$. The [η] values of Praestol solutions in 0.5 M NaCl were determined with an Ubbelohde viscometer (d_c = 0.54 mm) at 25°C.

The effective size of Praestol macromolecule in solution was evaluated from the reduced viscosity of its aqueous solution η_{sp}/C_p at a fixed copolymer concentration C_p [6–8]. The reduced viscosity was measured with a VPZh-3 viscometer (C_p 0.002%, d_c = 0.54 mm) at 25°C.

The pH of solutions was measured on a pH-121 pH meter with ESL-63-07 glass and chloride (EVL-1M3) silver electrodes.

Praestol B sample (see table) was subjected to degradation in 0.1% aqueous solition at 50°C in the presence of 0.008% potassium persulfate as a radical-generating agent. The degradation of Praestol was monitored viscometrically [9]. This reaction was performed in a cylindrical reaction vessel equipped with a thermostated water jacket, a magnetic stirrer, a control thermometer, and a sampling tube. In the course of degradation at certain intervals a portion of Praestol solution was sampled and both [η] and the efficiency of the color removal were determined. The table shows that the Praestol F, G, H and I samples prepared by chemical degradation of Praestol B are characterized by different [η] but identical chemical composition.

In our experiments we studied color removal from aqueous solutions of humic substances with a color index equal to 226° (cobalt bichromate scale). These solutions were prepared by dilution of biohumus [TU (Technical Specifications) 9891-007-111580–98] with water with stirring. The mixture was settled for 2 days, the precipitate and suspension were separated by filtration, and the resulting filtrate was diluted so as to achieve the above-indicated color index which varies in direct proportion with the optical density [4]. Color removal from a humus solution was carried out as follows. In the first stage a coagulant was introduced into a solution of humic substances and then, after 1 min, a flocculant was added. The mixture was stirred, kept for 1 h, and filtered through a Schott filter. The filtrate was poured into a 5-cm quartz optical cell, and the reference cell was filled with distilled water. The optical density was determined on a KFK-2 photocolorimeter at 400 nm. The color removal efficiency was evaluated by the expression

$$E = (n_0 - n)/n,$$

where n_0 and n are the optical densities of the initial aqueous solution of humic substances and that after introduction of the coagulant and flocculant, respectively.

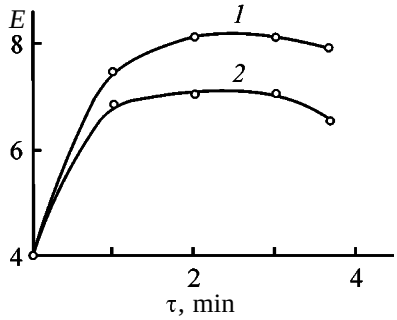

Fig. 1. Dependence of color removal efficiency E on time (τ) of introduction of the second component of the C + F mixture. C_p = 0.5 mg l^{-1}, C_c = 40 mg l^{-1}. Order of reagent introduction: (*1*) C + F and (*2*) F + C.

In the first experiments we studied the dependence of the color removal from solutions of humic substances on the order and time of introduction of a flocculant (Praestol C) in combination with a coagulant (C). Two series of experiments were performed which differ by the order of introduction of flocculant and coagulant. In the both series of experiments the coagulant (C_c) and flocculant (C_p) concentrations were constant and the second reagent was introduced at different intervals after introduction of the first reagent. Figure 1 shows the results of these experiments. It is seen that at simultaneous introduction of the flocculant and coagulant mixture F + C (τ = 0) the color removal efficiency is lower than that at separate introduction of the reagents ($\tau > 0$). The mutual arrangement of curves *1* and *2* in Fig. 1 shows that introduction of the flocculant after the coagulant (C + F) increases the color removal efficiency to a larger extent than introduction of the coagulant after the flocculant (F + C) at the same intervals. This result shows that irreversible sorption of flocculant macromolecules depends on the order of the reagent introduction. The maximum color removal efficiency E was observed when the flocculant was added 1 min after introducing the coagulant (Fig. 1, curve *1*). This is due to the fact that under these conditions the coagulant has time to be hydrolyzed to sufficient extent to form positively charged particles capable of associating with the negatively charged particles of humic acids. The resulting coagulant–humic acid aggregates rapidly coagulate. In further adding a flocculant the more complicated aggregates containing coagulant and humic acid particles and flocculant molecules can be formed. The humic acid–flocculant units in these aggregates are the interpolymeric complexes [10] formed by interaction of

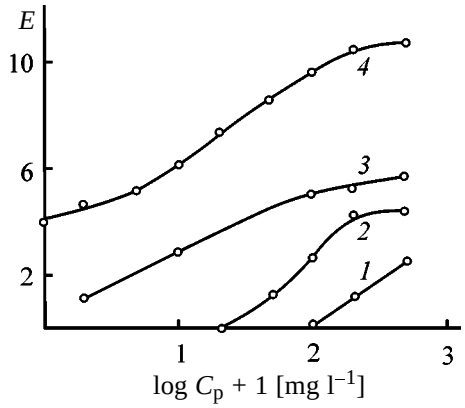

Fig. 2. Dependence of color removal efficiency E on flocculant concentration (Praestol C) C_p at varied coagulant concentrations. Order of reagent introduction C + F, the flocculant was added 1 min after introducing the coagulant.

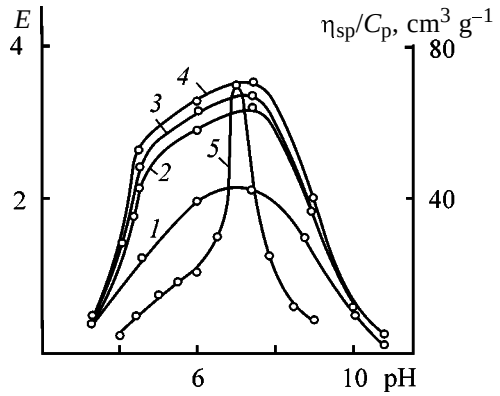

Fig. 3. Dependence of (*1–4*) color removal efficiency E and (*5*) parameter η_{sp}/C_p of flocculant (Praestol C) solutions on pH. (*1–4*) C_p = 0.5 mg l^{-1}; C_c = 16 mg l^{-1}. The parameter η_{sp}/C_p was determined at C_p = 0.1% at 50°C; the same for Fig. 5. Content of ionic groups in flocculant, mol %: (*1*) 9, (*2*) 33; (*3*) 20, and (*4, 5*) 27.

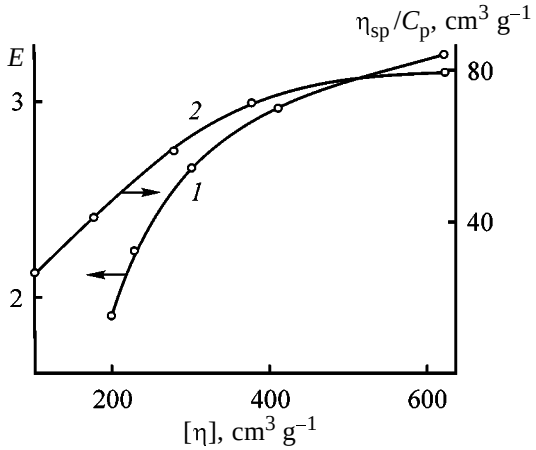

Fig. 4. Dependence of (*1*) color removal efficiency E and (*2*) parameter η_{sp}/C_p on [η] of flocculant (Praestol C) solutions. C_p = 0.5 mg l^{-1}, C_c = 24 mg l^{-1}.

the free carboxy and phenolic groups of humic acids with the amino groups of the flocculant. Due to this cooperative interaction between the coagulant and flocculant, coarse floccules are formed which precipitate, facilitating color removal from water. Based on these results, in further experiments we added flocculant 1 min after introducing the coagulant.

The efficiency of removal of colored humic substances from aqueous solutions at different flocculant concentrations was studied with the use of Praestol C. Figure 2 shows that the color removal efficiency increases with increasing C_p both in the absence of the coagulant (curve *1*) and in its presence in varied amounts (curves *2–4*). Comparison of these curves at constant C_p shows also that introduction of the coagulant and increase of its concentration (passing from curve *1* to curve *4*) improve the color removal. In accordance with the above-considered mechanisms, this effect is due to formation of bridging bonds connecting particles of coagulant and humic acids and flocculant macromolecules. These processes result in formation of coarse floccules capable of fast sedimentation.

The color removal from solutions of humic substances as influenced by pH was studied for Praestols A, B, C, and E of different chemical composition and close molecular weight (see table) at constant concentrations of both flocculant and coagulant. The required pH was adjusted by adding HCl and NaOH aqueous solutions. As seen from Fig. 3, the plots of E vs. pH show maximum for all flocculant samples irrespective of their chemical composition. The maximal E in these plots is observed at pH ~7. The similar maximum occurs in the plot of η_{sp}/C_p vs. pH (Fig. 3, curve *5*) which characterizes the pH dependence of the effective size of macromolecular globules of the flocculant. This fact is indicative of the correlation between the color removal efficiency of the flocculant and its conformational state in solution. At pH < 11 the dissociation degree of the ionic groups of the flocculant increases, the electrostatic repulsion between the positively charged sites along a polymeric chain increases, and, as a result, the flocculant macromolecules lengthen and the flocculant globules become larger. This effect is manifested as increase in η_{sp}/C_p. At pH < ~7 the concentration of counterions increases, compensating the fixed positive charges of the macromolecular chains and weakening the electrostatic repulsion along them. Therefore, the flocculant globules become more compact, which is manifested as the decrease in η_{sp}/C_p (Fig. 3, curve *5*). Figure 3 shows that the maximum color removal is observed for Pra-

estol C containing 27% ionic groups. This flocculant is characterized by the maximal η_{sp}/C_p parameter and, therefore, by the largest effective size of macromolecules. These results show that in the case of Praestol C the largest floccules are formed at pH 7. These floccules, due to their low aggregative stability in solution and fast sedimentation, facilitate color removal from water (Fig. 3).

The dependence of the color removal efficiency on $[\eta]$ of the flocculant solutions was studied for Praestols F, G, H, and I with the similar chemical composition of the macromolecules (see table) at constant C_p and C_c. These results show (Fig. 4, curve *1*) that with increasing $[\eta]$ the color removal efficiency increases. The dependence of η_{sp}/C_p on $[\eta]$ (Fig. 4, curve *2*) is similar, i.e., the increase in the color removal efficiency correlates with the increase in the macromolecule effective size. As a result, coarser floccules are formed incorporating larger amount of humic acids and accelerating the sedimentation.

CONCLUSIONS

(1) In introduction of flocculant in combination with coagulant into humic acid aqueous solutions the color removal efficiency increases with increasing $[\eta]$ of flocculant and coagulant and flocculant concentrations, in passing from simultaneous to successive introduction of reagents, and when changing the order of the reagent introduction from (coagulant after flocculant) to (flocculant after coagulant).

(2) The most efficient color removal from solutions of humic substances is provided by Praestol flocculant containing 27 mol % of ionic groups at pH 7 when the largest macromolecular globules are formed.

REFERENCES

1. Veitser, Yu.I. and Mints, D.M., *Vysokomolekulyarnye flokulyanty v protsessakh ochistki prirodnykh i stochnykh vod* (Macromolecular Flocculants in Processes of Decontamination of Natural and Wastewater), Moscow: Stroiizdat, 1984.
2. Zapol'skii, A.K. and Baran, A.A., *Koagulanty i flokulyanty v protsessakh ochistki vody: Svoistva, Poluchenie, Primenenie* (Coagulants and Flocculants in Processes of Water Decontamination: Properties, Preparation, Application), Leningrad: Khimiya, 1987.
3. Kurenkov, V.F., Snigirev, S.V., and Shishkareva, L.S., *Zh. Prikl. Khim.*, 2000, vol. 73, no. 2, pp. 257–261.
4. Kurenkov, V.F., Snigirev, S.V., Dervoedova, E.A., and Churikov, F.I., *Zh. Prikl. Khim.*, 1999, vol. 72, no. 11, pp. 1892–1896.
5. *Rukovodstvo po khimicheskomu i tekhnologicheskomu analizu vody* (Manual on Chemical and Technological Analysis of Water), Moscow: Khimiya, 1982.
6. Kargin, V.A., Mirlina, S.Ya., and Antipina, A.D., *Vysokomol. Soedin.*, 1959, vol. 1, no. 9, pp. 1428–1437.
7. Fernandes Prini, R. and Lagos, A.E., *J. Polym. Sci., Part A*, 1964, vol. 2, pp. 2917–2928.
8. Tsvetkov, V.N., Eskin, V.E., and Frenkel', S.Ya., *Struktura makromolekul v rastvorakh* (Structure of Macromolecules in Solutions), Moscow: Nauka, 1964.
9. Kurenkov, V.F. and Tazieva, E.D., *Zh. Prikl. Khim.*, 1994, vol. 67, no. 7, pp. 1162–1166.
10. Bekturov, E.A. and Bimendina, L.A., *Interpolimernye kompleksy* (Interpolymeric Complexes), Alma-Ata: Nauka, 1977.

Russian Journal of Applied Chemistry, Vol. 74, No. 1, 2001, pp. 90–94. Translated from Zhurnal Prikladnoi Khimii, Vol. 74, No. 1, 2001, pp. 87–91.

PROCESSES AND EQUIPMENT OF CHEMICAL INDUSTRY

Raising the Coefficient of Turbulent Diffusion in the Reaction Zone as Means To Improve Technical and Economical Parameters of Polymer Production

K. S. Minsker, V. P. Zakharov, R. G. Takhavutdinov, G. S. D'yakonov, and Al. Al. Berlin

Bashkortostan State University, Ufa, Bashkortostan, Russia
Kazan State Technological University, Kazan, Tatarstan, Russia
Semenov Institute of Chemical Physics, Moscow, Russia

Received July 19, 1999; in final form, July 2000

Abstract—Use of a new type of apparatus, high-output small-size tubular turbulent reactors of mainly diffuser–confuser design, in very fast processes, including polymerization, is considered. The turbulent diffusion coefficient D_t and its distribution over the apparatus volume were calculated as functions of the confuser divergence angle α. The calculations were confirmed by experimental data. New reactor designs for a number of processes of large-tonnage polymer production were proposed and put into practice.

One of the most important problems of chemical industry in performing both chemical and physical processes consists in organizing fast and high-quality mixing of fluid–fluid and gas–fluid flows, which requires intensification of mass-transfer processes. This problem is particularly topical in developing technologies for fast, primarily polymerization, processes in which mixing flows have strongly different densities and viscosities. This is clearly seen even in mixing infinitely soluble fluids, e.g., sulfuric acid or glycerol with water, when a phase boundary is preserved for a long time [1].

In industry, basic processes are commonly performed in volume mixing apparatus equipped with mechanical devices for vigorous stirring. However, in conducting fast exothermic processes in solution, e.g., cationic polymerization of isobutylene, copolymerization of isobutylene with isoprene or styrene, interaction of sulfuric acid with water, etc., volume mixing reactors have low efficiency, similarly to tubular plug-flow apparatus with laminar flows.

An ovel solution to the problem of developing technologies for fast chemical processes and improving the technical and economical parameters of the production process as a whole was to use reactors of new type. These were high-output small-size tubular apparatus operating in a quasi-plug-flow mode with turbulent flows and combining advantages of tubular plug-flow and volume mixing apparatus. These reactors also exhibited novel fundamental properties untypical of the conventional industrial apparatus [2–4]. The problems of achieving a vigorous stirring of the reaction medium, at which homogeneous reactant concentration fields are created in this kind of apparatus, are solved in a simpler and more efficient way.

The aims of this work were to analyze theoretically the turbulent mixing of fluid flows in tubular jet apparatus particularly efficient in fast chemical reactions (with characteristic reaction time $\tau_{ch} < 10^{-2}$ s) and physical mass-exchange processes, to provide recommendations for the reactor design on the basis of the analysis, and to discuss some examples of their industrial use.

As is known, the efficiency of mixing largely depends on the relative variation of the coefficient of turbulent diffusion along the reactor axis [2, 3]. The efficiency of mixing can be improved not only by raising the linear flow velocity u_0, but also by maintaining D_t at a certain high level along the direction of flow motion. This can be achieved by generating recirculation zones in a tubular apparatus, in particular, by changing the design (geometric arrangement) of the reactor [5]. Rather efficient in this regard are small-size tubular turbulent apparatus with identical repeating geometric units of diffuser–confuser design (Fig. 1b) ensuring a noticeable (by an order of magnitude and more) increase in D_t and maintaining con-

1070-4272/01/7401-0090$25.00

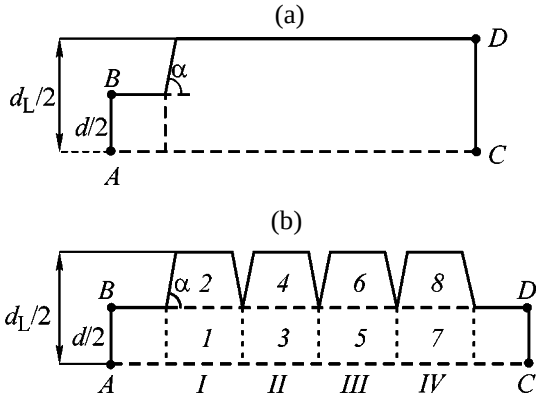

Fig. 1. Schematic of tubular turbulent apparatus of (a) cylindrical and (b) diffuser–confuser types. (α) Confuser divergence angle and (*d*) diameter of inlet and outlet orifices. (*1–8*) Apparatus zones and (*I–IV*) diffuser–confuser sections.

stant flow turbulence along the apparatus at arbitrary length [6].

The theoretical description is based on the following main model assumptions: The medium is Newtonian and incompressible; the flow is axially symmetrical and nonswirling; the turbulent flow can be described in terms of the so-called standard model [7] whose parameters are the specific kinetic energy of turbulence, *K*, and its dissipation ε; it is assumed that the coefficient of turbulent diffusion is equal to the kinematic coefficient of turbulent viscosity $D_t = K_t = \mu_t/\rho$. Let us write the mathematical model equations within the framework of these assumptions in the cylindrical system of coordinates: the continuity equation expressing the mass conservation law

$$\frac{1}{r}\frac{\partial(ru)}{\partial r} + \frac{\partial v}{\partial z} = 0; \quad (1)$$

the momentum transfer equation

$$\frac{\rho}{r}\frac{\partial(ruu)}{\partial r} + \rho\frac{\partial(uv)}{\partial z} = -\frac{\partial p}{\partial r} - \left[\frac{1}{r}\frac{\partial(r\tau_{11})}{\partial r} - \frac{\tau_{33}}{r} + \frac{\partial\tau_{21}}{\partial z}\right], \quad (2)$$

$$\frac{\rho}{r}\frac{\partial(ruv)}{\partial r} + \rho\frac{\partial(vv)}{\partial z} = -\frac{\partial p}{\partial r} - \left[\frac{1}{r}\frac{\partial(r\tau_{12})}{\partial r} + \frac{\partial\tau_{22}}{\partial z}\right], \quad (3)$$

with the components of the stress tensor given by

$$\tau_{11} = -2\mu\partial u/\partial r, \quad \tau_{22} = -2\mu\partial v/\partial z, \quad \tau_{33} = -2\mu u/r, \quad (4)$$

$$\tau_{12} = \tau_{21} = -\mu(\partial v/\partial r + \partial u/\partial z); \quad (5)$$

and the equations describing the transfer of specific kinetic energy of turbulence and its dissipation

$$\frac{\rho}{r}\frac{\partial(ruK)}{\partial r} + \rho\frac{\partial(vK)}{\partial z} = -\frac{1}{r}\frac{\partial}{\partial r}\left(\frac{\mu}{\sigma_K}\frac{r\partial K}{\partial r}\right) + \frac{\partial}{\partial z}\left(\frac{\mu}{\sigma_K}\frac{\partial K}{\partial z}\right) + \mu_t G - \rho\varepsilon, \quad (6)$$

$$\frac{\rho}{r}\frac{\partial(ru\varepsilon)}{\partial r} + \rho\frac{\partial(v\varepsilon)}{\partial z} = -\frac{1}{r}\frac{\partial}{\partial r}\left(\frac{\mu}{\sigma_E}\frac{r\partial\varepsilon}{\partial r}\right) + \frac{\partial}{\partial z}\left(\frac{\mu}{\sigma_E}\frac{\partial\varepsilon}{\partial z}\right) + \mu_t C_1 G\varepsilon/K - C_2\rho\varepsilon^2/K, \quad (7)$$

$$G = [(\tau_{11}^2 + \tau_{22}^2 + \tau_{33}^2)/2 + \tau_{12}^2]/\mu^2, \quad (8)$$

$$\mu_t = \rho\frac{C_\mu K^2}{\varepsilon}, \quad (9)$$

where *p* is pressure, *r* is the radial coordinate, *u* is the axial velocity component, *v* is the radial velocity component, *z* is the longitudinal component, μ is the effective dynamic viscosity coefficient, μ_t is the dynamic coefficient of turbulent viscosity, and ρ is density.

The following standard constants of the turbulence model were used:

$$C_1 = 1.44,\ C_2 = 1.92,\ C_\mu = 0.09,\ \sigma_K = 1.0,\ \sigma_E = 1.3. \quad (10)$$

The flow of a fluid with dynamic viscosity coefficient $\mu_m = 0.001$ Pa s and density $\rho = 1000$ kg m^{-3} is considered. The boundary conditions are conditions of symmetry along the *z* axis and condition of fluid adhesion to the solid wall surface. The pressure was set at the apparatus outlet (along the CD line), and the linear flow velocity $u_0 = 5$ m s^{-1}, at the inlet (AB line) along the symmetry axis. The lengths of the inlet and outlet orifices of the tubular apparatus exceeded its diameter manyfold ($L \gg d$). This ruled out any influence of the input and output turbulence parameters on the characteristics of turbulent flow in the diffuser–confuser part of the apparatus, which is the object of study. It was also taken that $D_t = V_t = \mu_t/\rho$.

To confirm the adequacy of the calculations performed, the obtained theoretical results were compared with the available experimental data for a cylindrical channel of constant diameter (Fig. 1a) at $\mathrm{Re} = 2 \times 10^5$ [8], with the obtained results also in agreement with the calculations done in [9]. In particular, Table 1 lists the lengths of the circulation zone appearing in the peripheral part of the tube, immedi-

Table 1. Calculated and experimental circulation zone lengths L_c/d

Divergence angle α, deg	L_c/d		
	experiment [8]	calculation	
		this study	[9]
30	4.1	3.4	3.5
90	4.6	4.7	4.7

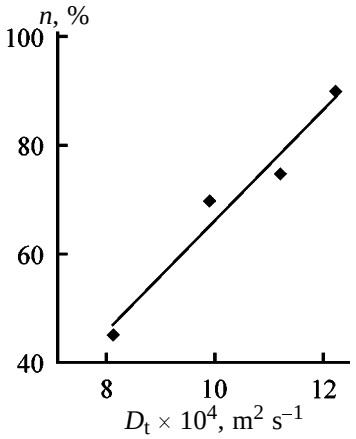

Fig. 2. Degree of emulsion homogeneity, *n*, vs. turbulent diffusion coefficient D_t in the diffuser–confuser channel of a tubular apparatus.

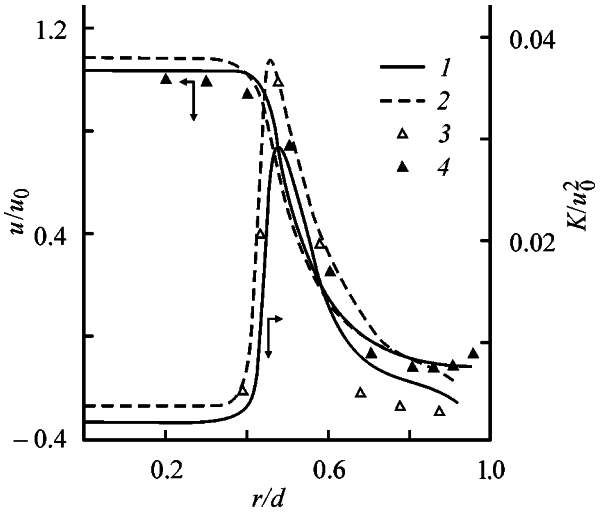

Fig. 3. Comparison of experimental and calculated axial velocities and specific kinetic energies of turbulence in the channel of a tubular apparatus. (*u*) Axial velocity component, (u_0) linear flow velocity, (*K*) kinetic energy of turbulence, (*r*) radial coordinate, and (*d*) diameter of the inlet and outlet orifices of the apparatus. Calculation: (*1*) this study and (*2*) [9]; (*3*, *4*) experiment [8].

ately downstream from the flow inlet into the diverging channel. A satisfactory agreement is observed (within 15%) between the calculated and experimental circulation zone lengths.

It was also shown experimentally that the quality of the forming emulsion (its homogeneity) strictly depends on the level of turbulence in the diffuser–confuser channel of the tubular jet apparatus (Fig. 2).

The agreement of the results is also observed for the axial velocity profiles and specific kinetic energy of turbulence (Fig. 3). The obtained results make it possible to calculate with confidence the characteristics of turbulent flow for analogous conditions and geometrically similar channels.

Calculations demonstrated that the best efficiency of fluid flow mixing is provided by tubular turbulent apparatus of diffuser–confuser design (Fig. 1b) with divergence angle α exceeding 20°–30°, with the convective velocity in the peripheral part of the apparatus much lower than that in its central part (Fig. 3). The transfer processes occur via turbulent exchange. This makes τ_m markedly shorter, which is rather important in performing fast chemical and mass-exchange processes. As a result, a tubular apparatus of diffuser–confuser design ensures, and this should always be kept in mind, a sufficiently homogeneous field of the turbulent diffusion coefficient D_t, with average D_t values in the central and peripheral parts of the tubular apparatus being only slightly different. The volume-averaged turbulent diffusion coefficients D_t are given in Table 2 for different parts of the apparatus and diffuser–confuser sections with different confuser divergence angles α. Noteworthy is the preservation of high numerical values of D_t at divergence angles α in the range 30°–85°.

The calculations performed allow apparatus of new type, not mentioned in the classification of apparatus for chemical industry [3, 4], to be recommended for use in fast chemical and mass-exchange physical processes. These are small-size tubular (0.03–0.3 m in diameter) apparatus of diffuser–confuser design, comprising several sections with divergence angles α ranging from 20° to 85°. Presently, apparatus of this kind are rather widely used in industry, including the manufacture of polymeric products. They are also highly efficient in the case of combined flows of fluids having strongly different densities and viscosities and in processing high-viscosity fluids. This results from the fact that a self-similar regime of fluid flow with viscosity-independent average character-

Table 2. Volume-averaged turbulent diffusion coefficients D_t in different parts and diffuser–confuser sections (Fig. 1b) of a tubular turbulent apparatus. Re = 250 000, d = 0.05 m, u_0 = 5 m s^{-1}, ρ = 1000 kg m^{-3}

Part of apparatus, section	Turbulent diffusion coefficients D_t at indicated α, deg							
	5	10	17	30	45	60	75	85
Parts of apparatus								
1	1.03	1.34	1.55	1.60	1.58	1.54	1.48	1.42
2	1.17	1.54	1.90	2.22	2.38	2.47	2.49	2.49
3	1.12	1.76	2.36	2.78	2.86	2.88	2.97	2.92
4	1.01	1.50	2.05	2.60	2.79	2.88	2.98	2.98
5	1.09	1.75	2.49	3.16	3.47	3.67	3.97	3.94
6	0.94	1.43	2.04	2.74	3.09	3.31	3.55	3.58
7	1.09	1.75	2.43	3.08	3.38	3.60	3.81	3.90
8	0.99	1.43	2.03	2.65	2.96	3.20	3.40	3.48
Diffuser–confuser sections								
I	1.12	1.47	1.79	2.03	2.14	2.18	2.18	2.16
II	1.05	1.59	2.15	2.66	2.81	2.88	2.98	2.97
III	0.99	1.54	2.18	2.87	3.21	3.42	3.68	3.69
IV	1.02	1.53	2.16	2.78	3.09	3.32	3.52	3.61

istics of the turbulent flow can be created in tubular turbulent jet apparatus [10].

Tubular turbulent apparatus of diffuser–confuser design show good performance in commercial production of elastomers based on binary and ternary copolymers of ethylene and propylene (preparation of gas–liquid mixtures, catalyst decomposition, introduction of stabilizers) [11–13], halobutyl rubber (chlorination of butyl rubber and also neutralization and washing of chlorobutyl rubber solutions) [14], and butadiene–styrene (emulsification, termination of the copolymerization reaction) [15], stereoregular *cis*-1,4-isoprene (prereactor, neutralization and washing of return solvent) [16, 17], stereoregular *cis*-1,4-butadiene (prereactor) rubbers, etc.

In all cases, the efficiency of reagent mixing increases markedly, which makes higher the sensitivity of the process to the action of various agents and improves the uniformity of the obtained polymeric products, including that between batches, and their technological, operational, and molecular characteristics. A quality level completely corresponding to the theoretical predictions could be achieved for a number of polymers. On the whole, all the processes are distinguished by pronounced energy and resource saving.

REFERENCES

1. Krekhova, M.G., Minsker, S.K., Prochukhan, A.A., and Minsker, K.S., *Teor. Osn. Khim. Tekhnol.*, 1994, vol. 28, no. 3, pp. 271–273.
2. Minsker, K.S. and Berlin, Al.Al., *Fast Polymerization Processes*, Gordon and Breach, 1996.
3. Berlin, Al.Al., Minsker, K.S., and Dyumaev, K.M., *Novye unifitsirovannye energo- i resursosberegayushchie vysokoproizvoditel'nye tekhnologii povyshennoi ekologicheskoi chistoty na osnove trubchatykh turbulentnykh reaktorov* (New Unified Power- and Resource-Saving High-Efficiency Technologies of Improved Environmental Safety Based on Tubular Turbulent Reactors), Moscow: NIITEKhIM, 1996.
4. Berlin, Al.Al., Minsker, K.S., and Zakharov, V.P., *Dokl. Ross. Akad. Nauk*, 1999, vol. 365, no. 3, pp. 360–363.
5. Berlin, Al.Al., Karpasas, M.M., Komapaniets, V.Z., *et al.*, *Dokl. Akad. Nauk SSSR*, 1989, vol. 305, no. 2, pp. 365–368.
6. Prochukhan, Yu.A., Minsker, K.S., Karpasas, M.M., *et al.*, *Vysokomol. Soedin., Ser. A*, 1988, vol. 30, no. 6, pp. 1259–1262.
7. Launder, B.E. and Spalding, D.B., *Mathematical Models of Turbulence*, London: Academic, 1972, 6th ed.

8. Chaturvedi, M.C., *J. Hydraul. Div., Proc. Am. Soc. Civil. Eng*., 1963, vol. 89, p. 61.
9. Turgeon, E. and Pelletier, D., *Papers of the 36th Aerospace Sci. Meet. and Exhibition: Proc. Am. Inst. of Aeronautics and Astronautics*, 1998, p. 501.
10. Landau, L.D. and Lifshits, E.M., *Teoreticheskaya fizika* (Theoretical Physics), vol. 6: *Gidrodinamika* (Hydrodynamics), Moscow: Nauka, 1988.
11. RF Patent 2141871.
12. RF Patent 2141872.
13. RF Patent 2141873.
14. Minsker, K.S., Zakharov, V.P., Ishtiryakov, A.D., *et al*., Abstracts of Papers, *Intensifikatsiya neftekhimicheskikh protsessov "Neftekhimiya-99": V Mezhdunarodnaya konferentsiya* (Intensification of Petrochemical Processes "Neftekhimiya-99": V Int. Conf.), Nizhnekamsk: Nizhnekamskneftekhim, 1999, vol. 1, pp. 124–126.
15. RF Patent 2059661.
16. RF Patent 2059656.
17. RF Patent 2059657.

Russian Journal of Applied Chemistry, Vol. 74, No. 1, 2001, pp. 95–98. Translated from Zhurnal Prikladnoi Khimii, Vol. 74, No. 1, 2001, pp. 91–95.

PROCESSES AND EQUIPMENT OF CHEMICAL INDUSTRY

Prediction of the Quality of Mixing of Disperse Materials

A. N. Verigin, V. G. Dzhangiryan, M. V. Emel'yanov, and V. G. Petrov

St. Petersburg State Technological Institute, St. Petersburg, Russia

Received June 1, 1998; in final form, July 2000

Abstract—An expression is derived allowing evaluation of the maximum achievable quality of mixing on the assumption that the key component particles are randomly distributed over the mixture volume.

Mixing of disperse materials, considered in a number of papers and monographs [1–9], is widely used in chemical industry. It is the stage of mixing that governs the quality of quite a number of final products, which determines the interest of a wide circle of researchers and engineers in this process.

Mixing consists in spatial distribution of components in order to obtain a mixture with uniform composition and physicochemical and chemical properties of the mixture [1]. The quality of a mixture is commonly assessed after its preparation by analysis of sample statistics, based on the distribution laws of their numerical characteristics or combinations of these. One of the most widely used criteria for assessment of the quality of a prepared mixture is the coefficient of heterogeneity (variation) or the variance of the key component distribution over its volume, calculated by analyzing samples of certain size. It is commonly believed that the practically achievable minimum variance corresponds to a random distribution of key component particles over the mixture bulk, except in the case when the variance is zero [1].

In practice, a problem is frequently encountered when it is necessary to assess, without performing the actual mixing, what is the achievable quality of the mixture and whether it can be improved in further operation of a mixer, i.e., the problem of quality prediction. Presently, there is no theoretically substantiated and experimentally verified technique for predicting the achievable quality of a mixture, i.e., finding the minimum variance of the key component distribution over its volume. Such a technique should take into account the size (volume) v_0 of particles of the key component, their volume-average content $c_0 = N_0 v_0 / V$, the mixer volume V, and, necessarily, the sample volume $V^* = \alpha V$, where $0 \le \alpha \le 1$. This problem has been commonly solved using statistical equations or empirically [1, 5, 7].

In the absence of segregation, the best mixture quality can be obtained on attainment of an equilibrium dynamic state, when the quality cannot be improved by random particle redistribution and the variance of the key component distribution over the mixture volume remains constant [5]. Thus, prediction of the quality of a mixture of disperse materials involves construction of a model of its equilibrium dynamic state. It is necessary to determine the possible deviation of the content of key component particles in an arbitrary volume (sample) from its mean value for a mixture with random particle distribution.

As an acceptable numerical characteristic of the equilibrium dynamic state of a system of disperse materials can serve the fractal dimension of a set of discrete objects (particles) [10]. The dimension of a point set can be determined in a number of ways [11–13]. Let us use its information dimension [14]. In analyzing the state of a mixture, measurement assumes its being partitioned into separate boxes of equal size. The measurement is done with a uniform scale with division value ε (resolving capacity). If we are interested in the number of key component particles in a box, then the mixture is divided into $1/\varepsilon$ boxes and the measurement is performed in one of these. Let $n(\varepsilon)$ be the number of boxes covering the mixture with nonzero probability (i.e., containing at least one particle of the key component). Some boxes will contain a greater number of particles than the others. The "natural measure" of the given partition is proportional to the frequency at which a key component particle is found within it. Following [14], we define $p_i(\varepsilon)$ as "probability density" of finding a particle in the ith box. The set of probabilities $\{p_i(\varepsilon)\}$ is termed "rough" or "coarse-grained" probability distribution at resolving capacity ε. Let N_0 be the total number of key component particles in the mixture (number of points in the set). To calculate the infor-

1070-4272/01/7401-0095$25.00

mation dimension, we find the number of particles N_i in each box $n(\varepsilon)$ of the partition and evaluate the probability $p_i(\varepsilon)$ of finding a particle in the ith box:

$$p_i(\varepsilon) = N_i/N_0, \qquad \sum_{i=1}^{N} p_i(\varepsilon) = 1. \tag{1}$$

We emphasize that $N_0 \neq n(\varepsilon)$. The average amount of information furnished by a single measurement with resolving capacity ε is given by

$$I(\varepsilon) = -\sum_{i=1}^{n(\varepsilon)} p_i(\varepsilon) \ln p_i(\varepsilon). \tag{2}$$

With decreasing ε (increasing resolving capacity), the number of boxes grows and we obtain a sequence of increasingly "fine-grained" probability distributions.

The information dimension d_I is the rate at which the amount of information grows with increasing measurement accuracy:

$$d_I = \lim_{\varepsilon \to 0} \frac{I(\varepsilon)}{\ln(1/\varepsilon)}. \tag{3}$$

It can be seen from formula (3) that d_I is determined by the asymptotic value of the slope of the plot of $I(\varepsilon)$ against $\ln(1/\varepsilon)$.

If the probabilities of all boxes in the partition are the same, then $I(\varepsilon) = \ln n(\varepsilon)$, and the information dimension reaches its maximum and coincides with the fractal dimension [14]:

$$d = \lim_{\varepsilon \to 0} \frac{\ln n(\varepsilon)}{\ln(1/\varepsilon)}. \tag{4}$$

The limit (4) may not always exist [15]. In the case when it does not, the notions of lower and upper information dimensions are introduced.

We can pass from a multicomponent mixture of volume V to analyzing a system uniting the set of coordinates of key component particles [8]. Provided that the particle sizes and, consequently, the ε value are finite, the fractal dimension of such a set (4) is given by the expression

$$d = \ln N/\ln(1/\varepsilon). \tag{5}$$

If the particle size is taken as the measure ε of the set (measurement accuracy), the latter can be written as

$$\varepsilon = (v_0/V)^{1/3}.$$

The number N of elements in a mixture having key component concentration c_0 and particle volume v_0 is given by

$$N = c_0 V/v_0 = N_0.$$

The expression for the fractal dimension of the mixture is written as

$$d = 3\ln N_0/\ln(V/v_0). \tag{6}$$

Correspondingly, we have for a sample

$$d^* = 3\ln(\alpha N_0)l/\ln(\alpha V/v_0). \tag{7}$$

Apparently, the condition $d^* < d$ must be fulfilled for $\alpha < 1$.

At sufficiently large mixture volume, when the number of particles of the key component is great, the concentrations at specific points can be considered a continuous source of information. It this case it seems natural to relate the uncertainty in the choice of a value of a random continuous variable to the density of probability distribution $p(c)$ of these values. If we assume that the mixture volume is unlimited, the expression for the entropy $I(C)$ of a continuous source of information has the form [16]

$$I(C) = -\int_{-\infty}^{\infty} p(c) \ln p(c) \mathrm{d}c - \lim_{\Delta c \to 0} \Delta c. \tag{8}$$

The second term in the right-hand side of relation (8) tends to infinity when the difference between the neighboring values of the random variable approaches zero: $\Delta c \to 0$, and it may be concluded that the entropy of the continuous distribution is infinitely large. There is nothing paradoxical in this conclusion; moreover, it would have been drawn beforehand. The uncertainty in the choice from an infinitely large number of possible values of the number of key component particles at specific points is infinitely large.

The first term in the right-hand side of relation (8) has a finite value depending on the distribution of the random variable C and independent of the accuracy of its determination Δc. It has the same structure as the entropy of the discrete source (2). The second term of the same relation, conversely, depends solely on the quantization step Δc (accuracy of determination) of

the random variable C. It is this term that is reason why $I(C)$ becomes infinite.

The finite characteristic of the information properties of a continuous source can be obtained using two known approaches.

On the one hand, the first term in relation (8) is taken as uncertainty. The entropy determined in this way, the so-called differential entropy, can be interpreted as mean uncertainty in the choice of a random variable C with arbitrary distribution with respect to the mean uncertainty in the choice of a random quantity varying within the range from zero to unity and having uniform distribution.

Let us assume that the domain of variation of a random continuous variable C with mean value c_0 is unbounded but its variance is known to be bounded. Then the maximum differential entropy will be observed for a normal distribution of the variable C with mean value c_0. For a mixture of two disperse materials, the first assumption follows from the assumption of a continuous distribution of the key component over the mixture volume, and the second, from the very formulation of the problem. To furnish proof [16], it is necessary to solve the problem of finding a function $p(c)$ ensuring the maximum value of the functional (9) under the following constraints:

$$\int_{-\infty}^{\infty} p(c)\mathrm{d}c = 1, \qquad \int_{-\infty}^{\infty} c^2 p(c)\mathrm{d}c = \sigma^2.$$

The sought-for distribution density $p(c)$ can be determined by the Lagrange multiplier method in the form of a Gaussian distribution

$$p(c) = \frac{1}{\sigma(2\pi)^{1/2}} \exp[-(c - c_0)^2/(2\sigma^2)]. \qquad (9)$$

Having calculated the functional (8) for this distribution, we obtain the maximum differential entropy I_c^*

$$I_c^* = -\int p(c) \ln p(c)\mathrm{d}c = \ln[(2\pi e)^{1/2}\sigma/c_0]. \qquad (10)$$

On the other hand, as applied to the problem in question, the concentration can be only determined at a sufficiently large sample volume, when the probability of finding in it at least one particle of the key component is close to unity. Therefore, the possible number of C values within the prescribed measurement accuracy (sample volume) is to be considered as a single value. It is necessary to subtract from the mean uncertainty of the choice by the source of a certain value (unit sample) the mean uncertainty of the same source, obtained under the condition that C is determined with a certain accuracy. Such a difference is the measure of eliminated uncertainty or amount of information. With a sample taken from the mixture at random, the average amount of information contained in any particular sample with respect to the amount of information contained in the mixture as a whole is equal to the difference of the *a priori* and *a posteriori* entropies of the source of information (mixture). The information entropy depends on the accuracy with which V^*, i.e., the sample volume, is measured. With account of (2) and (4), the expression for evaluating the maximum entropy of a mixture (source) becomes

$$I(\alpha) = -\sum_{i=1}^{n(\alpha)} d \ln \alpha = (d - d^*) + \ln(d - d^*). \qquad (11)$$

In this case, account was taken of the fact that there is no scaling invariance for the mixture and the fractal dimension depends on the sample volume. Comparison of expressions (10) and (11) gives

$$\ln[(2\pi e)^{1/2}\sigma/c_0] = (d - d^*) + \ln(d - d^*).$$

Simple transformations give the sought-for expression for evaluating the mixture quality

$$\sigma = \frac{c_0}{(2\pi e)^{1/2}}(d - d^*)\exp(d - d^*). \qquad (12)$$

where σ is the limiting minimal variance of the distribution of the key component over the volume of a mixture with prescribed properties, independent of the type of a mixer employed.

With account of expressions (7) and (8) allowing calculation of the fractal dimensions of the mixture, d, and sample, d^*, we get

$$d - d^* = \frac{3\ln\alpha \ln c_0}{\ln(V/v)\ln(\alpha V/v_0)}.$$

The possibility of using Eq. (12) was verified experimentally. Investigations were carried out on 5-l mixers with planetary stirring device [9]. To rule out the possible influence of physicochemical effects and gravity forces on the mixture quality, stirring experiments were done with particles of the same size and density (polystyrene, ca. 3 mm in size), differing only in color. The distribution of tracer particles over the mixer volume was studied. After the mixing process

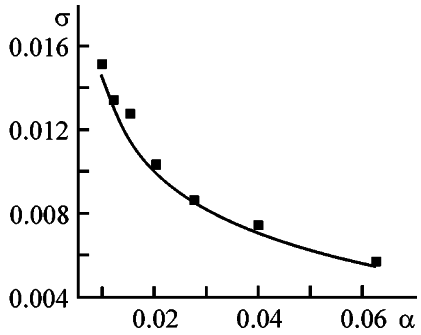

Variance σ of the key component distribution over the mixture volume vs. the relative sample volume α. (Line) calculation by Eq. (12); (points) experiment.

was complete, the mixture volume was divided into a certain number of samples. The number of tracer particles in a sample was determined by counting. Then the mixture variance was calculated. The experimental data are compared with results of calculations by Eq. (12) in the figure where the mixture variance is plotted against the sample volume determined as a fraction of the volume mixture. The observed discrepancy is accounted for by the fact that expression (12) is derived under the condition of a random distribution of the key component over the mixture volume. This condition can be only met if each dispersion particle can independently execute a certain finite motion in any direction during a finite interval of time. Such conditions cannot be provided in experiment. The character of motion of dispersion particles depends on specific features of the mixer operation, and the intensity of this motion depends on the energy expended in mixing.

CONCLUSION

Analysis of a mixture with random distribution of components gave an expression for calculating the limiting minimum variance of the key component distribution in the mixture volume in relation to the component properties, sample size, and mixer volume. The results of theoretical investigations are confirmed by the experiment.

REFERENCES

1. Kafarov, V.V., Dorokhov, N.N., and Arutyunov, S.Yu., *Sistemnyi analiz protsessov khimicheskoi tekhnologii* (Systems Analysis of Chemical Processes), Moscow: Nauka, 1985.
2. Generalov, M.B., Abstracts of Papers, *Vsesoyuznaya konferentsiya po tekhnologii sypuchikh materialov* (All-Union Conf. on Technology of Loose Materials), Yaroslavl: Yaroslav. Politekh. Inst., 1989, vol. 2, p. 178.
3. Zaitsev, A.I., Bytev, D.O., and Sidorov, V.N., *Zh. Vses. Khim. O–va. im. D.I. Mendeleeva*, 1988, vol. 33, no. 4, pp. 390–396.
4. Akhmadiev, F.G. and Aleksandrovskii, A.A., *Zh. Vses. Khim. O–va. im. D.I. Mendeleeva*, 1988, vol. 38, no. 4, pp. 448–453.
5. Makarov, Yu.I., *Apparaty dlya smesheniya sypuchikh materialov* (Apparatus for Mixing of Loose Materials), Moscow: Mashinostroenie, 1973.
6. Makarov, Yu.I., *Zh. Vses. Khim. O–va. im. D.I. Mendeleeva*, 1988, vol. 33, no. 4, pp. 384–389.
7. Grosz-Roell, F., *Int. Chem. Eng.*, 1980, vol. 20, no. 4, pp. 542–549.
8. Verigin, A.N., Ermakov, A.S., and Shashikhin, E.Yu., *Zh. Prikl. Khim.*, 1994, vol. 67, no. 9, pp. 1561–1562.
9. Osen'kina, V.A., A Study of the Process of Mixing of Loose Materials in Batch Mixers: High-Velocity, Centrifugal, and That with Planetary-Conveyor Stirrer, *Cand. Sci. Dissertation*, Moscow, 1972.
10. Moon, F.C., *Chaotic Vibrations. An Introduction for Applied Scientists and Engineers*, New York: Wiley–Interscience, 1987.
11. Bergé, P., Pomeus, Y., and Vidal, Ch., *L'ordre dans le chaos: Vers une approche détermeniste de la turbulence*, Paris: Hermann, 1988.
12. Lichtenberg, A.J. and Liberman, M.A., *Regular and Stochastic Motion*, New York: Springer, 1983.
13. Loskutov, A.Yu. and Mikhailov, A.S., *Vvedenie v sinergetiku* (Introduction to Synergetics), Moscow: Nauka, 1990.
14. Nicolis, J.S., *Dynamics of Hierarchical Systems: An Evolutionary Approach*, Berlin: Springer, 1986.
15. Neimark, Yu.I. and Landa, P.S., *Stokhasticheskie i khaoticheskie kolebaniya* (Stochastic and Chaotic Oscillations), Moscow: Nauka, 1987.
16. Dmitriev, V.I., *Prikladnaya teoriya informatsii* (Applied Theory of Information), Moscow: Vysshaya Shkola, 1989.

Russian Journal of Applied Chemistry, Vol. 74, No. 1, 2001, pp. 99–102. Translated from Zhurnal Prikladnoi Khimii, Vol. 74, No. 1, 2001, pp. 96–99.

ORGANIC SYNTHESIS AND INDUSTRIAL ORGANIC CHEMISTRY

Synthesis of a High-Energy-Capacity Compound, Tetrammine-*cis*-bis(nitro-2*H*-tetrazolato-N^2)cobalt(III) Perchlorate

A. Yu. Zhilin, M. A. Ilyushin, I. V. Tselinskii, and A. S. Brykov

St. Petersburg State Technological Institute, St. Petersburg, Russia

Received February 10, 2000; in final form, September 2000

Abstract—The conditions for preparing tetrammine-*cis*-bis(nitro-2*H*-tetrazolato-N^2)cobalt(III) perchlorate and the nature of impurities affecting the yield and purity of the target product were studied. The compound can be efficiently prepared using microwave heating.

To meet the requirements to the process, service, and environmental safety of explosives, which become more and more stringent, efforts are made to find new high-energy-capacity compounds to be used as primers among *d*-metal coordination compounds [1–3]. Tetrammine-*cis*-bis(nitro-2*H*-tetrazolato-N^2)cobalt(III) perchlorate (**I**), according to [4, 5], is one of the most promising explosives for safe primers (including laser initiation):

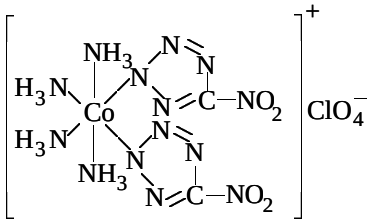

1

Some physicochemical and explosive properties of **I** are given below:

Density of single crystal, g cm^{-3}	2.05	[6]
Detonation rate at a single crystal density of 1.97 g cm^{-3}(calculation), km s^{-1}	8.1	[5]
Temperature of the onset of intense decomposition, °C (at heating rate of 20 deg min^{-1})	269	[7]
Sensitivity to the fire beam of fuse, cm	3–5*	[5]
Minimal charge for hexogen, g (KD8)	0.05	[5]
Time of transition from combustion to detonation, μs	~10	[4]

* Sensitivity limit: upper 3 cm, lower 5 cm.

In this work we studied the influence of the synthesis conditions on the yield and quality of **I**. Compound **I** can be prepared by the following scheme [7]:

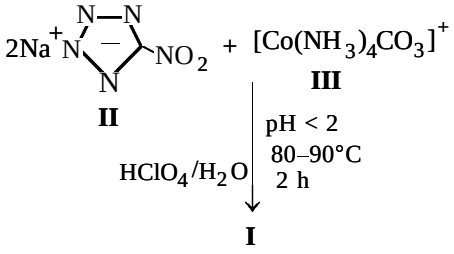

(1)

We found that the yield of the target product was 50–70%. The synthesis conditions were optimized by fractional factorial experiment (FFE) of the 2^{3-1} type with the generating ratio $X_3 = X_1X_2$. Analysis of the mathematical description revealed the effect on the process of the following factors: reaction (or exposure) time, x_1 (h); acidity of the medium, expressed through the perchloric acid concentration, x_2 (%); and reaction temperature, x_3 (°C). As the response function we chose the yield of the target product y (%). The *a priori* information suggested that the interaction effect X_1X_2 is insignificant; therefore, it was replaced in the design matrix by the factor X_3.

Main characteristics of the FFE of the 2^{3-1} type

Plan parameter	x_1	x_2	x_3
Zero level	2.0	7.5	80
Variation interval	1.0	2.5	10

The experimental results are given in the table.

The determining contrast and the system of simultaneous estimates of the coefficients have the form

$$1 = X_1X_2X_3;$$

$$b_1 \rightarrow \beta_1 + \beta_{23},$$

1070-4272/01/7401-0099$25.00

Fractional factorial experiment of the 2^{3-1} type

Run no.	Planning matrix			Response function	
	x_1	x_2	x_3	y_{ej}	y_{cj}
1	+1	–1	–1	23.1	23.85
2	–1	+1	–1	32.2	31.45
3	–1	–1	+1	60.3	60.85
4	+1	+1	+1	69.5	69.35

$$b_2 \rightarrow \beta_2 + \beta_{13},$$

$$b_3 \rightarrow \beta_3 + \beta_{12}.$$

By statistical processing of the experimental data, we obtained a regression equation adequately (acoording to the Student and Fisher tests [8]) describing the reaction:

$$y = 46.3 + 4.6x_1 + 4.5x_2 + 18.6x_3.$$

Analysis of the regression equation shows that the reaction temperature is the most significant factor of the process.

Further experiments on synthesis of **I** were performed with microwave heating (MWH). Recently there has been an increased interest in MWH as an alternative way of thermal activation of chemical reactions [9]. A chemical system containing polar molecules or ions can actively take up the energy of a UHF electromagnetic field, transform it to thermal energy, and thus warm up (in our case to ~102°C). The MWH accelerates anation in Co(III) ammine complexes [10]. By substitution of coordinated water with the 5-nitrotetrazole anion under MWH conditions (1 h), we prepared compound **I** in a 78% yield, which practically coincides with the value predicted by the mathematical description. Thus, microwave heating of the reactants ensures a high yield of **I** within a considerably shorter time.

In synthesis of **I**, we used sodium 5-nitrotetrazolate (**II**) prepared by the noncatalytic Sandmeyer reaction from 5-aminotetrazole [11]:

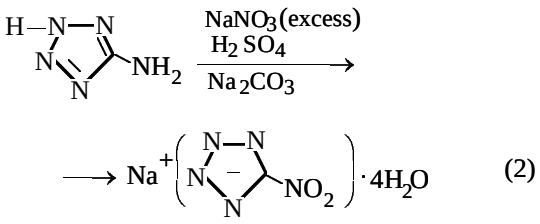

(2)

Salt **II** can contain sodium nitrite $NaNO_2$ as a natural impurity if the crude product is purified insufficiently. The NO_2^- ion competes with the nitrotetrazolate ion for the position in the inner sphere in the anation reaction [12]:

$$[Co(NH_3)_4(H_2O)_2]^{3+} + 2An \xrightarrow{H^+} [Co(NH_3)_4(An)_2]^+ + 2H_2O, \quad (3)$$

where

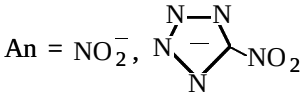

Therefore, it is very important to elucidate the influence of nitrite ion on formation of **I**. At +25°C, nitrite ion substituted both water molecules in **IV** within 170 h.

$$[Co(NH_3)_4(H_2O)_2]^{3+} + 2NO_2^- \xrightarrow{H^+} [Co(NH_3)_4(NO_2)_2]^+ + 2H_2O. \quad (4)$$

IV **V**

Complexes **IV** and **V** were isolated as sulfates: $[Co(NH_3)_4(H_2O)_2]_2(SO_4)_3$ (**IVa**) and $[Co(NH_3)_4 \cdot (NO_2)_2]_2SO_4$ (**Va**).

At the same temperature, simultaneous action of an excess of nitrite and nitrotetrazolate ions on cation **IV** for 170 h results in complete substitution of inner-sphere water and formation of complex **VI**:

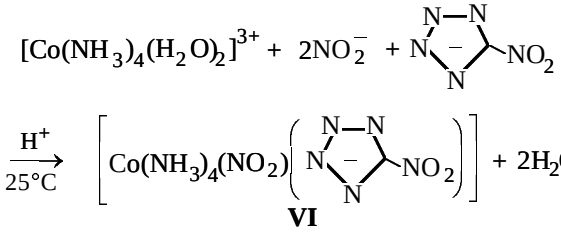

(5)

VI

Compound **VI** was isolated as crystal hydrate:

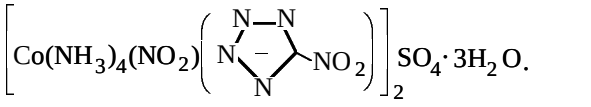

VIa

At the temperature increased to 80°C, instead of the expected product **I** we isolated from the reaction mixture salt **VII**:

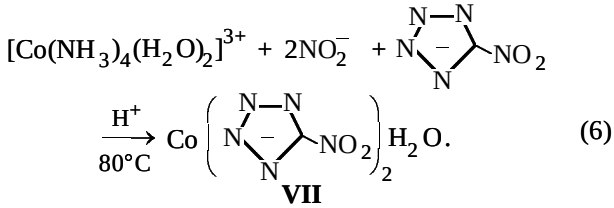

(6)

VII

Salt **VII** is very sensitive to mechanical actions and decomposes on heating with explosion. Hence, it is a primer [13]. Its impurity in **I** is inadmissible. Formation of **VII** involves breakdown of the inner sphere of **I** with reduction of Co(III) to Co(II). This process is probably due to possible combination of redox reactions initiated by the nitrite ion and to an appreciable *trans* effect of the nitrotetrazolate anion in the inner coordination sphere [14]. To confirm this assumption, we studied the reaction between **V** and 5-nitrotetrazolate anion in acid solution at 50–70°C. We found that the product composition depends on time. For example, 2 h after the start of the reaction the major product is complex **VIII**, but then its content decreases as compound **VII** is accumulated:

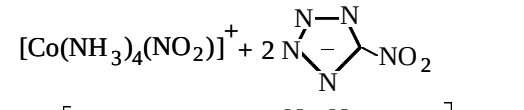

VIII

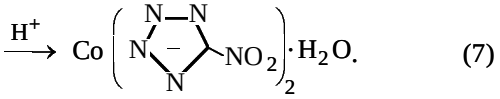

VII

Formation of complex **VIII** confirmed the assumption that in the course of synthesis of **I** in the presence of nitrite ions the ammine ligands become labile and can be substituted by other ligands.

Our experimental results show that the synthesis of **I** in aqueous solution should be performed at a temperature as high as possible and that the reactants should be thoroughly purified to remove sodium nitrite.

EXPERIMENTAL

The IR spectra were recorded on a Specord M-80 spectrophotometer from thin-film samples between KBr plates. The ^{1}H NMR spectra were taken on a Perkin–Elmer R-12 spectrometer operating at 60 MHz, with HMDS as internal reference. The reaction progress was monitored by TLC on Silufol UV-254 plates (eluent 3% aqueous $NaClO_4$).

The UHF heating device was a short-circuited waveguide of 9×4.5 cm cross section, connected to a UHF generator with the output capacity of 600 W and working frequency of 2450 MHz. The reaction vessel (a glass test tube 35 mm in diameter, equipped with a thermometer with an organic working liquid and a reflux condenser) was placed in the waveguide through a special hole.

Carbonatotetramminecobalt(III) perchlorate (IIIa) was prepared by the procedure in [15]. The yield of **IIIa** after drying was 77%. IR spectrum, ν, cm^{-1}: 1596 s, 1560 m (C=O, NH_3), 1084 s (ClO_4). ^{1}H NMR spectrum (DMSO-d_6), δ, ppm: 4.40 (12H, NH_3).

Found, %: C 4.6, H 4.7, N 20.1.
$CH_{12}ClCoN_4O_7$.
Calculated, %: C 4.2, H 4.2, N 19.6.

Tetrammine-*cis*-bis(nitro-2*H*-tetrazolato-N^2)cobalt(III) perchlorate (I). A 1-g portion of carbonatotetramminecobalt(III) perchlorate (**IIIa**) was dissolved in 10 ml of 10% perchloric acid until the CO_2 evolution ceased. The solution was filtered, and 34 ml of a 4.4% solution of sodium 5-nitrotetrazolate (**II**) was added. The reaction mixture was heated on a boiling water bath for 4 h and then cooled to 15°C; the precipitate was filtered off, washed with ethanol (2 ± 0.5 ml), and recrystallized from 1% $HClO_4$. Yield of **I** 0.92 g. IR spectrum, ν, cm^{-1}: 1588 m, 1316 m (NH_3, tetrazole), 1076 m (ClO_4), 1540 m (NO_2). ^{1}H NMR spectrum (DMSO-d_6), δ, ppm: 3.79, 4.29 (12H, NH_3).

Found, %: C 4.8, H 2.3, N 42.6.
$C_2H_{12}ClCoN_{14}O_8$.
Calculated, %: C 5.3, H 2.7, N 43.1.

Dinitritotetramminecobalt(III) sulfate (Va) was prepared according to [16]. Yield after drying 57%. IR spectrum, ν, cm^{-1}: 3120 m, 1620 m (NH_3), 1388 m, 1304 m (NO_2), 1120 m (SO_4).

Found, %: H 4.1, N 31.4.
$H_{24}Co_2N_{12}O_{12}S$.
Calculated, %: H 4.5, N 31.4.

Nitrito(nitrotetrazolato)tetramminecobalt(III) sulfate trihydrate (VIa). To a mixture of 16 ml of an aqueous solution containing 3.3 g of sodium nitrite and 60 ml of a 4.4% solution of sodium 5-nitrotetrazolate (**II**), we added 10 ml of a 1.5% sulfuric acid solution containing 1 g of diaquatetramminecobalt(III) sulfate (**IVa**) prepared according to [16]. The mixture was allowed to stand for 7 days. After drying, the yield of **VIa** was 70%. IR spectrum, ν, cm^{-1}: 1552 w (C–NO_2), 1400 m (NO_2), 1280 m (NH_3), 1052 m (SO_4).

Found, %: C 3.3, H 3.8, N 38.3.
$C_2H_{30}Co_2N_{20}S$.
Calculated, %: C 3.3, H 4.2, N 38.6.

Cobalt(II) nitrotetrazolate monohydrate (VII). To a mixture of 16 ml of an aqueous solution containing 3.3 g of sodium nitrite and 60 ml of a 4.4% solution of sodium 5-nitrotetrazolate (**II**), we added 10 ml of a 1.5% sulfuric acid solution containing 1 g of diaquatetramminecobalt(III) sulfate (**IVa**) prepared according to [16]. The mixture was heated to 80°C and kept at this temperature for 3 h. Yield of **VII** after drying 62%. IR spectrum, ν, cm^{-1}: 3544 w, 1616 m (H_2O), 1560 s, 1320 m (NO_2), 1440 m (tetrazole).

Found, %: C 7.8, H 0.6, N 45.6.
$C_2H_2CoN_{10}O_5$.
Calculated, %: C 7.9, H 0.7, N 45.9.

Triamminebis(5-nitrotetrazolato)nitritocobalt(III) hydrate (VIII). To a mixture of 16 ml of an aqueous solution containing 3.3 g of sodium nitrite and 60 ml of a 4.4% solution of sodium 5-nitrotetrazolate (**II**), we added 10 ml of a 1.5% sulfuric acid solution containing 1 g of diaquatetramminecobalt(III) sulfate (**IVa**) prepared according to [16]. The mixture was heated to 60°C and kept at this temperature for 2 h. Compound **VIII** precipitated on cooling. Yield after drying 39%. IR spectrum, ν, cm^{-1}: 3200 m (NH_3), 1544 s, 1332 m (C–NO_2), 1416 m, 1312 (NO_2).

Found, %: C 5.4, H 2.8, N 48.5.
$C_2H_{11}CoN_{14}O_7$.
Calculated, %: C 5.9, H 2.7, N 48.7.

The mother liquor was kept for 1 h at 60–70°C. An additional crop of **VII** was obtained; yield after filtration, washing, and drying 25%.

REFERENCES

1. Sinditskii, V.P. and Fogel'zang, A.E., *Ross. Khim. Zh.*, 1997, vol. 41, no. 4, pp. 74–80.
2. Ilyushin, M.A. and Tselinskii, I.V., *Ross. Khim. Zh.*, 1997, vol. 41, no. 4, pp. 3–13.
3. Ilyushin, M.A., Tselinskii, I.V. and Chernyi, A.V., *Ross. Khim. Zh.*, 1997, vol. 41, no. 4, pp. 81–88.
4. Bates, L.R., *Proc. Symp. Explos. Pyrotech.*, 1986, no. 13, pp. III/1–III/10.
5. Smirnov, A.V., Ilyushin, M.A., Tselinskii, I.V., and Khovaiko, V.I., in *Trudy nauchno-tekhnicheskoi konferentsii "Uspekhi khimii organicheskikh soedinenii azota"* (Proc. Scientific and Technical Conf. "Advances in Chemistry of Nitrogen Organic Compounds"), St. Petersburg: Sankt-Peterb. Gos. Tekhnol. Inst. (Tekh. Univ.), September 15–17, 1997, p. 21.
6. Morosin, B., Dunn, R.G., Assink, R., *et al.*, *Acta Crystallogr., Sect. C*, 1997, vol. 53, pp. 1609–1611.
7. Fronabarger, J., Schuman, A., Chapman, R.D., *et al.*, *AIAA Pap.*, 1995, no. 2858, pp. 1–7.
8. Akhnazarova, S.L. and Kafarov, V.V., *Metody optimizatsii eksperimenta v khimii i khimicheskoi tekhnologii* (Methods for Experiment Optimization in Chemistry and Chemical Technology), Moscow: Vysshaya Shkola, 1985.
9. Kuz'min, N.M. and Kubrakova, I.V., *Zh. Anal. Khim.*, 1996, vol. 51, no. 1, pp. 44–48.
10. Ilyushin, M.A., Lukogorskaya, A.S., Tselinskii, I.V., and Brykov, A.S., *Zh. Obshch. Khim.*, 1999, vol. 69, no. 3, pp. 449–451.
11. Ostrovskii, V.A. and Koldobskii, G.I., *Ross. Khim. Zh.*, 1997, vol. 41, no. 2, pp. 84–98.
12. Kostromina, N.A., Kumok, V.N., and Skorik, N.A., *Khimiya koordinatsionnykh soedinenii*, Moscow: Vysshaya Shkola, 1990.
13. Bagal, L.I., *Khimiya i tekhnologiya initsiiruyushchikh vzryvchatykh veshchestv* (Chemistry and Technology of Primer Explosives), Moscow: Mashinostroenie, 1975.
14. Nefedov, V.I., *Trans-vliyanie v khimii koordinatsionnykh soedinenii. Ser. "Problemy koordinatsionnoi khimii"* (*trans* Effect in Coordination Chemistry, Ser. "Problems of Coordination Chemistry"), Moscow: Nauka, 1979.
15. Novakovskii, M.S., *Laboratornye raboty po khimii kompleksnykh soedinenii* (Laboratory Works on Coordination Chemistry), Kharkov: Khar'kov. Univ., 1972.
16. Glikina, F.B. and Klyuchnikov, N.G., *Khimiya kompleksnykh soedinenii* (Coordination Chemistry), Moscow: Prosveshchenie, 1967.

Russian Journal of Applied Chemistry, Vol. 74, No. 1, 2001, pp. 103–105. Translated from Zhurnal Prikladnoi Khimii, Vol. 74, No. 1, 2001, pp. 100–102.

ORGANIC SYNTHESIS AND INDUSTRIAL ORGANIC CHEMISTRY

Efficient Procedure for Preparing Salicyl Alcohols

M. L. Belyanin, V. D. Filimonov, and E. A. Krasnov

Siberian State Medical University, Tomsk, Russia
Tomsk Polytechnic Institute, Tomsk, Russia

Received February 21, 2000

Abstract—A new convenient procedure was developed for selective *ortho*-hydroxymethylation of phenols by reaction of paraformaldehyde with a mixture of phenol and orthoboric acid. The method is general for phenols containing no strong electron-withdrawing substituents; it allows preparation of *o*-hydroxybenzyl alcohols of high purity in a high yield.

Salicyl (*o*-hydroxybenzyl) alcohol and its derivatives are of interest as intermediates in synthesis of many organic compounds: phenylchromones [1], isoflavones [2], etc.

Salicyl alcohol is an aglycone of a number of glycosides found in Salicaceae. Some of them exhibit antihelminth [3] and antiviral [4] activity.

One of the most widely used routes to salicyl alcohol is hydroxymethylation with formaldehyde or compounds generating it of phenyl metaborate PhOB=O (exists as trimers [5]). The initial metaborate is prepared by refluxing equimolar amounts of phenol and boric acid in aprotic aromatic solvents (toluene, xylene) with azeotropic distillation of the released water [5–9]. The yield of the crude target product, according to patents [6–8], depends on the initial phenol and does not exceed 65%; attempts to reproduce the synthesis of salicyl alcohol described in the patent resulted in a yield as low as 35% [5]. The conversion of phenol was incomplete, and polycondensation products formed, complicating purification of the target product [5].

Another route is hydroxymethylation of phenol in the presence of a 1.5-fold excess of arylboronic acids $ArB(OH)_2$. The reaction involves intermediate formation of cyclic esters of hydroxybenzyl alcohol and arylboronic acid. The desired alcohol is released by treatment of these esters with propylene glycol or hydrogen peroxide [10].

A simpler route to salicyl alcohols is reaction of paraformaldehyde with a mixture of phenol and excess boric acid in benzene under conditions of continuous azeotropic distillation of water, without preparing phenyl metaborate in advance. By this method we successfully performed selective *o*-hydroxymethylation of a series of phenols **1a**–**1k** and obtained the corresponding salicyl alcohols **2a**–**2k** (Table 1).

The structures of **2a**–**2k** were proved by the ^1H NMR (Table 2) and IR spectra and by comparison with the authentic samples. The IR spectra of **2a**–**2k** contain two strong absorption bands at 3475–3440 and 3240–3165 cm^{-1} characteristic of the intramolecular hydrogen bond and of O–H stretching vibrations, and also characteristic absorption bands ν(C–O) at 1015–1045 cm^{-1}:

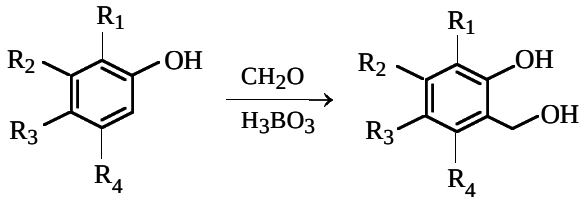

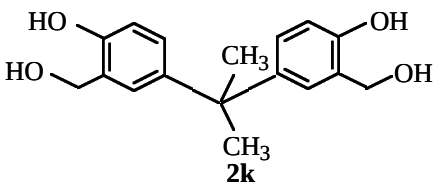

2k

where $R^1 = R^2 = R^3 = R^4 = H$ (**a**); $R^2 = R^3 = R^4 = H$, $R^1 = CH_3$ (**b**); $R^1 = R^2 = R^4 = H$, $R^3 = CH_3$ (**c**); $R^2 = R^3 = H$, $R^1 = CH(CH_3)_2$, $R^4 = CH_3$ (**d**); $R^1 = R^2 = R^4 = H$, $R^3 = OCH_3$ (**e**); $R^1 = R^2 = R^4 = H$, $R^3 = Cl$ (**f**); $R^1 = R^2 = R^4 = H$, $R^3 = F$ (**g**); $R^1 = R^2 = R^4 = H$, $R^3 = Ph$ (**h**); $R^1 = R^2 = R^4 = H$, $R^3 = OCOPh$ (**i**); $R^1 = R^3 = R^4 = H$, $R^2 = OCOPh$ (**j**).

ortho-Hydroxymethylation of phenols **1a**–**1k** by the suggested procedure occurs at lower temperature (up to 81°C), takes longer time, and requires a larger

1070-4272/01/7401-0103$25.00

Table 2. Synthesis of *o*-hydroxybenzyl alcohols **2a**–**2k** by reaction of phenols **1a**–**1k** with paraform

Compound	τ, h	Yield, %	mp, °C
2a	22	53	84–85 (C_6H_6) (85–86 [11])*
2b	37	48	25–27 (hexane) (5 [6], 33–34 [11])
2c	29	63	102–103 (C_6H_6) (104–105 [11])
2d	13	61	83–84 (hexane) (86 [12])
2e	21	40	79–80 ($CHCl_3$) (80–81 [11])
2f	53	54	92–93 (C_6H_6) (92–93 [11])
2g	38	34	69–70 (C_6H_6) (68–70 [13])
2h	46	68	162–163 ($C_6H_5CH_3$) (164–165 [13])
2i	52	60	114–115 (C_6H_6)
2j	33	35	125–126 (C_6H_6)
2k	49	56	144–145 (water)

* In parentheses are published data.

excess of boric acid (up to 1.5 mol) than hydroxymethylation of aryl metaborates [5–9]. Also, fresh portions of paraform should be added at regular intervals to compensate for its removal with the distillate. Nevertheless, there are important advantages: complete conversion of the initial phenol, absence of oligomeric products, and higher yield and purity of the target alcohols **2a**–**2k**.

It is important for practice that in hydroxymethylation of phenyl metaborate the resulting salicyl alcohol, as a rule, is isolated by treatment of the reaction mixture with alkali [5–7, 9], which makes this procedure unsuitable for preparing salicyl alcohols with substituents sensitive to bases. It was found that the boric acid esters formed under conditions of our procedure can be successfully saponified by keeping the reaction mixture in water without adding alkali. This approach allowed us to perform for the first time direct selective hydroxymethylation of phenols **1i** and **1j** containing phenyl benzoate moieties. The resulting alcohols **2i** and **2j** (Table 1) are synthetic equivalents of difficultly accessible dihydroxybenzyl alcohols.

The relatively low yield of **2j** is due to the fact that reaction of phenol **1j** with paraform yields, according to the ^{1}H NMR spectrum, a mixture of **2j** and its isomer, 2-hydroxymethyl-3-benzoyloxyphenol, inseparable by chromatography. In other words, hydroxymethylation occurs at both *o*-positions of the phenolic hydroxyl in **1j**. We were able to isolate only a portion of **2j** by single recrystallization of the mixture from benzene.

It should be noted that pyrocatechol monobenzoate appeared to be almost inert in hydroxymethylation (110 h). This is probably due to a strong intramolecular hydrogen bond blocking the phenolic hydroxyl in the *o*-position relative to the benzoate group.

Reaction of bisphenol **1k** containing two equivalent phenolic hydroxyls with paraform yields bis(hydroxymethyl) derivative **2k** within 49 h. At a shorter reaction time, the reaction mixture contained, according to TLC, unchanged **1k**, the monohydroxymethylation product, and alcohol **2k**; the latter is formed even in early stages of the reaction. Thus, hydroxymethylation of phenol **1k** occurs nonselectively at both phenyl rings.

Table 2. ^{1}H NMR spectra of salicyl alcohols **2a**–**2k** in DMSO-d_6

Compound	δ, ppm
2a	4.70 (s, 3H, CH_2OH), 6.70–7.18 (m, 4H, Ar), 8.80 (s, 1H, ArOH)
2b	2.13 (s, 3H, CH_3), 4.63 (s, 2H, CH_2OH), 6.52–6.95 (m, 3H, Ar)
2c	2.18 (s, 3H, CH_3), 4.43 (s, 2H, CH_2), 4.89 (s, 1H, CH_2OH), 6.61–7.07 (m, 3H, Ar), 9.03 (s, 1H, ArOH)
2d*	1.10–1.20 (d, 6H, $C\underline{H}_3$–CH–$C\underline{H}_3$), 2.02 (s, 4H, $ArC\underline{H}_3$, CH_3–$C\underline{H}$–CH_3), 3.28 (m, 1 H, OH), 5.04 (s, 2H, CH_2), 6.65–7.02 (m, 2H, Ar)
2e*	3.10 (s, 1H, OH), 3.60 (s, 3H, OCH_3), 4.63 (s, 2H, CH_2), 6.53–6.66 (m, 3H, Ar)
2f	4.74 (s, 2H, CH_2), 5.20 (s, 1H, $CH_2O\underline{H}$), 6.98–7.54 (m, 3H, Ar), 9.90 (s, 1H, ArOH)
2g	4.50 (s, 2H, CH_2), 4.80 (s, 1H, $CH_2O\underline{H}$), 6.70–7.26 (m, 3H, Ar), 9.40 (s, 1H, ArOH)
2h	4.80 (s, 2H, CH_2), 5.34 (s, 1H, $CH_2O\underline{H}$), 7.05–7.84 (m, 8H, Ar), 9.78 (s, 1H, ArOH)
2i	4.74 (s, 2H, CH_2), 5.30 (s, 1H, $CH_2O\underline{H}$), 7.08–8.36 (m, 8H, Ar), 9.73 (s, 1H, ArOH)
2j**	5.20 (s, 2H, $C\underline{H}_2OH$), 6.91–8.33 (m, 8H, Ar), 9.06 (s, 1H, ArOH)
2k	1.81 (d, 6H, $C\underline{H}_3CC\underline{H}_3$), 4.76 (s, 4H, $C\underline{H}_2OH$), 5.26 (s, 2H, $CH_2O\underline{H}$), 6.90–7.46 (m, 6H, Ar), 9.39 (s, 2H, ArOH)

* In $CDCl_3$. ** In pyridine-d_5.

Phenols with electron-withdrawing substituents in the ring (NO_2, CHO, COOH) remain inert under the reaction conditions and do not give the corresponding salicyl alcohols.

The positive effect reached in hydroxymethylation of phenols in the presence of excess boric acid can be explained as follows. In the case of equimolar amounts of phenol and boric acid [5–9], the presumable precursors of salicyl alcohol are cyclic borates [5]. We can assume with confidence that under the reaction conditions these cyclic borates are in equilibrium with free alcohol **2a** which enters further side transformations (dehydration, condensation with formaldehyde, etc.). Then excess boric acid under the suggested conditions decreases the concentration of free salicyl alcohol owing to shift of the equilibrium. Also, it is significant that the reaction is performed at a lower temperature (81°C) than suggested in the literature (90–95°C) [5–9]. It is known that salicyl alcohol is thermally unstable, and at temperatures above 100°C it rapidly forms polymeric products [14].

EXPERIMENTAL

The IR specrtra were taken on a Specord M-80 spectrophotometer in KBr pellets, and the ^{1}H NMR spectra, on a Bruker AC 200 spectrometer (200 MHz, DMSO-d_6, internal reference HMDS).

The reaction progress was monitored and the product purity checked by TLC on Silufol UV-254 plates, eluent benzene–ethanol (9 : 1). The plates were developed using filtered UV radiation, diazotized sulfanilic acid, or 5% $FeCl_3$ solution.

The typical procedure of hydroxymethylation of phenols **1a**–**1k** with paraform in the presence of boric acid was as follows. A mixture of 40 mmol of appropriate phenol, 3.72 g (60 mmol) of boric acid, and 1.8 g (60 mmol) of paraform in 70 ml of benzene was refluxed in a flask equipped with a Dean–Stark trap with continuous azeotropic distillation of water until the initial phenol was completely converted (TLC). Every 4 h, a fresh 0.45-g (15-mmol) portion of paraform was added. After reaction completion, excess benzene was distilled off under reduced pressure. To the residue 30 ml of water was added, and the mixture was allowed to stand for 5 h to ensure hydrolysis of the intermediate boric acid ester of the salicyl alcohol. The product was extracted with ether (three 40-ml portions), and the combined ether extracts were washed with watedr (20 ml). The solvent was removed, and alcohols **2a**–**2k** were purified by recrystallization.

CONCLUSIONS

(1) Reaction of paraform with phenols in the presence of excess boric acid under conditions of continuous azeotropic distillation of water results in selective *o*-hydroxymethylation of the substrates with complete conversion of the initial phenols and formation of salicyl alcohols.

(2) A general procedure was developed for preparing salicyl alcohols from phenols containing no strong electron-withdrawing substituents.

(3) The suggested procedure allowed for the first time preparation of the synthetic equivalents of dihydroxybenzyl alcohols.

ACKNOWLEDGMENTS

The study was financially supported by the Project of the Ministry of Education of the Russian Federation “Basic Research in the Field of Chemical Technologies” (project no. 98-8-3.1-127).

REFERENCES

1. Loic, R., *Synthesis*, 1989, no. 1, pp. 69–70.
2. Buruli, C., Desider, N., and Stein, M.L., *Eur. J. Med. Chem.*, 1987, vol. 22, no. 2, pp. 119–123.
3. Dudko, V.V., Lepekhin, A.V., Mefod’ev, V.V., *et al.*, in *Poisk, sozdanie i izuchenie novykh lekarstvennykh sredstv rastitel’nogo i sinteticheskogo proiskhozhdeniya* (Search for and Development and Study of New Drugs of Vegetable and Synthetic Origin), Biisk: NPO Altai, 1993, pp. 80–81.
4. Van Hoof, L., Totte, J., and Corthout, J., *J. Natur. Prod.*, 1989, vol. 52, no. 4, pp. 875–878.
5. Cerveny, L., Jenista, P., Markoul, A., *et al.*, *Chem. Techn.*, 1976, vol. 28, no. 9, pp. 557–559.
6. FR Patent 1 328 945.
7. JPN Patent 49-27 573.
8. FR Patent 2 105 291.
9. Yan, L., Zhiqiang, W., and Jiugping, W., *Chemistry*, 1996, no. 2, pp. 35–37.
10. Wataru, N., Kyo, O., Hiroshi, I., *et al.*, *Synthesis*, 1979, no. 5, pp. 365–368.
11. Casiraghi, G., Casnati, G., and Pugla, G., *Synthesis*, 1980, no. 1, pp. 124–125.
12. Strubell, N., *J. Prakt. Chem.*, 1959, vol. 9, nos. 3–4, pp. 153–159.
13. Arct, J., Eckstein, Z., and Krzywicka, H., *Przem. Chem.*, 1964, vol. 43, no. 2, pp. 87–91.
14. Vul’fson, N.S., *Preparativnaya organicheskaya khimiya* (Synthetic Organic Chemistry), Moscow: Goskhimizdat, 1959.

Russian Journal of Applied Chemistry, Vol. 74, No. 1, 2001, pp. 106–110. Translated from Zhurnal Prikladnoi Khimii, Vol. 74, No. 1, 2001, pp. 103–106.

ORGANIC SYNTHESIS AND INDUSTRIAL ORGANIC CHEMISTRY

Synthesis of Aryl-Substituted Propanols, Pentanediols, and Tetrahydropyran

R. R. Gataullin, T. V. Kazhanova, R. I. Galeeva, A. A. Fatykhov, L. V. Spirikhin, and I. B. Abdrakhmanov

Institute of Organic Chemistry, Ufa Scientific Center, Russian Academy of Sciences, Ufa, Bashkortostan, Russia

Bashkir State Agricultural University, Ufa, Bashkortostan, Russia

Received June 16, 2000

Abstract—Oxidation of *N*- and *C*-alkenylanilines with ozone under conditions of alcohol formation was studied. Depending on the structure of the alkenyl moiety, the reaction yields aryl-substituted propanols, pentanediols, or tetrahydropyran.

Since early 1960s, when the feasibility was demonstrated for preparative synthesis of Claisen rearrangement products from *N*-allylaniline [1, 2], there has been a great deal of interest in the chemistry of alkenylanilines. These compounds find extending use in organic synthesis, including preparation of practically useful substances. It is known that some *N*- and *C*-alkenylanilines exhibit activity as potato growth regulators and fungicides against potato phytophthora infection, inhibit biosynthesis of chitin of flour moth [3], show a pronounced local anesthetic effect [4], and are successfully used in synthesis of some valuable alkaloids [5]. Proceeding with studies [6–8] on transformations of *o*-alkenylarylamines, we studied oxidation of *N*- and *C*-alkenylanilines with ozone.

For example, from aniline (**I**) by a series of condensations we prepared *N*-methoxyacetyl-*N*-(2-penten-4-yl)aniline (**IV**) in a 68% yield:

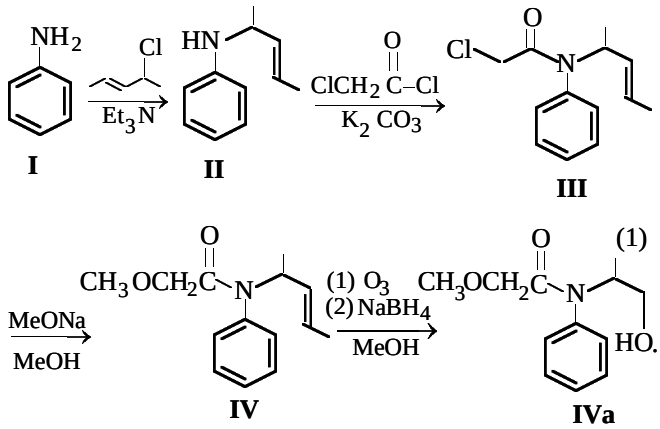

Previously field tests of the *N*-ethoxyacetyl analog of this compound demonstrated its efficiency against potato phytophthora infection, which was level with the known antiphytophthora agent Ridomil [ethyl *N*-methoxyacetyl-*N*-(2-methyl-6-ethylphenyl)aminobutyrate]; the productivity increased by 30%. Presumably, under the testing conditions involving the impact of soil, atmospheric oxygen, and sunlight, this compound could undergo transformations with participation of the unsaturated C=C bond of the pentenyl unit. Oxidation of amine **IV** with ozone is one of possible routes to hydroxy derivatives of this substance. We found that ozonation of **IV** followed by treatment with $NaBH_4$ gives *N*-methoxyacetyl-*N*-(1-hydroxyprop-2-yl)aniline in a 35–45% yield.

When an equimolar amount of ozone is passed through a solution of **IV** in cyclohexane–methanol, the reaction does not go to completion, and the ratio of the initial amine **IV** and product **IVa** is 1.5 : 1. When the similar reaction is performed in methanol, the ratio of these compounds [scheme (1)], according to the ^1H NMR data, varies from 1 : 1 to 1 : 0.7.

In contrast to *N*-alkenylaniline **IV**, ozonation in methanol of pentenylanilines **VIa** and **VIb** exhibiting local anesthetic activity [4] goes to completion; subsequent treatment of the reaction mixture with $NaBH_4$ gives propanols **VIIa** and **VIIb** in 50–60% yields [scheme (2)]. Oxidation of 2-cyclopentenylanilines **VIIIa**–**VIIIc** under these conditions yields pentanediols **IXa**–**IXc** in a 60–70% yield [scheme (3)].

1070-4272/01/7401-0106$25.00

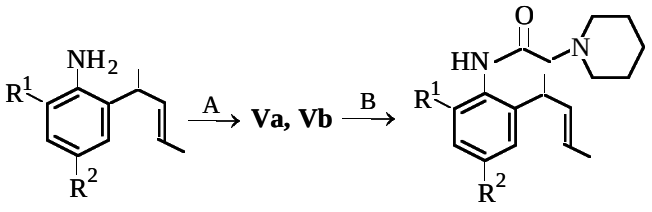

VIa, **VIb**

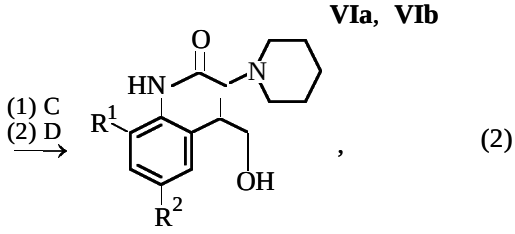

VIIa, VIIb

where R^1 = H, R^2 = Me (**a**); R^1 = R^2 = Me (b);

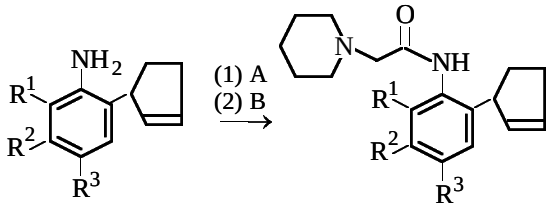

VIIIa–**VIIIc**

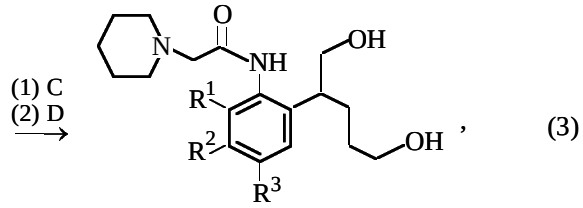

where R^1 = R^2 = R^3 = H (**a**); R^1 = Me, R^2 = R^3 = H (**b**); R^1 = H, R^2 = R^3 = F (**c**).

Reagents and conditions: A, $ClCH_2C(O)Cl$, K_2CO_3, 20°C; B, excess piperidine; C, O_3, MeOH, 0–5°C; D, $NaBH_4$, MeOH, 0–5°C.

Oxidation of *N*-acetyl-2-methyl-6-(cyclopent-1-enyl)aniline (**X**) [9] unexpectedly gave tetrahydropyran **XI** (yield 70%):

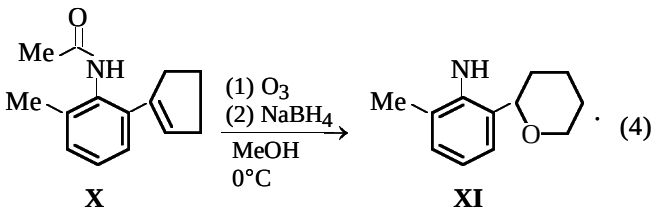

X **XI**

The structure of the products was proved by the IR and ^1H, ^{13}C NMR spectra and also by elemental analysis. The IR spectra of all the products contain a characteristic absorption band of the OH group at ν 3400–3600 cm^{-1}. In the ^1H NMR spectrum of amine **IVa**, the methyl protons of the propanol moiety give a doublet at δ 0.96 ppm (J 6.99 Hz). In the ^{13}C NMR spectrum, the signal of the methyl carbon of the propanol moiety is shifted upfield ($\delta_{C_{1'}}$ 14.73 ppm) as compared fo **IV**. The signals of the $C^{1'}$ and $C^{2'}$ atoms in **IVa** are observed at 64.45 and 53.62 ppm, respectively.

In the ^1H NMR specrta of amino alcohols **VIIa** and **VIIb**, the methyl groups give a doublet at 1.16 ppm (J 7.07 Hz). The methine proton $H^{2''}$ and the methylene protons $H^{1'}$ give multiplets at 4.33 and 3.64 ppm. The signals of the $C^{1''}$, $C^{2''}$, and $C^{3''}$ atoms of **VIIa** and **VIIb** in the ^{13}C NMR spectra are observed at 68, 35–37, and 17–18 ppm, respectively.

In the ^1H NMR spectra of diols **IXa**–**IXc**, the $H^{1''}$ and $H^{5''}$ protons of the pentanediol moiety give signals at 3.70 and 3.45 ppm, and the signal of OH protons is observed at 4.80 ppm. In the ^{13}C NMR spectra of **IXa**–**IXc**, the $C^{1''}$ and $C^{5''}$ signals are observed at 67 and 62 ppm, respectively. The signals of the $C^{2''}$, $C^{3''}$, and $C^{4''}$ atoms are observed at 41 and 28–29 ppm. The signals of the benzene carbon atoms in the ^{13}C NMR spectrum of **IXc** are split owing to coupling with F and give doublets with the coupling constants of 17–20 (for $C^{1'}$, $C^{2'}$, $C^{3'}$, and $C^{6'}$) and 216–223 Hz (for the $C^{4'}$ and $C^{5'}$ atoms directly bound to F).

The mass spectrum of the tetrahydropyranyl derivative **XI** contains a molecular peak M^+ (*m/z* 191).

EXPERIMENTAL

The ^1H and ^{13}C NMR spectra were taken on a Bruker AM-300 spectrometer (working frequency 300 and 75 MHz, respectively; solvent $CDCl_3$; internal reference TMS), and the IR spectra, on a UR-20 spectrometer. The product purity was checked by TLC (Silufol UV-254 plates). The mass spectrum was obtained with an MKh-1320 spectrometer (70 eV). The physicochemical characteristics of **VIb** and **VIIa**–**VIIc** are given in [10, 11].

***N*-(2-Methoxyacetyl)-*N*-(3-penten-2-yl)aniline (IV)** was prepared according to [1]. Yield 90%. R_f 0.48 (CH_2Cl_2–CH_3OH, 95 : 5), bp 123°C (1 mm Hg).

Found, %: C 70.41, H 8.35, N 6.07.
$C_{13}H_{19}NO_2$.
Calculated, %: C 70.59, H 8.60, N 6.33.

^{1}H NMR spectrum ($CDCl_3$, δ, ppm): 0.98 d (3H, *J* 6.61 Hz, CH_3), 1.50 d (3H, *J* 6.35 Hz, CH_3), 3.19 s (3H, OCH_3), 3.50 m (2H, CH_2), 5.25–5.45 m (3H, CH, HC=CH), 6.96–7.29 m (5H, ArH). ^{13}C NMR spectrum ($CDCl_3$, δ, ppm): 17.46, 17.63 (CH_3); 51.39 ($C^{1'}$); 56.76 (CH_3); 70.58 (CH_2); 127.21, 128.28, 128.92, 129.81, 130.59, 136.83 (C_{arom}, C=C); 167.77 (C=O).

***N*-Chloroacetyl-2-(3-penten-2-yl)-4-methylaniline (Va).** A three-necked flask equipped with a power-driven stirrer, a reflux condenser, and a dropping funnel was charged with dry K_2CO_3 and 17.1 g (0.1 mol) of 2-(3-penten-2-yl)-4-methylaniline in methylene chloride. A solution of 0.2 mol of freshly distilled chloroacetyl chloride in 80 ml of CH_2Cl_2 was slowly added dropwise with stirring. After reaction completion, the precipitate was filtered off, 100 ml of water was added, and the organic layer was washed with a 10% solution of $NaHCO_3$ until the CO_2 evolution ceased and then with two 100-ml portions of water. The organic solution was dried over $MgSO_4$. The solvent was vacuum-evaporated, and the residue was recrystallized from benzene. Yield of **Va** 15.4 g (90%), mp 109°C. IR spectrum, ν, cm^{-1}: 3275 (NH). ^{1}H NMR spectrum, δ, ppm (*J*, Hz): 1.35 d (3H, *J* 7.15, CH_3), 1.66 d (3H, *J* 7.05, CH_3), 2.35 s (3H, CH_3), 3.60 m (1H, $H^{1'}$), 4.28 s (2H, CH_2), 5.59 m (2H, HC=CH), 6.90 (1H, ArH), 6.87 (1H, ArH), 7.85 br.s (1H, NH). ^{13}C NMR spectrum ($CDCl_3$), δ, ppm (*J*, Hz): 20.25 (**Ia**), 35.80 ($C^{1'}$), 42.79 (C–Cl), 165.50 (C=O), 136.70 (C^1), 141.80 (C^2), 125.55 (C^3), 124.49 (C^5), 128.53 (C^4), 134.79 (C^6), 135.60 ($C^{2'}$), 130.45 ($C^{3'}$).

Found, %: C 64.00, H 7.16, N 5.98, Cl 15.46.
$C_{12}H_{18}NOCl$.
Calculated, %: C 63.29, H 7.91, N 6.15, Cl 15.60.

***N*-[(2-(3-propen-2-yl)-4-methylphenyl)aminocarbonylmethyl]piperidine (VIa).** Chloroacetylated aniline **Va** (2.3 g, 10 mmol) was dissolved in hot toluene (20 ml), and 5 ml of piperidine was added. The mixture was refluxed for 4 h. The amine hydrochloride precipitate was filtered off and washed with 5 ml of toluene. The filtrate was vacuum-evaporated, and the residue was recrystallized from a minimal amount of toluene. Yield of **VIa** 2.3 g (68%). R_f 0.48 (CH_2Cl_2).

Found, %: C 75.56, H 9.28, N 9.27.
$C_{19}H_{28}N_{20}$.
Calculated, %: C 76.00, H 9.33, N 9.33.

IR spectrum, ν, cm^{-1}: 3280 (NH). ^{1}H NMR spectrum ($CDCl_3$), δ, ppm (*J*, Hz): 1.49 d (3H, *J* 6.97, CH_3); 1.70 d (3H, *J* 6.46, CH_3); 2.30 s (3H, CH_3); 1.50, 1.60, 2.55 (m, 10H, H_{pip}); 3.08 s (2H, CH_2); 3.50 m (1H, CH); 5.35–5.65 m (2H, HC=CH); 7.00 s (1H, H^3); 7.05 d (1H, *J* 8.79, H^6); 7.90 d (1H, H^5); 9.25 s (1H, NH). ^{13}C NMR spectrum ($CDCl_3$, δ, ppm): 17.78, 20.03, 21.01 (C_{methyl}); 23.52, 26.08, 54.97 (C_{pip}); 63.03 ($C^{2''}$); 168.78 (C=O); 36.63 ($C^{1'}$); 134.75 (C^2); 122.62 ($C^{3'}$); 132.22 (C^1); 134.11 (C^2); 127.21 (C^3); 135.22 (C^4); 127.20 (C^5); 137.24 (C^6).

The general procedure of oxidation was as follows. Through a solution of 10 mmol of **IV**, **IVa**, **IVb**, **VIIIa**, **VIIIb**, or **X** in 10 ml of methanol at 0–5°C we passed a calculated amount of an ozone–oxygen mixture (controlled with a stopwatch). The mixture was kept for 5 min at this temperaturem after which 0.6 g of $NaBH_4$ was added at the temperature maintained no higher than 10–15°C. The mixture was allowed to stand at 20°C for 18 h and then diluted with a 10 : 1 mixture of H_2O and CH_3COOH. The product was extracted with CH_2Cl_2, washed with 5% $NaHCO_3$ and saturated NH_4Cl solution, and dried over Na_2SO_4. The solvent was evaporated, and alcohols **IVa**, **VIIa**, **VIIb**, and **IXa**–**IXc** or pyran **XI** was obtained.

***N*-(2-Methoxyacetyl)-*N*-(1-hydroxy-2-propyl)aniline (IVa).** Yield 91%. R_f = 0.27 (CH_2Cl_2–CH_3OH, 95 : 5).

Found, %: C 64.52, H 7.56, N 6.25.
$C_{12}H_{17}NO_3$.
Calculated, %: C 64.57, H 7.62, N 6.28.

^{1}H NMR spectrum ($CDCl_3$), δ, ppm (*J*, Hz): 0.96 d (1H, *J* 6.99, CH_3), 3.25 s (3H, CH_3), 3.40 m (2H, CH_2), 3.60 s (2H, CH_2), 4.81 m (1H, CH), 7.12 s (1H, OH), 7.22–7.50 m (5H, ArH). ^{13}C NMR spectrum ($CDCl_3$), δ, ppm: 14.73 ($C^{1'}$); 53.62 ($C^{2'}$), 64.45 ($C^{3'}$), 70.93 ($C^{2''}$); 58.97 ($C^{3''}$); 170.25 ($C^{1''}$); 128.42, 129.26, 129.87, 130.59, 137.24 (C_{arom}).

***N*-[2-(1-Hydroxy-2-propyl)-4-methylphenyl]-2-piperidinoacetamide (VIIa).** Yield 60%. R_f 0.36 (CH_2Cl_2–CH_3OH, 95 : 5).

Found, %: C 70.29, H 8.90, N 9.61.
$C_{17}H_{26}N_2O_2$.
Calculated, %: C 70.34, H 8.96, N 9.65.

IR spectrum, ν, cm^{-1}: 3312 (NH, OH), 1688 (C=O). ^{13}C NMR spectrum ($CDCl_3$), δ, ppm: 17.08 ($C^{3''}$), 21.09 (CH_3); 23.49, 25.92, 54.86 (C_{pip}); 35.71

($C^{2''}$), 68.20 ($C^{1''}$), 62.46 (C^2, CH_2); 132.76 (C^1); 136.31 (C^2); 127.39 (C^3); 135.19 (C^4); 127.19 (C^5); 137.24 (C^6), 169.47 (C^1, C=O).

***N*-[2-(1-Hydroxy-2-propyl)-4,6-dimethylphenyl]-2-piperidinoacetamide (VIIa).** Yield 60%. R_f 0.36 (CH_2Cl_2–CH_3OH, 90 : 10).

Found, %: C 65.01, H 8.38, N 8.36.
$C_{18}H_{28}N_2O_2$.
Calculated, %: C 65.06, H 8.43, N 8.43.

IR spectrum, ν, cm^{-1}: 3500 (OH, NH). ^1H NMR spectrum ($CDCl_3$), δ, ppm (*J*, Hz: 1.16 d (3H, *J* 7.07, CH_3), 1.40–2.60 m (10H, $5CH_2$), 2.16 s (3H, CH_3), 2.24 s (3H, CH_3), 3.12 s (2H, CH_2), 3.64 m (2H, CH_2), 4.33 m (1H, CH), 6.90 s (1H, OH), 6.96 s (1H, ArH), 7.03 s (1H, ArH), 8.90 s (1H, NH). ^{13}C NMR spectrum ($CDCl_3$), δ, ppm: 18.00 ($C^{3''}$), 37.38 ($C^{2''}$); 23.66, 26.26, 55.38 (C_{pip}); 62.46 (C^2); 170.56 (C^1); 18.83, 21.24 (C_{methyl}); 124.81, 128.71, 131.08, 135.84, 137.35, 142.83 (C_{arom}).

***N*-[2-(1,5-Dihydroxypent-2-yl)phenyl]-2-piperidinoacetamide (IXa).** Yield 63%. R_f 0.21 (CH_2Cl_2–CH_3OH, 90 : 10).

Found, %: C 67.48, H 8.70, N 8.71.
$C_{18}H_{28}N_2O_3$.
Calculated, %: C 67.50, H 8.75, N 8.75.

IR spectrum, ν, cm^{-1}: 3600 (OH, NH). ^1H NMR spectrum ($CDCl_3$), δ, ppm: 0.86–2.35 m (14H, $7CH_2$), 3.15 s (2H, CH_2), 3.44–3.73 m (5H, $2CH_2$), 3.44–3.73 m (5H, $2CH_2$, CH), 4.87 s (2H, 2OH), 9.56 s (1H, NH), 7.07–7.90 m (4H, Ar). ^{13}C NMR spectrum ($CDCl_3$), δ, ppm: 23.56, 26.06, 54.98 (piperidine); 27.99 ($C^{3''}$), 30.29 ($C^{4''}$), 41.54 ($C^{2''}$), 61.94 (C^2), 62.60 ($C^{5''}$), 67.13 ($C^{1''}$), 123.54 ($C^{4'}$); 125.97 ($C^{5'}$); 126.78 ($C^{3'}$); 135.48 ($C^{2'}$); 135.85 ($C^{1'}$); 135.94 ($C^{6'}$); 169.79 (C^1).

***N*-[2-(1,5-Dihydroxypent-2-yl)-6-methylphenyl]-2-piperidinoacetamide (IXb).** Yield 66%. R_f 0.23 (CH_2Cl_2–CH_3OH, 90 : 10).

Found, %: C 68.21, H 8.93, N 8.35.
$C_{19}H_{30}N_2O_3$.
Calculated, %: C 68.26, H 8.98, N 8.38.

IR spectrum, ν, cm^{-1}: 3600 (OH, NH). ^1H NMR spectrum ($CDCl_3$), δ, ppm: 0.85–2.30 m (14H, $7CH_2$), 2.29 s (3H, CH_3), 3.00 s (2H, CH_2), 3.45–3.75 m (5H, $2CH_2$, CH), 8.40 s (3H, OH, NH), 6.85 m (3H, Ar).

***N*-[2-(1,5-Dihydroxypent-2-yl)-4,5-difluorophenyl]-2-piperidinoacetamide (IXc).** Yield 59%. R_f 0.28 (CH_2Cl_2–CH_3OH, 90 : 10).

Found, %: C 61.00, H 6.73, F 10.71, N 6.89.
$C_{18}H_{24}F_2N_2O_3$.
Calculated, %: C 61.02, H 6.78, F 10.73, N 7.91.

IR spectrum, ν, cm^{-1}: 3600 (OH, NH). ^1H NMR spectrum ($CDCl_3$), δ, ppm (*J*, Hz): 6.90 d.d (1H, $J_{H^{6'}F^{5'}}$ 11.69, $J_{H^{6'}F^4}$ 8.66, $H^{6'}$), 1.40–3.70 m (23H, $10CH_2$, CH, 2OH), 7.50 d.d (1J, $J_{H^{3'}F^{4'}}$ 12.05, $J_{H^{3'}F^{5'}}$ 7.86, $H^{3'}$), 9.70 s (1H, NH). ^{13}C NMR spectrum ($CDCl_3$), δ, ppm: 23.14, 25.65, 54.55 (piperidine), 27.08 ($C^{3''}$); 29.75 ($C^{1''}$); 40.80 ($C^{2''}$); 61.56 ($C^{5''}$); 66.26 ($C^{1''}$); 62.08 (C^1); 112.44 d (C^3, $J_{C^{3'}F^{4'}}$ 17.55); 113.18 d ($C^{1'}$), 130.98 d ($C^{2'}$), 146.50 d.d (C^4, $J_{C^{4'}F^{4'}}$ 216); 146.59 d.d ($C^{5'}$, $J_{C^{5'}F^{5'}}$ 223, $J_{C^{5'}F^{4'}}$ 27); 169.81 (C^1).

6-Methyl-2-(tetrahydro-2-pyranyl)aniline (XI). Yield 67%. R_f 0.30 (CH_2Cl_2–MeOH 95 : 5).

Found, %: C 75.04, H 8.67, N 7.02.
$C_{12}H_{17}NO$.
Calculated, %: C 75.39, H 8.90, N 7.33.

IR spectrum, ν, cm^{-1}: 3600 (NH, OH). ^1H NMR spectrum ($CDCl_3$), δ, ppm (*J*, Hz): 1.60–2.30 m (6H, $3CH_2$), 3.65 d.d.t (2H, J_1 2.8, J_2 6.07, J_3 8.97, $H^{6a,b}$), 4.10 m (2H, NH_2), 4.42 d.d (1H, J_1 1.95, J_2 8.11, H^2), 6.67 t (1H, *J* 7.49, $H^{4'}$), 6.98 d (1H, $H^{5'}$), 7.02 d (1H, $H^{3'}$). ^{13}C NMR spectrum ($CDCl_3$), δ, ppm: 17.13 (CH_3), 23.44 (C^4), 25.64 (C^5), 29.28 (C^3), 68.45 (C^6), 79.78 (C^2), 117.19 ($C^{5'}$), 122.53 ($C^{3'}$), 124.70 ($C^{4'}$), 125.31 ($C^{1'}$), 129.36 ($C^{6'}$), 143.13 ($C^{2'}$). μ^+, *m/z* 191.

CONCLUSION

Reduction with sodium borohydride of ozonation products of *o*-alkenylanilines is a convenient route to *o*-hydroxypropyl-, *o*-dihydroxypentyl-, and *o*-tetrahydropyranyl-substituted anilines.

REFERENCES

1. Marcinkiewicz, S., Green, J., and Mamalis, P., *Tetrahedron*, 1961, nos. 3–4, pp. 208–222.
2. Marcinkiewicz, S., *Bull. Acad. Pol. Sci., Ser. Sci.*

Chem., 1971, vol. 19, no. 10, pp. 603–608.

3. RF Patent 2090556.
4. Gataullin, R.R., Kazhanova, T.V., Davydova, V.A., *et al.*, *Khim.-Farm. Zh.*, 1999, no. 4, pp. 17–19.
5. Danishefsky, S. and Phillips, G.B., *Tetrahedron Lett.*, 1984, vol. 25, p. 3159.
6. Gataullin, R.R., Kazhanova, T.V., Il'yasova, L.T., *et al.*, *Izv. Ross. Akad. Nauk, Ser. Khim.*, 1999, no. 5, pp. 975–978.
7. Gataullin, R.R., Afon'kin, I.S., Fatykhov, A.A., *et al.*, *Izv. Ross. Akad. Nauk, Ser. Khim.*, 2000, no. 1, pp. 118–120.
8. Gataullin, R.R., Kazhanova, T.V., Fatykhov, A.A., *et al.*, *Izv. Ross. Akad. Nauk, Ser. Khim.*, 2000, no. 1, pp. 171–173.
9. Gataullin, R.R., Afon'kin, I.S., Pavlova, I.V., *et al.*, *Izv. Ross. Akad. Nauk, Ser. Khim.*, 1999, no. 2, pp. 398–400.
10. Gataullin, R.R., Kazhanova, T.V., and Davydova, V.A., *Khim.-Farm. Zh.*, 1999, no. 5, pp. 29–32.
11. Gataullin, R.R., Kazhanova, T.V., and Kudashev, A.R., *Khim.-Farm. Zh.*, 2000, no. 2, pp. 18–21.

Russian Journal of Applied Chemistry, Vol. 74, No. 1, 2001, pp. 111–113. Translated from Zhurnal Prikladnoi Khimii, Vol. 74, No. 1, 2001, pp. 107–110.

ORGANIC SYNTHESIS AND INDUSTRIAL ORGANIC CHEMISTRY

Pathways of Acetol Formation in the Course of Production of Phenol and Acetone by Cleavage of Cumyl Hydroperoxide

I. I. Vasil'eva, V. M. Zakoshanskii, Yu. N. Koshelev, and V. P. Chulkov

Russian Research Institute of Petrochemical Processes, St. Petersburg, Russia

Received January 28, 2000; in final form, July 2000

Abstract—The mechanism of acetol formation in two-stage process of sulfuric acid cleavage of cumyl hydroperoxide was studied and confirmed by comparison with related reaction systems.

One of undesirable by-products in production of phenol and acetone by cleavage of cumyl hydroperoxide is hydroxyacetone (acetol). This impurity in commercial phenol dramatically deteriorates its color index. Acetol is removed from crude phenol catalytically by treatment with sulfonic cation-exchange resins. On an acid catalyst acetol partially reacts with phenol to form 2-methylbenzofuran (2-MBF). The amount of the forming 2-MBF is directly related to the content of acetol in the product to be catalytically purified. Separation of 2-methylbenzofuran from phenol is very difficult and is possible only by fractional azeotropic distillation with water. At the same time, 2-MBF, even when present in concentrations as low as 0.001 wt %, also dramatically impairs the color index of the commercial phenol.

The simplest way to improve the color index of commercial phenol is to prevent formation of acetol or sharply decrease its content in products fed to distillation. It is known that acetol is formed in the stage of sulfuric acid decomposition of cumyl hydroperoxide (CHP) into phenol and acetone; its concentration in the reaction mixture reaches 0.2 wt %. The mechanism of acetol formation and ways to decrease its concentration in CHP decomposition products were not elucidated. It was suggested that acetol forms with participation of acetone and CHP [1]. It was assumed that CHP directly reacts with acetone, or that CHP reacts with mesityl oxide formed by condensation of two acetone molecules in the presence of sulfuric acid. The mechanism of the direct reeaction was not described, and the second pathway was presented as a series of consecutive reactions:

$$2CH_3{-}\underset{\underset{O}{\|}}{C}{-}CH_3 \longrightarrow CH_3{-}\underset{\underset{O}{\|}}{C}{-}CH_2C(OH)(CH_3)_2$$

$$\longrightarrow CH_3{-}\underset{\underset{O}{\|}}{C}{-}CH{=}C(CH_3)_2,$$

$$CH_3{-}\underset{\underset{O}{\|}}{C}{-}CH{=}C(CH_3)_2$$

$$\xrightarrow[-R]{ROOH + H^+} CH_3{-}\underset{\underset{O}{\|}}{C}{-}CH_2(CH_3)_2COOH,$$

$$CH_3{-}\underset{\underset{O}{\|}}{C}{-}CH_2(CH_3)_2COOH$$

$$\xrightarrow[-(CH_3)_2CO]{H^+} CH_3{-}\underset{\underset{O}{\|}}{C}{-}CH_2OH.$$

It was also suggested [2] that acetol can form by reaction of acetone with hydrogen peroxide present in a small amount in the reaction mixture from cleavage of CHP.

EXPERIMENTAL

Acetol formation was studied under conditions of two-stage CHP decomposition into phenol and acetone in the presence of catalytic amounts of sulfuric acid [3]. The first stage, according to the adopted process scheme, was performed under conditions of almost complete decomposition of technical-grade CHP into target products, phenol and acetone, with simultaneous transformation of dimethylphenylcarbinol (DMPC) impurity into dicumyl peroxide (DCP). The experiment was performed in a glass flow-circulation system. The second stage, in which decomposition of CHP was completed and DCP was converted into α-methylstyrene, was performed in an autoclave equipped with a stirrer and a sampler. The composition of the products was determined by GLC [4].

The elucidate the mechanism of acetol formation in the first stage of CHP decomposition at various initial

1070-4272/01/7401-0111$25.00

Table 1. Concentration of acetol in the first stage of CHP decomposition

T, °C	τ, s	C_{acid}, M	C_{CHP}, M	C_A, wt %
46	80	0.0034	0.258	0.070
48	80	0.0030	0.188	0.067
49	80	0.0029	0.198	0.076
43	80	0.0032	0.544	0.115
45.8	70	0.0032	0.356	0.080
51.5	70	0.0010	0.197	0.051
51.5	80	0.0011	0.243	0.058
49	80	0.0021	0.227	0.078
48.1	80	0.0022	0.205	0.071
47.5	80	0.0038	0.178	0.091
40	80	0.0035	0.258	0.080
50	80	0.0034	0.246	0.099
64.5	80	0.0032	0.202	0.160

Table 2. Concentration of acetol in the second stage of CHP decomposition

τ, min	C_A, wt %, at indicated T, °C			
	100	110	120	130
0	0.077	0.079	0.085	0.087
5	0.087	0.087	0.102	0.120
7	–	0.093	0.110	0.120
9	–	–	–	0.120
10	0.091	–	0.119	–
12	–	0.112	–	0.123
15	0.100	–	0.123	0.127
18	–	0.113	–	–
20	0.105	–	0.127	–
25	–	0.119	–	–
30	0.107	–	–	–

concentrations C_{CHP}, we studied the dependence of the acetol concentration C_A in the reaction mixture on the main process parameters: temperature T, sulfuric acid concentration C_{acid}, and residence time τ.

The results show that the concentration of acetol in the reaction mixture in the circulation conduit depends on all the above-mentioned parameters; the concentration decreases with decreasing temperature, sulfuric acid concentration, and residence time.

To elucidate the specific features of acetol accumulation in the second stage of the process, we studied the dependence of its concentration in the reaction mixture on the sulfuric acid concentration and temperature at various residence times.

We found that the acid concentration has no appreciable efect on the rate of acetol accumulation, and the decisive factor affecting the reaction rate is the temperature. Data on variation of the acetol concentration in the reaction mixture with time at various temperatures are given in Tables 1 and 2.

In the course of studying accumulation of acetol in the second stage of CHP decomposition, we revealed some experimental trends. First, when we used as the feed the products obtained in the circulation unit, the acetol concentration in the reaction mixture considerably increased. Second, when the feed for the second stage was prepared in the first stage at the same sulfuric acid concentrations, temperatures, and circulation multiplicities, the final acetol concentrations after completion of the second stage were equal irrespective of its conditions. Third, when we used as the feed for the second stage a model mixture identical in the composition (according to GLC analysis) to the product of the first stage, the increase in the acetol concentration in the reaction mixture did not exceed 0.005 wt %.

These facts give some insight into possible pathways of acetol formation in the course of sulfuric acid decomposition of CHP. Apparently, the necessary condiiton for acetol formation is simultaneous presence in solution of acetone, hydroperoxide (HP), and catalytic amounts of sulfuric acid. The nature of HP and the presence of phenol are of no significance; additional experiments showed that acetol is efficiently formed in acetone solution in the presence of other HPs, in particular, hydrogen peroxide and *tert*-butyl hydroperoxide (TBHP). Data on acetol accumulation in the second stage of CHP decomposition are consistent with this conclusion; the only specific feature is that with the products from the first stage used as the feed the amount of the forming acetol, according to GLC data, exceeds several times that obtained with the model mixture of the same composition. This fact can be explained only by assuming that formation of acetol from acetone in the presence of CHP and acid occurs via formation of intermediate(s) undetectable by GLC. It is assumed that in the first stage of CHP decomposition this intermediate transforms into acetol only partially, and the reaction is completed in the second stage.

Possible intermediates that cannot be isolated and identified are 2-hydroxy-2-cumylperoxypropane **I** and 2,2-bis(cumylperoxy)propane **II**. It is known that compound **I** and related α-hydroxy peroxides derived from other HPs are formed reversibly in reactions of ketones with HPs at low temperatures [5]. These compounds are extremely labile, and their formation was

confirmed only by IR spectroscopy. Compound **II** was not described in the literature, but data are available on its analog prepared from acetone and TBHP [6].

Based on the above assumption and taking into account published data, we suggest the following scheme of acetol formation from acetone and CHP:

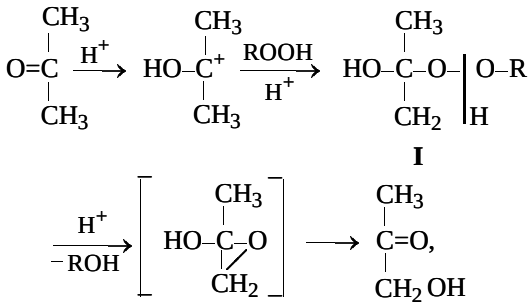

I

(1)

where R is the cumyl radical.

Decomposition of **I** with intermediate formation of the oxide is shown arbitrarily; most probably, decomposition with carbinol elimination and intramolecular rearrangement occur simultaneously.

The above hypothetical scheme can explain the pathway of acetol formation in the first stage of CHP decomposition, but, because of the low stability of α-hydroxy peroxides, in the second stage this pathway is improbable. The acetol precursor in the second stage should be a relatively stable compound. Presumably, along with the reactions shown in scheme (1), compound **I** reacts with CHP with formation of more stable compound **II** by the scheme

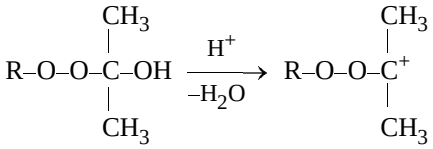

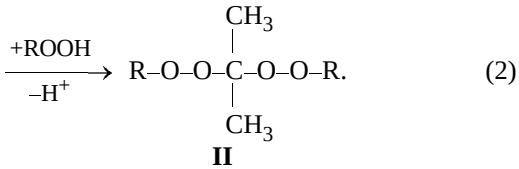

(2)

II

Compound **II**, presumably formed in the course of CHP decomposition in the first stage, in the second stage at elevated temperature decomposes to form CHP, DMPC, and acetol:

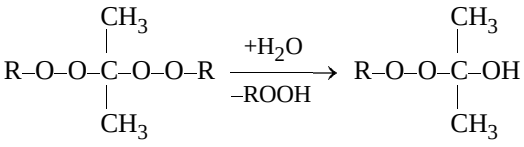

Since it is extremely difficult to confirm experimentally formation of acetol by pathway (1) because of the low stability of α-hydroxy peroxides, we examined the possibility of occurrence of reaction (2). An evidence in favor of this process could be formation of CHP, DMPC, and acetol in a stoichiometric ratio from specially prepared compound **II**. Since this compound does not exist in the neat form and since CHP formed from **II** by reaction (2) rapidly decomposes into phenol and acetone under conditions of acid catalysis, our proof of this mechanism was based on chemical analogies. To simulate formation of acetol in the second stage of CHP decomposition, we used an analog of **II**, which was specially prepared from acetone and TBHP according to [6]. This compound was subjected to decomposition in the presence of sulfuric acid in a solution of phenol in acetone. The GLC analysis showed that decomposition of this diperoxide yields equimolar amounts of TBHP, trimethylcarbinol, and acetol, which is an indirect evidence in favor of the suggested mechanism. In this process, acetol is formed via intermediate carbocations, as indicated by the absence of acetol in the products of thermal decomposition of the model hydroperoxide in aprotic CCl_4 without acid.

CONCLUSIONS

Formation of acetol in the course of sulfuric acid decomposition of cumyl hydroperoxide into phenol and acetone occurs by the carbocationic mechanism via intermediate formation of 2-hydroxy-2-cumylperoxypropane and 2,2-bis(cumylperoxy)propane.

REFERENCES

1. Messina, G., Lorezoni, L., Cappellazzo, O., and Gamba, A., *Chim. Ind.* (Milan), 1983, vol. 65, no. 1, pp. 10–17.
2. Pasterean, M., *C. R. Acad. Sci. Paris*, 1907, vol. 144, pp. 90–93.
3. USSR Patent 1 361 937.
4. Tsypysheva, L.G., Mishchenko, L.Ya., and Portnova, T.V., *Zh. Anal. Khim.*, 1987, vol. 42, no. 2, pp. 347–351.
5. Antonovskii, V.L. and Terent'ev, V.A., in *Uspekhi khimii organicheskikh perekisnykh soedinenii i autookisleniya* (Advances in Chemistry of Organic Peroxides and Autooxidation), Moscow: Khimiya, 1969, pp. 442–450.
6. Dickey, F.H., Rust, F., and Vaughan, W.E., *J. Am. Chem. Soc.*, 1949, vol. 71, pp. 1432–1434.

Russian Journal of Applied Chemistry, Vol. 74, No. 1, 2001, pp. 114–117. Translated from Zhurnal Prikladnoi Khimii, Vol. 74, No. 1, 2001, pp. 110–113.

ORGANIC SYNTHESIS AND INDUSTRIAL ORGANIC CHEMISTRY

3-Substituted Thietanes as Effective Inhibitors of Cumene Oxidation

V. M. Farzaliev, M. A. Allakhverdiev, A. M. Magerramov, N. A. Shirinova, L. A. Dzhavadova, I. A. Rzaeva, A. Z. Khalilova, and F. Yu. Aliev

Kuliev Institute of Chemistry of Additives, Academy of Sciences of Azerbaidzhan Republic, Baku, Azerbaidzhan

Baku State University, Baku, Azerbaidzhan

Received February 1, 2000; in final form, August 2000

Abstract—3-Substituted thietanes were prepared by reaction of 1,2-epithio-3-chloropropane with various nucleophiles in aqueous solutions and were characterized. The inhibiting power of these compounds in cumene oxidation was studied.

Previously we studied antioxidant activity of various thiiranes and thietanes. It was shown that the inhibiting mechanism involves both termination of an oxidation chain by reaction with peroxy radicals with oxidation of the inhibitors by cumyl hydroperoxide (CHP) and formation of substances catalyzing hydroperoxide degradation into molecular products and readily reacting with peroxy radicals.

In this work we synthesized 3-substituted thietanes and studied their antioxidant activity in cumene oxidation.

1,2-Epithio-3-chloropropane (**I**) was prepared by reaction of epichlorohydrin with thiourea in the presence of methanol [7]. Reaction of **I** with ammonium thiocyanate in an aqueous solution to form 3-thietanyl isothiocyanate (**II**) was studied in [8]. 3-Thietanyl-substituted thioureas **III** and **IV** were prepared by addition of 3-thietanyl isothiocyanate to benzylamine and morpholine, respectively:

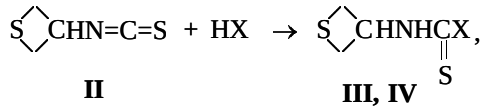

II **III, IV**

where X = $NHCH_2$– (**III**), –N⟨⟩O (**IV**).

3-Thietanol (V) was prepared by reaction of 1,2-epithio-3-chloropropane with sodium carbonate [9]:

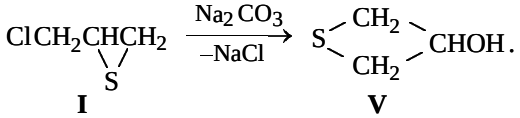

I **V**

The structure of the resulting compounds was confirmed by IR and 1H NMR spectroscopy and the purity, by elemental analysis and thin-layer and gas–liquid chromatography (GLC).

The IR spectra of 3-thietanyl-substituted thioureas **III** and **IV** contain the bands in the range 670–680, 720–730, and 1420–1435 cm^{-1}, which are typical for stretching vibrations of the four-membered thietane ring. The band in the range 1500–1520 cm^{-1} is assigned to stretching vibrations of the thiourea NHC(S) fragment.

In the range 2.65–3.65 ppm the ^1H NMR spectra of 3-thietanyl-substituted thioureas **III** and **IV** contain a quintet of four protons of two equivalent methylene groups of the thietane ring with the intensity ratio of 1 : 4 : 6 : 4 : 1. The signal of the single methine proton of the thietane ring appears as a quintet in the range 4.25–4.75 ppm. The broad strong signal of the NH protons of the thiourea skeleton is observed at 7.05–7.65 ppm. The signals of CH_2 protons of the benzyl fragment are observed in the range 2.5–2.9 ppm. The singlet in the range 6.61–6.89 ppm is assigned to five aromatic protons.

Reactions of **II**–**V** with CHP were performed in chlorobenzene under nitrogen at 110°C in a temperature-controlled glass reactor. The CHP content in the samples taken at regular intervals was determined by iodometric titration.

To determine the reaction stoichiometry, CHP was taken in excess. The stoichiometric coefficients calculated by the equation

1070-4272/01/7401-0114$25.00

$$\nu = \frac{[CHP]_0 - [CHP]_\infty}{[InH]_0},$$

(where $[CHP]_0$ and $[CHP]_\infty$ are the initial and final CHP concentrations, respectively, $[InH]_0$ is the initial concentration of the inhibitor) show that products formed from a single molecule of the inhibitors cause several thousand CHP molecules to decompose.

The kinetic parameters of the catalytic decomposition of CHP in the presence of **II**–**V** are presented in the table. High stoichiometric coefficients ν indicate the catalytic nature of CHP decomposition.

Analysis of the kinetic parameters of reaction of the tested compounds with CHP shows that their activity in this reaction appreciably depends on the nature of the substituent in a thietane molecule.

As in the case of the reaction with cumylperoxy radicals, compound **IV** is the most active in reaction with CHP. The rate constant K and the stoichiometic coefficient ν for this compound are higher by an order of magnitude than those for the other compounds.

The study of cumene autooxidation at 110°C in the presence of compounds **II**–**V** showed (Fig. 1) that all these thietanes inhibit the oxidation. To determine their antioxidant power in elementary reactions responsible for inhibition of cumene oxidation, we studied reactions of these compounds with cumylperoxy radicals and CHP. All the tested compounds (Fig. 2) inhibit initiated oxidation of cumene. The stoichiometric coefficient of inhibition equal to the number of oxidation chains terminated on single inhibitor molecule and products of its conversion was calculated from the induction period τ by the equation

$$f = \frac{\tau w_i}{[InH]_0},$$

where τ is the induction period (s), w_i is the initiation rate (under the conditions studied it is equal to 2×10^{-7} mol l^{-1} s^{-1}) [10].

The rate constant of the reaction of the tested inhibitors with peroxy radicals K was calculated form the rate of oxygen uptake. For this purpose the kinetic curves of oxygen uptake in the $\Delta[O_2]$ vs. t coordinates were transformed into the $\Delta[O_2]^{-1}$ vs. t^{-1} coordinates. From the slope of the straight line

$$\tan\alpha = \frac{fK_7[InH]_0}{K_2[RH]w_i}$$

the constant K_7 was calculated by the equation

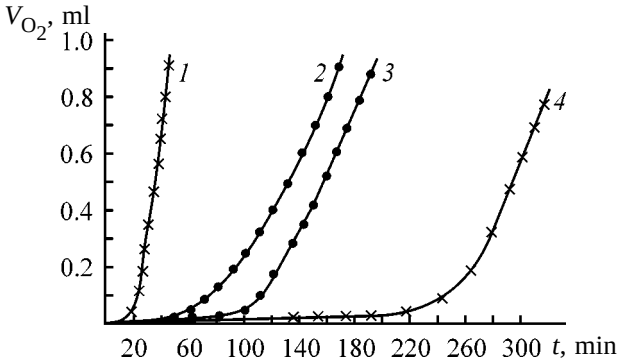

Fig. 1. Kinetic curves of cumene autooxidation at T = 110°C in the presence of the tested inhibitors with the concentration [InH] = (*1*) 0, (*2*, *3*) 5×10^{-5}, and (*4*) 5×10^{-6} M. (V_{O_2}) Oxygen volume and (t) time; the same for Fig. 2.

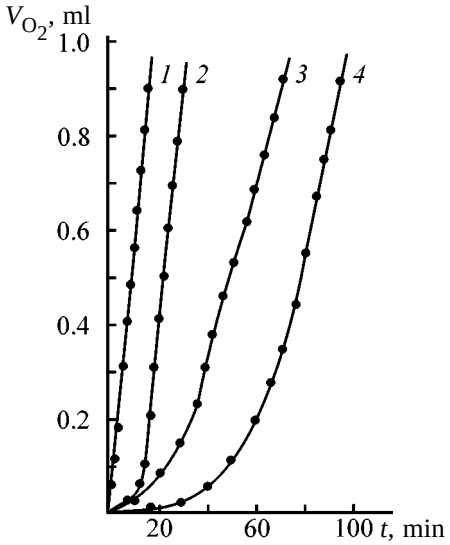

Fig. 2. Kinetic curves of initiated oxidation of cumene at [AIBN] = 2×10^{-2}, $w_i = 2 \times 10^7$ M, and T = 60°C: Inhibitor and concentration, M: (*1*) none; (*2*) **II**, 1×10^{-4} (*3*) **III**, 3×10^{-4}, and (*4*) **IV**, $5\ 10^{-6}$ M.

$$K_7 = \frac{\tan\alpha K_2[RH]w_i}{f[InH]_0},$$

where K = 1.51 l mol^{-1} s^{-1} [12], [RH] = 6.9 M.

As seen from the kinetic curves of initiated oxidation of cumene, the oxidation rate in the presence of the inhibitors after the induction period (Fig. 2, curves *2*–*4*) is lower than that in their absence (Fig. 2, curve *1*). This indicates that products of reaction of **II**–**V** with cumylperoxy radicals are also inhibitors. The kinetic parameters of reaction of **II**–**V** with cumylperoxy radicals are presented in the table.

As seen from the table, the stoichiometric coefficient f and the rate constant K_7 for **II**–**V** range from

Kinetic parameters* of reaction of 3-substituted thietanes with cumylperoxy radicals (60°C, [AIBN] = 2×10^{-2} M) and CHP (110°C)

Compound	f	$K_7 \times 10^{-4}$	K	ν
		l mol^{-1} s^{-1}		
II	0.96	2.23	20	53800
III	1.86	2.4	24	68600
IV	34	7.05	225	586000
V	0.24	2.0	12	23500

* AIBN is azobis(isobutyrolnitrile), f is the stoichiometric coefficient of inhibition, K_7 is the rate constant of reaction of the inhibitors with peroxy radicals, K is the rate constant of the reaction with CHP, and ν is the catalytic factor.

0.24 to 34 and from 2.0 to 7.05×10^{-4} l mol^{-1} s^{-1}, respectively. Analysis of the kinetic parameters of reaction of **II**–**V** with cumylperoxy radicals shows that the reactivity of these compounds strongly depends on the nature of the substituents at the thietane ring. Compound **IV**, unlike the other inhibitors, repeatedly terminates the oxidation chains (f = 34) and exhibits very high reactivity with respect to cumylperoxy radicals ($K_7 = 7.05 \times 10^{-4}$ l mol^{-1} s^{-1}).

Thus, all the tested inhibitors actively decompose CHP in three steps (Fig. 3): the first step is very slow (the induction period), the second is fast and autocatalytic, and the third is the final step of CHP degradation. The first two steps last different times depending on initial concentrations of hydroxperoxide and inhibitor. The induction period shortens with increasing the hydroperoxide concentration. The shape of the curves of CHP autocatalytic decomposition indicates that CHP decomposes under the action of products formed in the first slow step of the reaction

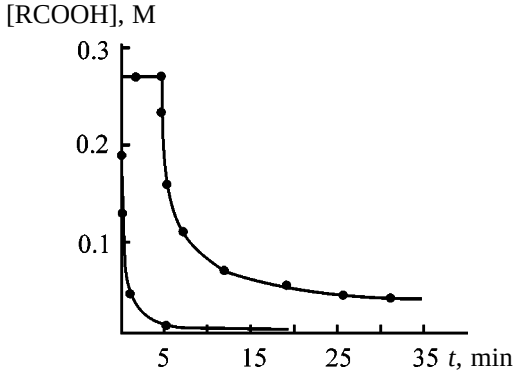

Fig. 3. Kinetic curves of CHP decomposition at T = 110°C under the action of **V**. [InH] 5×10^{-5} M. ([ROOH]) Concentration and (t) time.

of the inhibitors with CHP, but not under the action of the initial inhibitors.

EXPERIMENTAL

The IR spectra were recorded in a thin layer on a Specord 75-IR spectrometer. The ^{1}H NMR spectra were recorded on a Varian T-60 spectrometer operating at 60 MHz, with tetramethylsilane as the internal reference.

Thin-layer chromatography of **I**–**V** was performed on Silufol-254 plates using an ethanol–hexane mixture (1 : 5) as the eluent. In all case a single spot was observed after development with iodine.

1-Benzyl-3-(3'-thietanyl)thiourea (III). Benzylamine [10.7 g (0.1 mol)] was mixed with 3-thietanyl isocyanate [13.1 g (0.1 mol)]. The reaction mixture slightly warmed up. Crystalline target product was isolated after the reaction mixture was cooled to room temperature and diluted with benzene. The reaction course was monitored by TLC and IR spectroscopy. The yield of **III** was 24 g (87%), mp 165°C, R_f = 0.86.

Found, %: C 55.25, H 5.67, N 11.92, S 27.16.
$C_{11}H_{44}N_2S_2$.
Calculated, %: C 55.42, H 5.92, N 11.75, S 26.90.

Compound **IV** was prepared similarly in a 17.7 g (81%) yield from morpholine [8.7 g (0.1 mol)] and 3-thietanyl isothiocyanate [13.1 (0.1 mol)]; mp 165–166°C, R_f = 0.80.

Found, %: C 51.21, H 7.75, N 14.85, S 17.37.
$C_8H_{14}N_2OS_2$.
Calculated, %: C 51.58, H 7.58, N 15.04, S 17.21.

Cumyl hydroperoxide was purified by the known procedure [13] with subsequent distillation. Chlorobenzene and cumene were treated with concentrated sulfuric acid [14] to remove impurities. The CHP concentration was determined by iodometric titration [15]. Decomposition of CHP at 110°C in a chlorobenzene solution was studied in glass bubbling reactor under an inert atmosphere. The concentration of CHP and the tested compounds was varied from 0.23 to 0.45 and from 0.5×10^{-4} to 5×10^{-6} M, respectively. Cumene oxidation initiated by AIBN was studied on a manometric unit [10]. The rate constant of the initiation at 60°C is $K = 1.0 \times 10^{-5}$ s^{-1} [11]. The initiator concentration in all experiments was constant (2×10^{-2} M). The concentration of the inhibitors ranged from 1×10^{-4} to 5×10^{-6} M.

REFERENCES

1. Allakhverdiev, M.A., Akperov, N.A., Farzaliev, V.M., *et al*., *Khim. Geterotsikl. Soedin*., 1988, no. 12, p. 1619.
2. Allakhverdiev, M.A., Akperov, N.A., Farzaliev, V.M., *et al*., *Neftekhimiya*, 1988, vol. 28, no. 2, p. 251.
3. Allakhverdiev, M.A., Akperov, N.A., Farzaliev, V.M., *et al*., *Zh. Prikl. Khim*., 1988, vol. 61, no. 6, pp. 1411–1443.
4. Farzaliev, V.M., Allakhverdiev, M.A., Guseinova, G.M., *et al*., Abstracts of Papers, *V Moskovskaya nauchno-tekhnicheskaya konferentsiya po priborotekhnike i mashinostroeniyu* (V Moscow Scientific and Technical Conf. on Instrument Technique and Machine Building), Novgorod, 1991, p. 130.
5. Allakhverdiev, M.A., Akperov, N.A., and Farzaliev, V.M., *Khimiya tietanov* (Thietane Chemistry), Baku: Inst. Khimii Prisadok Akad. Nauk Azerbaidzhanskoi Respubliki, Available from VINITI, 1990, no. 369 590.
6. Farzaliev, V.M., Allakhverdiev, M.A., Akperov, N.A., and Liksha, V.B., *Neftekhimiya*, 1990, vol. 30, no. 5, p. 706.
7. Culvenor, C.C., Davies, W., and Pausacker, K.H., *J. Chem. Soc*., 1949, no. 11, p. 1050.
8. Huretdinova, N.O. and Guseva, F.F., *Izv. Akad. Nauk SSSR, Ser. Khim*., 1976, no. 3, p. 662.
9. Adams, E.R., Ayah, N.K., and Queen, A., *J. Chem. Soc*., 1960, no. 6, p. 2665.
10. Denisov, E.T., Kharitonov, V.V., and Fedorov, V.V., *Metody transformatsii kineticheskikh krivykh kak sposob otsenki effektivnosti ingibitorov okisleniya* (Transformation of Kinetic Curves as a Procedure for Estimating Efficiency of Oxidation Inhibitors), Chernogolovka, 1973.
11. Emanuel' N.M., Denisov, E.T., and Maizus, Z.K., *Tsepnye reaktsii okisleniya uglevodorodov v zhidkoi faze* (Chain Reactions of Hydrocarbon Oxidation In Liquid Phase), Moscow: Nauka, 1967.
12. Denisov, E.T., *Konstanty skorosti gomoliticheskikh zhidkofaznyk reaktsii* (Rate Constants of Homolytic Liquid-Phase Reactions), Moscow: Nauka, 1971.
13. Karnojitzki, V., *Les peroxides organiques*, Paris: Hermann, 1958.
14. Weissberger, A. and Proskauer, E.S., *Organic Solvents. Physical Properties and Methods of Purification*, Riddick, J.A. and Toops, E.E., Eds., New York: Interscience, 1955.
15. Houben–Weyl, *Methoden der Organischen Chemie*, vol. 2: *Analytische Methoden*, Stuttgart: Georg Thieme, 1953.

Russian Journal of Applied Chemistry, Vol. 74, No. 1, 2001, pp. 118–122. Translated from Zhurnal Prikladnoi Khimii, Vol. 74, No. 1, 2001, pp. 114–117.

ORGANIC SYNTHESIS AND INDUSTRIAL ORGANIC CHEMISTRY

Preparation of Amino Derivatives from Industrial Mixtures of Polychlorobiphenyls

T. I. Gorbunova, A. Ya. Zapevalov, V. E. Kirichenko, V. I. Saloutin, and O. N. Chupakhin

Institute of Organic Synthesis, Ural Division, Russian Academy of Sciences, Yekaterinburg, Russia

Received June 21, 2000

Abstract—Chemical utilization (conversion) of polychlorobiphenyls by nitration of their industrial mixture was studied. Reduction of the nitro derivatives gave mixtures of aminopolychlorobiphenyls.

One of the main sources of environmental pollution with highly toxic compounds, polychlorodibenzodioxins (PCDDs) and polychlorodibenzofurans (PCDFs), is continuing use of polychlorobiphenyls (PCBs) as liquid dielectrics. The first step to stop environmental pollution with PCDDs and PCDFs was made in early 1990s and implied total cessation of production of PCBs.

Today active efforts are made throughout the world to develop processes for utilization (conversion) of PCBs accumulated in large amounts, and state regulations are being adopted on determination and analysis of noxious impurities in air, water, and soil. Much attention is given to development and implementation of various projects aimed at normalization of the environment. A new program, Protection of the Environment and Population from Dioxins and Dioxin-Like Toxicants in 2000–2005, is to be adopted in Russia [1].

Procedures for utilization (conversion) of PCBs are summarized in [2]. Methods based on combustion of PCBs followed by trapping of off-gases seem to be economically unfeasible. Conversion of PCBs into useful nontoxic materials would be more acceptable.

Previously procedures were proposed for chemical processing of PCBs by substitution of two chlorine atoms in the initial industrial mixtures by alkoxy groups in the presence of alkali metal hydroxides [3].

In this work we continue a search for alternative chemical methods of conversion (utilization) of PCBs.

The goal of this study was development of procedures for preparing amino derivatives from the industrial PCB mixture. Such derivatives show promise in synthesis of polymeric compositions [4], dyes [5], analytical reagents [6–8], etc. The main precursors of aromatic amino derivatives are aromatic nitro compounds [5]. Both mono- [5, 9] and dinitro [10] derivatives of biphenyl are known. Mononitrobiphenyls are usually prepared by indirect procedures from various mononuclear derivatives [9], rather than by direct nitration of biphenyl. Treatment of biphenyl with nitrating mixture gives 4,4'-dinitrobiphenyl [10]. The by-product is 3,5,4'-trinitro-4-hydroxybiphenyl (less than 2%) [11]. In treatment of biphenyl with nitrating mixture, compounds with a greater degree of nitration were not detected. Other dinitro derivatives of biphenyl are also prepared by indirect procedures.

Scheme.

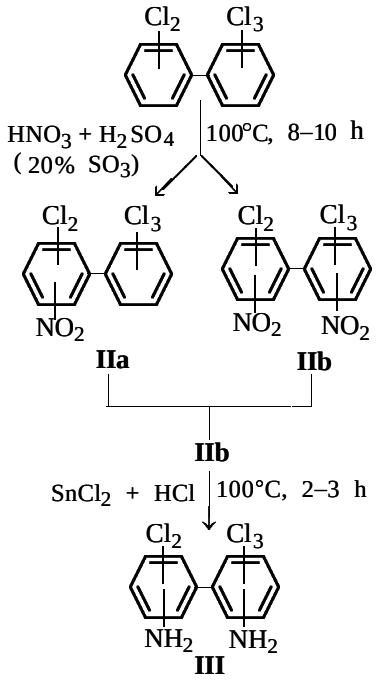

Preparation of diaminopentachlorobiphenyls.

1070-4272/01/7401-0118$25.00

Table 1. Data on nitration of PCB-5 (**I**)

Run no.*	Loaded				τ, h	Reaction product	Yield, %
	PCB-5 (**I**)		HNO_3	H_2SO_4 (20% SO_3)			
	mol	g	ml				
1	0.31	100.0	60	72	6	**I** + **IIa** + **IIb**	N/d**
2	0.3	98.0	60	72	9	**IIa** + **IIb**	″
3	0.2	65.3	40	48	9	**IIa** + **IIb**	″
			–	3	3		
4	0.2	65.3	60	72	12	**IIa** + **IIb**	″
			–	5	3		
5	0.3	98.0	60	72	12	**IIb**	98
			–	10	8		
			60	72	12		
6	0.6	195.9	120	144	8	**IIb**	99
			–	20	6		
			120	144	9		
7	0.3	98	60	72	12	**IIb**	99
			–	10	3		
			60	72	12		

* In run nos. 1 and 2 the loading was performed as recommended in [12]; in run nos. 3–7 the reactants were added in portions.
** (N/d) The yield was not determined, because it was difficult to separate **IIa** and **IIb**.

Table 2. Monitoring by the Yanovskii reaction of the progress of PCB-5 nitration

Run no.	Sampling time, h	Color of acetone solution	Amount of unchanged PCB-5 (**I**)	
			ml	g
1	2	Light brown, transparent	1.20	1.81
2	4		0.45	0.68
3	6		0.23	0.35
4	8		–	–
5*	10		–	–
6	12	Brown, transparent	–	–
7**	14		–	–
8	16		–	–
9	18		–	–
10	20		–	–
11	22	Reddish brown, nontransparent in transmitted light	–	–
22	24		–	–

* After sampling, an additional portion of oleum was introduced.
** After sampling, a portion of nitrating mixture was added.

A procedure was developed for nitration of a mixture of pentachlorobiphenyls PCB-5 (**I**), which are the main components of industrial PCBs. The isomeric composition of the industrial mixture of PCBs used in enterprises of the Ural region was determined by GLC; the results are reported elsewhere [3].

Nitration of PCB-5 (**I**) was performed by treatment with a mixture of nitric acid and oleum (20% SO_3) (see scheme). The reaction parameters (amount of the nitrating mixture, time, temperature) were determined (Table 1). The progress of nitration and the extent of PCB-5 conversion were monitored qualitatively by the Yanovskii reaction [6–8, 13] (see Experimental; Table 2).

Analysis of the nitration products **IIb** shows that under the reaction conditions two nitro groups are

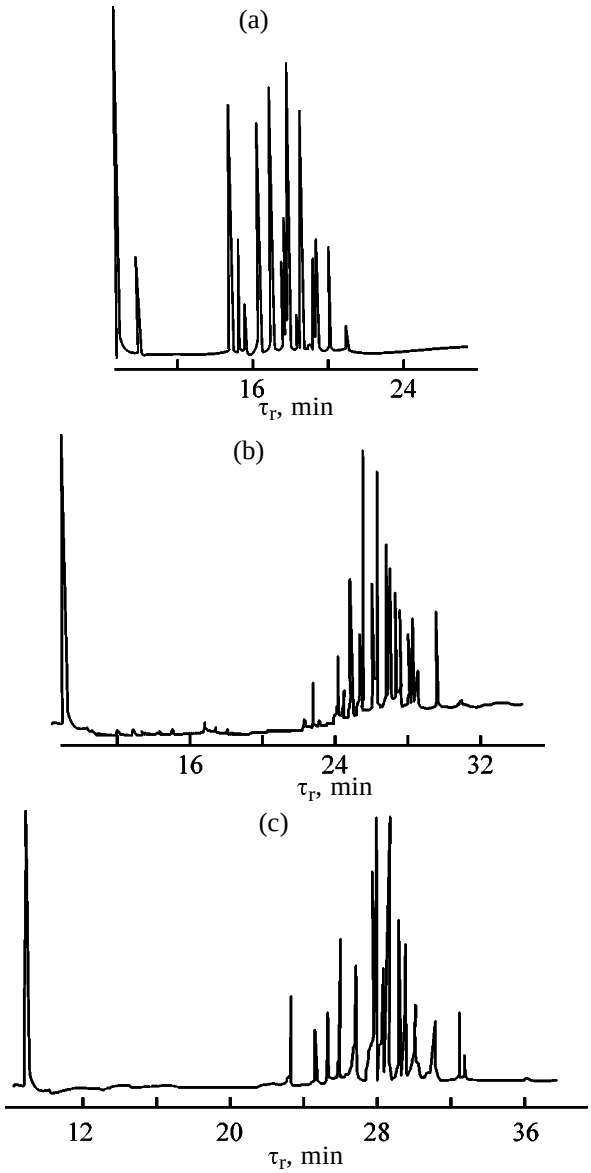

Fig. 1. Chromatograms of 5% solutions in toluene of (a) industrial PCB-5 mixture **I**, (b) mixture of dinitropentachlorobiphenyls **II**, and (c) mixture of diaminopentachlorobiphenyls **III**. (τ_r) Retention time.

introduced into the moleculees of the initial PCB-5. The presence of chlorine atoms in PCB-5 should favor deeper nitration. However, analysis of the isomeric composition of **I** [3] shows that accumulation of substituents (chlorine atoms) in positions 2 and 2' in the eleven major components distorts the coplanarity of the PCB-5 structure [10]. Furthermore, in six isomers of eleven both 4- and 4'-positions are occupied, and in the remaining five isomers one of these positions is occupied. All these factors prevent deep nitration of PCB-5 (**I**).

Figure 1 shows the GLC data proving complete conversion of the initial mixture **I** in the course of nitration.

Diamino derivatives **III** are prepared by reduction of nitro groups in mixture **IIb**. The most efficient laboratory procedure for reduction of dinitro derivatives **IIb** is their treatment with a solution of $SnCl_2$ in HCl (see scheme). The reaction occurs within 2 h and gives the crude product in a good yield (86%). After additional purification, the yield of target compounds **III** is 68–72% (Table 3):

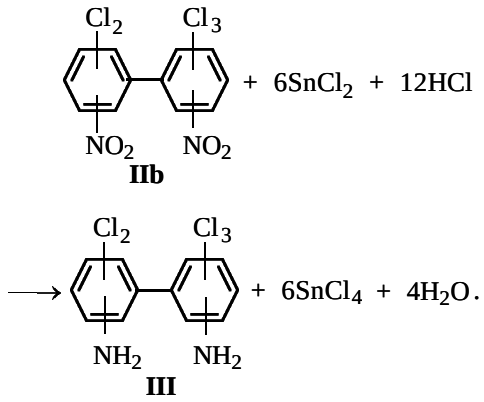

It should be noted that the temperature conditions of reduction of mixture **IIb** (about 100°C) exclude formation of dioxin-like structures from the initial substance [14]. This reduction procedure has significant advantages over the procedures used in industry and involving in most cases elevated temperatures and pressures [15].

Diaminopentachlorobiphenyls **III** can be used as starting compounds in production of dyes [5] and as components in polycondensation for preparing epoxy resins, polyamides, polymer blends [4], etc.

EXPERIMENTAL

The IR spectra were taken on a Specord 75-IR spectrophotometer from films of toluene solutions. The product purity was checked with a Shimadzu GC-14A gas–liquid chromatograph (Chromatopac C-RGA data processing system) equipped with a flame-ionization detector (HP-5 quartz capillary column, 30 m long, 0.2 mm i.d., carrier gas nitrogen). Compounds were injected as 10% solutions in hexane or methanol. The column temperature was kept at 100°C for 3 min with subsequent heating to 280°C at a rate of 10 deg min^{-1}. The vaporizer temperature was 280°C, and the detector temperature, 300°C.

The procedure of the Yanovskii reaction is described in detail elsewhere [16]. The blank experiment

Table 3. Results of reduction of dinitropentachlorobiphenyls **IIb**

τ, h	Loaded					Yield of **III**, %
	IIb		$SnCl_2 \cdot 2H_2O$		HCl concd., ml	
	mol	g	mol	g		
7	0.1	41.6	0.72	162.7	146	72
5	0.2	83.2	1.44	325.5	292	68
4	0.1	41.6	0.6	135.6	122	N/d*
2	0.09	39.0	0.72	162.7	146	71
1	0.1	41.6	0.72	162.7	146	N/d

* (N/d) The yield was not determined, because the isolated product contained **IIb** along with **III**.

(mixture of PCB-5, acetone, and NaOH solution) gives a three-layer system of immiscible initial reactants [from bottom to top: PCB-5 (**I**), colorless NaOH solution, and colorless acetone phase].

The control sample (a mixture of dinitropentachlorobiphenyls **IIb**, acetone, and NaOH solution) is a uniform liquid of intense reddish brown color, nontransparent in transmitted light.

A three-necked reactor equipped with a power-driven stirrer, a water-cooled reflux condenser, and a dropping funnel was placed on a boiling water bath and was charged with 195.9 g (0.6 mol) of pentachlorobiphenyl **I**. Then the nitrating mixture (120 ml of concd. HNO_3 and 144 ml of H_2SO_4 + 20% SO_3) was added dropwise with vigorous stirring. After addition completion, the mixture was stirred for 8 h, and 20 ml of oleum was added. The stirring was continued for 6 h, and a new portion of the nitrating mixture, similar to the first portion, was added. The stirring was continued for an additional 9 h, after which the nitration product was washed with hot water to pH 7. After drying, 247.4 g (99%) of dinitropentachlorobiphenyl **IIb** was obtained as a yellow solid, mp 72–75°C. IR spectrum, ν, cm^{-1}: 1550, 1335 (antisymmetrical and symmetrical stretching vibrations of the NO_2 groups).

Found, %: C 34.19, H 0.76, Cl 42.68, N 6.77.

$C_{12}H_3Cl_5N_2O_4$.
Calculated, %: C 34.61, H 0.73, Cl 42.57, N 6.73.

A three-necked vessel equipped with a power-driven stirrer, a water-cooled reflux condenser, and a dropping funnel was placed on a boiling water bath, 41.6 g (0.1 mol) of **IIb** was added, and a mixture of 162.7 g (0.72 mol) of $SnCl_2 \cdot 2H_2O$ and 146 ml of concd. HCl was added dropwise. After addition completion, the mixture was stirred for 2 h and washed with water, Na_2CO_3 solution, and again water until the medium became weakly acidic. The solid product was collected and dried. Then the dry substance was dissolved in toluene, and the $SnCl_4$ precipitate was washed by decanting. The solvent was distilled off, and the residue was kept in a vacuum. Yield of crude diaminopentachlorobiphenyl **III** 30.6 g (86%). Product **III** was distilled in a roughing-pump vacuum, bp 249–256°C/6 mm Hg. Yield of purified **III** 25.3 g (71%). IR spectrum, ν, cm^{-1}: 3460, 3365 (NH stretching vibrations), 1600 (NH bending vibrations).

Found, %: C 40.57, H 1.89, Cl 49.76, N 7.74.

$C_{12}H_7Cl_5N_2$.
Calculated, %: C 40.43, H 1.98, Cl 49.73, N 7.86.

CONCLUSIONS

(1) A procedure was developed for preparing dinitro derivatives from industrial mixture of polychlorobiphenyls.

(2) Reduction of dinitro derivatives of polychlorobiphenyls gave a mixture of diaminopolychlorobiphenyls in a yield of up to 72%.

(3) Diaminopolychlorobiphenyls can be valuable intermediates in production of polymers, dyes, etc.

ACKNOWLEDGMENTS

The study was supported by the State program for support of leading scientific schools, project no. 00-15-97390.

REFERENCES

1. Petrosyan, V.S., *Priroda*, 2000, no. 2, pp. 13–19.
2. Zanaveskin, L.N. and Aver'yanov, V.A., *Usp. Khim.*, 1998, vol. 67, no. 8, pp. 788–800.

3. Gorbunova, T.I., Zapevalov, A.Ya., Kirichenko, V.E., *et al.*, *Zh. Prikl. Khim.*, 2000, vol. 73, no. 4, pp. 610–614.
4. Shur, A.M., *Vysokomolekulyarnye soedineniya* (Macromolecular Compounds), Moscow: Vysshaya Shkola, 1971.
5. Vorozhtsov, N.N., *Osnovy sinteza promezhutochnykh produktov i krasitelei* (Principles of Synthesis of Intermediates and Dyes), Moscow: Goskhimizdat, 1955.
6. Pollitt, R.J. and Saunders, B.C., *J. Chem. Soc.*, 1965, no. 9, pp. 4615–4628.
7. Sawicki, E. and Stanley, T.W., *Anal. Chim. Acta.*, 1960, vol. 23, no. 6, pp. 551–556.
8. Sawicki, E., Noe, J., and Stanley, T.W., *Microchim. Acta*, 1960, no. 2, pp. 286–290.
9. Fieser, L.F. and Fieser, M., *Reagents for Organic Synthesis*, New York: Wiley–Interscience, 1968.
10. Nesmeyanov, A.N. and Nesmeyanov, N.A., *Nachala organicheskoi khimii* (Principles of Organic Chemistry), Moscow: Khimiya, 1970, book 2.
11. Bennett, G.M. and Grove, J.F., *J. Chem. Soc.*, 1945, pp. 378–380.
12. Becker, H., Berge, W., Domschke, G., *et al.*, *Organikum. Organisch-chemisches Grundpraktikum*, Berlin: Wissenschaften, 1976.
13. Kaminskii, A.Ya. and Gitis, S.S., *Zh. Obshch. Khim.*, 1964, vol. 34, no. 11, pp. 3743–3747.
14. Tarasov, V.V., *Sb. Nauchn. Tr. Ross. Khim.-Tekhnol. Univ. im. D.I. Mendeleeva*, 1995, issue 173, pp. 24–42.
15. Lebedev, N.N., *Khimiya i tekhnologiya osnovnogo organicheskogo i neftekhimicheskogo sinteza* (Chemistry and Technology of Basic Organic and Petrochemical Synthesis), Moscow: Khimiya, 1988.
16. Houben–Weyl, *Methoden der organischen Chemie*, vol. 2: *Analytische Methoden*, Stuttgart: Thieme, 1953.

Russian Journal of Applied Chemistry, Vol. 74, No. 1, 2001, pp. 123–126. Translated from Zhurnal Prikladnoi Khimii, Vol. 74, No. 1, 2001, pp. 118–121.

MACROMOLECULAR CHEMISTRY AND POLYMERIC MATERIALS

Viscosity of Melts of H Complexes Based on Acidic Diesters of Benzophenonetetracarboxylic Acid and Diaminodiphenylmethane or *m*-Phenylenediamine

T. A. Kosterova, V. N. Artem'eva, N. V. Kukarkina, V. P. Samarin, V. E. Yudin, Yu. N. Panov, and V. V. Kudryavtsev

Institute of Macromolecular Compounds, Russian Academy of Sciences, St. Petersburg, Russia

Received July 10, 2000

Abstract—The time dependences of the viscosity of melts of H complexes formed by dimethyl or diethyl dihydrogen 3,3',4,4'-benzophenonetetracarboxylate and 4,4'-diaminodiphenylmethane, *m*-phenylenediamine, or equimolar mixture of these diamines at 95 and 105°C were studied.

It is known that thermal imidization of H complexes formed by dimethyl dihydrogen 3,3',4,4'-benzophenonetetracarboxylate and aromatic diamines is the key step in preparation of light-weight polyimide foam composites containing felts and fabrics based on organic thermally stable fibers (including polyimide felt) as a reinforcing filler. Due to their low density along with high cryo- and thermal stability, refractoriness, and high thermal and sound insulation properties, these composites show promise for ship-building and aircraft industry [1].

In preparation of polyimide foam composites H complexes are used as prepolymers of polyimide binders. In the process, relatively low melting point (mp) of H complexes (from 70 to 130°C depending on the composition [2]) is a decisive factor. However, thermal imidization of H complexes also starts at low temperatures (100–120°C [3]). Thus, separation of melting and further intensive imidization of H complexes during prepreg preparation is of particular importance. This problem can be solved by preparing the prepreg at lower temperature (95–105°C) when the required H complexes occur in the molten state, but imidization is yet very slow.

To optimize the prepreg preparation the viscosity of the melt of the H complex (binder) and the kinetics of its variation should be determined. In this work we studied H complexes of dimethyl or diethyl dihydrogen benzophenonetetracarboxylate with aromatic diamine (diaminodiphenylmethane, *m*-phenylenediamine, or their mixture) under various preparation conditions.

EXPERIMENTAL

The initial H complexes were prepared as follows. 3,3',4,4'-Benzophenonetetracarboxylic dianhydride (0.03 mol) was dissolved with stirring in 15 ml of boiling methanol or ethanol (absolute or with addition 10 vol % water). The solution of dialkyl dihydrogen benzophenonetetracarboxylate was cooled to room temperature and the equimolar amount of the corresponding diamine (or diamines) was added dropwise with stirring. After solution homogenization the resulting solid H complexes were recovered by removing the solvent in a vacuum at room temperature. The abbreviations of the H complexes studied (depending on diamine and esterifying agent) are presented in the table.

Before use 3,3',4,4'-benzophenonetetracarboxylic dianhydride [BZP; TU (Technical Specifications) TSR 2159–69] was purified by refluxing in acetone (mp 225°C); 4,4'-diaminodiphenylmethane (DADPM) was distilled in a vacuum (1–3 mm Hg, mp 90–92°C); and *m*-phenylenediamine (*m*-PDA) was sublimed from zinc dust in a vacuum (mp 63°C).

The viscosity of the melts of H complexes was measured at 95 and 105°C on a PIRSP rheometer with a cone–plane working unit (1° angle at the cone apex, 40 mm cone diameter) [4].

The kinetic dependences of the viscosity of the melts of H complexes based on dimethyl dihydrogen benzophenonetetracarboxylates (BZPMe) prepared under various conditions are shown in Figs. 1a and 1b (in absolute methanol and in the mixture of methanol

1070-4272/01/7401-0123$25.00

H Complexes based on dialkyl dihydrogen benzophenonetetracarboxylates

Esterifying agent	H complexes with diamine		
	DADPM	*m*-PDA	DADPM + *m*-PDA
CH_3OH	BZPMe · DADPM	BZPMe · *m*-PDA	BZPMe · (DADPM + *m*-PDA)
CH_3OH + 10%H_2O	BZPMe · DADPM(H_2O)	BZPMe · *m*-PDA(H_2O)	BZPMe · (DADPM + *m*-PDA)(H_2O)
C_2H_5OH	BZPEt · DADPM	BZPEt · *m*-PDA	BZPEt · (DADPM + *m*-PDA)
C_2H_5OH + 10%H_2O	BZPEt · DADPM(H_2O)	BZPEt · *m*-PDA(H_2O)	BZPEt · (DADPM + *m*-PDA)(H_2O)

with 10 vol % water, respectively). As expected, with increasing temperature from 95 to 105°C the viscosity of melts increases more rapidly. The decrease in the viscosity, most pronounced at 105°C (Fig. 1a, curves *2*, *3*; Fig. 1b, curve *3*), is probably due to foaming of the molten sample and weight loss occurring in this case, because the foaming melt partially escapes from the rheometer cell (observed visually). The viscosity decrease is the more pronounced, the greater the melt foaming.

The time dependences of the viscosity of the melts of H complexes based on diethyl dihydrogen benzophenonetetracarboxylate (BZPEt) prepared under various experimental conditions are shown in Figs. 1c and 1d. With substitution of BZPEt for BZPMe in the H complex the life period of the melt increases,

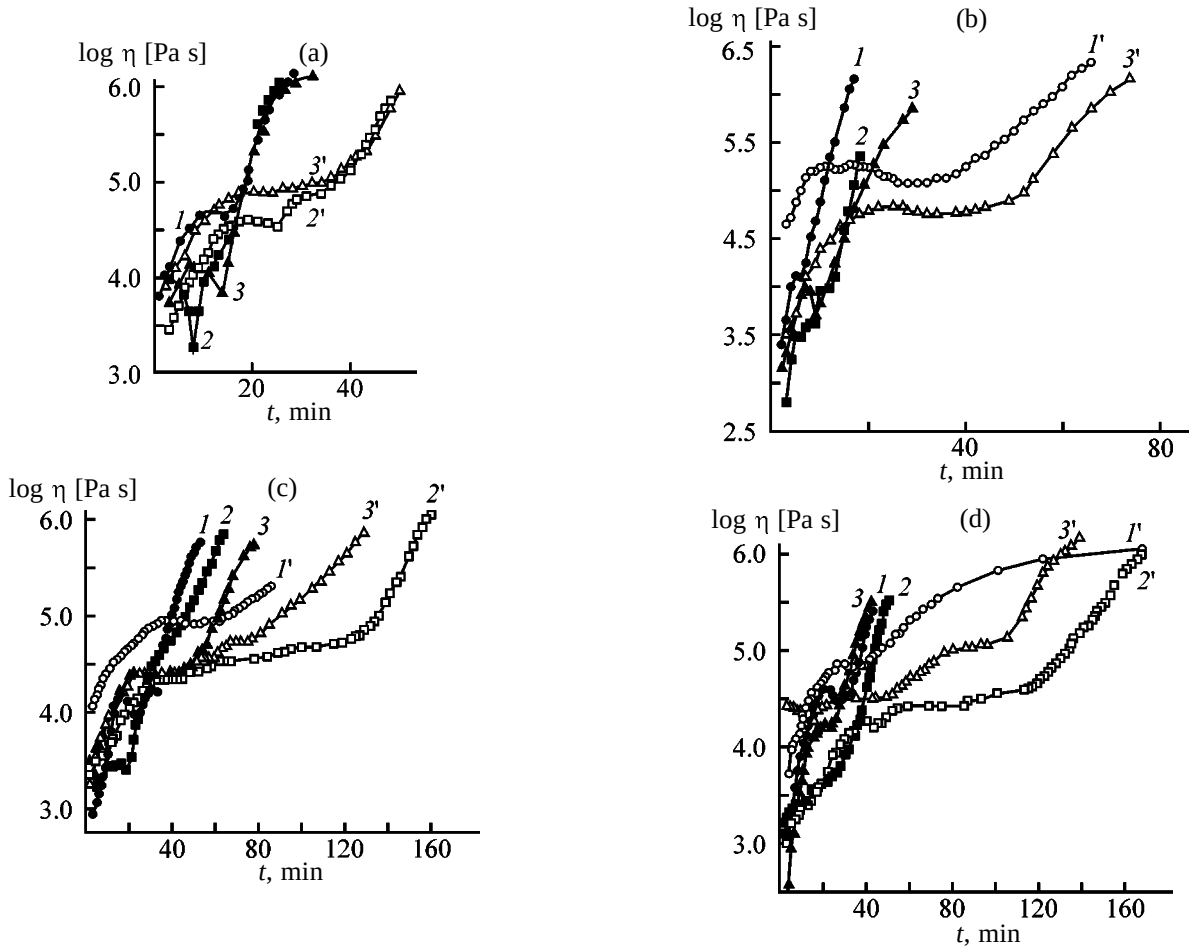

Fig. 1. Viscosity η of the melts of H complexes as a function of time *t*. (a): (*1*) BZPMe–DADPM, (*2*, *2*′) BZPMe–*m*-PDA, and (*3*, *3*′) BZPMe–(DADPM + *m*-PDA); (b): (*1*, *1*′) BZPMe–DADPM(H_2O), (*2*) BZPMe–*m*-PDA(H_2O), and (*3*, *3*′) BZPMe–(DADPM + *m*-PDA)(H_2O); (c) (*1*, *1*′) BZPEt–DADPM, (*2*, *2*′) BZPEt–*m*-PDA, and (*3*, *3*′) BZPEt–(DADPM–*m*-PDA); (d) (*1*, *1*′) BZPEt–DADPM(H_2O), (*2*, *2*′) BZPEt–*m*-PDA(H_2O), and (*3*, *3*′) BZPEt–(DADPM + *m*-PDA)(H_2O).

whereas the intensity of foaming significantly decreases.

Now, we consider the effect of the diamine nature in the H complex on the melt viscosity. As seen from Figs. 1a–1d, H complexes based on DADPM possess the greatest viscosity (curves *1*, *1*'). It should be noted that the temperature of 95°C is insufficient to melt the BZPMe-DADPM H complex prepared in absolute methanol (curve *1*' in Fig. 1a is absent). As a rule, H complexes based on *m*-PDA exhibit the lowest viscosity (Figs. 1a–1d, curves *2*, *2*'). The melts of H complexes based on the mixture of diamines (curves *3*, *3*') exhibit the intermediate viscosities.

Next, we analyze the effect of water present in the solvent used for esterification of BZP dianhydride and preparation of H complex on the melt viscosity. At 95°C the life period of the melts of H complexes prepared in aqueous alcohol (Figs. 1b, 1d, curves *1*'–*3*') is greater as compared with H complexes prepared in absolute solvents (Figs. 1a, 1b, curves *1*'–*3*'). However, at 105°C the relation is reverse: the life period of the melts of H complexes prepared in absolute alcohols (Figs. 1a, 1c, curves *1*–*3*) is greater than that of the complexes prepared in aqueous solvents (Figs. 1b, 1d, curves *1*–*3*).

Let us analyze how the structure of the H complex and the temperature of the experiment affect the rate of the increase in the melt viscosity at the final stage of the process, which is usually regarded as cross-linking and polymerization [5]. In our case it involves thermal imidization of H complexes. In all the cases the rate of the increase in the viscosity of the melt of the H complex based on BZPEt is significantly lower as compared with the H complex based on BZPMe. The rate constant of the increase of the melt viscosity of the H complex based on BZPEt–DADPM at 105°C is two times lower as compared with the H complex based on BZPMe–DADPM (2.7×10^{-3} and 5.2×10^{-3} s^{-1}, respectively). For H complexes based on the mixture of the diamines this difference is still greater (2.0×10^{-3} and 9.0×10^{-3} s^{-1}, respectively). Actually, the rate constant of imidization of the H complexes based on BZPEt is several times lower as compared with the H complexes based on BZPMe [3].

As for water present in the solvent during preparation of H complexes, it decelerates or accelerates the growth of the melt viscosity for H complexes based on BZPMe and BZPEt, respectively.

The dependence of the melt viscosity η on the shear rate $\dot{\gamma}$ was studied for the H complex based on BZPEt–(DADPM-*m*-PDA) (Fig. 2). This dependence can be approximated by the following expression:

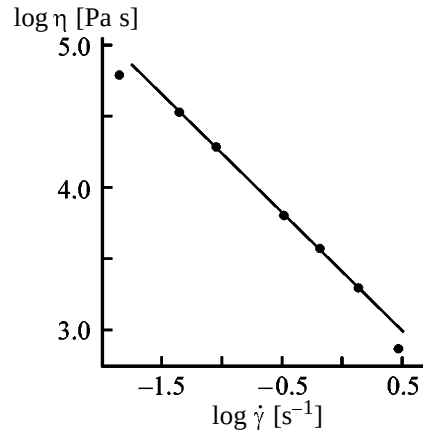

Fig. 2. Viscosity η of the melt of H complex based on BZPEt–(DADPM + *m*-PDA) as a function of the shear rate $\dot{\gamma}$ 40 min after the start of the experiment ($\log\dot{\gamma}$ = –1.88, T = 95°C); $n = \log\eta/\log\dot{\gamma}$ = 0.8.

$$\eta \sim \dot{\gamma}^{-n}.$$

For high-molecular-weight flexible-chain polymers n varies within 0.5–0.7 [5, 6]. In the case of structural ordering of the melt, e.g., typical for liquid-crystalline polymers, application of the shear stress breaks the melt structure and, as a result, n increases. In our case n = 0.8 (Fig. 2), which suggests formation of the mesomorphic rather than the liquid-crystalline structure in the melts of H complexes.

Our data allow some conclusions on the selection of the chemical composition of the binder for polyimide foam composites and conditions for preparing the corresponding precursors.

CONCLUSIONS

(1) Taking into account high viscosity of H complexes based on 4,4'-diaminodiphenylmethane, the use of binders based on the mixture of two diamines (4,4'-diaminodiphenylmethane and *m*-phenylenediamine) is the most promising.

(2) Preparation of binders in aqueous alcohols is advisable.

(3) Since curing of H complexes based on diethyl dihydrogen benzophenonetetracarboxylate at 95°C to prepare precursors is very slow, higher temperatures are recommended as compared with curing of H complexes based on dimethyl dihydrogen benzophenonetetracarboxylate.

REFERENCES

1. RF Patent 2 081 134.
2. Artem'eva, V.N., Kukarkina, N.V., Samarin, V.P., *et al.*, *Zh. Prikl. Khim.*, 2000, vol. 73, no. 7, pp. 1172–1179.
3. Artem'eva, V.N., Kudryavtsev, V.V., Chupans, P.I., *et al.*, *Izv. Ross. Akad. Nauk, Ser. Khim.*, 1995, no. 6, pp. 1060–1065.
4. Vinogradov, G.V., Malkin, A.Ya., Plotnikova, E.P., *et al.*, *Vysokomol. Soedin., Ser. A*, 1978, vol. 20, no. 2, pp. 226–230.
5. Vinogradov, G.V. and Malkin, A.Ya., *Reologiya polimerov* (Rheology of Polymers), Leningrad: Khimiya, 1977.
6. Van Krevelen, D.W., *Properties of Polymers*, New York: Elsevier, 1990, p. 875.

Russian Journal of Applied Chemistry, Vol. 74, No. 1, 2001, pp. 127–130. Translated from Zhurnal Prikladnoi Khimii, Vol. 74, No. 1, 2001, pp. 121–124.

MACROMOLECULAR CHEMISTRY AND POLYMERIC MATERIALS

Study of Polymerization of Ammonium Salts of *N,N*-Dimethylaminoethyl Methacrylate by Differential Scanning Calorimetry

D. Yu. Efimova, V. G. Shibalovich, and A. F. Nikolaev

St. Petersburg State Technological Institute, St. Petersburg, Russia

Received February 9, 2000; in final form, June 2000

Abstract—The kinetics of thermal polymerization of ammonium salts of *N,N*-dimethylaminoethyl methacrylate and mineral acids (HCl, HNO_3, H_2SO_4, and H_3PO_4) were studied by dynamic differential scanning calorimetry. The apparent rate constants, reaction orders, and thermal effect of polymerization of the salts were determined.

Water-soluble cationic polyelectrolytes based on aminoalkyl esters of (meth)acrylic acids and their derivatives, tertiary and quaternary salts, attract considerable interest, which is due, on the one hand, to the possibility of widely varying their chemical nature and physicochemical characteristics and, on the other hand, to their wide use in various branches of national economy, industry, technology, and medicine [1–5].

The most used procedure of their production is the liquid-phase polymerization in the presence of various initiators [1–4]. Of special interest are studies of solid-phase polymerization of ammonium salts using thermal methods, in particular, differential scanning calorimetry (DSC) and differential thermal analysis (DTA), allowing monitoring of the reaction kinetics, qualitative transformations of reactants, and the effect of various conditions on the reaction pathways [6–9].

In this work we studied solid-phase polymerization of ammonium salts of *N,N*-dimethylaminoethylmethacrylate (AS DM) and mineral acids by DSC in air.

AS DMs were synthesized by the reaction of equimolar amounts of DM and mineral acid in an organic solvent according to the scheme [10]

$$CH_2=C(CH_3)C(O)OCH_2CH_2N(CH_3)_2 + H^+A^-$$

$$\rightarrow [CH_2=C(CH_3)C(O)OCH_2CH_2N(CH_3)_2H^+]A^-,$$

where A^- is Cl^- (**I**), NO_3^- (**II**), HSO_4^- (**III**), and $H_2PO_4^-$ (**IV**).

The synthesized ammonium salts are white crystalline products, readily soluble in water and polar solvents.

Previously [11], when studying thermal transformations of AS DMs by DTA and TG in air, for all the studied salts we observed the endothermic peaks with maxima at 50–120°C and exothermic peaks with maxima at 105–210°C without weight loss, caused by melting of the crystalline phase of AS DMs and their polymerization, respectively. For salt **I**, polymerization and degradation proceed simultaneously.

The use of DSC, furnishing rich information on behavior of polymer systems under nonisothermal conditions, allows study of chemical and physical transformations in a wide temperature range, estimation of qualitative and quantitative characteristics of these transformations, and calculation of the kinetic parameters of the process [7–9].

In Fig. 1 are presented the DSC curves for salts **I**–**IV**. These curves reveal clearly pronounced endothermic and exothermic effects caused by melting and

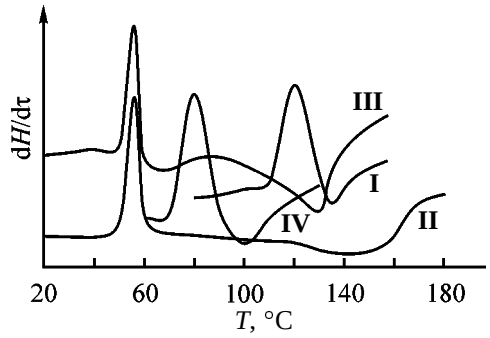

Fig. 1. DSC curves for ammonium salts **I**–**IV**. (d*H*/dτ) Rate of heat evolution, and (*T*) temperature (°C); the same for Fig. 2. Numbers at curves are numbers of compounds in Table 1.

1070-4272/01/7401-0127$25.00 © 2001 MAIK "Nauka/Interperiodica"

Table 1. Temperature ranges of melting and polymerization of AS DMs from DSC data

Salt	Temperature, °C			
	melting		polymerization	
	t_{init}	t_{fin}	t_{init}	t_{fin}
I	102	130	193	203
II	42	65	71	180
III	47	67	86	147
IV	75	83	92	123

polymerization of these salts, respectively. The temperature ranges of these processes are presented in Table 1.

Analysis of the DSC curves for salts **II**–**IV** (Fig. 2) registered at various heating rates (2.5, 5.0, and 10.0 deg min^{-1}) allowed unambiguous conclusion that the observed thermal effects correspond to polymerization; additional (concurrent) reactions were not found. For salt **I**, as mentioned above, the quantitative estimation of the polymerization parameters was not carried out owing to parallel polymerization and degradation processes.

The heat of polymerization for salts **II**–**IV**, determined by comparison of the peak areas of the sample and reference [6, 8], varies from 43 to 48 kJ mol^{-1}

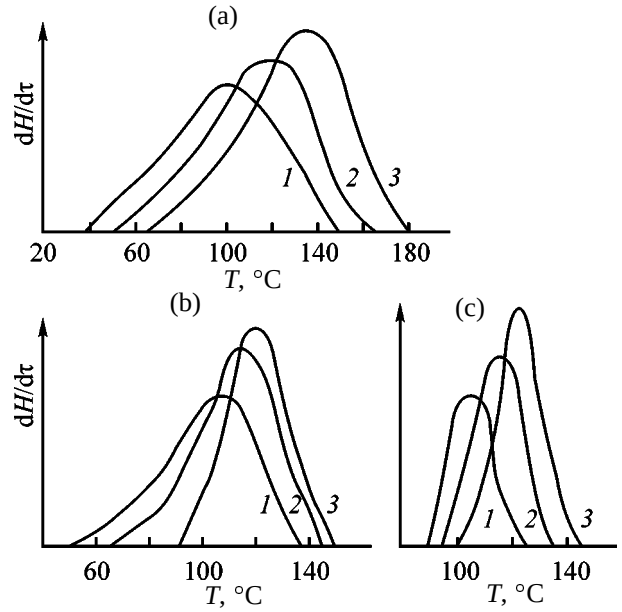

Fig. 2. DSC curves for polymerization of salts (a) **II**, (b) **III**, and (c) **IV**. Heating rate (deg min^{-1}): (*1*) 2.5, (*2*) 5.0, and (*3*) 10.0.

(Table 2). The relatively low enthalpies of polymerization of AS DMs (independent of the nature of the anion) are probably due to the effect of bulky substituent on the reactivity of the double bond in comparison with methacrylic acid.

To evaluate the apparent kinetic parameters of thermal polymerization of AS DMs, we used the methods of mathematical treatment of data [6–9, 12–14].

The apparent reaction orders, obtained by the Freeman–Carroll method [12], are in a good agreement with those evaluated by the Kissenger method [13] (deviation does not exceed 3%) (Table 2). Hence, considering the experimental errors, we can assume with sufficient accuracy that the reaction is second-order regardless of the salt nature.

The apparent total activation energy E_a of polymerization of salts varies from 23.0 to 83.0 kJ mol^{-1} depending on the nature of the anion (Table 2). For comparison, in Table 2 are presented the values of E_a for thermal polymerization of AS DMs, evaluated for the reactions performed under traditional isothermal conditions [15]. As seen from data listed in Table 2, the values of E_a obtained under isothermal and dynamic conditions are in a good agreement (deviation 6%), which suggests a possibility of using dynamic DSC for studying thermal polymerization of salts.

The comparative analysis of the kinetic parameters of thermal polymerization of AS DMs (Table 2) showed that these salts are fairly reactive; their polymerization proceeds at a high rate increasing in the order **IV** < **III** < **II**.

EXPERIMENTAL

AS DMs were synthesized by the procedure described in [10].

The DSC curves were recorded on a Perkin–Elmer DSC-2 scanning calorimeter with a heating rate of 1.5, 2.5, 5.0, 10.0, and 20.0 deg min^{-1}; the weighed portion was varied from 0.500 ± 0.001 to 1.500 ± 0.001 mg. Indium was used as a reference. Sealed small platinum crucibles were used. When studying thermal polymerization of salts **II**–**IV** by the dynamic DSC, we followed the main principles of thermal analysis [7–9].

To evaluate the kinetic and thermodynamic parameters of the process, we assumed that [7–9] (1) the heat Q_1, determined at a given time interval from the DSC curve, is in direct proportion to the degree of poly-

Table 2. Apparent kinetic parameters of polymerization of AS DMs from DSC data

Parameter	Salt		
	II	**III**	**IV**
Enthalpy $-\Delta H$, kJ mol^{-1}	48.28 ± 0.96	44.01 ± 0.88	43.03 ± 0.86
Entropy $-\Delta S$, J mol^{-1} K^{-1}	117.18 ± 2.34	109.48 ± 2.19	113.84 ± 2.28
Activation energy E_a, kJ mol^{-1}, by method:			
1	22.87	49.89	83.14
2	23.11	48.23	81.84
3	19.79	41.16	77.47
4	23.04	48.62	82.54
5 [15]	22.1	34.3	77.3
Reaction order n, by method:			
1	1.87	2.02	1.98
2	1.86	1.91	1.88
Reaction rate constant k, mol^{-1} min^{-1}, by method:			
1	4.67	1.94	1.13
2	4.73	1.98	1.09
3	4.05	1.81	0.93
4	4.71	1.92	1.10

Note: Method: (1) Freeman–Carroll, (2) Piloyan, (3) Kissenger, (4) Borchardt–Daniels, and (5) isothermal.

merization α throughout the process duration and (2) the total heat of polymerization Q_0, corresponding to the total area of the DSC peak, exactly corresponds to the process as a whole from the initial to final stage; $\alpha = 1 - (Q_1 Q_0)$.

These assumptions are true for chemical reactions with clearly pronounced initial and final stage, which is observed for salts **II**–**IV**.

The apparent kinetic parameters (reaction order, activation energy, and reaction rate constant) of polymerization of AS DMs were determined by the Freeman–Carroll [12], Kissenger [13], and Borchardt–Daniels [14] methods.

CONCLUSIONS

(1) Thermal polymerization of ammonium salts of *N*,*N*-dimethylaminoethyl methacrylate was qualitatively and quantitatively studied by the dynamic differential scanning calorimetry.

(2) The calculated main kinetic and thermodynamic characteristics of polymerization of these ammonium salts (enthalpy, entropy, apparent activation energy, order and rate constant of polymerization) suggest that the process parameters depend on the nature of anion; the reactivity varies in the order **II** > **III** > **IV**.

REFERENCES

1. Askarov, M.A., Mukhitdinova, N.A., and Nazarov, A.S., *Polimerizatsiya aminoalkylakrilatov* (Polymerization of Aminoalkyl Acrylates), Tashkent: Fan, 1977.
2. Askarov, M.A. and Dzhalilov, T.N., *Sintez ionogennykh monomerov* (Synthesis of Ionic Monomers), Tashkent: Fan, 1978.
3. *Ionogennye polimery* (Ionic Polymers), Askarov, M.A., Ed., Tashkent: Fan, 1986.
4. Bune, E.V., Sheiker, A.P., and Teleshov, E.N., *Vysokomol. Soedin., Ser. A*, 1989, vol. 31, no. 7, pp. 1347–1361.
5. Berov, M.V., Solovskii, M.V., Panarin, E.F., *et al.*, *Zh. Prikl. Khim.*, 1977, vol. 50, no. 1, pp. 126–129.
6. Wendlandt, W.Wm., *Thermal Methods of Analysis*, New York: Wiley, 1974.
7. Sazanov, Yu.N., *Termicheskii analiz organicheskikh soedinenii* (Thermal Analysis of Organic Compounds), Leningrad: Nauka, 1991.
8. Bernshtein, V.A. and Egorov, V.M., *Differentsial'naya skaniruyushchaya kalorimetriya v fizikokhimii polimerov* (Differential Scanning Calorimetry in Physical Chemistry of Polymers), Leningrad: Khimiya, 1990.
9. Zakunnaya, K.V., in *Novye metody polucheniya i is-*

sledovaniya polimerov: Sbornik trudov Akad. Nauk Ukr. SSR. Inst. khimii vysokomolekulyarnykh soedinenii (New Methods of Synthesis and Study of Polymers: Collection of Works of the Acad. Sci. of Ukrainian SSR. Inst. of Chemistry of Macromolecular Compounds), Kiev: Naukova Dumka, 1978, pp. 184–203.

10. Efimova, D.Yu., Shibalovich, V.G., Nikolaev, A.F., *et al*., *Zh. Org. Khim*., 1995, vol. 31, no. 12, pp. 1864–1865.
11. Efimova, D.Yu., Shibalovich, V.G., and Nikolaev, A.F., *Zh. Prikl. Khim*., 1996, vol. 69, no. 7, pp. 1170–1173.
12. Freeman, T.S. and Carroll, B., *J. Phys. Chem*., 1958, vol. 62, no. 4, pp. 394–397.
13. Kissenger, H.E., *Anal. Chem*., 1957, vol. 29, no. 11, pp. 1702–1706.
14. Borchardt, H.J. and Daniels, F., *J. Am. Chem. Soc*., 1957, vol. 79, no. 1, pp. 41–46.
15. Efimova, D.Yu., Synthesis and Polymerization of Ammonium Salts of *N*,*N*-Dimethylaminoethyl Methacrylate and Mineral Acids, *Cand. Sci. Dissertation*, St. Petersburg, 1998.

Russian Journal of Applied Chemistry, Vol. 74, No. 1, 2001, pp. 131–141. Translated from Zhurnal Prikladnoi Khimii, Vol. 74, No. 1, 2001, pp. 124–134.

MACROMOLECULAR CHEMISTRY AND POLYMERIC MATERIALS

Cluster Model of Aggregation of Epoxy–DPP Oligomers in Solutions. Structure of Coatings Based on Epoxy and Epoxy–Phenol Resins

A. N. Krasovskii, D. V. Novikov, V. A. Krasheninnikov, A. B. Plodistyi, A. A. Kharlampiev, and K. A. Bespalyi

St. Petersburg State University of Motion Pictures and Television, St. Petersburg, Russia
Institute of Macromolecular Compounds, Russian Academy of Sciences, St. Petersburg, Russia
Pigment Research and Production Association, Joint-Stock Company, St. Petersburg, Russia

Received July 26, 2000

Abstract—The IR MATIR spectra in the 1535–1680 cm^{-1} range were studied for epoxy–DPP resins (M_N = 1650–3400) in coatings on germanium substrate obtained from oligomer solutions in methylene chloride and Cellosolve with the concentration c = 10–50%. The concentration dependences of the relative viscosity of narrow-MWD fractions of epoxy oligomers (M_N = 1500–5300) in chloroform and Cellosolve solutions were studied. The structure of the network of cross-linked polymers based on epoxy (M_N = 2100–3400) and phenol–formaldehyde (M_N = 860) resins was studied by the electron-microscopic silver chloride decoration method. Based on the cluster lattice model, the optimal molecular weight and the concentration regimes were determined for epoxy oligomers in the lacquer composition for can protection.

Kurmakova *et al.* [1] found that the chemical stability of cross-linked polymer coatings obtained from solutions of epoxy-4,4'-isopropylidenediphenol (DPP) and phenol–formaldehyde resins [2] depends on the molecular weight M, functionality, and the density of cross-linking of epoxy oligomers [3–5]. It is believed [1] that the differences in the chemical stability of cured epoxy–phenol coatings on metal substrates [2] formed from narrow-MWD fractions of epoxy–DPP resins with close average molecular weights M and close amounts of epoxy and hydroxy groups [1] are due to nonlinear structure of the oligomers with M_N = 2000–5300 [4]. The fractions of epoxy resins containing branched macromolecules are more prone to aggregation in Cellosolve solution than linear macromolecules [1], and the corresponding coatings exhibit low chemical resistance to organic acids.

It is known [6] that the orientation ordering in the boundary layers of epoxy oligomers on the surface of optical crystals can be studied by IR MATIR spectroscopy [7]. This approach implies the use of Fresnel's and Kramers–Kronig formulas and takes into account the intermolecular interaction potential [6, 9]. This yields correct absorption æ(ν) and refraction $n(\nu)$ spectra, as well as complex polarizability $\alpha'(\nu)$ spectra of oligomers in their intrinsic absorption region and the orientation and polarizability anisotropy parameters of the macromolecules on the solid surface [7, 10].

As shown previously [10, 11], the orientation of the macromolecules on the surface of optical crystals of germanium and KRS-5 depends on the molecular weight M and concentration c of polymers in solution. In particular, the orientation parameter Σ of the macromolecules on the KRS-5 surface as calculated from the $\alpha'(\nu)$ spectra of epoxy oligomers (M_N = 450–3400) in chloroform solution takes a minimal value in the vicinity of a certain critical value c^*, and the maximal concentration excess of the molecules on the surface is observed at $c < c^*$ [7].

Dilute solutions of epoxy oligomers with a finite number of Kuhn segments N = 1–3 contain rod-like macromolecules which are self-associated at moderate concentrations in chloroform and Cellosolve solutions [4, 12]. The change in the slope of the concentration dependences of the relative viscosity of the narrow-MWD fractions of epoxy resin E-05 in Cellosolve solution is due to the difference in the hydrodynamic behavior of linear and branched macromolecules [1]. According to the Rayleigh scattering data [11, 12], DER-663 epoxy resin (N = 2) in chloroform solution in the vicinity of the critical concentration c^* exhibits a decrease in the light scattering intensity relative to

1070-4272/01/7401-0131$25.00

Table 1. Characteristics* of the samples of epoxy resins DER-664, DER-668, and E-05 and narrow-MWD fractions of oligomers in chloroform (CF), methylene chloride (MC), and Cellosolve (EC) solutions, 298 K

Sample no.	Epoxy oligomer	η_{rel}	$[\eta]$, $cm^3\ g^{-1}$			EN, %	M_v	M_N	M_w/M_N ±0.05	n_D
			CF	MC	EC					
1	DER-664	–	10.5	11.0	9.9	4.4–4.9	2100	1650	1.9	1.598
2	DER-668	84.7	17.5	17.5	13.4	1.0–2.0	3380	3400	2.7	1.623
3	E-05	61.6	–	15.0	12.3	1.0	2890	2500	2.5	–
4	E-05**	41.1	–	13.5	11.0	1.2	2590	2100	2.6	–
5	Fraction 1	–	–	–	15.9	0.9	–	4630	1.4	–
6	Fraction 2	–	–	–	11.0	0.8	–	5300	1.4	–

* Relative error of determining the intrinsic viscosity $[\eta]$ is ±5, relative viscosity η_{rel} of 42% solutions of oligomers in Cellosolve ±3, and epoxy number (EN), ±0.2%. The M_v parameters are calculated for solutions in chloroform, and M_N and M_w/M_N are determined by gel-permeation chromatography.

** Low-molecular-weight sample of E-05 resin.

the $c < c^*$ region corresponding to formation of discrete aggregates of macromolecules [7].

The cluster model [13] distinguishes two stages of aggregation of macromolecules in solutions. In dilute solutions, the probability p of formation of aggregates is determined by pair collisions of the molecules, and the degree of aggregation of macromolecules tends to slowly increase with increasing concentration c at $[\eta]c < 1$, where $[\eta]$ is the intrinsic viscosity. Indefinite growth of s at $[\eta]c > 1$ is due to aggregation of macromolecules by the cluster–cluster mechanism [13]. The concentration of the aggregates $c_s = c/s$ [14] is maximal at the probability $0.31 < p < 0.69$, where 0.69 is the threshold value of p_c for simple cubic lattice and Euclidean dimensionality $E = 3$ [13]. With growing molecular weight M of the macromolecules, p approaches the threshold value p_c, and in the case of the flexible-chain macromolecules in a thermodynamically good solvent the fractal dimension of the globules in the entangled state is $D = 5/3$ [15].

A transition from discrete clusters to infinite cluster on the surface of polymer films and coatings involves a change in the fractal dimension D appearing in the expression describing the density of the cluster cross-linking sites as a function of the radius R of the circumference incorporating the cluster of macromolecules [16]. The density of the points of the physical network of engagements on the polymer surface represented as a function of the cluster radius R asymptotically approaches a power funciton at $R > \zeta$, where ζ is the correlation radius [13], the fractal dimension D of the clusters of macromolecules being approximately equal to 5/3 at $R < \zeta$.

Densely cross-linked coatings based on epoxy–phenol resins experience internal stresses and degrade at a high rate, which decreses their protecting efficiency [4, 5]. It should be noted that loosely cross-linked networks based on epoxy oligomers with low molecular weight are permeable [17], and the corresponding coatings also have low protecting efficiency. The optimal protecting efficiency of epoxy–phenol resin-based coatings on metal substrates is achieved at the molecular weight M of the epoxy oligomers in the region of M_N = 2100–5000 [1, 4].

In this work, we studied the IR MATIR spectra in the 1535–1680 cm^{-1} range for epoxy resins (M_N = 1650 and M_N = 3400) in coatings on germanium substrates obtained from solutions of oligomers in methylene chloride and Cellosolve. Based on the spectra of absorption æ(ν) and reflection $n(\nu)$ indices, the concentration dependences were calculated for the orientation and polarizability anisotropy parameters for oligomers on the surface. The viscosity data obtained were used for determining the optimal concentration regimes of oligomers in solutions in terms of the cluster model. The structure of the surface of the cross-linked epoxy–phenol resins for epoxy oligomers with M_N = 2100–3400 was investigated by the electron-microscopic silver chloride decoration method.

The aim of the work is to study the aggregation of macromolecules in solutions and the orientation ordering of the macromolecules on the coating surface, as well as the structural parameters of the network of cross-linked epoxy–phenol resins, as influenced by the molecular weight and concentration of epoxy oligomers. It should be noted that these factors govern the physicochemical principles of designing oligomeric compositions, as well as the choice of the optimal concentration regimes of oligomers in lacquer compositions intended for can protection [2].

EXPERIMENTAL

We studied samples of DER-664 and DER-668 (Dow Corporation) and E-05 (Pigment Research and Production Association, Joint-Stock Company) epoxy resins, as well as narrow-MWD fractions of the E-05 resin whose characteristics are presented in Table 1. The latter fractions were prepared by precipitating with water from 10% solutions in acetone followed by distilling off the solvent. The concentration dependences of the relative viscosity η_{rel} of oligomeric samples in chloroform and Cellosolve solutions were obtained on an Ubbelohde capillary viscometer at 298 K in the concentration range c = 3–55 wt % (shear rate 110 s^{-1}, flow time of chloroform 86 s). The intrinsic viscosity [η] was determined by the conventional procedure [18], and the molecular weight of the samples, by liquid chromatography [19].

The IR MATIR spectra of the oligomers in coatings on the germainum surface under *s* and *p* polarization of the incident light were recorded on a Specord IR-75 double-beam spectrophotometer and a Perkin–Elmer 1720 X single-beam Fourier spectrometer using three- and four-mirror MATIR accessories and MATIR elements made of single-crystalline germanium ($N = 2 \times 14$, $\theta = 45°$) [6]. The spectra were recorded in the 1535–1680 cm^{-1} range with a resolution of 1 cm^{-1} (Fig. 1). In the single-beam procedure, the IR MATIR spectra of the oligomers on the substrate surface were recorded in the signal accumulation mode (10–100 scans) by subtracting from the IR spectrum of the sample the absorption of the MATIR element (germanium) in the reflection coefficient R (%) vs. wave number ν (cm^{-1}) coordinates with the relative error of ≤0.05%. The RPI-4 replica served as polarizer [6].

The absorption æ(ν) and refraction n(ν) indices were calculated by computer processing, according to Fresnel's and Kramers–Kronig procedures [8, 9], of the IR MATIR spectra of epoxy oligomers in coatings in the 1535–1680 cm^{-1} region corresponding to ν(C=C) vibrations of the double bonds in the aromatic fragments of the macrochain [7] (Fig. 2).

The 4–6-mm-thick coatings on germanium substrate were obtained from solutions of sample nos. 1–4 in methylene chloride and Cellosolve at c = 5–50% and dried in air at 373 K. The refraction index n(ν) at the reference points [8] was determined by extrapolation of the n_D values (16980 cm^{-1}) to the 1535–1665 cm^{-1} range [20]. The corresponding values for sample nos. 1 and 2 (Table 1) at the reference points

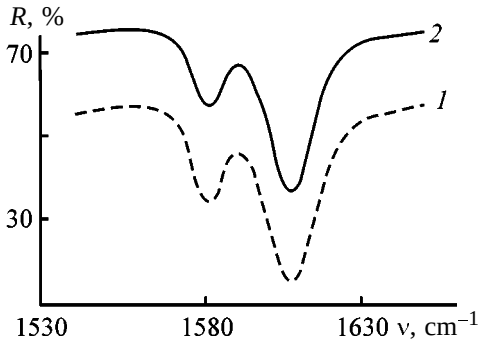

Fig. 1. IR MATIR spectra of epoxy–DPP resin in the 1530–1650 cm^{-1} range in (*1*) *p*- and (*2*) *s*-polarized incident light. Coating on germanium substrate ($N = 2 \times 14$, $\theta = 45°$) from solution of sample no. 2 in Cellosolve, c = 31%, 50 scans. (R) Reflection coefficient and (ν) wave number.

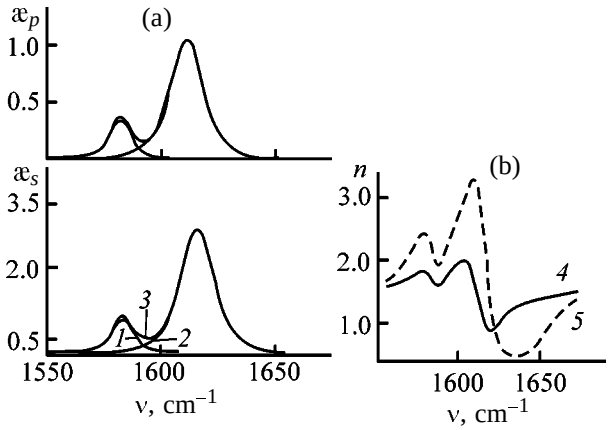

Fig. 2. Spectra of (a) (*1*–*3*) absorption indices æ(ν) and (b) refraction indices n(ν) in (*4*) *p*- and (*5*) *s*-polarized incident light in the 1550–1650 cm^{-1} range and decomposition of the ν(C=C) doublet into individual bands at (*1*) 1583 and (*2*) 1608 cm^{-1} [(*3*) aggregate curve)]. Coating on germanium from solution of sample no. 3 in Cellosolve, c = 31%, N = 28. (ν) Wave number.

[8] were estimated as follows: 1535 cm^{-1}, n_1 = 1.5336 and n_1' = 1.5366, and 1665 cm^{-1}, n_2 = 1.5338 and n_2' = 1.5368. The parameter æ at the reference points was calculated from the IR absorption spectra of oligomers in chloroform solutions using the values of the absorption coefficient $a = 4\pi\nu æ$ [6]. The corresponding values for sample nos. 1 and 2 were estimated at $æ_1(1535\ cm^{-1}) = æ_2(1665\ cm^{-1}) = 4 \times 10^3$.

The æ(ν) spectra were decomposed into individual components, 1583 and 1608 cm^{-1}, of the doublet due to the stretching vibrations of C=C double bonds in the aromatic fragments of the oligomer chain in the 1535–1665 cm^{-1} range, and the intensity æ and the integral intensity A(æ) of the band at 1608 cm^{-1} were calculated similarly to [7] (Fig. 2). The band

Table 2. Intensity æ of the band at 1608 cm^{-1}, anisotropy of the reflection index $n_s - n_p$, polarizability $\alpha'_s - \alpha'_p$, and orientation parameters $D_{p,s}$, Σ, and S of macromolecules as calculated from the æ(ν) and $n(\nu)$ spectra of oligomers in coatings on germanium substrates obtained from solutions of the samples in methylene chloride and Cellosolve

Sample no.	c, %	æ ± 5%, N = 28	$n_s - n_p$	$(\alpha'_s - \alpha'_p) \times 10^{-25}$ ±0.005, cm^3	$D_{p,s}$	Σ	S	φ ± 1, deg
					±0.03			
Solvent methylene chloride								
1	32*	0.87	0.29	0.87	0.59	–0.15	0.19	47
	40**	0.90	0.07	0.20	0.89	–0.04	0.04	53
	45	0.95	0.15	0.43	0.65	–0.11	0.15	49
2	18.7*	1.10	0.49	1.44	0.38	–0.26	0.35	41
	28**	1.21	0.05	0.13	0.90	–0.04	0.04	53
	31.7	1.21	0.59	1.74	0.34	–0.20	0.39	40
Solvent Cellosolve								
2	28**	0.91	0.06	0.17	0.90	–0.03	0.04	53
	31	0.86	–0.12	–0.33	1.32	0.12	–0.09	58
3	31	1.71	0.69	2.03	0.34	–0.34	0.39	40
4	31	1.72	0.65	1.91	0.35	–0.33	0.38	40

* Local maximum of orientation of the macromolecules on the surface.
** Local minimum of orientation of the macromolecules.

shape was approximated by superposing the Lorentz and Gauss functions, the former with the contribution of 0.8. The parameter æ was determined accurately to within less than 7%.

The polarizability spectra $\alpha'(\nu)$ were calculated by the expression [8]

$$\alpha'_{p(s)} = 3[(n^2_{p(s)} - 1)/(n^2 + 2)]/4\pi N_A, \quad (1)$$

where $n = (2n_p + n_s)/3$, $\alpha = (2\alpha'_p + \alpha'_s)/3$, and N_A is the Avogadro number [9].

The dichroic ratios $D_{p,s}(æ) = A_p/A_s$ (where A_p and A_s are the integral intensities of the band at 1608 cm^{-1} for *s*- and *p*- polarized incident light, respectively) and $D_{p,s}(\alpha') = \alpha'_p/\alpha'_s$ were calculated from the æ(ν) and $\alpha'(\nu)$ spectra, respectively (Table 2).

The second-order orientation parameter Σ was determined by the expression

$$\Sigma = (gD_{p,s} - 1)(1 - 3/2\sin^2\beta)(gD_{p,s} + 2). \quad (2)$$

Here, the factor g takes into account the light wave field effects and is approximately equal to the n_p/n_s ratio [9], and β is the angle between the direction of the dipole moment of transition M (1608 cm^{-1}) and the long axis of the oligomer molecule [7].

The parameter Σ was calculated from the dichroic ratios $D_{p,s}$ of the band at 1608 cm^{-1} in the æ(ν) and $\alpha'(\nu)$ spectra under assumption that β = 0° [7].

The orientation order was characterized by the polarizability anisotropy $\alpha'_s - \alpha'_p$ and the parameter $S = 1/2(3\langle\cos^2\varphi\rangle - 1)$, where φ is the angle between the transition moment M (1608 cm^{-1}) and the 0X axis of the XYZ larobatory coordinate system [9]. The effective depth of penetration of the light into oligomeric coatings on germanium substrate was calculated by the expression $d_{eff} = \ln(R_0/R)/4\pi\nu æ$ [6] as ≈1 μm.

Coatings with a thickness of 4–6 μm on electrolytically tin-plated sheet metal were prepared as prescribed for the EP-547 lacquer formulation [2] and formed from solution of epoxy and FPF-1 (M_N = 860) phenol–formaldehyde resins in Cellosolve at the epoxy resin concentration in the solution c = 31 wt % and the mass ratio of the components of 4 : 1. The coatings were cured at 473 K for 10 min and cooled in air at a rate of 20 deg min^{-1}. The preparations were produced by AgCl sputtering onto the external surface of the coatings in the 1.33×10^{-3} Pa vacuum to effective thickness of 0.4 nm and dissolved in hot chloroform. The carbon replicas were prepared by the standard procedure [16]. The AgCl molecules are accepted by hydroxy groups of epoxy and phenol–formaldehyde resins which are the AgCl nucleation centers [21]. The photomicrographs of the coatings were obtained with an EVM 100 L electron microscope; the

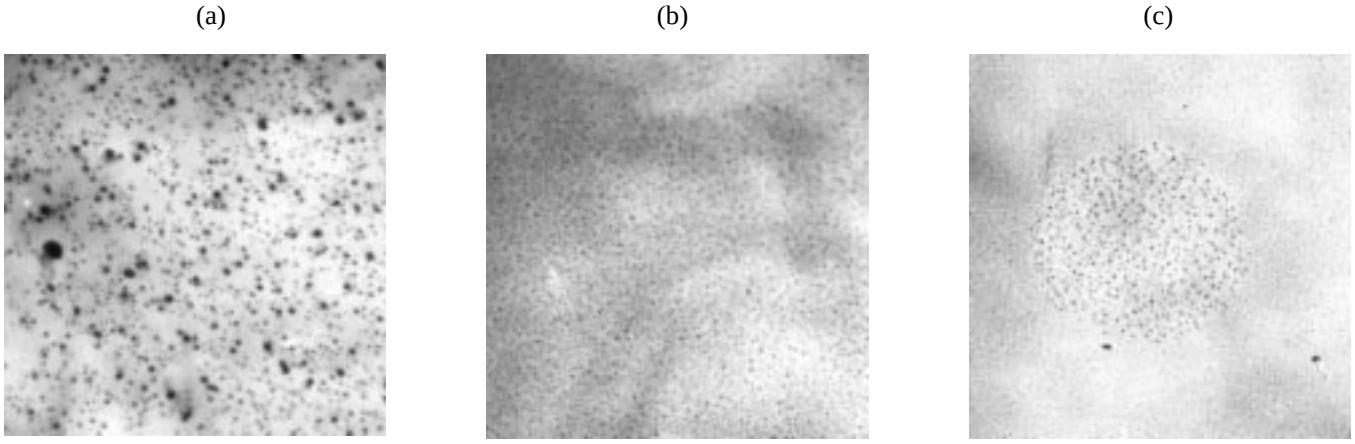

Fig. 3. Photomicrographs of the surface of cross-linked epoxy–phenol coatings on tin-plated sheet metal. Epoxy–DPP resin samples (a) no. 2 and (b, c) no. 4. Magnification: (a, b) ×30000 and (c) ×15000.

magnification in the computer processing of the decorograms was 100000 (Fig. 3).

Using the decorograms of the coating surface (Table 1, sample nos. 2–4), we determined the density ρ of the decorating AgCl particles corresponding to macromolecular clusters [22]. We used the model of percolation along the bound circumferences centered at particles [16]. With increasing radius $\langle R\rangle$, the circumferences overlap and get bound into clusters to form a percolation cluster. The lattice density ρ_l was calculated by the expression $\rho_l = \rho(\langle R\rangle)/\rho'$, where $\rho(\langle R\rangle)$ is the particle distribution density; ρ' is the density of the points of a two-dimensional lattice equivalent in the spatial distribution pattern of the particles and in the coordination number m corresponding to the area enclosed by the first maximum of the function $2\pi\rho\langle R\rangle g(\langle R\rangle)$, $g(\langle R\rangle)$ is the radial distribution function [23]. For $m = 3$, the relation $\rho' = 0.77/r^2$ [23] holds, where r is the most probable distance between the particles. The density of the cross-linking sites of the network of the cross-linked epoxy–phenol resin was calculated by the expression [21]

$$\rho(\langle R\rangle) = [1 + 2\pi\rho\int_0^R g(\langle R\rangle)\langle R\rangle d\langle R\rangle]/\pi\langle R\rangle^2. \qquad (3)$$

In the æ(ν) spectra of epoxy–DPP resins (Table 1, sample nos. 1 and 2) in coatings on germanium substrate, the intensity of the band at 1608 cm^{-1} for s polarization of the incident light exceeds that for p polarization [11]. Therefore, the dichroic ratio $D_{p,s}$ is under unity (Fig. 2, Table 2). The data obtained suggest that the orientation parameters $D_{p,s}$ and Σ of the oligomer molecules on the surface depend on the concentration c of the oligomers in the methylene chloride solution (Fig. 4). For sample no. 2, the parameter S takes a minimal value at the critical concentration c^* of 28±1%. In this case, the long axis of the macromolecules makes with the XY plane of the XYZ laboratory coordinate system an angle φ of about 54°, which corresponds to complete disordering of the

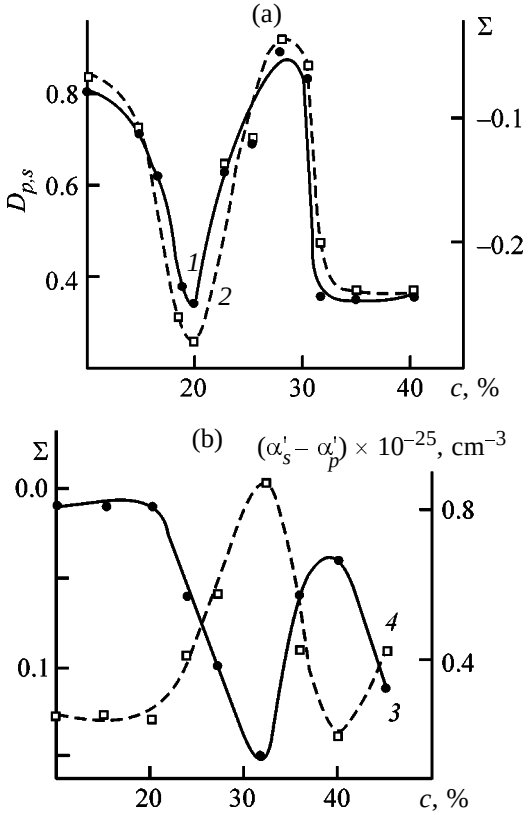

Fig. 4. (*1*) Orientation parameters $D_{p,s}$, (*2*, *3*) Σ, and (*4*) polarizability anisotropy $\alpha'_s - \alpha'_p$ of macromolecules as functions of the concentration c of the epoxy resin in methylene chloride solution. Coatings on germanium, samples no. (a) 1 and (b) 2.

Table 3. Concentration regimes and parameters of the aggregates of oligomer molecules in solutions of chloroform (sample nos. 1, 2) and Cellosolve (sample nos. 5, 6) as estimated by capillary viscometry, 298 K

Sample no.	c, %	$[\eta]c \pm 0.1$	c_s, g dl^{-1}	s ±0.05	D ±0.05	$p = (1 - 1/s)$ ±0.01	ρ	
							$E = 3$	$E = 2$
1	8.9	1.4	6.3	2.13	1.54	0.53	0.49	0.80
	17.9	2.8	5.3	5.03	1.54	0.80	0.21	0.62
	25*	4.0	4.0	9.44	2.0	0.89	0.12	0.51
	28.4	4.5	3.9	10.7	2.0	0.91	0.11	–
	33.3	5.2	3.7	13.7	2.0	0.93	0.10	–
2	9	2.4	3.6	3.67	1.54	0.73	0.29	0.68
	16.5	4.3	2.3	11.1	1.54	0.91	0.10	0.49
	25.4*	6.7	1.0	37.0	1.74	0.97	0.034	0.486
	30.3	8.0	0.9	51.3	1.74	0.98	0.027	0.455
5	15	2.4	8.5	1.77	1.42	0.43	0.53	0.80
	25	4.0	9.5**	2.63	1.42	0.62	0.34	0.67
	30*	3.8	8.7	3.43	1.65	0.71	0.25	0.60
	42	6.7	5.7	7.35	1.65	0.86	0.18	0.61
6	17	2.1	11.1	1.53	1.22	0.35	0.54	0.76
	25	3.0	11.5**	2.18	1.22	0.54	0.32	0.61
	30*	3.6	9.4	3.19	1.44	0.69	0.18	0.48
	40	4.8	7.2	5.57	1.44	0.82	0.16	0.51
	42	5.1	6.6	6.36	1.44	0.84	0.13	0.49

* Concentration c^* corresponding to the fractal-D_1–fractal-D_2 transition.
** Maximal concentration of the aggregates c_s.

molecules on the surface [6]. In the $c < c^*$ and $c > c^*$ regions, the increase in the orientation parameters of oligomer molecules on the substrate surface is due to a decrease in the angle φ. For example, at c = 18.7 and c = 31.7% the angle φ is about 40°, and the polarizability anisotropy $\alpha'_s - \alpha'_p$ of the oligomer molecules on the surface increases relative to the concentration regime at $c = c^*$ (Table 2).

For sample no. 1, virtually complete disordering of

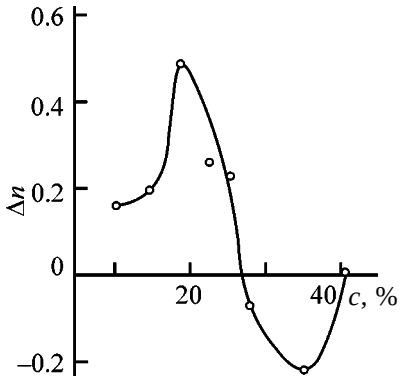

Fig. 5. $\Delta n = n_s - n_p$ parameter as a function of the concentration c of the oligomer in Cellosolve solution. Coating on germanium, sample no. 2.

the macromolecules in coatings on germanium obtained from oligomer solutions in methylene chloride is observed at c = 40%, which significantly exceeds the critical concentration for sample no. 2 (Fig. 4b, Table 2). Growth of the parameters S and $\alpha'_s - \alpha'_p$ at $c > c^*$ and $c < c^*$ is due to a decrease in the angle φ relative to the value of 54° corresponding to $c = c^*$.

In coatings obtained from Cellosolve solution of sample no. 2, the dependence of the anisotropy of the refraction index $\Delta n = n_s - n_p$ on the concentration c is nonmonotonic. The dichroism $D_{p,s}$ of the band at 1608 cm^{-1} is close to unity, and $\Delta n = 0$, which is due to disordering of the molecules on the surface at $c = 28 \pm 1\%$ (Fig. 5, Table 2). The inversion of the sign for Δn is observed at $c < c^*$ ($\Delta n > 0$) and $c > c^*$ ($\Delta n < 0$). The analogous inversion of the dichroism $D_{p,s}$ and the sign of Δn was revealed for coatings obtained for sample nos. 2–4 at c = 31%. With growing molecular weight of the samples, the orientation of the oligomers on the surface becomes less ordered, and, consequently, $\Delta n > 0$ (sample nos. 3 and 4) and $\Delta n < 0$ (sample no. 2).

As known [9], the Kerr constant describes the anisotropy of the polarizability of molecules in the

visible range of the spectrum. In solution of benzyl alcohol (or aniline) in CCl_4 the Kerr constant exhibits inversion of the sign [9]: positive values correspond to dilute solutions, and negative, to formation of aggregates of molecules in concentrated solutions. Therefore, virtually complete disordering of the macromolecules on the surface corresponds to minimal values of parameters S and $\alpha'_s - \alpha'_p$ (Δn) at the critical concentration c^* of oligomers in solution, and the growth of the parameters at $c < c^*$ and $c > c^*$ is due to the change in the degree of aggregation of macromolecules in solutions (Tables 2, 3). With growing molecular weight of oligomers, the orientation and optical anisotropy of macromolecules on the surface decrease at the concentration of epoxy resin in Cellosolve solution of 31%, which corresponds to the value prescribed for the composition based on epoxy and phenol–formaldehyde resins [2].

As known [13], the density ρ of the cross-linking sites of fractal aggregate tends to decrease with increasing degree of aggregation s or hydrodynamic volume $\langle V \rangle$ of the aggregate of macromolecules by the law valid for $E = 3$

$$\rho = Vs/\langle V \rangle = s^{(D-E)/D}, \quad (4)$$

where V is the hydrodynamic volume of the macromolecule.

In the case of fractal-D_1–fractal-D_2 transitions, the density ρ depends on the fractal dimension D of the aggregates [24]. In the first approximation, the relative viscosity η_{rel} in solution is described by the expression [14]

$$\ln \eta_{rel} = [\eta] c_s s^{(3-D)/D} = [\eta]_c c_s, \quad (5)$$

where $[\eta]_c$ is the current value of the intrinsic viscosity whose absolute analog is, as known [18], the parameter $(\eta_{rel} - 1)/c$.

As $Vs/\langle V \rangle = [\eta]/[\eta]_c$ [18], expressions (4) and (5) can easily be combined into the relation for the density ρ of the aggregates

$$\rho(s) = [\eta]/[\eta]c_s = s^{(D-3)/D}, \quad (6)$$

where $s = [\eta]_c c / \ln \eta_{rel}$ [14].

Expression (6) suggests that the slope of the $\rho(s)$ plot on the logarithmic scale is equal to $(D - 3)/D$, and $\rho(s)$ at $s \gg 1$ asymptotically approaches a power function [13, 15], which for polystyrene in bromoform solution at $[\eta]c > 3$ corresponds to $D \sim 5/3$.

For sample nos. 1 and 2 the dependences of the relative viscosity η_{rel} on the concentration c of oligomers in chloroform solution differ in the nature of

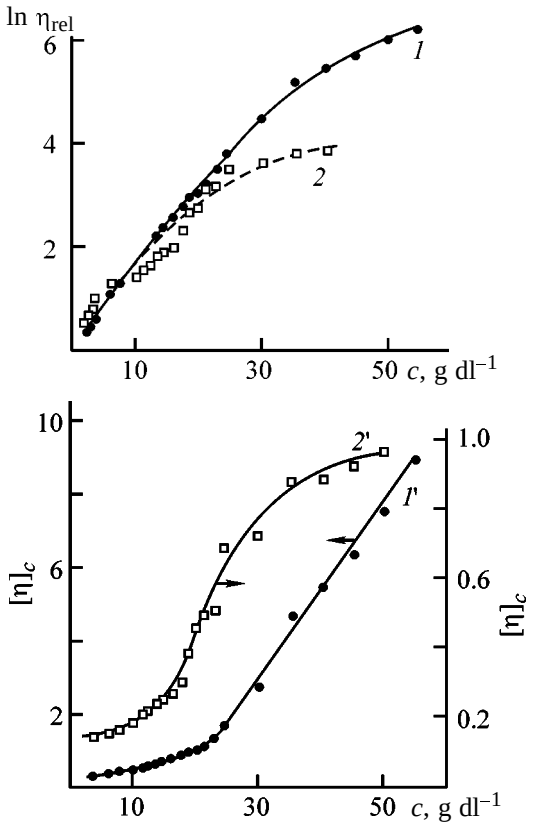

Fig. 6. (*1*, *2*) Relative η_{rel} and (*1'*, *2'*) current intrinsic $[\eta]_c$ viscosities as functions of the concentration c of oligomers in chloroform solution. Sample (*1*, *1'*) no. 1 and (*2*, *2'*) no. 2, 298 K.

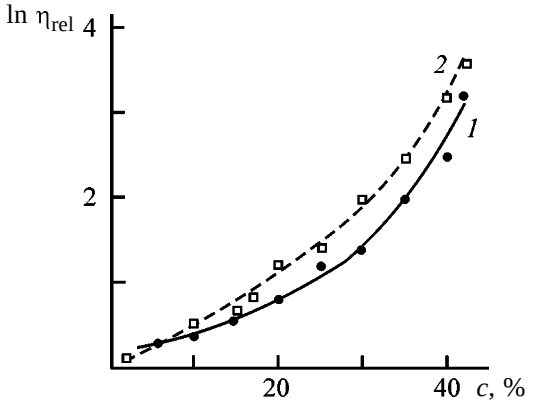

Fig. 7. Relative viscosity η_{rel} as a function of the concentration c of the oligomer in Cellosolve solution. Sample (*1*) no. 5 and (*2*) no. 6.

variation of $[\eta]_c$ with c (Fig. 6). For low-molecular-weight sample no. 1, the parameter $[\eta]_c$ attains saturation at $c > 35$ g dl^{-1}. For narrow-MWD fractions of epoxy resin E-05 (Tables 1, 3), $[\eta]_c$ varies with the oligomer concentration in Cellosolve solution by a power law. The shape of the curves $\rho(s)$ calculated from the $\eta_{rel}(c)$ dependences for solutions of oligomers in chloroform and Cellosolve (Figs. 6, 7) is in

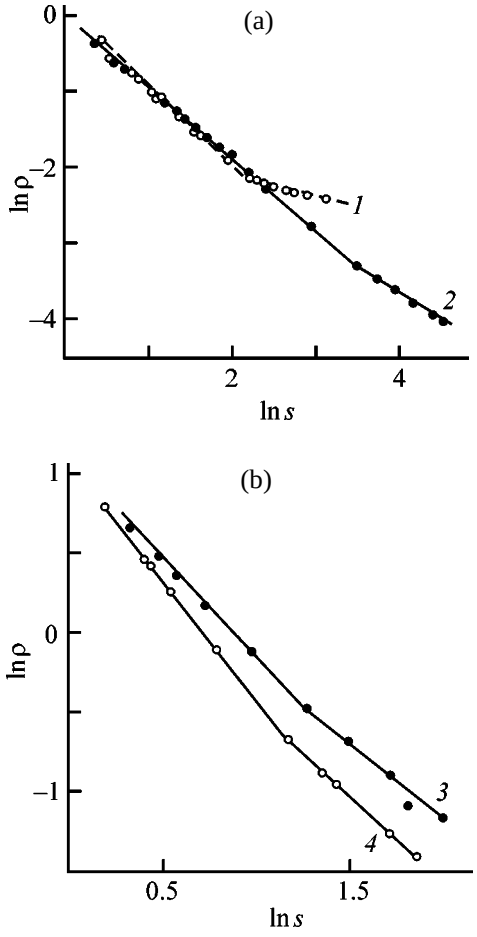

Fig. 8. Density of aggregates ρ as a function of the degree of aggregation *s* of the oligomer molecules in solutions of (a) chloroform and (b) Cellosolve in logarithmic coordinates. Sample (*1*) no. 1, (*2*) no. 2, (*3*) no. 5, and (*4*) no. 6.

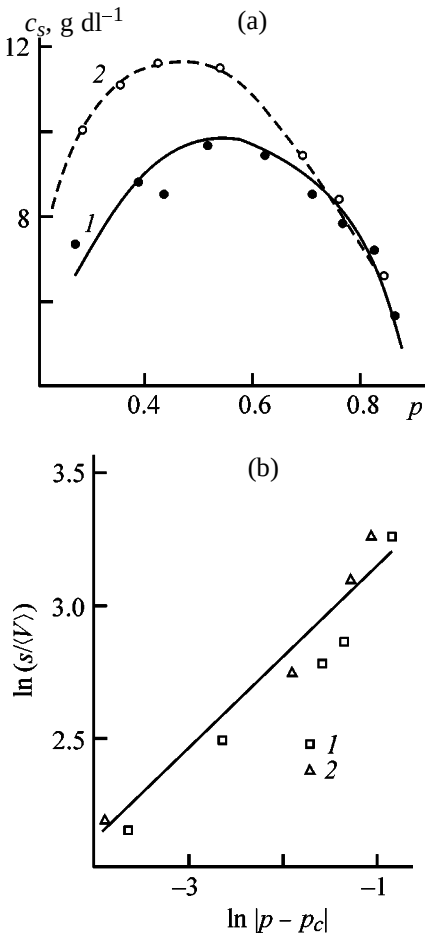

Fig. 9. (a) Concentration of the aggregates c_S of macromolecules in Cellosolve solution as a function of the flow probability *p* and (b) lattice density $s/\langle V\rangle$ as a function of the parameter $\Delta p = |p - p_c|$. Sample (*1*) no. 5 and (*2*) no. 6.

agreement with expression (6), these curves in the logarithmic coordinates consisting of two linear sections (Fig. 8).

It was found that the slope of the ρ(*s*) curves in the ln*p*–ln*s* coordinates for wide-MWD sample nos. 1 and 2 in chloroform solution changes at the critical concentration *c** corresponding to the flow probabilty $p > 0.69$ (Fig. 8a). At $c > c^*$, the aggregates of macromolecules forming in the case of sample no. 1 are more compact than for sample no. 2, the degree of aggregation *s* increasing with increasing molecular weight *M* (Table 3).

In solutions of narrow-MWD fractions of the E-05 resin (Table 3, sample nos. 5, 6) in Cellosolve, fractal-D_1–fractal-D_2 transitions occur at $c^* \sim 30\%$ and the flow probability $p_c = 0.69$. The resulting aggregates are looser than aggregates of the oligomer in chloroform. The concentration of the aggregates c_S varies nonmonotonically with increasing flow probability $p = 1 - 1/s$ [14] (Fig. 9). It is maximal in the region of $0.31 < p < 0.69$ and sharply decreases at $p > 0.69$. The appearance of the $c_S(p)$ curves suggests a transition to a continuous fluctuation network of engagements in solutions of oligomers in the vicinity of *c** [14], as the lattice density $\rho = s/\langle V\rangle$ of aggregates in the vicinity of the flow threshold $p_c = 0.69$ ($E = 3$) satisfies the expression $\rho \sim (\rho - 0.69)^a$, where $a = 0.4$ [13, 24].

The density ρ of the aggregates of macromolecules decreases with increasing molecular weight of the aggregates $M_S = Ms$ and the flow probability *p* (Table 3, Fig. 10). As follows from the dependence of the density of aggregates of macromolecules ρ on the parameter $\Delta p = p - 0.69$ obtained for nine fractions of the E-05 resin ($M_N = 1500$–5300, $M_w/M_N = 1.4$) in Cel-

Table 4. Cluster structure parameters for cross-linked epoxy–phenol polymers in coatings on sheet metal as estimated by electron microscopy

Sample no.	ρ_l, ±0.01	ζ, nm	$D_1(R < \zeta)$	$D_2(R > \zeta)$	m	ρ		$\langle R \rangle$	ζ_p
			±0.05			$E = 3$	$E = 2$	nm	
2	0.88	33	1.66	1.89	3	0.62	0.79	36	24
3	0.69	28	1.57	1.89	>3	0.70	0.77	26	18
4*	0.63	18	1.15	1.87	<3	0.74	0.53	19	11
4**	1.35	126	1.89	2.00	4	–	–	363***	116

Note: The density ρ of the aggregates of macromolecules was calculated for $E = 3$ and $E = 2$ using the viscosity data for sample nos. 2–4 in Cellosolve solution at $c = 30\%$. The ζ_p parameter was calculated from the average hydrodynamic radius of the aggregates $\langle R \rangle = 0.512(\langle V \rangle/\Phi)^{1/3}$, where Φ is the Flory constant [13, 18].

* For the first section of the network of small AgCl particles.

** For the second section of the network corresponding to densely packed clusters of macromolecules.

*** Maximal radius of aggregates of macromolecules [13].

losolve solutions at $c = 30\%$, for the threshold value $p_c = 0.69$ the density ρ is equal to 0.62 and $M_N = 3500 \pm 200$, which corresponds to the hexagonal ($m = 3$) planar lattice [25]. Thus, the most uniform network ($m = 3$, $E = 2$) of the cross-linked epoxy–phenol polymer can be expected for epoxy oligomer with $M_N = 3400$ (Table 4).

We found that the most uniform network of the decorating AgCl nanoparticles representing the chemical network of cross-linked epoxy–phenol polymer is characteristic of the oligomer sample no. 2 (Fig. 3a). The distribution pattern for small AgCl particles corresponds to the network of cross-linked epoxy oligomer, and larger AgCl particles correspond to aggregates of the high-modulus component (FPF-1 resin) uniformly distributed over the epoxy polymer matrix. The most probable distance r between the points of the small-scale network composed of regular hexahedrons ($m = 3$, $E = 2$) [23] is equal to 15 nm, and that for large-scale network, 150 nm.

The correlation radius ζ and the fractal dimension D of the clusters of macromolecules was determined by the expression for the lattice density [13]

$$\rho_l(\langle R \rangle) \sim \langle R \rangle^{D-2}, \quad (7)$$

where $\langle R \rangle = \zeta$ at the flow threshold $pD_c = 0.5$ ($E = 2$) [15, 21, 25].

The uniform network of macromolecules of the cross-linked polymer corresponds to $D_1 = 1.66$ and $D_2 = 1.89$ calculated from the slope of the $\rho_l(\langle R \rangle)$ dependence in the logarithmic coordinates (Fig. 11). The inflection point in the $\rho_l(\langle R \rangle)$ curve plotted in these coordinates corresponds to ζ [13, 22] equal to 33 nm (Table 4, sample no. 2). For sample no. 3 we found a marked decrease in the lattice density $\rho_l(\zeta)$, correlation radius ζ, and fractal dimension D_1 compared to sample no. 2.

In sample no. 4 the network containing units of epoxy and phenol–formaldehyde resins breaks into

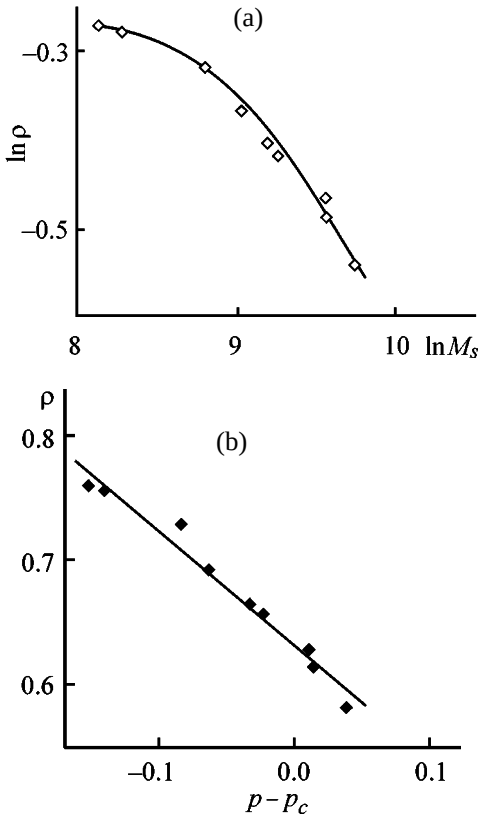

Fig. 10. Density of aggregates of macromolecules ρ in Cellosolve solution as a function of (a) molecular weight of aggregates M_s and (b) parameter $\Delta p = p - p_c$. $c = 30\%$, fractions of the E-05 resin, $M_N = 1500$–5300.

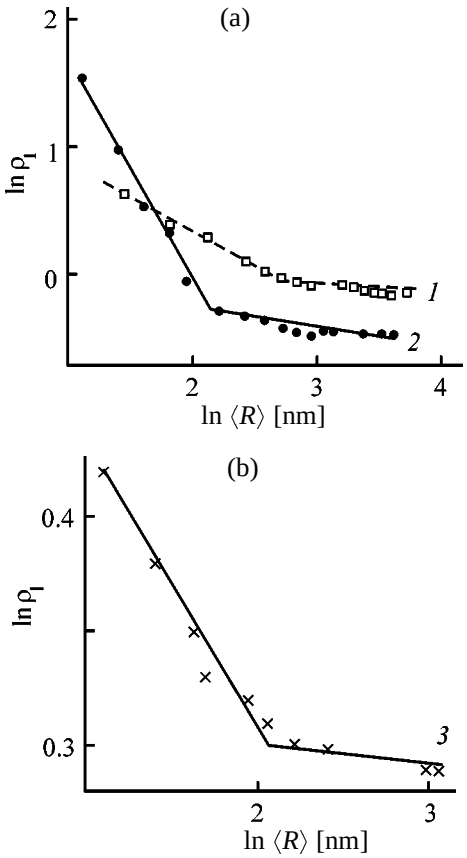

Fig. 11. Lattice density ρ_l of the decorating particles as a function of the radius $\langle R\rangle$, nm, of the circumference incorporating the cluster, as plotted in the logarithmic coordinates. Sample (*1*) no. 2 and (*2*) no. 4; (*3*) "lattice animals" fragment of sample no. 4. Radius dimension, nm: (a) with coefficient 2 and (b) with coefficient 15.

discrete clusters (Figs. 3b, 3c). In this case the decorogram of the polymer surface consists of sections lean (ρ_l = 0.63) and rich (ρ_l = 1.35) in small AgCl particles representing various fragments of the network of the epoxy resin. The discontinuity boundaries are the sites of localization of large AgCl particles attributed to FPF-1 resin, which suggests phase separation of the components [16, 17]. The average distance r between large AgCl particles is equal to 200 nm, and that between small particles, to 10 μm.

The values ρ_l = 0.63, D_1 = 1.15, and $m > 3$ (Table 4, sample no. 4) obtained for the first fragment of the network of small AgCl nanoparticles (Fig. 3b) support the conclusion concerning low local density of clusters of macromolecules. For the second fragment of the decorogram characterized by high local density of distribution of small AgCl nanoparticles (Fig. 3c) the values ρ_l = 1.36, D = 1.89, and m = 4 suggest formation of closely packed clusters of the "lattice animals" type [24]. For such clusters the correlation radius is by an order of magnitude greater than ζ corresponding to the first fragment of the network with a low density of AgCl particles (Fig. 11).

In accordance with the cluster approach [13], the density ρ of the aggregates as calculated from the viscosity data for narrow-MWD fractions of oligomers for three-dimensional (E = 3) and two-dimensional (E = 2) space increases with decreasing molecular weight M of the oligomers relative to the value M_N = 3400, as the concentration regime of the macromolecules in solution varies from $c = c^*$ to $c < c^*$ (Table 3, Fig. 10). For wide-MWD sample nos. 2–4, the density ρ of aggregates on the surface (E = 2) substantially decreases with decreasing M of the oligomers owing to a decrease in the fractal dimension D_1 of the aggregates (Table 4). This causes optical anisotropy to increase (Table 2), the network of the cross-linked epoxy–phenol resin to break down into discrete clusters, and the chemical resistance of the coatings to deteriorate.

CONCLUSIONS

(1) The orientation ordering in oligomer coatings on germanium substrate can be determined by IR MATIR spectroscopy. The ordering depends on the molecular weight and concentration of the oligomers in solutions. Complete disordering of the macromolecules on the surface is observed at the critical concentration c^* of epoxy oligomer (M_N = 3400) in Cellosolve solution of 28±1%. The increases of the orientation and polarizability anisotropy parameters of macromolecules on the surface are due to formation of discrete aggregates in solution at $c < c^*$.

(2) Based on the cluster lattice model, expressions were obtained for the density ρ(s) of the aggregates of macromolecules suitable for calculating, from the viscosity data, the critical concentrations c^* of oligomers in solutions. For narrow-MWD fractions of the E-05 resin (M_N = 1500–5300) in Cellosolve solution the density ρ(s) of aggregates of the macromolecules decreases with increasing molecular weight of epoxy oligomers and the flow probability p. For the threshold probability p_c = 0.69 and c^* = 30%, the value M_N = 3500±200 was obtained which is an optimal one. With decreasing molecular weight the average density of aggregates ρ(s) in solution and on the surface tends to increase. The value ρ = 0.62 for M_N = 3500 and c = 30% corresponds to a hexagonal planar lattice or the most uniform network of macromolecules on the surface.

(3) According to electron-microscopic data, epoxy oligomer with M_N = 3400 is characterized by the most uniform network of cross-linked epoxy–phenol polymer on the coating surface. A decrease in the molecular weight of epoxy resin from 3400 to 2100 causes breaking down of the continuous network of the cross-linked epoxy–phenol polymer into fragments with low and high local densities of discrete clusters of macromolecules, as well as a sharp decrease in the chemical stability of lacquer protecting coatings on sheet metal.

REFERENCES

1. Kurmakova, I.N., Novikov, N.A., Mozoleva, A.P., *et al.*, *Lakokras. Mater. Ikh Primen*., 1985, no. 5, pp. 11–13.
2. *Lakokrasochnye materialy dlya zachshity konservnoi tary* (Paint and Varnish Materials for Can Protection), Lyalyushko, S.M., Ed., Moscow: NIITEKhIM, 1981.
3. Chernin, I.Z., Smekhov, F.M., and Zherdyaev, Yu.M., *Epoksidnye polimery i kompozitsii* (Epoxy Polymers and Compositions), Moscow: Khimiya, 1982.
4. Markevich, M.A., Structural and Kinetic Aspects of the Processes of Formation of Epoxy–DPP Oligomers and Three-Dimensional Polymers Thereof, *Doctoral Dissertation*, Chernogolovka, 1986.
5. Markevich, M.A., Kuzaev, A.I., Shashkin, D.P., *et al.*, *Vysokomol. Soedin., Ser. A*, 1985, vol. 27, no. 3, pp. 1000–1007.
6. Harrick, N.J., *Internal Reflection Spectroscopy*, New York: Interscience, 1964.
7. Krasovskii, A.N., Kharlampiev, A.A., and Krasheninnikov, V.A., *Vysokomol. Soedin., Ser. A*, 1997, vol. 39, no. 2, pp. 250–258.
8. Saidov, G.V., *Spektroskopiya vnutri- i mezhmolekulyarnykh vzaimodeistvii* (Spectroscopy of Intra- and Intermolecular Interactions), Bakhshiev, N.G., Ed., Leningrad: Leningr. Gos. Univ., 1985, issue 4, pp. 5–14.
9. Vuks, M.F., *Elektricheskie i opticheskie svoistva molekul i kondensirovannykh sred* (Electrical and Optical Properties of Molecules and Condensed Media), Leningrad: Leningr. Gos. Univ., 1984.
10. Krasovskii, A.N., Kharlampiev, A.A., and Polyakov, D.N., *Zh. Prikl. Khim.*, 1994, vol. 67, no. 3, pp. 455–463.
11. Kharlampiev, A.A., Spectra of Optical Constants and Structure of Boundary (Surface) Layers of Polymers for Photography and Recording Media, *Cand. Sci. Dissertation*, St. Petersburg, 1999.
12. Krasovskii, A.N., Polyakov, D.N., Baranov, V.G., and Mnatsakanov, S.S., *Vysokomol. Soedin., Ser. A*, 1991, vol. 33, no. 6, pp. 1221–1227.
13. Feder, J., *Fractals*, New York: Plenum, 1988.
14. Krasovskii, A.N., Nikolaev, B.P., Shlyakov, A.M., and Mnatsakanov, S.S., *Kolloidn. Zh.*, 1994, vol. 56, no. 3, pp. 371–375.
15. Grosberg, A.Yu. and Khokhlov, A.R., *Statisticheskaya fizika makromolekul* (Statistical Physics of Macromolecules), Moscow: Nauka, 1989.
16. Novikov, D.V. and Varlamov, A.V., *Kolloidn. Zh.*, 1997, vol. 59, no. 3, pp. 355–359.
17. Markevich, M.A., Vladimirov, L.V., Prut, E.V., and Enikolopyan, N.S., *Mekh. Kompozits. Mater.*, 1985, no. 1, pp. 25–28.
18. Tsvetkov, V.N., Eskin, V.E., and Frenkel', S.Ya., *Struktura makromolekul v rastvorakh* (Structure of Macromolecules in Solutions), Moscow: Nauka, 1964.
19. Gorshkov, A.V., Verenich, S.S., Evreinov, V.V., and Entelis, S.G., *Chromatographia*, 1988, vol. 26, pp. 338–342.
20. Al'perovich, L.I., *Metod dispersionnykh sootnoshenii i ego primenenie dlya opredeleniya opticheskikh kharakteristik* (Method of Dispersion Relations and Its Application for Determination of Optical Characteristics), Dushanbe: Irfon, 1973.
21. Krasovskii, A.N. and Novikov, D.V., *Zh. Prikl. Khim.*, 1999, vol. 72, no. 9, pp. 1518–1527.
22. Novikov, D.V., Krasovskii, A.N., Andreeva, A.I., and Basov, S.V., *Kolloidn. Zh.*, 1999, vol. 61, no. 2, pp. 240–245.
23. Novikov, D.V. and Varlamov, A.V., *Poverkhnost'*, 1992, no. 6, pp. 117–121.
24. El'yashevich, A.M., Preprint of Report, *Soveshchanie "Problemy teorii polimerov v tverdoi faze"* (Meet. "Problems of the Theory of Polymers in Solid Phase"), Chernogolovka: Inst. Khim. Fiz. Akad. Nauk SSSR, 1985.
25. Ziman, J.M., *Models of Disorder: The Theoretical Physics of Homogeneously Disordered Systems*, Cambridge: Cambridge Univ. Press, 1979.

Russian Journal of Applied Chemistry, Vol. 74, No. 1, 2001, pp. 142–144. Translated from Zhurnal Prikladnoi Khimii, Vol. 74, No. 1, 2001, pp. 135–138.

MACROMOLECULAR CHEMISTRY AND POLYMERIC MATERIALS

Chemical Composition and Properties of Cultivated Wood-Rotting Fungi *Phanerochaete Sanguinea* and *Ganoderma Applanatum*

G. A. Petropavlovskii†, G. A. Pazukhina, I. V. Ovchinnikov, V. A. Petrova, and L. A. Nud'ga

Institute of Macromolecular Compounds, Russian Academy of Sciences, St. Petersburg, Russia
St. Petersburg State Academy of Forestry Engineering, St. Petersburg, Russia

Received July 20, 2000

Abstract—The fruit body composition of the cultivated wood rotting fungi *Phanerochaete sanguinea* 16–65, *Ganoderma applanatum* 4–94, and *Ganoderma applanatum* 40–90 and their sorption characteristics with respect to Cr(III) and Methylene Blue are studied.

The existing processes for cellulose bleaching with chlorine-containing reagents are necessarily accompanied by contamination of both the environment and the target product (bleached cellulose) with toxic chlorinated organic compounds (dioxins). In this connection searching for environmentally safe processes for cellulose bleaching using biological agents is a pressing problem. As known, it is possible to remove lignin from cellulose and thus increase its whiteness by direct treatment with white-rot fungus mycelium, pure hemicellulase (cleavage of ligno-carbohydrate bonds) and ligninase preparations (lignin degradation), and also with an enzymatic system from a mycelial culture. The latter case requires cultivation of lignin-degrading fungi having low cellulolytic activity. Efficient cellulose bleaching processes based on the use of lignin-degrading enzymes from various strains of wood-rotting fungi is under development at the St. Petersburg Academy of Forestry Engineering [1, 2]. Wastes from such processes represent fungal fruit bodies containing chitin, cellulose, melanin, and other components which can be used in various branches of industry and in medicine.

The goal of this work is to study the chemical composition of the cultivated wood-rotting fungi *Phanerochaete sanguinea* 16–65, *Ganoderma applanatum* 4–94, and *Ganoderma applanatum* 40–90 and to evaluate the sorption capacity of the fungal material and prospects for its utilization.

† Deceased.

EXPERIMENTAL

Three fungal strains *Ph. sanguinea* 16–65, *G. applanatum* 4–94, and *G. applanatum* 40–90 were grown by surface cultivation in 500-ml Erlenmeyer flasks at 26°C in a culture medium (175 ml) developed by Gavrilova [3]. Its composition was as follows ($g\ l^{-1}$): glucose 10.0, pentone 2.5, K_2HPO_4 0.4, $MgSO_4$ 0.5, $ZnSO_4$ 0.001, NaCl 0.3, $FeSO_4$ 0.005, and $CaCl_2$ 0.05. The culture medium was sterilized before use in an autoclave under pressure, cooled to room temperature, and inoculated with mycelial disks (0.5 mm) in Petri dishes on a pure culture agar. As the mycelium grew, the activity of oxidative enzymes in the culture medium was monitored. After reaching the peak activity the cultural liquors from different flasks, in which a given fungus was cultivated, were combined, filtered through a capron filter, and tested as cellulose bleaching agents.

The residual fungal fruit bodies were analyzed by successive extraction with hot water for 8 h, alcohol–benzene (1 : 2) mixture at bp for 8 h, and 6% NaOH at 100°C for 12 h. The residual insoluble chitin–glucan complex (CGC) was then hydrolyzed in concentrated HCl at 70°C for 7 h. The nonhydrolyzed fraction was additionally treated with a mixture of hydrogen peroxide and ammonia (1 : 10), and hydrolyzed again under the same conditions. The resulting hydrolyzates were combined and analyzed for glucose and glucosamine spectrophotometrically using color reactions of glucose with anthrone and of glucosamine with salicylaldehyde. The results are given in Tables 1 and 2.

1070-4272/01/7401-0142$25.00

Table 1. Fraction composition of fungi *Ph. sanguinea* 16–65, *G. applanatum* 4–94, and *G. applanatum* 40–90

Strain	Moisture, %	Fraction, %, soluble in indicated solvent			Insoluble residue, %
		hot water	alcohol–benzene mixture	6% NaOH	
Ph. sanguinea, 16–65	87.9	18.1	15.4	49.8	16.7
G. applanatum, 4–94	91.0	19.0	12.9	55.9	12.2
G. applanatum, 40–90	89.4	9.4	9.5	61.1	20.0

Note: Fraction composition is expressed in per cents from dry sample weight.

Infrared spectra were registered on a Specord 80/85 instrument (Carl Zeiss, Jena) using KBr technique.

Sorption experiments were conducted as follows. To a weighed portion of the sorbent (0.1 g recalculated to dry sample) we added 20 ml of a buffer solution and 10 ml of 0.01 M $CrCl_3$. After a lapse of time the sorbent was filtered off, and the residual Cr(III) was determined in the filtrate by chelatometric titration [4]. Sorption of Methylene Blue was performed as follows. To a 0.3-g sample 20 ml of 0.5% Methylene Blue and 80 ml of distilled water were added. After a lapse of time the sorbent was filtered off, and the filtrate was analyzed spectrophotometrically for Methylene Blue. The sorption capacity for *Esherichia coli* was estimated from the amount of adsorbed Methylene Blue (0.016 g of adsorbed Methylene Blue corresponds to 176×10^6 bacteria).

Table 1 shows that the highest moisture is observed for the fungus *G. applanatum* 4–94 and the least, for *Ph. sanguinea* 16–65, both growing on hardwood. Under natural conditions (in air, but not in aqueous medium as in this work) fruit bodied of these fungi are characterized by considerably lower moisture. The water-soluble fraction consisting of mineral salts and soluble hemicelluloses varies from strain to strain. The least content is found in *G. applanatum* 40–90 growing on softwood. The same strain contains the least amount of fats and resins representing the fraction soluble in the alcohol–benzene mixture. Hot aqueous NaOH dissolves proteins and melanin (partly). The percentage of this fraction is the highest (50–60%). The CGC content ranges from 12 to 20%, which is considerably lower than that in the mold fungus *Aspergillus niger* (50%), but comparable with that in the yeast *Saccharomycetes cerevisae* (12%) [5].

It was demonstrated by the IR spectra that the insoluble residue is represented by chitin–glucan complex. The spectra show the adsorption bands at 1203 and 1376 cm^{-1} (CH and CH_2 groups) typical of cellulose and other glucans [6] and also at 1652, 1555, and 1310 cm^{-1} (amide I, II, and III, respectively) [7] characteristic of chitin of various origins. The spectra are nearly identical with those obtained for CGC from mycelium of the fungus *Aspergillus niger*.

The elemental analysis data (Table 2) of the fungi after removal of the three soluble fractions demonstrate the presence of nitrogen, which is indicative of chitin.

Data on the composition of the insoluble fraction, obtained after it was totally hydrolyzed, confirmed the conclusion that this residue is represented by chitin–glucan complex. The hydrolyzed forms were demonstrated to be glucose, formed in cleavage of the glucan component of CGC, and glucosamine formed in hydrolysis of the chitin component to *N*-acetylglucosamine with simultaneous deacetylation. From these data we determined the composition of CGC isolated from the fungal fruit bodies (Table 3).

Table 3 shows that the chitin content in CGC is high in fruit bodies of all the strains studied, especial-

Table 2. Elemental composition of insoluble residue of fungi *Ph. sanguinea* 16–65, *G. applanatum* 4–94, and *G. applanatum* 40–90

Strain	Composition, %			
	C	H	N	ash
Ph. sanguinea, 16–65	41.5	6.5	2.2	0.7
G. applanatum, 4–94	42.8	7.0	2.2	0
G. applanatum, 40–90	42.0	6.6	1.6	0.9

Table 3. Composition of CGC isolated from *Ph. sanguinea* 16–65, *G. applanatum* 4–94, and *G. applanatum* 40–90

Strain	Content, %	
	chitin	glucan
Ph. sanguinea, 16–65	59.0	41.0
G. applanatum, 4–94	74.0	26.0
G. applanatum, 40–90	64.0	36.0

Table 4. Sorption characteristics of fungi *Ph. sanguinea* 16–65, *G. applanatum* 4–94, and *G. applanatum* 40–90 after treatment with hot water

Strain	Sorbed Cr(III), mg, at indicated pH and sorption time					SEC, mg-equiv g^{-1}, at pH 6.86
	1.68	4.60	6.86			
	t, min					
	1440	1440	10	60	1440	
Ph. sanguinea, 16–65	1.42	0.95	1.73	1.67	1.66	0.62
G. applanatum, 4–94	1.23	0.90	1.69	1.90	1.87	0.41
G. applanatum, 40–90	1.08	0.98	1.73	1.69	1.69	1.11

ly in *G. applanatum* 4–94 for which it is comparable with that in the wood rotting fungus *Fomes fomentarius* (71%) [5]. However, in contrast to the fungi studied, CGC from *F. fomentarius* additionally contains 10% intracellular melanin.

Such a high chitin content in CGC of the fungi studied and also the fact that their fruit bodies contain proteins suggest that these strains can be efficient ion exchangers for heavy metal ions. We studied the sorption properties of the fungi after treatment with hot water with an example of Cr(III). Sorption was performed over the pH range from 1.68 to 6.86. For all the fungi studied the maximal sorption in 24 h was observed at pH 6.86. The major fraction of Cr(III) was demonstrated to be sorbed in the first 10 min. The highest static exchange capacity (SEC) was shown by the strain *G. applanatum* 40–90 containing 61.1% proteins (Table 1) capable of fixing heavy metal ions.

Comparative analysis shows that CGC from the fungus *Aspergillus niger* demonstrates better sorption characteristics in strongly acidic solutions (depending on the composition, SEC for Cr(III) at pH 1.68 is 1.81–2.01 mg-equiv g^{-1} [8]). The strains studies in this work show better sorption from neutral solutions, and, although SEC obtained for these strains is lower, it should be taken into account that it refers not to CGC, but to fruit bodies only treated to remove the water-soluble fraction.

Finally, the fungal strains studied demonstrate high exchange capacity for Methylene Blue: recalculated to the sorbed amount of *Esherichia coli* it was found to be 176×10^6, 118×10^6, and 317×10^6 for *Ph. sanguinea* 16–65, *G. applanatum* 4–94, and *G. applanatum* 40–90, respectively.

CONCLUSIONS

(1) Fruit bodies of the cultivated fungi *Ph. sanguinea* 16–65, *G. applanatum* 4–94, and *G. applanatum* 40–90 contain up to 20% chitin–glucan complex, the relative content of chitin and glucan in CGC being dependent on the strain.

(2) The fungal strains studied show high sorption capacity for Cr(III), Methylene Blue, and *Esherichia coli*.

ACKNOWLEDGMENTS

The authors are grateful to V.A. Solov'ev and O.N. Malysheva for help in cultivating the wood-rotting fungi.

REFERENCES

1. Pashukhina, G.A., Soloviev, V.A., and Malysheva, O.N., Abstracts of Papers, *6th Int. Conf. on Biotechnology in the Pulp and Paper Industry*, Vienna (Austria), 11–15 June, 1995, p. 120.
2. Soloviev, V.A., Pashukhina, G.A., Malysheva, O.N., *et al.*, *Proc. 7th Int. Conf. on Biotechnology in the Pulp and Paper Industry*, Vancouver, BC (Canada), 16–19 June, 1998, p. B257–B259.
3. Yakovleva, N.S., Gavrilova, V.P., Solov'ev, V.A., *et al.*, *Mikol. Fitopatolog.*, 1993, vol. 27, no. 6, pp. 48–51.
4. Přibil, R., *Komplexony v chemické analyse*, Prague: Československ. Akad. Ved, 1957.
5. Nud'ga, L.A., Petrova, V.A., Ganicheva, S.I., *et al.*, *Materialy Pyatoi Konferentsii "Novye perspektivy v issledovanii khitina i khitozana"* (Proc. 5th Conf. "New Prospects in Studying Chitin and Chitosan"), Moscow: VNIRO, 1999, pp. 242–245.
6. Zhbankov, R.G., *Infrakrasnaya spektroskopiya tsellyulozy i ee proizvodnykh* (Infrared Spectroscopy of Cellulose and Its Derivatives), Minsk: Nauka i Tekhnika, 1964.
7. Panson, T.G., Marchessault, K.N., and Liang, C.G., *J. Polym. Sci.*, vol. 43, no. 141, pp. 101–106.
8. Nud'ga, L.A., Ganicheva, S.I., Petrova, V.A., *et al.*, *Zh. Prikl. Khim.*, 1997, vol. 70, no. 2, pp. 242–246.

Russian Journal of Applied Chemistry, Vol. 74, No. 1, 2001, pp. 145–148. Translated from Zhurnal Prikladnoi Khimii, Vol. 74, No. 1, 2001, pp. 138–142.

MACROMOLECULAR CHEMISTRY AND POLYMERIC MATERIALS

Comparative Study of Reactivity of Cellulose, Chitosan, and Chitin–Glucan Complex in Sulfoethylation

L. A. Nud'ga, V. A. Petrova, A. D. Ben'kovich, and G. A. Petropavlovskii†

Institute of Macromolecular Compounds, Russian Academy of Sciences, St. Petersburg, Russia

Received July 20, 2000

Abstract—Sulfoethylation of the chitin–glucan complex, isolated from mycelium of the mold fungus *Aspergillus niger*, by substitution with sodium β-chloroethylsulfonate or addition of sodium vinylsulfonate is examined. A comparative study is made of the reactivity of the chitin–glucan complex, chitosan, and cellulose in the both reactions. The sorption characteristics of the sulfoethylated products with respect to Cu(II) and Cr(III) are determined.

It is known that introduction of sulfo groups in cellulose and some other polysaccharides makes them water-soluble. Solutions of the resulting sulfo derivatives are stable in polymineral media, which is important in view of their use in metallurgy and oil production. Also sulfo derivatives can be used as cation exchangers and blood anticoagulants. Thus, chitin was sulfonated to synthesize a full analog of heparin [1].

The sulfoethyl group imparts the same properties to polysaccharides as the sulfo group, but additionally makes the resulting ether more resistant to hydrolysis in acid and alkaline solutions, since it is bound to the skeleton chain of the polysaccharide by an ether bond. It was reported also that sulfoalkyl derivatives of polysaccharides can exhibit biological, particularly anti-AID activity [2].

It is known [3–5] that sulfoethyl derivatives of cellulose and chitosan can be obtained, having a degree of substitution (DS) sufficiently high to make them water-soluble. At the same time, despite the fact that chitin–glucan complexes (CGCs) show promise as a source of chitin (utilization of various biochemical work wastes), there is only limited information on preparation of sulfoethyl derivatives of CGC [6]. The fact that chitin–glucan complexes contain both chitin and glucan fragments makes it possible to compare the CGC reactivity with that of cellulose and chitin in the same reactions.

Depending on an alkylating agent, sulfoalkylation can proceed either as substitution (with haloalkylsulfonates) or addition (with vinylsulfonate or alkane sultones). For alkylation of cellulose all the three types of reagents were used; selection of a reagent was governed by the length of the alkyl residue. Thus, for synthesis of sulfomethyl and sulfoethyl cellulose ethers haloalkylsulfonates were used [7]. Sulfoethyl cellulose was also obtained by addition of sodium vinylsulfonate [8] (this reaction is also known as sulfovinylation, despite the fact the product is a saturated sulfoethyl ether). In the case of higher homologs alkane sultones were also used [9].

Study of cellulose sulfoethylation by reaction of the first type showed that the yield increases when the reaction is performed in a diluent [7]. Additionally, this reduces the degradation of the macromolecules and improves the uniformity of the substituent distribution along the polysaccharide chain. Also the use of a diluent improves the product solubility and the quality of its solutions. It was demonstrated that the best suited diluents are branched alcohols or their mixtures with xylene. The optimal temperature of the reaction is 80°C from the viewpoint of competition of hydrolysis of sodium β-chloroethylsulfonate (β-NaCES) and substitution of the cellulose hydroxyls. The degree of substitution attained in this reaction was no more that 0.8, whereas in reaction of the second type [with sodium vinylsulfonate (NaVS)] products were obtained with SD of about 2.0.

In this work for CGC sulfoethylation we used substitution with β-NaCES and addition of NaVS.

In the case of substitution the reaction is written as

$$R(OH) + ClR_1SO_3Na + NaOH \rightarrow R\text{–}OR_1SO_3Na + NaCl + H_2O.$$

† Deceased.

1070-4272/01/7401-0145$25.00

Table 1. Results on substitution sulfoethylation of chitin–glucan complex in isopropanol (T = 80°C; N_2; CGC: β-NaCES : NaOH = 1 : 3 : 6)

Run no.*	τ, h	DD	Sulfur content, %	DS	*S*, %	[η]**
1	1	–	0.63	0.04	4.8	–
2	2	–	0.87	0.05	7.0	–
3	3	–	1.27	0.08	32.7	–
4	3	–	1.66	0.11	32.0	–
5	1	0	6.20	0.50	66.0	1.2
6	2	0.05	8.00	0.64	80.0	3.0
7	3	0.15	8.90	0.75	97.0	1.7
8	3	–	7.40	0.52	99.5	3.8
9	1.5	0.87	5.32	0.35	72.5	–

* (4) Reagent was added in portions at 30-min intervals; (5–7) initial CGC was included with isopropanol; and (8, 9) β-NaCES : NaOH = 1 : 1 : 3, the starting materials were, respectively, wood cellulose and chitosan from crab shells, the reagent was added in portions at 30-min intervals.

** Determined in 2% NaOH (for the soluble fraction).

Addition by the Michael reaction is written as

$$ClCH_2CH_2SO_3Na + NaOH \xrightarrow{-5^\circ C} CH_2{=}CHSO_3Na + NaCl + H_2O,$$

$$R(OH) + CH_2{=}CHSO_3Na \longrightarrow ROCH_2CH_2SO_3Na.$$

Finally, addition of alkane sultones is written as

$$ROH + \underset{\backslash\ /}{O{-}R_2}\ \underset{SO_2}{} \longrightarrow R{-}OR_2SO_3Na.$$

In these reactions R = Cell, Chit, CGC; $R_1 = CH_2$, C_2H_4; and $R_2 = C_3H_6$, C_4H_8, C_5H_{10}.

The sulfoethylated derivatives of CGC were examined as sorbents for Cu(II) and Cr(III), and their sorption characteristics were compared with those of chitosan and CGC.

EXPERIMENTAL

In experiments we used CGC isolated from mycelium of the mold fungus *Aspergillius niger*. The chitin and glucan contents in the product were 81.6 and 15.6%, respectively. In the reactions we used as-isolated CGC with a moisture content of 72.5%, or preliminary inclusion was performed with the same alcohol as was then taken as a diluent.

Chitosan was prepared from crab shells by alkaline deacetylation. The degree of deacetylation (DD) of the product was 0.88 and the molecular mass, M_v = 1.88×10^5. In the work we used TsA wood cellulose ($M_v = 1.1 \times 10^5$). β-NaCES was recrystallized from ethanol.

Sodium vinylsulfonate was preparad from β-NaCES by reaction with 28% NaOH at –5°C for 1 h. In sulfovinylation we used both crude vinylsulfonate containing NaCl and the product recrystallized from isopropanol or *tert*-butanol.

Sulfoethylation was carried out in isopropanol at 80°C under nitrogen with stirring. A calculated portion of β-NaCES was introduced either as one portion just at the beginning of the reaction or in equal portions at 0.5-h intervals.

The product was filtered off, washed to remove NaCl and residual alkali with 80% methanol, dehydrated with acetone, and, finally, dried at 60°C in a vacuum drier. All the products were analyzed for sulfur by Schoeniger. The solubility in water (*S*) was determined by conductometric titration. The intrinsic viscosity was determined in 0.5 M NaOH.

The sorption capacity of the products was determined in static experiments [10]. Sorption was performed from 0.01 M copper acetate or $CrCl_3$. The experiment time was 24 h. pH was adjusted by adding an appropriate buffer solution.

The kinetics of sulfoethylation with β-NaCES was studied as influenced by the alkylating agent concentration, procedure of its introduction, and CGC pretreatment procedure. The results are summarized in Table 1. As should be expected, with increasing reaction time (all other conditions being equal) the sulfur content in sulfoethylated CGC (SECGK) and, there-

fore, DS increase (see run nos. 1–3), though remaining at a low level. Introduction of β-NaCES in several portions somewhat increases DS (run no. 4) as a result of decreasing consumption of the reagent in hydrolysis. However, significant increase in DS was observed only when preliminary inclusion with isopropanol was used, providing replacement of water without deterioration of the highly developed inner surface of CGC. In experiment nos. 5–7 DS is above 0.50, and the products become substantially water-soluble. Alkaline conditions initiate partial deacetylation of the chitin fraction of CGC. Although DD increases with time in this case, it remains small (0.05–0.15). Therefore, the reaction products cannot be regarded as polyampholytes, in contrast to CGC carboxymethylation products in which DD reached 0.20–0.37 at DS of 0.16–0.81 [11].

The results obtained show that sulfoethylation proceeds to a greater degree with cellulose; in this case neither inclusion nor portionwise introduction of β-NaCES is needed. With chitosan DS 0.35 was obtained without inclusion, but with portionwise introduction of β-NaCES. It should be pointed out that with cellulose and chitosan higher solubility in water is attained at lower DS as compared to CGC. Similar result was obtained previously in carboxymethylation of CGC [11]. Evidently, in sulfoethylation also the substituent is nonuniformly distributed throughout the amorphous and ordered regions of the CGC supramolecular structure.

Addition sulfoethylation with NaVS was studied as influenced by the reaction medium and time and also by the quality of the alkylating agent and pretreatment of the starting material (Table 2). The results show that *tert*-butanol is the most suited diluent for the reaction. This is true for all the starting materials studied: CGC, chitosan, and cellulose. Evidently, the reason is that the accessibility of reaction centers of polysaccharides increases in diluents with bulky molecules.

The figure demonstrates the kinetic curves of sulfovinylation with cellulose, chitosan, and CGC, obtained under identical conditions without inclusion. The degree of substitution increases with time. The effect increases in the order CGC < chitosan < cellulose. Such a difference in the reaction rate for polysaccharides having the same reaction centers can be attributed to different supramolecular structure.

Purification of NaVS to remove NaCl somewhat increases DS, but to a lesser extent than preliminary inclusion of CGC, as in substitution sulfoethylation. Therefore, of primary importance in these reactions is a highly developed inner surface of CGC. In the case of addition sulfoethylation the reaction proceeds to a greater degree, providing higher DS and totally water-soluble products. Furthermore, in the addition NaOH acts only as a promoter; the consumption of this reagent is lower, eliminating deacetylation of the chitin fraction of CGC.

Table 2. Addition sulfoethylation of chitin–glucan complex (T = 80°C; N_2; CGC : NaVS : NaOH = 1 : 6 : 3)

Run no.*	Diluent	τ, h	Sulfur content, %	DS	*S*, %
1	Isopropanol	1	1.02	0.06	5.4
2	″	2	1.42	0.09	14.2
3	″	3	2.13	0.14	21.5
4	″	3	9.07	0.85	100
5	″	3	9.67	0.95	100
6	*tert*-Butanol	3	2.70	0.18	32.3
7	″	3	3.27	0.22	35.0
8	Isopropanol	3	11.30	1.05	100
9	*tert*-Butanol	3	12.08	1.21	100
10	Isopropanol	3	8.77	0.76	100
11	*tert*-Butanol	3	10.19	0.98	100

* (4) Inclusion with isopropanol; (5) CGC was included with isopropanol, NaVS was purified to remove NaCl; (7) NaVS was purified to remove NaCl by treatment with *tert*-butanol; (8, 9) cellulose was a starting material; and (10, 11) chitosan was a starting material.

Finally, despite the fact that one more stage (preparation of NaVS from β-NaCES) is needed, addition sulfoethylation is more preferable, as providing uniform highly substituted water-soluble products. Sodium vinyl sulfonate can be prepared from crude β-NaCES (the presence of NaCl only slightly influences DS in the product). It should be pointed out also that if preliminarily included CGC is used, the reactivity of CGC, chitosan, and cellulose in the reaction with NaVS is leveled.

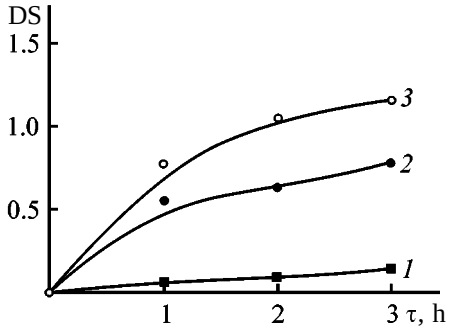

Kinetic curves of sulfovinylation of (*1*) CGC, (*2*) crab shell chitosan, and (*3*) wood cellulose in isopropanol at 80°C and polysaccharide : NaVS : NaOH = 1 : 6 : 3. (DS) Degree of substitution and (τ) time.

Table 3. Static exchange capacity of CGC and its derivatives

Sample	DD	DS	pH*	SEC, mg-equiv g^{-1}, for indicated ions	
				Cr^{3+}	Cu^{2+}
CGC	0	0	1.68	1.81	–
CANGC	0.31	0	1.68	1.90	–
CANGC	0.70	0	1.68	2.44	–
SECGC	0	0.18	1.68	–	7.60
			6.80	–	11.90
SECGC	0	0.74	1.68	1.30	10.80
			6.80	6.70	11.60
CAN	0.15	0	6.80	2.20	–
CAN	0.80	0	6.80	–	4.50

The sorption experiments were carried out with the iniital CGC, SECGC with DS of 0.18 and 0.74, partially deacetylated CGC (CANGC), and crab chitosan. The static exchange capacity (SEC) at various pHs is given in Table 3. The general trends are as follows. (1) All the sorbents studied better sorb Cu(II) than Cr(III). (2) The metals are better sorbed from neutral solutions than from acid solutions. (3) The greater the amount of adsorption centers in sorbents (amino groups in CAN and CANGC, sulfoethyl groups in SECGC), the higher SEC, regardless of the sorption mechanism on these groups. In the case of SECGC the ion-exchange sorption dominates, and the contribution of complexation with aminoacetyl group cannot be higher than SEC of CGC (free primary amino groups were not found in the CGC samples studied). In CAN and CANGC samples bearing primary amino groups sorption proceeds through complexation. Comparison of SEC obtained at pH 1.68 suggests that the ion-exchange mechanism is more favorable for the both cations.

CONCLUSIONS

(1) Sulfoethylation of the chitin–glucan complex, isolated from mycelium of the mold fungus *Aspergillius niger*, by substitution with sodium β-chloroethylsulfonate or addition of sodium vinylsulfonate is examined. The addition proceeds to a greater degree than the substitution. The addition products demonstrate more uniform distribution of substituents along the chain, which provides total solubility of sulfoethylated derivatives in water.

(2) In the both reactions the reactivity of the polysaccharides decreases in the order cellulose > chitosan > chitin–glucan complex.

(3) Preliminary activation of CGC by inclusion and sulfoethylation by the addition mechanism allow preparation of highly substituted CGC derivatives.

(4) The maximal sorption of Cu(II) and Cr(III) with sulfoethylated CGC was observed from neutral solutions.

REFERENCES

1. Tokura, S., Itoyama, K., Nishi, N., *et al*., *J. Macromol. Sci., Ser. A*, 1994, vol. 31, no. 11, pp. 1701–1718.
2. Ishikuro, Y., Inone, S., Meshusuka, G., *et al.*, *Sen-i-Gakkaishi* (Fiber), 1996, vol. 51, no. 12, pp. 571–579.
3. Nud'ga, L.A., Plisko, E.A., and Danilov, S.N., *Zh. Prikl. Khim.*, 1974, vol. 47, no. 4, pp. 872–876.
4. USSR Inventor's Certificate no. 757 540.
5. Simeonov, M. and Dimov, K., *Cellul. Chem. Technol*., 1976, vol. 10, no. 4, pp. 419–421.
6. Kogan, G., Rauko, P., Machova, E., *et al*., *Proc. 3rd Int. Conf. Eur. Chitin Soc*., Potsdam (Germany), August 31–September 3, 1999, vol. 4, pp. 176–181.
7. Plisko, E.A., and Danilov, S.N., *Zh. Prikl. Khim*., 1963, vol. 36, no. 9, pp. 2060–2064.
8. Dimov, K., Simeonov, M. and Dimitrov, D., *Papier* (Darmstadt), 1973, vol. 27, no. 4, pp. 129–135.
9. Kuznetsova, Z.I., Arkhipova, V.L., and Prostakova, V.M., *Vysokomol. Soedin.*, 1968, vol. 10, no. 6, pp. 438–441.
10. Přibil, R., *Komplexony v chemické analyse*, Prague: Ceskoslov. Akad. Ved, 1957.
11. Nud'ga, L.A., Petrova, V.A., Ganicheva, S.I., *et al*., *Zh. Prikl. Khim*., 2000, vol. 73, no. 2, pp. 297–301.

Russian Journal of Applied Chemistry, Vol. 74, No. 1, 2001, pp. 149–153. Translated from Zhurnal Prikladnoi Khimii, Vol. 74, No. 1, 2001, pp. 142–146.

MACROMOLECULAR CHEMISTRY AND POLYMERIC MATERIALS

Urethane Formation in the Presence of Stabilizers

M. M. Nazipov, A. A. Tabachkov, A. D. Elchueva, and A. G. Liakumovich

Kazan State Technological University, Kazan, Tatarstan, Russia

Received March 7, 2000

Abstract—The kinetics of urethane formation was studied in relation to the stabilizer type. A series of urethane elastomers (sealants, coatings, adhesives), derived from stabilized prepolymers and polyoxyalkylene-polyols of various molecular weights, were developed.

In production of cold-curable urethane elastomers [1–3], block copolymers of ethylene and propylene oxides with terminal hydroxy goroups (Laprols[1]) are widely used as polyether components. As compared to any polyester analogs, polyethers ensure higher frost and hydrolysis resistance of the composite materials.

Polyoxyalkylenepolyols readily react with toluene diisocyanate (TDI) to form reactive oligomers, prepolymers, which are intermediates in production of castable polyurethanes, sealants, corrosion-protective coatings, adhesives, etc.

The urethane formation processes are based on polycondensation of a polyol with the prepolymer, yielding urethane units:

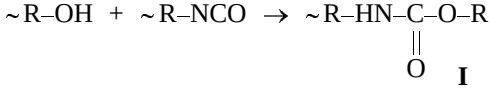

I

The main urethane formation reaction is always complicated by various side reactions somewhat distorting the structure of the final polymer, i.e., macromolecules of a highly elastic polyurethane consist of segments with different thermodynamic flexibility. "Soft" segments with weak intermolecular interaction and low glass-transition point are formed by oligomeric chains, and "hard" segments consist of products of reaction of the isocyanate group with low-molecular-weight compounds. Despite thorough drying of the polyol, amino groups **II** are formed in certain amounts; they very rapidly react with isocyanate groups to give urea units **III** in the macromolecules:

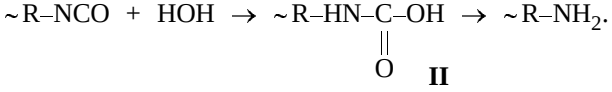

II

Urea groups are also formed by reaction of the isocyanate-containing prepolymer with amine-type curing agents:

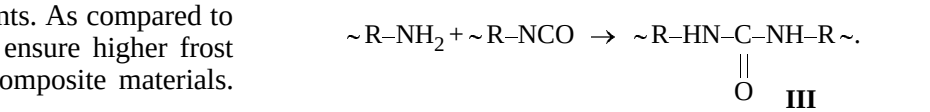

III

At the same time, curing of the prepolymer can occur by trimerization (**IV**) of the terminal isocyanate groups under the action of a catalyst:

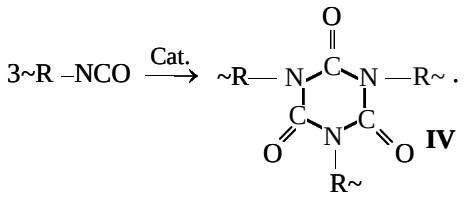

IV

Urethane and urea units in polymeric chains, owing to the presence of labile hydrogen atoms, react with isocyanate groups to form a three-dimensional cross-linked structure containing allophane (**V**) and biuret (**VI**) moieties:

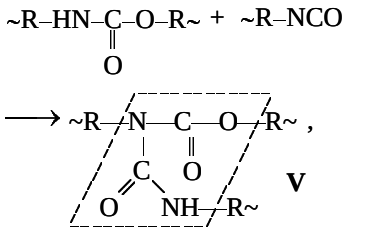

V

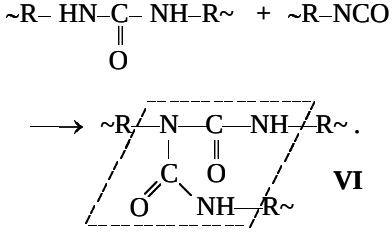

VI

[1] Laprols are produced on a large-tonnage scale by the Nizhnekamsknefteorgsintez Joint-Stock Company.

1070-4272/01/7401-0149$25.00

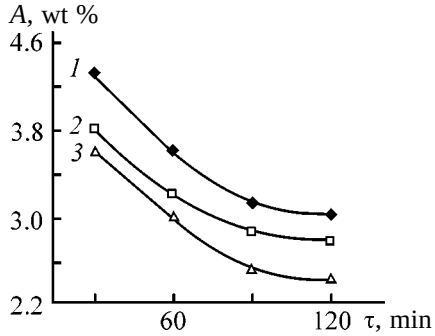

Fig. 1. Kinetic curves of synthesis of prepolymers from polyethers with various additions: (*A*) content of NCO groups and (τ) time; the same for Figs. 2 and 3. Synthesis: (*1*) with HCl, (*2*) with acetylacetone, and (*2*) from nonstabilized polyether.

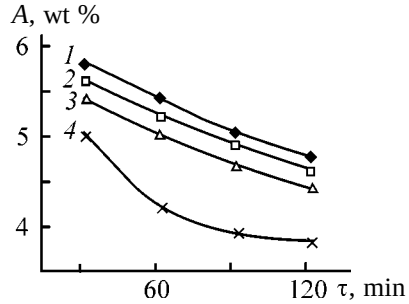

Fig. 2. Kinetic curves of synthesis of prepolymers from various TDI samples stabilized with HCl: (*1*) T-65/35, (*2*) T-80/20, (*3*) T-102T, and (*4*) nonstabilized TDI.

The presence of polar groups of different nature, randomly or regularly distributed in a relatively low-polar matrix of flexible oligomeric chains, is a specific feature of urethane elastomers, largely determining their supramolecular structure and chemical and physical properties. Owing to these groups, all types of urethane elastomers are characterized by fairly intense intermolecular interactions, mainly of the hydrogen bond type. The developed three-dimensional network of physical cross-links in network structures supplements the chemical cross-linking. The longer the chain of the hydroxyl-containing component, the lower the concentration of labile hydrogen atoms in urethane groups and hence the weaker the intermolecular interactions and the more flexible the polymeric chain. High rate of chain growth in reaction of a polyol with the prepolymer favors preparation of highly elastic materials, and high cross-linking rate results in preparation of stronger composites, up to formation of "glassy" polyuretyhane.

The main goal in urethane formation is to preserve the reactivity of the prepolymer and enhance its stability in storage. The effect of acetylacetone as a stabilizer in reaction of an ester polyol with TDI was studied in [4]. It is known that acetylacetone forms chelates with many metal ions occurring in the forms of salts, oxides, hydroxides, etc. Its reactivity toward isocyanates is very low; hence, in systems containing isocyanates and metal ions acetylacetone will form practically exclusively metal acetylacetonates, which catalyze the reaction between the NCO and OH groups and do not promote side reactions in the course of urethane formation.

In this work we examined for the first time the stabilizing effect of readily available hydrochloric acid on prepolymers based on polyoxyalkylenepolyols. The polyether is prepared in the presence of a base catalyst. Base impurities are strong catalysts of trimerization of prepolymers (**IV**), reducing their storage life and reactivity and even causing gelation. Addition of acid compounds into the reaction mixture in synthesis of prepolymers favors neutralization of alkali and more complete reaction between the NCO and OH groups.

EXPERIMENTAL

The polyether was placed in a vessel equipped with a stirrer and a jacket for heating or cooling and dried in a vacuum to a moisture content of about 0.05%; after that, a stabilizer (0.05 wt %) was added, the mixture was stirred for 5–10 min, and TDI was added in an amount required for preparing a prepolymer of a specified molecular weight. Urethane formation is exothermic; therefore, TDI was added in portions and the reactor was cooled through the jacket, so as to maintain the temperature at 70–75°C.

The process of sealant preparation includes the following stages: (a) preparation of a sealing paste (paste A) by mixing a reactive oligomer (thiokol or polyol), a filler, a catalyst, and the other additives; (b) preparation of a curing paste (paste B) by synthesis of a stabilized prepolymer from polyoxyalkylenepolyol with addition of a hydrophobic filler if required; (c) mixing of pastes A and B directly before application to a working surface. We used polyoxyalkylenepolyols of molecular weight 3000–5000 [TU (Technical Specifications) 2226-023-10488057–95) and a polysulfide oligomer (brand I thiokol). As curing catalysts we used dimethylaminomethylphenols (OM-1, OM-2, OM-3) of Agidol 51, 52, and 53 brands (TU 38-30356–86) in amount of 1.5–3.5 wt parts per 100 wt parts of polyol; the filler was P-803 industrial carbon [GOST (State Standard) 7885–77] in amount of 60–80 wt parts per 100 wt parts of polyol. The composites were tested on an RMI-250 tensile testing machine according to GOST 7762–74.

Figure 1 shows the kinetic curves of the synthesis of prepolymers from polyoxyalkylenepolyol of molecular weight 5000 and TDI (T-80/20) in the presence of HCl and acetylacetone and from the active polyether. In reactions of TDI with active polyols, side formation of allophanes **V** is possible. In storage, these prepolymers often undergo gelation due to formation of a three-dimensional cross-linked structure through side allophane bonds:

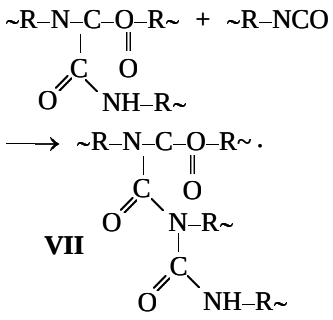

VII

By aminolysis, we detected in the prepolymer allophane groups in amount of 0.5–1.2 wt %, which are practically absent in the prepolymer based on stabilized polyols. IR examination revealed the presence of triisocyanurate structures in the prepolymer from active polyethers, which results in cross-linking of polyurethane macromolecules. In this process, the viscosity increases and the content of isocyanate groups decreases. It is known [5] that the rate of allophanate formation considerably exceeds the rate of trimerization of isocyanate groups. A sharp decrease in the content of NCO groups is particularly noticeable with the polyether of a lower molecular weight (Fig. 2, curve *4*). The brand of the TDI used does not play a significant role.

In the case of the stabilized prepolymer, urethane formation is characterized by occurrence of the main reaction [reaction (1)]. The type of the stabilizer has no significant effect on the kinetics of prepolymer synthesis; the content of the NCO groups becomes approximately constant within 90 min and does not change further (Fig. 3).

A process was suggested for preparation of polyurethane (TU 38.3 030 098–95, 38.4 030 103–95, 38.4 030 104–95, 222 600 201-3 013 487–95) and thiourethane sealants containing a stabilized prepolymer based on polyoxyalkylenepolyol of molecular weight 5000. The composite materials as compared to the industrial analogs are characterized by increased strength, elasticity, and water resistance and by good adhesion to various substrates. The use of a catalytic

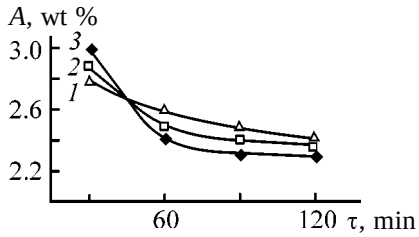

Fig. 3. Kinetic curves of synthesis of prepolymers in the presence of various stabilizers: (*1*) diisopropyl hydrogen phosphite, (*2*) diisooctyl hydrogen phosphite, and (*3*) phosphorochloridite.

curing coagent of reactive oligomers with various functional groups allows practically complete chemical binding with simultaneous improvement of physicomechanical parameters. The advantage of these sealants is that the sealing and curing pastes are taken in comparable amounts (ratio A : B varies from 2 : 1 to 1 : 1), which favors good mixing of the components under industrial conditions.

The physicomechanical parameters of polyurethane sealants determined in extended tests are listed in Table 1. The advantages of our formulations are simpler process and lower power consumption due to decreased amount of the components and curing at room temperature. Also, there are vast prospects for production of colored composites.

Polyoxyalkylenepolyols of molecular weight from 500 to 6000 are commercially available. Experiments showed (Table 2) that the best combination of elasticity and strength is attained when the molecular weight of the polyol is 3000–5000. With lower-molecular-weight polyethers, denser cross-linked materials are formed, which exhibit increased cohesion strength but low elasticity. With the molecular weight of the polyethers above 5000, the strength of the composites decreases. Introduction of a stabilizer (0.05 wt % HCl) into the prepolymer levels its reactivity toward polyols and suppresses side reactions. Formation of urethane elastomers occurs as a chain growth reaction. When the polymer contains no allophane cross-links, its reaction with polyol yields linear macromolecules, which is favorable for microphase segregation; such composites exhibit higher elasticity.

Phenol Mannich bases (PMBs), dimethylaminomethylphenols, are widely used catalysts of reactions of oligothiols and polyols with isocyanate-containing prepolymers. It was found previously [6] that the activity of these catalysts varies in parallel with their basicity. When the amount of the catalyst is low, the oligomers react slowly, which favors formation of a

Table 1. Properties of polyurethane sealants

Parameter	Ratio of pastes A : B		
	2.2 : 1.0	2.2 : 1.2	2.2 : 1.5
Normal curing conditions (25°C, 7 days)			
Nominal tensile strength, MPa	0.98–1.03	1.1–1.26	1.4–1.66
Relative elongation at break, %	500–530	510–550	400–510
Adhesion to metal (at exfoliation), kN m^{-1}	3.0–4.7	1.5–2.5	0.9–1.2
Hardness (TIR), arb. units	46–52	50–54	55–57
Keeping in water at 80°C, 6 h; rest, 3 days			
Nominal tensile strength, MPa	0.9–1.34	1.1–1.28	1.4–1.64
Relative elongation at break, %	350–420	220–260	350–370
Keeping at 100°C, 10 days			
Nominal tensile strength, MPa	1.3–1.5	1.25–1.7	1.4–1.6
Relative elongation at break, %	440–500	210–310	300–320
Extraction in water, 1 day			
Degree of swelling, wt %	0.06	0.14	5.1

Table 2. Main physicomechanical characteristics of composites

Parameter	*M* = 3000		*M* = 5000	
	1	2*	3	4*
Nominal tensile strength, MPa	2.6–2.9/2.1–2.2**	1.2–1.5/Gelation	2.4–2.7/2.1–2.5	2.8–3.0/1.8–2.1
Relative elongation at break, %	130–190/550–600	480–630/ –	530–780/350–420	350–380/250–320

* Stabilized prepolymer.
** (Denominator) values after storage of the prepolymer for 3 months.

low-defective network, and the resulting composites exhibit increased cohesion strength and elasticity (Table 3).

The increased content of the catalyst favors faster reaction of the oligomers, but the resulting network can become defective. Furthermore, at larger amounts of the catalysts formation of isocyanurates **IV**, which do not react with the polyether at room temperature, becomes more probable. As a result, the strength and adhesion characteristics of the product decrease.

Table 3. Influence of the catalyst amount on the physicomechanical characteristics of composites

Parameter	PMB content, wt parts per 100 wt parts of polyol	
	1.5	3.5
Nominal tensile strength, MPa	2.5–3.0	1.0–1.6
Relative elongation at break, %	350–400	280–340

We also examined the possibility of using Schiff bases derived from aliphatic diamines and various aldehydes as catalysts for curing of single-component sealants of the polyurethane and thiourethane nature. With aldimines it is possible to avoid a drawback characteristic of traditional single-component urethane systems: release of CO_2 at curing of isocyanate prepolymers with moisture present, as a rule, in fillers. We studied the reaction of mono- and diisocyanates with Schiff bases and hydrolysis of Schiff bases at various ratios of the components, curing temperatures, and pH values of the medium. With decreasing pH the hydrolysis of Schiff bases accelerates and the reaction of isocyanate groups with water decelerates. Electron-

donor substituents in aldimines accelerate with reaction with isocyanates.

CONCLUSION

Addition of an acid stabilizer to a prepolymer levels its reactivity toward a polyol or oligothiol and suppresses side reactions in the course of urethane formation. The use of the stabilized prepolymer opens prospects for preparation of a wide assortment of urethane elastomers.

REFERENCES

1. USSR Patent 2078789.
2. USSR Patent 2078781.
3. USSR Patent 2073053.
4. USSR Inventor's Certificate no. 1121974.
5. Saunders, J.H. and Frish, K.C., *Polyurethanes. Chemistry and Technology*, part 1: *Chemistry*, New York: Interscience, 1962.
6. Elchueva, A.D., Averko-Antonovich, L.A., and Sukhanov, P.P., *Kauchuk Rezina*, 1992, no. 5, pp. 18–20.

Russian Journal of Applied Chemistry, Vol. 74, No. 1, 2001, pp. 154–156. Translated from Zhurnal Prikladnoi Khimii, Vol. 74, No. 1, 2001, pp. 147–150.

MACROMOLECULAR CHEMISTRY AND POLYMERIC MATERIALS

Boric Acid Esters as Fungicide Additives and Heat Stabilizers of Elastomers Based on Siloxane Rubber

V. I. Grachek, N. N. Bukanova, A. V. Smolyakov, and A. N. Lukashik

Institute of Physical Organic Chemistry, Belarussian National Academy of Sciences, Minsk, Belarus

Received August 4, 2000

Abstract—New boric acid esters with an azomethine bond were prepared. These compounds exhibit an efficient fungicide and heat-stabilizing effect on elastomers based on SKTV-1 rubber.

Aging and stabilization of polymers is still an urgent problem. There is a growing interest in multifunctional stabilizers containing in the same molecule a number of functional groups acting by different mechanisms [1]. It is known that organoboron compounds exert a fungicide [2, 3] and heat-stabilizing effect [4–6] on polymeric materials. With the aim to develop promising fungicide additives and heat stabilizers for siloxane rubber, we prepared new boric acid esters containing azomethine groups, in view of the fact that compounds containing C=N groups are efficient heat-stabilizing agents for polysiloxanes [7].

Borates were prepared by heating of a mixture of boric acid with pyrocatechol and hydroxy compounds containing azomethine groups at 70–80°C in benzene with heteroazeotropic distillation of the released water.

The structure of the products was proved by IR and ^{1}H NMR spectroscopy, mass spectrometry, and elemental analysis.

The IR spectra of the compounds contain bands at 1040 ± 10 and 1350 ± 10 cm^{-1} characteristic of the symmetrical and antisymmetrical vibrations of the B–O group and at 1090 ± 10 and 1240 ± 10 cm^{-1} characteristic of the symmetrical and antisymmetrical vibrations of the C–O group. The band at 1640 ± 5 cm^{-1} is due to the CH=N vibrations, and that at 1754 cm^{-1}, to the stretching vibrations of the ester carbonyl (in **III** and **IV**).

The ^{1}H NMR spectra of the compounds are given in Table 1. The proton signals of the pyrocatechol ring are observed at 6.20 ± 0.04 and 5.60 ± 0.02 ppm. The azomethine proton gives a signal at 8.15 ± 0.03 ppm. The chemical shifts of protons of the substituents are also given in Table 1. In addition, the spectra of **III** and **IV** contain signals at 1.23 and 3.58 ppm, belonging to the methyl and methylene protons of the ethoxy group.

The mass spectra of the boric acid esters contain molecular peaks (Table 1), but their intensity is relatively low. The molecular peaks of all the compounds have a close intensity. Apparently, the extent and character of electron density delocalization in substituents, affecting the stability of the compounds to electron impact, yield of molecular ions, and formation of stable radicals, are similar in all the compounds.

The most characteristic and intense peaks in the mass spectra of the borates are those at *m/z* 135, 108, 92, and 65. They presumably originate from the $C_6H_4BO_3$ moiety, common for all the compounds.

All the compounds contain a strong peak at *m/z* 65, corresponding to the $C_5H_5^+$ ion, which can form only by rearrangement with hydrogen transfer from one part of the molecule to another.

The physicochemical characteristics of the compounds are listed in Table 2.

The synthesized esters were added to rubber stocks based on SKTV-1 siloxane rubber. The optimal content of the additives was 1 wt part per 100 wt parts of rubber. With larger amounts of the additives, the physicomechanical properties of the rubbers get worse. The rubber stocks were prepare on rollers using standard formulations. Boric acid esters do not exude to the surface of siloxane rubber and do not affect the peroxide curing of rubbers.

Rubbers with triaryl borate additives were tested for fouling with mold fungi. The fungus resistance of rubbers (extent of fungus growth on rubber samples) was evaluated in a six-point scale [GOST (State Standard) 9049–75]. The results are listed in Table 3. It is seen that the borate-containing rubbers are fouled

1070-4272/01/7401-0154$25.00

Table 1. NMR and mass spectra of the synthesized compounds

Compound*	^{1}H NMR spectrum, δ, ppm							Mass spectrum				
	CH^1	CH^2	CH^3	CH^4	CH^5	CH^6	CH^7	M^+ (I, %)	m/z = 135, $C_6H_4O_3B$	m/z = 108, $C_6H_4O_2$	m/z = 92, C_6H_4O	m/z = 65, C_6H_5
I	6.20	5.61	5.68	5.48	8.18		6.72	365 (32)	79	87	93	71
II	6.24	5.62	5.71	5.49	8.14		6.78	365 (34)	90	92	98	69
III	6.22	6.62	5.69	5.42	8.12	5.71	5.98	387 (30)	67	95	91	68
IV	6.20	5.60	5.61	5.40	8.13	5.71	5.98	403 (29)	72	95	90	66

*

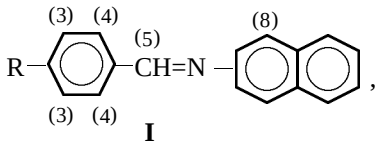

I,

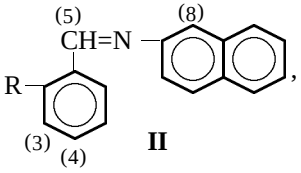

II,

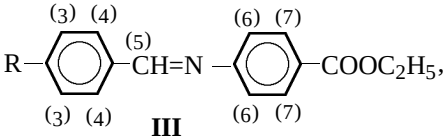

III

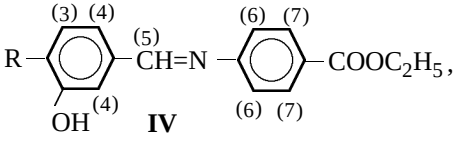

IV, where R is

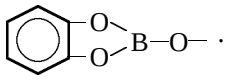

.

Table 2. Yields, melting points, and elemental analyses of triaryl borates

Compound	Yield, %	mp, °C	Found, %/Calculated, %				Formula
			C	H	N	B	
I	90	199–195	75.76/75.67	4.42/4.38	3.81/3.84	2.86/2.96	$C_{23}H_{16}BNO_3$
II	86	219–220	75.78/75.67	4.44/4.38	3.80/3.84	2.92/2.96	$C_{23}H_{16}BNO_3$
III	77	177–178	68.19/68.21	4.68/4.65	3.59/3.62	2.83/2.84	$C_{22}H_{18}BNO_5$
IV	72	155–156	65.64/65.53	4.53/4.49	3.44/3.47	2.59/2.68	$C_{22}H_{18}BNO_6$

with mold fungi to a considerably lesser extent than the rubbers with no additives. For example, the rubbers with the suggested additives remained fungus-resistant for 84 days, whereas the rubbers with no additives are intensely fouled in this period (5 points). Of the four examined triaryl borates, three are efficient fungicide additives to siloxane rubbers: **I**, **III**, and **IV**. Compound **II** showed a weak fungicide activity. This compound differs from **I** only in position of linking of the 2-naphthyliminomethyl group to the phenyl ring. It may be assumed that the more rigid molecule of **II** containing a substituent in the *o*-position of the phenyl ring diffuses to the rubber surface considerably more slowly, so that its surface concentration appears to be insufficient to suppress the fungus growth.

The heat resistance of the rubbers was evaluated from variation of their main physicomechanical properties: modulus of elasticity at 100% elongation M_{100}, nominal strength P, relative elongation at break L, and elongation set I. The inhibiting effect of the suggested additives was evaluated in comparison with the rubber containing no additives. The characteristics of rubbers at thermal aging, determined according to GOST 270–75, are listed in Table 4. It is seen that the synthesized triaryl borates inhibit thermal aging of rub-

Table 3. Evaluation of fungus growth on vulcanized siloxane rubbers in the six-point scale

Compound	Fouling, points, in indicated time, days			
	28	56	84	120
I	0	1	1–2	1–2
II	0	1–2	2	2–3
III	0	1–2	1	1–2
IV	0	0–1	1	1–2
No additive	4	4	5	5

Table 4. Thermal aging of vulcanized siloxane rubbers in the presence of triaryl borates

Compound	Before aging				After aging							
	M_{100}	P	L	l	250°C, 5 days				300°C, 1 days			
	MPa		%		M_{100}, MPa	K_P	K_L	l, %	M_{100}, MPa	K_P	K_L	l, %
I	1.8	7.0	390	4	2.0	0.60	0.51	8	2.5	0.56	0.50	9
II	2.2	6.8	330	5	3.4	0.75	0.42	7	Brittle			
III	2.4	7.2	320	6	3.0	0.68	0.56	5	2.5	0.58	0.62	6
IV	2.1	7.1	360	9	3.2	0.70	0.72	3	2.5	0.65	0.67	8
No additive	2.2	5.9	240	0	4.8	0.51	0.52	5	3.8	0.44	0.50	0

Note: $K_P = P/P_0$, $K_L = L/L_0$.

bers. For example, after keeping for 5 days at 250°C the modulus of elasticity of the rubbers with the additives increases to a lesser extent (by a factor of 1.5–2) than that of the rubber with no additives. This means that in the presence of the additives the cross-linking of the siloxane rubber occurs to a considerably lesser extent. The loss of the rubber strength in the presence of the additives is 10–20% smaller than in their absence. At a higher temperature (300°C), the changes in the modulus of elasticity and strength are also considerably less pronounced in the rubber samples containing additives (except **II**).

Compound **IV** is the most efficient heat stabilizer. This is due to the presence of the following atoms and groups: (1) boron atoms scavenging radicals owing to pronounced tendency to add groups containing free electrons; (2) nitrogen atoms capable of chain termination; (3) hydroxy groups enhancing the stabilizing effect owing to easy reaction of phenol radicals with peroxy radicals; and (4) ester group.

Our study showed than the synthesized triaryl borates exert a fungicide and heat-stabilizing effect on siloxane rubber. It is known [8] that siloxane rubber has a poor fungus resistance, and microorganisms accelerate degradation of rubbers.

Recently the requirements to environmental safety of additives to elastomer formulations became more stringent [9].

The synthesized triaryl borates meet the requirements imposed on fungicide additives: they are sufficiently toxic for mold fungi and nontoxic for humans (LD_{50} 590–640 mg kg^{-1}); they are well compatible with the rubber, do not prevent peroxide vulcanization, do not give rise to process complications, and enhance the heat resistance of the rubbers. With these additives, the service life of siloxane rubbers increases, and it becomes possible to use them in warm and humid climate at elevated temperatures without additional heat stabilizers.

CONCLUSION

New triaryl borates containing azomethine groups were prepared. The borates are heat stabilizers for vulcanized SKTV-1 rubbers and simultaneously protect them from fouling with mold fungi.

REFERENCES

1. Zaikov, G.E., *Usp. Khim.*, 1991, vol. 60, no. 10, pp. 2220–2249.
2. Chem, T.S.S., Chang, C., and Floss, H.G., *J. Org. Chem.*, 1981, vol. 46, no. 13, pp. 2661–2665.
3. Fedortsova, E.V., Idlis, G.S., Shvarts, E.M., *et al.*, *Zh. Obshch. Khim.*, 1994, vol. 64, no. 1, pp. 139–141.
4. JPN Patent Appl. 60-104148.
5. FRG Patent Appl. 4015844.
6. Radionov, Yu.M. and Danilov, S.I., *Dokl. Akad. Nauk SSSR*, 1986, vol. 288, no. 1, pp. 143–146.
7. JPN Patent Appl. 58-120651.
8. Borisova, N.N., Rebizova, V.G., and Kosenkova, A.S., *Vliyanie faktorov tropicheskogo klimata na svoistva kauchukov i rezin. Proizvodstvo RTI i ATI* (Effect of Tropical Climate Factors on Properties of Rubbers. Production of Rubber and Asbestos Items), Moscow: TsNIITEneftekhim, 1976.
9. Mukhutdinov, A.A. and Mukhutdinov, E.A., *Kauchuk Rezina*, 1997, no. 1, pp. 34–43.

Russian Journal of Applied Chemistry, Vol. 74, No. 1, 2001, pp. 157–161. Translated from Zhurnal Prikladnoi Khimii, Vol. 74, No. 1, 2001, pp. 151–156.

CHEMISTRY OF FOSSIL FUEL

Distribution of Varius Forms of Organic Nitrogen in a Lignite Macromolecule

V. V. Platonov, V. A. Proskuryakov, O. S. Polovetskaya, O. A. Shavyrina, and S. V. Ryl'tsova

Lev Tolstoi State Pedagogical University, Tula, Russia
St. Petersburg State Technological Institute, St. Petersburg, Russia

Received July 26, 1999

Abstract—The chemical composition of organic bases from tars of stepwise semicoking of lignite was studied. The features of distribution of organic nitrogen in a coal macromolecule and the most probable pathways of thermal degradation of the nitrogen-containing fragments were examined.

Up to now, fossil fuel is one of the sources of diverse nitrogen organic compounds (NOCs). Data on structural types of organic nitrogen and its distribution in a coal macromolecule are necessary for determining the chemical structure of coal and recovering in maximal yield the NOCs of the given structural-group and qualitative composition. Nitrogen organic compounds are valuable raw materials for preparing a wide set of pesticides, pharmaceuticals, dyes, heat-resistant fibers, special-purpose rubbers, ion-exchange resins, flotation agents for rare and rare-earth metals, surfactants, and vitamins. Recovery of NOCs from coals in high yield is hampered by the lack of detailed information on the chemical composition of the semicoking tars, which, in turn, does not allow scientifically substantiated selection of the initial brown coals and optimization of their processing.

The goals of this work were to study in detail the chemical composition of organic bases from tars of stepwise semicoking of lignite,[1] determine the features of distribution of organic nitrogen in the lignite macromolecule, and reveal the most probable pathways of thermal degradation of the nitrogen-containing fragments.

Semicoking was performed in a retort so as to minimize the pyrolysis of "primary" vapor–gas products [1]. Therefore, the major components of these products can be fairly reliably assigned to certain native fragments of the organic matter of lignite (OML). The tar was collected in three temperature ranges (°C): (I) <350, (II) 350–450, and (III) 450–500°C, corresponding, according to DTA, to the maximal yield of the tar. The tar yield (wt % based on OML) in stages I, II, and III was 1.5, 4.9, and 3.4, respectively.

The tars were subjected to total chemical group analysis [2]. The yield of organic bases in stages I, II, and III, wt % based on anhydrous tar (wt % based on OML), was 0.85 (0.013), 1.85 (0.091), and 1.17 (0.040), respectively.

The general characterization of the molecular structure of nitrogen organic compounds was based on data of IR, UV, ^{1}H and ^{13}C NMR spectroscopy, cryoscopy, elemental and quantitative functional analysis, and capillary gas–liquid chromatography (CGLC) [3–6].

The structural-group composition of organic bases from tars of stepwise semicoking of Near-Moscow lignite, calculated from the CGLC data, is listed in the table. It is seen that the organic bases recovered in different temperature ranges of OML degradation significantly differ in the structural-group composition.

For example, the tars recovered in the temperature range 350–450°C have a high content of picolines, lutidines, ethyl-, *n*-propyl-, isopropyl-, *n*-butyl-, and isobutylpyridines, and aliphatic and aromatic amines. The content of pyridine, quinoline, isoquinolines, benzoquinolines, benzoisoquinolines, indoles, carbazoles, hydrogenated quinolines and benzopyrroles, and polycyclic NOCs is the highest in the tars recovered in the range 450–550°C.

The distribution of NOCs in the coal macromolecule can be estimated more descriptively from the yield of separate groups of NOCs (see table). It is seen that the tar recovered in the second stage of

[1] Lignite from the Near-Moscow fields was studied (Kimovsk open pit).

1070-4272/01/7401-0157$25.00

Structural-group composition of organic bases and yield of separate groups of nitrogen-containing compounds from tars of stepwise semicoking of lignite

Sample no.	Group of compounds	Content, wt % based on whole fraction			Yield $A \times 10^4$, wt % based on OML		
		for indicated stage					
		I	II	III	I	II	III
1	Pyridine	0.50	1.15	2.45	0.65	10.62	9.80
2	Picolines	6.82	11.65	7.92	8.87	106.02	31.68
3	Lutidines	8.51	13.95	9.45	11.06	126.95	37.80
4	Ethylpyridines	0.90	1.65	0.92	1.17	15.02	3.68
5	C_3-Pyridines	7.91	9.45	6.65	10.28	86.00	26.60
6	$>C_4$-Pyridines	6.42	8.52	5.00	8.35	77.53	20.00
7	Quinolines	1.95	4.65	8.45	2.54	42.32	33.80
8	Isoquinolines	0.95	2.30	4.45	1.24	20.93	17.80
9	Benzoquinolines	0.65	1.82	5.55	0.85	16.57	22.20
10	Aromatic amines	1.95	2.50	1.25	2.54	22.75	5.00
11	Indoles	2.45	4.35	6.25	3.19	39.60	25.00
12	Carbazoles	0.65	1.50	2.85	0.85	13.65	11.40
13	Polycyclic NOCs	0.95	2.45	5.62	1.24	22.00	22.50
14	Aliphatic amines	1.65	1.90	0.85	2.15	17.30	3.40
15	Hydrogenated quinolines	8.90	10.50	13.45	11.57	95.60	53.80
16	Hydrogenated benzopyrroles	9.30	12.80	15.35	12.09	116.48	61.40

semicoking (350–450°C) is characterized by the highest content of NOCs. The major organic bases (content $A \times 10^4$, wt % based on OML) are picolines (106.02), lutidines (126.95), hydrogenated quinolines (95.60) and benzopyrroles (116.48), propyl- (86.00) and butylpyridines (77.53), quinolines (42.32), and indoles (39.60).

The table shows that the fragments of the molecular (or bituminous) fraction and the periphery of the macromolecular network of the lignite macromolecule contain pyridine and its alkyl derivatives (methyl-, dimethyl-, trimethyl-, ethyl-, *n*-propyl-, isopropyl, *n*-butyl-, isobutylpyridines). Also present in small amounts are aliphatic and aromatic amines. The macromolecular network of the lignite molecule is built of fragments of quinoline, isoquinoline, benzoquinolines, indole, carbazole, hydrogenated quinolines amd benzopyrroles, and polycyclic NOCs whose relative content in the organic bases increases with increasing temperature of OML degradation.

The scheme of the distribution of various nitrogen-containing fragments in the lignite macromolecule suggests ways to optimize semicoking of lignites to obtain tars enriched in given groups of NOCs or even in individual components.

Since ammonia is the main nitrogen-containing gaseous product of semicoking and, the more so, high-temperature coking of coals, it is important to elucidate the nature of its precursors.

To solve this problem, we calculated the structural and energy characteristics of separate components of organic bases. The calculation was based on data on the lengths of the C–N bonds and on the assumption that the bond length is inversely proportional to the bond dissociation energy.

The structures of separate representatives of lignite organic bases, identified in the tar, and the C–N bond lengths are given below:

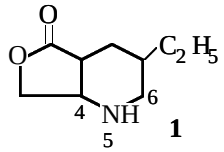

1

l_{4-5} 1.440 Å
l_{5-6} 1.4502 Å

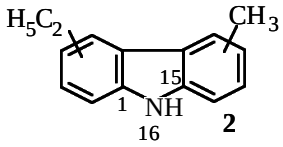

2

l_{1-16} 1.339 Å
l_{15-16} 1.325 Å

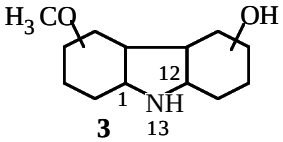

3

l_{1-13} 1.482 Å,
l_{12-13} 1.478 Å

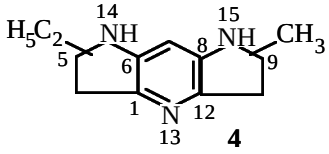

4

l_{5-14} 1.450 Å l_{9-15} 1.454 Å
l_{6-14} 1.343 Å l_{1-13} 1.265 Å
l_{8-15} 1.343 Å l_{12-13} 1.2640 Å

Scheme of distribution of various nitrogen-containing fragments in a lignite macromolecule

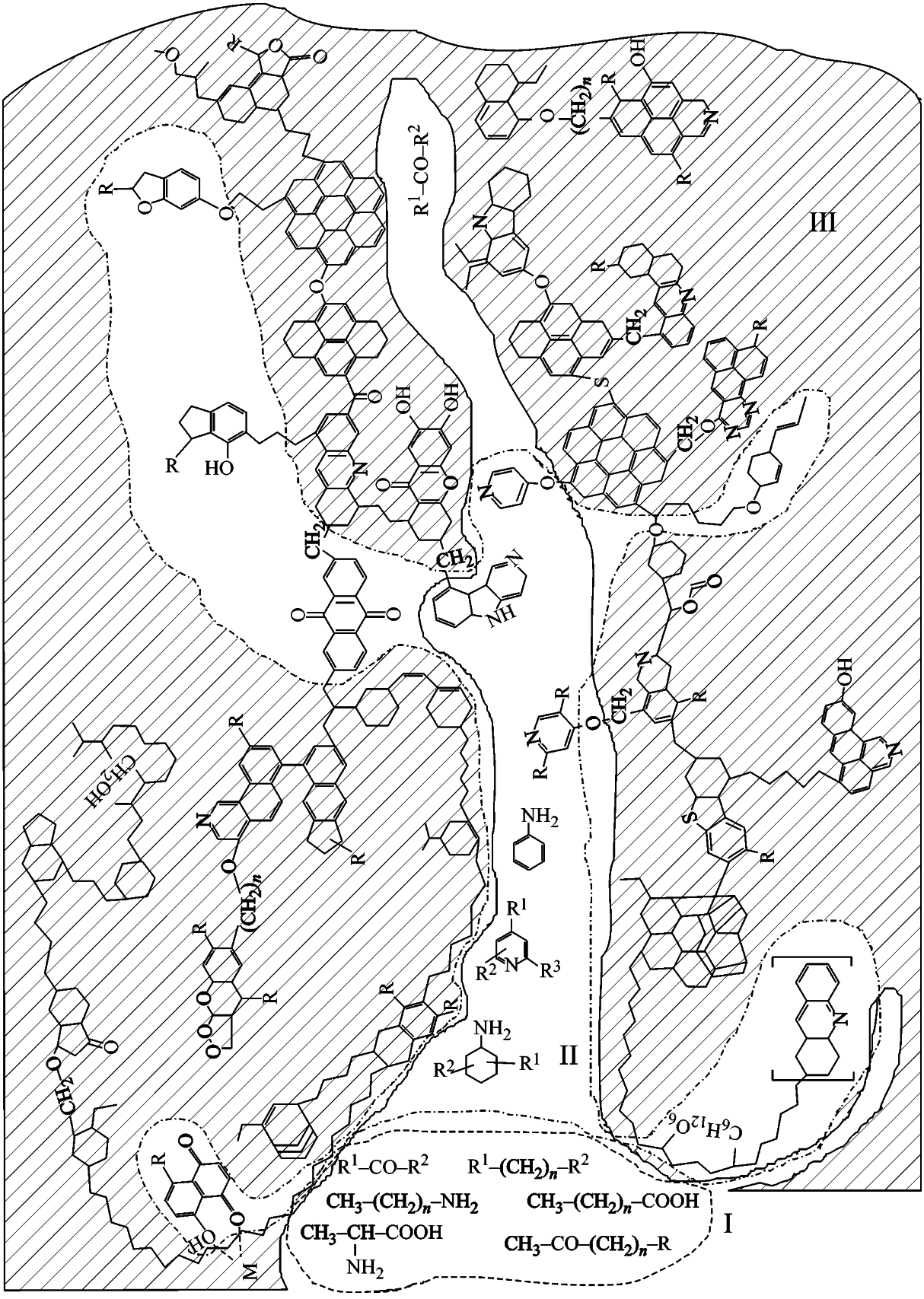

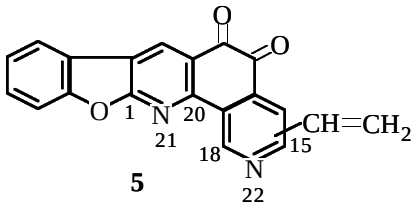

5

$l_{1–21}$ 1.261 Å $l_{18–22}$ 1.263 Å
$l_{20–21}$ 1.267 Å $l_{15–22}$ 1.266 Å

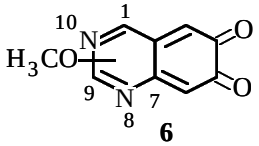

6

$l_{7–8}$ 1.265 Å $l_{1–10}$ 1.263 Å
$l_{8–9}$ 1.265 Å $l_{9–10}$ 1.266 Å

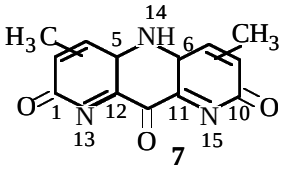

7

$l_{1–13}$ 1.398 Å
$l_{12–13}$ 1.322 Å
$l_{5–14}$ 1.473 Å
$l_{6–14}$ 1.472 Å
$l_{11–15}$ 1.321 Å
$l_{10–15}$ 1.400 Å

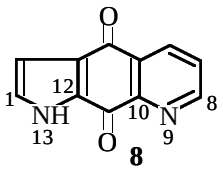

8

$l_{1–13}$ 1.330 Å
$l_{12–13}$ 1.325 Å
$l_{8–9}$ 1.343 Å
$l_{9–10}$ 1.325 Å

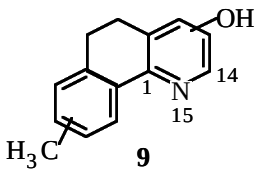

9

$l_{1–15}$ 1.265 Å
$l_{14–15}$ 1.265 Å

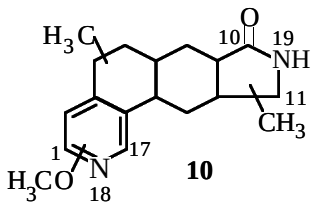

10

$l_{1–18}$ 1.264 Å
$l_{17–18}$ 1.462 Å
$l_{10–19}$ 1.371 Å
$l_{11–19}$ 1.443 Å

The bond lengths suggest that compounds **1, 3, 7, 8**, and **10** will decompose first, and compounds **4**–**6** and **9** will be more heat-resistant. Therefore, the following pathways of thermal degradation of components with formation of ammonia were suggested:

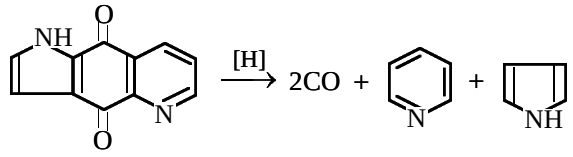

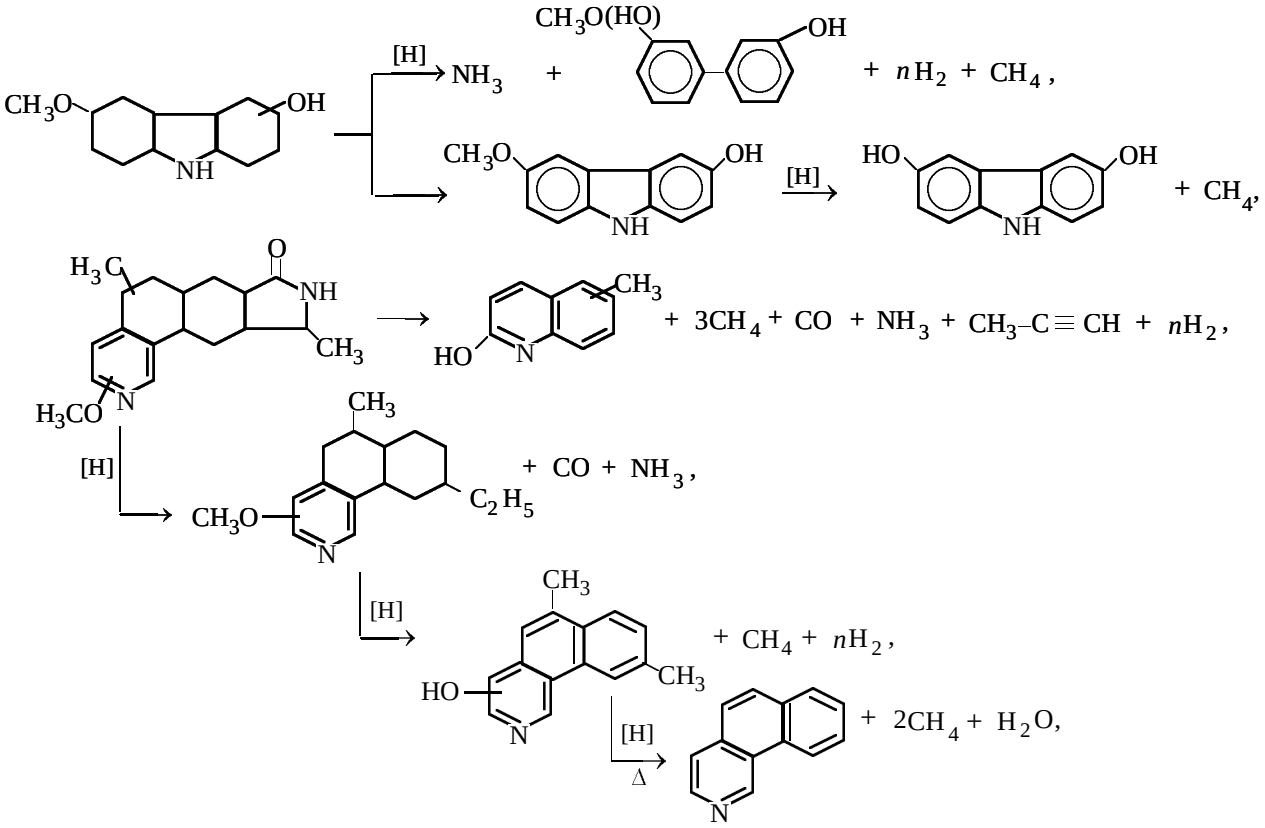

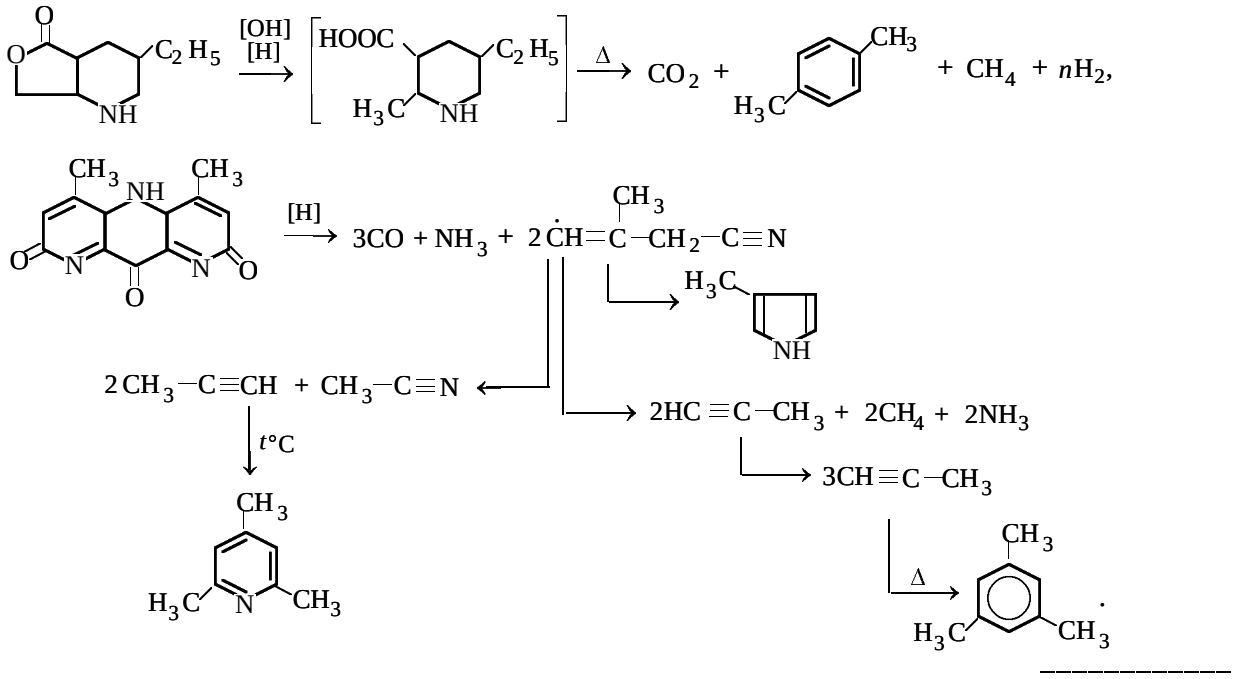

The lack of published data on the lengths and dissociation energies of the C–N bonds in complex molecules did not allow us to confirm the suggested degradation pathways by calculation of the activation energy for each process, e.g., by the Moin's method [7, 8]. However, it can be definitely concluded that the major sources of ammonia in high-temperature coking of lignites are structures containing pyrrole, pyrimidine, and piperidine rings, purine bases, five- and six-membered lactams, aliphatic and aromatic amines, and diamines.

CONCLUSIONS

(1) The chemical composition of organic bases from tars of stepwise semicoking of lignite from the Near-Moscow fields was studied.

(2) The dynamics of distribution of various nitrogen-containing fragments in the lignite macromolecule was elucidated, and the feasibility was demonstrated for thermal degradation of lignites to obtain tars enriched in a definite set of organic bases.

(3) Possible pathways of thermal degradation of separate organic bases with formation of ammonia were suggested. The main sources of ammonia are pyrrole, piperidine, pyrimidine, and lactam fragments of the coal macromolecule, and also purine bases, aliphatic and aromatic amines, and diamines.

REFERENCES

1. Platonov, V.V., Thermochemical Transformations of Coals from the Kuznetsk Fields, *Cand. Sci. Dissertation*, Moscow, 1972.
2. Kamneva, A.I. and Korolev, Yu.G., *Laboratornyi praktikum po khimii topliva* (Laboratory Course of Fuel Chemistry), Moscow: Mosk. Khimiko-Tekhnol. Inst. im. D.I. Mendeleeva, 1976.
3. Platonov, V.V., Tabolenko, N.V., Klyavina, O.A, and Ivleva, L.I., *Izv. Akad. Nauk Est. SSR, Khim.*, 1984, vol. 33, no. 2, pp. 102–109.
4. Platonov, V.V., Tabolenko, N.V., Klyavina, O.A., and Ivleva, L.I., *Izv. Akad. Nauk Est. SSR, Khim.*, 1985, vol. 34, no. 1, pp. 11–16.
5. Platonov, V.V., Tabolenko, N.V., Klyavina, O.A., *et al.*, *Khim. Tverd. Topl.*, 1987, no. 4, pp. 27–32.
6. Platonov, V.V., Proskuryakov, V.A., Polovetskaya, O.S., and Platonova, M.V., *Zh. Prikl. Khim.*, 1999, vol. 72, no. 2, pp. 314–318.
7. Moin, F.B., *Usp. Khim.*, 1967, vol. 36, no. 7, pp. 1223–1243.
8. Moin, F.B., *Dokl. Akad. Nauk SSSR*, 1963, vol. 152, no. 5, pp. 1169–1172.

Russian Journal of Applied Chemistry, Vol. 74, No. 1, 2001, pp. 162–163. Translated from Zhurnal Prikladnoi Khimii, Vol. 74, No. 1, 2001, pp. 157–158.

BRIEF COMMUNICATIONS

Thermodynamic Characteristics of Vaporization of Diethylarsine and Triethylmethoxystannane

A. K. Baev

Belarussian State Technological University, Minsk, Belarus

Received March 1, 2000; in final form, June 2000

Abstract—Saturated vapor pressures of diethylarsine and triethylmethoxystannane were measured in a wide temperature range. Thermodynamic characteristics of their vaporization and temperatures of the decomposition onset were determined.

The use of arsine in the synthesis of submicrometer structures of gallium arsenide by organometallic gas-phase epitaxy provides a high quality of the resulting products. However, from the environmental viewpoint, it is urgent to look for organoarsenic compounds with reduced toxicity and stability. The use of organotin compounds in the synthesis of thin-film articles enables their contact soldering and preparation of conductive oxide layers. Diethylarsine and triethylmethoxystannane are of interest in this connection, but published data on these compounds are limited to their spectra. Therefore, the goal of this work was to measure the vapor pressure of these compounds and to determine their thermal stability and thermodynamic characteristics of their vaporization.

The experiments were carried out under static conditions by a membrane method for samples containing 99.9 mol % main substance. A sample was introduced into a membrane chamber by distillation in vacuum using an all-glass sealed system, which was preliminarily heated under evacuation with a zeolite pump to remove moisture adsorbed on glass. Vapor pressures were measured with an MChR-3 manometer accurate to 0.1 mm Hg at fixed temperatures controlled by a liquid thermostat. A silicone liquid was used for the temperature control above 313 K and water, at lower temperatures. The accuracy of the temperature control in this temperature range was ± 0.05 K. Prior to and after the completion of an experiment the membrane chamber was cooled to the temperature of liquid nitrogen, and the residual vapor pressure was an evidence of side processes occurring in the system on heating. Experimental vapor pressures were treated by the least-squares method at a confidence level of 0.95.

The temperature dependences of the experimental saturated vapor pressures (Table 1) fit characteristic exponential curves. They are well reproduced on heating and cooling the systems. The semilogarithmic plots of vapor pressure against temperature are linear within the limits of experimental errors, which indicates that only vaporization processes occur in the temperature range under study.

Table 1. Vapor pressure of diethylarsine and triethylmethoxystannane

T, K	*P*, mm Hg	*T*, K	*P*, mm Hg
Diethylarsine			
281.05	23.4	332.05	219.0
288.45	34.0	337.45	265.2
294.15	45.0	342.55	315.4
298.25	54.2	346.35	368.1
305.05	73.4	349.95	403.3
310.35	93.0	353.35	445.1
316.75	121.2	357.85	514.0
324.25	163.8	362.95	602.6
328.95	195.0	366.35	661.8
Triethylmethoxystannane			
312.45	2.8	375.55	53.7
320.45	4.4	379.65	63.1
325.65	5.9	388.75	87.4
333.95	9.5	399.25	126.4
343.25	14.4	405.65	155.8
351.75	20.9	410.85	185.2
358.65	28.1	421.15	254.4
358.75	28.7	421.45	257.2
366.15	38.3	435.25	373.0

1070-4272/01/7401-0162$25.00

Table 2. Coefficients of the equation $\log P = -A/T + B$ and Antoine's equation $\ln P = -A/(C + t) + B$ and enthalpies and entropies of vaporization

A	B	$\Delta H^0(T)$,* kJ mol^{-1}	$\Delta S^0(T)$,* J mol^{-1} K^{-1}	A**	B**	C**
Diethylarsine						
1721.5 ± 2.7	7.52 ± 0.01	32.96 ± 0.05	88.92 ± 0.16	3155.3	16.08	37.176
Triethylmethoxystannane						
2374 ± 19	8.05 ± 0.05	45.45 ± 0.35	99.9 ± 1.0	4027.3	16.36	49.416

* Diethylarsine: T = 281–366 K; triethylmethoxystannane: T = 312–435 K. ** Antoine's equation.

The data on the vapor pressure P (mm Hg) were treated by the equation $\log P = -A/T + B$ and by the Antoine's equation. The calculated constants of the equations and enthalpies and entropies of vaporization are given in Table 2. The enthalpies of diethylarsine and triethylmethoxystannane vaporization found by the Antoine's equation are 35.15 (273.15 K), 34.24 (298.15 K), and 32.49 and 49.91 (273.15 K), 48.71 (298.15 K), and 42.61, respectively.

The average molecular weights of diethylarsine and triethylmethoxystannane, calculated using the experimental pressures of unsaturated vapors of diethylarsine and triethylmethoxystannane, well agree with the weights calculated from their formulas, which proves that monomeric molecules are present in the vapors. The pressures of unsaturated vapors obey the Gay–Lussac's law within a wide temperature range. Heating unsaturated vapors in steps of 1 K with sufficient in time thermostatic control at each fixed temperature allowed us to detect the temperatures of the onset of noticeable irreversible decomposition of diethylarsine (497.5 K) and triethylmethoxystannane (493.3 K).

As the enthalpies of vaporization of triethylarsine (38.52 ± 0.74 kJ mol^{-1}) [1] and diethylarsine (32.96 ± 0.15 kJ mol^{-1}) were obtained from the data on the vapor pressure in the same temperature range, their difference of 5.56 kJ mol^{-1} should be attributed to the change in the intermolecular interaction on the replacement of one C_2H_5 group by hydrogen. In view of the fact that the integral enthalpy of vaporization [2] is determined by the number and energy of bonds existing in solution, we can deduce $D(\mathrm{As}\cdot C_2H_5\text{–As})$ = 6.42 kJ mol^{-1}. This is a limiting value, as dispersion interactions in solution were not taken into account [3, 4]. With this value taken unchanged in liquid diethylarsine, we obtain $D(\mathrm{As–}C_2H_5\cdot\mathrm{As})$ equal to 3.64 kJ mol^{-1}, which can be used to estimate the enthalpies of vaporization of arsenic dialkyl derivatives.

The replacement of an ethyl group in $Sn(C_2H_5)_4$, having $\Delta H^0(T)$ = 46.6 ± 0.6 kJ mol^{-1} and $\Delta S^0(T)$ = 102.4 ± 1.7 J mol^{-1} K^{-1}, by a methoxy group in triethylmethoxystannane reduces the enthalpy of vaporization to 45.45 ± 0.36 kJ mol^{-1}, i.e., it only slightly affects the intermolecular interaction energy.

CONCLUSION

The obtained experimental data on the vapor pressure and thermodynamic properties can be used in the development of procedures for exhaustive purification of substances and in the gas-phase synthesis of semiconductor materials by decomposition of alkyl compounds.

REFERENCES

1. Baev, A.K., Silivanchik, I.P., and Kozyrkin, B.I., *Zh. Obshch. Khim.*, 1980, vol. 50, no. 9, pp. 1931–1937.
2. Baev, A.K., *Obshch. Prikl. Khim.* (Minsk), 1972, issue 5, p. 33.
3. Baev, A.K., *Zh. Khim. Thermodin. Termokhim.*, 1992, vol. 1, no. 2, pp. 143–158.
4. Baev, A.K., *Izv. Vyssh. Uchebn. Zaved., Khim. Khim. Tekhnol.*, 1999, vol. 42, no. 6, pp. 3–11.

Russian Journal of Applied Chemistry, Vol. 74, No. 1, 2001, pp. 164–166. Translated from Zhurnal Prikladnoi Khimii, Vol. 74, No. 1, 2001, pp. 159–161.

BRIEF COMMUNICATIONS

Microdosing on Evaporation from the Surface of a Porous Solid

S. I. Krichmar and Yu. N. Bardachev

Kherson State Technical University, Kherson, Ukraine

Received May 4, 2000

Abstract—The processes are examined that occur when dilute gas mixtures are prepared by the evaporation of a solution of impurities in an indifferent liquid solvent from the surface of a porous solid. Relationships between the concentrations of the impurities in the liquid and gas phases are given.

A procedure for dosing small amounts of volatile impurities in gases was suggested in [1]. This procedure enhances the capabilities of the known technique [2, 3] by increasing the surface area for the evaporation on a liquid–vapor interface owing to the use of a capillary-porous solid. The technique can be used on a larger scale if highly volatile components are dissolved in an indifferent liquid solvent with a vapor pressure lower than the vapor pressure of the impurities under study [4].

The aim of this work was to describe in more detail the possibilities of the suggested dosing procedure. We emphasize that this procedure can be used for the preparation of gas mixtures of pollutants with a given composition not only for calibration of gas sensors, but also in modern technologies of obtaining pure gases.

The operation of the leak device is the following. A solution of impurities in a liquid solvent is placed in narrow glass tube *2* with a widening in its top end filled with capillary-porous solid *3* (Fig. 1). Its bottom contacts the solution, and flat upper interface *4* is directed to the space through which a diluent gas is continuously flowing. The diameter of the glass tube is chosen in such a manner that the liquid does not flow out via its open lower end. The position of the liquid meniscus in the lower part of the tube is detected at regular time intervals with a cathetometer. In a conventional case the limitations in the choice of the tube diameter prevent measuring evaporation rates of poorly volatile liquids. The evaporation rate is proportional to the evaporation surface, all other factors being equal. The surface of a finely porous solid impregnated with a liquid is the most suitable for technical use of this property. A fine liquid film distributed over this solid evaporates evenly with a rate considerably higher than the rate of the liquid transport along the pores. Therefore, the process is almost independent of the equilibrium vapor pressures of the components.

In a steady-state mode the evaporation from the surface of a porous solid and from the meniscus in the tube results in changes in the position of the liquid level. The rate of its migration along the measuring tube (Fig. 1) is dl/dt, where l is the capillary length and t is the time. If the capillary cross section is S and the liquid density is ρ, the weight of substance evaporating in unit time is $S\rho(\Delta l/\Delta t)$. When the space velocity of the gaseous diluent is ϑ_p, the relative weight concentration of the ith component in the liquid containing several components will correspond

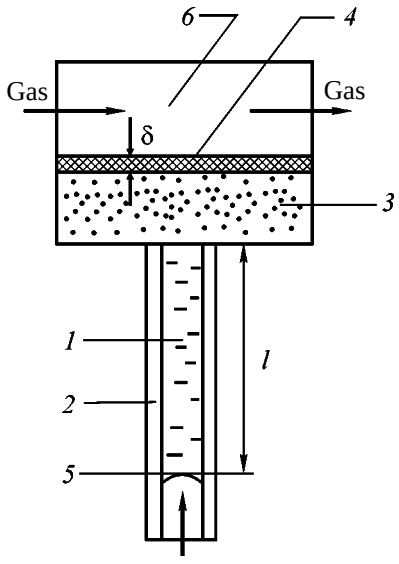

Fig. 1. Scheme of the leaking device: (*1*) liquid solution, (*2*) transparent tube, (*3*) porous solid, (*4*) evaporation surface (liquid–gas interface), (*5*) meniscus, and (*6*) gas space; (σ) effective diffusion layer and (l) capillary length (mm).

1070-4272/01/7401-0164$25.00

to the concentration X_i (g/cm^3) in the resulting gas:

$$X_i = x_i \frac{\rho S(\Delta l/\Delta t)}{\vartheta_p}. \quad (1)$$

With regard to the dependence of the volume of the vapor of the liquid on the absolute temperature T, the volume concentration of the ith component C_i (vol %) is calculated by the formula

$$C = 8.20 \times 10^3 \frac{S\rho T N_i(\Delta l/\Delta t)}{\vartheta_p \Sigma M_i N_i}, \quad (2)$$

where M_i and N_i are the molecular weights and mole fractions of the components of an evaporated liquid.

This relationship is similar to the relationship for the conventional installation [1].

At a constant cross section of a porous solid under steady-state conditions the flows of impurities J and of liquid solvent J_L are constant throughout the length (the averaged cross section of the pores is constant); hence,

$$J = Scu, \; J_L = S c_L u_L, \quad (3)$$

where u and u_L are linear migration rates of the components.

The starting nonstationary transfer process includes several stages, the diffusion being the limiting stage in the liquid layer adjacent to the interface. In the steady-state regime (operation) the transfer of an impurity component is described by the equation of linear convection–diffusion transfer in pores

$$D\frac{\partial^2 c}{\partial y^2} + u\frac{\partial c}{\partial y} = 0, \quad (4)$$

where D is the coefficient of impurity diffusion, C is its concentration, and y is a coordinate.

The limiting conditions are:

$$C_0 = C, \; y_0 = 0 \text{ at the interface,}$$
$$C = C^0, \; y = \infty \text{ far from the interface.} \quad (5)$$

The integration of Eq. (4) with regard to (5) gives

$$\frac{c - c_0}{c_i^0 - c_0} = 1 - e^{-uy/D}. \quad (6)$$

The diffusion density of the flow at the interface $y = 0$

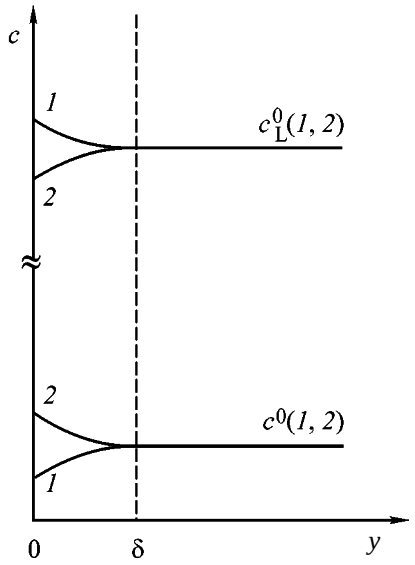

Fig. 2. Scheme of concentration distribution in the porous solid: (*1*) the impurity is more volatile than the diluent and (*2*) the impurity is less volatile; c^0 and c_L^0 are the same for both cases.

$$j_0 = D(\partial c/\partial y)_{y=0} = (c^0 - c_0)u = D\frac{c^0 - c_0}{\delta}, \quad (7)$$

where the effective diffusion layer is

$$\delta = D/u. \quad (8)$$

The time of attaining the steady-state regime is described in detail in [5]. We estimate the critical time of its setting τ as

$$\tau \approx \delta^2/D = D/u^2. \quad (9)$$

The ratio between the flows J/J_L and the section S along the whole length of the porous solid are constant, hence

$$J/J_L = \frac{uc - D(\partial c/\partial y)_{y=0}}{uc_L - D(\partial c/\partial y)_{y=0}} = c^0/c_L^0. \quad (10)$$

It is impossible to find from Eqs. (7) and (10) the concentrations in any point and, in particular, at the interface where $y = 0$. They can be found using the Raoult's equations by comparing the flows in the gas phase. Let the pressures of an impurity and solvent vapor in the gas phase be p and p_L, and p_0 and p_L^0 be their vapor pressures above the pure components,

Experimental test of the procedure

Mixture	Content, $\times 10^7$ vol %, at indicated air flow rate, $cm^3\ s^{-1}$		
	0.5	1.0	4.0
10.0% HCl + 90.0% H_2O*			
Taken HCl	14.08	7.04	3.17
Found HCl	14.0	7.00	3.10
Taken H_2O	126	63.4	28.5
Found H_2O	125	63.0	29.0
10.0% NH_3 + 90.0% H_2O**			
Taken NH_3	6.16	3.06	0.37
Found NH_3	6.10	3.00	0.37
Taken H_2O	55.44	27.94	33.3
Found H_2O	55.20	27.80	33.10
5.0% H_2O + 95.0% C_2H_5OH***			
Taken H_2O	5.76	3.88	1.44
Found H_2O	5.75	3.90	1.40

* Acidimetric determination of HCl, gravimetric determination of H_2O by absorption in a calcium chloride tube.
** Acidimetric determination of NH_3, determination of H_2O as in the previous case.
*** Back-titration of sodium thiosulfate with Fischer's reagent with starch as indicator; alcohol was not determined.

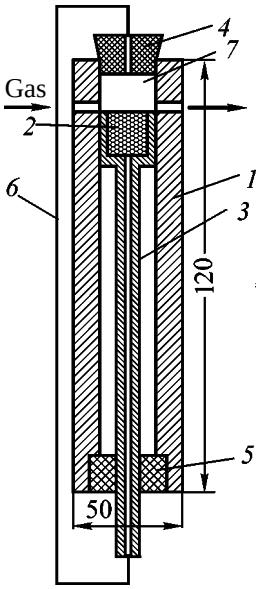

Fig. 3. Scheme of dosing unit: (*1*) body (polymethyl methacrylate), (*2*) porous solid (caked glass crumbs), (*3*) glass tube, (*4*, *5*) elastic sealing plugs, (*6*) by-pass, and (*7*) mixing chamber.

respectively, at a given temperature. Then in the gas

$$J_L/J = \frac{p_L^0(1 - N)}{p^0 N} = \frac{p_L^0(1/N - 1)}{p^0}. \quad (11)$$

Therefore,

$$N = (J_L p^0/J p_L^0 + 1)^{-1}, \quad (12)$$

or, with regard to the fact that the amount of impurities is noticeably smaller than that of the liquid solvent,

$$c_0 \approx \frac{p_L(J_L p^0/J p_L^0 + 1)}{M_L} = \frac{p_L(c_L^0/c^0 p_L^0 + 1)}{M_L}. \quad (13)$$

If $(c_L^0 p^0/c_0 p_L^0) \to 0$ on condition that $p^0/p_L^0 < c_L^0/c^0$ (vapor pressure of the impurity is very small), $c^0 \approx p_L/M_L$, which corresponds to the concentration of the pure solvent. If $c_L^0 p^0/c^0 p_L^0 \gg 1$, $c_0 \approx c^0 p_L^0/p^0$, i.e., the concentration of the impurity at the interface is lower than the starting concentration. The both situations are illustrated in Fig. 2.

The data of experimental tests of the procedure (see table) are taken from [5]. The drawing of the dosing unit is shown in Fig. 3.

As seen from the given experimental data, the dosing unit is able to operate with impurities whose partial pressure can be both lower and higher than the pressure of the diluent.

REFERENCES

1. Krichmar, S.I., *Vopr. Khim. Khim. Tekhnol.*, 1982, no. 97, pp. 96–98.
2. Desty, D.H., Geach, C.J., and Goldup, A., *Gas Chromatography. Proc. Third Symp. Organized by the Society for Analytical Chemistry*, Scott, R.P.W., Ed., London: Butterworths, 1960. Translated under the title *Gazovaya khromatografiya*, Moscow: Mir, 1964, p. 65.
3. Reiman, L.V., *Tekhnika mikrodozirovaniya gazov (spravochnik)* (Techniques of Gas Microdosing (Handbook)), Leningrad: Khimiya, 1985.
4. Krichmar, S.I., *Zavod. Lab. (Diagn. Mater.)*, 1996, vol. 62, no. 5, pp. 13–15.
5. Krichmar, S.I., *Zavod. Lab. (Diagn. Mater.)*, 1998, vol. 64, no. 8, pp. 8–11.

Russian Journal of Applied Chemistry, Vol. 74, No. 1, 2001, pp. 167–169. Translated from Zhurnal Prikladnoi Khimii, Vol. 74, No. 1, 2001, pp. 162–164.

BRIEF COMMUNICATIONS

Hydrolysis of Nitrosylsulfuric Acid

P. P. Kim, G. V. Pastukhova, and A. A. Peretrutov

Dzerzhinsk Branch, Nizhni Novgorod State Technical University, Dzerzhinsk, Russia

Received May 21, 1998; in final form, March 1999

Abstract—The statics and kinetics of hydrolysis of nitrosylsulfuric acid were studied at the initial sulfuric acid concentrations in the range 60–76 wt % and temperatures in the range 20–100°C or 30–130°C. The results were compared with the published data.

The reactivity of nitrosylsulfuric acid (NSA) depends on the degree of its hydrolysis and is determined by the concentration of nitrogen compounds formed in the solution in the free state in the course of hydrolysis. The NSA hydrolysis is an important industrial process, which has been little studied so far because of experimental difficultes. Data for diluted (60–70%) sulfuric acid are lacking.

In this work, the statics of NSA hydrolysis was studied with an SF-46 spectrophotometer. A cell with the nitrose sample and a reference cell were maintained at constant temperature using a special attachment in the form of a 1-mm-thick brass plate containing pockets for two cells and light-transmitting holes. Silicone oil delivered from a UH-8 thermostat through a heat-resistant pipe was circulated within the attachment. It was found that in the concentration range 0–5% N_2O_3 and 57.5–100% H_2SO_4 the Lambert–Beer law is fulfilled. The degree of NSA hydrolysis was calculated from the residual NSA concentration of the nitrose sample, as determined from comparison of its optical density with that of the nitrose sample containing 57.7 wt % of the initial sulfuric acid (assuming 100% hydrolysis of NSA).

The degrees of NSA hydrolysis are given in Table 1, and the dependences of the hydrolysis degree α on the initial sulfuric acid concentration $C_{H_2SO_4}$ at about 20°C are shown in the figure. The Shperling's data [1] for nitroses with about 0.2% N_2O_3 (curve *1*), the data of [2] for nitroses with 0.19% N_2O_3 (curve *2*), and experimental data obtained in this study (curve *3*) were compared. As seen, for the H_2SO_4 concentration exceeding 80% the data of [1, 2] are similar, whereas at concentrations less than 80% the hydrolysis degree is lower than that found in [1]. Our results are underestimated compared to [2]. The degree of NSA hydrolysis decreases considerably as the sulfuric acid concentration grows from 57.5 to 75 wt % (concave curve), passes through an inflection point at 73 wt % H_2SO_4, and then decreases more slowly (convex curve). Such behavior is observed over the entire studied range of N_2O_3 concentrations. The increase in the N_2O_3 concentration facilitates the NSA hydrolysis. The lower the sulfuric acid concentration, the wider the N_2O_3 concentration range corresponding to a drastic growth of the hydrolysis degree. For the H_2SO_4 concentrations up to 66 wt %, this range is 0–0.55%. At a further increase in the N_2O_3 concentration, the degree of NSA hydrolysis increases to a considerably lesser extent. At N_2O_3 concentrations above 1.2–1.6% the hydrolysis degree increases virtually linearly for temperatures within 20–100°C, depending on the decrease in the sulfuric acid concentration.

The experimental data obtained confirm once again that the hot regime is efficient for operation of sulfuric

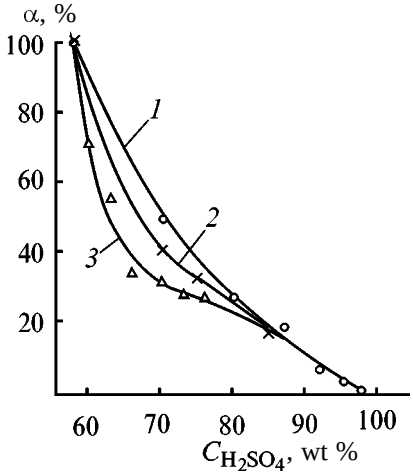

Degree α of NSA hydrolysis vs. the initial sulfuric acid concentration $C_{H_2SO_4}$. Temperature 20°C; N_2O_3 concentration 0.2%. (*1–3*) For comments, see text.

1070-4272/01/7401-0167$25.00

Table 1. Hydrolysis of nitrosylsulfuric acid

N_2O_3 concentration, %	Hydrolysis degree, %, at indicated temperature *T*, °C				N_2O_3 concentration, %	Hydrolysis degree, %, at indicated temperature *T*, °C			
	20	50	80	100		20	50	80	100
	76 wt % H_2SO_4					66 wt % H_2SO_4			
4.19	73.5	75.0	76.1	77.1	4.28	82.2	85.2	85.9	91.2
2.67	69.2	69.9	70.6	72.1	2.80	77.7	82.8	83.9	88.0
0.55	54.4	57.9	59.8	61.7	1.60	73.2	78.9	79.1	84.2
0.16	19.7	25.2	28.3	30.0	0.94	72.1	75.5	77.3	82.4
					0.47	48.6	51.2	54.2	56.6
	73 wt % H_2SO_4					63 wt % H_2SO_4			
4.22	74.3	75.1	77.8	77.9	5.26	88.1	89.5	90.5	91.6
1.05	71.6	74.9	76.0	77.0	2.62	81.9	83.2	87.3	88.6
0.80	68.6	69.9	74.8	75.0	1.73	77.2	83.0	84.5	85.7
0.54	60.0	62.0	62.7	65.4	1.12	75.4	82.3	83.8	84.9
0.37	37.6	41.1	43.6	44.8	0.15	53.2	54.0	57.9	59.9
	70 wt % H_2SO_4					60 wt % H_2SO_4			
4.22	76.1	78.5	79.7	80.2	4.54	92.8	92.9	97.3	98.0
1.57	71.3	77.6	77.8	79.2	2.67	88.0	90.6	96.0	97.0
1.29	70.9	76.5	77.7	79.2	1.15	81.6	90.3	91.4	93.0
0.62	66.2	68.6	69.2	70.8	0.69	78.6	86.5	88.1	89.2
0.40	46.2	49.7	50.9	52.4	0.28	76.7	85.8	87.0	88.1

acid system and NSA denitration. The high efficiency of utilization of high-nitrose solution was also confirmed. In the process, the nitrose activity increases not only owing to the increase in the N_2O_3 concentration, but also owing to the fact that the equilibrium in the nitrose is shifted toward the products of NSA hydrolysis.

The kinetics of NSA hydrolysis was studied on an Impul's KL-2 conductometer. The nitrose studied was charged into two cells of the conductometer and cooled to 0°C. Then, the cells were rapidly transported into a thermostat preheated to a specified temperature. After that, the time and the conductometer readings were recorded. In the course of the NSA hydrolysis the nitrose conductivity increased and then remained constant after the lapse of some time. This time was assumed as the time of complete hydrolysis. The second cell served for measuring temperature.

Table 2. Rate constants *k* of NSA hydrolysis

T, °C	*k*, l mol^{-1} min^{-1}, at indicated $HNSO_5$ concentration, wt %		
	4 (1.2% N_2O_3)	10 (3.0% N_2O_3)	15.2 (4.5% N_2O_3)
30	9.61×10^{-4}	5.52×10^{-3}	0.095
50	3.36×10^{-3}	1.43×10^{-2}	0.184
60	4.56×10^{-3}	1.69×10^{-2}	0.238
80	7.68×10^{-3}	3.24×10^{-2}	0.314
100	1.18×10^{-2}	5.90×10^{-2}	0.455
120	1.66×10^{-2}	7.58×10^{-2}	0.520
130	2.19×10^{-2}	9.72×10^{-2}	0.780

The reaction of NSA hydrolysis is of the overall second order and of the first order with respect to each component. The rate constant was calculated by the formula [3]

$$k = \frac{1}{\tau(C_{10} - C_{20})} \ln \frac{C_{20}(C_{10} - X_1)}{C_{10}(C_{20} - X_2)},$$

where C_{10} and C_{20} are the initial concentrations of $HNSO_5$ and H_2O (M), respectively, and X_1 and X_2, the concentrations of unchanged components (M).

The experimental data treated in the τ–$\ln[C_{20}(C_{10} - X_1)/C_{10}(C_{20} - X_2)]$ coordinates fall on a straight line, which confirms the value of 2 for the overall reaction order.

Table 2 shows how the kinetic parameters of NSA hydrolysis at the initial sulfuric acid concentration of 72.3 wt % change with temperature. As seen, the rate constant of the hydrolysis increases with N_2O_3 concentration and temperature. Depending on temperature, the increase in the N_2O_3 concentration from 1.2 to 3.0 and 4.5% increases the rate constant by a factor of 5.7–4.4 and 99–36, and the increase from 3.0 to 4.5%, by a factor of 17–8. At the temperature increased from 30 to 50 and 130°C at the N_2O_3 concentration of 1.2, 3.0, and 4.5% the rate constant of NSA hydrolysis increases by a factor of 3.5 and 22.8, 2.6 and 17.6, and 1.9 and 8.2, respectively, and the temperature coefficient increases from 0.57 to 1.75.

The obtained data on the statics and kinetics of NSA hydrolysis will be useful for intensifying the nitrose process.

CONCLUSIONS

(1) The degree of hydrolysis increases with increasing temperature and N_2O_3 concentration in solution and with decreasing sulfuric acid concentration.

(2) The hydrolysis rate is comparable with the rates of the other stages of the nitrose process.

REFERENCES

1. *Spravochnik sernokislotchika* (Handbook on Sulfuric Acid Manufacturer), Malina, K.M., Ed., Moscow: Khimiya, 1971.
2. Kuz'minykh, I.N. and Tantsova, N.N., *Zh. Prikl. Khim*., 1954, vol. 27, no. 6, pp. 594–599.
3. Stromberg, A.G. and Semchenko, D.P., *Fizicheskaya khimiya* (Physical Chemistry), Moscow: Vysshaya Shkola, 1988.

Russian Journal of Applied Chemistry, Vol. 74, No. 1, 2001, pp. 170–171. Translated from Zhurnal Prikladnoi Khimii, Vol. 74, No. 1, 2001, pp. 164–165.

BRIEF COMMUNICATIONS

Synthesis of Hexafluoroacetone by Catalytic Oxidation of Hexafluoropropylene

S. M. Igumnov, G. I. Lekontseva, A. A. Shipigusev, O. D. Gomzyakova, and V. A. Soshin

Perm Branch, Prikladnaya Khimiya Russian Scientific Center, Perm, Russia

Received May 17, 1999; in final form, August 2000

Abstract—Oxidation of hexafluoropropylene with molecular oxygen in a fixed bed of a catalyst (activated carbon promoted with alkali metal fluorides) was studied.

Catalytic oxidation of hexafluoropropylene (HFP) is a most promising route to hexafluoroacetone (HFA). In known procedures oxidation is carried out using as catalysts oxides of tin, iron, and indium [1] or fluorinated aluminum oxide [2], which in some cases is activated with water (0.001–0.003 mol per mole HFP [3]). Catalytic oxidation of HFP in the presence of palladium, platinum, rhodium, ruthenium, and iridium deposited on activated carbon was studied in [4].

In this work we found that the oxidation of HFP to HFA proceeds on a catalyst (activated carbon promoted with alkali metal fluorides NaF, KF, CsF, or RbF) at 50–300°C and the HFP : O_2 molar ratio of 1 : (0.1–10.0):

$$CF_3CF{=}CF_2 + 1/2\,O_2 \xrightarrow{C_{act}/MF,\ \Delta} (CF_3)_2C{=}O. \quad (1)$$

The reaction probably proceeds with intermediate formation of a carbanion generated by reaction with fluoride ion on the catalyst surface:

$$CF_3CF{=}CF_2 + F^- \rightarrow (CF_3)_2\bar{C}F + O_2 \rightarrow (CF_3)_2C{=}O + F^-.$$

Appearance of COF_2 in the reaction products is due to more profound oxidation:

$$CF_3CF{=}CF_2 + 1.5O_2 \rightarrow 3COF_2. \quad (2)$$

Formation of 1,1,1,2,3,3,3-heptafluoropropane is probably due to partial hydrolysis of COF_2 with residual moisture on the catalyst and further addition of hydrogen fluoride to HFP:

$$COF_2 + H_2O \rightarrow CO_2 + 2HF, \quad (3)$$

$$CF_3CF{=}CF_2 + HF \rightarrow CF_3CFHCF_3. \quad (4)$$

The required catalysts were prepared using a BAU-A brand crushed activated carbon with a particle size of 1.5–2.0 mm. In the tests the content of alkali metal fluorides was varied within 5–60 wt %; in this range the yield of HFA was almost constant. It was found that at the content of alkali metal fluoride smaller than 5 wt % the yield of HFA decreases, whereas the increase to more than 60 wt % is practically unfeasible. Oxidation at temperatures higher than 300°C and the HFP : O_2 molar ratio greater than 1 : 10 causes more profound oxidation of HFP yielding predominantly COF_2.

The catalyst activity remains stable for 1500 h. During this period the particle size also remains constant (1.5–2.0 mm). At longer operation the catalysts in question partially lose their activity because of changes in the grain-size distribution. The conditions of catalytic oxidation and experimental results are listed in the table.

EXPERIMENTAL

A tubular reactor (0.3 dm^3) equipped with an electrical heater, a thermocouple, and pipes to supply the initial components and O_2 and remove the oxidation products was filled with a catalyst (0.25 dm^3). The catalyst was activated carbon with 1.0–1.5 mm particle size, promoted with alkali metal fluorides. The catalyst was preliminarily activated by heating in a flow of dry nitrogen at 180–200°C for 4 h. Then the catalyst was cooled to the required temperature and HFP and O_2 were supplied at a rate of 1.0–3.0 l h^{-1} in the required molar ratio.

The gas mixture from the reactor was condensed in a trap cooled to –90°C and analyzed by gas–liquid

1070-4272/01/7401-0170$25.00

Catalytic oxidation of hexafluoropropylene*

Catalyst, wt %	T, °C	HFP : O_2 molar ratio	Composition of reaction product, %				B	α
			HFP	HFA	COF_2	Freon 227	%	
50 KF	100	1 : 3	11.8	55.4	29.3	2.5	62.8	88.2
25 CsF	220	1 : 2	13.1	48.4	36.1	2.4	55.7	86.8
30 KF	180	1 : 1	7.8	51.9	37.9	2.4	56.3	92.2
10 RbF	250	1 : 7	19.2	44.6	31.7	4.5	55.1	80.7
5 NaF	300	1 : 10	17.5	45.2	32.5	4.8	54.7	82.4

* (B) yield of HFA based on converted HFP; (α) conversion.

chromatography. The individual components were recovered by low-temperature fractional distillation.

The components were identified by IR and NMR spectroscopy. The yield of HFA was 55–62%, and conversion, 90%.

CONCLUSIONS

(1) Procedure was developed for preparing hexafluoroacetone by catalytic oxidation of hexafluoropropylene using activated carbon promoted with alkali metal fluorides.

(2) The main reaction is accompanied by side oxidation of hexafluoropropylene to CO_2 and 1,1,1,2,3,-3,3-heptafluoropropane.

REFERENCES

1. JPN Patent 60-55 049.
2. JPN Patent 58-22 017.
3. JPN Patent 58-23 856.
4. Kurosaki, A. and Okazaki, S., *Chem. Lett.*, 1988, no. 1, p. 17.

Russian Journal of Applied Chemistry, Vol. 74, No. 1, 2001, pp. 172–174. Translated from Zhurnal Prikladnoi Khimii, Vol. 74, No. 1, 2001, pp. 166–168.

BRIEF COMMUNICATIONS

Evaporation of Sulfur-Lean Melts of the System Cu–Ni–S

A. I. Golov, G. P. Miroevskii, E. B. Koklyanov, S. I. Lopatin, L. Sh. Tsemekhman, L. A. Pavlinova, and L. N. Parshukova

Kola Mining and Smelting Company, Murmansk, Russia
St. Petersburg State University, St. Petersburg, Russia
Gipronikel' Institute, Joint-Stock Company, St. Petersburg, Russia

Received October 16, 2000

Abstract—Differential high-temperature mass spectrometry was applied to study evaporation in sulfur-lean melts of the systems Cu–S and Cu–Ni–S at 1500 K. Data on partial pressures and activities of melt components were obtained.

Presently, a new autogenous technology for processing of a nickel-containing copper concentrate obtained in converter matte separation is being developed and put into practice. This technology has to produce copper with the minimum possible (for this process) impurity content.[1] The behavior of basic impurities (nickel and sulfur) in this process is governed by the thermodynamic properties of the Cu–Ni–S system at Ni content in the range 0.5–50% and up to 21.0% sulfur.

Here we report the results obtained in studying evaporation processes in sulfur-lean melts of the system Cu–Ni–S at a temperature of 1500 K by differential high-temperature mass spectrometry.

The investigation was performed on an MS-1301 mass spectrometer which, including apparatus units for measurements by the Knudsen effusion method and mass-spectrometric analysis of the vapor phase, allows experimental determination of partial vapor pressures of melt components. In this work, the evaporation occurred from a double effusion cell made of molybdenum and calibrated by the calcium fluoride vapor pressure [1].

The set of studies of evaporation from Cu–Ni–S melts also included investigations of evaporation from sulfur-lean Cu–S melts and measurements of partial vapor component pressures over the Cu_2S melt. The latter was necessary since Cu_2S was used as pressure standard in studying Cu–S and Cu–Ni–S melts.

The system Cu–S has more than once been the object of study by various methods in varied temperature ranges [2–10].

A previously described technique [10, 11] was applied to measure the partial pressures of copper and sulfur over Cu_2S (pure grade) melt in the temperature range 1359–1500 K. As standard substance was used copper of M00k brand, with partial vapor pressure at 1500 K P^0_{Cu} = 0.364 Pa. The copper and sulfur vapor pressures over Cu_2S melt were measured in [10]. It was found that at 1500 K the vapor over a Cu_2S melt contains only atomic copper and diatomic sulfur molecules, whose partial pressures are practically constant (0.043 ± 0.02 and 0.15 ± 0.02 Pa, respectively), being in sufficiently good agreement with published data [12–14].

The temperature dependences of the partial pressures (Pa) of copper and sulfur in the temperature range 1390–1550 K are described by

$$\log p_{Cu} = 12.40 \pm 0.05 - (19\,300 \pm 730)/T, \qquad (1)$$

Table 1. Partials pressures of copper and sulfur over Cu–S melt at 1500 K

Melt composition, at. %		Partial pressures, Pa	
Cu	S	p_{Cu}	p_{S_2}
98.2	1.8	0.33	0.047
98.4	1.6	0.34	0.024
98.6	1.4	0.32	0.025
98.7	1.3	0.33	0.020
98.9	1.1	0.34	0.020
99.0	1.0	0.34	0.009
99.1	0.9	0.34	0.007

[1] Gipronikel' Institute, Joint-Stock Company and Severonikel' Combine, Joint-Stock Company (Kola Mining and Smelting Company).

1070-4272/01/7401-0172$25.00

$$\log p_{S_2} = 10.71 \pm 0.12 - (17\,300 \pm 530)/T. \quad (2)$$

A Cu_2S preparation was used as pressure standard in measuring the partial pressures of copper and sulfur over a copper melt containing in the initial state 2.2 at. % sulfur at 1500 K. The partial pressures measured in the course of evaporation of this sample are presented in Table 1.

Table 1 shows that in the course of evaporation the partial pressure of copper is virtually constant and equal to the partial pressure over Cu_2S, and the partial pressure of sulfur falls from 0.047 to 0.007 Pa with decreasing content of sulfur in the melt.

The dependence of the partial pressure of sulfur on the content of sulfur in the melt at 1500 K is shown in the figure.

Published data on the partial pressure of sulfur in the given range of compositions and temperatures are diverse. For example, a value of 0.001 Pa was presented in [14]. Schuhmann and Moles obtained for compositions in this range at a temperature of 1523 K a partial pressure of sulfur equal to 0.025 Pa [15].

High-temperature mass spectrometry can be used as a variety of the classical "vapor pressure method" in determining the thermodynamic activity. The basic equation of the method $a_i = p_i/p_i^0$ gives directly the a_i value as a ratio of ion currents. Since $p_i = bI_iT$ and $p_i^0 = bI_i^0T$, then

$$a_i = I_i/I_i^0, \quad (3)$$

where p_i and p_i^0 are the partial pressures of ith component, measured over a composition under study and pure component, and I_i and I_i^0 are the respective ion currents.

If pure copper (p_{Cu}^0 = 0.364 Pa) at the same temperature is taken as the standard state of copper, then the activity of copper in molten Cu_2S and Cu–S melt containing ca. 2 at. % S is approximately unity. If the state of sulfur in the Cu_2S melt is taken as standard, then the activity of sulfur in a Cu–S melt containing ca. 2 at. % S is 0.31 and falls to 0.05 with its content in the melt decreasing to 0.09 at. % S. It is noteworthy that, in going from melts containing ca. 30 at. % S to melts with ~2 at. % S, the activity of sulfur decreases from 1 to 0.3 and the activity coefficient of sulfur increases from 0.03 to 0.15.

The evaporation from Cu–Ni–S melts was studied on preparations containing (at. %) copper 92.7 and 90.6, nickel 4.9 and 4.8, and sulfur 2.4 and 4.6. The working temperature was 1500 K. The experimental results are presented in Table 2.

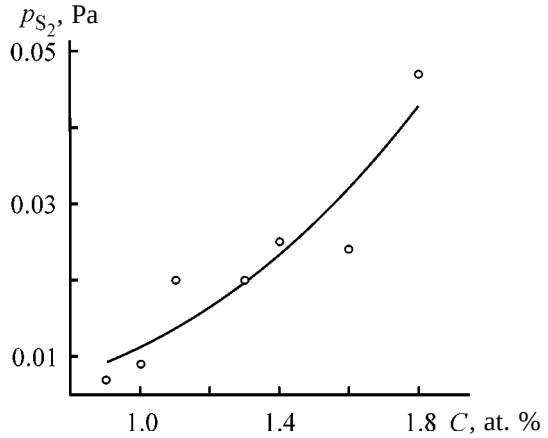

Partial pressure of sulfur p_{S_2} vs. content C of sulfur in the Cu–S melt.

Table 2 shows that the partial pressure of copper over melts is virtually constant, as also is the content of copper in the melt. The partial pressure of nickel over the melt at this temperature is $(0.4-0.5) \times 10^{-3}$ Pa, which is close to the detection limit of the

Table 2. Partial pressures of the components over Cu–Ni–S melt at 1500 K

Melt composition, at. %			Partial pressure, Pa		
Cu	Ni	S	p_{Cu}	$p_{Ni} \times 10^{-3}$	p_{S_2}
Sample no. 1					
90.4	7.5	2.1	0.320	~0.5	0.140
90.4	7.7	1.9	0.321	~0.5	0.149
90.4	7.9	1,7	0.332	~0.5	0.151
90.4	8.2	1.4	0.324	~0.5	0.156
90.3	8.5	1.2	0.339	~0.5	0.110
90.3	8.8	0.9	0.336	~0.5	0.095
89.9	9.5	0.6	0.338	~0.5	0.051
88.5	11.1	0.4	0.340	~0.5	0.020
Sample no. 2					
90.5	5.0	4.5	0.355	~0.4	0.153
90.5	5.1	4.4	0.345	~0.4	0.158
90.5	5.4	4.1	0.332	~0.4	0.164
90.5	5.6	3.9	0.332	~0.4	0.163
90.4	5.9	3.7	0.340	~0.4	0.158
90.4	6.2	3.4	0.386	~0.4	0.191
90.4	6.6	3.0	0.339	~0.4	0.162
90.4	7.0	2.6	0.360	~0.4	0.178
90.4	7.5	2.1	0.309	~0.4	0.138
90.4	8.2	1.4	0.315	~0.5	0.154
90.2	9.0	0.8	0.331	~0.5	0.084
89.5	10.0	0.5	0.308	~0.5	0.046
88.6	11.1	0.3	0.330	~0.5	0.025

measuring instrument. The partial pressure of sulfur depends on the content of sulfur in the melt, with this dependence expressed by the equation

$$p_{S_2} = -0.019[S]^2 + 0.12[S] - 0.0046. \quad (4)$$

The activity of copper in Cu–Ni–S melts is close to unity with the state of copper in Cu_2S ($p_{Cu\ in\ Cu_2S}$ = 0.34 Pa) as the standard state and somewhat less than unity if its state in metallic copper ($p_{Cu\ in\ Cu}$ = 0.364 Pa) is taken as the standard.

If the state of sulfur in Cu_2S (p_{S_2} = 0.15 Pa) is taken to be its standard state, then the activity of sulfur in the Cu–Ni–S melt decreases from about 1 to 0.1–0.2 with the content of sulfur in the melt decreasing from 4.5 to 0.3 at. %. In this case, the content of copper in the melt remains virtually constant, and that of nickel increases from 5.0 to 11.1 at. %.

REFERENCES

1. *Termodinamicheskie konstanty individual'nykh veshchestv: Spravochnik* (Thermodynamic Constants of Individual Substances: Reference Book), Glushko, V.P., Ed., Moscow: Nauka, 1978–1982, vols. 1–4.
2. Schuhmann, R. and Moles, O.W., *J. Met*., 1951, vol. 3, no. 3, pp. 139–146.
3. Rau, H., *Phys. Chem. Solids*, 1967, vol. 28, pp. 903–916.
4. Kellogg, H.H., *Can. Met. Quart*., 1969, vol. 8, no. 1, pp. 3–22.
5. Bale, C.W. and Toguri, J.M., *Can. Met. Quart*., 1976, vol. 15, no. 4, pp. 305–318.
6. Matousek, J.W. and Samis, C.S., *Trans. Met. Soc. Am. Inst. Met. Eng*., 1963, vol. 227, no. 4, pp. 980–985.
7. Nagamori, M. and Rosenquisn, T., *Met. Trans*., 1970, vol. 1, no. 1, pp. 329–330.
8. Jogannsen, F. and Spross, W., *Erzmetall*., 1961, vol. 14, no. 14, pp. 375–382.
9. Snurnikova, V.A., Bystrov, V.P., and Vanyukov, A.V., *Izv. Vyssh. Uchebn. Zaved., Tsvetn. Metall*., 1971, no. 6, pp. 34–36.
10. Golov, A.N., Miroevskii, G.P., Tsemekhman, L.Sh., *et al*., *Zh. Prikl. Khim*., 2000, vol. 73, no. 12, pp. 1936–1940.
11. Lopatin, S.I., Blatov, I.A., Kharlanov, A.S., *et al*., *Metally*, 1999, no. 5, pp. 33–35.
12. Kulikov, I.S., *Termicheskaya dissotsiatsiya soedinenii* (Thermal Dissociation of Compounds), Moscow: Metallurgiya, 1969.
13. Vanyukov, A.V., Isakova, R.A., and Bystrov, V.P., *Termicheskaya dissotsiatsiya sul'fidov metallov* (Thermal Dissociation of Metal Sulfides), Alma-Ata: Nauka Kaz. SSR, 1978.
14. Charma, R.C. and Chang, Y.A., *Met. Trans*., 1980, vol. 11B, no. 4, pp. 575–583.
15. Schuhmann, R. and Moles, O.W., *Trans. Am. Inst. Met. Eng*., 1951, vol. 191, no. 3, pp. 235–241.

Russian Journal of Applied Chemistry, Vol. 74, No. 1, 2001, pp. 175–177. Translated from Zhurnal Prikladnoi Khimii, Vol. 74, No. 1, 2001, pp. 169–171.

HISTORY OF CHEMISTRY AND CHEMICAL TECHNOLOGY

First Studies in the Field of Fixation of Atmospheric Nitrogen in Russia (Experiments of A.I. Gorbov and V.F. Mitkevich in 1906–1912)

The only sources of fixed nitrogen in the late XIX–early XX century were natural Chile saltpeter (sodium nitrate) and ammonia obtained in very limited amounts as a by-product of coal carbonization. Chile, a relatively small state, supplied saltpeter to, in fact, all the world's countries. No major deposits of saltpeter were known in any other region.

Chile saltpeter was used to manufacture nitric acid and served as fertilizer. A steady production of nitric acid in Russia was of interest for the Russian military. The agriculture needed fertilizers. The agrarian reforms started in 1906 gave rise to higher demand for fertilizers. For example, during the period from 1906 till 1912, the overall consumption of mineral fertilizers in Russia increased from 7.6 to 35.3 million poods (1 pood = 16 kg). The use of nitric fertilizers (Chile saltpeter) increased during the same period from 1.0 to 3.1 million poods, i.e., more than threefold [1]. The Russian–Japanese war demonstrated that, without domestic sources of fixed nitrogen, it is rather difficult to supply a sufficient amount of nitric acid to the industry of explosives.

It should be noted that, in addition to the gross expenditure for import of saltpeter, there were other factors stimulating the work aimed at obtaining nitric acid directly from atmospheric nitrogen. Russia received the whole amount of Chile saltpeter through its western boundary and Baltic ports. In case of military action in this region, a complete termination of saltpeter supply would be expected, which could deprive the armaments industry of the most important source of raw materials.

In December 1905, an interdepartmental Commission on the Problem of Obtaining Nitric Acid by Oxidation of Atmospheric Nitrogen was created at the Chief Engineering Department of the Ministry of Defense. The commission included staff members of the Artillery department: professors of the Mikhailovskaya Artillery Academy lieutenant-general G.A. Zabudskii (Chairman) and V.N. Ipat'ev, and colonels A.V. Sapozhnikov and N.M. Vittorf; Naval Department: P.P. Rubtsov and professor S.P. Vukolov,

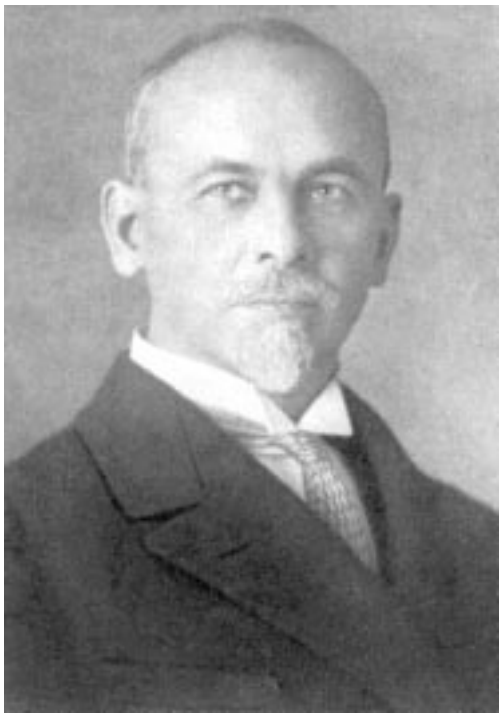

Vladimir Fedorovich Mitkevich

a known specialist in explosives; Ministry of Trade and Industry: professors N.S. Kurnakov and I.F. Shreder, prominent physical chemists, and professor V.F. Mitkevich, a specialist in electrical engineering; Chief Engineering Department: professor A.I. Gorbov, a chemist and initiator of commission's creation and its secretary [2, 3]. In its first meeting on February 14, 1906, the commission stated that "the Empire has no major deposits of saltpeter and, therefore, only manufacture of nitric acid from air is to be considered." Gorbov and Mitkevich were assigned to perform preliminary experiments in this direction.

Aleksandr Ivanovich Gorbov (1859–1939) graduated from the Natural Department of the Physicomathematical Faculty at St. Petersburg University in 1883. He was a pupil of A.M. Butlerov (1828–1886), who created the theory of structure of organic compounds, and a close friend of D.I. Mendeleev (1834–

1070-4272/01/7401-0175$25.00

1907). In 1883–1885, he worked at the University, and in 1885–1894, at the chemical laboratory of the St. Petersburg Academy of Sciences. Beginning in 1894, he taught at the Military Engineering Academy. Gorbov was a well-educated chemist and an active member of the Russian Physicochemical Society. His main scientific investigations were concerned with various problems of military technology. He also was one of the best-known popularizers of chemical science in the country [4–6]. Since 1926 and till the end of his life he had been Editor-in-Chief of *Zhurnal Prikladnoi Khimii* (Soviet Journal of Applied Chemistry) [7].

Vladimir Fedorovich Mitkevich (1872–1951), having graduated from the Physicomathematical Faculty of St. Petersburg University in 1895, taught electrical engineering and physics at higher school institutions in St. Petersburg and at the Electromechanical Department of the Polytechnic Institute beginning in 1902. He laid the groundwork of the course Theoretical Foundations of Electrical Engineering. In 1906, having backed his adjunct's dissertation, Mitkevich was elected a professor. During many years he held the chair of the fundamentals of electrical engineering, in 1927, he became a corresponding member, and in 1929, a full member of the Academy of Sciences of the USSR. Of exceptional importance are Mitkevich's studies concerned with the nature of electric arc, summarized in the monograph *O vol'tovoi duge* (On the Electric Arc). In 1907, he was awarded Popov Prize for these classical investigations [8–12].

At the end of the XIX century, William Crookes, the known English physicist and chemist, demonstrated experimentally that strong electric discharge in air may lead to oxidation of nitrogen to give nitric and nitrous acids. Further experiments revealed that 43.5 g of nitric acid per 1 kW h can be obtained in the oxidation of atmospheric nitrogen [2, 3]. Later, a yield of 60–75 g of HNO_3 per 1 kW h was achieved. In 1906, the first commercial installation for nitric acid production was constructed in Norway, a country rich in low-cost hydroelectric power. It is this method that Gorbov and Mitkevich became interested in.

Gorbov and Mitkevich studied the conditions for efficient production of nitrogen oxides and, in the end, nitric acid during several years. However, already in May 1906 the authors presented an original design of an arc furnace for fixing atmospheric nitrogen. The furnace design was patented in Russia, Norway, and Germany. Experiments were first done at the Mining Institute; later, M.A. Shatelen (1866–1957), the dean of the electromechanical department of the Polytechnic Institute, proposed to construct a pilot installation at the St. Petersburg Polytechnic Institute. Based on a vast experimental evidence, the authors established a clear dependence "...between the percentage of nitrogen oxide formed in burning of air under the action of an electric arc, volume of air introduced into the furnace during 1 h per kilowatt of electric arc power, and grams of nitric acid into which the nitrogen oxides can be converted..." In the authors' opinion, the equation had general character, being not related to any furnace design feature [13, 14].

Gorbov and Mitkevich established the influence of various factors on the efficiency of nitrogen fixing. In particular, it was found that the specific yield of the product per unit electric power expenditure decreases with increasing total power of the furnace. The possible reason was that zones with lower temperature appear in the furnaces, with reverse reactions occurring therein. The authors noted [14] that "...it is impossible to apply arbitrarily high power to a given furnace, and a power exists for this furnace of the maximum energy efficiency." Thus, it is necessary to find its own optimal process regimes for each furnace design. However, "it is important to have furnaces with as high power as possible, this making much simpler the monitoring of their correct operation" [14].

Eight furnaces were constructed for experiments, differing in the arrangement of electrodes, method of air supply, and design of condenser and combustion chamber. Two furnaces were single-phase, and the remaining six, three-phase. The power of seven furnaces was varied within 10–30 kW, and the eighth, three-phase furnace had power ranging from 60 to 220 kW. Special apparatus developed by the authors allowed monitoring of the process and variation of the experimental conditions.

Large-scale experiments were conducted under plant conditions at Sestroretsk, near St. Petersburg. The NO content of gases was on the average 2.44%, and the yield of nitric acid, 70.5 g per 1 kW h. In 1916, Gorbov and Mitkevich designed a 3000-kW furnace, and a plant started to be constructed at Kondopoga, on the northwestern bank of Lake Onega in Karelia. The site was chosen with account of the hydropower of River Suna flowing into Lake Onega. In 1918, the construction of the plant was suspended.

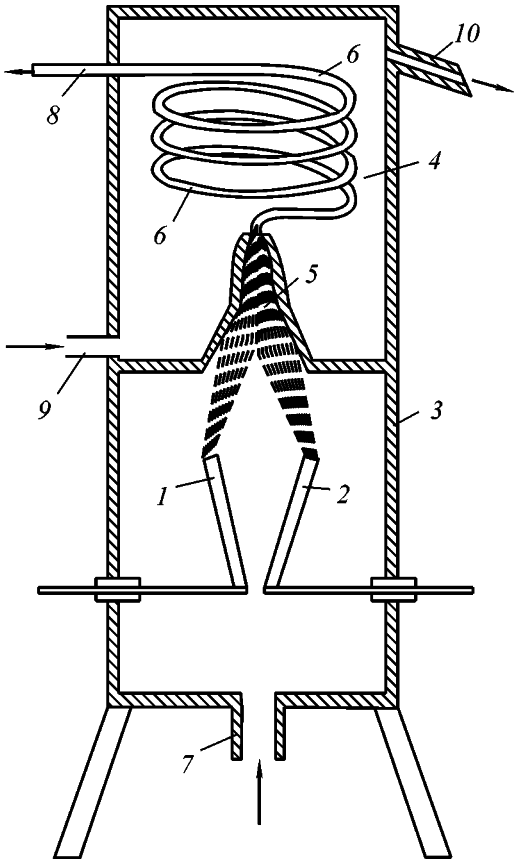

Gorbov and Mitkevich's furnace: (*1, 2*) electrodes creating the electric arc, (*3*) cylindrical furnace, (*4*) space for cooling water, (*5*) electric arc, (*6*) cooling coil for nitrogen oxides, (*7*) air inlet, (*8*) outlet for cooled nitrogen oxides, (*9*) pipe for supply of coil-cooling water, and (*10*) water outlet pipe.

REFERENCES

1. *Sel'sko-khozyaistvennyi promysel v Rossii* (Agriculture in Russia), Petrograd: Departament Zemledeliya, 1914.
2. Luk'yanov, P.M., *Tr. Inst. Istorii Estestvozn. Tekh*., 1960, vol. 30, pp. 307–332.
3. Sapozhnikov, A.V., *Azotnaya kislota iz vozdukha* (Obtaining Nitric Acid from Air), St. Petersburg, 1911.
4. Okatov, A.P., *Zh. Prikl. Khim.*, 1939, vol. 12, no. 6, pp. 795–801.
5. Mladentsev, M.N., *Priroda*, 1939, no. 12, pp. 114–115.
6. Arbuzov, A.E., *Izbrannye raboty po istorii khimii* (Selected Works on the History of Chemistry), Moscow: Nauka, 1975.
7. Morachevskii, A.G., *Zh. Prikl. Khim*., 1998, vol. 71, no. 1, pp. 3–6.
8. Mitkevich, V.F., *Izbrannye trudy* (Selected Works), Moscow: Akad. Nauk SSSR, 1956.
9. Shatelen, M.A., *Elektrichestvo*, 1947, no. 8, pp. 66–70.
10. Kalantarov, P.L. and Neiman, L.R., *Elektrichestvo*, 1947, no. 8, pp. 71–72.
11. Lebedinskii, V.K., *Elektrichestvo*, 1926, no. 10, pp. 416–417.
12. Kalantarov, P.L., *Elektrichestvo*, 1926, no. 10, pp. 417–418.
13. Gorbov, A.I. and Mitkevich, V.F., *Trudy 1-go Mendeleevskogo s"ezda po obshchei i prikladnoi khimii. Sankt-Peterburg, 20–30 dekabrya 1907 g.* (Proc. 1st Mendeleev Congr. on General and Applied Chemistry, St. Petersburg, December 20–30, 1907), St. Petersburg, 1909, pp. 268–275.
14. Gorbov, A.I. and Mitkevich, V.F., *Zh. Russk. Fiz.-Khim. O–va., Chast' Khim.*, 1913, vol. 45, part 2, pp. 1109–1136.

A. G. Morachevskii and V. V. Bashenko

Russian Journal of Applied Chemistry, Vol. 74, No. 2, 2001, pp. 179–183. Translated from Zhurnal Prikladnoi Khimii, Vol. 74, No. 2, 2001, pp. 177–181.

INORGANIC SYNTHESIS AND INDUSTRIAL INORGANIC CHEMISTRY

Formation of Nickel–Tantalum Compounds in NaCl–K_2TaF_7 Melts

E. S. Matychenko, O. A. Zalkind, V. Ya. Kuznetsov, V. M. Orlov, and S. L. Sukhorzhevskaya

Institute of Chemistry and Technology of Rare Elements and Mineral Raw Materials, Kola Scientific Center, Russian Academy of Sciences, Apatity, Russia

Received July 26, 2000

Abstract—The formation of nickel–tantalum compounds in halide fluorotantalate melts was studied at 750°C. The mechanism of electroless tantalum plating onto nickel is considered and it is suggested that disproportionation underlies the spontaneous transfer.

In electrolytic recovery of tantalum in a nickel crucible-cathode, the nickel impurity completely passes into the cathode deposit to form acid-resistant compounds [1]. Previously [2, 3], the behavior of nickel has been studied in salt mixtures containing 2.5 mol% K_2TaF_7, commonly used in electrolysis, and it has been found that electroless deposition of tantalum ions to form mainly the compound Ni_3Ta occurs at its surface. In view of the use of nickel in apparatus for metal-thermal production of high-capacity tantalum powders [4], it is of interest to study the interaction of nickel with a NaCl–K_2TaF_7 (14 mol %) melt having practical importance [5].

The aim of this study was to elucidate the mechanism of electroless tantalum plating onto nickel from halide melts containing K_2TaF_7, analyze the composition of nickel–tantalum intermetallic compounds in relation to their formation conditions, and obtain protective coatings on the nickel crucible walls directly in the process of obtaining sodium-reduced tantalum powders.

EXPERIMENTAL

The investigation was performed in a hermetically sealed steel retort in helium at 750°C. As a container for the melt served nickel or glassy carbon (SU 2000) crucible. Sodium chloride of special-purity grade was calcined in air at 600°C and melted in an atmosphere of pure helium. Potassium heptafluorotantalate was obtained from HF solutions and dehydrated by heating in a vacuum at 400°C. Working samples were cut-out from rolled nickel of 99.99% purity, treated with a mixture of HNO_3, H_2SO_4, and CH_3COOH acids, and washed with water and alcohol. The potential of the nickel plate was measured relative to a polished tantalum rod. Fusion cakes of salt mixtures were analyzed on an IK 20 IR spectrophotometer. X-ray patterns of the samples were taken on a DRON-2 diffractometer with graphite monochromator (Cu_{K_α} radiation, scan rate 2 deg min^{-1}, analysis depth ca. 1 μm). The highest peak in Figs. 1 and 2 is taken to be 100 on the relative intensity scale. Tantalum was determined in melts by X-ray fluorescence analysis with a SpaRK X-ray spectrometer (Ag anode, threshold sensitivity C_{th} = 0.001%, relative error 5–10%).

According to experimental data, the corrosion of nickel in chloride–fluorotantalate mixtures at 750°C was 2–5 g m^{-2} h^{-1}, depending on the sample exposure time, which contradicts the conclusions made in [6] about high corrosion resistance of the metal in a chloride melt with 4 mol % K_2TaF_7. The corrosion of nickel terminates when tantalum metal is introduced into a melt in the form of plates or a powder. Five intermetallic compounds exist in the Ni–Ta system: Ni_8Ta, Ni_3Ta, Ni_2Ta, NiTa, and $NiTa_2$ [7]. The compound Ni_3Ta, possessing the minimum Gibbs energy and having the highest growth rate constant as compared with the other phases, is the most stable [8]. It is this compound that was unambiguously identified on 350–400-μm-thick rolled nickel in melts containing 2.5 mol % K_2TaF_7 in those cases when two plates, of tantalum and nickel, were placed in the melt si-

1070-4272/01/7402-0179 $25.00 © 2001 MAIK "Nauka/Interperiodica"

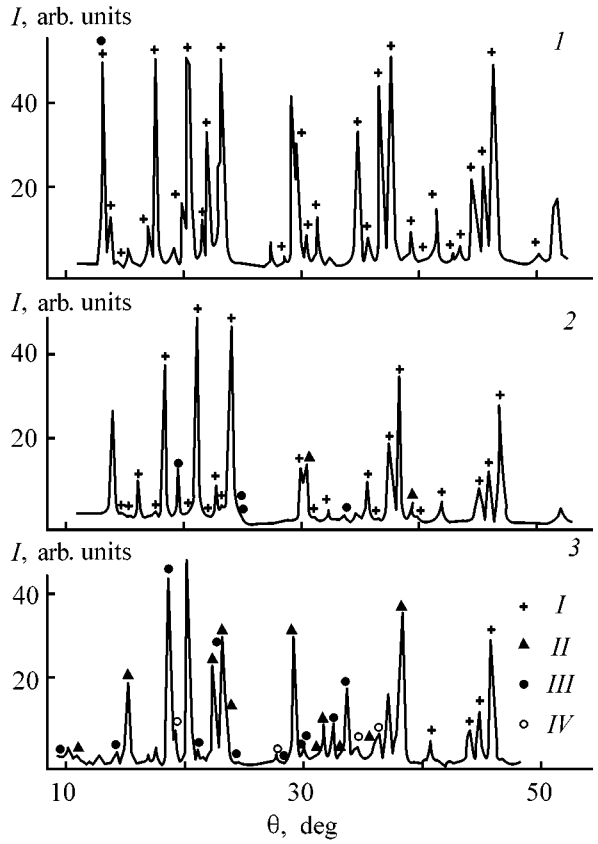

Fig. 1. X-ray diffraction patterns of nickel samples. (*I*) Relative intensity and (θ) Bragg angle; the same for Fig. 2. Background: 2KCl : KF (by weight) with 2.5 mol % K_2TaF_7, T = 750°C. (*1*) 350 μm rolled metal, (*2*) 50 μm foil, τ = 4 h, and (*3*) 50 μm foil, τ = 5 h. (*I*) Ni_3Ta, (*II*) Ni_2Ta, (*III*) NiTa, and (*IV*) Ta.

multaneously. The compound Ni_8Ta could not be detected in any of the numerous experiments. The pair—tantalum plate–50-μm-thick nickel foil—was used to obtain, at experiment duration of 4 h, coatings in which X-ray phase analysis (XPA) revealed, in addition to Ni_3Ta, two tantalum-richer intermetallic compounds, Ni_2Ta and $NiTa_2$ (Fig. 1, X-ray pattern no. *2*). Five hours after the beginning of an experiment, tantalum starts to be co-deposited together with the intermetallic compounds (Fig. 1, X-ray diffraction pattern no. *3*).

To obtain high-purity tantalum powders by the metal-thermal method, the time of formation of a protective coating on the nickel reactor walls should be the minimum possible. The metal loss from rolled tantalum about 500 μm thick at 750°C in a salt mixture NaCl–K_2TaF_7 (14 mol %) is approximately 380 g m^{-2} h^{-1} in the absence of nickel and becomes higher for the nickel–tantalum pair. Simultaneously, the concentration of tantalum in the melt grows. For example, introduction of a tantalum metal powder into the melt in amount of 5 or 10 wt % makes the tantalum concentration in the melt grow from 23.1 to, respectively, 24.1 or 25.4 wt % in 3 h. The rate of formation of surface diffusion alloys-coatings markedly increases since the introduction of a tantalum metal powder into the salt mixture immediately before an experiment rules out the possibility that the overall rate of electroless transfer of tantalum onto nickel is controlled by the first stage of the process—tantalum corrosion [9]. In NaCl–K_2TaF_7 (14 mol %) with 0.8 wt % dissolved tantalum powder, the mass of nickel samples increases already in the course of melting, and formation of intermetallic layers starts on their surface. During the time of experiments, including heating, melting, and keeping at 750°C for 15 min, protective layers are formed, composed, according to XPA, of a mixture of Ni_3Ta and tantalum-richer compound Ni_2Ta. This indicates that conditions more favorable for formation of protective coatings are created by the higher concentration of K_2TaF_7 in the melt and introduction of tantalum into the bath in the form of a metal powder. The maximum thickness of the obtained coatings was about 25 μm. On the whole, the process is controlled by the dynamic equilibrium

$$2Ni_3Ta + [Ta] \rightleftarrows 3Ni_2Ta, \quad \Delta G = -86.6 \text{ kJ g-at.}^{-1} \text{ Ta.} \quad (1)$$

However, no $NiTa_2$ compound or tantalum (foil thickness 50 μm) could be detected in dilute melts with 2.5 mol % K_2TaF_7 by XPA. The results of an analysis performed on an MS-46 Cameca X-ray microanalyzer of three samples with electroless coatings 18 to 23 μm thick demonstrate the same total content of tantalum in the range from 51.665 to 53.706 wt %, in agreement with XPA data. The phenomenon of electroless transfer is commonly associated with the presence in the melt of two charged species of a deposited metal [9]. In other words, disproportionation of tantalum ions underlies the spontaneous transfer of tantalum onto nickel.

Several studies of the mechanism of electrochemical reduction in the NaCl–KCl–K_2TaF_7 melt have been reported in the literature. Lantelme *et al.* [10] demonstrated that reduction of tantalum proceeds in a single reversible stage Ta(V) + 5e $\rightleftarrows$ Ta(0). The single-stage mechanism of tantalum discharge was confirmed by Kuznetsov [11] and Polyakova [12], but was identified as irreversible. The authors of [13, 14] allow for the presence of low-charge tantalum species in the molten mixtures and explain the formation of

carbides of high-melting metals by the disproportionation reaction.

The electrochemical behavior of tantalum was studied by linear and stationary voltammetry [10, 12] in chloride melts with low K_2TaF_7 concentration (0.04–0.25 mol %).

Chloride-fluorotantalate melts with high K_2TaF_7 content were chosen by the authors of the present study in view of the fact that salt melts with 2.5 and 14 mol % are of practical importance for obtaining tantalum powders by electrolysis and sodium-reduction. In addition, to make the formation of surface diffusion alloys-coatings faster, tantalum metal powder was added, directly in the course of the experiment, to the salt mixture before its being charged into the reactor, i.e., formation of low-charge compounds was promoted. When the content of tantalum powder introduced into the salt mixture prior to melting was raised to 5 wt % and more, XPA revealed the compound K_2TaCl_6 (Fig. 2), which points to the existence in the melt of two kinds of charged species in comparable amounts.

An IR spectral study demonstrated that the dissociation by the scheme

$$K_2TaF_7 \rightarrow KF + KTaF_6 \qquad (2)$$

becomes stronger with increasing content of tantalum metal in the chloride-fluorotantalate melt. The spectrum clearly shows a shift of the Ta–F absorption band from 535 (K_2TaF_7) to 545 cm^{-1} ($KTaF_6$), which is due to the fact that the Ta–F bond in the hexacoordinate complex becomes stronger because of the decreasing coordination number of tantalum ions (Fig. 3). This leads to the appearance of K^+ and F^- ions in the melt.

From the standpoint of the "autocomplex" model of the structure of molten alkali metal halides [15], the melting of an ionic crystal is accompanied by symmetry breakdown in the mutual arrangement of particles, resulting in that ion–dipole interaction is superimposed on the ion–ion interaction to give complexes. The role of a complexing agent in sodium chloride is played by the cation whose binding energy in the complex exceeds the cation energy in the second coordination sphere by 78 kJ mol^{-1}, i.e., complex ions $NaCl_4^{3-}$ are present in the starting chloride-fluorotantalate melt. The tendency of anions to form complexes becomes more pronounced with their increasing ionic moment and polarizability. The formal ionic moment ($1/r$, $Å^{-1}$) decreases in going from F^- to Cl^- (0.75–0.52), and the polarizability ($Å^3$) increases

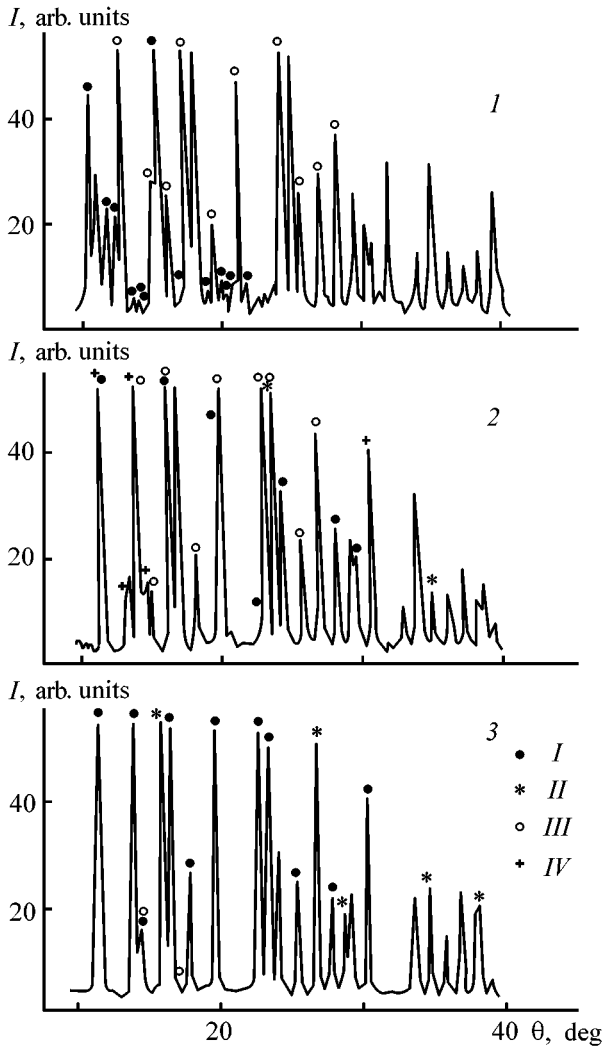

Fig. 2. X-ray pattern of a frozen melt. Background: NaCl–K_2TaF_7 (14 mol %) and tantalum metal (wt %): (*1*) 1.0, (*2*) 5.0, and (*3*) 10.0. (*I*) K_2TaF_7, (*II*) K_2TaCl_6, (*III*) K_3TaClF_7, and (*IV*) $KTaF_6$ (14 mol %).

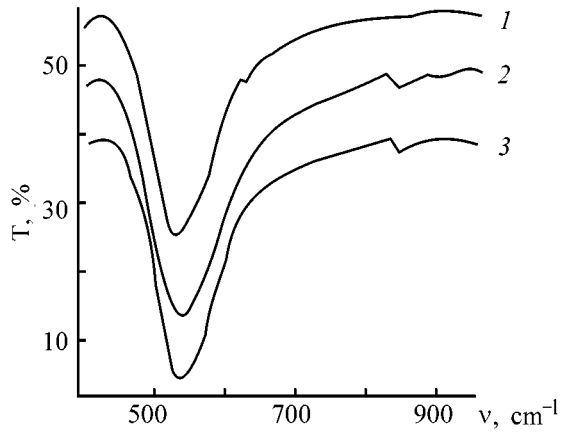

Fig. 3. IR spectra of potassium fluorotantalate in NaCl–K_2TaF_7 melt (14 mol %). (T) Transmission and (ν) wave number. Content of Ta metal powder (wt %): (*1*) 1.0, (*2*) 5.0, and (*3*) 10.0.

(0.64–2.96). As a result, the binding energy grows in passing from chloride to fluoride complexes because of a pronounced increase in their ionic momentum. Fluoride ions gradually replace chloride ions in autocomplexes, which leads to the appearance of free Cl^- ions in the melt. Fluoride complex compounds are formed in mixed chloride-fluoride melts at a relative excess of fluoride ions [16]. It is noteworthy that the amount of fluoride ions formed by reaction (2) in salt mixtures NaCl–K_2TaF_7 is negligible, compared with the content of chloride ions in the melt. Hence, the detection of just the chloride complex of a low-charge tantalum compound, K_2TaCl_6, by XPA in chloride-fluorotantalate melts with addition of up to 5 wt % tantalum metal and more is a well-established fact. The presence of potassium ions in the second coordination sphere of the tantalum(IV) complex K_2TaCl_6 cannot be accounted for in terms of the ion–ion interaction, since the ionic moment of K(I) is less than that of K(I). However, from the standpoint of the ion–dipole interaction, the potassium cation is more competitive since its polarizability exceeds that of the sodium cation [17]: $\alpha \times 10^{24}$ is 1.012 for K(I) at 800°C and 0.281 for Na(I). Probably, the ion–dipole interaction plays a key role in the case of formation of the K_2TaCl_6 compound.

The chemical reaction of tantalum(IV) compound formation can be written as follows

$$4K_2TaF_7 + Ta + 30NaCl + 2KF \rightarrow 5K_2TaCl_6 + 30NaF. \quad (3)$$

A calculation of the Gibbs energy of reaction (3) from reference data by the first Kireev method [18] demonstrated that the occurrence of this reaction is unlikely (ΔG_{298} = +853 kJ mol^{-1}). It becomes possible only in the simultaneous presence in the melt of the pair tantalum–nickel, when intermetallic compounds are formed on the nickel surface; ΔG = –118 kJ mol^{-1} for Ni_3Ta and –107.7 kJ mol^{-1} for Ni_2Ta [8]. This conclusion is confirmed by experiment: the compound K_2TaCl_6 (XPA data) and a shift of the equilibrium (2) (IR spectral data) are only observed on raising the content of tantalum metal powder to more than 5 wt % in the presence of a nickel plate. It is noteworthy that the reduction of tantalum pentachloride to tetrachloride $TaCl_4$ by tantalum foil has long been known [19].

The tantalum oxidation level was calculated using the corrosion current densities i (A cm^{-2}) obtained on shorting the external circuit of the electrodes with small resistances [3], by the formula [20]

$$i = \frac{K\bar{m}nF}{1000A} = Km\frac{n}{A}2.68 \times 10^{-3}, \quad (4)$$

where $K\bar{m}$ is the loss of Ta (g m^{-2} h^{-1}), n is the Ta oxidation level, F is the Faraday constant (A h g-equiv^{-1}), and A is the atomic weight of Ta.

At a current density of 0.003 A cm^{-2} and one-hour Ta loss of 50 g m^{-2} h^{-1} in a melt with 2.5 mol % K_2TaF_7, the lowest oxidation level of Ta was approximately +4.

The concentration gradient of potential-determining ions in various states of oxidation are the driving forces of the ion transfer occurring via diffusion at the electrodes and convection in the electrolyte bulk. Ions of the reduced form diffuse (j_{red}) from pure tantalum, where their concentration is higher, toward the alloy, where their concentration is lower, and disturb the equilibrium ratio of ions $[Ta^{4+}]/[Ta^{5+}]$ at the alloy surface. For the equilibrium to be restored, a reaction must occur, lowering the Ta^{4+} concentration at the surface of the positive nickel electrode. Nickel reacts with tantalum to give a surface alloy

$$3Ni + 2Ta^{4+} \rightarrow Ta^{5+} + Ni_3Ta. \quad (5)$$

Ta^{5+} ions with higher oxidation level, formed by reaction (5), diffuse toward the electrode made of pure tantalum, which, in turn, disturbs the equilibrium ratio of tantalum ions $[Ta^{4+}]/[Ta^{5+}]$ at its surface, creating an excess of Ta^{5+} ions. The response of the Ta/$[Ta^{4+}]$ system to the disturbing action of the j_{ox} flow has the form of the tantalum dissolution reaction to give ions of the reduced form Ta^{4+}, after which these ions again start their motion along the gradient toward the alloy. Thus, the transfer process is closed into the cycle occurring by the scheme [9].

$$Ta \left| \begin{array}{c} \nearrow [Ta^{4+}] \xrightarrow{j_{red}} [Ta^{4+}] \searrow \\ [Ta^{5+}] \xleftarrow{j_{ox}} [Ta^{5+}] \end{array} \right| Ni_3Ta \left| Ni \right.$$

CONCLUSIONS

(1) The composition of nickel–tantalum intermetallic compounds in chloride-fluorotantalate melts depends on the K_2TaF_7 concentration in the melt, amount of tantalum metal added to the melt, thickness of the nickel substrate, and experiment duration. In melts with high content of K_2TaF_7 (14 mol %), introduction of tantalum powder in amounts of ca. 1 wt % and more leads to faster formation of protective coatings on nickel. It follows from experiments that the nickel reactor walls are covered with Ni_3Ta and Ni_2Ta compounds.

(2) The compound K_2TaCl_6 was found in NaCl–K_2TaF_7 melts (14 wt %) upon introduction of tantalum powder in amounts of 5 wt % and more. A conclusion is made that the formation of surface intermetallic compounds is due to the disproportionation reaction. IR spectroscopy reveals the growing share of dissociation by scheme (2).

(3) The surface alloy is formed by reaction (5).

(4) The results of the study made it possible to obtain directly in the course of sodium-reduction tantalum powders with low content of nickel impurity.

REFERENCES

1. Konstantinov, V.I., *Elektroliticheskoe poluchenie tantala, niobiya i ikh splavov* (Electrolytic Production of Tantalum, Niobium, and Their Alloys), Moscow: Metallurgiya, 1977.
2. Matychenko, E. and Novichkov, V., *Proc. NATO Advanced Research Workshop "Refractory Metals in Molten Salts. Their Chemistry, Electrochemistry Technology,"* Dordrecht: Kluwer Acad. Publ., 1998, pp. 205–210.
3. Matychenko, E.S. and Novichkov, V.Yu., *Zashch. Met.*, 1999, no. 1, pp. 57–60.
4. US Patent 5 234 491.
5. Belyaev, K.Yu., Orlov, V.M., Prokhorova, T.Yu., and Miroshnichenko, M.N., *Abstr. NATO Advanced Research Workshop "Refractory Metals in Molten Salts. Their Chemistry, Electrochemistry Technology,"* Apatity, 1997, p. 112.
6. Kartsev, V.E., Kovalev, F.V., and Kazain, A.A., *Tsvetn. Met.*, 1993, no. 4, pp. 37–44.
7. Nash, A. and Nash, P., *Bull. Alloy Phase Diagr.*, 1984, vol. 5, no. 3, pp. 259–271.
8. Taxil, P., *J. Less-Common Met.*, 1985, vol. 113, p. 89.
9. Ilyushchenko, N.G., Anfinogenov, A.I., and Shurov, N.I., *Vzaimodeistvie metallov v ionnykh raspla-vakh* (Interaction of Metals in Ionic Melts), Moscow: Nauka, 1991.
10. Lantelme, F., Barhoun, A., Li, G., and Becce, J.P., *J. Electrochem. Soc.*, 1992, vol. 139, no. 5, pp. 1249–1255.
11. Kuznetsov, S.A., Glagolevskaya, A.L., and Belyaevskii, A.T., *Zh. Prikl. Khim.*, 1994, vol. 67, no. 7, pp. 1093–1099.
12. Polyakova, L.P., Kononova, Z.A., Kremenetskii, V.G., and Polyakov, E.G., *Zh. Prikl. Khim.*, 1996, vol. 69, no. 8, pp. 1307–1313.
13. Oki, T. and Tanikawa, J., *Proc. First Int. Symp. on Molten Salt Chem. Technol., April 20–22, 1983*, Kyoto, Japan, 1983, pp. 265–269.
14. Kuznetsov, S.A., Glagolevskaya, A.L., Kuznetsova, S.V., *et al., Zh. Prikl. Khim.*, 1990, vol. 63, no. 9, pp. 2078–2080.
15. Smirnov, M.V., Shabanov, O.M., and Khaimenov, A.P., *Elektrokhimiya*, 1996, vol. 32, no. 11, pp. 1240–1248.
16. Smirnov, M.V., *Elektrodnye potentsialy v rasplavlennykh khloridakh* (Electrode Potentials in Molten Chlorides), Moscow, 1973.
17. Kochedykov, V.A. and Khokhlov, V.A., *Rasplavy*, 1994, no. 5, pp. 38–43.
18. Ruzinov, L.P. and Gulyanitskii, B.S., *Ravnovesnye prevrashcheniya metallurgicheskikh reaktsii* (Equilibrium Transformations of Metallurgical Reactions), Moscow: Metallurgiya, 1975.
19. Fairbrother, F., *The Chemistry of Niobium and Tantalum*, Amsterdam: Elsevier, 1967.
20. Zhuk, N.P., *Kurs teorii korrozii i zashchity metallov* (A Theory of Corrosion and Metal Protection), Moscow: Metallurgiya, 1976.

Russian Journal of Applied Chemistry, Vol. 74, No. 2, 2001, pp. 184–187. Translated from Zhurnal Prikladnoi Khimii, Vol. 74, No. 2, 2001, pp. 181–185.

INORGANIC SYNTHESIS AND INDUSTRIAL INORGANIC CHEMISTRY

A New Technique for Synthesis of Nordstrandite

V. A. Lipin

All-Russia Aluminum-Magnesium Institute, St. Petersburg, Russia

Received June 19, 2000; in final form, November 2000

Abstract—Basic physicochemical characteristics of aluminum trihydroxide prepared for the first time by carbonization in the form of nordstrandite are described. Silicon-containing complexes present in the solution being carbonized act as stabilizers of the nordstrandite structure in the course of hydroxide precipitation from aluminate solutions.

Nordstrandite, synthesized in 1956 by Robert van Nordstrand, a known chemist, and named after him, is, together with bayerite, gibbsite, and doyleite, a polymorphic modification of aluminum hydroxide $Al(OH)_3$ [1–3]. Nordstrandite occurs in nature in eroded rocks, in association with carbonates, and in a number of bauxite ores [2–6].

A specific feature of thermal dehydration of nordstrandite is the formation of η-Al_2O_3 possessing a special type of crystal lattice defects and exhibiting thermal stability, which allows its use as a starting material in production of supports of catalysts for dehydration, isomerization, reforming, and some other catalytic processes [6, 7].

Synthesizing artificial nordstrandite involves certain technological difficulties. It can be obtained from X-ray-amorphous aluminum hydroxide by keeping ("aging") it in the presence of chelate-forming agents (ethylenediamine, ethylene glycol) under the conditions in which bayerite would be produced in the absence of these reagents. Also, nordstrandite mixed with bayerite can be obtained in reaction of aqueous solutions of aluminum with ammonium hydroxide, with subsequent many-day keeping at pH 7.5–13.0 [7, 8]. The complexity and long duration of synthesis hinder large-tonnage production of nordstrandite by conventional methods and restrain its practical use.

Nordstrandite described in this communication was for the first time obtained by carbonization from aluminate solutions produced in manufacture of alumina. The mechanism of the carbonization process is not completely clear despite numerous investigations. The reaction of aluminate solutions with carbon dioxide onsets at pH > 13 because of the excess of alkali in solution. Then, on introducing CO_2 into the solution, the pH decreases. With account of the modern concepts, the occurring reactions can be represented as

$$CO_2 + 2OH^- = CO_3^{2-} + H_2O, \quad (1)$$

$$[Al(OH)_4]^- + H_3O^+ = AlOOH + 3H_2O, \quad (2)$$

$$AlOOH + OH^- + H_2O = [Al(OH)_4]^-, \quad (3)$$

$$[Al(OH)_4]^- = Al(OH)_3 + OH^-, \quad (4)$$

$$CO_2 + 2H_2O = H_3O^+ + HCO_3^-, \quad (5)$$

$$2AlOOH + 2(Na, K)^+ + 2HCO_3^- = (Na, K)_2O \cdot Al_2O_3 \cdot 2CO_2 \cdot 2H_2O. \quad (6)$$

In processing aluminum-containing raw materials into alumina and other products, aluminum hydroxide is prepared in such a way that it should be obtained in the form of gibbsite. In addition, bayerite, pseudoboehmite, hydroaluminocarbonates of alkali metals (HAC), and X-ray-amorphous modification of these materials can be obtained under certain carbonization conditions [1]. Theoretical prerequisites for obtaining nordstrandite by carbonization of aluminate solutions had existed before [9], but have not been confirmed by practice.

The carbonization conditions were chosen in view of the specific features of nordstrandite formation in nature. A condition favoring nordstrandite formation is, as a rule, decomposition of basalt by weakly alkaline solutions via the compounds aluminohy-

1070-4272/01/7402-0184 $25.00 © 2001 MAIK "Nauka/Interperiodica"

Table 1. Effect of aluminate solution decomposition conditions on the chemical and phase composition of the precipitate [Composition of the starting solution (g dm^{-3}): R_2O_t 91.5, R_2O_c 74.8, Al_2O_3 84.5, SiO_2 1.46]

Carbonization conditions		Content in solution obtained, g dm^{-3}					Content in precipitate obtained, g dm^{-3}				Main phases in the precipitate
T, °C	τ, h	R_2O_t	R_2O_c	Al_2O_3	SiO_2	$NaHCO_3$	Al_2O_3	Fe_2O_3	SiO_2	R_2O	
50	5.5	92.5	88.4	0.21	0.026	11.1	63.4	0.03	1.50	0.91	Bayerite
50	8.5	93.5	84.5	–	0.005	23.6	62.9	0.04	1.60	1.17	Bayerite, gibbsite
70	2.0	93.0	87.1	–	0.010	16.0	63.2	0.03	1.78	1.62	Bayerite, HAC
70	4.5	92.8	88.3	0.05	0.025	12.1	63.4	0.03	1.85	1.28	Bayerite, gibbsite, HAC
70	6.0	92.4	92.4	0.56	0.042	0	62.0	0.03	1.60	0.97	Nordstrandite
80	2.5	93.1	83.8	–	0.005	25.3	60.3	0.03	1.40	1.32	Gibbsite, nordstrandite, HAC
80	2.5	93.0	87.9	0.01	0.025	13.7	63.1	0.01	1.76	1.46	Gibbsite, bayerite, HAC
80	4.0	93.1	84.4	–	0.004	23.6	63.3	0.03	1.89	1.32	Gibbsite, HAC

drocalcite $CaO \cdot Al_2O_3 \cdot 2CO_2 \cdot 5H_2O$ or dawsonite $(Na, K)_2O \cdot Al_2O_3 \cdot 2CO_2 \cdot 2H_2O$. Since nordstrandite is mainly formed in the presence of silicon-containing mineral compounds, aluminate solutions with increased, with respect to that in alumina production solutions, content of silicon were subjected to carbonization.

Nondesiliconized aluminate solutions produced in leaching of nepheline cake were used in experiments [10]. The carbonization was done with diluted carbon dioxide (16–25% CO_2) to pH 11.0–11.3. The formed solid phases and filtrates were separated on a Schott filter, with the precipitates washed with water at 30°C and analyzed for the content of main component gravimetrically and by the volumetric and photometric methods. The concentration of the "carbonate alkali" (R_2O_{cb}) in aluminate solutions, stoichiometrically proportional to the amount of CO_3^{2-} ions present in solution, was calculated in terms of sodium oxide as the difference between the "total" (R_2O_t) and "caustic" (R_2O_c) alkalis. The total and caustic alkalis were determined using titration by conventional techniques adopted in the alumina industry.

The granulometric composition of the obtained phases was determined with a SILAS laser granulometer. Crystal-optical measurements and microphotography were done with a COMIBAX microscope. The phase composition of the precipitates was determined by X-ray phase analysis and IR spectroscopy. X-ray patterns were taken on a Philips automated powder diffractometer with Cu_{K_α} radiation and graphite monochromator. IR spectra were obtained with a Perkin–Elmer spectrometer in the wave number range 400–3800 cm^{-1}. Samples for measurements were prepared by compaction of pellets with KBr. The solution pH was determined with an EV-74 ion meter.

The results obtained in carbonization of nondesiliconized aluminate solutions are presented in Table 1.

It follows from the data in Table 1 that a number of conditions is to be met for aluminum hydroxide to be formed as nordstrandite, including a temperature of 60–75°C and presence of a silica-containing phase in a solution being carbonized. In all probability, it is silica that stabilizes nordstrandite in the course of carbonization in a transition from metastable to crystalline phases. In the absence of silica in a solution being carbonized, all other conditions being the same, there occurs precipitation of the following phases conventional for the alumina production: gibbsite, bayerite, or aluminocarbonates of alkali metals [1].

Crystal-optical studies demonstrated the presence of finely crystalline aggregates of nearly radial-beam structure (Fig. 1). Inside the aggregates, there are point inclusions of the silicate phase. Nordstrandite has the following refractive indices of the crystalline phase: $\alpha = 1.582(1)$, $\beta = 1.582(1)$, $\gamma = 1.586(1)$.

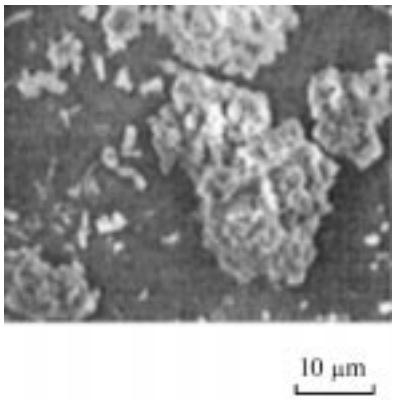

Fig. 1. Micrograph of nordstrandite sample obtained by carbonization of an aluminate solution.

Table 2. Comparative table of interplanar spacings and relative line intensities for nordstrandite

Nordstrandite synthesized by carbonization		Number of reference in ASTM file							
		24-6-97		15-141-96		12-401-96		18-31-96	
d, Å	*I*, rel. units	*d*, Å	*I*, rel. units	*d*, Å	*I*, rel. units	*d*, Å	*I*, rel. units	*d*, Å	*I*, rel. units
4.794	100	4.790	100	4.789	100	4.790	100	4.790	100
4.332	23	4.320	25	4.322	12	4.330	20	4.330	25
4.220	11	4.210	18	4.207	10	4.200	15	4.220	25
4.171	17	4.160	12	4.156	8	4.150	13	4.160	20
3.891	8	3.890	12	3.887	4	3.890	7	3.896	15
3.611	8	3.610	8	3.600	4	3.600	7	3.601	10
3.425	6	3.430	6	3.429	4	–	–	3.446	10
3.038	7	3.030	4	3.022	2	–	–	3.022	15
2.988	5	–	–	–	–	–	–	–	–
2.853	2	2.848	4	2.850	2	–	–	2.867	5
2.766	3	–	–	–	–	–	–	–	–
2.702	1	2.710	2	2.704	2	–	–	–	–
2.699	2	–	–	2.663	1	–	–	–	–
2.501	3	2.501	2	2.497	1	–	–	–	–
2.485	6	2.480	12	2.480	4	–	–	2.481	15
2.458	12	2.455	8	2.450	2	–	–	2.454	10
2.392	31	2.393	25	2.392	10	2.390	15	2.393	35
2.270	29	2.271	30	2.263	16	2.260	15	2.265	35
2.225	6	2.217	4	–	–	–	–	–	–
2.074	2	2.074	4	2.074	2	–	–	–	–
2.040	8	–	–	2.033	1	–	–	–	–
2.017	28	2.016	25	2.016	8	2.010	11	2.015	30
2.000	5	1.991	2	–	–	–	–	–	–
1.945	2	1.945	6	1.943	1	–	–	–	–
1.918	4	–	–	–	–	–	–	–	–
1.903	23	1.902	20	1.901	8	1.898	11	1.904	20
1.888	6	–	–	1.880	1	–	–	–	–
1.804	4	1.804	4	–	–	–	–	–	–
1.786	18	1.784	14	1.781	6	–	–	–	–
1.771	3	–	–	–	–	–	–	–	–
1.720	3	–	–	–	–	–	–	–	–
1.702	2	–	–	–	–	–	–	–	–
1.671	3	1.668	4	1.672	2	–	–	–	–
1.652	3	1.653	4	–	–	–	–	–	–
1.599	4	1.598	6	1.595	2	–	–	1.595	10
1.572	4	1.572	4	–	–	–	–	–	–
1.551	6	1.547	6	–	–	–	–	–	–
1.516	7	–	–	1.513	4	–	–	1.513	10
1.478	6	–	–	1.477	4	–	–	1.478	10
1.441	15	–	–	1.439	4	–	–	1.440	20
1.430	7	–	–	1.427	2	–	–	1.431	5
1.402	2	–	–	1.404	2	–	–	1.403	10
1.386	1	–	–	1.404	2	–	–	1.403	10
1.356	2	–	–	–	–	–	–	–	–

An IR spectrum of nordstrandite obtained by carbonization of a nondesiliconized solution is shown in Fig. 2. In the positions of the main bands, the spectrum is close to the spectra of both the natural mineral [2, 3] and synthetic nordstrandite samples prepared by other methods [7, 8]. The spectrum shows high intensity of stretching vibrations of OH^- groups in water molecules (3300–3700 cm^{-1}), deformation vibrations

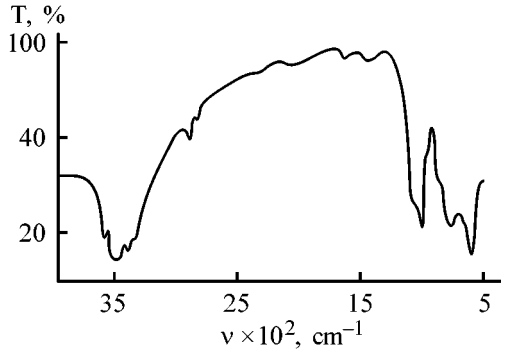

Fig. 2. IR spectrum of nordstrandite obtained by carbonization of an aluminate solution. (T) Transmission and (ν) wave number.

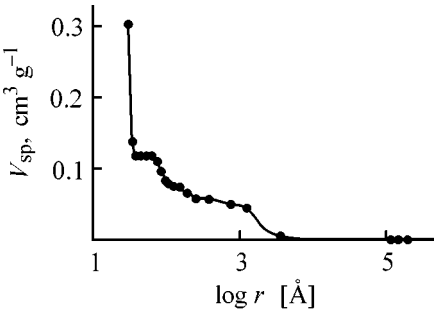

Fig 3. Integral porogram of aluminum oxide obtained by nordstrandite calcination at 550°C. (V_{sp}) Specific pore volume and (r) equivalent pore radius.

of OH^- groups (700–1100 cm^{-1}) and vibrations of the Al–O group (around 500 cm^{-1}).

An X-ray phase analysis of samples obtained by carbonization revealed virtual coincidence of the interplanar spacings and relative intensities of the obtained nordstrandite with the respective reference parameters in the ASTM file (Table 2).

The granulometric composition of nordstrandite was as follows:

d_{av}, μm	N, %
0–6	1.0–3.5
+6–12	0.7–4.9
+12–16	3.6–6.1
+16–24	36.7–44.7
+24–32	25.8–30.9
+32–48	15.4–29.7
+48	1.3–2.6

The average particle diameter is 24.6 μm. A specific feature of the obtained nordstrandite is that it has a monogranulometric composition and 80–95% of the material is constituted by particles 16–48 μm in size.

The porous structure of aluminum oxide prepared from nordstrandite produced by carbonization was studied by mercury porosimetry. A nordstrandite sample was heated at 550°C for 6 h. The measurements were done on a mercury porosimetric setup comprising high- and low-pressure porosimeters [11].

It follows from the obtained integral porogram, plotted in the coordinates pore volume–logarithm of equivalent pore radius (Fig. 3), that mesopores are predominant in the material under study. This is in agreement with the data of [6]. The high values of the average pore volume (0.60–0.67 $cm^3\ g^{-1}$), obtained in [7], were not observed in aluminum oxides prepared from nordstrandite.

CONCLUSIONS

(1) Nordstrandite was for the first time synthesized by carbonization and its basic characteristics are described. No significant difference in physicochemical properties between this kind of nordstrandite and that obtained by the conventional techniques was revealed.

(2) The experimentally confirmed possibility of obtaining nordstrandite by carbonization allows a substantial reduction in the price of the product and thereby expands the range of its practical use.

REFERENCES

1. Khanamirova, A.A., *Glinozem i puti umen'sheniya soderzhaniya v nem primesei* (Alumina and Ways To Reduce Its Impurity Content), Erevan: Akad. Nauk ArmSSR, 1983.
2. Chao, G.Y., Baker, J., Sabina, A.P., and Roberts, A.C., *Canad. Mineralogist*, 1985, vol. 23, no. 1, pp. 21–28.
3. Chao, G.Y. and Baker, J., *Canad. Mineralogist*, 1982, vol. 20, no. 3, pp. 77–85.
4. Saalfeld, H. and Jarchow, O., *Neues Jahrb. Mineral. Abh.*, 1968, vol. 109, no. 3. 185–191.
5. Novikov, V.M., Berkhin, S.I., Vitovskaya, I.V., *et al.*, *Problemy genezisa boksitov* (Problems of Genesis of Bauxites), Moscow: Nauka, 1975, pp. 257–265.
6. Benes, L., Stoica, L., Nicolescu, A., and Dardan, M., *Rev. Roum. Phys.*, 1966, vol. 11, no. 6, pp. 489–497.
7. US Patent 3328122.
8. Aldcroft, D. and Bye, G.C., *Sci. Ceramics*, 1967, vol. 3, no. 2, pp. 75–94.
9. Kulikova, G.V., Tsekhovol'skaya, D.I., and Shitov, V.A., *Dokl. Akad. Nauk SSSR*, 1974, vol. 217, no. 1, pp. 190–194.
10. Lipin, V.A., *Tsvetn. Met.*, 1998, no. 7, pp. 40–43.
11. *Tekhnologiya katalizatorov* (Technology of Catalysts), Mukhlenov, I.P., Ed., Leningrad: Khimiya, 1979.

Russian Journal of Applied Chemistry, Vol. 74, No. 2, 2001, pp. 188–192. Translated from Zhurnal Prikladnoi Khimii, Vol. 74, No. 2, 2001, pp. 186–190.

PHYSICOCHEMICAL STUDIES OF SYSTEMS AND PROCESSES

Polymorphism of Micelles in Aqueous Cetyltrimethylammonium Bromide Solutions

Chunsheng Mo and N. N. Kochurova

Research Institute of Chemistry, St. Petersburg State University, St. Petersburg, Russia

Received August 9, 1999; in final form, January 2000

Abstract—A viscometric study was made of the polymorphous transformation of micelles in an aqueous solution of cetyltrimethylammonium bromide in the presence of NaBr and sodium methylbenzenesulfonate. The effects of temperature and nature and concentration of additives on the second critical micelle concentration were studied. The thermodynamic characteristics of the micellar transition are estimated.

It is well known that inorganic electrolytes and polar organic compounds have a considerable effect on the physicochemical characteristics of aqueous solutions of ionic surfactants. Most clearly this effect is reflected in the viscosity of a micellar solution [1]. It has been demonstrated experimentally that small spherical micelles formed at the first critical micelle concentration (CMC_1) may transform into cylindrical micelles with increasing surfactant concentration or as a result of addition of polar compounds. Such a transformation results in higher viscosity of the solution and changes other thermodynamic characteristics. The use of certain organic electrolytes, such as benzenesulfonates, salicylates, etc., as additives to an aqueous surfactant solution allows preparation of highly viscous fluids, semisolid pastes, or gels. This phenomenon is widely used in pharmaceutical, food, and cosmetics industries, environmental protection, etc. Therefore, studying the indicated polymorphism is of considerable practical importance.

The asymmetrization of spherical micelles and the viscoelastic properties of aqueous solutions of cetyltrimethylammonium bromide (CTAB) in the presence of various additives have been studied extensively [2–13]. However, systems with low additive concentrations were considered in most of these works. Data on the thermodynamic characteristics of such systems are very scarce.

In this communication, we report the effects of the CTAB concentration and temperature on the polymorphism in dilute aqueous solutions of CTAB at relatively high NaBr concentrations (0.2 and 0.4 M) and in the presence of an organic additive, sodium methylbenzenesulfonate (NaMBS). The activation energy of viscous flow is estimated.

EXPERIMENTAL

As a surfactant we used CTAB (analytically pure grade) multiply recrystallized from a mixture of acetone and methanol (19 : 1). As the criterion of high quality served the absence of a minimum in the surface tension isotherm.

Sodium bromide and *p*-methylbenzenesulfonate (both of analytically pure grade) were used without further purification.

The viscosities at 30, 35, 40, 45, and 50°C were measured by capillary viscometry with an Ubbelohde viscometer on an experimental setup described in [14]. The dynamic viscosity η (Pa s) was determined from the outflow time of water and the solutions, using reference data on the viscosity of water.

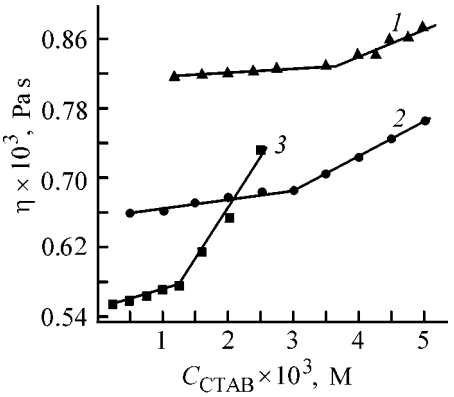

Fig. 1. Dynamic viscosity η of CTAB micellar solutions vs. the CTAB concentration $C_{CTAB} \times 10^3$ in the presence of various additives. Additive (M): (*1*) 0.2 NaBr, (*2*) 0.4 NaBr, and (*3*) 0.025 NaMBS. Temperature (°C): (*1*) 30, (*2*) 40, and (*3*) 50.

1070-4272/01/7402-0188 $25.00 © 2001 MAIK "Nauka/Interperiodica"

Table 1. Viscosity of aqueous salt solutions of CTAB

$C_{CTAB} \times 10^3$, M	Dynamic viscosity η (Pa s) and relative viscosity η_r at indicated temperature, °C									
	30		35		40		45		50	
	$\eta \times 10^3$	η_r	$\eta \times 10^3$	η_r	$\eta \times 10^3$	η_r	$\eta \times 10^3$	η_r	$\eta \times 10^3$	η_r
0.2 M NaBr										
1.17	0.8134	1.02	0.7266	1.01	0.6660	1.02	0.6020	1.01	0.5523	1.01
2.74	0.8294	1.04	0.7338	1.02	0.6725	1.03	0.6020	1.01	0.5523	1.01
5.05	0.8693	1.09	0.7554	1.05	0.6790	1.04	0.6079	1.02	.05523	1.01
7.60	0.9410	1.18	0.7841	1.09	0.6855	1.05	0.6079	1.02	0.5577	1.02
10.26	1.0128	1.27	0.8417	1.17	0.7117	1.09	0.6258	1.05	0.5577	1.02
15.25	1.2361	1.55	0.9424	1.31	0.7574	1.16	0.6616	1.11	0.5741	1.05
20.49	1.5705	1.97	1.1161	1.53	0.8161	1.25	0.6870	1.15	0.5944	1.09
30.12	2.2677	2.84	1.4509	2.02	1.0141	1.55	0.7780	1.31	0.6514	1.15
40.25	3.5185	4.41	2.0012	2.79	1.2829	1.97	0.8972	1.51	0.6769	1.24
50.26	5.8436	7.08	2.8631	3.98	1.6300	2.50	1.0619	1.78	0.7446	1.36
100.0	54.356	68.2	16.000	22.2	6.1391	9.40	2.9441	4.94	1.4933	2.73
0.4 M NaBr										
0.500	0.8055	1.01	0.7266	1.01	0.6594	1.01	0.6020	1.01	0.5523	1.01
1.00	0.8134	1.02	0.7338	1.02	0.6594	1.01	0.6020	1.01	0.5523	1.01
2.00	0.8533	1.07	0.7482	1.04	0.6725	1.03	0.6139	1.03	0.5577	1.02
4.00	0.9603	1.20	0.8245	1.15	0.7209	1.10	0.6358	1.07	0.5715	1.05
6.00	1.1186	1.40	0.9440	1.31	0.7868	1.21	0.6779	1.14	0.5920	1.08
10.0	1.5703	1.97	1.1897	1.65	0.9393	1.44	0.7706	1.29	0.6479	1.19
20.0	4.4000	5.52	2.5908	3.60	1.6876	2.58	1.1424	1.92	0.8503	1.56
30.0	11.221	14.1	5.4616	7.59	3.0285	4.64	1.7782	2.98	1.1829	2.16
0.25 M NaMBS										
0.75	0.9809	1.23	0.7985	1.11	0.6725	1.03	0.6139	1.03	0.5632	1.03
1.00	1.0687	1.34	0.8561	1.19	0.6986	1.07	0.6258	1.05	0.5687	1.04
1.25	1.1803	1.48	0.9208	1.28	0.7508	1.15	0.6437	1.08	0.5715	1.05
1.60	1.2580	1.58	0.9857	1.37	0.7937	1.22	0.6810	1.14	0.6104	1.12
2.00	1.6518	2.07	1.2895	1.79	0.9630	1.47	0.7423	1.25	0.6514	1.19
2.50	2.4952	3.13	1.8188	2.53	1.2317	1.89	0.8843	1.48	0.7258	1.33
3.38	4.9444	6.20	2.8990	4.03	1.6866	2.58	1.1490	1.93	0.8822	1.61
4.00	8.7085	10.92	4.2735	5.94	2.2186	3.40	1.4061	2.36	1.0192	1.86
5.15	14.648	18.37	6.0417	8.40	3.1283	4.79	1.8956	3.18	1.2964	2.37
7.64	35.390	44.38	12.748	17.72	6.1456	9.41	3.5157	5.90	2.1764	3.98
10.0	59.717	74.88	23.517	32.69	11.089	16.98	5.8115	9.75	3.2732	5.99

The densities of the tested fluids were measured pycnometrically.

The CMC_1 of CTAB in aqueous salt solutions was determined from the dependence of the surface tension on the surfactant concentration at a fixed temperature by the drop volume method [15]. In the measurements, the temperature was controlled to within 0.1°C. Doubly distilled water was used for solution preparation.

The dynamic viscosity η in water–CTAB–salt ternary systems, measured at various CTAB concentrations and temperatures, is given in Table 1 and Fig. 1. Table 1 also includes the relative viscosity η_r determined as the ratio of the outflow times of a solution tested and water.

The resulting dependences are broken straight lines consisting of two portions, which is consistent with the results reported in [16, 17]. The break point corresponds to the second critical micelle concentration CMC_2. CMC_2 values are given in Table 2 along with CMC_1 data obtained previously [15]. The results show that the viscosity gradually grows with the con-

Table 2. CMC_1 and CMC_2 in CTAB aqueous salt solutions

Electrolyte, M	$CMC_2 \times 10^3$, M					$CMC_1 \times 10^5$, M				
	at indicated temperature, °C									
	30	35	40	45	50	30	35	40	45	50
0.2 M NaBr	3.75	5.40	9.00	11.50	13.50	1.71	1.79	1.86	1.93	2.00
0.4 M NaBr	1.50	2.50	3.10	4.00	5.50	0.66	0.73	0.80	0.88	0.95
0.025 M NaMBS	0.40	0.65	0.90	1.10	1.25	10.0	11.3	12.5	13.9	15.1

centration incresing above CMC_1. Evidently, the shape of micelles is not changed between CMC_1 and CMC_2. Above CMC_2 the viscosity increases more rapidly with concentration.

Figure 1 illustrates the effects of the nature and concentration of additives on the sphere–cylinder micellar transition. It is seen that at 50°C the CTAB concentration at which transition occurs in 0.025 M NaMBS is lower than that for 0.4 and 0.2 M NaBr.

In micellar solutions, CMC_2 increases with temperature at a constant electrolyte concentration and decreases with increasing electrolyte concentration at constant temperature (Table 2). It is known that the temperature effect is about the same in the absence of additives [18]. Addition of NaMBS favors formation of cylindrical CTAB micelles at lower salt concentration as compared with the other salts. All these facts indicate that the nature and concentration of the additives play an important role in the asymmetrization of spherical CTAB micelles.

The mechanism of the electrolyte effect on the shape of micelles of ionic surfactants is associated to a considerable extent with the salting-out effect leading to closer packing of polar groups on a cylindrical micelle surface, which cannot be realized on a spherical surface [19].

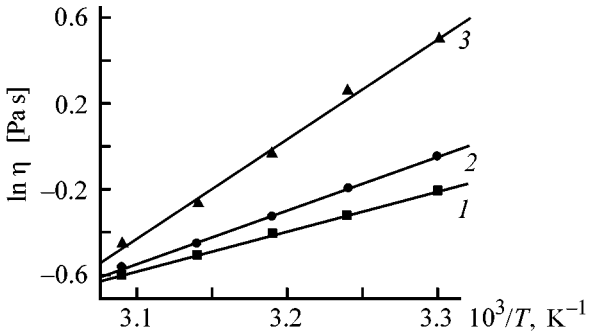

Fig. 2. Arrhenius plots for determining the enthalpy of activation. (η) Viscosity and (*T*) temperature. Solution composition: (*1*) H_2O + 1.17×10^{-3} M CTAB + 0.2 M NaBr, (*2*) H_2O + 4×10^{-3} M CTAB + 0.4 M NaBr, and (*3*) H_2O + 2×10^{-3} M CTAB + 0.025 M NaMBS.

According to Eyring's theory [20], the viscosity η is related to temperature *T* by

$$\eta = \frac{N_A h}{V} \exp\left(\frac{\Delta G^{\#}}{RT}\right), \quad (1)$$

where $\Delta G^{\neq}$ is the Gibbs activation energy of viscous flow in the solution (J mol^{-1}), *V* is the molar volume (m^3 mol^{-1}), η is the dynamic viscosity of the solution (Pa s), *T* is temperature (K), N_A is the Avogadro number, *h* is the Planck constant, and *R* is the gas constant.

The molar volume of surfactant in the equilibrium micellar solution, *V*, can be calculated by

$$V = \frac{100}{(100\rho - W)/M_0 + W/M}, \quad (2)$$

where *W* is the surfactant concentration (g/100 ml solution), M_0 and *M* are the molecular weights of water and surfactant, respectively, and ρ is the density of the micellar solution (g cm^{-3}).

Using Eq. (1) and taking into account that the standard enthalpy $\Delta H^{\neq}$, entropy $\Delta S^{\neq}$, and Gibbs energy $\Delta G^{\neq}$ of viscous flow activation are related by $\Delta G^{\neq} = \Delta H^{\neq} - T\Delta S^{\neq}$, we can write

$$\eta = \left(\frac{N_A h}{V}\right) \exp\left(\frac{-\Delta S^{\neq}}{R}\right) \exp\left(\frac{\Delta H^{\neq}}{RT}\right), \quad \eta = \exp\left(\frac{\Delta H^{\neq}}{RT}\right), \quad (3)$$

$$A = \left(\frac{N_A h}{V}\right) \exp\left(\frac{-\Delta S^{\neq}}{R}\right), \quad \ln \eta = \ln A + \frac{\Delta H^{\neq}}{RT}. \quad (4)$$

The dependence $\ln \eta = f(1/T)$ is expressed graphically as a straight line intersecting the ordinate axis. Examples of the Arrhenius plots for our experimental data (Table 1) are given in Fig. 2. The slope of the

Table 3. Thermodynamic characteristics of aqueous CTAB solutions in the presence of NaBr and NaMBS

$C_{CTAB} \times 10^3$, M	$\Delta G^{\neq}$ (J mol^{-1}) at indicated temperature, °C					$\Delta H^{\neq}$, kJ mol^{-1}	$\Delta S^{\neq}$, J K^{-1} mol^{-1}
	30	35	40	45	50		
0.2 M NaBr							
5.05	9265	9107	8946	8786	8626	19.00	32.10
7.60	9400	9209	9020	8826	8634	21.00	38.26
10.3	9620	9374	9128	8883	8637	24.50	49.08
15.3	10016	9686	9357	9025	8700	30.00	65.91
20.5	10614	10140	9661	9185	8710	39.50	95.27
30.1	11510	10865	10215	9568	8921	50.75	129.42
40.3	12600	11700	10813	9930	9044	66.25	176.95
50.3	13840	12690	11542	10394	9245	83.50	229.75
100	19420	17310	15200	13086	10975	147.50	422.42
0.4 M NaBr							
1.00	9084	8978	8873	8767	8661	15.50	21.16
2.00	9200	9067	8934	8802	8670	17.25	26.55
4.00	9501	9307	9114	8920	8726	21.25	38.75
6.00	9890	9625	9360	9095	8830	26.00	53.13
10.0	10702	10280	9860	9440	9018	36.25	84.26
20.0	13116	12280	11446	10610	9776	63.75	166.98
30.0	15565	14300	13030	11760	10490	92.50	253.74
0.025 M NaMBS							
1.60	10150	9805	9460	9115	8775	31.00	68.77
2.00	10850	10385	9920	9455	8990	39.00	92.85
2.50	11857	11220	10583	9945	9310	50.50	127.45
3.40	13480	12526	11573	10620	9667	71.25	190.54
4.00	14825	13605	12386	11166	9950	88.75	243.82
5.15	16020	14655	13290	11925	10560	98.75	272.86
7.64	18310	16695	15080	13460	11847	116.25	323.03
10.0	19796	18123	16450	14780	13105	121.25	334.61

straight line gives $\Delta H^{\neq}$, and then $\Delta S^{\neq}$ is determined to be $(\Delta H^{\neq} - \Delta G^{\neq})/T$.

The activation energy $\Delta G^{\neq}$ of viscous flow in aqueous-salt CTAB solutions at 30–50°C, calculated by Eq. (1) using the experimental values of η and ρ, and also $\Delta H^{\neq}$ and $\Delta S^{\neq}$, are given in Table 3. The results show that $\Delta G^{\neq}$ decreases with increasing temperature at constant CTAB concentration; the enthalpy and entropy of activation are practically independent of temperature. At constant temperature, $\Delta G^{\neq}$, $\Delta H^{\neq}$, and $\Delta S^{\neq}$ grow with increasing CTAB concentration. At constant CTAB concentration and constant temperature, $\Delta G^{\neq}$, $\Delta H^{\neq}$, and $\Delta S^{\neq}$ grow with increasing NaBr concentration. At constant CTAB concentration and any temperature from the experimental range, $\Delta G^{\neq}$, $\Delta H^{\neq}$, and $\Delta S^{\neq}$ are higher in aqueous NaMBS solutions, compared with the values in the presence of NaBr, indicating the significance of the counterion nature.

CONCLUSIONS

(1) The second critical micelle concentration was determined at 30–50°C in micellar aqueous solutions of cetyltrimethylammonium bromide in the presence of sodium bromide and methylbenzenesulfonate.

(2) The activation energy of viscous flow of the investigated aqueous solutions was estimated. The high positive $\Delta S^{\neq}$ compensates for the high enthalpy of activation $\Delta H^{\neq}$.

ACKNOWLEDGMENTS

The work was financially supported by the Russian Foundation for Basic Research (grant no. 00 015-97 357).

REFERENCES

1. Serdyuk, A.I. and Kucher, R.V., *Mitsellyarnye perekhody v rastvorakh poverkhnostno-aktivnykh veshchestv* (Micellar Transitions in Surfactant Solutions), Kiev: Naukova Dumka, 1987.
2. Candau, S.J., Hirsch, E., Zana, R., and Delsanti, M., *Langmuir*, 1989, vol. 5, no. 5, pp. 1225–1229.
3. Kryukova, G.N., Kasaikina, V.A., Markina, Z.N., and Seneva, A.V., *Kolloidn. Zh.*, 1981, vol. 43, no. 4, pp. 660–665.
4. Lin, Z., Cai, J.J., Scriven, L.E., and Davis, H.T., *J. Phys. Chem.*, 1994, vol. 98, no. 23, pp. 5984–5993.
5. Imae, T. and Ikeda, S., *J. Phys. Chem.*, 1986, vol. 90, no. 21, pp. 5216–5123.
6. Kern, F., Lemarechal, P., Candau, S.J., and Cates, M.E., *Langmuir*, 1992, vol. 8, no. 2, pp. 437–438.
7. Candau, S.J., Hirsch, E., Zana, R., and Adam, M., *J. Colloid Interface Sci.*, 1988, vol. 122, no. 2, pp. 430–438.
8. Candau, S.J., Merirhi, F., Waton, G., and Lemarechal, P., *J. Phys.* (Paris), 1990, vol. 51, no. 12, pp. 977–982.
9. Shikata, T., Hirata, H., and Kotaka, T., *Langmuir*, 1987, vol. 3, no. 6, pp. 1081–1088.
10. Striven, T.A., *Colloid Polym. Sci.*, 1989, vol. 267, no. 5, pp. 269–280.
11. Shikata, T., Hirata, H., and Kotaka, T., *Langmuir*, 1988, vol. 4, no. 2, pp. 354–461.
12. Shikata, T., Hirata, H., and Kotaka, T., *Langmuir*, 1989, vol. 5, no. 2, pp. 398–405.
13. Imae, T., Kamiya, R., and Iketa, S., *J. Colloid Interface Sci., 1985, vol. 108, no. 1, pp. 215–225.*
14. *Frolov, Yu.G., Grodskii, A.S., Razarov, V.V., et al., Laboratornye raboty i zadachi po kolloidnoi khimii* (Laboratory Course and Problem Book of Colloid Chemistry), Moscow: Khimiya, 1986.
15. Chunsheng Mo and Qian Zhong, *J. Jiangxi Normal Univ.* (Natural Sci. Ed.), 1997, vol. 21, no. 4, pp. 347–351.
16. Egorov, V.V. and Dembo, A.T., *Kolloidn. Zh.*, 1995, vol. 54, no. 1, pp. 52–56.
17. Verezhnikov, V.N. and Bashlykova, S.N., *Kolloidn. Zh.*, 1995, vol. 57, no. 3, pp. 431–434.
18. Rusanov, A.I., *Mitselloobrazovanie v rastvorakh poverkhnostno-aktivnykh veshchestv* (Micelle Formation in Surfactant Solutions), St. Petersburg: Khimiya, 1992.
19. Ekwall, P., Mandell, L., and Solyom, P., *J. Colloid Interface Sci.*, 1971, vol. 35, no. 4, pp. 519–528.
20. Glasstone, S., Laider, K.J., and Eyring, H., *The Theory of Rate Processes. The Kinetics of Chemical Reactions, Viscosity, Diffusion, and Electrochemical Phenomena*, New York: McGraw-Hill, 1941.

Russian Journal of Applied Chemistry, Vol. 74, No. 2, 2001, pp. 193–198. Translated from Zhurnal Prikladnoi Khimii, Vol. 74, No. 2, 2001, pp. 191–196.

SORPTION AND ION-EXCHANGE PROCESSES

Cation Exchange in Oxohydroxide Matrices of Niobium(V)

V. I. Ivanenko, I. A. Udalova, E. P. Lokshin, and V. T. Kalinnikov

Tananaev Institute of Chemistry and Technology of Rare Elements and Mineral Raw Materials, Kola Scientific Center, Russian Academy of Sciences, Apatity, Russia

Received January 19, 2000; in final form, September 2000

Abstract—Exchange of lithium, sodium, and potassium cations for hydrogen ions in oxohydroxide matrices of niobium(V), with alkali metal to niobium ratio of 1, was studied potentiometricaly. The possibility is considered of predicting the content of various singly charged cations in the case of their simultaneous presence in a complex hydrated oxide based on niobium(V).

Inorganic materials based on metaniobates of alkali metals possess specific electrical and optical properties, which enables their wide use in various fields of technology [1, 2]. However, the presence of impurity phases and deviations from a prescribed composition impairs the quality of the produced articles. In solid phase synthesis of metaniobates of alkali metals [2–4], low degree of homogenization gives rise to difficulties in obtaining a monophase product. The physicochemical properties of complex oxides of niobium and an alkali metal are substantially improved by creating alcoholate-based precursors and their subsequent hydrolysis [2, 5–7] and also direct reaction between hydroxides in aqueous solutions [8]. The quality of the obtained product depends on the composition and formation conditions of solid phases containing niobium(V) and an alkali metal.

To develop efficient approaches to manufacture of high-quality materials based on complex oxides, a knowledge is necessary of the formation conditions and composition of compounds obtained in aqueous solutions and thermodynamic characteristics of processes involving these compounds. The behavior of oxohydroxide forms of niobium(V) in aqueous electrolyte solutions is still a matter of discussion. Niobium(V), possessing high ionic potential, exhibits a strong tendency toward hydrolysis to give various oxygen- and hydroxide-containing complexes, including polynuclear complexes [9–20]. The compounds formed in the process can act as inorganic ion-exchangers. The authors of [12, 21] pointed to the formation of oxide compounds containing niobium(V) and an alkali metal in aqueous solutions; however, these data give no way of making an unambiguous conclusion about processes of solid phase formation.

The aim of this study was to analyze processes of competitive exchange of singly charged cations in oxohydroxide matrices of niobium(V).

EXPERIMENTAL

The processes of cation exchange were studied in aqueous chloride solutions. The electrolyte was chosen in view of the fact that chloride ions are characterized by a weak tendency toward association with polyvalent metals in the pH range studied (3–12) [17, 20], ruling out any influence of the anion background. In studying the exchange of alkali metal cations present in solution with the solid phase, a difficulty is encountered in monitoring the variation of their concentration. The most convenient and appropriate is an analysis of the exchange of an alkali metal cation for hydrogen ion. Therefore, the study was based on an analysis of curves of potentiometric titration of hydrated lithium, sodium, and potassium niobates with a 0.1 M solution of hydrochloric acid at constant ionic strength μ of a solution containing chloride of the respective alkali metal.

The starting hydrated amorphous lithium and sodium niobates of composition $Li_3NbO_4 \cdot 3.5H_2O$ and $Na_6Nb_4O_{13} \cdot 11.4H_2O$, and also water-soluble crystalline potassium niobate of composition $K_8Nb_6O_{19} \cdot 9H_2O$ were synthesized using freshly precipitated niobium(V) hydroxide. In preparing niobium(V) hydroxide [22], in the first stage, ammonium niobate was precipitated by gradually adding a hot acid fluoride solution of niobium ($C_{Nb(V)}$ = 1.13, C_{F^-} = 7.26 g-ion l^{-1}) to a concentrated solution of ammonia, taken in about 130% excess with respect to the stoichiometry, to pH > 9

1070-4272/01/7402-0193 $25.00 © 2001 MAIK "Nauka/Interperiodica"

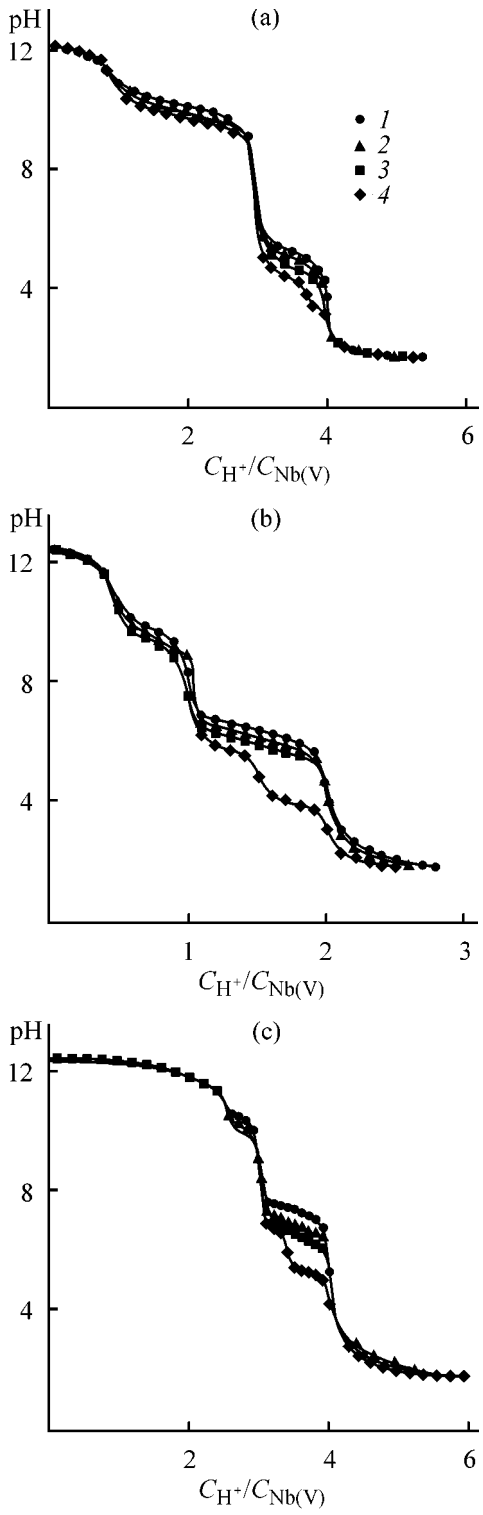

Fig. 1. PH value vs. $C_{H^+}/C_{Nb(V)}$ ratio. Initial conditions; temperature 20°C; (a) LiCl solution, $C_{Nb(V)} = 6.2 \times 10^{-2}$ M, $C_{OH^-}/C_{Nb(V)} = 0.96$; (b) NaCl solution, $C_{Nb(V)} = 5.6 \times 10^{-2}$ M, $C_{OH^-}/C_{Nb(V)} = 0.52$; (c) KCl solution, $C_{Nb(V)} = 4.9 \times 10^{-2}$ M, $C_{OH^-}/C_{Nb(V)} = 2.62$. Ionic strength, μ: (*1*) 0.1, (*2*) 0.2, (*3*) 0.4, and (*4*) 0.8.

with continuous stirring. After filtration, the obtained precipitate was "washed" to remove fluoride ions by triple repulpation in a 5% solution of ammonia. In the second stage, ammonium cations were exchange for hydrogen ions by adding hydrochloric acid to pH 4. The absence of ammonium ions was judged from IR spectra of a sample, taken on a UR-20 spectrophotometer. The sample was prepared in the form of a pellet with KBr. The thus obtained freshly precipitated niobium(V) hydroxide was repulped in a 0.5–1.0 M chloride solution of an alkali cation at pH ~12–13. After that, the solid phase was filtered off, washed with alcohol, and dried in air.

To prevent the possible hydrolysis, weighed portions of the starting samples were repulped in an alkaline solution with a prescribed $C_{OH^-}/C_{Nb(V)}$ ratio and then titration with HCl solution was carried out. The pH values were measured to within ±0.02 on an I-130 ion meter with an ESL-43-07 or ESL-63-07 glass electrode in a thermostated (±0.25°C) cell with continuous stirring.

Solid phases to be studied were isolated upon repulpation of the starting hydrated lithium, sodium, or potassium niobates in 0.2–0.4 M lithium, sodium, or potassium solutions, respectively, at pH values corresponding to the equivalence points found in potentiometric titration. The solutions were prepared from the above salts of chemically pure or special-purity grades in distilled water. The obtained suspensions were kept with stirring for 0.5 h. Further, the forming precipitates were filtered off with a vacuum filter, washed with alcohol on the filter, and dried in air. The content of alkali metal in hydrated and calcined at 700°C niobate samples taken from aqueous suspensions was determined by atomic-emission spectrophotometry with induction-coupled plasma and gravimetrically. The phase composition of compounds obtained upon thermal treatment was analyzed on a DRON-2 diffractometer with graphite monochromator (Cu_{K_α} radiation, counter velocity 2 deg min^{-1}). The total exchange capacity Γ^0 of a sample and the content of alkali metal cations, Γ_M, and hydrogen ions, Γ_H, in the solid phase were determined by comparing potentiometric data with the results of chemical and X-ray phase analyses with an accuracy of 3%.

Figures 1a–1c present the equilibrium pH values of the solution in relation to the ratio of concentrations of the acid introduced in titration and niobium(V). The first equivalence point at $C_{H^+}/C_{Nb(V)}$ ratios of 1, 0.5, and 2.5 (Figs. 1a, 1b, and 1c, respectively) is due to neutralization of free hydroxide ions in solution. The ratio of the content of alkali metal ions to that of

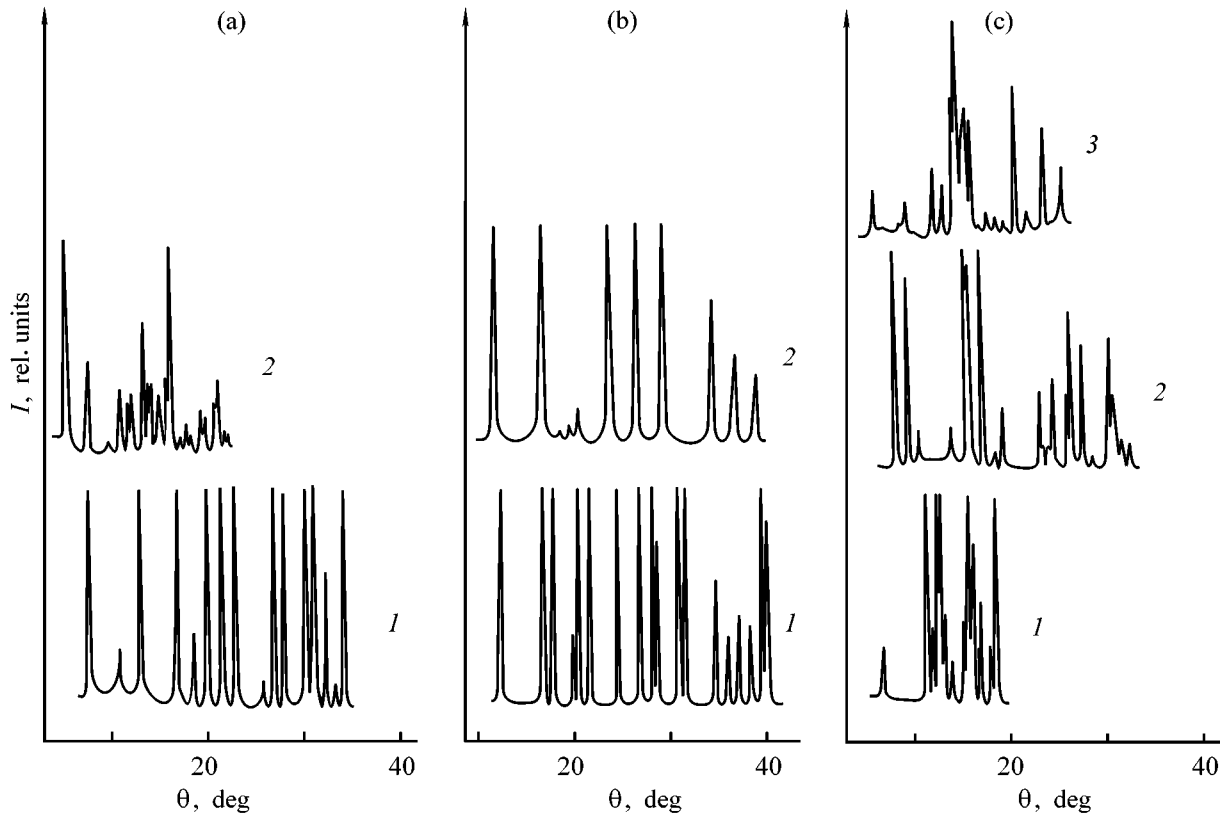

Fig. 2. X-ray diffraction patterns of lithium, sodium, and potassium niobate samples isolated from aqueous suspensions. (*I*) Intensity and (θ) Bragg angle. All the samples except crystalline $K_8Nb_6O_{19} \cdot 9H_2O$ were calcined at 700°C. (a) (*1*) Li_3NbO_4 and (*2*) $K_8Nb_6O_{19} \times 9H_2O$; (b) (*1*) $LiNbO_3$ and (*2*) $NaNbO_3$; (c) (*1*) $LiNb_3O_8$, (*2*) $Na_2Nb_4O_{11}$, and (*3*) K_4NbO_{17}.

niobium(V) in the niobate under study corresponds to the value in the starting sample. Further titration leads to the formation of, first, a hydrated metaniobate of the alkali metal M with M/Nb(V) = 1 ($C_{H^+}/C_{Nb(V)}$ = 3, 1, or 3; Figs. 1a, 1b, or 1c, respectively) and then niobium(V) hydroxide. Chemical and X-ray phase analyses of the solid phases formed confirmed the results of potentiometric measurements (Table 1; Figs. 2a and 2b).

Raising the ionic strength μ of the solution (Figs. 1a–1c), and, correspondingly, making higher the concentration of alkali metal ions in it, shifts the existence range of niobates to lower pH values and may strongly hinder the hydroxide formation. With the concentration of alkali metal in the solution raised substantially ($C_{M^+} > 0.8$ g-ion l^{-1}), two titration waves are observed instead of a single wave corresponding to niobium(V) hydroxide formation. The equivalence point of the first wave indicates the formation of niobates with the following alkali metal ion to niobium(V) ratios: Li : Nb = 1 : 3, Na : Nb = 1 : 2, K : Nb = 2 : 3. The results of chemical and X-ray phase analyses (Table 1; Fig. 2c) correlate well with the potentiometric data and indicate the formation of hydrated compounds of composition $LiNb_3O_8$, $Na_2Nb_4O_{11}$, and $K_4Nb_6O_{17}$, respectively, which are transformed into niobium(V) hydroxide upon further titration.

Table 1. Composition of alkali metal niobates isolated from aqueous suspensions

Solid phase	Composition, wt %, of a sample				
	air-dry			calcined	
	M_2O	Nb_2O_5	H_2O	M_2O	Nb_2O_5
Li_3NbO_4	19.6	55.2	26.1	26.9	72.7
$Na_6Nb_4O_{13}$	19.3	57.6	22.3	25.3	75.9
$K_8Nb_6O_{19}$	25.8	54.2	19.7	32.4	67.6
$LiNbO_3$	7.6	68.8	23.7	10.1	89.7
$NaNbO_3$	15.6	65.2	19.6	18.6	81.2
$LiNb_3O_8$	3.1	78.4	18.3	3.4	96.8
$Na_2Nb_4O_{11}$	8.8	73.6	17.8	10.8	88.7
$K_4Nb_6O_{17}$	16.5	68.9	14.9	19.5	80.8

Table 2. $\log K_p^t$, ΔH^0, and ΔS^0 values for ion exchange processes

Equilibrium	T, °C	$\log K_p^t$	ΔH^0, kJ mol^{-1}	ΔS^0, J mol^{-1} K^{-1}
LiR + H^+ ⇄ HR + Li^+	20	4.18	–19.5	13.4
	30	4.07		
	60	3.77		
NaR + H^+ ⇄ HR + Na^+	25	5.31	12.2	142.7
	40	5.42		
	60	5.54		
KR + H^+ ⇄ HR + K^+	20	6.28	17.6	180.1
	30	6.39		
	60	6.65		

Potentiometric studies revealed a rather wide range of hydrogen ion concentrations at which there exist hydrated forms of lithium, sodium, and potassium metaniobates with alkali metal ion to niobium(V) ratio of 1.

The formation of the disordered structure of the niobium(V) amorphous matrix via hydrogen bonds gives rise to high mobility of solution ions within the matrix and their free access to the solid phase, which results in that the process of heterogeneous cation exchange has bulk nature.

The ion exchange of alkali metal cations for hydrogen ions in hydrated metaniobate can be represented as

$$MR + H^+ \rightleftarrows HR + M^+, \qquad (1)$$

where R is the oxohydroxide matrix of niobium(V).

In the case when two solid phases are formed simultaneously, the constant of ion exchange by scheme (1) will be only controlled by the ratio of alkali metal ion and hydrogen ion activities in solution. Then, at constant ionic strength of the solution and equilibrium conditions, constant pH values would be expected at different degrees of exchange. Analysis of the obtained experimental data suggests that the cation exchange by scheme (1) involves only a single solid phase having the form of a hydrated oxohydroxide matrix of niobium(V) in which alkali metal cations are gradually replaced by hydrogen ions.

The content of alkali metal cations (MR) and hydrogen ions (HR) in the solid phase can be represented as a fraction of the total exchange capacity of the metaniobate sample. Since $\Gamma_M + \Gamma_H = \Gamma^0$, then $N_M = \Gamma_M/\Gamma^0$ and $N_H = \Gamma_H/\Gamma^0$. Then the expression for the cation exchange constant has the form

$$K_p = \frac{N_H a_{M^+}}{N_M a_{H^+}}.$$

At the same time, the apparent cation exchange constant, found from experimental data, is given by

$$K_H = \frac{N_H [M^+]}{N_M a_{H^+}}.$$

Analysis of the results of potentiometric titration (Figs. 1a–1c) shows that, despite μ = const, K_H has no constant value and its logarithm depends linearly on the degree of exchange of alkali metal cations for hydrogen ions. Since

$$\log K_H = \log K_p - \log f_{M^+}, \qquad (2)$$

the $\log K_p$ value must also linearly depend on Γ_H/Γ^0 at constant activity coefficient of the alkali metal in solution, f_{M^+}. The possible reason for such a dependence is the gradual change in the activity of cations in the solid phase from the value corresponding to a hydrate metaniobate of alkali metal to that characteristic of niobium(V) hydroxide. The true value of the thermodynamic constant K_p^t can be determined from the expression [23]

$$\log K_p^t = \int_0^1 \log K_p \, d(\Gamma_H/\Gamma^0).$$

With account of the linear dependence of $\log K_p$ on Γ_H/Γ^0, the $\log K_p^t$ value will correspond to $\log K_p$ at 50% substitution, i.e. at $\Gamma_H = \Gamma_M$. Substitution into (2) of the activity coefficient of alkali metal in solution yields

$$\log K_H = \log K_p^t + \frac{Az^2\sqrt{\mu}}{1 + aB\sqrt{\mu}}, \qquad (3)$$

$$\log K_H = \log [M^+] + pH,$$

where the solution pH corresponds to a value at 50% exchange of alkali metal cations for hydrogen ions in the oxohydroxide matrix of niobium(V).

The dependence of $\log K_H$ on the ionic strength of the solution is linear in the coordinates of Eq. (3). An extrapolation of this dependence to $\mu = 0$ gave the corresponding values of the logarithm of the thermodynamic constant at various temperatures and $\Gamma_H = \Gamma_M$ (Table 2).

The K_p^t values for exchange of alkali metal cations for hydrogen ions in hydrated metaniobates of sodium and potassium grow with increasing temperature, which shifts the existence region of niobium(V) hydroxide to higher pH values. In a similar exchange of cations in hydrated lithium metaniobate, the K_p^t value decreases with increasing temperature and the existence region of niobium(V) hydroxide is shifted to lower pH.

The thermodynamic exchange constant is determined from

$$\Delta G^0 = -2.3RT \log K_p^t, \quad (4)$$

where ΔG^0 is the change in the free Gibbs energy in ion exchange by scheme (1) and in the accompanying sorption and desorption of the solvent and dissolved electrolyte.

Substitution of $\Delta G^0 = \Delta H^0 - T\Delta S^0$ into expression (4) gives

$$\log K_p^t = \frac{\Delta S^0}{2.3R} - \frac{\Delta H^0}{2.3R}\frac{1}{T}. \quad (5)$$

An analysis of the dependence of $\log K_p^t$ on $1/T$ in the coordinates of Eq. (5) allowed a calculation of changes in the enthalpy, ΔH^0, and entropy, ΔS^0, in heterogeneous cation exchange (Table 2).

As it can be seen from Table 2, the affinity of the alkali metal cation for the oxohydroxide matrix of niobium(V) grows in order $K^+ < Na^+ < Li^+$. Decreasing ion radius and increasing size of the hydration shell favor firmer capture of cations into the solid phase. The course of the heterogeneous exchange process is presumably primarily determined by the difference between the degrees of hydration of the exchanging ions in the solid phase and in solution.

The parameter characterizing the degree of hydration of an alkali metal is the ratio between the radius of the hydrated ion, r_h, and the crystallographic radius r_c. Linear dependences of ΔH^0 and ΔS^0 on the degree of hydration of the cation being exchanged were obtained using the r_h and r_c values reported in [24, 25]. The destruction of the hydration shell in the course of sorption and the change in the coordination of bonds within the solid phase determine the ΔH^0 and ΔS^0 values. The change in entropy is the stronger, the lower the degree of hydration of the exchanged ion.

The results obtained in studying the heterogeneous cation exchange in oxohydroxides matrices of niobium(V) allow a choice of conditions under which hydrated compounds are formed with alkali metal cation to niobium(V) content ratio of 1 and high degree of homogenization with respect to singly charged cations. The isolation of the solid phase of this composition from aqueous suspensions with subsequent thermal treatment yields monophase metaniobate of alkali metal. On the basis of the investigations performed, a method was developed for synthesizing lithium metaniobate of stoichiometric composition in aqueous solutions [26, 27].

In synthesizing metaniobate, it is sometimes necessary to introduce simultaneously two or more cations of alkali metals into the oxohydroxide matrix of the solid phase. An important factor in this case is the relationship determining the exchange of several ions. Since the reactions

$$M_1R + H^+ \rightleftarrows HR + M_1^+,$$

$$M_2R + H^+ \rightleftarrows HR + M_2^+$$

are characterized by the constants

$$K_p^{(1)} = \frac{\Gamma_H[M_1^+]}{\Gamma_{M_1}a_{H^+}} \text{ and } K_p^{(2)} = \frac{\Gamma_H[M_2^+]}{\Gamma_{M_2}a_{H^+}},$$

$$K_p^{(1-2)} = \frac{\Gamma_{M_2}[M_1^+]}{\Gamma_{M_1}[M_2^+]} = \frac{K_p^{(1)}}{K_p^{(2)}}$$

corresponds to the constant of ion exchange by the scheme

$$M_1R + M_2^+ \rightleftarrows M_2R + M_1^+.$$

In the general case of a heterogeneous exchange process involving n singly charged cations

$$\Gamma = K_p^{(i-m)}\frac{[M_m^+]}{[M_i^+]}\Gamma_i,$$

where $m \neq i$. With account taken of the fact that $\Gamma_1 + \Gamma_2 + \ldots + \Gamma_n = \Gamma^0$, it can be written

$$K_p^{(i-1)}\frac{[M_m^+]}{[M_i^+]}\Gamma_i + \ldots + \Gamma_i + \ldots + K_p^{(i-n)}\frac{[M_n^+]}{[M_i^+]}\Gamma_i = \Gamma^0.$$

Therefore, the following expression is valid for calculating the solid phase composition

$$\Gamma = \frac{\Gamma}{1 + \sum\limits_{\substack{m=1,\\ m\neq i}}^{m=n} K_p^{(i-m)}\frac{[M_m^+]}{[M_i^+]}},$$

where i is the ion being exchanged and n is the number of ions involved in the exchange.

Thus, the obtained results make it possible to prognosticate the conditions necessary for synthesizing a solid phase containing various alkali metals in a prescribed ratio.

CONCLUSIONS

(1) The concentration and temperature limits of existence of hydrated lithium, sodium, and potassium metaniobates were determined. The thermodynamic characteristics of the heterogeneous exchange of al-

kali metal cations in these compounds for hydrogen ions were calculated.

(2) It is established that the affinity of alkali metal cations for the oxohydroxide matrix of niobium(V) grows in the order $K^+ < Na^+ < Li^+$ with increasing degree of their hydration.

(3) The possibility of synthesizing monophase metaniobates of alkali metals of prescribed composition in aqueous solutions is demonstrated.

(4) A model is proposed for calculating the content of various singly charged cations in their simultaneous incorporation into a complex niobium(V)-based hydrated oxide.

REFERENCES

1. Rez, I.S., *Zh. Vses. Khim. O–va im. D.I. Mendeleeva*, 1982, vol. 27, no. 3, pp. 53–61.
2. Shapiro, Z.I., Trunov, V.K., and Shishov, V.V., *Metody polucheniya niobatov shchelochnykh metallov* (Methods for Obtaining Niobates of Alkali Metals), Cherkassy: NIITEKhIM, 1978.
3. Agulyanskaya, L.A., Belov, V.V., Shapiro, Z.I., and Agulyanskii, A.I., *Vysokochist. Veshchestva*, 1989, no. 5, pp. 153–157.
4. RF Patent 2079469.
5. Turova, N.Ya. and Yanovskaya, M.I., *Neorg. Mater.*, 1983, vol. 19, no. 5, pp. 693–706.
6. Shinichi, H. and Kazumi, K., *Adv. Ceram. Mater.*, 1987, vol. 2, no. 2, pp. 142–145.
7. USSR Inventor's Certificate, no. 1101413.
8. USSR Inventor's Certificate, no. 570553.
9. Babko, A.K., Lukachina, V.V., and Nabivanets, B.I., *Zh. Neorg. Khim.*, 1963, vol. 8, no. 8, pp. 1839–1845.
10. Gridchina, G.I., *Zh. Neorg. Khim.*, 1963, vol. 8, no. 3, pp. 634–640.
11. Babko, A.K. and Nabivanets, B.I., *Problemy sovremennoi khimii koordinatsionnykh soedinenii* (Problems of Modern Chemistry of Coordination Compounds), Leningrad: Len. Gos. Univ., 1968, issue 2, pp. 111–129.
12. Lapitskii, A.V., *Vestn. Mosk. Gos. Univ., Ser. Matem., Mekhan., Astronom., Fiz., Khim.*, 1958, no. 6, pp. 121–126.
13. Reisman, A., Holtzberg, F., and Berkenblit, M., *J. Am. Chem. Soc.*, 1959, vol. 81, no. 6, pp. 1292–1295.
14. Jander, G. and Ertel, D., *J. Inorg. Nucl. Chem.*, 1960, vol. 14, nos. 1/2, pp. 71–76.
15. Jander, G. and Ertel, D., *J. Inorg. Nucl. Chem.*, 1960, vol. 14, nos. 1/2, pp. 77–84.
16. Jander, G. and Ertel, D., *J. Inorg. Nucl. Chem.*, 1960, vol. 14, nos. 1/2, pp. 85–91.
17. Neuman, G., *Acta Chem. Scand.*, 1964, vol. 18, no. 1, pp. 278–280.
18. Dartiquenave, Y., Lehne, M., and Rohmer, R., *Bull. Soc. Chim. France*, 1965, no. 1, pp. 62–66.
19. Goiffon, A., Grander, R., Bockel, C., and Spinner, B., *Rev. Chim. Minerale*, 1973, vol. 10, no. 3, pp. 487–502.
20. Spinner, B., Rev. Chim. Minerale, 1968, vol. 5, no. 4, pp. 839–852.
21. Ivanova, N.E., Sakharov, V.V., and Korovin, S.S., *Tem. Sb. Mosk. Inst. Tonkoi Khim. Tekhnol.*, 1977, no. 1, pp. 53–59.
22. Udalova, I.A., Ivanenko, V.I., and Kalinnikov, V.T., *Poluchenie gidroksidov niobiya(V), tantala(V), titana(IV) iz ftoridnykh rastvorov i kinetika ikh olyatsii i oksolyatsii* (Synthesis of Niobium(V), Tantalum(V), and Titanium(IV) Hydroxides from Fluoride Solutions and Kinetics of Their Oilation and Oxolation), Available from VINITI, 1999, Apatity, no. 2467-V99.
23. Helfferich, F., *Ionenaustauscher*, Bd 1, Weinheim: Chemie, 1959.
24. Dvořák, J., Koryta, J., and Bohačkova, V., *Elektrochemie*, Praha: Academia, 1975.
25. *Kratkii spravochnik fiziko-khimicheskikh velichin* (Concise Reference Book of Physicochemical Quantities), Mishchenko, K.P. and Ravdel', A.A., Eds., Leningrad: Khimiya, 1972.
26. RF Patent 2088530.
27. Udalova, I.A., Ivanenko, V.I., Lokshin, E.P., and Kalinnikov, V.T., *Sintez metaniobata litiya v vodnykh rastvorakh* (Synthesis of Lithium Metaniobate in Aqueous Solutions), Available from VINITI, 1999, Apatity, no. 2468-V99.

Russian Journal of Applied Chemistry, Vol. 74, No. 2, 2001, pp. 199–204. Translated from Zhurnal Prikladnoi Khimii, Vol. 74, No. 2, 2001, pp. 197–202.

SORPTION AND ION-EXCHANGE PROCESSES

A Sensitive Piezoelectric Crystal Sensor for Analyzing Phenols in Air

T. N. Ermolaeva, T. L. Lavrent'eva, A. E. Seredkin, and Ya. I. Korenman

Lipetsk State Technical University, Lipetsk, Russia

Voronezh State Technological Academy, Voronezh, Russia

Received December 15, 1999; in final form, June 2000

Abstract—A method was developed for analyzing volatile phehols in gaseous media by means of piezoelectric crystal sensors. The efficiency of the modifiers applied to the piezoelectric-crystal surface to improve the sensitivity and selectivity of analysis of toxic compounds was assessed. The choice of the conditions under which phenols are analyzed (nature and flow rate of carrier gas, mass of modifier film) is substantiated.

Monitoring of the atmosphere and air in the working area of industrial enterprises makes wide use of sensors of varied nature [1–3]. The subjects of the most active recent investigations have been mass-change-sensitive sensors with changing frequency of quartz crystal oscillations, operating on surface or volume acoustic waves [4–9]. Such sensors are easily incorporated into computer-based data acquisition and processing systems; they have low inertia and are suitable for remote detection of toxic compounds. The selectivity of the sensors is improved by their surface modification with sensitive sorbents of varied nature or specific biopolymers, as well as by incorporation into neutral polymers of compounds capable of reacting selectively with toxicants being analyzed. Among the most widely distributed organic toxicants to be monitored in air are phenol and its derivatives. The maximum permissible concentration (MPC) of volatile phenols in air in working areas is 5 mg m^{-3} [10].

The aim of this study was to assess the efficiency of various modifiers for piezoelectric crystal sensors (PECSs) and to develop a method for analyzing volatile phenols in air.

EXPERIMENTAL

Our studies were carried out on a setup comprising [11, 12] (Fig. 1) probe injection (*1a*) and gas mixture preparation (*1b*) units, detection cell *2*, quartz-crystal oscillation excitation circuit *3*, gas meter *4*, and data acquisition and processing unit *5*.

The analysis was carried out as follows. The gas mixture containing a compound to be analyzed was injected into a flow of dried carrier gas supplied from a gas cylinder and passed through the detection cell. The instrument was calibrated using standard gas mixtures prepared by passing carrier gas through a thermostated diffusion cell containing the compound to be analyzed. The carrier gas flow rate was measured with float rotameters. The passed volume of the gas was monitored with a rotary gas meter accurate within 0.0001 m^3.

The detection cell can incorporate 1–12 mass-sensitive AT-cut-off PECSs with a resonance oscillation frequency of 8–9 MHz, operating on the volume acoustic wave principle. The changes in the oscillation frequency of the PECS are recorded with a frequency meter or is transmitted with a 12-channel analog-digital converter to a Pentium 166 PC.

As analytical signal serves the change Δf in the oscillation frequency of PECS during sorption of a compound of interest with modifier films applied to the sensor surface. Both the mass of the film coatings applied and the mass of the compound sorbed by the PECS surface were determined using the Sauerbrey equation [13]

$$\Delta f = -2.3 \times 10^6 f_0^2 \Delta m/S.$$

Here, Δf is the change in the resonance oscillation frequency of the PECS owing to film application ($f_0 - f_f$) or sorption of the compound being analyzed ($f_f - f_a$), Hz; f_0 is the resonance (basic) oscillation

1070-4272/01/7402-0199 $25.00 © 2001 MAIK "Nauka/Interperiodica"

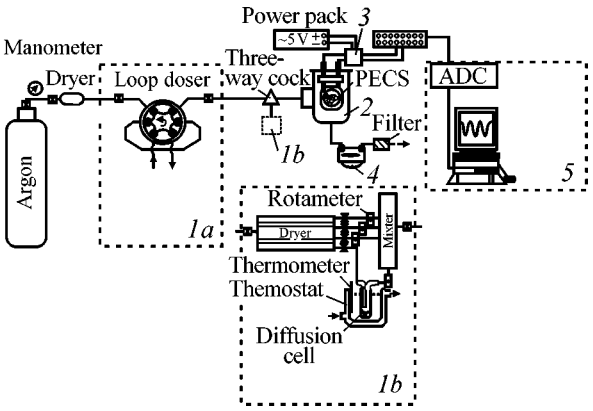

Fig. 1. Schematic of the setup for analyzing toxicants in air.

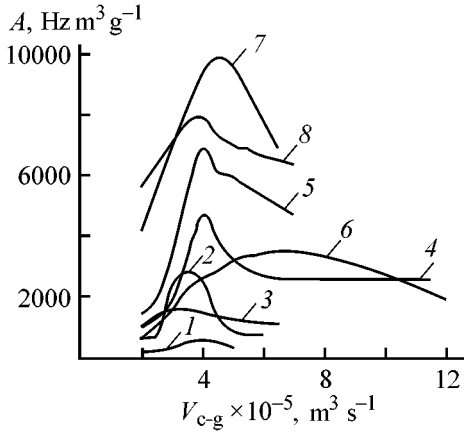

Fig. 2. Sensitivity A of phenol analysis using modified PECS as influenced by the carrier gas flow rate $V_{c\text{-}g}$. Modifier: (*1*) PMS-100, (*2*) BES, (*3*) TBPE, (*4*) TCEP, (*5*) PEGP, (*6*) MEA, (*7*) PEG-2000, and (*8*) PVP.

frequency of the PECS, MHz; Δm is the mass of the coating applied or the sorbate in the film, g; and S is the PECS surface area, cm^2.

The PECS were modified with low- and high-molecular-weight compounds (analytically pure) which can be conventionally classified into three groups [14]: (i) nonpolar saturated compounds (polymethylsiloxane liquid PMS-100, polymethylphenylsiloxane PMPS); (ii) polar compounds with locally concentrated negative charges, π bonds, and lone electron pairs at N and O atoms [1,2,3-tris(2-cyanoethoxy)propane TCEP, polyvinylpyrrolidone PVP, polyethylene glycol phthalate PEGP, polyethylene glycol adipate P-400, bis(2-ethylhexyl) sebacate BEC, pentaerythritol tetrabenzoate TBPE, polyphenyl ether PPE]; and (iii) polar compounds with surface-localized positive and negative charges (polyethylene glycols PEG-2000, PEG-3000; monoethanolamine MEA; polyvinyl alcohol PVA).

Using a microsyringe, 0.2–3.0 μl of the solution of the modifier with a concentration of 10 mg ml^{-1} was applied to the PECS surface. The solvents were double-distilled water, acetone (pure), ethanol (chemically pure), and dimethylformamide (chemically pure). The film was dried in a desiccator to constant weight at T = 65°C. After sorption of a compound being analyzed, the film was regenerated by passing pure carrier gas (argon, extra pure) through the detection cell.

The choice of the PECS modifier was based not only on the sorption properties of the coating but also on its elasticity ensuring adequate transfer of the signal from the piezoelectric crystal sensor. The efficiency of the modifiers was assessed using to the data obtained: sensitivity A calculated as the ratio between the change in the oscillation frequency of the PECS, Δf, and the concentration of the aromatic compound; dynamic sorption capacity (SC), i. e., sensitivity per unit mass of a modifier film; and the half-sorption and half-desorption times $t_{1/2}$ and $t'_{1/2}$, respectively.

The carrier gas flow rate was chosen on the basis of the rates of external and internal diffusion of volatile phenols to the PECS film surface and the sorption rate, taking into account the fact that at high rates of the carrier gas the pressure on the PECS increases and, therefore, the experimental error grows. The only optimal flow rate of the carrier gas was $(3.5–4.0) \times 10^{-5}$ $m^3 s^{-1}$ for virtually all the modifiers (Fig. 2). The only exception is the MEA-based coating for which sorption is almost instantaneous, and the PECS sensitivity is the greatest at a rate of 6.5×10^{-5} $m^3 s^{-1}$. An inert gas as carrier gas improves the kinetic parameters of analysis (the time of a single measurement decreases by 15 min relative to that in previous analyses in air [15, 16]).

The sensitivity of analyzing phenols in air, using sensors with coatings of varied nature, depends on the film modifier mass affecting the concentration of active functional groups on its surface. Therefore, the optimal mass of the film is estimated at (μg): 4.5 for low-molecular-weight MEA; 10–13 for linear polymers PMS-100, TCEP, PEG-2000, PEF-3000, P-400; and 17–20 for high-molecular-weight polymers PEGP, PVP, and PPE. A decrease in the modifier film mass to 3 μg and below impairs the film surface, which substantially decreases the sensitivity and reproducibility of the results of phenol determination.

The analytical response of PECS is governed both by the structure of a compound analyzed and the nature of modifier (Table 1). With increasing number of active functional groups in the phenol molecule,

Table 1. Efficiency of determining phenol and vanillin using PECS

Modifier	Δf, Hz	A, Hz m^3 g^{-1}	SC, Hz m^3 g^{-1} μg^{-1}	$t_{1/2}$, min	$t'_{1/2}$, min	Δm_a, μg
			Phenol			
PMS-100	130	140	39	0.45	1.50	0.15
PEG-2000	3840	4030	408	0.02	0.45	4.26
PEG-3000	3900	2400	235	0.17	0.23	4.50
P-400	1600	1080	114	0.20	0.25	1.77
TBPE	2780	2100	184	0.07	0.10	3.09
PEGP	7320	6900	535	2.50	1.70	8.13
PVP	5900	7800	650	0.30	1.25	6.75
MEA	2980	1840	441	0.40	0.75	3.42
BES	3080	3120	135	0.03	0.32	3.53
PPE	1400	3080	263	0.83	2.00	1.59
PMPS	1330	1500	111	1.67	4.50	1.52
PVA	2200	3540	170	1.48	3.08	2.24
			Vanillin			
PVP	500	18980	2116	0.94	2.05	0.52
MEA	300	1500	514	2.28	3.12	0.35
PEG-2000	190	4900	572	0.45	0.98	0.22

both the sensitivity of analysis A and the sorption–desorption time grow. The sensitivity of determining all the phenols studied is at a maximum for PECS modified with polyols and polylactams. The sensitivity A increases in the series of polyols as follows: P-400 < PEG-3000 < PVA < PEG-2000 < PEGP. For coatings with high sensitivity, the sorption–desorption time is typically greater. The exception are substrates based on polyethylene glycols, capable of efficient rapid sorption and desorption of phenols. High sorption activity of the films based on PEG-2000 (compared to PEG-3000) can be accounted for by the increase in the flexibility of the polymer chain because of the smaller number of functional groups.

The sorption–desorption kinetic parameters are determined by the nature and amount of the functional groups in the polymer molecule. For example, hydroxy groups in the PVA molecule, bound by intramolecular hydrogen bonds, sterically hinder sorption of phenol and prolong the sorption–desorption cycle, and bulky aromatic radicals in the PEGP molecule substantially retard sorption of phenols owing to the shielding of the ester oxygen atoms. The set of sorption and kinetic characteristics is optimal for PVP-based coatings which exhibit the maximal sensitivity and rate of sorption and desorption of phenols. The efficiency of the PVP-based coatings is due not only to the active centers present in its molecule but also to its arrangement favoring phenol sorption. Piezoelectric crystal sensors modified with PVP and PEGP can be recommended for monitoring of phenol in air at the working areas, in particular, for automated monitoring.

The kinetics of sorption of phenol on modifier films obtained by solvent evaporation were studied by IR spectroscopy [the spectra were recorded on an

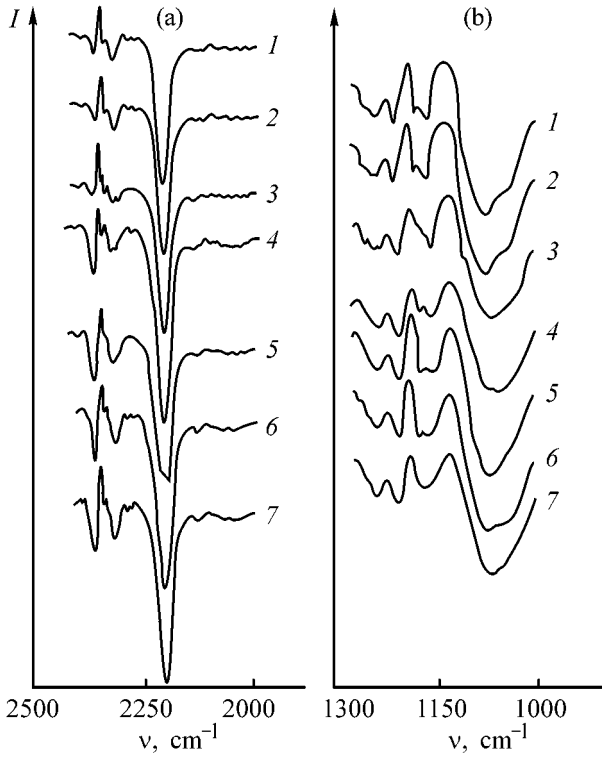

Fig. 3. IR spectra of TCEP-based modifiers with sorbed phenol in the region of the stretching vibrations of (a) nitrile and (b) ether groups. (*I*) Transmission and (ν) wave number. Film: (*1*) before phenol sorption and (*2*–*7*) after exposure to phenol vapor for 1, 2, 3, 5, 7, and 10 min, respectively.

Table 2. Sorption–desorption efficiency of phenol on films modified with chemical reagents

Modifier, wt %	Δf, Hz	A, Hz m^3 g^{-1}	$t_{1/2}$, min	$t'_{1/2}$, min	Δm_a, μg
TCEP + 4-AP, 2	4140	3750	0.07	0.33	4.60
TCEP + $FeCl_3 \cdot 6H_2O$, 2	3300	4300	0.08	1.08	3.90
PVP + 4-AP:					
2	18200	22160	0.53	2.00	20.16
5	48360	70900	0.83	–	53.69
10	53600	63060	0.92	–	61.59
PVP + AP, 2	6650	8070	0.05	–	7.39
PEG-2000 + 4-AP:					
2	18300	15550	0.08	2.5	21.02
5	21670	18850	0.50	–	24.90
PEG-3000 + 4-AP, 5	11750	7140	0.03	0.58	13.49

IKS-40 spectrophotometer (CaF_2 cell) after exposing the coatings to phenol vapor for 1–3, 5, 7, and 10 min. A comparison of the IR spectra showed that the substances being analyzed are sorbed by the TCEP-based film via hydrogen bonding with nitrile (Fig. 3a) and ether (Fig. 3b) groups of the modifier

$$CH_3-CH_2-C(-O-CH_2-CH_2-C\equiv N)_3.$$

The interaction is intensified on increasing the exposure time: the bands corresponding to the stretching vibrations of the nitrile (2252 cm^{-1}) and ether (1179 cm^{-1}) groups grow in intensity and broaden. Sorption of phenols by the support based on P-400

$$[-OC_2H_4-O-C(=O)-C_2H_4-C(=O)-]_n$$

initially involves interaction with only carbonyl oxygen atom (already after 3-min exposure) and then with the carbonyl (1609 cm^{-1}) and ester (1160 cm^{-1}) oxygen atoms. This is accompanied by broadening of the bands of the stretching vibrations of the functional groups and their shift to lower frequencies. Thus, all the reactive functional groups of the modifiers participate in hydrogen bonding during phenol sorption. The order in which functional groups interact with phenol depends not only on the reactivity of the complexing atoms, but also on the easiness of access to a group of interest.

To increase the sensitivity, the PECS supports were modified with chemical reagents that reacted quantitatively and selectively with phenols: 4-aminoantipyrine (4-AP), $FeCl_3 \cdot 6H_2O$ [15], and amidopyrine (AP) (Table 2). The maximal growth of the sensitivity observed in sorption of phenol by films containing up to 5 wt % 4-AP is accounted for by the formation of strong complexes between the reagent and phenol. Further increase of the 4-AP concentration decreases the sorption activity of the modifier owing to the growth of the film weight and mutual shielding of the functional group. Phenol desorption by the carrier gas is hindered as well, and PECS regeneration requires that heated air should be used or the modified sensor kept in a thermostat at 65°C. With piezoelectric crystal sensors coated with impregnated polymers (PEG-2000 with 4-AP, 5 wt % PVP with 4-AP, 5 wt %) it is possible to determine phenol in air of the working area in amounts of 0.3 and 0.08

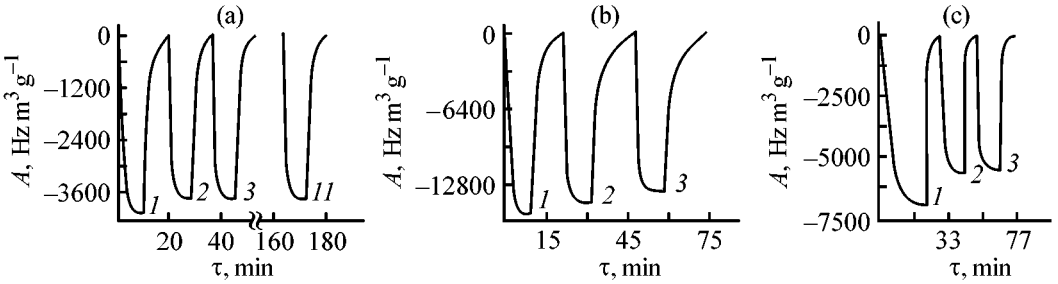

Fig. 4. Reproducibility of the response of PECS in repeated sorption–desorption cycles with phenols on modifier films. (*A*) Sensitivity and (τ) time. Film: (a) PEG, (b) PEG + 4-AP (5 wt %), and (c) PEGP. *Figures at curves* correspond to the sorption–desorption cycle no.

Table 3. Selectivity coefficients* in determining organic compounds, using PECS modified with (1) TCEP and (2) PVP

Compound B	The selectivity coefficient $K_{A/B}$									
	phenol		*o*-Cresol		*p*-Cresol		vanillin		TCP	
	1	2	1	2	1	2	1	2	1	2
Phenol			0.3	2.0	1.2	2.5	8.3	2.2	99.0	0.8
o-Cresol	3.2	0.5			3.8	1.3	26.7	1.2	319.5	0.4
p-Cresol	1.0	0.4	0.3	0.8			7.0	1.0	84.5	0.3
Vanillin	0.1	0.5	0.04	1.0	0.2	1.0			12.0	0.4
TCP	0.01	1.3	0.003	2.3	0.02	3.0	0.1	2.7		

* $K_{A/B} = \Delta m_A C_B/(\Delta m_B C_A)$, where Δm_A and Δm_B are the masses of the compounds sorbed and C_A and C_B are their concentrations.

MPC, respectively. However, inexhaustive desorption (≤90 %) reduces the service life of PECS and makes necessary additional calibration at regular intervals (Fig. 4).

When PECS is used in serial analysis, stable analytical response is important. After the first sorption–desorption cycle for phenol, all the coatings studied exhibit hysteresis depending on the nature and mass of the modifier film (Fig. 4). This is due to the structural changes in the film during its formation, as well as to the partial irreversibility of the sorption process. Repeatedly used PECSs modified with individual polymers (Figs. 4a, 4b) exhibit stable analytical signal (more than 10 sorption–desorption cycles for one film). The hysteresis is the most pronounced for films based on polyethylene glycol phthalate with its rigid polymer chain.

Piezoelectric crystal sensors modified with both individual polymers (PVP, PEG-2000, PEGP) and films containing specific reagents are characterized by low selectivity and are primarily intended for group analysis of volatile phenols in the presence of nonpolar substances (benzene, naphthalene, etc.). Comparison of the selectivity coefficients in determining individual phenols in gas mixtures (Table 3) suggests suitability of TCEP-based coatings for determining chlorophenols (2,4,6-trichlorophenol, TCP) and aromatic aldehydes in the presence of phenol and its alkyl derivatives, and phenol in the presence of certain *ortho* isomers. The gas mixture components can be separately analyzed using multisensor systems comprising a group of sensors arranged in the detection cell. This approach was described in detail for a set of nonspecific sensors employed in water monitoring [18].

We developed a procedure for determining volatile phenols in air, using PECS modified with a film based on polyvinylpyrrolidone and 4-AP (5 wt % solution in acetone) suitable for detecting phenols in 0.40 mg m^{-3} concentration (carrier-gas flow rate 3.7×10^{-5} m^3 s^{-1}). Each analytical run, including PECS regeneration, is complete within 10–15 min. The procedure based on the use of PECS, proposed in this work, compares favorably with the standard gas-chromatographic method [19] in simplicity, economic efficiency, and promptness. It can be used for determining phenols in remote or autonomous, including automated, regimes, which is of special importance for the environmental monitoring.

CONCLUSIONS

(1) The conditions for determining phenols using piezoelectric crystal sensors modified with macromolecular compounds of different nature were elucidated. The optimal experimental conditions are the carrier-gas flow rate of $(3.5–4.0) \times 10^{-5}$ m^3 s^{-1} and the modifier film mass of 10–13 μg.

(2) The efficiency of the modifiers was estimated by the piezoelectric-crystal microweighing. The most efficient coatings for piezoelectric crystal sensors employed for analyzing phenol in air are those based on polyols and polylactams. The kinetics of phenol sorption on various modifiers was studied by IR spectroscopy.

(3) A procedure was developed for determining volatile phenols by means of a modified piezoelectric-crystal sensor for which the detection limit is 0.40 mg m^{-3}.

REFERENCES

1. Zolotov, Yu.A., *Zh. Anal. Khim.*, 1990, vol. 45, no. 7, pp. 1255–1258.
2. Myasoedov, B.F. and Davydov, A.V., *Zh. Anal. Khim.*, 1990, vol. 45, no. 7, pp. 1259–1378.

3. Clements, J. *et al.*, *Sens. Actuators, B*, 1998, vol. 47, pp. 37–42.
4. Guilbault, G.G. and Jordan, J.M., *Anal. Chem.*, 1988, vol. 19, no. 1, pp. 1–28.
5. Ermolaeva, T.N. *et al.*, in *Ekologiya Tsentral'nochernozemnoi oblasti Rossiiskoi Federatsii* (Ecological State of the Central-Chernozem Region of the Russian Federation), Lipetsk: LEGI, 1998, no. 1, pp. 10–15.
6. Zhang, S. *et al.*, *Talanta*, 1998, vol. 45, pp. 727–733.
7. Chao, Y.-C. and Shih, J.-S., *Anal. Chim. Acta*, 1998, vol. 374, pp. 39–46.
8. McCallum, J.J., *Analyst*, 1989, vol. 114, no. 10, pp. 1173–1189.
9. Si, H.-S. *et al.*, *Anal. Chim. Acta*, 1999, vol. 390, pp. 93–100.
10. *Predel'no-dopustimye kontsentratsii vrednykh veshchestv v vozdukhe i vode* (Maximal Permissible Concentrations of Harmful Substances in Air and Water), Leningrad: Khimiya, 1975.
11. Korenman, Ya.I., Bel'skikh, N.V., and Kuchmenko, T.A., *Zh. Prikl. Khim.*, 1997, vol. 70, no. 4, pp. 626–629.
12. Alekhina, T.L., *et al.*, *Ekologiya Tsentral'nogo Chernozem'ya Rossiiskoi Federatsii* (Ecological State of the Central-Chernozem Region of the Russian Federation), Coll. of Works, Lipetsk: LEGI, 1998, pp. 150–155.
13. Sauerbrey, G., *Z. Phys.*, 1959, vol. 155, no. 2, pp. 205–222.
14. Kiselev, A.V., *Mezhmolekulyarnye vzaimodeistviya v adsorbtsii i khromatografii* (Intermolecular Interactions in Adsorption and Chromatography), Moscow: Vysshaya Shkola, 1986.
15. Korenman, Ya.I. *et al.*, *Zh. Anal. Khim.*, 1997, vol. 52, no. 3, pp. 313–318.
16. Ermolaeva, T.N. *et al.*, *Izv. Vyssh. Uchebn. Zaved., Khim. Khim. Tekhnol.*, 1999, vol. 42, no. 2, pp. 20–24.
17. Moskvin, L.N. and Tsaritsyna, L.G., *Metody razdeleniya i kontsentrirovaniya* (Methods of Separation and Concentration), Leningrad: Khimiya, 1991.
18. Vlasov, Yu.G., *Zh. Prikl. Khim.*, 1998, vol. 71, no. 9, pp. 1483–1486.
19. *Metodicheskie ukazaniya na opredelenie vrednykh veshchestv v vozdukhe* (Methodical Guidelines for Determining Harmful Substances in Air), Minzdrav SSSR, 1989, issue 24.

Russian Journal of Applied Chemistry, Vol. 74, No. 2, 2001, pp. 205–208. Translated from Zhurnal Prikladnoi Khimii, Vol. 74, No. 2, 2001, pp. 202–205.

SORPTION AND ION-EXCHANGE PROCESSES

Effect of Chemical Modification of Walnut Shell on the Yield and Pore Structure of Activated Carbon

A. A. Bagreev, A. P. Broshnik, V. V. Strelko, and Yu. A. Tarasenko

Institute of Sorption and Endoecology, National Academy of Sciences of Ukraine, Kiev, Ukraine

Received July 5, 1999; in final form, September 2000

Abstract—The effect of walnut shell treatment with solutions of inorganic salts prior to carbonization on the yield and properties of the obtained activated carbon was studied. The possibility of controlling the pore structure of the products in thermal treatment is demonstrated.

Recently, interest has again aroused in carbon sorbents prepared from fruit kernels and shells of various nuts [1–5]. This is due to their having much lower cost, compared with the traditional precursors (synthetic polymers and coals) used to produce activated carbons (ACs). However, a search for ways to increase the yield of the resulting product and to improve the structural-sorption characteristics of ACs prepared from fruit-kernel raw materials and, in particular, walnut shells (WS) is still urgent [6].

It has been noted [7–10] that, to improve ACs properties, make higher the yield, and obtain a more developed pore structure, the initial cellulose materials are treated with solutions of inorganic salts, which play the role of fire retardants and catalysts for carbonization and dehydration, ensuring a high yield of the products.

The character of WS dehydration in carbonization strongly affects all stages of ACs preparation. For example, intensifying the dehydration makes higher the ACs yield and hinders formation of resinous substances produced in cellulose degradation reactions competing with dehydration [7]. The choice of appropriate additives and dehydration conditions limiting the side processes resulting in carbon loss is an important problem in AC preparation. For example, the conventional thermal treatment of WSs (carbonization with subsequent activation) fails to yield high-quality AC for some reasons [11, 12].

Firstly, precursor is a macroporous material (the volume of macropores in the carbonization product is about 95% of the total pore volume. At the same time, to prepare highly porous ACs, it is necessary that the carbonization product should have some initial microporosity [9]. Secondly, WSs containing poorly structured components (lignin, hemicellulose, pectin, and proteins), and also mineral impurities, are carbonized to give a large amount of an amorphous coke residue impeding the evolution of pyrolysis gases. As a result, the forming "imperfect" carbon skeleton is contaminated with an amorphous coke residue.

Mineral impurities present in the initial WSs affect adversely the AC quality [9]. Mainly represented by carbonates, chlorides, sulfates, and nitrates of alkali and alkaline-earth metals, the impurities, on the one hand, make lower the onset temperature of carbonization, and, on the other, facilitate degradation of polymeric chains in cellulose, being catalysts for carbon oxidation.

At the same time, preliminary treatment of cellulose materials with phosphate-containing solutions increases the yield of raw carbon [7, 10]. In this case, three-substituted esters may be formed, along with one- and two-substituted esters, owing to the cross-linking of cellulose fragments [13]. Undoubtedly, the cross-linked fragments in the modified cellulose material subjected to pyrolysis strongly affect the structure and properties of raw carbon and ACs produced from this material.

The presence in cellulose-containing materials of phosphate groups, efficient catalysts of both intra- and intermolecular dehydration, accelerates these processes and makes slower the rate of the competing depolymerization reaction [7], which affects the yield and properties of carbonized residues. This concept sub-

1070-4272/01/7402-0205 $25.00 © 2001 MAIK "Nauka/Interperiodica"

Table 1. Effect of chemical modification of WSs on properties of carbonization product and ACs

Modifier, wt %	Carbonization		Activation	
	yield, %	pore volume, $cm^3\ g^{-1}$	yield, %	pore volume, $cm^3\ g^{-1}$
Initial WS	27.9	0.05	5.17	0.23
H_3PO_4	32.3	0.12	24.3	0.33
$(NH_4)_3PO_4$, 5	32.3	0.12	22.1	0.45
$(NH_4)_2HPO_4$:				
5	34.2	0.16	22.2	0.41
15	35.6	0.13	20.1	0.44
$NH_4H_2PO_4$:				
5	33.4	0.08	22.4	0.39
15	31.2	0.11	18.4	0.43
$Na_3B_4O_7$ + $(NH_4)_2HPO_4$: 5	34.9	0.1	26.7	0.33
15	41.7	0.14	25.5	0.34
$Na_2B_4O_7$ + H_3BO_3, 5	34.9	0.11	26.7	0.33
NH_4Cl	34.5	0.06	23.4	0.43
$(NH_4)_2SO_4$	33.4	0.03	27.7	0.24

Note: The AC parameters correspond to 90 min of activation.

stantiates the necessity for preliminary treatment of cellulose raw materials (i.e., for WS modification).

In this connection, the aim of this study was to analyze how impregnation (modification) of the initial WS with solutions of inorganic salts affects the yield and pore structure of carbonized products and activated carbons.

EXPERIMENTAL

As raw material served WSs. The method of shell preparation was described in [6]. The initial WS was impregnated with concentrated solutions of inorganic salts (chlorides, phosphates, sulfates, borates, or mixtures of these) so that the modifier content in the samples was 5–15 wt % (in terms of dry residue). After being separated from the solution, the nutshell was dried at 110°C.

The modified WS was subjected to thermolysis in argon at 800°C for 1 h on an installation described in [6]. To obtain AC samples with combustion loss from 6 to 50%, the thermolysis products were activated with steam at 750°C for varied time.

The mass change X (%) and yield R (%) of samples after each stage of thermal treatment, as well as the sorption volume of the pores V_s ($cm^3\ g^{-1}$) with respect to benzene, were estimated. The pore structure parameters of the materials—the micropore volume V_{mi} ($cm^3\ g^{-1}$); volume of sorbing pores V_t ($cm^3\ g^{-1}$), found from the isotherm of nitrogen adsorption at $P/P_0 = 0.95$; and the specific surface area S_{BET} ($m^2\ g^{-1}$), measured in different stages of thermolysis—were determined from sorption isotherms of carbon dioxide and nitrogen at 0°C and –196°C, respectively. The obtained isotherms were processed using modern methods of the adsorption theory [14, 15].

As noted in [16], the type and amount of introduced salt affect the thermal degradation of cellulose. The amount of salt required for WS modification is considerably lower than that commonly used for chemical activation [9]. This enables estimation of the true contribution of the salt additive and makes unnecessary washing of the final product.

The influence exerted by the nature of anion, salt concentration, and degree of exchange of the protons of phosphoric acid for ammonium ions on the yield and pore volume of ACs was studied. The results obtained are listed in Table 1. It can be seen that modification strongly affects the properties of the carbonization products and AC. In particular, the AC yield increases from 5.2% (unmodified WS) to 18.4–27.7% (modified samples). The activated carbons prepared from preliminarily modified WS possess higher pore volume than those prepared from unmodified WS (0.23 and 0.24–0.45 $cm^3\ g^{-1}$, respectively).

An estimate of the influence exerted by the amount of introduced salt (for the example of ammonium hydro- and dihydrophosphates) showed that AC samples prepared from WS with 5% of salts have the highest yield (22.2%) and the largest pore volume ($V_s \approx 0.39$–0.45 $cm^3\ g^{-1}$). For AC samples synthesized from WS with 15% ammonium phosphate, the yield is 18–20% and the pore volume, about 0.44 $cm^3\ g^{-1}$. It should be noted that the optimal concentration of ammonium orthophosphate in WS is 5%. Further increase in the amount of salt does not virtually affect the AC yield and pore volume.

It was found with various ammonium salts (chloride, sulfate, and phosphate) that the highest yield (27.7%) is observed for an AC sample prepared from WS modified with ammonium sulfate, and the largest pore volume (0.45 $cm^3\ g^{-1}$), for that prepared from WS preliminarily impregnated with ammonium ortho-

Table 2. Yield and parameters of pore structure of the carbonization products and ACs

Parameter	Carbonization product	AC	Parameter	Carbonization product	AC
R, %	35.6	20.1	V_{mi} (CO_2), $cm^3\ g^{-1}$	0.26	0.27
V_s, $cm^3\ g^{-1}$	0.12	0.44	V_t (N_2), $cm^3\ g^{-1}$	0.03	0.47
V_{mi} (N_2), $cm^3\ g^{-1}$	0.03	0.42	S_{BET} (N_2), $m^2\ g^{-1}$	50	850

phosphate. The yield and the pore volume for an AC sample prepared from WS impregnated with ammonium chloride solution are 23.4% and 0.43 $cm^3\ g^{-1}$.

The influence exerted by the degree of proton exchange in H_3PO_4 for ammonium ions was analyzed for samples modified with 5% solutions of $(NH_4)_3PO_4$, $(NH_4)_2HPO_4$, $(NH_4)H_2PO_4$, and H_3PO_4 to reveal the following tendency: the highest yield (24.3%) is observed for an AC sample based on phosphoric acid-impregnated WS and the largest pore volume (0.45 $cm^3\ g^{-1}$) for that prepared from WS impregnated with ammonium orthophosphate.

Borax taken alone and that with addition of boric acid or ammonium hydrophosphate give AC samples in 25.5–26.7% yield. For these AC samples, as well as for the AC samples synthesized from WS modified with ammonium phosphate, the highest yield corresponds to 5 wt % modifier. The pore volume in the ACs prepared from WS impregnated with borates is about 0.33 $cm^3\ g^{-1}$.

The treatment of WS with ammonium chloride, ammonium phosphate, boric acid, or its salts leads to a substantially larger pore volume in carbonized and activated materials, with the AC yield increasing nearly 2-fold.

Data on the formation and development of the pore structure in carbonized products and ACs were obtained from the results of an adsorption experiment. The figure shows, as an example, the nitrogen adsorption isotherms taken on carbonized samples and ACs prepared from WS containing 5 wt % ammonium hydrophosphate. The estimated yields R (%) and calculated pore structure parameters are listed in Table 2. For the carbonization product obtained from WS treated with ammonium hydrophosphate, the adsorption isotherm shows low slope and small adsorption of nitrogen over a wide range of pressures (curve *1* in the figure). This indicates that only a microporosity is present in the carbonized sample (Table 2), which is confirmed by the fact that the volume of sorbing pores V_t and that of micropores V_{mi} (N_2) coincide. As seen from the data on CO_2 sorption, this sample has a considerable volume of narrow micropores V_{mi} (CO_2).

The adsorption of nitrogen on AC prepared from WS pretreated with phosphates is 15 times that for the product of carbonization (curve *2* in the figure). As in the case of the carbonization products, these samples are characterized by low slope of the isotherms, which is typical of microporosity. The fact that the volume V_t of sorption pores and that of micropores V_{mi} (N_2) (Table 2) coincide also confirms the absence of mesoporosity in the prepared ACs.

Activation of a carbonized sample prepared from WS treated with ammonium hydrophosphate to 44% combustion loss (Table 2) leads to larger micropore volume determined from nitrogen sorption, whereas the pore volume found from CO_2 sorption does not virtually change. This suggests the formation of coarse micropores, which is confirmed by changes in the specific surface area and pore volume (Table 2). As a result of activation, S_{BET} increases 17-fold and V_s grows from 0.12 to 0.44 $cm^3\ g^{-1}$.

Thus, among all the salt additives used for preliminary impregnation of WSs, the highest AC yield is ensured by borates and ammonium sulfate, and the largest pore volume, by phosphates and ammonium chloride. Modification of WS with phosphates allows preparation of ACs with developed pore structure and

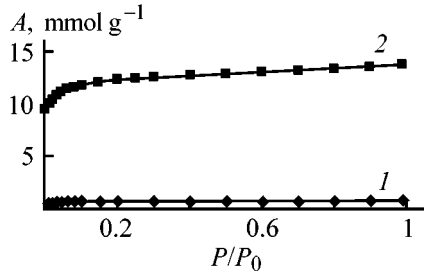

Isotherms of nitrogen adsorption on thermolysis products prepared from WS modified with ammonium hydrophosphate. (A) Adsorption and (P/P_0) relative pressure. (*1*) Carbonization product and (*2*) AC with a 44% combustion loss.

makes it possible to control the pore structure of the thermolysis products (i.e., to synthesize microporous sorbents).

CONCLUSION

Modification of walnut shell with inorganic salts prior to carbonization raises the yield of activated carbon and allows control of its structural-sorption characteristics. The activated carbons obtained in this process have reasonable operation characteristics.

REFERENCES

1. Gonzalez, M.T., Rodriguez-Reinoso, F., Garsia, A.N., and Marcilla, A., *Carbon*, 1997, vol. 35, no. 1, pp. 159–162.
2. Lupashku, T., Monahova, L., and Gonchar, V., *Rev. Roum. Chim.*, 1994, vol. 39, no. 8, pp. 909–916.
3. Limonov, N.V., Olontsev, V.F., Glushankov, L.V., and Solntsev, V.V., *Zh. Prikl. Khim.*, 1994, vol. 67, no. 10, pp. 1648–1650.
4. Lussier, M.G., Shull, J.C., and Miller, D.J., *Carbon*, 1994, vol. 32, no. 8, pp. 1493–1498.
5. Gergova, K. and Eser, S., *Carbon*, 1996, vol. 34, no. 7, pp. 879–888.
6. Bagreev, A.A., Broshnik, A.P., Strelko, V.V., and Tarasenko, Yu.A., *Zh. Prikl. Khim.*, 1999, vol. 72, no. 6, pp. 942–946.
7. Konkin, A.A., *Uglerodnye i drugie zharostoikie voloknistye materialy* (Carbon and Other Heat-Resistant Fibrous Materials), Moscow: Khimiya, 1974.
8. Ermolenko, I.N., Lyubliner, I.P., and Gul'ko, N.V., *Elementosoderzhashchie ugol'nye voloknistye materialy* (Fibrous Element-containing Carbon Materials), Minsk: Nauka i Tekhnika, 1982.
9. Von Kinle, H. and Bader, E., *Aktivkohle und ihre industrielle Anwendung*, Stutgart: Enke, 1980.
10. *Cellulose and Cellulose Derivatives*, Bikales, N.M. and Segal, L., Eds., New York: Wiley–Interscience, 1971, part 2.
11. Kartel', N.T., Chikhman, Yu. P., Mikhalovskii, S.V., and Strelko, V.V., *Ukr. Khim. Zh.*, 1984, vol. 50, no. 3, pp. 267–269.
12. Lupashku, F.G. and Dranka, I.V., *Izv. Akad. Nauk Resp. Moldova, Biol. Khim. Nauki*, 1991, no. 3, pp. 66–69.
13. Ermolenko, I.N., Buglov, E.D., Lyubliner, I.P., *et al.*, *Khim.-Farm. Zh.*, 1968, no. 12, p. 33.
14. Dubinin, M.M., *Usp. Khim.*, 1982, vol. 51, no. 7, pp. 1065–1074.
15. Jankowska, H., Swiatkoski, A., and Choma, J., *Active Carbon*, Ellis Horwood, 1991.
16. Golova, A.P., *Usp. Khim.*, 1975, vol. 44, no. 8, pp. 1454–1474.

Russian Journal of Applied Chemistry, Vol. 74, No. 2, 2001, pp. 209–213. Translated from Zhurnal Prikladnoi Khimii, Vol. 74, No. 2, 2001, pp. 206–210.

APPLIED ELECTROCHEMISTRY AND CORROSION PROTECTION OF METALS

Electrochemical Separation of Multicomponent Tin-based Alloys in Salt Melts

O. G. Zarubitskii, V. P. Opanasyuk, A. A. Omel'chuk, and N. F. Zakharchenko

Vernadskii Institute of General and Inorganic Chemistry, National Academy of Sciences of Ukraine, Kiev, Ukraine

Received July 26, 2000

Abstract—The results obtained in a study of the electrochemical separation of multicomponent tin-based alloys in salt melts are presented. The influence exerted by electrolysis conditions on the discharge at the auxiliary electrode of a number of metals accompanying lead and tin was determined.

Manufacture and purification of non-ferrous metals from polymetallic raw materials yield a great amount of polymetallic alloys [1, 2]. The qualitative and quantitative compositions of such alloys vary widely, depending both on the composition of starting raw materials and on the method of their processing. For example, purification of tin by vacuum refining yields alloys of the following composition (wt %): tin 30–40, bismuth up to 10, antimony up to 5–6, copper up to 3–5, silver up to 0.1–0.2, arsenic up to 0.3–1.5, iron up to 0.1–0.3, and lead the rest. The known methods for separation of such alloys into components are rather labor-consuming, involve large amounts of recirculated products, and are characterized by low recovery of the metals [2]. Silver and gold, accompanying non-ferrous metals, are, as a rule, distributed among the processing products and lost with them. It has been shown [2–4] that electrolysis in salt solutions, ensuring concentration of noble metals at the cathode, is an efficient method for processing alloys of this kind. A considerable progress in separation of multicomponent alloys by electrolysis in melts can be made with an auxiliary electrode hindering transfer of metals with more positive electrode potential from anode to cathode, thus favoring a higher degree of separation into components. This communication presents the results obtained in studying the electrochemical separation of tin-based multicomponent alloys in high-temperature electrochemical reactors of various kinds, including those with a porous electrode.

EXPERIMENTAL

A schematic of the electrochemical reactor for separation of multicomponent alloys is shown in Fig. 1. The experiments were done at current loads of 50 to 200 A. The developed electrolyzer design allows work in two modes: with and without auxiliary electrode mounted between the anode and cathode. Figure 1 shows an electrolyzer variant with an auxiliary electrode. A vessel *1* of arbitrary shape, made of an electrically conducting material and lined with graphite from inside, serves as cathode and receiver of metal deposited onto the cathode. Inside, this vessel contains a vessel *2* for anodic metal. The base of the anodic vessel *2* is made of a porous dielectric material *3*. The porosity of this material is chosen so as to rule out mechanical seepage of the anodic metal. Common-

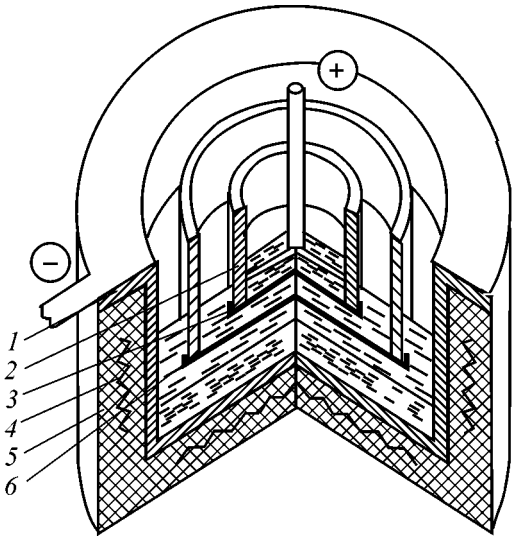

Fig. 1. Schematic of an electrochemical reactor for separation of tin-containing multicomponent alloys: (*1*) vessel for electrolyte and cathodic metal, (*2*) vessel for anodic metal, (*3*) porous diaphragm, (*4*) electric heaters, (*5*) external casing with heat insulation, and (*6*) auxiliary electrode.

1070-4272/01/7402-0209 $25.00 © 2001 MAIK "Nauka/Interperiodica"

Table 1. Half-wave potentials E of the cathodic reduction of non-ferrous metal ions in zinc chloride–based salt melts at 450°C

M^{n+}	E, V	RT/nF, V		M^{n+}	E, V	RT/nF, V	
		experiment	calculation			experiment	calculation
31.5 mol % $ZnCl_2$–68.5 mol % KCl				46.0 mol % $ZnCl_2$–19.5 mol % NaCl –34.5 mol % KCl			
Pb^{2+}	1.15	0.035	0.031	Pb^{2+}	1.52	0.029	0.031
Sn^{2+}	–	–	0.031	Sn^{2+}	1.48	0.030	0.031
Cu^{2+}	1.08	0.030	0.031	Cu^{2+}	1.32	0.034	0.031
Ag^{+}	0.94	0.060	0.062	Ag^{+}	1.23	0.052	0.062
Sb^{3+}	0.81	–	0.021	Sb^{3+}	1.20	0.019	0.021
Bi^{3+}	0.77	0.019	0.021	Bi^{3+}	1.03	0.022	0.021

ly, heat-resistant silica fabrics of various brands are used as porous diaphragm. Owing to the surface tension forces, the molten metal is contained within the anodic vessel and comes into contact with molten electrolyte through the pores. On passing a direct current, the metal dissolves at the anode and, after being transferred through the electrolyte layer, is deposited onto the cathode.

As molten electrolyte served salt mixtures based on zinc chloride. Zinc chloride and mixtures on its basis occupy a distinctive position among molten salts. They have low melting point and allow work in the interval 230–550°C. Zinc has more negative potential, compared with many non-ferrous metals, and, therefore, its compounds may be present in the electrolyte mixture, taking no part in the mass exchange between the electrodes. In molten state, zinc chloride forms associates of the type $(–Zn–Cl–)_n$, decomposing in the presence of weakly polarizing cations of alkali metals. The decomposition to give $[ZnCl_4]^{2–}$ anions is the stronger, the larger the cation of an alkali metal [7]. These anions can coordinate in the outer sphere cations of many non-ferrous metals, thus exerting influence on their discharge potential, and stabilize compounds with lower oxidation level. In addition, it has been established [8] that the electrical conductivity of mixtures based on zinc chloride also depends on the cation composition. Mixtures of this kind tend to segregate, with salts of heavy metals (e.g., lead) accumulated in the lower layers of the melt [9]. Thus, by controlling the composition of the electrolyte mixtures based on zinc chloride, one can change in a desirable direction the degree of metal separation, resistance of the electrolysis bath, and, consequently, the specific power consumption.

Table 1 lists the potentials of cathodic reduction half-waves for some non-ferrous metals relative to a chlorine reference electrode in molten zinc chloride–based electrolyte mixtures.

Current–voltage measurements were carried out in potentiodynamic mode on glassy carbon electrodes at potential sweep rate of 2 mV s^{-1}. It can be seen from the presented data that, in the mixtures under study, lead and tin have more negative potentials relative to such metals as copper, silver, antimony, and bismuth. Consequently, a lead–tin alloy must be deposited at the cathode in electrochemical separation of tin-based polymetallic alloys in the molten mixtures of the indicated composition, with metals having more positive potential—antimony, bismuth, silver, and copper—concentrated at the anode. The discharge–ionization potentials of metals have different values in mixtures of different compositions. In the ternary mixture, they are shifted to a more negative range. The order of ion discharge at the cathode is preserved, but the difference between the reduction potentials of some metals, e.g., lead and copper, lead and silver, etc., increases. This is apparently due to the nature of interaction between these ions and electrolyte components, which is poorly understood. It follows from the obtained data (Table 1) that, in mixtures ensuring a greater difference between the discharge–ionization potentials of lead and tin ions and those of accompanying metal ions with more positive potential (copper, silver, antimony, bismuth), these latter must pass into the salt phase in lesser amount. This must be promoted, to a certain extent, by the reducing action of lead and tin on cations of the above metals that have passed into the salt phase

$$2M^{n+} + nPb^0(Sn^0) \rightarrow nPb^{2+}(Sn^{2+}) + 2M^0, \quad (1)$$

where M^{n+} = Ag^+, Sb^{3+}, Bi^{3+}, and Cu^{2+}.

Table 2. Amount of accompanying elements passing into the salt phase in anodic dissolution of a multicomponent alloy containing (wt %): Pb 35.8, Ag 16.8, Cu 1.20, Bi 0.24, Sn 22.5, and Zn the rest

Electrolysis conditions		Melt-electrolyte	Concentration of metals in the salt phase, wt %			Electrolysis conditions		Melt-electrolyte	Concentration of metals in the salt phase, wt %		
$i \times 10^{-3}$, A m^{-2}	Q, A h		Cu	Ag	Bi	$i \times 10^{-3}$, A m^{-2}	Q, A h		Cu	Ag	Bi
10.0	18	Binary	0.0017	0.0026	0.0038	8.0	35	Binary	0.179	0.035	0.0060
	18	Ternary	0.0012	0.0020	0.0033		35	Ternary	0.151	0.026	0.0052

The investigations performed confirm this conclusion. Indeed, a lower degree of dissolution of electropositive components is observed in anodic polarization of polymetallic alloys in a ternary electrolyte (Table 2).

This fact is very important in those cases when the purified metal or alloy is obtained at the cathode. In this connection, a three-component mixture of zinc, sodium, and potassium chlorides, containing lead chloride for ensuring mass exchange between the electrodes, was used as molten electrolyte. In order to achieve more complete recovery of lead and tin by shifting the potential of the anodic alloy to more negative values, no tin chloride was introduced into the mixture. Owing to the close values of the electrode potentials of lead and tin, this component inevitably appears in the electrolyte on passing direct current. In the course of electrolysis, a certain component ratio is attained in the electrolyte, reflecting the mass exchange between the electrodes with account of changes in the alloy composition at the anode. The change in the concentrations of lead and tin chlorides in the course of electrolysis is presented in Fig. 2.

It can be seen from Fig. 2 that tin chloride is accumulated in the course of electrolysis. In the course of lead and tin recovery from the anodic alloy, the concentration of lead chloride in the electrolyte decreases. It was noticed that the concentration of zinc chloride changes somewhat only in the initial stage of electrolysis and remains virtually unchanged afterwards.

An alloy containing (wt %): Pb 39.6, Sn 50.1, Bi 7.5, Sb 2.2, Ag 0.12, and In 0.073 was subjected to electrochemical separation. The amount of metal charged into the anode chamber was 14.2 kg, and the electrolyte mass, 71 kg. The electrolysis was conducted at 400 ± 10°C, current of 50 A (current density of 0.125 A cm^{-2}), and average voltage drop of 2.5 V. As the anodic alloy gradually dissolved, its additional amounts (3 kg per 24 h) were introduced into the anode chamber. The quantity of electricity passed through the electrolyzer was 17 050 A h, and the total amount of alloy charged into the anode chamber, 53 kg. After passing 15 225 A h of electricity, the addition of the alloy into the anode chamber was terminated and additional amounts of lead and tin were recovered at the cathode. As a result, an alloy of the following composition was obtained at the anode (wt %): Pb 1.4, Sn 6.2, Bi 65.7, Sb 24.2, In not detected.

A typical dependence of the composition at the electrodes on the quantity of passed electricity is presented in Fig. 3. The dashed line denotes the instant when additional charging of the starting alloy into the anode chamber was terminated. In the initial stage of electrolysis, dissolution of metals having the most negative electrode potentials (In, Pb, Sn) was observed. This is indicated by the manner in which the content of lead and tin in alloys at the electrodes changes. With recovery of lead from the anodic alloy,

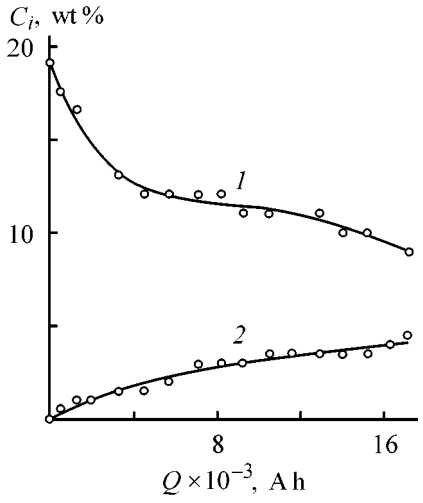

Fig. 2. Concentration C_i of (*1*) lead and (*2*) tin in electrolyte vs. the quantity Q of passed electricity. I = 60 A, j = 1500 A m^{-2}, T = 400°C.

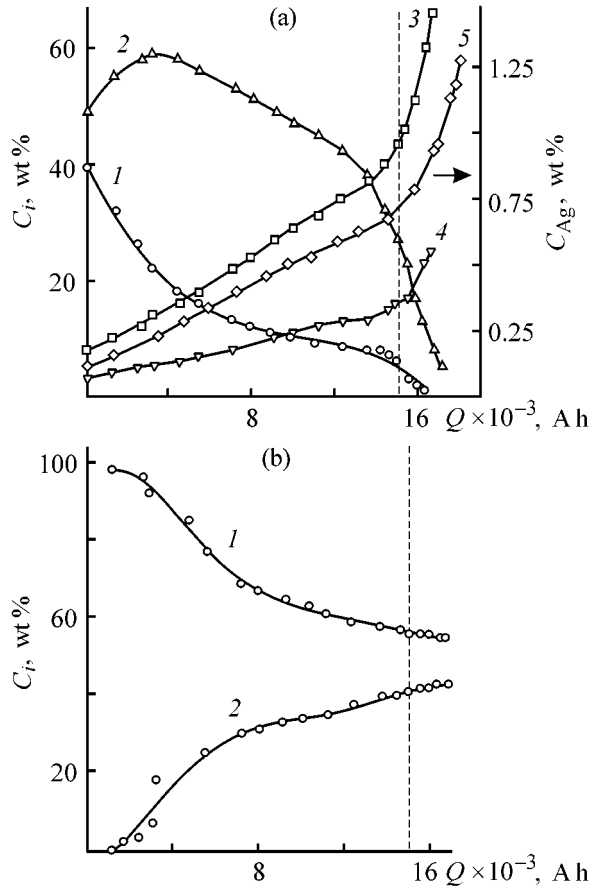

Fig. 3. (a) Anodic and (b) cathodic composition C_i vs. the quantity Q of passed electricity. (*1*) Lead, (*2*) tin, (*3*) bismuth, (*4*) antimony, and (*5*) silver. I = 60 A, j = 1500 A m^{-2}, U = 3 V, T = 400°C.

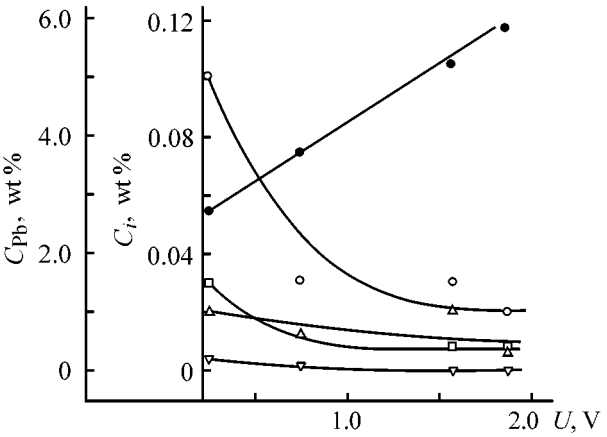

Fig. 4. Alloy composition C_i at the auxiliary electrode vs. the total voltage drop U across the electrolyzer. Q = 10 A h, T = 400°C. (*1*) Lead, (*2*) antimony, (*3*) silver, (*4*) bismuth, and (*5*) copper.

the concentration of tin in it grows. The alloy acquires a more positive potential, which favors simultaneous dissolution of lead and tin. Beginning in this instant of time (after passing 4000 A h of electricity in the given case), the content of both lead and tin in the anodic alloy starts to decrease, this occurring faster after the charging of additional amounts of the starting alloy is terminated. After passing 9350 A h of electricity, the concentration of indium in the anodic alloy was not higher than 5×10^{-3}%; further, virtually no indium was detected. Since the starting melt contained no tin ions, mainly lead was deposited at the cathode in the initial stage of electrolysis, and lead–tin alloy, in later stages, with accumulation of tin in the electrolyte. The concentration of silver in the cathodic alloy was not higher than 5×10^{-3}%, and that of Bi, 2×10^{-2}% during the entire course of electrolysis.

Generalization of the results of electrochemical separation of lead–tin alloys of varied composition demonstrates that at 95% recovery of Pb and Sn at the cathode, the anodic alloy contains 92–95% of the initial amount of Ag, 98–99% of Bi, and 93–96% of Sb.

If the anodic dissolution of the obtained alloy, enriched with Ag, Sb, and Bi, is continued, the concentration of Pb in it can be reduced to 0.04%, and that of Sn, to 0.01%. In doing so, the concentration of Ag decreases from 1.3 to 0.2% and an antimony–bismuth alloy containing up to 70% Bi remains at the anode.

In order to diminish the transfer of metals with more positive potential (Ag, Bi, Sb) from the anode to the cathode, electrolysis was studied in reactors with a porous auxiliary electrode made of graphitized carbon and placed between the anode and cathode.

It has been found [5, 6] that such an electrode hinders transfer of metals with more positive potential from the anode to the cathode. For example, the concentration of Ag in the cathodic metal was 5×10^{-3}% without the auxiliary electrode, whereas the use of a porous auxiliary electrode made it possible to reduce this concentration to 1×10^{-3}% under the same electrolysis conditions. The concentration of Sb and Bi decreased from 2×10^{-3}% to 1×10^{-3}%. The conditions of metal discharge on a porous auxiliary electrode of this kind were analyzed in detail in [5, 6]. It was shown that the discharge of metal ions at the porous electrode depends on the voltage drop across the electrolyzer, being only observed in those cases when the voltage drop across the porous electrode is greater than, or equal to, the decomposition voltage of a metal salt in a given molten electrolyte. In this connection, it is of practical interest to study how the composition of the alloy deposited at the auxiliary electrode depends on the total voltage drop across the electrolyzer. It follows from the data in Fig. 4 that the at small voltage drops and, consequently, at low electrode current densities the alloy

deposited at the auxiliary electrode contains a greater amount of metals with more positive potential (copper, bismuth, antimony, silver) and a lesser amount of lead. The main component of the alloy is tin.

The observed dependence is in qualitative agreement with the conclusions of [5, 6] and also with the general pattern of the cathodic deposition of impurity metals in refining of non-ferrous metals in salt melts [10], according to which their content N_i in the cathodic alloy is proportional to the electrode current density j

$$N_i = K_g(C_i/j^{i-n}), \quad (2)$$

where K_g is the mass-transfer constant, C_i is the impurity concentration in the salt phase, and n = 0.5–1.0, depending on the electrolysis mode.

The porous auxiliary electrode markedly diminishes the transfer of impurity metals with more positive potential from the anode to the cathode at small voltage drops across the electrolyzer, which are, however, sufficient for their discharge.

CONCLUSIONS

(1) A method was developed for electrochemical separation of tin-based multicomponent alloys, ensuring high recovery of pure lead and tin at the cathode, with 92–95% of the initial amount of silver, 98–99% of bismuth, and 93–96% of antimony remaining at the anode. The variation of the alloy composition at the electrodes with electrolysis time was determined.

(2) In order to diminish the transfer of accompanying impurity metals from the anode to the cathode, an electrolysis scheme is proposed with a porous auxiliary electrode made of graphitized carbon. The effect of electrolysis conditions on the recovery efficiency of metals accompanying lead and tin at the auxiliary electrode was determined.

REFERENCES

1. *Osnovy metallurgii* (Fundamentals of Metallurgy), Greiver, N.S., Ed., Moscow: Metallurgizdat, 1962, vol. 2.
2. Delimarskii, Yu.K. and Zarubitskii, O.G., *Elektroliticheskoe rafinirovanie tyazhelykh metallov v ionnykh rasplavakh* (Electrochemical Refining of Heavy Metals in Ionic Melts), Moscow: Metallurgiya, 1975.
3. Kleespies, E.K., Bennetts, J.P., and Henrie, T.A., *J. Metals*, 1970, vol. 22, no. 1, pp. 42–44.
4. Zarubitskii, O.G., Dugel'nyi, A.P., Omel'chuk, A.A., *et al.*, *Tsvetn. Met.*, 1991, no. 3, pp. 30–32.
5. Omel'chuk, A.A. and Zarubitskii, O.G., *Zh. Prikl. Khim.*, 1998, vol. 71, no. 4, pp. 609–613.
6. Omelshuk, A.A. and Zarubitskii, O.G., *Electrochim. Acta*, 1999, vol. 44, no. 11, pp. 1779–1787.
7. Markov, B.F. and Volkov, S.V., *Fizicheskaya khimiya rasplavlennykh solei* (Physical Chemistry of Molten Salts), Moscow: Metallurgiya, 1965, pp. 210–216.
8. Omel'chuk, A.A., Gorbach, V.N., and Zarubitskii, O.G., *Ukr. Khim. Zh.*, 1993, vol. 59, no. 8, pp. 795–800.
9. Zarubitskii, O.G., Barchuk, V.T., and Vorontsov, A.N., *Ukr. Khim. Zh.*, 1979, vol. 45, no. 3, pp. 211–215.
10. Zarubitskii, O.G. and Omel'chuk, A.A., *Elektrokhimiya ionnykh rasplavov* (Electrochemistry of Ionic Melts), Kiev: Naukova Dumka, 1979, pp. 74–87.

Russian Journal of Applied Chemistry, Vol. 74, No. 2, 2001, pp. 214–218. Translated from Zhurnal Prikladnoi Khimii, Vol. 74, No. 2, 2001, pp. 210–215.

APPLIED ELECTROCHEMISTRY AND CORROSION PROTECTION OF METALS

Electrodeposition of Nickel–Chromium Coatings from Chromium(III) Sulfate Electrolytes

B. A. Spiridonov and A. I. Falicheva

Voronezh State Technical University, Voronezh, Russia

Received March 14, 2000

Abstract—The kinetics of electrodeposition of nickel–chromium alloys from chromium(III) sulfate electrolytes containing succinic and malonic acids was studied. The effect exerted by the electrolysis mode and the pH of the electrolyte on the composition and quality of the obtained coatings was investigated. The possibility of obtaining protective and decorative nickel–chromium coatings containing 20–55% chromium is established.

In electroplating, chromium is deposited from chromic acid electrolytes [1–3]. However, this technique of obtaining chromium coatings has a number of essential drawbacks: very high toxicity of electrolytes, low cathode current efficiency by chromium ($CE_{Cr} \approx$ 10–15%), low electrochemical equivalent, and low throwing power [4]. To improve the process of chromium plating, modified electrolytes have been created on the basis of chromium(VI), and also new electrolytes containing chromium(III) have been developed [5–7]. Chromium(III)-based electrolytes are promising: they are harmless, their electrochemical equivalent is twice that in chromic acid solutions, and the current efficiency by chromium is greater (up to 40%) [8]. However, these electrolytes have not found wide application to the present day, which is in the first place associated with their instability caused by strong tendency of chromium toward complexation. The composition of chromium(III) complexes depends on a number of factors: chromium(III) concentration, temperature, nature of ligands, pH, etc. [9]. For example, on being dissolved in water, violet chromium(III) sulfate forms hexaaqua cations $[Cr(H_2O)_6]^{3+}$ [10] which are hydrolyzed to give $[Cr(OH)(H_2O)_5]^{2+}$ in concentrated solutions and $[Cr(OH)_2(H_2O)_4]^{+}$ in dilute solutions [11]. The hydrolysis is accelerated on heating, and the solution becomes blue-green at 40–45°C, and green [green chromium(III) sulfate, GCS] at 80–90°C [8]. The conversion of violet chromium(III) sulfate to GCS is accompanied by a shift of the peaks in their absorption spectra from λ_1 = 407 and λ_2 = 570 nm to λ_1 = 424–425 and λ_2 = 590–592 nm, respectively (λ_1 and λ_2 are the wavelengths of the absorption peaks), which confirms the occurrence of complexation [12].

It was shown in [9, 11] that GCS forms polynuclear anion complexes in moderately diluted and concentrated solutions. In these complexes Cr^{3+} ions are bound by hydroxo or oxo bridging groups and by SO_4^{2-} ions. The number of ligands in the complexes depends on the GCS concentration and the solution pH. The violet modification is converted to GCS on sufficiently fast heating (within several minutes), and the reverse transition is very slow (virtually occurring within a year) and involves transformation of bridging hydroxo groups into water molecules, and oxo groups into OH^--ions. This is accompanied by a gradual shift of the absorption peaks to shorter wave-lengths.

Chromium is known to be difficultly deposited from violet solutions [4] and deposited with very low current efficiency (CE_{Cr} 5–7%) from GCS solutions. The best results (with CE_{Cr} of up to 40%) have been achieved in chromium plating from solutions obtained by "aging" of GCS (keeping at 20–25°C for 20–25 days). The thus obtained chromium(III) sulfate was named "modified" GCS [4]. Unlike the violet and green solutions, modified GCS is rather stable: it retains its composition for a long time (within 6 months), as indicated by spectral measurements. The absorption peaks (λ_1 = 415 and λ_2 = 582 nm) occupy an intermediate position between the peaks for the violet solution and GCS [12].

However, chromium plating from solutions of modified GCS has an essential drawback: CE_{Cr} decreases with increasing electrolysis duration τ_{el} and cathode current density D_c. It was found by thermography [13] that the electrolyte temperature in the near-cathode lay-

1070-4272/01/7402-0214 $25.00 © 2001 MAIK "Nauka/Interperiodica"

er increases to 50°C and more, as τ_{el} and D_c increase. This is accompanied by fast conversion of modified GCS to GCS, which does not allow thick chromium coatings (more than 40 microns) to be obtained.

The use of pulsed current makes it possible to slow down the formation of GCS and to increase the thickness of chromium coatings to 50 μm [14].

Recently, new electrolytes based on chromium(III) salts have been developed, allowing the thickness of chromium coatings to be considerably increased (to 300 μm) and yielding hard chromium coatings [15]. However, despite this apparent progress, new chromium plating electrolytes have not found wide application.

In some cases, coatings with alloys of chromium and iron-group metals, e.g., nickel, can serve as an alternative to the coatings obtained from chromium(III) compounds [16, 17]. Solutions for depositing Ni–Cr alloy coatings are prepared from nickel plating electrolytes by addition of chromium(III) salts [3]. It is impossible to obtain Ni–Cr coatings using an electrolyte with chromic acid.

Nickel plating electrolytes are stable, and nickel is deposited with high current efficiency. Acid electrolytes for nickel plating have found the widest application. The deposition from these electrolytes involves two conjugated processes at the cathode: discharge of nickel(II) and discharge of hydrogen ions. The decrease in the concentration of the latter in the course of electrolysis results in a higher pH in the near-cathode layer (pH_s) and leads to the formation of nickel hydroxide and its basic compounds, which, being incorporated into the cathode precipitate, make higher the defectiveness of its crystalline structure. To stabilize the pH_s and obtain coatings with improved physicochemical properties, buffer components are introduced into nickel plating electrolytes, boric acid being the most widely used additive [3, 18]. However, it only exerts a buffer effect in a narrow pH range (5–6). The acid cannot be used as a buffer component in the electrolytes for deposition of Ni–Cr alloys, since chromium hydroxide is formed at much lower pH than nickel hydroxide (the solubility products $SP_{Ni(OH)_2}$ and $SP_{Cr(OH)_3}$ are 3.2×10^{-6} and 6.3×10^{-31}, respectively). More effective buffer components for plating of both nickel and Ni–Cr alloys are aminoacetic acid [19] and oxo- and dicarboxylic acids: tartaric H_2Tart, citric H_3Cit, malonic H_2Mal, succinic H_2Suc, glutaric H_2Glut, etc. [18, 20, 21].

Aqua complexes $[Ni(H_2O)_6]SO_4$, i.e. outer-orbital $4sp^3d^2$ octahedral ions, are formed in aqueous solutions of nickel(II) sulfate [9]. The introduction of oxo- and dicarboxylic acids into a nickel(II) sulfate solution is accompanied by complexation, which is confirmed by absorption spectra [20]. For example, the complex $[NiH_2Cit]^+$ is formed with citric acid. It has been found that the stability of the forming complexes with respect to a ligand decreases in the order: $Tart^{2-} > Cit^{3-} > Glut^{2-} > Suc^{2-} > Mal^{2-}$.

These results are in agreement with published data [22]. For example, in the series of acids H_2Mal–H_3Cit–H_2Tart the least stable complex is formed with malonic acid ($K_i = 7.3 \times 10^{-5}$), and the most stable, with tartaric acid ($K_i = 3.8 \times 10^{-6}$). The same buffer additives have been recommended for deposition of Ni–Cr alloys. For example, to obtain mirror-bright Ni–Cr coatings up to 3 μm thick with chromium content of 10–16%, aminoacetic acid is introduced into the sulfate electrolyte [19].

A preliminary study has shown that nickel–chromium coatings can be obtained from sulfate electrolytes (based on modified GCS) containing both succinic [23] and malonic acids as buffer and complexing additives. In the present study, we continued investigation of the electrodeposition of Ni–Cr alloys from sulfate electrolytes containing succinic and malonic acids.

EXPERIMENTAL

For the electrodeposition of Ni–Cr alloys we prepared a solution containing a brightener and nickel and chromium sulfates (modified GCS) (M): $NiSO_4 \times 7H_2O$ 1.0, $Cr_2(SO_4)_3$ 0.5; butyne-1,4-diol 1.5 ml l^{-1}. From this solution we obtained electrolytes containing succinic and malonic acids (M): electrolyte I H_2Suc 0.5, electrolyte II H_2Mal 0.1, and electrolyte III H_2Mal 0.5. For comparative studies we prepared electrolyte IV for chromium plating (0.5 M modified GCS and 0.2 M monoethanolamine) and electrolyte V for nickel plating (1.5 M $NiSO_4$, 30 g l^{-1} H_3BO_3, and 1.5 ml l^{-1} butyne-1,4-diol).

The current efficiency by the alloy (CE_{al}) was determined gravimetrically using a copper coulometer, with account taken of the alloy composition. The nickel content of the alloy was determined spectrophotometrically with dimethylglyoxime, and that of chromium, by the persulfate-silver method. The cathodic polarization was studied potentiodynamically (4 mV s^{-1}) on a P-5827 M potentiostat with a KSP self-recording potentiometer. All the potentials are given relative to a silver chloride electrode which served as a reference; platinum was used as an auxiliary electrode. Partial polarization curves were obtained by decomposition of the overall experimental curves on the basis

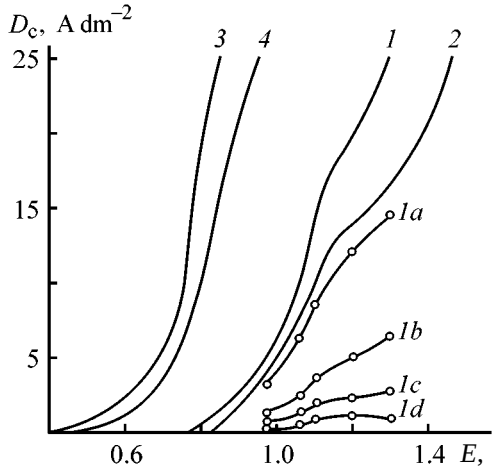

Fig. 1. Cathodic polarization curves obtained in deposition of nickel–chromium alloys from electrolytes with (*1*, *2*) succinic and (*3*, *4*) malonic acids at 50°C. D_c Current density and E potential; the same for Fig. 2. pH: (*1*, *3*, *4*) 1.0, (*2*) 1.5. H_2Mal concentration (M): (*3*) 0.1, (*4*) 0.5. (*1a–1d*) Partial polarization curves of H_2, Cr^{2+}, Ni^0, and Cr^0 formation.

of data on the current efficiencies by hydrogen, nickel, and chromium. The quality of the cathode deposits was judged from the outward appearance of the coatings; their reflectivity was studied with an FM-58 P photometer, and the morphology, with an MIM-7 microscope.

Analysis of the partial polarization curves derived from the overall curve of Ni–Cr alloy deposition from electrolyte I with succinic acid (Fig. 1) shows that chromium(III) is reduced to chromium(II) ($E^0_{Cr^{3+}/Cr^{2+}}$ = –0.41 V) simultaneously with the formation of hydrogen ($E^0_{H^+/H^0}$ = 0 V), nickel ($E^0_{Ni^{2+}/Ni^0}$ = –0.25 V), and chromium ($E^0_{Cr^{3+}/Cr^0}$ = –0.71 V). The rate of the last process (curve *1b*) exceeds that of nickel deposition (curve *1c*). One of the reasons why nickel formation is hindered is the adsorption of colloid surface-active $Cr(OH)_3$ on active sites of the cathode. The formation of chromium(III) hydroxide becomes possible at pH_s 2.9, a value that can be reached during the electrolysis [24].

With pH increasing from 1 to 1.5, the polarization curve shifts to the negative region, e.g., by 0.15 V at D_c = 15 A dm^{-2} (Fig. 1, curve *2*), which is accompanied by a decrease in the rate of hydrogen formation (Table 1). In the process, CE_{al} grows from 20 to 36%. The rate of nickel formation increases insignificantly (by a factor of ~1.2). Mention should be made of a decrease in the rate of the formation of Cr(II) ions. For example, at D_c = 25 A dm^{-2} the partial current density of chromium(II) ion formations decreases from 6.57 to 5.73 A dm^{-2}. Simultaneously, the partial current density of chromium formation increases from 1.05 to 2.91 A dm^{-2}, i.e., almost by a factor of three, and the alloy is enriched with chromium (from 32 to 51%).

It follows from these data that chromium(II) ions are formed at stronger polarization than chromium ions. It may be assumed that the process Cr^{3+} + 3e $\rightarrow$ Cr^0 is more probable, compared with $Cr^{3+} \rightarrow Cr^{2+} \rightarrow Cr^0$. A similar conclusion was made in [25]. Studies of the mechanism of chromium deposition from ammonium chromic alum have shown that the joint reduction of Cr^{3+} and Cr^{2+} ions to the metal is only possible when the fraction of Cr^{2+} ions in solution is no less than 50% of the total chromium (III) concentration in the electrolyte, which is impossible under the actual electrolysis conditions.

When pH exceeds 1.5, the rate of chromium deposition and CE_{al} decrease, the quality of the coatings is impaired, the coatings become dull, and burning appears along the cathode contour.

With D_c increasing to above 20 A dm^{-2}, the rate of chromium formation decreases (Table 1) and the alloy is enriched with nickel. Making the electrolysis duration longer has a similar effect. For example,

Table 1. Partial current densities of hydrogen, chromium(II), nickel, and chromium formation at T = 50°C

D_c, A dm^{-2}	i_{H^2}		$i_{Cr^{2+}}$		i_{Ni^0}		i_{Cr^0}	
	A dm^{-2}, at electrolyte pH							
	1.0	1.5	1.0	1.5	1.0	1.5	1.0	1.5
5	3.12	3.03	1.23	0.97	0.61	0.66	0.04	0.34
10	6.15	5.12	2.25	2.04	1.32	1.62	0.28	1.22
15	8.44	6.64	3.56	2.92	2.04	2.63	0.96	2.81
20	11.86	9.13	4.69	4.43	2.43	3.31	1.02	3.13
25	14.67	12.21	6.57	5.73	2.71	4.15	1.05	2.91

with τ_{el} increasing from 20 to 30 min, the content of chromium in the alloy decreases by approximately 20%. The hindrance to chromium deposition is due to a rise in pH_s with increasing τ_{el}, and it becomes more pronounced with growing D_c. With increasing pH_s, not only chromium(III) hydroxide is formed, but also the ionic composition of the electrolyte changes, which is accompanied by an increase in the concentration of green chromium(III) complexes whose reduction proceeds at higher cathode polarization [8].

It is evident from Fig. 1 that the overall polarization curves of Ni–Cr alloy deposition from electrolytes with malonic acid lie at more positive potentials (Fig. 1, curves *3* and *4*) than those for an electrolyte with succinic acid (curves *1* and *2*). This is apparently due to the lower stability of nickel complexes with H_2Mal.

Comparison of *E*–*i* curves for electrolytes II and III shows that the alloy is deposited with greater polarization from the electrolyte with higher H_2Mal concentration (curve *4*), which is attributable to the complexation involving not only nickel, but also chromium.

The overall polarization curve of joint deposition of nickel and chromium at room temperature lies between the curves of chromium deposition from electrolyte IV (Fig. 2, curve *2*) and nickel deposition from electrolyte V (Fig. 2, curve *1*).

The pH of electrolyte noticeably affects the position of the overall *E*–*D* curves. It is seen from Fig. 2 that the polarization curves are shifted to the negative region with pH increasing from 1 to 1.5. For example, at D_c = 15 A dm^{-2} the shift of the potential in electrolyte IV is 0.18 V (curve *2*'), and that in electrolyte V, 0.12 V (curve *1*').

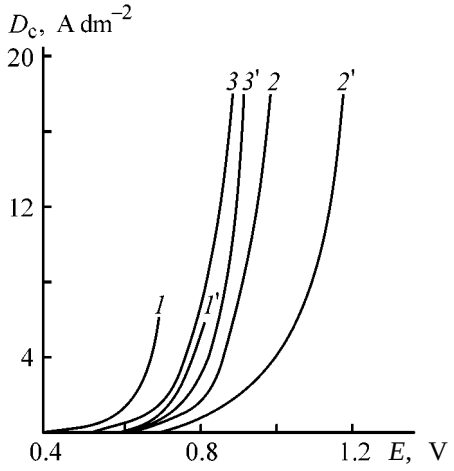

Fig. 2. Cathodic polarization curves of deposition of (*1*, *1*') nickel, (*2*, *2*') chromium, and (*3*, *3*') nickel–chromium alloy from sulfate electrolytes with H_2Mal (0.5 M) at 25°C. pH: (*1*–*3*) 1.0 and (*1*'–*3*') 1.5.

Comparison of curves *3* (Fig. 2) and *4* (Fig. 1) shows that, with temperature increasing from 25 to 50°C, the polarization of alloy deposition decreases, which is obviously due to an increase in the overvoltage of hydrogen evolution and higher solubility of chromium(III) hydroxide.

Table 2. Nickel content C_{Ni} of the alloy, CE_{al}, thickness δ, and outward appearance of coatings deposited from sulfate electrolytes with H_2Mal at *T*=50°C, τ_{el} = 20 min

pH	D_c, A dm^{-2}	CE_{al}, %	C_{Ni}, %	δ, μm	pH	D_c, A dm^{-2}	CE_{al}, %	C_{Ni}, %	δ, μm
Electrolyte II					Electrolyte III				
0.7	5	5.1	60.1	1.2 (L)	0.7	5	1.2	44.8	0.2 (L)
	10	10.2	63.0	4.5 (L)		10	2.6	46.3	1.2 (L)
	20	13.7	68.2	11.3 (SL)		20	3.5	50.5	3.1 (L)
	30	15.6	72.3	12.1 (D)		30	4.3	60.2	5.2 (SL)
1.0	5	6.4	61.2	1.5 (SL)	1.0	5	1.5	49.1	0.5 (L)
	10	13.7	63.8	5.6 (D)		10	3.0	52.8	2.5 (L)
	20	21.1	69.9	17.2 (D)		20	3.9	56.4	3.3 (SL)
	30	22.3	73.1	25.5 (D)		30	4.6	58.1	5.8 (SL)
1.5	5	14.1	66.5	2.9 (SL)	1.5	5	3.1	50.3	0.6 (L)
	10	16.7	72.2	6.8 (D)		10	6.3	54.4	2.8 (SL)
	20	21.7	76.4	17.7 (D)		20	7.4	58.1	8.1 (D)
						30	9.8	60.2	14.2 (D)

Note: L lustrous, SL semilustrous, D dull.

The effect of the electrolysis modes on the nickel content of an alloy, CE_{al}, and thickness and quality of coatings is illustrated in Table 2. It is evident that CE_{al} does not exceed 22% at the maximum thickness of 25 μm, and the deposited coatings are dull. Mirror-bright coatings have a thickness of 4–6 μm. With increasing D_c, the current efficiency by the alloy grows for both the electrolytes, CE_{al} being higher in all electrolysis modes for the electrolyte with lower H_2Mal concentration. Electrolyte III has a wider D_c range for obtaining bright coatings, but in this case the deposit has smaller thickness.

CONCLUSIONS

(1) It was found that joint electrodeposition of chromium and nickel is possible from electrolytes containing nickel and chromium sulfates [modified green chromium(III) sulfate] and succinic or malonic acid as buffer and complexing additives.

(2) Analysis of the partial curves shows that chromium(II) ions are formed in electrolysis; however, they do not exert any significant influence on the formation of metallic chromium, the process $Cr^{3+} + 3e \rightarrow Cr^0$ being, therefore, more probable.

(3) Sulfate electrolytes with succinic and malonic acids were developed for depositing protective and decorative nickel–chromium alloy coatings (20–55% Cr) at D_c 5–20 A dm^{-2}, T = 50°C, and pH 1–1.5; the current efficiency by the alloy is 20–35%.

REFERENCES

1. *Prikladnaya elektrokhimiya* (Applied Electrochemistry), Kudryavtsev, N. T., Ed., Moscow: Khimiya, 1975.
2. Bogoraz, L.Ya., *Khromirovanie* (Chromium Plating), Leningrad: Mashinostroenie, 1984.
3. *Gal'vanicheskie pokrytiya v mashinostroenii: Spravochnik* (Electroplating in Engineering: Reference Book), Shluger, M.F., Ed., Moscow: Mashinostroenie, 1985, vol. 1.
4. Falicheva, A.I., *Zh. Vsesoyuzn. Khim. Obshch. im. D. I. Mendeleeva*, 1964, vol. 9, no. 8, pp. 555–557.
5. USSR Inventor's Certificate, no. 1177398.
6. USSR Inventor's Certificate, no. 1636481.
7. Kudryavtsev, V.N. and Vinokurov, E.G., Abstracts of Papers, *15-i Mendeleevskii s"ezd po obshchei i prikladnoi khimii* (15th Mendeleev Congress on General and Applied Chemistry), Minsk, Belarus, 1993, pp. 166–167.
8. Falicheva, A.I. and Burdykina, R.I., *Gal'vanotekhn. Obrabotka Poverkhn.*, 1997, vol. 5, no. 1, pp. 15–19.
9. Remy, H., *Lehrbuch der Anorganischen Chemie*, vol. 2, Leipzig: Akademische Verlagsgesellschaft Geest and Portig K.-G., 1961.
10. Grinberg, A.A., *Vvedenie v khimiyu kompleksnykh soedinenii*, Leningrad: Goskhimizdat, 1951.
11. Lavrukhima, A.K. and Yukina, L.V., *Analiticheskaya khimiya khroma* (Analytical Chemistry of Chromium), Moscow: Nauka, 1979..
12. Falicheva, A.I., *Elektrokhim.*, 1968, vol. 4, no. 7, pp. 856–858.
13. Falicheva, A.I., Shalimov, Yu.N., and Ionova, I.G., *Zashch. Met.*, 1972, vol. 8, no. 4, pp. 499–503.
14. Shalimov, Yu.N., Falicheva, A.I., and Spiridonov, B.A., *Zashch. Met.*, 1977, vol. 13, no. 15, pp. 623–625.
15. Elinek, T.V., *Gal'vanotekhn. Obrabotka Poverkhn.*, 1997, vol. 5, no. 2, pp. 7–23.
16. Fedot'ev, N.P., Bibikov, N.N., Vyacheslavov, P.M., and Grilikhes, S.Ya., *Elektroliticheskie splavy* (Electrolytic Alloys), Moscow: Mashgiz, 1962.
17. Vyacheslavov, P.M., *Elektroliticheskoe osazhdenie splavov* (Electrodeposition of Alloys), Leningrad: Mashinostroenie, 1980.
18. Kudryavtsev, V.N. and Tsupak, T.E., *Issledovaniya v oblasti fizicheskoi khimii, analiticheskoi khimii i elektrokhimii* (Investigations in Physical Chemistry, Analytical Chemistry, and Electrochemistry), Moscow: Mendeleev Inst. Chem. Technol., 1963, no. 64, pp. 80–85.
19. Kudryavtsev, V.N. and Tsupak, T.E., *Issledovaniya v oblasti fizicheskoi khimii, analiticheskoi khimii i elektrokhimii* (Investigations in Physical Chemistry, Analytical Chemistry, and Electrochemistry), Moscow: Mendeleev Inst. Chem. Technol., 1963, no. 64, pp. 96–101.
20. Zvyagintseva, A.V., Falicheva, A.I., Spiridonov, B.A., and Shalimov. Yu.N., *Izv. Vyssh. Uchebn. Zaved., Khim. Khim. Tekhnol.*, 1988, vol. 31, no. 12, pp. 91–95.
21. Falicheva, A.I., Matantsev, A.I., and Lavrinova, A.E., *Zh. Prikl. Khim.*, 1964, vol. 37, no. 12, pp. 2600–2606.
22. Lur'e Yu.Yu., *Spravochnik po analiticheskoi khimii* (Handbook of Analytical Chemistry), Moscow: Khimiya, 1979.
23. Shalimov, Yu.N., Spiridonov, B.A., Satarov, V.V., and Falicheva, A.I., *Zashch. Met.*, 1986, vol. 22, no. 1, pp. 95–98.
24. Kublanovskii, V.S., Gorodyskii, A.V., Belinskii, L.N., and Glushchak, G.S., *Kontsentratsionnye izmeneniya v prielektrodnykh sloyakh v protsesse elektroliza* (Concentration Changes in Near-Electrode Layers in the Course of Electrolysis), Kiev: Naukova Dumka, 1978.
25. Zabotin, P.I. and Kozlovskii, M.T., *Izv. Akad. Nauk Kazakh. SSR, Ser. Khim.*, 1956, issue 6, no. 10, pp. 64–68.

Russian Journal of Applied Chemistry, Vol. 74, No. 2, 2001, pp. 219–223. Translated from Zhurnal Prikladnoi Khimii, Vol. 74, No. 2, 2001, pp. 215–220.

APPLIED ELECTROCHEMISTRY AND CORROSION PROTECTION OF METALS

Electrochemical Decomposition of Phenylhydrazine on a Fibrous Carbon Electrode

O. S. Zhukova, L. P. Lazareva, and V. Yu. Glushchenko

Institute of Chemistry, Far Eastern Division, Russian Academy of Sciences, Vladivostok, Russia

Received July 13, 2000

Abstract—Oxidation of phenylhydrazine by atmospheric oxygen in aqueous solution, its catalytic breakdown in the presence of Aktilen A carbon fiber, and electrochemical decomposition on a polarized carbon fiber were studied. Formation of various organic products of phenylhydrazine breakdown, remaining in solution after oxidation with air and catalytic decomposition on a carbon fiber, was studied by spectroscopy and chromatography. Feasibility of electrochemical decomposition on a carbon fiber for wastewater treatment to remove hydrazine derivatives was examined.

Hydrazine derivatives are a class of organic compounds widely used in various industries and in pharmacology. Hydrazines being highly toxic, various methods are used to remove hydrazine derivatives from wastewater. These methods are predominantly based on decomposition of the hydrazine group by various oxidants, such as chlorine, ozone, and oxygen [1].

At present, a process for oxidative decomposition of hydrazines on the electrode surface is being developed. However, the data on this process are scarce and mainly concern the mechanism of oxidation of hydrazine and its low-molecular-weight derivatives on a charged surface. Data on electrochemical oxidation of complex aromatic hydrazine derivatives are lacking.

In most works, the electrodes are built of various carbon materials, especially carbon fibers with excellent kinetic properties in sorption and electrochemical processes, ensured by the mobility of fibrils in the fiber structure [2, 3]. These fibrous carbon materials are used as matrices for preparing modified electrodes catalytically active with respect to hydrazine decomposition. Their surface is modified with noble metals [4–7] or metal complexes [8]. In all the cases, the electrolysis of hydrazine solution at controlled oxidation potential causes electrolytic oxidation of hydrazine to nitrogen. As shown in the above papers, no electrolytic oxidation of hydrazine is observed in the case of unmodified fibrous carbon electrodes in the range of potentials extending up to the potential of oxygen evolution from water.

It should be noted that data on electrochemical decomposition of hydrazine and its organic derivatives on unmodified fibrous carbon electrodes are almost lacking. As found in [9], electrolytic oxidation of phenylhydrazine on the surface of unmodified pyrographite yields benzene, nitrogen, and a number of complex organic compounds. Since carbon materials are suitable for hydrazine oxidation, investigating the electrochemical oxidation of more complex hydrazine derivatives on a carbon fiber for their removal from wastewater is of practical importance.

Published data [10, 11] indicate that hydrazines are unstable in aqueous solutions; they are oxidized by atmospheric oxygen and decompose in the presence of various catalysts. Hence, electrochemical oxidation of hydrazine derivatives in real wastewater on fibrous carbon electrodes will be accompanied by the above processes.

In this study, we analyzed the interaction of phenylhydrazine with the surface of a carbon electrode charged from an external electric current source and the feasibility of electrochemical decomposition on fibrous carbon electrodes for wastewater treatment to remove phenylhydrazine.

EXPERIMENTAL

In this study, we used Aktilen A brand carbon fiber with specific surface area S_{sp} 1000 $m^2 g^{-1}$ and average pore radius r_{av} 2.5 nm.

1070-4272/01/7402-0219 $25.00 © 2001 MAIK "Nauka/Interperiodica"

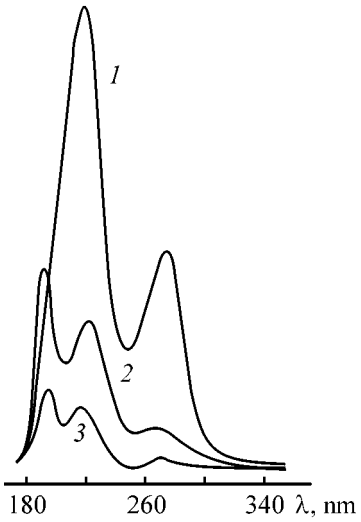

Fig. 1. UV spectra of a phenylhydrazine solution: (*1*) initial, (*2*) after contact with atmospheric oxygen, and (*3*) after contact with carbon fiber. (λ) Wavelength; the same for Fig. 6. Phenylhydrazine concentration C_0 7×10^{-3} M; the same for Figs. 2, 4–6.

Phenylhydrazine was prepared from crystalline phenylhydrazine hydrochloride [12]. Phenylhydrazine hydrochloride (200 g) was treated with a 30% solution of sodium hydroxide (100 ml), and phenylhydrazine was extracted with two 50-ml portions of benzene. The benzene extract was dried over potassium hydroxide and the solvent was removed on a rotary evaporator. Phenylhydrazine was purified by distillation in a vacuum; fraction with bp 120°C/12 mm Hg was collected.

The supporting electrolyte was a 0.1 N solution of chemically pure grade Na_2SO_4; the initial solutions of phenylhydrazine (0.2 M) were prepared in this electrolyte solution.

The electrochemical tests were carried out using a P-5827-M potentiostat and a three-electrode cell with cathode and anode volumes separated by an MB-2 bipolar membrane. The experimental procedure is presented elsewhere [13].

The spectral characteristics of the products of phenylhydrazine decomposition were registered on a Hitachi-220A spectrophotometer with the supporting electrolyte as reference. A chromatographic analysis of the products was performed on a Shimadzu LC 9A chromatograph equipped with a 250 × 4.6-mm Zorbax C18 column (ODS). Gradient elution was carried out with the concentration of isopropanol in the eluent varied between 0 and 100% in a single separation run; the elution rate was 0.6 ml min^{-1}. A UV detector was used; the analysis time was 1 h.

As seen from published data, the decomposition of hydrazine on the surface of a charged fibrous carbon electrode proceeds simultaneously with the oxidation of hydrazines by atmospheric oxygen and their catalytic oxidation on the fibrous carbon surface. Thus, to assess the feasibility of using carbon fibers as electrodes for electrolytic oxidation of phenylhydrazine it is necessary to elucidate the role of the above processes in the phenylhydrazine decomposition.

It is known that the oxidation of hydrazine derivatives involves formation of a diimide intermediate [14, 15]. The typical reaction is as follows:

(1)

This phenyldiimide can participate in several reactions yielding various oxidation products, such as benzene and nitrogen (main products) and hydrazobenzene, azobenzene, etc. [16]. Moreover, it was found that phenyldiimide radical participates in the radical dimerization yielding dimer **I** by the following reaction [9, 17]:

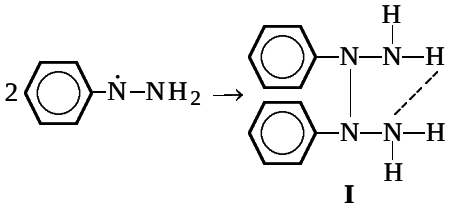

(2)

I

To elucidate the contribution of each reaction proceeding in phenylhydrazine solutions, we studied freshly prepared model solutions and phenylhydrazine solutions after their contact with air for 1–5 days. After contact with air, the model solution acquired an intense yellow-brown color, and a crystalline brown precipitate was formed and accumulated . This is probably due to the formation of product **I** by reaction (2).

The resulting solution was filtered, and a significant decrease in the phenylhydrazine concentration was found. The UV spectra (Fig. 1) show that the intensity of the peak at λ 272 nm, typical of phenylhydrazine, significantly decreases for solution brought in contact with air as compared with the freshly prepared solution. This result is confirmed by a chromatographic analysis of phenylhydrazine solutions, indicating that the concentration of phenylhydrazine in solution significantly decreases after its contact with air; moreover, additional peaks are observed in the chromatogram

(Fig. 2). One of these peaks was assigned to benzene, which was confirmed by the chromatogram of a reference benzene sample registered under the same conditions. Two other peaks belong to unidentified compounds. The decrease in the concentration of phenylhydrazine, evaluated from the peak areas, is 70%. The main pathway of phenylhydrazine consumption during contact of its solutions with air is probably precipitation of compound **I**.

Our data show that, after the oxidation of solutions with initial phenylhydrazine concentration of 300 mg l^{-1}, the residual content of phenylhydrazine in solution is as high as 36 mg l^{-1}, which significantly exceeds the maximal permissible concentration (MPC), 0.01 mg l^{-1}.

Thus, oxidation of phenylhydrazine solutions by air is characterized by insufficient conversion of phenylhydrazine, formation of significant amounts of compound **I**, and intense coloring of the solution.

Decomposition of hydrazine and its derivatives in the presence of catalysts proceeds more readily as compared with oxidation by air [18]. Published data show that hydrazine decomposes faster in the presence of such catalytically active materials as *d* metals [19], modified carbons [20, 21], and carbon fibers [22]. We studied the decomposition of phenylhydrazine in the presence of Aktilen A carbon fiber. The decrease in the concentration of phenylhydrazine is predominantly observed during its sorption on the fiber surface (Fig. 1). It should be noted that this process is accompanied by significant gas evolution associated with partial degradation of phenylhydrazine on the fiber, which is catalytically active in the phenylhydrazine oxidation. The gas evolution observed is probably due to catalytic decomposition of phenylhydrazine, which, by analogy with the case of hydrazine [18], can be described by the following equations:

$$2Ph{-}NHNH_2 + [O] \rightarrow 2Ph{-}NH_2 + N_2 + H_2O, \quad (3)$$

$$Ph{-}NHNH_2 + [O] \rightarrow C_6H_6 + N_2 + H_2O. \quad (4)$$

The chromatographic data (Fig. 2) show that, after 5-h contact with carbon fiber, the decrease in the phenylhydrazine concentration in solutions, calculated from the areas of the chromatographic peaks, reaches 70%. The decrease in the phenylhydrazine concentration after solution contact with carbon fiber for 4 days reaches 90%. All the chromatograms exhibit peaks belonging to various oxidation products. The main oxidation product is benzene. It should be noted that the content of these products in solution remains almost constant even after 4-day contact with carbon fiber.

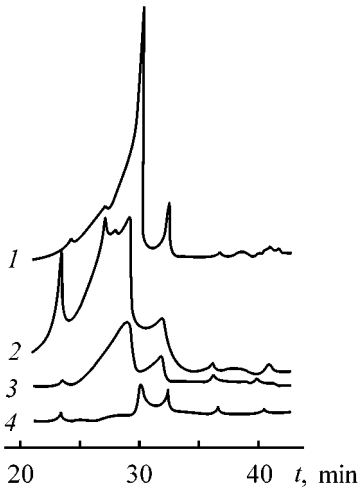

Fig. 2. Chromatograms of phenylhydrazine solution: (*1*) initial, (*2*) after contact with atmospheric oxygen for 5 days, and after contact with carbon fiber for (*3*) 5 h and (*4*) 5 days. (*t*) Time; the same for Figs. 3–5.

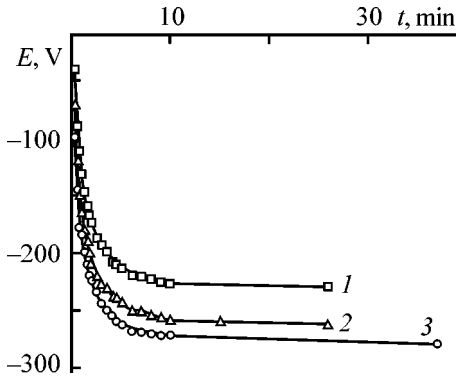

Fig. 3. Shift of the potential of Aktilen A fiber from the initial value upon addition of phenylhydrazine to 0.1 N Na_2SO_4 solution. (*E*) Potential. Phenylhydrazine concentration C_0 (mM): (*1*) 1, (*2*) 5, and (*3*) 7.

Our experimental data suggest that the decomposition of phenylhydrazine in solution in the presence of carbon fiber yields predominantly nitrogen and organic oxidation products, which are retained in solution and on the fiber surface. Thus, the catalytic decomposition of phenylhydrazine on the carbon fiber surface is unsuitable for wastewater treatment to remove phenylhydrazine. Although the catalytic conversion of phenylhydrazine is rather high, it takes too long time.

During our experiments on catalytic oxidation of phenylhydrazine on a fibrous carbon electrode with controlled potential, we found that the stationary electrode potential strongly shifts toward the cathodic region upon addition of phenylhydrazine to the solution (Fig. 3).

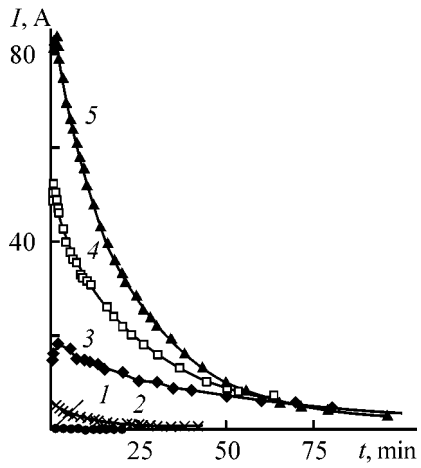

Fig. 4. Anodic current *I* on (*1, 2*) platinum gauze electrode and (*3–5*) Aktilen A fibrous carbon electrode in (*1*) 0.1 N Na_2SO_4 solution and (*2–5*) phenylhydrazine solutions. Potential *E* (V): (*1, 2, 4*) +0.25, (*3*) +0.15, and (*5*) +0.40.

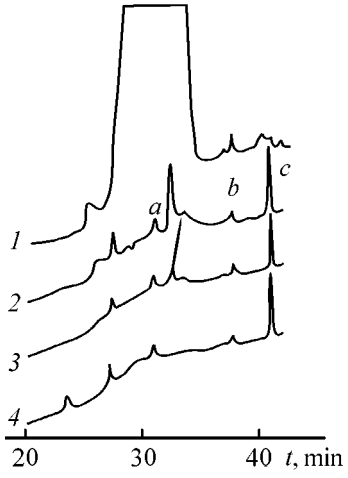

Fig. 5. Chromatograms of phenylhydrazine solutions: (*1*) initial and (*2–4*) that after contact with Aktilen A carbon fiber at various polarization potentials. Potential *E* (V): (*2*) +0.15, (*3*) +0.40, and (*4*) +0.60.

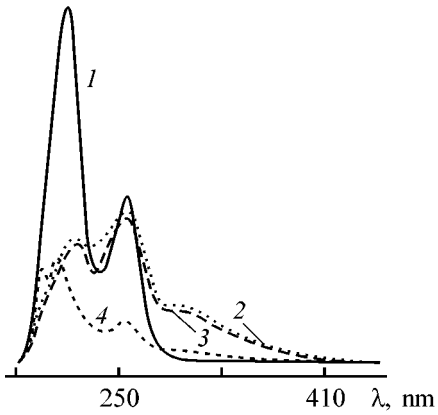

Fig. 6. UV spectra of (*1*) initial phenylhydrazine solution and (*2–4*) that after its contact with Aktilen A carbon fiber. Potential *E* (V): (*2*) +0.15, (*3*) +0.25, and (*4*) +0.40.

To study the effect of the carbon fiber potential on the oxidation efficiency, we measured the dependences of the current of anodic oxidation of phenylhydrazine carbon fiber surface at potentials of +0.15, +0.25, +0.40 (Fig. 4, curves *3–5*), and +0.60 V. All the curves have the same shape. Upon addition of phenylhydrazine the current first sharply increases and then decreases, which suggests intensive oxidation of phenylhydrazine on the charged fiber surface in the initial period. Then the oxidation current gradually decreases, which is due to the decrease in the phenylhydrazine concentration in solution, and reaches a certain constant value corresponding to the current of the Faraday reaction on the carbon fiber surface in the electrolyte solution in the absence of phenylhydrazine. This indicates that the decomposition of phenylhydrazine is practically complete at all the potentials studied.

With increasing potential of the carbon electrode, the initial current jump increases, i.e., the reaction rate depends on the polarization potential: the higher the polarization potential, the shorter the time in which the Faraday reaction current is attained.

It should be noted that the contribution from electrochemical decomposition of phenylhydrazine on the platinum current lead is insignificant. The currents of phenylhydrazine oxidation on the platinum electrode (Fig. 4, curve *2*) are significantly smaller than the total reaction current and thus the entire effect of electrocatalytic oxidation is due to the carbon fiber activity [23].

A chromatographic analysis of phenylhydrazine solutions brought in contact with polarized carbon fiber (Fig. 5) showed that the composition and content of the products of electrochemical oxidation of phenylhydrazine correlate with the electrode potential. As seen from the chromatogram of the phenylhydrazine solution after contact with the fibrous electrode at *E* +0.15 V, nearly 1% of phenylhydrazine is retained in solution along with various oxidation products (peaks *a–c*, peak *b* is assigned to benzene). Some of the oxidation products are colored, probably of aromatic nature, with a system of conjugated bonds requiring additional identification. The presence of the colored compound is manifested in the UV spectra of solutions as the band at λ 328 nm (Fig. 6).

At increased polarization potential of the carbon electrode, removal of the oxidation products from the solution is almost complete. The phenylhydrazine solutions obtained after oxidation at *E* +0.40 and +0.60 V are colorless; the oxidation of phenylhydra-

zine at these potentials is accompanied by vigorous gas evolution. The chromatograms of the resulting solutions are similar and contain peaks belonging to traces of organic compounds. Thus, the electrochemical decomposition of phenylhydrazine is almost complete even at +0.40 V. Our experimental results suggest that the unmodified carbon fiber is also active in electrochemical oxidation of phenylhydrazine and provides its almost complete decomposition and removal from solution.

Thus, the electrochemical decomposition of phenylhydrazine involves two simultaneous processes: oxidation of phenylhydrazine on the catalytic centers of carbon fibers and electrochemical oxidation in contact with the charged fiber surface. This suggests that the electrochemical decomposition of phenylhydrazine on the carbon fiber is an electrocatalytic process.

However, it should be noted that in some papers low activity of carbon fibers in the oxidation of hydrazine derivatives was observed, and it was recommended to modify the electrode surface to improve the oxidation efficiency [20–23].

CONCLUSIONS

(1) Even unmodified carbon fiber exhibits high electrocatalytic activity in electrochemical oxidation of phenylhydrazine and ensures its almost complete decomposition and removal from solution.

(2) The method of electrochemical decomposition can be recommended for wastewater treatment to remove phenylhydrazine, because the oxidation proceeds at low potentials and no additional contaminants are formed; as a result, phenylhydrazine is decomposed into environmentally safe products.

REFERENCES

1. Grekov, A.P. and Veselov, V.Ya., *Fizicheskaya khimiya gidrazina* (Physical Chemistry of Hydrazine), Kiev: Naukova Dumka, 1979.
2. Golub, D., Oren, Y., and Soffer, A., *J. Electroanal. Chem.*, 1987, vol. 227, nos. 1–2, pp. 41–53.
3. Sheveleva, I.V., *Cand. Sci. Dissertation*, Vladivostok, 1992.
4. Andonoglou, P.P., Jannakoudakis, A.D., Jannakoudakis, P.D., and Theodoridou, E., *Electrochim. Acta*, 1998, vol. 44, nos. 8–9, pp. 1455–1465.
5. Georgolios, N. and Karabinas, P., *J. Electroanal. Chem.*, 1990, vol. 280, no. 2, pp. 403–414.
6. Liu, J., Zhou, W., You, T., *et al.*, *Anal. Chem.*, 1996, vol. 68, no. 19, pp. 3350–3353.
7. Zhou, W., Xu, L., Wu., M., and Wang, E., *Anal. Chim. Acta*, 1994, vol. 299, no. 2, pp. 189–194.
8. Antoniadou, S., Jannakoudakis, A.D., Jannakoudakis, P.D., and Theodoridou, E., *Synth. Met.*, 1989, vol. 32, no. 3, pp. 309–320.
9. Goyal, R.N. and Srivastava, A.K., *Ind. J. Chem., Ser. A.*, 1995, vol. 34, no. 7, pp. 506–511.
10. Kost, A.N. and Sagitullin, R.S., *Usp. Khim.*, 1964, vol. 33, no. 4, pp. 361–395.
11. Overberger, C.G., Anselme, J.P., and Lombardino, J.G., *Organic Compounds with Nitrogen–Nitrogen Bonds*, New York: Roland, 1966.
12. *Organikum. Organisch-chemisches Grundpraktikum*, Berlin: VEB Deutscher Verlag, 1964.
13. Lisitskaya, I.G., Lazareva, L.P., Gorchakova, N.K., and Khabalov, V.V., *Khim. Tekhnol. Vody*, 1990, no. 12, pp. 3–6.
14. Canquis, G. and Genies, M., *Tetrahedron Lett.*, 1968, vol. 32, pp. 3537–3540.
15. Foner, S.N. and Hudson, R.L., *J. Chem. Phys.*, 1958, vol. 28, no. 4, pp. 719–720.
16. Kosower, E.R. and Huang, P.C., *J. Am. Chem. Soc.*, 1965, vol. 87, no. 20, pp. 4645–4646.
17. Huang, P.C. and Kosower, E.R., *J. Am. Chem. Soc.*, 1967, vol. 89, no. 15, pp. 3910–3911.
18. Korovin, N.V., *Gidrazin* (Hydrazine), Moscow: Khimiya, 1980.
19. Lin, Ch. and Bocarsly, A.B., *J. Electroanal. Chem.*, 1991, vol. 300, nos. 1–2, pp. 325–345.
20. Cerpia, G. and Castillo, J.R., *J. Appl. Electrochem.*, 1998, vol. 28, no. 1, pp. 65–70.
21. Isaacs, M., Aguirre, M.J., Toro-Labbe, A., *et al.*, *Electrochim. Acta*, 1998, vol. 43, nos. 12–13, pp. 1821–1827.
22. Korovin, N.V. and Kicheev, A.G., *Elektrokhimiya*, 1970, vol. 6, no. 9, pp. 1330–1333.
23. Lazareva, L.P., Zhukova, O.S., and Artem'yanov, A.P., *Elektrokhimiya*, 1999, vol. 35, no. 8, pp. 1027–1029.

Russian Journal of Applied Chemistry, Vol. 74, No. 2, 2001, pp. 224–228. Translated from Zhurnal Prikladnoi Khimii, Vol. 74, No. 2, 2001, pp. 220–225.

APPLIED ELECTROCHEMISTRY AND CORROSION PROTECTION OF METALS

Protective Properties of Lead Coating with Tin Sublayer for Copper Current Leads of Negative Electrodes in Lead-acid Batteries

Yu. B. Kamenev, M. V. Lushina, A. V. Kiselevich, A. I. Rusin, and E. I. Ostapenko

Scientific and Technical Center of Elektrotyaga Joint-Stock Private Company, St. Petersburg, Russia

Received December 23, 1999, in final form, October 2000

Abstract—The possibility of using a two-layer coating consisting of a tin sublayer and a lead layer for protection of copper current leads of negative electrodes in lead batteries was studied. The processes occurring on reflowing of the tin coating were investigated. The dependence of the protective characteristics of the tin coating on the heat treatment mode was shown to have extrema.

High per-unit-weight electrical characteristics and improved current distribution being of special importance for high-power lead-acid batteries, the cutting-through current leads of their negative electrodes are made of copper [1–3].

The use of copper current leads is due to the lower specific density of copper and its higher electrical conductivity, compared with that of lead, and also to the fact that copper has sufficient mechanical strength and is easily processed.

However, copper current leads can partially dissolve in sulfuric acid solutions, which is accompanied by oxygen depolarization. The subsequent electrodeposition of copper onto the paste surface in the negative electrode results in stronger gas evolution and self-discharge, lower capacity of the negative electrode, and lower efficiency of the charging current.

From the thermodynamic point of view, almost any quantity of copper ions in solution is sufficient for copper deposition onto lead surface. The minimum equilibrium concentration of copper in solution, $\alpha_{Cu^{2+}}$, at which this process begins, is 10^{-23} mol dm^{-3} as determined from the equation

$$\alpha_{Cu^{2+}} = \exp[nF(E_{Pb} - E^0_{Cu})/RT]. \quad (1)$$

Here n is the number of electrons involved in the reaction, F is the Faraday number, R is the gas constant, T is temperature, E_{Pb} is the potential of the lead electrode, and E^0_{Cu} is the standard potential of copper.

It is evident that there is no safe concentration of copper in solution, and, therefore, we can consider only its critical or practically insignificant level. It was shown in [4] that gas evolution is considerably enhanced at copper concentrations of about 4.8×10^{-4} mol dm^{-3}. Therefore, copper current leads should be protected with a coating from coming in contact with the electrolyte. The working conditions (strongly corrosive medium and cathodic-anodic polarization) impose very stringent requirements on the quality and stability of such a coating.

At present, electrodes with copper current lead protected by a galvanic lead coating are used in high-power lead-acid batteries [1–3]. The passivation of lead makes it stable in solutions of sulfuric acid, and, thus, continuous lead coatings are expected to have high protective characteristics. However, under conditions of cathodic-anodic polarization, typical of the operation of lead batteries, the surface of a lead coating is gradually loosened through $Pb \rightleftarrows PbSO_4$ transitions associated with considerable changes in the volume and morphology of the electrode material, giving rise to pores in the originally almost pore-free coatings. Simultaneously, the adhesion of the coating may deteriorate. This results in stronger self-discharge and gas evolution because of the lower overvoltage of hydrogen evolution on copper, compared with that on lead.

The protective properties of the lead coating can be improved by depositing a sublayer [3, 5]. In the present study, we analyzed the possibility of using a tin

1070-4272/01/7402-0224 $25.00 © 2001 MAIK "Nauka/Interperiodica"

sublayer deposited from a chloride-fluoride electrolyte [6].

The microstructure of electroplated coatings was studied by electron microscopy and X-ray microanalysis on a JEOL JSM-840A scanning electron microscope (Japan). When compiling X-ray images, we used a LINK ANALYTICAL AN10/85S energy-dispersion analyzer (UK). As samples were used 5×5-mm plates cut from middle parts of larger copper laminas with electrolytic coatings. Micrographs were taken at the same magnification of 2000. The mapped surface area was 5×10^3 μm^2.

The corrosion resistance of the coatings was studied in a sulfuric acid solution with density of 1.100 g cm^{-3}. The corrosion resistance was judged from the outward appearance of the coatings and from changes in their weight upon testing. After the tests, we determined the porosity of the coatings, and also the strength of coating adhesion to the copper base, by the method of marking a grid of scratches. The content of copper and tin in sulfuric acid solutions was determined by the atomic absorption method.

As shown by a microstructural study, electroplated tin coatings have a coarsely crystalline structure and are porous at layer thickness less than 25 μm. That is why we made an attempt to improve the protective properties of porous coatings by their reflowing.

To study the dependence of the structure of electroplated coatings on the reflowing duration, we used samples in the form of $105 \times 75 \times 0.2$ mm copper laminas with tin layer 5 μm thick. The samples were placed in a muffle furnace heated to 250°C and kept at this temperature for 5, 10, 20, 30, 45, and 60 s. A microstructural study demonstrated that a tin coating, subjected to reflowing for 10 s is uneven. With increasing duration of reflowing, the surface relief is smoothed out. Apparently, in the beginning of heating, a thin layer of tin covers copper at the bottom of through pores. On further heating, the thickness of the layer decreases with simultaneous relief leveling, to the point of formation of a mirror-like surface. For example, a tin coating subjected to reflowing for 30 s is a finegrained deposit.

Corrosion tests performed for three days demonstrated that the tin coating is completely absent on a sample not subjected to heat treatment. A sample heat-treated for 10 s retained a tin layer without visible imperfections. After 20 s of heat treatment, the tin layer on the sample was lost to a considerable extent, especially in those parts where tin had bright tint. Tin heat-treated for 45 s was almost completely dissolved.

Thus, with the duration of reflowing increasing to 30 s, on the one hand, the porosity of a tin coating becomes lower and, on the other, its corrosion is accelerated. The dependence of the protective characteristics of a tin coating on the duration of heat treatment shows an extremum, which points to the occurrence of at least two processes oppositely affecting the corrosion resistance of a tin layer on copper. In the absence of reflowing, tin has a certain through porosity, which ensures a contact of copper with solution. Therefore a copper–tin contact corrosion pair arises, in which tin is the anode, and copper, the cathode. Since a high hydrogen overvoltage is characteristic of tin, its corrosion takes place mainly with oxygen depolarization and depends on the rate of oxygen supply to the tin surface.

The rate of tin corrosion in a 0.1 N solution of sulfuric acid in the presence and absence of oxygen is 600 and 100–150 g m^{-2} day^{-1}, respectively [6]. Taking into account the known fact that tin corrosion occurs with oxygen depolarization, we can approximately calculate the corrosion rate V_{cor} in battery acid (density 1.280 g cm^{-3}). The weight of tin dissolved in a time τ is given by

$$M_{Sn} = Kj_{Sn}S\tau. \quad (2)$$

Here K is the electrochemical equivalent, j_{Sn} is the current density of tin dissolution, and S is the surface area of the electrode.

Under steady-state conditions

$$j_{Sn} = j_{O_2}, \quad (3)$$

$$j_{O_2} = 4FD_{O_2}C_{O_2}\delta^{-1}. \quad (4)$$

Here j_{O_2} is the current density of oxygen reduction, D_{O_2} and C_{O_2} are the diffusion coefficient and the concentration of dissolved oxygen, respectively, and δ is the diffusion layer width. Then

$$M_{Sn} = Kj_{O_2}S\tau = 4KFD_{O_2}C_{O_2}S\tau\delta^{-1}, \quad (5)$$

$$V_{cor} = M_{Sn}/S\tau = 4KFD_{O_2}C_{O_2}\delta^{-1}. \quad (6)$$

Substitution of $K = 2.1$ g A^{-1} h^{-1}, $F = 96500$ C mol^{-1}, $D_{O_2} = 2.5 \times 10^{-5}$ cm^2 c^{-1}, $C_{O_2} = 6.5 \times 10^{-7}$ mol cm^{-3}, $\delta = 10^{-2}$ cm, $S = 10^4$ cm^2, and $\tau = 24$ h [7] gives V_{cor} equal to 327 g m^{-2} day^{-1}. The corrosion rate must be much lower under real conditions, when 20 μm of lead, strongly hindering oxygen transfer, is deposited onto the tin sublayer. However, under the conditions when tin is in contact with a more noble metal (copper), which in addition

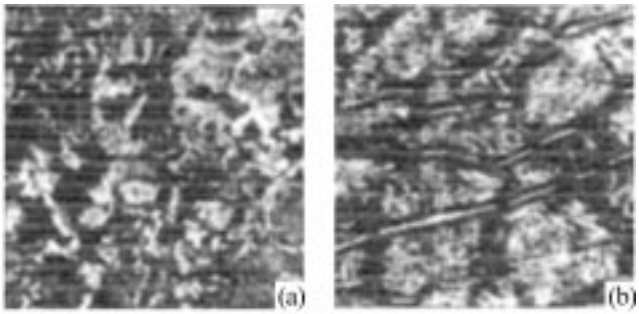

Fig. 1. Microstructure of surface layers of tin-plated samples subjected to reflowing for varied time. Reflowing duration (s): (a) 10 and (b) 30.

has hydrogen overvoltage much lower than that in tin, the mechanism of tin depolarization changes and the rate of its corrosion increases. This increase is also promoted by loosening of the lead layer in charging–discharge cycling of the battery. Thus, the absence of pores in the tin coating is a necessary condition for achieving its high protective properties. Therefore, reflowing of the tin sublayer is a necessary stage.

However, the reflowing of tin involves processes at the tin–copper interface, which strongly affect the protective characteristics of the tin coating. The distribution of copper and tin in the protective coatings on copper bases was determined by X-ray microanalysis. An analysis of such a distribution for a 5-μm-thick tin layer subjected to reflowing at 250°C for 10 s revealed the existence of a 2.5–3.0-μm-thick copper–tin transition layer on the copper side. A low-melting η-phase (Cu_6Sn_5) is formed at the tin–copper interface in the initial stage of tin reflowing as a result of copper dissolution in liquid tin. With increasing duration of reflowing, the thickness of the layer of intermetallic compounds grows noticeably. Raising the reflowing temperature also favors an increase in the thickness of this layer. Thus, the interaction of copper with molten tin results in the formation and growth of a layer of intermetallic compounds. This complicated process includes a reaction between copper and tin and the subsequent propagation of acicular crystals of intermetallic compounds across the thickness of the tin layer. It was found that the intermetallic compounds grow at a maximum rate within the first 5 s of reflowing. The intermetallic compounds of copper and tin are always of the cathodic nature with respect to tin, and, therefore, their emergence on the surface of the tin coating accelerates tin corrosion.

The microstructure of tin-plated samples subjected to reflowing in various modes is shown in Fig. 1. The structure of a coating subjected to reflowing in the optimum regime (10 s) has an appearance characteristic of electroplated tin—without acicular crystals (Fig. 1a). An X-ray analysis demonstrated the absence of copper on the surface. A coating subjected to reflowing for 30 s (Fig. 1b) has a structure of tin whose spherical crystals are pierced by acicular crystals of intermetallic compounds. An X-ray analysis demonstrated the presence of copper over the entire field under study. It is the presence of intermetallic compounds on the surface of such a coating that is responsible for its low corrosion resistance. The whole set of our experimental data confirms once more that the absence of copper in the surface layers of a nonporous coating is the condition for the high corrosion resistance of a tin coating on copper.

It follows from the aforesaid that an increase in the duration of reflowing of a tin sublayer may impair its protective characteristics, and, therefore, the choice of the duration of reflowing of the tin sublayer is one of key factors in preparing a two-layer coating.

To study the possibility of using a tin coating as a sublayer in lead-plating of copper current leads, we studied the corrosion resistance of the two-layer coating. The copper bases protected by a two-layer coating (a tin sublayer and a lead layer) were subjected to corrosion tests in sulfuric acid (density 1.100 g cm^{-3}) for 8 months. Samples with lead coating were used as reference. The results of the corrosion tests are presented in the table.

It may be safely suggested on the basis of these data that the processes occurring in a two-layer coating with tin sublayer, placed in a sulfuric acid solution, have the following mechanism. A coating without tin sublayer (sample no. 1) had good adhesion to the copper base after 5 months of tests, but the content of copper in solution was 145 mg l^{-1}, which points to rather poor protective characteristics of the coating. The accumulation of copper in solution results from the fact that the surface of lead is covered with a sulfate layer precluding contact deposition of copper from the solution.

The lead coating on a sublayer of tin not subjected to reflowing (sample no. 2), flaked away from the copper base after 5 months of tests. In this case, the content of copper in solution was 45 mg l^{-1}, which points to better protective properties of two-layer coating as compared with the coating without tin sublayer. However, the decrease in the content of copper in solution was accompanied by high content of tin (1286 mg l^{-1}). The initial weight of the tin sublayer and the concentration of tin in solution were used to determine that approximately 70–80% of the tin sub-

Results of corrosion tests of copper bases protected by two-layer coatings with tin sublayers

Sample no.	τ,* s	Outward appearance of a coating after 5 months	Content in solution, mg l^{-1}			
			copper		tin	
			in 5 months	in 8 months	in 5 months	in 8 months
		Pb coating				
1	–	Coating uniform, without visible traces of copper. Adhesion to base firm	145	283	0	0
		Sn–Pb coating				
2	–	Coating dark. Copper base visible to unaided eye. Strong flaking of the coating, adhesion to base poor	45	209	1286	1986
3	10	Minor flaking, adhesion to base satisfactory	5.6	24.8	<3	60.3
4	20	Coating dark and scaly. Separate copper points visible. Strong flaking of the coating, adhesion to base unsatisfactory	6.5	39.8	1156	1272

* τ is the duration of reflowing.

layer was dissolved in 5 months. Thus, on the one hand, tin protects copper from dissolution by the protection mechanism and, on the other, the high dissolution rate of tin not subjected to reflowing results in the loss of the coating adhesion to the base, with the resulting strong flaking, higher contact resistance, and uncovering of the copper base. An X-ray microanalysis of the copper base surface under a flaked away lead coating and of the surface of this coating from the copper base side for sample no. 2 demonstrated that, without reflowing, tin was almost completely dissolved at the copper–tin interface, as indicated by the absence of tin on the copper base surface. At the same time, the inner surface of the flaked-off lead coating consists of tin. These data indicate that in the case in question the corrosion of the two-layer coating is accompanied by a local (crevice) dissolution of the tin sublayer from the copper side. This mechanism of tin dissolution is responsible for the loss of adhesion of the protective layer to the copper base.

The lead coating deposited onto a sublayer of tin subjected to the optimal reflowing (sample no. 3, reflowing time 10 s) exhibited good adhesion to the base. After five months, the copper content in solution was 5.6 mg l^{-1}, and that of tin, less than 3 mg l^{-1}. All these facts point to a rather high corrosion resistance of tin subjected to the optimal reflowing. In this case, the corrosion of tin is accompanied by oxygen depolarization resulting from the high overvoltage of hydrogen evolution on tin under the conditions when the oxygen flow toward the tin surface is hindered by the lead layer. If a continuous layer of tin is disrupted either through the appearance of through pores (tin not subjected to reflowing) or because of the emergence of intermetallic compounds on its outer surface (on exceeding the permissible reflowing time), the mechanism of tin depolarization will change. Since copper and the intermetallic compounds have low overvoltage of hydrogen evolution, the oxidation of tin will occur with hydrogen depolarization, with the rate of hydrogen flow not limited by the layer of lead sulfate. All these factors will make higher the corrosion rate of the tin sublayer.

The lead coating deposited on a sublayer of tin subjected to reflowing in a non-optimal regime (sample no. 4, reflowing time 20 s) exhibited unsatisfactory adhesion to the base and strong flaking. The content of copper in sulfuric acid solution after five months was 6.5 mg l^{-1}, and that of tin, 1156 mg l^{-1}, which corresponds to dissolution of 65–70% of the tin sublayer. The aforesaid suggests that the increase in the reflowing time, resulting in disruption of a continuous tin sublayer through emergence of intermetallic compounds on the surface, makes higher the rate of its dissolution and, hence, leads to loss of adhesion of the protective coating to the copper base. An X-ray microanalysis demonstrated that the surface of the cop-

per base under the flaked-off coating contains 50–60% copper, and the inner side of the flaked-off coating consists of tin. The coatings with tin sublayer subjected to reflowing for 30, 45, and 60 s had similar characteristics. The data of corrosion tests performed during the subsequent three months confirmed this mechanism of the behavior of a two-layer coating with tin sublayer in sulfuric acid solutions.

Thus, our data demonstrate the exceptional importance of observing the regime of tin sublayer reflowing.

CONCLUSIONS

(1) A tin coating on a copper base, deposited from a chloride-fluoride electrolyte, is porous and shows rather poor anticorrosive characteristics. The fact that these characteristic are impaired in comparison with the corrosion rate of a compact tin is due to the accelerating effect of a $Cu/H_2SO_4/Sn$ contact pair, in which copper is cathode, on the corrosion rate.

(2) The range of heat treatment duration providing high-quality coatings was established. It was shown that making the reflowing longer results in a decrease in the corrosion resistance of a tin coating.

(3) Non-observance of the optimum regime of sublayer reflowing in fabricating a two-layer coating results in a considerable dissolution of the sublayer and loss of adhesion of the main lead layer to the copper base.

REFERENCES

1. Bagshaw, N.E., *Batteries on Ships*, Chichester: Studies Press, a Division of Wiley, 1982.
2. Goodman, S., *Batteries Int.*, 1992, no. 11, p. 105.
3. Kiessling, R., *J. Power Sourc.*, 1987, vol. 19, nos. 2–3, pp. 147–150.
4. Chunts, N.I., Rusin, A.I., and Simonova, M.V., *Issledovaniya v oblasti tekhnologii proizvodstva khimicheskikh istochnikov toka: Sbornik nauchnykh trudov Nauchno-issledovatel'skogo Akkumulyatornogo Instituta* (Studies of the Technology of Production of Chemical Power Cells: Coll. of Sci. Works of the Research Battery Institute), Leningrad: Energoatomizdat, 1986, pp. 22–27.
5. Lushina, M.V. and Kolikova, G.A., *Zh. Prikl. Khim.*, 1994, vol. 67, no. 2, pp. 296–299.
6. *Corrosion*, Shreir, L.L., Ed., 2nd Ed., London: Newnes-Butterworths, 1976.
7. Dasoyan, M.A. and Aguf, I.A., *Osnovy rascheta, konstruirovaniya i tekhnologii proizvodstva svintsovykh akkumulyatorov* (Principles of Calculation, Design, and Technology of Lead Battery Production), Leningrad: Energiya, 1978.

Russian Journal of Applied Chemistry, Vol. 74, No. 2, 2001, pp. 229–234. Translated from Zhurnal Prikladnoi Khimii, Vol. 74, No. 2, 2001, pp. 226–231.

CATALYSIS

Fe_2O_3–Li_2O Catalysts for Ammonia Oxidation

N. I. Zakharchenko

Zhukovskii State Aerospace University, Kharkov, Ukraine

Received June 13, 2000; in final form, October 2000

Abstract—The catalytic properties of the Fe_2O_3–Li_2O system in ammonia oxidation were studied in the high-temperature region. The influence of the phase composition of the system on the physicochemical and catalytic properties of the catalysts were revealed. The catalytic properties of lithium ferrite, which is the most active and selective component of the Fe_2O_3–Li_2O system, were studied. The mechanism of lithium ferrite deactivation at 1273 K is considered.

Catalytic oxidation of ammonia to nitrogen(II) oxide is the basic reaction for industrial production of nitric acid [1]. Owing to the high cost, deficiency, and irrecoverable loss of industrial catalysts (platinum, rhodium, and palladium alloys) in technological processes, a search for new efficient non-platinum catalysts (NPC) is urgent. Iron(III) oxide is a promising support for NPC, used industrially as a component in the second stage of a combined system for ammonia oxidation [1, 2]. To preserve the high activity and selectivity with respect to nitrogen(II) oxide and to enhance the thermal and chemical resistance of iron(III) oxide, various modifying additives are used, and metal oxides in particular [1–6]. The available data on catalysts for ammonia oxidation are empirical, because the modern theory of catalysis allows no unambiguous prediction of a set of properties for catalysts with various compositions, preparation procedures, and chemical prehistories. Accumulation of data on the catalytic properties of the systems is of practical and theoretical interest for the development of scientifically substantiated methods for creating catalysts with prescribed properties.

Lithium oxide (Li_2O) is used as modifying additive to iron oxide–containing catalysts, but the system Fe_2O_3–Li_2O has not been studied in a wide composition range [1, 3, 5–6]. The present work is concerned with the catalytic and physicochemical properties of the Fe_2O_3–Li_2O system in ammonia oxidation.

The catalyst was prepared by thermal decomposition in air of ferric nitrate hydrate $Fe(NO_3)_3 \cdot 9H_2O$ and lithium nitrate hydrate $Li(NO_3) \cdot 3H_2O$ (both analytically pure) mixed in a calculated ratio [7]. An X-ray phase analysis was performed on a URS-50I diffractometer in Fe_{K_α}-radiation. The phase composition of the Fe_2O_3–Li_2O catalytic system is presented in Table 1.

Table 1. Phase composition of the Fe_2O_3–Li_2O catalytic system

C_{Li_2O}, wt %	Phase composition	Properties of system components	
		crystal structure	unit cell parameter *a*, nm
0	α-Fe_2O_3	Trigonal α-Al_2O_3	0.5430
0–3.5	α-Fe_2O_3 + α-$Li_{0.5}Fe_{2.5}O_4$	–	–
3.6	α-$Li_{0.5}Fe_{2.5}O_4$	Cubic $MgAl_2O_4$	0.8330
3.7–15.7	α-$Li_{0.5}Fe_{2.5}O_4$ + α-$LiFeO_2$	–	–
15.8	α-$LiFeO_2$	Cubic NaCl	0.4156
15.9–48.2	α-$LiFeO_2$ + Li_5FeO_4	–	–
48.3	Li_5FeO_4	Rhombic Na_2O	0.9218
48.4–99.9	Li_5FeO_4 + Li_2O	–	–
100.0	Li_2O	Cubic antifluorite CaF_2	0.4628

1070-4272/01/7402-0229 $25.00 © 2001 MAIK "Nauka/Interperiodica"

Table 2. Properties of the Fe_2O_3–Li_2O catalytic system

C_{Li_2O}, wt %	S_{sp}, $m^2\ g^{-1}$	S_{NO}, % ($\tau = 6.77 \times 10^{-2}$ s)	$X \times 10^{-3}$, $m^3\ h^{-1}\ m^{-2}$	Y, rel. %	C_{Li_2O}, wt %	S_{sp}, $m^2\ g^{-1}$	S_{NO}, % ($\tau = 6.77 \times 10^{-2}$ s)	$X \times 10^{-3}$, $m^3\ h^{-1}\ m^{-2}$	Y, rel. %
0	5.9	94.7	6.50	0.30	30.0	2.2	24.3	2.42	1.33
2.0	6.4	95.0	7.05	0.26	35.0	1.9	19.1	2.09	1.41
3.0	6.8	95.3	7.49	0.24	40.0	1.7	15.5	1.87	1.48
3.6	7.1	95.5	7.82	0.21	45.0	1.6	12.2	1.76	1.50
4.0	6.9	92.9	7.60	0.23	48.3	1.5	11.2	1.65	1.53
5.0	6.6	85.5	7.27	0.25	50.0	1.4	9.2	1.54	1.55
6.0	6.3	78.6	6.94	0.27	53.0	1.3	6.8	1.43	1.58
8.0	5.7	70.2	6.28	0.40	56.0	1.2	5.5	1.32	1.64
10.0	5.0	62.9	5.50	0.55	60.0	1.0	3.8	1.10	1.71
13.0	4.2	55.7	4.63	0.75	65.0	0.9	2.6	0.99	1.73
15.0	3.6	52.0	3.97	0.91	70.0	0.8	1.9	0.88	1.78
15.8	3.5	51.0	3.86	0.93	80.0	0.6	1.1	0.67	1.87
18.0	3.1	42.1	3.42	1.02	90.0	0.5	0.7	0.55	1.92
20.0	2.9	37.7	3.19	1.10	100.0	0.4	0.4	0.44	1.97
25.0	2.5	30.2	2.75	1.22					

Note: X is the limiting AAM load, Y is ammonia breakthrough under the critical process conditions, and S_{NO} is selectivity by NO.

The specific surface area S_{sp} of the catalysts was measured by low-temperature adsorption of nitrogen and calculated by the BET equation (Table 2).

The catalyst selectivity by NO was determined on a flow-through installation with a quartz reactor 2×10^{-2} m in diameter [8]. The catalyst bed $(4–12) \times 10^{-2}$ m in height was composed of $(2 \times 3) \times 10^{-3}$-m granules; the ammonia concentration in the ammonia–air mixture (AAM) was about 10 vol %; the time of contact was 6.77×10^{-2} s, and the optimal pressure, according to previously obtained data [4], was 0.101 MPa. The test temperature corresponded to the maximum selectivity of a single-component iron oxide catalyst (1053 K) [7]. The compositions of the products of ammonia oxidation and thermal decomposition of nitrogen(II) oxide on the catalysts were determined by chromatographic analysis of the gas mixture for NH_3, O_2, N_2, NO, and N_2O before and after catalyst introduction, as in [9]. The sensitivity of analysis was (in 10^{-3} vol %): 3.0 for NH_3, 3.5 for NO, and 5.0 for O_2, N_2, and N_2O.

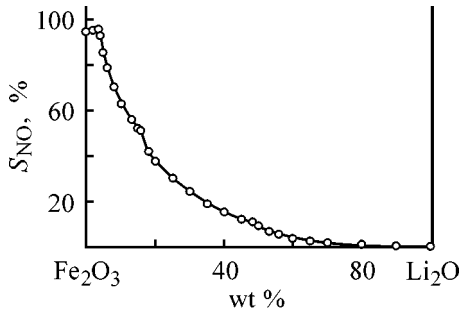

Fig. 1. Catalyst selectivity S_{NO} vs. composition of the Fe_2O_3–Li_2O system.

The limiting AAM load was determined by a procedure [3] consisting in that the catalyst is loaded to a critical state (dying), with the heat balance of a catalyst disturbed when the reaction passes from the diffusion to the kinetic region.

The results obtained in studying the catalytic properties of the Fe_2O_3–Li_2O system are presented in the Fig. 1 and Table 2.

Only two nitrogen compounds, N_2 and NO, were found among the reaction products of ammonia oxidation on the catalysts studied; under conditions far from critical no ammonia "breakthrough" occurred. Thus, the overall conversion of the initial substance is 100% and the only variable parameter of the catalytic process is the ratio between nitrogen(II) oxide and molecular nitrogen, i.e., the selectivity by NO (or by nitrogen). Thermal dissociation of NO may diminish the observed selectivity by nitrogen(II) oxide:

$$2NO = N_2 + O_2. \quad (1)$$

Experimental data on the degree of thermal dissociation of nitrogen(II) oxide on the catalysts of the system studied are presented in Table 3.

At the testing temperature and the optimal time of contact (6.77×10^{-2} s), nitrogen(II) oxide undergoes thermal dissociation in trace amounts (Li_2O and a mixture of Li_5FeO_4 with Li_2O) to 1.2% (on $Li_{0.5}Fe_{2.5}O_4$). The thermal dissociation of NO on lithium oxide does not virtually occur. At higher reagent flow velocities, i.e., with the time of contact decreasing to 1.2×10^{-3} s (critical conditions of catalyst dying), no thermal dissociation of nitrogen(II) oxide occurs, which is consistent with data on other NPC catalysts for ammonia oxidation [1, 10].

At lithium oxide concentrations of up to 3.6%, iron(III) oxide with a structure of α-Fe_2O_3 hematite (reflections with interplanar spacings of 0.3680, 0.2690, 0.2510, 0.2204, 0.1844, 0.1693, 0.1482, and 0.1452 nm) coexists with lithium ferrite α-$Li_{0.5}Fe_{2.5}O_4$ (main reflections with interplanar spacings of 0.589, 0.478, 0.374, 0.340, 0.2946, 0.2769, 0.2514, 0.2084, 0.1703, 0.1605, 0.1474, 0.1273, 0.1204, and 0.1115 nm) as a binary mixture. At the stoichiometric ratio $Li_2O : Fe_2O_3 = 1 : 5$ (3.6 wt % Li_2O) lithium ferrite is formed with a structure of the $Fe^{3+}[Li^{+}_{0.5}Fe^{3+}_{1.5}]O_4$ inverted spinel. The specific surface area of lithium ferrite (7.1 $m^2\ g^{-1}$) slightly exceeds that of iron(III) oxide (5.9 $m^2\ g^{-1}$). The selectivity of lithium ferrite by nitrogen(II) oxide is 95.5, i.e., exceeds the similar characteristic for α-Fe_2O_3 (94.7%). When the concentration of lithium ferrite, possessing the higher selectivity and specific surface area, is raised, the selectivity of catalysts of the α-Fe_2O_3–α-$Li_{0.5}Fe_{2.5}O_4$ system grows.

In the lithium oxide concentration range 3.7–15.7%, the ferrite phase α-$Li_{0.5}Fe_{2.5}O_4$ coexists with the α-modification of lithium metaferrite α-$LiFeO_2$ (main reflections with interplanar spacings of 0.239, 0.2073, 0.1467, 0.1252, 0.1200, 0.1089, 0.0925, 0.0845, 0.0640, and 0.0657 nm) as a binary mixture. The selectivity and the specific surface area of lithium metaferrite (51.0% and 3.5 $m^2\ g^{-1}$) are considerably lower than the similar characteristics for α-$Li_{0.5}Fe_{2.5}O_4$. The increase in the concentration of the low-active phase of lithium metaferrite in the α-$Li_{0.5}Fe_{2.5}O_4$–α-$LiFeO_2$ system leads to an abrupt monotonic decrease in the selectivity of catalysts by nitrogen(II) oxide.

X-ray phase analysis shows that, at lithium oxide concentrations of 15.9–48.2%, lithium metaferrite α-$LiFeO_2$ coexists with the Li_5FeO_4 phase as a binary mixture. Li_5FeO_4 ranks far below α-$LiFeO_2$, and especially α-$Li_{0.5}Fe_{2.5}O_4$, in selectivity and specific surface area (11.2% and 1.5 $m^2\ g^{-1}$). Raising the concentration of the low-active Li_5FeO_4 phase in the α-$LiFeO_2$–Li_5FeO_4 system drastically decreases the selectivity of catalysts by NO.

Table 3. Degree of NO decomposition on Fe_2O_3–Li_2O catalysts at 1053 K [Gas mixture composition (vol %): 9.5 NO, 71.3 N_2, 4.6 O_2, and 14.6 H_2O (vapor) ($\tau = 6.77 \times 10^{-2}$)]

C_{Li_2O}, wt %	Phase composition	γ,* %
0	α-Fe_2O_3	1.0
2.0	α-Fe_2O_3 + α-$Li_{0.5}Fe_{2.5}O_4$	1.1
3.6	α-$Li_{0.5}Fe_{2.5}O_4$	1.2
10.0	α-$Li_{0.5}Fe_{2.5}O_4$ + α-$LiFeO_2$	0.7
15.8	α-$LiFeO_2$	0.5
35.0	α-$LiFeO_2$ + Li_5FeO_4	0.2
48.3	Li_5FeO_4	0.1
70.0	Li_5FeO_4 + Li_2O	<0.1
100.0	Li_2O	<<0.1**

* Degree of NO decomposition.
** Virtually absent.

At lithium oxide concentrations exceeding 48.3%, Li_5FeO_4 coexists with the phase of lithium oxide as a mixture of two compounds. The selectivity and the specific surface area of lithium oxide (0.4% and 0.4 $m^2\ g^{-1}$) are lower than those of Li_5FeO_4 and all other system components. Raising the lithium oxide concentration in the Li_5FeO_4–Li_2O system leads to a monotonic decrease in the selectivity of catalysts by nitrogen(II) oxide. Thus, the selectivity of the system depends on its composition, in particular, on the ratio of phases in the two-component catalyst.

In the Fe_2O_3–Li_2O catalytic system, the only component of practical interest is lithium ferrite α-$Li_{0.5}Fe_{2.5}O_4$, the most active and selective compound surpassing even α-Fe_2O_3 in its characteristics. The other system components are low-active (α-$LiFeO_2$ and Li_5FeO_4) or virtually inactive (Li_2O).

The high-temperature oxidation of ammonia on catalysts occurs by two parallel reactions [1, 11]:

$$4NH_3 + 5O_2 = 4NO + 6H_2O, \quad (2)$$

$$4NH_3 + 3O_2 = 2N_2 + 6H_2O. \quad (3)$$

The redox mechanism of the reactions [11] is responsible for the correlation between the selectivity and strength of binding of chemisorbed oxygen to the catalysts [12]. The measure of the strength of oxygen binding to the catalyst is the heat of its chemisorption [11, 12]. For catalysts of certain nature (metals and

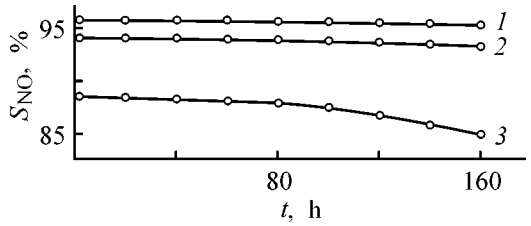

Fig. 2. Selectivity S_{NO} of lithium ferrite vs. operation time t. The linear velocity of AAM flow is 0.8 m s^{-1} (operation conditions). Temperature (K): (*1*) 1073, (*2*) 1173, and (*3*) 1273.

metal oxides) there exists an optimal energy of oxygen binding to the compound surface, ensuring the maximum selectivity by nitrogen(II) oxide [11–14]. The deviation of the binding energy from the optimal value impairs the NO selectivity and improves the selectivity by N_2. The binding energies of the surface oxygen to the individual components of the catalytic system in the oxidized state were determined from the temperature dependence of the pressure of oxygen in thermodynamic equilibrium with the surface oxygen of the compounds [15] (kJ mol^{-1} O_2): α-Fe_2O_3 143.5, α-$Li_{0.5}Fe_{2.5}O_4$ 138.2, α-$LiFeO_2$ 179.8, Li_5FeO_4 224.3, and Li_2O 242.5.

For hematite and lithium ferrite, the energies of oxygen binding to the surface are close and the selectivities differ only slightly. The energy of oxygen binding to the surface of α-$LiFeO_2$, and especially to the Li_5FeO_4 and Li_2O surfaces, much exceeds that for α-Fe_2O_3 and lithium ferrite. The product of stronger ammonia oxidation (i.e., nitrogen(II) oxide) is formed with breaking of a greater number of oxygen–catalyst bonds, compared with molecular nitrogen. This means that the selectivity by NO decreases with increasing binding energy of adsorbed oxygen [11, 13, 14], and it is this phenomenon that is observed for α-$LiFeO_2$, Li_5FeO_4, and Li_2O.

The limiting ammonia load grows with increasing specific surface area of the catalyst: it is the highest for lithium ferrite [7.82×10^3 m^3 NH_3 h^{-1} m^{-2}] and the lowest for lithium oxide (0.44×10^3 m^3 NH_3 h^{-1} m^{-2}] (Table 2). The limiting load for iron(III) oxide (6.50×10^3 m^3 NH_3 h^{-1} m^{-2}] is slightly lower than that for lithium ferrite. This parameter depends on the rate of the chemical reaction on the surface, which is, in turn, determined by the chemical composition of the catalyst. Under the critical process conditions ($\tau = 1.2 \times 10^{-3}$ s), no decomposition of nitrogen(II) oxide by pathway (1) is observed, but part of unreacted ammonia is found after the catalyst (breakthrough) (Table 2). With increasing specific surface area of the catalysts, the ammonia breakthrough decreases, which is consistent with the higher activity of such catalysts. The ammonia breakthrough is the highest for lithium oxide (1.97%) and the lowest for lithium ferrite (0.21%). In this respect, α-Fe_2O_3 is close to lithium ferrite (0.30%), their specific surface areas differing insignificantly.

The kinetic characteristics of the reaction on lithium ferrite, which is the most active and selective component of the Fe_2O_3–Li_2O system, were determined using the "burning" and "dying" temperatures of a lithium ferrite pellet, i.e., the temperatures at the critical points. The reaction rate was calculated by the method in which the temperature limits of the external diffusion region were determined using the "dying" of a catalyst pellet on lowering the AAM temperature [16]. The temperature of the catalyst surface was measured with a TPP-2 thermocouple inserted into the pellet from the side of AAM flow. A layer of lithium ferrite granules $(2.0–3.0) \times 10^{-3}$ m in size was placed between the pellet and the reactor walls to eliminate the heat loss. The kinetic parameters of the process were calculated by the Buben equation [17] solved for two reaction rates at a constant oxygen concentration. The equation has the form

$$(1 + a)\left[1 + (m - 1)\frac{a}{b}\right] - \frac{a}{\varepsilon}\left(1 - \frac{a}{b}\right) = 0, \quad (4)$$

$$a = T/T_0 - 1, \quad b = Q\beta C_0/(\alpha T_0), \quad \varepsilon = RT_0/E,$$

where m is the reaction order by ammonia, T is the catalyst surface temperature at the critical point (K), T_0 is the AAM temperature, C_0 is the ammonia concentration in the flow, α and β are the mass- and heat-transfer coefficients, Q is the heat effect of the reaction, and E is its activation energy.

The coefficients α and β were calculated from the known equations [18].

The kinetic parameters of ammonia oxidation on lithium ferrite are as follows: temperature of catalyst "burning," 527 K; ammonia concentration in AAM, 10 vol %; activation energy of the reaction, 9.54 kJ mol^{-1} NH_3; reaction order by ammonia, 0.19; and catalyst selectivity by NO (at 1053 K), 95.5%.

A study of the dependence of catalyst selectivity on operation time confirmed the high stability of lithium ferrite at 1073–1173 K (Fig. 2).

The selectivity of lithium ferrite at 1073 and 1173 K decreases by 0.4 and 0.7%, respectively, after 160 h of operation. The iron(III) oxide selectivity at

1073 K decreases by 3.5% after the same period of time [7]. With the process temperature raised to 1273 K, lithium ferrite undergoes deactivation under the influence of the elevated temperature and the reaction medium: the catalyst selectivity after 160 h of operation decreases by 3.5%. To elucidate the deactivation mechanism, the chemical and phase composition of the catalyst were studied along with its structure. X-ray diffraction patterns of the surface layer of a catalyst that operated at 1273 K contain lithium ferrite reflections and reflections with interplanar spacings of 0.485, 0.297, 0.253, 0.242, 0.2101, 0.1712, 0.1614, and 0.1485 nm, characteristic of magnetite Fe_3O_4 [19]. This conclusion is confirmed by IR spectral data. The IR spectra of the surface layer of a catalyst after operation contain the magnetite absorption peaks at 407, 427, 480, 557, 673, and 980 cm^{-1} [20]. Magnetite suppresses the catalyst selectivity, i.e., it is the low-active phase [7] (the magnetite selectivity at 1073 K is 7%). The intensity of the phase transformations occurring in the catalyst grows with increasing reaction temperature, as shown by X-ray diffraction analysis and IR spectroscopy. The increase in the concentration of the low-active phase with growing temperature results in a more abrupt decrease in the catalyst selectivity. In addition, the catalyst operated at 1273 K contains a new, relatively low-active phase—α-modification of lithium metaferrite α-$LiFeO_2$. The selectivity of α-$LiFeO_2$ at 1053 K is 51%. The appearance of the new, low-active phases of magnetite and α-$LiFeO_2$ at elevated temperatures is associated with the redox mechanism of ammonia oxidation [1, 5, 11] and is in good agreement with the results of thermodynamic calculations [21]. According to these data the high probability of lithium ferrite transformation at $T \geq 1273$ K (P_{O_2} = 0.021 MPa, air) by the reaction

$$6Li_{0.5}Fe_{2.5}O_4 = 3LiFeO_2 + 4Fe_3O_4 + O_2 \quad (5)$$

results in the formation of new phases, found in experimental studies. Similar transformations during heat treatment of lithium ferrite were observed in [22].

Under the influence of high temperature, the catalyst recrystallizes, with the specific surface area decreasing (Table 4). After 160 h of operation the size of lithium ferrite granules increases from 200 to 340 nm. The reaction conditions being far from critical, i.e., the reaction being limited by ammonia diffusion toward the catalyst surface, the specific surface area does not exert decisive influence on the selectivity of lithium ferrite [1, 3, 6]. This means that the drop in selectivity at 1273 K is mainly due to phase and chemical transformations of the catalyst. Under the critical conditions of the reaction (catalyst dying) the activity of lithium ferrite decreases and the limiting load falls from 7.49×10^3 to 2.97×10^3 m^3 NH_3 h^{-1} m^{-2}) as a result of recrystallization and a decrease in the specific surface area of the catalyst.

Table 4. Changes in selected structural and catalytic properties of lithium ferrite α-$Li_{0.5}Fe_{2.5}O_4$ during operation at 1273 K

t, h	S_{sp}, $m^2 g^{-1}$	Root-mean-square granule size, nm	Limiting load by ammonia, $A \times 10^{-3}$, $m^3 h^{-1} m^{-2}$
4	6.8	200	7.49
40	6.6	207	7.27
60	6.4	218	7.05
80	5.8	240	6.39
100	4.9	265	5.40
140	3.3	308	3.63
160	2.7	340	2.97

Thus, a set of chemical and phase transformations of the catalyst, yielding low-active and low-selective components (Fe_3O_4 and α-$LiFeO_2$) with rearranged structure is the reason for lithium ferrite deactivation. In the temperature range 1073–1173 K, lithium ferrite is a highly selective and stable catalyst for ammonia oxidation.

CONCLUSIONS

(1) The catalytic properties of the $Fe_2O_3Λi_2O$ system in ammonia oxidation were studied in the component concentration range 0–100 wt %.

(2) The catalytic properties of the individual components (α-Fe_2O_3, Li_2O, α-$Li_{0.5}Fe_{2.5}O_4$, α-$LiFeO_2$, and Li_5FeO_4) of the system were determined.

(3) The influence of the phase composition of the system on the physicochemical and catalytic properties of the catalysts, including the activity and selectivity by nitrogen(II) oxide, was revealed. The activity and the selectivity of the system depends on composition and, in particular, on the ratio of the amount of α-Fe_2O_3 phase to that of the α-$Li_{0.5}Fe_{2.5}O_4$ phase of a two-component catalyst. The same is true for the $Li_{0.5}Fe_{2.5}O_4$ and α-$LiFeO_2$, α-$LiFeO_2$ and Li_5FeO_4, and Li_5FeO_4 and Li_2O phases.

(4) The process parameters were determined on the ferrite catalyst, which is the most active and selective component of the Fe_2O_3–Li_2O system.

(5) A set of chemical and phase transformations of the $Li_{0.5}Fe_{2.5}O_4$ catalyst, resulting in the formation of low-active and low-selective components (Fe_3O_4 and α-$LiFeO_2$) with rearranged structure, is responsible for the deactivation of lithium ferrite at 1273 K.

(6) The obtained data on the catalytic properties of the Fe_2O_3–Li_2O system can be used in developing highly efficient modified catalysts for ammonia oxidation.

REFERENCES

1. Karavaev, M.M., Zasorin, A.P, and Kleshchev, N.F., *Kataliticheskoe okislenie ammiaka* (Catalytic Oxidation of Ammonia), Moscow: Khimiya, 1983.
2. Epshtein, D.A., Tkachenko, I.M., Dobrovol'skaya, N.V., *et al., Dokl. Akad. Nauk SSSR*, 1958, vol. 122, no. 5, pp. 874–877.
3. Morozov, N.M., Luk'yanova, L.I., and Temkin, M.I., *Kinet. Katal.*, 1966, vol. 7, no. 1, pp. 172–175.
4. Zakharchenko, N.I. and Seredenko, V.V., *Zh. Prikl. Khim.*, 1999, vol. 72, no. 11, pp. 1921–1923.
5. Zakharchenko, N.I. and Seredenko, V.V., *Vestn. Kharkov. Univ.*, 1998, no. 2, pp. 86–92.
6. Kurin, N.M. and Zakharov, M.S., *Kataliz v vysshei shkole* (Catalysis in Higher School), Moscow: Mosk. Gos. Univ., 1962, pp. 234–237.
7. Zasorin, A.P., Zakharchenko, N.I., and Karavaev, M.M., *Izv. Vyssh. Uchebn. Zaved., Khim. Khim. Tekhnol.*, 1980, vol. 23, no. 10, pp. 1274–1276.
8. *Analiticheskii kontrol' proizvodstva v azotnoi promyshlennosti* (Analytical Monitoring in Nitric Acid Production), Demin, L.A., Ed., Moscow: Goskhimizdat, 1958, no. 8.
9. Alkhazov, T.G., Gasan-zade, G.Z., Osmanov, M.O., and Sultanov, M.Yu., *Kinet. Katal.*, 1975, vol. 16, no. 16, pp. 1230–1234.
10. Zhidkov, B.A., Orlova, S.S., Bachenko, G.A., and Plygunov, A.S., *Khim. Tekhnol.*, 1979, no. 1, pp. 5–8.
11. Golodets, G.I., *Geterogenno-kataliticheskie reaktsii s uchastiem molekulyarnogo kisloroda* (Heterogeneous Catalytic Reactions Involving Molecular Oxygen), Kiev: Naukova Dumka, 1977.
12. Boreskov, G.K., *Geterogennyi kataliz* (Heterogeneous Catalysis), Moscow: Nauka, 1986.
13. Golodets, G.I., *Kinet. Katal.*, 1987, vol. 28, no. 2, pp. 337–341.
14. Il'chenko, N.I., Pyatnitskii, Yu.I., and Pavlenko, N.V., *Teor. Eksperim. Khim.*, 1998, vol. 34, no. 5, pp. 265–281.
15. Sazonov, V. A., Popovskii, V.V, and Boreskov, G.K., *Kinet. Katal.*, 1968, vol. 9, no. 2, pp. 307–314.
16. Beskov, V.S., Karavaev, M.M., Garov, D.V., and Arutyunyan, V.A., *React. Kinet. Catal. Lett.*, 1976, vol. 4, no. 3, pp. 351–357.
17. Buben, N.Ya., *Zh. Fiz. Khim.*, 1945, vol. 19, nos. 4–5, pp. 250–253.
18. Kasatkin, A.G., *Osnovnye protsessy i apparaty khimicheskoi tekhnologii* (Basic Processes and Apparatus of Chemical Engineering), Moscow: Khimiya, 1973.
19. *Powder Diffraction Data File, ASTM, Joint Committee in Powder Diffraction Standards*, Philadelphia, 1967.
20. Bogdanovich, N.P., Vorob'ev, Yu.P., Men, A.N., *et al., Opt. Spektrosk.*, 1970, vol. 29, no. 6, pp. 1151–1153.
21. Zakharchenko, N.I. and Protiven, I.N., Available from NIITEKhIM, 1994, Cherkassy, no. 9-khp-94.
22. Levin, B.E., Tret'yakov, Yu. D., and Letyk, L.M., *Fiziko-khimicheskie osnovy polucheniya, svoistva i primenenie ferritov* (Physicochemical Backgrounds of Fabrication, Properties, and Application of Ferrites), Moscow: Metallurgiya, 1979.

Russian Journal of Applied Chemistry, Vol. 74, No. 2, 2001, pp. 235–237. Translated from Zhurnal Prikladnoi Khimii, Vol. 74, No. 2, 2001, pp. 231–234.

CATALYSIS

Pyrolysis of Straight-Run Naphtha on ZSM-5 Zeolites Modified with Alkaline-Earth Metal Cations

V. I. Erofeev, L. V. Adyaeva, and Yu. V. Ryabov

Direction of Scientific and Technical Development, Tomsk Petrochemical Combine Joint-Stock Company, Tomsk, Russia

Received September 20, 2000

Abstract—The acid and catalytic properties of high-silica zeolites of ZSM-5 type, modified with alkaline-earth metal cations in pyrolysis of straight-run naphtha, were studied.

Until recently, lower C_2–C_4 olefins, which are important raw materials for petroleum chemical processes, have been prepared predominantly by pyrolysis of various hydrocarbons at high temperatures (800–850°C). Further intensification of the process by improving the design of tubular furnace pyrocoils or using more rigorous conditions is largely hindered by the chemical features of the process and technological factors. Therefore, pyrolysis of hydrocarbons in the presence of catalysts [1–6], allowing preparation of lower olefins at lower temperatures and with higher selectivity, is rather promising.

Although numerous oxide catalysts for pyrolysis of hydrocarbons are known, search for highly efficient systems for preparing C_2–C_4 olefins is still urgent.

Extensive studies of thermal pyrolysis and pyrolysis in the presence of oxide catalysts have shown that these processes are largely similar. It has been found that the catalyst does not affect the pathway of hydrocarbon pyrolysis, which predominantly proceeds by the heterogeneous–homogeneous radical-chain mechanism, and only makes higher the concentration of free radicals in the system [4]. However, only few reports are known of the use of zeolite catalysts for hydrocarbon pyrolysis [7, 8]. In this work, we studied the acid and catalytic properties of high-silica zeolites (HSZs) of ZSM-5 type, modified with alkaline-earth metal (AEM) cations in pyrolysis of straight-run naphtha.

The initial HSZs with silicate modulus of 30 were prepared by hydrothermal synthesis from alkaline aluminosilicates [9]. The zeolites were impregnated with AEM cations using appropriate metal nitrate solutions, and the resulting catalysts were dried at 110 and calcined at 600°C for 8 h. The content of AEM cations (M^{n+}) in HSZ was 1 wt % in terms of metal. The catalytic properties of zeolite-containing catalysts were studied on a flow-type setup in the 500–700°C range under atmospheric pressure at space velocity of 3 h^{-1}. The reagents and pyrolysis products were analyzed by gas chromatography [10]. As initial hydrocarbon raw material served straight-run naphtha (Surgut Gas Processing Plant) of the following composition, wt %: 56.89 paraffinic, 32.76 naphthenic, and 8.54 aromatic hydrocarbons.

The acid properties of catalysts were studied by thermal desorption of ammonia. A catalyst sample (0.7 g) was placed in a quartz reactor, the reactor was purged with helium (130 $cm^3\ min^{-1}$) at 600°C for 2 h and then cooled to 100°C, and the sample was saturated with ammonia. The thermal desorption of ammonia was carried out on heating at a rate of 10 deg min^{-1} to 650°C [11].

The curve of thermal desorption from HSZ-30 exhibits two forms of ammonia desorption: low-temperature form I with a peak at T_{max} 203°C, typical predominantly of Lewis acid centers, namely, coordination-unsaturated aluminum cations in H-HSZ-5, and high-temperature form II with T_{max} 400°C corresponding to stronger Brønsted centers, namely, hydrogen ions of the bridging hydroxy groups in HSZ (Fig. 1, curve *1*).

Incorporation of AEM cations into HSZ affects the strength and concentration of the acid centers in zeolite-containing catalysts. Modification of H-HSZ-30 with strontium and barium cations shifts their low-temperature forms I to higher temperatures: T_{max} 213 and 212°C, respectively (Fig. 1, curves *4*, *5*). At the same time, modification of HSZ-30 with any AEM cation strongly shifts T_{max} of the high-

1070-4272/01/7402-0235 $25.00 © 2001 MAIK "Nauka/Interperiodica"

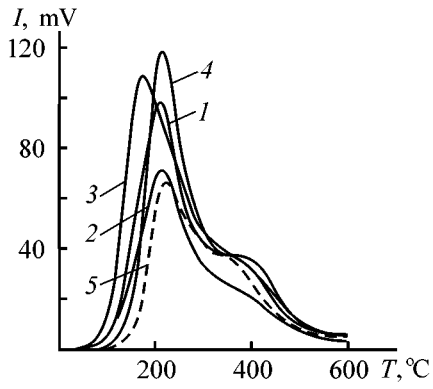

Fig. 1. Thermal desorption of ammonia from the HSZ surface as influenced by temperature. (*I*) Intensity and (*T*) temperature. Catalysts: (*1*) HSZ, (*2*) Mg-HSZ, (*3*) Ca-HSZ, (*4*) Sr-HSZ, and (*5*) Ba-HSZ; the same for Fig. 2.

temperature form II to lower temperatures, i.e., it strongly decreases the acidity of the corresponding centers. The greatest shift in T_{max} of the high-temperature form II to lower temperatures (335 and 350°C) is observed for HSZ modified with magnesium and barium, respectively (Fig. 1, curves *2* and *5*). Modification of HSZ-30 with magnesium and barium cations significantly decreases their total acidity to 610 and 525 μmol g^{-1}, respectively (Table 1) with respect to unmodified H-HSZ-30 (754 μmol g^{-1}). It should be noted that the concentration of the Lewis acid centers in the modified zeolite catalysts is 1.8–2.5 times greater than the concentration of the Brønsted acid centers, except in Ba-HSZ having close concentrations of the Lewis and Brønsted acid centers: 296 and 229 μmol g^{-1}, respectively. The common feature of all the zeolite-containing catalysts is that the addition of the AEM cations affects predominantly the strongly acidic Brønsted centers and causes their weakening, which is especially typical of Mg- and Ba-HSZs.

A study of the pyrolysis of straight-run naphtha, using zeolite catalysts modified with AEM cations, revealed a correlation between their acid and catalytic properties. In the 500–650°C range, the conversion of straight-run naphtha on HSZ-30 reaches 86–90%, which is three times the thermal conversion of naphtha on quartz powder in the same temperature range. With the temperature increasing from 500 to 650°C, the selectivity of formation of C_2–C_4 olefins increases to become 27% (11.95 and 10.52% ethylene and propylene, respectively), whereas the relative yield of aromatic hydrocarbons is 39.58% at 650°C.

Modification of HSZs with AEM cations lowers the total yield of pyrolysis products, with the relative yield of lower olefins increasing to 54.06% (Table 2, Fig. 2). With the temperature increasing from 550 to 700°C, the conversion and yield of C_2–C_4 alkenes grow for all the samples in question. The ef-

Table 1. Acid properties of HSZs modified with AEM cations

Sample	T_{max}, °C		Concentration of acid centers, μmol g^{-1}		
	form I	form II	form I	form II	total
HSZ	203	400	477	276	753
Mg-HSZ	189	375	415	196	611
Ca-HSZ	169	370	668	230	898
Sr-HSZ	213	355	528	252	780
Ba-HSZ	212	350	296	229	525

Table 2. Composition of the products of straight-run naphtha pyrolysis in the presence of HSZs modified with various AEM cations

Sample	*T*, °C	Conversion, %	Yield based on initial naphtha			Content, %	
			gas	alkenes C_2–C_4	arenes	alkenes in the gas phase	arenes in catalyzate
HSZ	700	88	58.49	26.01	35.81	44.46	86.29
Mg-HSZ	700	81	66.61	44.08	19.39	66.17	58.07
	750	89	70.4	45.81	24.41	65.06	92.59
Ca-HSZ	700	83	61.27	40.26	28.15	65.7	72.68
Sr-HSZ	700	77	59.86	40.41	21.50	67.5	53.31
Ba-HSZ	700	83	67.41	48.74	21.87	72.32	67.11

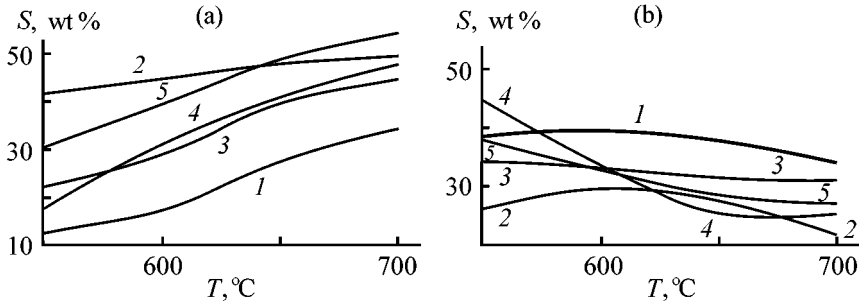

Fig. 2. Yield S of (a) C_2–C_4 alkenes and (b) arenes in conversion of straight-run naphtha. (T) Temperature.

fect of modification on the product composition is the most pronounced at lower temperatures of straight-run naphtha pyrolysis. Addition of Mg, Ca, and Ba to the zeolite increases the gas liberation from 58.5 (H-HSZ) to 67.4% (Ba-HSZ), with the content of alkenes simultaneously increasing from 44.5 to 72.3%. Addition of 1% strontium(II) to H-HSZ decreases the conversion of straight-run naphtha from 88 to 77 wt %. As compared with the initial H-HSZ, the gas evolution on the Sr-HSZ sample remains almost the same, whereas the content of alkenes in the gas phase increases from 44.5 to 67.5%.

Modification of HSZs with AEM cations by impregnation with solutions of the respective metal nitrates with subsequent calcination at 600°C leads to absorption and deposition of AEM cations in the HSZ pores and channels, decreasing the effective channel diameter, changing the diffusion and absorption characteristics, and lowering the activity and acidity of modified zeolite catalysts [12]. Modification of zeolites with AEM cations decreases not only the amount of the strongly acidic Brønsted centers (Table 1), but also the ratio between the Lewis and Brønsted acid centers, which affects the activity and selectivity of the catalysts. Dehydroxylation of the surface of zeolite-containing catalysts in the course of high-temperatures catalytic pyrolysis makes higher the concentration of the Lewis acid centers and Al^{3+} cations that escaped from the zeolite skeleton to form acid–base pairs $Al^{+}O^{-}$, which can activate hydrogen and saturated hydrocarbons yielding hydrocarbon radicals (the stage of heterogeneous generation of hydrocarbon radical). Then, during pyrolysis the hydrocarbon radical weakly bound to the surface passes into the bulk and the reaction proceeds in the homogeneous phase by the radical-chain mechanism [13, 14].

CONCLUSION

Modification of ZSM-5 high-silica zeolite with alkaline-earth metal cations increases the yield of lower C_2–C_4 olefins in pyrolysis of straight-run naphtha. High-silica zeolites modified with magnesium and barium cations exhibit the highest selectivity with respect to lower olefins in conversion of straightrun naphtha, which correlates with their acid properties.

REFERENCES

1. Novak, Z., Nametkin, N. S., and Rumyantsev, A.N., *Neftekhimiya*, 1979, vol. 19, no. 4, pp. 509–517.
2. Chernykh, S.P., Adel'son, S.V., and Mukhina, T.M., *Neftekhimiya*, 1991, vol. 31, no. 5, pp. 688–695.
3. Adel'son, S.V., Zhagfarov, F.G., Masloboishchikova, O.V., Trunina, E.V., *et al., Khim. Tekhnol. Topl. Masel*, 1989, no. 12, pp. 8–9.
4. Vasil'eva, N.A. and Buyanov, R.A., *Neftekhimiya*, 1979, vol. 19, no. 4, pp. 583–586.
5. Barabanov, N.L., *Neftepererab. Neftekhimiya*, 1995, no. 4, pp. 26–27.
6. Novak, Z., Nuenschel, G., Lanch, I., and Anders, K., *Neftekhimiya*, 1987, vol. 27, no. 6, pp. 736–740.
7. Minachev, Kh.M., Tagiev, D.B., Zul'fugarov, Z.G., and Sharifova, E.B., *Neftekhimiya*, 1980, vol. 20, no. 3, p. 408.
8. Mamedov, S.E., Aminbekov, A.F., and Mamedov, A.B., *Neftekhimiya*, 1998, vol. 38, no. 2, pp. 107–110.
9. RF Patent 1 527 154.
10. Erofeev, V.I., Korobitsyna, L.L., and Turkasova, G.I., *Fiziko-khimicheskie svoistva dispersnykh sistem i ikh primenenie. Sbornik nauchnykh trudov* (Physicochemical Properties of Dispersed Systems and Their Use. Collection of Scientific Works), Tomsk: Tomsk. Fil. Sib. Otd. Akad. Nauk SSSR, 1988.
11. Vosmerikov, A.V. and Erofeev, V.I., *Zh. Fiz. Khim.*, 1995, vol. 69, no. 5, pp. 787–790.
12. Mamedov, S.E., *Neftekhimiya*, 1998, vol. 38, no. 1, pp. 60–63.
13. Yampol'skii, Yu.P., *Elementarnye reaktsii i mekhanizm piroliza uglevodorodov* (Elementary Reactions and Mechanisms of Hydrocarbon Pyrolysis), Moscow: Khimiya, 1990, p. 150.
14. Rustamov, M.I., Farkhadova, G.T., Ismailov, E.G., *et al., Neftekhimiya*, 1997, vol. 37, no. 4, pp. 347–353.

Russian Journal of Applied Chemistry, Vol. 74, No. 2, 2001, pp. 238–240. Translated from Zhurnal Prikladnoi Khimii, Vol. 74, No. 2, 2001, pp. 235–237.

CATALYSIS

Catalytic Activity of Homogeneous Mixtures of Metal Chelates of Polyfluorinated β-Keto Esters with Tertiary Amines in Urethane Formation

M. S. Fedoseev and T. S. Vshivkova

Institute of Technical Chemistry, Ural Division, Russian Academy of Sciences, Perm, Russia

Received August 1, 2000

Abstract—A series of Cu(II), Co(II), Mn(II), Fe(III), and La(III) chelates with unsymmetrical fluorinated β-keto esters, taken separately and in mixtures with tertiary amines, were tested as catalysts in urethane formation and in synthesis of network elastomers.

Homogeneous catalysis in the liquid phase is widely used to effect oligomerization and dimerization of olefins, polymerization of acrylates and α-oximes, and oxidation, hydroxylation, and hydrogenation of oligomers. As for synthesis of polyurethanes, data on homogeneous catalysis of this process are much less extensive as compared, e.g., with those for synthesis of olefin oligomers. At the same time, significant rise in the industrial production of polyurethane materials by reactive injection molding (RIM) is impossible without using homogeneous catalytic systems. The process is based on the pseudo-prepolymer principle of formulating monomer–oligomer compositions to provide reliable compatibility of the reactants with active catalysts and fast curing of the mixture after molding.

The following catalysts are used in RIM processes: dibutyltin dilaurate, 1-methyl-3,5-diethylphenyl-2,4- and 2,6-diamines, 2,3-dimethyl-3,4,5,6-tetrahydropyrimidine, and their molecular complexes [1].

Studies of the newest RIM formulations show that the catalysts employed, such as dibutyltin dilaurate and tertiary amines, facilitate thermal oxidative degradation of the polymer [1]. Therefore, search for new catalytic systems free of these drawbacks is an urgent problem.

Previous studies of polyfluorinated copper β-diketonates have shown [2] that these compounds not only exhibit catalytic activity but also improve the structural organization of elastomers owing to donor–acceptor interaction with the polymer matrix. As a result, the properties of the materials become stable upon aging.

It is interesting to use this valuable property of fluorinated chelates in development of catalytic systems for RIM formulations. However, fluorinated copper chelates are less catalytically active than the existing catalysts [2], and the required curing rate cannot be ensured without adding cocatalysts with a synergistic effect. As such cocatalysts we chose tertiary amines whose synergistic effect on the catalysts is well known [3].

Here we report on a study of homogeneous catalysis with mixtures of Cu(II), Co(II), Mn(II), Fe(III), and La(III) chelates of fluorinated β-keto esters with an oligomeric tertiary amine, Lapromol-294.

Lapromol-294, a product of reaction of methyloxirane with ethylenediamine, has terminal functional hydroxy groups and is a reactive component of polyurethane compounds (chain-lengthening agent).

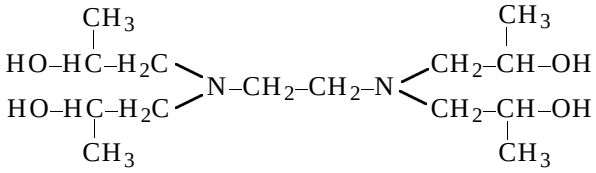

The rate constants of the reaction of phenyl isocyanate with *n*-butanol in cyclohexanone at 40°C in the presence of metal chelates of fluorinated β-keto esters (0.05 M) of the general formula

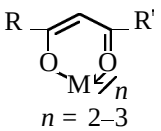

n = 2–3

are listed in Table 1. It is seen that all the chelates tested are homogeneous catalysts of urethane formation. Their catalytic activity increases in the order Co < Cu < La < Mn < Fe.

1070-4272/01/7402-0238 $25.00 © 2001 MAIK "Nauka/Interperiodica"

As seen from Table 2, addition of Lapromol-294 produces a pronounced synergistic effect. To understand its mechanism, special studies are required. The significant acceleration of urethane formation is probably due to the formation of molecular complexes of the fluorinated chelates with Lapromol-294:

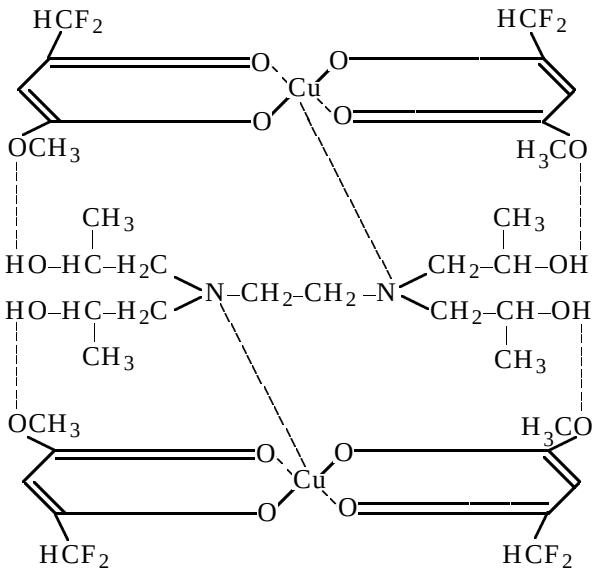

The interaction of the fluorinated chelates with Lapromol is manifested in the IR spectra as changes in the carbonyl absorption bands at 1640 and 1610 cm^{-1} and as a shift of the band of the Lapromol hydroxy groups at 3300 cm^{-1} because of the formation of a hydrogen bond with the oxygen atom of the alkoxy group in the coordinated β-keto ester anion.

Then we examined the influence of the homogeneous catalysts studied in the model reaction on the processing and physicomechanical properties of castable network polyurethanes.

The network polyurethanes were prepared and tested as described in [2]. Additionally, 20 wt % Lapromol-294 was added. The processing and physicomechanical properties of the stocks and catalytically cured elastomers are listed in Table 3.

It is seen that the examined catalyst mixtures substantially accelerate the polyurethane formation, which allows them to be recommended for production of polyurethane articles by the RIM process. It should also be noted that the polyurethanes exhibit highly stable properties in thermal aging.

Thus, Cu(II), Fe(III), Mn(II), Co(II), and La(III) chelates with florinated β-keto esters are homogeneous catalysts of urethane formation; their catalytic action is considerably enhanced in the presence of the synergistic additive Lapromol-294.

Table 1. Calculated and experimental rate constants of the reaction of phenyl isocyanate with *n*-butanol at 40°C in the presence of fluorinated chelates (homogeneous liquid, R = C_4H_9)

Chelate no.	R'	M	*n*	$K \times 10^{-4}$, l mol^{-1} s^{-1}	
				experiment	calculation
1	OCH_3	Cu	2	7.2	6.8
2	OC_2H_5	Cu	2	7.0	7.0
3	OC_2H_5	Fe	3	12	–
4	OC_2H_5	Mn	2	10	–
5	OC_2H_5	Co	2	6.5	–
6	OC_2H_5	La	3	8.0	–

Table 2. Synergistic catalysis of the reaction of phenyl isocyanate with *n*-butanol in cyclohexanone at 40°C (catalyst concentration 0.5 mol %)

Catalyst	Mutual solubility	$K \times 10^{-4}$, l mol^{-1} s^{-1}
–	–	0.39
Lapromol-294	Complete in mixed formulation	4.0
Lapromol-294 + chelate:		
no. 1	Complete	62
no. 3	〃	85
no. 4	〃	75
no. 5	〃	56
no. 6	〃	72

Table 3. Technological properties of polyurethane elastomers

Catalyst	*t*	τ	Tensile strength at 25°C, MPa	
	min		after curing	after aging at 100°C for 10 days
–	45	600	4.5	3.4
Lapromol-294	20	60	45	42
Chelate:				
no. 3	15	10	48	45
no. 4	10	5	46	44
no. 5	12	7	50	46
no. 6	17	14	44	42
no. 7	15	12	42	42

Note: (*t*) Working life at 25°C and (τ) curing time at 60°C.

EXPERIMENTAL

Chelates of Cu(II), Fe(III), Mn(II), Co(II), and La(III) with fluorinated β-keto esters were prepared at the Institute of Organic Synthesis, Ural Division, Russian Academy of Sciences, by the procedures described in [4–6]. The procedures for calculating and determining experimentally the rate constant of the reaction of phenyl isocyanate with *n*-butanol and preparing network polyurethanes were described in [2].

CONCLUSIONS

(1) A series of Cu(II), Fe(III), Mn(II), Co(II), and La(III) chelates with fluorinated β-keto esters were studied as catalysts of urethane formation (both taken separately and as mixtures with amine oligomer Lapromol-294). All the chelates exhibit catalytic activity, which is enhanced in the presence of Lapromol-294.

(2) The catalytic mixtures are active in synthesis of network polyurethanes. The processing and physicomechanical properties of the resulting castable polyurethanes were determined. These materials are highly stable in aging.

ACKNOWLEDGMENTS

The authors are sincerely grateful to V.I. Saloutin for submitting samples of fluorinated chelates.

REFERENCES

1. Lyubartovich, S.A., Morozov, Yu.L., and Tret'yakov, O.B., *Reaktsionnoe formovanie poliuretanov* (Reactive Molding of Polyurethanes), Moscow: Khimiya, 1990.
2. Fedoseev, M.S., Saloutin, V.I., and Sheshukova, T.S., *Zh. Prikl. Khim.*, 1999, vol. 72, no. 4, pp. 616–619.
3. Saunders, J.H. and Frish, K.C., *Polyurethanes. Chemistry and Technology*, part 1: *Chemistry*, New York: Interscience, 1962.
4. Pashkevich, K.I. and Saloutin, V.I., *Usp. Khim.*, 1985, vol. 54, no. 12, pp. 1997–2026.
5. Saloutin, V.I., Skryabina, Z.E., and Rudaya, M.N., *Izv. Akad. Nauk SSSR, Ser. Khim.*, 1984, no. 5, pp. 1106–1114.
6. Shapovalov, V.I., Saloutin, V.I., Pashkevich, K.I., and Piterskikh, I.A., *Zh. Obshch. Khim.*, 1980, vol. 50, no. 1, pp. 103–107.

Russian Journal of Applied Chemistry, Vol. 74, No. 2, 2001, pp. 241–246. Translated from Zhurnal Prikladnoi Khimii, Vol. 74, No. 2, 2001, pp. 238–243.

ENVIRONMENTAL PROBLEMS OF CHEMISTRY AND TECHNOLOGY

Measurement of the Solubility of Volatile Substances by Vapor-Phase Gas-Chromatographic Analysis

A. G. Vitenberg

Research Institute of Chemistry, St. Petersburg State University, St. Petersburg, Russia

Received January 27, 2000

Abstract—A new procedure is proposed for vapor-phase gas-chromatographic determination of the solubility of partly soluble volatile compounds in liquids. The method is based on successive pneumatic sampling to take small and equal portions of the equilibrium gas from the gas-liquid system containing an excess of the volatile component forming the second liquid phase. The gas-chromatographic determination of this component in the samples of the equilibrium gas makes it possible to find the slope of the isotherm describing the distribution of the substance between the liquid and gas phases near the saturation point, estimate the nonlinear portion of the isotherm, and calculate the substance content in the saturated solution.

Data on the solubility of volatile substances that are partly soluble and extremely poorly soluble in aqueous media are required to control the content of toxic impurities in industrial waste and in natural and drinking water. The shape of the distribution isotherm and, in particular, the interval of linearity and deviation from it in the region close to saturation are of interest for studying the thermodynamic properties of solutions and gas-liquid equilibrium in binary and more complex systems.

In the reference literature, data on the solubility of volatile compounds are scarce [1]. This is caused, on the one hand, by the reduced demand for such data and, on the other, by the lack of reliable methods for determining the solubility of volatile substances with an error of 0.1 wt% and less. At the same time, the development of sanitary-chemical and environmental monitoring requires reliable information on the content of volatile noxious impurities in dilute aqueous solutions at a level of 10^{-3}% and less, e.g., traces of aromatic and halogen-containing hydrocarbons in natural, drinking, and tap water. *A priori* calculation allows only approximate estimation of the content of volatile organic substances in saturated solutions.

Traditional methods for determining the solubility of partly or poorly soluble substances usually include measuring the maximal solubility of a volatile substance in a homogeneous solution; the excess soluble substance gives a second liquid phase. Such a state of the system is characterized by the practically constant concentration of the volatile component in the gas phase over the solution, independent of its amount in the liquid.

The content of the volatile substance in the saturated homogeneous solution is measured after thorough separation of two liquid phases. Fairly complex procedures using various devices are required for this purpose [2]. Their main drawback is the difficulty and sometimes impossibility of preparing and sampling a saturated homogeneous solution because of the formation of a supersaturated solution or an emulsion and evaporation of volatile components: it is very difficult to attain saturation of both phases without phase separation.

Substantial progress in determining the solubility of volatile substances in liquids is associated with the use of vapor-phase gas-chromatographic analysis (VPA) [3, 4]. This method includes measuring the content of volatile substances in the condensed phase by gas chromatography of the equilibrium gas phase. In this method, not a solution being studied but the vapor phase equilibrated with this solution at given temperature is introduced into the gas-chromatographic column. The vapor-phase analysis procedure is best adapted to analysis of a volatile component of a condensed matrix. One of the first publications on quantitative VPA is devoted to determining the solubility of hydrocarbons in water [5].

1070-4272/01/7402-0241 $25.00 © 2001 MAIK "Nauka/Interperiodica"

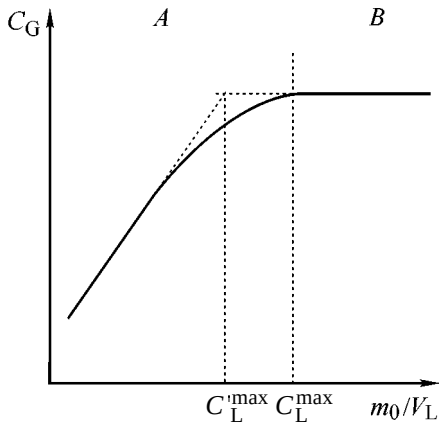

Fig. 1. Solubility of volatile substances in liquids, measured by VPA of a series of solutions with substance concentrations close to the saturation limit. (C_G) Concentration of volatile substance in the equilibrium gas; (m_0/V_L) substance concentration in the liquid phase. (*A*) Region of unsaturated homogeneous solutions and (*B*) region of phase separation of the liquid solution.

The use of VPA in measuring the solubility of volatile substances in liquids is based on the pattern of distribution of the solution components between the condensed and gas phases. The concentration dependence of the partial pressure of the volatile components of the liquid phase is described by the activity coefficients.

In dilute solutions with concentrations of volatile substances less than 0.01 wt %, the activity coefficient γ_i^∞ is practically constant [4, 6] and coincides with the activity coefficient for infinitely dilute solution:

$$\gamma_i^\infty = \lim_{x_i \to 0} \gamma_i. \quad (1)$$

In this case, Henry's law is fulfilled

$$P_i = H_i x_i. \quad (2)$$

According to this law the partial pressure P_i of the *i*th component over the solution is the product of its mole fraction x_i in the solution and Henry's constant H_i related to the saturated vapor pressure of this component P_i^0 by

$$H_i = P_i^0 \gamma_i^\infty. \quad (3)$$

At $\gamma_i \approx \gamma_i^\infty = \text{const}$ the system is characterized by a linear isotherm of distribution of the *i*th component between the liquid and gas phases. In such cases, the numerical value of the distribution coefficient

$$K = C_L/C_G, \quad (4)$$

equal to the ratio of the equilibrium weight concentrations of the substance in the liquid (C_L) and gas (C_G) phases, is practically independent of x_i.

In real solutions, at concentrations of volatile substances exceeding 0.1 wt %, the activity coefficient is usually a function of the mole fraction of the substance in the solution, i.e., $\gamma_i = f(x_i)$, and the system is characterized by a nonlinear distribution isotherm, with K depending on x_i.

In the region of liquid phase separation, the partial pressure of the *i*th component is independent of its amount in the system. In this case, the distribution isotherm is a straight line parallel to the concentration axis.

Based on such relations, the vapor-phase method for determining the solubility of the volatile substances was proposed as far back as the early 1980s [6]. The method involved preparation of a series of aqueous solutions with varied, and close to the saturation limit, concentrations of the components to be determined. The distribution isotherm $C_G = f(C_L)$ was derived from the data on the content of the component studied in the gas phase. The maximal solubility of the substance in the solution was determined by linear extrapolation of the sloping and horizontal sections of the isotherm, as shown in Fig. 1. The abscissa of the intersection point of these straight lines was taken as the maximal solubility of the substance. The method was tested by determining the solubility of chlorinated aromatic and saturated hydrocarbons in water.

Along with evident advantages, this method has a major constraint consisting in that it assumes a linear isotherm within the entire range of concentrations of unsaturated solutions up to the solubility limit. In other words, the method is based on the assumption that the activity coefficient is constant in the entire range of homogeneous solutions. When deviations of the isotherm from the linearity become substantial, the differences between the actual (C_L^{max}) and apparent extrapolated ($C_L^{'max}$) values (Fig. 1) may exceed the permissible value.

Another disadvantage of the above method is that it is labor-consuming, since it is necessary to prepare a great number of solution samples with the concentrations of volatiles less than 0.01–0.1 wt %.

We can avoid these difficulties by successively taking small and equal portions of the equilibrium gas from the gas–liquid system containing an excess of the volatile substance (i.e., in the case when a second

liquid phase exists). In the VPA method with pneumatic sample dosing into a chromatograph [7, 8], it is possible to take from the vessel containing the mass m_G of a volatile substance strictly specified mass fractions

$$m_g^i/m_G = (p' - p)/p' \quad (5)$$

(m_g^i is the weight of the substance sampled from the gas phase) and to vary them in a wide range by changing the pressures in the thermostated vessel with the solution studied, p', and in the chromatograph evaporator, p.

Repeated vapor-phase dosing of the samples into the chromatograph with a strictly fixed pressure jump from p' to p gives a series of chromatograms shown schematically in Fig. 2. The range of the phase separation of the liquid (even if it is not found visually) is characterized by chromatograms with constant height and area of peaks (section *I*) and, hence, constant weight of the substance taken. As the volatile substance is removed from the heterogeneous system, its amount decreases until the second liquid phase disappears, or, in other words, until the nonvariant equilibrium transforms into a monovariant one. This instant corresponds to the last chromatogram with the maximal peak height. Further vapor sampling decreases the concentration of the volatile substance in the solution, and the chromatograms of the equal portions of the equilibrium gas have the form of a series of peaks with decreasing height (sections *II* and *III*). The range of the constant ratios of peak heights (or areas) in the chromatograms of successive portions of the gas phase (section *III*) corresponds to the linear part of the distribution isotherm or to the region of infinite dilution, in which the distribution coefficient K is practically independent of the solute concentration. The range of the nonlinear isotherm (section *II*) is characterized by variable, and lower than unity, ratio of masses of the substance sampled from the system.

It should be noted that, in accordance with the features of VPA with pneumatic sampling [7, 8], the ratio of the gas (V_G) to liquid (V_L) phase volumes

$$r = V_G/V_L \quad (6)$$

in the vessel is the fundamental parameter determining the conditions of the experiment. The conditions for the use of the method with tolerable error can be expressed by the inequality

$$K \le r \le (p'/p). \quad (7)$$

These simple criteria allow, within the scope of the above method, determination of the boundaries of each portion of the distribution isotherm in the case

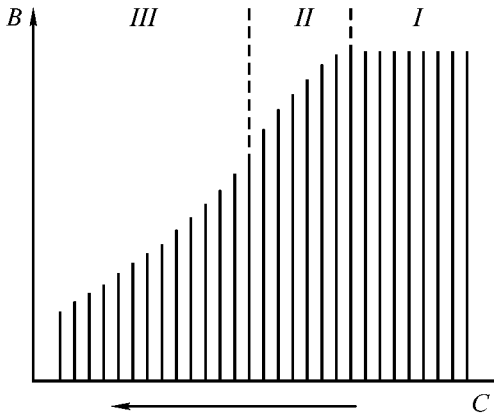

Fig. 2. Successive dosing of the equilibrium vapor into a chromatograph from a liquid–gas system with phase separation of the liquid phase: (*B*) detector signal and (*C*) successive dosing of the liquid phase. (*I*) Region of phase separation of the liquid phase, A_G^{n+1}/A_G^n = const; (*II*) nonlinear portion of the distribution isotherm, $A_G^{n+1}/A_G^n < 1$; and (*III*) linear portion of the distribution isotherm, $A_G^{n+1}/A_G^n = 1$. (A_G) Area of the chromatogram peak; (n) chromatogram ordinal number. Each vertical line is the amplitude of the detector signal or the peak height in the chromatogram.

of partly or poorly soluble volatile liquids with the distribution coefficient not exceeding several tens.

The thus obtained data can be used to calculate the substance solubility. One of the possible, and the simplest calculation procedures is as follows. In the case of a known saturated vapor pressure P_0 of the pure substance whose solubility is measured its concentration in the saturated solution C_L^0 can be calculated by the equation

$$C_L^0 = \frac{m_0 - m_g - m_0^n}{V_L}, \quad (8)$$

where m_0 is the mass of the substance introduced into the system before sampling, m_g is the calculated mass of the substance in the gas phase over the saturated solution, and m_g^n is found from VPA as the mass of the substance forming the second liquid phase and removed from the system in the first portion of the distribution isotherm (Fig. 2).

m_g is calculated with regard to the saturated vapor pressure of the volatile substance at the experiment temperature by the formula following from the fundamental gas equation of state:

$$m_g = \frac{P^0 \alpha_w V_G}{RT} M, \quad (9)$$

where R is the universal gas constant, M is the molecular mass of the volatile substance whose solubility

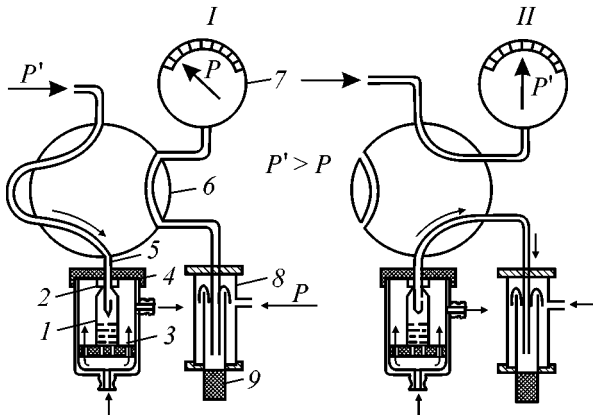

Fig. 3. Scheme of a device for pneumatic dosing of vapor phase samples into the chromatograph: (*1*) glass vessel; (*2*) elastic rubber plug; (*3*) screw chuck sealing and themostatically controlling the glass vessel; (*4*) rubber gasket; (*5*) steel needle with a side outlet; (*6*) two-positioned six-way gas cock; (*7*) standard manometer; (*8*) evaporator of the gas chromatograph; and (*9*) chromatographic column. (*I*) Producing elevated pressure in the vessel with a sample and (*II*) dosing the gas phase into the chromatograph.

is measured, and α_w is the coefficient reflecting the solubility of water in the organic phase.

When this solubility can be neglected, $\alpha_w = 1$. In other cases, α_w can be calculated by the formula

$$\alpha_w = \frac{P_i'}{P_i^0} = \frac{A_G''}{A_G^0} \quad (10)$$

from the saturated vapor pressure over pure (dry) organic substance, P_i^0, which is determined as the peak area A_G^0 in the chromatogram and that over the water-saturated organic phase, P_i'', also found as the peak area A_G'' in the chromatogram obtained under standard conditions.

The mass of the second organic phase can be calculated as the sum of masses of the volatile substance, m_g', sampled in each of n dosings into the chromatograph in the first portion of the distribution isotherm:

$$m_g^n = \sum_1^n m_g^i. \quad (11)$$

Since m_g'/m_g is the fraction of the substance sampled from the gas phase in each dosing of the saturated vapor into the chromatograph, we can write, in accordance with Eq. (5),

$$m_g^n = m_g^i n = m_g \frac{p' - p}{p'} n. \quad (12)$$

Then

$$C_L^0 = \frac{m_0 - m_g\{1 - n[(p' - p)/p']\}}{V_G}. \quad (13)$$

The condition for attaining the maximal accuracy of measurements is

$$(m_0 + m_g) >> m_g^n. \quad (14)$$

The inequality

$$n\frac{p' - p}{p'} \le \frac{\Delta C_L^0}{C_L^0}, \quad (15)$$

which relates the analysis conditions to the relative error of C_L^0 measurements, can serve as the criterion of the fulfillment of inequality (14). In practice, this condition is attained when no more than 3–5 samplings are performed on the horizontal portion of the distribution isotherm. In this case, the error of substance solubility measurement is determined by the procedure and the accuracy of introducing the mass m_0 and may be no worse than several percents.

EXPERIMENTAL

Measurements were performed on a Tsvet-500M chromatograph with a flame-ionization detector and a 200 × 0.4-cm glass column packed with 10% OV-101 as a stationary phase on Chromosorb W-AW (0.16–0.2 mm). The temperatures of the column, evaporator, and detector were 60, 120, and 180°C, respectively. The carrier gas flow rate in the chromatographic column was 20 ml min^{-1}, the detector signal was recorded by a TZ-4620 recording potentiometer and processed using Multikhrom package for Windows B.1.38 (IBM-486).

The equilibrium gas phase was dosed into the chromatographic column pneumatically by a special attachment for vapor-phase dosing of samples [8] heated to 150°C (Fig. 3). This attachment is installed on the evaporator of a standard chromatograph and provides introduction of a known volume (0.5–2.0 ml) of a gas phase from a vessel (in which the equilibrium is reached) into a chromatographic column through a short (5–7 cm) hot line.

Aqueous solutions with a given microcontent of benzene, toluene, chlorobenzene, chlorodibromomethane, dichlorobromomethane, 1,1-dichloroethane, and 1,2-dichloropropane were prepared using precisely weighed samples of the respective chemically pure grade substances under conditions excluding their loss.

The analysis procedure was as follows. Into a 15-ml standard vessel *1* for medical preparations (“penicil-

lin") was introduced 3–5 ml of water preliminarily checked for the absence of volatile organic substances. The vessel was plugged with elastic rubber plug *2* and hermetically sealed in a screw chuck *3*. To avoid sorption, the surface of the rubber stopper was protected with a Teflon film or aluminum foil. Then, 2–10 μl (accurate sample) of aromatic or halogenated hydrocarbon were introduced into the vessel with preliminarily calibrated Hamilton glass microsyringe by puncturing the rubber plug with the syringe needle. The vessel with the water sample was kept at 20, 25, and 30°C for 15 min with intermittent agitation of the liquid to reach the equilibrium. The sample temperature was controlled by water flow through screw chuck nipples *3* from a liquid thermostat. Then, the vessel with the sample in the temperature-controlled screw chuck was punctured with the needle *5* of a batcher through the elastic rubber plug to a length of 5–10 mm so that the needle end was in the gas phase. At this time, the cock *6* should be in position *I*, when the pressure p' in the vessel exceeds the pressure p in the chromatographic column. In this case, the standard manometer *7* shows the pressure of the carrier gas in the chromatograph evaporator *8*. By reversing the cock in position *II*, the gas space of the vessel *1* is connected with the chromatograph evaporator *8*. In this position, the sample of the equilibrium gas passes in pulsed mode into the chromatographic column owing to the pressure difference. At this time, manometer *7* shows the pressure p' in the auxiliary line. After a chromatogram was recorded, the stopcock *6* was returned to position *I*. The repeated dosing of the equilibrium gas into the chromatographic column was performed by reversing the cock *6* to position *II*. The pneumatic dosing of the gas into the chromatograph and the methods of the quantitative vapor-phase analysis were described in detail in [3, 7, 8].

The possibility of measuring the solubility of volatile substances in liquids by the above-described method was checked with aqueous solutions of the simplest aromatic and halogenated hydrocarbons. The choice of these compounds was governed by the availability of reliable reference data on their solubility in water and also by their high volatility and low VPA detection limit in solution (10^{-6}–10^{-8}%).

The measurement procedure is illustrated by an example of repeated pneumatic sampling of the equilibrium gas from a vessel with saturated aqueous solution of benzene with a minor (~1 mg) excess of pure benzene forming the second liquid phase. Data in Table 1 shows that the first eight chromatograms reflect the phase separation portion of the distribution isotherm, the ratio of the peak areas A_G^{n+1}/A_G^n being virtually unity. This isotherm portion is completed by a peak with the area of 9019 μV s^{-1}. Then, the system becomes two-phase (the liquid becomes homogeneous), and the portion of a nonlinear isotherm starts, which is completed with the 12th chromatogram with peak area of 7963 μV s^{-1}, giving way to the linear portion of the distribution isotherm. It should be noted that the upper limit of concentrations bounding the linear portion of the isotherm is only 15% less than the concentration of the maximal benzene solubility in water.

Table 1. Area of benzene peak on chromatograms in successive sampling of the equilibrium vapor from the three-phase system aqueous solution of benzene–benzene–argon

Chromatogram no. n	Peak area A_G, μV s^{-1}	$\frac{A_G^{n+1}}{A_G^n}$	Number of phases in the system and region of the distribution isotherm
1	9078	0.999	Three-phase system with liquid phase separation; horizontal portion of the isotherm
2	9073	0.999	
3	9069	0.998	
4	9053	1.001	
5	9065	0.999	
6	9053	0.999	
7	9040	0.998	
8	9019	0.983	
9	8866	0.975	Two-phase system with homogeneous liquid; nonlinear portion of the isotherm
10	8644	0.965	
11	8342	0.955	
12	7963	0.943	
13	7506	0.947	Two-phase system; linear portion of the isotherm
14	7111	0.947	
15	6737	0.946	
16	6373	0.945	
17	6023	0.945	
18	5691	0.944	
19	5375	0.949	
20	5101	0.947	
21	4833		

Similar series of chromatograms for toluene, chlorobenzene, 1,1-dichloroethane, and 1,2-dichloropropane allowed calculation of the solubility of these compounds in water. Data of Tables 2 and 3 show that our method provides acceptable accuracy in measuring the solubility of such volatile substances. Deviations from the reference data obtained by traditional methods [6, 9] do not exceed 10% and are within the error limits for the methods compared. However, differences between the results of the vapor phase extrapolation method [6] and our vapor-phase analysis

Table 2. Solubility of aromatic hydrocarbons in water

Substance	T, °C	Solubility,* g l^{-1}		Deviation $(b-a)/b$, %
		a	b	
Benzene	20	1.75	1.65 ± 0.09	6.0
	25	1.80	1.77 ± 0.09	1.7
	30	1.95	1.98 ± 0.11	1.5
Toluene	20	0.45	0.42 ± 0.03	7.1
	25	0.50	0.55 ± 0.025	9.0
	30	0.57	0.63 ± 0.03	9.5

* Solubility: (*a*) data of [2] and (*b*) measured by VPA method.

Table 3. Solubility of halogenated hydrocarbons in water at 30°C

Substance*	Solubility,** g l^{-1}			Deviation	
	reference data		experimental	$(c-a)/c$	$(c-b)/c$
	a	b	c		
CDBM	–	1.05 ± 0.04	1.35 ± 0.06	–	22.2
DCBM	–	3.03 ± 0.15	3.65 ± 0.14	–	16.9
1,1-DCE	5.00	4.83 ± 0.18	5.50 ± 0.32	9.1	12.2
1,2-DCP	2.70	2.42 ± 0.25	2.95 ± 0.12	8.5	18.0
CB	0.49	0.47 ± 0.03	0.52 ± 0.03	5.8	9.6

* (CDBM) chlorodibromomethane, (DCBM) dichlorobromomethane, (1,1-DCE) 1,1-dichloroethane, (1,2-DCP) 1,2-dichloropropane, and (CB) chlorobenzene.

** Solubility: (*a*) traditional methods [6, 9], (*b*) vapor-phase extrapolation [3]; (*c*) measured by VPA with repeated sampling of vapor from the same vessel.

with manifold sampling of the equilibrium vapor from the same vessel (Table 3) are somewhat greater. These deviations are systematical and probably associated with the above-noted features of the extrapolation calculation of the maximal solubility of volatile substances in liquids, which can give underestimated results.

CONCLUSION

The method was developed for determining the solubility of volatile substances, based on the principles and technique of vapor-phase gas-chromatographic analysis with repeated pneumatic sampling of the equilibrium vapor from the system and its dosing into a chromatographic column. Within the 0.1–10 g l^{-1} concentration range, the error of this method does not exceed 10%.

REFERENCES

1. Kogan, V.B., Fridman, V.M., and Kafarov, V.V., *Spravochnik po pastvorimosti* (Handbook on Solubility) vol. 1, book 1: *Binarnye sistemy* (Binary Systems), Moscow: Akad. Nauk SSSR, 1961.
2. Sutton, C.and Salder, J.A., *Environ. Sci. Technol.*, 1974, vol. 8, pp. 654–663.
3. Vitenberg, A.G. and Ioffe, B.V., *Gazovaya ekstraktsiya v khromatograficheskom analize: Parofaznyi analiz i rodstvennye metody* (Gas Extraction in Chromatographic Analysis: Vapor-Phase Analysis and Related Methods), Leningrad: Khimiya, 1982.
4. Kolb, B. and Ettre, L.S., *Static Headspace-Gas Chromatography*, New York: Wiley-VCH, 1997.
5. McAuliffe, C., *Chem. Technol.*, 1971, vol. 1, no. 1, pp. 46–52.
6. McNally, M.E. and Grob, R.L., *J. Chromatogr.*, 1983, vol. 260, no. 1, pp. 23–32.
7. Vitenberg, A.G., *Dokl. Akad. Nauk SSSR*, 1982, vol. 267, no. 1, pp. 113–117.
8. Vitenberg, A.G. and Reznik T.L., *Zh. Anal. Khim.*, 1984, vol. 39, no. 4, pp. 683–691.
9. Verschueren, K., *Handbook of Environmental Data Chemicals*, New York: Van Nostrand Reinhold, 1977.

Russian Journal of Applied Chemistry, Vol. 74, No. 2, 2001, pp. 247–252. Translated from Zhurnal Prikladnoi Khimii, Vol. 74, No. 2, 2001, pp. 249–254.

ENVIRONMENTAL PROBLEMS OF CHEMISTRY AND TECHNOLOGY

Diffusion, Osmotic, and Electroosmotic Permeability of Reverse-Osmosis Membranes

V. B. Korobov and S. I. Lazarev

Tambov State Technical University, Tambov, Russia

Received October 4, 1999; in final form, February 2000

Abstract—The diffusion, osmotic, and electroosmotic permeabilities of MGA-100 and OPM-K membranes in aniline- and morpholine-containing aqueous solutions were studied in the concentration range 0.4–12.5 kg m^{-3} at 20–45°C. The behavior of the permeabilities with solution concentration and temperature is analyzed and accounted for.

In [1–3] were presented results obtained in studying by the methods of reverse osmosis and electroosmofiltration the purification of wastewater produced at plants manufacturing chemicals-additives for polymeric materials. As objects of study served aniline- and morpholine-containing kinds of wastewater (both model and real) and polymeric reverse-osmosis membranes MGA-100 and OPM-K. It was shown that the baromembrane methods are promising for wastewater purification.

The present communication reports the results obtained in studying the diffusion, osmotic, and electroosmotic permeabilities to aniline and morpholine of reverse-osmosis membranes MGA-100 and OPM-K.

These data are necessary for analyzing transport phenomena and performing engineering calculations of membrane processes [4–5].

EXPERIMENTAL

A schematic of the experimental setup for studying the diffusion, osmotic, and electroosmotic permeabilities is presented in the figure.

The setup comprises a thermostated cell *I–II*, measuring capillary *1*, vessels for the starting (*2*, *3*) and spent (*4*, *5*) solutions, and a dc power source *6*.

The main unit of the setup is the *I–II* cell. It consists of two chambers, *I* and *II*, separated by a membrane *7* under study.

In analyzing the diffusion and osmotic permeabilities, a membrane is pressed between grids *8* made of acrylic resin in order to prevent its bending under the action of hydrostatic pressure and temperature stresses.

In studying the electroosmotic permeability, the membrane is fixed between chambers *I* and *II* in another way. A membrane under study is placed on a piece of Whatman paper, in its turn laid on the po-

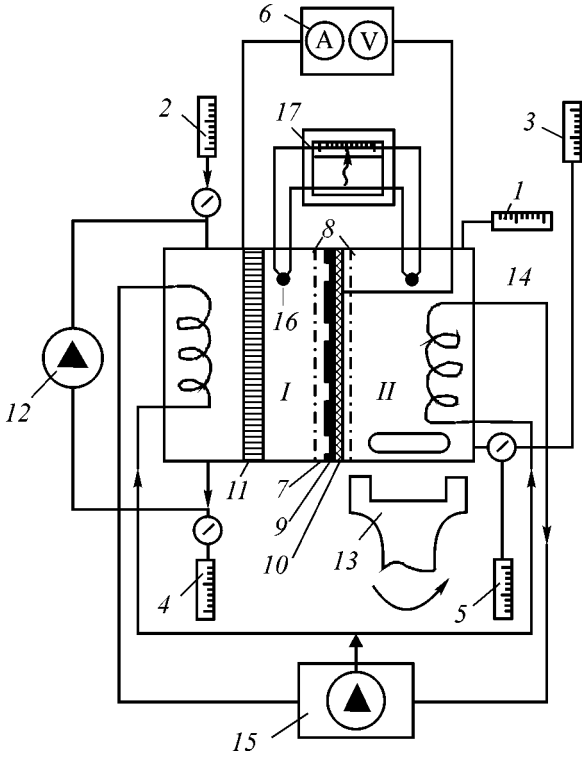

Schematic of the experimental setup. For explanations see the text.

1070-4272/01/7402-0247 $25.00 © 2001 MAIK "Nauka/Interperiodica"

rous electrode (cathode) *10*. The membrane, Whatman paper, and the porous electrode are pressed between the acrylic resin grids. In addition, one more porous electrode (anode) *11* is placed in chamber *I*.

The solution in chamber *I* is stirred by means of its continuous circulation effected by a centrifugal pump *12*, and that in chamber *II*, by a magnetic stirrer *13*. The necessary solution temperature in the cell chambers is maintained by heat-exchangers *14* in the cell chambers, through which water from thermostat *15* is circulated. The temperature in chambers *I* and *II* is monitored with Chromel-Copel thermocouples 16 connected to a potentiometer *17*. Constant temperature within the chambers is maintained automatically. The volume of the cell chambers is 0.6×10^{-3} m^3, and the working area of the membranes, 2.275×10^{-3} m^2. Chambers *I* and *II* are made of acrylic resin.

The diffusion and osmotic permeabilities were studied as follows. Preliminarily, a membrane to be studied was inspected and placed in a vessel with regularly renewed distilled water for 24 h and then used to assemble a measuring cell (figure). Chamber *I* was filled with a solution of certain concentration, and chamber *II*, with distilled water. To attain steady diffusion and osmotic flows, the solutions were kept in the chambers for a long time (11–13 h) and then discharged. After that the cell chambers were washed with distilled water for 15 min. Then the chambers were filled as in the preceding experiment: chamber *I*, with a solution of the same concentration, and chamber *II*, with distilled water. The content of the chambers was sampled through spent-solution vessels *4* and *5* and replenished through the starting-solution chambers *2* and *3*. Further, an experiment was performed to determine the diffusion and osmotic permeabilities. The experiment duration was 3 h.

The amount of water that passed across the membrane and the intensity of its osmotic transfer into chamber *I* were determined from the decrease in volume in the measuring capillary *1*. The amount of solute that passed across the membrane in the direction opposite to that of the osmotic transport as a result of diffusion was determined after an experiment was complete and the solutions were discharged into spent solution vessels *4* and *5*. The content of solutes in the samples was determined by photocolorimetry for aniline and by titrimetry for morpholine.

The coefficients of diffusion P_d (m^2 s^{-1}) and osmotic P_{os} (m^5 kg^{-1} s^{-1}) permeabilities were calculated under assumption of independent flows of solute and solvent (water) across the membrane by the formulas

$$P_d = \frac{C_2 V_2 X}{(C_1 - C_2) S \tau}, \quad (1)$$

$$P_{os} = \frac{\Delta V X}{(C_1 - C_2) S \tau}, \quad (2)$$

where V_1 and V_2 are volumes of chambers *I* and *II* (m^3); C_1 and C_2 are the concentrations of diffusate in, respectively, chambers *I* and *II* at the final instant of time (kg m^3); ΔV is the amount of solvent transferred across the membrane (m^2); S is the membrane surface area (m^2); X is the membrane thickness (m); and τ is the experiment duration (s).

The electroosmotic permeability was determined as follows. The cell was assembled and preliminary operations were performed: the chambers were filled with working solution and the solution allowed to stay until a steady state was attained, chambers *I* and *II* were washed with distilled water and again filled with the working solution, and a necessary temperature regime was estallished. After that, first a trial and then the main experiments were carried out. For this purpose, a voltage was applied to the electrodes and a necessary current density was set. In view of the intensive solvent transfer, the duration of the preliminary and main experiments was 30 min. The amount of solvent (water) that passed across the membrane and the intensity of its electroosmotic transfer into chamber *II* were determined from the increase in volume, ΔV, in the measuring capillary *1*.

The electroosmotic permeability coefficient P_{eos} (m^3 A^{-1} s^{-1}) was calculated by the formula

$$P_{eos} = \frac{\Delta V}{Si\tau}, \quad (3)$$

where i is the current density (A m^{-2}).

Tables 1 and 2 give the coefficients of diffusion and osmotic permeabilities of MGA-100 and OPM-K membranes in relation to the concentrations and temperatures of aqueous aniline and morpholine solutions. It follows from the presented data that the diffusion permeability to aniline changes with its concentration in solution in opposite directions for the MGA100 and OPM-K membranes: for the former, the diffusion permeability first grows with increasing concentration, passes through a maximum, and then starts to fall, whereas for the latter it first falls, passes through a minimum, and then starts to grow.

The dependences of the permeability on the morpholine concentration in solution are more complex, but also antibate for the MGA-100 and OPM-K membranes.

Let us analyze the behavior of the diffusion permeability with the solution concentration in more detail.

Table 1. Diffusion permeability coefficients in relation to the solution concentration and temperature

Aqueous solution	Type of membrane	C_{st}, kg m^{-3}	$P_d \times 10^{10}$ (m^2 s^{-1}) at indicated temperature, °C			
			20	25	32	45
Morpholine	OPM-K	0.6	0.57	0.66	0.91	1.84
		0.9	0.53	0.625	0.78	1.57
		2.18	0.36	0.475	0.63	1.31
		3.27	0.33	0.53	0.73	1.68
		8.28	0.37	0.55	0.83	1.7
		12.0	0.33	0.52	0.75	1.65
	MGA-100	0.6	0.77	1.29	1.68	3.3
		0.9	0.82	1.34	1.83	4.2
		2.18	0.935	1.35	2.24	4.66
		3.27	0.911	1.23	2.06	4.26
		8.28	1.015	1.47	2.1	4.6
		12.0	1.2	1.7	2.42	5.52
Aniline	OPM-K	0.5	1.72	2.1	2.9	4.0
		1.22	1.65	1.88	2.56	3.55
		2.7	1.35	1.63	2.0	2.55
		5.67	1.39	1.74	2.06	2.63
		9.85	1.45	1.87	2.25	2.9
		12.5	1.49	2.01	2.3	3.18
	MGA-100	0.42	1.57	2.3	2.9	6.0
		1.17	1.68	2.43	3.0	6.25
		4.93	1.67	2.31	3.0	6.08
		9.2	1.56	2.14	2.85	4.86
		12.5	1.49	2.0	2.4	4.5

It is known that the diffusion permeability depends on quite a number of factors: types of membranes and solutions [6]; nature of interaction between the solute and membrane, solvent and membrane [7]; etc. When passing across the membrane, the solute may diffuse both through the pore space filled with the solution and through amorphous regions of a swollen membrane. With increasing concentration of the solutions under study, molecules of aniline or morpholine, being incorporated into the matrix of cellulose acetate membrane, probably plasticize it [8–10], with the result that the diffusion permeability coefficient grows with increasing solute content of the solutions in the low-concentration range (Table 1).

Simultaneously with membrane plasticization, there possibly occurs the process of narrowing and even complete volume filling of pores, caused by solute sorption onto the membrane [11]. With this phenomenon dominating, the diffusion permeability coefficient decreases (Table 1).

However, for solutions of morpholine in water, the process of membrane "loosening" probably dominates, with the result that the diffusion permeability increases in this case (Table 1).

As mentioned above, the runs of the dependences of the diffusion permeability coefficients are the opposite for the OPM-K and MGA-100 membranes.

In addition, the diffusion permeability is somewhat lower for OPM-K membranes, compared with those of the MGA100 type. Apparently, the magnitude and the type of dependence of the diffusion permeability on the solution concentration are mainly affected by the membrane nature and the radius distribution of pores in the selective layer of membranes. Unfortunately, published data on the pore characteristics of reverse-osmosis polyamide membranes are extremely scarce and mostly unspecific [12, 13].

Sorption factors probably predominate for OPM-K membranes at low concentrations. With increasing solution concentration, the pore space decreases, as also does the diffusion permeability. With the solution concentration solution increasing further, the solute penetrates into the polymer matrix and the diffusion permeability coefficient starts to increase. However, for morpholine solutions, the diffusion permeability coefficient reaches a maximum after a certain increase and then (with the concentration growing futher) again falls, if only slightly (Table 1). This is probably due to the overall dehydration of the membrane.

Table 2. Osmotic permeability coefficients in relation to the solution concentration and temperature

Aqueous solution	Type of membrane	Temperature, °C							
		20		25		32		45	
		C_{st}, kg m^{-3}	$P_{osm} \times 10^{14}$, m^5 s^{-1} kg^{-1}	C_{st}, kg m^{-3}	$P_{osm} \times 10^{14}$, m^5 s^{-1} kg^{-1}	C_{st}, kg m^{-3}	$P_{osm} \times 10^{14}$, m^5 s^{-1} kg^{-1}	C_{st}, kg m^{-3}	$P_{osm} \times 10^{14}$, m^5 s^{-1} kg^{-1}
Morpholine	OPM-K	0.49	33.7	0.456	51.5	0.565	62.5	0.481	209.0
		1.05	26.8	1.145	28.4	1.062	36.5	1.107	63.1
		2.42	16.79	2.28	19.1	2.14	24.2	1.94	55.83
		5.097	15.1	5.0	20.2	5.0	22.6	4.44	28.5
		8.85	13.0	8.56	16.7	8.1	18.1	8.12	22.9
		13.1	10.3	13.1	12.2	13.04	13.7	13.08	17.0
	MGA-100	0.44	6.0	0.39	15.3	0.364	23.1	0.35	58.0
		1.175	3.9	1.018	8.0	1.044	11.6	1.018	22.4
		2.0	3.2	1.94	5.88	1.847	8.4	1.92	13.74
		4.5	2.77	4.36	4.97	4.27	5.7	4.1	6.87
		8.15	2.26	8.05	3.6	8.15	4.45	8.25	5.5
		12.5	1.7	12.5	2.15	12.9	2.92	11.6	3.62
Aniline	OPM-K	0.7	19.7	0.655	82.4	0.85	130.1	0.975	215.3
		1.375	13.5	1.075	62.05	1.375	98.4	1.45	182.9
		2.15	7.97	2.23	42.7	2.25	78.9	2.4	150.1
		5.2	3.81	5.5	24.7	5.2	28.1	5.4	67.1
		10.0	2.18	10.63	14.0	10.0	18.9	10.25	39.4
		13.0	1.48	12.6	3.4	13.05	5.86	12.2	30.1
	MGA-100	0.625	4.37	0.625	5.54	0.58	6.89	0.54	9.048
		2.75	1.2	2.43	1.5	2.65	2.3	2.59	4.91
		6.35	0.672	6.3	0.83	6.2	1.35	6.3	4.58
		9.8	0.615	9.76	0.78	9.7	1.0	9.93	4.45
		12.5	0.6	12.5	0.765	12.5	0.905	12.5	4.42

In addition to the already mentioned reasons for a change in the diffusion permeability coefficients, there presumably are also other factors affecting this parameter: nonlinear concentration dependence of the distribution coefficients of the solute [11], possibility of associate formation, membrane charge, etc. With increasing temperature, the diffusion permeability always grows for the investigated types of membranes (Table 1), in agreement with the commonly accepted concepts [8].

Let us consider the behavior of the osmotic permeability of membranes. Table 2 presents the osmotic permeability coefficient in relation to the solution concentration and temperature. It can be seen that the osmotic permeability of OPM-K membranes much exceeds that of MGA-100 membranes. This is probably due to differences in the nature of the membrane materials, their structural characteristics, and sign of charge on the membranes.

With increasing solution concentration, the sorption of solutes by membranes leads to their dehydration, to changes in their porous structure (because of membrane swelling and pore narrowing), and, as a result, to a dramatic decrease in osmotic permeability (Table 2). A similar pattern has been observed in studying the osmotic permeability of heterogeneous and homogeneous ion-exchange membranes [14, 15].

With increasing temperature, the osmotic permeability of the membranes grows (Table 2). This is in agreement with the commonly accepted concepts concerning the effect of temperature on the coefficients of water diffusion in polymers [8].

To conclude, it should be noted that the coefficients of osmotic permeability to aniline and morpholine solutions of the reverse-osmosis membranes studied are rather low, which also agrees with the commonly accepted concept of a rather low osmotic pressure of aqueous solutions of low-molecular organic substances [6].

Table 3 presents the electroosmotic permeability coefficients in relation to solution concentration and temperature. It follows from Table 3 that the electroosmotic permeability coefficients depend on the type

Table 3. Electroosmotic permeability coefficients in relation to the solution concentration and temperature

Aqueous solution	Type of membrane	Temperature, °C							
		20		25		32		45	
		C_{st}, kg m^{-3}	$P_{eos} \times 10^8$, m^3 A^{-1} s^{-1}	C_{st}, kg m^{-3}	$P_{eos} \times 10^8$, m^3 A^{-1} s^{-1}	C_{st}, kg m^{-3}	$P_{eos} \times 10^8$, m^3 A^{-1} s^{-1}	C_{st}, kg m^{-3}	$P_{eos} \times 10^8$, m^3 A^{-1} s^{-1}
Morpholine	OPM-K	0.45	9.98	0.45	9.2	0.45	8.0	0.45	5.8
		1.05	9.53	1.0	8.7	0.99	7.35	1.0	5.5
		2.22	8.4	2.15	7.75	2.2	6.2	2.2	4.75
		4.35	6.25	4.3	5.65	4.35	4.75	4.3	3.6
		8.3	4.28	8.25	3.8	8.3	3.0	8.3	2.23
		10.7	3.25	10.75	2.85	10.75	2.25	10.6	1.75
		12.5	2.63	12.4	2.4	12.5	2.0	12.5	1.37
	MGA-100	0.74	3.41	0.8	3.27	0.8	2.97	0.7	2.6
		1.5	3.35	1.4	3.22	1.5	2.93	1.5	2.56
		2.5	3.3	2.5	3.16	2.5	2.87	2.4	2.51
		5.0	3.2	5.2	3.06	5.0	2.82	5.0	2.45
		8.56	3.14	8.6	2.95	8.6	2.75	8.6	2.39
		13.0	3.05	13.0	2.88	13.1	2.67	13.2	2.32
Aniline	OPM-K	0.38	7.25	0.39	7.15	0.4	6.93	0.4	6.5
		1.13	6.98	1.03	6.85	1.04	6.62	1.04	6.3
		2.0	6.7	1.96	6.6	1.96	6.46	1.96	6.15
		4.0	6.34	4.0	6.26	4.0	6.1	4.0	5.8
		10.68	5.16	10.7	5.06	10.7	4.88	10.7	4.88
		12.6	4.96	12.6	4.84	12.6	4.64	12.6	4.64
	MGA-100	0.4	4.54	0.4	4.32	0.4	4.02	0.4	3.47
		0.74	4.51	0.74	4.28	0.74	3.98	0.74	3.45
		2.58	4.47	2.58	4.22	2.58	3.92	2.58	3.38
		4.8	4.43	4.8	4.18	4.8	3.87	4.8	3.3
		7.4	4.38	7.4	4.4	7.4	3.82	7.4	3.24
		11.4	4.33	11.4	4.09	11.4	3.76	11.4	3.18

of membrane (being higher for the OPM-K membrane, compared with MGA-100) and solution concentration (also falling with increasing concentration).

It is known [14, 16] that the electroosmotic flow of liquids depends on a number of factors, the most important of which are the solution viscosity, ion hydrability, nature of membrane matrix, its moisture content, degree of homogeneity, adsorption capacity, etc.

With increasing concentration of the solutions, their viscosity and electrical conductivity increase somewhat. Consequently, the electroosmotic permeability coefficient must decrease with increasing solution concentration. This is confirmed by the investigation performed (Table 3).

With increasing temperature, the viscosity of the solutions decreases somewhat, but their electrical conductivity grows to a greater extent. This suggests that the behavior of the electroosmotic permeability with temperature may vary. In the case in question, the key factor is, probably, the fast rise in electrical conductivity with increasing temperature, which leads to a substantial decrease in electroosmotic permeability with increasing solution temperature (Table 3).

As shown by experimental studies (Table 3), the electroosmotic permeability coefficient is independent of current density for the systems studied. The experiments were mainly performed at a current density of 13.5 A m^{-2}, and, in part, at 20°C and current densities of 8.8 and 19.8 A m^{-2}.

The difference between the electroosmotic permeability coefficients of the MGA-100 and OPM-K membranes is presumably due to the difference in the nature of the membrane materials, in their porosities, charge, etc.

CONCLUSIONS

(1) The diffusion, osmotic, and electroosmotic permeabilities of MGA-100 and OPM-K membranes strongly depend on the nature of solute and its concentration and temperature.

(2) The diffusion permeability of MGA-100 membranes exceeds that of OPM-K membranes. The dependences of the diffusion permeabilities on the concentration of aniline or morpholine are rather complex and show opposite kinds of behavior for these membranes.

(3) The osmotic permeability of MGA-100 membranes much exceeds that of OPM-K membranes. For all kinds of membranes and solutions studied, the osmotic permeability decreases dramatically with increasing solution concentration.

(4) Over a wide range of concentrations studied the electroosmotic permeability of MGA-100 membranes is lower than that of OPM-K membranes. With increasing concentration, the electroosmotic permeability falls.

(5) With increasing temperature, the diffusion and osmotic permeabilities increase, and the electroosmotic permeability falls.

REFERENCES

1. Lazarev, S.I., Korobov, V.B., Kliot, M.B., and Pirogov, P.A., *Izv. Vyssh. Uchebn. Zaved., Khim. Khim. Tekhnol.*, 1993, vol. 36, no. 5, pp. 76–80.
2. Korobov, V.B. and Lazarev, S.I., *Izv. Vyssh. Uchebn. Zaved., Khim. Khim. Tekhnol.*, 1995, vol. 38, nos. 4–5, pp. 73–79.
3. Korobov, V.B., Lazarev, S.I. and Konovalov, V.I., *Vestn. Tamb. Gos. Tekhn. Univ.*, 1995, vol. 1, nos. 3–4, pp. 296–303.
4. Korobov, V.B. and Konovalov, V.I., *Inzh.-Fiz. Zh.*, 1993, vol. 65, no. 3, pp. 356–357.
5. Konovalov, V.I. and Korobov, V.B., *Zh. Prikl. Khim.*, 1989, vol. 62, no. 9, pp. 1975–1982.
6. Yasminov, A.A., Kalgina, V.T., and Kozhevnikov, A.V., *Khim. Prom–st.*, 1978, no. 10, pp. 25–30.
7. Sourirajan, S., *Pure Appl. Chem.*, 1978, vol. 50, pp. 593–615.
8. Nikolaev, N.N., *Diffuziya v membranakh* (Diffusion in Membranes), Moscow: Khimiya, 1980.
9. Chalykh, A.E., *Diffuziya v polimernykh sistemakh* (Diffusion in Polymer Systems), Moscow: Khimiya, 1987.
10. Michaels, A.S., *Progress in Separation and Purification*, vol. 1, pp. 143–186.
11. Korobov, V.B. and Lazarev, S.I., *Izv. Vyssh. Uchebn. Zaved., Khim. Khim. Tekhnol.*, 1996, vol. 39, nos. 1–2, pp. 61–63.
12. Bryk, M.T. and Tsapyuk, E.A., *Ul'trafil'tratsiya* (Ultrafiltration), Kiev: Naukova Dumka, 1989.
13. Membrany na osnove aromaticheskikh poliamidov, *Plast. Massy*, 1980, no. 11, p. 60.
14. Pilipenko, A.T., Vakhnin, I.G., Gornovskii, I.T., *et al.*, *Kompleksnaya pererabotka mineralizovannykh stochnykh vod* (Integrated Processing of Mineralized Wastewater), Kiev: Naukova Dumka, 1984.
15. Grebenyuk, V.D. and Gudrid, T.D., *Kolloid. Zh.*, 1987, vol. 49, no. 2, pp. 336–339.
16. Tikhomolova, K.P., *Elektroosmos* (Electroosmosis), Leningrad: Khimiya, 1989.

Russian Journal of Applied Chemistry, Vol. 74, No. 2, 2001, pp. 253–258. Translated from Zhurnal Prikladnoi Khimii, Vol. 74, No. 2, 2001, pp. 249–254.

ENVIRONMENTAL PROBLEMS OF CHEMISTRY AND TECHNOLOGY

Deironing of Water with Natural Carbonate-containing Tripoli

I. L. Shashkova, A. I. Rat'ko, A. S. Panasygin, N. V. Mil'vit, and N. V. Bondareva

Institute of General and Inorganic Chemistry, Belarussian Academy of Sciences, Minsk, Belarus
Belarussian State Polytechnical Academy, Minsk, Belarus

Received September 15, 1998; in final form, March 2000

Abstract—The possibility of using natural carbonate-containing tripoli for water deironing was studied. Factors are considered determining the efficiency of tripoli in Fe(III) absorption.

Siliceous rocks constituted by various finely disperse opal-crystobalite formations (opokas, diatomites, tripolis) occur in nature either in pure form or with varied content of an associated component—most frequently of the carbonate-clay type [1]. The content of calcium carbonate in rocks of this kind is 0–60%, and that of clay, 0–15%, for different deposits.

In contrast to purely siliceous rocks, which are raw materials serving for various purposes and having their traditional areas of application (e.g., in manufacture of construction cement [1, 2]), carbonate-clay materials have not found wide use.

Large deposits of carbonate tripoli have been discovered in many regions of Belarus, Lithuania, and Russia. In this connection, it is of current interest to reveal the possibility of their use in the national economy.

With account of the ability of the carbonate component to absorb ions of heavy and non-ferrous metals from aqueous solutions [3–11], carbonate tripolis show ecological promise.

Compared with carbonates, carbonate-containing silicas are characterized by more developed porous structure and lower solubility [12], and also by ability to form strong granules [10], and, therefore, their use in water purification seems to be more promising than that of carbonates.

Previously, the high efficiency of carbonate-containing tripolis in recovery of a number of heavy metal ions: Cr(III), Pb(II), Zn(II), and Cu(II), has been demonstrated [9, 10]. The present communication reports the results obtained in studying their efficiency in deironing. A search for new high-efficiency materials for deironing of ground water and wastewater is an important task [13].

EXPERIMENTAL

The experiments were done with a tripoli containing 43.5% calcium carbonate, with its aqueous extract characterized by pH 8.6.[1] A representative sample of a natural carbonate tripoli and four its thermal modifications obtained by calcination in air at 500, 600, 700, and 800°C (designated as tripoli-500, tripoli-600, etc.) were used in the study.

The absorption of Fe(III) ions under static conditions from 0.001–0.1 N nitrate solutions with pH 1.7–2.3 was studied at 15–20°C at liquor ratio M = 1 : 125 [M = s : l, where s denotes the mass of solid sorbent (g), and l, the volume of liquid phase (ml)].

The experimental procedure was as follows: 25 ml of a solution was poured over 0.2 g of sorbent (0.09–0.25-mm fraction) and the mixture was kept for 1 day with periodic stirring. In studying the kinetics of the process, the experimental technique was similar, but the time of contact between the solution and the solid phase was varied between 10 min and several days. The solution was separated from the solid phase and the residual content of iron in the filtered solution was determined by complexometric titration or atomic-absorption spectrometry.

The solid phase was washed with water, dried in air, and subjected to X-ray phase analysis (DRON-2.0 diffractometer, Cu_{K_α} radiation).

The variation of the solution pH during sorption was monitored with an EV-74 ion meter.

[1] Stal'noe deposit, Mogilev oblast, Belarus.

1070-4272/01/7402-0253 $25.00 © 2001 MAIK "Nauka/Interperiodica"

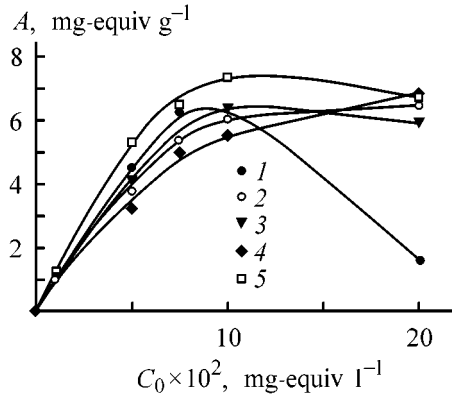

Fig. 1. Curves of Fe(III) ion absorption by natural tripoli and its thermal modifications. (*A*) Absorption and (C_0) initial concentration of $Fe(NO_3)_3$ solutions. (*1*) Starting tripoli, (*2*) tripoli-500, (*3*) tripoli-600, (*4*) tripoli-700, and (*5*) tripoli-800.

The experiments on deironing of real ground water under dynamic conditions were performed as described below.

Curves of Fe(III) ion absorption from $Fe(NO_3)_3$ of varied concentration by a carbonate-containing tripoli not subjected to thermal treatment and by samples calcined for 2 h at temperatures in the range from 500 to 800°C are shown in Fig. 1. It can be seen that the maximum amount of absorbed Fe(III) A_{Fe} is 7.5 mg-equiv g^{-1} [tripoli-800, $C_{Fe(NO_3)_3} = 10^{-1}$ g-equiv l^{-1}].

The absorption curves plotted in the coordinates A_{Fe}–$C_{0\,\{Fe(NO_3)_3\}}$ [$C_{0\,\{Fe(NO_3)_3\}}$ is the initial concentration of the iron(III) nitrate solution] for some of the samples pass through a maximum at $C_{0\,\{Fe(NO_3)_3\}} = 10^{-1}$ g-equiv l^{-1}, the most pronounced for the sample not subjected to thermal treatment.

According to published data [5–8, 14], calcium carbonate absorbs cations of doubly charged metals from acid and neutral solutions through formation of less soluble M(II) carbonates or hydrocarbonates. Carbonates of triply charged metal ions [Fe(III), Al(III)] cannot be obtained in aqueous solutions because of their hydrolytic decomposition [15]. When brought in contact with carbonates, these metals form hydroxides by the reaction

$$Fe(NO_3)_3 + CaCO_3 + HOH \rightarrow Fe(OH)_3 + CO_2 + Ca(NO_3)_2. \quad (1)$$

According to reference data, the pH of the onset of iron hydroxide precipitation depends on the Fe(III) concentration, being equal to 1.5 and 2.3 for solutions with concentrations of, respectively, 0.03 and 3 g-equiv l^{-1} [16]. Complete deironing of solutions of concentration 0.15 g-equiv l^{-1} with a calcium carbonate sorbent is observed at equilibrium solution pH 3.5 [14]. In deironing of solution with Fe(III) concentrations in the range $(5.4–43.0) \times 10^{-3}$ g-equiv l^{-1} with calcite, complete precipitation of iron hydroxide was observed in [17] at equilibrium solution pH exceeding 7.

The results obtained in deironing of aqueous solutions with the use of carbonate tripolis (Fig. 1, Table 1) also indicate that the amount of absorbed iron(III) and also the peak in the A_{Fe}–$C_{0\,\{Fe(NO_3)_3\}}$ curves (Fig. 1) correlate with how pH varies in the system under study. Table 1 lists the concentrations and pH values of the starting and equilibrium (brought in contact with the sorbent) $Fe(NO_3)_3$ solutions, and also the calculated degree of purification to remove iron(III) from solutions of various concentrations.

It can be seen from Table 1 that the pH of iron nitrate solutions with concentration lower than 10^{-1} g-equiv l^{-1} (Fig. 1, region before the peak in the curve) is 1.86–2.34 before the contact with the sorbent. After purification, i.e. after bringing the solution in contact with carbonate tripoli, the pH values increase to become 1.9–11.04. The degree of purification of such solutions to remove iron(III) is very high, but, nevertheless, it approaches 100% only in those cases when the pH of the equilibrium iron(III) solution exceeds 7, in agreement with the results of [17].

The pH of iron(III) nitrate solutions with concentrations exceeding 10^{-1} g-equiv l^{-1} (Fig. 1, region after the peak in the A_{Fe}–$C_{0\,\{Fe(NO_3)_3\}}$ curve) is 1.7–1.8 before and 1.6–1.8 after sorption. The absorption of iron(III) from these solutions is not accompanied by any significant change in pH. The extent of iron hydroxide precipitation in this region decreases, which is the reason for the appearance of the peak in the absorption curve.

For calcined tripoli modifications, the peak in the A_{Fe}–$C_{0\,\{Fe(NO_3)_3\}}$ curve is less pronounced. According to previously obtained data [9], thermal treatment of a carbonate tripoli in the range 500–800°C does not change significantly its phase composition, but is accompanied by a decrease in the intensity of calcite peaks. The alkaline properties of the tripoli are not

Table 1. Results of analysis of iron(III) nitrate solutions before and after contact with a carbonate-containing tripoli

Initial Fe(III) concentration $C_1 \times 10^3$, g-equiv l^{-1}	pH of the starting solution	Residual Fe(III) concentration $C_2 \times 10^2$, g-equiv l^{-1}	pH after sorption	Fe(III) sorption, mg-equiv g^{-1}	Degree of solution purification, %
		Starting tripoli			
1.0	2.34	0	7.03	1.25	100.0
5.0	1.93	1.3	3.35	4.53	72.4
7.5	1.86	2.4	1.89	6.28	66.9
10.0	1.82	4.9	1.78	6.35	50.8
20.0	1.70	18.7	1.64	1.63	6.5
		Tripoli-500			
1.0	2.34	0	7.32	1.25	100.0
5.0	1.93	2.0	3.05	3.75	60.0
7.5	1.86	3.2	1.85	5.38	57.3
10.0	1.82	6.8	1.76	6.06	32.5
20.0	1.70	14.8	1.63	6.50	26.0
		Tripoli-600			
1.0	2.34	0	7.20	1.25	100.0
5.0	1.93	1.8	3.68	4.03	64.4
7.5	1.86	3.6	1.90	4.79	51.1
10.0	1.82	4.9	1.80	6.44	51.5
20.0	1.70	15.2	1.71	6.00	24.0
		Tripoli-700			
1.0	2.34	0	9.58	1.25	100.0
5.0	1.93	2.0	4.68	3.25	60.0
7.5	1.86	3.5	1.96	5.03	53.6
10.0	1.82	5.6	1.81	5.56	44.5
20.0	1.70	14.5	1.64	6.88	27.5
		Tripoli-800			
1.0	2.34	0	11.04	1.25	100.0
5.0	1.93	0.8	5.15	5.31	85.0
7.5	1.86	3.5	1.96	5.03	53.6
10.0	1.82	4.1	1.81	7.38	59.0
20.0	1.70	14.6	1.64	6.75	27.0

changed significantly in the process. Table 2 lists the pH values of an aqueous extract and solubilities of carbonate tripoli before and after thermal treatment. It can be seen that the pH of the aqueous extract is three units higher for tripoli-800, compared with the starting carbonate tripoli, being equal to 11.99. The solubility of the carbonate-containing tripoli [calcium(II) content in solution] also grows. The thermal treatment is accompanied by partial decomposition of calcite to give a more soluble and more alkaline component—calcium oxide, and by an increase in the pH of the aqueous extract. The increase in the sorbent alkalinity levels out the peak in the absorption curves.

Table 2. Solubility in water and pH value of an aqueous extract of a carbonate tripoli before and after thermal treatment; pH of starting distilled water 5.1

Parameter	Starting tripoli	Tripoli-500	Tripoli-800
pH of aqueous extract	8.05	8.22	11.99
Ca(II) concentration in aqueous extract, mg-equiv l^{-1}	1.1	1.6	10.7

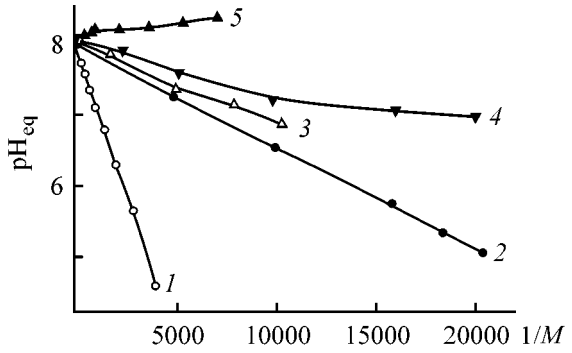

Fig. 2. pH of equilibrium solution vs. ratio of the tripoli mass to the volume of the starting aqueous solution. (*M*) Liquor ratio. pH of the starting solution: (*1*) 2.6, (*2*) 3.5, (*3*) 4.6, (*4*) 6.5, and (*5*) 7.5.

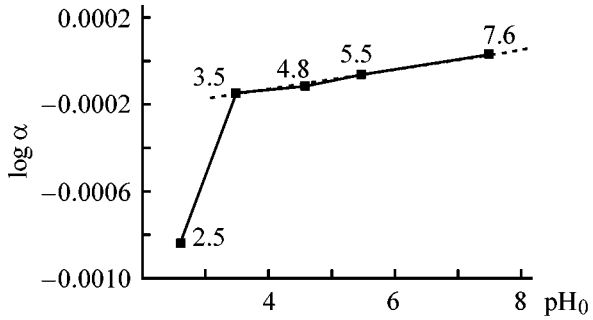

Fig. 3. Slope α of pH_{eq}–1/*M* straight lines vs. the pH_0 of the starting solution.

Thus, it is clear that the efficiency of iron(III) absorption from aqueous solutions by natural carbonate-containing tripoli is governed by the pH of equilibrium solution, pH_{eq}. This parameter is, in turn, a function of the pH of the starting solution and the liquor ratio used in purification, equal to the ratio of the solid sorbent mass to the volume of a solution being purified.

Table 3. Physicochemical characteristics of artesian water

Characteristic	Average value of parameter
Chromaticity	<20
pH	8.0
Chloride ions, mg l^{-1}	9.2
Sulfate ions, mg l^{-1}	15.1
NH_4^+, mg l^{-1}	0.52
Nitrate ions, mg l^{-1}	4.7
Nitrite ions, mg l^{-1}	Trace
Total iron, mg l^{-1}	3.65
Mn(II), mg l^{-1}	0.01
Fe(II), mg l^{-1}	3.31
Oxidizability by permanganate ions, mg l^{-1}	5.35
Alkalinity, mg-equiv l^{-1}	4.35
Temperature, °C	9.2

To determine the relationship between these parameters, the variation of the pH value in the system tripoli–water was studied in a wide range of s : l ratios and pH_0 values. A weighed portion of a sample was placed in distilled water with different pH_0 values adjusted using nitric acid or sodium hydroxide, kept for 1 day, and then the pH of the equilibrium liquid phase was determined. The obtained results are presented in Fig. 2 in the form of a set of pH_{eq}–1/*M* curves for solutions with different pH_0 values. As it can be seen from the figure, the value $pH_{eq} > 7$, necessary for complete purification to remove iron(III), is achieved for $Fe(NO_3)_3$ solutions with pH_0 in the range from 2.6 to 3.5 at 1/*M* of 1500–7000. For less acid solutions, this value is 20000 and more.

The initial portions of the pH_{eq}–1/*M* curves (Fig. 2) are approximated by a straight line with small standard deviation and are described by equations calculated by the least-squares method. All the approximated curves converge to a single point with sufficient accuracy. Hence follows that the existing system of five equations describing the dependence of pH_{eq} on 1/*M* at different pH_0 values can be combined into a single equation by determining the relationship between the slope of an experimental curve and the pH_0 value (Fig. 3). The data in Fig. 3 indicate the existence of a linear relation between tan α and pH_0 in the pH_0 range 3.5–7.5, expressed by the equation

$$\tan\alpha = -(-31.372 - 4.1627pH_0) \times 10^{-5}. \quad (2)$$

Thus, the relationship between pH_{eq}, pH_0, and liquor ratio M = s : l for solutions with pH falling within the above interval can be expressed as a linear equation

$$pH_{eq} = 7.98 - (31.372 - 4.1627pH_0) \times 10^{-5} M. \quad (3)$$

Relation (3) can be used to evaluate fast the efficiency of carbonate-containing materials in purification of real solutions. For example, at a weighed tripoli portion of 1 kg and prescribed pH_0 6, the solution volume V_l (l) that can be neutralized to pH 7 can be readily calculated using Eq. (3):

$$V_l = \frac{(31.37 - 4.16\,pH_0) \times 10^{-5} T}{7.98 - pH_{eq}} = 6.5 \times 10^5. \quad (4)$$

Equation (3) and its variations can also be helpful in evaluating the efficiency of a material in water pu-

Table 4. Efficiency of Fe_{tot} removal

Rate of water filtration, m h^{-1}	Content of iron at column outlet, mg l^{-1}		Charge bed height, cm	Rate of water filtration, m h^{-1}	Content of iron at column outlet, mg l^{-1}		Charge bed height, cm
	without aeration	with simplified aeration			without aeration	with simplified aeration	
3.8	0.48	0.11	60	10	2.07	1.51	22
10.5	1.10	0.23	60	10	1.73	1.14	34
16.0	1.35	1.02	60	10	1.22	0.97	47
20.0	1.72	1.34	60	10	0.51	0.28	63
28.0	2.31	1.72	60				

rification under dynamic conditions. In doing so, account should be taken of the kinetics of attainment of acid-base equilibria under dynamic conditions and the physical form of a sorbent.

The efficiency of carbonate-containing tripoli in deironing was confirmed in purification of artesian water.[1] The physicochemical characteristics of the water are presented in Table 3. It can be seen that, for this water source, the content of iron ions exceeds manyfold the maximum permissible concentration (MPC) of 0.3 mg l^{-1}.

As indicated by chemical analysis data, iron is present in the water of this source mainly in the form of Fe(II). According to published data, deironing is the most efficient in solutions of triply charged iron. The oxidation process Fe(II) $\rightarrow$ Fe(III) occurs in air under the action of atmospheric oxygen. Under the dynamic purification conditions, the process of saturation with oxygen of the solutions being purified is frequently intensified by additional aeration [13].

Water purification was performed in dynamic filtration mode with simplified aeration [13] on a column charged with granulated tripoli (column diameter 35 mm, charge bed height 600–650 mm, grain diameter 3 mm at 3-mm length). To obtain a granulated form of the sorbent, a humid mixture of carbonate tripoli with 10% addition of bentonite clay as binder was formed in an FP-015 granulator into cylindrical grains dried in air and then calcined at 650°C.

As it can be seen from the data in Table 4, water is purified to remove iron ions to the MPC standard. The rate of filtration is 10–12 m h^{-1} at sorbent bed height in the column of no less than 60–70 cm.

[1] Strumen' water intake (Pinsk).

CONCLUSIONS

(1) Carbonate-containing tripoli exhibit high efficiency in Fe(III) removal from aqueous solutions and are of interest as promising material for deironing of ground water and wastewater.

(2) Deironing is the most efficient under conditions when the relation between the tripoli mass and the starting solution volume ensures a pH value of the equilibrium solution higher than 7. The tripoli capacity with respect to iron reaches in this case the maximum value of 7.5 mg-equiv l^{-1}.

REFERENCES

1. *Kremnistye porody SSSR* (Siliceous Rocks of the USSR), Kazan: Tatar. Knizhn. Izd., 1976.
2. *Prirodnye corbenty SSSR* (Natural Sorbents of the USSR), Moscow: Nedra, 1990.
3. Tarasevich, Yu.I., *Prirodnye sorbenty v protsessakh ochistki vody* (Natural Sorbents in Water Purification), Kiev: Naukova Dumka, 1981.
4. Gudz', N.Ya. and Maksin, V.I., *Khim. Tekhnol. Vody*, 1991, vol. 13, no. 5, pp. 428–436.
5. Batalova, Sh.B., Likerova, A.A., Tabanova, Kh.G., and Zhaksylykova, M.Kh., *Izv. Akad. Nauk KazSSR, Ser. Khim.*, 1989, no. 3, pp. 83–87.
6. Hautala, E., Randall, J., Goodbau, A., and Waiss, A., *Water Res.*, 1977, vol. 11, no. 2, pp. 243–245.
7. Istomin, A.I., *Sborn. Nauchn. Tr. Nauchn.-Issled. Proekt. Inst. Obogashch. Rud Tsvet. Met., Kazmekhanobr.*, Alma-Ata: Kazmekhanobr, 1985, no. 28, pp. 149–162.
8. Mashkova, L.P. and Ogorodnikova, E.N., *Vestn. Mosk. Gos. Univ., Ser. 2, Khim.*, 1994, vol. 35, no. 5, pp. 456–459.
9. Rat'ko, A.I., Shashkova, I.L., Vecher, V.A., and

Gorbatsevich, N.V., *Vestsi Akad. Nauk Belarusi, Ser. Khim. Navuk*, 1997, no. 1, pp. 32–37.

10. Shashkova, I.L., Rat'ko, A.I., Mil'vit, N.V., *et al.*, *Zh. Prikl. Khim.*, 2000, vol. 73, no. 6, pp. 914–919.
11. Dijk, J.C., Scholler, Ir.M., and Wilms, D., *Chem.-Tech.* (BRD). 1988–1989, vol. 17, Sonderausg, pp. 23–27.
12. Kumok, V.N., Kuleshova, O.M., and Karabin, L.A., *Proizvedeniya rastvorimosti* (Solubility Products), Novosibirsk: Nauka, 1983.
13. *Obshchaya khimiya v formulakh, opredeleniyakh, skhemakh: Spravochnoe rukovodstvo* (General Chemistry in Formulas, Definitions, and Schemes: Handbook), Tikavoi, V.F., Ed., Minsk: Universitetskoe, 1987.
14. Lur'e, Yu.Yu., *Spravochnik po analiticheskoi khimii* (Handbook of Analytical Chemistry), Moscow: Khimiya, 1967.
15. Shanina, T.P., Poladyan, V.E., Marants, I.S., *et al.*, *Kompleks. Ispol'z. Miner. Syr'ya*, 1992, no. 4, pp. 87–89.
16. Batalova, Sh.B., Pak, N.D., Duimagambetova, S.D., *et al.*, *Kompleks. Ispol'z. Miner. Syr'ya*, 1979, no. 10, pp. 56–59.
17. Kul'skii, L.A. and Strokach, P.P., *Tekhnologiya ochistki prirodnykh vod* (Technology of Natural Water Purification), Kiev: Naukova Dumka, 1987.

Russian Journal of Applied Chemistry, Vol. 74, No. 2, 2001, pp. 259–264. Translated from Zhurnal Prikladnoi Khimii, Vol. 74, No. 2, 2001, pp. 254–259.

ENVIRONMENTAL PROBLEMS OF CHEMISTRY AND TECHNOLOGY

Mineralization of Detoxification Products of Yperite–Lewisite Mixture

V. G. Sakharovskii, V. I. Tugushov, E. V. Kashparova, A. M. Zyakun, A. I. Kochergin, and A. M. Boronin

Skryabin Institute of Biochemistry and Physiology of Microorganisms, Russian Academy of Sciences, Pushchino, Moscow oblast, Russia

State Institute of Technology of Organic Synthesis, Vol'sk-17, Saratov oblast, Russia

Received November 13, 1999; in final form, June 2000

Abstract—The mineralization of the products of detoxification (neutralization) of yperite–lewisite mixture by electrochemical oxidation was studied. A procedure for separation of potassium salts and arsenic compounds by electrocoagulation was developed. A possibility of using the resulting potassium salts as fertilizers for agriculture was discussed.

Russia's stock of chemical warfare includes nerve gases (sarin, soman, and VX) and blister gases [yperite, lewisite, yperite–lewisite mixtures (YLMs)]. The universally adopted concept of their disposal envisages two stages. In the first stage, war gases are neutralized to give reaction masses unsuitable for further use for military purposes. The second stage involves combustion or processing of the reaction mass into a commercial product.

The procedures for chemical detoxification of blister gases are rather well developed and tested at pilot plants; they can be used for practical purposes. It has been found that the detoxification products, excluding arsenic compounds, belong to compounds of hazard grade III [1].

It has been proposed to utilize the reaction masses by combustion. However, an analysis of the approaches to the development of processes based on the combustion of reaction masses showed that their realization results in the formation of large amounts of environmentally hazardous wastes [2]. This, in turn, caused counteraction of environmentalists and the public. In addition, the combustion of the reaction masses is highly expensive: the construction cost of gas-cleaning systems reaches 30% of the total expenditure [3].

The aim of this study was to develop a procedure for enviromentally safe conversion of detoxification products of YLMs into mineral fertilizers for agriculture and arsenic compounds serving as secondary raw materials for the reprocessing indusrtry.

As the object of study served a process solution from detoxification of YLM obtained by its alkaline treatment in the presence of monoethanolamine.[1] The process solution from YLM detoxification (so-called neutralizate) is a turbid brown-green liquid with black flakes.

The organic components of 300 ml of the YLM neutralizate were mineralized using a universal laboratory pilot setup (Fig. 1).

The electrolyzer parameters were as follows: operating volume 100 ml, anode (graphite) surface area 300 cm^2, voltage 6 V, and anodic current density 0.01 A cm^{-2}. The electrocoagulator parameters were as follows: operating volume 300 ml, surface area of aluminum electrodes 1040 cm^2, ac current density 0.01 A cm^{-2}, and voltage 6 V.

The electrolysis process and the composition and amount of organic products were monitored by high-resolution ^1H NMR spectroscopy [4].

The ^1H NMR spectra were recorded on a WP80SY NMR spectrometer (Bruker, Germany) under the standard conditions with compensation of ^1H signals from

[1] State Institute of Organic Synthesis Technology (Shikhany, Saratov oblast, Russia).

1070-4272/01/7402-0259 $25.00 © 2001 MAIK "Nauka/Interperiodica"

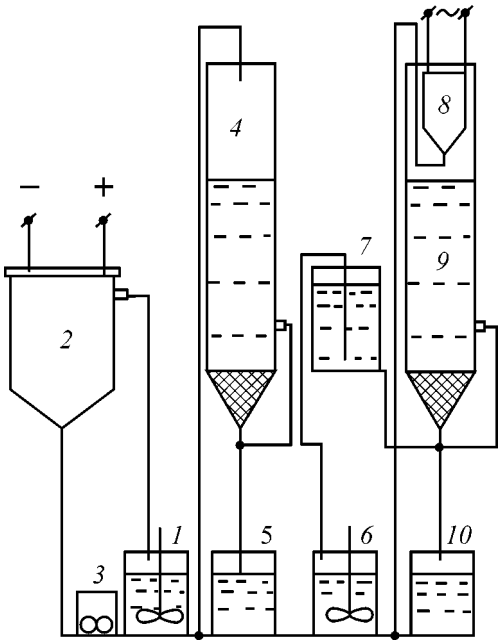

Fig. 1. Flow sheet of the laboratory setup for recovery of neutralizates of war gases: (*1*) mixer, (*2*) diaphragmless electrolyzer, (*3*) dosing pump, (*4*) settling filter, (*5*) vessel, (*6*) neutralizer, (*7*) CO_2 absorber, (*8*) electrocoagulator, (*9*) settling filter, and (*10*) crystallizer.

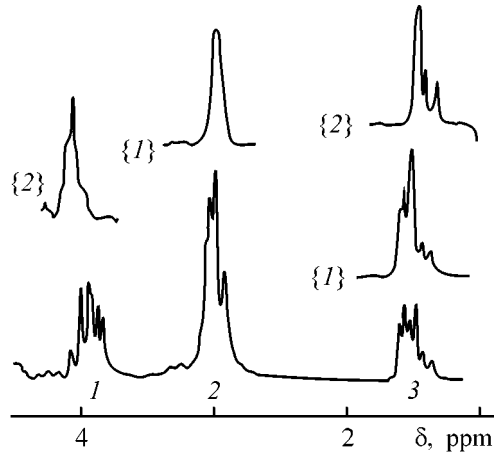

Fig. 2. ^{1}H NMR spectrum of the organic phase of YLM neutralizate at pH > 12. (δ) Chemical shift; the same for Figs. 3 and 4. ({*1*}, {*2*}) Signals obtained with spin–spin decoupling.

residual water, which were used as internal reference in determining the chemical shifts (δ = 5.00 ppm at pH > 2).

The arsenic content in the solutions was determined on an AAS-5100 Zeeman atomic-absorption spectrometer (Perkin–Elmer, US).

During electrolysis, the composition of the gas phase was determined on an MM8-80 mass spectrometer (VG, UK). Samples for mass-spectrometric analysis were withdrawn from the gas phase of the mixer (Fig. 1). Before the experiments, the reactor was purged with argon.

The total content of salts and organic substances in the solutions was determined gravimetrically from the weight of the dry residue after extraction separation of organic and inorganic fractions from the solid phase with chloroform.

The contents of sulfates, chlorides, nitrates, and carbonates in the YLM neutralizate and products of its processing were determined by the procedures described in [5, 6].

The pH in aqueous solutions was monitored with Lachema universal indicator paper (Czech Republic). The pH of ^1H_2O and ^2H_2O solutions was determined on an I-155 pH meter (Armenia). Potassium chloride, potassium hydroxide, nitric acid, and chloroform used in the experiments were of chemically pure grade.

From data presented in [1], the main products of alkaline detoxification of yperite, a YLM component, in the presence of monoethanolamine are *N*-(2-hydroxyethyl)thiomorpholine and monoethanolamine hydrochloride [Eq. (1)]. The main products of alkaline detoxification of lewisite [7], a YLM component, are acetylene, sodium arsenate, and sodium chloride [Eq. (2)]:

$$S(C_2H_4Cl)_2 + 2H_2NC_2H_4OH = [S{=}C_4H_8{=}NHC_2H_4OH]Cl + [HOC_2H_4NH_2]Cl, \quad (1)$$

$$ClCH{=}CHAsCl_2 + 4NaOH = CH{\equiv}CH + NaAsO_2 + 3NaCl + 2H_2O. \quad (2)$$

Thus, *N*-(2-hydroxyethyl)thiomorphine, monoethanolamine, sodium chloride, and sodium arsenate would be expected to be the main components of YLM neutralizate.

The ^{1}H NMR spectrum of the organic phase of YLM neutralizate, extracted with chloroform, contains three multiplets at δ 4.0, 3.0, and 1.5 ppm (Fig. 2).

The multplets at 4.0 and 3.0 ppm can be assigned to protons of free monoethanolamine (Fig. 3c) and *N*-(2-hydroxyethyl)thiomorpholine. In addition, ^{1}H signals from S–CH_2 groups of the thiomorpholine fragment may appear at 3.0 ppm [8].

The position of the ^{1}H NMR signals of N–NH_2 groups of the thiomorpholine fragment can be predicted by comparing the ^{1}H NMR spectral char-

acteristics of the organic fraction of the YLM neutralizate with those of the morpholine derivative 2-methylene-*N*-hydroxyethylmorpholine, for which the ^{1}H signals of the N–CH_2 groups are observed at 2.5 ppm [9]. In passing from morpholine to thiomorpholine, it is quite reasonable that the ^{1}H signals of thiomorpholine are shifted upfield by 0.3–0.4 ppm owing to the lower electronegativity of sulfur in comparison with oxygen. The additional upfield shift of the ^{1}H signals of the N–CH_2 groups of thiomorpholine by approximately 0.7 ppm can be attributed to the effect of the unshared electron pair of nitrogen atom, as was observed for festuclavine [10].

Thus, the multiplet at 1.5 ppm can be assigned to protons of the N–CH_2 group of *N*-(2-hydroxyethyl)-thiomorpholine. The spin–spin coupling of all the three multiplets observed in the ^{1}H NMR spectrum (Fig. 2) confirms this suggestion.

The fact that the main organic product of YLM neutralization is a thiomorpholine derivative is additionally confirmed by the ^{1}H NMR titration of the neutralizate (Figs. 3a, 3b), indicating a downfield shift of all the signals of the spectrum in passing from alkaline to acid medium. A similar shift is observed for the ^{1}H NMR signals of monoethanolamine (Figs. 3c, 3d). The pH ranges of the shift observed for the neutralizate and monoethanolamine are the same (pK 7.2), which is characteristic of the conversion of monoethanolamine and *N*-(2-hydroxyethyl)thiomorpholine into the corresponding hydrochlorides.

With account of the accumulated experience on degradation of some toxins and pollutants [8, 11–13], we selected electrolysis as the most universal and efficient technique and the method of electrocoagulation with the use of soluble aluminum electrodes, since arsenic salts that are formed in electrocoagulation as stable aluminum arsenates difficultly soluble in water.

The YLM neutralizate was subjected to electrolysis in the presence of potassium hydroxide on the laboratory pilot setup described above. The relation between the components of the starting reaction mixture to be used in electrolysis was evaluated using overall chemical equations (3) and (4) from the neutralizate composition, assuming that the electrolysis of organic components proceeds to complete mineralization with conversion of organic nitrogen into molecular form.

$$2C_6H_{13}ONS + 28KOH + 20.5O_2 = 12K_2CO_3 + 2K_2SO_3 + N_2 + 27H_2O, \quad (3)$$

$$2H_2NC_2H_4OH + 8KOH + 6.5O_2 = 4K_2CO_3 + N_2 + 11H_2O. \quad (4)$$

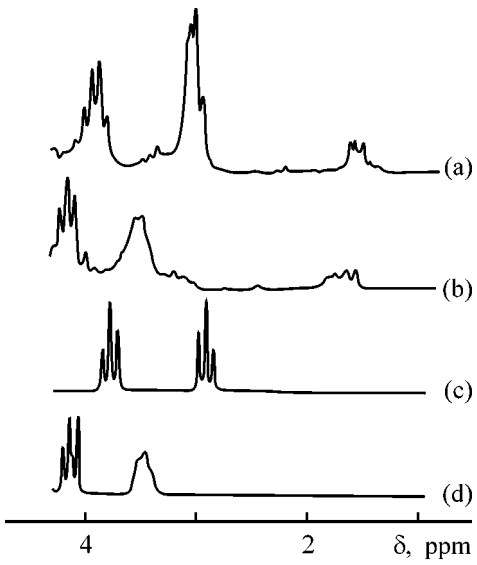

Fig. 3. ^{1}H NMR spectra of (a, b) the organic phase of YLM neutralizate and (c, d) monoethanolamine. pH: (a, c) 12 and (b, d) 5.5.

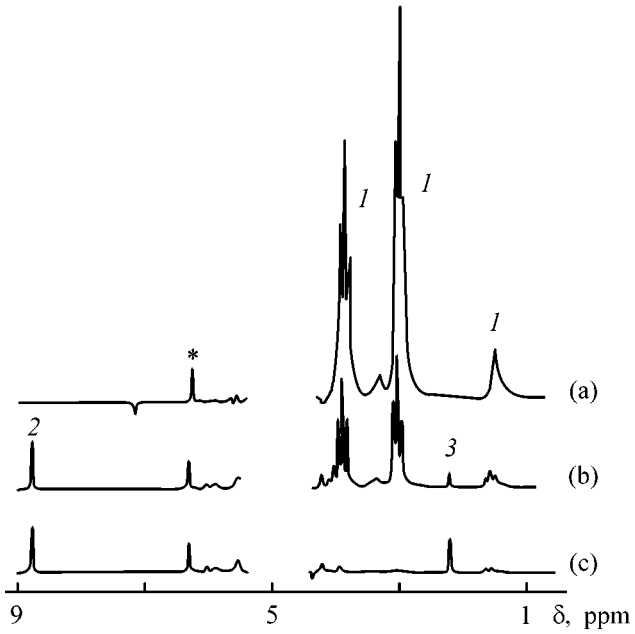

Fig. 4. ^{1}H NMR spectra of YLM neutralizate, taken during electrolysis. Neutralizate: (a) initial, (b) after 8 h, and (c) after 20 h of electrolysis. (*1*) Protons of organic compounds of neutralizate, (*2*) formate proton, and (*3*) protons of the methyl group of acetate. The ^{1}H signal of maleic acid used as internal reference is marked with an asteric.

Monitoring of the electrolysis of YLM neutralizate by the ^{1}H NMR (Fig. 4) showed that the intensities of all the signals decrease simultaneously and ^{1}H signals of acetate and formate appear. Analysis of the dynamics of consumption of the organic fraction

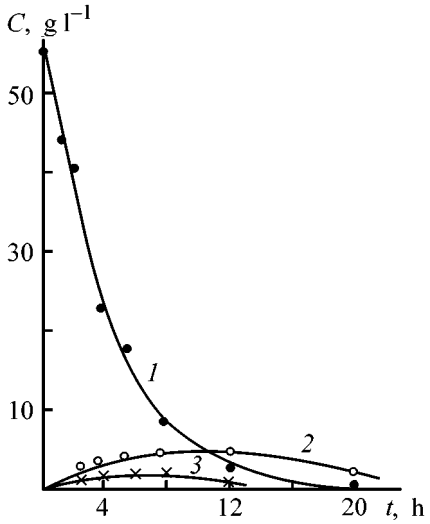

Fig. 5. Dynamics of variation of the content of organic components during electrolysis of YLM neutralizate. (*C*) Component concentration and (*t*) time. (*1*) Organic phase of neutralizate, (*2*) formate, and (*3*) acetate.

and accumulation of acetate and formate (Fig. 5) suggests exhaustive degradation of the organic fraction of YLM neutralizate during electrolysis. The relatively low content of acetate and formate in the reaction mixture during electrolysis indicates that these components are intermediates.

Comparison of the composition of YLM neutralizate before and after complete electrolysis (Table 1) confirms that the organic phase is for the most part mineralized to carbonates and sulfates. The relatively low content of nitrates in the electrolyzate (0.9 against calculated 9.7 g l^{-1}) suggests oxidation of organic nitrogen to the elemental state.

An analysis of the composition of the gas phase during electrolysis of a YLM neutralizate (Table 2) showed that the main components of the gas evolved during electrolysis are oxygen and nitrogen. The relatively high content of nitrogen in the gas phase confirms the conclusion that organic nitrogen is oxidized to elemental nitrogen.

The content of carbon oxides in the gas phase is relatively low, which can be attributed to their absorption by alkaline medium to give potassium and sodium carbonates.

In addition, the content of arsenic in the neutralizate decreases during electrolysis from 14.1 to 2.2 g l^{-1} (Table 1). Further purification of the electrolyzate to remove arsenic salts by electrocoagulation is impossible, because the medium is alkaline owing to a high content of sodium and potassium carbonates (Table 1). To decrease the arsenic concentration in the solution, the reaction mixture should be neutralized. The electrolyzate was neutralized with concentrated nitric acid to produce potassium nitrate as a target product. The resulting mixture was subjected to electrocoagulation, which decreased the arsenic content to 0.4 mg l^{-1} (Table 1).

The precipitates obtained after filtration of the reaction masses formed in electrolysis and electrocoagulation were combined, dried to constant weight, and weighed. The arsenic content was determined. As a result, 6.6 g of dry substance containing 67% arsenic was obtained from 300 ml of the initial neutralizate.

The purified electrolyzate and the solution of potassium carbonate, produced in the stage of treatment with HNO_3, were combined and evaporated with subsequent drying of the precipitate to constant weight (Table 1). As a result, 286 g of the salt product was obtained from 300 ml of the initial neutralizate. The composition of the product was as follows (wt %): potassium 40.6, sodium 4.2, carbonate 16.4, nitrate 34.0, chloride 3.2, and sulfate 1.6. The content of potassium and sodium was evaluated from the amount

Table 1. Composition of YLM neutralizate during processing

Component	Concentration, g l^{-1}		
	initial neutralizate	after electrolysis	final product
Organic substances	56.2	<0.2	<0.2
Inorganic substances	146.0	557.0	954.0
Acetate	<0.5	6.6	4.3
Arsenic	14.1	2.2	0.0004
Chlorides	36.6	28.4	30.3
Nitrates	0.0	0.9	324.0
Sulfates	2.6	13.7	15.4
Carbonates	28.3	157.5	157.0

Table 2. Composition of gas phase during electrolysis of YLM neutralizate

Component	Content (vol %) after indicated time, h		
	0	1.0	4.0
Hydrogen	0.004	11.90	14.10
Oxygen	5.700	17.10	18.86
Nitrogen	37.300	42.90	64.10
Carbon dioxide	0.040	0.04	0.05
Argon	56.900	28.60	2.83

of sodium and potassium hydroxides used in neutralization and mineralization.

Thus, the possibility of complete YLM mineralization was demonstrated. The process includes two main stages: (i) detoxification of war gases with alkali in the presence of monoethanolamine or a mixture of monoethanolamine with ethylene glycol and (ii) mineralization of the organic products of YLM detoxification by wet electrolytic combustion in the presence of alkalis with the use of electrocoagulation for purifying the reaction masses to remove arsenic and its salts.

As mentioned above, the first stage (stage of chemical weapon disposal proper) has been developed, tested on a semicommercial scale, and is ready to use [1].

In this work, we showed experimentally that, with potassium hydroxide used in all stages of the process, mineralization of the YLM neutralizate gives mixtures of potassium carbonates and nitrates with admixture of chlorides and sulfates.

Arsenic compounds contained in wastes formed in processing of YLM detoxification products are a mixture of metallic arsenic and aluminum arsenates with mechanical impurities. The amount of these waste products with arsenic content of 67% is 22% of the total amount of processed YLM. This conglomerate is a powder-like substance suitable for prolonged storage, transportation, and use as a raw material in industry, medicine, and agriculture.

Gases evolved in electrolysis of YLM detoxification products mostly contain oxygen and nitrogen, with relatively low content of hydrogen and without admixture of noxious components. They are not fire- and explosion-hazardous since the ratios of oxygen and hydrogen concentrations are far from those corresponding to the detonating mixture.

The main product of YLM neutralizate processing (potassium salts) was analyzed for the content of arsenic salts, which are enviromentally detrimental impurities in the case when this product is used as fertilizer in agriculture. The content of arsenic compounds (in terms of arsenic) in the final product of war gase processing is 0.4 mg per 1 kg of the product (Table 1), which is 5 times less than the maximum permissible concentration of arsenic in soil [7]. This means that the use of the final product as potassium fertilizer in agriculture will be enviromentally safe.

Further inprovement of the procedure of processing of YLM detoxification products could be aimed at reducing the expenditure of electrical energy and reagents (acids and alkalis). A promising approach to decreasing this expenditure is complex chemical biological processing of YLM detoxification products, including separation of the reaction mass formed in detoxification into organic and inorganic fractions, conversion of the residual organic substances in the inorganic fraction to mineral fertilizers by wet combustion, and biological utilization of the organic fraction with the use of microbes.

CONCLUSIONS

(1) Electrolysis of the products of alkaline detoxification of yprite-lewisite mixture in the presence of potassium hydroxide in a diaphragmless electrolyzer results in complete mineralization of the organic fraction of the neutralizate to potassium carbonates with admixture of chlorides and sulfates and partial reduction of arsenic to the elementary state. The waste gases formed are mixtures of nitrogen and oxygen with minor admixture of hydrogen.

(2) The use of electrocoagulation after treatment of the reaction mass with HNO_3 allows decontamination of potassium salts to remove arsenic and its compounds to a residual content below the maximum permissible concentration for soil, which makes possible their use as fertilizers in agriculture. The expected yield of potassium salts in mineralization is approximately 15 per ton of yperite–lewisite mixture. In this case, the yield of arsenic-containing wastes does not exceed 0.3.

ACKNOWLEDGMENTS

This work was supported by the subprogram “New Methods in Bioengineering” of the Federal Scientific and Technical Program “Research and Development in Priority Branches of Science and Technology for Civil Purposes,” project “Biotechnology of Environment Protection Against Anthropogenic Contaminants.”

REFERENCES

1. Luganskii, I.N., Sheluchenko, V.V., Krotovich, I.N., *et al., Ross. Khim. Zh.*, 1994, vol. 38, no. 2, pp. 34–36.
2. Shantrokha, A.V., Gormai, V.V., Gusarova, N.K., *et al., Ross. Khim. Zh.*, 1994, vol. 38, no. 2, pp. 23–25.
3. Dmitriev, V.N., *Zh. Vses. Khim. O–va*, 1988, vol. 33, no. 5, pp. 586–588.
4. Krivdin, L.B., Chekareva, T.G., Sakharovskii, V.G., *et al., Zh. Anal. Khim.*, 1981, vol. 36, no. 2, pp. 357–363.

5. Lur'e, Yu.Yu. and Rybnikova, A.I., *Khimicheskii analiz proizvodstvennykh stochnykh vod* (Chemical Analysis of Industrial Wastewater), Moscow: Khimiya, 1974.
6. Reznikov, A.A., Mulikovskaya, E.P., and Sokolov, I.Yu., *Metody analiza prirodnykh vod* (Methods of Analysis of Natural Waters), Moscow: Nedra, 1970.
7. Umyarov, I.F., Kuznetsov, B.A., Krotovich, I.N., *et al.*, *Ross. Khim. Zh.*, 1993, vol. 37, no. 3, pp. 25–29.
8. Boronin, A.M., Sakharovskii, V.G., Starovoitov, I.I., *et al.*, *Prikl. Biokhim. Mikrobiol.*, 1996, vol. 32, no. 1, pp. 61–68.
9. Shostakovskii, M.F., Atavin, A.S., Dmitrieva, Z.T., *et al.*, *Zh. Org. Khim.*, 1968, vol. 4, no. 7, pp. 1301–1302.
10. Sakharovskii, V.G. and Kozlovskii, A.G., *Zh. Strukt. Khim.*, 1983, vol. 24, no. 1, pp. 100–105.
11. RF Patent no. 2 117 507.
12. Boronin, A.M., Sakharovskii, V.G., Kashparov, K.I., *et al.*, *Prikl. Biokhim. Mikrobiol.*, 1996, vol. 32, no. 3, pp. 211–218.
13. RF Patent no. 2 023 670.

Russian Journal of Applied Chemistry, Vol. 74, No. 2, 2001, pp. 265–269. Translated from Zhurnal Prikladnoi Khimii, Vol. 74, No. 2, 2001, pp. 260–264.

ENVIRONMENTAL PROBLEMS OF CHEMISTRY AND TECHNOLOGY

Flocculating Efficiency of Polyelectrolytes Prepared from Wastes of Nitron Fiber Production

V. I. Grachek, A. A. Shunkevich, and O. P. Popova

Institute of Physical and Organic Chemistry, Belarussian National Academy of Sciences, Minsk, Belarus

Received December 18, 1998; in final form, August 1999

Abstract—Water-soluble cationic, amphoteric, and anionic polyelectrolytes were prepared from wastes of the Nitron fiber production. The extent to which the polyelectrolytes reduce the turbidity, content of petroleum products, and chemical oxygen demand was studied as a function of polyelectrolyte type and its concentration.

The cationic and anionic polyelectrolytes are widely used to intensify the separation of natural dispersed matter and decontamination of industrial wastewater [1–3]. In these processes, both separate polyelectrolytes of certain ionic type and their mixtures are used. Data on the acceleration of sedimentation with a flocculant mixture were reported in [4]. Amphoteric polyelectrolytes containing both cationic and anionic functional groups are the most promising for decontamination of aqueous solutions to remove suspended particles.

It is known [5–7] that derivatives of polyacrylamide are commonly used for wastewater decontamination. The flocculating efficiency of these reagents is mainly due to their ionic functional groups.

The aim of this study was to synthesize water-soluble polyelectrolytes with different charges of functional groups from wastes of production and reprocessing of acrylic polymers and analyze their flocculating characteristics. The wastes from Nitron fiber production (WNF)[1] containing 92.5% acrylonitrile were used as a raw material.

EXPERIMENTAL

In the experiments, we used an anionic polyelectrolyte prepared by alkaline hydrolysis of wet wastes from Nitron-C and Nitron-D fiber [8] production. Cationic polyelectrolyte was prepared by amination of WNF with ethylenediamine [9]. The amphoteric polyelectrolyte was prepared by two-stage synthesis. In the first stage, the fiber was aminated with ethylenediamine to reach an ion-exchange capacity of 4–6 mg-equiv g^{-1}. This product was hydrolyzed with 5% NaOH at 100°C for 2–3 h until a uniform mixture was formed.

In IR spectrum of amphoteric polyelectrolyte, a broad band at 3350 cm^{-1} due to the N–H stretching vibrations appears instead of the nitrile band at 2240 cm^{-1}. The spectrum also contains a strong absorption band at 1650 cm^{-1} due to C=O stretching vibrations and bands at 1550 and 1400 cm^{-1} associated with the symmetrical and antisymmetrical vibrations of the hydroxy groups.

The polyelectrolyte samples prepared by us were purified to remove oligomeric impurities and converted to the required form, and their exchange capacity was determined.

The exchange capacity of carboxy groups of the anionic flocculants was determined as follows. A commercial flocculant sample was acidified with 1 M HCl to pH 2. Under these conditions the polyelectrolyte was precipitated. This precipitate was washed with ten 20-ml portions of 0.1 M HCl and then with distilled water to pH 3. The washed precipitate was dissolved by treating it with 0.1 NaOH to pH 5. The resulting solution was acidified with 0.1 M HCl to reprecipitate the polyelectrolyte. The precipitate formed was washed to pH 3–3.5 and dried at 85 ± 5°C. A weighed sample of polyelectrolyte (50–100 mg) was dissolved in water and titrated potentiometrically with 0.1 N NaOH with stirring. pH value was monitored with a I-130 M ionometer. The exchange capacity of the polyelectrolyte was calculated from the titrant volume at the inflection point in the titration curve.

[1] Polimir Production Association, Novopolotsk.

1070-4272/01/7402-0265 $25.00 © 2001 MAIK "Nauka/Interperiodica"

Table 1. Characteristics of flocculants

Polyelectrolyte	Main functional groups	SEC,* mg-equiv g^{-1}
Anionic	$[-CH_2-\underset{\displaystyle CONH_2}{\underset{\vert}{CH}}-]_n[-CH_2-\underset{\displaystyle CONa}{\underset{\vert}{CH}}-]_m$	COOH, 8.83
Cationic	$[-CH_2-\underset{\displaystyle \begin{matrix}C\\ \diagup\ \ \diagdown\\ HN\quad\ N\\ \vert\quad\ \vert\\ CH_2-CH_2\end{matrix}}{\underset{\vert}{CH}}-]_n$	amino groups, 8.4
Amphoteric	$[-C_2H-\underset{\displaystyle COONH_2}{\underset{\vert}{CH}}-]_n\ [-CH_2-\underset{\displaystyle COONa}{\underset{\vert}{CH}}-]_m\ [-C_2H-\underset{\displaystyle \begin{matrix}C=O\\ \vert\\ NH\\ \vert\\ CH_2-CH_2-NH_2\end{matrix}}{\underset{\vert}{CH}}-]_p$	COOH, 4.5 amino groups, 3.2

* (SEC) Static exchange capacity.

Prior to determining the exchange capacity of the cationic polyelectrolyte, an aqueous solution of the commercial product was passed through a hollow-fiber filtering unit to remove impurities with molecular weight higher than 20 000. This purification procedure was performed at continuous washing with distilled water for 8 h to neutral reaction of the eluate. The concentration of the cationic polyelectrolyte in the eluate was determined gravimetrically. The exchange capacity of amino groups was calculated from the inflection point in the curve of the potentiometric titration of a weighed polyelectrolyte sample with 0.1 M HCl.

A commercial amphoteric polyelectrolyte containing Na-carboxylate groups and free amino groups was acidified with 0.1 M HCl to pH 2–2.1 and precipitated with a tenfold excess of acetone. The precipitate was kept in acetone for 15 min, filtered off, twice washed with acetone, and then dissolved in the minimal volume of distilled water. The polyelectrolyte obtained was again precipitated with acetone, dried in a vacuum to constant weight, and its 2 wt % aqueous solution was prepared. A 25-ml portion of this solution was titrated potentiometrically with 0.1 M NaOH. The amount of 0.1 M NaOH spent for reaction with a sum of amino groups combined with HCl and carboxy groups was determined from the inflection point in the curve of potentiometric titration. Separate determination of the amino groups associated with HCl molecules was carried out mercurimetrically [10]. The content of the carboxy groups in the amphoteric polyelectrolyte was calculated as the difference between the total amount of the functional groups and the amount of the amino groups.

The content of the functional groups in the anionic, cationic, and amphoteric polyelectrolytes is given in Table 1.

The flocculating efficiency of polyelectrolytes prepared by us was tested both with a model kaolin suspension in distilled water and with industrial wastewater. In these experiments, flocculant was introduced in combination with $Al_2(SO_4)_3$ as coagulant.

The flocculating efficiency of the polyelectrolytes was measured in a volumetric cylinder (50 cm^3) as the velocity of motion of the visible boundary between the columns of the calrified liquid and concentrated aqueous-kaolin suspension. In these experiments, we used the kaolin fraction with size no less than 0.1 mm [GOST (State Standard) 21 285]. In all experiments, the kaolin concentration in the suspension was 4 wt %. The samples were taken at a depth of 3 cm below the surface of the liquid and their optical density was measured on a KFK-2 photocolorimeter at 490 nm.

The flocculating efficiency of polyelectrolytes under consideration was also tested with industrial wastewater from the Naftan Production Association, Novopolotsk. In these experiments, the tested polyelectrolytes and commercial $Al_2(SO_4)_3$ were used as flocculants and coagulant, respectively. The degree of water decontamination was determined from its optical density at 440 nm. The chemical oxygen demand (COD) and the content of petroleum products was determined too. These tests were carried out as follows. A wastewater sample was poured into a 100-ml volumetric cylinder, and the flocculant and coagulant were added. This mixture was stirred for 30 s and allowed to stand for 60 min. Water samples were taken at a depth of 5 cm below the liquid surface, and their optical density was measured with a KFK-2 photocolorimeter. We also determined the chemical oxygen demand (COD) by the technique reported in [11] and the content of petroleum product with a Flyuorat-02 liquid analyzer.

In the first stage, the flocculating efficiency was studied as influenced by the type and concentration of a flocculant.

The curves of sedimentation of a kaolin suspension in the presence of anionic and amphoteric polyelectrolytes are given in Fig. 1. These curves show that the rate of sedimentation of the suspension depends on the type of polyelectrolyte and its concen-

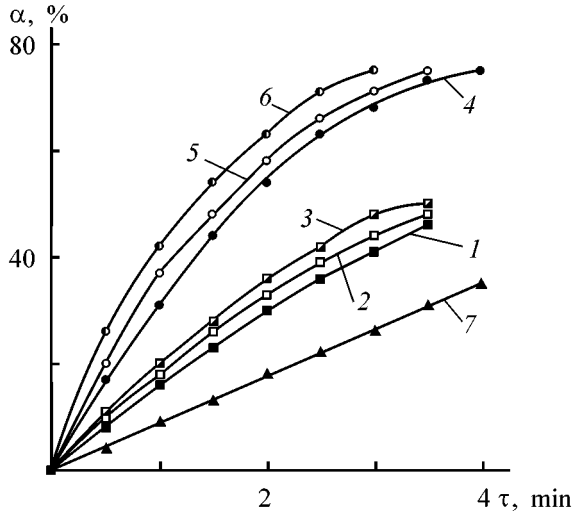

Fig. 1. Degree of clarification of the aqueous-kaolin suspension α vs. the sedimentation time τ. Type and concentration (mg l^{-1}) of polyelectrolyte: amphoteric, (*1*) 10, (*2*) 15, and (*3*) 20; cationic, (*4*) 10, (*5*) 15, and (*6*) 20; (*7*) with no flocculant.

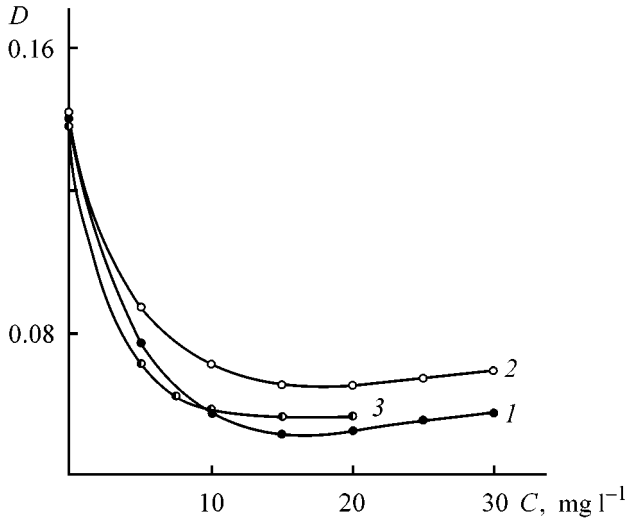

Fig. 2. Clarification of the aqueous-kaolin suspension vs. the polyelectrolyte concentration *C*. (*D*) Optical density; the same for Figs. 3, 4. Polyelectrolyte: (*1*) cationic, (*2*) amphoteric, and (*3*) commercial VA-2.

tration. Introduction of polyelectrolyte considerably increases the rate of sedimentation as compared with the system without flocculant. These curves also show that the cationic polyelectrolyte increases both the flocculation rate and the degree of clarification to a considerably larger extent than the amphoteric flocculant does. Introduction of anionic polyelectrolyte stabilizes the aque-on ous-kaolin suspension. We found that even an amount of the anionic polyelectrolyte as small as 5 mg l^{-1} stabilizes the aqueous-kaolin suspension to some extent and, as a result, decelerates the sedimentation. With increasing polyelectrolyte concentration, the suspension is further stabilized and the sedimentation stops.

Figure 2 shows the optical density of the aqueous-kaolin suspension as influenced by varied amounts of the cationic and amphoteric polyelectrolytes prepared by us and the commercial cationic flocculant VA-2. As seen from these results, the polyelectrolytes prepared by us provide the most efficient clarification at a concentration of 15–20 mg l^{-1}. According to [12], at these concentrations the globules of the flocculant macromolecules have the largest size and, therefore, provide the most efficient aggregation of particles of the aqueous-kaolin suspension. With the polyelectrolyte concentration increasing further, the flocculating efficiency decreases somewhat. Figure 2 shows that at polyelectrolyte content higher than 10 mg l^{-1} the polyelectrolyte synthesized by us becomes more efficient, whereas at low concentration of polyelectrolyte (5–10 mg l^{-1}) the flocculating efficiency of VA-2 flocculant slightly exceeds that of the cationic polyelectrolyte prepared in this work.

Since the optimal flocculant concentration C_{fl} required to clarity industrial wastewater may differ from that for the model aqueous-kaolin suspension, we studied the clarification of wastewater from the Naftan Production Association as influenced by the flocculant concentration. In these experiments, the flocculant was added in combination with a coagulant, because fast flocculation only occurred under these conditions.

Figure 3 shows that settling of the suspension for 1 h after simultaneous introduction of an flocculant and coagulant into the wastewater ensures an acceptable degree of clarification. Therefore, in further experiments, the flocculating efficiency of the polyelectrolytes was determined after settling of the suspension for 1 h after simultaneous introduction of the polyelectrolyte and coagulant.

Figure 4 shows the effect exerted by the concentration of the synthesized polyelectrolytes on the clarification of wastewater from the Naftan Production Association. According to these results, with increasing polyelectrolyte concentration, their flocculating efficiency first increases and then, after passing through a maximum, starts to decrease somewhat. These clarification curves are similar to those for the case of clarification of the aqueous-kaolin suspension (Fig. 2). The only difference is that in the clarification of wastewater the anionic polyelectrolyte in combination with the coagulant shows a slight flocculating effect.

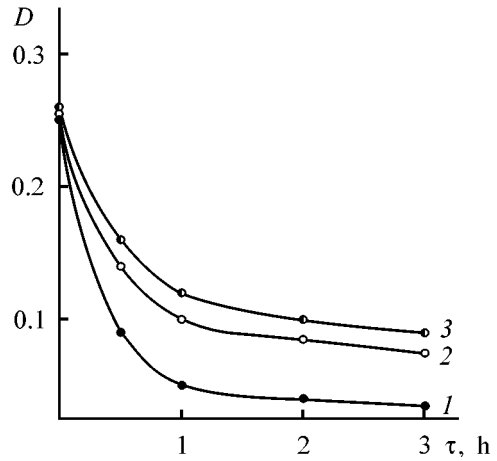

Fig. 3 Dependence of water clarification on the settling time τ. Coagulant concentration 100 mg l^{-1}, polyelectrolyte concentration 20 mg l^{-1}. Polyelectrolyte: (*1*) cationic, (*2*) amphoteric, and (*3*) anionic; the same for Fig. 4.

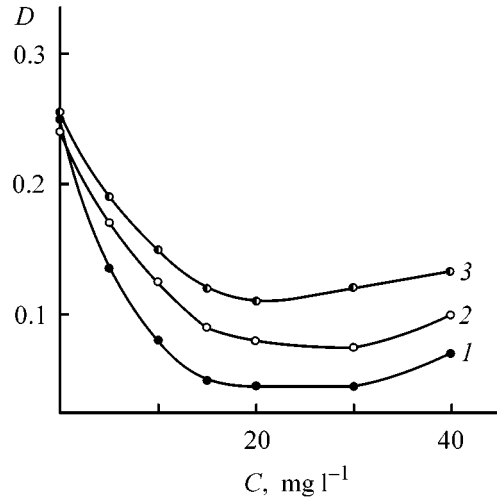

Fig. 4. Clarification of wastewater vs. polyelectrolyte concentration *C*. Coagulant concentration 100 mg l^{-1}.

Data on decontamination of wastewater from the Naftan Production Association are summarized in Table 2. The initial wastewater had the following characteristics: petroleum product concentration 34.48 mg l^{-1}, chemical oxygen demand (COD) 339 mg l^{-1}, and pH 7.8. Table 2 shows that all the polyelectrolytes tested improve the decontamination of the wastewater owing to their flocculating effect. The maximum degree of wastewater decontamination to remove petroleum products decreases in the order: cationic polyelectrolyte (68%), amphoteric polyelectrolyte (59%), and anionic polyelectrolyte (17%). For the same series of flocculants the maximum degree of wastewater decontamination evaluated from the COD decreases in the order: cationic (60%), amphoteric (45%), and anionic (40%). These data show that the cationic flocculant is preferable for decontamination of wastewater from petrochemical plants. Macromolecules of this polyelectrolyte are characterized by the optimal relation between of the sign and density of electric charge and flexibility of chains, ensuring the largest effective size of the flocculant globules and, as a result, the most efficient aggregation of dispersed particles in the wastewater.

Table 2. Characteristics of wastewater decontamination with flocculants prepared in this work

Flocculant	*C*, mg l^{-1}	pH	Content of petroleum products in wastewater before decontamination, mg l^{-1}	Degree of wastewater decontamination to remove petroleum products, %	COD, mg O_2 l^{-1}	Degree of decontamination, determined from COD, %
Cationic	10	7.9	21.4	38	188	45
	15	7.9	11.7	66	147	57
	20	8.0	11.0	68	136	60
Amphoteric	10	7.8	28.6	17	231	32
	15	7.9	16.4	52	199	41
	20	7.9	14.1	59	187	45
Anionic	10	7.8	29.8	13	260	23
	15	7.7	29.1	15	210	38
	20	7.6	28.4	17	203	40
Coagulant	50	7.7	29.9	13	261	23

CONCLUSION

Water-soluble cationic, amphoteric, and anionic polyelectrolytes were prepared from wastes of Nitron fiber production. It was found that the flocculating efficiency of these polyelectrolytes in clarification of the aqueous-kaolin suspension and wastewater from a petroleum processing plant decreases in the order: cationic, amphoteric, and anionic.

REFERENCES

1. Veitser, Yu.I. and Mints, D.M., *Vysokomolekulyarnye flokulyanty v protsessakh ochistki prirodnykh i stochnykh vod* (Macromolecular Flocculants in Decontamination of Natural and Wastewater), Moscow: Stroizdat, 1984.
2. Baran, A.A., *Polimersoderzhashchie dispersnye sistemy* (Polymer-containing Disperse Systems), Kiev: Naukova Dumka, 1986.
3. Tauserova, B.R., Taibagirova, K.S., Ergozhin, E.E., *et al.*, *Dokl. Akad. Nauk SSSR*, 1991, vol. 319, no. 3, pp. 627–631.
4. Kurenkov, V.F., Efimova, L.V., and Myagchenkov, V.A., *Zh. Prikl. Khim.*, 1989, vol. 62, no. 10, pp. 2298–2303.
5. Chen Boling and Tzin Tungui, *Khim. Tekhnol. Vody*, 1992, vol. 14, no. 10, pp. 729–736.
6. Stratulat, G.V., Lukashku, F.G., Moraru, V.N., *et al.*, *Khim. Tekhnol. Vody*, 1989, vol. 11, no. 6, pp. 519–522.
7. Jaeger, W., Gohike, U., Hahn, M., *et al.*, *Acta Polym.*, 1989, vol. 4, no. 3, pp. 161–170.
8. Osipenko, N.F., Mishkina, l.I., Tsvilik, G.L., *et al.*, *Vestsi Akad. Navuk Bel., Ser. Khim. Navuk*, 1992, no. 1, pp. 89–92.
9. Shunkevich, A.A., Grachek, V.I., Popova, O.P., *et al.*, *Resursosberegayushchie i ekologicheski chistye tekhnologii: Sbornik nauchnykh trudov II Nauchno-tekhnicheskoi konferentsii* (Resourse-Saving and Environmentally Clean Technologies. Proc. II Scientific and Technical Conf.), Grodno, 1997, part 1, pp. 179–185.
10. Polyansky, N.G., Gorbunov, G.V., and Polyanskaya, N.L., *Metody issledovaniya ionitov* (Methods for Studying Ionites), Moscow: Khimiya, 1976.
11. Novikov, Yu.V., Lastochkina, K.O., and Boldina, Z.N., *Metody opredeleniya vrednyh veshchestv v vode vodoemov* (Methods for Determining Toxic Compounds in Water of Ponds), Moscow: Meditsina, 1981.
12. Kurenkov, V.F., Shipova, L.M., and Karakuzina, S.V., *Zh. Prikl. Khim.*, 1995, vol. 68, no. 8, pp. 1371–1375.

Russian Journal of Applied Chemistry, Vol. 74, No. 2, 2001, pp. 270–273. Translated from Zhurnal Prikladnoi Khimii, Vol. 74, No. 2, 2001, pp. 265–269.

ORGANIC SYNTHESIS AND INDUSTRIAL ORGANIC CHEMISTRY

Synthesis and Tribological Characteristics of Oligoorganosiloxanes with Higher n-Alkyl Substituents

M. V. Sobolevskii, I. A. Lavygin, V. V. Zverev, V. I. Kovalenko, Yu. G. Zaslavskii, and M. I. Legkov

State Research Institute for Chemistry and Technology of Organoelement Compounds, State Scientific Center of the Russian Federation, Moscow, Russia

Received August 9, 2000

Abstract—A procedure was developed for hydrosilylation of α-olefins with oligohydrosiloxanes, and a series of comb-shaped organosiloxanes of the general formula $R_3SiO(R_2SiO)_m(RR'SiO)_nSiR_3$ (where R is CH_3, C_2H_5; R' is *n*-alkyl C_8–C_{18}) with random distribution of dimethylsiloxane (or diethylsiloxane) and methylalkylsiloxane (or ethylalkylsiloxane) units were obtained. The physicochemical characteristics of these oligomers were studied, with particular attention given to their lubricating properties (diameter of the wear spot and critical jamming load), which were compared to those of lubricating oils based on organosilicon compounds (PMS-100, KhS-2-1) and hydrocarbon-based MS-20 oil.

The presently available lubricating materials are inefficient in friction units of modern machines and mechanisms working under extreme conditions (boundary friction, high loads, temperature range from –60 to 250°C). The previously developed lubricants based on organosilicon liquids, in particular, polydimethyl- (PMS), polydiethyl- (PES), and polydimethylhaloorganosiloxanes (e.g., oligomethyldichlorophenylsiloxane KhS-2-1), have certain advantages over petroleum oils. Their heat resistance and chemical stability are fairly high; they remain liquid in a very wide temperature range, and their viscosity depends on temperature to a considerably lesser extent than that of mineral oils. These properties of the lubricants make them applicable at both high and low temperatures in the hydrodynamic friction mode. However, these materials are inefficient in the boundary friction mode because of the low carrying power of the boundary layer. This is due to the specific structure of the boundary phase of organosilicon liquids and to its lower viscosity as compared to the bulk phase [1]. At high loads the boundary layer is broken down, and the friction surfaces come in direct contact.

At the same time, mineral oils based on the hydrocarbons show high adhesion and cohesion characteristics, high carrying power of the boundary layer, and good lubricating properties in both friction modes; however, they have relatively narrow range of working temperatures, high temperature coefficient of viscosity, and low heat resistance.

It would be expected that replacement of a part of methyl (or ethyl) groups at the silicon atoms in a PMS (or PES) molecule by *n*-alkyl groups with 8 to 18 carbon atoms could give a lubricant combining the advantages of organosilicon liquids and mineral oils (a sort of "hybrid" of silicones with hydrocarbons).

Here, we report on synthesis of oligoorganosiloxanes with higher *n*-alkyl substituents and present their tribological characteristics.

One of simple and widely used routes to organosilanes and organosiloxanes with higher substituents at silicon atoms is hydrosilylation of α-olefins in the presence of a catalyst [2, 3].

However, the procedure developed in this work is not a simple interaction of a Si–H bond with an α-C=C bond. The oligomer molecule contains several Si–H bonds which successively react with olefin molecules. The reaction occurs in steps, with the rates of these steps being different. The growing steric hindrance can prevent completion of the reaction. It would be more adequate to consider hydrosilylation in systems of this kind as polyaddition of α-olefins to oligoorganohydrosiloxanes.

1070-4272/01/7402-0270 $25.00 © 2001 MAIK "Nauka/Interperiodica"

Table 1. Influence of reaction conditions on the degree of polyaddition

Run no.	Amount of reactants, mol		Conditions		Residual concentration of H_{Si}, wt %	Conversion, %
	octene	H_2PlCl_6	τ, h	*T*, °C		
1	1.1	2.42×10^{-7}	6	120	0.74	39.9
2	1.1	2.42×10^{-7}	6	130	0.75	38.5
3	1.1	2.42×10^{-7}	6	140	0.77	36.9
4	1.1	2.42×10^{-7}	6	150	0.98	19.7
5	1.1	2.42×10^{-7}	6	170	1.22	0
6	1.1	2.42×10^{-7}	6	110	1.22	0
7	1.1	2.42×10^{-7}	5	120–140	0.81	33.6
8	1.1	2.42×10^{-7}	7	120–140	0.72	41.0
9	1.0	2.42×10^{-7}	7	120–140	0.89	27.0
10	1.2	2.42×10^{-7}	7	120–140	0.73	40.2
11	1.1	0.8×10^{-7}	6	120–140	0.82	32.8
12	1.1	1.2×10^{-7}	6	120–140	0.73	40.2
Activation method						
14	1.1	1.1×10^{-7}	6	120–140	0.01	99.2

Table 2. Composition and physicochemical properties of oligoalkylsiloxanes with higher alkyl substituents of general formula $R_3SiO(R'_2SiO)_m(R'R''SiO)_nSiR_3$

Sample no.	Composition					Physicochemical properties				
	R	R'	R''	*m*	*n*	n_D^{20}	M_n	T_{flash}, °C	T_{solid}, °C	$\nu \times 10^6$, $m^2\ s^{-1}$
14	C_2H_5	C_2H_5	C_8H_{17}	–	18.7	1.458	2740	250	–58	1395
15	C_2H_5	C_2H_5	C_8H_{17}	5.8	10.3	1.454	3190	250	<–62	462
16	CH_3	C_2H_5	C_8H_{17}	–	5.6	1.445	1150	120	<–62	33
17	CH_3	CH_3	C_8H_{17}	7.2	6.3	1.431	–	250	–	84
18	CH_3	CH_3	C_8H_{17}	–	1.9	1.394	480	110	–	2.3
19	C_2H_5	C_2H_5	$C_{18}H_{37}$	5.8	10.3	1.457	–	170	34	–
20	CH_3	CH_3	$C_{18}H_{37}$	7.2	6.3	1.448	–	180	31	–

First, we studied the reaction of oligoorganohydrosiloxanes (with a known length of the siloxane chain and prescribed content of Si–H groups) with α-octene and α-octadecene. The overall reaction scheme can be represented as

$$R_3SiO(RRSiO)_m(RHSiO)_nSiR_3 + nCH_2{=}CH(CH_2)_pCH_3 \rightarrow R_3SiO(RRSiO)_m[R(CH_2(CH_2)_{p+1}CH_3)SiO]_nSiR_3.$$

Apparently, the structure and properties of the products must depend on the chemical nature and ratio of the diorganosiloxane units, length of the *n*-alkyl substituent, and molecular weight of the compound as a whole.

It was necessary to determine first the optimal conditions (temperature, time, reactant concentrations, stirring conditions) for preparing oligoorganosiloxanes with higher substituents.

We started from commercial hydrosiloxane samples differing in structure and content of hydride hydrogen. The purity of the initial olefins (octene and octadecene) was 98.3–99%.

The synthesis was performed in an inert atmosphere in the presence of the Speier catalyst (0.1% solution of H_2PtCl_6 in isopropyl alcohol).

The degree of conversion was judged from the consumption of Si–H groups, monitored by ^1H NMR. The results are given in Tables 1 and 2.

The experiments reflected in Table 1 were aimed at revealing conditions for maximal conversion of Si–H bonds in the reaction of octene with GKZh-94 com-

Table 3. Comparison of the lubricating power (wear spot diameter D_w, friction coefficient k_f) of oligoalkylsiloxanes with higher substituents and commercial organosilicon and petroleum oils (boundary friction mode, 200 min^{-1}, room temperature)

Sample	Viscosity ν (cSt) at 20°C	Load (kg) at indicated temperature, °C					
		20		45		90	
		D_w, mm	k_f	D_w, mm	k_f	D_w, mm	k_f
no. 14	1395	–	–	0.42	0.12	0.46	0.11
no. 15	462	–	–	0.33	0.13	0.45	0.13
no. 16	33	0.31	0.13	0.37	0.25	–	–
no. 17	84	–	–	0.33	0.12	0.41	0.13
no. 18	2.1	0.45	0.40	–	–	–	–
no. 19	–	0.30	0.12	0.38	0.12	0.43	0.09
no. 20	–	–	–	0.33	0.12	0.42	0.09
MS-20	–	–	–	0.34	0.09	0.46	0.10
PMS-1.5	1.5	0.44	0.35	0.58	>0.2	–	–
PMS-100	100	–	–	0.47	>0.2	0.90	0.2
KhS-2-1	48	–	–	0.82	>0.2	–	–

mercial oligoethylhydrosiloxane built of $–SiH(C_2H_5)O–$ units. The molar ratio of α-olefin to GKZf-94 was 1.0–1.1 in all experiments.

The results of experiments (Table 1) show that at temperature varied in the range 110–150°C, the amount of catalyst was within the range from 0.8×10^{-7} to 1.2×10^{-7} mol, and the reaction time, from 5 to 7 h, with the conversion not exceeding 40%. On raising the temperature to 170°C, α-olefin did not react with the hydrosiloxane because of the decomposition of the catalyst. The maximal conversion of 99.2% was attained with bubbling of an inert gas (activation by stirring), catalyst amount of 1.1×10^{-7} mol, temperature of 120–140°C, and reaction time of 6 h (run no. 14). The subsequent experiments were performed under these optimal conditions.

Oligoorganosiloxanes with *n*-alkyl radicals C_8H_{17} and $C_{18}H_{37}$ were prepared by reaction of oligomethyl-(ethyl-)hydrosiloxanes with octene and octadecene at molar ratios of 1 : 1.1 and 1 : 1, respectively. The composition and some physicochemical properties of the products are listed in Table 2.

Table 4. Critical jamming load at various temperatures

Sample	P_c (kg) at indicated temperature, °C	
	20	150
no. 14	126	63
no. 15	100	–
MS-20	63	24
PMS-100	<20	–
KhS-2-1	<20	–

Experimental results show that the high conversion (90–99.8%, residual concentration of hydride hydrogen 0.06–0.0016 wt %, respectively) was attained irrespective of the nature of alkyl groups at terminal and internal silicon atoms (methyl or ethyl), initial content of hydride hydrogen, and length of the hydrosiloxane and olefin chains.

At room temperature, oligosiloxanes with octyl radicals are uniform colorless transparent viscous liquids not solidifying on cooling to at least –50 (sample no. 14) or –60°C (sample no. 15). The kinematic viscosity of these liquids at these temperatures was 0.1193 and 0.0767 $m^2 s^{-1}$, respectively. At the same time, their analogs with octadecyl radicals are nontransparent pasty substances even at room temperature and become transparent viscous liquids only when heated to 34–35°C.

The tribological characteristics of the products were evaluated on a four-ball friction machine at various temperatures and loads on the friction couple in comparison with polymethylsiloxane liquids of linear (PMS-100) and branched (PMS-1.5r) structure, oligodimethyldichlorophenylsiloxane (KhS-2-1), and MS-20 lubricating oil on a hydrocarbon base. The obtained results are listed in Table 3.

As expected, partial replacement of methyl or ethyl groups by higher *n*-alkyl substituents (C_8H_{17} or $C_{18}H_{37}$) substantially improved the lubricating properties of oligoalkylsiloxanes, bringing them to the level characteristic of petroleum oils (Table 3).

Thus, the wear spot diameter D_2 and the friction coefficient k_f of oligodiethyl- (sample no. 15) and oligodimethylmethyloctylsiloxane (no. 17), oligodiethylethyloctadecylsiloxane (no. 19), and its methyl analog (no. 20) are close to those of MS-20 oil and are considerably smaller than those of PMS-100 and KhS-2-1.

The excellent lubricating properties of oligoalkylsiloxanes with higher alkyl substituents are manifested especially clearly when comparing the critical jamming loads P_c, determined by a standard procedure [GOST (State Standard) 9490–75] at 1500 min^{-1} in the course of 10 s. The results are listed in Table 4.

As seen from Table 4, in the case of oligodiethylethyloctylsiloxanes the load at friction destroying the lubricant layer is almost twice that with MS-20 hydrocarbon oil and considerably higher than that with PMS-100 and KhS-2-1. This means that oligoethyloctylsiloxanes form on friction surfaces a strong film with high carrying power and good adhesion and cohesion characteristics.

The temperature dependences (in Arrhenius coordinates) of the viscosities of MS-20 oil and oligoorganosiloxane nos. 15 and 17 are shown in the figure. The smaller, as compared with the case of MS-20, slope of the $\ln\eta$–$1/T$ curves for sample nos. 15 and 17 shows that the viscosity of these oligoorganosiloxanes is considerably less temperature-dependent, which extends the field of their possible application.

Thus, we developed a general route to a new class of liquid organosilicon oligomers with higher *n*-alkyl substituents. The optimal reaction conditions were found, and a series of compounds were prepared. Their lubricating properties are level with the case of MS-20 hydrocarbon oil, with the critical jamming load being higher and the temperature dependence of the viscosity being more favorable as compared with those of MS-20 oil.

EXPERIMENTAL

A five-necked flask equipped with a stirrer, a reflux condenser, a thermometer, a dropping funnel, and a tube for inert gas bubbling was charged with 82 g of alkylhydrosiloxane (GKZh-94, content of hydride

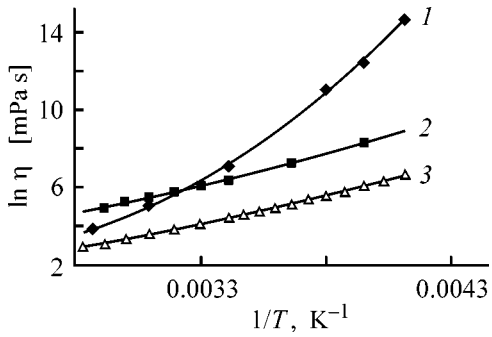

Temperature dependence of the viscosity η (in Arrhenius coordinates) of (*1*) MS-20 lubricating oil, (*2*) oligoorganosiloxane sample no. 15, and (*3*) sample no. 17.

hydrogen 1.22%), and nitrogen was passed for 20 min at a rate of 3 $l\,h^{-1}$ with continuous stirring to remove atmospheric oxygen. After the completion of purging, the reactor was heated to 120°C, and 123.2 g of octene containing the required amount of the catalyst was added from a dropping funnel at a rate at which the temperature of the reaction mixture could be kept below 140°C (initially the reaction is fast and is accompanied by considerable heat release). After adding the whole amount of octene, the mixture was stirred for 2 h, the unchanged octene was distilled off, the mixture was cooled to room temperature, and the product was unloaded.

The conversion of hydride groups was 98%. The ^{1}H NMR spectrum of the oligomer contained signals (ppm) from α-CH_2 (0.53–0.56), β-CH_2 (0.9–1.0), and more remote (1.3) protons.

REFERENCES

1. Deryaguin, B.V., Karasev, V.V., Lavygin, I.A., *et al.*, Abstracts of Papers, *Special Discussion on Thin Films and Boundary Layers*, Cambridge (England), September 28–30, 1970.
2. Lukevics, E.J. and Voronkov, M.G., *Gidrosililirovanie, gidrogermilirovanie, gidrostannirovanie* (Hydrosilylation, Hydrogermylation, Hydrostannylation), Riga: Akad. Nauk Latv. SSR, 1964.
3. Petrov, A.D., Mironov, V.F., Ponomarenko, V.A., and Chernyshev, E.A., *Sintez kremniiorganicheskikh monomerov* (Synthesis of Organosilicon Monomers), Moscow: Akad. Nauk SSSR, 1961.

Russian Journal of Applied Chemistry, Vol. 74, No. 2, 2001, pp. 274–276. Translated from Zhurnal Prikladnoi Khimii, Vol. 74, No. 2, 2001, pp. 269–272.

ORGANIC SYNTHESIS AND INDUSTRIAL ORGANIC CHEMISTRY

Photochemical Chlorination of α,α-Difluoroanisole

A. I. Shipilov and L. A. Kolpashchikova

Perm Branch, Prikladnaya Khimiya Russian Scientific Center, Perm, Russia

Received July 26, 2000

Abstract—Chlorination of α,α-difluoroanisole was performed. The yield of chlorodifluoromethoxybenzene was studied in relation to the mode of reaction initiation.

Trufluoromethoxy benzene derivatives are valuable intermediates in production of effective drugs [1].

One of synthetic routes to trifluoromethoxybenzenes is as follows:

$$ArOH + CHClF_2 \xrightarrow{\text{NaOH solution}} ArOCF_2H \xrightarrow{Cl_2} ArOCF_2Cl \xrightarrow{HF/SbCl_5} ArOCF_3.$$

In this work, we studied one of the stages of this scheme, namely, chlorination of difluoromethoxybenzene (α,α-difluoroanisole).

The chlorination of nonfluorinated anisoles is well studied. It occurs by the radical chain mechanism and can be successfully performed by various procedures. Chlorination of Cl–Ar–OCH_3 in the presence of PCl_5 at 150–180°C gives the corresponding trichloromethoxy derivative in approximately 76% yield [2]; chlorination of $ArOCH_3$ at 80–110°C, initiated by azobis(isobutyronitrile) (AIBN), occurs with a yield of about 80% [3], and UV-initiated chlorination of $ArOCH_3$, with a ~70% yield [4].

It is believed that the chlorination occurs by the radical chain mechanism, differing only in the way of the initial generation of atomic chlorine (substance, thermal, or photochemical initiation).

In contrast to unfluorinated anisoles, chlorination of α,α-difluoroanisole occurs difficultly. Despite the sufficient thermal stability of difluoromethoxybenzene (it is distilled without noticeable decomposition), attempts of its chlorination at 120–140°C in the presence of PCl_5 failed. Approximately 1–1.5 h after the start of chlorination, the mixture turned dark, which was followed by the formation of a dark brown tar. Among the identified liquid products, only traces of $ArOCF_2Cl$ were detected; the major components were unchanged α,α-difluoroanisole (~25%), products of chlorination in the ring (difluoromethoxypolychlorobenzenes, ~40%), and products of chlorine addition (~20%).

Chlorination with the use of radical initiators (e.g., AIBN) occurs more readily at moderate temperatures (80–110°C). Under these conditions, extensive tarring is usually avoided. However, the content of α-chlorination products does not exceed several percent, even on passing a fivefold excess of chlorine and taking up to 5% AIBN. The main reaction pathway is substitution of chlorine for hydrogen atoms of the aromatic ring.

In the case of UV initiation, chlorination of α,α-difluoroanisole occurs considerably more readily. The yield of the target product, chlorodifluoromethoxybenzene, depends on the intensity of the UV irradiation. With a 450-W UV lamp, the yield was as high as 95%, and with a 250-W lamp, it decreased to 70%, all other conditions being the same. With a common 150-W incandescent lamp, the yield was as low as 50%, with the major by-products being those of chlorination of the aromatic ring (see table).

Thus, the experimental results clearly show that the success or failure of α,α-difluoroanisole chlorination at the difluoromethoxy group depends on the initiation conditions. An acceptable result is obtained with UV initiation, with the yield of chlorodifluoromethoxybenzene increasing as the power of the UV source is raised.

In terms of the simple radical mechanism, it is difficult to explain the dramatic dependence of the reaction result on the mode of generation of atomic chlorine. An assumption that the chlorine atom generated by UV irradiation is more reactive than that generated by thermolysis of the chlorine molecule or

1070-4272/01/7402-0274 $25.00 © 2001 MAIK "Nauka/Interperiodica"

Chlorination of α,α-difluoroanisole

Run no.*	Substrate Ar–OCF_2H, g (mol)	Initiator	Chlorine, g (mol)	Conditions		Content of major reaction products, %			
				T, °C	τ, h	Ar–OCF_2Cl	Ar–OCF_2H	Cl–Ar–OCF_2Cl	Cl–Ar–OCF_2H
1	144 (1.0)	AIBN, 1.5 g	142 (2)	80	4.0	2.5	63.2	–	24
2	144 (1.0)	AIBN, 7.5 g	355 (5)	110	5.0	4.5	58.5	–	26
3	214 (1.5)	*hν* UV, 450 W	160 (2.25)	100	4.5	95	2.5	0.5	1.5
4	214 (1.5)	*hν* UV, 250 W	160 (2.25)	100	4.5	70	12	0.5	17
5	214 (1.5)	*hν*, 150 W	160 (2.25)	100	4.5	50	23	1.8	25

* Run nos. 3 and 4 were performed with a UV lamp, and run no. 5, with an incandescent lamp.

by the action of AIBN is not convincing, especially in view of the known fact that the actual reacting species in radical chlorination in aromatic solvents is a π complex of a chlorine atom with an aromatic molecule, rather than a free chlorine atom [5–7].

Such a π complex, **I**, is less reactive than a free chlorine atom and is more "remote" (along the reaction path) from the generation stage.

It seems more reasonable to account for the dramatic dependence of the yield of chlorodifluoromethoxyanisole on the initiation mode in terms of a reaction pattern with one-electron transfer.

Under UV irradiation, electron transfer is possible in the π complex of chlorine atom with the α,α-difluoroanisole molecule, yielding a radical cation **II** and a chloride anion:

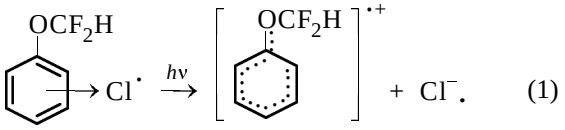

I **II** (1)

The resulting radical cation can be stabilized by release of a proton as an easily leaving group with the formation of radical **III**:

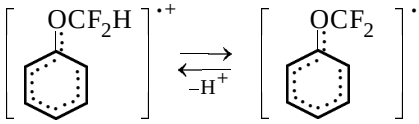

III (2)

The subsequent transformations are typical of radical chlorination:

$$ArOCF_2^{\cdot} + Cl_2 \rightarrow ArOCF_2Cl + Cl^{\cdot}.$$

Such a reaction pattern is confirmed by the following facts. It is well known that reactions involving electron transfer are considerably accelerated under electronic photoexcitation of the reacting molecules, i.e., irradiation initates electron transfer between a substrate and a reagent [8]. There is also some indirect evidence in favor of the intermediate formation of the radical cation. Proton-donor impurities (phenol, HCl, water) in the initial difluoroanisole cause extensive tarring and strongly inhibit formation of the desired $ArOCF_2Cl$. Probably, such impurities increase the current concentration of H^+ and thus prevent deprotonation of the radical cation, shifting to the left the equilibrium of reaction (2), and hence prevent formation of the radical $[ArOCF_2]^{\cdot}$ and the target product $ArOCF_2Cl$. In this case, the main transformation pathway of $[ArOCF_2H]^{\cdot +}$ is fragmentation with the cleavage of the O–C bond and formation of tars.

Apparently, to prove the reaction mechanism involving one-electron transfer from $ArOCF_2H$ to $Cl^{\cdot}$, it is necessary to detect the radical cation $[ArOCF_2H]^{\cdot +}$ by appropriate physical methods.

EXPERIMENTAL

Photoinitiated chlorination of α,α-difluoroanisole was performed in a 350-ml quartz flask equipped with an efficient stirrer and a bubbler. As sources of UV radiation were used DRL-250 and DRL-450 lamps and also a 150-W incandescent lamp. The lamps were placed at the side of the flask, at a distance of about 5 cm from the flask wall.

Chlorination of α,α-difluoroanisole in the presence of PCl_5 or AIBN was performed in a 250-ml glass flask equipped with an efficient stirrer and a bubbler. The calculated amount of PCl_5 was charged in a single portion, and AIBN was added in 0.2–0.3-g portions every 10 min.

The amounts of reactants taken, reaction conditions, and content of major products are listed in the

table. The reaction mixtures were analyzed using a Hewlett–Packard 5890 chromatograph equipped with a 30 000 × 0.25-mm capillary column (stationary phase SE-54). The products were identified by mass spectrometry (ITD-800 device) and ^{19}F NMR spectroscopy (Bruker WP-80 spectrometer).

CONCLUSIONS

(1) The yield of chlorodifluoromethoxybenzene in chlorination of α,α-difluoroanisole depends on the initiation mode. The highest yield is attained in the case of photoinitiation.

(2) The main pathway of photoinitiated chlorination of α,α-difluoroanisole presumably involves one-electron transfer in the π complex of α,α-difluoroanisole with a chlorine atom from the aromatic substrate to the chlorine atom, to give the radical cation $ArOCF_2^{\cdot +}$.

REFERENCES

1. Yagupol'skii, L.M., *Aromaticheskie i geterotsiklicheskie soedineniya s ftorsoderzhashchimi zamestitelyami* (Aromatic and Heterocyclic Compounds with Fluorinated Substituents), Kiev: Naukova Dumka, 1988.
2. *Sintezy ftorsoderzhashchikh soedinenii* (Syntheses of Fluorinated Compounds), Knunyants, I.L. and Yakobson, G.G., Eds., Moscow: Khimiya, 1973.
3. US Patent 5 440 051.
4. Louw, R. and Franken, P.W., *Chem. Ind.*, 1977, no. 3, pp. 127–128.
5. Aver'yanov, V.A., Zarytovskii, V.M., Shvets, V.F., *et al.*, *Zh. Obshch. Khim.*, 1981, vol. 17, no. 1, pp. 36–45.
6. Aver'yanov, V.A., Sycheva, N.A., Markov, B.A., and Mamzurin, B.V., *Kinet. Katal.*, 1989, vol. 30, no. 5, pp. 1033–1039.
7. Bunce, N.J., Ingold, K.U., Landers, J.P., *et al.*, *J. Am. Chem. Soc.*, 1985, vol. 107, no. 19, pp. 5464–5472.
8. Juliard, M. and Chanon, M., *Chem. Rev.*, 1983, vol. 83, no. 4, pp. 425–506.

Russian Journal of Applied Chemistry, Vol. 74, No. 2, 2001, pp. 277–279. Translated from Zhurnal Prikladnoi Khimii, Vol. 74, No. 2, 2001, pp. 272–274.

ORGANIC SYNTHESIS AND INDUSTRIAL ORGANIC CHEMISTRY

Synthesis, Structure, and Growth-Regulating Activity of 1-(6,9-Dimethyl-1,4-dioxa-8-azaspiro[4,5]dec-8-ylmethyl)-1*H*-pyridin-2-one

A. Sh. Sharifkanov, S. K. Alimzhanova, Zh. A. Abilov, and A. A. Bektibaeva

Al'-Farabi Kazakh State National University, Almaty, Kazakhstan

Received April 11, 2000; in final form, October 2000

Abstract—1-(6,9-Dimethyl-1,4-dioxa-8-azaspiro[4,5]dec-8-ylmethyl)-1*H*-pyridin-2-one was prepared by the Mannich reaction from 6,9-dimethyl-1,4-dioxa-8-azaspiro[4,5]decane, formaldehyde, and pyridin-2-one in alcohol. Its structure was proved by NMR spectroscopy. This compound exhibits a growth-regulating activity.

Pyridine derivatives exhibit a wide biological activity spectrum. Compounds based on them are used as drugs and plant growth regulators [1, 2].

The goal of this study was to prepare 1-(6,9-dimethyl-1,4-dioxa-8-azaspiro[4,5]dec-8-ylmethyl)-1*H*-pyridin-2-one, a new potentially bioactive compound [3], determine its structure, and study its biological activity.

1-(6,9-Dimethyl-1,4-dioxa-8-azaspiro[4,5]dec-8-ylmethyl)-1*H*-pyridin-2-one (**II**) was prepared in high yield by reaction of pyridin-2-one with 6,9-dimethyl-1,4-dioxa-8-azaspiro[4,5]decane (**I**) and formaldehyde in alcohol (pH 9) at room temperature:

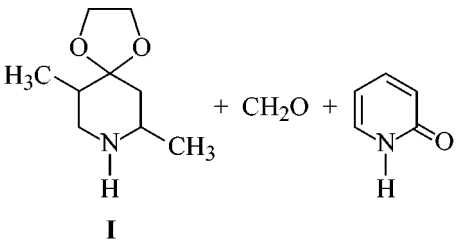

I

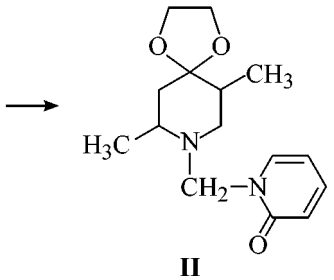

II

The structure of the product was proved by NMR spectroscopy.

Product **II** precipitates immediately; it is a white crystalline substance with mp 120–122°C (yield 60.5%). Product **IIa** was isolated from the mother liquor in 35% yield as pinkish crystals, mp 118–120°C. The proton chemical shifts of **II** and **IIa** (δ, ppm) are as follows (for atom numbering, see scheme below): **II** (mp 120–122°C), 1.13 d (3H, 2-CH_3) 0.79 d (3H, 5-CH_3), 2.80 m (2-H), 1.43 d.d (3-H_a), 1.72 d.d (3-H_e), 1.98 m (5-H), 2.40 t (6-H_a), 2.76 d.d (6-H_e), 3.93 m (7,8-CH_2), 4.69 d (9-H_a), 4.86 d (9-H_e), 7.61 d.d (10-H), 7.29 (11-H), 6.17 (12-H), 6.52 (13-H); **IIa** (mp 118–120°C), 1.08 d (2-CH_3), 0.84 d (5-CH_3), 2.88 m (2-H), 1.35 d.d (3-H_a), 1.68 d.d (3-H_e), 2.81 d.d (6-H_e), 7.36 d.d (10-H), 7.45 (11-H), 6.24 (12-H), 6.55 (13-H).

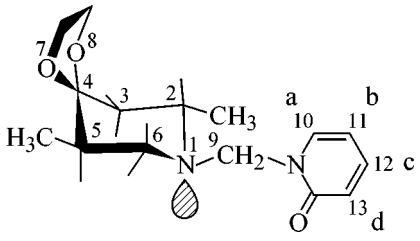

The proton coupling constants in **II** and **IIa** (*J*, Hz) are as follows: 2-H–2-CH_3 6.0; 5-H–5-CH_3 6.3; 2-H–3-H_a 11.7; 2-H–3-H_e 3.0; 5-H–6-H_a 11.7; 5-H–6-H_e 4.5; 3-H_a–3-H_e 12.9; 6-H_a–6-H_e 11.7; 9-H_a–9-H_e 13.2; ab 6.9; bc 6.9; cd 6.9; ac 2.1; db 1.2.

The ^{13}C NMR chemical shifts for **II** and **IIa** (δ, ppm) are as follows: 19.77 (2-CH_3), 10.40 (5-CH_3), 56.13 (C^2), 38.46 (C^3), 108.24 (C^4), 43.46 (C^5), 52.53 (C^6), 64.96 (C^7), 64.70 (C^8), 64.04 (C^9), 138.95 (C^{10}),

1070-4272/01/7402-0277 $25.00 © 2001 MAIK "Nauka/Interperiodica"

Effect of ShA-8 on the yield of potatoes Y_p

Growth stimulant, %	Y_{p1}, t ha^{-1}	ΔY_{p1},* %	Y_{p2}, t ha^{-1}	ΔY_{p2},* %
H_2O	19.6	–	21.0	–
Succinic acid, 2×10^{-3}	21.1	7.6	21.2	3.8
ShA-8, 1×10^{-3}	22.9	16.8	24.0	14.3
ShA-8, 1×10^{-4}	23.5	23.5	24.8	18.1

* (ΔY_{p1}) Increase in the yield due to soaking of tubercules, as compared to the control batch (H_2O); (ΔY_{p2}) increase in the yield due to leaf spraying.

105.18 (C^{11}), 120.41 (C^{12}), 135.59 (C^{13}), 162.87 (C^{14}).

The ^1H and ^{13}C NMR spectra of the compound with mp 120–122°C confirm structure **II**. An analysis of the compound with mp 118–120°C showed that it is structurally similar to **II** and contains a minor (10%) admixture of the *cis* isomer.

The coupling constants of vicinal protons in rigid chair-like cyclohexane systems lie within the following limits [4]: $^3J_{aa}$ 8–13, $^3J_{ae}$ 2–6, $^3J_{ee}$ 1–4 Hz. This fact is widely used in conformational analysis of cyclohexane and piperidine derivatives.

The ^1H NMR spectrum shows that the protons at C^9 are nonequivalent. Instead of a singlet that would be observed in the case of free rotation, these protons give two doublets at 4.69 and 4.86 ppm with a geminal coupling constant of 13.2 Hz, i.e., they are diastereotopic.

To determine the orientation of substituents at C^2 and C^5, it is sufficient to know the vicinal coupling constants of 2-H and 5-H with the adjacent protons.

The axial proton at C^3 gives a doublet of doublets at 1.43 ppm with coupling constants of 11.7 and 12.9 Hz. The large vicinal constant $^3J_{2\text{-H}-3\text{-H}_a}$ = 11.7 Hz suggests the axial orientation of the proton at C^2 and, hence, the equatorial orientation of the methyl group.

The signal of 6-H_a is a triplet at 2.40 ppm, *J* 11.7 Hz. This a signal shape is possible if the vicinal and geminal constants coincide: $^2J_{6\text{-H}_a-6\text{-H}_e}$ = $^3J_{5\text{-H}-6\text{-H}_a}$ = 11.7 Hz. This vicinal constant suggests the axial orientation of 5-H and, hence, the equatorial orientation of 5-CH_3.

The signals of the methyl groups are doublets with chemical shifts of 0.79 and 1.13 pm and the coupling constants $^2J_{2\text{-H}-2\text{-CH}_3}$ = 6.0 and $^2J_{5\text{-H}-5\text{-CH}_3}$ = 6.3 Hz. The high-field signal is assigned to the 5-CH_3 protons. The equatorial protons at C^3 and C^6 appear as doublets of doublets at 1.72 and 2.76 ppm with geminal coupling constants of 12.9 and 11.7 Hz and equatorial constants of 3.0 and 4.5 Hz. The complex multiplets at 2.80 and 1.98 ppm belong to the equatorial protons at C^2 and C^5.

A group of closely located signals at 3.93 ppm corresponds to methylene protons of the five-membered ring. In the range 6.0–8.0 ppm, signals of protons of the heteroaromatic ring are observed. In this range, we can clearly distinguish four separate multiplets. The first is the triplet of doublets from 12-H, δ 6.17 ppm. The doublet of doublets at 6.51 ppm belongs to 13-H. The lower-field signals at 7.29 and 7.61 ppm belong to 11-H (triplet of doublets) and 10-H (doublet of doublets), respectively. The chemical shifts and proton coupling constants in **II** (solution in $CDCl_3$) are given above.

Thus, the ^1H NMR data confirm the suggested composition of the product and show that the piperidine ring has a regular rigid chair conformation with equatorial orientation of methyl groups at C^2 and C^5.

The ^{13}C NMR spectrum of **II** contains signals from 15 carbon atoms, which were assigned on the basis of tabulated data and substituent effects, i.e., taking into account additive screening parameters. The composition and spectra of **IIa** are similar to those of **II**, which suggests identity of these compounds. However, product **IIa** contains a 10% admixture of the *cis* isomer.

The effect of **II** (code ShA-8; treatment of tubercules before planting and leaf spraying) on the yield and quality of potatoes[1] was studied under laboratory and field conditions during three years (see table).

Treatment of potato tubercules with ShA-8 before planting increases the potato yield by 23.5%, or by 4.6 t ha^{-1}, and enhances the resistance of plants to viral diseases.

EXPERIMENTAL

The NMR spectra were taken with Mercury-300 spectrometers ($CDCl_3$, internal reference TMS).

(6,9-Dimethyl-1,4-dioxa-8-azaspiro[4,5]decane (I). A round-bottomed flask equipped with a reflux con-

[1] Kazakh Research Institute of Potato, Vegetable, and Cotton Growing, Department of Potato Seed Growing and Technology.

denser with a calcium chloride tube was charged with 29 g (0.22 mol) of 2,5-dimethylpiperidin-4-one hydrochloride, 44 g (0.7 mol) of ethylene glycol, and 80 ml of anhydrous pyridine. The mixture was heated on an oil bath at 105–110°C for 3 h. After the reaction was complete, the pyridine was distilled off in a water-jet-pump vacuum, and excess ethylene glycol, in a roughing-pump vacuum. After being cooled, the residue was dissolved in 50 ml of water, and the solution was alkalized to pH 10 by adding a saturated NaOH solution from a dropping funnel with stirring and cooling with ice-cold water. The resulting aqueous solution was repeatedly extracted with ether. The ether extracts were dried over potassium carbonate, the solvent was distilled off, and the residue was vacuum-distilled to give 2 g (7%) of the initial 2,5-dimethyl-piperidin-4-one (bp 60–65°C/2 mm Hg, n_D^{20} 1.4670) and 13 g (60%) of 6,9-dimethyl-1,4-dioxa-8-azaspiro[4,5]decane as an almost colorless liquid, bp 77–79°C/2 mm Hg, n_D^{20} 1.4690.

1-(6,9-Dimethyl-1,4-dioxa-8-azaspiro[4,5]dec-8-ylmethyl)-1*H*-pyridin-2-one (II). A reaction flask was charged with 2.85 g (0.03 mol) of pyridin-2-ol and 2.25 g (0.075 mol) of 40% Formalin. To this mixture, a solution of 5.13 g (0.03 mol) of 6,9-dimethyl-1,4-dioxa-8-azaspiro[4,5]decane in 9 ml of alcohol (pH 9) was added dropwise with stirring. The mixture was stirred at room temperature for additional 3 h. The precipitate was separated and recrystallized from benzene to give a white crystalline substance; yield 5 g (60.5%), mp 120–122°C.

Found, %: C 64.4, H 8.2, N 9.6.

$C_{15}H_{22}N_2O_3$.

Calculated, %: C 64.7, H 7.9, N 10.1.

The solvent from the mother liquor was distilled off, and the precipitate was recrystallized from benzene to give a pinkish substance; yield 2.9 g (35%), mp 118–120°C.

Found, %: C 64.5, H 8.2, N 9.8.

$C_{15}H_{22}N_2O_3$.

Calculated, %: C 64.7, H 7.9, N 10.1.

CONCLUSIONS

(1) 1-(6,9-Dimethyl-1,4-dioxa-8-azaspiro[4,5]dec-8-ylmethyl)-1*H*-pyridin-2-one (ShA-8) was prepared; its structure was proved by NMR spectroscopy.

(2) Pyridin-2-ol reacts with formaldehyde and secondary amine under conditions of the Mannich reaction in alcohol (pH 9) in the pyridone form; condensation occurs at the nitrogen atom.

REFERENCES

1. Kurbat, N.M., Praliev, K.D., Stankevich, P.B., *et al.*, *Khim.-Farm. Zh.*, 1989, no. 9, pp. 1074–1076.
2. Prostakov, N.S., Mandal, T.K., Mobio, I.G., *et al.*, *Khim.-Farm. Zh.*, 1991, no. 6, pp. 28–33.
3. Kazakhstan Patent Appl. 8410.
4. Sergeev, N.M., *Spektroskopiya YaMR dlya khimikov-organikov* (NMR Spectroscopy for Organic Chemists), Moscow: Mosk. Gos. Univ., 1981.

Russian Journal of Applied Chemistry, Vol. 74, No. 2, 2001, pp. 280–285. Translated from Zhurnal Prikladnoi Khimii, Vol. 74, No. 2, 2001, pp. 274–280.

ORGANIC SYNTHESIS AND INDUSTRIAL ORGANIC CHEMISTRY

Alkenylation of Anilines with Dicyclopentadiene, Cyclopentadiene, and Piperylene

R. R. Gataullin, T. V. Kazhanova, I. A. Sagitdinov, A. A. Galyautdinov, A. A. Fatykhov, L. V. Spirikhin, and I. B. Abdrakhmanov

Institute of Organic Chemistry, Ufa Scientific Center, Russian Academy of Sciences, Ufa, Bashkortostan, Russia
Bashkir State Agricultural University, Ufa, Bashkortostan, Russia
Salavatnefteorgsintez Joint-Stock Company, Salavat, Bashkortostan, Russia

Received June 16, 2000

Abstract—Alkenylation of anilines with dicyclopentadiene, cyclopentadiene, and piperylene in the presence of mineral acids and Lewis acids was studied.

The discovery of the Claisen rearrangement of aromatic amines [1] provided access to 2-alkenyl-substituted arylamines, including cyclopentenyl- and pentenylanilines [2], which can be prepared from dicyclopentadiene (DCPD) or piperylene. A number of valuable compounds have been prepared from these amines, such as alkaloids [3], steel corrosion inhibitors, fungicides, plant growth stimulants, antiphytophthora agents, and local anesthetics [4–6]. The presence in allylaniline molecules of several reaction centers allows their transformations involving nitrogen atom, alkenyl fragment, or both centers simultaneously. The possibility of preparing new biologically active derivatives from 2-alkenylanilines by common reactions of amines or by certain specific reactions makes these compounds valuable synthons. To look for an alternative to the Claisen rearrangement of aromatic amines as a route to *o*-alkenylanilines, we studied alkenylation of anilines with DCPD, cyclopentadiene (CPD), and piperylene.

Reactions of DCPD with amines **I** and **II** in the presence of HCl at 130–220°C gave as main products the previously described [2] *o*-cyclopentenylanilines **III** and **IV** (yield of up to 45%) and also *N*-phenyl-(8*S*)- (**V**) and *N*-phenyl-(8*R*)-tricyclo[5.2.1.$0^{2,6}$]dec-3-en-8-amine (**VI**). Elevated temperatures (200°C) and longer reaction time favor cyclization of *o*-cyclopentenylanilines **III** and **IV** into hexahydrocyclopent[*b*]-indoles **VI** and **VIII** [7] and formation of *p*-cyclopentenylanilines **IX** and **X** [8] (Table 1). In the case of aniline (**I**), *o*,*o*-dicyclopentenylaniline (**XI**) [9] was also detected (<3%). When freshly distilled CPD is taken in reaction with aniline hydrochloride, the yield of a mixture of exo isomers **V** and **VI** decreases somewhat.

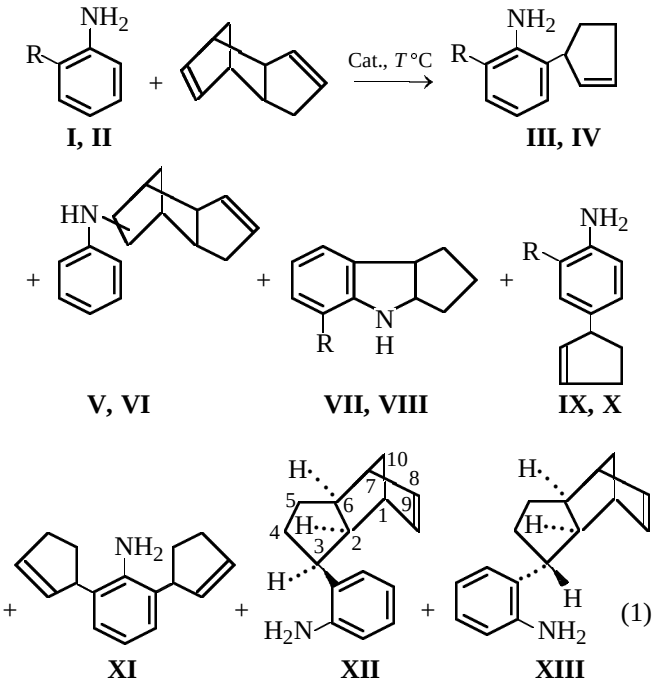

(1)

Here Cat. = HCl, $AlCl_3$, $FeCl_3$; R = H (**I**, **III**, **V**–**VII**, **IX**, **XI**); Me (**II**, **IV**, **VIII**, **X**).

With $AlCl_3$ used instead of HCl, the composition of the reaction products changes. The ratio of amines **I**, **IV** and **IX**, **X** is 1 : 1. The expected products **V** and

1070-4272/01/7402-0280 $25.00 © 2001 MAIK "Nauka/Interperiodica"

Table 1. Ratio of products of aniline (**I**) alkenylation with DCPD under various conditions (molar ratio aniline : DCPD 4 : 1)

Catalyst, mol	τ, h	*T*, °C	Product content, %					Total yield, %
			III	**VII**	**IX**	**V**, **VI**	**XII**, **XIII**	
HCl, 0.4	0.5	200	50	–	–	20	–	70
	2	150	45	–	–	15	–	60
	0.5	200	42	3	–	15	–	60
	5	200	29	14	2	14	–	57
$AlCl_3$:								
0.37	0.5	200	10	2	10	15	28	65
1.05	0.5	200	–	–	–	9	43	52
0.15	0.5	200	14	2	15	16	17	64
$FeCl_3 \cdot 6H_2O$, 0.15	0.5	200	20	–	21	14	13	68

Table 2. Substituted anilines in reaction with piperylene in the presence of KU-2 resin (reaction time 5 h, 180°C, molar ratio amine : piperylene 1 : 3)

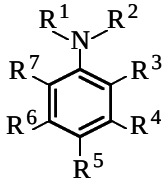

Initial amine	Substituent							Yield of products,* %			Total yield, %
	R^1	R^2	R^3	R^4	R^5	R^6	R^7	2-AA	4-AA	2,4-diAA	
II	H	H	Me	H	H	H	H	13	28	24	65
XIV	H	H	H	Me	H	H	H	21	25	18	64
XV	H	H	H	H	Me	H	H	38	–	26	64
XVI	H	H	Me	H	Me	H	H	58	–	–	58
XVII	H	H	Me	H	H	H	Et	–	61	–	61
XVIII	H	H	Me	H	H	Me	H	–	52	–	52
XIX	H	H	OMe	H	OMe	H	H	–	38	–	38
XX	H	H	Cl	H	H	H	H	26	22	15	63
XXI	Bu	Bu	H	H	H	H	H	–	19	–	19

* (AA) Alkenylated aniline.

VI are formed, as well as the products of alkenylation of the aromatic ring, 2-[(3*S*)- (**XII**) and 2-[(3*R*)-tricyclo-[5.2.1.$0^{2,6}$]dec-8-en-3-yl]amines (**XIII**). With increasing amount of $AlCl_3$, the relative content of **III** and **IX** decreases. At a 1 : 1 ratio of DCPD and $AlCl_3$, only amines **XII** and **XIII** are formed. With the $FeCl_3 \cdot 6H_2O$ catalyst taken in the same amount as $AlCl_3$, the relative content of **III** and **IX** is somewhat higher than that of **V**, **VI**, **XII**, and **XIII**. In the case of *o*-toluidine (**II**) and $AlCl_3$ catalyst, the composition of products, according to GLC, is the same as with that in the case of aniline (**I**).

The structure of **V**–**XIII** was confirmed by spectroscopic methods [10] and elemental analysis. The IR spectra [11] of **V** and **VI** contain a characteristic band of the NH group at 3430 cm^{-1}, and the spectra of **XII** and **XIII**, the bands of the NH_2 group at 3390 and 3470 cm^{-1}. The aromatic protons in the ^1H NMR spectrum of **IX** appear as two doublets (2H each) at 6.12 and 7.00 ppm. The methine 1'-H signal is a multiplet (1H) at 3.85 ppm. The broadened singlet of the NH group is observed at 3.50 ppm. Four protons of two CH_2 groups give rise to multiplets at 1.60 (1H) and 2.40 ppm (3H).

In *N*-substituted anilines, the C^2 and C^6 atoms, as well as the C^3 and C^5 atoms, are mutually equivalent. Therefore, the corresponding region of the ^{13}C NMR spectrum contains only four aromatic carbon signals and two signals of the olefin carbon atoms of the tricyclodecene moiety.

The ^{13}C NMR spectrum of *o*-substituted anilines **XII** and **XIII** contains in the region of aromatic carbon signals two sets of signals (eight signals each). Twelve of these 16 signals were assigned to the carbon atoms of the phenyl ring using the pulse train of a *J*-modulated spin echo.

In the case of *p*-substitution, the ^{13}C NMR spectrum would be simpler owing to the symmetrical structure of the aromatic moiety. Exo addition of the *N*-phenyl substituent to DCPD in **V** and **VI** is confirmed by the upfield shift (to 39.6 and 39.4 ppm) of the triplet of the bridging C^{10} atom. The formation of isomeric products **V** and **VI** is confirmed by characteristic doublets at 52.95 (56.42) ppm in the ^{13}C NMR spectrum and by single-proton doublets of doublets of *exo* protons at 3.34 (3.33) ppm (3 : 1 ratio) in the ^1H NMR spectrum. The ^{13}C NMR spectrum of **V** and **VI** contains only one signal of the C^3 cyclopentene carbon atom (in **V**; in **VI** it is C^5), whereas the spectrum of the mixture of diastereomers **XII** and **XIII** contains in the range 26.6–33.4 ppm six signals: 29.6, 32.6, and 36.6 ppm for *anti* diastereomer **XIII** and 32.2, 33.4, and 33.5 ppm for *syn* diastereomer **XII**. The *o*-substitution of the aromatic ring is confirmed by calculations using additive parameters.

The results of alkenylation of anilines **I**, **II**, and **XIV**–**XXI** with piperylene in the presence of KU-2 are listed in Table 2. The reaction is selective and, in the case of 2,4-xylidine (**XVI**) and 2-methyl-6-ethylaniline (**XVII**), yields a single product. This is due to the availability in these amines of only one position capable of alkenylation:

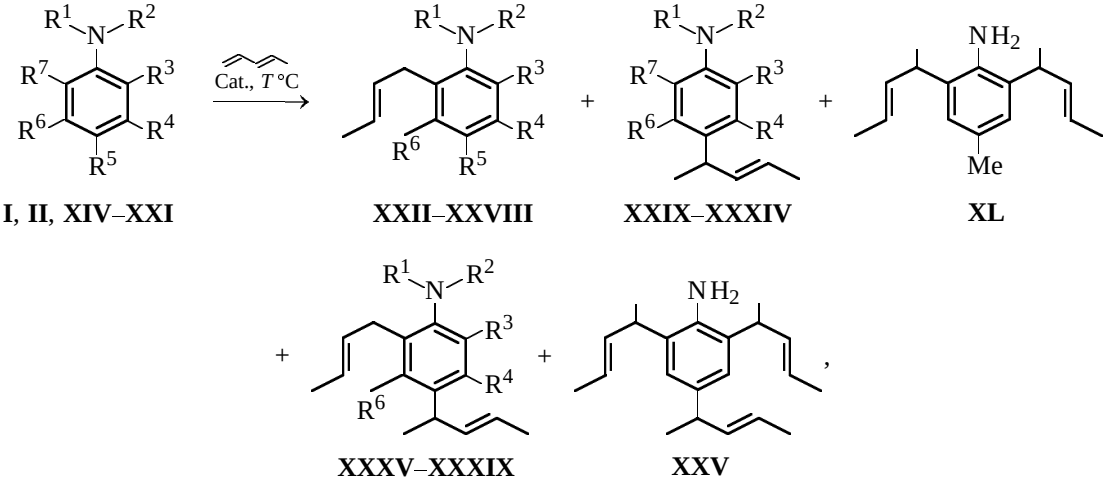

I, **II**, **XIV**–**XXI** **XXII**–**XXVIII** **XXIX**–**XXXIV** **XL**

XXXV–**XXXIX** **XXV** (2)

where $R^1 = R^2 = R^3 = R^4 = R^5 = R^6 = R^7 = H$ (**I**, **XXII**, **XXIX**, **XXXV**); $R^1 = R^2 = R^4 = R^5 = R^6 = R^7 = H$, $R^3 = Me$ (**II**, **XXII**, **XXX**, **XXXV**); $R^1 = R^2 = R^3 = R^5 = R^6 = R^7 = H$, $R^4 = Me$ (**XIV**, **XXIV**, **XXXI**; $R^1 = R^2 = R^3 = R^4 = R^6 = R^7 = H$, $R^5 = Me$ (**XV**, **XXV**); $R^1 = R^2 = R^4 = R^6 = R^7 = H$, $R^3 = R^5 = Me$ (**XVI**, **XXVI**); $R^1 = R^2 = R^4 = R^5 = R^6 = H$, $R^3 = Me$, $R^7 = Et$ (**XVII**, **XXXII**); $R^1 = R^2 = R^4 = R^5 = R^7 = H$, $R^3 = R^6 = Me$ (**XVIII**, **XXXIII**); $R^1 = R^2 = R^4 = R^6 = R^7 = H$, $R^3 = R^5 = OMe$ (**XIX**, **XXVII**); $R^1 = R^2 = R^4 = R^5 = R^6 = R^7 = H$, $R^3 = Cl$ (**XX**, **XXVIII**, **XXXIV**, **XXXVII**); $R^1 = R^2 = Bu$, $R^4 = R^6 = R^7 = R^3 = R^5 = H$ (**XXI**, **XXXIX**).

In the case of 2,5-xylidine (**XVIII**), and also with *N*,*N*-dibutylaniline (**XXI**), the formation of a single product is probably due to the steric and electronic effects of substituents. Alkylation of aniline (**I**) with piperylene in the presence of supported H_3PO_4 gives a large set of products in low total yield (Table 3). With $AlCl_3$ used as catalyst for alkenylation of piperylene, the best result was achieved in synthesis of 2,4-tri(1-methylbut-2-en-1-yl)aniline. In other cases, it is impossible to selectively obtain a single product although the total yield is sometimes high, (Table 4).

The physicochemical characteristics of compounds alkenylated with piperylene were reported in [12–14].

Table 3. Alkenylation of aniline (**I**) with piperylene in the presence of supported H_3PO_4 (reaction time 5 h, 150°C)

Catalyst	Aniline : piperylene molar ratio	Yield of products, %			Total yield, %
		2-AA	4-AA	2,4-diAA	
10% H_3PO_4 on silica gel	1 : 1	6.5	4.5	–	11
	1 : 2	12	6	–	18
	1 : 3	9	8	–	17
10% H_3PO_4 on kieselguhr	1 : 1	11.5	10.5	–	22
	1 : 2	14	12	Traces	26
	1 : 3	22	20	2	44
18% H_3PO_4 on silica gel	1 : 1	12	9	–	21
	1 : 2	18	21	3	42
	1 : 3	34	29	6	69
SF-300, polyphosphoric acid	1 : 1	4.5	4	–	8.5
	1 : 2	19	16	–	35
	1 : 3	30	14	6	50
10% H_3PO_4 on silica gel*	1 : 1	7	5	–	12
	1 : 2	9	8	5	22
	1 : 3	14	8	7	29

* τ = 5 h, T = 200°C.

Table 4. Alkenylation of aniline with piperylene in the presence of $AlCl_3$

T, °C	τ, h	Solvent	Aniline : piperylene molar ratio	Yield, %				Total yield, %
				2-AA	4-AA	2,4-diAA	2,4,6-triAA	
80	5	Toluene	1 : 1	3	24	4	–	34
80	4	″	1 : 1	2	15	2	–	21
80	3	″	1 : 1	1	10	1	–	13
100	5	″	1 : 1	6	20	5	–	32
100	5	″	1 : 3	2	22	17	2	43
130	5	″	1 : 1	2	13	5	–	19
130	5	″	1 : 3	4	16	5	3	28
100	5	Benzene	1 : 1	5	10	5	4	24
130	5	″	1 : 1	24	27	14	2	67
130	5	″	1 : 3	9	7	36	34	86
130	5	″	2 : 1	9	19	4	–	32
130	5	″	1 : 5	–	–	1	98	99
150	5	″	1 : 1	2	18	6	3	29
100	5	Hexane	1 : 1	12	33	8	2	55
130	5	″	1 : 1	21	45	16	2	84
130	5	″	1 : 3	19	25	44	5	93
150	5	″	1 : 1	15	18	21	2	56

EXPERIMENTAL

The IR spectra were taken on a UR-20 spectrometer, and the ^1H and ^{13}C NMR spectra, on a Bruker AM 300 spectrometer (working frequencies 300 and 75 MHz, respectively). Internal reference TMS, solvent $CDCl_3$. Elemental analysis was performed with an M-185B C–H–N analyzer, and the GLC analysis (including purity check), on a Chrom-5 chromatograph (carrier gas helium, flame-ionization detector, 1200 × 3-mm column, stationary phase SE-30, 5% on Chromaton N-AW DMCS, working temperature 50–300°C). Column chromatography was performed on silica gel LS 40/100 μm and Silpearl (eluent hexane). Qualitative TLC analysis was made with Silufol UV 254 and UV 254/366 plates; the chromatograms were developed under UV (λ = 254 nm) or with iodine vapor.

The alkenylation of anilines with DCPD, CPD, and piperylene was performed in a sealed heat-resistant

ampule or a 17-ml metallic autoclave, charged with the reactants and catalyst. The component ratios, reaction times and temperatures, and product yields are given in Tables 1–4. After the reaction was complete, the ampule or autoclave was cooled and opened, and the reaction mixture was transferred with chloroform into a separatory funnel. The mixture was treated with 5% KOH (2 × 100 ml), extracted with chloroform (2 × 50 ml), and dried over crystalline KOH. Then the mixture was filtered, the solvent was evaporated, and the residue was fractionated in a vacuum. With HCl catalyst, the reaction performed at 140–180°C gave after vacuum distillation monoalkenylated amine **III** or **IV**. Using the same reaction at 200°C with aniline **I** or **II**, we isolated, after vacuum distillation, amine **III** or **IV** with an admixture of indoline **VII** or **VIII** and *p*-substituted product **IX** or **X**. Indolines and *p*-substituted products were identified by GLC upon addition of authentic samples [3, 8]. The reaction with $AlCl_3$ catalyst gave, after vacuum distillation, a mixture of **III** + **IX** or **IV** + **X**, chromatographed on silica gel (eluent benzene). The products were identified by comparison of their ^1H and ^{13}C NMR spectra with those of authentic samples [2, 8, 9]. The fraction containing anilines **V** and **VI**, prepared by alkenylation of **I** in the presence of HCl, was analyzed as a mixture. The fraction containing N- (**V**, **VI**) and C-substituted products (**X**, **XI**), obtained by the reaction with $AlCl_3$ catalyst, was separated by chromatography on silica gel (eluent hexane). The **V** + **VI** and **X** + **XI** pairs were obtained as several fractions with varied component ratios. The physicochemical characteristics of 2-(cyclopent-2-enyl)anilines **II** and **IV** [2] indolines **VII** and **VIII** [7], and 4-(cyclopent-2-enyl)anilines **IX** and **X** [8, 9] were consistent with the relevant published data. Alkenylated anilines **XXII**–**XL** were isolated by column chromatography (alumina, eluent hexane), and their physicochemical characteristics were compared with those of authentic samples [12–14].

Mixture of anilines V and VI. IR spectrum, ν, cm^{-1}: 3430 (NH). ^1H NMR spectrum, δ, ppm (*J*, Hz): 1.12–2.75 m (10H, $3CH_2$, 4CH), 3.33 d.d (1H, J_1 3.57, J_2 7.60, NCH), 3.34 d.d (1H, J_1 3.53, J_2 7.69, NCH), 3.62 br.s (1H, NH), 5.49–5.80 m (2H, CH=CH), 6.66 d (2H, 2-H and 6-H, *J* 8.25), 6.70 1 (1H, 4-H), 7.20 t (2H, 3-H and 5-H).

Found, %: C 6.00, H 6.87, N 5.23.

$C_{16}H_{19}N$.

Calculated, %: C 6.27, H 7.45, N 5.49.

^{13}C NMR spectrum of *N*-phenyl-(8*S*)-tricyclo-[5.2.1.$0^{2,6}$]dec-4-en-8-amine (**V**), δ_C, ppm: 29.2 (C^3), 39.4 (C^{10}), 40.6 (C^9), 43.2 (C^2), 48.1 (C^8), 55.1 (C^7), 55.9 (C^1), 56.42 (C^6), 113.00 ($C^{2',6'}$), 129.30 ($C^{3',5'}$), 116.80 ($C^{4'}$), 131.70 (C^5), 132.30 (C^4), 147.70 ($C^{1'}$).

^{13}C NMR spectrum of *N*-phenyl-(8R)-tricyclo-[5.2.1.$0^{2,6}$]dec-4-en-8-amine (**VI**), δ_C, ppm: 29.2 (C^5), 36.6 (C^{10}), 40.5 (C^9), 42.3 (C^6), 45.5 (C^8), 52.9 (C^2), 55.8 (C^7), 55.9 (C^1), 113.2 ($C^{2',6'}$), 116.90 ($C^{4'}$), 129.30 ($C^{3',5'}$), 131.60 (C^3), 132 (C^4), 147.60 ($C^{1'}$).

2-Methyl-4-(cyclopent-2-enyl)aniline (X). R_f 0.42 (hexane–MeOH, 99 : 1). IR spectrum, ν, cm^{-1}): 1295, 3390, 3460 (NH_2). ^1H NMR spectrum, δ, ppm (*J*, Hz): 1.50–2.50 m (4H, $2CH_2$), 2.32 s (3H, CH_3), 3.62 br.s (2H, NH_2), 3.95 (1H, CH), 5.90–6.05 m (2H, CH=CH), 6.74 d (1H, *J* 7.69, 6-H), 7.04 d (1H, 5-H), 7.10 s (1H, 3-H). ^{13}C NMR spectrum, δ, ppm: 50.56 ($C^{1'}$), 17.40 (CH_3), 131.20 ($C^{2'}$), 135.02 ($C^{3'}$), 32.48 ($C^{4'}$), 34.01 ($C^{5'}$), 142.85 (C^1), 132.36 (C^2), 129.21 (C^3), 136.62 (C^4), 125.57 (C^5), 115.06 (C^6).

Found, %: C 83.09, H 8.51, N 7.77.

$C_{12}H_{15}N$.

Calculated, %: C 83.24, H 8.67, N 8.09.

2,6-Di(cyclopent-2-enyl)aniline (XI). Yield 3%, bp 168–170°C (2 mm Hg). The physicochemical characteristics agree with published data [2].

Mixture of anilines XII and XIII. IR spectrum, ν, cm^{-1}: 3390, 3470 (NH_2). ^1H NMR spectrum, δ, ppm (*J*, Hz): 1.20–2.80 m (10H, $3CH_2$, 4CH); 3.10, 3.23 (unresolved multiplets, Ar–CH); 3.60 br.s (2H, NH_2); 5.60–5.85 m (2H, CH=CH); 6.70 d (1H, *J* 7.80, 6'-H); 6.76 t (1H, 5'-H, *J* 7.80); 7.03 t (1H, 4'-H); 7.18 d (1H, 3'-H, *J* 7.70).

Found, %: C 6.12, H 6.79, N 5.00.

$C_{16}H_{19}N$.

Calculated, %: C 6.27, H 7.45, N 5.49.

^{13}C NMR spectrum of 2-[(3*S*)-tricyclo-[5.2.1.$0^{2,6}$]-dec-8-en-3-yl]aniline (**XII**), δ_C, ppm: 29.6 (C^5), 32.6 (C^4), 36.6 (C^3), 39.1 (C^{10}), 40.3 (C^7), 42.1 (C^1), 44.2 (C^2), 53.6 (C^6), 115.4 ($C^{6'}$), 118.3 ($C^{4'}$), 125.6 ($C^{5'}$),

126.2 ($C^{3'}$), 130.7 (C^{9}), 131.8 ($C^{2'}$), 132.1 (C^{8}), 144.1 ($C^{1'}$).

^{13}C NMR spectrum of 2-[(3*R*)-tricyclo-[5.2.1.$0^{2,6}$]-dec-8-en-3-yl]aniline (**XIII**), δ_C, ppm: 32.2 (C^{5}), 33.4 (C^{3}), 33.5 (C^{4}), 39.3 (C^{10}), 41.4 (C^{7}), 42.6 (C^{1}), 43.2 (C^{2}), 52.5 (C^{6}), 115.5 ($C^{6'}$), 118.1 ($C^{4'}$), 125.3 ($C^{5'}$), 126.2 ($C^{3'}$), 131.3 ($C^{2'}$), 132.1 (C^{8}), 132.8 (C^{9}), 144.2 ($C^{1'}$).

CONCLUSION

Alkenylation of anilines with dicyclopentadiene or cyclopentadiene in the presence of HCl yields *o*-cyclopentenylanilines as the main products. At higher temperatures (200°C) and longer reaction times, perhydrocyclopent[b]indolines are formed. With $AlCl_3$ catalyst, both *o*- and *p*-cyclopentenyl derivatives are obtained. Also, significant amounts of dicyclopentadiene substitution products are formed in both cases. Alkenylation of anilines with piperylene gives 2-, 4-, 2,4-di-, and 2,4,6-trialkenylated products. If the 4- or 2,4-positions of the aromatic ring are substituted, the alkenyl group is introduced at the free *o*- or *p*-position, respectively.

REFERENCES

1. Marchinkiewicz, S., Green, J., and Mamalis, P., *Chem. Ind.*, 1961, vol. 14, pp. 438–439.
2. Abdrakhmanov, I.B., Sharafutdinov, V.M., and Tolstikov, G.A., *Izv. Akad. Nauk SSSR, Ser. Khim.*, 1982, no. 9, pp. 2160–2162.
3. Danishefsky, S. and Phillips, G.B., *Tetrahedron Lett.*, 1984, vol. 25, pp. 3159–3162.
4. USSR Inventor's Certificate, no. 1489133.
5. Gataullin, R.R., Kazhanova, T.V., Davydova, V.A., *et al.*, *Khim.-Farm. Zh.*, 1999, no. 5, pp. 29–32.
6. Gataullin, R.R., Kazhanova, T.V., Davydova, V.A., *et al.*, *Khim.-Farm. Zh.*, 1999, no. 4, pp. 17–19.
7. Gataullin, R.R., Kazhanova, T.V., Kudashev, A.R., *et al.*, *Khim.-Farm. Zh.*, 2000, no. 2, pp. 18–21.
8. Gataullin, R.R., Kazhanova, T.V., Il'yasova, L.T., *et al.*, *Izv. Ross. Akad. Nauk, Ser. Khim.*, 1999, no. 5, pp. 975–978.
9. Gataullin, R.R., Kazhanova, T.V., Fatykhov, A.A., *et al.*, *Izv. Ross. Akad. Nauk, Ser. Khim.*, 2000, no. 1, pp. 171–173.
10. Myshko, V., Kozlikovskii, Ya.B., and Koshchii, V.A., *Zh. Org. Khim.*, 1992, vol. 28, pp. 950–954.
11. Ionin, B.I., Ershov, B.A., and Kol'tsov, A.I., *YaMR-Spektroskopiya v organicheskoi khimii* (NMR Spectroscopy in Organic Chemistry), Leningrad: Khimiya, 1983.
12. Kazitsyna, L.A. and Kupletskaya, N.B., *Primenenie UF-, IK-, YaMR- i mass-spektroskopii v organicheskoi khimii* (Use of UV, IR, NMR, and Mass Spectroscopy in Organic Chemistry), Moscow: Mosk. Gos. Univ., 1979, p. 77.
13. Abdrakhmanov, I.B., Sharafutdinov, V.M., Nigmatullin, N.G., *et al.*, *Zh. Org. Khim.*, 1982, vol. 18, no. 7, pp. 1466–1471.
14. Abdrakhmanov, I.B., Shabaeva, G.B., Nigmatullin, N.G., and Tolstikov, G.A., *Izv. Akad. Nauk SSSR, Ser. Khim.*, 1985, no. 6, pp. 1372–1378.
15. Abdrakhmanov, I.B., Shabaeva, G.B., Mustafin, A.G., and Tolstikov, G.A., *Zh. Org. Khim.*, 1984, vol. 20, no. 3, pp. 663–664.

Russian Journal of Applied Chemistry, Vol. 74, No. 2, 2001, pp. 286–291. Translated from Zhurnal Prikladnoi Khimii, Vol. 74, No. 2, 2001, pp. 281–286.

MACROMOLECULAR CHEMISTRY AND POLYMERIC MATERIALS

Hydrodynamic and Molecular Characteristics of Poly[1-(trimethylgermyl)propyne]

G. M. Pavlov, N. P. Evlampieva, N. A. Mikhailova, E. V. Korneeva, E. I. Ryumtsev, V. S. Khotimskii, E. G. Litvinova, and M. V. Chirkova

Institute of Physics, St. Petersburg State University, St. Petersburg, Russia
Institute of Macromolecular Compounds, Russian Academy of Sciences, St. Petersburg, Russia
Topchiev Institute of Petrochemical Synthesis, Russian Academy of Sciences, Moscow, Russia

Received October 25, 2000

Abstract—Samples and fractions of a membrane-forming polymer poly[1-(-trimethylgermyl)propyne], with the molecular weight within $4 < M \times 10^{-4} < 170$ were studied in cyclohexane by methods of molecular hydrodynamics (centrifugal sedimentation, translational isothermal diffusion, and viscometry). The molecular-weight dependences of the hydrodynamic characteristics were determined and analyzed. These dependences were used to estimate the equilibrium rigidities of the poly[1-(trimethylgermyl)propyne] chains. The size of the macromolecules was studied as influenced by the bulk effects. The results obtained are compared with published data for poly[1-(trimethylsilyl)propyne].

Glassy polymers based on silicon- and germanium-containing vinyl monomers exhibit high selectivity in gas separation [1–3]. These polymers include poly[1-(trimethylsilyl)propyne] (PTMSP) [3–4] which exhibits extraordinary gas permeability and dissolution and diffusion coefficients [3–5]. A distinguishing feature of PTMSP is the unprecedented level of selective gas transfer, exceeding by an order of magnitude that of high-permeability rubbers. These unique membrane properties of PTMSP are attributed to a combination of at least several features of its molecular structure: (1) presence of double bonds strengthening the molecular chain; (2) composition and specific features of distribution along the chain of the double –C=C bonds in *cis* and *trans* configurations, and (3) presence of weakly interacting bulky side substituents $Si(CH_3)_3$ [5–9]. All this is likely to ensure a large free volume in the polymer matrix, essential for the unique gas permeability of the polymer membranes. The great promise of such polymers for the membrane technology [10] makes necessary a thorough investigation of the molecular characteristics of membrane-forming polymers, in particular, by various methods of molecular physics.

To gain insight into the nature of facile gas transfer in glassy organoelement polymers, it is of interest to study analogous polymers. Of importance from this viewpoint is a study of the organogermanium analog of PTMSP, poly[1-(trimethylgermyl)propyne] (PTMGP) [11] with Si atoms in the side chain replaced by Ge atoms. In this work, samples and fractions of a new membrane-forming polymer, PTMGP, are studied by molecular hydrodynamics methods such as centrifugal sedimentation, translational diffusion, and viscometry.

A PTMGP sample was synthesized using $TaCl_5$/BuLi [11] as catalyst. According to the ^{13}C NMR data, the average (per cent) ratio of the *cis*-*trans* –C=C fragments was 9 : 91. The repeating unit of the polymer has the structural formula

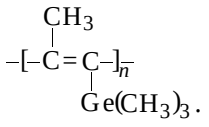

The sample was fractionated from a CCl_4 solution by fractional precipitation with ethanol. We obtained seven fractions (Table 1), and fraction no. 4 was subsequently refractionated (fraction nos. 8–11); as sample no. 12 served the initial unfractionated substance. The fractionation yield was 97%. The sample and its fractions were studied by the methods of molecular hydrodynamics.

1070-4272/01/7402-0286 $25.00 © 2001 MAIK "Nauka/Interperiodica"

Table 1. Hydrodynamic and molecular characteristics* of PTMGP in cyclohexane at 25°C

Fraction no.	$[\eta]$, $cm^3\ g^{-1}$	k'	$D \times 10^7$, $cm^2\ s^{-1}$	$\Delta n/\Delta c$, $cm^2\ g^{-1}$	$s_0 \times 10^{13}$, s	k_s, $cm^2\ g^{-1}$	$M_{sD} \times 10^{-4}$	$A_0 \times 10^{10}$, $g\ cm^2\ s^{-2}\ deg^{-1}\ mol^{-1/3}$	$\beta_s \times 10^{-7}$, $mol^{1/3}$	γ
1	324	0.48	0.77	0.093	15.4	370	119	3.48	1.22	1.37
3	286	0.57	0.72	0.100	15.2	380	126	3.17	1.17	1.33
4	350	0.49	0.81	–	15.0	330	110	3.66	1.20	0.90
5	305	0.54	0.64	0.106	17.8	485	165	3.17	1.24	1.58
6	225	0.53	–	–	10.2	145	40**	–	–	0.64
7	49	–	–	–	2.9	–	4.1***	–	–	–
8	350	0.39	–	–	16.7	–	150***	–	–	–
9	175	–	1.27	0.079	12.7	290	59	3.73	1.48	1.66
10	162	0.40	1.12	0.081	10.0	170	53	3.07	1.05	1.06
11	176	0.52	1.10	0.094	11.4	275	62	3.24	1.26	1.55
12	375	0.36	0.61	0.097	16.0	540	156	3.17	1.20	1.37

* $[\eta]$ is the intrinsic viscosity, k' is the Huggins constant, D is the diffusion coefficient, $\Delta n/\Delta c$ is the refraction index increment, s_0 is the sedimentation coefficient, k_s is the Gralen coefficient, M_{sD} is the molecular weight according to Swedberg, A_0 is the hydrodynamic invariant, β_s is the sedimentation parameter, and γ is a dimensionless parameter.

** $M_{s\eta}$ and M_{ks}.

*** $M_{s\eta}$.

Centrifugal sedimentation was carried out on an MOM 3180 analytical ultracentrifuge in a one-sector cell at 40 000 rpm. As the optical recording system served a Lebedev polarization interferometer [12, 13]. The sedimentation coefficients s were calculated from the shift of the sedimentation boundary X with time. Figure 1a shows the $\Delta \ln X$-vs.-Δt dependences whose slopes provided the values of the $s = \omega^{-2}(\Delta \ln X/\Delta t)$ parameter (ω is the angular velocity of rotation of the rotor). We studied the concentration dependence of the sedimentation coefficient, satisfying the linear approximation $s^{-1} = s_0^{-1}(1 + k_s c + ...)$. Figure 1b presents the s^{-1}-vs.-c dependence from which the coefficient s_0 and the Gralen coefficient k_s were determined. The following correlation was established between the s_0 and k_s parameters: $k_s = 2.5\ s_0^{1.85 \pm 0.3}$. The average value of the dimensionless parameter $k_s/[\eta] \equiv \gamma$ for all the fractions studied was $\gamma = 1.3 \pm 0.3$.

Translational diffusion was studied by the classic method of formation of a solution–solvent boundary whose position was determined at regular time intervals using a polarization interferometer. The setup (Tsvetkov's diffusometer) and the calculational algorithm for finding the diffusion coefficient D have been described in numerous publications [12, 13]. The refractive index increments $\Delta n/\Delta c$ were calculated from the area delimited by the diffusion curve.

The intrinsic viscosities $[\eta]$ were determined from the Huggins plots $\eta_{sp}/c = [\eta] + k'[\eta]^2 c + ...$ with $[\eta]_{sp} \equiv (\eta - \eta_0)/\eta_0 = (t - t_0)/t_0$, where η and η_0 are the viscosities of the solution and solvent, respectively, and t and t_0 are the times of flow of the solution and solvent in the Ostwald viscometer, respectively. The values of the parameters $[\eta]$ and Huggins parameter k' are presented in Table 1 together with other hydrodynamic characteristics. The floatability factor $(1 - \nu\rho_0)$ (or the density increment $\Delta\rho/\Delta c$) was estimated from the pycnometrically measured data for so-

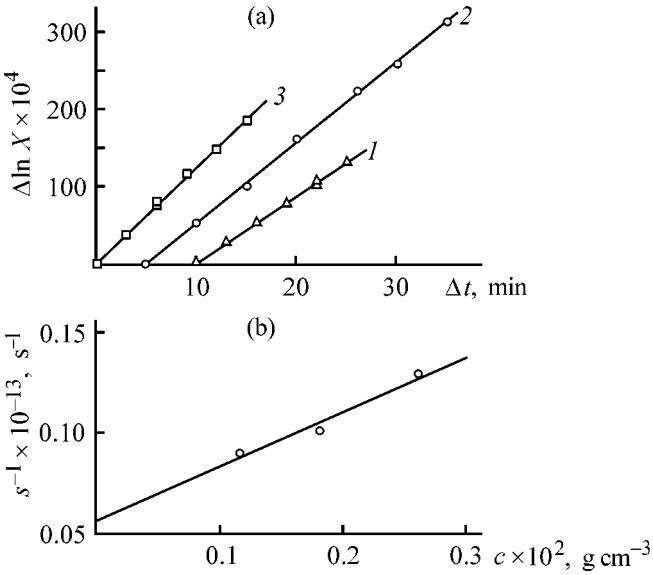

Fig. 1. (a) $\Delta \ln X$-vs.-Δt dependences for fraction no. 5 and (b) s^{-1}-vs.-c dependences for fraction no. 4 of PTMGP in cyclohexane. PTMGP concentration $c \times 10^2$, g cm^{-3}: (*1*) 0.261, (*2*) 0.181, and (*3*) 0.116.

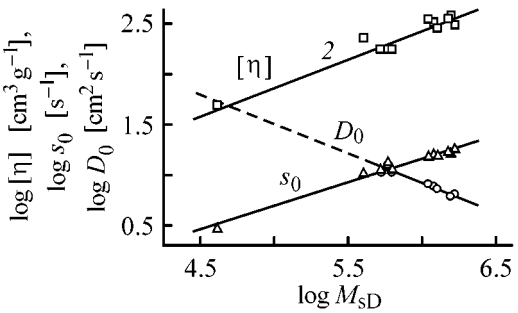

Fig. 2. K–M–H–S dependences for PTMGP in cyclohexane.

lutions in cyclohexane: $(1 - \nu\rho_0) = 0.417$. The viscosity of cyclohexane at 25°C η_0 is 0.859×10^{-2} poise.

The hydrodynamic characteristics presented in Table 1 made it possible to calculate the molecular weights M according to Swedberg [12] and to find of the hydrodynamic invariant A_0 [12] and the sedimentation parameter β_s [15], using the formulas

$$M_{sD} = R[s]/[D],$$
$$A_0 = (R[D]^2[s][\eta])^{1/3},$$
$$\beta_s = N_A(R[D]^2[s]k_s)^{1/3}.$$

Here, $[s] \equiv s_0\eta_0/(1 - \nu\rho_0)$, $[D] \equiv D_0\eta_0/T$, R is the universal gas constant, N_A is the Avogadro number, and T is the temperature, K.

The molecular weights and hydrodynamic invariants are presented for the PTMGP molecules in Table 1. The average value of the hydrodynamic invariant A_0 was estimated to be $(3.3 \pm 0.3) \times 10^{-10}$ g cm^2 s^{-2} deg^{-1} mol$^{-1/3}$, and the average value of the sedimentation parameter β_s, $(1.23 \pm 0.08) \times 10^7$ mol$^{1/3}$. These values are typical of linear polymer homologs [13, 15]; they were used in calculating the molecular weights of fraction nos. 6–8 and unfractionated sample no. 12 (Table 1) by the relations

Table 2. Parameters of scaling relations between the hydrodynamic characteristics and molecular weight for PTMGP in cyclohexane

Relation	b_i	Δb_i	K_i	r_i	n
$[\eta]$–M	0.53	0.05	0.173	0.9645	11
D_0–M	–0.59	0.06	2.79×10^{-4}	–0.9743	8
s_0–M	0.47	0.02	2.09×10^{-15}	0.9896	11

* b_i are the coefficients of the $D_0 = K_2M^{b2}$ type relations; r_i are the linear correlation coefficients for relations of the $\log k_s = \log K_4 + b_4 \log s_0$ type; n is the number of the points through which a straight line is drawn.

$$M_{s\eta} = (R/A_0)^{3/2}[s]^{3/2}[\eta]^{1/2},$$
$$M_{ks} = (N_A/\beta_s)^{3/2}[s]^{3/2}k_s^{1/2}.$$

The molecular weights obtained were used for plotting the Kuhn–Mark–Hauwink–Sakurada (K–M–H–S) dependences (Fig. 2) and calculating the corresponding scaling coefficients (Table 2). To within the root-mean-square errors, the scaling indices are described by the relations

$$|b_2| = (1 + b_1)/3, \quad (1)$$
$$|b_2| + b_3 = 1, \quad (2)$$
$$b_4 = (2 - 3b_3)/b_3, \quad (3)$$

which are typical of linear polymer homologs [12, 16, 17].

As follows from Table 1, the sample is fractionated not only with respect to the molecular weight. Certain role is probably played by uncontrolled variations in the content of the *cis* and *trans* fragments and by differences in the microblock structure (ratio of *cis* and *trans* blocks) of macromolecules for virtually identical compositions.

In view of the different numbers of the experimental points used for deriving the K–M–H–S relations and with account of expressions (1)–(3), the K–M–H–S relations were corrected within the root-mean-square errors to yield

$$[\eta] = 9.75 \times 10^{-2}M^{0.575},$$
$$D_0 = 1.19 \times 10^{-4}M^{0.525},$$
$$s_0 = 2.0 \times 10^{-15}M^{0.475}.$$

It should be noted that in this case the pre-exponential factors in the K–M–H–S equations are unambiguously related to the hydrodynamic invariant A_0

$$K_\eta^{1/3}K_D = A_0(T/\eta_0), \quad (4)$$
$$K_\eta^{1/3}K_s = A_0[(1 - \nu\rho_0)/(R\eta_0)]. \quad (5)$$

Relations (4) and (5) make it possible to estimate the average A_0 parameter for the PTMGP molecules in cyclohexane. It can be easily seen that this is identical to the average value obtained from the values presented in Table 1.

The size of the PTMGP macromolecules can be tentatively analyzed using the normalized scaling relations [18, 19], as it was done in [20]. Figure 3

presents a plot of this kind for the intrinsic viscosity. It is seen that the PTMGP molecules occupy an intermediate position between the rigid-chain and flexible-chain macromolecules. In this case we cannot rule out entirely the influence of bulk effects on the size of globules in solution. This is a common situation for macromolecules with intermediate rigidity [22, 23]; in particular, it has been observed for PTMSP molecules [23].

We will characterize the bulk effects by the parameter ε, for which holds $\langle h^2 \rangle \sim M^{1+\varepsilon}$, where $\langle h^2 \rangle$ is the root-mean-square distance between the chain ends. The parameter ε was calculated by the expressions $\varepsilon = (2b_\eta - 1)/3 = (2|b_D| - 1)$ [24]. Thus, the parameter ε may fall within $0 \le \varepsilon \le 0.05$. As is known [25, 26], the most general, and the only, theory describing the translational friction of a worm-like necklace with account of the bulk effects is the theory presented in [27], according to which for the following expression holds for [*s*]

$$[s]P_0N_A = [3/(1-\varepsilon)(3-\varepsilon)]M_L^{(1+\varepsilon)/2}A^{-(1+\varepsilon)/2}M^{(1-\varepsilon)/2} + (M_L P_0/3\pi)[\ln A/d - 1/3(A/d)^{-1} - \varphi(\varepsilon)]. \quad (6)$$

Here, *d* is the hydrodynamic diameter of the chain, and φ(ε) is a function that can be tabulated [27].

At ε = 0, formula (6) turns into relation obtained for the translational friction of a worm-like necklace without bulk interactions [28], and the corresponding φ(0) is 1.431. In terms of the theory of translational friction for a worm-like cylinder, the function φ(0) takes the value of 1.056 [29], which is known to entail slightly greater hydrodynamic cross section of the polymer chain (Table 3). Figure 4 presents the dependences corresponding to relation (6) for ε = 0 and ε = 0.05. The values estimated from these plots are presented in Table 3.

Assuming a constant size of the macromolecules in translational friction and viscosity phenomena and a constant hydrodynamic invariant A_0 in the homologous series of the polymer, we can write, similarly to [30, 31],

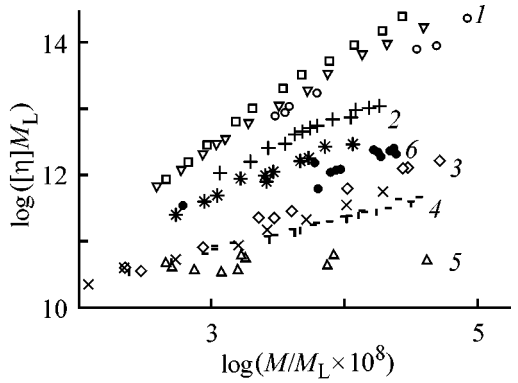

Fig. 3. Normalized scaling dependence $\log([\eta]M_L)$–$\log(M/M_L)$. Macromolecules: (*1*) extrarigid, (*2*) rigid, (*3*) flexible in thermodynamically good solvents, (*4*) flexible in θ-solvents, (*5*) globular [19, 20], and (*6*) data from Table 1.

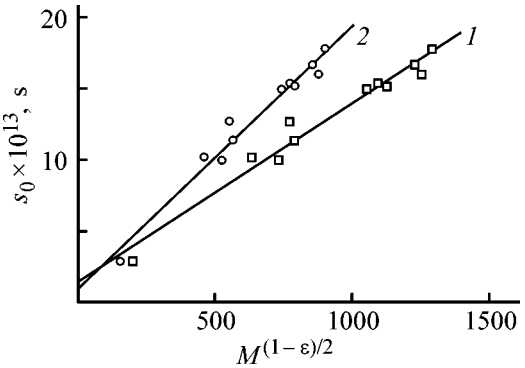

Fig. 4. Plot of s_0(c) vs. $M^{(1-\varepsilon)/2}$. ε: (*1*) 0 and (*2*) 0.05; the same for Fig. 5.

$$[s]P_0N_A = (M^2\Phi_0/[\eta])^{1/3}. \quad (7)$$

Thus, we consider the viscometric data in the coordinates $(M^2/[\eta])^{1/3} = f(M^{(1-\varepsilon)/2})$, where the function is defined by the right side of Eq. (6). This dependence was first used in [26]; for ε = 0 it turns into the known Bushin–Tsvetkov plot [13] for worm-like cylinder without bulk interactions. The plots corre-

Table 3. Estimated equilibrium rigidity *A* and hydrodynamic diameter *d* of PTMGP chains in cyclohexane

ε*	Slope	$(A \pm \Delta A) \times 10^8$, cm	Segment cut off	$(d \pm \Delta d) \times 10^8$, according to		*r*
				[26, 27]	[28]	
0*	$(12.6 \pm 0.8) \times 10^{-16}$	106 ± 13	$(1.38 \pm 0.8) \times 10^{-13}$	4 ± 4	6 ± 5	0.9821
0**	1.51 ± 0.07	68 ± 7	31 ± 71	16 ± 13	23 ± 19	0.9897
0.05*	$(18.6 \pm 1.1) \times 10^{-16}$	86 ± 11	$(0.91 \pm 0.78) \times 10^{-13}$	7 ± 6	–	0.9836
0.05**	2.21 ± 0.11	54 ± 6	–(22 ± 73)	30 ± 25	–	0.9899

* Estimated from the centrifugal sedimentation coefficients.

** Estimated from the intrinsic viscosities.

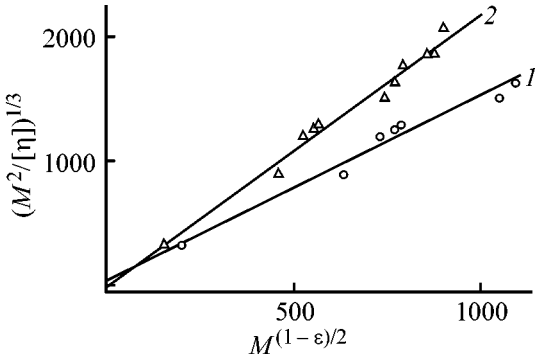

Fig. 5. Plot of $(M^2[\eta])^{1/3}$ vs. $M^{(1-\varepsilon)/2}$.

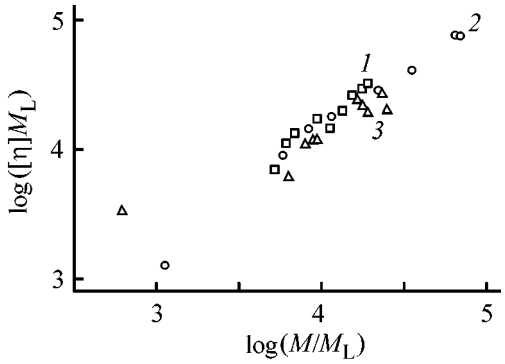

Fig. 6. $\log[\eta]M_L$–$\log(M/M_l)$ dependence for PTMGP and PTMSP. Data taken from: (*1*) [33] and (*2*) [7, 23]; (*3*) data from Tables 1 and 3.

sponding to relations (6) and (7) are presented in Fig. 5, and the data derived from these plots, in Table 3.

For objective reasons, the molecular weight range studied in this work is insufficiently wide, and the main body of the data corresponds to large M values ($M > 400 \times 10^3$). Therefore, the reliability of determining the hydrodynamic cross section of the macromolecules is not high, despite the fairly good correlation between the corresponding linear plots (linear correlation coefficients $r > 0.98$). At the same time, the Kuhn segment length is estimated with a sufficient reliability (Table 3). The translational friction measurements yielded $86 < A_f \times 10^8 < 106$ cm, and viscometric measurements gave $54 < A_\eta \times 10^8 < 68$ cm. These quantitative estimates agree well with the qualitative estimates in terms of normalized scaling relations (Fig. 3). The estimated A_f and A_η values typically disagree for linear polymers, which is explained by disagreements between the theories of translational and rotational friction of polymer chains [13].

In conclusion, we compare our results with the earlier data for PTMSP, a polymer analog of PTMGP [7, 32] differing in the presence of a Si atom in the side chain and in the ratio of *cis* to *trans* fragments. This comparison was also made for normalized scaling relations. The results are presented in Fig. 6, which suggests that the molecules of the compared polymers are close in size. This may be due to the competing influence of the composition and/or microblock structure of the polymers and the thermodynamic quality of the solvents in the polymer–solvent systems. Singling out each of these effects is not a trivial task, which calls for additional investigations over a wide range of molecular weights, including rather low M values.

CONCLUSION

Samples and fractions of a new membrane-forming polymer, poly[1-(trimethylgermyl)propyne] were studied by methods of molecular physics. The degrees of polymerization P of these fractions vary within $0.25 \le P \times 10^{-3} \le 10$. It was shown that poly[1-(trimethylgermyl)propyne] molecules belong to the intermediate group of semirigid macromolecules, for which the influence of both the hydrodynamic flow and the intrachain bulk effects on the chain size in solutions should be taken into account. Comparison of the characteristics of poly[1-(trimethylgermyl)propyne] and poly[1-(trimethylsilyl)propyne] revealed no large difference between the sizes of the chains when the Si atom in the side groups of the macromolecules was replaced with a Ge atom.

REFERENCES

1. Plate, N.A., Antipov, E.M., Teplyakov, V.V. *et al.*, *Vysokomol. Soedin., Ser. A*, 1990, vol. 32, no. 6, pp. 1123–1138.
2. Litvinova, E.G. and Khotimsky, V.S., Abstracts of Papers, *Second Int. Symp. "Progress in Membrane Science and Technology,"* Enschede (Netherlands), June 27–July 1, 1994, p. 57.
3. Masuda, H. and Higashimura, T., *Adv. Polym. Sci.*, 1987, vol. 81, pp. 121–159.
4. Masuda, H., Isobe, E., Higashimura, T., and Takada, K., *J. Am. Chem. Soc.*, 1983, vol. 105, no. 25, pp. 7473–7477.
5. Plate, N.A., Bokarev, A.K., Kaliuzhnyi, N.E., *et al.*, *J. Membr. Sci.*, 1991, vol. 60, no. 1, pp. 13–19.
6. Takada, K., Matsuya, H., Masuda, H., and Higashimura, T., *J. Appl. Polym. Sci.*, 1985, vol. 30, no. 4, pp. 1605–1616.
7. Savoca, A., Surnamer, A., and Tieu, Ch., *Macromolecules*, 1993, vol. 26, no. 23, pp. 6211–6216.

8. Shtennikova, I.N., Kolbina, G.F., Korneeva, E.V., *et al.*, *Zh. Prikl. Khim.*, 1998, vol. 71, no. 8, pp. 1350–1355.
9. Ryumtsev, E.I., Evlampieva, N.P., Shtennikova, I.N., *et al.*, *Vysokomol. Soedin., Ser. A*, 1999, vol. 41, no. 7, pp. 1169–1175.
10. Shtennikova, I.N., Kolbina, G.F., Yakimansky, A., *et al.*, *Eur. Polym. J.*, 1999, vol. 35, no. 12, pp. 2073–2078.
11. Khotimskii, V.S., Chirkova, M.V., Litvinova, E.G., *et al.*, *Vysokomol. Soedin., Ser. A*, 2000, vol. 42, no. 7, pp. 1169–1175.
12. Tsvetkov, V.N., Eskin, V.E., and Frenkel', S.Ya., *Struktura makromolekul v rastvorakh* (Structure of Macromolecules in Solutions), Moscow: Nauka, 1964.
13. Tsvetkov, V.N., *Zhestkotsepnye polimery* (Rigid-Chain Polymers), Leningrad: Nauka, 1986.
14. Pavlov, G.M. and Frenkel', S.Ya., *Vysokomol. Soedin., Ser. B*, 1986, vol. 20, no. 5, pp. 353–357.
15. Pavlov, G.M. and Frenkel', S.Ya., *Prog. Coll. Polym. Sci.*, 1995, vol. 99, pp. 101–108.
16. Budtov, V.P., *Fizicheskaya khimiya rastvorov polimerov* (Physical Chemistry of Polymer Solutions). St. Petersburg: Khimiya, 1992.
17. Pavlov, G.M. and Frenlel', S.Ya., *Vysokomol. Soedin., Ser. B*, 1982. vol. 24, no. 3, pp. 178–180.
18. Pavlov, G.M., Rowe, A.J., and Harding, S.E., *Trends Anal. Chem.*, 1997, vol. 16, no. 7, pp. 401–405.
19. Pavlov, G.M., Harding, S.E., and Rowe, A.J., *Prog. Coll. Polym. Sci.*, 1999, vol. 113, pp. 76–80.
20. Pavlov, G.M., Korneeva, E.V., Zhumel', K., *et al.*, *Zh. Prikl. Khim.*, 2000, vol. 73, no. 6, pp. 992–996.
21. Pavlov, G.M., Korneeva, E.V., Mikhailova, N.A., and Anan'eva, E.P., *Biofizika*, 1992, vol. 37, no. 6, pp. 1038–1043.
22. Pavlov, G.M., Korneeva, E.V., Mikhailova, N.A., *et al.*, *Vysokomol. Soedin., Ser. A*, 1993, vol. 35, no. 10, pp. 1647–1651.
23. Shtennikova, I.N., Kolbina, G.F., Khotimskii, V.S., *et al.*, *Vysokomol. Soedin., Ser. A*, 1998, vol. 40, no. 10, pp. 1569–1576.
24. Ptitsyn, O.B. and Eizner, Yu.E., *Zh. Tekh. Fiz.*, 1959, vol. 29, no. 9, pp. 1105–1111.
25. Bushin, S.V. and Astapenko, E.P., *Vysokoml. Soedin., Ser. A*, 1986, vol. 28, no. 7, pp. 1499–1503.
26. Pavlov, G.M., Panarin, E.F., Korneeva, E.V., *et al.*, *Vysokomol. Soedin., Ser. A*, 1990, vol. 32, no. 6, pp. 1190–1196.
27. Gray, H.B., Bloomfield, V.A., and Hearst, J.E., *J. Chem. Phys.*, 1967, vol. 46, no. 4, pp. 1493–1498.
28. Hearst, J.E. and Stockmayer, W., *J. Chem. Phys.*, 1962, vol. 37, no. 7, pp. 1425–1432.
29. Yamakawa, H. and Fujii, M., *Macromolecules*, 1974, vol. 7, no. 1, pp. 128–134.
30. Tsetkov, V.N., Lavrenko, P.N., Pavlov, G.M., *et al.*, *Vysokomol. Soedin., Ser. A.*, 1982, vol. 24, no. 11, pp. 2343–2351.
31. Pavlov, G.M., Selyunin. S.G., Shil'dyaeva, N.A., *et al.*, *Vysokomol. Soedin., Ser. A*, 1985, vol. 27, no. 8, pp. 1627–1632.
32. Masuda, H., Isobe, E., and Higashimura, T., *Macromolecules*, 1985, vol. 18, no. 5, pp. 841–847.

Russian Journal of Applied Chemistry, Vol. 74, No. 2, 2001, pp. 292–297. Translated from Zhurnal Prikladnoi Khimii, Vol. 74, No. 2, 2001, pp. 286–292.

MACROMOLECULAR CHEMISTRY AND POLYMERIC MATERIALS

Quantitative Determination of Phthalides in Molecules of Vinyl Polymers and Their Role in Radical Polymerization

Yu. I. Puzin, V. A. Kraikin, E. I. Galinurova, A. E. Egorov, E. M. Prokudina, and Yu. B. Monakov

Ufa State Petroleum Technical University, Ufa, Bashkortostan, Russia

Institute of Organic Chemistry, Ufa Scientific Center, Russian Academy of Sciences, Ufa, Bashkortostan, Russia

Received August 15, 2000

Abstract—The applicability to vinyl polymers of the procedure for quantitative determination of phthalide groups in polymeric molecules from the color of their sulfuric acid solutions was examined. The correlation between the intensity of the color of sulfuric acid solutions of polymers (polymethyl methacrylate, polystyrene) and the content of phthalide fragments incorporated into the polymer molecule was studied systematically on a quantitative level.

At present, active studies are being performed of transition of undoped polymers into a highly conducting state. Of the greatest interest in this respect are polymers containing phthalide groups [1, 2]. However, such polymers are prepared by polycondensation, and their film-forming properties are often unsatisfactory. Polyacrylates, in particular, polymethyl methacrylate (PMMA), are free of these drawbacks. Therefore, incorporation into PMMA macromolecules of phthalide fragments is of scientific and practical interest.

Phthalide fragments can be incorporated into a polymeric molecule in the course of radical polymerization by involving them in chain transfer or initiation reactions [3]. In this connection, determination of the content of phthalide units in a polymeric molecule becomes an urgent problem.

It is known [2, 4] that polyarylene phthalides dissolve in concentrated H_2SO_4 to form intensely colored solutions stable in time. The color probably originates from opening of the phthalide ring and formation of carbocations of the triphenylmethane series in the polymeric chain [5, 6]. The structure and properties of low-molecular-weight triphenylmethyl monocarbocations formed by dissolution of organic compounds of various classes in solvents with a high ionizing power and low nucleophilicity, such as liquid SO_2 and HCl, concentrated H_2SO_4 and $HClO_4$, etc. [7–9], have been studied in sufficient detail. It would be expected that phthalide groups incorporated into PMMA or polystyrene impart color to sulfuric acid solutions of these polymers.

In this work we studied sulfuric acid solutions prepared both from phthalides of various structures and from polymers obtained in their presence, with the aim to determine the content of phthalide units incorporated into a macromolecule and the role of phthalides in polymerization:

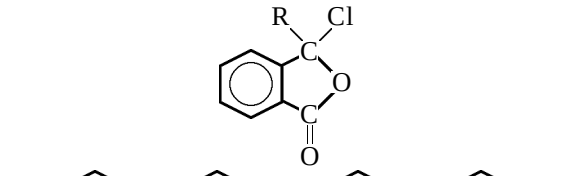

R = 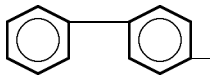 (**I**), 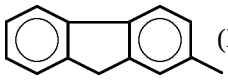 (**II**),

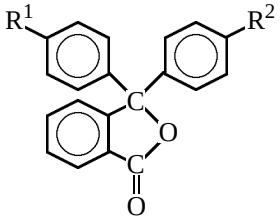

$R^1 = R^2$ = Cl (**III**), F (**IV**),

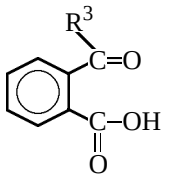

R^3 = 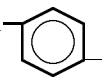 (**V**), 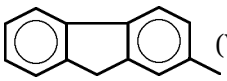 (**VI**),

1070-4272/01/7402-0292 $25.00

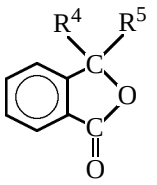

$R^4 = R^5 = H$ (**VII**), 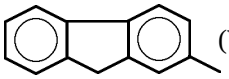 (**VIII**),

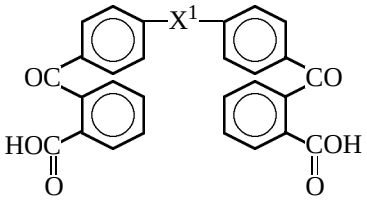

$X^1 = O$ (**IX**), S (**X**),

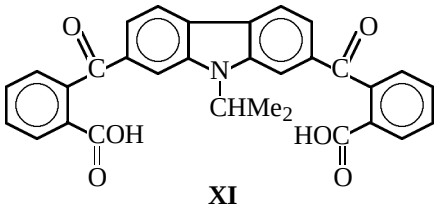

XI

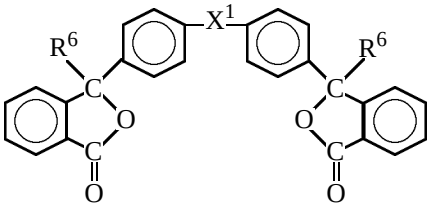

$X^1 = –$, R^6 = Ph- (**XII**); X^1 =  , R^6 = 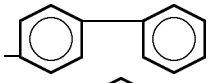 (**XIII**); X^1 =  , R^6 = 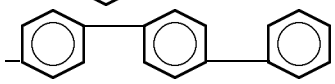 (**XIV**).

We also considered "pseudophthalides" **V**, **VI**, and **XI**–**XIV**, which contain no phthalide ring but can form it under appropriate conditions, e.g., under the action of sulfuric acid. It is known [10] that phthalides exhibit dual chemical activity owing to their possible existence as the cyclic and open tautomers:

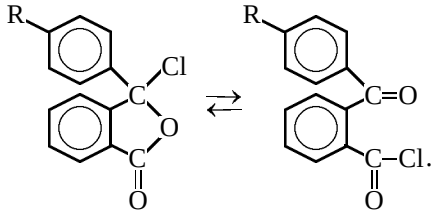

EXPERIMENTAL

The phthalides used in this work were prepared by the Friedel–Crafts reaction [11, 12]. The procedures of their synthesis and purification and some of their properties are given in [3, 12].

Sulfuric acid was doubly distilled; bp 278°C (98.3%).

Methyl methacrylate (MMA) and styrene were purified to remove the stabilizer by shaking with a 5–10% KOH solution, washed with water to neutral reaction, dried over $CaCl_2$, and doubly-distilled in a vacuum. The fractions with bp 42°C (13.3 kPa, MMA) and 70°C (8.0 kPa, styrene) were taken for polymerization.

Initiators were repeatedly recrystallized from methanol and dried at room temperature in a vacuum to constant weight.

Polymerization was performed in the bulk [13]. After reaching 5% conversion, the polymer was extracted with methanol or hexane and dried. Its molecular weight M_η was determined viscometrically in benzene at 25 ± 0.05°C from the intrinsic viscosity $[\eta]$ [13]:

$$[\eta] = KM_\eta^\alpha,$$

where $K = 0.94 \times 10^{-4}$, $\alpha = 0.76$ (PMMA); $K = 2.70 \times 10^{-4}$, $\alpha = 0.66$ (polystyrene).

Before determining the content of phthalide groups, polymer samples were repeatedly extracted with methanol in a Soxhlet apparatus, free phthalides **I**–**XIV** being readily soluble in methanol.

The molecular-weight distribution (MWD) curves were obtained with a KhZh-1302 gel chromatograph. Columns were packed with Waters styrogel, pore size 10^2–10^6 Å. The eluent was chloroform, flow rate 1 ml min^{-1}, 25°C. The columns were calibrated by polystyrene reference samples (Aldrich, US).

The electronic absorption spectra (solutions in 98% sulfuric acid) were taken on a Shimadzu UV-3100 UV–VIS–NIR spectrophotometer using 1-cm quartz cells. Solutions of other concentrations were prepared by dilution. The molar extinction coefficients ε (l mol^{-1} cm^{-1}) were calculated by the Bouguer–Lambert–Beer equation [14]

$$D = \varepsilon Cl.$$

where D is the optical density of solution, C is the solution concentration (M), and l is the cell thickness (cm).

Table 1. Aromatic phthalides used in PMMA synthesis and spectral characteristics of their solutions in concentrated H_2SO_4

Phthalide	λ_{max}, nm	Color	ε, l mol^{-1} cm^{-1}	Phthalide	λ_{max}, nm	Color	ε, l mol^{-1} cm^{-1}
I	537	Cherry	11684	**VIII**	585	Pinkish blue	11000
II	555	Cherry-red	43555	**IX**	461	Yellow	44279
III	481	Yellow	5209	**X**	545	Crimson-violet	39301
IV	453	Lemon-yellow	15448	**XI**	527	Claret	37160
V	438	Greenish yellow	5040	**XII**	524	Cherry	30176
VI	553	Cherry	43408	**XIII**	645	Sky-blue	72870
VII	296	Colorless	1407	**XIV**	687	Blue	100877

One of the most important problems in studying these polymers counsists in determining the content of phthalide groups incorporated into the polymeric molecule. Previously, polymerization of MMA has been performed in the presence of phthalide-containing compounds of various classes: ketocarboxylic acids, their chlorides, and arylene phthalides [3]. Attempts to determine the composition by elemental analysis failed, because the content of phthalide units was too low to be determined reliably. Therefore, we took advantage of the property of phthalides to form intensely colored solutions in concentrated H_2SO_4.

Solutions of phthalides in sulfuric acid are intensely colored except in the case of phthalide **VII** absorbing in the UV range (Table 1). In the examined phthalide concentration range $(0.5–8.5) \times 10^{-5}$ M, the Bouguer–Lambert–Beer law is valid. The concentration dependence of the spectra, used to calculate the extinction coefficients (Table 1), is illustrated in Fig. 1 for phthalide **II** as an example.

Figure 2 (curve *1*) shows the absorption spectra of phthalide **VIII** in 98% H_2SO_4. The spectrum underwent no changes in 25 h, which confirms the published data indicating the stability of phthalide solutions in concentrated H_2SO_4 [4].

Thus, solutions of phthalides in concentrated H_2SO_4 are intensely colored and fairly stable; the validity of the Bouguer–Lambert–Beer law and high extinction coefficients allow spectrophotometric determination of the content of phthalimide units in PMMA or polystyrene macromolecules.

Figure 2 (curve *2*) shows the spectrum of a PMMA solution obtained in the presence of phthalide **VIII**. It is seen that it practically coincides with the absorption spectrum of free phthalide. This means that

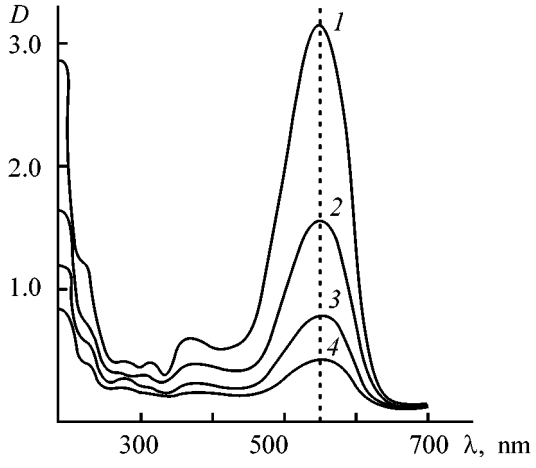

Fig. 1. Absorption spectra of sulfuric acid solutions of phthalide **II**. (*D*) Optical density and (λ) wavelength; the same for Figs. 2 and 3. Concentration of **II** in H_2SO_4, $C \times 10^5$, M: (*1*) 7.18, (*2*) 3.59, (*3*) 1.80, and (*4*) 0.90.

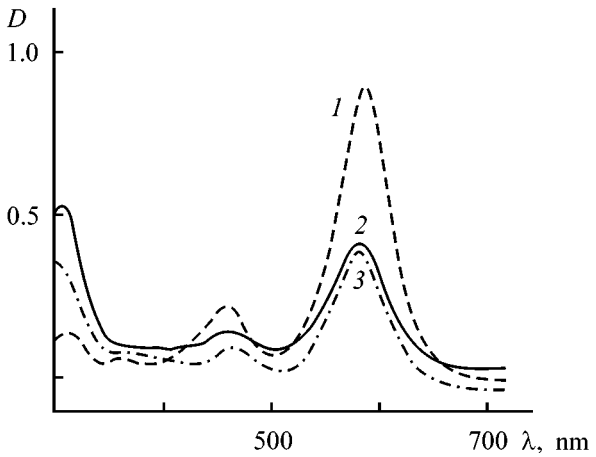

Fig. 2. Absortpion spectra of sulfuric acid solutions of (*1*) phthalide **III**, (*2*) PMMA prepared in the presence of phthalide **VIII**, and (*3*) PMMA prepared in the presence of phthalides **VIII** and **V**.

the polymeric chain of PMMA does not interfere with determination of the phthalide. Similar results are obtained in dissolution of polystyrene in H_2SO_4, but, in this case, the dissolution occurs very slowly on stirring the preliminarily pulverized polystyrene.

The visible-range spectra of PMMA and polystyrene solutions also remain unchanged during 24 h (Fig. 3).

A study of sulfuric acid solutions of PMMA, prepared in the presence of phthalides, showed that not all the phthalides were incorporated into the polymeric chain. Phthalides **X** and **XI** containing no active chain-transfer centers did not enter polymerization. The qualitative reaction of the samples (after extraction) with sulfuric acid was negative. The polymer prepared in the presence of pseudophthalide **V** is not colored on dissolution in concentrated H_2SO_4, either.

A sulfuric acid solution of the polymer prepared in the presence of phthalide **III** or **IV** is colored, which indicates that the phthalide fragments have been incorporated into the polymeric chain (Table 2). This fact contradicts the known data on the mechanism of chain transfer to haloaromatic compounds [13, 15] according to which the haloarene molecule is regenerated in the course of chain transfer [scheme (1), pathway (1.1)].[1] Hence, the chain transfer involves the phthalide molecule. The most probable is the cleavage of the bond at the tertiary carbon atom [scheme (1), pathway (1.2)], since the resulting radical A is stabilized by aromatic substituents. Furthermore, migration of the second substituent at the quaternary atom of the phthalide ring has been observed in numerous studies [10, 12].

As a result of this reaction, the phthalide ring can be incorporated into the polymeric molecule as a terminal group:

Scheme 1.

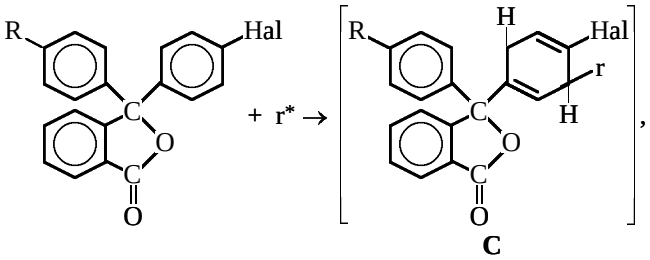

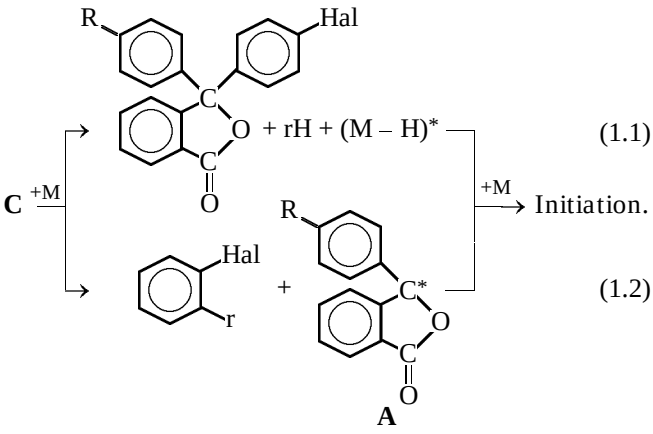

R = H, Hal (Hal = Cl, F).

Compounds **I** and **II,** containing a chlorine atom directly bound to the carbon atom of the phthalide ring, are also incorporated into the polymeric chain (Table 2); the content of phthalide units is approximately 1 unit per macromolecule. This means that phthalides **I** and **II** participate in chain transfer:

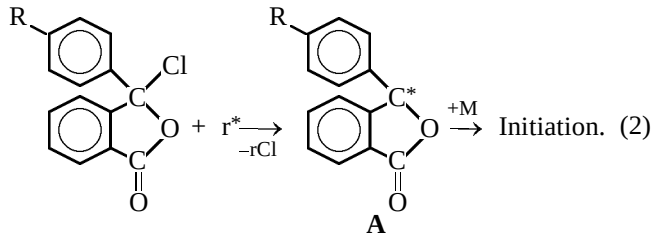

The polymer prepared by polymerization in the presence of a mixture of difluorenylphthalide (**VIII**) and chlorobenzoylbenzoic acid (**V**) forms a blue solution in sulfuric acid. The absorption spectrum of the sulfuric acid solution of this polymer is shown in Fig. 2 (curve *3*). It is seen that only difluorenylphthalide is incorporated into the polymeric chain. The absorption

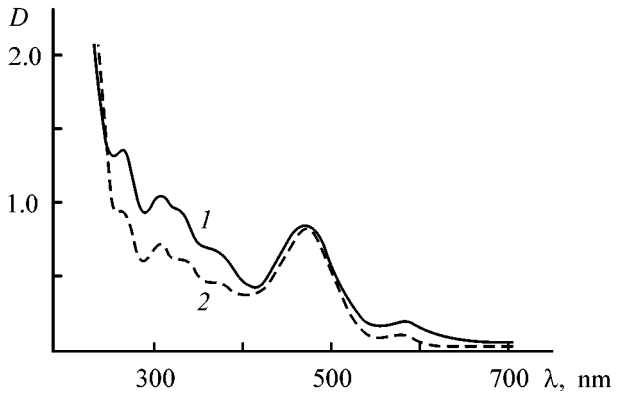

Fig. 3. Absorption spectra of sulfuric acid solutions of polystyrene prepared in the presence of phthalide **II**. The spectra were taken (*1*) 2 and (*2*) 25 h after the start of dissolution.

[1] Scheme (1) takes into account the fact that the chain transfer to phthalide **III** or **IV** involves the aromatic ring directly bound to halogen and also the fact that the radical attack at the *o*-position is more probable [15].

Table 2. Data on synthesis of polymers and content of phthalide groups in the polymer molecule

Compound	Monomer, initiator	Concentration, $C \times 10^3$, M		$M_\eta \times 10^{-5}$	Concentration of polymer in sulfuric acid solution [P]		λ, nm	D	Concentration of phthalide in sulfuric acid solution [Ph] $\times 10^5$, M	[Ph]/[P]
		initiator	phthalide		g l^{-1}	[P] $\times 10^5$, M				
I	MMA, AIBN*	3.65	10.0	3.213	11.07	3.45	536	0.454	3.902	1.13
			20.0	2.720	10.12	3.72	536	0.461	3.943	1.06
			30.0	2.420	7.85	3.24	536	0.416	3.564	1.10
II	MMA, AIBN	1.00	7.5	6.02	5.47	0.909	552	0.776	1.781	1.96
			15.0	5.75	6.73	1.171	552	1.079	2.47	2.11
	MMA, BP*	1.00	7.5	2.42	2.27	0.938	553	1.768	4.06	4.33
			15.0	2.695	1.19	0.442	553	0.273	0.627	1.42
	Styrene, AIBN	3.65	10.00	1.352	1.75	1.294	551	1.556	3.572	2.76
			24.90	0.520	0.24	0.462	552	0.841	1.931	4.18
III	MMA, AIBN	3.65	10.00	3.610	6.05	1.676	480	0.050	0.955	0.57
			25.0	3.270	8.15	2.492	481	0.080	1.545	0.62
			43.0	2.991	10.12	3.383	480	0.118	2.268	0.67
IV	MMA, AIBN	3.65	4.4	3.73	9.85	2.641	450	0.131	0.845	0.32
			9.9	3.63	10.16	2.779	452	0.160	1.036	0.37
			23.4	3.48	8.46	2.431	452	0.150	0.972	0.40
VI	MMA, AIBN	1.00	3.22	11.201	10.50	0.937	554	0.270	0.622	0.66
			6.43	9.415	4.50	0.480	555	0.327	0.753	1.57
	MMA, BP	1.00	3.22	11.20	10.26	0.916	554	0.022	0.329	0.36
			6.43	9.377	5.12	0.546	555	0.060	0.138	0.25
VIII	MMA, AIBN	1.00	2.73	7.169	14.90	2.078	580	0.368	3.345	1.61
			5.45	3.65	25.2	6.90	582	1.458	13.26	1.92
			10.90	8.437	9.40	1.11	582	0.285	2.59	2.33
	MMA, BP	1.00	2.73	10.964	12.14	1.107	581	0.380	3.455	3.12
			5.45	11.201	10.66	0.898	581	0.282	2.564	2.85
			10.90	12.000	8.15	0.679	580	0.204	1.855	2.73
	Styrene, AIBN	3.65	5.76	2.194	10.12	4.613	580	1.136	10.327	2.24
			11.55	2.132	20.31	9.526	578	4.038	36.709	3.85
			23.10	0.721	5.64	7.822	580	3.803	34.573	4.42
X	MMA, AIBN	1.00	0.25	15.9	10.97	0.688	300	0.756	53.70	78.1
			0.50	16.5	10.15	0.615	299	0.343	24.40	39.7
			0.75	18.11	5.93	0.327	298	0.139	9.91	30.3
			1.00	17.1	10.28	0.601	299	0.527	37.46	62.3
			1.50	15.7	9.75	0.621	298	0.530	37.695	60.7
	MMA, BP	1.00	0.25	12.445	10.15	0.815	297	1.471	104.50	128.24
			0.50	12.617	7.45	0.590	297	1.695	120.469	204.18
			0.75	12.943	6.85	0.529	298	2.213	157.285	297.33
			1.00	13.150	5.16	0.392	297	2.050	145.70	371.70
			1.50	13.934	5.05	0.362	299	2.018	143.426	396.20

* (AIBN) azobis(isobutyronitrile); (BP) benzoyl peroxide.

bands of **V** are not detected, i.e., this compound is not incorporated into the PMMA molecule. The polymer prepared in the presence of only difluorenylphthalide shows a similar spectrum, which convincingly proves the presence of difluorenylphthalide units in the macromolecules.

Using the calibration plot for this polymer, the content of phthalide fragments was found to be 1/1900 (mole per mole of monomeric units). The molecular weight of PMMA was determined by gel permeation chromatography (number-average M_n 340 000) and viscometry (viscosity-average M_η 365 000). Hence,

there are 1.80 phthalide groups per macrmolecule (1.92 according to viscometric data). This means that phthalide groups can be located both in terminal positions and inside the chain. Apparently, two fluorenyl fragments of the phthalide participate in the initiation, with the result that the additive becomes incorporated inside the macromolecule; this means that the additive and macromolecule are relatively independent of each other. The tentative scheme below illustrates how phthalides with fluorenyl substituents participate in the process:

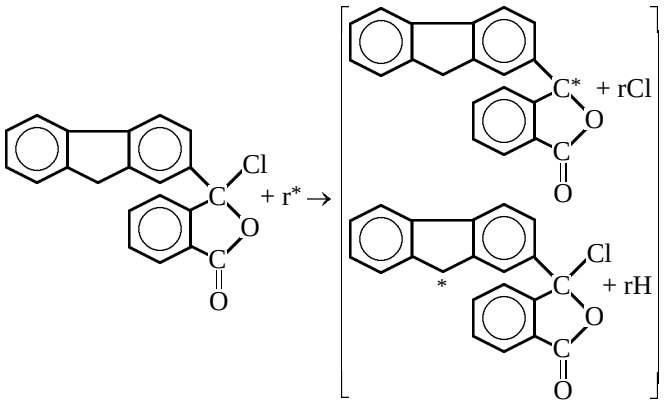

$\xrightarrow{+M}$ Initiation. (3)

Data on the content of the other phthalimides in the PMMA polymeric chain are listed in Table 2.

Thus, the obtained results show that phthalides of various structures take active part in radical polymerization and allow us to suggest the mechanism of their effect.

CONCLUSIONS

(1) Solutions of phthalides in concentrated H_2SO_4 are intensely colored, with the Bouguer–Lambert–Beer law obeyed, and exhibit high stability. The color of sulfuric acid solutions of polymethyl methacrylate and polystyrene prepared in the presence of phthalides is exclusively due to phthalide-containing compounds.

(2) The extinction coefficients of sulfuric acid solutions of phthalide-containing compounds of various structures were determined.

(3) The content of phthalide groups in polymeric molecules was determined. The main mechanism of their incorporation into the polymeric chain is participation in chain transfer.

ACKNOWLEDGMENTS

The study was financially supported by the Russian Foundation for Basic Research (project no. 98-03-33322).

REFERENCES

1. Petrov, A.A., Gonikberg, M.G., Salazkin, S.N., *et al.*, *Izv. Akad. Nauk SSSR, Ser. Khim.*, 1968, no. 2, p. 279.
2. Kraikin, V.A., Zolotukhin, M.G., Salazkin, S.N., and Rafikov, S.R., *Vysokomol. Soedin., Ser. A*, 1985, vol. 27, no. 2, pp. 422–427.
3. Puzin, Yu.I., Egorov, A.E., Khatchenko, E.A., *et al.*, *Vysokomol. Soedin., Ser. A*, 2000, vol. 42, no. 9, pp. 1524–1536.
4. USSR Inventor's Certificate, no. 1065741.
5. Berger, S., *Tetrahedron*, 1981, vol. 37, no. 8, pp. 1607–1611.
6. Hopkinson, A.C. and Wyatt, P.A.H., *J. Chem. Soc. B*, 1970, vol. 3, pp. 530–535.
7. Hart, H. and Sulzberg, J., *J. Am. Chem. Soc.*, 1963, vol. 85, no. 12, pp. 1800–1806.
8. Gold, V. and Tye, F.L., *J. Chem. Soc.*, 1951, no. 8, pp. 2102–2111.
9. Bethell, D. and Gold, V., *Carbonium Ions. An Introduction*, London: Academic, 1967.
10. Valters, R.E., *Kol'chato-tsepnaya izomeriya v organicheskoi khimii* (Ring–Chain Isomerism in Organic Chemistry), Riga: Zinatne, 1978.
11. Becker, H., Berge, W., Domschke, G., *et al.*, *Organikum. Organisch-chemisches Grundpraktikum*, Berlin: Wissenschaften, 1976.
12. Salazkin, S.N., Card Polymers, *Doctoral Dissertation*, Moscow, 1979.
13. Gladyshev, G.N. and Gibov, K.M., *Polimerizatsiya pri glubokikh stepenyakh prevrashcheniya i metody ee issledovaniya* (Polymerization at High Conversions and Methods for Its Investigation), Alma-Ata: Nauka, 1968.
14. Lyalikov, Yu.S., *Fiziko-khimicheskie metody analiza* (Physicochemical Analysis), Moscow: Khimiya, 1973.
15. Bagdasar'yan, Kh.S., *Teoriya radikal'noi polimerizatsii* (Theory of Radical Polymerization), Moscow: Akad. Nauk SSSR, 1959.

Russian Journal of Applied Chemistry, Vol. 74, No. 2, 2001, pp. 298–304. Translated from Zhurnal Prikladnoi Khimii, Vol. 74, No. 2, 2001, pp. 292–299.

MACROMOLECULAR CHEMISTRY AND POLYMERIC MATERIALS

Microstructure of Vinyl Chloride–Maleic Anhydride Copolymer in Condensed State

A. G. Filimoshkin, E. B. Chernov, G. A. Terent'eva, E. M. Berezina, and M. S. Safronova

Tomsk State University, Tomsk, Russia

Received May 4, 2000

Abstract—The structure of the macromolecule of an equimolar native vinyl chloride–maleic anhydride copolymer was studied. A mechanism of copolymerization of vinyl chloride with maleic anhydride is proposed.

Copolymers of maleic anhydride (MA) are used as starting substances in synthesizing ion exchangers, pharmaceuticals, cosmetics, and other substances, and also as enzyme carriers. To obtain materials with the desired properties, it is necessary to know the microstructure of the initial polymeric molecules. Macromolecules of the vinyl chloride–maleic anhydride (VCMA) copolymer undergo in solution cycloanhydride–enol tautomerism (CAET) cardinally altering the primary (native) microstructure of VCMA [1, 2]. The majority of methods for studying the composition and properties of chemical compounds are concerned with their solutions. These techniques are obviously unsuitable for studying the microstructure of VCMA copolymer, because in the course of dissolution the native microstructure formed in polyaddition is lost.

In this work we studied the VCMA microstructure by methods producing results that reflect the native microstructure, nonaltered by solvent. As such methods we chose thermogravimetry, spectroscopy, and gravimetric desorption analysis. For IR study, we cast VCMA films from THF under conditions of contact between VCMA and THF for 5–7 min. Since CAET transformations are slow, the native microstructure of VCMA is not altered within this period. A thermogravimetric study of thermal reactions in VCMA allowed us to avoid errors originating from the necessity to perform a series of experiments when the kinetics is studied in the isothermal mode; in our case all the necessary information is obtained with the same sample.

EXPERIMENTAL

The preparation conditions and characteristics of VCMA are given in [1]. Differential thermal analysis was performed on a Q 1500 derivatograph in helium at a heating rate of 10 deg min^{-1}. The DTA curves (Fig. 1) were processed taking into account the sequence of transformations: first H_2O is evolved and then HCl, CO_2, and CO. All calculations were performed proceeding from the mass balance of elimination of H_2O, HCl, CO_2, and CO, and the results

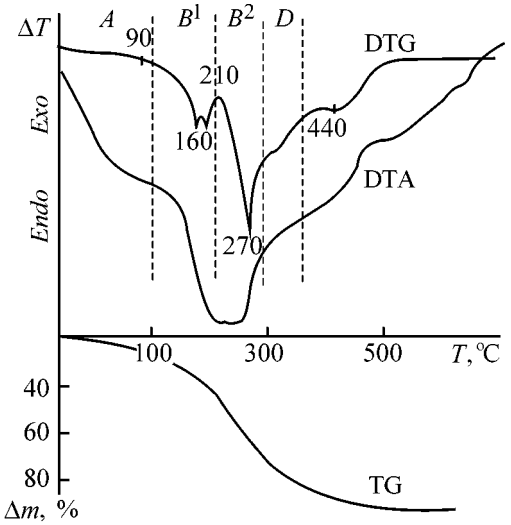

Fig. 1. DTA, DTG, and TG curves of copolymers: (Δm) weight loss and (T) temperature. Regions of thermograms along the abscissa, °C: (A) 40–100, (B^1) 100–200, (B^2) 200–300, and (D) 300–400.

1070-4272/01/7402-0298 $25.00 © 2001 MAIK "Nauka/Interperiodica"

Results of processing of TG curves

Characteristic	Temperature, °C									
	40–100	100–200	200–300		300–400		400–500			
Sample VCMA-22.0										
Region of thermogram	*A*	B^1	B^2			D				
Reaction product	H_2O	HCl	HCl	CO_2	CO_2	CO				
Mole fraction	(5.4)*	0.56	0.44	0.40	0.60	0.15				
Thermal effect	*Endo-*	*Exo-*		*Exo-*		*Exo-*				
n	0.03	2.05		2.42		4.03				
E_a, kJ mol^{-1}	79.4	72.3		120		234				
log(p*Z*) [s^{-1}]	13.5	7.8		13.3		21.9				
Sample VCMA-23.5										
Region of thermogram	*E*	F^1	F^2		F^3			G		
Reaction product	H_2O	HCl	HCl		HCl	CO_2		CO_2	CO	
Mole fraction	(3.6)*	0.53	0.43		0.035	0.59		0.41	0.51	
Thermal effect	*Endo-*	*Endo-*	*Exo-*			*Exo-*			*Exo-*	
n	1.68	1.14	1.15			4.8			6.4	
E_a, kJ mol^{-1}	54.3	69.8	322			195			392	
log(p*Z*) [s^{-1}]	9.1	6.5	35.3			19.6			31.8	
Sample VCMA-15.45										
Region of thermogram	*J*	K^1	K^2		L^1			L^2		
Reaction product	H_2O	HCl	HCl	CO_2	HCl	CO		CO_2		
Mole fraction	(3.7)*	0.91	0.09	0.61	0.39	0.2		0.75		
Thermal effect	*Endo-*	*Endo-*		*Exo-*		*Exo-*		*Exo-*		
n	1.63	1.83		2.68		3.13		2.96		
E_a, kJ mol^{-1}	56.0	95.4		173		116		234		
log(p*Z*) [s^{-1}]	9.4	10.8		21		12		18.8		

* The content of desorbed water (wt %) is given in parentheses.

were compared with those obtained in analyzing the products of thermal decomposition in a flow of oxygenfree nitrogen in a bubbling unit under isothermal conditions in the same temperature ranges. The gaseous decomposition products of VCMA-22.0 (22.0 wt % Cl as determined by the Schoeniger procedure) in regions *A*–*D* (Fig. 1) were trapped by selective absorbents: HCl, by an $Hg_2(NO_3)_2$ solution (solubility product of Hg_2Cl_2 2×10^{-18}); CO_2, by Ascarite; and CO, by a $PdCl_2$ solution. In the derivatograms of VCMA samples, we can distinguish the regions of "pure" dehydrochlorination B^1, F^1, K^1, and F^2 (see table). Above 250°C, HCl is eliminated simultaneously with CO_2 (regions B^2, F^3, and K^2). Thermal decomposition of VCMA is completed with release of CO_2 and CO (regions *D*, *G*, L^1, and L^2).

The mathematical processing of TG curves was performed by the equation

$$d\alpha/d\tau = k(1 - \alpha)^n,$$

where α is the conversion; $k = pZ\exp(-E_a/RT)$, p*Z* is the entropy parameter of the Arrhenius equation, E_a is the activation energy, *T* is temperature, and *R* is the gas constant [3].

The Arrhenius parameters and the values of *n* were computed [4, 5] (see table). All dependences were processed by the simple-iteration and Rosenbrock minimization procedures. Both methods gave consistent results.

The IR spectra were taken on a Specord M80 spectrophotometer. Films were prepared directly on NaCl plates from solutions of VCMA in THF and DMSO. The solvents were purified by conventional procedures [6]. An X-ray diffraction analysis confirmed the amorphous state of the VCMA samples (DRON-3M, Cu_{K_α} radiation).

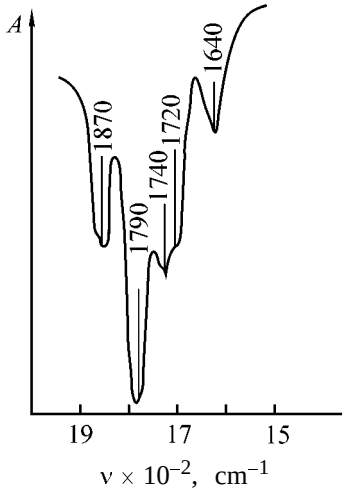

Fig. 2. IR spectrum of a VCMA-22.0 film cast from a 2% THF solution onto an NaCl plate: (*A*) absorption and (ν) wave number; the same for Fig. 3.

Along with the practically equimolar copolymer VCMA-22.0, we prepared two other samples: VCMA-15.45 enriched in MA and VCMA-23.5 containing, along with alternating segments, additional 6 mol % VC units decreasing the rigidity of the chain:

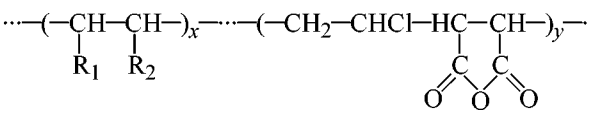
(I)

R_1 = H, R_2 = Cl, x = 0, y = 1.0 (VCMA-22.0); R_1 = H, R_2 = Cl, x = 0.06, y = 0.94 (VCMA-23.5); R_1 and R_2 = OC–O–CO, x = 0.3, y = 0.7 (VCMA-15.45).

Since dehydrochlorination of PVC (R_1 = H, R_2 = Cl, y = 0, x = 1) has been investigated in detail [7–9], we did not study it in this work.

Below we show as an example the Fischer projection of a macromolecule segment of alternating VCMA copolymer **II** incorporating succinic anhydride rings (*an*): two *r*- (*threo*) (^{1}C–^{2}C; ^{5}C–^{6}C) and one *m*- (*erythro*) (^{9}C–^{10}C):

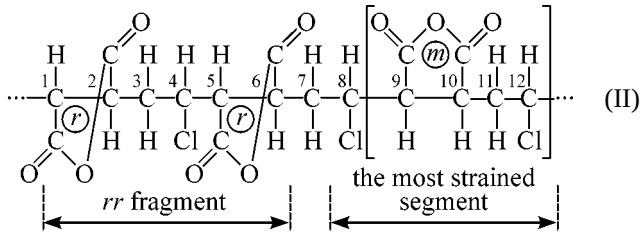

(II)

The ^{4}C, ^{8}C, and ^{12}C atoms may be both R- and S-chiral.

In view of the different chiralities of the ^{4}C, ^{8}C, and ^{12}C atoms, the C=O groups bound to ^{1}C, ^{2}C, ^{5}C, ^{6}C, ^{9}C, and ^{10}C **II** appear to be sterically and energetically nonequivalent; they are at different distances from the adjacent electronegative Cl atoms, which results in varied mutual repulsion and hence in different force constants of the C=O groups. This is manifested in the IR spectra in that the C=O groups in VCMA-22.0 films cast from THF give a set of absorption bands: one strong at 1790 cm^{-1}, two medium at 1870 and 1740 cm^{-1}, and a medium-intensity shoulder at 1720 cm^{-1}, which suggests the presence of four energetically nonequivalent states of the C=O groups (Fig. 2). Apparently, the group of bands at 1870–1720 cm^{-1} belongs to *an* structures and to the C=O groups in the enol tautomers Δ^6-*en* and Δ^7-*en*. A weak band at 1640 cm^{-1} most probably belongs to the C=C bond in *en* type macromolecule units. The fragments of microstructurally heterogeneous VCMA macromolecules are shown below.

Fragments of microstructurally heterogeneous VCMA macromolecules

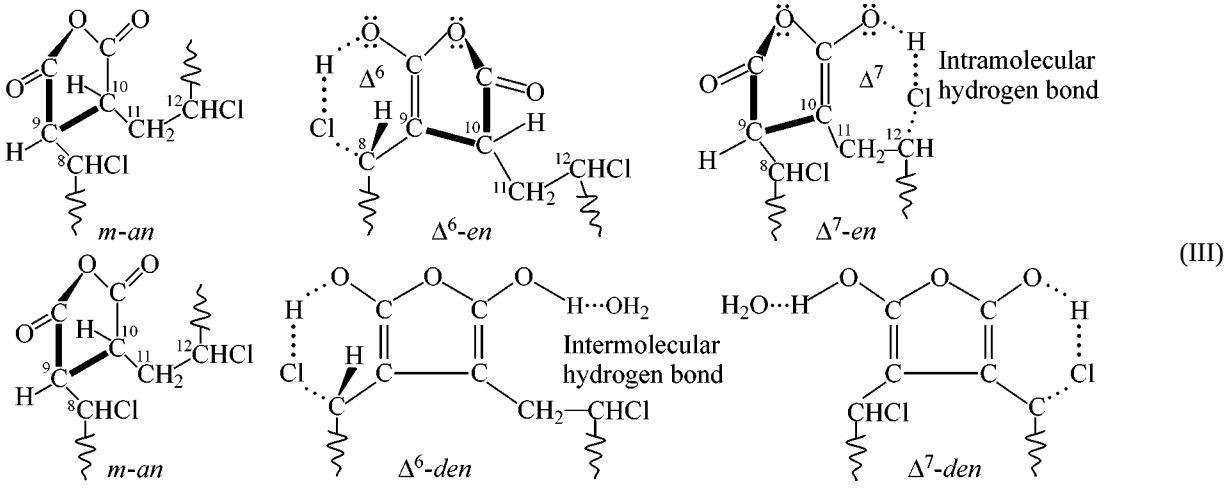

(III)

The IR data for DMSO solutions suggest distortion of the VCMA microstructure under the action of DMSO and formation of tautomeric forms containing hydroxy substituents. The IR spectrum of a VCMA film cast from DMSO but not dried to remove DMSO ("wet" film) and that of the same film dried in a vacuum at 40°C (Fig. 3) confirm the presence of the suggested structures. The IR spectrum of the wet film contains strong absorption bands related to vibrations of the C=C (1680 cm^{-1}) and OH (3450 cm^{-1}, broad) groups, and also a weaker band at 1730 cm^{-1}. The IR spectrum of the dry film contains a strong band at 1730 cm^{-1} [ν(C=O)] (Fig. 3).

One of the key questions to be answered in this work is whether this microstructural heterogeneity appears in the course of copolymerization or is formed under the action of the solvent. The following experiments were performed to solve this question.

In air, amorphous VCMA samples adsorb moisture. To evaluate, using DTA and gravimetry, the amount of atmospheric moisture adsorbed by VCMA macromolecules, we studied the kinetics of its desorption from native VCMA samples after their being kept in air for 5 days ("moist" samples).

The kinetics of isothermal desorption of water at room temperature from moist VCMA samples was monitored gravimetrically, in the course of storage of the samples in a desiccator over P_2O_5. The kinetic dependences of water desorption were processed by the equation [10]

$$\theta = \theta_{eq}[1 - \exp(-k\tau)], \quad (1)$$

where θ is the current amount of desorbed water, θ_{eq} is the amount of water at $\tau \to \infty$, and k is the rate constant of the adsorption–desorption process.

It was shown that desorption from the VCMA-22.0 sample occurs with $k = 5 \times 10^{-6}$ s^{-1}, $\theta_{eq} = 5.1$ wt %, which corresponds to one adsorbed H_2O molecule per two units of VCMA-22.0 copolymer (molecular weight 160.5).

The amounts of water desorbed from the same VCMA-22.0 sample, determined by DTA (see table) and gravimetrically under isothermal conditions, are reasonably consistent (5.40 and 5.29 wt %, respectively) and practically coincide with θ_{eq} calculated by Eq. (1), 5.1 wt %.

Desorption of water from moist VCMA-22.0 sample under nonisothermal conditions occurs with the apparent activation energy $E_a = 79.4$ kJ mol^{-1}, $n = 3.03$ (see table, region *A*). Because the physicochemical sense of the parameter of the thermal degradation reaction n is not quite clear, we considered several alternatives. The values of n may correspond to the numbers of possible stages (types) of one or another thermal reaction. It is natural to assume that the desorption of water involves cleavage of three types of intermolecular hydrogen bonds *den*···H_2O, two of which are shown in scheme (III): Δ^6-*den*···H_2O and Δ^7-*den*···H_2O. The third type is probably represented by other intermolecular hydrogen bonds, e.g., by the H bonds between H_2O molecules in the outer sphere of the associate: [(*den*···H_2O)···H_2O]. This assumption is supported by the fact that ΔH_v of water in the range 20–100°C varies from 44.2 to 40.7 kJ mol^{-1} [11], which is approximately half the E_a of water desorption from the VCMA-22.0 sample in the same temperature range.

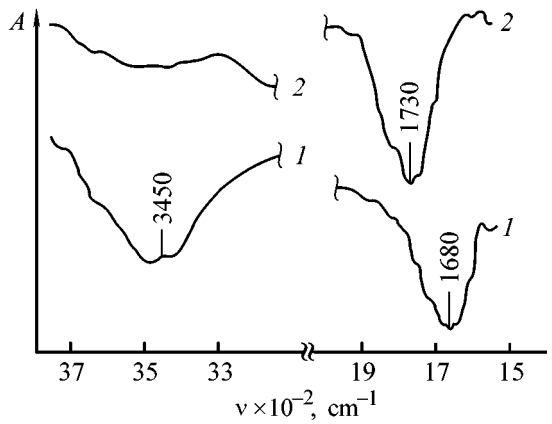

Fig. 3. IR spectra of VCMA-22.0 films cast from 2% DMSO solutions onto NaCl plates: (*1*) wet films containing DMSO and (*2*) films dried at 40°C.

In samples of the nonalternating VCMA copolymer, the content of water is a factor of 1.5 lower than that in the VCMA-22.0 sample (see table, regions *A*, *E*, *J*), and E_a of dehydration is only a factor of 1.3 higher than ΔH_v of water: 54.3 and 56.0 kJ mol^{-1}, with n equal to 1.68 and 1.63, respectively, which is due to the lower content of the *den* forms in these samples. The entropy parameter of dehydration $\log(pZ)$ = 9.1–13.5 (see table) suggests the formation of an ordered transition state of dehydration and allows water to be regarded as chemisorbed.

Thus, the microstructural heterogeneity of VCMA determines its capability to adsorb moisture from air and is responsible for the variability of VCMA properties. Namely, VCMA macromolecules permanently change their composition in the course of storage, depending on the storage time and air humidity; the composition may strongly differ from that of the freshly prepared samples.

The Arrhenius parameters of the dehydrochlorination of VCMA samples under nonisothermal condi-

tions also depend on their composition. For example, VCMA-22.0 eliminates 56 mol % of HCl with low E_a = 72.3 kJ mol^{-1} from two (n = 2.05) types of structures Δ^6-*en* and Δ^7-*en*; the VCMA-23.5 sample contains approximately the same amount of precursor groups that are readily dehydrochlorinated (53 mol %) and mostly belong to one type (n = 1.14). In the range 100–190°C, the VCMA-15.45 sample eliminates 91 mol % of HCl from two (n = 1.83) types of groups with higher E_{a_1} = 95.4 kJ mol^{-1} (see table, regions B^1, F^1, and K^1).

It is interesting that in the derivatogram of the VCMA-23.5 sample consisting of less rigid macromolecules there is a second range of pure dehydrochlorination (see table, region F^2) occurring very difficultly in a single (n = 1.15) stage. The high values of E_a = 322 kJ mol^{-1} and log(pZ) = 35.3 are close to the corresponding parameters of dehydrochlorination of low-molecular-weight analogs [8, 12] and exceed them because of the distortion of the favorable arrangement of units in substrates and the appearance of polyconjugated segments after the first stage of dehydrochlorination F^1. After stage F^1, there remains 43 mol % of CHCl groups incapable of forming Δ^6-*en* and Δ^7-*en* units from which elimination of HCl is facilitated. HCl is eliminated from such fragments without formation of the cyclic transition state, with E_a close to the value calculated for radical chain dehydrochlorination [8].

Thus, in regions B^1, F^1, and K^1 (see table) of pure VCMA dehydrochlorination, HCl is eliminated with considerably lower E_a and log(pZ) as compared with the same parameters for dehydrochlorination of PVC and model compounds [7–9, 13]. This is due to the concerted redistribution of bonds in the Δ^6-*den* and Δ^7-*den* rings and the formation of a low-energy zwitter-ion as one of the resonance structures of the final product [1]:

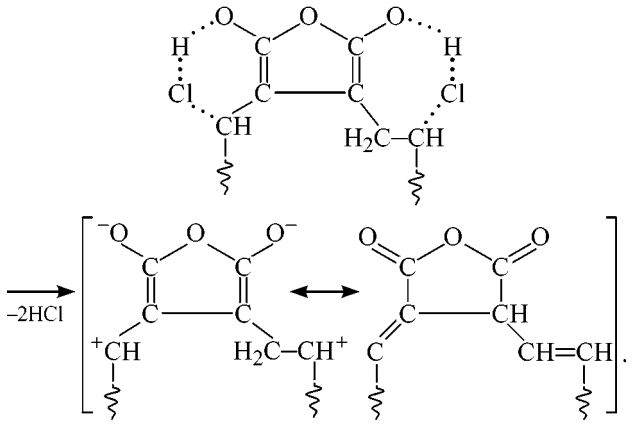

(IV)

For the sake of brevity, both mechanisms are shown with the same VCMA unit.

The products of thermal decomposition of VCMA under helium are black specular films, which suggests the formation of polyconjugated systems containing practically no oxygen, provided that CO_2 and CO are removed from VCMA macromolecules completely [13]. Based on the material balance of thermal reactions in VCMA in the nonisothermal mode (see table) and the results obtained in studying the isothermal decomposition at several temperatures in a bubbler unit, we suggest the following mechanism of VCMA decomposition on heating to 500°C under helium:

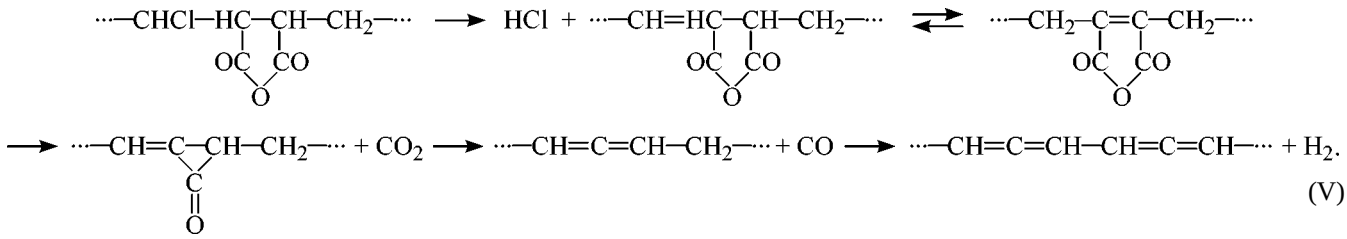

(V)

Whereas the presence of *m*- and *r*-anhydride rings in VCMA macromolecules is a known fact, the presence of tautomeric *en* and *den* forms in the macromolecules in the condensed state requires additional experimental support.

The IR spectra of VCMA in Figs. 2 and 3 show that the microstructure of VCMA is affected by a solvent. Let us return to considering the possibility of formation of *en* fragments during the chain growth process in the course of copolymerization. The necessary information can be obtained by computer processing of the kinetic dependences of the intensities of bands B and E (λ_{max} 246 and 268 nm, respectively) in the UV spectrum of VCMA in dioxane [2] by the equation

$$D_0 = D_{max}[1 - P\exp(-k\tau)], \quad (2)$$

where P is the factor related to the initial conditions; the concentration C of the tautomeric forms is pro-

portional to the current optical density of the corresponding absorption band D_λ, and C_{max} is proportional to D_{max} of the same band at $\tau \to \infty$.

At the instant when condensed VCMA macromolecules come in contact with the solvent ($\tau = 0$), the variation of both groups of bands *B* and *E* reflects the formation of the *en* and *den* tautomers by a pseudo-first-order reaction [2]. The group of bands with $\lambda_{max} = 246$ nm is due to $\pi \to \pi^*$ transitions in *en* forms, and that with $\lambda_{max} = 268$ nm, to $\pi \to \pi^*$ transitions in quasiaromatic structures [2]. Since D_λ is proportional to the content of the corresponding tautomeric *en* or *den* forms, Eq. (2) can be written as follows:

$$[en]_0 = [en]_{max}[1 - P\exp(-k\tau)],$$

$$[den]_0 = [den]_{max}[1 - P\exp(-kt)].$$

In this work, we processed with a computer the time dependences of the optical densities of the above UV absorption bands [2], which allowed us to calculate $[en]_0$ and $[den]_0$ at the instant of contact between native VCMA macromolecules and the solvent (mole fractions at $\tau = 0$):

λ_{max}, nm	D_{max}	P	$k \times 10^6$, s^{-1}	r^*	$[en]_0$	$[den]_0$
246	0.96	0.67	1.3	0.987	0.33	–
268	1.45	0.95	0.6	0.943	–	0.5

* Correlation coefficient.

It is significant that the results of all three independent methods: thermogravimetric, gravimetric, and UV spectroscopic [2], gave consistent values of $[en]_0$ in native VCMA-22.0 macromolecules: 33.8, 33.2, and 33.0 mol %, respectively, with $[den]_0$ in powdered VCMA not exceeding 5 mol %.

Thus, macromolecules of equimolar native copolymer VCMA-22.0 in the condensed state comprise a random sequence of alternating units VC–*r-an*, VC–*m-an* and anomalous structures Δ^6-*en* and Δ^7-*en*, which are formed in the course of copolymerization of VC with MA and are tautomerically labile units responsible for its dynamic microstructural heterogeneity:

$$\cdots\text{–[–(VC–}r\text{-}an\text{)–; –(VC–}m\text{-}an\text{)–]}_{0.67}\text{–}\cdots$$

$$\cdots\text{–[–(}\Delta^6\text{-}en\text{)-; –(}\Delta^7\text{-}en\text{)–]}_{0.33}\text{–}\cdots.$$

The mechanism of copolymerization of VC with MA is a matter of discussion. Equimolar copolymers were prepared at different VC to MA ratios by polymerization in the bulk and in benzene at 50°C with azobis(isobutyronitrile) as initiator [14, 15].

It is known that strictly alternating macromolecules are formed from molecular complexes of comonomers. Maleic anhydride forms complexes with many weak donors, such as vinyl ethers, olefins, styrene, acetone, DMF, DMSO, and even chloroform. The equilibrium constants *K* are, as a rule, low [14], which suggests that the concentration of the molecular complexes [VC·MA] is considerably lower than that of free molecules of VC and MA comonomers.

The fact of complexation between MA molecules and weak donors suggests that the equilibrium constant *K* of complexation between MA and VC at the copolymerization temperature (80°C) differs from zero. The formation of molecular complexes makes possible the chain growth by polyaddition of the complexes [VC·MA] to give alternating segments of the macromolecules of type **II**:

$$n[\text{VC}\cdot\text{MA}] \to \cdots\text{–[–(VC–}r\text{-}an\text{)–; –(VC–}m\text{-}an\text{)–]}_n\text{–}\cdots \quad \text{(VI)}$$

The incorporation of tautomeric *en* forms into growing macromolecules **VI** as segments of microstructural heterogeneity occurs as follows. An MA molecule in the biradical form **VIIb** forms a complex with a VC molecule at 80°C, yielding two biradicals **VIIIc** and **VIIId**.

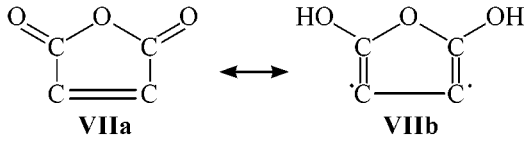

$HClC{=}CH_2$ + **VIIb**

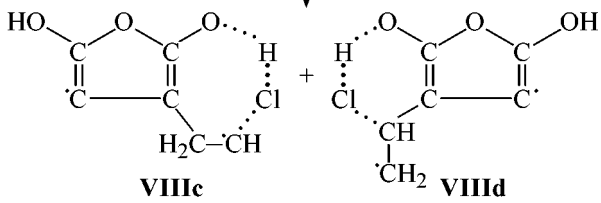

Then the chain growth continues by two pathways: polyaddition of molecular complexes [scheme (**VI**)] and their copolymerization with biradicals **VIIIc** or **VIIId** to form macromolecules containing the units –(VC-*r*- or -*m-an*)–, –(Δ^6-*en*)–, and –(Δ^7-*en*).

CONCLUSIONS

(1) Macromolecules of the equimolar native vinyl chloride–maleic anhydride copolymer prepared under

the chosen synthesis conditions comprise a random sequence of alternating comonomer units (67 mol %) and units containing the enol tautomer (33 mol %).

(2) The kinetics of desorption of atmospheric moisture and dehydrochlorination of vinyl chloride–maleic anhydride copolymer samples were studied. Elimination of HCl occurs both with low activation energy from enol tautomers and with high activation energy from segments consisting of vinyl chloride and anhydride rings.

(3) A mechanism of copolymerization of vinyl chloride with maleic anhydride was proposed, involving polyaddition of weak molecular complexes of comonomers in the ground state and in the form of biradical resonance structures.

REFERENCES

1. Filimoshkin, A.G., Terentieva, G.A., Berezina, E.M., and Pavlova, T.V., *J. Polym. Sci., Polym. Chem. Ed.*, 1993, vol. 31, pp. 1911–1914.
2. Pavlova, T.V., Terent'eva, G.A., Filimonov, V.D., *et al.*, *Zh. Prikl. Khim.*, 1999, vol. 72, no. 9, pp. 1515–1517.
3. Sestak, J., *Thermophysical Properties of Solids. Their Measurements and Theoretical Thermal Analysis*, Prague: Academia, 1984.
4. Reich, L. and Stivala, S.S., *Thermochim. Acta*, 1980, vol. 36, no. 3, pp. 103–106.
5. Coats, A.W. and Redfern, J.P., *Nature*, 1964, vol. 201, no. 2, pp. 68–72.
6. Gordon, A.J. and Ford, R.A., *The Chemist's Companion. A Handbook of Practical Data, Techniques, and References*, New York: Wiley, 1972.
7. Evsyukov, S.E., Kudryavtsev, Yu.P., and Korshak, Yu.V., *Usp. Khim.*, 1991, vol. 60, no. 4, pp. 764–798.
8. Troitskii, B.B. and Troitskaya, L.S., *Usp. Khim.*, 1985, vol. 54, no. 8, pp. 1287–1311.
9. Minsker, K.S., Kolesov, S.V., and Zaikov, G.E., *Starenie i stabilizatsiya polimerov na osnove vinilkhlorida* (Aging and Stabilization of Polymers Based on Vinyl Chloride), Moscow: Nauka, 1982.
10. *Khimicheskaya entsiklopediya* (Chemical Encyclopedia), Knunyants, I.L., Ed., Moscow: Sov. Entsiklopediya, 1988, vol. 1, p. 43.
11. *Khimicheskaya entsiklopediya* (Chemical Encyclopedia), Knunyants, I.L., Ed., Moscow: Sov. Entsiklopediya, 1988, vol. 1, p. 395.
12. Benson, S.W., *Thermochemical Kinetics. Methods for the Estimation of Thermochemical Data and Rate Parameters*, New York: Wiley, 1968.
13. Berlin, A.A., Geiderikh, M.A., Davydov, B.E., and Kargin, V.A., *Khimiya polisopryazhennykh sistem* (Chemistry of Polyconjugated Systems), Moscow: Khimiya, 1972.
14. Trivedi, B.C. and Culbertson, B.M., *Maleic Anhydride*, New York: Plenum, 1982.
15. Rzaev, Z.M., *Polimery i sopolimery maleinovogo angidrida* (Polymers and Copolymers of Maleic Anhydride), Baku: Elm, 1984.

Russian Journal of Applied Chemistry, Vol. 74, No. 2, 2001, pp. 305–308. Translated from Zhurnal Prikladnoi Khimii, Vol. 74, No. 2, 2001, pp. 300–303.

MACROMOLECULAR CHEMISTRY AND POLYMERIC MATERIALS

Molecular Characteristics of 1,4-*trans*-Polybutadiene and Nature of Organoaluminum Compound in Vanadium-Containing Catalytic Systems

N. N. Sigaeva, E. A. Shirokova, I. A. Ionova, I. R. Mullagaliev, and Yu. B. Monakov

Institute of Organic Chemistry, Ufa Scientific Center, Russian Academy of Sciences, Ufa, Bashkortostan, Russia

Received September 12, 2000

Abstract—The influence of the nature of an organoaluminum compound on the molecular characteristics of 1,4-*trans*-polybutadiene prepared with vanadium-containing catalytic systems was studied.

A study of coordinated ionic polymerization of dienes on *cis*-stereospecific catalytic systems showed that the nature of an organoaluminum compound (OAC) significantly affects both the activity of the catalytic system and the properties of the resulting polydienes. It has been found [1, 2] that, with different OACs, not only the rate constants of chain transfer to OAC (k_0^{Al}) but also the rate constants of chain growth k_g are different. The OAC nature affects the microstructure of the resulting polydiene [3] and its molecular characteristics [4]. It has been suggested [2] that the OAC molecule may be a part of the active center, which can be responsible for the kinetic nonuniformity of these catalytic systems. For the case of polymerization of dienes with *trans*-stereospecific catalytic systems, such data are lacking.

In this work, we studied how the OAC nature affects the molecular characteristics of 1,4-*trans*-polybutadiene (*trans*-PB) obtained with vanadium-containing catalytic systems.

It is known that vanadium-containing catalytic systems allow preparation of polydienes with high content of *trans* units. The resulting 1,4-*trans*-polydienes are highly crystalline polymers with good cohesion properties; they can be used in adhesive formulations, for preparing films, for manufacturing orthopedic articles, etc.

The best studied are catalytic systems based on VCl_3, VCl_4, or $VOCl_3$ and aluminum trialkyls [5, 6]. These systems are highly *trans*-stereospecific (from 80 to 99% *trans* units) and active. In this work, we chose the catalytic systems $VOCl_3$–OAC with OAC = Al(*i*-$C_4H_9)_3$ (TIBA), Al(*i*-$C_4H_9)_2Cl$ (DIBAC), and Al(*i*-$C_4H_9)_2H$ (DIBAH).

Figures 1 and 2 show the weight-average (M_w) and number-average (M_n) molecular weights and the polydispersity (M_w/M_n) of *trans*-PB as functions of the monomer conversion in the course of polymerization. It is seen that these catalytic systems allow preparation of *trans*-PB with fairly high molecular weight. The molecular weights and the M_w/M_n ratio increase throughout the course of polymerization. The rate of butadiene polymerization remains constant up to high conversions of the monomer.

It is seen that the highest M_w is attained with DIBAH as organoaluminum cocatalyst (Fig. 1), and the lowest, with DIBAC. The M_n values decrease in the order TIBA > DIBAC > DIBAH (Fig. 2). This means that *trans*-PB samples prepared with DIBAH show the widest molecular-weight distribution (MWD): the polydispersity reaches 10. This is probably due to the fact that the presence in the reaction mixture of a cocatalyst containing an Al–H bond makes the catalytic system more active in chain transfer to OAC as compared to compounds containing the Al–C and Al–Cl bonds. Data on the kinetic constants of polymerization k_g, k_0^{Al}, and k_0^m (rate constant of chain transfer to the monomer) confirm this assumption (see table). Replacement of the alkyl group in the OAC molecule by a hydrogen or chlorine atom affects not only the rate constants of chain transfer to OAC but also the rate constants of chain growth. Thus, the nature of OAC affects the probability of transfer to OAC (k_0^{Al}/k_g), whereas the probability of chain transfer to the monomer (k_0^m/k_g) remains unchanged for all

1070-4272/01/7402-0305 $25.00 © 2001 MAIK "Nauka/Interperiodica"

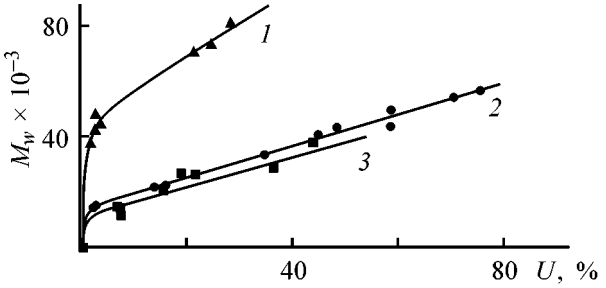

Fig. 1. M_w vs. conversion U of butadiene in polymerization with the catalytic system $VOCl_3$–OAC. Polymerization conditions: toluene; 25°C; C_m = 1.0, C_c = 5.0 × 10^{-3} M; Al/V ratio 4 (TIBA, DIBAC) or 2.5 (DIBAH); the same for Figs. 2–4. OAC: (*1*) DIBAH, (*2*) TIBA, and (*3*) DIBAC.

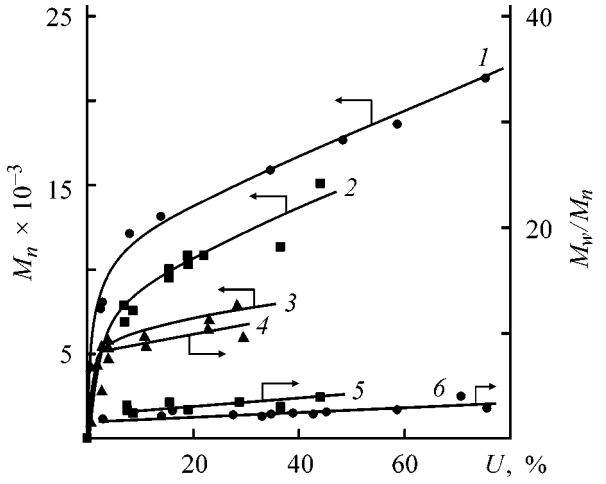

Fig. 2. (*1–3*) M_n and (*4–6*) M_w/M_n vs. butadiene conversion U in polymerization with the catalytic systems $VOCl_3$–OAC. OAC: (*1*, *6*) TIBA, (*2*, *5*) DIBAC, and (*3*, *4*) DIBAH.

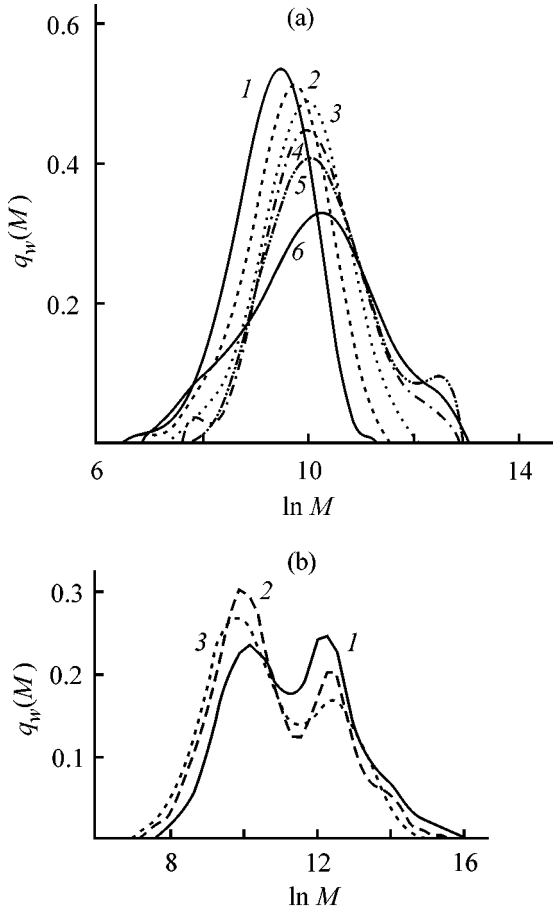

Fig. 3. MWD curves for *trans*-PB prepared with the catalytic systems (a) $VOCl_3$–TIBA and (b) $VOCl_3$–DIBAH. Monomer conversion, %: (a) (*1*) 2.5, (*2*) 14.0, (*3*) 34.7, (*4*) 45.0, (*5*) 58.7, and (*6*) 75.5; (b) (*1*) 4.7, (*2*) 16.8, and (*3*) 51.2.

the systems studied. This fact explains why polybutadienes prepared with these catalytic systems have different molecular weights.

Changing the type of OAC in the catalytic system affects not only the molecular weight but also the MWD shape.

The MWD curves of *trans*-PB at different monomer conversions are listed in Figs. 3a and 3b. At short time of butadiene polymerization on the catalytic system with TIBA (Fig. 3a), the MWD curves are unsymmetrical but unimodal, with broadening on the side of low molecular weights. With increasing conversion, the peak shifts to higher molecular weights, with simultaneous broadening on both sides. At large conversions, a shoulder appears on the side of high molecular weights, and finally MWD becomes bimodal. Similar changes in the shape of

Kinetic parameters of butadiene polymerization on the catalytic systems $VOCl_3$–OAC

OAC	k_g	k_0^m	$(k_0^m/k_g) \times 10^3$	k_0^{Al},	$(k_0^{Al}/k_g) \times 10^2$	C_a,* %
	l mol^{-1} min^{-1}			l mol^{-1} min^{-1}		
TIBA	260	0.70	2.7	5.6	2.0	8.2
DIBAH	30.0	0.08	2.7	2.0	6.7	7.5
DIBAC	50.0	0.13	2.6	1.5	3.0	11.0

* (C_a) Concentration of active centers.

MWD curves of polybutadiene were observed with DIBAC as OAC, whereas polymerization of butadiene with the catalytic system $VOCl_3$–DIBAH gives samples with polymodal MWD (Fig. 3b).

The shape of the dependences of the molecular characteristics of *trans*-PB on the concentrations of the catalytic system components and monomer is typical of Ziegler catalytic systems [7, 8]. With increasing monomer concentration, the molecular weights grow; with increasing catalyst concentration and Al/V ratio, both M_w and M_n decrease.

The dependence of the molecular characteristics of *trans*-PB on the polymerization temperature T_{pm} is unusual: In the range 20–25°C, M_w and M_w/M_n pass through a minimum, and M_n, through a maximum (Fig. 4).

Our experimental results show that one of specific features of *trans*-PB prepared with the tested catalytic systems is wide MWD, governed by the nature of OAC and synthesis conditions. This may be due to participation in the polymerization of several types of active centers differing in reactivity. Apparently, changing the nature of OAC as a component of catalytic systems affects the features of their reactivity.

EXPERIMENTAL

Butadiene was polymerized in toluene at 25°C without access of air or moisture. The catalytic complex was prepared in advance by combining solutions of $VOCl_3$ and OAC with addition of a small amount of the monomer [up to 5 mol per mole V(V)] and keeping for 0.5 h at 0°C. The polymerization was performed at monomer (C_m) and catalyst (C_c) concentrations of 1.0 and 5×10^{-3} M, respectively. The highest catalytic activity (the highest yield of the polymer) was observed at OAC/V ratio of 4.0 for TIBA and DIBAC and 2.5 for DIBAH.

The microstructure of polymers was studied by IR spectroscopy with a Specord M80 spectrophotometer [9]. The examined samples contained 83–90% 1,4-*trans* units and 17–10% 1,2-units. The gel fraction content did not exceed 1%.

Solutions of *trans*-PB were prepared by stirring the required amounts of the polymer and solvent at 80–90°C for 2–4 h just before measurements. The solutions were filtered while hot and then brought to the required temperature.

The molecular weights and MWD of polydienes were determined with a Du Pont liquid chromatograph

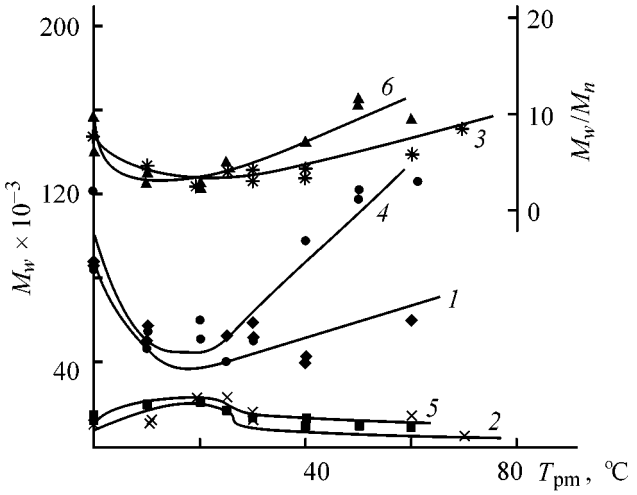

Fig. 4. (*1*, *4*) M_w, (*3*, *6*) M_n, and (*2*, *5*) M_w/M_n vs. polymerization temperature T_{pm} for samples of *trans*-PB prepared with the catalytic systems (*1–3*) $VOCl_3$–TIBA and (*4–6*) $VOCl_3$–DIBAC.

equipped with four columns packed with Shimadzu Microgel (pore size 1×10^3–10^6 Å). The separation was performed at 85°C with toluene as eluent. The column system was calibrated with polystyrene reference samples with narrow MWD ($M_w/M_n \le 1.2$), using the universal Benoit dependence [10] and the Mark–Houwink equation for *trans*-PB [11]. The MWD curves and molecular weights were corrected for instrumental broadening by the method described in [12, 13].

The kinetic constants k_g and k_0^m were calculated by the equations [14]

$$W_n = k_g C_m C_a,$$

$$1/P_n = 1/(\tau k_g C_m) + \Sigma (C_i k_0^i)/(k_g C_m),$$

$$1/P_n = 1/C_m \tau \Sigma k_0^i C_i - 1/k_g + k_0^m/k_g,$$

$$1/P_n = C_{Al} k_0^{Al}/k_g C_m + \tau \Sigma k_0^i C_i / k_g C_m,$$

where W_n is the polymerization rate, C_a is the concentration of active centers, P_n is the number-average polymerization rate, k_0^i is the rate constant of transfer with *i*th agent, C_{Al} is the OAC concentration, C_i is the concentration of the *i*th transfer agent, and τ is the polymerization time.

The constant k_g was determined using the equation

$$W_n \tau / P_n = C_a + W_0 \tau,$$

where W_0 is the overall chain-termination rate.

CONCLUSIONS

(1) The nature of the organoaluminum component of vanadium-containing catalytic systems affects both the average molecular weights of the resulting 1,4-*trans*-polybutadienes and the shape of their molecular-weight distribution.

(2) The influence of the nature of the organoaluminum compound on the molecular characteristics of 1,4-*trans*-polybutadienes is due to different probabilities of chain transfer to the organoaluminum compound, with the probability of chain transfer to the monomer remaining the same for all the systems studied.

(3) Polymerization of butadiene with vanadium-containing catalytic systems presumably occurs on centers differing in kinetic activity.

REFERENCES

1. Bubnova, S.V., Tverdov, A.I., and Vasil'ev, V.A., *Vysokomol. Soedin., Ser. A*, 1988, vol. 30, no. 7, pp. 1374–1379.
2. Kozlov, V.G., Nefed'ev, K.V., Marina, N.G., *et al.*, *Dokl. Akad. Nauk SSSR*, 1988, vol. 299, no. 3, pp. 652–656.
3. Hsien, H.L. and Yeh, G.H.C., *Rubber Chem. Technol.*, 1985, vol. 58, no. 1, pp. 117–145.
4. Sigaeva, N.N., Kozlov, V.G., Savel'eva, I.G., *et al.*, *Bashkir. Khim. Zh.*, 1998, vol. 5, no. 4, pp. 31–36.
5. Patterson, D.B. and Halasa, A.F., *Macromolecules*, 1991, vol. 24, no. 7, pp. 1583–1589.
6. Monakov, Yu.B. and Tolstikov, G.A., *Kataliticheskaya polimerizatsiya 1,3-dienov* (Catalytic Polymerization of 1,3-Dienes), Moscow: Nauka, 1990.
7. Monakov, Yu.B., Marina, N.G., Savel'eva, I.G., *et al.*, *Dokl. Akad. Nauk SSSR*, 1982, vol. 265, no. 6, pp. 1431–1433.
8. Sigaeva, N.N., Kozlov, V.G., Nefed'ev, K.V., *et al.*, *Bashkir. Khim. Zh.*, 1998, vol. 5, no. 2, pp. 30–34.
9. Anderson, J.N., Barsan, M.L., and Adams, H.F., *Rubber Chem. Technol.*, 1972, vol. 49, no. 5, pp. 1270–1276.
10. Benoit, H., Crubisic, L., and Rempp, P.A., *J. Polym. Sci. B*, 1967, vol. 5, no. 9, pp. 753–759.
11. Krentsel', B.A., *Entsiklopediya polimerov* (Encyclopedia of Polymers), Moscow: Sov. Entsiklopediya, 1972, vol. 1, p. 303.
12. Kislov, E.I., Zotikov, E.G., Podosenova, N.G., *et al.*, *Vysokomol. Soedin., Ser. A*, 1978, vol. 20, no. 8, pp. 1910–1912.
13. Budtov, V.P., Zotikov, E.G., Ponomareva, E.L., and Gandel'sman, M.I., *Vysokomol. Soedin., Ser. A*, 1985, vol. 27, no. 5, pp. 1094–1097.
14. Ermakov, Yu.I. and Zakharov, V.A., *Usp. Khim.*, 1972, vol. 41, no. 3, p. 377.

Russian Journal of Applied Chemistry, Vol. 74, No. 2, 2001, pp. 309–315. Translated from Zhurnal Prikladnoi Khimii, Vol. 74, No. 2, 2001, pp. 304–310.

MACROMOLECULAR CHEMISTRY AND POLYMERIC MATERIALS

Water-Resistant Films and Coatings Based on Cross-Linking Styrene–Acrylate Latex Copolymers

S. S. Ivanchev, V. N. Pavlyuchenko, N. A. Byrdina, M. Skrifvars, and J. Koskinen

St. Petersburg Branch, Boreskov Institute of Catalysis, Siberian Division, Russian Academy of Sciences, St. Petersburg, Russia

Neste Chemicals Oy, Porvoo, Finland

Received Septemper 19, 2000

Abstract—Water-resistant films and coatings were prepared from latexes of copolymers of styrene, *n*-butyl acrylate, 2-hydroxyethyl methacrylate, glycidyl methacrylate, and methacrylic acid. The degree of cross-linking of the copolymers in the course of film formation and the water resistance of the films and coatings, associated with this parameter and evaluated by the water absorption and mechanical properties of wet films, were studied in relation to the gross composition of the latex copolymer, conditions of its synthesis, distribution of functional groups responsible for cross-linking in a latex particle, and temperature of film formation.

The advantages of water-base polymer films and coatings consist in the convenience and environmental safety of their preparation. Especially promising are latex coatings prepared from highly concentrated systems, low-viscous at common temperatures, without using toxic and inflammable organic solvents. However, the specific features of film formation from latexes (by coalescence of latex particles) not always allow the potential of a polymeric system to be fully realized. Very often incomplete coalescence of particles and poor monolithization of a latex film result in poor water resistance of coatings, as judged from their equilibrium water absorption and mechanical strength of wet films.

One of the most efficient approaches to preparation of water-resistant latex coatings is the development of polymeric systems capable of cross-linking in the course of film formation. Previously, we have demonstrated the feasibility of preparing cross-linked coatings from latex copolymers containing epoxy and carboxy groups [1]. It is known that the reaction between these functional groups in homogeneous systems, e.g., in curing of epoxy resins, occurs at appreciable rate only at elevated temperatures. We found that in latex systems this reaction can be performed even at room temperature, probably owing to effects similar to micellar catalysis [2]. In [1], we introduced the required functional groups by using glycidyl methacrylate (GMA) and methacrylic acid (MAA) as comonomers in emulsion copolymerization. Usually up to 10 wt % GMA units was introduced. This, on the one hand, increased the cost of the copolymer and, on the other, resulted in partial cross-linking in the course of synthesis, which hindered coalescence of particles containing intraglobular cross-links.

Here we report the properties of films and coatings based on latex copolymers of styrene (ST), *n*-butyl acrylate (BA), 2-hydroxyethyl methacrylate (HEMA), MAA, and GMA, containing no more than 1 wt % GMA. The major comonomers ST and BA, determining the film-forming properties of latexes, were usually taken in amounts of 33–37 and 52–54 wt %, respectively; HEMA was added in an amount of 4–8% to increase the hydrophilicity of the copolymer and improve the coalescence of particles in the course of film formation. Three types of latex systems were studied.

In systems of type I, both reactive groups (epoxy and carboxy) are localized in the same reaction zone—latex particle shell.

In systems of type II, epoxy and carboxy groups are localized in different latex particles, i.e., system II is a mixture of two latexes: that of the ST–BA–HEMA–GMA copolymer and that of the ST–BA–HEMA–MAA copolymer. Both latexes were prepared using a seeding copolymer containing no functional groups. In such systems, a more efficient utilization

1070-4272/01/7402-0309 $25.00 © 2001 MAIK "Nauka/Interperiodica"

of functional groups would be expected, with their predominant participation in interglobular cross-linking in the course of coalescence.

Systems of type III are latexes with core–shell particles in which the core is ST–BA–HEMA–GMA copolymer and the shell is ST–BA–HEMA–MAA copolymer. In this system, both interglobular and intraglobular cross-linking is possible, although the latter process must be less pronounced than in systems of type I.

EXPERIMENTAL

Monomers used to synthesize latexes were purified by common procedures before copolymerization. The characteristics of the monomers agreed with reference data [3, 4]. The emulsion polymerization was initiated by potassium or ammonium persulfate. As emulsifiers were used anionic surfactant E-30 [sodium (C_{14}–C_{16})-alkylsulfonate] or nonionic surfactant OS-20 (C_{16}–C_{18} oxyethylated alcohol).

The emulsion copolymerization was performed in a 0.25–0.50 l glass vessel equipped with a stirrer, a reflux condenser, and tubes for feeding inert gas and adding reactants. In syntheses with gradual dosage of monomers, they were added from dropping funnels.

The dry residue of latexes was determined by drying a sample under an IR lamp to constant weight.

The size of latex particles was determined photometrically from the dependence of the optical density of dilute latexes on the transmitted light wavelength.

The films obtained from latex systems were cast on a glass support and studied in the free state.

The film quality was evaluated from the water absorption and gel fraction content. The water absorption was determined as the weight gain of films kept in distilled water for 24 h.

The gel fraction content and degree of swelling of the gel in the films were determined by separating the soluble fraction with acetone.

The mechanical properties of films were determined by a standard procedure [GOST (State Standard) 12589–78].

Latexes of type I were prepared in two stages. First, we prepared a seeding copolymer latex of composition (wt %) ST 54.6, BA 44.6, and HEMA 0.8 (no epoxy and carboxy groups). In the second stage, we added to the resulting seeding latex at various rates a monomeric mixture of composition (wt %) ST 35.0, BA 52.4, HEMA 5.2, MAA 6.4, and GMA 1.0. In each stage, the copolymerization was performed to practically complete conversion of the monomers, i.e., the composition of the copolymer corresponded to that of the monomer mixture. Thus, the gross composition of the copolymer (wt %) was as follows: ST 42.0, BA 49.6, HEMA 3.6, MAA 4.2, and GMA 0.6.

The two-stage process ensures increased concentration of functional groups in the surface layer, with the total content of the most expensive monomer, GMA, being less than 1%. Another advantage of the two-stage procedure is simple control of the latex particle size. The diameter of the latex particles after the second stage is actually determined by the size of the seeding particles. The conditions of latex syntheses are given in Table 1, and the characteristics of the latexes and films thereof, in Table 2.

Formation of films in this series of experiments was performed at 50°C, since films prepared at room temperature had worse strength in the wet state, which shows that the particle coalescence in unsatisfactory. It is seen that not all the latexes form cross-linked films, despite the same composition of the copolymers. Tables 1 and 2 show that the most important factors determining the possibility of preparing the cross-linked films are the rate of monomer mixture addition in the second stage of the latex synthesis and the size of the resulting particles. The highest content of the gel fraction and the lowest swelling were observed in films formed from latexes that were prepared by fast addition of the monomers, especially by their addition in a single portion (Table 2, copolymer no. 7). As seen from Table 2, the increasing particle size also favors higher gel fraction content in the film.

Our results can be accounted for by partial hydrolysis of epoxy groups, which are responsible for cross-linking, in the course of latex synthesis. The relatively fast hydrolysis of GMA in emulsion systems at elevated temperature (60°C) was observed in [5]. At fast addition of the monomer mixture, GMA units are localized in the particle volume owing to the high copolymerization rate, which prevents their hydrolysis. The increased particle diameter and hence their decreased surface area also hinder hydrolysis.

Although the water absorption of films does not strictly correlate with the gel fraction content, we see that the water absorption tends to decrease with increasing content of the gel freaction and decreasing degree of swelling of the films. As a rule, the highest water absorption is exhibited by fully soluble films (Table 2, copolymer nos. 1, 5) or by films containing a gel fraction with very high degree of swelling (copolymer no. 4).

Table 1. Conditions of synthesis of latex copolymers containing both types of functional groups in the latex particle shell (copolymerization temperature 70°C in both stages)

Copolymer no.	Synthesis conditions and some characteristics of seeding latex										Conditions of seeding copolymerization		
	composition of monomer mixture, wt %			monomer : water weight ratio	rate of monomer addition, % min^{-1}	content, wt % based on monomers		addition of initiator and emulsifier	dry residue, wt %	particle diameter, nm	rate of monomer addition,* % min^{-1}	content, wt % based on monomers	
	ST	BA	HEMA			initiator	emulsifier					initiator	emulsifier
1	55	45	–	1 : 5	0.337	0.65	2.0	At the beginning of the process	17.0	69	0.296	0.7	0
2	54.6	44.6	0.8	1 : 5	0.267	0.70	2.0		16.9	81	0.343	0.7	0
3	54.6	44.6	0.8	1 : 5	0.267	0.70	2.0		16.9	81	0.817	0.7	0
4	54.6	44.6	0.8	1 : 2.7	0.674	0.46	2.0		27.5	80	0.374	0.7	0
5	54.1	45.1	0.8	1 : 2.7	0.288	0.70	2.0	In the course of the process	27.3	96	0.251	0.9	0
6	54.1	45.1	0.8	1 : 2.7	0.288	0.70	2.0		27.3	96	0.521	1.24	1.07**
7	54.6	44.6	0.8	1 : 2.7	0.355	0.90	2.0		27.9	120	Added in one portion	0.7	0
8	54.6	44.6	0.8	1 : 2.6	Added in one portion	0.62	0.86		27.8	128	0.400	0.62	0.86***

* Composition of monomer mixture, wt %: ST 35.0, BA 52.4, GMA 1.0, MAA 6.4, and HEMA 5.2; weight ratio of monomers loaded in the first and second stages 1.0 : 1.8; initiator $K_2S_2O_8$; emulsifier sodium (C_{14}–C_{16})-alkylsulfonate.

** Emulsifier was added in portions during the process.

*** The whole amount of the emulsifier was added after the completion of the first stage.

Table 2. Characteristics of functionalized latexes and films thereof (film formation temperature 50°C)

Copolymer no.	Latex characteristics				Film characteristics, wt %		
	content, wt %		particle diameter, nm	pH	gel fraction content	degree of gel swelling	water absorption
	dry residue	coagulum					
1	28.8	0.70	87	2.55	0	–	11.2
2	32.5	0.65	92	2.50	41.1	5060	4.9
3	31.9	0.75	–	2.50	46.6	5300	9.5
4	40.2	0.95	118	2.59	41.3	7500	20.6
5	44.4	0.32	130	–	0	–	15
6	45.5	0.18	149	2.40	43.2	4120	12
7	48.5	2.3	192	–	56.9	2300	6.3
8	45.3	1.1	142	2.60	53.0	4400	6.0

Table 3 shows some mechanical properties of the films that exhibit the lowest water absorption (copolymer nos. 2, 8). It is seen that the film strength increases at high gel fraction content. However, films prepared from latex no. 2 are preferable. Although these films are less strong in the initial state as compared with those prepared from copolymer no. 8, their strength in the wet state decreases by no more than 15%, whereas the strength of the films prepared from latex no. 8 decreases almost by half after keeping in water for 24 h. Thus, films from copolymer no. 2 are more water-resistant. This may be due to better coalescence of the particles in the course of film formation from latex no. 2 owing to higher surface energy, since the diameter of particles of latex no. 2 is considerably smaller than that of latex no. 8 (Table 2).

Table 3. Mechanical properties of films and coatings formed from latexes with particles containing both types of functional groups in the shell (temperature of film and coating formation 50°C)

Copolymer no.	Ultimate tensile strength, MPa	Relative elongation at break, %	Adhesion strength, kN m^{-1}	Relative hardness
2	12.0* / 10.3	235 / 258	0.16	0.688
8	17.6 / 9.2	230 / 450	0.20	0.644

* (Numerator) initial state; (denominator) after keeping in water for 24 h.

Table 4. Conditions of synthesis of epoxide- and carboxyl-containing latexes. Initiator $K_2S_2O_8$ (0.4 wt % based on monomers); emulsifier OS-20 (1.5 wt % based on core polymer); core ST–BA copolymer (40 : 60 by weight); core : shell weight ratio 1 : 3; copolymerization temperature 65°C in both stages

Copolymer no.	Composition of monomeric mixture for shell, wt %						Rate of adding monomers, % min^{-1}
	ST	BA	GMA	MAA	HEMA	TDM*	
9	35	47	10	–	8	–	0.383
10	35	47	10	–	8	0.010	0.387
11	35	47	10	–	8	0.028	0.372
12	39	51	10	–	–	0.038	0.357
13	38	55	–	7	–	–	0.346
14	35	50	–	7	8	–	0.391

* Tertiary dodecyl mercaptan.

Table 5. Characteristics of epoxide- and carboxyl-containing latexes and films thereof (film formation temperature 50°C)

Copolymer no.	Latex characteristics			Film characteristics, wt %		
	dry residue, wt %	particle diameter, nm	pH	gel fraction content	degree of swelling of the gel	water absorption
9	24.1	510	2.40	84.7	1500	3.6
10	20.5	450	2.45	82.4	2000	4.6
11	22.0	540	2.35	68.3	1900	4.6
12	15.3	500	2.28	83.1	1700	27.3
13	17.6	510	–	0	–	45.2
14	23.0	570	2.10	0	–	22.2

Additional heat treatment of films at 125°C for 1 h increases the gel fraction content and decreases the water absorption. However, the effect is not significant. The water absorption of films prepared from latex no. 2 decreases from 4.9 to 4.0%.

Systems of type II are mixtures of epoxide- and carboxyl-containing latexes. When preparing the initial latexes, we also used the principles of seeding copolymerization and preparation of core–shell particles with incorporation of reactive functional groups in the shell copolymer only. The core copolymer was prepared by addition of an ST–BA monomer mixture (40 : 60 by weight) in a single portion to the aqueous phase containing OS-20 nonionic surfactant, followed by polymerization in the presence of $K_2S_2O_8$ at 65°C.

The shell was prepared by a semicontinuous process. To the latex of the core copolymer, we gradually added a monomer mixture containing the functional monomer. No additional amounts of the surfactant were introduced, which favored formation of the functionalized copolymer only in the shell. The conditions of latex syntheses are listed in Table 4.

Some characteristics of functionalized latexes and films thereof are listed in Table 5. It is seen that, owing to the relatively high GMA concentration, the initial epoxide-containing copolymers contain the gel fraction despite the presence in the reaction system of a small amount of the chain-terminating agent TDM. It should be noted that in most cases the gel fraction content is above 75%, which suggests that the core copolymer is partially involved in cross-linking, probably through formation of semiinterpenetrating networks. Films prepared from epoxide-containing copolymers have low water absorption, except copolymer no. 12 containing no HEMA units. Thus, HEMA introduced into the copolymer formulation improves the particle coalescence. This conclusion also refers to carboxyl-containing copolymers (nos. 13, 14).

In Fig. 1, the water absorption of films prepared from various latex mixtures is plotted vs. the content of the epoxy component. It is seen that the water absorption in these systems is not an additive quantity, which suggests interaction of the epoxide- and carboxyl-containing particles. A mixture of latex nos. 12 and 14 (curve *2*) at 50°C forms films with water absorption several times lower than that of the films formed from the individual latexes. It should be noted also that films with sufficiently low water absorption can only be formed in the case when at least one of the latex copolymers contains HEMA units (curve *2*). Otherwise, the formed films have very high water absorption (curve *1*). However, it is advisable that

HEMA units be present in both copolymers. In this case, it is possible to prepare films with low water absorption (about 4%) in a wide range of latex mixture compositions (curve *5*), including mixtures containing small amounts of the epoxide-containing copolymer at a total HEMA content of about 1 wt %.

These results suggest that the epoxy groups are the most efficient in cross-linking in systems with low content of the epoxide-containing copolymer. If the cross-linking efficiency is evaluated as the increase in the gel fraction content relative to the gel content in the initial epoxide-containing copolymer, we see that, indeed, the cross-linking efficiency increases as the content of the epoxide-containing copolymer in the latex mixture decreases (Fig. 2, curve *2*). As for the total gel fraction content in the compound film, it grows with increasing content of the epoxide-containing copolymer, although the water absorption of the films decreases to a lesser extent. This fact is consistent with the concept that the water absorption is determined to a larger extent by the cross-linking efficiency, i.e., by the number of interglobular bonds.

Despite the low water absorption of some compound films, their strength in the wet state is insufficient, which indicates insufficient interpenetration of the particles and poor monolithization of the film. However, on baking at 125°C for 2.5 h, the film strength sharply increases, and it becomes possible to form water-resistant coatings of high quality.

Systems of type III were prepared as follows. In the first stage, we formed the core of a latex particle containing epoxy groups. In the second stage, we added to the resulting seeding latex the monomer mixture ST–BA–HEMA–MAA at a rate of 0.620 % min^{-1}, with the initiator and emulsifier solutions added simultaneously. The conditions of latex synthesis are listed in Table 6.

As seen from Table 6, the formulations of latex nos. 15 and 16 are close. The main difference consists in the procedure for preparing the core copolymer. Whereas latex no. 15 was prepared with addition of the monomers in a single portion, in synthesizing latex no. 16 the monomer mixture was added gradually at a rate of 3.3 % min^{-1}. As already noted, in the first case, the epoxy groups undergo hydrolysis to a lesser extent, which results in better mechanical properties of the films prepared from latex no. 15 (Table 7).

The formed films exhibit fairly high water absorption, determined by the properties of the shell copolymers whose content in the composite particle is as high as 86.8 wt %. The shell copolymers are similar in composition and water absorption to carboxyl-containing copolymers used in mixed latex systems

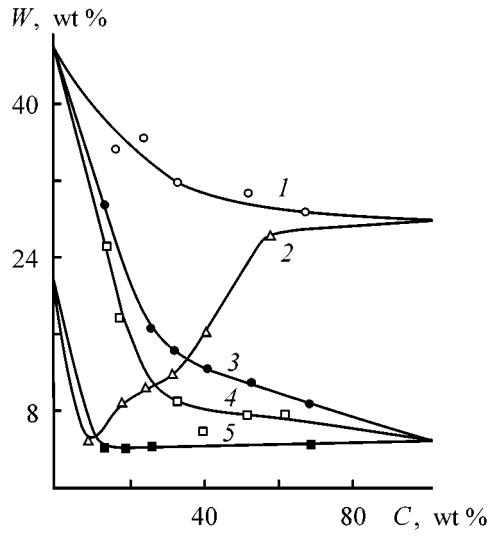

Fig. 1. Water absorption of latex films of system II *W* vs. the content of epoxide-containing copolymer in the latex mixture *C* (in terms of dry matter). Film formation temperature 50°C; the same for Fig. 2. Latex mixtures: (*1*) no. 12 + no. 13, (*2*) no. 12 + no. 14, (*3*) no. 9 + no. 14, (*4*) no. 10 + no. 13, and (*5*) no. 11 + no. 14.

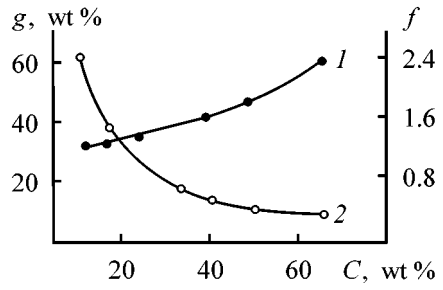

Fig. 2. (*1*) Gel fraction content *g* and (*2*) cross-linking efficiency *f* in films prepared from a mixture of latex nos. 11 and 14 vs. the content of the epoxide-containing copolymer in the latex mixture *C* (in terms of dry matter).

of type II (Tables 5, 7). The gel fraction content is low as compared with systems of type I and II, which may be due to an insufficient mobility of the functional groups fixed in different areas of the composite particle. The cross-linking efficiency can be improved by increasing the shell permeability, which, in turn, can be achieved by neutralization of carboxy groups with ammonia; simultaneously ammonia acts as cross-linking catalyst. However, formation of a very thick gel in this case apparently decreases the probability of formation of interglobular cross-links, which results in lower strength of the film and higher water absorption (Table 7). Thus, neutralization of carboxy groups in this system is not advisable.

Table 6. Preparation conditions and some characteristics of latex systems of type III [molar ratio core : shell 1 : 6.6; polymerization temperature in both stages 70°C; initiator $K_2S_2O_8$; emulsifier sodium (C_{14}–C_{16})-alkylsulfonate]

Copolymer no.	Composition of monomer mixture, wt %						Content, wt %		Latex characteristics		
	core*			shell**			initiator	emulsifier	dry residue, wt %	particle diameter, nm	Surface tension, mN m^{-1}
	ST	BA	HEMA	ST	BA	HEMA					
15	35.0	52.0	8.0	33.1	51.9	8.0	1.07	1.02	42.7	202	48.9*** 43.8
16	35.1	51.7	8.2	31.0	53.9	8.1	1.21	0.405	42.8	261	51.2 –

* Content of GMA in the core 5.0 wt %.
** Content of MAA in the core 7.0 wt %.
*** (Numerator) before neutralization; (denominator) after neutralization.

Table 7. Physicomechanical properties of films formed from latex systems of type III at room temperature

Copolymer no.	Ammonia content, g-equiv g-equiv^{-1} MAA	Ultimate tensile strength, MPa	Relative elongation at break, %	Gel fraction content	Degree of gel swelling	Water absorption
				wt %		
15	0	22.8* 10.8	210 290	48.1	3300	21.3
	1	22.2 5.8	175 285	60.0	2340	27.1
16	0	21.2 8.0	240 420	34.5	3590	21.6
	1	20.7 2.7	230 310	52.1	2340	32.3

* (Numerator) film in the initial state; (denominator) film kept in water for 24 h.

Despite the relatively high water absorption of the films, they can be regarded as fairly water-resistant, insofar as the strength of the wet films remains high, and in the case of the best sample (no. 15) it is even higher than that of films formed from latexes of type I (Table 3). The major advantage of latexes of type III is the feasibility of preparing from them films and coatings at room temperature.

To conclude, the properties of the materials obtained, mainly studied with free films, show that the synthesized latexes can be used for preparing sufficiently elastic coatings with adhesion strength [measured according to GOST (State Standard) 15140–78] within 0.20–0.50 kN m^{-1} and relative hardness (M-3 testing pendulum) of about 0.7. The temperature conditions of film formation determine the application fields of the latexes. Latexes of type III, forming a film at room temperature, can be recommended for fabrication of water-resistant water-dispersible paints. As for latexes of type I, it is appropriate to use them in the final stages of leather finishing, which can be performed at 50–60°C. Latex systems of type II can be used in special coatings when temperatures of 125°C are admissible in the process.

CONCLUSIONS

(1) Procedures were developed for preparing three types of latex systems capable of forming cross-linking water-resistant films: type I, latexes with core–shell particles with the shell formed from the random copolymer styrene–*n*-butyl acrylate–2-hydroxyethyl methacrylate–methacrylic acid–glycidyl methacrylate; type II, mixtures of latexes with the particle shell of the first latex formed from the styrene–*n*-butyl acrylate–2-hydroxyethyl methacrylate–glycidyl methacrylate copolymer, and the particle shell of the second latex, from the styrene–*n*-butyl acrylate–2-hydroxyethyl methacrylate–methacrylic acid copolymer; type III, la-

texes with core–shell particles with the core formed from the styrene–*n*-butyl acrylate–2-hydroxyethyl methacrylate–glycidyl methacrylate copolymer, and the shell, from the styrene–*n*-butyl acrylate–2-hydroxyethyl methacrylate–methacrylic acid copolymer.

(2) A study of the properties of the synthesized latexes and films thereof showed that each of the developed types of latex systems can be used to prepare cross-linked water-resistant films and coatings retaining sufficiently high mechanical strength in the wet state.

(3) Conditions of formation of water-resistant films depend on the type of the latex systems. Systems of type III allow preparation of water-resistant films at room temperature; formation of films from latexes of type I is possible at temperatures ≥50°C; and latex systems of type II form water-resistant films only after additional heat treatment at 125°C.

ACKNOWLEDGMENTS

The authors are grateful to Neste Chemical Oy company for financial support.

REFERENCES

1. Pavlyuchenko, V.N., Byrdina, N.A., and Ivanchev, S.S., Abstracts of Papers, *Int. Symp. "Polymers at the Phase Boundary,"* Lviv, October 25–29, 1994, p. 32.
2. Berezin, I.V., Martinek, K., and Yatsimirskii, A.K., *Usp. Khim.*, 1973, vol. 42, no. 10, pp. 1730–1736.
3. Vaculik, P., *Chemie Monomerů*, Prague: Československ. Akad. Ved, 1956, vol. 1.
4. *Entsiklopediya polimerov*, Moscow: Sov. Entsiklopediya, 1974, vol. 2, p. 180.
5. Geurts, J.M., Gottgens, C.M., Es, J.J.G.S. van, and German, A.L., Abstracts of Papers, *Int. Symp. "Free Radical Polymerization: Kinetics and Mechanism,"* Santa Margherita (Italy), May 26–31, 1996, pp. 221–223.

Russian Journal of Applied Chemistry, Vol. 74, No. 2, 2001, pp. 316–324. Translated from Zhurnal Prikladnoi Khimii, Vol. 74, No. 2, 2001, pp. 311–319.

MACROMOLECULAR CHEMISTRY AND POLYMERIC MATERIALS

Redox Activity of Poly-[PdSalpn-1,2] as Influenced by Thickness of Its Film and Composition of Supporting Electrolyte

L. P. Ardasheva and G. A. Shagisultanova

Herzen State Pedagogical University, St. Petersburg, Russia

Received February 29, 2000

Abstract—The electron transfer rate in the bulk of a [PdSalpn-1,2] polymeric film was studied as influenced by its thickness and the composition of the supporting electrolyte.

Procedures for preparing metal-containing polymeric films have been under development recently. Previously, brightly colored electrochromic heteronuclear and heteroligand Pd(II) complexes with bis(salicylidene)-1,2-propylenediamine ([PdSalpn-1,2]), bis(salicylidene)-1,3-propylenediamine ([PdSalpn-1,3]), and bis-(salicylidene)-*o*-phenylenediamine ([PdSalphen]) have been prepared by electrochemical oxidative polymerization [1–5] and their physicochemical properties (among which the most important are the electrical conductivity and photosensitivity) have been studied.

It should be noted that the properties of these polymers can be studied both in solutions of supporting electrolyte and in the solid state. Further study of the systems in question will give semiconductor characteristics of substances belongind to this class.

In this work the rate of electro-stimulated charge transfer in the polymers immersed in a solution of supporting electrolyte was studied as influenced by its composition and properties. In this case we deal with a system of three interrelated components: electrode, polymeric complexes immobilized on the electrode, and supporting electrolyte. A change in the properties of each component affects the properties of the whole system.

It is known that redox transformations of polymeric systems prepared by oxidative polymerization are accompanied by migration of anions of the supporting electrolyte inside and outside the polymeric matrix to maintain its electroneutrality. Such an overall process and the ions providing electroneutrality of the polymer are commonly termed [6] doping and dopants, respectively.

Levi *et al.* [7] found that the molecular structure of electron-conducting organic polymers is labile and may undergo conformational transformations caused by doping, swelling, and mechanical or electrochemical interactions of counterions and electrical charges of the polymeric chains. These transformations change the redox activity of the polymers.

The influence of various factors on the redox activity of organic polymers has been extensively studied [7–14]. However, polymeric metal complexes have not been investigated in this regard.

In this work, we studied the rate of electron diffusion in the bulk of the polymer as influenced by external factors (nature of the counterion and solvent and the concentration of the supporting electrolyte) and the thickness of the polymeric layer, one of the most important parameters of the polymer.

EXPERIMENTAL

Poly-[PdSalpn-1,2] was prepared by the procedure described in [15]. The polymer was identified by electronic absorption spectroscopy and X-ray photoelectron spectroscopy [16, 17]. The electrochemical experiments were performed in a three-electrode cell with separated compartments of the working, auxiliary, and reference electrodes.

A 0.1 M solution of tetrabutylammonium perchlorate (Bu_4NClO_4) in acetonitrile, deaerated with high-purity argon, was used as the supporting electrolyte. Acetonitrile (AN) was purified by the procedure described in [18]. To study the dependence of the redox conductivity of the polymer on the counterion

1070-4272/01/7402-0316 $25.00 © 2001 MAIK "Nauka/Interperiodica"

size, 0.1 M solutions of $Bu_4N[BF_4]$, Bu_4NF, and $Bu_4N[CF_3COO]$ in acetonitrile and dichloromethane were used. Dichloromethane (DCM), propylene carbonate (PC), and dimethylformamide (DMF) were purified as in [18].

As working electrode served platinum wire (99.99% Pt, 0.25 cm^2 surface area) sealed in glass. As auxiliary electrode was used a platinum gauze. All potentials were measured relative to a silver/silver chloride electrode filled with a saturated solution of sodium chloride.

Poly-[PdSalpn-1,2] was prepared under potentiostatic conditions by applying a 1.1 V potential to a 0.001 M solution of the monomer for a prescribed time.

Cyclochronovoltammograms (CCVA) recorded by sweeping the potential of an electrode coated with a film of poly-[PdSalpn-1,2] in a pure supporting electrolyte are shown in Fig. 1. These potentiodynamic curves indicate the occurrence of reversible redox processes in the solid phase of the polymeric film. Thus, the polymer exhibits electrical conductivity.

However, as seen from Fig. 1, the voltammograms of the polymer are bell-shaped and asymmetric relative to the abscissa axis. Levi *et al.* [7] believe that the broadening of the voltammetric peaks with respect to the theoretical peaks is due to repulsion of like-charged units of the polymeric chain, structural nonuniformity (alternation of amorphous and crystalline regions and cross-linking of the polymeric chains), and penetration of ions present in the solution and solvent molecules into the polymeric matrix.

The electrical conductivity in similar polymeric systems is provided by successive reactions of electron transfer from structural fragments, whose oxidation state is similar to that of the monomer, to the oxidized fragments of the polymeric chain through the polyconjugated system. This type of conductivity is designated redox conductivity and the systems of this kind, redoxactive systems.

There are two type of redox processes occurring in a conducting film at different potential sweep rates [7]. The first of these is the adsorption process which occurs via successive events of electron exchange between all units of the polymeric chain. This process occurs in relatively thin layers and is characterized by proportionality between the current and the potential sweep rate. The second is the diffusion process characterized by linear dependence between the peak currents of CCVA and the square root of the sweep rate. The occurrence of the diffusion process indicates that

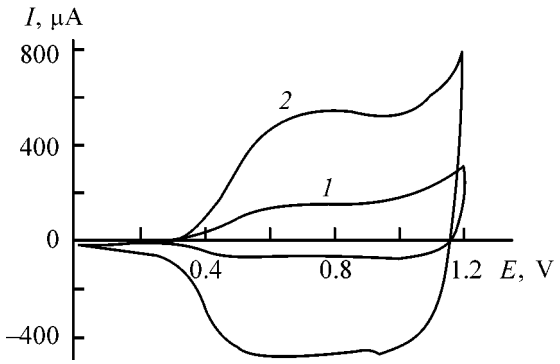

Fig. 1. Cyclochronovoltammograms of solid-phase redox processes in poly-[PdSalpn-1,2] at potential sweep rate of (*1*) 20 and (*2*) 100 mV s^{-1}. The time of polymer accumulation τ_a is 7 min; the accumulation potential E_a = 1.1 V; CH_3CN; TBAP. (*I*) current, (*E*) potential; the same for Figs. 3–5.

the rate determining step of the redox process is the ion transport (diffusion or migration) in the solution or(and) in the film. In this case, the rate of electron transfer in the bulk of the polymer between redox fragments of the polymeric chain is assumed to be considerably higher than that of ions in the electrolyte in which the polymer is immersed. If the porosity of the film is sufficiently high, i.e., there is larger polymer-free space inside the system, the deceleration of the ion transfer may be due either to interactions with cross-links in the macromolecule or to properties of the solvent and supporting electrolyte present in the pores.

Taking into account the fact that the propagation of an oxidation wave in a film is formally identical to diffusion of ions in a solution, the electron transfer rate can be characterized by the coefficient of electron diffusion along a polymeric chain D_{ct}. Thus, the electrical conductivity of a system is determined under the given conditions by the electron diffusion coefficient and depends on the properties of the medium and polymer, in particular, on the polymer thickness.

The electron diffusion coefficient D_{ct} was calculated by the Randles–Shevchik equation [19]. The peak currents were determined at the potential sweep rate $V_s \geq 100$ mV s^{-1}.

The thickness of the polymeric films was calculated from the quantity of electricity spent for complete reduction of the polymer, which, in its turn, was found by integrating cyclochronovoltammograms recorded at slow potential sweep rates (≤10 mV s^{-1}) [19]. Relatively stable polymeric films more than 2 μm thick were prepared in the course of a kinetic study of the polymer formation in acetonitrile. The time dependences of the thickness of poly-[PdSalpn-1,2] formed in di-

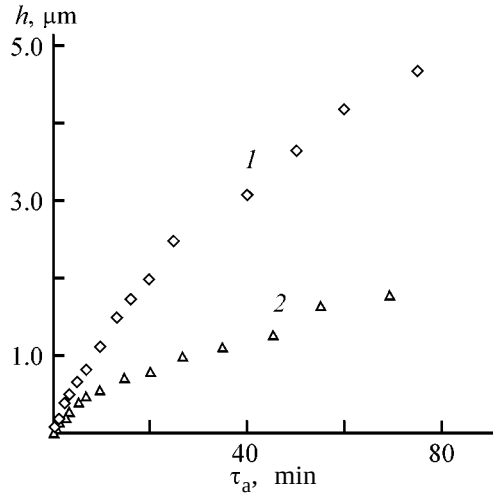

Fig. 2. Thickness of poly-[PdSalpn-1,2] film h grown in (*1*) CH_3CN and (*2*) CH_2Cl_2 vs. accumulation time τ_a. E_a = 1.1 V, TBAP.

chloromethane and acetonitrile at the optimal accumulation potential (1.1 V) are shown in Fig. 2.

It is known [19] that the diffusion coefficient D_{ct} in polymeric films may vary from 10^{-8} to 10^{-12} $cm^2\ s^{-1}$, i.e., in a wider range as compared with liquid solutions. This is due to the fact that the rate of electron transfer in a film is restricted by deformation of polymeric chains, long distances between electrochemically active fragments, diffusion of counterions from the solution, electron transfer between the oxidized and neutral fragments of the macromolecule, etc.

We studied the influence of the concentration of the supporting electrolyte on the redox activity of poly-[PdSalpn-1,2] prepared in acetonitrile at accumulation potential E_a = 1.1 V and accumulation time τ_a = 5, 10, and 20 min. A freshly prepared polymeric film was used in each experiment. As supporting electrolyte served 0.1 M tetrabutylammonium perchlorate (TBAP).

The shape of the potentiodynamic curves does not change with the Bu_4NClO_4 concentration increasing from 0.1 to 2 M. The electron diffusion coefficient along the polymeric chain also remains constant within the limits of experimental error. Thus, the redox activity of the polymer is not affected by the concentration of counterions. Apparently, the initial concentration of counterions in solution is sufficient to compensate the positive charges formed in polymer oxidation. An increase in the concentration of the supporting electrolyte has no effect on the formation and subsequent stabilization of new electrochemically active centers.

However, the diffusion coefficient D_{ct} decreases by 5–10, 10–20, 20–30, and 30–40% with the TBAP concentration in the solution decreasing to 0.08, 0.04, 0.02, and 0.01 M, respectively. The thicker the polymeric film, the stronger the decrease in D_{ct}. It should be noted that D_{ct} returned to the initial value when cyclochronovoltammograms of poly-[PdSalpn-1,2] prepared at low concentrations of the supporting electrolyte were recorded in solutions with the initial concentration of the counterions (0.1 M), used in the synthesis. Clearly, at a deficiency of counterions in solution, the probability of stabilization of all positively charged fragments formed in the polymeric chain decreases, and hence, the electron transfer in the polymer is decelerated.

The gap between the maxima of the anodic and cathodic peaks in the cyclochronovoltammograms (V_s = 100 mV s^{-1}) increases simultaneously with the decrease in D_{ct}. This difference is the most pronounced at [TBAP] = 0.01 and 0.02 M. Thus, it may be assumed that the considerable difference between in the potentials of the anodic and cathodic peaks at relatively fast potential sweep is due to kinetic restrictions. The diffusion of counterions to positively charged fragments of the polymeric chain is decelerated owing to insufficient concentration of ionic components of the solution in the polymeric matrix.

We also studied the influence exerted by BF_4^-, CF_3COO^-, and F^- ions on the redox activity of poly-[PdSalpn-1,2].

In each experiment we used a freshly prepared polymeric film. Acetonitrile solutions of Bu_4NClO_4, $Bu_4N[BF_4]$, $Bu_4N[CF_3COO]$, and Bu_4F were used as supporting electrolytes. Cyclochronovoltammograms of poly-[PdSalpn-1,2] prepared at E_a = 1.1 were recorded in (1) pure Bu_4NClO_4 solution, (2) a solution containing electrolyte ions whose influence is analyzed, and (3) pure Bu_4NClO_4 solution again. Simultaneously, the stability of poly-[PdSalpn-1,2] in supporting electrolyte containing the ions in question was studied. The results are presented in Table 1.

As seen from Table 1, the redox activities of the polymer in solutions containing ClO_4^- and BF_4^- anions are almost the same. This is clearly due to the fact that the crystallographic radii of these anions are similar [$r(ClO_4^-)$ = 0.236, $r(BF_4^-)$ = 0.232 nm] [20] and the dopant anion is known [13] to be incorporated in the polymer without solvation shell. However, it should be noted that the amount of the redox-active polymer decreases by 30% when the potential is continuously swept at a rate of 50 mV s^{-1} for 30 min in a solution containing BF_4^- anions, whereas its activity remains the same under similar conditions in the presence of ClO_4^- anions. Hence, the electrochemical inter-

Table 1. Influence of the nature of counterion on the electron diffusion coefficient in the bulk of poly-[PdSalpn-1,2] film of varied thickness (synthesis AN + TBAP)

Run no.	h, μm	D_{ct}, $cm^2\ s^{-1}$	h, μm	D_{ct}, $cm^2\ s^{-1}$	h, μm	D_{ct}, $cm^2\ s^{-1}$
		ClO_4^-		BF_4^-		ClO_4^-
1	0.7	1.1×10^{-10}	0.5	1.1×10^{-10}	0.6	8.3×10^{-11}
2	1.7	5.6×10^{-10}	1.6	6.0×10^{-10}	1.7	5.2×10^{-10}
3	2.6	1.2×10^{-9}	2.6	1.2×10^{-9}	2.6	1.2×10^{-10}
		ClO_4^-		CF_3COO^-		ClO_4^-
4	0.6	8.8×10^{-11}	0.2	4.7×10^{-11}	0.3	1.9×10^{-11}
5	1.7	5.9×10^{-10}	1.0	4.4×10^{-10}	1.3	3.7×10^{-10}
6	2.1	1.1×10^{-9}	1.5	8.4×10^{-10}	1.9	8.0×10^{-10}
		ClO_4^-		F^-		ClO_4^-
7	0.7	1.4×10^{-10}	0.2	5.1×10^{-11}	0.1	6.5×10^{-13}
8	1.9	8.0×10^{-10}	0.35	4.1×10^{-10}	0.6	9.5×10^{-12}
9	2.6	1.3×10^{-9}	0.38	3.2×10^{-10}	0.6	4.6×10^{-12}

action of BF_4^- with an oxidized fragment of the polymer is stronger as compared with that of ClO_4^- and higher energy is required for rupture of these bonds and passage of tetrafluoroborate anion in the solution. Thus, we suggest that some BF_4^- anions remain bound to monomeric units of the polymer and are not involved in the redox process.

A decrease in the redox activity of the polymer and in the diffusion coefficient D_{ct} was observed in cyclochronovoltammograms recorded in a solution containing CF_3COO^- ions. This confirms the assumption that a large counterion causes kinetic hindrances. Clearly, when anion is larger than that used in polymer preparation, there are steric hindrances to penetration of this anion to the space between the aromatic rings. Hence, stabilization of positive charge induced by oxidation is complicated in this case. Nevertheless the D_{ct} in a polymer placed in a solution containing perchlorate anions remains equal to that calculated for a trifuoroacetate solution and does not return to the initial value. A special study of the influence of the potential sweeping on the stability of the polymeric film in a solution containing CF_3COO^- anions showed that the redox activity almost completely disappeared after 15-min potential sweep at a rate of 50 $mV\ s^{-1}$.

A study of the influence of the F^- anion showed that after a film is again placed in a Bu_4NClO_4 solution the redox activity of the polymer does not reach the initial value, but, quite the reverse, decreases. Probably, in this case the role of counterions is played by solvated F^- anions [9]. They are not desolvated, presumable because of the higher energy of solvation as compared with the energy of interaction of the ion with a unit of the polymeric chain. This is typical of small ions with large solvation shell. Thus, the large solvation shell prevents free penetration of the counterion into the cavities of the polymeric membrane and causes irreversible changes in the polymeric structure, inducing its degradation.

The above experimental data mainly refer to the influence exerted by the nature of the supporting electrolyte on D_{ct}. However, we also observed the influence of the nature of the supporting electrolyte on the shape and parameters of the voltammograms. In going from ClO_4^- to BF_4^- and back, the shape of cyclochronovoltammograms does not change at potential sweep rates of both 10 and 100 $mV\ s^{-1}$. The redox processes remain reversible. By contast, in going from ClO_4^- to CF_3COO^-, the shape of the cyclochrono-

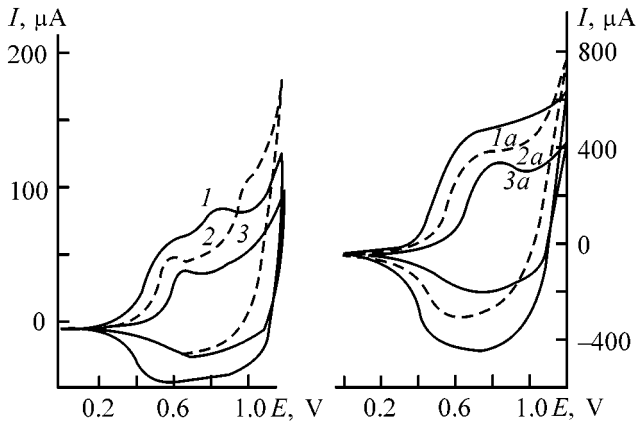

Fig. 3. Cyclochronovoltammograms of solid-phase redox processes in poly-[PdSalpn-1,2] at potential sweep rate of (*1–3*) 10 and (*1a–3a*) 100 $mV\ s^{-1}$ (the same for Fig. 4) in solutions containing (*1, 1a, 3, 3a*) ClO_4^- and (*2, 2a*) CF_3COO^- anions. τ_a = 3 min, E_a = 1.1 V, h = 0.58 μm, CH_3CN.

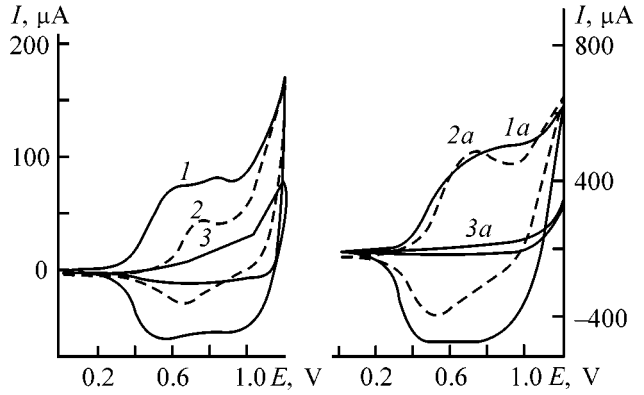

Fig. 4. Cyclochronovoltammograms of solid-phase redox processes in poly-[PdSalpn-1,2] in solutions containing (*1, 1a, 3, 3a*) ClO_4^- and (*2, 2a*) F^- anions. τ_a = 3 min, E_a = 1.1 V, h = 0.68 μm, CH_3CN.

voltammograms changes at both potential sweep rates (Fig. 3, curves *2*, *2a*). The voltammogram takes the initial shape after the polymeric system is again placed in the initial solution containing ClO_4^- anions (Fig. 3, curves *3*, *3a*). The shapes of cyclochronovoltammograms recorded in a fluoride solution at both slow and fast potential sweep rates strongly differ from that recorded in a perchlorate solution (Fig. 4, curves *2*, *2a*) and does not return to the initial state when the voltammogram is again recorded in a perchlorate solution (Fig. 4, curves *3*, *3a*).

Clearly, the total charge of the system must change in oxidation, i.e., upon appearance of positively charged sections of the polymeric chain. However, the oxidized polymer remains electroneutral owing to the compensation of the positive charge by counterions. There are two mechanisms of the compensation [7].

The cationic mechanism involves separation of the cations (C^+) of the supporting electrolyte whose molecules are partially located in the immediate vicinity of the polymer phase:

$$\{P, (C^+A^-)_m\} \rightarrow \{P^+, A^-, (C^+A^-)_{m-1}\} + C^+ + e.$$

In the case of the anionic mechanism, the charge is compensated by addition of anions of the supporting electrolyte contained in pores of the polymeric matrix:

$$\{P, (C^+A^-)_m\} + X^- \rightarrow \{P^+, X^-, (C^+A^-)_m\} + e.$$

The charge compensation by two different mechanisms results in different mechanisms of polymer functioning in solutions of different supporting electrolytes. Hence, the change in the shape of the voltammograms recorded in solutions containing CF_3COO^- and F^- anions can be accounted for using both the mechanisms. As seen from Figs. 3 and 4, the more positive current peak disappears and a pronounced peak with lower potential appears in the cathodic region of these cyclochronovoltammorgams. Migration of CH_3COO^- and solvated F^- anions in polymer pores must be sterically hindered, since their radii are greater than that of ClO_4^- in whose solution the polymer is prepared. Hence, the positive charge of the oxidized polymer must be compensated by the cationic, and not anionic mechanism. However, we suggest that the number of cations of the supporting electrolyte located in the immediate vicinity of the polymer phase is considerably smaller than that of the anions having smaller size. Hence, the number of charges of the polymeric chain compensated by the cationic mechanism is considerably smaller than that compensated by the anionic mechanism. This assumption is experimentally confirmed by the fact that current peaks corresponding to the cationic mechanism (less positive potential in the cathodic portion of the cyclochronovoltammograms) is smaller than those corresponding to the anionic mechanism of the charge compensation (more positive potential of the current peak). Thus, this explains the fast loss of the redox activity of the polymer is potential sweeping in solutions containing anions larger than those used in the synthesis. The electrical conductivity of the substance on the electrode sharply decreases because of the steric hindrances to charge compensation by the anions contained in the solution and irreversible compensation by cations fixed in the polymeric matrix.

The peak with the most positive potential is also present in the voltammograms recorded in solutions containing perchlorate and tetrafluoroborate anions. However, it is weak and overlaps with the stronger peaks located in the more positive region. There is no hindrance to migration of ClO_4^- and BF_4^- anions in pores of the polymeric matrix since their radii are almost identical and the polymeric film was prepared from a solution containing ClO_4^- anions. Hence, in this case the charge is compensated mainly by the anionic mechanism. However, the cationic mechanism is also possible. This is confirmed by the presence of current peaks at less positive potentials in the cathodic region of the cyclochronovoltammorgams.

The solvent plays an important role in the transfer of counterions in the solution and pores of the polymeric membrane. To study the influence of the solvent nature on the redox conductivity of the polymer, we calculated the electron diffusion coefficient along

Table 2. Influence of the solvent nature on the electron diffusion coefficient in poly-[PdSalpn-1,2] films of varied thickness

Run no.	h, μm	D_{ct}, $cm^2\ s^{-1}$	h, μm	D_{ct}, $cm^2\ s^{-1}$	h, μm	D_{ct}, $cm^2\ s^{-1}$	h, μm	D_{ct}, $cm^2\ s^{-1}$	h, μm	D_{ct}, $cm^2\ s^{-1}$	h, μm	D_{ct}, $cm^2\ s^{-1}$
	Synthesis in AN + TBAP						Synthesis in DCM + TBAP					
	AN		PC		AN		DCM		DMF		DCM	
1	0.6	1.1×10^{-10}	0.3	7.9×10^{-11}	0.4	3.1×10^{-11}	0.4	4.3×10^{-11}	0.06	1.7×10^{-11}	*	–
2	1.9	7.5×10^{-10}	0.9	3.4×10^{-10}	1.2	2.0×10^{-10}	0.9	1.5×10^{-10}	0.1	2.8×10^{-11}	*	–
3	2.7	1.7×10^{-9}	1.4	3.5×10^{-10}	1.5	1.9×10^{-10}	1.1	1.5×10^{-9}	0.2	9.0×10^{-11}	0.1	4.3×10^{-13}
	AN		DMF		AN		DCM		PC		DCM	
4	0.8	1.8×10^{-10}	0.3	6.2×10^{-11}	0.3	2.9×10^{-12}	0.4	3.7×10^{-11}	0.15	2.0×10^{-11}	0.1	3.0×10^{-12}
5	1.7	5.7×10^{-10}	0.4	2.3×10^{-10}	0.5	1.0×10^{-11}	0.8	1.2×10^{-10}	0.4	7.9×10^{-11}	0.3	1.1×10^{-11}
6	2.6	1.2×10^{-9}	0.9	5.8×10^{-10}	1.3	8.8×10^{-11}	1.2	1.9×10^{-10}	0.7	2.0×10^{-10}	0.6	3.5×10^{-11}
	AN		DCM		AN		DCM		AN		DCM	
7	0.8	1.4×10^{-10}	0.8	7.9×10^{-11}	0.8	1.5×10^{-10}	0.4	3.7×10^{-11}	0.35	3.9×10^{-11}	0.3	3.3×10^{-11}
8	1.9	7.1×10^{-10}	1.8	2.7×10^{-10}	1.9	6.7×10^{-10}	0.8	1.0×10^{-10}	0.9	1.6×10^{-10}	0.8	1.1×10^{-10}
9	3.1	1.9×10^{-9}	2.5	2.4×10^{-10}	3.0	1.8×10^{-9}	0.9	1.5×10^{-10}	1.1	2.2×10^{-10}	0.9	2.0×10^{-10}

* Disintegrated.

the polymeric chain in different solvents. In each experiment, a film freshly prepared from an acetonitrile solution was used. Propylene carbonate (PC), dichloromethane, and DMF were used as solvents. In all experiments, Bu_4NClO_4 served as supporting electrolyte. Cyclochronovoltammograms of poly-[PdSalpn-1,2] prepared at E_a = 1.1 V were recorded (1) in pure acetonitrile supporting electrolyte, (2) in tested solvent, and (3) again in pure acetonitrile solution. Simultaneously, the stability of the polymer in the tested solvent was studied. The results are presented in Table 2.

As seen from Table 2, dichloromethane is the most inert with respect to the polymer among the tested solvents. The calculated polymer thicknesses remain virtually unchanged. However, thick polymeric layers are oxidized and reduced incompletely in a single cycle even at a sweep rate of 10 mV s^{-1}. As a result, the calculated thickness decreases from 3.1 to 2.5 μm. Thus, at this sweep rate the electron transport in a polymer film of this thickness is controlled by diffusion. On the whole, in the case of dichloromethane solution, the diffusion coefficient decreases, especially in thick films. To maintain the macroscopic electroneutrality of the system in electron transfer in a polymer, counterions of the supporting electrolyte must diffuse into the matrix in the course of oxidation and out from the matrix in the course of reduction. Therefore, an increase in the solvent viscosity (η_{DCM} = 0.441×10^{-3} Pa s, η_{AN} = 0.341×10^{-3} Pa s) [21] makes lower the counterion mobility, thus decreasing the electrical conductivity of the material.

In dichloromethane, the potentials of anodic and cathodic peaks for thin polymeric films at fast poten-

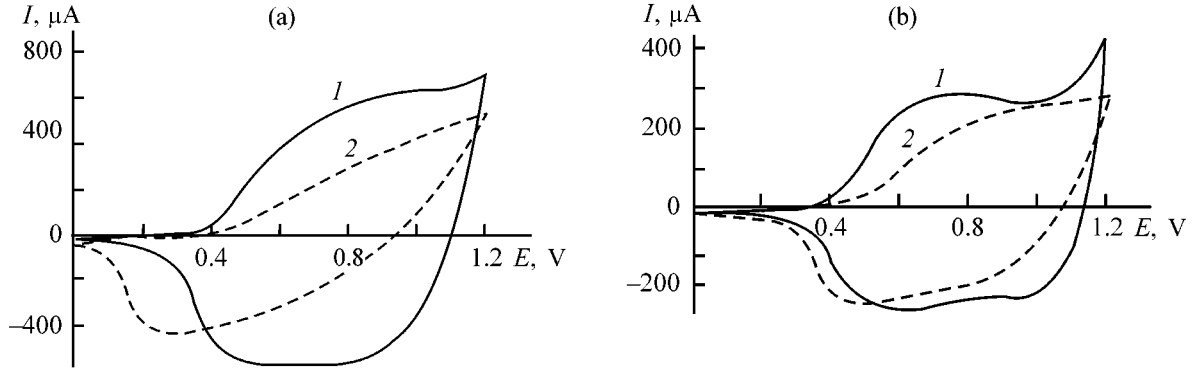

Fig. 5. Cyclochronovoltammograms of solid-phase redox processes in poly-[PdSalpn-1,2] films of thickness h (a) 0.8 and (b) 3.1 μm in TBAP in solutions of (*1*) acetonitrile and (*2*) dichloromethane at potential sweep rate V_s of (a) 100 and (b) 10 mV s^{-1}. τ_a: (a) 3 and (b) 15 min, E_a = 1.1 V.

tial sweeping and thick films at slow potential sweeping differ considerably (Figs. 5a, 5b). This may be due to kinetic hindrance to diffusion of ions of the supporting electrolyte in dichloromethane, more viscous than acetonitrile. Thus, the redox activity of the polymer is controlled by the counterion mobility.

In the case of a more viscous solvent, such as DMF ($\eta_{DMF} = 0.796 \times 10^{-3}$ Pa s) and PC ($\eta_{PC} = 2.513 \times 10^{-3}$ Pa s), the electron diffusion coefficient is lower. It should be noted that the amount of redox-active polymer on the electrode appreciably decreases after potential sweeping in PC and DMF solution and then in an acetonitrile solution ($V_s = 10$ mV s^{-1}). Thus, the polymer interacts with PC and DMF, which probably results in the swelling of the polymer and weakening of its adhesion to the electrode and bonds between the monomeric units. It should be noted that in DMF this interaction is stronger than in PC, which is possibly due to nucleophilic properties of DMF. Dimethylformamide, exhibiting more pronounced donor properties (the donor number of DMF and PC is 26.6 and 15.1, respectively) [21], interacts with positive sections of the oxidized polymeric chain and blocks their interaction with the counterions of the supporting electrolyte, thus decreasing the redox activity of the system. It should also be noted that the voltammograms of the tested polymer in DMF and PC considerably differ in shape from those recorded in acetonitrile and DCM at $V_s = 10$ and 100 mV s^{-1}.

We conclude that PC and DMF are unsuitable solvents for preparing polymers and studying their properties since they are not inert with respect to the tested polymers, decrease the redox activity of the polymers, and probably cause their physical degradation.

A study of the influence exerted by the solvent nature on D_{ct} in poly-[PdSalpn-1,2] prepared in TBAP solution in DCM at $E_a = 1.1$ V (Table 2) gave similar results.

Although the charge diffusion coefficient depends on the solvent nature, the polymer prepared in DMF exhibits a number of specific properties as compared with the polymer prepared in acetonitrile solution.

Clearly, in a solvent with low viscosity, such as acetonitrile, the electron diffusion coefficient increases negligibly and the amount of conducting polymer on the electrode does not virtually change at $V_s = 10$ mV s^{-1}. The thicker the film, the stronger the increase in D_{ct} in the polymer in acetonitrile. This is due to a strong overvoltage on the electrode coated with thick polymeric film at potential sweeping in dichloromethane, which restricts the electrical conductivity of the polymer. Strong kinetic hindrance appearing in relatively viscous solvent at fast potential sweep rates is caused by deceleration of the inward transport of counterions in the polymeric matrix. In acetonitrile this hindrance is less pronounced.

More viscous PC and DMF strongly decrease the redox activity of the polymer for the above reasons. In addition, DMF causes faster degradation of the polymer prepared from dichloromethane: the redox degradation is virtually completed in two cycles of potential sweep. Probably the films grown in dichloromethane are more friable and porous as compared with those prepared in acetonitrile. Since the difference in donor number between DCM and DMF is greater that that between acetonitrile and DMF, the displacement of charge-compensating molecules of dichloromethane by dimethylfomamide in pores of the polymeric membrane and the resulting addition of DMF molecules to the oxidized sections of the polymer prepared in DCM is faster than in the case of a polymer prepared in acetonitrile. Hence the degradation in DMF is considerably faster as compared with the case of films prepared in acetonitrile solutions.

Analysis of data presented in Table 2 confirms that the films prepared in DCM are more porous than those prepared in acetonitrile. The redox activities of the polymeric films with the same thickness in the solvent used in their preparation are virtually the same. We also found that in acetonitrile the diffusion coefficients D_{ct} for the films of similar thickness prepared in both acetonitrile and DCM are virtually the same ($D_{ct} \sim 1.6 \times 10^{-10}$ cm^2 s^{-1} at $h = 0.8$–0.9 μm). However, in DCM, the redox activity of the film prepared in acetonitrile ($D_{ct} \sim 7.2 \times 10^{-11}$ cm^2 s^{-1}) is lower than that of the films prepared in DCM [$D_{ct} \sim (1.4$–$1.6) \times 10^{-10}$ cm^2 s^{-1}] and having similar thickness ($h = 0.8$–0.9 μm). Although the redox activity of the polymer in more viscous DCM must seemingly decrease, the diffusion coefficient D_{ct} does not change. We suggest that the hindrance to diffusion of ions of the supporting electrolyte in more viscous DCM is compensated for by the larger pore space in the polymeric matrix prepared in this solvent.

Thus, the mobility of counterions depends on both the solvent viscosity and the number and size of pores in the polymeric matrix.

Acetonitrile and dichloromethane can be used as interchangeable solvents both for preparing these polymers and for studying their properties.

The dependences of the electron diffusion coefficient along the polymeric chains of poly-[PdSalpn-1,2]

films in acetonitrile and dichloromethane on their thickness h are shown in Fig. 6. The polymer was synthesized and studied in the same solvent.

As seen from Fig. 6, D_{ct} grows with increasing film thickness in the case of an acetonitrile solution. When DCM is used as the solvent, D_{ct} increases until the film thickness reaches approximately 1-μm and then decreases, tending to a constant value. The increase in the electrical conductivity of a film with its growing thickness is a somewhat surprising result. Nevertheless, this phenomenon is known for organic polymeric films.

However, no clear explanation of this phenomenon has been given. In this case, the charge diffusion front is assumed to move away from the charged centers in the bulk of the polymeric matrix rather than from the support–polymer interface [22, 23].

We offer the following explanation for this phenomenon. Thick polymeric films prepared by electrochemical polymerization are characterized by relatively high degree of cross-linking. These additional bonds facilitate electron transport in the polymeric phase. In addition, the number of structural defects (in particular, chain terminations), which can trap electrons, is negligible in the tested systems.

The fact that D_{ct} in polymeric films thicker than 1 μm does not change in DCM solutions may be due to the solvent properties. As noted above, the higher, compared with acetonitrile, viscosity of DCM prevents deeper penetration of counterions into the polymer. Clearly, the thickness of 1 μm is a threshold thickness, i.e., at definite sweep rate, counterions can penetrate only to a definite depth of the polymeric phase.

CONCLUSION

The electrochemical behavior of poly-[PdSalpn-1,2] was studied as influenced by the composition of the supporting electrolyte and thickness of the polymeric film. Contrary to fast electron transfer processes, the redox reactions in the film are subject to substantial kinetic limitations associated with the molecular movement of the polymeric chain and transport of ions and solvent molecules in the film.

ACKNOWLEDGMENTS

This work was financially supported by the Ministry of Science and Technology of the Russian Federation in the framework of the program “Photochemistry and Photoelectrochemistry of Supramolecular Complexes of Transition Metals on Solid Supports” (1996–1999).

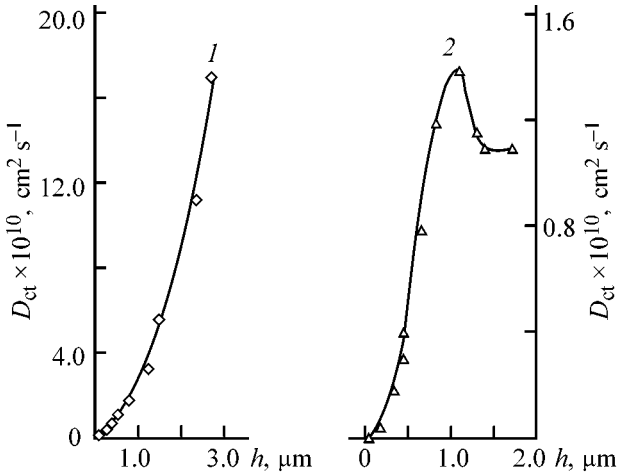

Fig. 6. Electron diffusion coefficient D_{ct} in the polymeric film in (*1*) CH_3CN and (*2*) CH_2Cl_2 vs. the film thickness h. E_a = 1.1 V, TBAP.

REFERENCES

1. Shagisultanova, G.A., *Teor. Eksp. Khim.*, 1991, vol. 27, no. 3, pp. 330–338.
2. Shagisultanova, G.A., Orlova, I.A., and Batrakov, Yu.F., *Zh. Prikl. Khim.*, 1995, vol. 68, no. 4, pp. 650–653.
3. Orlova, I.A., Synthesis and Properties of New Photo- and Electroactive Polymers Based on Transition Metal Complexes with Schiff Bases, *Cand. Sci. Dissertation*, Moscow, 1997.
4. Shagisultanova, G.A., Borisov, A.N., and Orlova, I.A., *J. Photochem. Photobiol., A: Chem.*, 1997, vol. 103, pp. 249–255.
5. Shagisultanova, G., Orlova, I., Ardasheva, L.P., and Popova, E., *J. Macromol. Symp.*, 1998, vol. 136, no. 12, pp. 91–97.
6. Vorotyntsev, M.A. and Levi, M.D., *Itogi Nauki, Ser. Elektrokhimiya*, 1991, vol. 34, pp. 154–220.
7. Levi, M.D., Lopez, C., Vieil, E., and Vorotyntsev, M.A., *Electrochim. Acta*, 1997, vol. 42, no. 5, pp. 757–769.
8. Dias, A.F., Castillo, J.I., Logan, J.A., and Lee, W.Y., *J. Electroanal. Chem.*, 1981, vol. 129, no. 1, pp. 115–132.
9. Shinohara, H., Aizawa, M. and Shirakawa, H., *J. Chem. Soc., Chem. Commun.*, 1986, no. 1, pp. 87–88.
10. Lapkowski, M. Zagorska, M., Kulszewicz-Bajer, I., and Pron, A., *J. Electroanal. Chem.*, 1992, vol. 151, no. 2, p. 341.

11. Imanishi, K., Sato, M., Yasuda, Y., *et al., J. Electroanal. Chem.*, 1988, vol. 242, nos. 1/2, p. 203–208.
12. Imanishi, K., Sato, M., Yasuda, Y., *et al., J. Electroanal. Chem.*, 1989, vol. 260, no. 2, pp. 469–473.
13. Alpatova, N.M., Levi, M.D., and Ovsyannikova, E.V., *Electrokhimiya*, 1994, vol. 30, no. 5, pp. 606–610.
14. Alpatova, N.M., Ovsyannikova, E.V., and Kazarinov, V.E., *Elektrokhimiya*, 1998, vol. 34, no. 1, pp. 83–89.
15. Shagisultanova, G.A. and Ardasheva, L.P., *Koord. Khim.*, 1999, vol. 25, no. 6, pp. 411–415.
16. *Handbook of X-ray Photoelectron Spectroscopy*, Chastein, J., Ed., New York: Perkin–Elmer, 1992.
17. Ardasheva, L.P., Spectral Luminescence, Photochemical, and Electrochemical Properties of Platinum(II) and Palladium(II) Complexes with Schiff Bases, *Cand. Sci. Dissertation*, Moscow, 1999.
18. Gordon, A.J. and Ford, R.A., *The Chemist's Companion. A Handbook of Practical Data, Techniques and References*, New York: Wiley–Interscience, 1972.
19. Khannanov, N.K., Yatsun, T.F., Shafirovich, V.Ya., and Strelets, V.V., *Izv. Akad. Nauk SSSR, Ser. Khim.*, 1983, no. 6, pp. 1282–1289.
20. Marcus, Y., *Ion Solvation*, New York: Wiley–Interscience, 1985.
21. Fialkov, Yu.A., *Rastvoritel' kak sredstvo upravleniya khimicheskim protsessom* (Solvent As Means to Control a Chemical Process), Leningrad: Khimiya, 1990.
22. Vorotyntsev, M.A. and Badiali, J.P., *Electrochim. Acta*, 1994, vol. 39, no. 2, pp. 289–306.
23. Alpatova, N.M., Ovsyannikova, E.V., and Kazarinov, V.E., *Elektrokhimiya*, 1996, vol. 32, no. 5, pp. 631–634.

Russian Journal of Applied Chemistry, Vol. 74, No. 2, 2001, pp. 325–329. Translated from Zhurnal Prikladnoi Khimii, Vol. 74, No. 2, 2001, pp. 320–324.

CHEMISTRY OF FOSSIL FUEL

Extraction Refining of Light Vacuum Gas Oil

A. A. Gaile, L. V. Semenov, O. M. Varshavskii, A. S. Erzhenkov, L. L. Koldobskaya, and E. A. Kaifadzhyan

St. Petersburg State Technological Institute, St. Petersburg, Russia

Kirishinefteorgsintez Production Association, Limited Liability Company, Kirishi, Leningrad oblast, Russia

Received September 25, 2000

Abstract—Highly selective refining of light vacuum gas oil by five-step countercurrent extraction of aromatic and heteroatomic compounds with *N*-methylpyrrolidone or dimethylacetamide in the presence of low-boiling nonpolar solvents was studied. The resulting refined oil can be used as high-quality raw material in hydrocracking and catalytic cracking.

Vacuum gas oils are used as raw material in lube oil production or for preparating lighter fractions by hydrocracking or catalytic cracking. In large petroleum refineries, it is cost efficient to combine hydrocracking with catalytic cracking, which improves the process flexibility and makes the fuel production more balanced [1].

It is known that rather strict requirements are imposed on the raw materials used in both hydrocracking and catalytic cracking, including the content of polycycloarenes, heteroatomic compounds, and heavy metals. Their increased content in vacuum gas oils promotes coke formation and catalyst poisoning and impairs the cracking level, yield of the petrol fractions, and the product quality [2]. Thus, when designing the catalytic cracking unit at the Ufa Petroleum Refinery, Joint-Stock Company, it was intended to produce diesel fuel with sulfur content below 0.2 wt % from light gas oil with sulfur content of 1.92 wt %. In fact, however, the obtained product contains 0.5 wt % sulfur [3]. The increased content of alkylaromatic hydrocarbons in the raw material and their oxidation by oxygen (presumably, adsorbed on a catalyst) resulted in that, after the unit was put in service, the level of phenols in wastewater increased by an order of magnitude from 0.27–0.62 to 3.59–5.34 mg l^{-1} [4].

Pretreatment of vacuum gas oils before hydrocracking or catalytic cracking can be performed by various methods such as hydrofining, primary hydrocracking, partial-conversion hydrocracking using two reactors in which hydrofining and hydrocracking proceed separately [5], and deep hydrogenation of the raw material at a pressure of about 30 MPa [6].

Also the raw material can be prepared for hydrocracking and catalytic cracking by extraction treatment with selective solvents [7, 8]. For example, refined oil containing 91.5 wt % saturated hydrocarbons was obtained by extraction of arenes from heavy vacuum gas oil (Romashki oil field). Catalytic cracking of the resulting refined oil provides petrol in yield higher by 7.3 wt % than that with crude vacuum gas oil [8].

The advantage of the extraction treatment of vacuum gas oils over the hydrogenation methods is that extraction can be performed under nearly atmospheric pressure, making the process more cost efficient. In its turn, the drawback of extraction treatment is that aromatic hydrocarbons and organoelement compounds are not sufficiently selectively removed with such solvents as phenol, furfural, and *N*-methylpyrrolidone. For example, the extracts after treatment oil distillates with phenol contain about 25 wt % saturated hydrocarbons [9]. Chernozhukov *et al.* [10] reported that extraction treatment of oils leads to loss of 5–15 wt % of the initial amount of saturated hydrocarbons.

The efficiency of extraction treatment can be improved by using an extraction system consisting of two partially miscible solvents, for example, furfural and isooctane [11]. It has been demonstrated [12] that addition of cetane to a polar extractant, e.g., to a mixture of *N*-methylpyrrolidone and ethylene glycol, increases the selectivity of extraction of benzene and its homologs from reforming catalyzates. It has also been reported [13] that addition of a mixture of toluene and

1070-4272/01/7402-0325 $25.00 © 2001 MAIK "Nauka/Interperiodica"

Table. 1. Characteristics of light vacuum gas oil

Characteristic	Sample no.		Characteristic	Sample no.	
	1	2		1	2
Fractional oil content, °C:			Density ρ_4^{20}	0.8892	0.8841
onset of boiling	305	270	Viscosity, mm s^{-1}:		
10%	323	283	at 20°C	31.18	13.58
30%	341	307	at 50°C	8.89	5.27
50%	355	328	Cloud point, °C	18	9
70%	368	349	Pour point, °C	15	5
90%	383	372	Sulfury content, wt %	43.4	32.5
end of boiling (96%)	390	380	Sulfur content, wt %	1.56	1.40
Refractive index n_D^{20}	1.4982	1.4919	Nitrogen content, wt %	0.22	0.10

Table 2. Conditions of five-step selective extraction refining of light vacuum gas oil

Parameter	Sample no. 1		Sample no. 2	
	experiment no.		experiment no.	
	1	2	3	4
Polar extractant	*N*-Methylpyrrolidone		Dimethylacetamide	
Moisture content in extractant, wt %	3	3	3	3
Mass ratio of extractant to raw material	5 : 1	3 : 1	5 : 1	5 : 1
Nonpolar solvent	Pentane	–	Pentane	Heptane/toluene (99 : 1 by mass)
Mass ratio of nonpolar solvent to raw material	1 : 1	–	1 : 1	0.5 : 1
Temperature, °C	30	30	30	50

octane to dimethylformamide makes higher the yield of refined oil in selective refining of oil fractions.

It was shown in [14, 15] that use of low-boiling polar extractants and pentane as a nonpolar solvent is efficient in extraction of aromatic hydrocarbons from middle oil.

The goal of this work was to improve the quality of light vacuum gas oil by selective removal of aromatic hydrocarbons and organoelement compounds using extraction with a polar extractant in pentane. In experiments we used two samples of light vacuum gas oil taken before (sample no. 1) and after (sample no. 2) upgrading a vacuum block at AVT-6 unit (Kirishinefteorgsintez Production Association). The upgrading (1999) included changing direct-flow sieve trays for a Vacupack regular packing and trays with buttress valves, and also improvement of the vacuum system [16]. The characteristics of the samples used are listed in Table 1.

As a result of more distinct fractional distillation of black oil, the light gas oil obtained after upgrading is characterized by lightened fractional oil content and lower content of aromatic hydrocarbons and organoelement compounds. A polar extractant for selective refining of the raw material was chosen so that there was no formation of azeotropic mixtures by the extractant with components of the raw material. It is known that *N*-methylpyrrolidone, one of the most efficient extractants for selective refining of oil fractions, does not form azeotropic mixtures with hydrocarbons boiling above 280°C [17]. Therefore, we used this extractant for selective refining of sample no. 1. For extraction of aromatic and organoelemental compounds from sample no. 2 (lower-boiling fraction) we used dimethylacetamide, which does not form azeotropic mixtures with hydrocarbons boiling above 250–270°C under standard conditions.

Selective refining of sample no. 1 of light vacuum gas oil was carried out by five-step countercurrent extraction with *N*-methylpyrrolidone in pentane or without diluent under conditions given in Table 2. In the case of sample no. 2, we used dimethylacetamide in pentane or in a mixture of heptane with tol-

Table 3. Material balance in selective refining of light vacuum gas oil (sample no. 1) with *N*-methylpyrrolidone in pentane (experiment no. 1)

Component	Input, g	Output			
		refined oil		extract	
		g	wt %	g	wt %
Raw material including:	100	66.2	44.0	33.8	6.2
saturated hydrocarbons	56.6	55.1	36.6	1.5	0.3
aromatic compounds	43.4	11.1	7.4	32.3	5.9
Polar extractant including:	500	15.0	10.0	485	88.2
N-methylpyrrolidone	485	14.6	9.7	470.4	85.6
water	15	0.4	0.3	14.6	2.6
Pentane	100	69.2	46.0	30.8	5.6
Total	700	150.4	100	549.6	100

Table 4. Results obtained in five-step selective extraction refining of light vacuum gas oil

Parameter	Experiment no.			
	1	2	3	4
Yield, wt %:				
refined oil	66.2	60.4	77.2	70.3
extract	33.8	39.6	22.8	29.7
Characteristics of refined oil				
Refractive index n_D^{20}	1.4780	1.4755	1.4752	1.4710
Density ρ_4^{20}	0.8428	0.8419	0.8540	0.8440
Viscosity, mm s^{-1}:				
at 20°C	25.0	24.8	13.0	–
at 50°C	7.76	7.66	5.22	–
Cloud point, °C	21	23	13	–
Pour point, °C	17	18	6	–
Sulfury content, wt %	17.1	15.8	13.7	9.5
Aromaticity factor (^{13}C NMR)	0.067	0.051	–	–
Sulfur content, wt %	0.60	0.58	0.45	0.37
Nitrogen content, wt %	0.08	0.12	0.04	0.05
Characteristics of extract				
Refractive index n_D^{20}	1.5642	1.5529	1.5708	1.5650
Density ρ_4^{20}	0.9830	0.9802	0.9868	0.9750
Viscosity, mm s^{-1}:				
at 20°C	139.5	72.7	37.1	–
at 50°C	21.4	12.8	8.65	–
Sulfury content, wt %	92.6	85.6	96.0	86.9
Aromaticity factor (^{13}C NMR)	0.429	0.407	0.557	0.447
Sulfur content, wt %	3.36	3.05	4.60	3.77
Nitrogen content, wt %	0.47	0.42	0.31	0.26
Degree of removal, wt %:				
aromatic hydrocarbons	74.4	78.1	67.4	79.4
sulfur-containing compounds	72.8	77.4	74.9	80.0
nitrogen-containing compounds	72.2	75.6	70.7	77.2

uene (1 wt %) modeling refined oil from an LG 35-8/300B benzene reforming unit. The use of higher-boiling nonpolar solvents allows an increase in the extraction temperature from 30 to 50°C at a total pressure in the extractors remaining close to atmospheric pressure.

As an example, Table 3 presents the material balance for experiment no. 1. Since pentane is more readily soluble in *N*-methylpyrrolidone than saturated hydrocarbons of the raw material, its use as a stripping solvent makes it possible to decrease their loss with the extractant phase from 10 (without pentane) to 2.65 wt % of the total amount of these components in the raw material (note that these components are valuable for further hydrocracking or catalytic cracking). The extract obtained using the extraction system *N*-methylpyrrolidone–pentane is characterized by higher content of aromatic compounds, as demonstrated by the higher sulfury content and aromaticity factor as compared with those in experiment no. 2 without pentane (Table 4). The aromaticity factors of the resulting extracts and refined oil obtained after regeneration of the extractants by fractional distillation on a 20-TP column was estimated as in [18], from ^{13}C NMR spectra (Bruker AM-500 instrument). Addition of the stripping nonpolar solvent also increases the content of sulfur- and nitrogen-containing compounds. In this case, the yield of refined oil increases by about 10%. Therefore, addition of pentane improves the selectivity of extraction refining of vacuum gas oil to remove undesired components. However, to maintain a high degree of extraction of aromatic and organoelemental compounds, one has to use an increased ratio of polar extractant to raw material.

Dimethylacetamide is a less selective solvent with respect to aromatic hydrocarbons than *N*-methylpyrrolidone [19]. However, refining of sample no. 2 with dimethylacetamide and pentane (experiment no. 3) appeared to be even more selective as compared with the refining of sample no. 1 in experiment no. 1 under the same conditions. The loss of saturated hydrocarbons with the extract is only 1.3 wt % of their total amount in the raw material, as demonstrated by the higher balance data; the content of aromatic compounds in the extract and the yield of refined oil are the highest among those obtained in all the experiments. These results can be attributed to the decreased content of undesired components in sample no. 2 and to the lower boiling end point of this fraction, i.e., to a shorter length of alkyl radicals in aromatic compounds.

In experiment no. 4, changing pentane for a mixture of heptane with toluene at simultaneously decreasing ratio of the nonpolar solvent to raw material and increasing process temperature results in lower selectivity of gas oil refining. In this case, the loss of saturated hydrocarbons with the extract increases to 5.8 wt % of their total in the raw material, and the yield of refined oil and the concentration of aromatic and sulfur-containing compounds in the extract decrease. As an advantage of the last variant we may note the highest degree of removal of aromatic and sulfur-containing compounds from refined oil.

CONCLUSIONS

(1) Extraction refining of light vacuum gas oil with *N*-methylpyrrolidone or dimethylacetamide in the presence of such nonpolar solvents as pentane and refined oil from a benzene reforming unit allows a decrease in the content of aromatic hydrocarbons in the refined gas oil by a factor of 2.5–3.5 at minimal loss of saturated hydrocarbons (1–3 wt % of their total in raw material).

(2) The degree of removal of sulfur- and nitrogen-containing compounds in extraction refining of light gas oil may be as high as 75–80%.

REFERENCES

1. Baral, V.I. and Huffman, G.S., in *Gidrokreking ostatkov i distillyatov, vklyuchaya gidroobesserivanie ostatkov i neftei* (Hydrocracking of Leavings and Distillates, Including Hydrodesulfurization of Leavings and Oils), Moscow: Vneshtorgizdat, 1971, pp. 3–30.
2. Ancheyta-Juarez, J., Lopez-Isunza, F., and Aguilar-Rodriguez, E., *Ind. Eng. Chem. Res.*, 1998, vol. 37, no. 12, pp. 4637–4640.
3. Kas'yanov, A.A., Sukhorukov, A.M., Prokopyuk, S.G., and Nikolaichuk, V.A., *Neftepererab. Neftekhim.*, 1998, no. 4, pp. 11–13.
4. Vezirov, R.R., Obukhova, S.A., Urmancheev, S.F., *et al.*, *Neftepererab. Neftekhim.*, 1998, no. 4, pp. 17–21.
5. Shorey, S.U., Lomas, D.A., and Kisom, U.G., *Neftegaz. Tekhnol.*, 2000, no. 2, pp. 93–102.
6. Moiseev, V.M., Gurdin, V.I., Reznichenko, I.D., *et al.*, *Khim. Tekhnol. Topl. Masel*, 2000, no. 3, pp. 25–28.
7. Omaraliev, T.O., *Kataliticheskii kreking gazoilevykh fraktsii neftei Zapadnogo Kazakhstana* (Catalytic Cracking of Light End of West Kazakh Oils), Alma-Ata: Nauka, 1988.
8. Orlowski, M., *Przem. Chem.*, 1981, vol. 60, nos. 9–10, pp. 462–465.
9. Podlesnaya, L.A., Shelikhov, V.V., Zhelobod'ko, V.F., *et al.*, in *Plastifikatory i voski* (Plasticizers and Waxes), Moscow: TsNIITEneftekhim, 1978, pp. 31–35.

10. Chernozhukov, N.I., Krein, S.E., and Losikov, B.V., *Khimiya mineral'nykh masel* (Chemistry of Mineral Oils), Moscow: Gostoptekhizdat, 1959.
11. Kolychev, V.M., Bondarenko, M.F., Pavlova, A.A., and Rudneva, O.N., in *Aromaticheskie uglevodorody iz produktov neftepererabotki i sintezy na ikh osnove* (Aromatic Hydrocarbons from Oil Refining Products and Syntheses on Their Basis), Moscow: Khimiya, 1969, pp. 17–23.
12. Raevskii, Yu.A. and Prokopets, M.M., *Neftepererab. Neftekhim.*, 1977, no. 4, pp. 32–33.
13. Prokopets, M.M. and Bushchak, V.B., *Vestn. L'vov. Politekh. Inst.*, 1988, no. 221, pp. 96–97.
14. *Ekstraktsiya i primenenie arenov srednedistillyatnykh neftyanykh fraktsii: Sbornik trudov OOO PO "KINEF"* (Extraction and Application of Arenes from Middle Oil: Collection of Works of KINEF Production Association, Limited Liabilityt Company), Gaile, A.A. and Somov, V.E., Eds., St. Petersburg: Sintez, 1998.
15. Gaile, A.A., Somov, V.E., Semenov, L.V., *et al.*, *Khim. Tekhnol. Topliv. Masel*, 1999, no. 5, pp. 3–7.
16. Vikhman, A.G., Kievskii, V.Ya., Pil'ch, L.M., *et al.*, *Khim. Tekhnol. Topl. Masel*, 1998, no. 5, pp. 41–42.
17. Shkol'nikov, V.M., Kolesnik, I.O., Oktyabr'skii, F.V., *et al.*, *Neftepererab. Neftekhim.*, 1989, no. 12, pp. 11–14.
18. Ogorodnikov, V.D., in *Instrumental'nye metody issledovaniya nefti* (Instrumental Methods in Petroleum Research), Novosibirsk: Nauka, 1987, pp. 49–67.
19. Deal, C.H. and Derr, E.L., *Ind. Eng. Chem. Process Des. Devel.*, 1964, vol. 3, no. 4, pp. 394–399.

Russian Journal of Applied Chemistry, Vol. 74, No. 2, 2001, pp. 330–332. Translated from Zhurnal Prikladnoi Khimii, Vol. 74, No. 2, 2001, pp. 324–327.

CHEMISTRY OF FOSSIL FUEL

Extraction Refining of Heavy Vacuum Gas Oil

A. A. Gaile, O. M. Varshavskii, L. V. Semenov, A. S. Erzhenkov, L. L. Koldobskaya, and E. A. Kaifadzhyan

St. Petersburg State Technological Institute, St. Petersburg, Russia

Kirishinefteorgsintez Production Association, Limited Liability Company, Kirishi, Leningrad oblast, Russia

Received September 25, 2000

Abstract—Selective refining of heavy vacuum gas oil and a combined fraction of light and heavy vacuum gas oils to remove aromatic and organoelement compounds and heavy metals by five-step countercurrent extraction with *N*-methylpyrrolidone or dimethylacetamide in the presence of heptane containing 1 wt % toluene was studied.

Heavy vacuum gas oil, similarly to the light one, is used as a raw material in lube oil and motor oil production. It is known that rather strict requirements are imposed on the raw material used in both hydrocracking and catalytic cracking, including the content of polycycloarenes, sulfur- and nitrogen-containing compounds, and heavy metals. The increased content of these undesirable components promotes coke formation and poisoning of catalysts and deteriorates the cracking level, yield of the petrol fractions, and the product quality [1, 2]. It is known that they can be removed from the raw material by the hydrogenation and extraction methods (for fuel-oil residue, by deasphalting).

The goal of this work was to improve the quality of heavy vacuum gas oil by selective extraction refining with polar and nonpolar solvents.

In experiments we used a sample of heavy vacuum gas oil taken after upgrading of AVT6 unit (Kirishinefteorgsintez Production Association). The upgrading (1999) included changing direct-flow sieve trays for a Vacupack regular packing with low hydrodynamic resistance, and also modification of the vacuum system. As a result, the content of the fraction boiling below 350°C in heavy vacuum gas oil decreased to 2.5 wt %, and the boiling end point (96% distillation) increased to 532°C [3]. The characteristics of the sample used are listed in Table 1.

As polar solvents were selected *N*-methylpyrrolidone and dimethylacetamide, forming no azeotropic mixtures with components of the raw material but showing high efficiency in selective refining of oil fractions [4, 5]. To raise the concentration of undesirable components in the extract and simultaneously to decrease the loss of saturated hydrocarbons, we also used a nonpolar solvent, heptane, containing 1 wt % toluene, modeling refined oil from an LG 35-8/300B benzene reforming unit.

Selective refining was carried out by five-step countercurrent extraction at 50°C and polar extractant (moisture content 3 wt %) to raw material ratio of 5 : 1. The mass ratio of the nonpolar solvent to the raw material was 1 : 1 and 0.5 : 1 in extraction with *N*-methylpyrrolidone and dimethylacetamide, respectively. Heavy metals were determined by X-ray spectral analysis on a BARS-2 instrument.

The results show that selective extraction refining of heavy vacuum gas oil with both *N*-methylpyrrolidone (Table 1) and dimethylacetamide (Table 2) ensures a sufficiently high degree of removal of undesirable components (62–75%) and high concentration of these components in the extract. The content of saturated hydrocarbons in the extract is 10–15 wt %, which corresponds to their loss with the extract at a level of only 6.2–11.4% of their initial content in the raw material. The extraction system with *N*-methylpyrrolidone provides more exhaustive refining, whereas the system with dimethylacetamide ensures more selective refining of the raw material to remove undesirable components. The difference between the obtained results can be attributed in part to different nonpolar solvent to raw material ratios.

We also studied the extraction refining of a wide vacuum gas oil fraction prepared by mixing samples of light and heavy vacuum gas oils at a mass

1070-4272/01/7402-0330 $25.00 © 2001 MAIK "Nauka/Interperiodica"

Table 1. Results obtained in five-step countercurrent selective extraction of aromatic hydrocarbons and organoelement compounds from heavy vacuum gas oil with *N*-methylpyrrolidone

Parameter	Raw material	Refined oil	Extract
Yield, wt %	100	60.0	40.0
Refractive index n_D^{20}	1.5018	1.4701	1.5610
Density ρ_4^{20}	0.892	0.846	0.961
Cloud point, °C	30	28	–
Pour point, °C	31	27	–
Sulfury content, wt %	47.6	22.6	85.05
Aromaticity factor	0.197	–	0.397
Element content, wt %:			
sulfur	1.38	0.57	2.60
nitrogen	0.24	0.10	0.45
W	1.53×10^{-4}	–	2.89×10^{-4}
V	0.90×10^{-4}	–	1.50×10^{-4}
Ni	0.40×10^{-4}	–	0.72×10^{-4}
Fe	0.49×10^{-4}	–	0.83×10^{-4}
Degree of removal, wt %:			
aromatic compounds	–	–	71.5
sulfur-containing compounds	–	–	75.4
nitrogen-containing compounds	–	–	75.0
W	–	–	75.6
V	–	–	66.7
Ni	–	–	72.0
Fe	–	–	68.0

Table 2. Results obtained in five-step extraction refining of heavy vacuum gas oil with dimethylacetamide

Parameter	Refined oil	Extract	Parameter	Refined oil	Extract
Yield, wt %	67.3	32.7	Sulfur content, wt %	0.76	2.65
Refractive index n_D^{20}	1.4858	1.5690	Nitrogen content, wt %	0.09	0.55
Density ρ_4^{20}	0.8620	0.9798	Degree of removal, wt %:		
Sulfury content, wt %	27.0	90.1	aromatic compounds	–	61.9
Aromaticity factor	–	0.438	sulfur-containing compounds	–	62.8
			nitrogen-containing compounds	–	74.9

Table 3. Results obtained in five-step extraction refining of wide vacuum gas oil fraction with dimethylacetamide

Parameter	Raw material	Refined oil		Extract	
		calculation	experiment	calculation	experiment
Yield, wt %	100	67.7	67.8	32.3	32.2
Refractive index n_D^{20}	1.5000	1.4839	1.4860	1.5685	1.5630 (20°C)
Density ρ_4^{20}	0.898	0.859	0.863	0.975	0.971
Sulfury content, wt %	45.0	24.8	25.7	89.7	85.6
Aromaticity factor	–	–	0.178	0.439	0.398
Sulfur content, wt %	1.38	0.71	0.91	2.79	2.38
Nitrogen content, wt %	0.22	0.08	0.11	0.51	0.49
Degree of removal, wt %:					
aromatic compounds				64.4	61.3
sulfur-containing compounds				65.3	55.5
nitrogen-containing compounds				74.9	71.7

ratio of 12.8 : 87.2. It is this ratio that is characteristic of the actual vacuum gas oil produced by AVT-6 unit [3].

Table 3 demonstrates that the parameters of extraction refining of this wide fraction are somewhat worse than those estimated theoretically using the additivity rule from data on extraction of undesirable components from light and heavy vacuum gas oils. The results obtained are consistent with the existing concept of the effect exerted by the fractional composition of the raw material on the efficiency of selective refining of oil fractions. According to this concept, extraction of arenes and organoelement compounds from wide fractions is relatively low-efficient [6]. The decreasing selectivity of extraction of undesirable components from the combined vacuum gas oil fraction can be attributed to the fact that the wider the gap between the initial and end boiling points of a raw material, the closer the solubilities in the extractant of high-boiling aromatic (or heterocyclic) compounds to be removed and low-boiling saturated hydrocarbons. This must be most clearly pronounced for strongly associated extractants whose selectivity is strongly dependent on the molecular weight of components to be removed [7]. However, neither *N*-methylpyrrolidone nor dimethylacetamide are classified with such extractants. Therefore, even in the case of a combined vacuum gas oil fraction, the degree of removal of undesirable components remains sufficiently high (55–72%).

CONCLUSIONS

(1) Extraction refining of heavy vacuum gas oil with *N*-methylpyrrolidone or dimethylacetamide in the presence of heptane containing 1 wt % toluene allows a 67–75% removal of aromatic hydrocarbons, sulfur- and nitrogen-containing compounds, and heavy metals. Addition of a nonpolar solvent to the polar extractant improves the extraction selectivity and reduces the loss of saturated hydrocarbons to 6% of their total in the raw material.

(2) The efficiency of extraction refining of the combined fraction of light and heavy vacuum gas oils is lower than the theoretical value estimated by the additivity rule. Nevertheless, in this case, too, the extraction systems proposed allow 55–72% removal of undesirable components.

REFERENCES

1. *Kreking neftyanykh fraktsii na tseolitsoderzhashchikh katalizatorakh* (Cracking of Oil Fractions on Zeolite-containing Catalysts), Khadzhiev, S.N., Ed., Moscow: Khimiya, 1982.
2. Ancheyta-Juarez, J., Lopez-Isunza, F., and Aguilar-Rodriguez, E., *Ind. Eng. Chem. Res.*, 1998, vol. 37, no. 12, pp. 4637–4640.
3. Vikhman, A.G., Kievskii, V.Ya., Pil'ch, L.M., *et al.*, *Khim. Tekhnol. Topl. Masel*, 1998, no. 5, pp. 41–42.
4. Kolesnik, I.O., Vavanov, V.V., and Shkol'nikov, V.M., *Proizvodstvo bazovykh masel uluchshennogo kachestva–osnova perspektivnogo assortimenta motornykh masel* (Manufacture of Basic Oils of Improved Quality as a Foundation of Promising Assortment of Engine Oils), Moscow: TsNIITEneftekhim, 1989.
5. Shkol'nikov, V.M., Kolesnik, I.O., Oktyabr'skii, F.V., *et al.*, *Neftepererab. Neftekhim.*, 1989, no. 12, pp. 11–14.
6. Kazakova, L.P. and Krein, S.E., *Fiziko-khimicheskie osnovy proizvodstva neftyanykh masel* (Physicochemical Principles of Petroleum Oil Production), Moscow: Khimiya, 1978.
7. Bittrich, H.J., Gaile, A.A., Lempe, D., *et al.*, *Razdelenie uglevodorodov s ispol'zovaniem selektivnykh rastvoritelei* (Separation of Hydrocarbons with Selective Solvents), Leningrad: Khimiya, 1987.

Russian Journal of Applied Chemistry, Vol. 74, No. 2, 2001, pp. 333–334. Translated from Zhurnal Prikladnoi Khimii, Vol. 74, No. 2, 2001, pp. 328–329.

BRIEF COMMUNICATIONS

Synthesis of Mordenite-like Zeolite from Secondary Silicon-containing Raw Materials

M. L. Pavlov, R. A. Makhamatkhanov, B. I. Kutepov, and U. M. Dzhemilev

Institute of Petrochemistry and Catalysis, Academy of Sciences of the Republic of Bashkortostan, Ufa Scientific Center of the Russian Academy of Sciences, Ufa, Bashkortostan, Russia

Received November 2, 2000

Abstract—A low-waste method is proposed for synthesizing a mordenite-like zeolite from secondary silicon-containing raw materials.

Specific features of the chemical composition and structure of the crystal lattice of a mordenite-like zeolite impart to it distinctive adsorption and catalytic properties and make it promising for practical use as support and component of catalysts for hydromerization of *n*-paraffins and hydrocracking of oil fractions and sorbents for drying of acid gases [1–3]. Therefore, development of techniques for synthesizing mordenite-like zeolites is a promising direction in the chemistry of zeolites.

The present communication describes, an industrially promising method for synthesis of mordenite from silicon-containing raw materials—wastes produced in manufacture of crystalline silicon (WMSC), with recycling of the mother liquor formed in the preceding synthesis of zeolite.

EXPERIMENTAL

Mordenite was synthesized from aqueous solutions of sodium aluminate and sodium hydroxide, and also from a new silicon-containing raw material—WMSC containing no less than 98 wt % SiO_2. The synthesis was done in an autoclave with a stirrer and a device that allowed sampling in the course of synthesis without disturbing the crystallization mode, in the interval 125–165°C with reaction mixtures of composition $(2.2–3.6)Na_2O \cdot Al_2O_3 \cdot (12–20)SiO_2 \cdot 300H_2O$.

The synthesized samples were washed to remove impurities, dried at 150°C for 3 h, and then calcined in air at 540°C for 4 h. The chemical composition of the liquid and solid phases was determined by the methods described in [4]. An X-ray diffraction analysis was done with a DRON-3 diffractometer with monochromatized Cu_{K_α} radiation (graphite monochromator in reflected beam). The adsorption properties of the obtained samples were characterized by static capacity with respect to H_2O, C_6H_6, and *n*-C_7H_{16} vapors.

Preliminary experiments demonstrated that WMSC can be used for mordenite synthesis. Further, the kinetic aspects of mordenite crystallization with the use of these raw materials were studied to reveal the influence exerted by the composition of the reaction mixture and by the temperature and duration of crystallization on the properties of the obtained product.

The figure shows kinetic curves describing the crystallization of a $2.2Na_2O \cdot Al_2O_3 \cdot 12SiO_2 \cdot 300H_2O$ reaction mixture at 125, 135, 145, and 155°C. The curves have S-like shape characteristic of similar curves taken in synthesizing other types of zeolites. The first portion of a curve reflects the induction period; the second, the period of exponential formation and growth of crystals; and the third, the period of a slowing-down crystallization.

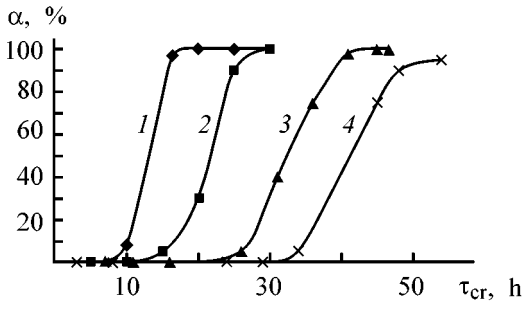

Crystallinity α of a sample vs. time τ_{cr} of crystallization of a reaction mixture of composition $2.2Na_2O \cdot Al_2O_3 \cdot 12SiO_2 \cdot 300H_2O$. Temperature (°C): (*1*) 155, (*2*) 145, (*3*) 135, and (*4*) 125.

1070-4272/01/7402-0333 $25.00 © 2001 MAIK "Nauka/Interperiodica"

Physicochemical properties of samples obtained under various conditions of crystallization of a $2.2Na_2O \cdot Al_2O_3 \cdot 12SiO_2 \cdot 300H_2O$ mixture*

T_{cr}, °C	τ_{cr}, h	XPA, %	Static zeolite capacity ($cm^3\ g^{-1}$) with respect to indicated vapor			Chemical composition, %		SiO_2/Al_2O_3
			H_2O	C_6H_6	C_7H_{14}	SiO_2	Al_2O_3	
145	5	0	0.02	0.07	0.05	73.8	15.4	8.1
	10	0	0.005	0.05	0.04	73.8	15.1	8.3
	15	5	0.013	0.05	0.04	73.8	14.7	8.5
	20	30	0.02	0.05	0.04	75.8	14.8	8.7
	25	90	0.11	0.13	0.11	75.2	14.9	8.6
	30	100	0.11	0.13	0.11	75.4	14.9	8.6
155	5	0	0.005	0.03	0.05	76.4	14.7	8.8
	10	8	0.002	0.05	0.04	73.9	15.1	8.3
	16.5	90	0.10	0.10	0.12	77.1	14.3	9.2
	20	100	0.10	0.12	0.12	76.2	14.1	9.2
	25	100	0.12	0.12	0.11	76.6	13.8	9.4
	30	100	0.12	0.12	0.12	77.3	14.1	9.3
160**	25	100	0.11	0.12	0.11	76.0	14.3	8.9

* T_{cr} is the crystallization temperature, and τ_{cr} is the time of crystallization.

** Sample synthesized by the conventional method.

It can be seen that formation of mordenite with high crystallinity at 145°C requires 28–30 h. With the synthesis temperature raised to 155°C, a sample of the same quality can be synthesized in 23–25 h, i.e., the duration of crystallization at which nearly 100% zeolite crystallinity can be achieved decreases with increasing crystallization temperature.

On the basis of the results obtained in the kinetic studies, conditions were chosen making it possible to synthesize from WMCS a mordenite with characteristics comparing well with the parameters of mordenite obtained from Na_2SiO_3, $NaAlO_2$, and NaOH (see the table). It should be noted that the crystallization times of mordenite with high phase purity by both variants are also close.

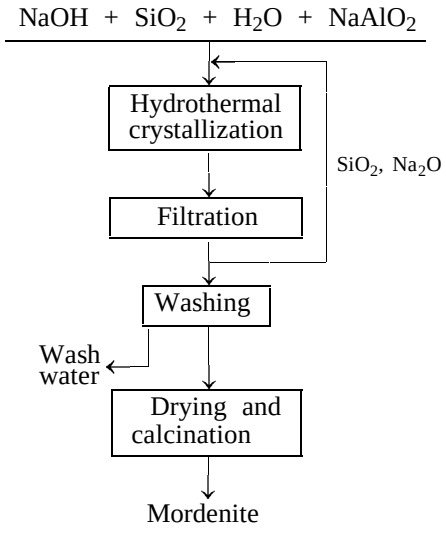

Scheme of synthesis of a mordenite-like zeolite.

In synthesis of mordenite, mother liquor containing silicon and sodium cations is formed in the stage of its hydrothermal crystallization. This solution is not always utilized, thereby making larger the amount of wastewater. The possibility was also studied of synthesizing mordenite with recycling of the mother liquor. The experiments performed demonstrated that such a technique is possible (see the scheme).

CONCLUSION

A method was developed for synthesizing mordenite from waste produced in manufacture of crystalline silicon used as silicon-containing raw material. The method assumes utilization of the mother liquor by its repeated use in zeolite synthesis.

REFERENCES

1. Isakov, Ya.I., *Neftekhimiya*, 1998, vol. 38, no. 6, pp. 404–438.
2. Breck, D.W., *Zeolite Molecular Sieves*, New York: Wiley, 1974.
3. Krupina, N.N., *Primenenie sinteticheskikh mordenitov v adsorbtsii, ionnom obmene i katalize* (Use of Synthetic Mordenites in Adsorption, Ion Exchange, and Catalysis), Moscow: TsNIITEneftekhim, 1990.
4. Kreshkov, A.P. and Yaroslavets, A.A., *Kurs analiticheskoi khimii* (A Course of Analytical Chemistry), Moscow: Khimiya, 1975, vol. 1.

Russian Journal of Applied Chemistry, Vol. 74, No. 2, 2001, pp. 335–337. Translated from Zhurnal Prikladnoi Khimii, Vol. 74, No. 2, 2001, pp. 330–332.

BRIEF COMMUNICATIONS

High-Temperature Fuel Cell Operating on Products of Incomplete Charcoal Combustion

N. M. Gamanovich, V. A. Gorbunova, A. I. Lamotkin, and G. I. Novikov

Belarussian State Technological University, Minsk, Belarus

Received April 12, 2000; in final form October 2000

Abstract—A high-temperature fuel cell operating on gaseous products of incomplete combustion of technical-grade charcoal and equipped with electrodes made of platinum and electrocatalytic oxide materials containing no noble metals was studied experimentally.

Previously [1], experimental data have been published obtained in testing a high-temperature fuel cell (HTFC) operating on gaseous products of incomplete combustion of coal (anthracite). As is known [2], this high-quality coal contains no sulfur that could poison HTFC electrodes. Lower-quality coals contain up to 12% sulfur and cannot serve as fuel for HTFC. In addition, in some CIS regions, the coal deposits are poor or coal is not mined at all, whereas there are ample opportunities for using charcoal. Charcoal is characterized [3] by calorific value of 31.4–34.2 mJ kg^{-1}, primary and storage humidity in the range from 2–4 to 7–15 wt %, ash content of no more than 3 wt %, content of volatiles (CO, CO_2, CH_4, etc.) of no more than 20 wt %, and porosity of 72 (birch charcoal) and 80 vol % (fir-tree charcoal). An important compositional feature of charcoal is the complete lack of sulfur. A sufficiently detailed thermodynamic analysis of the process in question was made in [1].

EXPERIMENTAL

Electrochemical oxidation of gases (CO and H_2) liberated in incomplete combustion charcoal (obtained by the method described [4]) was performed with an HTFC based on a solid oxide electrolyte of composition $0.9ZrO_2$–$0.1Y_2O_3$ (YSZ) [1] in the temperature range 770–1170 K.

The fuel cell comprising a cylindrical electrochemical cell with total working area of about 3.0 cm^2 was placed in the active zone of charcoal combustion. Charcoal was ignited and temperature was maintained with SNOL laboratory electric furnace [1].

The fuel electrode (anode) of the HTFC was prepared from Ni–YSZ nickel–zirconium-oxide cermet obtained using various techniques. Its specific consumption was about 0.100 kg per 1 m^2 of electrolyte surface. The air electrode (cathode) was deposited using two materials (synthesized by thermal decomposition of aqueous solutions of a mixture of nitrate salts prepared from pure and analytically pure reagents) based on rare-earth manganites of composition $La_{0.6}Sr_{0.4}MnO_3$ and $Ln_{0.8}Ca_{0.2}Mn_{0.94}Cr_{0.04}Ni_{0.02}O_3$ (close to that of the material used in [5]) where Ln is a mixture of La, Nd, Pr, and Ce. The specific expenditure of the cathode material was 0.120 kg m^{-2}, with its layer on the electrolyte being composite and including 10.0 wt % YSZ powder.

The fuel electrodes (anodes) of the HTFC were fabricated as follows. To obtain anode no. 1, finely dispersed Raney nickel (70%) and YSZ mass (30 wt %) were mechanically mixed and used to prepare an electrode paste (with 10% solution of rosin in C_2H_5OH). The paste was fired-in in a flow of technical grade helium at 1150 K in the course of 2.5 h. After depositing the anode, the cathode layer was fired-in in air at 1150 K for 2.5 h, with the anode layer of nickel simultaneously oxidized to NiO_x oxide.

In fabricating anode no. 2, an aqueous suspension of a finely dispersed YSZ powder in a solution of nickel nitrate $Ni(NO_3)_2 \cdot 6H_2O$ (70 wt % in terms of NiO) was prepared, dehydrated by evaporation, and finally calcined in air at 870 K. The obtained powder was used to prepare the electrode paste which was fired-in in air with the simultaneous firing-in of the cathode material into the electrolyte at 1470 K for 2.5 h.

The working cermet Ni–YSZ electrode was formed by reducing the nickel oxide phase in the NiO_x–YSZ

1070-4272/01/7402-0335 $25.00 © 2001 MAIK "Nauka/Interperiodica"

Potential differences *E*, voltages *U*, and current strengths *I* for HTFC with various electrodes (load resistance R = 1.0 kΩ)

Electrode no.	Type of HTFC electrode	*T*, K	*E*	*U*	*I*, mA
			V		
1	Anode, platinum; cathode, platinum	770	0.025	0.016	0.003
		870	0.127	0.10	0.01
		970	0.56	0.45	0.48
		1070	0.85	0.64	0.65
		1170	0.88	0.67	0.70
2	Anode, cermet no. 1; cathode, $La_{0.6}Sr_{0.4}MnO_3$	770	0.05	0.04	0.05
		870	0.86	0.60	0.68
		970	0.89	0.68	0.70
		1070	0.925	0.71	0.73
		1170	0.95	0.72	0.76
3	Anode, cermet no. 1; cathode, $Ln_{0.8}Ca_{0.2}Mn_{0.94}Cr_{0.04}Ni_{0.02}O_3$	770	0.20	0.18	0.18
		870	0.80	0.66	0.65
		970	0.86	0.66	0.70
		1070	0.89	0.68	0.71
		1170	0.94	0.72	0.75
4	Anode, cermet no. 2; cathode, $Ln_{0.8}Ca_{0.2}Mn_{0.94}Cr_{0.04}Ni_{0.02}O_3$	770	0.01	0.006	–
		870	0.10	0.09	0.10
		970	0.92	0.70	0.73
		1070	0.95	0.73	0.76
		1170	1.00	0.76	0.80

layer with fuel gases (CO, H_2) liberated in incomplete combustion of charcoal in operation of an electrochemical HTFC. The reduction of NiO_x to Ni favors the creation of porosity in the anode, necessary for the cell operation, and the sufficiently uniform distribution of disperse YSZ particles in the anode cermet hinders recrystallization of nickel particles via sintering [6], thereby ensuring prolonged electrochemical activity of the fuel electrode under the HTFC conditions.

As current lead was used 0.5-mm-thick platinum wire. As oxidizing agent served atmospheric oxygen supplied into the cathode space at a rate of 1.80 $cm^3\ min^{-1}$. To obtain comparative characteristics of HTFC, gases formed in incomplete combustion of charcoal were electrochemically oxidized in a cell with platinum layers as anode and cathode.

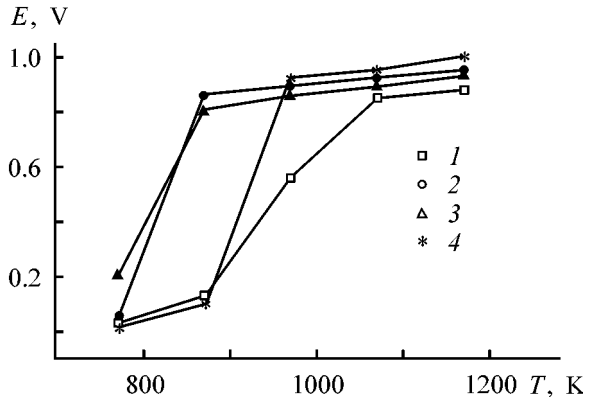

Potential difference *E* across an HTFC operating on products of incomplete charcoal combustion vs. temperature *T*. (*1*–*4*) Numbers of HTFC electrodes in the table.

The results obtained in measuring the potential difference, voltage, and current in the HTFC under study are presented in the table. It can be seen that the lowest potential difference is obtained with platinum electrodes, which can be attributed to the rather high polarizability of the platinum electrodes and their unipolar conductivity [7]. The best electrochemical parameters of an HTFC operating on gaseous products of incomplete combustion of charcoal (E = 1.0 V, U = 0.76 V, I = 0.80 mA) were obtained with cermet anode no. 2 and cathode of composition $Ln_{0.8}Ca_{0.2}Mn_{0.94}Cr_{0.04}Ni_{0.02}O_3$, which is apparently due to the high electrochemical activity of these electrodes (caused, among other factors, by the high permeability to oxygen of the electrode material with perovskite structure and by the catalytic activity of nickel in CO oxidation to CO_2) to be considered in further studies. On the whole, the given type of HTFC, operating on products of charcoal combustion, compares well in basic parameters with a similar cell operating on anthracite combustion gases [1].

The figure shows the potential difference across an HTFC in relation to its temperature. It can be seen

that the HTFC with platinum electrodes gradually passes into the optimal temperature mode of operation and yields the highest potential difference of 0.88 V at 1170 K. The HTFC with a Ni–YSZ cermet anode and manganite cathode is characterized by faster rise in potential, voltage, and current in the range 870–970 K, with nearly the best performance parameters reached. This steep change in the parameters is presumably due, in the first place, to chemical reduction of NiO_x at 870–970 K to give electrochemically active nickel metal in the anode cermet.

CONCLUSIONS

(1) It is established that the high-temperature fuel cell operating on gaseous products of incomplete combustion of technical-grade charcoal compares well in its electrochemical parameters with a similar cell operating on gases produced in anthracite combustion and can be recommended for practical use.

(2) The best parameters of HTFC (E = 1.0 V, U = 0.76 V, I = 0.80 mA) operating on the given fuel at a flow rate of the oxidizing agent—atmospheric oxygen, of 1.80 $cm^3\ min^{-1}$ were obtained with a cermet Ni–YSZ anode no. 2 and a $Ln_{0.8}Ca_{0.2}Mn_{0.94}Cr_{0.04}Ni_{0.02}O_3$ cathode at 1070–1170 K.

ACKNOWLEDGMENTS

The study was supported by the Foundation for Basic Research of the Republic of Belarus (grant no. Kh98-006).

REFERENCES

1. Novikov, G.I. and Gamanovich, N.M., *Zh. Prikl. Khim.*, 2000, vol. 73, no. 2, pp. 334–335.
2. Kukharenko, T.A., *Khimiya i genezis iskopaemykh uglei* (Chemistry and Genesis of Fossil Coal), Moscow: Gosgortekhizdat, 1960.
3. Koryakin, V.I., *Termicheskoe razlozhenie drevesiny* (Thermal Decomposition of Wood), Moscow: Goslesbumizdat, 1962.
4. Lamotkin, A.I., Protsevich, A.A., and Gurin, B.A., *Les. Ekologiya Resursy: Sb. Tr. MNTK* (Minsk), 1998, pp. 279–281.
5. Mori, M., *Proc. 2nd Int. Fuel Cell Conf.*, Tokyo, February 5–8, 1996, Tokyo, 1996, pp. 10–12.
6. Fukui, T., Ohara, S., and Mukai, K., *Electrochem. Solid-State Lett.*, 1998, vol. 1, no. 3, pp. 120–122.
7. Pal'guev, S.V., Gil'derman, V.K., and Zemtsov, V.I., *Vysokotemperaturnye oksidnye elektronnye provodniki dlya elektrokhimicheskikh ustroistv* (High-Temperature Oxide Electronic Conductors for Electrochemical Devices), Moscow: Nauka, 1990.

Russian Journal of Applied Chemistry, Vol. 74, No. 2, 2001, pp. 338–340. Translated from Zhurnal Prikladnoi Khimii, Vol. 74, No. 2, 2001, pp. 332–334.

BRIEF COMMUNICATIONS

Calculation of Current Strength in Reactor with Combined Anodes

T. N. Ostanina, V. M. Rudoi, N. I. Ostanin, and E. I. Kosheleva

Ural State Technical Univrersity, Yekaterinburg, Russia

Received February 16, 2000; in final form, May 2000

Abstract—A method is proposed for calculating the potentials of anodes made of various metals, total voltage across reactor, and current distribution among dissimilar anodes. Calculated data are compared with the performance parameters of a real reactor.

One of the most efficient methods for wastewater purification is electrocoagulation [1]. Anodes (made of iron and aluminum) dissolve in the reactor situated in a purification unit. In the process, metal cations pass into solution, which leads, in neutral medium, to formation of insoluble hydroxides. Molecules of hydroxides coagulate to form flakes onto which impurities (oil product wastes, fine suspended particles, etc.) are adsorbed. The purification process, as a rule, starts already in the reactor and is completed in the next chamber. The main process occurring at the anode is hydrogen evolution, which makes higher the degree of purification because of the carry-over of coagulating particles by gas bubbles. The basic problem in the operation of the reactor is the anode passivation. The passive film drastically retards the process of metal cation formation, the anode potential is shifted to the positive region, and oxygen evolution starts. In choosing technological conditions of reactor operation, it is necessary that the anode potential should be more negative than the potential of the onset of passivation of the corresponding metal. The calculation of the potential becomes complicated when anodes of different metals (iron and aluminum) are used, since it is not known how the current is distributed among the anodes.

In this communication, a method is proposed for calculating the potentials of anodes made of different metals and the distribution of the current in a reactor with combined anodes.

The voltage U across the electrolyzer is determined [2] by the difference of the potentials E_a and E_c of the anode and cathode, ohmic voltage drop across the electrolyte (ΔU_{el}), voltage drop across the electrode bulk ($\Delta U_{s.e}$), and that across the contacts (ΔU_{cont}).

$$U = E_a - E_c + \Delta U_{el} + \Delta U_{s.e} + \Delta U_{cont}. \quad (1)$$

If combined anodes are installed in the reactor [e.g., iron (1) and aluminum (2)], then, by virtue of the different kinetic parameters of ionization of the metals, their dissolution will proceed at different rates and, therefore, the current densities at different anodes and their potentials will differ. In this case, the electric balance will be preserved ($U_1 = U_2$). If the voltage drops across the electrode bulk and contacts are neglected, then it can be written

$$E_{a,1} + \Delta U_{el,1} = E_{a,2} + \Delta U_{el,2}. \quad (2)$$

The ohmic voltage drop across the electrolyte is determined, in accordance with Ohm's law, by the current load I of the electrolyzer, anode surface area S, distance L between the anode and cathode, and electrical conductivity of the electrolyte æ

$$\Delta U_{el} = I\frac{L}{æS} = \frac{iL}{æ}, \quad (3)$$

where i is the current density.

In the calculation it was assumed that the anodic process occurs by the retarded ionization mechanism [3] and the cathodic component can be neglected under the conditions considered

$$i_a = i_{ex}\exp\left[\frac{\beta zF}{RT}(E_a - E_{eq})\right], \quad (4)$$

where i_{ex} is the exchange current density, and E_{eq} is the equilibrium potential.

1070-4272/01/7402-0338 $25.00 © 2001 MAIK "Nauka/Interperiodica"

Taken as a whole, the processes of dissolution of the iron and aluminum anodes can be represented by the equations

$$Fe^0 - 2e \rightarrow Fe^{2+},$$
$$Al^0 - 3e \rightarrow Al^{3+}.$$

If account is taken of the dependence of the exchange current i_{ex} on the concentration C_{ox} of the oxidized form of a substance in solution (with metal being the reduced form), then it is necessary to introduce into the expression for the exchange current the accepted concentration standard St, equal, in SI units, to 1000 mol m^{-3} [4]:

$$i_{ex} = zFk^s C_{ox}^{\beta} St^{(1-\beta)}. \quad (5)$$

The equilibrium potential E_{eq} is found from the Nernst equation

$$E_{eq} = E^0 + \frac{RT}{zF} \ln \frac{C_{ox}}{St}. \quad (6)$$

On being transformed, Eq. (4) is written as

$$i_a = A\exp\left(\frac{\beta zF}{RT} E_a\right), \quad (7)$$

$$A = zFk^s St \exp\left(-\frac{\beta zF}{RT} E^0\right).$$

The anode current density is determined by the heterogeneous rate constant of the electrode process, k^s, transfer coefficient of the anodic process β, and standard potential E^0, i.e., depends on the nature of a metal being dissolved.

With account of (3) and (7), Eq. (2) takes the form

$$E_{a,1} + \frac{L}{æ}\left[A_1\exp\left(\frac{\beta_1 z_1 F}{RT} E_{a,1}\right)\right] = E_{a,2} + \frac{L}{æ}\left[A_2\exp\left(\frac{\beta_2 z_2 F}{RT} E_{a,2}\right)\right]. \quad (8)$$

The total current through the electrolyzer is the sum of the currents flowing through all the anodes

$$I = i_{a,1}S_1 + i_{a,2}S_2. \quad (9)$$

Solving the system of equations (8), (9) allows calculation of the potentials of anodes made of different metals (iron and aluminum). Then Eq. (7) can be applied to calculate the current densities for different anodes. If known, the anode potentials enable evaluation of the probability of passivation of electrodes made of various metals; a knowledge of the dissolution rates makes it possible to calculate the amount of iron and aluminum hydroxides in solutions, which is important for achieving the required level of water purification.

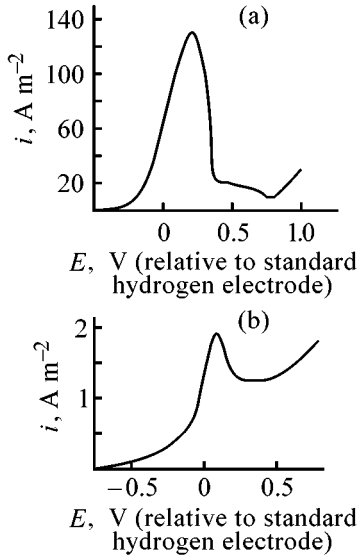

Fig. 1. Anodic polarization curves for dissolution of (a) iron and (b) aluminum in water subjected to purification, with addition of 1000 mol m^{-3} of sodium sulfate. (*i*) Current density and (*E*) potential (relative to standard hydrogen electrode).

The approach described above was used to analyze the technological mode of operation of the reactor in the UKOS-AVTO-5 unit employed to purify wastewater from car washes. The water subjected to purification contained 0.1 kg m^{-3} of oil products and 0.95 kg m^{-3} of suspended particles. The reactor of volume 1 × 0.38 × 0.73 m has 12 anodes (6 iron and 6 aluminum) and 12 iron cathodes of area 0.81 × 0.44 m each. The distance between the electrodes was 0.006 m. The overall load was 10 A.

An R-577 ac bridge was used to measure the electrical conductivity of the water being purified (æ = 0.38 S m^{-1}). Anodic polarization curves of iron and aluminum dissolution were taken with a P-5848 potentiostat (Fig. 1). The measurements were done in a three-electrode cell. The surface area of the working electrode was 0.36×10^{-3} and 0.09×10^{-3} m^2 for, respectively, iron and aluminum. An iron plate served as auxiliary electrode, and a saturated silver chloride electrode, as reference. In polarization studies, 1000 mol m^{-3} of sodium sulfate was added to the starting water to diminish the measurement error associated with the large voltage drop across the electrolyte. This compound has no effect on the anode passivation, but makes higher the electrical conductivity of the solution. The potentials of the onset of passivation, measured relative to the standard hydrogen elec-

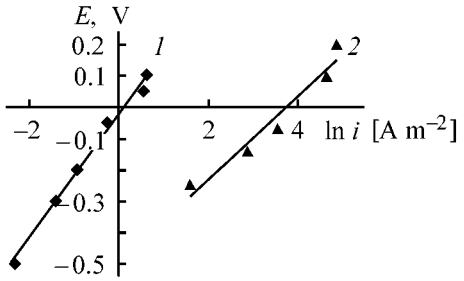

Fig. 2. E–ln i dependences taken with (*1*) aluminum and (*2*) iron electrodes. Solution: water subjected to purification, with addition of 1000 mol m^{-3} of sodium sulfate.

trode, were 0.21 and 0.09 V for iron and aluminum, respectively (Fig. 1). The dependence of the anode potential on the current density was obtained via transformation of Eq. (7)

$$E_a = -\frac{RT}{\beta zF}\ln A + \frac{RT}{\beta zF}\ln i_a. \qquad (10)$$

Analysis of the region of active dissolution of metals in the polarization curves plotted in the semilogarithmic coordinates does not contradict the assumption that the dissolution of both iron and aluminum electrodes occurs by the retarded ionization mechanism (Fig. 2). Regression analysis technique was applied to determine the coefficients in the straight-line equation (10) and then to calculate the kinetic parameters of iron and aluminum ionization (k^s and β). All the calculations were done on a PC with Mathcad 6 PLUS software. Solving the system of equations (8), (9) demonstrated that the potential of iron and aluminum anodes in the reactor E_{Fe} = –0.303 V and E_{Al} = –0.275 V. It can be seen from the polarization curves in Fig. 1 that no passivation must be observed at these potentials, which is the case. The dissolution current densities i_{Fe} = 2.055 A m^{-2} for the iron anode and i_{Al} = 0.283 A m^{-2} for the aluminum anode, which corresponds to the values found experimentally from the polarization curves (Fig. 1). The total voltage across the reactor, calculated by Eq. (1), was 0.4 V, which is also close to the measured value.

The agreement between the calculation results and the operation parameters of a real reactor suggests that the proposed method can be used to prognosticate the working conditions of an electrolyzer with combined anodes in choosing an optimal technological mode and intensifying the purification process.

CONCLUSIONS

(1) A method is proposed for calculating the potentials of anodes made of dissimilar materials and connected in parallel. A calculation using the basic equations of electrochemical kinetics was done taking in account the total number of electrons involved in the reaction.

(2) Anodic polarization curves were obtained for dissolution of iron and aluminum in water subjected to purification. The potentials of the onset of metal passivation under the experimental conditions were determined.

(3) The operation of the reactor in a unit for water purification was analyzed. The potentials of the iron and aluminum anodes and the current distribution among the anodes were calculated. It is shown that no anode passivation occurs under the conditions under consideration.

REFERENCES

1. Yakovlev, S.V., Krasnoborod'ko, I.G., and Rogov, V.M., *Tekhnologiya elektrokhimicheskoi ochistki vody* (Technology of the Electrochemical Purification of Water), Moscow: Stroiizdat, 1987.
2. *Prikladnaya elektrokhimiya* (Applied Electrochemistry), Tomilov, A.P., Ed., Moscow: Khimiya, 1984.
3. Damaskin, B.B. and Petrii, O.A., *Vvedenie v elektrokhimicheskuyu kinetiku* (Introduction into Electrochemical Kinetics), Moscow: Vysshaya Shkola, 1983.
4. Rudoi, V.M. and Murashova, I.B., *Zh. Fiz. Khim.*, 1998, vol. 72, no. 7, pp. 229–232.

Russian Journal of Applied Chemistry, Vol. 74, No. 2, 2001, pp. 341–343. Translated from Zhurnal Prikladnoi Khimii, Vol. 74, No. 2, 2001, pp. 335–337.

BRIEF COMMUNICATIONS

Combined Air Electrode Based on Polyaniline with Addition of Manganese Dioxide

M. O. Danilov and N. V. V'yunova

Institute of General and Inorganic Chemistry, National Academy of Sciences of Ukraine, Kiev, Ukraine

Received July 3, 2000

Abstract—Air electrodes based on polyaniline with an additive were studied in a prototype zinc–air power cell with salt electrolyte. Electrolytic manganese dioxide was chosen as additive. Discharge current–voltage (*I*–*V*) characteristics of the prototype chemical power cell based on a combined air electrode composed of polyaniline and manganese dioxide taken in 1 : 1 ratio are presented.

An electrically conducting polymer, polyaniline (PA), obtained by various methods from aniline, is widely used in electrochemical devices. One of its applications is that as a cathode material for chemical power cells with salt electrolyte [1–3]. The problem of obtaining this polymer and accounting for its electrical conductivity was discussed in [1, 4]. Polyaniline shows pronounced capacity for cycling in power cells, but has low working voltage [3]. To eliminate this disadvantage, it has been proposed to introduce into PA an additive possessing electrical conductivity and involved in the current-forming reaction at the air electrode.

The aim of this study was to verify the possibility of improving the electrical characteristics of PA-based electrodes by introducing into PA an additive having electrical conductivity higher than that of polyaniline and contributing to current generation at the air electrode. A possible additive of this kind is electrolytic manganese dioxide (EMD) possessing these properties.

A schematic of the conventional air electrode is presented in Fig. 1. The electrode comprises an active and a hydrophobic layers. It can be represented as a two-layer membrane separating the electrolyte and air. The layer adjacent to the electrolyte is hydrophilic, and that facing air, hydrophobic. In the operation of the air electrode, atmospheric oxygen diffuses through the hydrophobic layer and comes in contact with electrolyte penetrating through the active, hydrophilic layer. Therefore, the reaction of oxygen reduction is localized at the electrode–electrolyte–air interface.

In making a combined matrix, a mechanical mixture of PA and EMD was pressed in the hydrophobic layer to obtain a more diffuse electrode–electrolyte–air interface. Polyaniline was obtained by dc electrolysis of a 0.1 M solution of aniline in 1 M hydrochloric acid [5]. The starting aniline solution was colorless, i.e., unoxidized. All the reagents were of analytically pure grade. Polyaniline was deposited on a carbon fabric anode at current density of 5 mA cm^{-2}. A VT 1.0 titanium plate served as cathode. The PA layer was detached from the carbon fabric and dried at 90°C in a drying box. An EMD of chemically pure grade (Rustavi, Georgia) was used to prepare the mechanical mixture.

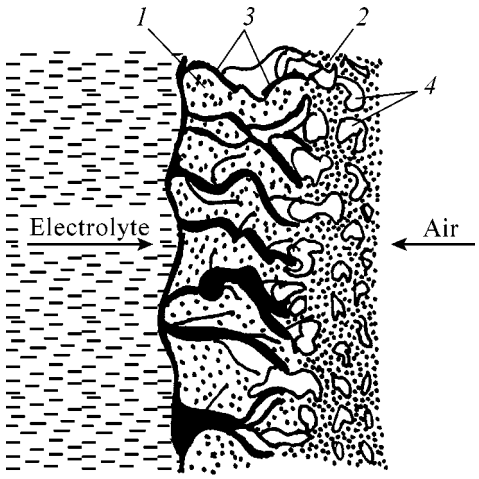

Fig. 1. Schematic of the air electrode: (*1*) active layer, (*2*) hydrophobic layer, (*3*) pores filled with electrolyte, and (*4*) pores filled with air.

1070-4272/01/7402-0341 $25.00 © 2001 MAIK "Nauka/Interperiodica"

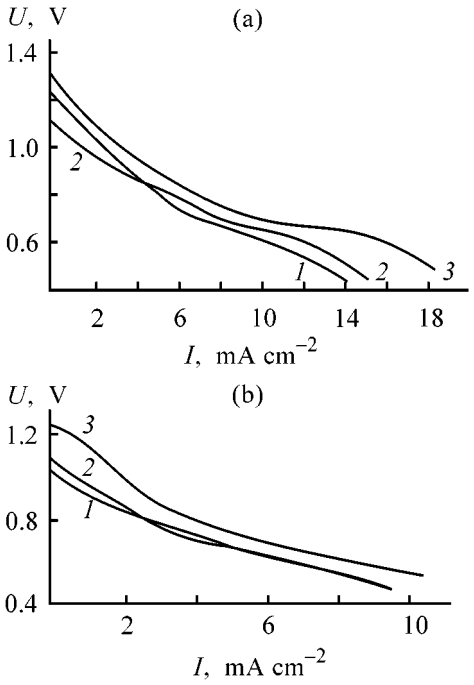

Fig. 2. *I–V* curves for prototype zinc–air power cell. Mass of the active layer in the air electrode (g): (a) 0.2 and (b) 0.1. (*U*) Voltage and (*I*) current density. Electrode material: (*1*) EMD, (*2*) PA, and (*3*) Combined PA–EMD matrix.

Electrodes used in the study were compacted in the form of pellets 3 cm in diameter from PA, EMD, and a 1 : 1 mechanical mixture of these compounds. Sets of electrodes with active layer mass of 0.2 and 0.1 g were fabricated. A hydrophobic layer of mass 0.3 g contained 70% acetylene black and 30% F-4D fluoroplastic emulsion in terms of dry substance.

Investigations were performed in galvanostatic mode with a prototype zinc–air power cell with electrolyte of composition 5 M NH_4Cl + 2 M $ZnCl_2$. The potentials of the air electrode were measured with high-resistance voltmeter relative to a silver chloride reference electrode. The prototype power cell voltage and the potential of the air electrode at each current density were recorded after a delay of 5 min.

Prior to cycling, the prototype power cell with a zinc–air electrode was discharged at a current density of 6 mA cm^{-2} until the voltage became 0.5 V. The current densities of power cell charging and discharge were the same and chosen in such a way that the charge capacity was twice the discharge capacity. The prototype power cell was cycled until the discharge capacity became less than half the charging capacity at a current density chosen for each air electrode.

Figure 2a presents *I–V* discharge curves for electrodes with active mass of 0.2 g. It can be seen from the discharge curves that a combined matrix of PA and EMD (Fig. 2a, curve *3*) with component ratio of 1 : 1 gives a better discharge curve than its separate components—PA (curve *2*) and EMD (curve *1*). Comparison of the discharge curves for PA and EMD shows that, at discharge current densities of up to 4 mA cm^{-2}, the working voltage of EMD electrodes exceeds that of electrodes made of polyaniline. At current densities in the range from 4 to 13 mA cm^{-2} the working voltage of polyaniline electrodes is the same as, or somewhat higher than the discharge voltage of the EMD electrodes.

Figure 2b shows *I–V* discharge curves for electrodes with active layer mass of 0.1 g. It can be seen that the combined matrix (curve *3*) has better discharge characteristics in this case, too. At current densities of up to 2 mA cm^{-2}, the electrode of pure PA (Fig. 2b, curve *2*) works better than the EMD electrode at smaller active layer mass. With the current density increasing from 2 to 8 mA cm^{-2}, the *I–V* discharge curves for PA and EMD are virtually the same.

Thus, the combined matrix of PA and EMD with component ratio of 1 : 1 shows better discharge characteristics, compared with air electrodes made of pure components. Cycling of PA + EMD electrodes in a prototype zinc–air power cell demonstrated the possibility of performing up to 30 charging–discharge cycles without capacity loss after the primary complete discharge of the power cell. These characteristics are inferior to those for pure PA (300 cycles), but better than the characteristics of EMD (10–15 cycles).

Possibly, the increase in the catalytic activity of the combined PA + EMD matrix is associated with the appearance of oxygen-containing groups on PA. These groups accumulate in the course of electrosynthesis on the surface of PA particles. When PA is combined with EMD, these oxygen-containing groups provides the electrode with oxygen, ensuring chemical oxidation of MnOOH to MnO_2. Therefore, the amount of EMD decreases in the course of discharge not so strongly owing to the conversion of MnO_2 into MnOOH. Intercalation by chlorine occurs in PA [3]. Schematically, all the processes occurring in the combined matrix of the air electrode can be represented by the reactions

$$2PACl_n + 2ne \rightarrow 2PA + 2nCl^-, \quad (1)$$

$$O_2 + 4H^+ + 4e \rightarrow 2H_2O, \quad (2)$$

$$MnO_2 + H_2O + e \rightarrow MnOOH + OH^-, \quad (3)$$

$$4MnOOH + O_2 \rightarrow 4MnO_2 + 2H_2O. \quad (4)$$

A conclusion can be made from reactions (1)–(4) that current generation at the combined matrix occurs by reactions (1)–(3). Reaction (4) gives, additionally, MnO_2 via chemical oxidation of MnOOH to MnO_2 by oxygen from the oxygen-containing groups on PA.

Thus, to improve the discharge characteristics of PA-based power cells, it is necessary to introduce into PA electrically conducting additives involved in the current-forming reactions. In particular, air electrodes with better electrolytic characteristics can be obtained on the basis of a combination of PA with EMD.

REFERENCES

1. Mengoli, G., Musiani, M.M., Pletcher, D., and Valcher, S., *J. Appl. Electrochem.*, 1987, vol. 17, no. 3, pp. 515–524.
2. Mengoli, G., Musiani, M.M., Pletcher, D., and Valcher, S., *J. Appl. Electrochem.*, 1987, vol. 17, no. 3, pp. 525–531.
3. Mu, S., Ye, G., and Wang, Y., *J. Power Sources*, 1993, vol. 45, no. 2, pp. 153–159.
4. Konig, U. and Schultze, J.W., *J. Electroanal. Chem.*, 1988, vol. 242, no. 1, pp. 243–254.
5. Danilov, M.O. and V'yunova, N.V., *Zh. Prikl. Khim.*, 2000, vol. 73, no. 3, pp. 418–420.

Russian Journal of Applied Chemistry, Vol. 74, No. 2, 2001, pp. 344–346. Translated from Zhurnal Prikladnoi Khimii, Vol. 74, No. 2, 2001, pp. 337–339.

BRIEF COMMUNICATIONS

Mechanism of Coagulation Purification of Wastewater with Aluminum Oxochloride

Yu. A. Feofanov and N. L. Litmanova

St. Petersburg University of Architecture and Construction, St. Petersburg, Russia

Received August 1, 2000

Abstract—Results of a coagulation purification of solutions modeling weakly contaminated wastewater from dairy shops are presented. The influents of detergents (HNO_3 and NaOH) and aluminum oxochloride on the process of contaminant removal from a milk solution in the pH range 2–12 is considered. Distinctions are noted in the behavior of model milk solutions with contaminant concentration. The results of studies performed at varied doses of aluminum oxochloride by the optical and electrophoretic methods are used to explain the mechanism of coagulation purification of model wastewater.

The great bulk of waste produced by plants is constituted by wastewater formed in washing of the dairy equipment. The washing process consists in several successive operations, each using one of the following reagents: acids, alkalis, or sterilizing agents, with the entire process completed by rinsing in pure water. As a result, the wastewater delivered to the purification facilities has qualitative and quantitative composition abruptly varying with time.

The results obtained in a study of the coagulation purification of solutions modeling strongly contaminated wastewater of dairy shops with the use of aluminum oxochloride (AOC) were reported in [1].

The aim of the present study was to analyze the behavior of wastewater with low content of impurities upon addition of various reagents: detergents and AOC. To reveal the influence exerted by each kind of contaminant on the process of coagulation, wastewater was replaced by model solutions.

The solution under study, obtained by diluting milk with distilled water, contained (mg l^{-1}): fat 350 and protein 280, and were characterized by chemical oxygen demand of 900 mg O_2 l^{-1}, which corresponds to the composition of dairy plant wastewater with moderate contamination. The pH was varied by adding industrial detergents: 1% solution of nitric acid and 0.1 N solution of sodium hydroxide. As coagulant was used freshly prepared 1% solution of AOC with basicity factor [$OH^-/(OH^- + Cl^-)$ ratio] of 5/6.

After mixing a milk solution with a coagulant by the procedure described in [2] and allowing the samples to stand for 1 h, the efficiency of purification was evaluated by the residual content of organic substances, determined from the loss in calcination of the dry residue [3].

The kinetics of impurity sedimentation was studied by measuring the optical density of solutions treated with a coagulant for 1 h on a KFK-2MP photocolorimeter in 1-cm-long cuvettes at light wavelength λ = 440 nm.

The electrokinetic potential of milk particles without AOC and with varied concentration of this compound was determined by microelectrophoresis [4] in a modified Abramson cell and PZO microscope (Poland). The ξ-potential was calculated using the Smoluchowski formula from the arithmetic-mean value of the electrophoretic velocity of 15–20 particles.

The efficiency of removal of organic impurities, E_{org}, is presented in Figs. 1 and 2 in relation to the pH value. The presence of only detergents without AOC in weakly contaminated solutions (Fig. 1, curve *1*) destabilizes the system (acid coagulation) at pH 4.75–5.10, with the maximum degree of purification (40%) observed at pH 5.0, which can be attributed to the electrical properties of the emulsion stabilizer—casein, whose isoelectric point lies in the above pH interval [5]. This is confirmed by the results of electrophoretic measurements (Fig. 1, curve *3*) indicating that the particle charge is the smallest in this pH range. In a more concentrated solution [1], the system coagulated at pH 4–5, with 50% removal of impurities

1070-4272/01/7402-0344 $25.00 © 2001 MAIK "Nauka/Interperiodica"

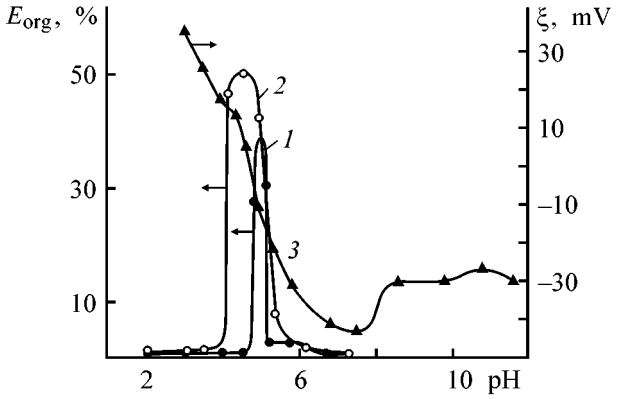

Fig. 1. (*1, 2*) Efficiency of organic substance removal, E_{org}, and (*3*) ξ-potential of particles vs. the pH of the model milk solution. Concentrations of fat and protein (mg l^{-1}): (*1, 3*) 350 and 280, (*2*) 1750 and 1450 {(*2*) data of [1]}.

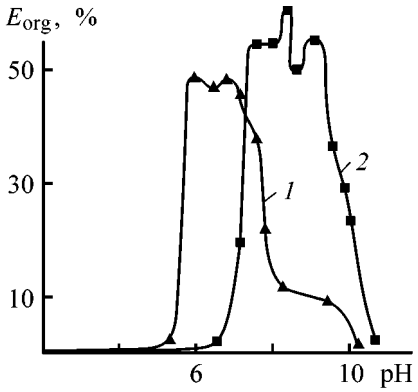

Fig. 2. Efficiency of organic substance removal, E_{org}, in the presence of AOC vs. the pH of the model milk solution. Concentrations of fat and protein 350 and 280 mg l^{-1}, respectively; the same for Fig. 3. Coagulant dose (mg l^{-1} in terms of Al_2O_3): (*1*) 60 and (*2*) 180.

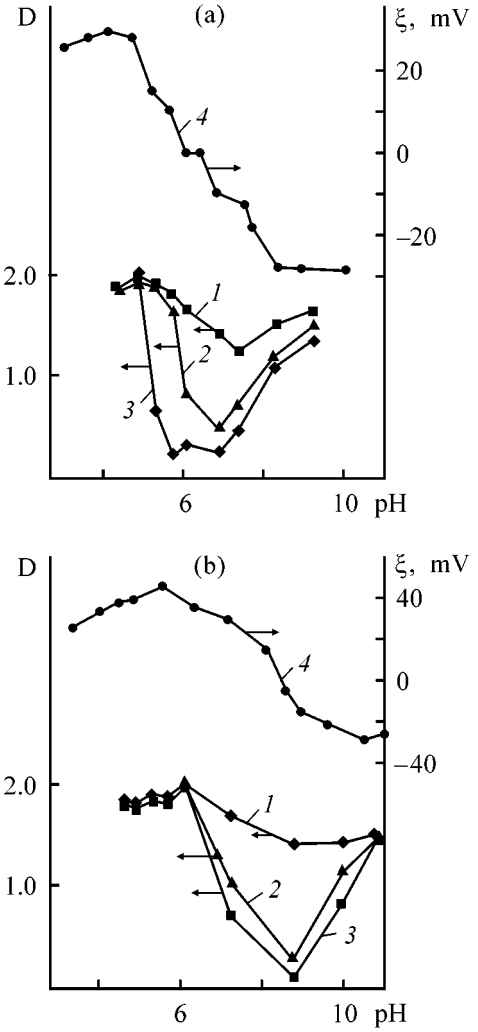

Fig. 3. (*1–3*) Optical density and (*4*) ξ-potential of particles vs. the pH of the model milk solution. AOC dose (mg l^{-1} in terms of Al_2O_3): (a) 60, (b) 180. Time of coagulation upon AOC introduction (min): (*1*) 1, (*2*) 10, and (*3*) 60.

achieved at pH 4.5 (Fig. 1, curve *2*). The observed slight differences in purification efficiency and pH ranges of efficient impurity removal between two model solutions can be accounted for by the fact that the number of collisions between protein particles grows with their increasing concentration. Under conditions close to the isoelectric state, when the stability of the system is the lowest, this leads to appearance of coarser aggregates of the disperse phase and its more complete sedimentation.

The peak in the curve describing the purification of a weakly contaminated solution is shifted to the less acid region (pH 4.9; Fig. 1, curve *1*), compared with that in a solution containing a greater amount of impurities (curve *2*), and, therefore, a smaller amount of acid is to be introduced to bring negatively charged protein molecules into the isoelectric (or nearly so) state. This can be attributed to the smaller density of surface charge of the colloid phase in the first case.

The run of the curves describing the efficiency of removal of organic impurities as a function of the pH of the medium is strongly affected by addition of AOC (Fig. 2). Adding 60 mg l^{-1} of coagulant (in terms of Al_2O_3) at pH < 5.1 does not destabilize the milk solution (curve *1*). This pH range is characterized by high, and invariable with time, values of the optical density of the system (Fig. 3a, curves *1–3*). With the AOC concentration increasing to 180 mg l^{-1} in terms of Al_2O_3 (3.6×10^{-3} M in terms of aluminum), a similar behavior is observed at pH < 6.1 (Fig. 3b, curves *1–3*).

It can be seen from the electrokinetic data that rather high positive ξ-potentials of the particles in the system under study are observed in these pH regions (Figs. 3a and 3b, curves *4*). The reason is that the strongly (positively) charged hydroxo complexes of aluminum, appearing at the above pH values and having high adsorbability, interact with the initially uncharged or weakly charged particles of the milk solution, recharging these latter and stabilizing the entire system. As it can be seen from Figs. 3a and 3b (curves *4*), the charge of particles formed as a result of such an interaction grows with increasing coagulant dose. This can be attributed to the favorable influence of the increasing concentration of aluminum on the hydrolytic polymerization, with polycations having greater charge formed in this pH range [6].

The coagulation of the given model solution and removal of impurities at AOC content of 180 mg l^{-1} in terms of Al_2O_3 is observed in the pH range 6.5–10.25 (Fig. 2, curve *2*). The process reaches the maximum efficiency (up to 60% removal of organic substances) in the pH range 7.3–9.5. Lowering the coagulant dose to 60 mg l^{-1} in terms of Al_2O_3 shifts this region to the left along the pH scale and restricts it to pH of 5.75–7.5 with the maximum purification of 48% (Fig. 2, curve *1*). It is in these pH ranges, where the peak efficiencies of purification to remove organic impurities are observed, that the electrokinetic potentials of particles belonging to the system under study are the lowest at both AOC concentrations (Figs. 3a and 3b). These data indicate a neutralization mechanism of coagulation.

However, a small coagulation zone observed in Fig. 2 (curve *2*) in alkaline medium (pH 9.5–10.25) at an AOC concentration of 180 mg l^{-1} coincides with the region of rather high negative values of the ξ-potential of particles (Fig. 3b, curve *4*). The partial sedimentation of the milk dispersion under these conditions is, in all probability, due to the occurrence of a heterocoagulation process with efficiency much lower than that of the neutralization coagulation.

CONCLUSIONS

(1) Use of aluminum oxochloride to purify weakly contaminated milk wastes allows efficient removal of organic impurities in a rather wide pH range.

(2) The maximum efficiency of purification of a model solution in the case of coagulant addition is ensured by the action of neutralization mechanisms.

(3) The pH range in which the neutralization coagulation proceeds depends on the concentration of aluminum oxochloride in solution.

(4) In the absence of aluminum oxochloride, the position of the peak in the curve describing the dependence of the purification efficiency on the pH value is determined by the initial concentration of contaminants.

REFERENCES

1. Feofanov, Yu.A. and Litmanova, N.L., *Zh. Prikl. Khim.*, 2000, vol. 73, no. 8, pp. 1390–1391.
2. Chernoberezhskii, Yu.M., Bykova, N.I., and Yanklovich, A.I., *Vestn. Len. Gos. Univ.*, 1982, no. 6, pp. 106–108.
3. *Unifitsirovannye metody analiza vod* (Unified Methods of Water Analysis), Lur'e, Yu.Yu., Ed., Moscow: Khimiya, 1973, 2nd revised ed.
4. Grigorov, O.N., Karpova, I.F., Koz'mina, Z.P., *et al.*, *Rukovodstvo k prakticheskim rabotam po kolloidnoi khimii* (Manual of Colloid Chemistry), Leningrad: Khimiya, 1964.
5. Töpel, A., *Chemie und Physik der Milch*, Leipzig: Fachbuchverlag, 1976.
6. Zapol'skii, A.K. and Baran, A.A., *Koagulyanty i flokulyanty v protsesse ochistki vody* (Coagulants and Flocculants in Water Purification), Leningrad: Khimiya, 1987.

Russian Journal of Applied Chemistry, Vol. 74, No. 2, 2001, pp. 347–349. Translated from Zhurnal Prikladnoi Khimii, Vol. 74, No. 2, 2001, pp. 340–342.

BRIEF COMMUNICATIONS

Sorption Capacity of Nitrogen-containing Derivatives of Wood for Ions of Various Metals

M. V. Efanov and A. G. Klepikov

Altai State University, Barnaul, Russia

Received July 13, 2000

Abstract—Sorption capacity of nitrogen-containing derivatives of aspen wood for Fe(III), Cu(II), Cd(II), and Ca(II) ions was studied. The possibility of using the products formed in oxyammonolysis of wood as sorbents of these metals from dilute aqueous solutions was examined.

Nitrogen-containing derivatives of lignin have ion-exchange properties and can be used as sorbents of heavy metal ions and organic dyes [1, 2]. The main drawbacks of these products are relatively low exchange capacity and low mechanical strength.

Previously, a procedure has been proposed for production of nitrogen-containing sorbents based on lignin by treatment of the industrial lignin with tetraalkylammonium salts [3]. The resulting sorbents exhibited improved mechanical strength and high sorption capacity for dyes (50–80 mg g^{-1}).

However, in the proposed procedure the yield of the target product is relatively low (up to 30–40% of the lignin weight in 1–3 days). To produce nitrogen-containing sorbents in quantitative yield, hydrolyzed lignin was treated with aqueous ammonia solutions of ammonium peroxodisulfate under mild conditions at 20°C for 1–5 days [4]. Along with hydrolyzed lignin, poor wood can be used as a raw material for production of nitrogen-containing sorbents.

In this work we studied the sorption capacity of nitrogen-containing derivatives of aspen wood, produced under conditions described in [4] and also by mechanochemical procedure, for ions of some metals.

EXPERIMENTAL

As raw materials we used air-dry sawdust of aspen wood approximately 50 years of age crushed to 0.4–0.75-mm fraction. The wood was analyzed by the well-known procedures [5]. The chemical composition of aspen wood was as follows:

Component	Content, % relative to absolutely dry raw material
Cellulose	49.6
Lignin	21.2
Pentosan	21.6
Extractives	3.96
Ash	0.26

Nitrogen-containing derivatives of wood were obtained by two procedures. According to the first procedure, the sawdust was treated with large excess of ammonia solution of ammonium peroxodisulfate at 20–25°C for 1–3 days [4]. According to the second, the sawdust combined with ammonium peroxodisulfate (0.1 g of available oxygen per 1 g of wood) was mechanically crushed in a ball mill in 25% aqueous ammonia (0.5 g of NH_3 per 1 g of wood) for 0.5–2 h.

Then, the products were washed with water to negative reaction for sulfate ion and dried in air to constant weight. The nitrogen content in the resulting samples was determined by the Kjeldahl semimicromethod [6], and the number of carboxyl groups, by conductometric titration [7]. The characteristics of the resulting products are listed in Table 1.

The sorption capacity of the resulting products was studied by establising equilibrium by means of the procedure described in [8]. For this purpose, weighed portions of samples (0.1–0.2 g) were placed in flasks, and 25 cm^3 of a solution of metal nitrates with concentration varying from 0.01 to 0.1 g-equiv dm^{-3} was added to each flask. When the equilibrium was

1070-4272/01/7402-0347 $25.00 © 2001 MAIK "Nauka/Interperiodica"

Table 1. Characteristics of nitrogen-containing derivatives of aspen wood. Oxygen 0.1 g per 1 g of wood

Sample no.	Oxidation conditions		Yield, %	Content, %	
	τ, h	NH_3, g per 1 g of wood		N	COOH
1	24	12.5	81.3	4.51	2.48
2	48	12.5	75.9	6.76	3.57
3	72	12.5	74.1	8.95	5.34
4*	0.5	0.5	97.4	1.86	2.54
5*	1	0.5	96.2	2.59	3.68
6*	2	0.5	95.8	4.76	5.47

* Product nos. 4–6 were obtained under conditions of mechanochemical synthesis (procedure 2); the same for Table 2.

Table 2. Sorption power of nitrogen-containing derivatives of aspen wood with respect to metal ions

Sample no.	τ, h	Content, %		Sorption, g-equiv g^{-1}			
		N	COOH	Cu^{2+}	Cd^{2+}	Fe^{2+}	Ca^{2+}
1	24	4.51	2.48	4.86	3.62	1.63	1.21
2	48	6.76	3.57	5.67	4.21	2.06	1.43
3	72	8.95	5.34	6.23	4.65	2.98	1.72
4*	0.5	1.86	2.54	4.27	3.42	1.37	1.02
5*	1	2.59	3.68	5.06	3.89	1.79	1.24
6*	2	4.76	5.47	7.05	5.42	3.78	1.89

Table 3. Effect of cation concentration in the initial solution C_{in} on the sorption power of some products of ammonolysis of aspen wood*

C_{in}, g-equiv dm^{-3}	Sorption, g-equiv g^{-1}			
	Cu^{2+}	Cd^{2+}	Fe^{2+}	Ca^{2+}
0.01	6.72	5.22	3.58	1.74
0.05	6.91	5.27	3.65	1.82
0.1	7.05	5.41	3.76	1.89

* Sample no. 6 obtained by procedure 2.

attained (after 24 h), the concentration of the corresponding ion in the solution was determined conductometrically.

The absorption was evaluated by the formula

$$A = (C_{in} - C_{eq})V/1000g, \quad (1)$$

where A is the absorption (g-equiv g^{-1}), C_{in} is the concentration of metal ion in the initial solution (g-equiv dm^{-3}), C_{eq} is the concentration of metal ion in the equilibrium solution (g-equiv dm^{-3}), V is the volume of the equilibrium solution (cm^3), and g is the weighed portion of the sorbent.

To estimate quantitatively the distribution of cations between the sorbent and solution, we evaluated the distribution coefficient K_d at low concentrations:

$$K_d = (C_{in} - C_{eq})V/1000gC_p. \quad (2)$$

The selectivity coefficient D characterizing the efficiency of separation of cations A and B was determined by the formula

$$D_{B/A} = K_{d(A)}/K_{d(B)}. \quad (3)$$

As the experimental results show, the sorption capacity of the products of oxidative ammonolysis of wood for the cations studied depends on the content of nitrogen and COOH groups (Table 2).

The sorption capacity of nitrogen-containing derivatives of wood is sufficiently high for all the cations studied, which is caused by the high content of carboxy groups and nitrogen (Table 2).

The high sorption power with respect to multicharged cations of the products of oxidative ammonolysis of wood with high content of COOH groups and nitrogen content of 1.86–8.95% is due to their chelating characteristics. Therefore, ions of *d* elements (Cu^{2+}, Cd^{2+}, and Fe^{3+}) are sorbed to the greatest extent, and Ca^{2+} ions, to the lowest. The sorption power with respect to the ions under the study decreases in the order: $Cu^{2+} > Cd^{2+} > Fe^{3+} > Ca^{2+}$ (Tables 2, 3). Making lower the concentration of ions in solution does not result in any significant decrease in their absorption with wood sorbents, i.e., the sorbents show high sorption power even in the case of dilute solutions (Table 3).

It was found that the sorbents produced from nitrogen-containing derivatives of wood are the most selective with respect to Cu(II) ions (Table 4).

The products obtained by the mechanochemical procedure (sample nos. 4–6) have, even at low nitrogen content and practically the same amount of COOH groups as in sample nos. 1–3, comparable sorption powers (Table 2). This can be explained by an increase in their specific surface area on milling.

Thus, the products of oxidative ammonolysis of aspen wood can be used as efficient sorbents with re-

Table 4. Selectivity coefficients of nitrogen-containing derivatives of wood with respect to the studied ions

Sample no.	Cu^{2+}/Ca^{2+}	Cu^{2+}/Cd^{2+}	Cu^{2+}/Fe^{3+}	Ca^{2+}/Cd^{2+}	Ca^{2+}/Fe^{3+}
1	4.62	3.65	2.31	1.12	0.46
2	5.31	3.82	2.53	1.57	0.64
5	5.94	4.28	2.76	1.26	0.71
6	6.29	5.17	3.04	1.78	0.95

spect to cations of transition metals in their recovery from dilute solutions.

CONCLUSIONS

(1) The sorption capacity of modified wood with respect to Fe(III), Cu(II), Cd(II), and Ca(II) ions depends only slightly on their concentration and decreases in the order: Cu(II) > Cd(II) > Fe(III) > Ca(II).

(2) The exchange capacity of nitrogen-containing derivatives of wood is sufficiently high (1.0–7.0 g-equiv g^{-1}) and depends on the content of nitrogen and carboxy groups.

(3) Nitrogen-containing sorbents based on wood are the most selective with respect to Cu(II) ions.

REFERENCES

1. Yaunzems, V.R., Mozheiko, L.N., and Sergeeva, V.N., *Khim. Drev.*, 1968, no. 2, pp. 115.
2. USSR Inventor's Certificate, no. 486033.
3. USSR Inventor's Certificate, no. 1010066.
4. USSR Inventor's Certificate, no. 363710.
5. *Prakticheskie raboty po khimii drevesiny i tsellyulozy* (Practical Works on Chemistry of Wood and Cellulose), Moscow, 1965.
6. Klimova, V.A., *Osnovnye mikrometody analiza organicheskikh soedinenii* (The Main Micromethods of Analysis of Organic Compounds), Moscow: Khimiya, 1975.
7. Mozheiko, L.N., Sergeeva, V.N., *et al.*, *Khim. Drev.*, 1969, no. 3, p. 139.
8. Garkusha, D.G., Kuznetsov, P.M., and Fogileva, R.S., *Zh. Anal. Khim.*, 1974, vol. 29, no. 11, p. 2295.

Russian Journal of Applied Chemistry, Vol. 74, No. 2, 2001, p. 350. Translated from Zhurnal Prikladnoi Khimii, Vol. 74, No. 2, 2001, pp. 342–343.

BRIEF COMMUNICATIONS

Alkylation of *p*-Cresol with Isohexyl Alcohol

I. M. Osadchenko and A. P. Tomilov

State Research Institute of Organic Chemistry and Technology, Moscow, Russia

Received June 23, 2000

Abstract—The feasibility of *p*-cresol alkylation with isohexyl alcohol, using phosphotungstic heteropoly acid as catalyst, was examined.

Alkyl derivatives of *p*-cresol find application as antioxidants, surfactants, and perfumes. In particular, products of *p*-cresol alkylation with isohexyl alcohol are used in synthesis of vetinone perfume (see scheme).

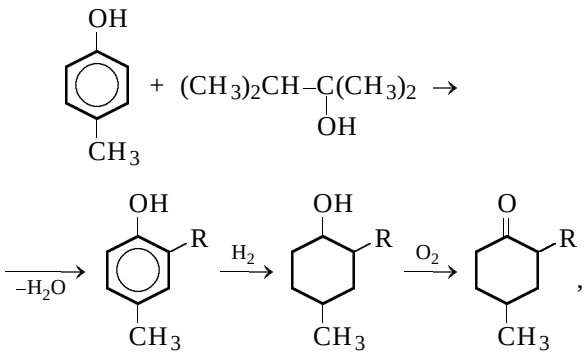

where R = $(CH_3)_2C(OH)–CH(CH_3)_2$.

Kheifits *et al.* [1, 2] studied the alkylation of *p*-cresol in the presence of various catalysts including $Fe_2(SO_4)_3$, $ZnCl_2$, BF_3, and H_2SO_4. Sulfuric acid appeared to be the most suitable. At a 2 : 1 molar ratio of *p*-cresol to alcohol and a temperature of 110–120°C, the target product was obtained in about 50% yield. A major drawback of the process is the appreciable tarring of the reaction mixture containing about 15 wt % tar.

The tarring, and also the high corrosive activity of sulfuric acid stimulated us to look for new catalysts for this process. We decided to test heteropoly acids which have recently found use as catalysts in many processes [3]. Among the tested heteropoly acids, the best results were obtained with reagent-grade phosphotungstic acid $H_7PW_{12}O_{42}$ [TU (Technical Specifications) 6-09-4376–78]. With this catalyst, the formation of tars under the conditions recommended for the process with sulfuric acid decreased by more than a factor of 2.

The experiment with phosphomolybdic acid $H_7PMo_{12}O_{42}$ failed, because the catalyst appeared to be reactive toward the starting compounds.

Below is given a typical procedure for condensation of *p*-cresol with isohexyl alcohol.

A reactor equipped with a reflux condenser with a Dean–Stark trap, a stirrer, a thermometer, and a dropping funnel was charged with 102 g (0.982 mol) of *p*-cresol and 2.0 g of $H_7PW_{12}O_{42}$. The mixture was heated on an oil bath to 85–95°C, and 51 g (0.50 mol) of isohexyl alcohol was added dropwise at this temperature over a period of 40 min. The temperature was gradually raised to 105–120°C, and the mixture was refluxed for 4 h 40 min. In the process, water was separated in the Dean–Stark trap. After the reaction was complete, the content of the target product was determined by GLC to be 50.5%. To isolate the product, the mixture was neutralized with 3 g of sodium carbonate. The neutralized mixture was vacuum-distilled. The target fraction (bp 125–140°C/8–10 mm Hg) contained, according to GLC, 97% 4-methyl-2-isohexylphenol. The product yield was 53 g (55.2% in terms of loaded isohexyl alcohol), and the amount of bottoms, 7.2 wt % relative to the target fraction (with sulfuric acid as catalyst, the amount of bottoms was 15 wt %).

The alkylation of *p*-cresol with 2-methyl-2-pentanol was performed similarly. The yield of the condensation product, 4-methyl-2-(2-methyl-2-pentyl)phenol, was 50%.

REFERENCES

1. Kheifits, L.A. and Podberezina, A.S., in *Problemy organicheskogo sinteza* (Problems of Organic Synthesis), Moscow: Nauka, 1965, pp. 124–132.
2. Kheifits, L.A., Podberezina, A.S., Klimakhina, S.T., and Grigor'eva, L.T., *Maslozhir. Prom–st.*, 1976, no. 7, pp. 32–34.
3. Kozhevnikov, I.V., *Usp. Khim.*, 1987, vol. 56, no. 9, pp. 1417–1442.

1070-4272/01/7402-0350 $25.00 © 2001 MAIK "Nauka/Interperiodica"

Russian Journal of Applied Chemistry, Vol. 74, No. 2, 2001, pp. 351–352. Translated from Zhurnal Prikladnoi Khimii, Vol. 74, No. 2, 2001, pp. 343–344.

BRIEF COMMUNICATIONS

New Processes in Bitumen Technology

N. A. Strakhova, D. A. Rozental', V. D. Shchugorev, L. P. Kortovenko, and O. Yu. Pavlyukovskaya

Astrakhan State Technical University, Astrakhan, Russia
St. Petersburg State Technological Institute, St. Petersburg, Russia
OOO Astrakhan'gazprom, Astrakhan, Russia

Received July 10, 2000

Abstract—The feasibility of high-paraffin raw material treatment by the action of ferromagnetic needles and electromagnetic field was examined with the aim to produce bitumens of improved quality.

Intensification of oil refining is possible on the basis of the theory of controlled phase transitions, according to which intermolecular interactions can be controlled by external actions converting the petroleum raw material to an active state. At the same time, traditional processes are only based on data on the chemical structure of molecules present in the petroleum raw material, without taking into account the origination and growth of supramolecular structures.

One of ways to exert effective influence on petroleum systems with the aim to convert them to an active state is physical activation (mechanical, electric, magnetic, ultrasonic, etc.) shifting the dynamic equilibrium dispersed phase–dispersion medium in the desired direction. For example, under the action of a strong nonuniform electromagnetic field in an apparatus with a vortical bed, paramagnetic particles become involved in directional motion, which results in their mutual approach and aggregation. The resulting aggregates of paramagnetic components are crystallization centers for solid hydrocarbons and favor their concentration in definite close-cut fractions.

There are different procedures, chemical and physical, for activating a raw material in bitumen production. By chemical activation is meant alteration of the group chemical composition of the dispersion medium by introducing special chemical additives (extract from selective purification of oils, sulfur with black solar oil, etc.) or removal of certain components, which alters the solvency of the dispersion medium and the particle size of the dispersed phase.

In physical activation of a bitumen raw material, the external effect is directed mainly at the dispersed phase, which causes changes in the composition and volume of the dispersion medium. For example, ultrasonic treatment of asphalt in the course of its oxidation raises the content of asphaltenes and the softening point of the resulting bitumen [1]. Owing to the high chemical activity of asphalt components as a consequence of the dispersing effect of ultrasonic treatment, and also to the high quality of bitumens, the process of asphalt oxidation under ultrasonic treatment has been implemented in industry.

Whereas mechanical and thermal actions, raising the extent and rate of breakdown of the petroleum structure, have only a minor effect on the subsequent formation of this structure after the end of treatment, such a treatment combined with application of an electromagnetic field will favor ordering of molecules having a dipole moment.

Experiments showed that, in an apparatus with a vortical bed, the sample properties are affected by electromagnetic field, and this effect depends on the treatment temperature. For example, on heating black oil to 140°C, its density somewhat decreases, but at higher temperatures (≥220°C) it noticeably increases. The black oil treated at high temperatures is characterized by increased content of asphaltenes. Since the temperature of 140°C is too low for thermal decomposition to occur, variation of the fractional and component compositions is probably due to rearrangement of the polar and nonpolar components of black oil with the formation of associates of varied structure.

On high-temperature treatment of black oil in a vortical-bed apparatus (280 and 320°C), the total con-

1070-4272/01/7402-0351 $25.00 © 2001 MAIK "Nauka/Interperiodica"

tent of light fractions (bp <350°C) increases by 1.1–1.5 wt %. The onset of sample boiling after high-temperature treatment is observed at a temperature 20°C higher than with the initial samples.

A combined effect of the electromagnetic field and the mechanical action of ferromagnetic needles placed in a capsule with samples results in phase redistribution in the disperse system and isolation of high-molecular-weight *n*-alkanes and ceresines in fractions with narrow boiling range. The fraction of modified black oil, boiling above 470°C, is characterized by low content of solid paraffins as compared with the same fraction of the initial black oil and can be of interest as raw material for production of petroleum bitumens.

Thus, application of various external actions affecting the chemical and structural transformations of petroleum disperse systems allows intensification of various oil refining processes, namely, pretreatment of high-paraffin raw materials with the aim to produce bitumen of improved quality.

REFERENCES

1. Volodin, Yu.A., Options of Improving the Efficiency of Oil Refining by Physicochemical Actions, *Cand. Sci. Dissertation*, Moscow, 1999.

Russian Journal of Applied Chemistry, Vol. 74, No. 2, 2001, pp. 353–354. Translated from Zhurnal Prikladnoi Khimii, Vol. 74, No. 2, 2001, pp. 345–346.

BRIEF COMMUNICATIONS

Copolymerization of *N*-Vinyl-4,5,6,7-tetrahydroindole with Acrylamide

O. V. Lebedeva, N. S. Shaglaeva, L. V. Kanitskaya, G. A. Pirogova, S. V. Fedorov, A. I. Mikhaleva, and A. K. Khaliullin

Irkutsk Institute of Chemistry, Siberian Division, Russian Academy of Sciences, Irkutsk, Russia

Received June 6, 2000

Abstract—Radical copolymerization of *N*-vinyl-4,5,6,7-tetrahydroindole with acrylamide in dimethylformamide was studied, and the relative activity constants of the monomers were determined.

N-Vinylpyrroles are reactive monomers in both cationic and radical polymerization processes and allow preparation of polymeric materials with a wide spectrum of valuable properties: special semiconductors, photosensitive materials, flotation agents, biologically active compounds, synthetic dyes, etc. [1].

In this work we studied the activity of *N*-vinyl-4,5,6,7-tetrahydroindole (VTHI) in radical copolymerization with acrylamide (AA).

Copolymerization of VTHI with AA in dimethylformamide (DMF) yields cream-colored powders soluble in DMF, DMSO, and *N*-methylpyrrolidone. The IR spectra of these products show that they contain units of both monomers (absorption bands of the pyrrole ring at 1300, 1380, 1490, and 1540 cm^{-1} and those of acrylamide at 510 and 965 cm^{-1}) and no double bonds (no bands at 859, 946, and 1585 cm^{-1}). The copolymers are free from homopolymer impurities, which is confirmed by the smooth shape of the turbidimetric titration curves.

The ^{13}C NMR spectra contain strongly broadened signals from the carbon atoms of the VTHI and AA fragments (ppm): 130.9–125.3 ($C^{8,9}$), 117.5–112.5 (C^{3}), 108.0–105.8 (C^{2}), 52.3–47.8 (C^{10}), 44.2–40.0 (C^{11}), 23.1–19.0 ($C^{4,5,6,7}$) and 180.0–174.0 (C=O), 38.8–33.6 (CH_2), respectively.

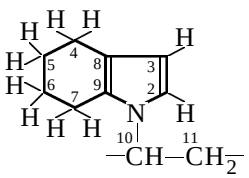

From the ^{13}C NMR spectra, we calculated the mole fractions of VTHI and AA and also the elemental composition of the copolymers (see table). The mole fraction of the VTHI units in the copolymer grows with increasing fraction of VTHI in the initial mixture, but does not exceed 0.4 even at the VTHI : AA ratio in the initial mixture of 4 : 1. This fact is consistent with the relatively low rates of radical polymerization of VTHI [2]. For the system VTHI–AA, the copolymerization constants are as follows: r_{VTHI} = 0.02, r_{AA} = 3.2.

With the fraction of VTHI units in the copolymer increasing by a factor of ~4, the viscosity of the product grows twofold.

EXPERIMENTAL

The copolymerization of the monomers was performed in sealed ampules at 60°C in the presence of azobis(isobutyronitrile) under argon. The reaction mixture was dissolved in DMF, and the copolymer was precipitated with acetone. Then the copolymer was reprecipitated from DMF solution into acetone and dried in a vacuum to constant weight. The intrinsic viscosity was determined in DMF at 20°C by the dilution procedure.

The relative activity constants were calculated by the Fineman–Ross and Kelen–Tudos procedures using G.I. Deryabina's program, with the Mortimer–Tidwell experimental design. The calculations were based on the results of experiments with conversion of ≤10%. The IR spectra were taken on a Specord 75-IR spectrometer from KBr pellets or mulls in mineral oil.

1070-4272/01/7402-0353 $25.00 © 2001 MAIK "Nauka/Interperiodica"

Characteristics of the initial mixture of VTHI and AA comonomers and their copolymers

Mole fraction				Yield, wt %	$[\eta]$, dl g^{-1}	Elemental composition of copolymers,* wt %			
initial mixture		copolymer				C	H	N	O
VTHI	AA	VTHI	AA						
0.291	0.709	0.102	0.898	10.3	0.12	56.6	7.4	17.8	18.2
0.434	0.566	0.163	0.837	7.3	0.19	59.7	7.6	16.8	15.9
0.523	0.477	0.206	0.794	5.2	0.20	61.5	7.7	16.2	14.6
0.825	0.175	0.391	0.609	4.6	0.27	68.3	8.1	13.9	9.7

* Calculated from the ^{13}C NMR spectra.

The ^{13}C NMR spectra of the copolymer samples (solutions in DMSO-d_6) were recorded on a Varian VXR-500S spectrometer (125.5 MHz) with the relaxation delay of 2.5 s and 90° pulse. As relaxant served chromium *tris*-acetylacetonate (0.02 M). The molar ratios of the copolymer components were determined from the ^{13}C NMR spectra by a common procedure: The relative intensity of the C=O signal q_{AA} was referred to one carbon atom and 1 mol of AA. The number of VTHI moles was calculated by the formula

$$M_{VTHI} = q_{VTHI}/q_{AA},$$

where q_{VTHI} is the relative intensity of the C^2 signal (or one of the signals from C^4, C^5, C^6, or C^7) of VTHI, $q_{VTHI} = I_{VTHI}/I_{tot}$ (I_{VTHI} and I_{tot} are the integral intensity of the C^2 signal and the total integral intensity, respectively).

The relative integration error was 3%. The relative error of the quantitative determination of the mole fractions of the comonomers and the elemental composition of the copolymers did not exceed 6.7%.

CONCLUSION

Radical copolymerization of *N*-vinyl-4,5,6,7-tetrahydroindole with acrylamide was studied. The second comonomer is more reactive. With increasing content of *N*-vinyl-4,5,6,7-tetrahydroindole in the initial mixture, its content in the copolymer and the viscosity of the reaction products become higher.

REFERENCES

1. Trofimov, B.A. and Mikhaleva, A.I., *N-Vinilpirroly* (*N*-Vinylpyrroles), Novosibirsk: Nauka, 1984.
2. Kruglova, V.A., Izykenova, G.A., Kalabina, A.V., *et al.*, *Vysokomol. Soedin., Ser. B*, 1982, vol. 24, no. 9, p. 691.

Russian Journal of Applied Chemistry, Vol. 74, No. 2, 2001, pp. 355–357. Translated from Zhurnal Prikladnoi Khimii, Vol. 74, No. 2, 2001, pp. 347–349.

INFORMATION

Tenth Kola Workshop on Electrochemistry of Rare Metals

On December 4–7, 2000, a regular workshop on electrochemistry of rare metals was held in Apatity (Murmansk oblast) at the Institute of Chemistry and Technology of Rare Elements and Mineral Raw Materials, Kola Scientific Center, Russian Academy of Sciences. Forty-five specialists, including representatives of research and higher school institutions of Moscow, St. Petersburg, Yekaterinburg, Novokuznetsk, Lipetsk, and Novomoskovsk took part. The Ukraine was represented by scientists from the Vernadskii Institute of General and Inorganic Chemistry, National Academy of Sciences of Ukraine. Among the co-authors of many reports were scientists from France (University of Provence, Marseilles; Sabatier University, Toulouse), Switzerland (University of Lausanne), Poland (Wroclaw University), and Finland (Technical University, Helsinki).

A wide variety of problems of general science and technology were discussed in 52 reports and brief communications. L.A. Petrii (Moscow) in his report "Electrochemistry at the End of the XX Century" considered topical problems of modern theoretical and applied electrochemistry and emphasized the important role of electrochemical science in solving energetic, ecological, and medical problems the mankind is confronted with. To the most important applied directions the author referred the development and optimization of chemical power cells and fuel cells, supercapacitors, electrochromic devices, membrane technologies, and electrochemical sensors. Particular attention was given to problems of electrocatalysis, possibility of using various rare metals in multicomponent metal and metal oxide catalysts. In the conclusion of his report, Petrii made an attempt to formulate some yet unsolved problems of fundamental electrochemistry. By contrast, the report by A.G. Morachevskii (St. Petersburg) was retrospective and concerned with the role played by Russian scientists in the development of high-temperature electrochemistry in the XX century. Prominent scientific schools, headed by Professors N.A. Pushin and P.P. Fedot'ev, formed at the beginning of the last century in St. Petersburg at the Electrotechnical and Polytechnic Institutes. This enabled the setting-up of the manufacture of light metals in Russia in the 1930s. An important stage in the development of physicochemical and electrochemical investigations of ionic melts is associated with the foundation in Sverdlovsk (Yekaterinburg) in 1957 of the Institute of High-Temperature Electrochemistry, Ural Division, Russian Academy of Sciences, and the activities of Professor M.V. Smirnov and his colleagues and pupils. An important contribution was made by the Kiev school of electrochemists, headed for a long time by Yu.K. Delimarskii, academician of the National Academy of Sciences of the Ukraine. The author noted that in the 1960s–1980s the USSR held the leading position in the world as regards the amount of information obtained in the field of physical chemistry and electrochemistry of molten salts and its scientific importance. Intensive investigations were being conducted in scientific centers of Moscow, Leningrad, Kiev, Tbilisi, Yekaterinburg, Krasnoyarsk, Irkutsk, Rostov-on-Don, Apatity, Nal'chik, and Novomoskovsk.

V.S. Kublanovskii (Kiev) considered and evaluated, on the basis of experimental data, components of the activation energy of the electrochemical process. A report by N.Kh. Tumanova and coauthors (Kiev) was concerned with passivation effects in dissolution of high-melting metals (Nb, Ta, Ti) in carbamide–halide melts.

A number of reports presented the results of new investigations in the field of high-temperature electrochemistry of niobium and tantalum. E.G. Polyakov, L.P. Polyakova, and P.T. Stangrit (Apatity) demonstrated by the example of oxofluoride complexes of tantalum that concentration changes in the near-electrode layer, affecting the course of an electrochemical reaction, are observed in melts with two ligands. By controlling the ligand composition of the electrolyte and current density, one can obtain materials with prescribed composition and structure. The reports by S.V. Kuznetsova and S.A. Kuznetsov (Apatity) were devoted to electrochemical synthesis of tantalum silicides and niobium–hafnium coatings from chloride–fluoride electrolytes. In particular, the authors demonstrated the possibility of obtaining continuous Nb–Hf coatings up to 20–30 μm thick. O.V. Makarova, Polyakova, and T.V. Stogova (Apatity) studied the thermal stability (700–730°C) of an oxofluoride electrolyte used to synthesize tantalum borides. Makarova

1070-4272/01/7402-0355 $25.00 © 2001 MAIK "Nauka/Interperiodica"

and co-authors (Apatuty, Moscow) confirmed experimentally the possibility of existence of heterocomplexes with tantalum and boron in oxofluoride melts.

V.V. Grinevich, A.V. Arakcheev, and Kuznetsov (Moscow, Apatity) reported the results obtained in studying the electrodeposition of niobium and its compounds from oxofluoride complexes dissolved in molten rubidium and cesium chlorides and fluorides. This study completed systematic investigations of the influence exerted by outer-sphere cations of alkali metals on the nature of cathodic processes occurring in electrolysis of niobium-containing halide-oxohalide melts. It was noted that stabilization of oxofluoro complexes of niobium with increasing size of solvent cation is only observed to rubidium inclusive, and not to cesium, as it might be assumed. Arakcheeva and co-authors (Moscow; Lausanne, Switzerland) presented the results obtained in preparing a new type of tantalum bronzes and studying their structure. The bronzes were grown at the cathode in electrolysis of oxofluoride melts, with Ta or TaO anodes. The electrolyte used contained K_2TaOF_5 or $K_3TaO_2F_4$. As solvent served ternary eutectic LiF–NaF–KF. Arakcheeva, Grinevich, and F.I. Shamrai (Moscow) studied the localization of oxygen atoms in cubic crystals of niobium suboxides in high-temperature electrolysis.

The report by Kolosov *et al.* (Apatity), concerned with the diffusion saturation of nickel with tantalum in a molten NaCl–K_2TaF_7 mixture in the presence of powdered tantalum metal, presented characteristics of the coatings obtained in the process. E.S. Matychenko and co-authors (Apatity) studied the formation of intermetallic compounds Ni_3Ta and Ni_2Ta through electroless transport of tantalum in chloride-fluorotantalate melts. V.Yu. Novikov and S.L. Sukhorzhevskaya reported the formation of tantalum carbide TaC on the surface of low-carbon St. 3 steel in a NaCl–K_2TaF_7 melt at 750°C in the electroless mode. V.P. Yurkinskii, E.V. Afonicheva, and E.G. Firsova (St. Petersburg) reported the results obtained in studying the growth kinetics of anodic oxide films on tantalum in low-melting nitrate mixtures (410–510 K).

G.A. Bukatova, E.G. Polyakov, and J. Aromaa (Apatity; Helsinki, Finland) demonstrated that electrolytically obtained pore-free tantalum coatings on such materials as St. 3 and Kh18N9T stainless steel impart to them high corrosion resistance in chloride-ion–containing media. The report by Yu.N. Zhirkova and co-authors (Novomoskovsk) was devoted to electrochemical synthesis of bimetallic powdered formulations containing rhenium, niobium, tantalum, and aluminum.

V.P. Baklanov, V.N. Bezumov, *et al.* (Moscow, Glazov) considered processes of optimization of the industrial manufacture of zirconium by electrolysis of fluoride-chloride melts. L.P. Polyakova and P. Taksil (Apatity; Toulouse, France) reported on investigations of the cathodic reduction of titanium in a NaCl–KCl–NaF melt containing K_2TiF_6 by a set of modern electrochemical methods.

Reports by Z.I. Valeeva, N.O. Esina, *et al.* (Yekaterinburg) were concerned with synthesis of cathode deposits of molybdenum and rhenium by electrolysis of chloride melts, investigation of the structure of the deposits, and vapor-phase deposition of molybdenum onto a nickel substrate. I.A. Novoselova and co-authors (Kiev) considered specific features of co-electroreduction of MoO_4^{2-} and SO_4^{2-} ions in melts of varied cationic composition.

Some reports were devoted to physicochemical investigations of molten systems containing compounds of rare earths and electrolysis processes involving them. Kuznetsov and co-authors (Apatity; Marseilles, France; Wroclaw, Poland) studied thermodynamic properties of molten mixtures of scandium(III) chloride with chlorides of alkali metals by means of electrochemical and calorimetric methods. A.V. Novoselova, V.Yu. Shishkin, and V.A. Khokhlov (Yekaterinburg) measured by the direct potentiometric method the redox potentials of Sm(III)/Sm(II) and Eu(III)/Eu(II) in molten cesium chloride. V.F. Goryushkin *et al.* (Novokuznetsk) determined, by measuring the emf of solid-phase cells, the standard thermodynamic characteristics of a number of lanthanide dichlorides. L.F. Yamshchikov and A.A. Zyapaev (Yekaterinburg) discussed from the thermodynamic standpoint the possibility of lanthanide separation on various liquid-metal electrodes (Al, Ga, In, Zn, Sn, and Bi) in molten salts. I.R. Elizarova, Polyakova, and Stangrit (Apatity) reported on a study of the Gd_2O_3 solubility in KCl–KF melt and electroreduction of gadolinium(III) complexes in chloride-fluoride melts. The report by A.I. Kononov (Lipetsk) was concerned with the cathodic process in a chloride neodymium-containing melt. Stangrit and A.I. Krasnoramenskii (Apatity; Zheltye Vody, Ukraine) demonstrated the possibility of obtaining aluminum–scandium alloys by electrolysis of Na_3AlF_6–Al_2O_3–Sc_2O_3 melts.

A.M. Potapov and M. Gaune-Escar (Yekaterinburg; Marseilles, France) studied the electrical conductivity of melts formed by $EuCl_2$ or $TbCl_2$ with chlorides of alkali metals in a wide range of compositions and temperatures. The same authors investigated, together with A.B. Salyulev (Yekaterinburg), absorption spectra

of diluted $TbCl_3$ solutions in chlorides of alkali metals. D.V. Makarov and co-authors (Apatity) compared various methods for synthesis of fluorides of rare-earth elements (yttrium, neodymium, and gadolinium).

Khokhlov (Yekaterinburg) discussed in detail in his report the investigations conducted at the laboratory of molten salts at the Institute of High-Temperature Electrochemistry, Ural Division, Russian Academy of Sciences. Its main direction of research is an integrated physicochemical study of molten salt electrolytes, including ionic-electronic melts. The laboratory proceeds with large-scale investigations commenced by Professor M.V. Smirnov and aimed at establishing fundamental relationships between the nature and energy of chemical bond and the structure, actual ionic composition, and properties of salt melts. The laboratory also studies complexation processes and conducts a search for ways of practical application of ionic melts.

I.A. Novoselova *et al*. (Kiev) reported the results obtained in studying the deposition of refractory coatings on nitride insulators (boron or aluminum nitrides) in their cathodic polarization in tungsten-containing melts at 850–900°C. O.I. Rebrin and co-authors (Yekaterinburg) studied the kinetics of anodic oxidation of beryllium and cathodic reduction of its ions in chloride melts. In a series of communications by A.V. Volkovich and co-workers (Novomoskovsk) considered the reaction of calcium, strontium, and barium oxides with individual chlorides of alkali metals and their binary mixtures in molten state (973–1173 K). The report by V.N. Zaichenko (Kiev) was concerned with the role of magnetic fields in the electrochemistry of ionic melts.

The workshop demonstrated that the most intensive and best-directed investigations in Russia in the field of high-temperature electrochemistry are conducted in Yekaterinburg and Apatity. The works in this field of other scientific centers are mainly occasional. In Yekaterinburg, investigations in a variety of directions, covering a wide range of problems, are being carried out at the Institute of High-Temperature Electrochemistry, Ural Division, Russian Academy of Sciences, and the Ural State University. The Institute of Chemistry, Kola Research Center, Russian Academy of Sciences, achieved the most pronounced success in the field of electrochemistry of niobium, tantalum, and rare-earth elements. Rather valuable, in the first place in methodological regard, are joint works carried out at scientific centers abroad.

One cannot but admit the high level of organization of the workshop and the friendly climate. The abstracts of all the presented reports are well published. The workshop was held with the support of the Russian Foundation for Basic Research, ZAO Rossiiskie redkie metally, the administration of Apatity town, and the Tananaev Institute Chemistry and Technology of Rare Elements and Mineral Raw Materials, Kola Scientific Center, Russian Academy of Sciences.

A. G. Morachevskii and L. P. Polyakova

Russian Journal of Applied Chemistry, Vol. 74, No. 3, 2001, pp. 359–362. Translated from Zhurnal Prikladnoi Khimii, Vol. 74, No. 3, 2001, pp. 353–356.

INORGANIC SYNTHESIS AND INDUSTRIAL INORGANIC CHEMISTRY

Crystallochemical Aspect of Phase Formation in the γ-FeOOH–H_2O–NaOH System

A. V. Tolchev, R. R. Bagautdinova, and D. G. Kleshchev

Chelyabinsk State Pedagogical University, Chelyabinsk, Russia

Received June 3, 2000

Abstract—Phase transition of metastable γ-FeOOH into α-FeOOH and its chemical transformation into α-Fe_2O_3 upon hydrothermal treatment in 0–5 M NaOH solutions at 100–230°C were studied. The regions of formation of the above phases were specified. The probable composition of the crystallizing complexes formed in the solutions and the reactions occurring at their incorporation into various atomically smooth faces of α-FeOOH and α-Fe_2O_3 were considered.

Metastable iron(III) oxyhydroxides of γ and δ modifications are formed by oxidation of aqueous solutions of iron(II) salts or iron(II) hydroxide suspensions under the conditions of high supersaturation. Upon thermal treatment in alkaline solutions they undergo phase transition (PT) or chemical transformation (CT) into the equilibrium phases α-FeOOH and α-Fe_2O_3, respectively, which are widely used as inorganic pigments and as starting materials for preparing magnetic powders, ceramics, etc. The kinetics and type of the transformation of metastable FeOOH as well as the crystal size and habit of the formed phases depend on many parameters, the main of which are thermal treatment temperature, alkali and FeOOH concentrations in suspension, and the structure and average size of crystals of the initial iron(III) oxyhydroxides.

In this work we studied possible factors affecting the phase composition and crystal habit of the iron(III) oxide compounds formed by hydrothermal treatment of γ-FeOOH in NaOH solutions.

The single-phase γ-FeOOH sample, as evidenced by X-ray phase analysis and electron microscopy, in the form of platelike crystals with the average size $60 \times 20 \times 5$ nm, was obtained by oxidation in air at 25 ± 2°C of aqueous solution of chemically pure grade iron(II) sulfate at pH 7.3 ± 0.5 adjusted by continuous addition of aqueous solution of chemically pure grade sodium hydroxide, similarly to [3]. The precipitate was separated from the mother solution on a Buchner funnel, washed with water to the absence of sulfate ions in the filtrate, and resuspended in distilled water and 0.1 to 5.0 M aqueous NaOH. The hydrothermal treatment of γ-FeOOH suspensions was performed in 0.07 dm^3 autoclaves filled to 0.8 volume at 110, 135, 170, 200, and 230°C for 2.5 h. The time of preheating the autoclave to prescribed temperature did not exceed 1 h. The temperature was controlled to within ±5°C.

The phase composition and dispersity were controlled by X-ray phase analysis (DRON-3 diffractometer, filtered FeK_α radiation) and electron microscopy (UEMV-100K microscope), and the solution composition was determined by chemical analysis. The mass fraction of α-FeOOH and α-Fe_2O_3 in the thermally treated samples was determined by the known procedure of quantitative X-ray phase analysis [7].

The experimental data show that, depending on C_{NaOH} and t, the hydrothermal treatment of the γ-FeOOH phase leads to phase transition or chemical transformation, which can occur in parallel (Fig. 1).

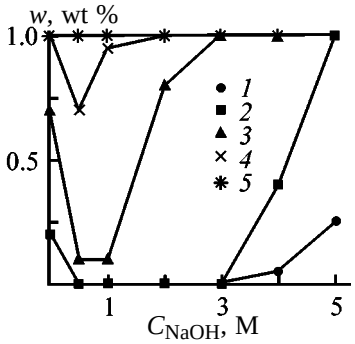

Fig. 1. Concentration w of the α-Fe_2O_3 phase in samples obtained at different temperatures of hydrothermal treatment vs. the NaOH concentration C_{NaOH} in the solution. Temperature (°C): (*1*) 110, (*2*) 135, (*3*) 170, (*4*) 200, and (*5*) 230. The same for Fig. 2.

1070-4272/01/7403-0359$25.00

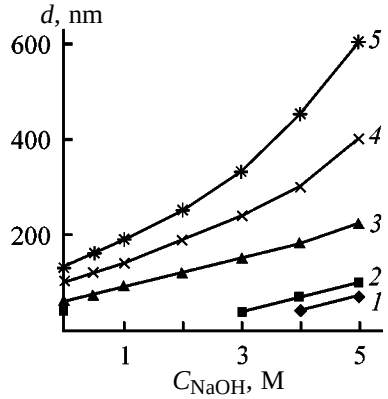

Fig. 2. Average size d of the α-Fe_2O_3 crystals vs. the NaOH concentration C_{NaOH} in the solution.

Note that at the fixed NaOH concentration in the solution the γ-FeOOH $\rightarrow$ α-FeOOH PT occurs at lower temperatures than CT γ-FeOOH $\rightarrow$ α-Fe_2O_3. The sequence of phase formation as a function of C_{NaOH} at T = const within 135–200°C is irregular: at C_{NaOH} < 0.5 and > 3 M the γ-FeOOH phase transforms into α-Fe_2O_3, whereas in the intermediate concentration region it transforms into α-FeOOH.

The average size and the habit of crystals of the forming phases are also functions of heat treatment parameters. For example, the α-FeOOH and α-Fe_2O_3 crystals, products of hydrothermal treatment of γ-FeOOH in distilled water, are acicular and isometric, respectively. With increasing NaOH concentration in the solution at T = const, the crystal habit of these phases changes regularly. In the process, the form factor f of the acicular α-FeOOH crystals increases from f = 2–4 at C_{NaOH} = 0 M to f = 6–8 at C_{NaOH} = 3 M, and at C_{NaOH} > 3 M a transition occurs from isometric habit of α-Fe_2O_3 crystals to the platelike habit. As the temperature or NaOH concentration in the solution grows at the fixed value of the other parameter, the average size of the α-FeOOH and α-Fe_2O_3 crystals in the directions of primary crystallization increases regularly (Fig. 2).

The fact that the habit and average size of crystals of the starting phase (γ-FeOOH) and those of the α-FeOOH and α-Fe_2O_3 phases formed by hydrothermal treatment change considerably indicates that in alkaline solutions, as in weakly acidic solutions, PT and CT of metastable FeOOH occur by the dissolution–precipitation mechanism (DPM) [4, 5, 8]. The latter involves the elementary stages of dissolution of metastable-phase crystals, formation of crystallizing complexes (CCs) in the solution, their transfer through the solution, and incorporation into the forming crystals of the equilibrium phase. It is generally accepted [9] that the formation of two-dimensional nuclei on an atomically smooth face is the limiting stage of layer-by-layer crystal growth. Since for sparingly soluble compounds, including α-FeOOH and α-Fe_2O_3, a two-dimensional nucleus is comparable in size with CCs present in the solution [7], the nucleation mechanism is reduced to the CC incorporation into the surface layer of these crystals. Let us consider the structure of the α-FeOOH and α-Fe_2O_3 faces and the CC composition and configuration in the solutions varying in compositions.

If the interaction of the crystal surface with the dispersion medium is negligible, as in neutral solutions including distilled water, then atomically smooth face (001) of α-FeOOH consists of the rows of water molecules (layer *I*) alternating with the rows of hydroxy groups (layer *II*), and faces (100) and (010) are formed by three and two adjacent rows of hydroxide ions, respectively, separated by one vacant row (Fig. 3a). The (100) face of α-Fe_2O_3 involves alternating layers of water molecules (layer *I*) and oxygen anions (layer *II*), and the (001) face, only the hexagonal network of hydroxy groups (Fig. 3b). The crystallizing complex in the given solutions consists of two octahedra sharing the base edge of the bipyramid (Fig. 3c) and has the composition $Fe_2(OH)_6 \cdot 4H_2O$ [10]. Incorporation of CCs into α-FeOOH crystals on the atomically smooth (001) face in points *1–4* is accompanied by olation. For the face (100) the oxolation reaction takes place in points *5* and *7* and the olation reaction, in point *6*. As for the face (010), oxolation occurs in points *8* and *10* and olation, in point *9*. For the (100) phase of α-Fe_2O_3, olation takes place in points *1–3* and dehydration, in points *4* and *5*. The face (001) is characterized by oxolation in points *6–8* and by olation in points *9* and *10*.

In alkaline solutions, especially at high temperatures, sodium hydroxide can react with the ligand molecules adsorbed on the crystal surface and incorporated into the crystallizing complexes. Therefore, in dilute NaOH solutions the reactions of complete or partial substitution of water molecules by hydroxide ions can occur on the (001) face of α-FeOOH and on the (100) face of α-Fe_2O_3. In concentrated solutions, along with these reactions, the oxolation reaction between the hydroxide ions of NaOH and those of the surface layer of (001), (010), and (100) faces of α-FeOOH or (001) face of α-Fe_2O_3 is probable. These reactions impart to the faces a negative charge, which is compensated by the positive charge of Na^+ ions in the near-crystal adsorption layer. Apparently, this fact can explain the increased solubility of iron(III) oxide compounds in alkaline solutions compared to neutral

and weakly acidic solutions, which is manifested as the increase in the equilibrium concentration of hydroxo aqua complexes (HACs) of iron(III) [11]. Second, the reaction of alkali with the electroneutral HACs $[Fe(OH)_3]_{aq}$ in alkaline solutions yields negatively charged HACs $[Fe(OH)_4]^-_{aq}$, the concentration of which changes regularly with growing C_{NaOH}. Thus, it can be presumed that, along with CCs of the composition $Fe_2(OH)_6 \cdot 4H_2O$, the negatively charged complexes $[Fe_2(OH)_7 \cdot 3H_2O]^-$ (Fig. 3d, CC') and $[Fe_2(OH)_8 \cdot 2H_2O]^{2-}$ (Fig. 3d, CC") can be present in NaOH solutions, with the maximum concentration of the first and the second complexes being attained in dilute and concentrated solutions, respectively.

As a result, the type of the reactions accompanying incorporation of CCs into the surface layer of crystals in alkaline solutions changes compared to neutral solutions. For example, incoprporation of CC' into α-FeOOH in dilute NaOH solutions is accompanied by olation on the (001) face in points *1–3* and by oxolation in point *4*, whereas on the (100) face in points *5* and *7* and on the (010) face in points *8* and *10* it is accompanied by oxolation. In points *6* and *9*, the dehydroxylation reaction occurs, resulting in release of OH^- ions from CC' into the solution: $O^{2-}_{cr} + OH^-_{CC} \rightarrow O^{2-}_{cr} + OH^-_{sol}$.

On the (100) face of α-Fe_2O_3 the oxolation takes place in points *1–3* and dehydration, in points *4* and *5*, whereas on the (001) face the oxolation occurs in points *6–8* and the olation, in points *9* and *10*. In concentrated NaOH solutions the incorporation of CC" into the (001) face of α-FeOOH is accompanied by olation in point *1*, dehydroxylation in points *2* and *3*, and oxolation in point *4*. On the (100) and (010) faces dehydroxylation proceeds in all the points *5–10*. In α-Fe_2O_3 the reaction type does not change on the (100) phase, but on the (001) face in points *6–8* there takes place dehydroxylation and in points *9* and *10*, dehydration.

Thus, depending on NaOH concentration in the solution, the incorporation of crystallizing complexes into α-FeOOH and α-Fe_2O_3 can be accompanied by the following concurrent reactions: dehydration, olation, oxolation, and dehydroxylation. The first two reactions, in which instead of weakly bound van der Waals complex [Fe(III)–H_2O] the strong hydroxide or oxide bridging bonds decreasing the Gibbs energy *G* of the crystal–CC system are formed between iron(III) ions adsorbed on the crystal surface and the crystallizing complex, are the most favorable from the thermodynamic standpoint. Compared to olation and dehydration reactions, the oxolation reaction $OH^-_{cr} + OH^-_{CC} \rightarrow O^{2-}_{cr} + H_2O_{sol}$ accompanied by deprotonation of the hydroxide ion with the strong covalent bond has the higher activation energy and, consequently, occurs at higher temperatures [13]. The activation energy of the dehydroxylation reaction is equal to the dissociation energy of the Fe(III)–OH^- bond of the crystallizing complex and is comparable with the dissociation energy of the hydroxide and oxide bridging bonds in the crystals, i.e., $\Delta G \sim 0$. Compared with the reactions considered, the latter reaction is noncompetitive.

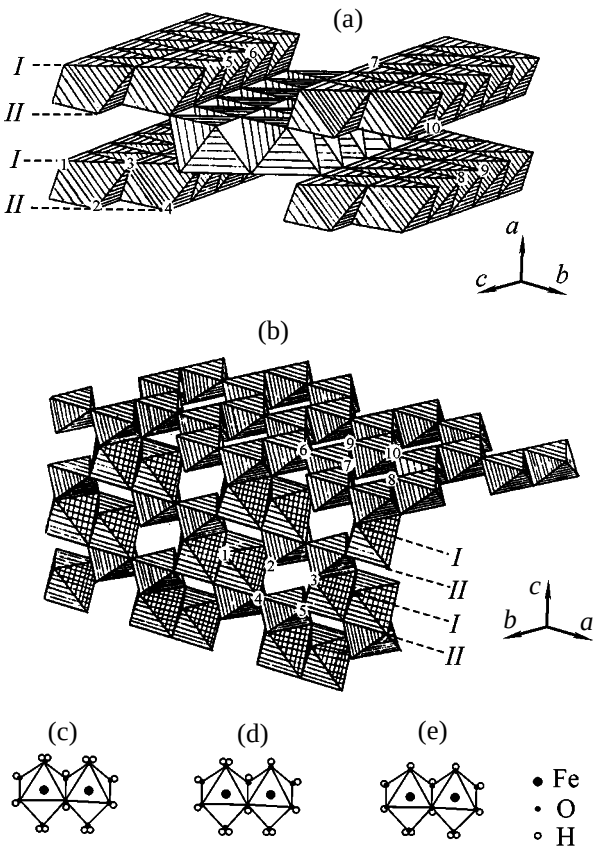

Fig. 3. Structure of (a) α-FeOOH and (b) α-Fe_2O_3 phases in polyhedral interpretation and structure of crystallizing complexes (c) $[Fe_2(OH)_6 \cdot 4H_2O]$, (d) $[Fe_2(OH)_7 \cdot 3H_2O]^-$, and (e) $[Fe_2(OH)_8 \cdot 2H_2O]^{2-}$.

The experimental data are analyzed based on the qualitative estimate of the probability of nucleation on the different crystal faces as determined from the number and type of the reactions occurring at incorporation of crystallizing complexes. For example, preferential growth of α-FeOOH crystals in the crystallographic direction *c*, and, consequently, their acicular habit were previously explained [10] by the smaller number of bonds (three bonds) formed on incorporation of CCs into the (100) and (010) faces

compared to that (four bonds) formed on incorporation into the (001) face. At higher temperatures of hydrothermal treatment at C_{NaOH} = const, all reactions, including oxolation, are activated on the (100) and (010) faces, which increases the average length and decreases the form factor of the α-FeOOH crystals. On the contrary, as the NaOH concentration in the solution increases owing to dehydroxylation, the probability of formation of nuclei on the (100) and (010) faces decreases, which predetermines the increase in the form factor of the α-FeOOH crystals. The incorporation of the complexes into the (100) and (001) faces of α-Fe_2O_3 involves formation of the similar number of bonds (five bonds). As a result, the α-Fe_2O_3 crystals formed upon CT of γ-FeOOH in neutral and weakly alkaline solutions are isometric. In concentrated alkalis, the nucleation on the (001) face is impeded by dehydroxylation and the platelike α-Fe_2O_3 crystals are formed, oriented normally to the crystallographic axis *c*, as evidenced by X-ray diffraction analysis [3, 4]. The influence of the hydrothermal treatment conditions on the γ-FeOOH transformations in alkaline solutions can also be understood in terms of the concept ot formation of crystallizing complexes. For example, as the number of oxide bridges formed upon α-Fe_2O_3 crystallization is two times higher, on the average, compared to those formed upon α-FeOOH crystallization, the chemical transformation γ-FeOOH → α-Fe_2O_3 at C_{NaOH} = const occurs at higher temperatures than the phase transition γ-FeOOH → α-FeOOH. For neutral solutions and dilute (C_{NaOH} < 1 M) and concentrated (C_{NaOH} > 3 M) NaOH solutions the type and the number of the reactions accompanying the incorporation of CC, CC', and CC" into the (001) face of α-FeOOH and the (100) face of α-Fe_2O_3 vary in the sequence: 4 olation reactions → 3 olation reactions + 1 oxolation reaction → 1 olation reaction + 1 dehydration reaction + 2 dehydroxylation reactions and 3 olation reactions + 2 dehydration reactions → 3 oxolation reactions + 2 dehydration reactions (for low and highly concentrated solutions, respectively). Therefore, compared to α-FeOOH, the probability of formation of the α-Fe_2O_3 nuclei at *T* = const is higher in neutral and concentrated alkali solutions and lower in the solutions of the intermediate concentrations, which is in line with the experimental data on phase formation in the γ-FeOOH–H_2O–NaOH system.

CONCLUSION

(1) The phase transition of metastable γ-FeOOH into α-FeOOH and its chemical transformation into α-Fe_2O_3 were studied upon hydrothermal treatment in 0–5 M NaOH solutions at 110–230°C. The regions of formation of the above phases were specified.

(2) The transformations of γ-FeOOH in alkaline solutions occur by the dissolution–precipitation mechanism. The probable composition of the crystallizing complexes formed in the solutions and the reactions occurring at their incorporation into various atomically smooth faces of α-FeOOH and α-Fe_2O_3 were considered. The established dependences of the phase composition and dispersity of the resulting products on the conditions of hydrothermal treatment were explained.

REFERENCES

1. *Gipergennye okisly zheleza* (Hypergene Iron Oxydes), Petrovskaya, N.V., Ed., Moscow: Nauka, 1975.
2. Feitknecht, W., *Z. Electrochem*., 1959, vol. 63, no. 1, pp. 34–43.
3. Hiller, J.E., *Werkstoffe Korros*., 1966, vol. 17, no. 11, pp. 943–951.
4. Tolchev, A.V., Bagautdinova, R.R., Kleshchev, D.G., *et al*., *Izv. Ross. Akad. Nauk, Neorg. Mater*., 1996, vol. 32, no. 11, pp. 1377–1380.
5. Bagautdinova, R.R., Kleshchev, D.G., Pletnev, R.N., *et al*., *Izv. Ross. Akad. Nauk, Neorg. Mater*., 1998, vol. 34, no. 5, pp. 584–586.
6. Krause, A., Moroniowna, K., and Przhybylski, E., *Z. Anorg. Allgem. Chem*., 1934, vol. 219, nos. 1–2, pp. 203–212.
7. Kitaigorodskii, A.I., *Rentgenosrukturnyi analiz melkokristallicheskikh i amorfnykh tel* (X-ray Diffraction Analysis of Finely Crystalline and Amorphous Solids), Moscow: GITTL, 1952.
8. Kleshchev, D.G., Sheinkman, A.I., and Pletnev, R.N., *Vliyanie sredy na fazovye i khimicheskie prevrashcheniya v dispersnykh sistemakh* (Influence of the Medium on Phase and Chemical Transformations in Disperse Systems), Sverdlovsk: Ural. Otd. Akad Nauk SSSR, 1990.
9. *Sovremennaya kristallografiya* (Modern Crystallography), vol. 3: *Obrazovanie kristallov* (Crystal Formation), Chernov, A.A., Ed., Moscow: Nauka, 1980.
10. Raspopov, Yu.G., Sheinkman, A.I., Bubnov, A.A., *et al*., *Izv. Akad. Nauk. SSSR, Neorg. Mater*., 1983, vol. 19, no. 2, pp. 299–301.
11. Kamnev, A.A., Ezhov, B.B., Malandin, O.G., and Vasev, A.V., *Zh. Prikl. Khim*., 1986, vol. 59, no. 8, pp. 1689–1693.
12. Perrin, D.D., *J. Chem. Soc*., 1959, no. 5, pp. 1710–1719.
13. Langmuir, D., *Am. J. Sci*., 1971, vol. 271, no. 2, pp. 147–156.

Russian Journal of Applied Chemistry, Vol. 74, No. 3, 2001, pp. 363–367. Translated from Zhurnal Prikladnoi Khimii, Vol. 74, No. 3, 2001, pp. 357–360.

INORGANIC SYNTHESIS AND INDUSTRIAL INORGANIC CHEMISTRY

Extraction Recovery of Tantalum(V) and Niobium(V) from Hydrofluoric and Hydrofluoric–Sulfuric Acid Aqueous Solutions with Octanol

V. G. Maiorov, A. I. Nikolaev, and V. K. Kopkov

Tananaev Institute of Chemistry and Technology of Rare Elements and Mineral Raw Materials, Kola Scientific Center, Russian Academy of Sciences, Apatity, Murmansk oblast, Russia

Received September 25, 2000

Abstract—Comparative study of extraction of tantalum(V) and niobium(V) with octanol and tributyl phosphate was made. The data on distribution of tantalum(V) and niobium(V) between octanol and hydrofluoric and hydrofluoric–sulfuric acid aqueous solutions were obtained. The flowsheet for preparation of pure tantalum and niobium oxides was developed.

Extraction technique is widely used for preparation of rare metal compounds. Octanol is the promising extractant for recovery of tantalum(V) and niobium(V) from aqueous solutions [1–4]. According to the data reported in [1], the extractive efficiency of octanol is not inferior to that of methyl isobutyl ketone (MIBK) commonly used in industrial preparation of tantalum(V) and niobium(V) compounds [5]. However, compared to octanol, MIBK exhibits such substantial drawbacks as the explosion hazard and high solubility in aqueous solutions.

In this work we made a comparative study of the extraction power of octanol and tributyl phosphate (TBP) with respect to tantalum(V) and niobium(V). TBP was chosen by us since this extractant is widely used for extraction of rare metals, among them tantalum(V) and niobium(V) [5]. We also studied the separation of tantalum(V) from niobium(V) in their simultaneous extraction from concentrated aqueous solutions and extractive purification of these metals to remove impurities.

In the experiments we used *n*-octyl alcohol $CH_3(CH_2)_6CH_2OH$ [1-octanol] (OCL). The main characteristics of octyl alcohol are as follows: solubility in water 0.05 wt %, density 0.824 g cm^{-3}, mp 15–16°C, bp 195°C, flash point 81°C, main substance content about 98%, and the maximum permissible concentration in air 10 mg m^{-3}. The equilibrium distribution of tantalum(V) and niobium(V) between aqueous phase and octanol is attained at a contact time less than 5 min. It was found in preliminary experiments that the extraction characteristics of OCL are close to those of other octanol isomers (2-octanol, 2-ethylhexanol). These organic solvents are commercially available and have acceptable cost. The extraction experimental technique was reported in detail in [6].

Figures 1 and 2 show the curves of extraction of tantalum(V) and niobium(V) from their dilute solutions in sulfuric–hydrofluoric acid mixtures used in several flowsheets of processing of Russian loparite [5]. The extraction was performed at the constant HF_{free} concentration equal to 3 M, where HF_{free} is the HF concentration calculated as the difference bet-

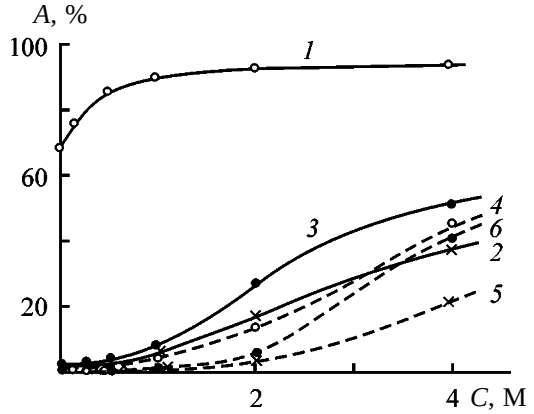

Fig. 1. Extraction of (*1–3*) Ta(V) and (*4–6*) Nb(V) from aqueous solution containing 0.005 M Ta(V), 0.1 M Nb(V), and 3 M HF_{free} with (*1, 4*) tributyl phosphate and (*2, 3, 5, 6*) 1-octanol. (*A*) Degree of recovery and (*C*) H_2SO_4 concentration; the same for Figs. 3 and 4. $V_o : V_{aq}$: (*1, 2, 4*) 1 : 10 and (*3, 6*) 1 : 5.

1070-4272/01/7403-0363$25.00

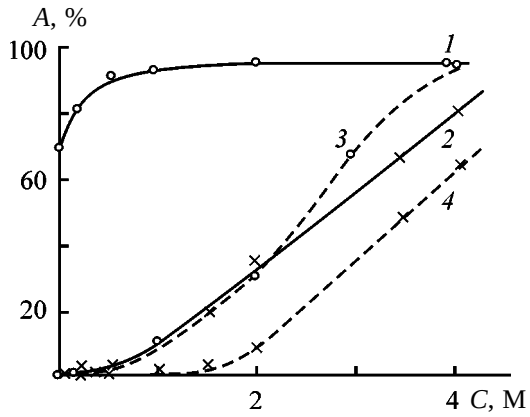

Fig. 2. Extraction of (*1*, *2*) Ta(V) and (*3*, *4*) Nb(V) at the ratio of organic and aqueous phases $V_o : V_{aq} = 1 : 10$ from aqueous solution containing 0.005 M Ta(V), 0.1 M Nb(V), and 3 M HF_{free} with (*1*, *3*) tributyl phosphate and (*2*, *4*) 1-octanol. (*A*) Degree of recovery and (*C*) H_2SiF_6 concentration.

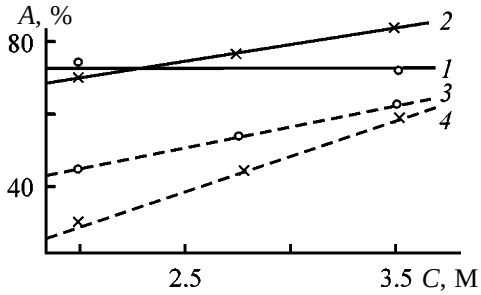

Fig. 3. Extraction of (*1*, *2*) Ta(V) and (*3*, *4*) Nb(V) from aqueous solution containing 0.45 M Ta(V), 0.75 M Nb(V), and 6 M HF_{free} with (*1*, *3*) tributyl phosphate and (*2*, *4*) 1-octanol. $V_o : V_{aq}$: (*1*, *2*) 0.75 : 1 and (*3*, *4*) 1.5 : 1.

ween the total HF concentration and the HF amount combined in the main complexes $HTaF_6$, $HNbF_6$, and H_2SiF_6 formed in the systems studied.

1-Octanol is less basic than TBP [7] and, therefore, the extraction of tantalum(V) and niobium(V) with octanol should be performed at higher ratio of the organic and aqueous phases $V_o : V_{aq}$. It is known [7] that niobium(V) and tantalum(V) are extracted from hydrofluoric acid solutions with neutral organic solvents by the mechanism of formation of $HMeF_6$ acids. The extraction of these complexes increases with increasing H^+ concentration. The difference between extraction recovery of these metals with OCL and TBP becomes the most pronounce at the deficiency of H^+ at the H_2SO_4 and H_2SiF_6 concentrations lower than 1 M. As compared to TBP, OCL virtually does not recover not only fluoroniobic acid $HNbF_6$ but even more extractable fluorotantalic acid $HTaF_6$. Therefore, to provide efficient extraction of tantalum(V) and niobium(V) with OCL, the higher concentration of acid in the aqueous phase is required.

It was found by us previously [6] that extraction of tantalum(V) and niobium(V) from hexafluosilicic acid solution with TBP exceeds that from sulfuric acid solutions. In extraction with OCL this effect is even more pronounced. Concentrated solutions of hexafluorosilicic acid are used, for example, in processing of several types of tantalite and columbite. We can expect that at the H_2SiF_6 concentration higher than 4 M the extraction powers of OCL and TBP are similar even at the equal ratio of volumes of the organic and aqueous phases. This fact shows that efficiency of extraction of tantalum(V) and niobium(V) is controlled not only by the acid type (tetrafluorooxotitanic, hexafluorosilicic, hexafluorostannic, sulfuric, hydrochloric [6, 8]), but also by the nature of the extractant. These facts call for systematic studies of extraction of the rare metals from fluorometallic acid aqueous solutions as influenced by the nature of the extractant. Such studies are of the current interest taking into account the increase in processing of the tantalum(V) and niobium(V)–lean raw materials including large amounts of foreign metals [titanium(IV), zirconium(IV), silicon(IV), etc.].

Along with the above-noted drawbacks of OCL as compared to TBP, OCL exhibits several advantages. The main advantage is its stability in long-term contact with process solutions. We found that with increasing contact time of OCL with solution containing 4 M HF and 5 M H_2SO_4 at the ratio of organic and aqueous phases $V_o : V_{aq} = 1 : 1$ to 280 h the degree of recovery of HF and H_2SO_4 decreases gradually from 36 to 26% and from 15 to 10%, respectively. After completion of these experiments OCL can be reused for further extraction. On contact of TBP with the aqueous phase under the identical conditions for 70 days the initial two-phase system was converted to a homogeneous solution. It is evident that homogenization of the system is due to decomposition of the extractant. The products of hydrolytic degradation of TBP contaminate niobium and tantalum materials with phosphorus(V) and other impurities [5], which prevents preparation of high-purity compounds of tantalum and niobium. Among other drawbacks of TBP are its toxicity and high density which deteriorates phase separation and, as a result, complicates and raises the price of the extraction installation [5].

Figure 3 shows extraction of tantalum(V) and niobium(V) from their concentrated solutions with OCL and TBP. These data show that the trends in extraction of tantalum and niobium with both TBP and OCL

Extraction of tantalum(V) and niobium(V) from hydrofluoric acid aqueous solutions

Run no.	Composition of initial solution, M				$V_o : V_{aq}$	Recovery, %	
	Ta(V)	Nb(V)	HF_{tot}	HF_{free}		Ta(V)	Nb(V)
1	0.45	0.75	5.7	–1.5	0.8 : 1	38	2.7
2	0.45	0.75	22.2	15	0.8 : 1	22	40
3	0.59	1.14	9.08	–1.3	0.8 : 1	33	2.1
4	0.59	1.14	9.08	–1.3	2.5 : 1	70	4.3

are similar. In extraction of tantalum from 2 M H_2SO_4 the degree of recovery of this metal with both OCL and TBP becomes identical. The degrees of niobium recovery with OCL and TBP become similar in extraction from approximately 3.5 M H_2SO_4. Figure 3 shows also that extraction of niobium and tantalum with octanol is more sensitive to variation in the H_2SO_4 content than extraction of these metals with TBP.

The results on extraction of tantalum(V) and niobium(V) from their concentrated solutions with OCL are analyzed below. In separate experiments we found that, in spite of the relatively low extractive power of OCL, the extracts containing the sum of Ta(V) + Nb(V) in amount of 0.8 M and larger can be obtained.

The data on recovery with octanol of tantalum(V) and niobium(V) from hydrofluoric acid aqueous solutions containing no sulfuric acid are listed in the table. These results show that with increasing HF concentration the separation of Ta(V) and Nb(V) is deteriorated (run nos. 1 and 2). It is known [5, 7], that tantalum(V) is extracted in the form of complex $HTaF_6$. Extraction by this mechanism is suppressed with excess HF due to a competitive extraction of hydrofluoric acid. In contrast to tantalum, extraction of niobium is mainly controlled by formation of the complex $HNbF_6$, and, therefore, excess HF increases the niobium transfer in the organic phase. To improve separation of Ta(V) from Nb(V), the extraction should be carried out at deficiency of HF and a large ratio of organic and aqueous phases (run nos. 3 and 4). In run no. 4 in continuos countercurrent extraction, tantalum(V) is virtually completely recovered with low coextraction of niobium(V).

Extraction of Nb and Ta with OCL sharply increases on introduction of sulfuric acid into the aqueous phase. For example, in extraction of tantalum(V) from aqueous solution containing 0.7 M Ta(V), 1.5 M HF_{free}, and 3 M H_2SO_4 at $V_o : V_{aq} = 1.2 : 1$ the degree of recovery of the metal is 86% in one cycle, increasing to 91% with decreasing HF_{free} concentration to 0.25 M. In extraction of niobium(V) and tantalum(V) from aqueous solution containing 0.45 M Ta(V), 0.75 M Nb(V), 6.5 M HF_{free}, and 4 M H_2SO_4 at $V_o : V_{aq} = 1.5 : 1$ the degree of extraction of tantalum(V) and niobium(V) is 85 and 88%, respectively, in one cycle. These data show that with continuous countercurrent extraction technique the exhaustive simultaneous recovery of tantalum and niobium can be reached in four extraction stages. The content of Ta(V) and Nb(V) in the resulting extract is 0.3 and 0.5 M, respectively.

Figure 4 shows the extractive separation of tantalum(V) from niobium(V) with *n*-octanol as influenced by sulfuric acid concentration. The mutual arrangement of curves *1* and *2* in Fig. 4 shows that at H_2SO_4 concentration higher than 2 M the increase in recovery of niobium(V) is more pronounced as compared to tantalum(V) and, as a result, the separation of these elements deteriorates. Therefore, taking into account the above-analyzed results, the separation of tantalum from niobium should be performed by extraction from solutions containing approximately 2 M H_2SO_4 at the minimal HF content.

We studied also separation of tantalum(V) from niobium(V) and their purification to remove foreign

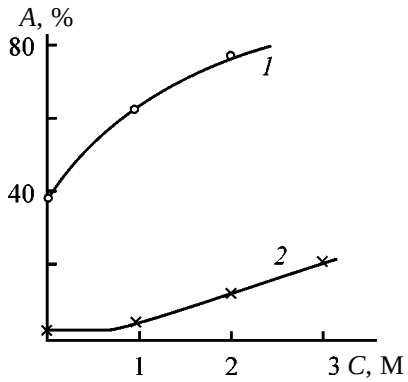

Fig. 4. Extraction of (*1*) Ta(V) and (*2*) Nb(V) from aqueous solution containing 0.45 M Ta(V) and 0.75 M Nb(V) with 1-octanol at $V_o : V_{aq} = 1 : 1$.

Flowsheet of extraction recovery of Ta(V) and Nd(V) from concentrated solutions with 1-octanol. Composition of initial solution (M): Ta(V) 0.45–0.65, Nb(V) 0.75–1.10, and H_2SO_4 ~2

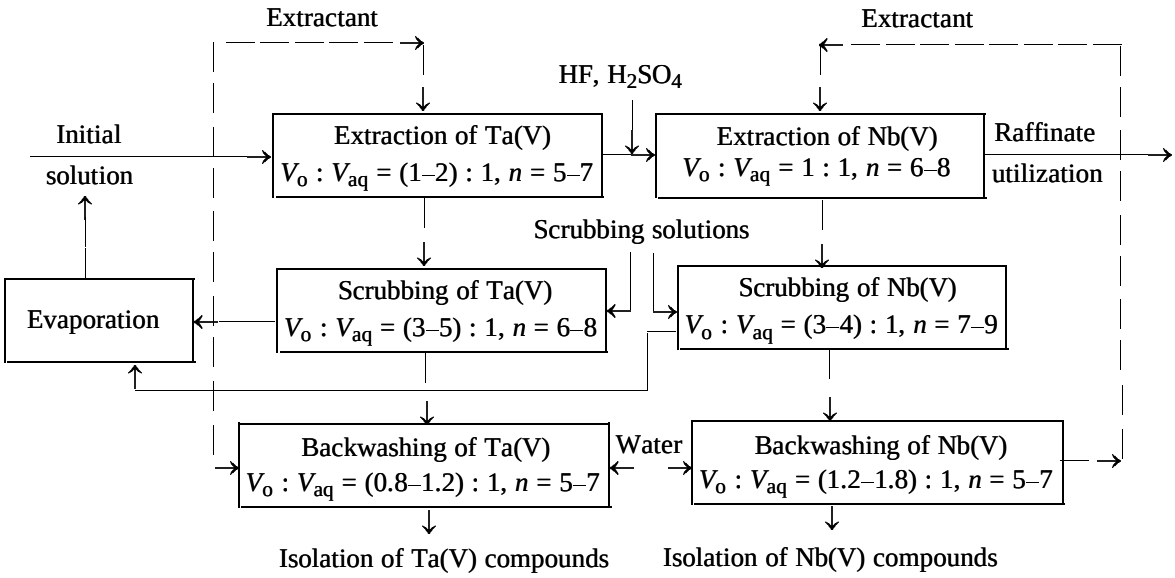

metals in the backwashing stage. In the case of the extraction system containing hydrofluoric acid only, the separation of tantalum(V) from niobium(V) is the most efficient at backwashing with water at $V_o : V_{aq}$ approximately equal to 10 : 1.5. We found that 72% of niobium(V) and only 10% of tantalum(V) pass into the aqueous phase in one backwashing stage. Sufficiently efficient purification of niobium(V) to remove titanium(IV), which is one of the most difficultly separable foreign metals [5], can be performed by backwashing with 15–20 M HF at $V_o : V_{aq}$ of about 10 : 1. In this case 86–68% of titanium(IV) and only 22–12% of niobium(V) pass into the aqueous phase in one backwashing stage. In the extraction systems containing an HF–H_2SO_4 mixture the purification of tantalum(V) in the organic extract is the most efficient at backwashing with 1.5–2 M H_2SO_4 at $V_o : V_{aq}$ = (3.5–4.5) : 1. The purification of niobium(V) in the organic extract is the most efficient at backwashing with 5–10 M HF and 5–6 M H_2SO_4 at $V_o : V_{aq}$ = (3–4) : 1.

The flowsheet for extraction recovery of tantalum(V) and niobium(V) is shown below. This technique allows recovery of the target metals from their concentrated solutions in hydrofluoric–sulfuric acid mixtures. Such solutions are used, for example, in processing of tantalite and (or) columbite. According to this flowsheet, tantalum(V) and niobium(V) are extracted successively. In contrast to the flowsheet based on extraction of the sum of niobium(V) and tantalum(V) followed by their separation in the backwashing stage, in the flowsheet developed in this work niobium(V) and tantalum(V) are extracted separately. Such modification results in the lower price of the process, improves its separation efficiency, and simplifies the process control [5]. The operative parameters were chosen from both the results of our studies and the reference data [1–5, 7].

With this flowsheet the samples of pure tantalum and niobium oxides were prepared using a batch extraction technique. The content of the metal impurities (recalculated on metal) in Ta(V) and Nb(V) oxides was as follows (wt %). Tantalum(V) oxide: Mn < 0.001; (Mg, Al, Sn, V, Cr, Fe) < 0.003; (Ca, Ti, Si, Pb, Nb, Mo) < 0.01; Zr ≪ 0.03. Niobium(V) oxide: Mn < 0.001; Sn < 0.003; (Mg, Al, Ti, Si, Pb, V, Ta, Cr, Mo, W, Fe) < 0.01, and Ca, Zr < 0.03. Our further studies showed that the content of the metal impurities in tantalum and niobium oxides can be decreased to the levels lower than 1×10^{-5}–1×10^{-3} wt %.

Thus, extraction of tantalum and niobium from their concentrated solutions with octanol is the promising technique for their purification to remove metal impurities and preparation of pure oxides.

CONCLUSION

(1) Comparative study of extraction of tantalum(V) and niobium(V) with octanol and tributyl phosphate shows that octanol can be used in industrial process for efficient separation of these metals.

(2) Separation of tantalum(V) from niobium(V)

and their purification to remove metal impurities by extraction with octanol were studied in relation to the process parameters. A flowsheet of the extraction process for preparation of pure tantalum(V) and niobium(V) oxides was developed.

REFERENCES

1. Hydrometallurgical Extraction of Tantalum and Niobium in China, *Bull. of Tantalum–Niobium International Study Center (TIC)*, 1998, no. 93, pp. 1–6.
2. Maiorov, V.G., Sklokin, L.I., and Nikolaev, A.I.. Abstracts of Papers, *XI Rossiiskaya konferentsiya po ekstraktsii* (XI Russian Conf. on Extraction), Moscow, 1998, p. 188.
3. Travkin, V.F., Agulyanskii, A.I., Glubokov, Yu.M., and Karamushko, E.V., *Tsvetn. Metall.*, 1998, nos. 8–9, pp. 18–22.
4. Travkin, V.F., Agulyanskii, A.I., Glubokov, Yu.M., and Karamushko, E.V., *Tsvetn. Metall.*, 1999, nos. 4, pp. 19–22.
5. Babkin, A.G., Maiorov, V.G., and Nikolaev, A.I., *Ekstraktsiya niobiya, tantala i drugikh elementov iz ftoridnykh rastvorov* (Extraction of Niobium, Tantalum, and Other Elements from Fluoride Solutions), Leningrad: Nauka, 1988.
6. Maiorov, V.G., Nikolaev, A.I., and Kopkov, V.K., *Zh. Prikl. Khim.*, 1999, vol. 72, no. 6, pp. 929–932.
7. Zolotov, Yu.A., Iofa, B.Z, and Chuchalin, L.K., *Ekstraktsiya galogenidnykh kompleksov metallov* (Extraction of Metal Halide Complexes), Moscow: Nauka, 1973.
8. Maiorov, V.G. and Nikolaev, A.I., *Hydrometallurgy*, 1996, vol. 41, pp. 71–78.

Russian Journal of Applied Chemistry, Vol. 74, No. 3, 2001, pp. 368–373. Translated from Zhurnal Prikladnoi Khimii, Vol. 74, No. 3, 2001, pp. 361–366.

INORGANIC SYNTHESIS AND INDUSTRIAL INORGANIC CHEMISTRY

Reaction of Manganese(II) Hydroxocarbonate with Calcium Aluminates in Aqueous Medium

V. A. Troshina, I. A. Mamaeva, G. I. Salomatin, G. M. Tesakova, M. A. Kruglova, and E. Z. Golosman

Novomoskovsk Institute of Nitrogen Industry, Joint-Stock Company, Novomoskovsk, Russia

Received September 19, 2000

Abstract—The reactions of manganese hydroxocarbonate $MnCO_3 \cdot mMn(OH)_2 \cdot nH_2O$ with calcium aluminates $CaAl_2O_4$ and $CaAl_4O_7$ in aqueous medium were studied by X-ray phase and differential thermal analyses and by IR spectroscopy.

Catalysts prepared by mixing metal hydroxocarbonates (MHCs) with calcium aluminates in various media show promise for industry and are widely discussed in the literature [1].

It was shown earlier [1–4] that the reactions of MHCs (M = Cu, Zn, Mg, Ni, Co) with calcium aluminates in aqueous medium occur as a heterogeneous ion exchange between an aqueous solution of calcium aluminates and solid metal hydroxocarbonates. As a result of such exchange the MHC crystal structure is either retained or rearranged to give the structure of the metal hydroxoaluminate or hydroxocarbonoaluminate.

In this work we studied specific features of reactions of manganese hydroxocarbonates (MnHCs) with calcium aluminates in aqueous medium, which directly concerns the problem of synthesizing manganese–aluminum–calcium catalysts for redox processes.

EXPERIMENTAL

Manganese hydroxocarbonate $MnCO_3 \cdot mMn(OH)_2 \cdot nH_2O$ [GOST (State Standard) 7205–77] and high-alumina cement of the Talyum[1] type [$CA : CA_2$ = 0.26, TU (Technical Specifications) 5737-006-00 284 345–99] were used as starting components for sample preparation. Manganese hydroxocarbonate was stirred with Talyum in aqueous medium at 75°C for 5 h. The resulting samples were dried for 2 h at 100°C. The manganese content (in terms of Mn_3O_4) was varied from 0 to 100%. Mechanical mixtures of the starting reagents were studied in parallel.

The X-ray phase analysis (XPA) was carried out on a DRON-2 X-ray diffractometer using CuK_α radiation and a graphite monochromator. The IR spectra of samples pressed with KBr were recorded on a Specord

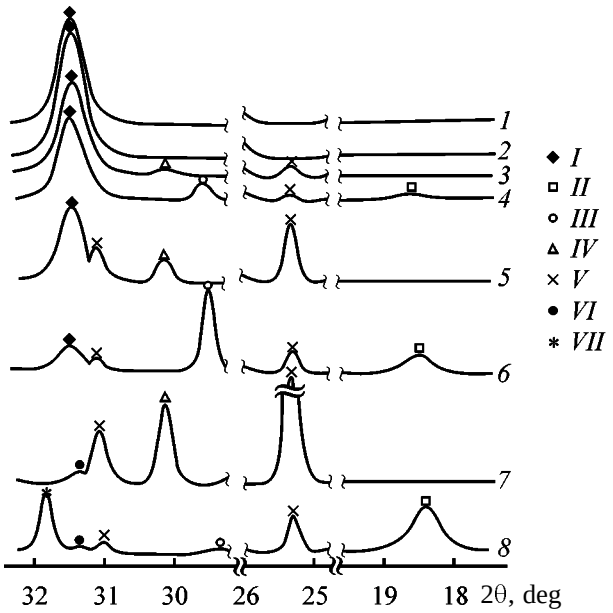

Fig. 1. Fragments of diffraction patterns of samples with various manganese content. (2θ) Bragg angle. Sample: before treatment with water: (*1*) MnHC, (*3*) 70% Mn_3O_4, (*5*) 30% Mn_3O_4, and (*7*) Talyum (0% Mn_3O_4); after treatment with water: (*2*) MnHC, (*4*) 70% Mn_3O_4, (*6*) 30% Mn_3O_4, and (*8*) 0% Mn_3O_4 (scanning rate v = 0.25 deg min^{-1}). (*I*) MnHC, (*II*) gibbsite, (*III*) $CaCO_3$, (*IV*) CA, (*V*) CA_2, (*VI*) CA_6, and (*VII*) C_3AH_6.

[1] Talyum is a mixture of calcium monoaluminate $CaO \cdot Al_2O_3$ and dialuminate $CaO \cdot 2Al_2O_3$. Here and hereinafter we use notations accepted in the chemistry of cements: (A) Al_2O_3, (C) CaO, and (H) H_2O.

1070-4272/01/7403-0368$25.00

75-IR spectrophotometer. The differential thermal analysis (DTA) was carried out on an OD-103 derivatograph in air. The heating rate (final temperature 1000°C) was 5 deg min^{-1}.

Fragments of diffraction patterns of the starting manganese hydroxocarbonate (MnHC), Talyum, and samples before and after treatment with water are shown in Fig. 1.

According to the XPA data, the components do not react during mechanical mixing; the mixture contains the phases of the starting MnHC and calcium aluminates (curves *3*, *5*). On mixing Talyum with water (without MnHC) it is hydrated to give calcium hydroxoaluminate C_3AH_6, gibbsite, and small amounts of calcium hydroxocarbonoaluminate owing to the reaction of calcium hydroxoaluminate with atmospheric CO_2 (curve *8*). The diffraction patterns of MnHC before and after treatment with water are identical (curves *1*, *2*). Mixing MnHC with calcium aluminates in aqueous medium results in the appearance of strong reflections of calcium carbonate (in the form of calcite) in the diffraction patterns of the samples. According to the earlier data [1–4], this is due to the reaction of Ca^{2+} ions with carbonate ions from metal hydroxocarbonates (in this case from manganese hydroxocarbonate). The dependence of the intensity of the $CaCO_3$ line (d = 3.03 Å) on the sample composition passes through a maximum at a 30–40% content of Mn_3O_4 (Fig. 2a) (this composition corresponds to the equimolar ratio $Ca^{2+} : CO_3^{2-}$ in the system). Along with this phase, the phases MnHC, $Al(OH)_3$ (gibbsite), calcium hydroxocarbonoaluminate, and unchanged CA_2 are present in the samples (curves *4*, *6*). Reflections characteristic of calcium hydroxoaluminate are observed only in the X-ray patterns with low content of manganese (less than 10–15% Mn_3O_4).

The integral intensity of MnHC reflections considerably decreases in the course of mixing with water; e.g., for samples with 30–40% Mn_3O_4 it is as low as 36–48% of the intensity measured for mechanical mixtures of the starting components. However, no other manganese compounds were detected.

These phenomena may be due to release of carbonate ions from the MnHC lattice and their possible replacement by aluminate and hydroxide ions generated on dissolution and hydrolysis of calcium aluminates [1–4]. Owing to a low solubility of MnHC in water (SP ~10^{-11}) the reaction is localized on the interface of the solid phase of MnHC and a solution of calcium aluminates. On the replacement of CO_3^{2-} by hydroxide ions, MnHC can be partially destroyed to give X-ray

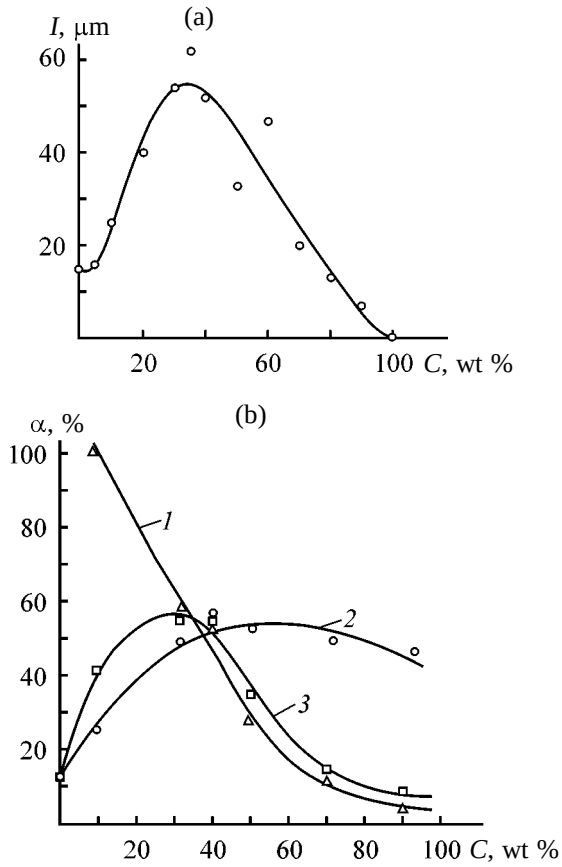

Fig. 2. (a) Intensity I of the $CaCO_3$ line (d = 3.03 Å) and (b) degree of the transformation of the starting compounds α as functions of the Mn_3O_4 content C in the system. (*1*) Degree of extraction of carbonate ions from the MnHC lattice, (*2*) degree of Ca^{2+} conversion to $CaCO_3$, and (*3*) total degree of conversion of the starting compounds to the reaction products.

amorphous manganese compounds such as $MnO_x \cdot yH_2O$, for example, by the scheme

$$MnCO_3 \cdot mMn(OH)_2 \cdot nH_2O \xrightarrow[-CaCO_3]{+Ca^{2+}} Mn\square mMn(OH)_2 \cdot nH_2O$$

$$\xrightarrow{+2OH^-} (m+1)Mn(OH)_2 \cdot nH_2O \xrightarrow{O_2, OH^-} (m+1)MnO_x \cdot yH_2O,$$

where a square means a vacancy.

The participation of aluminate ions in the exchange suggests formation of hydroxoaluminates or hydroxocarbonoaluminates in the system. However, such compounds (MnHA, MnHCA) were not detected. Nevertheless, the exchange of CO_3^{2-} with $[Al(OH)_4]^-$ can also occur without rearrangement of metal hydroxocarbonate, as was shown in [1–4]. The formation on heat treatment of disordered solid solutions

$MO \cdot Al_2O_3$ based on MO lattices suggests existence of aluminum-containing precursors; MnHC with aluminate ions dissolved in the lattice can be one of such precursors.

According to the XPA data, calcination of samples in air results in the formation of manganese oxides Mn_3O_4 and MnO_2. However, because of superposition of reflections of the forming oxides MnO_x and other phases (CA_2 and $CaCO_3$), it was impossible to estimate correctly the changes in the lattice parameters of these manganese oxides to make sure that $MnO_x \cdot Al_2O_3$ solid solutions are formed in the system.

In this connection we attempted to obtain manganese(II) oxide whose diffraction peaks would not overlap with those of the other phases. It was attained by heating samples to 500°C in an H_2 flow (at lower temperatures MnHC decomposed incompletely). It was found that the resulting MnO has a lower lattice constant compared to the tabulated value of 4.445 Å. For example, the decomposition of samples with 20 and 40% Mn_3O_4 gave MnO with a = 4.429 and a = 4.438 Å, respectively, whereas for MnO obtained by thermal decomposition of mechanical mixtures of MnHC with Talyum under similar conditions the lattice constant (4.444–4.446 Å) was close to the tabulated value. Therefore, we can conclude that solid solutions $MnO \cdot Al_2O_3$ based on the MnO lattice are formed in calcined samples, and, as the manganese(II) content in the system increases, the concentration of Al^{3+} dissolved in MnO seems to decrease.

Thus, taking into account our previous experience of studying similar systems [1–4], we can suggest that the above-mentioned phenomena occurring in the course of water treatment are due to formation of a solid solution based on the MnHC crystal lattice, in which carbonate ions are partially replaced by aluminate ions formed by hydration of Talyum. In this case the initial structure of MnHC is retained, and MnHC is decomposed on heating to form $MnO_x \cdot Al_2O_3$ solid solutions based on MnO_x lattices.

The examination of the diffraction patterns of the obtained samples shows that the diffraction maxima of the forming gibbsite are shifted relative to the tabulated values, and the shifts linearly correlate with the composition of the samples. For example, the maximum with d = 4.82 Å (hydrated Talyum) is shifted to d = 4.80 (sample with 30% Mn_3O_4) and d = 4.78 Å (sample with 70% Mn_3O_4). These data suggest distortion of the gibbsite crystal lattice, which is most likely due to insertion in its structure of manganese ions released from the initial MnHC in the course of its partial degradation. Their concentration in the gibbsite lattice seems to increase with increasing content of manganese in the system. The possibility of such insertion is provided by the layered structure of gibbsite and by significant content of octahedral vacancies in it [5].

When MnHC and calcium aluminates are mixed in an aqueous medium, they react with each other according to the following probable scheme: (a) dissolution of calcium aluminates in water with the formation of Ca^{2+} and $[Al(OH)_4]^-$ ions, (b) dissociation of tetrahydroxoaluminate ions with the formation of OH^- ions, and (c) chemical reaction of MnHC with the resulting dissociation products (scheme).

Scheme of the reaction of MnHC and products of $[Al(OH)_4]^-$ dissociation

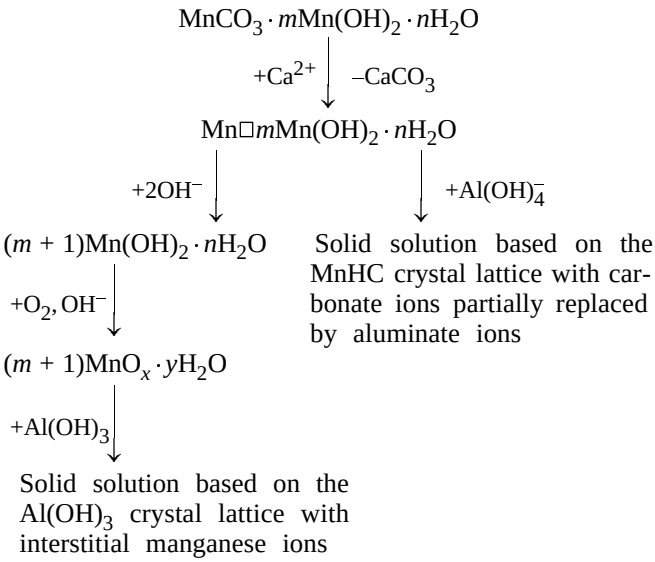

The IR spectra of the obtained samples are shown in Fig. 3. A number of absorption bands are present in the spectrum of hydrated Talyum (curve *1*). The absorption bands 750–800 and 500–700 cm^{-1} belong to the Al–O vibrations in the cases of tetrahedral and octahedral coordinations of oxygen atoms around aluminum, respectively. The absorption at 1400–1500 cm^{-1} is due to vibrations of the carbonate structures, which are formed by the reaction of Ca^{2+} ion with atmospheric CO_2; the absorption bands at 975 and 1030 cm^{-1} belong to the bending vibrations of OH^- groups of the forming gibbsite; the bands at 3465, 3530, 3620, and 3660 cm^{-1} are assigned to the stretching vibrations of the same groups.

The following changes in the IR spectra are observed on introduction of MnHC. As the manganese content in the system increases, the intensity of the

absorption bands of carbonate ions regularly increases; however, because of strong absorption in the 1400–1500 cm^{-1} range, it is impossible to resolve the bands of CO_3^{2-} ions in MnHC, $CaCO_3$, and calcium hydroxocarbonoaluminate. In the region of bending vibrations of OH^- groups of gibbsite the relative intensity of the observed absorption bands changes: the intensity of the band at 1030 cm^{-1} relative to the band at 975 cm^{-1} decreases. In the region of stretching vibrations of gibbsite OH^- groups the intensity of the band at 3660 cm^{-1} regularly decreases, and all the bands are broadened. Such changes in the IR spectra result from the formation of a system of new hydrogen bonds. The changes are the most pronounced in the spectra of the samples containing 30–40% Mn_3O_4 (curves *3*, *4*). In the region of OH^- stretching vibrations new absorption bands at 3550 and 3420 cm^{-1} appear, and all absorption bands in this region merge together to form a single broad band at 3420–3550 cm^{-1}. In the region of bending vibrations of OH^- groups of $Al(OH)_3$ the relative intensity of the absorption bands at 1030 and 975 cm^{-1} changes, their maxima shift to 1020 and 980 cm^{-1}, and a shoulder appears at 1020–1080 cm^{-1}.

On the whole, the spectrum of gibbsite becomes close to the spectrum of bayerite.

The observed changes in the IR spectrum of $Al(OH)_3$ are attributable to the insertion of manganese ions in the lattice with the formation of a system of new hydrogen bonds, to the changes in the characteristics of existing OH^- groups, and to the formation of new OH^- groups. The obtained data well agree with the XPA data on the shift of interplanar spacings in gibbsite.

Thus, the data of IR spectroscopy and XPA suggest that one more solid solution based on the gibbsite lattice is formed in the system, which is accompanied by the insertion of manganese ions in this lattice and by its partial reconstruction to the bayerite structure.

The fact that these changes in the IR spectrum are due to a reaction between the components of the system, but not to a change in their ratio, is obviously illustrated by the comparison of these spectra with the spectra of additionally prepared mechanical mixtures of MnHC with hydrated Talyum (Fig. 4). Furthermore, it follows from this comparison (namely, from the intensity of the absorption band at 870 cm^{-1} which is the most convenient to estimate the MnHC content) that MnHC has degraded to a considerable extent as a result of the reaction, which is confirmed by the XPA data.

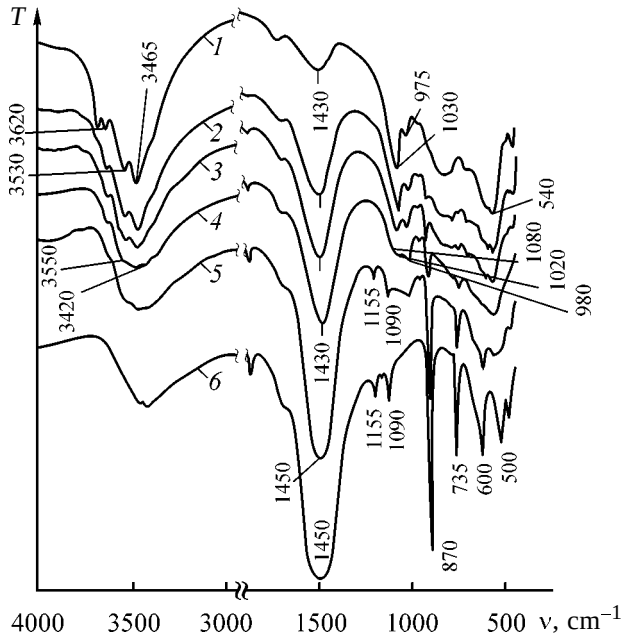

Fig. 3. IR spectra of samples with various content of manganese. (*T*) Transmittance and (ν) wave number; the same for Figs. 4 and 5. Mn_3O_4 content (wt %): (*1*) 0 (hydrated Talyum), (*2*) 20, (*3*) 30, (*4*) 40, and (*5*) 70; (*6*) MnHC.

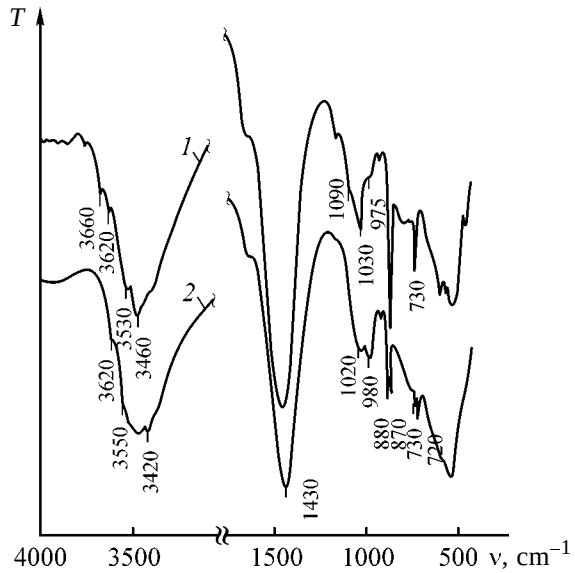

Fig. 4. IR spectra of (*1*) mechanical mixture of hydrated Talyum with MnHC (30% Mn_3O_4) and (*2*) sample of the same composition.

The formation in the system of solid solutions involving manganese compounds is proved by the fact that the intensity of the absorption bands of manganese oxides (in the range 490–650 cm^{-1}) in the IR spectra of the sample calcined in air is less than that of mechanical mixtures of calcined MnHC with cal-

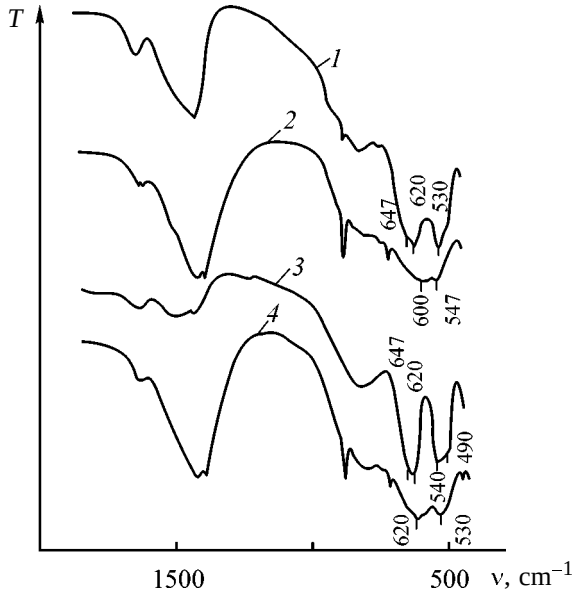

Fig. 5. IR spectra of (*1, 3*) mechanical mixture of calcined hydrated Talyum with calcined MnHC (40% Mn_3O_4) and (*2, 4*) calcined sample of the same composition. Calcination temperature (°C): (*1, 2*) 500 and (*3, 4*) 700.

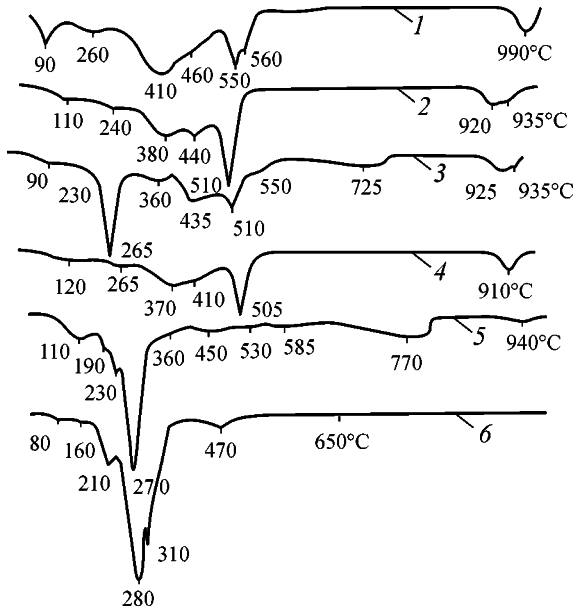

Fig. 6. DTG curves for (*1, 2, 4*) mechanical mixtures MnHC–calcium aluminates with various manganese content and (*3, 5, 6*) samples. Mn_3O_4 contents (wt %): (*1*) 100, (*2, 3*) 70, (*4, 5*) 30, and (*6*) 0 (hydrated Talyum).

cined hydrated Talyum of the same composition (Fig. 5).

The DTA data for the samples and mechanical mixtures of MnHC and calcium aluminates are given in Fig. 6. To interpret these data, we used the published data [6, 7] and the XPA data.

For example, the thermogram of the starting Talyum contains one endothermic peak at 90–100°C related to the removal of physically bound water. The curve of the decomposition of hydrated Talyum (curve *6*) involves seven endothermic peaks. The peak at 80°C corresponds to the loss of adsorbed water. At 160 and 210°C, calcium hydroxocarbonoaluminate is partially dehydrated. The strongest endothermic effect at 280°C is due to the dehydration of gibbsite with the formation of γ-Al_2O_3. At 310°C C_3AH_6 decomposes to lose 4.5 water molecules. The peak at 470°C corresponds to further dehydration of calcium hydroxoaluminate with the formation of $C_{12}A_7$. A very weak effect at 650°C corresponds to the decomposition of $CaCO_3$ formed in the samples as a result of the reaction of Ca^{2+} with atmospheric CO_2.

A number of endothermic peaks were detected in the thermogram of the starting MnHC (curve *1*). At 110°C adsorbed water is lost. At 240°C the decomposition of a γ-MnOOH impuirity and removal of structural water are possible. At 380 and 430°C MnHC decomposes stepwise with simultaneous oxidation of the forming MnO to β-Mn_2O_3, Mn_3O_4, and β-MnO_2. At 505 and 520°C β-MnO_2 is reduced to β-Mn_2O_3, and at 930°C β-Mn_2O_3 decomposes to Mn_3O_4. A very weak effect at 600°C is due to the conversion of small amounts of α-Mn_2O_3, formed by dissociation of MnHC and γ-MnOOH, to Mn_3O_4.

The same peaks as in the case of MnHC are detected in the thermograms of mechanical mixtures of MnHC with Talyum (curves *2, 4*).

The following pattern was observed in the case of samples obtained by mixing components in water. As the content of manganese in the samples increases, the amount of forming gibbsite decreases, the temperature of its dehydration is lowered, and the effect corresponding to the decomposition of C_3AH_6 at 300°C disappears. In the range 670–770°C an intense endothermic effect of $CaCO_3$ decomposition appears, the dependence of the amount of $CaCO_3$ on the composition passing through a maximum at a 30–40% content of Mn_3O_4. It is well consistent with the X-ray diffraction data (Fig. 1). Changes in the region of transformations of manganese compounds also take place: unlike mechanical mixtures, in the samples the intensity of the effect at 380°C decreases, as compared to 430°C, and new effects appear in the range 510–580°C.

The strongest changes are observed for the sample containing 30–40% Mn_3O_4: the effects of MnHC transformation are absent; instead of them endothermic effects are detected in the range 340–660°C.

Comparison with the XPA data allows these effects to be assigned to the removal of CO_3^{2-} and OH^- from the solid solution based on MnHC and to the transformation of manganese oxides.

Thus, the thermograms of samples obtained by mixing in water considerably differ from the thermograms of mechanical mixtures of the starting components and hydrated Talyum, which suggests a chemical reaction between the starting reagents.

We calculated the content of separate phases in samples of various compositions from the degrees of Talyum conversion, as determined by X-ray diffraction, and from the thermogravimetric and analytical data. We found that the amount of $Al(OH)_3$ formed in the sample with 30% Mn_3O_4 (DTG data) is less by 5–6% (in terms of Al_2O_3) than that calculated from the degree of Talyum transformation and analytical data. At the same time the contents of CAO in the system were in a good agreement. These facts suggest that approximately 10% of the total amount of Al_2O_3 in a sample takes part in the formation of a solid solution based on the MnHC crystal lattice. Furthermore, it follows from such calculations that in the case of a sample with 30% Mn_3O_4 about 60% of CO_3^{2-} ions from the MnHC structure seem to participate in the heterogeneous ion exchange.

It follows from the calculations for other samples that, as the content of manganese in the system increases, the degree of extraction of carbonate ions from the MnHC lattice decreases, the degree of the conversion of Ca^{2+} to $CaCO_3$ increases, the total degree of conversion of the starting substances to the reaction products being maximal at intermediate compositions (30–40% Mn_3O_4) corresponding to the equimolar ratio $Ca^{2+} : CO_3^{2-}$ in the system (Fig. 2b). Furthermore, as the manganese content in the system increases, the amount of $Al(OH)_3$ formed in the samples (by the DTG data) approaches the calculated value.

Our experimental and calculated data suggest that, as the manganese content in the system increases, the concentration of aluminate ions dissolved in the MnHC structure decreases, and the concentration of manganese ions in the gibbsite lattice, on the contrary, increases; the maximal amount of reaction products is formed at intermediate compositions.

CONCLUSIONS

(1) The reaction between manganese hydroxocarbonate and calcium aluminates in aqueous medium is similar in nature to the reactions in the systems cobalt hydroxocarbonate–calcium aluminate and nickel hydroxocarbonate–calcium aluminate. In these cases the structure of the metal hydroxocarbonate is retained and is not rearranged into the structure of the metal hydroxoaluminate (hydroxocarbonoaluminate).

(2) The concentration of aluminum ions dissolved in the lattice of manganese hydroxocarbonate tends to decrease with increasing manganese content in the system.

(3) A solid solution based on the gibbsite crystal lattice with interstitial manganese ions is formed in the system under study. The concentration of manganese ions in the gibbsite lattice tends to increase as the manganese content in the system increases.

(4) The maximal conversion of starting substances to the reaction products is reached in the samples containing 30–40% Mn_3O_4.

ACKNOWLEDGMENTS

The authors are grateful to M.P. Yaroshenko for valuable remarks.

REFERENCES

1. Yakerson, V.I. and Golosman, E.Z., *Katalizatory i tsementy* (Catalysts and Cements), Moscow: Khimiya, 1992.
2. Nechugovskii, A.I., Grechenko, A.N., and Golosman, E.Z., *Zh. Prikl. Khim.*, 1990, vol. 63, no. 8, pp. 1747–1751.
3. Grechenko, A.N., Zaldat, G.I., Bobrov, B.S., and Golosman, E.Z., *Zh. Neorg. Khim.*, 1992, vol. 37, no. 4, pp. 724–728.
4. Artamonov, V.I., Mamaeva, I.A., Boevskaya, E.A., *et al.*, *Zh. Neorg. Khim.*, 1978, vol. 23, no. 4, pp. 903–908.
5. Naray-Szabo, I., *Kristalykemia*, Budapest: Acad. Kiado, 1965.
6. *The Chemistry of Cements*, Taylor, H.F.W., Ed., New York: Academic, 1964, vol. 1.
7. Rode, E.Ya., *Kislorodnye soedineniya margantsa* (Oxygen Compounds of Manganese), Moscow: Akad. Nauk SSSR, 1952.

Russian Journal of Applied Chemistry, Vol. 74, No. 3, 2001, pp. 374–377. Translated from Zhurnal Prikladnoi Khimii, Vol. 74, No. 3, 2001, pp. 367–370.

INORGANIC SYNTHESIS AND INDUSTRIAL INORGANIC CHEMISTRY

Kinetic of Leaching of Cadmium and Zinc from Their Oxides and Hydroxides

V. V. Tarasov, A. D. Fedoseev, and Chzhan Dun Syan

Mendeleev Russian University of Chemical Technology, Moscow, Russia

Received August 28, 2000

Abstract—The rotating disc method was applied to study the kinetics of leaching of zinc and cadmium from their oxides and hydroxides by sulfuric acid at pH 2–5, temperature of 288–313 K, and disc rotation velocities of 300–3600 rpm. The kinetic regions of the topochemical processes of zinc and cadmium leaching were revealed.

A considerable amount of zinc- and cadmium-containing waste has been accumulated in Russia. One of the sources of such waste is the viscose production. Even though the manufacture of viscose fiber declines, vast amounts of zinc and cadmium hydroxide sludges have been accumulated as a result of many years' work of viscose plants. The content of zinc in the sludges may be as high as 20%, and that of cadmium, tenths of percent. The total amount of zinc in such "technological deposits" is as large as tens of thousands of tons, and that of cadmium, tens of tons. In view of the loss by Russia of the former sources of zinc, these deposits are of interest as potential sources of these metals. At the same time, sludge dumps have seized large areas of lands suitable for agricultural purposes and created a danger of groundwater contamination with heavy metals. Of particular interest from the environmental standpoint are the problems of migration of zinc and cadmium ions in underground water horizons, occurring as a result of acid rains. In contrast to the processes of the recovery of zinc and cadmium ions with concentrated acids, studied and described in ample detail [1–5], leaching by highly dilute acids, modeling acid rains, has been little studied.

The aim of this study was to establish kinetic laws of leaching of zinc and cadmium ions from their oxides and hydroxides by weak sulfuric acid solutions at pH ~2–5.

EXPERIMENTAL

The rate of reactions in the solid–liquid systems is commonly analyzed in terms of the topochemical kinetics [6, 7]. The specificity of such processes is determined by the development with time of the reaction zone in the solid and the related change of reaction regimes of the process. If we consider dissolution (leaching) of some components of a microscopically inhomogeneous solid, it seems reasonable to assume that the surface, "ideally smooth" in the beginning of the process, is gradually pierced by pores and covered with reaction products. This leads to the appearance of a surface porous layer largely determining the macrokinetics of the process. In this case, the surface reaction can be considered quasi-homogeneous and a description method can be used, similar to that used in describing the kinetics of gas absorption with a chemical reaction. The reaction kinetics and diffusion are closely related, and the rate of such a process may be independent of the stirring intensity [8].

One of the most widely used methods of investigation of topochemical reactions [6] is the so-called method of equally accessible surface [7], assuming that such hydrodynamic conditions are created under which all points on the solid surface react at equal rates with the reagent diffusing from the core. This is only possible when the thicknesses of the hydrodynamic and diffusion boundary layers do not vary between the points. It has been established using methods of physicochemical hydrodynamics that the necessary conditions are created when a solid disc is rotated far from the vessel walls [9, 10]. Indeed, in this case the thickness of the diffusion boundary layer, δ, can be expressed, as shown by Levich [9], as follows:

$$\delta = 1.62D^{1/3}\nu^{1/6}\omega^{-1/2}, \quad (1)$$

where D is the molecular diffusion coefficient, ν is the

1070-4272/01/7403-0374$25.00

kinematic viscosity coefficient, and ω is the angular velocity of disc rotation.

According to the first Fick's law, the mass flux j can be expressed in terms of the diffusion coefficient D and concentration gradient at the disc surface

$$j = -D\,\mathrm{grad}C = -D(C^* - C_i)/\delta. \quad (2)$$

Substituting (1) into Eq. (2), we have

$$j = 0.620\,D^{2/3}\nu^{-1/6}\omega^{1/2}(C^* - C_i). \quad (3)$$

The limiting disc dissolution rate is achieved in the external diffusion region, when the reagent concentration at the disc surface, C_i, becomes zero. In this case, the mass flux is proportional to the volume concentration of acid, C^*, and grows in proportion to $\omega^{1/2}$:

$$j = 0.620\,D^{2/3}\nu^{-1/6}\omega^{1/2}C^*. \quad (4)$$

In passing to the external kinetic, internal diffusion, or internal kinetic regions [7], the mass flux must become independent of ω, i.e., we have a self-similar mode with respect to the Reynolds number Re, which means that the Re number appears in Eqs. (3) and (4) to zero power. The theoretical values of the rate constants k_t were calculated by the formula

$$k_t = 0.620\,D^{2/3}\nu^{-1/6}\omega^{1/2}. \quad (5)$$

The rotating disc method is widely used for studying the kinetics of electrochemical processes and dissolution of various compounds [10].

The experiment was carried out with a rotating Teflon cylinder having a hollow 0.5 cm in diameter for a disc to be dissolved. A pellet of a substance under study was inserted into this hollow by means of an oil press developing a pressure of up to 40 kg cm^{-2}. The rotation velocity of the disc was varied between 330 and 3600 rpm. The leaching was done in a 200 cm^3 thermostated vessel. The pH value was monitored with an Anion 410 pH meter. Control measurements of the cadmium and zinc ion concentrations were performed by atomic absorption spectroscopy.

A schematic of the setup used to study the kinetics of leaching by the rotating disc method is presented in Fig. 1. The concentration change in the bulk of a solution flowing around the disc, dC/dt, can be expressed as

$$\mathrm{d}C/\mathrm{d}t = -aD(C^* - C_i)/\delta = -ak_e(C^* - C_i). \quad (6)$$

Thus, we can calculate from experimental data the effective rate constant of dissolution, k_e:

$$k_e = -(\mathrm{d}C/\mathrm{d}t)/a(C^* - C_i), \quad (7)$$

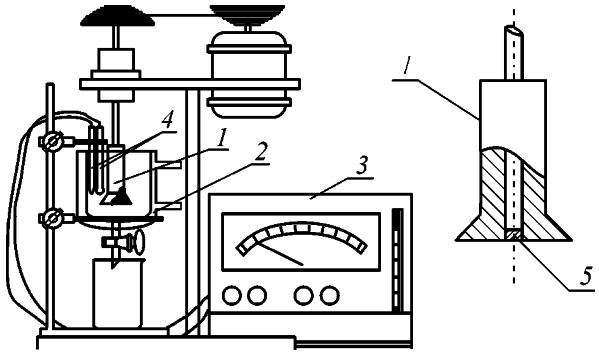

Fig. 1. Setup for studying the kinetics of leaching by the rotating disc method: (*1*) rotating disc with inserted pellet of a substance under study, (*2*) thermostated vessel, (*3*) Anion 410 A pH meter, (*4*) electrodes, and (*5*) pellet of a substance under study.

where $a = S/V$ is the specific surface area of the disc, i.e., the ratio of the apparent disc surface area S to the volume V of the solution flowing around the disc.

The k_e value coincides with the mass-transfer coefficient in the external diffusion region or with the rate constant k_c of a pseudo-first-order reaction in the external kinetic case. In the transition mode $k_e = f(k, k_c)$.

The k_e can also be found using the integral method. Separating variables in Eq. (6) and setting for simplicity $C_i = 0$ (i.e., taking that the process occurs in the external diffusion region), we get

$$-\int_{C^*}^{C} \mathrm{d}C/C = \int_0^t ak_e\,\mathrm{d}t. \quad (8)$$

Integration gives the equation for the kinetic curve

$$-\ln C = -\ln C^* + ak_e t, \quad (9)$$

or, with hydrogen ions consumed,

$$\mathrm{pH} = \mathrm{pH}^* + ak_e t. \quad (10)$$

Thus, having plotted the functions pH = $f(t)$, we can calculate the ak_e values from their slopes and, knowing a, determine k_e:

$$a = 0.785d^2/V, \quad (11)$$

where V is the volume of the leaching solution.

Figure 2 presents the pH of the aqueous medium in relation to the time of zinc oxide dissolution in the interval pH 2–5 at 298 K and disc rotation velocity of 1400 rpm.

Figure 2 shows that the dependence of pH on the

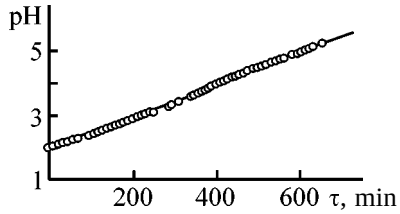

Fig. 2. pH of the reaction medium vs. the time τ of zinc oxide dissolution at 298 K and disc rotation velocity of 1400 rpm.

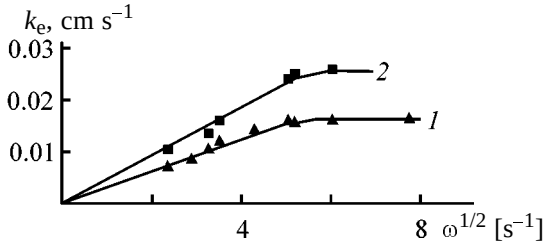

Fig. 3. Experimental rate constants k_e of zinc oxide leaching vs. the angular rotation velocity ω of the disc at (*1*) 293 and (*2*) 308 K.

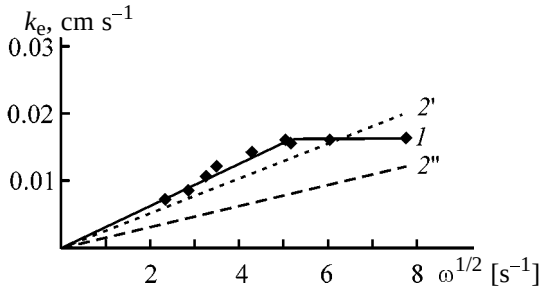

Fig. 4. Experimental rate constants k_e of zinc oxide leaching vs. the angular rotation velocity ω of the disc at 293 K. (*1*) Experiment; calculation: (*2*') for sulfuric acid and (*2*") for zinc sulfate.

process duration is linear, in accordance with Eq. (10). This indicates that the process rate is first-order with respect to the acid concentration. Indeed, as follows from extensive published evidence, the first order with respect to the leaching agent occurs the most frequently. For dissolution of zinc and cadmium hydroxides the time dependence of the pH is also linear. Changes in the concentrations of zinc(II) and sulfuric acid are exponential.

Figure 3 presents the experimental rate constants of zinc oxide leaching versus the square root of the angular velocity of disc rotation at 298 and 308 K. It can be seen that at disc rotation velocities in the range 330–1600 rpm (in the plot this interval corresponds to $\omega^{1/2}$ values up to 5.2 s$^{-1/2}$) the leaching rate constants k_e linearly depend on $\omega^{1/2}$. In this region the rate-determining stage of the process is either diffusion of acid toward the rotating disk of diffusion of zinc sulfate away from it.

At disc rotation velocities in the range 2200–3600 rpm the rate constants k_e of zinc oxide leaching are independent of the disk rotation velocity, which indicates a transition to the self-similar region. The nature of this self-similar region remains not quite clear. However, three reasons for such a kinetic behavior have been discussed, namely, transition of the process to (1) internal diffusion, (2) internal kinetic, or (3) external kinetic region. The last reason should be rejected since no significant dependence of k_e on T was observed in this region. In all probability, the true reason is the first one since the disc compacted from zinc oxide powder cannot be considered an absolutely smooth body and we have to reckon the possibility of development of a porous reaction zone. The second reason cannot be ignored, either, but it also assumes the development of a porous reaction zone.

Calculation by formulas (3)–(5) shows that, if the diffusion coefficient of sulfuric acid in the concentration range studied is taken to be 1.5×10^{-5} cm^2 s^{-1}, the calculated k_e are approximately 20% lower than the experimental values (Fig. 4). If we assume that the rate-determining stage of the process is the transport of zinc sulfate away from the disc ($D_{ZnSO_4} = 0.86 \times 10^{-5}$ cm^2 s^{-1}), then the agreement with experiment is much worse (the calculated k_e are half the experimental values). Presumably, it should be assumed that, up to a disc rotation velocity of 2000 rpm, the rate-determining stage is still the supply of sulfuric acid to the reaction zone, and a certain disagreement between the calculation and experiment can be attributed to the effect of the disc surface roughness, i.e., to a difference between the true and apparent surface areas. From the hydrodynamic standpoint, the roughness itself must only reduce the k_e value in a turbulent, but not laminar, mode of flow around the disc [9].

The obtained results indicate that (1) the reaction of sulfuric acid with zinc oxide is irreversible even at so low acid concentrations and (2) in the entire investigated range of sulfuric acid concentrations the rate-determining stage is the diffusion of sulfuric acid from the volume of the leaching aqueous solution.

As also in the case of zinc oxide, a linear dependence of experimental rates of the process on $\omega^{1/2}$ is observed in zinc hydroxide leaching at disc rotation velocities in the range 330–2600 rpm. However, in contrast to the oxides, this dependence is preserved up to 3600 rpm. This fact confirms once again the above assumption about the nature of the self-similar mode. Indeed, in the case of an essentially smooth and per-

Rate constants of the topochemical process of (a) zinc oxide, (b) zinc hydroxide, and (c) cadmium hydroxide leaching

ω, s^{-1}	Rate constant of leaching, k_e, cm s^{-1}, at indicated T, K				
	288	293	298	308	313
5.5	0.0065(a), 0.007(c)	0.005(b), 0.0065(c)	0.007(a)	0.007(b)	0.0085(a)
8.3			0.0085(a)		
10.6	0.009(a), 0.010(c)		0.011(a)		0.012(a)
12.3			0.012(a)		0.015(a)
18.3	0.014(a)		0.014(a)		0.024(a)
23.3		0.017(b), 0.016(c)			
25.3	0.017(a)		0.017(a)	0.024(b)	0.025(a)
26.8	0.017(a)	0.022(b, c)	0.016(a)	0.039(b)	0.026(a)

meable boundary of gel-like zinc hydroxide, there is no plateau in the $k_e = f(\omega^{1/2})$ plot. Thus, the plateau in this plot in dissolution of oxides is due to the porosity of the surface layer of the pellet.

The dependence of the experimental rate constants of cadmium hydroxide leaching on $\omega^{1/2}$ is also linear in the range ω = 330–2600 rpm.

The table lists the experimental rate constants of the topochemical process of leaching of zinc and cadmium oxides and hydroxides at various temperatures and disc rotation velocities. Comparison of the experimental rate constants of zinc oxide and hydroxide suggests that the rate of hydroxide dissolution somewhat exceeds the rate of oxide dissolution. We do not venture to account for this by higher kinetic hindrance in dissolution of the oxide, compared with that of the hydroxide, since such details already belong to the microkinetics of the process, which can only be discussed in the kinetic mode.

The dependence of $\ln k$ on $1/T$ in leaching of zinc oxide and zinc and cadmium hydroxides is linear. The following activation energies were obtained for the respective processes: 16 ± 2 (ZnO), 14 ± 2 [$Zn(OH)_2$], and 17 ± 3 kJ mol^{-1} [$Cd(OH)_2$]. These activation energies, coinciding within experimental error, are characteristic of diffusion-controlled processes.

CONCLUSIONS

(1) Rate constants of leaching of zinc oxide and hydroxide, and also cadmium hydroxide, with sulfuric acid solutions are obtained at pH 2–5 and 288–313 K at disc rotation velocities in the range 300–3600 rpm.

(2) Kinetic regions of the topochemical processes of zinc and cadmium leaching were revealed and it was demonstrated that under the conditions studied the dominant process is external diffusion of sulfuric acid from the bulk of the leaching solution. The activation energies of zinc oxide and hydroxide, and also cadmium hydroxide, were found.

(3) A transition of the kinetics of leaching to the self-similar mode region, possibly due to the roughness of the zinc oxide surface, was established.

ACKNOWLEDGMENT

The study was supported in part by INTAS (grant no. 971-30770).

REFERENCES

1. Lakernik, M.M. and Pakhomova, G.N., *Metallurgiya tsinka i kadmiya* (Metallurgy of Zinc and Cadmium), Moscow: Metallurgiya, 1969.
2. Syroezhkin, M.E. and Dzhakaev, Sh.I., *Pererabotka vel'tsokislov, shlakovozgonov i svintsovykh pylei na svintsovo-tsinkovykh zavodakh* (Processing of Weltz Oxides, Slag Fumes, and Lead Dusts at Lead–Zinc Plants), Moscow: Metallurgiya, 1971.
3. Ozberk, E., Collins, M.J., Makwana, M., *et al*., *Hydrometallurgy*, 1995, vol. 39, pp. 49–53.
4. Jankola, W.A., *Hydrometallurgy*, 1995, vol. 39, pp. 63–71.
5. Krysa, B.D., *Hydrometallurgy*, 1995, vol. 39, pp. 71–79.
6. Rozovskii, A.Ya., *Kinetika topokhimicheskikh reaktsii* (Kinetics of Topochemical Reactions), Moscow: Khimiya, 1974.
7. Frank-Kamenetskii, D.A., *Diffuziya i teploperedacha v khimicheskoi kinetike* (Diffusion and Heat-Transfer in Chemical Kinetics), Moscow: Nauka, 1962.
8. Danckwerts, P.V., *Gas–Liquid Reactions*, New York: McGraw-Hill, 1970.
9. Levich, V.G., *Fiziko-khimicheskaya gidrodinamika* (Physicochemical Hydrodynamics), Moscow: Fizmatgiz, 1959.
10. Pleskov, Yu.V. and Filinovskii, V.Yu., *Vrashchayushchiisya diskovyi elektrod* (Rotating Disc Electrode), Moscow: Nauka, 1972.

Russian Journal of Applied Chemistry, Vol. 74, No. 3, 2001, pp. 378–380. Translated from Zhurnal Prikladnoi Khimii, Vol. 74, No. 3, 2001, pp. 371–374.

INORGANIC SYNTHESIS AND INDUSTRIAL INORGANIC CHEMISTRY

Kinetics of Formation of Cobalt Carbonyls from Aqueous Solution of Cobalt Acetate in the Presence of Cyclohexanone in the Liquid–Liquid–Gas Heterogeneous System

Yu. T. Vigranenko, V. M. Gavrilova, and G. N. Gvozdovskii

VNIINeftekhim Joint-Stock Company, St. Petersburg, Russia

Received September 7, 2000; in final form, December 2000

Abstract—Cobalt carbonyls was prepared from an aqueous solution of cobalt acetate containing or not containing pyridine in the presence of the organic solvent immiscible with water. The product in the form of an organic solution can be used as hydroformylation catalyst. The kinetic equation taking into account the distribution of the reagents between the three phases was derived. The apparent rate constants and activation energies were calculated.

Industrial preparation of aldehydes form olefins and a CO + H_2 gas mixture is performed by hydroformylation [1]:

$$RCH{=}CH_2 + CO + H_2 \xrightarrow{\text{Cat.}} RCH_2CH_2CHO. \quad (1)$$

One of the steps of this process is preparation of the catalyst. The most suitable procedure for preparing cobalt carbonyls from solutions of cobalt salts is based on the reaction

$$4Co(RCOO)_2 + 16CO + 5H_2 \rightarrow Co_2(CO)_8 + 2HCo(CO)_4 + 8RCOOH. \quad (2)$$

We used cobalt acetate as the precursor since it is available and the resulting catalyst can be readily separated from the reaction products. Cyclohexanone was the solvent. Data on the kinetics of formation of cobalt carbonyls from an aqueous solution of $Co(OAc)_2$ in the presence of organic solvent in the liquid–liquid–gas system are lacking. It is only reported [2] that cobalt carbonyl is formed in a $Co(OAc)_2$ + toluene mixture. This reaction is heterogeneous and is controlled by diffusion. In this work we studied the kinetics of cobalt carbonyl formation in the above system.

Synthesis of cobalt carbonyls was studied in a 0.5-l ideal mixing batch reactor of the Vishnevskii screw type [3]. The unit consists also of high-pressure surge tanks for hydrogen, carbon oxide, and their mixture and a 0.25-l high-pressure charger for introducing the components of the reaction mixture into the reactor. The reactor purged with carbon monoxide was charged with cyclohexanone. A CO + H_2 mixture was fed at a pressure of 9.0 MPa, and stirring and heating were switched on. An aqueous solution of $Co(OAc)_2$ was poured into the charger. When pyridine was used it was introduced in the reactor with the organic solvent. The mixture was heated to the required temperature with stirring, and the $Co(OAc)_2$ solution was fed by the synthesis gas into the reactor. In the course of the synthesis the samples of the liquid were taken, and the aqueous and organic phases were separated. The cobalt(II) content was determined spectrophotometrically [4]; and the content of cobalt carbonyls, by iodometric titration [5].

Since cobalt acetate is practically nonvolatile, reaction (2), apparently, does not occur in the gas phase. The general kinetic equation of the reaction in the system of two immiscible liquid is as follows:

$$W = -\alpha\frac{d[Co(OAc)_2]^{(1)}}{dt} - (1-\alpha)\frac{d[Co(OAc)_2]^{(2)}}{dt}, \quad (3)$$

where α and $(1 - \alpha)$ are the volume fraction of the first (aqueous) and second (organic) phases, respectively.

Since $Co(OAc)_2$ is insoluble in cyclohexanone, $[Co(OOAc)_2]^{(2)} = 0$. Hence Eq. (3) can be written as

$$W = -\alpha\frac{d[Co(OAc)_2]^{(1)}}{dt}.$$

In accordance with the law of mass action

$$W = \alpha k[Co(OAc)_2]^{n_1} p_{H_2}^{n_2} p_{CO}^{n_3},$$

where n_1, n_2, and n_3 are the reaction orders with respect to $Co(OAc)_2$, H_2, and CO, respectively.

1070-4272/01/7403-0378$25.00

Finally, the kinetic equation of reaction (2) of formation of cobalt carbonyls is as follows:

$$W = k_{app}[Co(OAc)_2]^{n_1} p_{H_2}^{n_2} p_{CO}^{n_3}, \quad (4)$$

where $k_{app} = \alpha k$ is the apparent rate constant of reaction (2).

The kinetics of reaction (2) was studied as influenced by the salt concentration, partial pressures of hydrogen and carbon monoxide, and temperature. The rate of formation of cobalt carbonyls was calculated by numerical differentiation of the kinetic curves of $Co(OAc)_2$ consumption in the liquid phase. For this purpose we used the Lagrangian interpolation polynomial constructed using the experimental data [7]. The reaction order n_1 with respect to $Co(OAc)_2$, calculated by the van't Hoff procedure (Fig. 1a) from Eq. (5)

$$\log W_0 = \log [Co(OAc)_2]_0 + \text{const}, \quad (5)$$

was 1. This is also indicated by the fact that a given $Co(OAc)_2$ conversion at different salt concentrations (see table) is attained in the same time. The orders of reaction (2) with respect to hydrogen and carbon monoxide n_2 and n_3, calculated similarly, are 0.8 and 0.4, respectively (Figs. 1b, 1c).

The apparent rate constants of reaction (2) were calculated by the first-order equation [8]:

$$k_{app} = \tau^{-1} \ln \frac{[Co(OAc)_2]_0}{[Co(OAc)_2]_\tau}: \quad (6)$$

T, °C	135	150	165	180
$k_{app} \times 10^2$, min^{-1}	1.78	2.4	3.6	5.5

The activation energy E_A and the pre-exponential factor k_0 calculated form the temperature dependence of k_{app} are 41.7 kJ mol^{-1} and 2.9×10^3 min^{-1}, respectively.

Along with cobalt hydrocarbonyl $HCo(CO)_4$, cobalt carbonyl pyridine complex (CCP) is used as hydroformylation catalyst. This complex allows single-step preparation of alcohols form olefins [9]. The pyridine complex is a mixture of $[CoPy_6]^{2+}[Co(CO)_4]_2^-$ and $PyH^+Co(CO)_4^-$ salts and is formed by the reaction

$$8Co(OAc)_2 + 24CO + 9H_2 + 14Py \rightarrow 2[CoPy_6]^{2+}[Co(CO)_4]_2^- + 2PyH^+Co(CO)_4^- + 16HOAc. \quad (7)$$

Irreversibility of reaction (7) is also conformed by stability of CCP on relatively long storage. The kinetic equation (4) for reaction (7) takes the following form:

$$W = k'_{app}[Co(OAc)_2]^{n_1} p_{H_2}^{n_2} p_{CO}^{n_3} [Py]^{n_4}, \quad (8)$$

where k'_{app} is the apparent rate constant of reaction (7)

Influence of the initial concentration of cobalt acetate on the time of its 90% conversion in reaction (2) at T = 165°C, p = 29.4 MPa, CO : H_2 volume ratio = 1 : 1, and α = 0.5

$[Co(OAc)_2]$, M, in the aqueous phase	Time, min
1.94	65
3.77	63
6.0	64

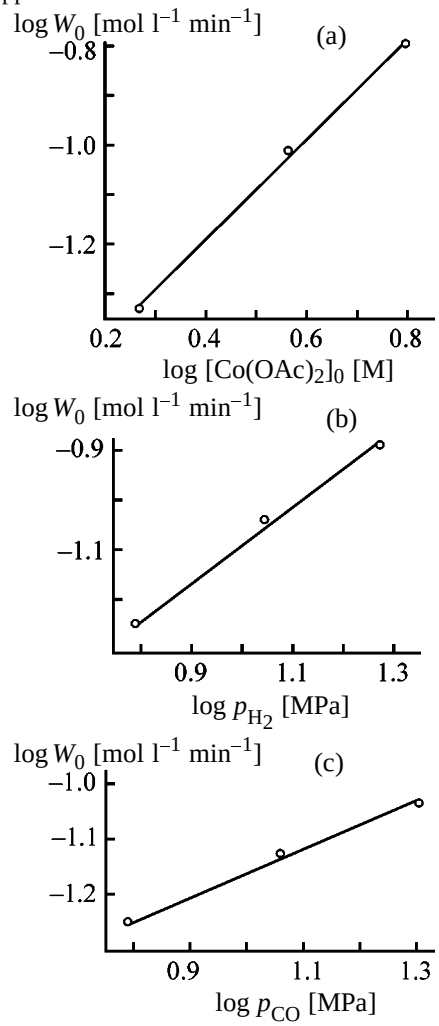

Fig. 1. Rate of $HCo(CO)_4$ formation W_0 at 150°C as a function of (a) the initial concentration $[Co(OAc)_2]_0$, (b) the partial pressure of hydrogen p_{H_2}, and (c) the partial pressure of carbon monoxide p_{CO}. (a) p_{CO+H_2} = 29.4 MPa, CO : H_2 volume ratio = 1 : 1; (b) p_{CO} = 6.0 MPa, $[Co(OAc)_2]_0$ = 6.0 M; (c) p_{H_2} = 6.0 MPa, $[Co(OAc)_2]_0$ = 6.0 M; the same for Fig. 2.

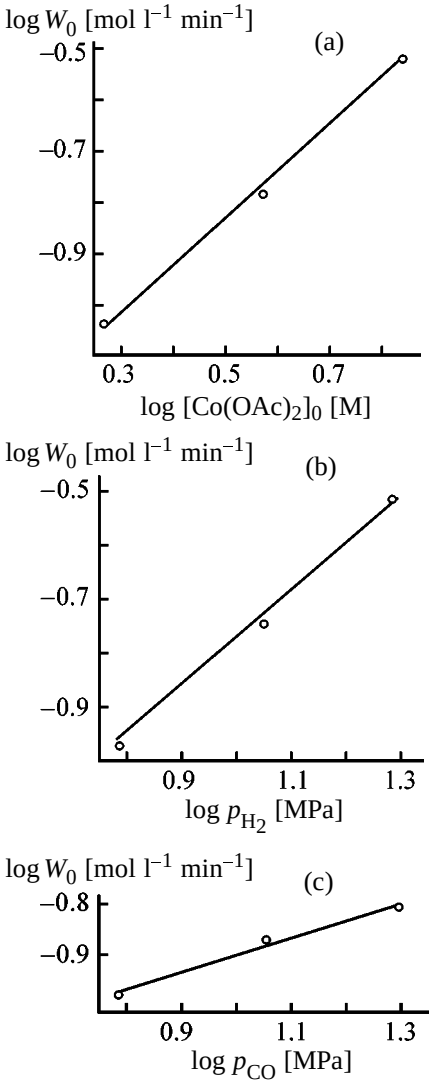

Fig. 2. Rate of CCP formation W_0 at 155°C as a function of (a) the initial concentration $[Co(OAc)_2]_0$, (b) the partial pressure of hydrogen p_{H_2}, and (c) the partial pressure of carbon monoxide p_{CO}.

and n_4 is the order of reaction (7) with respect to pyridine.

The kinetic features of CCP formation from $Co(OAc)_2$ and pyridine in cyclohexanone (Py/Co molar ratio 2, $\alpha = 0.5$) are similar to those of formation of $Co(CO)_8$ and $HCo(CO)_4$ (Figs. 2a–2c): the orders of reaction (7) with respect to $Co(OAc)_2$ ($[Co(OAc)_2] = 0–6.0$ M), H_2 (0–19 MPa), and CO (6–20 MPa) are 1, 0.9, and 0.3, respectively; E_A = 44.8 kJ mol^{-1} at 140–185°C; and $k_0 = 9.7 \times 10^4$ min.

The apparent rate constants of CCP formation by reaction (7) form $Co(OAc)_2$ and pyridine in cyclohexanone at $\alpha = 0.5$ and Py/Co molar ratio of 2 are as follows:

T, °C	140	155	175	185
$k'_{app} \times 10^2$, min^{-1}	2.76	4.37	6.0	10.5

CONCLUSIONS

(1) Formation of cobalt carbonyls from an aqueous solution of cobalt acetate, pyridine (or without pyridine), and the synthesis gas CO + H_2 in the presence of cyclohexanone in the liquid–liquid–gas heterogeneous system has the first order with respect to $Co(OAc)_2$ and the positive fractional orders with respect to H_2 and CO.

(2) The kinetic equation for calculation of the apparent rate constants and activation energies of formation of cobalt carbonyls in the liquid–liquid–gas heterogeneous systems were derived from the law of mass action.

REFERENCES

1. Gankin, V.Yu. and Gurevich, G.S., *Tekhnologiya oksosinteza* (Hydroformylation Process), Leningrad: Khimiya, 1981.
2. *Oksosintez. Poluchenie metodom oksosinteza al'degidov, spirtov i vtorichnykh produktov na ikh osnove* (Hydroformylation. Preparation of Aldehydes, Alcohols, and Their Secondary Products by Hydroformylation), Leningrad: Gostoptekhizdat, 1963.
3. Vishnevskii, N.E., Glukhanov, N.P., and Kovalev, I.S., *Mashiny i apparaty vysokogo davleniya s germetichnym elektroprivodom* (High-Pressure Machines and Apparatus with Hermetically Sealed Electric Drive), Leningrad: Mashinostroenie, 1977.
4. Fritz, J.S. and Schenk, G.H., *Quantitative Analytical Chemistry*, Boston: Allyn and Bacon, 1974.
5. Wender, I., Sternberg, H.W., and Orchin, M., *Anal. Chem.*, 1952, vol. 24, no. 1, pp. 174–175.
6. Lebedev, N.N., Manakov, M.N., and Shvets, V.F., *Teoriya tekhnologicheskikh protsessov osnovnogo organicheskogo neftekimicheskogo sinteza* (Theory of Main Industrial Processes of Basic Organic and Petrochemical Synthesis), Moscow: Vysshaya Shkola, 1984.
7. Bakhvalov, N.S., Zhidkov, N.P., and Kobel'kov, G.M., *Chislennye metody* (Numerical Methods), Moscow: Nauka, 1987.
8. Denisov, E.T., *Kinetika gomogennykh khimicheskikh reaktsii* (Kinetics of Homogeneous Chemical Reactions), Moscow: Vysshaya Shkola, 1988.
9. Vigranenko, Yu.T., Rybakov, V.A., and Borisov, R.B., *Zh. Prikl. Khim.*, 1983, vol. 56, no. 7, pp. 1619–1623.
10. Vigranenko, Yu.T., Rybakov, V.A., and Mukhenberg, K.M., *Koord. Khim.*, 1989, vol. 15, no. 1, pp. 103–107.

Russian Journal of Applied Chemistry, Vol. 74, No. 3, 2001, pp. 381–385. Translated from Zhurnal Prikladnoi Khimii, Vol. 74, No. 3, 2001, pp. 374–378.

INORGANIC SYNTHESIS AND INDUSTRIAL INORGANIC CHEMISTRY

Thermal Study of a Deposit Formed in Extraction of Hydrogen Chloride from Its Mixture with Air by Water-Sprayed Steel Chips

D. V. Klushin, A. I. Mikhailichenko, S. A. Volkov, and V. N. Klushin

Mendeleev Russian University of Chemical Engineering, Moscow, Russia

Received April 27, 2000; in final form, January 2001

Abstract—A deposit formed on the surface of steel chips in the course of prolonged interaction of their water-sprayed bed with air containing small amounts of hydrogen chloride was studied by thermogravimetry. The quantitative and qualitative composition of the deposit was established.

The absorption of HCl (0.01–0.05 g m^{-3}) by water-sprayed steel chips (4–6-mm fragments) from air at ambient humidity results in the formation of a dark suspension in solution and in formation of a black deposit on the surface of the chip bed. This deposit is not removed as the spraying intensity increases. At the same time it can be easily removed by mechanical stirring of the chips in the working solution or in water in a beaker. Particles of the deposit filtered off and dried at 105°C present a finely dispersed soot-like powder. In storage this powder randomly agglomerates into lumps of various size, easily crushed on weak pressing. The main part of the particles and agglomerates is magnetic. As the above-described procedure allows the residual content of HCl in air to be decreased to a level less than 0.02 mg m^{-3}, it is important to establish the composition of the deposit under discussion.

EXPERIMENTAL

According to the published data [1–5], reactions in the system air–HCl–water–steel chips yield, in particular, iron oxides and hydroxides whose properties directly depend on their genesis [2].

The presence of oxygen and HCl in gas and liquid phases, water, and iron in the steel chips, pH of the solution (ca. 5), and also the color and magnetic properties of the powder obtained suggest the following sequence of reactions in the system:

$$Fe + 2HCl \rightarrow FeCl_2 + H_2,$$

$$FeCl_2 + 2H_2O \rightarrow Fe(OH)_2 + 2HCl,$$

$$4Fe(OH)_2 + O_2 \rightarrow 4FeOOH + 2H_2O,$$

$$2FeOOH + Fe(OH)_2 \rightarrow Fe_3O_4 + 2H_2O.$$

Black magnetite Fe_3O_4 is deposited in similar systems at pH 5.2–12.4 [5]. Lepidocrocite γ-FeO(OH) colored from dark red to reddish black can be synthesized from iron(II) compounds [2]. Slow hydrolysis of Fe(II) and Fe(III) salts and the oxidation of iron powder in water [2] are possible ways of the formation of goethite α-FeOOH (dark brown or black powder). The magnetic properties of the main part of the powder under study and its color suggest that magnetite prevails in the powder.

The thermogravigram obtained on heating the powder in air in a derivatograph furnace at a heating rate of 9 deg min^{-1} (Fig. 1a) suggests a complicated pattern of the sample transformations.

The TG curve reflects minor weight changes (within 1%) up to 900°C. The weight loss in the range from the start of heating to approximately 550°C is surpassed within the 100–230°C range by a relatively significant weight gain. In the range 550–640°C the weight of the sample remains almost constant, and from 640°C to 900°C it gradually increases.

On the whole, the shape of the DTG curve is in a good agreement with that of the TG curve. In a flat concave part of the DTG curve corresponding to the total weight loss at 20–550°C there are a noticeable positive peak (at ~100–290°C with a maximum at 200°C) corresponding to the weight gain recorded in the TG curve and a much smaller negative peak (at ~480–540°C with a minimum at ~520°C) correspond-

1070-4272/01/7403-0381$25.00

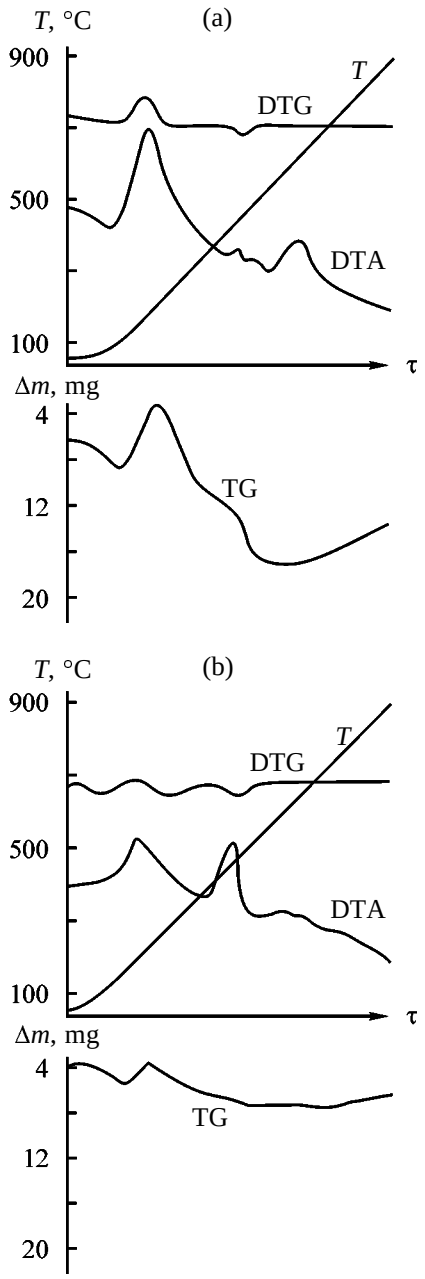

Fig. 1. Thermogravigram of the powder formed on water-sprayed steel chips through which an HCl–air mixture was filtered. The powder was dried at 105°C and kept in air. Heating rate 9 deg min^{-1}; (*T*) temperature, (Δm) weight change, and (τ) time. Sample (g): (a) 1.4243 and (b) 0.4271. Heating (a) in air and (b) in a helium atmosphere.

ing to the most intense weight loss. The weight gain within the 640–900°C range is not reflected in the DTG curve, which seems to result from its small value and insufficient sensitivity of the DTG galvanometer (1/15).

The initial portion (~20–80°C) of the DTA curve and its general downward trend at increasing temperature are indicative of a weak extended endothermic effect at 20–550°C with the weight loss. This effect overlaps with three exothermic transformations within this range. The first of them is the most pronounced (~100–460°C, maximum at ~220°C), it well agrees with the weight gain detected in the TG and DTG curves. The second (~480–525°C, maximum at ~505°C) and the third (~525–585°C, maximum at ~550°C) relatively weak peaks correspond to the weight loss at 480–585°C detected in the TG and DTG curves. The fourth clearly expressed exothermic deviation of the DTA curve corresponds to the part of the TG curve that reflects a very weak weight change at 585–730°C. The final almost linear part of the DTA curve is free of any peaks (temperatures above 730°C).

The final product of oxidative roasting of the deposit is a partially sintered powder containing rather easily crushed aggregates of characteristic red color typical for hematite α-Fe_2O_3. According to [2, 4, 5] this latter is a product of high-temperature treatment of magnetite in the presence of oxygen. Its magnetic properties are very weak.

Published data [2, 4, 5], as applied to Fig. 1, allow us to draw the following reasonable and reliable conclusions. The initial portion of the TG curve is obviously related to the loss of physically bound water. The weight growth at 100–230°C accompanied by the broad exothermic peak in the DTA curve, which is completed near 380°C, is attributable to the oxidation of magnetite (in practice, the oxidation of magnetite to maggemite γ-Fe_2O_3 is carried out at 200–250°C [5]) by the reaction

$$4Fe_3O_4 + O_2 \longrightarrow 6Fe_2O_3.$$

The weight growth in this reaction is

$$(1424.3 \times 32)/928 = 49.1 \text{ mg}.$$

This estimate is based on its stoichiometry and on the assumption that the whole mass of the sample under test (1.4243 g) is related to magnetite, which is a stable phase at room temperature [5].

However, the weight growth detected by the TG curve in this temperature range is significantly less. Moreover, the shape of the TG curve points to the simultaneous and finally prevailing competitive process of weight loss. It seems to be due to the presence of substances other than magnetite, which lose weight at this temperature. These substances, proba-

bly, mask (reduce) the real growth of the sample weight. Taking into consideration the color of the sample, we assume that γ-FeO(OH) and α-FeOOH can be such substances.

For example, goethite α-FeOOH transforms to hematite α-Fe_2O_3 upon dehydration at 50–500°C [2]. This transformation occurs without intermediate stages and is accompanied by a significant increase in surface area due to crystal destruction. Lepidocrocite γ-FeO(OH) is dehydrated at 180–300°C to give maggemite γ-Fe_2O_3, which is ferromagnetic like Fe_3O_4. On further heating maggemite also transforms to hematite with an exothermic effect.

Therefore, the total weight loss at 20–540°C can be assigned to the evaporation of both physically bound water and structural water. It should be noted that bonding of excess water in hydrated iron oxides and hydroxides is intermediate between adsorption and chemical bonds [2].

The TG curve allows us to estimate the composition of the powder under study. We assume that the resulting weight loss in the range 20–350°C (10.5 mg) is a consequence of two parallel processes, namely, the oxidation of magnetite and the dehydration of iron hydroxides by the reaction

$$2FeOOH \rightarrow Fe_2O_3 + H_2O.$$

If we denote weights (mg) of magnetite and iron hydroxide in a sample (1.4243 mg in total) as x and y, respectively, the weight gain due to the oxidation of Fe_3O_4 Δm_{ox} and the weight loss due to the dehydration of FeO(OH) and FeOOH Δm_{deh} in the chosen temperature range can be expressed, according to the stoichiometry of these reactions, as $\Delta m_{ox} = 32x/928$ and $\Delta m_{deh} = 18y/178$. This allows us to construct the following system of equations:

$$\begin{cases} 18y/178 - 32x/928 = 10.5, \\ x + y = 1424.3. \end{cases}$$

A solution of this system with respect to x and y shows that 69.14% of the sample weight is Fe_3O_4 and 30.86% is a sum of iron hydroxides FeOOH and FeO(OH).

The exothermic doublet in the DTA curve at 480–590°C corresponds to the parts of the TG curve with increasing intensity of weight loss. This doublet can be assigned to the transformation of maggemite into hematite. However, we cannot rule out a relation between this doublet and other modifications of Fe_2O_3 present in the starting sample (or formed by its thermal oxidation), which are capable of phase transformations (for example, δ-Fe_2O_3 and ε-Fe_2O_3). It is known [2] that ε-Fe_2O_3 is an unstable compound irreversibly transforming into α-Fe_2O_3 at 550°C. This temperature clearly corresponds to the maximum of the second peak in the doublet under discussion. Finally, there is an apparent, but not clearly explained in available literature, relation between this doublet and final (and definitely dissimilar) stages of dehydration of the sample in the temperature range under consideration.

A significant exothermic effect in the DTA curve at 580–710°C with a maximum at 660°C corresponds to the almost linear part of the TG curve. This effect is presumably related to the Curie point of γ-Fe_2O_3 (675°C) [4], which can exist in this region, and (or) to a change in magnetic properties of α-Fe_2O_3 (677°C).

When the temperature in similar systems rises to 700°C, traces of wustite FeO can appear [4]. Its oxidation seems to give rise to a weak growth of the sample weight detected in the final portion of the TG curve.

To refine our data, we recorded a thermogravigram of the powder heated in a helium atmosphere under the same conditions (Fig. 1b). The TG, DTG, and DTA curves of this thermogravigram differ essentially from the curves in Fig. 1a.

Despite general similarity of the TG curves, the curve in Fig. 1b even at room temperature exhibits a weak weight gain, which at approximately 30°C gives way to weight loss. In the range 180–255°C the sample weight grows again. At higher temperatures (up to 550°C) the weight loss again becomes prevailing, and then the sample weight remains almost constant up to 770°C. The weight of the sample grows only at higher temperatures up to the end of the heating.

The TG curve in Fig. 1b differs from the TG curve in Fig. 1a in the shape of the initial section, in much higher temperatures of the onset of weight gain (180 against 105°C), its maximum (~255 against 225°C), and completion (~415 against 380°C), of practical termination of weight loss (~550 against 540°C), and also of the beginning of the final weak and gradual weight gain (770 against 650°C).

In Fig. 1b the DTG curve is consistent in shape with the TG curve. A weak weight gain recorded in the TG curve at a near-room temperature is confirmed by the initial portion of the DTG curve. This increase is followed by a flat lowering of the DTG curve in the

range 30–500°C, which also confirms the total weight loss observed in the TG curve. There is a maximum in the DTG curve in Fig. 1b at 210°C in the range 100–325°C, which partially coincides with the range of the weight gain in the TG curve (~180–410°C). The subsequent negative peak in the DTG curve covers the range 460–600°C and has a minimum at 530°C. This minimum is in a good agreement with a well pronounced weight loss at 460–550°C in the TG curve. The region of the DTG curve above 600°C is almost linear, and a tendency to its extremely weak and gradual rise can be a very insignificant evidence for a certain weight growth detected in the TG curve above 770°C.

A comparison of the DTG curves in Figs. 1a and 1b shows that, in spite of their general similarity, the curve in Fig. 1b has a positive deviation near room temperatures, its peak with a maximum close to 200°C is more stretched and somewhat shifted to higher temperatures (~210 against ~200°C), its negative peak with a minimum at 530°C is also more stretched and shifted by approximately 5°C to higher temperatures, and its final portion has a certain slope.

It should be also noted that the products of calcination of the powder in a helium atmosphere and under oxidative conditions have the same color and properties.

The DTG curve in Fig. 1b is characterized by a broad exothermic peak in the 20–600°C range and by two well pronounced peaks covering the 20–450°C and 450–600°C ranges and having maxima at 235 and 520°C, respectively. Above 600°C there is a weak exothermic doublet in the DTA curve in the range 600–740°C with two maxima at 660 and 720°C. Above 740°C the DTA curve monotonically descends, exhibiting two very weak exothermic deviations with maxima at approximately 805 and 890°C.

The DTA curves in Figs. 1a and 1b differ to the greatest extent. The initial portion of the curve in Fig. 1b shows a definitely exothermic effect in contrast to that in Fig. 1a. The first exothermic peak in the curve in Fig. 1b spans the range 20–450°C, whereas the similar peak in Fig. 1a corresponds to the range 100–460°C. The maxima of these peaks are also situated at different temperatures: 235 and 220°C, respectively. In the range 450–600°C the curve in Fig. 1b has a well-pronounced second exothermic peak with a maximum at 520°C, and the curve in Fig. 1a has a significantly less distinct exothermic doublet with maxima at 500 and 560°C. On the contrary, in the range 600–740°C a well pronounced exothermic transformation with a maximum at 660°C in Fig. 1a corresponds to a weak exothermic doublet in Fig. 1b with maxima at 660 and 720°C. Finally, the region of the DTA curve in Fig. 1b above 740°C corresponds to the exothermic process in contrast to that in Fig. 1a.

The above-mentioned differences in thermogravigrams of Figs. 1a and 1b can be caused by the following reasons. At the beginning of the sample heating under helium, this gas is adsorbed by finely dispersed particles of the sample, which results not only in the weight gain detected in the TG and DTG curves, but also in heat liberation detected in the DTA curve below 100°C as an exothermic peak in Fig. 1b, unlike the same region in Fig. 1a where an endothermic deviation was found. The shapes of the both TG curves at temperatures higher than 100°C are almost the same. The dehydration of iron hydroxides and the oxidation of Fe_3O_4 on heating under helium begin and end at considerably higher temperatures, as follows from the comparison made above.

Calculations of the composition of the powder sample characterized by Fig. 1b gave 68.49% Fe_3O_4 and 31.51% iron hydroxides (the absolute difference from our earlier estimation is 0.65%).

Thus, as in the previous case, the weight gain in the range 180–250°C detected in the TG and DTG curves in Fig. 1b and the corresponding exothermic peak in the DTA curve are due to the oxidation of magnetite with oxygen, which is possibly present around crucibles in a small amount sufficient for oxidation. The limited oxygen content in this space causes the shift in the parameters of Fe_3O_4 oxidation (onset, end, and maximum) toward higher temperatures, as seen from the TG, DTG, and DTA curves.

The exothermic doublet in the DTA curve in Fig. 1a at 480–590°C corresponds to a single exothermic peak in the DTA curve in Fig. 1b at almost the same temperatures (460–600°C) with a maximum at 515°C. As in Fig. 1a, it probably results from the exothermic transformation of maggemite into hematite. The greater value of this peak suggests in this sample the increased content of lepidocrocite among iron hydroxides.

Probably, oxygen deficiency around crucibles suppresses the formation of one or more modifications of Fe_2O_3 and, in contrast, facilitates formation of other modification(s), which leads to degeneration of the doublet into a single peak. As a consequence, a single exothermic effect at 580–730°C in the DTA curve in Fig. 1a is transformed into a smooth exothermic effect, extended along the temperature axis (~600–

770°C) and having a clear tendency to splitting in two peaks. This effect also corresponds to the more extended portion of the TG curve, where no essential weight changes are observed. As assumed earlier, this effect is attributable to the magnetic properties of Fe_2O_3 modifications. Low oxygen content in the furnace atmosphere is probably responsible also for a significant shift of the onset of certain weight gain, completing sample heating, toward higher temperatures (from ~650 to ~770°C).

CONCLUSIONS

(1) Thermogravigrams were obtained under helium and in air for a deposit formed on steel chips at their treatment with humid air containing 0.01–0.05 g m^{-3} HCl. A comparative examination of the thermogravigrams was carried out.

(2) It was found that the deposit contains about 68.5–69.1% magnetite and 30.9–1.5% iron hydroxides. Lepidocrocite is the prevailing fraction among the hydroxides.

REFERENCES

1. *Fiziko-khimicheskie svoistva oksidov: Spravochnik* (Physicochemical Properties of Oxides: Reference Book), Moscow: Metallurgiya, 1969.
2. Ni, L.P., Gol'dman, M.M., Solenko, T.V., *et al*., *Okisly zheleza v proizvodstve glinozema* (Iron Oxides in Alumina Production), Alma-Ata: Nauka, 1971.
3. Levinskii, Yu.V., *Diagrammy sostoyaniya metallov s gazami* (Phase Diagrams of Metals with Gases), Moscow: Metallurgiya, 1975.
4. Zhuk, N.P., *Kurs teorii korrozii i zaschity metallov* (Theoretical Course of Corrosion and Metal Protection), Moscow: Metallurgiya, 1976.
5. Epikhin, A.N., Production of Magnetic Powders and Iron Oxide Pigments from Solid Industrial Wastes, *Cand. Sci. Dissertation*, Moscow, 1996.

Russian Journal of Applied Chemistry, Vol. 74, No. 3, 2001, pp. 386–389. Translated from Zhurnal Prikladnoi Khimii, Vol. 74, No. 3, 2001, pp. 379–383.

INORGANIC SYNTHESIS AND INDUSTRIAL INORGANIC CHEMISTRY

Fractionation of Sulfur Isotopes in the Course of High-Temperature Roasting of Copper–Nickel Sulfide Ores and Concentrates

L. Sh. Tsemekhman, L. B. Tsymbulov, A. G. Ryabko, B. A. Mamyrin, I. A. Blatov, and V. S. Velim

Gipronikel' Institute, Joint-Stock Company, St. Petersburg, Russia
Ioffe Physicotechnical Institute, Russian Academy of Sciences, St. Petersburg, Russia
Kola Mining and Smelting Company, Joint-Stock Company, Murmansk, Russia

Received November 29, 2000

Abstract—The fractionation of sulfur isotopes, namely, enrichment of the cinder with the heavy isotope ^{34}S in the course of roasting of various sulfide ores and concentrates in neutral and oxidative atmospheres at 773–973 K was studied.

High-temperature oxidative roasting is widely used today as one of main overhead stages in processing copper–nickel and copper sulfide concentrates. Therefore, roasting processes attract steady researches' interest. A significant attention is paid to the mechanisms of oxidation and dissociation of sulfur,[1] which is the major component removed upon the roasting.

It is well known that isotopes can be fractionated in the course of chemical reactions, i.e., fractions of isotopes in products can differ from those in the starting reagents. Therefore, it is not improbable that studying the fractionation of sulfur isotopes can give a new qualitative information on reaction mechanisms, as compared to traditional techniques (chemical analysis, XRD, X-ray spectral microanalysis, etc.).

The fractionation of sulfur isotopes in the course of high-temperature oxidative roasting of copper–nickel sulfide ore of Pechenga ore field was established previously [1]. However, the data obtained could not be considered as fully reliable because of insufficient number of the experiments.

In this work the possibility of fractionation of sulfur isotopes was confirmed not only for sulfide ores but also for Pechenga ore concentrates and natural pyrite at various temperatures in oxidative and neutral atmospheres.

[1] Oxidation of sulfur and dissociation of higher sulfides can occur simultaneously in spite of the fact that roasting is carried out in an oxidative atmosphere.

The composition of starting materials is given in Table 1. Pyrite was roasted at 773 and 873 K under argon in an installation shown in Fig. 1.

A 5-g pyrite sample in an alundum boat was first placed in a quartz tube and then in a furnace with a Silit heater. The tube was blown through with argon before switching on the furnace. On reaching a temperature of the experiment the quartz tube was moved to place the sample in the furnace hot area. In the course of the experiment the temperature was kept constant by an automatic apparatus. After roasting the sample was removed from the hot area by shifting the tube. The furnace was switched off, but the gas was passed through up to complete sample cooling.

After thorough grinding and mixing, the cooled sample was divided into two equal parts. One of them was chemically analyzed for the total sulfur and sulfate sulfur. The other part was used in the isotope mass-spectral analysis.

Copper–nickel sulfide ore and concentrate were roasted in air at 823 and 973 K. Preliminarily the ore and concentrate with the grain size less than 0.1 mm were pelletized with water added. A 4-g pellet sample was placed in a quartz reactor roughly modeling a fluidized-bed furnace (Fig. 2). The reactor was placed in a Silit furnace and heated. On reaching the required temperature, air was passed through the reactor bottom at a rate of 1.35 l min^{-1}. The oxidation time was varied from 1 to 15 min. On completion of the experiment, the air flow was ceased and the reactor

1070-4272/01/7403-0386$25.00

Table 1. Chemical composition of starting materials

Material	Content, wt %									
	Ni	Cu	Co	Fe_{total}	S_{total}	$S_{sulfate}$	SiO_2	Al_2O_3	CaO	MgO
Pyrite	0.09	0.10	0.01	39.8	44.60	1.01	8.4	0.42	0.24	0.22
Copper–nickel ore	2.44	0.65	0.06	27.4	13.78	0.41	22.0	0.66	1.90	19.20
Copper–nickel ore concentrate	7.68	4.00	0.23	30.4	20.18	0.13	16.8	3.70	0.66	11.20

was removed from the furnace. The cooled cinder was ground, weighed, and after thorough mixing divided into two parts. One of the parts was chemically analyzed for total sulfur and sulfate sulfur. The other part was used in the isotope analysis.

Determination of the sulfur isotope composition involves sample preparation, namely, complete conversion of sulfur in the sample to sulfur dioxide, and subsequent analysis of SO_2 by mass spectrometry [2].

A ground weighed sample was thoroughly mixed with a threefold excess of an oxidant. Copper(II) oxide of analytical pure grade was used as the oxidant. A mixture of the ore and copper(II) oxide was loaded in a porcelain boat placed in a quartz reactor. The system was evacuated to a pressure of 2×10^{-2} mm Hg. After evacuation the reactor was placed in a tubular furnace, the temperature was gradually raised to 573 K, and the sample was degassed within 30 min. Then the reactor was removed from the furnace, the temperature was raised to 1053–1083 K, and the reactor with the combustion boat was placed back in the furnace. The system was disconnected from the vacuum pump, and the trap was placed in a Dewar flask with liquid nitrogen. The evolved sulfur dioxide was frozen out in the trap. Sulfur from the sample was oxidized for 80 min. Sulfur dioxide from the trap was evaporated and refrozen in a quartz ampule, which was sealed and then analyzed by a standard technique on a double-beam mass spectrometer with a two-channel lap system. Sulfur from a reference sample was oxidized similarly.

Cinders after oxidative roasting of copper–nickel sulfide ore were analyzed on an MI-1330 mass spectrometer,[2] and cinders obtained by pyrite roasting and oxidative roasting of the ore concentrate, on an MI-1201V mass spectrometer.[3]

The sulfur isotope composition in the samples under study is usually characterized by the ratio $^{32}S/^{34}S$ of only two isotopes [3], because the concentration of the other natural isotopes, ^{33}S and ^{36}S, is negligible. Variations in the sulfur isotope composition are expressed by the value of $\delta^{34}S$ (‰), which is calculated by the equation

$$\delta^{34}S = \frac{^{34}S/^{32}S_s - {}^{34}S/^{32}S_{ref}}{^{34}S/^{32}S_{ref}} \times 1000, \quad (1)$$

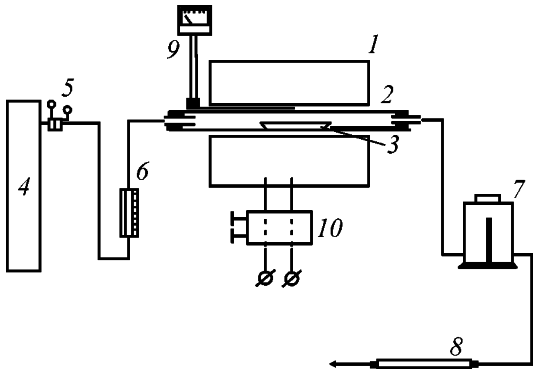

Fig. 1. Installation for pyrite roasting in a horizontal reactor: (*1*) electric furnace, (*2*) quartz tube, (*3*) boat with weighed sample, (*4*) cylinder with argon, (*5*) reducer, (*6*) flowmeter, (*7*) cooler, (*8*) packed filter, (*9*) thermocouple and potentiometer, and (*10*) transformer.

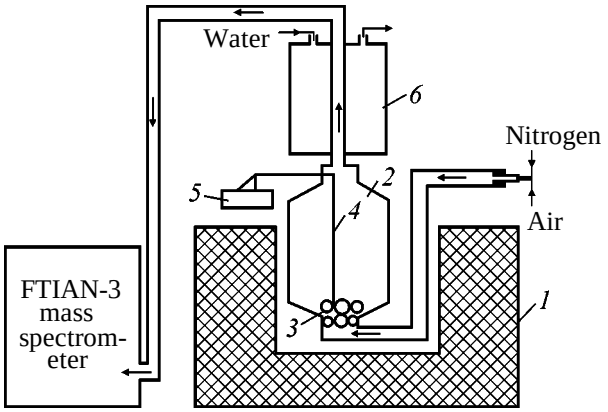

Fig. 2. Laboratory installation for pellet roasting in fluidized bed: (*1*) furnace with Silit heater, (*2*) quartz reactor, (*3*) pellets, (*4*) Chromel–Alumel thermocouple, (*5*) potentiometer, and (*6*) gas cooler.

[2] Isotope analysis was carried out in the Russian Research Institute of Geology (VSEGEI), St. Petersburg.

[3] Isotope analysis was carried out in the Institute of Microbiology, Russian Academy of Sciences, Moscow.

Table 2. Experimental conditions and data on pyrite roasting under argon

T, K	τ, min	S_{total}	$S_{sulfate}$	$\delta^{34}S$, ‰
		wt %		
initial sample		44.6	1.01	–2.0
773	1	44.4	1.03	5.6
773	2	44.2	0.17	5.2
773	10	43.9	1.03	0.1
873	5	44.1	0.84	1.4
873	10	44.7	0.74	0.5

where $^{34}S/^{32}S_s$ is the isotope ratio in a sample and $^{34}S/^{32}S_{ref}$ is that in a reference.

Troilite sulfur of the Canyon Devil meteorite is used as a universally recognized world [4]. In everyday practice an intermediate (working) reference is used instead of the absolute reference. The following formula is used for the conversion:

$$\delta^{34}S = (1 + \delta^{34}S_{ref/met}/1000)\delta^{34}S_{s/ref} + \delta^{34}S_{ref/met}, \quad (2)$$

where $\delta^{34}S_{ref/met}$ characterizes variations in the isotope composition of the working reference relative to the meteorite, and $\delta^{34}S_{s/ref}$ characterizes variations in the isotope composition of a sample relative to the working reference.

The positive sign of $\delta^{34}S$ indicates that sulfur is enriched with ^{34}S, and the negative sign, that sulfur is enriched with ^{32}S with respect to the meteorite sulfur. Further all analytical data are given relative to the above-mentioned international reference.

The accuracy of the $\delta^{34}S$ determination on MI-1330 and MI-1201V mass spectrometers was ±0.3 and ±0.1‰, respectively.

Experimental data on pyrite roasting are given in Table 2 and Fig. 3. They reveal appreciable fractionation of sulfur isotopes in the course of the pyrite dissociation. The maximal fractionation takes place in the initial stages of the roasting.

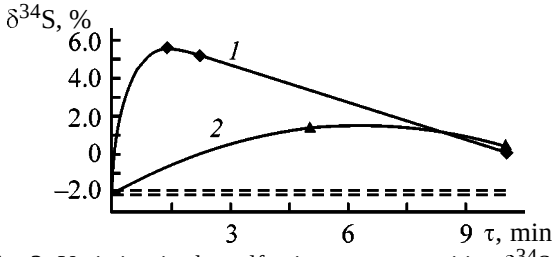

Fig. 3. Variation in the sulfur isotope composition $\delta^{34}S$ in a cinder obtained by pyrite roasting under argon. (τ) Time; the same for Fig. 4. Temperature (K): (*1*) 773 and (*2*) 873. Dashed lines denote limits of the accuracy of $\delta^{34}S$ determination in the initial sample; the same for Fig. 4.

Before discussing these data, we consider some aspects of the isotope separation theory. It was noted before that chemical transformations of molecules containing various sulfur isotopes are usually accompanied by their fractionation due to distinctions in their physicochemical properties, i.e., isotope distributions in the reagents and products change in a chemical reaction. This results from different mobility of molecules with light and heavy isotopes, which affects the reaction rate. Naturally, the rate is lower in the case of a heavier isotope.

The difference in rates may be partially caused by the difference in vibration frequencies of molecules with different isotopes [5]. However, this difference is unlikely to be significant at high temperatures.

The kinetic isotope effect is defined as the ratio of reaction rate constants of isotope species [6]:

$$k/k^* = (\mu^*/\mu)^{1/2} e^{-(E-E^*)/RT}, \quad (3)$$

where μ is the reduced mass of a molecule (asterisk designates a heavy isotope), E and E^* are activation energies of the reactions involving light and heavy isotopes, T is the absolute temperature, and R is the universal gas constant.

It is clear that the activation energy of the reaction involving a heavy-isotope species is higher that with a light-isotope form.

According to Eq. (3), the kinetic isotope effect depends on temperature and differences in the isotope masses and activation energies of various isotope forms. As the temperature increases, the isotope effect decreases. In the limiting case of $T \to \infty$ the exponential term approaches unity, and the isotope effect is determined by only the mass ratio. It should be noted that the mass difference between ^{32}S and ^{34}S is 7%.

Since bonds formed by a light isotope are weaker than those of a heavy isotope, the inequality $k/k^* > 1$ is valid, i.e., reaction products are usually enriched with a light isotope, and a heavy isotope is accumulated in the residue. Data in Fig. 3 are in a good agreement with these theoretical statements.

A significant enrichment of the cinder with ^{34}S is observed at the beginning of the dissociation (773 K), i.e., the $Fe^{32}S_2$ molecules dissociate preferentially. The enrichment decreases in time. The effect of cinder enrichment with ^{34}S at 873 K is less pronounced, which well agrees with Eq. (3).

Table 3. Experimental conditions and data on oxidative roasting of ore concentrate in fluidized bed

T, K	τ, min	S_{total}, wt %	$S_{sulfate}$, wt %	δS^{34}, ‰
Ore				
Starting	sample	13.78	0.41	5.3
973	1	11.48	0.14	5.6
973	5	4.73	0.37	5.0
973	10	0.90	0.58	6.8
Ore concentrate				
Starting	sample	18.9	1.48	8.2
823	3	14.5	1.00	9.5
823	10	10.6	1.78	9.2
823	15	10.2	2.02	7.5
973	1	16.9	0.57	7.9
973	3	13.3	0.71	9.4

To prove conclusively the fact of the enrichment with ^{34}S, it is necessary to correlate the content of sulfate sulfur with $\delta^{34}S$. Such a correlation is needed because ^{34}S is always accumulated preferentially in oxidized sulfur compounds in the following order: S^{2-}, S^0, SO_2, SO_3, SO_4^{2-}. This trend was the most completely demonstrated by Sakai and Bachinskii [4].

Consequently, if the sulfate content in pyrite samples strongly changes, a question arises whether the enrichment of a cinder with a heavy isotope results only from the lower content of sulfate sulfur in the sample under study. Table 2 demonstrates no explicit correlation between $\delta^{34}S$ and $S_{sulfate}$; however, during the first minutes of dissociation the cinder is appreciably enriched with ^{34}S irrespective of the content of sulfate sulfur in the sample.

The data on the oxidative roasting of the ore and concentrate are given in Table 3. Time dependences of the isotope compositions are presented in Fig. 4, which shows that the cinder is enriched with ^{34}S.

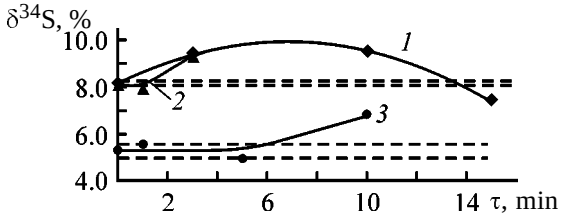

Fig. 4. Variation in sulfur isotope composition $\delta^{34}S$ in a cinder formed in the course of oxidative roasting of copper–nickel sulfide ore and ore concentrate. Sample: (*1*, *2*) concentrate and (*3*) ore. Temperature (K): (*1*) 823 and (*2*, *3*) 973.

At 823 K the enrichment is observed in the initial process stage, as is the case with pyrite dissociation.

In the case of roasting at 973 K the curves are differently shaped. However, in this case the cinder is also enriched with ^{34}S. We note that the enrichment at 973 K was found in the cases of various materials using different mass-spectrometric installations.

Thus, the experiments have shown that high-temperature (773–973 K) roasting of various sulfide ores and concentrates in neutral and oxidative atmospheres is accompanied by fractionation of sulfur isotopes, namely, enrichment of the cinder with ^{34}S.

The data on variation in time of the sulfur isotope composition in roasting gases would be no less valuable; however, such experiments require special equipment and development of appropriate technique.

CONCLUSIONS

(1) The greatest enrichment in roasting of natural pyrite under argon was observed within the first minutes at low temperatures. The maximal enrichment at 773 K was 6‰. In the case of roasting of copper–nickel sulfide ores and concentrates at 823 and 973 K, the maximal enrichment was 1.3–1.5‰.

(2) The regular trends revealed can be used in development of oxidative roasting theory for various sulfide materials.

REFERENCES

1. Tsymbulov, L.V., Kravtsova, O.A., Tsemekhman, L.Sh., *et al.*, in *Novye protsessy v metallurgii nikelya, medi i kobal'ta: Trudy OAO "Institut Gipronikel'"* (New Processes in the Metallurgy of Nickel, Copper, and Cobalt: Trans. of Gipronikel' Institute, Joint-Stock Company), Moscow: Ruda i Metally, 2000, pp. 214–219.
2. Ustinov, V.I. and Grinenko, V.A., *Pretsizionnyi mass-spektroskopicheskii metod opredeleniya izotopnogo sostava sery* (Precision Mass-Spectrometric Technique for the Determination of Sulfur Isotope Composition), Moscow: Nauka, 1965.
3. Rankama, K., *Isotope Geology*, London: Pergamon, 1954.
4. Grinenko, V.A. and Grinenko, L.N., *Geokhimiya izotopov sery* (Sulfur Isotope Geochemistry), Moscow: Nauka, 1974.
5. Hoefs, J., *Stable isotope Geochemistry*, Berlin: Springer, 1980, 2nd Ed.
6. Galimov, E.M., *Priroda biologicheskogo fraktsionirovaniya izotopov* (Nature of Isotope Biological Fractionation), Moscow: Nauka, 1981.

Russian Journal of Applied Chemistry, Vol. 74, No. 3, 2001, pp. 390–393. Translated from Zhurnal Prikladnoi Khimii, Vol. 74, No. 3, 2001, pp. 384–386.

PHYSICOCHEMICAL STUDIES OF SYSTEMS AND PROCESSES

On the Accuracy of Calculation by the Clapeyron–Clausius Equation

I. B. Sladkov and M. S. Nedoshivina

St. Petersburg State Technical University, St. Petersburg, Russia

Received October 8, 2000

Abstract—The accuracy of calculations by the Clapeyron–Clausius equation in the entire region of existence of a liquid phase is discussed in relation to temperature or pressure.

By now, equations have been developed allowing reliable prediction of the saturated vapor pressure over the entire region of existence of the liquid phase [1]. However, these methods rely upon a vast body of difficultly accessible input data and cannot be applied to poorly studied substances.

The Clapeyron–Clausius equation gives in the simplest form the temperature dependence of the vapor pressure and is widely used in thermodynamic calculations. For some substances it yields an acceptable error in comparatively narrow temperature intervals, which is accounted for by the assumptions made in deriving and integrating the equation. At the same time, the Clapeyron–Clausius equation is valid for many substances in rather wide temperature intervals, which has been substantiated by the compensation effect recently [1, 2].

The temperature at which the pressure is determined may vary within the existence range of the liquid phase, beginning at the triple point and ending at the critical point. The problem of how the choice of temperature affects the error of the Clapeyron–Clausius equation has not been studied. In the present study, data were obtained making it possible to relate the conditions of application of the Clapeyron–Clausius equation (range of temperatures or pressures in which a calculation is performed) to the expected error in calculating the saturated vapor pressure.

As objects of study were chosen 10 substances for which precise data on the saturated vapor pressure are available in the literature for the entire range of existence of the liquid phase. These substances, their fundamental constants [2], and also sources of tabulated data on the saturated vapor pressure are listed in Table 1.

For the above substances, calculations by means of the Clapeyron–Clausius equation were performed in the entire range of existence of the liquid phase, i.e., in the temperature interval between the triple and critical points.

As is known, in integrating the approximate Clapeyron–Clausius equation

$$\mathrm{d}\ln P/\mathrm{d}T = \Delta H_\mathrm{v}/(RT^2)$$

the enthalpy of vaporization is taken to be equal to its value at the boiling point, ΔH_b, and the constant of integration is found from the saturated vapor pressure at the boiling point. This yields the equation

$$\ln P = -A/T + B, \qquad (1)$$

$$A = \Delta H_\mathrm{b}/R, \qquad B = \Delta S_\mathrm{b}/(RT_\mathrm{b}).$$

The pressures calculated using Eq. (1) were compared with experimental values, and the relative error of pressure calculation by the Clapeyron–Clausius equation was determined. An example of calculations for two substances is given in Table 2.

Further, the absolute values of the above errors were averaged for some temperatures or pressures over all the 10 substances considered. This average error is given in Tables 3 and 4 and is considered a measure of the accuracy of the Clapeyron–Clausius equation.

It was found that the following behavior is observed in the temperature interval between the triple and critical points: for all of the substances the calculation error grows with decreasing temperature (which corresponds to decreasing pressure). In the temperature interval between the boiling and critical points,

1070-4272/01/7403-0390$25.00

Table 1. Physicochemical properties of substances

Substance	T_b, K	H_b, kJ mol^{-1}	T_c, K	P_c, MPa	Reference, source of data on vapor pressure
CCl_4	349.7	30.02	507.2	4.56	[3]
CCl_2F_2	243.4	20.51	385.2	4.15	[3]
$CHCl_2F$	282.1	24.49	451.6	5.19	[4]
$CHClF_2$	232.3	20.30	369.3	4.99	[5]
$CBrF_3$	215.5	18.25	340.2	3.97	[4]
$CBrClF_2$	269.1	23.15	427.0	4.25	[4]
$CBrCl_2F$	325.0	27.88	514.0	4.49	[4]
NH_3	239.7	23.36	405.5	11.35	[6]
$SiCl_4$	330.5	28.64	507.0	3.73	[7]
$SnCl_4$	387.0	33.98	592.2	3.84	[8]

Table 2. Error in calculation of the saturated vapor pressure by the Clapeyron–Clausius equation for NH_3 and $CHClF_2$

T, K	P, MPa, experiment	Calculation error, %	T, K	P, MPa, experiment	Calculation error, %
	NH_3			$CHClF_2$	
196	0.0064	15.4	193	0.0103	15.7
203	0.0109	11.1	203	0.0204	8.9
223	0.0408	2.7	218	0.0495	2.7
233	0.0717	0.4	223	0.0645	1.3
238	0.0931	–0.4	228	0.0829	0.2
253	0.1900	–1.7	243	0.1640	–1.9
293	0.8580	–0.9	253	0.2450	–2.3
313	1.555	0.9	273	0.4981	–2.5
343	3.312	3.9	293	0.9097	–1.7
353	4.139	4.9	313	1.533	–0.7
363	5.112	5.7	333	2.427	0.2
373	6.250	6.4	343	2.997	0.5
383	7.571	6.9	353	3.664	0.6
393	9.104	7.2	363	4.442	0.4
398	9.961	7.2	365	4.613	0.3

two types of behavior with temperature are observed for the calculation error Δ: for some substances Δ grows with increasing temperature, while for the others it remains approximately constant up to the critical point. Both types of dependences, plotted on the basis of the data in Table 1 for NH_3 and $CHClF_2$, are shown in Fig. 1. The difference $T - T_b$ is plotted along the abscissa, in order to bring into coincidence the zeros of the function and the argument (since the constant of integration of the Clapeyron–Clausius equation is found from the boiling point parameters, the equation gives zero error just for the boiling point).

The obtained data indicate that it is advisable to further analyze the accuracy of the Clapeyron–

Table 3. Accuracy of calculation by the Clapeyron–Clausius equation in the low-temperature region in relation to pressure

P, MPa	Error, %	
	average	maximum
0.01	12	16
0.02	7.0	10
0.03	5.1	8
0.04	3.6	5
0.05	2.4	4
0.06	1.5	3
0.07	1.1	2
0.08	0.6	1
0.09	0.4	0.7

Table 4. Accuracy of calculation by the Clapeyron–Clausius equation in the low-temperature (I) and high-temperature (II) regions in relation to temperature

$T - T_b$, K	Error, %		$T - T_b$, K	Error, %	
	average	maximum		average	maximum
Region I			Region II		
–5	0.5	1	20	0.8	3
–10	1.3	2	40	1.3	4
–20	3.1	5	60	1.5	4
–30	5.7	9	80	2.1	5
–40	10	14	100	2.7	7
–50	20	25	120	3.4	8
			140	3.6	9
			160	4.8	9
			180	5.0	10

Clausius equation for two temperature intervals: low-temperature ($T < T_b$) and high-temperature ($T > T_b$).

In the low-temperature region, the saturated vapor pressures of all the substances vary within the range from 0 to 0.1 MPa (the last figure is the rounding of a value of 0.10325 which gives in megapascals the saturated vapor pressure at the boiling point). Therefore, the accuracy of the Clapeyron–Clausius equation can be related both to pressure (Table 3) and to temperature (Table 4). Tables 3 and 4 show that the error in calculating the saturated vapor pressure becomes significant at pressures lower than 0.01 MPa or at temperatures deviating from the boiling point by more than 40 K.

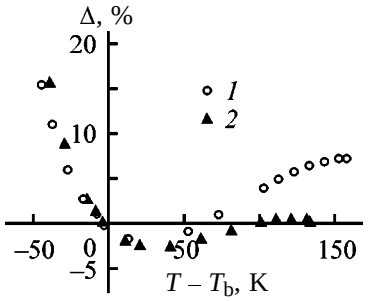

Fig. 1. Variation of the error of calculation by the Clapeyron–Clausius equation, Δ, with the distance from the boiling point. (*T*) Temperature. (*1*) NH_3 and (*2*) $CHClF_2$.

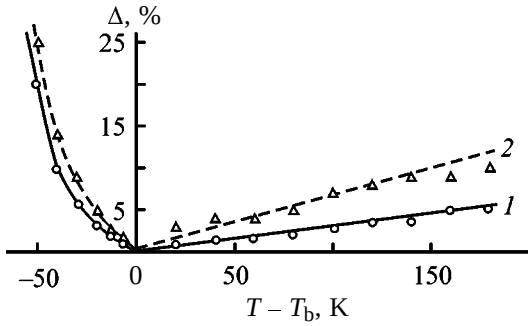

Fig. 2. (*1*) Average and (*2*) maximum error in calculating the saturated vapor pressure by the Clapeyron–Clausius equation vs. the calculation temperature *T*.

In the high-temperature region, it is impossible to set unambiguously the upper pressure limit because of the different critical pressures of all substances. Therefore, the accuracy of the Clapeyron–Clausius equation is given in relation to temperature (Table 4). It can be seen that in calculations above the boiling point the Clapeyron–Clausius equation ensures reliable prognosis of the saturated vapor pressure in sufficiently wide temperature intervals.

The results presented in Table 4 are summarized by the plot in Fig. 2, readily providing information about the expected average error in determining the pressure and the maximum error of calculation by the Clapeyron–Clausius equation in different temperature ranges. As seen from Fig. 2, the average error in calculating the saturated vapor pressure by the Clapeyron–Clausius equation in the temperature range from $T - T_b = -20$ to $T - T_b = 110$ K is relatively low and constitutes ±3%.

CONCLUSIONS

(1) It is shown that the accuracy of the Clapeyron–Clausius equation depends on calculation conditions (interval of temperatures or pressures for which a calculation is performed).

(2) In the low-temperature region ($T < T_b$) the calculation error increases dramatically when the pressure becomes lower than 0.01 MPa (or the calculation temperature deviates from the boiling point by more than 40 K).

(3) In the high-temperature region ($T > T_b$), the calculation error gradually grows when the critical point is approached, ensuring high reliability of the prediction of the saturated vapor pressure in a wide range of temperatures.

REFERENCES

1. Morachevskii, A.G. and Sladkov, I.B., *Fiziko-khimicheskie svoistva molekulyarnykh neorganicheskikh soedinenii* (Physicochemical Properties of Molecular Inorganic Compounds), St. Petersburg: Khimiya, 1996.

2. Waldenstrom, S., Stegavik, K., and Naqvi, K., *J. Chem. Ed*., 1982, vol. 59, no. 1, pp. 30–34.
3. *Teplofizicheskie svoistva freonov* (Thermal Properties of Freons), Rivkin, S.L., Ed., Moscow: GSSSD, 1985, vol. 2.
4. Maksimov, B.N., Barabanov, V.G., Serushkin, I.L., *et al*., *Promyshlennye ftoroorganicheskie produkty: Spravochnik* (Commercial Organofluorine Products: Reference Book), Leningrad: Khimiya, 1990.
5. Kletskii, A.V., *Tablitsy termodinamicheskikh svoistv gazov i zhidkostei* (Tabulated Thermodynamic Properties of Gases and Liquids), issue 2: *Freon-22* (Freon-22), Moscow: GSSSD, 1978.
6. Kletskii, A.V., *Tablitsy termodinamicheskikh svoistv gazov i zhidkostei* (Tabulated Thermodynamic Properties of Gases and Liquids), issue 4: *Ammiak* (Ammonia), Moscow: GSSSD, 1978.
7. Lapidus, I.I. and Nisel'son, L.A., *Tetrakhlorsilan i trikhlorsilan* (Tetrachlorosilane and Trichlorosilane), Moscow: Khimiya, 1970.
8. *Gmelin Handbuch der Anorganischen Chemie*, Weinheim: Chemie, 1968, vol. 46, part C1.

Russian Journal of Applied Chemistry, Vol. 74, No. 3, 2001, pp. 394–395. Translated from Zhurnal Prikladnoi Khimii, Vol. 74, No. 3, 2001, pp. 387–388.

PHYSICOCHEMICAL STUDIES OF SYSTEMS AND PROCESSES

Boiling Point Parameters of Di- and Trichlorostannane

I. B. Sladkov and Yu. A. Goncharova

St. Petersburg State Technical University, St. Petersburg, Russia

Received October 31, 2000

Abstract— The boiling point, molar volume of liquid at the boiling point, and enthalpy of vaporization at the boiling point were found by calculation for little-studied tin compounds SnH_2Cl_2 and $SnHCl_3$.

In the homologous series formed upon substitution of hydrogen atoms in the tin hydride molecule by chlorine (SnH_4, SnH_3Cl, SnH_2Cl_2, $SnHCl_3$, $SnCl_4$), only the end members of the series (SnH_4 and $SnCl_4$) have been studied in sufficient detail. Only scarce information is available about the properties of SnH_3Cl [1]. Published data on properties of dichlorostannane SnH_2Cl_2 and trichlorostannane $SnHCl_3$ are completely lacking. In particular, there is no information about such fundamental constants of the substances as boiling point parameters. In the present study, these properties of two poorly studied tin compounds are determined using calculation methods.

A reliable evaluation of the boiling point T_b of a compound under study can be made by comparative calculation methods, if boiling points are known for substances of the same type. Such methods are based on an analysis of variation in the boiling point in a series of compounds thermodynamically similar to the compound under study. The boiling points were determined using methods that were recommended in [1] and tested on a wide variety of molecular inorganic compounds. As compounds thermodynamically similar to those under study were chosen chlorosilanes. The properties of the compounds used to determine the physicochemical constants of little studied tin compounds are listed in Table 1.

The following relations were studied: (a) that between the boiling points of silicon and tin compounds in the homologous series EH_4, EH_3Cl, and ECl_4, where E is an element (Si or Sn); (b) that between the molar mass and the quantity $(T_bM)^{0.5}$ in the series of compounds SnH_4, SnH_3Cl, and $SnCl_4$; and that between the molar mass and the product of T_b by the parachor $\prod$ in the series of compounds SnH_4, SnH_3Cl, and SnH_4 (the parachor was calculated by the method described in [1]).

As an example, one of these dependences is shown in Fig. 1. It was established that all the three dependences are obviously linear. Their processing by the least-squares method gives the following equations:

$$T_b(SnH_mCl_n) = 0.98T_b(SiH_mCl_n) + 65.0, \quad (1)$$

$$(T_bM)^{0.5} = 1.07M + 40.81, \quad (2)$$

$$T_b\prod = 9.67M - 669.39. \quad (3)$$

The correlation coefficients and rms errors for dependences (1)–(3) are presented in Table 2.

Table 1. Input data for the calculation [1]*

Substance	M, g mol^{-1}	$\prod$, J$^{1/4}$ cm$^{5/2}$ mol^{-1}	T_b, K	V_b, cm^3 mol^{-1}
SnH_4	122.7	2.24	221.0	63.3
SnH_3Cl	157.2	2.87	306.7	83.0
$SnCl_4$	260.5	4.76	387.0	131.7
SiH_4	32.1	1.78	161.2	50.5
SiH_3Cl	66.2	2.48	242.6	65.1
SiH_2Cl_2	101.0	3.07	281.3	84.3
$SiHCl_3$	135.4	3.67	305.2	102.8
$SiCl_4$	170.0	4.30	330.5	121.2

* M is the molar mass, $\prod$ is the parachor, and V_b is the molar volume of liquid at boiling point.

Table 2. Correlation coefficient r and rms error S of Eqs. (1)–(6)

Equation	r	S, %
(1)	0.9992	1.2
(2)	0.9926	4.7
(3)	0.9993	4.0
(4)	0.9913	1.1
(5)	0.9992	1.9
(6)	0.9967	3.8

1070-4272/01/7403-0394$25.00

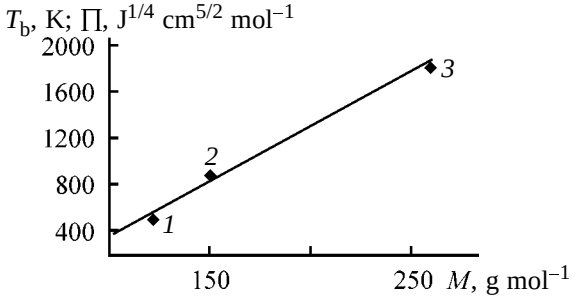

Fig. 1. Product of the boiling point T_b by the parachor ∏ vs. molar mass of a substance studied. (*1*) SnH_4, (*2*) SnH_3Cl, and (*3*) $SnCl_4$; the same for Fig. 2.

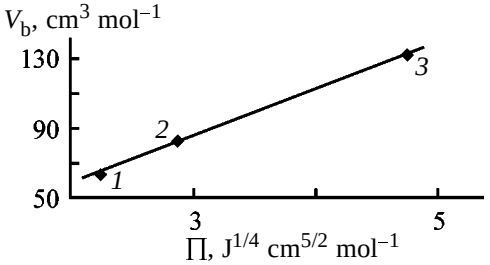

Fig. 2. Molar volume of the liquid at boiling point, V_b, vs. the parachor ∏.

To determine the molar volume of the liquid at the boiling point, V_b, the following relationships were studied: (a) that between the logarithm of V_b and the molar mass M in the series of compounds SnH_4, SnH_3Cl, and $SnCl_4$; (b) that between V_b and the parachor ∏ in the series of compounds SnH_4, SnH_3Cl, and $SnCl_4$; and (c) that between V_b of silicon and tin compounds in the homologous series EH_4, EH_3Cl, and ECl_4.

Table 3. Boiling point parameters of chlorostannane

Substance	T_b, K			V_b, cm^3 mol^{-1}		
	by equation					
	(1)	(2)	(3)	(4)	(5)	(6)
SnH_2Cl_2	340.7	315.8	339.4	94.0	98.3	97.4
$SnHCl_3$	364.2	354.0	368.4	112.1	115.2	114.2

Table 4. Recommended values of boiling point parameters of little studied chlorostannanes

Parameter	SnH_2Cl_2	$SnHCl_3$
T_b, K	332	362
V_b, cm^3 mol^{-1}	97	114
ΔH_b, kJ mol^{-1}	28.7	31.3

As an example, one of these dependences is presented in Fig. 2. It was established that all the three dependences are obviously linear. Their processing by the least-squares method gives the following equations:

$$\ln V_b = 0.00512M + 3.56, \quad (4)$$

$$V_b = 26.83\prod + 4.5, \quad (5)$$

$$V_b(SnH_mCl_n) = 0.94V_b(SiH_mCl_n) + 18.2. \quad (6)$$

The correlation coefficients and rms errors for dependences (4)–(6) are listed in Table 2.

The molar masses of SnH_2Cl_2 and $SnHCl_3$, equal to 192.0 and 226.5, and also the parachors of these substances (3.50 and 4.13, respectively) were used to calculate using Eqs. (1)–(6) the boiling points and molar volumes of liquids at the boiling points of these substances.

As seen from the data in Table 3, the T_b and V_b values obtained by various methods are reasonably consistent. The recommended values of the boiling point parameters of SnH_2Cl_2 and $SnHCl_3$ can be obtained by averaging data obtained by three independent methods (Table 4). The values in Table 4 are given with account of the expected error of ±2%.

The enthalpies of SnH_2Cl_2 and $SnHCl_3$ vaporization, lacking in the literature, were calculated for the boiling point by the equation

$$\Delta H_b = T_b[73 + 2.09\ln(T_bM/V_b)],$$

whose accuracy was estimated to be ±4% in [1] (Table 4).

CONCLUSIONS

(1) The applicability of calculation methods to predicting the boiling point parameters for two little studied tin compounds SnH_2Cl_2 and $SnHCl_3$ was demonstrated.

(2) The boiling point parameters of these compounds, lacking in the literature, were determined.

REFERENCES

1. Morachevskii, A.G. and Sladkov, I.B., *Fiziko-khimicheskie svoistva molekulyarnykh neorganicheskikh soedinenii* (Physicochemical Properties of Molecular Inorganic Compounds), St. Petersburg: Khimiya, 1996.

Russian Journal of Applied Chemistry, Vol. 74, No. 3, 2001, pp. 396–399. Translated from Zhurnal Prikladnoi Khimii, Vol. 74, No. 3, 2001, pp. 389–392.

PHYSICOCHEMICAL STUDIES OF SYSTEMS AND PROCESSES

Resistance to Hydrogen of Al–Sc Alloys

M. M. Antonova and V. B. Chernogorenko

Institute of Materials Science Problems, Ukrainian National Academy of Sciences, Kiev, Ukraine

Received August 24, 2000

Abstract—The behavior of aluminum–scandium alloys in hydrogen at an equilibrium pressure of 0.1 MPa was studied on a Sieverts apparatus.

The most efficient modifier of aluminum is scandium [1]. Addition of 1% Sc to AV000 aluminum yields the maximal number of grains (1090 per 1 cm^2) compared to other modifiers. Aluminum and aluminum alloys modified with scandium have the improved strength, plasticity, corrosion resistance, and other operation characteristics [2]. Scandium-doped aluminum has found application as structural material for aircrafts. Electrodes made of aluminum wire doped with 1% Sc facilitate welding of aluminum parts [3, 4], which allows fabrication of compact light articles. However, the strength of these materials, when operating for a long time under conditions of sharp temperature gradients, depends on their resistance to the environment in which they are exploited, in particular, air and hydrogen plasma.

In this work we studied the hydrogen absorption capacity of Al–Sc alloys. As known, compact aluminum does not interact with hydrogen. Aluminum hydride (AlH_3) as a white amorphous mass can be prepared solely by the chemical method from the ether solution [5]. Scandium absorbs hydrogen in the elemental state, forming the hydride ScH_2 [6], and also as a component of intermetallic compounds with metals that are not hydrogenated. For example, the intermetallic compound $ScMn_2$ yields hydrides $ScMn_2H_{3.8}$ [7]; $ScFe_2$, $ScFe_2H_4$; and $ScCo_2$, $ScCo_2H_4$ [8].

In the Al–Sc system, four intermetallic compounds are formed: Al_3Sc, Al_2Sc, AlSc, and $AlSc_2$ [9, 10]. The solubility of Al in Sc reaches about 6.25%. The limiting solubility of Al in Sc is 0.30%. At high crystallization rates the solubility of Sc can reach 5.1%. The data on the crystal structure of the phases in the Al–Sc system are given in Table 1. The crystal structures and the unit cell parameters of aluminum and the nearest intermetallic Al_3Sc are close. Therefore, as was shown by practical experience, cracks resulting from internal stresses do not appear in aluminum alloys containing up to 30% Sc at their various mechanical and thermal treatments. The behavior of these alloys in hydrogen-containing media was not studied previously.

EXPERIMENTAL

The alloys under study were obtained from aluminum (A999 ultrapure grade) and SkM-2 grade scandium containing (wt %) 99.88 Sc, 9×10^{-3} Fe, less than 0.001 Cu, 0.0051 Al, 0.05 Ca, 0.02 Mg, less than 0.001 Y, less than 0.0005 Yb, less than 0.005 Zr, less than 0.005 Ti, and 0.016 Si. The starting materials were smelted in an electric arc furnace with a permanent tungsten electrode under purified argon. Each sample was melted sixfold. The content of the elements in the alloys was determined by X-ray fluorescence analysis on a VRA-30 device. In some tests, chemical analysis was also used.

The alloys were hydrogenated at a 0.1 MPa hydrogen pressure on the improved quartz apparatus of the Sieverts type [6]. The volume of the reaction chamber was 60 cm^3. The pressure was measured with a mercury manometer. The hydrogen uptake was monitored by the pressure change in the system. The pressure was adjusted to the initial value every 5 min. Hydrogen was obtained by decomposing titanium hydride or $LaNi_5$ hydride in a reactor connected to the reaction chamber. Owing to plasticity, aluminum alloys containing up to 2% Sc were used as powder, which was prepared from finely disperse cuttings washed with ethyl alcohol and sieved. The other alloys were used as crushed ingots. Metallic scandium was hydrogenated without crushing.

We measured the sorption isobars at 0.1 MPa hydrogen pressure. Before hydrogenation, the alloys were activated by heating to 600–800°C at 13 Pa.

1070-4272/01/7403-0396$25.00

Table 1. Crystal structure of phases in the Al–Sc system [9, 11]

Phase	Prototype	Pearson's symbol	Space group	Structure designation	Lattice parameters, nm		
					a	*b*	*c*
Al	Cu	cF4	*Fm*3*m*	Al	0.4041	–	–
Al_3Sc	$AuCu_3$	cF4	*Pm*3*m*	Ll_2	0.4105	–	–
Al_2Sc	Cu_2Mg	cF24	*Fd*3*m*	Cl5	0.758	–	–
AlSc	CsCl	cP2	*Pm*3*m*	B2	0.5030	0.9895	0.3126
$AlSc_2$	$InNi_2$	hP6	$P6_3/mmc$	$B8_2$	0.488	–	0.6166
β-Sc	Cu	cI2	*Fm*3*m*	A2	0.454	–	–
α-Sc	Mg	hP2	$P6_3/mmc$	A3	0.3309	–	0.5273

Table 2. Sorption characteristics of scandium–aluminum solid solutions after activation at 600°C for 1 h

Sample	H_2 content, $cm^3\ g^{-1}$, at indicated temperature, °C							H_2 content in alloy, %
	600	500	400	300	200	100	20	
Al + 0.3% Sc:								
compact	0	1.4	2.0	4.3	5.3	7.1	8.9	0.08
powder	1.1	1.3	18.1	18.5	24.2	27.5	39.3	0.35
Al + 2% Sc:								
compact	0.4	2.0	3.5	4.0	7.1	13.1	13.9	0.14
powder	6.0	6.0	7.5	10.9	15.0	25.1	58.8	0.52

After activation, hydrogen was fed into the reactor, where the sample preheated to the maximal temperature was located, and the hydrogen sorption was observed and recorded at constant temperature till the saturation was complete. After that, the temperature was decreased by 100°C. The sorption process was resumed till the saturation was observed at the given temperature. The test was performed at stepwise decrease in the temperature to room temperature. The incubation period was observed in none of the cases. The total time of the experiment reached 3–5 days.

We found that all the compositions studied are hydrogenated reversibly and after decomposition in a vacuum and subsequent hydrogenation the final content of hydrogen in them is similar to the results of the first hydrogenation. The exception was metallic scandium. In the course of the first hydrogenation it took up only 86.6 cm^3 of H_2 per 1 g and disintegrated by cracking. No hydrogen was released in a vacuum at 900°C, and only at 1000°C it started decomposing. The results of the second hydrogenation are given in Table 2. Heating it in a vacuum was accompanied by intense cracking, indicative of transformation of the hydride structure. It can be presumed that, as in the Ti–H system [12, 13], hydrogen shifts the temperature of the β-Sc → α-Sc transition toward lower temperatures (the temperature of the α-Sc → β-Sc transition in air is 1337°C). In this case, as in the majority of studies, no scandium hydride of the composition ScH_2 was obtained. The hydrogen content in the hydride obtained corresponds to the composition $ScH_{1.39}$.

The hydrogen content in solid solution and scandium–aluminum alloys depends on dispersity (Table 2). Hydrogen absorption is stronger for powders owing to developed surface. On heating Al + 0.3% Sc and Al + 2% Sc samples to 600°C in a vacuum, about 7–10 cm^3 of adsorbed hydrogen per gram of the alloy is released, with most of hydrogen remaining in the alloy lattice. Concerning the effect of hydrogen on aluminum alloys, Dobatkin *et al*. [14] report that "...hydrogen content exceeding 0.2 cm^3 per 100 g drastically deteriorates impermeability of ingots. Also, it can affect impermeability of deformed semifinished products. Unfortunately, study of this effect, which is so important for estimating the potential of metals in spacecrafts, is given little attention yet."

The data on hydrogenation of the intermetallic compounds are given in Table 3. Before interaction with hydrogen, the alloys were activated in a vacuum

Table 3. Data on hydrogenation of intermetallic compounds of the Al–Sc system and scandium after the first cycle of hydrogenation–dehydrogenation

Sample	Activation		P_{H_2}, MPa	H_2 content, $cm^3\ g^{-1}$, at indicated temperature, °C									H_2, %**
	T, °C	τ, h		800	700	600	500	400	300	200	100	20	
Al_3Sc	600	1.0	0.1	–	–	0	2.5	24.5	24.5	25.6	42.5	44.6	0.40
Al_2Sc	900	0.7	0.1	7.6	14.3	17.7	25.5	32.5	38.4	41.4	69.5	75.6	0.67
AlSc	900	0.5	0.1	20.7	32.2	41.1	50.9	66.7	72.1	75.5	86.5	98.0	0.87
$AlSc_2$	800	0.5	0.1	104.0	105.9	106.6	107.1	126.9	129.4	131.4	150.2	189.5	1.15
$AlSc_2$*	200	0.5	2.5	–	–	–	–	–	–	–	10.0	241.9	2.16
Sc	900	0.5	0.1	320.9	321.0	321.0	321.0	322.0	326.0	327.0	338.0	338.0	3.0

* After the third cycle.
** Maximal H_2 content at 20°C.

at 800–900°C. The exception was Al_3Sc, which was activated at 600°C to prevent possible partial peritectic decomposition at 660°C. The maximum amount of hydrogen absorbed by $AlSc_2$ was smaller compared to similar AB_2 alloys (e.g., $NiMg_2$ and $NiTi_2$: 404 and 298 $cm^3\ g^{-1}$, respectively). As known [15], the solubility of hydrogen in aluminum and scandium and the diffusion rate of hydrogen in these metals grow with increasing pressure. It is presumed that the hydrogen pressure of 0.1 MPa is insufficient for complete saturation of $AlSc_2$. Therefore, the intermetallic compounds were hydrogenated at 2.5 MPa in a stainless steel installation. Additional activation of the alloy grains was performed by repeated hydrogenation–dehydrogenation cycles without removing the sample from the reaction chamber (Table 3).

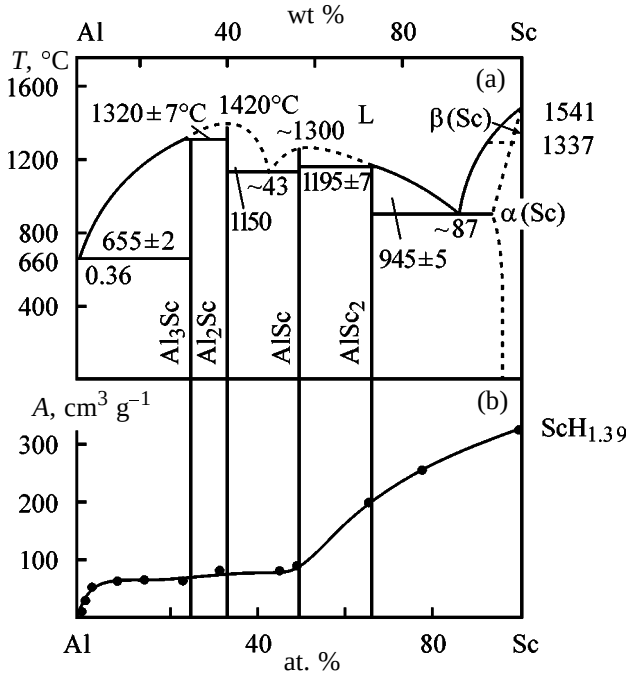

Fig. 1. (a) Phase diagram of the Al–Sc system and (b) maximal sorption capacity for hydrogen of the system alloys vs. alloy composition. (*T*) temperature and (*A*) sorption capacity at P = 0.1 MPa and 20°C.

We studied the influence of activation temperature and number of activation cycles on hydrogenation. After the third cycle the amount of sorbed hydrogen reached 241.9 cm^3 H_2 per gram of the alloy. Only minor amount of hydrogen (9.9 cm^3 H_2 per gram) was revealed by chemical analysis of the material hydrogenated at 200°C and 2.5 MPa. Thus, the hydride of $AlSc_2$ is extremely unstable, instantaneously decomposing at room temperature as the hydrogen pressure is quickly relieved from 2.5 to 0.1 MPa. For its storage the special stabilization procedures are necessary. Many hydrides, including $LaNi_5$ hydride, behave similarly. To stabilize them, the surface is saturated with oxygen or carbon dioxide at the temperature of liquid nitrogen.

The sorption capacity for hydrogen as a function of composition of the Al–Sc system is plotted in Fig. 1. All alloys of the system, especially intermetallic compounds, absorb hydrogen. If during fabrication of scandium-doped aluminum, namely, in the stage when aluminum–scandium charge is introduced into aluminum melt, the homogenization of the melt was not attained and scandium segregated in the course of subsequent crystallization, then, for example, in spacecraft articles and liquid-hydrogen cylinders, especially on warming them from the sun side, Al_3ScH_x or Al_2ScH_x can be formed with high probability. Scandium can segregate into intermetallic compounds in the course of rolling ingot and during welding with a scandium-containing wire owing to crystallization of a weld material. The resulting hydrides decompose with hydrogen evolution, resulting in the formation

of pores during diffusion. The hydrogen accumulation in a spacecraft in the presence of oxygen can cause explosion and fire.

In this work, the influence of the other components of traditional aluminum alloys, for example, magnesium and lithium alloys, on their resistance to molecular hydrogen was not studied. Presumably, the presence of these elements easily forming hydrides MgH_2 and LiH would deteriorate the hydrogen resistance of aluminum–scandium alloys.

CONCLUSION

(1) All alloys of the Al–Sc system interact with hydrogen. The intermetallic compounds Al_3Sc, Al_2Sc, AlSc, and $AlSc_2$ form hydrides.

(2) The amount of sorbed hydrogen grows with increasing hydrogen pressure.

(3) The $AlSc_2$-based alloy can be used for preparing hydrogen-accumulating materials.

(4) The aluminum alloys containing scandium can be recommended for aerospace technology only after testing them for hydrogen resistance.

REFERENCES

1. Lamikhov, L.K. and Samsonov, G.V., *Tsvetn. Met.*, 1964, vol. 37, no. 8, pp. 79–82.
2. Abstracts of Papers, *Skandii i perspektivy ego ispol'zovaniya: Mezhdunarodnaya nauchno-prakticheskaya konferentsiya* (Int. Scientific and Practical Conf. on Scandium and Prospects of Its Use), Moscow, 1994.
3. Filatov, Yu.A., Elagen, V.I., and Zakharov, V.V., *Tekhnol. Legk. Splavov*, 1997, no. 5, pp. 8–10.
4. Ishchenko, A.Ya., Lozovskaya, A.V., Poklyatskii, A.G., *et al*, *Avtom. Svarka*, 1993, no. 4, pp. 19–25.
5. Nekrasov, B.V., *Kurs obshchei khimii* (Course of General Chemistry), Moscow: Khimiya, 1967, part 2.
6. Antonova, M.M. and Morozova, R.A., *Preparativnaya khimiya gidridov* (Preparative Chemistry of Hydrides), Kiev: Naukova Dumka, 1976.
7. Kost, M.E., Raevskaya, M.V., Shilov, A.L., *et al*, *Zh. Neorg. Khim.*, 1979, vol. 24, no. 12, pp. 3239–3242.
8. Semenenko, K.N. and Burnasheva, V.V., *Dokl. Akad. Nauk SSSR*, 1976, vol. 231, no. 2, pp. 356–358.
9. *Diagrammy sostoyaniya dvoinykh metallicheskikh sistem: Spravochnik* (Phase Diagrams of Binary Metal Systems: Reference Book), Lyakishev, N.P., Ed., Moscow: Mashinostroenie, 1996.
10. Naumkin, O.P., Terekhova, V.T., and Savitskii, E.M., *Izv. Akad. Nauk SSSR, Metally*, 1965, no. 4, pp. 176–182.
11. Gschneidner, K.A., Jr., and Calterwood, F.M., *Bull. Alloy Phase Diagr.*, 1989, vol. 10, no. 1, pp. 34–36.
12. *Svoistva elementov: Spravochnik* (Element Properties: The Reference Book), Samsonov, G.V., Ed., Moscow: Metallurgiya, 1976.
13. *Metal Hydrides*, Mueller, W.M., Blackledge, J.P., and Libowitz, G.G., Eds., New York: Academic, 1968.
14. Dobatkin, V.I., Gabidulin, R.M., Kalachev, B.A., and Makarov, G.S., *Gazy i okisly v alyuminievykh deformiruemykh splavakh* (Gases and Oxides in Deformed Aluminum Alloys), Moscow: Metallurgiya, 1976.
15. Kalachev, B.A., Il'in, A.A., Lavrenko, V.A, and Levinskii, Yu.V., *Gidridnye sistemy: Spravochnik* (Hydride Systems: The Reference Book), Moscow: Metallurgiya, 1992.

Russian Journal of Applied Chemistry, Vol. 74, No. 3, 2001, pp. 400–403. Translated from Zhurnal Prikladnoi Khimii, Vol. 74, No. 3, 2001, pp. 393–396.

SORPTION AND ION-EXCHANGE PROCESSES

Sorption of Lead(II) from Aqueous Solutions by Synthetic Zeolites

I. V. Karetina, M. A. Shubaeva, L. F. Dikaya, and S. S. Khvoshchev

Grebenshchikov Institute of Silicate Chemisty, Russian Academy of Sciences, St. Petersburg, Russia
Corning Research Center, St. Petersburg, Russia

Received November 2, 1999; in final form, January 2000

Abstract—A comparative study of the sorption of lead(II) from dilute aqueous solutions by synthetic faujasites, chabazites, mordenites, erionites, phillipsites, and type A zeolites was performed. The most promising sorbents are low-silica chabazites and potassium erionites with relatively high SiO_2/Al_2O_3 ratio.

Recently, interest in the possibility of recovering heavy-metal ions from natural water and wastewater has been again aroused by the increasingly stringent environmental regulations. The high selectivity of zeolites with respect to lead ions has long been known [1–3]. For obvious reasons the preference has been given to natural zeolites [4–9]. At the same time, there are no published comparative data for main types of synthetic zeolites. This communication presents some results obtained in studying the ion-exchange capacity for lead(II) of synthetic faujasites, type A zeolites, chabazites, erionites, mordenites, and phillipsites treated with solutions with low concentration of Pb^{2+} ions in the presence of predominant amounts of Ca^{2+} ions.

All the zeolites studied were synthesized by the technique described in [10].[1] The composition of the crystals was determined by methods of chemical analysis (Table 1).

The estimates of the ion-exchange capacity of some zeolites for lead are presented in Table 2.

In the first case, weighed portions of zeolites (1.5–2.0 g) were treated with solutions containing lead(II) in amounts equivalent to the content of cations in crystals. In the second case, the solutions used for treatment contained the same amount of lead(II) and a 10-fold excess of calcium and magnesium ions. Each zeolite was thrice treated with the solution for 6 days at room temperature with intermediate washings. In the process, up to 2 l of the solution was used, depending on the required component ratios.

As seen from Table 2, Na^+ ions in zeolites are only in part replaced by Pb^{2+} ions even upon treatment with purely lead solutions. Under the conditions of competition with Mg^{2+} and Ca^{2+} ions, the degree of exchange for Pb^{2+} markedly decreases, but the selectivity order CHA > FAU > LTA remains unchanged. As seen from Table 2, the contents of PbO and CaO are comparable, even though the Ca^{2+} concentration in solutions is 10 times that of Pb^{2+}. At the same time, only an insignificant part of Na^+ ions is replaced under these conditions by Mg^{2+} ions.

The presence of Ca^{2+} ions has practically no effect, either, on the possibility of lead(II) recovery from solutions containing only 0.00006% Pb^{2+} (Table 3), with zeolites of different structural types exhibiting similar behaviors. A similar conclusion was made in [5] in reference to a number of natural zeolites. As seen from Table 3, the NaFAU-2 faujasite with SiO_2/Al_2O_3 ratio of 2.87 and low-silica chabazite NaCHA-1 show the highest capacity for lead(II).

The main results obtained in studying the absorption of Pb^{2+} ions by zeolites are presented in Table 4. Here, too, the solutions used contained 0.00006% lead(II). The treatment was performed at room temperature in the course of 15 days.

At so low degrees of exchange (the PbO/Al_2O_3 ratio in the zeolite crystals subjected to treatment was 0.001–0.004) it is difficult to speak of any clear relationship between the composition of zeolites and their ability to absorb lead(II). However, some conclusions can be made. Large cations are less firmly bound to the zeolite lattice, and, with increasing size of alkali metal cation in a zeolite, the ion-exchange sorption of lead(II), as a rule, becomes stronger. This is observed in going from Li^+ to Na^+ in the case of faujasites, and

[1] At the Corning Research Center.

1070-4272/01/7403-0400$25.00

Table 1. Composition of the starting crystalline samples and the corresponding ion forms

Zeolite	Composition of crystals
Faujasite (FAU):	
NaFAU-1	$0.94Na_2O \cdot Al_2O_3 \cdot 2.33SiO_2 \cdot 5.84H_2O$
NaFAU-2	$0.98Na_2O \cdot Al_2O_3 \cdot 2.87SiO_2 \cdot 6.19H_2O$
NaFAU-3	$1.03Na_2O \cdot Al_2O_3 \cdot 4.94SiO_2 \cdot 7.75H_2O$
CaFAU-1	$0.99CaO \cdot 0.03Na_2O \cdot Al_2O_3 \cdot 2.26SiO_2 \cdot 6.46H_2O$
LiFAU-1	$0.94Li_2O \cdot 0.02Na_2O \cdot Al_2O_3 \cdot 2.31SiO_2 \cdot 5.63H_2O$
MgCaFAU-1	$0.58MgO \cdot 0.43CaO \cdot 0.01Na_2O \cdot Al_2O_3 \cdot 2.34SiO_2 \cdot 6.01H_2O$
CaFAU-2	$0.97CaO \cdot 0.06Na_2O \cdot Al_2O_3 \cdot 2.94SiO_2 \cdot 6.94H_2O$
Chabazite (CHA):	
KCHA-1	$1.00K_2O \cdot Al_2O_3 \cdot 2.14SiO_2 \cdot 4.03H_2O$
KCHA-2	$0.97K_2O \cdot Al_2O_3 \cdot 3.12SiO_2 \cdot 4.28H_2O$
KCHA-3	$1.02K_2O \cdot Al_2O_3 \cdot 4.43SiO_2 \cdot 4.48H_2O$
NaCHA-1	$0.98Na_2O \cdot 0.04K_2O \cdot Al_2O_3 \cdot 2.11SiO_2 \cdot 4.50H_2O$
NaCHA-2	$0.80Na_2O \cdot 0.12K_2O \cdot Al_2O_3 \cdot 3.08SiO_2 \cdot 5.53H_2O$
NaCHA-3	$0.78Na_2O \cdot 0.18K_2O \cdot Al_2O_3 \cdot 4.39SiO_2 \cdot 6.23H_2O$
Erionite (ERI):	
KNaERI-1	$0.42K_2O \cdot 0.46Na_2O \cdot Al_2O_3 \cdot 7.65SiO_2 \cdot 6.26H_2O$
KNaERI-2	$0.70K_2O \cdot 0.37Na_2O \cdot Al_2O_3.7 \cdot 65SiO_2 \cdot 6.26H_2O$
NaKERI-1	$0.66Na_2O \cdot 0.18K_2O \cdot Al_2O_3 \cdot 5.33SiO_2 \cdot 5.68H_2O$
NaKERI-2	$0.68Na_2O \cdot 0.33K_2O \cdot Al_2O_3 \cdot 7.73SiO_2 \cdot 6.49H_2O$
NaA (LTA)	$Na_2O \cdot Al_2O_3 \cdot 2.03SiO_2 \cdot 4.74H_2O$
Mordenite (MOR)	$0.99Na_2O \cdot Al_2O_3 \cdot 10.19SiO_2 \cdot 6.49H_2O$
Phillipsite (PHI)	$0.79Na_2O \cdot 0.28R_2O \cdot Al_2O_3 \cdot 5.05SiO_2 \cdot 6.34H_2O$

Table 2. Composition of zeolite crystals after treatment with (1) 0.01 N $Pb(NO_3)_2$ and (2) 0.01 N $Pb(NO_3)_3$ + 0.1 N $Ca(CH_3COO)_2$ + 0.1 N $Mg(NO_3)_2$

Zeolite	Content of indicated oxides (mol mol^{-1} Al_2O_3) after treatment with solutions						
	1		2				
	PbO	Na_2O	PbO	Na_2O	K_2O	CaO	MgO
NaFAU-1	0.62	0.44	0.42	0.20	–	0.33	0.02
NaLTA	0.44	0.62	0.34	0.13	–	0.39	0.13
NaCHA-1	0.74	0.26	0.49	–	0.04	0.42	0.01

from Na^+ to K^+ for chabazites and erionites. The opposite tendency is only observed for a chabazite with the smallest SiO_2/Al_2O_3 ratio.

Ca^{2+} ions are bound to the lattice more firmly than Na^+ ions, and it could be expected that the ability of calcium zeolites to absorb lead(II) would be lower than that of sodium zeolites. For faujasites with $SiO_2/Al_2O_3 \cong 2.9$ this is indeed so, and further decrease in this ability is observed on replacing Ca^{2+} by Mg^{2+} ions. However, with the SiO_2/Al_2O_3 ratio decreasing to approximately 2.3, replacement of Na^+ by Ca^{2+} and Mg^{2+} has absolutely no effect on the sorption of lead(II) ions.

With decreasing total charge of the lattice and increasing SiO_2/Al_2O_3 ratio, the binding of cations to the lattice becomes weaker and they must be replaced more easily. Correspondingly, the ability of nearly all zeolites with like cations to absorb lead(II) grows within each structural type with increasing SiO_2/Al_2O_3 ratio. Only low-silica sodium chabazites and high-

Table 3. Effect of calcium ions on lead sorption: sorption from solutions containing (1) 0.6 mg l^{-1} Pb(II) and (2) 0.6 mg l^{-1} Pb + 250 mg l^{-1} Ca(II)

Zeolite	Content of Pb(II) in a zeolite, wt %, after treatment with indicated solution	
	1	2
NaFAU-1	1.0	0.9
NaFAU-2	1.7	1.7
CaFAU-2	1.3	1.4
NaFAU-3	1.1	0.9
NaLTA	1.0	1.2
NaCHA-1	1.6	1.5
NaMOR	0.8	0.8

Table 4. Recovery of lead(II) with zeolites from aqueous solutions containing (1) 0.6 mg l^{-1} Pb(II) + 250 mg l^{-1} Ca(II) and (2) 0.15 mg l^{-1} Pb(II) + 250 mg l^{-1} Ca(II)

Zeolite	SiO_2/Al_2O_3	Content of Pb(II) in zeolite, wt %, after treatment with indicated solution	
		1	2
Faujasite:			
NaFAU	2.01	–	1.0
NaFAU-1	2.33	0.9	–
LiFAU-1	2.31	0.5	–
CaFAU-1	2.26	0.9	–
MgCaFAU-1	2.34	1.0	–
NaFAU-2	2.87	1.7	1.3
LiFAU-2	2.9	1.0	–
CaFAU-2	2.94	1.4	–
MgCaFAU	2.9	1.0	–
NaFAU-3	4.94	–	0.9
Chabazite:			
NaCHA-1	2.14	1.5	1.5
KCHA-1	2.11	0.9	–
NaCHA-2	3.08	0.7	0.9
KCHA-2	3.12	1.0	–
NaCHA-3	4.39	0.9	–
KCHA-3	4.43	1.5	–
Erionite:			
NaKERI-1	5.33	0.7	–
KNaERI-1	5.26	1.3	0.8
NaKERI-2	7.73	1.1	–
KNaERI-2	7.65	1.8	1.7
Phillipsite			
NaPHI	5.05	–	1.0

Table 5. Influence exerted by the time of treatment with a solution containing 0.15 mg l^{-1} Pb(II) + 250 mg l^{-1} Ca(II) on the recovery of lead with NaCHA zeolite (SiO_2/Al_2O_3 = 5.0)

Number of treatments	Total time of treatments, days	Pb(II) in zeolite, wt %
1	1	1.3
1	2	1.6
1	5	1.8
4	9	2.1
Dynamic conditions (40 ml min^{-1})		0.9

silica faujasites remain outside this pattern. Presumably, the prevailing effect is exerted here already by the increasing number of bonds between cations and the aluminosilicate skeleton, rather than by their becoming stronger or weaker.

The noted relationships are, on the whole, also preserved in passing to solutions containing a four times smaller amount of lead(II). In this case, faujasite with particularly low SiO_2/Al_2O_3 ratio, synthesized by the method described in [11], and also phillipsite having rather high selectivity [6] exhibit under these conditions relatively low capacity for lead(II). It seems that the most promising are low-silica chabazites known as selective absorbers of strontium(II) from concentrated salt solutions [12] and potassium erionites with relatively high SiO_2/Al_2O_3 ratio. As seen from Table 4, both of these are low-sensitive to a fourfold decrease in the concentration of lead(II) in the solutions used.

It is possible to get a certain insight into the kinetics of lead(II) absorption from the data in Table 5. In all cases, the total volume of solution was 5 l at weighed portions of 0.5 g. The equilibrium state is not achieved even after several days; however, even under dynamic conditions the zeolite exhibits a quite appreciable capacity for lead(II) absorption.

CONCLUSION

Synthetic zeolites, especially low-silica chabazites and potassium erionite with relatively high SiO_2/Al_2O_3 ratio, show appreciable ion-exchange capacity for lead(II) in the presence of predominant amounts of calcium and magnesium ions in solutions.

REFERENCES

1. Chelishchev, N.F., Martynova, N.S., Fakina, L.K., and Berenshtein, B.G., *Dokl. Akad. Nauk SSSR,* 1974, vol. 217, no. 5, pp. 1140–1144.

2. Hertzenberg, E.P. and Sherry, H.S., *Adsorption and Ion Exchange with Synthetic Zeolites*, Flank, W.H., Ed., *ACS Symp. Ser*., Washington DC, 1980, vol. 135, pp. 187–194.
3. Assenov, A., Vassilev, Chr., and Kostova, M., *Chem. Tech*., 1985, vol. 37, no. 8, pp. 334–336.
4. Gradev, G.D., Stefanov, G.I., Ivanov, V.I., *et al*., *Trudy konferentsii po voprosam geologii, fiziko-khimicheskikh svoistv i primeneniya prirodnykh tseolitov* (Proc. Conf. on Problems of Geology, Physicochemical Properties, and Use of Natural Zeolites), Tbilisi: Metsniereba, 1985, p. 120.
5. Zamzov, M.J. and Murphy, J.E., *Separ. Sci. Technol*., 1992, vol. 27, no. 14, pp. 1969–1984.
6. Pansini, M., Colella, C., Caputo, D., *et al*., *Micropor. Mater*., 1996, vol. 5, no. 6, pp. 357–364.
7. Ali, A.A.H. and El-Bishtawi, R., *J. Chem. Technol. Biotechnol*., 1997, vol. 69, no. 1, pp. 27–34.
8. Tarasevich, Yu.I., Kardasheva, M.V., and Polyakov, V.E., *Kolloidn. Zh*., 1997, vol. 59, no. 6, pp. 813–818.
9. Torraca, E., Galli, P., Pansini, M., and Colella, C., *Micropor. Mesopor. Mater*., 1998, vol. 20, no. 1/3, pp. 119–127.
10. Zhdanov, S.P., Khvoshchev, S.S., and Samulevich, N.N., *Sinteticheskie tseolity* (Synthetic Zeolites), Moscow: Khimiya, 1981.
11. Kuhl, G.H., *Zeolites*, 1987, vol. 7, no. 5, pp. 451–457.
12. Chernyavskaya, N.B., Andreeva, N.R., Zhdanov, S.P., and Shubaeva, M.A., *Radiokhimiya*, 1988, vol. 30, no. 3, pp. 371–374.

Russian Journal of Applied Chemistry, Vol. 74, No. 3, 2001, pp. 404–408. Translated from Zhurnal Prikladnoi Khimii, Vol. 74, No. 3, 2001, pp. 396–400.

SORPTION AND ION-EXCHANGE PROCESSES

Sorption of Carbon Disulfide from Air–Gas Mixtures on Carbon Materials with Various Nature of the Surface

I. A. Tarkovskaya, S. S. Stavitskaya, and V. M. Luk'yanchuk

Institute of Sorption and Endoecology Problems, Ukrainian National Academy of Sciences, Kiev, Ukraine
Institute of Applied Problems of Physics and Biophysics, Ukrainian National Academy of Sciences, Kiev, Ukraine

Received May 30, 2000; in final form, November 2000

Abstract—The sorption of carbon disulfide on carbon materials was studied as influenced by the chemical nature of their surface and presence of surface oxygen-containing functional groups and metal ions differently bound on the sorbent surface. Cation-substituted carbons with considerably higher capacity as compared with the initial sorbents were prepared.

Activated carbons (ACs) are widely used for sorption recovery of carbon disulfide from industrial exhaust gases to decrease environmental contamination and to return this product in production [1–3]. However, in most cases the residual content of CS_2 in the exhaust gases significantly exceeds the maximal permissible concentration (MPC, 0.03 mg m^{-3}). More exhaustive removal of CS_2 and other toxic sulfur compounds is of particular importance for environmental safety; it is also required in systems for deep purification of air for operation of analytical and medical equipment, individual protection of breath organs, etc. Though the interaction of carbon disulfide with ACs was studied rather extensively [1–5], data on recovery of CS_2 to the levels about MPC and lower from low-concentrated air–gas mixtures (AGMs) are scarce. Thus, studies in this direction and search for more efficient sorbents are still urgent.

The sorption capacity of various carbon materials (CMs) with respect to certain gas mixtures can be increased by addition of various modifying agents (e.g., metal compounds) chemically interacting with the sorbed materials. Impregnation with various solutions is the most common way to modify CMs. For example, such chemical sorbents based on activated carbons are widely used in gas-protection apparatus [1–5]. As seen from published data [6–8], the ion-exchange substitution of the protons in the surface acidic functional groups of oxidized carbons (OCs) [9] with metal ions can be more efficient as compared with impregnation. In this case the surface complex OC–M^{n+} acts as a sorption center and the molecules of sorbed compounds (L) occupy the free sites of the metal coordination environment, forming the structures like –C–O–M···L_n. This process is termed "ligand" sorption [7–10]. It was found that, due to such processes, the cationic forms of OCs are more efficient in sorption of water vapor [8], ammonia [10, 11], sulfur dioxide [7, 11], carbon disulfide [7], etc., as compared with unmodified and even initial nonoxidized activated carbons.

In this work we studied the possibility of ligand sorption and the dependence of carbon disulfide sorption on carbon materials as influenced by the chemical nature of their surface and presence of the surface oxygen-containing functional groups (OCFGs) and metal ions differently bound with the carbon surface. It should be noted that the data on the feasibility and efficiency of CM modification with metal cations for carbon disulfide sorption are virtually lacking.

In our study we used various industrial carbons (AR-3, KAU, SKN, Sorbon). The samples were oxidized with air or nitric acid by the known procedures [9]. The cation-substituted forms of oxidized carbons containing copper, iron, and cobalt ions on the sorbent surface were prepared by the ion-exchange procedure [6, 9]. Moreover, some AC samples were modified by impregnation with solutions of the corresponding metal nitrates [6]. In this case we obtained the samples containing the modifying agents differently bound with the surface in amounts of 0.10–0.12 mg-ion g^{-1}. In the oxidized carbons (samples are denoted as AC-O-M-1) the metal cations substitute the protons in the OCFGs forming surface complexes. At certain preparation regimes during impregnation of nonoxi-

1070-4272/01/7403-0404$25.00

Table 1. Physicochemical characteristics of sorbents*

Sorbent	Pore volume, $cm^3\ g^{-1}$			S_{sp}, $m^2\ g^{-1}$	SEC, $mmol\ g^{-1}$	
	W_s	V_{mic}	V_{mes}		for HCl	for NaOH
Sorbon	0.87	0.58	0.29	915	0.6	0.0
KAU	0.70	0.42	0.28	720	0.0	2.2
KAU-O	0.68	0.40	0.28	700	2.2	0.1
SKN	0.85	0.58	0.27	840	0.2	1.6
AR-3	0.57	0.36	0.19	685	0.5	0.1
AR-3-O-Co-1	0.58	0.40	0.18	610	–	–
AR-3-Co-2	0.58	0.39	0.19	605	–	–
AR-3-O-Fe-1	0.74	0.61	0.13	840	–	–
AR-3-Fe-2	0.68	0.58	0.10	900	–	–
AR-3-O-Cu-1	0.70	0.42	0.28	720	–	–
AR-3-Cu-2	0.69	–	–	–	–	–

* W_s is the total pore volume; V_{mic}, V_{mes} are the volumes of micro- and mesopores; S_{sp} is the specific surface area; SEC is the static exchange capacity characterizing the content of the basic (for HCl) and acidic (for NaOH) surface groups; AC-O is the oxidized carbon; AC-O-M-1 are cation-substituted samples; and AC-M-2 are the metal-substituted samples prepared by impregnation.

dized carbons (AC-M-2 samples) metal compounds penetrate into the sorbent pores either in the initial (water-soluble) form, or as specifically sorbed whole molecules, or as hydroxides or basic salts formed in the side reactions [6, 9]. The physicochemical and sorption properties of CMs studied by common procedures [1, 9] are listed in Table 1.

The recovery of CS_2 from the air–gas mixtures was studied at various temperatures under the dynamic conditions in the columns containing 3–4 cm^3 of sorbent at constant flow rate of the gas mixture (200–250 ml min^{-1}). The concentration of carbon disulfide was determined by known chemical procedures [12]. In some cases the composition of the exhaust gas mixture at the column outlet was analyzed by gas chromatography. The desorption of carbon disulfide was also studied under the dynamic conditions in an argon flow. Our experimental data showed that the temperature of 100°C and argon flow rate of 100 ml min^{-1} are the optimal for efficient desorption.

Our tests showed that in the case of common ACs at 20–120°C the sorption of H_2S is reversible, decreasing with increasing temperature (Fig. 1); under the similar conditions it is mainly determined by the structural characteristics of the sorbent such as porosity, specific surface area, etc. The reversibility of CS_2 sorption is illustrated by almost complete removal of carbon disulfide with argon and by the possibility of performing several sorption–desorption cycles using a single sample (Table 2). At temperatures higher than 120°C the fraction of desorbed CS_2 significantly decreases, and the products of catalytic oxidation of carbon disulfide such as sulfur and carbon oxides appear in the exit gases. In the case of air–gas mixture containing 0.01–0.02 wt % ozone the protective life (up to appearance of CS_2 at the column outlet) remains constant up to 120°C, whereas at 130°C it strongly increases, which is probably due to intense oxidative decomposition of carbon disulfide.

The interaction of carbon disulfide with OCs differs from that described above. Under the similar conditions the sorption capacity of oxidized samples with respect to CS_2 was significantly lower as compared with the corresponding activated carbons (Fig. 2, Table 2), but the amount of reversibly sorbed carbon

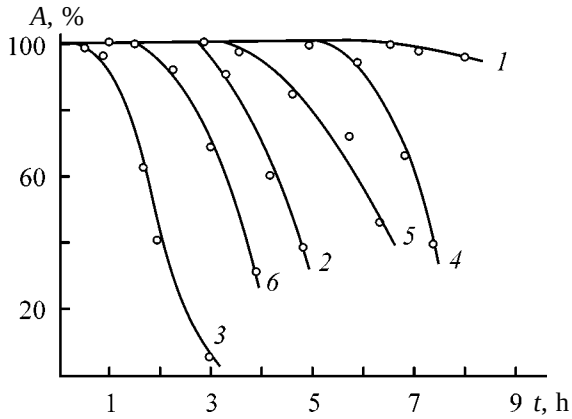

Fig. 1. Sorption *A* of carbon disulfide from (*1–3, 5*) dry and (*4–6*) wet air–gas mixtures on (*1–4*) Sorbon and (*5, 6*) AR-3 activated carbon at various temperatures. (*t*) Operation time; the same for Fig. 2. Temperature, °C: (*1, 4, 5*) 20, (*2, 6*) 50, and (*3*) 100.

Table 2. Sorption of carbon disulfide on various carbon materials*

Sorbent	Medium	*T*, °C	Cycle number	*m*, mg	Desorption, %	Oxidation products**	C_b, mg m^{-3}
Sorbon	AGM	20	1	600	95	–	1
	〃	20	2	580	100	–	1
	〃	20	3	610	100	–	1
	AGM + H_2O	20	1	460	98	–	1
	AGM + O_3	20	1	600	90	–	1
	〃	130	1	180	30	+	0.1
KAU	AGM	20	1	600	95	–	0.1
	〃	20	2	610	100	–	0.1
	〃	20	3	600	100	–	0.1
	〃	130	1	150	32	+	0.1
	AGM + O_3	130	1	190	25	+	0.1
KAU-O	AGM	20	1	50	47	–	1
KAU-O-Fe-1	〃	20	1	280	28	–	<0.1
	〃	80	1	250	22	+	<0.1
AR-3	〃	20	1	450	100	–	1
	〃	130	1	180	62	+	1
AR-3-O	〃	20	1	40	45	–	1
AR-3-Co-2	〃	20	1	500	40	–	0.1
	〃	80	1	220	35	+	0.1
	〃	130	1	280	28	+	0.1
AR-3-O-Co-1	〃	20	1	600	32	–	0.1
	〃	80	1	350	25	+	0.1
	〃	130	1	380	22	+	0.1
AR-3-Fe-2	〃	20	1	550	35	–	1
AR-3-O-Fe-1	〃	20	1	700	28	–	<0.1
	〃	80	1	510	18	+	<0.1
	〃	130	1	490	12	+	<0.1

* (*m*) Weight of sorbed carbon disulfide and (C_b) breakthrough concentration.
** Presence (+) and absence (–) of the oxidation products.

disulfide was smaller than in the case of ACs. Modification of the carbon surface with metal cations increased the recovery of CS_2 from air–gas mixtures (Table 2), and the amount of strongly bound or converted carbon disulfide increased to a still greater extent. The sorption of CS_2 (protective life) in the presence of water vapor decreases (Table 2, Fig. 1). In the cation-substituted sorbents the oxidation products appear at lower temperatures as compared with ACs (Table 2), which indicates that the sorbents containing metal cation are more efficient catalysts of carbon disulfide oxidation. Addition of ozone to the air–gas mixture at elevated temperatures promotes the recovery of CS_2, and this process is more efficient as compared with unmodified activated carbons (Fig. 3). It should be noted that the breakthrough concentration after the sorption (conversion) on the cation-substituted carbons is significantly lower than after sorption on unmodified sorbents (Table 2, Fig. 3), i.e., they provide more exhaustive purification of the exit gases.

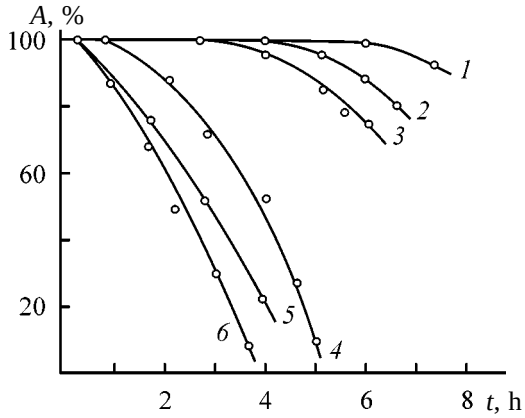

Fig. 2. Sorption of carbon disulfide *A* on (*1*) KAU, (*2*) SKN, (*3*) AR-3, (*4*) KAU-O, (*5*) SKN-O, and (*6*) Ar-3-O sorbents at 20°C.

As seen from Table 1, oxidation slightly decreases the volume of sorption pores and the specific surface area as compared with the initial AC, but the decrease in the carbon disulfide sorption on OC is probably due

not only to the above factors and blocking of the sorption pores, but also to certain chemical processes, because significant amount of CS_2 is sorbed irreversibly. However, the detailed analysis of this process requires further studies.

During interaction of CS_2 with the cation-substituted OCs the ligand sorption probably occurs yielding the surface complex –C–O–M···$(CS_2)_n$. The promoting effect of this surface complex –C–O–M··· on sorption and catalytic oxidation of carbon disulfide is also confirmed by the fact that in the case of modified sorbents prepared by impregnation and containing similar amounts of modifying metals the sorption and the amount of irreversibly sorbed CS_2 are significantly smaller (Table 2). Similar effects were observed for different carbon materials.

The decrease in the protective life in the case of wet air–gas mixtures is probably due to the competitive sorption of water molecules with formation of the complex –O–C–O–M···$(CS_2)_n(H_2O)_m$. The increase in sorption (conversion) in the presence of ozone can be due to reaction of the oxidant (ozone) with the substrate (CS_2) in the surface complex –O–C–O–M···$(CS_2)_n(O_3)_m$, i.e., to the catalytic activity of the cation-substituted carbons (as found in [13]).

We found that the prolonged (multicycle) operation of the cation-substituted carbons especially in the regimes of catalytic decomposition is rather difficult. At low temperatures this is due to the fact that significant amount of CS_2 is strongly sorbed on the sorbent surface and is not removed in the inert atmosphere. At elevated temperatures the catalytic conversion is observed, and the reaction products decrease the catalyst activity. Our experimental data suggest that one of the reaction products (elemental sulfur) can block the pores [1, 2], whereas sulfur oxides can react with metal cations.

Thus, we found that sorption of carbon disulfide on the carbon materials depends not only on the pore structure [1–3], but also on the chemical nature of their surface and on the presence of modifying agents. In this case the ion-exchange modification of the oxidized carbons with cations of such metals as iron, cobalt, and copper allows us to prepare efficient sorbents with high capacity and the protective life with respect to carbon disulfide significantly exceeding that of the initial ACs, including those containing metal cations, but prepared by impregnation.

Such modified carbon materials can be used in air treatment to remove CS_2 to the levels of MPC and lower. These sorbents are the most efficient in disposable filters for analytical and medical devices, individual breath-protection respirators, in the catalyst poisoning protection, etc.

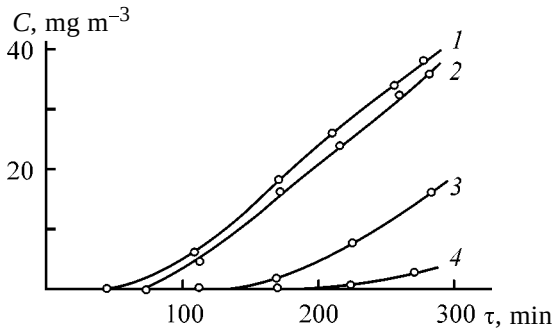

Fig. 3. Sorption of carbon disulfide on (*1, 2*) initial AR-3 and (*3, 4*) its oxidized forms modified by ion-exchange with iron (*1, 3*) in the absence and (*2, 4*) in the presence of ozone at 50°C. (*C*) Concentration of CS_2 and (τ) time.

These dependences are of practical importance in common use of activated carbons for gas purification or recuperation of carbon disulfide, because the operation of sorption columns requires taking into account gradual decrease in the sorption capacity of coals due to their oxidation (formation of OCFG). Such oxidized sorbents cannot be regenerated by treatment with steam or with solvents. In this case sorbents can be regenerated by high-temperature treatment.

CONCLUSIONS

(1) Sorption of carbon disulfide from air–gas mixtures on various carbon materials under various conditions was studied. This process is determined by the chemical nature of the sorbent surface and the presence of the surface oxygen-containing functional groups and modifying agents differently bound with the sorbent surface (ion-exchange treatment, impregnation with metal salts).

(2) Cation-substituted sorbents were prepared with the higher capacity and longer protective life with respect to carbon sulfide as compared with the initial sorbents.

(3) The fields of possible application of the modified carbon sorbents with the highest capacity for CS_2 are suggested.

REFERENCES

1. Kel'tsev, N.V. *Osnovy sorbtsionnoi tekhniki* (Principles of Sorption Processes), Moscow: Khimiya, 1984.
2. Von Kinle, H. and Bader, E., *Aktivkohle und ihre industrielle Anwendung*, Stuttgart: Enke, 1980.

3. Loskutov, A.I. and Khlopotnov, M.N., *Adsorb. Adsorb.*, 1982, no. 10, pp. 28–32.
4. Levit, R.M. and Sorokin, Ya.Z., *Khim. Volokna*, 1960, no. 1, pp. 34–39.
5. Belotserkovskii, G.M. and Levit, R.M., in *Khimiya i tekhnologiya serougleroda* (Chemistry and Technology of Carbon Disulfide), Leningrad: Khimiya, 1970, pp. 18–26.
6. Tarkovskaya, I.A. and Tomashevskaya, A.N., *Adsorb. Adsorb.*, 1984, no. 12, pp. 3–12.
7. Tarkovskaya, I.A., Tomashevskaya, A.N., Stavitskaya, S.S., *et al.*, *Khim. Tekhnol.*, 1991, no. 2, pp. 14–19.
8. Tarkovskaya, I.A., Stavitskaya, S.S., and Tikhonova, L.P., *Zh. Prikl. Khim.*, 1996, vol. 69, no. 4, pp. 602–606.
9. Tarkovskaya, I.A., *Okislennyi ugol'* (Oxidized Coal), Kiev: Naukova Dumka, 1981.
10. Tarkovskaya, I.A. and Stavitskaya, S.S., *Ross. Khim. Zh.*, 1995, vol. 39, no. 6, pp. 44–51.
11. Tomashevskaya, A.N., Tarkovskaya, I.A., and Baidenko, V.I., *Ukr. Khim. Zh.*, 1992, vol. 58, no. 2, pp. 155–160.
12. Blazhennova, A.N., Il'inskaya, A.A., and Rappoport, F.M., *Analiz gazov v khimicheskoi promyshlennosti* (Analysis of Gases in Chemical Industry), Moscow: Khimiya, 1954.
13. Tarkovskaya, I.A., Stavitskaya, S.S., Luk'yanchuk, V.M., *et al.*, *Khim. Tekhnol. Vody*, 1993, vol. 15, nos. 7–8, pp. 578–584.

Russian Journal of Applied Chemistry, Vol. 74, No. 3, 2001, pp. 409–413. Translated from Zhurnal Prikladnoi Khimii, Vol. 74, No. 3, 2001, pp. 401–405.

SORPTION AND ION-EXCHANGE PROCESSES

Sorption of CO_2 from Humid Gases on Potassium Carbonate Supported by Porous Matrix

V. E. Sharonov, E. A. Tyshchishchin, E. M. Moroz, A. G. Okunev, and Yu. I. Aristov

Novosibisk State University, Novosibirsk, Russia
Boreskov Institute of Catalysts, Siberian Division, Russian Academy of Sciences, Novosibirsk, Russia

Received May 23, 2000; in final form, November 2000

Abstract—Kinetics of sorption of carbon dioxide on potassium carbonate supported by different porous matrices was studied in a flow reactor at 40°C. The structural and chemical changes of potassium carbonate–aluminum oxide composite sorbents were studied by powder X-ray diffraction, thermogravimetry, and low-temperature nitrogen sorption.

The capacity and selectivity of porous sorbents can be increased by introduction in their pores of a compound which reversibly reacts with the gaseous adsorbate. For example, the most promising composites of this type are silica gel containing calcium chloride or lithium bromide in its pores and used as a water sorbent [1, 2] and potassium carbonate–activated carbon and potassium carbonated–aluminum oxide systems used for sorption of carbon dioxide [3, 4]. In particular, the sorption capacity of these systems with respect to CO_2 is several times higher than that of conventional sorbents such as activated carbons, aluminum oxide, and zeolites [4]. Important advantages of these composites are the absence of corrosion, low regeneration temperature, and effective sorption of CO_2 form humid gaseous mixtures. These sorbents can be used for removal of CO_2 form waste gases of thermal power plants, in creation of protecting and reducing atmospheres, in survival systems of submarines, in hydrogen production by steam conversion of methane, etc. [3, 5].

Carbon dioxide sorption from humid gas mixtures in a flow adsorber was studied and the time dependence of the outlet CO_2 concentration was measured by Hayashi *et al*. [3, 4]. They suggest that potassium carbonate–porous matrix composites sorb carbon dioxide owing to occurrence of reversible chemical reaction

$$K_2CO_3 + H_2O + CO_2 \rightleftarrows 2KHCO_3. \quad (1)$$

At $T < 100$°C the forward reaction prevails and the reverse reaction used for sorbent regeneration occurs at $T > 150$°C. The important parameters of composite sorbents are the residual concentration of carbon dioxide at the outlet of an adsorber C_{out} and the dynamic sorption capacity A_{dyn}. Hayashi *et al.* [4] showed that the dynamic capacity of the tested sorbents strongly depends on the nature of the support matrix and on the distribution of the active component in its pores. For example, low activity of potassium carbonate supported by silica gel can be due to reaction of these components to form inert surface potassium silicates, which is confirmed by electron microscopy [5]:

$$K_2CO_3 + SiO_2 = K_2SiO_3 + CO_2. \quad (2)$$

When activated carbon is used as the matrix, large salt crystals blocking penetration of the reagents in the sorbent pores can be formed on the hydrophobic surface of the carbons depending of their pore structure. As a result, the reactive surface of potassium carbonate decreases, thus decelerating the sorption of carbon dioxide [4]. Hayashi *et al.* [4] also studied sorption of carbon dioxide from smoke on the potassium carbonate–porous carbon composite. It was found that the dynamic capacity of the sorbent can be as high as 1 mol CO_2/1 g sorbent. Unfortunately, Hayashi *et al.* [4, 5] gave little attention to sorption properties of potassium carbonate on other supports and did not substantiate the choice of porous carbons for practical application.

In this work we studied not only potassium carbonate supported by silica gel and activated carbon but also the potassium carbonate–vermiculite composite and systematically studied the potassium carbonate–aluminum oxide system. The detailed study of the

1070-4272/01/7403-0409$25.00

Table 1. Texture parameters of the initial matrices and the potassium carbonate content in the sorbents

Matrix	Size and shape of granules, mm	S_{sp} (BET), $m^2\ g^{-1}$	Moisture capacity, ml g^{-1}	Salt content, wt %	Sorbent
Al_2O_3-1	Spheres, d = 0.2–0.25	248	0.7	28.4	A1
Al_2O_3-2	Fraction 1–2	280	1.5	45.9	A2
Carbon-1	Spheres, d = 3–5	450	0.6	25.3	C1
Carbon-2	Cylinders, d = 1	>1150	0.5	22.0	C2
Silica gel KSK	Fraction 1–2	350	1.0	36	S1
Vermiculite	Fraction 1–2	2.3	1.6	47.5	V1

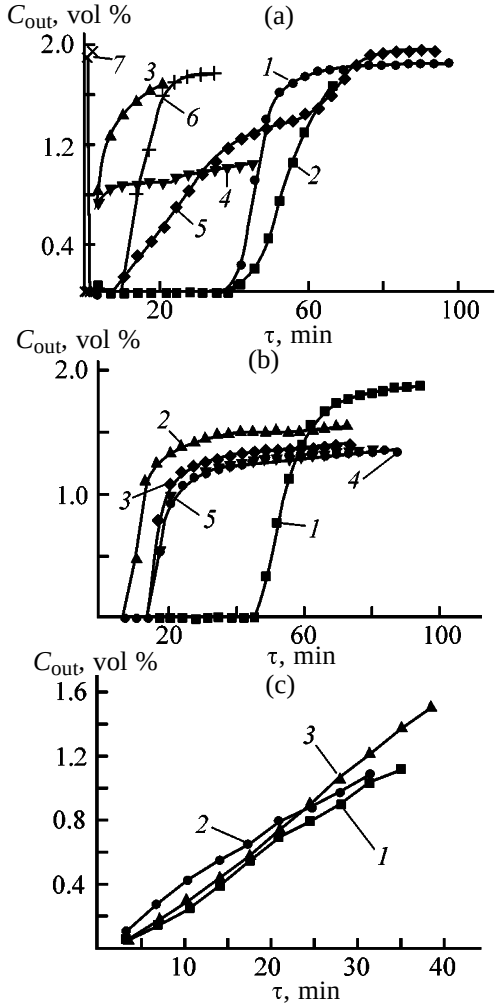

Fig. 1. Carbon dioxide concentration at the outlet of adsorber C_{out} as a function of time τ. (a) (*1*) A1, (*2*) A2, (*3*) S1, (*4*) V1, (*5*) C1, and (*6*) C2 freshly prepared samples; (*7*) initial Al_2O_3 matrix. (b) Sample A1: (*1*) freshly prepared, (*2*) after the first sorption–regeneration cycle at 200°C, (*3*) freshly prepared and calcined at 350°C, (*4*) freshly prepared at calcined at 200°C, and (*5*) after the first sorption–regeneration cycle at 350°C. (c) Sample C1: (*1*) freshly prepared, (*2*) after the first sorption–regeneration cycle at 200°C, and (*3*) after the second sorption–regeneration cycle at 200°C.

latter composite was caused by the fact that it can be used for removal of CO_2 form gas mixtures, for example, in short-cycle adsorption of carbon dioxide [7]. To study the influence of the nature of the porous matrix-host on the sorption of carbon dioxide by supported potassium carbonate, we used both hydrophilic (silica gel, aluminum oxides, inflated vermiculite) and hydrophobic (porous carbon) matrices. Inflated vermiculite is a mainly macroporous sorbent; the other matrices are mainly mesoporous. Along with the sorption kinetics of carbon dioxide in a flow adsorber, we also studied, using X-ray diffraction (XRD), thermogravimetry (TGA), and low-temperature nitrogen sorption, the changes in the texture and phase composition of the sorbents during the sorption and regeneration.

EXPERIMENTAL

The sorbents were prepared by impregnation of porous supports (the parameters are presented in Table 1) with 40% aqueous K_2CO_3, followed by drying on a water bath (T = 100°C) at continuous removal of water vapor with a water-jet pump. The content of potassium carbonate in the samples ranged from 22 to 47% depending on the moisture capacity of the sample. We studied sorption of carbon dioxide at 40°C in an 5-ml adsorber (a 180-mm glass tube 6 mm i.d.). Air fed in the adsorber was saturated with a water vapor to the dew point of 30°C. Then CO_2 was introduced to its content in the inlet gas flow of 2 vol %. The flow rate of the gas fed in the adsorber was 150 $cm^3\ min^{-1}$. The CO_2 content at the outlet was measured chromatographically with an accuracy of 2% in the range of 10^{-2}–2.0 vol %.

As seen from Fig. 1a, the general shape of the time dependences of the CO_2 concentration at the outlet of the adsorber depends on the nature of the sorbent matrix. Freshly prepared alumina composites A1 and A2 almost completely sorb carbon dioxide

within the first 40–50 min. The residual CO_2 concentration does not exceed $(20–25)\times10^{-4}$ vol %. Then the CO_2 concentration at the outlet C_{out} increases up to the inlet value. The dynamic capacity of these sorbents A_{dyn} defined as the ratio of the CO_2 amount adsorbed by the moment when the outlet CO_2 concentration starts to increase (i.e., by the start of breakthrough) to the initial weight of the sorbent reaches 0.06–0.094 g g^{-1}. This is 65–75% of their limiting capacity calculated in accordance with the stoichiometry of reaction (1). The measured dynamic capacity of the samples is about 20 times higher than that of the initial Al_2O_3 matrix (Fig. 1a), i.e., the main part of carbon dioxide is adsorbed by reaction (1).

The time of CO_2 sorption on C1 and C2 sorbents based on porous carbon is considerably shorter (5–12 min) (Fig. 1a). Then the outlet carbon dioxide concentration increases monotonically, with the increase slightly decelerating at C_{out} = 1.0–1.2 vol %. The curves of CO_2 sorption on potassium carbonate supported by silica gel (S1) and vermiculite (V1) indicate breakthrough of CO_2 already at the first steps of the experiment. In the case of vermiculite sorbent the curve flattens out at 50% adsorption of CO_2 fed at the inlet. The dynamic capacity of these sorbents is low and does not exceed 0.006 g g^{-1} (Table 2).

Thus, among the tested sorbents only potassium carbonate–aluminum oxide composites having high dynamic capacity and providing low CO_2 concentration at the adsorber outlet are of practical interest. We studied these composites in more detail. Since at T > 150°C equilibrium (1) is shifted to decomposition of potassium carbonate, regeneration of the samples was performed at 200–350°C in an air flow. However, under these conditions the dynamic capacity of alumina composites does not return to the initial value. As seen from Fig. 1b, in the first step carbon dioxide is completely sorbed on the initial A1 sorbent and the sorbents regenerated at 200 and 350°C. Then CO_2 breakthrough is observed, and the curve flattens out at the level of 25–40% sorption. The time to the breakthrough increases with increasing the regeneration temperature from 200 to 350°C but does not exceed 15–30% of the time for the initial freshly prepared sorbent A1. It should be noted that calcination of the initial A1 and A2 sorbents at 200–350°C decreases their dynamic capacity several times (Fig. 1b).

For comparison we studied regeneration of C1 and C2 sorbents, since Hayashi *et al.* [4] found that the sorption properties of composites based on porous carbons can be completely regenerated by calcination.

Table 2. Dynamic capacity for carbon dioxide

Sorbent	A_{dyn}, g g^{-1} (% of the maximal value*), to indicated C_{out}, vol %	
	0.005	1.0
A1	0.063 (73)	0.067 (78)
A2	0.094 (64)	0.121 (82)
C1	0.008 (10)	0.044 (55)
C2	0.025 (35)	0.034 (48)
S1	0 (0)	<0.001 (<1)
V1	0 (0)	0.006 (4)

* The maximal capacity of the sorbents was calculated in accordance with the stoichiometry of reaction (1).

Table 3. Specific surface area S_{sp} and mesopore volume V_{me} of A1 sorbent calcined at different temperatures T_c

Sample	T_c, °C	S_{sp} (BET), m^2 g^{-1} support	V_{me}, m^3 g^{-1} support
Initial A1 support	200	248	0.41
Initial sorbent	200	142	0.34
	350	149	0.40
After CO_2 sorption	200	173	0.35
	350	174	0.38

Indeed, C1 and C2 sorbents were completely regenerated by heating at 150–200°C for 1–2 h (Fig. 1c).

To understand the different behavior of the sorbents, the changes in their texture and phase composition during the sorption and regeneration were studied by XRD, low-temperature nitrogen sorption, and TGA. The TG curves of A1 sorbent, measured on a Rigaku Thermoflex thermobalance, have two regions

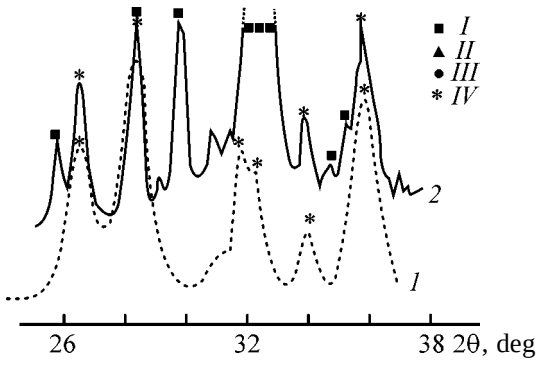

Fig. 2. Powder X-ray diffraction patterns of pure potassium aluminocarbonate (*1*) $KAl(CO_3)_2\cdot1.5H_2O$ and (*2*) freshly prepared A2 sorbent. (2θ) Braggs' angle; the same for Figs. 3 and 4. (*I*) $K_2CO_3\cdot1.5H_2O$, (*II*) K_2CO_3, (*III*) $KHCO_3$, and (*IV*) $KAl(CO_3)_2\cdot1.5H_2O$.

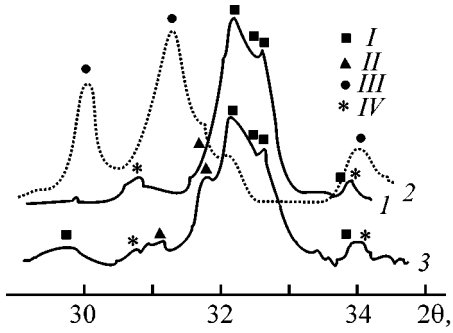

Fig. 3. Powder X-ray diffraction patterns of A2 sorbent: (*1*) freshly prepared, (*2*) after the first sorption cycle, and (*3*) regenerated at 200°C.

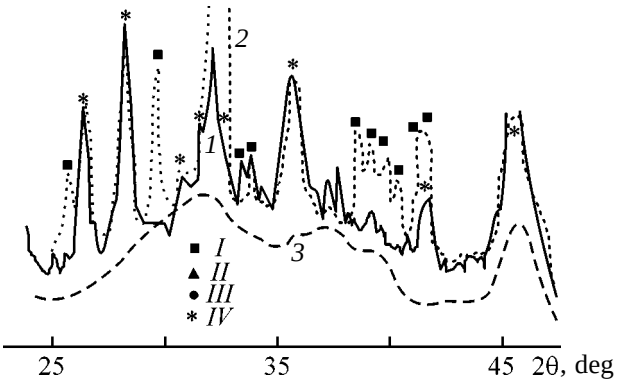

Fig. 4. Powder X-ray diffraction patterns of freshly prepared (*1*) A1 and (*2*) A2 sorbent and (*3*) of A1 sorbent calcined at 350°C.

of weight loss at 80–100 and 320–350°C. The first peak is assigned to elimination of the crystallization water from $K_2CO_3 \cdot 1.5H_2O$. The second peak is probably due to CO_2 liberation in reaction of potassium carbonate with the matrix. Similar reaction [reaction (2)] was observed [5] between potassium carbonate and silica gel. The TG curve of pure alumina contains a single peak at 50–130°C due to removal of physically and chemically bonded water.

The specific surface area and pore size distribution of the samples were determined by low-temperature nitrogen adsorption performed on an ASAP-2400 Micromeritics unit. The results show that the surface area accessible for nitrogen slightly decreases after introduction of the salt (Table 3). Knowing the density of potassium carbonate $\rho_{K_2CO_3} = 2.428$ g cm^{-3}, we can estimate its content in pores accessible for nitrogen. The specific weight of potassium carbonate (g g^{-1}) in alumina pores, normalized to the weight of alumina Al_2O_3-1, is

$$m_{K_2CO_3} = V_w \rho_s \times 0.4 = 0.396,$$

where $\rho_s = 1.414$ g cm^{-3} is the density of a 40% solution of potassium carbonate at the impregnation temperature (25°C).

The volume occupied by potassium carbonate, $m_{K_2CO_3}/\rho_{K_2CO_3} = 0.163$ cm^3 g^{-1} Al_2O_3, is larger than the decrease in the pore volume measured by nitrogen porosimetry (Table 3). This is likely due to partial fixation of potassium carbonate particles in the macropores of the support. Interestingly, an increase in the pore volume of the sorbents with increasing regeneration temperature indirectly confirms reaction of potassium carbonate with alumina matrix to form carbon dioxide.

The phase transformations in the sorbents were studied by powder X-ray diffraction performed *ex situ* (HXG-4 diffractometer, graphite monochromator, CuK_α radiation). Freshly prepared A1 and A2 sorbents contain, along with anhydrous potassium carbonate and its sesquihydrate, also potassium aluminocarbonate $KAl(CO_3)_2 \cdot 1.5H_2O$ (Fig. 2) formed during preparation of the sorbent. After sorption the reflections of anhydrous potassium carbonate disappear and reflections of potassium hydrogen carbonate formed by reaction (1) appear (Fig. 3), whereas the amount of the aluminocarbonate phase decreases negligibly. The reflections of the X-ray patterns of the composites calcined at 350°C are strongly blurred, which makes it impossible to determine the phase composition of the samples (Fig. 4). The X-ray patterns of the spent and initial A1 sorbents calcined at 200°C are similar to that of the initial sample. However, some redistribution of the intensities of the reflections and their broadening are observed.

As determined by XRD, the initial C1 sorbent contains only the sesquihydrate and anhydrous potassium carbonate. Potassium carbonate completely reacts with carbon dioxide to form potassium hydrogen carbonate which reversibly decomposes to the initial K_2CO_3 at 200°C. These transformations are similar to those described by Hirano *et al.* [3]. Potassium aluminosilicate prepared by the procedure in [6] and isolated in the pure state weakly sorbs CO_2. This can cause the difference between the experimental dynamic capacity of A1 and A2 sorbents and the maximal dynamic capacity of these samples calculated from the stoichiometry of reaction (1).

CONCLUSIONS

(1) Sorption of carbon dioxide on supported potassium carbonate strongly depends on the chemical nature and pore structure of the host matrix. Freshly prepared composites based on γ-alumina have the

highest dynamic capacity (0.06 – 0.094 g g^{-1}, which is 65–75% of the limiting value) at 2-s contact of the gas flow with the sorbent, with the CO_2 concentration at the adsorber outlet being less that 25×10^{-4} vol %.

(2) The dynamic sorption capacity of the alumina composites decreases 3–4 times after the first sorption–regeneration cycle, whereas the sorbents based on porous carbons are regenerated reversibly.

(3) As determined by XRD, in the course of preparation of A1 and A2 samples a solution of potassium carbonate reacts with alumina to form $KAl(CO_3)_2 \cdot 1.5H_2O$ which does not sorb CO_2.

(4) Although the alumina composite has low dynamic capacity, it can be used in gas purification when application of zeolites is impossible because of high humidity of the gas phase and adsoption purification requires large investments (primarily in laboratories and small plants).

ACKNOWLEDGMENTS

This work was partially financially supported by the Russian Foundation for Basic Research (project no. 99-03-32312a), Russian Universities—Basic Research program (project no. 991065), and the Siberian Division of the Russian Academy of Sciences (Program of Support of Young Scientists).

REFERENCES

1. Aristov, Yu.I., Tokarev, M.M., Cacciola, G., and Restuccia, G., *React. Kinet. Catal. Lett.*, 1996, vol. 59, no. 2, pp. 325–334.
2. Gordeeva, L.G., Resticcia, G., Cacciola, G., and Aristov, Yu.I., *React. Kinet. Catal. Lett.*, 1998, vol. 63, no. 1, pp. 81–88.
3. Hirano, S., Shigemoto, N., Yamada, S., and Hayashi, H., *Bull. Chem. Soc. Jpn.*, 1995, vol. 68, no. 3, pp. 1030–1035.
4. Hayashi, H., Taniuchi, J., Furuyashiki, N., *et al.*, *Ind. Eng. Chem. Res.*, 1998, vol. 37, no. 1, pp. 185–191.
5. Hayashi, H., Hirano, S., Shigemoto, N., *et al.*, *J. Chem. Soc. Jpn., Chem. Ind. Chem.*, 1995, vol. 12, pp. 1006–1012.
6. Tomilov, N.P., Berger, A.S., and Boikova, A.I., *Zh. Neorg. Khim.*, 1969, vol. 14, no. 3, pp. 674–679.

Russian Journal of Applied Chemistry, Vol. 74, No. 3, 2001, pp. 414–416. Translated from Zhurnal Prikladnoi Khimii, Vol. 74, No. 3, 2001, pp. 406–408.

SORPTION AND ION-EXCHANGE PROCESSES

Sorption Purification of Scandium(III) To Remove Zirconium(IV) Impurity in Hydrochloric Acid Solutions

Yu. V. Sokolova

Moscow State Institute of Steel and Alloys (Technological University), Moscow, Russia

Received December 20, 1999; in final form, September 2000

Abstract—A study was made on separation of the Zr(IV) impurity from scandium(III) in hydrochloric acid solutions by sorption with KRF-20t-60 cation exchanger, including sorption kinetics and sorption under dynamic conditions. The sorbent regeneration with 5% ammonium fluoride or 10% potassium carbonate at 22°C was considered.

Separation of Zr(IV) impurity from scandium(III) is a complicated problem because of close chemical properties of these elements. OS-99.9 grade scandium oxide with 0.005% and lower ZrO_2 content [1] was prepared using precipitation methods (e.g., zirconium iodate precipitation), or extraction with mixed extractants. However, these methods do not always provide the required purity of the product. In this work, we removed Zr(IV) from scandium(III) by sorption from hydrochloric acid solution with the H form of KRF-20t-60 cation exchanger containing phosphonic $PO(OH)_2$ functional group.

It was shown earlier that the recovery of cations with KRF-20t-60 cation exchanger is characterized with a mixed kinetics. The equilibrium in multicomponent salt solutions is attained in several weeks. A series of cation sorption selectivity (including the above elements) in acid solution (i.e., under conditions suppressing dissociation of phosphonic group) is as follows: REE(III) $\ll$ Sc(III) < Zr(IV) [2, 3].

Filatova *et al.* [4] believe that functional groups of swollen phosphonic cation exchangers in the H form are bound with each other by water molecules. Probably, this feature of such resins explains the high selectivity of KRF-20t-60 resin with respect to multicharged cations and the long time required to attain the sorption equilibrium, because during sorption from the multicomponent solution under conditions suppressing dissociation of the ionogenic groups of the resin the complex formation proceeds repeatedly.

The ability of KRF-20t-60 cation exchanger to separate REE(III) and the other cations from Sc(III) in acid solution was used for primary scandium concentration [5]. To separate Zr from scandium, we used in this work the greater affinity of the resin for Zr(IV) as compared to Sc(III) and the capability of Zr(IV) to displace Sc(III) from the resin phase because of complex formation.

EXPERIMENTAL

The main physicochemical characteristics of KRF-20t-60 cation exchanger are as follows: total static exchange capacity 6.6 mg-equiv g^{-1}, bulk density 0.38 g ml^{-1}, equivalent moisture capacity coefficient 2.90 H_2O g^{-1}, total pore volume 0.31 cm^3 g^{-1}, pK_{dis} for the first stage 3.0–3.2, divinylbenzene content 20%, and grain size 0.5–1.0 mm.

Cation exchanger samples were preliminarily conditioned by the standard method [6]. The scandium chloride solution was prepared by dissolution of OS-99.0 grade scandium oxide with the ZrO_2 content less than 0.1 wt % in chemically pure grade hydrochloric acid under boiling; the insoluble residue was separated by filtration. The scandium and zirconium concentrations were about 3 g l^{-1} and 3 mg l^{-1}, respectively.

The scandium concentration in the solution was determined by titration with EDTA in the presence of xylenol orange as an indicator. The impurity contents were determined using inductively-coupled plasma on a Labtam V-310 Plasma spectrometer and a Model 300 Perkin–Elmer AA spectrometer. The Zr detection limit was 10^{-5}%; the determination error was no more than 20%.

The degree of Zr sorption is independent of hydrochloric acid concentration within the 1–8.5 M range, and at the taken water-to-sorbent volume ratio V_w/V_s is close to 100% (Fig. 1). Experiments on scandium

1070-4272/01/7403-0414$25.00

purification procedure were performed with 1 M HCl. This acidity is enough to suppress dissociation of the cation exchanger phosphonic groups and to realize complexing properties of the cation exchanger.

The kinetics of Zr(IV) sorption on KRF-20t-60 cation exchanger from the scandium chloride solution was studied by the method of the limited solution volume. The degree of conversion equal to the ratio of Zr(IV) sorption at the instant τ to the equilibrium sorption value, after 6 h of sorption was equal to 84 and 74% for cation exchanger in the H and Sc forms, respectively, i.e., Zr sorption is slow (Fig. 2). Therefore, for sorption under dynamic conditions, we used a sorption column with the sorbent bed height to column diameter ratio d/h no less than 10: the solution flow velocity through the sorbent V did not exceed 0.4 ml min^{-1} cm^{-2}.

During the experiment, the H form of the sorbent was transformed into the Sc form by passing the scandium chloride solution through the sorbent. The comparison of the Sc(III) and Zr(IV) elution curves, when metals are sorbed by the H form of KRF-20t-60 from solutions of various compositions (Fig. 3), shows that Zr is efficiently sorbed by the cation exchanger also after the Sc concentration in the eluate becomes equal to the initial Sc concentration. This is explained by the preferential sorption of Zr(IV) during complex formation.

It follows from the data obtained that at Sc concentration of 3 g l^{-1}, Zr concentration of 3 mg l^{-1}, h/d ratio of 10, and the solution flow velocity of 0.4 ml min^{-1} cm^{-2} sorption with KRF-20t-60 allows removal of Zr impurity from a scandium chloride solution with a purification coefficient of 50 in the solution volume greater than 42 resin volumes. When the Sc and Zr concentrations were 2.94 g l^{-1} and 28.1 mg l^{-1}, respectively (Zr was introduced additionally), the purification efficiency under the same conditions decreased. In this case, the required purification degree for obtaining OS-99.9 grade scandium oxide (~1.5 mg l^{-1} of Zr) is attained for solution volume equal to 1.5–2 resin volumes (V_{rel} = 1.5–2).

Calculation showed that in run no. 1 the sorbent capacity was about 100 mg of Zr per liter of the resin; in run no. 2 (V_{rel} = 2) 55 mg of Zr was sorbed. The characteristics of the sorbent show that Zr occupies 0.02 and 0.03% of the ion exchanger capacity in run nos. 2 and 1, respectively. Hence, poor separation of Zr(IV) impurity in run no. 2 is probably due to the insufficient time of cation exchanger contact with the solution (~0.5 h), rather than to Zr excess over the ion exchanger capacity. This problem can be solved by repeated sorption under static conditions.

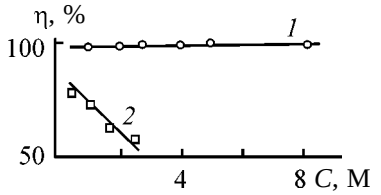

Fig. 1. Degree of Zr sorption η from scandium chloride solution on KRF-20t-60 cation exchanger in the Sc form as a function of acid concentration C. $C_{Sc(III)}$ = 9.80 and $C_{Zr(IV)}$ = 10^{-4} g l^{-1}; V_w/V_r = 2.0. Acid: (*1*) HCl and (*2*) H_2SO_4.

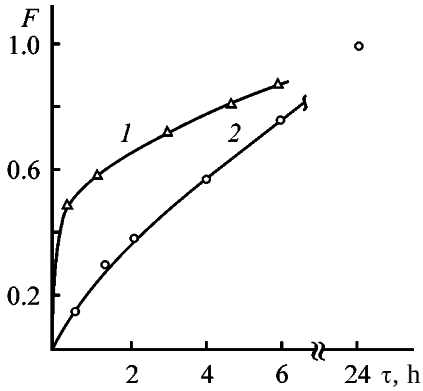

Fig. 2. Kinetic curves of Zr(IV) sorption on KRF-20t-60 cation exchanger in (*1*) H and (*2*) Sc form. Solution composition (g l^{-1}): Sc(III) 2.91, Zr(IV) 0.027, and HCl 80; V_w/V_r 20. (F) Degree of conversion equal to the ratio of the sorption at the instant τ to the equilibrium sorption; (τ) time.

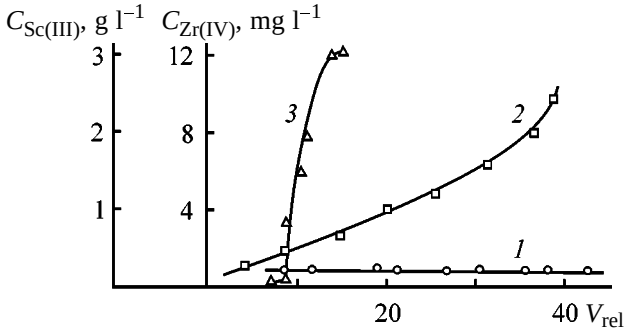

Fig. 3. (*1, 2*) Output curves of Zr and (*3*) Sc at their sorption on KRF-20t-60 in H form under dynamic conditions. h/d = 10, v = 0.4 ml min^{-1} cm^{-2}. ($C_{Sc(III)}$) Sc(III) concentration, ($C_{Zr(IV)}$) Zr(IV) concentration; (V_{rel}) volume of the solution passed, expressed in the resin volumes. Solution composition (g l^{-1}): (*1*) Sc(III) 3.00, Zr(IV) 0.0023, HCl 73 (run no. 1); (*2*) Sc(III) 3.00, Zr(IV) 0.0281, HCl 73 (run no. 2); (*3*) Sc(III) 3.00, Zr(IV) 0.003, HCl 80.

To regenerate the ion exchanger, it was washed with distilled water to remove the initial solution and

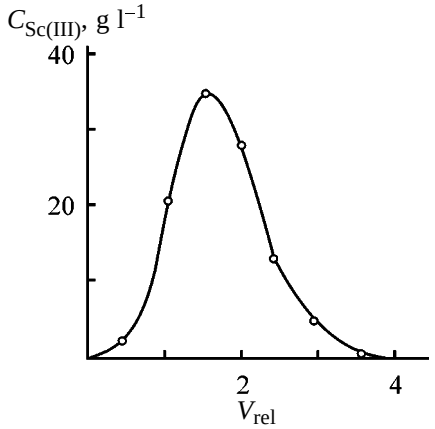

Fig. 4. Sc(III) desorption from KRF-20t-60 cation exchanger with 5% NH_4F. ($C_{Sc(III)}$) Sc(III) concentration in NH_4F solution; (V_{rel}) volume of NH_4F solution expressed in the resin volumes.

with 2% ammonia to neutralize the acid in the ion exchanger pores, and then Sc(III) was desorbed with 5% NH_4F at 20–25°C (Fig. 4). The degree of Sc(III) desorption was 90 and 99% when elution was performed by the volume of the NH_4F solution V_{rel} equal to 4 and 8. Then, Sc(III) was recovered as scandium fluoride by adding hydrochloric (or another) acid to the resulting solution up to free acid concentration of about 100 g l^{-1} and calcination of the precipitate at 450°C. The residual Sc concentration in the mother liquor did not exceed 10–20 mg l^{-1}.

If required, scandium can be recovered as oxide by calcination of scandium(III) hydroxide. In this case, scandium desorption is performed with 10% potassium carbonate at room temperature. The desorption degree is close to 100% when the regenerating solution for scandium elution is taken in amount of V_{rel} = 10. Scandium hydroxide is precipitated from the carbonate medium by neutralization with hydrochloric acid to pH ~ 7. The residual Sc concentration in the solution is 20–30 mg l^{-1}.

After conversion of the cation exchanger into the H form by treatment with 3% HCl, it can be used again for scandium purification to remove Zr impurity.

Scandium oxide recovered from the solution in run no. 1 by precipitation of scandium hydroxide with 25% NH_4OH (chemically pure grade) followed by drying and calcination contained less than 0.005% ZrO_2.

We should expect that the high affinity of phosphonic acid cation exchanger KRF-20t-60 for multicharged cations allows also efficient separation of Th(IV) and U(VI) impurity from scandium under conditions suppressing the dissociation of the phosphonic acid group, when the complexing properties of resin ionogenic groups can be realized.

CONCLUSION

A study of the kinetics and dynamics of the Zr(IV) sorption from acidic scandium chloride solution with KRF-20t-60 cation exchanger showed that the Zr concentration can be decreased by a factor of 50 and more by sorption purification. Procedures of the sorbent regeneration with 5% NH_4F or 10% potassium carbonate at room temperature were proposed.

REFERENCES

1. Korshunov, B.G., Reznik, A.M., and Semenov, S.A., *Skandii* (Scandium), Moscow: Metallurgiya, 1987.
2. Sokolova, Yu.V., Medvedev, A.S., and Kurdyumov, G.M., in *Metallurgiya redkikh metallov: Poroshkovaya metallurgiya* (Less-Common Metal Metallurgy: Powder Metallurgy), Moscow: Metallurgiya, 1987, pp. 72–78.
3. Sokolova, Yu.V., Kurdyumov, G.M., Smirnov, A.V., *et al.*, *Zh. Prikl. Khim.*, 1991, vol. 64, no. 8, pp. 1766–1768.
4. Filatova, L.N., Shelyakina, M.A., and Kurdyumova, T.N., *Sbornik nauchnykh trudov Inst. khimicheskikh reaktivov i osobochistykh veshchestv* (Proc. Inst. of Chemical Reagents and Ultrapure Substances), Moscow: IREA, 1984, issue 46, pp. 72–78.
5. RF Patent 2037548.
6. Polyanskii, N.G., Gorbunov, G.N., and Polyanskaya, N.P., *Metody issledovaniya ionitov* (Methods of Studying Ion Exchangers), Moscow: Khimiya, 1976.

Russian Journal of Applied Chemistry, Vol. 74, No. 3, 2001, pp. 417–420. Translated from Zhurnal Prikladnoi Khimii, Vol. 74, No. 3, 2001, pp. 413–415.

APPLIED ELECTROCHEMISTRY AND CORROSION PROTECTION OF METALS

K-Selective Solid-Contact Electrodes Based on Electron-Conducting Polymers

N. N. Markuzina, K. N. Mikhel'son, E. V. Molodkina, and A. Levenstam

Research Institute of Chemistry, St. Petersburg State University, St. Petersburg, Russia
Abo Academy, Turku, Finland

Received November 20, 2000

Abstract—K-Selective solid-contact electrodes with potential-stabilizing transient layers based on two different electron-conducting polymers, poly(3-octyl)thiophene, polyaniline, and also on their mixture are developed. These electrodes are characterized by the operation limits, selectivity, and stability of the potentiometric response as well as by their electrochemical impedance.

Improvement of the design of ion-selective electrodes (ISEs) and search for novel materials for their construction are regarded as the most important lines in chemical sensor research. From the practical standpoint solid-contact electrodes (SCEs), i.e., electrodes having no inner filling solution, show considerable advantages such as eliminated need in regular change of the inner filling solution, possibility of any spatial orientation of a sensor, easier transportation, etc.

The first SCEs were coated wire electrodes with a film membrane in direct contact with an electronic conductor [1, 2]. The potential of such electrodes strongly and randomly varies in time. To stabilize the potential at the membrane/lead interface, Stefanova and others [3–5] proposed to introduce a polymer-based redox system in the inner membrane layer contacting with the electronic conductor. As such potential-stabilizing systems they successfully used powdered EO-7 and EI-21 ion-exchange redox resins (redoxites). The potential of thus modified electrodes appeared to be much more stable as compared to the first wire electrodes with film membranes. However, the modified electrodes were characterized by sudden change in their potential by 0.5–1 mV, which causes a need in regular (at interval of several hours) recalibration of the sensors. In industrial process control such a frequent calibration is not always permitted, so that further search for new potential-stabilizing materials for SCEs still remains urgent.

One of the reasons for insufficient stability of the potential of SCEs with redoxites can be heterogeneity of the transient layer. Indeed, even if every particle of a finely dispersed resin is in ion-exchange equilibrium with the membrane organic phase and the bulk of each particle of the resin is in the state of the redox equilibrium, these are insufficient conditions to maintain the equilibrium potential in the transition zone from ionic to electronic conductance. Keeping of the equilibrium potential requires realization of a direct contact of a lead with a great number of the resin particles. Only in this case one may expect that the electron current from the lead to the resin particles (and back) will be sufficiently high to provide certain value of the electrode potential stable in time and within a series of electrodes. In this context redox couples seems to be more favorable as compared to polymer resins. In its turn, it was demonstrated in [3–5] that the intrinsic drawback of these SCEs is that they are sensitive to the redox potential of test solutions as a result of diffusion of soluble redox couples from the intermediate layers to the outer side of the membrane.

The combination of solubility and low mobility of redox couples can be realized with the use of soluble electron-conducting polymers (EPs) introduced in the intermediate layer between the membrane and the lead. More or less successfully such polymers were used in various SCEs [6–10]. The electronic conductance of EPs is caused by the presence of delocalized π electrons in the polymer structure. Electron-conducting polymers become electron-ionic transducers by the *p* and *n* doping mechanisms according to Eqs. (1) and (2):

$$p \text{ doping: } P^0 + X^- = p^+X^- + e, \quad (1)$$

$$n \text{ doping: } P^0 + C^+ + e = P^-C^+. \quad (2)$$

The existing EPs are characterized by low conductivity [6–9]. The goal of this work is to develop a

1070-4272/01/7403-0417$25.00

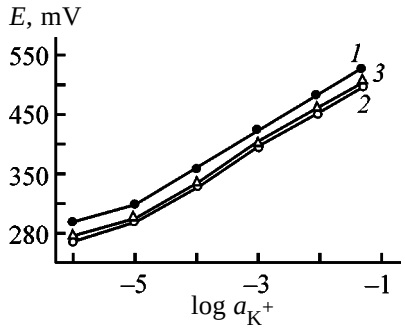

Fig. 1. emf of voltaic cell II E as a function of $\log a_{K^+}$ for K^+-SCEs based on various EPs: (*1*) PA, (*2*) POT, and (*3*) POT + PA; the same for Fig. 2.

K-selective SCE stabilized with soluble EPs. The distinctive feature of this work is that we used not only the individual EPs, poly(3-octyl)thiophene (POT) and polyaniline (PA), as was the case in [6–9], but also their mixtures. Furthermore, we used a partly soluble electron-conducting composite as a lead material, instead of carbon glass used in [6–9], providing more continuous transition from one type of conductance to another in the transition layer.

In this work we used the electron-conducting polymers POT and PA (Application Technologies, France) as ion-electronic transducers for K-selective SCEs.

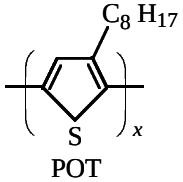

POT

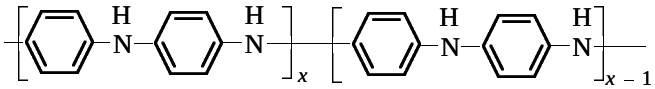

PA

POT is soluble in most organic solvents. In the undoped form it is a *p* semiconductor, showing nonselective cationic response toward some alkali and alkaline-earth metals [6]. Undoped PA in the form of emeraldin base (EB) is poorly soluble in organic solvents. However, PA can be doped (protonated) by introducing organic acid molecules in its structure [9]. The resulting electron-conducting emeraldin salt (ES) is readily soluble in certain organic solvents. In this work PA was doped with di-(2-ethylhexyl) hydrogen phosphate (HDEHP) (Aldrich).

Solutions of POT in THF were obtained by dissolution of 0.015 g of POT in 2 ml of freshly distilled THF. To obtain a solution of PA in THF, 0.02 g of PA in the form of EB was added to 0.05 M HDEHP in THF (2 ml) [9]. In doped PA the molar ratio of HDEHP to PA monomeric unit was 0.5. The resulting mixture was allowed to stand for 3 days, and the insoluble fraction was then filtered off. The filtrate (soluble fraction of PA-HDEHP in THF, where PA is in the ES form) was used in manufacture of SCEs.

The K-selective membranes were prepared as follows. Polyvinyl chloride (PVC) (matrix material), dioctyl phthalate (DOP) (plasticizer), valinomycin (membrane active compound), and potassium tetra-*p*-chlorophenylborate (ion exchanger) were dissolved in THF. The PVC and DOP were taken in 1 : 3 ratio. The valinomycin and potassium tetra-*p*-chlorophenylborate concentrations were 2×10^{-3} and 1×10^{-1} mol kg^{-1}, respectively. The electron-conducting polymers (POT, PA, or POT + PA equimolar mixture) were added in amount of 1 wt % against the membrane composition of the transition layer.

The membrane of SCEs consisted of two layers successively applied to a support of an electron-conducting composite (PVC : carbon black : DOP = 1 : 1 : 0.5). The inner transition layer contacting the support was prepared by applying 200 μl of the appropriate composition using an HTL V-3 micropipet. The outer layer directly contacting an aqueous solution was represented by the membrane composition without EP, applied similarly over the transition layer after it became dry. The thickness of the inner and outer layers was the same (about 200 μm).

The electrode characteristics of K-selective electrodes were studied with liquid–junction voltaic cells I and II (see below).

Ag	AgCl, KCl	Variable-composition solution: KCl, $MeCl_z$	Membrane	KCl (0.01M), AgCl	Ag	(I)

Electrode with inner filling solution

Ag	AgCl, KCl	Variable-composition solution: KCl, $MeCl_z$	Membrane	Membrane + EP	EP	Cu	(II)

Solid-contact electrode

First of all we studied the K^+ function of SCEs in pure KCl solutions.

For comparison we performed measurements with the ordinary K-selective electrodes with inner filling solution. The results obtained for K^+-SCEs 3 days after they were brought in contact with 0.01 M KCl solution are given in Fig. 1. The time of establishment of stationary potential was 1–3 min, which practically does not differ from that for the corresponding elec-

trodes with inner filling solution. Figure 1 demonstrates that for all K^+-SCEs studied, regardless of the nature of a polymer entering the composition of the inner membrane layer, the operation limit was 1×10^{-1}–1×10^{-5} M at a slope of the K^+ function of 57 ± 2 mV/pK^+. Similar results were obtained for the corresponding electrodes with inner filling solution. It should be pointed out that the SCEs with two different polymers, POT and PA, showed K^+ function throughout the observation time (4 months).

However, in contrast to the electrodes with inner filling solution, the potential of SCEs measured in 0.01 M KCl drifts with time (Fig. 2). It is seen that the potential of SCEs with POT and PA decreased quite rapidly (by 5–7 mV day^{-1}) in the first three weeks and then the drift was at a level of 1–2 mV day^{-1} in the entire observation period (4 months).

For SCEs with POT + PA the potential increased in the first several days and then decreased at a rate of 4–5 mV day^{-1} in the entire observation period (about 40 days for these electrodes).

To elucidate the source of the observed instability of the potential of the SCEs, they were studied by the electrochemical impedance method in 0.01 and 0.1 M KCl. The impedance spectra were registered and processed with an Autolab PGstat FRA 2 impedance analyzer (Eco Chemie) over the frequency range of the polarizing sine-shaped signal from 100 kHz to 0.01 Hz. The polarization amplitude was ± 5 mV. The typical impedance spectra are presented in Fig. 3. The spectra distinctly demonstrate semicircles corresponding to the bulk of the membrane phase, whose resistance is practically independent of the solution concentration. We found no indication of a process decelerating the establishment of the electrochemical equilibrium at the membrane/lead interface.

In fact, electrochemical impedance data provide information on the polarizability of an object (SCE in our case) with electric current of a given amplitude and frequency. The results obtained suggest that at the membrane/lead interface the electrochemical equilibrium is established between the oxidized (doped) and reduced (undoped) forms of EP. At each moment of time this equilibrium is controlled by the ratio of the thermodynamic activities of these forms. The corresponding electric potential should be stable for certain time until this activity ratio is changed. However, this ratio can change as a result of, for example, oxidation of the membrane components by atmospheric oxygen, resulting in long-term drift of the electrode potential.

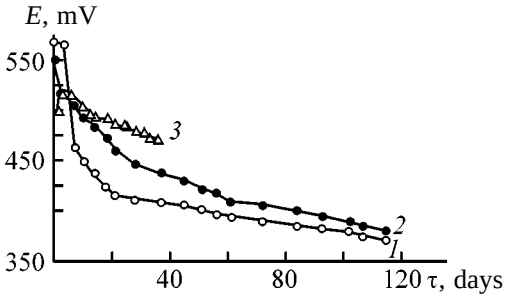

Fig. 2. emf of voltaic cell II E as a function of the contact time with 0.01 M KCl τ for K^+-SCEs based on various EPs.

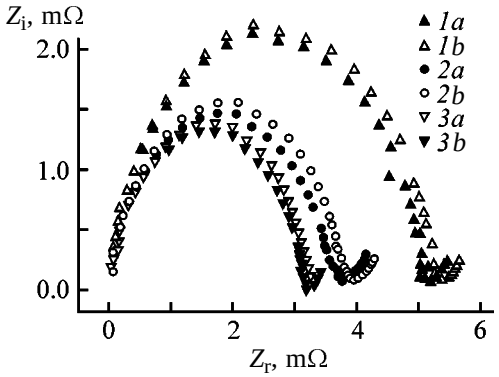

Fig. 3. Impedance spectra in KCl solutions of K^+-SCEs based on various EPs. Z_r and Z_i are the real and imaginary parts of the total resistance Z. KCl concentration (M): (*1a*–*3a*) 0.1 and (*1b*–*3b*) 0.01. EP: (*1a, 1b*) PA, (*2a, 2b*) POT, and (*3a, 3b*) POT + PA.

Figure 2 shows that the potentials of all the SCEs studied drift toward less positive values. But oxidation of EP should initiate potential drift in the opposite direction. Therefore, it is unlikely that oxidation with atmospheric oxygen may be regarded as the major reason for the insufficient stability of SCE operation. Another possible reason can be spontaneous reduction of the doped form of EP. It is this process that can provide the observed potential drift.

At last we studied the K^+ selectivity of SCEs in the presence of various interfering cations. The selectivity coefficients were estimated by the Nikol'skii equation from the biionic potentials measured in 0.1 M solutions of the corresponding chlorides (see table). The results show that initially (in the first 10 days) the SCEs studied practically do not differ from the electrodes with inner filling solution in their selectivity with respect to K^+ in the presence of Na^+, NH_4^+, Ca^{2+}, and Mg^{2+}. However, the K^+ selectivity of the SCEs decreases with time, which can be attributed to diffusion of the membrane-active components, primarily valinomycin, from the outer layer to the

Selectivity coefficients of K^+-ISEs determined by BIP method

Contact time	$\log K^{sel}_{K^+/M^{z+}}$ for indicated M^+				
	Na^+	NH_4^+	H^+	Ca^{2+}	Mg^{2+}
K^+-ISE with inner filling solution					
–	–3.82	–1.91	–4.50	–4.11	–5.12
K^+-SCE with POT					
3 h	–4.14	–1.73	–3.66	–4.04	–4.88
7 days	–3.61	–1.67	–3.39	–3.86	–4.55
14 days	–3.72	–1.64	–2.65	–2.93	–4.19
21 days	–3.31	–1.51	–2.99	–2.85	–3.52
102 days	–3.28	–1.49	–1.61	–2.65	–3.33
K^+-SCE with PA					
3 h	–3.79	–1.68	–3.24	–3.93	–4.61
7 days	–3.54	–1.64	–3.16	–3.62	–4.42
14 days	–3.37	–1.52	–2.34	–2.89	–4.01
21 days	–2.92	–1.33	–2.29	–2.41	–3.01
102 days	–3.27	–1.51	–1.54	–2.40	–2.72

plasticized supporting layer. As a result, the ionophore concentration in the membrane gradually decreases, causing deterioration in the selectivity.

It is typical that the SCE selectivity with respect to K^+ in the presence of hydrogen ions is lower than that of the corresponding electrodes with inner filling solution, and this parameter tends to substantially decrease with time (see table). This is probably due to the fact that the electron-conducting polymers (especially PA) entering the composition of the membrane inner layer are pH-sensitive [10]. It follows from data given in the table that SCEs with POT in the membrane inner layer generally demonstrate higher selectivity as compared to the PA-containing SCEs.

CONCLUSIONS

(1) The K-selective solid-contact electrodes studied demonstrate the K function over the concentration range 1×10^{-1}–1×10^{-5} M at a slope of 57 ± 2 mV/pK^+, which is well consistent with the characteristics of the corresponding electrodes with inner filling solution. The K^+ function is preserved over the entire observation period (4 months).

(2) The K selectivity of the SCEs in the presence of various interfering cations in the first 10 days practically does not differ from that of the electrodes with the classical design, but gradually decreases in the subsequent period.

(3) The potential of the SCEs drifts at a rate of 5–7 mV day^{-1} in the first 10 days and of 1–2 mV day^{-1} thereafter. The electrodes can operate for 10 h without recalibration.

REFERENCES

1. James, H., Carmack, G., and Freiser, H., *Anal. Chem.*, 1972, vol. 44, no. 4, pp. 856–857.
2. Cattral, R.W., Tribuzio, S., and Freiser, H., *Anal. Chem.*, 1974, vol. 46, no. 14, pp. 2223–2224.
3. Stefanova, O.K., Rozhdestvenskaya, N.V., and Gorshkova, V.F., *Elektrokhimiya*, 1983, vol. 19, no. 9, pp. 1225–1230.
4. Stefanova, O.K., Rozhdestvenskaya, N.V., Mukhitdinova, B.A., *et al.*, *Zh. Prikl. Khim.*, 1989, vol. 62, no. 5, pp. 995–999.
5. Rozhdestvenskaya, N.V. and Pugacheva, E.V., *Zh. Prikl. Khim.*, 1992, vol. 65, no. 5, pp. 2205–2210.
6. Cadogan, A., Gao, Z., Levenstam, A., and Ivaska, A., *Anal. Chem.*, 1992, vol. 64, no. 21, pp. 2496–2501.
7. Bodacka, J., McCarrick, M., Levenstam, A., and Ivaska, A., *Analyst*, 1994, vol. 119, no. 9, pp. 1985–1991.
8. Hulanicki, A., Michalska, A., and Levenstam, A., *Talanta*, 1994, vol. 41, no. 2, pp. 323–325.
9. Bodacka, J., Lindfors, T., McCarrick, M., *et al.*, *Anal. Chem.*, 1995, vol. 67, no. 20, pp. 3819–3824.
10. Karyakin, A.A., Lukachova, L.V., Karyakina, E.E., *et al.*, *Anal. Commun.*, 1999, vol. 36, no. 4, pp. 153–156.

Russian Journal of Applied Chemistry, Vol. 74, No. 3, 2001, pp. 421–423. Translated from Zhurnal Prikladnoi Khimii, Vol. 74, No. 3, 2001, pp. 413–415.

APPLIED ELECTROCHEMISTRY AND CORROSION PROTECTION OF METALS

Electrolytic Deposition of the Zinc–Cobalt Alloy

O. S. Vinogradov and Yu. P. Perelygin

Penza State University, Penza, Russia

Received February 3, 2000; in final form, June 2000

Abstract—The influence of the electrolyte composition and process conditions on electrolytic deposition of the zinc–cobalt alloy was studied.

Corrosion-resistant electroplated coatings for items used in marine atmosphere are mainly prepared from cadmium. However, cadmium and its salts are toxic, which severely restricts their application. When looking for a substitute for cadmium, it is necessary to ensure not only high corrosion resistance of a coating in marine atmosphere but also the low friction coefficient, so that screw joints be readily dismantlable and articles be soft-solderable with acid-free fluxes. The most promising in this respect can be zinc–cobalt coating. The zinc–cobalt alloy can be electroplated from acidic and weakly acidic [1–6], ammonium chloride and sulfate [7–11], and diphosphate [12] electrolytes.

The goal of this work was to study the influence of the composition of the ammonium chloride electrolyte and electroplating conditions on the composition of the zinc–cobalt alloy, current efficiency (CE), and physicomechanical properties and corrosion resistance of the coating.

Semilustrous and lustrous coatings of the alloy are deposited from ammonium chloride electrolyte. The alloy composition and properties are influenced by the concentration of discharging metal ion and electroplating conditions. The cobalt content in the alloy increases with increasing Co(II) concentration in the electrolyte at a Zn(II) concentration of 35 g l^{-1}, current density of 1.5 A dm^{-2}, temperature of 20°C, and pH 4.75 (Fig. 1, curve *1*).

In the range of Co(II) concentrations 2.5–15 g l^{-1}, under optimal electroplating conditions, the dependence of the cobalt content in the alloy (%) on the cobalt concentration in the electrolyte (g l^{-1}) is described by the equation

$$[Co]_{all} = 2.04 + 6.86\log[Co(II)] \quad (R = 0.976). \quad (1)$$

The alloy composition correlates with the concentration ratio of Zn(II) and Co(II) in the electrolyte as follows:

$$\log\frac{[Zn]_{all}}{[Co]_{all}} = 0.79 + 0.43\log\frac{[Zn(II)]}{[Co(II)]} \quad (R = 0.955). \quad (2)$$

As the Co(II) concentration in the electrolyte is increased, the current efficiency (Fig. 1, curve *2*) decreases, which is due to the fact that the overvoltage of hydrogen evolution decreases with increasing content of cobalt in the alloy [13]. The current efficiency of alloy deposition (%) linearly correlates with the Co(II) concentration in the electrolyte:

$$CE = 94.67 - 0.37[Co(II)] \quad (R = 0.996). \quad (3)$$

When examining the influence of electroplating conditions on the alloy composition and current efficiency, each parameter was varied at fixed values of the other parameters. With increasing current efficiency from 1 to 2 A dm^{-2}, temperature from 20 to 40°C, and electrolyte pH from 4 to 5.5, the cobalt content in the alloy increases (Fig. 2, curves *1–3*); the current efficiency decreases with inceasing current density (Fig. 2, curve *4*) and grows with temperature (curve *5*) and with increasing pH (curve *6*). The decrease in the current efficiency at increased current densities may

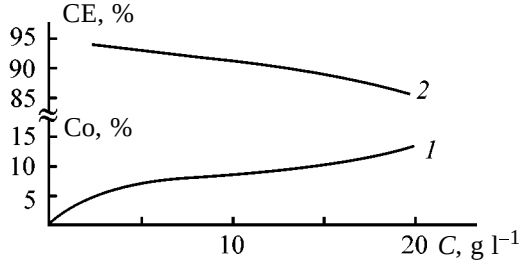

Fig. 1. (*1*) Alloy composition (Co content) and (*2*) current efficienct CE as functions of the Co(II) concentration in the electrolyte *C*.

1070-4272/01/7403-0421$25.00

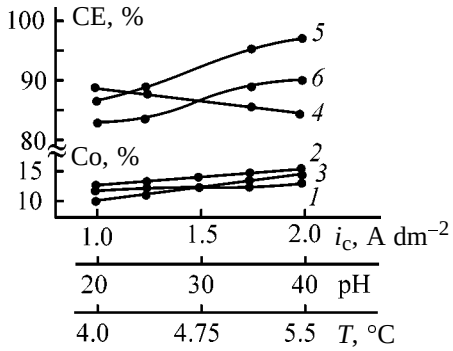

Fig. 2. (*1–3*) Co content in alloy and (*4–6*) current efficiency CE as functions of the (*1, 4*) current density i_c, (*2, 5*) temperature, and (*3, 6*) pH.

be due to a shift of the cathode potential toward negative values and hence to increased contribution of hydrogen evolution. The increase in the current efficiency with temperature is due to the shift of the cathode potential toward positive values and to increasing ion mobility in the electrolyte.

To obtain lustrous coatings containing 3–5% Co in the alloy, the following electrolyte composition can be suggested (g l^{-1}): $ZnCl_2$ (in terms of metal) 30–40, $CoCl_2$ (in terms of metal) 2–4, NH_4Cl 220–260, boric acid 20–30, and bone glue 2–3. Electroplating is performed at room temperature, current density of 1–2 A dm^{-2}, and pH 4.5–5.0.

To optimize the compositions of the alloy and electrolyte and the electroplating conditions for preparing the alloy containing 3–5% Co, we performed a four-factorial experiment. The optimization parameter was the Co content in the alloy *Y*, which should be 3–5%. The factors affecting the alloy composition are Co(II) concentration in the electrolyte x_1, current density x_2, temperature x_3, and electrolyte pH x_4.

After determining the coefficients of the regression equation, we evaluated their significance by the Student's test. For this purpose, we performed three parallel experiments in the plan center (at the base level of all the factors). The chemical analysis of the alloy samples obtained gave Y_1 = 3.6, Y_2 = 4.0, and Y_3 = 4.4. Then, the insignificant coefficients of the regression equation were canceled, and the resulting model was checked for adequacy using the Fisher's test. The regression equation adequately describing the effect of the process parameters on the Co content in the alloy is as follows:

$$Y = 4.2 + 0.9x_1 + 1.15x_2 + 1.0x_3 + 0.8x_4 + 0.15x_1x_2 + 0.15x_2x_3 + 0.15x_2x_4. \quad (4)$$

As seen from Eq. (4), the alloy composition is influenced both by separate factors (Co concentration in the electrolyte, current density, temperature, and pH of the electrolyte) and by a combination of factors (to an insignificant extent) current density–Co(II) concentration in the electrolyte, current density–temperature, and current density–pH of the electrolyte.

The phase composition of the coating at a cobalt content in the alloy of 1–6% was studied with a DRON-2 X-ray diffractometer. The alloy is a solid solution of cobalt in zinc and consists of the homogeneous phase γ^2 + zinc. Such a structure ensures enhanced corrosion resistance of the coating.

The electroplated coatings of the alloy without passivation are white, lustrous, and smooth under magnification of 300, 1000, and 3000.

The solderability of the alloy coating was evaluated by the time τ and area *S* of spilling of POS-61 solder with an alcohol–rosin flux. The results obtained with a 0.13-g portion of POS-61 are given in the table.

It is seen that, as the cobalt content in the alloy is increased, the solderability is improved, and the alloy containing 12% Co surpasses in this paremeter the cadmium coating.

The antifriction properties of the Zn and Zn–6%Co coatings were studied without passivation of the coating on a special unit allowing determination of the friction force at various loads on the couple. The friction coefficient at a load of 50–200 g for Zn and Zn–6% Co is 0.27 and 0.25, i.e., coating with the alloy makes screw joints more readily dismantlable than coating with zinc.

Climatic tests performed in a chamber with a humid (93±3%) atmosphere at 40±2°C for 56 days and in a chamber containing salt aerosol for 7 days [GOST (State Standard) 9.308–85] showed that the corrosion resistance of the coating depended on the cobalt content. Tests in a chamber with humid atmosphere

Solderability of coatings of zinc, cadmium, and zinc–cobalt alloy

Coating	*S*, mm	τ, s
Zn	18.3	6
Cd	170	8
Alloy with Co content, %:		
1	18.5	6
3.5	18.5	2
12	172	2

showed that the coatings containing 3–5% Co with or without passivation well compare with the cadmium coating in the corrosion resistance. The only change observed was the change in the color of the passive film. Tests with salt aerosol showed no corrosion for the passivated alloy coating, whereas without passivation corrosion products were observed as a white deposit. Thus, the passivated coatings of alloy containing 3–5% Co well compare in the corrosion resistance with the cadmium coating.

Based on the results obtained, we suggested the electrolyte composition and process conditions for deposition of alloys containing 1, 3–5, and 9–11% Co. Coatings with different cobalt content can be used under different service conditions. The coating containing up to 1% Co is more corrosion-resistant than the purely zinc coating and can be used as protective and decorative coating instead of zinc coatings. The coating containing 3–5% Co approaches the cadmium coating in corrosion resistance and can be used as protective and decorative coating for items subjected to impact of marine atmosphere. The coating containing 9–11% Co well compares with the cadmium coating in corrosion resistance and can be used as a protective and decorative coating with a low friction coefficient for parts subjected to impact of marine atmosphere.

REFERENCES

1. Yur'ev, B.P. and Ezrokhina, L.M., *Zh. Prikl. Khim.*, 1974, vol. 47, no. 6, p. 1424.
2. Mazur, T.S., Nikiforova, A.F., and Repka, V.V., *Vopr. Khim. Khim. Tekhnol.*, 1973, issue 30.
3. Kirilova, I.V., Karbasov, B.G., and Tikhonov, K.I., Abstracts of Papers, *Teoriya i praktika elektroosazhdeniya metallov i splavov: Zonal'naya konferentsiya* (Theory and Practice of Electrolytic Deposition of Metals and Alloys: Regional Conf.), Penza, 1989, p. 31.
4. Fratesi, R. and Roventi, E., *Mater. Chem. Phys.*, 1989, vol. 23, no. 45, p. 529.
5. Short, N.R., Abibsi, A., and Dennis, J.K., *Galvanotechnik*, 1990, vol. 81, no. 3, p. 834.
6. Shears, A.P., *Trans. Inst. Metal Finish.*, 1989, vol. 67, no. 3, p. 67.
7. Vinogradov, S.N., Mal'tseva, G.N., and Rambergenov, A.K., *Gal'vanotekh. Obrab. Poverkhn.*, 1993, vol. 2, no. 4, p. 37.
8. Kirilova, I.V., Karbasov, B.G., Bodyagina, M.M., and Tikhonov, K.I., in *Teoriya i praktika elektroosazhdeniya metallov i splavov* (Theory and Practice of Electrodeposition of Metals and Alloys), Penza: Penz. Dom Nauchno-Tekh. Propagandy, 1986, p. 58.
9. Vinogradov, S.N., Mal'tseva, G.N., and Nikolaeva, N.P., in *Teoriya i praktika elektroosazhdeniya metallov i splavov* (Theory and Practice of Electrodeposition of Metals and Alloys), Penza: Penz. Dom Nauchno-Tekh. Propagandy, 1986, p. 32.
10. Vinogradov, S.N., Mal'tseva, G.N., and Nikolaeva, N.P., in *Progressivnaya tekhnologiya i voprosy ekologii v gal'vanotekhnike* (Advanced Technology and Environmental Problems in Electroplating), Penza: Penz. Dom Nauchno-Tekh. Propagandy, 1991, p. 6.
11. Panasenko, S.A., Grishchuk, V.I., Oleshchenko, N.N., *et al.*, *Zashch. Met.*, 1990, vol. 26, no. 2, p. 327.
12. Kudryavtsev, N.T., Smirnova, T.G., Tsesarskii, V.M., and Yakovlev, Yu.G., *Zashch. Met.*, 1969, vol. 5, no. 5, p. 577.
13. Lur'e, Yu.Yu., *Spravochnik po analiticheskoi khimii* (Handbook on Analytical Chemistry), Moscow: Khimiya, 1967.

Russian Journal of Applied Chemistry, Vol. 74, No. 3, 2001, pp. 424–426. Translated from Zhurnal Prikladnoi Khimii, Vol. 74, No. 3, 2001, pp. 416–418.

APPLIED ELECTROCHEMISTRY AND CORROSION PROTECTION OF METALS

Deposition of Copper from Dilute Solutions onto Disperse Graphite Cathode

G. M. Zagorovskii, G. P. Prikhod'ko, V. M. Ogenko, and I. G. Sidorenko

Institute of Surface Chemistry, Ukrainian National Academy of Sciences, Kiev, Ukraine

Received March 22, 2000; in final form, June 2000

Abstract—Results obtained in studying copper(II) recovery from sulfate solutions with concentrations less than 1 g l^{-1} in an electrolyzer with disperse graphite cathode are presented.

Closed systems with circulating water supply are environmentally the safest. Technologies of this kind can be used in electroplating, hydrometallurgy, and other industries provided that washing water having the form of low-concentration (< 1 g l^{-1}) solutions of salts of non-ferrous metals is purified by nonchemical methods.

One of promising methods for solving this problem is electrolysis making it possible to obtain metals in the most concentrated state requiring minimum energy expenditure for further processing. However, electrolytic recovery of non-ferrous metals from low-concentration aqueous solutions is hindered by diffusion limitations on the current. This problem can be solved by using bulk-porous flow-through electrodes and, in particular, cathodes made of fibrous carbon materials [1–3].

The effect of carbon fiber splicing by crystals of deposited metal and the resulting deterioration of the electrode characteristics [4] necessitates a search for disperse carbon materials with developed surface, which would enable fabrication of a "pseudofluidized" cathode devoid of this shortcoming.

The present study used thermally expanded graphite as a material of this kind [5].

EXPERIMENTAL

Thermally expanded graphite with a bulk density of 8–10 g l^{-1} was obtained by fast heating of GAK-2 natural graphite intercalated with sulfuric acid in an electric furnace preliminarily heated to 900°C, with $(NH_4)_2S_2O_8$ as oxidizing agent [5].

Voltammograms were taken with a PI-50-1.1 potentiostat in a three-electrode glass cell, with the working electrode polarized at potential sweep rate of 5 mV s^{-1}. As auxiliary electrode served a $40 \times 10 \times$ 3-mm graphite plate. As reference electrode was used saturated silver chloride electrode. The working electrode was fabricated from compacted thermally expanded graphite by pressing the disperse material in a glass tube with inner diameter of 3 mm, placed in a cell filled with electrolyte. The role of the working surface was played by the lower edge of the obtained graphite rod, and that of a current lead, by a copper wire pressed into graphite.

The disperse working electrode was fabricated by pouring 10 mg of thermally expanded graphite in a glass tube 3 mm in diameter, placed in a cell filled with electrolyte. A copper current lead 2.5 mm in diameter was dipped into the tube to such a depth that the lower edge of the column of thermally expanded graphite was level with the edge of the glass tube.

As supporting electrolyte was used 0.01 N sodium sulfate solution.

Copper(II) was deposited from solution in a flow-through electrolyzer made of a glass tube 30 mm in diameter and 150 mm long, with a disperse cathode in its upper part. As current lead served a nickel foil circle 29.5 mm in diameter and a Nichrome wire. The electrolyte flow was effected through a clearance between the edge of the nickel circle and the electrolyzer wall. As anode was used graphite rod 6 mm in diameter, placed in a glass tube to prevent its coming in contact with cathode particles.

The electrolyte was pumped through using an RR1-05 peristaltic pump providing solution flow rate in the range from 0.1 to 200 ml min^{-1}. The pumping rate was chosen so that the quantity of electricity passed through a given solution volume (at a current

1070-4272/01/7403-0424$25.00

established at voltage of 35 V across the electrolyzer terminals) was sufficient for recovery of the entire amount of copper contained in the solution. The electrolyzer was connected to a B5-49 dc stabilized power supply. The current strength was monitored with an Shch-4300 multimeter.

The content of copper(II) in solution was determined by the method described in [6] with a KFK-2MP photoelectric concentration colorimeter.

The solutions were prepared from analytically pure grade chemicals.

Because of the specific character of the preparation technology, thermally expanded graphite contains a residual amount of the intercalating agent (sulfuric acid) in its crystal lattice and various oxygen-containing groups (lactone, quinone, etc.) on its surface [5]. Therefore, cathodic polarization of electrodes made of thermally expanded graphite is accompanied by deintercalation and reduction of oxygen-containing groups.

The fact that the concentration of reducible oxygen-containing groups on the working surface of the electrode will decrease with increasing time of cathodic polarization can account for the decrease in current in electrode cycling. This made necessary a study of the time dependence of the polarization current. For this purpose, the electrode was polarized for 5 min in the supporting electrolyte in the potentiostatic mode at a potential of 1 V, and after that a voltammogram was taken. Then the procedure was repeated. The obtained voltammograms are shown in Fig. 1.

Upon cathodic polarization of a compacted electrode for 30 min the current ceases to change. Therefore, all further studies were performed on electrodes subjected to preliminary polarization in a supporting electrolyte for 30 min.

Introduction of Cu(II) ions into the solution changes the shape of the polarization curves, and, at a copper(II) content in solution of 20 mg l^{-1}, the process of copper deposition on thermally expanded graphite becomes predominant. The polarization curves show portions of limiting currents depending on the concentration of the depolarizing agent (Fig. 2).

The results of polarization studies on an electrode made of compacted thermally expanded graphite indicate that hydrogen starts to evolve on reaching a potential of –1.3 V, which enables this material to be used in recovery of non-ferrous metals from aqueous solutions.

The same phenomena are observed on a disperse electrode made of thermally expanded graphite

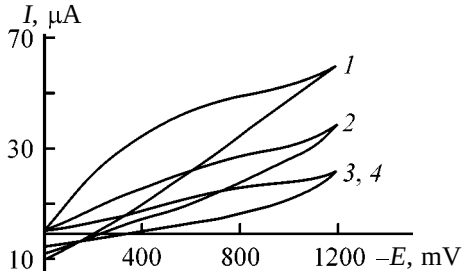

Fig. 1. Voltammograms of an electrode made of compacted thermally expanded graphite, taken in the supporting electrolyte. (*I*) Current and (*E*) potential; the same for Fig. 2. (*1*) Without preliminary polarization; after polarization for (*2*) 10, (*3*) 30, and (*4*) 40 min.

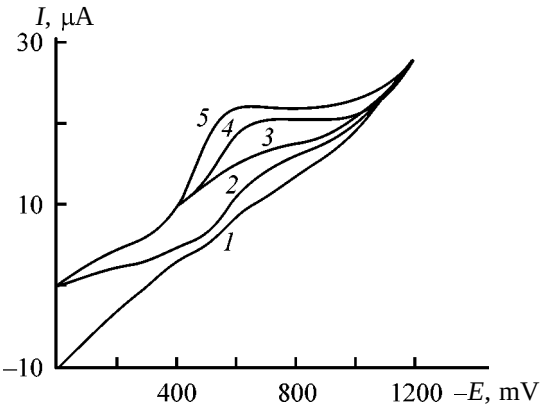

Fig. 2. Cyclic voltammograms of a compacted electrode, taken in solutions with varied copper(II) content. Copper(II) content (mg l^{-1}): (*2*) 5, (*3*) 10, (*4*) 20, and (*5*) 50; (*1*) curve taken with reverse potential sweep for (*2*–*5*).

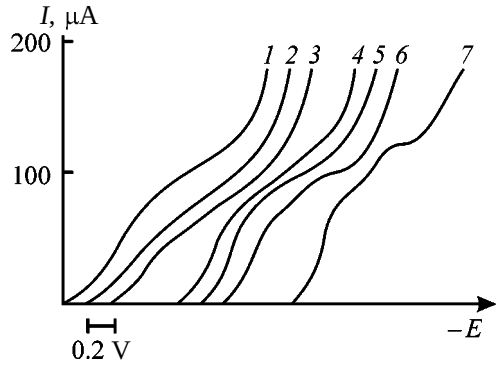

Fig. 3. Polarization characteristics of a disperse electrode in solutions with varied copper(II) content. (*I*) Current and (*E*) voltage. Copper(II) content (mg l^{-1}): (*1*) 0, (*2*) 0.1, (*3*) 0.2, (*4*) 0.5, (*5*) 1.0, (*6*) 2.0, and (*7*) 5.0.

(Fig. 3), but the currents are an order of magnitude higher than those in the case of compacted electrodes and limiting currents of copper deposition start to be observed at a copper content in solution of 2 mg l^{-1}. The cathode current density is as high as 0.15 A dm^{-2},

Current efficiency CE by copper at varied copper content in solution

Run no.	I, mA	C_{in}	C_{out}	Degree of copper recovery, %	CE %
		mg l^{-1}			
1	4.0	1	0.08	92.0	2.5
2	2.0	1	0.4	60.1	5.3
3	2.2	5	0.6	88.4	9.5
4	2.5	10	0.1	99.0	15.6
5	2.8	20	0.3	98.5	17.2
6	3.5	50	0.2	99.5	29.8
7	3.7	100	0.5	99.5	37.2
8	4.0	200	0.7	99.6	44.5
9	6.0	500	0.6	99.8	50.0

calculated per visible working surface area of the electrode, which is quite acceptable for performing electrolysis with sufficient intensity.

Owing to the occurrence of side processes at the cathode made of thermally expanded graphite, the current efficiency by the metal will not reach 100%, which is confirmed by the results of electrolysis, presented in the table.

As would be expected, the current efficiency by the metal steadily grows with increasing copper(II) concentration in solution.

Comparison of the results of run nos. 1 and 2 shows that aqueous solutions can be purified to remove copper ions to residual concentrations corresponding to the maximum permissible concentration in an electrolyzer with disperse cathode made of thermally expanded graphite at higher power consumption.

CONCLUSION

The possibility is demonstrated of copper recovery from dilute aqueous solutions in electrolyzers with disperse cathode made of thermally expanded graphite. Electrolyzers of this kind can be employed in straight-flow water consumption schemes, although their use in circulation schemes is preferable.

REFERENCES

1. Varentsov, V.K., in *Intensifikatsiya elektrokhimicheskikh protsessov: Sbornik nauchnykh trudov Inst. elektrokhimii Akad. Nauk SSSR* (Intensification of Electrochemical Processes: Coll. of Scientific Works of Inst. of Electrochemistry, USSR Acad. Sci.), Tomilov, A.P., Executive Ed., Moscow: Nauka, 1988, pp. 94–118.
2. Varentsov, V.K. and Varentsova, V.I., *Elektrokhimiya*, 1995, vol. 31, no. 3, pp. 304–306.
3. Varentsov, V.K. and Varentsova, V.I., *Zh. Prikl. Khim.*, 1997, vol. 70, no. 1, pp. 83–86.
4. Varentsov, V.K. and Yudkina, A.A., *Sovremennye khimicheskie i gal'vanicheskie protsessy v proizvodstve pechatnykh plat: Materialy nauchno-tekhnicheskogo seminara obshchestva "Znanie" RSFSR* (Proc. of Scientific and Technical Workshop of Znanie Society, RSFSR, on Modern Chemical and Electroplating Processes in Printed Circuit Board Production), Leningrad: Leningr. Dom Nauchno-Tekh. Propagandy, 1991, pp. 68–70.
5. Chernysh, I.G., Karpov, I.I., Prikhod'ko, G.P., and Shai, V.M., *Fiziko-khimicheskie svoistva grafita i ego soedinenii* (Physicochemical Properties of Graphite and Its Compounds), Kiev: Naukova Dumka, 1990.
6. Lur'e, Yu.Yu., *Analiticheskaya khimiya promyshlennykh stochnykh vod* (Analytical Chemistry of Industrial Wastewater), Moscow: Khimiya, 1984.

Russian Journal of Applied Chemistry, Vol. 74, No. 3, 2001, pp. 427–429. Translated from Zhurnal Prikladnoi Khimii, Vol. 74, No. 3, 2001, pp. 419–421.

APPLIED ELECTROCHEMISTRY AND CORROSION PROTECTION OF METALS

Effect of Lead(II) Complexation on Solubility of β-PbO in Alkaline Solutions in the Presence of Certain Alcohols

V. P. Yurkinskii, N. V. Sokolova, and V. A. Popov

St. Petersburg State Technical University, St. Petersburg, Russia

Received September 9, 1999; in final form, November 2000

Abstract—Complex formation of lead(II) was studied, and the solubility of β-PbO was determined by potentiometric titration in solutions containing sodium hydroxide (0.3–4 M) and a series of mono- and polyhydric alcohols. A correlation between the lead monoxide solubility and Pb(II) complex formation function was considered.

The major fraction of the secondary lead raw material is lead(II) oxide. Its processing involves treatment with alkaline solutions in which fairly high solubility of PbO is caused by formation of strong Pb(II) hydroxo complexes [1–3]. To increase the PbO solubility, it is suggested to add alcohols (e.g., glycerol [1]) into the alkaline solution.

In this work, the solubility of β-PbO in alkaline solutions containing additives of mono- and polyhydric alcohols (1-propanol, ethanol, ethylene glycol, glycerol, and sorbitol) was determined. Simultaneously, complex formation of Pb^{2+} ions in these solutions was studied to determine the correlation between the PbO solubility and the lead(II) complex formation function.

To determine the complex formation function, we used potentiometric titration [2, 3].

It is known that in alkaline solutions Pb^{2+} ions form strong complexes, mainly $Pb(OH)_3^-$ [2].

To determine the composition of lead(II) hydroxo-alcoholic complexes, we used a method developed by us previously for studying complex formation of Pb(II) in alkaline solutions with glycerol [3]. The average ligand number n in the complex was determined as a slope of the linear dependence of the indicating lead amalgam electrode on the logarithm of the ligand (hydroxide ion, alcohol) concentration [3]. The calculated $\bar{n}_{OH^-}$ and $\bar{n}_{alc}$ are listed in the table.

As seen, $\bar{n}_{OH^-}$ is close to 3 for all alcohols, similarly to glycerol [3]. Hence, complexes $Pb(OH)_3^-$ prevail in the solution [2]. The n_{alc} value shows that the Pb(II)-to-alcohol ratio is 1 : 1 for sorbitol and 2 : 1 for the other alcohols.

Thus, the composition of the prevailing complexes in the solution can be presented by the formula $[Pb(OH)_3 \cdot C_6H_8(OH)_6]^-$ for sorbitol and $[2Pb(OH)_3 \cdot$ alcohol molecule$]^{2-}$ for the other alcohols.

Using the known equation [4]

$$\Delta E = \frac{RT}{zF} \ln \frac{C^0_{Pb^{2+}}}{[Pb^{2+}]} = \frac{RT}{zF} \ln \Phi,$$

where ΔE is the experimental difference between potentials of the indicating electrode in the initial solution and in the solution containing sodium hydroxide, we calculated the complex formation function Φ as influenced by the hydroxide ion concentration for all the solutions studied.

Then, the functions Φ were obtained for solutions with fixed $[OH^-]$ and variable concentrations of alcohols. In Fig. 1, these dependences are shown for $[OH^-] = 0.3$ M. For the other sodium hydroxide concentrations such dependences are similar.

The presence of 1-propanol or ethanol in alkaline solutions changes the lead(II) complex formation function weakly (by no more than 10%). As for ethyl-

Average number of ligands in lead(II) complexes

Alcohol	$\bar{n}_{OH^-}$	$\bar{n}_{alc}$
–	2.96 ± 0.05	–
1-Propanol	2.7 ± 0.1	0.5 ± 0.1
Ethanol	2.7 ± 0.1	0.5 ± 0.1
Ethylene glycol	2.8 ± 0.1	0.5 ± 0.1
Sorbitol	3.0 ± 0.1	1.0 ± 0.1

1070-4272/01/7403-0427$25.00

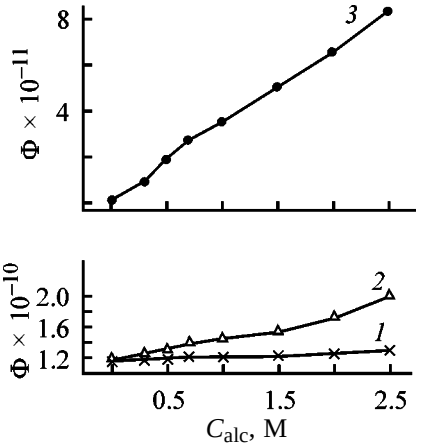

Fig. 1. Complexation function Φ as influenced by the alcohol concentration C_{alc} in 0.3 M NaOH. Alcohol: (*1*) 1-propanol, (*2*) ethylene glycol, and (*3*) sorbitol.

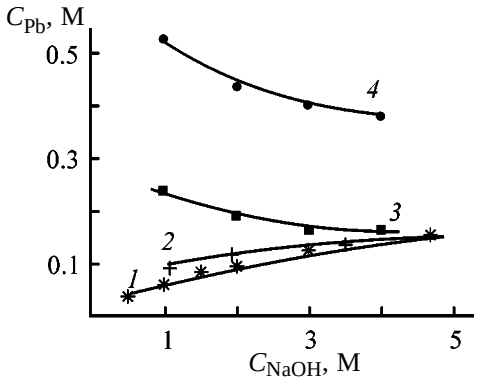

Fig. 2. β-PbO solubility C_{Pb} as a function of sodium hydroxide concentration C_{NaOH} at C_{alc} = 0.5 M. Alcohol: (*1*, *2*) none {(*2*) data of [8]}, (*3*) glycerol, and (*4*) sorbitol.

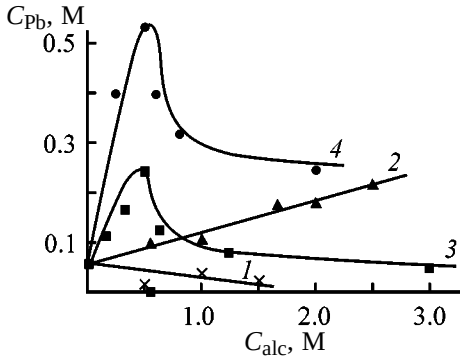

Fig. 3. β-PbO solubility C_{Pb} as a function of the alcohol concentration C_{alc} in 1 M NaOH. Alcohol: (*1*) 1-propanol, (*2*) ethylene glycol, (*3*) glycerol, and (*4*) sorbitol.

ene glycol or sorbitol, Φ increases practically linearly with the alcohol concentration (Fig. 1). The Φ values exceeded those for alcohol-free solutions maximally by about 70% for ethylene glycol and by a factor of 70 for sorbitol. It was shown in [3] that glycerol addition increases F maximally by a factor of 4.5.

Spectroscopic study of Pb(II) complex formation with ethylene glycol, glycerol, and xylitol [5] showed that these alcohols are active ligands and form 1 : 1 complexes with lead(II). Participation of hydroxide ions in complex formation and the Pb-to-OH^- ratio in the complexes were not considered in that work.

The solubility of β-PbO in the solutions studied was determined as follows. Solutions were stored for a long time in a thermostat at 298 ± 0.1 K contacting with the solid phase at intermittent agitation. The lead content in the solution was determined complexometrically [6]. The equilibrium was thought to be reached when in two successive measurements at a 7-day interval the lead concentration changed by no more than 1%. On the average, the equilibrium was reached in 30 days. After determination of the equilibrium lead(II) concentration, the potential of the indicating lead electrode was measured to calculate the lead(II) complexation function Φ.

The solubility of β-PbO in alcohol-free solutions was studied within the 0.5–4.7 M NaOH concentration range and in solutions containing one of the above alcohols with its concentration varied from 0.06 to 3.0 M and NaOH concentration varied from 1.0 to 4.0 M (Figs. 2, 3).

Earlier, the PbO solubility in the PbO–NaOH–H_2O system was studied in [7, 8] (in [8], at 298 K). For comparison, the data of [8] are presented in Fig. 2.

In solutions free of organic additives, the PbO solubility increases with the NaOH concentration. The results reasonably agree with data of [8]. In solutions containing glycerol and sorbitol, the PbO solubility weakly decreases with increasing alkali concentration; the optimal alkali concentration is about 1.0 M.

Curves in Fig. 3 show that the PbO solubility in 1.0 M NaOH initially increases with increasing concentration of glycerol or sorbitol, passes through a maximum at C_{alc} 0.5 M, and then noticeably decreases. For ethylene glycol, the solubility increases monotonically with increasing alcohol concentration.

Visual observation showed that the decrease of the PbO solubility in the solutions containing glycerol and sorbitol at C_{alc} > 0.5 M is caused by the change of the solid phase composition: Dense yellow β-PbO precipitate converts into voluminous white precipitate (its composition was not determined). In solution containing 2.5 M ethylene glycol, the PbO solubility is 3.7 times greater as compared to the solution containing no alcohol. In such solutions, the β-PbO phase is

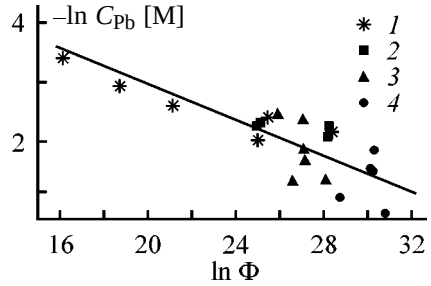

Fig. 4. β-PbO solubility C_{Pb} as influenced by complexation function Φ. Alcohol: (*1*) none, (*2*) glycerol, (*3*) ethylene glycol, and (*4*) sorbitol.

stable for all ethylene glycol concentrations studied. Propanol does not noticeably affect the PbO solubility.

In Fig. 4, the correlation between the PbO solubility and Pb(II) complex formation function is shown for all solutions studied. As seen, within the experimental error this correlation is linear in $\ln C_{Pb}$–$\ln \Phi$ coordinates. Hence, in the systems under consideration the PbO solubility is determined by Pb(II) complex formation, with both hydroxide ions and alcohols acting as ligands.

CONCLUSIONS

(1) In the β-PbO–NaOH–H_2O–alcohol systems studied, the hydroxo–alcoholic complexes of Pb(II) are formed.

(2) The β-PbO solubility in the above systems depends on the Pb(II) complexation.

(3) The optimal concentrations of sodium hydroxide (1.0 M) and alcohols were determined in solutions intended for β-PbO dissolution.

REFERENCES

1. Morachevskii, A.G., Vaisgant, Z.I., and Demidov, A.I., *Pererabotka vtorichnogo svintsovogo syr'ya* (Processing of the Secondary Lead Raw Material), St. Petersburg: Khimiya, 1993.
2. Yurkinskii, V.P. and Sokolova, N.V., *Zh. Prikl. Khim.*, 1999, vol. 72, no. 10, pp. 1592–1595.
3. Yurkinskii, V.P. and Sokolova, N.V., *Zh. Prikl. Khim.*, 1999, vol. 72, no. 11, pp. 1917–1919.
4. Kravtsov, V.I., *Ravnovesie i kinetika elektrodnykh reaktsii kompleksov metallov* (Equilibrium and Kinetics of Electrode Reactions of Metal Complexes), Leningrad: Khimiya, 1985.
5. Baiborodov, P.P., *Zh. Prikl. Khim.*, 1975, vol. 48, no. 12, pp. 2690–2693.
6. Přibil, R., *Komplexony v chemické analyse*, Prague: Československ. Akad. Ved, 1957.
7. Sokolova, E.I. and Chizhikov, D.M., *Zh. Neorg. Khim.*, 1957, vol. 2, no. 7, pp. 1662–1666.
8. Bruile, E.S. and Dombrovskaya, N.S., *Zh. Neorg. Khim.*, 1959, vol. 4, no. 9, pp. 2091–2099.

Russian Journal of Applied Chemistry, Vol. 74, No. 3, 2001, pp. 430–433. Translated from Zhurnal Prikladnoi Khimii, Vol. 74, No. 3, 2001, pp. 422–424.

APPLIED ELECTROCHEMISTRY AND CORROSION PROTECTION OF METALS

Role of Heterophase Interactions between Cadmium and Nickel in Cadmium Electrode Activation

I. A. Kazarinov, M. M. Burashnikova, and A. N. Stepanov

Chernyshevskii State University, Saratov, Russia

Received February 23, 1999; in final form, July 1999

Abstract—The structural and electrochemical characteristics of cadmium electrodes with nickel introduced in metallic state into the active material of the electrode by electroless plating were studied. The specific role played by heterophase interactions between nickel and cadmium in the mechanism of cadmium electrode activation was substantiated experimentally.

The key role in the mechanism of the activating action exerted by nickel on the operation of a cadmium electrode is played by the interaction of cadmium and nickel metallic phases in charged state [1, 2], resulting in the formation of nonequilibrium solid solutions of nickel in cadmium in the course of cycling. This system being unstable, it decomposes under certain electrode operation conditions into more stable phases, in particular, into an intermetallic compound (IMC) of cadmium and nickel, $Cd_{21}Ni_5$ [3–5].

Analysis of the whole body of experimental data and theoretical concepts concerning the activating effect of nickel suggests that the "concept of nonequilibrium solid solution" as the sole reason for the formation of a highly dispersed state of the charged cadmium electrode is of limited value. For example, it follows from the experimental data [4] that the dispersity of the active material of a charged cadmium electrode grows by an order of magnitude in the presence of nickel(II), which points to a rather strong interatomic interaction between cadmium and nickel to give covalent or mixed covalent-ionic type of bonding [6]. At the same time, data on the saturated vapor pressure of cadmium over cadmium–nickel melts indicate the absence of noticeable departures from the Raoult law for the cadmium vapor [7], suggesting a weak interatomic interaction between the components. The same is indicated by the Gibbs energy of $Cd_{21}Ni_4$ IMC formation ($\Delta G_f^0 \approx -1$ kJ mol^{-1} [8]), by the type of crystal lattice (γ-brass) [9, 10] characterized by metallic bonding between the atoms [6], and by close electronegativities of the metals (1.7 for cadmium and 1.8 for nickel) [11]. Consequently, the mechanism of the high dispersing action of nickel on the charged state of the cadmium electrode cannot be accounted for only in terms of the interatomic interaction of cadmium and nickel in the formation of solid solutions.

With account of the fact that, according to chemical phase analysis, the amount of reduced nickel in the cadmium electrode may be as high as 1–6 wt % [12], the following conclusion is justified: Under equilibrium conditions, metallic nickel exists in charged cadmium electrodes in two forms: as a highly diluted solid solution in cadmium and as an intrinsic finely crystalline phase, which is X-ray amorphous [13]. The lack of a consistent concept of the dispersing action of metallic nickel on the charged state of a cadmium electrode is, in the authors' opinion, due to the misjudgment of the role played by the heterophase interaction between metallic nickel and cadmium, despite the apparent probability of the predominant existence of nickel as an independent phase in ultramicrodispersed state.

The present study is devoted to an experimental substantiation of the important role played by heterophase interactions between nickel and cadmium in the activation of the cadmium electrode. A direct proof of the possibility of a heterophase interaction between nickel and cadmium could be furnished by high structural and electrochemical characteristics of cadmium electrodes with metallic nickel introduced in the active material. However, a complicated problem of achieving high dispersity and uniformity of nickel distribution in the active material is to be solved in this case. Such a dispersity of mixture components can be achieved either through occurrence of chemical processes in the solution bulk [e.g., by coprecipitation of cadmium and nickel(II) hydroxides] or by depositing nickel onto the surface of the disperse phase.

1070-4272/01/7403-0430$25.00

Introduction of highly dispersed nickel by electroless plating onto cadmium oxide in hypophosphite nickel-plating solutions was found to be a promising method [14, 15]. In [15], the possibility was demonstrated of obtaining a highly dispersed metallic phase with grain size on the order of 0.01 μm, depending on the solution composition and thermolysis regime.

EXPERIMENTAL

To solve the problem at hand, we studied the structural and electrochemical characteristics of cadmium electrodes made of cadmium oxide treated under special conditions with hypophosphite-based electroless nickel plating solution. The cadmium electrodes were fabricated by the technology of porous metallic cadmium electrodes with 1 wt % polyvinyl alcohol introduced as a binder in the form of an aqueous suspension [16]. The cadmium electrodes under study differed in the method of introduction of the nickel additive and in its amount and had the following composition: electrode 1 (control), cadmium oxide and 3 wt % Ni/Cd in the form of coprecipitated nickel and cadmium hydroxides; electrode 2, cadmium oxide treated with blank electroless nickel plating solution containing no nickel(II) ions; electrodes 3–7, cadmium oxide treated with electroless nickel plating solution containing 0.8, 1.4, 2.4, 4.1, and 7.0 wt % Ni/Cd, respectively.

Figure 1 shows the coefficient of cadmium utilization, K_u, in the electrodes under study in cycling in an 8.1 M KOH solution (i_{disch} = 0.01 A cm^{-2}, i_{ch} = 0.005 A cm^{-2}). The electrodes with addition of metallic nickel (Fig. 1, curve *2*) introduced by electroless nickel plating onto cadmium oxide show higher K_u values [75–80% against 68% for the control (curve *1*)].

Eliminating nickel from electroless plating solutions (curve *3*) leads to a dramatic decrease in K_u from 64% in the first cycle to 35% in the seventh. This result, which is in good agreement with the behavior of cadmium electrodes without activating additives [12], indicates that the other components of the electroless nickel plating solution exert neither positive nor negative influence on how the high-activity state of the cadmium electrode is formed.

The introduction of metallic nickel into the active material of the cadmium electrode by the method of electroless nickel plating also leads to a pronounced increase in the specific surface area of the cadmium electrodes, determined by the pulsed potentiostatic method [17] (Fig. 2): with the nickel content increasing from 0.8 to 7.0 wt % Ni/Cd, the specific surface area changes from 8.8 to 27 m^2 g^{-1}. The most pronounced increase in the specific surface area of the electrodes is observed on raising the concentration of nickel to 2–3 wt % Ni/Cd.

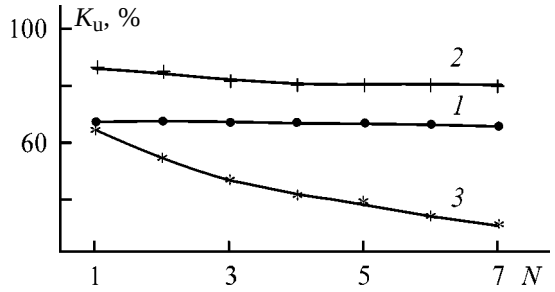

Fig. 1. Variation of K_u of cadmium in porous cadmium electrodes in the course of cycling. (*N*) Cycle number. Method of nickel compound introduction: (*1*) coprecipitation of $Ni(OH)_2$ + $Cd(OH)_2$ (3 wt % Ni/Cd) and (*2*) electroless nickel plating; and (*3*) no nickel additive.

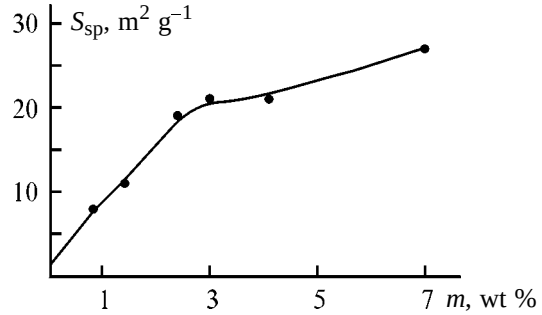

Fig. 2. S_{sp} of charged cadmium electrode vs. the nickel content m in its active material produced by electroless nickel plating of cadmium oxide.

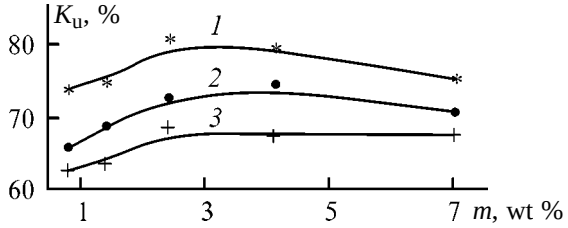

Fig. 3. K_u of cadmium in the active material of cadmium electrodes vs. its nickel content m at different discharge current densities. i_{disch} (A cm^{-2}): (*1*) 0.005, (*2*) 0.0135, and (*3*) 0.027.

The dependence of K_u on the nickel content in the active material shows a maximum at 2–4 wt % Ni/Cd (Fig. 3).

The presented structural and electrochemical characteristics of cadmium electrodes fabricated from cadmium oxide subjected to electroless nickel plating point to the high activating effect of metallic nickel

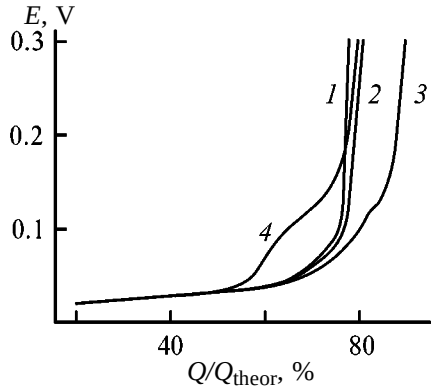

Fig. 4. Discharge curves for porous cadmium electrodes (fabricated from cadmium oxide subjected to electroless nickel plating and containing varied amount of nickel) in an 8.1 M KOH solution in the second cycle (i_{disch} = 0.01 A cm^{-2}). (*E*) Potential and (Q/Q_{theor}) discharge capacity normalized to the theoretical electrode capacity. Nickel content (wt %): (*1*) 0.82, (*2*) 1.4, (*3*) 4.1, and (*4*) 7.0.

introduced into the cadmium electrode as an independent phase in a highly dispersed state.

Figure 4 presents discharge curves for cadmium electrodes 3, 4, 6, and 7 in the second forming cycle (with the electrode potentials measured relative to a reversible cadmium electrode in the same alkali solution). With the nickel content of cadmium oxide increasing to 4 wt % Ni/Cd, a second potential delay appears in the discharge curves of the cadmium electrodes at polarizations of 120–140 mV. This delay is associated with the formation in the course of electrode charging of the $Cd_{21}Ni_5$ intermetallic phase [3–5].

The formation of the $Cd_{21}Ni_5$ IMC already in charging of the cadmium electrode can only be accounted for by the occurrence of interphase interaction of nickel with cadmium formed in the course of charging.

In [18, 19], the possibility of occurrence of solid-state diffusion processes with a sufficiently high rate at temperatures lower than the melting points of the systems in ultradispersed state (0.01–0.10 μm) was substantiated theoretically and confirmed experimentally. Phenomena of this kind are characteristic of some diffusion pairs with strongly different interdiffusion coefficients of the components [20–22]. A certain contribution to the mechanism of development of mechanical strain in the diffusion zone may come from the difference in density between the starting components and the phase formed in the diffusion zone. The initial introduction of nickel in the form of an individual highly dispersed metallic phase enabled a heterophase interaction between cadmium and nickel already in the first forming cycles.

CONCLUSION

The heterophase interaction of cadmium and nickel in the active material of charged electrodes, resulting in the formation of $Cd_{21}Ni_5$ IMC, accounts for the particularly strong activating effect of the nickel additive on the charged state of the cadmium electrode. The mechanism of this activating effect can be understood as follows: heterodiffusion in the cadmium–nickel binary system gives rise to mechanical stresses in the boundary region of the interphase contact with the subsequent relaxation through formation of micropores and cracks on the surface of active material grains.

REFERENCES

1. Reshetov, V.A., Pen'kova, L.I., and L'vova, L.A., *Khimicheskie istochniki toka* (Chemical Power Sources), Novocherkassk: Novocherkassk. Politekh. Inst., 1981, pp. 26–33.
2. Reshetov, V.A., L'vova, L.A., and Baranov, A.P., Abstracts of Papers, *II Vsesoyuznaya nauchnaya konferentsiya "Elektrokhimicheskaya energetika"* (II All-Union Scientific Conf. "Electrochemical Power Engineering"). Moscow: Mosk. Energ. Inst., 1984, p. 96.
3. Kazarinov, I.A., Reshetov, V.A., L'vova, L.A., and Ryabskaya, I.A., in *Issledovaniya v oblasti khimicheskikh istochnikov toka* (Research in the Field of Chemical Power Sources), Saratov: Saratov. Gos. Univ., 1977, issue 5, pp. 39–49.
4. Reshetov, V.A., Grachev, D.K., L'vova, L.A., *et al.*, in *Issledovaniya v oblasti khimicheskikh istochnikov toka* (Research in the Field of Chemical Power Sources), Saratov: Saratov. Gos. Univ., 1979, issue 6, pp. 17–25.
5. Reshetov, V.A., Grachev, D.K., Pen'kova, L.I., *et al.*, *Zh. Prikl. Khim.*, 1979, vol. 52, no. 3, pp. 586–589.
6. *Intermetallic Compounds*, Westbrook, J.H., Ed., New York: Wiley, 1967.
7. Critchley, J.K. and Jeffery, J.W., *J. Appl. Crystallogr.*, 1969, no. 2, pp. 273.
8. Terent'ev, N.K., Investigations in Technology of Metal–Ceramic Cadmium Electrode in Nickel–Cadmium Batteries, *Cand. Sci. Dissertation*, Leningrad, 1975.
9. Lihl, F., *Z. Metallkunde*, 1955, vol. 46, no. 1, pp. 434–437.
10. Lott, R.J. and Critchley, J.K., *Nature*, 1963, vol. 200, no. 4908, p. 773.

11. Bokii, G.B., *Kristallokhimiya* (Crystal Chemistry), Moscow: Nauka, 1971.
12. Reshetov, V.A., Kazarinov, V.A., and L'vova, L.A., in *Issledovaniya v oblasti prikladnoi elektrokhimii* (Research in the Field of Applied Electrochemistry), Saratov: Saratov. Gos. Univ., 1989, pp. 18–26.
13. Sivakumar, R. and Char, T.L. Rama, *Electrodep. Surface Treat.*, 1973, vol. 1, no. 3, pp. 227–237.
14. Gorbunova, K.M., Nikiforova, A.A., and Sadakov, G.A., *Itogi Nauki, Ser.: Elektrokhimiya*, 1966, pp. 5–55.
15. Walker, G.A. and Goldsmith, C.C., *Thin Solid Films*, 1978, vol. 53, no. 2, pp. 217–222.
16. Anan'ev, L.G., Volynskii, V.A., and Kosholkin, V.N., Abstracts of Papers, *7-ya Vsesoyuznaya konferentsiya po elektrokhimii* (7th All-Union Conf. on Electrochemistry), Chernovtsy, October 10–14, 1988, vol. 1, pp. 116–117.
17. USSR Inventor's Certificate no. 935 778.
18. Belluffi, R.W. and Cahn, I.W., *Acta Met.*, 1981, vol. 29, no. 3, pp. 493–500.
19. Novikov, V.I., Trusov, L.I., Lapovak, V.N., and Geleichivit, T.P., *Fiz. Tverd. Tela*, 1983, vol. 25, no. 12, pp. 3696–3698.
20. Shewmon, P.G., *Diffusion in Solids*, New York: McGraw-Hill, 1963.
21. Bokshtein, B.S., Bokshtein, S.Z., and Zhukhovitskii, A.A., *Termodinamika i kinetika diffuzii v tverdykh telakh* (Thermodynamics and Kinetics of Diffusion in Solids), Moscow: Metallurgiya, 1974.
22. Geguzin, Ya.E., *Diffuzionnaya zona* (Diffusion Zone), Moscow: Nauka, 1979.

Russian Journal of Applied Chemistry, Vol. 74, No. 3, 2001, pp. 434–439. Translated from Zhurnal Prikladnoi Khimii, Vol. 74, No. 3, 2001, pp. 425–430.

ENVIRONMENTAL PROBLEMS OF CHEMISTRY AND TECHNOLOGY

Nanocrystalline Metal Oxides as Promising Materials for Gas Sensors for Hydrogen Sulfide

M. N. Rumyantseva, M. N. Bulova, T. A. Kuznetsova, L. I. Ryabova, A. M. Gas'kov, G. Loucaseau, and M. Labeau

Lomonosov State University, Moscow, Russia
National Polytechnic Institute of Grenoble, France

Received November 17, 1999; in final form, February 2000

Abstract—Results of investigations aimed at creating a material possessing selective sensitivity to gaseous hydrogen sulfide are presented. Polycrystalline films of doped tin dioxide were obtained by pyrolysis of an aerosol of appropriate organometallic compounds. The effect of copper and nickel oxides on the electrical properties, actual structure, and composition of polycrystalline tin dioxide films was studied. The influence of trace amounts of gaseous H_2S on the electrical conductivity of the films was analyzed in detail.

The problem of determining trace amounts of hydrogen sulfide in the atmosphere is of particular interest for environment protection in large cities, at chemical centers, and at oil and gas fields. The high toxicity of hydrogen sulfide and the presence, together with H_2S, of appreciable amounts of hydrogen, hydrocarbons, and other noxious gases in natural gas additionally complicate detection of hydrogen sulfide. In this connection, a search for materials that could be used in gas sensors for hydrogen sulfide is aimed at achieving their high sensitivity and selectivity [1–4].

Tin dioxide films are widely used in resistive chemical sensors, which are of particular interest because of their high sensitivity, simple design, and low cost [5, 6]. The principle of operation of such sensors is based on the dependence of the electrical conductivity of the material on the content of trace amounts of reducing or oxidizing gases in the ambient atmosphere. The change in the electrical conductivity of polycrystalline films can, as a rule, be accounted for by the interaction at the surface of SnO_2 grains between chemisorbed O_2^- ions and molecules adsorbed from the gas phase. Such interactions result in that the electron concentration in the conduction band of tin dioxide increases or decreases. The sensor characteristics of the material: sensitivity, response time, selectivity, and stability, are determined by a number of factors, of which the most important are the microstructure of the films, their thickness, departures from stoichiometry, and the type and concentration of dopants. In the present study, it is proposed to improve the sensitivity to hydrogen sulfide by using a heterogeneous nanocrystalline system composed of two oxides, one of which is chemically stable and provides for the semiconducting properties of the material, and the other enters into selective reaction with a gas being analyzed (Fig. 1).

The oxides were chosen on the basis of criteria among which of fundamental importance is the possibility of reversible chemical reaction with the system upon a change in the composition of the ambient atmosphere. Thermodynamic estimates of reactions in heterogeneous systems including solid oxides, metal sulfides, and gaseous hydrogen sulfide and air demonstrated that in the range 100–500°C nickel and copper oxides form sulfides in the presence of trace amounts of hydrogen sulfide in air, whereas tin dioxide remains a stable phase. Such compositional changes are reversible and may strongly affect the

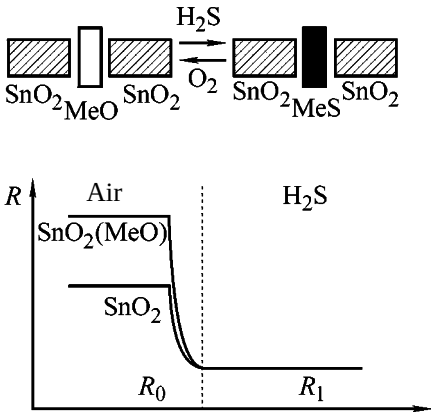

Fig. 1. Model of a heterogeneous nanocrystalline system.

1070-4272/01/7403-0434$25.00

electrical properties of the system, since copper and nickel oxides are *p*-type wide-band-gap semiconductors and sulfides of these metals are characterized by metallic conduction. The possibility of using SnO_2(CuO) for detecting trace amounts of hydrogen sulfide was first demonstrated in [7]. The increase in the sensitivity of tin dioxide samples to H_2S in the concentration range 50–1200 ppm upon doping with copper oxide was confirmed in later studies [8, 9]. However, the main effort has gone into achieving high sensor parameters, whereas the mechanism by which the system reacts with hydrogen sulfide has not been studied in detail and the role played by copper ions in sensor signal formation has not been revealed.

EXPERIMENTAL

Synthesis of polycrystalline SnO_2(CuO) and SnO_2(NiO) films by aerosol pyrolysis was described in detail in [9–11]. The film thickness was determined on cross sections with a Jeol JSM-35 scanning electron microscope. The phase composition and microstructure of the films were studied by means of X-ray diffraction analysis on a Siemens Cristalloflex instrument with CuK_α radiation.

The content of copper and nickel in the films was determined using local X-ray fluorescence analysis (Cameca-SX50). The analysis was made at four electron energies of 8, 12, 16, and 20 kV, with average intensity ratio of sample and reference lines calculated for each energy for the lines SiK_α, SnL_α, CuK_α, NiK_α, and OK_α. The obtained results were processed using SAMx-Strata special-purpose software for thin films and multilayer objects. The film composition was calculated in terms of the Pouchou–Pichoir model [12] for an SnO_2(MO)/SiO_2/Si(substrate) two-layer structure.

The surface composition of the films was determined and layer-by-layer composition analysis across the film thickness was made by Auger electron spectroscopy (AES) on a Jeol Jump IO-CCS instrument. Local analysis was done at 6–8 points, with spectra recorded in differential form in the energy range 50–1000 eV and intensities of the following Auger transitions used in the analysis: Sn (432 eV), O (510 eV), C (272 eV), Ni (848 eV), and Cu (924 eV).

The electrical resistance of the films was measured in the temperature range 77–523 K in the stabilized voltage mode at U = 1 V. The change in the circuit current, proportional to the conductivity of the films under study, was recorded. The distance between the current leads was 5 mm, and the film width was 4 mm.

The interaction of the obtained films with various gas mixtures was studied in an automated cell allowing control over the gas phase composition and temperature. The measurement scheme was described in detail in [13]. The electrical conductivity of the films was measured in the temperature range 100–450°C in an atmosphere of dry synthetic air and in gas mixtures of varied composition (ppm): 300 CO, 80 C_2H_5OH or 1000 CH_4 in dry air and 100 H_2S in nitrogen. The kinetics of variation of the electrical conductivity of the films, measured in air (G_0) and in the atmosphere of the above gas mixtures (G_t) at different temperatures, allowed estimation of the film sensitivity $S_t = (G_t - G_0)/G_0$.

The mechanism of interaction between SnO_2(CuO) and hydrogen sulfide was studied *in situ* by Raman spectroscopy with electrical properties recorded simultaneously. The Raman spectra were obtained on a Dilor XY multichannel spectrometer with Ar laser as radiation source (λ = 514.5 nm, 50 mW). The area of the analyzed section was 1 μm^2.

Sets of SnO_2 and SnO_2(MO) films were prepared, with copper concentration varying within 0.09–2.5 at. %, and nickel concentration, within 0.16–2.83 at. %. According to X-ray phase analysis data, the SnO_2 phase (tinstone) is present in all the synthesized films, with no copper- or nickel-containing phases found in the samples. This may be due both to the insufficient concentration of these phases and to the small size of their crystallites. The average dimensions of SnO_2 crystal grains were evaluated using the Debye–Scherrer formula on the basis of the reflection broadening in X-ray diffraction spectra and was found to be in the range from 3 to 10 nm, depending on synthesis conditions. The obtained data were confirmed by studying the film microstructure by transmission electron microscopy. No significant influence of copper or nickel in the concentration range 0–2.0 at. % on the SnO_2 grain size was revealed. An analysis of the real structure of the films by scanning electron microscopy indicated that they possess porous structure and are formed from agglomerates 50–100 nm in size.

A study of the composition of SnO_2(CuO) and SnO_2(NiO) films across their thickness by AES with the use of ion etching by means of an Ar^+ beam demonstrated that films doped with copper and nickel oxides exhibit different kinds of impurity distribution across the thickness. Films doped with nickel oxide are characterized by uniform distribution of nickel

Energy difference $\Delta = E(\mathrm{O1}s) - E(\mathrm{Sn3}d_{5/2})$ in XPS spectra of films

Sample	[M], at. %	Δ, eV	Δ – Δ1, eV (Δ_1 = 43.95 eV)
SnO_2	–	44.00	0.05
SnO_2(CuO)	1.26	43.90	–0.05
SnO_2(NiO)	1.25	44.80	0.85

across the entire thickness of a film. An analysis of the composition of an SnO_2(NiO) film (0.89 at. % Ni) gave values coinciding within measurement error for the surface composition ($I_{Ni}/I_{Sn} = 0.13 \pm 0.1$) and the bulk average ($I_{Ni}/I_{Sn} = 0.13 \pm 0.1$). In the case of SnO_2(CuO), a significant decrease in copper concentration was observed in going from the surface of a film into its bulk: $I_{Cu}/I_{Sn} = 0.24 \pm 0.1$ and 0.06 ± 0.1, respectively, for a film containing 1.84 at. % Cu. This effect may be due to segregation of copper on the surface of SnO_2 grains. In this case the total concentration of copper can be represented as the sum

$$[\mathrm{Cu}] = [\mathrm{Cu}]_s + [\mathrm{Cu}]_v,$$

where $[\mathrm{Cu}]_s$ and $[\mathrm{Cu}]_v$ are, respectively, the concentrations at the surface of a grain and in its bulk.

If we assume that $[\mathrm{Cu}]_s > [\mathrm{Cu}]_v$, then the obtained experimental data can be explained by taking into account the fact that $[\mathrm{Cu}]_s$ makes a major contribution to the composition of the surface layer of the film.

The state of copper and nickel in the synthesized films was analyzed by X-ray photoelectron spectroscopy (XPS). It was shown that the dopants are in oxidized state. The electronic state of nickel corresponds to NiO, whereas the data obtained for copper indicate an intermediate oxidation level (CuO, Cu_2O). The intermediate oxidation level of copper, also observed in studying the films by AES, may be due to the effect of high vacuum and ion sputtering on the composition of the surface being analyzed.

It is of interest to study the effect of copper and nickel ions on the Sn–O bond energy. The table lists the energy differences $\Delta = E(\mathrm{O1}s) - E(\mathrm{Sn3}d_{5/2})$ for films of pure and doped SnO_2, compared with a similar value calculated from reference data for pure SnO_2 (Δ_1 = 43.95 eV). The obtained data indicate that copper ions have no effect on the Sn–O bond energy ($\Delta - \Delta_1 = 0.05$ eV). Introduction of nickel in the same concentration leads to a pronounced change in the Sn–O bond energy ($\Delta - \Delta_1 = 0.85$ eV). The different effects of the same concentration of copper and nickel ions on the Sn–O bond energy may be due to differences between the distributions of copper and nickel ions between the crystal lattice and the surface of SnO_2 grains. It may be assumed that, at equal total concentrations, most part of copper is distributed in the form of segregates over the surface of tin dioxide grains, whereas nickel is mostly incorporated in the SnO_2 crystal lattice, occupying Sn sites. This assumption is in agreement with the results of layer-by-layer analysis of the composition of SnO_2(CuO) and SnO_2(NiO) films by AES. Calculations in terms of the percolation theory [14] demonstrated that the concentration of copper ions in the samples studied is insufficient for a thin (1 nm) copper oxide layer to be formed on the surface of every SnO_2 grain: a percolation cluster can be formed in the case of copper oxide distribution over boundaries of SnO_2 agglomerates.

A study of the electrical properties of the obtained films revealed a high sensitivity of the electrical conductivity of the material to the content of copper and nickel ions. Raising steadily the concentration of dopants results in the increasingly pronounced rise in resistance on lowering the temperature [15]. A portion of thermally activated behavior appears in the $\log R$–$(100/T)$ curves, with the activation energy E_a, determined from the relation $R \approx \exp(E_a/kT)$, gradually growing with increasing dopant concentration to become 0.5–0.6 eV in films containing 1.45 at. % Cu and 0.45 at. % Ni. Raising the dopant concentration further does not lead to any changes in the behavior of the conductivity of the films. The data obtained indicate that doping with copper or nickel oxides changes the mechanism of conduction in tin dioxide films. Presumably, with growing Cu and Ni concentration, the barrier mechanism plays an increasingly important role, with the barrier height (E_a) depending on the concentration of doping impurities. The temperature dependence of the electrical conductivity is in this case expressed as $G = G_0 \exp(-E_a/kT)$. The appearance of an energy barrier upon doping may be due to lowering of the Fermi level because of the compensation of donor oxygen vacancies $V_O^{\cdot\cdot}$ by acceptor-type substitution defects $Cu_{Sn''}$ ($Ni_{Sn''}$) or to formation of a *p*-CuO(NiO)/*n*-SnO_2 junction near the surface of tin dioxide grains.

The dynamic sensitivity of the films, $S_t = (G_t - G_0)/G_0$, was studied in relation to temperature, dopant concentration, and gas phase composition. Figure 2 shows typical dynamic curves in the S_t–t coordinates for SnO_2, SnO_2(CuO), and SnO_2(NiO) films under the conditions of a cyclic change in the gas phase composition at a temperature of 200°C. In the interac-

tion of the samples with a 100 ppm $H_2S + N_2$ gas mixture, the electrical conductivity of the films grows and then decreases reversibly on replacing the atmosphere with dry air. Multiple cycling of the gas phase composition (>100 cycles) has no effect on the nature and magnitude of changes in the electrical conductivity of the doped films. The long time necessary for the maximum change in electrical conductivity to be achieved is due to the relation between the measuring cell volume (2 l) and the gas mixture flow rate (4 $l\,h^{-1}$). The maximum sensitivities are observed at 150°C for SnO_2(CuO) films and at 250°C for SnO_2(NiO).

Figure 3a shows in the form of a three-dimensional diagram the dependence of the sensitivity of SnO_2(CuO) films to 100 ppm $H_2S + N_2$ on the content of copper in the films and size of SnO_2 crystalline grains. The maximum sensitivities to hydrogen sulfide correspond to average grain size of 5–6 nm and copper content in the films of 1.2–1.4 at. %. A similar analysis for SnO_2(NiO) films demonstrated (Fig. 3) that the maximum gas sensitivity is observed for films with the same average grain size of 5–6 nm, but containing 0.6–0.7 at. % Ni. The obtained optimal SnO_2 grain size corresponds to doubled thickness of the depleted layer in polycrystalline SnO_2, evaluated in [16].

An analysis of the whole set of the obtained experimental data revealed the main distinctions between the effects of copper and nickel oxides on the properties of SnO_2:

(1) According to AES and XPS data, copper oxide is mainly concentrated on the surface of SnO_2 grains, whereas nickel oxide is evenly distributed between the surface and the bulk of the crystalline grains.

(2) The interaction of SnO_2(NiO) films with the gas phase is much slower, compared with the case of SnO_2(CuO) films, in the entire temperature range studied.

(3) In determining hydrogen sulfide, the optimal working temperature of SnO_2(NiO) films is 100°C higher than that of SnO_2(CuO) films.

(4) In contrast to the case of copper, introduction of nickel into SnO_2 increases the sensitivity of this material to CO, C_2H_5OH, and CH_4.

Thus, it would be expected that the reaction of the SnO_2(CuO) and SnO_2(NiO) systems with hydrogen sulfide gas occurs by different mechanisms.

The mechanism of the reaction between polycrystalline SnO_2(CuO) and SnO_2(NiO) films and hydrogen sulfide was studied. Changes in the state of surface atoms upon interaction of SnO_2 and SnO_2(CuO) nanocrystalline films with an atmosphere containing 300 ppm of hydrogen sulfide in nitrogen was studied by *in situ* Raman spectroscopy at T = 150°C (Fig. 4). It was found that the intensity of vibrations of surface SnO_2 molecules (broad band at 570 cm^{-1}) decreases; copper sulfide Cu_2S (472 cm^{-1}) is formed in the

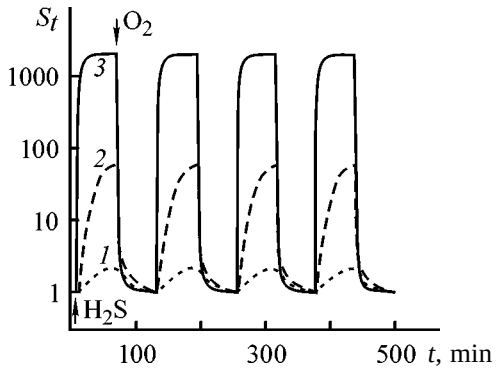

Fig. 2. Relative electrical conductivity S_t of (*1*) SnO_2, (*2*) SnO_2(CuO), and (*3*) SnO_2(NiO) films in cyclic replacement of dry air by a 100 ppm $H_2S + N_2$ gas mixture at 200°C. (*t*) Time.

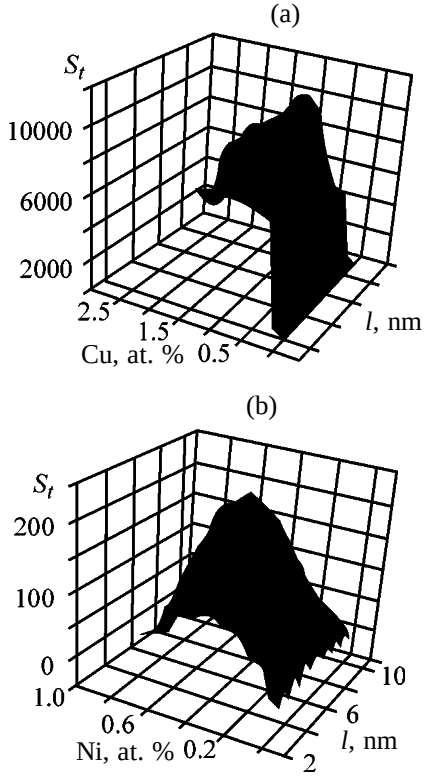

Fig. 3. Sensitivity S_t of (a) SnO_2(CuO) and (b) SnO_2(NiO) films to 100 ppm $H_2S + N_2$ vs. content of doping impurities of Cu and Ni ions in the films and size l of SnO_2 crystalline grains.

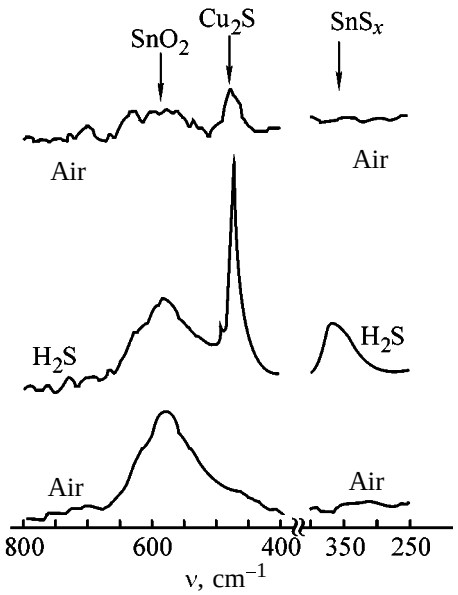

Fig. 4. Changes in Raman spectra of SnO_2(CuO) in cycling replacement of dry air with 300 ppm $H_2S + N_2$ gas mixture at 150°C. (ν) Wave number.

atmosphere of hydrogen sulfide in samples doped with copper oxide; tin sulfide SnS_x (broad band at 350 cm^{-1}) is formed in pure and doped tin dioxide.

Thus, the mechanism of interaction of SnO_2(CuO) with the gas phase involves the following basic processes.

(1) Adsorption of oxygen molecules onto the tin dioxide surface, with a depleted layer formed and the electrical conductivity decreasing because of the binding of a part of conduction band electrons by the adsorbed oxygen

$$O_{2g} \rightleftarrows 2O_s,$$

$$O_s + 2e \rightleftarrows O_s^{2-}.$$

(2) Adsorption of hydrogen sulfide molecules and their interaction with adsorbed oxygen

$$H_2S_g + 3O_s^{2-} = SO_{2g} + H_2O + 6e.$$

This reaction leads to an increase in the electron concentration n in the SnO_2 conduction band and makes higher the electrical conductivity

$$G = en\mu,$$

where e is the electron charge, $\mu = \mu_0 \exp(-E_a/kT)$ is the electron mobility, and E_a is the height of the barrier appearing at the p-CuO/n-SnO_2 interface, proportional to the concentration of introduced copper in the range 0–1.5 at. %.

(3) Chemical reaction of copper oxide with hydrogen sulfide gas to give copper(I) sulfide

$$6CuO_s + 4H_2S_g = 3Cu_2S_s + SO_{2g} + 4H_2O.$$

This reaction eliminates the energy barrier and thereby leads to a dramatic increase in the electron mobility μ and, consequently, in the electrical conductivity.

In the absence of hydrogen sulfide molecules, copper sulfide is reversibly converted into copper(II) oxide upon reaction with atmospheric oxygen

$$Cu_2S_s + 2O_{2g} = 2CuO_s + SO_{2g}.$$

(4) Chemical reaction of tin dioxide with hydrogen sulfide to give tin sulfide exerting no significant influence on the electrical properties of the system but changing the state of the material surface.

(5) Oxygen diffusion from the bulk of SnO_2 grains toward their surface to give neutral and doubly ionized vacancies

$$O_O^x = V_O^x + O_s$$

$$V_O^x = V_O^{\cdot\cdot} + 2e.$$

The role of nickel in the interaction of SnO_2(NiO) with the gas phase may be due to the effect of Ni redistribution between the bulk and the surface of an SnO_2 grain, depending on the redox properties of the atmosphere. In an oxidizing medium (in air), Ni^{2+} cation [$r(Ni^{2+})$ = 0.70 Å] may occupy sites on the cationic sublattice of SnO_2 [$r(Sn^{4+})$ = 0.69 Å], whereas in a reducing atmosphere containing hydrogen sulfide, CO, C_2H_5OH, or CH_4, reduction of nickel(II) is possible, with its transport toward the SnO_2 grain surface. This eliminates the effect of compensation of donor oxygen vacancies $V_O^{\cdot\cdot}$ by acceptor-type substitution defects $Ni_{Sn''}$, making higher the electrical conductivity of the material.

CONCLUSION

Nanocrystalline systems based on metal oxides are of interest as sensitive materials for resistive gas sensors. Introduction of copper and nickel oxides into the tin dioxide matrix gives high-resistivity samples. The increase in the resistance of SnO_2(MO) films is due to the compensation of intrinsic atomic defects by impurity centers and the formation of energy barriers at contacts between grains of semiconductors with different conduction types. Copper and nickel oxides were found to exert strong influence on the sensor

properties of tin dioxide films, leading to a 10^2–10^3-fold increase in the sensitivity of films to hydrogen sulfide. The obtained results can be used in developing high-sensitivity sensors for hydrogen sulfide gas. The mechanism of gas sensitivity is associated with changes in the electronic state of copper and nickel in the surface layer in relation to the gas phase composition.

ACKNOWLEDGMENTS

The study was financially supported by the Russian Foundation for Basic Research (project no. 98-03-32 843).

REFERENCES

1. Mangamma, G., Jayaraman, V., Gnanasekaran, T., and Periaswami, G., *Sensors Actuators B*, 1998, vol. 53, pp. 133–139.
2. Royster, T.L.J., Chatterjee, D., Paz-Pijalt, G.R., and Marrese, C.A., *Sensors Actuators B*, 1998, vol. 53, pp. 155–162.
3. Solis, J.L. and Lantto, V., *Sensors Actuators B*, 1998, vol. 48, pp. 322–327.
4. Tamaki, J., Shimanoe, K., Yamada, Y., *et al*., *Sensors Actuators B*, 1998, vol. 49, pp. 121–125.
5. Gopel, W., *Sensors Actuators A*, 1996, vol. 56, pp. 83–102.
6. Gopel, W. and Schierbaum, K.D., *Sensors Actuators B*, 1995, vol. 25–26, pp. 1–12.
7. Tamaki, J., Maekawa, T., Miura, N., and Yamazoe, N., *Sensors Actuators B*, 1992, vol. 9, pp. 197–203.
8. Sarala Devi, G., Manorama, S., and Rao, V.J., *J. Electrochem. Soc*., 1995, vol. 142, pp. 2754–2757.
9. Rumyantseva, M.N., Labeau, M., Senateur, J.P., *et al*., *J. Mater. Sci. Eng. B*, 1996, vol. 41, pp. 228–234.
10. Rumyantseva, M.N., Gaskov, A.M., Ryabova, L.I., *et al*., *J. Mater. Sci. Eng. B*, 1996, vol. 41, pp. 333–338.
11. Rumyantseva, M.N., Ryabova, L.I., Kuznetsova, T.A., *et al*., *Izv. Ross. Akad. Nauk, Neorg. Mater*., 1999, vol. 35, pp. 1–7.
12. Pouchou, J.L. and Pichoir, F., *Rech. Aerospat*., 1984, vol. 5, pp. 349–367.
13. Gautheron, B., Labeau, M., Delabouglise, G., and Schmatz, U., *Sensors Actuators B*, 1993, vol. 15–16, pp. 357–362.
14. Takayasu, H., *Fractals in the Physical Science*, Manchester: Manchester Univ. Press, 1990.
15. Akimov, B.A., Gas'kov, A.M., Labeau, M., *et al*., *Vestn. Mosk. Gos. Univ., Ser. 3: Fiz., Astron*., 1996, no. 5, pp. 60–65.
16. Ogawa, H., Nishikawa, M., and Abe, A., *J. Appl. Phys*., 1982, vol. 53, pp. 4448–4454.

Russian Journal of Applied Chemistry, Vol. 74, No. 3, 2001, pp. 440–444. Translated from Zhurnal Prikladnoi Khimii, Vol. 74, No. 3, 2001, pp. 430–434.

ENVIRONMENTAL PROBLEMS OF CHEMISTRY AND TECHNOLOGY

Nature of Gas Sensitivity in Nanocrystalline Metal Oxides[1]

A. M. Gas'kov and M. N. Rumyantseva

Moscow State University, Moscow, Russia

Received November 17, 1999; in final form, May 2000

Abstract—Problems associated with developing gas-sensitive inorganic materials are discussed. The principle of operation of a semiconductor gas sensor of resistive type is considered, and main band structure parameters sensitive to the gas phase composition are determined. Ways to solve the problem of selectivity of semiconducting oxides are discussed. The influence of microstructure, dopants, and analysis temperature is looked into on the basis of experimental results obtained in studying nanocrystalline tin dioxide and zinc oxide. Prospects for use of systems based on two or more nanocrystalline oxides (nanocomposites) are considered.

Nanocrystalline materials are being extensively studied with the aim of a search for novel properties [1, 2]. Much progress has been made in the field of directed synthesis of nanocrystalline systems based on metal oxides possessing high gas sensitivity, which can be used as catalysts and materials for gas sensors [3, 4]. With decreasing crystallite size, the contribution from the surface energy to the total free energy of the system increases dramatically, which leads to high activity of materials of this kind in heterogeneous interactions. The fact that the geometric dimensions of nanocrystallites and molecular sizes are comparable predetermines the difference between the kinetics of chemical transformations in nanocrystalline systems and similar processes in coarsely crystalline materials. These specific features make nanocrystalline semiconducting oxides very promising for development of high-sensitivity fast-response gas sensors, in which just surface processes play the key role in the formation of a sensor signal.

Despite the achieved high gas sensitivities, putting semiconducting oxides into practice is hindered by the poor selectivity of these materials and the lack of data on the mechanism of their interaction with the gas phase. The high rates of adsorption and redox processes make difficult studying the mechanism of surface reactions experimentally by the conventional methods. Under these conditions, the most complete information could be furnished by *in situ* investigation techniques.

The present communication discusses the nature of the gas sensitivity of semiconducting nanocrystalline metal oxides, the principle of operation of gas sensors on their base, and ways to improve the selectivity of the sensors.

Scheme of compositional analysis of the ambient atmosphere with a gas sensor

Object to be analyzed
↓
Sampling
↓
Filter, membrane
Sensor
Sensitive material
Signal converter
↓↑
Control circuits
↓↑
Data storage and transfer
Data processing

The main elements in analyzing the composition of the ambient atmosphere are (see scheme) object being analyzed, sampling system, filter, sensitive unit, signal converter, and a system for analysis control with the possibility of processing of the electric signal and information storage and transfer. According to the classification presented in [5], semiconducting gas sensors belong to the group of electric chemical sensors furnishing information about the ambient composition directly in the form of an electric signal. The possibility of combining in the same material the functions of a sensitive element and signal converter markedly simplifies the design of a sensor and constitutes the main advantage of resistive-type sensors over biochemical, optical, acoustic, and other devices.

[1] Reported at I Russian Conference "Surface Chemistry and Nanotechnology."

1070-4272/01/7403-0440$25.00

The principle of operation of semiconducting gas sensors is based on the dependence of the electrical properties of a material on the concentration of chemisorbed molecules. The formation of surface acceptor levels in real semiconductors may be due to oxygen adsorption from the gas phase. This process involves physical adsorption of O_2 molecules and capture by these molecules of electrons from the surface layer of the semiconductor.

$$1/2O_{2(gas)} + V_O^x \rightleftarrows O_s, \quad (1)$$

$$O_s + 2e \rightleftarrows O_s^{2-}, \quad (2)$$

where V_O^x are oxygen vacancies, and O_s is oxygen adsorbed onto the surface.

As a result, a depletion layer is formed near the crystal surface, with the electron concentration lower than that in the bulk. Figure 1 presents a band diagram illustrating the effect of adsorption on the parameters of the semiconductor band structure. The main of these: band gap E_g, Fermi level position E_F, electronic work function φ, and depletion layer width L, determine the electrical properties of a semiconducting material [7]. It should be noted that, in selecting a material for gas sensors, the absolute values of these parameters are not so important as their change upon chemisorption. The depletion layer width L is determined by the Debye screening length in the given material L_D [7] and the height of the surface Schottky barrier V_s [8].

$$L = L_D(eV_s/kT), \quad (3)$$

where e is the electron charge, k is the Boltzmann constant, and T is absolute temperature.

The Debye screening length in a given material is determined by the equation

$$L_D = \varepsilon kT/e^2n, \quad (4)$$

where ε is the dielectric constant of the material, and n is the carrier concentration.

The surface barrier height is, in its turn, determined by the surface charge Q_s^2:

$$V_s = Q_s^2/2\varepsilon\varepsilon_0 en. \quad (5)$$

The presence in the atmosphere of molecules of gases differing in their redox properties from atmospheric oxygen may lead, even under normal conditions (T = 25°C), to a pronounced change in electrical properties. Reducing gases, such as H_2, CO, and

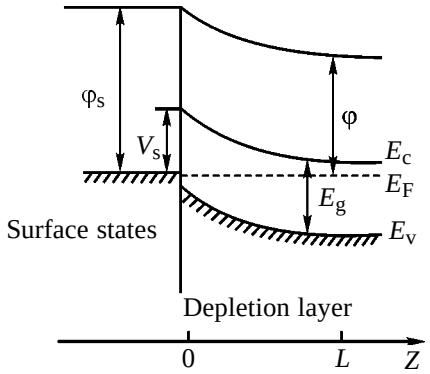

Fig. 1. Band structure of the surface layer of the semiconductor: (E_v) valence band top, (E_c) conduction band bottom, (E_g) band gap, (E_F) Fermi level position, (φ) electronic work function, (φ_s) work function for emission of an electron from a surface level, (V_s) surface barrier, and (L) depletion layer width.

NH_3, make the electronic work function lower and the electrical conductivity higher, whereas the presence of oxidizing gases (O_3, NO_2) leads to the opposite effect. The interaction of the surface of a semiconducting oxide with a reducing gas, e.g., CO, can be described by the equations

$$CO_{gas} \rightleftarrows CO_s, \quad (6)$$

$$CO_s + O_s^{2-} \rightleftarrows CO_{2(s)} + 2e, \quad (7)$$

$$CO_{2(s)} \rightleftarrows CO_{2(gas)}. \quad (8)$$

Reactions (6)–(8) decrease the concentration of oxygen adsorbed on the surface of crystal grains and lead to delocalization of electrons, making the electrical conductivity of *n*-type material higher (Fig. 2, curve *1*) and that of the *p*-type material lower. The presence of oxidizing gases in the atmosphere leads to decrease in the concentration of electrons in the surface layer, increase in the height of intergrain barriers, and decrease in the electrical conductivity of *n*-type materials (Fig. 2, curve *2*). The atmosphere-induced changes in the electrical properties of semiconducting materials are reversible in the temperature range 100–500°C.

The height of the surface barrier is also fundamentally important in selecting a material for gas sensors. By analogy with the Schottky barrier at the metal–semiconductor interface, the height of the barrier at the semiconductor surface can be represented as [6, 8]

$$V_s = X(\varphi_s - \varphi), \quad (9)$$

where φ_s is the work function for emission of an electron from a surface level, φ is the thermionic work

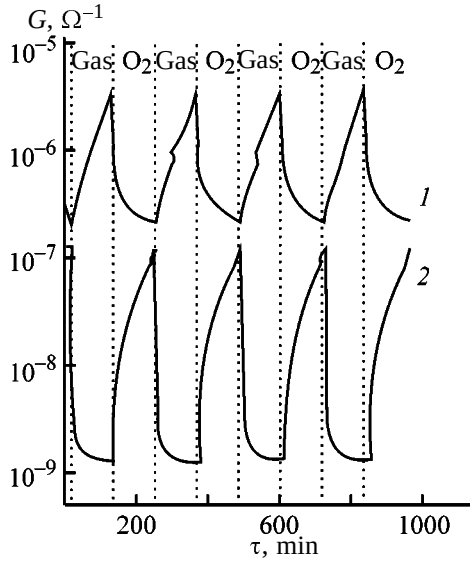

Fig. 2. Variation of the electrical conductivity G of polycrystalline ZnO with time τ in the presence of (*1*) reducing gas and (*2*) oxidizing agents.

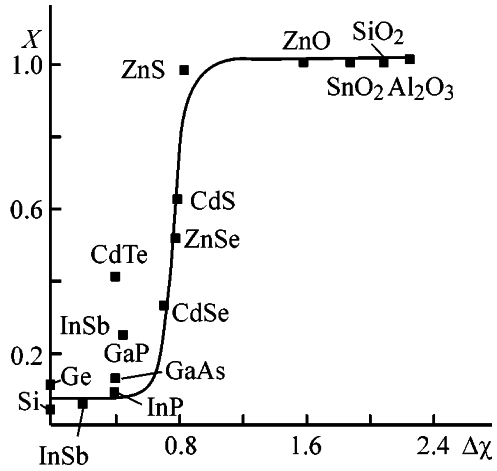

Fig. 3. Parameter X vs. difference of electronegativities $\Delta\chi$ of the anion and cation forming the semiconductor.

function, and X is a chemical parameter depending on the nature of a semiconductor.

The parameter X is defined as a coefficient of a linear dependence relating V_s and φ_s and can be interpreted as a manifestation of the sensitivity of the electrical properties of a semiconductor to the state of its surface. Figure 3 presents the parameter X in relation to the difference of electronegativities $\Delta\chi$ (by Pauling) of the anion and cation forming the semiconductor. The abrupt change in the X value at $\Delta\chi = 0.8$ corresponds to a transition from materials with covalent bonding (Si, Ge, GaAs) to those in which ionic bonds predominate (ZnO, SnO_2). Thus, the highest sensitivity to changes in the concentration of molecules adsorbed onto the surface and, consequently, to changes in the gas phase composition is exhibited by materials with predominantly ionic bonding. Oxides characterized by exceedingly high resistivity, SiO_2 and Al_2O_3, are not used in resistive gas sensors in pure state because of the difficulties encountered in electrical conductivity measurements.

Despite the considerable success in improving the sensitivity and speed of response of semiconducting gas sensors, there remain a number of problems among which the most important are the poor selectivity and the sensitivity to atmospheric moisture, which is due to the nonselective nature of adsorption. Let us consider successively the effect of microstructure and dopants on the gas-sensitive properties of the material.

The contribution of the surface to the electrical properties of a semiconductor can be achieved by passing from a single crystal to a polycrystalline system. In this case, each crystalline grain is to be considered a closed volume with a depletion layer near its surface (Fig. 4). The decrease in the carrier concentration at grain boundaries leads to formation of intergrain energy barriers whose height determines the electrical conductivity of a polycrystalline material as a whole. The strongest influence of the state of the surface on the electrical properties of the material is observed when the following condition [3] is met:

$$l/2 \le L, \tag{10}$$

where l is the crystallite size and L is the depletion layer width, varying between 3 and 10 nm for various oxides.

All other conditions being the same, the depletion layer width depends on the redox properties of chemisorbed molecules. The reducing gases H_2, CO, H_2S, and NH_3 make the depletion layer narrower, whereas the oxidizing gases O_3 and NO_2, conversely, lead to an increase in the depletion layer width, being involved in competitive adsorption together with atmospheric oxygen. Thus, when forming the real structure of an oxide, account should be taken of the chemical nature of a gas being analyzed: the optimal grain size for detecting molecules possessing reducing properties is to be smaller, compared with the case of oxidizing gases.

In order to raise the adsorption activity, semiconducting oxides are doped with noble metals: Pt, Pd, Au, and Ru. It has been established that these metals form on the oxide surface clusters whose presence facilitates adsorption and dissociation of reducing

gases. The presence of Pd, Pt, or Au clusters, in particular, lowers the electronic work function and decreases the activation energy of the reaction occurring on the surface of the semiconducting oxide. However, in addition to the catalytic effect, the above metals exert influence on the electrical properties and real structure of the polycrystalline matrix and can also change the intrinsic chemical state on the oxide surface. It has been shown that the state of Pt (Pt or PtO_2) in SnO_2 depends on the cluster size and changes depending on the gas phase composition. The authors believe that the transition of platinum from the oxidized state (in air) to the metallic state (in a gas mixture of 900 ppm CO in N_2) leads to high gas sensitivity of SnO_2(Pt) films. Reaction with a gas mixture containing 1% H_2 in nitrogen results in the reduction of palladium to metallic state, accompanied by a 1000-fold increase in the electrical conductivity of the films. The photoelectron spectrum of the surface of an SnO_2(Pd) film annealed in an inert atmosphere of N_2 contains peaks corresponding to both states of palladium: Pd and PdO. The manifestation of reducing properties by an inert medium is due in this case to the lack of oxygen in the gas phase, which makes lower the concentration of adsorbed oxygen on the oxide surface.

Recently, complex nanocrystalline systems (nanocomposites) containing two or more oxides have been widely used for solving the problem of selectivity of materials. The nanocomposite composition can be represented as M_1O/M_2O, where M_1O is the nanocrystalline matrix and M_2O is the doping oxide distributed between the surface and the bulk of the M_1O nanocrystalline grain. The advantage of nanocomposites over simple nanocrystalline oxides, when used in gas sensors, is associated with the redistribution of M_2 between the bulk and the surface of M_1O grain, depending on the redox properties of the gas phase. Low oxidation levels of M_2 cation, corresponding to larger ionic radius and predominant distribution of M_2 over the surface of M_1O grains, occur in the reducing atmosphere. By contrast, cations in higher oxidation states are formed in an oxidizing atmosphere, with increasing probability that M_2 cations occupy regular cationic positions in M_1O. The lability of the chemical state of the M_2 cation in the nanocrystalline system may result in a dramatic change in the state of grain boundaries and in modification of the electronic properties of the material in the presence of even trace amounts (0.1–10 ppm) of reducing or oxidizing gas molecules in the gas phase. The table lists as examples nanocomposites that are of interest for creating gas-sensitive materials. The oxides to be used in creating nanocomposites are chosen with account of the ionic radii of the elements [12].

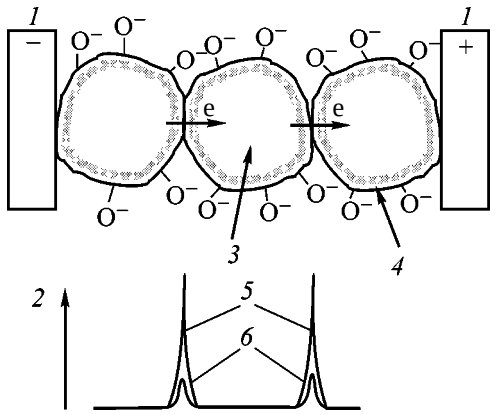

Fig. 4. Scheme of formation of intercrystallite electrical barriers in the polycrystalline system: (*1*) electrode, (*2*) potential barrier, (*3*) crystallite bulk, (*4*) depletion layer, (*5*) height of potential barrier in air, and (*6*) height of potential barrier in the presence of a reducing gas.

CONCLUSION

The effect of gas sensitivity of nanocrystalline metal oxides is based on the chemisorption process and chemical reactions on the surface, involving chemisorbed oxygen. High gas sensitivity can be achieved with systems based on simple and complex semiconducting oxides. An important parameter is the high dispersity of a material with microstructure stable under conditions of prolonged annealing at 60–100°C.

M_1O/M_2O nanocomposites for creating gas-sensitive materials

M_1O/M_2O	$r(M_1)$, Å	$r(M_2)$, Å	
		oxidized form	reduced form
Cr_2O_3/SnO_2	Cr^{3+} 0.61 $3d^34s^0$	Sn^{4+} 0.69 $4d^{10}5s^0$	Sn^{2+} 0.93 $4d^{10}5s^2$
SnO_2/CuO	Sn^{4+} 0.69 $4d^{10}5s^0$	Cu^{2+} 0.73 $3d^94s^0$	Cu^{1+} 0.96 $3d^{10}4s^0$
SnO_2/MoO_3	Sn^{4+} 0.69 $4d^{10}5s^0$	Mo^{6+} 0.42 $4d^05s^0$	Mo^{5+} 0.63 $4d^15s^0$
Ga_2O_3/Fe_2O_3	Ga^{3+} 0.62 $3d^{10}4s^0$	Fe^{3+} 0.64 $3d^54s^0$	Fe^{2+} 0.77 $3d^64s^0$
In_2O_3/NiO	In^{3+} 0.79 $4d^{10}4s^0$	Ni^{3+} 0.60 $3d^74s^0$	Ni^{2+} 0.70 $3d^84s^0$
WO_3/TiO_2	W^{6+} 0.58 $5d^06s^0$	Ti^{4+} 0.60 $3d^04s^0$	Ti^{3+} 0.67 $3d^14s^0$

ACKNOWLEDGMENTS

The study was financially supported by the Russian Foundation for Basic Research (project no. 98-03-32 843).

REFERENCES

1. Khairutdinov, R.F., *Usp. Khim.*, 1998, vol. 67, no. 2, pp. 125–139.
2. Shull, R.D., *J. Nanostruct. Mater.*, 1993, vol. 2, pp. 213–216.
3. Gopel, W., *Sensors Actuators A*, 1996, vol. 56, pp. 83–102.
4. Moseley, P.T., *Sensors Actuators B*, 1992, vol. 6, pp. 149–156.
5. Myasoedov, B.F. and Davydov, A.V., *Zh. Anal. Khim.*, 1990, vol. 45, no. 7, pp. 1259–1278.
6. Henrich, V.E. and Cox, P.A., *The Surface Science of Metal Oxides*, Cambridge: Cambridge Univ. Press, 1993.
7. Bechstedt, F. and Enderlein, R., *Semiconductor Surface and Interface: Their Atomic and Electronic Structure*, Berlin: Akademie, 1988.
8. Souteyrand, E., *Transduction electrique pour la detection de gaz, dans les capteurs chimiques*, Lyon: CMC2, 1997.
9. Norris, J., *Solid State Gas Sensors*, Mosely, P.T. and Tofield, B.C., Eds., Bristol: Alam Higer, 1987, pp. 124–138.
10. Tofield, B.C., *J. Chem. Soc., Faraday Trans. 1*, 1988, vol. 84, no. 2, pp. 441–457.
11. Gaidi, M., Labeau, M., Chenevier, B., and Hazemann, J.L., *Sensors Actuators B*, 1998, vol. 48, pp. 277–284.
12. Shannon, R.D. and Prewitt, C.T., *Acta Crystallogr., Sect. B*, 1969, vol. 25, no. 5, pp. 925–949.

Russian Journal of Applied Chemistry, Vol. 74, No. 3, 2001, pp. 445–448. Translated from Zhurnal Prikladnoi Khimii, Vol. 74, No. 3, 2001, pp. 435–438.

ENVIRONMENTAL PROBLEMS OF CHEMISTRY AND TECHNOLOGY

Preparation of Anionic Flocculant by Alkaline Hydrolysis of Polyacrylamide (Praestol 2500) in Aqueous Solutions and Its Use for Water Treatment Purposes

V. F. Kurenkov, S. V. Snigirev, F. I. Churikov, A. A. Ruchenin, and F. I. Lobanov

Kazan State Technological University, Kazan, Tatarstan, Russia
Kazan'orgsintez Joint-Stock Company, Kazan, Tatarstan, Russia
Moscow Office, Stockhausen GmbH and KG, Moscow, Russia

Received October 19, 2000

Abstract—A study was made of the low-temperature hydrolysis of high-moleculer-weight polyacrylamide Praestol under the action of NaOH in dilute aqueous solution. The performance of the hydrolyzed and nonhydrolyzed polymer when combined with aluminum sulfate in treatment of natural water was estimated.

The most important reaction in polymer-analogous transformations of polyacrylamide (PAA) is alkaline hydrolysis. It is often used for partial replacement of the amide groups in PAA macromolecules by carboxylate groups. The degree of hydrolysis can affect the flocculating power, viscosity, and adhesion properties of the polymer [1, 2]. There are numerous publications on hydrolysis of PAA and its behavior in various media, but published data on low-temperature hydrolysis of PAA in dilute aqueous solutions are scarce [3, 4]. These investigations are motivated by the possibility of modifying PAA during application. For this reason, hydrolyzed PAA in a number of cases is preferable over acrylamide–sodium acrylate copolymers. In this connection, we studied in this work hydrolysis of high-molecular-weight PAA Praestol 2500[1] which currently receives much attention.

EXPERIMENTAL

We used Praestol 2500 produced by Stockhausen (Krefeld, Germany) with $[\eta] = 1550$ cm^3 g^{-1} and $M_\eta = 8.7 \times 10^6$; pure grade aluminum sulfate $Al_2(SO_4)_3 \cdot 18H_2O$ [GOST (State Standard) 3758–65]; pure grade SO brand kaolin [TU (Technical Specifications) 21-5494310–92]; and distilled water. Other chemicals were of chemically pure grade.

In the laboratory experiments, Praestol 2500 was dissolved at room temperature under continuous stirring (stirrer rotation rate 600 rpm during feeding of the polymer and 300 rpm during the subsequent 1-h period). Hydrolysis was carried out in a three-necked flask equipped with a power-driven stirrer, a thermometer, and a tube for taking samples. In the course of the reaction we took samples from the reaction solution at regular intervals so as to determine the degree of hydrolysis of the polymer A [mol % of the units of sodium acrylate (SA)] by potentiometric titration [5]. The relative standard deviation and relative error of determination were within 1.4 and 3.3%, respectively [5].

In industrial tests, hydrolysis of Praestol 2500 was combined with its dissolution in the acting unit for preparing the polymer solution,[2] and the degree of hydrolysis was monitored [5].

Potentiometric measurements were carried out with a pH-121 pH-millivoltmeter with an ESL-43-07 glass inidicating electrode and an EVL-1M3 silver chloride reference electrode.

The intrinsic viscosity $[\eta]$ was determined in 0.5 M NaCl solution at 25°C, and the data obtained were used for calculating the viscosity-average molecular weight of the hydrolyzed Praestol 2500 by the Mark–Houwink equation $[\eta] = kM_\eta^\alpha$, with the constants k and α varied depending on the degree of hydrolysis of the polymer; their values were taken from [6]. In accordance with [7–9], we judged the effective size of the macromolecular coils $\langle r^2 \rangle^{1/2}$ of the hydrolyzed

[1] Moscow–Stockhausen–Perm Russian–German enterprise, Joint-Stock Company.

[2] Water treatment works of the Kazan'orgsintez Joint-Stock Company.

1070-4272/01/7403-0445$25.00

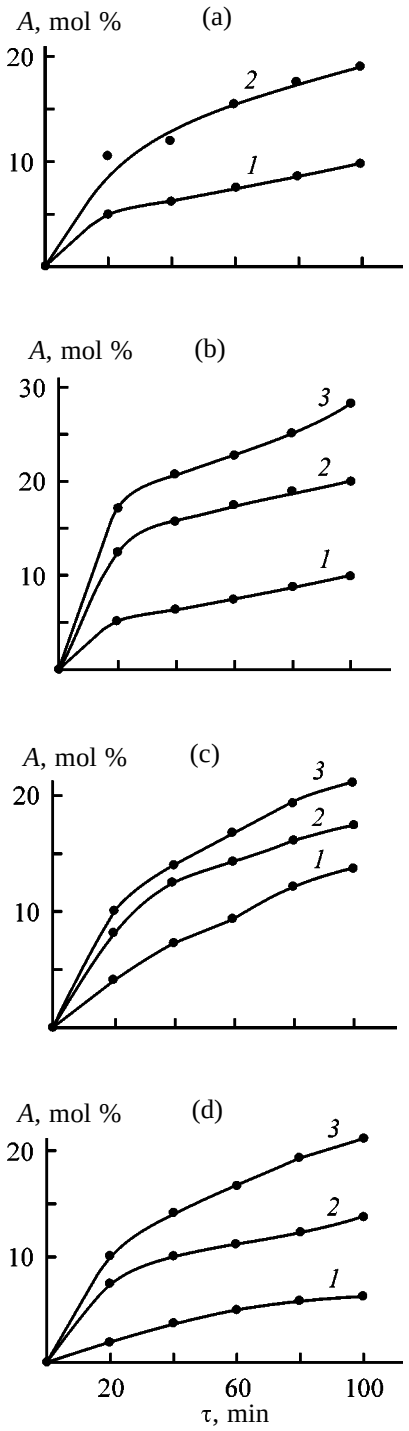

Fig. 1. Content of the SA units in the copolymer *A* as a function of the time τ in hydrolysis of PAA. (a) Initial mass ratio [PAA]/[NaOH] = 5; 20°C; [PAA], %: (*1*) 0.005 and (*2*) 0.1. (b) [PAA] = 0.05%, 22°C, initial mass ratio [PAA]/[NaOH]: (*1*) 3.3, (*2*) 1.6, and (*3*) 0.5. (c) [PAA] = 0.05%, initial mass ratio [PAA]/[NaOH] = 1.6. Temperature, °C: (*1*) 5, (*2*) 15 and (*3*) 25. (d) [PAA] = 0.5%, initial mass ratio [PAA]/[NaOH] = 1.6; 25°C. Water: (*1*) riverine, (*2*) tap, and (*3*) distilled.

Praestol 2500 indirectly, from the reduced viscosity η_{sp}/C_p (as measured in water at C_p = const).

Sedimentation analysis was carried out in 0.14% kaolin suspensions in a sedimentometer with VT-500 torsion balance scales after tenfold stirring of the suspension with a disk stirrer with perforations.

In industrial tests, the quality of the water after treatment was monitored basing on the standards set in the Sanitary Rules and Regulations (SanPiN) [10].

To prepare modified PAA suitable for natural water treatment [11], we chose the hydrolysis conditions at which the degree of hydrolysis of the polymer did not exceed 30 mol %. Namely, hydrolysis was carried out for 1.5 h in dilute aqueous solutions ([PAA] = 0.05–0.1%) intended for preparing polymer solutions at water treatment plants, in the presence of NaOH at 5, 15, and 25°C.

Under the actual conditions, PAA is hydrolyzed by the scheme

$$-(-CH_2-\underset{\displaystyle CONH_2}{\underset{|}{CH}}-)_{n-} + m\mathrm{NaOH} + H_2O$$

$$\rightarrow -(-CH_2-\underset{\displaystyle CONH_2}{\underset{|}{CH}}-)_{n-m}-(-CH_2-\underset{\displaystyle COO^-Na^+}{\underset{|}{CH}}-)_{m-} + m\mathrm{NH_4OH}.$$

Figure 1a presents the kinetic curves for PAA hydrolysis obtained by the potentiometric method. The polymer concentration in the experiments was varied at [PAA]/[NaOH] = const. Figure 1a shows that with increasing concentration of the polymer the initial rate of hydrolysis and the content of the SA units in the hydrolysis products tend to increase (going from curve *1* to curve *2*). Individual kinetic curves in Fig. 1a evidence high rates of hydrolysis in the initial stages of the reaction, which can, probably, be attributed to anchimeric promotion of hydrolysis of the amide groups by the neighboring hydrolyzed (carboxylate) groups [12]. Figure 1a also evidences deceleration of hydrolysis in the course of the reaction. This is probably due to the electrostatic repulsion between the OH^- ions and the carboxylate anions COO^- accumulating in the macromolecules during hydrolysis.

The influence of the NaOH concentration on the hydrolysis kinetics was elucidated at [PAA] = const, other conditions remaining unchanged. As seen from Fig. 1b, with increasing NaOH concentration the initial rate of hydrolysis tends to increase, and the macromolecules of the forming copolymer get enriched with

the SA units (going from curve *1* to curve *3*). This is due to increase in the concentration of OH^- ions in the reaction system.

Figure 1c presents the kinetic curves characterizing hydrolysis of Praestol 2500 over the 5–25°C range at constant concentrations of the polymer and NaOH. It is seen that the initial rate of hydrolysis and the content of the SA units in the macromolecules of the forming copolymer tend to increase with rising temperature (going from curve *1* to curve *3*). This dependence is consistent with the general relationships in alkaline hydrolysis of polyvinylamides.

Figure 1d demonstrates the influence of the medium on hydrolysis of Praestol 2500. The reaction was run in distilled, tap (turbidity 1.1 mg l^{-1}, color index 15 deg), and riverine (turbidity 4.9 mg l^{-1}, color index 46 deg, total alkalinity 1.6 mg l^{-1}) water. In this series of runs, the concentrations of the polymer and NaOH, as well as the temperature (25°C), were kept constant. Figure 1d shows that the initial rate of hydrolysis and the SA content in the forming copolymer tend to decrease in the series distilled water > tap water > riverine water.

This is explained by the fact that this series characterizes the decrease in the efficiency of alkaline hydrolysis of the polymer with increasing content of the impurity.

The impurity hydrocarbonates contained in tap, and in a greater amount, in riverine water could react with NaOH, thus decreasing its concentration and, thereby, the hydrolysis efficiency.

To determine the degree of hydrolysis of Praestol 2500 ensuring the greatest flocculation effect, we studied sedimentation of the model kaolin suspension under the action of aluminum sulfate and Praestol 2500 samples differing in the degree of hydrolysis and having close M_η values (Table 1). The sedimentation conditions were chosen basing on the results of our previous investigations [13]. As known [14], when added to an aqueous kaolin suspension, aluminum sulfate is hydrolyzed to form positively charged particles of aluminum hydroxide adsorbed on the negatively charged kaolin particles (ζ potential of the kaolin surface was –4.2 mV) forming complex aggregates. Upon subsequent introduction of Praestol 2500, larger floccules formed, which caused joint flocculation of all the partciles. Figure 2 demonstrates the flocculation effect as a function of the content of the SA units in the hydrolyzed Praestol 2500. The flocculation effect was estimated by the formula

$$D = (t_0 - t)/tz,$$

Table 1. Characterization of Praestol 2500 based flocculants

Sample no.	[η], $cm^3\ g^{-1}$	$M_\eta \times 10^{-6}$	Content of indicated units, mol %	
			AA	SA
1	1500	4.4	89	11
2	1500	4.0	83	17
3	1500	3.8	80	20
4	1500	3.2	76	24
5	1600	4.4	72	28

where t_0 and t are the times required for accumulation of 50% of the sediment mass on the pan of the torsion balance with and without polymer, respectively (for 0.14% kaolin suspension t_0 = 30 min).

The $D = f(A)$ dependence presented in Fig. 2 (curve *1*) has an extremum due to the parallel run of the $\eta_{sp}/C_p = f(A)$ plot (curve 2). This fact suggests that the flocculation effect D is strongly dependent on the parameter $\langle r^2\rangle^{1/2}$ for hydrolyzed Praestol 2500. It takes a maximal value at $A \approx 20$ mol % (curve *1*), which corresponds to the greatest η_{sp}/C_p values (curve *2*). It can be assumed that this composition of the macromolecule corresponds to the optimal relation between the charge density and the flexibility of the chains and, therefore, the largest $\langle r^2\rangle^{1/2}$ values. As a result, polymer bridges link a greater number of kaolin particles, which favors formation of large floccules and accelerates their sedimentation. The greatest flocculation power of the hydrolyzed Praestol was observed at $A \approx 20$ mol %, which is consistent with the previous data [15]. For this reason, in industrial tests Praestol was hydrolyzed up to the degree of hydrolysis of 19 mol %, and the resulting hydrolyzed polymer (HP) was used for water tretament. Its performance was compared with that of nonhydrolyzed

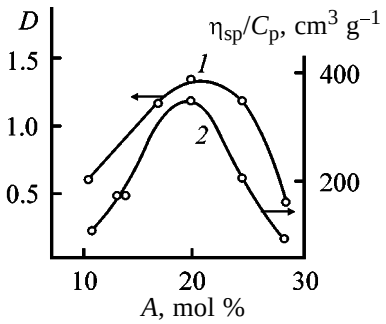

Fig. 2. (*1*) Flocculation effect D and (*2*) reduced viscosity η_{sp}/C_p as functions of the content of the SA units in the copolymer A in hydrolyzed Praestol 2500. $C_c = 6.4 \times 10^{-4}$%, η_{sp}/C_p was measured in water at 25°C at C_p = 0.0002%.

Table 2. Efficiency of treatment of natural water under the action of flocculants P and HP with A = 19 mol % in combination with aluminum sulfate coagulant*

Date	C_c, mg l^{-1}	C_f, mg l^{-1}	Purified water: turbidity, mg l^{-1}		Purified water: Al(III), mg l^{-1}	
			P	HP	P	HP
1.06	13	0.015	1.10	0.97	0.33	0.28
2.06	13	0.017	1.16	1.09	0.32	0.27
3.06	14	0.013	1.12	1.02	0.30	0.24
5.06	13	0.010	1.34	1.26	0.38	0.29
10.06	16	0.017	1.16	1.15	0.24	0.17
11.06	14	0.013	1.20	1.11	0.19	0.16
12.06	16	0.016	1.01	0.90	0.21	0.15
13.06	16	0.013	1.31	0.61	0.18	0.16

* (C_c, C_f) Concentrations of coagulant and flocculant, respectively.

polymer (P) combined with coagulant, aluminum sulfate, in treatment of the water samples taken from the Volga river and intended for potable water and industrial water supply purposes. Praestol 2500 was hydrolyzed in the operating unit for preparing polymer solution.

The water treatment flowsheet comprised two lines with identical sets of the water treatment facilities (flocculation chambers, horizontal settlers, and quartz filters) with the capacity of 1700 $m^3 h^{-1}$. The P polymer was fed to one line, and HP, to the other, and in both lines the quality of the treated water was assessed basing on the standards of SanPiN [10]. The results are summarized in Table 2. It is seen that the indices of water treated with P and HP satisfy the standards (SanPiN [10] sets the MPC for turbidity at 1.5 mg l^{-1} and for aluminum(III), at 0.5). Other indices of the water after treatment also satisfied the SanPiN standards. It should be noted that owing to large M_η values, very low doses of Praestol 2500 were sufficient for improving the standardized indices. The tabulated data also evidence that on changing from P to HP the turbidity of the treated water decreased by 18%, and the content of Al(III), by 26%. The latter fact is due to the presence in the HP macromolecules of carboxylate groups able of forming complexes with Al(III) ions. Thus, low doses of HP afforded more efficient treatment of natural water compared to P.

CONCLUSIONS

(1) Alkaline hydrolysis of Praestol 2500 in dilute aqueous solutions at 5–25°C yields polymers with controllable degree of hydrolysis (up to 30 mol %).

(2) The water treatment efficiency was improved on going from P to HP with the degree of hydrolysis of 19 mol% when the polymers were used in combination with aluminum sulfate.

REFERENCES

1. Abramova, L.I., Baiburova, T.A., Grigoryan. E.P., *et al*., *Poliakrilamid* (Polyacrylamide), Kurenkov, V.F., Ed., Moscow: Khimiya, 1992.
2. Nikolaev, A.F. and Okhrimenko, G.I., *Vodorastvorimye polimery* (Water-Soluble Polymers), Leningrad: Khimiya, 1979.
3. Kurenkov, V.F., Aleeva, Yu.V., Zabbarov, A.N., and Myagchenkov, V.A., *Zh. Prikl. Khim*., 1992, vol. 65, no. 11, pp. 2543–2546.
4. Kurenkov, V.F., Il'ina, I.V., Gerkin, R.V., and Karnaukhov, N.A., *Izv. Vyssh. Uchebn. Zaved., Khim. Khim. Teknnol*., 1996, vol. 39, nos. 1–2, pp. 71–73.
5. Churikov, F.I., Snigirev, S.V., and Kurenkov, V.F., *Zavod. Lab. Diagn. Mater*., 1998, no. 6, pp. 9–10.
6. Klein, J. and Conrad, K.-D., *Macromol. Chem*., 1978, vol. 178, pp. 1635–1642.
7. Butle, J.A.V., Robins, A.V., and Shooter, K.V., *Proc. Roy. Soc.* (London), 1957, vol. A241, pp. 299–303.
8. Nagasawa, M. and Kagawa, I., *J. Polym. Sci*., 1957, vol. 25, pp. 61–65.
9. Fernandez Prini, R. and Lagos, A.E., *J. Polym. Sci., Part A*, 1964, vol. 2, pp. 2917–2928.
10. *SanPiN* (Sanitary Rules and Regulations) *2.1.4.559–96: Potable Water. Sanitary Requirements to the Quality of Potable Water in Central Potable Water Supply Systems. Quality Control*, Moscow: Goskomepidnadzor, 1996.
11. Kurenkov, V.F., Churikov, F.I., and Snigirev, S.V., *Zh. Prikl. Khim*., 1999, vol. 72, no. 9, pp. 1485–1489.
12. Nagase, K. and Sakaguchi, K., *J. Polym. Sci., Part A*, 1965, vol. 3, no. 7, pp. 2475–2486.
13. Kurenkov, V.F., Snigirev, S.V., Len'ko, O.A., and Churikov, F.I., *Vestn. Kazan. Tekhnol. Univ.*, Kazan: Novoe Znanie, 1999, nos. 1–2, pp. 97–100.
14. Frog, B.N. and Levchenko, A.P., *Vodopodgotovka* (Water Treatment), Nikoladze, G.I., Ed., Moscow: Mosk. Gos. Univ., 1996.
15. Kurenkov, V.F., Churikov, F.I., and Snigirev, S.V., *Zh. Prikl. Khim*., 1999, vol. 72, no. 5, pp. 828–831.

Russian Journal of Applied Chemistry, Vol. 74, No. 3, 2001, pp. 449–454. Translated from Zhurnal Prikladnoi Khimii, Vol. 74, No. 3, 2001, pp. 439–444.

ENVIRONMENTAL PROBLEMS OF CHEMISTRY AND TECHNOLOGY

Intensification of the Flotation Treatment of Water with Natural Polyelectrolytes

I. N. Konovalova, N. V. Stepanova, P. B. Vasilevskii, and I. G. Bereza

Murmansk State Technical University, Murmansk, Russia

Received August 24, 2000

Abstract—The influence of natural polyelectrolytes, sodium alginate and chitosan, on the efficiency of water treatment by flotation to remove fish oil was elucidated by studying the kinetics of formation of adsorption layers at the aqueous polyelectrolyte solution–air and aqueous polyelectrolyte solution–fish oil interfaces. The stability of fish oil emulsions stabilized by sodium alginate and chitosan was studied.

Removal of fatty substances from water and aqueous solutions has become an especially urgent problem [1]. Fat-containing wastewater is not appropriate for biological and other water treatment works because fat impurities depositing on pipeline walls prevent transportation of wastewater and disturb operation of the water treatment works. Fat removed from wastewater can find use as a valuable supplement to mixed feed for domestic animals and poultry.

The biopolymers studied in this work, sodium alginate ANa and chitosan, are not toxic and exhibit a set of properties making them suitable for removal of fat and protein substances from wastewater generated by food industry enterprises with their subsequent utilization as food supplement [2–7].

Wastewaters generated at fish enterprises are complex disperse systems whose main components are fat and protein. Fat occurs in wastewater as emulsions and films.

Coarsely dispersed systems are treated, in particular, by flotation and settling; finer emulsions are broken down by coagulation, flocculation, and chemical and biological methods. Additives of natural polyelectrolytes such as ANa and chitosan can be used for intensifying the flotation treatment of water, as they can affect the stability of fat droplets and air bubbles and their hydrophobic and hydrophilic properties. The suitability of ANa and chitosan as flocculants in wastewater treatment was pointed out in a number of publications [2, 5, 7–11]. However, in Russia these polymers have not as yet found wide application because of their relative expensiveness [5]. Recently, a fairly inexpensive electrochemical method of preparing polyelectrolytes of diverse nature from hydrobiontics has been developed [12].[1] Sodium alginate and chitosan prepared by this method have low prime cost and are suitable for development of waste-free technologies and closed water circuits, e.g., in production of hydrolyzates, isolates, and concentrates from hydrobiontics.

The aim of this work was to elucidate how natural polyelectrolytes ANa and chitosan affect the efficiency of the flotation treatment of water to remove fish oil.

EXPERIMENTAL

We used ANa and chitosan with molecular weights of 13000 and 14000, respectively.[1] As fat additives served food-grade fish oil [GOST (State Standard) 3714–72]. We prepared aqueous solutions of ANa with concentrations ranging from 0.000025 to 0.25 g l^{-1}. Chitosan solutions of the same concentrations were prepared in 1% acetic acid. The acidity of the medium was adjusted using 0.1 M HCl and 0.1 M NaOH. The pH value was measured with an I-135 pH-meter. The kinetics of formation of the adsorption layers at the water–air and water–fish oil interfaces were monitored by variation of the surface tension of the solution σ at the interface with time τ. The surface tension of the solutions was determined by the Wilhelmi's method [13]. The half-relaxation time was calculated by the procedure described in [14]. The fish oil–water emulsions were prepared using a PT-2 tissue microcrusher (rotation rate 20 rps, stirring time 15 s), and the content of ANa and chitosan additives in the aqueous phase was varied within 0.2–1 g l^{-1}. The

[1] Protein Joint-Stock Company, Murmansk.

1070-4272/01/7403-0449$25.00

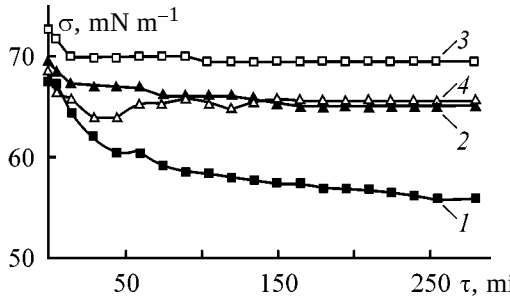

Fig. 1. Variation with time of the surface tension σ of solutions of (*1, 3*) ANa and (*2, 4*) chitosan at (*1, 2*) solution–air and solution–fish oil interface. Solution concentration 0.000025 g dl^{-1}, T = 20°C, pH 5.5–6; the same for Fig. 2. (τ) Time.

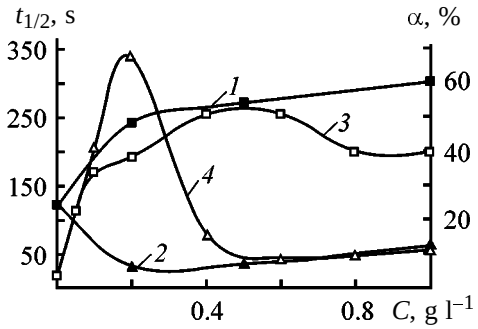

Fig. 3. Variation of (*1, 2*) half-time of breakdown $t_{1/2}$ and (*3, 4*) degree of removal of oil by flotation α with the polyelectrolyte concentration C. Oil content in the emulsion 40% of the total amount; initial oil concentration in the solutions subjected to flotation treatment 0.5 g l^{-1}; T = 20°C; flotation time 15 min.

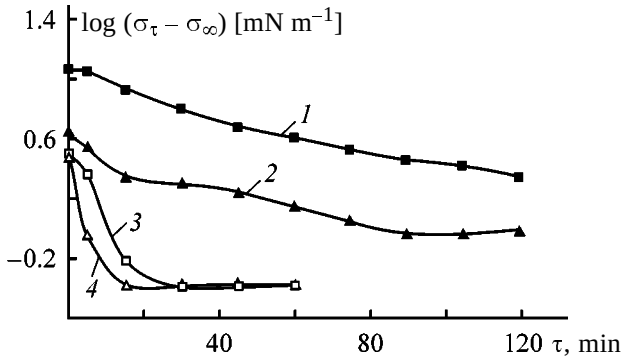

Fig. 2. Variation of $\log(\sigma_\tau-\sigma_\infty)$ with time τ of formation of the adsorption layers of (*1, 3*) ANa and (*2, 4*) chitosan at (*1, 2*) solution–air and (*3, 4*) solution–fish oil interface. (σ_τ, σ_∞) Surface tension of the solution at the moment τ and equilibrium surface tension, respectively.

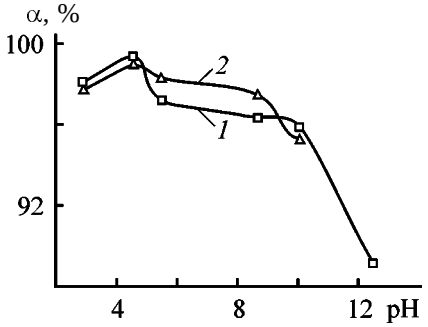

Fig. 4. Variation of the degree of removal of oil from water α by pressure flotation in the presence of (*1*) ANa and (*2*) chitosan with the pH of solution. Initial oil concentration 0.25 g dl^{-1}; flotation time 15 min.

stability of the emulsions was estimated from the time of breakdown of the half of the initial amount of the emulsion $t_{1/2}$ [15] and from the lifetime of droplets at the interface [16]. The conformations taken by the molecules of the biopolymers were determined by the procedure proposed in [17]. To this end, we measured the viscosity of aqueous solutions of ANa and chitosan with a capillary viscometer at various pH values.

The flotation treatment of water to remove oil impurities was carried out on a pilot setup for pressure flotation.[2] The flotation time was 15 min at the pressure of 0.25 Pa cm^{-1}. The oil content before and after flotation was determined photometrically using phosphovanillin reagent [18]. The experimental results are presented in Figs. 1–4 and in Tables 1 and 2.

The efficiency of removal of emulsified hydrophobic substances by flotation is governed by a number of factors [19]. The deciding factor is the state of the adsorption layers on the surface of the particles and air bubbles being floated [20]. The maximal degree of removal will, evidently, be achieved in the case when the adsorption layers form at both interfaces with equal intensity. This will involve flocculation of the oil molecules by the "bridge" mechanism and coalescence of oil droplets with air bubbles via the polymer "bridge." If the polyelectrolyte is adsorbed predominantly at the solution–air interface, only polyelectrolyte is removed from the solution. In the case of the predominant adsorption at the solution–oil interface, the oil–surfactant macromolecule complex will remain in the solution. The removal will be less intensive. Thus, it can be assumed that the degree of oil removal by flotation will be at a maximum for a polymer for which the rates of formation of the adsorption layers at the solution–air and oil–air interfaces will be approximately the same. It is believed that efficient flotation implies surface tension at the interface of 60–65 mN m^{-1}. At greater surface tensions intense frothing is observed, and at smaller, the size of the bubbles increases and their number decreases. As a result, the flotation efficiency decreases [21].

[2] Murmansk State Technical University.

Figure 1 presents the kinetic curves showing a decrease in the surface tension of the polyelectrolyte solutions of interest (concentration 0.000025 g l^{-1}) at the solution–air and solution–fish oil interfaces at the solution temperature of 20°C and pH 5.5–6. For polyelectrolytes with the concentrations of 0.00025 and 0.0025 g l^{-1} we obtained analogous curves.

Since the procedure of interest implies taking the first measurement within 4–5 s after formation of the layer, the σ_0 values shown in the figure are essentially the surface tensions at the initial moment of the layer formation which differ from the surface tension of the solvent. For double-distilled water σ_0 = 72.44 mN m^{-1} at 25°C.

As seen from Fig. 1, the surface tension decreases to the greatest extent within the first 10–15 min of formation of the adsorption layer for both polyelectrolytes studied and for both interfaces. The equilibrium surface tension is achieved for chitosan at the solution–air and solution–oil interfaces 100 min after the onset of formation of the adsorption layer (curves *2*, *4*) and for ANa, after 100 min at the solution–oil interface (curve *3*) and after 250 min at the solution–air interface (curve *4*). In the case of ANa under the actual conditions the surface tension decreases to the greatest extent at the solution–air interface: 15–20 min after the onset of formation of the adsorption layer the surface tension is equal to 62–65 mN m^{-1} (curve *1*). Our experimental data suggest that both ANa and chitosan exhibit surface activity at the solution–oil interface. The surface activity $(d\sigma/dC)_{C \to 0}$ calculated from the σ–*C* plots for ANa and chitosan at the solution–air interface is equal to 0.4×10^{-4} and 2.4×10^{-3} N m^2 mol^{-1}, respectively, and at the solution–oil interface, to 2.61×10^{-6} and 2.65×10^{-6} N m^2 mol^{-1}, respectively. Low surface activity of certain derivatives of chitin was mentioned in [22]. It should be noted that in the case of chitosan at the aqueous solution–oil interface (curve *4*), 30 min after the onset of formation of the adsorption layer the curve σ–τ exhibits a minimum. This is, evidently, due to formation of a microemulsion at the chitosan–fish oil interface. The influence of the impurities contained in chitosan on its surface activity also cannot be ruled out [23].

Formation of the adsorption layers was quantitatively estimated by the procedure described in [14], using the equation proposed originally by Rebinder:

$$\log(\sigma_\tau - \sigma_\infty) = \log(\sigma_0 - \sigma_\infty) - (\tau/2.3\theta),$$

where, σ and σ_τ are the surface tensions of the solution at the initial moment and the moment τ, mN m^{-1}, respectively; σ_∞ is the equilibrium surface tension, mN m^{-1}; θ is the relaxation time, min; and τ is the time, min.

Table 1. Relaxation time θ of solutions (0.000025 g dl^{-1}) of ANa and chitosan at the solution–air and solution–fish oil interface. Temperature 20°C; pH 5.5–6

Biopolymer	θ, min, at indicated interface	
	solution–air	solution–fish oil
ANa	45	18
Chitosan	15	10

Table 2. Lifetime of oil droplets at the oil–aqueous polyelectrolyte solution interface τ_{av} at various values of solution pH. Temperature 20°C; time of formation of the adsorption layer 150 min; polyelectrolyte concentration 0.25 g l^{-1}

pH	τ_{av}, min
Chitosan	
2.8	0.7
3.5	2.1
4.14	4.2
4.5	12.1
5.1	10 (day)
5.4	10 (day)
7.1	1.5 (day)
8.0	0.2
9.0	0.3
9.9	9.5
11.6	10.8
Sodium alginate	
3.8	0.3
6.6	1.1
9.7	0.2
12.0	5

By graphically solving this equation, we determined the relaxation times for the systems under study.

Trapeznikov *et al*. [24] studied solutions of an amphoteric polyelectrolyte (protein) and found that initially the surface tension sharply decreased and then $\log(\sigma_0 - \sigma_\infty) = f(\tau)$ exhibited a linear section with a smaller slope. From the $\log(\sigma_0 - \sigma_\infty)$ plot, we can estimate the so-called relaxation time θ corresponding

to adsorption and rearrangement of the adsorption layers and desorption [24].

Figure 2 presents the $\log(\sigma_\tau - \sigma_\infty) = f(\tau)$ plots for the adsorption layers of ANa and chitosan. Basing on the procedure proposed in [24], we estimated from the initial straight-line sections of these plots the relaxation times for ANa and chitosan at the solution–air and solution–oil interfaces (Table 1).

Table 1 shows that the maximal relaxation time of 45 min is characteristic of ANa at the solution–air interface. For chitosan the relaxation time is smaller compared to ANa for both interfaces. As seen from Fig. 2, for both polymers and the solution–oil interface (curves *3*, *4*) the slope of the second section in the plot is very small. This suggests that virtually no rearrangement of the adsorption layers and desorption occur [24]. This can probably be explained by formation at the interface of a thin oil microemulsion stabilized by polyelectrolytes. In the case of chitosan, irreversible adsorption is probably due to electrostatic interaction of the positively charged functional groups of the chitosan macromolecules with negatively charged groups of oil molecules.

The rate of formation of the adsorption layers of a surfactant affects the stability of the emulsions: The higher the rate, the greater the stability of the emulsion by the moment of its formation [25].

Figure 3 (curves *1*–*4*) shows the stability of the fish oil emulsions stabilized by the biopolymers studied and the degree of removal of oil by flotation α as functions of polyelectrolyte concentration in solution (pH of the polyelectrolyte solutions 5.5–6). Figure 3 shows that at concentrations lower than 0.2 g l^{-1} (Fig. 3, curve *2*) chitosan exerts a sensitizing effect: $\tau_{1/2}$ tends to markedly decrease, and at concentrations up to 1 g l^{-1} it does not exceed $t_{1/2}$ for emulsions without these additives. In accordance with Fig. 2, chitosan has a somewhat greater surface activity at the solution–oil interface compared to ANa. At low concentrations chitosan is rapidly adsorbed at the surface of oil droplets, favoring coalescence of droplets and affecting flocculation by the "bridge" mechanism [26]. At chitosan concentrations corresponding to formation of saturated adsorption layer (over 0.2 g l^{-1}) the macromolecules are adsorbed on the entire surface of the oil droplets, thus increasing the stability of the emulsions within this range of the polyelectrolyte concentration. Figure 3 suggests that the most stable emulsions are formed in the presence of ANa (curve *1*): $t_{1/2}$ for them is by a factor of 5–6 greater than for emulsions forming in the presence of chitosan. It should be emphasized that although ANa is somewhat less surface-active than chitosan, it is superior to chitosan in the emulsifying power. This can be explained in our case by a greater viscosity of chitosan solutions, which is responsible for the fact that under identical intensity of stirring the emulsions stabilized by chitosan will be less dispersed and will break down at a higher rate than those stabilized by ANa.

Figure 3 shows the degree of removal by flotation of oil from water (curves *3*, *4*) depending on the polyelectrolyte concentration. The oil–polyelectrolyte solution contact time was 15 min, which correponds to the maximal rate of decrease in the surface tension at the interface (Fig. 1). The maximal degree of removal of oil by flotation in the case of chitosan is achieved at the concentration of 0.2 g l^{-1}. This can be explained by the flocculation effect of chitosan: The minimum in the $\tau_{1/2}$–C curve corresponds to the maximum in the α–C curve (Fig. 3, curves *2*, *4*, respectively). In the case of ANa the decrease in the degree of removal of oil from water in the concentration range 0.2–0.6 g l^{-1} is probably due to its relatively high surface activity at the solution–air interface (Fig. 1, curve *3*). This is responsible for formation of stable air bubbles during frothing and, thereby, for increased degree of removal of oil from water. In the case of ANa the removal of oil is less efficient (Fig. 3, curve *3*), as ANa, compared to chitosan, forms more stable emulsions with oil. With increasing time of contact between oil particles and polyelectrolyte solution before flotation to 100–150 min the residual amount of oil in water significantly increases.

It is known that the stability of the adsorption layers widely varies with time and attains maximal values after establishment of the adsorption equilibrium [25]. This effect is, evidently, manifested not only under static conditions of formation of the adsorption layer but also under treatment of emulsions by flotation. Thus, under actual conditions the optimal time of contact of oil with polyelectrolyte solution during flotation is 10–15 min. To explain the influence of the polyelectrolyte on the stability of the emulsions and the removal of oil by flotation it is also necessary to take into account the conformation of the polyelectrolyte macromolecules in solution, which is markedly affected by the pH of the solution.

The influence of pH on the stability of the emulsions was estimated from the average lifetime of oil droplets at the oil–aqueous polyelectrolyte solution interface τ_{av}. The time of formation of the adsorption layer was 150 min, which corresponds to the time required for establishment of the adsorption equilibrium at this interface (Fig. 1). The concentration of

the polyelectrolyte corresponded to formation of saturated adsorption layer and was equal to 0.25 g l^{-1}. The results obtained are presented in Table 2.

As follows from Table 2, the longest τ_{av} for chitosan is observed at pH 5.1–7 and 9–12, and for ANa, at pH 6.6 and 12. The influence of pH on the lifetime of the droplets is probably due to the conformational changes in the polyelectrolyte macromolecules.

Our findings concerning the conformation taken by the chitosan macromolecules as influenced by pH of the medium suggest that in acidic medium (pH < 3) the chitosan macromolecules take the most unfolded conformation. At pH 4–7 they roll up into loose globules. In alkaline medium compact dense structures, globules, form. This is consistent with the nature of the macromolecules of chitosan, which are cationic surfactants, and with the solubility of chitosan whose isoelectric point is at pH 5.2 [3].

The ANa macromolecules in alkaline medium take the most unfolded conformation. On going to acidic medium, the viscosity of the solution of this polyelectrolyte decreases, which suggests formation of compact structures. Acidification of the medium (pH < 4) does not change the viscosity, as this pH value, evidently, corresponds to the most compact polymeric ANa chains. This dependence is explained by the fact that ANa is anionic surfactant which is virtually insoluble in acidic media [3, 27].

Thus, under actual conditions (at pH 5.5–6) the chitosan and ANa macromolecules take loose coil conformation corresponding to formation of the most stable oil–water emulsion (Table 2). It should be noted that in strongly alkaline medium (pH 11–12) the lifetime of droplets also increases. A possible reason is the presence of a large amount of alkali in the polyelectrolyte solution. Probably, owing to oil hydrolysis certain amount of the molecules (more precisely, alkaline salts) of free fatty acids forms at the polyelectrolyte solution–oil interface. These molecules present an additional structural and mechanical barrier in the form of ultramicroemulsion and hinder coalescence of oil droplets with the allied surface.

Figure 4 presents the degree of removal of oil by flotation depending on the pH of the polyelectrolyte solutions. It is seen that the maximal degree of removal of oil from water corresponds to pH 5.5–6. At this pH the macromolecules of the polyelectrolytes occur in a loose coil conformation.

Our results suggest complex interaction between the natural polyectrolytes and fat components contained in water. Evidently, it is also necessary to take into account the fact that polyelectrolytes are solubilized by lipid substances as pointed out in [28].

CONCLUSION

The polyelectolytes sodium alginate and chitosan acting as surfactants at the solution–air and solution–oil interfaces affect the stability of the oil–water emulsions and intensify removal of fat and protein components from water by flotation. The stability of the emulsions and the efficiency of water treatment by flotation depends on the conformation taken by the polyelectrolyte macromolecules in solution.

REFERENCES

1. Matov, B.M., *Flotatsiya v pishchevoi promyshlennosti* (Flotation in Food Industry), Moscow, Pishch. Prom–st., 1976.
2. Bykov, V.P., *Ryb. Khoz.*, 1995, no. 1, pp. 49–53.
3. Bogdanov, V.D., and Safonova, T.M., *Strukturoobrazovateli i rybnye kompozitsii* (Structure-Forming Agents and Fish Compositions), Moscow: Pishch. Prom–st., 1993.
4. Jirgensons, B., *Natural Organic Macromolecules*, Oxford: Pergamon, 1962.
5. Veitser, Yu.I. and Mints, D.M., *Vysokomolekulyarnye flokulyanty v protsessakh ochistki vody* (Macromolecular Flocculants in Water Treatrment Processes), Moscow: Stroiizdat, 1980.
6. Podkorytova, A.V., Aminina, N.M., and Sokolova, V.M., *Ryb. Khoz.*, 1996, no. 5, pp. 63–64.
7. Maslova, G.V., Kuprina, E.A., Shchedrina, N.A., *et al.*, *Ryb. Khoz.*, 1996, no. 3, pp. 60–61.
8. Baran, A.A. and Teslenko, A.Ya., *Flokulyanty v biotekhnologii* (Flocculants in Biotechnology), Leningrad: Khimiya, 1990.
9. Babenkov, E.D., *Ochistka stochnykh vod koagulyantami* (Wastewater Treatment with Coagulants), Moscow: Nauka, 1977.
10. Vinogradov, B.D., Efimov, A.A., and Lukina, L.N., in *Proc. 3rd All-Union Conf. "Sovershenstvovanie proizvodstva khitina i khitozana iz pantsir'soderzhashchikh otkhodov krilya i puti ikh ispol'zovaniya"* (Improvement of Production of Chitin and Chitosan from Shell-Containing Wastes of Krill and the Ways of Using Them), Moscow: VNIRO, 1992, pp. 105–107.
11. No, H.K. and Meyres, S.R., *J. Agr. Food Chem.*, 1989, vol. 37, no. 3, pp. 580–583.
12. USSR Inventor's Certificate no. 1 751 888.
13. Adamson, A.W., *Physical Chemistry of Surfaces*, New York: John Wiley and Sons, 1976.

14. Derkach, S.R., Zotova, K.V., Izmailova, V.N., and Panaeva, S.A., *Zh. Prikl. Khim.*, 1993, vol. 66, no. 3, pp. 633–638.
15. Alekseev, G.I. and Bogdanov, N.I., *Izv. Vyssh. Uchebn. Zaved., Severokavkaz. Region, Tekh. Nauki*, 1993, nos. 1–2, pp. 76–79.
16. Baranova, V.I., Bibik, E.E., Kozhevnikova, N.M., *et al.*, *Praktikum po kolloidnoi khimii: uchebnoe posobie dlya khimiko-tekhnologicheskikh spetsializirovannykh vuzov* (Laboratory Manual on Colloid Chemistry: Educational Manual for Chemicotechnological Special Higher Educational Establishments), Lavrov, I.S., Ed., Moscow: Vysshaya Shkola, 1983.
17. *A Laboratory Manual of Analytical Methods of Protein Chemistry*, vol. 1–3, Alexander, P. and Bloch, R.I., Eds., London, Pergamon, 1960–1961. Translated under the title *Analiticheskie metody belkovoi khimii*, Moscow: Inostrannaya Literatura, 1963, p. 233.
18. Lur'e, Yu.Yu. and Rybnikova, A.N., *Khimicheskii analiz proizvodstvennykh stochnykh vod* (Chemical Analysis of Indistrial Wastewaters), Moscow: Khimiya, 1974.
19. Rulev, N.N., Deryagin, B.V., and Dukhin, S.S., *Kolloidn. Zh.*, 1977, vol. 39, no. 4, pp. 314–323.
20. Deryagin, B.V., Rulev, N.N., Dukhin, S.S., *Kolloidn. Zh.*, 1977, vol. 79, no. 4, pp. 680–691.
21. Yakovlev, S.V., Karelin, Ya.A., Zhukov, A.I., and Kolobanov, S.K., *Kanalizatsiya* (Sewage System), Moscow: Stroiizdat, 1975.
22. Babak, V.K., Anchipolovskii, M.A., Vikhoreva, G.A., and Lukina, I.G., *Kolloidn. Zh.*, 1996, vol. 58, no. 2, pp. 155–162.
23. *Praktikum po kolloidnoi khimii (kolloidnaya khimiya lateksov i poverkhnostno-aktivnykh veshchestv)* [Laboratory Manual on Colloid Chemistry (Colloid Chemistry of Latexes and Surfactants)], Neiman, R.E., Ed., Moscow: Vysshaya Shkola, 1971.
24. Trapeznikov, A.A., Vins, V.G., and Shirokova, T.Yu., *Kolloidn. Zh.*, 1981, vol. 43, no. 2, pp. 322–328.
25. Markhasin, I.L., Nazarov, V.D., and Kozlova, T.I., *Vodosnabzh. San. Tekh.*, 1981, no. 4, pp. 7–8.
26. Baran, A.A. and Solomentseva, I.M., *Khim. Tekhnol. Vody*, 1983, vol. 5, no. 2, pp. 120–137.
27. Zikeev, B.V., *Pererabotka vodnogo nerybnogo syr'ya* (Processing of Nonfish Water Resources), Moscow: Pishchepromizdat, 1950.
28. Izmailova, V.N. and Rebinder, P.A., *Strukturoobrazovanie v belkovykh sistemakh* (Structure Formation in Protein Systems). Moscow: Nauka, 1974.

Russian Journal of Applied Chemistry, Vol. 74, No. 3, 2001, pp. 455–460. Translated from Zhurnal Prikladnoi Khimii, Vol. 74, No. 3, 2001, pp. 445–450.

PROCESSES AND EQUIPMENT OF CHEMICAL INDUSTRY

Hydrodynamic Model of a Free Jet of Atomized Fluid

S. V. Aniskin and O. I. Protod'yakonova

St. Petersburg State Technological University of Plant Polymers, St. Petersburg, Russia

Received December 20, 2000

Abstract—The formation and development of a gas–fluid jet outflowing from a single-flare atomizer of a spray absorber are analyzed theoretically, and a hydrodynamic model taking into account the nonuniformity of spraying density and gas flow velocity across the jet is developed on the basis of this analysis.

Developing methods for calculating mass-exchange processes in spraying apparatus requires a detailed theoretical study of jet flows. Such flows occur, in particular, in direct-flow spray absorbers.

One of important kinds of jet flows is a flow of drops formed in spraying a fluid with a single-flare atomizer. It is known that a gas jet is always formed inside such a drop flow. Thus, the jet of atomized fluid, considered as a whole, is a gas–fluid jet.

The main distinction of single-jet atomizers is that fluid drops are present within the entire flare cone.

Let us represent the structure of the jet flow under consideration as the following scheme (Fig. 1). The gas–fluid jet is conventionally divided into three zones. In the first zone, the fluid jet outflowing from the atomizer *1* is deformed and then disintegrates into drops and some coarse formations of indeterminate shape, which, in turn, also disintegrate into large and fine drops. There are no formations of this kind in the second and third zones, and inclusions of the disperse phase are only composed of large and fine drops. The mechanisms of interaction between phases are different in these zones.

As the gas–fluid jet moves, its flare expands, with the volume density of the fluid phase, correspondingly, decreasing:

$$\beta = \frac{V_l}{V_g + V_l}, \quad (1)$$

where V_l and V_g are, respectively, the fluid and gas volumes in the gas–fluid jet.

In the initial part of the first zone, the forming drops are so close to one another that their hydrodynamic boundary layers come in contact. This gives rise to a certain structure of interconnected fluid phase inclusions, with the motion of gas through this structure comparable with the filtration process.

In the final part of the first zone, beginning with the instant when the β value becomes approximately equal to 0.02 [1], there is no mutual influence of drops any more and they move further entirely independently of one another. In this case, the momentum exchange between the fluid and the gas will depend on the size, shape, and relative velocities of drops and of fluid formations whose disintegration into drops continues in the flow zone in question.

In accordance with the results obtained in experimental studies of the hydrodynamics of the gas–fluid jet by the photographic method [2], the mentioned disintegration is complete at the instant when β becomes 0.003. It should be noted that the estimated β values at which moving drops cease to affect one another may be somewhat different for atomizers of special types. For example, for atomizers in which

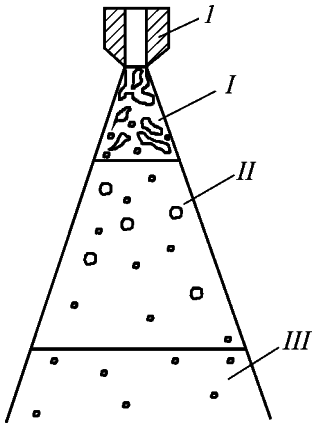

Fig. 1. Structure of gas–fluid jet in fluid spraying with a single-flare atomizer: (*1*) atomizer and (*I–III*) jet zones.

1070-4272/01/7403-0455$25.00

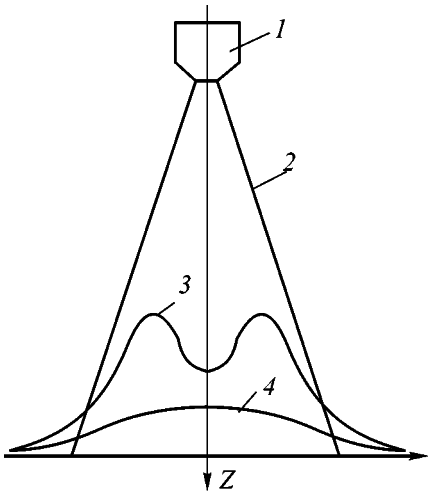

Fig. 2. Distribution of gas flow velocity and fluid spraying density across the flare: (*1*) atomizer, (*2*) conventional flare boundary, (*3*) distribution of spraying density J (m s^{-1}), and (*4*) distribution of gas flow velocity v_i (m s^{-1}).

the fluid flow is divided into separate small jets forming chains of drops this β value may be much lower than 0.02.

In the second zone, the momentum of the gas jet formed inside the drop flow steadily grows because of the drop deceleration [2] which can be described by the known hydrodynamic equations [3]. Here, it is important to take into account the fact that drops in this zone do not change their shape and size.

A distinctive feature of the third zone is that the drops in it have already lost a major part of the initial momentum. Therefore, the momentum that can be transferred by drops to gas in this stage of development of the gas–fluid jet can be considered negligibly small as compared with the momentum of the gas jet formed in the second zone.

Consequently, the momentum of the gas jet in the third zone remains constant. The motion of a jet satisfying the conditions of the third zone corresponds to the known model of a submerged gas jet with disperse inclusions [4].

Thus, the relative phase motion velocities are comparatively low in the third zone of the gas–fluid jet. It is this fact that gives no way of effectively performing in this zone such mass-exchange processes in which the main resistance to mass transfer is associated with the gas phase. In this connection, it is advisable to ensure by using one or another factor (pressure of the fluid outflowing from the atomizer nozzle, drop size, shape and size of apparatus, directed jet flow, fluid jet flare angle, etc.) sufficiently high relative velocities of phases throughout the reaction volume of the apparatus. Under such conditions, no third zone appears in the gas–fluid jet.

Therefore, it is advisable, when studying the flow of gas–fluid jets in spray mass-exchange apparatus intended to perform processes with the main resistance to mass transfer associated with the gas phase, to limit the zone of problem setting to the first two flow zones.

Models have peen proposed [5–7] describing the flow of a gas–fluid jet in the first and second of the considered zones. In describing the relative motion of gas and fluid in these zones [6], the flow of a gas was identified with the process of its filtration through a disperse fluid medium. In doing so, the Ergun equation, originally proposed for describing the process in an apparatus with solid filter, was employed as an equation relating the hydraulic resistance of the disperse medium to the relative velocity of phases and the volume concentration of the disperse phase.

However, the use of this approach in modeling the flow in question is only justified for the first zone of the jet. In the second zone, the volume concentration of the disperse phase goes beyond the validity limits of the Ergun equation.

A shortcoming of [5] consists in the assumption of a uniform distribution of the gas flow velocity over the gas–fluid jet. In doing so, the authors determine the jet boundary from the initial flare angle and trajectory of drop motion at the thus determined jet boundary.

Actually, as indicated by the results obtained in experimental studies of flows of this kind [2, 8], the distribution of the gas flow velocity in the jet is not uniform, but resembles a Schlichting profile.

Figure 2 shows a typical gas flow velocity distribution and spraying density (amount of fluid passing through unit cross-section of the gas–fluid flow) across the flare at a certain distance from the atomizer [9].

In using [5] the assumption of a uniform gas flow velocity distribution in the gas–fluid jet, it is rather essential how a method for reliably determining the gas jet boundary is chosen (Fig. 2). Galustov [5] determines the boundary of the gas flow with gas velocity uniformly distributed across the gas–fluid jet from the boundary of the drop flow. The latter is preliminarily found from the prescribed spraying density J defined as a fluid flow Q_l passing through a jet flare cross-section S

$$J = Q_l/S. \quad (2)$$

Meanwhile, it is known that the gas flow boundary should be found from the type of gas flow velocity distribution across the jet. However, with this method used, the boundaries of the drop and gas flows are found to be in different places of the flare. Thus, the condition used to introduce the gas flow boundary determines the cross-section area of the gas–fluid jet and the intensity of momentum exchange between the fluid and gas in the jet. Consequently, the adequacy of the hydrodynamic model [5] describing the flow of a gas–fluid jet with uniform cross-sectional distribution of the gas to the actual process strongly depends on a method used to determine the jet boundary, not specified in [5]. It should be noted that developing such a method is a complicated independent task.

The main problem to be solved in a theoretical analysis of a gas–fluid jet flow in the first and second zones, made in this study, is to construct a flow model free of the above shortcomings. The model was developed under the following assumptions. The jet flow is considered to be established. There is no drop fragmentation or coagulation in the second zone of the jet. There is no heat exchange within the jet. The distribution of the spraying density in the gas–fluid jet is axially symmetric. The stresses in the turbulent gas jet developed inside the flare in the first and second zones of the gas–fluid flow are negligibly small as compared with the stresses created in this jet by the moving fluid.

The size distribution of drops formed in fluid jet fragmentation is the same across the flare. The process of drop fragmentation in the gas–fluid jet is complete at a volume concentration of the disperse phase $\beta = 0.003$. Since the intensity of new drop formation markedly decreases along the first zone, it is natural to use in constructing the model the assumption that changes in the average drop size with β varying between 0.02 and 0.003 can be considered negligible.

In order to take into account the nonuniformity of spraying density distribution across the jet flare, let us divide the flare with conical surfaces into n separate jets within which the flow rate remains the same (Fig. 2a), i.e. the following condition is met for an arbitrary ith jet:

$$G_i = \text{const}, \tag{3}$$

where G_i is the mass flow rate of the fluid (kg s^{-1}).

Let us determine the variation of the gas flow momentum along the Z-axis within ith jet. To do so, let is distinguish a thin layer of the cone with height dz, as shown in Fig. 3a. Let us consider the cross-section of this layer in a plane passing through the Z-axis (Fig. 3b). We assume that the velocity v_i and pressure P_i of the gas are constant within each ith layer. Changes in the momentum of the gas flow between the cross-sections ab and cd occur for the following three reasons: stresses appearing in fluid deceleration, partial momentum transfer resulting from the shift of the gas flow through lateral surfaces bd and ac toward the Z-axis, and pressure drop ΔP across the distance Δz.

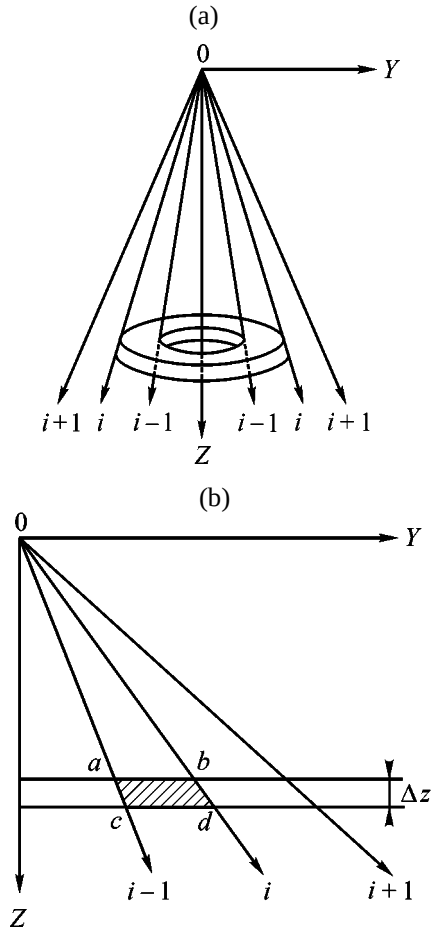

Fig. 3. Schematic of how the gas–fluid flow flare is subdivided by flow lines: (a) volume scheme and (b) section in a plane passing through the Z-axis.

With account of the aforesaid, the following equation can be written for the variation of momentum in the distinguished ith layer of the cone:

$$\Delta(\rho_g Q_{gi} v_{zi}) + \rho_g v_{z(i+1)} \Delta Q^y_{g(i+1)} - \rho_g v_{zi} \Delta Q^y_{gi} + S_i \Delta P_i + G_i \Delta u_{zi} = 0, \tag{4}$$

where ρ_g is the gas density (kg m^{-3}); S_i, the area of cross-section ab (m^2); v_i, the gas velocity within ith layer (m s^{-1}); Q_{gi}, the volumetric flow rate of gas

through area S_i ($m^3 s^{-1}$); $\Delta Q^y_{g(i+1)}$ and ΔQ^y_{gi} are, respectively, the part of the volumetric gas flow rate coming to layer i from layer $i + 1$ and that coming to layer i from layer $i - 1$; P_i, the gas pressure in layer i ($N m^{-2}$); and u_{zi}, the fluid velocity along the Z-axis ($m s^{-1}$).

With account of the introduced designations, the quantity ΔQ_{gi}, equal to the change in the gas flow rate in ith layer from section ab to section cd, is defined by the equation

$$Q_{gi} = \Delta Q^y_{g(i+1)} - \Delta Q^y_{gi}. \quad (5)$$

The quantity $\Delta Q^y_{g(i+1)}$ appearing in Eq. (4) can be determined from the condition for conservation of the gas flow rate in a jet of radius y_i:

$$\Delta Q^y_{g(i+1)} = \sum_{i+1}^{i} \Delta Q_{gi}. \quad (6)$$

Let us denote the radial gas flow velocity in ith element of space (i.e., in the $abcd$ element) by v_{yi}, and that in $(i + 1)$th element, by $v_{y(i+1)}$. With account of these designations the volumetric flow rate of gas coming into ith element through its lateral surface from $(i + 1)$th element of a distinguished layer of a gas–fluid jet of height dz can be expressed as

$$\Delta Q^y_{g(i+1)} = -2\pi y_{i+1} v_{y(i+1)}. \quad (7)$$

From relations (6) and (7) we obtain, passing from finite differences to differentials, the following conservation equation for the gas flow rate in the form

$$\sum_{i=1}^{i} (dQ_{gi}/dz) = -2\pi y_{i+1} v_{y(i+1)}. \quad (8)$$

In order to obtain equations describing changes in the momentum in a layer of the cone, bounded by a lateral surface of radius y_i and horizontal sections z and $z + \Delta z$, we sum Eq. (4) from $i = 1$ to i. In doing so, account should be taken of the fact that, by virtue of the axial symmetry, there is no gas flow along the Y-axis at the Z-axis of the jet, and, therefore, $\Delta Q^y_{g1} = 0$. As a result of the summation, we obtain, passing from Δz to dz, the sought-for equation in the following form:

$$\frac{d}{dz}\sum_{i=1}^{i} (\rho_g Q_{gi} v_{zi}) + \rho_g v_{z(i+1)} \sum_{i=1}^{i} (dQ_{gi}/dz) + \sum_{i=1}^{i} G_i (du_{zi}/dz) + \sum_{i=1}^{i} S_i (dP_i/dz) = 0. \quad (9)$$

To determine the P_i value, we use the following considerations. Within an elementary volume $abcd$ of the jet (Fig. 3b) there exists some gas pressure P_i. The gas flow velocity along the Y-axis is constant within the volume $abcd$. Under these conditions, the variation of the pressure P_i in the direction of the Y-axis will be entirely determined by the stress created by the flow of drops along the Y-axis in the elementary volume in question. This dependence is expressed by the relation

$$(P_{i+1} - P_i) \times 2\pi y_i dz + G_i du_{yi} = 0. \quad (10)$$

Further, we derive an expression describing the variation of the fluid flow velocity in ith elementary volume of the $abcd$ space. Let us assume that the direction of the Z-axis coincides with that of the gravity force. In obtaining this expression, account should be taken of the fact that, by virtue of the different kinds of mutual influence of moving drops within these regions, this expression will have different forms for regions of the first zone of the jet, satisfying the conditions $\beta > 0.02$ (initial region of the first zone) and $\beta < 0.02$ (final region of the first zone and the second zone).

Let us first find the expression describing the variation of the fluid flow velocity along the Z-axis in the initial part of the first zone of the gas–fluid jet, satisfying the condition $\beta > 0.02$. For this purpose, let us write an equation characterizing the deceleration of the fluid flow G under the action of the gas-medium resistance force F_{ri} and the gravity force F_{gri}:

$$G_i du_{zi} = -(F_{ri}\cos\alpha - F_{gri}), \quad (11)$$

where α is the angle between the Z-axis and the direction of action of the resistance force F_{ri}.

The F_{gri} value is given by

$$F_{gri} = g G_i \Delta z_i / u_{zi}, \quad (12)$$

where g is the acceleration of gravity.

In deriving the expression for the mentioned resistance force for the initial part of the first zone of the jet, we can rely upon an analogy between the mechanism of gas–fluid interaction in the gas–fluid jet and that of gas filtration through a packing bed moving as a whole [6]. The reason for applying the above analogy is the sufficiently high volume density of the fluid phase in the considered initial part of the first zone of the jet, where, as mentioned above, $\beta \geq 0.02$. With account of the analogy, the force arising in the

fluid deceleration in *i*th elementary volume of the *abcd* space will be given by the filtration pressure drop dP_{fi} across the mentioned volume

$$F_{ri} = S_{fi}dP_{fi}. \quad (13)$$

If a straight line is drawn through the planes *ab* and *cd* in the direction coinciding with that of the F_{ri} force, then these planes will intercept a portion d*l* on the straight line. To obviate unnecessary graphical complications, this line portion is not shown in Fig. 3. Apparently, the ratio of S_i to S_{fi} will be proportional to the ratio of d*l* and d*z*, which allows use of the following relation in further analysis:

$$S_i/S_{fi} = dl/dz. \quad (14)$$

Then, for the considered initial part of the first zone of the jet, the variation of the fluid velocity u_{zi} in a layer of thickness d*z* will be given, with account taken of expressions (11)–(14), by

$$du_{zi}/dz = (S_i dP_{fi}\cos\alpha)/G_i dl + g/u_{zi}. \quad (15)$$

To determine dP_{fi}/dl, we use the known calculation procedure [10] based on the Darcy equation

$$dP_f/dl = \xi\rho_g u_{rel}^2/2d_{eq}, \quad (16)$$

where u_{rel} is the relative motion velocity of fluid and gas, d_{eq} is the equivalent packing channel diameter, and ξ_f is the filtration resistance coefficient.

For packings of arbitrary shape the ξ_f value can be determined using the Ergun relations [11]

$$\xi_f = 133/Re_g + 2.34. \quad (17)$$

The equivalent dimater of packing channels is determined using the known relation [10]

$$d_{eq} = 4\varepsilon/a, \quad (18)$$

where *a* is the specific surface area of the packing (m^{-1}) and ε is the packing bed porosity.

To apply this method for dP_f/dz calculation to the gas–fluid jet in the region in question, it is necessary to find the relationship between d_{eq} and the size of the forming drops. We assume that d_{eq} is constant in fluid jet disintegration into drops. Then, with account of $\varepsilon = 1 - \beta$, it follows from (18) that

$$d_{eq} = 4(1 - \beta)/a. \quad (19)$$

At the end of the zone in which the jet disintegrates into drops the β value is small and the specific surface area of the fluid becomes equal to the specific surface area a_d of drops in the disintegrated jets. The a_d value can be determined from the average volume-surface diameter, or the Sauter diameter d_{32}, using the relation

$$a_d = 6/d_{32}. \quad (20)$$

From (19) and (20) follows that

$$d_{eq} = 2d_{32}/3. \quad (21)$$

Relation (21) gives an expression describing the variation of the velocity u_{zi} within *i*th elementary volume *abcd*. This expression can be written, with account of Eqs. (15)–(17), in the form

$$du_{zi}/dz = 3S_i\xi_f 3\rho_g u_{rel}^2\cos\alpha/4G_i d_{32} + g/u_{zi}. \quad (22)$$

The same equation written for the projections onto the *Y*-axis has the form

$$du_{yi}/dz = 3S_i\xi_f\rho_g u_{rel}^2\sin\alpha/4G_i d_{32}. \quad (23)$$

In deriving Eq. (23), which is simpler than Eq. (22), account was taken of the fact that the *Y*-component of the gravity force is zero.

In the part of the gas–fluid jet satisfying the condition $\beta < 0.02$, drops move independently of one another. Therefore, the variation of the fluid motion velocity can be evaluated from that of the velocities of separate drops. The expression describing this variation has the form

$$du_{zi}/dz = -3\xi_d\rho_g u_{rel}^2\cos\alpha/4d_{32}u_{zi} + g/u_{zi}, \quad (24)$$

$$du_{yi}/dz = 3\xi_d\rho_g u_{rel}^2\sin\alpha/4d_{32}u_{zi}, \quad (25)$$

where ξ_d is the resistance coefficient of a drop moving in a gas medium.

A formula for determining the ξ_d value is chosen depending on the Reynolds number Re. For the conditions under consideration, we can use the formula valid for the range $0.1 < Re < 1000$ [3]:

$$\xi_d = 24(1 + 0.125Re^{0.72})/Re. \quad (26)$$

Using the apparent relations $u_y = dy/dt$, we can obtain an expression necessary for determining the dependence $y_i(z)$

$$dy_i/dz = u_{yi}/u_{zi}. \quad (27)$$

Thus, the developed hydrodynamic model of a free

flare of atomized fluid includes 6*n* first-order differential equations for 10*n* unknowns: Q_{gi}, v_{zi}, v_{yi}, u_{zi}, u_{yi}, u_{rel}, P_i, S_i, y_i, and α_i, which are to be supplemented with an appropriate number of closing relations with apparent meaning. These are algebraic equations of the form

$$Q_{ri} = S_i v_{zi}, \quad (28)$$

$$S_i = \pi(y_i^2 - y_{i-1}^2), \quad (29)$$

$$u_{rel} = [(u_{yi} - v_{yi})^2 + (u_{zi} - v_{zi})^2]^{1/2}, \quad (30)$$

$$\alpha_i = \arctan[(u_{yi} - v_{yi})/(u_{zi} - v_{zi})]. \quad (31)$$

In accordance with the assumption of a practically instantaneous establishment of a stationary gas–fluid jet flow immediately after the fluid outflow from the atomizer nozzle, the constructed system of equations of the hydrodynamic model should only be supplemented with boundary conditions. At $z = 0$, $G_i = G_i^{(0)}$, $u_{zi} = u_{zi}^{(0)}$, $u_{yi} = u_{yi}^{(0)}$, $v_{zi} = u_{zi}^{(0)}$, $v_{yi} = u_{yi}^{(0)}$, $y_i = y_i^{(0)}$, $\alpha_i = \alpha_i^{(0)}$; at $y = 0$, $v_{y1} = 0$.

On the outer boundary of the jet, i.e., at $y > y_n$, $v_{y(n+1)} = 0$, $v_{z(n+1)} = 0$, $G_{n+1} = 0$, $P_{i+1} = P_a$, where P_a is the atmospheric pressure (Pa). This system can be solved numerically by the Runge–Kutta method.

CONCLUSIONS

(1) A detailed theoretical analysis of the gas–fluid jet formed by an atomizer in a spraying apparatus served as a basis for constructing a hydrodynamic model taking into account the nonuniformity of gas velocity distribution and the variation of gas pressure in the jet.

(2) The main advantage of the developed model consists in that there is no need to preliminarily determine the gas jet boundaries in applying the model to calculations of spraying mass-exchange apparatus.

REFERENCES

1. Soo, S.L., *Fluid Dynamics of Multiphase Systems*, Waltham (Massachusetts): Blaisdell, 1967.
2. Torf, A.I., Pasechnik, S.P., and Aniskin, S.V., in *Mezhvuzovskii sbornik nauchnykh trudov "Okhrana okruzhayushchei sredy ot zagryazneniya proizvodstvennymi vybrosami"* (Intercollegiate Coll. of Sci. Works "Environment Protection from Pollution with Industrial Wastes"), Leningrad, 1977, issue 5, pp. 181–186.
3. Sternin, L.E., Maslov, B.N., Shraiber, A.A., and Podvysotskii, A.M., *Dvukhfaznye mono- i polidispersnye techeniya gaza s chastitsami* (Two-Phase Mono- and Polydisperse Gas Flows with Particles), Moscow: Mashinostroenie, 1960.
4. Abramovich, G.N., *Teoriya turbulentnykh strui* (Theory of Turbulent Jets), Moscow: Nauka, 1966.
5. Galustov, V.S., *Pryamotochnye raspylitel'nye apparaty v teploenergetike* (Direct-Flow Spraying Apparatus in Heat-and-Power Engineering), Moscow: Energoatomizdat, 1969.
6. Basargin, B.N., Zvezdin, Yu.G., and Denchuk, E.Ya., in *Massoobmennye i teploobmennye protsessy khimicheskoi tekhnologii* (Mass- and Heat-Exchange Processes in Chemical Technology), Yaroslavl: Yaroslav. Politekh. Inst., 1975, issue 1, pp. 8–13.
7. Aniskin, S.V., in *Mezhvuzovskii sbornik nauchnykh trudov "Okhrana okruzhayushchei sredy ot zagryazneniya proizvodstvennymi vybrosami"* (Intercollegiate Coll. of Sci. Works "Environment Protection from Pollution with Industrial Wastes"), Leningrad, 1977, issue 5, pp. 179–181.
8. Katalov, V.I., Gushchin, Yu.I., and Basargin, B.N., in *Massoobmennye i teploobmennye protsessy khimicheskoi tekhnologii* (Mass- and Heat-Exchange Processes in Chemical Technology), Yaroslavl: Yaroslav. Politekh. Inst., 1975, issue 2, pp. 13–16.
9. McVey, J.B., Russell, S., and Kennedy, J.B., *J. Propulsion*, 1988, vol. 3, no. 3, pp. 202–209.
10. Ramm, V.M., *Absorbtsiya gazov* (Absorption of Gases), Moscow: Khimiya, 1976.
11. Ergun, S., *Chem. Eng. Progr.*, 1952, vol. 48, no. 2, pp. 89–94.

Russian Journal of Applied Chemistry, Vol. 74, No. 3, 2001, pp. 461–465. Translated from Zhurnal Prikladnoi Khimii, Vol. 74, No. 3, 2001, pp. 451–455.

PROCESSES AND EQUIPMENT OF CHEMICAL INDUSTRY

Effect of Stirring Devices on the Intensification of Gas–Fluid Processes

V. N. Ivanets, S. N. Al'brekht, and G. E. Ivanets

Kemerovo Technological Institute of Food Industry, Kemerovo, Russia

Received April 3, 2000; in final form, November 2000

Abstract—A comparative analysis is made of the operation of apparatus of rotary-pulsation and ejector types with self-suction turbine agitator. The dependence of the efficiency of operation on the output capacity and energy-related characteristics determining power consumption for agitation of gas–fluid mixtures were determined experimentally.

One of the main parameters characterizing the efficiency of a gas–fluid apparatus is the phase surface contact area. Present attempts to raise its value are commonly associated with reducing the geometric dimensions of gas bubbles by using, as a rule, various bubbling and mechanical stirring devices [1–3]. However, gas–fluid apparatus presently used in chemical and other industries have a number of serious disadvantages and frequently fail to satisfy modern requirements to the output capacity, quality, and energy expenditure per unit product. Therefore, development of new absorber designs and improvement of the existing types of apparatus are, beyond any doubt, urgent tasks. One of possible ways to solve this problem is to provide intensive stirring ensuring a significant rise in the phase boundary area and concentration of a considerable amount of energy in small volumes. It is known that the use of low-frequency (20–20 000 Hz) acoustic elastic vibrations allows in most cases a substantial intensification of the homogenization process. In this case, such phenomena as cavitation, acoustic pressure, and pulsing microflows occur in the medium being treated, making higher the rate of physicochemical processes in heterogeneous systems [3].

Acoustic vibrations are generated by means of hydrodynamic transmitters. In transmitters of this kind, acoustic vibrations are generated by rotary-pulsation devices. In view of their great potentiality, it may be assumed that that use of gas–fluid rotary-pulsation apparatus (RPA) for performing absorption will allow a substantial intensification of this process.

The goal of this study was to analyze the efficiency of conventional gas–fluid apparatus (of ejector type and with turbine agitator) and RPA for performing nitrosation of diphenylamine (DPA) in an organic solvent (trichloroethylene, TCE, fluid phase) with a mixture of nitrose gases, NO and NO_2 (gas phase), with the aim to develop a multifunction apparatus for intensifying processes of absorption, homogenization, and dispersion.

In the first stage, the influence exerted by the main parameters (temperature, concentration, solubility of the gas phase, its amount and means of delivery) on the time of process completion was studied. For this purpose, a laboratory rig was designed and fabricated. The experiments were performed as follows. A pretreated 1.01 : 1 gas mixture of nitrogen oxides, NO + NO_2, was fed through a rotameter into the reactor, together with a 15% solution of DPA in TCE. The temperature of the reaction mixture was monitored with a thermocouple; its prescribed value was maintained with thermostat and supply lines for a cooling agent. The reactor of volume 0.65×10^{-3} m^3 was equipped with a mechanical agitator and a bubbling device. Samples were taken at 30-s intervals and analyzed for the content of DPA in solution by thin-layer chromatography and spectrometry on an SF-46 instrument.

Originally, the effect of the nitrosing agent flow rate on the time of complete DPA conversion was studied. Analysis of the results furnished by mathematical processing of experimental data shows that at a gas phase flow rate exceeding 0.3 $m^3 h^{-1}$ the time in which the process is complete remains practically unchanged. Therefore, in further experiments, the gas phase flow rate was taken to be, in a certain excess, 0.35 $m^3 h^{-1}$. Then the dependence of the time of complete DPA conversion on the process temperature was

1070-4272/01/7403-0461$25.00

Table 1. Time of process completion τ at varied flow rates of the gas (Q_g) and fluid (Q_f) phases in the extractor

Q_g, $m^3\ h^{-1}$	τ, min, at indicated Q_l, $m^3\ h^{-1}$		
	0.2	0.275	0.35
0.66	70	70	70
1	59	58	57
1.5	38	33	28.7
2	32	26.7	21.4

Table 2. Maximum output capacity V_l of ejector-type apparatus at varied gas component flow rate Q_l and working phase flow rate W

Q_g, $m^3\ h^{-1}$	V_l, $m^3\ h^{-1}$, at indicated W, $m^3\ s^{-1}$		
	10.46	14.38	18.3
0.66	0.01543	0.01543	0.01543
1	0.0183	0.01862	0.1895
1.5	0.02842	0.03273	0.03763
2	0.03375	0.04045	0.05047

studied in the range 10–30°C with a step of 5°C. It was found that the shortest time (1.5 min) is achieved at a temperature of 20 ± 2°C [4]. The dependences of the process duration on the intensity of stirring and method of gas phase feeding into the reactor (into the over-solution space or through a bubbler situated at the bottom) were studied. It was found that the time of complete DPA conversion decreases with increasing agitator speed. The minimum time corresponds to an agitator rotation rate of 157 s^{-1}. In this case, the method by which the gas phase is fed has virtually no effect on the time of process completion. Analysis of experimental data shows that under the found optimal conditions [temperature 20 ± 2°C, atmospheric pressure, nitrogen oxide mixture composition $NO : NO_2$ = (1.01–1.04) : 1, initial DPA concentration 15 wt %, stirring intensity $Re = 5 \times 10^3$] the DPA nitrosation is kinetically controlled. Vigorous stirring eliminates the effect of the mass exchange at the phase boundary on the rate of the chemical reaction.

After the basic process parameters were found, the most efficient of the three kinds of gas–fluid apparatus (with ejector, with self-suction turbine agitator, and of rotary-pulsation type) was determined. The DPA nitrosation was studied on a semicommercial installation comprising rotameters and control equipment serving to vary the flow rates of components within prescribed limits, reaction unit including one of the compared apparatus, and redox potentiometer for determining the completion time of the chemical reaction. The reaction mixture volume was constant (0.018 m^3) in all the experiments.

As a criterion for comparing the operation of the three apparatus served the efficiency

$$E = V/(N\tau), \quad (1)$$

where V is the reaction mixture volume (m^3), N is the power consumed for performing the process (W), and τ is the process duration (min).

The power consumed for performing the process consists of the following components:

$$N = N_1 + N_2 + N_3 + N_4 + N_5,$$

where N_1, N_2, N_3, N_4, and N_5 are, respectively, the powers consumed for stirring of the gas–fluid system, preparing the starting solution, cooling the oxidizing agent, pumping the cooling agent to lower the temperature of the reaction unit, and feeding the gas. The N_2–N_5 values are approximately the same in performing the same process in apparatus of different types. Therefore, they can be disregarded in comparing the efficiencies of the apparatus under study. The N_1 values were determined for each apparatus experimentally.

In each experiment the duration of DPA nitrosation is a function of the flow rates of fluid and gas phases without taking into account conditions common to all of the three apparatus studied. The ejector-type apparatus comprises an ejector and a bottom reactor. A chemical reaction occurs in the mixing chamber of the ejector during motion of the fluid and gas phases, with the fluid simultaneously saturated with dissolved gas. The reaction continues in the lower part of the reactor, but the amount of gas phase dissolved in the fluid phase is smaller, compared with that in the ejector. The residual kinetic energy of the jet goes to agitation of the reaction mixture, which leads to leveling of substance concentrations over the entire volume. For the studied flow rate ranges for the fluid (0.2–0.35 $m^3\ h^{-1}$) and gas phases (0.66–2 $m^3\ h^{-1}$), the minimum (10 $m\ s^{-1}$) and maximum (20 $m\ s^{-1}$) velocities of the fluid outflowing from the ejector nozzle of diameter 2.6×10^{-3} m were taken according to the known recommendations [5]. The obtained experimental data are presented in Table 1. Mathematical processing of these data for the batch mode yielded the dependence

$$\tau = 115.43 - 68.26Q_g - 32.22Q_gQ_l + 16.15Q_g^2. \quad (2)$$

In the continuous mode, the maximum output capacity V_l of the ejector-type apparatus was studied experimentally at different velocities W of working medium outflow from the nozzle and different gas flow rates (Table 2). Analysis of the experimental results shows that shorter time τ is achieved in the batch mode at ejector flow velocity of 20 m s^{-1} and gas phase flow rate of 2 m^3 h^{-1}. In the continuous mode, the maximum output capacity of the installation is achieved at the same flow rates.

The total hydraulic loss of pressure, ΔP, in the circulation circuit consists of losses in suction and pumping lines and in the ejector itself. The working-medium pressure at the nozzle outlet P_w = 0.1 MPa, whereas the total loss of pressure in the circulation circuit will be given, with account of the working-medium pressure, by

$$\Delta P = \Delta P_{suc} + \Delta P_{pump} + \Delta P_{ej} + P_w. \quad (3)$$

Figure 1 shows the dependence of ΔP on the fluid phase flow rate Q_l, described by the equation

$$\Delta P = 8.02Q_l^2 - 1.256Q_l + 1.97. \quad (4)$$

With account of (4), the power consumed for pumping the working medium through the circulation circuit is given by

$$N = \frac{724.35Q_l^2 - 267.22Q_l + 35.81}{\eta}, \quad (5)$$

where η = 0.55 is the pump efficiency.

With account of expressions (1), (2), and (5) and V = 0.018 m^3, the formula for determining the efficiency of ejector-type apparatus will have the form

$$E = [(73.17Q_l^2 - 26.99Q_l + 3.6)(115.43 - 68.26Q_g - 32.22Q_gQ_l + 16.15Q_g^2)]^{-1}. \quad (6)$$

Analysis of (6) shows that the highest efficiency is achieved for apparatus of this type at a fluid phase nozzle velocity of 10.43 m s^{-1} and gas phase flow rate of 2 m^3 h^{-1} (Table 2).

In studying the operation of a self-suction turbine agitator (STA), the gas phase was delivered, under the action of the pumping effect created by the mixer, into the central, hollow part of the rotating shaft and dispersed directly into the fluid phase. The flow rate of the nitrose gases was varied between 1 and 2 m^3 h^{-1}. The rotation speed of the mixer was 110 s^{-1}, volume

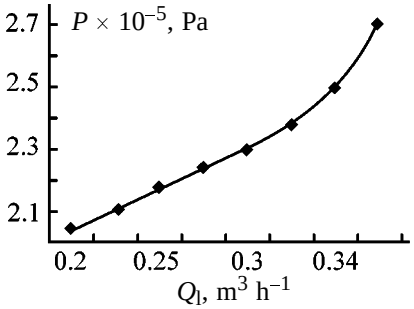

Fig. 1. Total loss of the pressure P of the working medium in the circuit vs. the fluid phase flow rate Q_l.

of the reaction mixture 0.018 m^3, and volume of apparatus with STA 0.01 m^3. In the batch mode, the time of process completion in the entire volume of the reaction mixture was determined. The obtained experimental data are presented in Table 3.

The equation describing the time τ (min) of complete conversion in relation to the flow rate of the gas phase in an apparatus with STA has the form

$$\tau = 9.9Q_g^2 - 43.02Q_g + 66.3. \quad (7)$$

The self-suction turbine-type agitator used in the experiments had the following characteristics: diameter 0.1 m, number of blades 6, blade width 0.01 m. In calculating the power consumed by the STA for agitation of the gas–fluid system, two circumstances were taken into account: (1) the dynamic viscosity coefficient of the main component was chosen as

Table 3. Process completion time τ for apparatus with STA and RPA

Run no.	τ, min, at indicated Q_g, m^3 h^{-1}				
	1	1.25	1.5	1.75	2
Self-suction turbine agitator					
1	33.04	28.44	24.34	21.47	19.94
2	33.07	28.34	24.33	21.34	19.83
3	33.04	28.42	24.39	21.42	19.96
Average	33.05	28.4	24.35	21.41	19.91
Rotary-pulsation apparatus					
1	32.53	26.05	21.71	18.24	16.57
2	32.56	26.03	21.68	18.27	16.59
3	32.56	26.04	21.72	18.23	16.61
Average	32.56	26.04	21.70	18.25	16.59

Table 4. Experimental values of power N_e

Flow rate, $m^3\ h^{-1}$		N_e, W
gas phase in RPA	fresh solution	
1	0.03318	37.70
1.25	0.04147	36.62
1.5	0.04976	35.77
1.75	0.05916	35.16
2	0.06510	34.80

the key factor for a reaction mixture with gas saturation $\varphi < 0.3$, and (2) the reaction mixture density ρ_m ($kg\ m^{-1}$) in the apparatus was calculated at gas flow rates in the range from 1 to 2 $m^3\ h^{-1}$ by the equation

$$\rho_m = 38.86Q_g^2 - 181.37Q_g + 1327.8. \quad (8)$$

Under these conditions, the values of the centrifugal criterion Re_c are within $(2.18–24) \times 10^5$. For the turbine agitator of the given type [1], the power criterion K_N remains constant (0.76) in the above range of Re_c values. Then, use of the known formula [1] and expression (8) gives a theoretical relation for determining the power consumption N_t (W) for agitation with STA:

$$N_t = 0.041\rho_m = 1.59Q_g^2 - 7.43Q_g + 54.4. \quad (9)$$

However, analysis of the experimental dependence

$$N_e = 1.68Q_g^2 - 8.9Q_g + 56.1 \quad (10)$$

shows that, with increasing flow rate of the gas component, the experimental power values are somewhat lower than the theoretical values, which is presumably due to lower density of the reaction mixture near the agitator.

With account of (7) and (10), the dependence of the efficiency of a gas–fluid apparatus with STA on the flow rate of the gas component can be represented as

$$E = 1\times10^{-3}(0.92Q_g^4 - 8.9Q_g^3 + 58.3Q_g^2 - 166.78Q_g + 206.56)^{-1}. \quad (11)$$

Analysis of (11) shows that the efficiency of an apparatus with STA grows with increasing flow rate of the gas phase because of the decreasing power consumed for agitation and shorter process duration. An RPA of original design has been developed to intensify gas–fluid processes [5].

The rotary-pulsation apparatus operates as follows. The fluid phase is fed into the working cavity via the inlet pipe. Under the action of inertia forces created by a rotating rotor it passes through rectangular slits in the rotor and stator rings. With the shaft rotating, the slits are periodically closed. In this zone of strong turbulence, there exist pulsation forces and high velocity gradients. The gas phase delivered via two pipes goes through channels inside the stator teeth and arrives in the space formed by slits in the rotor ring. During rotor rotation, the outlet channels are periodically closed at the same frequency, which favors fine dispersion of the gas phase.

Thus, to achieve complete interaction of the gas and fluid phases, a unit volume of fluid is subjected to multiple treatment in the active zone of the RPA. The clearance between the rotor and stator teeth was 1×10^{-4} m, and the speed of rotation, 314 s^{-1}. The main goal of the performed sets of experiments was to determine the time τ of completion of diphenylamine nitrosation in RPA at gas phase flow rates in the range from 1 to 2 $m^3\ h^{-1}$ and reaction mixture volume of 0.001 m^3. The obtained experimental data are presented in Table 3.

The equation obtained by processing the data in Table 3 has the form

$$\tau = 12.37Q_g^2 - 53.02Q_g + 73.16. \quad (12)$$

The power N_e consumed for agitation of the gas–fluid mixture in RPA was measured experimentally at varied flow rates of the gas and fluid phases; the averaged results are given in Table 4.

The obtained experimental data are described by the regression equation

$$N_e = 1.95Q_g^2 - 8.76Q_g + 44.5. \quad (13)$$

Analysis of Eq. (13) clearly shows that the consumed power decreases somewhat with increasing flow rate of the gas phase, which is presumably due to a decrease in the density of the gas–fluid mixture in the active zone of the apparatus.

The operation efficiency of an installation with STA can be calculated using Eqs. (12) and (13). Then the dependence of the RPA efficiency on the gas phase flow rate has the form

$$E = 1\times10^{-3}(1.34Q_g^4 - 11.75Q_g^3 + 64.34Q_g^2 - 166.75Q_g + 181.1)^{-1}. \quad (14)$$

To compare the efficiencies of the apparatus under

study, the following parameter values are taken: for apparatus with ejector, Q_g = 2 $m^3 h^{-1}$, flow velocity of the fluid phase 10.46–18.3 m s^{-1}; for apparatus with STA and for RPA, Q_g = 1–2 $m^3 h^{-1}$, output capacity 0.032–0.065 $m^3 h^{-1}$.

Graphical interpretation of the obtained relations describing the dependence of the efficiency of the apparatus on their output capacity is done in Fig. 2.

Analysis of the experimental data in Fig. 2 shows that the apparatus with STA has much lower efficiency than its competitors, becoming comparable with an ejector-type apparatus only at an output capacity of 0.05 $m^3 h^{-1}$. In contrast to the apparatus under consideration, the ejector-type apparatus shows high efficiency only at low output capacities, and its efficiency steeply decreases when this parameter grows. Already at an output capacity of 0.0425 $m^3 h^{-1}$ it becomes comparable in efficiency with RPA. An undisputed leader in efficiency, beginning with output capacity of 0.045 $m^3 h^{-1}$, is RPA, and it is this apparatus that should be used to perform the process under consideration.

The results obtained in studying the operation of a semicommercial RPA in performing gas–fluid processes were used to produce an intermediate, *N*-nitrosodiphenylamine, in manufacture of an antioxidant for rubber articles Diafen FP[1] and commercial *p*-nitrosophenol.[2]

CONCLUSIONS

(1) The dependences of the time in which diphenylamine nitrosation is complete on the flow rates of the gas and fluid phases were obtained for apparatus with a self-suction turbine agitator and those of rotary-pulsation and ejector types. Mathematical models of the occurring processes were developed for these cases. The power expenditure for agitation of the gas–fluid system under study was found for these apparatus.

(2) The efficiencies as functions of the output capacity were compared for apparatus with ejector or self-suction turbine and apparatus of rotary-pulsation type in performing a gas–fluid process. It was found that the ejector-type apparatus is the most efficient at low output capacities (up to 0.042 $m^3 h^{-1}$), and the rotary-pulsation apparatus, at higher values of this parameter (more than 0.045 $m^3 h^{-1}$).

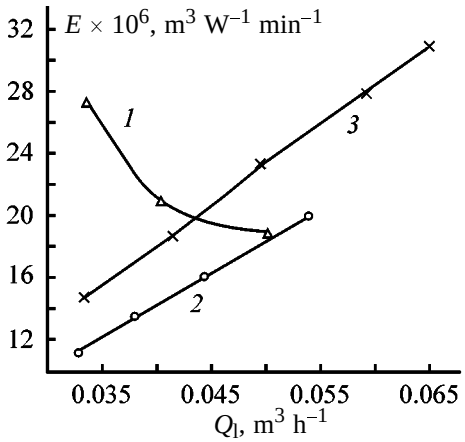

Fig. 2. Efficiency *E* of an installation vs. its output capacity *Q*. Apparatus: (*1*) with ejector, (*2*) with STA, and (*3*) of rotary-pulsation type.

REFERENCES

1. Braginskii, B.P., Begachev, V.I., and Barabash, V.M., *Peremeshivanie v zhidkikh sredakh: Fizicheskie osnovy i inzhenernye metody rascheta* (Agitation of Fluid Media: Physical Foundations and Methods of Engineering Calculation), Leningrad: Khimiya, 1984.
2. Barabash, V.M. and Belevitskaya, M.A., *Teor. Osn. Khim. Tekhnol.*, 1995, vol. 29, no. 4, pp. 362–372.
3. Aksel'rod, Yu.V., *Gazozhidkostnye khemosorbtsionnye protsessy: Kinetika i modelirovanie* (Gas–Fluid Chemisorption Processes: Kinetics and Modeling), Moscow: Khimiya, 1989.
4. Ivanets, V.N. and Al'brekht, S.N., in *KemTIPP 25 let: dostizheniya, problemy, perspektivy: Sbornik nauchnykh trudov* (25th Foundation Aniversary of Kemerovo Technological Institute of Food Industry: Achievements, Problems, and Prospects: Coll. of Sci. Works), Kemerovo, 1988, part 2, pp. 3–7.
5. Ivanets, G.E., Plotnikov, P.V., and Al'brekht, S.N., in *Tekhnologii i protsessy pishchevykh proizvodstv: Sbornik nauchnykh trudov KemTIPP* (Technologies and Processes of Food Industry: Coll. of Sci. Works of Kemerovo Technological Institute of Food Industry), Kemerovo, 1999, pp. 133–134.

[1] Azot Joint-Stock Company, Kemerovo.
[2] NVKh Khimtekh (Berezniki, Perm oblast).

Russian Journal of Applied Chemistry, Vol. 74, No. 3, 2001, pp. 466–468. Translated from Zhurnal Prikladnoi Khimii, Vol. 74, No. 3, 2001, pp. 456–459.

ORGANIC SYNTHESIS AND INDUSTRIAL ORGANIC CHEMISTRY

Base Hydrolysis and Use of Cationic Ammonium Dyes in Which the Chromophore System Is not Conjugated with the Nitrogen Atom

A. P. Mikhailovskaya, T. Yu. Dyankova, and N. P. Novoselov

St. Petersburg State University of Technology and Design, St. Petersburg, Russia

Received July 26, 2000; in final form, October 2000

Abstract—The capability of cationic dyes in which the onium group is not conjugated with the chromophore system to form aqueous dispersions in a weakly alkaline medium was examined. Such dyes can be fixed on a fiber in increased amounts owing to their binding not only in the cationic form but also in the hydrolyzed monomolecular form.

Dispersible dyes are widely used for dyeing of manmade fibers, including heat-resistant fibers based on polyheteroarylenes (PHAs). These dyes are practically insoluble in water but can be used in the form of aqueous dispersions. The degree of dispersity of the dye in the aqueous phase strongly affects the coloristic properties and color fastness.

One of the ways to prepare the molecularly dispersed form of a dye is to use cationic dyes in which the onium group is not conjugated with the chromophore system. Owing to the presence of such a cationic center, these dyes are water-soluble. In a weakly alkaline solution, the onium groups are eliminated to give particles of size close to that of separate molecules [1, 2]. Of interest in this connection are ammonium compounds derived from tertiary amines (including heterocyclic amines) with hydrogen, alkyl, or arylalkyl substituents. Quaternization of tertiary amines with alkyl halides occurs in organic solvents. The resistance of quaternary ammonium salts to hydrolysis depends on the nature of substituents at nitrogen. Published data on cationic dyes of such structure are consistent with the well-known stabilizing effect of alkyl substituent on onium compounds. Alkyl substituents exert a *+I* effect and weaken the polar character of NH and NC bonds [1]. Cationic dyes in which the ammonium group is not conjugated with the chromophore are hydrolyzed in alkaline solutions with release of the tertiary amines. The presence of electron-withdrawing substituents at nitrogen (as, e.g., in aniline and diphenylamine derivatives) facilitates cleavage of the onium compounds. The hydrolysis pathways of quaternary ammonium bases are as follows [1]:

$$OH^- + R{-}CH_2{-}CH_2{-}N^+(CH_3)_3 \xrightarrow{+H_2O} \begin{cases} R{-}CH_2{-}CH_2{-}OH + :N(CH_3)_3 \\ R{-}CH{=}CH_2 + H_2O + :N(CH_3)_3 \\ R{-}OH + CH_3{-}CH_2{-}OH + :N(CH_3)_3. \end{cases}$$

EXPERIMENTAL

Below are the structural formulas of the selected cationic (**I**) and dispersible (**II**–**IV**) dyes:

\$(91©)

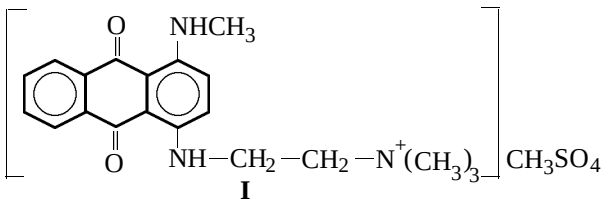

I

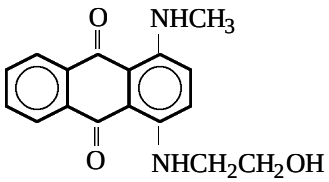

II

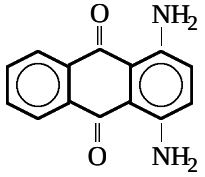

III

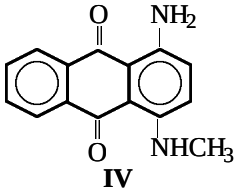

IV

1070-4272/01/7403-0466\$25.00 © 2001 MAIK "Nauka/Interperiodica"

Spectrophotometric studies showed that the state of cationic dyes depends on pH of the aqueous solution. This is illustrated in Fig. 1. As pH is increased from 3 to 11, the absorption intensity decreases, and at pH > 12 a dispersion of the base released from the cationic dye is formed (Fig. 2). Figure 3 shows the spectra of the cationic dye and its hydrolyzed form. Hydrolysis of the dye was performed in 1 N NaOH at 98°C for 30 min. Comparison of the spectra of dispersible dyes **II**–**IV** and of the hydrolyzed form of cationic dye **I** shows that the changes in the spectra are due to base hydrolysis of the cationic dye and release of a new dye in the form of a dispersion.

The kinetics of cleavage of the initial cationic dye was monitored by measuring the amount of the molecularly dispersed form from the hypsochromic shift of the short-wave absorption band with $\lambda_{D\max} = 610$ nm, which corresponds to a 100% content of the cationic dye. The short-wave absorption band at $\lambda_{D\max} = 565$ nm was considered to correspond to a 100% content of the hydrolyzed form. This is confirmed by analysis of fiber samples dyed with the cationic dye under conditions of hydrolysis and with a dispersible dye as a component of a composite dye bath in the presence of appropriate tertiary amine. Hydrolysis of the cationic dye was performed in aqueous solution at pH 10.5 for 100 min at 90 and 98°C. The content of the hydrolyzed dye was evaluated from the shift of the absorption bands in the range 500–600 nm, monitored with a 2-nm step. The results are shown in Fig. 4. The kinetic curves of hydrolysis of the cationic dye exhibit two sections. In the section corresponding to the content of the hydrolyzed form of up to 7–9%, the hydrolysis proceeds actively with increasing rate. The amount of the dye hydrolyzed in the first 20 min is 6.88% at 90°C and about 10% at 98°C. As the molecularly dispersed form of the dye accumulates, the degree of aggregation increases; it is determined by the solubility of the chromophore at these values of pH and temperature.

Comparison of the electronic absorption spectra of alcoholic solutions of dispersible dyes **II**–**IV** and hydrolyzed form of cationic dye **I** shows that the product of base hydrolysis of the onium dye containing the chromophore structure is structurally similar to dye **II**.

Thus, cationic dyes containing onium fragments can be cleaved with release of the insoluble chromophore structure in the monomolecular state, which facilitates its diffusion into the substrate. This property of cationic dyes in which the onium group is not conjugated with the chromophore allows dyeing to be

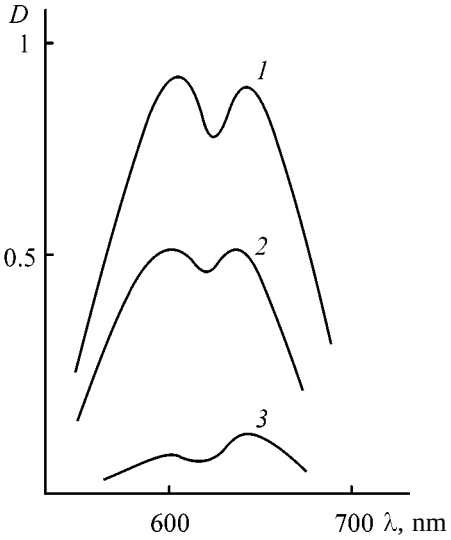

Fig. 1. Absorption spectra of aqueous solutions of the cationic dye at pH (*1*) 3, (*2*) 7, and (*3*) 11. (*D*) Optical density and (λ) wavelength; the same for Fig. 3.

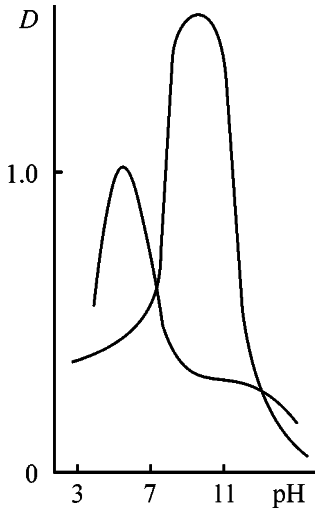

Fig. 2. Effect of pH on the absorption spectra of cationic dyes. (*D*) Optical density.

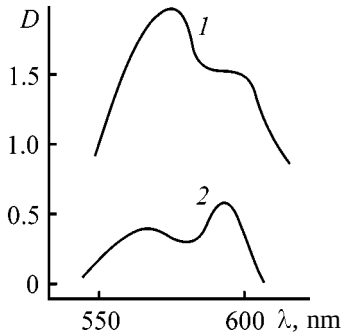

Fig. 3. Absorption spectra in 3.2×10^{-4}% solutions of (*1*) cationic dye and (*2*) its hydrolyzed form in aqueous acetic acid.

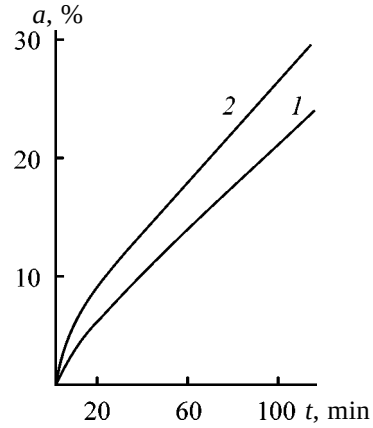

Fig. 4. Kinetic curves of hydrolysis of the cationic dye at (*1*) 90 and (*2*) 98°C. (*a*) Amount of the hydrolyzed form relative to the amount of the initial sample; (*t*) time.

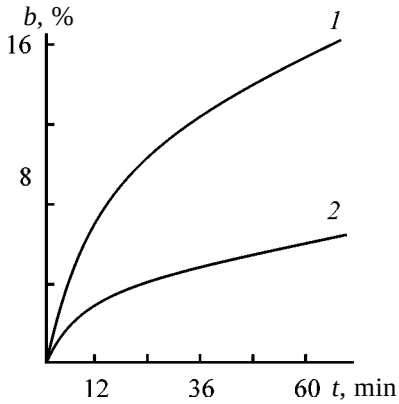

Fig. 5. Kinetic curves of uptake by the fiber of the hydrolyzed form of the cationic dye at (*1*) pH 10.33 and (*2*) pH 9.05. (*b*) Uptake relative to the amount of the initial sample; (*t*) time.

combined with treatment of aramide fibers with alkaline agents to remove or neutralize structurally bound acidic impurities. Furthermore, the hydrolysis conditions can be adjusted so as to make the rate of sorption of the hydrolyzed form equal to the rate of cleavage of the initial dye (Fig. 5). As follows from the Langmuir and Henry's data, dyeing under such conditions allows simultaneous fixation of the soluble and insoluble forms of the cationic dye, which increases the extent of dyeing of PGA fibers with a dense chemically inert microstructure and difficultly accessible nanostructure.

The process suggested in [2] successfully passed industrial trials at the Gor'kii Silk-Twisting Factory (Moscow) and Sport Private Company.

Dyeing of PGA fibers with cationic dyes in which the ammonium group is not conjugated with the chromophore moiety gives intense uniform colorings highly resistant to wet treatments [3].

CONCLUSIONS

(1) The cationic onium dye is hydrolyzed in an alkaline solution with release of the chromophore structurally similar to the dispersible dye.

(2) Quaternary ammonium bases in which the positively charged nitrogen atom is not conjugated with the chromophore moiety can be efficiently used for dyeing of highly oriented polyheteroarylene fibers.

REFERENCES

1. Avdyunina, Z.P., Properties and Use of Dyes in Which the Onium Group Is not Conjugated with the Chromophore System, *Cand. Sci. Dissertation*, Leningrad, 1969.
2. USSR Inventor's Certificate no. 1175199.
3. Dyankova, T.Yu. and Mikhailovskaya, A.P., *Tekhnologiya krasheniya termostoikoi tkani na osnove volokna SVM na mashinakh tipa MKP: Informatsionnyi listok* (Process for Dyeing of Heat-Resistant Fabric Based on SVM Fiber on MKP-Type Machines: Information Bulletin), St. Petersburg: Sankt-Peterb. Gos. Univ. Tekhnologii i Dizaina, 1998.

Russian Journal of Applied Chemistry, Vol. 74, No. 3, 2001, pp. 469–472. Translated from Zhurnal Prikladnoi Khimii, Vol. 74, No. 3, 2001, pp. 459–462.

ORGANIC SYNTHESIS AND INDUSTRIAL ORGANIC CHEMISTRY

New Route to Vicasol, a Water-Soluble Form of Vitamin K_3

K. I. Matveev, V. F. Odyakov, and E. G. Zhizhina

Boreskov Institute of Catalysis, Siberian Division, Russian Academy of Sciences, Novosibirsk, Russia

Received June 23, 2000

Abstract—A procedure was suggested for preparing vicasol in an approximately 85% yield in a two-phase system consisting of concentrated (~5–6 M) aqueous solution of $NaHSO_3$ and a solution of 2-methyl-1,4-naphthoquinone in an incombustible organic solvent (e.g., chloroform or trichloroethylene).

Vicasol (sodium 2-methyl-1,2,3,4-tetrahydronaphthalene-1,4-dione-2-sulfonate) is a water-soluble form of vitamin K_3 [1, 2]. More than 90% of the produced vicasol is used in cattle-breeding [3], and only up to 10%, in medicine. The use of vicasol in cattle-breeding increases the productivity by 17–23% depending on the species and age of animals [4]. Vicasol is added to forage in amount of 2–4 g per ton of forage [5] in the form of vitamin additives (premixes) together with vitamins A, E, and D and with microelements. The demand of Russia for vicasol today is about 45–50 tons annually and tends to grow.

Vitamins of group K are noy produced in Russia and CIS countries. In some other countries, vicasol is produced from 2-methylnaphthalene by outdated processes [1] which cannot be used in Russia because of environmental problems and the lack of the required raw materials.

We have developed the principles of the new Vikasib process for production of vicasol and other vitamins of group K [6] starting from α-naphthol which is, in turn, a petrochemical product.[1] In this process, the final stage is reaction of 2-methyl-1,4-naphthoquinone (menadione) dissolved in an organic solvent with an aqueous solution of sodium hydrosulfite [7, 8]:

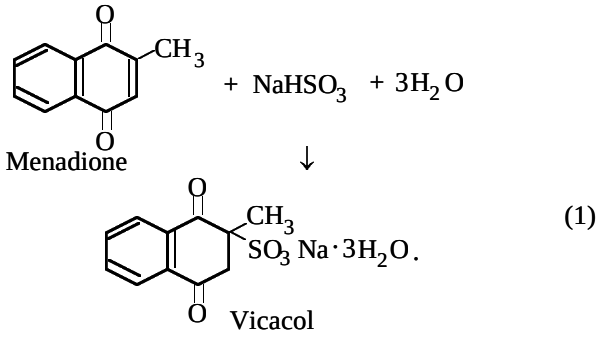

(1)

[1] Institute of Catalysis, Siberian Division, Russian Academy of Sciences.

The equilibrium constant of reaction (1) is high (~1×10^6 l mol^{-1} [9]); therefore, the 100% yield of vicasol is readily attainable. However, isolation of vicasol from the reaction mixture involves problems. Vicasol is readily soluble in water [2], and therefore it cannot be quantitatively recovered from aqueous solution. Furthermore, vicasol is thermally unstable and in the course of boiling readily isomerizes into sodium 3-methyl-1,4-dihydroxynaphthalene-2-sulfonate [10, 11] showing no vitamin properties:

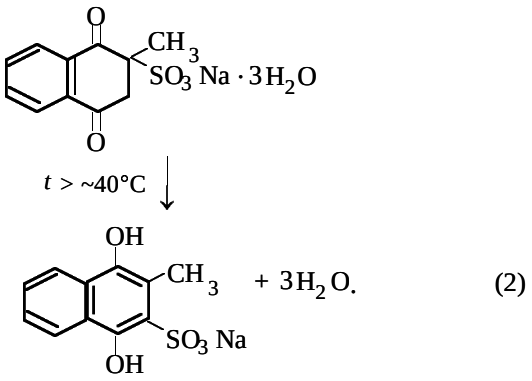

(2)

Such isomerization slowly proceeds even in the course of prolonged storage of vicasol at elevated temperatures [12]. Therefore, aqueous solutions of vicasol should not be concentrated by evaporation, and crystallization of vicasol should occur without heating.

Previously [13], crystallization of vicasol was performed in the presence of a large excess of $NaHSO_3$ which acted as a salting-out agent. However, the resulting vicasol contained up to 33% $NaHSO_3$ [14]. At the same time, the presence of only up to 2% $NaHSO_3$ in vicasol is prescribed by the State Pharmacopeia [15], and this amount is necessary and sufficient for enhancing the resistance of vicasol to light at subsequent storage [16].

1070-4272/01/7403-0469$25.00

Up to the 1970s, vicasol was prepared by mixing solid menadione with an aqueous solution of $NaHSO_3$ containing Na_2SO_3 impurities [17]. The resulting vicasol was contaminated with unchanged menadione and its decomposition products. In [14] it was suggested to dissolve menadione in CCl_4 with subsequent addition of water and excess $Na_2S_2O_5$ and vigorous stirring of the resulting two-phase system. We suggested [8] to perform reaction (1) in the two-phase system $CHCl_3$–H_2O, with the aqueous phase containing 4–6 M $NaHSO_3$ prepared from pure Na_2SO_3 and SO_2. In this case the amount of water taken for synthesis is reduced, and pure vicasol can be obtained even from crude menadione prepared in the preceding stage of the Vikasib process [6].

EXPERIMENTAL

Menadione was prepared by catalytic methylation of 1-naphthol [18] followed by oxidation of the resulting 2-methyl-1-naphthol with solutions of phosphomolybdovanadic heteropoly acids [19, 20]. Along with the main substance (88–90%), the product contained an impurity of dimeric quinones C_{22} and polymers $C_{x.11}$. Recrystallization from methanol gave 98–99% pure menadione.

Aqueous 4.0–6.5 M solutions of $NaHSO_3$ were prepared from analytically pure grade anhydrous Na_2SO_3 and pure gaseous SO_2 from a cylinder. These solutions were stored in the dark for no more than a week, because of occurrence of slow oxidation $HSO_3^- \rightarrow SO_4^{2-}$ [21].

Vicasol was prepared in a 1.1-l three-necked flat-bottomed shaked cylindrical vessel with one wide neck. The vessel was placed in a shaker operating at a rate of 400 shakings per minute. As solvents for menadione we used pure grade chloroform and trichloroethylene. For washing of vicasol and its additional precipitation from aqueous solution we used chemically pure grade isopropanol.

The sum of HSO_3^- + SO_2 in $NaHSO_3$ solution was determined by iodometric titration [22], and the content of Na^+ was calculated from the weight of the initial Na_2SO_3.

The menadione content in solutions was determined by GLC using a 40-m capillary column coated with SE-30; the internal reference was duroquinone. Analysis was performed with a Tsvet-500 chromatograph; the results were processed with a Multichrom automated system [23].

The main substance content in crystalline vicasol was determined by iodometric titration after hydrolysis of vicasol to menadione in the presence of $LiIO_4$ and lithium borate buffer solution [24]. The content of excess $NaHSO_3$ in vicasol was determined by iodometric titration, and the content of Na_2SO_4 impurity, colorimetrically with poorly soluble barium chloranilate $Ba(C_6Cl_2O_4)_2 \cdot xH_2O$ whose colored $C_6Cl_2O_4H^-$ anion passed into solution in the presence of SO_4^{2-} anions [25].

Concentrated solutions of $NaHSO_3$ were prepared from the calculated amount of anhydrous Na_2SO_3 by bubbling of SO_2 through an aqueous suspension of $Na_2SO_3 \cdot 7H_2O$. A 1-l volumetric cylinder containing 700 ml of water and a 361.5-g portion of anhydrous (98%) Na_2SO_3 (2.81 mol) were weighed. The first (~120–150 g) portion of Na_2SO_3 was suspended and partially dissolved with vigorous stirring, so as to avoid formation of $Na_2SO_3 \cdot 7H_2O$ clots. Through the resulting solution of Na_2SO_3 containing suspended $Na_2SO_3 \cdot 7H_2O$, SO_2 was bubbled at a rate of 50–200 ml min^{-1} through a glass tube with a capillary tip. The bubbling rate was adjusted so as to ensure complete dissolution of the rising SO_2 bubbles. In the process, the solution warmed up, and its volume increased by approximately 15%.

After the first portion of Na_2SO_3 mostly dissolved, the remaining Na_2SO_3 (~210–240 g) was gradually added, with the bubbling of SO_2 being continued. The cylinder with the Na_2SO_3 + SO_2 solution was intermittently cooled and weighed. After the solution took up 180–182 g of SO_2 (2.81–2.84 mol), the feeding of SO_2 was stopped, and the solution volume was brought to 1 l.

The resulting 5.62 M solution of $NaHSO_3$ had pH ~4–5. Its composition was as follows (M): $[Na^+]$ = 5.62, $[S^{IV}] = [HSO_3^-] + 2[S_2O_5^{2-}] + [SO_2\ (\text{impurity})]$ = 5.62–5.65.

Vicasol was prepared at a molar ratio $[NaHSO_3]$: [menadione] from 1.5 to 1.7, starting from both purified and crude menadione. For example, 75.4 g of crude (88%) menadione was dissolved in chloroform to obtain 200 ml of a brown solution containing 66.4 g (0.347 mol) of menadione. The solution was filtered and transferred into the reactor, and 105 ml of a 5.62 M aqueous solution of $NaHSO_3$ (0.58 mol) was added. The solution was purged with nitrogen or CO_2, and the vessel was sealed and vigorously shaken. In the course of shaking, a thick suspension of fine vicasol crystals formed, and the mixture warmed up from 20 to 40°C. Intermittently the shaking was stopped, a sample was taken for analysis, and the reactor was

turned to change the shaking direction and eliminate dead zones. The total time of reaction (1) was ~2 h.

The resulting suspension having a brown color due to tar impurities was transferred onto a Nutsch filter, and the liquid phases were thoroughly separated. The filtrate consisting of aqueous and organic phases was separated for subsequent recovery of the second portion of vicasol from the aqueous phase. The crystals on the filter were washed first with 40 ml of $CHCl_3$ and then with 4–6 20-ml portions of anhydrous isopropanol until the filtrate became colorless.[2] The resulting yellowish white finely crystalline mass was placed on an enameled tray and air-dried to constant weight (101 g). The product composition was as follows (%): main substance (vicasol) 96.3, $NaHSO_3$ + $Na_2S_2O_5$ 0.8, Na_2SO_4 2.7, which meets the requirements of the State Pharmacopeia [15]. The yield of vicasol recalculated on dry substance was 97.3 g (0.295 mol, 85%).[3]

From the filtered aqueous phase, after combining with the filtrates containing isopropanol, we isolated an additional 15 g of vicasol. The main substance content in this fraction was 65–85%, the remainder being $NaHSO_3$ ($Na_2S_2O_5$) (15–25%) and Na_2SO_4.

With pure (recrystallized) menadione, the synthesis is performed similarly. In this case, however, there is no need to wash the obtained vicasol crystals with chloroform.

To prepare $NaHSO_3$ solution, it is preferable to use analytically pure grade Na_2SO_3[4] rather than technical-grade $Na_2S_2O_5$ containing much more impurities.

In synthesis of vicasol by reaction (1), solvents other than $CHCl_3$ (preferably incombustible, e.g., trichloroethylene [8]) can be also used. In any case the reaction takes about 2 h.

The long time of reaction (1) is due to two factors. First, concentrated aqueous solutions of $NaHSO_3$ are a complex system containing three anions. The dimeric anion $S_2O_5^{2-}$ (hydrosulfite) prevailing in solution occurs in equilibrium with the monomeric anions $HOSO_2^-$ (protonated sulfite with the O–H bond) and HSO_3^- (sulfonate with the S–H bond) [26, 27]:

$$2HOSO_2^- \xrightleftharpoons{K_{iSO}} 2HSO_3^- \xrightleftharpoons[-H_2O]{K_{dim}} S_2O_5^{2-}. \qquad (3)$$

The active nucleophile attacking the molecule of menadione (or another quinone) is apparently sulfonate HSO_3^-.[5] The equilibrium between it and the $HOSO_2^-$ anion is shifted toward HSO_3^- (K_{iSO} ~4.9 [28]). However, at a high total concentration of $NaHSO_3$ the equilibrium between the monomers and the dimer $S_2O_5^{2-}$ is shifted toward the dimer.[6] Therefore, the low rate of vicasol formation may be due to the low concentration of HSO_3^- in concentrated aqueous solutions which are actually solutions of $Na_2S_2O_5$ and contain $HOSO_2^-$ and HSO_3^- only in low equilibrium concentrations.

The second and apparently the major cause of the low rate of reaction (1) is the high viscosity of the three-phase system consisting of the aqueous $Na_2S_2O_5$ solution, solution of menadione in $CHCl_3$, and suspension of the forming vicasol. Reaction (1) occurs on the boundary of the aqueous and organic phases and is controlled by diffusion of menadione from the bulk of the organic phase to the phase boundary. When the third phase (suspended vicasol) appears, the concentration of menadione in the organic phase decreases, the viscosity grows, and hence the diffusion of menadione and the reaction as a whole decelerate.

Although the rate of reaction (1) is low, the use of ~5–6 M solutions of $NaHSO_3$ (~2.5–3 M solutions of $Na_2S_2O_5$) containing the minimal amount of water ensures the most complete crystallization of vicasol and its isolation in up to 85% yield. In less concentrated (~2–3 M) solutions of $NaHSO_3$ [7] reaction (1) is faster but it is possible to isolate no more than 60% of the forming vicasol.

CONCLUSIONS

(1) The use of a two-phase system consisting of a concentrated (~5–6 M) aqueous solution of $NaHSO_3$ and a solution of menadione in chloroform or trichlo-

[2] After washing the filtrate containing $CHCl_3$ was combined with the organic phase, and the filtrates containing *i*-C_3H_7OH, with the aqueous phase.

[3] If required, vicasol was sieved through a 0.2-mm sieve. It was stored at room temperature in a dark glass vessel.

[4] Analytically pure grade Na_2SO_3 can contain an Na_2SO_4 impurity. Therefore, to prepare very pure solutions of $NaHSO_3$, it is appropriate to start from $NaHCO_3$ or Na_2CO_3.

[5] Sulfonate ions HSO_3^- attack by hidride atom the 3-position of menadione having the lowest electron density; this results in formation of vicasol and not of the isomeric 3-methyl-1,4-dihydroxynaphthalene-2-sulfonate.

[6] Published data on the dimerization equilibrium constant K_{dim} are contradictory; in any case, it increases with increasing ionic strength of the $NaHSO_3$ solution. In ~4.9 M $NaHSO_3$ solution it is about 0.34 l mol^{-1} [29]; therefore, in the 5.62 M solution the fraction of the reactive species HSO_3^-, apparently, does not exceed 5–10%.

roethylene allows preparation of the purest vicasol in a yield of about 85% owing to its more complete crystallization from aqueous solutions containing smaller amount of water.

(2) By addition of anhydrous isopropanol to the aqueous phase of the mother liquor, it is possible to isolate an additional amount of 65–85% vicasol.

REFERENCES

1. Shnaidman, L.O., *Proizvodstvo vitaminov* (Production of Vitamins), Moscow: Pishchevaya Prom–st., 1973, 2nd ed.
2. Odyakov, V.F., Titova, T.F., Matveev, K.I., and Krysin, A.P., *Khim.-Farm. Zh.*, 1992, vol. 26, nos. 7–8, pp. 69–77.
3. Val'dman, A.R., *Vitaminy v zhivotnovodstve* (Vitamins in Cattle-Breeding), ch. 4: *Vitamin K* (Vitamin K), Riga: Zinatne, 1977.
4. Motovilov, K.Ya. and Matveeva, K.I., in *Sovershenstvovanie metodov kormleniya i soderzhaniya sel'skokhozyaistvennykh zhivotnykh: Sbornik nauchnykh trudov* (Improvement of Methods for Cattle Feeding and Keeping: Coll. of Scientific Works), Novosibirsk, 1995, pp. 37–40.
5. Biryukova, D.Yu., Effect of Stimulating Forage Additive and Vicasol Prepared from α-Naphthol on the Metabolism and Productivity of Broiler Chickens, *Cand. Sci. Dissertation*, Novosibirsk, 2000.
6. Matveeva, K.I., Zhizhina, E.G., and Odyakov, V.F., *Khim. Prom–st.*, 1996, no. 3, pp. 173–179.
7. RF Patent 1 822 554.
8. RF Patent 2 126 792.
9. Shin, N.T. and Petering, D.H., *Biochim. Biophys. Res. Comm.*, 1974, vol. 55, no. 4, pp. 1319–1325.
10. Asahi, Yo., *J. Pharm. Soc. Jpn.*, 1956, vol. 76, pp. 370–372.
11. Greenberg, G.F., Leung, Kwok Kee, and Leung, M., *J. Chem. Educ.*, 1971, vol. 48, no. 9, pp. 632–634.
12. Valdes Santurio, J.R., Lukats, V., and Alfonso Manso, A., *Rev. Cub. Farm.*, 1982, vol. 16, no. 3, pp. 204–221.
13. US Patent 2 367 302.
14. US Patent 3 657 286.
15. *Gosfarmakopeya SSSR* (USSR State Pharmacopeia), Moscow: Meditsina, 1968, 10th ed., pp. 733–735.
16. Shu-Yuan Yeh and Wiesse, G.A., *Drug Stand.*, 1958, vol. 26, pp. 22–29.
17. Shmuk, A. and Guseva, A., *Zh. Prikl. Khim.*, 1948, vol. 21, no. 11, pp. 1180–1182.
18. RF Patent 2 050 345.
19. Matveev, K.I., Zhizhina, E.G., Odyakov, V.F., and Parmon, V.N., *Izv. Ross. Akad. Nauk, Ser. Khim.*, 1994, no. 7, pp. 1208–1211.
20. Matveev, K.I., Odyakov, V.F., and Zhizhina, E.G., *J. Mol. Catal. A: Chem.*, 1996, vol. 114, nos. 1–3, pp. 151–160.
21. Ermakov, A.N., Poskrebyshev, G.A., and Purmal', A.P., *Kinet. Katal.*, 1997, vol. 38, no. 3, pp. 325–338.
22. Williams, W.J., *Handbook of Anion Determination*, London: Butterworths, 1979.
23. Kalambet, Yu.A. and Kozmin, Yu.P., *J. Chromatogr.*, 1991, vol. 542, pp. 247–261.
24. Odyakov, V.F., Zhidina, E.G., and Matveev, K.I., *Khim.-Farm. Zh.*, 1996, vol. 30, no. 1, pp. 50–53.
25. Bertolacini, R.J. and Barney, J.E., *Anal. Chem.*, 1957, vol. 29, no. 1, pp. 281–283.
26. Simon, A. and Waldmann, K., *Z. Anorg. Allg. Chem.*, 1955, vol. 281, nos. 3–4, pp. 135–150.
27. Litlejoin, D., Walton, S.A., and Chang Shih Ger, *Appl. Spectrosc.*, 1992, vol. 46, no. 5, pp. 848–851.
28. Horner, D.A. and Connick, R.E., *Inorg. Chem.*, 1986, vol. 25, no. 14, pp. 2414–2417.
29. Connick, R.E., Tam, T.M., and Deuster, E. von, *Inorg. Chem.*, 1982, vol. 21, no. 1, pp. 103–107.

Russian Journal of Applied Chemistry, Vol. 74, No. 3, 2001, pp. 473–477. Translated from Zhurnal Prikladnoi Khimii, Vol. 74, No. 3, 2001, pp. 463–467.

MACROMOLECULAR CHEMISTRY AND POLYMERIC MATERIALS

Properties of Crystalline Polyvinylenes Prepared by Phase-Transfer Dehydrochlorination of Vinyl Chloride Copolymers

V. N. Salimgareeva, Yu. A. Prochukhan, N. S. Sannikova, and Z. Kh. Kuvatov

Institute of Organic Chemistry, Ufa Scientific Center, Russian Academy of Sciences, Ufa, Bashkortostan, Russia

Received January 10, 2000; in final form, June 2000

Abstract—Crystalline polyvinylenes were prepared by phase-transfer dehydrochlorination of binary copolymer of vinyl chloride with vinyl acetate (9 : 1 molar ratio) and ternary copolymer with vinyl acetate and vinyl alcohol (27 : 1 : 2 molar ratio), and the chemical and electrical properties of these substances and of products of their thermolysis were studied.

Polymers with a system of conjugated bonds in the main chain, including polyvinylenes, are of particular interest due to their semiconductor, paramagnetic, and other properties, which are not typical of common macromolecular compounds. The variety of specific properties is due to the features of their electronic structure and conformation of conjugated molecules. These properties depend on the polymer structure; and the presence of the crystalline phase in the polymer increases the electrical conductivity and decreases the concentration of paramagnetic centers as compared with the amorphous sample [1]. The crystalline structure provides high anisotropy of the polymer properties, necessary for application in microelectronics.

The properties of crystalline polyvinylenes formed by acetylene polymerization using Ziegler–Natta catalysts are described in detail (e.g., [2, 3]). A method for preparing highly crystalline polyvinylene by dehydrochlorination of polyvinyl chloride under the conditions of phase-transfer catalysis was developed in [4]. The resulting polyvinylene exhibits unique chemical and physical properties. It is highly stable with respect to oxidants and is easily dehydrogenated at high temperatures [4]. The products of its thermolysis exhibit high strain sensitivity [5] and paramagnetic properties [6].

Crystalline polyvinylenes were also prepared by phase-transfer dehydrochlorination of a binary copolymer of vinyl chloride with vinyl acetate and a ternary copolymer with vinyl acetate and vinyl alcohol [7]. Some properties of these polyvinylenes were studied in this work.

EXPERIMENTAL

In our work we studied crystalline polyvinylenes prepared by phase-transfer dehydrochlorination of commercial samples of a binary copolymer of vinyl chloride with vinyl acetate (9 : 1 molar ratio) and a ternary copolymer of vinyl chloride with vinyl acetate and vinyl alcohol (27 : 1 : 2 molar ratio) in aqueous solutions of potassium hydroxide in the presence of phase-transfer catalysts [7].

The properties of crystalline polyvinylenes were compared with those of amorphous samples prepared from the same vinyl chloride copolymers [7] and of crystalline polyvinylenes prepared from polyvinyl chloride (PVC) [4]. The products of conversion of vinyl chloride homo- and copolymers are coarse black or dark brown powders (0.8–1.0 mm particle size).

The polymer structure was studied using polarization-optical microscopy. The polyvinylene crystals prepared from copolymers are significantly smaller than those prepared from polyvinyl chloride and larger than the crystals obtained by acetylene polymerization: the crystal size is 1–2 [7], 1×10^3 [4], and $(2–5) \times 10^{-3}$ μm [8], respectively.

The thermal treatment of the samples at 100–1200°C was carried out in a quartz tube in a vacuum ($\approx 10^{-3}$ mm Hg); at higher temperatures a ceramic tube was used. The sample was heated with a heating rate of 1.5 deg min^{-1} and kept at chosen temperature for 2 h. All manipulations were performed under argon.

The specific electrical resistivity was measured by the four-probe procedure in cells equipped with stain-

1070-4272/01/7403-0473$25.00

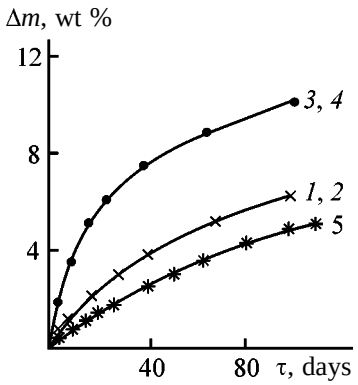

Fig. 1. Kinetic curves of oxidation with atmospheric oxygen of polyvinylenes of (*1, 2, 5*) crystalline and (*3, 4*) amorphous structure prepared by dehydrochlorination of (*1, 3*) copolymer of vinyl chloride with vinyl acetate, (*2, 4*) copolymer of vinyl chloride with vinyl acetate and vinyl alcohol, and (*5*) polyvinyl chloride. (Δ*m*) Weight gain and (τ) oxidation time.

less-steel electrodes using an E 7–8 ac potentiometer (1 kHz). The design of the measuring cells allowed preparation of 50–300-μm thick polymer pellets. The samples were oxidized with air dried over P_2O_5. The stability with respect to thermal oxidative degradation was studied using an MOM derivatograph (0.08 deg s^{-1} heating rate, 0.1×10^{-3} kg sample weight).

The nucleophilic properties of polyconjugated systems determine their interaction with electrophilic reagents, e.g., molecular oxygen. Polyvinylenes are the polymers with a system of conjugated double bonds prepared by phase-transfer dehydrochlorination of vinyl chloride copolymers; they are easily oxidized with oxygen, with the color changing from black to red and light yellow. The reactivity of polyvinylenes is also determined by packing of the polymer molecules. On passing from crystalline to amorphous samples the X-ray diffraction (XRD) patterns of these polymers demonstrate shifting of the diffraction peaks toward larger scattering angles. Due to higher ordering of crystalline polyvinylenes as compared with amorphous polymers, the rate and the extent of their oxidation are lower. As seen from Fig. 1 (curves *1, 2* and *3, 4*), the kinetic curves of oxygen uptake, illustrating the polymer oxidation, by the crystalline samples lie below those corresponding to the amorphous samples.

Polyvinylenes prepared from copolymers of vinyl chloride with vinyl acetate and vinyl alcohol are the products with the polyene structure of the *trans* polyacetylene type. The IR spectra of these compounds, similar to those prepared from PVC, contain no stretching (3044–3057 cm^{-1}) and in-plane (1249, 1329 cm^{-1}) and out-of-plane (740 cm^{-1}) bending vibrations of the =C–H group of the *cis* configuration. The IR spectra exhibit the bands at 1292, 3010–3015 cm^{-1} belonging to the in-plane bending and stretching vibrations of the =C–H group of the *trans* configuration. The IR spectrum of the product of PVC conversion exhibits a strong peak at 1000–1015 cm^{-1} belonging to the out-of-plane bending vibrations of =C–H in the *trans* configuration of the $–(CH=CH)_n$ units ($n \gg 2$). In the spectra of the conversion products of the vinyl chloride copolymer this band is split in two bands at 1008 and 996 cm^{-1}. Moreover, new peaks appear at 980 and 940 cm^{-1}, which are due to the vibrations of shorter polyvinylene series ($n = 2$ and $n = 1$) [9]. The presence of smaller conjugation blocks in the macromolecules of polyvinylenes prepared from vinyl chloride copolymers, in contrast to those prepared from PVC, decreases their reactivity toward oxygen, because the nucleophilicity of polyconjugation systems decreases with decreasing conjugation length [10]. However, as seen from Fig. 1, these polyvinylenes react with oxygen more actively than the product of PVC dehydrochlorination: their kinetic curves of oxygen uptake (curves *1, 2*) lie higher as compared with curve *5*.

As for molecules forming a crystal, their reactivity, determined by the electronic structure, is less decisive for the reaction than the mode of crystal packing [11]. The diffraction peak in the XRD pattern of crystalline polyvinylene prepared from vinyl chloride copolymer is shifted toward larger angles ($2\theta = 21°$) as compared with the sample prepared from vinyl chloride homopolymer ($2\theta = 20°$), which suggests lower ordering of the polymer structure. The oxidation of crystalline samples is probably controlled by diffusion of the oxidant gas into the polymer bulk, which is more hindered in the perfect crystal lattices of polyvinylenes prepared from PVC as compared with those prepared from vinyl chloride copolymer with less ordered structure. Moreover, the polyvinylene crystals prepared from vinyl chloride copolymers are smaller than those prepared from PVC (1–2 and 1×10^3 μm, respectively).

Oxidation of polyvinylenes with similar supramolecular structure prepared from binary and ternary vinyl chloride copolymers proceeds with similar rate (Fig. 1, curves *1, 2* and *3, 4*). Since the history of these polyvinylenes does not affect their heat resistance and electrophysical properties, in our further work we studied only the products of conversion of the binary copolymer of vinyl chloride with vinyl acetate.

The thermal oxidative degradation of polyvinylene

prepared from vinyl chloride copolymer with significant weight loss starts at 200–220°C and yields volatile (predominantly benzene) and viscous products of aromatic nature. At higher temperature almost no benzene is observed in the pyrolysis products. The supramolecular polymer structure affects the degradation processes. In the crystalline polyvinylene the degradation of the polymer macromolecules proceeds with a lower rate than in the amorphous samples (Fig. 2, curves *1*, *2*). As compared with the product of PVC dehydrochlorination, the less ordered polyvinylene prepared from vinyl chloride copolymer promotes degradation processes: curve *1* lies above curve *3* (Fig. 2).

The rigid crystalline structure hinders cleavage of the polyvinylene fragments of the macromolecule, but promotes carbonization during its thermal treatment. Dehydrogenation of the crystalline polymer prepared from vinyl chloride copolymer starts at 350–400°C, proceeds with a greater rate as compared with amorphous polymer (Fig. 3, curves *1*, *2*), and yields completely carbonized samples at 1400–1500°C, whereas the carbonization of the amorphous polyvinylenes starts at 450–500°C and is completed at temperatures higher than 2000°C. The less ordered structure of crystalline polyvinylene prepared from vinyl chloride copolymer shifts the processes of hydrogen elimination toward higher temperatures as compared with the polymer prepared from PVC (Fig. 3, curves *1*, *3*). In the latter case elimination of hydrogen starts at 250–300°C and terminates at 1100–1200°C.

Dehydrogenation of polyvinylenes follows the common dependences of hydrocarbon dehydrogenation. At a given temperature the following dehydrogenation–hydrogenation equilibrium is attained:

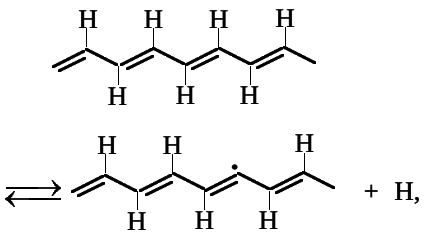

which is confirmed by the fact that the kinetic curve of hydrogen loss is a curve with saturation. The above equilibrium shifts toward dehydrogenation with increasing temperature. At thermal treatment at 300°C of polyvinylenes prepared from vinyl chloride homo- and copolymers, virtually constant C/H ratio in the polymer is attained within 2 h (Fig. 3, curves *1'*, *3'*). With increasing temperature to 400°C the C/H ratio increases and reaches a constant value within for 2 h

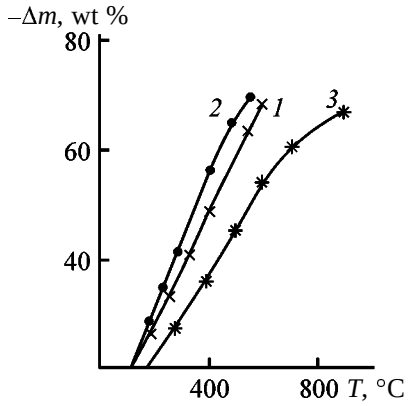

Fig. 2. Weight loss Δm as a function of temperature during thermal oxidative degradation of polyvinylenes of (*1, 3*) crystalline and (*2*) amorphous structure prepared from vinyl chloride (*3*) homo- and (*1, 2*) copolymers.

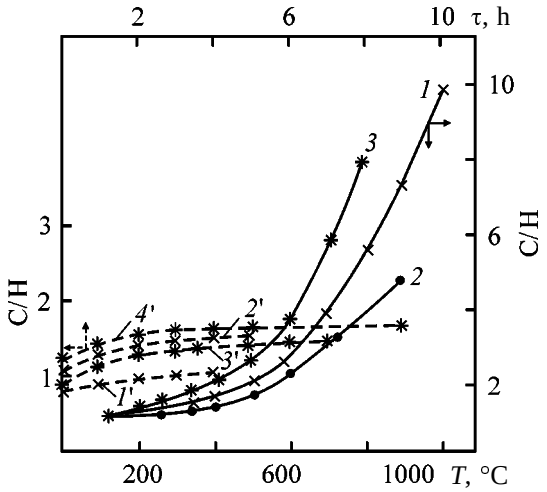

Fig. 3. C/H ratio as a function of (*1'–4'*) time and (*1–3*) temperature *T* of thermal treatment of polyvinylenes of (*1'–4'*, *1, 3*) crystalline and (*2*) amorphous structure. Polyvinylenes prepared from vinyl chloride (*3, 3'*, *4'*) homo- and (*1, 2, 1'*, *2'*) copolymers. Thermal treatment: (*1'*, *3'*) at 300°C after preliminary heating of polyvinylenes to 200°C and (*2'*, *4'*) at 400°C after preliminary heating of polyvinylenes to 300°C.

(Fig. 3, curves *2'*, *4'*). Hydrogen elimination proceeds without catalysts and hydrogen acceptors at temperatures significantly lower than the temperature of olefin dehydrogenation (>500°C).

The chemical and electrophysical properties of the polymers in question are determined by the specific electronic structure of polyvinylenes and especially by conjugation chains and delocalization of π electrons in them. The synthetic polymers with a linear conjugation system exhibit low electrical conductivity at room temperature [1]. The specific electrical conductivity σ_{20} of crystalline and amorphous polyvinylenes pre-

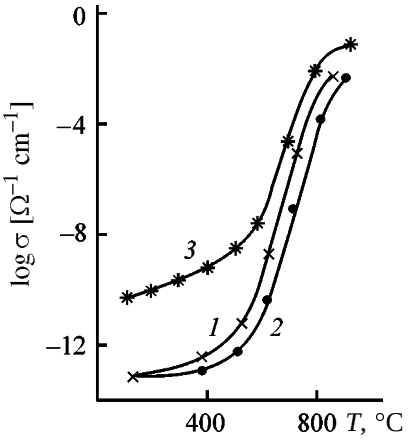

Fig. 4. Specific electrical conductivity σ of polyvinylenes of (*1, 3*) crystalline and (*2*) amorphous structure as a function of the temperature of thermal treatment *T*. Polyvinylenes prepared from vinyl chloride (*3*) homo- and (*1, 2*) copolymers.

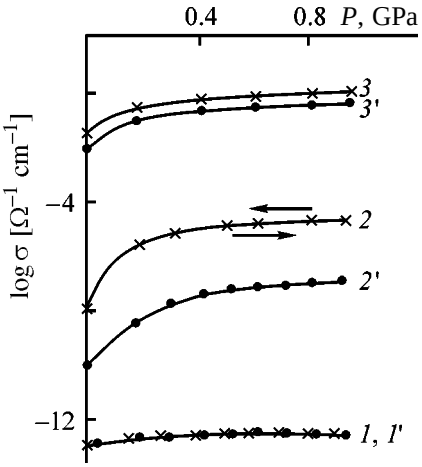

Fig. 5. Specific electrical conductivity σ of (*1*–*3*) crystalline and (*1*'–*3*') amorphous polyvinylenes prepared from copolymer of vinyl chloride and vinyl acetate and heat-treated at (*1, 1*') 100, (*2, 2*') 600, and (*3, 3*') 900°C as a function of pressure *P*.

pared from vinyl chloride copolymers does not exceed 10^{-13} Ω^{-1} cm^{-1}, i.e., they are actually insulators. It is known that the charge transfer involves the intrachain transfer along the conjugated chains and the interchain transfer. The transfer of the charge carriers along the conjugated bond system in macromolecules and between the molecules is probably more hindered in these polymers than in the product of PVC conversion (σ_{20} = 10^{-9} Ω^{-1} cm^{-1}). This is due to more random packing of macromolecules and the presence of shorter blocks of conjugated bonds as compared with the above copolymer. The decrease in the length of conjugated blocks decreases the polymer conductivity due to the increase in the band gap and in the number of intermolecular barriers.

The probability of the electron exchange, i.e., the mobility of the charge carriers should increase with decreasing distance between the separate sections during thermal treatment [12]. In this case, the supramolecular structure of polyvinylenes affects the resulting electrical conductivity. The carbonized samples of crystalline polyvinylene have greater electrical conductivity as compared with the pyrolysis products of amorphous polymer, because the dependences of the specific electrical conductivity of the polymer samples on the temperature of their thermal treatment for crystalline polyvinylenes lie above those of the amorphous samples (Fig. 4, curves *1*, *2*). This phenomenon is probably due to easier transfer of the charge carriers between macromolecules as compared with the amorphous polymer. During pyrolysis of these polyvinylenes at low temperatures (up to 400–500°C) σ_{20} monotonically increases. In this temperature range these polymers undergo transformations accompanied by formation of three-dimensional structures and accumulation of double bonds. The σ_{20} values of these products are lower as compared with the pyrolysis products of polyvinylenes prepared from PVC and fired at the same temperatures (Fig. 4, curves *1*, *3*). The specific conductivity of the products of polyvinylene pyrolysis at 600–700°C becomes approximately equal. As seen from Fig. 3, the composition of the products obtained at 600–700°C can be described by the formula $-(C_xH)_n-$, where $x \geq 2.0$.

High-temperature pyrolysis (above 400–500°C) increases σ_{20} by 9–10 orders of magnitude to values typical of semiconductors. Such a sharp change in the electrical properties is probably due to the steep increase in the number and size of conjugated blocks, which facilitates the electron transfer.

The increase in the electrical conductivity with increasing mobility of the charge carriers can be also attained by compression of the polymer sample, which decreases the intermolecular distances and increases the overlap of the electron orbitals of the neighboring atoms, and thus decreases the energy barrier between the conjugation blocks [1]. With increasing pressure, the electrical conductivity reaches saturation at 0.2 GPa. At the same time, the electrical conductivity of the crystalline polyvinylenes prepared from vinyl chloride copolymers only slightly changes with increasing pressure (Fig. 5, curves *1, 1*'). The effect of pressure is stronger on passing to the heat-treated samples and increases at pyrolysis temperatures of 600–700°C. Sharp increase in the electrical conduc-

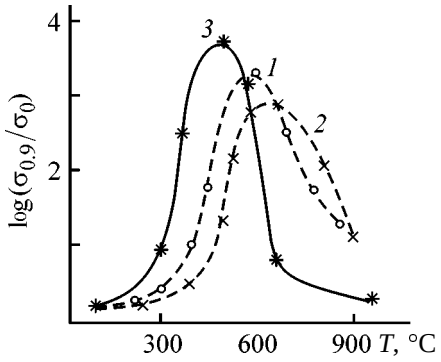

Fig. 6. Relative change in the electrical conductivity $\sigma_{0.9}/\sigma_0$ in the samples of heat-treated polyvinylenes of (*1*, *3*) crystalline and (*2*) amorphous structure as influenced by the pyrolysis temperature *T*. Polyvinylenes are the products of conversion of (*1*, *2*) vinyl chloride and vinyl acetate copolymer and (*3*) polyvinyl chloride. $\sigma_{0.9}$ and σ_0 are the specific electrical conductivities at uniaxial pressure of 0.9 GPa and without pressure.

tivity is observed for the samples treated at 600–700°C with the $(C_2H)_n$– composition: The increase in the specific electrical conductivity with increasing pressure to 0.9 GPa reaches nearly three orders of magnitude (Fig. 5, curve *2*). With increasing pyrolysis temperature above 700°C the effect of pressure on the electrical conductivity of the polymers in question decreases.

The extrema are the most pronounced in the temperature dependence of the function $\log(\sigma_{0.9}/\sigma_0)$, where $\sigma_{0.9}$ and σ_0 are the specific electrical conductivities at uniaxial pressure of 0.9 GPa and without pressure, respectively (Fig. 6).

The strain sensitivity of the heat-treated crystalline polyvinylene prepared from vinyl chloride copolymer is higher than that of the amorphous polymer, but lower as compared with the heat-treated polymer prepared from PVC.

There is no hysteresis in the pressure dependence of the specific electrical conductivity of the heat-treated crystalline polyvinylenes (Fig. 5, curve *2*). This feature is also typical for the pyrolysis products of polyvinylenes prepared from PVC and vinyl chloride copolymer, but distinguishes them from known semiconductors.

CONCLUSIONS

(1) As compared with amorphous samples, the ordered structure of crystalline polyvinylenes prepared by phase-transfer dehydrochlorination provides smaller rate and extent of their oxidation with atmospheric oxygen, lower rate of the weight loss, and higher rate of hydrogen elimination at high temperatures.

(2) The electrical conductivity and strain sensitivity of heat-treated crystalline polyvinylenes (conversion products of vinyl chloride copolymer) are higher than those of the amorphous samples, but smaller than those of the heat-treated products of polyvinyl chloride conversion.

REFERENCES

1. *Organicheskie poluprovodniki* (Organic Semiconductors), Kargin, V.A., Ed., Moscow: Nauka, 1968.
2. Lopyrev, V.A., Myachina, G.F., Shevalevskii, O.I., *et al*., *Vysokomol. Soedin., Ser. A*, 1988, vol. 30, no. 10, pp. 2019–2033.
3. Matnishyan, A.A., *Usp. Khim.*, 1988, vol. 57, no. 4, pp. 656–683.
4. Leplyanin, G.V. and Salimgareeva, V.N., *Izv. Ross. Akad. Nauk, Ser. Khim*., 1995, no. 10, pp. 1886–1893.
5. Salimgareeva, V.N., Prochukhan, Yu.A., Sannikova, N.S., *et al.*, *Vysokomol. Soedin., Ser. A*, 1999, vol. 41, no. 4, pp. 667–672.
6. Salimgareeva, V.N., Prochukhan, Yu.A., Korepanova, O.E., *et al., Zh. Prikl. Khim*., 1999, vol. 72, no. 5, pp. 831–836.
7. Salimgareeva, V.N., Prochukhan, Yu.A., and Sannikova, N.S., *Zh. Prikl. Khim.*, 2000, vol. 73, no. 3, pp. 490–495.
8. Shimamura, K., Karasz, F.E., Hirch, J.A., *et al*., *Macromol. Chem. Rapid Commun*., 1981, vol. 2, no. 8, pp. 473–480.
9. Shirakawa, H. and Ikeda, S., *Polym. J*., 1971, vol. 2, no. 2, pp. 231–244.
10. Berlin, A.A., Geiderikh, M.A., Davydov, B.E., *et al*., *Khimiya polisopryazhennykh sistem* (Chemistry of Polyconjugated Systems), Moscow: Khimiya, 1972.
11. Legasov, V.A. and Buchachenko, A.L., *Usp. Khim*., 1986, vol. 55, no. 12, pp. 1949–1961.
12. Dulov, A.A., Slinkin, A.A., Rubinshtein, A.M., *et al*., *Izv. Akad. Nauk SSSR, Ser. Khim*., 1963, no. 11, pp. 1910–1920.

Russian Journal of Applied Chemistry, Vol. 74, No. 3, 2001, pp. 478–482. Translated from Zhurnal Prikladnoi Khimii, Vol. 74, No. 3, 2001, pp. 468–472.

MACROMOLECULAR CHEMISTRY AND POLYMERIC MATERIALS

Some Properties of Crystalline Polyacetylenes of Various Density

V. N. Salimgareeva, N. S. Sannikova, S. V. Kolesov, and Z. Kh. Kuvatov

Institute of Organic Chemistry, Ufa Scientific Center, Russian Academy of Sciences, Ufa, Bashkortostan, Russia

Received July 13, 2000; in final form, December 2000

Abstract—The resistance of crystalline polyacetylenes of various density to oxidants and high temperatures was studied. The electrophysical and magnetic properties of these polymers and of the products of their thermolysis were determined.

Polyacetylene (PAc) is a polymer with a linear system of conjugated double bonds, which possesses semiconductor and magnetic properties due to the presence of delocalized π electrons in the macromolecule [1]. This compound is promising for electronics, which utilizes predominantly crystalline semiconductor materials in the form of single crystals or thin mono- and polycrystalline layers [2].

Crystalline PAc is prepared by polymerization of acetylene using Ziegler–Natta catalysts [3]. The PAc films and powders are agglomerates of randomly bound fibrils with the thickness of 10–80 nm and length of tens micrometers. The resulting films are rather porous; the pore volume reaches 2/3 of the total polymer volume, and the apparent volume density is 0.4 g cm^{-3}. The PAc samples with the density reaching 0.7–1.1 g cm^{-3} were also prepared [4]. The properties of these samples are significantly different. For example, the specific electrical conductivity of the foam-type material (0.02–0.04 g cm^{-3}) is nearly two orders of magnitude smaller than that of the pressed films (0.1–0.4 g cm^{-3} density) [5].

Crystalline PAc can be prepared by conversion of polyvinyl chloride (PVC) under the conditions of phase-transfer catalysis [6]. The crystals of the polymer prepared by this method are the largest; their size reaches 1.0×10^3 μm. This procedure allows control of the packing density of the polymer crystals and yields samples with a density of 1.15–1.20 and 1.30–1.35 g cm^{-3}.

Here we report on some properties of crystalline PAc of various densities prepared by phase-transfer dehydrochlorination of PVC.

EXPERIMENTAL

We studied crystalline PAc prepared by phase-transfer dehydrochlorination of PVC with 50% aqueous solutions of potassium hydroxide in the presence of phase-transfer catalysts [6]. The polymer of 1.2 g cm^{-3} density was obtained using potassium hydroxide solution in the amount of 0.42 g (recalculated on the dry weight) per 1 ml of the organic phase (PVC solution in nitrobenzene), and that of 1.35 g cm^{-3} density, with a smaller amount of KOH (0.25 g ml^{-1}). The product of PVC conversion is a coarse black or dark brown powder (0.8–1.0 mm particle size).

The polymer structure was studied using optical (Amplival Poi U unit) and electron (EMMA-4 unit) microscopy. The X-ray diffraction (XRD) patterns were registered on a DRON-2 diffractometer (CuK_α radiation).

The thermal treatment of the samples was carried out in a quartz tube in a vacuum ($\approx 10^{-3}$ mm Hg); at higher temperatures a ceramic tube was used. The sample was heated with a heating rate of 1.5 deg min^{-1} and kept at a chosen temperature for 4 h. All manipulations were performed under argon. The thermal stability was studied using a du Pont 900 derivatograph at a 3 deg min^{-1} heating rate in a helium flow (40 ml min^{-1}).

The specific electrical resistivity was measured by the four-probe procedure in cells equipped with stainless-steel electrodes using an E 7–8 ac potentiometer (1 kHz). The design of the measuring cells allowed preparation of 50–300-μm thick pellets. The magnetic susceptibility of the powdered PAc samples was measured by the Faraday procedure [7] in the 20–100°C

1070-4272/01/7403-0478$25.00

temperature range and at the 2–15 kOe magnetic field intensity.

The samples were oxidized with atmospheric oxygen and ozone; oxygen was dried over P_2O_5. The ozone–oxygen mixture (1–2 vol % ozone concentration) was passed through a 7×0.5-cm tube packed with the polymer at room temperature, at a rate of 2–5 l h^{-1}.

According to the data of electron microscopy, the PAc sample (1.20 g cm^{-3} density) prepared by phase-transfer dehydrochlorination of PVC contains the crystals of three modifications with the following lattice parameters (Å): hexagonal $a = b = 5.2$, $c = 2.52$; orthorhombic $a = 4.0$, $b = 7.9$; and monoclinic $a = c = 3.9$, $b = 2.52$. It was found that the crystal modifications with analogous parameters are also present in the PAc sample (1.35 g cm^{-3} density), which is confirmed by similar electron microscopic patterns. Their diffraction patters are also similar: The scattering angles ($2\theta = 20°$) and reflection intensities are equal. Thus, the XRD densities of both PAc samples are equal, whereas their pycnometric densities are different. These difference in the XRD and pycnometric densities can be due to different content of closed pores [8]. At similar XRD density the porosity is lower in the samples with higher pycnometric density.

As seen from the reactions of PAc with electrophilic reagents, in particular atmospheric oxygen and ozone, the volume of micropores affects the chemical and physical properties of crystalline PAc. The PAc sample with the pycnometric density of 1.20 g cm^{-3} absorbs up to 1.2 wt % of atmospheric oxygen in 60 h, whereas the polymer with the 1.35 g cm^{-3} density does not noticeably absorb oxygen. The polymer with a small density flames up immediately on contact with ozone, whereas the reaction of ozone with the high-density polymer is relatively slow: the polymer weight increases by only 5% after ozone bubbling for 5 h. Thus, the polymer oxidation is probably controlled by diffusion of oxygen and ozone into the sample bulk, and in the high-density polymer the diffusion is significantly hindered.

The behavior of PAc samples with different crystal packing at high temperature is also different. In general, thermal degradation of the macromolecules of the crystalline polymer with significant weight loss starts at 300–320°C and is complete at 600–650°C with formation of a coke residue (yield 35–45%). In the PAc sample of 1.20 g cm^{-3} density the polymer degradation proceeds at a higher rate and with a lower yield of the coke residue as compared with the less-

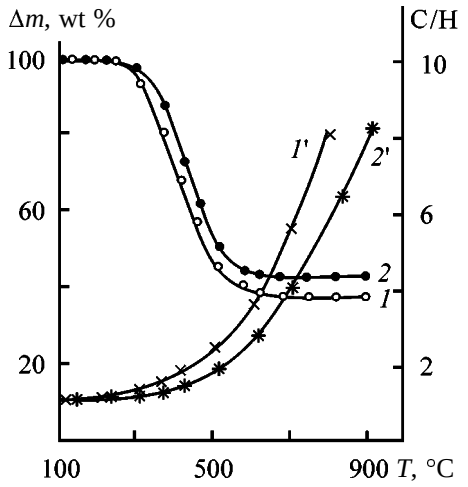

Fig. 1. (*1*, *2*) Weight loss Δm and (*1'*, *2'*) C/H ratio of crystalline PAc as functions of pyrolysis temperature *T*. Polymer density (g cm^{-3}): (*1*, *1'*) 1.20 and (*2*, *2'*) 1.35.

porous high-density polymer: curve *1* of the weight loss lies below curve *2* (Fig. 1).

The decrease in the content of closed pores in crystalline PAc hinders release of the volatile products of the polymer degradation and carbonization. The dehydrogenation of crystalline PAc of 1.20 g cm^{-3} density starts at 250°C and yields, via formation of several intermediate structures, completely carbonized samples at 1100–1200°C. In the high-density polymer elimination of hydrogen is hindered: The dependence of the C/H ratio characterizing hydrogen loss with temperature for the PAc sample of 1.35 g cm^{-3} density lies below that for the sample of 1.2 g cm^{-3} density (Fig. 1). The elevated thermal stability of high-density PAc is probably due to the hindered diffusion of hydrogen in the compact sections and possible hydrogen bonding between the π electrons and H atoms of the neighboring molecules.

The samples of crystalline PAc with different densities exhibit different electrophysical properties. The polymer with a high density (i.e., with a low porosity) exhibits higher specific electrical conductivity σ than the low-density sample: 10^{-9} and 10^{-10} Ω^{-1} cm^{-1}, respectively. High density and regular packing of the polymer probably facilitate the transfer of the charge carriers (e.g., electrons in the case of electronic conductivity) between macromolecules owing to high stability of high-density crystalline PAc to oxidation with atmospheric oxygen; its increased electrical conductivity is preserved for about 500 h on storage under argon or in air.

The electrical conductivity of the PAc sample slowly increases on heating to 400–500°C, and this

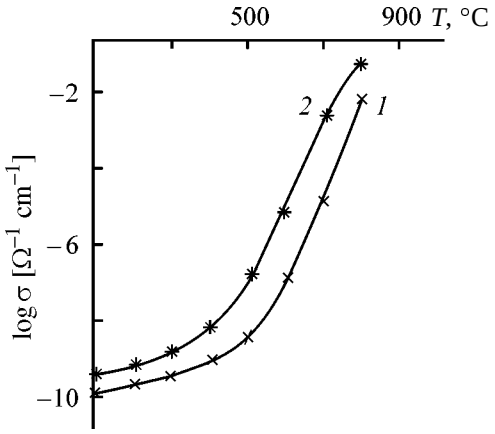

Fig. 2. Specific electrical conductivity σ of crystalline PAc as a function of the pyrolysis temperature *T*. Polymer density (g cm^{-3}): (*1*) 1.20 and (*2*) 1.35.

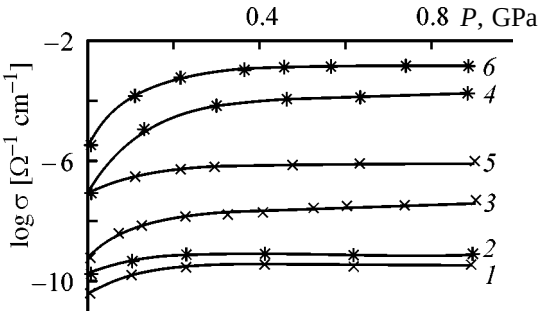

Fig. 3. Specific electrical conductivity σ of (*1, 2*) initial samples of crystalline PAc and samples heat-treated at (*3, 4*) 500 and (*5, 6*) 600°C. (*P*) Pressure. Polymer density (g cm^{-3}): (*1, 3, 5*) 1.20 and (*2, 4, 6*) 1.35.

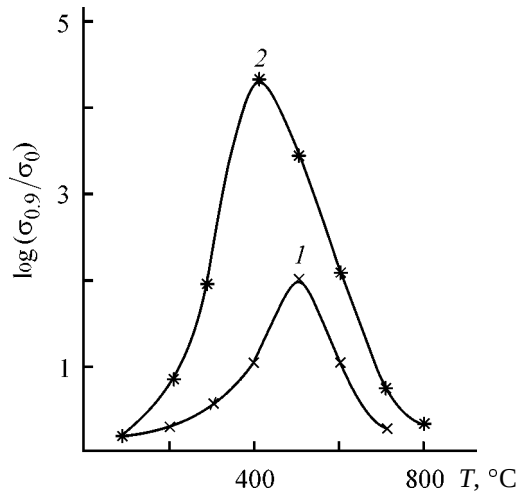

Fig. 4. Relative change in the electrical conductivity $\sigma_{0.9}/\sigma_0$ of crystalline PAc provided by uniaxial pressure of 0.9 GPa as influenced by the pyrolysis temperature *T*. Polymer density (g cm^{-3}): (*1*) 1.20 and (*2*) 1.35.

process intensifies at higher temperatures (Fig. 2). This is probably due to the fact that the probability of electron exchange, i.e., the mobility of charge carriers should increase with decreasing distance between the separate conjugated blocks during the thermal treatment [9]. The difference in the electrical conductivity is also observed in the products of PAc pyrolysis with the initial density of 1.20 and 1.35 g cm^{-3} (Fig. 2).

The increase in the mobility of the charge carriers can be also attained by compression of the polymer sample, which probably decreases the intermolecular distances and thus decreases the energy barrier between the neighboring conjugation blocks [7]. The uniaxial pressure only slightly increases the PAc conductivity (Fig. 3), which reaches a constant value at 0.20–0.24 GPa.

The thermal treatment of crystalline polymer yields the products whose electrical conductivity significantly increases with compression. At the same temperatures of heat treatment, in the pressure range 0–0.9 GPa, crystalline PAc with high density of crystal packing exhibits higher electrical conductivity than the low-density polymer samples (Fig. 3, curves *3, 4* and *5, 6*). As seen from the dependences of σ of the polymers at pressure of 0.9 GPa on the temperature of their thermal treatment, the heat-treated samples of PAc polymer with a high density are more strain-sensitive than the low-density samples (Fig. 4). The curve for the high-density PAc sample lies higher than that for the low-density polymer in the entire temperature range studied. These curves pass through a maximum; the greatest change in σ (by nearly 4.5 orders of magnitude) is observed for the high-density polymer (1.35 g cm^{-3}) heat-treated at 400°C.

The intrinsic paramagnetism of the polymers with a system of conjugated double bonds distinguishes PAc from the other polymers. We observe a single strong signal in the ESR spectrum with g = 2.003 typical for a free electron. The π electron is a paramagnetic center or a defect, which determines the magnetic properties of the polymer including its magnetization in an applied magnetic field.

The crystalline PAC prepared by phase-transfer dehydrochlorination of PVC is a weakly magnetic material; its static magnetic susceptibility does not exceed 10^{-6} g^{-1}. The static magnetic susceptibility χ is a response of the material on the applied magnetic field and characterizes the electronic effects related to structural features of the solid polymer and determined by only the physical nature of the given material [10]. The PAc susceptibility depends on the field intensity (Fig. 5a) with the saturation attained at relatively low

field intensities, which suggests that the polymer contains certain ordered areas where the cooperative spin interaction is possible. This polymer belongs to magnetically hard materials, because magnetization takes place at the magnetic field intensities $H \geq 10^{-3}$ Oe. In the area of field intensities studied (2–15 Oe) the magnetic susceptibility χ of the samples with densities of 1.20 and 1.35 g cm^{-3} is negative, which suggests their diamagnetism.

The crystalline polymer with the lower density is more diamagnetic than the high-density polymer. This is due to the fact that the magnetic susceptibility depends on the mutual location of the molecules in the solid. The stronger electron interaction in the sample with higher density probably increases χ.

The susceptibility of the molecules without intrinsic magnetic moment is equal to the sum of diamagnetic χ_d component characterizing the Langevin diamagnetism and paramagnetic component χ_p characterizing the van Vleck paramagnetism [7]:

$$\chi = \chi_d + \chi_p.$$

Diamagnetism originates from the interaction of the magnetic field with the partially or completely occupied electron orbitals, whereas paramagnetism is due to the interaction with unpaired electrons and uncompensated electron orbital moments. Therefore, the van Vleck paramagnetism should be proportional to the number of electrons.

Obviously, the contribution of the van Vleck paramagnetism to the susceptibility of the PAc molecule is predominant, because with increasing magnetic field intensity the polymer magnetization increases, which is typical for classical paramagnets (Fig. 5a). With increasing temperature (H = 14 kOe) χ of crystalline polymer with low density (1.2 g cm^{-3}) decreases, whereas in the high-density polymer (1.35 g cm^{-3}) it linearly increases (Fig. 5b).

The magnetic susceptibility is sensitive to the changes in the electronic structure occurring in the course of thermal treatment. Upon thermolysis, PAc passes from the diamagnetic to paramagnetic state; χ becomes positive and decreases with increasing field intensity (Fig. 5a). The increase in the packing density of the PAc crystals decreases their paramagnetism: The curve of χ vs. field intensity for the pyrolysis products of high-density polymer lies below the curve determined for low-density crystalline PAc (1.20 g cm^{-3}) heat-treated at the same temperature (Fig. 5a). The temperature dependence of the magnetic susceptibility of the pyrolysis products differs

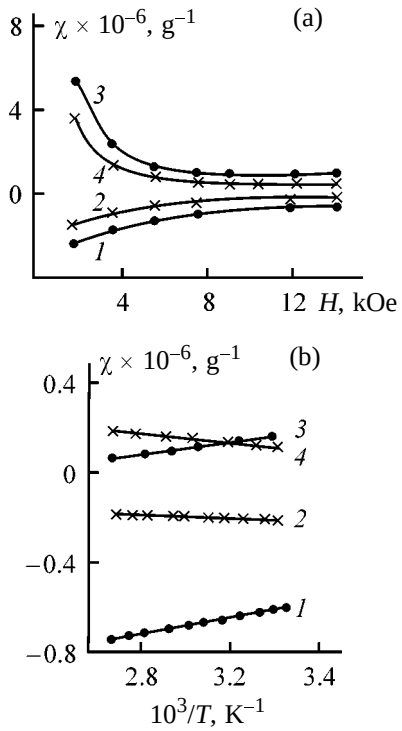

Fig. 5. Static magnetic susceptibility χ of the (*1*, *2*) initial and (*3*, *4*) heat-treated at 450°C samples of crystalline PAc as a function of (a) field intensity H and (b) temperature T. (a) Temperature 20°C; (b) field intensity 14 kOe. Polymer density (g cm^{-3}): (*1*, *3*) 1.20 and (*2*, *4*) 1.35.

from that found for the crystalline samples with low density. It increases with temperature, which corresponds to the increase in the number of paramagnetic centers due to the activation process. The apparent activation energy of the appearance of paramagnetic carriers is 1.1 eV.

Thus, the density of crystal packing in the initial polymer sample determines the properties of crystalline PAc and of the products of its thermal treatment.

CONCLUSIONS

(1) The chemical, electrophysical, and magnetic properties of crystalline polyacetylene prepared by phase-transfer dehydrochlorination of polyvinyl chloride depend on its density. As compared with low-density polyacetylene (d = 1.20 g cm^{-3}), the high-density polymer (d = 1.35 g cm^{-3}) is more resistant to atmospheric oxygen, ozone, and high temperatures.

(2) This polymer and the products of its pyrolysis exhibit higher electrical conductivity and strain sensitivity as compared with the low-density samples.

(3) The initial crystalline high-density polyace-

tylene exhibits lower diamagnetism, whereas the products of its thermolysis exhibit lower paramagnetism as compared with the corresponding low-density polymer samples.

REFERENCES

1. *Organicheskie poluprovodniki* (Organic Semiconductors), Kargin, V.A., Ed., Moscow: Nauka, 1968.
2. Kaner, R.B. and MacDiarmid, A.D., *Sci. Am.*, 1988, vol. 258, no. 2, pp. 50–56.
3. Ito, T., Shirakawa, H., and Ikeda, S., *J. Polym. Sci., Polym. Chem. Ed*., 1974, vol. 12, no. 1, pp. 11–20.
4. Shen, Z., Yang, M., and Farona, M., *Inorg. Chim. Acta*, 1984, vol. 94, nos. 1–3, pp. 26–27.
5. Wnek, G.E., Chien, J.C.W., Karacz, F.E., and Druy, M.A., *J. Polym. Sci., Polym. Lett. Ed*., 1979, vol. 17, no. 12, pp. 779–786.
6. Leplyanin, G.V. and Salimgareeva, V.N., *Izv. Ross. Akad. Nauk, Ser. Khim*., 1995, no. 10, pp. 1886–1893.
7. Vyatkin, S.E., Deev, A.N., Nagornyi, V.G., *et al*., *Yadernyi grafit* (Nuclear Graphite), Moscow: Atomizdat, 1967.
8. Dulov, A.A., Slinkin, A.A., Rubinshtein, A.M., *et al*., *Izv. Akad. Nauk SSSR, Ser. Khim*., 1963, no. 11, pp. 1910–1920.
9. Swenberg, Ch.E. and Pope, M., *Electronic Processes in Organic Crystals*, Oxford: Clarendon, 1982.
10. Blyumenfel'd, L.A., Berlin, A.A., Slinkin, A.A., and Kalmanson, A.E., *Zh. Strukt. Khim*., 1960, vol. 1, no. 1, pp. 103–108.

Russian Journal of Applied Chemistry, Vol. 74, No. 3, 2001, pp. 483–488. Translated from Zhurnal Prikladnoi Khimii, Vol. 74, No. 3, 2001, pp. 468–472.

MACROMOLECULAR CHEMISTRY AND POLYMERIC MATERIALS

Preparation of Chemically Cross-Linked Swollen Gels from Spent Rubbers and Their Use as Components of Rubber Stocks

S. V. Usachev, O. Yu. Solov'eva, M. E. Solov'ev, D. N. Babyuk, and V. M. Voronov

Yaroslavl State Technical University, Yaroslavl, Russia

Received December 23, 1999; in final form, March 2000

Abstract—A study was made of cross-linking of gelatinous compositions to obtain products classed with gels of the first type in which a part of the plasticizer is firmly retained by the gel structure of the elastomer. The elastic-hysteresis properties of the rubbers were studied.

According to the existing physicochemical concepts of structure formation and properties of elastomer blends, enhancement of fatigue-strength properties of rubbers based on them is due to a specific structure of the boundary zone between the polymer phases, incorporating along with the segmental interdiffusion layer also the boundary layers [1]. A thin contacting layer of one of the phases is characterized by a less close packing of macromolecules and in some cases by the lower degree of cross-linking [2]. The thinned layers provide efficient relaxation of stresses, which is one of the causes of the mutual reinforcement effect. Apparently, addition and distribution in a rubber stock of microparticles of a polymeric substance with *a fortiori* thinned stated of macromolecules due to filling of the interchain space with a plasticizer could enhance the conformational mobility of chains and accelerate relaxation of local overstresses arising under applied mechanical field.

In this work we examined the efficiency of using as such disperse phase swollen chemically cross-linked polymer gels. Usually swollen polymer gels (polymer jellies) are obtained from primary polymers [3]. However, in our case it is interesting to prepare gels from secondary polymeric materials, e.g., from spent rubbers, since products of spent rubber reprocessing are widely used as components of rubber stocks, decreasing their cost and modifying their properties.

EXPERIMENTAL

Polymer jellies were prepared by plasticization of crushed resins (CRs) of model composition and of crushed spent heating tubes (HTs) which are an inevitable waste of tire production. Plasticization was performed in hydrocarbon media at 160–200°C; the CR : plasticizer ratio was 1 : 3. Model rubbers were prepared from SKI-3 rubber; the polymer base of HT rubbers was a combination of SKI-3 and SKD rubbers. As a plasticizer we used Vaseline oil which is well compatible thermodynamically with SKI-3 and SKD rubbers, and also PN-6sh aromatic oil whose thermodynamic affinity for these rubbers is lower.

Plasticization at 160–200°C was performed until visually uniform compositions were obtained; owing to a low content of the polymer gel fraction and a high content of the plasticizer, these gels can be classed with jellies of the second type (swollen gels with a physical network) [4]. Degradation of the vulcanization structure of CRs was monitored by variation of the content of the sol (S) and gel (G) fractions and from the variation of the equilibrium swelling Q of the insoluble fraction in toluene.

We calculated the index of degradation of the vulcanization structure of the resins I_d by the formula [5]

$$I_d = Q(100 - S),$$

where Q and S are expressed in percents.

For example, at the process temperature of 180°C I_d of the rubber in the final product obtained from vulcanized unfilled SKI-3 rubber was 40.5, and the viscosity-average molecular weight of the sol fraction of the rubber was 42 000.

Figure 1 shows variation with time of the gel fraction content in HT reprocessing products heated in air and in the Vaseline oil medium. It is seen that the

1070-4272/01/7403-0483$25.00

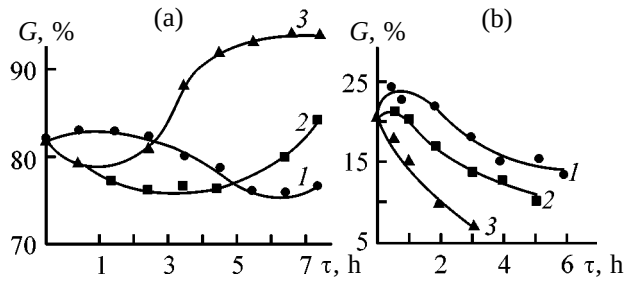

Fig. 1. Variation of the gel fraction content *G* in HTs in the course of heating (a) in air and (b) in Vaseline oil (1 : 3) at (*1*) 160, (*2*) 180, and (*3*) 200°C. (τ) Heating time.

initial stage of plasticization in the oil at 160–180°C is characterized by increase in the content of the insoluble fraction until a maximum is reached. This is probably due to cross-linking of the elastomer under the action of vulcanizing agents that had not reacted in the course of primary vulcanization and subsequent crushing. Cross-linking can also be effected by active sulfur fragments released in rearrangements of polysulfide bonds. On further heating, the gel fraction content decreases. At 200°C, no maximum is detected, which shows that degradation essentially prevails. With increasing temperature the apparent rate constant of gel degradation increases (Table 1).

Heating of HTs in air at 180 and 200°C in the absence of the plasticizer initially also causes the gel fraction content to decrease. After reaching a certain minimum, the amount of the gel starts to grow, suggesting the prevalence of cross-linking.

The degradation processes are more pronounced at 160°C. Comparison of the curves in Figs. 1a and 1b shows that addition of oil prevents cross-linking and accelerates thermal degradation of the gel. Analysis of the obtained curves shows that it is appropriate to perform thermal degradation of HTs at 180°C. At 160°C the process takes long time: After heating for 6 h, gel particles of ~1 mm size are still detected visually in the composition. When the process is performed at 200°C, the polymer strongly degrades before the composition becomes visually uniform, which is indicated by a decrease in viscosity.

Table 1. Kinetics of gel degradation during thermal plasticization of HTs in Vaseline oil

T, °C	Apparent rate constant of gel degradation, h^{-1}
160	0.426
180	0.616
200	0.912

When developing a procedure for preparing swollen chemically cross-linked gels, we took into account the following facts. The high content of the plasticizer certainly determines the specific features of cross-linking of rubber macromolecules. As noted in [3], an important condition for cross-linking of the polymer in such systems is the contact of separate molecules. Otherwise, either three-dimensional aggregates can form from a limited number of macromolecules, or separate macromolecules can undergo intramolecular cross-linking. The concentration of the polymer in the jellies under consideration exceeds the level theoretically required to ensure mutual contact of the revolution spheres of separate macromolecules in the unrolled state (several tenth fractions of percent [3]). Nevertheless, in the presence of a plasticizer the relative contribution of intramolecular cross-linking inevitably increases, and that of intermolecular cross-linking decreases [3, 6]. Another specific feature of the swollen gels in hand is the decreased (owing to strong degradation in the stage of secondary reprocessing) molecular weight of the rubber component. Therefore, it seems apparently necessary to take cross-linking agents in larger amounts as compared to cross-linking of a high-molecular-weight rubber. When choosing the type and content of cross-linking agents, we took into account in this case the recommendations given in [7].

The curing of the compound prepared by thermal degradation of HTs in Vaseline oil at 180°C [vulcanizing group, wt parts per 100 wt parts of rubber component): mercaptobenzothiazolyl disulfide 6.0, diphenylguanidine 3.0, zinc oxide 15.0, stearic acid 9.0, sulfur 45.0] is characterized by data in Fig. 2. It is seen that addition of sulfur is accompanied by an increase in the content of the insoluble fraction and a decrease in the degree of its swelling. At a certain instant marked with a triangle in the curves, the viscosity of the compound sharply increases, and its stirring with a power-driven propeller stirrer becomes impossible. This instant was identified as gelation point.

However, when a jelly prepared from HTs and Vaseline oil at 200°C was heated under similar conditions with the same amounts of the cross-linking agents, no gelation was observed at the vulcanization temperature. Apparently, in this case vulcanizing agents add mostly intramolecularly without formation of a common three-dimensional structure, which is probably due to the significantly decreased molecular weight of the rubber and fairly uniform distribution of macromolecules in the plasticizer. After cooling to

room temperature, this compound acquires a jelly-like consistence.

Figure 3 shows the kinetics of curing of compounds prepared by dispersion of HTs in PN-6sh oil at 200°C with various amounts of sulfur (20 and 40 wt parts per 100 wt parts of rubber) in the presence of accelerators and activators whose content and type are given above. As seen, compounds with PN-6sh oil as plasticizer differ from those with Vaseline oil in the higher concentration of free sulfur at the same curing time. Gelation occurs also in compounds prepared at 200°C. This is presumably due to worse thermodynamic compatibility of SKI-3 and SKD with aromatic PN-6sh oil, owing to which the fragments of the rubber chains can be more densely packed in microvolumes and hence can be cross-linked more readily. The gel content in all the examined compounds does not exceed a definite level of 15–18 wt %. The initial gel content in the compounds before degradation of HTs in the plasticizers is 20%. This means that the degree of cross-linking of the rubber macromolecules is fairly high. After cooling, the compound vulcanized at 143°C for 60 min with the vulcanizing group containing 40 wt parts of sulfur is a soft elastic pasty mass. After heating for 5 h and subsequent cooling, the product becomes solid. The jelly-like consistence of the compound with 20 wt parts of sulfur is preserved after curing.

We have examined the possibility of accelerating curing of swollen gels with ultraaccelerators, in particular, zinc dimethyldithiocarbamate (Zimate). In parallel, we performed for comparison vulcanization of jellies with sulfur in the presence of other, less active accelerators. In both cases we also used activators. The content of vulcanizing substances in the jellies and the vulcanization temperatures are listed in Table 2.

The vulcanization time of the jellies was 60 min. The products were added to tread rubber stocks in amounts of 10 and 15 wt parts per 100 wt parts of rubber. The stocks containing chemically cross-linked jellies prepared by cross-linking of the components with sulfur at 143°C and with sulfur in the presence of various amounts of zinc dimethyldithiocarbamate at 70 and 90°C are similar to the common rubber stock in the vulcanization rate. The physicomechanical characteristics of tread rubbers with additions of swollen gels, prepared using various vulcanizing systems, are listed in Table 3.

Data in Table 3 show that the properties of rubbers depend on the content and composition of jellies and on the temperature of their vulcanization. The best

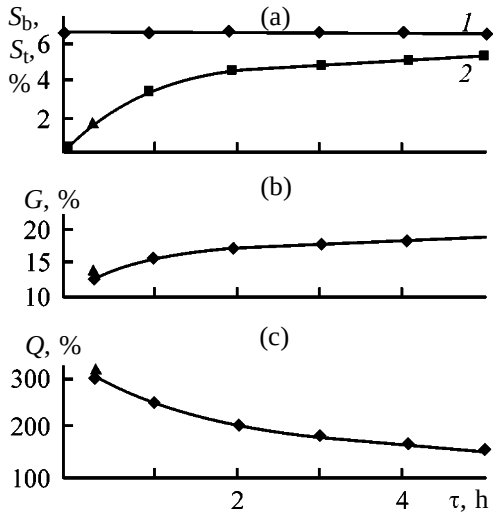

Fig. 2. Kinetic curves of curing of the HT–Vaseline oil compound (1 : 3) prepared at 180°C. Vulcanization temperature 143°C; the same for Fig. 3. (S_t, S_b) Content of total and bound sulfur; (*G*) gel content; (*Q*) equilibrium degree of swelling; (τ) process time; the same for Fig. 3. Sulfur: (*1*) total and (*2*) bound.

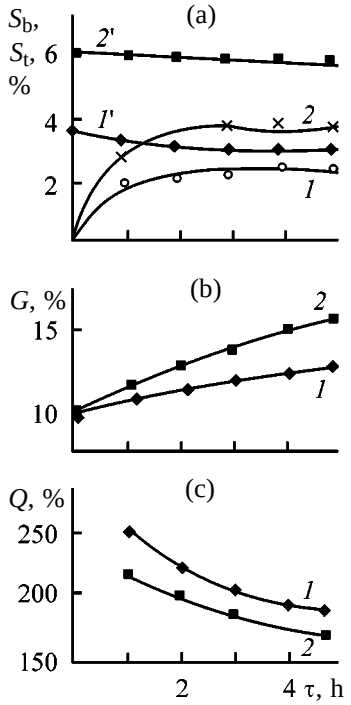

Fig. 3. Kinetic curves of curing of the HT–PN-6sh oil compound (1 : 3) prepared at 200°C. Content of (*1*, *2*) bound and (*1*', *2*') total sulfur. Amount of added sulfur, wt parts per 100 wt parts of rubber: (*1*, *1*') 20 and (*2*, *2*') 40.

combination of the elastic-strength and endurance characteristics is attained with chemically cross-linked jellies formed at 143°C in the presence of 20 and 25 wt parts of sulfur in combination with Altax and

Table 2. Composition of the vulcanizing group of ingredients at various temperatures of vulcanization of swollen gels. Content, wt parts: ZnO 15, stearic acid 9

Compound no.	*T*, °C	Content, wt parts per 100 wt parts of rubber component			
		sulfur	Zimate	Altax	diphenylguanidine
1	70	20	4	–	–
2	70	25	4	–	–
3	90	20	1	–	–
4	90	25	1	–	–
5	143	20	–	6	3
6	143	25	–	6	3

Table 3. Physicomechanical parameters of tread rubbers with addition of swollen gels obtained with vulcanizing systems of various compositions

Parameter	Initial rubber	Content of swollen gel, wt parts per 100 wt parts of rubber					
		10	15	10	15	10	15
		vulcanizing composition no.					
		1		2		3	
Nominal stress at 300% elongation, MPa	10.0	9.8	10.0	10.0	10.5	9.9	9.8
Nominal tensile strength, MPa	19.0	17.5	15.0	16.0	16.0	18.0	16.1
Relative elongation at break, %	520	500	480	460	420	500	480
Abradability (MIR-1 machine), $m^3\ TJ^{-1}$	55.6	63	69	63	78	57	91
Heat build-up, °C	25	21	20	21	21	23	23
Endurance at repeated stretching (ε_0 = 150%), thousand cycles	17.4	24.5	21.1	22.0	8.3	48.6	46.8
Parameter	Initial rubber	Content of swollen gel, wt parts per 100 wt parts of rubber					
		10	15	10	15	10	15
		vulcanizing composition no.					
		4		5		6	
Nominal stress at 300% elongation, MPa	10.0	9.8	7.9	9.7	9.9	9.3	9.8
Nominal tensile strength, MPa	19.0	17.6	15.5	18.5	18.4	18.4	18.6
Relative elongation at break, %	520	510	500	550	540	570	520
Abradability (MIR-1 machine), $m^3\ TJ^{-1}$	55.6	63	87	48	49	47	50
Heat build-up, °C	25	20	20	20	22	21	20
Endurance at repeated stretching (ε_0 = 150%), thousand cycles	17.4	54.9	52.6	36.3	36.8	42.8	36.2

diphenylguanidine. The rubbers containing these jellies, exhibiting the modulus of strength similar to that of serial samples, show higher endurance, lower heat build-up, and lower abradability. The rubbers containing jellies prepared using zinc dimethyldithiocarbamate exhibit somewhat worse characteristics.

When evaluating the structural features of rubbers prepared with addition of swollen gels with a chemical network of cross-links between rubber macromolecules, it should be taken into account that a part of the plasticizer is firmly retained in the gel structure. This is suggested by the fact that, when such samples are

treated with toluene, the amount of the extracted plasticizer is appreciably lower (60.7, 66.2, and 55.3 wt % for compound nos. 2, 4, and 6, respectively) than its total amount in the swollen gel (73–75 wt %). It should be noted also that in the case of vulcanization with sulfur in the presence of Altax and diphenylguanidine at 143°C the vulcanization network incorporates a larger amount of the plasticizer then in vulcanization in the presence of Zimate at 70 and 90°C. This may be due the higher density of the vulcanization network formed at 143°C. Apparently, the effect of the ultraaccelerator at a large amount of the plasticizer is manifested in more efficient intramolecular addition of sulfur.

The properties of rubbers containing swollen gels are largely affected by the character of dispersion of the gels in the matrix rubber stock. The particle-size distribution of swollen chemically cross-linked gels dispersed in the matrix of butadiene–styrene rubber by stirring [8, 9] is given in Table 4.

Table 4 shows that the swollen gels whose polymeric fraction is cross-linked in the presence of common accelerators of sulfur vulcanization at 143°C are readily dispersed in the rubber matrix. The content of fine (50–200 μm) particles is 70%. At the same time, in the jellies cross-linked using Zimate the majority of particles have a size of 250–350 μm. These data suggest that the prevalence in the swollen gel of intramolecular sulfur bridges (compound no. 4) makes the resulting compound more rigid, since vulcanization is accompanied by formation of a new type of the polymer with the molecular structure containing chemically bound sulfur. As a result, the cohesion energy density increases, the difference in solubility between the butadiene–styrene rubber and the newly prepared polymer becomes more pronounced, and coarser jelly particles are formed on mixing.

Thus, the structure of the rubber stock containing swollen chemically cross-linked polymer gels can be represented as a combination of elastomers of different chemical nature. The specific feature of such structure is the increased conformational mobility of macromolecules in dispersed phase particles and the decreased particle modulus, which enhances the endurance of the compounds [10]. The mass transfer of excess plasticizer to the matrix mixture forms a boundary layer around particles with a higher plasticizer content and hence with a decreased modulus. This layer also enhances the endurance, since it provides relaxation of local stresses. A valuable property of such compositions is decrease in the hysteresis loss, manifested in decreased heat build-up under conditions of repeated deformations at constant elastic-strength characteristics.

Table 4. Particle-size distribution of swollen chemically cross-linked gels in the rubber matrix

Compound no.	Particle size, mm	Volume fraction of particles, %
2	0.05–0.10	6.5
	0.11–0.20	18
	0.21–0.25	11
	0.26–0.35	64.5
4	0.05–0.10	4
	0.11–0.20	8
	0.21–0.25	8
	0.26–0.35	80
6	0.05–0.10	44
	0.11–0.20	26
	0.21–0.25	15
	0.26–0.35	15

CONCLUSIONS

(1) Thermal plasticization of crushed model rubbers based on SKI-3 rubber and spent heating tubes based on SKI-3 + SKD rubbers in plasticizers and in air at 160–200°C was studied. The kinetic features of degradation of the three-dimensional structure of the vulcanized rubbers were found, and the apparent rate constants of gel degradation were determined. Swelling in hydrocarbon media makes formation of jellies of the second type less probable. At decreased molecular weight, rubber macromolecules preserve the long-chain structure in thermal plasticization products.

(2) The process for preparing chemically cross-linked gels by sulfur cross-linking of thermal plasticization products of the above-mentioned rubbers in the presence of accelerators and activators was studied. When added to rubber stocks, swollen chemically cross-linked gels are broken down to microparticles in the course of mixing under the influence of shear stress and give the disperse phase. The resulting elastomer compounds acquire enhanced elastic-hysteresis properties after vulcanization.

ACKNOWLEDGMENTS

The study was supported by the Ministry of Education of the Russian Federation (project no. 9808-2.2-120).

REFERENCES

1. Kuleznev, V.N., *Smesi polimerov* (Polymer Blends), Moscow: Khimiya, 1980.
2. Kuleznev, V.N. and Usachev, S.V., in *Mezhdunarodnaya konferentsiya po kauchuku i rezine IRC-94* (Int. Rubber Conf. IRC-94), Moscow, September 27–October 1, 1994, vol. 3, pp. 288–298.
3. Papkov, S.P., *Studneobraznoe sostoyanie polimerov* (Gelatinous State of Polymers), Moscow: Khimiya, 1974.
4. Tager, A.A., *Fizikokhimiya polimerov* (Physical Chemistry of Polymers), Moscow: Khimiya, 1978, 3rd ed.
5. Makarov, V.M. and Drozdovskii, V.F., *Ispol'zovanie avtomobil'nykh shin i otkhodov proizvodstva amortizovannykh rezinovykh izdelii* (Utilization of Automobile Tires and Spent Rubber Items), Leningrad: Khimiya, 1986.
6. Dontsov, A.A., Kanauzova, A.A., and Litvinova, T.V., *Kauchuk-oligomernye kompozitsii v proizvodstve rezinovykh izdelii* (Rubber–Oligomer Compounds in Production of Rubber Items), Moscow: Khimiya, 1986.
7. USSR Inventor's Certificate no. 1 781 246.
8. Gradus, A.Ya., *Rukovodstvo po dispersnomu analizu metodom mikroskopii* (Manual on Dispersion Analysis by Microscopy), Moscow: Khimiya, 1979.
9. Basov, N.I., Lyubartovich, V.A., and Lyubartovich, S.A., *Kontrol' kachestva polimernykh materialov* (Quality Control of Polymeric Materials), Leningrad: Khimiya, 1990.
10. Usachev, S.V., Zakharov, N.D., Vetoshkin, A.B., and Zubov, V.A., in *Materialy i tekhnologiya rezinovogo proizvodstva: Preprinty mezhdunarodnoi konferentsii po kauchuku i rezine "Rubber 84"* (Materials and Processes of Rubber Production: Preprints of Int. Conf. on Rubber "Rubber 84"), Moscow, September 4–8, 1984, no. C60.

Russian Journal of Applied Chemistry, Vol. 74, No. 3, 2001, pp. 489–493. Translated from Zhurnal Prikladnoi Khimii, Vol. 74, No. 3, 2001, pp. 478–482.

MACROMOLECULAR CHEMISTRY AND POLYMERIC MATERIALS

Synthesis of Polymethyl Methacrylate Microspheres in the Presence of Dextran and Its Derivatives

A. Yu. Men'shikova, T. G. Evseeva, N. A. Chekina, and S. S. Ivanchev

Institute of Macromolecular Compounds, Russian Academy of Sciences, St. Petersburg, Russia

Received October 3, 2000; in final form, November 2000

Abstract—Emulsion polymerization of methyl methacrylate initiated by a carboxyl-containing azo initiator in the presence of a polymeric stabilizer (dextran or its functionalized derivatives) was studied with the aim to prepare monodisperse microspheres of polymethyl methacrylate with surface carboxy, amido, and aldehyde groups. The optimal conditions for formation of monodisperse microspheres were found, allowing control of their diameter in the submicrometer range and of the nature and content of surface functional groups.

Synthesis of monodisperse microspheres in the presence of polymeric stabilizers shows promise since stabilizers not only enhance the aggregative stability of particles in the course of polymerization but also, in subsequent transformations, play the role of spacers containing functional groups for covalent binding of ligands. With biologically active substances (BASs) as ligands, such microspheres are used in immunoassay as immunoreagents visualizing the progress of immunochemical reactions. Most often BASs are bound to microspheres via surface carboxy groups capable, after activation, to form amide bonds with BAS amino groups, or via aldehyde groups reacting with a amino groups under very mild conditions to form Schiff bases [1–3]. Suitable polymeric stabilizers in preparation of microspheres can be dextran and its functionalized derivatives which are widely used for modification of water-soluble pharmaceuticals with the aim to prolong their effect and reduce the toxicity [4, 5]. Preparation of polystyrene [6] and polyalkyl cyanoacrylate [7] microspheres in the presence of dextran and β-cyclodextrin was reported previously. Of interest for immunoassay are also microspheres based on polymethyl methacrylate (PMMA), a polymer with a higher density and a lower refractive index, which is advantageous for processes involving fast sedimentation or optical monitoring of immunochemical reactions [8]. Samples of PMMA microspheres obtained both in the absence and in the presence of dextran were tested in immunization processes [9, 10]. The microspheres in this case acted not only as carriers of immunoreagents but also as an adjuvant enhancing the immune response. It was found that the microspheres undergo slow biodegradation, which facilitates elimination of PMMA from the body. At present, additional surface modification of dextran-coated microspheres is performed with the aim to obtain active functional groups. For example, hydroxy groups of dextran are oxidized to aldehyde groups with periodate. To obtain directly in the course of synthesis monodisperse PMMA particles with the carboxylated surface coated with a polymeric stabilizer, it seems promising to perform emulsion polymerization of MMA initiated with a carboxyl-containing azo initiator in the presence of dextran. It is also interesting to study the features of a similar process performed in the presence of functionalized dextran derivatives, with the aim to introduce into the microsphere surface layer not only carboxy but also other functional groups, to increase the surface concentration of functional groups, and to control their content depending on the nature of the derivative in hand.

EXPERIMENTAL

Methyl methacrylate, isoamyl alcohol, and dimethylformamide (DMF) were purified by standard procedures. The procedures for purification and characteristics of 4,4'-azobis(4-cyanovaleric acid) (CVA) are described elsewhere [2]. Synthesis was performed in double-distilled water as dispersion medium. Dextran (M 60 000 ± 10 000) produced by the St. Petersburg Academy of Pharmaceutical Chemistry was used without additional purification.

Dextran derivatives differing in the nature of functional groups and degree of substitution (DS) were prepared and characterized according to [4, 5]. We

1070-4272/01/7403-0489$25.00

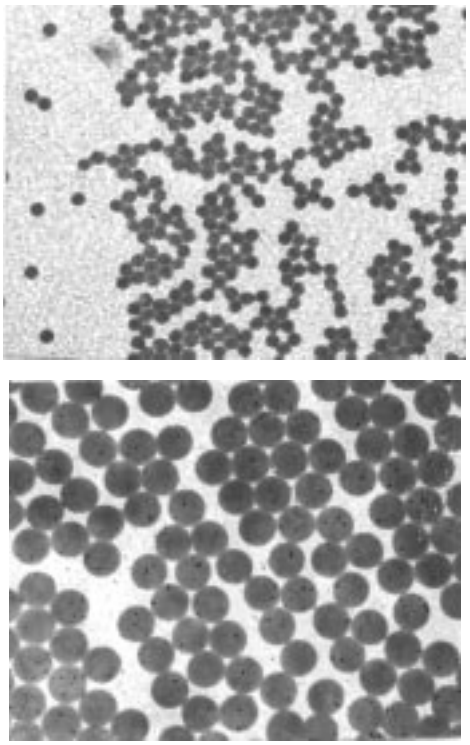

Fig. 1. Influence of the nature of the initiator on the size of PMMA microspheres. Initiator: (a) potassium persulfate and (b) CVA.

prepared carboxymethyl dextran (CMD) (DS 0.6), carboxyethyl dextran (CED) (DS 0.91), dextran polyaldehyde (DPA) (DS 1.15), and carboxyethyl dextran amides (CEDAs) containing both carboxy and amide groups ($CEDA_1$: DS_{carb} 0.31, DS_{amide} 0.32; $CEDA_2$: DS_{carb} 0.27, DS_{amide} 0.58).

The CVA-initiated emulsion polymerization was performed at 348 ± 1 K by the procedure described in [2, 3] in the presence of dextran or its derivatives. The ratio of MMA to the aqueous phase was 1 : 10, the initiator concentration was 0.2 wt % relative to water, and the dextran content was varied from 0.1 to 0.4 wt % relative to water. To reveal the effect of the nature of the initiator on the characteristics of the forming PMMA microspheres, polymerization in the presence of dextran (0.2 wt %) was also initiated with potassium persulfate, which is commonly used for preparing monodisperse latexes. The polymerization temperature in this synthesis was decreased to 343 K, since even at this temperature the rate constant of persulfate decomposition ($\log K = -1.3$ [11]) is higher than that of CVA at 353 K ($\log K = -3.94$ [12]). In some runs the conversion of the monomer in the course of polymerization was monitored by gas chromatography, with isoamyl alcohol as internal reference (determination error 5%).

Table 1. Influence of dextran concentration in the reaction mixture on the diameter *d* of PMMA latex particles*

Dextran, wt %	*d*, μm
0.10	0.29–0.48
0.15	0.30–0.43
0.20	0.42
0.25	0.37
0.30	0.46
0.35	0.54
0.40	0.36

* Concentrations: MMA 10 wt %, CVA 0.2 wt %, Na_2HPO_4 0.02 M, and NaOH 0.0168 M.

The particle diameters in the forming latexes were determined with a JEM 100 S electron microscope (JEOL, Japan). After triple washing of the latexes to remove water-soluble impurities by successive centrifuging and redispersion, the surface concentration of carboxy groups was determined by conductometric titration [2]. The surface concentration of aldehyde groups was determined by the same method, after reaction of the aldehyde groups with hydroxylamine hydrochloride [13].

We found that monodisperse PMMA particles (Fig. 1) are formed when the polymerization is initiated with both carboxyl-containing azo initiator CVA and persulfate. However, in synthesis with CVA the particle diameter was larger (0.42 μm) than with persulfate (0.18 μm). Also considerably higher was the concentration of carboxy groups on the particle surface (1.47 vs. 0.42 μg-equiv m^{-2}), which is advantageous for subsequent chemical binding of BASs. Thus, the carboxyl-containing azo initiator is apparently more efficient for preparing PMMA microspheres in the presence of dextran.

As shown in [3], in emulsifier-free emulsion polymerization of styrene initiated by CVA the diameter of the forming microspheres is largely affected by the ionic strength and pH of the dispersion medium [3]; therefore, to control the particle size, it is advisable to choose appropriate buffer systems. Therefore, we performed a series of experiments on preparation of PMMA microspheres in the presence of Na_2HPO_4 (to provide weakly alkaline medium) and 0.2 wt % dextran (Table 1). We found that PMMA particles obtained in the presence of dextran and without it at low concentration of the buffer additive Na_2HPO_4 have a comparable size (Fig. 2). As the concentration of Na_2HPO_4 was increased to 0.08 M, the diameter of PMMA microspheres formed in the presence of

dextran linearly increased, with the monodispersity and stabillity of the latex being preserved. On the contrary, in the absence of dextran the particle size drastically increased with increasing ionic strength, a large amount of coagulum formed, and the latex lost monodispersity. Thus, at high Na_2HPO_4 concentration the electrostatic barrier produced by repulsion of ionized carboxy groups appears to be insufficient to provide the aggregative stability of the forming latex, whereas steric stabilization of microspheres with dextran imparts to them additional stability in the course of polymerization. This fact makes it possible to finely control, by varying the salt concentration, the diameter of microspheres in the submicrometer range, with the monodispersity being preserved.

As shown in [6], dextrans with the molecular weight ranging from 70 000 to 2 000 000 enhance the resistance of polystyrene dispersions formed in their presence to the action of electrolytes. This trend was explained in [6] by formation of highly viscous strong surface adsorption layers consisting of dextran and the forming polymer, preventing the particle coalescence. The highest stability is attained at $M \geq 500\,000$. However, experiments in [6] were performed at constant molar concentration of dextrans of different molecular weights, so that with increasing M the weight content of dextran in the reaction mixture increased, and the surface concentration of the polymeric stabilizer could increase also. By contrast, in this work, to determine the synthesis conditions ensuring aggregative stability and monodispersity of the resulting PMMA latexes, we took the same dextran sample (M = 60 000) and varied its concentration in the range 0.1–0.4 wt %, at an Na_2HPO_4 concentration of 0.02 M (Table 1). We found that the aggregative stability of the latex in the course of the synthesis, evaluated by the amount of the forming coagulum, largely depends on the dextran concentration in the reaction mixture (Fig. 3). At a dextran concentration of 0.20–0.25 wt %, no coagulum was formed. At lower concentrations of the steric stabilizer, as expected, the aggregative stability of the latex decreased. However, the latex stability also decreased at dextran concentrations above the optimal level; it is interesting that the concentration of the carboxy groups on the particle surface increased in parallel with the amount of the coagulum. If the aggregative stability were controlled by the electrostatic factor, an opposite trend would be expected. Apparently, the experimentally observed decrease in the aggregative stability of microspheres with increasing concentration of carboxy groups in the surface layer consisting of dextran and the forming polymer is due

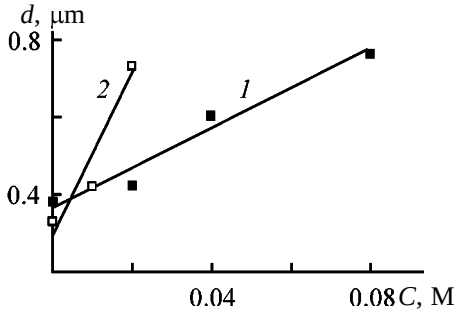

Fig. 2. Diameter d of the forming PMMA microspheres as a function of the concentration C of Na_2HPO_4 (*1*) in the presence (0.2 wt %) and (*2*) in the absence of dextran.

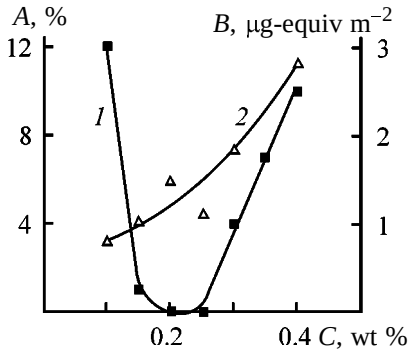

Fig. 3. Influence of dextran concentration C in the reaction mixture (*1*) on formation of coagulum A and (*2*) on concentration of surface carboxy groups B.

to destabilization of the surface layer as a result of mutual repulsion of the ionic groups.

To obtain microspheres with different surface functional groups, we performed a series of experiments in the presence of various dextran derivatives, taken in a concentration of 0.25 wt % (Table 2). We found that the concentration of carboxy groups on the surface of particles obtained in the presence of CMD, $CEDA_1$, and $CEDA_2$ is higher as compared to the microspheres prepared in the presence of dextran (Fig. 3). This may be due to incorporation of carboxyl-containing polymeric stabilizers into the surface layer of the microspheres. The diameter of these microspheres is somewhat larger than that of the particles formed in the presence of unmodified dextran. This fact suggests differences in the character of the particle stabilization and hence in the structure and strength of the forming surface layer, which may be caused by mutual repulsion of the ionic carboxy groups of the dextran derivatives as it was observed in preparation of microspheres in the presence of large amount of unmodified dextran.

The degree of ionization of carboxy groups in the surface layer of the particles was decreased by replac-

Table 2. Characteristics of PMMA latexes prepared in the presence of dextran derivatives*

Stabilizer	MMA conversion, % (by the end of synthesis)	Coagulum, % (by the end of synthesis)	pH (by the end of synthesis)	*d*, μm	Concentration of surface –COOH groups, μg-equiv m^{-2}
			Na_2HPO_4		
Dextran	99	0	7.38	0.37	1.10
CMD	99	2	7.00	0.51	2.70
CED	98	0	7.20	0.49	1.12
$CEDA_1$	81	18	7.20	0.49	1.42
$CEDA_2$	99	14	7.30	0.50	1.57
			KH_2PO_4		
Dextran	99	0	6.70	0.63	1.18
CMD	96	1	5.25	0.50–1.60	–
$CEDA_1$	72	0	6.20	0.38–0.56	–
DPA	96	0	6.30	0.44	0.82 1.22 (–CHO)

* Concentrations: polymeric stabilizer 0.25 wt % and salt 0.02 M.

ing Na_2HPO_4 by KH_2PO_4 providing a more acidic medium. We found that, in the presence of dextran and KH_2PO_4, coarser monodisperse microspheres are formed (Table 2), which suggests that the electrostatic factor also contributes to their stabilization. This assumption is also supported by the polydispersity of latexes prepared in the presence of carboxylated dextran derivatives in a weakly acidic medium. By contrast, synthesis under the same conditions of a PMMA latex in the presence of a dextran derivative with nonionic aldehyde groups (DPA) gave a monodisperse latex in a good yield.

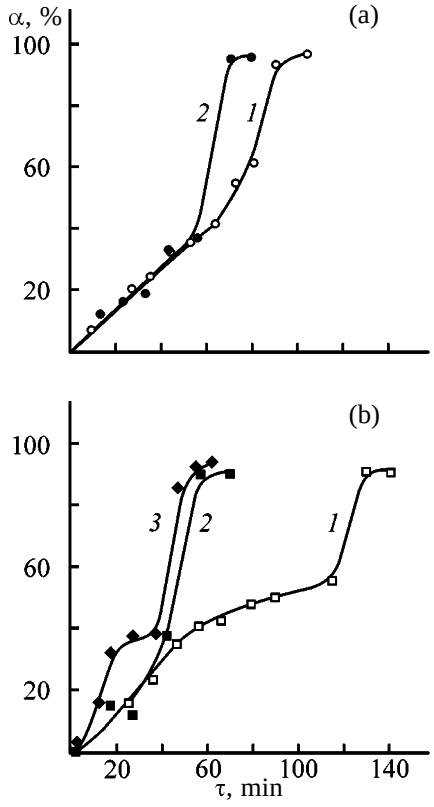

Fig. 4. Variation with time τ of MMA conversion α. Polymer added: (*1*) none, (*2*) dextran, and (*3*) DPA (0.25 wt %). Salt added: (a) Na_2HPO_4 and (b) KH_2PO_4.

To examine the influence of the composition of the reaction mixture on polymerization, we studied the conversion of MMA in the course of the synthesis in the presence of dextran or DPA, or without addition of a polymeric stabilizer. The reaction medium also contained Na_2HPO_4 or KH_2PO_4 (Fig. 4). In the weakly alkaline medium (Fig. 4a), the initial linear sections of the kinetic curves coincide for experiments performed in the presence and in the absence of dextran. However, in the presence of dextran this section is followed by sharp acceleration of the process, and the resulting particles are appreciably smaller than the microspheres obtained without adding dextran (Table 3). In the weakly alkaline medium, the kinetic curves of synthesis of PMMA microspheres in the presence of dextran or DPA show practically no linear section (Fig. 4b). The shape of the conversion curves depends on the nature of the steric stabilizer, which may be due to different structures of the forming surface layers. In the presence of dextran, highly viscous surface adsorption layers can form, restricting penetration of the growing radicals from the aqueous phase inside polymer–monomer particles (PMPs); as a result, the lifetime of the macroradical in PMP becomes

Table 3. Diameter d and number N of particles formed in experiments on determination of MMA conversion (Fig. 4)*

Stabilizer	d, μm	Number of particles $N \times 10^{-12}$, ml^{-1}
	Na_2HPO_4	
–	0.73	0.40
Dextran	0.50	1.20
	KH_2PO_4	
–	0.72	0.39
Dextran	0.63	0.58
DPA	0.30	5.80

* Concentrations: polymeric stabilizer 0.25 wt % and salt 0.02 M.

longer and the gel effect is enhanced. Presumably, with DPA formation of adsorption layers can be accompanied by grafting of PMMA by reaction of the growing radicals with DPA aldehyde groups. This process accelerates formation of PMPs at the beginning of the synthesis and enhances the aggregative stability of the PMPs owing to formation of stronger surface layers with chemical links between PMMA and DPA. Therefore, the number of particles formed in the presence of DPA appreciably increases (Table 3).

CONCLUSION

Emulsion polymerization of methyl methacrylate, initiated with a carboxyl-containing azo initiator and performed in the presence of dextran or its derivatives, allows preparation of monodisperse polymethyl methacrylate microspheres. The optimal preparation conditions were found, allowing control of the particle diameter (in the submicrometer range) and functionality (introduction into the surface layer of carboxy and aldehyde groups required for binding immunoreagents and of amide groups improving the biocompatibility of these microspheres).

ACKNOWLEDGMENTS

The study was financially supported by the Program of the St. Petersburg Scientific Center, Russian Academy of Sciences for the year 2000 (initiative project no. 19).

REFERENCES

1. Prokopov, N.I., Gritskova, I.A., Cherkasov, V.R., and Chalykh, A.E., *Usp. Khim.*, 1996, vol. 65, no. 2, pp. 178–192.
2. Lishanskii, I.S., Men'shikova, A.Yu., Evseeva, T.G., *et al.*, *Vysokomol. Soedin.*, 1991, vol. 33, no. 6, pp. 413–416.
3. Men'shikova, A.Yu., Evseeva, T.G., Shabsel's, B.M., *et al.*, *Kolloidn. Zh.*, 1997, vol. 59, no. 5, pp. 671–675.
4. Iozep, A.A., Bessonova, N.K., and Passet, B.V., *Zh. Prikl. Khim.*, 1998, vol. 71, no. 2, pp. 320–323.
5. Iozep, A.A., Bessonova, N.K., Strokach, D.A., and Passet, B.V., *Zh. Prikl. Khim.*, 1997, vol. 70, no. 5, pp. 824–828.
6. Bakeeva, I.V., Borodina, I.A., and Gritskova, I.A., *Vysokomol. Soedin., Ser. B*, 1997, vol. 39, no. 5, pp. 868–871.
7. Yen, S.P.S., Rembaum, A., Molday, R.W., and Dreyer, W., in *Emulsion Polymerization: Am. Chem. Soc. Symp. Ser.*, Washington: Am. Chem. Soc, 1976, pp. 236–244.
8. Amiral, J. and Migaud, M., *Eur. Clin. Lab.*, 1991, vol. 10, no. 6, pp. 28–29.
9. Kreutor, J., *Vaccine*, 1986, vol. 4, pp. 125–129.
10. Zhao, Z., *J. Pharm. Sci.*, 1996, vol. 85, no. 12, pp. 1261–1270.
11. Brandrup, J. and Immergut, E.H., in *Polymer Handbook*, Wiley, 1989, 3rd ed.
12. Cavell, E.A.S. and Meeks, A.C., *Macromol. Chem.*, 1967, vol. 108, pp. 304–306.
13. Yan, C., Zanhg, X., and Sun, Z., *J. Appl. Polym. Sci.*, 1990, vol. 40, pp. 89–98.

Russian Journal of Applied Chemistry, Vol. 74, No. 3, 2001, pp. 494–497. Translated from Zhurnal Prikladnoi Khimii, Vol. 74, No. 3, 2001, pp. 483–486.

MACROMOLECULAR CHEMISTRY AND POLYMERIC MATERIALS

Controlled Polymerization of Methyl Methacrylate in the Presence of *C*-Phenyl-*N*-*tert*-Butylnitrone and Commercial Radical Initiators

D. F. Grishin, L. L. Semenycheva, and E. V. Kolyakina

Research Institute of Chemistry, Nizhni Novgorod State University, Nizhni Novgorod, Russia

Received August 9, 2000

Abstract—Radical polymerization of methyl methacrylate initiated by dicyclohexyl peroxydicarbonate in the presence of a chain-terminating agent, *C*-phenyl-*N*-*tert*-butylnitrone, as a potential source of stable nitroxyl radicals, was studied.

"Pseudoliving" radical polymerization is a relatively new field of synthetic polymer chemistry; in the past decade, it received much researchers' attention [1–6]. The main feature of such processes is termination of material chains by recombination of macroradicals with stable radicals added to control the chain propagation. In this case, a labile bond is formed at the end of the polymer chain, capable of cleavage with regeneration of the active macroradical:

$$\sim P_n^{\cdot} + A^{\cdot} \rightleftarrows [\sim P_n\text{–}A], \quad (1)$$

$$[\sim P_n\text{–}A] + M \rightarrow [\sim P_{n+m}\text{–}A], \quad (2)$$

where $A^{\cdot}$ is a stable radical.

As a result, the periods of "sleep" and "life" of polymer chains alternate, and the molecular weight of the polymer successively increases; as a result, polymers with narrow MWD are formed. The most widely used stable radicals acting as chain-terminating agents are sterically hindered nitroxyls [1–3]. In this case the "pseudoliving" mechanism is realized at relatively high temperatures exceeding 100°C. Under these conditions the chain termination on nitroxyls becomes reversible. It was shown previously that polymerization of methyl methacrylate (MMA) initiated by azobis(isobutyronitrile) (AIBN) in the presence of spin traps as potential sources of stable nitroxyl radicals, e.g., *C*-phenyl-*N*-*tert*-butylnitrone (PBN) [7] or 2-methyl-2-nitrosopropane (MNP) [8], occurs by the mechanism of pseudoliving chains at lower temperatures (323–343 K).

In this connection, it is interesting to study polymerization of MMA in the presence of PBN, initiated by the widely used commercial initiator, dicyclohexyl peroxydicarbonate (CPC).

EXPERIMENTAL

The monomer was purified by a common procedure [9]. PBN was prepared following the protocol in [10]. The physicochemical constants of the compounds agreed with published data. The polymerization kinetics was monitored gravimetrically, dilatometrically [11], and calorimetrically [12]. The samples were pretreated by the following procedure: The monomer was placed in a glass ampule, degassed by three freeze–pump–thaw cycles, and polymerized at a residual pressure of 1.3 Pa. The molecular weight was determined viscometrically [13]. The molecular-weight distribution (MWD) of polymethyl methacrylate (PMMA) was determined by gel-permeation chromatography (GPC) using a set of five styrogel columns with a pore diameter of 1×10^5, 3×10^4, 1×10^4, 1×10^3, and 250 Å (Waters, the United States). The detector was an R-403 differential refractometer (Waters), and the eluent was tetrahydrofuran. Narrow-MWD polystyrene references were used for calibration [14]. The recalculation of the average molecular weight from polystyrene to PMMA was done by the formula $\log M_{PMMA} = 1.019 \log (0.664 M_{PS})$.

We found that PBN as a potential source of stable nitroxyl radicals can efficiently control the kinetic parameters of CPC-initiated polymerization of MMA and the molecular-weight characteristics of the resulting polymer. Figure 1 shows the kinetic curves of polymerization, obtained gravimetrically. It is seen that addition of PBN in amount comparable with that

1070-4272/01/7403-0494$25.00

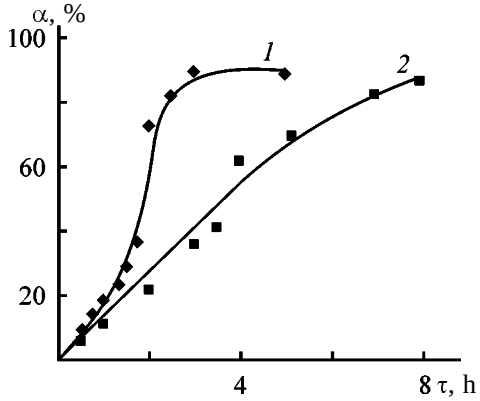

Fig. 1. Kinetic curves of MMA polymerization in the presence of PBN at 323 K. Initiator: 0.1 M CPC; the same for Fig. 2. (α) Conversion and (τ) time; the same for Fig. 2. (*1*) No additives; (*2*) 0.4 mol % PBN added.

of the initiator suppresses the autoacceleration effect.

It is interesting and important from the practical viewpoint that PBN exerts no appreciable inhibiting effect on the propagation rate of the polymer chain (Table 1): The initial polymerization rate V_p, determined dilatometrically, in the presence of PBN decreases insignificantly. This fact is of major practical importance, because a significant drawback of presently known chain-terminating agents is their substantial decelerating effect on polymerization [1–3], which somewhat limits the efficiency of their industrial use.

Table 1. Kinetic parameters of MMA polymerization in the presence of PBN and molecular-weight characteristics of polymers. [Initiator] = 0.1 mol %; T = 323 K

[PBN], mol %	$V_p \times 10^4$, mol l^{-1} s^{-1}	Conversion, %	Polydispersity coefficient of polymer
	AIBN initiator		
–	–	11.8	2.1
0.4	–	7.2	1.8
0.8	–	2.2	1.8
0.8	–	7.3	1.8
0.8	–	31.4	1.8
0.8	–	61.4	1.7
0.8	–	74.3	1.7
	CPC initiator		
–	5.8	9.1	1.6
–	5.8	82.0	>3
0.1	4.6	7.3	–
0.2	4.1	10.1	–
0.4	3.0	5.8	–
0.8	1.7	7.5	–
0.4	–	3.1	1.6
0.4	–	11.0	1.7
0.4	–	35.8	1.9
0.4	–	62.1	2.5
0.4	–	82.2	2.5

The effect of nitrone on the kinetics of CPC-initiated polymerization of MMA is revealed still more clearly from the differential kinetic curves obtained calorimetrically at 323 K (Fig. 2). At successively increased concentration of nitrone, the autoacceleration effect considerably decreases and the lifetime of the polymer chain increases, which allows the gel effect, undesirable in commercial polymerization processes, to be practically totally suppressed.

The decrease in the gel effect is indirectly confirmed by the ratio of V_p of CPC-initiated MMA polymerization in the presence of various concentrations of PBN to the maximal rate, i.e., the rate in the stage of the gel effect V_g. As seen from Table 2, this ratio gradually decreases as the PBN concentration is increased and becomes close to 3.5 at a PBN concentration of 0.4 and 0.8 mol %.

Our results show that in the presence of CPC and PBN polymerization of MMA occurs by the mechanism of pseudoliving chains. The chain-terminating agents are stable nitroxyl radicals containing a macromolecular fragment and formed by the scheme

$$\sim P_n^{\cdot} + \underset{\displaystyle H\ \ O}{\overset{\displaystyle |\ \ \downarrow}{Ph–C=N–C_4H_9}} \rightarrow \underset{\displaystyle Ph\ \ O^{\cdot}}{\overset{\displaystyle |\ \ |}{\sim P_n Ph–CH–N–C_4H_9}} \quad (3)$$

$$A^{\cdot}$$

Then, the chain grows in the "living" chain mode [Eqs. (1), (2)].

The most exhaustive information on the possibility of realization of this mechanism under specific experimental conditions is furnished by measuring the molecular weight of the polymeric product as a function of conversion and by studying in detail the MWD of the synthesized samples.

The dependence on conversion of the MWD of PMMA prepared using the PBN–CPC system at a fixed concentration of nitrone is shown in Fig. 3. With increasing conversion, the curve shifts toward higher-molecular-weight products. The polydispersity coefficients somewhat increase with conversion but remain considerably lower than those of PMMA prepared with CPC initiator in the absence of PBN (Table 1). The increased polydispersity of PMMA synthesized with CPC initiator may be due to occurrence, along with the living mechanism, of bimolecular chain termination resulting in formation of a certain amount of the "dead" polymer.

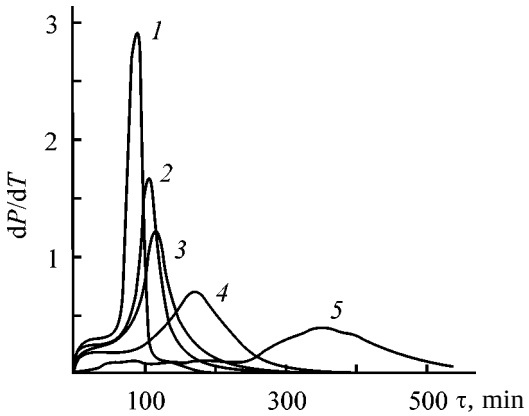

Fig. 2. Differential kinetic curves (d*P*/d*T*) of MMA polymerization in the presence of PBN at 323 K. (τ) Time. [PBN], mol %: (*1*) 0, (*2*) 0.1, (*3*) 0.2, (*4*) 0.4, and (*5*) 0.8.

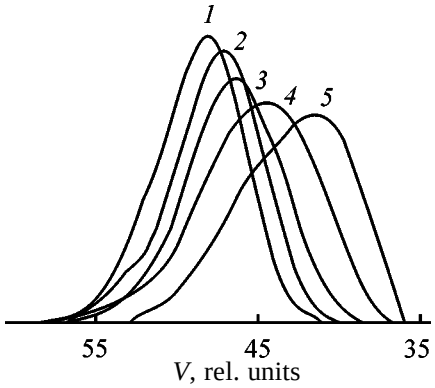

Fig. 3. GPC curves for PMMA samples of various conversions prepared at 323 K in the presence of 0.1 mol % CPC and 0.4 mol % PBN. (*V*) Volume. Conversion, %: (*1*) 3.1, (*2*) 11.0, (*3*) 35.8, (*4*) 62.1, and (*5*) 82.2.

Considerable differences between the polydispersity coefficients of polymers synthesized in the presence of PBN with AIBN and CPC initiators are probably due to the following factors.

First, the rate constants of the reactions of nitrone with the radicals produced by decomposition of these initiators differ. The rate constant of scavenging by the spin trap of the alkoxy radical $RO^{\cdot}$ generated by thermal decomposition of CPC is 10^7–10^8 l mol^{-1} s^{-1}, whereas for tertiary carbon-centered radicals, e.g., $[(CH_3)_2C(C{\equiv}N)^{\cdot}]$ or polymethyl methacrylate propagating radical, it is less than 0.8×10^4 l mol^{-1} s^{-1} [15]. In polymerization of MMA, the propagation rate constant is 0.7×10^3 l mol^{-1} s^{-1} [16], and the rate constant of addition of the alkoxy radical across the >C=C< bond is about 10^3–10^4 l mol^{-1} s^{-1} [17]. Probably, in the initial period of CPC-initiated MMA polymerization nitrone will be largely consumed for reaction with radicals generated by decomposition of CPC, in contrast to the AIBN-initiated MMA polymerization, because the constants of scavenging of alkoxy radicals with PBN are 2–4 orders of magnitude higher than those of the radicals generated by decomposition of AIBN and of similar radicals. Thus, in CPC-initiated MMA polymerization the chain propagation is controlled by nitroxyl radicals with the lower-molecular-weight fragment as compared to the AIBN-initiated polymerization when the nitroxyl spin adducts contain macromolecular polymeric chains. The structural differences between the nitroxyl spin adducts are responsible for some specific features of CPC-initiated MMA polymerization in the presence of PBN and for the increased polydispersity coefficients. Thus, nitroxyl radicals incorporating macromolecular fragments react with the propagating macroradical to form a less strong and hence more labile bond, which allows living polymerization to be performed under milder conditions.

Table 2. Ratio of the rate in the gel effect stage to the initial rate of MMA polymerization. T = 323 K, [CPC] = 0.1 mol %

[PBN], mol %	$V_g \times 10^4$	$V_p \times 10^4$	V_g/V_p
	mol l^{-1} s^{-1}		
–	45.9	5.8	7.9
0.1	25.9	4.6	5.6
0.2	18.9	4.1	4.6
0.4	10.9	3.0	3.6
0.8	5.8	1.7	3.4

Second, as noted above, the propagation constant in MMA polymerization and the rate constant of addition of the alkoxy radical to the double bond are 3–4 orders of magnitude lower than the rate constant of scavenging of the alkoxy radical by PBN. However, as the concentration of PBN is as low as 0.2–0.8 mol % relative to the monomer, the probability of reaction of the alkoxy radical with the monomer is many times higher than that of the reaction with PBN, which can result in formation of the dead polymer.

Third, at a relatively high initial concentration of nitroxyl radicals at the beginning of the process the decay of the propagating radicals mainly occurs by reversible recombination with nitroxyl radicals. In a certain period, polymerization continues owing to both reinitiation and initiation due do decomposition of the initiator. It should be noted that the half-life of CPC is much longer than that of AIBN at 323 K (40 and 4.5 h, respectively). Apparently, PBN initially reacts mostly with alkoxy radicals generated by decomposition of CPC to form a labile adduct capable

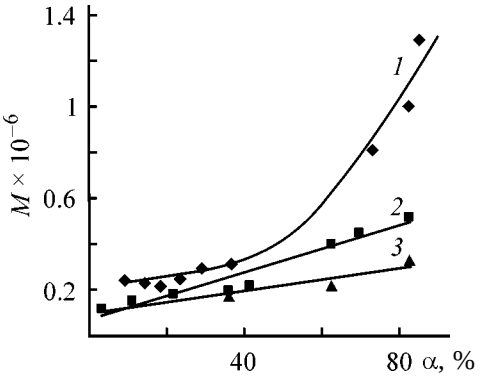

Fig. 4. Molecular weight M of PMMA as a function of conversion α. Initiator: 0.1 mol % CPC. Molecular weight: (*1*, *2*) viscosity-average and (*3*) number-average. [PBN], mol %: (*1*) 0 and (*2*, *3*) 0.4.

of subsequent decomposition and chain propagation. Owing to further radical generation by CPC, common radical polymerization occurs along with the living process, which results in formation of the dead polymer and hence in the increased polydispersity coefficient.

The data obtained indirectly show that polymerization is accompanied by steady growth of the average molecular weight of the resulting PMMA. To experimentally confirm this assumption, we studied the molecular weight of PMMA as a function of conversion (Fig. 4). The results show that in the presence of PBN the molecular weight linearly increases with conversion. This fact proves that the number of propagating chains remains constant in the course of polymerization, which is typical for polymerization in the pseudoliving chain mode.

CONCLUSIONS

(1) The kinetic features of polymerization of methyl methacrylate in the presence of *C*-phenyl-*N*-*tert*-butylnitrone and the molecular-weight characteristics of the resulting polymer show that in this system radical polymerization occurs in the living chain mode. In the presence of excess *C*-phenyl-*N*-*tert*-butylnitrone relative to dicyclohexyl peroxydicarbonate, the main decay pathway of the propagating radicals is their reaction with nitroxyl radicals. This fact determines the living character of polymerization, namely, steady increase in the molecular weight throughout the process, with practical absence of the gel effect.

(2) Our results allow *C*-phenyl-*N*-*tert*-butylnitrone to be considered as agent terminating the polymeric chain and controlling its lifetime; it shows promise for preparing macromolecules of preset structure under conditions of industrial synthesis of polymethyl methacrylate.

ACKNOWLEDGMENTS

The study was financially supported by the Competitive Center for Basic Natural Science, Education Ministry of the Russian Federation, and by the Russian Foundation for Basic Research (project no. 99-03-83346).

REFERENCES

1. Smirnov, B.N., *Vysokomol. Soedin., Ser. A*, 1990, vol. 32, no. 3, pp. 583–589.
2. *Controlled Radical Polimerization*, Matyizewski, K., Ed., Oxford Univ. Press, 1998.
3. Korolev, G.V. and Marchenko, A.P., *Usp. Khim.*, 2000, vol. 69, no. 5, pp. 447–475.
4. Hawker, C.J., *J. Am. Chem. Soc.*, 1994, vol. 116, no. 12, pp. 11185–11188.
5. Veregin Richard, P.N., Odell, P.G., Michalak, L.M., and Georges, M.K., *Macromolecules*, 1996, vol. 29, no. 8, pp. 2746–2754.
6. Yoshida, E. and Tanimoto, S., *Macromolecules*, 1997, vol. 30, no. 14, pp. 4018–4023.
7. Grishin, D.F., Semenycheva, L.L., and Kolyakina, E.V., *Vysokomol. Soedin., Ser. A*, 1999, vol. 40, no. 4, pp. 609–614.
8. Grishin, D.F., Semionicheva, L.L., and Koliakina, E.V., *Mendeleev Commun.*, 1999, no. 6, pp. 45–47.
9. *Analytical Chemistry of Polymers*, Kline, G.M., Ed., New York: Interscience, 1959.
10. Terabe, S. and Konaka, R., *J. Chem. Soc., Perkin Trans. 2*, 1972, no. 14, pp. 2163–2166.
11. *Praktikum po khimii i fizike polimerov* (Practical Course of Polymer Chemistry and Physics), Kurenkov, V.F., Ed., Moscow: Khimiya, 1990.
12. *Entsiklopediya polimerov* (Polymer Encyclopedia), Kabanov, V.A. *et al.*, Eds., Moscow: Sov. Entsiklopediya, 1972, vol. 1, p. 932.
13. Rafikov, S.R., Pavlov, S.A., and Tverdokhlebova, I.I., *Metody opredeleniya molekulyarnykh vesov i polidispersnosti vysokomolekulyarnykh soedinenii* (Methods for Determination of Molecular Weights and Polydispersities of Macromolecular Compounds), Moscow: Khimiya, 1963.
14. Moris, S., *J. Liq. Chromatogr.*, 1990, vol. 13, no. 9, p. 1719.
15. Zubarev, V.E., *Metod spinovykh lovushek* (Method of Spin Traps), Moscow: Mosk. Gos. Univ., 1984, p. 26.
16. Odian, G., *Principles of Polymerization*, New York: McGraw-Hill, 1970.
17. Denisov, E.T., *Konstanty skorostei gomoliticheskikh zhidkofaznykh reaktsii* (Rate Constants of Homolytic Liquid-Phase Reactions), Moscow: Nauka, 1971.

Russian Journal of Applied Chemistry, Vol. 74, No. 3, 2001, pp. 498–500. Translated from Zhurnal Prikladnoi Khimii, Vol. 74, No. 3, 2001, pp. 487–489.

MACROMOLECULAR CHEMISTRY AND POLYMERIC MATERIALS

Effect of Molecular Weight of Poly-(1,2-Dimethyl-5-Vinylpyridinium Methyl Sulfate) on Flocculation of Aqueous Kaolin Suspension

A. V. Navrotskii, I. A. Novakov, S. M. Makeev, V. V. Orlyanskii, V. A. Kozlovtsev, O. O. Kotlyarevskaya, and V. A. Navrotskii

Volgograd State Technical University, Volgograd, Russia

Received April 21, 2000

Abstract—Effect of molecular weight of poly-(1,2-dimethyl-5-vinylpyridinium methyl sulfate) on flocculation of aqueous kaolin suspension is studied.

Up-to-date water treatment processes suggest the use of reagents providing destabilization and enhanced separation of a dispersed phase contained in water [1, 2]. Among these reagents cationic polymer electrolytes usually show high performance. Their dissociation in a solution with formation of high-molecular-weight polycations ensures a complex flocculating effect by virtue of neutralization of a negative surface charge of suspended particles and simultaneous formation of bridging bonds between them [2, 3]. In our opinion, poly-(1,2-dimethyl-5-vinylpyridinium methyl sulfate) (poly-1,2-DM-5-VPMS) shows promise as such a cationic polyelectrolyte.

Previously we demonstrated that poly-1,2-DM-5-VPMS with desired molecular and rheological characteristics can be synthesized in the presence of a series of peroxide initiators, *tert*-butylperoxypropanol being the most efficient among them [4, 5]. Based on this result a process for synthesis of poly-1,2-DM-5-VPMS was developed and production of KF-91 cationic flocculant based on it was organized. This flocculant was tested in various processes [6], and its high performance as a reagent for water treatment is beyond question. However, we believe that the efficiency of using KF-91 may be increased by virtue of optimization of the process conditions.

In this work we studied the effect of the molecular weight of poly-1,2-DM-5-VPMS on flocculation of aqueous kaolin suspension.

EXPERIMENTAL

Poly-1,2-DM-5-VPMS was synthesized and isolated as in [5]. As a dispersion phase we used kaolin (KSD brand) with a mean particle size of 7 μm.

In flocculation experiments the kaolin concentration was 4%, and the poly-1,2-DM-5-VPMS concentration C_p was 0.0125–2.0 mg/g kaolin. The system was stirred, and the travel time of the flocculi/supernatant boundary from the first to the second mark on a cylinder was measured to estimate the sedimentation rate V_s. Also the turbidity of the supernatant τ was measured 30 min after.

From the experimental data thus obtained we determined the optimal concentrations of the polyelectrolytes. The criterion was the minimal turbidity of the supernatant, i.e., the maximal degree of clarification, and the maximal rate of floccule sedimentation. The clarification and flocculation factors D_τ and D_V were estimated by the following equations:

$$D_\tau = (\tau_0/\tau_{min}) - 1, \quad D_V = (V_{max}/V_0) - 1,$$

where τ_0 and τ_{min} are the supernatant turbidity, respectively, without and with the polyelectrolyte added in the optimal concentration; and V_0 and V_{max} are the floccule sedimentation rates under the same conditions.

Introduction of poly-1,2-DM-5-VPMS of various molecular weights considerably increases both the suspension sedimentation rate and the rate of sedimentation of flocculi of the kaolin suspension (Fig. 1). The supernatant turbidity plotted against the flocculant concentration shows extrema (Fig. 1a), which is typical of the systems solid–water–polyelectrolyte [1]. The polyelectrolyte concentration providing flocculation of the dispersed system ranges from 0.025 to

1070-4272/01/7403-0498$25.00

0.750 mg g^{-1}. Beyond this range the turbidity of treated water increases. In the case of lower concentrations this can be attributed to the presence of unflocculated and partially flocculated particles. At C_p > 0.750 mg g^{-1} this is due to stabilization of the suspension by the polyelectrolyte, which is particularly pronounced in the case of the lower-molecular-weight poly-1,2-DM-5-VPMS with $M_\eta = 1.7 \times 10^6$. For this sample efficient flocculation is observed only at a concentration of 0.125–0.200 mg g^{-1}. With increasing molecular weight of the flocculant the instability range of the system kaolin–water–flocculant expands.

Data on the floccule sedimentation rate are given in Fig. 1b. The concentration dependences of the sedimentation rate have extrema also. For the poly-1,2-DM-5-VPMS sample with M_η 1.7×10^6 the sedimentation rate only slightly changes with the concentration, ranging within 0.003–0.004 m s^{-1}. For the other samples the maximal sedimentation rate is observed at the flocculant concentration of 0.750–0.875 mg g^{-1}.

Figure 2 demonstrates the effect of the molecular weight of the polyelectrolyte on the clarification and flocculation factors. The clarification factor characterizing the degree of suspension sedimentation remains practically unchanged for the samples having lower molecular weights, and considerably increases with increasing molecular weight to $(3–5) \times 10^6$. The flocculating effect increases rapidly to M_η 3.5×10^6 and remains practically unchanged with further increasing molecular weight of the flocculant.

The results show a considerable effect of the molecular weight of poly-1,2-DM-5-VPMS on flocculation (Fig. 2). Most likely this effect is due to different flocculation mechanisms (surface charge neutralization and bridging bond formation mechanisms) prevailing at a given M_η. In the case of the flocculant with lower M_η having a high charge density on the polycation, flocculation proceeds predominantly by the charge neutralization mechanism. As a result, the clarification effect remains constant at $M_\eta = (1.7–3) \times 10^6$ (Fig. 2). In this case bridge formation contributes insignificantly because of small size of the macromolecules, as clearly demonstrated by data on the sedimentation rate, which does not increase with increasing concentration of the lowest-molecular-weight flocculant with $M_\eta = 1.7 \times 10^6$ (Fig. 1b). Increasing sedimentation rate and flocculation effect with increasing M_η is associated with increasing size of the flocculi primarily by the bridging bond formation mechanism. Therefore, a combination of a high molecular weight [$M_\eta = (3–5) \times 10^6$] and charge density (~ 4 mequiv g^{-1}) provides a condition for effective

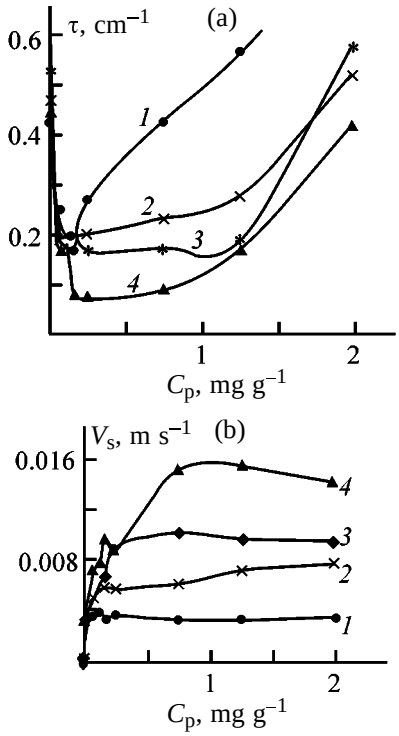

Fig. 1. (a) Residual turbidity of the supernatant τ and (b) floccule sedimentation rate V_s as functions of the concentration C_p of the polyelectrolyte of various molecular weights. $M_\eta \times 10^{-6}$: (*1*) 1.7, (*2*) 2.62, (*3*) 2.75, and (*4*) 5.31.

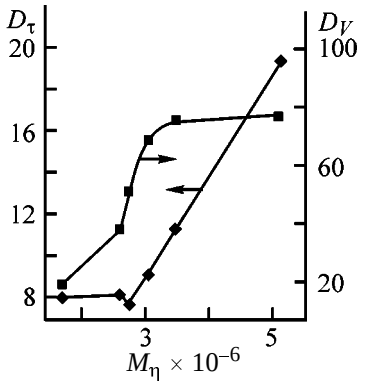

Fig. 2. Flocculation factor D_τ and clarification factor D_V as functions of the molecular weight of poly-1,2-DM-5-VPMS M_η.

adsorption of the polymer on the dispersed particles, decreasing surface charge, and formation of bridging bonds. However, to confirm the proposed flocculation mechanism, it is necessary to study adsorption of poly-1,2-DM-5-VPMS on the dispersed particles as well as the polyelectrolyte effect on the electrokinetic properties and disperse composition of the dispersions in more detail.

At present time widely spread flocculants are various cationic and anionic derivatives of polyacrylamide

(PAA). It was demonstrated [7, 8] that sequential introduction of PAA cationic and anionic derivatives provides the best flocculation effect for kaolin. However, in this case D_V changes from 3 after introduction of a cationic derivative to 10 after additional treatment with an anionic PAA [9], whereas introduction of poly-1,2-DM-5-VPMS increases D_V to 9–70.

The results obtained showed that the flocculation efficiency of poly-1,2-DM-5-VPMS as a function of M_η is the highest at $M_\eta = (3–5) \times 10^6$. This fact should be taken into account in practical use of commercial flocculants based on poly-1,2-DM-5-VPMS from various sources. Thus, the molecular weight of poly-1,2-DM-5-VPMS of PPS brand is $(1.5–1.8) \times 10^6$ [10] or 2.5×10^6 [9]. Therefore, according to our results, its flocculating effect is relatively low. KF-91 flocculant has a higher M_η [$(3–4) \times 10^6$] [5, 6], so that it can be recommended for separation of dispersions.

Indeed, it was demonstrated in [6] that KF-91 flocculant shows higher performance in treating wastewater of various origins as compared to other flocculants. Water treated with KF-91 is characterized by the lowest residual content of suspended and oxidizable (organic) compounds. The performance of this flocculant is well comparable with that of Sedipur (BASF) [6]. Furthermore, KF-91 has the maximal biodissimilation coefficient (BDC = COD/BOD) characterizing biodegradation of the residual flocculant in water. The high BDC of KF-91 (0.84) (for comparison, BDC of Sedipur is 0.58) characterizes it as the most environmentally friendly reagent among the related ones.

CONCLUSION

Poly-(1,2-dimethyl-5-vinylpyridinium methyl sulfate) demonstrates high flocculation effect on aqueous kaolin suspension, which allows recommendation of this polyelectrolyte for treatment of water to remove suspended material. The results obtained suggest that higher-molecular-weight samples of poly-1,2-DM-5-VPMS with $M_\eta = (3–5) \times 10^6$ should provide stronger flocculation effect in separation of concentrated suspensions and dewatering of precipitates. The optimal flocculant concentration was found to be 0.03–0.90 mg g^{-1}, depending on the dispersion nature and concentration.

REFERENCES

1. Zapol'skii, A.G. and Baran, L.A., *Koagulyanty and flokulyanty v protsessakh ochistki vody: Svoistva, Poluchenie, Primenenie* (Coagulants and Flocculants in Water Treatment: Properties. Preparation. Applications), Leningrad: Khimiya, 1987.
2. Baran, A.A. and Teslenko, A.Ya., *Flokulyanty v biotekhnologii* (Flocculants in Biotechnology), Leningrad: Khimiya, 1990.
3. Baran', Sh. (Baran, A.A.) and Gregory, D., *Kolloidn. Zh.*, 1996, vol. 58, no. 1, pp. 13–18.
4. RF Patent 2 048 479.
5. Navrotskii, A.V., Polymerization of 1,2-Dimethyl-5-vinylpyridinium Methyl Sulfate in the Presence of Water-Soluble Peroxides and Characterization of the Polymer, *Cand. Sci. Dissertation*, Volgograd, 1997.
6. Meshcheryakov, S.V., Orlyanskii, V.V., Mazlova, E.A., and Navrotskii, V.A., *Neft. Gaz. Prom–st. Zashch. Korroz. Okhr. Okruzh. Sredy*, 1996, nos. 5–6, pp. 22–27.
7. Bulidorova, G.V. and Myagchenkov, V.A., *Kolloidn. Zh.*, 1995, vol. 57, no. 6, pp. 778–782.
8. Kurenkov, V.F., Efremova, L.V., and Myagchenkov, V.A., *Zh. Prikl. Khim.*, 1989, vol. 62, no. 10, pp. 2298–2303.
9. Onishchenko, A.V., Kuz'min, A.A., Starostin, V.N., *et al.*, *Khim. Tekhnol. Vody*, 1996, vo. 18, no. 4, pp. 352–355.
10. Zubakova, L.B., Tevlina, A.S., and Davankov, A.B., *Sinteticheskie ionoobmennye materialy* (Synthetic Ion-Exchange Materials), Moscow: Khimiya, 1978.

Russian Journal of Applied Chemistry, Vol. 74, No. 3, 2001, pp. 501–504. Translated from Zhurnal Prikladnoi Khimii, Vol. 74, No. 3, 2001, pp. 490–493.

MACROMOLECULAR CHEMISTRY AND POLYMERIC MATERIALS

Viscometric Study of Fixation of Cations in Aqueous Solutions of Polyelectrolytes Based on Salts of 2-Acrylamido-2-Methylpropanesulfonic Acid

V. F. Kurenkov, I. Yu. Kolesnikova, and D. A. Solov'ev

Kazan State Technological University, Kazan, Tatarstan, Russia

Received March 16, 2000; in final form, August 2000

Abstract—An experimental study is made of the effect of the solution ionic strength and the nature of a cation (Li, Na, K, Mg, Ca, Sr, and Ba) on fixation of counterions on polysulfonate anions in aqueous solutions of poly-2-acrylamido-2-methylpropanesulfonic acid and copolymers of acrylamide and *N*-vinylpirrolidone with 2-acrylamido-2-methylpropanesulfonic acid.

It is well known that the nature of interaction of polyions with counterions considerably influences the thermodynamic and hydrodynamic properties of polyelectrolyte solutions [1] and also controls the conformation state and reactivity of macroradicals growing in radical polymerization of ionic monomers in ionizing media [2]. It was demonstrated previously that the nature of a cation has an effect on radical polymerization of Li, Na, and K [3] and Mg, Ca, and Ba salts of 2-acrylamido-2-methylpropanesulfonic acid (HAMS) [4] and copolymerization of acrylamide (AA) with Li, Na, and K salts of HAMS in aqueous solutions [5] and also on flocculating properties of poly-2-acrylamido-2-methylpropanesulfonic acid (HPAMS) salts [6]. To gain a better insight into the effect of the nature of cations on polymerization and copolymerization of HAMS salts in aqueous solutions and also on the properties of the resulting polymers, in this work we studied the features of fixation of single-charged (Li, Na, K) and double-charged cations (Mg, Ca, Ba) on polysulfonate anions in aqueous solutions of HPAMS and copolymers of acrylamide and *N*-vinylpirrolidone (*N*-VP) with HAMS salts.

EXPERIMENTAL

In the work we used samples of NaPAMS and copolymers of AA and *N*-VP with NaAMS obtained by radical polymerization and copolymerization of the monomers in aqueous solutions. For polymerization we used HAMS [Lubrizol 2404, mp 185°C (Lubrizol Corp., the Great Britain)]; acrylamide [mp 84.5°C (Mitsubishi Chem. Ind., Ltd., Japan)]; and *N*-vinylpirrolidone (Merck, FRG) purified by vacuum distillation in the presence of 0.1% KOH. All other chemicals used were of chemically or analytically pure grade. NaAMS was prepared by neutralization of HAMS to pH 9 in an aqueous solution by titration with NaOH. The copolymerization procedure was as in [7]. After copolymerization the resulting polymers were precipitated by adding aqueous solutions into acetone, filtered, washed with acetone, and vacuum-dried to constant weight at room temperature. The characteristics of the polymers used in this work are summarized in the table.

Before carrying out viscometric measurements the samples of NaPAMS and AA/NaAMS and *N*-VP/NaAMS copolymers were converted into the H form on KU-2×8 cation-exchange resin.

The intrinsic viscosity $[\eta]$ of the polymers was determined in 0.5 NaCl at 25 ± 0.5°C using an Ubbelohde viscometer (capillary diameter 0.56 mm). The viscosity-average molecular weight of the polymers M_η was estimated as follows [8]:

$$[\eta] = 1.95 \times 10^{-5} M_\eta^{0.83},$$

where $[\eta]$ is expressed in dl g^{-1}.

The composition of AA/NaAMS and *N*-VP/NaAMS copolymers (SO_3H group content) was determined by titration with NaOH after conversion of the copolymers into the H form on KU-2×8 cation-exchange resin.

The reduced viscosity η_{sp}/C_p, where η_{sp} is the specific viscosity and C_p is the copolymer concentration, was determined at various solution ionic strengths μ

1070-4272/01/7403-0501$25.00

Characteristics of polymers and copolymers studied

Sample index*	$[\eta]$, $cm^3\ g^{-1}$	$M_\eta \times 10^{-6}$	Monomeric unit content, mol %		
			N-VP	AA	HAMS
A	130	0.63	–	–	100
B	84	037	–	–	100
C	157	–	–	61	39
D	130	–	–	88	12
E	180	–	11	–	89
F	169	–	23	–	77

* Structural formulas of the macromolecules:

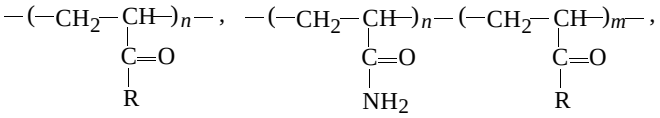

A, B **C, D**

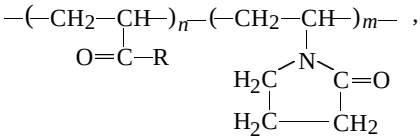

E, F

where R = –NH–C(CH$_3$)$_2$–CH$_2$–SO$_3$Na.

provided by adding inorganic salts. The measurements were performed with a VPZh-3 viscometer (capillary diameter 0.43 mm) at 30°C and C_p = const. In determination of η_{sp}/C_p the viscosities of the polymer solutions and a solvent was measured at the same μ.

In studying the state of the macromolecules of HPAMS salts and copolymers of AA and *N*-VP with HAMS salts in water and aqueous salt solutions one should take into account the effect of the medium on the ionization equilibrium of ionic groups:

$$\underset{\mathbf{I}}{A^-X^+} \rightleftarrows \underset{\mathbf{II}}{A^- \| X^+} \rightleftarrows \underset{\mathbf{III}}{A^- + X^+},$$

where A^- is a macroanion, X^+ is a cation, and **I, II**, and **III** are, respectively, contact ion pairs, ion pairs separated by a solvent, and free ions.

Increasing μ and the degree of association of cations with polysulfonate anions results in a shift of the ionization equilibrium to the left and hence in weakening of the Coulombic repulsion between similarly charged units along the macromolecular chain. This leads also to decreasing effective size of the macromolecular globules $\langle r^2 \rangle^{1/2}$ and manifests itself in decreasing η_{sp}/C_p measured at C_p = const. Therefore, the shape and size of the polyelectrolyte macromolecules can be characterized on the basis of η_{sp}/C_p [9, 10]. The reduced viscosity can be used also in solving the reverse task, i.e., in determination of the degree of association of cations with the polyanions, as we made in this work. The effect of the nature of cations on the degree of their association with the polyanions was studied with HPAMS samples of various molecular weights (samples **A** and **B**), and in the case of copolymers of AA and *N*-VP with HAMS, with samples of various molecular weights (estimated from $[\eta]$) and various chemical compositions of the macromolecules (samples **C, D, E, F**).

Let us analyze the dependence of η_{sp}/C_p of HPAMS (sample **A**) solutions on μ preset by additions of inorganic salts of single-charged (Li_2CO_3, NaCl, KCl) and double-charged cations ($MgCl_2$, $CaCl_2$, $SrCl_2$, $BaCl_2$) (Fig. 1a). The results show that the reduced viscosity decreases with increasing μ, which can be attributed, as noted above, to decreasing effective size of the macromolecular globules as a result of weakening Coulombic repulsion between similarly charged units along the macromolecular chain. At a given μ the reduced viscosity decreases in the order $Li^+ > Na^+ > K^+ > Mg^{2+} > Ca^{2+} > Sr^{2+} > Ba^{2+}$ (Fig. 1a, curves *1*–*7*). Similar pattern was observed for another HPAMS sample (B) at C_p = 0.5%. These effects are due to increasing degree of association of the counterions with polysulfonate anions with increasing μ and cationic radius in the order $Li^+ < Na^+ < K^+ < Mg^{2+} < Ca^{2+} < Sr^{2+} < Ba^{2+}$.

These results are consistent with the fact that the degree of association of Na^+ in NaPMS solutions increases with the ionic strength [11] and also with data on the degree of association of alkali and alkaline-earth metal ions in solutions of other strong polyelectrolytes such as poly-*p*-styrenesulfonic and polyethenesulfonic acids, obtained by various physicochemical methods [12].

The degree of association of single- and double-charged cations with the polyions of AA/HAMS copolymers was determined for samples **C** and **D** having different chemical composition and $[\eta]$. Data on η_{sp}/C_p for sample **C** (AA/HAMS copolymer) as a function of μ preset by addition of salts of single- (LiCl, NaCl, KCl) and double-charged cations ($MgCl_2$, $CaCl_2$, $SrCl_2$, $BaCl_2$) are given in Fig. 1b. The results show that as μ increases, the reduced viscosity decreases as a result of reduction of the size of macromolecular globules $\langle r^2 \rangle^{1/2}$. At μ = const η_{sp}/C_p decreases in the order $K^+ < Na^+ < Li^+ < Ba^{2+} < Sr^{2+} <$

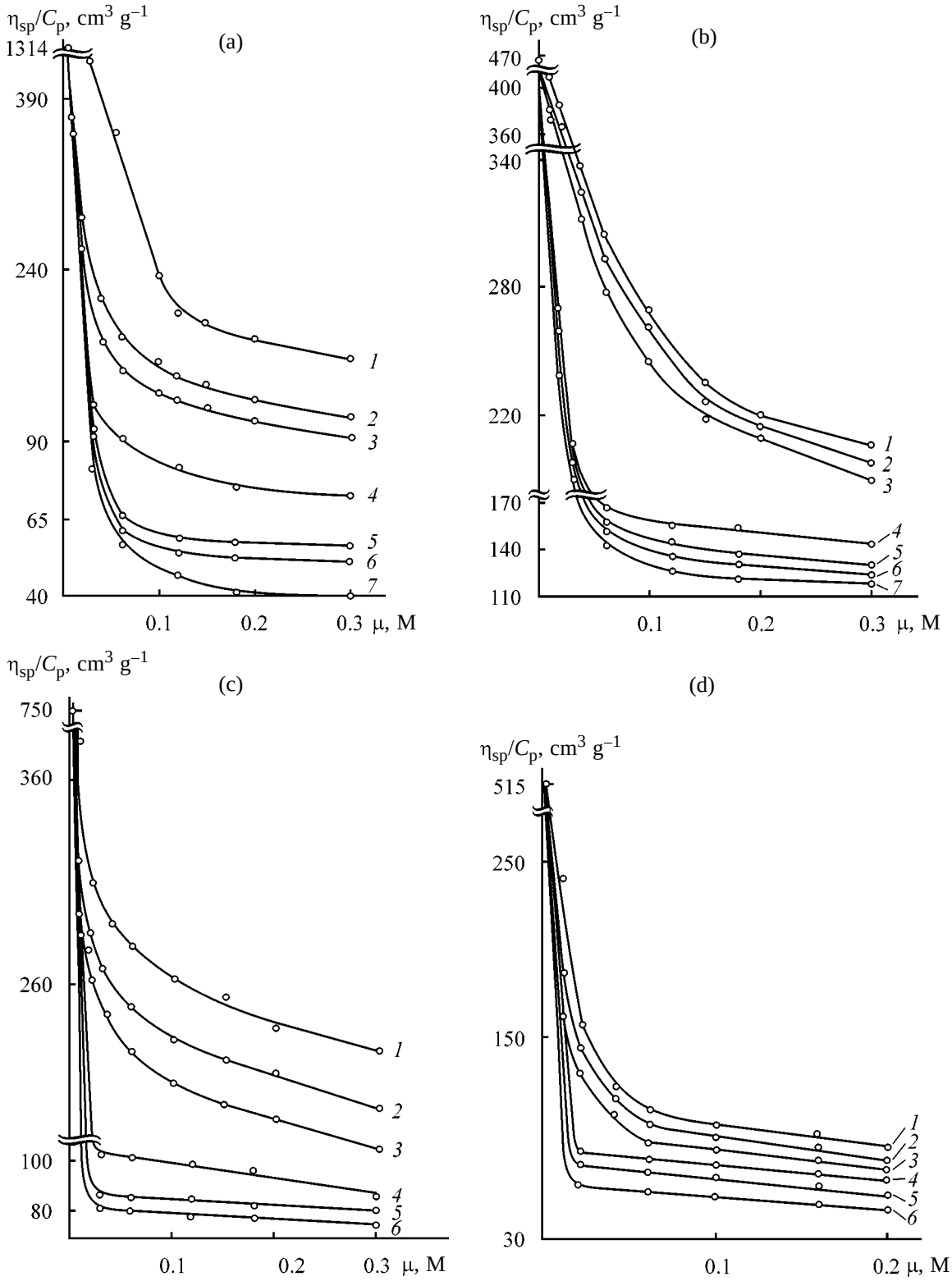

Fig. 1. Reduced viscosity η_{sp}/C_p of aqueous solutions of samples (a) **A**, (b) **C**, (c) **E**, and (d) **F** as a function of the ionic strength μ at C_p = 0.1%. Supporting electrolyte: (a) (*1*) Li_2CO_3, (*2*) NaCl, (*3*) KCl, (*4*) $MgCl_2$, (5) $CaCl_2$, (6) $SrCl_2$, and (*7*) $BaCl_2$; (b) (*1*) KCl, (*2*) NaCl, (*3*) LiCl, (*4*) $BaCl_2$, (*5*) $SrCl_2$, (*6*) $CaCl_2$, and (*7*) $MgCl_2$; and (c, d) (*1*) KCl, (*2*) NaCl, (*3*) Li_2CO_3, (*4*) $BaCl_2$, (*5*) $CaCl_2$, and (*6*) $MgCl_2$.

$Ca^{2+} < Mg^{2+}$ (Fig. 1b, curves *1–7*). The similar pattern was obtained for sample **D** also. Figure 1b demonstrates strong decrease in η_{sp}/C_p on passing from single- to double-chagred cations (at C_p = const), which can be attributed to more effective shielding by them of the polyanion charges and also to contraction caused by the chelation effect. Results obtained with copolymers with various molecular characteristics over a wide range of the supporting electrolyte concentrations suggest that the degree of association of the cations with polysulfonate anions of the AA/HAMS copolymers increases with increasing μ. Depending on the nature of the cation the degree of association increases in the order $K^+ < Na^+ < Li^+ < Ba^{2+} < Sr^{2+} < Ca^{2+} < Mg^{2+}$.

As in the case of AA/NaAMS copolymers (Fig. 1b), for *N*-VP/HAMS copolymers with various molecular characteristics (samples **E** and **F**) the degree of association of cations with the polyanions increases with increasing μ. Similarly, depending of the nature of the cation the degree of association increases in the order $K^+ < Na^+ < Li^+ < Ba^{2+} < Ca^{2+} < Mg^{2+}$ (Figs. 1c and 1d).

Thus, in the case of AA/HAMS and *N*-VP/HAMS copolymers the effect of the nature of cations on the degree of association differs from that observed for HPAMS homopolymers. It should be pointed out that under the experimental conditions changing chemical composition and molecular weight of the polymers (see table) did not change the order of variation of the degree of association of cations with the polyanions. It may be suggested that the observed trends are caused by interaction between the sulfonate and amide groups in the case of AA/HAMS [13] and *N*-VP/HAMS copolymers [14].

To conclude, the general nature of observed trends of counterionic association in solutions of the polyelectrolytes studied was demonstrated in experiments with polymers and copolymers with various molecular characteristics over wide concentration ranges of copolymers and supporting electrolytes. The results obtained allows general interpretation of the effect of the nature of a cation on the kinetics of homopolymerization of HAMS salts [3, 4] and of their copolymerization with AA [5] and *N*-VP in aqueous solutions.

CONCLUSIONS

(1) In poly-2-acrylamido-2-methylpropanesulfonic acid solutions the degree of association of cations with the polyanions increases with increasing ionic strength and cationic radius in the order $Li^+ < Na^+ < K^+ < Mg^{2+} < Ca^{2+} < Sr^{2+} < Ba^{2+}$.

(2) In the case of AA/HAMS and *N*-VP/HAMS copolymers the degree of association of cations with the polyanions increases with increasing ionic strength also, but the effect of cations on the degree of association differs from that for HPAMS, changing, respectively, in the order $K^+ < Na^+ < Li^+ < Ba^{2+} < Sr^{2+} < Ca^{2+} < Mg^{2+}$ and $K^+ < Na^+ < Li^+ < Ba^{2+} < Ca^{2+} < Mg^{2+}$.

ACKNOWLEDGMENTS

The work was financially supported by the Foundation for Basic Research in Natural Science, Ministry of Education of the Russian Federation (project no. 97-0-9.4-59).

REFERENCES

1. Morawetz, H., *Macromolecules in Solution*, New York: Wiley, 1965.
2. Kabanov, V.A. and Topchiev, D.A., *Polimerizatsiya ioniziruyushchikhsya monomerov* (Polymerization of Ionizable Monomers), Moscow: Nauka, 1975.
3. Kurenkov, V.F. and Safin, A.G., *Zh. Prikl. Khim*., 1998, vol. 71, no. 1, pp. 136–140.
4. Kurenkov, V.F., Safin, A.G., and Almazova, E.I., *Zh. Prikl. Khim*., 1998, vol. 71, no. 10, pp. 1704–1708.
5. Kurenkov, V.F. and Rodina, Yu.G., *Zh. Prikl. Khim*., 1999, vol. 72, no. 10, pp. 1699–1704.
6. Kurenkov, V.F., Safin, A.G., and Merkanina, O.N., *Zh. Prikl. Khim*., 1998, vol. 71, no. 6, pp. 1015–1018.
7. Kurenkov, V.F., Khairullin, M.R., and Utikeeva, A.R., *Zh. Prikl. Khim*., 1999, vol. 72, no. 7, pp. 1177–1181.
8. Fisher, L.W., Soher, A.R., and Tan, J.S., *Macromolecules*, 1977, vol. 10, pp. 949–954.
9. Kargin, V.A., Mirlina, S.Ya., and Antipina, A.D., *Vysokomol. Soedin*., 1959, vol. 1, no. 9, pp. 1428–1437.
10. Fernandez-Prini, R. and Lagos, A.E., *J. Polym. Sci., Ser. A*, 1964, vol. 2, pp. 2918–2928.
11. Tan, J.S. and Markus, P.S., *J. Polym. Sci., Polym. Phys*., 1976, vol. 14, pp. 235–250.
12. Marina, N.G. and Monakov, Yu.B., in *Khimiya vysokomolekulyarnykh soedinenii* (Macromolecular Chemistry), Ufa: Inst. Khimii, Bashkir. Fil., Akad. Nauk SSSR, 1976, pp. 116–146.
13. Valueva, S.V., Kipper, A.I., Lyubina, S.Ya., *et al*., *Vysokomol. Soedin., Ser. A*, 1992, vol. 34, no. 12, pp. 35–44.
14. Olson, K.G. and Butler, G.B., *Macromolecules*, 1984, vol. 17, pp. 2486–2498.

Russian Journal of Applied Chemistry, Vol. 74, No. 3, 2001, pp. 505–509. Translated from Zhurnal Prikladnoi Khimii, Vol. 74, No. 3, 2001, pp. 494–498.

MACROMOLECULAR CHEMISTRY AND POLYMERIC MATERIALS

Kinetics of Radical Copolymerization of Acrylamide with Magnesium 2-Acrylamido-2-Methylpropanesulfonate in Aqueous Solutions

V. F. Kurenkov, O. A. Zaitseva, and D. A. Solov'ev

Kazan State Technological University, Kazan, Tatarstan, Russia

Received October 25, 2000

Abstract—Kinetic features of homogeneous radical copolymerization of acrylamide with magnesium 2-acrylamido-2-methylpropanesulfonate in concentrated aqueous solutions in the presence of the initiating system potassium peroxosulfate–sodium hydrosulfite at pH 9 and 50°C were studied by dilatometric technique.

Copolymers of acrylamide (AA) with salts of 2-acrylamido-2-methylpropanesulfonic acid (H-AMS) are the efficient flocculants, stabilizers, lubricants, and thickening agents. They are used in water purification, hole drilling, and oil production [1, 2]. Valuable commercial characteristics of copolymers, insufficient data on their synthesis, and specific kinetic effects in copolymerization of ionogenic monomers [3, 4] motivate the urgency of studying copolymerization of AA with salts of H-AMS. It is well known [3, 4] that one of the factors of the efficient control of (co)polymerization of ionogenic monomers is ionic strength of a solution μ. The effect of the ionic strength μ on polymerization [5, 6] and copolymerization of AA with salts of single-charged cations and H-AMS [7] was studied previously. In this report, we considered the effect of μ on the features of radical copolymerization of AA with magnesium salt of H-AMS (Mg-AMS) in aqueous and aqueous-salt solutions.

EXPERIMENTAL

We used acrylamide produced by the Mitsubishi Chem. Ind. Ltd. (mp 84.5°C), H-AMS (mp 185°C) produced by the Labrizol Corp., cation exchanger KU-2 × 8 [GOST (State Standard) 10896–78], distilled water, and other chemicals of chemically pure grade. The copolymer of Mg-AMS was produced by neutralization of H-AMS to pH 9 in aqueous solution under the action of 20% suspension of $Mg(OH)_2$ and was used in the form of aqueous solution.

Copolymerization was carried out in dilatometers to low conversion (x < 4%) and in glass weighing bottles to high conversion. The procedures of copolymerization and dilatometric study of copolymerization kinetics were similar to those described in [7]. After completing the copolymerization, the copolymers were precipitated from aqueous solutions to acetone, washed with acetone, and dried at room temperature in a vacuum drier to constant weight. The yield of copolymers was determined gravimetrically, and the chemical composition was determined by elemental analysis for sulfur [8].

Potentiometric measurements were carried out on a pH-121 unit with the use of glass (ESL 63-07) and silver chloride (EVL 1M3) electrodes at 25°C.

The molecular weight of copolymers was evaluated from the intrinsic viscosity [η] of the solutions, determined by isoionic dilution in 0.5 M NaCl in an Ubbelohde viscometer (d_c = 0.5 mm) at 25°C.

Copolymerization of AA (M_1) with Mg-AMS (M_2) was carried out in concentrated aqueous solutions of the monomeric mixture ([M_1 + M_2] = 10–20%) at pH 9 and 50°C. The reaction was initiated by the system potassium peroxosulfate (PP)–sodium hydrosulfite (SHS), which is widely used and is highly efficient in polymerization of water-soluble monomers. The reaction was carried out at PP concentration of 5.2×10^{-4} and SHS concentration of 3.5×10^{-4} M. The pH was kept at the level of 9, which excluded hydrolysis of Mg-AMS [9] and imidization of amide groups [10] and also provided highly efficient initiation of copolymerization by the system PP–SHS [11] and constancy of the initiation rate at variation of Mg-AMS concentration and addition of low-molecular-weight salts, since the rate of PP decay in alkaline media is independent of μ [12]. Preliminary experi-

1070-4272/01/7403-0505$25.00

Table 1. Parameters of copolymerization of AA with Mg-AMS in aqueous solutions. [AA] = 0.35 [PP] = 5.2×10^{-4}, [SHS] = 3.5×10^{-4} M

[Mg-AMS], M	$v_0 \times 10^5$, mol l^{-1} s^{-1}	k_c	Yield in 2 h, %	[η], cm^3 g^{-1}
0.13	1.9	0.11	–	–
0.16	2.7	0.12	–	–
0.20	4.1	0.13	–	94
0.23	4.4	–	41	102
0.35	9.0	0.15	62	–
0.39	12.3	0.17	63	133
0.46	15.8	0.16	63	142
0.53	20.0	0.16	73	152
0.59	23.8	0.16	68	172

ments confirmed that under experimental conditions copolymerization of AA with Mg-AMS does not proceed in the absence of initiators and, in the presence of initiators, proceeds under homogeneous conditions at any conversion owing to sufficiently high solubility of the monomers and copolymers in water.

The effect of the ionic strength on copolymerization of AA with Mg-AMS was evaluated in experiments with variation of the initial concentration of Mg-AMS and addition of the low-molecular-weight salt $MgCl_2$. In so doing, we took into account that the apparent reactivity in copolymerization of AA is independent of μ [13, 14]. The kinetic data on the process were obtained from the linear portions of the kinetic curves of copolymerization, plotted from the dilatometric data at low conversions ($x < 4\%$). The kinetic parameters of copolymerization are listed in Table 1. It is seen that with increasing initial concentration of Mg-AMS the initial rate of copolymerization v_0, yield, and molecular weight of copolymers increase in parallel. The rate v_0 also increased with an increase in the concentration of the low-molecular-weight electrolyte $MgCl_2$ in the range 0.1–0.5 M in the experiments performed at a constant concentration of the mixture M_1 + M_2 (Fig. 1). To determine the reaction order of copolymerization with respect to Mg-AMS concentration, we analyzed data in Fig. 2. In the studied range of Mg-AMS concentrations the dependence $\log v_0$–log[Mg-AMS] is not linear (Fig. 2a, curve *1*). In passing to solutions with higher concentrations of the monomer (0.35–0.59 M) the reaction order with respect to Mg-AMS increases from 1.5 to 1.7. The similar variation of the reaction order with respect to the monomer was observed in polymerization of *N*,*N*-diethylaminoethyl methacrylate hydrochloride [15], potassium and sodium salts of H-AMS [5, 6], and also in copolymerization of AA with Na salt of H-AMS [7], which is caused by an increase in viscosity of the reaction mixture [5].

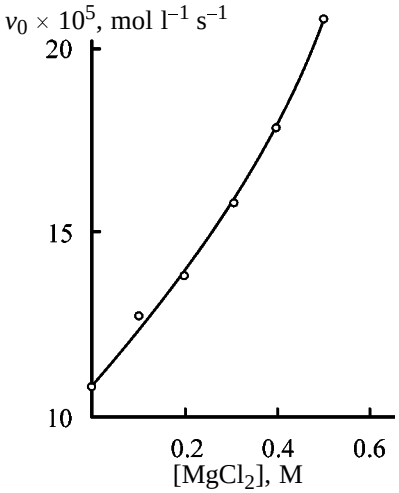

Fig. 1. Initial rate of copolymerization of AA with Mg-AMS v_0 in aqueous solutions as a function of concentration [$MgCl_2$]. [AA + Mg-AMS] = 10%, molar ratio [AA] : [Mg-AMS] = 5 : 5.

To establish the equation for the total rate of copolymerization of AA with Mg-AMS, we performed the experiments for variable concentrations of AA and the components of the initiating system with the concentrations of the other components and the reaction conditions kept constant. The effect of the AA concentration on copolymerization was evaluated in the range 0.14–0.48 M. It is evident from Fig. 2a (curve *2*) that with an increase in AA concentration v_0 decreases, and the reaction order of copolymerization with respect to AA is equal to 1. The effect of PP and SHS concentrations on copolymerization is illustrated in Fig. 2b and Table 2. From Fig. 2b and Table 2 it follows that with increasing concentrations of PP and SHS v_0 and the yield of the copolymers increase and the molecular weight decreases. The decrease in the molecular weight with increasing concentration of PP (Table 2) is caused by the increase in the concentration of free radicals in the system, which is typical of radical copolymerization. The decrease in the molecular weight with increasing concentration of SHS (Table 2) may be due to growing contribution of chain transfer to the macroradical ~M$^{\cdot}$, which can be represented by the scheme

$$\sim M^{\cdot} + HSO_3^- \longrightarrow \sim MH + SO_3^{-\cdot}. \qquad (1)$$

In aqueous solutions, HSO_3^- ions are formed at 20°C when [SHS] < 10^{-3} M, which can be presented

Table 2. Effect of concentrations of PP and SHS on copolymerization of AA with Mg-AMS. $[M_1 + M_2]$ = 10%, AA : Mg-AMS = 3 : 7

PP (SHS) concentration, M	$v_0 \times 10^5$, mol l^{-1} s^{-1}	Yield in 2 h, %	$[\eta]$, cm^3 g^{-1}	PP (SHS) concentration, M	$v_0 \times 10^5$, mol l^{-1} s^{-1}	Yield in 2 h, %	$[\eta]$, cm^3 g^{-1}
Potassium peroxosulfate				Sodium hydrosulfite			
0.031	11.3	60	85	0.00035	6.4	69	112
0.044	13.9	69	68	0.00084	6.7	72	108
0.070	18.2	77	74	0.00168	7.7	77	102
0.079	20.6	81	47	0.00224	9.5	80	60

by the scheme

$$S_2O_5^{2-} + H_2O \longrightarrow 2HSO_3^-. \quad (2)$$

From data in Fig. 2b, we determined the orders of the copolymerization with respect to the concentrations of PP and SHS, which are 0.5 and 0.1, respectively. Based on the results of the experiment, we found the empirical equation for the total rate of copolymerization of AA with Mg-AMS, which is as follows:

$$v_c = k_c[AA]^{1.0}[\text{Mg-AMS}]^{1.5}[PP]^{0.5}[SHS]^{0.1}, \quad (3)$$

where k_c is the rate constant of copolymerization.

In Eq. (3) $k_c = (k_g/k_t^{1/2})(2fk_{dec})^{1/2}$, where k_g, k_t, and k_{dec} are the rate constants of chain growth and termination and of initiator decomposition, respectively; f is the initiation efficiency.

Taking into account the reaction orders found by Eq. (3), we evaluated the k_c values presented in Table 1. It is seen that with increasing the initial concentration of Mg-AMS the k_c values initially increase and then become constant at [Mg-AMS] > 0.35 M. This variation of k_c can be caused by variation of μ. The effect of μ on the rate constant of the reaction between A and B ions can be determined from the Debye–Hückel theory by the simplified equation

$$\log k = \log k_0 + 2Z_AZ_B\gamma\mu^{1/2}, \quad (4)$$

where k_0 is the rate constant of the reaction at $\mu = 0$, Z_A and Z_B are the degrees of oxidation of A and B ions, and γ is a constant for the given solvent and temperature. Equation (4) can be used for estimation of the effect of μ on copolymerization with participation of ionogenic monomers. The experimental data presented in the coordinates of Eq. (4) are shown in Fig. 3. The increase in $k_c = (k_g/k_t^{1/2})(2fk_{dec})^{1/2}$ with increasing μ, observed in Fig. 3 at low μ, is caused by an increase in the k_g/k_t ratio, since under the experimental conditions $k_{dec} \neq f(\mu)$ [12]. An increase of μ weakened the electrostatic repulsion of sulfonate

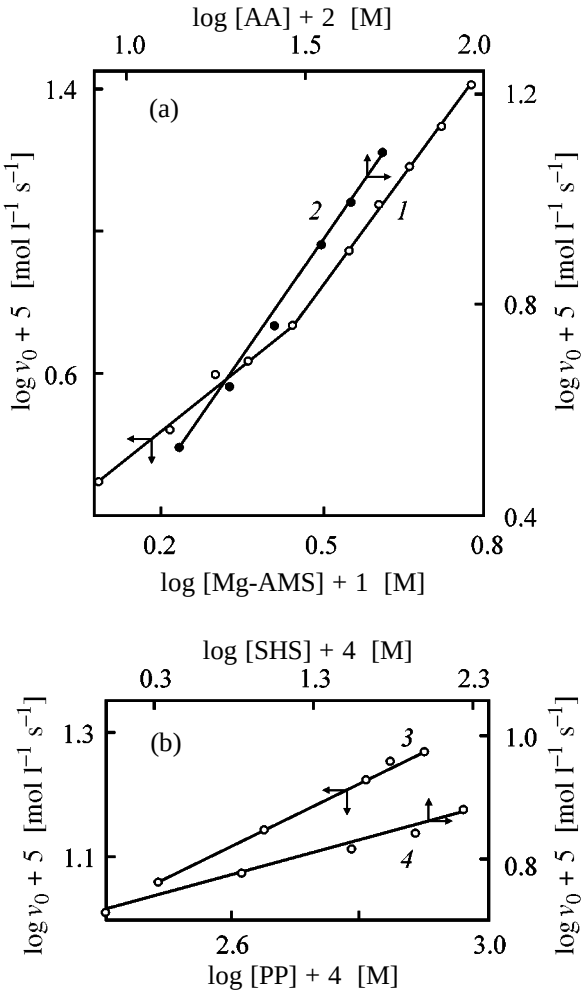

Fig. 2. Initial rate of copolymerization of AA with Mg-AMS (v_0) as a function of concentration of (*1*) Mg-AMS, (*2*) AA, (*3*) PP, and (*4*) SHS. (*2–4*) [Mg-AMS] = 0.4, (*4*) [PP] = 5.2×10^{-4}, and (*3*) [SHS] = 3.5×10^{-4} M. [AA] (M): (*1*) 0.35 and (*3, 4*) 0.17. (a, b) For comments, see text.

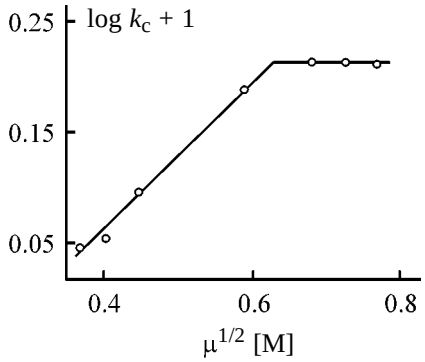

Fig. 3. Dependence of $\log k_c$ on $\mu^{1/2}$ [M] in copolymerization of AA with Mg-AMS in aqueous solutions. [AA] = 0.4 M.

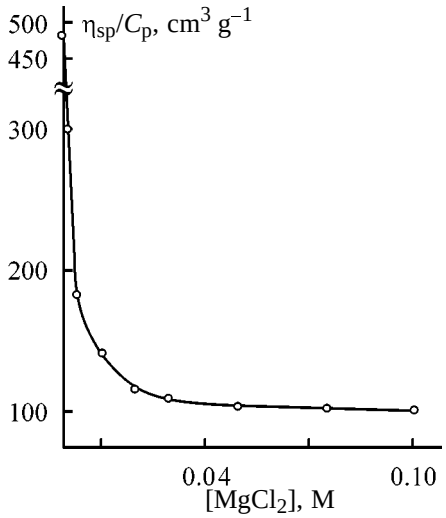

Fig. 4. Reduced viscosity η_{sp}/C_p of copolymer of AA with H-AMS in water as a function of $MgCl_2$ concentration. C_p = 0.1%; 30°C; [η] = 157 cm^3 g^{-1}, content of H-AMS units 38.7 mol %.

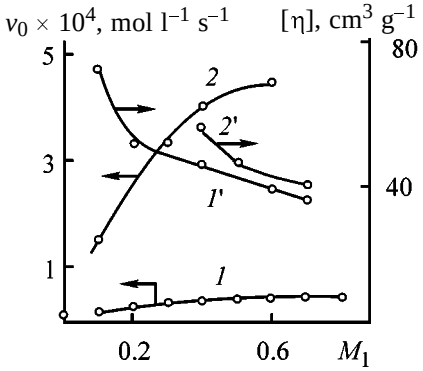

Fig. 5. Dependences of (*1*, *2*) copolymerization initial rate v_0 and (*1*', *2*') [η] of copolymers of AA with Mg-AMS on the mole fraction of AA in the initial monomeric mixture M_1. [AA + Mg-AMS] (%): (*1*, *1*') 10 and (*2*, *2*') 20.

anions in Mg-AMS and in terminal units of Mg-AMS macroradicals (in the events of chain growth) and also between sulfonate anions at the ends of two macroradicals (in the events of chain termination). This should favor increase in k_g and k_t. It is evident that with increasing μ the predominant increase in k_g is the reason of an increase in $k_g/k_t^{1/2}$ and k_c values, since in this case the molecular weights of the resulting copolymers increased (Table 1). In the range of low μ the conformation state of the macromolecules also varied, which was confirmed by data presented in Fig. 4. As seen, with increasing μ η_{sp}/C_p decreased (at C_p = const) owing to weakening of electrostatic repulsions of like charges of macromolecules and contraction of macromolecular globules in the solution. At high μ, η_{sp}/C_p varied slightly at changing μ (Fig. 4). This is caused by stabilization of the size of the copolymer macromolecules, which evidently leveled the accessibility of the growing macroradical for the ionogenic monomer and the reactivity of Mg-AMS in copolymerization. As a result, k_g and k_t did not vary and the ratio $k_g/k_t^{1/2}$ and k_c were constant in the range of high μ (Fig. 3).

Let us consider the effect of the composition of the initial monomeric mixture on copolymerization of AA with Mg-AMS. As seen from Fig. 5, throughout the studied range of the initial ratios of monomers at $[M_1 + M_2]$ = const an increase in the AA content in the monomeric mixture results in an increase in v_0 (curves *1*, *2*) and a decrease in [η] (curves *1*', *2*') of the copolymers. These data suggest higher reactivity of AA in copolymerization in comparison with Mg-AMS and formation of copolymers with higher molecular weight in monomeric mixtures enriched with Mg-AMS units. It is also seen from Fig. 5 that with increasing initial concentration of the monomeric mixture $M_1 + M_2$ the v_0 values (passing from curve *1* to curve *2*) and the molecular weights (passing from curve *1*' to curve *2*') increase.

In Fig. 6 is presented the instant composition of the copolymer as a function of composition of the initial monomeric mixture in copolymerization of AA with Mg-AMS. This curve corresponds to the relative activities of monomers $r_{AA} < 1$ and $r_{Mg\text{-}AMS} < 1$. The values of r_{AA} and $r_{Mg\text{-}AMS}$ were not determined, since in the system under consideration the variation of the ionic strength of the solution under conditions of synthesis (owing to variation of μ with variation of the Mg-AMS concentration and in the course of the reaction) results in variable copolymerization constants; therefore, copolymerization cannot be de-

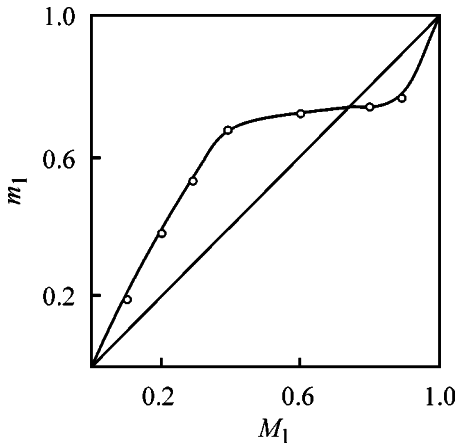

Fig. 6. Composition of copolymer of AA with Mg-AMS as a function of AA mole fraction in the initial monomeric mixture M_1 at the conversion $x < 4\%$. [AA + Mg-AMS] = 10%. (m_1) Mole fraction of AA units in the copolymer.

scribed by fixed constants with the use of classic equations [4].

The above data suggested the possibility of production of macromolecular copolymers of AA with Mg-AMS with a high yield and controllable values of v_0, molecular weight, and copolymer composition by copolymerization of monomers in concentrated solutions in water and aqueous-salt solutions.

CONCLUSIONS

(1) The copolymerization rate v_0 increases with increasing concentration of the monomeric mixture acrylamide + Mg 2-acrylamido-2-methylpropanesulfonate, acrylamide, Mg 2-acrylamido-2-methylpropanesulfonate, potassium peroxosulfate, and sodium hydrosulfite, and also on addition of $MgCl_2$. The k_g/k_t ratio increases with increasing μ in the range of low μ and does not vary in the range of high μ.

(2) The intrinsic viscosities [η] of copolymers increase with increasing concentration of the mixture acrylamide + Mg 2-acrylamido-2-methylpropanesulfonate and Mg 2-acrylamido-2-methylpropanesulfonate and also with decreasing concentration of potassium peroxosulfate and sodium hydrosulfite.

(3) The reactivity of acrylamide in copolymerization is relatively high in comparison with Mg 2-acrylamido-2-methylpropanesulfonate.

ACKNOWLEDGMENTS

This work was financially supported by the Foundation for Basic Natural Science, Education Ministry of the Russian Federation (project no. 97-0-9.4-59) and the Foundation for Research and Development Works of the Tatarstan Republic [project no. 19-03/2000 (F)].

REFERENCES

1. McCormick, C.I., *J. Macromol. Sci.: Chem., Ser. A*, 1985, vol. 22, no. 5, pp. 955–982.
2. Lisovtsev, V.V., Rostokin, G.A., and Kulikova, A.E., *Khimicheskaya promyshlennost': Akrilaty i polivinilkhlorid* (Chemical Industry: Acrylates and Polyvinyl Chloride), Moscow: NIITEKhim, 1984, pp. 1–20.
3. Kabanov, V.A. and Topchiev, D.A., *Polimerizatsiya ioniziruyushchikhsya monomerov* (Polymerization of Ionizable Monomers), Moscow: Nauka, 1975.
4. Kurenkov, V.F. and Myagchenkov, V.F., *Zh. Prikl. Khim.*, 1999, vol. 72, no. 6, pp. 881–890.
5. Kurenkov, V.F. and Safin, A.G., *Vysokomol. Soedin., Ser. A*, 1997, vol. 39, no. 11, pp. 1749–1754.
6. Kurenkov, V.F. and Safin, A.G., *Zh. Prikl. Khim.*, 1997, vol. 70, no. 12, pp. 2030–2034.
7. Kurenkov, V.F. and Utikeeva, A.R., *Vysokomol. Soedin., Ser. A*, 2000, vol. 42, no. 4, pp. 587–593.
8. Charlot, G., *Les methods de la chimie analytique. Analyse quantitative minerale*, Paris: Masson, 1961, 4th ed.
9. *2-Acrylamido-2-Methylpropane Sulfonic Acid Monomer*, Wickliffe, Ohio (USA): Lubrizol, 1994.
10. USSR Inventor's Certificate no. 235997.
11. Kholodnova, L.V., Pavlyuchenko, V.K., Alekseeva, Z.M., and Andreeva, A.I., *Kataliticheskie i initsiiruyushchie sistemy dlya sinteza i modifikatsii polimerov* (Catalytic and Initiating Systems for Synthesis and Modification of Polymers), Leningrad: ONPO Plastpolimer, 1984, pp. 99–104.
12. Kolthoff, I.M. and Miller, I.K., *J. Am. Chem. Soc.*, 1951, vol. 73, no. 7, pp. 3055–3059.
13. Osmanov, T.O., Gromov, V.F., Khomikovskii, P.M., and Abkin, A.D., *Vysokomol. Soedin., Ser. A*, 1980, vol. 22, no. 3, pp. 668–675.
14. Topchiev, D.A., Shakirov, R.Z., Kalinina, L.I., *et al.*, *Vysokomol. Soedin., Ser. A*, 1972, vol. 14, no. 3, pp. 581–586.
15. Loginova, R.R., Gavurina, R.K., and Aleksandrova, M.L., *Vysokomol. Soedin., Ser. B*, 1969, vol. 11, no. 9, pp. 643–645.
16. Paul, T.K., Sathpathy, U., and Konar, R.S., *J. Appl. Polym. Sci.*, 1982, vol. 27, no. 5, pp. 1501–1511.

Russian Journal of Applied Chemistry, Vol. 74, No. 3, 2001, pp. 510–515. Translated from Zhurnal Prikladnoi Khimii, Vol. 74, No. 3, 2001, pp. 499–504.

MACROMOLECULAR CHEMISTRY AND POLYMERIC MATERIALS

Ionic Polyacrylamide Flocculants as Promoters of Sedimentation of Ocher Suspension and Thickening of Its Precipitates in Aqueous and Aqueous-Salt Solutions

V. E. Proskurina and V. A. Myagchenkov

Kazan State Technological University, Kazan, Tatarstan, Russia

Received June 8, 2000

Abstract—The kinetic features of flocculation of an ocher suspension and thickening of its precipitate in aqueous and aqueous-salt solutions containing ionic and nonionic acrylamide copolymers with different composition and molecular properties were studied.

Water-soluble arylamide (co)polymers produced in large scale are widely used in industry as highly efficient, cheap, readily available, and technologically safe flocculants and stabilizers of various dispersion systems (DSS) [1–3].

The performance of polyacrylamide flocculants (PAAFs) depends not only on their chemical nature and molecular parameters, the nature and physicochemical properties of the dispersed phase (DP) (first of all the specific surface area, concentration of the adsorption centers, lyophilic nature of the surface, etc.), and the nature of dispersion medium, but also on the conditions of sedimentation of the DP (free or hindered) and parameters of the flocculation process [4]. The study of the correlation between flocculation processes under conditions of hindered sedimentation and thickening of the precipitates [5, 6] is of scientific and practical interest since kinetics of these processes is poorly understood [7, 8].

It should be noted that the liquid phase of a number of DSs used in practice contains various active additives (in particular, salt additives) which can strongly affect the flocculation.

In this work we studied the kinetic features of flocculation of model DS, an ocher suspension, and thickening of the precipitate in aqueous and aqueous-salt (0.5 N NaCl) media in the presence of nonionic and ionic (anionic and cationic) PAAFs with different compositions and molecular properties.

EXPERIMENTAL

We studied five samples of PAAFs differing in the chemical nature of the copolymer and molecular parameters: nonionic polyacrylamide (N) and ionic (A_1, A_2, C_1, and C_2) copolymers of acrylamide with different concentrations of ionic units. The viscosity-average molecular weight of sample N with the structural formula

$$(-CH_2-\underset{\displaystyle CONH_2}{\underset{|}{CH}}-)_n$$

is $\overline{M}_\eta = 7.4 \times 10^6$. Anionic PAAFs ($A_1$ and A_2) are random copolymers of acrylamide with sodium acrylate with viscosity-average molecular weight $\overline{M}_\eta = 5.4 \times 10^6$ and $\overline{M}_\eta = 7.66 \times 10^5$ and content of ionic units $\beta = 17.4$ and $\beta = 80\%$, respectively. Samples C_1 and C_2 are random copolymers of acrylamide and dimethylaminoethyl methacrylate hydrochloride with $\overline{M}_\eta = 2.3 \times 10^6$ and 1.06×10^6, $\beta = 16.3$ and 62%, respectively.

The viscosity-average molecular weight $\overline{M}_\eta$ of the flocculants was calculated from the intrinsic viscosity $[\eta]$ by the Mark–Houwink equation

$$[\eta] = K\overline{M}_\eta^a, \quad (1)$$

where K and a are tabulated constants [9, 10].

To eliminate the polyelectrolytic effect in determination of $[\eta]$, 0.5 N aqueous solution of NaCl was used as the solvent.

To provide more reliable and comprehensive estimation of the flocculating properties of acrylamide (co)polymers, we also studied polyoxyethylene (POE) widely used in industry. The viscosity-average molecular weight of POE having the structural formula $(CH_2–CH_2–O)_n$ is $\overline{M}_\eta = 2.2 \times 10^6$.

1070-4272/01/7403-0510$25.00

The kinetics of sedimentation of an ocher suspension ["golden" trade name, TU (Technical Specifications) 301-019–90] under hindered conditions [4] in the presence of the tested polymeric additives (in all experiments the initial concentration of DP was C_d = 8%) was studied in 2000-ml volumetric cylinders by the shift of the boundary between the clarified and nonclarified suspension. This method allows reliable monitoring of the sedimentation in the steps of both accelerated sedimentation (flocculation) and thickening of the precipitate [11, 12].

Ocher was kept in the dispersion medium for 1 day. The suspension was mixed by 10-fold overturn of the cylinders just before the experiment.

The flocculation effect was quantitatively characterized by the specific dimensionless parameter D:

$$D = (\bar{V}/\bar{V}_0) - 1, \quad (2)$$

where $\bar{V}$ and $\bar{V}$ are average sedimentation rates of DF in the presence and in the absence of the flocculants, respectively.

It should be noted that in all experiments $\bar{V}$ and $\bar{V}_0$ were measured at constant degree of clarification of the working suspension Q = 0.5.

The efficiency of the polymeric additives was quantitatively estimated by the flocculating power λ [1]:

$$\lambda = \frac{(\bar{V}/\bar{V}_0 - 1)}{C} = \frac{D}{C}, \quad (3)$$

where C is the flocculant concentration.

When D and λ are positive, a polymeric additive is a flocculant; at $D < 0$ and $\lambda < 0$ it is a stabilizer.

Viscometric analysis of PAAF and POE solutions was performed on an Ostwald viscometer with a capillary 0.54×10^{-3} m in diameter. The correction for the kinetic energy of the flowing liquid was less than 1.5% and was neglected in calculation of the viscosity numbers:

$$\frac{\eta_{sp}}{C} = \frac{\tau - \tau_0}{\tau_0 C}, \quad (4)$$

where τ and τ_0 are the time of effluence of solution with the polymer concentration C and the solvent, respectively.

Let us consider the kinetics of flocculation of an ocher suspension in water in the presence of PAAF and POE. The kinetic curves are shown in Fig. 1. To simplify comparison of curves *2–7*, the amount of flocculants introduced in the suspension was the same (2×10^{-3}%). Considerable differences in the location of curves *5*, *7* and *2*, *4* (Fig. 1) and hence in the flocculation effects D and flocculation power λ (see table) can be due to differences in the molecular weights $\bar{M}_\eta$ of the tested polymers and in the charge densities on their macromolecules β.

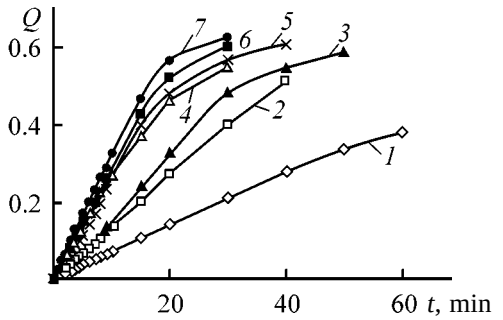

Fig. 1. Kinetic curves of sedimentation of an aqueous ocher suspension. Flocculant: (*1*) none, (*2*) C_2, (*3*) POE, (*4*) A_2, (*5*) C_1, (*6*) PAA, and (*7*) A_1. [PAAF] = [POE] = 2×10^{-3}%. (*Q*) The degree of clarification and (*t*) time; the same for Figs. 2 and 3.

The molecular weights $\bar{M}_\eta$ of copolymers A_1 and C_1 are considerably higher than those of copolymers A_2 and C_2. The root-mean-square size of these macromolecules $\langle \bar{R}^2 \rangle^{0.5}$ varies in parallel with $\bar{M}_\eta$ [9]. The fact that $\langle \bar{R}^2 \rangle^{0.5}$ of A_1 and C_1 is larger than that of A_2 and C_2 is also due to lower parameters β for A_2 and C_1 since the shielding of the charges localized along the macromolecules of A_2 and C_2 with higher content of ionic groups is more pronounced. The stronger shielding decreases the electrostatic potential of repulsion between similarly charged units of the macromolecules and hence decreases $\langle \bar{R}^2 \rangle^{0.5}$ [13, 14]. The higher $\langle \bar{R}^2 \rangle^{0.5}$, the higher is probability of formation of bonds of a macromolecule with two and more ocher particles (bridge formation). As a consequence, experimental D and λ of copolymers A_1 and C_1 are considerably higher than those of copolymers A_2 and C_2. These correlations between the flocculation parameters and M of ionic PAAF (A_1, A_2, C_1, and C_2) confirm additionally the bridge mechanism of flocculation in the tested systems.

As seen from kinetic curves *5* and *7* (Fig. 1) and values of parameters D and λ (see table), anionic copolymer A_1 is stronger flocculant with respect to ocher than cationic copolymer C_1.

Taking into account the negative charge of DP particles, the ratio between the flocculation parameters of copolymers A_1 and C_1 additionally supports the bridge mechanism of flocculation in the tested systems.

Summary of data on flocculation of an ocher suspension and thickening of the precipitate in aqueous and aqueous-salt (0.5 N NaCl) solutions in the presence of PAAF and POE

Parameter	Sequence of introduction of components	Flocculant					
		N-2000	POE	A_1	C_1	A_2	C_2
$D_{0.5}$	F	83.0	0.300	154	2.56	3.25	1.13
	NaCl + F	54.5	–	142	1.94	3.25	3.25
	F + NaCl	19.0	0.660	37.5	1.08	3.25	1.13
	(NaCl + F)	36.6	0.850	9.00	1.50	4.72	1.13
$\lambda \times 10^{-3}$, $m^3\ kg^{-1}$	F	4.15	0.015	7.73	0.128	0.163	0.057
	NaCl + F	2.73	–	7.09	0.097	0.163	0.163
	F + NaCl	0.950	0.033	1.88	0.054	0.163	0.057
	(NaCl + F)	1.83	0.043	0.45	0.075	0.236	0.057
$\gamma \times 10^5$, s^{-1}	F	132	18.3	95.0	35.4	10.1	14.7
	NaCl + F	21.2	2.03	109	24.3	10.8	12.2
	F + NaCl	52.7	18.1	64.8	19.3	14.9	10.3
	(NaCl + F)	113	22.7	101.7	20.1	29.8	10.6
$\rho_{pr} \times 10^{-3}$, $kg\ m^{-3}$	F	1.25	1.28	1.24	1.24	1.26	1.19
	NaCl + F	1.24	1.26	1.24	1.24	1.18	1.21
	F + NaCl	1.24	1.26	1.24	1.24	1.21	1.22
	(NaCl + F)	1.24	1.26	1.24	1.25	1.21	1.21

Note: F is flocculant; γ is the constant of precipitate thickening; ρ_{pr} is the precipitate density; $\gamma \times 10^5$, s^{-1} and $\rho_{pr} \times 10^{-3}$, $kg\ m^{-3}$ for ocher and ocher + 0.5 N NaCl are 4.22 and 16.3; 1.30 and 1.29, respectively.

The experimental relations $D(A_1) \gg D(C_1)$ and $\lambda(A_1) \gg \lambda(C_1)$ indicate different nature of ocher sorption on polymer A_1 and C_1 since these results cannot be explained by the differences in $\overline{M}_\eta$ and $\langle \overline{R}^2 \rangle^{0.5}$ because D and λ of polymers with $\overline{M} > 1 \times 10^6$ are almost independent of $\overline{M}_\eta$ [1, 4]. If the numbers of PAAF macromolecules forming "bridge" and "anchor" bonds (since adsorption occurs on a single DF particle, these macromolecules are not involved in the flocculation) with particles of the DP are denoted as N_1 and N_2 [4], respectively, then, apparently, $y_1(A_1) \gg y_2(C_1)$ and $y_2(A_1) < y_2(C_1)$ where

$$y_1 = \frac{N_1}{N_1 + N_2}, \qquad y_2 = \frac{N_2}{N_1 + N_2},$$

The strong differences in parameters y_1 and y_2 for copolymers A_1 and C_1 can be due to the presence of both positively (owing to Fe^{3+}) and negatively (owing to silanol groups) charged areas on the surface of DP particles [15]. To complete the analysis, it should be noted that the tested PAAFs are irreversibly and almost completely adsorbed on ocher particles (the degree of adsorption is $\alpha > 0.98$) [16].

The parameters y_1 and y_2 depend not only on the macroion charge but also on the nature and concentration of active centers on DP particles and the [PAAF]/C_d ratio [1, 4].

As seen from curves *3* and *6* (Fig. 1) and the table, PAA is more efficient flocculant than POE. The fact that D and λ of POE are lower than those of PAA is due to more compact conformation of POE macromolecules. This, in particular, is indicated by considerably smaller values of $\langle \overline{R}^2 \rangle^{0.5}$ for POE, which can be indirectly estimated by comparing the viscosity numbers at C = const. For example, $(\eta_{sp}/C) \times 10^{-3}$ for PAA and POE at $C = 0.1\%$ are 3.58 and 0.635 $cm^3\ g^{-1}$, respectively.

Let us consider ocher sedimentation when PAAF (or POE) and inorganic electrolyte (NaCl) are present simultaneously. The influence of the ionic strength on flocculation of ocher suspension in the presence of PAAF under conditions of hindered sedimentation (C_d = 6%) was studied in [17].

It was of interest to estimate the influence of the ionic strength on the kinetics of ocher sedimentation in the presence of not only anionic but also other samples of PAAF and POE. The influence of process parameters on ocher sedimentation should be also

taken into account, since, as noted in [18–20], the sedimentation stability strongly depends on the sequence of introduction of the active additives in the system.

Three modes of flocculant (F) introduction were tested: (1) first NaCl and then F; (2) first F and then NaCl; (3) simultaneous introduction of NaCl and the flocculant in an ocher suspension. It should be noted that the amount of PAAP and NaCl additives was the same in all experiments. As seen from Fig. 2, the flocculation effect strongly depends on the sequence of introduction of the cationic flocculants C_1 and C_2 and NaCl electrolyte.

When F is introduced after NaCl, the flocculation effect D is maximal (Fig. 2, curves *5*, *7*).

These results suggest that introduction of NaCl into an ocher suspension yields dense coagulation aggregates of DP particles, which are suitable "nuclei" for formation of relatively large floccules in subsequent introduction of the flocculant. The floccules contain, along with DP particles and NaCl, macromolecules of cationic acrylamide copolymers with a medium and high content of ionic groups β.

The kinetic curves of ocher sedimentation in the presence of copolymers A_1 and A_2 and NaCl electrolyte are shown in Figs. 3a and 3b. Even visual comparison of the kinetic curves shows that the flocculation parameters of copolymer A_1 are considerably higher than those of A_2 at all sequences of introduction of PAAF and NaCl. The quantitative difference in these parameters is seen from the table: $D(A_1) > D(A_2)$ and $\lambda(A_1) > \lambda(A_2)$.

The flocculation parameters D an λ of ionic PAAF, C_1, C_2 (Fig. 2) and A_1 (Fig. 3b) in 0.5 N NaCl, as influenced by the introduction mode, decrease in the order F after NaCl > NaCl after F > NaCl + F simultaneously. Our experimental results show that macromolecular globules strongly "contract" at direct contact of polymeric additives C_1, C_2, A_1, with NaCl coagulant. This is clearly confirmed by the results of viscometric analysis (Fig. 4). Sharp decrease in the viscosity numbers $\langle \bar{R}^2 \rangle^{0.5}$ changes similarly) with increasing electrolyte concentration is due to weakening of electrostatic repulsion of similarly charged groups of the macromolecules owing to shielding of negative charges of A_1 and positive charges of C_1 and C_2. As a result, the macromolecules roll up in globules. The parameters $\langle \bar{R}^2 \rangle^{0.5}$, D, and λ change similarly (see table).

It should be noted that the flocculation parameters of PAA and POE nonionic polymers with respect to

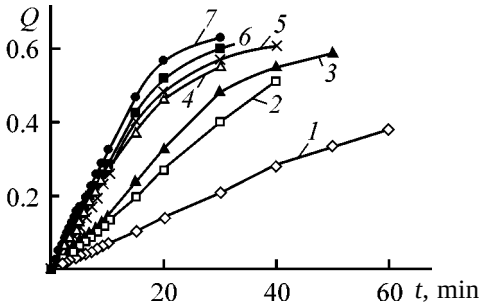

Fig. 2. Kinetic curves of sedimentation of an aqueous ocher suspension (*1*) in the absence and (*2–7*) in the presence of PAAF cationic flocculant [(*2, 3, 5*) C_2 and (*4, 6, 7*) C_1] and NaCl electrolyte. Introduction mode: (*5, 7*) F after NaCl, (*2, 4*) NaCl after F, and (*3, 6*) NaCl + F simultaneously. $[C_1] = [C_2] = 2 \times 10^{-3}$%, [NaCl] = 0.5 M.

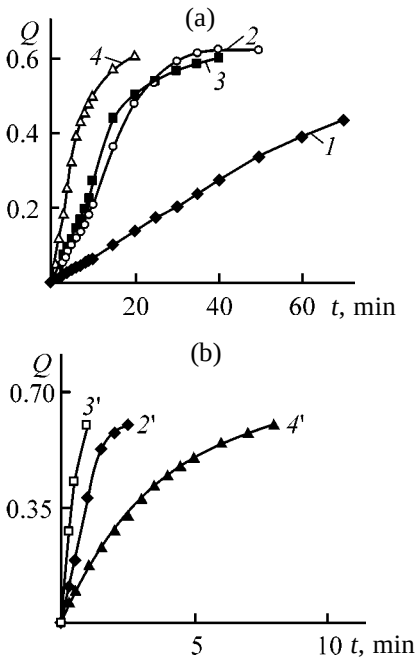

Fig. 3. Kinetic curves of sedimentation of an aqueous ocher suspension (*1*) in the absence and (*2–4*, *2'–4'*) in the presence of anionic acrylamide copolymers (a, *2–4*) A_2 and (b, *2'–4'*) A_1 and NaCl electrolyte. Introduction mode: (*3*, *3'*) F after NaCl, (*2*, *2'*) NaCl after F, and (*4*, *4'*) NaCl + F simultaneously. $[A_1] = [A_2] = 2 \times 10^{-3}$%, [NaCl] = 0.5 M.

ocher in aqueous media fundamentally differ from those in aqueous salt media (see table). Unlike PAA, introduction of inorganic electrolyte has virtually no effect of the flocculation parameters of POE. This is mainly due to globular conformation of POE macromoleculs. Low flocculation parameters of POE were noted in [22].

This is also confirmed by the weak dependence of the viscosity numbers of POE (Fig. 4, curves *4*) on

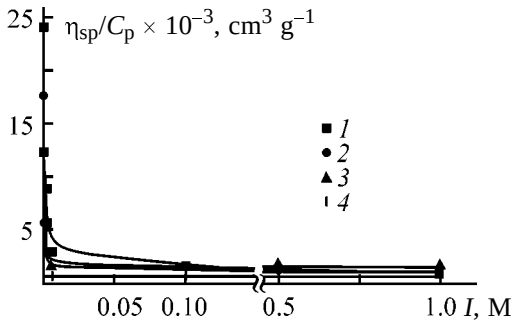

Fig. 4. Viscosity number η_{sp}/C of (*1*) A_1, (*2*) C_2, (*3*) N, and (*4*) POE flocculants as a function of the ionic strength of the solution I = [NaCl]. [PAAF] = [POE] = 0.1%.

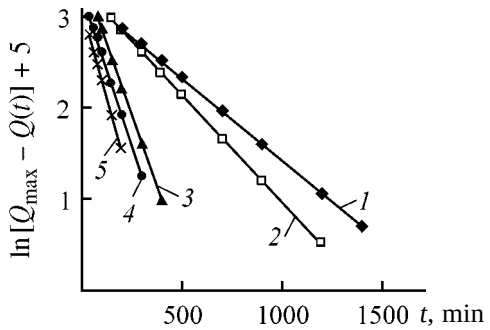

Fig. 5. Kinetic curves of thickening of precipitates of an ocher suspension (*1*) in the absence of additives, (*2*) in the presence of NaCl ([NaCl] = 0.5 M) and (*3*–*5*) in the presence of C_2 PAAF ([C_2] = 2×10^{-3}%) and NaCl. Introduction mode: (*4*) F after NaCl, (*5*) NaCl after F, and (*3*) NaCl + F simultaneously. (Q) Degree of clarification and (t) time.

the ionic strength of the solution I. These results indirectly indicate that $\langle \bar{R}^2 \rangle^{0.5}$ of POE remains virtually the same since the dependences $\eta_{sp}/C = f(I)$ and $\langle \bar{R}^2 \rangle^{0.5} = f(I)$ are similar.

As seen from Fig. 4 (curve *3*), η_{sp}/C of PAA appreciably decreases with increasing [NaCl]. This is probably due to the fact that PAA contains small amount (1–2 mol %) of carboxy groups formed by hydrolysis of the amide groups during preparation of the polymer. The decrease in the flocculation parameters D and λ of sample N with increasing I is manly due to the decrease in the size of its macromolecules.

The aim of second step of our work was to study the kinetics of thickening of ocher precipitates in the presence of the same PAAFs. The kinetic curves of thickening of an ocher precipitate in the presence of copolymer C_2 or NaCl or of their mixture are shown in Fig. 5. Using the procedure described in our previous work [7], we calculated the constant of the precipitate thickening γ from the slope of the $\ln[Q_{max} - Q(t)] = f(t)$ curves constructed from the experimental data (Fig. 5).

As seen from the table, in all the tested systems the constants of thickening of ocher precipitates γ in the presence of PAAF and POE exceed those for pure ocher and the ocher–NaCl system. This is obviously due to flocculation in the first step of ocher sedimentation in the presence of the polymers and NaCl coagulant depending of the sequence of their introduction.

It should be noted that the most important parameter of the precipitate is its density ρ_{pr}. The structure of the precipitate and the degree of its thickening and dehydration can be estimated from ρ_{pr}. The precipitate density ρ_{pr} depends on the weight content and density of its solid phase [6] and is calculated by the equation

$$\rho_{pr} = \frac{m + (V_{pr} - m/\rho)\rho_0}{V_{pr}}, \quad (5)$$

where ρ and ρ_0 are the density of ocher ($\rho = 2.7 \times 10^3$ kg m^{-3}) and water ($\rho_0 = 2.7 \times 10^3$ kg m^{-3}), respectively, and m is the ocher weight.

The precipitate volume is calculated by the equation

$$V_{pr} = (1 - Q_{max})V_0, \quad (6)$$

where V_0 is the working volume of an ocher suspension in a volumetric cylinder.

The experimental results presented in the table show that ρ_{pr} of the precipitates formed in the presence of the flocculants and NaCl coagulant is slightly lower than that of the ocher precipitate formed in the absence of these additives. This is due to formation of macromolecular bridges between particles of DP. The floccules thus formed are more friable including the region of Q values close to Q_{max}.

CONCLUSIONS

(1) The kinetics of flocculation of an ocher suspension and thickening of the precipitates in aqueous and aqueous-salt (0.5 N NaCl) media in the presence of nonionic and ionic (anionic and cationic) acrylamide copolymers having different composition and molecular parameters was studied.

(2) The flocculation power was correlated with the molecular parameters of the flocculants. The sedimentation stability strongly depends on the sequence of introduction of the flocculants and the electrolyte.

(3) The thickening constants and densities of ocher precipitates formed in the presence of the flocculants

in aqueous and aqueous-salt (0.5 N NaCl) media were calculated.

REFERENCES

1. Myagchenkov, V.A., Baran, A.A., Bekturov, E.A., and Bulidorova, G.V., *Poliakrilamidnye flokulyanty* (Polyacrylamide Flocculants), Kazan: Tekhnol. Univ., 1998.
2. Veitser, Yu.I. and Mints, D.M., *Vysokomolekulyarnye flokulyanty v protsessakh ochistki prirodnykh i stochnykh vod* (Macromolecular Flocculants in Purification of Natural and Waste Waters), Moscow: Stroiizdat, 1984.
3. Babenkov, E.D., *Ochistka vody koagulyantami* (Purification of Water with Coagulants), Moscow: Nauka, 1977.
4. Baran, A.A., *Polimersoderzhashchie dispersnye sistemy* (Polymer-Containing Disperse Systems), Kiev: Naukova Dumka, 1986.
5. Turovskii, I.S., *Obrabotka osadkov stochnykh vod* (Treatment of Wastewater Sludges), Moscow: Stroiizdat, 1982.
6. Lyubarskii, V.M., *Osadki prirodnykh vod i metody ikh obrabotki* (Sludges of Natural Waters and Methods of Their Treatment), Moscow: Stroiizdat, 1980.
7. Proskurina, V.E. and Myagchenkov, V.A., *Zh. Prikl. Khim.*, 1999, vol. 72, no. 10, pp. 1704–1708.
8. Myagchenkov, V.A. and Proskurina, V.E., *Kolloidn. Zh.*, 2000, vol. 62, no. 5, pp. 654–659.
9. Rafikov, S.R., Budtov, V.P., and Monakov, Yu.B., *Vvedenie v fizikokhimiyu polimerov* (Introduction to Physical Chemistry of Polymers), Moscow: Nauka, 1978.
10. Klein, J. and Conrad, K.D., *Makromol. Chem.*, 1978, vol. 179, pp. 1635–1638.
11. Kul'skii, L.A., *Osnovy khimii i tekhnologii vody* (The Fundamentals of Chemistry and Technology of Water), Kiev: Naukova Dumka, 1991.
12. Zapol'skii, A.K. and Baran, A.A., *Koagulyanty i flokulyanty v protsessakh ochistki vody* (Coagulants and Flocculants in Purification of Water), Leningrad: Khimiya, 1987.
13. Gennes, P.-G. de, *Scaling Concepts in Polymer Physics*, Ithaca: Cornell Univ. Press, 1979.
14. Klenin, V.I., *Termodinamika sistem s gibkotsepnymi polimerami* (Thermodynamics of Systems Containing Polymers with Flexible Macromolecules), Saratov: Saratov. Gos. Univ., 1995.
15. Belen'kii, V.F. and Riskin, I.V., *Khimiya i tekhnologiya pigmentov* (Chemistry and Technology of Pigments), Leningrad: Khimiya, 1974.
16. Myagchenkov, V.A., Bulidorova, G.V., and Evdokimova, L.E., *Khim. Tekhnol. Vody*, 1995, vol. 17, no. 3, pp. 252–256.
17. Myagchenkov, V.A., Kurenkov, V.F., and Nagel', M.A., in *Mezhvuzovskii sbornik: Fiziko-khimicheskie osnovy sinteza i pererabotki polimerov* (Intercollegiate Collection: Physicochemical Principles of Synthesis and Processing of Polymers), Gor'kii: Gor'k. Univ., 1983.
18. Bulidorova, G.V. and Myagchenkov, V.A., *Kolloidn. Zh.*, 1995, vol. 57, no. 6, pp. 778–782.
19. Kurenkov, V.F., Nurutdinova, F.S., Churikov, F.I., and Myagchenkov, V.A., *Khim. Tekhnol. Vody*, 1991, vol. 13, no. 4, pp. 309–312.
20. Myagchenkov, V.A., Proskurina, V.E., and Bulidorova, G.V., *Kolloidn. Zh.*, 2000, vol. 62, no. 2, pp. 222–227.
21. Bekturov, E.A. and Bakauova, Z.Kh., *Sinteticheskie vodorastvorimye polimery v rastvorakh* (Synthetic Water-Soluble Polymers in Solutions), Alma-Ata: Akad. Nauk Kaz. SSR, 1981.
22. Slipenyuk, T.S., *Kolloidn. Zh.*, 1998, vol. 60, no. 1, pp. 70–72.

Russian Journal of Applied Chemistry, Vol. 74, No. 3, 2001, pp. 516–518. Translated from Zhurnal Prikladnoi Khimii, Vol. 74, No. 3, 2001, pp. 505–507.

BRIEF COMMUNICATIONS

Effect of Aqueous Solutions of Biuret, Dimethyl Sulfoxide, and Acetamide on the Paper-Forming Properties of Cellulose

I. I. Osovskaya and G. M. Poltoratskii

St. Petersburg State Technological University of Plant Polymers, St. Petersburg, Russia

Received June 20, 2000

Abstract—Chemical activation of cellulose material was studied as a means to improve the mechanical characteristics of experimental paper.

This report is a continuation of our previous article [1] in which we suggested a principally new approach to choosing a cellulose activator, based on thermodynamic studies and a few available publications [2–8]. We showed in [1] that the degree of cellulose activation with an aqueous solution of a chemical reagent depends on the structure of the solvent (liquid water), which is, in turn, determined by the nature and concentration of the solute. Based on thermodynamic studies (calorimetry, densimetry), we proved that water in the presence of structure-breaking and structure-making electrolytes transforms the hydrophilic and sorption properties of cellulose by affecting its structure [1–3]. It was shown that the most promising activating agent is biuret which, when added in small concentrations (3–5 wt %), facilitates maximal development of the capillary-porous structure of cellulose and makes it more accessible for the liquid medium.

The goal of this study was improvement of the paper-forming properties of the cellulose material by optimization of cellulose activation with aqueous solutions of organic substances. We studied the physicomechanical properties of experimental paper that was obtained from cellulose activated with aqueous solutions of biuret, dimethyl sulfoxide (DMSO), and acetamide. Experiments were performed with bleached sulfate cellulose (Arkhangelsk Pulp-and-Paper Plant, Joint-Stock Company) which had the following characteristics: α-cellulose content 91.8%, degree of polymerization 1700, degree of crystallinity 65%, and ash residue 6%. Activated cellulose was prepared by stirring a 6% cellulose suspension for 2 min in the presence of an activator, washed with distilled water, and squeezed to a cellulose concentration of 50 wt %. Experimental castings of 100 ± 1 g m^{-2} weight were prepared on a sheet-casting machine and subjected to standard physicomechanical tests. The concentration of the organic component was varied within 0–5 wt %. The results of physicomechanical tests are given in Figs. 1 and 2 and in the table.

Figures 1a and 1b show that the effect of cellulose activation with aqueous solution of an organic substance depends on its nature and concentration. The breaking length BL and relative elongation ε_0 of paper substantially increase as the concentrations of biuret and DMSO are increased to 1.5 and 5 wt %, respec-

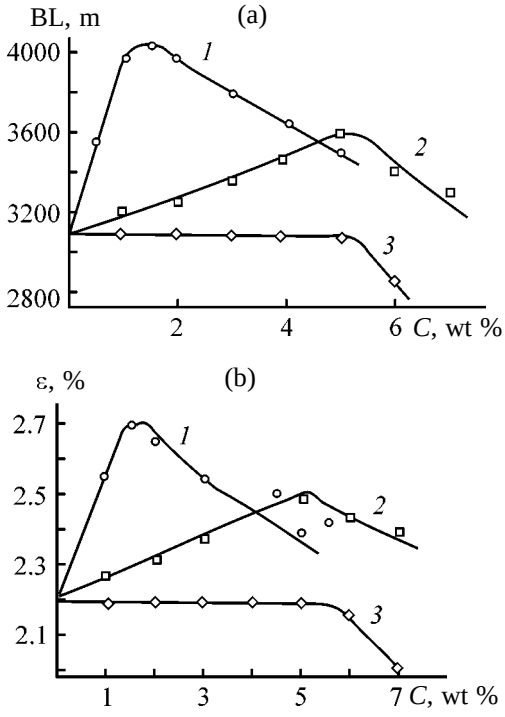

Fig. 1. Effect of concentration *C* of (*1*) biuret, (*2*) DMSO, and (*3*) acetamide in aqueous solution on the (a) breaking length BL and (b) relative elongation ε_0 of paper formed by the traditional procedure.

1070-4272/01/7403-0516$25.00

tively (Figs. 1a, 1b). As the concentration of the organic substance is increased further, these parameters decrease. As seen from the table, the tear resistance E varies in parallel with BL and ε_0.

Figure 2 shows the influence of cellulose activation with biuret on the degree of polymerization of cellulose and strength of a single fiber BL_0. The degree of polymerization was determined viscometrically at 25°C in a solution of the sodium iron tartrate complex (SITC).

As seen from Fig. 2, treatment of cellulose with biuret is accompanied by insignificant degradation of cellulose and the loss of the strength of a single fiber.

The physicomechanical characteristics of the experimental paper sample (see table; Figs. 1, 2) are consistent with the previously measured [1] physicochemical properties of cellulose (heat of wetting, water-retaining power, and density) activated with biuret, DMSO, and acetamide.

The parallel variation of the mechanical characteristics of paper and physicochemical properties of activated cellulose allows us to explain the dependence of these properties on the nature and concentration of the organic agent. Addition of biuret and DMSO, which are structure-breaking agents with respect to water, increases the content of weakly associated water molecules whose penetration into previously inaccessible very fine pores and capillaries of the cellulose fiber becomes possible. For development in cellulose of microareas comparable in size with water molecules, biuret is preferable, since it contains a larger number of groups actively interacting with water and breaking its clusters. From this standpoint, it is possible to explain the dependence of the physicomechanical characteristics of paper on the nature and concentration of the organic additives.

Figures 1a and 1b show that BL, ε_0, and E increase only at small concentration of the activator. This is due to formation and growth of the total volume of microareas of the cellulose fiber. In such a fiber, in the course of dehydration of the fibrous mass for paper production, the pores are closed to a greater extent, ensuring formation of a uniform and less strained macrostructure [1]. An increase in the pore size at a higher content of the activator causes formation of fibers with a more strained and less regular, and hence more defective, structure [1]. Furthermore, swelling of cellulose in a biuret aqueous solution is accompanied not only by weakening of hydrogen bonds and alteration of the capillary-porous structure

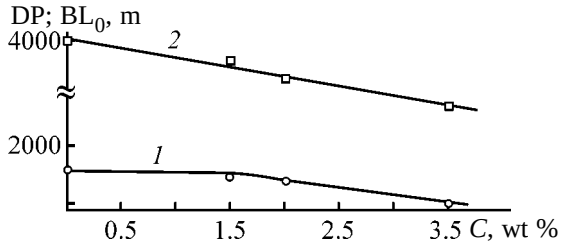

Fig. 2. Effect of concentration C of biuret aqueous solution on the (*1*) degree of polymerization DP and (*2*) strength of the single fiber BL_0.

of the polymer, but also by chemical processes decreasing the degree of polymerization (Fig. 2). Degradation of cellulose macromolecules is responsible for a decrease in the strength of single fibers and hence in the strength of paper as a whole (Fig. 2). At a biuret concentration less than 1.5 wt %, BL_0 and the degree of polymerization also slightly decrease (Fig. 2), but the paper-forming properties of cellulose are not noticeably affected.

Figures 1a and 1b show that acetamide (structure-making agent with respect to liquid water) does not enhance the strength of the experimental paper, and at its content higher than 5 wt % the mechanical characteristics of the paper drastically decrease. Measurements [1] of the density, water-retaining power, and sorption showed that addition of acetamide to the cellulose–water system favors formation of a coarse-porous structure of cellulose. The lack of developed submicroscopic system of pores and capillaries impairs the paper-forming properties of the cellulose fiber and decreases the paper strength.

Tear resistance of paper produced from activated fibers

Modifier (aqueous solution)	Activator concentration, wt %	Tear resistance E, g
–	0	52
Biuret	1.2	56
	1.6	64
	2.1	62
	3.7	58
	4.1	56
DMSO	4.8	58
	6.1	54
	6.5	53
Acetamide	3.5	52
	4.6	50
	5.3	47
	6	44

ACKNOWLEDGMENTS

The study was financially supported by the Integration and Combined Utilization of Wood Resources federal target programs.

REFERENCES

1. Osovskaya, I.I. and Poltoratskii, G.M., *Zh. Prikl. Khim.*, 1999, vol. 72, no. 4, pp. 676–679.
2. Osovskaya, I.I. and Poltoratskii, G.M., *Izv. Vyssh. Uchebn. Zaved., Khim. Khim. Tekhnol.*, 1997, vol. 40, no. 3, pp. 30–32.
3. Mishchenko, K.P. and Poltoratskii, G.M., *Termodinamika i stroenie vodnykh i nevodnykh rastvorov elektrolitov* (Thermodynamics and Structure of Aqueous and Nonaqueous Electrolyte Solutions), Leningrad: Khimiya, 1976.
4. Terent'ev, O.A., *Gidrodinamika voloknistykh suspenzii v tsellyulozno-bumazhnom proizvodstve* (Hydrodynamics of Fiber Suspensions in Pulp-and-Paper Production), Moscow: Lesnaya Prom–st., 1980.
5. Sivaraja, H., *Colourage*, 1987, vol. 34, no. 15, pp. 15–20.
6. *Water in Polymers*, Rowland, S.P., Ed., Washington, DC: Am. Chem. Soc., 1980.
7. Ossovskaja, I. and Poltoratsky, G., *Colloid Polym. Sci.*, 1993, vol. 93, p. 85.
8. Russian Inventor's Certificate no. 154915.

Russian Journal of Applied Chemistry, Vol. 74, No. 3, 2001, pp. 519–521. Translated from Zhurnal Prikladnoi Khimii, Vol. 74, No. 3, 2001, pp. 507–510.

BRIEF COMMUNICATIONS

Synthesis and Some Characteristics of Magnetic Matrices for Fixation of Biologically Active Substances

S. S. Airapetyan, G. G. Balayan, and A. G. Khachatryan

Yerevan State University, Yerevan, Armenia

Received August 1, 2000

Abstract—A possibility of production of nonporous magnetic matrices with two-layer coating based on cobalt ferrite with the aim to use these matrices for fixation of biologically active substances was considered. The function of the first layer (silica coating) is to shield the cobalt ferrite surface and provide conditions for applying the second (polymer) layer containing various functional groups.

With advances in modern procedures of recovery and purification of various chemical compounds, particularly biologically active substances, the necessity arises to produce matrices with a set of useful specific characteristics. In this connection, production of matrices that, among other things, are capable of magnetization is an urgent problem. These matrices can be used for fixation in bioengineering and also for recovery and purification of enzymes and other biologically active substances, when the use of standard matrices is impossible (e.g., in the case of highly viscous homogenate of biologically active substances). In addition, carriers based on magnetic matrices can be recovered from a suspension by applying magnetic fields instead of centrifuging [1].

At present, magnetic matrices for affine sorbents and supports are produced by KLB Co. (Sweden), IBF (France), etc. They consist of agarose and acrylamide gels, swelling in solvents, with admixed magnetite (up to 7 wt %).

However, these matrices do not fully meet the requirements placed upon them; the main requirements are mechanical strength of the matrix material, chemical resistance to biologically active substances and chemical reagents, insolubility in a wide range of solution pH, the features of wettability and swelling in the eluent, and the reactivity providing the possibility of chemical modification [2].

Instead of the above gels of the organic origin, a silica gel shell having low nonspecific sorption, ideal rigidity, and soft hydroxyl cover can be used [3]. However, it should be borne in mind that in modification of these matrices with hydrophobic radicals (ethyl C_2, octyl C_8, and others) only about 40% of silanol groups at the matrix surface are involved in the modification. The residual silanol groups can cause undesirable silanol reactions deteriorating the quality of the operations. To avoid this, after modification the surface of these matrices is additionally treated with a low-molecular-weight hydrophobic modifier, e.g., trimethylchlorosilane. However, in this case, too, shielding of the residual silanol groups is incomplete.

Another drawback of silica gel matrices is their operating range of pH restricted to neutral and acidic solutions (pH 3–8).

To eliminate the above drawbacks and produce magnetic matrices most fully meeting the imposed requirements, it seems appropriate to apply two-layer coatings on the surface of powdered magnetic materials. As the first layer, silica having active silanol groups at its surface can be used, owing to which a great variety of chemical compounds with various functional groups can be fixed at the silica surface. The second layer can be formed by macromolecular compounds chemisorbed at the SiO_2 surface and shielding all the surface silanol gropus.

The possibility of applying silica coating on various supports is described in sufficient detail in [4–6], where the application conditions and characteristics of protecting silica coatings on the surface of nickel, iron, aluminum, and other oxides, and also various metals and alloys are presented.

Thus, the aim of this work is to study a possibillity of production of nonporous two-layer magnetic matrices based on cobalt ferrite for fixation of biologically active substances.

1070-4272/01/7403-0519$25.00

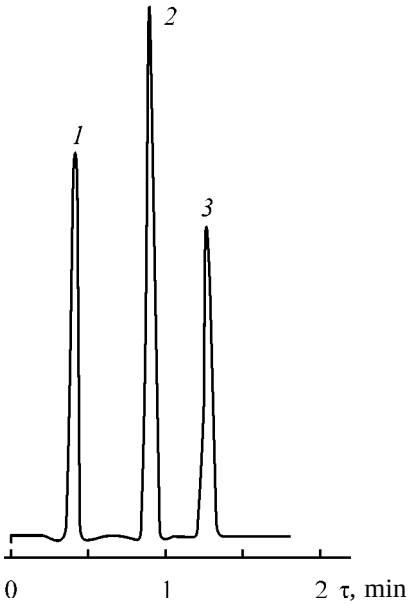

Fig. 1. Chromatogram of the test mixture uracil (*1*)–benzene (*2*)–toluene (*3*). Support: cobalt ferrite with silica coating and grafted C_8 phase, pressure 154 bar. (τ) Time; the same for Fig. 2.

EXPERIMENTAL

As the initial magnetic material we used finely dispersed powdered cobalt ferrite synthesized by the procedure described in [7]. All chemicals (cobalt and iron chlorides, and also sodium hydroxide) were of chemically pure grade.

The procedure of applying silica coating on the surface of cobalt ferrite particles was as follows. Powdered cobalt ferrite was suspended at continuous stirring in distilled water heated to boil. Then, dilute sodium silicate solution with a concentration of 2 wt % recalculated to SiO_2 and a silicate modulus (SiO_2/Na_2O molar ratio) no less then 3 was slowly added to the resulting suspension. The amount of sodium silicate solution ensured the weight ratio of cobalt ferrite to silicon dioxide of approximately 7–8. In addition of sodium silicate solution, the volume of the initial suspension was kept constant.

After addition of the required amount of sodium silicate solution, heating was stopped, and the suspension was cooled to room temperature, decanted, washed with distilled water on a filter, and filtered. The resulting powder was dried in a drying chamber at 150°C and subjected to heat treatment at 900°C in a muffle for 5 h.

To rehydroxylate the silica surface and to provide a possibility of its modification, the resulting powder was kept in boiling 20% nitric acid for 20 h. In so doing, dissolution of the magnetic support was not observed. This suggests that the surface of cobalt ferrite particles is completely coated with silica.

The second, polymeric, layer was applied on the silica surface according to the procedure described in [8, 9]. As a macromolecular compound, we used copolymer of methyl methacrylate with octadecyl methacrylate at a molar ratio of 1 : 1.

To assess the quality of coatings, the resulting magnetic matrices with single- and two-layer coatings were tested by the reversed-phase high-performance liquid chromatography (HPLC).

This procedure was selected owing to its higher efficiency and accuracy in comparison with the other well-known procedures. The surface of magnetic matrices with single-layer silica coating was modified with octylsilane (C_8).

In all chromatographic experiments, we used columns 4.6 mm in diameter and 50 mm long. A Beckman HPLC chromatograph equipped with double-beam UV detector operating at 254 nm was used. As an eluent, we used an acetonitrile–acetone mixture with the component ratio of 30 : 70; the flow rate of the eluent was 1 ml min^{-1}.

Figure 1 illustrate separation of a test mixture (uracil, benzene, and toluene) in a column packed with the magnetic matrix (particle size 1.5 μm) with a single-layer coating containing a grafted C_8 phase. The chromatogram shows that on the magnetic support it is possible to obtain a high-grade silica coating with active silanol groups, to which the C_8 phase can be covalently grafted. However, the use of these matrices as packing materials for reversed-phase chromatography is beyond the scope of this report. This chromatogram should be considered only as illustration of possibility of applying a high-quality thin-layer silica coating to magnetic support and blocking its surface.

Figure 2 illustrates separation of a test mixture (uracil, pyridine, phenol, and toluene) in a column filled with the magnetic matrix (particle size 1.5 μm) with a two-layer coating. The chromatogram shows that the retention time of pyridine (Fig. 2c, 0.475 min) is less than that of phenol (Fig. 2d, 0.512 min). This fact proves that "silanol" interaction of the surface of the resulting matrices with pyridine is not manifested, i.e., the surface of magnetic matrices with the two-layer coating contains no silanol groups [10].

Thus, this study showed that film magnetic matrices can be produced by applying a two-layer coating

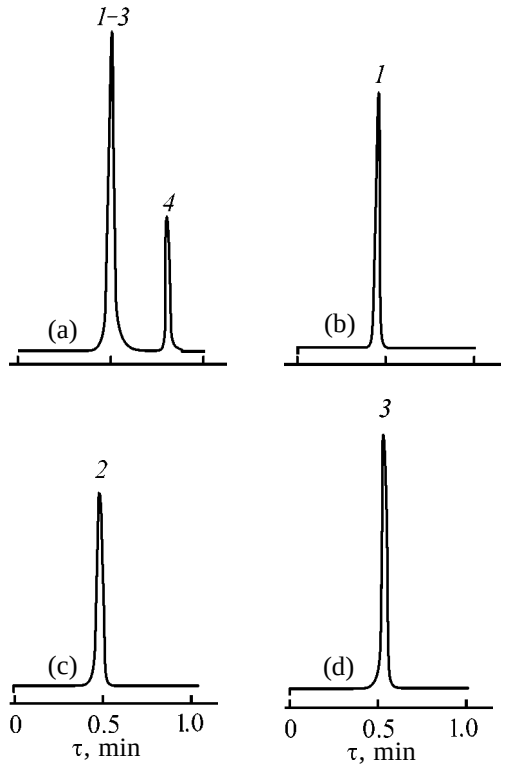

Fig. 2. Chromatogram of (a) the test mixture uracil (*1*)–pyridine (*2*)–phenol (*3*)–toluene(*4*) and (b–d) its components. Support: cobalt ferrite with silica and polymer coatings, pressure 130 bar.

to the surface of highly dispersed particles of magnetic materials. These film magnetic matrices completely conform to the requirements imposed on matrices used for fixation of biologically active substances [2]. The specific surface area of the resulting magnetic matrices is relatively low (1–3 $m^2 g^{-1}$) owing to their minimum porosity. Therefore, they are more suitable for bulky biomolecules, for which the problem of intraporous penetrability becomes of decisive importance.

CONCLUSIONS

(1) On a magnetic support (cobalt ferrite), it is possible to prepare a nonporous silica coating with active silanol groups to which aliphatic chains of various length can be covalently grafted.

(2) Application of the second layer, polymeric coating, provides inactivation of silanol groups at the matrix surface and also the presence of functional groups required for fixation of biologically active substances.

REFERENCES

1. Osterman, L.A., *Khromatografiya belkov i nukleinovykh kislot* (Chromatography of Proteins and Nucleic Acids), Moscow: Nauka, 1985.
2. Turkova, J., *Affinity Chromatography*, Amsterdam: Elsevier, 1978.
3. *Modifitsirovannye kremnezemy v sorbtsii, katalize i khromatografii* (Modified Silicas in Sorption, Catalysis, and Chromatography), Lisichkin, G.V., Ed., Moscow: Khimiya, 1986.
4. US Patent 4873353.
5. Iler, R.K., *The Chemistry of Silica*, New York: Wiley, 1979, part 2.
6. Sayor, M. and Sreenivas, K., *Science*, 1990, vol. 247, no. 4946, pp. 1056–1060.
7. Levin, B.E., Tret'yakov, Yu.R., and Letyuk, L.M., *Fiziko-khimicheskie svoistva i primenenie ferritov* (Physicochemical Characteristics and Application of Ferrites), Moscow: Metallurgiya, 1979.
8. Hanson, M., Unger, K., Mant, C., and Hodges, R., *J. Chromatogr*., 1992, no. 599, pp. 65–75.
9. Hanson, M. and Unger, K., *J. Chromatogr.*, 1990, no. 517, pp. 269–284.
10. *Catalog of the Keystone Sci. Co*., 2000, pp. 150–153.

Russian Journal of Applied Chemistry, Vol. 74, No. 3, 2001, pp. 522–523. Translated from Zhurnal Prikladnoi Khimii, Vol. 74, No. 3, 2001, pp. 510–511.

BRIEF COMMUNICATIONS

Synthesis of Dioxolanylmethyl Methacrylates from Aldehydes, Glycerol, and Methyl Methacrylate

A. S. Shevchuk, V. A. Podgornova, and O. P. Yablonskii

State Technical University, Yaroslavl, Russia

Received February 12, 2000; in final form, July 2000

Abstract—The feasibility of preparing dioxolanylmethyl methacrylates from aldehydes in two stages (without purification of intermediate 4-hydroxymethyl-1,3-dioxane) was examined.

Proceeding with studies on synthesis of dioxolanylmethyl methacrylates (DMMs), we examined the feasibility of their synthesis from aldehydes. Previously [1, 2] we found conditions for preparing DMMs from ketones and revealed specific features of preparation of 4-hydroxymethyl-2-alkyl-1,3-dioxolanes (HMDs), intermediates in DMM synthesis. We suggested that these compounds are formed as mixtures of isomers. The goal of this study is synthesis of DMMs both from separate HMD isomers and their mixture.

The two-stage procedure for preparing dioxolanylmethyl methacrylates from aldehydes can be represented by the scheme

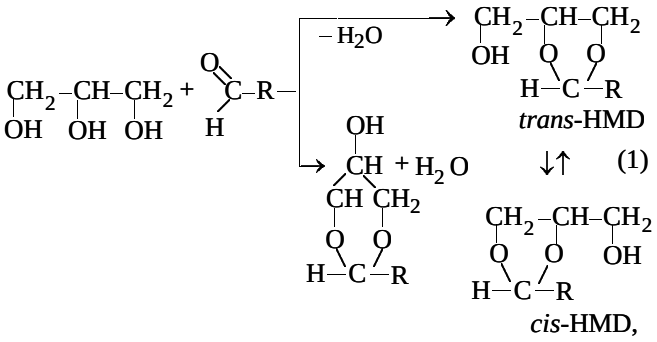

(1)

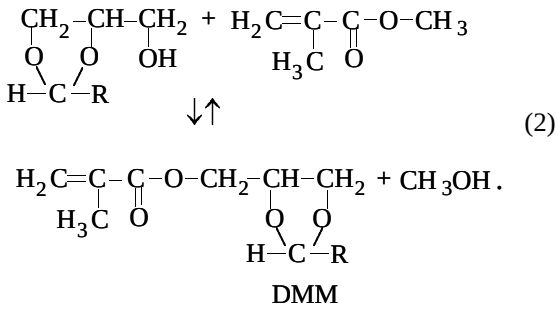

(2)

DMM

Studies were performed with acetaldehyde (in the form of paraldehyde) and propionaldehyde, following the previously described synthetic and analytical procedures [2]. First, we examined the possibility of formation of isomeric 1,3-dioxan-5-ol. For this purpose we performed an independent synthesis of HMD from 4-hydroxymethyl-2,2-dimethyl-1,3-dioxolane:

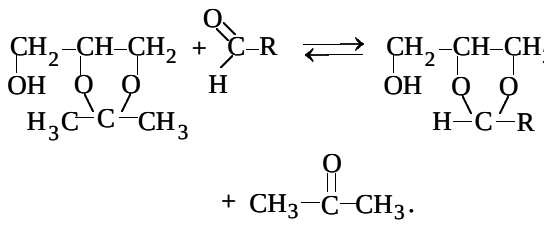

(3)

Formation of the six-membered ring in reaction (3) is impossible, and the occurrence of reaction (3) can be judged from the release of acetone. The reaction product in the chromatogram gave the same peaks with the same retention time as the HMD prepared from glycerol. This fact confirms the assumption about the isomeric composition of HMD. Furthermore, these results showed that reaction (3) can be used for preparing 1,3-dioxolane alcohols difficultly accessible by the direct route, since reaction (3) occurred under fairly mild conditions. We also prepared HMD from glycidol, i.e., by reaction also excluding formation of 1,3-dioxan-5-ol. The retention times of HMD isomers prepared by this reaction and from glycerol coincided. These facts convincingly prove that reaction of glycerol with aldehyde does not yield 1,3-dioxan-5-ol, and HMD is formed as a mixture of isomers.

To elucidate the full pattern of the two-stage synthesis, it was important to determine whether all the isomers undergo ester interchange. For this purpose, we performed thorough fractional distillation of HMD prepared from glycerol and propionaldehyde under

1070-4272/01/7403-0522$25.00

reduced pressure in a nitrogen atmosphere on a 60-cm column. Separation gave two low-boiling fractions (68–70°C at 5–7 mm Hg and 72–74°C at 5–6 mm Hg) and bottoms.

Chromatographic analysis of the fractions performed on two different stationary phases showed that the first fraction was a practically individual substance (92–95% purity). The second fraction was, apparently, a mixture of *cis* and *trans* isomers (approximately 66 and 28%) with an impurity of a third isomer. Published data on isomerism of heterocyclic compounds suggest the possibility of formation of *cis* and *trans* isomers; with different substituents, the number of isomers increases to four (two isomers for each of the *cis* and *trans* forms) [3, 4]. The first fraction, practically consisting of a single isomer, was analyzed by ^{1}H NMR spectroscopy (Tesla BS-567 spectrometer, 100 MHz). The spectrum was consistent with the structure of 1,3-dioxolane containing one hydroxy group. The signal at 3.4 – 4.2 ppm (relative to HMDS) corresponds to the 1,3-dioxolane ring [5]. Thus, the ^{1}H NMR and GLC data showed that a rather complex mixture of isomers was formed. Detailed study of its composition is beyond the scope of this work.

The second stage involving reaction of HMDs with methyl methacrylate (MMA) was performed under conditions of ester interchange with HMDs based on ketones [1]. The reaction vessel was equipped with a distillation column. HMD was taken as a single isomer and as an isomeric mixture. The results were as follows. After removal of unchanged reactants by distillation under reduced pressure in a nitrogen atmosphere, DMM was obtained as a mixture of two isomers, irrespective of whether the initial HMD was an individual isomer or an isomeric mixture. It should be noted that the ratio of the HMD isomers is determined by reaction conditions, mainly by the nature of the acid catalyst. Thus, to prepare dioxolanylmethyl methacrylates from glycerol, MMA, and aldehydes, there is no need to separate the isomers formed in the first stage. The yield of DMM based on glycerol is about 60%. The physicochemical characteristics of one of DMMs, 2-methyl-1,3-dioxolan-4-ylmethyl methacrylate, are as follows: colorless transparent liquid; bp 84–86°C at 5–6 mm Hg; d_4^{20} = 1.079 g cm^{-3}; n_D^{20} = 1.4540; molecular refraction: calculated 46.35, found 46.40.

CONCLUSIONS

(1) Dioxolanylmethyl methacrylates are formed from aldehydes, glycerol, and methyl methacrylate as mixtures of two isomers, irrespective of whether the intermediate 4-hydroxymethyl-1,3-dioxolane was taken as individual isomer or isomeric mixture.

(2) 1,3-Dioxan-5-ol is not formed in reaction of aldehydes with glycerol.

REFERENCES

1. RF Patent 2089545.
2. Shevchuk, A.S., Podgornova, V.A., and Piskaikina, E.G., *Zh. Prikl. Khim.*, 1999, vol. 72, no. 5, pp. 815–818.
3. Shabarov, Yu.S., *Organicheskaya khimiya* (Organic Chemistry), Moscow: Khimiya, 1996, part 2.
4. March, J., *Advanced Organic Chemistry. Reactions, Mechanisms, and Structure*, New York: Wiley–Interscience, 1987, vol. 1.
5. Chernyshova, A.T., Rol'nik, L.E., Zlotskii, S.S., and Rakhmankulov, D.L., *Zh. Org. Khim.*, 1994, vol. 30, no. 5, pp. 787–788.

Russian Journal of Applied Chemistry, Vol. 74, No. 3, 2001, pp. 524–526. Translated from Zhurnal Prikladnoi Khimii, Vol. 74, No. 3, 2001, pp. 512–513.

BRIEF COMMUNICATIONS

Feasibility of Depth Processing of Astrakhan Condensate

N. A. Strakhova, D. A. Rozental', L. P. Kortovenko, and G. I. Litvinova

Astrakhan State Technical University, Astrakhan, Russia
St. Petersburg State Technological Institute, St. Petersburg, Russia

Received July 10, 2000; in final form, December 2000

Abstract—The fractional composition of black oil from Astrakhan condensed gas was studied with the aim of its processing to produce commercial fuel.

The Astrakhan Gas Complex is the leading gas-processing plant in the lower Volga region. The rated annual production of separation gas is 12.0×10^9 m^3. Also, commercial petroleum products are produced: gas sulfur, gasoline, diesel fuel, and black oil. The Astrakhan Gas-Processing Plant (AGPP) sells black oil containing 2.8–3.2 wt % sulfur as M-100 boiler fuel. Because of high sulfur content, the demand for such fuel is limited, and it is sold at a low price, since the majority of heat and electric power plants in the region tend to use gas as environmentally cleaner fuel. The physicochemical characteristics of two samples of black oil taken in different times are listed in Table 1.

As seen from Table 1, black oil from the Astrakhan condensed gas deposit is characterized by a high congealing point (30–31°C) and a low coking capacity (1.05–1.11%); it contains three groups of compounds in comparable amounts: (1) paraffins and naphthenic compounds, (2) aromatic compounds, and (3) resins and asphaltenets. The content of solid paraffins is about 18%, and the sulfur content, 3%.

To examine the feasibility of depth processing of the black oil, we obtained and examined its close-cut fractions. Deep-vacuum distillation of the residual components of the condensate under laboratory conditions was performed with a Manovyan flask [1] allowing distillation at temperatures up to 560–580°C at a residual pressure of 40–70 Pa without noticeable decomposition. We also used a MINITOP automated installation, following the ASTM D 2892–90 testing procedure. The characteristics of close-cut (10°C) fractions of averaged black oil samples are listed in Table 2.

It is seen that the content of sulfur in fractions is approximately equal, being within 2.8–3.4 wt %. Solid paraffins are distributed nonuniformly. For example, in the 320–400°C fraction the content of C_{20}–C_{25} is 8.77 wt % relative to black oil; the content of C_{26}–C_{28} in the 400–430°C fraction, C_{29}–C_{31} in the 430–450°C fraction, and C_{32}–C_{36} in the 450–500°C fraction is 29.94, 17.94, and 37.20 wt %, respectively. Oil distillates (320–500°C fraction) amount to 13.5 wt % of stable condensate. They are characterized by a high viscosity index; however, the necessity of labor-consuming removal of sulfur and paraffins makes unfeasible production of base oils in the course of processing of condensed gas. The most

Table 1. Physicochemical characteristics of black oil from Astrakhan Gas-Processing Plant

Parameter	Sample no.	
	1	2
Nominal viscosity ^{0}NV at 80°C	10.0	10.7
Ash residue, %	0.10	0.09
Weight fraction, %:		
mechanical impurities	0.20	0.15
water	–	–
sulfur	2.7	3.0
water-soluble acids and alkalis	–	–
hydrogen sulfide	–	–
Coking capacity, %	1.05	1.11
Density at 20°C, kg m^{-3}	934.5	935.0
Flash point in closed crucible, °C	85.0	85.3
Open flash point, °C	117.0	115.0
Congealing point, °C	31.0	30.0
Heat of combustion (lower) for dry fuel, kJ kg^{-1}	41 680	41 590
Component content, wt %:		
paraffins and naphthenic compounds	37.8	38.5
aromatic compounds	32.0	31.8
resins	27.8	27.3
asphaltenes	2.4	2.4

1070-4272/01/7403-0524$25.00

Table 2. Characteristics of close-cut (10°C) fractions of black oil*

Fraction, °C	*m*, %	ρ, kg m^{-3}	η, mm^2 s^{-1}	C_p	C	C_S
				%		
320–360	10.97	920	8.9	8.670	0.027	3.0
360–380	3.39	921	9.0	8.709	0.028	3.3
380–390	4.73	925	11.61	9.832	0.039	3.4
390–400	5.61	929	12.75	8.118	0.053	3.1
400–410	3.95	929	15.52	28.626	0.078	3.4
410–420	5.72	935	18.42	28.787	0.092	3.0
420–430	4.62	935	27.02	32.509	0.092	2.8
430–440	6.70	936	50.85	17.652	0.164	3.2
440–450	1.72	938	39.36	19.098	0.190	2.9
450–460	2.40	942	49.81	40.212	0.284	2.8
460–470	3.21	944	50.80	34.657	0.295	3.2
470–480	5.75	944	66.70	37.547	0.336	3.2
480–490	6.08	945	83.0	37.086	0.560	3.0
490–500	2.20	947	83.1	37.110	0.561	3.1
>500	32.95	–	–	–	–	–

* (*m*) Fraction amount (by weight), (ρ) density at 20°C, (η) viscosity at 50°C, (C_p) paraffin content, (*C*) coking capacity, and (C_S) sulfur content.

appropriate way to utilize wide-cut vacuum gas oil and its close-cut fractions is production of high-viscosity and motor fuel for low- and medium-speed ship engines, since the requirements to the quality of such fuel are less stringent.

As components of ship fuel we used black oil of grade 100, wide-cut vacuum gas oil (320–500°C fraction), and its close-cut fractions (320–400, 400–450, and 450–500°C); for dilution and modification of the structure and properties of petroleum residues, we used straight-run and hydrorefined diesel fraction from AGPP. The compounds prepared ensured the optimal conditions of transportation and pumping of the fuel; the sulfur content did not exceed the level permitted by the standard [2].

The ship fuel compounds contained, along with diesel fuel, 60% vacuum gas oil (320–400°C), 60 or 50% wide-cut distillate (320–500°C), or 20% black oil and 40% 320–500°C fraction. The quality of these compounds met the requirements imposed on high-viscosity ship fuels [TU (Technical Specifications) 38.1 011 314–90] of the following grades: light high-viscosity SL, high-viscosity SVL, and also on DT and DM motor fuels [GOST (State Standard) 1667–68].

At present, AGPP has no facilities for vacuum distillation; therefore, we examined the possibility of preparing ship fuel by compounding black oil with diesel fuel in a vortical-bed apparatus (VBA) of V-105K-04 type. Compounds were prepared by the vigorous stirring and dispersion in combination with acoustic and electromagnetic treatments [3].

The compound containing 35% black oil and 65% diesel fuel, prepared in a VBA at 140°C and treatment time of 30 s, shows a high resistance to phase separation and a congealing point as low as –10°C, whereas the mechanical stirring as the only kind of treatmnent, performed for 30 min, gives a product with a congealing point of –5°C. Because of improved low-temperature properties of the fuel, the weight fraction of high-paraffin black oil could be increased to 45%. In this case, the congealing point of the fuel was –7°C. The total sulfur content in the fuel was 1.5%, which met the requirements of the standard.

The decreased congelaing point of the ship fuel is apparently due to favorable conditions for dispersion of black oil components in the bulk of the diesel fuel, provided in VBA, so that the sizes of crystallizing paraffins decrease and the structure of the compound becomes more uniform and cross-linked.

CONCLUSIONS

(1) From black oil of stable condensate from the Astrakhan Gas-Processing Plant, it is feasible to produce standard fuel for low-speed diesels by its compounding with diesel fuel, followed by treatment in a vortical-bed apparatus.

(2) Using vacuum distillation facilities, it is feasible to produce from this black oil, by direct compounding with diesel fuel, commercial fuel of the SL and SVL grades according to TU 38.1 011 314–90 and motor fuels of the DT and DM grades according to GOST 1667–68.

REFERENCES

1. Manovyan, A.K., Khachaturova, D.A., and Lozin, V.V., *Laboratornaya peregonka i rektifikatsiya neftyanykh smesei* (Laboratory and Industrial Distillation of Petroleum Mixtures), Moscow: Khimiya, 1984.
2. Badyshtova, K.M., Berdshtat, Ya.M., Bogdani, Sh.K., *et al.*, *Topliva, smazochnye materialy, tekhnicheskie zhidkosti: Assortimenty izgotovleniya; sposoby polucheniya* (Fuels, Lubricants, Technical Fluids: Production Assortments and Procedures), Shkol'nikov, V.M., Ed., Moscow: Khimiya, 1989.
3. Vershinin, N.P., *Voprosy teorii i praktiki ispol'zovaniya vrashchayushchegosya elektromagnitnogo polya* (Theoretical and Practical Problems of Applying Rotating Electromagnetic Field), Podolsk, 1997.

Russian Journal of Applied Chemistry, Vol. 74, No. 3, 2001, pp. 527–529. Translated from Zhurnal Prikladnoi Khimii, Vol. 74, No. 3, 2001, pp. 514–515.

BRIEF COMMUNICATIONS

Utilization of Gas Sulfur from Astrakhan Gas-Processing Plant as Additive to Bitumens

N. A. Strakhova, D. A. Rozental', B. I. Belinskii, L. P. Kortovenko, and O. Yu. Pavlyukovskaya

Astrakhan State Technical University, Astrakhan, Russia
St. Petersburg State Technological Institute, St. Petersburg, Russia

Received July 10, 2000; in final form, December 2000

Abstract—The feasibility was examined for improving the quality of commercial bitumen by its plasticization with high-paraffin black oil and sulfur from the Astrakhan Gas-Processing Plant, with treatment of the mixed components in a vortical-bed apparatus at 130–140°C for 25 s.

In the context of urgent problems of improving the quality of bitumens produced in Russia, finding new ways to involve sulfur in industrial processes, and developing new sulfur-containing products, we performed studies on modification of commercial bitumens with sulfur. It is known that the influence of sulfur on the structure of petroleum bitumens is the most pronounced when sulfur is present as a condensation structure and sulfur-containing asphaltenes are formed at relatively low mixing temperatures (140°C). Sulfur–bitumen binder was prepared by continuous stirring of the components with a mechanical stirrer for an optimal time [1, 2].

It is interesting to study the effect of electromagnetic field in combination with mechanical treatment on activation of compounding of the sulfur–bitumen binder in a V-150K-04 vortical-bed apparatus. No data are available on the combined effect of mechanical treatment and electromagnetic field, in particular, on preparation of sulfur-containing bitumens. Therefore, we examined the feasibility of obtaining, using a combined effect of electromagnetic field and mechanical activation, the optimal disperse structure of sulfur-containing bitumens by compounding viscous bitumens with residual components of stable condensate and sulfur from the Astrakhan Gas-Processing Plant (AGPP).

As components of sulfur–bitumen binders we used samples of viscous bitumen of the BND 60/90 grade from West-Siberian oils, technical-grade sulfur, and high-paraffin black oil from AGPP. Commercial BND 60/90 bitumen exhibits insufficient adhesion and practically no margin with respect to the softening point. The residual components of the stable condensate from AGPP were used as diluents for the viscous bitumen and plasticizers for the petroleum sulfur–bitumen binder. Sulfur acts as a bitumen modifier owing to interaction with active groups of asphaltenes [2]; it also acts as a filler enhancing the heat resistance of the compound.

Mechanochemcial activation of compound components was performed in a vortical-bed apparatus (VBA) with application of the rotating electromagnetic field at the melting point of sulfur. As grinding bodies were used iron needles. The sulfur–bitumen compound was prepared as follows. A VBA ampule was charged with BND 60/90 bitumen and black oil in various proportions. The mixture was kept for several minutes at 130–140°C. Then sulfur was added in the molten or finely divided form. Electromagnetic treatment of the mixture in VBA was performed at 130°C for 5–25 s depending on the amount of the added sulfur. At the mixing temperature, sulfur melts and, under vigorous stirring, is uniformly dispersed in the bulk of the binder.

Data on the influence of sulfur on commercial characteristics of sulfur-containing bitumens with various ratios of the dispersed phase to dispersion medium are listed in the table. It is seen that the compound prepared from BND 60/90 bitumen and black oil in a 4 : 1 ratio exhibits a relatively narrow plastic range, which is due to high concentration in high-boiling black oil fractions of paraffins and naphthenic hydrocarbons, including solid paraffins with a high melting point (52–70°C). Addition of sulfur (up to 5 wt %) increases the softening point and decreases

1070-4272/01/7403-0527$25.00 © 2001 MAIK "Nauka/Interperiodica"

Commercial characteristics of sulfur-containing bitumens

BND 60/90 bitumen : black oil weight ratio	Sulfur content, wt %	Penetration × 10, mm	Softening point, °C	Brittle point, °C
4 : 1	0	200	27.0	–12.0
	5	140	39.0	–18.5
	10	89	47.3	–25.0
	15	76	50.5	–14.0
	20	70	53.0	–12.5
3 : 1	0	260	21.0	–11.5
	5	200	25.5	–15.0
	10	180	31.0	–16.0
	15	160	35.5	–18.0
	20	120	38.0	–19.0
	25	96	40.5	–20.5
	30	72	47.0	–22.0
	35	68	49.0	–20.0
2 : 1	0	300	15.5	–13.0
	5	280	17.0	–14.0
	10	250	21.0	–14.5
	15	210	25.5	–16.0
	20	160	31.0	–18.0
	25	110	38.5	–20.0
	30	86	45.5	–25.0
	35	79	47.5	–20.5
1 : 1	0	380	–	–11.0
	10	280	25.0	–12.5
	20	220	29.0	–18.0
	30	160	33.0	–22.0
	40	110	41.5	–24.0
	50	89	47.5	–26.5
	60	78	49.5	–21.0

penetration, which is due to increase in the heat resistance and viscosity of the medium as a result of partial dissolution of sulfur in the dispersion medium and formation of an additional disperse phase of sulfur particles. Low brittle points are due to relative increase in the content of oil fractions of the compounds as a result of partial dissolution of sulfur. As the sulfur concentration is increased further (>10 wt %), the plastic range of bitumens increases. However, simultaneously the frost resistance gets worse, and with respect to the brittle point such sulfur–bitumen binders no longer meet the requirements of the standard. Such a behavior is apparently due to separation of sulfur from oil fractions.

As the amount of the dispersion medium is increased, it becomes feasible to introduce sulfur in high concentrations. For example, in compounds of bitumen with black oil at 3 : 1 and 2 : 1 ratios the optimal concentration of sulfur is 30 wt %, and at a 1 : 1 ratio, 50 wt %. As seen from the table, the low-temperature properties of the binders at various ratios of the components (bitumen, black oil, and sulfur) are improved, with the penetration (0.1 mm) being in the range 72–89 and the softening point, in the range 45.5–47.5°C. This is apparently due to treatment conditions in VBA, providing the favorable structure of the binder at optimal ratio of the components (oils, resins, and asphaltenes).

Microscopic studies of the compound structure show that sulfur is uniformly distributed in the bulk of the binder, with colloidal size of sulfur crystals. Thus, by adding 10–50 wt % gas sulfur, it is feasible to prepare high-quality sulfur–bitumen binders operating in a wide temperature range and meeting the main requirements of GOST (State Standard) 22 245–90 to BND 60/90 paving bitumens.

CONCLUSIONS

(1) Electromagnetic and mechanochemical treatment of compound components in a vortical-bed apparatus at 130–140°C for 25 s allows preparation of a sulfur–bitumen binder resistant to phase separation.

(2) Addition of finely dispersed gas sulfur and residual components of the condensate from the Astrakhan Gas-Processing Plant improves the frost-resistant properties and plasticity of commercial BND 60/90 paving bitumen.

(3) With increasing ratio of the dispersion medium to the dispersed phase in the compounds, the concentration of gas sulfur can be increased to 50 wt %.

REFERENCES

1. Gurarii, E.M., *Puti uluchsheniya svoistv asfal'tobetonnykh i drugikh bitumomineral'nykh smesei: Sbornik nauchnykh trudov SoyuzdorNII* (Ways To Improve the Properties of Asphalt Concrete and Other Bitumen–Mineral Mixtures: Coll. of Sci. Works of the All-Union Research Institute of Road Building), Balashikha, 1971, issue 44, pp. 137–146.
2. Plotnikova, I.A., Gurarii, E.M., Stepanyan, I.V., *et al.*, *Avtomob. Dorogi*, 1985, no. 6, pp. 13–14.
3. Veren'ko, V.A., *Izv. Vyssh. Uchebn. Zaved., Stroit. Arkhitekt.*, 1985, no. 14, pp. 62–66.

Russian Journal of Applied Chemistry, Vol. 74, No. 3, 2001, pp. 530–534. Translated from Zhurnal Prikladnoi Khimii, Vol. 74, No. 3, 2001, pp. 516–520.

HISTORY OF CHEMISTRY AND CHEMICAL TECHNOLOGY

Academician V. A. Kistyakovskii's Works in the Theory of Passive State and Corrosion of Metals (To 250th Anniversary of the Discovery of Metal Transition into Passive State)

The first scientific description of the transition of a metal into passive state was given by M.V. Lomonosov (1711–1765) in the paper *O deistvii khimicheskikh rastvoritelei* (On the Action of Chemical Solvents), published 250 years ago in 1750. Unfortunately, this work, and also other scientist's works in the field of physics and chemistry, written in Latin, had been little known to the scientific community till the early XX century. Lomonosov observed and described fast termination of the dissolution of iron in concentrated nitric acid, and attributed this to a change in the solvent properties [1]. Later, the behavior of iron in nitric acid solutions was studied by quite a number of other researchers [2, 3]. In 1836, a Swiss scientist C. Schonbein (1799–1868) was, probably, the first to name "passive" the state of iron appearing on its being immersed in a sufficiently concentrated (50%) solution of HNO_3. In Schonbein's opinion, "the anomalous behavior of iron has nothing to do with its affinity for oxygen, but, rather, is based on something else." In the same year, by Schonbein's initiative, M. Faraday (1791–1867) repeated and extended his experiments. Faraday came to a conclusion that the reason for passivation is the formation on the metal surface of a very thin invisible film. The argument between Faraday and Schonbein was considered in sufficient detail by A.M. Sukhotin in his monograph [3].

In the beginning of the XX century, a great contribution to investigations of the passivity and corrosion of metals was made by V.A. Kistyakovskii, an outstanding Russian scientist.

Vladimir Aleksandrovich Kistyakovskii was born on October 12, 1865, in Kiev, into a family of intellectuals, whose representatives gained wide acceptance. His father, A.F. Kistyakovskii (1833–1885), was a professor of criminal law at Kiev University, the author of scientific works on the history of law and justice in the Ukraine. Vladimir Aleksandrovich's younger brother, B.A. Kistyakovskii (1868–1920), who also went into law, was a doctor of law, public figure, and minister of the Ukrainian government in 1918. B.A. Kistyakovskii's son, Georgii (George) Kistyakovskii (1900–1982), a known chemist, professor of Harvard University, held a number of positions of responsibility in the United States, and was an advisor in science and technology to President Dwight Eisenhower (1890–1969) [4, 5].

Academician V.A. Kistyakovskii (photo taken in 1945–1946)

In 1883, V.A. Kistyakovskii finished Second Kiev Gymnasium and entered the physicomathematical faculty of Kiev University. In 1885, he went to the natural department of the physocomathematical faculty at St. Petersburg University, having a very highly skilled teaching staff at that time. Among the professors of the natural department were chemists D.I. Mendeleev (1834–1907) and N.A. Menshutkin (1842–1907), physiologist I.M. Sechenov (1829–1905), soil scientist V.V. Dokuchaev (1846–1903),

1070-4272/01/7403-0530$25.00

and biologists A.O. Kovalevskii (1840–1901) and A.N. Beketov (1825–1902). When being a senior student, V.A. Kistyakovskii worked under direct supervision of Professor M.D. L'vov (1848–1899), an organic chemist and A.M. Butlerov's (1828–1886) pupil. The first Vladimir Aleksandrovich's scientific work *Deistvie vodnykh rastvorov mysh'yakovoi kisloty na zhidkii izobutilen i amilen* (The Action of Aqueous Solutions of Arsenic Acid on Liquid Isobutylene and Amylene), published in 1899, was his only study in the field of organic chemistry. Already his diploma work was devoted to analysis of modern concepts in the field of chemistry of solutions: *Gipoteza Planka–Arreniusa* (Planck–Arrhenius Hypothesis) [6, 7]. This was one of the first works in Russia, which presented the standpoints of S. Arrhenius (1859–1927), J. van't Hoff (1852–1911), W. Ostwald (1853–1932), and M. Planck (1858–1947) concerning the nature of electrolyte solutions and dissociation processes. In the final part of the work V.A. Kistyakovskii discussed the possibility of bringing into accord various theories of solutions by introducing the concept of ion hydration. In 1889, he graduated from the university with a candidate degree awarded by the physicomathematical faculty.

In 1889–1890, V.A. Kistyakovskii continued, by his own initiative, his education at Prof. Ostwald's laboratory in Leipzig (Germany), the center of the nascent new disciplines, physical chemistry and electrochemistry [7–9]. W. Nernst (1864–1941) and Arrhenius worked together with Ostwald at that time. All the three scientists were later awarded, in different years, Nobel Prizes (in, respectively, 1903, 1909, and 1920). The work at Ostwald's laboratory was very important for the entire subsequent scientific activities of Vladimir Aleksandrovich. He became particularly closely associated with Arrhenius, having lived with him for more than a month in Paris in 1889, during the World Exhibition; their friendly relationship had been preserved for years. Arrhenius became a foreign corresponding member of the St. Petersburg Academy of Sciences in 1903, an honorary member of the Russian Physicochemical Society in 1909, and an honorary member of the Academy of Sciences of the USSR in 1926.

Having returned to Russia, V.A. Kistyakovskii became, together with I.A. Kablukov (1857–1942), a professor of Moscow University, a convinced supporter and propagandist of new concepts concerning the theory of solutions, not supported at that time by leading Russia's chemists. In 1890, Vladimir Aleksandrovich published an important work concerned with the theory of aqueous solutions of double salts [10], in which he considered complicated cases of electrolytic dissociation and introduced the concept of complex compounds into the Russian chemical literature. Results of more detailed physicochemical and electrochemical studies of double salt solutions were published by the scientist in 1901–1902.

In December 1901, V.A. Kistyakovskii presented a large report *Razbor vozrazhenii na teoriyu elektroliticheskoi dissotsiatsii* (Analysis of Objections to the Theory of Electrolytic Dissociation) at the XI Congress of Natural Scientists and Physicians in St. Petersburg. Vladimir Aleksandrovich demonstrated once more his adherence to modern concepts of the nature of electrolyte solutions and emphasized that "it will be possible in the future to reveal the close relationship between the chemical nature and electrolytic dissociation" [5, 11].

In 1891–1895, V.A. Kistyakovskii was compelled to teach in schools (gymnasiums), and only in 1896 he became privatdocent of St. Petersburg University and delivered courses of lectures on physical chemistry, electrochemistry, and photochemistry. Only in August 1902, for the first time after graduating from the university, V.A. Kistyakovskii was appointed regular lecturer at a higher school institution: He was invited to occupy the position of a senior laboratory assistant in the newly formed St. Petersburg Polytechnic Institute [12, 13]. In June 1903, having backed his master's dissertation at Moscow University, he was elected professor, and backed his doctoral dissertation in chemistry at the same place in 1910.

Vladimir Aleksandrovich created at the Polytechnic Institute the first Russia's laboratory of physical chemistry and theoretical chemistry, with excellent, by that time, equipment. He delivered lectures on physical chemistry and electrochemistry, himself did laboratory with students, and supervised diploma works. The central position among quite a number of research directions pursued by V.A. Kistyakovskii was held by investigations of the electrochemical behavior of metals in aqueous media. Being an excellent experimenter himself, Vladimir Aleksandrovich got a chance to perform various electrochemical investigations.

As far back as 1901, when determining the electrode potential of magnesium in a potassium cyanide solution, V.A. Kistyakovskii observed the passivity phenomenon in this metal for the first time. In more detail, he studied the electrochemical behavior of magnesium in various media in 1907 [14]. Originally, the passive behavior of magnesium was only attributed to the formation of an invisible oxide film.

Professor V.A. Kistyakovskii with a group of young lecturers of St. Petersburg Polytechnic Institute (from left to right): sitting: I.I. Zhukov, V.A. Kistyakovskii, and F.E. Dreier; standing: F.F. Rotarskii and L.A. Rotinyants (photo taken in 1909).

Later, Vladimir Aleksandrovich interpreted this process as formation of magnesium oxide hydrate. This initiated analysis of thin films from the colloid-electrochemical standpoint. Beginning in 1909, the scientist developed his own original film theory of metal passivity and corrosion as applied to magnesium, iron, chromium, and, in part, aluminum. The obtained experimental data were first summarized in V.A. Kistyakovskii's doctoral dissertation, which, in conformity with the regulations of that time, was published in full as a separate book [15].

The developed theory is based on the concept that the electrodes under study are covered with an oxide film both in active and in passive states. In the passive state, this film has amorphous glassy structure, and in the active, partly disintegrates through corrosion. V.A. Kistyakovskii particularly emphasized (1912) that the amorphous passivating film is also present on iron, nickel, and chromium surfaces showing metallic luster. The potentials of the passive electrodes are regarded as oxygen potentials.

In studying the electrode processes, Vladimir Aleksandrovich discovered and explained a number of phenomena named by motor chemical or motor electric effects. These phenomena are based on the influence exerted by fluid motion on the transition of a metal from the active into passive state. The concepts of metal and passivity put forward by V.A. Kistyakovskii were developed to a full extent only in the second half of the 1920s.

In 1912–1916 was published in several parts a comprehensive course of electrochemistry, actually the first textbook on this subject in Russia, written by the scientist. The course also included the basic concepts of the film theory of the passive state of metals. In the summer of 1918, in connection with his mother's illness, Vladimir Aleksandrovich went to Kiev, where his mother and brother lived. After Soviets came to power in February 1919 and the Ukrainian Academy of Sciences was organized in March of the same year, V.A. Kistyakovskii was elected its member. He became the chairman of the Chemical Committee intended to fulfil tasks assigned by the Red Army. However, in view of deteriorating health, he was forced to go away for medical treatment to the North Caucasus already in January 1920. All difficulties associated with his stay there were described in detail in the scientist's autobiography, which became open to public only recently (publication by Yu.I. Solov'ev [5]). Only in the autumn of 1922 V.A. Kistyakovskii could return to St. Petersburg and resume his pedagogical and research activities at the Polytechnic Institute, interrupted for four years and later continued till 1934, the time of his moving to Moscow.

Beginning in 1925, the concepts of the film theory of passivity took their final shape in V.A. Kistyakovskii's works, and the relationship of the theory with corrosion processes was underlined [16–19]. The scientist considered the film theory to be a variant of the electrochemical theory of metal corrosion. The reason for the occurrence of the passive state is the formation of an amorphous, glassy electrically conducting film of oxides, covering the metal with a continuous layer. The passivity effect can be observed both in aqueous solutions and in air. The formation of such a film, e.g., on iron placed in humid air, occurs in three stages. The first, obligatory stage is the formation of an amorphous film, in all probability having a structure of colloid type, under the action of oxygen. The second stage consists in the thickening of the film, becoming pseudoamorphous, composed of crystallites. In the third stage, certain crystallites of iron oxides are formed. The second and third stages may be more or less pronounced, depending on the corrosion conditions. According to the film theory, the surface of metals that can become passive (Mg, Fe, Cr, Ni, Co, Al, etc.) in humid air is covered with a film of the corresponding metal oxides. The film structure strongly affects the corrosion processes. Disintegration of the film, its "solidation" (the term introduced by V.A. Kistyakovskii, with broader sense than crystallization), leads to metal corrosion. The film theory of corrosion was at that time a major contribution to the theory of electrode potentials, serving as a basis for the development of the theory of metal corrosion [20].

The many-year's all-round scientific activities of V.A. Kistyakovskii were highly appreciated in our country and abroad. In 1925, he was elected a corresponding member, and in 1929, a full member of the Academy of Sciences of the USSR. He was also a member of the Paris Physicochemical Society and Electrochemical Society of New York.

In 1930, V.A. Kistyakovskii organized in Leningrad, at the Academy of Sciences of the USSR, the Colloid-Electrochemical Laboratory (LAKE) [21]. The laboratory had the minimum number of staff members (2 in 1930 and 7 in 1934) and several postgraduate students and occupied part of a building on Vasilyevsky Island (Volkhovskii lane, 1). The same building housed quite a number of other scientific institutions of the Academy of Sciences of the USSR. The laboratory was aimed to study colloid-electrochemical phenomena and, in particular, to investigate disperse systems, thin films, problems of metal corrosion at temperatures of up to 50°C, and electrocrystallization of metals. The closest associates of V.A. Kistyakovskii at LAKE were A.N. Strel'nikov (department of disperse chemistry), I.V. Krotov (metal corrosion), and K.M. Gorbunova (electrochemistry). There is no escape from mentioning that the presently widely accepted term "electrocrystallization" was introduced by Vladimir Aleksandrovich. Among V.A. Kistyakovskii's pupils at LAKE were also P.D. Dankov, A.T. Vagramyan, Ts.A. Adzhemyan, and others.

In 1934 (May 30–June 3) was held the 1st conference on metal corrosion at the Academy of Sciences of the USSR. V.A. Kistyakovskii was elected its chairman and presented a large report concerned with the problems of passive state and metal corrosion [22].

After the laboratory was transferred from Leningrad to Moscow, together with a number of other institutions of the Academy of Sciences, LAKE was much expanded by V.A. Kistyakovskii's initiative and transformed into the Colloid-Electrochemical Institute (KEIN), Academy of Sciences of the USSR, and the total number of staff members increased from 10–12 to 70 by 1936. Among those who worked at KEIN were A.N. Frumkin (1895–1976), P.A. Rebinder (1898–1972), N.A. Izgaryshev (1884–1956), B.V. Deryagin (1902–1994), and other known scientists. The scope of the institute covered a wide variety of problems [13]. Academician Frumkin became director of the Institute in 1939; in 1945, he initiated transformation of KEIN into the Institute of Physical Chemistry, Academy of Sciences of the USSR.

In 1937, V.A. Kistyakovskii formulated rather clearly the goals of the science he was developing, colloid electrochemistry [23, 24]. It is based on the hypothesis that the phase boundary is a transition layer composed of mutually penetrating, by diffusion, molecules, or adsorbed molecules, or a layer of chemical reaction products (oxide, oxide–adsorption, or other films). The description of these transition layers involves, in close association, concepts of colloid chemistry and electrochemistry. Faraday's idea, accounting for the passive state of iron and steel, was extended by V.A. Kistyakovskii to other metals subject to passivation, with much attention given to the nature of a film. The colloid electrochemistry includes the theory of electrocrystallization of metals as processes related to the corrosion of these metals. The film concept of the passive state, and the adsorption concept which appeared later, do not contradict, but only supplement each other [25].

In 1945, Vladimir Aleksandrovich's 80th birthday anniversary was celebrated. Reports concerned with the life and activities of the scientist, his contribution to the development of electrochemistry and the theory

of metal passivity were delivered by Frumkin [26], Izgaryshev [27], and Dankov [28]. V.A. Kistyakovskii's achievements in studying the passive state of metals were also noted in a monograph by Frumkin and co-authors [29].

In a very brief review we in the first place dwelled upon V.A. Kistyakovskii's electrochemical investigations, leaving aside his works in the field of thermodynamics of fluids, chemical kinetics, photochemistry, and general problems of physical chemistry. We did not consider the intensive scientific-organizational activities of the scientist in the field of corrosion protection of metals.

V.A. Kistyakovskii died in Moscow on October 19, 1952, at the age of 86. He devoted more than sixty years of his life to research and teaching. These 60 years made an epoch in the development of physical chemistry, electrochemistry, and theory of corrosion and corrosion protection of metals. Academician V.A. Kistyakovskii made a major contribution to the coming-to-be and advances of these scientific disciplines in Russia.

REFERENCES

1. Lomonosov, M.V., *Polnoe sobranie sochinenii. Trudy po fizike i khimii* (Complete Coll. of Works: Physics and Chemistry), Moscow: Akad. Nauk SSSR, 1950, vol. 1.
2. *Gmelin's Handbuch der anorganischen Chemie*, 1930, 8th ed., vol. 59A, issue 3, pp. 313–358.
3. Sukhotin, A.M., *Fizicheskaya khimiya passiviruyushchikh plenok na zheleze* (Physical Chemistry of Passivating Films on Iron), Leningrad: Khimiya, 1989.
4. *World Who's Who in Science*, Marquis–Who's Who, 1968, 1st ed., p. 940.
5. Solov'ev, Yu.I., *Vestn. Ross. Akad. Nauk*, 1995, vol. 65, no. 12, pp. 1130–1134.
6. Solov'ev, Yu.I., *Zh. Fiz. Khim.*, 1956, vol. 30, no. 8, pp. 1910–1915.
7. Solov'ev, Yu.I., *Istoriya ucheniya o rastvorakh* (History of the Theory of Solutions), Moscow: Akad. Nauk SSSR, 1959.
8. Figurovskii, N.A. and Roman'kov, Yu.I., *Vladimir Aleksandrovich Kistyakovskii*, Moscow: Nauka, 1967.
9. Solov'ev, Yu.I. and Makarenya, A.A., *Vopr. Estestvozn. Tekh.*, 1962, issue 13, pp. 94–101.
10. Kistyakovskii, V.A., *Zh. Russk. Fiz.-Khim. O–va., Chast' Khim.*, 1890, vol. 22, no. 6, pp. 411–430.
11. Kistyakovskii, V.A., *Zh. Russk. Fiz.-Khim. O–va., Chast' Khim.*, 1902, vol. 34, no. 1, pp. 19–32.
12. Morachevskii, A.G., *Zh. Prikl. Khim.*, 1999, vol. 72, no. 9, pp. 1574–1579.
13. Polukarov, Yu.M., *Zh. Fiz. Khim.*, 1999, vol. 73, no. 10, pp. 1720–1722.
14. Kistyakovskii, V.A., *Zh. Russk. Fiz.-Khim. O–va., Chast' Khim.*, 1907, vol. 39, no. 8, pp. 1445–1446, 1453–1455.
15. Kistyakovskii, V.A., *Elektrokhimicheskie reaktsii i elektrodnye potentsialy nekotorykh metallov* (Electrochemical Reactions and Electrode Potentials of Some Metals), St. Petersburg: Schroeder, 1910.
16. Kistyakovskii, V.A., in *Elektricheskie i elektrokhimicheskie svoistva metallov. Soobshcheniya o nauchno-tekhnicheskikh rabotakh v Respublike* (Electrical and Electrochemical Properties of Metals: Reports on Research and Development Works in the Republic), Leningrad: Nauchnoe Khimiko-Tekhnicheskoe, 1928, issue 24, pp. 193–215.
17. Kistyakovskii, V.A. and Krotov, I.V., *Izv. Akad. Nauk SSSR, VII Ser., Otd. Fiz.-Mat. Nauk*, 1930, no. 8, pp. 715–726.
18. Kistyakovskii, V.A., in *Trudy Noyabr'skoi yubileinoi sessii Akademii Nauk SSSR 12–19 noyabrya 1932 g.* (Proc. November Jubilee Session of USSR Acad. Sci., November 12–19, 1932), Leningrad: Akad. Nauk SSSR, 1933, pp. 253–265.
19. Kistyakovskii, V.A., *Usp. Khim.*, 1933, vol. 2, no. 2, pp. 237–247.
20. Dankov, P.D., *Zh. Fiz. Khim.*, 1945, vol. 19, no. 10–11, pp. 485–496.
21. Kistyakovskii, V.A., *Vestn. Akad. Nauk SSSR*, 1935, no. 2, pp. 7–14.
22. Kistyakovskii, V.A., *Trudy Pervoi konferentsii po korrozii metallov* (Proc. I Conf. on Metal Corrosion), Moscow: Akad. Nauk SSSR, 1935, pp. 9–17.
23. Kistyakovskii, V.A., *Izv. Akad. Nauk SSSR, Ser. Khim.*, 1937, no. 5, pp. 1049–1063.
24. Kistyakovskii, V.A., in *Matematika i estestvoznanie v SSSR* (Mathematics and Natural Science in the USSR), Moscow, 1938, pp. 416–430.
25. Tomashov, N.D. and Chernova, G.P., *Passivnost' i zashchita metallov ot korrozii* (Passivity and Corrosion Protection of Metals), Moscow: Nauka, 1965.
26. Frumkin, A.N., *Izv. Akad. Nauk SSSR, Otd. Khim. Nauk*, 1946, no. 2, pp. 121–125.
27. Izgaryshev, N.A., *Izv. Akad. Nauk SSSR, Otd. Khim. Nauk*, 1946, no. 2, pp. 127–135.
28. Dankov, P.D., *Izv. Akad. Nauk SSSR, Otd. Khim. Nauk*, 1946, no. 2, pp. 137–142.
29. Frumkin, A.N., Bagotskii, V.S., Iofa, Z.A., and Kabanov, B.N., *Kinetika elektrodnykh protsessov* (Kinetics of Electrode Processes), Moscow: Mosk. Gos. Univ., 1952.

A. G. Morachevskii and V. S. Shpak

Russian Journal of Applied Chemistry, Vol. 74, No. 3, 2001, pp. 535–536. Translated from Zhurnal Prikladnoi Khimii, Vol. 74, No. 3, 2001, pp. 521–522.

========== INFORMATION ==========

IV International Conference "Polymeric Materials of Decreased Combustibility"

The IV International Conference "Polymeric Materials of Decreased Combustibility" took place on November 17–18, 2000 in Volgograd on the base of the Volgograd State Technical University (VGTU). The conference was supported by the Russian Foundation for Basic Research (RFFI). The co-chairmen of the conference were Corresponding Member, Russian Academy of Sciences, Director of the Institute of Chemical Physics, Russian Academy of Sciences (IKhF) A.A. Berlin and Dr. Sci. (Chem.), Head of VGTU, Prof. I.A. Novakov. The members of the Organizing Committee were well-known Russian scientists in the field of polymer combustion: R.A. Andrianov (Moscow State Building University, MGSU), A.N. Baritov (MGSU), G.E. Zaikov (Institute of Biochemical Physics, Russian Academy of Sciences, IBKhF, Moscow), A.D. Kuntsevich (IKhF), A.M. Lipatov (Udmurt State University, Izhevsk), A.M. Merzhanov (Institute of Macrokinetics, Russian Academy of Sciences, Chernogolovka, Moscow oblast), A.I. Rakhimov (VGTU), and Tsyganov (RFFI).

About 400 scientists from 30 research centers of Russia, Uzbekistan, South Korea, Ukraine, the United States, and Belarus took part in the conference. The program included 17 plenary lectures and 50 poster presentations. The conference was opened by Berlin and Novakov who emphasized the urgency and the scientific and practical importance of the conference subject field.

The scientific program of the conference was opened by the N.A. Khalturinskii's (IKhF) report *Physical Aspects of Polymer Combustion and the Mechanism of Inhibitor Action*. Problems of using nanocomposites as fireproofing compounds for polymers and composite materials were discussed in the report made by Zaikov. O.I. Tuzhikov (VGTU) reported on recent achievements of VGTU in the field of using phosphorus-containing compounds as fireproofing compounds for polymers and polymeric compositions (phosphorus-containing polymers and low-molecular-weight additives to polymers). An active interest was taken in results of development of difficultly combustible foamed plastics for building (Andrianov). The L.G. Panova's (Saratov State Technical University) report was devoted to physicochemical principles of fabrication of blended textiles of decreased combustibility and of hybrid composite materials based on them. P.M. Vasil'ev (Splain Research and Production Center, Volgograd) reported on the use of the Mikrokosm integrated computer system for predicting the properties of fireproofing compounds for polymeric compositions. R.M. Aseeva (IBKhF) made two reports one of which was devoted to carbooligoarylenes for composite materials of decreased combustibility and the other, to new environmentally safe fireproofing coatings based on oxidized polysaccharides. G.D. Bakhtina (VGTU) reported on the use of phosphorus-containing methacrylates for preparing polymeric materials of decreased combustibility. Kim Von Duk (Samchok National University, Samchok, South Korea) reported on synthesis of new organosilicones of decreased combustibility for industry. Advances in the field of modified intumescent epoxy compounds were discussed by S.G. Shukman (Research and Educational Center of Chemical Physics, Udmurt Scientific Center, Ural Division, Russian Academy of Sciences, Izhevsk). Yu.M. Evtushenko (Elektroizolit Joint-Stock Company, Moscow) reported on modification of epoxy resins with methylphosphonoamidic acid. The problem of preventing migration of fireproofing compounds in polymers was discussed by A.Ya. Korol'chenko (MGSU). The last three plenary lectures concerned development of processes for production of new fireproofing compounds (F.M. Mudryi, Khimprom Joint-Stock Company, Volgograd), certification of polymeric materials for aircraft interior with respect to fire safety (Barbot'ko, Russian Institute of Aviation Materials, Moscow), and modification of elastic polyurethanes with phosphorus- and boron-containing compounds (S.N. Bondarenko, Volzhskii Polytechnic Institute, Volzhskii, Volgograd oblast).

Among poster presentations, studies on the following subjects should be mentioned above all: features of flame distribution over the surface of thin polymer films containing microencapsulated fireproofing compounds; structure of the surface of epoxy polymers containing microencapsulated fireproofing compounds under thermal impact, physical aspects of combustion, and ways to optimize the composition of fireproofing

1070-4272/01/7403-0535$25.00 © 2001 MAIK "Nauka/Interperiodica"

mixtures with a synergistic effect; coking, structure and properties of the carbonized layer formed in the course of thermal oxidative degradation and combustion of highly reinforced composite materials. Also presented were poster reports concerning the mechanism of coking in the presence of various additives, theory of combustion of polymeric materials, synthesis of new high-performance inhibitors of polymer combustion, mechanism of the action of combustion inhibitors, development of new polymeric materials and compositions of decreased combustibility, toxicity, and fuming in the course of combustion, equipment and procedures for evaluating the fire resistance of polymeric materials.

The conference demonstrated undoubted theoretical and practical interest in the problems of combustibility of polymeric materials. Combustibility of polymers is a cause of many fires, and polymer combustion is accompanied by release of large amounts of toxic substances.

The next International Conference "Polymeric Materials of Decreased Combustibility" will be held in 2002.

The conference proceedings are available from the library of the Institute of Chemical Physics, Russian Academy of Sciences.

G. E. Zaikov

Russian Journal of Applied Chemistry, Vol. 74, No. 3, 2001, pp. 537–538. Translated from Zhurnal Prikladnoi Khimii, Vol. 74, No. 3, 2001, pp. 522–523.

INFORMATION

Addcon World 2000: Plastics Additives and Modifiers Conference

The 6th International Plastics Additives and Modifiers Conference took place on October 25–26 in Basel, Switzerland. It was organized by Rapra Technology and financially supported by Ciba Specialty Chemicals, Clariant Huningue, DSM, Lonzagroup, and Uniqema. The conference continued a series of annual meetings held previously in Switzerland, Belgium, Singapore, the United Kingdom, and Czechia.

Every year Addcon brings to participants' notice from 20 to 30 reports made by the leading companies and worldwide known scientists on recent achievements in the field of development and practical use of additives to polymers. Recently, cardinal changes occurred in this field. Thanks to efforts of environmental protection movement, the use of polyvinyl chloride (PVC) was significantly restricted, which had an effect on the use of the corresponding additives. It should be noted, however, that rigid vinyl polymers are still widely used in the building industry.

First and foremost, active attempts are made in Europe to replace halogen-containing fire retardants with environmentally clean fireproofing agents. Novel stabilizers are being developed; nanocomposites gradually gain the market.

Naturally, the producers of additives make efforts to improve their products, facilitate their use, and decrease the production cost. The goal of this (and previous) conference was to aid in improving the quality and performance of additives.

The conference program included 26 reports made by scientists from the United States, Europe, Asia, and Australia. The opening speech was made by Vice President of the Great Lakes Chemicals corporation (the United States) J. Teat who emphasized the urgency and prospects of the conference.

R. Adams, a representative of BP Amoco Chemicals (the United States) reported on parameters of some plasticizers for flexible vinyl compounds and actually initiated a discussion on the use of stabilizers in various materials. Representatives of the British and American Divisions of Velsicol Chemical (T. Bohnert *et al.*) reported on development of an aromatic plasticizer reducing the viscosity of plastisol. The use of a model oxidation reaction for quantitative evaluation of the performance of a stabilizer based on a phenolic antioxidant in polypropylene was reported in a joint presentation by E. Zeinalov (Institute of Problems of Chemical Physics, Academy of Sciences of Azerbaijan) and H. Schroeder (BAM Company, Germany). Unfortunately, this was the only report made by CIS scientists. The Belgian division of Great Lakes Chemicals (C. Callierotti *et al.*) reported on achievements in the use of physical methods for improving the performance of additives. J. Malik and I. Bachert (Clariant Huningue SA, France) proved that the package of stabilizers developed by them is useful for development of new criteria for testing materials.

Consideration of environmental aspects of using additives was initiated by the survey report made by T. Galvanek (BRG, the United States). Successful cooperation of basic and applied science was demonstrated by representatives of the University of Sussex (the United Kingdom) and divisions of EPI in the United Kingdom, Canada, the United States, and Malaysia, who reported on environmentally clean degradable plastics based on polyethylene. J. van Haveren (Agrotechnological Research Institute, the Netherlands) discussed the possibilities and trends in using additives based on renewable materials.

A. Litzenberger (DSBG BV, Germany) discussed the criteria of optimal choice of flame retardants for plastics. R. Herbiet (Alusuisse Martinswerk GmbH, Germany) described in detail new metal hydroxides which proved to be highly efficient as fireproofing compounds. D. Eisermann (Ciba Specialty Chemicals, Switzerland) reported on increase in productivity of polypropylene film production through stabilization with lactone technology. The first day of the conference was completed with a report made by R. Beswick (BMS AG, Switzerland) on the role of market research in development of the additives business.

The second day of the conference was opened with a report of I. Wheeler (Silberline) on the properties of metal pigments. Then D. Deutsch and J. Catino (Specialty Minerals, the United States) presented a method for quick electron-microscopic analysis of service properties of hybrid antiblocks. R. Rangaprasad and Y. Vasudeo (Reliance Industries, India) reported on

1070-4272/01/7403-0537$25.00

studies of the efficiency of using special additives in production of linear polyethylene.

S. Al-Malaika (Aston University, the United Kingdom) reported on an effective bioantioxidant for polymer stabilization and brilliantly demonstrated the significance of basic research for development of new products. The results of cooperation of scientists from different countries were presented in reports made by staffmembers of the University of Sussex (the United Kingdom) and Victoria University of Technology (Australia) (N. Billingham *et al.*, *Evaluation of the Stabilizer Performance in Polymers*) and of the Institute of Macromolecular Chemistry (Czechia) and Institute of Organic Chemistry (Germany) (J. Pospišil *et al.*, *Optimization of Activity, Performance, and Durability of UV Absorbers*).

However, the majority of reports, as follows from the conference goals, were devoted to commercial systems and products. J.-M. van Maren (Bennet Europe, the Netherlands) reported on composites prepared from polymer solutions. Compatible block copolymers of PVC with polyolefins developed by BF Goodrich Performance Materials were described by N. Pourahmady *et al.* J. Williams and K. Geick (Lonzagroup, the Netherlands) described the effect of the plasticizer on the properties of low-density polyethylene films. Additives used in polymer processing were considered by D. De Corte (Dyneon, Belgium).

The most recent advances were discussed by J. McGowan (General Electric Specialty Chemicals Europe, the Netherlands) in the report *A New Class of Polyolefin Process Stabilizer*; N. Ergenc (Ciba Specialty Chemicals, Switzerland) in the report *New Effect Additives*; I. Vulic (Cytec Industries, the Netherlands) in the report *UV Stabilisation of Pigmented Systems*; J. Ehretsmann (Aptechnologies, Switzerland; Propension, France) in the report *Novel Additives for Improvement of Polymer Properties.*

In the concluding speech, the conference chairman D. Pritchard (the United Kingdom) emphasized that the conference was successful and announced that the next conference will take place in 2001 in Berlin.

G. E. Zaikov and A. Ya. Polishchuk

Russian Journal of Applied Chemistry, Vol. 74, No. 3, 2001, p. 539. Translated from Zhurnal Prikladnoi Khimii, Vol. 74, No. 3, 2001, p. 524.

BOOK REVIEWS

Nikolaev, V.M., Karelin, E.A., Kuznetsov, R.A., and Toporov, Yu.G., *Tekhnologiya transplutonievykh elementov* (Technology of Transplutonium Elements)

Dimitrovgrad: Nauchno-Issled. Inst. Atomnykh Reaktorov, Gos. Nauchn. Tsentr RF, 2000

Discovery of the phenomenon of radioactivity in the very end of the XIX century has produced a very striking effect on the progress of science in the XXth century, becoming one of the most important factors determining the major research lines in physics, chemistry, and chemical technology all over the world. Among the most distinguished achievements of the XXth century is discovery, characterization, and development of production processes of near transuranium elements, neptunium and plutonium. Of a great interest are also the transplutonium elements (TPEs) (americium, curium, berkelium, californium, and einsteinium). It is worth noting that the technology of TPEs is closely related to the problem of nuclear waste management.

The monograph written by a group of expert researchers from the Research Institute of Nuclear Reactors, Russian State Scientific Center, summarizes and critically evaluates the methods for preparation, separation, and use of TPEs (including the methods used in spent fuel reprocessing). Also a wide spectrum of technological, economic, and environmental problems is discussed. The book includes an introduction and six chapters. Each of them is supplemented with vast bibliography (677 references on the total).

In the introduction (pp. 3–6) the authors justify the urgency of the problems discussed in the book, noting the point that no monograph dealing with the technological aspects of production, separation, purification, and practical applications of TPEs was published in Russia till now.

The first chapter (pp. 7–24) is devoted to the physical principles of production of TPEs. By the essence successive neutron capture in nuclear reactors is the only method for production of practically significant amounts of TPEs. The authors examine physical principles of formation of TPEs by irradiation and the methodology of estimating the yield of the resulting nuclides as well as accumulation of actinides in the irradiated fuel of power reactors.

In the second, central chapter (pp. 25–152) are examined the existing methods for TPE separation and purification to remove fission products and nonradioactive elements. It is indicated that in the chemical technology of TPEs a preference is given to the extraction and chromatographic methods as the most suitable for organization of remote-controlled processes providing high partition coefficients. For concentration and isolation of TPEs the precipitation methods are mostly used. In this chapter extraction of TPEs with neutral extractants, amines, and organophosphorus acids is reviewed.

The third chapter (pp. 153–195) represents data on partitioning of TPEs. The complexity of this problem is caused by the similarity in the properties of TPEs in their typical oxidation state (III) and difficulties in preparation of TPEs in oxidation states other than III because of their low stability.

In the fourth chapter (pp. 196–226) a comparative analysis is made of the existing methods of separation of TPEs from irradiated targets.

The fifth chapter (pp. 226–257) is devoted to the urgent problem of separation of TPEs from spent nuclear fuel. The authors indicate that at present only a few countries (France, the Great Britain, Russia, and Japan) regenerate uranium and separate plutonium from spent fuel. At the same time the United States, Germany, Sweden, Spain, and other countries prefer long cooling of spent fuel followed by its disposal in geological formations. In the chapter are discussed the processes for recovery of actinides from high-level radioactive waste, including wet and molten salt processes.

The concluding sixth chapter (pp. 258–355) summarizes data on ionizing radiation sources based on TPEs. Production of such sources is presently the major practical application area of TPEs.

The book is of indisputable interest for a wide spectrum of specialists working in the field of radiochemistry. The style of rendering makes the monograph intelligible enough to be used as a handbook for teaching staff and students specialized in chemistry and chemical technology

A. G. Morachevskii

1070-4272/01/7403-0539$25.00 © 2001 MAIK "Nauka/Interperiodica"

Russian Journal of Applied Chemistry, Vol. 74, No. 3, 2001, pp. 540–541. Translated from Zhurnal Prikladnoi Khimii, Vol. 74, No. 3, 2001, p. 525.

BOOK REVIEWS

Geiss, F., *Osnovy tonkosloinoi khromatografii (planarnaya khromatografiya)*

Moscow, 1999, Russian translation of *Fundamentals of Thin-Layer Chromatography*, Mamaroneck, NY: Huethig, 1987

Thanks to an open sorbent layer, thin-layer chromatography (TLC) is more simple and versatile technique as compared to other chromatographic methods. At the same time the fact that in TLC a sorbent is in contact with the gas phase makes it more difficult to describe the partition processes. Because of their complexity the molecular interactions between a sorbent, sorbate, and solvent in TLC systems are poorly understood, which does not allow formulation of criteria for *a priori* decision on optimal solvents and sorbents for solving a given task. Therefore, knowledge of TLC fundamentals as well as of the principles common for all the chromatographic techniques is the necessary condition for successful application of TLC.

The translation of the worldwide known monograph by Geiss became the first book in Russian devoted to the principles of TLC, including new techniques, sorbents, solvents, and methods for optimization of TLC procedure.

Russian translation of the monograph was initiated by V.G. Berezkin. The book was submitted for publishing in 1989. However, only in 1998 V.G. Berezkin and L.N. Kolomiets succeeded (after changing the publishing house) in organization of printing the monograph. Conscientious and competent translation of the book was made by B.P. Lapin and M.A. Koshevnik.

The first chapter of the monograph represents the guidance to the monograph and comparative examination of advantages and drawbacks of TLC and liquid column chromatography.

The second chapter gives the background of TLC, emphasizing the solvent flow in a porous medium under the action of capillary forces. The factors responsible for erosion of chromatographic bands are analyzed. With reference to the works by Giddings and Guiochon the author examines various methods for estimating the layer efficiency (mean theoretical plate height, separation number).

The third chapter is important from the practical standpoint. It is devoted to representation and analysis of the TLC data. Attempts are made to assess the applicability of various methods for correcting R_f. A particular attention is paid to the resolving power equation. To compare the applicability of different multicomponent eluents to separation of the same test mixture, the author recommends to use the discriminating power equation. Also a comparative analysis is given of the potentialities of various elution modes.

With the advent of chemically grafted phases, particularly reversed phases, the requirements to the layer activity control became less strict. However, the traditional sorbents such as silica gel and alumina remain the most widely popular because of their low cost. Therefore, the separation quality may depend on the sorbent activity. In this connection the fourth chapter, reviewing the properties of TLC sorbents and the methods for activity control of hydrophilic sorbents, is interesting and important for understanding the processes occurring in TLC separations.

The fifth chapter deals with the problems of optimization of R_f and the selectivity, i.e., the parameters characterizing solvents and eluents. The methods for characterization of the eluting power are examined.

The system solvent–gaseous phase–sorbent is examined in the sixth chapter, including such topics as saturation of a TLC box, presaturation of a sorbent layer and its consequences, and changing composition of the moving phase. The effects of the temperature, pH, sorbent layer thickness, quality of a solvent, etc. are discussed in the seventh and eighths chapters.

The theoretical and practical aspects of gradient TLC are examined in the ninth chapter.

In the tenth chapter the points considered in the fourth chapter are analyzed as applied to the problem of how the results obtained in TLC separations can be used for optimization of liquid column chromatography separations. The author formulates the criteria of successful application of TLC data to liquid column chromatography separations and analyses the commonly spread sources of failure on this way.

1070-4272/01/7403-0540$25.00

The eleventh chapter entitled *Quantitative Processing of TLC Data* is written by S. Ebel. The chapter outlines briefly the basic principles and methods of quantization of TLC data.

In the twelfth chapter an algorithm is given for optimization of separation conditions, and also recommendations how to eliminate the typical errors.

Finally, in the Appendix are given the basic equations used in TLC, brief glossary of terms, and tables for recalculation of the retention factors.

The book is of indisputable interest for a broad spectrum of specialists working in the field of chromatography, including organic and medical chemists, biologists, criminalists, and also analysts dealing with analysis of drug preparations, environmental objects, and foods.

L. S. Litvinova

Russian Journal of Applied Chemistry, Vol. 74, No. 4, 2001, pp. 543–554. Translated from Zhurnal Prikladnoi Khimii, Vol. 74, No. 4, 2001, pp. 529–540.

REVIEWS

Alkaline Hydrolysis of Polyacrylamide

V. F. Kurenkov, H.-G. Hartan, and F. I. Lobanov

Kazan State Technological University, Kazan, Tatarstan, Russia
Stockhausen GmbH & Co. KG, Krefeld, Germany
Moscow Office, Stockhausen GmbH & Co. KG, Moscow, Russia

Received September 12, 2000; in final form, December 2000

Abstract—Specific features of the hydrolysis of polyacrylamide and its derivatives under various conditions are characterized. The most efficient procedures for performing hydrolysis in dilute and concentrated aqueous solutions and suspensions, as well as during acrylamide polymerization in aqueous solutions and emulsions, are discussed.

Polymer-analogous transformations involving a low-molecular-weight reagent are successfully employed for modification of natural and synthetic polymers with the aim to prepare products with improved set of performance characteristics [1, 2]. A good example of this is the hydrolysis of polyacrylamide (PAA) and its derivatives, yielding partially hydrolyzed polymers with greater application potential, compared with the initial polymers. Such hydrolyzed polymers differing in the molecular weight M and MWD pattern, chemical composition, and distribution of the hydrolyzed units along the chain (linear, branched, and cross-linked) have different functional purposes and different application fields (water treatment, flocculation of the raw material flotation residue, concentration and recovery of minerals, intensification of petroleum production, paper and textile processing) [3–6]. For example, high polymers [$M = (2–18) \times 10^6$], whose efficiency grows with increasing M, serve as flocculants, thickeners, structure- and film-forming agents and lubricants, and low-molecular-weight polymers [$M = 5 \times 10^3–4 \times 10^5$] can be used as petroleum thinning agents, dispersing and stabilizing agents for muds, and additives for hermetic sealing and for decreasing the loss of cement slurries [3–9]. With regard to preparing partially hydrolyzed polymers with various molecular characteristics, it is worthwhile to consider the potentialities of the chemical modification of PAA and its derivatives by various methods. The relationships in acid and alkaline hydrolysis of polyvinylamides were discussed in review [10] and monograph [6]. In view of these data, supplemented by more recent publications, we consider in this work the specific features of hydrolysis of PAA and its derivatives and the most efficient hydrolysis procedures in dilute and concentrated aqueous solutions and suspensions and during polymerization of acrylamide (AA) in the presence of hydrolyzing agents in aqueous solutions and emulsions. We do not consider copolymerization of AA and other unsaturated amides with acrylic (AAc) and methacrylic acid, since various aspects of copolymerization in the systems of interest have been discussed in monographs [6, 11, 12].

SPECIFIC FEATURES OF HYDROLYSIS OF POLYACRYLAMIDE IN AQUEOUS SOLUTIONS

Without hydrolyzing agents, polyacrylamide is resistant to hydrolysis in aqueous solutions at room temperature [13, 14], and at high temperatures (93°C) it is hydrolyzed at an appreciable rate [15–19]. The chemical stability of aqueous solutions of PAA at 60 and 100°C at pH 4–10 was studied in [20, 21]. The hydrolysis rate is at a maximum at pH 4, and at a minimum at pH ~ 10. Hydrolysis of PAA in the presence of acid catalysts yields AA–AAc copolymers:

$$-(-CH_2-\underset{\displaystyle CONH_2}{\underset{|}{CH}}-)_n- \;+\; mH_2O$$

$$\rightarrow\; -(-CH_2-\underset{\displaystyle CONH_2}{\underset{|}{CH}}-)_{n-m}-(-CH_2-\underset{\displaystyle COOH}{\underset{|}{CH}}-)_m- \;+\; mNH_3.$$

As hydrolysis catalysts are used strong mineral acids (hydrochloric, sulfuric, phosphoric, etc.) and polysulfonic acid [20, 21]. Acid hydrolysis of PAA is

1070-4272/01/7404-0543 $25.00 © 2001 MAIK "Nauka/Interperiodica"

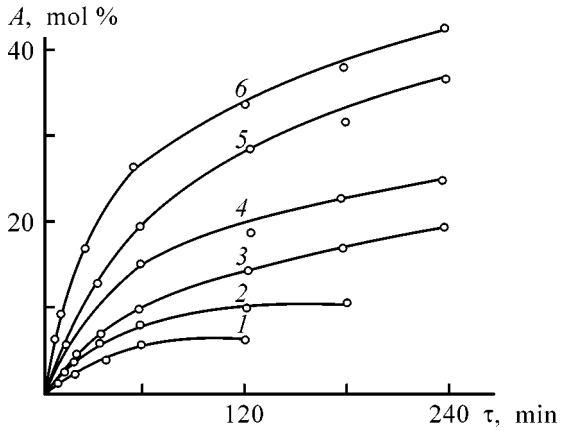

Fig. 1. Variation of content of SA units in copolymer *A* with time τ in hydrolysis of PAA with $M_\eta = 3.2 \times 10^6$ at different NaOH concentrations. [PAA] = 0.14 base-mol l^{-1}, T = 50°C. [NaOH] (M): (*1*) 0.014, (*2*) 0.042, (*3*) 0.070, (*4*) 0.097, (*5*) 0.14, and (*6*) 0.278.

typically accompanied by intra- and intermolecular imidization yielding the following structures:

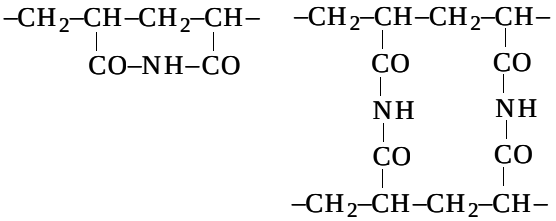

Imidization yields partially or completely insoluble products. The lost solubility can be recovered by treating the polymer with weakly alkaline solutions to break down the secondary amide bridges between the macromolecules:

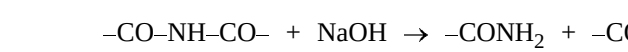

Imidization of PAA in acidic media occurs at an appreciable rate at 75, accelerates at 85, and is very fast at 110°C [21] and at high polymer concentrations. Polymethacrylamide (PMAA) undergoes exhaustive imidization at 65°C [3]. In contrast to PAA, *N*-alkylacrylamide polymers do not undergo imidization. Because of the occurrence of imidization, acid hydrolysis of the polymer has not found application in preparing hydrolyzed derivatives of polyvinylamides. Therefore, alkaline hydrolysis seems to be more suitable for these purposes.

Hydrolysis of PAA in the presence of base catalysts (alkalis, carbonates and bicarbonates of alkali metals, etc.) yields random copolymers of AA and AAc salts whose macromolecules contain no block structures [21]:

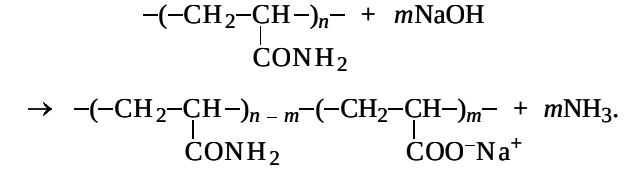

The kinetics of alkaline hydrolyis of PAA in aqueous solutions has been extensively studied [20, 22–30]. The reaction proceeds at a higher rate compared with low-molecular-weight amides, but, in contrast to them, it involves two stages. The first stage is characterized by the highest rate and is complete at a degree of hydrolysis equal to 40 mol %. This is a first-order reaction with respect to PAA and alkali. The second stage of hydrolysis proceeds at a 10 times lower rate, compared with that in the first stage and is complete at a degree of hydrolysis equal to 70%. The high initial rate of the reaction is due to the fact that the carboxylate groups formed in hydrolysis accelerate the hydrolysis of the neighboring amide groups (anchimeric contribution) [2]. The deceleration with increasing conversion is due to the enhanced electrostatic repulsion between the OH^- ions and the accumulating carboxylate anions $-COO^-$. Deceleration is also due to the growing size of the macromolecular globules, making higher the viscosity of the solutions and hindering the diffusion of the reacting species. Raising the NaOH concentration accelerates the hydrolysis and enriches the forming copolymer in sodium acrylate (SA) units (Fig. 1) [31]. Raising the temperature also accelerates the PAA hydrolysis. The activation energy of PAA hydrolysis grows with increasing conversion and is estimated at 59.5, 74.0, 81.5, and 99.5 kJ mol^{-1} for degrees of hydrolysis equal to 2, 8, 12, and 19 mol %, respectively [32]. A similar pattern of variation of the activation energy with conversion in the alkaline hydrolysis of PAA was observed in [29]. Along with the regular influence of the temperature on the hydrolysis rate, the temperature-related changes in the degree of dissociation of carboxylate groups, in the character of the electrostatic interaction between the carboxylate anions and OH^- ions, and in the conformation taken by the macromolecules, affected the activation energies of hydrolysis.

Hydrolysis in dilute aqueous solutions (0.05–0.2%) of PAA with $M_\eta = 5.7 \times 10^6$ under the action of NaOH was studied in [33]. The reaction was carried out at 3, 25, and 50°C for a period of time ranging from 3 h to 20 days. Lowering the polymer concentration (at [NaOH] = const) made higher the initial rate and degree of hydrolysis of PAA owing to an increase in the [NaOH]/[PAA] ratio. The hydrolysis was intensified by raising the temperature and NaOH concentration (at [PAA] = const). The experiments showed that

low-temperature hydrolysis of PAA in dilute aqueous solutions is suitable for preparing copolymers with controllable content of the SA units, which can be used, e.g., for treatment of natural water.

Influence of the neighboring units. The influence of the hydrolyzed groups on hydrolysis of the neighboring amide groups in alkaline hydrolysis of PAA was studied by Higuchi and Senju [25]. They analyzed the reactivity of the amide units (B) of the macromolecules with zero, one, or two neighboring carboxylate units (A), characterized by hydrolysis rate constants k_0, k_1, and k_2, respectively. For the initial rate of hydrolysis, Higuchi and Senju proposed the equation

$$dx/d\tau = k_0[a - (3 - 2k_1/k_0)x][OH^-], \quad (1)$$

where x is the concentration of the hydrolyzed groups at the instant τ, and a is the initial concentration of the amide groups.

In the course of the reaction, the amide groups having no neighboring carboxylate groups disappear at a degree of hydrolysis equal to 43 mol %, and the amide groups with one carboxylate neighbor at a degree of hydrolysis equal to 57 mol %. At a degree of hydrolysis within 43–57 mol % the reaction rate can be described by the equation

$$dx/d\tau = 2k_2(0.57a - x)[OH^-]. \quad (2)$$

The experimental data on the PAA hydrolysis are adequately described by the relation $k_0 : k_1 : k_2 = 1 : 0.2 : 0$ [25] and indicate a decelerating (with increasing conversion) effect of the $-COO^-$ groups (repulsion of OH^- ions) on the hydrolysis of the neighboring amide groups. For describing the rate of alkaline hydrolysis of PAA with account of the influence exerted by the neighboring groups, Fuoss *et al.* [34] proposed the equation

$$dx/[(a - x)(b - x)] = [k_0 e^{-\alpha\tau} + k_2(1 - e^{-\alpha\tau})]d\tau, \quad (3)$$

where a and b are the initial concentrations of PAA and NaOH, respectively, and α is the probability factor.

Data comparison made by Truong *et al.* [35] showed that the kinetics of alkaline hydrolysis is adequately described by Eqs. (1) and (2). It was also found that the experimentally established (by NMR spectroscopy) pattern of distribution of the carboxylate units in the macromolecules of the hydrolyzed polymer is in good agreement with that calculated for the $k_0 : k_1 : k_2 = 1 : 0.2 : 0$ ratio (Fig. 2). This suggests the decisive role played by the effect of neighboring groups in the kinetics of alkaline hydrolysis of PAA.

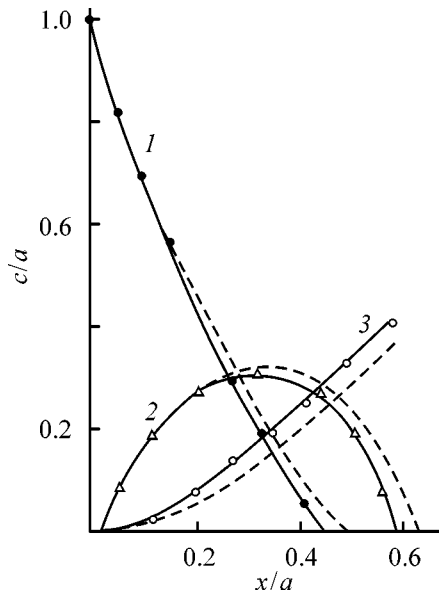

Fig. 2. Relative content of triads in hydrolysis of PAA. (c, a, x) Concentrations of the triads and amide and carboxylate groups, respectively. (*1*) BBB, (*2*) (BBA + ABB); and (*3*) ABA. (*Points*) Experimental data and (*dashed lines*) calculation for $k_0 : k_1 : k_2 = 1 : 0.2 : 0$.

Influence of the macromolecule structure. The hydrolysis reaction is affected by the structure of the polymer molecule. As shown in [36, 37], hydrolysis of PAA and PMAA, similarly to that of low-molecular-weight amides, involves an intermediate imidization stage. This was confirmed by spectral studies: The characteristic absorption band of imide at $\lambda = 235$ nm appeared and subsequently disappeared during hydrolysis. The transformations of low-molecular-weight amides in alkaline hydrolysis can be represented as

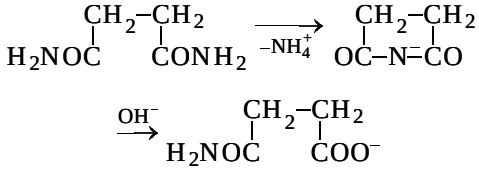

The rate constants of imidization, k_i, and hydrolysis, k_h, for low-molecular-weight amides, such as succinimide, glutarimide, and PAA, are estimated at 25°C as follows: $k_i \times 10^{-4}$ (s^{-1}): 2.7, 0.62, 4.4; $k_h \times 10^{-4}$ (s^{-1}): 1.03, 1.78, 1.06 [38]. These constants evidence that the PAA macromolecules contain "head-to-head" linked units that underwent imidization and subsequent hydrolysis. The imidization and hydrolysis become faster with increasing temperature, with the activation energy of imidization exceeding that of hydrolysis [22].

Unlike low-molecular-weight amides that can be hydrolyzed quantitatively [39], PAA is hydrolyzed in

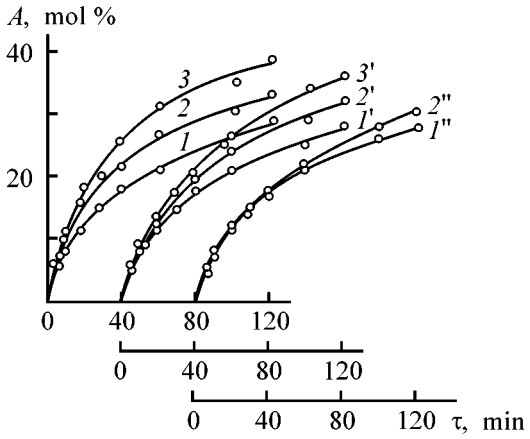

Fig. 3. Variation of the content of SA units in copolymer *A* with time τ in hydrolysis of PAA with $M_\eta = 3.2 \times 10^6$ for various concentrations of NaCl. [PAA] = 0.14 base-mol l^{-1}, [NaOH] = 0.14 M, *T* = 60°C. [NaCl], M: (*1*, *1*', *1*'') 0, (*2*, *2*') 1.71, and (*3*, *3*', *2*'') 3.42. $M_\eta \times 10^{-6}$: (*1*–*3*) 9, (*1*'–*3*') 3.42, and (*1*'', *2*'') 0.4.

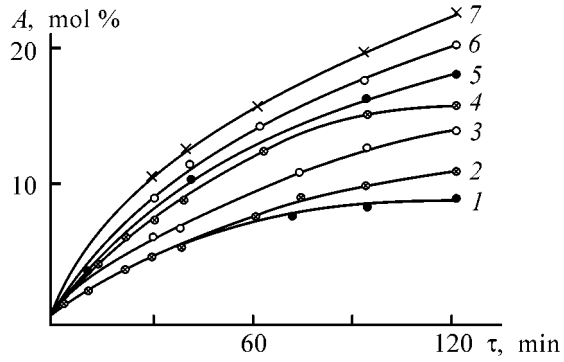

Fig. 4. Variation of the content of Li (Na, K) acrylate units in copolymer *A* with time τ in PAA hydrolysis for various concentrations of (*1*, *3*, *5*) LiOH, (*2*, *4*, *6*) NaOH, and (*2*, *4*, *7*) KOH. [PAA] = 0.14 base-mol l^{-1}, *T* = 50°C. [Alkali], M: (*1*, *2*) 0.07, (*3*, *4*) 0.096, and (*5*–*7*) 0.139.

the presence of base catalysts to typically no more than 70 mol %. This is due to the fact that the amide groups blocked by two neighboring carboxylate groups become inactive [24], which can be represented schematically as

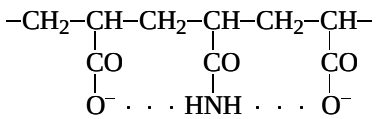

Copolymers of AA with AAc and AA with allyl alcohol [20], polymethacrylamide, as well as copolymers of methacrylamide with methacrylic acid, are also hydrolyzed incompletely [38, 40]. The degree of PAA hydrolysis can be increased by carrying out the reaction in 10 M NaOH at 100°C [20]. Also, the degree of hydrolysis can be brought to 96% in a two-stage reaction, with the hydrolysis initially carried out in the presence of NaOH at 20°C to the degree of hydrolysis equal to 67 mol % and then in the presence of HCl at 100°C [41]. Similar results were obtained when PAA was initially hydrolyzed at 95–97°C for 2 h to 60 mol % conversion and then at 100–210°C [42]. It should be noted that at high temperatures the hydrolysis may be accompanied by degradation of the macromolecules [20, 43].

Influence of the ionic strength. The influence of salt additives on the alkaline hydrolysis of PAA in aqueous solutions was discussed in a number of works. It was found that these additives accelerate hydrolysis at 50 [29, 33] and 93°C [44]. In [31], alkaline hydrolysis of PAA with different molecular weights in 1% aqueous solutions at 20–60°C was studied as influenced by addition of NaCl. In [45], the kinetics of the process was studied potentiometrically. As seen from the kinetic curves shown in Fig. 3, the initial rate of hydrolysis of PAA remains unchanged with M_η varied within $(0.4–9.2) \times 10^6$ and upon addition of NaCl. With increasing conversion, the influence of NaCl on hydrolysis becomes appreciable, (compare curves *1* and *3*, *1*' and *3*', and *1*'' and *2*''), and this effect is enhanced with increasing *M*. This follows from the changes with conversion in the electrostatic interactions in the system and in the conformation taken by the macromolcules, as indicated by measurements of the dynamic viscosity of the reaction solutions.

The above data show that the degree of PAA hydrolysis grows with increasing ionic strength of the solutions and molecular weight *M* of the initial polymer.

Kurenkov *et al.* [31] studied the influence of the ammonium sulfate impurity on the alkaline hydrolysis of PAA, this impurity being typical of PAA produced by ammonia procedure. The experiments showed that the initial rate of the reaction and the degree of hydrolysis of the polymer decrease with increasing concentration of the added ammonium sulfate. This is due to the decrease in the concentration of NaOH consumed in the reaction with ammonium sulfate. Thus, the degree of hydrolysis of the forming copolymer may decrease in the presence of impurities contained in PAA produced by ammonia procedure.

Influence of the nature of hydrolyzing agents. The kinetics of hydrolysis of PAA with $M_\eta = 6.5 \times 10^6$ in 1% aqueous solutions in the presence of LiOH, NaOH, and KOH at 50°C was studied in [46]. The kinetic curves of hydrolysis are shown in Fig. 4. It is

seen that the initial rate and degree of hydrolysis of the polymer grow with increasing concentration of the hydrolyzing agent (going from curves *1*, *2* to curves *3*, *4* and *5*–*7*). Data in Fig. 4 for fixed concentrations of added alkali show that the initial rate and degree of hydrolysis of the polymer in the region of low alkali concentrations increase in the order LiOH < NaOH (KOH) (curves *1*, *2* and *3*, *4*), and at higher alkali concentrations, in the order LiOH < NaOH < KOH. According to the findings of Marina and Monakov [47] and the measured dynamic viscosities of the reaction solutions, the degree of binding of the cations to the copolymers of AA with AAc salts increases in the order $Li^+ < Na^+ < K^+$. Therefore, the electrostatic repulsion between the carboxylate anions and OH^- ions, which enhances the catalytic activity of the alkalis, must weaken in the order LiOH > NaOH > KOH. This dependence becomes more pronounced with increasing alkali concentration and time of hydrolysis.

The PAA hydrolysis can be carried out in the presence of sodium silicate—liquid glass which is an aqueous solution of oligomers of general formula $[Na(OH_2)_x]_2Si_mO_{2m+1}$, where m is the silicate modulus ($m = [SiO_2] : [Na_2O] \times 1.032$). Sodium silicate exhibits strong alkaline properties: pH 13–14 and alkalinity corresponding to 3–4 N NaOH [14, 48]. This is due to dissociation of the oligomers in water

$$[Na(OH_2)_x]_2 Si_mO_{2m+1} \rightleftarrows (Si_mO_{2m+1})^{2-} + 2Na(OH_2)^+$$

and the subsequent hydrolysis of the oligomer ions

$$(Si_mO_{2m+1})^{2-} + 2H_2O \rightleftarrows 2OH^- + H_2Si_mO_{2m+1}.$$

As known [49], alkaline hydrolysis of polyacrylonitrile at 92–96°C yields AA–SA copolymers. As hydrolyzing agent can serve sodium silicate [50]. However, high-temperature hydrolysis of polyacrylonitrile is a multistage reaction complicated by the heterophase nature of the process and degradation of the macromolecules [51]. Therefore, it is more advisable to prepare AA–SA copolymers by hydrolysis of PAA at moderate temperatures (20–50°C), which was studied in [52, 53]. In these works, hydrolysis was carried out in 0.5% aqueous solutions at 50°C for 1.5 h. It was shown that the initial rate and degree of hydrolysis increase with growing silicate modulus of sodium silicate owing to the increasing alkalinity and, hence, hydrolyzing power. Raising the sodium silicate concentration within 0.3–1.0% accelerated the reaction and increased the degree of PAA hydrolysis. Similar trends were observed on raising the polymer concentration within 0.05–0.5% [52], as well as on elevating the temperature from 20 to 50°C [53].

Table 1. Characterization of hydrolyzing agents

Hydrolyzing agent	Density at 20°C, g cm^{-3}	Akali content, %
Etching bath effluent	1.435	40.0
Solid alkali wastes	1.020	1.94
Degreasing solution	1.023	2.03

This is the first-order reaction with respect to PAA and sodium silicate, which is in agreement with the data on the hydrolysis under the action of NaOH [22, 24]. The results cited above confirmed the suitability of sodium silicate for preparation at an acceptable rate of efficient flocculants with various degrees of hydrolysis [48].

Partially hydrolyzed PAA with various molecular weights can be prepared by a two-stage procedure, when hydrolysis under the action of sodium silicate is followed by partial degradation of the polymer in 0.4% aqueous solutions under the action of potassium peroxosulfate (5% relative to the polymer) at 50°C for 4 h [54]. It was shown that M can be lowered by factors of 2.3 and 3.5, compared with the initial PAA, the degree of hydrolysis of the products being 42.0 and 16.2 mol %, respectively.

As hydrolyzing agents for PAA can serve various alkaline process wastes. In [55, 56], hydrolysis of PAA in 0.5% aqueous solutions at 30–70°C under the action of alkaline electroplating wastes was studied (these wastes are characterized in Table 1). It was shown that PAA samples with different molecular weights M_η within $(0.9–5.3) \times 10^6$ can be hydrolyzed at room temperature to a degree of 30 mol %. Figure 5 illustrates how the hydrolysis is influenced

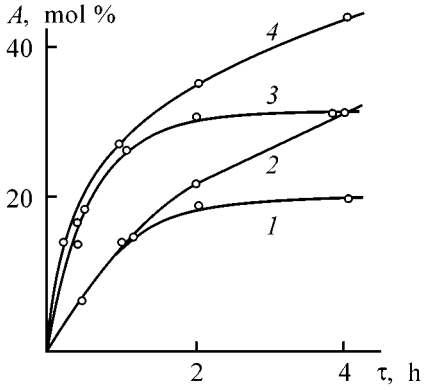

Fig. 5. Variation of the content of acrylate units in copolymer A with time τ in hydrolysis of PAA with $M_\eta = 5.3 \times 10^6$ for various hydrolyzing agents. [PAA] = 0.07 base-mol l^{-1}, T = 21°C. Hydrolyzing agent (0.01%): (*1*) solid alkali wastes, (*2*) sodium hydroxide, (*3*) degreasing solution, and (*4*) etching bath effluent.

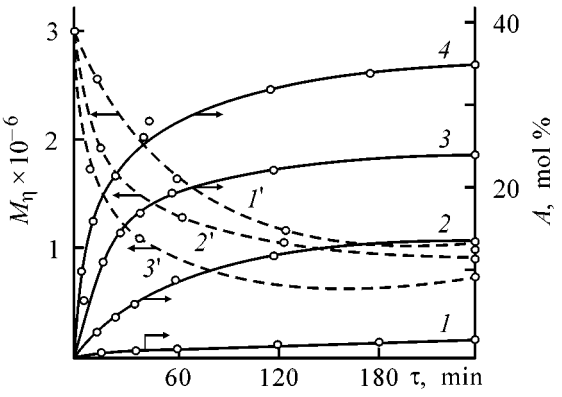

Fig. 6. Variation of (*1*–*4*) content of SA units in copolymer *A* and (*1*'–*3*') M_η with time τ in PAA hydrolysis at various concentrations of NaOH. [PAA] = 0.343 base-mol l^{-1}; $[K_2S_2O_8]$ = 0.033% of [PAA], T = 60°C. [NaOH], M: (*1*, *1*') 0, (*2*) 0.116, (*3*, *2*') 0.437, and (*4*, *3*') 0.734.

by various hydrolyzing agents. It is seen that all the hydrolyzing agents exhibit high catalytic activity with respect to PAA. In the order of increasing catalytic activity, the reagents can be arranged as follows: solid alkali wastes (sodium hydroxide) < degreasing solution < etching bath effluent. The difference between the efficiencies of the hydrolyzing agents is evidently due to the impurities contained in the wastes.

The aforesaid suggests that alkaline electroplating wastes are suitable for preparing partially hydrolyzed PAA, a promising reagent for intensifying the treatment of process wastewater and, in particular, electroplating effluents [57, 58].

METHODS FOR PREPARATION OF ACRYLAMIDE–SODIUM ACRYLATE COPOLYMERS

Hydrolysis of PAA in aqueous solutions in the presence of destructive agents. Alkaline hydrolysis of PAA in the presence of minor amounts of destructive agents is suitable for controlling the chemical composition and molecular weight M of the forming products. The hydrolysis of PAA, combined with its degradation, was studied in [59]. The reaction was carried out at 30–70°C in 2.4% aqueous solutions of PAA with M_η 3×10^6 in the presence of $K_2S_2O_8$ as degradative agent. Hydrolysis was monitored potentiometrically [45], and degradation, viscometrically. Alkaline hydrolysis of PAA [60] and partially hydrolyzed PAA [61] in the absence of $K_2S_2O_8$ did not involve degradation, which is consistent with published data [62]. Introducing $K_2S_2O_8$ and raising its concentraiton did not affect the hydrolysis but were accompanied by a decrease in M as a result of degradation of the macromolecules. Figure 6 illustrates how the NaOH concentration affects the process. Without NaOH, hydrolysis does not occur (curve *1*), whereas with increasing NaOH concentration, the hydrolysis becomes faster (going from curve *2* to curve *4*). It is seen that the degradation reactions are intensified with increasing NaOH concentration (going from curve *1*' to curve *3*'). Raising the temperature affected the degradation in a similar way. In the 30–70°C range, the activation energy of alkaline hydrolysis of PAA in the presence of the destructive agent is estimated at 46.3 kJ mol^{-1}. The studies described demonstrated the possibility of preparing partially hydrolyzed polymer with controllable molecular weight M and chemical composition of the macromolecules.

PAA hydrolysis in suspensions. This method is based on hydrolysis of the already prepared PAA in a concentrated aqueous solution dispersed in a water-immiscible organic solvent (benzene, toluene, heptane, hexane, cyclohexane, etc.). First, a suspension of an aqueous PAA solution is prepared (20–50% water + 20–50% PAA) in an organic liquid containing 0.1–30% of an oil-soluble emulsifying agent with low hydrophilic–lipophilic balance. Also, an alkali-resistant surfactant and 0.2–30% (relative to the suspension mass) of 50% aqueous solution of the hydrolyzing agent (NaOH, KOH, Na_2CO_3, K_2CO_3, etc.) are introduced into the suspension. The reaction is run at 10–70 [63–65] or 125°C under pressure to prevent boiling of the reaction mixture [66]. Also, the hydrolyzing agent can be added in the form of an alkali suspension in a hydrophobic organic liquid [63, 64]. As stabilizing additives can serve oxyethylated alcohols (oleyl and lauryl) [63, 65, 66] and oleic acid isopropylamide [67].

Also described was hydrolysis of a PAA suspension with particle size of 0.001–1.0 cm under the action of alkaline agents in the form of solutions [68, 69] or emulsions [68]. The degree of hydrolysis of the polymer is controlled by varying the concentrations of the hydrolyzing agents, temperature, and reaction time.

Powdered PAA can be hydrolyzed in aqueous-organic media in the presence of an alkali with such organic liquids as C_{4-6} alcohols [69–72], ketones, ethers, and nitriles readily miscible with water [71].

The reaction rate and the degree of hydrolysis of the polymer are governed by the ratio of the aqueous and organic phases. Raising the fraction of water in the mixture leads to higher degree of swelling of the polymer particles and makes the amide groups of the macromolecules more accessible to OH^- ions [73].

The kinetic features of alkaline hydrolysis of PAA with $M_\eta = 3.4 \times 10^6$ and uniform particle size (average size 0.04 cm) have been studied in water–toluene suspensions ([PAA] = 14.2–71.0%, water : toluene volume ratio 1 : 8) at 60°C [45, 74]. NP-3 Sulfonol (sodium alkylbenzenesulfonate of general formula $C_nH_{2n+1}C_6H_4SO_3Na$ with n = 10–12) in amount of 0.5% relative to that of toluene served as stabilizing agent. The data reported in [45, 74] suggest the possibility of changing the degree of hydrolysis of the polymer by varying the NaOH concentration. It was shown that alkaline hydrolysis in suspensions, similarly to that in aqueous solutions, is a second-order reaction (first-order with respect to the alkali and PAA). Hydrolysis is accelerated by raising the temperature; the activation energy is estimated at 63 kJ mol^{-1}.

In [45], the inflence of nonuniform particle-size distibution pattern on alkaline hydrolysis of PAA was studied. Figure 7 presents the kinetic curves of hydrolysis of a PAA sample with nonuniform particle size (particle size 0.015–0.24 cm) and fractions with uniform particle size. In the initial stage of hydrolysis, the PAA samples with nonuniform and uniform particle sizes differ in the degree of hydrolysis. For samples with uniform particle size the initial rate of hydrolysis increases with decreasing particle size. This is due to increase in the degree of swelling of PAA and easier accessibility of the amide groups of the polymer to OH^- ions. As seen from Fig. 7, at high conversions (>40 mol %) the samples with nonuniform and uniform particle sizes exhibit identical degrees of hydrolysis. This is evidently due to the fact that the swelling degree in the aqueous phase of the polymer attained the limiting value for all the samples and the amide groups became equally accessible to the hydrolyzing agent. This demonstrates the possibility of preparing polymers with controllable degree of hydrolysis by PAA hydrolysis in suspensions.

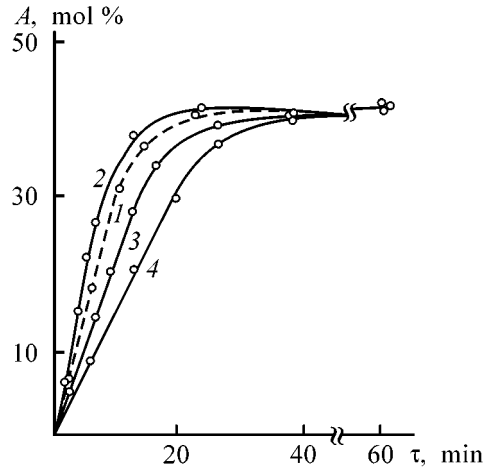

Fig. 7. Variation of content of the SA units in copolymer A with time τ in hydrolysis of (*1*) unfractionated PAA and (*2–4*) PAA fractions with the average particle size d. [PAA] = 3.352 base-mol l^{-1}, [NaOH] = 6.704 M, water : toluene = 1 : 8, [NP-3] = 0.5% relative to toluene, T = 60°C. $d \times 10$, cm: (*2*) 0.25, (*3*) 0.75, and (*4*) 1.2.

Polymerization of AA in concentrated aqueous solutions in the presence of hydrolyzing agent. In review [75], the AA polymerization in aqueous solutions was studied as influenced by the pH of the medium. Various procedures for AA polymerization in the presence of hydrolyzing agents were described in patents [76, 77]. This process occurs in the presence of free radicals $R^\cdot$ and the OH^- ions, originating from NaOH dissociation and catalyzing the hydrolysis. The process can be represented by the general scheme

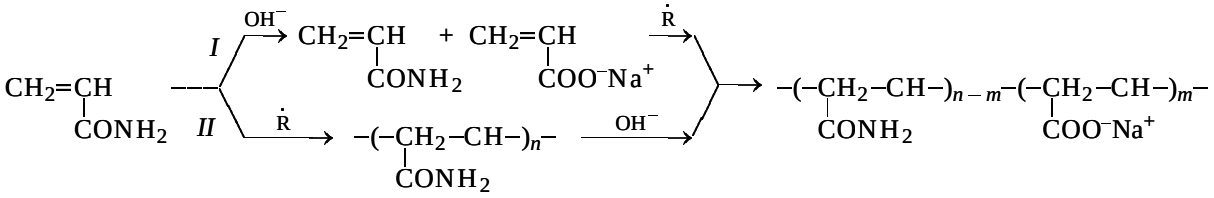

Of the two possible reaction routes *I* and *II*, the main route is copolymerization *I*. Only at low conversions (<3%) the contribution from route *II* is comparable with that from route *I*; for high conversions (>30–40%) the contribution from route *II* is negligible. The reaction is carried out with concentrated solutions of monomers to prepare macromolecular products. However, it is accompanied by cross-linking as a result of imidization coused by hydrogen ions present in aqueous solutions. Adding alkali to an aqueous monomer solution makes imidization and cross-linking of the polymer less probable but decreases the molecular weight of the polymer. Formation of water-soluble products is also favored by tris(2-carbamoylethyl)amine (CEA), characterized by high proton-accepting power. Under the polymerization conditions,

Table 2. Influence of hydrolyzing agents on μ_η and composition of the AA–SA copolymers [90]

Hydrolyzing agent, M	Content of indicated unit, mol %		$M_\eta \times 10^{-6}$
	AA	SA	
Water*			
–	98.4	1.6	9.70
[NaOH]:			
0.003	92.4	7.6	2.54
0.005	83.2	16.8	0.83
0.025	72.6	27.4	0.18
Water : toluene** = 1 : 8			
–	99.5	0.5	3.00
[NaOH]:			
0.028	98.0	2.0	1.66
0.083	96.6	3.4	1.53
0.220	92.0	8.0	0.32
0.443	79.0	21.0	0.20
$[Na_2CO_3]$:			
0.052	96.5	3.5	2.60
0.083	94.6	5.4	1.73
0.150	90.9	9.1	1.09
0.3	81.6	18.4	0.27

* [AA] = 0.704 M, $[(NH_4)_2S_2O_8]$ = 0.1% of AA, 50°C, 5 h.
** [AA] = 0.625 M, $[K_2S_2O_8]$ = 0.1% of AA, 40°C, 2 h.

CEA is formed in the reaction of AA with sodium hydroxide and ammonia by the scheme

$$CH_2{=}CHCONH_2 \xrightarrow{OH^-} CH_2{=}CHCOO^- + NH_3,$$

$$3CH_2{=}CHCONH_2 + NH_3 \rightarrow (CH_2CH_2CONH_2)_3N.$$

CEA forms redox systems with persulfates and affects the initiation rate of polymerization [78]. Also, CEA is a chain-transfer agent, and low-molecular-weight products are formed in its presence, even in concentrated monomer solutions [78–80]. For example, the intrinsic viscosity of the polymers produced by radiation-induced polymerization of AA ([AA] = 70%) in binary eutectic systems (AA + H_2O) decreases from 1350 to 400 $cm^3\ g^{-1}$ with the NaOH concentration increasing from 0.45 to 1.46% [81].

Kurenkov *et al.* [82] studied the AA polymerization in 20% aqueous solutions in the presence of Na_2CO_3 and NaOH under adiabatic conditions (initial temperature 25°C), with peroxosulfate-hydrosulfite as initiating system. The heat released in polymerization decreases the viscosity of the system and shifts the gel effect to high temperatures. The decrease in the viscosity of the reaction mixture facilitates diffusion of the hydrolyzing agent toward the amide groups of the macromolecules and makes the hydrolysis of the polymer more efficient. It was found under conditions simulating the polymerization [82] that CEA is not formed in the presence of Na_2CO_3 and the degree of hydrolysis of AA is not high. The initial polymerization rate tends to decrease with increasing concentration of CEA, NaOH, and Na_2CO_3 additives in the order CEA < NaOH < Na_2CO_3 (at fixed concentration of the additives). The reaction order with respect to CEA, NaOH, and Na_2CO_3 is 1.0, 0.8, and 0.1, respectively. The molecular weight M of the resulting copolymers tends to decrease in the presence of CEA and NaOH additives. In contrast to NaOH, raising the Na_2CO_3 concentration is not accompanied by any increase in the CEA concentration or the molecular weight M of the copolymer. The copolymers prepared in the presence of Na_2CO_3 are characterized by $M < 4.2 \times 10^{-6}$ and content of the SA units of up to 15 mol %.

In [83, 84], AA copolymers with SA or AAc were prepared under the conditions of adiabatic polymerization of AA in 28% aqueous solutions in the presence of alkalis (pH < 13.5) and acids (boric, phosphoric). On introducing radical initiators, the temperature increased from 27 to 92°C owing to the exothermic character of polymerization. Polymerization yielded high copolymers containing 13 mol % ionic units. To increase their content to 30–35 mol %, the reaction mass after polymerization was kept at elevated temperature for 4–20 h.

In [85], synthesis of macromolecular AA–SA copolymers in AA polymerization in 40% aqueous solutions at initial temeprature of 20–50°C [85] was described. The reaction was run in buffer solutions of a mixture of sodium tertraborate and sodium hydroxide (molar ratio 1 : 3) or disubstituted sodium orthophopshate with sodium hydroxide (molar ratio 1 : 1), or sodium carbonate with sodium hydroxide (at salt concentration in the buffer solution of 0.02–0.36 and sodium hydroxide concentration of 0.04–0.5 M) at pH 12.0–12.4. The resulting reaction mass was kept at 60–75°C for 5 h in a vacuum or inert medium. Drying yielded powdered AA–SA copolymer with particle size of 0.01–0.5 cm.

The AA–SA copolymers with content of SA units of 30 mol % and $M = 12 \times 10^6$ can be prepared by radiation-induced polymerization of AA in the presence of sodium hydroxide and boric acid [86]. Polymerization of AA in 20–50% aqueous solutions in the presence of a buffer mixture (pH > 12) under the action of ionizing radiation (^{60}Co) and with chem-

ical initiation can yield AA–SA copolymers of various compositions [87]. At low NaOH concentrations, hydrolysis of the salt component of the buffer mixture increased the alkali content in the reaction mixure and enabled control over the composition of the forming copolymer.

Of indubitable interest is the possibility of preparing AA–SA copolymers in inverse emulsions. To this end, a concentrated aqueous solution of the monomer, with a hydrolyzing agent as additive, is dispersed in a hydrophobic organic liquid (benzene, toluene, xylene, cyclohexane, etc.) in the presence of a water-in-oil emulsifying agent [88]. Polymerization is initiated by an oil- or water-soluble initiator. In this case, polymerization and hydrolysis proceed in the aqueous phase. The advantages of this method are the facile heat removal and the occurrence of the reaction in low-viscosity media (viscous aqueous solution of the forming copolymer is the internal phase). The reaction yields a latex suitable as a ready-to-use product. The latex can easily be concentrated by azeotropic distillation; if followed by drying, this yields a powdered polymer [6, 88]. Various aspects of the AA polymerization in the presence of hydrolyzing agents in inverse emulsions with various organic solvents, emulsifying agents, and initiators have been discussed [89–98]. It was shown that the polymerization can be accelerated by raising the NaOH concentration. This is due to the enhanced influence of the SA monomer yielded by hydrolysis, whose polymerization is accelerated by the increasing NaOH concentration [11]; the AA polymerization rate in alkaline media is independent of pH [99]. Raising the NaOH concentration results in enrichment of the copolymer in the SA units and a decrease in M (Table 2). The observed decrease in M was ascribed to the increasing contribution of chain transfer to CEA, whose content in the reaction mixture increased with growing NaOH concentration. The data in Table 2 show that the characteristics of the copolymers in inverse emulsions are in agreement with those in aqueous solutions under comparable conditions. The investigations demonstrated the possibility of preparing high AA–SA copolymers of various compositions in inverse emulsions.

Polymerization of AA in concentrated aqueous solutions with subsequent hydrolysis of the polymer. A two-stage procedure for preparing partially hydrolyzed PAA was described in the patents cited in [76, 78]. Initially, AA is polymerized or copolymerized with vinyl monomers in 10% aqueous solutions in the presence of a radical initiator, and the resulting viscous mass of the (co)polymer is treated with alkali at 50–90°C [100, 101]. In other cases [102–109], polymerization is carried out in 10–50% aqueous solutions, predominantly under adiabatic conditions. To facilitate the subsequent hydrolysis, the viscous polymer mass is treated after polymerization in an extruder to obtain particles of size 0.2–2.0 cm, and the resulting granules are treated with solutions of alkalis [102–109], alkali metal carbonates [103, 109, 110], or sodium or potassium hydrocarbonates [110]. Next, the hydrolyzed polymer is once again granulated to particle size of 0.2–0.5 cm, dried at 40–130°C, and crushed to particle size of 0.01–0.1 cm [103, 106, 107]. This yields a copolymer with varied content of SA units and water content of 10–15%. Polymer samples can be uniformly hydrolyzed without mechanical degradation of macromolecules by mixing the gel-like polymer mass with a solid alkali in a screw extruder [101]. A specially designed mixer [110] can be used for preventing agglutination of the polymer granules during mixing with the hydrolyzing agent.

In [111], a procedure was described for preparing products with degree of hydrolysis 1.3–3 times exceeding that calculated for the taken NaOH amount. This procedure involves treatment of the PAA granules with an alkali solution at 55–99°C for 12 h, followed by drying of the polymer. NaCl and KCl can serve as hydrolysis activators [110].

Another two-stage procedure for preparing hydrolyzed polymers [112] deserves attention. Initially, a 35–50% aqueous solution of the monomer (AA, 2-acrylamido-2-methylpropanesulfonic acid, etc.) is prepared, which is poured onto a moving infinite band cooled from the back side with a liquid cooling agent. Thus, a 0.5–1.5-cm thick solution layer is created. This is followed by polymerization in an inert atmosphere at a temperature <80°C under UV irradiation with λ = 300–400 nm or with the use of radical initiators. This yields within 15–60 min a gel-like polymer containing 50–65% water. It is reduced to 0.05–0.2-cm particles and mixed at 10–40°C with alkaline-earth metal (Ca, Mg) oxides taken in amount of <30 mol % relative to that of the polymer unit. Hydrolysis is carried out at 60–80°C for 12 h. The resulting polymer is dried at 80–100°C to a residual moisture content of under 10%, which yields 0.03–0.1-cm granules.

Preparation of hydrolyzed PAA was also described in [113]. First, AA is polymerized in 25% aqueous solutions at 20°C for 5 h, yielding PAA solutions with viscosity of 125 cP. These are granulated in a screw extruder to 0.25-cm particles. The resulting particles are mixed with 20% aqueous NaOH and

dried with hot air for 3 h, which yields a polymer with a degree of hydrolysis of 95 mol % and viscosity of 145 cP.

The reviewed studies show that alkaline hydrolysis of PAA and its derivatives is strongly affected by the characteristics of the initial polymers and hydrolyzing agents, as well as by the reaction conditions. This is manifested in the effect of the neighboring groups, as well as electrostatic, conformational, and concentration effects influencing the kinetics of chemical transformations of polymers and the structure of the forming products. Undoubtedly, with these factors taken into account, it is possible to carry out controllable hydrolysis of polyvinylamides and prepare products with various molecular characteristics and, therefore, various properties.

REFERENCES

1. *Chemical Reactions of Polymers*, Fettes, E.M., Ed., New York: Interscience, 1964.
2. Plate, N.A., Litmanovich, A.D., and Noa, O.V., *Makromolekulyarnye reaktsii* (Macromolecular Reactions), Moscow: Khimiya, 1977.
3. MacWilliams, D.C., *Funct. Monom.*, 1973, vol. 1, pp. 1–197.
4. Nikolaev, A.F. and Okhrimenko, G.I., *Vodorastvorimye polimery* (Water-Soluble Polymers), Leningrad: Khimiya, 1979.
5. Myagchenkov, V.A. and Kurenkov, V.F., *Polym.-Plast. Techn. Eng.*, 1991, vol. 30, nos. 2–3, pp. 109–135.
6. Abramova, L.I., Baiburdov, T.A., Grigoryan, E.P., *et al.*, in *Poliakrilamid* (Polyacrylamide), Kurenkov, V.F., Ed., Moscow: Khimiya, 1992.
7. Kurenkov, V.F. and Myagchenkov, V.A., in *Polymeric Materials Encyclopedia*, Boca Raton, Florida: CRC, 1996, vol. 1, pp. 47–54.
8. Kurenkov, V.F., *Handbook of Engineering Polymeric Materials*, Morganville: Marcel Dekker, 1997, ch. 3, pp. 61–72.
9. Kurenkov, V.F., *Soros. Obrazov. Zh.*, 1997, no. 5. pp. 48–53.
10. Kurenkov, V.F. and Baiburdov, T.A., *Izv. Vyssh. Uchebn. Zaved., Khim. Khim. Tekhnol.*, 1989, vol. 32, no. 7, pp. 3–15.
11. Kabanov, V.A. and Topchiev, D.A., *Polimerizatsiya ionizuyushchikhsya monomerov* (Polymerization of Ionizable Monomers), Moscow: Nauka, 1975.
12. Myagchenkov, V.A. and Frenkel', S.Ya., *Kompozitsionnaya neodnorodnost' sopolimerov* (Compositional Inhomogeneity of Copolymers), Leningrad: Khimiya, 1988.
13. Skal'skaya, U.L., Kravchuk, Yu.M., and Kruglitskii, N.N., *Ukr. Khim. Zh.*, 1966, vol. 32, no. 3, pp. 299–301.
14. Veitser, Yu.I. and Mints, D.M., *Vysokomolekulyarnye flokulyanty v protsessakh ochistki prirodnykh i stochnykh vod* (Macromolecular Flocculants in Processes of Natural Water and Wastewater Treatment), Moscow: Stroiizdat, 1984.
15. Zil'berman, E.N., Starkov, A.A., and Pomerantseva, E.G., *Vysokomol. Soedin., Ser. A*, 1977, vol. 19, no. 12, pp. 2714–2718.
16. Zil'berman, E.N., Starkov, A.A., Eremeev, P.V., *et al.*, *Vysokomol. Soedin., Ser. A*, 1979, vol. 21, no. 1, pp. 31–33.
17. USSR Inventor's Certificate, no. 643 512.
18. JPN Appl. 64-11083.
19. Maurer, J.J., Harvey, G.D., and Klemann, I.P., *Polym. Mater. Sci. Eng., Proc. ACG, Div. Polym. Mater. Sci.*, 1986, vol. 55; *Fall Meet.*, Anaheim, California, 1986, pp. 705–709.
20. Fun Sin'-to and Te-Shchu-kou, *Khim. Tekhnol. Polim.*, 1959, no. 9. pp. 80–94.
21. Sakurada, I., Ohmara, Y., and Sakaguchi K., *Kobunshi Kagaku*, 1967, vol. 24, pp. 618–723.
22. Moens, J. and Smets, G., *J. Polym. Sci.*, 1957, vol. 23, no 4, pp. 931–948.
23. Klein, J. and Heitzman, R., *Makromol. Chem.*, 1978, vol. 179, no. 8, pp. 1895–1904.
24. Nagase, K. and Sakaguchi, K., *J. Polym. Sci., part A*, 1965, vol. 3, pp. 2475–2482.
25. Higuchi, M. and Senju, R., *Polym. J.*, 1972, vol. 3, no. 3, pp. 370–377.
26. Mamedov, M.F., Serebryakov, B.R., Buniyat-zade, A.A., *et al.*, *Vysokomol. Soedin., Ser. A*, 1972, vol. 14, no. 1, pp. 107–110.
27. Gunari, A.A. and Gundiah, S., *Makromol. Chem.*, 1981, vol. 182, no. 1, pp. 1–8.
28. Muller, G., Laine, J.P., and Fenyo, J.C., *J. Polym. Sci., Polym. Chem. Ed.*, 1979, vol. 17, pp. 659–672.
29. Went, P.M., Evans, R., and Nappe, D.H., *J. Polym. Sci., Polym. Symp.*, 1975, vol. 49, pp. 159–167.
30. Kulicke, W.M., Kniewske, R., and Klein, J., *Progr. Polym. Sci.*, 1982, vol. 8, pp. 373–468.
31. Kurenkov, V.F., Baiburdov, T.A., and Stupen'kova, L.L., *Zh. Prikl. Khim.*, 1985, vol. 58, no. 3, pp. 701–703.
32. Korosteleva, E.A.and Mishchenko, K.P., *Zh. Prikl. Khim.*, 1980, vol. 53, no. 8, pp. 1921–1923.
33. Kurenkov, V.F., Aleeva, Yu.V., Zabbarov, A.N., and Myagchenkov, V.A., *Zh. Prikl. Khim.*, 1992, vol. 65, no. 11. pp. 2543–2546.
34. Fuoss, R.M., Watanabe, M., and Coleman, B.D., *J. Polym. Sci.*, 1960, vol. 48, pp. 5–15.
35. Truong, N.D., Galin, J.C., and Francois, J., *J. Polym. Sci.*, 1986, vol. 27, no. 3, pp. 459–466.
36. Morawetz, H., *Nouv. J. Chim.*, 1982, vol. 6, no. 12, pp. 659–660.

37. Sawant, S. and Morawetz. H., *J. Polym. Sci., Polym. Lett. Ed.*, 1982, vol. 20, pp. 385–388.
38. Acrus, C.L., *J. Chem. Soc.*, 1949, no. 3, pp. 2732–2736.
39. Smets, G. and Hesbain, A.M., *J. Polym. Sci.*, 1959, vol. 40, no. 136, pp. 217–226.
40. Pinner, S.H., *J. Polym. Sci.*, 1953, vol. 10, no. 4, pp. 379–384.
41. Kulicke, W.H. and Horl, H.H., *Colloid. Polym. Sci.*, 1985, vol. 263, no. 7, pp. 53–54.
42. Zil'berman, E.N., Starkov, A.A., and Gladyshev, N.M., *Vysokomol. Soedin., Ser. B*, 1976, vol. 18, no. 6, pp. 453–454.
43. Savitskaya, M.N. and Kholodova, Yu.D., *Poliakrilamid* (Polyacrylamide), Kiev: Tekhnika, 1969.
44. Maurer, J.J., Barvey, G.D., and Klemann, J.P., *Proc. Am. Chem. Soc.*, 1986, vol. 55, pp. 705–709.
45. Kurenkov, V.F., Baiburdov, T.A., and Stupen'kova, L.L., in *Fiziko-khimicheskie osnovy sinteza i pererabotki polimerov* (Physicochemical Foundations of Synthesis and Processing of Polymers), Gor'kii: Gor'k. Gos. Univ., 1985, pp. 79–86.
46. Kurenkov, V.F., Baiburdov, T.A., and Stupen'kova, L.L., *Zh. Prilk. Khim.*, 1989, vol. 62, no. 8, pp. 1901–1903.
47. Marina, N.G. and Monakov, Yu.V., *Khimiya i fizikokhimiya vysokomolekulyarnykh soedinenii* (Chemistry and Physical Chemistry Macromolecular Compounds), Ufa: Inst. Khimii, 1976, pp. 116–146.
48. Iler, R.K., *The Chemistry of Silica*, New York: Wiley-Interscience, 1979.
49. Zil'berman, E.N., Starkov, A.A., Zlotnik, D.E., *et al., Zh. Prilk. Khim.*, 1974, vol. 47, no. 11, pp. 2610–2612.
50. Zainutdinov, S.A. and Akhmedov. K.S., *Issledovanie mineral'nogo i rastitel'nogo syr'ya Uzbekistana* (Study of Mineral and Plant Raw Materials of Uzbekistan), Tashkent: Akad. Nauk Uzb. SSR, 1962, pp. 63–66.
51. Zil'berman, E.N., *Usp. Khim.*, 1986, vol. 55, no. 1, pp. 62–68.
52. Kurenkov, V.F., Gerkin, R.V., and Karnaukhov, N.A., *Zh. Prikl. Khim.*, 1995, vol. 68, no. 7, pp. 1193–1197.
53. Kurenkov, V.F. and Gerkin, R.V., in *Khimiya i tekhnologiya elementoorganicheskikh soedinenii i polimerov* (Chemistry and Technology of Organoelement Compounds and Polymers), Kazan: Kazan. Khim.-Tekhnol. Inst., 1997, pp. 67–73.
54. Kurenkov, V.F., Gerkin, R.V., Ivanov, V.S., and Luk'yanov, V.S., *Izv. Vyssh. Uchebn. Zaved., Khim. Khim. Tekhnol.*, 1998, vol. 41, no. 2. pp. 73–77.
55. Kurenkov, V.F., Gerkin R.V., and Karnaukhov, N.A., *Zh. Prikl. Khim.*, 1995, vol. 68. no. 8, pp. 831–834.
56. Kurenkov, V.F., Il'ina, I.V., Gerkin, R.V., and Karnaukhov, N.A., *Khim. Tekhnol. Vody*, 1990, vol. 12, no. 9, pp.822–825.
57. Kurenkov, V.F., Trubina, I.R., Churikov, F.I., and Myagchenkov, V.A., *Izv. Vyssch. Uchebn. Zaved., Khim. Khim. Tekhnol.*, 1996, vol. 39, nos. 1–2, pp. 71–73.
58. Kurenkov, V.F., Aleeva, Yu.V., Churikov, F.I., and Myagchenkov, V.A., *Izv. Vyssh. Uchebn. Zaved., Khim. Khim. Tekhnol.*, 1991, vol. 34. no 4. pp. 93–96.
59. Kurenkov, V.F., Baiburdov, T.A., and Stupen'kova, L.L., in *Khimiya i tekhnologiya elementoorganicheskikh soedinenii i polimerov* (Chemistry and Technology of Organoelement Compounds and Polymers), Kazan: Kazan. Khim.-Tekhnol. Inst., 1985, pp. 47–51.
60. Myagchenkov, V.A., Kurenkov, V.F., and Akhmed'yanova R.A., *Vysokomol. Soedin., Ser B*, 1984, vol. 26, no. 5, pp. 340–344.
61. Kurenkov, V.F., Nagel', M.A., Kosterina, E.N., and Myagchenkov, V.A., in *Khimiya i tekhnologiya elementoorganicheskikh soedinenii i polimerov* (Chemistry and Technology of Organoelement Compounds and Polymers), Kazan: Kazan. Khim.-Tekhnol. Inst., 1984. pp. 34–36.
62. Chmeler, M., Kunchner, A., and Barther, E., *Angew. Makromol. Chem.*, 1980, vol. 89. pp. 145–152.
63. US Patent 3 998 777.
64. US Patent 4 151 140.
65. US Patent 4 171 296.
66. US Patent 4 283 507.
67. JPN Appl. 57-202 308.
68. JPN Appl. 53-121 091.
69. USSR Inventor's Certificate, no. 956 488.
70. JPN Patent 53-4117.
71. JPN Patent 54-50096.
72. Romanian Patent 57 653.
73. Cincu, C., Boghina, C., Marinescu, N., *et al., Mater. Plast.*, 1982, vol. 19, no. 3, pp. 151–157.
74. Kurenkov, V.F., Baiburdov T.A., and Stupen'kova, L.L., in *Khimiya i tekhnologiya elementoorganicheskikh soedinenii i polimerov* (Chemistry and Technology of Organoelement Compounds and Polymers), Kazan: Kazan. Khim.-Tekhnol. Inst., 1983, pp. 50–53.
75. Kurenkov, V.F. and Myagchenkov, V.A., *Eur. Polym. J.*, 1980, vol. 16, no. 11, pp. 1229–1239.
76. Gromov, V.F. and Teleshov, E.N., *Plast. Massy*, 1984, no. 10, pp. 9–13.
77. Kurenkov, V.F. and Abramova, L.I., *Polym.-Plast. Techn. Eng.*, 1992, vol. 31, nos. 7–8. pp. 659–704.
78. Zil'berman, E.N., Abramova, L.I., and Petrova, T.N., *Vysokomol. Soedin., Ser. A*, 1982, vol. 24, no. 7, pp. 1511–1515.
79. Gromov, V.F., Sheinker, A.A., Khomikovskii, P.M., and Abkin, A.V., *Vysokomolek. Soedin., Ser. A*, 1974, vol. 16, no. 2., pp. 365–369.
80. Shapiro, L.V., Lukhovitskii, V.I., and Polikarpov, V.V., *Vysokomol. Soedin., Ser. A*, 1984, vol. 26, no. 4, pp. 650–654.

81. Korneeva, G.P., Mamin, E.B., Sheinker, A.P., *et al.*, *Plast. Massy*, 1973, no. 5, pp. 12–15.
82. Kurenkov, V.F., Baiburdov, T.A., and Stupenkova, L.L., *Eur. Polym. J.*, 1990, vol. 26, no. 8, pp. 915–918.
83. US Patent 3 968 083.
84. JPN Appl. 52-137 483.
85. RF Patent 2 078 772.
86. Wada, T. *et al.*, *Radiat. Phys. Chem.*, 1983, vol. 22, pp. 1064–1070.
87. Sheinker, A.P., Bune, E.V., Tolstikova, L.P., *et al.*, Abstracts of Papers, *3 Vsesoyuznaya konferentsiya "Vodorastvorimye polimery i ikh primenenie"* (3rd All-Union Conf. "Water-Soluble Polymers and Their Application," Irkutsk, May 26–29, 1987, p. 10.
88. Kurenkov, V.F. and Myagchenkov, V.A., *Polym.-Plast. Techn. Eng.*, 1991, vol. 30, no. 4, pp. 367–404.
89. Kurenkov, V.F., Verizhnikova, A.S., and Myagchenkov V.A., *Vysokomol. Soedin., Ser. A*, 1984, vol. 26, no. 3, pp. 535–540.
90. Kurenkov, V.F., Verihznikova, A.S., and Myagchenkov, V.A., *Eur. Polym. J.*, 1984, vol. 20. no. 4, pp. 357–360.
91. Kurenkov V.F., Verizhnikova, A.S., and Myagchenkov, V.A., *Dokl. Akad. Nauk SSSR*, 1984, vol. 278, no. 5, pp. 1173–1178.
92. Kurenkov, V.F., Vagapova, A.K., and Myagchenkov, V.A., in *Khimiya i tekhnologiya elementoorganicheskikh soedinenii i polimerov* (Chemistry and Technology of Organoelement Compounds and Polymers), Kazan: Kazan. Khim.-Tekhnol., 1985, pp. 58–61.
93. Kurenkov, V.F., Verizhnikova, A.S., and Myagchenkov, V.A., *Vysokomol. Soedin., Ser. A*, 1986, vol. 28, no. 3, pp. 5488–5492.
94. Kurenkov, V.F., Vagapova, A.K., Logunova, M.N., and Myagchenkov, V.A., *Fiziko-khimicheskie osnovy sinteza i pererabotki polimerov* (Physicochemical Foundations of Synthesis and Processing of Polymers), Gor'kii: Gor'k. Gos. Univ., 1986, pp. 28–32.
95. Kurenkov, V.F., Trifonova, M.N., Vagapova, A.K., and Myagchenkov, V.A., *Izv. Vyssh. Ucheb. Zaved., Khim. Khim. Tekhnol.*, 1986, vol. 29, no. 10, pp. 105–109.
96. Kurenkov, V.F., Trifonova, M.N., and Myagchenkova, V.A., *Eur. Polym. J.*, 1987, vol. 23, no. 9, pp. 685–688.
97. Kurenkov, V.F., Verizhnikova, A.S., and Myagchenkov, V.A., in *Fizikokhimiya protsessov sinteza i svoistva polimerov* (Physical Chemistry of Synthesis Processes and Properties of Polymers), Gor'kii: Gor'k. Gos. Univ., 1988, pp. 35–40.
98. Kurenkov, V.F., Trifonova M.N., Baiburdov, T.A., and Myagchenkov, V.A., *Vysokomol. Soedin., Ser. A*, 1989, vol. 31, no. 9, pp. 1898–1903.
99. Blauer, G., *Trans. Faraday Soc.*, 1960, vol. 56, no. 4, pp. 606–612.
100. US Patent 3 247 717.
101. JPN Patent 49-17 668.
102. JPN Appl. 54-102 390.
103. JPN Appl. 58-8681.
104. JPN Appl. 61-29 964.
105. JPN Appl. 57-179 204.
106. JPN Appl. 56-16 505.
107. JPN Appl. 59-184 203.
108. JPN Appl. 52-5295.
109. JPN Appl. 56-167 705.
110. Romanian Patent 84 876
111. JPN Appl. 1 271 373.
112. JPN Appl. 2-173 102.
113. US Patent 4 146 690.

Russian Journal of Applied Chemistry, Vol. 74, No. 4, 2001, pp. 555–559. Translated from Zhurnal Prikladnoi Khimii, Vol. 74, No. 4, 2001, pp. 541–545.

INORGANIC SYNTHESIS AND INDUSTRIAL INORGANIC CHEMISTRY

Manufacture of High-Purity Sodium by Distillation

E. P. Lokshin

Tananaev Institute of Chemistry and Technology of Rare Elements and Mineral Raw Materials, Kola Scientific Center, Russian Academy of Sciences, Apatity, Murmansk oblast, Russia

Received January 31, 2000; in final form, May 2000

Abstract—The efficiency of purification of technical-grade sodium to remove potassium impurity by distillation is evaluated theoretically. A technology and apparatus for obtaining high-purity sodium by high-vacuum distillation were developed. The metal quality was assessed by means of a variety of chemical and physical methods.

High-purity sodium is necessary for precision studies of its physical properties, synthesis of some special-purity compounds of sodium, and manufacture of high-capacitance tantalum and niobium capacitor powders [2, 3], photoelectric devices [4, 5], illuminating lamps, high-temperature heat pipes, etc.

A number of methods have been proposed for purification of sodium, relying upon the difference in physical and chemical properties between sodium and impurities contained in it. The methods based on low solubility of some impurities in the metal being refined (filtration, melting with settling, purification with cold traps), are suitable for rough purification, e.g., to remove stock particles or a major part of oxygen [6, 7]. It has been reported [8] that the content of Fe, Si, Al, and Cr impurities can be lowered by filtration of sodium heated to 200–500°C from, respectively, 0.003, 0.03, 0.01, and 0.001 wt % to 0.001, 0.001, 0.003, and 0.0001 wt %. These methods failed to ensure the required degree of purification to remove poorly soluble impurities and could not separate soluble impurities. Attempts have been made to improve their efficiency through chemical binding of impurities into compounds having low solubility [9–27]. The chemical binding techniques markedly extended the number of separable impurities; however, special reagents and conditions of chemical binding reactions should be selected for each impurity or group of impurities, which complicates practical use of these approaches.

A technology for manufacture of "reactor" purity sodium has been proposed [9], according to which the technical-grade metal obtained by electrolysis is purified by combined application of methods for oxidative binding of impurities and two-stage filtration; however, no quality characteristics of the obtained metal have been reported. The characteristics of the purification methods used for obtaining the metal make it possible, however, to maintain that for a number of impurities (potassium, gas impurities, calcium, iron, etc.) the achieved purification level was insufficiently high for some fields of application. Also inefficient were electrochemical [28, 29] and crystallization [30] purification techniques.

High-quality sodium can be obtained by reduction of its special-purity compounds. This technique is commonly used to produce small amounts of sodium directly in photoelectric devices [4]. The most frequently used salts are chlorides, chromates, and dichromates, among the commonest reducing agents are calcium, aluminum, titanium, and zirconium. The high-temperature processes employed in this case hinder the development of large-scale apparatus. The obtained metals require further purification, since during the purification process the metal vapor carries away stock particles and gas impurities are evolved, both of these being absorbed by the condensing metal [4]. The metal quality decreases dramatically with increasing scale of the process.

The aim of the present study was to develop a technology for obtaining high-purity sodium from the commercially produced technical-grade metal by the vacuum distillation method.

1070-4272/01/7404-555 $25.00 © 2001 MAIK "Nauka/Interperiodica"

EXPERIMENTAL

Impurities in sodium can form chemical compounds and be present as true solutions or mechanical inclusions. According to GOST (State Standard) 3273–63, sodium used in the study could contain up to (wt %): 0.25 K, 0.2 Ca, and 0.005 Fe. The technical-grade metal was also contaminated with oxygen, lead ($<5 \times 10^{-3}$%), copper ($>3 \times 10^{-5}$%), bound chlorine and sulfur, organic compounds. Some impurities are present as various compounds, e.g., oxygen may enter into the composition of oxides, hydroxides, or carbonates. The potassium impurity must be the most difficultly separable in distillation of sodium, since the equilibrium pressures of sodium and potassium vapors are close. Therefore, it is necessary to study in the first place the conditions for effective sodium purification to remove potassium.

The possible efficiency of sodium purification to remove potassium by single-stage distillation was evaluated using Rayleigh's equation [31]

$$\ln \frac{W_2}{W_1} = \int_{x_1}^{x_2} \frac{dx}{y - x}, \quad (1)$$

where indices 1 and 2 refer to the intial and current instant of distillation, W is the amount of fluid distilled in the still, and x and y are the concentrations of the volatile component in, respectively, fluid and vapor.

The concentration of the volatile component in vapor and fluid are related by the known expression

$$y = \frac{\gamma_K x P_K^0}{\gamma_K x P_K^0 + \gamma_{Na}(1 - x) P_{Na}^0}, \quad (2)$$

where γ_K, γ_{Na} are the activity coefficients of potassium and sodium; P_K^0, P_{Na}^0 are the equilibrium vapor pressures over pure potassium and sodium.

Theoretically possible yield of pure sodium in equilibrium single-stage distillation of technical-grade sodium (x_1 = 0.25 wt %)

T, K	b_T	Yield (%) of fraction with indicated upper limit of potassium content, wt %			
		0.01	0.005	0.001	0.0005
523	0.0201	93.6	92.3	89.3	88.0
573	0.0305	90.4	88.4	84.1	82.2
623	0.0442	86.2	83.4	77.5	75.0
673	0.0491	84.7	81.7	75.2	72.5

At low impurity concentration the activity coefficient of potassium was considered independent of its concentration in melt. Then, introducing designation

$$b_T = \frac{P_{Na}}{\gamma_K P_K} \quad (3)$$

and taking into account that $\gamma_{Na} \approx 1$ at $x \to 0$, we obtain from (2)

$$y = \frac{x}{x + b_T}, \quad (4)$$

where b_T is independent of the composition of the metal being distilled, but depends on temperature.

Substituting (4) into Eq. (1) and taking into account that $b_T \ll 1$ for the sodium–potassium system, we finally obtain upon integration the following expression

$$\ln \frac{W_2}{W_1} = \frac{b_T}{1 - b_T} \ln \frac{x_2}{x_1}. \quad (5)$$

The activity coefficients at 523, 573, 623, and 673 K were calculated from the experimental activity coefficient at 473 K [32] on the assumption that the entropy of mixing is equal to its ideal value, which gives the equation

$$\ln \gamma_i^{T_1} = \left(\frac{T}{T_1}\right) \ln \gamma_i^T, \quad (6)$$

where $\gamma_i^{T_1}$, γ_i^T are the activity coefficients of i-th component at, respectively, temperatures T_1 and T.

The results of calculation by Eq. (5), presented in the table, indicate that, theoretically, single-stage distillation can ensure deep purification of sodium to remove potassium.

The purification of technical-grade sodium by distillation was studied on a setup shown schematically in Fig. 1. The setup comprised a Kh18N9T steel distillation still *1* with a condensation pipe *2*, charging pipe *3*, evacuation pipe *4*, cover *5* with a pocket for thermocouple *6*, still-heating furnace *7*, S52-1 glass receiving ampules *8*, and an evacuating system (not shown in the figure) comprising a forevacuum and oil-diffusion pumps, a liquid nitrogen trap, transducers, and vacuum meter for measuring the residual gas pres-sure. The bell nipple *9* in the unit connecting the steel condenser and glass members precluded any contact between molten sodium and the metal (Kovar alloy)–glass joint, improving the reliability of the set-up operation.

Sealed containers with technical-grade sodium stored under a layer of paraffin–Vaseline mixture were

opened, metal ingots were extracted, washed with naphtha, and placed in a melting vessel, and the vessel was then evacuated. Sodium was melted and poured through pipe *3* into a pre-evacuated, and tested for air-tightness, distillation setup, with excess pressure of inert gas created over the sodium surface. The major part of oxide films was detained by a steel grid installed at the melting vessel bottom. The melting vessel was disconnected, and the poured-in metal was rapidly heated to a prescribed temperature, with the residual gas pressure maintained at $\leq 6.7 \times 10^{-3}$ Pa. Separate fractions of the distillate were collected into ampules, which were sealed-off when filled. The performed corrosion tests [33] made it possible to establish the conditions under which S 52-1 glass should be used in working with high-purity sodium.

At 573–593 K, the distillation was slow, since the equilibrium pressure of saturated vapor pressure of sodium did not exceed 4 Pa. On raising the distillation temperature to 603 K, the distillation rate was 0.8 g $cm^{-2} h^{-1}$. Although the first fractions of the condensate were enriched in potassium impurity (the potassium content was determined by the atomic-absorption method), sodium containing less than 0.01% potassium could not be obtained. This can be accounted for by fast depletion in potassium of the surface layer of the melt, resulting from metal evaporation from only a thin surface layer [34]. Vapor formation in the bulk of a metallic melt is hindered, since, the metals having high heat conductivity, it is difficult to create the necessary temperature gradient along the melt height. Because of the high heat conductivity and absence of regions with markedly different densities, the role played by convective flows in the agitation of the metal being distilled is also unimportant. Thus, the purification process is limited by potassium diffusion from the bulk toward the surface layer. When the surface layer is depleted of potassium, the process of equilibrium distillation is disrupted and the efficiency of separation markedly decreases.

An acceptable degree of purification can be achieved if distillation of a minor amount of sodium is performed in two stages: first at 523–563 K, with the main amount of potassium and organic compound impurities removed, and then at 623–633 K, to remove difficultly volatile impurities (calcium, heavy metals, sodium oxide, etc.). Two-stage distillation gave metal containing less than 0.01% potassium; however, the duration of the first stage was 48 h at metal height of 10 cm in the distillation still.

Fabrication of reliable and safe stirring devices suitable for operation with alkali metals at high temperature is a complicated task. To ensure effective melt stirring, a distillation apparatus shown schematically in Fig. 2 has been developed [35]. It comprised a distiller *1* with an extension *2*; central tube *3* with vertical slits *4* for metal circulation; and cover *5* with welded-in pipes *6* and *7* for, respectively, pouring-in black metal and condensing vapor. To extensions of the condensation pipe were connected an evacuating system and vessels-receivers for the evaporated metal (not shown in Fig. 2). A filling *8*, made of perforated steel disks, was fixed inside the central tube. An entrainment trap *9* was mounted above the central tube. The distiller was heated with a furnace *10*, and the extension *2*, with an independent electric heater *11*, with the power of both controlled by varying the applied voltage by means of autoformers.

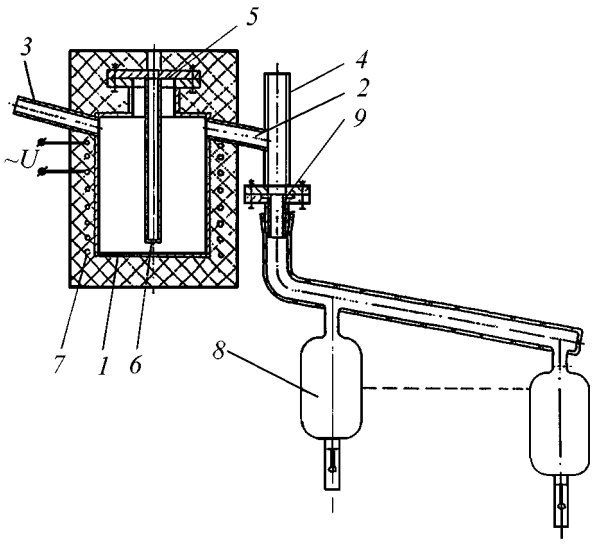

Fig. 1. Schematic of high-vacuum distiller.

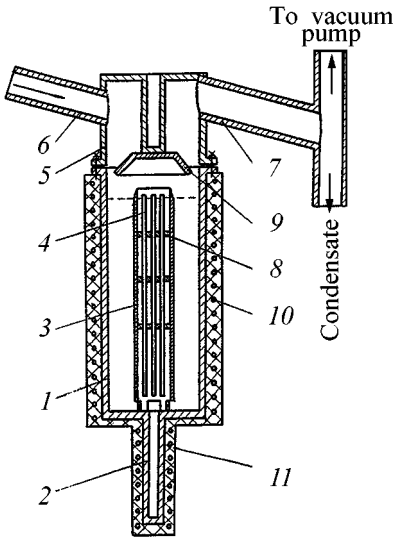

Fig. 2. Schematic of a device for metal distillation in the boiling mode.

The distillation was done as follows. An assembled apparatus was evacuated and heated to 400–410 K, and technical-grade sodium was poured-in. The extension whose length exceeded approximately 20-fold its diameter was heated with the furnace, which allowed sodium overheating in the extension to 1030–1050 K, with the temperature of sodium in the distiller being 510–550 K. A vapor was formed in the extension, whose pressure exceeded the hydrostatic pressure of the column of sodium poured into the distiller. The vapor moved along the central tube upwards, with the vapor flow disintegrated in the filling into fine bubbles and intensively agitating the melt. After potassium-rich fractions were evaporated, the distiller was cooled and fractions of the condensate and still bottoms were fractionated.

Upon 2-h distillation of 5500 g of technical-grade sodium containing 0.28% potassium, 95.5% of the metal remaining in the still contained 0.007% potassium. Potassium was concentrated in two fractions, 125 g each, containing 11.4 and 0.52% potassium, respectively. On making the distillation longer (5 h), the content of potassium impurity in the still bottoms decreased to 0.0015–0.003%, with 88.5–90% of sodium obtained as purified product. At distillation duration of 7 h, the potassium impurity became 0.0006% with 85% of sodium obtained as purified product. Organic residues were distilled off simultaneously with potassium.

Final purification of sodium was carried out by means of repeated distillation in the setup shown in Fig. 1 at a temperature of 650–690 K and residual gas pressure of no more than 6.7×10^{-3} Pa. With this done, the most difficultly volatile impurities—calcium, heavy metals, chlorides, oxides, etc.—were separated. The purified metal was analyzed by atomic-absorption and spectral methods. Below is given the content of impurities in high-purity sodium purified by the developed technique:

Impurity	K	Rb	Cs	Cu	Ag	Mg
Content, wt %	6×10^{-4}	$<1 \times 10^{-3}$	$<1 \times 10^{-3}$	$<5 \times 10^{-6}$	$<5 \times 10^{-7}$	$<2 \times 10^{-5}$
Impurity	Ca	Zn	Al	Ga	In	Tl
Content, wt %	2×10^{-5}	1×10^{-5}	$<1 \times 10^{-5}$	$<5 \times 10^{-6}$	$<5 \times 10^{-6}$	$<8 \times 10^{-6}$
Impurity	Ti	Sn	Pb	Sb	Bi	V
Content, wt %	$<9 \times 10^{-6}$	$<5 \times 10^{-6}$	$<5 \times 10^{-6}$	$<5 \times 10^{-5}$	$<5 \times 10^{-6}$	$<5 \times 10^{-7}$
Impurity	Cr	Mo	Mn	Fe	Co	Ni
Content, wt %	$<5 \times 10^{-6}$	$<5 \times 10^{-6}$	$<5 \times 10^{-6}$	$<1 \times 10^{-5}$	$<2 \times 10^{-6}$	1×10^{-6}

The quality of sodium obtained using the developed technology exceeds that of the best of the known foreign samples [36, 37].

The content of oxygen, found by vacuum evaporation of sodium from a sample, with subsequent titration of unevaporated residue, was not higher than 2×10^{-4} wt %.

The ratio of the residual electrical resistance ρ_0 (at $T \to 0$) of high-purity sodium to the resistance at 293 K was 1.54×10^{-4}, which corresponds to a total impurity content of about 0.001 wt %.

CONCLUSIONS

(1) It was shown theoretically and experimentally that vacuum evaporation of a minor amount of technical-grade sodium can yield metal with impurity content of less than 0.01 wt %. The rate-limiting stage of the process is potassium diffusion from the bulk toward the surface layer of the melt being refined. A distiller design and a process regime were developed, making it possible to overcome kinetic hindrances.

(2) Final purification of sodium to remove alkalineearth and heavy metals, oxygen, organic and other impurities is achieved by its additional high-vacuum distillation. A distiller design and regimes of finishing sodium purification were developed.

(3) The developed technology and equipment were used in commercial manufacture of high-purity sodium in conformity with TU (Technical Specification) 48-4-475–86.

REFERENCES

1. Vershinin, S.L. and Churbanov, M.F., *Vysokochist. Veshchestva*, 1993, no. 1, pp. 77–80.
2. Elyutin, A.V., Vaisenberg, A.I., and Kolchin, O.P., *Giredmet na sluzhbe nauchno-tekhnicheskogo progressa* (Giredmet in the Service to the Progress of Science and Technology), Moscow: Giredmet, 1981, pp. 127–150.
3. Zelikman, A.N., Krein, O.N., and Samsonov, G.V., *Metallurgiya redkikh metallov* (Metallurgy of Rare Metals), Moscow: Metallurgiya, 1978.
4. Reichel, T. and Jedlička, M., *Fotokatody*, Praha: Státni nakl. Technické literatury, 1963.
5. Aleksandrov, E.M., Aleksandrova, T.V., Markova, V.V., and Abdullaev, B.F., *Elektron. Tekh., Ser. 4*, 1990, no. 2, pp. 62–64.
6. Alabyshev, A.F., Grachev, K.Ya., Zaretskii, S.A., *et al.*, *Natrii i kalii* (Sodium and Potassium), Leningrad: Goskhimizdat, 1959.
7. Sittig, M., *Sodium: Its Manufacture, Properties, and Uses*, New York: Reinhold Pub. Corp., 1956.
8. Aleksandrovskii, S.V., Geilikman, M.B., and Gaidamako, I.M., *Zh. Prikl. Khim.*, 1995, vol. 68, no. 6, pp. 892–897.
9. Morachevskii, A.G., Shesterkin, I.A., Busse-Machukas, V.B., *et al.*, *Natrii. Svoistva, proizvodstvo, primenenie* (Sodium: Properties, Manufacture, Use), St. Petersburg: Khimiya, 1992.
10. Subbotin, V.I., Kirillov, P.L., and Kozlov, F.A., *Teplofiz. Vys. Temp.*, 1965, vol. 3, no. 1, pp. 154–163.
11. US Patent 3 243 280.
12. USSR Inventor's Certificate, no. 246 066.
13. French Appl. 2 251 627.
14. French Patent 1 484 647.
15. USSR Inventor's Certificate, no. 387 013.
16. USSR Inventor's Certificate, no. 246 056.
17. USSR Inventor's Certificate, no. 231 844.
18. US Patent 3 287 109.
19. Karabash, A.G., Bogdanovich, N.G., Kopytov, V.S., *et al.*, Abstracts of Papers, *2-i Mendeleevskii s"ezd po obshchei i prikladnoi khimii* (2nd Mendeleev Congress on General and Aplied Chemistry), Moscow: Nauka, 1981, vol. 1, pp. 158.
20. USSR Inventor's Certificate, no. 377 372.
21. Jpn Appl 61-149 446.
22. Jpn Appl. 12 217.
23. Jpn Appl. 9971.
24. Jpn Appl. 62-127 433.
25. Kalandarishvili, A.G., Kuchukhidze, V.A., Shartava, Sh.Sh., and Chkadua, S.S., *Atomn. Energiya*, 1989, vol. 66, no. 1, pp. 22–24.
26. USSR Inventor's Certificate, no. 387 013.
27. RF Patent 2 123 061.
28. US Patent 3 947 334.
29. US Patent 3 387 969.
30. Dulony, J. and Holzhauer, W., *Zesz. Nauk. U. J. Pr. chem.*, 1971, vol. 264, no. 16, pp. 291–297.
31. Gel'perin, N.I., *Distillyatsiya i rektifikatsiya* (Distillation and Rectification), Moscow: Goskhimizdat, 1947, vol. 1.
32. Lokshin, E.P. and Ignat'ev, O.S., *Teplofiz. Vys. Temp.*, 1971, vol. 9, no. 1, pp. 94–100.
33. Lokshin, E.P., Ivanova, V.S., and Presser, R.F., *Khimicheskaya tekhnologiya i metallurgiya mineral'nogo syr'ya Kol'skogo poluostrova* (Chemical Technology and Metallurgy of Mineral Raw Materials from the Kola Peninsula), Apatity: Kola Nauchn. Tsentr Akad. Nauk SSSR, 1991, pp. 97–99.
34. Pazukhin, V.A. and Fisher, A.Ya., *Razdelenie i rafinirovanie metallov v vakuume* (Metal Separation and Refining), Moscow: Metallurgiya, 1969.
35. USSR Inventor's Certificate, no. 254 108.
36. Goates, J.R., Ott, J.B., and Hsu Chen, C., *Trans. Faraday Soc.*, 1970, vol. 66, no. 565, pp. 25–29.
37. Aldrich, *Catalog Handbook of Fine Chemicals*, 1996–1997, Milwaukee, USA, p. 1324.

Russian Journal of Applied Chemistry, Vol. 74, No. 4, 2001, pp. 560–563. Translated from Zhurnal Prikladnoi Khimii, Vol. 74, No. 4, 2001, pp. 545–548.

INORGANIC SYNTHESIS AND INDUSTRIAL INORGANIC CHEMISTRY

Influence of Intensive Mechanical Treatment on Decomposition of Barium Peroxide

I. A. Massalimov and Yu. A. Sangalov

Research Institute of Low-Tonnage Chemical Products and Reagents, Ufa, Bashkortostan, Russia

Received May 11, 1999; in final form, November 1999

Abstract—The effect of mechanical treatment on the properties of barium peroxide—high-temperature source of oxygen—is considered.

Peroxide compounds of alkaline-earth metals attract attention of researchers and technologists as a source of chemically bound and readily evolved oxygen. These compounds have pronounced thermal stability and are widely used in metallurgy, polymer chemistry, medicine, etc. [1]. The basic technological parameter ensuring the possibility of using the peroxides is the temperature of their decomposition into an oxide and active oxygen. The most stable of the known metal peroxides—barium peroxide, starts to actively evolve oxygen at 500°C, with complete loss of oxygen at 900°C [2]. The change in enthalpy in the process is 75 kJ mol^{-1} {$\Delta H_f(BaO_2)$ = –623, $\Delta H_f(BaO)$ = –548 kJ mol^{-1} [3]}. BaO_2 decomposition is accompanied by rupture of the peroxide bond and liberation of oxygen [4].

The kinetics of BaO_2 dissociation depends on external pressure and atmosphere composition. In the atmosphere of oxygen, BaO_2 is more thermally stable, as would be expected, whereas in the atmosphere of water vapor or carbon dioxide it starts to decompose already at 200°C [5]. However, the presence of water vapor or carbon dioxide in the reaction volume is not always desirable or acceptable. The synthesis temperature (with peroxide used) may be lower than the temperature at which intensive oxygen evolution occurs. In such cases, modification of barium peroxide is desirable, lowering the temperature of its dissociation.

In the present communication, a method for controlling the temperature of barium peroxide decomposition in air under normal pressure is proposed, relying upon intensive mechanical treatment.

Barium peroxide [GOST (State Standard) 6054–75] was preliminarily dried at 105°C. Barium peroxide powders—both initial and mechanically treated—were stored in a desiccator over calcium chloride. An analysis of the IR spectra of the samples demonstrated the absence of water and carbon dioxide adsorbed from air.

The mechanical treatment of barium peroxide was done in the working chamber of a D-109 disintegrator. Powders mechanically treated to varied extent were obtained by repeated or multiple grinding in the same apparatus. Sedimentation, thermal, and X-ray diffraction analyses of the initial and mechanically treated BaO_2 samples were made under identical conditions.

The sedimentation analysis was made on a Retsch Lumosed photoelectric instrument (Germany). A 2-g sample was placed in a chamber filled with cyclohexanol, thoroughly stirred, and the chamber was mounted on the analyzer. In the course of particle settling, the intensity of a light beam passing through the chamber changed, which was recorded by the analyzer. A computer connected to the analyzer calculated by means of appropriate software the size distribution of the particles.

Thermal analysis was done on a Q-1000 derivatograph (Hungary), with differential-thermal (DTA) and thermogravimetric (TG) curves recorded. The thermal effects were evaluated from the DTA curves, using reference samples.

X-ray analysis was made on a DRON-2.0 diffractometer. The BaO_2 unit cell is tetragonal, with two molecules and each barium ion surrounded by six peroxide ions forming an octahedron. The unit cell parameters of the initial powder were as follows: a = 3.818 and c = 6.854 Å.

1070-4272/01/7404-0560 $25.00 © 2001 MAIK "Nauka/Interperiodica"

A sedimentation analysis of BaO_2 samples mechanically treated to varied extent demonstrated that considerable changes in particle size are only observed after the first two treatments: the broad asymmetric particle size distribution lying in the interval 0.05–0.30 mm (Fig. 1a) is transformed into a narrow peak with maximum corresponding to particle size of 0.005–0.010 mm (Fig. 1b). Further multiple treatment of the powder did not lead to any significant changes in the curve (Fig. 1b).

Intensive mechanical treatment of peroxide powders leads to the appearance in the DTA curves (Fig. 2) of new exothermic peaks in the temperature range 240–350°C, with the height and shape of the peaks dependent on the extent of mechanical treatment. The appearance of these peaks upon mechanical treatment indicates the occurrence of some changes caused by mechanical impact. In mechanochemistry, the additional energy imparted to a substance by mechanical treatment is conventionally named excess enthalpy

$$\Delta H_{ex} = H_T^* - H_T,$$

where H_T^* is the enthalpy of a mechanically treated active solid, and H_T is the enthalpy of the same substance in the initial equilibrium state at temperature T.

The energy is accumulated in distorted chemical bonds appearing as a result of atomic displacements relative to regular crystal lattice sites. Since the excess enthalpy affects both the equilibrium and the rate of the solid-state reaction, it is a rather important quantitative characteristic of the reactivity of a substance. The excess enthalpy is determined by measuring the area under the peak in the DTA curve corresponding to annealing of defects formed in the solid as a result of mechanical treatment. To compare ΔH_{ex} values obtained in different stages of mechanical treatment with the energy of barium peroxide decomposition equal to 75 kJ mol^{-1} [3], ΔH_{ex} was evaluated for reference samples: $AgNO_3$, Sn, $LiNO_3$, $NaNO_3$, and KNO_3 characterized by heat effects in the range 200–350°C. In the initial stage of mechanical treatment, ΔH_{ex} grows, but then decreases despite the continued intensive treatment. This fact indicates that, in a certain stage, part of energy accumulated in the preceding treatment is released.

An analysis of curves describing the loss of mass of peroxide samples as a function of temperature demonstrated that the curves are shifted to lower temperatures, i.e. oxygen evolution starts at lower temperatures. For clarity, points corresponding to 50% loss of active oxygen were chosen in these curves and

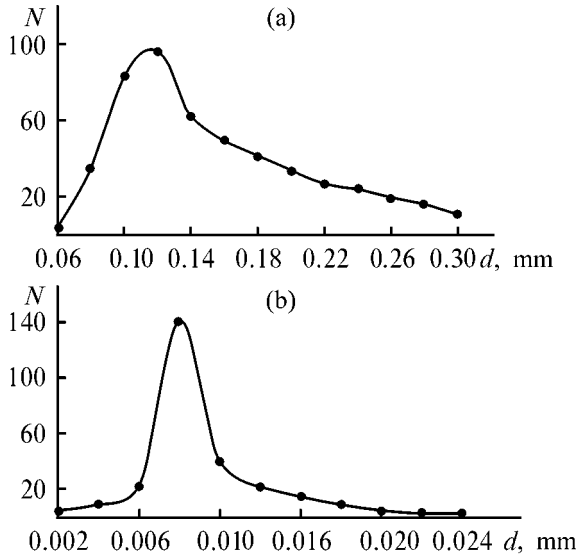

Fig. 1. BaO_2 particle size distribution functions. (N) Number of particles and (d) particle diameter. Powder: (a) initial and (b) twice treated.

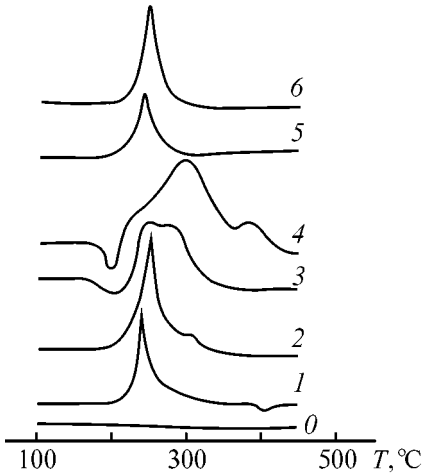

Fig. 2. DTA curves for mechanically treated barium peroxide powders. (T) Temperature. *Digits* at curves indicate the number of treatments; curve *0* is for the initial sample.

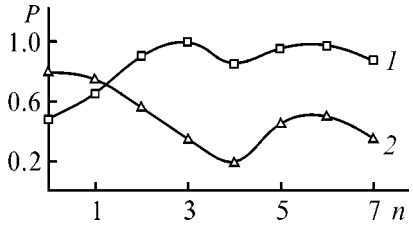

Fig. 3. Parameters P of BaO_2 samples vs. the number n of mechanical treatments. Parameter P: (*1*) S/S_{max} (for explanation see text), (*2*) $T \times 10^{-3}$ (°C) corresponding to liberation of 50% of active oxygen.

the corresponding temperatures were calculated for these points for each sample treated to varied extent. Figure 3 (curve *2*) presents the dependence of this temperature on the extent of treatment.

X-ray studies of samples subjected to varied extent of mechanical loading demonstrated that their crystal structure undergoes noticeable changes. X-ray diffraction patterns measured under identical conditions revealed changes in reflection intensity ratios. For example, for certain samples the intensity of the reflection (101) becomes equal or even smaller than 59% of the intensity of the reflection (002). Changes in the intensities of the reflections from different planes indicates varied degree of disordering of their constituent atoms under the action of mechanical treatment of varied intensity. The increase in the intensity of (002) reflections with respect to other reflections indicates that the employed extent of mechanical treatment does not cause any significant shifts from the (002) plane containing barium atoms. Presumably, the role of a stabilizing factor is played in this case by the presence of a pair of oxygens between barium atoms from different planes, contributing to the (002) reflections. At the same time, it is easier to cause disordering of atoms from the (101) plane by mechanical treatment. The process of a general decrease in intensity with its subsequent growth is observed several times with increasing duration of mechanical treatment.

The periodically observed general decrease in reflection intensity is due to partial disordering of atoms throughout the crystal lattice, giving way, in the course of subsequent mechanical treatment, to ordering of lattice atoms.

It should be noted that, despite the significant changes in X-ray reflection intensities, no already present peaks disappear and no new peaks appear in the X-ray diffraction patterns. No significant broadening of X-ray profiles is observed either.

For quantitative comparison of changes in X-ray diffraction patterns, the quantity

$$S = \sum_{hkl} I(hkl)$$

was calculated, where $I(hkl)$ is the intensity of an X-ray reflection with Miller indices (hkl).

S values were calculated for each sample. For convenience of presentation of S in relation to treatment duration, the maximum value, S_{max}, was chosen among all the S values corresponding to each sample, and all these values were normalized to it.

The effect of mechanical loading on the S/S_{max} value is illustrated in Fig. 3 (curve *1*).

An analysis of how the BaO_2 lattice constants depend on mechanical loading demonstrated that the parameters a and c change insignificantly with loading, except in the case of a fourfold treatment for which the microstrain $\Delta a/a$ is 1%.

Mechanically treated barium peroxide was used to perform solid-state synthesis of a high-temperature superconductor, $Y_1Ba_2Cu_3O_y$. As a result, the synthesis temperature was lowered by 150°C and more homogeneous samples were obtained, having no inclusions of the undesirable "green" phase of $BaCuO_2$. Thus, mechanical treatment made "milder" the synthesis conditions and improved the product quality even at higher temperatures, where the common untreated barium peroxide yields better results, compared with barium oxides.

Use of mechanically modified barium peroxide could produce even greater effect in polymer chemistry and organic synthesis, in purification of wastewater and organic and inorganic materials, in metallurgy, etc.

CONCLUSIONS

(1) Application of considerable mechanical loads leads to noticeable structural rearrangements in barium peroxide. The effect of periodic changes in reflection intensity with mechanical load points to relaxation of a deformed crystal into its initial state under mechanical impact. The doses of mechanochemical action leading to the highest microstrains were determined.

(2) Mechanical activation of barium peroxide gives rise to a number of new thermal effects in the temperature range 200–350°C and also leads to a significant change in the dynamics of liberation of active oxygen. The areas under exothermic peaks in DTA curves change nonmonotonically with applied load.

(3) To the maximum values of the exothermic peaks in the DTA curves correspond minimum reflection intensities in X-ray diffraction patterns, indicating the most disordered state with the maximum microdeformation parameter. To these values correspond the lowest temperatures of BaO_2 decomposition.

(4) The existence of a correlation between X-ray and thermal data points to the bulk nature of crystal-structure changes occurring in the substance in the course of its mechanical treatment and to the possibility of lowering substantially the BaO_2 dissociation temperature.

REFERENCES

1. Vol'nov, I.I., *Perekisnye soedineniya shchelochnozemel'nykh metallov* (Peroxide Compounds of Alkaline-Earth Metals), Moscow: Nauka, 1983.
2. Schumb, W.C., Satterfield, Ch. N., and Wentworth, R.L., *Hydrogen Peroxide*, New York: Reinhold, 1955.
3. Efimov, A.I., Belokurova, L.P., Vasil'kova, I.V., *et al.*, *Svoistva neorganicheskikh soedinenii: Spravochnik* (Properties of Inorganic Compounds: Reference Book), Leningrad: Khimiya, 1983.
4. Kuprii, V.Z., A Study of the Mechanism of Decomposition of Metal Peroxides, Peroxosalts of Sulfur and Boron, and Some Peroxohydrates, *Cand. Sci. Dissertation*, Kiev, 1970.
5. Azuma, Y., Mizuide, M., and Sachiro, K., *Gypsum Lime*, 1979, no. 162, pp. 175–183.
6. Heinicke, G., *Tribochemistry*, Berlin: Akademie-Verlag, 1984.

Russian Journal of Applied Chemistry, Vol. 74, No. 4, 2001, pp. 564–568. Translated from Zhurnal Prikladnoi Khimii, Vol. 74, No. 4, 2001, pp. 549–553.

PHYSICOCHEMICAL STUDIES OF SYSTEMS AND PROCESSES

Thermodynamic Analysis of Alloying in the System Lithium–Tellurium

A. G. Morachevskii

St. Petersburg State Technical University, St. Petersburg, Russia

Received January 16, 2001

Abstract—Data on thermodynamic properties of alloys of the system lithium–tellurium in liquid and solid states are compared and analyzed.

Tellurium forms with all alkali metals intermetallic compounds commonly possessing very narrow homogeneity regions. In addition, formation of tellurium-based solid solutions is uncharacteristic of these systems [1–4]. The lack of solid solutions allows use of polarization measurements for estimating the thermodynamic properties of the solid phases and makes simpler the necessary calculations.

In the system Li–Te, congruently melting compounds Li_2Te (mp 1477 ± 10 K) and $LiTe_3$ (mp 733 ± 1 K) are formed, with the latter compound characterized by a very flat maximum [1, 5]. The optimized phase diagram of the system (Fig. 1), presented by Sangster and Pelton [6], is very close to the data of [5].

The first data on thermodynamic properties of the system Li–Te were presented by Foster and Liu [7] who measured the potentials of lithium alloys with tellurium in the melt LiF–LiCl relative to a lithium–bismuth reference electrode (Li–Bi alloy saturated with Li_3Bi). The authors studied the lithium-lean part of the system ($0.056 \le x_{Li} \le 0.520$, x_{Li} is the molar fraction of Li in the alloy, 14 compositions) at a single temperature (798 K). The excess partial molar Gibbs energy of lithium ΔG_{Li}^{exc} (J mol^{-1}) at this temperature as a function of composition can be represented as

$$\Delta G_{Li}^{exc} = -153000 - 24000x_{Li} + 48850x_{Li}^2. \quad (1)$$

Equation (1) covers solely the region of liquid alloys of the system Li–Te at 798 K ($x_{Li} \le 0.38$). At infinite dilution ($x_{Li} \to 0$) ΔG_{Li}^{exc} is –153.0 kJ mol^{-1}, and the activity coefficient of lithium, γ_{Li}^{∞}, 9.6×10^{-11}. It follows from Eq. (1) that the ΔG_{Li}^{exc} value varies only slightly with increasing lithium content in the alloy: –154.9 (x_{Li} = 0.10), –155.8 (x_{Li} = 0.20) and –155.8 kJ mol^{-1} (x_{Li} = 0.30). The average value of ΔG_{Li}^{exc} in the region of liquid alloys is -155.4 ± 0.6 kJ mol^{-1} [7].

At 798 K and $x_{Li} > 0.38$ the process in the cell is associated with the reaction

$$Li(l) + 0.5Te(l) = 0.5Li_2Te(s). \quad (2)$$

The change in the standard Gibbs energy ΔG_{798}^0 upon formation of 1 mole of Li_2Te is -325.9 ± 1.7 kJ mol^{-1} [7]. The same value is given in the reference book compiled by Mills [8]. The standard entropy of Li_2Te, found by approximate calculation, is $S_{298}^0 = 77.4 \pm 12.6$ J mol^{-1} K^{-1} [8]. A close value, $S_{298}^0 = 80.8 \pm 12.6$ J mol^{-1} K^{-1}, was obtained using a different calculation procedure by Voronin [9]. The standard enthalpy of Li_2Te formation, ΔH_{298}^0, was estimated to be -355.6 ± 20.9 kJ mol^{-1}, using the

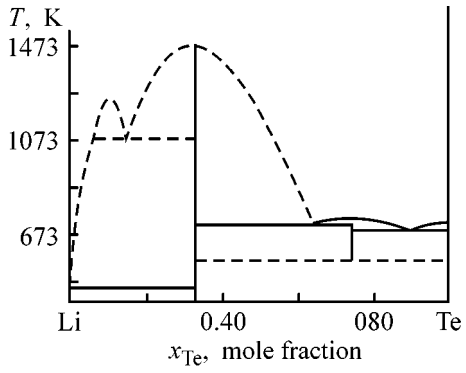

Fig. 1. Phase diagram of the lithium–tellurium system [6]. (T) Temperature and (x_{Te}) tellurium content in the system.

1070-4272/01/7404-0564 $25.00 © 2001 MAIK "Nauka/Interperiodica"

standard entropy and ΔG^0_{298} from the reference book [8]. The same values of ΔH^0_{298} and S^0_{298} were used by Barin *et al.* [10] to estimate the thermodynamic functions of Li_2Te in a wide temperature range (298–1100 K).

For liquid lithium–tellurium alloys, close results were obtained in [11]. In a set of systematic investigations concerned with thermodynamic properties of liquid alloys formed by lithium and Group III–V elements of the periodic system, alloys of the system Li–Te ($0.016 \le x_{Li} \le 0.222$, 7 compositions, 823 K) were studied by the emf method [12, 13]. As electrolyte served a eutectic mixture LiF–LiCl. The limiting value of ΔG^{exc}_{Li} at infinite dilution is –154.3 kJ mol^{-1} and $\gamma^{\infty}_{Li} = 1.6 \times 10^{-10}$. In the composition range studied here, ΔG^{exc}_{Li} is virtually constant (–154.3 kJ mol^{-1}) [11].

In a more recent study [14], a lithium–fluoroborate glass was used in emf measurements to avoid interaction of Li–Te alloys with molten electrolyte. Li_2Te is possibly soluble in molten salts [15–17]. On the basis of the whole set of properties, the following glass composition was taken to be the optimal (mol %): 15.9 Li_2O, 69.0 B_2O_3, and 15.1 LiF [18, 19]. The lithium–tellurium alloys under study were prepared electrochemically [20].

In [14], the alloys were studied in the range 733–803 K ($0.008 \le x_{Li} \le 0.283$, 10 compositions) and the partial and integral thermodynamic characteristics at 785 K were given. The activity coefficient of lithium is virtually constant in the composition range studied [$(3.44 \pm 0.39) \times 10^{-11}$ at 785 K]. The dependence of the emf on $\log x_{Li}$ is nearly linear (Fig. 2). In this case, the expression

$$E = -2.303 \frac{RT}{F} \log x_{Li}\gamma_{Li}$$

can be represented as

$$E = a - b\log x_{Li}.$$

The least-squares processing of the data reported in [14] yields the dependence

$$E = 1.661 - 0.124\log x_{Li}.$$

The correlation coefficient is 0.993, and the root-mean-square error, 0.35%. It should be noted that the obtained coefficient of the logarithm in the above expression slightly differs from the theoretical value (0.156 at 785 K).

The activity coefficient of tellurium was determined by integrating the Gibbs–Duhem equation in the form

$$\ln \gamma_{Te} = -\alpha_{Li}x_{Li}x_{Te} + \int_0^{x_{Li}} \alpha_{Li} dx_{Li},$$

where $\alpha_{Li} = \ln \gamma_{Li}/(1 - x_{Li})^2$.

Below, the activities and activity coefficients of lithium and tellurium in liquid alloys at 785 K are given for the composition interval ($0.08 \le x_{Li} \le 0.28$) with a step of 0.04 molar fraction:

x_{Li}	$a_{Li} \times 10^{12}$	$\gamma_{Li} \times 10^{11}$	a_{Te}	γ_{Te}
0.08	2.67	3.34	0.957	1.04
0.12	3.57	2.97	0.928	1.06
0.16	5.30	3.31	0.876	1.04
0.20	7.08	3.54	0.821	1.03
0.24	7.85	3.27	0.798	1.05
0.28	8.23	2.94	0.793	1.10

The average activity coefficient, as determined from smoothed data, is $(3.23 \pm 0.14) \times 10^{-11}$ for lithium and -1.05 ± 0.02 for tellurium. If Henry's law is fulfilled for a solute (lithium in the given case), then Raoult's law must be fulfilled for the solvent (tellurium) in the same range of compositions [21].

According to [14], the ΔG^{exc}_{Li} value in the concentration range ($0.008 \le x_{Li} \le 0.280$) at 785 K lies within the range from –152.8 to –158.5 kJ mol^{-1}, which is close to the previously obtained results [7].

In [22], the vapor pressure of Te_2 over molten $LiTe_3$ at 733–1030 K was measured by absorption spectrometry. In this case, the temperature dependence of tellurium activity is expressed by the equation ($x_{Te} = 0.75$)

$$\log a_{Te} = -0.471 + 296.5T^{-1}.$$

At 785 K the tellurium activity is 0.807 and its activity coefficient, 1.08, in good agreement with the above data obtained on the basis of [14].

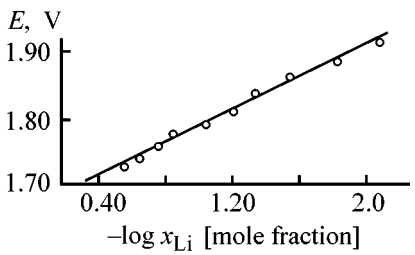

Fig. 2. Electromotive force E vs. lithium concentration x_{Li} in the alloy at 785 K.

In the same study [22], the vapor pressure of tellurium over a $LiTe_3$–Li_2Te mixture in solid state at 653–722 K was also determined. For the equilibrium

$$4LiTe_3(s) = 2Li_2Te(s) + 5Te_2(g)$$

$\log P_{Te_2} = 5.326 - 6726/T$, where P is pressure (atm).

For the reaction

$$0.5Li_2Te(s) + 2.5Te(s) = LiTe_3(s) \quad (3)$$

the change in the Gibbs energy (kJ) is given by

$$\Delta G_T^0 = 30.51 - 5.293 \times 10^{-2}T. \quad (4)$$

The authors of [22] emphasize that the ΔG_T^0 value becomes positive below 577 K and the compound $LiTe_3$ decomposes into two phases: Li_2Te and Te [22]. This fact is reflected in the phase diagram of the Li–Te system (Fig. 1).

In [23–28], the thermodynamic properties of the compounds formed by lithium and other alkali metals were determined by means of polarization measurements, with polarization curves measured in pulsed galvanostatic mode and switching-off curves recorded on a specially designed setup [29, 30]. The method consists in that the potential of tellurium electrode polarized by dc rectangular pulses of increasing amplitude is recorded at the moment when the circuit is broken. The setup allowed switching-on the polarizing current for a prescribed time (from 1 to 32 s), turning-on the tape drive of the recorder 1 s before the polarization circuit is broken, current switching-off, and delivery of a pulse to a digital voltmeter. Measurements in the potentiodynamic mode could be used for obtaining preliminary results and estimating the number of phase regions in alloying.

The above technique for measuring polarization curves in pulsed galvanostatic mode is fast and, at the same time, ensures high accuracy (not worse than ±1%) in determining the phase-region potential. However, the interpretation of results depends on the reliability of data obtained in studying a particular phase diagram. In the Li–Te system, only two compounds are formed whose compositions are beyond any doubt. Consequently, polarization measurements yield rather reliable results in this case.

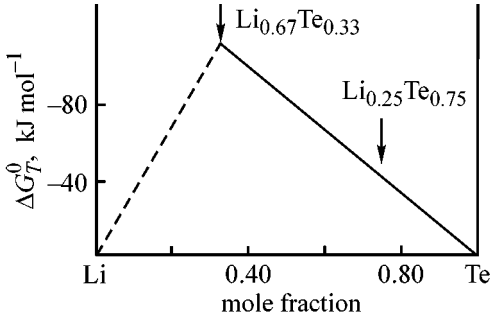

Fig. 3. The integral molar Gibbs energy ΔG_T^0 vs. alloy composition in the system lithium–tellurium at 650 K.

The Li–Te system was studied at 650 K, with a LiF–LiCl–LiI melt as electrolyte [25]. Two regions with constant potentials relative to lithium reference electrode (1.774 ± 0.002 and 1.721 ± 0.002 V), attributable to the phase regions Te + $LiTe_3$ and $LiTe_3$ + Li_2Te, were clearly revealed in the polarization and switching-off curves. The first phase region is related to the reaction

$$Li(l) + 3Te(s) = LiTe_3(s). \quad (5)$$

In accordance with reaction (5), the standard changes in the Gibbs energy in the formation of $LiTe_3$ and $Li_{0.25}Te_{0.75}$ from pure components are -171.2 ± 0.2 and -42.8 ± 0.1 kJ mol^{-1}, respectively.

The second phase region corresponds to the occurrence of the reaction

$$LiTe_3(s) + 5Li(l) = 3Li_2Te(s). \quad (6)$$

The change in the Gibbs energy at 650 K for this reaction is -830 ± 0.2 kJ. Taking into account the ΔG_{650}^0 value for $LiTe_3$, we have -333.8 ± 0.4 and -111.3 ± 0.2 kJ mol^{-1} for the change in the Gibbs energy in the formation of, respectively, Li_2Te and $Li_{0.67}Te_{0.33}$ from pure components. These values are close to those obtained previously by Foster and Liu [7] at 798 K. For reaction (3) at 650 K, Eq. (4) gives, on the basis of data reported in [22], $\Delta G = -3.89$ kJ; according to our data, $\Delta G = -1.30$ kJ.

The dependence of the Gibbs energy on composition for the Li–Te system at 650 K [25] is presented in Fig. 3. As seen, there is virtually no clearly visible break in the curve at $LiTe_3$ composition. Indeed, it follows from the obtained potentials that the partial molar Gibbs energy of lithium ΔG_{Li}, determining the slope of the straight lines, is –166.1 and –171.2 kJ mol^{-1} at 650 K in the phase regions $LiTe_3$ + Li_2Te and Te + $LiTe_3$, respectively. With the adopted scale of the ordinate axis in Fig. 3, this difference is very small.

Data on integral molar Gibbs energy ΔG (kJ mol^{-1}) at 798 K, obtained in [7, 14], are close in the comparable part of the homogeneity region:

x_{Li}	ΔG_{798} [7]	ΔG_{798} [14]	Discrepancy, %
0.04	–7.31	–7.32	0.14
0.08	–14.22	–14.41	1.32
0.12	–20.97	–21.90	4.20
0.16	–27.63	–28.30	2.37
0.20	–34.23	–35.11	2.51
0.24	–40.79	–41.87	2.58
0.28	–46.99	–48.52	3.15

In studying the tellurium cathode polarization, we used, along with the halide electrolyte, a nitrate–nitrite electrolyte with addition of lithium hydroxide ($LiNO_3$–$LiNO_2$–LiOH, 423 K) and also electrolytes with dissimilar cations, LiCl–KCl (650 K) and $LiNO_3$–KNO_3 (423 K). No significant differences between the potentials of the two-phase regions of interest were revealed; however, in electrolytes with dissimilar cations, a region with constant potential relative to the lithium reference electrode (1.959 ± 0.008 V at 423 K and 1.896 V at 650 K) was additionally observed. Most likely, this is due to the involvement of potassium ions in alloying.

It should be particularly emphasized that, in an electrolyte with a single kind of cations, both two-phase regions are recorded at 423 K, although the difference between the potentials corresponding to these regions does not exceed 0.02 V (1.770 ± 0.010 and 1.751 ± 0.002 V).

The potential of the Te + Li_2Te two-phase region relative to lithium reference electrode (1.779 ± 0.003 V), determined in [31] at 298 K by the electrochemical method (coulometric titration) with the use of a propylene–carbonate electrolyte containing LiF_6As, corresponds to the standard Gibbs energy of Li_2Te formation from pure solid components (-343.5 ± 1.3 kJ mol^{-1}). The obtained potential of the phase region at 298 K [31] is close to the potentials of the phase regions at 423 K [25].

Data on the potential of lithium reduction from molten electrolytes on a liquid tellurium cathode are available [23, 32]. The discharge of lithium ions with the formation of an alloy on both solid and liquid cathodes should be considered a single electrochemical process [33]. This concept is of fundamental importance and governs the thermodynamics of alloying. Not only electron transfer occurs, but also a simultaneous interaction of the reduced metal with the cathode material. In reduction of lithium on a liquid tellurium cathode, the observed value of the potential cannot serve as a basis for any thermodynamic calculation because of the undetermined lithium content in the surface layer of the liquid alloy. Nonetheless, the depolarization value and the difference between the potentials of lithium reduction on an inert solid cathode and a liquid cathode allow qualitative estimation of the degree of component interaction in the liquid alloy. It should be kept in mind, however, that the depolarization depends, to a certain extent, on the measurement technique. For this reason, the potentials of lithium reduction on various liquid cathodes can be compared solely under identical measurement conditions. The depolarization value in lithium reduction on the liquid tellurium cathode lies within 1.95–2.10 V. For comparison, this value is 0.94 V for bismuth and 0.68 V for lead at 723 K [34].

The switching-off curves measured at 823 K, after polarizing the liquid tellurium cathode with 2–3 A cm^2 current density for 1 h, show two plateaus of potential decay. In the LiF–LiF electrolyte, the plateau potentials, averaged over 30 tests, are 0.72 ± 0.05 and 1.64 ± 0.01 V relative to a lithium reference electrode [32]. The latter potential is close to the potential corresponding to liquid lithium–tellurium alloy saturated with Li_2Te (1.67 V, 798 K) [7]. The plateau in potential decay at 0.72 ± 0.05 V cannot be explained yet, since part of the system Li–Li_2Te has virtually not been studied at all.

The aforesaid suggests that there is rather good agreement between the results obtained in studying the thermodynamic properties of liquid alloys and solid phases in the system Li–Te by different methods.

REFERENCES

1. Drits, M.E. and Zusman, L.L., *Splavy shchelochnykh i shchelochno-zemel'nykh metallov* (Alloys of Alkali and Alkaline-Earth Metals), Moscow: Metallurgiya, 1986.
2. Morachevskii, A.G., Busse-Machukas, V.B., Shesterkin, I.A., *et al.*, *Natrii: Svoistva, proizvodstvo, primenenie* (Sodium: Properties, Manufacture, and Use), St. Petersburg: Khimiya, 1992.
3. Morachevskii, A.G., Beloglazov, I.N. and Kasymbekov, B.A., *Kalii: Svoistva, proizvodstvo, primenenie* (Potassium: Properties, Manufacture, and Use), Moscow: Ruda i Metally, 2000.
4. Lokshin, E.P. and Voskoboinikov, N.B., *Rubidii i Tsezii* (Rubidium and Cesium), Apatity: Kola Nauch. Tsentr, Ross. Akad. Nauk, 1996.
5. Cunningham, P.T., Johnson, S.A., and Cairns, E.J., *J. Electrochem. Soc.*, 1973, vol. 120, no. 3, pp. 328–330.
6. Sangster, J. and Pelton, A.D., *J. Phase Equilibria*, 1992, vol. 13, no. 3, pp. 300–303.

7. Foster, M.S. and Liu, C.C., *J. Phys. Chem.*, 1966, vol. 70, no. 3, pp. 950–952.
8. Mills, K.C., *Thermodynamic Data for Inorganic Sulphides, Selenides and Tellurides*, London: Butterworths, 1974.
9. Voronin, G.F., *Zh. Fiz. Khim.*, 1970, vol. 44, no. 3, pp. 3013–3017.
10. Barin, I., Knacke, O., and Kubaschewski O., *Thermochemical Properties of Inorganic Substances: Supplement*, Berlin: m.b.H. Stahleisen Verlag, Dusseldorf, 1977.
11. Demidov, A.I., Morachevskii, A.G., and Ivantsova, M.N., *Elektrokhimiya*, 1975, vol. 11, no. 5, pp. 819–820.
12. Morachevskii, A.G., Gerasimenko, L.N., and Demidov, A.I., *Termodinamicheskie svoistva metallicheskikh splavov* (Thermodynamic Properties of Metal Alloys), Baku: Elm, 1975, pp. 239–241.
13. Morachevskii, A.G. and Demidov, A.I., *Zh. Fiz. Khim.*, 1983, vol. 57, no. 9, pp. 2113–2128.
14. Chekoev, N.G. and Morachevskii, A.G., *Zh. Prikl. Khim.*, 1979, vol. 52, no. 3, pp. 685–687.
15. Gruen, D.M., *Quart. Rev.*, 1965, vol. 19, pp. 349–368.
16. Gruen, D.M., McBeth, R.L., Foster, M.S., and Crouthamel, C.E., *J. Phys. Chem.*, 1966, vol. 70, no. 2, pp. 472–477.
17. Morachevskii, A.G., Demidov, A.I., Bulatova, V.F., and Klebanov, E.B, *Issledovaniya v oblasti khimii ionnykh rasplavov i tverdykh elektrolitov* (Study of the Chemistry of Ionic Melts and Solid Electrolytes), Kiev: Naukova Dumka, 1985, pp. 100–105.
18. Chekoev, N.G. and Morachevskii, A.G., *Primenenie tverdykh stekloobraznykh elektrolitov pri issledovanii termodinamicheskikh svoistv splavov litiya* (Applicaton of Solid Glass Electrolytes in Studies of Thermodynamic Properties of Lithium Alloys), Available from VINITI, 1984, no. 6973–84.
19. Chekoev, N.G. and Morachevskii, A.G., Abstracts of Papers, *IX Vsesoyuznaya konferentsiya po fizicheskoi khimii i elektrokhimii ionnykh rasplavov i tverdykh elektrolitov* (IX All-Union Conf. on Physicochemistry and Electrochemistry of Ionic Melts and Solid Electrolytes), Sverdlovsk: Ural'sk. Nation. Tsentr, Akad. Nauk SSSR, 1987, vol. 3, part 1, p. 193.
20. Chekoev, N.G. and Morachevskii, A.G., *Izv. Vyssh. Uchebn. Zaved., Tsvetn. Metall.*, 1987, no. 6, pp. 124–126.
21. Morachevskii, A.G. and Sladkov, I.B., *Termodinamicheskie raschety v metallurgii: Spravochnik* (Thermodynamic Calculations in Metallurgy: Handbook), Moscow: Metallurgiya, 1993.
22. Hitch, B.F., Toth, L.M., and Brynestad J., *J. Inorg. Nucl. Chem.*, 1978, vol. 40, no. 1, pp. 31–34.
23. Temnogorova, N.V., Demidov, A.I., and Morachevskii, A.G., *Zh. Prikl. Khim.*, 1979, vol. 52, no. 4, pp. 929–930.
24. Morachevskii, A.G., Demidov, A.I., and Temnogorova, N.V., *Fizicheskaya khimiya i elektrokhimiya rasplavlennykh i tverdykh elektrolitov* (Physicochemistry and Electrochemistry of Molten and Solid Electrolytes), Sverdlovsk: Ural'sk. Nation. Tsentr, Akad. Nauk. SSSR, 1979, part 2, pp. 119–120.
25. Demidov, A.I., Dukhanin, G.P., Simikov, I.A., and Morachevskii, A.G., *Elektrokhimiya*, 1983, vol. 19, no. 8, pp. 1125–1129.
26. Demidov, A.I., Morachevskii, A.G., Dukhanin, G.P., and Simikov, I.A., Abstracts of Papers, *VI Vsesoyuznaya konferentsiya po khimii i tekhnologii redkikh shchelochnykh elementov* (VI All-Union Conf. On Chemistry and Technology of Rare Alkali Elements), Moscow: Nauka, 1983, pp. 83–84.
27. Morachevskii, A.G., Klebanov, E.B, and Shesterkina, I.I., Abstracts of Papers, *V Vsesoyuznaya konferentsiya po termodinamike metallicheskikh splavov* (V All-Union Conf. on Thermodynamics of Metal Alloys), Moscow: TsNIIchermet, 1985, p. 30.
28. Klebanov, E.B, Shibalovskaya, I.I., and Morachevskii, A.G., *Izv. Vyssh. Uchebn. Zav., Tsvetn. Metall.*, 1989, no. 1, pp. 126–127.
29. Nikitin, A.V., *Zh. Prikl. Khim.*, 1979, vol. 52, no. 1, pp. 2039–204.
30. Nikitin, A.V., Study of the Alloying Processes Accompanying Precipitation of Lithium from Molten Salts on Liquid and Solid Cathodes of Bismuth, Antimony, Tellurium and Their Alloys, *Cand. Sci. Dissertation*, Leningrad, 1980.
31. Fleming, J.G. and Stevenson, D.A., *J. Electrochem. Soc.*, 1989, vol. 136, no. 12, pp. 3859–3869.
32. Demidov, A.I., Nikitin, A.V., and Morachevskii, A.G., *Zh. Prikl. Khim.*, 1979, vol. 52, no. 8, pp. 1881–1882.
33. Morachevskii, A.G., Abstracts of Papers, *Pervyi Ukrainskii Elektrokhimicheskii S'ezd* (The First Ukrainian Electrochemical Congress), Kiev, 1995, p. 147.
34. Temnogorova, N.V, Demidov, A.I., and Morachevskii, A.G., *Izv. Vyssh. Uchebn. Zav., Tsvetn. Metall.*, 1979, no. 3, pp. 89–96.

Russian Journal of Applied Chemistry, Vol. 74, No. 4, 2001, pp. 569–571. Translated from Zhurnal Prikladnoi Khimii, Vol. 74, No. 4, 2001, pp. 553–555.

PHYSICOCHEMICAL STUDIES OF SYSTEMS AND PROCESSES

Thermodynamic Analysis of Alloying in the System Lithium–Selenium

A. G. Morachevskii

St. Petersburg State Technical University, St. Petersburg, Russia

Received January 16, 2001

Abstract—Data on the thermodynamic properties of liquid alloys and the solid phase in the system lithium–selenium are compared and discussed.

Lithium and selenium form only a single compound, Li_2Se (mp 1575 ± 5 K), and there exists a separation region in the selenium-rich part of the system [1]. The optimized phase diagram of the system is presented in Fig. 1 [2]. Other properties of lithium–selenium alloys are considered in a review [2]. However, it seems reasonable to discuss results obtained in thermodynamic studies of the alloys in more detail.

First data on thermodynamic properties of liquid alloys of the system Li–Se were obtained in [3] by measuring the emf of concentration cells with lithium–selenium alloys ($x_{Li} \le 0.464$, x_{Li} is the molar fraction of lithium in the alloy) in contact with molten LiBr–RbBr (mp 540 K) or LiF–LiCl–LiI electrolyte (mp 614 K), and experimental data were represented as graphs. The interaction of lithium–selenium alloys with salt melts [4] makes interpretation of the emf measurements rather complicated.

In [5], thermodynamic properties of liquid lithium–selenium alloys ($0.002 \le x_{Li} \le 0.159$, 12 compositions) were studied by the emf method, with glass ($Li_2O : B_2O_3 : LiF = 8.3 : 84.7 : 15.3$ wt %) used as solid electrolyte to prevent interaction of Li–Se alloys with molten electrolyte LiCl–KCl. All the compositions studied lie within the separation region. The average cell emf is 2.085 ± 0.002 V at 693 K. In the separation region of the Li–Se system, where a mixture of molten salts is additionally present as a third phase, the emf is 2.10 V at both temperatures (633 and 663 K) [4], which is close, within 0.7%, to the above value. This suggests that the influence exerted by the interaction with the salt phase on the thermodynamic properties of the Li–Se itself is insignificant. The average partial molar Gibbs energy of lithium ΔG_{Li} at 693 K in the separation region is (201.2 ± 0.2) kJ mol^{-1} [5]. The average Li activity, a_{Li}, at this temperature is $(6.83 \pm 0.24) \times 10^{-16}$.

It was indicated in [4] that the interaction of lithium with selenium in the liquid state should be described by the reaction

$$2Li + xSe = Li_2Se_x.$$

For this reason, the activity coefficient and activity of Li_2 are used. This approach seems to be inconvenient for systematic studies of the thermodynamic properties of liquid lithium alloys [6] and is not substantiated to a sufficient extent.

In the composition range studied [5], the integral molar Gibbs energy ΔG of the system Li–Se can be estimated with regard to the constant ΔG_{Li} value by taking into account that virtually pure selenium (ΔG_{Se} approaches zero) is in equilibrium with the lithium alloy at 693 K. This energy can also be calculated in the conventional manner without taking into account the specificity of interaction between the components:

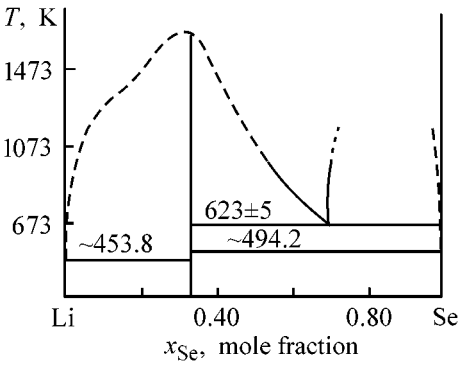

Fig. 1. Phase diagram of the lithium–selenium system according to [2]. (T) Temperature and x_{Se} selenium content in the alloy.

1070-4272/01/7404-0569 $25.00 © 2001 MAIK "Nauka/Interperiodica"

$$\Delta G = (1 - x_{Li})\int_0^{x_{Li}} \frac{\Delta G_{Li}^{exc}}{(1 - x_{Li})^2}\, dx_{Li} + \Delta G^{id},$$

where ΔG_{Li}^{exc} is the partial excess Gibbs energy of lithium and ΔG_{Li}^{id} is the change in the Gibbs energy for the ideal solution at a given composition and temperature.

Both the approaches give similar results (693 K, ΔG, kJ mol^{-1}):

x_{Li}	ΔG	x_{Li}	ΔG	x_{Li}	ΔG
0.02	–4.06	0.08	–16.11	0.14	–28.17
0.04	–8.06	0.10	–20.16	0.16	–32.20
0.06	–12.08	0.12	–24.21	0.18	–36.22

As shown above, only a single, rather stable compound Li_2Se is formed in the Li–Se system. This fact and the constant ΔG value in the composition range studied enable an approximate estimate of the change in the Gibbs energy for the reaction

$$0.667Li(l) + 0.333Se(l) = Li_{0.667}Se_{0.333}(s). \quad (1)$$

The point of intersection of the dashed straight lines in Fig. 2 corresponds to the limiting Gibbs energy for reaction (1) at a given temperature (–134.1 kJ mol^{-1}). The true value of ΔG must be somewhat lower in absolute value (probably, -131 ± 2 kJ mol^{-1}). The change in the Gibbs energy of reaction (1) at 633 K, calculated from the results of emf measurements for compositions in equilibrium with the solid phase Li_2Se, is –131.1 kJ mol^{-1} [4]. With the slight difference in measurement temperatures (693 and 633 K) disregarded, these results agree quite satisfactorily. The corresponding value for Li_2Se is –393.3 kJ mol^{-1}.

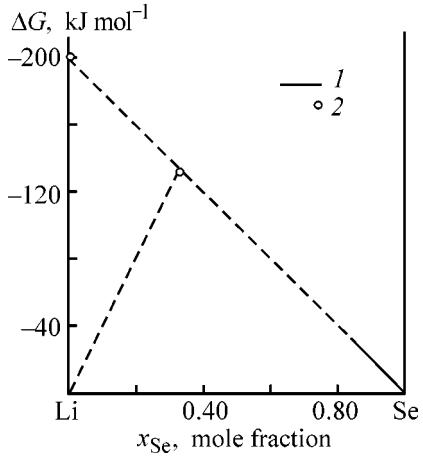

Fig. 2. Integral molar Gibbs energy ΔG vs. composition. (x_{Se}) Selenium content in the alloy. Data, temperature (K): (*1*) [5], 693 and (*2*) [3], 633.

In a study [7], not mentioned in review [2], the polarization of a solid selenium electrode in the $LiNO_3$–$LiNO_2$–LiOH melt was studied at 423 K. The polarization curve measured in pulsed galvanostatic mode has a clearly pronounced portion of constant potential (2.098 ± 0.002 V) relative to a solid lithium reference electrode. This potential is associated with the presence of a two-phase mixture Se + Li_2Se in the surface layer of the electrode being polarized. Thus, for the reaction

$$2Li(s) + Se(s) = Li_2Se(s) \quad (2)$$

the change in the Gibbs energy at 423 K is –404.9 kJ mol^{-1}. Correspondingly, ΔG = 135.0 kJ mol^{-1} in the case of formation of the $Li_{0.667}Se_{0.333}$ compound by reaction (2). Recalculation to the liquid supercooled state of the initial components, corresponding to reaction (1), yields –135.6 and –406.8 kJ mol^{-1} for $Li_{0.667}Se_{0.333}$ and Li_2Se, respectively (at 423 K).

The standard entropy S_{298}^0 of lithium selenide is estimated unambiguously. Calculation by Latimer's method [8] yields 96.2 ± 20.9 J mol^{-1} K^{-1}, and that by Voronin's method, 69.9 ± 12.6 J mol^{-1} K^{-1} [9]. In Mills's handbook [10], the S_{298}^0 value of 71.1 ± 12.6 J mol^{-1} K^{-1} is reported. The same value (with unspecified error) is used as a basis for calculations in the reference book [11].

The change in the enthalpy in Li_2Se formation from pure solid components at 423 K can be calculated with reasonable accuracy by means of the equation

$$\Delta H_T = \Delta G_T + T\Delta S_{298}^0 + T\Delta C_p \ln(T/298),$$

where ΔS_{298}^0 characterizes the enthalpy change under the standard conditions and ΔC_p is the change in the average heat capacity in the temperature range under consideration.

According to the data presented in the reference book [11], S_{298}^0 = 29.08 J mol^{-1} K^{-1} for Li(s) and 42.26 J mol^{-1} K^{-1} for Se(s). Closely similar values (29.10 and 42.43 J mol^{-1} K^{-1}, respectively) were used in calculations in [8]. If we accept S_{298}^0 = 96.2 J mol^{-1} K^{-1} for Li_2Se, then the ΔS_{298}^0 value for the process considered will be –4.22 J mol^{-1} K^{-1}. In its turn, the other S_{298}^0 values given above for Li_2Se yield ΔS_{298}^0 –30.52 and –29.32 J mol^{-1} K^{-1}. The average heat capacities of the components in the range 298–623 K are (J mol^{-1} K^{-1}): 17.1 (Li_2Se), 6.21 (Li), and 6.38 (Se) [11]. With these values taken into account by using equation (3) for 423 K at ΔG_{423} = –404.9 kJ mol^{-1}, we obtain, depending on ΔS_{298}^0, the following ΔH_{423} values (kJ mol^{-1}): –406.9, –418.0,

and –417.5. The last two values are preferable, and they are close to the ΔH^0_{298} value for Li_2Se (-425.9 ± 8.4 kJ mol^{-1}), obtained by fluorine calorimetry in [8].

Thus, the results of electrochemical measurements yield the following values of the integral molar parameters for compounds Li_2Se (kJ mol^{-1}): 404.9 (ΔG_{423}), –418.0 (ΔH_{423}), and –393.3 (ΔG_{633}). The changes in the Gibbs energy are obtained on the basis of a series of experimental studies [3, 5, 7]. The enthalpy change depends on the method chosen for estimating the standard energy of lithium selenide, but seems to be rather reasonable.

REFERENCES

1. Cunningham, P.T., Johnson, S.A., and Cairns, E.J. *J. Electrochem. Soc.*, 1971, vol.118, no.12, pp. 1941–1944.
2. Sagster, J. and Pelton, A.D., *J. Phase Equilibria*, 1997, vol. 18, no. 2, pp. 181–184.
3. Cairns, E.J., Kucera, G.H., and Cunningham, P.T., *J. Electrochem. Soc.*, 1973, vol. 120, no. 5, pp. 595–597
4. Cunningham, P.T., Cairns, E.J., Hathaway, E.J., *et al. J. Electrochem. Soc.*, 1973, vol. 120, no.5, pp. 591–594.
5. Chekoev, N.G. and Morachevskii, A.G., *Zh. Prikl. Khim.*, 1978, vol. 51, no. 10, pp. 2348–2349.
6. Morachevskii, A.G. and Demidov, A.I., *Zh. Fiz. Khim.*, 1983, vol. 57, no. 9, pp. 2113–2128.
7. Dukhanin, G.P., Demidov, A.I., and Morachevskii, A.G., *Elektrokhimiya*, 1983, vol. 19, no. 9, pp. 1264–1266.
8. Ader, M., *J. Chem. Thermodyn.*, 1974, vol. 6, no. 6, pp. 587–597.
9. Voronin, G.F., *Zh. Fiz. Khim.*, 1970, vol. 44, no. 12, pp. 3013–3017.
10. Mills, K.C., *Thermodynamic Data for Inorganic Sulphides, Selenides and Tellurides*, London: Butterworths, 1974.
11. Barin, I., Knacke, O., and Kubaschewski O., *Thermochemical Properties of Inorganic Substances: Supplement*, Berlin: m.b.H. Stahleisen Verlag, Dusseldorf, 1977.

Russian Journal of Applied Chemistry, Vol. 74, No. 4, 2001, pp. 572–575. Translated from Zhurnal Prikladnoi Khimii, Vol. 74, No. 4, 2001, pp. 556–559.

PHYSICOCHEMICAL STUDIES OF SYSTEMS AND PROCESSES

Improvement of the Procedure for Thermodynamic Calculation of the Equilibrium Composition of Gas Mixture Formed in Concurrent-Consecutive Reactions

N. V. Trusov

Kharkov State Polytechnic University, Kharkov, Ukraine

Received May 12, 2000; in final form, September 2000

Abstract—Criteria are proposed that make it possible to exclude interactions distorting the results that can be obtained in a thermodynamic calculation of the equilibrium composition of the gas mixture formed in concurrent-consecutive reactions. The proposed improvement is verified on the basis of the available experimental data.

In [1], a thermodynamic calculation of the equilibrium composition was performed using the modified Hook–Jeaves method [2]. The choice of a process for catalytic oxidation of ammonia as a test object of study can be attributed to the exhaustive scientific substantiation of this technology [3–7] allowing precise evaluation of the validity of calculated data.

The calculation of the equilibrium composition formed in ammonia oxidation, performed in [1], made it possible to ascertain some specific features of the process, on the one hand, and clearly established the possibility of using the proposed technique for thermodynamic analysis of processes occurring in complex chemical systems, on the other. However, there was evidence indicating the insistent need for further improvement of this method.

For example, a completely unacceptable circumstance was revealed in solving the test problem, namely, the reactions of nitrogen(II) oxide oxidation to NO_2 and NO_x hydrogenation were included into the set of reactions under consideration. This was done because the change in the Gibbs energy gave no reason to exclude these reactions. Both the reactions occur in the industrial process for nitric acid production, but take place in the stages of afteroxidation–absorption of nitrose gas and in purification of the discharged flow to remove nitrogen oxides. In the stage of ammonia oxidation, these reactions do not occur [3, 4] and the problem in question can only be solved with the given stage modeled as precisely as possible by means of a thermodynamic calculation.

Noteworthy in this connection is the influence exerted by the number of reactions taken into account on the calculated composition of the equilibrium gas. For example, if only the following reactions are considered

$$4NH_3 + 5O_2 = 4NO + 6H_2O, \quad (1)$$

$$2NH_3 = 3H_2 + N_2, \quad (2)$$

$$4NH_3 + 3O_2 = 2N_2 + 6H_2O, \quad (3)$$

$$4NH_3 + 4O_2 = 2N_2O + 6H_2O, \quad (4)$$

then the obtained equilibrium composition (Table 1) is in rather good agreement with experimental data [3, 4]. However, if only the reaction

$$2NO + O_2 = 2NO_2 \quad (5)$$

is added, the calculated composition of the nitrose gas changes dramatically (Table 1). It can be seen that it is reaction (5) that is the reason for the discrepancy between the calculated thermodynamic data and experimental results. This evidence required thorough analysis.

Table 1. Equilibrium composition of nitrose gas in relation to the number of reactions considered (T = 1200 K, P = 0.1 MPa, initial ratio O_2/NH_3 = 2 mol mol^{-1})

Set of reactions	Production gas component, vol %						NO_x yield, %
	N_2	O_2	H_2O	NO	N_2O	NO_2	
(1)–(4)	70.0	7.1	13.9	8.9	0.1	–	95.3
(1)–(5)	74.3	8.5	11.1	0.4	0.43	5.28	86.9

1070-4272/01/7404-0572 $25.00 © 2001 MAIK "Nauka/Interperiodica"

It was evident that, despite the thermodynamic probability, there exists a group of reactions (*n*) that cannot be included into the set of concurrent-consecutive chemical interactions (*m*). The reason is that they have different durations τ, which cannot be accounted for by a thermodynamic analysis by definition. With the reaction duration $\tau(m) << \tau(n)$, the calculated equilibrium composition is the composition that could be formed in a real process at infinitely long exposure.

In the system under study, $NH_3 + O_2$, reactions of this kind can be revealed and excluded from consideration on the basis of extensive published evidence [3–7]. However, on passing to a less studied system of reagents and chemical processes, such an operation might prove impossible or erroneous, which would naturally distort the final calculated result, and to such an extent that its practical value would be completely depreciated. Therefore, the problem of finding a criterion that would reveal such reactions already in the preliminary stage is of primary importance. The present communication reports the results of this search.

To solve the problem, it is in the first place necessary to select reactions reliably known to proceed (A) or not proceed (B) in the real process of catalytic oxidation of ammonia.

Group A includes reactions (1)–(4). This choice was substantiated using the results obtained in [3, 4]. As for group B, it comprises reaction (5) and

$$5H_2 + 2NO = 2NH_3 + 2H_2O, \quad (6)$$

$$2H_2 + 2NO = N_2 + 2H_2O. \quad (7)$$

As would be expected, the subsequent direct comparison between the thermodynamic potentials of the chosen reactions (Gibbs energy ΔG_T^0 and enthalpy ΔH_T^0) failed to reveal in both the groups any common pattern that would allow identification of those of the reactions that distort the results of thermodynamic calculation as compared with experimental data. However, relating the thermodynamic potentials of a particular reaction (*i*) to the ΔG_T^0 and ΔH_T^0 of reaction (1) governing the composition of the equilibrium gas [i.e. is basic[1] (b)] revealed an interesting pattern. The characteristics presented in Table 2 require some explanation.

The ratios $\Delta G_T^0(i)/\Delta G_T^0(b)$ and $\Delta H_T^0(i)/\Delta H_T^0(b)$ used for criterial evaluation and denoted, respectively, by $\mathrm{Rel}[\Delta G_T^0(i)]$ and $\mathrm{Rel}[\Delta H_T^0(i)]$ vary differently with increasing reaction temperature for reactions belonging to groups A and B. A typical pattern demonstrating the difference between the two groups of reactions with regard to one of the criteria is shown in Fig. 1. This difference is reflected by the schematic representation of the obtained correlation with indication of the sign of criterion application within the temperature interval under study (900–1400 K).

Table 2. Behavior with temperature of the criteria $\mathrm{Rel}[\Delta G_T^0(i)]$ and $\mathrm{Rel}[\Delta H_T^0(i)]$ for some reactions (T = 900–1400 K, P = 0.1 MPa)

Reaction *i*	Criterion	
	$\mathrm{Rel}[\Delta G_T^0(i)]$	$\mathrm{Rel}[\Delta H_T^0(i)]$
Proceeding reactions		
(2)	+\+	+\+
(3)	+\+	+\+
(4)	+\+	+\+
Non-proceeding reactions		
(5)	+\−	+\+
(6)	+\+	+/\+
(7)	+\+	+/\+

There is no escape from noticing the fact that, for all reactions whose occurrence under conditions of catalytic oxidation of ammonia has been confirmed experimentally, the behavior of the functions $\mathrm{Rel}[\Delta G_T^0(i)]$

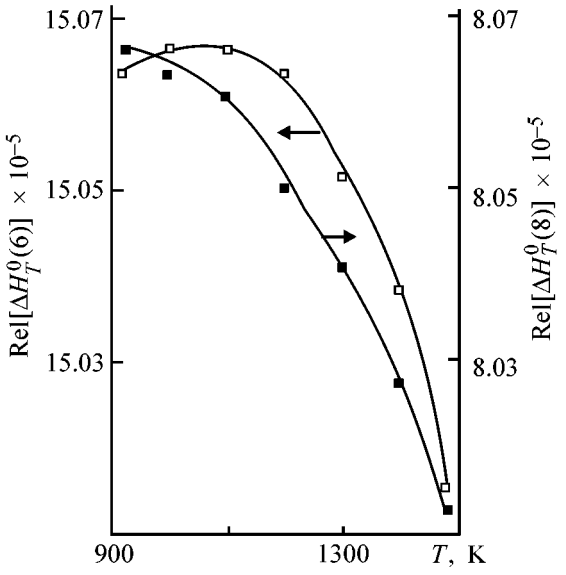

Fig. 1. Typical behavior with temperature T of the criterion $\mathrm{Rel}[\Delta G_T^0(i)]$ for reactions (6) and (8).

[1] In the given case, the choice of the gas reaction is unambiguously predetermined a priori [3–7]. However, in the general case, a search for such a reaction is an independent scientific problem.

Table 3. Effect of the AAM composition and reaction temperature on ammonia conversion into NO_x, γ (P = 0.1 MPa)

O_2/NH_3, mol mol^{-1}	γ (%) at indicated temperature, K		
	1100	1200	1300
1.00	74.1	75.0	75.0
1.25	78.5	78.5	78.9
1.50	85.1	85.1	94.3
1.75	94.0	94.0	89.1

and Rel[$\Delta H_T^0(i)$] with T and their sign remain invariable over the entire temperature range studied. This circumstance cannot be understood as a mere coincidence, as it is equally impossible to consider accidental the fact that at least a single characteristic for all reactions of group B (run of the curve or the sign of the criterion at the boundary of the temperature interval) differs from that for group A.

Detailed theoretical substantiation of the revealed pattern is far beyond the scope of the present study. It should be noted that this would require a special analysis including as a not the least important part a mathematical approximation to the Le Chatelier principle as applied to the set of the reactions under study. However, even a formal application of the revealed relationship allows successful solution of the problem at hand—to reveal and exclude already in the preliminary stage the reactions distorting the results of a thermodynamic calculation of the equilibrium composition.

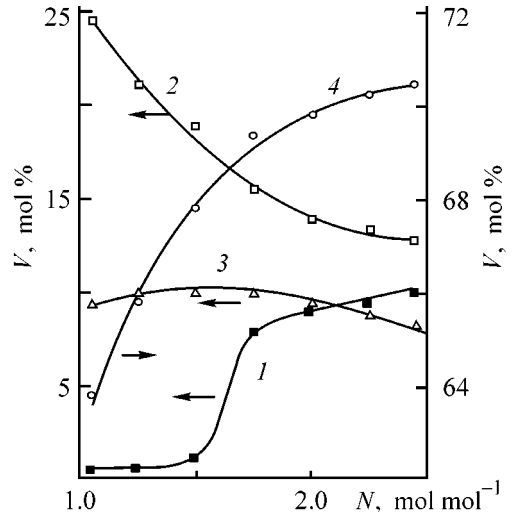

Fig. 2. Content V of a component in the equilibrium mixture vs. the initial ratio O_2/NH_3 N in the AAM. T = 1200 K, P = 0.1 MPa; calculation after a criterial estimate of the entire set of reactions. Component: (*1*) O_2, (*2*) H_2O, (*3*) NO, and (*4*) N_2.

To verify the possibility of using the proposed characteristics, a criterial analysis was made of the entire set of reactions considered in [1]. It was found that only four more reactions should be added to reactions (1)–(4)

$$4NH_3 + 6NO = 5N_2 + 6H_2O, \quad (8)$$

$$2NO = N_2 + O_2, \quad (9)$$

$$4NH_3 + 7O_2 = 6H_2O + 4NO_2, \quad (10)$$

$$4NO = N_2 + 2NO_2. \quad (11)$$

The criterial characteristics of the reaction

$$H_2 + 2NO = H_2O + N_2O \quad (12)$$

seemingly allow its inclusion into the set of the considered interactions; however, none of the selected 11 reactions proceeds to give hydrogen.

The last circumstance indicates that formal use of the proposed criteria in no way rules out a chemical-technological assessment of information. It is quite evident that a meaningless set of concurrent-consecutive reactions would be obtained without taking this aspect into account. In the given case, an absurd member of the set would be hydrogenation of nitrogen(II) oxide in the absence of at least a single reaction leading to appearance of hydrogen in the gas mixture.

A part of the results obtained in a thermodynamic calculation is presented in Table 3.

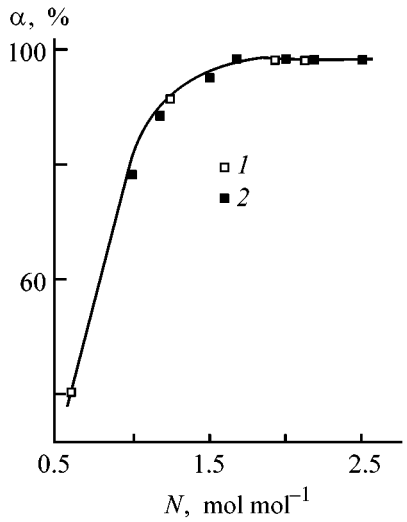

Fig. 3. Yield α of nitrogen oxides NO_x vs. initial O_2/NH_3 ratio N in AAM. Data: (*1*) [3] and (*2*) present study.

It can be seen that temperature has practically no effect on the yield of NO_x at O_2/NH_3 ratios less than the stoichiometric value for reaction (1). Raising the content of oxygen has positive effect on the NO + NO_2 yield, which points to the necessity for preliminary heating of the initial air–ammonia mixture (AAM). However, at $O_2/NH_3 > 1.75$ (mol mol^{-1}), temperature becomes an adversely affecting factor. A detailed analysis of the results obtained in a thermodynamic calculation of the equilibrium composition demonstrated that the reason is that thermal dissociation of nitrogen(II) oxide by reaction (11) is markedly intensified, causing unavoidable partial loss of the forming target product. All this is in good agreement with Atroshchenko's opinion [3] that, in some cases, temperature may be a more important factor than the initial mixture composition, and its influence may be both positive and negative.

As for the "straight" (i.e. that at fixed temperature) effect of the AAM composition, it is evident from the analysis in Fig. 2.

Figure 2 more precisely corresponds to experimental data of various authors [3–7] than the results presented in [1]. It should be emphasized that the coincidence of the calculated thermodynamic characteristics with experimental results [3] is virtually ideal for the dependence of the NO_x yield on the initial gas composition (Fig. 3).

The presented results can serve as direct proof of the adequacy of the proposed technique for revealing reactions that distort results obtained in thermodynamic calculations of the equilibrium composition as compared with the actual process. All this makes it possible to pass to considering more complicated tasks. In particular, a direct possibility opens up of studying whether or not application of Andrussow's nitroxyl theory [8] and Wendlandt's hydroxylamine mechanism [9] to the mechanism of catalytic ammonia oxidation is justified. This is all the more important as the first theory was created at the time when the very existence of HNO was purely hypothetical (no experimental evidence in favor of the existence of this compound existed), and the presence of NH_2OH as an intermediate in catalytic oxidation of ammonia has not been confirmed experimentally up to now [10].

CONCLUSION

Based on a comparative analysis of experimental results obtained by different researchers, criteria are proposed allowing exclusion of reactions distorting the results of thermodynamic calculations of the equilibrium composition. The coincidence of the obtained calculated results with experimental data is virtually ideal.

REFERENCES

1. Trusov, N.V., *Zh. Prikl. Khim.*, 1998, vol. 71, no. 8, pp. 1270–1274.
2. Bunday, B.D., *Basic Optimization Methods*, London: Edward Arnold, 1984.
3. Atroshchenko, V.I. and Kargin, S.I., *Tekhnologiya azotnoi kisloty* (Technology of Nitric Acid), Moscow: Khimiya, 1970.
4. Karavaev, M.M., Zasorin, A.P., and Kleshchev, N.F., *Kataliticheskoe okislenie ammiaka* (Catalytic Oxidation of Ammonia), Moscow: Khimiya, 1970.
5. *Metody raschetov po tekhnologii svyazannogo azota* (Procedures for Calculation in Technology of Bound Nitrogen), Atroshchenko, V.I., Ed., Kiev: Vysshaya Shkola, 1978.
6. *Proizvodstvo azotnoi kisloty v agregatakh bol'shoi edinichnoi moshchnosti* (Manufacture of Nitric Acid in High-Unit-Power Apparatus), Olevskii, V.M., Ed., Moscow: Khimiya, 1985.
7. *Spravochnik azotchika* (Handbook of Nitrogen Worker), Karavaev, M.M., Ed., Moscow: Khimiya, 1987.
8. Andrussow, L., *Bull. Soc. chim. France*, 1951, nos. 1–2, pp. 45–50.
9. Wendlandt, R., *Z. Electrochem.*, 1949, vol. 53, no. 5, pp. 307–319.
10. Trusov, N.V., Grin', G.I., Loboiko, A.Ya., and Koshovets, N.V., *Poluchenie sinil'noi kisloty po metodu Andrussova* (Manufacture of Hydrocyanic Acid by Andrussow's Method), Kharkov: Osnova, 1999.

Russian Journal of Applied Chemistry, Vol. 74, No. 4, 2001, pp. 576–579. Translated from Zhurnal Prikladnoi Khimii, Vol. 74, No. 4, 2001, pp. 560–563.

PHYSICOCHEMICAL STUDIES OF SYSTEMS AND PROCESSES

Physicochemical Properties of Lithium Perchlorate Solutions in Mixtures of Sulfolane with 1,3-Dioxolane

V. S. Kolosnitsyn, N. V. Slobodchikova, N. V. Karichkovskaya, and L. V. Sheina

Institute of Organic Chemistry, Ural Scientific Center, Russian Academy of Sciences, Ufa, Bashkortostan, Russia

Received March 22, 2000; in final form, July 2000

Abstract—The electrical conductivity, viscosity, and density of sulfolane–1,3-dioxolane mixtures and 1 M lithium perchlorate solutions on their base were studied. The activation energies of viscous flow and electrical conductivity were calculated. Departures of some of the measured values from additivity are demonstrated.

It is known that individual highly polar solvents are strongly associated because of the formation of hydrogen bonds and dipole–dipole and electron-donor–acceptor (EDA) interactions. The extent of association reaches tens and, occasionally, hundreds of units. This leads to an increase in viscosity and, thereby, impairs the transport properties of polar solvents, which is extremely undesirable when high-conductivity electrolyte solutions are to be obtained. Mixtures of solvents, as a rule, have lower viscosity that it would be expected on the basis of their composition. The reason is that heteromolecular associates are formed, with molecular weight lower than that of homomolecular associates existing in individual solvents. It could be assumed that the composition of heteromolecular associates and their strength are in the first place determined by the EDA properties and stereochemistry of interacting molecules. However, it is difficult to make *a priori* an unambiguous conclusion about the composition of heteromolecular associates formed in one or another system on the basis of the available reference data. Therefore, investigations are necessary, aimed to elucidate the stereochemistry of associates formed in various systems and to relate the EDA and structural properties of interacting molecules to the composition and strength of heteromolecular associates being formed.

To obtain high-conductivity electrolyte solutions, solvents are prepared on the basis of mixtures of highly polar compounds, having high solvating power, with low-polar compounds having low viscosity. Most frequently, propylene carbonate [1, 2] and ethylene carbonate are used as highly polar components, and tetrahydrofuran (THF), dimethoxyethane (DME), and dioxolane, as low-polar components. A promising group of highly polar solvents is formed by sulfolanes [3]. However, the physicochemical properties of mixed solvents on their base are little studied. Previously, electrolyte systems based on a mixture of sulfolane (Sl) with THF and DME have been studied [4].

The aim of the present study was to analyze in detail the physicochemical properties of lithium perchlorate solutions in mixtures of sulfolane with 1,3-dioxolane.

EXPERIMENTAL

The solvents and lithium perchlorate were thoroughly purified and dried. According to gas-liquid chromatography, the purity of the solvents was no less than 99.5–99.8%. The solutions used were prepared in a box dried with phosphorus(V) oxide. The content of water in the electrolyte solutions, found by biamperometric titration in Fischer's reagent, did not exceed 0.03%. The electrical conductivity χ was measured with an E7-8 ac bridge in capillary cells with platinum-plated electrodes. The solution viscosity η was measured in Ubbelohde viscometers with suspended level of closed type, and the density ρ was found picnometrically. The errors in determining the viscosity and electrical conductivity did not exceed 0.2%, the error in density was 0.02%, the temperature was maintained to within ±0.01°C. The molar volume V_m was calculated as described in [5].

1070-4272/01/7404-0576 $25.00 © 2001 MAIK "Nauka/Interperiodica"

Table 1. Physicochemical properties of mixtures of sulfolane with 1,3-dioxolane

C_{Sl},* mol %	$\eta \times 10^3$, N s m^{-2}					ρ, g cm^{-3}					V_m, cm^3 mol^{-1}				
	at indicated temperature, °C														
	30	35	40	45	50	30	35	40	45	50	30	35	40	45	50
0.0	0.62	0.58	0.55	0.53	0.51	1.0471	1.0414	1.0350	1.0297	1.0218	70.7	71.1	71.6	71.9	72.5
20.7	0.89	0.85	0.82	0.78	0.75	1.1161	1.1112	1.1061	1.1011	1.0955	74.9	75.3	75.6	75.9	76.3
43.0	1.49	1.39	1.24	1.21	1.17	1.1690	1.1641	1.1602	1.1557	1.1492	80.3	80.7	80.9	81.2	81.7
65.8	3.04	2.53	2.32	2.12	1.99	1.2125	1.2075	1.2035	1.1993	1.1919	86.1	86.5	86.8	87.1	87.6
100	10.25	9.05	8.02	7.17	6.42	1.2644	1.2594	1.2564	1.2535	1.2512	95.0	95.4	95.6	95.9	76.3

* C_{Sl} is the content of sulfolane in a mixture; the same for Table 2.

Table 2. Physicochemical properties of 1 M $LiClO_4$ solutions in mixtures of sulfolane with 1,3-dioxolane

C_{Sl}, mol %	$\chi \times 10^3$, Ω^{-1} cm^{-1}					$\eta \times 10^3$, N s m^{-2}					ρ, g cm^{-3}				
	at indicated temperature, °C														
	30	35	40	45	50	30	35	40	45	50	30	35	40	45	50
0.0	3.2	–	–	–	–	1.00	0.93	0.89	0.85	0.81	1.1279	1.1222	1.1166	1.1098	1.1040
11.9	4.63	4.82	4.97	5.05	5.12	1.41	1.31	1.25	1.16	1.12	1.1657	1.1603	1.1560	1.1510	1.1460
20.4	5.5	5.72	5.91	6.11	6.29	1.731	1.63	1.52	1.43	1.35	1.1866	1.1814	1.1768	1.1700	1.1650
41.5	6.3	6.58	6.95	7.31	7.68	3.151	2.94	2.69	2.50	2.35	1.2323	1.2298	1.2251	1.2206	1.2159
68.6	4.64	5.09	5.53	6.02	6.54	8.54	7.61	6.78	6.10	5.50	1.2791	1.2749	1.2709	1.2659	1.2618
100	2.22	2.61	2.90	3.20	3.49	28.57	24.56	20.83	18.28	16.02	1.3168	1.3132	1.3103	1.3057	1.3022

A study of the physicochemical properties of sulfolane mixtures with dioxolane demonstrated that the dependence of their viscosity on composition is strongly non-linear (Table 1). The composition dependence of the mixture density is also nonlinear, but to a much lesser extent. For example, the departure of molar volumes from additivity does not exceed 1%. The significant negative deviations from linearity, observed for viscosity isotherms, indicate a manifestation of specific intermolecular interactions in the solvents. The weakly pronounced deviations of the molar volume from additivity are in all probability due to the close molar volumes of homo- and heteromolecular associates in the solvents.

The physicochemical properties of lithium perchlorate solutions in sulfolane–dioxolane mixtures are presented in Table 2. The isotherms of electrical conductivity of 1 M solutions of lithium perchlorate solutions in solvent mixtures pass through a maximum at a 1 : 1 molar ratio of components. This indicates that the specific interactions between sulfolane and dioxolane are preserved in the presence of lithium perchlorate.

The increase in the electrical conductivity may be due to a decrease in the solution viscosity or to a change in the degree of salt association. To reveal the factors responsible for the change in electrical conductivity, the correlated electrical conductivity $\chi\eta$ was calculated. It was found that the isotherms of correlated electrical conductivity are convex with respect to the mixture composition axis (Fig. 1). The correlated electrical conductivity decreases with increasing temperature.

It is known [6] that the dependences of the correlated electrical conductivity of salt solutions in solvent mixtures on their composition are linear only in those cases when the solvating powers of the solvents are the same or differ widely, which is due to the invariable composition of the solvation shells of the salts. The positive deviations of the $\chi\eta$ isotherms from linearity are observed in the case of preferential solvation of lithium ions by molecules of solvents with large molar volume. The preferential solvation is done by solvents possessing high donor properties. For example, the authors of [7] attributed the positive deviations of the correlated electrical con-

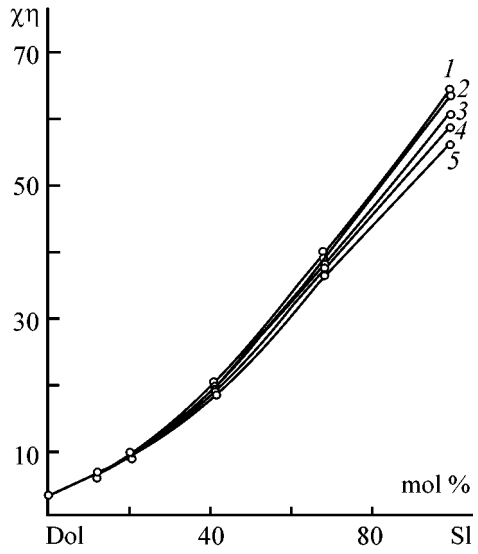

Fig. 1. Isotherms of correlated electrical conductivity χη of 1 M lithium perchlorate solutions in mixtures of sulfolane with dioxolane. Temperature (°C): (*1*) 30, (*2*) 35, (*3*) 40, (*4*) 45, and (*5*) 50.

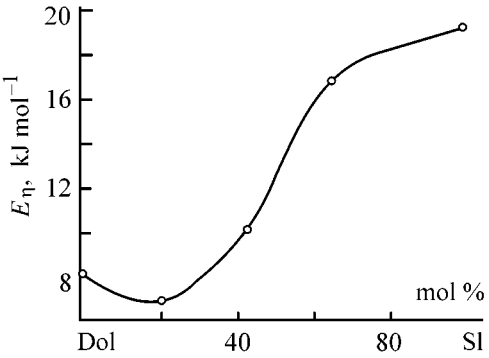

Fig. 2. Concentration dependence of the activation energy E_η of viscous flow of sulfolane–dioxolane mixtures.

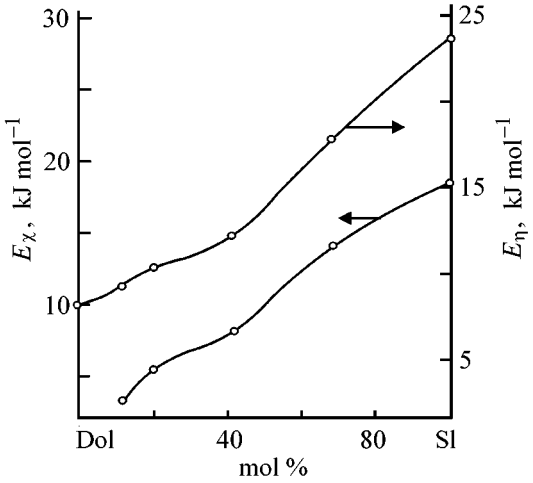

Fig. 3. Concentration dependences of the activation energy of electrical conductivity, E_χ, and viscous flow, E_η, of 1 M lithium perchlorate solutions in mixtures of sulfolane with dioxolane.

ductivity of lithium tetrafluoroborate solutions in mixtures of propylene carbonate with dimethoxyethane from linear concentration dependence to preferential solvation of lithium ions by dimethoxyethane molecules, possessing higher donor properties than propylene carbonate.

The negative deviations of the correlated electrical conductivity from a linear concentration dependence indicate a higher degree of lithium perchlorate association in mixtures of sulfolane with dioxolane than it would be expected on the basis of the solvent mixture composition. The decrease in the χη value with growing temperature points to an increase in the degree of lithium perchlorate association.

The higher degree of salt association in solvent mixtures is due to the fact that the solvate shell of lithium perchlorate is mainly composed of dioxolane molecules. Since the molar volume of dioxolane (68.6 $cm^3\ mol^{-1}$) is much smaller than that of sulfolane (95.2 $cm^3\ mol^{-1}$), resolvation leads to a decrease in the interionic distance, because of the decreasing size of the solvate shell of the lithium ion, and thereby makes higher the degree of lithium perchlorate association.

The activation energy of viscous flow of solvent mixtures exhibits a minimum as a function of concentration at a sulfolane : 1,3-dioxolane molar ratio of 2 : 1 (Fig. 3) and an inflection point at 1 : 2 molar ratio of the components. Since the activation energy is a structure-sensitive parameter, such a behavior of the activation energy as a function of concentration suggests that sulfolane : 1,3-dioxolane molecular associates of compositions 1 : 2 and 2 : 1 exist in solvent mixtures. The concentration dependences of the activation energies of viscous flow and electrical conductivity are also nonlinear, but to a much lesser extent, compared with solvent mixture. Only slight negative deviations from linearity are observed at a sulfolane : 1,3-dioxolane ratio close to 1 : 1. Probably, binding of most part of 1,3-dioxolane molecules in the solvate shell of a lithium ion leads to disintegration of sulfolane–1,3-dioxolane intermolecular associates.

CONCLUSION

The the isotherms of electrical conductivity of lithium perchlorate in mixtures of sulfolane with 1,3-dioxolane exhibit a maximum at a molar ratio of the components close to 1 : 1. The appearance of the maximum is due to a decrease in the solution viscosity, resulting from the formation of heteromolecular associates with lower degree of association, compared

with homomolecular associates. The degree of lithium perchlorate association in mixtures of sulfolane with 1,3-dioxolane is lower than it would be expected judging from the composition of the system. This is attributed to a decrease in the volume of the solvate shell of a lithium ion as a result of preferential solvation by 1,3-dioxolane.

REFERENCES

1. Volkov, O.V., Skundin, A.M., and Ignat'ev, N.V., *Elektrokhimiya*, 1992, vol. 28, no. 12, pp. 1852–1855.
2. Volkov, O.V., Kanevskii, L.S., Radchenko, A.F., and Skundin, A.M., *Elektrokhimiya*, 1991, vol. 27, no. 9, pp. 1198–1200.
3. Kolosnitsyn, V.S., Sheina, L.V., Karichkovskaya, N.V., and Mochalov, S.E., *Zh. Fiz. Khim.*, 1999, vol. 63, no. 6, pp. 1112–1115.
4. Slobodchikova, N.V., Kolosnitsyn, V.S., and Sheina, L.V., Abstracts of Papers, *XIX Vsesoyuznoe Chugaevskoe soveshchanie po khimii kompleksnykh soedinenii* (XIX All-Union Chugaev Symp. on Chemistry of Complex Compounds), Ivanovo, 1999, p. 282.
5. Anosov, V.Ya., Ozerova, M.I., and Fialkov, Yu.Ya., *Osnovy fiziko-khimicheskogo analiza* (Fundamentals of Physicochemical Analysis), Moscow: Nauka, 1978.
6. Domracheva, E.P., Zhuk, E.G., Karapetyan, Yu.A., and Eichis, V.N., *Mezhvuzovskii sbornik nauchnykh trudov* (Intercollegiate Coll. Sci. Works), Ivanovo, 1985, pp. 39–44.
7. Plakhotkin, V.N., Tovmash, N.F., and Mishustin, A.I., *Elektrokhimiya*, 1988, vol. 24, no. 7, pp. 964–968.

Russian Journal of Applied Chemistry, Vol. 74, No. 4, 2001, pp. 580–583. Translated from Zhurnal Prikladnoi Khimii, Vol. 74, No. 4, 2001, pp. 564–567.

SORPTION AND ION-EXCHANGE PROCESSES

Sorption of Lanthanum(III) by Natural Mordenite-containing Tuff

B. B. Mitypov, E. L. Zonkhoeva, N. M. Kozhevnikova, and B. V. Pashinova

Baikal Institute of Nature Management, Siberian Division, Russian Academy of Sciences, Ulan-Ude, Buryatia, Russia

Institute of Geology, Siberial Division, Russian Academy of Sciences Russia

Received August 10, 1999; in final form, November 2000

Abstract—The equilibrium in the mordenite-containing tuff–lanthanum(III) solution system was studied within a wide metal concentration range (1–2000 μg ml^{-1}). Kinetic parameters of La(III) sorption were determined.

Rare-earth elements, exhibiting high biological activity, are widely used as microfertilizers [1–4]. Lanthanum(III) sulfate catalyzes the fixation of atmospheric nitrogen by nitrogen-fixing bacteria [3]. Lanthanum, cerium, and samarium nitrates are efficient microfertilizers improving the germination of seeds of wheat, pea, corn, and sugar beet and raising their productivity by 22–40% and dry substance gain by 11–14% [1–3]. Acceleration of bean crops ripening by 4–6 days has also been observed [1].

To obtain REE-based microfertilizers, it is appropriate to use the sorption technology, with natural zeolites as sorbents. Zeolites are prolonging carriers of microelements, releasing them into the soil solution during a long period of time. Published data on the kinetics of REE sorption by natural zeolites and on the solution–zeoilite equilibrium, which are necessary for preparing and using new microfertilizers, are lacking.

EXPERIMENTAL

A mordenite-containing tuff from Mukhor-Talin perlite–zeolite deposit (Buryatia) with the composition (wt %): SiO_2 70.96, Al_2O_3 11.97, MgO 0.18, CaO 0.92, Na_2O 2.38, and K_2O 5.22, and Si/Al molar ratio of 5.2, was used as a sorbent. The content of zeolite in the rock determined with a PTsL-2 zeolite portable laboratory [5] was 62%. To analyze the sorption kinetics and equilibrium sorption of lanthanum ions, the mordenite-containing tuff was crushed, with 0.25–0.5- and 1–2-mm fractions separated from the dust and dried at room temperature for 24 h. The sorption equilibrium was studied under static conditions. Solutions of lanthanum sulfate and nitrate with La^{3+} concentrations from 1 to 2000 μg ml^{-1} and the solid-to-liquid (s : l) ratios of 1 : 10 and 1 : 50 were taken. The lanthanum content was determined photometrically with arsenazo III, which is a very sensitive and selective procedure [6]. The sorption capacity was calculated as the difference of the lanthanum concentrations before and after sorption (average of three measurements); the relative determination error was no more than 3%.

The kinetics of lanthanum sorption from solutions with lanthanum concentrations of 0.01, 0.02, 0.005, and 0,007 g-ion l^{-1} was also studied under static conditions. The time of sorbent–solution contact was varied from 5 min to 6 days. The kinetic curves were plotted in the Q–τ coordinates, where Q is the amount of lanthanum ions sorbed and τ is the time of the contact between solution and sorbent. The kinetic parameters were calculated by the method described in [7]. During the initial period, when lanthanum sorption proceeds on the sorbent surface and the process is controlled by external diffusion, the rate constant R was calculated by the equation

$$R = \frac{dQ}{d\tau}\frac{1}{CK}, \quad (1)$$

where C is the lanthanum concentration in the solution and K is the equilibrium distribution coefficient.

With increasing contact time, the amount of the metal ion sorbed is determined by the rate of exchange inside the sorbent grain. To calculate the effective diffusion coefficient D and the exchange rate constant B characterizing the internal-diffusion mech-

1070-4272/01/7404-0580 $25.00 © 2001 MAIK "Nauka/Interperiodica"

anism, the equation derived for spherical particles was used:

$$F = Q_\tau/Q_\infty = (6/r)\sqrt{D\tau/\pi}, \quad (2)$$

$$B = \pi^2 D/r^2, \quad (3)$$

where Q_τ/Q_∞ is the degree of ion exchange and r is the average radius of sorbent particles.

The obtained data are presented in the table and in Figs. 1–3. In spite of the wide concentration range (1–2000 μg ml^{-1}), all isotherms of equilibrium sorption are similar. Figures 1a and 1b show the isotherms of lanthanum sorption from solutions of lanthanum nitrate and sulfate by mordenite tuff with grain size of 0.25–0.5 and 1–2 mm at s : l ratios of 1 : 10 and 1 : 50.

As seen, all isotherms have three portions: (1) the initial portion, whose points lie on the ordinate axis; which means quantitative (100%) recovery of lanthanum from dilute solution; (2) portion ascending to the maximum, and (3) descending portion. The lanthanum recovery depends on the anion nature: it is somewhat higher for nitrate than for sulfate.

With increasing lanthanum concentration, isotherms pass through maximum and then sorption starts to decrease. Thus, the study performed in a wide range of La(III) concentration revealed complex character of lanthanum sorption by mordenite tuff, from complete recovery to drastic decrease of sorption.

The maximum in the isotherm may be associated with the existence in solution of intermediates with enchanced chemical affinity for tuff [8]. The REE ions are strong complex-forming species. In the neutral and acid aqueous solutions, lanthanum ions exist as aqua complexes $[La(H_2O)_n]^{3+}$ or $[La(H_2O)_n(OH)]^{2+}$, where n = 5–8 [9, 10]. In sulfate solutions, complexes $[La(SO_4)_n]^{3-2n}$, where n = 1–3, are also found. At low sulfate ion concentrations (<0.1 g-ion l^{-1}), $[La(SO_4)]^+$ cations prevail [11], although anionic complexes may also be formed under the same conditions [12]. In aqueous solutions of lanthanum nitrate, complexes $[LaNO_3]^{2+}$, $[La(NO_3)_2]^+$, and $[La(H_2O)_nNO_3]^{2+}$ with n = 5–6 exist [13, 14].

Probably, at concentrations below that corresponding to the sorption peak, lanthanum aqua and hydroxo complexes are sorbed, since the enhanced zeolite selectivity with respect to lanthanum ions in the initial portion of the isotherm (where they are sorbed completely) can be accounted for by the large charge of the ion. The mechanism of sorption of the lanthanum aqua complex by a synthetic zeolite is described in [15]. The inversion of the sorbent selectivity after

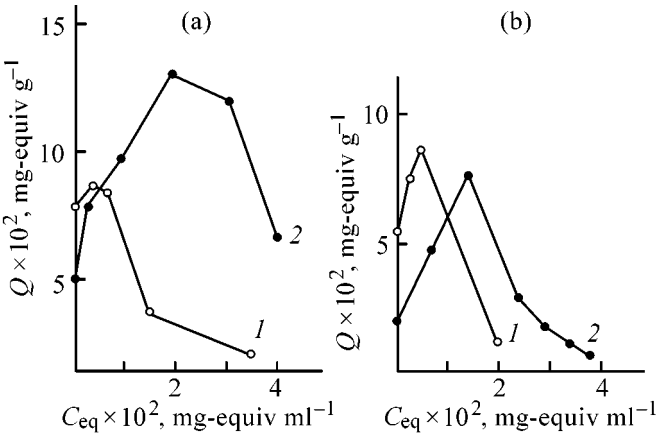

Fig. 1. Isotherms of equilibrium sorption of lanthanum ions from solutions of (a) $La(NO_3)_3 \cdot 6H_2O$ and (b) $La_2(SO_4)_3$ by mordenite-containing tuff. (Q) Exchange capacity and (C_{eq}) equilibrium concentration of lanthanum ions in solution. (*1*) d = 0.25–0.5 mm, s : l = 1 : 50 and (*2*) d = 1–2 mm, s : l = 1 : 10.

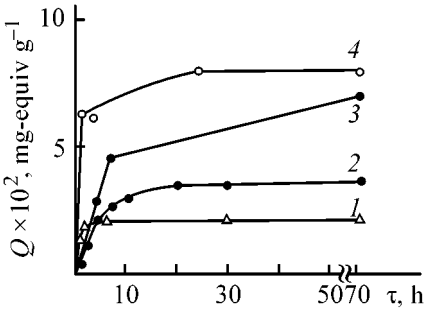

Fig. 2. Kinetics of lanthanum(III) sorption from solutions by mordenite-containing tuff. (Q) exchange capacity and (τ) time. (*1*) $La_2(SO_4)_3$, 0.02 N, d = 1–2 mm, s : l = 1 : 10; (*2*) $La_2(SO_4)_3$, 0.01 N, d = 1–2 mm, s : l = 1 : 10; (*3*) $La(NO_3)_3 \cdot 6H_2O$, 0.007 N, d = 1–2 mm, s : l = 1:10; and (*4*) $La_2(SO_4)_3$, 0.005 N, d = 0.25–0.5 mm, s : l = 1 : 50.

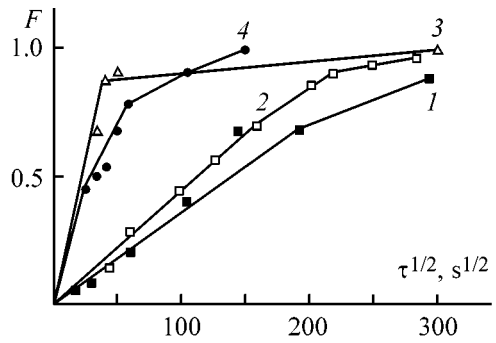

Fig. 3. Degree of ion exchange, F, vs. time τ. $F = Q_\tau/Q_\infty$, where Q_τ is the amount of lanthanum sorbed from solutions during time τ, and Q_∞ is equilibrium sorption. (*1*) $La(NO_3)_3 \cdot 6H_2O$, 0.007 N, d = 1–2 mm, s : l = 1 : 10; (*2*) $La_2(SO_4)_3$, 0.01 N, d = 1–2 mm, s : l = 1 : 10; (*3*) $La_2(SO_4)_3$, 0.005 N, d = 0.25–0.5 mm, s : l = 1 : 50; and (*4*) $La_2(SO_4)_3$, 0.02 N, d = 1–2 mm, s : l = 1 : 10.

Kinetic parameters of lanthanum(III) sorption from solutions with natural mordenite-containing tuff

Parameter	$La_2(SO_4)_3$			$La(NO_3)_3 \cdot 6H_2O$
	0.005 N, d = 0.25–0.5 mm, s : l = 1 : 50	0.01 N, d = 1–2 mm, s : l = 1 : 10	0.02 N, d = 1–2 mm, s : l = 1 : 10	0.007 N, d = 1–2 mm, s : l = 1 : 10
$\tau_{1/2}$, s	2160	11520	600	21600
τ_∞, s	86400	108000	86400	259200
$(dQ/d\tau) \times 10^{-5}$, mg-equiv g^{-1}	9.6	0.3	5.6	0.2
K, ml g^{-1}	23.7	5.6	8.2	461.3
$R \times 10^{-5}$, s^{-1}	77	5	30	0.07
$D \times 10^{-8}$, $cm^2\ s^{-1}$	2.4	1.0	30	0.5
$B \times 10^{-5}$, s^{-1}	67	1.7	55	1.0

reaching a certain lanthanum concentration, which is a manifestation of electroselectivity, supports this mechanism: upon dilution, the equilibrium is shifted toward stronger sorption of ions with larger charge, whereas in concentrated solutions the opposite trend is observed [8].

The grain size and the s:l ratio affect the position of the isotherm peak. At d = 0.25–0.5 mm and s : l ratio of 1 : 50 (Figs. 1a, 1b, curves *1*) the maximum exchange capacity (EC) is observed at lower equilibrium concentrations than in the case of larger grain size and s : l ratio of 1 : 10 (Figs. 1a, 1b, curves *2*), i.e., on small tuff grains the maximal *EC* is reached at lower sorbent consumption. This result was used in selecting the regime of saturation of mordenite-containing tuff with lanthanum salts.

The kinetic curves of lanthanum sorption by mordenite-containing tuff are similar (Fig. 2). The degree of filling of the zeolite phase, F, is in all cases a linear function of $\tau^{1/2}$ up to high values of F (Fig. 3). This confirms the fairly high contribution of the internal-diffusion mechanism of sorption [16]. The kinetic parameters listed in the table show how the rate of lanthanum sorption depends on the tuff grain size, lanthanum concentration, and nature of anion.

With decreasing grain size, the sorbent surface area grows and, hence, the rate of sorption controlled by external diffusion $dQ/d\tau$ increases. With increasing concentration of lanthanum sulfate, the time of half-exchange $\tau^{1/2}$ and the time of attaining the equilibrium, τ_∞, become shorter. The rate of sorption of the lanthanum ion by the external-diffusion mechanism $dQ/d\tau$, the rate constant of external-diffusion sorption R, and the distribution coefficient K are also higher in sorption from more concentrated solutions. The metal concentration also affects the parameters of the internal-diffusion process: the rate constant B and effective diffusion coefficient D increase with concentration. The B value is of the same order of magnitude as R. Hence, the sorption of lanthanum ions from the sulfate solution occurs by the mixed mechanism.

Let us consider the effect of the anion nature on the kinetic parameters. The data in the table show that the distribution coefficient K for sorption from a nitrate solution is greater than that for a sulfate solution. The sorption proceeds with lower rate both across the grain–solution boundary and within the grain itself, which is caused by lower mobility of nitrate ions, compared with that of sulfate ions [17]. The internal diffusion is the limiting stage of the lanthanum sorption from a nitrate solution, because R is an order of magnitude lower than B.

CONCLUSIONS

(1) The sorption equilibrium in the mordenite-containing tuff–lanthanum(III) system was studied. The sorption isotherms show a maximum, suggesting complex interactions in the system.

(2) The rate of lanthanum(III) sorption depends on the nature of anion, grain size, metal concentration, and s : l ratio and is described by the mixed mechanism in sorption from sulfate solutions and by the external-diffusion mechanism for nitrate solution.

REFERENCES

1. Drobkov, A.A., *Dokl. Akad. Nauk SSSR*, 1941, vol. 32, no. 9, pp. 666–667.
2. Drobkov, A.A., *Dokl. Akad. Nauk SSSR*, 1941, vol. 32, no. 9, pp. 668–669.

3. Kogan, B.I., *Ekonomicheskie ocherki po redkim zemlyam* (Economical Sketches on Rare Earths), Moscow: Akad. Nauk SSSR, 1961.
4. Moskalev, Yu.I., *Mineral'nyi obmen* (Mineral Exchange), Moscow: Meditsina, 1985.
5. Belitskii, I.A., Drobot, I.V., Valueva, G.P., *et al.*, *Opyt ekspressnogo opredeleniya soderzhaniya tseolitov v gornykh porodakh s ispol'zovaniem portativnykh zeolitnykh laboratorii PTsL-1 i PTsL-2* (Practice of Express Determination of Zeolite Content in Rocks Using PTsL-1 and PTsL-2 Portable Zeolite Laboratories), Novosibirsk: Nauka, 1979.
6. Jefferi, P.G., *Chemical Methods of Rock Analysis*, Oxford: Pergamon, 1970.
7. Chelishchev, N.F., Volodin, V.F., and Kryukov, V.L., *Ionoobmennye svoistva prirodnykh vysokokremnistykh tseolitov* (Ion-Exchange Properties of Natural High-Silicon Zeolites), Moscow: Nauka, 1988.
8. Kokotov, Yu.A., Zolotarev, P.P., and El'kin, G.E., *Teoreticheskie osnovy ionnogo obmena: slozhnye ionoobmennye sistemy* (Theoretical Foundations of Ion Exchange: Complex Ion-Exchange Systems), Leningrad: Khimiya, 1986.
9. Serebrennikov, V.V., *Khimiya RZE: scandii, ittrii, lantanidy* (Chemistry of REE: Scandium, Yttrium, Lanthanides), Tomsk: Tomsk. Gos. Univ., 1959, vol. 1.
10. Yatsimirskii, K.B., Kostromina, N.A., Shcheka, Z.A., *et al.*, *Khimiya kompleksnykh soedinenii RZE* (Chemistry of REE Complex Compounds), Kiev: Naukova Dumka, 1966.
11. Spedding, F.H. and Iaffe, S., *J. Am. Chem. Soc.*, 1954, vol. 76, no. 4, pp. 882–884.
12. Secine, T., *J. Inorg. Nucl. Chem.*, 1964, vol. 26, no. 7, pp. 1463–1465.
13. Choppin, G.R., *et al.*, *Inorg. Chem.*, 1965, vol. 4, no. 6 pp. 1250–1254.
14. Kumok, V.N. and Serebrennikov, V.V., *Zh. Neorg. Khim.*, 1965, vol. 10, no. 9, pp. 2011–2018.
15. Breck, D.W., *Zeolite Molecular Sieves*, New York: Wiley, 1974.
16. Kokotov, Yu.A. and Pasechnik, V.A., *Ravnovesie i kinetika ionnogo obmena* (Equilibrium and Kinetics of Ion Exchange), Leningrad: Khimiya, 1970.
17. Lur'e, Yu.Yu., *Spravochnik po analiticheskoi khimii* (Handbook of Analytical Chemistry), Moscow: Khimiya, 1967.

Russian Journal of Applied Chemistry, Vol. 74, No. 4, 2001, pp. 584–587. Translated from Zhurnal Prikladnoi Khimii, Vol. 74, No. 4, 2001, pp. 567–570.

SORPTION AND ION-EXCHANGE PROCESSES

Sorption of Copper(II) from Chloride Solutions by Carbonate-containing Technological Waste

T. G. Lupeiko, T. I. Ivleva, and L. A. Solov'ev

Rostov State University, Rostov-on-Don, Russia

Received December 17, 1999; in final form, October 2000

Abstract—Absorption of copper(II) ions from copper chloride solutions by a technological carbonate-containing waste was studied in relation to concentration of starting solutions (1–25 wt %), amount of sorbent added, and time.

The problem of industrial waste purification to remove heavy metals and, in the future, recovery of these metals from natural water and contaminated soil, have been and will be a major problem of importance increasing year after year. Tackling with this problem requires a large amount of relatively low-cost and readily available sorbents. Of particular interest in this connection is the possibility of using as sorbents technological wastes with appropriate properties.

There is published evidence that calcium carbonate [1] or calcium and magnesium carbonates [2] can be used as sorbents removing heavy metals from water. The sorption capacity of calcium (magnesium) carbonate is associated with the exchange of calcium (magnesium) ion for a heavy metal ion in aqueous solutions. Since the effectiveness of ion exchange of a solid carbonate-containing product is the higher, the larger its solubility product (SP), it would be expected that a mixture of calcium and magnesium carbonates is a more effective sorbent than pure calcium carbonate in view of the fact that the SP ($CaCO_3$) is 9.9×10^{-9}, and SP ($MgCO_3$), 4×10^{-5} [3].

The present communication reports on a study of copper(II) sorption from copper chloride solutions by activated technological waste containing calcium and magnesium carbonates (for brevity, henceforth—sorbent).

EXPERIMENTAL

For experiments, copper(II) chloride dihydrate of chemically pure grade was used to prepare 20 ml of copper chloride solutions of the following concentrations: 1.02, 2.05, 4.13, 8.38, 12.70, 16.37, 20.43, 25.24 wt % or, respectively, 0.0103, 0.0208, 0.0427, 0.0903, 0.1423, 0.1908, 0.2477, 0.3200 g cm^{-3} (solutions nos. 1–8, respectively). To these solutions was added 1 g of sorbent predried to constant weight at 100°C and the mixtures were kept at 20°C with stirring at regular intervals. After a certain time elapsed, the liquid phase was filtered and analyzed for the content of residual copper. Copper was determined complexometrically with murexide [4] or, at low concentrations, by spectrophotometry of ammonia complexes [5]. The error was not higher than 0.5%. To eliminate

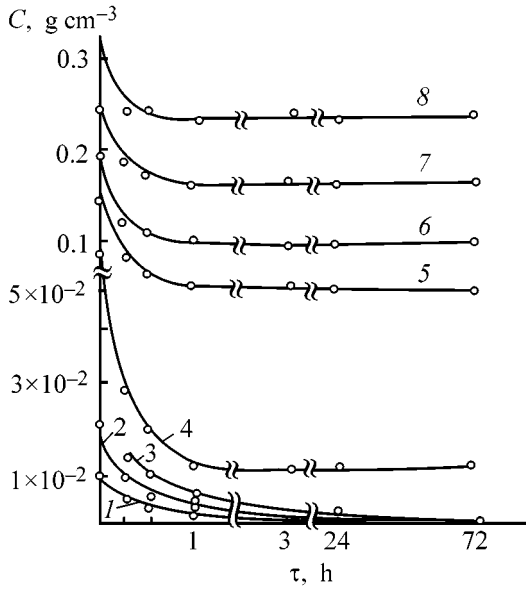

Fig. 1. Variation of copper(II) concentration C in copper chloride solutions nos. 1–8 in the course of sorption. (τ) Time. Digits *1–8* at the curves denote solution numbers; the same for Fig. 2.

1070-4272/01/7404-0584 $25.00 © 2001 MAIK "Nauka/Interperiodica"

the interference of calcium and magnesium ions, these were masked by adding sodium fluoride prior to titration. Also, the pH of the starting solutions and solutions was measured in the course of sorption (PRL no. 517 pH-meter with silver chloride and glass electrodes; accuracy of pH measurement in the optimal mode ±0.01 pH units). The solution density, necessary for calculations, was found picnometrically. The error in determining the solution density was ±0.0005 density measurement units [6]. To ascertain the composition of the product obtained as a result of sorption, it was subjected to X-ray phase analysis on a DRON-2 installation with Cu_{K_α} radiation. The error in determining the interplanar spacings was not higher than 0.01 Å. The common feature of all experiments is that carbon dioxide evolution was observed upon addition of sorbent to the solutions under study, becoming more pronounced with increasing concentration of the initial solution.

As it can be seen from Fig. 1, the process of copper sorption from copper(II) chloride solutions proceeds intensively, being complete in approximately 1 h. However, sorption from solutions nos. 1–3, also proceeding intensively during the first hour, is not complete, but continues further, although being much slower. For example, in the case of starting solution no. 2, the concentration of copper(II) chloride decreases to 0.0036 g cm^{-3} 1 h after the beginning of sorption, and becomes an order of magnitude lower in 3 days. The specificity of sorption from solutions nos. 1–3 is apparently associated with their comparatively high dilution resulting in that the amount of copper ions contained in these solutions is insufficient for saturating the added sorbent. This conclusion is especially clearly confirmed by Fig. 2. Indeed, it can be seen that the maximum amount of copper sorbed per 1 g of sorbent grows steadily with increasing copper content in the starting solution. The highest value (~0.83 g g^{-1}) is reached for solution no. 5, initially containing approximately 1.34 g of copper. Hence follows that solutions nos. 1–3, containing in 20 ml of solution about 0.1, 0.2, and 0.4 g of copper, respectively, cannot ensure saturation of the added 1 g of sorbent.

It can also be seen from Fig. 3 (curve *1*) that, on reaching a value of 0.83 g g^{-1} for solution no. 5, the specific amount of sorbed copper starts to decrease. This tendency is more pronounced in the case of a more prolonged contact between the sorbent and solution (Fig. 2). No unambiguous explanation has been given for this fact, but it should be taken into account to ensure effective use of the sorbent.

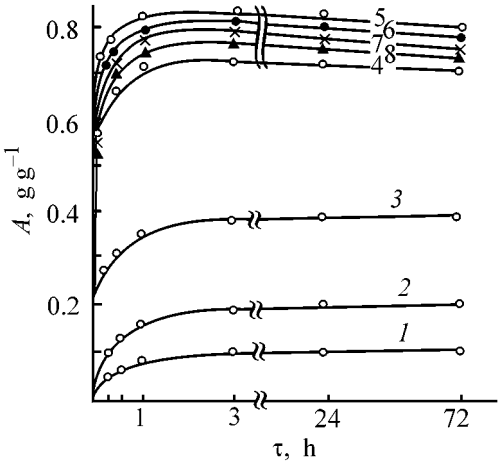

Fig. 2. Amount *A* of copper bound with sorbent in solutions nos. 1–8 vs. time τ.

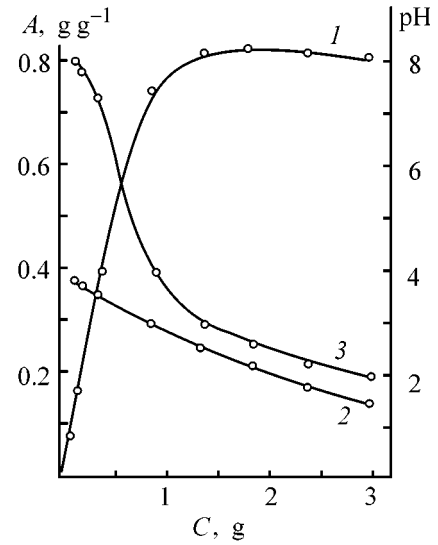

Fig. 3. (*1*) Amount A of copper bound by 1 g of sorbent in 1 h, (*2*) pH of the starting solutions, and (*3*) that in 72 h vs. copper content *C* in the starting solutions nos. 1–8.

The obtained data suggest that the processes of sorption from solutions nos. 5–8, on the one hand, and nos. 1–4, on the other, are markedly different. In the first case, the process ends with sorbent saturation in approximately 1 h, whereas in the second, the sorption, also being intensive during the first hour, later passes into a slowed-down phase continuing for days and presumably terminating only after formation of an equilibrium copper-containing sorption product.

Since the sorption process, consisting in an exchange interaction of calcium and copper carbonates in the sorbent with copper(II) ions in solution, is associated with hydrolysis, the possible final products of interaction between the carbonates and copper ions are hydrolysis products—basic salts and even copper(II)

X-ray phase analysis data for sorbent and sorption products*

Sorbent		Products of sorption from solutions								
		nos. 1–3						no. 8		
		after 1 h			after 3 days			after 3 days		
d, Å	I_{rel}	d, Å	I_{rel}	phase	d, Å	I_{rel}	phase	d, Å	I_{rel}	phase
–	–	5.45	100	F	5.45	100	F	5.45	100	F
–	–	5.04	40	F	5.04	50	F	5.04	50	F
–	–	–	–	–	–	–	–	4.02	30	–
3.81	20	3.81	12	S	3.81	7	S	–	–	–
3.33	10	3.33	6	S	–	–	–	–	–	–
3.03	100	3.03	70	S	3.03	30	S	–	–	–
–	–	2.83	50	F	2.83	55	F	2.83	60	F
–	–	2.78	70	F	2.70	80	F	2.70	80	F
–	–	–	–	–	–	–	–	2.62	20	–
2.48	12	2.48	5	S	–	–	–	–	–	–
–	–	2.28	85	F	2.28	90	F	2.28	85	F
2.27	45	2.27	30	S	2.27	10	S	–	–	–
2.08	30	2.08	20	S	2.08	5	S	–	–	–
–	–	–	–	–	–	–	–	2.01	7	–
1.90	45	1.90	20	S	1.90	8	S	–	–	–
1.87	45	1.87	20	S	1.87	8	S	–	–	–
1.81	5	–	–	–	–	–	–	–	–	–
1.62	6	–	–	–	–	–	–	–	–	–
1.60	11	1.60	3	S	1.60	1	S	–	–	–
1.51	8	1.51	2	S	–	–	–	–	–	–
1.46	5	–	–	–	–	–	–	–	–	–
1.47	7	1.47	1	S	–	–	–	–	–	–
1.41	8	1.41	2	S	–	–	–	–	–	–

* S stands for sorbent, and F, for $Cu_2Cl(OH)_3$.

hydroxide. The apparent key factors in the given case are their solubility products and changes in solution pH in the course of sorption. As indicated by the obtained results, the behavior of the solution pH (Fig. 3, curves *2* and *3*) strongly depends on the copper(II) content in the starting solutions. In solutions nos. 4–8, the change in pH is relatively small and terminates in approximately 1 h. In the case of starting solutions nos. 1–3, the pH changes during much longer time and to a greater extent. For example, the pH reaches a value of 7.45 in solution no. 3 and 7.75 in solution no. 2. These data are in good agreement and confirm the fact that 1 g of sorbent is insufficient for neutralizing initial acid solutions in copper sorption from solutions nos. 5–8. At the same time, in sorption from solutions nos. 1–3, the amount of copper in these solutions is not enough for saturating the sorbent. Sorbents binds hydrogen ions by the reaction

$$2H^+ + MCO_3 \rightarrow M^{2+} + H_2O + CO_2$$

thereby shifting to the right the hydrolysis reaction

$$Cu^{2+} + nH_2O \rightleftarrows [Cu(OH)_n]^{2-n} + nH^+.$$

An indirect evidence in favor of the occurrence of this reaction is the intense evolution of carbon dioxide upon addition of sorbent to copper(II) chloride solutions. The equilibrium of hydrolysis reactions is shifted in solutions nos. 1–3 to such an extent that the initially acid solutions become neutral or even weakly alkaline. It would be expected, with account of the fact that the reached pH values exceed the pH of the onset of copper(II) hydroxide precipitation (5.5) and approach the pH of its complete precipitation (8–10) [7], that even copper(II) hydroxide ($n = 2$) may be the final product of sorption in the case of an excess of sorbent.

In this connection, with an excess of sorbent, the residual concentration of copper may reach values determined by the solubility product of copper hydroxide. In particular, at pH 8 this concentration is 6.03×10^{-9} g cm^{-3}. Presumably, just this value is that final concentration to which tends in the course of time the residual concentration of copper in a solution treated with an excess of sorbent. However, products with $n < 2$ can be formed in intermediate stages. Indeed, according to X-ray phase analysis of sorption products [8] (see the table), the main phase

formed in sorption from dilute solutions nos. 1–3 is $Cu_2Cl(OH)_3$. This phase is detected in corresponding sorption products after both 1h and 3 days of contact between the sorbent and solution. This may be due to either lower solubility of $Cu_2Cl(OH)_3$, compared with the solubilities of other possible phases (including copper hydroxide), or to the fact that this phase is originally formed in sorption and its subsequent transformation into products of deeper hydrolysis is rather slow. The last variant (possibly combined with the first) is indirectly confirmed by the presence of reflections corresponding to this phase also in X-ray diffraction patterns of sorption products formed in more concentrated solutions.

CONCLUSIONS

(1) Carbonate-containing sorbent of technological origin can be used to sorb copper(II) from chloride solutions. Addition of the sorbent to solutions of this kind leads to intense evolution of carbon dioxide, accompanied by a decrease in the acidity of the starting solutions. With solutions originally containing more than 1.3–1.5 g of copper per 1 g of sorbent added, the sorption process ends with sorbent saturation in approximately 1 h. The maximum sorbent capacity is in this case 0.83 g g^{-1}.

(2) With an excess of sorbent, the sorption process is vigorous initially and then becomes slower, with the latter stage not complete even after 3 days. The solution pH becomes in this case equal to, or greater than 7, with the $Cu_2Cl(OH)_3$ phase being the main product of copper precipitation.

REFERENCES

1. Gudkova, N.N. and Kornyakova, L.N., *Sovershenstvovanie inzhenernogo oborudovaniya zdanii i sooruzhenii* (Improvement of the Enginery of Buildings and Constructions), Chelyabinsk: Chelyab. Gos. Tekhn. Univ., 1990, pp. 104–112.
2. US Patent 5 098 579.
3. Goronovskii, I.T., Nazarenko, Yu.P., and Nekryach, E.F., *Kratkii spravochnik po khimii* (Concise Handbook of Chemistry), Kiev: Akad. Nauk USSR, 1963.
4. Schwarzenbach, G., *Die Komplexometrische Titration*, Stutgart: Enke, 1955; Přibil, R., *Komplexometrie*, Praha: Chemapol, 1955. Translated under the titles Shvartsenbakh, G. and Prshibil, R., *Kompleksonometriya* Moscow: Goskhimizdat, 1958.
5. Malkina, T.G. and Podchainova, V.N., *Zh. Anal. Khim.*, 1964, vol. 19, no. 4, pp. 668–670.
6. Rae, W.N. and Reilly, J., *Physico-Chemical Practical Exercises*, London: Methuen, 1934.
7. Podchainova, V.N. and Simonova, L.N., *Analiticheskaya khimiya elementov: Med'* (Analytical Chemistry of Elements: Copper), Moscow: Nauka, 1990.
8. Mirkin, L.I., *Rentgenostrukturnyi analiz: Spravochnoe rukovodstvo* (Handbook of X-ray Phase Analysis), Moscow: Nauka, 1976.

Russian Journal of Applied Chemistry, Vol. 74, No. 4, 2001, pp. 588–591. Translated from Zhurnal Prikladnoi Khimii, Vol. 74, No. 4, 2001, pp. 571–574.

SORPTION AND ION-EXCHANGE PROCESSES

Sorption of Cations of the Zn^{2+}–Hg^{2+}–NO_3^-–H_2O System by Biomass of Ostreatus Agaricaceae Basidiomycete and KB-4(H^+) Cation Exchanger

T. L. Zalevskaya and E. V. Radion

Belarus State Technological University, Minsk, Belarus

Received February 3, 2000; in final form, October 2000

Abstract—Sorption of cations of the Zn^{2+}–Hg^{2+}–NO_3^-–H_2O system by the biomass of basidiomycete (line 21 *Pl. ostreatus f. florida*) and by KB-4(H^+) cation exchanger at pH 1.00 was studied. The results are discussed with regard to the state of cations in the solution before contact with the sorbent, sorbent properties, and sorption behavior of cations.

Previously, we studied the sorption of Cu(II), Pb(II), Hg(II), or Fe(III) by the biomass of *Pl ostreatus f. florida* basidiomycete from nitrate solutions containing a single cation or two metal cations simultaneously [1, 2]. The results were considered from the viewpoint of hydrolytic properties of metal ions. Proceeding with these studies, we examined the sorption of Hg(II) by a basidiomycete biomass from 0.1 M solution in the presence of 0.1 M Zn(II).

To examine the nature of sorption bonds, we also studied the sorption of Hg(II) and Zn(II) by carboxylic cation exchanger KB-4(H^+) whose functional groups can act as centers of electrovalent interaction and are able to participate in ion-dipole interaction, H-bond formation, and complexation [3].

EXPERIMENTAL

Analytically pure zinc nitrate and the solution of Hg(II) nitrate prepared by dissolution of metallic mercury in chemically pure nitric acid (1 : 1) were used. The fruit bodies of basidiomycete *Pl. ostreatus f. florida*, line 21 were provided by the Wood Institute, Belarussian National Academy of Sciences. Samples of air-dry basidiomycete biomass crushed to 0.5-mm particles were brought in contact with metal salt solution in hermetically sealed vessels for one day. Preliminary kinetic experiments showed that this the time is enough for equilibrium to be attained in the system [1]. The required solution pH was adjusted by adding chemically pure KOH or HNO_3. The solution pH was measured on an EV-74 universal pH meter with an error of 0.05 pH units. In blank tests performed for each system, a biomass sample was brought in contact with a zinc- and mercury-free solution at a given pH.

Mixtures were kept in a TS-80 M-2 air thermostat with intermittent agitation. After one day, equilibrated solutions were separated from the basidiomycete biomass, and the content of metal ions in them was determined.

The cation exchanger was pretreated by the method described in [4]. Its moisture content, determined as in [5], was 16.22%. The sorption was studied at 25 ± 0.1°C under static conditions; the attainment of the equilibrium distribution of metal ions between the solution and cation exchanger was proved in all runs.

To determine the effect of metal ion concentration, the sorption was studied at Hg(II) and Zn(II) concentrations of 0.01 and 0.1 M. The solutions prepared were kept for 7 days at 25 ± 0.1°C to attain equilibrium. The effect of pH could not be studied, because HgO deposition begins even at pH > 1.20. Therefore, all studies were done at pH 1.00.

The amounts of Hg(II) and Zn(II) simultaneously present in the solution were determined complexometrically. Initially the total metal content was determined by back-titration with a standard solution of zinc salt with eriochrome black T in ammonia buffer, then potassium iodide was added to displace equivalent amount of EDTA from its mercury complex, and the displaced EDTA was titrated with the zinc salt. The Zn(II) content in the mercury-free solution was

1070-4272/01/7404-0588 $25.00 © 2001 MAIK "Nauka/Interperiodica"

Sorption of Hg(II) and Zn(II) with sorbents at pH 1.00

Ion	System	Sorption S		V/m_0,* ml g^{-1}	K_d
		mmol g^{-1}	mg g^{-1}		
KB-4(H^+) cation exchanger, $C_{Zn} = C_{Hg} = 0.01$ M					
Zn^{2+}	Zn^{2+}–NO_3^-–H_2O	0	0	33.67	0
Hg^{2+}	Hg^{2+}–NO_3^-–H_2O	0.19	38.11	42.57	29.72
Zn^{2+}	Zn^{2+}–Hg^{2+}–NO_3^-–H_2O	0.01	0.65	36.21	1.11
Hg^{2+}	Zn^{2+}–Hg^{2+}–NO_3^-–H_2O	0.15	30.09	36.21	23.40
KB-4(H^+) cation exchanger, $C_{Zn} = C_{Hg} = 0.1$ M					
Zn^{2+}	Zn^{2+}–NO_3^-–H_2O	0	0	55.36	0
Hg^{2+}	Hg^{2+}–NO_3^-–H_2O	1.60	320.94	32.61	28.03
Zn^{2+}	Zn^{2+}–Hg^{2+}–NO_3^-–H_2O	1.24	81.08	52.70	16.19
Hg^{2+}	Zn^{2+}–Hg^{2+}–NO_3^-–H_2O	2.29	459.35	52.70	36.68
Basidiomycete biomass, $C_{Zn} = C_{Hg} = 0.1$ M					
Zn^{2+}	Zn^{2+}–NO_3^-–H_2O	2.38	155.63	89.54	19.52
				160.37	37.10
				147.46	43.63
Hg^{2+}	Hg^{2+}–NO_3^-–H_2O	0.92	184.54	87.15	16.68
				99.53	16.12
				91.31	16.69
Zn^{2+}	Zn^{2+}–Hg^{2+}–NO_3^-–H_2O	0	0	98.46	0
Hg^{2+}	Zn^{2+}–Hg^{2+}–NO_3^-–H_2O	1.11	222.65	98.46	16.75
				79.86	20.73
				88.70	25.20

* (V) solution volume and (m_0) sorbent sample weight.

determined by direct complexometric titration with eriochrome black T in ammonia buffer at pH 10 [6].

The metal sorption by the sorbent, S (mmol and mg per g of absolutely dry sorbent), and distribution coefficients K_d between the sorbent and solution were calculated from the chemical analysis data (table).

In discussing the sorption of simultaneously present metals, we should take into account the action of many factors: (1) the state of metal ions in the solution before coming in contact with the sorbent, which is determined by the hydrolytic behavior of each ion, by mutual influence of ions on their hydrolysis, and by probable interaction of hydrolyzed species of different metals; (2) the ion-exchange properties of the sorbent, determined by the number of ionogenic groups, degree of their dissociation at given pH, and the nature of exchanging ion [5]; and (3) the sorption behavior of metal ions, which is individual and depends on the chemical nature of the metal ion and sorbent.

We determined the pH at which HgO and $Zn(OH)_2$ start to precipitate (>1.20 and >5.50, respectively) from 0.1 M metal ion solution. At the same time, the solution containing 0.1 M Hg(II) and 0.1 M Zn(II) cannot be prepared at pH > 1.00 because of the precipitate formation. It is this fact that determined the pH at which we studied the metal sorption in the Hg(II)–Zn(II)–NO_3^-–H_2O system. As seen, the Hg(II) hydrolysis is facilitated in a mixed Hg(II)–Zn(II) solution, i.e., Zn(II) affects the hydrolytic behavior of Hg(II).

To obtain preliminary data on the possible hydrolytic interaction of Hg(II) with Zn(II), we performed pH-metric titration of solutions by the method described in [7] (see figure). Two titration jumps in curve *3* are observed after the onset of precipitation. To find whether HgO and $Zn(OH)_2$ coprecipitate, we performed some calculations [7]. In accordance with the solubility products SP(HgO) 3.0×10^{-26} and SP($Zn(OH)_2$) 1.4×10^{-17} [8], at the instant when $Zn(OH)_2$ starts to precipitate, the concentration of untitrated Hg(II) is

$$C(\mathrm{Hg}) = \frac{\mathrm{SP(HgO)}}{\mathrm{SP[Zn(OH)_2]}}\, C_{in}(\mathrm{Zn}) \approx 2 \times 10^{-11} C_{in}(\mathrm{Zn}).$$

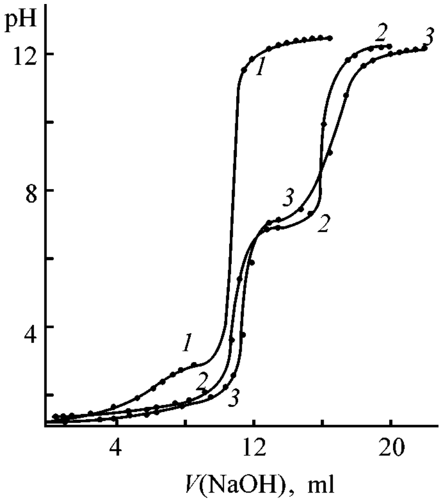

Curves of potentiometric titration of (*1*) Hg(II), (*2*) Zn(II), and (*3*) Hg(II)–Zn(II). $C_{Hg} = C_{Zn} = 0.01$ M. (*V*) Volume.

Thus, at practically any initial concentration of metal ions, two jumps corresponding to successive precipitation of HgO and $Zn(OH)_2$ must be observed in the curve of titration of an Hg(II)–Zn(II) solution with alkali in the absence of chemical interaction between Hg(II) and Zn(II). This is, indeed, observed in the experiment (curve *3*). However, the curve shape suggests that certain interaction between Hg(II) and Zn(II) does occur, because the curve contains no titration jump related to titration of pure Hg(II) in the acid medium (curve *1*), and the second jump is distorted and shifted to the right relative to curve *2* owing to superposition of some other process. Hence, Hg(II) and Zn(II) ions affect the hydrolysis of each other, with Hg(II) hydrolysis facilitated. Interaction of these ions in the solution is also possible.

At pH 1.00, when the degree of cation exchanger ionization is negligible, we should expect negligible sorption of Hg(II) and Zn(II) with KB-4 ion exchanger (pK ≈ 7 [3]. Indeed, only Zn(II) is not sorbed from solutions free of the other metal (see table), i.e., the ion exchange properties of KB-4 resin depend on the nature of the exchanging ions. The higher affinity of KB-4 for Hg(II) may be due to a number of specific properties of Hg^{2+} ion distinguishing it from the other metal ions. Firstly, no hydroxides are known for Hg^{2+}, with HgO directly precipitated instead. Secondly, Hg^{2+} shows low hydrolysis susceptibility; nevertheless, HgO is precipitated from strongly acidic solutions. Thirdly, a number of Hg^{2+} compounds are covalent (they are weak electrolytes), which is due to the strong polarizing effect of Hg^{2+}. It is known that the bond covalence grows with increasing polarization and the H^+ ion exhibits a particularly high polarizing effect. Since H^+ and Hg^{2+} ions participate in the ion exchange:

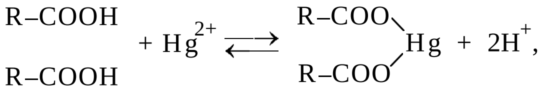
$$\begin{matrix} R\text{–}COOH \\ R\text{–}COOH \end{matrix} + Hg^{2+} \rightleftarrows \begin{matrix} R\text{–}COO \\ R\text{–}COO \end{matrix}\!\!>\!Hg + 2H^+, \quad (1)$$

the sorption of Hg^{2+} by the ion exchanger in a strongly acidic medium can be accounted for by the abnormally high polarizing power of exchanging ions. In addition, Hg and H have close electronegativities of, respectively, 2.00 and 2.2; i.e., the degrees of covalence of the Hg–O and H–O bonds are approximately the same. Since the charge of the Hg^{2+} ion is higher than that of H^+, the exchange (1) of these ions is possible under the above conditions. The measurement of pH of solutions before and after sorption confirmed the ion-exchange character of the process.

In the presence of Hg(II), Zr(II) is also sorbed by KB-4 at both metal concentrations (see table). Taking into consideration that Zn(II) is not sorbed from mercury-free solutions, we can suggest that the Zn(II) sorption in the presence of Hg(II) is caused by the formation of a compound between them in solution.

The sorption of Hg(II) grows by a factor of 8.4 with the metal concentration increasing by an order of magnitude (see table), with the distribution coefficient remaining practically unchanged, which indicates the participation in the ion-exchange process of the same sorption-active species. As shown in [2], these are Hg^{2+} ions.

When the metal ions are present simultaneously, the sorption behavior of each ion changes substantially. The main change is that Zn(II) is noticeably sorbed by KB-4 in the presence of Hg(II). For instance, 1.24 mM of Zn(II) per g of KB-4 is sorbed at a metal concentration of 0.1 M; K_d is 16.9 (see table). Since Zn(II) is not sorbed itself under these conditions, its sorption by the cation exchanger can be accounted for by the formation of a Zn(II) complex with Hg(II), which is not destroyed upon sorption and is strongly retained by the cation exchanger. Another argument for the formation of a heteronuclear compound is the substantial change in K_d of Hg(II) in the presence of Zn(II) (see table); in a 0.01 M solution the Hg(II) sorption decreases somewhat, but in a 0.1 M solution it substantially increases as compared with the Zn-free solution. Thus, mutual influence of metal ions on their hydrolytic and sorption behavior is observed in the Hg(II)–Zn(II) solution. At pH 1.00, a heteronuclear compound is formed in solution and is specifically sorbed by the carboxylic cation exchanger. The data in the table show that this compound contains more Hg(II) than

Zn(II). Since the Hg(II) sorption by the cation exchanger is the ion-exchange process and Zn(II) is sorbed only via interaction with Hg(II), we can suggest that the sorption of heteronuclear oxocompound Hg(II)–Zn(II) proceeds in accordance with the scheme

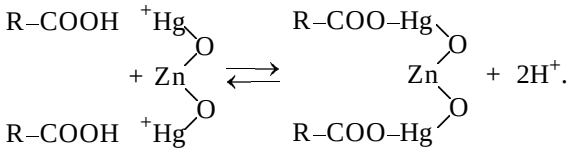

(Fragment of heteronuclear oxocompound)

The data in the table also show that, in the absence of the other metal, Zn(II) is sorbed by the basidiomycete biomass to a greater extent than Hg(II). When these metals are present simultaneously, their sorption behavior changes: the Zn(II) sorption stops, while the Hg(II) sorption increases somewhat.

The high K_d values for Zn(II) in the mercury-free solution deserve attention. To clarify whether ionic or nonionic forms of metals are sorbed by the basidiomycete biomass, we varied the V/m_0 ratio. In this case, for Zn(II) in a mercury-free solution, K_d changes (see table), and we can suggest in accordance with Schubert's rule that nonionic forms of Zn(II) are sorbed [9]. For Hg(II) in a zinc-free solution, K_d is constant at varied V/m_0. Hence, ionic forms of Hg(II) are sorbed. As shown in [2], these are Hg^{2+} ions. In solutions containing both ions, K_d for Hg(II) changes somewhat with V/m_0. This indicates a change in the Hg(II) sorption behavior (as compared with zinc-free Hg(II) solutions), caused by the formation of a heteronuclear Hg(II)–Zn(II) compound.

Comparison of the metal ion sorption by the basidiomycete biomass and KB-4 under the same conditions allows a conclusion that sorption by the KB-4 ion exchanger of Hg(II), Hg(II) in the presence of Zn(II), and Zn(II) in the presence of Hg(II), is greater than sorption by the basidiomycete biomass. The mechanism of Hg(II) sorption is the same in all cases: the ion exchange of Hg^{2+} for H^+. The Zn(II) sorption from mercury-free solution cardinally differs for the examined sorbents. Zn(II) is not sorbed by the cation exchanger at all and strongly sorbed by the basidiomycete biomass. As shown above, nonionic forms of Zn(II) are sorbed. The nature of the Zn(II)– biomass bonds remains unclear, and further studies are required to reveal the role of various functional groups in the interaction of Zn(II) with the basidiomycete biomass.

Since the sorption behavior of Hg(II) and Zn(II) in their sorption by the basidiomycete biomass are strongly different, we can suggest that the heteronuclear Hg(II)–Zn(II) compound existing in the solution decomposes upon sorption, and preferential Hg^{2+} sorption occurs because of the above-mentioned features of this ion.

CONCLUSIONS

(1) In the Hg(II)–Zn(II) solution, the mutual influence of the metals on their sorption and hydrolytic behavior is observed.

(2) The heteronuclear Hg(II)–Zn(II) compound formed in the solution is strongly sorbed by the KB-4 ion exchanger, but decomposes when brought in contact with the biomass of *Pl. ostreatus f. florida* basidiomycete.

REFERENCES

1. Zalevskaya, T.L. and Baev, A.K., *Koord, Khim.*, 1996, vol. 22, no. 6, pp. 499–501.
2. Zalevskaya, T.L., Radion, E.V., Baev, A.K., and Sheremet, E.N., *Koord, Khim.*, 1998, vol. 24, no. 5, pp. 339–342.
3. Shataeva, L.K., Kuznetsova, N.N., and El'kin, G.E., *Karboksil'nye kationity v biologii* (Carboxylic Cation Exchangers in Biology), Leningrad, 1979.
4. Starobinets, G.L., Borshchevskaya, T.I., and Maksimova, S.G., *Dokl. Akad. Nauk BSSR*, 1983, vol. 27, no. 2, pp. 138–140.
5. Ol'shanova, K.M., Potapova, M.A., and Morozova, N.M., *Praktikum po khromatograficheskomy analizy* (Laboratory Course of Chromatographic Analysis), Moscow: Vysshaya Shkola, 1970.
6. Schwarzenbach, G. and Flashka, H., *Die Komplexometrische Complexometric Titration*, Stuttgart: Ferdinand Euke Verlag, 1965.
7. Radion, E.V., *Vestsi Akad. Navuk Belarusi, Ser. Khim. Navuk*, 1996, no. 2, pp. 8–13.
8. Lur'e, Yu.Yu., *Spravochnik po analiticheskoi khimii* (Handbook of Analytical Chemistry), Moscow: Khimiya, 1985.
9. Davydov, Yu.P., Efremenkov, V.M., Bondar', Yu.I., *et al., Vestsi Akad. Navuk Belarusi, Ser. Fiz.-Energ. Navuk*, 1997, no. 3, pp. 29–33.

Russian Journal of Applied Chemistry, Vol. 74, No. 4, 2001, pp. 592–595. Translated from Zhurnal Prikladnoi Khimii, Vol. 74, No. 4, 2001, pp. 575–578.

SORPTION AND ION-EXCHANGE PROCESSES

Sorption Characteristics of "Food Fibers" in Secondary Products of Processing of Vegetable Raw Materials

S. S. Stavitskaya, T. I. Mironyuk, N. T. Kartel', and V. V. Strelko

Institute of Sorption and Endoecological Problems, National Academy of Sciences, Kiev, Ukraine

Received May 30, 2000; in final form, November 2000

Abstract—Some structural-sorption characteristics of a series of secondary products (wastes) obtained in processing of vegetable raw materials, such as wheat straw, buckwheat peel, sunflower husk, and beet pulp, containing fibrous cellulose skeleton ("food fibers"), were determined. The effect of chemical and mechanochemical modification of these products on the characteristics of their pore structure and sorption activity with respect to organic substances, heavy metal ions, and ^{90}Sr radionuclides was studied.

Previuos studies [1, 2] have shown that linear regular homopolysaccharides (cellulose, mannans, and chitin), contained in products of vegetable origin (grasses, legumes, vegetables, fruits, berries, algae, mushrooms, etc.) and also called "food fibers" (FFs), which are insoluble in water owing to strong intramolecular association, have noticeable binding ability with respect to a number of heavy metals and radionuclides, among them transuranium elements. It has been found experimentally that, in human and animal gastrointestial tracts, FFs are able to sorb calcium, copper, zinc, and iron ions, and also cholic acids, nitrous slags, phenols, and other toxic substances and to detoxicate the organism [3–5]. Medical and biological studies indicate that FFs used as sorbing food additives facilitate removal of various toxicants from the organism in curing many diseases, which appreciably increases the efficiency of therapeutic procedures and reduces their duration.

Because of the need for widening the assortment of sorbents (enterosorbents and food additives), it is an urgent task to study sorption, ion-exchange, and complexing characteristics of a number of vegetable products, which appear most often as nonutilizable wastes of agricultural industry.

The aim of this work was to study comprehensively the sorption characteristics of some FF-containing products, such as wheat straw, buckwheat peel, sunflower husk, and beet pulp. These products were subjected to chemical or mechanochemical modification: (1) lyophilic drying of the product after treatment with buffer solutions of varied acidity and (2) thermal extrusion of a moistened product.

Lyophilic drying (cold vacuum dehydration) of the products was carried out on a laboratory setup at temperatures ranging from –10 to –15°C after swelling of these products during boiling in buffer solutions with pH 3.56 ($KC_4H_5O_6$), 7.05 (KH_2PO_4 + Na_2HPO_4), and 9.18 (K_2HPO_4) for 1 h and keeping the resulting suspensions at room temperature for 7 days, washing of the solid phase with distilled water to neutral wash water pH, and filtration.

The mechanochemical treatment of the samples was carried out on a pilot two-worm extruder.[1] Its technical characteristics were as follows: length 1.5 m, outlet diameter 63 mm, rotation speed of the worms 30–45 rpm, and temperature in the area of maximum compression 160–180°C. The initial product fed into the extruder had moisture content of 25%.

The main goal of the modification of these products was to raise their internal adsorption surface area and facilitate the access to active centers of FF-containing materials. Therefore, it was of interest to estimate the sorption characteristics of the modified products with respect to organic substances, toxic metals, and radionuclides.

The features of the pore structure of the products and their capacity for molecular and ion-exchange sorption were studied by common procedures [6, 7]. The specific surface area S_{sp} was measured gas-chromatographically from the thermal desorption of argon. The volume of sorption pores, W_s, was de-

[1] Ukrainian Research Institute of Machines for Plastic Production (Kiev).

1070-4272/01/7404-0592 $25.00 © 2001 MAIK "Nauka/Interperiodica"

termined by the dessicator technique from the sorption of benzene, methanol, and water vapor.

The sorption capacity of the sorbents under consideration was estimated from the isotherms of adsorption from aqueous solutions of substances-markers with various molecular weights, such as Methylene Blue (M = 319) and vitamin B_{12} (M = 1355), representing groups of organic compounds with, respectively, low and medium molecular weight. In doing so, we used the method of individual weighed portions; the solid phase to solution weight ratio was 1 : 2000, and the contact time of the material with solutions of various initial concentrations, 4 h.

The ion-exchange characteristics of the samples (static exchange capacity) were judged from the sorption of acid and alkali from 0.01 M HCl and 0.1 M NaOH solutions.

The structural changes in the products (degradation of polysaccharide chains) upon mechanochemical modification were estimated from the concentration of paramagnetic centers, determined by ESR. The ESR spectra of dry sorbent samples were recorded on an SEPR-03 radiospectrometer (Svetlana Production Association, Russia) in air at room temperature.

The limiting sorption capacity of the samples for heavy metal cations was determined from the corresponding plateaus in the isotherms of sorption from solutions of lead acetate and strontium chloride. The equilibrium concentrations of metals in the solutions were measured by the atomic-absorption spectroscopy on a KAS-120.1 device (Elektropribor Production Association, Ukraine).

The sorption selectivity with respect to radiostrontium was estimated from the distribution coefficient K_d of the isotope between the sorbent and radioactive solution. The initial activity of the solution was 1.6×10^{-5} Ci l^{-1}. The specific activities were measured by the standard procedure [8]: after evaporation of 1 ml of an aliquot, the dry residue was analyzed with a 1211 RackBeta liquid scintillation β-counter (Finland) tuned to the ^{90}Sr emission energy.

Table 1 presents data characterizing the porosity of lyophilized materials treated with buffer solutions. The initial products were practically nonporous. Swelling in the electrolytes and subsequent lyophilic drying resulted in the appearance of sorption pores and development of the specific surface area of the materials. In acidic media, the porosity develops considerably more slowly than in neutral and alkaline solutions. The S_{sp} values for products treated with acidic and alkaline buffer solutions differ by a factor as large as 3–5. In addition, the samples treated with alkaline solutions have fairly high adsorption activity with respect to organic substances in aqueous solutions. For example, it follows from the isotherms of Methylene

Table 1. Characteristics of porosity of FF-containing lyophilized materials treated with buffer solutions with various acidities

Parameter	pH of suspension	Material		
		wheat straw	buckwheat peel	sunflower husk
S_{sp}, $m^2\ g^{-1}$	3.56	2	3	11
	7.05	10	11	20
	9.18	13	13	37
W_s ($cm^3\ g^{-1}$) with respect to				
C_6H_6	7.05	0.10	0.08	0.09
CH_3OH	7.05	0.22	0.22	0.20
H_2O	7.05	0.24	0.18	0.19

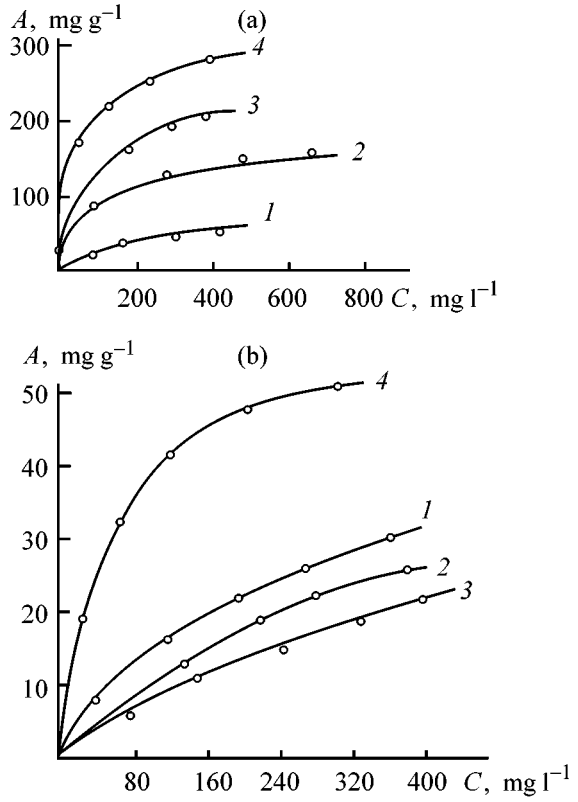

Fig. 1. Isotherms of sorption of (a) methylene blue and (*b*) vitamin B_{12} with FF-containing samples treated with alkaline solution (pH 9.18). (*A*) Sorption, (*C*) concentration of an equilibrium solution of (a) Methylene Blue and (b) vitamin B_{12}. (*1*) Wheat straw, (*2*) buckwheat peel, (*3*) sunflower husk, and (*4*) KAU activated carbon.

Table 2. Structural and sorption characteristics of FF-containing materials before and after high-temperature extrusion

Material	Stage of treatment	Concentration of PCs $N \times 10^{-15}$, spin g^{-1}	SEC (mg-equiv g^{-1}) for		Sorption capacity (mg g^{-1}) for		K_d of Sr, ml g^{-1}
			Cl^{-1}	Na^+	Pb^{2+}	Sr^{2+}	
Buckwheat peel	Initial	2.4	0.4	1.8	1.4	0.9	20
	After extrusion	7.9	0.5	2.0	1.6	1.7	310
Sunflower husk	Initial	1.1	0.4	0.8	0.5	0.7	–
	After extrusion	2.7	0.5	1.4	1.0	1.6	–
Beet pulp	Initial	1.1	0.4	1.4	1.8	2.2	30
	After extrusion	3.1	0.5	2.0	2.3	3.1	270

Blue adsorption (see Fig. 1a) that the adsorption capacity of these samples reaches 150–200 mg g^{-1}, which is comparable with some classic sorbents (activated carbons, silicas, clays, and others) recommended as adsorbents for medicine.

However, the sorption activity of the resulting samples with respect to medium-molecular-weight molecules, represented by vitamin B_{12}, is lower than that of activated carbons (Fig. 1b) with a broad pore-size distribution. It is likely that the resulting FF-containing materials have ultramicroporous structure accessible to small polar molecules (water, methanol), but the access is hindered for larger nonpolar molecules of benzene and impossible at all for large molecules of vitamin B_{12}. This is evident from the data on W_s for various adsorbates (Table 1): the values determined for comparatively small molecules of methanol and water (critical size of up to 0.3 nm) are higher by a factor of 2–2.5 that those for benzene (critical size of up to 0.6 nm). Medium-sized and large molecules are most probably sorbed in macropores whose contribution to the specific surface area of the sorbent sample is, as a rule, insignificant (no more than 1 $m^2 g^{-1}$).

The results of titrations of FF-containing materials with 0.1 N NaOH and 0.01 HCl show rather strong sorption of alkali metal cations. Their static exchange capacity (SEC) with respect to Na^+ cations is 0.8–1.8 mg-equiv g^{-1} even for the initial materials, which suggests the presence of proton groups, most probably of alcohol type (as suggested by the structure of the cellulose skeleton). This is responsible for the ion-exchange and complexing sorption of multicharged alkali and transition metal cations.

It was of interest to improve the sorption characteristics of FF-containing materials by thermal extrusion treatment, which, in our opinion, must result in an increase in the accessibility to ions of active centers in a rather rigid three-dimensional skeleton of the material. It is well known [9] that the mechanochemical treatment of the material in extrusion may result in numerous ruptures (degradation) of polysaccharides chains, indicated, e.g., by an increase in the concentration of defective structures of the free-radical type, i.e., paramagnetic centers (PCs). Actually, an abrupt increase (by a factor of 2–2.5) in the concentration of PCs in FF-containing materials is registered after extrusion in the ESR spectra (Table 2). It is evident that the presence of PCs of the macroradical type should be considered a positive factor for food additive or enterosorbent, since macroradicals can inhibit free-radical chain processes at the cell level, initiated by both external ionizing radiation and internal radiation caused by incorporated radionuclides.

It was found that, upon extrusion, the SEC of the materials with respect to Cl^- anions increases insignificantly, while the SEC with respect to Na^+ cations grows noticeably (by 0.2–0.6 mg-equiv g^{-1}). This treatment of the materials has positive effect on their binding power with respect to multicharged metal cations: the sorption capacity of the materials with respect to Pb^{2+} and Sr^{2+} increases by 30–40% (Table 2).

Still more interesting are data on changes in the selectivity of radioactive strontium sorption by FF-containing materials after thermal extrusion. The resulting distribution coefficients K_d with respect to ^{90}Sr suggest that the mechanochemical treatment of these ma-

terials increases their sorption selectivity practically by an order of magnitude. In other words, modified FF-containing materials can be compared, as radioactive strontium sorbents, with adsorbents of the ion-exchange type, e.g., oxidized carbons [10].

CONCLUSIONS

(1) After proper chemical or mechanochemical modification, secondary products of processing of agricultural plants can be considered fairly efficient adsorbents in molecular or ion-exchange sorption. Their sorption characteristics with respect to organic substances (e.g., Methylene Blue and vitamin B_{12}), heavy metal ions (e.g., lead and strontium), and strontium radionuclide compare well with those for classic adsorption materials based on carbons, silica, aluminosilicates, etc.

(2) Modified materials based on secondary vegetable products and containing food fibers can be considered potential food additives with therapeutic and prophylactic effect or as components of enterosorbents.

REFERENCES

1. Vanshtein, S.G. and Masik, A.M., *Pishchevye volokna v profilakticheskoi i lechebnoi meditsine* (Food Fibers in Prophylactic and Therapeutic Medicine), Moscow: Vsesoyuzn. Inst. Med. Issled., 1985, issue 3.
2. *Prirodnye sorbenty* (Natural Sorbents), Belyakov, N.A., Ed., St. Petersburg: Tsentr Sorbtsionnykh Tekhnologii, 1992.
3. *Sorbents and Their Clinical Applications*, Giordano, C., Ed., New York: Academic, 1980.
4. *Enterosorbtsiya* (Enterosorption), Belyakov, N.A., Ed., Leningrad: Tsentr Sorbtsionnykh Tekhnologii, 1991.
5. Davydov, V.I., Stavitskaya, S.S., Strelko, and Kartel', N.T., *Enterosorption: Present State, Problems, and Prospects of Application*, Preprint of Inst. of Sorption and Endoecological Problems, Kiev, 1993.
6. Kel'tsev, N.V., *Osnovy adsorbtsionnoi tekhniki* (Principles of Adsorption Technology), Moscow: Khimiya, 1984.
7. Aivazov, B.V., *Praktikum po khimii poverkhnostnykh yavlenii i adsorbtsii* (Practical Course of Surface Chemistry and Adsorption), Moscow: Vysshaya Shkola, 1973.
8. Sinitsyn, S.S., Kogochigov, P.M., Golutvinova, M.M., *et al.*, *Metody raboty s primeneniem radioaktivnykh indikatorov* (Methods of Working with Radioactive Tracers), Moscow: Akad. Nauk SSSR, 1966.
9. Pshezhetskii, S.Ya., Kotov, A.G., Roginskii, V.A., *et al.*, *EPR svobodnykh radikalov v radiatsionnoi khimii* (ESR of Free Radicals in Radiation Chemistry), Moscow: Khimiya, 1972.
10. Kartel', N.T. and Bortun, L.N., *Ukr. Khim. Zh.*, 1992, vol. 58, no. 1, pp. 24–27.

Russian Journal of Applied Chemistry, Vol. 74, No. 4, 2001, pp. 596–602. Translated from Zhurnal Prikladnoi Khimii, Vol. 74, No. 4, 2001, pp. 579–585.

APPLIED ELECTROCHEMISTRY AND CORROSION PROTECTION OF METALS

Voltammetry with a Fluoride-Selective Electrode with Solid-Phase Reference System

M. S. Turaeva, S. A. Kot, O. V. Glumov, and I. V. Murin

Research Institute of Agrophysics, St. Petersburg, Russia
St. Petersburg State University, St. Petersburg, Russia

Received October 30, 2000

Abstract—Experimental results obtained in a study of the voltammetric response of an all-solid fluoride-selective electrode based on LaF_3 (Eu^{2+} 0.8 mol %), LaF_3 (Sr^{2+} 5 mol %) and CeF_3 (Sr^{2+} 5 mol %) single crystals brought in contact with Ag, Bi, and Sn metal samples are presented. The method of cathodic inversion voltammetry was applied to study the reduction of La^{3+} and Ce^{3+}—cations from the rigid sublattice of solid electrolytes, which determines the threshold of the electrochemical stability of a membrane. Anodic inversion voltammetry was used to investigate the characteristics of solid-phase generation of metal fluorides at the interface between the fluoride-selective electrode and metals.

The fluoride-selective electrode (FSE) with a single-crystal membrane of LaF_3 solid electrolyte activated with Eu^{2+} (0.8 mol %), one of the most specific ion-selective electrodes, is widely used for measuring the activity of the fluoride ion in solutions [1]. In addition, it has been proposed to use FSE in an electrochemical cell with a metal working electrode as voltammetric sensor (VAS) sensitive to changes in the elemental composition of solid surfaces [2, 3]. The operation of FSE and VAS is based on different processes. In FSE, the potential-determining process is the reversible transfer of the fluoride ion at the solid electrolyte–solution interface

$$F^-_S \leftrightarrow F^-_{s.e} \text{ (FSE)}. \quad (1)$$

In VAS, the voltammetric response is due to solid-phase reactions of metal fluoride formation, proceeding at the interface between the FSE membrane and metal and involving mobile ions of the solid electrolyte, $F^-_{s.e}$:

$$nF^-_{s.e} + M \leftrightarrow MF_n + ne\text{(VAS)}, \quad (2)$$

whose reduction is characterized by curves with a single peak [2–4]. It is proposed to use the output signals of the sensor: peak current and potential and stationary potential, to determine the nature of a metal and its content [2, 3].

The present communication reports on a study of the voltammetric response of FSE with a solid-state reference system in the case of contact between LaF_3 single-crystal membrane (Eu^{2+} 0.8 mol %) and metals. The study was undertaken in order to expand the use of FSE and single-crystals of other nonstoichiometric fluorides with tysonite structure [LaF_3 (Eu^{2+} 0.8 mol %), LaF_3 (Sr^{2+} 5 mol %), and CeF_3 (Sr^{2+} 5 mol %)] in detection of metal impurities on the surface of solids without aqueous or nonaqueous solutions and without reagents. Previously, all-solid FSEs with LaF_3 membrane (Eu^{2+} 0.8 mol%), and single crystals of LaF_3 (Sr^{2+} 5 mol%) and CeF_3 (Sr^{2+} 5 mol %), have not been considered in the voltammetric mode.

EXPERIMENTAL

Two types of FSE were fabricated, with liquid and solid inner reference systems. Polished membranes made of a lanthanum fluoride single crystal activated with Eu^{2+} (0.8 mol %) were 10 mm in diameter and 1–1.5 mm thick. Some experiments were done with all-solid FSEs based on LaF_3 (Sr^{2+} 5 mol %) and CeF_3 (Sr^{2+} 5 mol %) single crystals.

The electrochemical behavior of the interface between the solid electrolyte and metal can be strongly affected by structural defects and crystallographic in-

1070-4272/01/7404-0596 $25.00 © 2001 MAIK "Nauka/Interperiodica"

homogeneities of the solid electrolyte. Since preliminary experiments revealed that the voltammetric signal intensity depends on the conductivity-related properties of the single-crystal solid electrolyte, membranes with resistance not exceeding 50 kohm were chosen.

Particular attention was given to pretreatment of the FSE membrane surfaces and metallic electrodes, since dynamic voltammograms are exceedingly sensitive to contamination of contact surfaces and reflect the presence of uncontrollable impurities in trace amounts. The procedure for treatment of the solid electrolyte surface and preparation of metal samples for experiments was described in [2].

The study was performed in two-electrode electrochemical cells FSE | M

$$\text{Sn, SnF}_2 \,|\, \text{LaF}_3 \,|\, \text{M} \qquad (3)$$

using a PU-1 polarograph or PI-50-1.1 potentiostat with PR-8 programming unit. The metal served as working electrode with area varied in the experiment between 0.05 and 1 mm^2. The fluoride-selective electrode with a solid-phase reference system served in voltammetric measurements as auxiliary and reference electrodes. Solid-phase Sn, SnF_2 electrodes, commonly used in LaF_3-based gas sensors [5, 6], were fabricated by mixing Sn and SnF_2 powders and compacting the mixture, with subsequent fusion.

The emf was measured with an I-120 ion meter or ITN-7 electrometer (R_{in} = 10^{16} ohm).

The operation of an all-solid FSE in contact with metal electrode was studied in the inversion voltammetry mode. As experimental metal samples were tested Ag, Sn, and Bi, whose electrochemical behavior has been considered previously for an FSE with liquid inner reference system [7, 8].

A most important condition for studying the response of the interface between the FSE membrane and metal is the descrimination of the processes occurring in half-cells of the cell with solid electrolyte. It is more difficult to ensure nonpolarizability of the interface between the solid electrolyte and the solid-phase reference system in voltammetric measurements, compared with the case of potentiometry [9], especially with anionic conductors. The requirements to the solid-phase reference systems can be formulated as follows: (i) the reference system must contain a sufficient number of active ions ensuring charge transfer across the interface between the reference electrode and the solid electrolyte, (ii) metal particles must form an electrically conducting network, (iii) large contact surface area between the ionic and electronic conductors is necessary for diminishing the polarization at the metal–salt interface, (iv) it is advisable to make as thin as possible the salt layer between the surface of the single-crystal solid electrolyte and metal particles for reducing the ohmic polarization of the layer, and (v) it is necessary to ensure high rate of exchange at the metal–salt and salt–solid electrolyte phase boundaries of the reference half-cell.

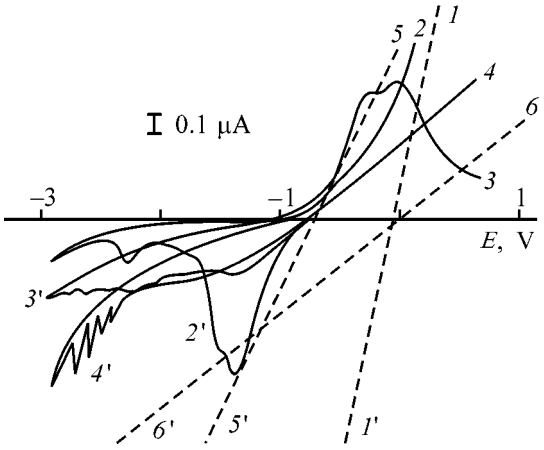

Fig. 1. Dynamic voltammograms of cells. Potential sweep rate V = 0.03 V s^{-1}; the same for Fig. 2. (E) Potential; the same for Fig. 2. Cell: (*1*, *1'*) (4), (*2*–*5*, *2'*–*5'*) (5), and (*6*, *6'*) (6). For explanation see text.

The choice of a solid-phase reference system based on SnF_2 is governed by the sufficiently high ionic conductivity of SnF_2 ($\sigma \approx 2 \times 10^{-7}$ S cm^{-1} at 20°C) and by the fact that the reaction $SnF_2 + 2e \leftrightarrow Sn + 2F^-$ is reversible under certain conditions [4, 7]. The fabricated solid Sn, SnF_2 electrodes were tested by successive comparison of voltammograms of the cells

$$\text{Ag, AgCl} \,|\, \text{KCl 1 M, KF 1 M} \,|\, \text{LaF}_3 \,|\, \text{KF 1 M, KCl 1 M} \,|\, \text{AgCl, Ag;} \qquad (4)$$

$$\text{Ag, AgCl} \,|\, \text{KCl 1 M, KF 1 M} \,|\, \text{LaF}_3 \,|\, \text{SnF}_2\text{, Sn;} \qquad (5)$$

$$\text{Sn, SnF}_2 \,|\, \text{LaF}_3 \,|\, \text{SnF}_2\text{, Sn,} \qquad (6)$$

measured at potential sweep rates in the range 0.02–0.05 V s^{-1}.

The current–voltage (I–E) characteristic of the symmetric cell (4), linear within ±3 V and independent of the potential sweep rate (Fig. 1, curves *1* and *1'*), was used for evaluating the ohmic voltage drop in the solid electrolyte [7].

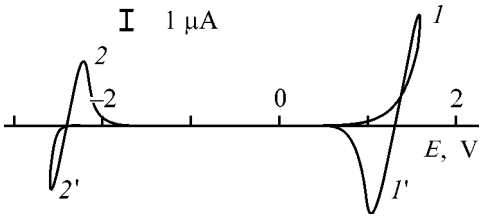

Fig. 2. Cyclic voltammogram of the Sn, $SnF_2|LaF_3|Ag$ cell. For explanation see text.

It was found that the voltammograms of cell (5), comprising two types of reference electrodes: silver chloride electrode in an aqueous solution and a solidphase electrode, measured at potentials ranging from –2 to +2 V, were different for different samples. With some solid electrodes, a single-peak SnF_2 decomposition curve was observed at E = –0.6 V after anodic polarization of the $LaF_3|SnF_2$, Sn contact in the range from –0.5 to +1.5 V and subsequent cathodic sweep (Fig. 1, curves *2* and *2*'). With other solid electrode samples, an anodic peak was clearly manifested at E = 0.05 V, associated with the reaction of tin fluoride formation (Fig. 1, curves *3* and *3*'). In other cases, irregular current fluctuations appeared in the cathodic region, indicating, in all probability, a poor contact between the reference electrode and the surface of the single-crystal membrane. The observed diversity of voltammetric responses does not always affect the cell emf, i.e., the stationary potential of the Sn, SnF_2, LaF_3 electrode was reproducible, E_{st} = –(0.621 ± 0.003) V. However, when effects of this kind did appear, interpretation of processes at the $LaF_3|M$ interface was either strongly hindered or at all impossible. In this connection, attention was paid to the technology of fabrication of the solid-phase reference system whose efficiency was verified by measuring voltammograms of cell (5). The fabrication technology of the Sn, SnF_2 electrodes was modified so as to ensure, by changing the salt to metal ratio, compaction pressure, and time and temperature of fusion, a linear *I–E* characteristic of cell (5) at potentials ranging from E = –2.0 to E = +2 V (Fig. 1, curves *5* and *5*'). It was found that raising the potential sweep rate ($dE/dt > 0.06$ V s^{-1}) led to the appearance of a hysteresis in the dynamic *I–E* curve. Therefore, voltammetric testing of solid-phase electrodes was also used to select the working range of potential sweep rates. A comparison of the *I–E* curves for cells (1) and (5) revealed an additional polarization resistance that remained unchanged under the experimental conditions.

The voltammogram of cell (6) with two solid-phase contacts (Fig. 1, curves *6* and *6*') is characterized, as would be expected, by an increase in polarization resistance, but remains linear in the range of potentials in question and exhibits no hysteresis at sweep rates of 0.01 to 0.04 V s^{-1}. Similar behavior is observed with $LaF_3:Sr^{2+}$ and $CeF_3:Sr^{2+}$ single crystals. All-solid FSEs, ensuring this type of dynamic *I–E* curves in contact with Sn, SnF_2, were used to study the $LaF_3|M$ interface, with the *I–E* curve of cell (5) monitored at regular intervals, in the case when there occurred a Nernst dependence of the FSE emf on the activity of the fluoride ion in solution in the range 1–5 pF^-.

The working range of potentials at which solid-phase reactions at the $LaF_3|M$ interface (M = Ag, Bi, or Sn) was verified using the cyclic voltammogram of the Sn, $SnF_2|LaF_3|Ag$ cell (Fig. 2), since the potential of silver fluoride formation is the most positive among the metal electrodes under study: E^0 (Ag|AgF) = 0.95 V [7]. After anodic charging of the interface from E = 0.5 to E = 2 V, a current appears at E > +1 V as a result of AgF formation. A single-peak curve of silver reduction is observed in subsequent cathodic potential sweep (Fig. 2, curves *1* and *1*'). Further shift of the potential in the negative direction gives rise to a current at E = –2.35 V (Fig. 2, curve *2*'). Changing the sweep direction to anodic is accompanied by the appearance of curves with a single peak (Fig. 2, curve *2*). The nature of the curves depends on the contact zone area, potential sweep rate, and interface potential in inversion. In cathodic polarization of the $LaF_3|M$ interface at –2.35 V, cations belonging to the rigid sublattice of the single crystal are reduced to form $LaF_3|La|Ag$ electrodes, and potential inversion in the anodic direction leads to La oxidation and regeneration of the solid electrolyte. A similar behavior is characteristic of an FSE with liquid inner reference system the case of contact between a $LaF_3:Eu^{2+}$ membrane and metals [4, 9]. The redox reactions involving lanthanum contained in the solid electrolyte are important as regards the possible use of nonstoichiometric fluorides in analytical practice, since they determine the working range of potentials.

The reactions limiting the cathodic region of electrochemical stability of the solid fluorine-conducting electrolyte were analyzed using LaF_3 (Eu^{2+} 0.8 mol %), LaF_3 (Sr^{2+} 5 mol %), and CeF_3 (Sr^{2+} 5 mol %) single crystals in the cathodic inversion voltammetry mode. It was found that the voltammograms of the contact between Ag and the single crystals used were similar, but the reduction potential was dependent on the cations of the rigid sublat-

tice. The initial portions of the dynamic voltammograms, reflecting the transition to a Faraday cathodic process, were, as a rule, independent of the potential sweep rate. (dE/dt = 0.02–0.05 V s^{-1}). Further, the slope of the *I–E* curves coincided with the ohmic polarization of the contact FSE membrane–Ag. The dynamic anodic curves measured from the level of the stationary potential were characterized by a single peak and reflected the transition from the $LaF_3|La|Ag$ electrode to a $LaF_3|Ag$ one with regeneration of the FSE|Ag interface. Figure 3 presents $CeF_3:Sr^{2+}|Ag$ interface regeneration curves taken after cathodic forming of the $CeF_3:Sr^{2+}|Ce|Ag$ cell at generation potential $E_{g.c}$ = –2.6 V and Q_c = 8.36 μC.

Reduction of La^+ in $LaF_3:Eu^{2+}$ and $LaF_3:Sr^{2+}$ single crystals and Ce^{3+} in $CeF_3:Sr^{2+}$ single crystal was studied by analyzing the influence exerted on the characteristics of anodic processes by the potential of cathodic charging of the interface to form $LaF_3:Eu^{2+}|La|Ag$, $LaF_3:Sr^{2+}|La|Ag$, and $CeF_3:Sr^{2+}|Ce|Ag$ electrodes. It was found that at generation potentials ranging from $E_{g.c}$ = –2.5 to $E_{g.c}$ = –2.7 V the current of the peak in the anodic curves linearly depends on the square root of the potential sweep rate $I_{a.p} = f(V^{1/2})$ in the range 0.01–0.05 V s^{-1} for all of the interfaces studied (Fig. 4a). The same dependence is preserved when the data are corrected for the ohmic polarization of the contact [10]. The accumulation potential exerts only slight influence on the slope of the $\log I_{a.p} = f(\log V)$ dependence, varying between 0.5 and 0.6 for the experimental data and those corrected for the ohmic polarization. Probably, the interface regeneration process is of diffusion nature. A linear dependence of the anodic peak current on the amount of passed electricity, $I_{a.p} = f(Q_c)$ (Fig. 4b) is observed at Q_c ranging from 7.27 to 23.4 μC for the $LaF_3:Eu^{2+}|Ag$ interface (curves *1–3*) and from 8.36 to 17.6 μC for the $CeF_3:Sr^{2+}|Ag$ interface (curve *4*). The emf of the formed cells is within –(2.380 ± 0.005) V for the Sn, $SnF_2|LaF_3:Eu^{2+}|La|Ag$ cell, –(2.370 ± 0.005) for Sn, $SnF_2|LaF_3:Sr^{2+}|La|Ag$, and –(2.340 ± 0.005) for Sn, $SnF_2|CeF_3:Sr^{2+}|Ce|Ag$.

The reactions of metal fluoride formation at the $LaF_3:Eu^{2+}|M$ interface in the solid-phase cell (3) (M = Ag, Bi, or Sn) were studied in the anodic inversion voltammetry mode. Previously, it has been shown in studying an FSE with water reference system that the nature of the decomposition curves of anodically generated compounds depends on the generation potential $E_{g.a}$, and, after the formation of an intermediate phase of metal fluorides at the op-

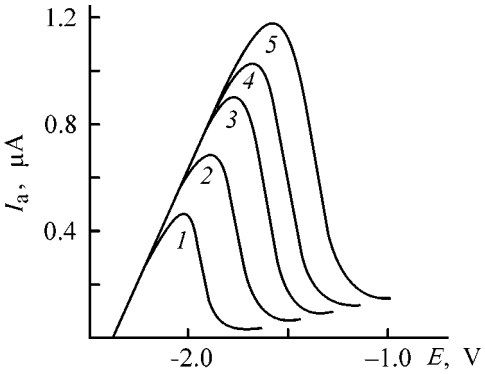

Fig. 3. $CeF_3:Sr^{2+}|Ag$ interface regeneration (*I–E*) curves taken after cathodic forming of the $CeF_3:Sr^{2+}|Ce|Ag$ cell at $E_{g.c}$ = –2.6 V (Q_c = 8.36 μC). Potential sweep rate *V* (V s^{-1}): (*1*) 0.01, (*2*) 0.02, (*3*) 0.03, (*4*) 0.04, and (*5*) 0.05; the same for Fig. 5.

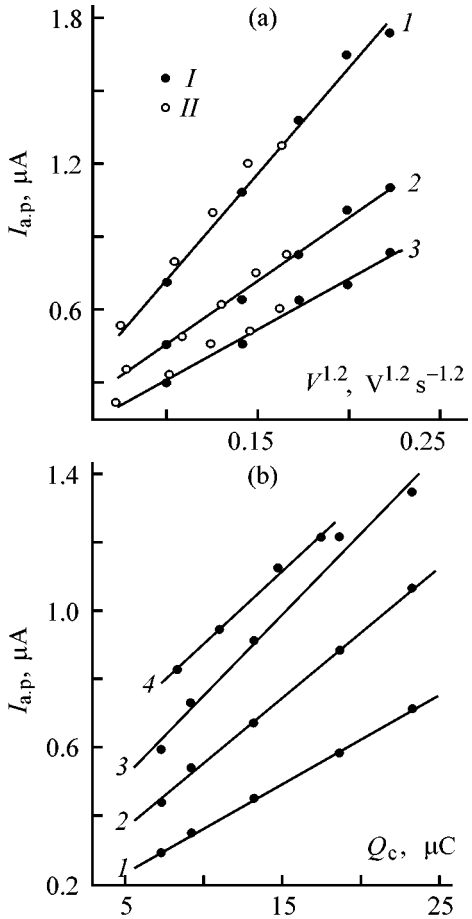

Fig. 4. Anodic peak current $I_{a.p}$ of cation oxidation in the FSE membrane after charging of the FSE|Ag (–) interface at $E_{g.c}$ = –2.6 V vs. (a) potential sweep rate *V* and (b) amount of passed charge Q_c. FSE: (*1*) $LaF_3:Eu^{2+}$, (*2*) $LaF_3:Sr^{2+}$, and (*3*) $CeF_3:Sr^{2+}$. (a) Data: (*I*) experimental and (*II*) corrected for the ohmic polarization of the contact; the same for Fig. 6a. (b) Potential sweep rate *V* (V s^{-1}): (*1*) 0.01, (*2*) 0.02, and (*3*) 0.03. For explanation see text.

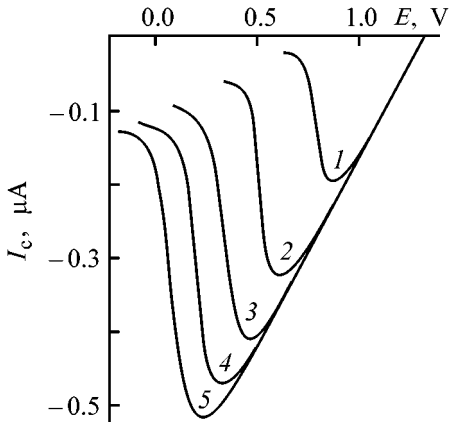

Fig. 5. $LaF_3:Eu^{2+}|Ag$ interface regeneration curves I_c–E after anodic formation of AgF at $E_{g.a}$ = 1.9 V.

timal potential $E_{g.a}$, the cathodic curves are characterized by a single peak [2, 7]. Guided by the prospects for use of this kind of curves in analytical practice, the authors of the present study paid primary attention to data analysis allowing the most adequate assessment of the chosen optimal potential $E_{g.a}$ of compound accumulation in studying the processes at the interface between M and FSE membrane with a solid-phase reference system.

For this purpose, the effect of $E_{g.a}$ on how the cathodic peak current $I_{c.p}$ and peak potential $E_{c.p}$ depend on the potential sweep rate V and amount of electricity Q_a consumed for generation of metal fluorides in potentiostatic charging of the $LaF_3:Eu^{2+}|M$ interface was studied. It is known that the conditions of electrolysis in aqueous and nonaqueous solutions affect the properties of a deposit at its equal amounts. Deviation from the optimal accumulation potential leads to a change in the run of dynamic I–E characteristics, e.g. affects the peak width [11]. Possibly, the mechanism by which the nucleation and growth of a deposit of metal fluorides occur at the interface between the FSE membrane and metal in air medium is manifested in a change in relative rates of separate stages of the multistage solid-phase process. As a criterion for optimizing the electrolysis conditions in order to decrease the number of stages limiting the rate of the solid-phase process is chosen the potential of the cathodic charging of the interface, at which the $I_{c.p}$ of the anodic curve is a linear function of V^n with n close to 0.5. In the voltammetry of aqueous solutions, such a behavior is characteristic of processes controlled either by the rate of mass transfer under linear diffusion conditions [12] or by the ohmic resistance of passive films [13, 14].

Preliminary choice of nearly optimal potentials $E_{g.a}$ was done with regard to the $E_{g.a} - E_{st}$ values obtained previously [8, 10]. A linear dependence of the peak current of cathodic curves on $V^{1/2}$ in the range 0.01–0.04 V s^{-1} was observed at the chosen $E_{g.a}$ for the contacts under consideration. Experiments demonstrated that changes in $E_{g.a}$ affect in different ways the characteristics of the cathodic processes, namely, the behavior of $E_{c.p}$ and slope of the $\log I_{c.p} = f(\log V)$ dependence and also exert influence on the emf of the formed cells.

As shown by investigations of anodic processes at the $LaF_3:Eu^{2+}|Ag$ interface, the cathodic curves recorded from the level of the stationary potential after accumulation of an intermediate compound exhibit a single peak. Figure 5 presents cathodic curves taken at potential sweep rates in the range 0.01–0.05 V s^{-1} after anodic polarization of the $LaF_3:Eu^{2+}|Ag$ interface at $E_{g.a}$ = 1.9 V (Q_a = 32.16 μC). The ratio $\Delta\log I_{c.p}/\Delta\log V$ for the $LaF_3|Ag$ interface is independent of the accumulation potential and approximately equal to 0.5 for experimental and ohmic-polarization–corrected data, which confirms the diffusion nature of the solid-phase process [10, 12]. With increasing potential sweep rate, the peak potential is shifted in the negative direction and linearly depends on $V^{1/2}$. Such a behavior is characteristic of processes controlled by the ohmic resistance of passive films [12, 14]. The peak potential corrected for the ohmic polarization of the solid electrolyte remains constant. With correction made for the ohmic polarization of the contact, the potential difference between the half-peak potential and the current peak potential ($E_{c.p/2} - E_{c.p}$) = 0.06 V, which corresponds to a reversible process with transfer of a single electron. The emf of the cells formed at accumulation potentials of 1.9, 2.0, and 2.1 V is in the range (1.345 ± 0.003) V.

It is important to note that a deviation of $E_{g.a}$ from the optimal value within ±0.1 V is tolerable for the given structure does not lead to any significant change in its characteristics. Attention should be paid to the fact that insufficient treatment of the interfacial surface exerts much more pronounced influence on the properties of cathodic curves, with the half-peak potential becoming more negative than the stationary potential ($E_{c.p/2} \neq E_{st}$), the dependence of the peak potential $E_{c.p}$ on $\log V$ turning linear, and processes at the interface becoming irreversible even upon generation of compounds at the optimal $E_{g.a}$.

Upon generation of an intermediate phase at the $LaF_3:Eu^{2+}|Sn$ interface at $E_{g.a}$ = 0.9 and $E_{g.a}$ = 0.8 V, the cathodic curves measured from the level of the stationary potentials, with V varied between 0.01 and 0.05 V s^{-1}, are also characterized by a single peak. However, the generation potential affects the way in which in fluoride is formed and the $LaF_3:Eu^{2+}|Sn$ regenerated, making $\Delta\log I_{c.p}/\Delta\log V$ increase from 0.60 (for $E_{g.a}$ = 0.9 V) to 0.637 (for $E_{g.a}$ = 0.8 V), which is accompanied by peak broadening. The peak potential $E_{c.p}$ shows a linear dependence on log *V*, which is a criterion of process irreversibility and disagrees with the data obtained for an FSE with aqueous reference system. Also, a change in the emf of the formed Sn, $SnF_2|LaF_3|SnF_2$, Sn cells is observed (0.03 V for $E_{g.a}$ = 0.8 V and 0.01 V for $E_{g.a}$ = 0.09 V).

The $LaF_3:Eu^{2+}|Bi$ interface regeneration curves obtained after potentiostatic charging at $E_{g.a1}$ = 1.1, $E_{g.a2}$ = 1.2, $E_{g.a3}$ = 1.28, and $E_{g.a4}$ = 1.3 V, all exhibiting a single peak, strongly differ from the dynamic voltammograms of the FSE|Ag interface. The initial portion of the cathodic polarization curve is independent of the potential sweep rate and has a shape characteristic of charge-transfer-controlled processes. The peak potentials $E_{c.p}$ show linear dependence on log *V*, similarly to the FSE|Sn interface. The slope of the linear dependence $\log I_{c.p} = f(\log V)$ grows from 0.72 to 0.83 as $E_{g.a}$ is changed from 1.2 to 1.3 V, with the peak in the cathodic curves broadening and the ratio of the area under the cathodic peak to amount of charge consumed in deposit accumulation increasing. Presumably, the reaction of bismuth fluoride formation at the contact of the FSE membrane with Bi and the cathodic regeneration of the interface are irreversible. The emf of formed cells is within (0.400 ± 0.010) V.

Figure 6a presents linear dependences of the peak current $I_{c.p}$ on $V^{1/2}$ for the interfaces $LaF_3:Eu^{2+}|Ag$ ($E_{c.p}$ = 1.9 V, Q_a = 5.12 μC), $LaF_3:Eu^{2+}|Bi$ ($E_{g.a}$ = 1.3 V, Q_a = 54 μC), and $LaF_3:Eu^{2+}|Sn$ ($E_{g.a}$ = 0.8 V, Q_a = 18.7 μC) for data obtained in experiment and those corrected for the ohmic polarization of the contact by means of approximate equations [12].

For solving analytical problems, it was of interest to study the dependence of $I_{c.p}$ on the amount of charge consumed for generation of metal fluorides. It was found that the dependence $I_{c.p} = f(Q_a)$ measured upon AgF accumulation at E_g = 2.0 V is linear within the range from 1.5 to 7 μC (Fig. 6b, curve *1*) and

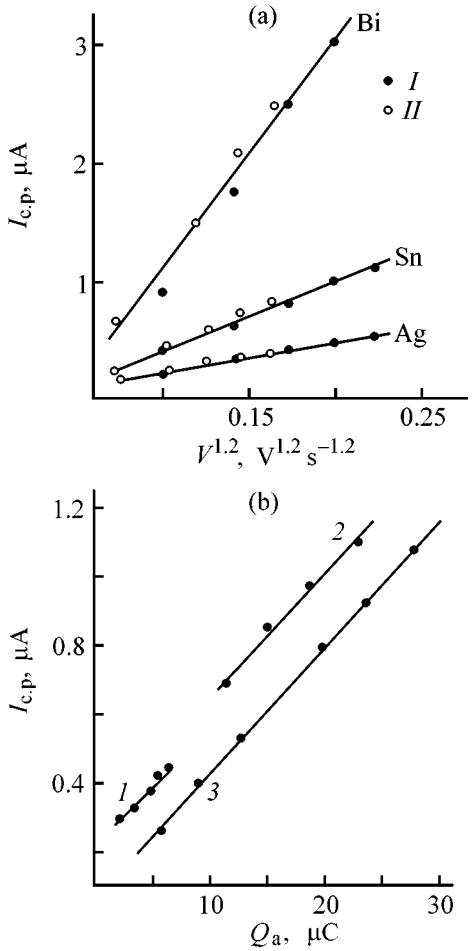

Fig. 6. Cathodic current peak $I_{c.p}$ after anodic charging of the FSE|M (+) interface at $E_{g.a}$ vs. (a) potential sweep rate *V* and (b) amount of passed electricity Q_c. (a) M: Ag: $E_{g.a}$ = 1.9 V, Q_a = 5.12 μC; Sn: $E_{g.a}$ = 0.8 V, Q_a = 18.7 μC; Bi: $E_{g.a}$ = 1.3 V, Q_a = 54 μC. (b) Potential sweep rate *V* (V s^{-1}): (*1*) 0.04 (Ag, $E_{g.a}$ = 2 V), (*2*) 0.03 V (Bi, $E_{g.a}$ = 1.28 V), and (*3*) 0.02 (Bi, $E_{g.a}$ = 1.1 V). For explanations see text.

25 to 95 μC at larger area of contact between silver and the FSE membrane. Interestingly, despite the irreversible nature of the process of $LaF_3:Eu^{2+}|Bi$ interface regeneration, the dependence of $I_{c.p}$ on Q_a measured after polarization of a contact between the membrane and bismuth is also linear in the Q_a range from 5.8 to 27.7 μC at E_g = 1.1 V (Fig. 6b, curve *3*) and 11.6 to 23 μC at E_g = 1.28 V (Fig. 6b, curve *2*).

CONCLUSIONS

(1) In studying the voltammetric behavior of an all-solid fluoride-selective electrode based on LaF_3 (Eu^{2+} 0.8 mol %), LaF_3 (Sr^{2+} 5 mol %), and CeF_3 (Sr^{2+} 5 mol %) single crystals, it is advisable to

verify the *I–E* characteristic of the Sn, SnF_2|FSE membrane|aq F^-, Cl^-|AgCl, Ag cell. Provided that it is linear in the working range of potentials and potential sweep rates, the voltammetric response of an all-solid fluoride-selective electrode in contact with metal is similar to that of the commercial fluoride-selective electrodes.

(2) The threshold of electrochemical stability of a solid fluorine-conducting electrolyte was determined, characterizing the cathodic part of the working range for voltammetry of an all-solid fluoride-selective electrode in contact with metals.

(3) The influence exerted by the potential of anodic accumulation of metal fluorides at the interface between an all-solid fluoride-selective electrode and metal (Ag, Bi, Sn) on the dependence of the peak current of interface regeneration processes on the potential sweep rate was considered. The revealed pattern is also characteristic of redox reactions involving cations from the rigid sublattice in the membrane of a fluoride-selective electrode; these reactions occur on the surface and in the bulk of the solid electrolyte without involvement of the contact metal in the electrode reaction.

(4) The obtained dependences of the stationary potential and peak potential on the nature of metal, and also the linear dependence of the peak current on the amount of charge consumed for product formation, are of interest for analytical practice, since these results can be used for voltammetric detection of the metals considered in this study with all-solid cells in the air medium.

REFERENCES

1. *Spravochnoe rukovodstvo po primeneniyu ionoselektivnykh elektrodov* (Handbook of the Use of Ion-Selective Electrodes), Petrukhin, O.M., Ed., Moscow: Mir, 1986.
2. Turaeva, M.S., Pegova, I.A., Vasilevskii, V.L., and Grilikhes, M.S., *Zh. Prikl. Khim.*, 1996, vol. 69, no. 8, pp. 1321–1331.
3. Turaeva, M.S., Pegova, I.A., Vasilevsky, V.L., and Grilikhes, M.S., *Proc. 10th Eur. Conf. on Solid-State Transducers, Eurosensors-10*, Leuven, Belgium, September 8–11, 1996, pp. 191–195.
4. Turaeva, M.S., Lyalin, O.O., and Vasilevskii, V.L., *Elektrokhimiya*, 1992, vol. 28, no. 10, pp. 1505–1511.
5. Yamazoe, N., Hisamoto, J., and Miura, N., *Sensors Actuators*, 1987, vol. 11, no. 12, pp. 415–423.
6. Harke, S., Wiemhofer, H.-D., and Gopel, W., *Sensors Actuators B*, 1990, vol. 1, no. 1–6, pp. 188–194.
7. Turaeva, M.S., Pegova, I.A., and Vasilevskii, V.L., *Elektrokhimiya*, 1996, vol. 32, no. 4, pp. 491–497.
8. Turaeva, M.S., *Elektrokhimiya*, 1996, vol. 32, no. 4, pp. 498–502.
9. Lyalin, O.O., Turaeva, M.S., and Mogilevskii, B.M., *Elektrokhimiya*, 1977, vol. 13, no. 11, pp. 1716–1718.
10. Delahay, P., *New Instrumental Methods in Electrochemistry; Theory, Instrumentation and Application to Analytical and Physical Chemistry*, New York: Interscience, 1954.
11. Vydra, F., Štulik, K., and Julákova, E., Rozpouštécí *Polarografic a Voltametrie*, Praha: Nakladatelstvi technicke literatury, 1977.
12. Galus, Zb., *Teoretyczue Podstawy Elektroanalisy Chemicznej*, Warszawa: Panstwowe Wydawnictwo Naukowe, 1971.
13. Macdonald, D.D., *Transient Techniques in Electrochemistry*, New York: Plenum, 1981.
14. Calandra, A.J., de Tacconi, N.R., Pereiro, R., and Arvia, A.J., *Electrochim. Acta*, 1974, vol. 19, no. 12, pp. 901–905.

Russian Journal of Applied Chemistry, Vol. 74, No. 4, 2001, pp. 603–606. Translated from Zhurnal Prikladnoi Khimii, Vol. 74, No. 4, 2001, pp. 585–588.

APPLIED ELECTROCHEMISTRY AND CORROSION PROTECTION OF METALS

Effect of Anodic Polarization of Fibrous Carbon Electrode in Alkaline and Acid Solutions on the Distribution of Electrical Conductivity across the Electrode Thickness

V. K. Varentsov and V. I. Varentsova

Institute of Solid-State Chemistry and Mineral Processing, Siberian Division, Russian Academy of Sciences, Novosibirsk, Russia

Received May 5, 2000; in final form, June 2000

Abstract—The effect exerted by anodic treatment of electrodes with varied thickness, made of NT-1 low-conductivity carbonized material, in 0.07 M KOH and 0.25 M H_2SO_4 solutions on the distribution of the electrical conductivity across the electrode thickness at various anodic polarization conditions was studied.

It has been shown previously that cathodic treatment of electrodes of varied thickness, made of a high-resistivity NT-1 carbonized material, in solutions of sulfuric acid and potassium hydroxide yields electrodes with electrical conductivity varying across the electrode thickness [1]. The conductivity profile depends on polarization conditions and electrode thickness. It has been established that anodic treatment of electrodes made of fibrous carbon materials (FCM) in acid and alkaline solutions can be used to change the electrical conductivity of FCMs [2]. The most pronounced changes are observed for carbonized FCMs—depending on anodic polarization mode their conductivity may vary within a factor of several tens. This suggests that anodic treatment of FCM can serve as efficient method for obtaining non-isoconducting electrodes.

The present communication reports on a study of the influence exerted by anodic polarization of NT-1 FCM electrodes in potassium hydroxide and sulfuric acid solutions on the distribution of electrical conductivity across the electrode thickness.

EXPERIMENTAL

The experimental procedure was identical to that described previously [1]. The anodic polarization was performed using a B5-49 dc power source with solutions containing (M): (1) 0.07 KOH, (2) 0.1 KOH and 1.5 $(NH_4)_2SO_4$, and (3) 0.25 H_2SO_4 circulated through the electrode at a rate of 0.18 ml cm^{-2} s^{-1}. A cell of special design, described in [3], was equipped with a special insert allowing measurement of the electrode thickness. The study was carried out with electrodes consisting of several layers of NT-1 FCM with electrical conductivity of 0.04 Ω^{-1} cm^{-1}. After anodic treatment the electrode was thoroughly washed with distilled water and dried to constant weight, and then the electrical conductivity of each of the FCM layers was measured [1].

The theory of flow-through three-dimensional electrodes shows that the polarization profile across the electrode thickness, determining the electrode efficiency, largely depends on the relative electrical conductivities of the electrode material and the solution. In this connection, it is of importance to consider the effect of this factor on the possible electrical conductivity profile across the electrode thickness. These studies were performed with a 0.07 M KOH solution with electrical conductivity lower than that of NT-1. To raise the electrical conductivity of the KOH solution, 1.5 M of NH_4NO_3 salt was added, with the electrical conductivity of the resulting solution exceeding that of NT-1.

Figures 1 and 2 present the distributions of the electrical conductivity of the electrode across its thickness L for varied conditions of its anodic polarization in the above alkaline solutions. For convenience of comparison of the obtained results, the ratio of electrical conductivities of the fibrous carbon electrode (FCE) before, χ_{in}, and after, χ_t, its anodic treatment is plotted along the ordinate axis. It can be seen from Figs. 1

1070-4272/01/7404-0603 $25.00 © 2001 MAIK "Nauka/Interperiodica"

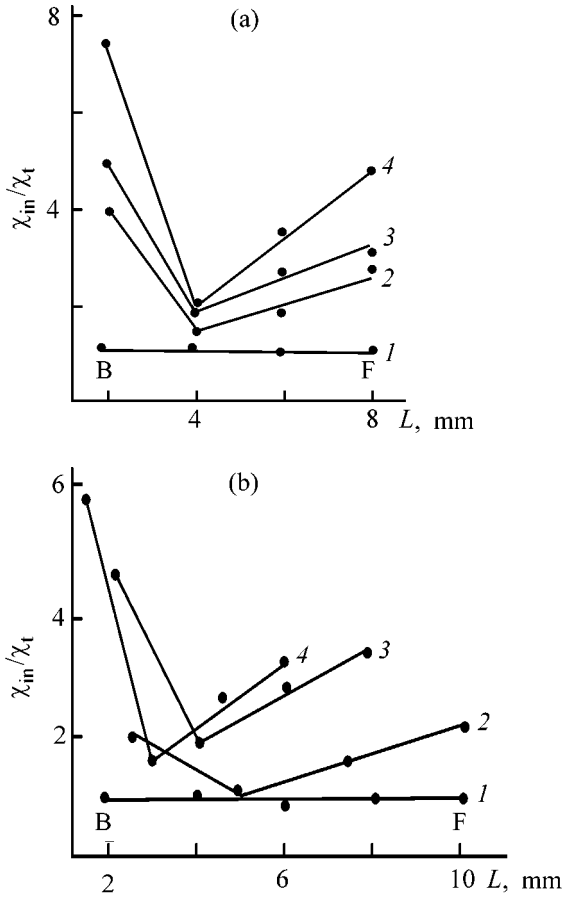

Fig. 1. Distribution of electrical conductivity χ_{in}/χ_t across the electrode thickness L after anodic polarization in a solution of 0.07 M KOH and 1.5 M NH_4NO_3. Solution conductivity χ_s = 0.2 Ω^{-1} cm^{-1}. (a) Electrode thickness 8 mm. Current density (A m^{-2}): (*1*) 0, (*2*) 250, (*3*) 1000, and (*4*) 2500. Treatment duration (min): (*1*) 0, (*2, 3*) 15, and (*4*) 5. (b) Current density 1000 A m^{-2}. Electrode thickness (mm): (*1, 2*) 10, (*3*) 8, and (*4*) 6.

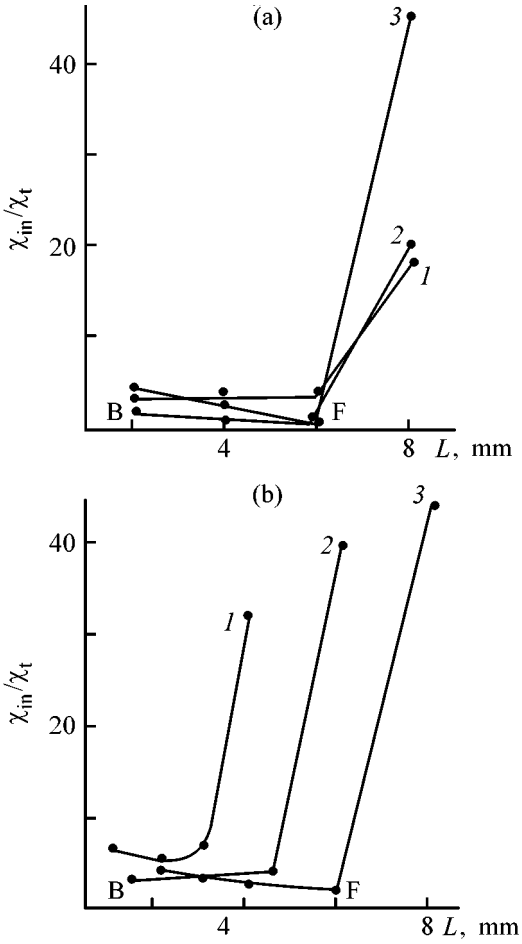

Fig. 2. Distribution of electrical conductivity χ_{in}/χ_t across the electrode thickness L after anodic polarization in a 0.07 M KOH solution. χ_s = 0.015 Ω^{-1} cm^{-1}. (a) Electrode thickness 8 mm. Current density (A m^{-2}): (*1*) 250, (*2*) 1000, and (*3*) 2500. Treatment duration (min): (*1, 3*) 15, and (*2*) 5. (b) Current density 1000 A m^{-2}, treatment duration 15 min. Electrode thickness (mm): (*1*) 4, (*2*) 6, and (*3*) 8.

and 2 that different χ distributions across the electrode thickness can be obtained with alkaline solutions having different electrical conductivities. Figure 1 demonstrates the effect exerted by anodic polarization of FCE in an alkaline solution whose electrical conductivity exceeds χ_{NT-1} fivefold. The dependence χ_{in}/χ_t–L shows an extremum, the largest changes in electrical conductivity are observed at the backside of the electrode. The electrical conductivity profile depends on the anodic polarization conditions. Raising the anodic treatment current density makes the electrical conductivity profile more pronounced, with the FCM resistivity increasing not only in the back (B), but also in the front part (F) of the electrode. The electrical conductivity at the electrode edges and in its middle part differ 1.6–3.5-fold (Fig. 1a). The electrode thickness is important—the extremum in the χ_{in}/χ_t–L curve is more pronounced for a thinner electrode and tends to disappear with increasing electrode thickness (Fig. 1b).

Another situation is observed in performing anodic treatment of FCE in an alkaline solution with electrical conductivity 3 times lower than that of FCE (Fig. 2). The most pronounced change in the electrical conductivity is observed at the front side of the electrode. Varying the conditions of anodic polarization and the electrode thickness affects the slope of the ascending portion of the χ_{in}/χ_t–L curve. It should be noted that the electrical conductivities at the front side of the electrode and in its middle part differ by more than a factor of 40.

The observed changes in the electrical conductivity profile in the electrode, depending on the relative initial electrical conductivities of the electrode material and the solution, electrode thickness, and overall anodic treatment current density are in good agreement with the theoretically predicted and experimentally confirmed distribution of polarization across the electrode thickness, depending on the above-mentioned factors [4–8]. For example, it is known that, in the case when the electrical conductivity of FCM, χ_{FCM}, exceeds that of the solution, χ_s, the process is localized at the front side of the electrode. In the opposite case, at $\chi_{FCM} < \chi_s$, the process is localized at the back side of the electrode [4, 8]. Raising the current density favors stronger polarization at the electrode edges, in good agreement with the data presented in Fig. 2.

Anodic polarization on NT-1 in sulfuric acid solutions does not lead to such pronounced changes in the electrical conductivity across the electrode, compared with that in alkali solutions. In contrast to the results presented above, the variation of χ_{FCM} across the electrode (Fig. 3) and the change in χ_t relative to χ_{in} are much weaker as compared with the case of FCM treatment in alkaline solutions. The electrical conductivities in the middle part of the electrode and at its edges differ by no more than a factor of 1.1–1.5. The most pronounced changes in χ_{FCM} are observed at the front side of the electrode, and not at its back side as it would be expected on the basis of the fact that $\chi_s > \chi_{FCM}$ ($\chi_s = 0.12\ \Omega^{-1}\ cm^{-1}$). The conceivable reason for such a change in the electrical conductivity of NT-1 is that FCM intercalation compounds are formed with sulfuric acid, with the electrical conductivity of graphite even possibly growing somewhat [9–11]. It is known that the forming compounds are unstable and decompose already at room temperature both in solution and in air. The experimental procedure included sample drying at 80–100°C, which favored decomposition of these intercalation compounds. As a result, the obtained χ_{in}/χ_t–L dependences deviate from the expected dependences and theoretical polarization profiles, even though the occurrence of a minimum in the middle part of the electrode is in agreement with the polarization distribution across its thickness. No data on how χ_{FCM} changes in the course of decomposition of intercalation compounds could be found in the literature. Apparently, more adequate interpretation of the obtained dependences requires special additional investigations, which are beyond the scope of the present study.

It should also be noted that comparison of the results reported in this communication and those obtained in [1] indicates that changes in χ_{FCM}, measured on a single-layer electrode 2–3 mm thick and multilayer electrode are about the same under comparable conditions. For example, the $\chi_{NT\text{-}1}$ decreases upon anodic polarization in a KOH solution 50–80-fold for a single-layer electrode 3 mm thick [1]. It can be seen from Fig. 1 that the electrical conductivity of the front part of the electrode decreases 45–50-fold as compared with the starting material. These results also confirm the adequacy of representing a single-layer electrode as a multilayer electrode composed of FCMs of the same type. This approach has been successfully used in studying FCM operation by means of numerical and experimental methods [5–8].

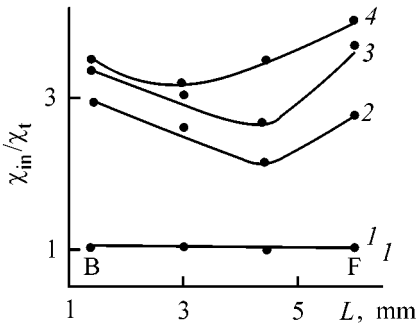

Fig. 3. Distribution of electrical conductivity χ_{in}/χ_t across the electrode thickness L after anodic polarization in a 0.25 M H_2SO_4 solution. Electrode thickness 6 mm. Current density (A m^{-2}): (*1*) 0, (*2*) 1000, (*3*) 250, and (*4*) 2500. Treatment duration (min): (*1*) 0, (*2*, *3*) 15, and (*4*) 5.

Thus, the results obtained in studying the influence exerted by anodic polarization on the electrical conductivity of FCM and its distribution across the electrode allow tentative assessment of the promise of electrolysis as a method for creating fibrous carbon electrodes with electrical conductivity varying across the electrode thickness. The variation of the electrical conductivity across an electrode subjected to anodic treatment in an alkaline solution is in qualitative agreement with the theoretically predicted polarization profile. This allows fabrication of nonisoconducting electrodes with prescribed electrical conductivity profile across the electrode thickness.

CONCLUSIONS

(1) Anodic treatment of electrodes made of high-resistivity carbonized fibrous carbon material NT-1 in alkaline and acid solutions changes the electrical conductivity of the electrode across its thickness. Depending on the solution composition, relative initial conductivities of the electrode material and the solution, and anodic polarization current density, different

electrical conductivity profiles across the electrode can be obtained.

(2) In the case of treatment in alkaline solutions, the experimentally obtained electrical conductivity profiles across the electrode thickness are in qualitative agreement with the theoretical polarization profile.

(3) The lack of correspondence between the polarization profile and electrical conductivity profiles across a fibrous carbon electrode treated in sulfuric acid solutions is probably due to formation of intercalation compounds of sulfuric acid and graphite.

REFERENCES

1. Varentsov, V.K. and Varentsova, V.I., *Zh. Prikl. Khim.*, 2000, vol. 73, no. 10, pp. 1661–1664.
2. Varentsov, V.K. and Varentsova, V.I., *Zh. Prikl. Khim.*, 1999, vol. 72, no. 4, pp. 609–613.
3. Varentsov, V.K. and Varentsova, V.I., *Zh. Prikl. Khim.*, 1999, vol. 72, no. 4, pp. 605–609.
4. Gurevich, I.G., Vol'fkovich, Yu.M., and Bagotskii, V.S., *Zhidkostnye poristye elektrody* (Porous Fluid Electrodes), Minsk: Nauka i Tekhnika, 1974.
5. Varentsov, V.K. and Koshev, A.N., *Izv. Sib. Otd. Akad. Nauk SSSR, Ser. Khim. Nauk*, 1988, no. 7, pp. 117–123.
6. Zherebilov, A.F. and Varentsov, V.K., *Izv. Sib. Otd. Akad. Nauk SSSR, Ser. Khim. Nauk*, 1985, no. 3, pp. 35–39.
7. Zherebilov, A.F. and Varentsov, V.K., *Izv. Sib. Otd. Akad. Nauk SSSR, Ser. Khim. Nauk*, 1987, no. 2, pp. 19–24.
8. Varentsov, V.K., Zherebilov, A.F., and Bek, R.Yu., *Elektrokhimiya*, 1982, vol. 18, no. 3, pp. 366–370.
9. Ubbelohde, A.R. and Lewis, F.A., *Graphite and Its Crystal Compounds*, Oxford: Clarendon Press, 1960.
10. Chernysh, I.G., Karpov, I.I., Prikhod'ko, G.P., and Shai, V.M., *Fiziko-khimicheskie svoistva grafita i ego soedinenii* (Physicochemical Properties of Graphite and Its Compounds), Kiev: Naukova Dumka, 1990.
11. Rashid, H., Lake, M., Wcollen, J., *et al.*, *Carbon*, 1986, vol. 24, no. 4, pp. 511–513.

Russian Journal of Applied Chemistry, Vol. 74, No. 4, 2001, pp. 607–610. Translated from Zhurnal Prikladnoi Khimii, Vol. 74, No. 4, 2001, pp. 589–592.

APPLIED ELECTROCHEMISTRY AND CORROSION PROTECTION OF METALS

Participation of Zincate Ions in Processes Occurring on Nickel Oxide Electrode of Nickel–Zinc Battery

Z. P. Arkhangel'skaya, R. P. Ivanova, T. B. Kas'yan, and L. B. Raikhel'son

Rigel' Joint-stock Company, St. Petersburg, Russia

Received May 12, 2000; in final form, October 2000

Abstract—A mechanism of zinc transfer from the negative to the positive electrode of a nickel–zinc battery was studied.

A study of the distribution of components in a nickel–zinc (NZ) battery under cycling has shown that approximately 20% of the active material in the negative electrode is transferred to the nickel oxide electrode (NOE) in the initial cycles [1]. According to X-ray data, the active material is present in NOE pores as zinc oxide, forming no compounds with nickel oxides. The dynamics of its accumulation corresponds to the loss of weight by the negative electrode.

The mechanism of transfer of zinc compounds has not been established. This issue was considered in [2] with the purpose to reveal the reasons for NOE "poisoning" in NZ batteries. The authors assumed that the observed reduction in the electrode capacity is due to zinc oxide precipitation in its pores, caused by a decrease in the KOH concentration in the electrolyte, associated with oxygen evolution in charging.

The precipitation of zinc oxide in NOEs with a cermet base hardly affects the efficiency of such electrodes at moderate discharging rates, but impairs the specific characteristics of the NZ battery, because part of the active material of the negative electrode is not used properly. Therefore, elucidation of the reasons for the interelectrode zinc transfer in NOEs is of considerable interest.

EXPERIMENTAL

We studied processes in ventilated NZ-25, NZ-80, and NZ-180 batteries with rated capacity of 25, 80, and 180 A h, respectively. Paired cermet nickel-oxide electrodes of thickness 1 mm and zinc electrodes with active material consisting of zinc oxide, metallic zinc, and inhibitors and surfactants as additives were used in the batteries. The ratio of the initial capacities of the negative and positive electrodes in all the batteries was 3 : 1. Hydrated cellulose and nonwoven polypropylene were used as separators.

The electrolyte in the NZ-25 and NZ-180 batteries contained 480 and 15 g l^{-1} of KOH and LiOH, respectively, and that in the NZ-80 batteries, 380 and 25 g l^{-1}, respectively. The volume of the electrolyte was 4 cm^3 per 1 A h of rated capacity, which corresponds to the total volume of pores in the electrodes and separators.

The batteries were charged during 8–10 h with stepwise decreasing currents (A) to a voltage of 1.98 V in each stage: NZ-25: I_1 = 5, I_2 = 3, I_3 = 1.5; NZ-80: I_1 = 10, I_2 = 5; and NZ-180 I_1 = 20, I_2 = 10. The imparted capacity was 25, 80, and 150 A h, respectively. The current expenditure for oxygen evolution did not exceed 1–2% per cycle. This hardly affected the KOH concentration, and only resulted in its gradual decrease because of the accumulation of carboxylic ions in the electrolyte. In this connection, we reduced after 100–200 cycles the capacity supplied to the batteries in charging. The discharge currents corresponded to a 5-h mode (5, 16, and 40 A, respectively), i.e., the conditions of electrolyte diffusion and convection were the same for all the batteries.

In the course of the tests, some batteries were periodically disassembled in charged or discharged state, and the content of ZnO and Zn_{met} in zinc electrodes and also that of KOH, K_2CO_3, LiOH, and Zn^{2+} in free electrolyte, zinc electrodes, and NOEs were determined.

The transfer of zinc compounds from the negative electrode to the NOE in battery cycling is character-

1070-4272/01/7404-0607 $25.00 © 2001 MAIK "Nauka/Interperiodica"

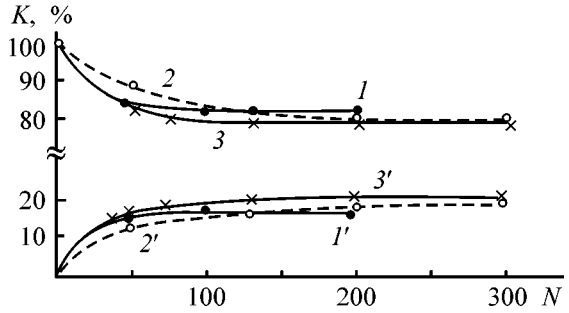

Fig. 1. Variation of the zinc content in (*1*–*3*) negative and (*1*′–*3*′) positive electrodes in cycling of (*1*, *1*′) NZ-25, (*2*, *2*′) NZ-80, and (*3*, *3*′) NZ-180 batteries. (*K*) Ratio of the zinc weight to its initial amount and (*N*) number of cycles.

ized by correspondence between the loss of Zn weight from the negative electrode and its accumulation in the positive electrode (Fig. 1). Approximately 10% of zinc is transferred during the first 10 cycles from the negative electrode to the NOE, which corresponds to 1.2 g per cycle for the NZ-25 battery. Then the transfer slows down and stops by 50–70th cycle. The total amount of zinc accumulated in the NOE was 20–22%.

The concentration of zincate ions in the electrolyte of charged NZ-25 and NZ-80 batteries was 10–15 g l^{-1}, whereas in discharged batteries it decreased with increasing number of cycles, from 50 to 30 g l^{-1}, in contrast to silver-zinc batteries (having no nickel oxide electrode) where it was 80–100 g l^{-1} under the same conditions [3] and changed only slightly in cycling.

These results confirm the pattern established in [1], and demonstrate that fundamental changes in macrokinetic processes occurring at zinc electrodes are associated with the operation of the NOE in the alkaline battery.

The limiting concentration of zincate ions formed in anodic zinc dissolution in KOH solutions depends on the KOH concentration:

$$Zn + 4OH^- - 2e = [Zn(OH)_4]^{2-}. \quad (1)$$

When hydroxide ions are deficient in the zone of the electrochemical process, the hydroxo complex is decomposed to liberate these ions, which serves to prolong the discharge of the zinc electrode:

$$[Zn(OH)_4]^{2-} \rightarrow ZnO + H_2O + 2OH^-. \quad (2)$$

In the process, the consumption of hydroxide ions decreases from 2 to 1 mol per faraday (26.8 A h) of electricity. Reverse reactions occur in the cathodic process. The redox reaction on NOE proceeds as follows

$$Ni(OH)_2 + OH^- - e \rightarrow NiOOH + H_2O. \quad (3)$$

Oxides with higher oxygen content are scarcely formed under the considered conditions (charging to no more than 80% of the maximum NOE capacity), which allows us to determine the consumption of hydroxide ions with sufficient accuracy. The following reaction may occur in parallel with reaction (3)

$$2OH^- - 2e \rightarrow H_2O + 1/2O_2. \quad (4)$$

To reduce the fraction of current consumed for reaction (4), we limited the final charging voltage. In the case when the main processes occur without side reactions, the consumption and formation of OH^- ions at the electrodes are counterbalanced during both charging and discharging of NZ batteries. Since this compensation is provided by reactions at the opposite electrodes, it depends on the conditions of OH^- ion delivery to the reaction zones.

The correspondence between the loss of zinc from the negative electrode and the accumulation of zinc in the NOE (Fig. 1) means that these processes are closely related in the NZ battery. To elucidate the transfer mechanism, it is necessary to determine this relationship.

The OH^- ions participating in the reaction migrate and diffuse under the influence of KOH concentration gradient directed from the negative to the positive electrode in charging a battery, and in the opposite direction during its discharge. Correspondingly, the concentration gradient of zincate ions has the same direction. In both cases, the appearance of a considerable concentration gradient is due to the occurrence of migration processes under the conditions of slowed-down diffusion of reagents, which is unable to compensate for concentration changes occurring in porous electrodes when a complicated system of separators is used [4].

The second feature of the observed transfer consists in that the kinetics of zinc oxide accumulation in the NOE (percentage of zinc weight in the negative electrode) is similar in all the batteries under study, in spite of their different sizes and capacities (Fig. 1). Thus, under identical polarization conditions, the change in the concentration of zinc oxide in NOE pores depends not on its surface area, but on the capacity per unit of its volume [5], i.e., on the NOE thickness, equal for all the batteries under study.

Change in component weights and electrolyte concentration in NOE pores in charging an NZ-25 battery {initial concentration: KOH 8.03 M, $[Zn(OH)_4]^{2-}$ 0.93 M; charging capacity 25 A h (0.93 faraday); volume of pores in NOE 33 cm^3}

Process stage	Contents of components, mol				Concentration, g l^{-1}		
	KOH	$[Zn(OH)_4]^{2-}$	ZnO	OH^-	KOH	$[Zn(OH)_4]^{2-}$	Zn^{2+}
Before charging	0.265	0.0308			450	124.5	61
Change during charging	–0.25	–0.0262	+0.0262	+0.052*	–424	–105.9	–51.9
After charging	0.015	0.0046	0.0262		26.0	18.6	9.1
	+0.052*				+88.2*		
Final content:							
mol	0.067	0.0046	0.0262				
g	3.75	0.6	2.13				
g l^{-1}	–	–	–		114.2	18.6	9.1

* Replenishment with hydroxide ions liberated upon hydroxo complex decomposition.

The analytically determined electrolyte compositions in charged and discharged NZ batteries (Fig. 2) are diffusion-averaged. However, these data indicate that the concentrations of KOH and zincate ions in the electrolyte of the charged and discharged batteries are not completely equalized, which results from changes occurring in NOE pores. In this case, the content of zincate ions in the electrolyte of a charged battery is low (approximately 15 g l^{-1}), and that in a discharged battery, 25–30 g l^{-1}, i.e., it does not exceed 50 g l^{-1} even in the initial cycles.

On the basis of the obtained data and taking into account the data of [5] on changes in the electrolyte composition under charging conditions, we calculated the amount of KOH in NOE pores by the end of charging of an NZ-25 battery in the third cycle (see the table). It was assumed that only NiOOH is formed in the NOE and no oxygen is evolved. The component diffusion was disregarded, being suppressed in the given case because of liberation of OH^- ions directly within NOE pores.

The decrease in the KOH content was determined using Eq. (3) in view of its being equal to K mol per faraday of passing current. Here K is the potassium transfer number equal to 0.27 [6], as calculated from the limiting equivalent electric conductivity of K^+ and OH^- ions. The increase in the amount of water by reaction (3), namely, 1 mol per faraday, was disregarded, since the excess water is displaced from the pore space [5].

In the calculations, account was taken of the electrolyte replenishment with hydroxide ions liberated upon decomposition of the hydroxo complex in the NOE pores (see the table). Their amount was determined on the assumption that $[Zn(OH)_4]^{2-}$ ions do not participate in the reactions occurring in NOE in battery charging. Therefore, changes in the content of hydroxide ions are only related to a decrease in the $[Zn(OH)_4]^{2-}$ solubility with diminishing KOH concentration.

Comparison of the data in the table and Fig. 2 shows that the KOH concentration in NOE pores decreases by approximately a factor of 2.5 in the course of charging, compared with the averaged electrolyte concentration. These data reflect the slowing down of the diffusion processes in the battery's electrolyte.

The variation of the concentrations of KOH and zincate ions in NOE pores in the third charging–discharge cycle, determined from the experimental data

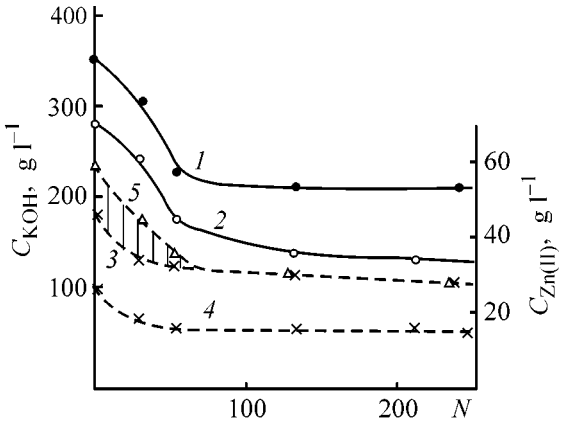

Fig. 2. Variation of the concentration C of (*1, 2*) KOH and (*3–5*) zincate ions in terms of Zn(II) in the electrolyte of an NZ-80 battery in cycling of (*1, 3, 5*) discharged battery [(*5*) at the negative electrode] and (*2, 4*) charged battery. (*N*) Number of cycles.

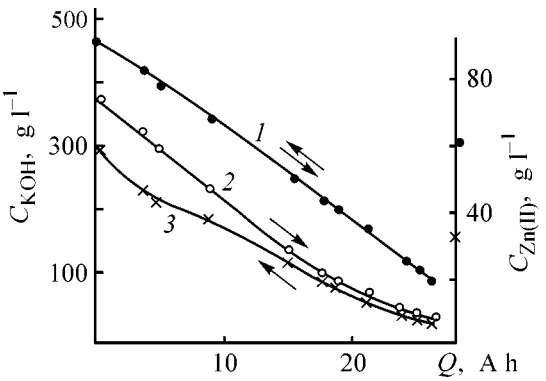

Fig. 3. Changes in concentration *C* of (*1*) KOH and (*2, 3*) zincate ions in terms of Zn(II) in NOE pores in the course of (*1, 2*) charging and (*1, 3*) discharge of an NZ-25 battery. (*Q*) Capacity.

obtained in this study and those reported in [3, 7], in good agreement with our data, is illustrated in Fig. 3. The curves describing the variation of the KOH concentration in charging and discharge coincide in accordance with the reversibility of reaction (1), and the plots for zincate ions disagree owing to the low solubility of zincates formed in chemical dissolution of ZnO.

Thus, the per-cycle loss of zinc from the negative electrode results from the transition of such an amount of zincate ions from it into the electrolyte, which is necessary to maintain the level characteristic of the processes occurring at this electrode. This amount corresponds to that of zinc remaining in the NOE in the form of ZnO.

Zincate solutions being unstable, the scheme in Fig. 3 is unsuitable for precise quantitative determinations. However, it gives basic notion of the processes resulting in the transfer and accumulation of zinc oxide in NOE pores. It also shows that, with decreasing KOH concentration in the electrolyte, the transfer of zinc falls, since in this case the limiting concentrations of zincate ions formed in electrochemical and chemical dissolution approach each other.

Comparison of Figs. 2 and 3 allows assessment of the influence exerted by diffusion processes on the variation of the content of the electrolyte components. It is evident that the averaged concentrations of KOH and zincate ions in a charged battery are greater by approximately a factor of 2.5 than the calculated minimum concentrations in pores shown in Fig. 3. Since the volume of the electrolyte in the NOE pores corresponds to 1/3 of its total volume in the battery, the calculated change in the concentration in pores is close to the actual value, i.e., the effect of the diffusion of OH^- ions into the pore space of NOE during charging and discharge of the battery is insignificant, and their formation directly in the NOE pores upon decomposition of hydroxo complexes contained in the pores is of greater importance.

The run of curves *3* and *5* in Fig. 2 shows that at number of cycles less than 70 the region between them reflects the kinetics of zinc oxide accumulation in the NOE, and the approach of these curves to each other is related to a decrease in the KOH content in the electrolyte.

CONCLUSIONS

The transfer of zinc from the negative electrode to the nickel oxide electrode in a nickel–zinc battery is associated with the formation of electrolyte flows oppositely directed in charging and discharge. A greater concentration of zincate ions is established at the negative electrode, compared with the concentration reached upon chemical dissolution of zinc oxide precipitated in the nickel oxide electrode. The deficiency in zincate ions returning to the zone of the negative electrode in discharge of the nickel oxide electrode is compensated for by the anodic process at the zinc electrode, maintaining equilibrium with respect to hydroxide and zincate ions.

The transfer of zinc is slowed down as the KOH concentration in the electrolyte decreases, because the solubilities of the zincate ion in electrochemical and chemical processes approach each other.

REFERENCES

1. Alekseeva, M.E., Arkhangel'skaya, Z.P., Ivanova, R.P., *et al., Zh. Prikl. Khim.*, 1997, vol. 70, no. 1, pp. 73–78.
2. Dmitrienko, V.E., Zubov, M.S., Barsukov, V.Z., and Sagonyan, L.N., *Elektrokhimiya*, 1987, vol. 23, no. 9, pp. 1240–1241.
3. Shapot, M.B., Levenfish, P.G., Levin, N.I., and Kochetova, T.I., *Sbornik rabot po khimicheskim istochnikam toka* (Coll. of Works on Chemical Power Sources), Leningrad: Energiya, 1970, no. 5, pp. 124–131.
4. Reshetov, V.A., Reshetova, G.N., and Arkhangel'skaya, Z.P., *Elektrokhimiya*, 1972, vol. 8, no. 9, pp. 1345–1348.
5. Boldin, R.V., Akbulatova, A.D., and Mel'nikova, T.A., *Khimicheskie istochniki toka* (Chemical Power Sources), Leningrad: Energoatomizdat, 1983, pp. 47–51.
6. *Kratkii spravochnik fiziko-khimicheskikh velichin* (Brief Reference Book of Physicochemical Data), Mishchenko, K.P. and Ravdel', A.A., Eds., Leningrad: Khimiya, 1972, pp. 116–117.
7. Romanov, V.V., *Zh. Prikl. Khim.*, 1962, vol. 35, no. 6, pp. 1293–1302.

Russian Journal of Applied Chemistry, Vol. 74, No. 4, 2001, pp. 611–615. Translated from Zhurnal Prikladnoi Khimii, Vol. 74, No. 4, 2001, pp. 593–597.

APPLIED ELECTROCHEMISTRY AND CORROSION PROTECTION OF METALS

Kinetics of Sn(II) Contact Reduction in Alkaline Solutions with Compact and Dispersed Aluminum

A. F. Dresvyannikov and I. O. Grigor'eva

Kazan State Technological University, Kazan, Tatarstan, Russia

Received September 19, 2000

Abstract—The kinetics of contact reduction of tin on aluminum from alkaline stannite solutions was studied by atomic absorption analysis, iodometry, gravimetry, X-ray phase analysis, and method of polarization diagrams.

Tin finds wide application in various industries. Since the cost of tin is rather high, a necessity arises to recover it from spent industrial solutions. The known methods of tin recovery in the form of metal from aqueous solutions are rather few in number and mainly performed in acid media. These are electrolytic reduction, characterized by low current efficiency owing to the low concentration of tin ions in solution, and also cementation (contact reduction). For example, it was proposed in [1] to recover tin by the contact reduction on aluminum or aluminum alloys from wastewater by its acidification with hydrochloric, sulfuric, or nitric acid to pH ≤ 4. Tin of more than 99% purity is precipitated from solutions within 1–4 h as a powder or granules.

It is necessary to note that the contact reduction process is widely applied in electroplating of coatings onto aluminum. In this case [2], stannate alkaline solutions are used in which aluminum articles are covered with a film of contact tin serving as an independent coating improving the antifriction properties of the surface [3]. During the first 10–20 s after the onset of the reaction, there are about 2000 atoms of dissolved aluminum [4, 5] per single deposited atom of tin; further, this ratio changes sharply, reaching a value of 6 : 1. Simultaneously, the rate of aluminum dissolution and hydrogen evolution decrease because of the blocking of the main part of the surface area of the base metal by the contact deposit.

The contact reduction of tin(IV) in alkaline solutions has been studied in sufficient detail [3–5], whereas there are scarcely any data on the contact reduction of tin(II).

Previously, it has been proposed to use dispersed aluminum for recovery of tin from solutions of its compounds [6]. Therefore, the aim of this work was to study the contact reduction of tin (II) ions in alkaline solutions by compact and dispersed aluminum.

Polydisperse aluminum of PA-1, PA-3, and ASD-0 grades (as-delivered) with average particle size of 343, 169.5, and 77.8 μm and variation factor of, respectively, 0.31, 0.48, and 0.29 was used. The content of the main component was determined from the volume of hydrogen evolved upon dissolution of aluminum in alkali. Chemically pure $SnSO_4$ and NaOH were used. The compositions of the reaction mixture are given in Table 1.

Table 1. Composition of reaction mixture in tin(II) reduction with dispersed aluminum

Composition no.	Composition, M		Aluminum	*m*(Al), g
	Sn(II)	NaOH		
1	0.069	0.8	PA-1	0.36
2	0.069	0.8	PA-3	0.36
3	0.069	0.8	PA-3	0.18
4	0.069	0.8	PA-3	0.54
5	0.069	0.8	PA-3	0.72
6	4×10^{-2}	0.5	PA-3	0.18
7	5×10^{-3}	0.08	PA-3	0.018
8	10^{-3}	0.025	PA-3	0.009
9	0.069	0.8	ASD-0	0.36

1070-4272/01/7404-0611 $25.00 © 2001 MAIK "Nauka/Interperiodica"

Table 2. Conditions of electrochemical measurements on compact aluminum and tin

Run no.	Solution composition, M		*T*, °C
	Sn(II)	NaOH	
1	0.0365	0.4	25
2	0.0365	0.5	25
3	0.0365	0.8	25
4	0.0365	1.2	25
5	0.0365	0.4	45
6	0.0365	0.4	65
7	0.0365	0.4	25
8	0.0102	0.2	25
9	0.0010	0.4	25
10	0	0.4	25

The procedure of Sn(II) reduction by suspended aluminum was described in [7, 8].

The content of Sn(II) ions was determined by iodometric titration of reaction mixture aliquots taken at certain time intervals. In addition, the content of tin ions in the reaction mixture was monitored at regular intervals by atomic absorption spectrometry (AAS-1N spectrometer, Carl Zeiss). The evolved hydrogen was determined volumetrically.

The content of the main component and additives in the deposit was determined by X-ray fluorescent (VRA-20L spectrometer, Carl Zeiss) and X-ray phase analyses (DRON-3M installation) with the use of long-wavelength Fe_{K_α} radiation with a β-filter.

Electrochemical studies were carried out with A999 aluminum samples of 99.8% purity [TU (Technical Specification) 6-09-2705–78]. Cathodic polarization curves (2 mV s^{-1}) were measured on tin in solutions under study with a P-5848 potentiostat (Table 2), and the anodic curves, on aluminum in similar electrolytes containing no tin ions. The potentials are given relative to a silver chloride reference electrode. Aluminum samples, dried in a drying box and cooled to constant weight, were weighed before and after obtaining a deposit, and also after its dissolution in dilute HNO_3 (1 : 1).

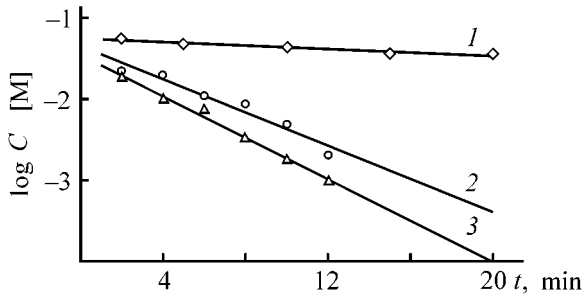

Fig. 1. Kinetics of Sn(0) deposition on aluminum of varied dispersity. C_{Sn} = 0.069 M. (*C*) Current Sn(II) concentration and (*t*) time. Aluminum: (*1*) PA-1, (*2*) PA-3, and (*3*) ASD-0.

The difference between standard potentials of aluminum and tin in alkaline stannite solutions is rather significant (approximately 1.4 V [9]), and, therefore, intensive contact exchange of the Al–Sn(II) pair is thermodynamically possible.

When aluminum is brought in contact with an alkaline stannite solution, first the natural oxide film on its surface is dissolved, and then there occurs contact reduction of tin, followed by dissolution of aluminum with hydrogen evolution:

$$Al_2O_3 + 2OH^- + 3H_2O = 2[Al(OH)_4]^-,$$

$$3[Sn(OH)_4]^{2-} + 2Al = 3Sn + 2[Al(OH)_4]^- + 4OH^-,$$

$$2Al + 2NaOH + 6H_2O = 2Na\,[Al\,(OH)_4] + 3H_2.$$

The experiments demonstrate that about 90% of metallic tin is precipitated with PA-3 or ASD-0 dispersed aluminum within the first 5–8 min (Fig. 1). The use of sufficiently dispersed aluminum powders (d_{av} < 200 μm) results in the loss of suspension's aggregate stability in the course of tin deposition and in the association of its particles into large formations (granules) from several fractions of millimeter to several millimeters in size, with shape from flat, "tablet-like" to spherical. These granules have high mechanical strength, which points to considerable interaction forces between the particles.

The kinetics of tin(II) reduction by dispersed aluminum is described by a first-order equation (Fig. 1), in agreement with the general concept of the process of contact exchange: the deposition occurs under diffusion control of metal ions being reduced, following the law of a monomolecular reaction on the outer surface of a deposit with approximately constant surface area [10, 11]. In view of the aforesaid, we calculated the apparent rate constants K_{app} of tin(II) reduction as follows [8]:

$$K_{app} = \frac{2.303}{t}\frac{V}{S}\log\frac{C_0}{C}.$$

Here *S* is the metal surface area (cm^2), *V* the volume of the reaction mixture (cm^3), C_0 the initial tin(II) concentration (M), *C* the current tin(II) concentration (M), and *t* the process duration (s).

In doing so, it was accepted that the surface area, on which tin is reduced, is invariable for each particular type of aluminum powder.

The experiments show that K_{app} decreases with increasing amount of aluminum and concentration of Sn(II) ions and increases with growing concentration of alkali and degree of aluminum dispersion:

Composition no.	K_{app}, cm s^{-1}
1	0.0063
2	0.0192
3	0.0283
4	0.0184
5	0.020
6	0.044
7	0.987
8	2.256
9	0.0157

The experimental data are in complete agreement with the concept of the related chemical activity of dispersed aluminum and the thickness of the oxide layer on its surface, which is, in turn, determined by particle size [12].

Since the process under consideration is of electrochemical nature, we calculated by Faraday's law from titrimetric data the apparent current density for the contact exchange:

$$j = m/qSt.$$

Here m is the weight of tin reduced by instant of time t, q is the electrochemical equivalent of tin, and S is the surface area of aluminum particles.

The apparent current density corresponding to this process was calculated from the volume of evolved hydrogen. These experiments show that not only the current density of hydrogen evolution (Fig. 2a), but also its ratio to the current density of the contact exchange (Fig. 2b) changes with time. Both curves exhibit a maximum, which is characteristic of topochemical transformations [11]. It is believed that the occurrence of a maximum is related to the increase in the surface area of precipitated metal (tin) and in the current density of partial reaction of tin reduction. The fast growth of the tin surface area in the initial stage results in that the rate of contact exchange increases with time. However, owing to a decrease in the concentration of tin(II) ions, the contact exchange current also decreases. The surface area becomes constant, since the rate of contact exchange decreases.

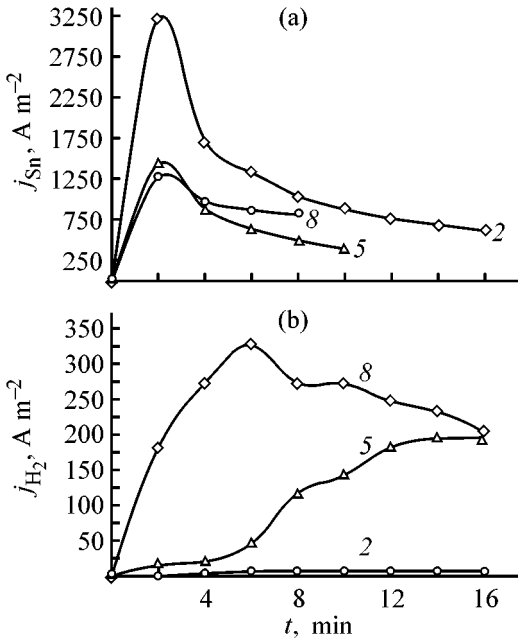

Fig. 2. Kinetics of (a) tin deposition and (b) hydrogen evolution on PA-3 aluminum particles. (j) Current density and (t) time. Numbers at the curves correspond to the numbers of compositions in Table 1.

In concentrated tin(II) solutions ($C_{Sn} \geq 10^{-2}$ M), the rates of metal deposition and hydrogen evolution differ by more than two orders of magnitude, and in dilute solutions ($C_{Sn} \leq 10^{-3}$ M), by a factor of 2–3.

The behavior of compact aluminum under similar conditions is different: at $C_{Sn} \geq 10^{-1}$ M the rates of tin reduction and hydrogen evolution are comparable, whereas in dilute ($C_{Sn} \approx 10^{-3}$ M) solutions the rate of metal reduction is almost two orders of magnitude less than the rate of hydrogen evolution (Table 3). This fact confirms the assumption that the physicochemical properties of compact and dispersed aluminum are essentially different. According to the data reported in [13, 14], compact and dispersed kinds of aluminum have different structures of surface oxide layers, and also clear distinctions in crystal lattice characteristics (unit cell parameters, sizes of mosaic units, microstresses, etc.).

Since the reaction of hydrogen liberation makes lower the current efficiency of the cathodic reduction of tin in dilute solutions (10^{-3}–10^{-2} M) at sufficiently high current densities of aluminum dissolution, the compromise electrode potential is frequently close to the corrosion potential of aluminum in the supporting solution. This fact suggests that the reaction of hydrogen reduction, occurring simultaneously with the reduction of tin complexes on the surface of a freshly

Table 3. Data of electrochemical measurements on compact aluminum and tin

E_{cor}, V		$-E_{min}$	$-E_{max}$	j, A m^{-2}			Current efficiency, %	
Al	Sn	V, according to E–t		Al	Sn	H	Sn	H
1.620	1.080	1.600	1.745	165	80	85	48.5	51.5
1.540	1.080	1.560	1.680	202	87	115	43.1	56.9
1.540	1.080	1.440	1.610	256	104	152	40.6	59.4
1.540	1.080	1.460	1.690	372	132	240	35.5	64.5
1.620	1.080	1.670	1.860	246	121	125	49.3	50.7
1.620	1.080	1.660	1.770	326	165	161	50.6	49.4
1.480	1.080	1.413	1.660	198	87	111	43.9	56.1
1.420	1.080	1.551	1.695	108	24	84	22.2	77.8
1.580	1.120	1.490	1.721	132	2	130	1.5	98.5
–	–	1.471	1.680	132	0	132	0	100

precipitated metal, substantially affects the contact exchange (Fig. 3).

The compromise potential of such a composite electrode first shifts in the positive direction, which is associated with the blocking of the aluminum surface by reduced tin (Fig. 4). The range of potentials at which contact exchange occurs corresponds to the cathodic reduction of tin in diffusion mode (Fig. 3) and, therefore, this reaction is rate-determining.

With increasing alkali concentration, the potential of the aluminium electrode shifts to a more positive region, which is attributable to the formation of a more compact layer of the deposit. Comparison of the currents of cathodic reduction of tin and anodic dissolution of aluminum shows that the contact deposition of tin from concentrated solutions involves a minor fraction of side reduction of hydrogen. The process of contact exchange in these conditions can be approximately described by polarization (corrosion) diagrams. For a specified concentration of tin ions the limiting current of 30–40 A m^{-2} in run no. 1 (Table 2) is reached at potentials of –1.2…–1.6 V (Fig. 3).

At a sufficiently high concentration of tin(II) ions (≥10 M), tin is precipitated as a dense spongy deposit poorly adherent to the compact base metal and periodically detached from the surface. Such a deposit does not preclude electrolyte access to the aluminum surface, and, therefore, the contact exchange can theoretically occur to the point of complete dissolution of aluminum or complete precipitation of tin. The reduction of tin ions at the limiting diffusion current under a considerable cathodic polarization may be the reason for tin precipitation as a spongy deposit [10, 11]. The gravimetric data (Table 3) show that the rate of hydrogen evolution in dilute solutions essentially grows, reaching a value that exceeds severalfold the rate of tin reduction j_c(Sn):

$$j_a(\mathrm{Al}) = j_c(\mathrm{Sn}) + j_c(\mathrm{H}),$$

$$j_c(\mathrm{H}) = j_a(\mathrm{Al}) - j_c(\mathrm{Sn}).$$

The intensity of aluminum dissolution grows, in accordance with its anodic behavior, with increasing NaOH concentration (Table 3). The evolution of hydrogen in dilute solutions leads to a dramatic decrease

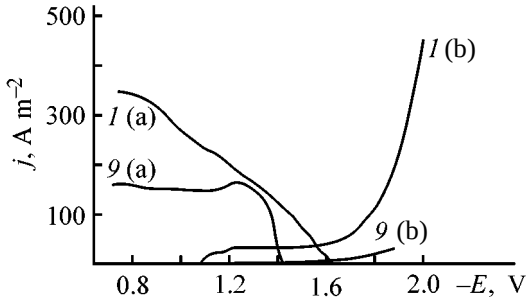

Fig. 3. (a) Anodic and (b) cathodic polarization curves for precipitation of tin on aluminum at varied concentration of tin(II) ions in solution. (j) Current density and (E) potential. The numbers at the curves correspond to run numbers in Table 2; the same for Fig. 4.

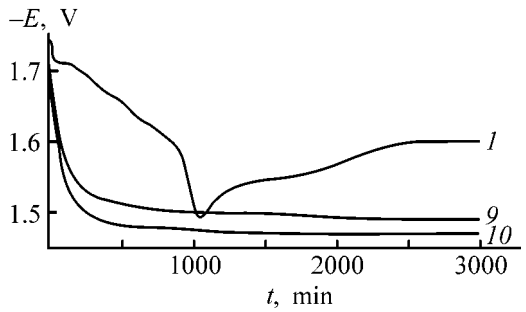

Fig. 4. Chronopotentiograms of A999 aluminum in solutions with varied concentration of tin(II) ions. (E) Potential and (t) time.

in the cathode current efficiency by tin at rather high current density of aluminum dissolution (Fig. 3), with the compromise electrode potential frequently being lower than the potential of "free" aluminum corrosion in a supporting solution (Table 3). This fact points to a complicated relationship between all the three reactions and, in particular, to the overall effect of aluminum surface activation, e.g., owing to its development, accumulation of alkali in the cathode layer, intensification of dissolution product removal, etc. (Fig. 4).

The aforesaid shows that the method of polarization diagrams is inapplicable in its frequently used simplified version to determination of the contact exchange current in those systems in which the current corresponding to side reactions is comparable with this current. This is rather evident, because the polarization curve of corroding metal reflects not the anode current of metal dissolution, but the difference between this parameter and the cathode current of oxidant reduction.

Thus, the behavior of the aluminum electrode in stannite alkaline solutions is determined by a combination of reactions: anodic dissolution of aluminum, cathodic reduction of tin, and, finally, cathodic evolution of hydrogen, which proceeds on both aluminum and tin. In this case, the total rate of the process is determined by the anodic dissolution of aluminum and depends at any instant of time on the current values of the electrode potential and the state of the electrode surface.

It is necessary to note that a coarse fern-shaped deposit is formed on compact aluminum at sufficiently high Sn(II) concentrations in solution ($\geq 10^{-2}$ M). According to the data of X-ray diffractometry, this deposit is identified as β-tin ("white" tin) with minor admixture of SnO_2. A similar pattern is also observed in reduction of Sn(II) with dispersed aluminum. In this case, weak lines of residual aluminum are observed in the X-ray diffraction patterns.

The purity of the deposited tin can be improved by additional treatment of the deposit with a concentrated alkali solution removing residual aluminum or its oxo and hydroxo compounds.

Our experiments and their theoretical interpretation suggest that the reduction of tin(II) ions to free metal on compact and dispersed aluminum has both common features and certain distinctions resulting from the dissimilar nature and structure of the outer layer of natural aluminum oxide, and also from different diffusion conditions on a flat electrode and suspension metal particles.

CONCLUSIONS

(1) Tin can be deposited as metallic granules or powder from stannite solutions in a wide concentration range (10^{-1}–10^{-3} M) via reduction with compact and dispersed aluminum.

(2) The process kinetics is of diffusion nature, which is caused by the formation of a continuous layer of tin on aluminum in the initial stage of the process.

(3) The resulting deposits mainly consist of β-tin with minor admixture of aluminum metall and SnO_2.

(4) The method of polarization curves is inapplicable in its traditional version to the determination of the contact exchange current in the systems in which the current of side reactions is comparable with the contact exchange current.

REFERENCES

1. Jpn. Patent Pending 59-190 334, IPC C 22 B 5/00.
2. Lukomskii, Yu.Ya., Priyatkin, G.M., and Mulina, T.V., *Usp. Khim.*, 1991, vol. 60, no. 5, pp. 1077–1103.
3. Byarnotas, A.K., Bubyalis, Yu.S., and Matulis, Yu.Yu., *Trudy Akad. Nauk LitSSR*, 1968, ser. B, no. 3, pp. 81–88.
4. Stoichev, D.I., Stoyanova, E.A., and Rashkov, S.R., *Bolgar. Akad. Nauk, Izv. Khimii*, 1983, vol. 16, no. 4, p. 418.
5. Kaushpedas, Z.P., Stoyanova, E.A., and Stoichev, D.I., *Trudy Akad. Nauk LitSSR*, 1987, ser. B, no. 4(161), pp. 43–49.
6. RF Patent 2 096 501.
7. Dresvyannikov, A.F., Petukhova, L.P., and Sopin, V.F., *Zh. Prikl. Khim.*, 1998, vol. 71, no. 10, pp. 1656–1659.
8. Dresvyannikov, A.F., Sopin, V.F., and Khairullin, M.G., *Zh. Prikl. Khim.*, 1999, vol. 72, no. 4, pp. 601–605.
9. *Spravochnik po elektrokhimii* (Handbook of Electrochemistry), Sukhotin, A.M., Ed., Leningrad: Khimiya, 1981.
10. Antropov, L.I. and Donchenko, M.I., *Korrosiya i zashchita ot korrozii. Itogi nauki i tekhniki* (Corrosion and Corrosion Protection. Advances of Science and Technology), Moscow: VINITI, 1973, vol. 2, pp. 113–170.
11. Rotinyan, A.L. and Kheifets, V.L., *Teoreticheskie osnovy protsessa kontaktnogo vytesnenia metallov* (Theoretical Foundations of Contact Displacement of Metals), Leningrad: Leningrad. Tekhnol. Inst., 1979.
12. Lokenbakh, A.K., Zaporina, N.A., and Lepin', L.K., *Izv. Akad. Nauk LatvSSR, Ser. Khim.*, 1981, no. 1, pp. 45–49.
13. Lepin', L.K., *Izv. Akad. Nauk LatvSSR, Ser. Khim.*, 1974, no. 1, pp. 18–27.
14. Zhilinskii, V.V., Lokenbakh, A.K., and Lepin', L.K., *Izv. Akad. Nauk LatvSSR, Ser. Khim.*, 1986, no. 2, p. 157.

Russian Journal of Applied Chemistry, Vol. 74, No. 4, 2001, pp. 616–620. Translated from Zhurnal Prikladnoi Khimii, Vol. 74, No. 4, 2001, pp. 598–602.

APPLIED ELECTROCHEMISTRY AND CORROSION PROTECTION OF METALS

Transport Limitations on Anodic Dissolution of Steels in Phosphoric Acid Electrolyte with Conditioning Additives

E. A. Fedorova

Nizhnii Novgorod State University, Nizhnii Novgorod, Russia

Received July 5, 2000; in final form, January 2001

Abstract—Transport limitations on anodic dissolution of steels with varied level of alloying were studied in the repassivation region in modified electropolishing solutions with addition of alkali metal sulfates, glycerol, adamantane, and remantadine.

Good performance in the practice of electrochemical treatment of steel and alloy surfaces has been exhibited by modified solutions for electrochemical polishing with conditioning additives of the type of adamantane [1], possessing a number of advantages over the conventional sulfuric–phosphoric–chromic acid electrolyte [2]. A most important information, necessary for selecting optimal solution compositions and electrochemical polishing modes for alloys with varied degree of alloying can be obtained by studying the kinetics and revealing the limiting stages of anodic oxidation of alloys in the transpassive state.

If oxygen is evolved in the course of anodic polishing, which is characteristic of steels [3, 4], this unambiguously indicates that a continuous solid (apparently of oxide nature) film is formed on the anode surface. This film possesses ionic conductivity and *p*- or *n*-type semiconductivity. The rate of anodic oxidation of the alloy is determined in this case by three components of potential drops across the alloy–film and film–electrolyte interfaces and the film itself. It is still a matter of discussion which one of these plays the decisive role and what is the driving factor of the process—ion migration within the anodic oxide film (AOF) under the action of electric field, diffusion mass transfer of reagents in the near-electrode layer [5], acceptor mechanism of control, or the mechanism of salt film formation [6, 7].

The kinetics of anodic dissolution of transpassive steel anodes was studied for the example of 12Kh18N10T, 20Kh13, 95Kh18, and 08kp steels with varied degree of alloying and diffusion coefficients were evaluated for phosphoric acid (PhA) electrolytes with alkali metal sulfates (and K_2SO_4 [4] in the first place), glycerol $C_3H_8O_3$, adamantane (Ad), and its derivative—remantadine (Re) as conditioning additives.

EXPERIMENTAL

Electrochemical measurements were carried out with a P5848 potentiostat and KSP-4 recorder in a three-electrode cell with separated electrode spaces and saturated silver chloride reference electrode. The potentials are given relative to the standard hydrogen electrode. The steel working electrodes, fabricated in the form of disks with reactive surface area of 0.2–0.5 cm^2, were cleaned mechanically and weighed prior to each experiment. All the experiments were done at 323 K.

Partial polarization curves were plotted with account of the current efficiencies of ionization of steel components, determined gravimetrically and by quantitative analysis of anolytes in an electrolyzer with separated electrode spaces. The electrochemical equivalents of the steels were calculated with account of the percentage content of components and their final oxidation states. The fraction of current consumed for evolution of oxygen gas was evaluated volumetrically. The quantitative content of metal ions of the dissolving components of a steel in the anolyte was determined by atomic-absorption analysis on an AAS-1 spectrophotometer with detection limit of 0.05–0.1 mg l^{-1} [8]. Voltammograms were measured at potential sweep rates V_s (V s^{-1}): 0.01, 0.02, 0.05, 0.1, and 0.2. Measurements on a rotating disk electrode were done at rotation velocities w = 25–324 rad s^{-1}.

It has been shown previously that, in the case of joint use of adamantane and potassium sulfate con-

1070-4272/01/7404-0616 $25.00 © 2001 MAIK "Nauka/Interperiodica"

ditioning additives to a PhA electrolyte, the current efficiencies of anodic dissolution of the components of 12Kh18N10T steel decrease, making the service life of polishing solutions 1.5 times longer. Replacing water with glycerol in electrolytes of this kind ensures the necessary smoothing of the surface of steels with heterogeneous structure (20Kh13, 95Kh18, and 08kp), with the rate of their anodic dissolution becoming lower.

Figure 1 presents the experimental data obtained in studying the factors retarding the oxidation of steel components in the presence of conditioning additives to a PhA solution for the example of 12Kh18N10T steel at current peak (j_p) potentials and limiting currents j_l at the inflection point of current–voltage (*I–E*) curves. Figure 2 shows the results of partial-current measurements on a rotating disk electrode. The initial portions of the j_p–$V_s^{1/2}$ and j_p–$w^{1/2}$ curves were approximated in all solutions by straight lines corresponding to a diffusion-controlled process. With increasing V_s and w, the anodic dissolution process first passes into the region of mixed diffusion-activation–controlled kinetics and then into that of purely activation control, where mixing already has no effect on the process rate (Fig. 2a).

With the anodic polarization increasing further, when two processes—ionization of steel components and oxygen evolution at the AOF–electrolyte interface—occur in parallel, the portion intercepted on the ordinate axis by the straight line plotted in the j_p–$w^{1/2}$ coordinates is equal [9] to the fraction of current consumed for oxygen evolution (Fig. 2b). In the transpassive region, with increasing V_s, the process becomes irreversible (Fig. 2b).

According to the theory of thin-film voltammetry applied to quasi-reversible and irreversible electrochemical processes [9–12], including anodic oxidation [10, 11], the peak currents j_p in the *I–E* curves can be used to evaluate the diffusion coefficients of ions in anodic dissolution of metallic electrodes.

About the same peak currents were observed in voltammetric curves obtained with 08kp, 20Kh13, and 95Kh18 steel electrodes in PhA solutions with conditioning additives. For the 95Kh18 alloy the currents were higher than those with other steels at one and the same anode potential. The same pattern was observed in constructing anodic partial curves $\log j_{st}$–*E* (Fig. 3).

The obtained voltammetric characteristics of steel electrodes were used to find the diffusion coefficient *D* of ions, with account of the procedures for cal-

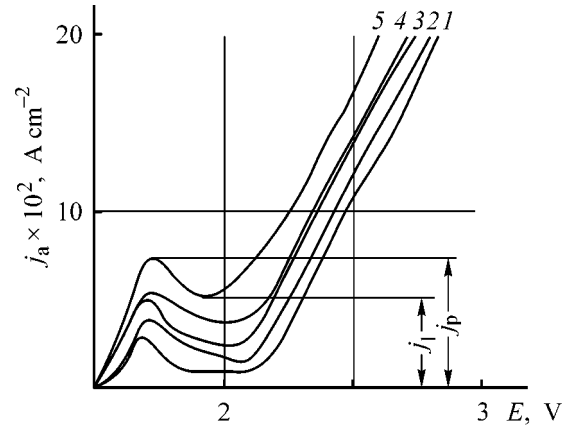

Fig. 1. Voltammetric curves of anodic dissolution of 12Kh18N10T steel at 323 K. 13.5 M H_3PO_4 solution with additives (M): $C_3H_8O_3$ 2.0, H_2SO_4 0.5. (j_a) Anode current density and (*E*) potential. Potential sweep rate (V s^{-1}): (*1*) 0.004, (*2*) 0.008, (*3*) 0.01, (*4*) 0.02, and (*5*) 0.04.

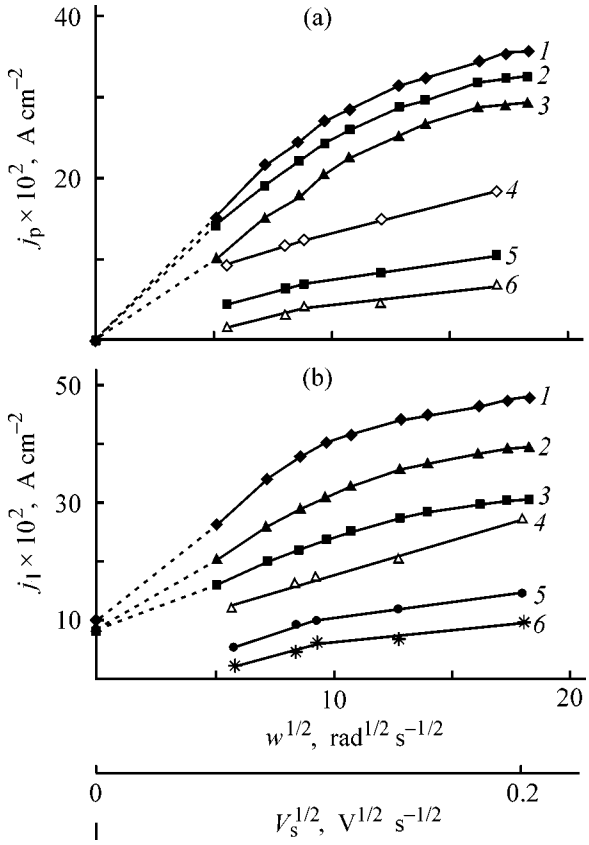

Fig. 2. Currents (a) j_p and (b) j_l for 12Kh18N10T steel vs. (*1–3*) $w^{1/2}$ and (*4–6*) $V_s^{1/2}$. (j_p, j_l) Peak current and current at the inflection point of the *I–E* curve, (*w*) disk rotation velocity, and (V_s) potential sweep rate. H_3PO_4 solution (*1–3*) 11 M and (*4*, *5*) 13.5 M with additives (M): (*2*) 5.7 K_2SO_4; (*3*) 5.7 K_2SO_4, 7.3×10^{-3} Ad; (*4*) 0.5 H_2SO_4; (*5*) 2.0 $C_3H_8O_3$, 0.5 H_2SO_4, 7.3×10^{-3} Ad; (*6*) 2.0 $C_3H_8O_3$, 0.5 H_2SO_4; and (*1*) no additive.

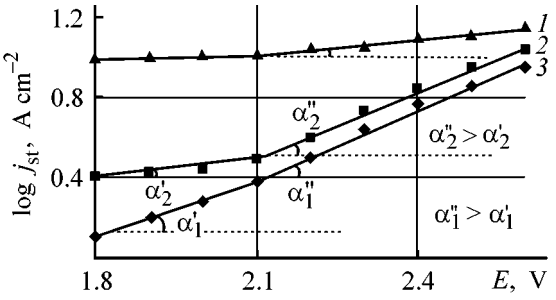

Fig. 3. Anodic partial curves $\log j_{st}$–E. Solution (M): H_3PO_4 13.5, $C_3H_8O_3$ 2.0, H_2SO_4 0.5, Re 2.9×10^{-2}. Steel: (*1*) 08kp, (*2*) 20Kh13, and (*3*) 95Kh18.

culation of diffusion and kinetic parameters of irreversible processes [9], by means of the equation

$$J_p = 3.0 \times 10^5 n(\alpha n)^{1/2} SCD^{1/2} V_s^{1/2}, \quad (1)$$

where J_p is the experimental peak current in the voltammetric curve (A), S the electrode area (cm^2), C the concentration of dissolving ions of steel components in the anolyte (M), V_s the potential sweep rate (V s^{-1}), n the number of electrons exchanged in an elementary process, and α the transfer coefficient for electrons.

The αn values were calculated using a quantity that is a reciprocal of the slope of the linear dependence of the peak potential $E_p = f(\ln V_s)$ and the Delahey equation [9] for the irreversible process:

$$dE_p/d\ln V_p = 2.303RT/2\alpha nF. \quad (2)$$

The diffusion coefficients of iron ions, mainly contained in the alloys under study, in the anodic dissolution of the alloys in a PhA electrolyte with conditioning additives in the range of electropolishing potentials are listed in Table 1. The obtained values of diffusion coefficients reflect the occurrence of an intermediate state between the liquid- and solid-phase diffusion of ions of components of the dissolving steels [13]. Of the two main driving factors of the process—ion migration under the action of electric field within AOF and diffusion of products formed in anodic dissolution of the steel components under the action of the concentration gradient—the first is apparently the limiting factor. In this case it becomes possible to account for the observed increase in the rate of anodic dissolution of steels with the growing extent of their alloying with chromium in the order 95Kh18 > 20Kh13 > 08kp (Fig. 3). Easier migration of ions through the AOF (γ-Fe_2O_3) exhibiting semiconducting properties with *p*-type conduction is possible if the motion of ions (Fe^+) of one of the two main components of chromium steels—iron and chromium—is slower. Cr^{6+} ions, being incorporated into the semiconducting γ-Fe_2O_3 film will increase the number of cationic vacancies and, as a result, make higher the rate of iron ionization. The incorporation of chromium ions in the γ-Fe_2O_3 oxide layer is possible since the difference between the atomic radii of Fe (r_{Fe} = 1.26 Å) and Cr (r_{Cr} = 1.30 Å) [16] does not exceed 15%.

The partial dependences $\log j_{st}$–E reflecting the anodic dissolution of iron, the dominant component of 08kp, 20Kh13, and 95Kh18 steels, show a break (Fig. 3). The slope of the semilogarithmic curves is greater after the break, which corresponds to the stage mechanism of metal ion ionization [17] and is due to the dissimilar dependences of the rates of these stages on potential.

With multicharge ions (Fe^{2+}, Fe^{3+}, Cr^{3+}, Cr^{6+}) formed in the end, abstraction of electrons from metal ions presumably occurs in stages. The initially formed subions (Fe^+ and, possibly, Cr^{2+}) will overcome the potential barrier at the metal–oxide interface and then potential barriers inside the forming oxide film, migrating via cationic vacancies and, possibly, being in part additionally oxidized inside the film. The subions going out of the film must react with atomic oxygen. Therefore, the rate of the oxygen process must be determined by two processes—evolution of oxygen

Table 1. Diffusion coefficients of iron ions, D_{Fe}, in anodic dissolution of steels in a PhA electrolyte with conditioning additives

Steel brand	Electrolyte composition, M	D_{Fe}, cm^2 s^{-1}
12Kh18N10T	H_3PO_4 11, K_2SO_4 5.7	$(3.1–6.1) \times 10^{-6}$
	H_3PO_4 13.5, H_2SO_4 0.5, $C_3H_8O_3$ 2.0	$(1.0–1.3) \times 10^{-7}$
	H_3PO_4 13.5, H_2SO_4 0.5, $C_3H_8O_3$ 2.0, Ad 7.3×10^{-3}	$(7.0–8.6) \times 10^{-7}$
20Kh13	H_3PO_4 13.5, H_2SO_4 0.5, $C_3H_8O_3$ 2.0	$(1.5–2.1) \times 10^{-7}$
	H_3PO_4 13.5, H_2SO_4 0.5, $C_3H_8O_3$ 2.0, Re 2.9×10^{-2}	$(2.2–3.5) \times 10^{-7}$
95Kh18	H_3PO_4 13.5, H_2SO_4 0.5, $C_3H_8O_3$ 2.0	$(2.7–4.6) \times 10^{-7}$
	H_3PO_4 13.5, H_2SO_4 0.5, $C_3H_8O_3$ 2.0, Re 2.9×10^{-2}	$(3.0–5.1) \times 10^{-7}$

Table 2. Current efficiencies CE^{st} for anodic oxidation of 12Kh18N10T steel in a PhA electrolyte with conditioning additives and fraction of current consumed for evolution of oxygen gas, Q_{O_2}, at varied current density j_a

j_a, A dm^{-2}	CE^{st}	Q_{O_2}	CE^{st}	Q_{O_2}	CE^{st}	Q_{O_2}	CE^{st}	Q_{O_2}
	%, for indicated electrolyte*							
	no. 1		no. 2		no. 3		no. 4	
20	63.8	26.9	59.4	30.6	58.8	29.8	60.2	27.8
30	53.6	38.2	48.3	42.7	44.5	38.7	49.6	33.6
40	46.8	47.3	43.1	50.6	40.9	43.0	42.7	39.2
50	42.5	52.3	40.0	54.0	37.8	47.5	41.5	43.8
60	40.2	54.2	34.3	58.5	35.8	49.3	37.6	46.4

* Electrolyte composition (M): no. 1, H_3PO_4 11, K_2SO_4 5.7; no. 2, H_3PO_4 11, K_2SO_4 5.7, Ad 7.35×10^{-3}; no. 3, H_3PO_4 11, H_2SO_4 0.5, $C_3H_8O_3$ 2.0; no. 4, H_3PO_4 11, H_2SO_4 0.5, $C_3H_8O_3$ 2.0, Ad 7.35×10^{-3}.

Table 3. Effect of glycerol, adamantane, and remantadine additives to solution of composition (M): H_3PO_4 13.5, H_2SO_4 0.5, on the rate of anodic dissolution and smoothing of steel surface

Steel brand	Additive, M	Process mode		Rate of anodic dissolution of steel, μm min^{-1}	Relative smoothing, %
		j_a, A dm^{-2}	τ, min		
12Kh18N10T	–	60	4	7.6	50.6
20Kh13	–	60	6	7.8	48.1
95Kh18	–	60	6	8.1	42.4
12Kh18N10T	$C_3H_8O_3$ 2.0, Ad 7.3×10^{-3}	75	2	6.4	78.6
20Kh13	$C_3H_8O_3$ 2.0, Ad 7.3×10^{-3}	75	2	6.6	64.5
20Kh13	$C_3H_8O_3$ 2.0, Re 2.9×10^{-2}	60	4	5.1	64.1
95Kh18	$C_3H_8O_3$ 2.0, Ad 7.3×10^{-3}	60	4	7.2	62.7
95Kh18	$C_3H_8O_3$ 2.0, Re 2.9×10^{-2}	60	4	5.8	63.8

gas and oxygen consumption for additional oxidation of the products formed in anodic oxidation of steel components.

Experiments on collection of gas evolved from the surface of 12Kh18N10T steel anodes in a PhA solution with conditioning additives (Table 2) confirmed the assumption made.

The fraction of current consumed for oxygen gas evolution, Q_{O_2}, was smaller than the theoretically calculated current efficiencies by O_2 [$CE^{O_2} = 100 - CE^{st}$ (%)] in solutions containing either K_2SO_4 or glycerol and adamantane. Therefore, the observed inequality $Q_{O_2} < CE^{O_2}$ cannot be accounted for only by the possible oxidation of organic additives in the course of electrolysis.

The conditioning additives to the PhA solution affected the kinetics of anodic dissolution of steels in different ways (Table 2). Raising the content of cations K^+ and adamantane in a wide range of concentrations in an aqueous PhA solution makes lower the current efficiencies by the steels under study, which is due, as shown in [18], to their adsorption onto the steel anode surface.

In the case of simultaneous presence of glycerol and adamantane additives in a conditionally nonaqueous phosphoric acid solution, the rates of ion migration in the film (Table 1) and current efficiencies by steel increased somewhat, and the fraction of oxygen gas decreased (Table 2).

It may be assumed that, since the surface anodic film must be in dynamic equilibrium with the solution, unstable subions going out of the film will transform into stable ions under the action of oxygen and solution, with precipitation of the solid phase. If this occurs in the close vicinity of the film, it grows somewhat. Under the action of additives (adamantane and remantadine in the first place), subions probably acquire a certain extent of stability and may pass into solution, being preserved for a certain time and forming supersaturated solutions. According to the Schottky mechanism [19], this must make the film thinner, facilitate somewhat the anodic process, especially at

microscopic projections, and accelerate the smoothing of the microscopic roughness, and this was actually observed in practice (Table 3).

CONCLUSIONS

(1) Anodic dissolution of steels in phosphoric acid electrolyte with such conditioning additives as potassium sulfate, glycerol, and adamantane (or remantadine) proceeds in the transpassive region in stages, with ion migration in the AOF under the action of electric field as limiting factor, film thinning, and accelerated smoothing of the surface microroughness.

(2) It is recommended to use remantadine [$(2.0–4.0) \times 10^{-2}$ M], lowering the rate of anodic dissolution of steels as compared with adamantane, in electrochemical treatment of chromium and carbon steels as an additive to a solution of composition (M): H_3PO_4 13.5, H_2SO_4 0.5, $C_3H_8O_3$ 2.0, with the required quality of surface treatment preserved.

REFERENCES

1. Fedorova, E.A., *Ekologiya Prom–st. Ross.*, 1999, no. 1, pp. 12–16.
2. Vinogradov, S.S., *Ekologicheski bezopasnoe gal'vanicheskoe proizvodstvo* (Ecologically Safe Electroplating Shop), Moscow: Globus, 1998.
3. Fedorova, E.A., Mitrofanov, E.V., and Flerov, V.N., *Zh. Prikl. Khim.*, 1985, vol. 58, no. 8, pp. 1897–1899.
4. Fedorova, E.A., *Modification of Compositions of Solutions for Electropolishing of Titanium-containing Steels*, Available from VINITI, 1999, no. 2364-V99.
5. Maslikov, S.V. and Saushkin, B.P., *Zh. Prikl. Khim.*, 1999, vol. 72, no. 9, pp. 1551–1554.
6. Landolt, D., *Elektrokhimiya*, 1995, vol. 31, no. 3, pp. 228–234.
7. Magaino, S., Matlosz, M., and Landolt, D., *J. Electrochem. Soc.*, 1993, vol. 140, no. 8, pp. 1365–1368.
8. Bripke, M.E., *Atomno-absorbtsionnyi spektrokhimicheskii analiz* (Atomic-Absorption Spectral-Chemical Analysis), Moscow: Khimiya, 1982.
9. Galus, Zb., *Teoretyczue Podstawy Elektroanalisy Chemicznej*, Warszawa: Panstwowe Wydawnictwo Naukowe, 1971.
10. Wieckowski, A., Ghah, E., and Huy Ha La, *J. Electrochem. Soc.*, 1984, vol. 131, no. 10, pp. 2024–2034.
11. Survila, A.A., *Elektrokhimiya*, 1986, vol. 22, no. 8, pp. 1045–1049.
12. Protsailo, T.A. and Rez', Ya.F., *Elektrokhimiya*, 1996, vol. 32, no. 5, pp. 639–641.
13. Tret'yakov, Yu.D., *Tverdofaznye reaktsii* (Solid-Phase Reactions), Moscow: Khimiya, 1978.
14. Sukhotin, A.M., Andreeva, O.S., and Dudenkova, L.A., *Elektrokhimiya*, 1985, vol. 21, no. 2, pp. 251–255.
15. Valeev, A.Sh., *Elektrokhimiya*, 1981, vol. 12, no. 11, pp. 1830–1836.
16. Rabinovich, V.A. and Khavin, Z.Ya., *Kratkii khimicheskii spravochnik* (Concise Reference Book of Chemistry), Moscow: Khimiya, 1977.
17. Kabanov, B.N., *Elektrokhimiya metallov i adsorbtsiya* (Electrochemistry of Metals and Adsorption), Moscow: Nauka, 1966.
18. Fedorova, E.A. and Naumov, V.I., *Elektrokhimiya*, 1993, vol. 29, no. 5, pp. 585–591.
19. Kubaschewski, O. and Hopkins, B.E., *Oxidation of Metals and Alloys*, New York: Akademic, 1962, 2nd ed.

Russian Journal of Applied Chemistry, Vol. 74, No. 4, 2001, pp. 621–625. Translated from Zhurnal Prikladnoi Khimii, Vol. 74, No. 4, 2001, pp. 603–607.

CATALYSIS

Synthesis of Monosilane by Catalytic Disproportionation of Trichlorosilane in a Reaction-Rectification Apparatus with Recycle

V. M. Vorotyntsev, G. M. Mochalov, and O. V. Nipruk

Nizhnii Novgorod State Technical University, Nizhnii Novgorod, Russia

OOO Firma Khorst, Moscow, Russia

Received February 21, 2000; in final form, October 2000

Abstract—Basic principles of a procedure for calculating a reaction-rectification apparatus for synthesizing silane by catalytic disproportionation of trichlorosilane are presented. Technological parameters are substantiated and the process of silane synthesis in the reaction-rectification apparatus is optimized.

Silane is one of the most important starting materials used to manufacture semiconducting silicon and epitaxial structures on its base. The quality of semiconducting silicon is mainly determined by the purity of silane, and, therefore, the use of silane in microelectronics imposes strict requirements on its purity. Since the impurity composition of silane is formed in the stage of its synthesis, much attention is paid presently to selecting a synthesis technique allowing easy purification of the obtained product.

Until recently, disproportionation of organosubstituted silanes [1], namely, that of triethoxysilane, has been the main industrial method for silane synthesis. However, silane obtained in this way contains difficultly removable impurities of organic substances and, therefore, fails to satisfy the growing requirements of microelectronics.

The highest-purity silane can be obtained by disproportionation of trichlorosilane in the presence of a catalyst [2–7]. However, the proposed method has long been in disuse in the industry because of the lack of catalyst that would not contaminate the product and could retain its activity for a sufficiently long time. According to the patent literature, the best catalysts for disproportionation of trichlorosilane are anion-exchange resins combining high activity of functional groups and ability to bind molecules containing electroactive atoms—As, B, and P. The highest catalytic activity is exhibited by resins of the following types: Amberlyst A-21, Amberlyst-26, gel quaternary-ammonium resin IRA-400, AN18-12P, and AV27-12P.

Synthesis of silane by disproportionation of trichlorosilane has not been used in Russia until now, and, therefore, calculation and optimization of the technological scheme and of the procedure for synthesizing silane by this method are of interest.

When reactions of redistribution of hydrogen and chlorine atoms among molecules of chlorosilanes from the series $SiCl_4$, $SiHCl_3$, SiH_2Cl_2, SiH_3Cl, SiH_4 proceed in the course of catalysis on anion-exchange resins at nearly normal temperature, bimolecular interactions may occur simultaneously, described by the following equations of reversible reactions [1]:

$$2SiHCl_3 \rightleftarrows SiCl_4 + SiH_2Cl_2, \quad (1)$$

$$2SiH_2Cl_2 \rightleftarrows SiHCl_3 + SiH_3Cl, \quad (2)$$

$$2SiH_3Cl \rightleftarrows SiH_2Cl_2 + SiH_4, \quad (3)$$

$$2SiH_2Cl_2 \rightleftarrows SiCl_4 + SiH_4, \quad (4)$$

$$SiCl_4 + SiH_3Cl \rightleftarrows SiHCl_3 + SiH_2Cl_2, \quad (5)$$

$$SiHCl_3 + SiH_4 \rightleftarrows SiH_2Cl_2 + SiH_3Cl. \quad (6)$$

Reactions (1)–(4) involve disproportionation; reactions (5) and (6) are of dismutation type.

Thus, synthesis of silane by disproportionation proceeds in stages, with dichlorosilane and monochlorosilane formed as intermediates. Therefore, it is advisable to synthesize silane in the recycle mode, i.e., with separation of target products and recycling of intermediates into the reactor. A reaction-rectification apparatus described in [8] (Fig. 1) was used for this purpose.

1070-4272/01/7404-0621 $25.00 © 2001 MAIK "Nauka/Interperiodica"

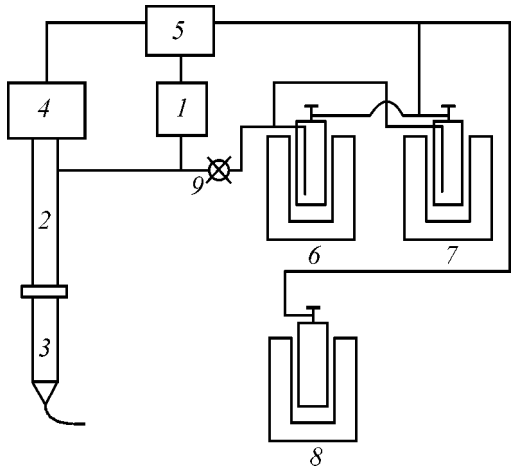

Fig. 1. Schematic of a reaction-rectification apparatus for synthesizing silane by catalytic disproportionation of trichlorosilane: (*1*) Vessel, (*2*) rectification column, (*3*) evaporator, (*4*) reactor, (*5*) dephlegmator, (*6, 7*) condensers, (*8*) silane receiving vessel, and (*9*) cock.

The starting trichlorosilane is fed from vessel *1* into the upper part of the separation section of rectification column *2* and then into condenser *3*. Trichlorosilane vapor is delivered from the evaporator into the lower part of the separation section of rectification column and then into reactor *4*. The reactor has the form of a thermostated vessel charged with a catalyst. In the reactor occurs the disproportionation of silane, with the composition of the mixture of reaction products close to the equilibrium composition at the reactor temperature.

Synthesis gas is fed into dephlegmator *5* where partial condensation of reaction products occurs. The condensate, containing trichlorosilane, silicon tetrachloride, and other chlorosilanes, is returned into vessel *1*, being mixed there with the starting trichlorosilane. As a result, the reaction products are accumulated in vessel *1*. A mixture of chlorides is delivered from the vessel into the separation section of the rectification column whose operation results in that silicon tetrachloride is concentrated in the evaporator and discharged from the apparatus. The process of silicon tetrachloride accumulation in vessel *1* continues until the rates of its synthesis in the reactor and discharge from the evaporator become equal. After this occurs, the apparatus is operating further in the stationary mode. The vapor not condensed in dephlegmator *5*, enriched in silane and light chlorosilanes, is discharged from the apparatus and condensed in receiving vessel *6* or *7* at liquid nitrogen temperature. At regular intervals, silane is evaporated from the receiving vessel into vessel *8*, and light chlorosilanes are returned through cock *9* into the apparatus and, arriving at the reactor, are again involved in the reaction of disproportionation. The products of this reaction are again subjected to partial condensation in dephlegmator *5*. Thus, the apparatus is operating in a closed cycle.

It can be seen from the described technological cycle that an important condition for operation of the apparatus is the concerted action of the reactor and the rectification column. The rate of silicon tetrachloride discharge depends on the degree of extraction, separation factor, and silicon tetrachloride concentration in the upper part of the rectification column. In its turn, the rate of synthesis of silicon tetrachloride is determined by the difference in its concentrations before and after passing through the reactor, and the concentration at the reactor inlet coincides with that in the upper part of the rectification column. In accordance with the equations of reactions (1)–(6), the content of silicon tetrachloride in the starting mixture fed into the reactor affects the concentration of silane and chlorosilanes in the gas mixture discharged from the reactor. Consequently, the concentration of silicon tetrachloride at the reactor inlet and in the upper part of the rectification column determines the efficiency of both the reactor and the rectification column. Therefore, the algorithm for calculation of the above technological cycle is aimed to search for the concentration of silicon tetrachloride at the reactor inlet and the upper part of the rectification column. This problem was solved as follows.

(1) Controllable parameters of the process were set: reaction temperature T_r; dephlegmator temperature T_d; pressure in the apparatus, P_0; $SiCl_4$ concentration in the lower part of the column, X_l; separating capacity of the rectification column, represented by the number n of theoretical plates in the zero-takeoff mode.

(2) The composition of the starting mixture fed in the reactor was introduced: $DI(1)$, $DI(2)$, $DI(3)$, $DI(4)$, and $DI(5)$—concentrations of, respectively, silane, mono-, di-, and trichlorosilane, and silicon tetrachloride.

(3) The composition of the equilibrium mixture discharged from the reactor at T_r was calculated using the following algorithm.

(a) The equilibrium constants were calculated from the Gibbs energies; the thermodynamic constants necessary for calculations were taken from [9, 10].

(b) The equilibrium concentrations of the components in reaction (1) were calculated by passing to a three-dimensional coordinate system and introducing a variable reaction coordinate z reflecting

changes in component concentrations in the course of the reaction:

$$X(3) = DI(3) + 0.5z,$$

$$X(4) = DI(4) - z,$$

$$X(5) = DI(5) + 0.5z,$$

where $X(3)$, $X(4)$, and $X(5)$ are, respectively, the equilibrium concentrations of di- and trichlorosilane and silicon tetrachloride.

The solution was found in the form of the following quadratic equation

$$K_{eq}1 = X(5)X(3)/X(4)^2.$$

The physically realizable solution must satisfy the condition $0 \le X(4) \le 1$, $0 \le X(3) \le 1$, $0 \le X(5) \le 1$.

(c) Using the obtained z value, the equilibrium concentrations of the reactants of reactions (1)–(6) were calculated at appropriate equilibrium constants, with the z value and the mixture composition corrected each time. The calculation was repeated until the quasi-equilibrium composition of the system stabilized at the values corresponding to the chosen convergence criterion. This gave a set of equilibrium concentrations of all the components of the system: $X(1)$ silane, $X(2)$ monochlorosilane, $X(3)$ dichlorosilane, $X(4)$ trichlorosilane, and $X(5)$ silicon tetrachloride.

(4) The saturated vapor pressure was calculated for each component of the system at T_d by the following equations [9–11]:

$$\mathrm{SiH_4} - \log P_1 = 68.07 - 2020/T + 5.1847 \times 10^{-5}T^2 - 25.771 \log T,$$

$$\mathrm{SiH_3Cl} - \log P_2 = 7.3948 - 1095.7/T,$$

$$\mathrm{SiH_2Cl_2} - \log P_3 = -1297.2T + 1.75\log T - 2.4827 \times 10^{-3}T + 3.9022,$$

$$\mathrm{SiHCl_3} - \log P_4 = -1170/(T + 246) + 7.09119,$$

$$\mathrm{SiCl_4} - \log P_5 = 7.6414 - 1572.3/T.$$

(5) The separation factor defined as the ratio of the $SiCl_4$ concentrations at the top and bottom of the column; degree of extraction, p; rate of synthesis in the reactor; and rate of $SiCl_4$ discharge from the apparatus were calculated. The degree of extraction was found using the equation [12]

$$F = \frac{1 - \alpha\theta}{(1 - p)F_0^{-(1 - \alpha\theta)/(1 - p)} - \theta},$$

where $\theta = p(\alpha - 1)$, F is the separation factor in the takeoff mode, F_0 the separation factor in the zero-takeoff mode, $F_0 = \alpha^n$, n the number of theoretical plates, p the degree of extraction, and α the separation coefficient.

The following comparison was made: if the rate of discharge was lower than the rate of synthesis, then the concentration of silicon tetrachloride at the inlet of the reactor and the separation section was raised: otherwise, it was reduced and step 3 was executed again. The calculation procedure was repeated until the rates of synthesis and discharge of silicon tetrachloride became close, to satisfy the chosen convergence criterion.

(6) The saturated vapor pressure was calculated for the equilibrium mixture, liquefied at T_d and having concentrations $X(1)$–$X(5)$ (steps 3b and 3c) of the components discharged from the reactor, using the equation

$$P = P_1X(1) + P_2X(2) + P_3X(3) + P_4X(4) + P_5X(5).$$

(a) In the case of $P < P_0$, the composition $X(1)$–$X(5)$ was used in step 3 [instead of $DI(1)$–$DI(5)$] and the calculation procedure was repeated until condition 6b was satisfied.

(b) At $P > P_0$, the procedure went to calculating by the method of iterations the degree of extraction of light fractions from dephlegmator *5*.

(7) The composition of equilibrium liquid and vapor phases in dephlegmator *5* at temperature T_d and pressure P_0 was calculated using a set of equations for i components, having the form

$$x_0(i) = y_0(i)P_0/[P_0(1 - S) + SP_1],$$

where i is the number of a mixture component, S the degree of extraction of light fractions, P_0 the working pressure, P_i the equilibrium pressure at T_d, $x_0(i)$ the concentration of ith component in the liquid phase, and $y_0(i)$ the same in the vapor phase.

(8) The system of equations was solved by iterations of the degree of extraction.

(9) Since the liquid of composition $x_0(i)$ comes from dephlegmator *5* into the feeding vessel *1* and thence arrives at the reactor inlet and the upper part of the rectification column, this composition was used in passing to step 3.

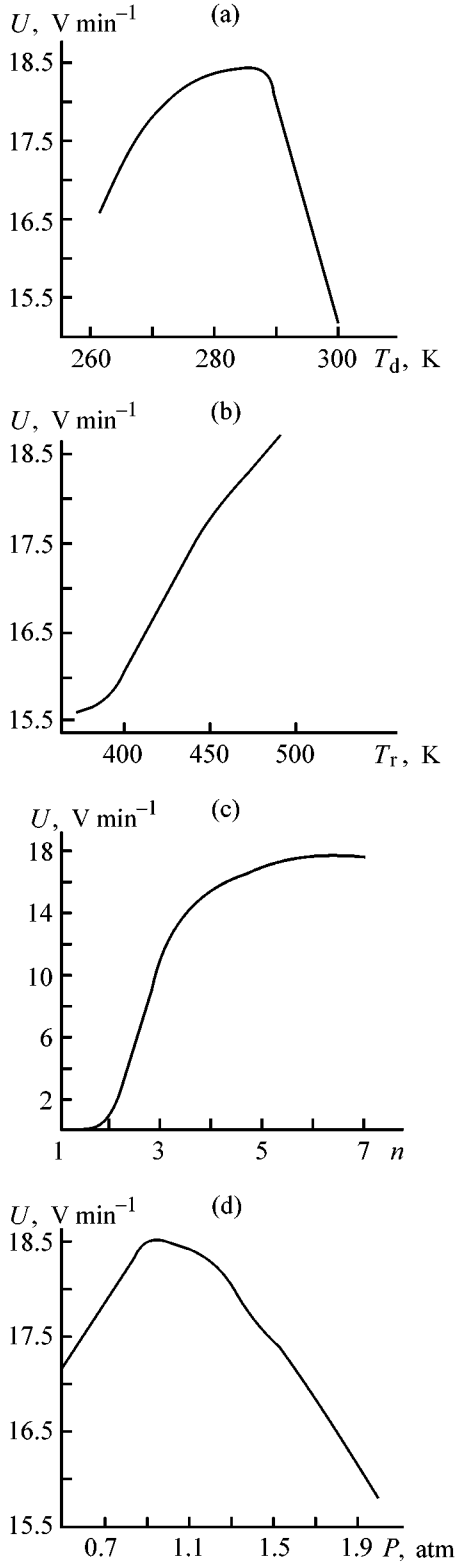

Fig. 2. Calculated dependences of the output capacity U of the apparatus on (a) dephlegmator temperature T_d, (b) reactor temperature T_r, (c) number n of theoretical plates in the rectification column, and (d) pressure P in the column.

(10) The calculation procedure was repeated until stationary values of S, $x_0(i)$, and $y_0(i)$ were obtained with the satisfied condition for equal rates of synthesis and discharge of silicon tetrachloride.

(11) Since the vapor of composition $y_0(i)$ is discharged from dephlegmator *5* and condensed in receiving vessel *6* or *7*, light chlorosilanes remaining in the receiving vessels after silane is evaporated therefrom into vessel *8* are returned into the reactor (recycled). The $y_0(i)$ values were used to calculate the composition of the liquid in vessels *6* and *7* after the evaporation of silane. This composition was used in step 3 to calculate the concentration of silane in the mixture discharged from the reactor; degree of vapor mixture extraction from dephlegmator *5* in recycle, S_r; and concentration of silane in the mixture, y_{1r}.

(12) Then the output capacity U (g g^{-1}) of the apparatus was found for a conventional reactor load of 1 mol min^{-1}:

$$U = [Sy_1 + (S_rSy_{1r})(1 - y_1)][1 + S(1 - y_1)] \times 32 \times 60,$$

where Sy_1 is the amount of silane taken-off in 1 min, y_r the concentration of silane in the vapor in a recycle, $S_rS(1 - y_1)y_{1r}$ the amount of silane taken-off during a recycle, and 32 the molecular weight of silane (g mol^{-1}).

The data obtained in the calculations are graphically in Figs. 2a–2d.

It can be seen from Fig. 2a that, with the dephlegmator temperature increasing to 278 K, the output capacity of the apparatus grows. It may be assumed that this is due to the fact that the solubility of silane in the condensate decreases with increasing temperature. This prevents silane from coming back to the reactor, which diminishes the influence exerted by the reverse reaction of dismutation. At higher temperatures (T > 285 K), a greater amount of light chlorosilanes is discharged from the apparatus instead of being returned into the reactor, which impairs the output capacity of the apparatus.

It is seen from Fig. 2b that the output capacity of the apparatus grows steadily with increasing reactor temperature, since the reaction equilibrium is shifted toward formation of light products, this reaction being endothermic.

The influence of the number of theoretical plates, n, is illustrated in Fig. 2c. It can be seen that, at n < 3 and $SiCl_4$ concentration in the lower part of the column equal to 99%, the output capacity of the apparatus is nearly zero. This is due to the low efficiency of

the column in $SiCl_4$ removal from the reaction zone. Then the output capacity increases and, having reached the maximum value at $n = 6$, remains further unchanged, since the rectification column already shows its maximum separation efficiency in the technological process in question. Consequently, raising the number of theoretical plates to more than six is inexpedient.

Elevating the pressure in the apparatus to 1.2 atm leads to an increase in output capacity because of the higher concentration of light chlorosilanes in the condensate and to their recycling into the reactor, with the result that the rate of silane synthesis becomes higher (Fig. 2d). Raising the pressure to more than 1.2 atm makes the output capacity lower because of the increasing solubility of silane in the condensate and its penetration into the reactor where it is involved in the reverse reaction of dismutation.

The described technological scheme for manufacture of silane was implemented in a pilot installation. An experimental study of the silane synthesis demonstrated that the calculated dependence of the output capacity of the installation on the dephlegmator temperature, pressure, and number of theoretical plates is in agreement with the experiment, with, however, the experimental output capacity constituting only 70% of the calculated value. Possibly, this is due to kinetic limitations affecting the attainment of chemical equilibrium in the reactor, disregarded by the calculation procedure (step 3c). A gas-chromatographic analysis of a mixture of chlorosilanes before and after the reactor confirmed this assumption. The kinetic limitation on the reaction is associated with the fact that only the first disproportionation reaction is kinetically unhindered in the multistage consecutive-concurrent process of trichlorosilane disproportionation to silane [see reactions (1)–(3)]. The same effect was observed in a laboratory study of the kinetics of trichlorosilane disproportionation [13]. Probably, the kinetic limitation is associated with hindrances to desorption of a higher-boiling reaction product from the catalyst surface.

CONCLUSIONS

(1) The calculations demonstrated that the most expedient way to synthesize silane is in a reaction-rectification apparatus at the maximum possible reactor temperature (limited by the thermal stability of the catalyst used and of intermediate reaction products), dephlegmator temperature T_d = 278–285 K, pressure P = 1–1.2 atm, and number of theoretical plates in the rectification column of no less than six.

(2) An experimental study of the silane synthesis by the proposed technological scheme established that the experiment is in good agreement with the calculations.

(3) The practical implementation of this technology and synthesis conditions made it possible to create the first Russia's facility for manufacture of monosilane satisfying the requirements of microelectronics.

REFERENCES

1. Zhigach, A.F. and Stasinevich, D.S., *Khimiya gidridov* (Chemistry of Hydrides), Leningrad: Khimiya, 1969.
2. US Patent 4 395 389.
3. US Patent 4 613 489.
4. FRG Patent 2 162 537.
5. French Patent 2 118 725.
6. US Patent 4 113 845.
7. FRG Patent 2 507 864.
8. RF Patent 2 152 902.
9. Lapidus, I.I. and Nisel'son, L.A., *Tetrakhlorsilan i trikhlorsilan* (Tetrachlorosilane and Trichlorosilane), Moscow: Khimiya, 1970.
10. *Spravochnik khimika* (Chemist's Handbook), Nikol'skii, B.P., Ed., Moscow: Khimiya, 1971.
11. Vorotyntsev, V.M., Balabanov, V.V., Mochalov, G.M., *et al.*, *Poluchenie i analiz chistykh veshchestv* (Synthesis and Analysis of Pure Substances), Gorki: Gor'k. Gos. Univ., 1984, p. 77.
12. Devyatykh, G.G. and Elliev, Yu.E., *Vvedenie v teoriyu glubokoi ochistki veshchestv* (Introduction to the Theory of Deep Purification of Substances), Moscow: Nauka, 1981.
13. Grishnova, N.D., Gusev, A.V., Moiseev, A.I., *et al.*, *Zh. Prikl. Khim.*, 1999, vol. 72, no. 10, pp. 1667–1672.

Russian Journal of Applied Chemistry, Vol. 74, No. 4, 2001, pp. 626–630. Translated from Zhurnal Prikladnoi Khimii, Vol. 74, No. 4, 2001, pp. 608–612.

CATALYSIS

Oxidation and Stabilization of Dioxane Alcohol Formals

E. M. Kuramshin, V. K. Gumerova, S. S. Zlotskii, M. L. Verizhnikov, E. M. Gotlib, N. G. Nugumanova, S. V. Bukharov, and N. A. Mukmeneva

Ufa State Technical University of Petroleum, Ufa, Bashkortostan, Russia

Received June 23, 2000; in final form, February 2001

Abstract—The kinetic parameters of liquid-phase oxidation of dioxane alcohol formals were determined. The inhibiting activity of a number of phenol and organophosphorus antioxidants is evaluated and methods are proposed for decelerating the destruction of dioxane alcohol formals, occurring via thermal oxidation.

High-boiling by-products of isoprene synthesis by the dioxan method are multicomponent mixtures [1]. After evaporation of light fractions, the products are mainly composed of dioxane alcohol formals (DAF) of the following composition [1]:

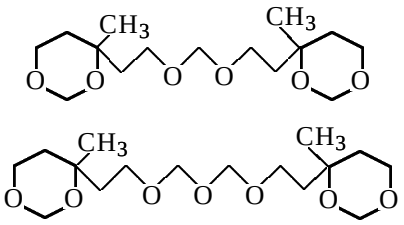

At present, DAFs find application as plasticizers in polyvinylchloride-based formulations [2]. However, wide use of DAF is hindered by their poor thermal oxidation stability.

The aim of the present study was to analyze the autooxidation and initiated oxidation of DAF and to choose on this basis antioxidants able to hinder undesirable processes of thermal-oxidation destruction.

EXPERIMENTAL

The rate of O_2 uptake in DAF oxidation was studied on a gasometric setup of static type [3]. A thermostated glass reactor of conical shape, equipped with a magnetic stirrer, was charged with 5 ml of DAF and purged with oxygen for 10 min. The amount of absorbed oxygen $\Delta[O_2]$ (mol l^{-1}) was calculated using the formula

$$\Delta[O_2] = V_{O_2}/V_s \times 22.4,$$

where V_{O_2} is the amount of absorbed oxygen (ml), and V_s is the sample volume (ml).

The rate of oxidation $V_{O_2} = \Delta[O_2]/t$ was determined as the slope of the straight line in the coordinates $\Delta[O_2]$–time.

The temperature range of DAF oxidation, ensuring the occurrence of the process in the chain mode, is 100–130°C. To this interval of working temperatures corresponds the initiator *tert*-butyl peroxide (TBP) with rate constant of decomposition equal to $\log k_d = 14.9 - 146.300/19.15T$ [4]. The TBP concentration was varied within the range $(2–30) \times 10^{-3}$ M.

The parameter a, characterizing the oxidability of a DAF ($a = k_d[DAF]/2k_t^{1/2}$) containing a DAF hydroperoxide (DAFHP) with unknown initiation rate $v_{i,DAF}$, was determined by the method of mixed initiation. According to this technique, a DAF with chains generated at an unknown rate $v_{i,DAF}$ was oxidized in the presence of TBP initiator for which the rate constant of initiation, k_i, is known [4]. For this purpose, the initial rate of oxidation, v_{O_2}, was measured in a set of experiments with different TBP concentrations, and the parameter a and $v_{i,DAF}$ were found from the dependence of v_{O_2} on [TBP], using the expression $v_{O_2} = a^2/v_{i,DAF} + a^2k_i[TBP]$ [4].

The parameter b characterizing the susceptibility of DAF to auto-oxidation is a combined factor [$b = (1/2)ak_i^{1/2}$] including the parameter a determining the rate of chain oxidation at v_i = const and $k_{i,DAF}$—the effective rate constant of auto-oxidation [4]. The autooxidation of DAF proceeds with acceleration, and the kinetics of O_2 absorption is described by the known expression $(\Delta[O_2])^{1/2} = bt$, characteristic of hydrocarbons, fuels, and acetals [3, 4]. In the coordinates $\Delta[O_2]^{1/2}$–t, the experimental points fall on a straight line. The parameter b is determined as the slope of the experimental straight line, with the upwards shift

1070-4272/01/7404-0626 $25.00 © 2001 MAIK "Nauka/Interperiodica"

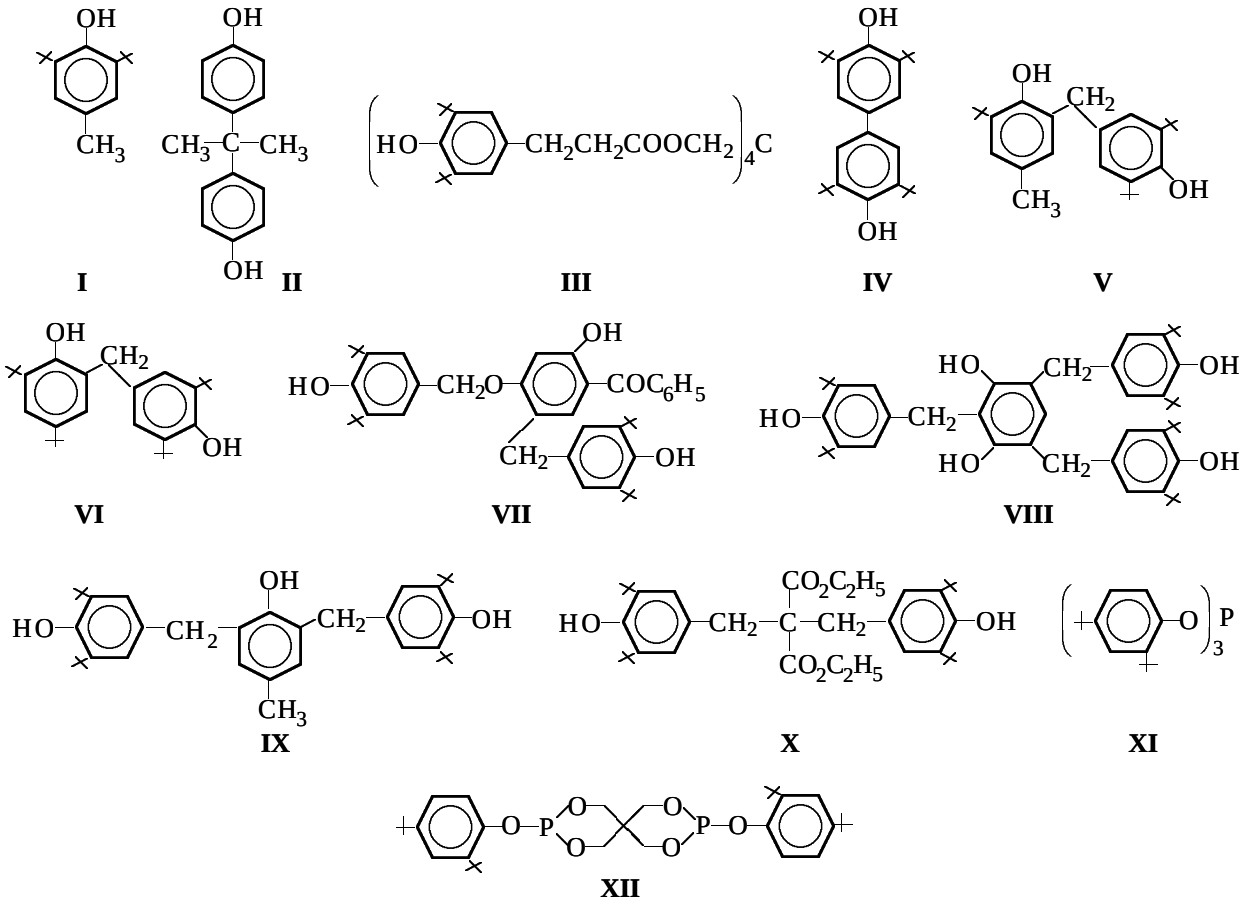

of the straight line away from the origin of coordinates related to the presence in DAF of hydroperoxides accumulated in storage.

DAF hydroperoxides were analyzed using a iodometric method based on reduction of the peroxide group by the iodide ion [5]. Oxidants of phenol type **I**–**X**, used to suppress autooxidation of DAF, were synthesized by the method described in [6]; organophosphorus compounds **XI** and **XII**, tested as DAF oxidation inhibitors, were obtained as described in [7].

In manufacture and storage of DAF in contact with atmospheric oxygen, the corresponding hydroperoxides (DAFHP) are accumulated, with their concentration in some samples equal to $(2–4) \times 10^{-3}$ M. The auto-oxidation of DAF at elevated temperature (>120°C) is accompanied by intensive absorption of oxygen to give DAFHP (Table 1). The yield of DAFHP per absorbed oxygen is nearly quantitative in the initial stage of autooxidation (ca. 90% at $\Delta[O_2] \le 1 \times 10^{-2}$ M). With increasing extent of the process, the DAFHP yield decreases to become about 30% by the end of experiment, with the decomposition rate much exceeding under these conditions the rate of DAFHP formation. With increasing temperature, the parameter b characterizing the rate of auto-oxidation grows from 4×10^{-5} to 27×10^{-5} $(M\ s^{-2})^{1/2}$; the Arrhenius dependence has the form $\log k = 6.36 - 76\,500/(19.5T)$. The activity of DAF in auto-oxidation (Table 2) is comparable with that for individual cyclic acetals [1,3-dioxane (DO) and 4,4-dimethyl-1,3-dioxane (DMDO)]—$b_{DO} : b_{DMDO} : b_{DAF} = 18.9 : 14.7 : 11.5$ (120°C).

Table 1. Rate of oxygen absorption and accumulation of hydroperoxides in DAF auto-oxidation (120°C)

t, min	$\Delta[O_2] \times 10^2$, M	$\Delta[DAFHP] \times 10^2$, M	$\frac{\Delta[DAFHP]}{\Delta[O_2]} \times 100$, %
0	0	0.4	–
10.5	1.0	1.3	90.0
30.5	3.2	2.2	56.3
71.5	7.0	3.5	44.3
117	10.7	4.5	38.3
165	14.3	4.8	30.8
189	17.7	5.6	24.4

Table 2. Kinetic parameters of initiated oxidation and auto-oxidation of individual DO and DAF (120°C)

Parameter	DO*	DMDO*	DAF
DO, M	11.7	8.3	–
$k_d/2k_t^{1/2} \times 10^3$, $(M s)^{-1/2}$	6.6	17.7	–
$a \times 10^2$, $(M s^{-1})^{1/2}$	7.7	14.7	2.1
$k_i \times 10^5$, s^{-1}	2.4	0.4	12.0
$b \times 10^5$, $(M s^{-2})^{1/2}$	18.9	14.7	11.5

* Data of [8].

Table 3. Kinetic parameters of initiated oxidation of DAF (Initiator TBP)

T, °C	[TBP] $\times 10^3$, M	$k_i \times 10^5$, s^{-1}	$v_{O_2} \times 10^5$, $M s^{-1}$	$a \times 10^2$, $(M s^{-1})^{1/2}$	$\nu = v_{O_2}^2 : v_i$
110	0	0.69	0.28	1.45	–
	3.0		0.35		169
	6.0		0.40		96
	12.0		0.50		6
120	0	2.9	1.0	2.10	–
	6.0		1.35		77
	18.0		1.92		37
	21		2.0		33
130	0	6.8	2.08	3.7	–
	1.8		2.28		187
	3.0		2.70		124
	6.0		3.22		79
	31.0		5.50		26

Table 4. Effect of inhibitor (InH) structure on the DAF auto-oxidation hindrance factor n (120°C)

Inhibitor	[InH], wt %	$b \times 10^5$, $(M s^{-2})^{1/2}$	$n = b/b_{InH}$
I	0	11.5	–
	0.018	3.6	3.2
	0.4	2.8	4.1
	0.1	2.2	5.2
II	0.1	3.6	3.2
	1.23	6.9	1.7
III	0.1	3.1	3.7
IV	0.1	2.6	4.4
V	0.1	3.4	3.4
VI	0.1	3.3	3.5
VII	0.1	3.2	3.6
VIII	0.1	4.1	2.8
IX	0.1	4.5	2.6
X	0.1	6.5	1.8
XI	0.1	33.7	0.34
XII	0.1	7.5	1.5
II + XII (3 : 2)	0.1 1.23	10.7 3.6	11 3.2

The dependence of squared rate of initiated DAF oxidation, $v_{O_2}^2$, on the TBP concentration is linear and described by the equation $v_{O_2}^2 = a^2 v_{i,DAF} + a^2 k_i[TBP]$. The chain length, varying within the range 75–200 (Table 3), depends on temperature and initiator concentration. The effect of temperature on the parameter a characterizing the oxidability of DAF is described by the equation $\log a = 6.12 - 58\,200/(19.15T)$. The oxidability of DAF is much lower (Table 2) than that of the compounds DO and DMDO.

However, the high initiating activity of the accumulating hydroperoxides (120°C, $k_i = 4b^2/a^2 = 1.2 \times 10^{-4}$ s^{-1}) is the main reason for the poor oxidation stability of DAF in operation at elevated temperatures.

To suppress the undesirable auto-oxidation and improve the thermal-oxidation stability of DAF, the effect of phenol **I**–**X** and organophosphorus **XI** and **XII** compounds on the rate of O_2 absorption was studied. In the absence of inhibitors, DAFs oxidize at virtually constant rate with slight acceleration in accordance with the expression

$$\Delta[O_2] = b^2 t^2.$$

Introduction into the oxidizing system of ionol **I** makes the rate of O_2 absorption lower, with no induction period observed, which is presumably due to the presence in the mixture of DAFHP accumulated during storage. The kinetic curves of DAF auto-oxidation are linearized in the coordinates $\Delta[O_2]^{1/2}$–t, the auto-oxidation parameter b decreases from 11.5×10^{-5} to 2.2×10^{-5} $(M s^{-2})^{1/2}$ (120°C) with the concentration of **I** increasing from 0.018 to 0.10 wt % (Table 4). The influence exerted by the inhibitors was evaluated on the basis of the auto-oxidation deceleration factor n equal to the ratio of the auto-oxidation rate in the absence of inhibitor to that in its presence ($n = b/b_{InH}$). For example, the process deceleration factor for inhibitor **I** grows with increasing inhibitor concentration to reach the limiting value ($n_\infty = 5.2$) at [InH] $\geq$ 0.1 wt %.

The organophosphorus inhibitor **XII**, taken at concentration of 0.1 wt % (2×10^{-3} M), affects the auto-oxidation of DAF only slightly ($n = 1.5$). Raising the concentration of **XII** to 1.25 wt % (2.5×10^{-2} M; this concentration ensures stability of PVC-based polymer formulation plasticized with DAF) strongly decelerates the auto-oxidation of DAF ($n = 8.8$) and, after absorption of 4×10^{-3} M O_2 in the course of 40 min (120°C) the process virtually terminates. Consequently, the effect of process deceleration under the action of the organophosphorus inhibitor is manifested only in the case of its manyfold excess over the content of

DAFHP accumulated in DAF storage; [DAFHP] = 2×10^{-3} M $[InH]_0 = 2.5 \times 10^{-2}$ M.

Under these conditions, DAFHPs initiating auto-oxidation are presumably transformed into inactive molecular products, with virtually no free radicals formed. Introduction of an organophosphorus inhibitor (0.1 wt %) into the system being oxidized makes the rate of auto-oxidation higher ($n = 3$), presumably because of the catalytic decomposition of DAFHP by the homolytic mechanism.

The inhibitors studied show no synergistic effect. For example, a mixture of two inhibitors, **II + XII**, taken in a 3 : 2 ratio at a total concentration of 0.1 wt %, exhibits antagonism, since the deceleration factor of the mixture of inhibitors ($n = 1.1$) is much lower than that for each of the individual compounds **II** and **XII**. Raising the total concentration of the mixture of inhibitors to 1.25 wt % leads to only a slight increase in the DAF autooxidation deceleration factor ($n = 3.2$).

As already mentioned, use of high inhibitor concentrations ($\geq 10^{-2}$ M) fails to preclude auto-oxidation completely and kinetic curves show no induction period. Therefore, the efficiency of the inhibitors was evaluated on the basis of the parameter $\alpha = k_{InH}/k_d[DAF]$ [4]. According to this expression, the faster the reaction of an inhibitor with peroxy radicals leading the oxidation chain, the greater the α value and the higher the inhibitor's efficiency. If inhibited oxidation proceeds by the chain mechanism and chain termination occurs via reaction between the inhibitor with peroxy radicals, then the oxidation rate is described by the equation [4]

$$v_{O_2} = \frac{k_d[DAF]v_i}{fk_{InH}[InH]} = \alpha^{-1}\frac{v_i}{f[InH]},$$

whence follows that under the conditions of oxidation at $v \leq 30$

$$\alpha = \frac{v_i}{(v_{O_2} - v_i)f[InH]},$$

with $f = 2$ (Table 2).

The above procedure for determining the α value was used to measure the efficiency of the decelerating action of compound **I** and other phenol inhibitors. The obtained data are compared with a similar characteristic for the organophosphorus compound **XII** in Table 5.

It can be seen from the presented data that introduction of inhibitors in the case of DAF auto-oxidation makes the process rate lower, with the chain length decreasing from 54 to 7 units; however the chain mode is preserved even at rather high inhibitor concentrations in the range $(1.2–24.6) \times 10^{-3}$ M. The observed behavior is presumably due to the presence in DAF of DAFHPs effectively stimulating the oxidation. This assumption is confirmed by the low value of the parameter α characterizing the efficiency of inhibitors in DAF oxidation ($\alpha < 10^2$ M^{-1}), much exceeded by those in inhibited oxidation of a mixture of hydrocarbons ($\alpha \geq 10^3$ M^{-1}) [4]. In addition, molecules containing an acetal group form hydrogen bonds with phenol inhibitors, much impairing their activity in the reaction with peroxy radicals, terminating the chains [8].

Table 5. Evaluation of inhibitor efficiency in DAF auto-oxidation (120°C, $v_{i,DAF} = 2.2 \times 10^{-7}$ M s^{-1}, $f = 2$)

Inhibitor	$[InH] \times 10^3$, M	$v_{O_2} \times 10^5$, M s^{-1}	ν	α, M^{-1}
I	0	1.20	54	–
	1.3	0.44	20	19
	2.8	0.35	16	11
II	5.2	0.32	15	7
III	1.3	0.25	11	34
IV	2.6	0.22	10	19
V	3.1	0.33	15	11
VI	2.6	0.26	12	16
VII	1.2	0.32	15	29
VIII	1.4	0.40	18	20
IX	2.0	0.69	31	8
	24.6	0.15	7	3

CONCLUSIONS

(1) A mixture of dioxane alcohol formals intensely absorbs oxygen at elevated temperatures (100–300°C) to form the corresponding hydroperoxides. The parameter characterizing the rate of auto-oxidation of DAFs is close to those for individual 1,3-dioxanes and much exceeds the parameters for hydrocarbons. The high initiating activity of the forming hydroperoxides accounts for the low thermal-oxidation stability of DAFs.

(2) Introduction of phenol inhibitors into the system substantially lowers the rate of auto-oxidation, with the process deceleration factor markedly changed. For organophosphorus inhibitors this parameter is somewhat lower.

REFERENCES

1. Chugunov, Yu.V., Fazylova, M.G., Efremov, Yu.Ya., *et al., Zh. Prikl. Khim.*, 1996, vol. 69, no. 7, pp. 1160–1162.
2. RF Patent 2 100 356.
3. Kuramshin, E.M. and Imashev, U.B., *Okislenie i stabilizatsiya dizel'nykh topliv* (Oxidation and Stabilization of Diesel Fuels), Moscow: TsNIITEneftekhim, 1995.
4. Denisov, E.T. and Kovalev, G.N., *Okislenie i stabilizatsiya reaktivnykh topliv* (Oxidation and Stabilization of Propellant Fuels), Moscow: Khimiya, 1983.
5. Antonovskii, V.L. and Buzlanova, M.M., *Analiticheskaya khimiya organicheskikh soedinenii* (Analytical Chemistry of Organic Compounds), Moscow: Khimiya, 1978.
6. Mukmeneva, N.A., Kadyrova, V.Kh., Bukharov, S.V., and Nugumanova, G.N., *Zh. Obshch. Khim.*, 1996, vol. 66, no. 10, pp. 1725–1727.
7. RF Patent 2 140 938.
8. Rakhmankulov, D.L., Zorin, V.V., Kuramshin, E.M., *et al., Metody issledovaniya reaktsionnoi sposobnosti organicheskikh soedinenii* (Methods for Studying the Reactivity of Organic Compounds), Ufa: Reaktiv, 1999.

Russian Journal of Applied Chemistry, Vol. 74, No. 4, 2001, pp. 631–635. Translated from Zhurnal Prikladnoi Khimii, Vol. 74, No. 4, 2001, pp. 613–617.

ENVIRONMENTAL PROBLEMS OF CHEMISTRY AND TECHNOLOGY

Electrokinetic Removal of Hydrophobic Organic Compounds from Soil

A. Yu. Kolosov, K. I. Popov, N. A. Shabanova, A. A. Artem'eva, B. M. Kogut, A. S. Frid, V. Yu. Zel'venskii, and E. M. Urinovich

Mendeleev University of Chemical Engineering, Moscow, Russia

Moscow State University of Food Industries, Moscow, Russia

Dokuchaev Soil Institute, Moscow, Russia

IREA Federal State Unitary Enterprice, Moscow, Russia

Received March 14, 2000, in final form, January 2001

Abstract—Electrokinetic technique for soil decontamination to remove hydrophobic organic compounds, based on application of direct electric field to soil sample preliminarily treated with solutions of chelating agent and a nonionic surfactant, was developed. The influence of various factors on electroosmotic flow in soddy podzolic soil sample was studied.

Decontamination of soils to remove organic contaminants is an urgent problem [1, 2]. This problem can be solved with the use of various techniques, including thermal [3] or biological [4] treatment of soil, pumping of solutions containing agents capable of extracting the toxic contaminants throngh soil [5, 6], and application of electric field [7, 8]. However, these techniques are suitable for decontamination of specific objects only. For example, treatment with heated gas is efficient in removal of organic impurities from sandy soil but is unsuitable for decontamination of clay. Furthermore, such techniques are mainly suitable for removal of highly volatile organic compounds [3].

In this work, we studied decontamination of heavy soil containing large amount of clay to remove hydrophobic organic compounds (HOCs). Decontamination of such soils is one of the most difficult remediation problems. The main aim of our experiments was to study on model systems the possibility of increasing the efficiency of electrokinetic decontamination of soil to remove neutral toxic organic compounds with the use of chemical reagents.

The electrokinetic technique for decontamination of soil is based on removal of impurities by electroosmosis, electromigration, electrophoresis, and diffusion. The most efficient among these processes is electroosmosis. The efficiency of impurity removal by this mechanism is mainly controlled by the electrokinetic potential (ζ-potential) [9]. It is known that the surface of soil particles is charged negatively [10] and characterized by relatively low ζ-potential [11, 12]. The ζ-potential can be increased by treatment of soil with aqueous solutions of chelating agents, such as 1-hydroxyethylidenediphosphonic (HEDP), ethylenediaminetetraacetic (EDTA), and citric acids. Introduction of these compounds, especially HEDP, into a soil sample in amount of 1×10^{-2} M leads to an approximately 10-fold increase in the ζ-potential [11–13].

The ζ-potential is also influenced by the pH of solutions of chelating compounds added to soil. It was found that for HEDP and EDTA solutions the maximum ζ-potential is attained at pH 6–8 [13, 14].

To remove HOCs from soil it is necessary not only to increase the electroosmotic flow but also to ensure HOC solubilization in the pore solution. For this purpose, a contaminated soil sample should be simultaneously treated with chelating agent and nonionic surfactant. It should also be taken into account that introduction of nonionic surfactant in the soil can affect the rate of the electroosmotic flow. Therefore, we studied in this work the dependence of soil decontamination on the nature of a nonionic surfactant.

In our experiments, we used nonionic surfactants, since these compounds are to a considerably lesser ex-

1070-4272/01/7404-0631 $25.00 © 2001 MAIK "Nauka/Interperiodica"

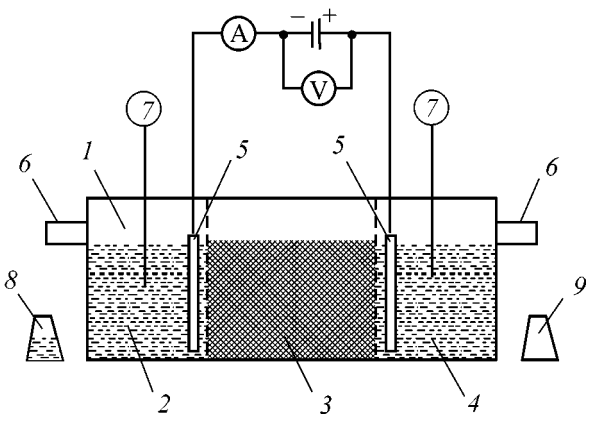

Fig. 1. Scheme of the experimental unit: (*1*) electroosmotic cell, (*2*) cathode compartment, (*3*) chamber for soil sample, (4) anode compartment, (5) drain pipes, (6) electrodes, (7) glass electrode , (8) receiving flask for cathodic solution, and (9) receiving flask for anodic solution

tent sorbed on the soil surface as compared with cationic surfactants. Furthermore, in contrast to anionic surfactants, the use of nonionic surfactants is not accompanied by electromigration of micelles in the direction opposite that of the electroosmotic flow, deteriorating electroosmotic transfer of the impurities.

EXPERIMENTAL

Our experiments were performed with a sample of clayey loam soddy-podzolic soil taken from the top soil horizon (0–15 cm) at the divide territory of an experimental field located at the Dokuchaev base station (Zelenograd). The main characteristics of this soil sample were as follows:

Characteristic	Value
pH (salt extract)	5
Hydrolytic acidity, mg-equiv kg^{-1}	17
Exchangeable calcium, mg-equiv kg^{-1}	160
Exchangeable magnesium, mg-equiv kg^{-1}	70
Free iron (by Jackson), %	0.17
Mobile iron (by Tamm), %	0.05
Total organic carbon, %	1.2

The initial soil sample was air-dried, broken down, and sifted through a sieve with 3-mm mesh.

Figure 1 shows schematically the experimental unit. The unit consists of an electroosmotic cell, a dc power supply, and devices for measuring the pH, current strength, and voltage. The electroosmotic cell is divided by perforated membranes into three compartments: cathode, anode, and that for a soil sample. The total surface area of perforations in each membrane is 10 cm^2. The perforated membranes are covered with filter paper. The cross section of the unit is 5.1×5.3 cm^2. The lengths of the soil compartment and electrode compartments are 8.3 and 5.5 cm, respectively. The platinum electrodes are installed at the minimal spacing from the membranes. A constant level of solution in the compartments is ensured by overflow of the excess solution into the receiving flasks through the drain pipes.

In our experiments, we used readily water-soluble nonionic surfactants Triton X-100 (9-10-oxyethylated isooctylphenol $R–C_6H_4–O(C_2H_4O)_mH$, where R is the isooctyl radical, (m = 9, 10), OS-20 [monoalkyl ethers of polyethylene glycol prepared from primary aliphatic alcohols $C_nH_{2n+1}O(C_2H_4O)_{20}H$, n = 14–18], and ALM-10 [monoalkyl ethers of polyethylene glycol prepared from primary aliphatic alcohols $C_nH_{2n+1}O(C_2H_4O)_{10}H$, n = 12–14]. The critical micelle concentration (CMC) of the nonionic surfactants tested were as follows (M): Triton X-100 9×10^{-4} M, OS-20 2×10^{-4}, and ALM-10 1.6×10^{-4} [15, 16].

The effect of nonionic surfactants Triton X-100 and OS-20 on the electroosmotic flow through a soil sample was studied by the following technique. The air-dried soil sample was moistened with aqueous solutions containing chelating agent and nonionic surfactant to moisture-saturated state. The moisture-saturated capacity of the soil sample used in our experiments was 0.47 ml H_2O per 1 g air-dried soil. The pH of the chelating agent (HEDP) solution was adjusted to 6–8 by adding 40% NaOH. The concentration of the chelating agent was 1×10^{-2} M; the surfactant concentration was varied from 0 to 10-fold CMC and higher. The moistened soil sample was allowed to stand in a dessicator for 1 day to attain equilibrium. After equilibration the soil sample was placed in the strictly horizontal soil compartment of the experimental unit. The aqueous solution containing the surfactant and chelating agent in amounts equal to those in the pore solutions (pH 6–8) was poured into the anode compartment. The presence of the surfactant in the anode solution ensures its constant concentration in the soil sample throughout the experiment. The cathode compartment was filled with 1×10^{-2} M HEDP solution with pH equal to that in the anode compartment. The solution volume in both the anode and cathode compartments was 150 cm^3. Under these conditions, the surface of the liquid phase in the electrode compartments coincides with level of the overflow pipes. The weight of the moist soil sample was 445 g (330 g of air-dried soil). The level of the soil surface in the soil compartment exceeds the level of the solution surface in the side compartments by 3–4 mm. The higher level of the soil surface prevents overflow of the anode and cathode solutions above the soil

sample. The cathode solution volume drained into the receiving flask was intermittently balanced by pouring an equal amount of the fresh solution into the anode compartment.

In the course of electroosmosis, the pH in both the anode and cathode compartments was adjusted to 6–8 by adding concentrated sulfuric acid and 40% NaOH. We used the concentrated reagent solutions to eliminate the inaccuracy in determining the rate of the electroosmotic flow V_{eo} due to dilution.

The field strength E between the electrodes was 2 V cm^{-1}. The experiments were carried out at room temperature. Table 1 shows our results concerning the influence of the surfactant concentaration on V_{eo} in the presence of 1×10^{-2} M HEDP.

The electrokinetic treatment was used by us for decontamination of the soil sample to remove both moderately volatile [chlorobenzene (CB)] and highly volatile [trichloroethylene (TCE)] organic compounds. The rate of TCE evaporation exceeds that of CB by more than a factor of 3.5 [17].

In decontamination of the soil sample to remove chlorobenzene, ALM-10 and HEDP were used as nonionic surfactant and chelating agent, respectively. In removal of tricloroethylene, Triton X-100 was used instead of ALM-10 as the nonionic surfactant, all other factors being the same.

The experiments on decontamination of the soil sample to remove HOC were carried out as follows. A certain amount of HOC was added to an air-dried soil sample; the sample was thoroughly mixed and allowed to stand for 1 day for equilibration. Thereafter, the soil sample was treated with an aqueous solution containing nonionic surfactant and chelating agent and kept for 1 day. After electrokinetic treatment, the content of CB and TCE was determined in the electrode and soil compartments. Chlorobenzene and trichloroethylene were recovered from the anode and cathode solutions and soil sample by treatment with hexane at the following ratios of the organic and aqueous phases: anode solution 3 : 1, cathode solution 3 : 1, and soil pore solution 2 : 1. The chlorobenzene content was determined spectrophotometrically on an M 40 UV-VIS spectrophotometer, TEC was determined by gas chromatography on an HP-5890 gas chromatograph with an MSD-5972 mass-selective detector.

Our data on electroosmotic removal of CB from a sample of soddy-podzolic soil preliminarily contaminated with this organic compound are given in Table 2 and Fig. 2.

Table 1. Effect of surfactant concentration on the electroosmotic flow rate V_{eo}

Reagent, M	Surfactant concentration, M	V_{eo}, ml h^{-1}
1×10^{-2} KCl	0	2.0 ± 0.6
1×10^{-2} HEDP	0	6.0 ± 6.0
1×10^{-2} HEDP + OS-20	2×10^{-3}	5.5 ± 0.6
1×10^{-2} HEDP + Triton X-100	9×10^{-3}	5.3 ± 0.6
	2.7×10^{-2}	4.8 ± 0.6

We found that introduction of various surfactants into the soil sample decreases the electroosmotic flow rate. As seen from Table 1, at the same ratios of the surfactant content in the pore solution to CMC, introduction of Triton X-100 decreases V_{eo} to a larger extent than that of OS-20. These results show also that, with the Triton X-100 concentration in the pore solution increasing from 0 to 2.7×10^{-2} M, V_{eo} decreases by approximately 20%. However, although the nonionic surfactant makes lower the electroosmotic flow rate, the acceleration of osmosis under the action of the chelating agent remains significant even at surfactant concentrations substantially exceeding CMC. For comparison it should be noted that for a soil sample treated with 1×10^{-2} M KCl V_{eo} is equal to 2.0 ± 0.6 ml h^{-1}.

In order to intensify the transfer of organic toxic impurities into the pore solution, the nonionic surfactant should be introduced in amounts much exceeding the CMC. Under these conditions, the colloid dissolution of HOCs may occur via both solubilization and formation of microemulsions [18].

We found that, in electrokinetic treatment of the soil sample contaminated with HOCs, the toxic contami-

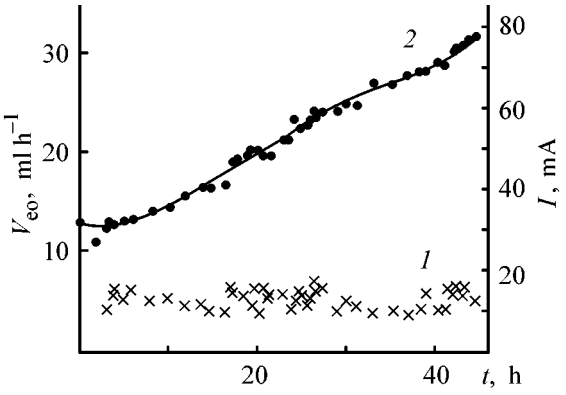

Fig. 2. Variation with time t of (*1*) electroosmotic flow rate V_{eo} and (*2*) current in the course of the electroosmotic treatment of a sample of soddy-podzolic soil contaminated with chlorobenzene.

Table 2. Results of electrokinetic treatment of soddy-podzolic soil sample contaminated with chlorobenzene.* Reagent HEDP + ALM-10, treatment time 45 h, initial chlorobenzene amount in the soil sample 46 g

E, V cm^{-1}	V_{eo}^{av}, ml h^{-1}	N	Chlorobenzene amount (g) and concentration (%) after electrokinetic experiment				Degree of soil decontamination from chlorobenzene
			in cathodic solution	in soil sample	in anodic solution	total	
0	0	0	0.05 (12.5)	0.26 (75)	0.05 (12.5)	0.36 (100)	28
2	5.1	1.6	0.17** (47**)	0.14 (39)	0.05 (14)	0.36 (100)	61

* E field strength; (V_{eo}^{av}) average electroosmotic flow rate; (N) number of volumes of the pore solution transferred from soil sample by osmotic flow during the electrokinetic experiment.

** Chlorobenzene amount (g) and concentration (%) in both cathodic solution and corresponding receiving flask.

nants are transferred not only to the cathode but also to the anode compartment.

This fact shows that, along with the transfer of an HOC with electroosmotic flow into the cathode compartment, HOC also passes into the anode compartment by diffusion. However, it is the electroosmotic flow that contributes to the greatest extent to the total transfer of the contaminants. As seen from Table 2, chlorobenzene is equally distributed between the cathode and anode compartments in the absence of electric current. At the same time, in the presence of the electroosmotic flow, the contaminant concentration in the cathode compartment exceeds that in the anode compartment by a factor of 3.4. For example, at $E = 2$ V cm^{-1} the amount of the contaminant removed mainly by the electroosmotic flow increases by a factor of 2.2 as compared with that via diffusion (at $E = 0$).

Figure 2 shows the time dependence of both the electroosmotic flow rate and the current in electrokinetic treatment of a soil sample contaminated with chlorobenzene. The gradual increase in the current in the course of an electroosmosis under constant voltage is indicative of increase in the conductivity of solutions. With pH maintained at 6–8, we observed an increase in the current in all the experiments on electrokinetic treatment of soddy-podzolic soil. In our opinion, the increase in the current is caused by intermittent neutralization of the cathode and anode solutions in the course of electrokinetic treatment.

In the experiments on soil decontamination to remove TCE and CB, we found that, with increasing surfactant concentration in pore solution, the rate of removal of these contaminants grows. For example, with the Triton X-100 concentration increasing from 9×10^{-3} to 2.7×10^{-2} M, the average rate of contaminant removal increases by approximately a factor of 3.

Our experiments showed (Table 2) that, after an uninterrupted 45-h electrokinetic treatment of soil sample contaminated with chlorobenzene, 61% of this contaminant was removed. In this experiment, the initial chlorobenzene content in the soil sample was 0.12 wt %, and the ALM-10 concentration in pore solution, 2.8×10^{-3} M. The soil sample contaminated with TCE was electrokinetically treated for 34 h in the presence of 9×10^{-3} M Triton X-100 in the pore solution. Such treatment lowered the contaminant content from 0.1 to 0.015 wt %, i.e., 85% of the contaminant was removed. Comparison of our experimental results on TCE removal from soil sample with those reported in [7] shows that the use of a mixed reagent containing chelating agent and neutral surfactant increases the efficiency of electroknetic decontamination of soil to remove this toxic impurity.

Our experiment showed also that TCE is removed from soil faster than CB. We believe that this difference is caused by hindrance to CB solubilization in pore solution.

CONCLUSIONS

(1) Introduction of nonionic surfactants into a soil sample in amounts significantly exceeding the critical micelle concentration in pore solution decreases the electroosmotic flow rate in electrokinetic decontamination of soil to remove organic toxic impurities. However, the overall increase in the volume rate of the electroosmotic flow under the action of HEDP present in solution as the chelating agent remains significant.

(2) Treatment of a soil sample with mixed reagent containing chelating agent and surfactant in the electrokinetic technique for removal of toxic hydrphobic organic compounds substantially raises its efficiency,

as shown by experiments on removal of chlorobenzene and trichloroethylene from soddy podzolic soil.

REFERENCES

1. Stolker, G.N., Extended Abstracts, *I@EC Spec. Symp. Am. Chem. Soc.*, Atlanta, 1994, p. 484.
2. *Rossiya: ekologiya i armiya. Geoekologicheskie problemy voenno-promyshlennogo kompleksa i voenno-oboronoi deyatel'nosti* (Russia: Geoenvironmental Problems of Military-Industrial Complex and Military-Defense Activity), Bulatov, V.I., Ed., Novosibirsk: TsERIS, 1999.
3. Heron, G., Zutphen Van, M., Christiansen, T.H., and Enfield, C.G., *Environ. Sci. Technol.*, 1998, vol. 32, no. 10, p. 1474.
4. Wilson, J.T. and Wilson, B.N., *Appl. Environ. Microbiol.*, 1985, vol. 49, p. 242.
5. Smith, J.A., Sahoo, D., McLellan, H.M., and Imbrigiotta, T.E., *Environ. Sci. Technol.*, 1997, vol. 31, no. 11, p. 3565.
6. Sahoo, D., Smith, J.A, Imbrigiotta, T.E., and McLellan, H.M., *Environ. Sci. Technol.*, 1998, vol. 32, no. 12, p. 1686.
7. Ho Sa, V., Athmer, C., Sheridan, P.W., *et al.*, *Environ. Sci. Technol.*, 1999, vol. 33, no. 7, pp. 1086–1092.
8. Acar, Y.B., Li, H., and Gale, R., *J. Geotechn. Eng.*, 1992, vol. 118, no. 11, p. 1837.
9. Tikhomolova, K.P., *Elektroosmos* (Electroosmosis), Leningrad: Khimiya, 1989.
10. Ponizovskii, A.A., Pinskii, D.L., and Vorob'eva, L.A., *Khimicheskie protsessy i ravnovesiya v pochvakh* (Chemical Processes and Equilibria in Soils), Moscow: Mosc. Gos. Univ, 1986.
11. Popov, K.I., Shabanova, N.A., Artem'eva, A.A., *et al.*, *Kolloidn. Zh.*, 1997, vol. 59, no. 2, pp. 233–235.
12. Popov, K.I., Kruglov, S.V., Tarasova, N.P., and Komarova, N.I., *Ross. Khim. Zh.*, 1996, vol. 40, nos. 4–5, pp. 179–189.
13. Popov, K., Yachmenev, V., Kolosov, A., and Shabanova, N., *Colloids Sur. A: Physicochem. Eng. Aspects*, 1999, vol. 160, no. 2, p. 135.
14. Kolosov, A.Yu., Popov, K.I., and Shabanova, N.A., Abstracts of Papers, *Mezhdunarodnaya konferentsiya po kolloidnoi khimii i fiziko-khimicheskoi mekhanike* (Int. Conf. on Colloid Chemistry and Physicochemical Mechanics), Moscow: Mosk. Gos. Univ., 1998, p. 85.
15. *Poverkhnostno-aktivnye veshchestva: Spravochnik* (Surfactants: Handbook), Abramzon, A.A. and Gaevoi, G.M., Eds., Moscow: Khimiya, 1976.
16. Schonfeldt, N., *Oberflachenaktive Anlagerungs-produkte des Athylenoxydes. Ihre Herstellung, Eigenschaften und Anwendung*, Stuttgart: Wissenschaftliche Verl.-Ges., 1959.
17. *Spravochnik khimika* (Chemist's Handbook), Nikol'skii, B.P., Ed., vol. 6: *Syr'e i produkty promyshlennosti organischeskikh veshchestv* (Raw Materials and Products of Industrial Organic Synthesis), Leningrad: Khimiya, 1967.
18. *Micellization, Solubilization, and Microemulsions*, vols. 1, 2, Mittal, K.L., Ed., New York: Plenum, 1976.

Russian Journal of Applied Chemistry, Vol. 74, No. 4, 2001, pp. 636–639. Translated from Zhurnal Prikladnoi Khimii, Vol. 74, No. 4, 2001, pp. 617–620.

ENVIRONMENTAL PROBLEMS OF CHEMISTRY AND TECHNOLOGY

Monitoring of the Sources of Environmental Pollution with Crude Oil

O. Yu. Begak and A. M. Syroezhko

St. Petersburg State Technological Institute, St. Petersburg, Russia;
Mendeleev All-Russian Research Institute of Metrology, St. Petersburg, Russia

Received December 28, 2000

Abstract—The possibility of preliminary identification of sources of environmental pollution with crude oil was studied by IR Fourier spectroscopy, gamma-ray spectrometry, chromatography–mass spectrometry, and capillary gas-liquid chromatography with oil samples from six fields of the Khanty-Mansi Autonomous District and samples of soil and ground water contaminated with these oils.

Conclusive identification of sources of pollution with oil is the most important environmental problem. At present nearly 160–170 Mt of crude oil is recovered annually in the Khanty-Mansi Autonomous District, which is more than half of the oil production in Russia. At such a scale of oil recovery, environmental pollution due to various accidents on the pipelines is inevitable. However, determining the culprit is rather difficult because of the absence of reliable procedures for identifying the origin of a crude oil. Such a problem is dealt with for the first time for a single geographical region with a large number of oil wells located in rather close proximity.

In this work, we attempted to determine the differences in the composition of six oil samples recovered from various fields of Khanty-Mansi Autonomous District and two samples of contaminated soil and water. It should be noted that, when brought in contact with soil and water, oil undergoes various transformations depending on the temperature gradient, humidity, solar activity, wind rose, etc. (typical of a given geographical region [1]) and proceeding at different rates for different petroleum hydrocarbons. In 1994, the Ministry for Environmental Protection and Natural Resources of the Russian Federation issued an instruction on how sources of water pollution with crude oil are to be identified, based on successive use of IR spectroscopy and gas-liquid chromatography [2]. In addition, in 1993, the Federal Department of Hydrometeorology and Environmental Monitoring brought into use "The System of Identification of Oil Spillages in Sea" [3], based on spectrophotometry and high-pressure liquid and capillary chromatography. The above documents were taken into account in this study.

EXPERIMENTAL

Crude oil samples from six fields (Alekhinskoe, Lyantorskoe, Prirazlomnoe, Priobskoe, Krasnoleninskoe, and Trekhozernoe) and samples of soil (Alekhinskoe field) and water (Petelinskoe filed) contaminated with oil were taken in November 1997 (Table 1).

Table 1. Crude oil samples studied

Sample no.	Field
1	Alekhinskoe, Nizhnesortyskneft' Oil and Gas Producing Department
2	Lyantorskoe, Lyantorneft' Oil and Gas Producing Department
3	Alekhinskoe, soil sample taken from contaminated territory
4	Krasnoleninskoe, Kondpetroleum Joint-Stock Company
5	Trekhozernoe, Lukoil-Uralneftegaz Fuel Processing Plant
6	Prirazlomnoe, Yuganskneftegaz Joint-Stock Company
7	Priobskoe, Yuganskneftegaz Fuel Processing Plant
8 (flooded)	Petlinskoe, Yuganskneftegaz Fuel Processing Plant

1070-4272/01/7404-0636 $25.00 © 2001 MAIK "Nauka/Interperiodica"

The samples were studied using IR spectrometry, capillary gas-liquid chromatography (GLC), chromatography–mass spectrometry, and gamma-ray spectrometry.

The IR spectra were recorded on computerized IR Fourier spectrometer (FSL-05 software, SpbInstruments, St. Petersburg) in automated mode in the 650–800 cm^{-1} region (resolving power 1 cm^{-1}) in 80-μm thick cells with KBr windows [4].

The capillary GLC of the oil samples was performed on a Tsvet-500 chromatograph equipped with a flame-ionization detector and a quartz capillary column (0.32 mm in diameter and 50 m long) with OV-101 stationary phase.

The chromatography–mass spectrometry of crude oil, soil, and water samples was carried out on an MD 800 unit with a capillary column and a system for computer processing of the results.

The gamma-ray spectra were registered on a gaged gamma-ray spectrometer with a DGDK-80V-3 Ge(Li) semiconductor detector, equipped with an ES 1840 PC for automated recording and processing of the results. Samples of oil, soil, and flooded oil (300 ml volume) were placed in a special cell on the semiconductor detector. Owing to the low specific activity of the samples, the gamma-ray spectra of the samples were accumulated for 8 h.

The IR spectra of crude oil samples recorded on an IR Fourier spectrometer are presented in Fig. 1. We compared the spectra in the 600–1800 cm^{-1} range by means of computer subtraction of one spectrum from another, with the maximum error in recording the optical absorption of no more than 0.5%. Curve 1 corresponds to the absorption spectrum of sample no. 1. The other curves were obtained by subtraction of the spectra of the other samples from the spectrum of sample no. 1. As seen, the resulting spectra exhibit significant differences in the "fingerprint" area, except the spectrum of sample no. 6 (Table 1) for which the difference in the intensities of most of the bands is smaller than 10%. Nevertheless, the absorption spectra of the samples in question exhibit significant differences in the 650–800 cm^{-1} range in Fourier absorption (Fig. 2). Thus, the Fourier spectrometry allows reliable identification and distinguishing of various sorts of crude oil as environmental contaminants, including oil in soil and water. It was found that a short-term UV irradiation with simultaneous bubbling of oxygen through the samples (artificial aging) did not give rise to any new bands and did not cause significant transformation of the existing bands (Fig. 3).

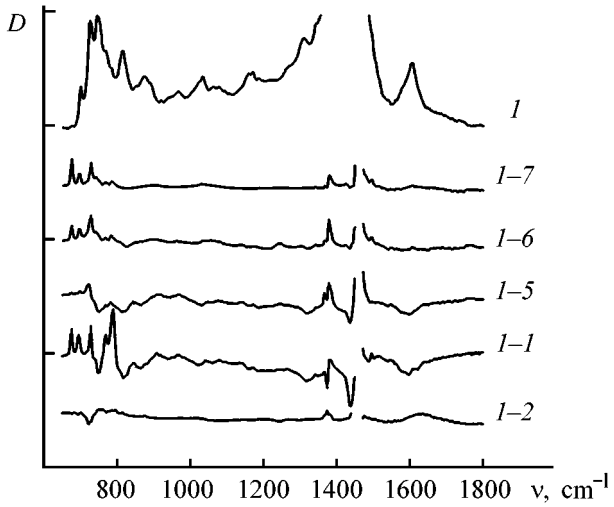

Fig. 1. Spectra of crude oil samples. (*D*) Optical density and (ν) wave number; the same for Figs. 2 and 3. (*1*) Sample no. 1; (*1–1*, *1–2*, *1–5*, *1–6*, *1–7*) the differences of the spectra of sample no. 1 and sample nos. 2, 4, 5, 6, and 7, respectively. Runouts at 1450 cm^{-1} are due to the low transmission of the sample. The distance between the marks on the vertical axis corresponds to a change in *D* by 1; the same for Figs. 2 and 3.

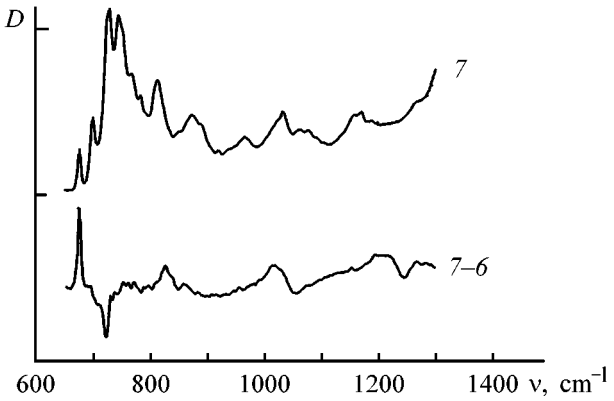

Fig. 2. Comparison of the spectra of sample nos. 6 and 7. (*7*) Sample no. 7; (*7–6*) the differences of the spectra of sample nos. 7 and 6 (Magnification ×5).

The chromatographic data showed that the oil samples from the Lyantorskoe and Petelinskoe fields differ significantly from the other samples, whereas the composition of the other oil samples is nearly the same. We found that the quantitative and qualitative reproduction of chromatograms (peak intensity and retention time) recorded on a Tsvet-500 chromatograph are insufficient for reliable identification of oil samples.

Investigation of the oil samples by chromatography-mass spectrometry before and after aging (heating to 90°C, UV irradiation with a 1000-W lamp) showed

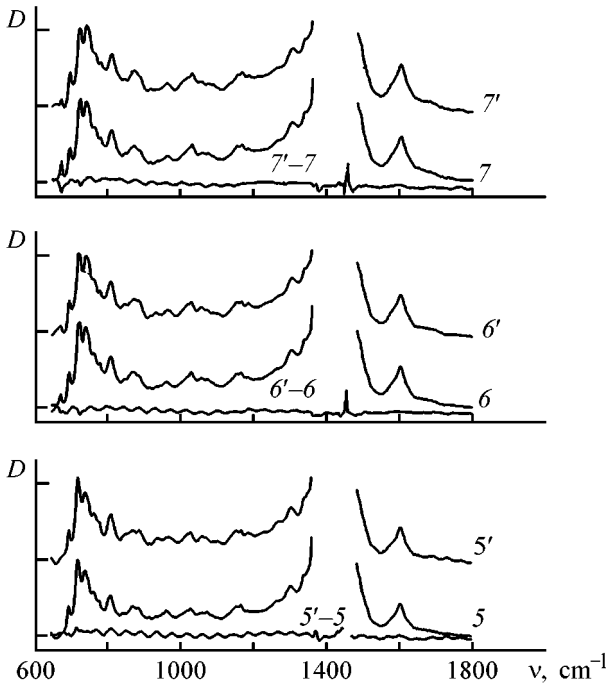

Fig. 3. Comparison of the spectra of sample nos. 5–7. Spectra registered (*5–7*) before and (*5*′*–7*′) after aging; (*5–5*′, *6–6*′, *7–7*′) the difference of the spectra of the corresponding crude oil samples.

that the ratio of ^{12}C and ^{13}C isotopes is nearly constant in all of the oil samples studied. Their hydrocarbon compositions are also similar, with slight difference observed only in the content of isopropenoid alkanes (pristane, phytane, and norpristane). However, these differences are not so significant as to ensure reliable identification of the initial oil samples.

Since the crude oil in each field occurs in rock materials differing in chemical composition and content of natural nuclides (NRNs) [5], the content of NRN in the oil samples taken from different fields must also be different (Table 2). All the samples contain nuclides of the thorium and uranium series, and the soil sample, also potassium-40. The samples differ in qualitative radionuclide composition, except sample nos. 5 and 7 exhibiting nearly twofold difference in the content of bismuth-214. As seen from Table 2, gamma-ray spectrometry only allows identification of the potential source of oil pollution using seven nuclides: four members of the thorium series (thallium-208, bismuth-212, lead-212, and actinium-228), two members of the uranium series (bismuth-214, lead-214), and potassium-40 (for soil samples).

Thus, each crude oil sample taken from a different field is characterized by individual nuclide composition. It should be noted that the total content of radioactive nuclides in the samples of the Khanty-Mansi oil district is relatively low. The highest content of radionuclides was determined for sample no. 3 (soil sample taken from a spillage territory at the Alekhinskoe field), whose specific activity of 23.8 ± 4.2 Bq kg^{-1} is more than an order of magnitude smaller than the maximal permissible level (370 Bq kg^{-1} according to nuclear safety regulations NBR-96). In the other oil samples, the specific activity is even lower and nuclides of the thorium and uranium series were only recorded owing to the high sensitivity of gamma-ray spectrometry (special computer program was used in processing the obtained gamma-ray spectra). Further study of oils by the given method requires wider statistics. It should be noted that this procedure, combined with the other methods, may be promising for oil identification in the case of two and more sources of oil pollution.

Table 2. Data of gamma-ray spectrometric analysis of oil samples

Sample no. (according to Table 1)	Specific activity A_s, Bq kg^{-1}					
	uranium series		thorium series			
	^{214}Bi	^{214}Pb	^{208}Tl	^{219}Bi	^{212}Pb	^{228}Ac
1	–	–	–	–	–	5.3 ± 7.5
2	–	4.8 ± 4.7	–	–	–	8.9 ± 6.0
3*	3.2 ± 2.6	6.0 ± 4.3	3.7 ± 2.0	–	5.3 ± 3.9	13.3 ± 6.0
4	–	–	–	–	–	–
5	11.3 ± 11.3	12.1 ± 7.9	–	–	–	–
6	11.5 ± 12.5	–	2.7 ± 2.1	–	–	–
7	24.8 ± 10.6	11.8 ± 6.1	–	–	–	–
8	10.9 ± 15.7	15.1 ± 10.1	–	–	–	5.5 ± 4.7

* Potassium-40 was found only in sample no. 3 (soil), its specific activity was 157.5 Bq kg^{-1}.

CONCLUSIONS

(1) A study of six samples from different oil fields of Khanty-Mansi Autonomous District demonstrated that it is advisable to perform preliminary search for the source of oil pollution of soil and water by means of IR Fourier spectroscopy and gamma-ray spectrometry.

(2) Chromatography–mass spectrometry and capillary chromatography are of little use in solving this environmental problem.

REFERENCES

1. Izmailov, V.V. *Transformatsiya neftyanykh plenok v sisteme okean–led–atmosfera* (Transformation of the Oil Films in the Ocean–Ice–Atmosphere System), Leningrad: Gidrometeoizdat, 1988.
2. *Instruktsiya po identifikatsii istochnika zagryazneniya vodnogo ob"ekta neft'yu* (Instruction concerning Identification of the Source of Contamination of a Water Object with Crude Oil), Moscow: Ministerstvo Ekolog. Okhran. Okruzh. Sredy, 1994.
3. *RD 52.10.243-92, Rukovodstvo po khimicheskomu analizu morskikh vod* (Instruction concerning Chemical Analysis of Seawaters), St. Petersburg, 1993.
4. *Fur'e-spektrometr laboratornyi FSL-05. Tekhnicheskoe opisanie. Instruktsiya po ekspluatatsii* (FSL-05 Laboratory Fourier Spectrometer. Technical Specification. Operation Guide), SpbInstruments, 1988.
5. *Khimiya urana: Sbornik nauchnykh trudov* (Chemistry of Uranium: Collection of Scientific Papers), Laskorin, B.N. and Myasoedov, B.F., Eds., Moscow: Nauka, 1989.

Russian Journal of Applied Chemistry, Vol. 74, No. 4, 2001, pp. 640–643. Translated from Zhurnal Prikladnoi Khimii, Vol. 74, No. 4, 2001, pp. 621–624.

PROCESSES AND EQUIPMENT OF CHEMICAL INDUSTRY

Dispersion and Coalescence in Fluid-Gas Jet Apparatus with Elongated Mixing Chamber

A. N. Blaznov, V. A. Kunichan, and D. V. Chashchilov

Biisk Technological Institute of Polzunov Altai State Technical University, Biisk, Russia

Received October 16, 2000

Abstract—The problem of application of fluid-gas jet apparatus with elongated cylindrical mixing chamber as mixers is considered. Results obtained in studying the dispersion and coalescence of bubbles of the gas phase are presented. The obtained experimental data are processed in terms of Kolmogorov's theory of isotropic turbulence.

Fluid-gas jet apparatus can be effectively used as absorbers. Their application in chemical, food, and pharmaceutical industries to remove noxious impurities from gases to be discharged into the atmosphere has been described [1–3]. Fluid-gas jet apparatus with elongated (no less than 30–35 diameters long) cylindrical mixing chamber show promise as absorbers of this kind. Such apparatus are characterized by simple design of the mixing chamber (without confuser or diffuser) and make it possible to achieve high injection coefficients [3]. There exists a procedure for calculating these apparatus as water-jet vacuum pumps [3, 4]. However, the available published data are insufficient for calculating the absorption characteristics of jet apparatus with elongated mixing chamber.

It is known that the intensity of absorption is determined by the interface area and mass-transfer coefficient. In [1, 2], studies were reported concerned with jet-injection shell-and-tube absorbers similar in design to fluid-gas jet apparatus with elongated cylindrical mixing chamber. The presented equations enable calculation of averaged values of the interface surface area at uncontrolled gas content. With fluid-gas jet apparatus allowing control over the injection coefficient and, consequently, over the gas content, evaluation of their mass-exchange characteristics requires such calculation techniques which take into account, together with other factors, the dependence of the interface surface area on the gas content and residence time of the gas-fluid emulsion in the mixing chamber of the absorber.

A schematic of an absorber based on a jet apparatus with elongated mixing chamber is presented in Fig. 1. The working fluid is delivered at high velocity into the mixing chamber and is mixed there with the gas being injected, to form a gas-fluid emulsion. Two zones can be conventionally distinguished in the mixing chamber, differing in the flow motion modes [3, 5]. The first zone is that of unsteady flow, in which the jet of the working fluid expands, is mixed with the gas phase, and fills the entire cross-section of the mixing chamber at some distance L from the nozzle exit. This zone is characterized by enhanced turbulence. At a distance L from the nozzle exit the

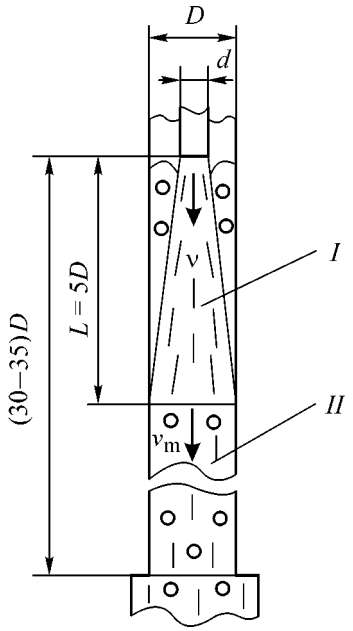

Fig. 1. Schematic of jet absorber. Flow zone: (*I*) unsteady and (*II*) steady.

1070-4272/01/7404-0640 $25.00 © 2001 MAIK "Nauka/Interperiodica"

intensity of agitation decreases and the gas-fluid flow passes into the steady-flow zone in which a homogeneous gas-fluid emulsion moves. Mainly dispersion of gas bubbles in the turbulent flow is observed in zone *I*, and coalescence of these bubbles, in zone *II*.

The process of dispersion in a turbulent flow can be described using Kolmogorov's theory of isotropic turbulence [6]. In this case, the expression for determining the average volume-surface diameter of gas bubbles, $d^0_{32_{\varphi\to 0}}$, at very low content of the dispersed phase ($\varphi \to 0$) has the form

$$d^0_{32_{\varphi\to 0}} = K(\sigma^{3/5}/\rho^{1/5}\varepsilon^{2/5}), \quad (1)$$

where K is a constant, σ the surface tension (N m^{-1}), and ρ the density of the continuous phase (kg m^{-3}).

The parameter ε in (1), named the energy dissipation rate, is calculated as

$$\varepsilon = N/V, \quad (2)$$

where N is the amount of energy dissipated in the turbulent flow per unit time (W), and V is the volume within which this occurs (m^3).

Applying this approach to a jet absorber, we define the energy loss by fluid jet per unit time in the unsteady-flow zone (Fig. 1) as

$$N = Gv^2/2 - Gv_m^2/2, \quad (3)$$

where G is the mass flow rate of the working fluid (kg s^{-1}), v the velocity of the fluid jet at the nozzle exit (m s^{-1}), and v_m the fluid velocity in the mixing chamber (m s^{-1}).

The condition for fluid flow continuity in the nozzle and the chamber gives

$$N = \frac{\rho v^3}{2}\frac{\pi d^2}{4}\left(1 - \frac{d^4}{D^4}\right), \quad (4)$$

where d and D are the diameters (m) of, respectively, the nozzle and the mixing chamber.

The volume of the unsteady-flow zone is approximately equal to the volume of a cylinder of diameter D and length L:

$$V = (\pi D^2/4)L. \quad (5)$$

The length of the mixing chamber can be expressed in terms of the mixing chamber diameter as $L = mD$. The coefficient m varies within the range from 4.5 to 6 [7–9].

Thus, the rate of energy dissipation can be finally found from the expression

$$\varepsilon = \frac{\rho v^3 d^2}{2mD^3}\left(1 - \frac{d^4}{D^4}\right). \quad (6)$$

It is noteworthy that at d/D ratios smaller than 0.5 the numerical value of the expression in parentheses in (6) is close to unity. In this case, expression (6) can be simplified:

$$\varepsilon = \rho v^3 d^2/2mD^3. \quad (7)$$

The effect of gas content φ on the bubble diameter can be taken into account by means of a linear function, $f(\varphi) = 1 + k\varphi$, where k is a proportionality factor [10].

Then, the final expression for determining the diameter of bubbles formed in the unsteady-flow zone takes the form

$$d^0_{32} = K\frac{\sigma^{3/5}}{\rho^{1/5}\varepsilon^{2/5}}(1 + k\varphi). \quad (8)$$

In further motion of the gas-fluid emulsion in the turbulent flow along the mixing chamber in zone *II* (Fig. 1), the interface surface area changes through coalescence of separate bubbles. This phenomenon is due to collisions of bubbles under the action of turbulent pulsation. The process of bubble coalescence in the fluid–fluid systems was described in [11]. A formula was proposed for calculating the drop collision frequency in terms of Kolmogorov's theory of isotropic turbulence. For a monodisperse heterogeneous system the collision frequency can be determined for a particle (drop, bubble) from the expression [11]

$$\theta = \left(\frac{24\varphi w^2}{d_b^2}\right)^{1/2}, \quad (9)$$

where w^2 is the averaged squared rate of turbulent pulsation and d_b is the bubble size (m).

According to Kolmogorov's theory, the averaged squared rate of turbulent pulsation

$$w^2 = C\left(\frac{\varepsilon_{dr} d_b}{\rho}\right)^{2/3}, \quad (10)$$

where C is a constant and ε_{dr} is the rate of energy dissipation in the steady-flow zone.

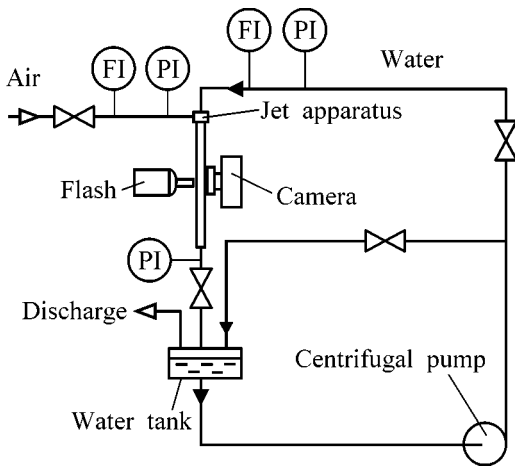

Fig. 2. Schematic of the experimental setup.

For a cylindrical mixing chamber, the following expression can be written for calculating the average ε_{dr} as flow losses in a pipe [12]:

$$\varepsilon_{dr} = \lambda \frac{\rho v_m^3}{2D}, \qquad (11)$$

where λ is the friction coefficient.

The coalescence frequency θ_c is related to the collision frequency θ of a bubble and the collision efficiency factor K_e by [11]:

$$\theta_c = K_e \theta. \qquad (12)$$

If n_τ gas bubbles are present in a unit volume of the flow at a current instant of time, then $n_\tau\theta/2$ collisions occur in unit volume. If the initial number of bubbles in a unit volume is denoted by n_0, and the number of bubbles coalesced by the given instant of time, by n, then the following equation can be written for the frequency of collisions occurring in a unit volume:

$$\theta^V = \frac{(n_0 - n)}{2}\theta. \qquad (13)$$

Then the coalescence frequency in a unit volume can be found from

$$\theta_c^V = K_e \frac{(n_0 - n)}{2}\theta. \qquad (14)$$

Since $\theta_c^V = dn/d\tau$ and the number and diameter of bubbles are related by

$$d_b = \left[\frac{6\varphi}{\pi(n_0 - n)}\right]^{1/3}, \qquad (15)$$

substitution of (9) and (15) into Eq. (14) and integration of the obtained expression from, respectively, 0 to τ and 0 to n yields

$$d_b = d_b^0\left[1 + K_e \frac{\varphi^{1/2}(\varepsilon_{dr}/\rho)^{1/3}\tau}{(d_b^0)^{2/3}}\right]^{3/2}, \qquad (16)$$

where d_b^0 is the bubble diameter at the initial instant of time (m).

Expression (16) can be used for describing the dependence of the bubble diameter on the time of emulsion motion in the mixing chamber of the jet apparatus at a given gas content. For polydisperse systems, the average volume-surface bubble diameter d_{32} is used as a quantity determining the bubble size d_b.

EXPERIMENTAL

With the aim to study experimentally the dispersion and coalescence of gas bubbles and to determine numerically the coefficients K, k, and K_e appearing in (8) and (16), an experimental setup shown schematically in Fig. 2 was developed. The setup comprises a vertical jet apparatus with a replaceable nozzle and an elongated cylindrical glass chamber of the same kind, a water tank, and a centrifugal pump. The setup is equipped with means of control and monitoring of the rate and pressure of the working gas and injected gas flows, and also with a camera and a flash for recording the bubble size.

The setup was used to study the dispersion and coalescence of the gas phase in the mixing chamber of the jet apparatus for the water–air system. The experiments were carried out for nozzles 4, 6, 8, 10, and 12 mm in diameter and mixing chambers of diameter 10 and 15 mm. The jet velocity at the nozzle exit was varied within 0.86–25 m s^{-1}. The temperature of fluid and gas was maintained at 25°C. The average volume-surface bubble diameter d_{32} was determined photographically.

The bubble size at the initial instant of time was determined by taking photographs of the gas-fluid emulsion at a distance $L = 5D$ from the nozzle exit at volume gas content φ of 0.01, 0.1, and 0.2.

Figure 3 shows as points the experimental data obtained in determining the average volume-surface bubble diameter d_{32}^0 at the initial instant of time in relation to the energy dissipation rate calculated using (7). The solid lines represent the results of experimental data processing by the least-squares method with the use of Eq. (8). $K = 1.05$ was found at low gas

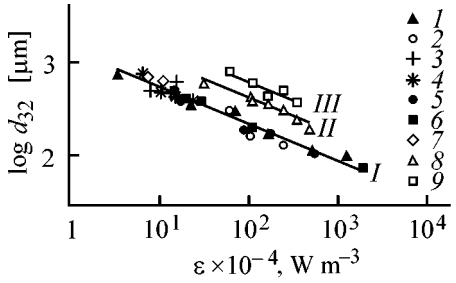

Fig. 3. Bubble size d_{32} vs. energy dissipation rate ε for an apparatus with nozzles of diameter d and mixing chambers of diameter D at gas content φ. d (mm), D (mm), φ: (*1*) 4, 15, 0.01; (*2*) 6, 15, 0.01; (*3*) 10, 15, 0.01; (*4*) 12, 15, 0.01; (*5*) 4, 10, 0.01; (*6*) 6, 10, 0.01; (*7*) 8, 10, 0.01; (*8*) 6, 15, 0.1; (*9*) 6, 15, 0.2. (*I–III*) Calculated curves at gas content φ of, respectively, 0.01, 0.1, and 0.2.

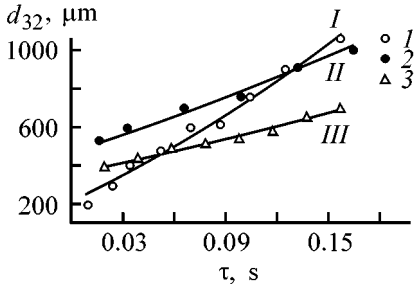

Fig. 4. Bubble size d_{32} vs. residence time τ of bubbles in the mixing chamber for an apparatus with nozzle of diameter d = 4 mm and mixing chambers of diameter D at fluid jet velocity at the nozzle exit v and gas content φ = 0.3. D (mm), v (m s^{-1}): (*1*) 10, 25; (*2*) 10, 13.3; and (*3*) 15, 25. (*I–III*) Calculated curves.

content, and k = 9, at φ = 0.1 and 0.2. The calculated values are in agreement with experiment within ±15%.

The variation of the interface area along the mixing chamber as a result of gas bubble coalescence was studied in several flow motion modes at a gas content that is the maximum possible for the photographic method to be applicable. The results obtained in a number of experiments in a jet apparatus with a nozzle 4 mm in diameter and mixing chambers 10 and 15 mm in diameter at a gas content φ = 0.3 are represented by points in Fig. 4 in the form of the dependence of the bubble size on the time of bubble residence in the mixing chamber. For comparison, the figure shows lines obtained by processing the experimental data by the least-squares method with the use of expression (16). It was found that the collision efficiency factor K_e = 0.014. The maximum difference between the calculated values and experimental data is ±10%.

CONCLUSIONS

(1) An approach to describing the dispersion and coalescence of the gas phase in fluid-gas jet apparatus with elongated mixing chamber, employed as jet absorbers, is proposed on the basis of Kolmogorov's theory of isotropic turbulence.

(2) The adequacy of the proposed approach is confirmed experimentally. Expressions are obtained for determining the average volume-surface diameter of gas bubbles in relation to the rate of energy dissipation in the fluid jet, volumetric gas content, and time of residence of gas bubbles in the mixing chamber of the apparatus. These expressions can be used to calculate mass exchange characteristics of jet absorbers.

REFERENCES

1. Tishin, V.B., Ibragimov, S.Kh., Lepilin, V.N., and Novoselov, A.G., *Zh. Prikl. Khim.*, 1985, vol. 58, no. 2, pp. 460–461.
2. Lepilin, V.N., Novoselov, A.G., Tishin, V.B., and Ibragimov, S.Kh., *Zh. Prikl. Khim.*, 1986, vol. 59, no. 10, pp. 2203–2208.
3. Lyamaev, B.F., *Gidrostruinye nasosy i ustanovki* (Water-Jet Pumps and Installations), Leningrad: Mashinostroenie, 1988.
4. Korennov, B.E., A Study of Water-Air Ejectors with Elongated Cylindrical Mixing Chamber, *Cand. Sci. Dissertation*, Moscow, 1980.
5. Sokolov, E.Ya. and Zinger, N.M., *Struinye apparaty* (Jet Apparatus), Moscow: Energiya, 1970, 2ng ed.
6. Kolmogorov, A.N., *Dokl. Akad. Nauk SSSR*, 1949, vol. 66, no. 5, pp. 325–328.
7. Kamenev, P.N., *Gidroelevatory i drugie struinye apparaty* (Hydraulic Elevator and other Jet Apparatus), Moscow: MSPM, 1950.
8. Vasil'ev, Yu.N., *Lopatochnye mashiny i struinye apparaty* (Impeller Machines and other Jet Apparatus), Moscow: Mashinostroenie, 1971, issue 5, pp. 175–201.
9. Abramovich, G.N., *Teoriya turbulentnykh strui* (Theory of Turbulent Jets), Moscow: Fizmatgiz, 1960.
10. Coulaloglou, C.A. and Tavlarides, L.L., *Am. Inst. Chem. Eng. J.*, 1976, vol. 22, no. 2, pp. 289–297.
11. Tronov, V.P. and Rozentsvaig, A.K., *Zh. Prikl. Khim.*, 1975, vol. 48, no. 5, pp. 1265–1266.
12. Piterskikh, G.P. and Valashek, E.R., *Khim. Prom–st.*, 1956, no. 1, pp. 35–41.

Russian Journal of Applied Chemistry, Vol. 74, No. 4, 2001, pp. 644–648. Translated from Zhurnal Prikladnoi Khimii, Vol. 74, No. 4, 2001, pp. 625–629.

MACROMOLECULAR CHEMISTRY AND POLYMERIC MATERIALS

Influence of Synergistic Effects on Ion-Exchange Chromatographic Separation of Proteins

A. A. Demin, K. P. Papukova, E. S. Nikiforova, and E. N. Pavlova

Institute of Macromolecular Compounds, Russian Academy of Sciences, St. Petersburg, Russia

Received June 7, 2000

Abstract—Formation of strong bonds between proteins and polyelectrolyte chains of ion-exchange sorbents gives rise to synergistic effects in multicomponent sorption and chromatographic separation of proteins. A series of heteronetwork-cross-linked polymeric bases with varied content of ionic groups was prepared. Consecutive sorption and cosorption of insulin and α-lactalbumin on these materials were studied.

Correct understanding of the interaction of multicomponent protein mixtures with the sorbent surface is very important in developing chromatographic procedures for recovery and purification of proteins. In most cases, studies of multicomponent sorption and chromatography are based on the concept on competitive sorption of the sorbate molecules on a limited number of sorption centers on the sorbent surface. At the same time, it is known that, at strong interaction of a protein with the sorbent surface, adsorbed protein layers with different structures and energies of intermolecular bonds are formed under certain conditions. Zimina *et al*. [1–2] observed formation of such nonuniform layers during interaction of γ-globulin with polyethylene or polydimethylsiloxane films and of human serum albumin with a film of siloxane-carbonate copolymer. The first, irreversibly or strongly adsorbed layer consists of molecules directly interacting with the surface active centers. The second layer contains molecules adsorbed on the active centers of protein molecules of the first layer.

The energy barrier preventing competitive protein sorption (causing "irreversible protein sorption") is due to either a change in the conformation of an adsorbed protein molecule [3] or multicenter interaction of the macromolecule with the surface [4]. For a protein to be desorbed, external conditions—solution pH, ionic strength, and content of an organic solvent—are to be changed.

Polymeric materials are the most preferable sorbents for recovery and purification of biologically active compounds (BACs). The high sorption capacities of these materials for BACs are due to the polyfunctional nature of the interaction with BACs and to the highly permeable crosslinked structure of the polymers having pores and channels larger than diameters of solvated molecules of a target compound. Ion-exchange sorbents with high capacity for proteins (up to several grams of protein per 1 g of the sorbent) were prepared in the course of studies aimed at improving the selectivity of protein sorption [5–7]. The target component was recovered under conditions providing the strongest sorption of the protein on the sorbent.

Studies of the consecutive sorption and cosorption of model protein pairs on ion-exchange sorbents of different types have shown that multicomponent protein sorption under the conditions of the strongest sorption, determined by pH, is complicated by synergistic effects: there is no desorption of one protein by another and, furthermore, the sorption of one protein grows in the presence of the other under static conditions [8–11]. It has been demonstrated that, at the same ratio between the components of a mixed protein solution and the sorbent, the protein content in the sorbent may depend on the sequence in which the proteins was brought in contact with the sorbent. The selectivity of protein sorption may be reversed during sorption.

The above data show that synergistic effects in multicomponent sorption are caused by strong bonding between a protein and a sorbent. After the sorption centers are filled, further binding is effected by protein–protein interactions. It is clear that synergistic effects deteriorate the protein separation, since fine chromatographic separation is only possible when the sorp-

1070-4272/01/7404-0644 $25.00 © 2001 MAIK "Nauka/Interperiodica"

tion energies of each component of the mixture are different. For efficient separation of the components, competitive sorption conditions are necessary.

Previously [12] we studied sorption of insulin and ribonuclease on Polysorb molecular sorbent as influenced by the degree of its sulfonation. It was found that realization of either synergistic effect or competitive sorption is determined by the number of ionic groups of the sorbent per protein molecule. However, protein separation on the Polysorb sorbent is complicated by strong hydrophobic interaction of the proteins with the sorbent matrix (macroporous copolymer of styrene with divinylbenzene). To determine the influence of synergistic effects on the protein separation, we prepared a series of cross-linked polymeric bases (CPBs) with the following properties: (1) hydrophilicity to prevent hydrophobic interactions, (2) variable content of ionic groups, and (3) heteronetwork-cross-linked structure providing high permeability for protein molecules. In the present study we analyzed the multicomponent sorption of proteins on these CPBs under static conditions and demonstrated how the kinetics of protein separation depends on the mechanism of the multicomponent sorption.

To determine the conditions for synthesis of hydrophilic structurally stable CPBs with varied content of ionic groups, we studied copolymerization of *N*-dimethylaminopropylmethacrylamide (DMAM) with *N*,*N*'-ethylenedimethacrylamide (EDMA) in aqueous solutions. Previously we showed [13] that DMAM copolymerizes with hexahydro-1,3,5-triacryloyltriazine in an aqueous solution under heterogeneous conditions to form structurally stable CPBs with strong swellability. Three-dimensional copolymerization of these monomers in aqueous or aqueous-organic solution yields highly hydrated copolymers. The structure of the resulting CPBs consists of both densely cross-linked regions containing microglobules and loosened regions disappearing on drying. Swollen cross-linked polymeric bases contain a large amount of the solvent, which ensures high permeability for BAC macromolecules.

Copolymerization of DMAM with EDMA in water also occurs under heterogeneous conditions to form CPBs of the ADE type (anion exchangers based on dimethylaminopropylmethacrylamide–ethylenedimethacrylamide copolymers). The monomer concentration in the solution is 20%. The relative swelling K_{rel}, expressed as the ratio of the swelling coefficient K_{swell} of the Cl form of CPB to that of the OH form and characterizing the structural stability of ADE CPBs, remains virtually the same (close to unity) on changing EDMA content in CPB (Fig. 1). Taking into account this fact, structurally similar hydrophilic CPBs with varied content of ionic groups $-N(CH_3)_2$ were prepared by copolymerization of appropriate hydrophylic nonionic amide with DMAM and EDMA [14]. *N*-(2-hydroxypropyl)methacrylamide (HPMA), which is similar in reactivity to DMAM and EDMA, was used as a hydrophilic nonionic monomer. The EDMA content was constant (10 mol %).

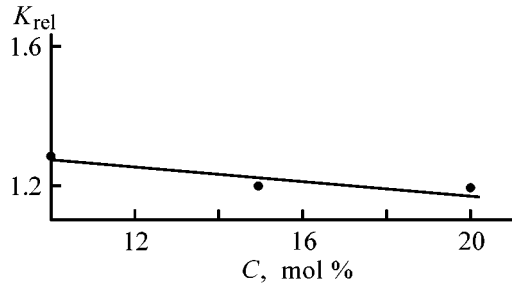

Fig. 1. Relative swelling coefficient K_{rel} of CPB vs. the content of the cross-linking agent *C*.

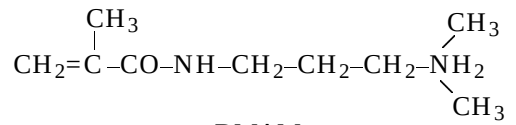

DMAM

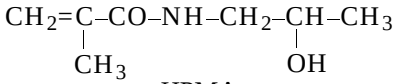

HPMA

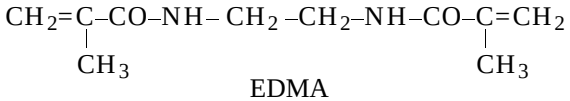

EDMA

A series of CPBs: ADE-10, ADGE-10-1, ADGE-10-4, and ADGE-10-10 was prepared. The first and the second figures in the CPB name denote the molar percentage of EDMA and the number of HPMA moles per mole of DMAM, respectively. GPE-10 is an EDMA–HPMA copolymer. Some properties of CPBs are summarized in Table 1.

Table 1. Properties of CPBs*

CPB	V_{sp}, ml g^{-1}	EC, mg-equiv g^{-1}	K_{rel}
ADE-10	10.0	5.0	1.3
ADGE-10-1	8.1	2.8	1.2
ADGE-10-4	7.7	1.2	1.2
ADGE-10-10	7.7	0.4	1.0
GPE-10	5.9	–	1.0

* V_{sp} and EC are the specific volume and the exchange capacity for chloride ion, respectively.

Table 2. Selectivity coefficient of protein sorption on CPB at pH 8.0

Sorbent	Selectivity coefficient	
	insulin	α-lactalbumin
ADE-10	2200	460
ADGE-10-1	1100	330
ADGE-10-4	230	90
ADGE-10-10	50	20
GPE-10	1	1

The degree of swelling of CPB weakly changes with the DMAM–HPMA ratio. The structural stability of CPB was estimated from the relative swelling coefficient K_{rel}. As seen from Table 1, K_{rel} changes weakly and approaches unity with decreasing DMAM content. This indicates that the CPB structure is stable during ionization. Thus, copolymerization of DMAM and HPMA with EDMA in a 20% aqueous solution yields structurally stable CPB characterized by strong swellability, irrespective of the terpolymer composition.

The ion-ion interaction between a protein and a sorbent can be controlled by the DMAM–HPMA ratio. Since the selectivity of sorption of model proteins (insulin and α-lactalbumin) on these CPBs at pH 8.0 falls with decreasing content of the ionic monomer and the proteins do not interact with GPE-10 (Table 2), we suggest that the sorption of these proteins on the CPB is mainly due to ion-ion interactions. The selectivity coefficients were calculated from the isotherm sections measured at low degrees of sorption.

The multicomponent sorption of proteins on the tested anion exchangers was studied under static conditions for the example of the insulin–α-lactalbumin pair at pH 8.0 (the conditions providing the maximal insulin sorption). When consecutive sorption was studied, the second protein was introduced after the attainment of equilibrium in the system sorbent–first protein. After the sorption was complete, the protein concentrations in the binary solution were determined by reversedphase high-performance liquid chromatography. Then the protein amount sorbed by 1 ml of the sorbent was calculated. When the cosorption was studied, a binary protein solution with the same weight concentrations of the components was used. The results are presented in the form of histograms (Fig. 2).

As seen from Fig. 2, in the case of the consecutive sorption on ADE-10, the second protein not only does not desorb the first protein but also promotes its additional sorption. In the case of cosorption, the total amount of proteins sorbed on ADE-10 is higher than the sum of the sorption capacities of the anion exchanger for the components, i.e., the proteins are sorbed by the synergistic mechanism. Addition of the second protein to the system comprising ADGE-10-1 and the first protein does not increase the sorption of the first protein. At the same time no desorption of the first protein is not observed either. Consecutive sorption of the proteins on ADGE-10-4 is a competitive process: addition of a solution of the second protein results in desorption of the first protein from the ion exchanger. Similarly, the mechanism of sorption of insulin and ribonuclease on the sorbents with different

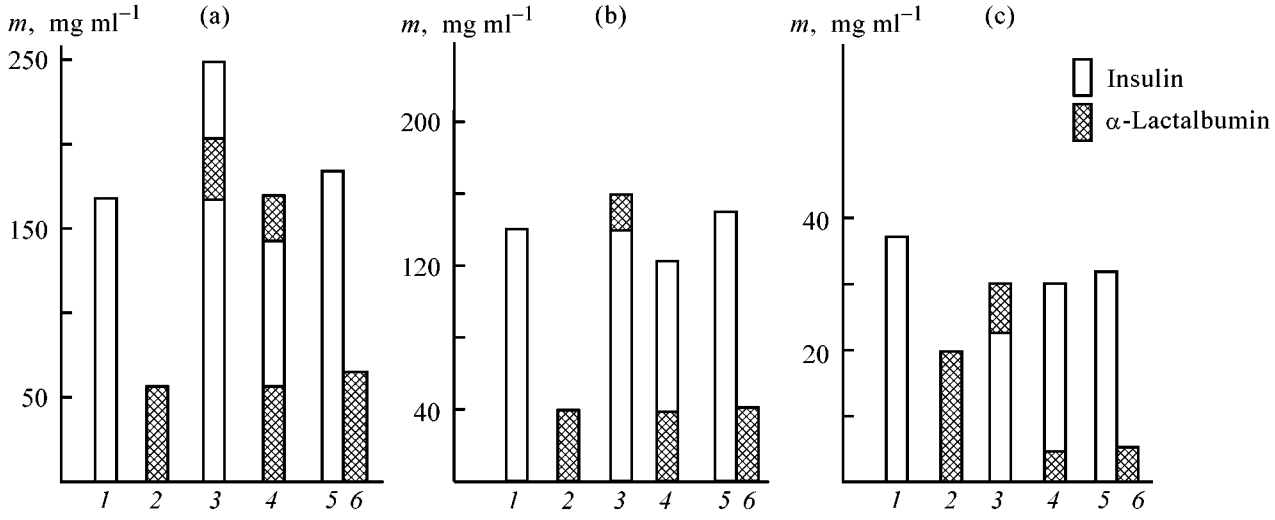

Fig. 2. Consecutive sorption and cosorption of insulin and α-lactalbumin on (a) ADE-10, (b) ADGE-10-1, and (c) ADGE-10-4. (*m*) Amount of protein sorbed by 1 ml of the sorbent. Sorption mode: (*1*, *2*) from separate component solutions, (*3*, *4*) consecutive, and (*5*, *6*) from two-component solution.

degrees of sulfonation goes from synergistic to competitive with decreasing content of the ionic groups in a sorbent.

To accelerate the protein sorption under dynamic conditions and to approach the conditions of equilibrium sorption, we aslo used composites based on the tested CPBs, so-called cellosorbents. Cellosorbents were prepared by impregnation of a highly permeable cellulose hydrate matrix with 3–10 μm sorbent particles in forming spherical cellosorbents granules [15, 16]. We prepared TsS-ADM-10 and TsS-ADG-10-4 cellosorbents with 100–315-μm granules. The exchange capacities of these materials for the chloride ion are 0.78 and 0.24 mg-equiv g^{-1} of dry sorbent, respectively. The water content in the hydrated sorbent is 90%.

In the dynamic experiments, a sorbent tested was placed in a 2×62-mm Milichrom steel column. A 1 mg ml^{-1} protein solution was fed at a 5 μl min^{-1} rate. A solution of the second protein was passed trough the column after the sorbent was saturated with the first protein. Then the column was washed with water and the proteins were desorbed with 0.3% orthophosphoric acid, with the eluate dived into fractions. It was shown preliminarily that the tested proteins are completely desorbed under these conditions. In each fraction, the protein concentration was determined by HPLC. When the cosorption was studied, we used a solution with the same concentrations of insulin and α-lactalbumin and a total protein concentration of 2 mg ml^{-1}.

When a solution of the second protein is passed through a column with ADE-10 and ADGE-10-1 saturated with the first protein, the desorption of the first protein is low. Probably the second protein substitutes only the molecules of the first protein sorbed by the protein-protein interactions. The sorption layer thus formed contains two proteins: the first is bound mainly to the amino groups of the sorbent and the second is sorbed owing to the protein–protein interactions. The content of insulin and α-lactalbumin in ADE-10 and ADGE-10-1 after passing a binary solution containing both the proteins is close to that in the initial solution. The eluate obtained in desorpton with an acid solution contains insulin and α-lactalbumin. The sorption properties of cellosorbents based on ADE-10 and ADGE-10-1 are similar. The composition of the eluate fractions formed in desorption from TsS-ADE-10 cellosorbent is shown in Fig. 3a. Thus, sorbents with high content of ionic groups are inefficient for the most economic frontal displacement processes. In the case of consecutive sorption on the ADGE-10-4 sorbent, the protein sorbed in the first step is completely desorbed with a solution of the second protein. When an insulin–α-lactalbumin solution is passed through a column packed with this sorbent, the sorbent is gradually enriched with insulin selectively sorbed under these conditions. The elution peak obtained after passing 2 ml of an insulin–α-lactalbumin solution through a column with TsS-ADGE-10-4 is shown in Fig 3b.

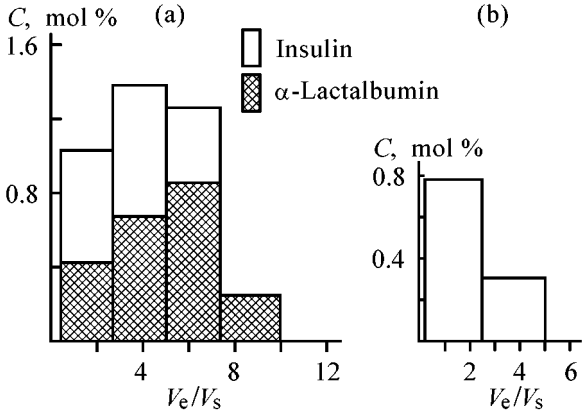

Fig. 3. Elution of proteins sorbed from an insulin–α-lactalbumin solution with equal weight concentrations of the proteins (C_{tot} = 2 mg ml^{-1}) on (a) TsS-ADE-10 and (b) TsS-ADGE-10-4. (V_e) Total eluate volume (ml), and (V_s) sorbent volume.

CONCLUSIONS

(1) Consecutive sorption and cosorption of model proteins (insulin and α-lactalbumin) on specially prepared heteronetwork polymeric bases with varied content of ionic groups (with capacity for Cl^- ranging from 0.4 to 5.1 mg-equiv g^{-1}) was studied under static conditions. With decreasing content of ionic groups in the sorbents, the protein sorption weakens, which leads to a competitive mechanism of multicomponent sorption.

(2) A study of the sorption-desorption kinetics of proteins on sorbents with varied content of ionic groups showed that the efficient frontal displacement process of ion-exchange chromatography is only possible in the case of competitive sorption.

ACKNOWLEDGMENTS

This work was financially supported by the St. Petersburg Scientific Center (project no. 21).

REFERENCES

1. Zimina, L.A., Iordanskii, A.L., Polishchuk, A.Ya., *et al.*, *Vysokomol. Soedin., Ser. A*, 1980, vol. 22. no. 9, pp. 2143–2148.
2. Iordanskii, A.L., Ulanov, B.P., Zimina, L.A., and Zaikov, G.E., *Dokl. Akad. Nauk SSSR*, 1979, vol. 249, no. 2, pp. 480–482.
3. Norde, W., *Adv. Colloid. Interface Sci.*, 1986, vol. 25, no. 2, pp. 267–340.
4. Andrade, J.D. and Hlady, V., *Ann. N.Y. Acad. Sci.*, 1987, vol. 516, no. 1, pp. 158–172.
5. Shataeva, L.K., Kuznetsova, N.N., and El'kin, G.E., *Karboksil'nye kationity v biologii* (Carboxylic Cation Exchangers in Biology), Leningrad: Nauka, 1979.
6. Samsonov, G.V. and Melenevskii, A.T., *Sorbtsionnye i khromatograficheskie metody fiziko-khimicheskoi biotekhnologii* (Sorption and Chromatographic Methods of Physicochemical Biotechnology), Moscow: Nauka, 1986.
7. Samsonov, G.V., *Ion Exchange Sorption and Preparative Chromatography of Biologically Active Molecules*, New York: Plenum, 1986.
8. Demin, A.A. and Dynkina, I.M., *Zh. Fiz. Khim.*, 1995, vol. 69, no. 4, pp. 718–721.
9. Demin, A.A., Mogilevskaya, A.D., and Samsonov, G.V., *Zh. Fiz. Khim.*, 1996, vol. 70, no. 11, pp. 2059–2062.
10. Demin, A.A., Mogilevskaya, A.D., and Samsonov, G.V., *Zh. Prikl. Khim.*, 1996, vol. 69, no. 1, pp. 31–34.
11. Demin, A.A., Mogilevskaya, A.D., and Samsonov, G.V., *J. Chromatogr.*, 1997, vol. 760, no. 1, pp. 105–115.
12. Demin, A.A., Papukova, K.P., Nikiforova, E.S. and Samsonov, G.V., *Zh. Fiz. Khim.*, 2000, vol. 74, no. 4, pp. 689–693.
13. Papukova, K.P., Demin, A.A., Samsonov, G.V., *et al.*, *Vysokomol. Soedin., Ser. A*, 1995, vol. 37, no. 10, pp. 1644–1648.
14. Papukova, K.P., Demin, A.A., and Nikiforova, E.S., *Vysokomol. Soedin., Ser. B*, 2000, vol. 42, no. 11, pp. 1936–1940.
15. USSR Patent no. 1819272.
16. Demin, A.A., Dubinina, N.I., Melenevskii, A.T., *et al.*, *Zh. Prikl. Khim.*, 1984, vol. 57, no. 10, pp. 2212–2217.

Russian Journal of Applied Chemistry, Vol. 74, No. 4, 2001, pp. 649–652. Translated from Zhurnal Prikladnoi Khimii, Vol. 74, No. 4, 2001, pp. 629–633.

MACROMOLECULAR CHEMISTRY AND POLYMERIC MATERIALS

Anion Exchangers Based on Allyl Compounds and Some Nitrogen- and Oxygen-Containing Monomers and Oligomers

E. E. Ergozhin, A. K. Chalov, R. A. Iskakova, and A. I. Nikitina

Bekturov Institute of Chemical Sciences, Ministry of Education and Science of Kazakhstan Republic, Almaty, Kazakhstan

Received December 19, 2000

Abstract—Anion exchangers containing different basic groups and having good physicochemical and sorption properties were prepared by polycondensation of polyallylamine and various allyl halides, diglycidyl ethers of dihydroxybenzenes, and aromatic amines with some aliphatic polyamines.

Synthesis of allyl polymers with high chemical and thermal stability is being extensively studied [1–3]. New ion-exchange resins with high sorption capacity for transition metal ions have been prepared by polycondensation of allyl monomers with epoxy compounds. The kinetics and mechanism of reactions of various allyl compounds have been studied and described quantitatively [4–6]. Abdusattarova *et al*. [5] analyzed the kinetic features of radical polymerization of diallyl monomer formed from allyl bromide and piperidine. Pavlova *et al*. [6] studied the mechanism of intramolecular cyclization in radical polymerization of diallyl isophthalates, preceding gelation.

In this work, we studied the synthesis and properties of polyfunctional anion exchangers based on polyallylamine (PAA), allyl bromide (AB), allyl chloride (AC), diglycidyl ethers of resorcinol (DGER) and hydroquinone (DGEH), and various amines: polyethylenepolyamine (PEPA), polyethylenimine (PEI), and hexamethylenediamine (HMDA). The reaction kinetics were studied by polarography, IR spectroscopy, and chemical analysis.

EXPERIMENTAL

Diglycidyl ethers of resorcinol and hydroquinone were prepared by the procedure described in [7]. The content of epoxy groups, determined by the procedure described in [8], was 31.7 and 30.2%, respectively. The anion exchangers were prepared in dimethylformamide (DMF) at various temperatures. The resulting gel was cured at 80–120°C. Condensation of DGER and DGEH with PAA was performed at a temperature of 40 to 80°C for a time ranging from 1 to 2 h. When AG was used, the temperature and time of the reaction were 13–24°C and 0.5–2 h. The cured polymer was crushed and sifted, with the 0.25-mm fraction taken.

The static exchange capacity (SEC, mg-equiv g^{-1}), moisture content, swellability, and chemical and thermal stability of the anion exchangers were determined by the conventional procedures [9].

The polarographic study was performed on a PU-1 universal polarograph. The parameter $m^{2/3}t^{1/6}$ of the capillary was 4.38 $mg^{2/3}\ s^{-1/2}$. As reference electrode served saturated calomel electrode. As supporting electrolyte was used 0.02 M $(C_2H_5)_4NI$ solution in 50% DMF.

The IR spectra of the initial compounds and intermediate and final reaction products were recorded on a Specord M 80/M 85 spectrophotometer KBr pellets (200 mg KBr + 1 mg of a sample) or thin films between plates.

The IR spectra of DGER and DGEH contain the bands of epoxy groups in the ranges 850–950, 1200–1250, and 3000–3100 cm^{-1}. The bands at 1424 and 1000 cm^{-1} in the spectrum of allylamine are assigned to the double bond of the allyl group.

No bands of epoxy groups or the double bond of the allyl group were found in the IR spectrum of the anion exchanger prepared from PAA, DGER, and DGEH. The bromine number of the allylamine oligomer (6.3) [10] also suggests the opening of the double bonds.

1070-4272/01/7404-0649 $25.00 © 2001 MAIK "Nauka/Interperiodica"

Table 1. Influence exerted by the nature of the starting compounds on the nitrogen content, SEC, and sorption capacity of the anion exchangers

Anion exchanger based on	N, %	SEC, mg-equiv g^{-1}	Sorption capacity, mg-equiv g^{-1}		
			Cu^{2+}	Ni^{2+}	Co^{2+}
PEPA : AB : DGER	12.97	9.9	9.8	4.6	3.9
PEI : AB : DGER	16.55	8.7	7.7	4.1	3.9
HMDA : AB : DGER	6.56	5.0	5.0	3.5	3.1
PEPA : AC : DGER	13.15	10.2	10.2	5.4	5.3
PEI : AC : DGER	16.17	6.6	5.4	3.5	3.1
HMDA : AC : DGER	6.98	5.1	5.0	2.9	2.3
PEPA : AB : DGEH	11.02	8.9	8.6	4.0	3.6
PEI : AB : DGEH	15.40	7.8	7.2	4.0	3.4
HMDA : AB : DGEH	5.62	4.3	4.1	2.8	2.5
PAA : H_2O : DGER	8.57	6.2	4.3	3.1	3.0

Copolymers with the maximum exchange capacity (6.2 mg-equiv g^{-1}) are formed at PAA : DGER : H_2O = 0.3 : 0.7 : 2.5.

Water catalyzes the reaction of epoxy compounds with amines and increases the swellability of the resulting anion exchanger. At a deficiency of water the reaction mixture is overheated in the initial precondensation step, and the reaction becomes less homogeneous.

Copolymers prepared from allyl halides and DGER at high amine content in the reaction mixture are water-soluble or strongly swelling. The physicochemical properties of these anion exchangers deteriorate. For example, the SEC and swellability of the anion exchanger based on PEPA grow from 6.5 to 9.9 mg-equiv g^{-1} and from 6.1 to 8.4 mg l^{-1}, respectively, with the amine concentration increasing from 1 to 2 wt parts. The SEC of the anion exchanger based on PEI increases from 3.5 to 8.7 mg-equiv g^{-1} with increasing amine concentration from 1 to 3.5 wt parts. Copolymerization of HMDA at amine concentrations higher than 1 wt part yields soluble products.

We found that the exchange capacity of the anion exchangers based on PAA decreases to 2.6 mg-equiv g^{-1} with the fraction of the cross-linking agent increasing from 0.7 to 1.0 wt parts. As the DGER content increases from 1 to 2.5 wt parts, the SEC and the swellability of the anion exchangers based on allyl halides (AHs) decrease from 8.9 to 5.9 mg-equiv g^{-1} and from 9.3 to 5.2 mg l^{-1}, respectively, which is probably due to an increase in the cross-linking density. This makes lower the accessibility of the functional groups in ion exchange.

The physicochemical properties of the anion exchangers prepared at the optimal ratio of the starting components were studied as influenced by the temperatures of precondensation and curing. The exchange capacity of the ion exchanger increases from 5.3 to 9.9 mg-equiv g^{-1} on elevating the precondensation temperature from 13 to 24°C. As the curing temperature is raised from 80 to 120°C, the SEC of the anion exchangers decreases from 9.9 to 7.4 mg-equiv g^{-1}, which is probably due to an increase in the cross-linking density owing to deamination and dehydration.

The influence exerted by the nature of the initial components on the static exchange and sorption capacities of the anion exchangers is shown in Table 1.

The static exchange and sorption capacities of the anion exchangers for transition metal ions strongly depend on the amine nature. The SEC of the polymers prepared with PEPA, which is the most effective, is as high as 9.9–10.2 mg-equiv g^{-1}. The capacities are almost independent of the nature of allyl compounds and diglycidyl ethers (DGE).

The sorption capacity of all anion exchangers for copper(II) cations is high. Nickel(II) and cobalt(II) cations are more effectively sorbed by anion exchangers based on PEI, HMDA, and PAA.

Thus, the best preparation conditions of the anion exchangers based on DGER are as follows: PAA : H_2O : DGER = 0.3 : 0.7 : 2.5; precondensation temperature 80°C and time 2 h. The best conditions of condensation of AH with DEG are as follows: PEPA : AH : DGE = 2.0 : 2.0 : 1.5; PEI : AH : DGE = 3.5 : 2.0 : 1; HMDA : AH : DGE = 2 : 2 : 1.5; precondensation temperature 24°C and curing temperature 80°C; preparation time 2 h.

The chemical stability of the anion exchangers was estimated from the change in the exchange capacity in solutions of 5 N sulfuric acid, sodium hydroxide, and 10% H_2O_2. The polymers based on PEPA exhibit the lowest stability with respect to the oxidizing agent and sulfuric acid. A study of the thermal stability of the anion exchangers on heating at 100°C for 12 h in hermetically sealed ampules showed that the decrease in the capacity does not exceed 8%.

It was of interest to study the kinetic features of precondensation of AHs with DGEs and amines. Previously, the mechanism of polycondesation of allyl bromide, DGER, and PEPA has been studied by polarography, IR spectroscopy, and chemical analysis. This reaction has been found [11] to be a two-step process. In the first step, AB reacts with DGER via opening of the epoxy ring and rupture of the C–Br bond in allyl bromide. Addition of PEPA in the second step yields cross-linked anion exchanger owing to

rupture of both the C–Br bond in the intermediate and the N–H bond in the amino group and opening of the double bond of the allyl group.

We studied the kinetics of each step of this reaction by polarography. This method offers a number of advantages in studying the kinetics of homogeneous reactions, one of which is the possibility of an *in situ* study without isolation of the components from the reaction mixture [12]. If during chemical reaction one or several polarographically active compounds are formed or consumed in a solution, the time dependences of their concentration can be followed by polarography.

Among AB, DGER and PEPA, only allyl bromide is polarograpically active. A great number of halogen-containing organic compounds is known to be reduced on a mercury dropping electrode at a half-wave potential $E_{1/2}$ ranging from 0 to –2.5 V. Electrochemical rupture of the carbon–halogen bond in monohalogenated derivatives usually involves two electrons. In this case a halide anion is formed and the position of the halogen atom in the organic molecule is occupied by a hydrogen atom.

$$C_3H_5Br + 2e \rightarrow C_3H_6 + Br^-.$$

This reaction is manifested in polarograms as single-step two-electron diffusion-controlled waves. We used 0.02 M $(C_2H_5)_4NI$ in 50% DMF as supporting electrolyte, since DMF is strongly adsorbed on the surface of a mercury dropping electrode, thus preventing appearance of polarographic maxima [13]. From the polarograms of AB recorded in this electrolyte we determined the half-wave reduction potential of allyl bromide, –1.29 V, which agrees with published data [14].

The kinetic curves describing a decrease in the concentration of AB during its polycondensation with DGER and PEPA at different temperatures were constructed from the results of polarographic analysis (Fig. 1), since the intensity of the polarographic wave *h* is directly proportional to the AB concentration. These curves show that the reaction is accelerated with increasing temperature and is vigorous in both steps during the first 60 min. Thus, the optimal time of precondensation of these monomers is 2 h.

A study of the polycondensation kinetics showed that the rate constants of both steps remain virtually constant. This indicates that the polycondensation of AB, DGER, and PEPA is a first-order reaction [15]. The kinetic parameters of the polycondensation are summarized in Table 2.

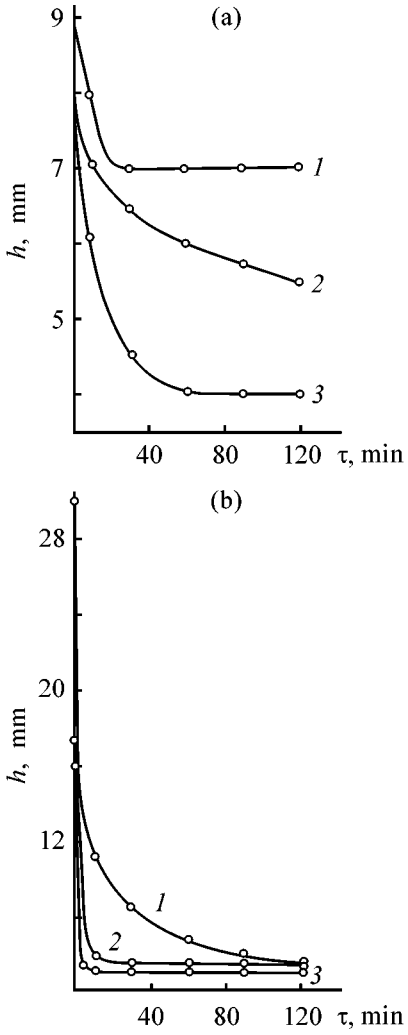

Fig. 1. Kinetics of the (a) first and (b) second steps of AB polycondensation with DGE and PEPA at (*1*) 13, (*2*) 18, and (*3*) 24 °C. (*h*) Intensity of polarographic wave and (τ) time.

As seen from Fig. 2, the fact that the temperature dependences of the rate constants are linear in the Arrhenius coordinates in both steps confirms that the polycondensation can be described by the Arrhenius equation.

Table 2. Kinetic parameters of the first and second steps of polycondensation of AB, DGER and PEPA

Step	*T*, K	log *k*	*E*, kJ mol^{-1}
AB + DGER	286	–3.7	32
	291	–3.4	
	297	–3.2	
AB + DGER + PEPA	286	–8	28
	291	–2.5	
	297	–2.3	

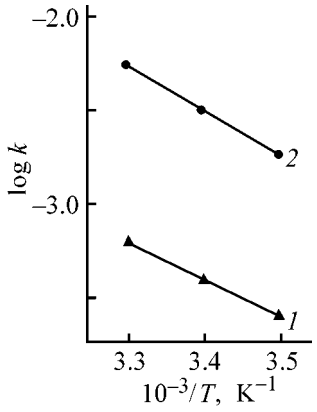

Fig. 2. Rate constants *k* of the (*1*) first and (*2*) second steps of polycondensation of AB, DGER, PEPA vs. temperature *T*.

Thus, new polyfunctional anion exchangers with high exchange capacity and improved physicochemical properties were prepared by polycondensation of allyl compounds and diglycidyl ethers of dihydroxybenzenes with various amines in DMF, followed by curing of the resulting gel. The optimal preparation conditions were determined and some properties of the anion exchangers were studied. As determined by polarography, IR spectroscopy, and chemical analysis, the use of AHs allows preparation of three-dimensional polymers cross-linked not only by amines, but also by the double bonds of allyl groups. Polycondensation of AB, DGER, and PEPA is a first-order reaction. The low activation energies indicate that both the steps are fast at low temperatures, with the second step being faster than the first. This is likely to be due to the exothermic nature of the second step.

REFERENCES

1. Fadel, H., Schwark, S., Lunkwitz, K., and Jakobach, H., *J. Angew. Makromol. Chem.: Appl. Macromol. Chem. Phys.*, 1998, vol. 263, p. 7894.
2. Stroganov, V.F., Mikhal'chuk, V.M., Maklanov, L.I., *et al.*, Abstracts of Papers, *6-ya Mezhdunarodnaya konferentsiya po khimii i fizikokhimii oligomerov* (Sixth Int. Conf. on Chemistry and Physical Chemistry of Ologomers), Chernogolovka, 1997.
3. Mukhamedgaliev, B.A. and Mirkamilov, T.M., *Lakokras. Mater. Ikh Primen.*, 1999, no. 10, p. 21.
4. Shoinbekova, S.A., Mukhitdinova, B.A., Nikitina, A.I., *et al.*, *Izv. Minist. Obraz. Nauki Resp. Kaz., Nats. Akad, Nauk Resp. Kaz., Ser. Khim.*, 1999, no. 2, pp. 90–93.
5. Abdusattarova, S.P., Safaev, U.A., and Dzhalilov, A.T., *Vysokomol. Soedin., Ser. B*, 1990, vol. 32, no. 12, pp. 930–932.
6. Pavlova, O.V., Kireeva, S.M., Romantsova, I.I., and Sivergin, Yu.M., *Vysokomol. Soedin., Ser. A*, 1990, vol. 32, no. 6, pp. 1256–1260.
7. US Patent 3121727.
8. Paquin, A.M., *Epoxydverbindungen und Epoxydharze*, Berlin: Springer, 1958.
9. *GOSTs* (State Standards) *10898–84*, *10898.2–74*, *10898.5–84*.
10. Toropseva, A.M., Belgorodskaya, K.V., and Bondarenko, V.M., *Laboratornyi praktikum po khimii i tekhnologii vysokomolekylyarnykh soedinenii* (Laboratory Course on Chemistry and Technology of Macromolecular Compounds), Leningrad: Khimiya, 1972, pp. 74–75.
11. Chalov, A.K., Erozhin, E.E., Iskakova, R.A., and Nikitina, A.I., *Izv. Minist. Obraz. Nauki Resp. Kaz., Nats. Akad, Nauk Resp. Kaz. Ser. Khim.*, 2000, no. 5, pp. 30–35.
12. Bezuglyi, V.D., *Polarografiya v khimii i tekhnologii polimerov* (Polarography in Polymer Chemistry and Technology), Leningrad: Khimiya, 1968.
13. Mairanovskii, S.G., Stradyn', Ya.P., and Bezuglyi, V.D., *Polyarografiya v organicheskoi khimii* (Polarography in Organic Chemistry), Moscow: Khimiya, 1975.
14. Terent'ev, A.P. and Yanovskaya, L.A., *Polyarograficheskii metod v organicheskoi khimii* (Polarography in Organic Chemistry), Moscow: Khimiya, 1957.
15. Berlin, A.A., Vol'fson, S.A., and Enikolopyan, N.S., *Kinetika polimerizatsionnykh protsessov* (Kinetics of Polymerization Processes), Moscow: Khimiya, 1978.

Russian Journal of Applied Chemistry, Vol. 74, No. 4, 2001, pp. 653–656. Translated from Zhurnal Prikladnoi Khimii, Vol. 74, No. 4, 2001, pp. 633–636.

MACROMOLECULAR CHEMISTRY AND POLYMERIC MATERIALS

Formation, 3D Structure, and Strength Characteristics of Interpenetrating Polymer Networks Based on Cold-Curing Oligomer–Oligomer Systems

Yu. N. Anisimov and S. N. Savin

Mechnikov State University, Odessa, Ukraine

Received September 25, 2000; in final form, December 2000

Abstract—The kinetics of low-temperature formation of interpenetrating polymer networks based on modified epoxy resins and copolymers of unsaturated oligoester resin with oligoether acrylates were studied in relation to the composition of the initial mixture. The influence of the parameters of the three-dimensional structure (cross-linking density, content of lattice points, number of monomeric units in cross-links) on the strength characteristics of the resulting polymer networks was examined, and the best conditions were found for preparing shockproof materials.

The properties and structure of interpenetrating polymer networks (IPNs) of various types are favorable for preparing materials with valuable service characteristics [1, 2]. The three-dimensional (3D) structure and properties of polyurethane-based IPNs are largely influenced by the kinetics of formation of these materials [2]. Curing of a series of modified epoxy resins has been studied, and the main characteristics of their network structure have been determined; the shock resistance of these materials is relatively poor [3, 4]. We have studied previously the 3D structure and physicomechanical characteristics of network copolymers based on unsaturated oligoester resins and oligoether acrylates [5], and also the kinetics of formation, 3D structure, and strength characteristics of semi-IPNs based on modified epoxy resins and oligoether acrylates [6]. In this work we studied the process of formation, 3D structure, and strength characteristics of IPNs based on modified epoxy resins and network copolymers of cold-curing oligoester resins with the aim of preparing polymeric materials with enhanced strength.

EXPERIMENTAL

We studied the kinetics of IPN formation from two network components. The first component was UP-637 epoxy–resorcinol resin [TU (Technical Specifications) 6-05-241–74] containing 32 wt % epoxy groups; for comparison we used ED-20 epoxy–4,4'-isopropylidenediphenol resin [GOST (State Standard) 10587–84] containing 22 wt % epoxy groups. The choice of UP-637 was governed by the higher strength of composites based on it, as compared with other modified resins [3, 6]. The epoxy resins were cured at 20°C with polyethylenepolyamine (PEPA) of B brand (TU 6-02-594–85), taken in amounts of 20 and 14 wt %, respectively, relative to the above-mentioned epoxy resins. The second component of IPN was a network copolymer based on polyethylene glycol maleate phthalate (PGMP) (GOST 27952–88) containing 98.2 wt % main substance and oligoether acrylates (OEAs): triethylene glycol dimethacrylate (TGM) and di(triethylene glycol) phthalate dimethacrylate (MGP) containing 98.6 and 98.2 wt % main substance, respectively. The characteristics of these compounds agree with data reported in [5, 7]. For comparison, we prepared copolymers of PGMP with methyl methacrylate (MMA). Copolymerization was performed at weight fraction of the oligomers in the initial mixtures of 0.45 at 20°C in the presence of the effective initiating system methyl ethyl ketone peroxide (MEKP)–cobalt diacetylacetonate (CDA), proposed in [5].

The kinetics of network formation was studied by two independent methods: IR spectroscopy and measurement of the electrical conductivity of curing systems. In the first case, IPNs were formed in special

1070-4272/01/7404-0653 $25.00 © 2001 MAIK "Nauka/Interperiodica"

Characteristics of 3D structure and physicomechanical characteristics of IPNs based on oligomer–oligomer systems* (formation temperature 20°C)

Sample no.	Resin	OEA copolymer	C_1, wt fraction	$W \times 10^4$, mol l^{-1} s^{-1}			C_2, wt fraction	ρ_{cl}	$\gamma \times 10^4$, mol cm^{-3}	$\bar{P}_{cl}$	ΣF	σ_c, MPa	a_{im}, kJ m^{-2}
				W_1	W_2	W_{app}							
1	ED-20	–	–	5.6	–	5.0	0.96	4.2	15.0	–	8528	96	12
2	UP-637	–	–	7.4	–	6.8	0.97	4.9	20.2	–	8560	102	14
3	–	PGMP + MMA	1.0	–	6.2	5.8	0.74	1.3	5.2	16	9275	66	9
4	–	PGMP + TGM	1.0	–	7.6	7.0	0.78	1.4	6.8	12	9816	80	16
5	–	PGMP + MGP	1.0	–	9.4	8.6	0.81	1.5	7.6	8	9856	94	18
6	ED-20	PGMP + MMA	0.5	6.0	6.8	11.6	0.82	1.5	9.1	12	8902	81	11
7	〃	PGMP + TGM	0.3	6.6	6.9	13.2	0.76	1.4	7.8	12	–	78	13
			0.45	6.2	8.1	14.0	0.84	1.8	10.4	10	9170	90	18
			0.6	6.4	8.5	14.6	0.80	1.5	8.1	11	–	82	15
8	〃	PGMP + MGP	0.45	6.3	10.2	15.1	0.86	1.9	12.2	7	9192	92	20
9	UP-637	PGMP + TGM	0.45	8.0	8.8	15.7	0.87	2.0	12.6	8	9196	95	22
10	〃	PGMP + MGP	0.45	8.2	10.4	17.4	0.89	2.1	14.0	6	9228	98	26

* (C_1, C_2) Content of copolymer and gel fraction, respectively; (ρ_{cl}) cross-linking density; (γ) content of chemical lattice points; ($\bar{P}_{cl}$) mean content of OEA units in cross-links; and (ΣF) total cohesion.

cells between NaCl plates directly in the cell compartment of a Specord 75-IR spectrometer. The extent of curing of epoxy resins was determined by measuring the optical density at the absorption peak of the epoxy groups at 930 cm^{-1}, and the degree of copolymerization of the second component, by measuring the optical density at the absorption peak at 1630 cm^{-1}, associated with stretching vibrations of the double bond in PGMP and OEA [6]. The transmission at these wave numbers varied within 15–80% in the course of network formation, which allowed the degree of conversion of the components to be measured with an accuracy of ±0.5%. The advantage of this method as compared with dilatometry and calorimetry is the possibility of monitoring the transformation of each component to high conversions, irrespective of the growing viscosity [6]. The rate of network formation from the epoxy resins, W_1, and the copolymerization rate W_2 were calculated by the least-squares method with error not exceeding 3%. The electrical conductivity of the curing system was measured in a temperature-controlled Teflon cell with an E7–8 digital meter by the previously described procedure [6] allowing calculation of the apparent rate of network formation W_{app}, which includes the overall rate of curing of the epoxy resin and the rate of copolymerization of the second component, with a relative error of 3%.

The formed IPNs were extracted with boiling acetone in a Soxhlet apparatus in the course of 12 h, after which the yield of the 3D-cross-linked gel fraction was determined. The extraction was performed with IPN materials formed by curing at 20°C for no less than 24 h. The strength characteristics of the materials were determined as follows. The breaking compression stress σ_c was measured according to GOST (State Standard) 4861–82 for cylindrical samples 12 mm in diameter and 15 mm high on a TsD-10 testing machine; the relative error did not exceed 2%. The impact resilience of the composites a_{im} was measured for 60 × 5 × 5-mm rectangular samples without notches using an MK-05 pendulum impact machine with distance of 40 mm between the bearings, according to GOST (State Standard) 3458–88; the relative error was 2%.

The kinetic parameters of IPN formation (see table) show that the rates of formation of individual network structures of the first and second components are

rather close; the curing rate of UP-637 resin and the copolymerization rate in the system PGMP + MGP are somewhat higher. The kinetic parameters of curing of the individual components, determined by IR spectroscopy (W_1) and evaluated from the electrical conductivity (W_{app}), are reasonably consistent. In preparing IPNs from two components, the rates of formation of the networks based on epoxy resin increase in going from ED-20 to UP-637, remaining close to the rates of curing of the individual resins (see table). Copolymerization of the second component occurs under the conditions when a network based on the epoxy resin is formed, with significant increase in the viscosity in the initial period, which favors manifestation of the gel effect; the rate W_2 is higher than that in the absence of the epoxy resin. The rates of formation of the network from the second component increase in going from TGM to MGP, all other conditions being the same, which is consistent with our data [5] on the relative reactivity of these OEAs in copolymerization. It should be noted that the apparent rates of IPN formation, W_{app} are, on the whole, additive with respect to W_1 and W_2 and can be used as a measure of the overall rate of IPN formation. The rates of IPN formation are the highest in formulations based on the epoxy–resorcinol resin and the PGMP–MGP copolymer: The IPN formation is complete at 20°C within 60–100 min.

The 3D structure of the IPNs was characterized by the cross-linking density ρ_{cl} {calculated by Charlesby's formula (1) [7]} and the content of chemical lattice points γ (see table).

$$\rho_{cl} = \frac{1/(\sqrt{m_s} - 1)}{1 - m_s}, \quad (1)$$

where m_s is the content of the soluble sol fraction in the composites, determined by extraction with acetone.

The parameter ρ_{cl} is dimensionless and allows only qualitative evaluation of the cross-linking density in IPNs as influenced by the initial formulation and the curing conditions. It is preferable to use the parameter γ, calculated from the known molecular weights of the IPN components and their content in the composites by the procedure similar to that described in [2, 6]; the relative error does not exceed 3%. Knowing γ and the molecular weights of the corresponding OEAs, we calculated the mean number of OEA units in the cross-links $\overline{P}_{cl}$ of the second IPN component. In total, these parameters characterize the 3D structure of the IPNs and reveal correlations between the structural parameters and

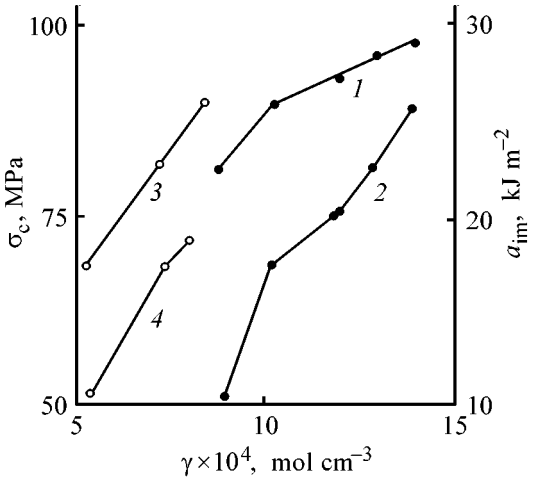

(*1, 3*) Breaking compression stress σ_c and (*2, 4*) impact resilience a_{im} of IPNs vs. the content of chemical lattice points γ in polymeric materials: (*1, 2*) polymeric materials with IPN based on epoxy resin and PGMP–OEA network copolymers; (*3, 4*) PGMP–OEA network copolymers. For compositions, see table.

strength characteristics (see table, figure). We found that both σ_c and a_{im} grow with increasing γ, which agrees with the trends observed previously in semi-IPNs [5, 6]. Among the materials prepared from the individual components, the highest strength is exhibited by the materials based on the epoxy–resorcinol resin and PGMP–MGP copolymers (see figure). As for IPNs prepared from two components, with the weight fraction of the second component (copolymer) raised from 0.3 to 0.6, the parameters ρ_{cl}, γ, and a_{im} first increase, reaching a maximum at C_1 = 0.45, and then decrease (see table). The trend in the variation of $\overline{P}_{cl}$ is the opposite. Estimation of the density of the chemical cross-links in copolymers of the oligoester resin with OEA showed that the content of the chemical lattice points increases in going from TGM to MGP, especially as compared with the copolymers based on MMA. The highest strength characteristics (both σ_c and a_{im}) are exhibited by the IPNs based on the epoxy–resorcinol resin and PGMP–MGP copolymers; the parameters of the 3D network for these IPNs are also the highest.

The physicomechanical properties of 3D-cross-linked polymers are determined by the content of not only chemical network points but also potential physical network points facilitating energy dissipation in mechanical treatment of the polymeric material [1, 8]. At present, there are no experimental procedures for measuring the physical network parameters in network polymers and IPNs [3, 7, 8]. The physical network density in polymers is estimated from the cohesion,

using the molar attraction constants F for various atomic groups in macromolecules, following the recommendations given in [7, 8]. Previously, such calculations of the total cohesion ΣF have been performed for TGM and MGP homopolymers; it was found that ΣF and the impact resilience of the polymers vary in parallel [9]. Using a similar procedure, we calculated the total cohesion both for the individual components and for IPNs prepared from them (see table); the error in calculating ΣF did not exceed 0.1%. It is seen that the strength grows with increasing cohesion, especially the dynamic strength characterized by a_{im}. The higher impact resilience of IPNs based on MGP copolymers, as compared with those based on TGM copolymers, may be due to the higher calculated values of total cohesion of such IPNs, since the MGP copolymers contain atomic groups with high internal rotation barrier—phthalate groups, and hence to larger zone in which cross-links are stabilized. The absolute values of the impact resilience of the resulting IPNs with the optimal composition are 1.5–2 times higher than the similar characteristics of the corresponding individual network components and correspond to the parameters of shockproof polymeric materials [7, 10].

CONCLUSION

The effect exerted by the content and nature of components on the kinetics of low-temperature formation of interpenetrating polymer networks from oligomer–oligomer systems was elucidated.

REFERENCES

1. Sperling, L.H., *Interpenetrating Polymer Networks and Related Materials*, New York: Plenum, 1982.
2. Lipatov, Yu.S. and Alekseeva, T.T., *Vysokomol. Soedin., Ser. A*, 1996, vol. 36, no. 6, pp. 940–944.
3. Zaitsev, Yu.S., Kochergin, Yu.S., Pakter, M.K., and Kucher, R.V., *Epoksidnye oligomery i kleevye kompozitsii* (Epoxy Oligomer and Adhesive Formulations), Kiev: Naukova Dumka, 1990.
4. Anisimov, Yu.N., Kolodyazhnyi, A.V., and Grekhova, O.B., *Zh. Prikl. Khim.*, 1999, vol. 72, no. 8, pp. 1385–1390.
5. Anisimov, Yu.N., Kolodyazhnyi, A.V., and Savin, S.N., *Zh. Prikl. Khim.*, 1998, vol. 71, no. 11, pp. 1867–1871.
6. Anisimov, Yu.N. and Savin, S.N., *Ukr. Khim. Zh.*, 2000, vol. 66, no. 4, pp. 48–52.
7. Sedov, L.N. and Mikhailova, Z.V., *Nenasyshchennye poliefiry* (Unsaturated Polyethers and Polyesters), Moscow: Khimiya, 1977.
8. Van Krevelen, D.W., *Properties of Polymers. Correlations with Chemical Structure*, Amsterdam: Elsevier, 1972.
9. Anisimov, Yu.N. and Kolodyazhnyi, A.V., *Zh. Prikl. Khim.*, 1996, vol. 69, no. 7, pp. 1179–1182.
10. Babaevskii, P.G. and Kulik, S.G., *Treshchinostoikost' otverzhdennykh polimernykh kompozitsii* (Fracturing of Cured Polymer Compounds), Moscow: Khimiya, 1991.

Russian Journal of Applied Chemistry, Vol. 74, No. 4, 2001, pp. 657–662. Translated from Zhurnal Prikladnoi Khimii, Vol. 74, No. 4, 2001, pp. 637–642.

MACROMOLECULAR CHEMISTRY AND POLYMERIC MATERIALS

Directional Synthesis of Hybrid Polymers from 2- and 4-Vinylpyridines

L. A. Shibaev, N. M. Geller, T. A. Antonova, A. V. Gribanov, M. V. Mokeev, S. I. Klenin, and B. L. Erusalimskii

Institute of Macromolecular Compounds, Russian Academy of Sciences, St. Petersburg, Russia

Received December 18, 2000

Abstract—Formation of hybrid three-dimensional structures by treatment of copolymers of 2- and 4-vinylpyridine with butyllithium, followed by grafting of *tert*-butyl acrylate molecules, was studied by mass-spectrometric thermal analysis and ^{13}C NMR spectroscopy.

The specific feature of anionic polymerization of 2- and 4-vinylpyridine (2-VP, 4-VP) is the high activity of the pyridine rings in the monomers and polymers in reactions with initiator molecules and active centers (ACs) formed in the course of polymerization. Thanks to this property, it is possible to construct macromolecules of complex "architecture," including hybrid polymers based on copolymers of 2- and 4-VP and *tert*-butyl acrylate (TBA), under the action of butyllithium.

The process of formation of three-dimensional (3D) hybrid structures, which can be transformed into polyelectrolyte networks with predictable parameters, can be monitored by mass-spectrometric thermal analysis (MTA) and solid-state ^{13}C NMR spectroscopy.

Synthesis of homopolymers and hybrid polymers of 2- and 4-VP is of interest as one of possible routes (along with polymerization of some other polar monomers) to polymers that can be functionalized and used in various branches of chemistry, pharmacology, medicine, biology, etc., in particular, in the fields where pH-sensitive polymeric systems are required. A study of the mechanism of anionic polymerization of polar monomers, effected by allyl derivatives of Cr, Mo, and W, and a structural analysis of the resulting macromolecules [1–3] revealed a number of structural forms of the polymers, originating from two types of active polymerization centers that arise on the growing chains: nitrogen–metal and carbon–metal, capable of interconversion in the course of growth of the polymeric molecules. Polymerization of 2- and 4-VP, as well as that of *N*,*N*-dimethylacrylamide [4], yields macrocyclic, network, branched, star-shaped, and linear structures. The revealed relations allow control of the macromolecular architecture within wide limits and construction of polymeric materials with new chemical, mechanical, optical, and hydrodynamic properties. These relations are also to a certain extent applicable to other initiators of anionic polymerization, such as organolithium, -sodium, -potassium, and -magnesium compounds. To reveal the specific features of polymerization under the influence of the above compounds, it is appropriate to examine the results of synthesis of hybrid polymers in the presence of an organolithium compound.

In this work, taking into account the high activity of pyridine rings in reactions with organometallic compounds and different activities of the N–Met bond in 2- and 4-VP polymers, we made an attempt to construct polymeric chains, using as the base element an assembly of characterized 2- and 4-VP copolymers prepared by radical polymerization. The copolymers were treated with butyllithium to generate active centers along the polymer chain for subsequent grafting of pendant chains of poly-*tert*-butyl acrylate (PTBA). We expected that, by varying the molecular weight and composition of the copolymer, it would be possible to change the content of active centers along the copolymer chain and hence the number of pendant chains of the grafted polymer. It would be thus possible to control the parameters of the branched polymer and, in the limiting case, the parameters of the forming 3D network.

To analyze the polymers and reveal the mechanism of the reaction of organometallic compounds with polyvinylpyridines, we used MTA and solid-state ^{13}C NMR spectroscopy.

1070-4272/01/7404-0657 $25.00 © 2001 MAIK "Nauka/Interperiodica"

EXPERIMENTAL

Homo- and copolymers of 2- and 4-VP were prepared by polymerization of freshly distilled 2- and 4-VP at 70°C in the bulk in the presence of 0.5% azobis(isobutyronitrile) (AIBN). The polymer was precipitated into petroleum ether, purified by fourfold reprecipitation from chloroform solution into petroleum ether, and vacuum-dried at 50°C for 24 h. Butyllithium was prepared by reaction of Li with C_4H_9Cl in hexane. The reaction of the polymers and copolymers with C_4H_9Li was performed at temperatures from +5 to –65°C, polymer concentration of 0.1 M, and molar ratios C_4H_9Li/monomer unit of 1, 0.8, 0.3, and 0.1. After a definite time (from 1 min to several hours), either the process was stopped by adding 1 ml of a cooled CH_3OH–H_2O mixture (10 : 1), or pendant TBA chains were grafted by adding 1 ml of TBA. The polymer was precipitated by adding water, washed several times with fresh portions of water (until pH of the wash water reached 6–7), and vacuum-dried at 50°C.

Mass-spectrometric thermal analysis of the polymers [3] was performed with an MKh-1320 device. A 0.1–0.2-mg sample was fixed with aluminum foil on a thermocouple placed in the thermal degradation chamber. The sample was heated from 293 to 773 K at a rate of 5 deg min^{-1}. The mass spectra of the thermal degradation products were recorded at 2-min intervals, and a mass thermogram (temperature dependence of the characteristic ion currents) was obtained.

High-resolution solid-state ^{13}C NMR spectra were obtained at room temperature on a Bruker CXP-100 spectrometer (25.18 MHz for ^{13}C) using magic angle spinning (3–4 kHz) and cross polarization techniques. The chemical shifts (ppm) are given relative to TMS.

The reaction of butyllithium with pyridine was described for the first time by Ziegler [5]. Nucleophilic substitution at the α-position yielded 2-butylpyridine. Ziegler also prepared 2,6-dibutylpyridine by reaction of butyllithium with 2-butylpyridine, and also some other related derivatives of pyridine and quinoline [6]:

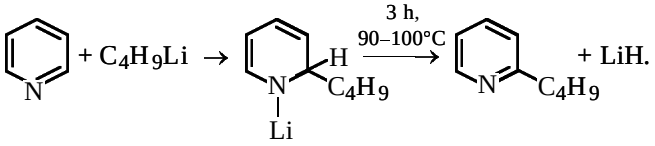

Reaction of pyridine with C_4H_9Li involves alkylation with the formation of a cyclic diene structure, followed by rearomatization. Much later, Schmitz *et al.* [7] studied by chromatography and mass spectrometry the products of reaction of pyridine, cumyl, and ethylpyridine with C_4H_9Li. Some conclusions of [7] can be applied to reactions accompanying the anionic polymerization of 2-VP. Alkylation of the ring by the nucleophilic attack at the α-position occurred in all cases (at varied component ratio, reaction temperature, chain-terminating agents). In some cases, products formed by attack of C_4H_9Li at the alkyl group of the model compound were detected. The products of ring alkylation undergo rearomatization, but dihydro- and tetrahydroalkylpyridines were also detected.

The first step in the development of a procedure for directional synthesis of hybrid polymers was to reveal specific features of the mechanism by which occurs

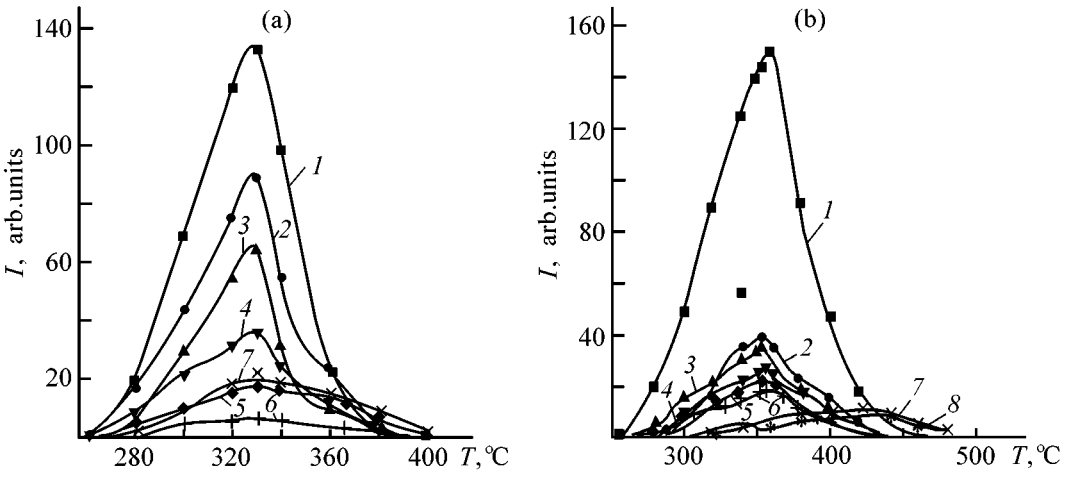

Fig. 1. Curves of evolutiuon of volatile products in thermal degradation of P-2-VP: (a) initial polymer and (b) polymer treated with butyllithium (P-2-VP-1). (*I*) Intensity and (*T*) temperature. Mass of characteristics ions: (a) (*1*) 105, (*2*) 79, (*3*) 104, (*4*) 106, (*5*) 118, (*6*) 119, and (*7*) 132; (b) (*1*) 119, (*2*) 132, (*3*) 175, (*4*) 105, (*5*) 106, (*6*) 79, (*7*) 163, and (*8*) 137.

the reaction of poly-2-vinylpyridine (P-2-VP) with C_4H_9Li. It was of interest to find how readily are the pyridine rings in the polymer chains alkylated:

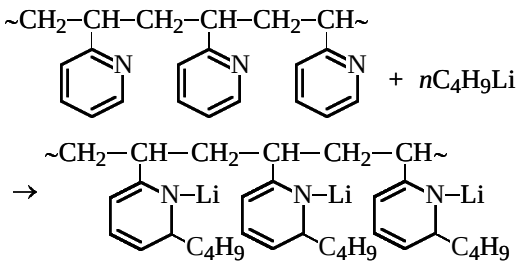

Figure 1a shows a mass thermogram of P-2-VP prepared by radical polymerization of 2-VP in the bulk, initiated by AIBN. Treatment of this polymer in toluene at +5°C with butyllithium (monomer unit : C_4H_9Li = 1 : 0.8) yields a product (P-2-VP-1) whose mass thermogram (Fig. 1b) significantly differs from that given in Fig. 1a both in the set of characteristic peaks and in the temperature dependence of the ion currents. Below are given the mass spectra of the thermal degradation products of the initial P-2-VP at 370°C

m/*e*	105	79	104	106	78
I	1000	685	428	135	112
m/*e*	93	132	118	210	119
I	90	78	71	26	26

and P-2-VP treated with C_4H_9Li (P-2-VP-1) at 355°C:

m/*e*	119	133	132	175	161	105	146
I	1000	815	250	230	137	164	157
m/*e*	93	107	79	162	189	78	
I	133	131	130	79	59	52	

The fragmentation pattern of P-2-VP[1] is shown in Scheme 1.

Scheme 1.

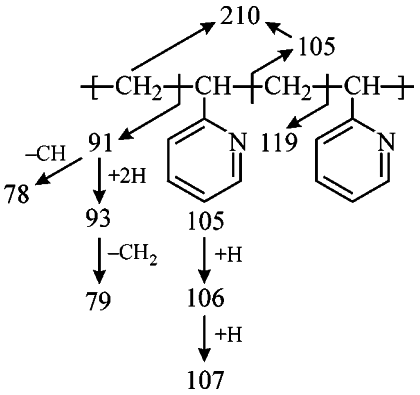

Fragmentation of P-2-VP.

[1] It should be taken into account that the mass spectrum reflects a superposition of two processes: thermal degradation of polymeric molecules and fragmentation of low-molecular-weight degradation products in the ion source.

Since, as already noted, the reaction of P-2-VP with C_4H_9Li can yield both alkylcyclodiene and aromatic products, for we should consider two fragmentation patterns P-2-VP-1 (Schemes 2, 3).

As seen from the mass spectrum of P-2-VP-1, the strongest peak is that at *m*/*e* 119, in contrast to the mass spectrum of the initial P-2-VP with the strongest peak at *m*/*e* 105. Simple fragmentation by Scheme 2 does not produce an ion with *m*/*e* 119 without further additions or rearrangements. Fragmentation by Scheme 3 does produce an ion with *m*/*e* 119, but in this case its peak would hardly be the strongest in the mass spectrum.

Scheme 2.

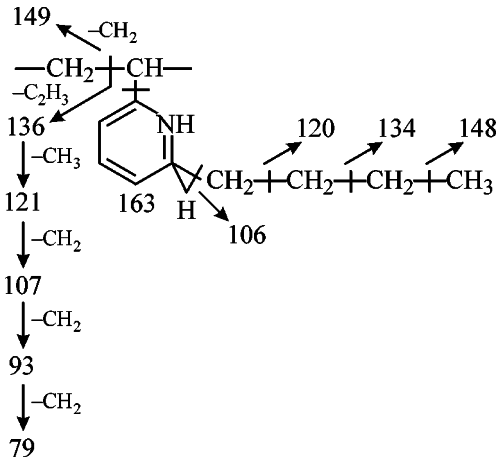

Fragmentation of P-2-VP-1 (without rearomatization).

Scheme 3.

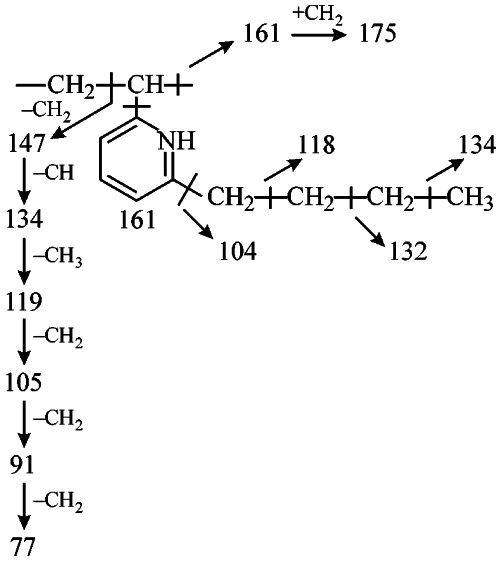

Fragmentation of P-2-VP-1 (with rearomatization).

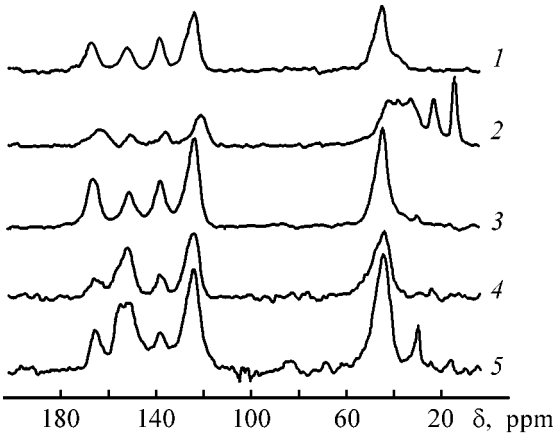

Fig. 2. High-resolution solid-state ^{13}C NMR spectra: (*1*) initial P-2-VP; (*2*) P-2-VP treated with butyllithium (P-2-VP-1); (*3*) P-2-VP treated with butyllithium at 0°C with addition of TBA; (*4*) copolymer of 2-VP and 4-VP (1 : 1); and (*5*) graft copolymer based on 2-VP : 4-VP (1 : 1) and TBA. (δ) Chemical shift.

The more probable pathway of formation of the ion with *m*/*e* 119 is the loss of the C_3H_7 group followed by addition of hydrogen to the remaining fragment:

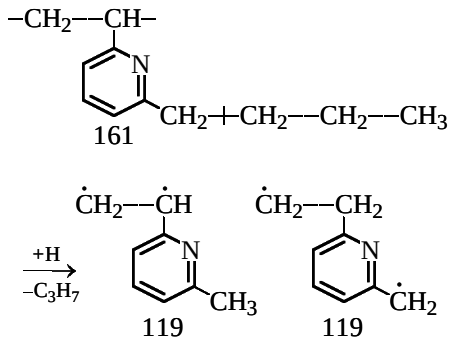

At the chosen ratio of the polymer and C_4H_9Li, the alkylation of P-2-VP occurs to no more than 80%. The P-2-VP units remaining unchanged give the fragmentation peak at *m*/*e* 105. Since depolymerization is hindered by the presence of alkylated units, another pathway of thermal degradation of P-2-VP units may become preferable:

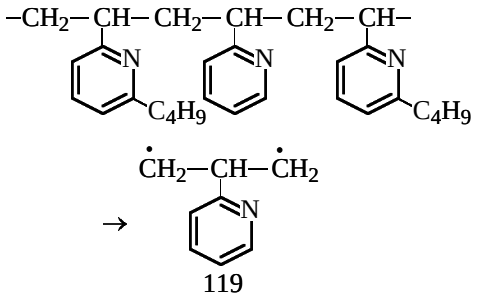

From the two above-given fragmentation patterns of P-2-VP-1, that shown in Scheme 3 is more consistent with the observed set of charactestic ions. In other words, under the chosen conditions, alkylation of the pyridine rings is followed by complete (or considerable) rearomatization of the alkylated cyclodiene fragments.

This conclusion is supported by the fact that ions with *m*/*e* 161 (molecular ion in Scheme 3, one of the strongest peaks in the mass spectrum), 132, 177 ($M + CH_2$) and 189 ($M + C_2H_4$) are present in the mass spectrum.

This result of MTA was confirmed by solid-state ^{13}C NMR spectroscopy. Figure 2 (curve *1*) shows the NMR spectrum of the initial P-2-VP. The signals (ppm) are assigned as follows: 42.7, CH and CH_2 groups of the vinyl chain; carbon atoms of the pyridine ring: 121.7, C^2 and C^4; 136.4, C^3; 149.9, C^5; and 164.9, C^1. The spectrum is fully consistent with the structure of P-2-VP.

Figure 2 (curve *2*) shows an NMR spectrum of the polymer treated with butyllithium (P-2-VP-1). The spectrum contains lines corresponding to the carbon atoms in the chain of the butyl fragment (12.4, 21.2, 30.9, 36.2 ppm). In the downfield region, the positions and shapes of some lines changed. The lack of signals at about 100 and 50 ppm ($C^{2'}$ and $C^{4'}$ atoms in the cyclodiene moiety) suggests a practically complete rearomatization of the pyridine rings alkylated with butyllithium. The signals at 163 ($C^{1'}$, $C^{5'}$), 134 ($C^{3'}$), and 119 ppm ($C^{2'}$, $C^{4'}$) have downfield shoulders, which, in combination with the presence of a signal at 148.5 ppm belonging to the C^5 atom in the intact pyridine ring, suggests incomplete alkylation of the pyridine ring and agrees with our expectations when account is taken of the reaction conditions.

Thus, the MTA and ^{13}C NMR data show that alkylation of the pyridine rings in P-2-VP under the action of C_4H_9Li readily occurs at +5°C; the reaction products contain vinylpyridine and vinylalkylpyridine fragments, whereas fragments with cyclodiene structure are practically absent. However, such structures are detected by ^{13}C NMR spectroscopy in the products of the reaction of P-2-VP with C_4H_9Li, performed at lower temperature (e.g., –65°C); thus, we can conclude that, in the range from +5 to –65°C, rearomatization of cyclodiene structures formed by alkylation of P-2-VP with C_4H_9Li significantly depends on temperature.

The next step in the synthesis of hybrid polymers is the reaction of "living" polyvinylpyridine with TBA at the N–Li bond. It has been noticed [8] that in the case of P-2-VP, active centers show low activity in anionic polymerization, especially at low temperatures; by contrast, in the case of P-4-VP, N–Li

active centers are highly reactive. Therefore, for further directional synthesis of hybrid polymers we decided to use copolymers of 2-VP and 4-VP obtained by radical polymerization in the bulk at 70°C under the action of AIBN. The copolymerization constants were determined by the Fineman–Ross method: r_1 = 0.50 (4-VP), r_2 = 0.79 (2-VP). The composition of the copolymers was determined from the ^{1}H NMR spectra (in $CDCl_3$); the molecular and conformational characteristics of the copolymers were studied by sedimentation–diffusion analysis, viscometry, and light scattering (see table).

Molecular weight M_{sd} and composition of copolymers

Molar ratio of 4-VP and 2-VP		M_{sd}
in monomer mixture	in copolymer*	
0.80 : 0.20	0.75 : 0.25	20000
0.50 : 0.50	0.42 : 0.58	48000
0.20 : 0.80	0.22 : 0.78	100000

* The composition of the copolymers was determined from the ^{1}H NMR spectra by the intensity ratio of the peaks (ppm) at 8.2 (S_1), 6.8 (S_2), and 6.25 ppm (S_3); content of 2-VP $C = 2S_2/(S_1 + S_2) = 2S_2/(S_2 + S_3)$.

Figure 2 (curve *3*) shows a ^{13}C NMR spectrum of P-2-VP treated with C_4H_9Li at 0°C, with TBA added at the same temperature. No hybrid polymer is detected. The MTA data confirm this fact, though traces of PTBA are detected (a certain amount of the homopolymer may be present). The same result (and even more apparent) was obtained when the same process was performed at –65°C. By contrast, the NMR spectrum of the copolymer containing 58% 2-VP and 42% 4-VP (Fig. 2, curve *4*), treated with C_4H_9Li at –65°C and subjected to grafting with TBA, is quite different (Fig. 2, curve *5*). Both the intensities and positions of the characteristic signals change. For example, signals from the $–CH_2–$ (22.7 ppm) and $–CH_3$ (14 ppm) groups are observed (other butyl signals are obscured by signals of the polymer chain atoms). Also, there are signals corresponding to the TBA structures: 80 (–O–C–), 28 ($–CH_3$), and a shoulder at 176 ppm (–C=O). The shoulder at about 52 ppm corresponds to the TBA methylene group bound to the nitrogen atom of the pyridine ring, which confirms grafting of TBA to the pyridine ring. Also, the shape of the lines corresponding to the carbon atoms of the pyridine ring changes (range 170–110 ppm). The signal at 66.8 ppm corresponds to the carbon atoms of the pyridine rings directly bound to the butyl group (C^3 in 2-VP and C^5 in 4-VP fragments). The signal at 60 ppm is due to the same carbon atoms in the pyridine rings transformed into the diene structures. The ratio of the pyridine and diene rings, evaluated from the integral intensities of the C^3 and C^5 signals and the signals of methylene groups of the TBA chains, is approximately 1 : 1.

The above results prove grafting of TBA chains to the N–Li active centers in the 4-VP fragments of the 2-VP–4-VP copolymer. This fact suggests the possibility of controlling within wide limits the content of pendant PTBA chains by varying the content of 4-VP in the copolymer. Furthermore, this result furnishes an opportunity to evaluate the amount of active centers along the backbone molecules of the hybrid polymer and, hence, to determine quantitatively the composition of the whole hybrid polymer. It should be noted also that our results provide a basis for synthesis of a 3D network from the hybrid copolymer by appropriately choosing the concentration of the 2-VP–4-P copolymer in the reaction solution and the size of the pendant TBA chains. For example, with these parameters increased, the reaction of the active centers at the end of the growing PTBA chain with the pyridine ring of the adjacent backbone copolymer molecule becomes possible.

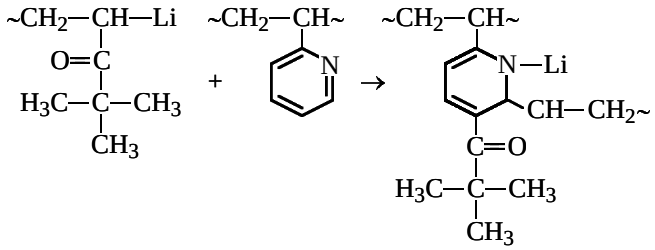

For clearer presentation of the obtained results and further progress of the study, we give the general scheme of formation of hybrid copolymers based on 2-VP, 4-VP, and TBA.

(1) Synthesis of 2-VP and 4-VP copolymer.

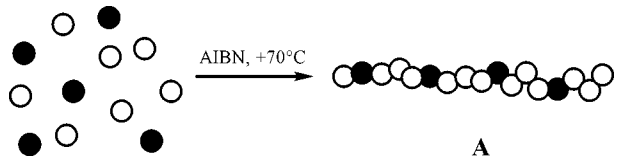

(2) Formation of active centers along the copolymer chain.

(3) Synthesis of the graft copolymer with pendant TBA chains.

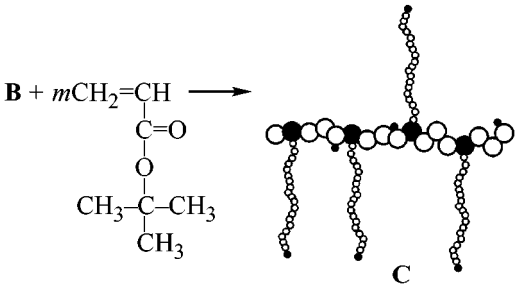

(4) Formation of a 3D structure by grafting of a pendant chain of the hybrid polymer to the backbone copolymer molecule.

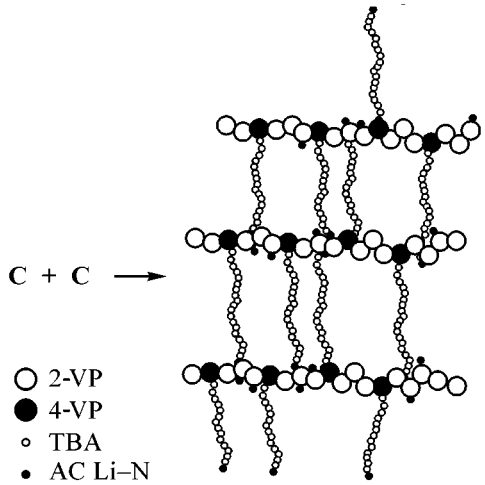

This scheme shows that the parameters of the 3D structure can be controlled by the composition and molecular weight of the initial copolymer **A**, concentration of butyllithium, amount of reacted TBA, and concentration of the hybrid polymer **C** in the reaction solution.

The 3D structure of the hybrid polymer can be subsequently converted into a polyelectrolytic pH-sensitive network by transforming the backbone moiety into a salt of the polybase (e.g., by reaction of the polymer with HCl) and of pendant PTBA chains into polyacrylic acid (e.g., by pyrolysis at 200°C) [9]:

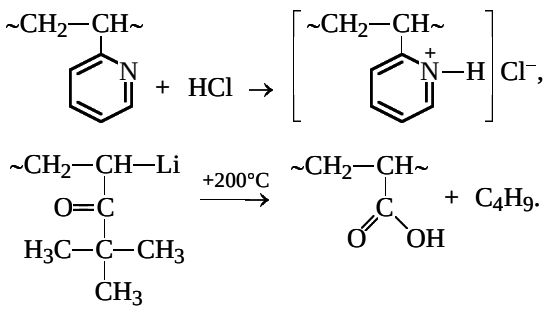

CONCLUSION

A study by mass-spetrometric thermal analysis and high-resolution solid-state ^{13}C NMR spectroscopy showed that butyllithium is active in alkylation of pyridine rings of polymers and copolymers of 2- and 4-vinylpyridine. The extent of rearomatization of the alkylated pyridine rings is temperature-dependent in the range from +5 to –65°C. In this temperature range, the N–Li active centers in the 2-vinylpyridine units are weakly active in grafting of *tert*-butyl acrylate units. By contrast, similar centers in the 4-vinylpyridine units are active, which allows preparation of a hybrid copolymer of 2-vinylpyridine, 4-vinylpyridine, and *tert*-butyl acrylate. The revealed trends allowed us to propose a scheme for preparing 3D structures that can be converted into polyelectrolytic networks with controllable structural parameters.

ACKNOWLEDGMENTS

The study was financially supported by the Russian Foundation for Basic Research (project no. 99-03-33333).

REFERENCES

1. Erussalimsky, B.L., Fedorova, L.A., Klenin, S.I., and Shibaev, L.A., *Macromol. Symp.*, 1998, vol. 128, pp. 221–230.
2. Shibaev, L.A., Antonova, T.A., Fedorova, L.A., *et al.*, *Vysokomol. Soedin., Ser. A*, 1995, vol. 37, no. 11, pp. 1874–1880.
3. Shibaev, L.A., Fedorova, L.A., Antonova, T.A., *et al.*, *Vysokomol. Soedin., Ser. A*, 1996, vol. 38, no. 11, pp. 1808–1811.
4. Shibaev, L.A., Fedorova, L.A., Antonova, T.A., *et al.*, *Zh. Prikl. Khim.*, 1999, vol. 72, no. 8, pp. 1354–1359.
5. Ziegler, K. and Zeiser, H., *Ber. Deutsch. Chem. Ges.*, 1930, vol. 63, pp. 1847–1852.
6. Ziegler, K. and Zeiser, H., *Justus Liebigs Ann. Chem.*, 1931, vol. 485, no. 6, pp. 174–179.
7. Schmitz, F.P., Hilgers, H.H., and Gemmel, B., *Makromol. Chem.*, 1990, vol. 191, pp. 1033–1049.
8. Krasnosel'skaya, I.G., D'yakonova, N.V., Turkova, L.D., *et al.*, *Vysokomol. Soedin.*, 1999, vol. 41, no. 7, pp. 1093–1101.
9. Hirochi, I. and Mitsuru, U., *Macromolecules*, 1988, vol. 21, no. 5, pp. 1475–1482.

Russian Journal of Applied Chemistry, Vol. 74, No. 4, 2001, pp. 663–668. Translated from Zhurnal Prikladnoi Khimii, Vol. 74, No. 4, 2001, pp. 643–648.

MACROMOLECULAR CHEMISTRY AND POLYMERIC MATERIALS

Synthesis of Water-Soluble Chemically Degradable Polymers from Glutaraldehyde and *N*-Vinylpyrrolidone–Allylamine Copolymers

M. V. Solovskii, N. V. Nikol'skaya, E. V. Korneeva, N. A. Mikhailova, and G. M. Pavlov

Institute of Macromolecular Compounds, Russian Academy of Sciences, St. Petersburg, Russia

Institute of Physics, St. Petersburg State University, St. Petersburg, Russia

Received November 29, 2000

Abstract—Water-soluble chemically degradable copolymers of *N*-vinylpyrrolidone with allylamine, containing azomethine links between the polymeric chains, were prepared. The composition and molecular-weight characteristics of the polymers were determined.

Polymers based on *N*-vinylpyrrolidone (VP) are widely used in medicine as detoxicants, plasma substitutes, and means for prolonging the effect of various drugs [1]. At the same time, these materials, being carbon-chain polymers, are not biodegradable. The task is to restrict their molecular weight (*MW*) so as to facilitate their elimination from a living body after having fulfilled the biological function. Relatively low-molecular-weight (*MW* 10 000–15 000) polymers can be used only as detoxicants; their molecular weight is too low for use as plasma substitutes or prolongation means, because such polymers will be rapidly eliminated from the living body and will not ensure the required biological effect. At the same time, use of higher-molecular-weight (*MW* 80 000–100 000) polymers, suitable as prolongation means, involves problems associated with their slow elimination and accumulation of high-molecular-weight fractions causing undesirable side biological effects.

Published data show [2] that the maximal molecular weight of poly-VP at which its macromolecules can be filtered through kidneys is 40 000. Distribution of poly-VP in a body and its elimination with urine should be considered as biological fractionation of a heterogeneous mixture of macromolecules of different sizes, some of which (smaller) pass through biological membranes and the others are retained.

It is convenient to use as carriers of biologically active substances (BASs) water-soluble VP polymers with the *MW* lower than the critical value for filtration through kidneys, containing, at the same time, chemically or biologically degradable links between macromolecular chains. In this case the polymer would be retained in a body for a long time, gradually degrading into low-molecular-weight fragments subsequently eliminated by the kidney filtration mechanism [3].

Thus, from the practical viewpoint, it is appropriate to synthesize water-soluble macromolecules of reactive low-molecular-weight VP copolymers undergoing chemical (hydrolysis) or biological degradation in a living body to low-molecular-weight fragments that can be readily eliminated from the living body. Preliminary addition of drugs to such chemically degradable copolymers will ensure their prolonged effect.

This paper reports on synthesis and study of water-soluble VP–allylamine copolymers (VP–Aam) treated with glutaraldehyde to form readily hydrolyzable azomethine links between the polymeric chains. Such polymer systems have not been described previously.

The interest in VP–Aam copolymers (compared, e.g., with VP–vinylamine copolymers) is due to the fact that copolymerization of VP with Aam, similar to other allyl monomers, is accompanied by degradation transfer of a chain to the allyl monomer. Thus, copolymerization of VP with allyl monomers yields low-molecular-weight copolymers without formation of blocks of the reactive units. Copolymers with just these features were required as starting substances for our study.

1070-4272/01/7404-0663 $25.00 © 2001 MAIK "Nauka/Interperiodica"

Table 1. Radical copolymerization of VP (M_1) with Aam (M_2) in isopropanol at 70°C, [AIBN] = 1.0 wt %

Starting monomer mixture		Yield in 48 h, %	Copolymer	VP–Aam copolymer		
$[M_2]$, mol %	$[M_1+M_2]$, wt %			$[m_2]$, mol %	$[\eta]$, dl g^{-1}	$\overline{M}_v$
20	30	44.9	**Ia**	6.2	0.13	20000
25	30	45.6	**Ib**	6.0	0.11	15000
25	40	49.6	**Ic**	7.0	0.11	15000
25	50	45.2	**Id**	8.8	0.10	13000
30	40	46.0	**Ie**	9.7	0.10	13000
25	50	49.0	**If**	8.70	0.09	11000
15	30	92.5	**Ig***	6.30	0.15	28000
20	30	89.1	**Ih***	8.4	0.08	9000

* Copolymers **Ig** and **Ih** were prepared by radiation-induced copolymerization at a dose of 100 kGy.

Table 2. Reaction of VP–Aam copolymers with glutaraldehyde (GA) in aqueous solution at 45°C in a flask without purging with argon

Initial copolymer		C_{cop},* wt %	[GA] : [NH_2]	τ, h	Reaction product		
NH_2, mol %	$[\eta]$, dl g^{-1}				yield, %	$[NH_2]$, mol %	$[\eta]$, dl g^{-1}
6.0	0.11	12.0	0.20 : 1	Gel formed			
6.0	0.11	12.0	0.15 : 1	〃			
6.0	0.11	12.0	0.10 : 1	6	72.0	5.10	0.20
6.2	0.13	8.2	0.10 : 1	9.5	90.0	2.10	0.25

* (C_{cop}) Copolymer concentration.

It should be noted that radical copolymerization of VP with Aam as a base in solution has been poorly studied [4]. Panarin *et al*. [5] reported copolymerization of VP with allylammonium salts in aqueous solution in the presence of a water-soluble initiator, 2,2'-azo-bis-(2-amidinylpropane) dichloride. They prepared in 98% yield VP–Aam · HX copolymers containing 10.8–27.1 mol % Aam · HX units. At the same time, it seemed appropriate to study single-stage copolymerization of VP with Aam in the form of a base in an organic solvent (acting as transfer agent for the growing polymeric chain) using a readily available initiator, azobis(isobutyronitrile) (AIBN), to evaluate the potentialities and limitations of this route to VP–Aam copolymers, to study the properties of the resulting copolymers, and to bring them into reaction with glutaraldehyde.

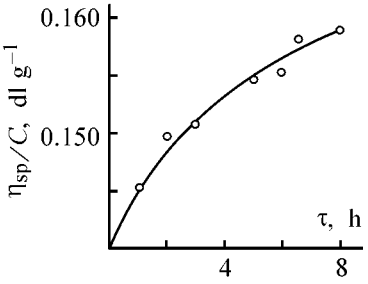

Fig. 1. Variation with time τ of the reduced viscosity η_{sp}/C of aqueous solution of **Ia** in the presence of glutaraldehyde. 45°C; C_{cop} = 5.0 wt %; [GA] : [NH_2] = 0.2 : 1.

Radical copolymerization of VP with allylamine was performed in isopropanol at 70°C in the presence of 1 wt % AIBN; the total concentration of the monomers in the starting mixture $[M_1 + M_2]$ was 30–50 wt %, $[M_2]$ = 20–30 mol % (Table 1). Isopropanol is a well-known chain-transfer agent, which also facilitated the preparation of low-molecular-weight copolymers. As shown in Table 1, low-molecular-weight ($\overline{M}_v$ = 11000–20000) copolymers **Ia**–**If** are formed under these conditions in 45–50% yield; the content of the allylamine units is from 6.0 to 9.7 mol %.

It is known [6, 7] that radiation-induced copolymerization allows difficultly polymerizable monomers to be involved in the process, because it ensures increased concentration of initiating radicals. Allylamine is among monomers of this kind. Radiation-induced copolymerization of VP with Aam was performed in isopropanol at irradiation dose of 100 kGy. Table 1 shows that initiation of copolymerization by radiation is more efficient than that by a substance. Copolymers **Ig** and **Ih** are similar in composition to, respectively, copolymers **Ia** and **If** (Table 1). However, the yields are different: 92.5 and 89.1% for **Ig** and **Ih** against 44.9 and 49.0% for, respectively, **Ia** and **If**.

In the preliminary stage of the study, reactions of copolymers **I** with glutaraldehyde were performed in aqueous solution at 45°C in a flask without argon purging (Table 2). As seen from Table 2, gelation is avoided when copolymer **I** is taken in a concentration of 8–12 wt % at a molar ratio of GA to NH_2 groups approximately equal to 0.1 : 1. The main part of experiments were performed in aqueous solution at 45°C in sealed ampules preliminarily purged with argon. The concentration of copolymers **I** was varied from 8.5 to 11.0 wt %, and the molar ratio of GA to NH_2 groups was in the range from 0.10 : 1 to 0.15 : 1. The concentration of copolymers **I** was chosen so as to exclude gelation and keep above unity the product $c[\eta]$ characterizing the degree of solution filling with polymer globules. Under such conditions, polymeric chains can undergo intermolecular cross-linking to

give copolymers **II**. This process manifested itself as an increase in the *MW* of the starting copolymers (Table 3) and in the reduced (Fig. 1) and intrinsic (Table 3) viscosities. The reaction of copolymers **I** with glutaraldehyde to give copolymers **II** can be schematically represented as:

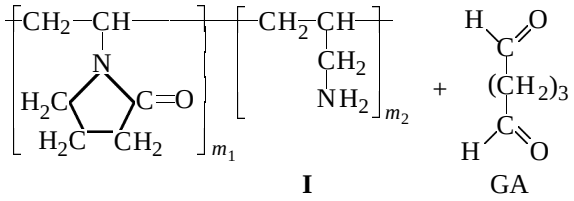

I GA

$m_1 + m_2 = 100$ mol %

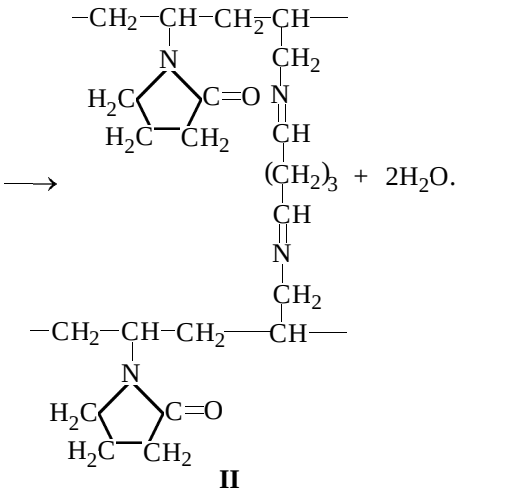

II

This process resembles the cross-linking below gel point of linear polystyrene with a bifunctional compound, 9,10-bis(chloromethyl)anthracene, studied in detail by Krakovyak *et al*. [8]. Intrachain cross-links with glutaraldehyde of type **III** are also possible.

$$–CH_2–N=CH–(CH_2)_3–CH=N–CH_2– \quad \textbf{(III)}$$

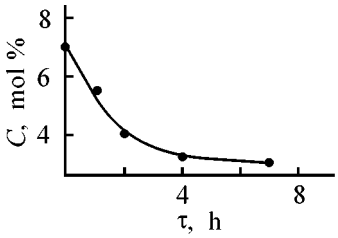

Fig. 2. Variation with time τ of the content C of NH_2 groups in copolymer **Ic** in the course of its reaction with glutaraldehyde in aqueous solution. 45°C; C_{cop} = 10.5 wt %; [GA] : [NH_2] = 0.15 : 1.

Cross-linking is accompanied by a decrease in the molar content of NH_2 groups in the starting copolymer **I** (Fig. 2, Table 3). Copolymer **IIa** was formed at complete conversion of the NH_2 groups. The conversion of the NH_2 groups in the formation of copolymers **IIb**–**IIe** was 47–57%. The resulting cross-linked copolymers **IIb**–**IIe** containing azomethine cross-links between the polymer chains are readily soluble in water, which allowed us to study their molecular characteristics in 0.1 N aqueous solution of sodium acetate. Table 4 lists the intrinsic viscosities [η], diffusion (D_0) and sedimentation (S_0) coefficients, and molecular weights M_{SD} of soluble cross-linked copolymers **IIa**, **IIc**, and **IIe**, determined by combination of the diffusion and sedimentation methods.

Copolymer **IIa** was prepared from linear VP–Aam copolymer with small (4.94 mol %) content of NH_2 groups, which were completely converted in the reaction with glutaraldehyde. The reaction yielded a VP–Aam polymer with M_{SD} = 52 000. In the course of reaction with glutaraldehyde to form polymer **IIa**, the molecular weight of the starting linear VP–Aam copolymer increased by approximately a factor of 3. For copolymer **IIa**, $D_0 = 3.7 \times 10^{-7}$ cm^2 s^{-1} and $S_0 = 1.7 \times 10^{-13}$ Svedberg units (Sv).

Table 3. Reaction of VP–Aam copolymers with glutaraldehyde in aqueous solution at 45°C in a sealed ampule purged with argon

Initial copolymer			C_{cop}, wt %	[GA] : [NH_2]	τ, h	Reaction product*						
NH_2, mol %	[η], dl g^{-1}	$\bar{M}_v$				copolymer	yield, %	[NH_2], mol %	[η], dl g^{-1}	$D_0 \times 10^7$, cm^2 s^{-1}	$S_0 \times 10^{13}$, Sv	M_{SD}
4.9	0.12	18 000	10.0	0.1 : 1	9	**IIa**	64.0	0	0.18	3.7	1.7	52 000
7.0	0.11	15 000	10.0	0.1 : 1	9	**IIb**	72.2	3.7	0.25	–	–	–
7.0	0.11	15 000	10.5	0.1 : 1	9	**IIc**	72.0	3.4	0.26	3.3	2.75	94 000
7.0	0.11	15 000	10.5	0.1 : 1	8	**IId**	78.0	3.3	0.27	2.9	2.65	103 000
7.0	0.11	15 000	10.5	0.15 : 1	7	**IIe**	80.0	3.00	0.26	2.9	2.15	84 000
7.0	0.11	15 000	11.0	0.15 : 1	7	Gel formed						

* (D_0) diffusion coefficient; (S_0) sedimentation coefficient, Svedberg units (Sv); (M_{SD}) molecular weight determined by combination of the diffusion and sedimentation methods.

Table 4. Variation of pH of the aqueous solution containing cross-linked copolymer **IIc**

τ, days	pH	Q_{pH}, %	τ, days	pH	Q_{pH}, %
C_{cop} = 0.1 wt %, 25°C			C_{cop} = 0.05 wt %, 37°C		
0	5.50	0	0	5.0	0
3	6.78	38.0	3	7.38	61.6
7	7.25	52.0	7	7.58	66.8
12	7.48	58.9	14	7.65	68.7
26	7.51	59.6	25	7.69	69.7
33	7.58	61.9	32	7.80	72.5

Copolymers **IIc**–**IIe** have close [η] (0.26–0.27) and M_{SD} (84000–103000). The low [η] of copolymers **IIc**–**IIe** at high M_{SD} suggests compaction of macromolecular globules through reaction with glutaraldehyde. The formation of polymers **IIc**–**IIe** is accompanied by growth of the molecular weight by a factor of 5–7 as compared with the starting non-cross-linked copolymer **Ic**. Copolymer **IIe** was prepared at higher content of glutaraldehyde in the starting solution, 0.15 mol %, at C_{cop} = 10.5 wt %. Under these conditions an *MW* of 84000 is reached in 7 h, with the content of residual NH_2 groups decreasing to 3.0 mol %. For copolymer **IIe**, $D_0 = 2.9 \times 10^{-7}$ and $S_0 = 2.15 \times 10^{-13}$. On raising C_{cop} to 11.0 wt % at [GA] : [NH_2] = 0.15 : 1, a cross-linked gel is formed.

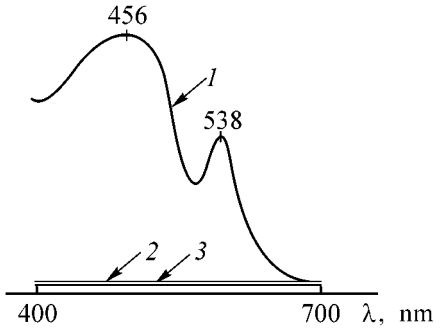

Fig. 3. UV spectra in physiological solution in the range 400–700 nm: (*1*) cross-linked copolymer **IId**, C_{cop} = 0.65 wt %; (*2*) starting linear copolymer **Ic**, C_{cop} = 58.2 wt %; (*3*) glutaraldehyde, [GA] = 6.67 μl ml^{-1} of buffer solution, pH 3.9. (λ) Wavelength.

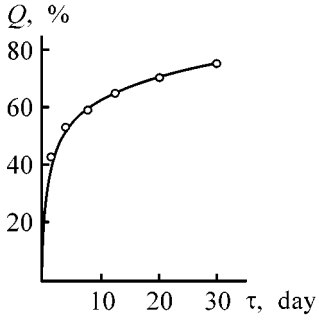

Fig. 4. Kinetics of hydrolysis, judged from variation of the reduced viscosity of cross-linked copolymer **IIe** (M_{SD} = 84000) in physiogical solution. 25°C; C_{cop} = 1.0 wt %. (*Q*) Degree of hydrolysis and (τ) time.

The presence in copolymers **II** of azomethine bonds between the polymer chains cross-linked with glutaraldehyde to the gel point was proved by UV spectroscopy (Fig. 3). The spectrum of **IId** in the range 400–700 nm in aqueous solution contains two absorption bands peaked at 456 and 538 nm, associated with the absorption of the –N=CH bonds. The starting copolymer **Ia** exhibits no absorption in the range 400–700 nm.

It was important to evaluate the hydrolytic stability of cross-linked copolymers **II** in water and in physiological solution at 25 and 37°C. The hydrolysis of copolymers **II** was monitored by measuring the pH of an aqueous solution of **IIc** in the course of hydrolysis and the reduced viscosity of a solution of **IIe** in physiological solution. In both cases we calculated the degree of hydrolysis Q_{pH} (or *Q*) at instant τ. As seen from Table 4, hydrolysis of copolymer **IIc** (M_{SD} = 94000) in aqueous solution, evaluated from pH variation, is fast: Q_{pH} reaches 62.0% in 33 days (25°C, C_{cop} = 0.1 wt %). With temperature raised to 37°C and concentration of the copolymer solution decreased to 0.05 wt %, Q_{pH} increases, reaching 72.5% in 32 days.

Figure 4 shows the kinetics of hydrolysis of high-molecular-weight branched polymer **IIe** in a physiological solution at 25°C, pH 6.8, and C_{cop} = 1 wt %, plotted using data on the reduced viscosity of this copolymer η_{sp}/C. As seen from Fig. 4, the degree of hydrolysis is as high as 75% after 30 days under these conditions. Knowing the *MW* of **IIe** before hydrolysis and the degree of hydrolysis in 30 days, we can calculate the *MW* of **IIe** after hydrolysis for 30 days. We obtained a value of 21000, which is below the critical value for kidney filtration. Thanks to easy hydrolysis, copolymers **IIc**–**IIe** containing reactive NH_2 groups can be used as BAS carriers.

Thus, using two independent procedures, we found that polymers **II** obtained by treatment with glutaraldehyde are readily hydrolyzed in water and in physiological solution at both 37 and 25°C. This means that the azomethine bond is very labile in aqueous solutions, and the chemically degradable VP copolymers obtained can be used as carriers of biologically active substances.

EXPERIMENTAL

N-Vinylpyrrolidone was purified by threefold distillation in a vacuum from KU-2 cation-exchange resin in the presence of hydroquinone. The fraction with bp 75–77°C/667–800 Pa was collected. n_D^{20} = 1.5125, d_4^{20} = 1.0458 g cm^{-3}; MR_D: found 32.00, calculated 31.74 cm^3 mol^{-1}. Allylamine was distilled twice from molecular sieves, bp 58°C. n_D^{20} = 1.4230, d_4^{20} = 0.7627 g cm^{-3}; MR_D: found 19.00, calculated 19.03 cm^3 mol^{-1}. Glutaraldehyde was purchased from Vekton as 50% aqueous solution and purified as follows. First, water was distilled off in a vacuum (22°C, 133 Pa, bath temperature 30°C). The residue was vacuum-distilled. A fraction boiling at 62°C/266 Pa (bath temperature 120°C) was collected and immediately dissolved in water. The concentration of glutaraldehyde was determined by reaction with hydroxylamine hydrochloride, followed by titration of the released HCl with 0.1 N NaOH (bromophenol blue indicator) [9]. The concentration of glutaraldehyde in the resulting aqueous solution was 30 wt %. The purity of glutaraldehyde was judged from the lack of absorption in the UV spectrum of aqueous solution at 235 nm [10]. The initiator, AIBN, was recrystallized three times from chloroform–ethanol (1 : 5) at temperatures ≤ 40°C; mp 103°C.

Copolymerization of VP with allylamine was performed in 2-propanol in the presence of AIBN at 70°C in sealed ampules preliminarily purged with argon. After the copolymerization was complete, the ampules were opened and the copolymers were precipitated by adding the reaction mixture to diethyl ether. The product was collected on a Schott filter and dried in a vacuum to constant weight. The content of primary amino groups in VP–Aam copolymers was determined spectrophotometrically (λ = 424 nm) after complexation with trinitrobenzenesulfonic acid [11]. The molecular weights of copolymers **I** were calculated from their intrinsic visocsities, measured in 0.1 N aqueous solution of sodium acetate. As a first approximation, we used the Mark–Kuhn–Houwink equation known for poly-*N*-vinylpyrrolidone [12]. The radiation-induced copolymerization of VP with allylamine was performed in 2-propanol at a dose of 100 kGy in evacuated ampules on an MRKh-γ-20 installation with a ^{60}Co source.

Reaction of glutaraldehyde with 0.5 g of VP–Aam copolymer was performed in aqueous solution at 45°C in a sealed ampule preliminarily purged with argon. After the reaction was complete, the ampule was opened, and the resulting viscous solution was diluted with 25 ml of distilled water, transferred into a separatory funnel, and shaken with three 20-ml portions of diethyl ether to remove unchanged GA. The aqueous solution was kept under vacuum to remove residual ether and subjected to lyophilic drying. The content of unchanged primary amino groups in the dried product was determined. The intrinsic viscosity of the cross-linked copolymer was measured at 25°C in 0.1 N sodium acetate.

The products of reaction of VP–Aam copolymers with glutaraldehyde were studied by molecular hydrodynamics. The translational friction of macromolecules in the free state (diffusion) and in a centrifugal field (sedimentation, MOM 3180 analytical ultracentrifuge) was studied in 0.1 N aqueous solution of sodium acetate. In both cases the technique of artificial boundary formation was used. The diffusion and sedimentation boundaries were determined after varied periods of time with Lebedev polarization interferometers [13]. The diffusion curves and sedimentograms were processed using standard techniques [14]. The sedimentation experiments were performed at 40 000 rpm. The floatability factor (density increment) $1 - v\rho_0 = 220$ for poly-VP has been determined previously [12]. The molecular weights were calculated from the diffusion (D_0) and sedimentation (S_0) coefficients using the Svedberg formula

$$M_{SD} = \frac{RT}{1 - v\rho_0}\frac{S_0}{D_0},$$

where R is the universal gas constant and T is temperature (K).

The hydrolysis of the cross-linked VP–Aam copolymer was monitored by measuring the variation with time of the pH of the copolymer aqueous solution at 25°C and 37°C and of the reduced viscosity of the copolymer solution in physiological solution at 25°C. In the first case, the degree of hydrolysis Q_{pH} was calculated by the formula

$$Q_{pH} = \frac{pH_\tau - pH_{\tau_0}}{pH_{ip}} \times 100\%,$$

where pH_τ is the pH of a solution of the cross-linked copolymer by instant of time τ, pH_{τ_0} is the initial pH of the solution of the cross-linked copolymer, and pH_{ip} is the pH of the solution of the starting (non-cross-linked) copolymer.

In the second case, the degree of hydrolysis was calculated by the formula

$$Q = \frac{M_{\tau_0} - M_\tau}{M_{\tau_0} - M_{ip}} \approx \frac{(\eta_{sp}/C)_{\tau_0}^{1/\alpha} - (\eta_{sp}/C)_\tau^{1/\alpha}}{(\eta_{sp}/C)_{\tau_0}^{1/\alpha} - [\eta]_{ip}^{1/\alpha}} \times 100\%,$$

where $(\eta_{sp}/C)_{\tau_0}$ is the initial reduced viscosity of the cross-linked copolymer (dl g^{-1}); $(\eta_{sp}/C)_\tau$ is the re-

duced viscosity of the cross-linked copolymer at instant of time τ (dl g^{-1}); $[\eta]_{ip}$ is the intrinsic viscosity of the starting linear non-cross-linked VP–Aam copolymer (dl g^{-1}); α is the empirical constant characteristic of a given polymer in a given solvent and reflecting the shape of polymer macromolecules in solution; to a first approximation, $\alpha = 0.5$; M_{τ_0}, M_τ, and M_{ip} are the corresponding molecular weights.

The UV spectra of the cross-linked and starting copolymers were measured in aqueous solution on a Specord M-40 spectrophotometer in 1-cm cells.

CONCLUSIONS

(1) The reaction of copolymers of *N*-vinylpyrrolidone and allylamine with glutaraldehyde was studied. Water-soluble polymers containing free NH_2 groups and having molecular weights 5–7 times those of the starting copolymers were obtained.

(2) The high-molecular-weight copolymers obtained readily undergo hydrolysis under physiological conditions.

ACKNOWLEDGMENTS

The study was financially supported by the Russian Foundation for Basic Research (project no. 00-15-97318).

REFERENCES

1. Plate, N.A. and Vasil'ev, A.E., *Fiziologicheski aktivnye polimery* (Physiologically Active Polymers), Moscow: Khimiya, 1986.
2. Hulme, B., *Clin. Sci.*, 1968, vol. 43, pp. 515–529.
3. Shtil'man, M.I., Brudz', S.P., and Dergunova, O.N., Abstracts of Papers, *VIII Vsesoyuznyi simpozium "Sinteticheskie polimery meditsinskogo naznacheniya"* (VIII All-Union Symp. "Manmade Polymers for Medical Purposes"), Kiev: Naukova Dumka, 1989, pp. 81–82.
4. Shlimak, V.M., Shtil'man, M.I., Kozlov, A.A., *et al.*, *Vysokomol. Soedin., Ser. B*, 1984, vol. 26, no. 12, pp. 901–903.
5. Panarin, E.F., Tarasova, N.N., and Gorbunova, O.P., *Zh. Prikl. Khim.*, 1993, vol. 66, no. 11, pp. 2525–2530.
6. Solovskii, M.V., Ushakova, V.N., Panarin, E.F., *et al.*, *Khim. Vys. Energ.*, 1987, vol. 21, no. 2, pp. 143–147.
7. Solovskii, M.V., Gudaitis, A.A., Panarin, E.F., *et al.*, *Khim. Vys. Energ.*, 1991, vol. 25, no. 4, pp. 375–377.
8. Krakovyak, M.G., Anan'eva, T.D., Anufrieva, E.V., *et al.*, *Vysokomol. Soedin., Ser. A*, 1984, vol. 26, no. 10, pp. 2071–2076.
9. Toroptseva, A.M., Belogorodskaya, K.V., and Bondarenko, V.M., *Laboratornyi praktikum po khimii i tekhnologii vysokomolekulyarnykh soedinenii* (Laboratory Manual on Chemistry and Technology of Macromolecular Compounds), Leningrad: Khimiya, 1972.
10. Kuznetsova, N.P., Mishaeva, R.N., and Gudkin, L.R., *Zh. Prikl. Khim.*, 1999, vol. 72, no. 7, pp. 1171–1177.
11. Snyder, S.L. and Sobocinski, P.Z., *Anal. Biochem.*, 1975, vol. 64, no. 2, pp. 284–288.
12. Pavlov, G.M., Panarin, E.F., Korneeva, E.V., *et al.*, *Vysokomol. Soedin., Ser. A*, 1990, vol. 32, no. 6, pp. 1190–1196.
13. Tsvetkov, V.N., *Zhestkotsepnye polimernye molekuly* (Rigid-Chain Polymeric Molecules), Leningrad: Nauka, 1986.
14. Tanford, Ch., *Physical Chemistry of Macromolecules*, New York: Wiley, 1961.

Russian Journal of Applied Chemistry, Vol. 74, No. 4, 2001, pp. 669–672. Translated from Zhurnal Prikladnoi Khimii, Vol. 74, No. 4, 2001, pp. 649–652.

MACROMOLECULAR CHEMISTRY AND POLYMERIC MATERIALS

Heat Resistance of Polyamidobenzimidazoles

V. V. Khakhinov, Zh. P. Mazurevskaya, D. M. Mognonov, and O. V. Il'ina

Baikal Institute of Nature Management, Siberian Division, Russian Academy of Sciences, Ulan-Ude, Buryatia, Russia

Buryat State University, Ulan-Ude, Buryatia, Russia

Received November 16, 2000

Abstract—Thermal degradation of polymers based on polyamidobenzimidazoles was studied in relation to the monomeric units structure and mole fraction of the initial monomers.

Of particular interest among synthetic macromolecular compounds are polyheteroarylenes whose macromolecule contains amino groups along with thermally stable benzimidazole rings. Such polymers are amorphous; they possess elevated softening points and exhibit high heat resistance depending on the structure of the monomeric units [1]. Mixed polyamidobenzimidazoles (PABIs) based on bis-*o*-phenylenediamines, diphenyl esters of aromatic or aliphatic dicarboxylic acids, and ε-caprolactam, being somewhat less heat-resistant than the corresponding commercial homopolybenzimidazoles, are more soluble in organic solvents. Therefore, their processing into commercial items such as adhesives, films, fibers, lacquers, plastics, and fiber glasses is more convenient [2, 3]. However, wide use of the polymers for preparing heat-resistant film materials is restricted by the lack of data on the mechanisms of thermal degradation and on the qualitative and quantitative composition of the degradation products. Such data are important not only for industrial practice but also for development of approaches to construction of polymers with the preset service properties.

In this work we studied the degradation of PABIs differing in the structure of chemical units of the macromolecular chain. As investigation objects were chosen copolymers prepared from aromatic tetramines, diphenyl esters of aromatic dicarboxylic acids, and ε-caprolactam at different molar ratios of the initial monomers.

EXPERIMENTAL

In this work, we used 3,3',4,4'-tetraaminodiphenyl ether (TADPE) and 3,3',4,4'-tetraaminodiphenylmethane (TADPM), produced by the Novosibirsk Institute of Organic Chemistry, Siberian Division, Russian Academy of Sciences. Diphenyl adipate (DPA) and diphenyl isophthalate (DPI) were prepared by fusion of the corresponding acid dichlorides with phenol [2]; pure-grade ε-caprolactam was additionally purified by vacuum distillation. Thermogravimetric studies were performed with a Q-1000 derivatograph (MOM, Hungary) in platinum crucibles in air or under argon; the sample weight was 100 mg. The IR spectra were taken with a Specord 75-IR spectrometer equipped with an attachment for measuring the spectra in the temperature range 20–250°C. Samples were prepared as pellets with KBr. Thermal degradation products were analyzed with an LKhM-80 gas chromatograph equipped with a thermal conductivity detector and a dynamic pyrolytic cell heated at a rate of 1–10 deg min^{-1}, as in thermogravimetric analysis. The composition of low-molecular-weight degradation products was determined by chromatography; the columns were packed with CaA molecular sieves or Porapak Q sorbent.

A condensation test tube, first empty and then filled with the reactants, was purged with an inert gas by repeated cycles of evacuation and inert gas admission and then placed in a bath heated to 200°C. The temperature was gradually raised over a period of 1–1.5 h. After 20–30 min, the melt solidified and the reaction continued in the solid phase. After 3.5–4 h, when the melt transformed into a solid mass, polycondensation was continued for an additional 1 h at the same temperature in a vacuum (1–2 mm Hg), after which the mixture was slowly cooled to room temperature in an inert gas flow.

1070-4272/01/7404-0669 $25.00 © 2001 MAIK "Nauka/Interperiodica"

Characteristics of copolymer*

Molar ratio of initial monomers	η_r, dl g^{-1}	T_s, °C	Molar ratio of initial monomers	η_r, dl g^{-1}	T_s, °C
TADPM : DPA : CL:			TADPM : DPI : CL:		
1 : 1 : 0	8.16	295–300	1 : 1 : 0	1.82	385–390
0.8 : 0.8 : 0.2	1.63	215–220	0.8 : 0.8 : 0.2	1.50	345–350
0.6 : 0.6 : 0.4	1.43	205–210	0.5 : 0.5 : 0.5	1.34	255–260
0.5 : 0.5 : 0.5	1.23	195–200	0.4 : 0.4 : 0.6	1.12	215–220
0.4 : 0.4 : 0.6	1.10	180–185			
TADPE : DPA : CL:			TADPE : DPI : CL:		
1 : 1 : 0	6.36	255–260	1 : 1 : 0	2.86	375–380
0.8 : 0.8 : 0.2	5.96	235–240	0.8 : 0.8 : 0.2	1.04	345–350
0.6 : 0.6 : 0.4	5.50	205–210	0.5 : 0.5 : 0.5	0.98	265–270
0.5 : 0.5 : 0.5	3.63	205–210	0.4 : 0.4 : 0.6	1.31	255–260

* (η_r) Reduced viscosity of a 0.5% solution of the polymer in HCOOH, 20°C; (T_s) softening point; (CL) caprolactam.

The resulting PABIs are yellow-brown powders. The elemental analyses of the products correspond to the composition of the copolymers. The IR spectra are identical to those of the model compounds and contain absorption bands at 1630–1680 cm^{-1}, characteristic of CO stretching vibrations (amide I band), and at 1515–1570 cm^{-1}, characteristic of NH bending vibrations (amide II band) [4].

Polybenzimidazoles are known [5] to exhibit high heat resistance, but their hardness and insolubility in common organic solvents complicate their processing into finished items by modern industrial methods. Introduction of amide bonds into the macromolecule increases the solubility of PABIs in amides and other available organic solvents, with insignificant decrease in the heat resistance. Polymers prepared by the above scheme have high molecular weight, with the solution viscosity also depending on the molar ratios of the reactants:

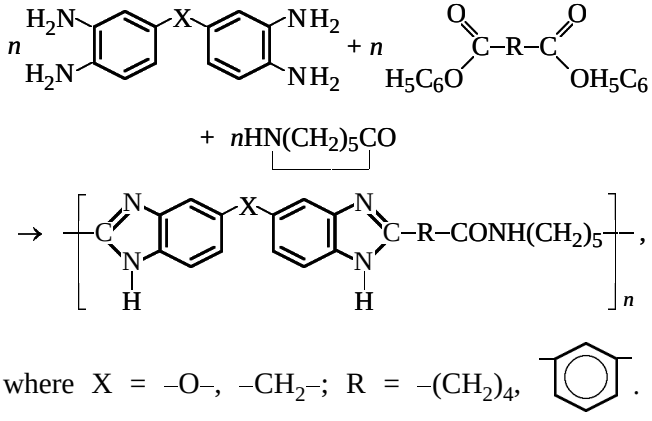

where X = –O–, –CH_2–; R = –$(CH_2)_4$, .

All the synthesized polymers are soluble at room temperature in sulfuric and formic acids and, on heating, in acetic acid, DMF, tricresol, and benzyl alcohol. The solubility grows with increasing mole fraction of ε-caprolactam. The copolymers with mole fraction of ε-caprolactam greater than 0.4 are in most cases completely dissolved in tricresol and benzyl alcohol at room temperature. As seen from the table, the synthesized PABIs soften on heating, in contrast to the known polybenzimidazoles [5]; the softening point decreases with increasing mole fraction of ε-caprolactam. According to the results of thermomechanical analysis, the softening point lies within 180–390°C, being lower in polymers with bridging methylene group. Depending on the structure of their monomeric units, polyamidobenzimidazoles exhibit different thermal characteristics; with increasing content of benzimidazole fragments the onset of degradation shifts to higher temperatures. Thermal analysis data show that degradation of PABIs in air in the range 300–600°C occurs in two stages (Figs. 1a, 1b). The first stage, in which the weight loss does not exceed 5%, occurs within 330–400°C. Degradation of PABI in air occurs similarly to degradation in an inert atmosphere. The IR spectra of samples heated to these temperatures do not differ from those of the initial samples, except for a decrease in the intensity of some absorption bands due to cross-linking of the polymer. Presumably, the degradation processes occurring in this stage do not involve the backbone chain, although the polymer becomes insoluble. An appreciable (>5%) weight loss occurs at 380–460°C, which is due to extensive degradation of PABI. With respect to heat resistance,

PABIs prepared from ε-caprolactam, diphenyl esters, and aromatic tetramines can be ranked in the following order (X is the bridging group in the tetramine and R is that in the dicarboxylic acid):

X	R	X	R	X	R	X	R
$-(CH_2)-$	$-(CH_2)_4-$	< $-O-$	$-(CH_2)_4-$	< $-CH_2-$	$-C_6H_4-$	< $-O-$	$-C_6H_4-$.

The relatively low heat resistance of PABI with a bridging methylene chain is probably due to insufficient conjugation with the benzimidazole system and insufficient degree of polymer cyclization. The copolymers with an oxygen bridge are the most heat-resistant. As expected, the polymer containing no bridging groups between aromatic rings is more heat-resistant than the polymers studied in this work, but its solubility drastically decreases [6].

To gain insight into the degradation mechanism, we studied the thermolysis of PABIs by pyrolytic gas chromatography. The gaseous degradation products were assigned to specific macromolecular fragments. Chromatographic curves (Fig. 2) show that the primary gaseous degradation product is hydrogen. The relatively low temperature of hydrogen evolution from the majority of PABIs is mainly due to the lability of the hydrogen atom in the benzimidazole group. Presumably, the polymer is cross-linked in this stage via the nitrogen atom of the benzimidazole ring with evolution of hydrogen and low-molecular-weight side products [7]. This assumption is confirmed by the results of thermal analysis (see above). The evolution of carbon dioxide is due to hydrolysis of amino amide structures with the formation of carboxy groups, followed by their decarboxylation. The increase in the content of carbon oxides suggests decomposition of the linear fragments of the macromolecules and cleavage of bridging bonds with release of volatile degradation products and polycyclization of the polymer. On further heating, minor amounts of CO_2, CH_4, C_2H_4, ammonia, and cyano compounds are detected, suggesting decomposition of aromatic and heterocyclic fragments of the copolymer.

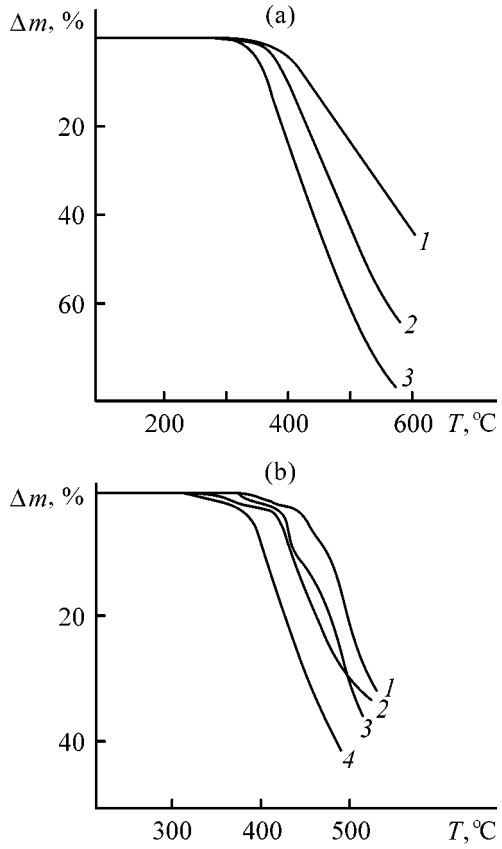

Fig. 1. TG curves for PABIs. (a) Equimolar ratio of components; (*1*) TADPE–DPI–CL, (*2*) TADPM–DPI–CL, and (*3*) TADPE–DPA–CL. (b) (*1*) TADPE–DPI–CL, molar ratio 0.8 : 0.8 : 0.2; (*2*) the same, 0.4 : 0.4 : 0.6; (*3*) TADPM–DPI–CL, 0.4 : 0.4 : 0.6; and (*4*) TADPM–DPA–CL, 0.6 : 0.6 : 0.4. (Δ*m*) Weight loss and (*T*) temperature.

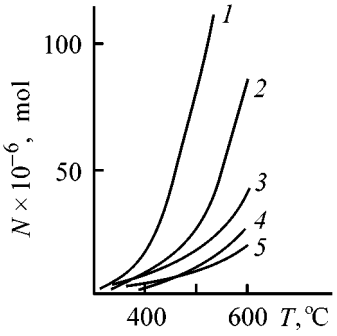

Fig. 2. Release of gaseous products in pyrolysis of PABI of composition TADPM–DPI–Cl, 0.4 : 0.4 : 0.6: (*1*) H_2, (*2*) CO_2, (*3*) CO, (*4*) CH_4, and (*5*) C_2H_4. (*N*) Amount of volatile degradation products and (*T*) temperature.

CONCLUSION

The synthesized polyamidobenzimidazoles have high molecular weight, high heat resistance, and good mechanical characteristics and exhibit film-forming properties. These characteristics depend on the structure of the monomeric units and molar ratio of the initial monomers. Being the most heat-resistant, the copolymers derived from 3,3',4,4'-tetraaminodiphenyl ether and diphenyl isophthalate are of practical interest.

REFERENCES

1. Korshak, V.V., *Termostoikie polimery* (Heat-Resistant Polymers), Moscow: Nauka, 1969.
2. Izyneev, A.A., Korshak, V.V., and Mazurevskaya, Zh.P., *Dokl. Akad. Nauk SSSR*, 1974, vol. 217, no. 3, pp. 585–591.
3. Izyneev, A.A., Korshak, V.V., Mazurevskaya, Zh.P., *et al.*, *Vysokomol. Soedin., Ser. B*, 1986, vol. 28, no. 7, pp. 489–494.
4. Bellamy, L.J., *The Infra-Red Spectra of Complex Molecules*, London: Methuen, 1954.
5. Mognonov, D.M., Khomutov, V.A., Izyneev, A.A., and Doroshenko, Yu.E., *Izv. Sib. Otd. Akad. Nauk SSSR, Ser. Khim. Nauk*, 1978, no. 2, issue 2, pp. 1244–1247.
6. Mognonov, D.M. and Khakhinov, V.V., *Zh. Prikl. Khim.*, 1998, vol. 71, no. 4, pp. 641–645.
7. Mognonov, D.M., Samsonova, V.G., Khakhinov, V.V., and Pinchuk, I.N., *Vysokomol. Soedin., Ser. B*, 1997, vol. 39, no. 7, pp. 1250–1257.

Russian Journal of Applied Chemistry, Vol. 74, No. 4, 2001, pp. 673–677. Translated from Zhurnal Prikladnoi Khimii, Vol. 74, No. 4, 2001, pp. 652–656.

MACROMOLECULAR CHEMISTRY AND POLYMERIC MATERIALS

Polymer Complexes and Their Flocculation Power

R. K. Zakirov, F. Yu. Akhmadullina, N. N. Valeev, and D. G. Pobedimskii

Kazan State Technological University, Kazan, Tatarstan, Russia

Received April 19, 2000

Abstract—Complexation of various complementary polymers and the flocculating power of the resulting complexes were studied. Regression equations adequately describing the recovery of phenol by polymeric complex reagents are presented.

Polymer complexes are the products of interaction of complementary polymers. They possess specific physical and mechanical properties that strongly differ from those of the initial polymers. The operation stability of polymer complexes determines their wide use as ion exchangers, soil structuring materials, supporting compounds and membranes for medicine purposes, and high-performance flocculants.

In this work, the interaction in binary systems of dissimilar polymers and the flocculating power of the resulting complexes was studied with the aim to develop high-performance macromolecular reagents for pretreatment of wastewater of complex composition with toxic components, produced in base organic synthesis.

In our tests we used a modified ampholyte gelatin—phthaloylgelatin [PG, molecular weight $(60–80) \times 10^4$)], nonionic polyethylene oxide (PEO, 9×10^5), proksanol (PR, 3×10^3), and cation-active polymer VPK-402 (1.1×10^6), which show high-performance in water treatment [1, 2].

Data on complexation and prevailing binding mechanism in the PG–PEO, PG–PR, and PG–VPK systems were obtained by viscometry, conductometric titration of isomolar series, and IR spectroscopy.

The viscosity and conductometric characteristics of individual compounds and their binary systems were measured by common procedures at 25°C using 0.1–1.0% solutions of macromolecular compounds (MMCs). First, we compared the results of the above measurement with the theoretical (additive) dependences that would be observed in the absence of specific interaction in the systems. As a result, certain deviations between the experimental and theoretical data were observed suggesting the formation of associates. The ranges corresponding to maximum extent of complexation between the polymer reagents were determined using the procedure proposed in [3]: the relative viscosities or electrical conductivities corresponding to the additive curve were taken as unity, and then the experimental results were converted into relative quantities ($\eta/\Sigma\eta$ or $\chi/\Sigma\chi$).

For each polymer pair, dependences of the above parameters on the MMC content were recorded (Figs. 1a–1c). The experimental viscosity and electrical conductivity in the binary systems differ from the additive values, which indicates intermolecular

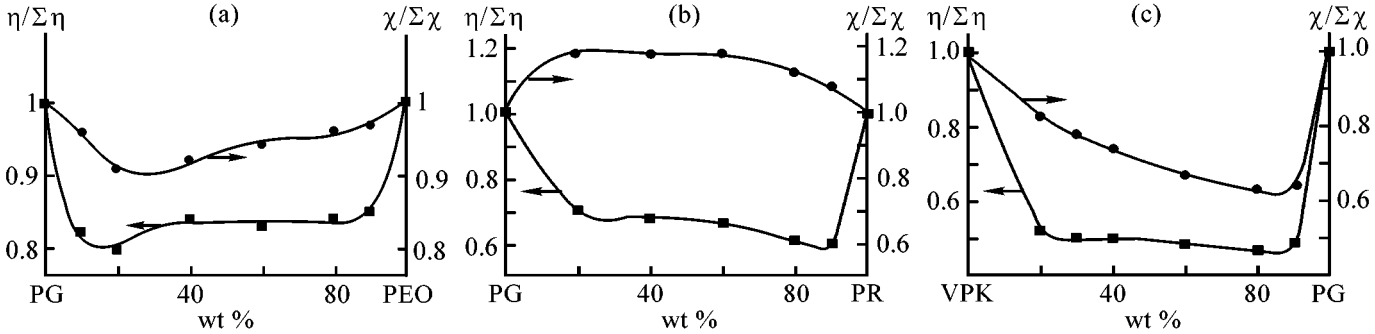

Fig. 1. Reduced electrical conductivity $\chi/\Sigma\chi$ and viscosity $\eta/\Sigma\eta$ in the (a) PG–PEO, (b) PG–PR, and (c) VPK–PG binary systems as influenced by variations in the system composition.

1070-4272/01/7404-0673 $25.00 © 2001 MAIK "Nauka/Interperiodica"

the association with the formation of polymer complexes in these systems.

As seen from Fig. 1a, polymer complexes are formed in the PG–PEO system in a wide concentration range (20–80 wt %). Almost similar dependence is observed for the dependence of the electrical conductivity; a minimum in this parameter is observed in the same concentration region.

Proxanol and PG form polymeric complexes in almost the entire concentration range (Fig. 1b), but the strongest and most stable complexes are formed at PR : PG = 86 : 14. The minimum in the viscosity curve corresponds to $\eta/\Sigma\eta = 0.56$, i.e., a nearly twofold decrease in the solution viscosity (as compared with the theoretical data) is observed, which suggests they formation of stable associates in this system. The significant increase in the electrical conductivity in the system is probably due to an increase in the uncompensated charge of phthaloylgelatin macromolecules in complexation of proksanol with modified gelatin.

As seen from Fig. 1c, in the VPK–PG binary system, the viscosity ($\eta/\Sigma\eta = 0.47$) and the electrical conductivity ($\chi/\Sigma\chi = 0.63$) change most significantly suggesting the strongest, among the systems studied, interaction between the components. Complexation also proceeds in a wide concentration range. The most stable complexes are formed in a narrow PG : VPK range (80–90) : (20–10), which is confirmed by the conductivity data and suggests a compact structure of macromolecular globules of the given polymeric complexes.

An IR study allowed us to analyze the nature of the forces stabilizing the structure of the polymer complexes.

The intermolecular interaction of the polar groups of polyampholyte, polyethylene oxide, and proksanol molecules via hydrogen bonds is a decisive factor in the formation of associates between modified gelatin and nonionic polymers. This is confirmed by the IR spectra of the polymer complexes and starting compounds, which are strongly different in the regions of stretching vibrations of the –NH and –OH bonds. In the 3600–3300 cm^{-1} range, the IR spectrum of PG exhibits a strong band at 3315 cm^{-1} and the stretching vibrations of the terminal hydroxy groups in PEO and PR appear as broad weak bands at 3390 and 3370 cm^{-1}, respectively.

In the case of PG and nonionic VPK complexes, the ν(OH, NH) band is shifted by nearly 30 cm^{-1} to higher frequencies as compared with the spectrum of PG, whereas the vibrations of terminal OH groups in associates with PG are shifted to lower frequencies in comparison with PEO and PR by 28 and 50 cm^{-1}, respectively. This suggests the formation of a new system of hydrogen bonds in the binary systems, which confirms the structure formation via intermolecular hydrogen bonds. It should be noted that these bonds are weaker than the hydrogen bonds in the PG macromolecule and stronger as compared with PEO and PR. Oxygen atoms of the carbonyl and ether groups of polymeric macromolecules are also involved in macromolecule binding, which is confirmed by changes in the shape of the absorption bands of the C=O and C–O–C stretching vibrations in the spectra of polymer complexes.

In the PG–VPK system, another mechanism of macromolecule binding is preferable. Apparently, electrostatic forces play a significant role in the formation of polymer structures in a wide range of component ratios, and the hydrophobic interactions additionally stabilize the resulting complex.

The flocculating power of the copolymers was studied by the known procedure in flow-type aerated apparatus including the units for preliminary clarification and biological purification [1]. The tests were carried out using real industrial wastewaters and slurry suspension under conditions close to those of the industrial process.

The performance of the polymer complexes in the treatment of industrial wastewater was evaluated with respect to phenol (which is the main biological toxin) and calculated as the ratio of the difference between the content of phenols in the wastewater after biological treatment and after preliminary clarification to the content of phenols in the initial wastes (control sample).

To evaluate the mutual influence of various polymers and the effect of the degree of the wastewater contamination on the quality of water purification with respect to the control sample, we performed a mathematical processing of the experimental results. Taking into account the complex and unstable composition of the industrial wastewater, a regression equation in the form of a second-order polynomial was used as a mathematical model:

$$y = b_0 + \sum_{j=1}^{k} b_j x_j + \sum_{j=1}^{k-1} \sum_{l=j+1}^{k} b_{j1} x_j x_1 + \sum_{j=1}^{k} b_{jj} x_j^2,$$

where y is the efficiency of wastewater purification to remove phenol (%), b_j are the coefficients of the regression equation, and x_j are the concentrations of phenol in the initial sample or those of the corresponding flocculants (mg l^{-1}).

Table 1. Coefficients of the regression equation $y = b_0 + b_1c_{PG} + b_2c_{MMC} + b_3x_P + b_{11}c_{PG}^2 + b_{22}c_{MMC}^2 + b_{33}x_P^2 + b_{12}c_{PG}c_{MMC} + b_{13}c_{PG}x_P + b_{23}c_{MMC}x_P$

Flocculating agent	Coefficient										R, %
	b_0	b_1	b_2	b_3	b_{11}	b_{22}	b_{33}	b_{12}	b_{13}	b_{23}	
PG–PEO	13.0	8.78	–0.338	–18.5	–0.312	0.186	2.29	–1.25	0.628	1.68	79.1
PG–PR	7.85	–11.0	5.84	13.7	2.35	0.778	–0.735	–1.08	–0.206	–1.96	58.7
PG–VPK	16.3	4.23	16.6	–2.40	–0.18	–4.30	0.030	–1.00	0.177	0.408	74.7

The results of mathematical processing of the experimental data are listed in Table 1.

Analysis of the resulting dependences and determination coefficients shows fair convergence of the experimental and theoretical values (coefficient of regression R in Table 1).

Since the target function is determined by three variables, the mutual effect of the decisive factors was analyzed using the $y = f(c_i, c_j)$ surfaces at fixed third parameter.

The most complex dependence was plotted for the PG–VPK binary composition (Fig. 2a). These results suggest the decisive role of the polymeric ampholyte; with increasing concentration of this compound in the complex reagent, the efficiency of phenol recovery grows significantly. As for the effect of cation-active VPK, the maximum efficiency with respect to phenol is attained at medium concentrations of the cationic flocculant in the polymeric reagent. Further increase in its concentration impairs the performance of the binary system.

The dependences plotted in Figs. 2b and 2c illustrate mutual effect of a given reagent and the initial concentration of phenol (toxicant) on the quality of purification of wastewater treated with PG–VPK binary system. The resulting dependences have a rather complex saddle shape and confirm the above conclusions on the decisive role of modified gelatin and insignificant effect of VPK (Fig. 2a). With increasing phenol concentration in the wastewater (within the limits of the emergency discharge), the recovery of the toxicant is enhanced, which is obviously due to the increase in the probability of contact between the binary flocculant and phenol molecules.

The binary systems based on PG and nonionic polymers of various molecular weights exhibit an analogous effect of the polyampholyte and phenol concentrations on the quality of the purified water. At the same time, the surfaces obtained for these systems are less complex in shape and smoother.

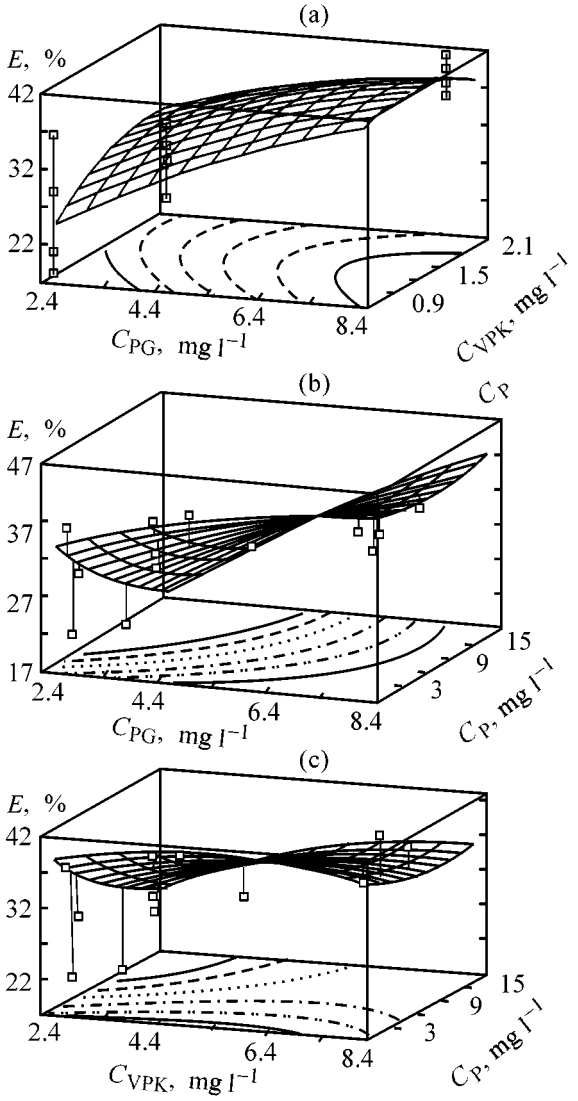

Fig. 2. Mutual effect of (a) modified gelatin and cation-active polymer, (b) modified gelatin and phenol, and (c) cation-active polymer and phenol on the efficiency E of phenol recovery. Concentration of (a) phenol, (b) VPK, and (c) modified gelatin 5 mg l^{-1}.

Table 2. Comparison of experimental and theoretical results

Flocculant	Optimal charge, mg l^{-1}		Optimal ratio			Efficiency, %	
	experiment	calculation	experiment	calculation		experiment	calculation
				model	complexation		
PG–PEO	7–10	7	4 : 1–6 : 1	4 : 1–6 : 1	4 : 1–6 : 1	57–64	60
PG–PR	12–13	10–12	1 : 1–3 : 1	1 : 1–3 : 1	1 : 6	40–55	45–50
PG–VPK	10	8–9	4 : 1–6 : 1	4 : 1–7 : 1	4 : 1–7 : 1	35–38	40

The data presented in Table 2 confirm the feasibility of using the obtained mathematical models to predict the degree of decontamination to remove the most toxic component with polymeric complex flocculants from wastewater formed in base organic synthesis taking into account the initial degree of the wastewater contamination.

As seen, such principal parameters as optimal charges and component ratio in the polymer reagents, ensuring their maximum flocculating power, are consistent with the experiment for the systems studied.

Comparison of the optimal component ratios in the binary reagents, determined experimentally in a study of complexation and theoretically (from the regression analysis), shows that the efficiency of flocculants is the highest at the ratios corresponding to the formation of the most stable polymeric complexes.

The only exception is the PG–PR system. This is probably due to an increase in the uncompensated charge of PG macromolecules in the course of complexation with PR (Fig. 1b), which deteriorates the conditions of phenol recovery. The increase in the content of the polyampholyte improves the efficiency of the complex reagent, which is probably due to the growing concentration of active centers forming hydrogen bonds with proton-donor compounds. The presence of intermolecular hydrogen bonds providing interaction between the binary reagent and phenol with its subsequent recovery from wastewater is confirmed by IR data; it was found that new hydrogen bonds are formed in the complex reagent–phenol system.

As seen from Table 2, the polymeric flocculant based on PG and PEO exhibits the highest efficiency. The use of low-molecular-weight nonionic and cation-active polymers significantly decreases the flocculating power of the complex reagents.

Comparison of the results for the PG–PEO and PG–PR binary systems reveals the contribution from the molecular weight of components of the complex flocculant. As seen, low-molecular-weight PR decreases the flocculating power of the binary reagent by 10–15% on the average [4].

Despite the rather close molecular weights of the complexes of PG with PEO and VPK (similar conditions of complexation, comparable molecular weights of nonionic and cation-active polymers), the PG–VPK system exhibits lower flocculation efficiency. This is probably due to the predominant mechanism of phenol binding with copolymer associates.

With account taken of the composition, structure, and nature of macromolecular compounds forming interpolymer complexes, it is obvious that the binary flocculant based on PG and PEO possesses a greater number of proton-donor and proton-acceptor groups, not involved in the polymer-polymer interaction and forming intermolecular bonds with wastewater components, in particular, phenol. These are carboxy, hydroxy, amido, and other groups of modified gelatin and ether groups of polyethylene oxide. The replacement of a nonionic polymer by a cation-active one makes lower the efficiency of interaction of the resulting copolymer and phenol because of the decrease in the number of the active centers capable of hydrogen bonding.

EXPERIMENTAL

The viscosity of the polymer solutions was measured on a Ubbelohde viscometer with a capillary diameter of 0.73 or 0.86 mm.

To prepare a solution of a macromolecular flocculant, a weighed portion of a polymer was added to a required volume of water and the mixture was agitated with a magnetic stirrer at a rate of no more than 200 rpm. Before measurements, the solutions were filtered through a coarse glass filter.

The conductometric parameters were measured on a P-5021 ac potentiometer, an F582 unit (zero reader),

in a special conductometric cell with a 0.6-mm distance between platinum electrodes (1 cm^2 area).

The mathematical processing of the results was done using a STATGRAPHICS Plus 3.0 software.

CONCLUSIONS

(1) Phthaloylgelatin–polyethylene oxide, phthaloylgelatin–proksanol, and phthaloylgelatin–VPK binary systems are promising for water treatment to decrease the toxicity of wastewater produced in base organic synthesis.

(2) Simulation of the processes of phenol recovery by polymeric complex flocculants allows formulation of recommendations on use of the given flocculants to cope with real emergency discharges of phenol.

REFERENCES

1. USSR Inventor's Certificate, no. 789 422.
2. Veitser, Yu.I. and Mints, D.M., *Vysokomolekulyarnye flokulyanty v protsessakh ochistki prirodnykh i stochnykh vod* (Macromolecular Flocculants in the Treatment of Natural and Waste Waters), Moscow: Stroiizdat, 1984.
3. Tarasenko, Yu.G., Uskova, E.T., Ezhova, T.G., *et al.*, *Khim. Tekhnol. Vody*, 1980, vol. 2, no. 1, pp. 38–41.
4. Zapol'skii, A.K. and Baran, A.A., *Koagulyanty i flokulyanty v protsessakh ochistki vody* (Coagulants and Flocculants in Water Treatment), Leningrad: Khimiya, 1987.

Russian Journal of Applied Chemistry, Vol. 74, No. 4, 2001, pp. 678–680. Translated from Zhurnal Prikladnoi Khimii, Vol. 74, No. 4, 2001, pp. 657–659.

MACROMOLECULAR CHEMISTRY AND POLYMERIC MATERIALS

Radical Graft Polymerization of Glycidyl Methacrylate and Polycaproamide Fiber

I. V. Lavnikova and V. F. Zheltobryukhov

Volgograd State Technical University, Volgograd, Russia

Received July 13, 2000; in final form, December 2000

Abstract—Graft polymerization of glycidyl methacrylate to polycaproamide fiber, initiated by the highly effective redox system Cu^{2+}–H_2O_2, was studied. The kinetic parameters affecting the yield of grafted polyglycidyl methacrylate and the efficiency of the graft polymerization were determined.

Analysis of the existing procedures for preparing new polymeric fibrous materials and the possibilities of controlling their physicomechanical and chemical properties shows that graft polymerization is a promising procedure for production of manmade (in particular, polycaproamide, PCA) fibers [1–3]. Modification of a PCA macromolecule with glycidyl methacrylate (GMA) containing reactive epoxy groups can be a route to ion-exchange fibers; therefore, development of an efficient process for modification of PCA fiber is of practical interest. The use of GMA in emulsion polymerization of the monomer makes fiber production environmentally appropriate; the process is sufficiently fast and does not involve homopolymer formation, which is typical of the emulsion polymerization [4].

Our goals were to improve the existing procedures [1] for preparing polycaproamide graft copolymers (PGCs) and to find the best conditions for grafting GMA to PCA. The main parameters of graft polymerization of PCA and GMA in the presence of the redox system Cu^{2+}–H_2O_2 are the concentration of the monomer and components of the redox system, and the polymerization temperature and time.

Graft polymerization can be apparently represented by the following scheme. The redox reaction between copper ions and hydrogen peroxide generates $\dot{O}H$ radicals whose reaction with PCA yields long-lived macroradicals initiating graft polymerization [1].

The influence of the GMA concentration on the amount of grafted polyglycidyl methacrylate (PGMA) and on the monomer conversion was studied in the range of GMA concentrations 0.24–16.5 M. Graft polymerization was performed in emulsion, with polyvinyl alcohol (0.1%) as emulsifier:

$$[NH(CH_2)_4CO]_n + \dot{O}H \rightarrow [NH\dot{C}H(CH_2)_4CO]_n,$$

$$[NH\dot{C}H(CH_2)_4CO]_n + m\,CH_2{-}\underset{O}{\overset{}{}}{-}CHCH_2OC(O){-}\underset{CH_3}{C}{=}CH_2 \rightarrow [NHCH(CH_2)_4CO]_n.$$

$$\begin{array}{l} \qquad\qquad\qquad\qquad\qquad\qquad\quad CH_3 \\ \qquad\qquad\qquad\qquad\qquad\qquad\quad | \\ \qquad\qquad\qquad\qquad\qquad\qquad CH_2{-}C]_m \\ \qquad\qquad\qquad\qquad\qquad\qquad\quad | \\ CH_2{-}CHCH_2OC{=}O \\ \diagdown\,O\,\diagup \end{array}$$

We found that graft polymerization is fast in the initial stage (Table 1). Raising the monomer concentration above 2.35 M is not appropriate, because the amount of PGMA increases insignificantly. Based on the data obtained in the [GMA] range from 1.2 to 2.35 M and using the procedure described in [5], we calculated the reaction order with respect to the monomer to be 1.93. This value is somewhat higher than

1070-4272/01/7404-0678 $25.00 © 2001 MAIK "Nauka/Interperiodica"

the values typical of heterogeneous polymerization, which is probably due to the capture of the macroradicals by the polymer phase [4].

At present, PGCs are prepared using redox systems, with initiation based on addition of one of the components to the PCA macromolecule. This method ensures very high efficiency of graft polymerization, because the peroxy compound decomposes either at the fiber itself or in its close vicinity. As a result, an active polymeric center is generated, at which graft polymerization of various monomers subsequently occurs [1]. Experiments at varied H_2O_2 concentration confirmed the trend revealed in studies of graft polymerization [6, 7]: with increasing $[H_2O_2]$, the amount of the graft polymer first increases and then, after reaching a maximum, decreases drastically, which is probably due to participation of H_2O_2 in termination of the growing PGMA chains. The kinetic parameters of graft polymerization with the redox system are listed in Table 2. These data suggest that copper ions catalyze graft polymerization. Without copper, grafting does not occur, and, even at a copper concentration as low as 0.0049 M, the reaction rate is 2.3×10^{-4} mol l^{-1} s^{-1}, and the amount of grafted PGMA, 22 wt %. The reaction rate is higher with the initiating system Cu^{2+}–H_2O_2, compared with the known initiating system Fe^{2+}–H_2O_2 [8]. It should be noted that, with increasing $[Cu^{2+}]$, the initial rate grows by a factor of 2.7, to 6.1×10^{-4} mol l^{-1} s^{-1}. The calculated reaction orders with respect to hydrogen peroxide and copper are somewhat lower than those in heterogeneous polymerization. This is probably due to the fact that the constants of chain transfer to the monomer are low and the escape of radicals from particles is insignificant; however, our results agree with data in [9].

A study of the graft polymerization in relation to temperature showed that at 0–60°C the yield of grafted PGMA is as low as 0.1 wt %, whereas at 70°C it becomes as high as 43 wt %.

The kinetic data in Table 3 show that graft polymerization initially occurs at a high rate in the examined temperature range. For example, the initial polymerization rate is 0.6×10^{-4} at 62°C, and as high as 7.4×10^{-4} mol l^{-1} s^{-1} at 70°C, with simultaneous increase in the yield of PGMA to 43 wt %.

The kinetic curves obtained in studing the temperature dependence of the reaction rate were used to calculate the activation energy of heterophase graft polymerization, found to be equal to 53.33 kJ mol^{-1}, which is typical of radical graft polymerization based on chain transfer from the low-molecular-weight radical

Table 1. Influence of GMA concentration on parameters of graft polymerization*

[GMA], M	Amount of grafted PGMA, wt %	Monomer conversion, wt %	Initial rate of polymerization $v_p \times 10^4$, mol l^{-1} s^{-1}
0.3	5.3	14.0	0.5
1.2	17.0	7.4	1.6
1.8	19.1	6.9	4.3
2.35	34.5	8.9	9.2
5.9	46.5	10.0	9.7
11.8	46.4	3.6	9.7
16.5	46.5	2.2	9.8

* Reaction conditions: initiation with H_2O_2 (0.08 M)–Cu^{2+} (0.018 M) at 60°C, τ = 50 min; grafting at 70°C, τ = 60 min, bath ratio 30.

Table 2. Influence of the content of the redox system components on the kinetic parameters of graft polymerization of GMA*

Component of redox system	Concentration, M	Amount of grafted PGMA, wt %	$v_p \times 10^4$, mol l^{-1} s^{-1}	$v_p^{max} \times 10^4$, mol l^{-1} s^{-1}	Reaction order with respect to component
H_2O_2	0.0098	11	12	3.8	0.71
	0.078	15	1.8	4.3	
	0.118	30	3.5	8.1	
	0.198	35	6.1	11	
Cu^{2+}	0	0	0	0	0.2
	0.0049	22	2.3	7.8	
	0.01	24	2.6	9.1	
	0.018	37	6.1	12.9	

* Reaction conditions: initiation at 80°C, τ = 60 min; grafting at [GMA] = 2.35 M, 80°C, τ = 60 min, bath ratio 30.

Table 3. Influence of polymerization temperature T_p on parameters of graft polymerization

T, °C	Amount of grafted PGMA, wt %, at indicated reaction time, min						$v_p \times 10^4$, mol l^{-1} s^{-1}	$v_p^{max} \times 10^4$, mol l^{-1} s^{-1}
	20	40	60	80	100	120		
62	2.3	3.6	5.6	5.6	6	6	0.6	1.5
65	6.1	19	24	25	26	26	3.7	6.3
70	19	35	41	42	43	43	7.4	12.3

* Reaction conditions: initiation with H_2O_2 (0.08 M)–Cu^{2+} (0.018 M), 80°C; grafting at [GMA] = 2.35 M, bath ratio 30.

Table 4. Influence of the time of graft polymerization on the amount of grafted PGMA

τ, min	Amount of grafted PGMA, wt %, at indicated GMA concentration, M		
	1.175	1.76	2.35
0–20	2.6	15.2	19.2
20–40	3.2	30.1	36.7
40–60	4.9	34.7	40.2
60–80	5.1	36.0	45.0
80–100	5.2	36.1	45.0
100–120	5.3	36.0	45.1

* Reaction conditions: initiation with H_2O_2 (0.08 M)–Cu^{2+} (0.018 M), 80°C; grafting at 70°C, bath ratio 30.

to the polymer [9]. Data in Table 4 show that graft polymerization decelerates with time and fully stops in 80 min.

EXPERIMENTAL

Polycaproamide in the form of staple fiber (1 g) was placed in a flask equipped with a reflux condenser and was activated with the Cu^{2+}–H_2O_2 redox system. For this purpose, PCA was treated with a 0.098–0.198 M aqueous solution of H_2O_2 in the presence of 0–0.018 M Cu^{2+} at 50–100°C for 10–90 min. Copper(II) was taken in the form of sulfate. The bath ratio was 30. Activated PCA was thoroughly washed with water for 60 min to remove excess H_2O_2 and copper salts. The washing completeness was checked by analysis for active oxygen.

Then PCA was treated with a 0.3–16.5 M emulsion of GMA in a flask equipped with a reflux condenser for 10–120 min at 60–80°C. The amount of the grafted polymer was determined gravimetrically and calculated from the content of epoxy groups. The overall activation energy was calculated from the temperature dependence of the rate constant.

CONCLUSIONS

(1) The main features of graft polymerization of glycidyl methacrylate and polycaproamide fiber in the presence of the redox system Cu^{2+}–H_2O_2 were determined.

(2) Under the optimal conditions, the maximal amount of the grafted polyglycidyl methacrylate is 46.5% and no homopolymer is formed.

REFERENCES

1. Zheltobryukhov, V.F., Development of Technological Principles and Semicommercial Implementation of the Process for Production of Graft Polycaproamide Copolymers, *Doctoral Dissertation*, Volgograd, 1987.
2. Druzhinina, T.V. and Druzhinin, S.I., *Khim. Volokna*, 1995, no. 5, pp. 7–11.
3. Smirnova, N.V. and Gabrielyan, G.A., *Khim. Volokna*, 1995, no. 1, pp. 27–30.
4. Ivanchev, S.S., *Radikal'naya polimerizatsiya* (Radical Polymerization), Leningrad: Khimiya, 1985.
5. Toroptseva, A.M., Belogorodskaya, K.V., and Bondarenko, V.M. *Laboratornyi praktikum po khimii i tekhnologii vysokomolekulyarnykh soedinenii* (Laboratory Manual on Chemistry and Technology of Macromolecular Compounds), Leningrad: Khimiya, 1972.
6. Andrichenko, Yu.D., Druzhinina, T.V., and Bondarenko, G.N., *Khim. Volokna*, 1994, no. 3, pp. 17–20.
7. Rogovin, Z.A. and Gal'braikh, L.S., *Khimicheskie prevrashcheniya i modifikatsiya tsellyulozy* (Chemical Transformations and Modification of Cellulose), Moscow: Khimiya, 1979.
8. Zaikov, V.G., Druzhinina, T.V., and Gal'braikh, L.S., *Khim. Volokna*, 1992, no. 3, pp. 11–12.
9. Eliseeva, V.I., Ivanchev, S.S., Kuchasnova, S.I., and Lebedev, A.V., *Emul'sionnaya polimerizatsiya i ee primenenie v promyshlennosti* (Emulsion Polymerization and Its Use in Industry), Moscow Khimiya, 1976.

Russian Journal of Applied Chemistry, Vol. 74, No. 4, 2001, pp. 681–686. Translated from Zhurnal Prikladnoi Khimii, Vol. 74, No. 4, 2001, pp. 660–666.

MACROMOLECULAR CHEMISTRY AND POLYMERIC MATERIALS

Carboxymethylated Wood as a Chemical Reagent for Preparation of Drilling Fluids

N. G. Bazarnova, P. S. Chubik, A. G. Khmel'nitskii, A. I. Galochkin, and V. I. Markin

Altai State University, Barnaul, Russia

Tomsk Polytechnic University, Tomsk, Russia

Vorozhtsov Novosibirsk Institute of Organic Chemistry, Siberian Division, Russian Academy of Sciences, Novosibirsk, Russia

Received April 12, 2000; in final form, July 2000

Abstract—Properties are studied of drilling solutions modified with carboxymethylated wood prepared by the suspension method under various conditions. Carboxymethylated wood is recommended as a chemical reagent for modification of drilling fluids.

Carboxymethyl cellulose (CMC) was one of the first cellulose-based chemical reagents for modification of drilling fluids. Presently it is a cellulose ether the most widely used for this purpose [1, 2].

Carboxymethyl cellulose sodium salt (NaCMC) (anion-active polymer) is adsorbed on clays. Even at low concentrations of NaCMC (especially with NaCMC having higher molecular weight, and consequently, higher viscosity) filtration can be markedly reduced. Low-viscosity NaCMC is used to reduce filtration of drilling fluids of very high density, and medium-viscosity NaCMC is added to drilling solutions with ordinary concentration of the solid phase.

NaCMC suspensions have the property of shear thinning, they possess high relative viscosity at very low shear rate. Similarly to other polymer suspensions, NaCMC suspensions have relative viscosity decreasing with increasing temperature. The efficiency of NaCMC as an agent reducing the filtration and increasing the viscosity decreases with increasing salt concentration. Some of Ca-containing drilling fluids are thinned out by adding small amount of NaCMC. Carboxymethyl cellulose shows strong effect in neutral and weakly basic solutions (pH 6.0–9.0), but is low-efficient in acidic media. NaCMC precipitates at pH < 6 and coagulates at pH > 9.0 [3].

Addition of NaCMC favors better operation of rock cutting tools, increases boring speed and headway per drill bit, and improves mud pumping. Carboxymethyl cellulose is compatible with most of drilling reagents, providing a synergistic effect. Only chromates, are practically incompatible with NaCMC, being strong oxidants (in the presence of chromates, NaCMC undergoes oxidative degradation, especially at elevated temperatures).

Thermal degradation of carboxymethyl cellulose can be inhibited by adding phenol, aniline, amine hydrochloride, or other compounds. In this case, the clay solution preserves its characteristics up to 180–190°C. However, simultaneous use of several clay suspension inhibitors (to provide synergistic effect) has a number of drawbacks, such as increased consumption of inhibiting reagents (up to 100% relative to the NaCMC weight) and filler, difficulties in transportation (especially in winter time), and high toxicity of phenol-containing inhibitors. The protecting effect of the inhibitors is based on their preferential oxidation, compared with NaCMC [4], as it has been clearly demonstrated for the example of oxidation of phenol fragments of lignin in separation of cellulose from wood by the oxygen–alkaline method, studied with model compounds [5]. It has been shown that it is possible to overcome in part the indicated problems and to improve the inhibiting effect of phenol if NaCMC is synthesized in its presence [6, 7]. Note also that such synthetic reagents as Karbofen (based on phenol) and Karbanil (based on aniline and urea) improve the thermal and salt resistance of drilling fluids.

Among lignin-based chemical reagents used in drilling, mention can be made of Sunil. It is synthesized

1070-4272/01/7404-0681 $25.00 © 2001 MAIK "Nauka/Interperiodica"

Table 1. Conditions of synthesis and characteristics of aspen wood carboxymethylation products in reactor mixer

Sample	Liquid-to-solid ratio	τ_1, h	T_1, °C	τ_2, h	T_2, °C	CMG, g	S, %	η_{rel}
CMD-1	0.7	2	65	1.0	65	18.3	92	1.08
CMD-2	0.6	4	55	0.5	55	19.9	89	1.04
CMD-3	0.5	3	60	0.5	60	16.8	92	1.03
CMD-4*	1.7	1	45	0.5	45	19.9	86	1.05

* Preliminarily defibered sample.

by treatment of wood lignin with concentrated nitric acid, followed by partial reduction of the introduced nitro groups to amino groups with sulfite. Sunil provides a considerable decrease in the viscosity and gel strength of drilling fluids. Additionally, Sunil demonstrates such useful properties as bio- and atmosphere resistance.

In our opinion, synthesis of a carboxymethyl derivative of wood without its preliminary decomposition, i.e., containing carbohydrate and aromatic fragments [8–10], will combine in this reagent a set of properties useful in its application as a modifier of drilling fluids [11].

EXPERIMENTAL

Carboxymethylated aspen wood was prepared by successive treatment of sawdust (0.4–0.7-mm fraction) with NaOH and sodium monochloroacetate in 10-l SMKS-10 reactor mixer at a wood-to-NaOH-to-sodium monochloroacetate ratio of 1.0 : 0.6 : 1.5. The moisture content of the reaction mixture was 40%. The yield of the carboxymethylated product was 0.3–3 kg.

Carboxymethylation of wood in organic solvents was carried out as follows. A weighed portion (10 g) of sawdust (0.4–0.75-mm fraction) was placed in a porcelain mortar and vigorously ground with a pestle with 5.83 g of preliminarily crushed NaOH. Then 70 ml of a solvent was added; the mixture was triturated, placed in a reaction flask, and allowed to stand at 80°C for 3 h. Then the reaction mixture was transferred from the flask to a porcelain mortar, 2.4 g of sodium monochloroacetate was added, and the content was thoroughly ground with a pestle to obtain a homogeneous mass. The resulting mass was placed in a reaction flask and allowed to stand at 40°C for 1 h. The resulting product was air-dried and then washed with 96% ethanol. During washing, 90% acetic acid was added to a negative reaction for alkali (with phenolphthalein) and chloride (with silver nitrate).

The solubility of the resulting carboxymethylated products in water, relative viscosity of their alkaline solutions, and content of carboxymethyl groups were determined by the procedures recommended in [12].

The characteristics of drilling fluids [relative viscosity (RV), plastic viscosity (PV), filtration index (FI), yield point (YP), and gel strength (GS)] were determined by the standard procedures used to test drilling fluids [13].

The rheological properties of model drilling fluids were studied with a Haake Viscotester VT550 rotary viscometer. As model drilling fluids served aqueous suspensions containing 8% bentonite clay (< 0.1-mm fraction) and 0.3% of a chemical reagent (carboxymethylated aspen wood prepared in various organic solvents).

Methods are known for carboxymethylation of cellulose in the presence of minor amounts of water in pug mills or reactor mixers [14]. In the present work, we studied for the an example of aspen wood the possibility of carboxymethylation of lignocarbohydrate materials in 10-l SMKS-10 reactor mixer. The conditions of synthesis and characteristics of the products are given in Table 1 (τ_1 and T_1 are the alkaline treatment time and temperature, τ_2 and T_2 are the carboxymethylation time and temperature, CMG is the carboxymethyl group content, S is the solubility in water, and η_{rel} is the relative viscosity of alkaline solutions).

Properties of the products obtained in the reactor mixer are close to those of the products obtained in a laboratory homogenizer [15, 16]. The temperatures of thermal treatment and carboxymethylation were maintained obviously lower than those in [15, 16], assuming that shear stress makes carboxymethylation in a reactor mixer more efficient, which may result in a considerable decrease in the sample viscosity at higher temperatures.

Sample CMD-5 was obtained in aqueous alcohol (isopropanol) solution under the following conditions: liquid-to-solid ratio 13 (weight ratio of isopropanol to water 4.3 : 1); alkaline treatment and carboxymethylation times 6 and 3 h, respectively (the total process

Table 2. Results of testing of drilling fluids modified with chemical reagents

Drilling fluid composition, %		Characteristics of drilling fluids						
clay	reagent	RV, s	PV, mPa s	YP, dPa	FI, cm^3 in 30 min	pH	GS_1	GS_{10}
							dPa	
8	–	16.5	–	–	22	9.4	0	0
16	–	19.0	6.09	17.05	15.0	7.8	1.72	2.31
8	0.56 CMC-Toros	25.0	–	–	10	8.0	1.76	5.92
16	0.30 CMC-Toros	114.5	19.36	73.20	11.0	8.3	82.9	146.4
16	0.30 CMC-600	59.0	14.60	60.75	10.0	8.3	10.9	13.91
16	0.30 CMD-1	20.0	7.48	21.43	16.0	7.3	12.1	15.88
16	0.30 CMD-2	19.5	6.31	34.45	12.0	7.3	21.5	27.49
16	0.30 CMD-3	19.0	6.02	28.67	12.5	7.4	9.8	13.99
16	0.30 CMD-4	19.0	6.43	28.93	13.5	7.5	12.9	17.01
16	0.30 CMD-5	22.3	10.53	8.51	13.5	8.2	6.8	17.20
8	0.56 CMD-5	17.5	–	–	15.5	8.0	0	0.44

time was 18 h, the carboxymethylation stage being performed twice); and alkaline treatment and carboxymethylation temperatures 50°C. Characteristics of CMD-5: carboxymethyl group content 18.9%, relative viscosity 1.11, and solubility in water 93%.

The carboxymethylation products directly obtained from wood contained carboxymethylated cellulose, hemicelluloses, and lignin, as demonstrated by spectral and chemical analysis. As characteristics of model drilling fluids prepared on the basis of clay (the main structure- and crust-forming component of drilling solutions) we measured the relative viscosity, plastic viscosity, filtration index, clay crust thickness *K*, yield point, gel strengths after 1 and 10 min (GS_1 and GS_{10}, respectively), and pH, i.e., the most significant properties influenced by addition of NaCMC. The results are given in Table 2.

Alkaline solutions of carboxymethylated wood obtained by the suspension method in aqueous alcohol medium show higher relative viscosity (1.11) as compared with samples obtained at low liquid-to-solid ratio in aqueous solutions under conditions of vigorous mechanical agitation.

It should be pointed out that the solubility of carboxymethylated cellulose varies within 86–93%. This value is lower than that of commercial NaCMC (mostly having solubilitions of 98–100%), which does not deteriorate the performance characteristics of drilling fluids modified with CMD.

The suitability criterion of drilling fluids is that the gel strength should be higher than the stress provided by the mass of suspended particles of drill cuttings or a filler (clay). Otherwise these particles start to precipitate when circulation of a drilling fluid in a borehole stops. A general requirement to the structural mechanical properties of a drilling fluid is that its structure should ensure stabilization of a suspension of drill cuttings under non-circulation conditions. To characterize the evolution of the drilling fluid structure strength in the course of time, the gel strength is measured 1 and 10 min after the state of rest is established.

Suspensions modified with CMD are weakly structured as compared with the dispersion medium (16% clay suspension). The disperse phase particles weakly interact each with other, forming no sufficiently stable structures in the state of rest.

GS_1 of drilling fluids modified with various CMDs ranges from 6.80 (CMD-5) to 21.51 dPa (CMD-2), which is considerably lower as compared with that of drilling fluids modified with commercial reagent CMC-Toros, being comparable in this parameter with CMC-600.

For drilling fluids modified with any of CMD samples obtained, GS_{10} increases by about 3–4 dPa, except in the case of CMD-5 (for this sample the rise was about 10 dPa, which is comparable with that for CMC-600). GS_1 and GS_{10} of drilling fluids modified with CMC-Toros are high, indicating that these fluids are highly structured, i.e., have a spatial structure with high mechanical strength. Use of drilling fluids with very strong structure, i.e., with high gel strength, deteriorates the conditions for drilling fluid treatment in chutes to remove drill cuttings, and also results in strongly fluctuating pressure on borehole walls during running and pulling-out of a drill string. The pressure differences caused by motion of a drill string across

a well bore are the higher, the stronger the structure of a drilling fluid in the borehole. During pulling-out of a drill string, the pressure on borehole walls decreases, which may result in distortion of the borehole stability and also in gas (or oil) show or water development. In running of a drill string, the pressure on the walls increases, so that it may reach a value sufficient for formation breakdown and lost return [17].

The most significant rheological characteristics of drilling fluids are the relative viscosity, plastic viscosity, and yield point.

In drilling, it is advisable to use a drilling fluid with as low viscosity as possible, but having a sufficiently high supporting power. A possible exception from this rule are cases of large-size hole boring, when the hole clearance cross-section is so high that, even at the maximal slush pump delivery, it is impossible to provide a return velocity sufficient for cutting transport. A higher viscosity of drilling fluids may improve the cutting transport.

The relative viscosity of CMD-modified drilling fluids ranges from 17.5 to 22.3 s (RV of the initial clay suspension 19 s), i.e., addition of CMD has virtually no effect on this rheological parameter. By contrast, CMC-Toros increases RV to 114.5 s, and CMC-600, to 59.0 s, which impairs well-boring parameters.

The plastic viscosity of the initial 16% clay solution is 6.09 mPa s. For fluids modified with carboxymethylated wood samples CMD_1–CMD-5 this value is 6.02–7.48 mPa s. Addition of CMD-5 increases PV to 10.53 mPa s. The commercial reagents increase PV of the clay suspension by a factor of 2–3 relative to the values obtained for the reagents proposed in this work: PV of model fluid with CMC-600 is 14.60 mPa s, and with CMC-Toros, 19.36 mPa s. Thus, again, the proposed carboxymethylated derivatives of wood are preferable as regards this parameter.

The observed RV and PV of the carboxymethylated reagents proposed may be lower, compared with the known commercial reagents, for two reasons: (1) lower degree of polymerization of the products and (2) lower viscosity caused by the presence of carboxymethylated lignin in the composition of the CMDs. Modified lignins (chlorolignin, Sunil, and Igetan) are widely used, together with NaCMC, as additives to drilling fluids acting as thinners of clay suspensions [3]. The carboxymethylated wood products proposed in this work are multifunctional, containing both the carbohydrate and aromatic fragments.

Addition of CMDs has a stronger effect on the yield point of the initial clay suspensions: depending on a CMD sample, the initial value (17.05 dPa) changes within the range from 8.51 (CMD-5) to 34.45 dPa (CMD-2). As seen, addition of CMD-5 considerably (by a factor of 2) decreases the initial value. The maximal increase in YP is observed with CMD-2. Addition of CMC-600 or CMC-Toros makes YP a factor of 3–4 higher, which is unfavorable in well-boring too, since the yield point characterizes the shearing resistance of the fluid, unlike the gel strength reflecting the strength of the fluid structure in the state of rest. Therefore, the greater the YP, the stronger the resistance of the fluid to a well bore, which is accompanied by such unfavorable effects as gage wear, increasing power consumption, etc.

It is well known that pH considerably affects the properties of drilling fluids. The minimal viscosity of the initial clay suspensions is observed at pH 8.5–9.5. The optimal pH was demonstrated to be 9–11. However, raising the pH of drilling fluids deteriorates the stability of borehole walls built of a clay material as a result of its disintegration, decreases the formation productivity because of the swelling of the clay constituents of the formation material, and leads to rapid corrosion of drill pipes made of light aluminum alloys. The acidic medium accelerates corrosion of steel drill pipes and other steel facilities operating in contact with drilling fluids. The pH of drilling fluids modified with CMD-1–CMD-4 ranges from 7.25 to 7.50, which is somewhat lower than that of drilling fluids with the known commercial reagents. The pH of clay suspension modified with CMD-5 is 8.25, which is comparable with that of drilling fluids modified with commercial reagents.

Thus, addition of carboxymethylated derivatives of wood provides simultaneous decrease in the filtration index, yield point, and gel strength of drilling fluids, having practically no effect on their basic rheological characteristics, such as the relative and plastic viscosities. Commercial reagents CMC-600 and CMC-Toros decrease the filtration index even more efficiently, but, simultaneously, they initiate considerable increase in all or nearly all of the rheological characteristics (relative viscosity, plastic viscosity, yield point) and structural mechanical properties of drilling fluids. Therefore, carboxymethylated wood demonstrates significant advantage over commercial CMC. The reagents proposed in this work constitute a new class of chemical reagents that can be used as modifiers of drilling fluids [11].

The majority of the methods for preparation of CMC are based on treatment of alkaline cellulose in organic

Table 3. Rheometric data for clay suspensions modified with carboxymethylated wood prepared in various organic solvents and water (shear rate 72.5–906.9 s^{-1})

Solvent	Bingham–Shvedov model			Ostwald–de Waale model		
	YP, dPa	PV, mPa s	δ, %	C, mPa s	*n*	δ, %
Reagent: Sovetskaya CMC						
–	101.209	14.312	2.9	2363.8	0.33	1.8
Reagent: CMD						
Ethyl acetate	105.46	15.52	1.9	2550.0	0.32	3.9
Water	125.25	11.93	1.4	4631.6	0.23	3.4
Dimethyl sulfoxide	128.41	14.13	2.1	4094.8	0.26	1.9
Acetone	137.42	12.88	1.5	5010.2	0.23	2.4
2-Propanol	140.50	14.98	2.6	5037.2	0.24	4.7
Benzene	162.84	13.72	1.2	5949.1	0.22	1.7
1,4-Dioxane	171.56	10.83	1.0	8868.5	0.15	3.6
n-Butanol	183.17	13.85	1.9	8439.5	0.18	4.9
2-Methyl-1-propanol	185.11	15.01	0.9	8179.2	0.19	4.7
Ethanol	185.15	13.14	2.1	9452.3	0.16	5.8
Methanol	186.87	11.02	1.1	9643.4	0.15	2.2
Chloroform	212.69	11.74	1.0	11949.3	0.13	3.6

Note: C is the consistency index, *n* is the non-Newtonian behavior factor, and δ is the mean error of approximation of experimental data by the rheological models.

or aqueous-organic solvents. In this work, we synthesized carboxymethylated derivatives of aspen wood in various organic solvents by the method described in [10] and studied the rheological properties of clay suspensions (8% bentonite clay in water) modified with them. The reagent content was 0.3% in all experiments.

The dynamic viscosity was measured at various shear rates with a Haake Viscotester VT550 rotary viscometer. Figure 1 shows the yield point of the clay suspension modified with carboxymethylated aspen wood, prepared in various protic (Fig. 1a) and aprotic solvents (Fig. 1b), as a function of the shear rate. For comparison, data are given for a drilling fluid modified with 0.3% CMC-600. The shape of the curves is similar in all the cases, despite that the properties (solubility in water, content of carboxymethyl groups, and relative viscosity of alkaline solutions) of the carboxymethyl derivatives vary widely, depending on an organic solvent in which they were prepared [18].

The presented results show that all the model drilling fluids demonstrate behavior typical of non-Newtonian fluids. The systems studied are pseudoplastic, since the yield point depends on the shear rate. It follows from a comparative analysis of the curves given in Fig. 1 that the yield point grows more slowly with increasing shear rate for carboxymethylated aspen wood.

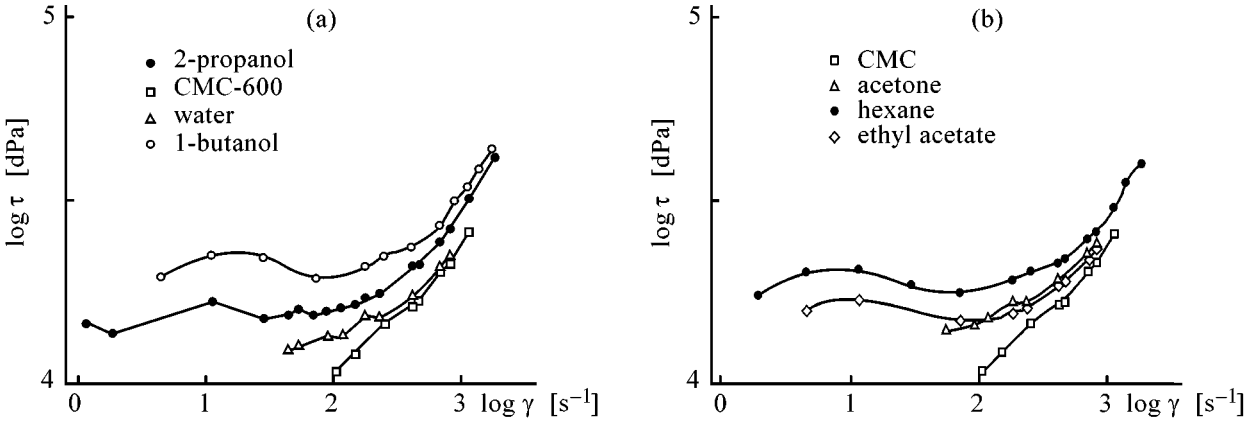

Fig. 1. Yield point τ of bentonite clay suspensions modified with 0.3% carboxymethylated aspen wood, prepared in various (a) protic and (b) aprotic solvents, vs. the shear rate γ.

Table 3 summarizes the rheometric data for clay suspensions modified with carboxymethylated wood prepared in various organic solvents and water.

The list of parameters characterizing the rheological properties of drilling solutions is determined by selection of a theoretical model, i.e., an equation relating the stress τ to the deformation or shear rate γ [18].

It follows from Table 3 that in most cases the rheological properties of the tested modified clay suspensions are described more adequately by the Bingham–Shvedov model.

For carboxymethylated wood samples obtained in chloroform, 1,4-dioxane, methanol, and isopropanol, the yield point is nearly constant over a wide range of shear rates. Chemical reagents based on carboxymethylated aspen wood demonstrate a wider spectrum of rheological parameters as compared with CMC, which allows them to be recommended as modifiers for drilling fluids used in gas and oil-well drilling.

CONCLUSIONS

(1) Carboxymethylated aspen wood reduces the filtration index, gel strength, and yield point of bentonite clay composites without changing their elastic and relative viscosities, which allows use of such composites for preparing drilling fluids.

(2) Rheological properties of clay suspensions modified with carboxymethylated aspen wood, obtained in various organic solvents, can be described more adequately in terms of the Bingham–Shvedov model.

REFERENCES

1. Kister, E.G., *Khimicheskaya obrabotka burovykh rastvorov* (Chemical Treatment of Drilling Fluids), Moscow: Nedra, 1972.
2. Gray, G.P. and Darley, H.C.H., *Composition and Properties of Oil Well Drilling Fluids*, Houston: Gulf, 1980.
3. Ryazanov, Ya.A., *Spravochnik po burovym rastvoram* (A Reference Book of Drilling Fluids), Moscow: Nedra, 1979.
4. Koz'mina, O.P., Teslenko, V.N., and Timokhin, I.M., *Zh. Prikl. Khim.*, 1982, vol. 55, no. 10, pp. 2367–2370.
5. Gierer, J. and Imsgard, F., *Svensk. Papperstidn.*, 1977, vol. 16, p. 510.
6. Gorodnov, V.D., Timokhin, I.M., Teslenko, V.N., *et al., Khimicheskie reagenty i termoustoichivye burovye rastvory* (Chemical Reagents and Heat-Resistant Drilling Fluids), Tashkent: Fan, 1977.
7. Timokhin, I.M., Zalesskii, V.I., Teslenko, V.N., *et al.*, *Ivz. Vyssh. Uchebn. Zaved., Neft' Gas*, 1971, no. 6, pp. 23–25.
8. RF Patent Appl. no. 96 115 827/04.
9. Markin, V.I., Bazarnova, N.G., and Galochkina, A.I., *Khim. Rast. Syr'ya*, 1997, no. 1, pp. 26–28.
10. Markin, V.I., A Study of Wood Carboxymethylation by the Suspension Method, *Cand. Sci. Dissertation*, Krasnoyarsk, 1999.
11. RF Patent no. 2 127 294.
12. *TU* (Technical Specifications) *6-55-40-90: Carboxymethyl Cellulose Sodium Salt*.
13. Chubik, P.S., *Praktikum po promyvochnym zhidkostyam* (Practical Course of Drilling Fluids), Tomsk: Tomsk. Politekh. Inst., 1991.
14. Grigor'eva, T.A. and Davydova, M.I., *Plast. Massy*, 1981, no. 11, pp. 42–43.
15. Markin, V.I., Bazarnova, N.G., Galochkin, A.I., and Gorulev, O.A., *Trudy Mezhdunarodnogo foruma po problemam nauki, tekhniki i obrazovaniya* (Proc. Int. Symp. on Problems of Science, Engineering, and Education), Savinykh, V.P. and Vishnevskii, V.V., Eds., Moscow: Akad. Nauk Zemle, 1997, issue 1, pp. 49–51.
16. Bazarnova, N.G., Katrakov, I.B., Markin, V.I., *et al.*, *Trudy Mezhdunarodnogo foruma po problemam nauki, tekhniki i obrazovaniya* (Proc. Int. Symp. on Problems of Science, Engineering, and Education), Savinykh, V.P. and Vishnevskii, V.V., Eds., Moscow: Akad. Nauk Zemle, 1997, issue 1, pp. 53–55.
17. Ryabchenko, V.I., *Upravlenie svoistvami burovykh rastvorov* (Control of Drilling-Fluid Characteristics), Moscow: Nedra, 1990.
18. Chubik, P.S., *Kvalimetriya burovykh promyvochnykh zhidkostei* (Quality Control of Drilling Fluids), Tomsk: Nauch.-Tekhn. Lit., 1999.

Russian Journal of Applied Chemistry, Vol. 74, No. 4, 2001, pp. 687–690. Translated from Zhurnal Prikladnoi Khimii, Vol. 74, No. 4, 2001, pp. 667–670.

CHEMISTRY OF FOSSIL FUEL

Extractive Refining of the Kerosene Fraction with Recovery of Aromatic Petroleum Solvents

A. A. Gaile, L. V. Semenov, O. M. Varshavskii, A. S. Erzhenkov, L. L. Koldobskaya, and E. A. Kaifadzhyan

St. Petersburg State Technological Institute, St. Petersburg, Russia

Kirishinefteorgsintez Production Association, Kirishi, Leningrad oblast, Russia

Received September 25, 2000

Abstract—Jet fuel containing less than 10 wt % arenes and aromatic petroleum solvents of the Nefras AR-120/200 type was prepared by combination of arene extraction from the hydrorefined kerosene fraction with the acetonitrile–pentane system, followed by concentration of arenes in the course of acetonitrile regeneration from the extract phase, based on the formation of azeotropes of acetonitrile with saturated C_9–C_{10} hydrocarbons.

Environmentally clean jet fuels can be produced by extraction of aromatic hydrocarbons and sulfur-containing compounds with aqueous acetone with addition of pentane [1, 2]. Despite its relatively low selectivity, acetone has significant advantahes as polar extractant: It does not form azeotropic mixtures with feed components and can be readily regenerated by distillation. Addition of water and pentane increases the selectivity; however, in production of environmentally clean jet fuels containing ≤10% aromatic hydrocarbons, their concentration in the extract usually does not exceed 85–90 wt %.

One of the best ways to utilize extracts of middle petroleum fractions is to produce such aromatic petroleum solvents as Nefras AR-120/200 and AR-150/330, analogs of Solvesso and Cyclosol (petroleum naphtha) [3]. These solvents are produced by catalytic reforming of hydrorefined petroleum fractions, followed by extraction of arenes, or by pyrolysis followed by sulfuric acid refining of the pyrocondensate to remove unsaturated hydrocarbons [4–6]. It seems more economically advantageous to produce aromatic petroleum solvents by extraction of hydrorefined middle distillates without using power-consuming catalytic or high-temperature processes. The main problem is how to ensure the required high concentration of arenes in the product: In Nefrases and their analogs the content of arenes is, as a rule, no less than 98 wt % [4, 7]. The requirements to petroleum naphthas are less stringent: 96 wt % according to GOST (State Standard) 10214–78 and 90 wt % according to TU (Technical Specifications) 38001196–79.

Our goal was to produce simultaneously the environmentally clean jet fuel containing ≤10 wt % arenes and aromatic petroleum solvents containing ≥98 wt % arenes from the hydrorefined kerosene fraction by means of the extractive process.

As an extractant we chose the heterogeneous acetonitrile–water–pentane system, successfully used previously for extractive refining of the diesel fraction [8]. Acetonitrile does not form azeotropic mixtures with C_9 arenes but forms them with saturated C_9–C_{10} hydrocarbons, which are components of the kerosene fraction [9]. Saturated hydrocarbons remaining in the extract must mainly include cycloalkanes and C_9–C_{10} alkanes, which are better soluble in acetonitrile than their higher-boiling homologs also present in the kerosene fraction. This fact somewhat complicates the flowsheet of acetonitrile regeneration from the extract phase; on the other hand, it must lead to higher content of arenes in the aromatic concentrate as compared with the extract, since the major fraction of saturated hydrocarbons will be removed as azeotropic mixtures with acetonitrile.

As the feed we used the hydrorefined kerosene fraction (154–220°C) from the Kirishinefteorgsintez Production Association, with the following characteristics: n_D^{20} = 1.4380; ρ_4^{20} = 0.781; content of arenes 14.0 wt %, including 13.2 wt % monocyclic arenes

1070-4272/01/7404-0687 $25.00 © 2001 MAIK "Nauka/Interperiodica"

Table 1. Conditions of extractive refining of hydrorefined kerosene fraction (5 TP, 25°C, 5 wt % water in acetonitrile)

Run no.	Solvent : feed weight ratio	
	acetonitrile	pentane
1	2 : 1	0.7 : 1
2	3 : 1	0.7 : 1
3	3 : 1	1.0 : 1

and 0.8 wt % bicyclic arenes. The aromaticity factor determined from the ^{13}C NMR spectrum (Bruker AM-500 spectrometer) according to [10] was 0.09.

The 5-TP extractive refining of the kerosene fraction was performed with countercurrent supply of aqueous acetonitrile containing 5 wt % water and of the feed with addition of pentane. The conditions are listed in Table 1, and the results, in Table 2.

The solvents were regenerated by distillation of the extract and raffinate phases in 20-TP columns. In the course of distillation of the extract phase, the following fractions were obtained: <36°C, azeotrope of pentane with acetonitrile; 36–76°C, azeotropes of acetonitrile with water and saturated hydrocarbons; 76–81°C, mainly acetonitrile with admixture of water. The bottom residue was the aromatic concentrate.

By backwashing of acetonitrile from the 36–76°C fraction with water, we recovered arene-free saturated hydrocarbons distilled-off from the extract phase. These saturated hydrocarbons can be combined with the raffinate.

The characteristics of the raffinates and extracts, and also of aromatic concentrates recovered after distillation of the solvents and removal of the major fraction of saturated hydrocarbons from the extract in the form of azeotropes with acetonitrile and water, are listed in Table 2. The concentration of saturated hydrocarbons decreases from 11.3–15.5 wt % in the extract to 0.5–3.4 wt % in the aromatic concentrate. With increasing acetonitrile : feed ratio, as expected, the degree of arene recovery increases, their

Table 2. Results of 5-TP countercurrent extraction of arenes from hydrorefined kerosene fraction

Parameters	Run		
	no. 1	no. 2	no. 3
	Raffinate		
Yield, wt %	93.8	92.2	92.7
Arene content, wt %:	9.34	8.31	8.52
including monocyclic	9.0	8.12	8.32
bicyclic	0.34	0.19	0.20
Refractive index n_D^{20}	1.4352	1.4340	1.4345
Density ρ_4^{20}	0.775	0.774	0.774
	Extract		
Yield, wt %	6.2	7.8	7.3
Arene content, wt %:	84.5	80.8	83.6
including monocyclic	76.1	73.2	75.2
bicyclic	8.4	7.6	8.4
Refractive index n_D^{20}	1.4913	1.4885	1.4906
Density ρ_4^{20}	0.872	0.864	0.870
	Aromatic concentrate		
Yield, wt %	5.37	6.52	6.13
Arene content, wt %:	97.3	96.6	99.5
including monocyclic	88.1	87.6	89.5
bicyclic	9.2	9.0	10.0
Aromaticity factor	0.521	0.515	0.538
Degree of arene recovery, %:	37.3	45.0	43.6
including monocyclic	35.8	44.2	41.6
bicyclic	61.2	73.8	74.7
Refractive index n_D^{20}	1.5008	1.5004	1.5025
Density ρ_4^{20}	0.882	0.879	0.887

Table 3. Fractional composition of the aromatic concentrate (run no. 3) and of aromatic solvents prepared by its distillation

Parameter	Aromatic concentrate	Nefras AR-120/200	Solvesso 150	Component of Nefras AR-150/330
Standard distillation, °C:				
onset of boiling	160	156	176	194
10%	174	168	186	198
30%	182	175	191	202
50%	188	181	195	205
70%	196	185	201	209
90%	208	192	207	214
end of boiling	215	206	215	230

Table 4. Characteristics of aromatic solvents recovered by distillation of the aromatic concentrate (run no. 3)

Parameter	Nefras AR-120/200	Solvesso 150	Component of Nefras AR-150/330
Yield, wt %	80	15	5
Arene content, wt %	99.5	99.4	99.8
Refractive index n_D^{20}	1.4973	1.4981	1.5173
Density ρ_4^{20}	0.876	0.913	0.933

concentration in the raffinate decreases, with, however, simultaneously decreasing content of arenes in the extract and aromatic concentrate (run nos. 1, 2). By contrast, with increasing pentane : feed ratio, the content of arenes in the extract and aromatic concentrate increases, but, at the same time, the degree of arene recovery decreases somewhat (run nos. 2, 3). Raising simultaneously the acetonitrile : feed and pentane : feed ratios allows both the degree of arene recovery and the content of arenes in the aromatic concentrate to be increased (run nos. 1, 3).

After combining the raffinates with the saturated hydrocarbons recovered from the extract phase in the course of acetonitrile regeneration, the yield of the refined jet fuel in run nos. 1–3 increases to 94.63, 93.48, and 93.87 wt %, with the content of arenes decreasing to 9.26, 8.20, and 8.41 wt %.

The bicyclic arenes, whose presence in an environmentally clean jet fuel is particularly undesirable, are recovered to a much greater extent than monocyclic arenes. The content of bicyclic arenes in the raffinate is an order of magnitude lower than the level permitted for Jet A-1 fuel (≤3%) [11].

By distillation on a 20-TP column of the aromatic concentrate obtained under optimal conditions (run no. 3), we isolated three fractions whose characteristics are listed in Table 3. The data in Tables 3 and 4 show that the first fraction corresponds to Nefras AR-120/200. Its density ρ_4^{20} should be no less than 0.865, and the content of compounds undergoing sulfonation, no less than 98 wt %.

The second, with respect to the boiling limits and arene content, fraction corresponds to the solvent Solvesso 150, and the third fraction (bottoms) can be used as a component of Nefras AR-150/330. It is also possible to use as a component of Nefras AR-150/330 the combined second and third fractions.

CONCLUSIONS

(1) Extractive refining of the kerosene fraction with acetonitrile–pentane, combined with azeotropic distillation of acetonitrile with saturated hydrocarbons in the course of regeneration of acetonitrile from the extract, yields under optimal conditions an aromatic concentrate containing up to 99.5 wt % arenes, compared with 83.6 wt % in the extract.

(2) The proposed procedure of extractive refining of the kerosene fraction yields, without using power-consuming catalytic reforming, a jet fuel containing less than 10 wt % arenes and aromatic petroleum solvents of the Nefras AR-120/200 type.

REFERENCES

1. Gaile, A.A., Somov, V.E., Semenov, L.V., *et al.*, *Khim. Tekhnol. Topl. Masel*, 1999, no. 5, pp. 3–7.

2. Varshavskii, O.M., Gaile, A.A., Kaifadzhyan, E.A., *et al.*, *Ekstraktsiya i primenenie arenov srednedistillyatnykh neftyanykh fraktsii: Sbornik trudov OOO "KINEF"* (Extraction and Use of Arenes from Middle Petroleum Distillates: Coll. of Works of KINEF Ltd.), Gaile, A.A. and Somov, V.E., Eds., St. Petersburg: Sintez, 1998, pp. 2–10.
3. Gaile, A.A., Somov, V.E., Varshavskii, O.M., and Semenov, L.V., *Ekstraktsiya i primenenie arenov srednedistillyatnykh neftyanykh fraktsii: Sbornik trudov OOO "KINEF"* (Extraction and Use of Arenes from Middle Petroleum Distillates: Coll. of Works of KINEF Ltd.), Gaile, A.A. and Somov, V.E., Eds., St. Petersburg: Sintez, 1998, pp. 91–138.
4. Stekol'shchikov, M.N., *Uglevodorodnye rastvoriteli: Svoistva, proizvodstvo, primenenie: Spravochnik* (Hydrocarbon Solvents: Properties, Production, Use: Handbook), Moscow: Khimiya, 1986.
5. Kayumov, R.P., Khaimova, T.G., Podol'skaya, D.V., and Konopleva, S.V., in *Fiziko-khimicheskie metody issledovaniya produktov neftekhimicheskogo sinteza* (Physicochemical Methods for Studying Products of Petrochemical Synthesis), Moscow: TsNIITEneftekhim, 1990, issue 9, pp. 126–132.
6. Rakhimov, M.G., Sushko, L.G., Parshin, I.V., *et al.*, *Neftepererab. Neftekhim.*, 1987, no. 7, pp. 21–23.
7. Sharafutdinova, L.G., Isyanov, I.Ya., Pavlova, A.A., *et al.*, in *Proizvodstvo uglevodorodnykh rastvoritelei* (Production of Hydrocarbon Solvents), Moscow: TsNIITEneftekhim, 1979, issue 3, pp. 110–124.
8. Varshavskii, O.M., Gaile, A.A., Semenov, L.V., and Somov, V.E., *Ekstraktsiya i primenenie arenov srednedistillyatnykh neftyanykh fraktsii: Sbornik trudov OOO "KINEF"* (Extraction and Use of Arenes from Middle Petroleum Distillates: Coll. of Works of KINEF Ltd.), Gaile, A.A. and Somov, V.E., Eds., St. Petersburg: Sintez, 1998, pp. 11–18.
9. Ogorodnikov, S.K., Lesteva, T.M., and Kogan, V.B., *Azeotropnye smesi: Spravochnik* (Azeotropic Mixtures: Handbook), Leningrad: Khimiya, 1971.
10. Ogorodnikov, V.D., in *Instrumental'nye metody issledovaniya nefti* (Instrumental Methods for Studying Crude Oils), Novosibirsk: Nauka, 1987, pp. 49–67.
11. Nasirov, R., *Neft' Ross.*, 1997, no. 11, pp. 38–42.

Russian Journal of Applied Chemistry, Vol. 74, No. 4, 2001, pp. 691–695. Translated from Zhurnal Prikladnoi Khimii, Vol. 74, No. 4, 2001, pp. 670–674.

CHEMISTRY OF FOSSIL FUEL

Recovery of Isobutylene from Commercial Butane–Butylene Fractions

K. G. Sharonov, A. M. Rozhnov, S. Ya. Karaseva, Yu. B. Myshentseva, V. I. Barkov, and V. I. Alenin

Samara State Technical University, Samara, Russia

Received February 28, 2000; in final form, September 2000

Abstract—A possibility of recovery of isobutylene with high concentration and purity from abgases of petroleum production and oil refining, e.g., from gases released in pyrolysis or catalytic cracking, by reversible reaction of isobutylene with isobutanol was studied.

In recent years, the production of methyl *tert*-butyl ether (MTBE) and methyl *tert*-amyl ether (MTAE) by alkylation of methanol with isoolefins has increased in many countries. These compounds are used as additives to motor fuel.

The hydrocarbon fractions C_4–C_5 of gases released in pyrolysis and catalytic cracking can be used as low-cost raw materials for production of isoolefins. A review of procedures for recovery of isoolefins from hydrocarbon gases was given in [1]. The procedures are based on the high reactivity of the tertiary carbon atom at the double bond in reactions of electrophilic addition. With many reagents (water, alcohols, and acids), such reactions are reversible, which allows recovery of concentrated isoolefins by subsequent decomposition of these products.

Strong acids, such as sulfuric, hydrochloric, organic sulfonic acids, and Friedel–Crafts catalysts can catalyze this reaction. The common drawback of these acids is their high corrosion activity and the low selectivity of the process. The use of weak acids, e.g., phosphoric, is inefficient owing to the low rate of the process. Of most interest as catalysts are sulfonic cation exchangers, allowing the reaction to be performed with high selectivity at low temperatures (85–90°C).

However, the procedure for hydration recovery of isobutylene via trimethylcarbinol (TMC), in which sulfonic cation exchangers are used as catalysts, has significant drawbacks: (1) the use of aqueous solutions decreases the catalytic activity of sulfonic cation exchanger, and (2) concentrated isobutylene-containing fractions (with isobutylene content of no less than 50 wt %) are used.

These drawbacks are lacking in the case of the reaction of isobutylene with aliphatic alcohols C_4–C_5. The reaction yields *tert*-alkyl ethers, which are subsequently decomposed.

The procedure for synthesizing MTBE and MTAE was thoroughly studied and discussed in [1]. As regards synthesis, and especially decomposition of ethers of higher alcohols, a number of problems still remain unsolved. It is well known [2, 3] that the reactivity of alcohols and the equilibrium degree of their conversion in the reaction with isobutylene decrease with increasing molecular weight of alcohol (Table 1). In addition, butyl alcohols do not undergo intermolecular dehydration on sulfonic cation exchanger (contrary to methanol and ethanol) and have higher boiling point. Therefore, the use of butyl alcohols as chemical extracting agents for recovery of isoolefins is of practical interest.

In this work the possibility of recovery of isobutylene from pyrolysis gases by the reaction with isobutanol was demonstrated by calculations and experiments.

Table 1. Rate constants b and equilibrium constants K_c for alkylation of alcohols with isobutylene at 323 K [2, 3]*

Alcohol	b, H^+-equiv mol^{-1} h^{-1}	K_c
Methanol	0.28	12.8 ± 2.0
Ethanol	1.58	76.1 ± 2.0
Propanol	2.63	137.6 ± 1.8
Butanol	3.53	150.3 ± 1.8
Pentanol	5.92	160.6 ± 1.8

* For stoichiometric ratio of the initial components.

1070-4272/01/7404-0691 $25.00 © 2001 MAIK "Nauka/Interperiodica"

Table 2. Data on the equilibrium of reaction (1) in the liquid phase in the presence of sulfonic cation exchanger KU-23 at molar ratio alcohol : isobutylene = 4 : 1

T, K	Catalyst content, mol %	Number of tests	τ, h	Composition of equilibrium mixture, mole fraction			$K_c = \alpha_{eth}/\alpha_{al}\alpha_{ol}$	Activity coefficient γ_i			$K_a = K_c K_\gamma$ *
				iso-C_4H_8	*iso*-C_4H_9OH	BTBE		*iso*-C_4H_9OH	BTBE	olefin	
343	10–15	13	9–23	0.01360	0.7534	0.2330	2270 ± 0.36	1.079	2.087	1.551	28.46
363	10–15	14	9–15	0.02439	0.7561	0.2195	11.90 ± 0.31	1.073	2.033	1.544	14.64
383	10–12	12	10–17	0.04251	0.7606	0.1968	6.09 ± 0.18	1.066	1.995	1.546	7.37
403	8–10	12	1.5–5	0.06459	0.7661	0.1693	3.42 ± 0.21	1.058	1.965	1.555	4.10
423	8–10	13	0.75–5	0.08946	0.7724	0.1382	2.00 ± 0.13	1.049	1.941	1.568	2.36

* $K_\gamma = \gamma_{eth}/\gamma_{al}\gamma_{ol}$.

Table 3. Concentration equilibrium constants K_c of reaction (1) at various *iso*-C_4H_9OH : *iso*-C_4H_8 molar ratios

T, K	K_a	Molar ratio *iso*-C_4H_9OH : *iso*-C_4H_8									
		1 : 1		2 : 1		5 : 1		10 : 1		20 : 1	
		K_c	K_c'	K_c	K_c'	K_c	K_c'	K_c	K_c'	K_c	K_c'
343	27.66	114.18	140.42	57.46	59.44	28.65	28.65	21.56	21.53	18.46	18.45
363	13.73	47.34	57.21	26.72	27.91	14.27	14.28	10.89	10.88	9.38	9.37
383	7.33	21.75	25.64	13.38	14.00	7.62	7.63	5.90	5.90	5.11	5.11
403	4.17	1–.97	12.54	7.16	7.48	4.32	4.41	3.41	3.40	2.97	2.97
423	2.50	6.00	6.65	4.09	4.98	2.59	2.59	2.07	2.07	1.81	1.81

It has been shown in a number of studies concerned with synthesis of MTBE and MTAB [4, 5] that the concentration equilibrium constant K_c does not correspond to the thermodynamic constant K_a owing to deviation of the system alcohol–ether–isobutylene from ideality. At the same time, at the molar ratio alcohol : isobutylene equal to 3 : 1 and higher the concentration equilibrium constant becomes stable. The equilibrium of the reaction

$$CH_3–CH–CH_2OH + CH_2=C(CH_3)_2 \rightleftarrows CH_3–CH–CH_2–O–C(CH_3)_3 \quad (1)$$

was studied in the liquid phase in the range 343–423 K. The experiments were carried out in hermetically sealed glass ampules in the presence of KU-23 sulfonic cation exchanger as catalyst. For the study, we used isobutylene (99.8 wt %), isobutanol (99.8 wt %), and isobutyl *tert*-butyl ether (ITBE) (98.5 wt %).

Isobutyl *tert*-butyl ether was produced by the reaction of isobutylene with isobutanol, with subsequent rectification. The equilibrium for each temperature was reached for both direct and reverse reactions.

The reaction products were analyzed by gas-liquid chromatography on a KhROM-3.1 device equipped with a flame-ionization detector and temperature programming unit on a 6-m-long column packed with 15% PEG-20M on silanized Chromaton AW-HDMS. The results of the experiments are given in Table 2 listing the activity coefficients γ_i of the mixture components and the thermodynamic equilibrium constants K_a. The values of γ_i were calculated by the UNIFAC technique [6], using the quantitative data for molecular fragments given in [7]. The resulting equilibrium constants K_a are described by the equation

$$\log K_a = -4.08 + 1894/T. \quad (2)$$

With the use of K_a values, we calculated the equilibrium composition of the products of reaction (1) by the scheme

$$K_a \rightarrow \text{(composition)} \rightarrow \text{UIFAC} \rightarrow K_\gamma \rightarrow K_c = K_a/K_\gamma. \quad (3)$$

In doing so, the butane-butylene fraction with isobutylene content of 20 mol % was used as isobutylene-containing fraction. The calculations were carried out for the range 343–423 K and *iso*-C_4H_8 : *iso*-C_4H_9OH molar ratios of 1 : 1, 1 : 2, 1 : 5, 1 : 10, and

Table 4. Material balance of IBTBE synthesis at 333 K and molar ratio isobutanol : isobutylene of 2 : 1

Component	Passed		Obtained			
			liquid phase		gas phase	
	g h^{-1}	wt %	g h^{-1}	wt %	g h^{-1}	wt %
Isobutane	4.1	2.88	0.4	0.44	3.7	7.33
n-Butane	2.6	1.83	0.3	0.33	2.3	4.56
1-Butene	28.0	19.69	4.9	5.34	23.1	45.73
trans-2-Butene	7.9	5.56	0.2	0.22	7.7	15.25
cis-2-Butene	6.2	4.36	0.9	0.98	5.3	10.50
Isobutylene	25.2	17.72	1.2	1.31	1.2	2.38
Butadiene	0.1	0.07	0.01	0.01	0.09	0.18
C_4-acetylene	1.5	1.05	0.05	0.05	1.45	2.87
Isobutanol	66.6	46.84	35.0	38.17	2.07	4.10
IBTBE	–	–	48.1	52.47	3.30	6.54
Isobutene dimers	–	–	0.23	0.25	0.10	0.20
Trimethylcarbinol	–	–	0.30	0.33	0.18	0.36
Total	142.2	100.0	91.69	100.0	50.49	100.0

1 : 20. The value of K_c was determined using approximation procedure by the scheme

$$K_a \rightarrow (\text{composition}, K_\gamma) \rightarrow K_c \rightarrow (\text{composition}, K''_\gamma) \rightarrow K'_c = (\text{composition}, K'''_\gamma) \rightarrow K''_c. \quad (4)$$

The approximation was considered acceptable when the discrepancy in K_c values did not exceed 10 rel. %.

The results of calculations performed by scheme (4), presented in Table 3, suggest that even the first approximation gives K_c constants coinciding with K'_c within 10 abs. %. A plot of the equilibrium conversion of isobutylene against temperature at various alcohol : isobutylene ratios is presented in Fig. 1. The calculations showed that the equilibrium conversion of isobutylene is close to 100% at low temperature andalcohol : isobutylene molar ratio exceeding 5 : 1. The calculations also confirmed that hydrocarbon gases with isobutylene content of approximately 5 wt % are suitable as feed.

The obtained calculated and experimental data were verified on a continuous laboratory setup in a temperature-controlled sectional vertical reactor packed with KU-23 cation exchanger, using butane–butylene fraction from the catalytic cracking installation[1] and isobutanol. The initial isobutanol-containing mixture was fed from the top of the reactor, and the gaseous butane-butylene fraction, from the bottom through a bubbler. The material balance of the synthesis is presented in Table 4. The degree of isobutylene recovery was 90–92%.

[1] "Sintezkauchuk" (Togliatti).

The experimental values of the concentration equilibrium constant K_c for IBTBE synthesis were used to evaluate the equilibrium degree of conversion of ether in its decomposition. The evaluation was carried out for the range 353–403 K and isobutanol : IBTBE molar ratios of 1 : 1, 2 : 1, and 3 : 1. The results of evaluation are represented by lines in Fig. 2. Also

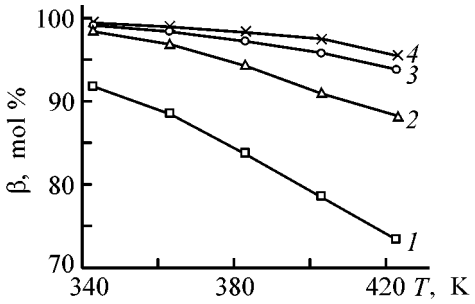

Fig. 1. Equilibrium conversion of isobutylene, β, vs. temperature *T* in IBTBE synthesis.

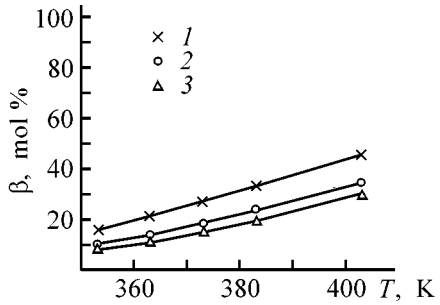

Fig. 2. Equilibrium conversion of IBTBE, β, vs. temperature *T* in its decomposition. Isobutanol : IBTBE molar ratio: (*1*) 1 : 1, (*2*) 2 : 1, and (*3*) 3 : 1. (*Line*) calculation and (*points*) experimental data.

Table 5. IBTBE decomposition in a flow-type reactor at 363 K and equimolar ratio of the ether and alcohol

v, h^{-1}	Composition of the reaction mass, wt %				IBTBE conversion	Selectivity with respect to isobutylene	Relative error of material balance, %
	iso-C_4H_8	*iso*-C_4H_9OH	IBTBE	isobutylene dimers	mol %		
0.3	2.38	88.33	8.86	0.43	85.24	99.17	0.35
0.5	6.60	82.83	8.48	2.09	85.87	96.11	0.49
1.0	2.16	92.70	5.04	0.10	91.60	99.82	1.09
3.0	4.09	89.52	6.20	0.19	89.67	99.65	1.50
5.0	4.96	86.24	8.57	0.23	85.07	99.55	0.60
8.0	6.02	77.76	16.05	0.17	73.27	99.62	0.34
12.0	8.23	68.23	23.39	0.15	61.04	99.61	0.72

given are the experimental IBTBE conversions (*points*) in IBTBE decomposition at 363 K, isobutanol : IBTBE molar ratio in the feed of 1 : 1, 2 : 1, and 3 : 1, and volumetric flow rate of feed equal to 1 h^{-1}. The results of these experiments showed that removal of isobutylene from the reaction zone increases the IBTBE conversion to 91.6%, compared with the equilibrium value of 21%.

The calculations showed that the optimal dilution is the alcohol : ether ratio of 1 : 1. With increasing dilution, the conversion of the ether decreases. Although the ether decomposition is a high-temperature reaction, the temperature should not be raised above 120°C because of the probable polymerization of isobutylene and degradation of sulfonic cation exchanger.

The experiments on IBTBE decomposition were carried out in the liquid phase in a temperature-controlled flow-type reactor packed with KU-23 cation exchanger. A system of traps was mounted at the outlet of the reactor. The first trap served to collect the liquid reaction mass, and the second trap contained a 0.5 N solution of bromine in acetic acid to absorb the released isobutylene. The reaction mass of the first trap was analyzed on a chromatograph without any pretreatment. The material balance was stricken for each run. The maximum error with respect to material balance was 6.54 rel. %.

The experiments were performed at varied temperature, isobutanol : IBTBE molar ratio, and volumetric feed flow rate v. In each run, we determined the conversion and selectivity of ether decomposition. The results of one of ether decomposition runs are presented in Table 5.

This study allows us to propose the following scheme of isobutylene recovery from the butane–butylene fraction of catalytic cracking or pyrolysis gas: etherification of isobutyle with alcohols C_4 → blowing off of unreacted hydrocarbons from the ether fraction → decomposition of ether to isobutylene → successive washing of isobutylene with alcohol C_4 cooled to 263 K and water. Isobutylene produced by this scheme was of no less than 99.9 wt % purity.

CONCLUSIONS

(1) The equilibrium of synthesis and decomposition of isobutyl *tert*-butyl ether in the presence of sulfonic cation exchanger KU-23 was studied. The equilibrium conversion of isobutylene in synthesis is close to 100% at alcohol : isobutylene molar ratios of 5 : 1 and 10 : 1. An experimental verification of the equilibrium data showed that the isobutylene conversion is 90–92%.

(2) The calculations showed that it is appropriate to carry out the decomposition of isobutyl *tert*-butyl ether in a solution of isobutanol at the optimal alcohol : ether molar ratio of 1 : 1. The ether conversion in a flow-type reactor at 363 K reaches 91% and the selectivity is more than 99% at a volumetric flow rate of feed equal to 1 h^{-1}.

(3) A scheme for recovery of isobutylene from dilute gas mixtures was proposed.

ACKNOWLEDGMENTS

The study was financially supported in part by the Russian Foundation for Basic Research (project no. 99-03-32312a), the Russian Universities—Basic Research Intercollegiate Program (project no. 991065), and the Siberian Division of the Russian Academy of Sciences (Program for Support of Young Scientists).

REFERENCES

1. Pavlov, S.Yu., *Vydelenie i ochistka monomerov dlya sinteticheskogo kauchuka* (Recovery and Purification of Monomers for Synthetic Rubber), Leningrad: Khimiya, 1987.
2. Sharonov, K.G., Rozhnov, A.M., Barkov, V.I., and Vigdergauz, A.M., *Zh. Prikl. Khim.*, 1987, vol. 60, no. 9, pp. 2177–2179.
3. Sharonov, K.G., Rozhnov, A.M., Barkov, V.I., and Cherkasova, R.I., *Zh. Prikl. Khim.*, 1987, vol. 60, no. 2, pp. 359–366.
4. Colombo, P., Corl, L., and Dalloro, L., *Ind. Eng. Chem. Fundam.*, 1983, vol. 22, p. 219.
5. Gicquel, A. and Tork, B., *J. Catal.*, 1983, vol. 83, no. 2, pp. 9–18.
6. Reid, R.C., Prausnitz, J.M., and Sherwood, T.K., *The Properties of Gases and Liquids*, New York: McGraw–Hill, 1977, 3rd ed.
7. Fredenslung, A., Gmeling, J., and Michelsen, M.L., *Ind. Eng. Chem. Process Dev.*, 1977, no. 16, p. 450.

Russian Journal of Applied Chemistry, Vol. 74, No. 4, 2001, pp. 696–699. Translated from Zhurnal Prikladnoi Khimii, Vol. 74, No. 4, 2001, pp. 617–620.

CHEMISTRY OF FOSSIL FUEL

Prediction of the Quality of Petroleum Bitumens

O. Yu. Begak and A. M. Syroezhko

St. Petersburg State Technological Institute, St. Petersburg, Russia

Mendeleev Russian Research Institute of Metrology, St. Petersburg, Russia

Received December 4, 2000

Abstract—The common and specific features of quality standard and substandard bitumens were studied by elemental analysis and by determining the yield and composition of toluene-insoluble substances, the composition and concentration of impurities in standard and substandard bitumens, and the group composition of bitumens before and after aging.

At present, about 2/3 of crude oil in Russia is extracted from West-Siberian fields. At the Kirishi Oil-Refining Plant, vacuum residues from a commercial mixture of West-Siberian crude oils from the Surgut fields are used to produce oxidized bitumens for paving and building. The technical characteristics of these bitumens are determined by their colloid structure, which, to a first approximation, depends on the group composition [1, 2]. The optimal group composition of bitumens produced from vacuum residues of various crude oils (of methane, naphthene, arene base) has not been determined. However, it is commonly accepted that, to attain high technical characteristics, paving bitumens should consist of ~50% mono-, bi-, and polycycloaromatic and paraffin–naphthene compounds, 30–34% resins, and 21–23% asphaltenes. At similar group (and hence chemical) composition, bitumens obtained from the same raw material often exhibit different heat resistances (which is often manifested in a drastic decrease in ductility upon heating). Therefore, bitumens are subdivided with respect to this parameter into quality standard and substandard, despite compliance with the requirements of GOST (State Standard) 7847–93 concerning other technical characteristics (softening point, penetration, flash point, brittle point).

The goal of this study was to reveal, using modern physicochemical methods of analysis, the factors responsible for the difference between the heat-resistant (standard) and non-heat-resistant (substandard) bitumens.

EXPERIMENTAL

Samples of standard and substandard bitumens of BDUS 100/130 and BDUS 70/100 brands (21 samples) were studied by elemental analysis (C, H, N, O, S) and exclusion chromatography.

From each bitumen sample[1] we recovered substances insoluble in toluene and analyzed them by ICP–MS on a VG Plasma Quad Turbo Plus spectrometer (UK). The content of microimpurities in bitumen samples was determined by the same method.

Asphaltenes were recovered from bitumens by exhaustive precipitation with hot pentane in a Soxhlet apparatus. Their elemental analysis was performed with a Carlo Erba analyzer (model 1106, Italy).

HPLC studies were performed on a Gold Systems liquid chromatograph (Beckman, the United States) equipped with a fast-response spectrophotometric detector (model 168) and a 6.2 × 250-mm Zorbax PSM 300 S column for exclusion chromatography (Du Pont, the United States).

Standard samples of BDUS 100/130 bitumens (five samples) have the following parameters: ring-and-ball softening point 43–45°C; penetration (needle 0.1 mm in diameter, 25°C) 103–118; ductility before heating

[1] Produced on a bitumen installation at the Kirishinefteorgsintez Production Association, Joint-Stock Company, in May 2000.

1070-4272/01/7404-0696 $25.00 © 2001 MAIK "Nauka/Interperiodica"

140–150 cm, after heating 112–140 (25°C); brittle point after heating ≤–12°C.

Substandard BDUS 100/130 bitumens (four samples) differed from the standard samples in that their ductility at 25°C was considerably lower (49–74 cm) upon heating, being below the prescribed level of 100 cm.

Standard BDUS 70/100 bitumens (five samples) have the following parameters: ring-and-ball softening point 43–46°C; penetration at 25°C 92–97; ductility before heating 147–150 cm, after heating 113–125 cm at the prescribed level of 100 cm; brittle point after heating ≤–15°C.

Substandard BDUS 70/100 bitumens (seven samples) exhibited the same parameters except that their ductility at 25°C after heating was considerably lower (47–71 cm), being below the prescribed level of 100 cm.

We found no significant differences between the total content of malthenes and asphaltenes in standard and substandard BDUS 100/130 bitumens. The content of malthenes in the studied samples of the standard and substandard bitumens was, respectively, 77.8–79 and 77.9–78.1 wt %.

For standard and substandard samples of BDUS 70/100 bitumens, these differences are also insignificant: The content of malthenes is 77.7–79.4 and 78.7–79.1 wt %, respectively.

The content of toluene-insoluble residue in the substandard samples varies by a factor of 24–25, but in standard samples the variation range is still wider: by a factor of 58. On the whole, no quantitative relationship can be revealed.

The maximal content of toluene-insoluble residue is 0.88% in standard bitumens and 0.73% in substandard bitumens.

The chemical composition of the toluene-insoluble residue was determined by ICP–MS upon dissolution in aqua regia (Table 1). It is seen that the major component of insoluble bitumen residues is iron, apparently present in the form of oxides. Also, the residues contain significant amounts of calcium, magnesium, barium, and aluminum. Zinc, copper, vanadium, manganese, and nickel are present in smaller amounts.

It should be noted that, on the whole, the content of Mg, Al, Ca, Ba, Zn, Cu, and Mn impurities is higher in the residues from standard bitumens (BDUS 70/100 and 100/130), compared with those from the substandard samples. The only exception is iron whose content in residues from substandard bitumens is approximately two times that in standard bitumens of the same brand.

Table 1. Results of ICP–MS analysis of residues after dissolution of bitumen samples

Element	Element content, mg kg^{-1}			
	BDUS 70/100	BDUS 100/130	BDUS 100/130	BDUS 70/100
	standard		substandard	
Mg	2700	2200	3300	6900
Al	2600	3600	4600	10500
Ca	6100	3100	11200	8200
Fe	10500	21300	6400	11500
Ba	1400	1300	2400	3200
Zn	610	580	840	960
Cu	450	380	450	630
V	350	230	300	220
Mn	190	210	200	350
Ni	300	130	170	230

Table 2. Characteristics of bitumen samples studied by HPLC, ICP–MS, ^{1}H and ^{13}C NMR, and X-ray diffraction

Parameter	BDUS 70/100	BDUS 100/130	BDUS 100/130	BDUS 70/100
	standard		substandard	
Elemental composition, %:				
C	81.10	81.08	81.08	81.06
H	10.54	10.26	10.36	10.30
N	0.50	0.66	0.40	0.72
S	1.94	0.98	0.66	1.19
O	5.92	7.20	7.50	6.73
Ash content, %	0.110	0.054	0.090	0.085
Weight loss in aging, %	0.11	0.13	0.06	0.08

From the whole set of 21 samples, we selected two standard and two substandard samples whose characteristics are listed in Table 2. A comparative study of these samples was performed by HPLC.

Table 2 shows that standard bitumen samples have higher sulfur content than the substandard samples. This phenomenon is due to the fact that the crude oil delivered for processing to the Kirishinefteorgsintez Production Association has significantly varying sulfur content. For example, according to the data of X-ray spectral analysis, the sulfur content in

Table 3. Content of impurities in standard and substandard bitumens (average values)

Element	Content, mg kg^{-1}, in bitumens		Ratio of impurity contents	Element	Content, mg kg^{-1}, in bitumens		Ratio of impurity contents
	standard	substandard			standard	substandard	
Mg*	**160**	**87**	**1.8**	**Zn**	**7.7**	**5.3**	**1.4**
Si	1535	1657	0.9	Ni	35.5	35	1.01
S	225	235	0.95	P	32	37	~0.9
V	13	12	1.08	**B**	**11.3**	**8.1**	**1.4**
Na	140	148	0.95	**Ba**	**9.3**	**4.8**	**1.9**
Al	**263**	**165**	**1.6**	**Pb**	**1.6**	**3.1**	**0.5**
Ca	**167**	**119**	**1.40**	**Sr**	**1.1**	**0.53**	**~2.0**
Fe	247	206	1.2	**As**	**1.1**	**0.53**	**~2.0**
Br	23.5	25	0.9	**Cu**	**12.3**	**1.6**	**7.7**
Mn	2.1	2.2	0.95	Ti	4.9	5.6	0.9
Co	2.8	2.3	1.2	W	1.8	1.6	1.1
Se	9.9	12.7	0.8				

* Data for impurities whose contents differ the most significantly are printed bold.

the crude oil delivered to the oil-refining plant varied from 0.3 to 1.66 wt %, being within 1.2–1.4 wt % in most samples.

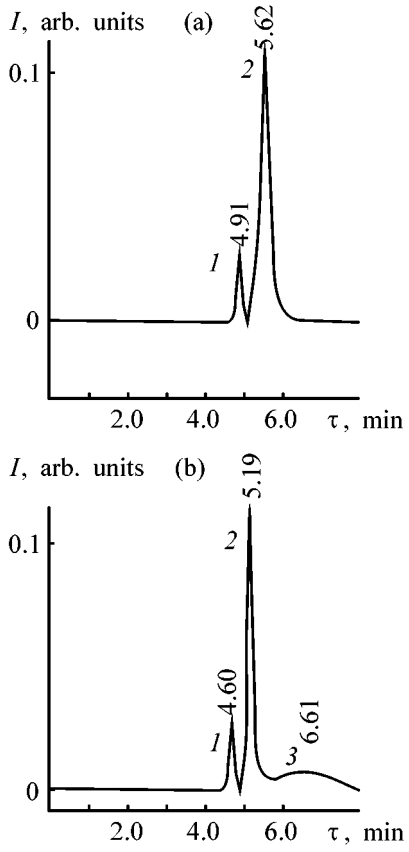

Fig. 1. Chromatograms of standard BDUS 100/130 bitumen. Eluent: (a) THF and (b) THF–CH_3CN (1 : 1). (*I*) Intensity and (τ) retention time. Fraction no.: (*1*) 1, (*2*) 2, and (*3*) 3.

An HPLC analysis of the four selected bitumen samples was performed in a column packed with silanized silica gel based sorbent, with THF (flow rate 1 ml min^{-1}) as eluent. A typical chromatogram is shown in Fig. 1a. It is seen that each bitumen sample is separated in two fractions with similar UV spectra. The area of the first peak with a shorter retention time, corresponding to the fraction that mainly consists of monocyclic aromatic compounds of oils, is higher for standard bitumens than for the substandard samples. The ratio of the areas of the first and second peaks for standard bitumens is 0.13 for BDUS 70/100 and 0.23 for BDUS 100/130, whereas for substandard bitumens this ratio is 0.10 and 0.14, respectively. Thus, standard bitumens are characterized by the higher degree of aromaticity of oils. This may be due to the fact that polycyclic aromatic compounds, resins, and asphaltenes are among the compounds giving in the chromatogram a peak with a long retention time.

The bitumens samples in hand, after aging for 2 h at 160°C and subsequent elution with THF–CH_3CN (1 : 1), also show two peaks in the chromatogram (Fig. 1b). The ratio of the areas of the first and second peaks is different in standard and substandard samples. This ratio changes after heating as compared to the initial samples. Apparently, the fraction with the shorter retention time mainly consists of paranaphthenic (PNCs), monocyclic aromatic (MCACs), bicycloaromatic (BCACs), and toluene (TCs) compounds, and also alcohol–toluene resins (ATRs) in the monomeric and partially associated form. Asphaltenes show a longer retention time. The intensity ratios of these peaks in both initial and aged bitumens suggest

that the structure of bitumens primarily differs on the associative level, with the chemical composition being similar. Samples with more closely packed structural units (a micelle with associated asphaltene molecules in the center, with resins in the shell and MCACs, BCACs, and PNCs in the remote surrounding) exhibit higher ductility, including the ductility after aging. If a sample forms "looser" structures because of the lower aromaticity of asphaltenes, resins, and oils, it will exhibit lower ductility as well.

Table 3 gives experimental data on the content of microimpurities in standard and substandard bitumens, as determined by ICP–MS. Since the total error of the ICP–MS method does not exceed 20%, the difference in the average content of some impurity elements between the bitumen samples can be considered significant (Table 3). As a rule, the content of impurities in standard bitumens is considerably higher than that in substandard samples, except in the case of lead impurity (Table 3). This fact is consistent with the increased content of the same impurities in the residues upon dissolution of standard bitumens in toluene, as compared with the insoluble residues of substandard bitumens (Table 1). The weight content of impurities in standard bitumens is higher than that in substandard bitumens by 80% for Mg, 40% for Ca, 90% for Ba, 270% for Sr, 60% for Al, 40% for B and Zn, and 100% for As.

The most significant difference between the standard and substandard bitumen samples is observed for the Cu content: by a factor of 7.7.

It should be noted that the obtained data on the increased content of impurity elements in standard bitumens as compared with the substandard samples are fully consistent with the results of analysis of toluene-insoluble substances. The insoluble residues of standard bitumens contain increased amounts of alkalineearth metals, aluminum, zinc, copper, and manganese as compared with the toluene-insoluble residues of the substandard samples.

Apparently, the increased content of a number of impurity elements in standard bitumen samples as compared with the substandard samples suggests a stronger catalytic effect of these elements on the oxidation of the initial vacuum residue, resulting in higher quality of the bitumen. Since the oxidation occurs by oxidative dehydrogenation, this assumption also accounts for the increased aromaticity of malthenes and asphaltenes in standard bitumens.

CONCLUSIONS

(1) A study by ICP–MS, HPLC, and elemental analysis showed that samples of standard and substandard paving bitumens have virtually identical qualitative chemical compositions of the base (organic part) but differ in the degree of aromaticity of malthenes and asphaltenes and in the content of ash, sulfur, oxygen, and microelements [alkaline-earth elements (Mg, Ca, Sr, Ba), 3*d* elements (Cu, Co, Zn), and also Al, B, Pb, and Ag].

(2) Aging is accompanied by changes in the group composition of bitumens, primarily on the associative level. The standard and substandard bitumens differ the most significantly in the ratio of monomeric and associated forms of oil, resin, and asphaltene molecules, which is particularly manifested in aging of the bitumens.

REFERENCES

1. Kolbanovskaya, A.S. and Mikhailov, V.V., *Dorozhnye bitumy* (Paving Bitumens), Moscow: Transport, 1973.
2. Khudyakova, T.S., Rozental', D.A., and Malikova, I.A., *Adgezionnye svoistva neftyanykh bitumov i sposoby ikh korrektirovki: Tematicheskii obzor* (Adhesion Properties of Petroleum Bitumens and Ways To Adjust Them: Topical Review), Moscow: TsNIITEneftekhim, 1991, issue 3.

Russian Journal of Applied Chemistry, Vol. 74, No. 4, 2001, pp. 700–701. Translated from Zhurnal Prikladnoi Khimii, Vol. 74, No. 4, 2001, pp. 679–680.

BRIEF COMMUNICATIONS

Effect of Chlorine and Nitrosyl Chloride on Nitrogen(II) Oxide Oxidation into Nitrogen(IV) Oxide

A. I. Morozovskii, A. B. Solomonov, and V. I. Skudaev

Perm State Technical University, Perm, Russia

Received July 7, 2000; in final form, November 2000

Abstract—The effect of chlorine and nitrosyl chloride impurities on the regeneration of nitrogen(IV) oxide—oxidizing agent in oxychlorination of hydrocarbons—was studied at two temperatures. An assumption is made that the process occurs by radical-chain mechanism and involves chlorine oxides.

The substitution of oxygen by nitrogen(IV) oxide in oxidative chlorination of a number of organic compounds allows a 2–10-fold acceleration of the process, depending on the chosen technological scheme. To prevent discharge of the forming hydrogen chloride and nitrogen oxides into the atmosphere, nitrogen oxides are used in a closed cycle

$$RH + HCl + NO_2 \rightarrow RCl + H_2O + NO, \quad (1)$$

$$NO + 1/2O_2 \rightarrow NO_2, \quad (2)$$

$$2NO_2 + 4HCl \rightarrow Cl_2 + 2NOCl + 2H_2O. \quad (3)$$

Reaction (2) has been studied in a wide temperature range [1]. In the course of oxychlorination, the reaction may proceed either at room temperature in a separate apparatus, conventionally named the oxidizing vessel, simultaneously with the oxidation of hydrogen chloride [reaction (3)], or directly in the oxychlorination reactor simultaneously with reaction (1) at relatively high temperatures. However, in both cases, it will proceed in the presence of chlorine and nitrosyl chloride—products of hydrogen chloride oxidation by nitrogen(IV) oxide, which may affect the reaction rate. The aim of the present study was to elucidate this influence.

EXPERIMENTAL

The effect of chlorine and nitrosyl chloride was studied by IR spectroscopy on a Specord 75-IR instrument in a 214-ml high-temperature quartz cuvette under atmospheric pressure at 298 and 523 K. The content of chlorine and nitrosyl chloride was up to 25 mol % relative to nitrogen(II) oxide. The reaction conditions were chosen with account of reagent concentrations and temperatures in the oxidizing vessel and oxychlorination reactor. The components of the reaction mixture were introduced into the cuvette with a medical syringe, the cuvette was purged, and the reaction mixture was diluted, with argon. The reaction course judged from the rate of nitrogen(IV) oxide formation measured by recording kinetic curves of NO_2 accumulation at a wave number of 1626 cm^{-1}.

The results of the experiments are presented in Figs. 1a and 1b. At 298 K, the presence of chlorine and nitrosyl chloride has no effect on the rate of nitrogen(II) oxide oxidation into nitrogen(IV) oxide, whereas at 523 K their presence accelerates the process.

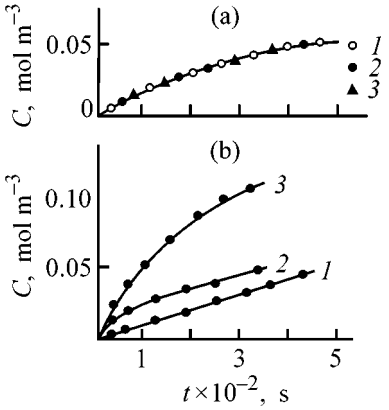

Fig. 1. NO_2 concentration C vs. time t in (a) oxidizing vessel and (b) oxychlorination reactor. Temperature (K): (a) 298 and (b) 523. Initial reagent concentration (mol m^{-3}): NO 0.194 and O_2 0.388. Impurity concentration (mol m^{-3}): (*1*) 0, (*2*) 0.0485 Cl_2 (a) and 0.0291 NOCl (b); (*3*) 0.0485 Cl_2.

1070-4272/01/7404-0700 $25.00 © 2001 MAIK "Nauka/Interperiodica"

The apparent temperature-independence of the reaction rate is accounted for by the low negative activation energy, growing with increasing temperature through a change of the dominant reaction path [1].

Chlorine may affect the rate of NO oxidation into NO_2 through a decrease in the NO concentration caused by the occurrence of a concurrent reaction

$$2NO + Cl_2 \rightarrow 2NOCl. \quad (4)$$

However, the rate of reaction (4) is three orders of magnitude lower than that of reaction (2). The absence of effect of nitrosyl chloride can be attributed to its inertness with respect to nitrogen(II) oxide and oxygen at low temperature.

To account for the acceleration of NO oxidation into NO_2 in the presence of chlorine at high temperature, an assumption should be made that oxygen compounds of chlorine may be formed, exhibiting markedly higher activity in nitrogen(II) oxide oxidation, compared with oxygen. Rather probable is the radical-chain mechanism of the process, according to which a $ClO\dot{O}$ radical is formed upon decomposition of a chlorine molecule

$$\dot{Cl} + O_2 \rightarrow ClO\dot{O}. \quad (5)$$

The reaction of NO with the $ClO\dot{O}$ radical proceeds in two stages [2]

$$NO + ClO\dot{O} \rightarrow NO_2 + Cl\dot{O}, \quad (6)$$

$$NO + Cl\dot{O} \rightarrow NO_2 + \dot{Cl}, \quad (7)$$

with a chain developed after that.

The presence of nitrosyl chloride increases the rate of nitrogen(IV) oxide formation, especially strongly in the first 60–100 s, which can be attributed to thermal decomposition of nitrosyl chloride

$$NOCl \rightarrow NO + \dot{Cl}. \quad (8)$$

This, firstly, makes higher the nitrogen(II) oxide concentration and, secondly, gives rise to a chain process involving oxygen compounds of chlorine, which are, as mentioned above, much more active in nitrogen(II) oxide oxidation as compared with oxygen.

REFERENCES

1. Mal'ko, M.V. and Nesterenko, V.V., *Kinetika i mekhanizm khimicheskikh reaktsii v dissotsiiruyushchem teplonositele – chetyrekhokisi azota* (Kinetics and Mechanism of Chemical Reactions in Dissociating Hear Transfer Agent—Nitrogen Tetroxide), Minsk: Nauka i Tekhnika, 1974.
2. Nikitin, I.V., *Khimiya kislorodnykh soedinenii galogenov* (Chemistry of Oxygen Compounds of Chlorine), Moscow: Nauka, 1986.

Russian Journal of Applied Chemistry, Vol. 74, No. 4, 2001, pp. 702–703. Translated from Zhurnal Prikladnoi Khimii, Vol. 74, No. 4, 2001, pp. 680–682.

BRIEF COMMUNICATIONS

Determination of Carbonyl Compounds by High-Performance Liquid Chromatography

K. A. Dychko, V. V. Khasanov, G. L. Ryzhova, and T. T. Kuryaeva

Tomsk State University, Tomsk, Russia

Received March 10, 2000; in final form November, 2000

Abstract—Carbonyl compounds in the form of 2,4-dinitrophenylhydrazones in alcoholic solutions were analyzed by high-performance liquid chromatography. This simple procedure is characterized by high sensitivity and reproducibility.

Detection of formaldehyde, acetaldehyde, and propionaldehyde in alcoholic solutions by gas chromatography is rather difficult because of the low sensitivity of flame ionization detectors to carbonyl compounds with small number of atoms (especially to formaldehyde) and, in the case of gas-liquid chromatography, because of the poor separation of acetaldehyde and propionaldehyde from the main component (ethanol), which hinders their quantitative determination [1, 2]. In this work we used high-performance liquid chromatography (HPLC) with preliminary preparation of 2,4-dinitrophenylhydrazine (DNPH) derivatives [3]. These derivatives can be easily separated and determined under the conditions of the reversed-phase HPLC.

Carbonyl compounds (aldehydes and ketones) present in the alcoholic solutions determine their quality. These compounds can serve as fragrant additives (aromatic aldehydes and some others) and toxins (formaldehyde, acetaldehyde, glutaraldehyde, etc.). The content of some compounds (e.g., formaldehyde and acetaldehyde) in alcohol liquors is strictly standardized and controlled.

In this work, we studied the behavior of DNPH derivatives under the conditions of the reversed-phase HPLC.

EXPERIMENTAL

The measurements were carried out by reversed-phase HPLC on a Pharmacia-LKB unit equipped with a UV 430 nm detector and a 4×250-mm column packed with LiChrosorb RP-8 (10 μm) silica gel under the isocratic conditions using an acetonitrile–0.1 N acetic acid (2 : 1) eluent with an elution rate of 0.9 ml min^{-1}.

The required derivatives were prepared before placing the sample in the column as follows. A solution of a sample (0.5 ml) containing no more than 1 mg of the carbonyl compound was mixed with a 0.03 M

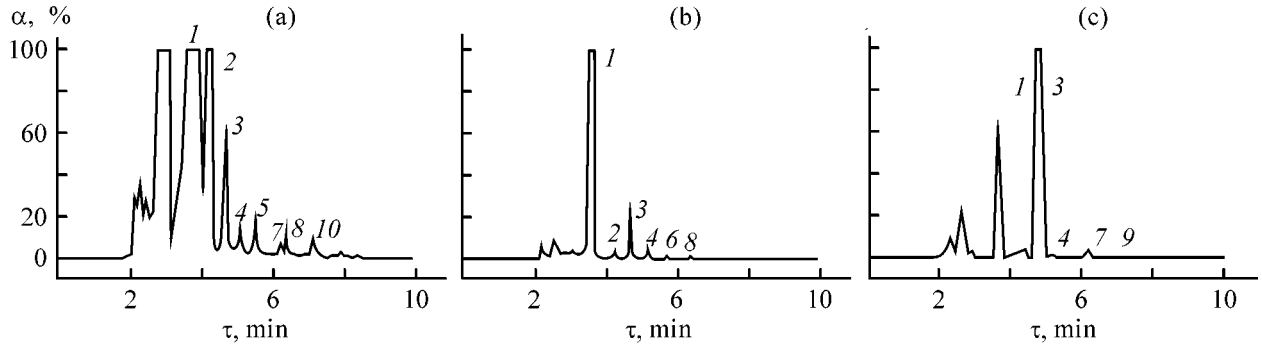

Fig. 1. Chromatograms of samples (a) *III*, (b) *II*, and (c) *IV*. (α) Absorption and (τ) retention time. Content: (*1*) initial DNPH, (*2*) formaldehyde, (*3*) acetaldehyde, (*4*) acetone, (*5*) propionaldehyde, (*6*) isobutyraldehyde, (*7*) butanone, (*8*) benzaldehyde, (*9*) isopentanal, and (*10*) pentanal.

1070-4272/01/7404-0702 $25.00 © 2001 MAIK "Nauka/Interperiodica"

DNPH solution in acetonitrile (0.5 ml), acidified with a drop of concentrated hydrochloric acid, and kept at 50–90°C for 10–15 min. Then the mixture was cooled; if the solution was turbid, it was diluted tenfold with the eluent. In the case of alcoholic liquors, 0.5-ml samples were analyzed without dilution. The reaction conditions ensured quantitative conversion of carbonyl compounds.

The HPLC procedure was performed using 20-μm samples. The retention parameters and the peak areas were determined on a Spectra-Physics SP4290 integrator. The chromatograms are shown in Fig. 1.

As seen, the separation order of the DNPH derivatives of the carbonyl compounds corresponds to the number of carbon atoms in the carbonyls. Moreover, the derivatives with branched carbon chains are eluted before the normal compounds with the same number of carbon atoms. Unchanged DNPH is eluted first and does not hinder detection of the carbonyls in question.

The elution order was determined by comparison with chromatograms of individual carbonyls; the content of carbonyls was found using the gaging dependence for the DNPH–acetaldehyde derivative.

The results of the analysis of alcoholic liquors are listed in the table.

Such compounds as acetaldehyde, propionaldehyde, acetone, and methyl ethyl ketone, difficultly detectable by gas-liquid chromatography, can be determined at concentrations lower than 0.5 mg l^{-1} with increased sample volume. This procedure is fairly promising in analysis of the quality of the alcoholic liquors and in quantitative determination of carbonyl compounds in various objects. However, it should be noted that analysis of herb infusions may be hindered by various extracted compounds. For example, very high content of formaldehyde in sample *III* is probably due to the overlap with a peak of extracted compound. This problem can be solved by using a diode-matrix detector. On the whole, the sensitivity of the developed procedure is higher as compared with that of gas–liquid chromatographic procedure and constitutes at least 0.5 mg l^{-1} with an rms error of no more than 10%.

Content of carbonyl compounds *C* in alcoholic liquors

τ_r,* min	*C*, mg/100 ml				Compound
	I	*II*	*III*	*IV*	
4.37	19.1	2.60	163.1	–	Formaldehyde
4.76	–	25.7	73.4	212.9	Acetaldehyde
5.28	7.95	3.96	18.1	2.54	Acetone
5.42	–	–	28.4	–	Propionaldehyde
5.74	0.82	–	–	–	Isobutyraldehyde
6.14	10.13	–	–	6.40	Butanone
6.50	–	1.62	31.2	–	Benzaldehyde
6.66	–	–	–	1.14	Isopentanal
7.21	3.77	–	15.3	–	Pentanal
7.94	–	–	3.49	–	U.i.**
8.44	–	–	2.42	–	″
8.83	–	–	0.97	–	″

* (τ_r) Retention time.

** (U.i.) Unidentified; dash designates that the content of the corresponding compound is lower than 0.5 mg/100 ml.

REFERENCES

1. *Chromatographic Analysis of the Environment*, Grob, R.L., Ed., New York: Dekker, 1975.
2. Haszlo, Maros, *Acta Chim. Hung.*, 1985, vol. 118, no. 3, pp. 215–220.
3. Shatts, V.D. and Sakhartova, O.V., *Vysokoeffektivnaya zhidkostnaya khromatografiya* (High-Performance Liquid Chromatography), Riga: Zinatne, 1988.

Russian Journal of Applied Chemistry, Vol. 74, No. 4, 2001, pp. 704–705. Translated from Zhurnal Prikladnoi Khimii, Vol. 74, No. 4, 2001, pp. 682–683.

BRIEF COMMUNICATIONS

Initiation of Low-Temperature Polymerization with Hexafluoropropylene Ozonide

D. P. Kiryukhin, I. M. Barkalov, and I. L. Ismoilov

Institute of Problems of Chemical Physics, Russian Academy of Sciences, Chernogolovka, Moscow oblast, Russia

Received December 7, 2000

Abstract—The feasibility of using hexafluoropropylene ozonides for initiating low-temperature polymerization and copolymerization of tetrafluoroethylene, hexafluoropropylene, and some other monomers was demonstrated.

The mechanism of low-temperature ozonolysis of tetrafluoroethylene (TFE) and hexafluoropropylene (HFP) has been studied in detail [1, 2]. It was found that the decomposition products of TFE ozonide effectively initiate the radical polymerization of TFE. In this work, we studied the initiating power of HFP ozonide in low-temperature polymerization of TFE and some other monomers.

EXPERIMENTAL

Studies of the low-temperature ozonolysis, thermal stability of ozonolysis products, and polymerization kinetics were performed by calorimetry, successfully used for this purpose previously [3]. Gaseous TFE and HFP were purified by being passed through a sulfuric acid solution and a column packed with activated carbon, followed by low-temperature fractionation.

Ozone was generated by means of electric discharge; an oxygen flow was passed through a glass ozonizer. To obtain pure ozone, its solution in liquid oxygen was subjected to low-temperature fractionation. Crystalline ozone was additionally purified by sublimation. All experiments were performed in glass calorimetric cells. The IR spectra of polymers prepared as films were taken on an H-800 (Higler) spectrometer.

To evaluate the initiating power of HFP ozonide, we performed the following experiments. First, we prepared HFP ozonide at low temperatures. For this purpose, ozone and HFP in an equimolar ratio were frozen in a calorimetric cell with a vacuum stop-cock at 77 K and then slowly warmed to 220 K (see figure, curve *1*). An endothermic peak of HFP melting was observed at T_m = 117 K. Then, in the range 160–220 K, was observed an exothermic peak due to formation of the ozonide and the corresponding acid fluorides. As shown in [1, 2], HFP molozonide $CF_3–\overset{\diagup O_3 \diagdown}{CF}–CF_2$ is first formed in this temperature interval and then transformed into the ozonide $CF_3–CF\underset{\diagdown O \diagup}{–O–O}–CF_2$ and acid fluorides. After the formation of HFP ozonide, the warming was stopped, the calorimeter with the cell was cooled to 77 K, the cell was connected to a vacuum unit, a certain portion of TFE was condensed, and the cell was again placed in the calorimeter. The calorimetric curve was recorded in the course of slow thawing. The calorimetric curve of thawing of such the system (see figure, curve *2*) shows endothermic peaks associated with dissolution of products of low-tempera-

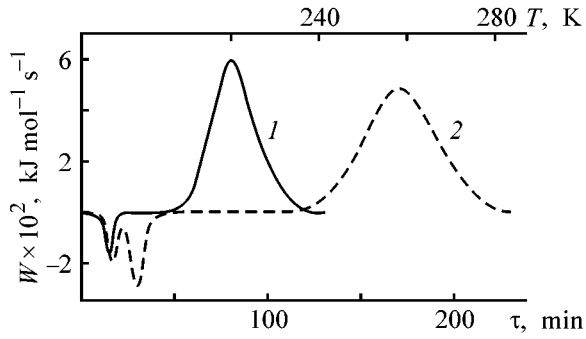

Calorimetric curves of warming of an HFP (0.0289 g)–O_3 (0.0092 g) mixture: (*1*) initial mixture and (*2*) after warming to 220 K, cooling to 77 K, and addition of 0.096 g of TFE. (W) Heat release, (T) temperature, and (τ) time.

1070-4272/01/7404-0704 $25.00 © 2001 MAIK "Nauka/Interperiodica"

ture HFP ozonolysis and melting of TFE (T_m = 141 K). Further warming in the range 240–290 K is accompanied by vigorous heat evolution related to polymerization of TFE. Note that it is in this range that HFP ozonide decomposes to give a very reactive bipolar ion which can initiate TFE polymerization [1]:

$$F_3C-\overset{\diagup O-O\diagdown}{CF}-O-CF_2 \rightarrow [F_3C-\overset{\diagup O-O^-}{C^+F} + F_2CO]$$
$$\rightarrow F_3-CFO + F_2CO + 1/2O_2.$$

For the initial molar ratio HFP ozonide : TFE = 1 : 50, the conversion of the monomer, determined gravimetrically after the process completion, was 100%. Thus, the decomposition products of HFP ozonide effectively initiate TFE polymerization.

This conclusion is confirmed by the following experiment. If TFE is introduced into the cell after warming the system HFP–ozone to 300 K, when decomposition of the ozonide is already complete and the cell contains only stable decomposition products, no polymer is formed.

It should be noted that low-temperature decomposition of HFP ozonide also initiates copolymerization of TFE with HFP. A mixture of TFE and HFP in a 4 : 1 molar ratio was frozen at 77 K in a cell in which HFP ozonide was prepared. In the course of thawing of this system, we also observed in the range 240–290 K vigorous heat release associated with copolymerization. The yield of the copolymer in such experiments was about 100%. Hence, the resulting TFE–HFP copolymer contains no less than 25% HFP, since it is known [3] that HFP does not undergo homopolymerization under these conditions and can only enter copolymerization. The IR spectra of the resulting copolymer contain absorption bands characteristic of the TFE–HFP copolymer.

With the HFP content in the initial mixture raised further (e.g., to HFP : TFE = 1 : 2), the copolymerization rate decreases and the yield of the polymeric product becomes as low as ~50%.

Note that the products of ozonide decomposition can also initiate polymerization of other monomers, e.g., acrylonitrile and methyl methacrylate. For example, the yield of the polymer in 24 h at 290 K was 65% with acrylonitrile and 30% with methyl methacrylate.

Thus, we have demonstrated the feasibility of using the decomposition products of HFP ozonide for initiating polymerization and copolymerization processes.

ACKNOWLEDGMENTS

The study was financially supported by the Russian Foundation for Basic Research (project no. 00-03-32212).

REFERENCES

1. Ismoilov, I.L., Atakulov, Sh.B., Muidinov, M.R., *et al.*, *Dokl. Akad. Nauk SSSR*, 1987, vol. 295, no. 5, pp. 1159–1163.
2. Ismoilov, I.L., Kiryukhin, D.P., Barkalov, I.M., and Teshebaev, S.T., *Khim. Fiz.*, 1989, vol. 8, no. 1, pp. 98–101.
3. Barkalov, I.M. and Kiryukhin, D.P., *Int. Rev. Phys. Chim.*, 1994, vol. 13, no. 2, pp. 337–357.

Russian Journal of Applied Chemistry, Vol. 74, No. 4, 2001, pp. 706–707. Translated from Zhurnal Prikladnoi Khimii, Vol. 74, No. 4, 2001, pp. 684–685.

BRIEF COMMUNICATIONS

Resistance of Rosin-Modified Polyester Resin to Thermal Oxidative Degradation

N. I. Polezhaeva, I. V. Polezhaeva, V. A. Levdanskii, M. Ya. Nikulin, and B. N. Kuznetsov

Institute of Chemistry and Chemical Technology, Siberian Division, Russian Academy of Sciences, Krasnoyarsk, Russia

Received September 7, 2000; in final form, December 2000

Abstract—The resistance of rosin-modified polyester resin to thermal oxidative degradation was studied. This resin can be used as organic binder in low-temperature corrosion-inactive soldering pastes.

Among microelectronic devices under development, a prominent place is occupied by devices produced by hybrid integrated technology. The assembling and mounting of hybrid integrated microcircuits are accelerated and the mounting quality is improved when tin-plating or soldering pastes are used [1, 2].

At present, various resins and polymeric materials are used as organic binders in soldering pastes. A binder imparting to the paste the required viscosity and adhesive power should not evaporate at ambient temperature, but should completely volatilize on heating before the solder starts to melt. Furthermore, it should be inert with respect to the solder in both storage and paste fusion. The most used as the main component of the organic binder are traditional products of wood chemical industry: rosin and products of its processing [3–5]. Studies showed that rosin solutions do not ensure the required process properties of soldering pastes. Rosin has low softening point T_s (60–68°C) and poor heat resistance [6]. Many solutions of polymeric materials are unsuitable for binder preparation because of the high softening point, which results in that the organic matter is not separated from the solder in the course of soldering.

To ensure the required adhesion, heat resistance, and softening point of the organic binder, we prepared a polyester resin modified with rosin. Because the working temperature of fusion of low-temperature soldering pastes is, depending on the solder composition, 200–450°C for template printing and 140–350°C for the dosing unit, the heat resistance of the polymeric product is of crucial importance for development of the organic binder.

In this work, we studied the resistance to thermal oxidative degradation of a rosin-modified polyester resin.

EXPERIMENTAL

The polyester resin was prepared from ethylene glycol (bp 198–200°C, d_4^{20} = 1.115), glycerol (bp 290°C, d_4^{20} = 1.260), maleic anhydride (bp 202°C, d_4^{20} = 0.934), and phthalic anhydride (bp 285°C, d_4^{20} = 1.527). To prevent side reactions, the synthesis was performed under argon. The initial mixture was heated at 195–198°C for 4 h. Then commercial oleoresin pine rosin (OPR) was added, and the addition reaction was performed for 1 h at 198–200°C. The polycondensation equilibrium was shifted by removal of the released water using a Dean–Stark trap. The yield of the polyester was 90% based on the initial charge. The product is a dark yellow transparent solid. The softening point T_s and acid number AN were determined by the procedure given in [7]. The physicochemical characteristics of the samples are as follows: OPR, T_s = 65°C, AN = 165 mg KOH g^{-1}; polyester resin, T_s = 95–100°C, AN = 110 mg KOH g^{-1}.

The parameters of thermal oxidative degradation of the resulting polyester resin were determined by dynamic thermogravimetry [8]. To determine the onset temperature of the resin degradation more accurately by means of thermogravimetric analysis, we recorded along with the TG curves also the DTG and DTA curves [9]. The study was done with an MOM Q-1000 derivatograph (Hungary) in programmed sample heating mode. A 0.1-g sample was heated in a platinum crucible in air at a rate of

1070-4272/01/7404-0706 $25.00 © 2001 MAIK "Nauka/Interperiodica"

5 deg min^{-1}. The instrument sensitivities were as follows: balance, 100 mg; DTA galvanometer, 1/3; and DTG galvanometer, 1/10.

Because the polyester resin contains the solvent, free water, residual alcohol, and unsaponifiable substances boiling in the range 100–250°C, the weight loss starts at relatively low temperatures. Therefore, the heat resistance of the sample was judged from the onset temperature of degradation (T_d^{DTA} is the onset temperature of the exothermic effect in the DTA curve, associated with the onset of oxidation; T_d^{DTG} is the temperature at which the DTG curve starts to deviate from the horizontal), rather than from the temperatures of 5% and 10% weight loss [9]. The activation energy of thermal degradation E_d was estimated by the Freeman–Carrol procedure [8]. Data on the thermal oxidative degradation of the polyester resin are listed in the table.

Data in the table show that, as regards all the criteria: T_s = 95–100°C, T_d^{DTG}, T_d^{DTA}, T_d^{av} (average degradation onset temperature from the DTG and DTA data), the synthesized polyester resin meets all the requirements to organic binders for low-temperature soldering pastes.

In the course of fusion of the soldering paste, a major fraction of the binder evaporates and burns out; the residue should be corrosion-inactive and nonconducting. The polyester resin was tested for corrosion activity on copper plates according to GOST (State Standard) 20.57.406–8 in a humid (93 ± 3% humidity) chamber for 21 days at 40 ± 2°C. An assessment of the results according to GOST 275.97–88 showed that the resin is corrosion-inactive. This fact makes assembling and mounting of hybrid integrated microcircuits less labor-consuming, because the washing stage is eliminated.

The volume resistivity of the polyester resin after partial fusion and storage in a humid chamber was, on the average, 1.7×10^{13} Ω m.

CONCLUSIONS

(1) A new product, rosin-modified polyester resin, was prepared.

Parameters of the heat resistance of samples, as determined by dynamic thermogravimetry

Sample	T_d^{DTG}, °C	T_d^{DTA}, °C	T_d^{av}, °C	E_d, kJ mol^{-1}
OPR	200	160	180	50
Polyester resin	540	460	500	80

* $T_d^{av} = (T_d^{DTG} - T_d^{DTA})/2$.

(2) As shown by dynamic thermogravimetry, the modified polyester resin is resistant to thermal oxidative degradation.

(3) The modified polyester resin can be used as organic binder in low-temperature corrosion-inactive soldering pastes.

REFERENCES

1. Krasov, V.G., Petrauskas, G.B., and Chernozubov, Yu.S., *Tolstoplenochnaya tekhnologiya v SVCh mikroelektronike* (Thick-Film Technology in UHF Microelectronics), Moscow: Radio i Svyaz', 1985.
2. Chigonin, N.N., Fomina, E.N., and Krasov, V.G., *Elektron. Tekh. Mater.*, 1979, issue 7, pp. 26–31.
3. Trizna, Yu.P., Panov, L.I., Koretskii, V.N., and Rogovskii, V.F., *Tekh. Sredstv Svyazi. TPO*, 1979, issue 2, pp. 61–64.
4. USSR Inventor's Certificate, no. 1489955.
5. USSR Inventor's Certificate, no. 1745478.
6. Klyuev, A.Yu., Shlyashinskii, R.G., Prokopchuk, N.R., *et al.*, *Zh. Prikl. Khim.*, 1999, vol. 72, no. 2, pp. 288–292.
7. Vershuk, V.I. and Gurich, N.A., *Metody analiza syr'ya i produktov kanifol'no-skipidarnogo proizvodstva* (Methods for Analysis of Raw Materials and Products of Rosin and Turpentine Production), Moscow: Goslesbumizdat, 1960.
8. Wendlandt, W.Wm., *Thermal Methods of Analysis*, New York: Wiley–Interscience, 1974.
9. Prokopchuk, N.R., *Vestsi Akad. Navuk Bel., Ser. Khim. Navuk*, 1984, no. 4, pp. 119–121.

Russian Journal of Applied Chemistry, Vol. 74, No. 4, 2001, pp. 708–710. Translated from Zhurnal Prikladnoi Khimii, Vol. 74, No. 4, 2001, pp. 686–688.

OBITUARY

In Commemoration of Professor Gleb Aleksandrovich Mamantov (1931–1995)

G.A. Mamantov, one of the best known specialists in chemistry and electrochemistry of molten salts, honored professor and head of the chemical faculty at the University of Tennessee, Knoxville, USA, would be 70.

G.A. Mamantov was born on April 10, 1931 in a small town of Karsava, situated in the eastern part of Latvia. There lived during the Civil war in Russia his parents, Elena and Aleksandr G.A. Mamantov, general practitioners, both St. Petersburg born. In 1944, the G.A. Mamantov family was taken out of Latvia and they found themselves in a camp for displaced persons at Kleinkotz (West Germany). In 1945–1949, G.A. Mamantov was studying there at a Latvian gymnasium. In 1949, the G.A. Mamantov family moved to the US. In the same year, G.A. Mamantov entered the University of Louisiana, and in 1953 was awarded there the degree of a bachelor of chemistry. At the same university (in 1954) he backed his master's dissertation "Studies in Voltammetry"). In 1957, G.A. Mamantov received his PhD degree in electrochemistry. The title of his PhD dissertation was "Anodic Stripping Voltammetry and Other Studies of Electrode Processes." In final stages of G.A. Mamantov's education, his work was supervised by P. Delahay, the most prominent American electrochemist, author of a number of monographs, two of which have been translated into Russian [Delahay, P., *Novye pribory i metody v elektrokhimii* (New Devices and Methods of Electrochemistry), Moscow: Inostrannaya Literatura, 1957; *Dvoinoi sloi i kinetika electrodnykh protsessov* (Double Layer and Kinetics of Electrode Processes), Moscow: Mir, 1967]. The first of these books had strong impact on the development of voltammetric measurements in the USSR. The second, with a foreword written by Academician A.N. Frumkin, was highly appreciated by him. In 1954–1958, G.A. Mamantov published, together with Delahay, four papers concerned with the theory and practice of voltammetry. In particular, they derived equations for the transient time in the case of linear diffusion and simultaneous migration, and also for the case of spherical diffusion. G.A. Mamantov studied at Delahay's laboratory the reproducibility of the transient time in voltammetric (chronopotentiometric measurements) and reduction of complex ions in aqueous solutions. In 1957–1958, the scientist worked as a researcher chemist at Dupont Corp. (Niagara Falls, NY). In 1958–1960, he served in the US Air Force in California. On having finished his military service, G.A. Mamantov for some time (1960–1961) conducted scientific research together with Prof. J.L. Margrave at the University of Wisconsin. Their publication (1961) was concerned with decomposition of liquid borazine.

G. A. Mamantov (photograph taken in the 1960s).

Beginning in 1961 and till the end of G.A. Mamantov's life, his pedagogical and scientific activities had been associated with the University of Tennessee. In 1971 he became professor, and in 1979, head of the chemical faculty. Simultaneously, he had been a consultant at Oak Ridge National Laboratory since 1962, and held a similar position at Los Alamos National Laboratory since 1986. In 1987, G.A. Mamantov founded a small company Molten Salt Technology and became its president. In the summer of

1070-4272/01/7404-0708 $25.00 © 2001 MAIK "Nauka/Interperiodica"

1991, the scientist delivered lectures at Paris University as an invited professor.

The scientific legacy of G.A. Mamantov is vast and diverse. The list of his works, compiled by the scientist himself shortly before his death, includes 261 items. Let us make an attempt to distinguish the main directions of research. During 1963–1973, more than 30 publications were concerned with the application of modern electrochemical and spectroscopic methods to investigation of fluoride melts which are of interest for the nuclear reactor technology. Particular attention was paid to the behavior of various compounds dissolved in the mixtures $LiF–BeF_2–ThF_4$, $LiF–BeF_2–ZrF_4$, and LiF–NaF–KF. The results obtained in studying fluoride systems were summarized in reviews [1, 2]. In some studies, the behavior of compounds of uranium with various oxidation levels in fluoride melts was analyzed.

G.A. Mamantov and co-workers proposed an original design of a reference electrode for molten fluorides and fluoroborates [3].

About 60 publications (1970–1975) were devoted to investigation of various systems based on chloroaluminate melts by optical and electrochemical methods. In the initial stage of this series of works, the nature of the system $AlCl_3$–NaCl and the behavior of various ions introduced into melt were studied.

Changing the composition of a chloroaluminate melt alters its acid–base properties and affects redox processes involving the dissolved substances and their coordination characteristics. The composition of the species present in a melt was determined by Raman spectroscopy, the equilibria were studied quantitatively by potentiometry. Voltammetric measurements were also widely used to study specific features of electrode reactions. With the chemistry of chloroaluminate solutions and acid–base equilibria in these melts was concerned a summarizing paper by G.A. Mamantov and R. Osteryoung [4]. In 1980, G.A. Mamantov and coworkers were the first to develop and apply an original—spectroelectrochemical—technique for investigation of electrode reactions. Optically transparent electrodes allowed observation of the absorption spectra of substances involved in the electrode process [5, 6]. Particular attention was given by G.A. Mamantov during a succession of years to application of optical methods in studying the behavior of compounds of sulfur in higher oxidation states in chloroaluminate melts and to electrochemical reactions involving these compounds. These investigations were for the most part summarized in [7].

Gleb and Charmaine Mamantov.

In 1980, G.A. Mamantov published an extensive review [8] concerned with the use of molten salts in rechargeable secondary power cells. Together with coworkers, he proposed and comprehensively studied a rather efficient secondary chemical power cell with sodium anode, solid electrolyte composed of β"-alumina, and cathode in the form of a chloroaluminate melt with S(IV) ions [9–11]. Also, quite a number of other cathode formulations were considered. Later, the possibility was demonstrated of using glassy solid electrolyte instead of β"-alumina [12].

A numerous series of works with G.A. Mamantov's participation was devoted to low-temperature spectroscopic and spectroelectrochemical studies of organic compounds [13, 14].

G.A. Mamantov's scientific activities were characterized by an exceedingly close attention to the experimental technique and account of all the factors affecting the interpretation of a result obtained. For example, he was the first to point to the necessity for a repeated study of the electrochemical behavior of a number of rare metals in halide melts when, after the appearance of a number of reports (by Russian scientists, in the first place) in the late 1980s, it became clear that oxygen-containing impurities exert strong influence on the complexation in these media.

By G.A. Mamantov's initiative, and under his and his colleagues' (J. Braunstein, G.P. Smith) editorship, six collections of works *Advances in Molten Salt Chemistry* were published in 1971–1987, together with some other books, the last of which appeared in print in 1994 [15].

The scientific and organizational activities of G.A. Mamantov were distinguished by exceptional intensity. He was a member of the American Chemical Society, Electrochemical Society, Society of Applied Spectroscopy, and other scientific societies, took part in the organization and holding of a great variety of

conferences and symposia. G.A. Mamantov initiated the establishment of M. Bredig's prize awarded for the best works in chemistry of molten salts. G.A. Mamantov was elected a foreign member of the Latvian Academy of Sciences.

The list of G.A. Mamantov's scientific awards is vast. Gleb Aleksandrovich Mamantov had not lived in Russia, but he was brought up in a Russian family, had a perfect command of the Russian, and always showed keen interest in our country. Twice, in 1974 and 1989, the scientist was in the USSR for a long stay, visited scientific centers in Kiev, Moscow, and Leningrad. G.A. Mamantov translated into English B.B. Damaskin's book *Printsipy sovremennykh metodov izucheniya electrokhimicheskikh reaktsii* (Moscow: Mos. Gos. Univ., 1965) (Principles of Modern Techniques for Analysis of Electrochemical Reactions). G.A. Mamantov's elder brother, Il'ya Aleksandrovich, taught Russian philology at the University of Dallas and had repeatedly been to the USSR before 1978.

When the financing of the scientific research and higher school dropped dramatically in the early 1990s, G.A. Mamantov was truly worried about the fate of our scientific schools. He invited to his laboratory several young scientists from Russia, Ukraine, and Latvia for postgraduate education and scientific training. Despite falling severely ill in 1993, G.A. Mamantov was always ready to help in training of young scientists. G.A. Mamantov died on March 12, 1995, at the age of sixty-three at the height of his pedagogical and scientific activities. He was true scientist, excellently educated, talented, and vigorous. And he will be remembered as such by all of those who knew him.

The authors wish to thank Professor Ch. Hussey (University of Mississippi, USA), Dr. G. Stafford (National Institute of Standards and Technology, USA), and I.A. Mamantov's son, Igor Mamantov (Dallas, USA) for help in obtaining the necessary materials.

REFERENCES

1. Fung, K.W. and Mamantov, G., *Adv. in Molten Salt Chemistry*, Braustein, J., Mamantov, G., and Smith, G.P., Eds., New York: Plenum, 1973, vol. 2, pp. 199–254.
2. Manning, D.L. and Mamantov, G., *Characterization of Solutes in Nonaqueous Solvents*, Mamantov, G., Ed., New York: Plenum, 1978, pp. 289–309.
3. Clayton, F.R., Mamantov, G., and Manning, D.L., *High Temper. Science*, 1973, vol. 5, no. 5, pp. 358–364.
4. Mamantov, G. and Osteryoung, R., *Characterization of Solutes in Nonaqueous Solvents*, Mavantov, G., Ed., New York: Plenum, 1978, pp. 223–249.
5. Mamantov, G., Norvell, V.E., and Klatt, L., *J. Electrochem. Soc.*, 1980, vol. 127, no. 8, pp. 1768–1772.
6. Norvell, V.E. and Mamantov, G., *Molten Salt Techniques*, Lovering, D.G. and Gale, R.J., Eds., New York: Plenum, 1978, vol. 2, pp. 223–249.
7. Marassi, R. and Mamantov, G., *The Sulfur Electrode: Fused Salts and Solid Electrolytes*, Tischer, R.P., Ed., New York: Academic, 1983, pp. 191–217.
8. Mamantov, G., *Materials for Advanced Batteries*, Murphy, D.W., Bronchead, J., and Steele, B.C.H., Eds., New York: Plenum, 1980, pp.111–122.
9. Mamantov, G., Marassi, R., Matsunaga, V., *et al.*, *J. Electrochem. Soc.*, 1980, vol. 127, no. 11, pp. 2319–2325.
10. Mamantov, G., Tanemoto, K., and Ogata, Y., *J. Electrochem. Soc.*, 1983, vol. 130, no. 7, pp. 1528–1531.
11. Mamantov, G. and Hvistendahl, J., *J. Electrochem. Soc.*, 1984, vol. 168, no. 1–2, pp. 451–466.
12. Orchard, S.W., Sato, Y., Schebrechts, J.-P., and Mamantov, G., *J. Electrochem. Soc.*, 1990, vol. 137, no. 7, pp. 2194–2195.
13. Wehry, E.L. and Mamantov, G., *Modern Fluorescence Spectroscopy*, Wehry, E.L., Ed., New York: Plenum, 1981, vol. 4, pp. 193–250.
14. Stout, P.J. and Mamantov, G., *Chemical Analysis of Polycyclic Aromatic Compounds*, Tuan Vo-Dinh, Ed., New York: Wiley, 1989, pp. 411–432.
15. *Chemistry of Nonaqueous Solutions. Current Progress*, Mamantov, G. and Popov, A.I., Eds., New York: VCH Publishers, 1994.

A. G. Morachevskii, V. R. Okorokov, and E. G. Polyakov

Russian Journal of Applied Chemistry, Vol. 74, No. 4, 2001, pp. 711–712. Translated from Zhurnal Prikladnoi Khimii, Vol. 74, No. 4, 2001, pp. 689–?690.

OBITUARY

Ivan Yakovlevich Tyuryaev (1920–2001)

Ivan Yakovlevich Tyuryaev, a known scientist in the field of industrial catalysis, doctor of technical science, Professor, Honored Scientist and Technologist of Russia, died on March 5, 2001, at the age of 80.

I.Ya. Tyuryaev was born on September 12, 1920. In 1948, he graduated from the Lomonosov Institute of Fine Chemical Technology, Moscow, having returned to the institute in 1946 after being discharged from the army where he went as a volunteer after finishing his first year as a student. He backed his candidate dissertation in 1954, and doctoral dissertation in 1963.

Tyuryaev started his labor activity in 1948, first as a production engineer and then as deputy head of a pilot shop at the Pilot plant (Yaroslavl). From 1952 till 1956, when doing his military service, he was appointed a military representative of the Ministry of Defense. In 1956, by request of the Ministry of Chemical Industry, he was discharged and then worked as a senior researcher at research institutes in Yaroslavl, Leningrad, and Moscow, being also a senior researcher at the Research Institute of Synthetic Alcohols (Moscow). In 1958, he was invited to head the newly organized laboratory of contact-catalytic processes at the Research Institute of Monomers for Synthetic Rubber (Yaroslavl). From 1963 till 1965 he headed the laboratory of catalytic synthesis and was deputy director for science at the Institute of Macromolecular Compounds, Academy of Sciences of the Ukraine (Kiev). From 1965 to 1997, Tyuryaev headed the newly organized laboratory of catalysts and leading researcher at the Prikladnaya Khimiya Russian Scientific Center [former GIPKh (State Institute of Applied Chemistry)].

Tyuryaev's half-century's scientific activities covered the following three main directions of research: petrochemistry, organic synthesis, and catalysis.

Tyuryaev became widely known for his works in the field of petrochemistry (1948–1965, Yaroslavl, Kiev). Tyuryaev developed theoretical foundations of the technology of manufacture of basic monomers (butadiene, isoprene, isobutylene) for synthetic rubbers by dehydration of hydrocarbons. He studied

the chemistry, equilibrium, and rates of the main and all side reactions; dynamics of, and reasons for changes in catalyst activity; chemistry and kinetics of catalyst regeneration.

He developed theoretical basis for calculation of reactors and regenerators with suspended catayst bed and performed mathematical modeling of dehydrogenation reactors of various kinds. The research and development culminated in designing and creating a number of large-tonnage productions of butadiene and isoprene in our country and abroad.

Tyuryaev is the founder of a new scientific direction in monomer synthesis: he (together with coauthors) discovered a new reaction—oxidative dehydrogenation of hydrocarbons to give dienes. He studied the chemistry and kinetics of these reactions and found appropriate catalysts.

Tyuryaev also studied the chemistry and kinetics of the reactions occurring in the three-stage process for isoprene production (propylene $\rightarrow$ 2-methylpentene-1 $\rightarrow$ 2-methylpentene-2 $\rightarrow$ isoprene). He developed a theoretical approach to the choice of a homogeneous catalyst for the last stage.

1070-4272/01/7404-0711 $25.00 © 2001 MAIK "Nauka/Interperiodica"

In the field of industrial organic synthesis (1965–1980, Leningrad), Tyuryaev was in charge of the development of an industrial technology for manufacture of ε-caprolactam via εcaprolactone and studied the chemistry and kinetics of the involved reactions and found appropriate catalysts.

Tyuryaev developed industrial techniques for manufacture of a number of amino acids for agriculture, food industry, health protection service (*L*-lysine, *L*-sodium glutamate, *DL*-tryptophane, *L*-DOFA), from synthesis of starting compounds to separation of racemates and racemation of *D*-isomers. Catalysts for the catalytic stages were found. Extensive research and development work and tests were carried to the stage of industrial production design.

Under Tyuryaev's supervision was developed (1966–1990, Leningrad) a group of catalysts for organic synthesis (production of indole, furan, tetrahydrofuran, ethylenediamine, organofluorine products, etc.) and a set of catalysts for aerospace and defense technology, altogether more than twenty in number. In developing these catalysts, the chemistry and kinetics of the main production stages were studied, comprehensive stand and full-scale studies were carried out, and manufacturing facilities were created. The catalysts developed for the aerospace and defense technologies are unique in their activity and service characteristics and ensure fabrication and reliable operation of the obtained articles and objects.

As a result of his scientific research activities, Tyuryaev published more than two hundred works, including 2 monographs, and received about 50 inventor's certificates.

Together with conducting research studies, Tyuryaev carried out extensive scientific-organizational and pedagogical work. During the period from 1960 to 1990, he was a permanent member of the scientific council of catalysis at the State Committee on Science and Technology; from 1982 till 1990 Tyuryaev was chief chemist for catalysts of the Ministry of Chemical Industry; from 1979 to 1990, he was dean of the base faculty of the Leningrad Technological Institute (LTI) at GIPKh, organized with his direct participation, and a professor of the chair of special catalysts at this faculty; from 1967 till the last days of his life Tyuryaev was a permanent member of a number of qualifying councils awarding the degrees of candidate and doctor of science (GIPKh, VNIINeftekhim, Leningrad Technological Institute); he was one of organizers and a co-chairman of the Leningrad city seminar on catalysis and a member of the Editorial board of *Zhurnal Prikladnoi Khimii*.

Tyuryaev shared his profound knowledge and vast experience with his pupils. Twenty candidate and two doctoral dissertations have been prepared under his supervision.

Tyuryaev was active citizen and a man of principle.

For his services in the development of the domestic chemical science, Tyuryaev was decorated with an Order of Friendship among Nations and a number of medals.

We lost an excellent, nice, and sympathetic person, a truly intelligent man, and a professional of great vigor.

The blessed memory of Ivan Yakovlevich, an outstanding scientist, colleague, and teacher, will be cherished forever in the hearts of those who were lucky to have known him.

Prikladnaya Khimiya Russian Scientific Center,

St. Petersburg Technological Institute,

Editorial board and editorial staff of Zhurnal Prikladnoi Khimii

Russian Journal of Applied Chemistry, Vol. 74, No. 4, 2001, p. 713. Translated from Zhurnal Prikladnoi Khimii, Vol. 74, No. 4, 2001, p. 691.

BOOK REVIEWS

Reznik, I.D., Ermakov, G.P., and Shneerson, Ya.M., *Nikel'* (Nickel), Moscow: Mashinostroenie, 2000, vol. 1, 384 pp.

The first volume of a three-volume monograph *Nikel'* (Nickel) written by such known specialists as I.D. Reznik, (Gintsvetmet Institute, Moscow), G.P. Ermakov (Severonikel' Combine, Monchegorsk), and Ya.M. Shneerson (Gipronikel' Institute, St. Petersburg) was published in the end of 2000. All the authors have rich experience of work at plants and institutes of the nickel industry. The book comprises 10 chapters, grouped in three parts. The first chapter considers in detail the problems of technical development of nickel plants in the USSR in the postwar years (1945–1991). First batches of nickel metal were obtained in Russia as far back as 1933 at the Ufalei nickel plant (Chelyabinsk oblast); in 1938–1939, Yuzhuralnikel' (Orsk) and Severonikel' combines were put into operation. In 1991, 282 thousand tons of nickel were manufactured in Russia, which constituted 34% of the world's nickel output. In the subsequent years, the manufacture of nickel by the domestic plants decreased, whereas the world's output approached 1 million tons in 2000. The authors discuss separately groups of plants processing oxidized nickel ores (ch. 1) and sulfide copper–nickel ores (ch. 2). The second chapter gives special attention to the Noril'sk mining and smelting combine and the history of its construction. In 1942, the combine produced the first electrolytic nickel. The second chapter also includes information about the Krasnoyarsk plant of nonferrous metals where sludges produced in electrolysis at the Noril'sk mining and smelting combine are processed and platinum-group metals are refined. Both chapters captivate the reader and mention a large number of engineers and researchers who contributed to the creation and development of the domestic nickel industry and to designing and implementing new technological schemes.

Nickel ore processing has its own specificity consisting in the wide variety of ore types, the variability and complexity of their composition, low nickel content, necessity for performing numerous preliminary treatments, and impossibility of ore dressing by the common mechanical methods. The second part of the book describes in ample detail the methods for preparation of ores and concentrates for metallurgical conversion. Such issues are covered as ore blending (ch. 3), sampling (ch. 4), drying (ch. 5), briquetting (ch. 6), agglomeration (ch. 7), and balling (ch. 8). The ninth chapter is concerned with reductive calcination of oxidized nickel ores for subsequent ammonia-carbonate leaching. The third part of the monograph (ch. 10) describes various methods for dressing of oxidized nickel ores. The authors consider the segregation calcination with flotation or magnetic separation of the calcine to be the most efficient method for dressing this kind of ores. The method is in the development stage and has not been used under industrial conditions (segregation calcination could make profitable the processing of lean oxidized ores of the Ural region).

Each part of the book is provided with a list of references to a total of 257 works of domestic and foreign authors. The monograph has clearly technological orientation and analyzes production processes at, in the first place, domestic plants.

The book is of interest for engineers and researchers working in the field of processing of nickel-containing raw materials. The manner of presentation makes the book recommended reading for senior students, masters, and postgraduate students specializing in metallurgy of heavy nonferrous metals.

A. G. Morachevskii, I. N. Beloglazov

1070-4272/01/7404-0713 $25.00 © 2001 MAIK "Nauka/Interperiodica"

Russian Journal of Applied Chemistry, Vol. 74, No. 4, 2001, p. 714. Translated from Zhurnal Prikladnoi Khimii, Vol. 74, No. 4, 2001, p. 692.

BOOK REVIEWS

Gaile, A.A., Somov, V.E., and Varshavskii, O.M., *Aromaticheskie uglevodorody: Vydelenie, primenenie, rynok: Spravochnik* (Aromatic Hydrocarbons: Isolation, Use, and Market: Reference Book), St. Petersburg: Khimizdat, 2000, 544 pp.

The reference-monographic edition systematizes the advances in chemistry and technology of aromatic hydrocarbons with account of numerous publications of, mainly, the last decade. The bibliography of the book, given separately for each chapter, includes about 1900 references.

The first chapter "Isolation and Separation of Arenes" briefly considers, with due regard to the existence of specialized literature, the sources of arenes. The main attention is given to extractive isolation of aromatic hydrocarbons from catalysts for reforming of benzine fractions and pyrocondensates, straight-run medium-distillate petroleum fractions with simultaneous production of ecologically safe jet-engine and diesel fuels. Also considered are methods for isolation and purification of arenes obtained in coal carbonization from "crude benzene" and coal tar and techniques for separation of C_8–C_{10} arenes. Also, this chapter reflects the results obtained by the authors of the book in studies performed at the St. Petersburg State Technological Institute in cooperation with PO Kirishnefteorgsintez.

Chapters 2–4 consider various ways to use benzene and its homologues, naphthalene, and polycycloarenes. Of particular interest are some new promising fields of application of arenes and, in particular, production of phenol by means of vapor-phase oxidation of benzene by nitrogen(I) oxide in the presence of zeolites modified with iron oxide.

The fifth chapter presents technological schemes of industrial processes for production of aromatic hydrocarbons and their most important derivatives—styrene, cumene, phenol, cyclohexane, linear alkylbenzenes, bisphenol A, aniline, caprolactam, phthalic anhydride, terephthalic acid, etc. Performance characteristics of various processes for manufacture of aromatic compounds are compared.

The sixth chapter is concerned with the fields of application of petroleum aromatic solvents and aromatic concentrates—promising products that can be isolated in extraction manufacture of ecologically safe motor fuels, an alternative to hydrocracking, which requires gross investment and involves high energy consumption.

The seventh chapter presents data on the scale of manufacture, consumption structure, and prices of aromatic hydrocarbons and their most important derivatives.

The use of the reference book is facilitated by the provided subject index.

For this reference-monographic edition to be comprehensive, it would be advisable to supplement the book with sections concerning the arene formation processes (catalytic reforming and pyrolysis of oil fractions, coal carbonization), composition of arenes present in oils, and mechanisms of the reactions considered. However, the authors did not aim to cover all arene-related issues in an encyclopedic manner, restricting themselves to provision of references on some of these topics.

The book is well published, contains an ample body of concrete data on industrial processes and advanced investigations in the field of isolation and use of aromatic hydrocarbons. It seems to be a valuable manual both for specialists in petroleum refining and petrochemistry and in organic synthesis and for teachers, postgraduate students, and students of chemical-technological and oil higher school institutions.

I. V. Tselinskii

1070-4272/01/7404-0714 $25.00 © 2001 MAIK "Nauka/Interperiodica"

Russian Journal of Applied Chemistry, Vol. 74, No. 4, 2001, pp. 715–719. Translated from Zhurnal Prikladnoi Khimii, Vol. 74, No. 4, 2001, pp. 693–696.

INFORMATION

The Second Russian Kargin Symposium "Chemistry and Physics of Polymers at the Beginning of XXI Century"

The Second All-Russia Kargin Symposium "Chemistry and Physics of Polymers at the Beginning of the XXI Century" (Chernogolovka, May 29–31, 2000) was organized by the Russian Academy of Sciences (Department of General and Technical Chemistry and Scientific Council on Macromolecular Compounds) with active participation of the Institute of Problems of Chemical Physics, Institute of Synthetic Polymeric Materials, Institute of Organoelement Compounds, and Moscow State University.

Among the Symposium participants were more than 400 scientists and specialists from 19 Russian towns (Moscow, St. Petersburg, Kazan, Nizhni Novgorod, Chernogolovka, Irkutsk, Ufa, Yekaterinburg, Novosibirsk, Saratov, Samara, Birsk, Barnaul, Tver, Izhevsk, Al'met'evsk, Balakovo, Troitsk), CIS (Azerbaijan, Armenia, Belarus Republic, Uzbek Republic), and also scientists from Egypt, Romania, the United States, France, Switzerland, and Japan. Participants from Russia represented 21 institutions of the Russian Academy of Sciences, 28 universities, and 11 research institutes for various branches of industry.

The symposium program included 19 plenary lectures and 375 posters presented at four poster sessions. By the amount of related contributions, all of them can be arbitrarily subdivided into the following 13 topics.

(1) Polymers and biology. Various aspects of this complex problem were outlined in six plenary lectures. The general strategy of synthesis of biopolymers based on lactic and glycolic acid was analyzed in the lecture given by M. Vert (France). A. Grosberg (US) examined in his lecture the geometry and topology of proteins and also phase transitions in polymers and biopolymers. E. Shakhnovich (US) reviewed recent achievements in computer modeling of the structure/function relationship in proteins. The potentialities of the modern chemistry of medical biopolymers for development of new materials modeling certain functions of organs and tissues of living bodies were discussed in the lecture given by L.I. Valuev (Moscow).

The poster presentations by V.A. Alinovskaya, S.A. Belyaev, S.M. Butrim, and P.M. Bychkovskii (Minsk, Belarus) reported data on immobilization of various drug preparations on monocarboxycellulose. E.A. Baryshnikova and I.I. Vointseva (Moscow) demonstrated the possibility of synthesizing water-soluble *m*-carborane-containing oligo salts for boron-neutron-capture therapy of cancer and biocidic interpolymers based on polyhexamethyleneguanidine and chlorosulfonated polyethylene. T. Budtova (St. Petersburg) reported on a study of polyelectrolyte gels based on cross-linked sodium polyacrylate as models for new drug preparations. Immobilization of lipases into a complex of two oppositely charged polyelectrolytes was reported by I.V. Gorokhova (Moscow). E.N. Danilovtseva (Irkutsk) presented data on synthesis and characteristics of new water-soluble copolymers based on 1-vinyl-4,5,6,7-tetrahydroindole.

It is known that dendrimers bearing amino groups on the surface of their molecules show promise for transport of a genetic material into a cell. M.V. Zhiryakova (Moscow) synthesized for the first time water-soluble positively charged nonstoichiometric polyelectrolyte complexes with polypropylenimine dendrimers. The composition and properties of complexes of polylysine with negatively charged liposomes were reported by O.E. Kuchenkova (Moscow). The contribution by I. Zorin (St. Petersburg) was concerned with synthesis of mesogenic polyamido ethers with amino acid units in the main chain. N.A. Kas'yanenko (St. Petersburg) and O.A. Pyshkina (Moscow) reported the results of a spectroscopic study of interaction of DNA with synthetic polymers and of native DNA and its single-chain analog with distearyldimethylammonium chloride in solution. Synthesis and characterization of collagen–apatite composite for medical use were reported by S.D. Litvinov (Samara). The contribution by A.V. Makeev (St. Petersburg) was devoted to synthesis of polyfunctional polymeric coatings for medical use, based on polyvinyl alcohol and lactic acid.

(2) Synthesis and properties of composites and polymers. The corresponding plenary session included eight lectures covering particular aspects of this complex problem. They were as follows. Rigidity and Plasticity in Solid Polymers (E.F. Oleinik, Moscow); Polymer Chemical Structure, Free Volume, and

1070-4272/01/7404-0715 $25.00 © 2001 MAIK "Nauka/Interperiodica"

Prediction of Membrane Properties (Yu.P. Yampol'skii, Moscow); Liquid-Crystal Elastomers: Features and Mechanisms of Orientation Induced by Mechanical Field (R.V. Tal'roze, Moscow); Ceramic-Reinforced Polymers and Polymer-Modified Ceramics (J.E. Mark, US); New Principles of Development of Photosensitive Multifunctional Materials Based on Chiral Photochromic Copolymers (V.P. Shibaev, Moscow); Langmuir–Blodgett Ferroelectric Polymer Films (L.M. Blinov, Moscow); Block Ionomer Complexes (A.V. Kabanov, US); and Photochemical Effects on Polymer Films and Fibers (A. Mousa, Egypt).

Poster presentations by V.S. Avinkin and M.Yu. Vdovin (Moscow) and by B.N. Anfimov (Moscow) were devoted to the effect of ethylene–vinyl acetate copolymer (EVAC) or paraffins on the mechanical and elastic properties of the LDPE–rubber powder composite and also to the contribution of chemical cross-linking between the components to the properties of polymer composites. O.V. Stoyanov (Kazan) reported the structural mechanical characteristics of mixtures of EVAC and LDPE. The properties of biocompatible implants based on polymers and phosphates modified with polyacrylic acid were reported by E.N. Andreeva (Moscow). Generalized data on the phase composition and structure of fibers of thermotropic liquid-crystal copolyethers were reported by E.A. Antipin (Moscow). The principles of closed-cycle processing of wood by alkylation and etherefication to obtain polymer composites and the molecular topological structure of such composites and various celluloses were reported by N.G. Bazarnova (Barnaul) and Yu.A. Ol'khov (Chernogolovka).

Also, many other aspects related to the topic were considered in poster sessions, including modification of polymers in the solid state under the simultaneous action of pressure and shear stress, studied for the example of mixtures of cellulose and chitosan (T.A. Akopova, Moscow); features of the processes occurring in polyethylene-based metal-containing polymer mixtures and solid-state polymerization of acrylamide (V.A. Zhorin, Moscow); characterization by various methods of the structure and compatibility of such mixtures (N.L. Voropaeva, Tashkent); effect of high pressure on the structure and thermal properties of mixtures of polyethylene terephthalate with liquid-crystal (LC) polymer (H. Al-Itavi, Moscow); and the thermodynamics and structure of polymer mixtures under stress conditions (E.V. Rusinova, Yekaterinburg). The general features and nature of heat-induced relaxation of polymer glasses and a procedure for calculating the quasi-equilibrium stress relaxation curve were considered in the contributions presented by M.S. Arzhakov and G.M. Lukovkin (Moscow). A.P. Safronov (Yekaterinburg) reported a thermodynamic model taking into account the features of dissolution of polymer glasses. The contributions of V.G. Vasil'ev, V.S. Papkov, A.Yu. Rabkin, and M.M. Levitskii (Moscow), V.A. Kovyazin (Moscow), D.D. Korochkin (Moscow), and O.G. Nikol'skii (Moscow) were devoted to various aspects of synthesis and characterization of polyorganosiloxanes.

(3) Theoretical polymer research. In this session two plenary lectures were given: Computer Modeling of Self-Organized Polymers (P.G. Khalatur, Tver) and Multiscaled Modeling of Polymer Properties and Behavior (A. Gusev, Switzerland).

In more than 20 poster presentations, such problems were treated as orientational self-organization in molten rigid-chain polymers (A.E. Arinshtein, Moscow); effect of diblock copolymer on the final stages of phase separation in a polymer mixture (E.N. Govorun, Moscow); computer modeling of systems containing polymer chains and colloid particles (N.V. Davydov) (Moscow); properties of a solution of a flexible-chain polymer under conditions of "contraction" in the field of substrate surface forces (A.I. Dolinnyi, Moscow); adsorption of a polymer chain on a spherical surface (E.I. Zheligovskaya, Moscow); structure of associates of acrylic ester series (A.A. Il'in, Yaroslavl); effect of chemical defects on the structure, dynamics, and macroscopic properties of the *n*-paraffin C_{50} and of ethylene/propylene copolymers (I.A. Karmilov, Moscow); conformation behavior of comb-like macromolecules (A.A. Klochkov, Moscow); evolution of the molecular-mass distribution (MMD) in the interchain exchange reaction in polymer mixtures (Ya.V. Kudryavtsev, Moscow); concentration limits of the phase instability range in polymer–particle systems in the case when the particles are larger than the globules (A.A. Litmanovich, Moscow); phase behavior of a two-dimensional polymer comb in an A–B binary solvent (A.A. Merkur'eva, St. Petersburg); analysis of the spinodal equation for a binary polymer mixture in terms of the contractible lattice model (N.N. Nikitina, Kazan); theory of high-frequency twisting-vibrating relaxation processes in polymer chains (V. Toshchevikov, St. Petersburg); and numerical calculation of the self-diffusion coefficient distribution function (E.B. Shakir'yanov, Birsk).

(4) Polyelectrolytes. A.A. Yaroslavov and V.A. Kabanov (Moscow) reported in their plenary lecture on a study of the interaction of polyelectrolytes with lipid membranes. The session included more than 20 poster

presentations. S.B. Zezin, V.A. Kasaikin, A.A. Zinchenko, S.I. Kargov, A.S. Andreeva, S.A. Andreenko, and I.R. Nasimova (Moscow) reported on a theoretical and experimental study of the structure and conformation behavior of polyelectrolyte–surfactant complexes in weakly polar organic solvents, including the features of phase separation of such complexes, reversible gelation in polyelectrolyte solutions, electrical conductivity of polyelectrolytes, and effect of the polymer matrix structure on the adsorption properties of polyelectrolyte gels. The contributions by A.V. Lezov (St. Petersburg) and E.A. Lysenko (Moscow) were devoted, respectively, to interaction of Cu(II) with azole-containing polyelectrolytes in aqueous solutions and to molecular properties and association of polypeptide–surfactant complexes of block polyelectrolytes in organic solvents of various polarities. T.F. Lelyukh (Novosibirsk) reported on synthesis of cationic polyelectrolyte with tertiary amino groups and their application as flocculants for treatment of wastewater contaminated with mercury. The capability of hydrophobized polyelectrolyte gels to absorb hydrophobic compounds from aqueous solutions was reported by A.V. Tazina (Moscow).

(5) Radical polymerization. The plenary lecture given by K. Matyjaszewski (Poland) was devoted to new promoting systems for "live" radical polymerization of various monomers. Under this topic several poster contributions were also presented. They were devoted to synthesis of alkoxyamines (new class of agents of live radical polymerization) and methods for determining the rate constants of their reversible homolytic decomposition and copolymerization of dimethacrylates with styrene in their presence (G.M. Bakova, M.P. Berezin, and I.S. Kochneva, Chernogolovka). Other contributions discussed specific features of radical polymerization of hydrophobic derivatives of acrylamide (A.I. Barabanova, Moscow) and salts of 2-acrylamido-2-methylpropanesulphonic acid with acrylamide in water and aqueous salt solutions (V.F. Kurenkov, Kazan); mechanism and kinetics of polymerization of tetrafluoroethylene promoted by mechanically activated silica and fluorinated carbonaceous materials (V.P. Mel'nikov, Moscow); radical copolymerization of vinyl acetate with *N*-vinylpyrrolidone and styrene (M.O. Pastukhov, Nizhni Novgorod); possibility of preparing stereoregular polymers by radical polymerization (Yu.I. Puzin, Ufa); and polymerization of acrylonitrile in supercritical carbon dioxide (E.U. Said-Galiev, Moscow). New approaches to chain growth control under conditions of pseudolive radical polymerization were examined in three contributions presented by D.F. Grishin and others (Nizhni Novgorod). The effect of temperature on the kinetics of nitroxylinhibited copolymerization of styrene with butyl acrylate was reported by M.G. Pavlov (Moscow).

R.Z. Azanov (Kazan) reported on a study of cationic polymerization of isobutylene catalyzed by $AlCl_3$ and BF_3. The thermodynamics and features of synthesis of polyurethanes and their reactions with alcohols were discussed in the contributions by T.A. Bykova (Nizhni Novgorod) and E.R. Badamshina and I.V. Doronina (Chernogolovka). Several poster contributions were devoted to such problems as radiation cryopolymerization and copolymerization of HCN and radiationinduced postpolymerization of isoprene and butadiene with sulfur dioxide (D. Kiryukhin and G.A. Kichigina, Chernogolovka); radiation-induced grafting to polyolefins of vinylsilanes that do not enter into homopolymerization (A.M. Mesh, St. Petersburg); and radiation-chemical synthesis of crown-containing gels (S.V. Nesterov, Moscow). The development and practical applications of perfluoroolefin ozonides (new class of promoters for polymerization of fluorinated olefins) and the role of radicals long-lived in solution in polymerization of fluorinated olefins were reported by M.R. Muidinov and S. Allayarov (Chernogolovka).

(6) Nanoparticles in polymers. This session included two plenary lectures: Macromolecular Reactions at Phase Boundary as a Direct Method for Synthesis of Polymeric Nanosystems (V.P. Zubov, Moscow) and Nanosponges and Clusters of These: New Macromolecular Particles and Their Self-Association (V.A. Davankov, Moscow). Of particular interest among the poster contributions were those devoted to self-immobilization of reactive nanoparticles of polyoxometallates in monolayers and Langmuir–Blodgett films of network polymers (V.V. Arslanov, Institute of Physical Chemistry, Moscow); formation mechanism and structure of polymeric nanocomposites with copper and cadmium sulfides (A.V. Volkov, Moscow); structure and properties of cellulose hydrate films containing dispersed silver (N.E. Kotel'nikova, St. Petersburg); polycarbonate-based adamantine nanocomposites (S.V. Krasheninnikov, Moscow); electroluminescence in polymer composites (E.M. Mal'tsev, Moscow); formation of carbonaceous micro- and nanostructures from functionalized polymers (O.V. Nikolaeva, Izhevsk); poly-*p*-xylylene-based metal-containing polymer nanocomposites (S.A. Ozerin, Moscow); formation of nanophases in porous polymer matrices of varied nature, such as polyethylene terephthalate, PVC, and isotactic polypropylene (E.S. Trofimchuk, Moscow).

(7) Dendrimers. A.M. Muzofarov (Moscow) clearly demonstrated in his plenary lecture that, in the recent decade, dendrimers, initially regarded only as exotic illustration to theoretical developments, became one of the most popular objects in the polymer chemistry research. E.V. Agina, E.A. Makeeva, M.V. Zhiryakova, and others (Moscow) considered in their poster presentations synthesis and phase behavior of five generations of LC dendrimers with terminal mesogenic groups (anisic acid derivatives) bound to carbosilane dendritic matrix via an undecyl spacer, and also carbosilane dendrimers with terminal aliphatic groups; synthesis (for the first time) of water-soluble electrically charged nonstoichiometric polyelectrolyte complexes with dendrimer as a lyophilizing polycation; and ionization equilibrium in aqueous Astramol solutions of the first five generations of poly(propylenimine) dendrimers and their interaction with network polyelectrolytes containing peripheral carboxy groups. The properties of the first three generations of dendrimers based on *L*-aspartic and *L*-glutamic acids, containing terminal ester groups and BOC-amino acids as base dendrons were reported by A.Yu. Bilibin, St. Petersburg). S.P. Molchanov (Moscow) discussed a new method for studying individual molecules and small clusters of dendrimers by microscopy. This method was used to study the structure of carbosilane LC dendrimers (S.A. Ponomarenko, Moscow). M.V. Ryabkov reported on a thermodynamic study of a first-generation carbosilane dendrimer with methoxyundecyl terminal groups at 0–340 K. The phase diagram of the system third-generation LC dendrimer–CCl_4 was reported by Yu.V. Panina (Saratov). The effect of methylene and allyl terminal groups on the molecular characteristics of carbosilane dendrimers was studied by G.E. Polushina (St. Petersburg). The translation flexibility of phosphorus-containing dendrimers of fifth and eighth generations in CCl_4 was reported by A.I. Sagidullin (Kazan). A.S. Tereshchenko (Moscow) discussed synthesis of a dendrimer bearing three HO groups at each terminal spacer. New approaches to synthesis of dendrimers without use of protecting groups were presented by G.N. Khimich (St. Petersburg).

(8) Liquid-crystal polymers. The plenary lecture given by R.V. Tal'roze (Moscow) was concerned with LC elastomers prepared through chemical cross-linking or reactions induced by gamma-ray and UV radiation, and also through noncovalent interactions stabilizing both the network structure and LC order under conditions of self-organization of matter. The poster presentations concerned with this topic reported results of a systematic and comparative analysis of the effect of temperature on the structure and mechanical characteristics of highly oriented fibers of LC copolyethers (E.M Antipov, I.A. Volegova, and A.A. Levchenko, Moscow); data on the phase behavior, structure, and magnetic properties of comb-like LC ionomers containing Cu, Ni, Co, Mn, Na, Ca, and Rb cations (E.B. Barmatov and D.A. Pebalk, Moscow); and data on the structure and mechanical properties of H-bonded LC polymer networks (M.A. Koval', Moscow). D.D. Grinshpan (Minsk) reported on formation of LC structures in aqueous solutions of cellulose sulfate sodium salt.

(9) Metal-containing polymers. This class of polymers is of a great scientific and practical interest. In the poster session, reports were presented concerned with synthesis, structure, and properties of metal-containing epoxy polymers (L.M. Amirova, Kazan); metal oxide structures synthesized by thermal treatment of salt forms of carboxyl-containing nitrocellulose with metal ions (I.A. Bashmakov, Minsk); chemical deposition of silica in a polymer matrix (E.A. Burlova, Kazan); properties of metal-coordinated polyurethanes (Davletbaeva, I.M., Kazan); polymers based on unsaturated metal oxacarboxylates and the role of the topography of macromolecular metal complexes in catalysis (G.I. Dzhardimalieva and A.D. Pomogailo, Chernogolovka); molecular properties of metal-containing disubstituted polyacetylene (E.I. Ryumtseva, St. Petersburg); and polyfunctional polymerizable systems based on methacrylates and alkali metal ions (N.A. Gavrilenko, Tomsk).

(10) Synthesis of new polymers. In the plenary lecture A.L. Rusanov (Moscow) discussed new Diels–Alder aromatic adducts based on hexaphenyl-substituted bis-cyclopentadienones and dienophiles. In principle, several poster contributions presented in other sessions can also be regarded as related to this topic. Nevertheless, mention can be made here of reports devoted to synthesis of such polymer materials as polyarylene sulfoxides (new class of sulfur-containing polymers), new fluorine-containing polyether-α-diketones, hydroxyl-containing polyimides (2,4,6-trinitrotoluene derivatives), cyclolinear permethylpolysilanesiloxanes, polyarylenethynylenes with 3-hexyl-multisubstituted oligothiophene blocks, and card polyaryleneetherketones (B.A. Zachernyuk, M.L. Keshtov, L.G. Komarova, D.Yu. Larkin, I.A. Khotina, and V.V. Shaposhnikova, Moscow); new copolymers based on methacrylic acid esters with chromophoric groups capable of heterocyclization; thermostable nonlinearly optically active polyamidoimides, polybenzoxazinones, and their complexes with Cu(I); copolymethacrylates with heteroaromatic nonlinear-

ly optically active chromophoric groups possessing high molecular hyperpolarizability (G.K. Lebedeva, N.L. Loretsyan, N.N. Smirnov, and I.V. Podeshvo, St. Petersburg); and copolymers of butadiene monoxide and propylene oxide (A.V. Nemirovskaya, Kazan).

(11) Conducting polymers. The poster session included reports concerned with electrochemical synthesis of conducting polymers based on metal phthalocyanines (N.P. Alpatova, Moscow); preparation and transport characteristics of microporous polyethylene films with conducting layer (polyaniline and polypyrrole) (G.K. Elyashevich and E.Yu. Rosova, St. Petersburg); electrical and electrochemical properties of composites based on polyaniline and polyacetylene with graphite and zinc (G.I. Kozub, Chernogolovka); synthesis of polyaniline-based interpolymer complexes (N.A. Koryabina, Moscow); and molecular and supramolecular structure of stable electroconducting copolymers of ethylene and acetylene (V.A. Marikhin, St. Petersburg).

(12) Synthesis and properties of polyolefins and aliphatic polyketones. In the poster session, O.N. Babkina and N.M. Brava (Chernogolovka) reported the results obtained in measurements of the electrical conductivity of various metallocene complexes and Al alkyls, boranes, and borates as components of high-performance catalytic systems for polymerization of olefins. These contributions discussed the role of ions in the indicated processes, conditions of synthesis of polyethylene with a broad spectrum of molecular weights and structures. Interesting data on the kinetics of metallocene-catalyzed homo- and copolymerization and molecular structure of polyethylene and copolymers of ethylene with 1-hexene, 1-octene, and 4-methyl-1-pentene were obtained by L.G. Echevskaya (Novosibirsk) and N.I. Ivancheva (St. Petersburg). Ternary copolymerization of propylene with ethylene and diene was considered by A.N. Klyamkina (Moscow). P.M. Nedorezova (Moscow) and N.M. Pakostina (Chernogolovka) discussed synthesis of polypropylene with controllable microstructure and MMD (high-modulus isotactic, syndiotactic, and hemiisotactic polypropylene) and its thermal, mechanical, and optical properties.

A series of poster presentations were devoted to synthesis and characterization of a new generation of functionalized copolymers (so-called aliphatic polyketones) based on olefins and carbon monoxide.

The reports by A.M. Kal'sin (Moscow) was concerned with new ruthenium and palladium complexes as catalysts for copolymerization of ethylene and CO. Other contributions were devoted to studies of the structure and deformation mechanism of new elastomers based on aliphatic polyketones (V.M. Neverov, Moscow); photolysis and photooxidation (S.I. Kuzina, Chernogolovka) and thermodynamics of copolymers of carbon monoxide with ethylene, propylene, and styrene at 0–600 K (A.V. Tsvetkova, Nizhni Novgorod); determination of the surface free energy and acid–base properties (O. Shashkina, Kazan), computer modeling of the crystal structure, phase transitions, and dynamics (N.B. Shenogina, Moscow), and IR spectroscopic study of the phase composition of films of ethylene–CO copolymer (D.M. Shkrabo, Troitsk).

(13) Experimental methods in polymer research. Although mention was already made of the application of particular techniques to studies of various polymer properties, it seems appropriate to say several words about other experimental methods reported by the conference participants. These include scanning electron-probe microscopy for determining the local rigidity of polymer surface (A.M. Alekseev, Moscow). Low-frequency dielectrometry was applied to study films of polyheteroarylenes in methyl methacrylate (L.G. Bradulina, Moscow), epoxyamine polymer mixtures (T.L. Elizarova, Chernogolovka), and segnetoelectric films (N.I. Kuznetsova, Moscow). The phase formation and thermal stability of epoxy polymers and copolymers were studied by the methods of photoactive probe, ESR, solid echo, and local NMR in radiofrequency scattering fields (S.B. Brichkin, B.E. Krisyuk, and N.N. Bolkov, Chernogolovka). M.I. Motornov (Moscow) used PALS (Positron Annihilation Lifetime Spectroscopy) for monitoring volume changes associated with deformations in glassy, partially crystalline, and LC polymers.

Of course, this brief review does not exhaust the diversity of problems discussed at the symposium. Most of the plenary lectures and posters represented scientific research supported financially by the Russian Foundation for Basic Research and other foundations. The 3rd Kargin Symposium is planned to be held in three years as an international conference.

G. P. Belov

Russian Journal of Applied Chemistry, Vol. 74, No. 4, 2001, pp. 720–721. Translated from Zhurnal Prikladnoi Khimii, Vol. 74, No. 4, 2001, pp. 698–699.

========== INFORMATION ==========

1st International Conference on Polymer Modification, Degradation, and Stabilization (MoDeSt 2000)

The 1st International Conference on Polymer Modification, Degradation, and Stabilization was held from September 3 to 7, 2000, in Palermo (Italy). The conference was organized by the Department of Chemical Engineering and Materials (University of Palermo). The conference participants were more than 500 scientists from 27 European Countries (Italy, Switzerland, Sweden, Russia, UK, Hungary, Romania, France, Poland, Netherlands, Germany, Czech Republic, Slovak Republic, Portugal, Belgium, Denmark, Ukraine, Austria, Norway, Spain, Slovenia, Finland, Greece, Belarus Republic, Croatia, Azerbaijan, and Georgia), 3 African countries (Egypt, Algeria, South Africa), 7 Asian countries (Saudi Arabia, Israel, Japan, Malaysia, China, India, Turkey), 5 American countries (US, Canada, Mexico, Venezuela, Brazil), and also from Australia.

The international advisory board of the conference included G. Audisio, C. Bastioli, E. Martuscelli, and C. Neri (Italy), N. Hadjichristidis and C. Papaspyrides (Greece), W. Habicher (Germany), A. Krzan (Slovenia), G. Marosi (Hungary), A. Okuwaki (Japan), A. Queiros (Portugal), F. Shutov (US), L. Utracki (Canada), Jianqi Wang (China), and G. E. Zaikov (Russia). The conference Chairman was Prof. F.P. La Mantia (University of Palermo) and Co-chairman, Prof. G. Camino (University of Torino). Thirteen organizations were sponsors of the conference, among them the University of Palermo, Provincia Regionale di Palermo, and such well-known companies as Alitalia, Banco di Sicilia, CIBA Specialty Chemicals, Rheometric, Belotti Strumenti, and Solvay.

More than 100 oral reports and a plenary lecture entitled Polymer Oxidation and Stabilization—Personal Outlook on the Past and Future (Norman Billingham, University of Brighton, Sussex, UK), were presented. Seven general lectures covered the topical problems of the conference. G. George (Queensland University of Technology, Brisbane, Australia) reported on chemiluminescence mechanisms in heterochain oxidation of polypropylene. Dennis Price (Fire Chemistry Research Group, University of Salford, UK) gave a lecture on polymer pyrolysis studies of relevance to polymer combustion and flame retardance. The effect of processing on melt degradation and stabilization of polymers was discussed in the lecture given by E. Kramer (University of Applied Sciences of Aargau, Windisch, Switzerland). The next general lecture was devoted to photostabilization of polymeric materials by surface modification (C. Decker, Department of Polymer Photochemistry, University of Mulhouse, France). Samuel J. Huang (University of Connecticut, Institute of Material Science, Storrs, Connecticut, US) gave a lecture on biodegradable polymers design, synthesis, and applications. Two last general lectures were devoted to the contribution of organometallic catalysis to reactive processing of thermoplastics (A. Michel, Laboratory of Polymeric Materials and Biomaterials, University of Claude Bernard Lyon I, Villeurbanne, France) and prediction of lifetimes of polymeric materials in environmental conditions from accelerated and ultraaccelerated photooxidation experiments (J. Lemaire, Laboratory of Molecular and Macromolecular Photochemistry, University Blaise Pascal, Aubiere, France).

Further the Conference was held in the form of a number of minisymposia on 9 dedicated topics. The 1st technical session (Oxidation and Stabilization) included 34 oral presentations and 39 posters. In this session the problems of the kinetics and mechanism of oxidation of various polymers in solution, melt, and solid phase were discussed, and also those of polymer stabilization and prediction of lifetimes.

The second session (Thermal Degradation, Combustion, and Fire Retardance) included 35 oral presentations and 35 posters. Of primary concern were the problems of nanocomposites as fireproofing compounds, and also combustion mechanisms of polymeric materials.

In the third session (Processing and Melt Stabilization), 18 oral presentations and 9 posters were given.

The topic of the fourth session was High Energy Radiation in Polymers: New Materials and Technologies. The session included 18 oral presentations and 33 posters. Particular attention was paid to polymer photochemistry and processes occurring upon irradiation of polymers with X-rays, electrons, protons, neutrons, and recoil atoms.

1070-4272/01/7404-0720 $25.00 © 2001 MAIK "Nauka/Interperiodica"

The fifth session (Biodegradation and Biodegradable Polymers) included 6 oral presentations and 20 posters. Of primary concern were the problems of applications of polymers in medicine, particularly in surgery operations.

In the sixth session (Ageing of Polymers and Composites), 12 oral presentations and 15 posters were given, devoted to selective and accelerated ageing of the polymers and composites, and also to prediction of the evolution of the performance characteristics in aging under various conditions of storage and exploitation.

The seventh session (Functionalization and Reactive Processing) included 24 oral presentations and 23 posters. The major attention in this session was paid to reactive processing of polymers, preparation of polymer blends and composites, and solubility (compatibility) of polymers in polymer blends and ways to its improvement.

In the eighth session (Testing and Life Predicition) covered 22 oral presentations and 11 posters were given. In this session, problems of climatic aging of polymers, development of new generations of weatherometers, testing methods for studying polymer aging, and analysis of polymer degradation products were discussed.

Finally, the ninth session (Recycling and Material and Energy Recovery) was devoted to polymer reprocessing and energy recovery from polymer wastes. The session included 25 oral presentations and 34 posters.

A proposal was discussed at the conference to create a permanent MoDeSt forum which would plan and organize future activities encompassing conferences, workshops, seminars, and courses. G. Camino and F. La Mantia became the co-chairmen of the organizing committee of this forum.

It was accepted a good choice to held such interdisciplinary conferences with a broad spectrum of topics. The Conference has demonstrated good potentialities of meetings where lectures are combined with discussions and live contacts of a large number of scientists. The 2nd International Conference on Polymer Modification, Degradation, and Stabilization, MoDeSt-2002, will be held in Budapest (Hungary).

G. E. Zaikov and M. I. Artsis

Russian Journal of Applied Chemistry, Vol. 74, No. 4, 2001, pp. 722–724. Translated from Zhurnal Prikladnoi Khimii, Vol. 74, No. 4, 2001, pp. 699–701.

INFORMATION

IV All-Russia Conference with Participation of CIS Countries "Scientific Foundations of Preparation and Technology of Catalysts" III All-Russia Conference with Participation of CIS Countries "Problems of Catalyst Deactivation"

The conferences were organized by the initiative of the Institute of Catalysis, Siberian Division, Russian Academy of Sciences; Institute of Petrochemistry and Catalysis, Academy of Sciences of the Republic of Bashkortostan, Ural Scientific Center of the Russian Academy of Sciences; with the support of the Academy of Sciences of the Republic of Bashkortostan; Government of the Republic of Bashkortostan; Russian Foundation for Basic Research; Ministry of Industry, Science, and Technology of the Russian Federation; Scientific Council of catalysis, Russian Academy of Sciences; and ZAO Kaustic (Sterlitamak).

Among the participants of the conferences were more than 140 scientists and leading specialists from 16 institutes of the Russian Academy of Sciences, 12 universities, 13 applied-research institutes and companies, 15 industrial plants of Russia, and 9 institutes of Ukraine, Belarus, Armenia, and Uzbekistan, who synthesize, study, and use various (heterogeneous and homogeneous) catalysts in large-tonnage industrial processes of hydrogenation, dehydrogenation, isomerization, polymerization, etc. Nineteen plenary talks (including 5 concerned with metal-complex catalysis) were delivered and more than 60 reports (including 15 on metal-complex catalysis) presented at the conferences.

The main scientific directions of the reports presented at IV Conference were the following:

fundamental physicochemical and kinetic aspects of synthesis of heterogeneous catalysts and supports in all stages of their fabrication;

control over catalyst formation to obtain catalysts with prescribed properties;

new methods for catalyst fabrication;

scientific basis for development of technologies, versatile technological lines, and apparatus for the main stages of catalyst and support fabrication; effect of the scaling factor;

present state of the industrial production of catalysts.

The scientific directions of the III Conference were the following:

nature and mechanism of catalyst deactivation;

kinetics and modeling of deactivation processes;

investigation techniques;

ways of extending the service life of catalysts.

Reports on "Metal-Complex Analysis in Organic and Metal-Organic Synthesis" were delivered at a separate section.

Within the first direction, the report by G.R. Kotel'nikov (Yaroslavl) considered the state and problems of production and service life of catalysts for synthesis of styrene, α-methylstyrene, methyl vinylpyridine, and isoprene, and for dehydrogenation of paraffins C_4–C_5 into olefins, and also the provision of rare-earth metals for catalyst production plants. It was pointed out that, because of the lack of the necessary equipment and raw materials of appropriate quality, the possibilities of domestic catalyst production technologies are not always realized. Of much interest was the report by A.A. Galkin (Moscow) on preparation of oxide catalysts and supports in "sub- and above-critical" water.

Five interesting reports were presented by the Institute of Catalysis, Siberian Division, Russian Academy of Sciences (Novosibirsk). The scientific foundations of mechanochemical methods as the ecologically safest technology for fabrication of catalysts, supports for these, and adsorbents were discussed by V.V. Molchanov; the development of a technology of highly dispersed skeleton zirconium phosphates—catalysts for isomerization of paraffins and their selective oxidation into olefins, were analyzed by V.A. Sadykov; methods of preparation and production technology of block catalysts with cellular structure for purification

1070-4272/01/7404-0722 $25.00 © 2001 MAIK "Nauka/Interperiodica"

of exhaust gases of automobiles, selective reduction of nitrogen oxides in fume gases of thermal power plants, and purification of volatile organic substances in oxidation of ammonia in nitric acid production were considered by Z.R. Ismagilov; the development and use of domestic microspherical cracking catalysts were discussed by V.P. Doronin; synthesis, properties, and use of highly dispersed zirconium-containing oxide systems were reported by A.S. Ivanova.

New tendencies in the development of methods for preparation of catalysts for chlororganic synthesis were discussed in the report by I.I. Kurlyandskaya (Moscow). In particular, various techniques for catalyst formation by support impregnation were considered, especially the method making no use of a solvent. E.Z. Golosman (Novosibirsk) analyzed fundamental mechanisms of synthesis and formation of cement-containing catalysts for various processes of organic, inorganic, and ecological catalysis. The industrial production of these catalyst by means of a low-waste technology was commenced at catalyst shops of NIAP and some other domestic plants; the catalysts were introduced into practice of low-temperature conversion of CO, methanization, creation of protective atmospheres, synthesis of a number of organic compounds, and purification of discharge gases at more than 150 plants of Russia, CIS countries, and countries beyond the boundaries of the former Soviet Union.

At the section "Metal-Complex Catalysis in Organic and Metalorganic Synthesis," Y.M. Dzhemilev discussed in detail recent advances of domestic and foreign researchers in the field of application of metal-complex catalysts in promising chemical technologies for production of a wide variety of practically important monomers (α-olefins, isopentanes, vinylarenes, higher mono- and dicarboxylic acids, anhydrides, alcohols, glycols, amines, nitrogen-containing heterocycles, sulfides, sulfoxides, and sulfones).

The reports by V.I. Smetanyuk and E.I. Bagrii (Moscow) considered production techniques and possibilities of metal-complex gel-immobilized catalytic systems for the example of dimerization and oligomerization of ethylene and propylene, and also the biomimetic approach to development of promising catalytic systems for functionalization of saturated hydrocarbons. To a new direction—use of homogeneous catalysts based on palladium complexes for synthesizing a new class of polymers, alternating copolymers of olefins with carbon monoxide—was devoted report by G.P. Belov (Chernogolovka). The results of a quantum-chemical study of the geometric and electronic structure of models of active centers in lanthanide catalysts for diene polymerization were considered by Z.M. Sabirov (Ufa).

Oral reports presented the results obtained in the development of enzyme-modeling catalysts, immobilization of metal-complex catalysts on polymeric supports, and synthesis of catalysts for production of mono- and dicarboxylic acids and alcohols and for selective functionalization of hydrocarbons to give oxygen- and chlorine-containing products.

At the conference on catalyst deactivation, N.M. Ostrovskii and N.A. Pakhomov (Novosibirsk) presented in their reports new models of catalyst deactivation by coke, tested for concrete examples of deactivation of catalysts for cracking and hydrogenation, and also Pt/Al_2O_3 catalysts, in isomerization of paraffins, dehydrogenation of cyclohexane, and dehydrocyclization of paraffins. They also considered problems of reversible and irreversible deactivation of supported bimetallic catalysts for dehydrogenation of lower paraffins. The factors leading to deactivation of V/Ti catalysts for partial oxidation of durene in the temperature range 360–480°C in the course of prolonged operation were discussed in a report by B.I. Kutepov (Ufa).

It was repeatedly emphasized in plenary talks and oral reports that the catalyst deactivation is one of the problems of industrial catalysis. The industry of the developed countries produces annually many hundred thousand tons of catalysts only because of their limited service life, irreversible poisoning, and loss of activity and selectivity; the unstable or periodic (with regular regeneration) work of catalysts leads to markedly higher investment, energy expenditure, and higher-cost products. An important task, whose accomplishment would make faster the solution of the problem as a whole, is to develop methods for fast catalyst testing to prognosticate the rate of their deactivation and their stability under industrial conditions.

The participants of the conference noted that the designs by Russian specialists and the investigations performed retain their high level, but, if the present extent of science is not changed, our scientific achievements will soon become outdated. In the last 10 years the domestic output of catalysts dropped dramatically, constituting at present 10–25% of the level of the early 1990s. The decline in the investment in the catalyst industry has led to physical aging and obsolescence of the equipment used and poorer quality of catalysts. The actively aggressive, to the point of illegal search for consumers, policy of foreign com-

panies at the Russian market leads to purchase of imported catalysts, which have much higher cost, but not higher quality, compared with the domestic catalysts.

Among the recommended measures intended to improve the domestic catalyst industry was mentioned the necessity for address state financing of pilot-evaluation shops for production of catalysts meeting the world's best standards at promising plants, including AO Katalizator (Novosibirsk), catalyst shops at Omsk and Ryazan oil refineries, and some others.

During the conferences, a round-table discussion was held, with the participation of managers of industrial plants and presentation of institutes and production facilities; the state of, prospects for, and problems of the development, manufacture, and consumption of domestic catalysts were discussed. In order to ensure prompt exchange of scientific and technological information and coordination of efforts at the catalyst market, it was proposed that the Institute of Catalysis, Siberian Division, Russian Academy of Sciences, should initiate creation of an association of major manufacturers and consumers of catalysts and set-up a periodic collection of works (journal) devoted to problems of industrial catalysis. The conference participants consider the first experience of holding a joint conference with participation of specialists in homogeneous and heterogeneous catalysis to be a success and recommend the Organizing committee of the future conference to adopt the same way. Full texts of plenary talks are to be published in *Kinetika i Kataliz* journal.

G. P. Belov

Russian Journal of Applied Chemistry, Vol. 74, No. 5, 2001, pp. 725–728. Translated from Zhurnal Prikladnoi Khimii, Vol. 74, No. 5, 2001, pp. 705–708.

INORGANIC SYNTHESIS AND INDUSTRIAL INORGANIC CHEMISTRY

Kinetics of Natural Langbeinite Conversion in Magnesium Chloride Solutions

T. V. Mazur, I. Yu. Kostiv, and V. T. Yavorskii

State Research Institute of Halurgy, Kalush, Ukraine
L'vivs'ka Politekhnika State University, Lviv, Ukraine

Received December 18, 1998; in final form, December 2000

Abstract—The mechanism of conversion of natural langbeinite with magnesium chloride solutions was studied. The dependence of the degree of conversion on the process time, temperature, $MgCl_2$ concentration in solution, and grain size of natural langbeinite was studied.

The halurgical scheme of processing potassium polymineral ores ensures 18–22% recovery of langbeinite to a solution [1]. Most of it remains in the undissolved halite–langbeinite residue as a waste product. At the same time langbeinite is one of the main minerals of the ore (content up to 20 wt %) and is of special value as potassium–magnesium sulfate mineral. Different ways of langbeinite recovery were suggested. Washing-out of halite with water or salt solutions [2, 3] makes it possible to obtain a langbeinite concentrate used as a fertilizer or processed into schoenite and potassium sulfate. The conversion of langbeinite into schoenite under the action of water is also used [4]. The recovery of langbeinite from the ore increases to 80–85% when it is preliminarily recrystallized into schoenite [5]. However, water is rapidly saturated, which decelerates the process. Moreover, the humidified paste solidifies. The degree of langbeinite conversion does not exceed 80% in 30 days [5]. One more feature of processing of such ores into fertilizers is formation of excess solutions of magnesium chloride, which must be utilized. This is a complicated problem for ore fields that are remote from the magnesium production.

The soluble part of potassium polymineral ores is a five-component system of salts containing a great number of solid phases [6]. Slow reactions occur between these phases depending on the composition of the liquid phase. Langbeinite is known to participate in paragenesis with kainite, as described by the equations

$$K_2SO_4 \cdot 2MgSO_4 + MgCl_2 + 6H_2O \rightleftarrows 2[KCl \cdot MgSO_4 \cdot 3H_2O] + MgSO_4, \quad (1)$$

$$K_2SO_4 \cdot 2MgSO_4 + MgCl_2 + KCl + 9H_2O \rightleftarrows 3[KCl \cdot MgSO_4 \cdot 3H_2O], \quad (2)$$

$$K_2SO_4 \cdot 2MgSO_4 + KCl \cdot MgCl_2 \cdot 6H_2O + 3H_2O \rightleftarrows 3[KCl \cdot MgSO_4 \cdot 3H_2O]. \quad (3)$$

The reactions occur in an $MgCl_2$ solution and in the absence of KCl are accompanied by the formation of $MgSO_4$. The reaction rate is affected by the interface area, the concentrations of $MgCl_2$ and $MgSO_4$ in solution, temperature, and the reactant ratio.

We studied the interaction of natural langbeinite with $MgCl_2$ solutions under laboratory conditions. Natural langbeinite was taken from an operating open pit, crushed to a particle size of <2.5 mm, washed to remove halite impurity with water, treated with acetone to remove intercrystal moisture, dried at 50°C, and sieved. The resulting product contained (wt %) K^+ 18.6, Mg^{2+} 11.64, Ca^{2+} 0.06, Na^+ 0.07, Cl^- 0.05, SO_4^{2-} 69.16, and H_2O 0.42 (or 98.76% langbeinite, less than 0.1% halite, and minor amounts of polyhalite, kieserite, and water). The starting solution to be studied had the following composition (wt %): K^+ 1.38, Mg^{2+} 6.50, Na^+ 0.94, Cl^- 19.39, SO_4^{2-} 3.08, and H_2O 68.71 ($MgCl_2$ 22.4%). This solution was used to prepare 15–36% $MgCl_2$ solutions from $MgCl_2 \cdot 6H_2O$ (analytically pure grade) and distilled water. Pure grade KCl was also used.

A solution of magnesium chloride of a specified concentration was mixed with langbeinite in glass beakers in a weight ratio of 1 : 1. Stoichiometric amounts of KCl [according to reaction (2)] were

1070-4272/01/7405-0725$25.00

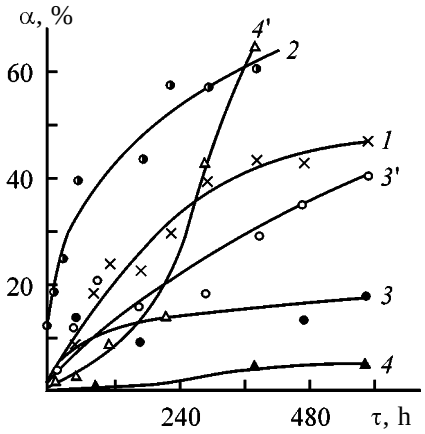

Fig. 1. Degree of langbeinite conversion α into kainite as a function of the process time τ. Temperature (°C): (*1*) 25, (*2*) 50, (*3*, *3*') 75, and (*4*, *4*') 95. (*3*', *4*') Crystalline KCl was added to a system.

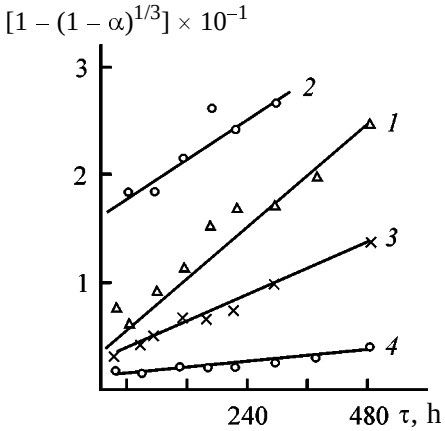

Fig. 2. Graphical confirmation of the fact that the conversion of langbeinite into kainite follows the "compressing sphere" mechanism: (α) conversion and (τ) process time; the same for Fig. 3. Temperature (°C): (*1*) 25, (*2*) 50, (*3*) 75, and (*4*) 95.

added to langbeinite. The components were heated to the required temperature and mixed. The mixture in closed beakers was placed in an air thermostat and kept there at 50 ± 0.5°C for 480 h with intermittent mixing and sampling. The samples were filtered on a Büchner funnel, the filtrate was collected in a preliminarily weighed test tube, the intercrystal solution was removed by washing the solid phase with refined vegetable oil and acetone, and the solid was dried at 50°C. The liquid and solid phases were analyzed for K^+ and Na^+ by flame photometry, for Mg^{2+} and Ca^{2+} by complexometric titration, for Cl^- by mercurimetric titration, and for SO_4^{2-} gravimetrically [7]. The material balance was calculated by solving a system of equations involving the content of ions in the liquid and solid phases; the degree of conversion was determined from the material balance with respect to Cl^- and SO_4^{2-} ions and from the equations of reactions (1) and (2).

The effects of temperature and process time on the degree of langbeinite conversion into kainite were studied. Natural langbeinite with a grain size of 1.0–2.5 mm and a 23.7% solution of $MgCl_2$ were preheated to the reqiured temperature and mixed in a desiccator. The mixture was kept in a desiccator at 25, 50, 75, and 95°C for 480 h with intermittent stirring and sampling.

The data obtained (Fig. 1) show that the degree of langbeinite conversion into kainite at 25°C gradually increases and reaches 47% in 480 h. Under these conditions the rate of conversion remains low. It is known [8] that the degree of kainite formation even from readily soluble carnallite and magnesium sulfate hexahydrate (in the stoichiometric ratio) at 25°C reaches only 35% in 240 h, with the process gradually decelerating. At 50°C the process accelerates, the conversion reaching 61.5% in 312 h. The further temperature rise to 75°C drastically decelerates the process, with the maximal conversion being as low as 18.3% in 480 h.

The addition of crystalline KCl at 75°C facilitates reaction (2). Langbeinite converts into kainite with a higher rate. Heating to 95°C (without adding KCl) favors langbeinite stabilization. Under these conditions the field of kainite crystallization is absent from the stable diagram; the maximal temperature of kainite existence under stable conditions is 83°C [8]. However, kainite can exist as a metastable phase at temperatures up to 105°C [9]. In the presence of a kainite seed the degree of the langbeinite conversion into kainite at 95°C is 5.8% in 480 h. In the presence of KCl this value increases to 65.2%.

The above-given data have shown that the highest degree of langbeinite conversion into kainite is reached at 50°C. The acceleration of the process is affected by the addition of KCl, which salts-out kainite at elevated temperatures [10].

The dissolution of langbeinite in a solution of magnesium chloride is the slowest stage of the process. It follows the "compressing sphere" mechanism. According to the equation describing this mechanism, the plots of $[1 - (1 - \alpha)^{1/3}]$ (where α is the conversion) vs. process time τ are linear (Fig. 2); this fact suggests that the reaction occurs near the surface of spherical langbeinite bodies.

Topochemical reactions involving a solid phase are frequently described by the Erofeev's equation [11]

$$\alpha = 1 - \exp(-K\tau^n), \quad (4)$$

where n is the reaction order.

Transformation of this equation gives

$$n\log\tau = \log(1/K) + \log[-\ln(1 - \alpha)]. \quad (5)$$

The plots of the langbeinite conversion into kainite in the $\log[-\ln(1 - \alpha)]$–$\log\tau$ coordinates are linear (Fig. 3). The rate constant of the reaction can be determined graphically from the condition

$$K = -\ln(1 - \alpha_{\tau=1}). \quad (6)$$

At 25°C K is equal to 0.00602, at 50°C to 0.07079, and at 75°C to 1.46. Substitution of these data in the Arrhenius equation gives the activation energy of 78.9 kJ mol^{-1} for the range 25–50°C. Hence, the conversion of langbeinite into kainite is kinetically controlled [11]. To accelerate the process, it is necessary to heat to at least 50°C and maintain this temperature throughout the process.

The reaction order can be determined from Eq. (5). At 25°C it is 0.83 and at 50°C, 0.47. This means that the reaction is multistage; it is limited by the reaction of crystalline langbeinite yielding intermediate compounds.

The effect of the $MgCl_2$ concentration in solution on the langbeinite conversion into kainite at 50°C was also studied. For these experiments we took the initial langbeinite (grain size 1.0–2.5 mm) after washing. Crystalline KCl was added to the reaction mixture in the stoichiometric ratio to langbeinite corresponding to the equation of reaction (2). Weighed samples of the solution of definite concentration and langbeinite were placed in separate sealed vessels. Samples of liquid and solid phases were taken after 24, 120, and 240 h.

The data obtained (Fig. 4) show that at concentrations of magnesium chloride in the reaction mixture less than 18.0% virtually no conversion occurs. As the $MgCl_2$ concentration increases, the degree of langbeinite conversion also increases. In a 35.9% $MgCl_2$ solution it is 72.9% in 24 h and 84.3% in 120 h.

In the reaction mixture free from KCl the conversion proceeds by Eq. (1); after the process termination the solid phase contained a mixture of kainite, epsomite, and unchanged langbeinite.

In the course of the conversion $MgCl_2$ is incorporated into the solid phase, and its concentration in the liquid decreases. At low initial $MgCl_2$ concentrations a high degree of the conversion cannot be attained. At any concentration of the solution reaction (1) can go to completion only with respect to langbeinite, and $MgCl_2$ should be in excess. To reach a high degree of the langbeinite conversion into kainite, the concentration of $MgCl_2$ in the initial solution should be 24.3–35.9% at the weight ratio of the phases of 1 : 1. Therefore, on completion of the process, the kainite suspension should be separated into the liquid and solid phases. The liquid phase is recycled for concentrating and converting, and the solid phase is processed into a fertilizer.

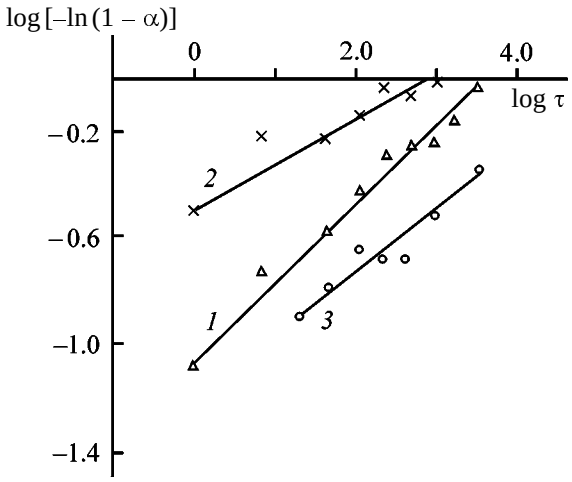

Fig. 3. Graphical determination of the rate constants of reaction (1) by the Erofeev's equation. Temperature (°C): (*1*) 25, (*2*) 50, and (*3*) 75.

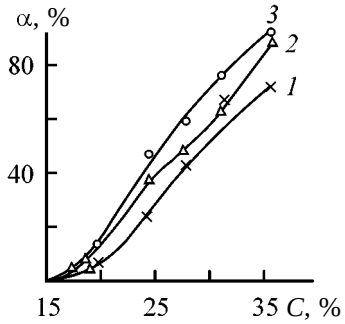

Fig. 4. Degree of langbeinite conversion α as a function of $MgCl_2$ concentration in the liquid phase C. Process time τ (h): (*1*) 24, (*2*) 120, and (*3*) 240.

Magnesium chloride wastes concentrated by evaporation contain carnallite in the solid phase and magnesium chloride in the liquid phase. They can be utilized for langbeinite conversion in the course of processing of polymineral potassium ores. In this case the reaction follows Eqs. (2) and (3), which results in reduced demand for potassium chloride. After the separation of sodium chloride and unchanged $MgCl_2$ solution, the solid phase is a mixture of kainite, sylvite or epsomite, unchanged langbeinite, and impuri-

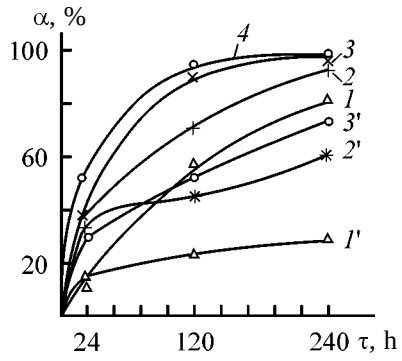

Fig. 5. Degree of langbeinite conversion α as a function of process time τ at various concentrations of $MgCl_2$ *C* and sizes of langbeinite grains *f*. *C* (wt %): (*1*'–*3*') 22.4 and (*1*–*4*) 28.3. *f* (mm): (*1*, *1*') 1.0–2.5, (*2*, *2*') 0.5–1.0, (*3*, *3*') 0.315–0.5, and (*4*) less than 0.315.

ties of anhydrite, kieserite, and polyhalite. After drying it contains (wt %) K_2O 20–25, MgO 10–15, Cl^- up to 20, and NaCl up to 3. When the formation of magnesium chloride waste is undesirable, the solid phase can be processed into chlorine-free potassium fertilizers.

The conversion of langbeinite with an $MgCl_2$ solution is a heterogeneous process influenced by the interface area. Therefore, we studied the dependence of the conversion on the size of langbeinite grains. To do this, we took the initial concentrations of $MgCl_2$ in the liquid phase of 22.4 and 28.3 wt % and langbeinite fractions of 1.0–2.5, 0.5–1.0, 0.315–0.5, and less than 0.315 mm. The temperature was 50°C, and the process time and KCl amount were the same as in the previous experiments.

The results obtained show (Fig. 5) that at the $MgCl_2$ concentration of 22.4 wt % for the 1.0–2.5 mm fraction the conversion degree is 15.1 in 24 h, 22.5 in 120 h, and 29.0% in 240 h. For the 0.5–1.0 mm langbeinite fraction it is 37.0, 43.2, and 58.5%, respectively, and for the 0.315–0.5 mm fraction, 30.8, 52.8, and 72.6%, respectively.

In a more concentrated solution (28.3 wt % $MgCl_2$) the degree of conversion is considerably higher. Its acceptable value is reached for the 0.5–1.0 mm fraction in 240 h (94.5%), for the 0.315–0.5 mm fraction in 120 (91.6%) and 240 h (97.5%), and for the <0.315 mm fraction, in 120 (93.5%) and 240 h (97.3%). Therefore, the size of langbeinite grains less than 0.55 mm and the process time of 120 h can be recommended for practical purposes.

CONCLUSIONS

(1) Natural langbeinite converts into kainite in 24.3–35.9% magnesium chloride solution at 25–75°C. The highest degree of conversion is reached at 50°C and, with KCl added, at 75°C. In the presence of kainite seeds and KCl the conversion is fairly complete also at 95°C.

(2) The degree of conversion increases with increasing $MgCl_2$ concentration in solution within the limits 24.3–35.9% and with decreasing langbeinite grain size. The >90% conversion is reached in 120 h with a grain size less than 0.5 mm.

(3) The data obtained can be used as the basis for the technology of processing polymineral potassium ores without formation of magnesium chloride waste.

REFERENCES

1. Kovalishin, I.I., Grebenyuk, D.V., and Okrepkii, I.M., *Tr. Vses. Inst. Galurgii*, 1975, no. 74, pp. 75–78.
2. Kashkarov, O.D. and Sokolov, I.D., *Tekhnologiya kaliinykh udobrenii* (Technology of Potassium Fertilizers), Leningrad: Khimiya, 1978.
3. USSR Inventor's Certificate no. 1562320.
4. Grebenyuk, D.V., Opanasyuk, N.P., Podobailo, N.N., and Kozel'skii, R.P., *Zh. Prikl. Khim.*, 1985, vol. 58, no. 9, pp. 2118–2120.
5. Grebenyuk, D.V., Davybida, V.I., and Okrepkii, I.M., *Ref. Sb. Kaliin. Prom–st.*, 1980, no. 3, pp. 11–13.
6. Yanat'eva, O.K. and Orlova, V.T., *Dokl. Akad. Nauk SSSR*, 1962, vol. 142, no. 1, pp. 102–104.
7. *Metody analiza rassolov i solei* (Methods of Analysis of Brines and Salts), Morachevskii, Yu.V. and Petrova, E.M., Eds., Leningrad: Khimiya, 1965.
8. Nikolaev, V.I. and Fradkina, Kh.B., *Izv. Sekt. Fiz.-Khim. Anal. Akad. Nauk SSSR*, 1952, vol. 20, pp. 269–276.
9. Autenrieth, H., *Kali Steinsalz*, 1969, vol. 5, no. 5, pp. 158–165.
10. Orlova, V.T. and Yanat'eva, O.K., *Zh. Neorg. Khim.*, 1976, vol. 16, no. 10, pp. 2779–2781.
11. Pozin, M.E. and Zinyuk, R.Yu., *Fiziko-khimicheskie osnovy neorganicheskoi tekhnologii* (Physicochemical Principles of Inorganic Technology), Leningrad: Khimiya, 1985.

Russian Journal of Applied Chemistry, Vol. 74, No. 5, 2001, pp. 729–732. Translated from Zhurnal Prikladnoi Khimii, Vol. 74, No. 5, 2001, pp. 709–712.

SORPTION AND ION-EXCHANGE PROCESSES

Sorption Recovery of Transplutonium Elements from Nitric Acid Solutions with Arsenazo Group Reagents

N. P. Molochnikova, B. F. Myasoedov, and O. P. Shvoeva

Vernadsky Institute of Geochemistry and Analytical Chemistry, Russian Academy of Sciences, Moscow, Russia

Received May 30, 2000

Abstract—Sorption recovery of actinides and lanthanides from nitric acid solution with arsenazo group reagents, activated carbon modified with these reagents, and chelating sorbents containing arsenazo functional groups was studied.

Recovery of transplutonium elements from acidic solutions is an important industrial problem, and search for reagents suitable for sorption and extraction recovery of these elements is urgent. It is known [1, 2] that arsenazo group reagents are widely used in analysis, because they form strong complexes with more then 30 elements including actinides and lanthanides. Reagents based on chromotropic acid, arsenazo I (monoazo derivative) and arsenazo III (bisazo derivative), are used for highly sensitive spectrophotometric determination of certain elements [1, 2] including americium and curium [3, 4]. The use of these reagents for metal extraction is limited because of their low solubility in organic solvents, which increases only in the presence of higher alcohols. Arsenazo III can be used for recovery and separation of actinides and lanthanides [5] including americium(III) and (V) [6] in two-phase, free of organic solvents aqueous systems based on water-soluble polymers. For sorption recovery, we synthesized a series of chelating sorbents containing arsenazo group reagents.[1] It is known [7] that chelating sorbents exhibit enhanced selectivity, which is due to the nature of functional groups reacting with metal ions. These groups are introduced into the polymeric matrix by appropriate chemical reactions or are formed during the synthesis of the polymeric sorbent. The chelating sorbent prepared by azo coupling of diazotized aminopolystyrene with arsenazo I was used for selective concentration of many elements [8–11] and determination of trace elements in uranium ores and concentrates, carbonate and silicate rocks, natural water, and wastewater [2, 7, 12, 13]. Cellulose fibrous sorbent with arsenazo groups is selective toward uranium and lanthanides and was used for selective recovery of these elements form solutions with high concentration of alkali and alkaline-earth metals [14]. A new fibrous chelating sorbent POLIORGS 33A containing amidoxime, hydrazine, oxy, and arsonoazo groups selectively recovers plutonium from acidic saline solutions and allows its separation from the other elements [15, 16].

In this work, we studied the recovery and concentration of transplutonium and rare-earth elements from nitric acid solutions with sorbents containing arsenazo fragments.

EXPERIMENTAL

Nitric acid solutions containing radiochemically pure radionuclides $^{242–244}$Cm, ^{243}Cm, ^{241}Am, ^{239}Pu, and $^{152–154}$Eu were used. Sorption was studied under static conditions by mixing nitric acid solution (V = 2–4 ml) containing a definite amount of radionuclide with the sorbents (m = 5–200 mg) for 0.1–20 h. Sorbents in form of powders were separated by centrifuging after the radionuclide sorption. The degree of radionuclide recovery (%) was estimated from the α- or γ-activity of the initial and resulting solutions (after sorption). The α-activity was determined on a proportional counter with 2π geometry, while the γ-activity was measured on an LP-4900 analyzer.

The following reagents were used: analytically pure grade arsenazo I [2-(2-arsonophenylazo)-1,8-dihydroxynaphthalene-3,6-disulfonic acid]

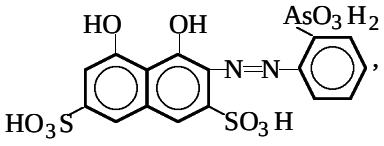

[1] In the Vernadsky Institute of Geochemistry and Analytical Chemistry, Russian Academy of Sciences.

1070-4272/01/7405-0729$25.00

Table 1. Degree of curium and europium sorption from nitric acid solutions on carbons modified with arsenazo group reagents. V/m = 200, sorption time 2 h

C_{HNO_3}, M	Degree of sorption, %, on indicated carbon					
	Daukh					Alkaline-A
	unmodified		modified with arsenazo III		modified with arsenazobenzene	modified with arsenazo III
	Cm	Eu	Cm	Eu	Eu	Eu
2.5×10^{-4}	78	75	95	88	68	99
0.1	22	59	33	61	31	24

arsenazo III [2,7-bis-(2-arsonophenyazo)-1,8-dihydroxynaphthalene-3,6-disulfonic acid] prepared by the reaction between chromotropic and aminophenylarsonic acid

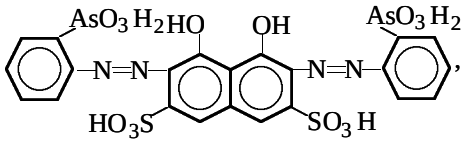

and arsenazobenzene [2-(2-arsonophenylazo)-7-(phenyl-azo)-1,8-dihydroxynaphthalene-3,6-disulfonic acid]

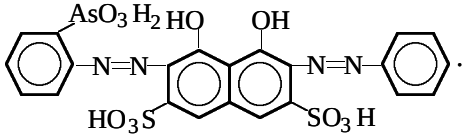

Daukh and Alkaline A activited carbons were used as sorbents. Iron-free carbon was prepared by washing with hydrochloric acid and water. Then it was saturated with reagent solution at agitation for 2 h, washed with water, and dried at 100°C.

The following chelating sorbents (all synthesized in Vernadsky Institute) were used. Polystyreneazoarsenazo was prepared by the reaction of diazotized aminopolystyrene with arsenazo I. It is a dark violet powder insoluble in water and acids. The exchange capacity of this sorbent for KOH is 1.6–2.8 mmol g^{-1}:

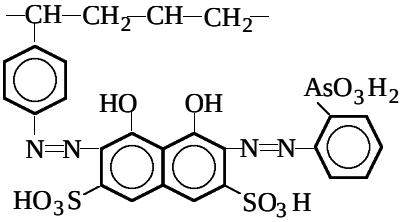

Arsenazo I polymers with benzidineazoarsenazo (BAAI and BPVAI):

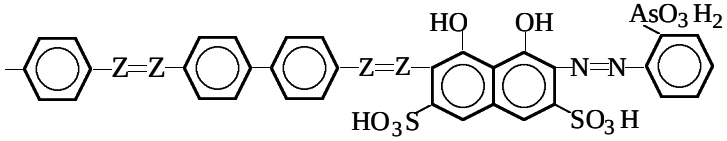

(Z are various substutuents).

Polyarsenazo-n is filled fibrous chelating sorbent composed of polyacrylonitrile fiber and polystyreneazoarsenazo sorbent containing sulfo, *peri*-dihydroxy-, and *o*-hydroxy-*o*'-arsonoazo groups. The filling degree of the sorbent is 50%. It is a black fibrous material stable in strongly acidic, weakly alkaline, and neutral solutions. Its sorption exchange capacity for NaOH is 2.2 mmol g^{-1}.

We studied sorption of actinides and lanthanides from nitric acid solutions on activated carbons modified with arsenazo group reagents. It is known that a coomon procedure for concentrating and separating elements is sorption on matrices with active surface preliminarily saturated with complexing agents. Modified activated carbons are widely used to concentrate microelements. We modified carbons with arsenazobenzene and arsenazo III, which form the most stable complexes with transplutonium and rare-earth ions. The study of curium and europium recovery as influenced by the arsenazo III content showed that 1.2×10^{-4} M arsenazo III is required to saturate 1 g of carbon. Curium and europium sorption is strongly dependent on the solution acidity and is possible only from weakly acidic medium (<0.1 M HNO_3, Table 1). Car-

Table 2. Degree of metal sorption with chelating sorbents from nitric acid solutions. V/m = 200 (100 for polyarsenazo-n); sorption time 2 h

C_{HNO_3}, M	Sorption degree, %											
	BAAI		BPVAI		polystyreneazoarsenazo				polyarsenazo-n			
	Cm	Eu	Cm	Eu	Cm	Am	Pu	Eu	Cm	Am	Pu	Eu
0.1	98	99	97	96	>99	99	99	97	99	99	97	99
1.0	84	74	82	88	94	94	98	87	87	94	94	81
3.0	56	11	27	32	70	72	98	58	61	42	97	51

bons modified with arsenazo III recover metals better than the unmodified carbons. However, quantitative recovery of curium (98%) with unmodified carbons can also be reached at the ratio of the solution volume to sorbent mass equal to 200, when the time of contact of the solution with the sorbent increases to 18 h.

To recover elements from more acidic solutions, we studied their sorption with sorbents containing arsenazo functional groups in relation to the nitric acid concentration. As seen, quantitative recovery of actinides and lanthanides(III) is possible from solutions with nitric acid concentration no more than 1 M (Table 2). Plutonium can be recovered from 3 M HNO_3.

The kinetics of europium sorption from 1 and 3 M HNO_3 with polystyreneazoarsenazo and benzidineazoarsenazo is shown in Fig. 1. At the ratio of the solution volume to the sorbent mass of 200, the equilibrium recovery of europium with polystyreneazoarsenazo at stirring is reached within 1 h, and with benzidineazoarsenazo, within 4–6 h. The study of the degree of europium recovery from 1 M HNO_3 in 2 h as a function of the ratio of the solution volume (V) to the sorbent mass (m) showed that europium is quantitatively sorbed with polystyreneazoarsenazo and benzidineazoarsenazo at V/m 200 and 40, respectively. To recover metals from more concentrated HNO_3 solutions, the polystyreneazoarsenazo mass should be increased (Fig. 2, Table 3): e.g., at V/m 100, 60% europium is recovered even from 5 M HNO_3.

Since polystyreneazoarsenazo and benzidineazoarsenazo are fine powders, they should be separated from the solution by centrifuging, which is inconvenient with radioactive elements.

Fibrous chelating sorbents with high kinetic and selective characteristics are the most promising for recovery of actinides and lanthanides. To increase the efficiency of metal concentration (especially from large volumes), filled fibrous sorbents with higher kinetic characteristics and higher selectivity were used [17]. The study of metal sorption from nitric acid solutions with the filled fibrous chelating sorbent poyarsenazo-n containing polyacrylic fiber as a polymeric matrix and polystyreneazoarsenazo as a filler showed that this material well compares with the above-studied sorbents in sorption properties but has better kinetic characteristics (Fig. 1), since it exhibits

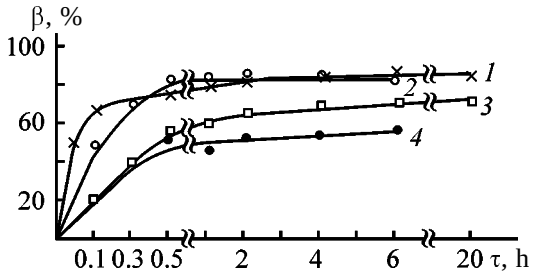

Fig. 1. Degree of europium sorption β with (*1*) polyarsenazo-n, (*2*, *4*) polystyreneazoarsenazo, and (*3*) BAAI as a function of sorption time t. HNO_3 concentration (M): (*1*–*3*) 1 and (*4*) 3. V/m: (*1*) 100 and (*2*–*4*) 200.

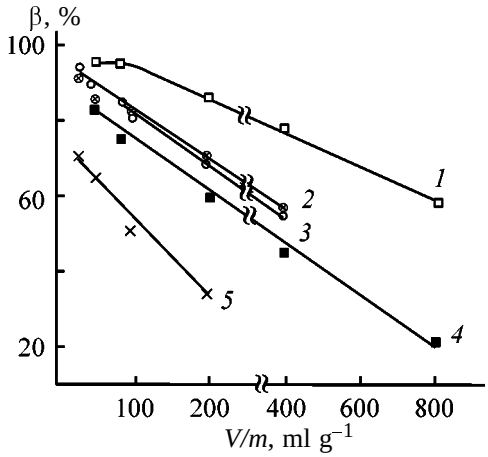

Fig. 2. Degree of europium sorption β with (*1*, *4*) polystyreneazoarsenazo, (*2*, *5*) polyarsenazo-n, and (*3*) BAAI as a function of V/m ratio. Sorption time 2 h. HNO_3 concentration (M): (*1*–*3*) 1 and (*4*, *5*) 3.

Table 3. Degree of europium sorption from nitric acid solutions. Sorption time 2 h

C_{HNO_3}, M	Degree of sorption, %, at indicated V/m			
	polystyreneazoarsenazo		polyarsenazo-n	
	200	100	100	50
3	58	72	48	56
4	54	69	42	53
5	46	60	30	53

rapid swelling and larger surface area. Triple-charged metals can be quantitatively recorded with polyarsenazo-n from nitric acid solution with concentration lower than 1 M, and plutonium, from solutions with higher acid concentration. As for polystyreneazoarsenaso, the increase of the polyarsenazo-n mass (Fig. 2, Table 3) increases the degree of metal recovery.

CONCLUSION

Chelating sorbents with arsenazo functional groups can be successfully used for sorption recovery and concentration of actinides and lanthanides from nitric acid solutions. Sorption can be accompanied by both chelation and ion exchange, because, along with chelating groups, these sorbents contain sulfo groups, which can be sites of usual ion exchange. It was shown that chelating sorbents with azo groups (especially those based on fibrous polymers) recover radionuclides from nitric acid solutions better than modified carbons.

REFERENCES

1. Savvin, S.B., *Arsenazo III* (Arsenazo III), Moscow: Atomizdat, 1966.
2. Savvin, S.B., *Organicheskie reagenty gruppy Arsenazo III* (Arsenazo III Group Organic Reagents), Moscow: Atomizdat, 1971.
3. Milyukova, M.S., Myasoedov, B.F., and Ryzhova, L.V., *Zh. Anal. Khim.*, 1972, vol. 27, no. 5, pp. 1769–1774.
4. Myasoedov, B.F., Milyukova, M.S., and Ryzhova, L.V., *Radiochem. Radioanal. Lett.*, 1972, vol. 11, no. 1, pp. 39–44.
5. Shkinev, V.M., Molochnikova, N.P., Zvarova, T.I., *et al.*, *J. Radioanal. Nucl. Chem., Articles*, 1985, vol. 88, no. 1, pp. 115–120.
6. Molochnikova, N.P., Frenkel', V.Ya., Myasoedov, B.F., *et al.*, *Radiokhimiya*, 1987, vol. 29, no. 1, pp. 39–45.
7. Myasoedova, G.V. and Savvin, S.B., *Khelatoobrazuyushchie sorbenty* (Chelating Sorbents), Moscow: Nauka, 1984.
8. Savvin, S.B., Eliseeva, O.P., and Rozovskii, Yu.G., *Dokl. Akad. Nauk SSSR*, 1968, vol. 180, no. 2, pp. 374–377.
9. Savvin, S.B., Myasoedov, B.F., and Eliseeva, O.P., *Zh. Anal. Khim.*, 1969, vol. 24, no. 7, pp. 1023–1026.
10. Myasoedov, B.F., Eliseeva, O.P., and Savvin, S.B., *J. Radioanal. Chem.*, 1969, vol. 2, nos. 5–6, pp. 369–376.
11. Myasoedov, B.F. and Molochnikova, N.P., *J. Radioanal. Chem.*, 1970, vol. 6, no. 1, pp. 67–73.
12. Dorokhova, E.M., Shvoeva, O.P., Cherevko, A.S., and Myasoedova, G.V., *Zh. Anal. Khim.*, 1979, vol. 34, no. 6, p. 1140.
13. Kazinskaya, I.E., Myasoedova, G.V., Pavlotskaya, F.I., and Frenkel', V.Ya., Absracts of Papers, *3-ya Vsesoyuznaya konferentsiya po khimii neptuniya i plutoniya* (3rd All-Union Conf. on Neptunium and Plutonium Chemistry), Leningrad, November 1987, p. 29.
14. Ryzhova, L.V., Myasoedova, G.V., Khitrov, L.M., *et al.*, *Radiokhimiya*, 1980, vol. 22, no. 2, pp. 284–288.
15. Myasoedova, G.V., Molochnikova, N.P., Lileeva, L.V., and Myasoedov, B.F., *Radiokhimiya*, 1999, vol. 41, no. 5, pp. 456–458.
16. Shvoeva, O.P., Kuchava, G.P., and Myasoedova, G.V., *Zh. Anal. Khim.*, 1987, vol. 42, no. 11, pp. 1995–1997.
17. Myasoedova, G.V., Nikashina, V.A., and Molochnikova, N.P., *Zh. Anal. Khim.*, 2000, vol. 55, no. 6, pp. 611–615.

Russian Journal of Applied Chemistry, Vol. 74, No. 5, 2001, pp. 733–736. Translated from Zhurnal Prikladnoi Khimii, Vol. 74, No. 5, 2001, pp. 713–716.

SORPTION AND ION-EXCHANGE PROCESSES

Extraction-Chromatographic Separation and Concentration of Phenol and Guaiacol with the Use of Organic Solvent Mixtures as Stationary Phases

Ya. I. Korenman, I. V. Vatutina, and A. T. Alymova

Voronezh State Technological Academy, Voronezh, Russia

Received January 26, 2001

Abstract—Extraction-chromatographic concentration and separation of phenol and guaiacol was studied as influenced by the composition of binary tributyl phosphate–pentyl acetate, tributyl phosphate–dinonyl phthalate, tributyl phosphate–didecyl sebacate, and ternary tributyl phosphate–dicyclohexano-18-crown-6–toluene and tributyl phosphate–dicyclohexano-18-crown-6–chloroform stationary phases.

Extraction chromatography with the use of nonpolar polymeric sorbents as supports and mixtures of organic solvents as stationary phases (SPs) is a promising technique for concentration of microamounts of chemical compounds [1]. For example, phenol can be recovered from aqueous solution with tributyl phosphate (TBP) organic solution applied to the surface of a polymeric sorbent (Polysorb S) [2, 3]. At the same time, extraction-chromatographic concentration of guaiacol exhibiting physicochemical features close to those of phenol but significantly differing from the latter in toxicological characteristics was not studied. In this work we studied extraction-chromatographic concentration of phenol and guaiacol from aqueous solutions with the use of TBP or dicyclohexano-18-crown-6 (DCH18C6) organic solutions as the stationary phases.

The aim of this work was to study the effect of composition of the stationary phase on extraction-chromatographic separation of phenol and guaiacol.

EXPERIMENTAL

Polysorb S was pretreated, impregnated with stationary phase (SP), and packed into a chromatographic column by a common procedure [3]. The choice of the optimal composition of the mixed stationary phase was governed by the data on the selectivity coefficients β and distribution factor D of phenol and guaiacol between immiscible aqueous and organic phases. It was found that TBP–alcohol and TBP–hydrocarbon mixtures commonly used as stationary phases in extraction chromatography are more weakly retained by Polysorb matrice in filtration of aqueous phenol and desorbing solutions than the compounds previously tested for this purpose [4].

Extraction of phenol and guaiacol under static conditions with TBP–pentyl acetate (PA), TBP–didecyl sebacate (DDC), and TBP–dinonyl phthalate (DNP) mixtures is characterized by high values of D and β (Table 1, SP nos. 1–3). In extraction of phenol with DCH18C6 (0.3 mole fraction) solution in chloroform or toluene D = 20–25. Relatively low distribution factors in extraction of phenol and guaiacol with organic solutions of the crown ether can be caused by the lower polarity of the ether oxygen atoms in DCH18C6 as compared to TBP. In extraction of phenol and guaiacol with DCH18C6 solution in toluene their distribution factors are virtually similar (~25). In extraction with DCH18C6 solution in chloroform (SP no. 6) the distribution factor of phenol exceeds that of guaiacol by a factor of 2. The stationary phase no. 6 has the minimum kinematic viscosity η, which facilitates diffusion of the components and increases the separation efficiency. Therefore, in separation of phenol and guaiacol with the use of frontal chromatography stationary phase no. 6 is preferable.

The ternary stationary phases TBP–DCH18C6–toluene (SP no. 4) and TBP–DCH18C6–chloroform (SP no. 5) exhibit larger sorption power as compared to the TBP–DCH18C6 binary stationary phase. We found also that with ternary stationary phase no. 5 the separation coefficient β is maximal (Table 1).

Large distribution factors of phenol and guiacol

1070-4272/01/7405-0733$25.00

Table 1. Composition and features of stationary phases

SP no.	Composition, mole fraction		η, $mm^2 s^{-1}$	*D*		β
	main component	additive		phenol	guiacol	
1	TBP, 0.6	PA	2.8	320	95	3.3
2	TBP, 0.8	DNP	6.7	395	95	4.1
3	TBP, 0.9	DDS	7.0	360	90	4.0
4	TBP, 0.3	Toluene; DCH18C6, 0.2	2.2	260	70	3.7
5	TBP, 0.3	Chloroform; DCH18C6, 0.2	2.3	235	53	4.4
6	DCH18C6, 0.3	Chloroform	1.4	22	11	2.0

between aqueous solution and the binary and ternary stationary phases (nos. 1–5) indicate the high sorption capacity of the columns with respect to the compounds concerned. In experiments on extraction-chromatographic concentration of phenol and guaiacol and determination of the operating parameters, the columns were packed with Polysorb (2.9 g) impregnated with SP (2.9 ml). The bed height of the modified sorbent *h* was 14 cm. More efficient columns used for separate determination of phenol and guiacol contained less viscous stationary phase no. 6, and the bed height was 5 cm.

In our experiments the sorption capacity of the column *E* was conventionally determined from the concentration of the target compound in the initial solution and the solution volume passed by the moment when the component concentration in the eluate became 16% of the initial level [1]. We found that the solution volume passed through the column under these conditions remains constant irrespective of the initial concentration of the compounds being separated [5]. At the same time, the *E* value determined from the eluate volume passed through the column by the moment of breakthrough of the first amounts of the target compound increases with decreasing initial concentration of phenol or guaiacol.

Table 2. Column characteristics*

SP no.	*E*, μg g^{-1}	HETP, cm	*D*'	V_r, ml	V_e, ml
			Phenol		
1	683	2.5	290	2.8	10.5
2	720	2.4	303	2.8	9.5
3	645	3.4	293	2.6	11.0
4	323	2.1	179	2.4	9.0
5	292	2.1	172	2.4	8.5
6	58	1.6	22	1.4	3.5
			Guaiacol		
1	302	5.2	110	2.1	8.5
2	293	5.6	109	2.1	8.0
3	276	5.8	103	1.9	8.0
4	190	2.3	56	1.7	6.0
5	155	2.8	48	1.7	7.5
6	20	1.6	11	1.3	3.5

* V_r and V_e are the retention and elution volumes, respectively.

The highest *E* value was observed in filtration of phenol aqueous solution (pH 3) through the column with SP no. 2 (filtration rate 0.4 l h^{-1}). The columns with SP nos. 1 and 2 have a high sorption capacity with respect to guaiacol. Table 2 shows that in passing from the column with SP no. 3 to the column with SP no. 6 containing DCH18C6 instead of TBP the sorption capacity significantly decreases.

In extraction-chromatographic systems the distribution factor *D*' of a component is determined under dynamic conditions as the ratio of the volume of the eluate containing half concentration of the component (relative to the initial solution) to the SP volume [1, 6]. The distribution factors *D*' of phenol and guaiacol determined by this procedure (Table 2) are comparable to those determined under static conditions (Table 1).

As seen from Table 2, increase in the SP viscosity, hindering diffusion of phenol and guaiacol [6, 7], is responsible for decrease in HETP. The HETP is the largest in the case of SP no. 3. The most efficient column with SP no. 6 is characterized by relatively small HETP. It is that column that was used to study the possibility of separate determination of phenol and guaiacol in their mixtures by frontal chromatography (Fig. 1). The differential output curve $\Delta A/\Delta V = f(V)$

has two maxima corresponding to two different retention volumes. The areas under maxima of the differential output curve correspond to the amounts of guaiacol and phenol, respectively [6, 8].

The elution volumes V_e of phenol and guaiacol were determined by their desorption with an aqueous solution containing 0.5 g of NaOH and 5 g of NaCl per 100 g of the solution. As with HETP, V_e decreases with decreasing SP viscosity facilitating diffusion of phenol and guiacol (Table 2).

Table 2 shows that the values of extraction-chromatographic characteristics of guaiacol are lower than those of phenol. We assume that this decrease is caused by introduction of the less hydrophobic OCH_3 group into the phenol molecule, which virtually does not affect the specific interaction with SP but enhances nonspecific interactions with eluent (water) [7]. This assumption is confirmed by the fact that V_r of guaiacol is less than that of phenol, i.e., guaiacol exhibits larger affinity for the aqueous desorbing solution.

In elution of phenol the retention volume V_r can decrease owing to phenol ionization in the alkaline eluent and strong hydration of the resulting ionic species. Table 2 shows that V_r of phenol and guaiacol is close, so that their elution peaks superimpose and separation of the compounds by elution with aqueous alkaline solution becomes impossible.

In analysis of a 1-l sample of solution containing a phenol–guaiacol mixture we found that the column with SP no. 2 has a high sorption capacity for these compounds and provides their 100-fold concentration (V_e < 10 ml). Therefore, it is SP no. 2 that was used for concentrating phenol and guiacol.

We studied also the degree of recovery (*R*, %) of the compounds from aqueous solution (1 l) at a filtration rate of 0.4 l h^{-1} as influenced by the bed height of the modified sorbent. As seen from Fig. 2, the degree of recovery of phenol increases with increasing the sorbent bed height (Fig. 2). The feasibility of selective recovery of phenol from a phenol–guaiacol mixture on the column with h = 3 cm was reported by us previously [9]. Concentration of phenol–guaiacol mixture can be performed on a column with h = 8 cm. In analysis of smaller sample of the phenol–guaiacol mixture (10 ml) on the column with SP no. 5 having a lower sorption capacity but a higher selectivity coefficient, we obtained the similar dependence of the degree of recovery on the sorbent bed height. With this column phenol is selectively recovered within

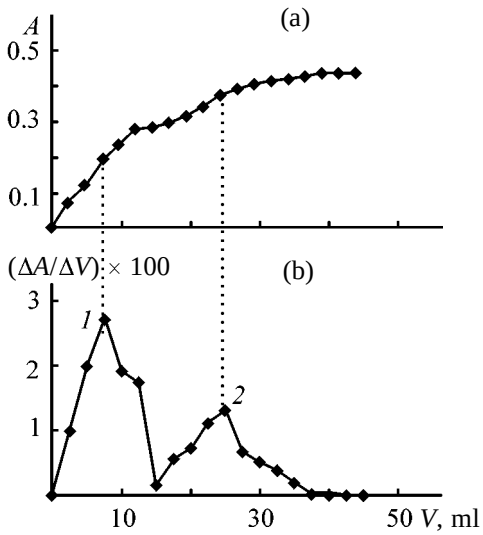

Fig. 1. (a) Integral and (b) differential output curves of (*1*) guaiacol and (*2*) phenol sorption. (*A*) Eluate optical density and (*V*) eluate volume.

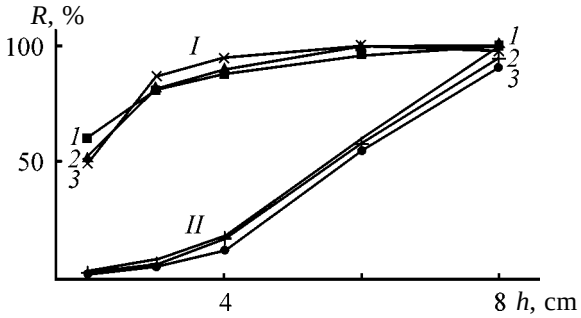

Fig. 2. Degree of recovery *R* of (*I*) phenol and (*II*) guaiacol as a function of the bed height *h* of the modified sorbent. Initial compound content (μg l^{-1}): (*1*) 1.0, (*2*) 2.5, and (*3*) 5.0.

a 2-cm sorbent bed, and guiacol is virtually completely recovered within 6 cm.

In extraction-chromatographic concentration of phenol–guaiacol mixtures on the column with SP no. 2 at a high filtration rate the sorption bands of the compounds are smeared and overlapped [6]. Therefore, the effect of the rate of solution filtration on the degree of recovery was studied on the column with a higher sorbent bed (14 cm). Figure 3 illustrates the recovery of phenol (initial concentration 1.0, 2.5, and 5.0 μg l^{-1}) and guaiacol (initial concentration 1 μg l^{-1}) from aqueous solution (1 l) at variable filtration rate. At a filtration rate within 0.4 – 0.8 l h^{-1} the recovery of phenol is virtually complete (100%). Further increase in the filtration rate causes partial breakthrough and loss of phenol. At the filtration rate of 1.1 l h^{-1} the degree of recovery of phenol does not exceed 60%.

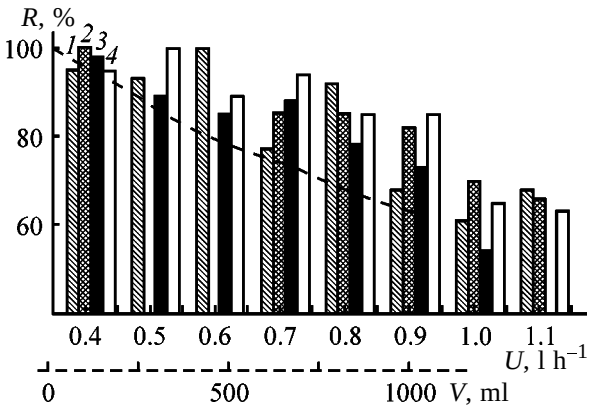

Fig. 3. Degree of recovery *R* of phenol as a function of the (bars) rate of eluate filtration *U* and (dashed line) eluate volume. Content (μg l^{-1}): phenol (*1*) 1.0, (*2*) 2.5, and (*3*) 5.0; guaiacol (*4*) 1.0.

As seen from Fig. 3, the similar relationships occur for guaiacol (Fig. 3).

Figure 3 (dashed line) shows also the degree of recovery of phenol (initial concentration 5 μg l^{-1}) as a function of the solution volume passed through the column (SP no. 2) at a constant filtration rate, approximately equal to 1.1 l min^{-1}. It is seen that at such a rapid filtration phenol can be efficiently recovered only from small volume of solutions. At $V <$ 250 ml phenol is virtually completely recovered from aqueous solution. With increasing solution volume to 500 and 1000 ml recovery of phenol does not exceed 80 and 65%, respectively. Thus, at a filtration rate of 1.1 l h^{-1} recovery of phenol is the most complete at $V <$ 250 ml.

CONCLUSIONS

(1) The optimal compositions of binary stationary phases for separate determination of phenol and guaiacol (dicyclohexano-18-crown-6–chloroform) and concentration of phenol–guaiacol mixtures (tributyl phosphate–dinonyl phthalate) by frontal extraction chromatography were established.

(2) The efficiency of concentration of phenol–guaiacol mixtures was studied as a function of the bed height of the modified sorbent, the filtration rate, and the eluate volume.

REFERENCES

1. *Extraction Chromatography*, Braun, T. and Ghersini, G., Eds., Budapest: Akad. Kiado, 1975.
2. Korenman, Ya.I., Alymova, A.T., and Bobrinskaya, E.V., *Zh. Prikl. Khim.*, 1993, vol. 66, no. 10, pp. 2305–2310.
3. Korenman, Ya.I., Alymova, A.T., and Vatutina, I.V., *Zh. Prikl. Khim.*, 1999, vol. 72, no. 10, pp. 1645–1648.
4. Korenman, Ya.I., Alymova, A.T., and Vatutina, I.V., *J. Radioanal. Nucl. Chem.*, 2000, vol. 246, no. 3, pp. 629–634.
5. Pilipenko, A.T., Yurchenko, V.V., Zhuk, P.F., and Zul'figarov, O.S., *Khim. Tekhnol. Vody*, 1987, vol. 9, no. 5, pp. 420–422.
6. Perry, S.G., Amos, R., and Brewer, P.I., *Practical Liquid Chromatography*, New York: Plenum, 1972.
7. *Osnovy analiticheskoi khimii* (Fundamentals of Analytical Chemistry), Zolotov, Yu.A., Ed., Moscow: Vysshaya Shkola, 1999, vol. 1.
8. RF Patent no. 2155957.
9. RF Patent no. 2157522.

Russian Journal of Applied Chemistry, Vol. 74, No. 5, 2001, pp. 737–741. Translated from Zhurnal Prikladnoi Khimii, Vol. 74, No. 5, 2001, pp. 717–721.

APPLIED ELECTROCHEMISTRY AND CORROSION PROTECTION OF METALS

Kinetics of Leaching of Nickel Compounds from Spent Electrodes of Nickel–Iron Batteries in Ammonia Solutions

A. I. Demidov and O. A. Krasovitskaya

St. Petersburg State Technical University, St. Petersburg, Russia

Received August 4, 2000

Abstract—The extent of nickel recovery from spent electrodes of nickel–iron batteries in ammonia solutions was studied in relation to time and leaching temperature. The optimal time and the temperature at which the extent of nickel recovery in leaching solutions containing ammonium salts is the highest were determined and the dependence of the process efficiency on the anionic composition of the solution was analyzed. The apparent activation energies of nickel leaching from the active mass preliminarily extracted from lamellas are calculated, and the adequacy to the actual process of the model of leaching controlled by external diffusion is assessed.

The problems of utilization and recycling of raw materials containing non-ferrous metals, including nickel, are presently the matter of strong interest. The priority direction in this field is the development of hydrometallurgical processing techniques characterized by environmental safety and low energy consumption [1–4].

Complexation in ammonia solutions underlies nickel recovery from oxidized ores [5–7]. Previously, it has been shown that this approach is promising for processing of positive electrodes of nickel–iron batteries. Nickel is present in lamellas of spent batteries in the form of hydroxides, mainly $Ni(OH)_2$ dissolving in aqueous ammonia by the overall reaction

$$Ni(OH)_2(s) + 6NH_3(aq) \rightarrow [Ni(NH_3)_6]^{2+}(aq) + 2OH^-(aq). \quad (1)$$

Ammonium salts added to aqueous solutions make higher the dissolution efficiency because of their buffer action preventing accumulation of OH^- ions by reaction (1), which takes the form

$$Ni(OH)_2(s) + 4NH_3(aq) + 2NH_4^+(aq) \rightarrow [Ni(NH_3)_6]^{2+}(aq) + 2H_2O. \quad (2)$$

It was established that the extent of nickel recovery may be as high as 99% in some cases of leaching of lamella fragments in ammonia solutions containing ammonium salts [8]. However, revealing the possibility of such processing on industrial scale requires more detailed studies of the process kinetics.

The rate of leaching (generally dependent on reagent concentration, temperature, rate of stirring, extent to which the surface of the solid phase is developed, etc.) may vary in the course of the process. The heterogeneous process of leaching includes at least three main stages, namely, transport of reagents toward the reaction surface, chemical reactions proper, and removal of dissolved products into the solution bulk. Therefore, one of the basic tasks in studying the kinetics of a complex process consists in finding the apparent activation energy of the process and in determining its limiting stage.

In this study, we analyzed the efficiency of the process in relation to the time and temperature of leaching for several solution compositions. The leaching was performed from a spent active paste, both contained within lamella fragments and preliminarily extracted from it. The leaching solutions were prepared using the following reagents: aqueous ammonia NH_4OH (ultrapure grade) and ammonium salts (chemically pure grade) NH_4Cl, NH_4NO_3, $(NH_4)_2SO_4$, and $(NH_4)_2CO_3$.

The extent of nickel recovery was calculated from the results of spectrophotometric analysis for nickel in the leaching solutions by the technique described in [8]. The leaching process was studied in solutions of the following compositions (M): 2 NH_4OH and 1 NH_4NO_3 (solution A), 2 NH_4OH and 1 NH_4Cl

1070-4272/01/7405-0737$25.00

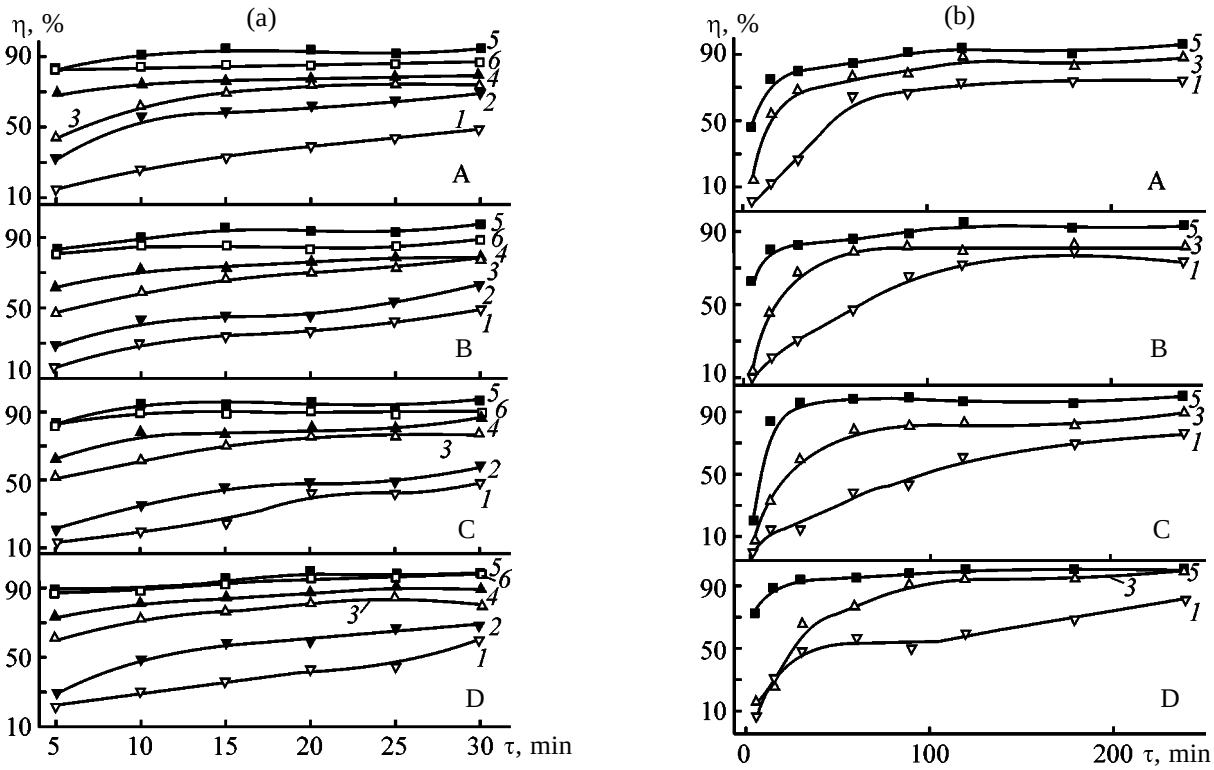

Fig. 1. Kinetics of nickel recovery from (a) active paste and (b) lamella fragments into ammonia solutions A–D at various temperatures. (η) Extent of nickel recovery and (τ) time; the same for Fig. 3. Leaching temperature (°C): (*1*) 30, (*2*) 40, (*3*) 50, (*4*) 60, (*5*) 70, and (*6*) 80.

(solution B), 1.5 NH_4OH and 1 $(NH_4)_2SO_4$ (solution C), and 1.5 NH_4OH and $(NH_4)_2CO_3$ (solution D).

The leaching was done from 1.0-g portions of spent active paste and also from closed lamella fragments containing approximately the same amount of the active paste. A sample was placed in a preliminarily thermostated flask with 50 ml of leaching solution, equipped with a magnetic stirrer. In this stage of the investigation, the rate of agitation was maintained constant. The duration of leaching was varied from 5 to 240 min for lamellas and from 5 to 30 min for the active paste without lamellas.

Figure 1a illustrates the progress in time of isothermal leaching of nickel from the active paste into solutions containing various ammonium salts. Several tentative conclusions follow from the presented plots: (1) the curve shapes are basically the same for all of the studied leaching solution compositions; (2) recovery of nickel is strongly temperature-dependent, especially in the initial stage of the process (first 10 min) and at temperatures lower than 50°C; the maximum extent of recovery is observed at 70°C and then, with temperature raised to 80°C, decreases somewhat; (3) above 50°C the rate of leaching tends to decrease with time, except for the initial stage; (4) at 70–80°C the optimal time of nickel recovery is 10–20 min and 1–2 h for leaching from, respectively, the active paste and lamellas in ammonia solutions, irrespective of their anionic composition.

This suggests that, in its initial stage, the leaching proceeds in a mixed diffusion-kinetic mode and then tends to pass into the predominantly diffusion region [9–11].

The results obtained in leaching of nickel compounds from lamella fragments (Fig. 1b) on the whole agree with the aforesaid, with correction made for the even more pronounced decrease in the leaching rate with time. The shapes of the curves obtained at 30°C differ from those of the curves taken at 50 and 70°C to a greater extent than these latter differ from each other. Comparison of the data in Figs. 1a and 1b shows that direct leaching through the lamella sheath at a given temperature imposes on the process obvious diffusion limitations, which is one more evidence in favor of the above tentative conclusions.

To confirm these conclusions quantitatively, the obtained kinetic dependences were processed to eval-

uate the apparent activation energy of the process. To construct a plot in the Arrhenius coordinates, the rate of leaching was determined from the initial portions of the curves. Figure 2 presents the results of mathematical processing of the kinetic curves obtained in leaching in ammonia solutions of the active paste not enclosed in a lamella. In the same coordinates are shown experimental points describing leaching from lamella fragments under similar conditions. The slope of the straight line presented in the figure was used to determine the activation energy of leaching of the active paste to be, on the average, 30 kJ mol^{-1}, which is a quantitative indication of the occurrence of the process in the transition diffusion-kinetic region [10, 11].

At the same time, the experimental dependence in Fig. 2, well described by a straight line in the Arrhenius coordinates (with correlation coefficients exceeding 0.95) at $1/T > 2.95 \times 10^{-3}$ K^{-1} ($T < 65$°C), shows an obvious tendency toward a decrease in its slope (and, consequently, in the apparent activation energy). These results confirm the assumption that the process tends to pass into the diffusion region with time and with increasing leaching temperature. In addition, the closeness of the experimental points in Fig. 2 indicates that the leaching parameters affect in about the same way the percentage of nickel recovery from the active paste and lamella fragments. It should be noted that no significant differences were revealed between the activation energies obtained for all of the four leaching solutions: 29.9, 32, 33, and 27.4 kJ mol^{-1} for, respectively, solutions A, B, C, and D.

Erofeev and Kolmogorov derived a generalized kinetic equation that can be used to derive, without composing differential equations, formulas of chemical kinetics for homogeneous and heterogeneous reactions. In particular, the equation for topochemical processes has the form

$$E = 1 - \exp(-k\tau^n), \quad (3)$$

where E is the fraction of substance reacted by the instant of time τ, having the meaning of the probability that a molecule has reacted by the time τ.

Bulanov *et al.* [13] used for describing the kinetics of leaching of iron-containing raw materials in obtaining ferrous chloride a similar equation

$$C_i = C_i^0[1 - \exp(\alpha_i\tau)], \quad (4)$$

where $\alpha_i < 0$ is a constant accounting for specific features of the reagent diffusion, C_i^0 is the concentration of ith leached substance in the starting concentrate, and C_i is its concentration in solution.

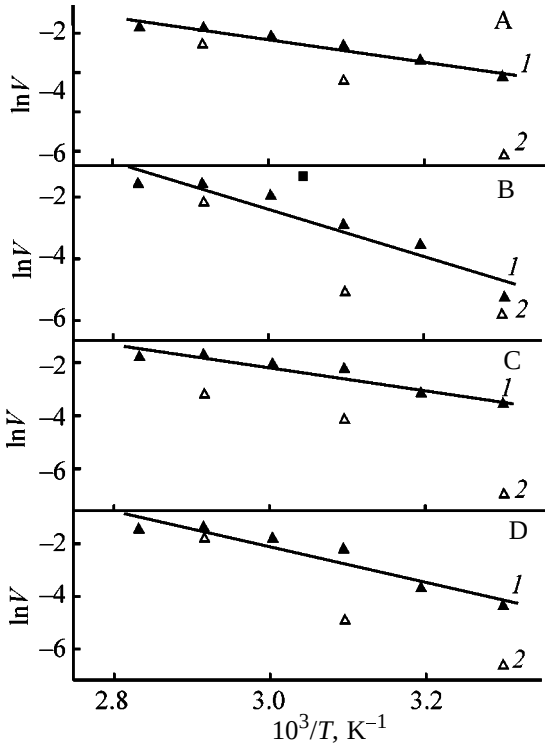

Fig. 2. Dependence of the leaching rate $\ln V$ (for explanation, see text) in ammonia leaching solutions A–D on temperature T. (*1*) Active paste and (*2*) lamella fragments.

The numerical values of the coefficients can be obtained by means of linear regression analysis of experimental data. Such a model of the leaching process requires some assumptions, which idealize somewhat the process in question, but are rather frequently used in modeling. At the same time, the validity of the following assumptions is the criterion for the possibility of regarding the process as an ideal mixing process [13]: (1) all solid particles have spherical shape which is preserved during the chemical reaction; (2) the average granulometric composition of particles is the same throughout the reaction volume; (3) the solid particles and the solution are homogeneously mixed in the reaction volume; (4) the active surface of the particles is proportional to the concentration of the substance being dissolved in the solid phase; (5) the sludge temperature is constant in time and the same throughout the reaction volume; (6) the leaching of the active paste is diffusion-controlled, the substance transfer within pores of a particle toward its boundary (internal diffusion) can be neglected and only external diffusion (substance transfer from the particle surface into the bulk of the liquid) be con-

Results of linear regression analysis of the kinetics of nickel leaching from the active paste and lamella fragments in ammonia solutions at 70°C

Solution	$G = \ln(1 - \eta)$	R
	Active paste	
A	$-1.540 - 7.61 \times 10^{-2}\tau$	0.840
B	$-1.927 - 3.931 \times 10^{-2}\tau$	0.746
C	$-2.119 - 4.945 \times 10^{-2}\tau$	0.764
D	$-1.467 - 1.113 \times 10^{-1}\tau$	0.865
	Lamella fragments	
A	$-1.229 - 8.344 \times 10^{-3}\tau$	0.869
B	$-1.504 - 6.131 \times 10^{-3}\tau$	0.796
C	$-1.888 - 1.307 \times 10^{-2}\tau$	0.704
D	$-2.047 - 1.776 \times 10^{-2}\tau$	0.836

sidered; (7) the concentration of the leached component at the surface of the solid phase is close to the saturation concentration; (8) surface adsorption can be neglected in considering heterogeneous chemical reactions and the rate at which the adsorption equilibrium is attained greatly exceeds the rate of the chemical reaction; (9) all reactions occur on the surface of the solid phase; (10) ammonia leaching solutions are in excess in the apparatus; (11) the diffusion surface can be taken to be proportional to the nickel hydroxide concentration in the solid phase in considering Ni^{2+} diffusion flows; (12) the leaching process can be considered under conditions excluding hydrolytic decomposition of ammonia solutions.

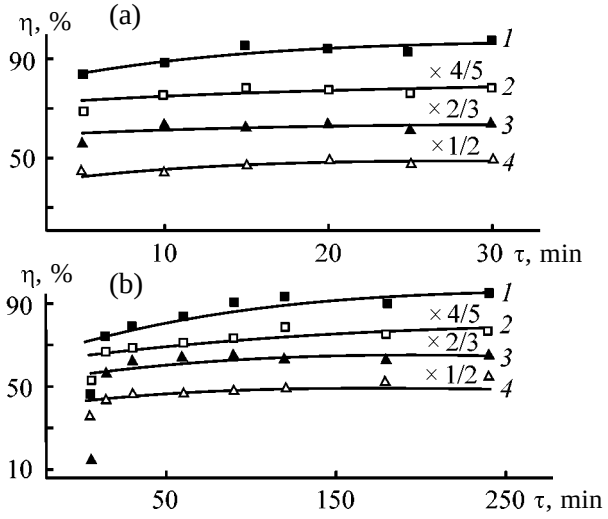

Fig. 3. Comparison of model kinetic curves with experimental data for nickel leaching from (a) active paste and (b) lamella fragments at 70°C. Solution: (*1*) A, (*2*) B, (*3*) C, and (*4*) D.

With account of the fact that the C_i/C_i^0 ratio is in the given case equivalent to the extent of recovery η, an attempt was made to describe the leaching process in terms of the model proposed in [13]. For this purpose, the experimental data were subjected to regression analysis in the coordinates G–τ, where $G = \ln(1 - \eta)$, with the slope of the straight line yielding in this case the coefficient α. The results of the analysis are presented in the table (R is the correlation coefficient).

Thus, the coefficients of the models are significant, since t (Student's test) gives significant correlation coefficients $R \geq 0.67$. Hence, we can obtain theoretical and experimental models describing how nickel passes into solution in the course of time. Model kinetic curves of nickel recovery, plotted using the equations (see table), are in good agreement with the experimental data for the active paste (Fig. 3a). Leaching from lamella fragments is also satisfactorily described by the equations of the model, except in the initial stage when, as shown above, the share of the kinetic component is still relatively high (Fig. 3b).

Analysis of the model suggests that the process of nickel passing into solution can indeed be considered an ideal mixing process with sufficient accuracy. The coincidence of the calculated and experimental data suggests that the process of nickel leaching in ammonia solutions from both the active paste itself and lamellas with active paste is diffusion-controlled.

CONCLUSIONS

(1) A study of the kinetics of nickel leaching from spent electrodes of nickel–iron batteries demonstrated that, in the initial stage (especially at temperatures below 50°C), the process occurs in a mixed diffusion-kinetic mode and then tends to pass into the diffusion region.

(2) The anionic composition of ammonia leaching solutions exerts no fundamental effect on the efficiency of nickel recovery from the active paste and lamella fragments.

(3) The optimal time of leaching at 70–80°C is about 10–20 min for the active paste and 1–2 h for lamella fragments.

(4) The model of outer-diffusion-controlled leaching satisfactorily describes the kinetics of nickel recovery from the active paste and lamella fragments taken from spent positive electrodes of nickel–iron batteries.

REFERENCES

1. Sittig, M., *Metal and Inorganic Waste Reclaiming Encyclopedia*, New York: Park Ridge, 1980.
2. Khudyakov, I.F., Doroshkevich, A.P., and Karelov, S.V., *Metallurgiya vtorichnykh tyazhelykh tsvetnykh metallov* (Metallurgy of Secondary Heavy Non-Ferrous Metals), Moscow: Metallurgiya, 1987.
3. Zhang, P., Yokoyama, T., Itabashi, O., *et al*., *Hydrometallurgy*, 1998, vol. 50, no. 1, pp. 61–75.
4. Nogueira, C.A. and Delmas, F., *Hydrometallurgy*, 1999, vol. 52, no. 3, pp. 267–287.
5. Borbat, V.F. and Leshch, I.Yu., *Novye protsessy v metallurgii nikelya i kobal'ta* (New Processes in Metallurgy of Nickel and Cobalt), Moscow: Metallurgiya, 1976.
6. Khudyakov, I.F., Tikhonov, A.M., Deev, D.I., and Naboichenko, S.S, *Metallurgiya medi, nikelya i kobal'ta* (Metallurgy of Copper, Nickel, and Cobalt), Moscow: Metallurgiya, 1977, vol. 2.
7. Bukin, V.I., Reznik, A.M., Vasil'chenko, S.V., and Granat, N.A., Present State of, and Prospects for Use of Extraction in Ammonia Processing of Nickel- and Cobalt-Containing Raw Materials, *Obzor. Inform. TsNIIEI TsM, Ser. Proizv. Tyazh. Tsvetn. Met*., 1983, issue 3.
8. Demidov, A.I. and Krasovitskaya, O.A., *Zh. Prikl. Khim*., 2000, vol. 73, no. 10, pp. 1656–1660.
9. Bretsznajder, S., Kawecki, W., Zeyko, G., and Marcinkowski, R., *Podstawy ogolnetechnologii chemicznej*, Warsaw: Naukowo-Technicznej, 1973.
10. Habashi, F., *Principles of Extractive Metallurgy*, New York: Gordon and Breach, 1969.
11. Zelikman, A.N., Vol'dman, G.M., and Belyaevskaya, L.V., *Teoriya gidrometallurgicheskikh protsessov*, Moscow: Metallurgiya, 1983.
12. Beloglazov, I.N., Morachevskii, A.G., and Zhmarin, E.E., *Kineticheskie zakonomernosti protsessov rastvoreniya i vyshchelachivaniya* (Kinetics of Dissolution and Leaching), Moscow: Ruda i Metally, 2000.
13. Bulanov, V.Ya., Vatolin, N.A., Zalazinskii, G.G., and Volkova, P.I., *Gidrometallurgiya zheleznykh poroshkov* (Hydrometallurgy of Iron Powder), Moscow: Nauka, 1984.

Russian Journal of Applied Chemistry, Vol. 74, No. 5, 2001, pp. 742–745. Translated from Zhurnal Prikladnoi Khimii, Vol. 74, No. 5, 2001, pp. 721–724.

APPLIED ELECTROCHEMISTRY AND CORROSION PROTECTION OF METALS

Dynamics of Changes in the Anionic Composition of Sodium Chloride Solutions in a Flow-through Electrolyzer

R. G. Romanova, S. I. Agadzhanyan, G. V. Korshin, and V. F. Sopin

Kazan State Technological University, Kazan, Tatarstan, Russia

Received July 7, 2000

Abstract—Products theoretically obtainable by electrochemical treatment of sodium chloride solutions in the dynamic mode are considered. Hydrated chlorine, and hypochlorous and hydrochloric acids are determined quantitatively by iodometric titration, spectrophotometry, and potentiometry. A comparative analysis is made of theoretical and experimental results obtained in determining chlorine-containing ions.

Electrochemically treated solutions of sodium chloride find increasingly wide application in medical practice. At the same time, the mechanism of effective action of these solutions remains unclear because the ionic and gas species in them occur in a labile equilibrium. In this connection, the composition of electrochemically treated sodium chloride solutions in a flow-through electrolyzer with a canvas dam was studied. The obtained experimental data are compared with the results of approximate theoretical calculations.

A wide variety of reactions may occur at electrodes in electrolysis of chloride solutions [1, 2]. Depending on electrochemical treatment (ET) conditions, electrolyzer parameters (type of diaphragm, distribution of current over electrodes, electrode material, stationary or dynamic mode), solution (nature and concentration of electrolytes), and temperature, the resulting solutions may have different chemical compositions. The most probable and practically important are reactions involving chloride ions and products of their oxidation (HClO, ClO^-, Cl_3^-, Cl_2). Reactions leading to deeper oxidation (ClO_2^-, ClO_3^-, ClO_4^-) are kinetically hindered [3], being only possible as a result of redox reactions in the bulk at high content of precursors and elevated temperatures.

Anolyte being of primary practical importance, we restrict consideration to processes occurring in the anode part of the electrolyzer.

At the current densities (1–10 A dm^{-2}) and electrolyte concentrations used, two competitive reactions may proceed at the electrodes:

$$2Cl^- = Cl_2 + 2e, \quad E_0 = 1.359 \text{ V}; \qquad (1)$$

$$2H_2O = 4H^+ + O_2 + 4e, \quad E_0 = 1.229 \text{ V}. \qquad (2)$$

Experiments show that processes (1) and (2) may actually proceed simultaneously; however, with ORTA (ruthenium oxide–titanium) electrodes used, the fraction of current α consumed for process (1) is 98–99% in electrolysis of sodium chloride solutions [4]. At low sodium chloride concentrations, α is much lower, as indicated by the experimental data presented below.

Let us consider processes occurring in the solution bulk. The reaction of molecular chlorine with aqueous solutions proceeds via hydration stage

$$Cl_2(g) = Cl_2(aq), \quad K = 0.104–0.003 \ (25–80°C), \qquad (3)$$

where K is the temperature-dependent equilibrium constant of hydration [5].

Then proceeds disproportionation, with the thermodynamic constant $K = 3.94 \times 10^{-4}$ [5]:

$$Cl_2 + H_2O = H^+ + Cl^- + HOCl. \qquad (4)$$

Also possible is formation of the trichloride ion

$$Cl_2 + Cl^- = Cl_3^-. \qquad (5)$$

The equilibrium constant of reaction (5) is 0.18 at 25°C [1].

In view of the aforesaid, it may be assumed that with the electrolyzer and ET modes used, only molecular chlorine is formed at the electrode from chlorine compounds, and conditions for existence of only hydrated molecular chlorine and hypochlorous and hydrochloric acids are created in the anolyte solution. In addition, thrichloride ions can theoretically exist in the solution; however, under real conditions, the con-

1070-4272/01/7405-0742$25.00

Table 1. Determination of active chlorine by iodometric titration (IM) and spectrophotometry (SP) for various ET modes

j, A dm^{-2}	Content of active chlorine $C \times 10^3$, M		Content of active chlorine species (SP)			
	IM	SP	Cl_2	HClO	fraction of indicated component, %	
			$C \times 10^3$, M		Cl_2(aq)	HClO
1	1.70	1.85	0.31	1.54	16.8	73.2
2	4.00	3.40	0.95	2.09	31.2	68.8
3	5.90	5.79	2.31	3.48	39.9	60.1
4	9.56	8.80	4.17	4.63	47.4	52.6
5	12.80	11.35	5.91	5.45	52.1	47.9

tent of chloride ions is less than 1–2% of the total amount of active chlorine even at the highest current density.

The total amount of oxidants in solution can be determined by iodometric titration. Hydrated molecular chlorine and chlorine-containing ions can be identified spectrophotometrically by their absorption in the UV range [6]. In addition, the content of active chlorine can be found by potentiometric titration of hypochlorous acid. Coincidence of the results obtained by the three methods can validate the assumption made.

Absorption in the UV spectral region is observed for ClO_2^-, ClO^- ions, HClO molecules, and hydrated chlorine [3, 6]. Chlorate and perchlorate ions cannot be identified using UV spectra, having no pronounced absorption bands in this range.

The UV spectra of chemically obtained chlorine water were measured in order to study the direct products of chlorine hydrolysis under conditions when there are no reactions occurring in the case of ET. In doing so, the total content of active chlorine was determined iodometrically. A preset pH value in model solutions was maintained by adding hydrochloric acid or sodium hydroxide. The obtained spectra of chlorine water and sodium chloride after ET were identical at equal pH values (see figure), which indicates that the composition of the solutions is the same as regards the absorbing components. If the formation of the trichloride ion, whose concentration is, as already mentioned, not higher than 1–2%, is disregarded, then measurements at two wavelengths are sufficient for determining separately the concentrations of hydrated chlorine and hypochlorous acid.

Solution of the system of equations describing the absorption of solutions containing hydrated chlorine and hypochlorous acid gives the following expressions, which can be used to determine their concentrations:

$$C(\mathrm{HClO}) = (6.696A_{290} - 2.556A_{320}) \times 10^{-2}, \quad (6)$$

$$C(\mathrm{Cl_2}) = (2.268A_{320} - 1.075A_{290}) \times 10^{-2}, \quad (7)$$

where A_{290} and A_{320} is the absorption by the solutions at, respectively, 290 and 320 nm.

The results obtained in determining spectrometrically various active chlorine species are presented in Tables 1 and 2 for various ET modes in comparison with the data furnished by iodometric titration.

For the cathode fraction the results yielded by the two methods coincide, which is due to the presence in the catholyte of the only active chlorine species, namely, hypochlorite ion penetrating into the catholyte by electromigration. For the anolyte the spectrophotometric method gives somewhat underestimated

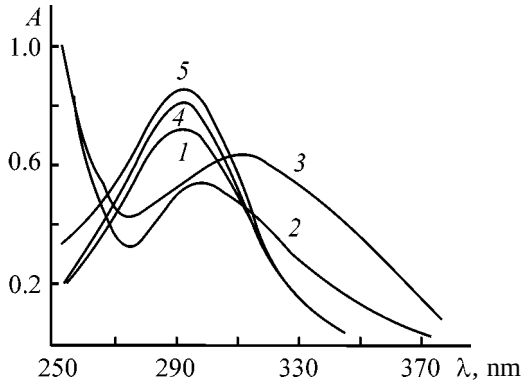

Absorption spectra: (*A*) optical density and (λ) wavelength. Chlorine water (C = 1.138 M): (*1*) pH 11.65, l = 0.2 cm; (*2*) pH 2.18, l = 2.0 cm; 0.137 M NaCl solution subjected to ET (i = 3 A dm^{-2}, v = 10 l h^{-1}, flow-through electrolyzer); (*3*) anolyte, pH 2.5, l = 5.0 cm; (*4*) anolyte, pH 11.0, l = 1.0 cm; and (*5*) catholyte, pH 11.3, l = 5 cm.

Table 2. Determination of active chlorine in the catholyte by iodometric titration and spectrophotometry

j, A dm^{-2}	Content of active chlorine $C \times 10^3$, M	
	IM	SP
1	0.200	0.183
2	0.300	0.801
3	0.404	0.418
4	0.605	0.643
5	4.29	4.31

Table 3. Theoretically calculated amounts of various active chlorine species accumulated in electrolysis of a 0.137 M NaCl solution in a flow-through cell (α = 100%)

j, A dm^{-2}	Total content of active chlorine $C \times 10^3$, M	Fraction of indicated component, %		
		Cl_2(aq)	HClO	Cl_3^-
1	2.742	19.1	80.5	0.5
2	5.498	31.8	67.4	0.8
3	8.228	46.0	58.0	1.0
4	10.97	47.9	50.9	1.2
5	13.72	53.3	45.5	1.3
6	16.46	57.5	41.1	1.4
7	19.2	61.1	37.5	1.5
8	21.94	64.0	34.5	1.5
9	24.68	66.5	31.9	1.6
10	27.43	68.6	29.7	1.7
11	41.15	75.9	22.3	1.8

values as compared with the iodometric titration data, which is probably due to the departure of the reaction from the 100% efficiency by chlorine. Actually, the efficiency by chlorine may be lower, especially in the initial stages of electrolysis, when the probability of the competing reaction of oxygen evolution grows at high pH values.

Approximate theoretical calculations of the accumulation of various active chlorine species were performed for α of 100, 80, and 60%. It was assumed in the calculations that HClO is not involved in migration processes owing to its being electroneutral, and the contributions of ClO^- and Cl_3^- to migration are negligible because of their low concentration, compared with the concentrations of Na^+, H_3O^+, and Cl^- ions. As a simplifying assumption, it was taken that only Cl^- and Na^+ ions are transferred across the membrane, whereas H^+ and OH^- ions formed at the electrode surface have not enough time to reach the diaphragm. The presented equations are of semiquantitative nature; however, to a first approximation, too, it is possible to obtain the predominant forms of active chlorine accumulation in solution. The calculated data presented in Table 3 indicate that active chlorine is mainly present in solution in the hydrated form and as hypochlorous acid molecules. The share of trichloride ions in the total active chlorine is not more than 2%, and that of hypochlorite ions is negligibly small. HClO predominates in the initial stages of electrolysis, but at current densities exceeding 5 A dm^{-2} the content of hypochlorous acid decreases and most of active chlorine is present in the form of hydrated molecular chlorine.

Hydrolysis of molecular chlorine proceeds, upon shifting the equilibrium, to give hypochlorous and hydrochloric acids. In addition, hydrochloric acid is also formed if the chlorine electrolysis proceeds with less than 100% efficiency. Since the dissociation constants of these two acids are markedly different, hypochlorous acid can be titrated separately and the content of active chlorine can be determined from the results of titration.

The content of HCl and HClO was calculated from the titration curves of sodium chloride solutions electrochemically treated in various modes. The titration curves show two jumps both for chlorine water solutions and for electrochemically treated sodium chloride solutions, with $V_1 = V_2$ for the former and $V_1 > V_2$ for the latter (V_1 and V_2 are the titrant volumes spent for titration to, respectively, the first and second equivalence points). The obtained results are presented in comparison with iodometric titration data in Table 4.

Thus, comparison of the results of spectrophotometric, potentiometric, and iodometric data on active chlorine shows their satisfactory agreement. However, iodometric titration gives 5–20% higher content of active chlorine, compared with the other two methods. The higher concentration of hydrochloric acid, compared with the maximum possible concentration in hydrolysis of hydrated chlorine, indicates that oxidation of water to give oxygen occurs in electrolysis in addition to the oxidation of chloride ions, which is in agreement with practical data [2].

EXPERIMENTAL

Electrochemical treatment was applied to 0.137 M solutions of analytically pure sodium chloride in distilled water. The electrochemical flow-through cell comprised two planar-parallel ORTA electrodes separated by a canvas dam.

Table 4. Results of iodometric and potentiometric (PM) determination of active chlorine in the anode chamber of a flow-through electrolyzer

j, A dm^{-2}	Content of acid $C \times 10^3$, M			Content of active chlorine $C \times 10^3$, M (IM)
	HCl	HClO	active chlorine	
1	1.34	0.89	1.78	1.70
2	2.05	1.79	3.58	3.80
3	3.25	2.90	5.80	5.90
4	4.68	4.29	8.58	9.56
5	5.69	5.14	10.28	12.08

The ET process was performed in a galvanostatic configuration in the dynamic mode, i.e., the liquid flow moved along the electrodes without mixing with subsequent portions of the liquid.

The iodometric determination of active chlorine was done by the procedure described in [7]. The spectrophotometric measurements were performed on an M-40 instrument. Standard solutions of chlorine water were prepared by passing chlorine gas through distilled water. Chlorine was generated by oxidizing hydrochloric acid with potassium permanganate [8]. The potentiometric titration was done with a pH-673M pH meter, using glass and silver chloride electrodes.

REFERENCES

1. *Spravochnik po elektrokhimii* (Handbook of Electrochemistry), Sukhotin, A.M., Ed., Leningrad: Khimiya, 1991.
2. Dobos, D., *Electrochemical Data*, Budapest: Akad. Kiado, 1978.
3. Eigen, M. and Kustin, K., *J. Am. Chem. Soc*., 1962, vol. 84, no. 8, pp. 1355–1361.
4. Yakimenko, L.M., *Proizvodstvo khlora, kausticheskoi sody i neorganicheskikh khlorproduktov* (Manufacture of Chlorine, Caustic Soda, and Inorganic Chlorine Products), Moscow: Khimiya, 1974.
5. Cotton, F.A. and Wilkinson, G., *Advanced Inorganic Chemistry*, New York: Interscience, 1966.
6. Connick, R.E. and Chia, X.T., *J. Am. Chem. Soc*., 1959, vol. 81, no. 6, pp. 1280–1284.
7. Williams, W.J., *Handbook of Anion Determination*, London: Butterworths, 1979.
8. Karyakin, Yu.V. and Angelov, I.N., *Chistye khimicheskie veshchestva* (Pure Chemical Substances), Moscow: Khimiya, 1974.

Russian Journal of Applied Chemistry, Vol. 74, No. 5, 2001, pp. 746–749. Translated from Zhurnal Prikladnoi Khimii, Vol. 74, No. 5, 2001, pp. 725–728.

APPLIED ELECTROCHEMISTRY AND CORROSION PROTECTION OF METALS

Oxidation of Alcohol–Ammonia Mixtures in High-Temperature Fuel Cell with Various Electrodes

N. M. Gamanovich, V. A. Gorbunova, and G. I. Novikov

Belarussian State Technological University, Minsk, Belarus

Received July 26, 2000; in final form, February 2001

Abstract—A high-temperature fuel cell with zirconium oxide electrolyte and various electrode materials, efficiently operating at 1070–1170 K on alcohol–ammonia fuel and air as oxidizing agent, was studied.

The development and practical use of fuel cells (FCs) and, in particular, high-temperature fuel cells (HTFCs) based on a ZrO_2–Y_2O_3 (YSZ) solid electrolyte and operating at 1070–1370 K for direct generation, with high conversion efficiency, of electric power from fuels have been a topical scientific and technological problem for more than a decade [1–3]. Here, mention should be made of the increasing interest (especially in such industrially developed countries as the United States, Japan, Germany, etc.) in use of FCs and HTFCs for obtaining "environmentally clean" electric power [3–6]. For example, a large research center dealing with FC problems has been organized recently in Germany and R&D work in this direction has been commenced, aimed at putting into industrial practice FCs with fuel conversion efficiency of up to 55% [7].

HTFCs based on solid oxide electrolytes and operating on vaporous fuels can be improved by optimizing both the cell design and the composition of the electrolyte and electrode layers and current leads. This could yield in the future an HTFC with power density of 1.5–2.0 W cm^{-2} in dc current generation [8]. A nearly as high power density (0.3–0.8 W cm^{-2} at cell voltage of 1.0–1.2 V) has already been achieved in recent years in HTFCs of planar and tubular design and units on their base with power in the range 1–100 kW, operating on H_2, CH_4, and diesel fuels [5, 8–10].

Recent investigations have been aimed to search for efficient fuels for HTFCs, and one of those found was a fuel based on alcohol–ammonia mixtures. A rather detailed thermodynamic analysis of the electrochemical oxidation of these mixtures in HTFCs was made in [1].

In addition, industrial use of HTFCs requires that noble metals in their electrodes should be replaced by lower-cost materials. By now, a number of materials of different kinds (for cathode and anode) have been developed for HTFCs. These are mainly alkaline-earth- (in position A) and transition-metal-doped (in position B) manganites, chromites, and cobaltites of rare-earth elements of the type ABO_3 [3] and metal–ceramic (cermet) anode materials (of the type of nickel–YSZ composites) [2, 12].

EXPERIMENTAL

The basic element of the employed HTFC is an electrochemical cell based on a solid oxide electrolyte of composition $0.9ZrO_2 + 0.1Y_2O_3$ (YSZ). The electrolyte for these cells was fabricated on a specially designed laboratory installation by hot die slip casting [1, 4]. The cells have tubular shape and the following dimensions (mm): diameter 10.0, working (central) part length 10.0, and wall thickness in the working area 0.35–0.40. The thus obtained electrolyte cells were degreased in C_2H_5OH and the cathode and anode layers were deposited onto them.

Various kinds of electrodes were used in the study: metallic (Pt), metal–ceramic (nickel-based), and ceramic (based on rare-earth manganites). To obtain stable layers close to the YSZ electrolyte in the thermal expansion coefficient, 10–35 wt % YSZ powder was introduced in the electrode paste composed of the above materials. Experiments with Pt electrodes were only carried out to obtain comparative characteristics of HTFCs. The main part of the study was done with lower-cost and more efficient electrodes: anodes based on the Ni–YSZ cermet and ceramic cathodes.

To perform electrochemical oxidation of the alcohol–ammonia mixture, an HTFC with a cermet

1070-4272/01/7405-0746$25.00

anode and a cathode made of an $La_{0.4}Ln_{0.4}Ca_{0.2}Mn_{0.94}Cr_{0.04}Ni_{0.02}O_3$ manganite (where Ln is a mixture of cerium-group rare-earth elements) doped in positions A and B was fabricated. This composition is sufficiently economical (having lower cost as compared with chemically purified compounds of lanthanum or other individual rare earths), being prepared from a mixture obtained industrially as half-product in hydrometallurgical processing of rare-earth-containing ores of the bastnaesite type [13, 14]. It is known that the electrochemical activity of electrodes can be substantially raised by introducing into their composition oxides with mixed-type conduction (oxygen-ion and electronic), such as CeO_2, V_2O_5, PrO_{2-x}, or Bi_2O_3 [1]. Commonly, oxides of this kind are introduced already in the stage of electrode layer formation on the electrolyte [4]. In this study, cathode materials were synthesized from manganites of a mixture of cerium-group rare earths, with increased (due to Pr and Ce ions) oxygen-ion conductivity [13].

Cathode material powders were synthesized by isothermal decomposition (at 1170–1270 K) of a mixture of nitrate salts prepared with the use of an industrial hydrometallurgical half-product: nitrate solution with rare-earth concentration of 300 g l^{-1} (in terms of total rare-earth oxides) and 30 g l^{-1} of free HNO_3 [14]. The specific consumption of the cathode material deposited onto the electrolyte cell was 12.0 mg cm^{-2}, with the material being a composite and containing 10.0 wt % YSZ powder.

The anode (fuel electrode) of the HTFC was made of an Ni–YSZ nickel zirconium cermet obtained by various methods. The specific consumption of the anode material was about 10.0 mg cm^{-2}.

Finely dispersed Raney nickel (70 wt %) and YSZ dross (30 wt %) were mechanically mixed, and the electrode paste was formed on the basis of this mixture (using 10% solution of rosin in C_2H_5OH). The paste was fired-in in a flow of technical-grade helium at 1550 K in the course of 2.5 h. After depositing the anode, the cathode layer was fired-in at 1420–1470 K in air for 2.5 h, which resulted simultaneously in oxidation of the anode layer of nickel to NiO_x oxide.

The cermet working electrode was formed through reduction of the nickel oxide phase in the NiO_x–YSZ layer by high-temperature alcohol–ammonia mixture in the course of operation of the electrochemical HTFC. The process of Ni reduction from NiO_x creates pores, necessary for the operation of HTFC, in the anode material, and the sufficiently uniform distribution of disperse YSZ particles in the anode cermet hinders collective crystallization of nickel particles in sintering, thereby ensuring prolonged electrochemical activity of the fuel electrode [12].

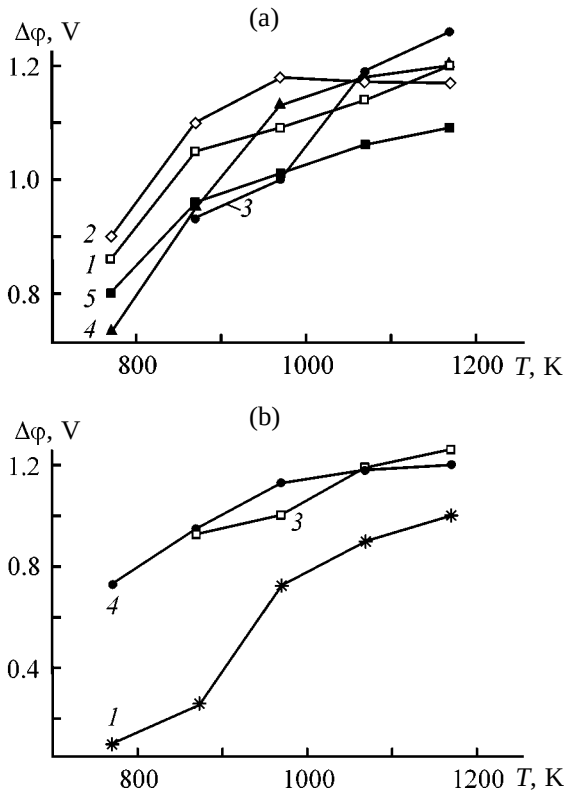

Fig. 1. Potential difference Δφ for an HTFC operating on alcohol–ammonia mixture, alcohol, and ammonia vs. temperature *T*. Digits at curves (a) *1*–*5* and (b) *3*, *4* denote the numbers of HTFC fuels in the table. (b) (*3*, *4*) HTFC with non-platinum electrodes; (*1*) alcohol–ammonia mixture in HTFC with Pt electrodes [11].

As current lead was used platinum wire 0.5 mm thick. As oxidizing agent in the HTFC served atmospheric oxygen supplied into the cathode space (at a pressure of 10^5 Pa).

Figures 1a and 1b show the obtained temperature dependences of the HTFC parameters. Previously [11], the current–voltage characteristics of electrochemical oxidation of an alcohol–ammonia mixture in HTFC on platinum electrodes (Fig. 1b, curve *1*) have been obtained. The maximum potential differences, voltages, and currents in HTFCs with platinum electrodes in oxidation of an alcohol–ammonia mixture are the following: Δφ = 1.0 V, V = 0.9 V, I = 0.85 mA (with an external load resistance R = 1000 Ω).

Preliminarily, electrochemical oxidation of separate components of the mixture, ammonia and ethanol, was performed in an HTFC of this kind. Ammonia and alcohol vapors were obtained by heating a 25% aqueous solution of ammonia and 96% ethanol. After

Potential differences Δφ, voltages *V*, and currents *I* measured in an HTFC operating on alcohol–ammonia mixtures. Load resistance $R = 1000\ \Omega$

Fuel no.	*T*, K	Δφ, V	*V*, V	*I*, mA
		C_2H_5OH, carrier gas N_2		
1	770	0.86	0.67	0.70
	870	1.05	0.80	0.81
	970	1.09	0.82	0.86
	1070	1.14	0.87	0.90
	1170	1.20	0.92	0.96
		NH_3		
2	770	0.90	0.70	0.75
	870	1.10	0.84	0.90
	970	1.18	0.90	0.95
	1070	1.17	0.90	0.95
	1170	1.17	0.84	0.90
		$NH_3 + C_2H_5OH$*		
3	870	0.93	0.70	0.75
	970	1.00	0.84	0.85
	1070	1.19	0.91	0.95
	1170	1.26	0.97	1.00
4	770	0.73	0.54	0.60
	870	0.95	0.72	0.76
	970	1.13	0.86	0.90
	1070	1.18	0.90	0.94
	1170	1.20	0.91	0.95
5	770	0.80	0.59	0.64
	870	0.96	0.73	0.76
	970	1.01	0.78	0.82
	1070	1.06	0.81	0.85
	1170	1.09	0.83	0.88

* Method of fuel preparation: passing NH_3 over the surface of alcohol heated to 300 (fuel no. 3) and 315 K (no. 4); bubbling of NH_3 vapor through alcohol at 293 K (no. 5).

drying (to remove water vapor), the vapors of the alcohol and ammonia were delivered into the anode space of the HTFC. The obtained potential differences, voltages, and currents are presented in the table. It can be seen that the parameters of HTFCs operating on, separately, ammonia and alcohol are rather close.

The alcohol–ammonia mixture used for electrochemical oxidation was prepared by methods providing different concentrations of the components in the working fuel mixture (see table). As oxidizing agent served atmospheric oxygen under ambient pressure. The potential differences, voltages, and currents measured in oxidation of the alcohol–ammonia mixtures are also given in the table. It is noteworthy that the *I* value recorded in a practically important case of HTFC operation in a circuit with an external resistance $R < 1000\ \Omega$ (in a short-circuited mode, in the limiting case) is as high as 0.3 A, which corresponds to a current density $i = 0.1\ \text{A cm}^{-2}$.

As seen from the table and Fig. 1a, the HTFC parameters depend on how an alcohol–ammonia mixture is prepared. The fluctuations of these parameters (potential difference, voltage, and current) are probably due to variations in the alcohol concentration in the mixture.

Analysis of the influence exerted by the HTFC electrode materials on the efficiency of electrochemical oxidation of the alcohol–ammonia mixture (Fig. 1b) suggests that the nickel–cermet anode and manganite cathode have higher activity (yielding $\Delta\varphi = 1.26$ V, $V = 0.97$ V, $I = 1.0$ mA) as compared with HTFCs having platinum electrodes [11]. This may be associated both with an increase in the polarization of the platinum electrode as a result of its surface oxidation to PtO_x and with sintering of platinum grains in the course of HTFC operation, making lower the electrode porosity [1, 3].

CONCLUSIONS

(1) The electrochemical characteristics of a tubular high-temperature fuel cell operating on alcohol–ammonia mixtures with air as oxidizing agent were determined experimentally. It is established that the method by which the alcohol–ammonia mixture is prepared affects the electrochemical parameters of the cell.

(2) The optimal values of the parameters of a high-temperature fuel cell: potential difference $\Delta\varphi = 1.26$ V, voltage $V = 0.97$ V, and current $I = 1.0$ mA (under load $R = 1.0\ \text{k}\Omega$) were obtained for a mixture prepared by passing NH_3 vapor over the surface of ethanol heated to 300 K. The best characteristics of the high-temperature fuel cell operating on this fuel were obtained with an Ni–YSZ cermet anode and a cathode made of a new material, $La_{0.4}Ln_{0.4}Ca_{0.2} \cdot Mn_{0.94}Cr_{0.04}Ni_{0.02}O_3$ (where Ln is a mixture of cerium-group rare earths introduced in the form of an industrial hydrometallurgical half-product), synthesized at 1070–1170 K.

ACKNOWLEDGMENTS

The study was supported by the Foundation for Basic Research of the Republic of Belarus (grant no. Kh98-006).

REFERENCES

1. *Vysokotemperaturnyi elektroliz gazov* (High-Temperature Electrolysis of Gases), Perfil'ev, M.V., Ed., Moscow: Nauka, 1988.
2. Murygin, I.V., *Elektrodnye protsessy v tverdykh elektrolitakh* (Electrode Processes in Solid Electrolytes), Moscow: Nauka, 1991.
3. Pal'guev, S.F., Gil'derman, V.K., and Zemtsov, V.I., *Vysokotemperaturnye oksidnye elektronnye provodniki dlya elektrokhimicheskikh ustroistv* (High-Temperature Electronic Oxide Conductors for Electrochemical Devices), Moscow: Nauka, 1990.
4. Gamanovich, N.M. and Novikov, G.I., *Vestsi Akad. Navuk Belarusi, Ser. Khim. Navuk*, 1995, no. 4, pp. 5–7.
5. Hamnett, A., *Phil. Trans. Roy. Soc. London, Ser. A*, 1996, vol. 354, no. 1712, pp. 1653–1669.
6. Avakov, V.B., *Ross. Khim. Zh.*, 1994, vol. 38, no. 3, pp. 15–20.
7. Naumovich, E.N., Kharton, V.V., and Vecher, A.A., in *Khimicheskie problemy sozdaniya novykh materialov i tekhnologii: Sbornik statei NII fiziko-khimicheskikh problem Belarusskogo Gos. Univ.* (Chemical Problems in Development of New Materials and Technologies: Coll. of Works of Research Inst. of Physicochemical Problems, Belarussian State Univ.), Minsk: Belorus. Gos. Univ., 1998, pp. 431–450.
8. Veziroglu, T.N., *Proc. 13th World Hydrogen Energy Conf.*, June 12–15, 2000, Beijing (China), 2000, vol. 1, pp. 3–19.
9. Korovin, N.V., *Elektrokhimicheskaya energetika* (Electrochemical Power Engineering), Moscow: Energoatomizdat, 1991.
10. Henne, R.H., Lang, M., Muller, M., *et al*., *Ann. New York Acad. Sci*., 1999, vol. 891, pp. 124–136.
11. Novikov, G.I. and Gamanovich, N.M., *Zh. Prikl. Khim*., 1998, vol. 71, no. 11, pp. 1911–1912.
12. Fukui, T., Ohara, S., and Mukai, K., *Electrochem. Solid-State Lett.*, 1998, vol. 1, no. 3, pp. 120–122.
13. Mori, M., *Proc. 2nd Int. Fuel Cell Conf*., February 5–8, 1996, Tokyo, 1996, pp. 10–12.
14. Gorbunov, A.V., Plasmochemical Treatment of Solutions of Group II–III Metal Nitrates in Electric Arc Reactor, *Cand. Sci. Dissertation*, Minsk, 1998.

Russian Journal of Applied Chemistry, Vol. 74, No. 5, 2001, pp. 750–754. Translated from Zhurnal Prikladnoi Khimii, Vol. 74, No. 5, 2001, pp. 728–732.

APPLIED ELECTROCHEMISTRY AND CORROSION PROTECTION OF METALS

Electrocatalytic Determination of Oxalate Ions on Chemically Modified Electrodes

L. G. Shaidarova, S. A. Zaripova, L. N. Tikhonova, G. K. Budnikov, and I. M. Fitsev

Kazan State University, Kazan, Tatarstan, Russia

Received May 18, 2000; in final form, December 2000

Abstract—The electrocatalytic activity with respect to oxalate ions of spongy osmium immobilized within a carbon-paste electrode was studied. A procedure is proposed for electrocatalytic determination of oxalate ions on a chemically modified electrode based on spongy osmium under conditions of flow-through–injection analysis.

The necessity for analytical monitoring of oxalate ions is due to the biological importance of these compounds. For example, oxalic acid and its salts play an important part in the human body [1–3], quite a number of diseases being associated with disruption of the oxalate exchange. Therefore, it is advisable to use simple, proximate, and accurate analytical techniques in clinical diagnostics.

Analytical laboratories more frequently employ classical methods of analysis, gravimetry and titrimetry, for determining oxalate ions, with potentiometric titration with ion-selective or glass electrodes [4] occasionally used among electrochemical methods. Voltammetric techniques have not found use for this purpose. This is due to the fact that anions, including oxalates, are oxidized or reduced on indicator electrodes with a high overvoltage. However, as reported in [5], the overvoltage effects can be diminished by means of the so-called redox mediators. That is why interest has been aroused recently in electrochemical analytical techniques based on the use of chemically modified electrodes (CMEs) possessing electrocatalytic properties [6–8]. These electrodes are already being used successfully for electrochemical detection of a wide variety of compounds, such as oxygen, hydrogen peroxide, anions, alcohols, aldehydes, carbohydrates, amino acids, etc., including application in flow-through analysis systems [9].

A search for new redox mediators for CME and their use in flow-through–injection analysis (FIA) of biologically important compounds for the purpose of introducing automation and improving the efficiency of determination is a currently pressing problem.

The present study is concerned with the possibility of electrocatalytic determination of oxalic acid and oxalate ions, using carbon-paste electrodes (CPE) modified with spongy osmium under FIA conditions.

Carboxylic acids and their salts are oxidized at graphite electrodes with high overvoltage [10]. When using a CME based on a redox mediator, the overvoltage can be made lower. It was found that CPE modified with spongy osmium exhibits electrocatalytic activity toward oxalic acid. To elucidate the electrocatalysis mechanism, electrooxidation of the modifier and substrate on the CPE and CME was studied.

Oxalic acid is oxidized at CPE at $E > 1.2$ V (Fig. 1, curve *1*). The anodic voltammogram of the supporting electrolyte, recorded with CME in the absence of sub-

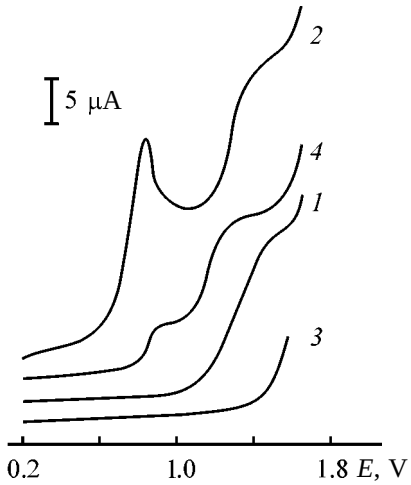

Fig. 1. Voltammograms of oxalic acid oxidation at (*1*) CPE and (*2*) osmium-based CME with borate buffer solution with pH 9.0 as supporting electrolyte. Concentration of oxalic acid 1×10^{-3} M; the same for Fig. 2. (*E*) Potential. Background curve: (*3*) at CPE and (*4*) at CME.

1070-4272/01/7405-0750$25.00

strate in the potential range E = 0.0–1.5 V, shows two waves (Fig. 1, curve *4*). According to published data [4], electron transfer occurs at first-wave potentials ($E \approx 0.8$ V) to give metal oxide, probably OsO_2, oxidizing at second-wave potentials. On adding substrate to the solution, the first electrochemical signal grows in intensity, being now recorded in the form of a peak (Fig. 1, curve *2*). The peak current depends on the substrate concentration. In performing electrolysis in a solution containing oxalate ions, bubbles of a gas, probably CO_2, accumulate on the electrode surface at $E \approx 0.8$ V. No gas evolution at CME in a supporting electrolyte solution was observed in this range of potentials. Similar results were obtained with sodium oxalate as substrate. This circumstance indicates that oxalate ions are oxidized at $E \approx 0.8$ V, i.e., at potentials of modifier oxidation, at CMEs based on spongy osmium. It was found in studying the dependence of the peak current i_p on the potential sweep rate v that the rate coefficient of the electrode process, $\Delta \log i / \Delta \log v$, is 0.27 for CME, which indicates that the process is complicated by a chemical reaction, i.e., electrooxidation of oxalate ions at CME proceeds by the EC mechanism including a preceding electrochemical stage and the subsequent chemical reaction. In the first stage, there occurs electrooxidation of the modifier to form osmium oxides oxidizing the substrate. A similar electrocatalytic behavior of osmium has been also observed in oxidation of other organic molecules [11]. The scheme of the electrode process can be represented as [11]

$$[OsO_x \cdot nH_2O] - e + OH^- \rightleftarrows [OsO_xOH \cdot nH_2O],$$

$$[OsO_xOH \cdot nH_2O] + 1/2C_2O_4^{2-} \rightarrow [OsO_x \cdot nH_2O] + CO_2 + OH^-.$$

Thus, spongy osmium immobilized within CPE exhibits electrocatalytic activity toward oxalic acid and its salts. The catalytic effect consists in that the overvoltage is lowered by 0.5 V. In addition, a significant excess of the anodic current over the modifier oxidation current recorded in the absence of substrate is observed in oxidation of oxalate ions at CME. In the system in question, catalysis occurs with respect to both current and potential.

The influence exerted by the solution pH and nature of supporting electrolyte on the current–voltage characteristics of the first wave of modifier oxidation (anodic current and peak position along the potential axis) was studied with and without the substrate. As seen from Fig. 2a, the peak potential decreases with

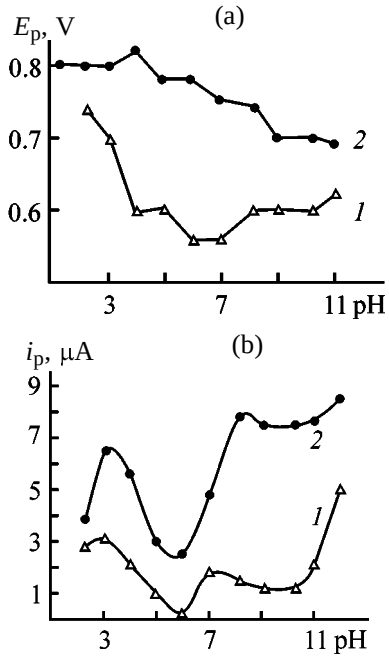

Fig. 2. (a) Peak potential E_p and (b) peak current of modifier oxidation i_p vs. pH value (*1*) without and (*2*) with oxalic acid, with 0.1 M Na_2SO_4 solution as supporting electrolyte and pH adjustment with H_2SO_4 or NaOH.

increasing pH in the range 2–5 and increases at pH from 6 to 12 (Fig. 2a, curve *1*). Presumably, this is due to changes in the position of the acid–base equilibrium between the members of the redox couple. The peak potential of electrocatalytic oxidation of oxalic acid at the modified electrode steadily shifts to less positive potentials (Fig. 2a, curve *2*). This can be attributed to the dependence of mole fractions α of the protonated and deprotonated oxalic acid species on pH [12]: $\alpha_{C_2O_4^{2-}}$ grows with increasing pH, which shifts the potential to less positive values.

The rise in the anodic current in the alkaline medium both with and without substrate (Fig. 2b) is due to the increasing number of catalytically active species on the electrode surface.

The pH value is chosen with the aim of achieving the maximum decrease in the overvoltage of substrate oxidation, on the one hand, and recording the highest catalytic current, on the other. These conditions are met by using high pH values. However, the reproducibility of the catalytic signal is impaired at pH > 11. Therefore, supporting electrolytes with pH ~ 9.0 were used. The following buffer solutions were chosen to maintain stable pH: phosphate, ammonia, and borate. In determining oxalate ions the best metrological characteristics were obtained with borate buffer solution with pH 9.0 as supporting electrolyte.

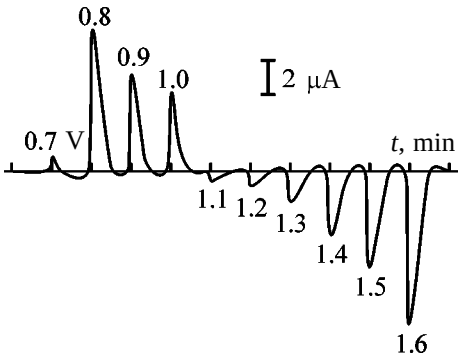

Fig. 3. FIA signal obtained in electrocatalytic oxidation of oxalic acid at an osmium-based CME at different applied potentials E with borate buffer solution with pH 9.0 as supporting electrolyte. (t) Time.

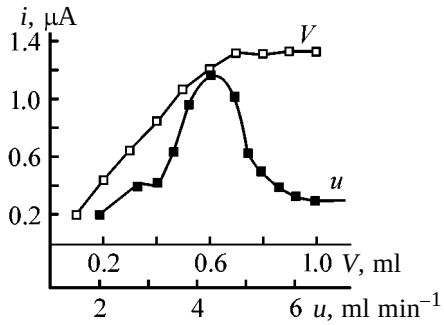

Fig. 4. FIA signal of electrocatalytic oxidation of oxalic acid at osmium-based CME vs. flow rate u and injected sample volume V with borate buffer solution with pH 9.0 as supporting electrolyte. (i) Peak current.

The osmium-based chemically modified electrode can be used for detecting electrochemically oxalate ions in flow-through analysis. In performing FIA, the electrocatalytic signal was recorded in the potentiostatic mode, and, therefore, the dependence of the peak current on the applied potential was studied.

The specific feature of how the FIA signal depends on the discretely applied potential (Fig. 3) is the change in the direction of the recorded peak with the potential shifted to the anodic region, which is due to a change in the charge of the electrophilic species. In order to find out whether this is due to a change in the form of mediator or substrate, a similar dependence was studied on an electrode modified with a complex of cobalt(II) with phthalocyanine. There is published evidence of the use of this redox mediator for amperometric detection of hydroxy acids [13]. In electrooxidation of oxalic acid at such an electrode in the potentiostatic mode, no change in the recording direction was observed with increasing potential. Consequently, the direction of recording of the FIA signal for the osmium-based CME is in all probability affected by a change of the existing modifier species, caused by alteration of the level of its oxidation on applying a more positive potential. Further studies are necessary for this process to be described in more detail.

As shown in Fig. 3, the FIA signal grows at potentials of up to 0.8 V, which confirms the assumption that modifier species formed at first-wave potentials are involved in electrocatalysis. In further studies, the FIA signal was recorded at E = 0.8 V, when the maximum analytical signal is observed.

In studying how the electrocatalytic response of CME in flow-through systems depends on hydrodynamic parameters, it was found that the maximum signal is observed at a flow rate u = 4.3 ml min^{-1} and injected sample volume V = 0.7 ml (Fig. 4).

Thus, the optimal conditions of FIA are as follows: E = 0.80 V, u = 4.3 ml min^{-1}, and V = 0.7 ml. Under these conditions, an FIA capacity of 60 samples per hour can be achieved.

The dependence of the FIA signal intensity on the substrate concentration is linear in the range 0.05–350 μmol, being described by the following equation (i, μA; c, μmol)

$$i = (5.8 \pm 0.7) \times 10^{-2} + (5.6 \pm 0.4) \times 10^{-3} c,\ r = 0.9991.$$

The detection limit calculated using the 3s criterion [14] is 10 nmol.

In evaluating the metrological parameters of the proposed method, it is necessary to consider the precision of analysis. The difficulties encountered in determining oxalate ions with solid electrodes under stationary conditions are due to the formation of carbon dioxide in electrooxidation of these anions. Gas bubbles screen the surface of the indicator electrode. Therefore, to obtain reproducible results, it is necessary to continuously clean the electrode surface. In a flow-through system, all the forming bubbles are carried away by a fluid flow; in addition, the electrode surface itself is renewed in the carrier flow. As a result, the signal reproducibility remains practically unchanged in a prolonged use of an indicator electrode without cleaning in a flow-through cell. The calculated S_r value does not exceed 5% within the working concentration range (Table 1).

The adequacy of the procedure was assessed by comparing the results of a flow-through–injection analysis for oxalic acid of artificial mixtures with data of potentiometric titration with a glass electrode. A statistical analysis of the obtained results by means of

t and *F* tests [14] demonstrated (Table 2) that there is no systematic error in determination of oxalate ions. The chosen methods are equally accurate in the range of concentrations to be determined ($F_{calc} < F_{tab}$), with the discrepancies between means being insignificant ($t_{calc} < t_{tab}$).

It was found that the determination is hindered by compounds exhibiting catalytic activity in the region of potentials under consideration and by those involved in the reaction of heterogeneous catalysis on osmium-based CME.

Thus, osmium-based CME can be used as electrochemical sensor for amperometric detection of oxalate ions in FIA.

The proposed technique can be used for determining oxalate ions in biological fluids, including the case of enzyme analysis.

EXPERIMENTAL

The dc voltammograms were recorded on a PU-1 polarograph with a three-electrode cell. CPE and CME served as indicator electrodes, silver chloride electrode was used as reference, and platinum wire, as anode. The carbon-paste electrode was prepared by mixing activated carbon and paraffin, taken in 6 : 4 ratio. In fabricating CME, a modifier (spongy osmium) was introduced into the carbon paste in amount of 2–5 wt %. After thorough mixing, the mixture of the components was placed in a glass tube 2.6 mm in diameter. The electrode surface was renewed mechanically with the use of abrasives and filter paper.

FIA was made using a setup including a peristaltic pump, injector, flow-through electrochemical cell, and recording device. The solutions used were supplied and discharged through flowing pipes made of silicone tubes with inner diameter of 2.0 mm. The injection was done with a microsyringe through the sealing membrane. A schematic of the flow-through membrane is presented in Fig. 5.

Electrical conductivity was imparted to the solutions with the use of a 0.5 M aqueous solution of Na_2SO_4 with NaOH or H_2SO_4, added to adjust the pH value, and also borate, ammonia, or phosphate buffer solutions. The pH value was monitored using a pH-150 pH meter. Solutions of oxalic acid and sodium oxalate were prepared by dissolving accurately weighed portions of chemically pure geade reagents in distilled water. Solutions with lower concentrations were obtained by successive dilution of the starting solutions.

Table 1. Results of analysis for oxalic acid and sodium oxalate on osmium-based CME (n = 7, P = 0.95)

Substrate	Substrate content, μmol		S_r
	introduced	found ($x \pm \Delta x$)	
Oxalic acid	0.5	0.47 ± 0.02	0.05
	5.0	4.8 ± 0.2	0.04
	10.0	10.0 ± 0.3	0.03
	100.0	99 ± 1	0.01
Sodium oxalate	1.0	0.95 ± 0.05	0.05
	5.0	4.9 ± 0.3	0.05
	10.0	10.2 ± 0.4	0.04
	100.0	101 ± 1	0.01

Table 2. Results of analysis for oxalic acid by voltammetry with osmium-based CME (method I) and by potentiometric titration (method II) (N = 6, P = 0.95, t_{tab} = 2.57, F_{tab} = 5.05)

$c \pm \delta$, g l^{-1}		F_{calc}	t_{calc}
method I	method II		
0.8 ± 0.1	1.0 ± 0.2	4.0	2.47
1.2 ± 0.2	1.4 ± 0.2	1.0	2.00
1.5 ± 0.3	1.7 ± 0.4	1.8	1.12

CONCLUSIONS

(1) The carbon-paste electrode modified with spongy osmium exhibits electrocatalytic activity toward oxalic acid and its salts. The substrates considered are oxidized at graphite electrodes, including the carbon-paste one, with high overvoltage at E > 1.2 V. For the electrode modified with spongy osmium, the overvoltage decreases by 0.5 V, and the anodic current much exceeds the current of oxidation

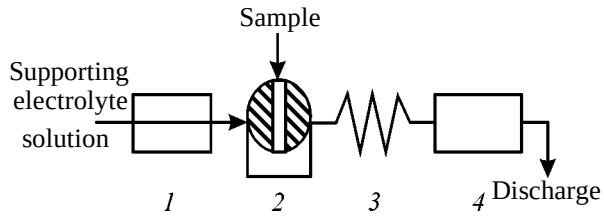

Fig. 5. Schematic of the flow-through–injection system: (*1*) peristaltic pump, (*2*) injector, (*3*) mixer, and (*4*) flow-through electrochemical cell.

of the modifier itself. The electrode process involves electrooxidation of the modifier, probably with the formation of osmium(IV) oxide oxidizing the substrate.

(2) Chemically modified electrode based on spongy osmium can be used for amperometric determination of oxalate ions in flow-through–injection analysis. The optimal conditions of analysis are as follows: E = 0.80 V, u = 4.3 ml min^{-1}, and V = 0.7 ml. The dependence of the analytical signal on the substrate concentration is linear in the range 0.05–350 μmol. The detection limit is 10 nmol. The signal reproducibility S_r = 0.034 (for c = 1 μmol, n = 10). The analysis capacity is 60 samples per hour.

ACKNOWLEDGMENTS

The study was supported by the Russian Foundation for Basic Research (project no. 00-03-32 389).

REFERENCES

1. Filippovich, Yu.B., *Osnovy biokhimii* (Foundations of Biochemistry), Moscow: Vysshaya Shkola, 1993.
2. *Metabolic Pathways*, Greenberg, D.M., Ed., New York: Academic, 1967.
3. *Rukovodstvo po klinicheskim laboratornym issledovaniyam* (Handbook of Clinical Laboratory Investigations), Smirnova, L.G. and Kost, E.A., Eds., Moscow: Medizdat, 1960.
4. Williams, W.J., *Handbook of Anion Determination*, London: Butterworths, 1979.
5. Budnikov, G.K., Maistrenko, V.N., and Murinov, Yu.I., *Vol'tamperometriya s modifitsirovannymi i ul'tramikroelektrodami* (Voltammetry with Modified Electrodes and Ultramicroelectrodes), Moscow: Nauka, 1994.
6. Labuda, J., *Selective Electrode Rev*., 1992, vol. 14, pp. 33–86.
7. Anderson, J.L., Bowden, E.F., and Pickup, P.G., *Anal. Chem.*, 1996, vol. 98, no. 12, pp. 379R–444R.
8. Kutner, W., Wang, J., Lher, M., and Buck, R.P., *Pure Appl. Chem*., 1998, vol. 70, no. 6, pp. 1302–1318.
9. Budnikov, G.K., *Zh. Anal. Khim*., 1996, vol. 51, no. 2, pp. 156–162.
10. *Organic Electrochemistry, An Introduction and a Guide*, Baizer, M.M. and Lund, H., Eds., New York: Marcel Dekker, 1983.
11. Petrii, O.A. and Kalinin, V.D., *Elektrokhimiya*, 1999, vol. 35, no. 6, pp. 699–707.
12. *Osnovy analiticheskoi khimii: Obshchie voprosy: Metody razdeleniya* (Fundamentals of Analytical Chemistry: General Problems: Separation Techniques), Zolotov, Yu.A., Moscow: Vysshaya Shkola, 1996.
13. Santos, L.M. and Baldwin, R.P., *Anal. Chem*., 1986, vol. 58, no. 4, pp. 848–852.
14. Charykov, A.K., *Matematicheskaya obrabotka rezul'tatov khimicheskogo analiza: Metody obnaruzheniya i otsenki oshibok* (Mathematical Processing of Chemical Analysis Data: Methods of Error Detection and Evaluation), Leningrad: Khimiya, 1984.

Russian Journal of Applied Chemistry, Vol. 74, No. 5, 2001, pp. 755–761. Translated from Zhurnal Prikladnoi Khimii, Vol. 74, No. 5, 2001, pp. 733–739.

APPLIED ELECTROCHEMISTRY AND CORROSION PROTECTION OF METALS

Plating of Iron–Nickel Alloy in the Presence of Triphenylmethane Derivatives and Azo Dyes

A. S. Milushkin

Kaliningrad State University, Kaliningrad, Russia

Received April 27, 2000; in final form, July 2000

Abstract—The inhibiting action of hydrogen absorption in the course of plating of iron–nickel alloy from a sulfate electrolyte in the presence of triphenylmethane derivatives and azo dyes was studied. An electrolyte suitable for plating of iron–nickel alloy on articles susceptible to hydrogen embrittlement was developed.

Iron–nickel alloys as electroplated coatings are used instead of nickel, which is in short supply, to protect articles against corrosion and impart protection-decorative properties [1–8]. With such coatings not only the performance characteristics are improved, but also the productivity of parts is increased along with their reliability and life [7]. The presence of additives complicates composition and requires frequent replacement of electrolyte. Probably, for this reason, plating of the alloy instead of pure nickel is not widely used yet [9].

In this work, the alloy of the composition 80% nickel and 20% iron was used. Triphenylmethane derivatives and azo dyes were additives. Their names and structural formulas are listed in Table 1.

Table 1. Triphenylmethane derivatives and azo dyes

Additive no.	Additive name	Molecular weight
1	Bromocresol green (tetrabromo-*m*-cresolsulfophthalein)	662
2	Eriochrome black	465
3	Methyl red (4'-*N*,*N*-dimethylaminoazobenzene-2-carboxylic acid)	269
4	Eriochrome blue SE (acid chrome dark blue, acid chrome blue T)	520
5	Fuchsin new, rosaniline (3,3'-dimethyl-*p*-triaminotriphenylcarbinol chloride)	365
6	Pararosaniline (tri-*p*-aminotriphenylcarbinol chloride)	323
7	Additive **5** + additive **2**	
8	Additive **5** + Progress ($C_nH_{2n+1}CH(CH_3)OSO_2Na$, n = 6–16)	

Structural formulas of the additives

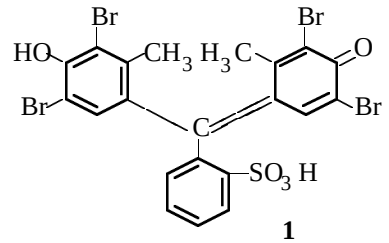

1

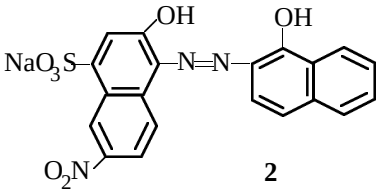

2

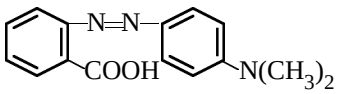

3

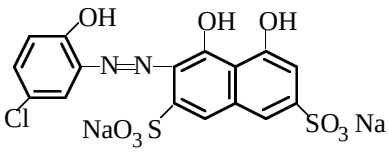

4

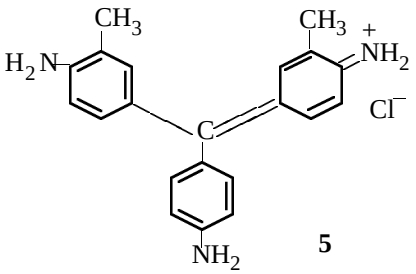

5

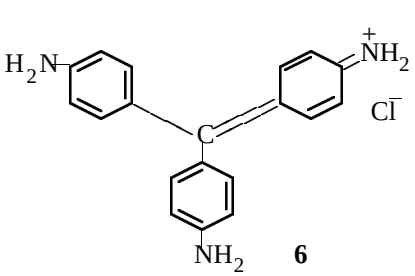

6

1070-4272/01/7405-0755$25.00

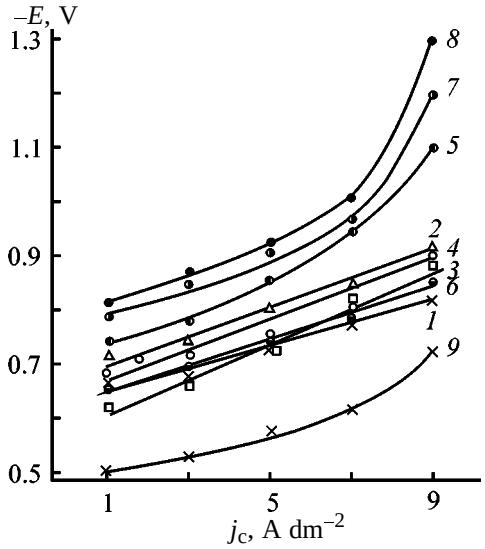

Fig. 1. Cathode potential E vs. current density j_c in the presence of triphenylmethane derivatives and azo dyes (C = 2 mM). The curve numbers are the same as the additive numbers in Table 1; (*9*) no additive; the same for Figs. 2 and 3.

The sulfate–chloride electrolyte in the presence of additives allows preparation of high-quality electroplated coatings with finely crystalline structure, provides good adhesion, and ensures the minimal hydrogen absorption by the steel support. Also, it allows preparation of corrosion-resistant decorative coatings with lustrous surface.

The iron–nickel alloy was plated from an electrolyte containing (g l^{-1}) $NiSO_4 \cdot 7H_2O$ 240, $NiCl_2 \cdot 6H_2O$ 38, $FeSO_4 \cdot 7H_2O$ 80, and H_3BO_3 40 under the following conditions: pH 1.8–2.0, j_c = 1.9–9 A dm^{-2}, 45–55°C, stirring with a magnetic stirrer. The electrolyte was treated for 4 h at the minimal current density. Solutions were prepared from chemically pure grade reagents. The hydrogen absorption was estimated on a U8–A spring wire (100 mm long and 1 mm in diameter) twisted on a K-5 unit. Before plating, the samples were polished with a micrometric abrasive cloth, degreased with lime, and washed with distilled water. This treatment removes the oxide surface layer and eliminates the hydrogen absorption in the course of the preparation of the sample surface.

The hydrogen absorption was performed during the electrolysis time of 12.5, 26, and 52 min and judged from the decrease in the plasticity of the twisted wire samples: $N = (a/a_0) \times 100\%$, where a and a_0 are the number of rotations before failure of the unplated and plated sample, respectively. The cathodic current efficiency (CE) was determined coulometrically.

The $40 \times 40 \times 2$ mm plates were used for studying the physicomechanical properties of the alloy. The iron–nickel alloy was coated to a 20 μm thickness. The silver chloride reference electrode was used. Polarization measurements were recorded on a multigraph. The luster γ was measured on an FB-5 luster meter vs. a uviol glass as reference (luster 65 arb. units). The nonworking side of the plate was protected with a BF-2 glue. The adhesion of the alloy to the support was tested by methods of intersecting scratches or twisting on a K-5 unit. The corrosion resistance of iron–nickel coatings was studied in a chamber filled with a salt fog [10]. The solution containing 30 g l^{-1} NaCl was spread every 15 min for 7 h. The spread time was 3 min. The corrosion protection was calculated by the formula:

$$Z = \frac{K_{corI} - K_{corII}}{K_{corI}} \times 100\%,$$

where K_{corI} and K_{corII} are the corrosion rates (g m^{-2} day^{-1}) for samples coated with the alloy with and without additives, respectively.

In the other conditions, the procedure was similar to that described previously [11].

Plating of iron–nickel alloy is accompanied by strong hydrogen absorption by the steel support, which is reflected as a 15–27% decrease in the plasticity at j_c from 1 to 9 A dm^{-2}. With the electrolysis time decreased to 52 min the further decrease in the plasticity to 65% was observed (Table 2, no inhibitor). The cathodic potential at j_c = 1 A dm^{-2} is –0.48 V, decreasing to a value of –0.72 V as the current is increased to 9 A dm^{-2} (Fig. 1, curve *9*). The deposits are finely crystalline, rough, partially cracked, with satisfactory adhesion to the support. Such deposits do not impede diffusion into the steel support. The surface is dull and semilustrous, with pitting and filament dendrites (Fig. 2, no additive, a luster of 38–20 arb. units). The current efficiency by the alloy is 71–65% (Fig. 3, curve *9*).

Introduction of triphenylmethane derivatives and azo dyes into a sulfate chloride electrolyte decreases considerably the hydrogen absorption by the steel support and enhances the performance characteristics of the iron–nickel alloy. However, the inhibiting and luster-producing action of all the additives is different (Table 2).

The inhibitors on the surface of a cathode metal are adsorbed electrostatically, specifically, and chemically [12]. The bond strength of molecules with a cathode surface is affected by the electron density on the atom

Table 2. Characteristics of the iron–nickel alloy in the presence of triphenylmethane derivatives and azo dyes

Inhibitor no.	j_c, A dm^{-2}	C, mM	Plasticity, %, in indicated time, min			CE, %	γ, arb. units	$-E$, V	Appearance and structure of coating
			12.5	26	52				
1	1	1	91	86	83	82	60	0.66	Finely crystalline, with strong internal stresses, good adhesion to the support, semilustrous and lustrous surface
	3		89	86	82	81	45	0.67	
	5		84	85	80	81	40	0.67	
	7		82	80	80	79	25	0.72	
	9		80	79	75	78	25	0.86	
	1	2	94	90	85	–	–	–	Dense, cracked from the edges with increasing current density
	3		91	90	84	–	–	–	
	5		89	87	83	–	–	–	
	7		85	87	80	–	–	–	
	9		83	83	80	–	–	–	
2	1	1	93	90	88	89	70	0.70	Finely crystalline, with good adhesion, slightly cracked from the edges with increasing current density, with lustrous surface
	3		91	89	87	91	68	0.71	
	5		89	88	84	90	65	0.81	
	7		86	84	82	86	60	0.89	
	9		84	82	80	85	52	0.95	
	1	2	96	94	92	–	–	–	″
	3		93	91	90	–	–	–	
	5		92	90	91	–	–	–	
	7		89	90	88	–	–	–	
	9		89	86	85	–	–	–	
3	1	1	87	83	80	75	50	0.60	Finely crystalline, with good adhesion to the support, dense, lustrous, and partially cracked from the edges
	3		85	80	78	74	48	0.63	
	5		81	79	75	73	40	0.66	
	7		79	75	72	72	40	0.71	
	9		77	75	70	72	38	0.85	
	1	3	89	85	82	84	55	0.68	Semilustrous and lustrous, with satisfactory adhesion to the support
	3		88	83	81	83	53	0.73	
	5		85	82	80	81	50	0.75	
	7		84	81	78	81	45	0.85	
	9		80	79	76	79	30	0.90	
4	1	0.5	87	80	79	79	55	0.55	Finely crystalline, exfoliated from the edges, with semilustrous and lustrous surface
	3		85	79	78	77	50	0.56	
	5		81	79	75	76	48	0.65	
	7		79	76	75	75	40	0.71	
	9		76	73	71	75	38	0.82	
	1	1	92	90	88	–	–	–	Finely crystalline, with satisfactory adhesion to the support, gray, semilustrous
	3		89	89	87	–	–	–	
	5		86	86	85	–	–	–	
	7		83	82	82	–	–	–	
	9		80	80	79	–	–	–	
5	1	1	95	94	92	93	50	0.73	Finely crystalline, cracked from the edges, gray, semilustrous and lustrous
	3		93	93	89	92	60	0.86	
	5		90	90	89	90	55	0.94	
	7		85	87	88	90	45	0.99	
	9		83	82	82	89	25	0.99	
	1	3	98	98	95	96	45	0.76	Finely crystalline, dense, regular, with good adhesion to the support and lustrous surface
	3		97	96	94	95	75	0.81	
	5		96	94	94	95	70	0.80	
	7		93	94	93	94	55	0.94	
	9		90	90	90	93	40	1.20	

Table 2. (Contd.)

Inhibitor no.	j_c, A dm^{-2}	C, mM	Plasticity, %, in indicated time, min			CE, %	γ, arb. units	$-E$, V	Appearance and structure of coating
			12.5	26	52				
6	1	1	90	85	82	84	45	0.58	Finely crystalline, cracked from the edges with increasing current density, dense, gray, semilustrous
	3		86	84	80	83	40	0.60	
	5		84	82	80	82	42	0.72	
	7		80	80	78	81	35	0.80	
	9		78	79	77	79	25	0.82	
	1	2	92	90	85	–	–	–	"
	3		90	87	83	–	–	–	
	5		88	86	82	–	–	–	
	7		85	85	80	–	–	–	
	9		83	83	80	–	–	–	
7	1	–	96	93	90	–	–	–	Finely crystalline, dense, smooth, strongly adherent to the support, lustrous
	3		94	92	88	–	–	–	
	5		91	91	87	–	–	–	
	7		88	90	86	–	–	–	
	9		86	86	85	–	–	–	
8	1	–	100	100	98	–	–	–	Finely crystalline, regular, smooth, with good adhesion to the support and lustrous surface
	3		99	99	95	–	–	–	
	5		95	95	95	–	–	–	
	7		93	92	92	–	–	–	
	9		92	92	92	–	–	–	
None	1	–	85	78	75	–	–	–	Finely crystalline, with satisfactory adhesion, cracked, rough, with pitting and dendrites, dull, semilustrous
	3		81	75	71	–	–	–	
	5		80	74	70	–	–	–	
	7		75	70	69	–	–	–	
	9		73	70	65	–	–	–	

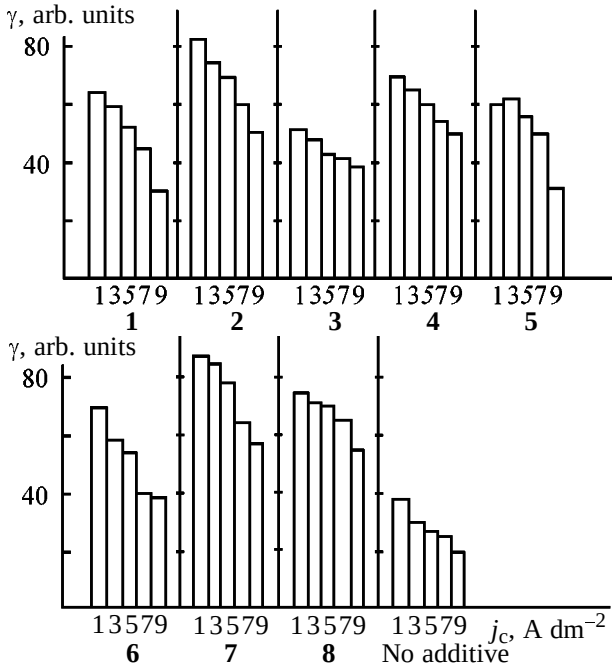

Fig. 2. Luster γ vs. j_c in the presence of additives (C = 2 mM).

acting as adsorption center. With increasing electron density the chemisorption bond between the cathode metal and the inhibitor strengthens [13].

Let us consider the suppression of hydrogen absorption (SHA) in the presence of organic additives (triphenylmethane derivatives and azo dyes) as influenced by their molecular structures.

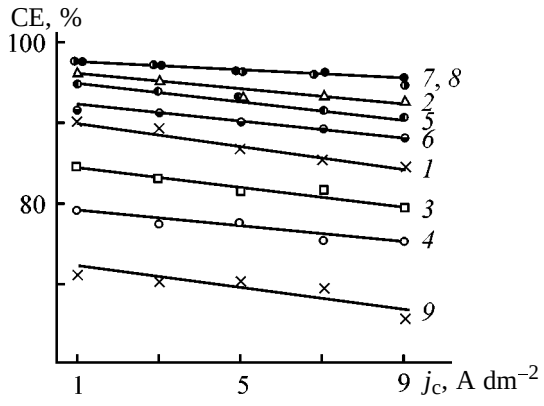

Fig. 3. Current efficiency CE vs. j_c in the presence of additives (C = 2 mM).

The additives of the first group, i.e., azo dyes (Table 1) eriochrome black (**2**), methyl red (**3**), and eriochrome blue SE (**4**) show the inhibiting and luster-producing action. The SHA efficiency of the azo dyes decreases in the following order: **2** > **3** > **4**.

For example, the plasticity of the steel samples in the presence of methyl red is the lowest (76–89% at C = 3 mM) and CE, 79–84% (Table 2, inhibitor **3**). Since the surface of the iron–nickel alloy is charged negatively, not only nitrogen of the NH_2 group but also π-conjugated ensemble of azobenzene carboxylated in *p*-position can be adsorption centers. As a result, the adsorption of this compound increases. The cathodic potential ranges from –0.60 to –0.90 V. The coatings have finely crystalline structure and gray color, are satisfactorily adherent to the support, and crack with increasing current density. The luster is 30–55 arb. units at C = 3 mM. The corrosion damages are of degree IV, and the corrosion protection is 65% (Table 3, **3**). The weak luster-producing action of the additive is due to the presence of electron-donating carboxy group –COOH, which itself actively interacts with the metal, thus competing with the conjugated system and disturbing the equilibrium electron distribution in the chain. As a result, the luster-producing power of this compound decreases [14].

Compared to methyl red, eriochrome blue SE (**4**) is the stronger inhibitor. The plasticity is 79–92% at C = 1 mM (Table 2, **4**). The adsorption of the inhibitor is provided by the N, O, and S atoms, two sulfonate groups as anionic centers, and –N=N– double bonds, possessing a fairly mobile electronic cloud capable of donating π electrons [14]. The high resistance of aromatic azo compounds arises from the conjugation of the –N=N– double bond with the π electrons of the core [15]. An electron-accepting Cl substituent, which serves as acceptor for π electrons of the core, decreases adsorption of the additive. This can explain a decrease by –0.07 to –0.24 V in the cathodic potential compared to that of the initial electrolyte (Fig. 1, curve *4*; Table 2, inhibitor **4**). The coatings are of lower quality; their adhesion to the support is satisfactory but they exfoliate from the edges at higher j_c; the coatings are semilustrous and lustrous. The corrosion damages are of degree IV. The protecting action is 72% (Table 3, additive **4**).

Among compounds of this group, eriochrome black (**2**) is the most efficient inhibitor ensuring the highest plasticity (86–96% at C = 2 mM). CE is 92–96% (Table 2, **2**). The adsorption of the given compound is provided by two electron-donating alcohol groups (–OH), nitrogen group ($–NO_2$), azo group (–N=N–), by the $–SO_3H$ sulfonate group as anionic center, and by two naphthalene cores.

Table 3. Corrosion resistance of iron–nickel alloys as 20-μm-thick coatings plated in the presence of additives (C = 2 mM and j_c = 1 A dm^{-2})

Additive no.	Degree of corrosion damage	K, g m^{-2} day^{-1}	Z, %
1	III	1.51	88
2	II	0.96	92
3	IV	4.20	65
4	IV	3.38	72
5	II	1.04	91
6	III	2.1	82
7	I	0.85	93
8	I	0.71	94
No additive	IV	5.5	55

As a result, the inhibitor is stronger bonded to the cathode surface. The cathodic potential ranges from –0.72 to –0.92 V, which agrees with the coating quality. The deposits are smooth and are characterized by finely crystalline structure, good adhesion to the support, and a luster of 50–83 arb. units. The corrosion rate is 0.96 g m^{-2} day^{-1}. The corrosion damages are of degree II, i.e., the corrosion products are in the form of dots or spots covering 10–15% of the sample surface. The corrosion protection is 92%.

The additives of the second group are triphenylmethane derivatives: bromocresol green (**1**), fuchsin new (**5**), pararosaniline (**6**), a mixture of additives **5** and **2** (**7**), and a mixture of additives **5** and Progress (**8**). The SHA efficiency of triphenylmethane derivatives decreases in the order **8** > **7** > **5** > **1** > **6**.

Introduction of fuchsin new (**5**) into an electrolyte decreases the cathodic potential to the value from –0.65 to –0.85 V. The deposits are dense, gray, and cracked from the ends with increasing j_c. The plasticity of the steel samples is 80–92% and CE, 88–92% at C = 2 mM. The inhibiting action of hydrogen absorption of this additive is due to three benzene rings and three electron-donating NH_2 groups. The luster is 39–70 arb. units and the corrosion damages are of degree III (Tables 2 and 3, additive **6**).

Bromocresol green (**1**) is a stronger inhibitor. The plasticity is 80–94% and CE, 84–90% (Table 2, **1**). The inhibiting action of this additive on hydrogen

absorption can be ascribed to the O and S reaction centers of higher electron density and to electron-donating methyl substituent (CH_3) strengthening this action. The Br electron-accepting substituent reduces the reactivity of the additive. The cathodic potential is from –0.66 to –0.81 V (Fig. 1, curve *1*). The deposits are dense, exfoliating from the support at high current densities, and semilustrous or lustrous (Table 2, **1**). The corrosion damages are of degree III, i.e., the corrosion products occupy 20–40% of the sample surface (Table 3, **1**).

The best inhibitor of hydrogen absorption is fuchsin new (**5**). In the presence of this additive the plasticity N = 90–98% and CE is equal to 93–96% (Table 2, **5**). The strong SHA of this additive is due to the presence of three amino groups NH_2 and two methyl groups CH_3 at three benzene rings [15]. The cathode potential is considerably lower (by –0.28 to –0.48 V) compared to the pure electrolyte (Fig. 1, curve *5*). The quality deposits with good adhesion to the support and semilustrous and lustrous surface were obtained. The presence of the NH_2 groups in the additive, which itself react with the metal, thus competing with the conjugated system and disturbing the equilibrium electron distribution in the chain, reduces the luster-producing power of this compound [14]. The luster was 40–75 arb. units at C = 3 mM. The corrosion damages correspond to degree II. The corrosion protection is 91% (Table 3, **5**).

To enhance the inhibiting and luster-producing power in a sulfate–chloride electrolyte, we studied two mixtures: the strongest inhibitor fuchsin new (**5**) and the most efficient luster-producing agent eriochrome black (**2**). The plasticity of the samples is rather high (85–96%) and CE is 95–98% (Table 2, **7**). The corrosion rate is 0.85 g m^{-2} day^{-1} and the corrosion protection, 93%, i.e., the surface slightly turns dark (Table 3, no. 7).

A mixture of additive **5** and Progress (**8**) is the strongest inhibitor of hydrogen absorption; N = 92–100% and CE is 94–97% (Table 2, **8**). The potential is considerably decreased and ranges from –0.81 to –1.3 V (Fig. 1, curve *8*). The luster is enhanced only slightly (55–75 arb. units). Progress is the efficient antipitting additive ensuring wetting of the cathode surface. Due to its adsorption on the surface, the phase boundary tension weakens, thus facilitating escape of hydrogen bubbles from the surface [16]. The corrosion is the lowest (0.71 g m^{-2} day^{-1}), the corrosion protection amounts to 94%, and the corrosion damage is of degree 1.

CONCLUSIONS

(1) Plating of iron–nickel alloy from a sulfate–chloride electrolyte is accompanied by strong hydrogen absorption by the steel support, which is manifested as a 15–35% drop of the plasticity at j_c = 1–9 A dm^{-2}.

(2) Triphenylmethane and azo dyes are the efficient inhibitors of hydrogen absorption. The strongest inhibiting action was exerted by fuchsin new (N = 90–95%), fuchsin new + eriochrome black (N = 85–96), and by fuchsin new + Progress (N = 92–100%). At the same time, these dyes are efficient corrosion inhibitors (Z 91, 93, and 95%).

(3) Sulfate–chloride electrolyte containing fuchsin new + Progress, fuchsin new + eriochrome black, and fuchsin new can be recommended for industrial plating of iron–nickel alloy on articles susceptible to hydrogen embrittlement. The electrolyte yields quality coatings with lustrous surface and the minimal hydrogen absorption and ensures the high current efficiency and corrosion resistance.

REFERENCES

1. Patel, N.K., Das F.M., and Patel, J.S., *Plat. Surface Finish.*, 1976, vol. 63, no. 8, pp. 13–14.
2. Law, M.J. and Hutchinson, P.S., *Bull. Electrochem.*, 1985, vol. 32, no. 10, pp. 417–420.
3. Singh, D. and Singh, V., *Indian J. Technol.*, 1975, vol. 13, no. 11, pp. 520–523.
4. USSR Inventor's Certificate no. 857306.
5. US Patent 3878067.
6. US Patent 3969198.
7. Milushkin, A.S., *Zashch. Met.*, 1996, vol. 32, no. 2, pp. 190–195.
8. Kruglikov, S.S., Bakhchisaraits'yan, N.G., and Veleeva, E.V., *Materialy seminara "Intensifikatsiya tekhnologicheskikh protsessov pri osazhdenii metallov i splavov"* (Proc. Seminar "Intensification of Deposition of Metals and Alloys in Industry"), Moscow: Avtotransizdat, 1971, pp. 143–145.
9. Vyacheslavov, P.M., *Elektrolitichеskoe osazhdenie splavov* (Electroplating of Alloys), Leningrad: Mashinostroenie, 1986, pp. 46–53.
10. Loshkarev, Yu.M., Plating of Metals under Conditions of Surfactant Adsorption on Electrodes, *Doctoral Dissertation*, Dnepropetrovsk, 1973.
11. Milushkin, A.S. and Beloglazov, S.M., *Ingibitory navodorazhivaniya i elektrokristallizatsii pri mednenii*

i nikelirovanii (Inhibitors of Hydrogen Absorption and Electrocrystallization during Copper and Nickel Plating), Leningrad: Leningr. Gos. Univ., 1986.

12. Zhuk, N.P., *Kurs teorii korrozii i zashchity metallov* (Theoretical Course of Corrosion and Protection of Metals), Moscow: Metallurgiya, 1976.
13. Matulis, Yu.Yu., *Tr. Akad. Nauk Lit. SSR, Ser. B*, 1972, vol. 2, issue 2, pp. 39–46.
14. Mozolis, V.V. and Iokubaite, S.P., *Zavisimost' bleskoobrazuyushchikh svoistv organicheskikh soedinenii ot ikh stroeniya* (Luster-Producing Action of Organic Compounds as Influenced by Their Structure), Available from LitNIINT, Vilnius, 1983, no. 1055–83.
15. Nesmeyanov, A.N. and Nesmeyanov, N.A., *Nachala organicheskoi khimii* (Principles of Organic Chemistry), Moscow: Khimiya, 1974, 2nd ed.
16. Grilikhes, S.Ya. and Tikhonov, K.I., *Elektroliticheskoe i khimicheskoe pokrytie* (Electrolytic and Electroless Plating), Leningrad: Khimiya, 1990.

Russian Journal of Applied Chemistry, Vol. 74, No. 5, 2001, pp. 762–765. Translated from Zhurnal Prikladnoi Khimii, Vol. 74, No. 5, 2001, pp. 739–742.

APPLIED ELECTROCHEMISTRY AND CORROSION PROTECTION OF METALS

Release Coatings on Apparatus for Fabrication of Electrodes for Chemical Power Sources

M. Yu. Serbinovskii and G. A. Danyushina

South-Russian State Technical University, Novocherkassk, Russia

Received August 9, 2000

Abstract—The influence exerted by the composition and properties of formulations for electrodeposition on the characteristics of release coatings on rollers for rolling of ribbon-type cathodes is described. A composition based on VUPFS-35 resin and magnesium zirconate powder is recommended for use in the formulations.

The well-known problem encountered in manufacture of electrodes for chemical power cells is the high adhesion of the cathode paste to working surfaces and tools of the equipment employed. One of ways to tackle with this problem is to use release coatings of polymeric nature with mineral fillers. The requirements imposed upon coatings of this kind are as follows: chemical inertness and low adhesion to the materials being processed; good cohesion with equipment parts; high hardness, strength, and wear resistance; and, in some cases, dimension precision.

As criteria for assessing the quality of the coatings chosen in the course of the present study served the following parameters: adhesion strength of the active paste–coating system and also wear and roughness of the coating surface. The last two criteria were used in assessing the quality of coatings on roller tools, perforated disks of granulators, and extruder parts. These items are subject to the action of high pressure and abrasive wear, and, at the same time, their dimension precision directly affects the accuracy of fabrication of rolled electrodes or extruded grains. Therefore, the wear resistance and evenness of coating thickness are particularly important for these equipment parts. In this case, the most promising technique for coating deposition is electroplating. This method yields coatings of uniform thickness on articles of complex shape and makes it possible to control the coating structure, producing functional coatings with prescribed properties.

The adhesion strength was evaluated from the rupture stress of two cylindrical samples [GOST (State Standard) 209–75] between whose edges a plate made of copper(II) oxide, manganese(IV) oxide, or carbon was preliminarily squeezed. The sample compression stress was 1.25 MPa for the coal plate and 1.60 MPa for the two others. The wear resistance of coatings was tested on an end friction machine, with plates made of the same CuO, MnO_2, or C serving as counter bodies. The average sliding velocity was 0.048 m s^{-1}, and the load, 0.20 MPa for the carbon plate and 0.25 MPa for two other kinds of materials. The surface roughness was evaluated by parameter R_a (GOST 2789–73).

The service characteristics of electrodeposited organomineral coatings are determined by the formulation composition, deposition conditions, and thermal treatment of the obtained coatings. Commonly, a formulation for electrodeposition contains a water-soluble film-forming agent, neutralizer, and various additives.

A number of film-forming materials are manufactured commercially in the form of insoluble acid pastes. As bases for formulations to be used for electrodeposition of coatings were studied V-KF-093 and V-K-Ch-0207 primers, KCh-0125 varnish, Residrol VA-133, VEP-2100 and UR-1154 enamels, and VUPFS-35 and VUPFS-35A resins. The film-forming materials were converted to the water-soluble state by means of neutralizers: diethylamine, triethylamine, triethanolamine, 2-diethylaminoethanol, and ammonia.

To make the coatings harder and more wear-resistant, oxide powders were introduced into the formulations. Al_2O_3, SiO_2 (Aerosil), MgO, ZrO_2, $MgO \cdot ZrO_2$, and TiO_2, exhibiting high chemical resistance against the materials rolled, were studied. All the oxide powders were of pure grade and had particle size of less than 60 μm; Aerosil of A-175 brand was used [1]. The influence exerted by the type of additive

1070-4272/01/7405-0762$25.00

and its concentration on the properties of the formulations and coatings was analyzed.

In preliminary studies, the best results in rolling of positive electrodes and granulation of the cathode paste were obtained with coatings based on an alkyd–urethane resin VUPFS-35A [2], and, therefore, further studies described below were done with formulations based on this resin. Diethylamine is the most efficient in neutralization of the VUPFS-35A resin. The obtained results indicate that, to obtain high-quality coatings, the formulation pH should be maintained within 8.7–8.9. This can be done with diethylamine.

Studies of the effect of the resin concentration on the coating properties demonstrated that the optimal content of VUPFS-35A is 10–14 wt %. Making the resin concentration higher leads to higher electrical conductivity of the formulation, with the result that the obtained coatings are loose and porous. Lowering the concentrations leads first to a decrease in the strength of the coatings and then disrupts their continuity. The content of the VUPFS-35A resin was taken to be 10 wt %, and further studies were aimed at selecting a mineral additive and determining the optimal composition of the formulation.

To prepare formulations and electrodeposit coatings, the VUPFS-35A resin was neutralized with diethylamine to pH 8.7–8.85, and then the calculated amounts of water and necessary additives were added and the mixture was stirred for 2–3 h. The viscosity, pH, and electrical resistivity of the obtained formulations were monitored. Coatings were deposited onto articles made of carbon construction (45, 40Cr, 40CrNi) and stainless steels (30Cr13, Cr18Ni10Ti, etc.). Prior to depositing the coatings, the surface of the articles to be coated was treated by the known methods [2, 3]. The coatings were deposited on an installation comprising a controlled dc current source and a bath for electrodeposition, equipped with a stirrer. The deposition time was 2 min. The bath voltage in depositing coatings with the use of formulations with Al_2O_3, MgO, and TiO_2 additives was 100 V, and that for SiO_2, ZrO_2, and $MgO \cdot ZrO_2$ additives, 60 V. After depositing the coatings, the samples were thoroughly washed with tap and distilled water and kept at 180 ± 5°C for 40–60 min.

The stability of the electrodeposition process and the quality of the obtained coatings are strongly affected by the pH of the formulation used and its electrical conductivity. As mentioned above, the most effective agent for neutralization of the VUPFS-35A resin is diethylamine. The introduced amount of neutralizer depends on the acid number of the binder. The optimal amount of neutralizer is ca. 0.7 ± 0.1 wt %. Such a content of the neutralizing agent maintains the pH value within the range 8.7–8.9, which favors fabrication of high-quality coatings. The introduction of oxide additives alters the acidity and may impair the coating quality, leading to appearance of beads, craters, and porosity. For this reason the pH of the formulation was adjusted in the appropriate way. Figure 1a shows the dependence of the pH value on the content of additives. Raising the concentration of the chosen additives leads to significant changes in pH only in the case of a formulation with SiO_2. For this composition the pH decreases to below the admissible level, which leads to deposition of poor-quality coatings, and, therefore, an additional, compared with other formulations, pH adjustment is necessary in this case.

The electrical conductivity of a formulation exerts strong influence on the stability of the electrodeposition process and the coating quality. Introduction of Al_2O_3, MgO, TiO_2, and ZrO_2 into formulations does not change their electrical conductivity noticeably (see Fig. 1b). The increase in electrical conductivity on making the content of $MgO \cdot ZrO_2$ or SiO_2 higher than 5 wt % impairs the quality and service characteristics of the obtained coatings. For coatings with $MgO \cdot ZrO_2$, a practically appreciable quality deterioration is observed at additive content exceeding 6.5 wt %. The electrical conductivity of a formulation with $MgO \cdot ZrO_2$ is presumably higher because of the greater charge of colloid particles. Magnesium zirconate does not virtually dissociate in the formulation, and, therefore, the pH value changes only slightly on increasing its content.

With Aerosil, the outward appearance and service characteristics of the coatings are markedly deteriorated already at an SiO_2 content of 5.0–5.5 wt %. This concentration corresponds to an electrical conductivity as high as 120×10^{-3} S m^{-1}, which is the upper limit for obtaining high-quality coatings. The rise in electrical conductivity in formulations with Aerosil is probably due to the high activity of this oxide, which can, under certain conditions, partly dissolve to form H_2SiO_3 and H_4SiO_4 whose dissociation is responsible for the increase in electrical conductivity. The decrease in pH for the formulation with SiO_2 confirms the probability of acid formation (Fig. 1a). The abrupt change in electrical conductivity, observed in this case, and the corresponding deterioration of the coating quality restrict or completely rule out use of SiO_2 in formulations with VUPFS-35A.

Figure 1c shows how the concentration of additives

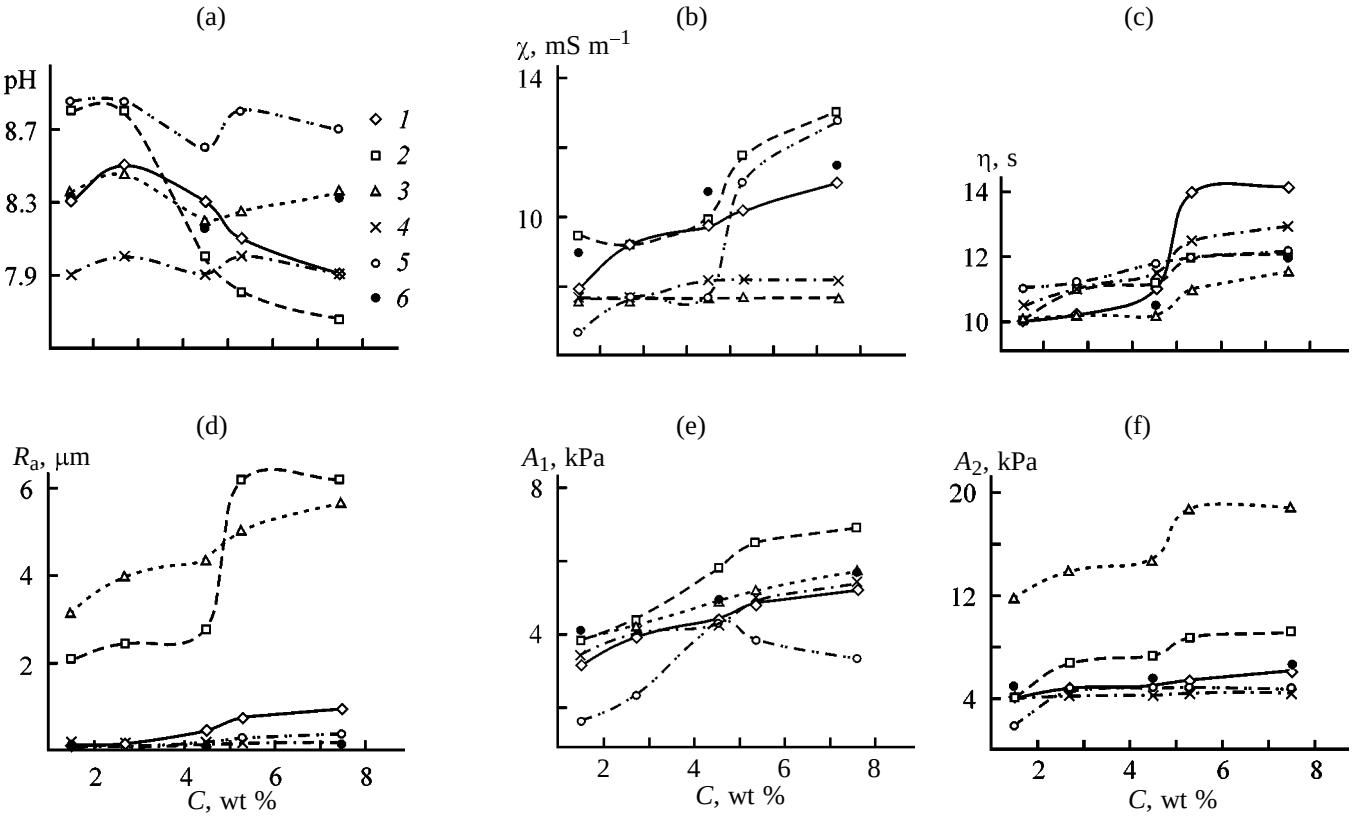

Fig. 1. Effect of additive content C on (a) pH, (b) electrical conductivity χ, (c) viscosity η measured as outflow time from a VZ-4 viscometer, (d) coating surface roughness R_a, and also adhesion of a plate based on (e) PME-100V carbon black, A_1, and (f) MnO_2, A_2, to coatings deposited using VUPFS-35A. Additive: (*1*) Al_2O_3, (*2*) SiO_2, (*3*) MgO, (*4*) ZrO_2, (*5*) $MgO \cdot ZrO_2$, and (*6*) TiO_2.

affects the formulation viscosity, which grows with increasing content of oxides in the suspension. The substantial rise in the viscosity of the formulation with Al_2O_3 in the oxide content range 4–6 wt % is presumably due to formation of larger colloid particles lowering the formulation fluidity. Higher coating quality corresponds to VZ-4 viscosity equal to 10–12.5 s. With increasing viscosity, the adhesion of the cathode paste to the coatings grows. Figure 1d demonstrates the effect of additive content on the surface roughness of the coatings, and Figs. 1e and 1f, the influence exerted by the content of additives on the adhesion of plates based on PME-100V carbon black and MnO_2 to the coatings. The results obtained in testing the wear resistance of the coatings are presented in the table.

The main criteria for suitability of the coatings under study for rolling of plates based on carbon black (technical-grade carbon), manganese dioxide, and copper(II) oxide are the adhesion strength of the system cathode plate–coating and coating wear. However, the surface roughness also affects the characteristics of coatings. For example, the high surface roughness of coatings based on VUPFS-35A resin

Wear of coatings based on VUPFS-35A with oxide additives (5 wt %)

Plate	Wear, μm h^{-1}, of coatings with indicated additives					
	Al_2O_3	SiO_2	MgO	ZrO_2	$MgO \cdot ZrO_2$	TiO_2
PME-100V	0.05	0.03	0.04	0.88	0.04	0.03
MnO_2	0.12	0.06	0.09	1.92	0.09	0.07
CuO	0.10	0.05	0.07	1.61	0.07	0.06

with SiO_2 or MgO additives leads to higher adhesion of the coatings to the active paste of the plate, and, therefore, such coatings are not release coatings for the materials tested. The best combination of processing and service characteristics are observed for coatings based on VUPFS-35A with addition of $MgO \cdot ZrO_2$.

CONCLUSIONS

(1) It is recommended that electrodeposition should be performed using a formulation of the following composition (wt %): VUPFS-35A resin 10, diethylamine 0.7, $MgO \cdot ZrO_2$ 4.5–6.5, surfactant 0.10–0.30, and water the rest.

(2) The optimal properties of the formulation to be used: pH 8.70–8.85, viscosity measured by VZ-4 (GOST 8420–74) 11.0–12.2 s, and electrical conductivity $(66–120) \times 10^{-3}$ S m^{-1}.

(3) The following parameters are recommended for deposition: voltage 60 V, time 2 min, and thermal treatment temperature 180 ± 5°C and time 40–60 min.

(4) The coatings of this kind can be recommended for deposition onto rolls of installations for rolling of carbon, copper oxide, and manganese dioxide electrodes.[1]

REFERENCES

1. *Entsiklopediya neorganicheskikh materialov v dvukh tomakh* (Encyclopedia of Inorganic Materials in Two Volumes), Fedorchenko, I.M., Ed., Kiev: Glavnaya Redaktsiya Ukrainskoi Sovetskoi Entsiklopedii, 1977, vol. 1.
2. Krylova, I.A., Kogan, N.D., and Ratnikov, V.N., *Okraska elektroosazhdeniem* (Painting by Electrodeposition), Moscow: Khimiya, 1982.
3. Shabel'skii, V.A. and Myshlennikova, V.A., *Okrashivanie metodom elektroosazhdeniya: Tekhnologiya i oborudovanie protsessa* (Painting by Electrodeposition: Process Technology and Apparatus), Leningrad: Khimiya, 1983.

[1] The coatings were successfully tested on rolls of experimental installations for chemical power cell electrodes and parts of granulators for cathode paste processing at OKTB Orion (Novocherkassk) and laboratory for mechanization and automation of chemical power cell production, Suth-Russian State Technical University (Novocherkassk Polytechnic Institute).

Russian Journal of Applied Chemistry, Vol. 74, No. 5, 2001, pp. 766–770. Translated from Zhurnal Prikladnoi Khimii, Vol. 74, No. 5, 2001, pp. 743–747.

CATALYSIS

Catalytic Decomposition of Cumyl Hydroperoxide under the Action of Aspartic Acid Derivatives

B. V. Pekarevskii, V. A. Ivanov, and V. M. Potekhin

St. Petersburg State Technological Institute, St. Petersburg, Russia

Received June 5, 1997; in final form, 2000

Abstract—The inhibiting activity of aspartic acid derivatives in the stage of degenerate chain branching in decomposition of cumyl hydroperoxide was studied. The kinetic and thermodynamic parameters of the reaction were established.

Petroleum products can be oxidized with atmospheric oxygen during storage and recovery with deterioration of their service characteristics. To stabilize organic materials, antioxidant additives are used. The mechanism of the inhibiting effect of the vast majority of additives (among them Ionol) involves termination of oxidation chains by the reaction with peroxide radicals. However, it is well known [1] that at low extents of oxidation of hydrocarbons hydroperoxides are accumulated in the substrate. These hydroperoxides are capable of spontaneous decomposition with formation of free radicals, which results in additional initiation of oxidation chains (stage of degenerate branching).

At present it is well known that heteroatomic nitrogen-, sulfur-, and phosphorus-containing compounds (esters of xanthic, dithiocarbamic, and dithiophosphoric acids) catalytically decompose hydroperoxides by the molecular mechanism [2], showing no inhibiting activity in the stage of chain propagation reactions, and have a low thermal stability, which restricts their fields of application.

At the same time, sterically hindered phenols used as commercial antioxidants are practically incapable of inhibiting the oxidation in the stage of degenerate chain branching as a result of their partial or complete deactivation with radicals formed by decomposition of the hydroperoxide. In this connection the search for polyfunctional inhibitors capable of termination of the oxidation chains by the reaction with peroxide radicals and decomposition of hydroperoxides with formation of molecular products is an urgent problem.

Previous studies [3] show that derivatives of aspartic acid of the general formula

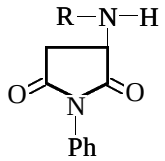

where R = C_6H_4OH-*o* (HIn_1), $C_6H_4CH_3$-*o* (HIn_2), and C_6H_5 (HIn_3), are highly efficient scavengers of peroxide radicals. Published data on possible participation of hydroxyls and amino groups [4] suggest that these compounds will participate in the stage of degenerate chain branching. In this connection we studied the effect of *N*-phenylarylaminosuccinimides on decomposition of cumyl hydroperoxide.

The kinetics of decomposition of cumyl hydroperoxide (CHP) in the presence of aspartic acid derivatives were studied at 80–110°C in an inert medium at concentrations of acceptors varying in the range 10^{-4}–10^{-3} M. Under experimental conditions the rate of thermal decomposition of CHP is negligible (10^{-7}–10^{-8} mol l^{-1} s^{-1}) [5]. As seen from Fig. 1, the rate of CHP decomposition in the presence of aspartic acid derivatives considerably increases even at moderate temperatures.

Taking into account the difference in concentrations of reactants ([ROOH]/[HIn] > 1000), we can confirm that CHP catalytically decomposes under the action of the test compounds at a high capacity of the inhibitor with respect to hydroperoxide

$$\nu = \frac{[ROOH]_0 - [ROOH]_{res}}{[HIn]_0}, \quad (1)$$

where $[ROOH]_0$ and $[ROOH]_{res}$ are the initial and residual concentrations of hydroperoxide (M), respec-

1070-4272/01/7405-0766$25.00

tively, $[HIn]_0$ is the initial concentration of the inhibitor (M), and ν is the efficiency of the inhibitor with respect to hydroperoxide.

The kinetic curves of CHP decomposition in the presence of HIn_1–HIn_3 have the shape typical for deactivation of the acceptor with hydroperoxide at a high degree of conversion. When $[ROOH]_0 \gg [HIn]_0$, the process can be described by the equation [6]

$$\frac{d[ROOH]}{dt} = k_{cat}([ROOH] - [ROOH]_0) + k_{ir}([ROOH] - [ROOH]_0), \quad (2)$$

where k_{cat} and k_{ir} are the overall rate constants of the catalytic and irreversible stages (s^{-1}).

Integration of Eq. (2) from $[ROOH]_0$ to $[ROOH]_{res}$ gives the relation

$$[ROOH] = ([ROOH]_0 - [ROOH]_{res})\exp[-(k_{cat} + k_{ir})t] + [ROOH]_{res}. \quad (3)$$

Indeed, in the semilogarithmic coordinates the kinetic curves for CHP decomposition in the presence of aspartic acid derivatives are linear, which suggests the first order of the reaction with respect to hydroperoxide (Fig. 1). It was established that the dependence of the rate of CHP decomposition on the acceptor concentration is linear as well (Fig. 2). This suggests that the reaction is first-order with respect to acceptor, and one HIn molecule participates in the event of hydroperoxide decomposition. The rate of CHP decomposition is affected by both the acceptor concentration and the initial concentration of the starting hydroperoxide. When [ROOH] > 0.15 M, the dependence of the decomposition rate on the initial concentration of the hydroperoxide is linear (Fig. 3), which confirms the first order of CHP decomposition with respect to ROOH. In the second portion of the curve, the rate of CHP decomposition is practically independent of the hydroperoxide concentration, and the reaction order approaches zero. This "limiting" dependence of the rate of CHP decomposition on its initial concentration can be the evidence for formation of the acceptor–hydroperoxide complex. In view of these results, the scheme of CHP decomposition in the presence of HIn_1–HIn_3 can be represented as follows:

$$n\text{ROOH} + \text{HIn} \underset{}{\overset{K_m}{\rightleftarrows}} n\text{ROOH}\cdot\text{HIn},$$

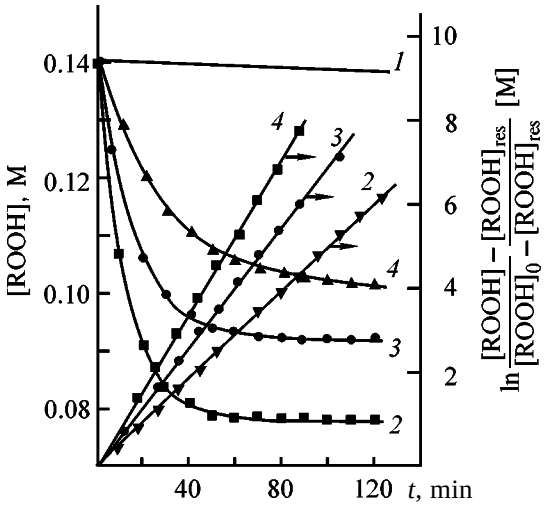

Fig. 1. Kinetic curves of CHP decomposition in the presence of aspartic acid derivatives and their semilogarithmic plots. Temperature 90°C, solvent 1,2-dichlorobenzene, $[HIn]_0 = 5 \times 10^{-4}$ M; the same for Figs. 3 and 4. ([ROOH]) Concentration of hydroperoxide and (*t*) time. Inhibitor: (*1*) none, (*2*) HIn_1, (*3*) HIn_2, and (*4*) HIn_3.

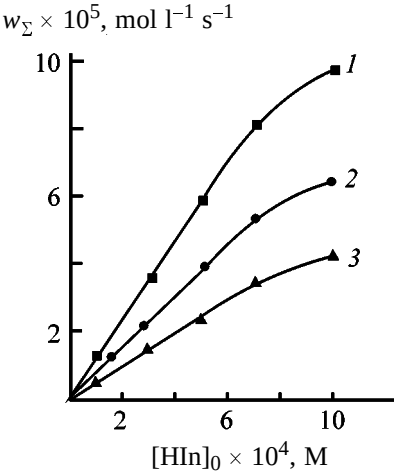

Fig. 2. Initial rate of CHP decomposition w_Σ as a function of the acceptor concentration $[HIn]_0$. $[ROOH]_0$ = 0.14 M, temperature 90°C, solvent 1,2-dichlorobenzene. (*1*) HIn_1, (*2*) HIn_2, and (*3*) HIn_2; the same for Figs. 3 and 4.

$$n\text{ROOH}\cdot\text{HIn} \xrightarrow{k_\Sigma} \begin{cases} \xrightarrow{k_r} \text{Radical products}, \\ \xrightarrow{k_m} \text{Molecular products}, \end{cases}$$

$$n\text{ROOH} + \text{HIn} \xrightarrow{k_{ir}} \text{Reaction products}.$$

Provided that $[ROOH]_0 \gg [HIn]_0$, $n = 1$, and the reaction scheme is adequately described by the

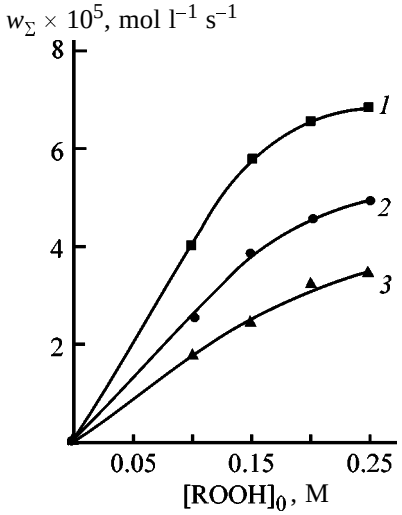

Fig. 3. Initial rate of CHP decomposition w_Σ as a function of the hydroperoxide concentration $[ROOH]_0$.

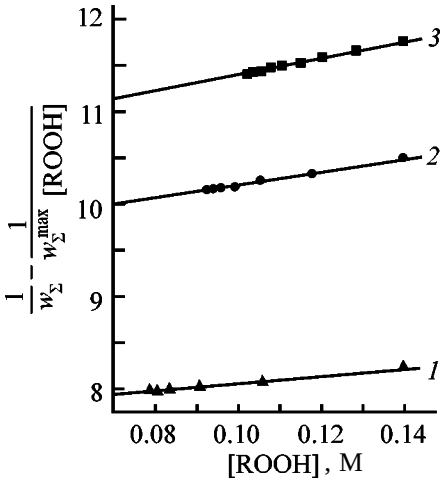

Fig. 4. Dependence of the parameter $(w_\Sigma)^{-1} - (w_\Sigma^{max}[ROOH])^{-1}$ on CHP concentration [ROOH].

Michaelis–Menten equation [7]

$$w_\Sigma = \frac{k_\Sigma K_m [HIn]_0 [ROOH]}{1 + K_m [ROOH](1 + k_{ir}^{-1}[ROOH])}, \qquad (4)$$

where K_m is the constant of complex formation (l mol^{-1}), k_Σ is the rate constant of hydroperoxide decomposition in the complex (s^{-1}), and k_{ir} is the rate constant of oxidation with hydroperoxide (s^{-1}).

Graphical solution of Eq. (4) (Fig. 4) gave the k_Σ, k_{ir}, and K_m values.

The values of the kinetic and thermodynamic parameters of CHP decomposition in the presence of HIn_1–HIn_3 are listed in Table 1.

With increasing probability of formation of the intermediate HIn·ROOH, the rate of hydroperoxide decomposition increases. The calculated thermodynamic parameters of complex formation (Table 1) suggest energetically favorable formation of the complex HIn·ROOH.

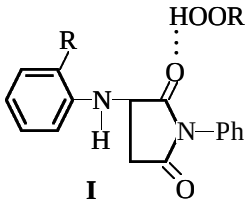

I

In view of published data on the reactivity of aminophenols [8, 9], formation of complex **I** with a hydrogen bond is the most preferable.

The effect of the substituent in the *ortho* position to the nitrogen atom of the amino group is one of the factors governing the kinetic parameters of CHP decomposition in the presence of the compounds in hand. For example, as the electron-donor power increases in passing from HIn_2 to HIn_3, the rate constant of hydroperoxide decomposition grows owing to decreasing activation energy of the process. However, it should be noted that this effect is insignificant.

It is well known that the effect of inhibitor in the stage of degenerate chain branching in the total oxidation process is mainly governed by the pathway by which the hydroperoxide decomposes (molecular or radical). An increase in the inhibition activity of antioxidants is caused by the increase in the fraction of hydroperoxide decomposition catalyzed by these antioxidants with formation of active radicals. To determine the relative contribution of radical decomposition of the hydroperoxide with addition of aspartic acid derivatives, we studied decomposition of CHP under the action of inhibitors in the presence of radical scavenger *N*,*N*'-di-β-naphthyl-*p*-phenylenediamine (DPA), which reacts with free radicals to give colored quinone diimine (QDI) [10]

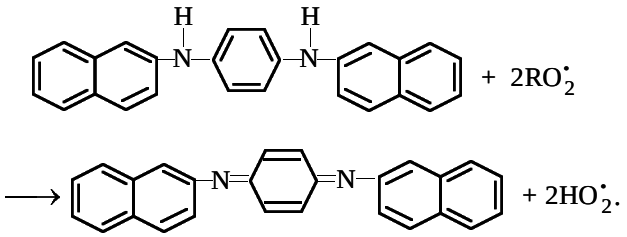

The rate of DPA consumption was measured from the rate of accumulation of QDI whose concentration was determined spectrophotometrically from absorption in the visible range (λ = 480 nm).

Since aspartic acid derivatives are polyfunctional

Table 1. Kinetic and thermodynamic parameters of CHP decomposition in the presence of aspartic acid derivatives.* $[ROOH]_0 = 0.14$ M, $[HIn]_0 = 5 \times 10^{-4}$ M, 1,2-dichlorobenzene, 90°C

HIn	k_Σ, s^{-1}	E_Σ, kJ mol^{-1}	K, l mol^{-1}	E, kJ mol^{-1}	$-\Delta S^{\neq}$, J mol^{-1} K^{-1}	k_{ir}, s^{-1}	E_{ir}, kJ mol^{-1}
HIn_1	2.8	78	0.34	27	81	0.71	86
HIn_2	2.1	89	0.27	30	90	0.66	96
HIn_3	1.9	97	0.19	33	96	0.60	99

* k_Σ and E_Σ are the apparent constant and the apparent activation energy of catalytic decomposition of CHP, respectively; K, E, $\Delta G^{\neq}$, and $\Delta S^{\neq}$ are the equilibrium constant, activation energy, Gibbs energy, and entropy of formation of the HIn·ROOH intermediate, respectively; k_{ir} and E_{ir} are the rate constant and activation energy of oxidation of the inhibitor with the hydroperoxide, respectively; the relative error of determination of the parameters is 5–10%.

Table 2. Kinetic and energy characteristics of radical decomposition of CHP in the presence of aspartic acid derivatives ($[ROOH]_0 = 0.14$ M, $[HIn]_0 = 5 \times 10^{-4}$ M, 1,2-dichlorobenzene, 90°C)

HIn	k_{in}, l mol^{-1} s^{-1}	E_r, kJ mol^{-1}	$w_\Sigma \times 10^5$	$w_r \times 10^6$	$\alpha \times 100\%$
			mol l^{-1} s^{-1}		
HIn_1	0.13 ± 0.03	74.4 ± 0.8	6.2 ± 0.2	9.1 ± 0.3	16.2 ± 0.2
HIn_2	0.11 ± 0.01	81.2 ± 0.6	4.3 ± 0.2	8.2 ± 0.1	20.4 ± 0.5
HIn_3	0.08 ± 0.01	86.1 ± 0.6	2.8 ± 0.2	6.0 ± 0.1	21.3 ± 0.5

* k_{in}, w_r, and E_r are the rate constant of initiation and the rate and activation energy of radical decomposition of the intermediate HIn·ROOH, respectively; w_Σ is the total rate of decomposition of the intermediate HIn·ROOH; α is the relative contribution of radical decomposition of the hydroperoxide in the complex.

inhibitors, they can react with radicals formed in decomposition of hydroperoxide after passing of these radicals from the solvent cage to the solvent bulk. However, this reaction is unlikely under the experimental conditions since free radicals react primarily with dissolved DPA, which is a more efficient radical scavenger than HIn. It was found that the rate of CHP decomposition under the action of DPA is 1.2×10^{-6} mol l^{-1} s^{-1} at 90°C, which is substantially lower than the rate of catalytic decomposition of CHP under the action of aspartic acid derivatives. Hence, the effect of DPA on decomposition of hydroperoxide can be neglected. The relative contribution of radical decomposition of CHP is determined as

$$\alpha = w_r/w_\Sigma, \quad (5)$$

The kinetic and energy characteristics of radical decomposition of CHP are listed in Table 2. These data show that aspartic acid derivatives inhibit oxidation of hydrocarbons in the stage of degenerate chain branching, directing hydroperoxide decomposition for the most part to the molecular pathway as compared to thermal decomposition ($\alpha_{therm} \sim 80\%$). In this case, the relative contribution of radical decomposition of CHP in the presence of HIn_1–HIn_3 is practically independent of the nature of the substituent in the *ortho* position to the nitrogen atom of the amino group.

EXPERIMENTAL

Decomposition of CHP was carried out in 1,2-dichlorobenzene in a glass reactor of bubbling type at 85–110°C in high-purity argon. To remove dissolved oxygen, argon was bubbled through the reaction mixture for 30 min before experiments. The temperature was maintained with an accuracy of 0.1°C. The total volume of the samples withdrawn during an experiment did not exceed 10–15% of the volume of the reaction mixture. The discrepancy between the results of parallel runs did not exceed 4–6%. The hydroperoxide content in a sample was determined by iodometric titration in concentrated acetic acid [11]. The discrepancy between the results of parallel runs did not exceed 3%.

The relative contribution of radical decomposition of CHP was determined by the inhibitor technique with the use of spectroscopy. The electronic absorption spectra were recorded on an SF-56 spectrophotometer. The optical density of the samples of the reaction mixture withdrawn from the reactor at certain

intervals was measured at a wavelength of 480 nm at 20°C.

CONCLUSIONS

(1) Aspartic acid derivatives exhibit inhibition activity in the stage of degenerate chain branching caused by their ability for catalytic decomposition of hydroperoxide by the molecular mechanism (relative contribution of molecular decomposition 80–85%). For the compounds studied, the capacity of the antioxidant with respect to hydroperoxide is 58–150, and the overall decomposition constants are in the range 1.8–2.8 s^{-1}.

(2) Based on kinetic and thermodynamic characteristics of decomposition of cumyl hydroperoxide under the action of aspartic acid derivatives, it was proposed that catalytic decomposition of hydroperoxide proceeds with formation of a complex with a hydrogen bond HIn·ROOH.

REFERENCES

1. Denisov, E.T. and Kovalev, G.I., *Okislenie i stabilizatsiya reaktivnykh topliv* (Oxidation and Stabilization of Jet Fuels), Moscow: Khimiya, 1983.
2. Kuliev, A.M., *Khimiya i tekhnologiya prisadok k maslam i toplivam* (Chemistry and Technology of Additives to Oils and Fuels), Moscow: Khimiya, 1972.
3. Pekarevskii, B.V., Ivanov, V.A., Potekhin, V.M., and Kochueva, S.A., *Zh. Prikl. Khim.*, 1995, vol. 68, no. 10, pp. 1676–1679.
4. Pobedimskii, D.G., *Usp. Khim.*, 1971, vol. 40, no. 2, pp. 254–255.
5. Denisov, E.T., *Konstanty skorostei gomoliticheskikh zhidkofaznykh reaktsii* (Rate Constants of Homolytic Liquid-Phase Reactions), Moscow: Nauka, 1971.
6. Denisov, E.T., *Kinetika gomogennykh khimicheskikh reaktsii* (Kinetics of Homogeneous Chemical Reactions), Moscow: Vysshaya Shkola, 1978.
7. Skibida, I.P., Bel'kov, V.G., and Maizus, Z.K., *Izv. Akad. Nauk SSSR., Ser. Khim.*, 1970, no. 8, pp. 1780–1785.
8. Emanuel', N.M., Denisov, E.T., and Maizus, Z.K., *Tsepnye reaktsii okisleniya uglevodorodov v zhidkoi faze* (Chain Reactions of Liquid-Phase Oxidation of Hydrocarbons), Moscow: Nauka, 1965.
9. Skibida, I.P., *Usp. Khim.*, 1975, vol. 44, no. 10, pp. 1729–1747.
10. Denisova, L.N., Denisov, E.T., and Metelitsa, D.I., *Zh. Fiz. Khim.*, 1970, vol. 44, no. 7, pp. 1870–1876.
11. Kruzhalov, E.D. and Golovanenko, B.I., *Sovmestnoe poluchenie fenola i atsetona* (Simultaneous Production of Phenol and Acetone), Moscow: Goskhimizdat, 1963.

Russian Journal of Applied Chemistry, Vol. 74, No. 5, 2001, pp. 771–776. Translated from Zhurnal Prikladnoi Khimii, Vol. 74, No. 5, 2001, pp. 748–753.

PROCESSES AND EQUIPMENT OF CHEMICAL INDUSTRY

A Model of Joint Absorption of Hydrogen Sulfide and Carbon Dioxide in a Moving Drop of Alkaline Solution

S. V. Aniskin, O. I. Protod'yakonova, and S. V. Marasev

St. Petersburg State Technological University of Plant Polymers, St. Petersburg, Russia

Received March 1, 2001

Abstract—A mathematical model of hydrogen sulfide and carbon dioxide absorption by a moving drop of alkaline solution is proposed on the basis of a theoretical analysis of the process. The results obtained in solving numerically the equations of the model are presented and analyzed.

The cost efficiency of jet scrubbers in absorption purification of fume gases formed in recovery units of pulp and paper industry to remove hydrogen sulfide depends on how the problem of reducing the consumption of the alkaline solution absorbing hydrogen sulfide is solved.

As known, the fume gases of recovery units contain, in addition to hydrogen sulfide, also carbon dioxide in amounts much exceeding the content of the former. If the absorption purification of fume gases to remove hydrogen sulfide is performed at comparable rates of hydrogen sulfide and carbon dioxide absorption, this entails an unjustified increase in the absorbent consumption. This poses the problem of reducing the intensity of carbon dioxide absorption, compared with that of hydrogen sulfide. Solving this problem requires a theoretical analysis of the joint absorption of hydrogen sulfide and carbon dioxide in a moving drop of an alkaline solution, which is one of the main components of the gas–fluid jet formed in the absorption apparatus under consideration.

Constructing a model of this process at the level of inclusion of a disperse phase (developing a model of the elementary transfer event) is the aim of the present study. The model is defined under the following assumptions. The drop is spherical. There is no fluid flow inside the drop. The drop moves at a constant velocity. A diffusion boundary layer is formed in the gas phase near the drop surface. Outside this boundary layer, i.e., in the gas flow core, the concentrations of hydrogen sulfide and carbon dioxide are taken to be constant. It is assumed that the main resistance to mass transfer in carbon dioxide absorption by a drop of an alkaline solution rests in the fluid phase. Then the carbon dioxide concentration at the drop surface can be taken to differ only slightly from that in the gas flow core.

The diffusion coefficients of all the chemical components involved in the process in question are the same and constant in time. It is assumed that the heat effect of absorption is negligible, and the temperature of the physical system, constant. The reaction of hydrogen sulfide with the alkaline solution is considered to be instantaneous, which allows use of the Olender condition [1] assuming the existence of a local equilibrium at any point of the drop volume for hydrogen sulfide and products of reaction with OH^- ions. This assumption makes it possible to use in the model equilibrium equations relating the concentrations of chemical components in reactions involving hydrogen sulfide and sodium hydrosulfide.

The reactions of carbon dioxide, involving interactions with water and OH^- ions, are not instantaneous. For the reaction

$$CO_2 + H_2O \rightleftarrows H^+ + HCO_3^- \qquad (1)$$

the expression for the rate constant k_1 has the form [1]

$$\log k_1 = 329.8 - 110.541 \log T - 17\,265.4/T, \qquad (2)$$

where T is temperature (K), and k_1 is the rate constant of the pseudo-first-order reaction (s^{-1}).

In alkaline medium, H^+ ions are neutralized as a result of the following instantaneous chemical reaction:

$$H^+ + OH^- \rightleftarrows H_2O. \qquad (3)$$

The result of two successive reactions (1) and (3)

1070-4272/01/7405-0771$25.00

can be written in the form

$$CO_2 + OH^- \rightleftarrows HCO_3^-. \quad (4)$$

The rate of reaction (4) is governed by the rate of its slower first stage.

Carbon dioxide can also react directly with OH^- ions. This reaction is written in the same way as reaction (4). The reaction is not instantaneous, its rate constant k_2 is expressed as

$$\log k_2 = 13.835 - 2895/T, \quad (5)$$

where k_2 is the rate constant of a second-order reaction ($m^3\ kmol^{-1}\ s^{-1}$).

The overall rate q of the chemical reaction of carbon dioxide with the alkaline solution ($kmol\ m^{-3}\ s^{-1}$) can be expressed in terms of the rate constants k_1 and k_2 as follows:

$$q = k_1[CO_2] + k_2[OH^-][CO_2]. \quad (6)$$

The nature of the dependence of k_1 and k_2 on the ionic strength of the solution was reported in [1].

All other reactions occurring in the alkaline solution in absorption of hydrogen sulfide and carbon dioxide are considered instantaneous. To these belong

$$HCO_3^- + OH^- \rightleftarrows CO_3^{2-} + H_2O, \quad (7)$$

$$H_2S + OH^- \rightleftarrows HS^- + H_2O, \quad (8)$$

$$HS^- + OH^- \rightleftarrows S^{2-} + H_2O. \quad (9)$$

The absorption of hydrogen sulfide by a drop of the alkaline solution can be described using diffusion equations written for each chemical component involved in the process. With account of the assumptions made, these equations are written as follows:

$$\frac{\partial c_1}{\partial t} = D\nabla^2 c_1 - q_1 - q_2, \quad (10)$$

$$\frac{\partial c_2}{\partial t} = D\nabla^2 c_2 + q_1 + q_2 - q_3, \quad (11)$$

$$\frac{\partial c_3}{\partial t} = D\nabla^2 c_3 + q_3, \quad (12)$$

$$\frac{\partial c_4}{\partial t} = D\nabla^2 c_4 - q_1 - q_2 - q_3 - q_4 - q_5, \quad (13)$$

$$\frac{\partial c_5}{\partial t} = D\nabla^2 c_5 - q_4, \quad (14)$$

$$\frac{\partial c_6}{\partial t} = D\nabla^2 c_6 + q_4 - q_5, \quad (15)$$

$$\frac{\partial c_7}{\partial t} = D\nabla^2 c_7 + q_5, \quad (16)$$

where $\nabla^2 = \frac{1}{r^2}\frac{\partial}{\partial r}(r^2\partial/\partial r)$ is a Laplacian; r is the current drop radius; D is the diffusion coefficient of reagents in the fluid phase; c_1, c_2, ..., c_7 are the concentrations of, respectively, CO_2, HCO_3^-, CO_3^{2-}, OH^-, H_2S, HS^-, and S^{2-}; q_1, q_2, ..., q_5 are the rates of chemical reactions (1), (3), (7), (8), and (9).

In order to simplify the written system of equations, let us introduce the following designations:

$$c_1 + c_2 + c_3 = x, \quad (17)$$

$$c_2 + 2c_3 + c_4 + c_6 + 2c_7 = y, \quad (18)$$

$$c_5 + c_6 + c_7 = z. \quad (19)$$

With account of expressions (17)–(19), Eqs. (10)–(16) take the form

$$\frac{\partial x}{\partial t} = D\nabla^2 x, \quad (20)$$

$$\frac{\partial y}{\partial t} = D\nabla^2 y, \quad (21)$$

$$\frac{\partial z}{\partial t} = D\nabla^2 z, \quad (22)$$

The system of Eqs. (17)–(22) contains ten unknowns c_1–c_7, x, y, and z and is nonclosed. It should be supplemented with four closing relations. As three relations of this kind can be used, in accordance with the Olender conditions, equilibrium equations for those chemical components reactions between which are considered to be instantaneous. These relations have the form

$$c_6 = K_1 c_5 c_4, \quad (23)$$

$$c_7 = K_2 c_6 c_4, \quad (24)$$

$$c_3 = K_3 c_2 c_4, \quad (25)$$

where K_1–K_3 are the equilibrium constants (kmol m^{-3}).

The formulas for calculating the equilibrium constants were reported, e.g., in [2]. The fourth closing relation can be derived from Eq. (10) by expanding the terms q_1 and q_2 in accordance with (6). Let us write this relation in the form

$$\frac{\partial c_1}{\partial t} = D\nabla^2 c_1 - k_1 c_1 - k_2 c_1 c_4, \quad (26)$$

The thus obtained system of equations (17)–(26) is closed. The initial conditions for this system can be written as

at $t = 0$ $c_i = c_{0i}$, $i = 1, 2, ..., 7$,

$$x = x_0, \ y = y_0, \ z = z_0. \quad (27)$$

By virtue of the central symmetry of the spherical drop, the following natural boundary conditions can be written

$$\text{at } r = 0 \quad \frac{\partial x}{\partial r} = \frac{\partial y}{\partial r} = \frac{\partial z}{\partial r} = \frac{\partial c_1}{\partial r} = 0. \quad (28)$$

The boundary condition for the variable y has the form

$$\text{at } r = R \quad \partial y/\partial r = 0, \quad (29)$$

where R is the drop radius.

This boundary condition expresses the known fact of zero ion transfer across the phase boundary.

For the variable z, representing the total content of sulfur at each point of the drop, a boundary condition of third kind can be written

$$\text{at } r = R \quad \partial z/\partial R = \beta(A - \mathrm{He}_5 c_5)/D, \quad (30)$$

where β is the mass-transfer coefficient in the gas phase (m s^{-1}), A is the hydrogen sulfide concentration in the gas flow core (kmol m^{-3}), and He_5 is Henry's constant for hydrogen sulfide.

This boundary condition expresses the equality of the hydrogen sulfide flow rate in the gas medium and the flux of the quantity z (the so-called total sulfur) in the fluid medium at the phase boundary.

The flow of hydrogen sulfide transferred in the gas phase toward the drop surface depends on the mass transfer coefficient β which is a function of parameters determining the conditions of gas flow around the drop. The coefficient β can be found using the known Fressling formula [1]:

$$\beta = D(2 + 0.5\mathrm{Re}^{0.33}\mathrm{Sc}^{0.5})/2R, \quad (31)$$

where Re is the Reynolds number and Sc is the Schmidt number.

As known, the main resistance to the transport of carbon dioxide is exerted by the fluid phase, and, consequently, its concentration at the phase boundary can be considered to be equal to the concentration of this component in the gas flow core with sufficient precision. Then the following boundary condition of first kind can be written for Eq. (26):

$$\text{at } r = R, \quad c_1 = c_{R_1}. \quad (32)$$

The c_{R_1} value can be found from the carbon dioxide concentration B in the gas flow core (kmol m^{-2}), using the relation

$$c_{R_1} = B/\mathrm{He}_1, \quad (33)$$

where He_1 is Henry's constant for carbon dioxide. A condition of the third kind for the variable x can be written as follows:

$$\text{at } r = R, \quad \frac{\partial x}{\partial r} = \frac{\partial c_1}{\partial r} = 0. \quad (34)$$

Equation (21) with boundary conditions (28), (29) and initial conditions (27) has a trivial solution

$$y = y_0. \quad (35)$$

Thus, the constructed mathematical model, describing nonstationary diffusion in joint absorption of hydrogen sulfide and carbon dioxide by a moving drop of alkaline solution, includes three parabolic differential equations (20), (22), and (26), involving second-order partial derivatives, with initial and boundary conditions (27), (28), (30), (32), and (34) and seven algebraic equations (17)–(19), (23)–(25), and (35). This system can only be solved numerically. For this purpose, a calculational scheme was developed, having the following specific features. The scheme is marching with respect to time.

An iteration process is performed within each time slice. A finite-difference model is constructed on a four-point T-shaped gage. A grid nonuniform along the spatial coordinate r and uniform in time t was

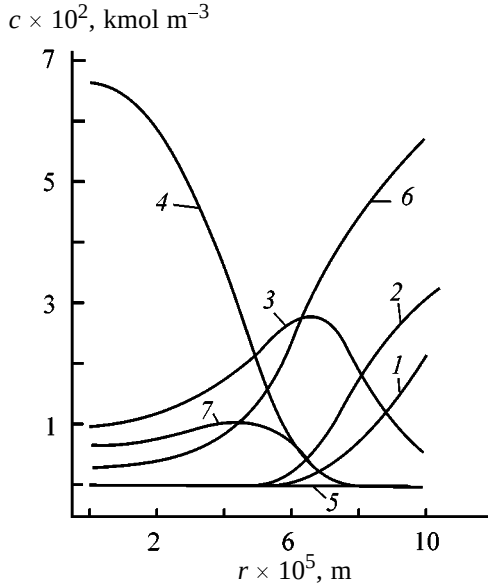

Fig. 1. Distribution of the concentrations c of chemical components involved in hydrogen sulfide and carbon dioxide absorption along the drop radius r. $R = 10^{-4}$ m, $t = 0.8$ s, $E = 520$, $A = 5\times10^{-5}$ kmol m^{-3}, $c_3 = 0$, $c_4 = 0.1$ kmol m^{-3}. c: (*1*) c_1, (*2*) c_2, (*3*) c_3, (*4*) c_4, (*5*) c_5, (*6*) c_6, and (*7*) c_7.

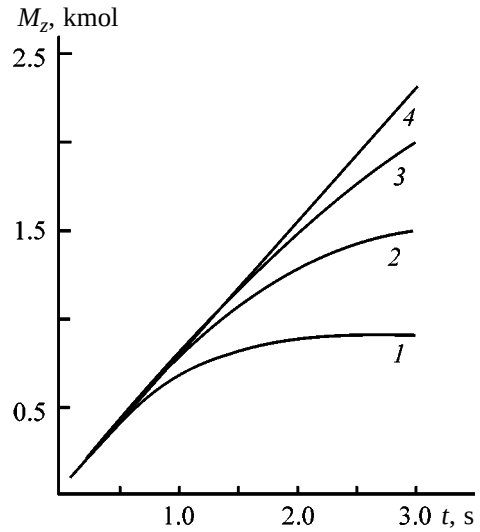

Fig. 2. Amount of hydrogen sulfide, M_z, absorbed by a drop of alkaline solution vs. absorption time t at varied initial concentration of sodium hydroxide in the drop, c_{04}. $R = 10^{-4}$ m, $A = 6\times10^{-6}$ kmol m^{-3}, $c_{03} = 0$, $c_{R_1} = 3\times10^{-3}$ kmol m^{-3}. c_{04} (kmol m^{-3}): (*1*) 5×10^{-2}, (*2*) 0.1, (*3*) 0.2, and (*4*) 0.5.

used. The differential equations were approximated with respect to the parameters x, z, and c_1, using implicit schemes with approximation of first order with respect to time and second order with respect to spatial coordinate. The finite-difference analogs of differential equations are transformed into three-point relations, which, taken together with the initial and boundary conditions also written in the finite-difference form, are solved by the sweep method.

The calculation of the algebraic part of the system consists in solving a fourth-order equation in c_4 and then finding the unknowns c_2, c_3, and c_5–c_7 with the use of the already calculated values of x, z, c_1, and c_4.

To ensure the uniqueness of solution, it is necessary to single out the only positive root of the fourth-order equation in c_4. In finding the numerical solution, the temporal, Δt, and spatial, Δr, steps of the grid are chosen in such a way that, with their values decreasing further, the dependence of the sought-for numerical solution on the grid steps becomes inessential. Thus, the convergence of the scheme chosen for solving the problem in question is established.

Figures 1–4 show the results obtained in solving the equations of the model under the following common initial conditions: $c_{01} = c_{02} = c_{05} = c_{06} = c_{07} = 0$ and constant $D = 10^{-9}$ m s^{-1}, $\beta = 0.1$ m s^{-1}, $He_5 = 0.283$, $He_1 = 1.33$, and $T = 293$ K appearing in the equations of the model as coefficients. The calculations were done at ionic strength $I = 1$ kmol m^{-3}. The values of the other parameters used to obtain the results presented in Figs. 1–4 are given in the figure captions.

Figure 1 shows the curves describing the distribution along the drop radius of the concentrations of the chemical components involved in the absorption of hydrogen sulfide and carbon dioxide. The curves indicate a complex nature of the diffusion processes occurring in the drop of the alkaline solution. The curves were obtained under the condition that $E = 520$, where

$$E = B/A, \tag{36}$$

i.e., under condition that the concentration of carbon dioxide exceeds manyfold that of hydrogen sulfide. It can be seen from Fig. 1 that the sum of the areas under curve nos. *1–3* is approximately equal to that under curve nos. *5–7*. Consequently, the amounts of the absorbed components (hydrogen sulfide and carbon dioxide) can be considered equal. Their concentrations being strongly different, it is apparent that the intensity of hydrogen sulfide absorption much exceeds that for carbon dioxide. Thus, the model is in agreement with the known data [3], which qualitatively confirms its validity.

Figure 2 shows how the amount of hydrogen sul-

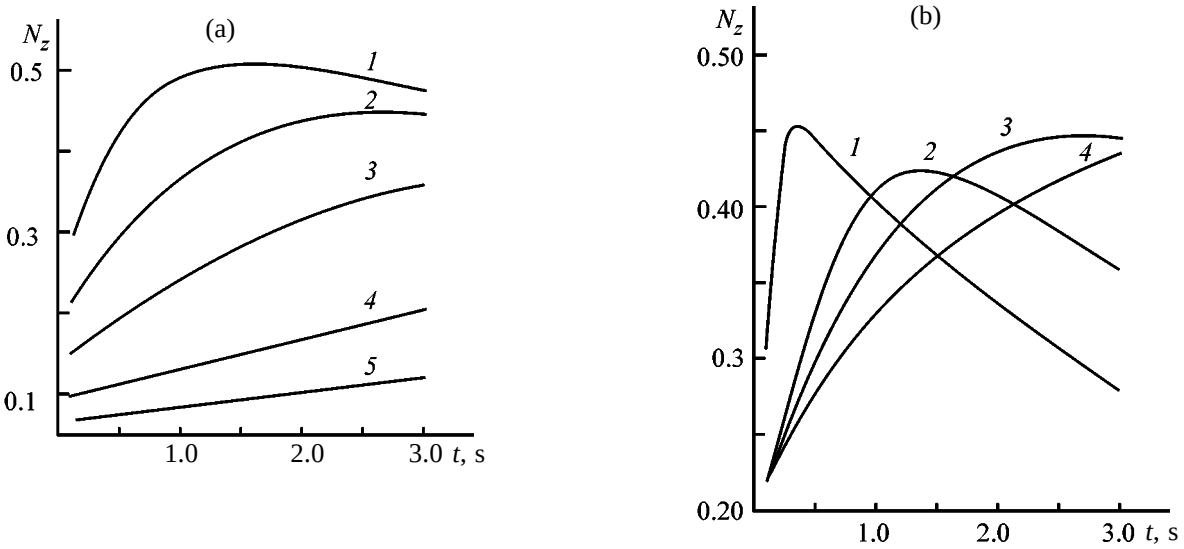

Fig. 3. Mole fraction N_z of hydrogen sulfide absorbed by drop vs. absorption time t. $A = 6\times10^{-6}$ kmol m^{-3}, $c_R = 3\times10^{-3}$ kmol m^{-3}, $c_{03} = 0$. (a) $R = 10^{-4}$ m. c_4 (kmol m^{-3}): (*1*) 5×10^{-2}, (*2*) 0.1, (*3*) 0.2, (*4*) 0.5, and (*5*) 1. (b) $c_4 = 0.1$ kmol m^{-3}. R (m): (*1*) 10^{-5}, (*2*) 5×10^{-5}, (*3*) 10^{-4}, and (*4*) 5×10^{-4}.

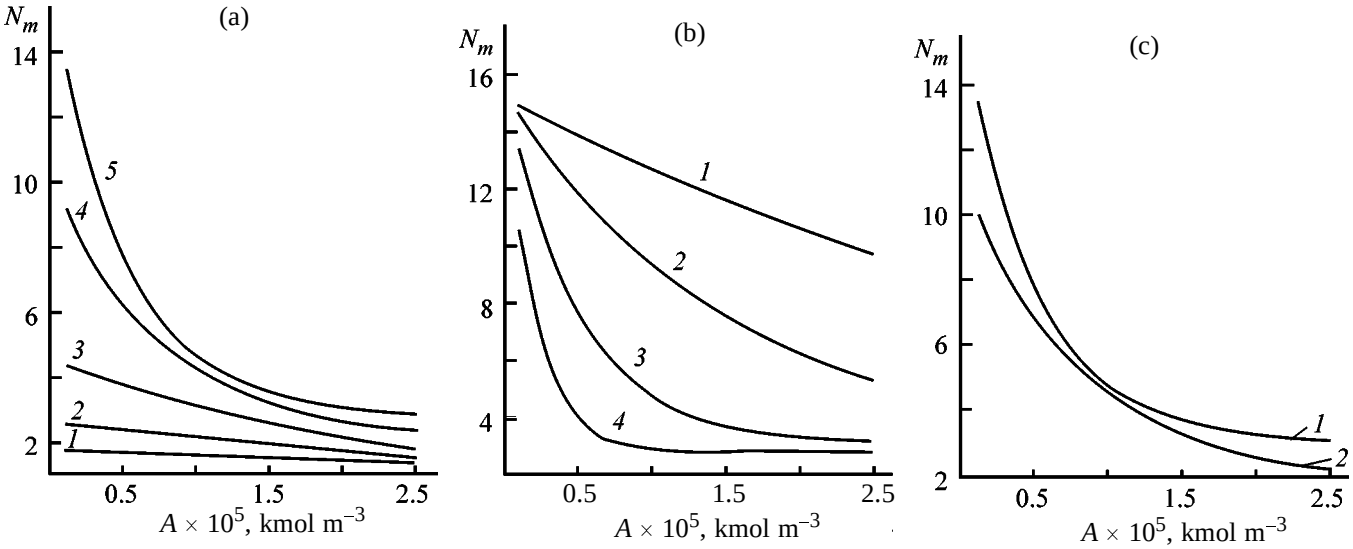

Fig. 4. Relative amount of sodium hydroxide, N_m, consumed for chemical reaction with hydrogen sulfide and carbon dioxide absorbed by the drop vs. hydrogen sulfide concentration A in the gas flow core. $R = 10^{-4}$ m, $c_{04} = 0.1$ kmol m^{-3}. (a) $c_{03} = 0$, $t = 0.5$ s. E: (*1*) 0, (*2*) 60, (*3*) 2×10^2, (*4*) 6×10^2, and (*5*) 10^3. (b) $c_{03} = 0$, $E = 10^3$. t (s): (*1*) 2×10^{-2}, (*2*) 0.1, (*3*) 0.5, and (*4*) 2. (c) $E = 10^3$, $t = 0.5$ s. c_{03} (kmol m^{-3}): (*1*) 0 and (*2*) 1.

fide, M_z (kmol), absorbed by a drop of alkaline solution in the presence of carbon dioxide depends on time. This quantity is given by

$$M_z = 4\pi\int_0^R r^2 z\,dr. \qquad (37)$$

It should be noted that the obtained kinetic curves of absorption of the above two components are similar to the curves characterizing the absorption kinetics of a single component, hydrogen sulfide, by alkaline solution. The initial linear portions of all of the presented kinetic curves correspond to that stage of absorption in which the main resistance to mass transfer is exerted by the gas phase. The rate of this stage is determined by the mass-transfer coefficient β. With the amount of sodium hydroxide in a drop decreasing through absorption of hydrogen sulfide and carbon

dioxide, the resistance to transfer of these components in the fluid phase grows. Correspondingly decreases the absorption rate, which reflects on the shape of the calculated kinetic curves in Fig. 2.

Figure 3 shows the curves characterizing the change with time of the mole fraction N_z of hydrogen sulfide in the total amount of carbon dioxide and hydrogen sulfide absorbed by the drop. The N_z value is given by

$$N_z = \frac{\int_0^R r^2 z\,dr}{\int_0^R r^2(z + x)dr}. \quad (38)$$

From Fig. 2a follows that the largest relative amount of hydrogen sulfide absorbed by the drop in the presence of carbon dioxide in the gas phase is observed at the lowest initial concentration of sodium hydroxide in the drop. Thus, the selectivity of hydrogen sulfide absorption from a gas mixture including also carbon dioxide grows with decreasing absorbent concentration. However, as follows from Fig. 2, this leads to lower total amount of absorbed hydrogen sulfide.

The plots in Fig. 3 demonstrate that the selectivity of hydrogen sulfide absorption varies with time nonsteadily, with the corresponding curves exhibiting a maximum. This is accounted for by the fact that the rate of hydrogen sulfide absorption exceeds that for carbon dioxide in the initial stage of the process. It also follows from Fig. 3b that the absorption time elapsed until the $N_z(t)$ function reaches its maximum is the shorter, the smaller the drop radius.

The plots in Fig. 4 make it possible to evaluate the consumption of sodium hydroxide for hydrogen sulfide absorption, which is important from the technological standpoint. Figure 4 presents the N_m–A dependences in which the quantity N_m defined by

$$N_m = \frac{\int_0^R r^2(c_{04} - c_4)dr}{\int_0^R r^2 z\,dr} \quad (39)$$

expresses the ratio of the amount of sodium hydroxide chemically bound to hydrogen sulfide and carbon dioxide to the amount of hydrogen sulfide absorbed by the drop. It follows from Fig. 4a that the relative consumption N_m of sodium hydroxide decreases with increasing concentration of hydrogen sulfide in the gas phase and grows with increasing carbon dioxide concentration E. This is accounted for by the fact that part of sodium hydroxide is consumed for absorption of carbon dioxide.

Figure 4b demonstrates that the relative consumption of sodium hydroxide, N_m, decreases with increasing absorption time. This result casts doubt on the concept occurring in the scientific literature, namely, that the absorption of hydrogen sulfide by sodium hydroxide in carbon dioxide should be performed at short time of contact between the fluid and gas phases.

From Fig. 4c follows that the presence of sodium carbonate in a sodium hydroxide solution at the initial instant of time (curve *2*) makes lower the relative consumption of sodium hydroxide, N_m, for hydrogen sulfide absorption.

Thus, the presence at the initial instant of time in the alkaline solution of other components (possibly contained in spraying solution circulated in the absorption apparatus) may exert influence on the consumed amount of sodium hydroxide.

CONCLUSIONS

(1) An analysis was made of chemical reactions occurring in absorption of hydrogen sulfide and carbon dioxide in an aqueous solution of sodium hydroxide.

(2) The results of the analysis were used to construct a closed system of differential equations describing the nonstationary diffusion of components involved in these chemical reactions, and the corresponding boundary-value problem was formulated.

(3) Numerical solution of the boundary-value problem yielded relations making it possible to evaluate the selectivity of hydrogen sulfide absorption and the consumption of sodium hydroxide for hydrogen sulfide and carbon dioxide absorption.

REFERENCES

1. Sherwood, T.K., Pigford, R.L., and Wilke, C.R., *Mass Transfer*, New York: McGraw-Hill, 1975.
2. Aniskin, S.V. and Protod'yakonov, I.O., *Zh. Prikl. Khim.*, 1995, vol. 68, no. 7, pp. 1158–1161.
3. Astarita, G., *Mass Transfer with Chemical Reaction*, Amsterdam: Elsevier, 1967.

Russian Journal of Applied Chemistry, Vol. 74, No. 5, 2001, pp. 777–783. Translated from Zhurnal Prikladnoi Khimii, Vol. 74, No. 5, 2001, pp. 754–761.

PROCESSES AND EQUIPMENT OF CHEMICAL INDUSTRY

Simulation of Extraction from a Capillary-Porous Particle with Bidisperse Structure

R. Sh. Abiev

St. Petersburg State Technological Institute, St. Petersburg, Russia

Received October 30, 2000

Abstract—A mathematical model of extraction from a capillary-porous particle with bidisperse structure is described. Results of numerical simulations are presented together with the criterial equation for calculating the effective diffusion coefficient, obtained on processing these results. A criterion is established for selecting the optimal oscillation frequency. The criterion is tested on a physical model, with the obtained numerical results qualitatively confirmed.

Capillary-porous particles with bidisperse structure, possessing capillaries of two, strongly different sizes, frequently occur in nature and technology. Into this category may be placed tissues of plant or animal origin, and also many kinds of catalysts [1]. Neglecting the polydispersity of capillary sizes in capillary-porous particles makes less accurate the obtained results and gives no way of elucidating some physical mechanisms of substance transfer inside the particles. The bidisperse model of a capillary-porous particle is the analytically simplest variety of the polydisperse model, making it possible to reveal fundamental aspects of mass transfer in real polydisperse particles.

The present study is concerned with the process of extraction from a bidisperse model of a capillary-porous particle.[1] In the simplest case the model of a bidisperse particle can be represented as fine capillaries, which are the main channels for solutions of target components, branching-off from coarse pores (blind or through). As a rule, there is virtually no fluid motion within the capillaries, with substance transfer occurring by the molecular-diffusion mechanism. However, at certain amplitudes, pulsation of the external pressure in coarse pores may give rise to oscillatory motion of fluid because of the compression of gas trapped in capillaries [2, 3]. Thus, coarse pores play the role of transport channels with convective substance transfer, with the resulting manyfold acceleration of solute extraction from the particle as a whole.

In order to simplify the analysis, a planar model [4, 5] of a capillary-porous particle with bidisperse structure was adopted (Fig. 1). The ensemble of fine capillaries was replaced by an anisotropic porous structure with preset porosity ε, a porous block whose pores are filled at the initial instant of time with a concentrated solution of the target component; the anisotropy is manifested in that the diffusion occurs only along the *y*-axis. A transport channel whose side walls border on the porous block passes through the particle. Molecular diffusion of the substance from the porous block into the channel occurs (shown by arrows in Fig. 1) through these boundaries. The diffusion in the channel itself is convective.

The mathematical model of the extraction process in the particle under consideration can be described by the following system of equations [indices: (0) initial state, (1) porous block, and (2) transport channel].

Diffusion equation for the porous block:

$$\partial C_1/\partial t = D(\partial^2 C_1/\partial y^2), \quad (1)$$

where C_1 is the substance concentration in the porous block (kg m^{-3}), t is time (s), and D is the molecular diffusion coefficient (m s^{-1}).

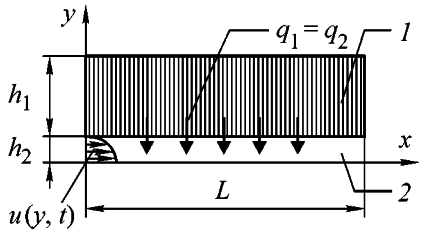

Fig. 1. Planar model of a particle with bidisperse structure and through transport pores: (*1*) porous block and (*2*) transport channel.

[1] The mathematical model was developed with participation of G.M. Ostrovskii (St. Petersburg State Technological Institute).

1070-4272/01/7405-0777$25.00 © 2001 MAIK "Nauka/Interperiodica"

Convective diffusion equation for the transport channel:

$$\partial C_2/\partial t + u\partial C_2/\partial x = D(\partial^2 C_2/\partial x^2 + \partial^2 C_2/\partial y^2), \quad (2)$$

where C_2 is the substance concentration in the transport channel (kg m^{-3}), and u is the longitudinal (along the x-axis) fluid velocity (m s^{-1}).

Initial conditions:

$$C_1(x, y) = C_{10}, \ 0 \le x \le L, \ h_2 < y \le h_1 + h_2; \quad (3)$$

$$C_2(x, y) = C_{20}, \ 0 \le x \le L, \ 0 < y \le h_2, \quad (4)$$

where h_1 and h_2 are the half-widths of the porous block and the transport channel, respectively (m), and L is the particle length (m).

Boundary conditions:

$$C_2(x, h_2) = C_1(x, h_2), \quad (5)$$

$$q_2(x, h_2) = q_1(x, h_2), \quad (6)$$

$$C_2(0, y) = C_2(L, y) = C_{20}, \quad (7)$$

$$q_1(x, h_1 + h_2) = 0, \quad (8)$$

$$q_2(x, 0) = 0, \quad (9)$$

where q_1 and q_2 are the substance fluxes (kg m^{-2} s^{-1}).

With account of the smallness of the actual velocities in the transport channels and the dimensions of these, the fluid flow mode was taken to be laminar, and the velocity profile can be taken, without any significant loss of accuracy, to be parabolic in space and harmonic in time:

$$u(x, t) = u_{\max}[1 - (y/h_2)^2]\sin(\omega t), \quad (10)$$

where ω is the angular velocity of oscillation (rad s^{-1}).

The substance fluxes at the interface between the porous block and the channel (at $y = h_2$) are given, with the diffusion coefficient D assumed to be independent of the substance concentration, by

$$q_1 = -\varepsilon D(\partial C_1/\partial y), \quad (11)$$

$$q_2 = -D(\partial C_2/\partial y). \quad (12)$$

Equation (7) characterizes, in the case of good agitation within the volume of a continuous apparatus, the boundary conditions at the channel ends, which can be taken as conditions of constant concentrations. In the general case, the conditions (7) of the first kind should be replaced by boundary conditions of the third kind, and, with account taken of the variation of the substance concentration in a batch apparatus, by conditions of fifth or sixth kind [6].

Equation (8) corresponds to the absence of a flow through the blind ends of fine capillaries, and Eq. (9), to the symmetry condition along the channel axis.

The coefficient ε in Eq. (11) accounts for the fraction of the surface area across which the substance transfer from the porous block side occurs.

The system of Eqs. (1)–(12) was solved by the grid method, using for approximation of Eq. (2) the modified Pismen–Rackford method of variable directions, accurate to first order, with approximation error [Δt, $(\Delta x)^2$, $(\Delta y)^2$], where Δt is the time step of the grid (s); Δx, Δy are the grid steps along the x- and y-axes, respectively (m), with the grid being absolutely stable in the linear case [7]. Equation (1) was approximated using the absolutely stable Krank–Nicholson method, accurate to second order. The boundary conditions were approximated by expressions accurate to second order.

The fluid volume contained within the transport channel is described by the balance equation expressing the law of mass conservation with respect to the substance being extracted:

$$\partial M_1/\partial t = G_{\text{bc}} - G_0,$$

where $\partial M/\partial t$ is the rate at which the mass of the substance being extracted grows in the transport channel (kg s^{-1}), G_{bc} is the substance flux at the boundary between the porous block and the transport channel (kg s^{-1}), and G_0 is the outward flux from the transport channel (kg s^{-1}):

$$\frac{\partial M_1}{\partial t} = \frac{\partial}{\partial t}\int_0^{h_2}\int_0^{L} C_2 \mathrm{d}x\mathrm{d}y, \quad G_{\text{bc}} = D\int_0^{L} \left.\frac{\partial C_2}{\partial y}\right|_{y=h_2} \mathrm{d}x,$$

$$G_0 = D\int_0^{h_2}\left(\left.\frac{\partial C_2}{\partial x}\right|_{x=0} - \left.\frac{\partial C_2}{\partial x}\right|_{x=L}\right)\mathrm{d}y.$$

The developed software made it possible to observe dynamically the concentration fields at grid nodes and record in a data file instantaneous values of G_{bc}, G_0, and $\partial M/\partial t$ (Fig. 2).

Several numerical experiments were performed. At Peclet numbers

$$\mathrm{Pe}_L = \bar{u}L/D \le 1$$

($\bar{u} = \omega\pi^{-1}\int_0^{\pi/\omega}\int_0^{h_2} u(y, t)\partial y\partial t = 4u_{\max}/3\pi$ is the fluid motion velocity averaged over the half-period and the

transport channel cross-section), the convective transfer in the channel has virtually no effect on the extraction rate. Therefore, the main calculations were done at

$$\mathrm{Pe}_L = \bar{u}L/D > 1. \quad (13)$$

Numerical experiments demonstrated that, all other conditions being the same, there exists the optimal frequency of fluid oscillations in the channel, ω_{opt}, at which the minimum process duration can be achieved.

Analysis of the curves in Fig. 2 shows that two stages exist at any oscillation frequency. The first is the attainment of regularity, with the substance content in the porous block falling fast because of high concentration gradients. In the process, one part of molecules of the substance being extracted goes from the transport channel outwards, and the other is accumulated in the transport channel (for all plots in Fig. 2 this stage is over when curve *2* intersects the abscissa axis and curve *3* has inflection).

The second stage (mode which is "regular" when period-averaged) depends of the oscillation frequency (with all other parameters of the model fixed).

At low frequencies, the role played by convective substance transfer is insignificant; for example, curves *1* and *3* in Fig. 2a are monotonic and the lower portion of curve *2* tends asymptotically to the abscissa axis. At higher frequencies (Fig. 2b), curve *3* exhibits a weakly pronounced maximum nearly coinciding in phase with the minimum in curve *2*; at the same time the intensity of substance transfer is still rather low. This is due to the fact that the molecules of the substance being extracted have to pass a longer way toward the opening of the transport channel virtually by means of diffusion only.

At a nearly optimal frequency (Fig. 2c) all the three curves show clearly pronounced extrema virtually coinciding in phase. The outflow of the substance from the transport channel (curve *2*) is virtually immediately followed by its transfer from the particle outwards, into the fluid surrounding the particle (curve *3*). In addition, transfer from the porous block into the transport channel is enhanced (curve *1* exhibits a pronounced maximum), since the fluid in the transport channel rapidly "releases" the substance outwards, with all the three lines having large amplitudes. This type of substance transfer resembles exchange of potential and kinetic energies in mechanical oscillatory systems and, therefore, quite deserves being termed the "resonance" in mass transfer. It may be stated that the frequency of external action coin-

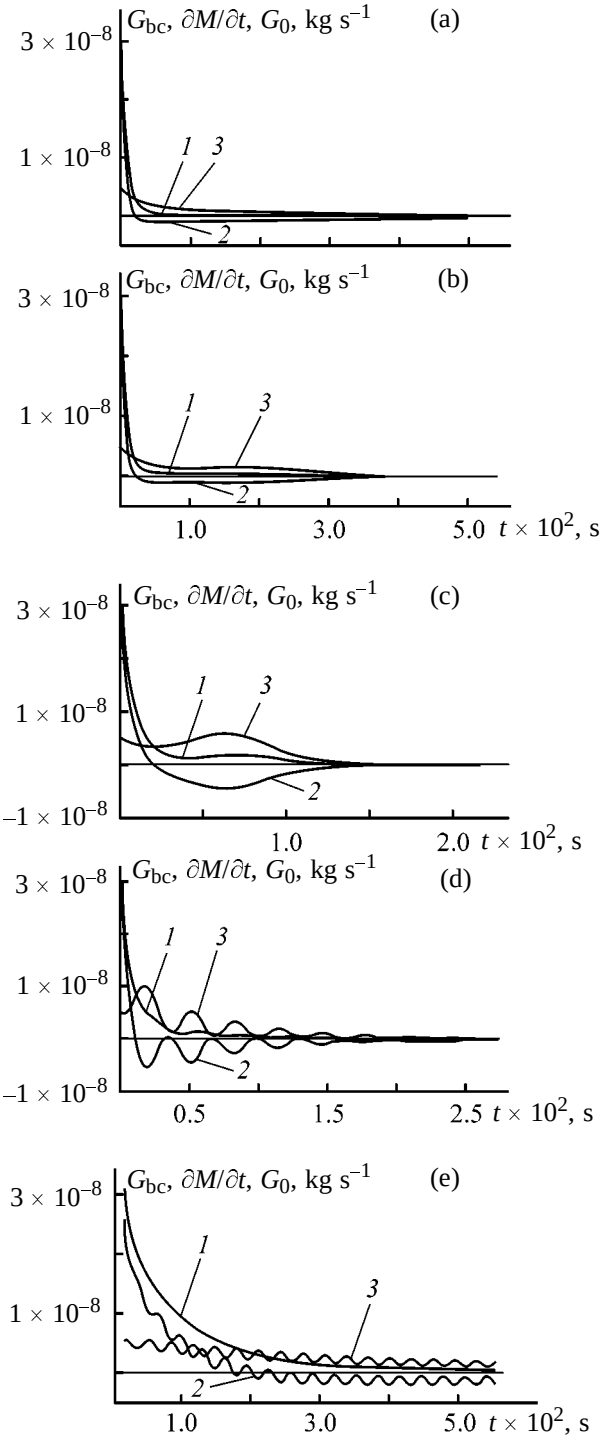

Fig. 2. Variation with time t of the (*1*) substance flux at the block–channel interface, G_{bc}; (*2*) rate of mass gain in the transport channel, $\partial M/\partial t$; and (*3*) substance flux from the transport channel outwards, G_0. Calculated parameters: $h_1 = h_2 = 10^{-6}$ m, $L = 10^{-5}$ m, $D = 0.5 \times 10^{-9}$ m^2 s^{-1}, $\varepsilon = 0.4$, $u_{max} = 5 \times 10^{-3}$ m s^{-1}, $C_{10} = 10$ kg m^3, $C_{20} = 0$. Angular frequency ω (s^{-1}): (a) 1, (b) 10, (c) 100, (d) 1000, and (e) 10000.

cides with the characteristic fundamental frequency of mass transfer inside the capillary-porous particle.

At fluid oscillation frequencies exceeding the optimal frequency severalfold (Fig. 2d), the amplitude of oscillations of curves *2* and *3* decays fast; in addition, curve *2* intersects the abscissa axis at maxima in curve *3*, with the minimum in curve *3* nearly reaching zero. This is accounted for by the fact that the fluid in the transport channel moves, together with the point of maximum concentration, so fast that the substance does not have enough time to be removed from the transport channel outwards. As a result, the maximum concentration in the channel becomes higher than that in the adjacent layers of the porous block, i.e., the transverse concentration gradient is reversed. Thus, the substance in the high-concentration zone starts to penetrate from the transport channel back into the porous block (back transfer), which on the whole hinders the process of substance extraction from the particle [4, 5].

This fact indicates that, in different parts of the transport channel, the G_{bc} flux may change not only its magnitude, but also its sign. This leads to an indisputable conclusion that the rate of molecular diffusion, characterized by the coefficient D, exerts no direct influence on the optimal frequency of oscillations. Indeed, let us assume that, all other parameters being the same, the diffusion coefficient becomes two times greater. Then, the local flux of substance across the boundary between the porous block and the transport channel will increase twofold in accordance with the Fick law. However, further, being saturated fast with the substance being extracted, the fluid in the channel will move to the region in which the porous block is depleted (i.e., the local concentration in the porous block is lower than that in the transport channel), and the local back flux of the substance at the same boundary will also increase twofold. Thus, the faster the fluid in the transport channel is saturated with the substance being extracted, the faster it returns the substance to the depleted porous block. Naturally, these considerations refer to "long" transport channels ($L/h_2 \gg 1$), since the molecular diffusion plays very important role in "short" channels. Numerical experiments demonstrated that at $L \approx h_2$ there is no optimal frequency: The short way to the opening of the transport channel is traveled by molecules fast because of the occurrence of molecular diffusion.

At frequencies exceeding the optimal frequency by an order of magnitude and more (Fig. 2e), the amplitude of oscillations of curves *2* and *3* markedly decreases. Curve *1* becomes monotonic, as in the case of low frequencies (Figs. 2a, 2b), since the concentration field has not enough time to change substantially during a period of oscillation. The dramatic decrease in the total rate of mass transfer can be understood as follows. The fluid flowing into the channel at high velocity has no time to be saturated with the substance and flows back after a short period of time. In doing so it returns the substance that has passed into the fluid in the channel to the depleted layers of the porous block at the ends of the transport channel.

A detailed analysis of the concentration field and fluxes at the channel wall at these frequencies demonstrated the following. The transverse concentration gradient in the channel rapidly approaches zero owing to intense convection; macroscopic volumes of fluid with relatively high concentration at the channel axis rapidly move from its middle part ($x \approx L/2$) into zones with low concentration, where occurs back substance transfer, and the flux signs are reversed, i.e., the substance passes from the fluid in the channel into the porous block.

Thus, too "fast" fluid oscillations within the channel (at, e.g., ultrasonic frequencies) are as inefficient as too "slow" oscillations.

Let us make an attempt to evaluate qualitatively the optimal frequency of fluid oscillations in the channel at fixed other parameters.

In order that the convective transfer of substance from a particle with bidisperse structure occur with the highest intensity it is necessary that, at the highest velocity, the concentration at the right-hand edge of the channel (Fig. 1, at $x = L$) should also be the highest, since the convective flux of the substance $q_{conv} = uC_2$. The velocity reaches its highest value in a time equal to a quarter of the oscillation period; $t_0 = (1/4)2\pi/\omega = \pi/2\omega$. During this time the fluid front must pass a distance on the order of the channel length L, being saturated, on its way, with the substance being extracted. In the model in question, the instantaneous velocity of the fluid front $u_f = (2/3)u_{max}\sin(\omega t)$, and, during a time t_0, it will travel through a distance $x_f = \int_0^{t_0} u_f dt = 2u_{max}/3\omega = u_{av}/\omega$, and just this distance should be on the order of L. Thus, the optimal frequency of fluid oscillations can be found from the condition

$$\mathrm{Sr} = \omega L/u_{av} \sim 1. \qquad (14)$$

The results obtained in calculating the Struchal number Sr at the optimal frequency of fluid oscillations are presented in Table 1.

Engineering calculations require simple relations, e.g., in the form of criteria. An analysis of the mathematical model demonstrated that the determining criteria include the fine-pore porosity ε of the porous block, geometric simplexes $\Gamma_1 = h_1/L$ and $\Gamma_2 = h_2/L$, and the Struchal number Sr, and the dependent criterion is the inverse effective Peclet number: $K_d = 1/\mathrm{Pe}_{eff} = D_{eff}/\bar{u}L$, where $\bar{u} = (4/3\pi)u_{max}$ is the fluid velocity in the transport channel, averaged over the cross-section and the half-period. The effective diffusion coefficient D_{eff} was found from the slope of the kinetic curve [4] in the regular process regime. Processing of results obtained in more than 80 numerical experiments gave the following criterion equation

$$D_{eff}/\bar{u}L = 0.218\mathrm{Sr}^{0.5}\exp(-1.2\mathrm{Sr})\varepsilon^{-0.22}\Gamma_1^{-0.63}\Gamma_2^{0.29}. \quad (15)$$

The exponential factor is introduced into the equation to account for the "resonance" dependence of the effective diffusion coefficient on the Struchal number [Fig. 3 shows the function (15) for fixed ε, Γ_1, Γ_2]. This curve exhibits a maximum at Sr = 0.42, i.e., at Sr on the order of unity.

EXPERIMENTAL

To verify the numerically obtained relations, an experimental setup shown schematically in Fig. 4a was assembled. The oscillatory motion of the fluid through the central channel in the particle was effected by means of a system comprising a compressor *1*, a solenoid-and-pressure-operated valve *2*, and a control unit (pulse generator) *3* with variable repetition frequency and off duty factor of rectangular pulses. The valve *2* was connected by a tube *4* with inner diameter D_t = 15 mm and hose *5* to the model *6* of a capillary-porous particle with bidisperse structure, which, in turn, is connected by means of a tight joint in the form of a plug *7* to a 5-l glass vessel *8*. The amplitude of fluid oscillations was controlled by means of bypass *9* and throttling *10* valves. The U-shaped part of the hose was 5–350 mm long, the length of the pipe connecting the particle model *6* to the plug *7* was 105 mm.

The model of a capillary-porous particle with bidisperse structure is shown schematically in Fig. 4b. In a glass tube *11* is mounted a coaxial polyvinyl chloride plastic tube *12* with through holes *13* of diameter 0.1–0.2 mm, arranged in staggered rows with a step of 2–3 mm. At both ends the tube *11* is sealed with rubber plugs *14*, between which is placed a dense bed *15* of washed river sand (particle size 300–400 μm). After being placed in the model, the sand was impregnated with 10.0 ml of 2 N HCl solution to saturation. It could be seen through the transparent tube *11* that the entire intergrain space of the sand was being homogeneously impregnated with the acid solution, with air removed through holes *13* in the tube *12*. The bed saturation was also judged from the onset of drop fall from the pore space. The volume of the drops was measured with a volumetric cylinder.

Table 1. Struchal number estimated at the optimal frequency of fluid oscillations ($h_1 = h_2$ = 1 μm, L = 10 μm)

$u_{max} \times 10^3$, m s^{-1}	ω_{opt}, rad s^{-1}	Pe_L by formula (13)	Sr by formula (14)
0.5	40	4.24	1.2
1.0	70	8.49	1.05
2.5	150	21.2	0.9
5.0	200	42.4	0.6
7.5	300	63.7	0.9

Thus, a dense grainy bed saturated with liquid was formed in the annular channel between tubes *11* and *12*. The bed was connected to the inner space of tube *12* only through fine holes *13*. This allowed the bed to be regarded as incompressible, and substance transport within this bed, as having purely diffusion nature. The fluid flowing inside the tube *12* provided for the convective transport of the substance.

In this experimental model, the pore space of the bed *15* is analogue of fine capillaries in capillary-porous particles of plant origin, and the tube *12*, analogue of a transport channel.

After switching-on the compressor *1* and control unit *3* and filling the vessel *8* (Fig. 4a) with 1 l of 0.01 N NaOH solution, a stopwatch was set going. The duration τ (s) of the extraction process was judged from the instant of decolorization (neutralization) of the alkali solution to which 1 ml of 1% alcoholic solution of phenolphthalein was preliminarily

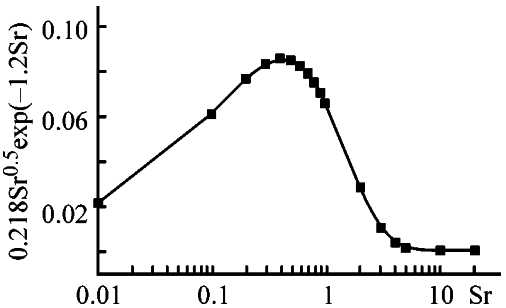

Fig. 3. Typical plot of the quantity $0.218\mathrm{Sr}^{0.5}\exp(-1.2\mathrm{Sr})$ vs. Struchal number.

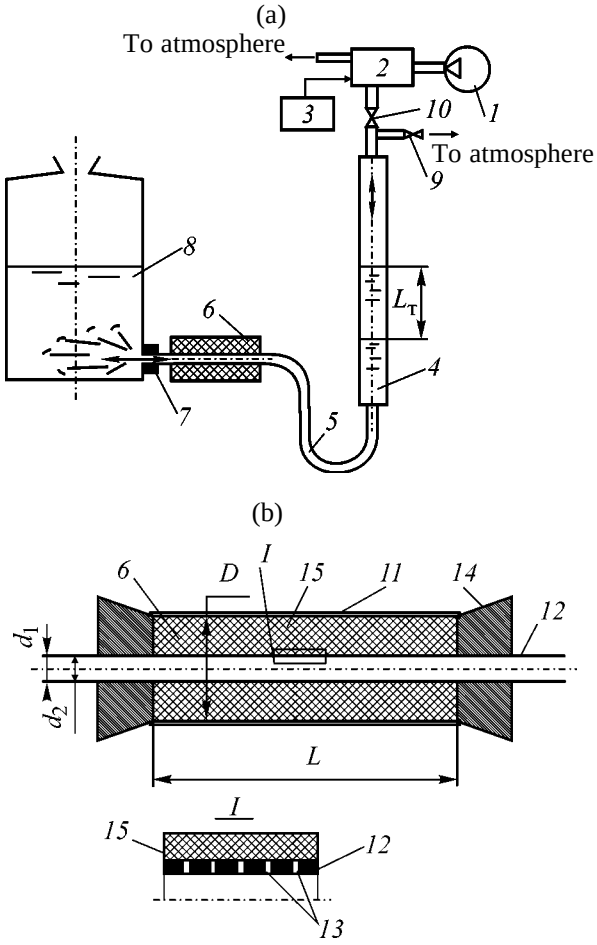

Fig. 4. Setup for modeling extraction from capillary-porous particle with bidisperse structure: (a) overall scheme and (b) cartridge simulating the porous particle. L = 78 mm, D = 23 mm, d_1 = 10 mm, and d_2 = 7.5 mm. (*1*) Compressor, (*2*) solenoid-and-pressure-operated valve, (*3*) control unit (pulse generator), (*4*) glass tube, (*5*) hose, (*6*) particle model, (*7*) plug, (*8*) vessel with bottom neck, (*9, 10*) valves, (*11*) glass tube, (*12*) polyvinyl chloride plastic tube, (*13*) holes, (*14*) rubber plugs, and (*15*) dense bed of sand.

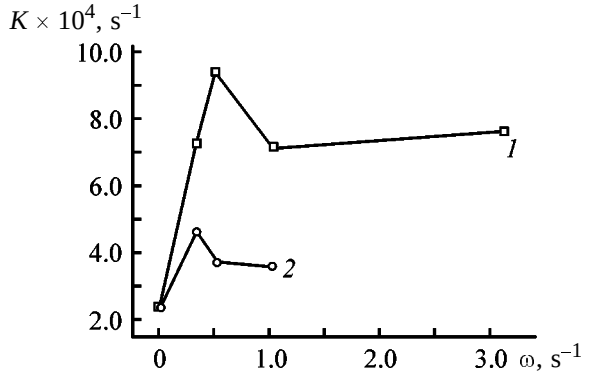

Fig. 5. Extraction index K vs. angular velocity ω of oscillations at different amplitudes A of fluid oscillations in the particle model. A (m): (*1*) 0.60 and (*2*) 0.12.

added. The amount of acid present in the pore space of sand twice exceeded that required by the stoichiometry. In experiments with large oscillation amplitude, the fluid in the vessel was rather well agitated by a pulsing jet; in other cases, the fluid was additionally agitated, in order to equalize concentrations, by slightly rocking the vessel *8*. In an experiment with "immobile" fluid, when no fluid oscillations were generated in tube *2*, the particle model was placed in a volumetric cylinder in which fluid was agitated with a slowly rotating glass rod (with rotation frequency of 1 s^{-1}). These measures were taken to enable the outer-diffusion resistance to substance transfer (outside the particle model) to be considered infinitely small as compared with the inner-diffusion resistance (inside the particle model). Also measured were the pulse duration T_p, interval duration T_i, and the amplitude L_t of fluid motion in the tube *4* (Fig. 4a).

The amplitude of fluid motion in the tube *2* was determined using the formula

$$A = L_t(D_t/d_2)^2, \quad (16)$$

and the average velocity of the fluid in the tube was found as

$$u_{av} = A/T_p. \quad (17)$$

The angular frequency of oscillations were calculated using the relation

$$\omega = 2\pi/(T_p + T_i), \quad (18)$$

and the off-duty factor of pulses was found as the ratio of the pulse duration to the oscillation period:

$$\Psi = T_p/(T_p + T_i). \quad (19)$$

As a similarity criterion, characterizing the simultaneous (homochronous) nature of the diffusion extraction of substance from the intergrain space into the transport channel (tube *12* in Fig. 4b), on the one hand, and the convective transfer of the extracted substance from this channel into the bulk of the fluid in the apparatus, on the other, was taken the Struchal number calculated using the formula

$$Sr = \omega L_{eff}/u_{av}, \quad (20)$$

with the sum of the lengths of tube *12* and hose and tube connections taken as the effective channel length L_{eff} = 0.533 m. As the characteristic of the process intensity was chosen a reciprocal of the extraction process duration: $K = 1/\tau$.

The results of the experiments are presented in Table 2, and dependences of K on ω and Sr in, respectively, Figs. 5 and 6. The run of these dependences

Table 2. Results obtained in modeling the process of extraction from a capillary-porous particle with bidisperse structure

T_i	T_p	L_t	A	ω, s^{-1}	u_{av}, m s^{-1}	Ψ	Sr	τ, s
s		m						
∞	0	0	0	0	0	0	0	4200
9	1	0.145	0.58	0.628	0.58	0.10	0.577	1200
3	1	0.15	0.6	1.57	0.6	0.25	1.39	852
6	1	0.15	0.6	0.897	0.6	0.143	0.797	1380
3	1	0.15	0.6	1.57	0.6	0.25	1.39	789
2.5	1.5	0.28	1.12	1.57	0.747	0.375	1.12	740
6	6	0.21	0.84	0.523	0.14	0.50	1.99	1065
3	3	0.18	0.72	1.05	0.24	0.50	2.32	1405
1	1	0.05	0.2	3.14	0.2	0.50	8.37	1320
9	9	0.15	0.6	0.349	0.0667	0.50	2.79	1380
3	3	0.03	0.12	1.05	0.04	0.50	13.9	2820
6	6	0.03	0.12	0.523	0.02	0.50	13.9	2697
9	9	0.03	0.12	0.349	0.0133	0.50	13.9	2182
9	9	0.06	0.24	0.349	0.0267	0.50	6.97	1380
6	6	0.035	0.14	0.523	0.0233	0.50	12.0	1260
3	3	0.02	0.08	1.05	0.0267	0.50	20.9	3000

corresponds to the nature of the numerically obtained relations. In particular, the dependence represented by experimental points in Fig. 6 is in qualitative agreement with the approximation yielded by processing the results of numerical simulations and shown in Fig. 3.

CONCLUSIONS

(1) For each fluid oscillation amplitude there exists the optimal oscillation frequency at which the extraction process has the highest intensity.

(2) At a certain Struchal number, approximately equal to unity, the extraction proceeds the most intensely.

(3) In particles with long transport channels practically no effect on the optimal oscillation frequency.

(4) Too high oscillation frequencies, and also too low frequencies (at equal amplitude), do not lead to ($L/h_2 \gg 1$) the molecular diffusion coefficient has any noticeable acceleration of the extraction process as compared with simple infusion, being, therefore, energetically unfavorable.

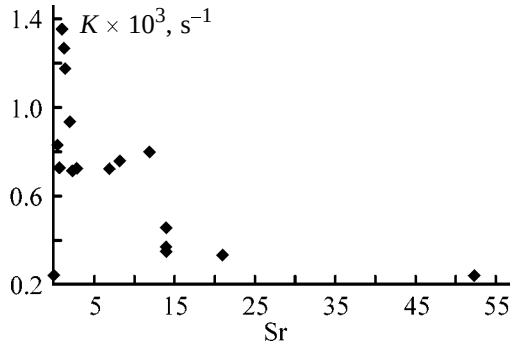

Fig. 6. Extraction index K vs. the Struchal number Sr.

(5) The obtained relations make it possible to provide recommendations for determining the optimal extraction conditions on measuring the pore size in real particles.

REFERENCES

1. Aksel'rud, G.A. and Al'tshuler, M.A., *Vvedenie v kapillyarno-khimicheskuyu tekhnologiyu* (Introduction to Capillary-Chemical Technology), Moscow: Khimiya, 1983.
2. Ostrovskii, G.M., Ivanenko, A.Yu., and Aksenova, E.G., *Teor. Osn. Khim. Tekhnol.*, 1995, vol. 29, no. 6, pp. 607–611.
3. Abiev, R.Sh., *Zh. Prikl. Khim.*, 2000, vol. 73, no. 7, pp. 1141–1144.
4. Abiev, R.Sh. and Ostrovskii, G.M., *Teor. Osn. Khim. Tekhnol.*, 2001, vol. 35, no. 3, pp. 1–7.
5. Abiev, R.Sh., Ostrovskii, G.M., and Aletdinova, N.G., *Sbornik trudov Mezhdunarodnoi nauchnoi konferentsii "Matematicheskie metody v tekhnike i tekhnologiyakh – MMTT-2000"* (Proc. Int. Sci. Conf. "Mathematical Methods in Technology—MMTT-2000"), St. Petersburg, June 23–26, 2000, vol. 3, section 3, pp. 89–91.
6. Sterlin, M.D., *Upravlenie teplofizicheskimi protsessami: novye modeli i algoritmy* (Control over Thermal Processes: New Models and Algorithms), St. Petersburg: Sankt-Peterb. Gos. Tekh. Univ., 1997.
7. Anderson, D.A., Tannehill, J.C., and Pletcher, R.H., *Computational Fluid Mechanics and Heat Transfer*, New York: Hemisphere, 1984.

Russian Journal of Applied Chemistry, Vol. 74, No. 5, 2001, pp. 784–787. Translated from Zhurnal Prikladnoi Khimii, Vol. 74, No. 5, 2001, pp. 762–766.

ENVIRONMENTAL PROBLEMS OF CHEMISTRY AND TECHNOLOGY

Identification of Oil Pollution Sources by a Set of Modern Instrumental Methods

O. Yu. Begak and A. M. Syroezhko

St. Petersburg State Technological Institute, St. Petersburg, Russia
Mendeleev Russian Research Institute of Metrology, St. Petersburg, Russia

Received December 28, 2000

Abstract—Source of contamination of the soil and water with oil can be exactly identified by a set of instrumental methods such as atomic absorption spectrometry, inductively coupled plasma mass spectrometry, atomic emission spectroscopy, X-ray fluorescence analysis, and inductively coupled plasma emission spectrometry.

Sources of pollution of environmental objects (soil, water) can be exactly identified using a set of instrumental methods including FTIR, γ-ray spectrometry, and up-to-date analytical methods for determination of impurities in oil. Identification is carried out by both quantitative analysis for impurities such as S, Na, Ca, Fe, Ni, Cu, V, Mn, Zn, Mg, Al, Ba, and Ti and their relative content.

In the previous work [1] on the basis of analytical data on oils of six oil fields of the Khanty-Mansi autonomous district we recommended to use FTIR and γ-ray spectrometry for preliminary identification of oil pollution sources. Gas chromatography–mass spectrometry and capillary GLC appeared to be low-informative in this respect.

EXPERIMENTAL

For reliable identification of oil pollution sources, in addition to the methods employed in [1] (FTIR, γ-ray spectrometry, gas chromatography–mass spectrometry, and capillary GLC) we used five more up-to-date methods: (1) inductively coupled plasma mass spectrometry (ICP-MS), (2) atomic absorption spectrometry (AAS) in the flame or unflame atomization modes [2], (3) X-ray fluorescence analysis (XFA) [3], atomic emission spectroscopy, and inductively coupled plasma emission spectrometry (ICP-ES) [4].

Metal impurities in samples of oil, oil-polluted soil, and watered oil sample were determined by ICP-MS with a VG inductively coupled plasma mass spectrometer (the United Kingdom). Standards of each of element to be determined were prepared in nitric acid gravimetrically.

Metal impurities were determined by electrothermal atomic absorption spectrometry (ETAAS) with a Perkin–Elmer Model 4100 ZL instrument. Hollow cathode lamps of the same manufacturer were used.

We examined a combined scheme of identification of oil pollution sources by impurities (metal and nonmetal) using two different methods: (1) atomic emission spectroscopy of oil dry ash residue with Ar high-frequency plasma as a light source and an STE-1 crossed dispersion spectrograph and (2) ICP-ES of mineralized acidic solutions of test oil samples on a PS1000 instrument (Leeman Labs Inc., the United States), which allowed determination of a wide variety of impurities in test oils. Also we used a Hitachi 180/80 polarized Zeeman flame atomic absorption spectrophotometer (Hitachi, Japan) with atomization in stoichiometric acetylene–air flame.

XFA examination of oil samples was performed on a Philips PW 1220C automatic scanning spectrometer.

In Fig. 1a are given data on the V, Cu, Ni, and Cr content in the initial oil samples (oil field numbering is as in [1]). Basing on these data, all the oil samples can be arbitrarily subdivided into three groups with high, medium, and low content of the indicated metals. The first group (total content of the four metals above 40 mg kg^{-1}) includes sample nos. 1 (Alekhinskoe oil field), 2 (Lyantorskoe oil field), and

1070-4272/01/7405-0784$25.00

7 (Priobskoe oil field); the second group (10–40 mg kg^{-1}) includes sample nos. 5 (Trekhozernoe oil field), 6 (Prirazlomnoe oil field), and 8 (Petelinskoe oil field); and the third group (<10 mg kg^{-1}) is represented by sample no. 4 (Krasnoleninskoe oil field).

Figure 1b demonstrates the relative metal content in the oil samples. The results obtained by ICP-MS (Figs. 1a, 1b) allow identification of oil from the indicated oil fields. The most difficultly distinguishable are sample nos. 1 and 2 (Alekhinskoe and Lyantorskoe oil fields, respectively). However, in this case also the relative content of impurities differs by more than 10% (effective criterion of the Russian State Ecological Committee). Artificial aging of oil did not change the indicated trends somewhat significantly. Therefore, oil of different oil fields of the West Siberia can be objectively distinguished by the content of the indicated four metals, as determined by ICP-MS.

Also oil samples are unambiguously identified by ETAAS. This method was used for determination of V, Ni, and Cr [5].

The final stage of this study was performing of multi-technique identification of oil pollution sources by impurities. All oil samples were analyzed by atomic emission spectroscopy (vaporization of ash residue in ac arc) for 25 foreign elements (Mn, Cu, Ni, Fe, Zn, Ca, Cr, Mg, Al, Ag, V, Na, B, Ba, Ti, Pb, Co, Be, As, Sb, Cd, Bi, Hg, Se, and S). In none of the samples studied we found As, Sb, Se, Bi, Cd, Hg, Ag, and Be. The content of Co, B, Cr, and Pb was found to be near the detection limits of the indicated analytical techniques. Therefore, it was advisable to develop a multi-technique procedure of oil identification involving determination of 13 foreign elements: S, Na, Ca, Fe, Ni, Cu, Zn, Mg, Al, V, Ba, Mn, and Ti. Combined employment of ICP-ES, AAS, and XFA allows reliable determination of all the indicated 13 foreign elements. In this case Ca, Fe, Ni, Cu, and Zn can be determined by all the three techniques or by any of them separately. Also, if needed, FTIR or γ-ray spectrometry can be attracted.

It should be pointed out that sulfur is best determined by XFA. Na, Al, Mn, and Ti are most reliably determined by ICP-ES; and Mg, Ba, and V, by combination of AAS and ICP-ES.

All the three indicated techniques are applicable to thorough characterization of oil from the Khanty-Mansi autonomous district. The results are summarized in Table 1. They suggest that all the samples studied, including oil-polluted soil and water, are clearly distinct in the absolute and relative content of

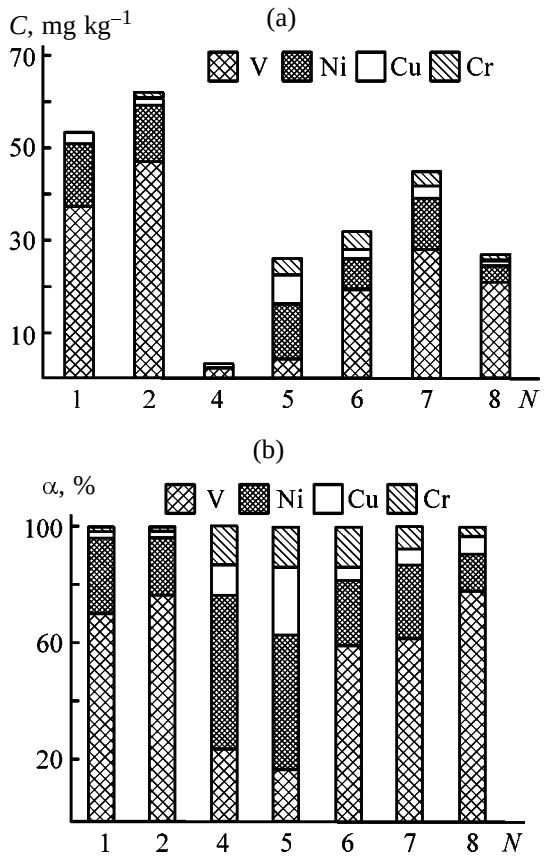

Fig. 1. Identification of oil from various oil fields by (a) the content of metal impurities *C* and (b) their relative content α. (*N*) Sample no.

individual foreign elements and their total content. The concentrations of such foreign elements as Na, Cu, V, Mn, and Ti can differ from sample to sample by a factor of up to several tens. For Ca, Ni, Mg, and Ba this factor is about 10, and for Zn and Al, 5–7.

The total content of 12 foreign elements varies over the range 319–3556 μg cm^{-3}, i.e., by a factor of 11.

The results show a strong variation in the sulfur content from sample to sample. The maximal content (0.95–0.99%) was observed in sample nos. 1 (Alekhinskoe oil field) and 7 (Priobskoe oil field). The minimal content (0.3–0.4%) was found in sample nos. 4 (Krasnoleninskoe oil field) and 5 (Trekhozernoe oil field). The minimal and maximal contents of sulfur in the samples studied differ by a factor of 3.1.

The individuality of the oil samples studied is manifested even more distinctly in comparative analysis of data on the relative content of foreign elements (Table 2). In sample no. 1 the ratio Mg/Ba = 37.5 is maximal among all the samples. Sample no. 2 is characterized by the maximal Mg/Zn ratio (12.5), sam-

Table 1. Foreign elements in oil samples

Element	Element content, μg cm^{-3}, in indicated sample							C_{max}/C_{min}
	no. 1	no. 2	no. 4	no. 5	no. 6	no. 7	no. 8	
S	9500	8100	3200	4350	7600	9900	5900	3.1
Na	295	2730	215	260	355	115	790	23.7
Ca	92	400	180	40	250	50	170	10.0
Fe	90	110	35	30	90	20	80	5.5
Ni	20	46	20	20	65	15	6	10.8
Cu	15	20	25	5	160	10	20	32.0
Zn	18	10	15	10	60	15	20	6.0
Mg	75	125	115	25	210	20	30	10.5
Al	40	65	50	15	50	35	10	6.5
V	35	20	1.4	1.2	10	35	10	29.2
Ba	2	10	5	20	7	2	6	10.0
Mn	1.2	1.3	2.4	0.4	2.9	0.4	0.1	29.0
Ti	5	20	0.8	0.6	1.3	1.2	1.0	33.3
Σ foreign elements (without S)	688	3556	665	427	1261	319	1143	–

Table 2. Distinguishing features of oil samples

Parameter	Element ratio in indicated sample						
	no. 1	no. 2	no. 4	no. 5	no. 6	no. 7	no. 8
Mg/Ba	37.5*	12.5	23	1.25	30	10	5
Mg/Zn	4.2	12.5	7.7	2.5	3.5	1.3	1.5
Ca/V	2.6	20	129	33	25	1.4	17
Ca/Ba	46	40	36	2	35.7	25	28
Cu/Σ	0.022	0.006	0.037	0.012	0.127	0.031	0.017
Ca/Mg	1.2	3.2	1.6	1.6	1.2	2.5	5.7

* The maximal values are underlined.

ple no. 4, by the maximal Ca/V ratio (12.9), and sample no. 8, by the maximal Ca/Mg ratio (5.7). Sample no. 7 is characterized by the maximal ratio of Cu to the total of foreign elements (Cu/Σ = 0.127). In sample nos. 5 and 7, respectively, the ratios Ca/Ba = 2 and Ca/V = 1.4 are the minimal.

To conclude, the results obtained show that oil from each oil field of the Khanty-Mansi autonomous district has its individual composition of foreign elements and can be identified by a set of up-to-date analytical techniques. One of the possible flowsheets of identification of oil pollution source in the Khanty-Mansi autonomous district is given in the scheme.

CONCLUSIONS

(1) It was demonstrated with an example of oils of the Khanty-Mansi autonomous district that oil pollution sources can be identified by impurity content using such methods as γ-ray spectrometry, atomic absorption analysis, atomic emission analysis, X-ray fluorescence analysis, ICP-MS, and ICP-ES. For primary identification FTIR can be used.

(2) Identification is performed by computer comparison of absorption bands of oil samples in the fingerprint range, and also by the radionuclidic composition of elements of the thorium and uranium

Possible flowsheet of identification of oil pollution source in the Khanty-Mansi autonomous district

Sample collected from oil spill

Sample collected from the source

↓

First stage. FTIR examination of test sample and of samples collected from all probable pollution sources

↓

If IR spectra are similar, identification is continued

If IR spectra are not similar, identification is completed

↓

Quantitative comparative analysis of characteristic parameters of IR spectra ⟶ Parameters of IR spectra are not identical. Identification is completed

↓

Parameters of IR spectra meet the identity criterion. Selection of oil samples for the second stage of identification

↓

Second stage. γ-Ray spectrometry or ICP-MS (or AAS, ICP-ES, XFA). Determination of foreign metals and their ratios for the group of samples selected in the first stage

↓

Characteristic parameters of the samples meet the identity criterion. Selection of oil samples for the third stage of identification

Characteristic parameters of the samples do not meet identity criterion. Identification is completed

↓

Third stage. Statistical treatment of the results

↓

Characteristic parameters of the samples meet the identity criterion. Identification is completed. Samples are identical

Characteristic parameters of the samples do not meet the identity criterion. Identification is completed

series, the composition of metallic and nonmetallic impurities in oil such as S, Na, Ca, Fe, Ni, Cu, Zn, Mg, Al, V, Ba, Mn, and Ti, and their relative content.

REFERENCES

1. Begak, O.Yu. and Syroezhko, A.M., *Zh. Prikl. Khim.*, 2001, vol. 74, no. 4, pp. 617–620.
2. Sturgeon, R., *Spectrochim. Acta*, 1997, vol. 52, nos. 9–10, pp. 1451–1457.
3. Afonin, V.P., Komyak, N.I., Nikolaev, V.P., and Plotnikov, R.I., *Rentgenofluorestsentnyi analiz* (X-ray Fluorescence Analysis), Novosibirsk: Nauka, 1991.
4. Employment of ICP-ES in Geological and Environmental Research, *ICP Inf. Newslett.*, 1996, vol. 21, no. 8, pp. 512–514.
5. Begak, O.Yu., Borodin, A.V., Dolinger, V.A., *et al.*, *Zavod. Lab. Diagnost. Mater.*, 1999, vol. 65, no. 12, pp. 16–19.

Russian Journal of Applied Chemistry, Vol. 74, No. 5, 2001, pp. 788–791. Translated from Zhurnal Prikladnoi Khimii, Vol. 74, No. 5, 2001, pp. 767–770.

ORGANIC SYNTHESIS AND INDUSTRIAL ORGANIC CHEMISTRY

Solubility of Synthetic Pyrethroids in Organic Solvents

O. I. Mikhailenko, O. A. Kolyadina, and Yu. I. Murinov

Institute of Organic Chemistry, Ufa Scientific Center, Russian Academy of Sciences, Ufa, Bashkortostan, Russia

Received March 30, 2000; in final form, July 2000

Abstract—The solubilities of four synthetic pyrethroids in organic solvents at 0–50°C were determined, and the enthalpies of solution were calculated. The enthalpies of solution of pyrethroids in benzene were measured calorimetrically.

Synthetic pyrethroids show considerable promise as insecticides, being safe for humans, useful fauna, and environment as a whole and meeting in this respect the modern requirements to chemical means for plant protection [1]. The most convenient form of insecticides is their liquid form, in particular, an emulsifiable concentrate [2]. Up to now, pesticide formulations for practical use were selected semiempirically [3]. The emulsifiable concentrate is a multicomponent solution whose properties are determined by a set of physicochemical processes occurring in this system. The scientifically substantiated approach to development of pesticide formulations for practical use requires understanding of these physicochemical processes. In this work we studied the solubility of various pyrethroids in organic solvents.

EXPERIMENTAL

The pyrethroids were prepared in the laboratory of fine organic synthesis. The structure and physicochemical properties of the pyrethroids are listed in Table 1. At various temperatures we determined the solubilities of these pyrethroids in heptane, toluene, tetrachloromethane, and ethanol, and also of Alphametrin and Decametrin in hexane and cyclohexane and of Phenvalerate in chloroform. The solvents were purified by standard procedures [4].

The solubility of synthetic pyrethroids in organic solvents N_s (mole fraction) was determined gravimetrically in the temperature range 0–50°C. Saturated solutions of pyrethroids were prepared by continuous shaking of a solvent with excess pyrethroid in closed temperature-controlled test tubes. The time required to attain the equilibrium varied from 1 to 5 h depending on the solution viscosity and concentration; the process was monitored refractometrically. The temperature was maintained to within ±0.1°C. The relative error of solubility determination was 2–5%.

The enthalpy of solution of pyrethroids in benzene was measured with a Calvet differential microcalorim-

Table 1. Physicochemical characteristics of synthetic pyrethroids*

Pyrethroid	Name	Purity, %	mp, °C	d^{25}, kg dm^{-3}	n_D^{25}
I	Permetrin	97	15–16	1.191	1.5672
II	Phenvalerate	98	17–18	1.172	1.5689
III	Alphametrin	99	79–80	–	–
IV	Decametrin	99	97–98	–	–

* Structural formulas:

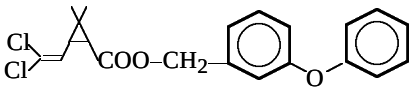

I

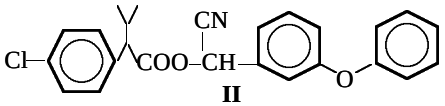

II

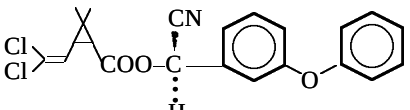

III

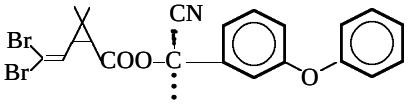

IV

1070-4272/01/7405-0788$25.00

Table 2. Solubility of synthesic pyrethroids in organic solvents at various temperatures

T, K	Solubility, mole fraction				*T*, K	Solubility, mole fraction			
	I	**II**	**III**	**IV**		**I**	**II**	**III**	**IV**
	In hexane					In ethanol			
283.2	–	–	0.00056	0.00025	308.2	0.25955	0.0380 (306.2 K)	0.00543	0.00166
288.2	–	–	0.00123	0.00038					
293.2	–	–	0.00143	0.00050	313.2	–	–	0.00777	0.00228
298.2	–	–	0.00199	0.00069					
303.2	–	–	0.00265	0.00110		In toluene			
308.2	–	–	0.00385	0.00131					
313.2	–	–	0.00559	0.00191	273.2	–	0.278	0.0687	–
					283.2	0.477	0.334	0.0929	0.0363
	In cyclohexane				288.2	–	0.356	0.109	0.0458
					293.2	0.590	0.388	0.125	0.0578
283.2	–	–	0.00290	0.00093	298.2	0.626	–	0.153	0.0708
288.2	–	–	0.00366	0.00140	303.2	0.682	–	–	0.0840
293.2	–	–	0.00615	0.00212					
298.2	–	–	0.00799	0.00275		In tetrachloromethane			
303.2	–	–	0.01214	0.00360					
308.2	–	–	0.01904	0.00537	273.2	–	–	0.0686	–
313.2	–	–	0.02264	–	280.2	0.436	–	–	–
					283.2	0.455	–	–	0.0121
	In heptane				286.2	0.466	–	0.0784 (285.2 K)	–
283.2	0.0985	–	0.00391 (284.2 K)	0.00041	288.2	0.469 (290.2 K)	–	0.0820	0.0155
288.2	0.1241	0.0309	0.00419	0.00052	293.2	0.479	–	0.0893	0.0236
293.2	0.1514	0.0374	0.00464	0.00064	298.2	–	0.398 (299.2 K)	0.0914	0.0309
298.2	0.1798	0.0488	0.00527	0.00080	303.2	–	–	–	0.0458
303.2	0.2355	0.0670	0.00570	0.00100	307.2	–	0.514	–	–
308.2	–	0.0924	0.00627	–	310.2	–	0.568	–	–
					315.2	–	0.651	–	–
	In ethanol				318.2	–	0.716	–	–
					320.2	–	0.769	–	–
273.2	–	0.00808	–	–					
283.2	0.09724	0.0157 (285.2 K)	0.00131	0.00039		In chloroform			
288.2	0.11906	0.0162	0.00172	0.00055					
293.2	0.14464	0.0217 (291.2 K)	0.00232	0.00074	283.2	–	0.366	–	–
298.2	0.16779	0.0240 (296.2 K)	0.00293	0.00094	288.2	–	0.417	–	–
300.2		0.0267	–	–	293.2	–	0.467	–	–
303.2	0.1981	0.0345	0.00403	0.00127	298.2	–	0.490	–	–
					300.2	–	0.539	–	–

eter (Setaram, France) at 30°C. The temperature was maintained to within ±0.005°C. The device was calibrated by the heat due to the Joule effect. The calibration accuracy was ±0.5°C.

The experimental solubility data are listed in Table 2. From the polythermal data, using the equation $\partial \ln N_s / \partial (1/T) = -\Delta H_s / R$, we calculated the enthalpies of solution of the pyrethroids (Table 3).

Our results show that the solubility of the pyrethroids in all the tested solvents decreases in the order Permetrin > Phenvalerate > Alphametrin > Decametrin. According to [5], the degree of self-association of

Table 3. Enthalpies of solution of synthetic pyrethroids in various organic solvents

Solvent	ΔH_s, kJ mol^{-1}			
	I	**II**	**III**	**IV**
Hexane	–	–	51.7 ± 3.7	49.3 ± 1.6
Cyclohexane	–	–	53.4 ± 2.3	49.2 ± 1.8
Heptane	30.2 ± 1.3	40.9 ± 2.8	14.6 ± 0.4	31.6 ± 0.4
Ethanol	27.3 ± 1.3	31.9 ± 1.6	41.0 ± 1.1	42.4 ± 0.8
Toluene	12.7 ± 0.8	11.0 ± 0.4	21.3 ± 0.9	30.2 ± 0.8
Tetrachloromethane	3.2 ± 0.6	24.7 ± 0.3	8.1 ± 0.6	47.8 ± 2.5
Chloroform	–	13.9 ± 1.7	–	–

pyrethroids in organic solvents increases in the opposite order: Permetrin < Phenvalerate < Alphametrin < Decametrin. For enantiomerically pure Alphametrin and Decametrin, the solubility, apparently, is largely affected by the crystal lattice strength.

The synthetic pyrethroids are considerably less soluble in saturated hydrocarbons and ethanol, as compared to toluene and chlorinated solvents. As for the solubility of Alphametrin and Decametrin in saturated hydrocarbons, it increases in the order hexane < heptane < cyclohexane. The enthalpies of solution of these pyrethroids in hexane and cyclohexane coincide within experimental error. Hence, the different solubility is due to the entropy factor: More compact cyclohexane molecules, apparently, penetrate more readily into the rigid crystal lattice of Alphametrin and Decametrin and promote their dissolution. The enthalpies of solution in heptane are considerably lower, especially for Alphametrin.

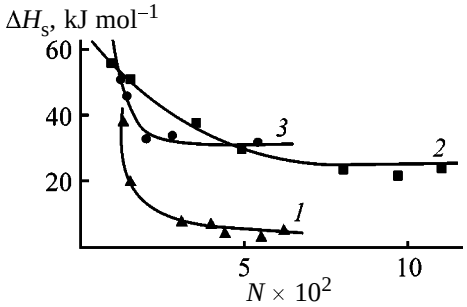

Fig. 1. Enthalpy of solution of pyrethroids in benzene ΔH_s, determined calorimetrically at 30°C, as a function of solute mole fraction *N*. Pyrethroid: (*1*) Phenvalerate, (*2*) Alphametrin, and (*3*) Decametrin.

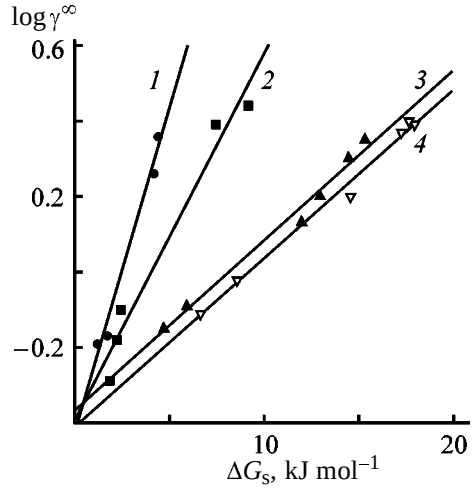

Fig. 2. Correlations between the Gibbs energies of solution of pyrethroids ΔG_s (298 K) and limiting activity coefficients γ^∞ of organic solvents in pyrethroids, calculated from the GLC data (373 K). Pyrethroid: (*1*) Permetrin, (*2*) Phenvalerate, (*3*) Alphametrin, and (*4*) Decametrin.

In dissolution of pyrethroids in CCl_4, the intermolecular interactions with the solvent are largely determined by the dichlorovinyl fragment: The enthalpies of solution of Permetrin and Alphametrin containing this fragment are appreciably lower than those of Phenvalerate and Decametrin.

The concentration dependences of the enthalpies of solution of pyrethroids in benzene, determined calorimetrically, are shown in Fig. 1. At 30°C, in the range of pyrethroid mole fractions 0.03–0.05 and higher, the enthalpies of solution of Phenvalerate, Alphametrin, and Decametrin are 4.3 ± 2.1, 23.8 ± 2.8, and 33.3 ± 2.3 kJ mol^{-1}, respectively. These values are consistent with the values obtained from the temperature dependences of the solubility in another aromatic solvent, toluene: 11.0 ± 0.4, 21.3 ± 0.9, and 30.2 ± 0.8 kJ mol^{-1}, respectively. The lowest enthalpy of solution of Phenvalerate could be expected from the fact that pyrethroid molecules can interact with aromatic hydrocarbons by the π–π mechanism, and Phenvalerate contains three benzene rings in the molecule and exhibits the loosest structure of the crystal lattice. Figure 2 shows that Phenvalerate is characterized by stronger interactions with aromatic hydrocarbons than Alphametrin and Decametrin.

CONCLUSIONS

(1) The solubility of pyrethroids in organic solvents varies in opposite direction with the degree of their self-association.

(2) The calorimetrically measured enthalpies of solution of pyrethroids are comparable with the values calculated from the temperature dependences of the solubility.

REFERENCES

1. Mel'nikov, N.N., *Zh. Vses. Khim. O–va. im. D.I. Mendeleeva*, 1988, vol. 33, no. 6, p. 602.
2. *The Pesticide Manual: A World Compendium*, Worthing, Ch.R., Ed., Nottingham, 1979, 6th ed.
3. Hulpke, H., *Pesticide Chemostry: Humam Welfare and Environment: Proc. 5th Int. Congr. on Pesticide Chemistry (Kyoto, Japan, 1982)*, Miyamoto, J. and Kearney, P.C., Eds., Oxford: Pergamon, 1983, vol. 4, pp. 241–244.
4. Weissberger, A. and Proskauer, E.S., *Organic Solvents. Physical Properties and Methods of Purification*, Riddick, J.A. and Toops, E.E., Eds., New York: Interscience, 1955.
5. Mikhailenko, O.I., Kolyadina, O.A., and Murinov, Yu.I., *Zh. Fiz. Khim.*, 1996, vol. 70, no. 12, p. 2290.

Russian Journal of Applied Chemistry, Vol. 74, No. 5, 2001, pp. 792–795. Translated from Zhurnal Prikladnoi Khimii, Vol. 74, No. 5, 2001, pp. 770–774.

ORGANIC SYNTHESIS AND INDUSTRIAL ORGANIC CHEMISTRY

Antiradical and Antioxidant Activity of Phenylhydrazones of Aromatic Aldehydes

E. I. Pleskushkina, A. N. Nikolaevskii, and T. A. Filippenko

Donetsk State University, Donetsk, Ukraine

Received April 29, 2000

Abstract—With the aim of searching for new antioxidants, including those of the biogenic type, the antioxidant properties of phenylhydrazones of some aromatic aldehydes were studied under conditions of ascorbate-dependent peroxide oxidation of oleic acid residues in Tween-80. Also the reactivity of these hydrazones toward a stable radical, diphenylpicrylhydrazyl, was studied. The correlation between the antioxidant and antiradical activities of phenylhydrazones was examined.

The reactions of free-radical peroxide oxidation of lipids (POL) in biomembranes not only play an important role in the normal cell physiology but also often act as key units of the mechanisms of various pathological states, including the radiation sickness, infection and oncological diseases, etc. [1]. Therefore, search for physiologically active substances exhibiting antioxidant and antiradical properties and favoring normalization of the level of peroxide oxidation of lipids in biomembranes is an urgent problem. It is interesting to study in this respect phenylhydrazones, which exhibit a wide spectrum of physiological activity. It is known that phenylhydrazones (PHs) of some ketones exhibit antitubercular and antiviral activity [2, 3]. Salicylaldehyde benzoylhydrazone inhibits DNA synthesis in cells of radiation-sensitive tissues and is an effective low-toxic radioprotector [4]. It is believed that the pharmacological effect of phenylhydrazone compounds is associated, directly or indirectly, with their effect on the free-radical processes occurring in a living body. Data on the antioxidant activity of phenylhydrazones were obtained only recently [5]. The quantitative evaluation of the antioxidant and antiradical activity of phenylhydrazones will give insight into the mechanisms of their biological effect, on pathways of their transformations in radical processes, and on the structure–antioxidant activity relationships.

In this work we studied the antiradical and antioxidant activity of phenylhydrazones and the correlation of their reactivity in radical reactions with their composition and molecular structure.

EXPERIMENTAL

The antiradical activity of phenylhydrazones was studied relative to a stable radical, diphenylpicrylhydrazyl (DPPH), as substrate. The reaction was monitored photocolorimetrically with a KFK-3 device. Phenylhydrazones [6] of the formulas

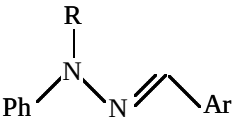

R = –H, Ar = –Ph (**1**);

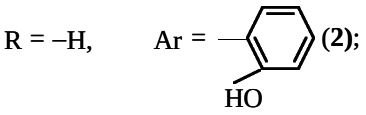

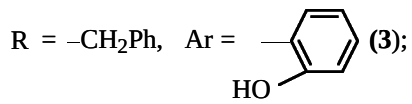

R = –CH_2Ph, Ar = (**3**);

R = –CH_2Ph, Ar = –Ph (**4**)

and DPPH [7]

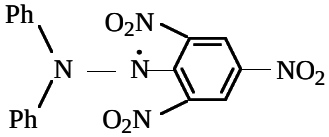

were prepared and purified by standard procedures. The purity of phenylhydrazones was evaluated by elemental analysis and IR spectroscopy, and that of DPPH, by IR, UV, and ESR spectroscopy. Solutions

1070-4272/01/7405-0792$25.00

of DPPH in hexane ($\varepsilon = 1.4 \times 10^3$ l mol^{-1} mm^{-1}), benzene ($\varepsilon = 1.24 \times 10^3$ l mol^{-1} mm^{-1}), and methanol ($\varepsilon = 1.18 \times 10^3$ l mol^{-1} mm^{-1}) exhibit an absorption maximum in the visible range (520 nm) and are stable in storage. Solutions of phenylhydrazones and DPPH were mixed in an equimolar ratio at 293 K in the range of reactant concentrations 10^{-4}–10^{-5} M, after which variation of the optical density of the DPPH solution was monitored in time and the kinetic curves of DPPH consumption were constructed (DPPH solutions in this concentration range obey the Lambert–Beer law).

The antioxidant activity of phenylhydrazones was studied in oxidation of Tween-80 (polyoxyethylene sorbitan monooleate), which is a model of lipid oxidation. Tween-80 purchased from Laba Chemie Fischamend, Austranal Präparate was used without additional purification. Oxidation of Tween-80 in dilute aqueous solutions was performed for 48–50 h at 313 K in the presence of optimal concentrations of Fe(II) and ascorbic acid. The concentration of malondialdehyde (MDA), which is the peroxidation product, was determined photocolorimetrically from the absorption of a pink complex of MDA with thiobarbituric acid ($\lambda = 540$ nm, $\varepsilon = 1.56 \times 10^4$ l mol^{-1} mm^{-1}) [8]. The performance of phenylhydrazones as antioxidants was evaluated from the decrease in the concentration of malondialdehyde as compared to the control experiment.

Figure 1 shows the kinetic curves of consumption of the DPPH radical in its reaction with phenylhydrazones of salicylaldehyde and benzaldehyde in hexane. Study of the reaction rate as a function of the DPPH and phenylhydrazone concentrations (Fig. 2) showed that the reaction is first-order with respect to both DPPH and phenylhydrazone. Such reaction orders are preserved in hexane for all the compounds studied. Thus, the kinetic equation for the reaction rate can be given as follows:

$$W = k_{app}[\text{DPPH}][\text{PH}].$$

The constants k_{app} calculated by this equation from the initial rates of DPPH consumption are listed in Table 1. It is seen that the rate constants of this reaction depend on the composition and structure of phenylhydrazones. Benzaldehyde benzylphenylhydrazone containing no labile hydrogen atom at nitrogen lacks antioxidant activity. This fact suggests that in the reaction with DPPH the reactive center in the phenylhydrazone molecule is the NH group of the hydrazone moiety. Thus, the reaction pattern can be represented

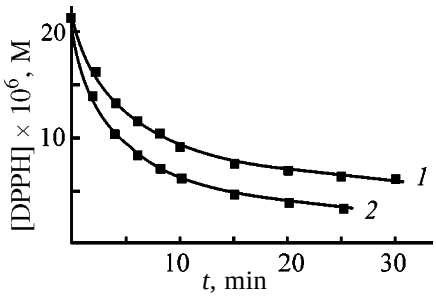

Fig. 1. Kinetic curves of the reactions of DPPH with phenylhydrazones of (*1*) benzaldehyde and (*2*) salicylaldehyde in hexane solution at 293 K. (*t*) Time.

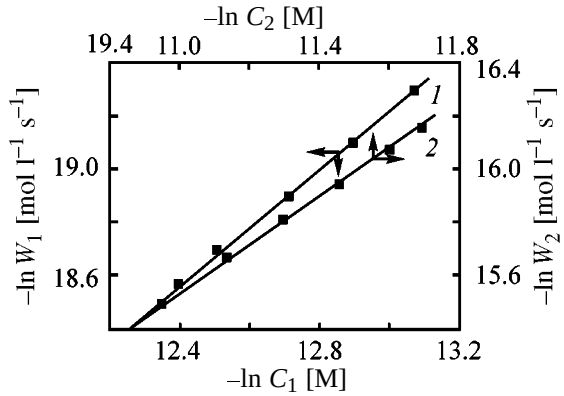

Fig. 2. Rate of reaction of DPPH with benzaldehyde phenylhydrazone as a function of the concentrations of (*1*) phenylhydrazone C_1 and (*2*) DPPH C_2.

as follows:

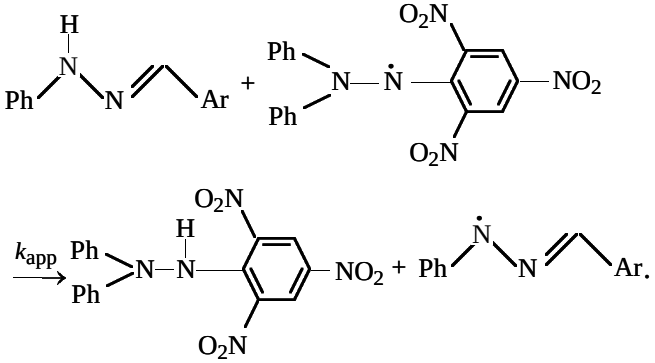

The final products of this reaction, along with the reduced form of diphenylpicrylhydrazyl (DPPH–H), are probably recombination products of the phenylhydrazone radicals with DPPH and of two phenylhydrazone radicals.

Comparison of the rate constants for different phenylhydrazones in hexane (Table 1) shows that introduction of the hydroxy group into the aldehyde moiety of the phenylhydrazone (compound **2**) significantly increases k_{app} as compared to **1**. This fact is

Table 1. Kinetic parameters of the reactions of aromatic aldehyde phenylhydrazones with DPPH in various solvents (T = 293 K)

Compd. no.*	k_{app}, l mol^{-1} s^{-1}		
	hexane	benzene	methanol
1	115 ± 5	11 ± 1	6.2 ± 0.6
2	201 ± 7	16 ± 20	155 ± 2
3	0.10 ± 0.01	Weak reaction	3.6 ± 0.5
4	No reaction with DPPH		
5	1.5 ± 0.2	0.27 ± 0.01	4.5 ± 0.6

* Compounds: (**1**) benzaldehyde phenylhydrazone, (**2**) salicylaldehyde phenylhydrazone, (**3**) salicylaldehyde benzylphenylhydrazone, (**4**) benzaldehyde benzylphenylhydrazone, and (**5**) Ionol.

due to additional contribution of the OH group to the reaction with DPPH, which occurs with the homolytic cleavage of the O–H bond. This contribution can be estimated by determining the antiradical activity of the hydrazone containing the hydroxy group in the aldehyde moiety but lacking the labile hydrogen atom at N (compound **3**). Table 1 shows that this activity is low, i.e., the main contribution to the reaction with DPPH (and hence to the antiradical activity) is made by the NH group.

Study of the solvent effect on the reaction kinetics showed that the reaction order is the same in all the tested solvents but the rate constant k_{app} strongly depends on the solvent.

The apparent rate constants of the reaction of DPPH with benzaldehyde phenylhydrazone in various solvents (k_{app}, l mol^{-1} s^{-1}) were measured at various temperatures in the range 293–323 K, and the following relations were obtained:

$$k_{app} = 2.29 \times 10^3 \exp[(-6800 \pm 380)/RT] \quad \text{(hexane)},$$

$$k_{app} = 2.27 \times 10^7 \exp[(-36\,000 \pm 1200)/RT] \quad \text{(benzene)},$$

$$k_{app} = 2.33 \times 10^4 \exp[(-20\,000 \pm 1000)/RT] \quad \text{(methanol)}.$$

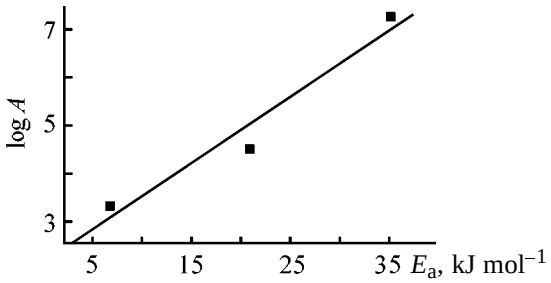

Fig. 3. Correlation between the preexponential term A and activation energy E_a of the reaction of DPPH with benzaldehyde phenylhydrazone in various solvents.

The decrease in the apparent rate constants, increase in the activation energy, and variation of the preexponential term in going from hexane to benzene and methanol show that the reactivity of the hydrazones decreases in going from hexane to benzene and methanol. The logarithm of the preexponential term linearly correlates with the activation energy (Fig. 3), which suggests the presence of a compensating effect. This effect is due to the localized interaction of the reagent with the solvent. For example, in benzene the decrease in the reaction rates is due to the well-known capability of DPPH to form π complexes with aromatic hydrocarbons, in which the radical is considerably less reactive than in the nonsolvated state [9]. In methanol, the reaction center of phenylhydrazone is blocked as a result of hydrogen bonding with the solvent [10]. The decrease in k_{app} and increase in E_a are in this case due to a decrease in the concentration of free, more active phenylhydrazone molecules. A considerably higher rate constant of the reaction with **2** in methanol, as compared to **1**, is due to active participation in the reaction of the hydroxy group in the aldehyde fragment of **2**. Owing to the high dielectric permittivity of methanol, the hydroxy group dissociates in this solvent to a greater extent.

The activity of the examined phenylhydrazones in the reaction with DPPH considerably exceeds that of the commercial inhibitor Ionol.

Our data on the antiradical activity of phenylhydrazones correlate with data on their antioxidant activity in oxidation of ethylbenzene [5]. This fact shows that the antioxidant properties of these compounds are due to their capability for reacting with radicals and confirms the suggested mechanism of the antioxidant action of these compounds in oxidation of hydrocarbons. Study of aromatic aldehyde phenylhydrazones as antioxidants of the ascorbate-dependent peroxide oxidation of oleic acid residues in Tween-80 showed, however, that their activity parameters do not always correlate with the characteristic of the antiradical activity (Table 2). This may be due to specific features of oxidation in this system, and also to possible operation of alternative mechanisms of the antioxidant effect of phenylhydrazones. At present, the mechanism of lipid oxidation in the presence of peroxide oxidation cofactors, Fe(II) and ascorbic acid, is not fully understood. Along with the radical-chain mechanism [1], oxidation by the ionic mechanism [11] is also probable. As seen from Table 2, the antioxidant activity of phenylhydrazones increases in the order **1** < **2** < **4** < **3**. The high antioxidant activity of **3** and **4**, with their low antiradical effect, is due to the possi-

Table 2. Effect of phenylhydrazones of aromatic aldehydes on the rate of accumulation of malondialdehyde (MDA) in oxidation of Tween-80

Compd. no.	MDA concentration $C \times 10^6$, M		Decrease in MDA accumulation rate, %
	control	experiment	
1	1.94	1.46	25
2	2.50	1.47	41
3	2.35	0.67	71
4	1.93	0.65	66

bility of their reaction with hydroperoxides initiating POL and of complexation with iron ions affecting the reaction rate. Also, interaction of oleic acid residues with phenylhydrazones, accompanied by structural changes, can enhance the oxidation resistance of the system.

CONCLUSIONS

(1) The kinetic study of the reactions of aromatic aldehyde phenylhydrazones with a stable radical, diphenylpicrylhydrazyl, in various solvents showed that the parameters of the antiradical activity of phenylhydrazones depend both on the compound structure and on the solvent.

(2) Reactions of diphenylpicrylhydrazyl with phenylhydrazones involve abstraction of hydrogen atom from the NH group of the hydrazone moiety. The contribution of the hydroxy group in the aldehyde moiety to the antiradical activity of phenylhydrazones is significant only in methanol.

(3) The antiradical activity of phenylhydrazones correlates with their antioxidant activity in oxidation of hydrocarbons and does not fully correlate with their antioxidant activity in ascorbate-dependent peroxide oxidation of oleic acid residues in Tween-80 in aqueous solutions. This is due to specific features of oxidation of this system and to possible operation of alternative mechanisms of antioxidant action.

REFERENCES

1. Kagan, V.E., Orlov, O.N., and Prilipko, L.L., *Itogi Nauki Tekh., Ser.: Biofiz.*, 1986, vol. 18, pp. 3–23.
2. Shverev, V.I., Galstukhova, N.B., Pankina, Z.A., *et al.*, *Khim.-Farm. Zh.*, 1978, vol. 12, no. 12, pp. 88–92.
3. Mirskova, A.N., Levkovskaya, G.G., Medina, P.V., *et al.*, *Khim.-Farm. Zh.*, 1977, vol. 11, no. 3, pp. 74–78.
4. Vladimirov, V.G., Krasil'nikov, I.I., and Aranov, O.V., *Radioprotektory: struktura i funktsii* (Radioprotectors: Structure and Functions), Kiev: Naukova Dumka, 1989.
5. Nikolaevskii, A.N., Filipenko, T.A., and Pleskushkina, E.I., *Neftekhimiya*, 2000, vol. 40, no. 2, pp. 145–148.
6. Kitaev, Yu.P. and Buzykin, B.I., *Gidrazony* (Hydrazones), Moscow: Nauka, 1974.
7. Tietze, L. and Eicher, Th., *Reaktionen und Synthesen im organisch-chemischen Praktikum und Forschungslaboratorium*, Stuttgart: Thieme, 1991.
8. Blagorodov, S.G., Shepelev, A.P., Dmitrieva, N.A., *et al.*, *Khim.-Farm. Zh.*, 1987, vol. 21, no. 3, pp. 292–296.
9. Buchachenko, A.L. and Vasserman, A.M., *Stabil'nye radikaly: Elektronnoe stroenie, reaktsionnaya sposobnost' i primenenie* (Stable Radicals: Electronic Structure, Reactivity, and Use), Moscow: Khimiya, 1973.
10. Barslay, L.R.C., Edwards, C.E., and Vingvist, M.R., *J. Am. Chem. Soc.*, 1999, vol. 121, no. 26, pp. 6226–6231.
11. Minotti, G. and Aust, S.D., *Chem. Phys. Lipids*, 1987, vol. 44, pp. 191–195.

Russian Journal of Applied Chemistry, Vol. 74, No. 5, 2001, pp. 796–799. Translated from Zhurnal Prikladnoi Khimii, Vol. 74, No. 5, 2001, pp. 775–777.

MACROMOLECULAR CHEMISTRY AND POLYMERIC MATERIALS

Determination of the Esterification Degree of Polygalacturonic Acid

A. M. Bochek, N. M. Zabivalova, and G. A. Petropavlovskii†

Institute of Macromolecular Compounds, Russian Academy of Sciences, St. Petersburg, Russia

Received January 16, 2001

Abstract—The number of free and esterified carboxy groups of polygalacturonic acid was determined by conductometric titration.

Pectins are abundant in nature. They are present in almost all plants and, in relatively great amounts, in fruits and vegetables [1]. Pectins are also contained in pedicels and plant fibers [2–5]. Pectins are conventionally used in food and pharmaceutical industries and in cosmetics [1, 6, 7].

The number of methoxylated groups of pectin (polygalacturonic acid, PGA) is one of the main parameters determining the properties of its aqueous solutions and gels. The solubility of pectin in water, its gelating power, and sorption properties with respect to heavy metal ions also depend on the number of methoxy groups. The content of methoxy groups in a PGA molecule is characterized by the number of methoxy groups K_{MeO} and the esterification degree (ED, number of esterified carboxy groups per the total number of carboxy groups):

$$ED = (K_e/K_t) \times 100 = [(K_t - K_f)/K_t] \times 100 = [(1 - K_f)/K_t] \times 100, \quad (1)$$

where K_e is the number of esterified carboxy groups; K_f the number of free carboxy groups; and K_t is the total number of carboxy groups, $K_t = K_f + K_e$.

The esterification degree is usually determined by potentiometric titration and by the Ca acetate procedure [1, 8].

When the potentiometric procedure is used, the number of esterified groups is determined by back-titration. It should be noted that determination of both the number of esterified carboxy groups and free carboxy groups contributes to the determination error of ED of pectins. In addition, since polygalacturonic acid is a weak acid, the equivalence point of the titration cannot be precisely determined. We developed a conductometric titration procedure for more accurate determination of the number of free and esterified carboxy groups of pectins.

† Deceased.

EXPERIMENTAL

We studied apple pectin. Its ED was determined by potentiometric titration and conductometric titrations.

When the number of free carboxy groups K_s of PGA was determined by the potentiometric procedure, a weighed portion of the pectin (0.2 g) was placed in a weighing bottle for titration and wetted with ethanol. Distilled water heated at 40°C (20 ml) was added with stirring. The polymer was dissolved with stirring for 2 h. The resulting solution was titrated with 0.1 N NaOH in the presence of phenolphthalein to pail rose color. The pH of the solution was also measured by a laboratory pH meter. The number of free carboxy groups (%) was calculated by the equation

$$K_f = \frac{N_{NaOH} V_{NaOH} \times 0.045}{a} \times 100, \quad (2)$$

where a is the weighed portion of pectin with absorbed water (g); N_{NaOH} and V_{NaOH} the normality and volume (ml) of the alkali solution spent for titration.

The number of esterified carboxy groups (K_e) was determined as follows. 0.1 N NaOH solution (10 ml) was added to a neutralized PGA sample after deter-

1070-4272/01/7405-0796$25.00

mination of the free carboxy groups. The weighing bottle was plugged with a stopper. The content was stirred at room temperature for 2 h to saponify the esterified carboxy groups of the polymer. Then 0.1 N HCl (10 ml) was added. Excess HCl was titrated with 0.1 N NaOH. The number of the esterified carboxy groups was calculated from the volume of 0.1 NaOH solution spent for titration:

$$K_e = \frac{N_{NaOH} V_{NaOH} \times 0.045}{a} \times 100. \quad (3)$$

The total number of the COOH groups (%) is equal to the sum of the free and esterified groups: $K_t = K_f + K_e$.

The number of methoxy groups in PGA can be calculated from the ED by the equation:

$$K_{MeO} = \frac{100ED \times 31}{176 + ED \times 14}, \quad (4)$$

where ED is necessarily expressed in fractions of unity.

The conductometric determination of the number of carboxy groups by was performed similarly.

To determine the total amount of carboxy groups, 0.1 N NaOH (10 ml) was added with the aid of a volumetric pipet to a neutralized sample after determination of the free carboxy groups. The weighing bottle was plugged with a stopper. The content was stirred at room temperature for 2 h to saponify the esterfied carboxy groups of the polymer. The polymer solution was titrated with 0.1 N HCl. The equivalence point was determined form the conductometric titration curves (see Fig. 1a, curve *2*). The total content of the carboxy groups, %, of the polymer was calculated by the equation:

$$K_t = \frac{N_{HCl} V_{HCl} \times 0.045}{a} \times 100, \quad (5)$$

where $V_{HCl} = V_2 - V_1$.

The number of esterified carboxy groups was calculated as $K_e = K_t - K_f$.

As seen from Fig. 1b, neutralization of free COOH groups of pectin is completed at pH 8.5–9.0 (curve *1*). The equivalence point is rather blurred. Usually the titration is performed in the presence of phenolphthalein to appearance of a pail-rose color of the solution [1]. It should be noted that the color of the indicator

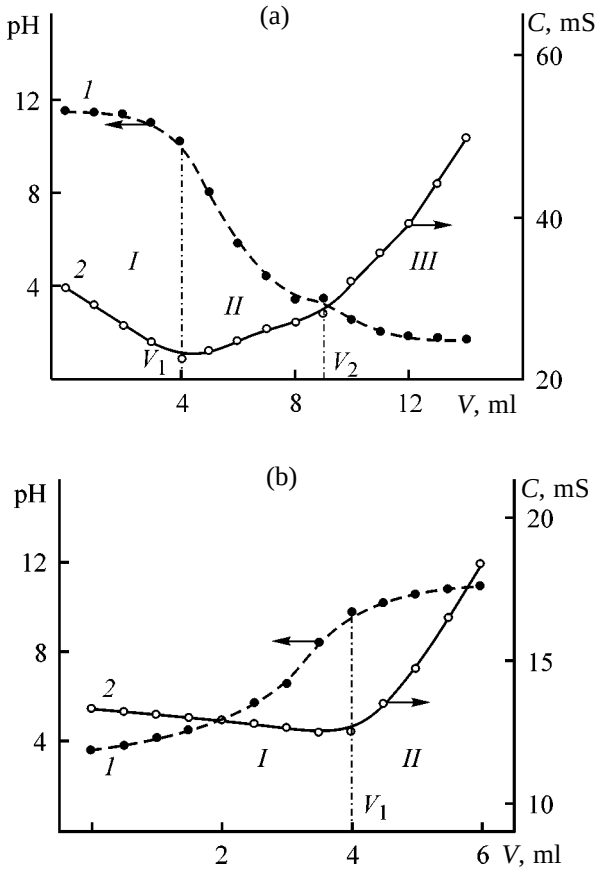

Fig. 1. (*1*) Potentiometric and (*2*) conductometric titration curves constructed for determination of (a) the total number of carboxy groups and (b) the number of free carboxy groups in PGA. (*C*) Electrical conductivity; (*V*) the volume of (a) 0.1 N HCl or (b) 0.1 N NaOH added to the sample.

changes from colorless to rose in a relatively wide pH range (8.2–10.0), which can results in appreciable error. The conductometric procedure is free of this drawback. In this case the electrical conductivity of the solution is measured. The electrical conductivity depends on the mobility, concentration, and nature of the ions present in the solution. The mobility of protons is the highest and it decreases in going to OH^- and then to single-, double-, and higher charged ions. The conductometric titration curve of PGA (Fig. 1b) has a minimum and consists of two sections. Section I is due to conversion of the COOH groups into COONa groups. In the course of this process the proton concentration in the solution decreases and the concentration of Na^+ cations increases owing to dissociation of the COONa groups. Since polygalacturonic acid is a weak acid, its carboxy groups are incompletely dissociated in a solution. Sodium polygalacturate is dissociated completely. The slight decrease in

Esterification degree ED and the concentration of methoxy groups K_{MeO} in PGA, determined by potentiometric and conductometric titration

Method	ED	K_{MeO}
	%	
Potentiometric	72.30 ± 0.35	12.04
Conductometric	67.8 ± 0.15	11.30
Published data	60.0 – 68.0	10.0 – 11.4

the electrical conductivity during titration is caused by the fact that the effect of the introduced Na^+ cations cannot compensate for the decrease in the conductivity due to consumption of H^+ ions, because Na^+ ions are less mobile than protons. As excess NaOH appears after completion of neutralization of the COOH groups the conductivity sharply increases proportionally to the concentration of OH^- and Na^+ ions (section *II*). Thus, conductometric titration allows more reliable and accurate, as compared to the potentiometric titration, determination of the equivalence point of neutralization of the pectin COOH groups with NaOH (Fig. 1b).

The titration curves of PGA saponified with an HCl solution are shown in Fig. 1a. The completion of neutralization of unreacted alkali with hydrochloric acid and the onset of protonation of ionized carboxy groups

$$R–COONa + HCl = R–COOH + NaCl$$

can be determined in the presence of the same indicator from the potentiometric titration curve (curve *1*). The conversion of COONa groups into COOH groups (and appearance of free HCl) is completed at pH 3.2–3.5 and is difficult to detect. Hence in the case of the potentiometric titration the additional manipulation is used: after pectin saponification an HCl solution is added in the amount equivalent to that of NaOH solution used for PGA saponification. The alkali not spent in the saponification is neutralized with the acid. The number of esterified (saponified) carboxy groups in a PGA sample is calculated from the results of titration of the excess acid with an NaOH solution [1].

The above operations are eliminated when the conductometric procedure is used (curve *2*). A saponified pectin sample is titrated with an HCl solution and the total number of carboxy groups in the polymer is determined. Two sharp knees in the titration curves divide it into three sections. Section *I* is assigned to neutralization of the strong base with the strong acid. After the neutralization the concentration of OH^- anions and hence the electrical conductivity decrease. Section *II* is due to conversion of the sodium form of the carboxy groups into the H form. The increase in the electrical conductivity of the solution is typical for titration of a weak acid salt with a strong acid, i.e., is proportional to the proton concentration formed by dissociation of the weak polyacid. Finally section *III* is due to appearance of free HCl. The electrical conductivity increases more sharply owing to an increase in the proton concentration in the solution. Thus, conductometric titration, unlike the potentiometric procedure, allows reliable determination of the onset and the end of protonation of ionized carboxy groups with HCl. Section *II* corresponds to the total amount of PGA carboxy groups. The esterification degree as the arithmetic mean of five measurements performed by the potentometric and conductometric procedures is presented in the table. As seen from the table, the scatter of ED determined by potentiometric titration is higher than that of ED determined by conductometric titration. The average ED of apple pectin determined by conductometric titration agrees well with the published data (ED 0.60 – 0.68). At the same time, ED and K_{MeO} obtained by the potentiometric titration are slightly overestimated [1]. The reasons of the overestimation were discussed above. Thus, conductometric titration allows determination of the esterification degree of polygalacturonic acid with higher accuracy as compared to the potentiometric procedure.

CONCLUSION

Advantages of the conductometric titration over potentiometric titration in determination of the esterification degree were demonstrated.

REFERENCES

1. Aimukhamedova, G.B., Alieva, D.E., and Shelukhina, N.P., *Svoistva i primenenie pektinovykh sorbentov* (Properties and Application of Pectin Sorbents), Frunze: Ilim, 1984.
2. Sobolev, M.A. and Krasivskaya, A.A., *Tekstil. Prom–st.*, 1954, no. 7, pp. 39–41.
3. *Spravochnik po khimicheskoi tekhnologii obrabotki l'nyanykh tkanei* (Handbook on Chemical Treatment of Linen Fabric), Fridlyand, G.I., Ed., Moscow: Leg-

kaya Industriya, 1973, pp. 14–33.

4. Bochek, A.M., Zabivalova, N.M., Shamolina, I.I., *et al.*, Abstracts of Papers, *The First Central Eur. Conf. on Fibre Grade Polymer, Chemical Fibres and Special Textiles*, Lodz (Poland), October 3–4, 2000, Lodz, 2000, p. A2.
5. Meijer, W.J., Vertregt, N., Rutgers, B., and Vande Waart, M., *Ind. Groups Prod.*, 1995, vol. 4, pp. 273–284.
6. Vasilenko, Yu.K., Kaishev, N.N., Komnantsev, V.A., *et al.*, *Khim.-Farm. Zh.*, 1993, no. 11, pp. 44–46.
7. Ashumbaeva, Z.Zh., Mokrashev, A.M., Dzhumkaliev, *et al.*, *Primenenie pektinov v meditsine* (Medical Application of Pectins), Frunze: Ilim, 1989.
8. Shelukhina, N.P., Ashubaeva, Z.D., and Aimukhamedova, G.B., *Pektinovye veshchestva, ikh nekotorye svoistva i proizvodnye* (Pectins, Their Some Properties, and Derivatives), Frunze: Ilim, 1970.

Russian Journal of Applied Chemistry, Vol. 74, No. 5, 2001, pp. 800–803. Translated from Zhurnal Prikladnoi Khimii, Vol. 74, No. 5, 2001, pp. 778–780.

MACROMOLECULAR CHEMISTRY AND POLYMERIC MATERIALS

Thermal Chlorination of Methyltrichlorosilane

M. G. Voronkov, V. K. Stankevich, B. F. Kukharev, and K. A. Abzaeva

Irkutsk Institute of Chemistry, Siberian Division, Russian Academy of Sciences, Irkutsk, Russia

Received October 12, 1999; in final form, February 2000

Abstract—The procedure for thermal chlorination of methyltrichlorosilane to chloromethyltrichlorosilane in a circulation flow system was developed. The yield of $ClCH_2SiCl_3$ was studied as influenced by the reaction temperature and the reactant ratio.

Chloromethyltrichlorosilane, $ClCH_2SiCl_3$ (CMTS), is a valuable reagent for preparing carbofunctional organosilicon monomers and polymers (surface-modifying and cross-linking agents, adhesion promoters, immobilized catalysts, etc. [1–6]) and is used in synthesis of sorbents, ion exchangers, and bioprotecting coatings. This compound is also a precursor of widely used biostimulant, 1-(chloromethyl)silatrane (Mival) [7, 8]. Chloromethyltrichlorosilane is usually prepared by free-radical chlorination of methyltrichlorosilane (MTS) with gaseous chlorine:

$$Cl_2 + CH_3SiCl_3 \rightarrow ClCH_2SiCl_3 + HCl.$$

The reaction is performed either in the vapor phase on exposure to UV [9, 10] or visible [11] radiation or in a solution in the dark in the presence of azobis(isobutyronitrile) as the initiator [9, 10]. It should be noted that, since chlorination of mono- and dichloromethyltrichlorosilanes ($ClCH_2SiCl_3$ and $Cl_2CHSiCl_3$) is considerably faster than that of the initial MTS, the monochloro derivative is prepared at its continuous removal form the reaction mixture or at a large excess of MTS. The first procedure is based on photochemical chlorination of $MeSiCl_3$ vapor with gaseous chlorine on exposure to UV [9, 10] or visible light [9].

Large-scale photochemical chlorination of MTS is complicated by the lack of industrial reactors containing parts made form optical quartz and by the need for intermittent removal of the polymeric film absorbing UV–Vis radiation from the surface of the transparent window or from the built-in light sources. It is difficult to construct powerful photochemical reactors since the light intensity decreases proportionally to the square of the distance form the light source. In some cases the photochemical reaction can be accompanied by spontaneous combustion or explosion of a mixture of gaseous reactants [10]. The industrial process of dark chlorination of MTS in the presence of asobis(isobutyronitrile) is performed in a distillation column under inversion conditions (the temperature in the reaction zone and in the still is 64 and 110°C, respectively) [12]. The CMTS yield based on the spent $MeSiCl_3$ is 75%. In this case the steady-state inversion conditions in the upper part of the column and the working temperature in the reaction zone are difficult to maintain, and large amount of the expensive initiator and large excess of $MeSiCl_3$ are required. In addition, $Cl_2CHSiCl_3$ and Cl_3CSiCl_3 are formed in considerable amounts, i.e., the selectivity of the process is low.

Another procedure for preparing CMTS is based on photochemical chlorination of $MeSiCl_3$ with sulfuryl chloride [13, 14]:

$$SO_2Cl_2 + CH_3SiCl_3 \xrightarrow{h\nu} SO_2 + ClCH_2SiCl_3 + HCl.$$

This reaction is catalyzed by yttrium chloride, lanthanum chloride, and manganese chloride [14]. Although this procedure does not require complex equipment, it is more expensive as compared to the chlorination with gaseous chlorine.

We developed a new procedure for preparing CMTS by chlorination of $MeSiCl_3$ with gaseous chlorine at 300–400°C in a circulation system.

This reaction occurs by the radical mechanism similar to that of thermal chlorination of alkanes [15]. The chain propagation involves formation of Cl and CH_2SiCl_3 radicals:

$$Cl_2 \xrightarrow{300\text{–}400^\circ C} 2Cl^{\cdot},$$

$$Cl^{\cdot} + CH_3SiCl_3 \rightarrow CH_2SiCl_3 + HCl,$$

$$Cl_2 + {}^{\cdot}CH_2SiCl_3 \rightarrow ClCH_2SiCl_3 + Cl^{\cdot}.$$

1070-4272/01/7405-0800$25.00

Yield of $ClCH_2SiCl_3$ as influenced by the conditions of thermal chlorination of $MeSiCl_3$.

$T_{reactor}$, °C	Feed rate of $MeSiCl_3$, g h^{-1}	Flow rate of Cl_2, l h^{-1}	$MeSiCl_3 : Cl_2$, mol : mol	τ, h	CMTS yield, %	α,* %
350	829.4	1.18	105 : 1	12	82.2 (42)**	51.1
300	222.7	1.27	26 : 1	12	72.3 (35)	48.4
350	576.0	2.42	36 : 1	6	77.7 (38.5)	49.5
400	783.3	2.63	45 : 1	6	76.3 (40.6)	53.2
450	852.5	1.66	77 : 1	12	66.7 (40.2)	60.3
500	844.8	3.18	40 : 1	6	62.5 (35.2)	56.3
300	238.1	1.20	30 : 1	12	77.0 (37.8)	49.0
250	162.8	0.22	111 : 1	20	85.9 (7.7)	9

* α is the MTS conversion.
** Yield of CMTS based on reacted and initial (in parentheses) MTS.

It is known that the rate constants and activation energies of radical-chain consecutive chlorination reactions yielding mono-, di-, and trichloro derivatives are almost the same [15]. Hence, for CMTS to be selectively formed, large excess of MTS with respect to chlorine should be used and CMTS being formed should be removed from the reaction mixture.

The chlorination was performed at $MeSiCl_3 : Cl_2$ ~100 : 1 (see table). At 350°C the selectivity of the process (the CMTS yield based on consumed MTS) was higher than 82% and the MTS conversion in 12 h was 51%. With a larger MTS excess, the output of CMTS is lower. At $MeSiCl_3 : Cl_2$ = 25 : 1 49.5% of MTS is converted within 6 h; however the selectivity decreases to 77%. Thus, taking into account the output of the reactor and the process selectivity, the $MeSiCl_3 : Cl_2$ molar ratio can be varied from 25 : 1 to 100 : 1 depending on the technical and economical requirements.

The temperature influence on the MTS chlorination is similar to that of alkane chlorination. With increasing temperature the reaction is accelerated, and its selectivity decreases. In addition, at 500°C the reactor nozzle is strongly clogged with coke.

At the same time the process occurs even at 250°C. However, in this case, despite high selectivity (the CMTS yield based on consumed MTS is 86%), a 9% conversion of MTS is reached only in 20 h.

Thus, as seen from the table, the best reaction temperature is 350–400°C.

EXPERIMENTAL

Methyltrichlorosilane was chlorinated on a circulation unit (see figure). The unit consists of a 0.5-l heated flask (*1*), connected through a packed column (*2*) and a condenser with a dosing apparatus and then with an electrically heated flow reactor. The reactor is connected with two condensers (straight-run *6* and reflux *7*). The condensate formed in the first condenser goes in the accumulator with a siphon and then back in the flask. Gaseous HCl and unchanged Cl_2 pass to the absorbers through the reflux condenser. The reactor is a quartz tube 12.5 mm in diameter and 250 mm long, packed with quartz chips.

An MTS vapor formed in the flask passes through the packed column, is condensed in the condenser, and is fed into the dosing apparatus form which it is fed with a controlled rate to the reactor heated to

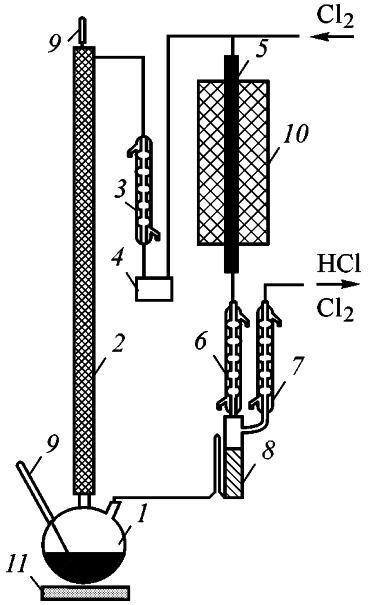

Scheme of the unit for gas-phase thermal chlorination of methyltrichlorosilane: (*1*) 0.5-l flask, (*2*) packed column, (*3, 6, 7*) condensers, (*4*) dosing pump, (*5*) reactor, (*8*) condensate accumulator, (*9*) thermometer, (*10*) tubular furnace, and (*11*) electric heater.

300–400°C. Chlorine is fed simultaneously form a cylinder. The flow rate of chlorine is measured with a rheometer. The flask temperature in the first and final steps of the process is 65 and 105°C, respectively. The temperature of the column head is about 65°C. The $MeSiCl_3 : Cl_2$ molar ratio at the outlet of the reactor was maintained constant.

An example of the CMTS synthesis is presented below. Methyltrichlorosilane (149.5 g, 1 mol) is placed in the still of the packed column and is heated to boil. When the temperature of the top of the column reaches 65°C, MTS condensate formed in the condenser is fed into the dosing apparatus and then with a 830 g h^{-1} (5.55 mol h^{-1}) flow rate into the reactor heated to 350°C. Simultaneously gaseous chlorine is fed with a 1.18 l h^{-1} (0.0526 mol h^{-1}) flow rate into the reactor. The $MeSiCl_3 : Cl_2$ molar ratio is 105 : 1. The process lasts for 12 h. In this period 14.2 l (0.63 mol) of chlorine is passed through the system. Fractionation of the bottoms on a 20-TP column yields the initial MTS (73.1, 0.49 mol) with bp 65–66°C (720 mm Hg) and CMTS (77.3 g, 0.42 mol) with bp 117–119°C (720 mm Hg), n_D^{20} = 1.4530, d_4^{20} = 1.4420, and a 99.7% purity determined by GLC {published data [14]: bp 118–120°C (760 mm Hg), n_D^{20} = 1.4530}.

Found (%): C 6.56, H 1.03, Cl 77.00, Si 15.07, 6.25, 1.12, 76.91, 15.14.
CH_2Cl_4Si.
Calculated (%): C 6.53, H 1.10, Cl 77.10, Si 15.27.

The CMTS yield based on the initial $MeSiCl_3$ and spent MTS is 82.2 and 42%, respectively. The MTS conversion is 51.1%.

The weight of the remaining bottoms is 10.2 g. As determined by GLC, the bottoms contain 31% $Cl_2CHSiCl_3$ and 69% Cl_3CSiCl_3. $Cl_2CHSiCl_3$ (2.6 g, 0.012 mol) was isolated by fractionation of the bottoms; bp 141–142°C (720 mm Hg), 99.3% purity determined by GLC, n_D^{20} = 1.4715, d_4^{20} = 1.5503 {published data [14]: bp 144°C (760 mm Hg), n_D^{20} = 1.4715}.

Found (%): C 5.40, H 0.41, Cl 81.27, Si 12.32, 5.44, 0.53, 81.21, 13.05.
CH_2Cl_5Si.
Calculated (%): C 5.50, H 0.46, Cl 81.18. Si 12.86.

The purity of the chlorine-containing products was determined by GLC on an LKhM-80 chromatograph equipped with a catharometer. Helium was the carrier gas. A 3000 × 3 mm steel column was packed with 3% OV-17 on Inerton Super (0.160–0.200 mm). The column was heated form 40 to 180°C at a rate of 4 deg min^{-1}.

The ^1H NMR spectra were recorded at 25°C on a Tesla 480 C spectrometer operating at 80 MHz, with TMS as the internal reference. The spectra of $ClCH_2SiCl_3$ and $Cl_2CHSiCl_3$ contain only one singlet at 3.24 and 5.44 ppm, respectively. The chemical shifts agree with the published data [14].

The ^{35}Cl NQR spectrum of $ClCH_2SiCl_3$ recorded on an IS-3 spectrometer contains the following signals, ν^{77}, MHz: 36.77 ($ClCH_2$); 19.555, 19.470 ($SiCl_3$) (cf. [16]).

CONCLUSION

Thermal chlorination of methyltrichlorosilane with elemental chlorine in the gas phase at 300–400°C yields chloromethylchlorosilane in a 63–82% yield based on reacted $MeSiCl_3$.

REFERENCES

1. Sobolevskii, M.V., Muzovskaya, O.A., and Popeleva, G.S., *Svoistva i oblasti primeneniya kremniiorganicheskikh produktov* (Properties and Fields of Application of Organosilicon Compounds), Sobolevskii, M.V., Ed., Moscow: Khimiya, 1975.
2. Motsarev, G.F., Sobolevskii, M.V., and Rozenberg, V.R., *Karbofunktsional'nye organosilany i organosiloksany* (Carbofunctional Organic Silanes and Siloxanes), Moscow: Khimiya, 1990.
3. Edwin, P., *Pludeman Silane Coupling Agents*, New York: Plenum, 1982.
4. Makarskaya, V.M., Pashchenko, A.A., and Krupa, A.A., *Povyshenie kachestva stekloplastikov s pomoshch'yu appretov* (Improvement of Fiber Glass Quality with the Aid of Dressings), Kiev: UkrNIINTI, 1976.
5. Voronkov, M.G., Vlasova, N.N., and Pozhidaev, Yu.N., *Zh. Prikl. Khim.*, 1996, vol. 69, no. 5, pp. 705–718.
6. Voronkov, M.G., Chernov, N.F., and Baigozhin, A., *Zh. Prikl. Khim.*, 1996, vol. 69, no. 10, pp. 1594–1601.
7. Voronkov, M.G., *Silatrany* (Silatranes), Novosibirsk: Nauka, 1978.
8. Voronkov, M.G., *Top. Curr. Chem.*, 1970, vol. 84, pp. 77–135.
9. Motsarev, G.F., Andrianov, K.A., and Zetkin, V.I., *Usp. Khim.*, 1971, vol. 40, no. 6, pp. 980–1013.

10. Andrianov, K.A. and Khananashvili, L.M., *Tekhnologiya elementoorganicheskikh monomerov i polimerov* (Technology of Organoelement Monomers and Polymers), Moscow: Khimiya, 1973.
11. Voronkov, M.G., Velikanov, A.A., Stankevich, V.K., and Tsyrendorzhieva, I.P, *Zh. Prikl. Khim*., 1990, vol. 69, no. 4, pp. 912–914.
12. USSR Inventor's Certificate no. 154543.
13. Voronkov, M.G. and Davydova, V.P., *Dokl. Akad. Nauk SSSR*, 1959, vol. 125, no. 3, pp. 553–556.
14. Voronkov, M.G., Vlasova, N.N., Bol'shakova, S.A., *et al*., *Dokl. Akad. Nauk SSSR*, 1981, vol. 256, no. 1, pp. 90–95.
15. Krentsel', B.A., *Khlorirovanie parafinovykh uglevodorodov* (Chlorination of Paraffin Hydrocarbons), Moscow: Nauka, 1965.
16. Biryukov, I.P., Voronkov, M.G., Motsarev, T.V., *et al*., *Dokl. Akad. Nauk SSSR*, 1965, vol. 162, no. 1, pp. 130–132.

Russian Journal of Applied Chemistry, Vol. 74, No. 5, 2001, pp. 804–812. Translated from Zhurnal Prikladnoi Khimii, Vol. 74, No. 5, 2001, pp. 781–788.

MACROMOLECULAR CHEMISTRY AND POLYMERIC MATERIALS

Effect of the Medium on the (Co)polymerization Kinetics and Properties of *N*-Vinyl-3(5)-methylpyrazole (Co)polymers

N. A. Lavrov

St. Petersburg State Technological Institute, St. Peterburg, Russia

Received December 27, 2000

Abstract—The kinetics of homopolymerization of *N*-vinyl-3(5)-methylpyrazole and its copolymerization with vinyl acetate, 2-hydroxyethyl methacrylate, and acrylic acid, as influenced by the reaction medium, were studied. The properties of the resulting (co)polymers were determined.

(Co)polymers of *N*-vinyl-3(5)-methylpyrazole (VMP) show promise in preparation of coatings, adhesives, films, flocculants, ion-exchange resins, physiologically active substances, etc. [1, 2]. Various procedures were developed for preparing VMP (co)polymers: radical (co)polymerization in the bulk, in an organic solvent, in suspension, in emulsion, or in aqueous-organic media; there are indications that the (co)polymerization can be initiated by ionizing radiation [1, 3–8]. By varying the nature of the comonomer, the composition of the monomeric mixture, and the reaction conditions, it is possible to prepare copolymers with various molecular weights and solubilities, including water-soluble products.

However, published papers, as a rule, are applied and do not involve the kinetic analysis of (co)polymerization; the possibility of controlling the reactivity of the monomers by varying the process conditions and the reaction medium is not examined. Only scarce data are available on the properties of VMP (co)polymers, in particular, of VMP–vinyl acetate (VA) copolymers prepared in the bulk [9]. This paper considers the effect of the medium (comonomer, initiator, solvent) on the kinetic features of the synthesis of VMP (co)polymers and on their properties.

VMP–VA copolymers were prepared by three procedures: in the bulk, in emulsion, and in aqueous-organic solutions. Bulk copolymerization was performed at 70°C with azobis(isobutyronitrile) (AIBN) as initiator (0.1–1.0% relative to the total weight of the monomers); the copolymers were prepared and isolated as described in [10]. Copolymerization in aqueous emulsion was performed at 60°C using the initiating system manganese tris(acetylacetonate)–acetic acid. The initiator concentration was 3.4×10^{-3} M; the emulsifier, sodium laurylsulfonate or Sol'var (VA–vinyl alcohol copolymer with the mole fraction of VA units of 0.12), was added in an amount of 24–29 g l^{-1}; the polymers were prepared and isolated as described in [11]. Copolymerization in a water–dimethyl sulfoxide (DMSO) mixture was performed at 25–45°C with the initiating system ammonium persulfate (AP)–ascorbic acid (AscA); the concentration of the monomers was 1–2 M, and that of the components of the initiating system, 0.02–0.2 M; the copolymers were prepared and isolated as described in [5].

Copolymers of VMP with 2-hydroxyethyl methacrylate (HEMA) and with acrylic acid (AA) were prepared in a water–DMSO mixture at 25–45°C. Copolymerization of the monomers and isolation of the reaction products were performed according to [12, 13]; the component concentrations were similar to those used in copolymerization of VMP with VA. Base hydrolysis of VMP–VA copolymers was performed according to [14].

Samples for physicomechanical, thermal, and dielectric tests were prepared and the properties of the (co)polymers wee determined by the procedures in [15]. The thermal analysis was performed according to [16]. The composition of the copolymers was determined from the nitrogen content using a CHN analyzer. The copolymerization constants were calculated taking into account the monomer conversion [17].

A structural feature of the VMP molecule is p–π conjugation between the lone electron pair of the nitrogen atom and the double bond of the vinyl group. As a result, the electron density on the double bond increases. This feature is typical of *N*-vinyl compounds and determines the electron-donor character of VMP.

1070-4272/01/7405-0804$25.00

Although the VMP heterocycle contains two nitrogen atoms imparting the acceptor properties to the heterocycle, this fact will not reduce significantly the polarity of the vinyl group. For example, vinylazoles containing two and more nitrogen atoms in the heterocycle are regarded as electron-donor monomers [18]. The donor properties of VMP should be more pronounced than those of *N*-vinylsuccinimide (VSI) whose molecule contains two electron-withdrawing carbonyl groups. The electron-donor character of VMP should facilitate its radical copolymerization with electron-withdrawing monomers.

The existing synthesis procedures allow preparation of VMP as a mixture of two isomers: *N*-vinyl-3-methylpyrazole and *N*-vinyl-5-methylpyrazole:

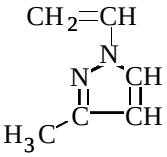

N-Vinyl-3-methylpyrazole

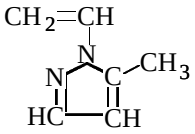

N-Vinyl-5-methylpyrazole

Irrespective of the catalyst used, the ratio of the 3-methyl and 5-methyl isomers in the monomer is 60 : 40 [4]. The heterocycle of the VMP molecule contains double bonds. Therefore, conjugation in this molecule is stronger than in VSI. It can be expected that the VMP monomer will be more active in copolymerization than VSI. However, the activity of the VMP radical should be relatively low.

Our experimental results are nicely consistent with theoretical analysis of the structural features and reactivity of VMP.

Kinetic study of bulk copolymerization of VMP with VA showed that the reaction rate increases to a definite limit with increasing AIBN concentration. At similar reaction times, the conversion of the monomers increases as the AIBN concentration is increased from 0.1 to 0.5 wt %, but at higher AIBN concentrations the conversion did not increase further. As the relative content of VMP in the initial mixture is increased, the overall copolymerization rate increases (Fig. 1). At the same time, the homopolymerization rate is higher for VA than for VMP. These facts show that the VMP radical is more active than the VA radical. The shape of the dependences shown in Fig. 1 suggests occurrence of the gel effect characteristic of radical (co)polymerization in the bulk and associated with occlusion of the macroradicals in the polymer matrix; as a result, the chain termination rate constant abruptly decreases.

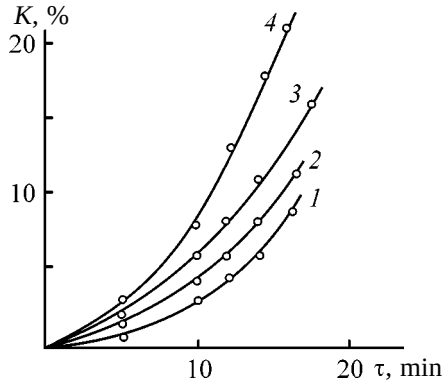

Fig. 1. Conversion of monomers *K* as a function of copolymerization time τ. AIBN content 0.5% relative to the weight of the monomers. VMP mole fraction in the monomer mixture: (*1*) 0.05, (*2*) 0.10, (*3*) 0.15, and (*4*) 0.25.

The copolymers are enriched in VMP units as compared to the initial mixture (Table 1). The VA–VMP copolymerization constants (Table 2) show that VMP is considerably more active. The r_1/r_2 ratio shows that

Table 1. Compolsition of VMP–VA copolymers prepared under various conditions

VMP mole fraction in monomer mixture	Conversion, %	VMP mole fraction in copolymer
Bulk copolymerization		
0.05	3.0	0.399
0.05	5.2	0.388
0.10	4.4	0.513
0.10	6.8	0.501
0.15	6.6	0.640
0.15	9.3	0.618
0.25	7.4	0.749
0.25	12.5	0.735
Emulsion copolymerization		
0.22	13.6	0.410
0.22	21.6	0.370
0.30	9.7	0.667
0.30	14.6	0.610
0.46	17.6	0.714
0.46	34.5	0.634
Copolymerization in water–DMSO mixture (7 : 2 by volume)		
0.25	7.5	0.887
0.25	16.1	0.831
0.50	16.5	0.891
0.50	33.9	0.852
0.75	37.5	0.922
0.75	47.1	0.910

Table 2. Copolymerization constants of VMP (M_1) with other monomers (M_2)

Comonomer M_2	Copolymerization	T, °C	r_1	r_2	r_1/r_2
VA	Bulk	70	6.90 ± 0.10	0.03 ± 0.01	230
	Emulsion	60	1.58 ± 0.26	0.10 ± 0.02	15.8
	In H_2O–DMSO	25	4.20 ± 0.07	0.01 ± 0.01	420
HEMA	"	25	0.03 ± 0.01	1.94 ± 0.10	0.015
AA	"	25	0.02 ± 0.01	1.54 ± 0.20	0.013

the rate constant of the reaction of VMP macroradical with VMP monomer exceeds by a factor of 230 the rate constant of the reaction of VA macroradical with VA monomer. The calculated relative activities of the monomers toward radicals $1/r$ show that in the course of copolymerization VA reacts faster with VMP radical than with VA radical.

Comparison of the VMP–VA copolymerization constants with the results obtained from studies of the bulk copolymerization of VSI with VA (r_{VSI} = 5.1, r_{VA} = 0.17, r_{VSI}/r_{VA} = 30) [19] shows that the activities of VMP and VA differ to a greater extent than those of VSI and VA, i.e., VMP is a more active monomer than VSI. The same conclusion follows from the Alfrey–Price parameters calculated for VMP. Taking for VA Q = 0.026 and e = –0.22 [20], we obtain for VMP Q = 1.14 and e = –1.47, whereas for VSI Q = 0.13 and e = –0.34 [20].

Preparation of polymers in aqueous media is advantageous from the technological and environmental viewpoints. With high-performance initiating systems, the reaction temperature can be decreased, and the process can be made power-saving. Therefore, we examined the possibility of preparing VMP polymers in aqueous solutions in the presence of emulsifiers, and also in aqueous-organic mixtures.

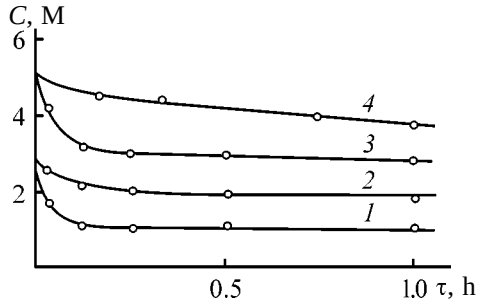

Fig. 2. Concentration C in the reaction mixture: (*1*) VMP, (*2*) VA, and (*3*, *4*) total of monomers, as a function of copolymerization time τ, with (*1*–*3*) Sol'var and (*4*) sodium laurylsulfonate as emulsifiers. Concentrations, M: $Mn(acac)_3$ 3.4×10^{-3} and CH_3COOH 0.84.

Kinetic study of the (co)polymerization of VMP with VA in emulsion in the presence of the initiating system $Mn(acac)_3$–CH_3COOH showed that under these conditions it is possible to prepare both homopolymers of VMP and VA and their copolymers of a wide range of compositions. Homopolymerization of VA is faster (13.8×10^{-3} mol l^{-1} s^{-1}) than that of VMP (8.32×10^{-3} mol l^{-1} s^{-1}), which is due to the higher activity of the VA radical as compared to VMP. VMP monomer is more active than VA monomer; therefore, similar to bulk copolymerization, VMP is consumed in the monomer mixture faster than VA (Fig. 2, curves *1*, *2*). The gel effect characteristic of bulk copolymerization is not manifested in this case. Sol'var as emulsifier is more efficient than sodium laurylsulfonate, as it ensures higher copolymerization rates (Fig. 2, curves *3*, *4*). Emulsion copolymerization does not require elevated temperatures; it can be performed in the range 20–60°C [21].

Similar to bulk copolymerization, the copolymers are enriched in VMP units (Table 1). With increasing conversion of monomers, the differences in compositions are leveled out. The copolymerization constants for the emulsion process differ less significantly than those for the bulk copolymerization (Table 2). This may be due to complexation of VA monomer with $Mn(acac)_3$ [22], affecting the VA reactivity and increasing its relative activity in copolymerization with VMP owing to polarization of the double bond in VA. VMP monomer forms no complexes with $Mn(acac)_3$, as such complexation is characteristic of vinyl esters only [22].

VMP monomer is water-insoluble; therefore, its (co)polymers cannot be prepared in aqueous solutions. We have studied the solubility of VMP and its mixtures with other monomers (VA, HEMA, AA) in aqueous-organic media (water–acetone, water–dimethylformamide, water–DMSO) and examined the possibility of preparing (co)polymers in these media using the redox initiating systems AP–AscA, AP–sodium sulfite, etc. The best results were obtained with the system AP–AscA in a water–DMSO mixture [23].

The reaction can be performed at 25–45°C. Copolymerization of VMP with VA in the presence of the system AP–AscA occurs with an induction period which is longer when the reaction is performed in air. Furthermore, in the presence of atmospheric oxygen the reaction decelerates (Fig. 3a, curves *3*, *5*). Increase in the total concenration of monomers from 1 to 2 M has virtually no effect on the copolymerization rate; the experimental points fall on a common kinetic straight line. Therefore, taking into account the solubility of the monomers in water–DMSO mixtures, it is not appropriate to take the monomers in concentrations higher than 1 M.

Under the chosen conditions, it is possible to prepare both VMP–VA copolymers of a wide composition range and VMP homopolymers. However, the VA homopolymerization under these conditions does not occur even at the concentration of the initiating system increased to 0.2 M. This is probably due to the inhibiting effect of atmospheric oxygen dissolved in water.

The monomer ratio significantly affects the copolymerization rate and the copolymer yield. Similar to the bulk process, VMP monomer is more active: The reaction rate and the copolymer yield increase with increasing contyent of VMP in the monomer mixture (Fig. 3a, curves *2–4*), and the copolymer is enriched in VMP as compared to the initial mixture (Table 1). In the course of the reaction, with increasing conversion the content of VMP in the copolymer decreases, becoming close to the composition of the monomer mixture. The copolymerization constants are as follows: $r_{VMP} = 4.20 \pm 0.07$ and $r_{VA} = 0.01 \pm 0.01$. The activation energy of copolymerization in the range 25–45°C was 41.2 kJ mol^{-1}, which is close to the values obtained for polymerization of the other monomers in the presence of this initiating system [24].

The copolymerization rate and the copolymer yield are affected by the water : DMSO ratio (Fig. 3b). This is probably due to different solubilities of the monomers and copolymer in water and in DMSO and to the heterophase nature of the process, which affects the rates of the elementary reaction events. The effect of the medium on the reaction kinetics was also noted for homopolymerization of VMP in water–acetone mixtures [25].

Copolymerization of VMP with HEMA is sufficiently fast at room temperature; the yield of the copolymer in 1 h exceeds 80% at the monomer ratio varied in a wide range. Similar to copolymerization of VMP with VA, an induction period is observed. In

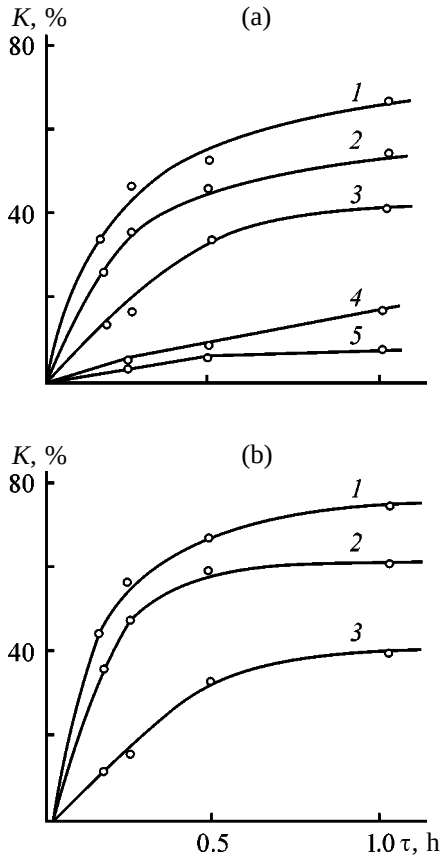

Fig. 3. Conversion of monomers *K* (*1–4*) in argon and (*5*) in air as a function of copolymerization time τ. Concentration, M: monomers 1.0; AP and AscA 0.02 M each. 25°C. VMP mole fraction in monomer mixture: (a) (*1*) 1.00 (homopolymerization), (*2*) 0.75, (*3*, *5*) 0.50, and (*4*) 0.25; (b) 0.50. Water : DMSO volume ratio: (a) 7 : 2; (b) (*1*) 1 : 2, (*2*) 4 : 5, and (*3*) 7 : 2.

copolymerization with *N*-vinyl compounds, HEMA is more reactive [26]. The same trend is observed with VMP: The reaction rate increases from 2.2×10^{-4} to 2.8×10^{-4} mol l^{-1} s^{-1} as the mole fraction of the less active monomer VMP is decreased from 0.75 to 0.25; the copolymer is enriched in HEMA units as compared to the composition of the initial monomer mixture (Table 3).

The copolymerization rate constants were as follows: $r_{VMP} = 0.03 \pm 0.01$ and $r_{HEMA} = 1.94 \pm 0.10$. With conversion, the content of the less active monomer, VMP, in the copolymer increases, approaching its content in the initial monomer mixture (Table 3), which corresponds to the copolymerization constants $r_1 < 1$ and $r_2 > 1$ and is characteristic of copolymerization of *N*-vinyl compounds with acrylates.

Similar trends were also observed in copolymerization of VMP with AA: The copolymers were enriched

Table 3. Composition of VMP–HEMA and VMP–AA copolymers prepared in an H_2O–DMSO mixture (volume ratio 7 : 2)

VMP mole fraction in monomer mixture	Conversion, %	VMP mole fraction in copolymer
Copolymerization of VMP with HEMA		
0.25	38	0.156
	81	0.183
0.50	73	0.324
	80	0.378
0.75	65	0.605
	69	0.611
Copolymerization of VMP with AA		
0.25	68	0.171
0.50	64	0.386
	65	0.408
0.75	59	0.538

in AA units as compared to the initial monomer mixtures (Table 3); the copolymerization constants are listed in Table 2.

The probability of diad formation and the statistical mean length of blocks and chains of VMP–VA copolymers are largely affected by the reaction medium (Table 4).

Since the rate constant of the reaction of VMP macroradical with VMP monomer considerably exceeds the rate constant of the reaction of VA macroradical with VA monomer, the probability of formation of VMP–VMP diads is higher compared to VA–VA diads. For copolymerization in the bulk and in the water–DMSO mixture, this relation is observed at any content of VMP in the monomer mixture. In emulsion copolymerization, this is characteristic of monomer mixtures with the mole fraction of VMP greater than 0.3. In the copolymer prepared in the water–DMSO

Table 4. Influence of reaction medium on the probability of diad formation f and the statistical mean block length L in chains of VMP (M_1)–VA (M_2) copolymers

VMP mole fraction in monomer mixture	f_{11}	f_{22}	$f_{12} = f_{21}$	L_1	L_2
Bulk copolymerization					
0.1	0.253	0.089	0.330	1.77	1.27
0.2	0.449	0.031	0.260	2.73	1.12
0.3	0.588	0.014	0.199	3.96	1.07
0.4	0.692	0.007	0.151	5.60	1.04
0.5	0.773	0.003	0.112	7.90	1.03
0.6	0.837	0.002	0.081	11.4	1.02
0.7	0.889	0.0007	0.055	17.1	1.01
0.8	0.932	0.0003	0.034	28.6	1.008
0.9	0.969	0.0001	0.016	63.1	1.003
Emulsion copolymerization					
0.1	0.057	0.293	0.325	1.18	1.90
0.2	0.141	0.143	0.358	1.40	1.40
0.3	0.233	0.080	0.344	1.68	1.23
0.4	0.329	0.047	0.312	2.05	1.15
0.5	0.429	0.027	0.272	2.58	1.10
0.6	0.534	0.015	0.225	3.37	1.07
0.7	0.644	0.008	0.175	4.69	1.04
0.8	0.757	0.003	0.120	7.32	1.03
0.9	0.876	0.0007	0.062	15.2	1.01
Copolymerization in H_2O–DMSO mixture (7 : 2)					
0.1	0.183	0.035	0.391	1.47	1.09
0.2	0.340	0.013	0.324	2.05	1.04
0.3	0.471	0.006	0.262	2.80	1.02
0.4	0.581	0.003	0.208	3.80	1.015
0.5	0.676	0.002	0.161	5.20	1.010
0.6	0.758	0.001	0.120	7.30	1.006
0.7	0.830	0.0004	0.085	10.8	1.004
0.8	0.894	0.0001	0.053	17.8	1.003
0.9	0.950	0	0.025	38.8	1.001

Table 5. Probability of diad formation f and the statistical mean block length L in chains of copolymers of VMP (M_1) with acrylic monomers (M_2), prepared in the water–DMSO mixture

VMP mole fraction in monomer mixture	f_{11}	f_{22}	$f_{12} = f_{21}$	L_1	L_2
		M_2 = HEMA			
0.1	0.0002	0.897	0.051	1.003	18.5
0.2	0.0008	0.795	0.102	1.007	8.76
0.3	0.002	0.692	0.153	1.013	5.53
0.4	0.004	0.590	0.203	1.02	3.91
0.5	0.008	0.489	0.252	1.03	2.94
0.6	0.014	0.387	0.300	1.05	2.29
0.7	0.024	0.287	0.345	1.07	1.83
0.8	0.046	0.186	0.384	1.12	1.49
0.9	0.109	0.087	0.402	1.27	1.22
		M_2 = AA			
0.1	0.0001	0.874	0.063	1.002	14.9
0.2	0.0006	0.754	0.123	1.005	7.16
0.3	0.002	0.641	0.179	1.009	4.59
0.4	0.003	0.534	0.231	1.01	3.31
0.5	0.006	0.433	0.281	1.02	2.54
0.6	0.010	0.336	0.327	1.03	2.03
0.7	0.017	0.244	0.370	1.05	1.66
0.8	0.033	0.156	0.406	1.08	1.39
0.9	0.077	0.073	0.425	1.18	1.17

mixture, the content of diads with alternating units is higher than in the product of bulk copolymerization but lower than in the product of emulsion copolymerization.

In copolymers of VMP with acrylic monomers, the relation is inverse (Table 5): The probability of formation of VMP–VMP diads is lower compared to HEMA–HEMA or AA–AA diads at a mole fraction of VMP less than 0.9.

By comparing the copolymerization constants (Table 2) and the probabilities of diad formation in copolymer chains (Tables 4, 5), we can compare the relative activities of VMP, VSI, VA, HEMA, and AA in copolymerization. The ratio r_1/r_2 suggests that AA in copolymerization with VMP is more active than HEMA: r_{AA}/r_{VMP} = 77 and r_{HEMA}/r_{VMP} = 64.7. However, it is seen from Table 5 that the probability of formation of HEMA–HEMA diads in copolymerization of VMP with HEMA is higher than that of formation of AA–AA diads in copolymerization of VMP with AA at any monomer ratio. Figure 4 shows that copolymerization of VMP with HEMA is faster than that with AA; therefore, the monomers can be ranked in the following order with respect to activity: VA < VSI < VMP < AA < HEMA.

The VMP homopolymer is a white powder soluble in alcohols and aromatic and chlorinated hydrocarbons but insoluble in water and petroleum ether. VMP–VA and VMP–HEMA copolymers are also isolated as white powders soluble in dimethylformamide and methanol. VMP–AA copolymers are white powders soluble in methanol.

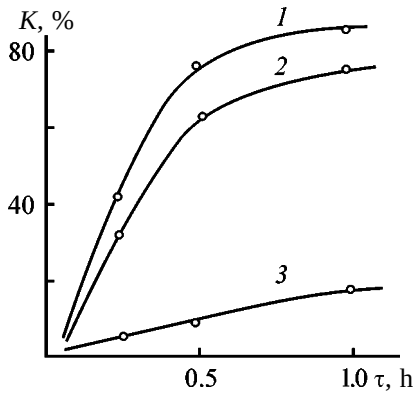

Fig. 4. Monomer conversion K as a function of copolymerization time τ. Concentration, M: monomers 1.0; AP and AscA 0.02 each; VMP mole fraction in the monomer mixture 0.75; volume ratio water : DMSO 7 : 2; 25°C. Comonomer: (*1*) HEMA, (*2*) AA, and (*3*) VA.

Table 6. Properties of VMP homopolymers [27] prepared at 70°C

Copolymerization	AIBN concentration, mol %	$[\eta]$, dl g^{-1}, in benzene at 20°C	T_f, °C
Bulk	0.1	1.15	238–245
In toluene	0.5	0.98	180–200
	1.0	0.89	165–180
	1.5	0.75	150–165
	2.0	0.69	160–170

It is known [6] that homopolymers of VMP with the highest molecular weight (up to 1.3×10^6) are formed by bulk polymerization with AIBN initiator. In organic solvents in the presence of AIBN, poly-*N*-vinyl-3(5)-methylpyrazole (PMVP) of a lower molecular weight is formed: $(0.6–1.0) \times 10^5$ in benzene and $(1.0–3.0) \times 10^4$ in ethyl acetate [7].

As the initiator concentration is decreased, the molecular weight of PMVP decreases, as indicated by decrease in the intrinsic viscosity of polymer solutions $[\eta]$; the flow point T_f also decreases (Table 6).

The properties of VMP–VA copolymers prepared by bulk copolymerization are listed in Table 7. The samples were prepared from the monomer mixtures with the VMP mole fraction varying from 0.05 to 0.75, in the presence of AIBN initiator (0.5% of the total weight of the monomers).

The properties of the copolymers (Table 7) show that, as the content of VMP units increases, the strength, heat resistance, and glass transition point increase. The pyrazole rings of VMP are less polar than the acetate groups of VA; therefore, with increasing content of VMP units the dielectric properties of the copolymers are improved. The thermal properties of the copolymers are as follows: heat conductivity 0.10–0.18 W m^{-1} K^{-1}, temperature conductivity $(4–6) \times 10^{-8}$ m^2 s^{-1}, and specific heat 1.2–3.2 kJ kg^{-1} K^{-1}.

Thermal analysis of the polymers shows that the temperatures of the onset and maximal rate of degradation increase with increasing VMP content. Decomposition of the samples occurs in two stages: At 190–360°C vinyl acetate units degrade, which is followed by degradation of VMP units at 360–500°C (Fig. 5). The homopolymers decompose in one stage.

The preparation conditions affect the intrinsic viscosity of solutions of VMP–VA copolymers (Table 8); the thermal and dielectric properties change insignificantly (within the determination error).

The properties of VMP–HEMA copolymers prepared in the water–DMSO mixture at a VMP mole fraction of 0.50 are as follows: Brinell hardness 116 MPa, Vicat softening point 72°C, temperature of maximal degradation rate 412°C, and water absorption in 2 h 50%.

VMP (co)polymers are highly resistant to hydrolysis. Base hydrolysis of VMP homopolymer at 20–90°C occurs neither under heterogeneous (in aqueous NaOH) nor under homogeneous (in aqueous-methanolic NaOH) conditions. The IR spectrum of the hydrolyzed polymer is identical to that of the initial polymer; the bands at 1530 (stretching vibrations of substituted heteroaromatic five-membered rings) and 780 cm^{-1} (out-of-plane ring vibrations) are preserved.

In VMP–VA copolymers, only VA units are sub-

Table 7. Properties of copolymers of *N*-vinyl-3(5)-methylpyrazole with vinyl acetate

Parameter	Copolymer with indicated VMP mole fraction				PVMP
	0.05	0.25	0.50	0.75	
Intrinsic viscosity in toluene at 25°C, dl g^{-1}	0.21	0.52	0.75	0.89	–
Breaking bending stress, MPa	–	–	25	28	–
Specific impact resilience, kJ m^{-2}	5–8	5–8	3–4	1–2	1–2
Brinell hardness, MPa	–	45	75	102	145
Glass transition point, °C	–	40	48	59	78
Temperature of degradation onset, °C	190	205	240	245	255
Temperature of 5% weight loss, °C	300	–	300	305	380
Temperature of maximal degradation rate, °C	330	–	425	435	445
Dielectric permittivity at 10^6 Hz	3.0	2.8	2.8	2.5	2.3
Tangent of dielectric loss angle at 10^6 Hz	0.01–0.02				

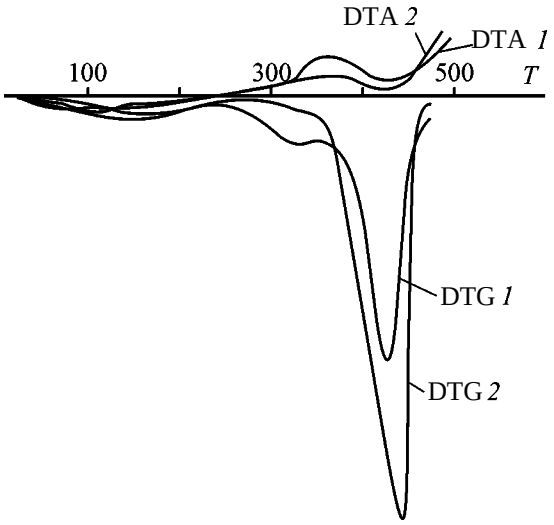

Fig. 5. DTA and DTG curves of (*1*) copolymer of VMP with VA (VMP mole fraction 0.50) and (*2*) PVMP.

ject to hydrolysis; VMP–VA copolymers are hydrolyzed faster than VA homopolymers prepared under the similar conditions. This is probably due to the fact that the microstructure of the copolymer macrochains makes the VA units in the copolymer more accessible to the hydrolyzing agent. Separate VA units alternating with VMP blocks are hydrolyzed more readily, and the maximal degree of hydrolysis is close to the content of VA units in the copolymers, so that their conversion is practically 100%.

Thus, hydrolysis of VMP–VA copolymers yields copolymers of VMP with vinyl alcohol. These substances are yellow or yellowish powders. Depending on the composition, the products can be soluble in organic solvents or water. VMP–HEMA copolymers undergo practically no changes at attempted base hydrolysis, because the HEMA units are also highly resistant to hydrolysis up to 80–100°C. The AA units in VMP–AA copolymer in hydrolysis with NaOH solutions transform into sodium acrylate units.

Table 8. Effect of the medium on the intrinsic viscosity [η] of VMP–VA copolymers in toluene at 25°C

Copolymerization	[η], dl g^{-1}, at indicated VMP mole fraction	
	0.25	0.75
Bulk	0.52	0.89
Emulsion	0.54	0.76
In water–DMSO mixture	0.77	1.18

CONCLUSIONS

(1) The reaction medium affects the relative activity of *N*-vinyl-3(5)-methylpyrazole in copolymerization and the alternation of units in the resulting copolymers. The kinetics of (co)polymerization in the bulk, emulsion, and water–dimethyl sulfoxide mixtures were studied, and the copolymerization constants were determined.

(2) *N*-Vinyl-3(5)-methylpyrazole in copolymerization with vinyl acetate is more active, which results in formation of compositionally nonuniform copolymers. Copolymers with a better unit alternation can be obtained by performing the reaction in emulsion in the presence of the initiating system manganese tris(acetylacetonate)–acetic acid.

(3) Copolymers of *N*-vinyl-3(5)-methylpyrazole with vinyl acetate, 2-hydroxyethyl methacrylate, and acrylic acid of a wide composition range can be prepared in a water–dimethyl sulfoxide mixture (volume ratio 7 : 2).

(4) The physicomechanical, thermal, and dielectric properties of *N*-vinyl-3(5)-methylpyrazole were studied. The strength, heat resistance, and glass transition point increase with increasing content of *N*-vinyl-3(5)-methylpyrazole.

(5) The possibility of modification of *N*-vinyl-3(5)-methylpyrazole (co)polymers by base hydrolysis was examined. The *N*-vinyl-3(5)-methylpyrazole units are not hydrolyzed. Depending on the nature of the comonomer, copolymers soluble in water or organic solvents can be thus prepared.

REFERENCES

1. Lavrov, N.A., Redina, N.V., and Stulova, O.V., in *Khimicheskaya tekhnologiya, svoistva i primenenie plastmass: Mezhvuzovskii sbornik nauchnykh trudov* (Chemical Technology, Properties, and Use of Plastics: Intercollegiate Coll. of Scientific Works), Leningrad: Leningr. Tekhnol. Inst. im. Lensoveta, 1990, pp. 55–61.
2. Lavrov, N.A., Stulova, O.V., Vinogradova, M.V., *et al.*, in *Plastmassy so spetsial'nymi svoistvami: Materialy nauchno-tekhnicheskogo seminara* (Plastics with Special Properties: Proc. Scientific and Technical Seminar), St. Petersburg: Sankt-Peterb. Dom Nauchno-Tekh. Propagandy, 1992, pp. 7–9.
3. Lavrov, N.A., *Plast. Massy*, 1989, no. 11, pp. 16–17.
4. Lavrov, N.A., Novatskii, A.G., Nesterenko, V.D., and Zaitseva, E.V., in *Khimicheskaya tekhnologiya, svoistva i primenenie plastmass: Mezhvuzovskii sbornik*

nauchnykh trudov (Chemical Technology, Properties, and Use of Plastics: Intercollegiate Coll. of Scientific Works), Leningrad: Leningr. Tekhnol. Inst. im. Lensoveta, 1984, pp. 21–27.

5. Lavrov, N.A. and Stulova, O.V., *Zh. Prikl. Khim.*, 1992, vol. 65, no. 11, pp. 2619–2621.
6. Gzyryan, A.G., Danielyan, V.A., and Barkhudaryan, V.G., *Vysokomol. Soedin., Ser. B*, 1982, vol. 24, no. 7, pp. 521–525.
7. Karamzina, L.V., Pochinok, V.Ya., Gurash, G.V., *et al.*, *Ukr. Khim. Zh.*, 1976, vol. 42, no. 8, pp. 850–852.
8. Gzyryan, A.G., Barkhudaryan, V.G., and Danielyan, V.A., *Vysokomol. Soedin., Ser. B*, 1982, vol. 24, no. 7, pp. 518–521.
9. Lavrov, N.A. and Nikolaev, A.F., *Zh. Prikl. Khim.*, 1990, vol. 63, no. 5, pp. 1204–1205.
10. Lavrov, N.A., Nikolaev, A.F., and Vedernikov, V.V., *Izv. Vyssh. Uchebn. Zaved., Khim. Khim. Tekhnol.*, 1987, vol. 30, no. 10, pp. 89–92.
11. Lavrov, N.A. and Tsynbal, E.M., *Zh. Prikl. Khim.*, 1992, vol. 65, no. 9, pp. 2108–2110.
12. Lavrov, N.A., *Zh. Prikl. Khim.*, 1993, vol. 66, no. 6, pp. 1420–1422.
13. Lavrov, N.A., *Zh. Prikl. Khim.*, 1994, vol. 67, no. 11, pp. 1915–1916.
14. Lavrov, N.A., Vedernikova, A.A., and Novatskii, A.G., in *Khimicheskaya tekhnologiya, svoistva i primenenie plastmass: Mezhvuzovskii sbornik nauchnykh trudov* (Chemical Technology, Properties, and Use of Plastics: Intercollegiate Coll. of Scientific Works), Leningrad: Leningr. Tekhnol. Inst. im. Lensoveta, 1987, pp. 80–83.
15. Kryzhanovskii, V.K., *Issledovanie polimernykh materialov metodami prikladnoi fiziki: Uchebnoe posobie* (Study of Polymeric Materials by Methods of Applied Physics: Textbook), Leningrad: Leningr. Tekhnol. Inst. im. Lensoveta, 1984.
16. Shul'gina, E.S. and Vinogradov, M.V., *Termicheskie svoistva polimerov: Metodicheskie ukazaniya* (Thermal Properties of Polymers: Methodical Regulations), Leningrad: Leningr. Tekhnol. Inst. im. Lensoveta, 1988.
17. Sautin, S.N., Lavrov, N.A., Punin, A.E., and Hartmann, K., *Metody rascheta otnositel'nykh aktivnostei monomerov pri sopolimerizatsii: Uchebnoe posobie* (Methods for Calculating the Relative Activities in Copolymerization: Textbook), Leningrad: Leningr. Tekhnol. Inst. im. Lensoveta, 1986.
18. Smirnov, A.I., Reactivity of *O*- and *N*-Vinyl Monomers in Alternating Radical Copolymerization Reactions, *Doctoral Dissertation*, Moscow, 1989.
19. Lavrov, N.A., Bondarenko, S.G., Nikolaev, A.F., and Sautin, S.N., *Zh. Prikl. Khim.*, 1984, vol. 57, no. 3, pp. 618–621.
20. *Copolymerization*, Ham, G.E., Ed., New York: Interscience, 1964.
21. RF Patent 2021291.
22. Nikolaev, A.F., Belogorodskaya, K.V., and Duvakina, N.I., in *Khimicheskaya tekhnologiya, svoistva i primenenie plastmass: Mezhvuzovskii sbornik nauchnykh trudov* (Chemical Technology, Properties, and Use of Plastics: Intercollegiate Coll. of Scientific Works), Leningrad: Leningr. Tekhnol. Inst. im. Lensoveta, 1976, pp. 11–18.
23. USSR Inventor's Certificate no. 1812180.
24. Lavrov, N.A., Bondarenko, V.M., and Nikolaev, A.F., *Zh. Prikl. Khim.*, 1984, vol. 57, no. 3, pp. 610–613.
25. Gzyryan, A.G., Danielyan, V.A., and Matsoyan, S.G., *Arm. Khim. Zh.*, 1982, vol. 35, no. 8, pp. 543–546.
26. Lavrov, N.A., *Plast. Massy*, 1995, no. 3, pp. 24–26.
27. Darbinyan, E.G., Amazyan, G.A., Abramyan, T.G., *et al.*, *Arm. Khim. Zh.*, 1974, vol. 27, no. 9, pp. 790–795.

Russian Journal of Applied Chemistry, Vol. 74, No. 5, 2001, pp. 813–817. Translated from Zhurnal Prikladnoi Khimii, Vol. 74, No. 5, 2001, pp. 789–792.

MACROMOLECULAR CHEMISTRY AND POLYMERIC MATERIALS

Copolymerization of Acrylamide with Salts of 2-Acrylamido-2-methylpropanesulfic Acid in Aqueous Solutions as Influenced by the Nature of Double-Charged Cation

V. F. Kurenkov, O. A. Zaitseva, D. G. Vazeeva, and D. A. Solov'ev

Kazan State Technological University, Kazan, Tatarstan, Russia

Received September 25, 2000

Abstract—The kinetics of copolymerization of acrylamide with magnesium, calcium, and strontium 2-acrylamido-2-methylpropanesulfonates in aqueous solutions in the presence of potassium persulfate–sodium hydrosulfite initiating redox system at pH 9 and 50°C was studied as influenced by the cation nature.

The radical copolymerization in aqueous solutions is the main, but still not clearly studied procedure for preparing copolymers of acrylamide (AA) with salts of 2-acrylamido-2-methylpropanesulfonic acid (H-AMS), which are widely used in various branches of industry thanks to their valuable properties [1, 2]. One of the typical features of copolymerization of the salts of weak [3] and strong [4] unsaturated acids is the dependence of the kinetic parameters of synthesis and characteristics and properties of the resulting polymers on the cation nature [5]. Such dependences were found previously for polymerization of salts of H-AMS with single- [6] and double-charged [7] cations, and in the course of copolymerization of AA with single-charged metal 2-acrylamido-2-methylpropanesulfonates [8]. In this work we studied the kinetics of radical copolymerization of acrylamide with magnesium, calcium, and strontium 2-acrylamido-2-methylpropanesulfonates in water and aqueous salt solutions as influenced by the cation nature.

EXPERIMENTAL

In our work we used acrylamide purchased from Mitsubishi Chem. Ind. Ltd. (Japan) (mp 84.5°C), H-AMS purchased from Lubrizol Corp. (Great Britain) (mp 186°C), distilled water, and other chemically pure grade reagents. Magnesium, calcium, and strontium 2-acrylamido-2-methylpropanesulfonates were prepared by neutralization of H-AMS (upon cooling and mixing) in aqueous solution to pH 9 with suspensions of $Mg(OH)_2$, $Ca(OH)_2$, and $Sr(OH)_2$, respectively, with subsequent filtration of the undissolved residue and were used as aqueous solutions. The procedures of copolymerization, dilatometric measurements, and tests were presented previously in [9]. The shift of the meniscus of the reaction mixture in a dilatometer capillary in the course of reaction was controlled with a KM-8 cathetometer.

After copolymerization the resulting polymers were precipitated from aqueous solutions into acetone, filtered off, washed with acetone, and dried to constant weight in a vacuum at room temperature.

The intrinsic viscosity [η] of copolymer solutions was measured in a 0.5 M NaCl solution at 25°C using a VPZh-3 viscometer (d_c = 0.56 mm).

The content of ionic groups in copolymer was determined from the content of sulfur [10].

Copolymerization of AA (M_1) with H-AMS salts (M_2) was carried out in concentrated aqueous solutions ([M_1 + M_2] = 5–15 wt %) at pH 9 and 50°C with the potassium persulfate (PP)–sodium hydrosulfite (SHS) redox initiating system. Variation in the ionic strengths of solutions μ at changing concentrations of the ionic monomer and low-molecular-weight nonpolymerizing salts does not affect the AA reactivity, because the rate of its polymerization in aqueous solutions is independent of salt addition [11, 12]. Solution pH 9 maintained during copolymerization and utilization of PP initiator provide constant rates of initiation at changing ionic strength μ, because the rate of PP decomposition in alkaline solutions is independent of μ [13]. Moreover, constant pH 9 provides high polymerization efficiency of the PP–SHS system

1070-4272/01/7405-0813$25.00

Table 1. Parameters of AA copolymerization with H-AMS salts in aqueous solutions, initial molar ratio $[M_1 + M_2] = 3 : 7$

Monomer	$[M_1 + M_2]$, M	Salt added, M	$v_0 \times 10^5$, mol l^{-1} s^{-1}	Yield in 2 h, %	$[\eta]$, cm^3 g^{-1}
Mg-AMS	0.29	–	0.58	63	57
	0.57	–	4.08	68	84
	0.57	$MgCl_2$, 0.4	5.13	80	89
	0.57	$MgCl_2$, 0.8	6.09	89	88
	0.86	–	17.02	76	100
Ca-AMS	0.28	–	0.68	62	–
	0.56	–	4.36	62	107
	0.56	$CaCl_2$, 0.4	5.43	98	106
	0.56	$CaCl_2$, 0.8	6.37	99	105
	0.84	–	19.78	64	112
Sr-AMS	0.26	–	0.82	47	–
	0.51	–	6.24	60	–
	0.51	$SrCl_2$, 0.4	7.72	83	–
	0.51	$SrCl_2$, 0.8	8.32	86	–
	0.76	–	20.13	61	–

[14], and hinders hydrolysis of H-AMS salts [15] and imidization of the amide groups possible during polymerization of AA in concentrated aqueous solutions [16].

Copolymerization was carried out under the homogeneous conditions at any conversions, and no spontaneous polymerization was observed in the absence of the PP–SHS initiating system.

The effect of the cation nature on copolymerization of AA and Mg-, Ca-, and Sr-AMS was studied at various concentrations of the initial monomer mixtures $M_1 + M_2$; the initial molar ratio $[M_1] : [M_2]$ was 3 : 7. The kinetic curves of copolymerization were obtained by the dilatometric procedure and are shown in Fig. 1. In all cases the initial sections of the kinetic curves were linear, and, using them, we determined the copolymerization initial rates v_0 at low conversions ($x < 3\%$). The resulting v_0 values are listed in Table 1. As seen from Fig. 1 and Table 1, v_0, conversion, and $[\eta]$ of copolymers increase with increasing concentration of $M_1 + M_2$ in the reaction mixture. The copolymerization rates v_0 and conversion also increase with increasing concentration of low-molecular-weight salts ($MgCl_2$, $CaCl_2$, and $SrCl_2$) at constant $[M_1 + M_2] = 10$ wt % (Table 1). Such a change in v_0 with increasing concentrations of the monomer mixture $M_1 + M_2$ and low-molecular-weight additives is due to the increase in μ, which decreases the electrostatic repulsion between similarly charged sulfonate groups of the ionic monomers and macroradicals and the terminal ionic groups in the events of the chain growth [9].

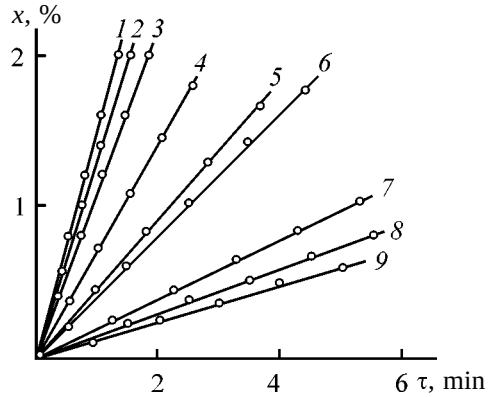

Fig. 1. (*1–3*) Initial sections of the kinetic curves of copolymerization of AA with (*1, 4, 7*) Sr-AMS, (*2, 5, 8*) Ca-AMS, and (*3, 6, 9*) Mg-AMS in aqueous solutions. Initial molar ratio $[M_1] : [M_2] = 3 : 7$; $[PP] = 3.9 \times 10^{-4}$, $[SHS] = 2.6 \times 10^{-4}$ M. (*x*) Conversion and (τ) time. $[M_1 + M_2]$, wt %: (*1–3*) 15, (*4–6*) 10, and (*7–9*) 5.

Table 1 shows that at fixed compositions of the monomer mixture $M_1 + M_2$ v_0 increases in the order $Mg^{2+} < Ca^{2+} < Sr^{2+}$. This dependence is observed in the absence and in the presence of low-molecular-weight salts; v_0 and $[\eta]$ increase in parallel in going from copolymers of AA with Mg-AMS to copolymers with Ca-AMS (Table 1).

The data on copolymerization at various initial molar ratios $[M_1] : [M_2]$ (Figs. 2, 3) confirm the

dependence of v_0 and [η] on the nature of double-charged cation. With Sr-AMS at $[M_1] : [M_2] > 4 : 6$ (Fig. 2) the system was microheterogeneous (the reaction solutions were turbid), and therefore we failed to determine v_0. As seen from Fig. 3, the higher-molecular-weight copolymers of AA with Ca-AMS and Mg-AMS are formed in the monomer mixtures enriched with the ionic monomers.

To explain the observed dependence of the copolymerization parameters on the cation nature in H-AMS salts, we consider the ionization equilibrium of the ionic groups of the monomers and macroradicals in the salt solutions:

$$\underset{\mathbf{I}}{A^-X^+} \rightleftarrows A^- \;\|\; \underset{\mathbf{II}}{X^+} \rightleftarrows A^- + \underset{\mathbf{III}}{X^+}, \qquad (1)$$

where A^- is the anion of the monomer or macroradical; X^+ is the cation; and **I, II**, and **III** are the contact ion pairs, ion pairs separated with a solvent, and free ions, respectively.

The increase in μ and degree of binding of the cations with polyanions shifts the ionization equilibrium (1) to the left, decreasing the intra- and intermolecular interactions in the reaction system. This affects the reactivity of H-AMS salts and their macroradicals and causes instability in the polymerization rate constants and copolymerization constants. As a result, the copolymerization with participation of the ionic monomer could not be described by classical equations with fixed r_1 and r_2.

It is known [17] that with increasing cation radius r (0.72×10^{10}, 1.00×10^{10}, and 1.26×10^{10} m for Mg^{2+}, Ca^{2+}, and Sr^{2+}, respectively [18]) the degree of the cation binding with polysulfonate anions increases in the series $Mg^{2+} < Ca^{2+} < Sr^{2+}$.

As a result, the electrostatic repulsion of similarly charged H-AMS salts with the similar macroradical decreases in the order $Mg^{2+} > Ca^{2+} > Sr^{2+}$, which causes the increase in v_0 and [η] in the reverse order $Mg^{2+} < Ca^{2+} < Sr^{2+}$.

The effect of the monomer molar ratio $[M_1]/[M_2]$ in the initial reaction mixture on the composition of AA copolymers with Mg-AMS and Ca-AMS was studied at $[M_1 + M_2] = 10$ wt %, other conditions being equal (Fig. 4). In these two copolymer systems the rate constants of the monomer addition to the dissimilar macroradical are higher than that to the similar one, i.e., for AA $r_1 = k_{11}/k_{12} < 1$ and for H-AMS salts $r_2 = k_{22}/k_{21} < 1$. The data given in Fig. 4 for $[M_1]/[M_2]$ = const indicate the enrichment of copoly-

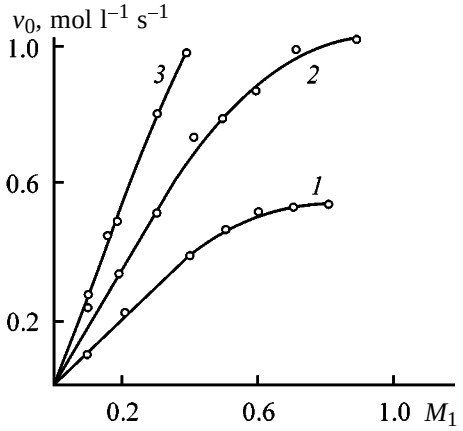

Fig. 2. Initial rate of copolymerization v_0 of AA with (*1*) Mg-AMS, (*2*) Ca-AMS, and (*3*) Sr-AMS as a function of the AA content in the initial monomer mixture M_1 (mole fraction). $[M_1 + M_2] = 10$ wt %, $[PP] = 5.2 \times 10^{-4}$ M and $[SHS] = 3.5 \times 10^{-4}$ M; the same for Fig. 4.

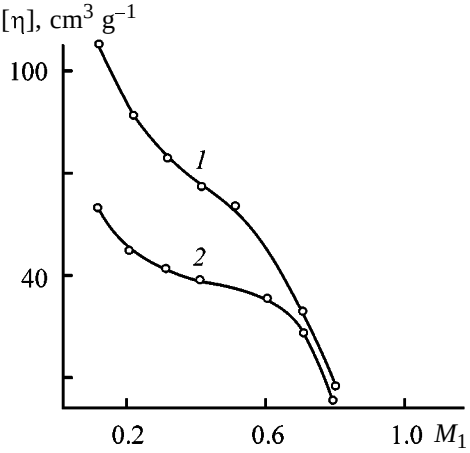

Fig. 3. Intrinsic viscosity of solutions [η] of AA copolymers with (*1*) Ca-AMS and (*2*) Mg-AMS as a function of the AA content in the initial monomer mixture M_1 (mole fraction), $\tau = 2$ h.

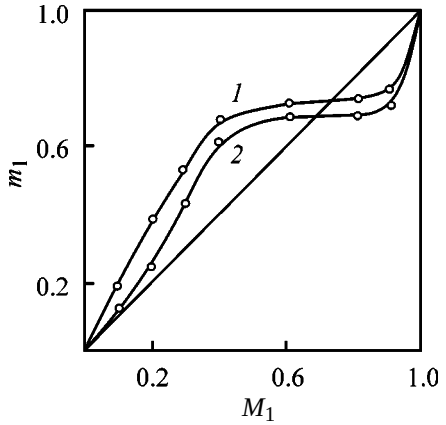

Fig. 4. Composition of AA copolymer with (*1*) Mg-AMS and (*2*) Ca-AMS as influenced by the mole fraction of AA in the initial monomer mixture M_1. (m_1) Mole fraction of AA units in copolymer.

Table 2. Composition of AA copolymer with H-AMS salts as influenced by the concentration of the initial monomer mixture (initial molar ratio $[M_1] : [M_2] = 3 : 7$)

Monomer	$[M_1 + M_2]$, M	Contents of indicated units in copolymer	
		AA	H-AMS salt
Mg-AMS	0.57	53.0	47.0
	0.86	47.0	53.0
Ca-AMS	0.56	44.0	56.0
	0.84	43.0	57.0
Sr-AMS	0.51	39.3	60.7
	0.76	37.7	62.3

mers with ionic monomers on passing from Mg- to Ca-AMS (passing from curve *1* to curve *2*).

The data listed in Table 2 illustrate the effect of the cation nature on the composition of AA copolymers with Mg-, Ca-, and Sr-AMS at various concentrations of the monomer mixture $M_1 + M_2$, other conditions being equal. The experimental data at $[M_1 + M_2] =$ const illustrate the increase in the content of the ionic units in the copolymer macromolecule in the series $Mg^{2+} < Ca^{2+} < Sr^{2+}$, which agrees with results given in Fig. 4. Our data (Table 2) also show that the increase in the concentration of the reaction mixture $M_1 + M_2$ causes the enrichment of the copolymers with ionic units. This concentration effect is due to the increase in the ionic strength of the solutions μ. With increasing μ and binding of cations with polysulfonate anions in the order $Mg^{2+} < Ca^{2+} < Sr^{2+}$ the electrostatic repulsion of similarly charged particles becomes weaker, which increases k_{22}. As a result, the copolymers are enriched with ionic units (Fig. 4, Table 2). Similar increase in v_0 with increasing cation radius was found previously in polymerization of Mg-, Ca-, and Ba-AMS [7] and Ca, Sr, and Ba- *p*-styrenesulfonates [19]. This fact suggests that the effect of cations on (co)polymerization is a general feature for salts of strong unsaturated acids.

Thus, the kinetic parameters of copolymerization of AA with H-AMS salts of double charged cations and the properties of the resulting copolymers can be controlled by varying μ and the nature of cations in the ionic monomer.

CONCLUSIONS

(1) The v_0 values increase with increasing concentration of monomers in the $M_1 + M_2$ reaction mixture and with addition of low-molecular-weight salts in the order $Mg^{2+} < Ca^{2+} < Sr^{2+}$.

(2) The intrinsic viscosity of copolymers [η] increases with increasing concentration of the reaction mixture $M_1 + M_2$ in the following order: $Mg^{2+} < Ca^{2+}$.

(3) The content of the ionic groups increases with increasing concentration of the reaction mixture $M_1 + M_2$ and in the order $Mg^{2+} < Ca^{2+} < Sr^{2+}$.

ACKNOWLEDGMENTS

The work was financially supported by the Foundation of Basic Natural Science of the Ministry of Education of the Russian Federation (project no. 97-0-9.4-59) and the Foundation of Research and Development of the Tatarstan Republic (project no. 19-03/2000).

REFERENCES

1. McCormick, C.L., *J. Macromol. Sci. Chem., Ser. A*, 1985, vol. 22, nos. 5–7, pp. 955–982.
2. Lisovtsev, V.V., Rostokin, G.A., and Kulikova, A.E., in *Khimicheskaya promyshlennost': Akrilaty i polivinilkhlorid* (Chemical Industry: Acrylates and Polyvinyl Chloride), Moscow: NIITEKhIM, 1984, pp. 1–20.
3. Kabanov, V.A. and Topchiev, D.A., *Polimerizatsiya ionizuyushchikhsya monomerov* (Polymerization of Ionizing Monomers), Moscow: Nauka, 1975.
4. Kurenkov, V.F. and Myagchenkov, V.A., *Zh. Prikl. Khim.*, 1999, vol. 72, no. 6, pp. 881–890.
5. Pomogailo, A.D. and Savost'yanov, V.S., *Metallosoderzhashchie monomery i polimery na ikh osnove* (Metal-Containing Monomers and Polymers on Their Basis), Moscow: Khimiya, 1988.
6. Kurenkov, V.F. and Safin, A.G., *Zh. Prikl. Khim.*, 1998, vol. 71, no. 1, pp. 136–140.
7. Kurenkov, V.F., Safin, A.G., and Almazova, E.I., *Zh. Prikl. Khim.*, 1998, vol. 71, no. 10, pp. 1704–1708.
8. Kurenkov, V.F. and Rodina, Yu.G., *Zh. Prikl. Khim.*, 1999, vol. 72, no. 10, pp. 1699–1704.
9. Kurenkov, V.F. and Utikeeva, A.R., *Vysokomol. Soedin., Ser. A*, 2000, vol. 42, no. 4, pp. 587–593.
10. Charlot, G., *Les methods de la chimie analytique. Analyse quantitative minerale*, Paris: Masson, 1961, 4th ed.
11. Topchiev, D.A., Shakirov, R.Z., Kalinina, L.P., *et al.*,

Vysokomol. Soedin., Ser. A, 1972, vol. 14, no. 3, pp. 581–586.

12. Osmanov, T.O., Gromov, V.F., Khomikovskii, P.M., and Abkin, A.D., *Vysokomol. Soedin., Ser. A*, 1979, vol. 21, no. 8, pp. 1766–1770.
13. Kolthoff, I.M. and Miller, I.K., *J. Am. Chem. Soc.*, 1951, vol. 73, pp. 3055–3059.
14. Kholodnova, L.V., Pavlyuchenko, V.N., and Alekseeva, Z.M., in *Kataliticheskoe i initsiiruyushchie sistemy dlya sinteza i modifikatsii polimerov* (Catalytic and Initiating Systems for Synthesis and Modification of Polymers), Leningrad: Plastpolimer, pp. 90–104.
15. *2-Acrylamido-2-methylpropane Sulfonic Acid Monomer*, Wickliffe, Ohio (USA): Lubrizol, 1994.
16. USSR Inventor's Certificate no. 235997.
17. Marina, N.G. and Monakov, Yu.B., in *Khimiya i fiziko-khimiya vysokomolekulyarnykh soedinenii* (Chemistry and Physical Chemistry of Macromolecular Compounds), Ufa, 1976, pp. 116–146.
18. Shannon, R.D., *Acta Crystallogr., Sect. A*, 1974, vol. 32, pp. 751–758.
19. Kurenkov, V.F., Vagapova, A.K., and Myagchenkov, V.A., *Eur. Polym. J.*, 1982, vol. 18, no. 9, pp. 763–767.

Russian Journal of Applied Chemistry, Vol. 74, No. 5, 2001, pp. 818–821. Translated from Zhurnal Prikladnoi Khimii, Vol. 74, No. 5, 2001, pp. 793–796.

MACROMOLECULAR CHEMISTRY AND POLYMERIC MATERIALS

Synthesis and Absorption Power of New Polyelectrolyte Tetrazole-Containing Acrylic Hydrogels

A. V. Igrunova, N. V. Sirotinkin, and M. V. Uspenskaya

St. Petersburg State Technological Institute, St. Petersburg, Russia

Received December 21, 2000; in final form, February 2001

Abstract—The kinetic features of formation and equilibrium swelling in water and aqueous solutions of metals were considered for new hydrogels based on acrylic acid and methylenebisacrylamide modified with 2-methyl-5-vinyltetrazole in the polymerization stage. The influence of the concentration of the reactants on the gelation rate and the degree of equilibrium swelling was studied, as well as the influence of 2-methyl-5-vinyltetrazole on the properties of the copolymers prepared. Possible application fields for the new hydrogels were proposed.

Polyacrylate hydrogels find wide application owing to their unique water-absorbing and immobilizing power with respect to various media. These properties are of special value in the context of the present-day problems of biological medicine and ecology [1, 2]. Incorporation into the polymer structure of complexones, in particular, nitrogen-containing heterocyclic moieties, intensifies the absorption of aqueous solutions of electrolytes [3]. High complexing power of the tetrazole ring with respect to heavy and noble metal ions makes these gels suitable for water treatment application. The immunobiological activity of polyvinyltetrazoles and copolymers of vinyltetrazoles with acrylic acid (AA) makes these hydrogels promising for application in living bodies [4, 5].

The aim of this work is to study the kinetic features of gelation and the behavior of the gels in electrolyte solutions, as well as to analyze the mechanism of formation and interaction of the gel prepared with solutions of salts of copper, cobalt, nickel, and other metals.

EXPERIMENTAL

Network copolymers were prepared by radical polymerization of AA partially neutralized with sodium hydroxide (degree of neutralization α = 0.8–0.9), 2-methyl-5-vinyltetrazole (MVT), and methylenebisacrylamide (MBAA) as cross-linking agents in an aqueous solution at 40–60°C. The initiator was the ammonium persulfate–tetramethylethylenediamine (TMED) redox system. The initial concentrations of the reactants in polymerization were as follows: monomer 30, MVT 0–70 wt % of the AA mass, and MBAA 0–0.9 wt % of the monomer mass. Prior to polymerization, 2-methyl-5-vinyltetrazole[1] was purified by vacuum distillation (bp 80°C at 20 mm Hg). The other reactants, as well as their purification and copolymerization procedures, were characterized in [6]. Polymerization was carried out in ampules; the reaction mixture was deoxygenated prior to adding the initiator by passing argon through the solution for 2–3 min. A specific feature of the experiment was freezing of AA in a refrigerator at 3–5°C prior to the reaction.

The kinetic parameter to be measured was the gelation time as estimated from the time of the onset of the fluidity loss by the reaction mixture.

The gel structure was investigated by ^{13}C NMR spectroscopy and differential thermal analysis (DTA). The presence of the tetrazole moiety in the polymer was judged from the peaks in the IR spectrum at ν 1100, 1208, and 1635 cm^{-1} (tetrazole ring vibrations). The resulting copolymers are thermally stable, as evidenced by the thermal oxidation analysis data as processed by the Freeman and Carrol's method (E_a = 420 kJ mol^{-1}).

The copolymers synthesized were kept in distilled water to remove the sol fraction. The equilibrium swelling of the gels and the swelling kinetics were studied by the standard gravimetric method. The degree of equilibrium swelling was calculated by the equation $Q = (m_s - m_d)/m_d$, where m_s, g, is the mass

[1] Synthesized at the St. Petersburg State Technological Institute.

1070-4272/01/7405-0818$25.00

of the swollen sample, and m_d, g, is the mass of the dried sample [6].

The macrokinetics of the three-dimensional copolymerization of AA, MVT, and MBAA have a number of specific features. As seen from Fig. 1, the plot of the gelation time (induction period) vs. the MVT concentration has a maxumim at the MVT concentration of 10–20 wt % with respect to AA. The cross-linking agent, MBAA, exerts the expected effect: the induction period tends to increase, and the gelation rate, to decrease with decreasing MBAA concentration from 0.5 to 0.05 wt %. This is consistent with the mass action law in the gelation macrokinetics. The fact that at the MBAA concentrations over 0.5 wt % the gelation point is observed at a later time is due to the specific features of the gelation mechanism. The gel based on AA and MBAA, most likely, was formed by the colloidal-chemical mechanism, as indirectly noted in a number of works [7]. Dissimilar reactivities of AA and MBAA are responsible for the formation at high MBAA concentrations of blocks from the MBAA units with a low activity of side double bonds and of intramolecular rings, divinyl loops, and network of engagements [7]. Thus, at the MBAA concentration of 0.9 wt % the hydrogel has a heterogeneous structure.

The nonlinear dependence of the induction period on the MVT concentrtation in the reaction mixture can be explained by the difference in the relative copolymerization activity constants: r_{AA} = 0.67 and r_{VT} = 0.29 in the AA–5-vinyltetrazole system [8], $r_{AA} < r_{MBAA}$ [9], as well as by the influence of complexing with TMED [10, 11], formation of an interpolymeric complex in AA and MVT polymerization [12], and formation of ion pairs [8, 12]. It was found [8] that the carboxy groups from AA participate in hydrogen bonding with the proton from the tetrazole ring of unsubstituted 5-vinyltetrazole. As a result, the initial polymerization rate and the degree of conversion of the monomers tend to decrease with increasing content of vinyltetrazole in the monomer mixture. In our case, MVT can also induce polarization of the COO^-H^+ (Na^+) group of AA. A greater reactivity of the AA–MVT–MBAA system compared to the system without MVT is indicated by the calculated activation energies of the reaction, namely, E_{app} of 120 and 140 kJ mol^{-1} in the former and latter cases, respectively [these parameters were calculated form the plots of the gelation time t_g, min, vs. the synthesis temperature T (K)]. This fact can be explained by formation of the redox complex MVT–ammonium persulfate [13] initiating AA copymerization. Formation of a

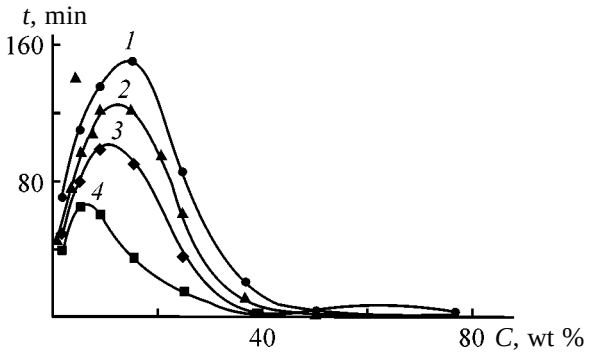

Fig. 1. Gelation time t as a function of the MVT concentration C at different proportions of the cross-linking agent (MBAA). Initiator (ammonium persulfate) concentration 0.4 wt %. MBAA concentration, wt %: (*1*) 0.1, (*2*) 0.2, (*3*) 0.9, and (*4*) 0.5.

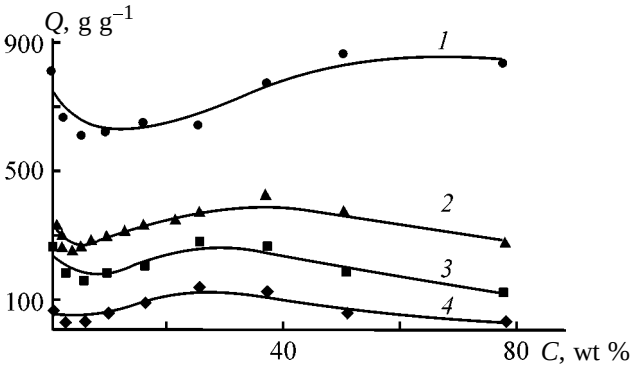

Fig. 2. Equilibrium degree of swelling Q of hydrogels in distilled water as a function of the MVT concentration C in the reaction mixture at different concentrations of MBAA. MBAA concentration, wt %: (*1*) 0.1, (*2*) 0.2, (*3*) 0.5, and (*4*) 0.9.

complex with the charge transfer between the persulfate ions and the "pyridinium type" nitrogen atom of MVT, i.e., of the tetrazole–ammonium persulfate redox system, was observed earlier [12]. Gel formation was observed in the system without ammonium persulfate. In that case, weakly cross-linked networks of predominantly physical nature were formed, as judged from a large amount of the sol fraction. The mechanism of such initiation is, evidently, due to formation of the MVT–TMED complex [10]. A high reactivity of MVT in gelation is supported by the ^{13}C NMR data: the sol fraction contains no MVT. At MVT concentrations over 30%, a strong gel is formed which retains its elasticity and the shape in the equilibrium swollen state. The analysis of the gelation mechanism should, probably, take into account the gel effect, which is indicated by the dependence of the gelation time on the MBAA concentration.

The influence of the MVT concentration on the

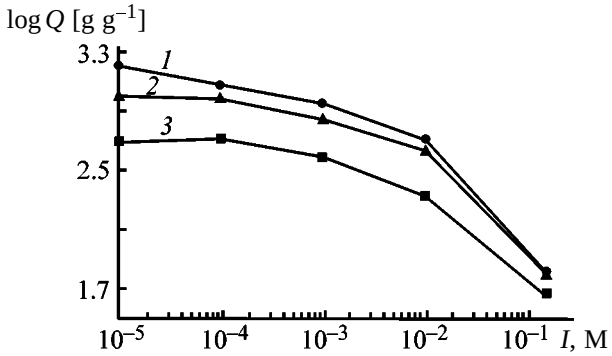

Fig. 3. Equilibrium degree of swelling Q of hydrogels based on AA and MVT as a function of the ionic strength of the external electrolyte I. MVT concentration in the reaction mixture 36 wt %. MBAA concentration, wt %: (*1*) 0.05, (*2*) 0.1, and (*3*) 0.2.

equilibrium degree of swelling of the hydrogel at different proportions of the cross-linking agent MBAA at 20°C is shown in Fig. 2. Based on data in Figs. 1 and 2, it is possible to prepare gels with desired properties within a certain period. This is essential for solving specific technical problems. e.g., fabrication of hollow fibers filled with a water-swelling absorbent. This problem can be solved, e.g., by selecting appropriate concentrations of the reactants.

Figure 2 shows that with decreasing proportion of the cross-linking agent the equilibrium degree of swelling tends to increase. The influence of the MVT concentration is ambiguous. In loosely cross-linked polymers the equilibrium degree of swelling tends to increase with increasing MVT concentraiton (to 80 wt %). With MBAA concentrations over 0.1 wt % the plot of the degree of swelling vs. the MVT concentration passes through a maximum, which shifts to lower MVT concentrations with increasing network density. The decrease in the equilibrium degree of swelling is due to increase in the proportion of the gel fraction.

In electrolyte solutions, the hydrogels of interest behave as three-dimensional membranes. The ion distribution pattern for the hydrogel–solution system varies with the composition of the surrounding solution (e.g., concentration and the nature of salt of polyvalent metal) [14]. Figure 3 presents a typical plot of the equilibrium degree of swelling vs. the ionic strength of the surrounding solution for polyelectrolyte hydrogels differing in the cross-linking density. It is seen that at the salt (sodium chloride) concentrations over 10^{-4} M the degree of swelling tends to decrease. The increased concentration of the ions outside the hydrogel was observed at salt concentrations under 1×10^{-4} M. Budtova *et al*. [2] theoretically interpreted these phenomena in terms of the Donnan theory and the diffusion approach. Those authors treated the gel as an ionic sorbent, and the thermodynamic basis of the phenomenon was considered in [15, 16]. The equilibrium degree of swelling for the gel with the metal salt concentrations of 1×10^{-4} M increases relative to that in distilled water. This can be explained by the structurization of the solution surrounding the gel, owing to participation of the MVT units in the system of intermolecular and ionic bonds [10, 17]. The gels under study collapse with the salt concentration increasing to 1×10^{-1} M.

Equilibrium degree of swelling Q of the hydrogels based on AA and MVT at different concentrations of $NiCl_2$, $CoCl_2$, and $CuCl_2$. MVT concentration 36.6, and MBAA concentration 0.2 wt %

Salt concentration, M	Q, g g^{-1}, in salt solution		
	$NiCl_2$	$CoCl_2$	$CuCl_2$
1×10^{-5}	544	556	546
1×10^{-4}	604	521	466
1×10^{-3}	110	212	238
1×10^{-2}	17	11	26

The table shows how the equilibrium degree of swelling varies with the concentrations of selected salts for hydrogels based on AA and MVT at 16°C.

It is seen that with increasing salt concentration the equilibrium degree of swelling tends to decrease. The hydrogels based on AA and MVT have high degrees of equilibrium swelling in salts compared to those based on AA. This is due to formation of chelate complexes with the Co^{2+}, Ni^{2+}, and Cu^{2+} ions involving both the tetrazole ring [18] and the acrylate groups [19]. It was found that the tetrazole-containing gels decolorize the salt solutions, and the hydrogels based on AA only partly sorb metals ion.

The swelling of the gels based on AA, MBAA, and MVT in salt solutions exhibit the following characteristic features that can be explained basing on the Donnan principle and the diffusion approach. In the initial stage the hydrogel swells faster in a more concentrated solution, and in salt solutions equilibrium is attained faster than in distilled water.

The swelling of the synthesized hydrogels can be described by an S-shaped curve (Fig. 4). It is seen that with increasing MVT proportion in the copolymer the degree of equilibrium swelling in distilled water tends to increase. The swelling rate of the copolymers in the initial stage of the process tends to increase with increasing MVT proportion in the monomer mixture.

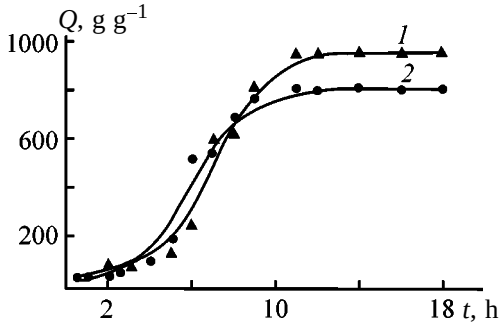

Fig. 4. Degree of swelling Q of hydrogels as a function of the time t at the cross-linking agent (MBAA) concentration of 0.1 wt %. MVT concentration in the reaction mixture, wt %: (*1*) 77 and (*2*) 36.

Our experiments suggest that the synthesis conditions ensuring the maximal absorption capacity of hydrogels based on AA, MVT, and MBAA as cross-linking agent are as follows: ammonium persulfate concentration 0.8 wt %, and synthesis temperature 60°C.

CONCLUSIONS

(1) Tetrazole-containing hydrogels based on acrylic acid, methylenebisacrylamide, and 2-methyl-5-vinyltetrazole were synthesized for the first time by radical copolymerization of monomers in aqueous solution.

(2) The kinetic features of gelation and the properties of the forming products were studied as influnced by the monomer ratio and the initiator concentration. The optimal conditions of preparing hydrogels with the maximal degree of equilibrium swelling and the shortest gelation time were determined.

(3) The equilibrium swelling of the gels in distilled water and solutions of copper, nickel, cobalt, and sodium salts at room temperature was studied. The gels exhibit high water-absorbing power in solutions with the salt concentration under 1×10^{-3} M, namely, up to 600 g g^{-1} for the gels synthesized at the methylenebisacrylamide concentration in the monomer mixture of 0.2 wt %. The high absorbing power of the gels in salt solutions is due to formation of chelate complexes.

(4) High immobilizing power of the gels prepared makes them promising for water treatment and selective binding of metals from salt solutions.

REFEFERCES

1. *Superabsorbent. Polymer Science and Tecnology*, Buchholz, F.L. and Peppas, N.A., Eds., *ACS Symp. Ser*., vol. 573, Washington, DC: Am. Chem. Soc., 1994, pp. 3–7.
2. Budtova, T.V., Suleimenov, I.E., and Frenkel', S.Ya., *Zh. Prikl. Khim*., 1997, vol. 70, no. 4, pp. 529–539.
3. Shatalov, G.V., *Monomery i polimery s azol'nymi i azinovymi tsiklami* (Monomers and Polymers with Azole and Azine Rings), Voronezh: Voronezh. Univ., 1984, pp. 67–84.
4. Kizhnyaev, V.N., Smirnov, A.I., Biryukova, Yu.I., *et al*., *Khim.-Farm. Zh*., 1992, vol. 26, nos. 11–12, pp. 55–57.
5. Kruglova, V.A., Annenkov, V.V., Moskvina, L.G., *et al*., *Khim.-Farm.* Zh., 1989, vol. 23, no. 2, pp. 195–198.
6. Uspenskaya, M.V., Yankovskii, S.A., and Bobasheva, A.S., *Zh. Obshch. Khim.*, 1998, vol. 68, no. 5, pp. 784–787.
7. Zhao, X., Zhu, S., Hamielec, A.E., and Pelton, R.H., *Macromol. Symp*., 1995, no. 92, pp. 253–300.
8. Kruglova, V.A., Voropaeva, E.F., Annenkov, V.V., and Kizhnyaev, V.N., *Izv. Vyssh. Uchebn. Zaved., Khim. Khim. Tekhnol*., 1987., vol. 30, no. 12, pp. 105–109.
9. Kishi, R., Hasebe, M., and Osada, Y., *Polym. Adv. Technol*., 1990, vol. 1, no. 1, pp. 19–25.
10. Kizhnyaev, V.N., Kruglova, V.A., and Vereshchagin, L.I., *Zh. Prikl. Khim*., 1990, vol. 63, no. 12, pp. 2721–2724.
11. Pavlova, M.A. and Kastel'yanos-Domingo, O.M., *Zh. Prikl. Khim*., 1996. vol. 69, no. 9, pp. 1558–1563.
12. Gaponik, P.N., Ivashkevich, O.A., Kovaleva, T.B., *et al*., *Vysokomol. Soedin., Ser. B*., 1988, vol. 30, no. 1, pp. 39–42.
13. Kizhnyaev, V.N., Kruglova, V.A., Ivanova, N.A., and Buzilova, S.R., *Izv. Vyssh. Uchebn. Zaved., Khim. Khim. Tekhnol*., 1990, vol. 33, no. 7, pp. 106–109.
14. Budtova, T.V., Sichetskii, D.A., Kuranov, A.L., and Suleimenov, I.E. *Zh. Prikl. Khim*., 1997, vol. 71, no. 3, pp. 511–513.
15. Kazanskii, K.S. and Dubrowski, S.A., *Advances in Polymer Science*, 1992, vol. 104: *Polyelectrolytes, Hydrogels, Chromatographic Materials*, pp. 97–133.
16. Dubrovskii, S.A. and Kazanskii, K.S., *Vysokomol. Soedin., Ser. B*., 1993, vol. 35,. no. 10, pp. 1712–1721.
17. Kizhnyaev, V.N. and Smirnov, A.I., *Vysokomol. Soedin., Ser. A*, 1993, vol. 35, no. 12, pp. 1997–2000.
18. Kizhnyaev, V.N. and Kruglova, V.A., *Zh. Prikl. Khim*., 1992, vol. 65, no. 8, pp. 1879–1884.
19. Rivas, B.L. and Sequel, G.H., *Polyhedron*, 1999, vol. 18, no. 19, pp. 2511–2518.

Russian Journal of Applied Chemistry, Vol. 74, No. 5, 2001, pp. 822–829. Translated from Zhurnal Prikladnoi Khimii, Vol. 74, No. 5, 2001, pp. 797–804.

MACROMOLECULAR CHEMISTRY AND POLYMERIC MATERIALS

Comparative Analysis of the Methods for Calculating the Viscosity of Binary Nonelectrolyte Mixtures

E. D. Totchasov, M. Yu. Nikiforov, I. A. Luk'yanchikova, and G. A. Al'per

Institute of Solution Chemistry, Russian Academy of Sciences, Ivanovo, Russia

Received April 8, 1999; in final form, June 2000

Abstract—The results of calculating the viscosity of binary nonelectrolyte systems by methods obviating fitting parameters were compared. A method was proposed for calculating the viscosity of *n*-alkanol–*n*-alkane solutions with account of the molecular association by the free-volume theory accurately to within 7.9%.

Studies of the concentration dependence of the viscosity of liquid solutions have recently generated much interest in the context of many practical problems [1–4]. The viscosity as a physicochemical property is very sensitive to intermolecular interactions. For example, experimental data in [5, 6] suggest that in the water–dimethylformamide (DMF) system the maximal deviations from additivity make 2% for density, 9% for heat capacity, and 24% for adiabatic compressiblity against 197% for viscosity. This trend is observed for other nonelectrolyte systems as well. Development of methods for calculating the viscosity of multicomponent liquid systems is in the scope of the theory of solutions [7–9].

By now, the theory of viscosity of liquids has by no means been developed to completion, and the viscosity of solutions can be calculated practically in terms of semi-theoretical concepts like the Eyring theory [10], the free-volume theory [11], or their combination [12]. Also, caclulations can be made by formulas utilizing fitting parameters to be determined using one or several preset experimental points [13–15].

In this work we carry out a comparative analysis of selected methods for calculating the viscosity of binary nonelectrolyte mixtures obviating fitting parameters.

The deviation of the physicochemical properties of mixtures from their additive values is the greatest in the vicinity of the equimolar composition. This makes reasonable analysis of the predictive power of the calculational methods either for the composition corresponding to the maximal deviation from additivity, or for all the systems at the equimolar composition. In this work, we chose the latter option.

In [16], we calculated the viscosity of nonelectrolyte solutions in terms of the Eyring concept of the activation nature of viscous flow. The viscosity of organic liquids and their mixtures is adequately described by the formula

$$\eta = A\exp(\Delta H^{\#}/RT), \quad (1)$$

where $\Delta H^{\#}$ is the activation enthaply of viscous flow.

Following the Eyring's assumption that the activation enthalpy is a fraction of the cohesion energy E_{coh}:

$$\Delta H^{\#} = E_{coh}/n, \quad (2)$$

we obtained eventually for equimolar mixtures [$X_A = X_B = 0.5$ mole fraction (m.f.)] the relation [16]

$$\Delta\ln\eta = -H^E/RT(0.5/n_A + 0.5/n_B) + (\Delta H_A^{vap} - \Delta H_B^{vap})/2RT$$

$$\times [(0.5 + \varphi_A)\times 0.5/n_B + (0.5 + \varphi_B)\times 0.5/n_A], \quad (3)$$

where $\Delta H_A^{vap} = E_{A,coh} + RT$, $\Delta H_B^{vap} = E_{B,coh} + RT$ is the enthalpy of vaporization of the components A and B, respectively; $\Delta\ln\eta = \ln\eta - 0.5\ln\eta_A - 0.5\ln\eta_B$; η is the dynamic viscosity of the equimolar solution; η_A and η_B are the dynamic viscosities of the components A and B, respectively; and φ_A and φ_B are the volume fractions of these components, respectively.

Herefrom, the viscosities of the pure components η_A and η_B are assumed to be known. The ΔH^{vap} values for the pure components were taken from [17], and H^E, from reference books [18, 19]. The experimental values of the viscous flow activation energy for solution $\Delta H^{\#}$ were determined from the dependence $\ln\eta_{exp} = 1/T$, i.e, from the experimental η_{exp}

1070-4272/01/7405-0822$25.00

values for a binary solution taken from the reference book [20].

One of the semi-theoretical methods for describing the viscosity of liquids that obviate fitting parameters is that based on the free-volume theory relating the viscosity η to the so-called reduced volume $\tilde{V}$ [11]:

$$\eta = A\exp[1/(\tilde{V} - 1)], \quad (4)$$

where

$$\tilde{V} = V/V^*, \quad (5)$$

V is the molar volume, and V^* is the volume occupied by the liquid molecule (the occupied volume).

The term "occupied volume" is an ambiguous physical notion that has different definitions [21, 22]. In this work we took advantage of the Flory theory [23] for calculating $\tilde{V}$. This theory relates the reduced volume to the volume expansion coefficient α as

$$\tilde{V}^{1/3} - 1 = \alpha T/3(1 + \alpha T). \quad (6)$$

As the α values are usually known for pure solvents only, formulas (5) and (6) enable calculating $\tilde{V}_A$, $\tilde{V}_B$ and V_A^*, V_B^*. In view of the fact that the occupied volume V^* is physically an additive parameter, for binary mixtures holds

$$V^* = V_A^* X_A + V_B^* X_B. \quad (7)$$

Hence, the reduced volume of the equimolar mixture can be determined by the formula

$$\tilde{V} = V/V^* = V/(0.5V_A^* + 0.5V_B^*). \quad (8)$$

The viscosity of the equimolar mixture can be calculated as

$$\ln\eta = 0.5\ln\eta_A + 0.5\ln\eta_B + (\tilde{V} - 1)^{-1} - 0.5(\tilde{V}_A - 1)^{-1} - 0.5(\tilde{V}_B - 1)^{-1}. \quad (9)$$

Lastly, the Lobe formula [24] enables calculating the kinematic viscosity ν of liquid mixtures by the empirically established relation

$$\nu = \varphi_B\nu_B e^{\alpha_A\varphi_A} + \varphi_A\nu_A e^{\alpha_B\varphi_B}, \quad (10)$$

$$\alpha_B = -1.7\ln(\nu_A/\nu_B),$$

$$\alpha_A = 0.27\ln(\nu_A/\nu_B) + [1.3\ln(\nu_A/\nu_B)]^{0.5}, \quad (11)$$

where the α_B, ν_B, and φ_B parameters characterize the component with a lower viscosity. To change to the dynamic viscosity η, ν is to be multiplied by the density ρ ($\eta = \nu\rho$).

Table 1 presents the results of calculating the dynamic viscosity in terms of various theories for 30 binary systems containing components of different chemical nature (η_1 was calculated in terms of the Eyring theory, η_2, in terms of the free-volume theory, and η_3, in terms of the Lobe theory). Also presented are the rms and the maximal deviations of the calculated values from the experiment, σ_Σ and σ_{max}. The calculations were carried out for the equimolar ratio of the components at 298.15 K. The experimental viscosities of the solutions η_{exp} and pure liquids (Table 2) were taken from [20, 25, 26]. The volume expansion coefficients α of the components required for calculating the reduced volume by formula (6) were taken from the reference book [20]; they are presented in Table 3 along with some other properties of the pure components. The molar volumes of the equimolar mixtures of nonelectrolytes taken from [20, 25, 26] and the V^* and $\tilde{V}$ values calculated by formulas (7) and (8) are presented in Table 4.

All the systems are classified into three groups: both polar components, a polar and a nonpolar component; and both nonpolar components.

Table 1 shows that semi-theoretical methods of calculating the viscosity, afford, on the average, an rms deviation under 10%. For systems polar–nonpolar and polar–polar components, the best results are afforded by the Eyring theory (rms deviation of 4.9 and 5.6%, respectively), and for systems nonpolar–nonpolar components, by the free-volume theory ($\sigma_\Sigma = 4.5\%$).

We separately calculated the viscosities of 15 binary systems *n*-alkanol–*n*-alkane for which the free-volume theory fairly correctly takes into account the molecular association (up to now, this was done only in calculations of thermodynamic properties [27]).

The occupied volume V_{Aass}^* of the associated component, similar to the K and φ_{A1} parameters, becomes in this case a function of the temperature and the composition of the mixture

$$V_{Aass}^* = V_{A1}^* + \Delta V^0 K\varphi_{A1}, \quad (12)$$

where φ_{A1} is the mole fraction of the monomers of A in the mixture as defined by the ratio

$$\varphi_{A1} = [2K\varphi_A + 1 - (4K\varphi_A + 1)^{1/2}]/2K^2\varphi_A, \quad (13)$$

Table 1. Calculated η_1–η_3 and experimental η_{exp} values of the dynamic viscosity of binary nonelectrolyte systems at the equimolar ratio of the components T = 298.15 K)

System	$\eta_1 \times 10^3$	$\eta_2 \times 10^3$	$\eta_3 \times 10^3$	$\eta_{exp} \times 10^3$
	Pa s			
Polar components				
Acetone–DMF	0.479	0.499	0.503	0.502
Acetone–methanol	0.349	0.382	0.353	0.342
Acetone–ethanol	0.399	0.510	0.489	0.430
Acetone–ethyl acetate	0.346	0.356	0.363	0.361
Methanol–THF	0.457	0.539	0.521	0.469
Methanol–triethylamine	0.517	0.488	0.417	0.486
Methanol–chloroform	0.516	0.511	0.566	0.604
Ethanol–triethylamine	0.625	0.634	0.498	0.598
Ethanol–ethyl acetate	0.500	0.557	0.575	0.536
Chloroform–methyl acetate	0.495	0.404	0.474	0.495
Ethyl acetate–methyl acetate	0.389	0.398	0.420	0.387
σ_Σ, %	4.9	8.6	7.8	
σ_{max}, %	15 Methanol–chloroform	19 Acetone–ethanol	17 Ethanol–treiethylamine	
Polar–nonpolar components				
Acetone–benzene	0.402	0.428	0.453	0.403
Acetone–hexane	0.263	0.311	0.317	0.298
Acetone–tetrachloromethane	0.512	0.600	0.642	0.514
Benzene–methanol	0.521	0.558	0.595	0.551
Benzene–Propanol	0.828	0.967	0.956	0.846
Benzene–Chloroform	0.579	0.549	0.602	0.563
Benzene–ethanol	0.661	0.707	0.768	0.712
Benzene–ethyl acetate	0.501	0.491	0.525	0.470
Chloroform–hexane	0.310	0.371	0.423	0.372
Chloroform–tetrachloromethane	0.684	0.651	0.757	0.665
Acetonitrile–tetrachloromethane	0.522	0.598	0.720	0.574
Cyclohexane–ethanol	0.826	0.763	1.004	0.868
Cyclohexane–isopropanol	0.983	1.211	1.247	1.018
σ_Σ, %	5.6	6.8	14	
σ_{max}, %	17 Chloroform–hexane	19 Cyclohexane–iso-propanol	26 Acetonitrile–tetra-chloromethane	
Nonpolar components				
Benzene–heptane	0.502	0.441	0.488	0.413
Benzene–cyclohexane	0.646	0.648	0.768	0.610
Benzene–chlorobenzene	0.720	0.665	0.701	0.672
Hexane–heptane	0.357	0.342	0.364	0.341
Hexane–cyclohexane	0.482	0.489	0.479	0.438
Cyclohexane–tetrachloromethane	0.873	0.848	0.970	0.855
σ_Σ, %	8.6	4.5	13	
σ_{max}, %	22 Benzene–heptane	12 Hexane–cyclohexane	26 Benzene–cyclohexane	

V^*_{A1} refers to a hypothetical liquid consisting of the monomers; $\Delta V^0 = -5.6$ cm^3 mol^{-1} is the change in the volume in the association reaction [27], and K is the alcohol association constant in the Kraetschmer–Wiebe continuous association model [27].

The V^*_{A1} and K values were taken equal to those in [27]; they are presented, along with some other properties of the pure components, in Table 5. For the occupied volume of the binary equimolar solution we obtain:

$$V^*_{ass} = (V^*_{A1} + \Delta V^0 K\varphi_{A1})\times 0.5 + V^*_B \times 0.5. \quad (14)$$

Consequently, in terms of the association model considered, Eq. (8) for the reduced volume of a binary equimolar mixture takes the form

$$\tilde{V}_{ass} = \frac{V}{V^*_{ass}} = \frac{V}{(V^*_{Al} + \Delta V^0 K\varphi_{Al})\times 0.5 + V^*_B \times 0.5}. \quad (15)$$

Using the calculated $\tilde{V}$ value for solutions, we calculated by formula (9) the dynamic viscosity of the mixtures. The molar volumes V of the equimolar *n*-alkanol–*n*-alkane solutions required for calculating the reduced volumes $\tilde{V}_{ass}$ and $\tilde{V}$ were taken from [20, 28–34]. They are presented in Table 6 along with the V^*_{ass}, V^*, $\tilde{V}_{ass}$, and $\tilde{V}$ parameters.

Table 7 presents the calculated dynamic viscosities for *n*-alkanol–*n*-alkane systems at the equimolar ratio of the components at 298.15 K (η_1 in terms of the Eyring theory, η_2 in terms of the free-volume theory, η_3 in terms of the free-volume theory with account of molecular association, and η_4 by the empirical Lobe method). The experimental viscosities for these solutions and pure liquids (Table 2) were taken from [20, 31, 32, 34–38]. The calculated results (Table 7) show that the empirical Lobe formula is suitable for *n*-alcohol–*n*-alkane mixtures (with the rms deviation of 4.2%). The free-volume theory with the molecular association taken into account affords a closer agreement with the experiment than the classical free-volume theory (rms deviations 7.9 and 10%, respectively). On the whole, there is no interconnection between the nature (polarity) of the mixture components and the accuracy of the calculational method.

As an illustration, we will calculate the dynamic viscosity for the equimolar butanol–hexane mixture by all the calculational methods discussed in this work.

Eyring theory. (1) Using relation (3), we will determine $\Delta \ln \eta$ for the equimolar mixture $\{X_A = X_B =$

Table 2. Dynamic viscosity of pure liquids at T = 298.15 K

Liquid	$\eta \times 10^3$, Pa s
Acetone [20]	0.301
Acetonitrile [20]	0.348
Benzene [20]	0.598
Butanol [31]	2.550
Hexane	0.286 [31], 0.296 [35]
Heptane [35]	0.391
Decane [26]	0.832
DMF [20]	0.796
Methanol [20]	0.553
Methyl acetate [25]	0.360
Nonane [26]	0.647
Octane [32]	0.506
Pentanol [34]	3.513
Propanol [35]	1.968
Isopropanol [20]	2.036
Tetrachloromethane [20]	0.897
Tetrahydrofuran [20]	0.466
Triethylamine [20]	0.356
Chlorobenzene [20]	0.750
Chloroform [20]	0.533
Cyclohexane [20]	0.869
Ethanol [35]	1.087
Ethyl acetate [25]	0.422

Table 3. Properties and parameters of the pure components at T = 298.15 K

Component	$\alpha \times 10^4$, K^{-1} [20]	V^*, cm^3 mol^{-1} [formula (5)]	$\tilde{V}$ [formula (6)]
Acetone	15.20	54.99	1.346
Acetonitrile	14.00	39.92	1.324
Benzene	12.60	68.87	1.299
Hexane	14.00	99.34	1.324
Heptane	12.47	111.5	1.296
DMF	10.35	61.72	1.255
Methanol	12.05	31.60	1.288
Methyl acetate	14.85	59.40	1.339
Propanol	9.15	61.09	1.230
Isopropanol	11.50	60.21	1.278
Tetrachloromethane	11.30	76.19	1.274
Tetrahydrofuran	12.35	63.25	1.294
Triethylamine	15.35	103.5	1.348
Chlorobenzene	9.95	81.96	1.247
Chloroform	13.45	61.43	1.314
Cyclohexane	13.05	83.26	1.307
Ethanol	10.15	46.90	1.251
Ethyl acetate	14.30	74.07	1.330

Table 4. Properties and parameters of equimolar mixtures of nonelectrolytes at T = 298.15 K

System	V [20]	V^* [formula (7)]	$\tilde{V}$ [formula (8)]
	$cm^3\ mol^{-1}$		
Acetone–DMF	75.40	58.36	1.292
Acetone–methanol	57.19	43.30	1.321
Acetone–ethanol	66.29	50.95	1.301
Acetone–ethyl acetate	86.34 [25]	64.53	1.338
Methanol–THF	61.00	47.43	1.286
Methanol–triethylamine	88.22	67.55	1.306
Methanol–chloroform	60.76	46.52	1.306
Ethanol–triethylamine	97.04	75.20	1.290
Ethanol–ethyl acetate	78.76	60.49	1.302
Chloroform–methyl acetate	80.66	60.42	1.335
Ethyl acetate–methyl acetate	88.90	66.74	1.332
Acetone–benzene	81.76	61.93	1.320
Acetone–hexane	102.6	77.17	1.330
Acetone–tetrachloromethane	84.81	65.59	1.293
Benzene–methanol	65.11	50.24	1.296
Benzene–propanol	82.37	64.98	1.268
Benzene–chloroform	95.86	75.42	1.271
Benzene–ethanol	74.27	57.89	1.283
Benzene–ethyl acetate	94.09	71.47	1.316
Chloroform–hexane	106.6	80.39	1.326
Chloroform–tetrachloromethane	89.28	68.81	1.298
Acetonitrile–tetrachloromethane	74.95	58.06	1.291
Cyclohexane–ethanol	84.32	65.08	1.296
Cyclohexane–isopropanol	93.29	71.74	1.300
Benzene–heptane	117.8	90.19	1.306
Benzene–chlorobenzene	95.86	75.42	1.271
Hexane–heptane	138.0 [26]	105.4	1.309
Hexane–cyclohexane	120.4	91.30	1.319
Cyclohexane–tetrachloromethane	103.1	79.73	1.293
Benzene–cyclohexane	99.88	76.07	1.313

0.5 m.f.; H^E = 527 [18], for butanol ΔH^V_A = 52 300 [17], for hexane ΔH^V_B = 31 380 [17], $H^{\#}_A$ = 18 872 [20], $H^{\#}_B$ = 6629 J mol^{-1} [20]; $E_{A,coh} = \Delta H^V_A - RT$ = 52 300 – 8.314 × 298.15 = 49 821, $E_{B,coh} = \Delta H^V_B - RT$ = 31 380 – 8.314 × 298.15 = 28 901 J mol^{-1}; $n_A = E_{A,coh}/H^{\#}_A$ = 2.64, $n_B = E_{B,coh}/H^{\#}_B$ = 4.36; φ_A = 0.412, φ_B = 0.588}:

Table 5. Properties and parameteres of associated components (alkanols) and alkanes at T = 298.15 K [27]

Component	K	V	V^*_{Al}	V^*
		$cm^3\ mol^{-1}$		
Ethanol	317	58.66	52.19	46.90
Propanol	197	75.12	66.32	61.09
Butanol	175	91.98	80.89	75.70
Pentanol	153	108.7	94.37	89.20
Hexane	–	131.5	–	99.34
Heptane	–	144.5	–	111.5
Octane	–	163.5	–	127.7
Nonane	–	178.8	–	141.6
Decane	–	196.0	–	156.0

$$\Delta \ln \eta = -0.493.$$

(2) We will calculate the dynamic viscosity of the equimolar mixture (for butanol, $\eta_A = 2.55 \times 10^{-3}$ [31], and for hexane, $\eta_B = 0.286 \times 10^{-3}$ Pa s [31]):

$$\eta = \exp(\Delta \ln \eta + 0.5 \ln \eta_A + 0.5 \ln \eta_B) = 0.522 \times 10^{-3} \text{ Pa s}.$$

Free-volume theory. (1) Using formula (5), we will calculate the reduced volumes of butanol $\tilde{V}$ and hexane $\tilde{V}$ (for butanol at T = 298.15 K V^*_A = 75.7 [27], V_A = 91.98 $cm^3\ mol^{-1}$ [27]; for hexane at T = 298.15 K V^*_B = 99.34 [27], V_B = 131.5 $cm^3\ mol^{-1}$ [27]):

$$\tilde{V}_A = \frac{V_A}{V^*_A} = 1.215,$$

$$\tilde{V}_B = \frac{V_B}{V^*_B} = 1.324.$$

(2) Using formula (7), we will calculate the occupied volume for the equimolar mixture:

$$V^* = 0.5V^*_A + 0.5V^*_B = 87.52 \text{ cm}^3 \text{ mol}^{-1}.$$

(3) Using formula (8), we will determine the reduced volume of the equimolar mixture (for the molar volume of the equimolar mixture butane–hexane V = 111.6 $cm^3\ mol^{-1}$ [31]):

$$\tilde{V} = \frac{V}{V^*} = 1.275.$$

(4) We will determine $\Delta \ln \eta$ of the equimolar mix-

Table 6. Properties and parameters of equimolar mixtures alkanol–alkane at T = 298.15 K

System	V	V^* [formula (7)]	V^*_{ac} [formula (14)]	$\tilde{V}$ [formula (8)]	$\tilde{V}_{ass}$ [formula (15)]
	$cm^3\ mol^{-1}$				
Ethanol–hexane	95.51 [20]	73.12	73.24	1.306	1.304
Ethanol–heptane	102.1 [20]	79.20	79.33	1.289	1.287
Propanol–hexane	103.5 [28]	80.22	80.34	1.290	1.288
Propanol–heptane	110.2 [20]	86.30	86.43	1.277	1.275
Propanol–nonane	127.7 [29]	101.4	101.5	1.259	1.258
Propanol–decane	136.0 [30]	108.6	108.7	1.252	1.251
Butanol–hexane	111.6 [31]	87.52	87.63	1.275	1.274
Butanol–octane	128.0 [32]	101.7	101.8	1.259	1.257
Butanol–nonane	135.8 [33]	108.7	108.8	1.249	1.248
Butanol–decane	144.3 [30]	115.9	116.0	1.245	1.244
Pentanol–hexane	119.5 [20]	94.27	94.37	1.268	1.266
Pentanol–heptane	126.6 [20]	100.4	100.5	1.261	1.260
Pentanol–octane	136.3 [34]	108.5	108.6	1.256	1.255
Pentanol–nonane	144.4 [33]	115.4	115.5	1.251	1.250
Pentanol–decane	152.6 [30]	122.6	122.7	1.245	1.244

Table 7. Calculated η_1–η_4 and experimental (η_{exp}) values of the dynamic viscosity of the systems *n*-alkanol–n-alkane at the equimolar ratio of components (T = 298.15 K)

System	$\eta_1 \times 10^3$	$\eta_2 \times 10^3$	$\eta_3 \times 10^3$	$\eta_4 \times 10^3$	$\eta_{exp} \times 10^3$
	Pa s				
Ethanol–hexane	0.391	0.433	0.422	0.425	0.439 [35]
Ethanol–heptane	0.569	0.522	0.506	0.520	0.515 [35]
Propanol–hexane	0.476	0.583	0.569	0.514	0.549 [35]
Propanol–heptane	0.604	0.681	0.660	0.617	0.627 [35]
Propanol–nonane	1.054	0.911	0.864	0.874	0.848 [36]
Propanol–decane	1.299	1.092	1.036	1.069	1.008 [36]
Butanol–hexane	0.522	0.677	0.664	0.574	0.639 [31]
Butanol–octane	0.814	0.885	0.872	0.816	0.798 [32]
Butanol–nonane	1.059	1.040	1.008	0.969	0.955 [37]
Butanol–decane	1.300	1.196	1.156	1.157	1.093 [37]
Pentanol–hexane	0.544	0.927	0.923	0.693	0.783 [20]
Pentanol–heptane	0.716	1.018	0.997	0.807	0.846 [38]
Pentanol–octane	–	1.133	1.107	0.945	0.982 [34]
Pentanol–nonane	1.084	1.234	1.203	1.076	1.069 [37]
Pentanol–decane	1.326	1.464	1.424	1.241	1.258 [37]
σ_Σ, %	14	10	7.9	4.2	
σ_{max}, %	31 Pentanol–hexane	20 Pentanol–heptane	18 Pentanol–hexane	12 Pentanol–hexane	

ture by the relation

$$\Delta \ln \eta = (\tilde{V} - 1)^{-1} - 0.5(\tilde{V}_A - 1)^{-1} - 0.5(\tilde{V}_B - 1)^{-1} = -0.232.$$

(5) We will calculate the dynamic viscosity of the equimolar mixture as

$$\eta = \exp(\Delta \ln \eta + 0.5 \ln \eta_A + 0.5 \ln \eta_B)$$
$$= 0.677 \times 10^{-3}\ \text{Pa s}.$$

Free-volume theory with molecular association taken into account. (1) Using formula (13), we will determine the mole fraction of the butanol monomers

Table 8. Calculated η_1–η_4 and experimental η_{exp} values of the dynamic viscosity of the system butanol (A) + hexane (B) at T = 298.15 K

X_A, m.f.	$\eta_1 \times 10^3$	$\eta_2 \times 10^3$	$\eta_3 \times 10^3$	$\eta_4 \times 10^3$	$\eta_{exp} \times 10^3$
	Pa s				
0.073	0.293	0.315	0.309	0.311	0.306
0.185	0.321	0.373	0.364	0.357	0.348
0.338	0.389	0.478	0.469	0.441	0.440
0.438	0.461	0.588	0.575	0.516	0.539
0.648	0.743	0.935	0.931	0.775	0.909
0.738	0.963	1.166	1.159	0.970	1.169
0.868	1.489	1.701	1.693	1.459	1.688

* η_1 by the Eyring theory, η_2 by the free-volume theory without association taken into account, η_3 with association taken into account, and η_4 by the Lobe method.

in the system φ_{Al} (for butanol K = 175 at T = 298.15 K [27], φ_A = 0.412):

$$\varphi_{A1} = [2K\varphi_A + 1 - (4K\varphi_A + 1)^{1/2}]/(2K^2\varphi_A) = 0.00508.$$

(2) Using formula (12), we will calculate the occupied volume for the associated component V^*_{ass} (for butanol V^*_{A1} = 80.89 [27], ΔV^0 = –5.6 cm^3 mol^{-1} [27]):

$$V^*_{Aass} = V^*_{A1} + \Delta V^0 K\varphi_{A1} = 75.91 \text{ cm mol}^{-1}.$$

(3) We will determine the reduced volume of the associated component (butanol) $\tilde{V}_{ass}$ with account of association:

$$\tilde{V}_A = \frac{V_A}{V^*_A} = 1.212.$$

(4) Using formula (14), we will determine the occupied volume for the binary equimolar mixture

$$V^*_{ass} = (V^*_{A1} + \Delta V^0 K\varphi_{A1}) \times 0.5 + V^*_B \times 0.5 = 87.63 \text{ cm}^3 \text{ mol}^{-1}.$$

(5) Using formula (15), we will determine the reduced volume of the equimolar solution with account of association $\tilde{V}_{ass}$:

$$\tilde{V}_{ass} = \frac{V}{V^*_{ass}} = 1.274.$$

(6) We will calculate $\Delta \ln \eta$ for the equimolar system by the relation

$$\Delta \ln \eta = (\tilde{V}_{ass} - 1)^{-1} - 0.5(\tilde{V}_{Aass} - 1)^{-1} - 0.5(\tilde{V}_B - 1)^{-1} = -0.252.$$

(7) We will determine the dynamic viscosity of the equimolar mixture

$$\eta = \exp(\Delta \ln \eta + 0.5 \ln \eta_A + 0.5 \ln \eta_B) = 0.664 \times 10^{-3} \text{ Pa s.}$$

Lobe method. (1) Using formula (10), we will calculate the kinematic viscosity of the equimolar mixture (at T = 298.15 K the kinematic viscosity of butanol $\nu_A = 3.165 \times 10^{-6}$ [31], and that of hexane, $\nu_B = 0.437 \times 10^{-6}$ m^2 s^{-1} [31]):

$$\nu = \varphi_B\nu_B e^{\alpha_A\varphi_A} + \varphi_A\nu_A e^{\alpha_B\varphi_B} = 0.8 \times 10^{-6} \text{ m}^2 \text{ s}^{-1},$$

$$\alpha_B = -1.7 \ln(\nu_A/\nu_B) = -3.366,$$

$$\alpha_A = 0.27 \ln(\nu_A/\nu_B) + [1.3 \ln(\nu_A/\nu_B)]^{0.5} = 2.139.$$

(2) The density of the equimolar mixture butanol–hexane at T = 298.15 K is equal to 0.7178×10^3 kg m^{-3} [31]. Hence, the dynamic viscosuty of this system can be calculated as $\eta = \rho\nu = 0.7178 \times 10^3 \times 0.8 \times 10^{-6} = 0.574 \times 10^{-3}$ Pa s.

Along with the equimolar composition, we also calculated the viscosity throughout the concentration range by all the methods utilized in this work for the butanol–hexane system. The calculated viscosities (Table 8) show that the results of analysis do not markedly change for nonequimolar mixtures either.

CONCLUSIONS

(1) The semi-theoretical methods for calculating the viscosity of the binary mixtures based on the Eyring theory or the free-volume theory afford virtually identical accuracy (rms deviation of 4–9%). The empirical method affords a lower accuracy (8–14%) for all classes of nonelectrolyte systems (classified into polar–polar, polar–nonpolar, and nonpolar–nonpolar component mixtures). The maximal inaccuracy for all the methods can reach 20–26%.

(2) For systems *n*-alkanol–*n*-alkanel set apart for the viscosity calculations as a separate series, because they were extensively studied previously, the best results are afforded, however, by the Lobe method (4.2%). By taking into account the molecular association in terms of the free-volume theory, it is possible to improve the accuracy (from rms deviation of 10 to 7.9%) in predicting the viscosity of the *n*-alkanol–*n*-alkane solutions.

REFERENCES

1. Krasovskii, A.N., Kharlampiev, A.A., and Tkach, V.P., *Zh. Prikl. Khim.*, 1997, vol. 70, no. 7, pp. 1165–1174.
2. Sumarokova, G.N. and Berger, E.N., *Zh. Prikl. Khim.*, 1997, vol. 70, no. 9, pp. 1432–1442.
3. Stupishina, G.N. and Vershinina, V.I., *Biokhimiya*, 1998, vol. 63, no. 11, pp. 1503–1508.
4. Abramzon, A.A. and Petel'skii, M.B., *Zh. Prikl. Khim.*, 1998, vol. 71, no. 8, pp. 1282–1285.
5. Afanas'ev, V.N., Efremova, L.S., and Volkova, T.V., *Fizikokhimicheskie svoistva binarnykh rastvoritelei: Vodosoderzhashchie sistemy* (Physicochemical Properties of Binary Solvents: Water-Containing Systems), Ivanovo, 1988, part 1.
6. V'yugin, A.I., Zverev, V.A., and Krestov, G.A., in *Termodinamika i stroenie rastvorov* (Thermodynamics and Structure of Solutions), Ivanovo, 1976, issue 5, pp. 50–53.
7. Kanti, M., Lagourette, B., Alliez, J., and Boned, C., *Fluid Phase Equil.*, 1991, vol. 65, pp. 291–304.
8. Syrnikov, Yu.P., Penkina, N.V., Kiselev, M.G., and Pukhovskii, Yu.P., *Zh. Fiz. Khim.*, 1992, vol. 66, no. 3, pp. 185–189.
9. Luk'yanchikova, I.A., Nikiforov, M.Yu., and Al'per, G.A., *Zh. Fiz. Khim.*, 1998, vol. 72, no. 7, pp. 1230–1235.
10. Glasstone, S., Laidler, K.J., and Eyring, H., *The Theory of Rate Processes. The Kinetics of Chemical Reactions, Viscosity, Diffusion, and Electrochemical Phenomena*, New York: McGraw-Hill, 1941.
11. Cohen, M.H. and Turnbull, D., *J. Chem. Phys.*, 1959, vol. 31, no. 5, pp. 1164–1169.
12. Bloomfield, V.A. and Dewan, R.K., *J. Phys. Chem.*, 1971, vol. 75, no. 20, pp. 3113–3119.
13. McAlister, R.L., *Am. Inst. Chem. Eng. J.*, 1960, vol. 6, no. 3, pp. 427–431.
14. Katti, R.K. and Chaudry, M.M., *J. Chem. Eng. Data*, 1964, vol. 9, no. 5, pp. 442–443.
15. Heric, E.L., *J. Chem. Eng. Data*, 1966, vol. 11, no. 1, pp. 66–68.
16. Nikiforov, M.Yu., Al'per, G.A., and Krestov, G.A., *Zh. Fiz. Khim.*, 1988, vol. 62, no. 6, pp. 1684–1686.
17. Lebedev, Yu.A. and Miroshnichenko, E.A., *Termokhimiya paroobrazovaniya organicheskikh veshchestv: Teploty ispareniya, sublimatsii i davleniya nasyshchennogo para* (Thermochemistry of Vaporization of Organic Substances: Heats of Vaporization and Sublimation and Saturated Vapor Pressure), Moscow: Nauka, 1981.
18. Belousov, V.P. and Morachevskii, A.G., *Teploty smesheniya zhidkostei* (Heats of Liquid Mixing), Leningrad: Khimiya, 1970.
19. Belousov, V.P., Morachevskii, A.G., and Panov, M.Yu., *Teplovye svoistva rastvorov neelektrolitov* (Thermal Properties of Nonelectrolyte Solutions), Leningrad: Khimiya, 1981.
20. Krestov, G.A., *Fiziko-khimicheskie svoistva binarnykh rastvoritelei* (Physicochemical Properties of Binary Solvents), Leningrad: Khimiya, 1988.
21. Macedo, P.B. and Litovitz, T.A., *J. Chem. Phys.*, 1965, vol. 42, no. 2, pp. 245–256.
22. Erdey-Gruz, T., *Transport Phenomena in Aqueous Solutions*, Budapest: Akad. Kiado, 1974.
23. Flory, P.J., Orwoll, R.A., and Vrij, A., *J. Am. Chem. Soc.*, 1964, vol. 86, no. 17, pp. 3507–3520.
24. Reid, R.G., Prausnitz, J.M., and Sherwood, T.K., *The Properties of Gases and Liquids*, New York: McGraw-Hill, 1977.
25. Petrino, P.J., Gaston-Bonhomme, Y.H., and Chevalier, J.L.E., *J. Chem. Eng. Data*, 1995, vol. 40, no. 1, pp. 136–140.
26. Aucejo, A., Cruz Burguet, M., Munoz, R., and Marques, J.L., *J. Chem. Eng. Data*, 1995, vol. 40, no. 1, pp. 141–147.
27. Heintz, A., *Ber. Bunsenges. Phys. Chem.*, 1985, vol. 89, no. 2, pp. 172–181.
28. Heintz, A., Schmittecker, B., Wagner, D., and Lichtenthaler, R.N., *J. Chem. Eng. Data*, 1986, vol. 31, no. 4, pp. 487–492.
29. Wagner, D. and Heintz, A., *J. Chem. Eng. Data*, 1986, vol. 31, no. 4, pp. 483–487.
30. Bender, M. and Heintz, A., *Fluid Phase Equil.*, 1991, vol. 67, pp. 241–257.
31. Franjo, C., Jimenes, E., Iglesias, T.R., *et al.*, *J. Chem. Eng. Data*, 1995, vol. 40, no. 1, pp. 68–70.
32. Franjo, C., Menaut Consolacion, P., Jimenes, E., *et al.*, *J. Chem. Eng. Data*, 1995, vol. 40, no. 4, pp. 992–994.
33. Treszczanowicz, A.J. and Benson, G.C., *Fluid Phase Equil.*, 1993, vol. 89, pp. 31–56.
34. D'Aprano, A., Donato, I.D., and Turco Liveri, V., *J. Solution Chem.*, 1990, vol. 19, no. 7, pp. 711–720.
35. Papaioannou, D. and Panayiotou, C., *J. Chem. Eng. Data*, 1994, vol. 39, no. 3, pp. 463–466.
36. Totchasov, E.D., Luk'yanchikova. I.A., Nikiforov, M.Yu., and Al'per, G.A., *Vyazkost' binarnykh rastvorov neelektrolitov na osnove propanola i izopropanola* (Viscosity of Binary Nonelectrolyte Solutions Based on Propanol and Isopropanol), Available from VINITI, 1998, no. 1097-V98.
37. Totchasov, E.D., Luk'yanchikova, I.A., Nikiforov, M.Yu., and Al'per, G.A., Abstracts of Papers, *VII Mezhdunarodnaya konfertentsiya "Problemy sol'vatatsii i kompleksoobrazovaniya v rastvorakh"* (VII Int. Conf. "Problems of Solvation and Complexation in Solutions"), Ivanovo, 1998, p. 64.
38. Rappon, M. and Kaukinen, J.A., *J. Mol. Liq.*, 1988, vol. 38, no. 2, pp. 107–133.

Russian Journal of Applied Chemistry, Vol. 74, No. 5, 2001, pp. 830–833. Translated from Zhurnal Prikladnoi Khimii, Vol. 74, No. 5, 2001, pp. 805–808.

MACROMOLECULAR CHEMISTRY AND POLYMERIC MATERIALS

Electrophysical Properties of Coordination Compounds Based on Cobalt(II) and Manganese(II) Chlorides and ε-Caprolactam

I. M. Davletbaeva, A. R. Khairutdinov, R. A. Bylinkin, and V. V. Parfenov

Kazan State Technological University, Kazan, Tatarstan, Russia
Kazan State University, Kazan, Tatarstan, Russia

Received June 13, 2000

Abstract—The metal complex systems based on Co(II) and Mn(II) chlorides and ε-caprolactam were studied. Temperatures of the phase transition, activation energy of the electrical conductivity, and mobility of the charge carriers in the compounds obtained were determined.

In [1–3], we found that a series of coordination compounds of transition metal [Co(II), Mn(II), Cu(II), and V(III)] chlorides cross-link polymers containing electron-donor groups. Up to now, aromatic diisocyanates and related urethane-forming systems were the main objects of the study of interaction with metal complexes.

The initial components forming metal-complex modifying systems can be subdivided in two types. In the first group, 3*d* metal chlorides with variable metal oxidation state [Cu(II), Fe(III), V(III), and Cr(III)] are used as coordinating centers, and *N*,*N*'-diethylhydroxylamine and polyoxyethylene glycol, as ligands. Interaction is accompanied by redox process, and yields polynuclear complexes in which 3*d* metal ions exist in two oxidation states. The resulting reactive system cross-links polyurethane matrix, enhances its physicomechanical properties, and substantially (by a factor of 10^4–10^5) increases the electrical conductivity. It was shown that the cross-linking effect in the urethane-forming system occurs at a low content of metal chloride (0.1–1%).

In the second case, 3*d* metal chlorides in the lower oxidation state [Co(II) and Mn(II)] and monoethanolamine (MEA) were the initial components for obtaining a metal-complex modifier. It was found that the reaction of $CoCl_2$ with MEA is completed by formation of a mixture of mono-, bi-, and polynuclear tetrahedral cobalt complexes in which the metal ions keep their oxidation state and are bound with each other by chloride bridges.

The ability of metal ions to coordinate the urethane amide group and thus to cross-link macromolecules was used in synthesis and studying modifying systems based on Co(II) and Mn(II) chloride complexes with ε-caprolactam.

It was found that on addition of a $CoCl_2$ ($MnCl_2$)–MEA mixture the ε-caprolactam melt becomes turbid, and its viscosity increases. Thermooptical study on a polarization microscope with a thermal stage showed that the resulting turbid melt is a smectic liquid crystal phase, which is readily identified through characteristic "schlieren" textures. These results were confirmed by DSC (Fig. 1).

The intrinsic viscosity was measured for the initial ε-caprolactam and products of the final stage of its reaction with $MnCl_2$–MEA and $CoCl_2$–MeA. For caprolactam, the intrinsic viscosity is close to zero, while for coordinated ε-caprolactam it is 0.027 dl g^{-1}. Such a small increase in the intrinsic viscosity in-

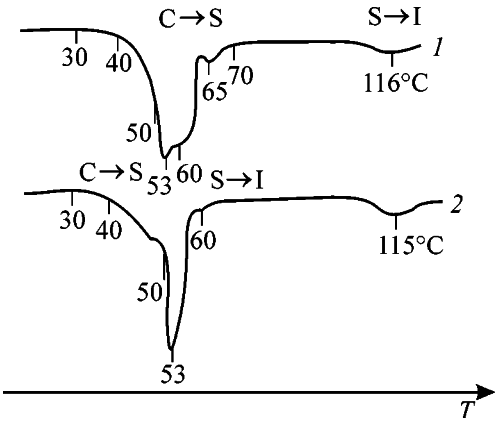

Fig. 1. DSC curves for the (*1*) $CoCl_2$–MEA–ε-caprolactam and (*2*) $MnCl_2$–MEA–ε-caprolactam systems. Heating rate 8 deg min^{-1}. (*T*) Temperature. Phase state of the substance: (C) crystalline, (S) smectic liquid crystal, and (I) isotropic liquid.

1070-4272/01/7405-0830$25.00

dicates that ε-caprolactam does not polymerize under reaction conditions.

The change of the chemical composition of ε-caprolactam caused by interaction with the metal-complex system was controlled by IR spectra. The most characteristic absorption band for ε-caprolactam caused by stretching vibrations of the amide carbonyl group lies at 1672 cm^{-1}. After interaction with the metal-complex system it shifts to 1678 cm^{-1} and noticeably broadens. Such changes are characteristic for coordinated carbonyl group and suggest that ε-caprolactam forms coordination bonds with metal complexes in the $CoCl_2$–MEA system.

To study features of mesomorphic phase formed, we measured the temperature dependences of electrical conductivity in the systems $CoCl_2$–MEA–ε-caprolactam and $MnCl_2$–MEA–ε-caprolactam. These dependences are shown in Fig. 2 in semilogarithmic coordinates. Three sections of the curves are observed. They can correspond to the crystalline state (C), mesomorphic state of the smectic type (S), and state of isotropic liquid (I).

At phase transitions S → I (at heating) and I → S (at cooling), the electrical conductivity changes by more than an order of magnitude. At C → S phase transition, no jump of the electrical conductivity is observed; however, the break appears in the $\ln\sigma$–$1/T$ curve, caused by the change of the activation energy. The position of this break in the temperature curve approximately corresponds to the C → S phase transition temperature in the DSC curve. Since it is known that the temperature dependence of the electrical conductivity for organic semiconductors is well fitted by the Arrhenius equation, we used the equation

$$\sigma = \sigma_0 \exp[-E_a/kT] \quad (1)$$

to determine the activation energies E_a of the electrical conductivity. The activation energies, phase transition temperatures, and conductivities are listed in the table.

The shape of DSC dependences and the values of E_a obtained in our work are similar to published data for other systems [4–6]. However, we can note certain features characteristic for the systems studied: the activation energies of high-frequency and dc electrical conductivity for the isotropic phase are practically the same; the temperature range of the mesophase existence is fairly broad; the electrical conductivity is several orders of magnitude larger than that described in the literature (up to 10^{-3} Ω^{-1} cm^{-1} in the I phase); the pronounced temperature hysteresis occurs, i.e.

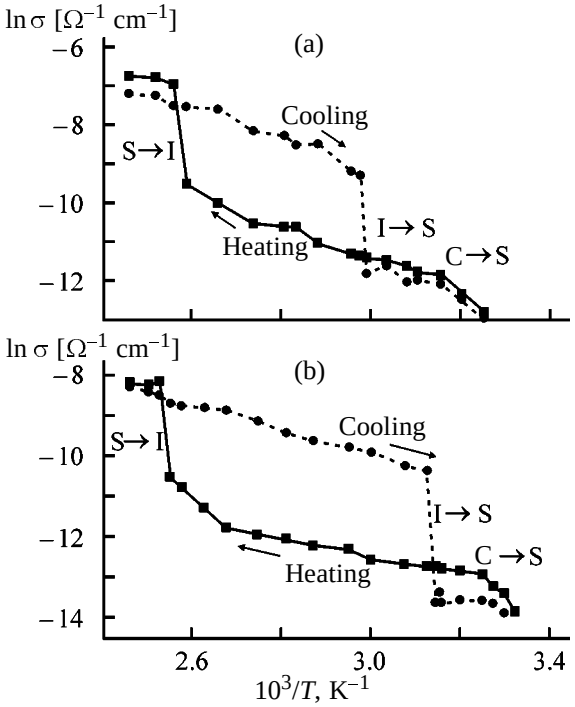

Fig. 2. Temperature dependence of the electrical conductivity σ for the (a) $CoCl_2$–MEA–ε-caprolactam and (b) $MnCl_2$–MEA–ε-caprolactam systems.

at sample cooling the temperature interval of the existence of the mesophase is fairly narrow.

The DSC curves are shown in Fig. 1. For both systems the melting point varies within the range 50–60°C. The DSC curves were measured up to the corresponding S → I transitions. The temperature of the transition into the isotropic liquid was determined from both the corresponding jumps in the curves of temperature dependence of the electrical conductivity and the DSC curves. It is 116–120°C and 115–119°C for the $CoCl_2$–MEA–ε-caprolactam and $MnCl_2$–MEA–ε-caprolactam systems, respectively.

Phase transfer temperatures T, activation energies E_a, and electrical conductivity σ for systems MCl_2–MEA–ε-caprolactam; M = Co, Mn

Parameter	Co	Mn
T, °C: C → S	55	57
S → I	116	115
I → S	65	45
E_a, eV: for C	1.06	1.29
for S	0.43	0.14
for I	0.38	0.24
σI/σS	15	23
Δσ, Ω cm^{-1}	8.35×10^{-7}–1.00×10^{-3}	1.21×10^{-6}–2.75×10^{-4}

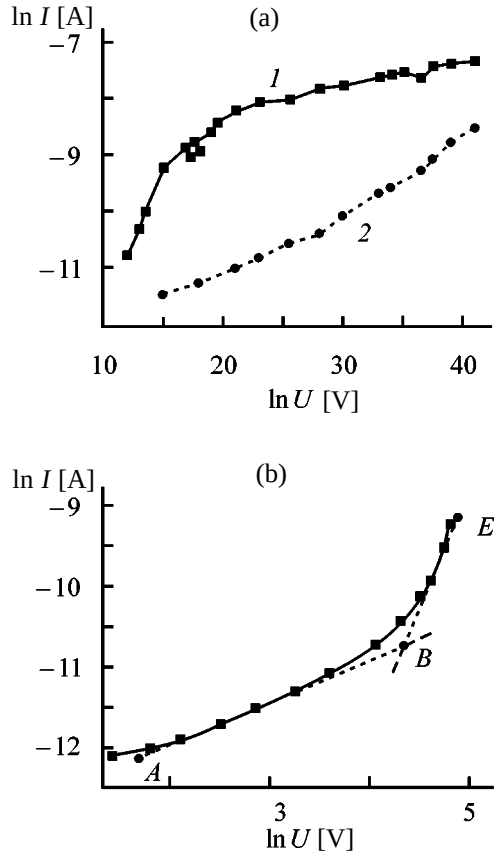

Fig. 3. Volt-ampere characteristics of the (a) $MnCl_2$–MEA–ε-caprolactam and (b) $CoCl_2$–MEA–ε-caprolactam systems. (*I*) Current and (*U*) voltage. Sample: (*1*) initial and (*2*) after electrochemical purification.

The volt–ampere characteristics (VAC) measured for freshly prepared samples are linear at a low field intensity. At fields $E > 4 \times 10^3$ V cm^{-1} they become sublinear up to saturation. Moreover, the current decreases with time. Such a phenomenon is known for liquid crystals and the other systems with the ionic conductance and is due to the electrochemical purification to remove extrinsic ions. After standing for 30 min in the maximal electric field of 2×10^4 V cm^{-1}, the current through the sample decreases and becomes independent of time. Probably, after the electrochemical purification to remove extrinsic ions, the volt–ampere characteristic of samples is mainly caused by the electronic component of the current. The volt–ampere characteristics for $MnCl_2$–MEA–ε-caprolactam and $CoCl_2$–MEA–ε-caprolactam systems are shown in Figs. 3a and 3b, respectively. For the system with $CoCl_2$, both ohmic and nonohmic sections are described by the Child–Langmuir law. Such a behavior of VAC is caused by the following two effects. At a relatively high current density corresponding to the strong electric field, the concentration of current carriers moving in the gap between the electrodes is fairly large, and these carriers form a space charge. The next reason of the VAC nonlinearity is the existence of traps such as impurities, defects of crystal packing, dislocations, and other lattice defects. These defects give rise to additional localized levels in the band gap [7].

At low voltages, injection of current carriers from the electrode is negligible, and the current obeys the Ohm law (section *AB*). In the absence of traps, the current is restricted by the space charge at the voltage corresponding to point *B*. In this point, the concentration of free carriers injected from the electrode begins to prevail over the thermally equilibrium concentration of carriers. After this point, VAC obeys the Child–Langmuir law and follows the *BE* line, and the current I (A cm^{-2}) is determined by the equation

$$I \cong 10^{-13}\frac{\mu\varepsilon U}{d^3}, \qquad (2)$$

where U is applied voltage (V), μ is the carrier mobility (cm^2 V^{-1} s^{-1}), ε is the dielectric constant, and d is the distance between the electrodes (cm).

The current stops to be ohmic beginning from the definite voltage U_{tr} (point *B*) at which the currents start to be limited by the space charge. After determining U_{tr} from the experimental VAC curve for the substance studied ($CoCl_2$–MEA–ε-caprolactam system) and its substitution in Eq. (2), we obtain a formula for determination of the carrier mobility μ:

$$\mu = 10^{13} Id^3/(\varepsilon U^2)$$

All liquid crystal compounds are characterized by anisotropy of dielectric parameters. In this case, the average dielectric constant equal to 41 was used for the $CoCl_2$–MEA–ε-caprolactam system.

After substitution of U_{tr} = 73 V from the VAC curve for the $CoCl_2$–MEA–ε-caprolactam system in Eq. (3), we calculated the mobility of charge carriers: $\mu = 7 \times 10^{-4}$ cm^2 V^{-1} s^{-1}, which corresponds to the electronic mobility characteristic typical of organic semiconductors in the case of hopping (electronic) conductance.

The volt–ampere characteristic for the $MnCl_2$–MEA–ε-caprolactam system after the electrochemical purification is ohmic; transition to the quadratic section at field intensities up to 2×10^4 V cm^{-1} was not observed.

EXPERIMENTAL

The crystal hydrate $MnCl_2 \cdot 4H_2O$ was dried to $MnCl_2 \cdot 3H_2O$ at 106°C, and $CoCl_2 \cdot 6H_2O$ was dried at 60°C in a thermal box. Monoethanolamine was purified by vacuum distillation. Chemically pure grade ε-caprolactam was prepared by recrystallization of commercial grade ε-caprolactam from ethyl acetate. The reaction of $CoCl_2$ and $MnCl_2$ with MEA was performed with vigorous agitation and heat removal. The molar ratios $MnCl_2$: MEA and $CoCl_2$: MEA was 1 : 10 and 1 : 3.6, respectively. The resulting complex was introduced directly into the ε-caprolactam melt at the molar ratio [$MnCl_2$] and [$CoCl_2$] : [ε-caprolactam] = 1 : 9. The reaction mass was agitated at 90°C for 30 min. Catalytic amounts of acetonitrile and 2,4-toluylene diisocyanate were also introduced into the reaction mass.

The IR spectra were registered on a Perkin–Elmer 16PC FT-IR spectrometer with precise fixation of the light radiation (±1%). The thickness of the spectrometric cell was 0.022 cm. Thermograms were obtained on a DSM-2M differential scanning microcalorimeter (rate of heating to 200°C 8 deg min^{-1}). The intrinsic viscosity was determined on a Ubbelohde viscometer at 20°C. Phase transitions were registered with a Polam P-211 polarization microscope equipped with a thermal stage.

The study of electrophysical characteristics was reduced to measurement of the temperature dependences of the dc electrical conductivity within the 290–420 K range by the standard method. Platinum electrodes with optimal size were introduced into the vessel with the sample studied. To avoid field end effects, the fixed distance between the electrodes was substantially smaller than their linear sizes. The temperature was controlled through the change of the voltage on a thermostat heater and monitored with a Chromel–Alumel thermocouple (connected with a V7-21 voltmeter) placed directly in the vessel with the sample. The electrical resistance of the latter was measured with a E6-13A teraohmmeter with an error of 2.5%.

The charge carrier mobility was determined through recording volt–ampere characteristics at 290 K. The sample was installed into a specially fabricated cell of the "sandwich" type: two flat glass plates with the applied transparent conducting layer of SnO_2 were separated by a mica layer with a small window in which the sample was placed. The thickness of the gap between the glass plates was equal to the thickness of the mica layer, which in our case was 4×10^{-5} m. The voltage on the sample (40 V) was fed from a stabilized V5-9 source. The current was recorded on a V7-21 universal voltmeter. The electric field intensity was varied up to 2×10^3 V cm^{-1}.

CONCLUSIONS

(1) Data on electrical conductivity and conductivity activation energy show that the compounds obtained by the reaction between $MnCl_2$ (or $CoCl_2$), monoethanolamine, and ε-caprolactam and existing in the crystalline, liquid-crystalline, and isotropic state are organic semiconductors.

(2) Phase transitions crystal–liquid crystal and liquid crystal–isotropic liquid appear in the temperature dependence of the electrical conductivity as a break or sharp jump (at the liquid crystal–isotropic liquid transition). The pronounced temperature hysteresis in the heating–cooling cycle is observed.

(3) The electrical conductance of freshly prepared samples has a mixed ionic-electronic character. After the electrochemical purification, volt–ampere characteristics of the systems studied are characteristic for organic semiconductors with hopping electronic conductance.

(4) The transition from ohmic to quadratic (the Child–Langmuir dependence) section in the volt–ampere curves of the $CoCl_2$–MEA–ε-caprolactam system is observed. The mobility of charge carriers was calculated from the inflection point.

REFERENCES

1. Davletbaeva, I.M., Kirpichnikov, P.A., and Rakhmatullina, A.P., *Macromol. Symp.*, 1996, vol. 106, no. 4, pp. 87–90.
2. Davletbaeva, I.M., Ismagilova, A.I., Tyut'ko, K.A., *et al.*, *Zh. Obshch. Khim.*, 1998, vol. 68, no. 6, pp. 1021–1027.
3. Davletbaeva, I.M., Kirpichnikov, P.A., Rakhmatullina, A.P., and Kuzaev, A.I., *Vysokomol. Soedin., Ser. B*, 1998, vol. 40, no. 4, pp. 667–671.
4. Baessler, H. and Labes, M.M., *Phys. Rev. Lett.*, 1968, vol. 21, no. 27, pp. 1791–1793.
5. Kusabayshi, S. and Labes, M.M., *Mol. Cryst. Liq. Cryst.*, 1969, vol. 7, no. 6, pp. 395–405.
6. Gorskii, F.K. and Bashuk, M.A., *Sbornik trudov II Vsesoyuznoi konferentsii po zhidkim kristallam i ikh prakticheskomu primeneniyu* (Proc. II All-Union Conf. on Liquid Crystals and Their Application), Ivanovo, 1973, pp. 103–107.
7. Gutmann, F. and Lyons, L.E., *Organic Semiconductors*, New York: Wiley, 1967.

Russian Journal of Applied Chemistry, Vol. 74, No. 5, 2001, pp. 834–838. Translated from Zhurnal Prikladnoi Khimii, Vol. 74, No. 5, 2001, pp. 809–813.

MACROMOLECULAR CHEMISTRY AND POLYMERIC MATERIALS

Epoxidation of 5-Vinyl-2-norbornene with *tert*-Butyl Hydroperoxide, Catalyzed with Transition Metal Compounds

M. Yu. Osokin, O. P. Karpov, Yu. G. Osokin, A. A. Surovtsev, B. N. Bychkov, and S. I. Kryukov

Yaroslavl State Technical University, Yaroslavl, Russia
Yarsintez Research Institute, Joint-Stock Company, Yaroslavl, Russia

Received August 15, 2000; in final form, February 2001

Abstract—Epoxidation of 5-vinyl-2-norbornene with *tert*-butyl hydroperoxide in the presence of Mo, V, and Ti compounds was studied. The optimal conditions for synthesis of 2,3-epoxy-5-vinylnorbornane were found.

Recently there has been a great deal of interest in preparation of new polymeric materials for electronics, electrical and medical engineering, etc. Incorporation into polymers of hydrocarbon or functional derivtives of norbornene ensures high thermal and chemical resistance of the resulting materials [1–3]. Among alicyclic epoxy compounds, the demand for 2,3-epoxy-5-vinylnorbornane increases because of its extending application field [3–12].

Development and mastering on the pilot scale in Russia of a process for production of ethylidenenorbornene [13] made 5-vinyl-2-norbornene (VNB) available and created prerequisites for setting up production of 2,3-epoxy-5-vinylnorbornane. The feasibility of selective epoxidation of VNB into mono- and diepoxides was demonstrated in [14–16].

Recent reviews [17–19] reflecting most exhaustively the present state of studies in the filed of epoxidation of unsaturated cyclic hydrocarbons contain practically no data on oxidation of VNB with alkyl hydroperoxides. Among commercially available alkyl hydroperoxides [20], we chose *tert*-butyl hydroperoxide (TBHP), since with this agent the products of hydroperoxide epoxidation of VNB can be separated most readily.

In this work we studied the features of VNB epoxidation with *tert*-butyl hydroperoxide, catalyzed with transition metal compounds.

EXPERIMENTAL

5-Vinyl-2-norbornene was prepared by the Diels–Alder reaction from cyclopentadiene and 1,3-butadiene [21]; the main substance content in the product isolated by sharp fractional distillation in a vacuum was no less than 98.5 wt %. TBHP (99 wt %) was prepared by oxidation of *tert*-butyl sulfate with hydrogen peroxide [22]. As epoxidation catalysts were tested molybdenyl ethanediolate $MoO_2(OC_2H_4OH)_2$, molybdenyl 2,3-butanediolate $MoO_2[OCH(CH_3)CH\cdot(CH_3)OH]_2$, molybdenyl 2-methyl-2,3-butanediolate $MoO_2[OC(CH_3)_2CH(CH_3)OH]_2$, molybdenyl ethylene-1,2-bis(salicylidenimine) MoO_2(salen), molybdenyl resinate $MoO_2(OCOC_{19}H_{29})$, molybdenum boride MoB, vanadium acetylacetonate $V(acac)_3$, vanadyl acetylacetonate $VO(acac)_2$, and tetrabutoxytitanium $Ti(OC_4H_9)_4$, which were prepared by appropriate procedures [20, 23, 24] or taken as commercial chemicals. The solvents (chemically pure grade) were dried before use.

Epoxidation of VNB was performed under nitrogen in a glass or metallic temperature-controlled vessel equipped with a magnetic stirrer. In the course of the experiments, samples of the reaction mixture were taken and analyzed for the content of TBHP (by iodometric titration [25]) and VNB epoxidation products (chromatographically, after treatment of the sample with triphenylphosphine to reduce the unchanged hydroperoxide). An LKhM-80 chromatograph equipped with a thermal conductivity detector and a 3000 × 3-mm column was used; the stationary phase was 5% XE-60 on Chromaton N-AW-DMCS (0.20–0.25 mm). The column temperature was 125°C, and the carrier gas (hydrogen) flow rate, 30 $cm^3\ min^{-1}$. The content of VNB and its monoepoxide was determined using an internal reference (*n*-tridecane).

The consumption of the initial reactants, VNB and TBHP, and accumulation of the epoxidation products

1070-4272/01/7405-0834$25.00

were monitored. As kinetic characteristic was used the initial rate of consumption of TBHP or VNB W_0 or the apparent rate constant k_{app}, calculated graphically from the slopes of the kinetic curves of TBHP consumption in the semilog coordinates. The determination error of these quantities did not exceed 5%.

The ^{1}H NMR spectrum was taken on a Tesla BS-567 spectrometer (100 MHz) from a 20% solution of the sample in CCl_4, with HMDS as internal reference. The IR spectrum was taken on a Shimadzu IR-4354 spectrophotometer in the range 4000 – 400 cm^{-1} from a thin film between NaCl plates. VNB monoepoxide isolated from the reaction mixture by fractional vacuum distillation had the following constants: bp 64.5–65.5°C at 1.13 kPa, d_4^{20} = 1.0224 g cm^{-3}, and n_D^{20} = 1.4875. Published data: bp 53–56°C at 4.5 mm Hg [26], 37°C at 20 mm Hg [4] (the latter value is probably a misprint; 2.0 mm Hg seems to be correct); n_D^{20} = 1.4870 [14].

Catalytic epoxidation of VNB with *tert*-butyl hydroperoxide at 80–100°C and molar ratio VNB : TBHP = 3 : 1 yields exclusively a mixture of isomeric monoepoxides exo-2,3-epoxy-5-vinylnorbornane (**I**) and 5-epoxyethyl-2-norbornene (**II**):

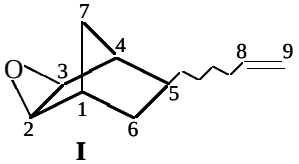

I

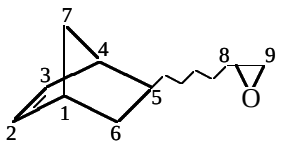

II

The chromatogram of the VNB epoxidation product contains two peaks in a 92 : 8 ratio. The structure of the VNB epoxidation product was studied by ^{1}H NMR and IR spectroscopy [27–29]; the spectra were compared with those of the initial VNB [30]. The major signals in the ^{1}H NMR spectrum of the VNB epoxidation product can be assigned to **I**, δ, ppm: 5.75 m (H^8), 5.0 q (H^9), 2.95 q (H^2 and H^3), 2.25 m (H^5), 2.4 m (H^1 and H^4), 1.7 m and 0.75 m ($2H^6$), 1.35 m and 1.1 m ($2H^7$); these parameters are identical to those obtained in [3, 4]. Compound **II** is detected as an impurity; the corresponding signals are weak, δ, ppm: 6.10 m, 5.95 m (H^3 and H^2); 2.8 m (H^8); 2.65 m, 2.15 m ($2H^9$).

IR spectrum, ν, cm^{-1}: 3068 m, 3040 s (ν_{C-H} in epoxy ring), 2966 s, 2864 s, 1636 s ($\nu_{C=C}$, –C=CH_2), 1461 m, 1446 m, 1424 w, 1377 s, 1321 m, 1280 w, 1265 m, 1236 w, 1223 w, 1158 w, 1087 w, 1028 w, 994 s ($\delta_{=C-H}$), 980 s, 910 s ($\delta_{=C-H}$), 866 s, 845 s (ν_{C-O}), 790 w, 764 w, 723 w, 661 w. The spectrum also confirms formation of **I** as the major product [4]. Selective hydroperoxide oxidation of VNB across the norbornene double bond was also noted in [14, 16]. Diepoxide derivatives of VNB are formed only with a large excess of TBHP, or by epoxidation of VNB monoepoxides.

Epoxidation of VNB in the presence of metal complexes can be accompanied by side reactions: radical decomposition of TBHP and reaction of the resulting VNB epoxide with *tert*-butyl alcohol. Experiments showed that the contribution of these reactions is small, and VNB epoxidation occurs selectively with a high conversion of TBHP. Also, epoxidation and subsequent isolation of the products can be accompanied by formation of polymers; this was prevented by adding an inhibitor, 4-*tert*-butylpyrocatechol (5×10^{-3} wt %), to the initial VNB.

We have performed several series of experiments in which we varied the initial concentrations of TBHP and catalyst in the reaction mixture, the molar ratio VNB : TBHP, and the reaction temperature and time. The influence of various factors on epoxidation of VNB is illustrated by Table 1.

The concentration of the catalyst, $MoO_2(OC_2H_4 \cdot OH)_2$, was varied from 1.9×10^{-4} to 23.3×10^{-4} M, which corresponds to the molar ratio Mo : TBHP from 1×10^{-4} : 1 to 12×10^{-4} : 1. We found that, as the catalyst concentration is increased, the TBHP conversion grows and the yield of VNB epoxide (mixture of isomers **I** and **II**) based on reacted TBHP (reaction selectivity) passes through a maximum. At the molar ratio Mo : TBHP = 12×10^{-4} : 1 the reaction selectivity decreases owing to accelerated thermocatalytic decomposition of TBHP. In further experiments on epoxidation of VNB we took the molar ratio Mo : TBHP = 6×10^{-4} : 1 ensuring reproducibly high yield of the target product.

With increasing initial concentration of TBHP in the reaction mixture from 0.97 to 1.95 M at the molar ratio VNB : TBHP = 3 : 1, the TBHP conversion increases, but the yields of VNB epoxide based on reacted TBHP and VNB decrease insignificantly. The best concentration of TBHP is 1.95 M (19.8 wt %); in this case the output of VNB epoxide from the unit of the reactor volume is the highest.

As noted in [20], olefins facilitate heterolytic decomposition of organic hydroperoxides. As the molar ratio VNB : TBHP is increased from 1 : 1 to 3 : 1, the conversion of TBHP increases from 77 to 98% and the yield of VNB epoxide based on reacted TBHP increases from 84.0 to 96.7 mol %. Taking VNB in more than threefold molar excess is not appropriate,

Table 1. Influence of various factors on epoxidation of VNB with *tert*-butyl hydroperoxide in the presence of the catalyst, $MoO_2(OC_2H_4OH)_2$

Initial concentration, M			Solvent	*T*, °C	τ, min	*K*,* %	Yield,** mol %
TBHP	VNB	[Mo] × 10^4					
1.95	5.85	1.9	–	100	60	92.3	93.5/95.2
1.94	5.85	5.8	–	100	60	97.6	97.4/96.0
1.95	5.85	11.8	–	100	60	98.1	96.7/95.8
1.94	5.85	23.3	–	100	60	99.5	78.4/93.9
0.97	2.90	5.8	Toluene	100	60	77.8	98.9/98.6
1.30	3.90	7.8	″	100	60	93.3	97.8/97.2
1.95	1.95	11.8	″	100	60	77.0	84.0/95.6
1.95	3.90	11.8	″	100	60	93.5	93.3/96.2
1.95	5.85	11.8	–	80	60	86.1	98.2/98.5
1.94	5.85	11.7	–	90	30	86.3	99.0/99.2
1.94	5.85	11.7	–	90	60	92.0	97.5/96.8
1.94	5.85	11.7	–	90	90	95.4	96.8/94.7
1.95	5.85	11.8	–	100	30	94.7	97.9/97.6
1.94	5.85	11.7	–	110	60	98.8	92.4/94.3

* (*K*) Conversion of TBHP; ** yield of VNB based on reacted TBHP (in numerator) and on reacted VNB (in denominator).

because it will require additional power consumption for recovery of recycled VNB.

With increasing tempertature, the conversion of TBHP increases, but the epoxidation selectivity decreases, especially above 110°C. At 100°C epoxidation is practically complete in 60 min. The residual TBHP concentration is less than 0.4 wt %, which allows safe isolation of VNB epoxide from the reaction mixture.

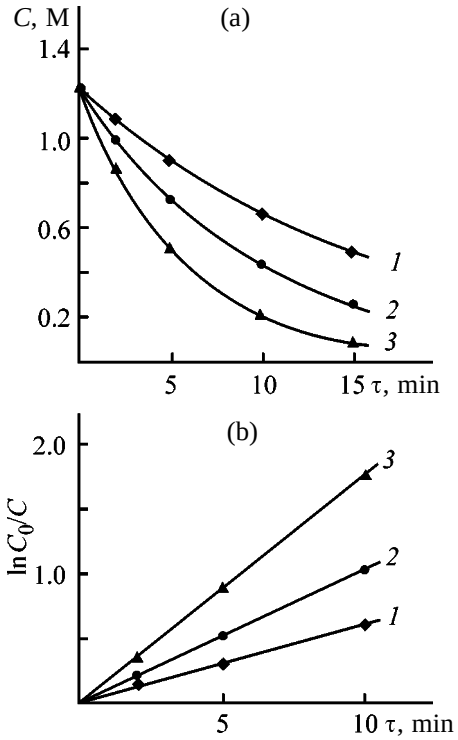

Fig. 1. (a) Variation with time τ of the TBHP concentration *C* in the course of VNB epoxidation and (b) the same curves in the semilog coordinates. Solvent toluene; initial concentration C_0, M: TBHP 1.23, VNB 3.65, and Mo 7.4 × 10^{-4}. Temperature, °C: (*1*) 80, (*2*) 90, and (*3*) 100.

Kinetic study of VNB epoxidation at 80–100°C showed that the hydroperoxide is consumed without noticeable induction period owing to high reactivity of VNB; the reaction rate is described by a first-order equation with respect to TBHP (Fig. 1). Certain deceleration of VNB epoxidation is observed at hydroperoxide conversions exceeding 70%. The temperature dependence of the apparent rate constant k_{app} (s^{-1}) of VNB epoxidation with *tert*-butyl hydroperoxide in toluene, catalyzed with $MoO_2(OC_2H_4OH)_2$, has the form $k_{app} = 5.26 \times 10^5 \exp(-58\,968/RT)$.

It is known [20] that the solvent used in hydroperoxide epoxidation of olefins appreciably affects each elementary stage of oxidation, primarily by affecting the solvation environment of the catalyst and the complexing power of the solvated catalyst toward the components of the reaction mixture. As a result, the epoxidation rate and selectivity are largely solvent-dependent. Studies of the solvent effect (Table 2) showed that the initial rate of TBHP consumption W_0 in the course of VNB epoxidation decreases in the order toluene > chlorobenzene > octane > isobutanol. There is no clear correlation of W_0 with the dielectric permittivity of the solvent. With a mixed solvent alcohol–aromatic hydrocarbon, epoxidation of VNB is accelerated, which is probably due to activation of

Table 2. Solvent effect on epoxidation of VNB, catalyzed with $MoO_2(OC_2H_4OH)_2$ at 100°C. Initial concentration of TBHP 1.95 M, molar ratio VNB : TBHP = 2 : 1, Mo : TBHP = 6×10^{-4} : 1

Run no.	Solvent	ε [34]	$W_0 \times 10^3$, mol l^{-1} s^{-1}	*K*,** %	*S*,** mol %
1	Octane	1.95	3.5	77.5	90.8
2	Toluene	2.38	5.1	87.2	94.5
3	Chlorobenzene	5.61	4.6	82.0	88.9
4	Isobutanol	17.7	1.7	56.8	76.6
5	Isobutanol–toluene	–	8.3	99.5	82.1
6	Isopropanol–toluene	–	9.2	98.9	82.6
7	–	–	6.5	94.7	97.9

* Molar ratio VNB : TBHP 1 : 1 in run nos. 5 and 6 and 3 : 1 in run no. 7.
** (*K*) Conversion of TBHP in 30 min and (*S*) selectivity.

the molybdenum catalyst. Under certain conditions alcohol forming a stronger complex with the catalyst weakens the ligand–molybdenum bonds to such an extent that their fast exchange with the olefin becomes possible. The influence of alcohol on epoxidation of olefins was discussed in [31]. To ensure higher selectivity, it is appropriate to perform epoxidation of VNB without a solvent.

As VNB epoxidation catalysts we used the compounds of the most active transition metals [32]: Mo, V, and Ti (Table 3). It is seen from these data that in the presence of molybdenum catalysts, which are readily soluble in the reaction mixture, epoxidation of VNB occurs selectively with a high conversion of TBHP. The catalytic activity of the tested Mo catalysts shows no noticeable dependence on the ligand. The heterogeneous catalyst MoB ensures a higher selectivity of VNB epoxidation, but the reaction rate is lower. Sapunov *et al.* [33] revealed a correlation of the catalytic activity of organometallic epoxidation catalysts with the acceptor power of the metal ion, characterized by the specific charge of the metal ion z/r^2, where *z* is the charge and *r*, the radius of the metal ion [34]. Table 3 shows that the activity of the catalysts decreases in the order Mo > V > Ti, i.e., with decreasing specific charge of the metal ion.

CONCLUSIONS

(1) The optimal conditions were determined for epoxidation of 5-vinylnorbornene with *tert*-butyl hydroperoxide in the presence of a soluble molybdenum catalyst, providing the reaction selectivity of 96–98 mol %: initial concentration of *tert*-butyl hydroperoxide 1.95 M, molar ratios 5-vinyl-2-norbornene : *tert*-butyl hydroperoxide = 3 : 1 and Mo : *tert*-butyl hydroperoxide = 6×10^{-4} : 1, 100°C, and reaction time 60 min.

(2) The apparent activation energy of epoxidation of 5-vinyl-2-norbornene is 59 kJ mol^{-1}.

(3) Analysis by gas–liquid chromatography and ^1H NMR and IR spectroscopy shows that epoxidation of 5-vinyl-2-norbornene yields *exo*-2,3-epoxy-5-vinylnorbornane and a minor amount of isomeric 5-epoxyethyl-2-norbornene.

(4) The activity of catalysts in epoxidation of 5-vinyl-2-norbornene decreases in the order Mo > V > Ti,

Table 3. Catalytic activity of transition metal compounds in epoxidation of VNB with *tert*-butyl hydroperoxide. 90°C; reaction rime 30 min; initial concentration of TBHP 1.94 M; molar ratios VNB : TBHP = 3 : 1, Mo : TBHP = 6×10^{-4} : 1, V : TBHP = 6×10^{-4} : 1, and Ti : TBHP = 6×10^{-3} : 1

Catalyst*	*K*, %	*S*, mol %	*A*,** s^{-1}	z/r^2**
$MoO_2(OR^1)_2$	86.3	99.0	1.54	15.61
$MoO_2(OR^2)_2$	95.8	98.6	1.70	15.61
$MoO_2(OR^3)_2$	96.6	98.6	1.71	15.61
$MoO_2(OCOR^4)$	98.9	94.8	1.68	–
MoO_2(salen)	97.8	98.2	1.72	–
MoB	68.2	96.3	1.18	–
$V(acac)_3$	43.0	85.1	0.66	–
$VO(acac)_2$	50.9	86.4	0.79	14.36
$Ti(OC_4H_9)_4$	23.7	77.9	0.03	8.65

* R^1 = C_2H_4OH, R^2 = $CH(CH_3)CH(CH_3)OH$, R^3 = $C(CH_3)_2 \cdot CH(CH_3)OH$ or $CH(CH_3)C(CH_3)_2OH$, R^4 = $C_{19}H_{29}$ (residue of a tricyclic carboxylic acid like abietic acid), salen = *N*,*N*-bis(salicylidene)ethylenediamine $OC_6H_4CH{=}NC_2H_4N{=}CHC_6H_4OH$, acac = acetylacetonate $OC(CH_3){=}CHCOCH_3$.
** (*A*) Molar catalytic activity equal to the amount of VNB epoxide (moles) formed in 1 s on 1 mol of the catalyst; (z/r^2) specific charge on the metal ion.

with a decrease in the specific charge of the metal ions.

ACKNOWLEDGMENTS

The authors are grateful to V.V. Volynets and T.B. Ushakova for recording the spectra.

REFERENCES

1. Makovetskii, K.L., *Vysokomol. Soedin., Ser. B*, 1999, vol. 41, no. 9, pp. 1525–1543.
2. Artem'eva, V.N., Kudryavtsev, V.V., Kukarkina, N.V., and Yakimanskii, A.V., *Zh. Prikl. Khim.*, 2000, vol. 73, no. 1, pp. 117–122.
3. Crivello, J.V. and Narayan, R., *Macromolecules*, 1996, vol. 29, no. 1, pp. 433–445.
4. LeCamp, L., Vaugelade, C., Yossef, B., and Bunel, C., *Eur. Polym. J.*, 1997, vol. 33, no. 9, pp. 1453–1462.
5. JPN Patent 06220158.
6. JPN Patent 06207126.
7. JPN Patent 06172550.
8. JPN Patent 06116358.
9. JPN Patent 06033029.
10. JPN Patent 06087916.
11. US Patent 5292827.
12. JPN Patent 02199115.
13. Titova, L.F., Osokin, Yu.G., Bazhanov, Yu.V., *et al.*, Abstracts of Papers, *Pervyi neftekhimicheskii simpozium sotsialisticheskikh stran (Baku, 21–25 noyabrya 1978 g.)* (First Petrochemical Symp. of Socialist Countries (Baku, November 21–25, 1978), Moscow: Nauka, 1978, p. 60.
14. Yur'ev, V.P., Gailyunas, G.A., Tolstikov, G.A., and Valyamova, F.G., *Neftekhimiya*, 1972, vol. 12, no. 3, pp. 353–357.
15. Kas'yan, L.I., Bombushkar', M.F., Malinovskii, M.S., *et al., Ukr. Khim. Zh.*, 1978, vol. 44, no. 9, pp. 956–959.
16. Voronenkov, V.V., Osokin, Yu.G., Baidin, V.N., *et al.*, *Neftekhimiya*, 1985, vol. 25, no. 2, pp. 234–236.
17. Kas'yan, L.I., Seferova, M.F., and Okovityi, S.I., *Alitsiklicheskie epoksidnye soedineniya: Metody sinteza* (Alicyclic Epoxy Compounds: Preparation Procedures), Dnepropetrovsk: Dnepropetrovsk. Gos. Univ., 1996.
18. Kas'yan, L.I., *Usp. Khim.*, 1998, vol. 67, no. 4, pp. 299–316.
19. Dryuk, V.G. and Kartsev, V.G., *Usp. Khim.*, 1999, vol. 68, no. 3, pp. 206–225.
20. Tolstikov, G.A., *Reaktsii gidroperekisnogo okisleniya* (Oxidations with Hydroperoxides), Moscow: Nauka, 1976.
21. Plate, A.F. and Belikova, N.A., *Zh. Obshch. Khim.*, 1960, vol. 30, no. 12, pp. 3045–3053.
22. Karnojitzki, V., *Les peroxides organiques*, Paris: Hermann, 1958.
23. USSR Inventor's Certificate no. 1171088.
24. Gavrilenko, V.A., Evzerikhin, E.I., Kolosov, V.A., *et al., Izv. Akad. Nauk SSSR, Ser. Khim.*, 1974, no. 9, pp. 1954–1956.
25. Antonovskii, V.L. and Buzlanova, M.M., *Analiticheskaya khimiya organicheskikh peroksidnykh soedinenii* (Analytical Chemistry of Organic Peroxides), Moscow: Khimiya, 1978.
26. US Patent 3183249.
27. Brand, J.C.D. and Eglinton, G., *Applications of Spectroscopy to Organic Chemistry*, London: Oldborne, 1965.
28. Cross, A.D., *An Introduction to Practical Infra-Red Spectroscopy*, London: Butterworths, 1960.
29. Shriner, R.L., Fuson, R.C., Curtin, D.Y., and Morrill, T.C., *The Systematic Identification of Organic Compounds. A Laboratory Manual*, New York: Wiley, 1980, 6th ed.
30. Osokin, Yu.G., Yablonskii, O.P., Lapuka, L.F., *et al.*, in *Osnovnoi organicheskii sintez i neftekhimiya: Mezhvuzovskii sbornik nauchnykh trudov* (Basic Organic Synthesis and Petrochemistry: Intercollegiate Coll. of Scientific Works), Leningrad: Leningr. Tekhnol. Inst., 1979, issue 11, pp. 55–62.
31. Stozhkova, G.A., Leonov, V.N., Prenglaev, V.B., *et al.*, in *Osnovnoi organicheskii sintez i neftekhimiya: Mezhvuzovskii sbornik nauchnykh trudov* (Basic Organic Synthesis and Petrochemistry: Intercollegiate Coll. of Scientific Works), Yaroslavl, 1987, issue 23, pp. 28–32.
32. Jorgensen, K.A., *Chem. Rev.*, 1989, vol. 89, no. 3, pp. 431–458.
33. Sapunov, V.N., Sharykin, V.G., Logvinov, A.S., *et al.*, *Kinet. Katal.*, 1983, vol. 24, no. 3, pp. 586–590.
34. *Spravochnik khimika* (Chemist's Handbook), Nikol'skii, B.P., Ed., Leningrad: Goskhimizdat, 1962, vol. 1.

Russian Journal of Applied Chemistry, Vol. 74, No. 5, 2001, pp. 839–844. Translated from Zhurnal Prikladnoi Khimii, Vol. 74, No. 5, 2001, pp. 814–819.

MACROMOLECULAR CHEMISTRY AND POLYMERIC MATERIALS

Thermal Degradation of Polyvinylpyrrolidone on the Surface of Pyrogenic Silica

V. M. Bogatyrev, N. V. Borisenko, and V. A. Pokrovskii

Institute of Surface Chemistry, National Academy of Sciences of Ukraine, Kiev, Ukraine

Received November 20, 2000

Abstract—Thermal degradation of polyvinylpyrrolidone was studied by thermogravimetry, IR spectroscopy, and thermal-desorption mass spectrometry.

Due to high complexing and adhesion properties, nontoxicity, and solubility in water and most organic solvents polyvinylpyrrolidone (PVP) is widely used in various branches of industry [1]. Along with common use of PVP in medicine, pharmacology, and textile industry, studies are actively pursued aimed at preparing new materials on its basis. Among them preparation of new copolymers and polymer blends including organic-inorganic hybrid materials and nanocomposites is the most promising. Such polymer–silica composites based on PVP were prepared by adsorption procedure [2, 3] or by grafting to the surface of solid particles with formation of covalent bonds between the polymer and SiO_2 [4, 5]. Previously, the PVP–silica materials were used to prepare selective membranes [6, 7], optical materials [8, 9], and chromatographic supports [10, 11].

In highly filled polymeric systems the fraction of PVP units directly contacting with the silanol surface groups of silica increases. It is known that the degree of filling and the nature of the surface active groups of dispersed filler significantly affect thermal and thermal oxidative degradation of polymeric materials [12]. Since for PVP such data are lacking, the study of thermal transformations of PVP in the adsorption layers of various thickness on the surface of finely dispersed silica is urgent.

EXPERIMENTAL

In our work we used medical-grade PVP (Sintvita, Russia) with an average molecular weight of 10 700 and A-300 Aerosil pyrogenic silica (Khlorvinil, Ukraine) with a specific surface area of 320 $m^2 g^{-1}$.

The samples were prepared as follows. First, a dispersion of silica and a 10% solution of PVP in distilled water were prepared, and the required amount of the PVP solution was added to the silica dispersion. Then the resulting mixture was thoroughly mixed and after 1-h storage deposited on glass plates as thin layers, which were dried at 80°C for 4–5 h. The product was ground in an agate mortar and additionally dried at 80°C for 1 h.

The silica samples with sorbed PVP were analyzed for the carbon content on an AN-7529 express analyzer by combustion in an oxygen flow. The specific surface area was determined by low-temperature desorption of argon according to the standard procedure. The properties of the resulting PVP–silica samples are listed in Table 1.

Thermal analysis was carried out using a Q-1500 D derivatograph. The measurement parameters were as follows: 500, 500, and 250 μV for TG, DTA, and DTG, respectively; sensitivity 200 mg, and heating rate 10 deg min^{-1}. The samples (300.16 ± 0.24 mg) were heated in a ceramic crucible.

The IR spectra were taken from pressed samples (5–6 mg cm^{-2}). The thermal transformations were studied using a heated quartz cell (CaF_2 optics). The

Table 1. Properties of PVP–silica samples

Sample no.	Carbon content, %	PVP content		S_{sp}, $m^2 g^{-1}$
		%	mmol g^{-1}	
1	3.8	5.8	0.52	258
2	8.2	12.6	1.14	217
3	11.0	16.9	1.52	183
4	15.8	24.3	2.19	128
5	19.0	29.3	2.64	65

1070-4272/01/7405-0839$25.00

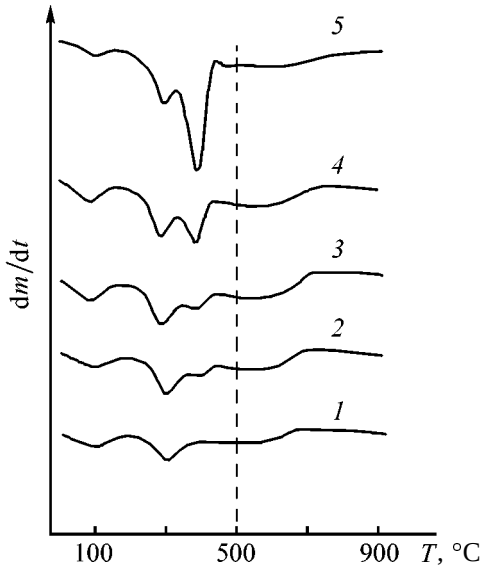

Fig. 1. DTG curves of the samples of pyrogenic silica with sorbed PVP: (d*m*/d*t*) rate of the weight loss and (*T*) temperature. The figures at the curves correspond to sample nos. in Table 1; the same for Fig. 4.

sample was heated in a spectral cell for 15 min in air and then evacuated for 1–1.5 min without cooling. The IR spectra were registered after cooling of the sealed cell to room temperature. Then the temperature of the spectral cell was increased and the measurement cycle was repeated. The IR spectra were registered on a Specord M-80 spectrophotometer.

The mass-spectrometric measurements were carried out on a vacuum thermal-desorption unit with a heated quartz cell. The mass spectra were registered on an MKh 7304 spectrometer equipped with a computer system for registration and treatment of the experimental results. The sample weight was 2.0 ± 0.3 mg.

The average molecular weight of the PVP used indicates that the polymer molecule contains about 96 monomeric units

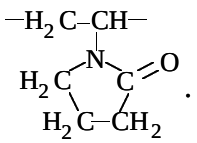

High solubility of PVP in water allowed preparation of silica dispersions in the PVP solution in a wide concentration range of components. The presence of the silanol groups on the silica surface and the tertiary amine and carbonyl groups in the polymer molecule suggests strong adsorption interaction. However, it was found [13] that in the hybrid PVP–silica material the polymer and SiO_2 are bound only through the hydrogen bonds between the carbonyl and silanol groups.

The IR spectra of the PVP–silica samples studied exhibit the bands of stretching vibrations of the SiO–H groups (3748 cm^{-1}) that do not participate in bonding with carbonyl groups. With increasing polymer concentration the intensity of the absorption band of the C=O group (1664 cm^{-1}) increases, whereas the band at 3748 cm^{-1} decreases and finally completely disappears. With decreasing PVP concentration the fraction of the units in the polymer chain interacting with the silanol groups on the silica surface increases. These results agree with the data on the sorption of PVP on silica [3].

With increasing content of the polymer the specific surface area of the samples decreases because of the increase in the layer thickness of sorbed PVP (Table 1).

The DTG curves of the PVP–silica layers are shown in Fig. 1. The first peak with the maximal weight loss for all the samples occurs at 100–115°C and corresponds to the removal of water physically sorbed on the silica surface [14]. The DTG curves for sample nos. 2–5 exhibit three steps of the weight loss, and only in the case of sample no. 1 thermal oxidative degradation proceeds in two steps. The parameters of the weight loss during thermal degradation are given in Table 2. The weight loss in the 200–1000°C range is taken as 100%. In each sample the temperature boundary between the degradation steps was determined as the point of the minimal rate of the weight loss.

As seen from the above data, despite different width of the temperature range of the first step of oxidative degradation, the temperature maxima of all the samples occur in the narrow range: 315–325°C. Similar pattern is observed for the second step of oxidative thermolysis: T_{max} is 420–425°C, except sample no. 1.

The third stage of degradation is characterized by a lower rate of the weight loss. In this case the DTG curves exhibit a broad peak whose T_{max} increases from 570 to 660°C with increasing content of PVP in the sample.

The TG analysis reveals two stages of thermal oxidative degradation with nearly equal weight losses. The first stage proceeds in two steps, and their parameters change depending on the amount of sorbed PVP. With decreasing content of PVP in the sample the relative contribution of the weight loss in the second step decreases. As seen, in sample no. 1 the first stage of thermolysis proceeds in one step. The second stage

Table 2. Weight loss Δm in the steps of thermal oxidative degradation of the PVP–silica samples

Parameter	Sample no.					
	1	2	3	4	5	PVP_{in}
Temperature range, °C	200–415	200–390	200–380	200–370	200–340	200–395
Δm, %	43.6	41.4	38.7	23.6	23.6	13.4
Temperature range, °C	–	390–465	380–470	370–465	360–485	395–495
Δm, %	–	17.1	19.5	20.6	27.1	58.1
Temperature range, °C	415–1000	465–1000	470–1000	465–1000	485–1000	495–1000
Δm, %	56.4	41.5	41.8	55.8	49.3	20.3

of thermal oxidative degradation occurs in one step, with similar weight loss for all the samples.

For comparison, we performed the TG analysis of the initial PVP under the conditions similar to those used for the PVP–silica samples. The weight composition of the sample was comparable with that of sample no. 5: 100 mg of the polymer was mixed with 200 mg of the inert filler. As seen, the parameters of thermal oxidative degradation of this sample are significantly different. The first peak of the weight loss at T_{max} 105°C belongs to the removal of water, whose presence is manifested by a broad band at 3000–3600 cm^{-1} in the IR spectrum. The most intense weight loss is observed in a narrow temperature range (Table 2). Thermal degradation of the initial PVP powder without filler (137 mg) exhibits nearly similar results. The main weight loss (75%) occurs in the 330–430°C temperature range.

As seen from the data on the weight loss (Table 2), adsorption of PVP on the pyrogenic silica surface induces intense oxidative degradation of the polymer at lower temperatures, but hinders oxidation of the carbonized residue.

Adsorption of the PVP molecules on the silica surface decreases the flexibility of the molecular chains, causing the nonequilibrium strained state of the polymer chain [15]. As a result, the strained sections that appeared in macromolecule more readily undergo thermal oxidation, and thus the volatile products can appear under milder conditions. According to [16], the volatile products of PVP oxidation at 300–400°C are carbon dioxide and pyrrolidone. We assume that the TG peak at T_{max} 320°C belongs specifically to the stage of thermal oxidative degradation of the strained sections of the polymer chain. The relative weight loss in this stage decreases with decreasing weight fraction of silica and thus with decreasing surface area of silica in the sample.

The stage of oxidative degradation at T_{max} 420°C was observed for all the samples containing more than 12% PVP. This stage involves thermal degradation of the polymer chains occurring in the adsorption layer at a larger distance from the silica surface. The relative weight loss in this step increases with increasing content of PVP in the sample.

The IR spectroscopic study of thermal oxidative degradation of the PVP–silica samples in air was performed by heating in steps according to the procedure given above. The IR spectra of sample no. 1 registered in the 20–600°C range are shown in Fig. 2a. As seen, a new absorption band appears at 1600–1800 cm^{-1}.

The dependences of the intensity of the selected absorption bands on the temperatures of thermal degradation are shown in Fig. 2b. Above 200°C a new absorption band appears at 1712 cm^{-1} and reaches the highest intensity at 300°C. At this temperature the majority of the C–H groups is broken down (Fig. 2b, curves *1, 4*) and the sample becomes brown. The IR spectrum of sample no. 5 with the highest content of PVP exhibits an absorption band at 1770 cm^{-1} after heating to 300–350°C (Fig. 2c).

Appearance of new absorption bands in the course of thermal degradation is probably due to the change in the environment of the carbonyl groups of the sorbed polymer, with formation of double bonds. The stretching vibration band of the C=O groups conjugated with these double bonds is observed at 1720 cm^{-1} [17]. With increasing layer thickness of the adsorbed polymer more complex cyclic structures involving carbonyl groups and oxygen atoms in the polymer chain can appear. The frequencies of the C=O groups in such structures are 1740–1800 cm^{-1} [17].

The thermal degradation of the adsorbed polymer in vacuum was monitored by the composition of the

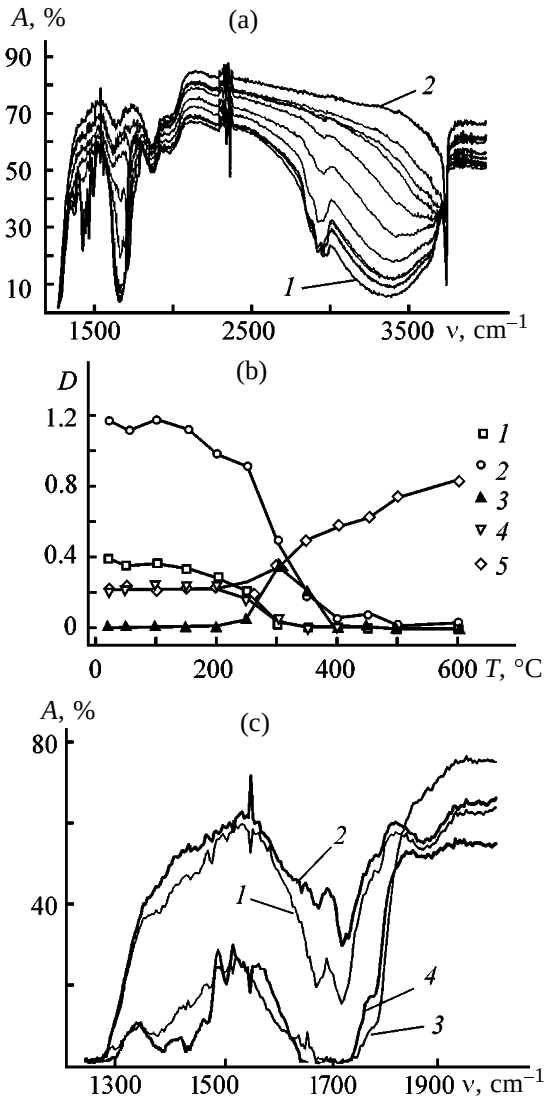

Fig. 2. (a) IR spectra of sample no. 1 (*1*) at room temperature and (*2*) after heating for 15 min to 600°C in air and evacuation for 1 min (intermediate spectra correspond to intermediate heating temperatures); (b) optical density $D = \log I_0/I$ at (*1*) 1428, (*2*) 1660, (*3*) 1712, (*4*) 2924, and (*5*) 3748 cm^{-1} as influenced by the temperature of thermal treatment *T*, and (c) IR spectra of sample nos. (*1*, *2*) 1 and (*3*, *4*) 5 after heating for 15 min in air at 300 and 350°C and evacuation for 1 min. (*A*) Transmission and (ν) wave number.

volatile degradation products using mass spectrometry. It was found that the degradation of PVP with liberation of pyrrolidone begins at approximately 100°C in all the samples studied. This low-temperature step in the PVP degradation suggests that similar process occurs in air simultaneously with removal of water from the samples. We failed to separate the contributions of these processes to the weight loss using IR and DTG data.

The degradation of the PVP–silica and initial PVP samples involves different number of stages (Fig. 3). The low- and high-temperature stages proceed at T_{max} 90–105 and 350–390°C, respectively. Additional step is observed for the initial PVP at 280–300°C. To confirm that this intermediate step involves thermal degradation of the initial polymer, we studied the PVP samples with an average molecular weight of 10000. For this purposed we used another PVP sample from Sintvita (Russia), K-15 PVP (Fluka), and PVP after dissolution in water and drying in air at 75°C. In all the cases the intermediate stage of thermal degradation was observed. Simultaneous appearance of various ions in the mass spectra (Fig. 3) indicates degradation of the polymer with formation of volatile products and their further fragmentation in the ionization source of a mass spectrometer.

As seen from the mass spectra registered at T_{max} for low- and high-temperature degradation stages, the difference in the yields of the molecular ions of pyrrolidone (85^+) and vinylpyrrolidone (111^+) is the most significant. These two ions can be used to analyze thermal degradation of PVP, because the relative intensity of the ion 85^+ in the mass spectra of vilylpyrrolidone is lower than 8.1% [18], whereas in the spectrum of pyrrolidone the vinypyrrolidone molecular ion (111^+) is absent.

The mass thermograms for the ions 85^+ and 111^+, taken in the course of degradation of the samples with adsorbed polymer, are shown in Fig. 4. As seen, pyrrolidone is released in two stages, whereas vinylpyrrolidone appears only in one stage; the ratio of the release of pyrrolidone in both stages was determined. For sample nos. 1, 3, 5 the ratio I_{85^+}(2nd stage)/I_{85^+}(1st stage) is 6.56, 2.75, and 1.66, respectively; in the case of the initial PVP it is 1.04.

The degradation of vinyl polymers (polyvinyl alcohol, polyvinyl acetate, polyvinyl chloride) starts with breakdown of the side groups [19] with formation of the corresponding double bonds. Similar scheme of breakdown of the pyrrolidone ring with formation of the intermediate cyclic complex was suggested for PVP in [16].

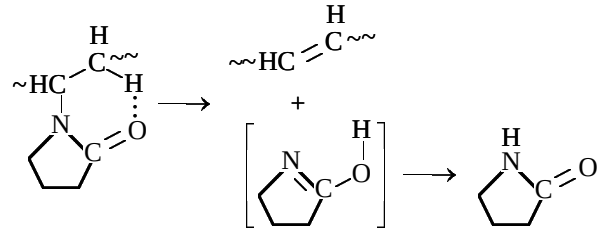

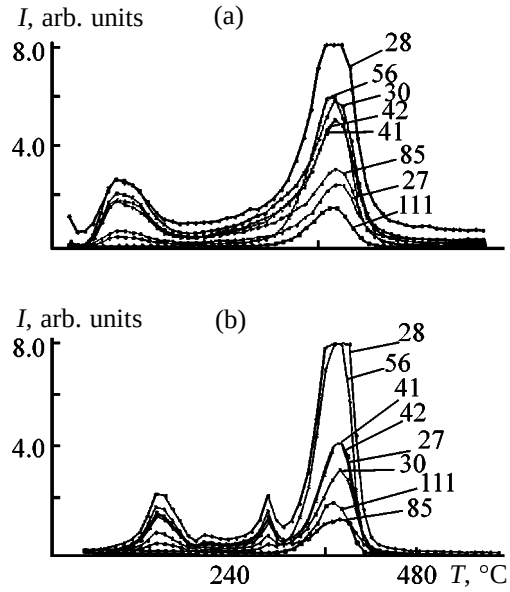

Fig. 3. Mass thermograms of (a) sample no. 5 and (b) initial PVP. (*I*) Relative intensity and (*T*) temperature; the same for Fig. 4. The numbers at the curves are the weights of the positive ions.

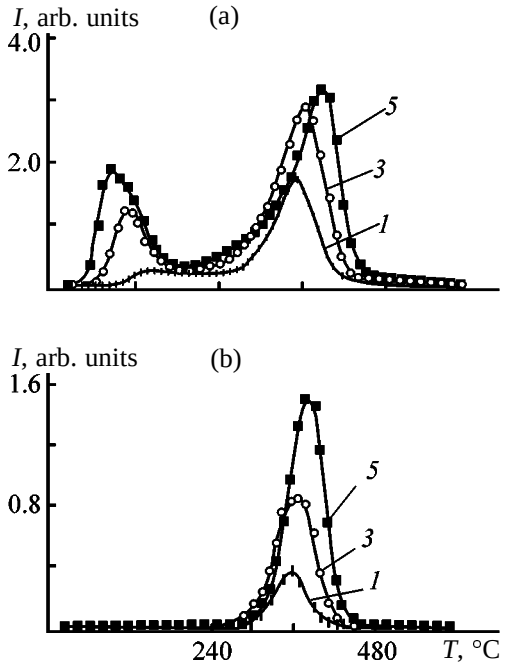

Fig. 4. Mass thermograms for the ions (a) 85^+ (pyrrolidone) and (b) 111^+ (vinylpyrrolidone).

The hydrogen bond between the C=O group in PVP and the silanol group of the SiO_2 surface can block formation of such cyclic complex and thus hinder elimination of pyrrolidone from the polymer chain. This phenomenon is observed in the low-temperature stage of thermolysis. With decreasing amount of adsorbed polymer the fraction of the carbonyl groups bound by hydrogen bonds decreases, which, in turn, decreases pyrrolidone release. Restricted flexibility of the polymer molecules sorbed on the support can also decrease the yield of the intermediate complexes.

Vinylpyrrolidone is released only in the high-temperature stage of PVP degradation. We found certain correlation between the ratio I_{85^+}/I_{111^+} and the content of PVP in the sample. This ratio changes from 4.35 to 2.03 for sample nos. 2 and 5, respectively. In the case of various initial PVP samples I_{85+}/I_{111+} varies within the range 0.53–0.68.

Thermal degradation of the polymer macromolecule is accompanied by breakdown of both side and main chains. This process involves elimination of the monomer units from the ends of the main chain and with increasing number of the breaks in the main chain the polymerization rate increases. Variation of the ratio of the degradation products (ions 85^+ and 111^+) suggests changes in the thermal degradation mechanism.

In all the PVP–silica samples a pronounced dependence is observed between the amount of the adsorbed polymer and degradation with release of pyrrolidone and depolymerization with formation of vinylpyrrolidone. In the samples with a lower content of PVP, i.e., with a higher content of the units of adsorbed macromolecule directly bound to the silica surface, thermal degradation in the high-temperature stage is characterized by a greater contribution of elimination of the pendant rings and smaller contribution of depolymerization. Thermal treatment in a vacuum at 700°C gives a carbonized residue on the silica surface. After vacuum thermolysis in the course of mass spectrometric studies the samples studied became black.

Our experimental results give the following qualitative pattern of PVP degradation. At temperatures of up to 200°C certain fraction of pyrrolidone rings is removed and double bonds in the chains appear. As a result, cross-links in the polymer are formed, which hinder the flexibility of macromolecule. With increasing temperature, separate units of the initial PVP molecules acquire the mobility required to form intramolecular complexes promoting elimination of the pyrrolidone rings (T_{max} 280–300°C). In contrast, in the case of PVP–silica samples the solid matrix significantly affects macromolecules occurring in the adsorption layer, which additionally hinders flexibility of macromolecules and thus elimination of the pen-

dant groups. As a result, the stage with T_{max} 280–300°C in the PVP–silica samples is absent.

Further heating causes the homolytic cleavage of the polymer chains in both initial and adsorbed polymer (T_{max} 360–400°C). In this degradation stage sorbed polymer hinders cleavage of the main chain and thus promotes carbonization of the silica surface.

CONCLUSIONS

Thermal and thermal oxidative degradation of polyvinylpyrrolidone sorbed on the pyrogenic silica surface and of that occurring in the initial state differs in the number of degradation stages and amount of the volatile products appearing in these stages. In both cases adsorption of polyvinylpyrrolidone shifts the processes completing the polymer degradation toward higher temperatures. The increased fraction of the polymer units directly bound with the silanol groups on the silica surface hinders release of pyrrolidone in the low-temperature degradation stage and depolymerization of polyvinylpyrrolidone at high temperatures.

ACKNOWLEDGMENTS

This work was financially supported by the Ukrainian Science and Technology Center (project no. 1068).

REFERENCES

1. Sidel'kovskaya, F.P., *Khimiya N-vinilpirrolidona i ego polimerov* (Chemistry of *N*-Vinylpyrrolidone and Its Polymers), Moscow: Nauka, 1970.
2. Carrado, K.A. and Xu, L.Q., *Chem. Mater.*, 1998, vol. 10, no. 5, pp. 1440–1445.
3. Guzenko, N.V., Pakhlov, E.M., Lipkovskaya, N.A., and Voronin, E.F., Abstracts of Papers, *1-ya Vserossiiskaya konferentsiya po khimii poverkhnosti i nanotekhnologiyam* (1st Russian Conf. on Surface Chemistry and Nanoprocesses), St. Petersburg–Khilovo, Sept. 27–Oct. 1, 1999, p. 24.
4. Chaimberg, M. and Cohen, Y., *Ind. Eng. Chem. Res.*, 1991, vol. 30, no. 12, pp. 2534–2542.
5. Yoshinaga, K., Yokoyama, T., and Kito, T., *Polym. Adv. Technol.*, 1993, vol. 4, no. 1, pp. 38–42.
6. Tamaki, R., Chujo, Y., Kuraoka, K., and Yazawa, T., *J. Mater. Chem.*, 1999, vol. 9, no. 8, pp. 1741–1746.
7. Castro, R.P. and Cohen, Y., *J. Membrane Sci.*, 1996, vol. 115, no. 2, pp. 179–190.
8. Yoshida, M. and Prasad, P.N., *Appl. Opt.*, 1996, vol. 35, no. 9, pp. 1500–1506.
9. Yoshida, M. and Prasad, P.N., *Chem. Mater.*, 1996, vol. 8, no. 1, pp. 235–241.
10. Litvinova, L.S. and Zgonnik, V.N., *J. AOAC Int.*, 1999, vol. 82, no. 2, pp. 227–230.
11. Kurganov, A., Puchkova, Y., Davankov, V., and Eisenbeiss, F., *J. Chromatogr., Ser. A.*, 1994, vol. 663, no. 2, pp. 163–174.
12. Bryk, M.T., *Destruktsiya napolnennykh polimerov* (Degradation of Filled Polymers), Moscow: Khimiya, 1989.
13. Toki, M., Chow, T.Y., Ohnaka, T., *et al.*, *Polym. Bull.*, 1992, vol. 29, no. 6, pp. 653–660.
14. Belyakova, L.A., Tertykh, V.A., and Bortun, A.I., *Khim. Tekhnol.*, 1987, no. 2, pp. 3–10.
15. Lipatov, Yu.S. and Sergeeva, L.M., *Adsorbtsiya polimerov* (Adsorption of Polymers), Kiev: Naukova Dumka, 1972.
16. Peniche, Z., Zaldivar, D., Paros, M., *et al.*, *J. Appl. Polym. Sci.*, 1993, vol. 50, no. 3, pp. 458–493.
17. Nakanishi, K., *Infrared Absorption Spectroscopy*, Tokyo: Nankido, 1962.
18. Cornu, A. and Massot, R., *Compilation of Mass Spectral Data*, London: Heyden, 1966.
19. Madorsky, S.L., *Thermal Degradation of Organic Polymers*, New York: Interscience, 1964.

Russian Journal of Applied Chemistry, Vol. 74, No. 5, 2001, pp. 845–850. Translated from Zhurnal Prikladnoi Khimii, Vol. 74, No. 5, 2001, pp. 820–825.

MACROMOLECULAR CHEMISTRY AND POLYMERIC MATERIALS

Grafting of Methylenebutanedioic Acid to Low-Density Polyethylene in the Course of Reactive Extrusion, Initiated with Carborane-Containing Peroxides

Yu. M. Krivoguz, A. P. Yuvchenko, T. D. Zvereva, and S. S. Pesetskii

Belyi Institute of Mechanics of Metal–Polymer Systems, Belarussian National Academy of Sciences, Gomel, Belarus
Institute of Chemistry of New Materials, Belarussian National Academy of Sciences, Minsk, Belarus
Institute of Physical Organic Chemistry, Belarussian National Academy of Sciences, Minsk, Belarus

Received November 23, 2000

Abstract—The influence of carborane-containing peroxides on the efficiency of grafting of methylenebutanedioic acid to low-density polyethylene in a single-screw extrusion reactor equipped with a static mixer was studied.

Grafting of monomers containing chemically active functional groups to polyolefin macromolecules is a subject of active study in many research centers [1–6], which is due to growing use of grafted products in preparation of polymeric composites, mostly of polymer blends and alloys. As a rule, grafting is performed in a polyolefin melt; as continuous reactors are used special extruders acting simultaneously as high-performance mixers of the components and providing controllable feeding of the components, removal of by-products, accurate temperature control, control of the velocity of the reaction mixture transport, etc. [1, 6]. The yield of the grafted product and the course of side processes are determined both by the extruder design features and by the reaction mixture composition [1, 5, 6]. In particular, we showed in [5, 6] that the course of grafting of methylenebutanedioic acid (MA) to low-density polyethylene (LDPE), at identical apparatus design and process (thermal) parameters, is largely influenced by the nature and concentration of the peroxide initiator. Use for these purposes of commercial peroxides [dicumyl peroxide (DCP), 2,5-dimethyl-2,5-di-*tert*-butylperoxyhexane, etc.] results in active chemical cross-linking of the macromolecules, occurring simultaneously with grafting of MA. As a result, strongly cross-linked products are formed, which limits their use for fabrication of composites. Furthermore, the product obtained by grafting of MA to LDPE (LDPE-*graft*-MA) with traditional peroxides exhibits a poor resistance to thermal oxidative degradation in air and in aqueous solution [7].

In [8–10] we described the synthesis of unsaturated carborane-containing peroxides. These peroxides can be used for cross-linking of polyethylene [11], initiating high-temperature radical cross-linking reactions. In contrast to cross-linked polyethylene prepared with traditional peroxides, the product obtained with carborane peroxides exhibits enhanced resistance to thermal oxidative degradation [11]. Presumably, the thermostabilizing effect of carborane peroxides is due to grafting of carborane-containing fragments formed by thermolysis of the peroxide to macromolecules and intermolecular cross-linking through boron atoms. The possibility of grafting to polyolefin molecules of functional groups of unsaturated peroxides is indicated, e.g., by Assoun *et al.* [12] who studied grafting of carboxy groups to polypropylene macromolecules in the melt under the action of peroxy acids.

It is interesting to evaluate the effect of carborane-containing peroxides as initiators of grafting of functional monomers to polyethylene macromolecules. Here this problem is studied with grafting of MA to LDPE as example.

EXPERIMENTAL

We used LDPE of 15803–020 brand [GOST (State Standard) 16337–77, Polimir Production Association, Novopolotsk; density 0.92 g cm^{-3}, mp 105°C] and MA purchased from Chemical Division Pfizer, the United States. The following carborane-containing peroxides were chosen (Table 1): peroxy esters **I** and

1070-4272/01/7405-0845$25.00

Table 1. Characteristics of peroxide initiators*

Peroxide	Name	Available oxygen content, %	
		found	calculated
DCP	Dicumyl peroxide	–	5.92
I	3-Methyl-3-(*o*-carboranoylperoxy)-1-butyne	5.66	5.92
II	3-Methyl-3-(*m*-carboranoylperoxy)-1-butyne	5.62	5.92
III	1,7-Bis(*tert*-butylperoxymethylvinylsilyl)-*m*-carborane	6.32	6.95
IV	Bis(3-methyl-3-*tert*-butylperoxy-1-butynyl)-1-*m*-carboranylmethanol	–	6.63
V	Bis(3-methyl-3-*tert*-butylperoxy-1-butynyl)-1-(7-isopropyl)-*m*-carboranylmethanol	–	6.1
VI	Bis(3-methyl-3-*tert*-pentylperoxy-1-butynyl)-1-*o*-carboranylmethanol	–	6.44
VII	Bis(3-methyl-3-*tert*-pentylperoxy-1-butynyl)-1-(2-isopropyl)-*o*-carboranylmethanol	–	5.94

*Structural formulas of peroxides:

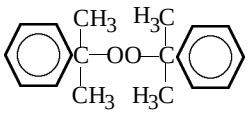

DCP

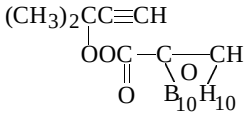

I

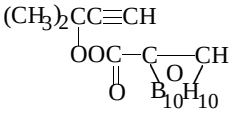

II

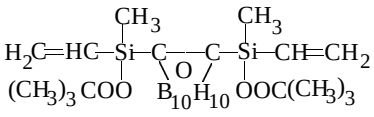

III

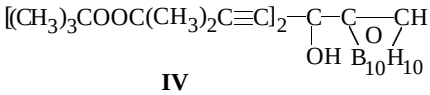

IV

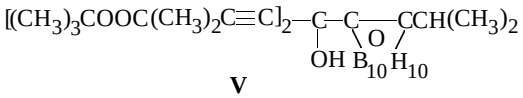

V

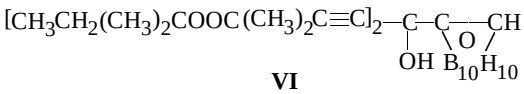

VI

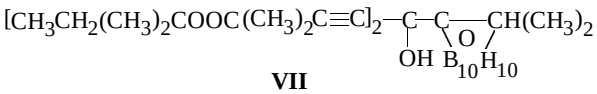

VII

II [8], silylcarborane **III** [9], and mixtures of peroxy alcohols with alkylperoxy groups **IV**–**VII** [10]. For comparison, we also used DCP whose effect on grafting of MA to LDPE, as well as the properties of the resulting products, are relatively well studied [5, 6, 13]. Also we tested mixtures of carborane-containing peroxides with DCP.

Grafting was performed in a single-screw extruder additionally equipped with a static mixing head, under the following conditions: nitrogen atmosphere; screw rotation rate 35 rpm; temperatures, °C: zone I 160 and zones II–IV and mixing head 185. The scheme of the extrusion reactor is similar to that shown in [6] for the Brabender plastograph equipped with a static mixer. The process for preparing the reaction mixture is also described in [6].

As parameter characterizing the progress of grafting, we used the grafting efficiency α: the weight ratio of the grafted acid to its total amount introduced into the polymer [6]. The quantity α was calculated from the content of MA in LDPE before and after extraction with ethanol at 70°C, determined by IR absorption spectroscopy [6, 14].

The viscosity of the polymer melt was evaluated by the melt flow index (MFI), which was determined at 190°C and a load of 10 kg with an IIRT-AM device (Ekodatchik Private Company, Tula, Russia).

The thermal stability of peroxides was evaluated with an MOM derivatograph (Hungary) under argon; the sample weight was 100 mg, and the linear heating rate, 7 deg min^{-1}. The reaction order n of thermal decomposition of peroxides was calculated by the Kissinger method [15]. The apparent activation energy E_a was determined from the exothermic peak in the DTA curve in the temperature range where the linear dependence was preserved (up to 130°C for **I** and **II**, 160°C for **III**, and 155–160°C for **IV**–**VII**) [15]. The thermal analysis of the polymeric samples was performed with a derivatograph in air; the sample weight was 500 mg, and the heating rate, 2.5 deg min^{-1}.

Tables 1 and 2 show that in peroxy esters **I** and **II** the available oxygen content is similar to that in DCP, but the thermal stability of **I** and **II** (T_{od} denotes the temperature of the onset of degradation) is lower: T_{od} = 116–118°C; for *ortho* isomer **I** n = 1.89 and E_a = 153 kJ mol^{-1}; for *meta* isomer **II** n = 1.63 and

Table 2. Characteristics of thermal stability of carborane-containing peroxides

Peroxide	Process stages	DTG, °C			TG, Δm, %	DTA				
		T_{onset}	T_{end}	$T_{maximum}$		mp, °C	exothermic peak, °C		n	E_a, kJ mol^{-1}
							T_{onset}	$T_{maximum}$		
DCP	1	127	177	162	43.0	43	127	163	1.16	154
	2	177	202	–	32.0					
I	1	118	150	134	55.0	95	118	136	1.89	153
	2	179	230	192	13.0					
II	1	116	158	140	20.0	85	115	142	1.63	112
	2	180	287	248	40.0					
	3	342	470	–	4.0					
III	1	135	192	164	25.0	–	136	167	1.68	179
IV	1	125	186	171	47.0	80	123	173	1.45	132
	2	186	485	–	7.0					
V	1	127	192	166	30.5	99	126	168	1.60	153
	2	192	257	–	5.0					
	3	257	463	–	32.0					
VI	1	125	185	170	50.0	–	124	172	1.43	130
	2	185	480	–	14.0					
VII	1	123	194	157	31.0	51	122	163	1.61	153
	2	194	272	–	8.0					
	3	272	470	–	41.0					

E_a = 112 kJ mol^{-1}; at the same time, for DCP T_{od} = 127°C, n = 1.16, and E_a = 154 kJ mol^{-1}. Peroxides **I** and **II** initiate grafting of MA to LDPE under experimental conditions (concentration 0.15 wt %) with an efficiency of 23–25% (with DCP α = 66.7%, Table 3). In diperoxy alcohols **IV**–**VII**, the available oxygen content is somewhat higher than in DCP (Table 1), and their thermal stability is similar to that of DCP (T_{od} = 123–127°C); however, the character of decomposition of **IV**–**VII** is different (n = 1.43–1.61, E_a = 130–153 kJ mol^{-1}). The performance of diperoxy alcohols in grafting MA to LDPE approaches that of DCP. At concentrations of the mixtures **IV** + **V** and **VI** + **VII** of 0.15 wt %, α = 37.5–40.9% (Table 3, entries 6 and 7). At a concentration of the mixture **VI** + **VII** of 0.3 wt %, the grafting efficiency is 83.1%, being similar to the grafting efficiency attained with DCP (84.4%) (Table 3, entries 6 and 7).

An important advantage of carborane-containing peroxides **I**, **II**, and **IV**–**VII** over DCP is suppression, to a large extent, of the concurrent cross-linking of polyethylene macromolecules. The parameter sensitive to cross-linking accompanying MA grafting is MFI

Table 3. Influence of peroxides on the MA grafting efficiency and MFI of the polymer

Entry	Initial composition	MFI, g/10 min	α, %
1	LDPE	16.9	–
2	LDPE/MA + 0.15DCP	10.2	66.7
3	LDPE/MA + 0.3DCP	2.8	84.4
4	LDPE/MA + 0.15(**I**)	16.5	23.1
5	LDPE/MA + 0.15(**II**)	16.9	24.9
6	LDPE/MA + 0.15(**IV** + **V**)	12.0	37.5
7	LDPE/MA + 0.15(**VI** + **VII**)	15.9	40.9
8	LDPE/MA + 0.15(**III**)	18.5	18.4
9	LDPE/MA + 0.3(**VI** + **VII**)	6.5	83.1
10	LDPE/MA + 0.3(**III**)	20.3	29.1
11	LDPE/MA + 0.15(DCP + **I**)	15.1	44.5
12	LDPE/MA + 0.3(DCP + **I**)	5.5	64.3
13	LDPE/MA + 0.15(DCP + **II**)	13.4	46.5
14	LDPE/MA + 0.3(DCP + **II**)	6.0	56.0
15	LDPE/MA + 0.15(DCP + **IV** + **V**)	14.2	46.7
16	LDPE/MA + 0.3(DCP + **IV** + **V**)	3.7	74.2

Note: Weight ratio of components in peroxide mixtures 1 : 1.

[6]. A significant decrease in MFI on grafting of MA to LDPE is one of the main drawbacks of the process based on using DCP. For example, Table 3 shows that MFI of the initial LDPE is 16.9 g/10 min. Grafting of MA in the presence of 0.15 and 0.3 wt % DCP yields a functionalized product with MFI of 10.2 and 2.8 g/10 min, respectively. Thus, with DCP it is impossible to graft MA to LDPE with a high (>80%) yield and therewith avoid strong cross-linking.

In contrast to the product obtained with DCP, MFI of polyethylene grafted with MA in the presence of peroxy esters **I** and **II** (0.15 wt %) is similar to that of the initial LDPE, which suggests practically no cross-linking. The occurrence of concurrent cross-linking of LDPE macromolecules with diperoxy alcohols **IV** + **V** and **VI** + **VII** depends on the structure of the *tert*-alkyl group at the O–O bond. For example, in the case of diperoxy alcohols **VI** + **VII** with *tert*-pentylperoxy groups (0.15 wt %) the cross-linking of macromolecules is insignificant (MFI 15.9 g/10 min), and with compounds **IV** + **V** containing *tert*-butylperoxy groups MFI of LDPE-*graft*-MA is 12.0 g/10 min (Table 3). It should be noted also that in the case of grafting initiation with peroxides containing *tert*-pentylperoxy groups grafting of MA to LDPE is more efficient (α = 40.9%) as compared to peroxy alcohols with *tert*-butylperoxy groups (α = 37.5%).

As seen from Table 3, addition of carborane-containing peroxide **I** or **II** or of a mixture of diperoxides **IV** + **V** to DCP allows significant reduction of the yield of the cross-linked product with a sufficiently high grafting efficiency. For example, the materials obtained with a mixture of DCP with **I**, **II**, or **IV** + **V** are characterized by MFI = 13.4–15.1 g/10 min and α = 44.5–46.7% (Table 3, entries 11, 13, 15).

With a concentration of the peroxide mixtures of 0.3 wt %, MFI is lower, 3.7–5.5 g/10 min, at α = 56–74.2%; with straight DCP MFI = 2.8 g/10 min and α = 84.4% (Table 3, entries 3, 12, 14, 16).

Among the tested carborane-containing peroxides, the most thermostable is silylcarborane **III** (T_{od} = 135°C), which can be simultaneously considered as a peroxide monomer owing to the presence of two vinyl groups; however, under the experimental conditions (0.15 and 0.3 wt %) it is the least efficient initiator of MA grafting to LDPE (Table 3, entries 8, 10; α = 18.4 and 29.1%, respectively). This is probably due to partial consumption of radicals generated by decomposition of **III** for initiation of oligomerization of the carborane-containing fragment via double bonds and its grafting to polyethylene macromolecules. This processes can be represented as follows [12, 13].

Thermal decomposition of peroxide:

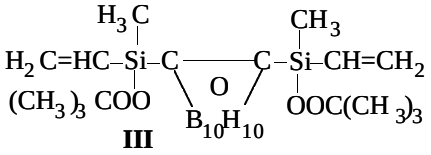

III

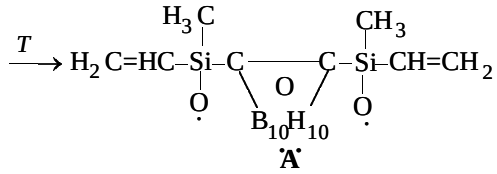

A

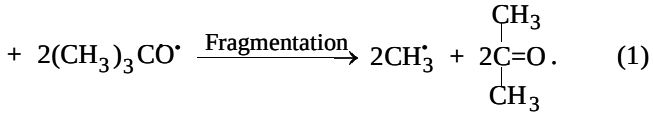

(1)

Oligomerization of peroxide:

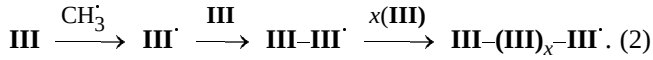

(2)

Grafting of peroxide to LDPE macromolecules:

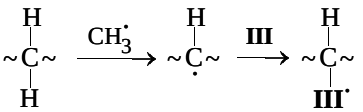

or

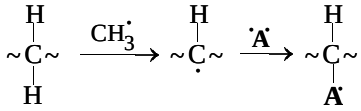

(3)

Grafting of oligoperoxide:

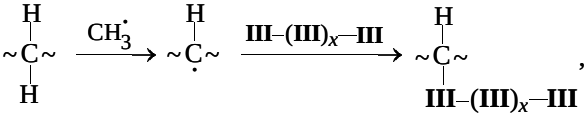

(4)

It should be noted that biradical **·A·** owing to steric hindrance is low-mobile and should not exhibit appreciable initiating power as compared to $^{\cdot}OC(CH_3)_3$ and $^{\cdot}CH_3$. Therefore, oligomerization of peroxide **III** by scheme (2) is improbable. Hence, grafting to LDPE of oligomeric fragments of **III** [scheme (4)] is also improbable. The most probable pathway is formation of products with monomolecular grafted fragments of peroxide **III** [scheme (3)].

The noticeably higher MFI (18.5 and 20.3 g/10 min) of the sample obtained with silylcarborane **III**, as compared to the initial LDPE (MFI 16.9 g/10 min) (Table 3, entries 1, 8, 10) indicates that a material with new physical (rheological) characteristics is formed. The higher MFI of LDPE-*graft*-MA obtained in the presence of silylcarborane **III** may be due to

Table 4. DTA data for the polymeric materials prepared

Entry	Initial composition, wt %	T_{od}	T_{10}	T_{50}	T_{ox}
		°C			
1	LDPE	360	390	445	170
2	LDPE/MA + 0.3DCP	360	385	440	160
3	LDPE/MA + 0.3(DCP + **I**)	358	380	445	162
4	LDPE/MA + 0.3(DCP + **II**)	351	380	455	162
5	LDPE/MA + 0.3(DCP + **IV** + **V**)	360	375	450	175
6	LDPE/MA + 0.3(**VI** + **VII**)	362	397	442	180
7	LDPE/MA + 0.3(**III**)	360	388	450	190

Note: (T_{od}, T_{10}, T_{50}, T_{ox}) temperatures of the onset of degradation, 10 and 50% weight loss, and onset of oxidation, respectively.

degradation of the macromolecules, which is hardly probable [9], or to the lubricating effect of grafted (and nongrafted) organosilicon fragments in the polymer melt. It is known [16] that organosilicon compounds are good lubricants. Therefore, the increase in MFI on grafting in the presence of **III** should be mainly due to the lubricating effect of the thermolysis products of **III**.

The use of carborane-containing peroxides (straight or mixed with dicumyl peroxide) noticeably enhances the resistance of LDPE-*graft*-MA to thermal oxidative degradation as compared to the material prepared in the presence of DCP (Table 4). Thermal oxidation of functionalized polyethylene prepared using a mixture of diperoxy alcohols **VI** + **VII** (0.3 wt %, Table 4, entry 6) and a mixture of **IV** + **V** with DCP (0.3 wt %, entry 5) is accompanied by the weight gain in the TG curve, with the onset at 180 and 175°C, which is 15–20°C higher compared to the material prepared with DCP (Table 4, entry 2). The material prepared with peroxide monomer **III** exhibits the highest resistance to thermal oxidative degradation: Its thermal oxidation starts only at 190°C, which is 30°C higher than the onset temperature of oxidation of the functionalized polyethylene formed in the presence of DCP. Presumably, the thermostabilizing effect of carborane-containing peroxides is due to grafting of carborane-containing fragments to polyethylene macromolecules. This effect is especially characteristic of **III**.

CONCLUSIONS

(1) The performance of peroxides containing carborane fragments in initiation of grafting of methylenebutanedioic acid to low-density polyethylene macromolecules depends on the chemical structure of the peroxides.

(2) Initiation of grafting with a mixture of diperoxy alcohols **VI** + **VII** containing alkylperoxy groups ensures formation of the functionalized polymer with the grafting efficiency comparable to that attained with dicumyl peroxide initiator, with the appreciably reduced degree of cross-linking of the macromolecules.

(3) Peroxide silylcarborane monomer **III** used as initiator allows preparation of the material with the melt flow index 10–20% higher than that of the initial LDPE.

(4) Functionalized low-density polyethylene prepared in the presence of carborane-containing peroxides exhibits enhanced resistance to thermal oxidative degradation as compared to the product obtained in the presence of dicumyl peroxide.

REFERENCES

1. *Reactive Extrusion: Principles and Practice*, Xanthos, M., Ed., Munich: Hanser, 1992.
2. De Roover, B., Devanx, J., and Zegras, R., *J. Polym. Sci., Part A: Polym. Chem.*, 1998, vol. 34, pp. 1195–1202.
3. Vainio, T., Hu, G.-H., Lambla, M., and Seppala, J.V., *J. Appl. Polym. Sci.*, 1996, vol. 61, pp. 843–852.
4. Vainio, T., Hu, G.-H., Lambla, M., and Seppala, J.V., *J. Appl. Polym. Sci.*, 1997, vol. 63, pp. 883–894.
5. Pesetskii, S.S., Krivoguz, Yu.M., Jurkowski, B., and Urbanowicz, R., *Zh. Prikl. Khim.*, 1998, vol. 71, no. 1, pp. 122–127.
6. Pesetskii, S.S., Jurkowski, B., Krivoguz, Yu.M., and Urbanowicz, R., *J. Appl. Polym. Sci.*, 1997, vol. 65, pp. 1493–1501.
7. Pesetskii, S.S., Jurkowski, B., Krivoguz, Yu.M., and Kuzavkov, A.I., *Polymer*, 2000, vol. 41, pp. 1037–1043.

8. Yuvchenko, A.P., Zvereva, T.D., and Zhukovskaya, I.A., *Zh. Obshch. Khim.*, 1992, vol. 62, no. 4, pp. 855–860.
9. Yuvchenko, A.P. and Zvereva, T.D., *Vestsi Akad. Navuk Bel., Ser. Khim. Navuk*, 1994, no. 1, pp. 55–60.
10. Yuvchenko, A.P. and Zvereva, T.D., *Zh. Obshch. Khim.*, 1994, vol. 64, no. 3, pp. 447–449.
11. Yuvchenko, A.P., Markina, A.Ya., Prokopchuk, N.R., *et al.*, *Zh. Prikl. Khim.*, 1998, vol. 71, no. 3, pp. 472–475.
12. Assoun, L., Manning, S.C., and Moore, R.B., *Polymer*, 1998, vol. 39, pp. 2571–2577.
13. Pesetskii, S.S., Krivoguz, Yu.M., and Yuvchenko, A.P., *Zh. Prikl. Khim.*, 1998, vol. 71, no. 8, pp. 1364–1370.
14. Pesetskii, S.S., Kuzavkov, A.I., Kasperovich, O.M., and Krivoguz, Yu.M., *Vestsi Akad. Navuk Bel., Ser. Khim. Navuk*, 1997, no. 3, pp. 15–19.
15. Gorshkov, V.S., Timashev, V.V., and Savel'ev, V.G., *Metody fiziko-khimicheskogo analiza vyazhushchikh veshchestv*, Moscow: Vysshaya Shkola, 1981, pp. 37–40.
16. Sobolevskii, V.M., Organosilicon Liquids, *Khimicheskaya entsiklopediya* (Chemical Encyclopedia), Moscow: Sovetskaya Entsiklopediya, 1990, vol. 2, pp. 509–510.

Russian Journal of Applied Chemistry, Vol. 74, No. 5, 2001, pp. 851–854. Translated from Zhurnal Prikladnoi Khimii, Vol. 74, No. 5, 2001, pp. 825–828.

MACROMOLECULAR CHEMISTRY AND POLYMERIC MATERIALS

Chromatographic Retention Parameters of Certain Benzimidazole Derivatives on Octadecyl Silica Gel

A. I. Zhebentyaev, N. A. Alekseev, and D. A. Rozhdestvenskii

Vitebsk State Medical University, Vitebsk, Belarus

Received October 19, 2000; in final form, February 2001

Abstract—Certain trends in chromatographic retention of benzimidazole derivatives on octadecyl silica gel (mobile phase phosphate buffer–acetonitrile) are considered. Retention parameters of compounds being separated are estimated and interpreted in terms of the reversed-phase HPLC theory.

Benzimidazole (BI) derivatives are widely used in medical practice as spasmolytic (Dibasol), antihypoxanthic (Bemityl) [1], and antisecretory (Omeprazole) drugs. Some of BI derivatives are now studied as potential drugs (Tomerzole, etc.). Therefore, development of universal methods for detection of compounds of this group in medical products and also in biological fluids in studying pharmacokinetics of these drug preparations is an urgent problem. Furthermore, it was demonstrated in [2, 3] that knowledge of the retention parameters in reversed-phase chromatography allows prediction of the lipophilicity of biologically active compounds and, therefore, their behavior in the body, which is particularly important in developing novel drugs by structural modification of known compounds.

In this work we studied the chromatographic characteristics of BI derivatives under conditions of reversed-phase HPLC.

EXPERIMENTAL

In the work we used the following BI derivatives: Bemityl (2-ethylthiobenzimidazole hydrobromide), Dibasol (2-benzylbenzimidazole hydrochloride), Omeprazole (5-methoxy-2-{[(4-methoxy-3,5-dimethyl-2-pyridyl)methyl]sulfonyl}benzimidazole), and Tomerzole (2-ethylthio-5-ethoxybenzimidazole hydrochloride) with 99% content of the main component. As a model compound we used 2-benzyl-5,6-dimethylbenzimidazole hydrochloride (BDB). The samples were 10^{-4} M aqueous solutions of the indicated compounds.

Chromatographic study was carried out with a Milikhrom-4 liquid chromatograph (Nauchpribor Research and Production Association, Russia) (spectrophotometric detector; 64×2 mm steel column packed with Separon-C_{18} sorbent, grain size 5 μm). Mobile phases were prepared by mixing acetonitrile with aqueous KH_2PO_4 of a fixed concentration; pH of the eluent was adjusted with KH_2PO_4, orthophosphoric acid, and KOH. The sample volume was 5 μl. Acetonitrile (Kriokhrom, Russia) of ultrapure grade was distilled with a dephlegmator prior to use. Also double-distilled water and potassium dihydrogen phosphate of chemically pure grade were used. The retention volume of an unsorbable component (sodium nitrite) was 110 μl. The analytical wavelengths were 300 nm for Tomerzole and Bemityl, 274 nm for Dibasol and BDB, and 214 nm for Omeprazole.

For separation of the BI derivatives we used reversed-phase HPLC, since these compounds differ from each other by the structure of alkyl, alkoxy, and other substituents in the BI system. When studying sorption of the tested compounds on a nonpolar sorbent, their tendency to ionization with decreasing pH should be taken into account as well as the contribution of various substituents to the sorption equilibrium constant.

The dependence of the chromatographic retention on the eluent pH is given in Fig. 1. The observed dependence is typical of weak organic bases. The decrease in the retention of the compounds in an acidic medium is primarily due to protonation of the nitrogen atom of the benzimidazole ring and the decrease in the lipophilicity of the molecule. The selectivity coefficient α for the pair Tomerzole/Bemityl is independent of pH of the mobile phase, since these compounds have, evidently, the same pK_{BH^+}. For the pair Tomerzole/Dibasol, on the contrary, the selectivity coefficient depends on the eluent pH (pH_{opt} 4–5),

1070-4272/01/7405-0851$25.00

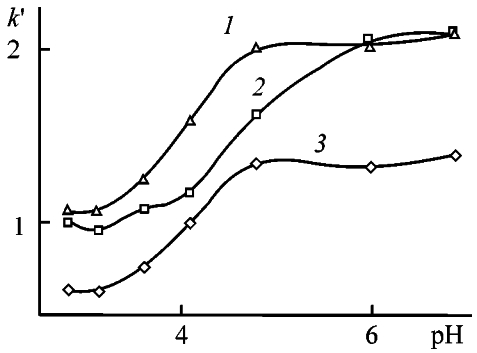

Fig. 1. Retention of (*1*) Tomerzole, (*2*) Dibasol, and (*3*) Bemityl on the sorbent Separon C_{18} as a function of pH of the mobile phase. Eluent 0.01 M KH_2PO_4–MeCN (60 : 40). (k') Capacity coefficient.

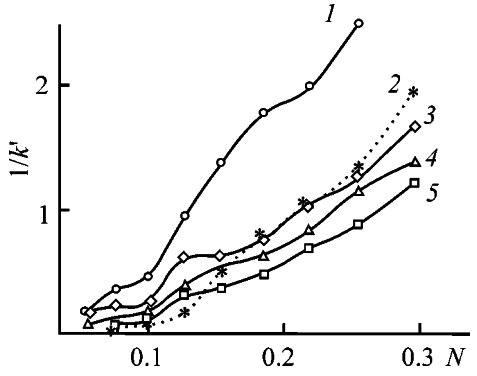

Fig. 2. Capacity coefficient k' of (*1*) BDB, (*2*) Omeprazole, (*3*) Bemityl, (*4*) Dibasol, and (*5*) Tomerzole as a function of the MeCN concentration N (mole fraction) in the mobile phase.

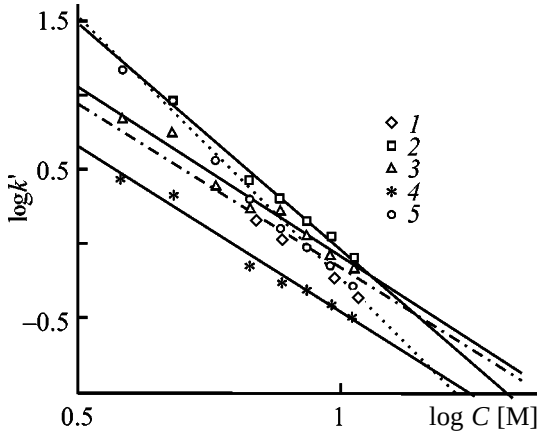

Fig. 3. Capacity coefficient k' of (*1*) Bemityl, (*2*) Tomerzole, (*3*) Dibasol, (*4*) BDB, and (*5*) Omeprazole as a function of the MeCN concentration C in the mobile phase.

which can be attributed to the difference in their structure and properties. In the Dibasol molecule there is an electron-donor benzyl radical in the position *2*, causing a higher electron density on the nitrogen atom (according to [4], pK_{BH^+} of Dibasol in water is 4.2).

With increasing the MeCN mole fraction the retention of the organic sorbates decreases under reversed-phased HPLC conditions, which corresponds to the displacement retention models (Figs. 2, 3). The observed deviation from linearity of these dependences is indicative, evidently, of association of molecules of the organic modifier of the mobile phase [5]. The results were treated by linear regression analysis [6, 7] using Eqs. (1) and (2).

$$1/k' = aN + c, \quad (1)$$

$$\log k' = b - p \log C, \quad (2)$$

where k' is the capacity coefficient, N is the mole fraction of MeCN in the mobile phase, C is the MeCN concentration in the eluent (M), and a, c, b, p are the linear regression coefficients.

The results are summarized in Table 1 (equation coefficients are given for the linear section of the dependence).

The coefficient p of Eq. (2) corresponds to the number of moles of MeCN displaced from the sorbent surface in adsorption of 1 mol of the sorbate. Analysis of this parameter allows certain conclusions about the arrangement of the sorbate molecules on octadecyl silica gel. It follows from Table 2 that benzyl radical occupies nearly the same area as the ethylthio group. Introduction of the ethoxy group in the BI ring considerably increases the retention, so that Tomerzole and Bemityl are satisfactorily separated over the MeCN concentration range 20–45 vol %. Introduction of methyl substituents in the Dibasol or BDB molecule does not practically change the sorption site area, which can be attributed to the electron-acceptor effect of the BI system.

Data presented in Fig. 3 are not consistent with those predicted by the theory [8], according to which the dependences described by Eq. (2) must intersect in the same point. This inconsistency can be attributed to the fact that the BI derivatives are polar compounds. Therefore, they tend to ionization, being capable of specifically interacting with the mobile phase and residual silanol groups. As a result, the hydrophobic mechanism of chromatographic separation has certain limitations in the investigated system. The chromatographic data were described by Eq. 3 [8]

$$b = b_0 + b_1 p/p_1, \quad (3)$$

where b_1/p_1 is the ratio of the capability of a compound to be retained to its capacity of competing with

Table 1. Coefficients of Eqs. (1) and (2) for BI derivatives (sorbent Separon C_{18})

Sorbate	Eq. (1)			Eq. (2)		
	a	*c*	r^2	–*p*	*b*	r^2
Bemityl	7.26	–0.53	0.988	2.20	2.04	0.990
Tomerzole	4.63	–0.33	0.982	3.03	3.00	0.991
Dibasol	5.94	–0.38	0.990	2.28	2.19	0.985
BDB	12.23	–0.61	0.991	2.10	1.76	0.990
Omeprazole	9.34	–0.94	0.985	3.48	3.58	0.989

an organic modifier (MeCN) for the site on octadecyl silica gel, and b_0 is the coefficient reflecting the degree of consistency of the retention mechanism to the purely hydrophobic one.

Retention of the tested five BI derivatives is described by the equation $b = -0.70 - 1.23p$ (r^2 0.992), which is in a satisfactory agreement with the results obtained in [8]. The coefficient b_0 is somewhat lower (by the absolute value) that that given in [8] for weakly polar organic sorbates. However, this parameter is close to the value given for 5-fluorouracil derivatives ($b_0 = -0.635$).

The capacity coefficients of BI derivatives with water as a mobile phase (value proportional to the Henry coefficient) were estimated by Eq. (4) [9]

$$\log k' = \log k'_w - SF, \quad (4)$$

where k'_w is the capacity coefficient of a compound with the use of water as a mobile phase, F is the MeCN volume fraction, and S is the empirical constant. The estimated k'_w are well consistent with the coefficients p (Table 1). The results obtained allow comparison of the hydrophobicity of the tested compounds and also estimation of the relative contributions of the substituents to the sorption interaction of the BI derivatives.

To select the optimal chromatographic systems for separation of the BI derivatives, we estimated the separation efficiency and selectivity, and also the effect of the MeCN concentration and eluent pH on these characteristics. It appeared typical that the curves of the dependence of the height of equivalent theoretical plate (HETP) on the MeCN concentration in the mobile phase pass through a minimum. The minimal HETP for Bemityl, Tomerzole, and Dibasol (0.05–0.08 mm) is observed at 25–35 vol % MeCN. Increase and decrease in the MeCN concentration in the mobile phase relative to this value decreased the separation efficiency. For Omeprazole the optimal MeCN concentration in the mobile phase was found to be 25–30%. Decreasing eluent pH from 7.5 to 3.5–4.5 somewhat increases the separation efficiency of the BI derivatives by virtue of a less pronounced erosion of the rear front of the bands. The latter can be attributed to a decreased amount of ionized residual silanol groups on the stationary phase surface [10].

The selectivity coefficient α for the pair Tomerzole/Bemityl decreases from 2.5 (20 vol % MeCN) to 1.5 (40–45 vol % MeCN). At higher MeCN concentration the selectivity coefficient changes only slightly (α = 1.3 at 55 vol % MeCN). This trend can be interpreted in terms of decreasing adsorption of the ethoxy group on octadecyl silica gel with increasing MeCN concentration. The coefficient α for the pair Dibasol/BDB is practically independent of the MeCN concentration in the eluent.

The pharmaco effect of a drug is determined by its concentration in the vicinity of a target cell (receptor) and also by the affinity for the receptor. In its turn, the concentration of a biologically active compound (BAC) at the receptor is determined by such pharmacokinetic characteristics as the bioavailability *f*, comparative distribution volume V_d, and distribution constant [11]. All these parameters are controlled by the ionization constant of a compound and its lipophilicity. As seen from Table 2, Tomerzole is characterized by a higher lipophilicity than Bemityl, which is well consistent with their bioavailability (7 and

Table 2. Coefficients of Eq. (4) for BI derivatives

Sorbate	–*S*	$\log k'_w$	r^2	k'_w
Bemityl	0.03	1.16	0.987	14.45
Tomerzole	0.03	1.74	0.991	54.95
Dibasol	0.03	1.54	0.991	34.67
BDB	0.03	1.11	0.992	12.88
Omeprazole	0.04	1.93	0.995	85.11

20% for Bemityl and Tomerzole, respectively) and V_d (1.3 and 18.3 l kg^{-1}, respectively) [12, 13]. A good correlation (r 0.97) is also observed between k'_w and data of [14], in which the antisecretory activity of BI derivatives (Bemityl, Tomerzole, and Omeprazole) was studied. The pharmaco effect of these compounds on H^+–K^+-ATP-ase was found to be 17.6, 38.0, and 78.1%, respectively. The affinity of a BAC for a receptor is controlled not only by the presence of functional groups, but also by the size of the hydrocarbon fragment of the molecule, i.e., its lipophilicity. Therefore, the chromatographic retention parameters of BI derivatives can be used to predict the dissociation constants of the complex receptor–BAC [15].

CONCLUSIONS

(1) On the basis of experimental chromatographic parameters a comparative analysis is made of the adsorption properties of benzimidazole derivatives on octadecyl silica gel.

(2) The estimated adsorption and chromatographic parameters are in a satisfactory agreement with the pharmacokinetic characteristics of drugs of the benzimidazole group.

REFERENCES

1. Mikhailov, I.B., Kuzeva, V.I., Sharf, M.Ya., *et al*., *Eksp. Klin. Farmakol*., 1997, vol. 60, no. 3, pp. 20–22.
2. *High Performance Liquid Chromatography in Biochemistry*, Henschen, A., Hupe, K.-P., Lottspeich, F., and Voelter, W., Eds., Weinheim: VCH, 1985.
3. Polunina, I.A. and Roldugin, V.I., *Kolloidn. Zh.*, 1999, vol. 61, no. 2, pp. 259–263.
4. *Gosudarstvennaya farmakopeya SSSR* (USSR State Pharmacopoeia), Moscow: Meditsina, 1987, 11th ed., vol. 1, p. 130.
5. Lanin, S.N., Lanina, N.A., and Nikitin, Yu.S., *Zh. Fiz. Khim.*, 1995, vol. 69, no. 11, pp. 2045–2051.
6. Murakami, F., *J. Chromatogr*., 1979, vol. 178, no. 2, pp. 393–399.
7. Shatts, V.D. and Sakhartova, O.V., *Vysokoeffektivnaya zhidkostnaya khromatografiya* (High-Performance Liquid Chromatography), Riga: Zinatne, 1988.
8. Shatts, V.D., *Zh. Fiz. Khim.*, 1986, vol. 60, no. 1, pp. 1–8.
9. Melander, W.R. and Horvath, C., *High-Performance Liquid Chromatography: Advances and Perspectives*, New York: Academic, 1980, vol. 2, p. 113.
10. Kabulov, B.D. and Zalyalieva, S.V., *Zh. Fiz. Khim*., 1992, vol. 66, no. 8, pp. 2001–2012.
11. Kholodov, L.E. and Yakovlev, V.P., *Klinicheskaya farmakokinetika* (Clinical Pharmacokinetics), Moscow: Meditsina, 1985.
12. Boiko, S.S., Bobkov, Yu.G., and Zherdev, V.P., *Khim.-Farm. Zh*., 1987, no. 11, pp. 1288–1291.
13. Boiko, S.S., Bobkov, Yu.G., Zherdev, V.P., and Dvoryaninov, A.A., *Farmakol. Toksikol*., 1987, no. 5, pp. 54–57.
14. Kovalev, T.V., Spasov, A.A., Bakulev, P.A., *et al*., *Khim.-Farm. Zh*., 1990, no. 2, pp. 127–130.
15. Dukes, G.E., *ASHP Midyear Clinical Meet.*, 1989, vol. 24, no. 12, pp. 1–8.

Russian Journal of Applied Chemistry, Vol. 74, No. 5, 2001, pp. 855–859. Translated from Zhurnal Prikladnoi Khimii, Vol. 74, No. 5, 2001, pp. 829–832.

MACROMOLECULAR CHEMISTRY AND POLYMERIC MATERIALS

Effect of Calcium Cation on the Structure of Silica Gel Formed from Decationized Sol

T. F. Kuznetsova

Institute of General and Inorganic Chemistry, Belarussian National Academy of Sciences, Minsk, Belarus

Received August 1, 2000; in final form, March 2001

Abstract—Isotherms of sorption of water and tetrachloromethane vapors on a silica gel formed from decationized sol in the presence of calcium chloride are identified on the basis of the IUPAC classification. The manner in which the structure and sorption properties of the samples studied vary with $CaCl_2$ concentration and kind of adsorbate is analyzed.

When the silica gel structure is formed from decationized monodisperse silica sol, the presence of dense SiO_2 particles is ensured till the onset of gelation [1]. In an evolution of this method, silica gel was prepared from a sol with elongate and lamellar shape of particles, acquired under the action of calcium salts [2] or as a result of SiO_2 flocculation with a quaternary ammonium base [3]. Because of their uncommon structure and unique structural properties, laminated silica gels are regarded as potential sensors, membranes, binders, or coatings for obtaining inorganic fibers. However, their microstructure, whose practical importance is determined by their sorption properties and the dependence of these on the kind of adsorbate, by the molecular sieve action, and by the reversibility and kinetics of adsorption has been little studied so far.

The aim of this study was to analyze the effect of calcium chloride on how the silica gel structure is formed from decationized sol, and the primary objective, to establish within the possible limits the relationship between such characteristics as pore size, size distribution and specific surface area of pores, on the one hand, and the sorption properties and dependence of these on the kind of adsorbate, on the other.

A decationized silica sol with pH 3.5 and silicic acid content of 4 wt % was obtained by passing an aqueous solution of sodium metasilicate through a column packed with KU-2 sulfonic acid cation-exchange resin in the hydrogen form. The sol was mixed with aqueous solutions of potassium chloride, with Ca/Si molar ratios in the range 5×10^{-4}–1×10^{-1}. An $NH_3 \cdot H_2O$ solution was added to the mixture to adjust pH 7.5, and a gel was precipitated with hydrochloric acid at constant pH 5.6. After syneresis and aging for 16 h, the gel was thoroughly washed with distilled water, with vigorous stirring to break down clots, till complete absence of chloride ions in washing water, and then dried in air at room temperature and in a drying box at 393 K for 4 h.

The adsorption–desorption isotherms of water and tetrachloromethane vapors were measured gravimetrically at 293 K after preliminary "evacuation" of samples at 413 K for 16 h. The specific surface area A was calculated from the monolayer capacity by the linear BET equation at relative pressures p/p_0 = 0.05–0.25, using landing area of 0.125 nm^2 for water molecule and 0.322 nm^2 for CCl_4 molecule [4]. The limiting sorption pore volume V_p was calculated by the Gurvich method [5] in the form of the amount of vapor sorbed to saturation and expressed in terms of water volumes. The distribution $\Delta V/\Delta r$ of the volumes V of mesopores with respect to their radii r was calculated from desorption curves by the Kelvin equation, and the pore shapes were analyzed on the basis of the form of the vapor adsorption–desorption hysteresis loop [6]. The average pore radius r_p was found for cylindrical and bottle-shaped pores, using the formula

$$r_p = 2V_p/A, \quad (1)$$

and for slotlike pores as a slot halfwidth [6] by the formula

$$r_p = V_p/A. \quad (2)$$

The refractive index n_D of the silica sols was determined using a Zeiss Abbe refractometer at 293 K; the zero-charge point of the silica gels was found by titration [7].

1070-4272/01/7405-0855$25.00

Structural and sorption properties of silica gels formed in the presence of calcium cation contained in decationized sols

Sample no.	Ca/Si, mol/mol	Type of isotherm	Shape of hysteresis loop	$V \times 10^3$, $m^3\ kg^{-1}$	$A \times 10^{-3}$, $m^2\ g^{-1}$	r, nm
			Adsorbate H_2O			
1	–	I	–	0.29	434*	1.34*
2	5×10^{-4}	IV	H2	0.42	555	1.51
3	1×10^{-3}	IV	H2	0.60	718	1.67
4	1×10^{-2}	IV	H2	0.42	680	1.23
5	1×10^{-1}	IV	H1	0.36	163	4.42
			Adsorbate CCl_4			
1	–	I	–	0.28	1120*	0.50*
2	5×10^{-4}	IV	H4	0.40	1097	0.36
3	1×10^{-3}	IV	H4	0.58	1600	0.36
4	1×10^{-2}	IV	H4	0.34	800	0.42
5	1×10^{-1}	IV	H2	0.30	209	2.87

* Apparent values.

The isotherms of sorption of water and tetrachloromethane vapors by the samples under study differ in the type, presence, and shape of capillary-condensation hysteresis (see table, Fig. 1). The isotherms give insight into stages of gradual modification of the structure of silica gel with increasing content of calcium chloride, with micropores transformed into macropores in the process. The isotherms indicate complete pore filling by various adsorbates and satisfactory observance of the Gurvich rule.

The reversible isotherm *1* of H_2O vapor sorption, which is of type I characteristic of microporous adsorbents, takes the form of an irreversible type IV isotherm for mesoporous adsorbents on passing to sample nos. 2–5 (Fig. 1) [6]. The hysteretic curve of H2 shape in isotherm *2*, indicating the presence of bottle-like mesopores, is transformed into H1 hysteresis in isotherm *5*, characteristic of cylindrical pores formed by particle agglomerates or spheres [6]. The shape of the narrow hysteresis in isotherms *3* and *4* of water vapor sorption is difficult to determine.

The reversible type I isotherm of CCl_4 vapor sorption, characterized by the presence of a nearly horizontal plateau, indicates filling of narrow micropores (Fig. 1). Isotherms *2–5* of CCl_4 vapor sorption are irreversible at medium relative pressures $p/p_0 > 0.2$–0.3. The isotherms belong to type IV characteristic of sorption on mesoporous adsorbents, their hysteresis loops of H4 (isotherms *2–4*) and H2 shape (isotherm *5*) confirm the presence in the structure of, respectively, predominantly narrow slotlike or bottle-shaped mesopores.

Isotherm *3* of sorption of water and tetrachloromethane vapors by a silica gel obtained at a molar ratio Ca/Si = 1×10^{-3} is characterized by the strongest absorption in the entire p/p_0 range (Fig. 1), with the sample demonstrating the expected apparent increase in the pore volume and specific surface area, compared with the other samples (see table). Silica gel no. 3 shows approximately the same saturation adsorption for different adsorbates (0.60×10^{-3} $m^3\ kg^{-1}$), but different specific surface areas (718×10^3 and 1600×10^3 $m^2\ kg^{-1}$) found from the monolayer capacities of, respectively, water and CCl_4. The overestimated A values in calculation from the CCl_4 vapor adsorption are due to the predominance of the dispersive interaction: the isotherm of tetrachloromethane sorption is of type I for microporous sample and is more concave with respect to the p/p_0 axis in mesoporous samples. The fact that the Gurvich rule is observed for type I isotherms commonly indicates that the pore size is equal to at least several molecular diameters of the adsorbate to ensure packing of its molecules with a density close to that of the normal liquid [8]. An additional evidence in favor of the overestimated A value in calculation from the CCl_4 adsorption is that $r_p < 0.595$ nm values are obtained, smaller than the kinetic diameter of the CCl_4 molecule (see table). The fact that the adsorption portions of isotherms *2–4* of CCl_4 vapor sorption are of type I indicates the presence of a certain volume of micropores in the structure.

Thus, sample no. 1 is characterized as microporous on the basis of adsorption of both water and tetra-

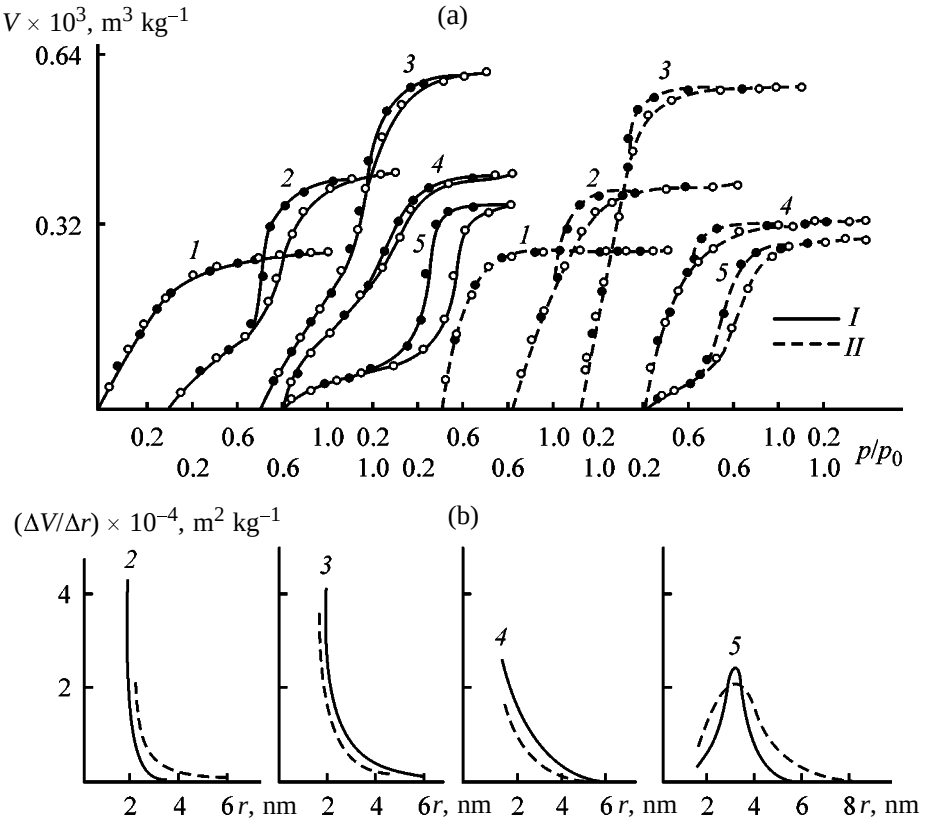

Fig. 1. (a) Isotherms of adsorption–desorption of (*I*) H_2O and (*II*) CCl_4 vapors and (b) distributions, calculated from the isotherms, of the adsorption volumes of (*I*) H_2O and (*II*) CCl_4 with respect to mesopore radii in silica gels obtained (*1*) without and (*2*–*5*) in the presence of calcium cations. (*V*) Amount of adsorbed vapor recalculated to the liquid state of the adsorbate, (p/p_0) relative pressure of adsorbate vapor, and (p_0) saturated vapor pressure of the adsorbate (Pa). ($\Delta V/\Delta r$) Density of mesopore volume distribution with respect to mesopore radius and (r) mesopore radius found from the Kelvin equation. Ca/Si molar ratio: (*2*) 5×10^{-4}, (*3*) 1×10^{-3}, (*4*) 1×10^{-2}, and (*5*) 1×10^{-1}.

chloromethane vapors. The pores in this sample are cylindrical, formed by densely packed globules. Numerous fine pores are formed in the silica gel in the presence of calcium cations in amounts not exceeding 1×10^{-3} M Ca^{2+}, which is indicated by the increase in the specific surface area (see table). The narrow hysteresis in isotherms *3* and *4* of H_2O vapor sorption points to filling of these pores via polymolecular adsorption. Judging from the shape of hysteresis in the isotherms of CCl_4 vapor sorption, the pores are determined as very narrow slotlike pores.

The specific features of adsorption and capillary condensation of H_2O and CCl_4 vapors suggest that the pore system is constituted in the obtained samples by (i) spaces between agglomerates of SiO_2 particles elongated under the action of the calcium cation, (ii) spaces between compact three-dimensional agglomerates composed of densely packed interwoven chains, and (iii) intra-agglomerate pores. The loop appears at high relative pressures as a result of condensation of H_2O and CCl_4 vapors within secondary mesopores, i.e., outside the intra-agglomerate pores. It is not improbable that the most open structure is formed by long chain segments and spaces between these at molar ratios Ca/Si $\leq 1 \times 10^{-3}$.

The reason for the above changes in the porous structure of silica gel is that the silica gel inherits the microstructure that existed in the hydrogel after coagulation of the SiO_2 hydrosol in the presence of the calcium cation [9]. Changes in the structural and sorption parameters under the action of different amounts of calcium cations are due to the varied extent of neutralization by this cation of the charge of SiO_2 particles. This charge is a factor determining the aggregative stability of the sol, preventing particle agglomeration via condensation of surface (≡SiOH) and ionized (≡SiO^-) groups to form Si–O–Si bonds. In the beginning of gelation, silica sol particles, dispersed in solution and negatively charged, are held together at points of the weakest electrostatic repul-

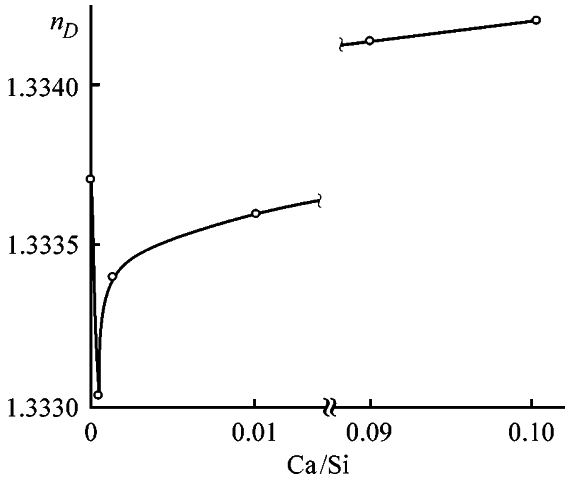

Fig. 2. Effect of the calcium cation on the refractive index n_D of decationized silica gel. (Ca/Si) Molar ratio.

sion under the action of calcium cations. On adding an $NH_3 \cdot H_2O$ solution, there proceeds a special type of chain coagulation of globules, when their mutual repulsion occurs with a force that can overcome interglobule bonds [3]. Agglomerates of SiO_2 particles grow mainly in chains because of the attachment of particles to one another at the ends of the growing chains. Chain-like agglomerates may include regions several particles thick, with arbitrary distribution. Possibly, precipitation of excess SiO_2 on chain agglomerates formed in the presence of calcium cations leads to formation of dense fibers and development of a partially fibrous gel structure [3].

The greater the amount of cations in a gel, to a larger extent is disrupted the binding of the SiO_2 surface to water, and globule cohesion occurs at "hydrophobized" regions [10]. Since the zero-charge point of liquid silica gel nos. 1–5 increases from pH 5.7 for the initial sample to pH 7.0 in a sample containing 1×10^{-1} mol Ca^{2+}, it is also possible that calcium hydroxide nuclei are formed on the SiO_2 surface [11, 12]. Under conditions of strong attraction, rather compact particle agglomerates are formed. In the process, the specific surface area decreases, thin capillaries gradually disappear, being transformed into wider pores responsible for the H1 hysteresis in sample no. 5 for H_2O absorption or H2 hysteresis for absorption of CCl_4 (Fig. 1). This hysteresis can be attributed either to open cylindrical pores with various cavity shapes or to bottle-shaped pores with very wide openings into cavities.

Although the distribution of the volume of bottle-shaped pores with respect to pore size is difficult to interpret, mention can be made, for comparison purposes, of the absence of maxima in curves *2–4* calculated from the desorption of water and tetrachloromethane, in contrast to curve *5* exhibiting maxima corresponding to a predominant mesopore radius of approximately 3.0 nm in the sample (Fig. 1).

Determining the specific surface area by BET gives no way of distinguishing the external surface, formed by globule agglomerates, and the internal surface formed by intra-agglomerate pores. Therefore, the agglomeration and changes in the agglomerate radius with increasing Ca/Si ratio were judged from the variation of the refractive index n_D of the corresponding silica sols in Fig. 2.

The total number N of colloid particles in clusters with nonequilibrium structure formed as a result of a random Brownian motion of colloid particles is related to the cluster radius R, particle radius R_0, and density ρ by Eq. (3) [13]. With increasing size of a cluster composed of N particles, it density decreases following the equation

$$N = \rho(R/R_0)^D, \quad (3)$$

where D is the fractal dimension of the cluster, quantitatively characterizing the space filling by the cluster.

Since, according to Eq. (3), the cluster density increases with decreasing cluster size, the refractive index must also increase. Therefore, the hydrodynamic radius of agglomerates of sol particles, formed on introducing calcium cations in amounts equal to, or less than 1×10^{-3} M Ca^{2+}, must be greater than that in the initial SiO_2 hydrosol and decrease with the amount of Ca^{2+} cations increasing further. The drop in n_D is due to the formation of chain agglomerates of particles on introducing calcium cation, and its subsequent increase, to the decrease in the radii of sol particle agglomerates with increasing Ca/Si ratio, occurring because of their densification.

CONCLUSIONS

(1) The formation of the silica gel structure from a decationized sol in the presence of calcium cations is accompanied by the appearance of mesopores, significant changes in the prehysteresis portion of vapor sorption isotherms, and a decrease in the specific surface area of the xerogel.

(2) Under the action of calcium cations, type I isotherms are transformed into isotherms of type IV. The type of isotherm and the sorption properties of a silica gel depend on the kind of adsorbate and salt concentration.

(3) Chain agglomerates of particles formed at low calcium concentrations are combined with increasing calcium content into dense three-dimensional agglomerates. The specific surface area decreases, without any increase in the limiting adsorption volume of pores in the process.

ACKNOWLEDGMENTS

The author wishes to thank S.I. Eremenko and G.S. Lemeshonok for help in the experiments.

REFERENCES

1. US Patent 224435.
2. Eur. Patent Appl. 0335195.
3. Iler, R.K., *The Chemistry of Silica*, New York: Wiley–Interscience, 1979.
4. McClellan, A.L. and Harnsberger, H.E., *J. Colloid Interface Sci*., 1967, vol. 23, no. 4, pp. 577–599.
5. Gurvich, L.G., *Zh. Ross. Fiz.-Khim. O–va., Chast' Khim*., 1915, vol. 47, issue 4, pp. 805–827.
6. IUPAC, *Pure Appl. Chem*., 1985, vol. 57, no. 4, pp. 603–619.
7. Subramanian, S., Schwarz, J.A., and Hejase, Z., *J. Catal*., 1989, vol. 117, no. 2, pp. 512–518.
8. Gregg, S.J. and Sing, K.S.W., *Adsorption, Surface Area and Porosity*, London: Academic, 1982.
9. Barby, D., *Characterization of Powder Surfaces*, Parfitt, G.D. and Sing, K.S.W., Eds., New York: Academic, 1976, pp. 353–425.
10. Neimark, I.E. and Chertov, V.M., in *Adsorbtsiya i adsorbenty* (Adsorption and Adsorbents), Moscow: Nauka, 1987, pp. 193–199.
11. James, R.O. and Healy, I.W., *J. Colloid Interface Sci*., 1972, vol. 40, no. 1, pp. 42–52.
12. Kuznetsova, T.F., *Izv. Ross. Akad. Nauk, Neorg. Mater*., 1993, vol. 29, no. 6, pp. 788–790.
13. Tuel, A., Dautry, P., Hommel, H., *et al*., *Prog. Colloid Polym. Sci*., 1988, vol. 76, no. 1, pp. 32–36.

Russian Journal of Applied Chemistry, Vol. 74, No. 5, 2001, pp. 860–863. Translated from Zhurnal Prikladnoi Khimii, Vol. 74, No. 5, 2001, pp. 833–837.

MACROMOLECULAR CHEMISTRY AND POLYMERIC MATERIALS

Synthesis of Single-Component Urethane Sealants

A. D. Elchueva, N. V. Aristova, I. V. Bortnikov, and A. A. Tabachkov

Kazan State Technological University, Kazan, Tatarstan, Russia

Received October 5, 2000; in final form, February 2001

Abstract—Single-component urethane sealing formulations with aldimines as cross-linking agents were developed. The temperature dependence of the curing time of the sealants was examined. The influence of the –CH=N–/–NCO ratio and of fillers (industrial carbon and chalk) on their physicochemical properties was studied.

Polyurethane elastomers are widely used in various branches of industry. With progress of studies in the field of development of single-component formulations, their performance is improved and the application field is expanded. The procedures used in industry for curing of polyurethane sealants have significant drawbacks. All sealants of this type are two-component; they are not quite convenient in service and require performing certain manipulations directly before use. Their curing is effected with diamines and glycols. Curing of a single-component urethane sealant based on an isocyanate-containing prepolymer results in formation of defects (blisters, cavities) due to release of carbon dioxide on contact of isocyanate groups with atmospheric moisture. The goal of this work was to develop single-component urethane formulations with aldimines as cross-linking agents. Aldimines, when reacting with atmospheric moisture, release active curing agents which react with isocyanate groups without releasing CO_2, so that formation of defects in the cured sealant can be avoided.

Urethane elastomers show considerable promise for practice. Polyurethanes are prepared from compounds containing highly reactive isocyanate groups. Their transformations yield polymeric structures with diverse types of chemical bonds and allow preparation, within the same class of polyurethanes, of materials of widely varying properties.

An important factor determining the physicomechanical properties of polyurethanes, especially at elevated temperatures, is the nature of cross-links in the three-dimensional polymer network, depending on the curing agent used.

Studies of the effect of diamines and water as curing agents in single-component systems on the properties of composites based on various diisocyanates showed [1] that strong intermolecular interaction in polymers results in increased modulus of elasticity and tensile strength. The rigid segments in the chain (bulky aromatic diisocyanates and aromatic amines) also enhance the cohesion strength. Flexible groups (e.g., aliphatic amines) contribute to the elastic properties of the elastomers.

Thus, polyurethanes can be considered as block copolymers [2] with flexible polyether or polyester segments and rigid segments formed by urethane or urea fragments. Flexible segments increase the elasticity and relative elongation at break, whereas rigid segments with enhanced intermolecular interactions increase the hardness, tensile strength, melting point, and glass transition point.

The structure of the three-dimensional polyurethane network is determined by the synthesis conditions, in particular, by the preparation procedure (single-stage or two-stage). When the polymer is prepared by a two-stage procedure via a prepolymer, formation of a more regular network can be expected. Elastomers prepared via prepolymer [3] exhibit higher cohesion strength but lower values of the adhesion strength and modulus of elasticity and are less elastic.

In a two-stage procedure for production of polyurethanes the prepolymers are usually highly viscous, and special equipment is required for their mixing and feeding to reaction vessels without air access. The properties of the final product can largely depend on the accuracy of temperature control and on the storage time and stability of the prepolymer.

The advantage of the single-stage preparation of polyurethanes is the stability of the reaction mixture. With aromatic diamines, an additional advantage is

1070-4272/01/7405-0860$25.00

the possibility of dosing these relatively high-melting crystalline substances using standard dosing units. The major problem, however, is to balance the reactivities of the backbone polyol and curing agent to attain the required degree of cross-linking. If both components are diols, it is not difficult, but with amine cross-linking agents it is necessary to add a catalyst accelerating the reaction of the hydroxide with the isocyanate. The advantages of the single-stage procedure are also simpler process and wider range of suitable raw materials.

Analysis of the present state of production of single-component polyurethane elastomers [4] reveals the following trends: improvement of the curing system and development of optimal formulations.

The goal of this study was preparation of single-component urethane formulations with azomethines (Schiff bases) as cross-linking agents. These systems, reacting with atmospheric moisture without release of carbon dioxide, facilitate reaction of the polymer backbone chain with isocyanate groups.

EXPERIMENTAL

In our study we used toluene 2,4-diisocyanate [TDI, TU (Technical Specifications) 6.03331–79), Laprol-5003 polyether (TU 6-05-1513–87), P-803 industrial carbon [GOST (State Standard) 7885–77), and chalk (GOST 842–52). The deformation and strength properties were determined according to GOST 21 751–76, and the Shore hardness, according to GOST 263–75.

Aldimines were prepared by reaction of an aldehyde with a diimine in a 2 : 1 molar ratio (see table).

Schiff bases are prepared [5] by condensation of aldehydes and ketones **I** with various amino compounds **II**, resulting in elimination of water and formation of the corresponding azomethines **III**. The kinetic data suggest a two-stage mechanism [Eq. (1)] of formation (and reverse hydrolysis) of azomethines, involving formation of a tetrahedral intermediate, carbinolamine **IV**, which in some cases can be isolated (e.g., reaction of chloral with hydroxylamine) or detected in solution by ^{1}H NMR spectroscopy:

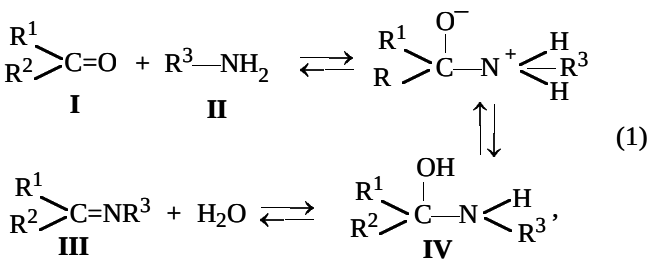

(1)

Initial substances for synthesis of aldimines

Diamine	Aldehyde	mp, °C
Ethylenediamine	Benzaldehyde	42–44
〃	Nitrobenzaldehyde	145
〃	Furfural	51–52
Hexamethylenediamine	Benzaldehyde	(l)
〃	Nitrobenzaldehyde	86–88
〃	Furfural	43
Phenylenediamine	Benzaldehyde	110–113
〃	Nitrobenzaldehyde	85–90
〃	Furfural	(l)
Diaminodiphenylmethane	Benzaldehyde	121
〃	Nitrobenzaldehyde	172
Diaminodiphenylmethane	Furfural	(l)

where R^1, R^2 = H, Alk, Ar; R^3 = Alk, Ar, OH, OR, NHR, Hal.

Aldehydes and dialkyl ketones smoothly condense with primary amines to give the corresponding Schiff bases, whereas the reactivity of aryl ketones is relatively low, and in this case longer reaction time and Brønsted acid catalysis are required.

Hydrolysis of azomethines to the initial amines and carbonyl compounds is an example of the nucleophilic attack at the C=N bond. This two-stage process involves addition of water molecules to the C=N bond to form a carbinolamine intermediate which subsequently decomposes into the amine and carbonyl compound. The rates of azomethine hydrolysis and formation are pH-dependent.

Cycloaddition of Schiff bases to simple isocyanates **VI** is preceded by reversible formation of zwitter-ionic intermediate **VII** [Eq. (2)] which in some cases can be isolated. The further transformations are determined by the stability of the zwitter-ionic intermediate (i.e., mainly by the steric and electronic effects of substituents in the azomethine molecule) and by the reaction conditions (kinetic or thermodynamic control). On the whole, when the benzylidene moiety of Schiff base **V** contains electron-donor *para* substituents and the reaction is performed at low temperatures (i.e., under conditions of kinetic control), direct ring closure in the zwitter-ion to give [2+2]-cycloadduct **VIII** is favored:

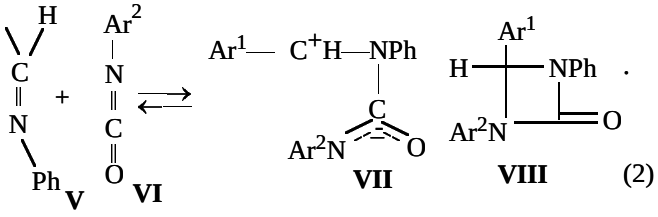

(2)

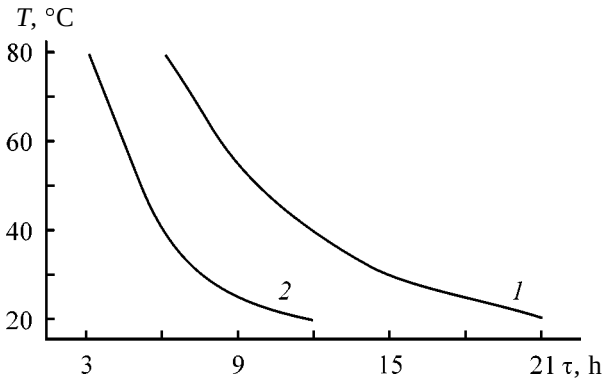

Fig. 1. Correlation between the temperature T and time τ of sealant curing with aldimines based on (*1*) benzaldehyde and (*2*) nitrobenzaldehyde and furfural.

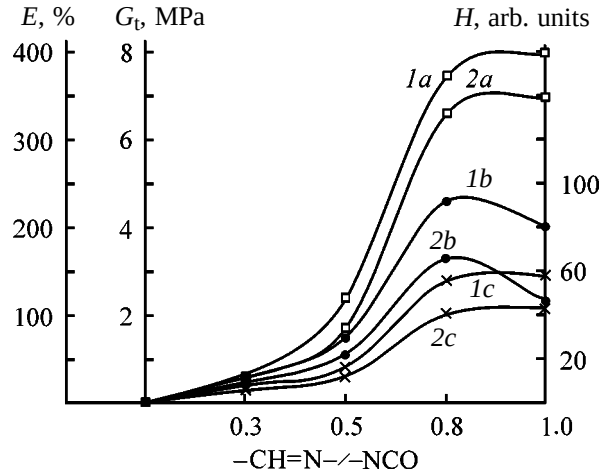

Fig. 2. Influence of the –CH=N–/–NCO ratio on the physicomechanical properties of sealants containing 60 wt parts of industrial carbon, cured with (*1a–1c*) aromatic and (*2a–2c*) aliphatic imines: (*1a*, *2a*) relative elongation E, (*1b*, *2b*) nominal tensile strength G_t, and (*1c*, *2c*) Shore hardness H; the same for Fig. 3.

It was suggested to use Schiff bases for preparing composites from polyisocyanate and aldimine for coatings stable in storage [6, 7]; also, Schiff bases can be used as latent hardeners for low-temperature curing of epoxy oligomers [8].

However, studies by Arbizov and his disciples [9] showed that Schiff bases react with isocyanates only at 100–160°C. Therefore, preparation of cold-curable sealants using the reactions of Schiff base formation is practically impossible. We have studied the hydrolysis of Schiff bases as sealant components.

It is known [10] that aldimines **IX** in the presence of atmospheric moisture are hydrolyzed to the initial compounds: aldehydes and diamines. This reaction, in particular, occurs on a support:

$$R'–CH=N–R''–N=CH–R' + H_2O \rightarrow 2R'–CHO + H_2N–R''–NH_2. \quad (3)$$

The released diamine reacts with the OCN groups of the prepolymer to give a three-dimensionally cross-linked polymer.

Curing of sealants depends on several factors, in particular, on the temperature and structure of substituent R' in the aldehyde molecule (Fig. 1). With increasing temperature, the time of sealant curing decreases. Curing is also accelerated when electron-withdrawing substituents such as NO_2, Br, I, or OCH_3 are introduced into the *para* position of benzaldehyde. These substituents decrease the electron density on the electrophilic center ($–C^+=N–$ carbon atom) and enhance its affinity for water, accelerating the hydrolysis. The amino groups released in the course of hydrolysis react with the isocyanate group even at 0–25°C; as a result, the sealant curing accelerates.

Figure 2 shows the dependences of the physicomechanical properties of sealants on the ratio of the reactive groups –NCO/–CH=N in the oligomeric system. As this ratio is increased, the strength and hardness of the urethane elastomers increase. This is due to the increased degree of cross-linking. The increase in the –NCO/–CH=N ratio to 0.5 has a weak effect on the properties. However, at further increase the strength of the sealants is enhanced, reaching a maximum at the –NCO/–CH=N ratio equal to 0.8–0.85. At the –NCO/–CH=N ratio higher than unity the physicomechanical parameters start to decrease.

The deformation and strength characteristics of sealants are influenced by the structure of the amine moiety in aldimines. For example, the selanats cured with aromatic imines considerably surpass in strength those cured with aliphatic analogs, owing to incorporation of aromatic ring into the polymer structure.

Unfilled sealants are used seldom because of their poor physicomechanical parameters and high cost. To improve the properties and reduce the cost, various fillers are added. In this work we used active (industrial carbon) and neutral (chalk) fillers. Figure 3b shows the dependences of the main physicomechanical parameters of the sealants on the content of industrial carbon and chalk. These data show that, irrespective of the imine type and component ratio, the parameter values as functions of the filler content pass through maxima. The nominal tensile strength and the relative elongation vary in parallel with varying filler content.

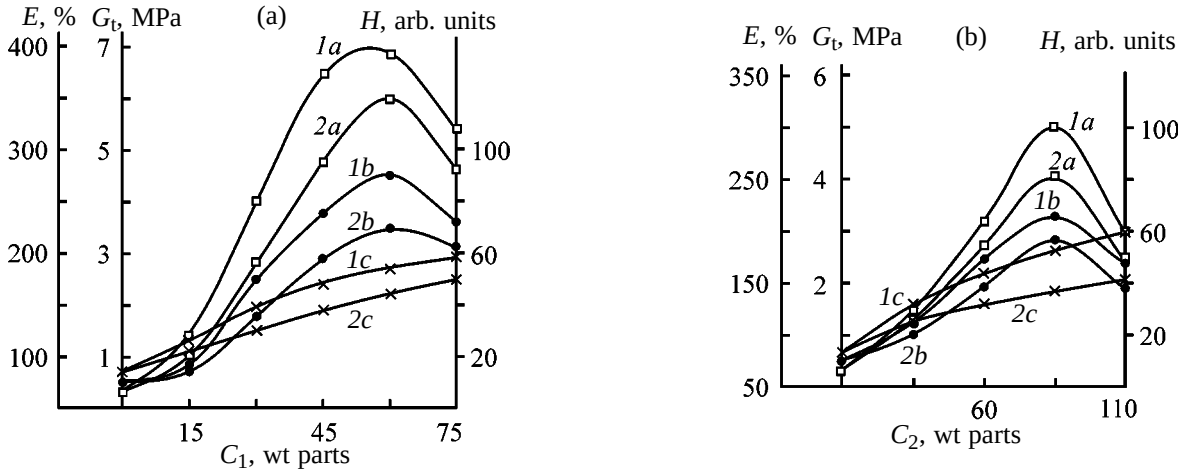

Fig. 3. Influence of the content of (a) P-803 industrial carbon C_1 and (b) chalk C_2 on the properties of sealants cured with (*1a–1c*) aromatic and (*2a–2c*) aliphatic imines.

The hardness of the composites increases monotonically. The physicomechanical properties of polyurethane sealants filled with industrial carbon are considerably better than those of the sealants filled with chalk. However, at high filling (more than 60 wt parts of industrial carbon or more than 90 wt parts of chalk per 100 wt parts of oligomer) the curing becomes complicated because of hindered diffusion. Highly active industrial carbon should be introduced in smaller amounts than chalk; the optimal dosage is 40 wt parts. This filler strongly affects the efficiency of macromolecule binding and formation of the physical network comprising from 60 to 80% of the total content of bonds in the polymer. Replacement of industrial carbon by neutral chalk at the same filler content (60 wt parts per 100 wt parts of prepolymer) decreases the physicomechanical properties of sealants.

CONCLUSIONS

(1) Single-component urethane sealants with aldimines as cross-linking agents were developed.

(2) The effect of temperature on the curing time of sealants was studied. With increasing temperature from 20 to 80°C, the curing time decreases from 12–15 to 2–4 h.

(3) The ratio of the –CH=N– and –NCO groups affects the physicomechanical properties of the sealants, with its optimal value being 0.8–0.85.

(4) The properties of sealants were studied in relation to the filler content. The strength parameters pass through maxima at the following filler content: industrial carbon 60 wt parts and chalk 90 wt parts.

REFERENCES

1. Lipatov, Yu.S., Kercha, Yu.Yu., and Sergeeva, L.M., *Struktura i svoistva poliuretanov* (Structure and Properties of Polyurethanes), Kiev: Naukova Dumka, 1970.
2. Saunders, J.H., *J. IRI*, 1968, vol. 2, pp. 21–22.
3. Rausch, R. and Sayigh, A., *Ing. Eng. Chem.*, 1965, vol. 57, pp. 92–94.
4. *Tematicheskii obzor TsNIITEneftekhim. Seriya: "Promyshlennost' sinteticheskogo kauchuka. Proizvodstvo uretanovykh elastomerov v SShA"* (Topical Review of the Central Research Inst. of Technical and Economical Studies in Petrochemical Industry, Ser.: Chemical Rubber Industry. Production of Urethane Elastomers in the United States), 1979.
5. *Comprehensive Organic Chemistry. The Synthesis and Reactions of Organic Compounds*, Barton, D. and Ollis, W.D., Eds., vol. 2: *Nitrogen Compounds*, Oxford: Pergamon, 1979.
6. US Patent 5 569 706.
7. US Patent 5 523 376.
8. Blagonravova, A.A. and Nepomnyashchii, A.I., *Lakovye epoksidnye smoly* (Varnish Epoxy Resins), Moscow: Khimiya, 1970.
9. Zobova, N.N., Rusanov, G.N., and Arbuzov, B.A., *Izv. Akad. Nauk SSSR, Ser. Khim.*, 1972, no. 2, pp. 2016–2020.
10. Sorokin, M.F., Onosova, L.A., and Tarasov, A.V., *Zh. Prikl. Khim.*, 1986, vol. 2, no. 8, pp. 17–21.

Russian Journal of Applied Chemistry, Vol. 74, No. 5, 2001, pp. 864–869. Translated from Zhurnal Prikladnoi Khimii, Vol. 74, No. 5, 2001, pp. 838–842.

CHEMISTRY OF FOSSIL FUEL

Production of Environmentally Friendly Diesel Fuel and Petroleum Aromatic Solvents by Extraction Combined with Azeotropic Distillation

A. A. Gaile, G. D. Zalishchevskii, O. M. Varshavskii, L. V. Semenov, A. S. Erzhenkov, L. L. Koldobskaya, and E. A. Kaifadzhyan

St. Petersburg State Technological Institute, St. Petersburg, Russia
Kirishinefteorgsintez Production Association, Limited Liability Company, Kirishi, Leningrad oblast, Russia

Received December 26, 2000

Abstract—A method is proposed for production of environmentally friendly diesel fuel, including five-step countercurrent extraction of aromatic hydrocarbons from the hydrofined diesel fraction with dimethylformamide or dimethylacetamide containing 3–5 wt % H_2O and pentane followed by regeneration of the extractants from the extract phase by azeotropic distillation. The process allows production of diesel fuel with the content of aromatic hydrocarbons below 10 wt %. Another product is a petroleum aromatic solvent like Nefras AR-150/330.

In the previous works we demonstrated that environmentally friendly diesel fuel with a content of aromatic hydrocarbons below 15 wt % and sulfur content below 0.003 wt % can be produced by five-step countercurrent extraction of the hydrofined diesel fraction with acetonitrile containing pentane [1–3]. Acetonitrile was selected as a polar solvent, since it does not form azeotropic mixtures with components of the feed and can be readily regenerated by distillation. However, even with additions of water and pentane, increasing the selectivity of separation, the arene concentration in the extract is at a level of 90 wt %.

One of the most promising lines in using extracts of mid oils is production of petroleum aromatic solvents like Nefras AR-120/200 and AR-150/330 [4, 5]. These solvents find use in varnish-and-paint industry and photography, in preparation of cleansing reagents, extraction of precious metals, and flotation of minerals. Petroleum aromatic solvents are produced by catalytic reforming of hydrofined oil fractions followed by extraction of arenes or pyrolysis with sulfuric acid refining of the condensate to remove unsaturated hydrocarbons. Nefras AR-120/200 can be also produced more simply by extraction of arenes from the hydrofined kerosene fraction with acetonitrile containing pentane. In regeneration of acetonitrile, forming azeotropic mixtures with saturated hydrocarbons C_9–C_{10}, from the extract phase, the arene content increases from 85 to 98–99 wt %, which meets the requirements for Nefras AR-120/220 [6]. The hydrofined diesel fraction can be a source of Nefras AR-150/330 without using such power-consuming processes as catalytic reforming or pyrolysis.

The goal of this work is to develop a combined extraction–azeotropic distillation process providing simultaneous production of both environmentally friendly diesel fuel with an arene content below 10 wt % and Nefras AR-150/330 from the diesel fraction.

The criterion for selection of an extractant is that it should not form azeotropic mixtures with arenes C_{10+} and also with saturated hydrocarbons over the range of at least C_{10}–C_{14}. The diesel fraction contains even higher-boiling saturated hydrocarbons C_{15}–C_{20}, but their content in the extract phase is insignificant by virtue of a lower solubility in polar solvents. Thus, the critical temperature of solution of *n*-hexadecane, *n*-decane, and *trans*-decalin in dimethylformamide (DMF) is 112 [7], 84.6, and 64.9°C, respectively [8].

In [9] DMF and also dimethylacetamide (DMAA) and acetonitrile were proposed to be used as azeotropizers for separation of alkylbenzenes C_9–C_{10} from the catalytic reforming fraction containing also about 20 wt % of saturated hydrocarbons C_{10}–C_{11}.

DMF and DMAA can form azeotropic mixtures with higher-boiling saturated hydrocarbons also. In formation of azeotropic mixtures the condition

1070-4272/01/7405-0864$25.00

Table 1. Limiting activity coefficients of hydrocarbons in DMF and DMF to hydrocarbon saturated pressure ratio at 140°C

Hydrocarbon	γ_i^0	bp, °C	P_i^0, kPa [11]	P_{DMF}^0/P_i^0
n-Decane	13.1 [12]	174.1	38.92	1.99
n-Dodecane	17.3	216.3	10.70	7.24
n-Tridecane	20.0	235.4	5.72	13.5
n-Tetradecane	23.3	253.5	3.06	25.3
2-Methyltridecane	~23	247.9	3.92	19.8
trans-Decalin	11.55 [12]	187.3	29.53	2.62
p-Cymene	1.91 [12]	177.2	35.42	2.19
Durene	2.37	196.8	20.26	3.82
DMF	–	153	77.43	–

Table 2. Limiting activity coefficients of hydrocarbons and solvent selectivity

Solvent	*T*, °C	γ_i^0 [14, 15]			γ_h^0/γ_b^0	$1/\gamma_b^0$	γ_{hp}^0/γ_h^0
		hexane	heptane	benzene			
Acetonitrile	25	25.5	41.41	2.7	9.44	0.370	1.62
DMF	25	17.0	22.7	1.4	12.1	0.714	1.34
DMAA	30	9.767	11.60	1.143	8.55	0.875	1.19

$\gamma_i^0 > P_s^0/P_i^0$ should be met, i.e., the limiting activity coefficient of the *i*th component in the solvent *s* is higher than the solvent to component saturated pressure ratio [10]. The experimental γ^0 of *n*-decane, *trans*-decalin, and *p*-cymene at 140°C (temperature close to the expected boiling point of azeotropic mixtures of DMF with the hydrocarbons) is given in Table 1. The limiting activity coefficients of the higher-boiling alkanes were estimated by extrapolation of data for heptane, octane, and decane using the linear relationship $\log\gamma_i^0 = a + bn_C$, where n_C is the number of carbon atoms in the *n*-alkanes. Similarly γ_i^0 of durene was estimated by extrapolation of data on the activity coefficients of toluene and *o*-xylene.

It follows from Table 1 that DMF should form azeotropic mixtures with alkanes C_{10}–C_{13} and branched alkanes C_{14}. At the same time the systems DMF–arenes C_{10+} are zeotropic, except for mixtures with the lowest-boiling alkylbenzenes C_{10} like *p*-cymene, which goes not to the diesel but to the kerosene fraction. The saturated vapor pressure of DMAA, estimated by the Antoine equation [13], at 140°C is 47.6 kPa, which is lower than that of DMF by a factor of 1.6. However, the nonideality of systems DMAA–saturated hydrocarbons is also lower than that of the corresponding systems with DMF by about the same factor. For example, γ^0 of octane at 50°C in DMF and DMAA is 21.2 and 13.0, respectively [14]. Therefore, the probability of formation of azeotropic mixtures of hydrocarbons with DMAA is nearly the same as with DMF. Another requirement to extractants is that they should demonstrate high group selectivity toward components to be separated. This property can be characterized, for example, by the ratio of the limiting activity coefficients of hexane to benzene γ_h^0/γ_b^0. Additionally the effective extractant should be characterized by high solvency $1/\gamma_b^0$ and low molecular-weight selectivity expressed as the ratio of the limiting activity coefficients of homologous hydrocarbons, for example, of heptane and hexane (γ_{hp}^0/γ_h^0). DMF surpasses acetonitrile in all these parameters (Table 2). DMAA, having nearly the same group selectivity toward arenes as acetonitrile, is considerably more efficient by the solvency and molecular-weight selectivity, i.e., by the characteristics which are particularly important in extraction of arenes from relatively high-boiling fractions with a wide boil-off range, with which the diesel fractions are classified.

As a feed we used the hydrofined diesel fraction (Kirishinefteorgsintez Production Association, Limited Liability Company) having the following characteristics: boil-off range (standard distillation) 223–330°C, refractive index n_D^{20} = 1.4684, density ρ_4^{20} = 0.836, and content of aromatic hydrocarbons 24.8 wt %.

Table 3. Parameters of single-stage extraction of aromatic hydrocarbons at 25°C estimated by UNIQUAC method [feed composition (wt %): *n*-dodecane 37.5, *n*-hexadecane 37.5, *n*-hexylbenzene 20.0, and 1-methylnaphthalene 5.0]

Parameter	Experiment no.				
	1	2	3	4	5
Weight ratio:					
DMF : feed	3 : 1	3 : 1	5 : 1	5 : 1	5 : 1
pentane : feed	–	1 : 1	0.5 : 1	1 : 1	1.5 : 1
Yield of extract phase, wt %:	83.72	73.85	88.48	85.44	81.98
Composition of extract phase, wt %:					
n-dodecane	3.05	1.42	2.16	1.61	1.22
n-hexadecane	1.47	0.59	1.06	0.74	0.52
n-hexylbenzene	4.65	3.25	2.87	2.56	2.28
1-methylnaphthalene	1.41	1.19	0.83	0.79	0.75
pentane	–	12.64	6.25	10.85	14.11
DMF	89.42	80.91	86.83	83.45	81.12
Composition of raffinate phase, wt %:					
n-dodecane	41.92	24.68	33.51	27.33	22.21
n-hexadecane	50.03	27.01	41.96	32.48	25.36
n-hexylbenzene	6.81	6.13	4.65	4.60	4.44
1-methylnaphthalene	0.45	0.47	0.28	0.29	0.30
pentane	–	40.78	18.81	34.43	46.76
DMF	0.79	0.93	0.79	0.87	0.93
Composition of extract, wt %:					
n-dodecane	28.82	22.00	31.19	28.32	25.53
n-hexadecane	13.93	9.19	15.31	12.91	10.99
n-hexylbenzene	43.96	50.38	41.48	44.97	47.79
1-methylnaphthalene	13.29	18.43	12.02	13.80	15.69
Yield of extract, wt %	35.41	23.81	39.82	34.05	29.28
Separation coefficients:					
$\beta_{3/1}$	9.4	9.3	9.6	9.5	9.4
$\beta_{3/2}$	23.6	24.3	24.4	24.4	25.1
$\beta_{4/1}$	42.9	44.4	46.0	46.3	45.5
$\beta_{4/2}$	108.0	116.2	117.2	119.6	122.0
Degree of recovery, %:					
n-hexylbenzene	77.8	60.0	82.6	76.6	70.0
1-methylnaphthalene	94.1	87.8	95.8	94.0	91.9

Using the UNIQUAC procedure, we estimated parameters of single-step extraction of aromatic hydrocarbons from the model system dodecane–hexadecane–*n*-hexylbenzene–1-methylnaphthalene at 25°C with straight DMF and DMF containing pentane (Table 3).

The theoretical results suggest that (1) at the same concentrations of dodecane and hexadecane in the initial mixture the dodecane content in the extracts is higher than that of hexadecane by a factor of 2–2.3; (2) separation coefficients β, estimated as the ratio of the distribution coefficients of the arenes and alkanes, are higher in the presence of pentane as compared to straight DMF; (3) arene content in the extract is higher in extraction with DMF–pentane also (see experiment nos. 1, 2); (4) to increase the degree of recovery of aromatic hydrocarbons in extraction with DMF–pentane, it is necessary to use an increased DMF to feed ratio (experiment nos. 1, 3); and (5) at weight ratios of DMF to feed and pentane to feed of 5 : 1 and 1 : 1, respectively (experiment no. 4), the same degree of recovery of 1-methylnaphthalene as in experiment no. 1 is realized at higher arene concentration in the extract and β, and also at a lower loss of the raffinate.

Table 4. Conditions of extractive purification of diesel fraction (number of theoretical plates 5; temperature 25°C)

Parameter	Experiment no.			
	1	2	3	4
Extractant	DMAA	DMAA	DMAA	DMF
Moisture content in extractant, wt %	5	5	5	3
Mass ratio:				
extractant : feed	3 : 1	4 : 1	5 : 1	4 : 1
pentane : feed	1 : 1	1 : 1	1.5 : 1	1 : 1

The advantages of extraction of arenes with a mixture of the polar (DMF) and nonpolar (pentane) solvents over extraction with straight DMF, which are not clearly distinct in the case of single-step extraction, should be more pronounced in multistep countercurrent extraction. The parameters of five-step countercurrent extractive purification of the diesel fraction are given in Table 4. As a result of higher selectivity and lower solvency of DMF as compared to DMAA, the moisture content in the extractants was 3 and 5 wt %, respectively.

Data on extraction of the arenes are given in Table 5. Pentane and the polar extractant were removed from the raffinate phase by fractional distillation. The yield of the extract and the arene content in it were estimated from the material balance equations. Regeneration of the solvents from the extract phase was performed also by distillation with a 20 TP column. As a result of formation of azeotropic mixtures of DMAA or DMF with saturated hydrocarbons of the extract phase, the arene content in the extract increases from 93–95 wt % in the extract to 98–99 wt % in the concentrate of aromatic hydrocarbons.

Simultaneous increase in the DMAA : feed and pentane : feed ratios (experiment nos. 1, 3) improves all the parameters of the extraction/azeotropic distillation process, including the degree of recovery of arenes, their content in the concentrate of aromatic hydrocarbons, and raffinate quality.

The arene contents in the resulting diesel fuel and concentrate of aromatic hydrocarbons, meeting the requirements for environmentally friendly diesel fuel and Nefras AR-150/330 (≤10 wt % [16] and ≥98 wt %, respectively [17]), are realized in experiment nos. 2 and 4, i.e., under similar conditions for DMAA and DMF. The latter is due to similar values of the selectivity and solvency of DMAA and DMF with a 5 and 3 wt % moisture content, respectively.

Note that, in contrast to DMAA, commercial DMF is available in Russia. DMF finds industrial use

Table 5. Parameters of countercurrent extraction of arenes from hydrofined diesel fraction

Parameter	Experiment no.			
	1	2	3	4
Raffinate				
Yield, wt %	85.5	82.1	83.3	82.5
Arene content, wt %	12.85	9.9	10.7	10.0
Sulfur content, wt %	0.020	0.014	0.016	0.014
Refractive index n_D^{20}	1.4600	1.4579	1.4585	1.4580
Density ρ_4^{20}	0.822	0.819	0.930	0.937
Extract				
Yield, wt %	14.5	17.9	16.7	17.5
Arene content, wt %	95.2	93.1	95.1	94.6
Concentrate of aromatic hydrocarbons				
Yield, wt %	14.0	17.0	16.0	16.9
Arene content, wt %	98.4	98.0	99.0	98.0
Sulfur content, wt %	0.20	0.197	0.198	0.197
Degree of recovery of arenes, %	55.7	67.2	64.1	66.7
Refractive index n_D^{20}	1.5367	1.5360	1.5380	1.5362
Density ρ_4^{20}	0.930	0.928	0.937	0.930

Table 6. Parameters of chromatographic distillation of feed, raffinate, and concentrate of aromatic hydrocarbons (experiment no. 2)

Parameter	Feed	Raffinate	Concentrate of aromatic hydrocarbons
Fraction composition, °C:			
initial boiling point	203	202	220
10%	233	236	236
30%	259	260	263
50%	281	281	283
70%	302	302	304
90%	322	322	331
dry point	352	346	357

for recovery and purification of isoprene by extractive distillation; the same process is used also for recovery of benzene from the benzene fractions of reformer naphtha or pyrolysis condensate. Commercial production of DMAA by condensation of acetic acid with dimethylamine was formerly realized at the Salavat Petroleum Chemical Combine [18], but now it is not manufactured in Russia.

Samples of the feed and concentrate of aromatic hydrocarbons separated in experiment no. 2 were characterized by ^{13}C and ^{1}H NMR spectra on a Bruker AM-500 instrument. The spectra were analyzed by the procedure described in [19]. The results demonstrated that the aromaticity factor characterizing the relative amount of aromatic carbon atoms in a molecular-weight-average molecule increases from 0.111 in the feed to 0.506 in the concentrate, the number of aromatic carbon atoms, from 1.74 to 7.49, and the number of hydrogen atoms bound to aromatic carbon atoms, from 1.03 to 4.3.

Table 6 demonstrates the results of chromatographic distillation, corresponding to the TBP (true boiling point) curve, of samples of the feed, raffinate, and concentrate of aromatic hydrocarbons, obtained in experiment no. 2. TBP curves of the raffinate and feed differ only slightly (raffinate dry point somewhat decreases). The initial boiling and dry points of the concentrate increase as compared to the feed. Nevertheless, practically the whole concentrate can be used as a component of Nefras AR-150/330.The concentrate of aromatic hydrocarbons separated from the diesel fraction can be combined with the component of Nefras 150/330 separated from the jet engine fuel fraction [6].

CONCLUSIONS

(1) In the process including extractive purification of the diesel fraction with dimethylformamide or dimethylacetamide in pentane and regeneration of polar extractants from the extract phase by azeotropic distillation, providing removal of azeotropic mixtures of amides with saturated hydrocarbons C_{10}–C_{14}, the arene content in the concentrate of aromatic hydrocarbons increases to 98–99 wt % against 93–95% in the extract.

(2) The proposed extraction–azeotropic distillation method allows production of environmentally friendly diesel fuel with an arene content below 10 wt %. Another product is a petroleum aromatic solvent like Nefras AR-150/330.

REFERENCES

1. Varshavskii, O.M., Gaile, A.A., Semenov, L.V., and Somov, V.E., in *Sbornik trudov OOO "KINEF"* (Coll. of Works of Kirishinefteorgsintez Production Association, Limited Liability Company), Gaile, A.A. and Somov, V.E., Eds., St. Petersburg: Sintez, 1998, pp. 11–18.
2. Gaile, A.A., Somov, V.E., Semenov, L.V., *et al.*, *Khim. Tekhnol. Topl. Masel*, 1999, no. 5, pp. 3–7.
3. RF Patent 2148070.
4. Gaile, A.A., Somov, V.E., Varshavskii, O.M., and Semenov, L.V., *Sbornik trudov OOO "KINEF"* (Coll. of Works of Kirishinefteorgsintez Production Association, Limited Liability Company), Gaile, A.A. and Somov, V.E., Eds., St. Petersburg: Sintez, 1998, pp. 91–138.
5. Gaile, A.A., Somov, V.E., and Varshavskii, O.M., *Aromaticheskie uglevodorody: vydelenie, primenenie, rynok* (Aromatic Hydrocarbons: Separation, Applications, and Market), St. Petersburg: Khimizdat, 2000.
6. Gaile, A.A., Semenov, L.V., Varshavskii, O.M., *et al.*, *Zh. Prikl. Khim.*, 2001, vol. 74, no. 2, pp. 320–324.
7. Rogalski, M. and Stryjek, R., *Bull. Acad. Pol. Sci., Ser. Sci. Chim.*, 1980, vol. 28, no. 2, pp. 139–147.
8. Antosik, M., Stafiej, A., and Stryjek, R., *Fluid Phase Equil.*, 1990, vol. 58, no. 3, pp. 325–333.
9. GDR Patent 108510.
10. Kogan, V.B., *Azeotropnaya i ekstraktivnaya rektifikatsiya* (Azeotropic and Extractive Distillation), Leningrad: Khimiya, 1971.
11. *Fiziko-khimicheskie svoistva individual'nykh uglevodorodov* (Physicochemical Properties of Individual Hydrocarbons), Tatevskii, V.M., Ed., Moscow:

Gostoptekhizdat, 1960.

12. Mukhopadadhyay, M. and Malleshwara, R.B.D., *Indian Chem. Eng.*, 1987, vol. 29, no. 4, pp. 52–56.
13. Lesteva, T.M. and Logunova, G.I., *Zh. Prikl. Khim.*, 1979, vol. 52, no. 9, pp. 1986–1989.
14. Gmehling, J., Menke, J., and Schiller, M., *Activity Coefficients at Infinite Dilution*, DECHEMA Chemistry Data Ser., Frankfurt on Main, 1994, vol. 9, part 3, pp. 919–1389.
15. Mollmann, C. and Gmehling, J., *J. Chem. Eng. Data*, 1997, vol 42, no. 1, pp. 35–40.
16. Kaminskii, E.F., Osipov, L.N., Khavkin, V.A., *et al.*, *Neftepererab. Neftekhim.*, 1996, no. 2, pp. 12–14.
17. Kayumov, R.P., Khaimova, T.G., Konopleva, S.N., and Stekol'shchikov, M.N., *Fiz.-Khim. Metody Issled. Prod. Neftekhim. Sinteza*, 1990, issue 9, pp. 126–132.
18. Yakushkin, M.I., *Neftepererab. Neftekhim.*, 1979, no. 10, pp. 40–42.
19. Ogorodnikov, V.D., in *Instrumental'nye metody issledovaniya nefti* (Instrumental Methods in Petroleum Research), Novosibirsk: Nauka, 1987, pp. 49–67.

Russian Journal of Applied Chemistry, Vol. 74, No. 5, 2001, pp. 870–876. Translated from Zhurnal Prikladnoi Khimii, Vol. 74, No. 5, 2001, pp. 843–849.

CHEMISTRY OF FOSSIL FUEL

The Use of Pulse Nuclear Magnetic Resonance for Studying the Mechanism of Solvation Separation of Natural Bitumen

V. G. Kozin, A. Yu. Kopylov, and R. S. Kashaev

Kazan State Technological University, Kazan, Tatarstan, Russia

Received April 12, 2000; in final form, November 2000

Abstract—A mechanism of deasphalting and fractionation of Ashal'chinsk natural bitumen with acetone was studied by pulse NMR. The features of distribution of components of the initial material in acetone solutions in deasphalting and also structural variations in the colloidal system resulting in separation of fractions when water is added in portions to the solution were studied. The structural-group composition of the separation products was characterized on the basis of NMR and IR data.

Previously [1, 2] we suggested a procedure of solvation deasphalting and fractionation of natural bitumens (NBs). This separation procedure is of large applied significance and calls for further investigation aimed at studying the mechanism of complicated multistage extraction of components from NB at discrete variation of the solvency of the polar solvent. However, the mechanism of separation of NB, which is a complex colloidal system, by a polar solvent is not adequately studied. The procedures widely used for studying petroleum dispersion systems (PDSs) with preseparation of these systems by distillation, extraction, adsorption, and other methods with subsequent use of chromatography, IR spectroscopy, and polarography allow determination of the elemental, chemical, and structural-group compositions of the separation products [3]. However, all these methods destroy the colloidal system during analysis and do not allow sudying structural variations in PDSs under the action of various factors. These methods should be replaced by noncontact methods which do not destroy the colloidal system and furnish information on the composition and structure of the system components but also on the parameters of molecular motion, structural ordering, and phase transitions of the "living" colloidal system. At present, among these methods, pulse NMR spectroscopy finds expanding application [4, 5].

EXPERIMENTAL

For measurements of NMR relaxation parameters we used an 08RS/BK pulse relaxometer, which is a modification of previously developed pulse relaxometers [6]. The unit is based on the Hahn and Carr–Purcell–Meiboom–Gill methods [5]. We measured the spin–spin relaxation times T_2i (ms) of the components of phases found in NB, its solutions in acetone, and also in the products of deasphalting and fractionation. The number of phases characterized by certain T_2i values and proton population density Pi was determined by expansion of envelope of spin–echo signals to individual components with subsequent separation of linear portions [7, 8]. In studying acetone solutions in NB and solution of the deasphalting product in hydrated acetone, the possibility of finding more than three phases in the system arised owing to using two steps of measurements at various regimes of relaxometer operation. First, the envelope of spin echo was divided in two portions at the fracture point, and then the resulting portions were individually expanded into components whose number did not exceed three. Associated and free acetone molecules and also their associates with the most mobile molecules of oils with long relaxation times (approximately 1000 ms) make the main contribution into the approximately linear portion of the curve at the end of the envelope. The initial portion of the envelope corresponds to less mobile components of the solution.

To study the effect of the solvent amount on restructurization proceeding in deasphalting, we prepared the solution of NBs in acetone in the range of solvent to NB ratio from 0.25 to 1. At the ratio higher than 1 the solution separated in two phases, i.e., deasphalting proceeded; therefore, at the ratio of 3–5 the solutions of asphalt (lower layer) and deasphalting product (upper layer) were studied individually. To study the effect of temperature on the parameters of

1070-4272/01/7405-0870$25.00

molecular motion, the resulting solutions were prepared and analyzed at 20 and 35°C.

To study the mechanism of solvation fractionation, we carried out deasphalting of Ashal'chinsk NB with acetone (ratio of 5) at 20°C. Then, the solution of deasphalting product was fractionated by separation of fractions on adding water in portions in the amounts of 4, 8, 12, and 16 wt %, respectively. The process was carried out similarly at 30 and 40°C. Then, the compositions of the upper (the solution of deasphalting product in wet acetone) and the lower (solutions of asphalt and fractions) phases were studied individually by pulse NMR. The spectrometer was equipped with a temperature-controlled unit for measurement of the spin–spin relaxation time at the same temperature at which the fractionation was carried out.

The initial materials and also asphalt and the fractions produced by the same scheme but at 55°C were also studied by pulse NMR in the temperature range 20–100°C.

To study the structural-group composition of solutions of asphalt and deasphalting product obtained at 20°C and also solutions of asphalt and fractions obtained at 55°C, we registered high-resolution ^{1}H NMR spectra on a Tesla-567A spectrometer operating at 100 MHz. In addition, the fractionation products were studied by IR spectroscopy [3] using a Specord M-85 spectrophotometer.

The spin–spin relaxation time T_2i and proton populations Pi of NB components, products of its separation, and their solutions in acetone were the main characteristics used for studying this colloidal system by pulse NMR.

The temperature dependences of the spin–spin relaxation time of NB components are presented in Fig. 1. It is seen from Fig. 1 that this colloidal system exists in the form of three phases with different molecular mobilities. Curve *1* can be assigned to the most mobile phase whose molecules most likely form the dispersion medium and enter into the composition of the outer solvation shell of a complex structural unit (CSU) being in direct contact with the dispersion medium. Oil molecules and long, fairly mobile aliphatic fragments of resin molecules can be among these components of the system. Curve *2* can be assigned to resin molecules that form the inner solvation shell being in direct contact with the CSE nuclei, asphaltenes. The asphaltene phase is represented by curve *3* characterizing the components of the initial material with the lowest molecular mobility. In this case, asphaltenes as the third phase of the system

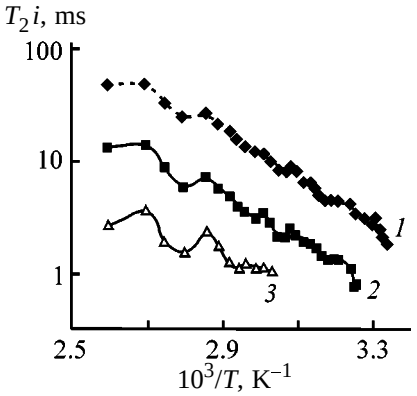

Fig. 1. Relaxation time T_2i of components of Ashal'chinsk NB as a function of temperature T. (*1*) Oils, (*2*) resins, and (*3*) asphaltenes.

begin to be detected by the device only at a temperature above 50°C, since at lower temperatures the structured asphaltene components have too short relaxation time.

As seen from Fig. 1, there are abrupt step variations of the spin–spin relaxation time for the phase corresponding to asphaltenes. These variations characterize the restructurization proceeding in each of the three suggested phases. Thus, each jump in the temperature dependence is apparently caused by variation of the structure of CSU and associates of NB components. Naturally, this restructurization for oils is less pronounced than that for asphaltenes having a stack structure close to the graphite-like structure. Resins have an intermediate structure.

It is of great scientific interest to study by pulse NMR the structural variations occurring in NB in its mixing with acetone. With this purpose we studied the NMR spectra of acetone–NB solutions at 20 and 35°C. In the absence of acetone two phases are revealed by the dependence of T_2i of NB components on the solvent ratio (Fig. 2) at these temperatures, similarly to data in Fig. 1. It should be noted that all the curves corresponding to 35°C lie above the curves characterizing the solution at 20°C, which is due to increase in the molecular mobility with increasing temperature. In addition of acetone to the colloidal system in hand at the acetone : NB ratio of 0.25, these two phases can be observed but the T_21 and T_22 values characterizing their molecular mobilities are significantly higher. In this case a new phase with the relaxation time T_23 appears in the solution; in its formation acetone plays a dominant role. Polar molecules of acetone have formed presumably associates primarily with heteroatomic and aromatic components previously incorporated into the outer solvation shell of CSU. Addition of the next portion of acetone to the

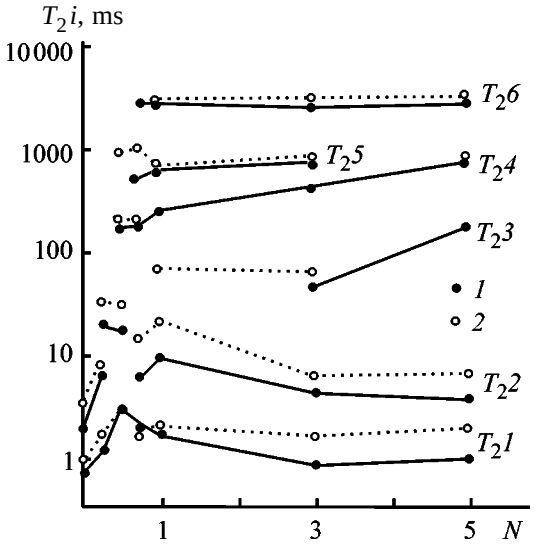

Fig. 2. Relaxation time T_2i of NB components as a function of the degree of dilution of NB with acetone. (*N*) Ratio of acetone to NB. Temperature, °C: (*1*) 20 and (*2*) 35.

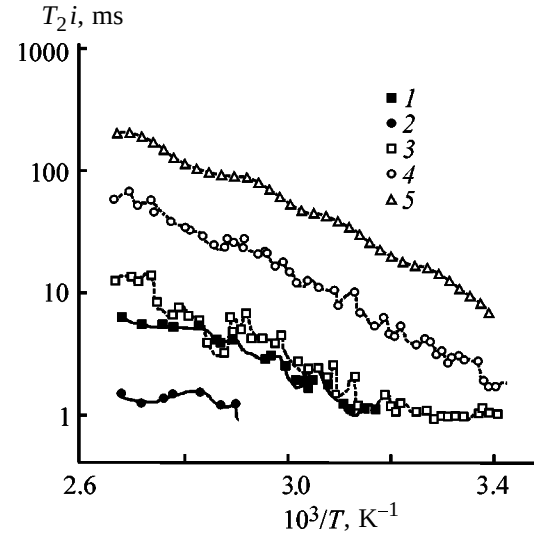

Fig. 3. Temperature dependence of relaxation time T_2i for components of (*1, 2*) asphalt and (*3, 4*) deasphalting product. (*1, 3*) *T1*, (*2, 4*) *T2*, and (*3*) *T3*.

system (the acetone : NB ratio of 0.5) results in an increase in the molecular mobility of the initially coexisting phases *1* and *2*. Phase *3* formed on addition of the first portion of acetone does not change the molecular mobility, and a new phase *4* with a longer relaxation time T_24 appears. It can be assumed that in this case not only the outer solvate layer but also the layer directly adjacent to asphaltenes, CSU nucleus, starts to destroy. This assumption is based on the fact that addition of the next portion of acetone (acetone : NB ratio of 0.75) results in CSU restructurization accompanied by significant decrease in the molecular mobility of asphaltene phase *1* and appearance of new phases *5* and *6* enriched with acetone. From our data in neat acetone, there are two phases with different molecular mobilities, free and associated molecules with relaxation times T_2a = 2800 and T_2b = 1000 ms at 20°C, respectively. Hence, it can be concluded that the relaxation time T_25 is close to the relaxation time of the associated phase and T_26 is close to that of the free phase of neat acetone. Thus, at this ratio of acetone to NB in the system, asphaltenes start to separate as individual microphase, in which the resin and oil molecules in the solvate shell are replaced by acetone molecules.

Further addition of acetone to the system under consideration does not result in formation of new phases, and the initial colloidal system separates in layers forming two coexisting thermodynamically equilibrium colloidal systems: asphalt solution in which asphaltene and heavy resinous components of the initial materials with lower molecular mobility are concentrated and solution of deasphalting product containing molecules of oils and resins and small amount of finely dispersed solvated asphaltenes. When analyzing the dependences of NMR parameters separately for solutions of asphalt and deasphalting product it should be noted that phases *1* and *2* refer to solutions of both asphalt and deasphalting product. The phases having the relaxation times T_23, T_24, and T_26 are present only in the solution of deasphalting product, and the phase with the relaxation time T_25 is distributed between phases *4* and *6* at the ratio of acetone to NB higher than 3. The fact that components of NB dissolved in acetone are separated with respect to their molecular mobility is confirmed by the temperature dependence of the relaxation time of asphalt and deasphalting product components, produced by deasphalting of NB at 55°C and acetone ratio equal to 3 (Fig. 3). In this dependence there are two phases of asphalt whose relaxation times correspond to T_21 and T_22 presented in Fig. 1. These two phases are also present in the deasphalting product; however, their components have considerably higher molecular mobility owing to breakdown of the three-dimensional graphitic structure of asphaltenes which most likely retained only the platelike two-dimensional structure. The most mobile phase in deasphalting product (the upper line in the plot) corresponds to oils.

It is well known that it is the oil fraction of NB, consisting of paraffin naphthene hydrocarbons forming the major fraction of the dispersion medium and the outer solvate shell of CSU, that passes primarily into the deasphalting product. The analysis of the high-resolution NMR spectrum showed that polycondensed aromatic components with short aliphatic

chains also pass predominantly into the deasphalting product solution, while at the same degree of aromaticity and condensation molecules with longer aliphatic substituents remain in the asphalt solution. Association of polar molecules of acetone with polycondensed aromatic components with short aliphatic chains is less hindered sterically and therefore these components predominantly pass into the deasphalting product solution. This suggestion is confirmed in [9], according to which aromatic hydrocarbons with the largest average molecular polarization have the highest solubility in a polar solvent.

The mechanism of solvation fractionation (SF) was studied on the basis of data on distribution of components with various molecular mobilities in solutions of deasphalting product and fractions at portional addition of water. Figure 4 shows the dependence of T_2i on the amount of water added for components of solutions of fractions (lower layer) and deasphalting product (upper layer). It is evident that with increasing amount of water the number of phases in the system increases; however, asphaltene phase *1* is the same in the solutions of all fractions, and its relaxation time T_21 increases with increasing temperature of the process. The presence of asphaltenes in all fractions is confirmed by the data obtained in studying physicochemical characteristics of products of the fractionation carried out at the same solvent ratio but different temperature [2].

Phase *2*, corresponding mainly to the resins incorporated into CSU shells partially retained in deasphalting, is not registered in NMR experiments at 20°C. During SF at 30°C and 40°C this phase is not registered in this colloidal system at water content no more than 8% when the first two fractions are precipitated. Phase *3* with the relaxation time T_23 can be observed only at 20°C at a water content of up to 12%. After isolation of the first three fractions the concentration of acetone molecules (free molecules with the relaxation time T_25 and also self-associated molecules and molecules associated with water and deasphalting product components with the relaxation time T_24) increases to such an extent that the relaxation time of the other components of the system cannot be detected.

Thus, the pulse NMR technique reveals some differences between the mechanisms of deasphalting and fractionation. Thus, in deasphalting an increase in the concentration of acetone is accompanied by appearance of new phases involving deasphaling product and acetone molecules with a higher molecular mobility, whereas in SF with increasing water content the

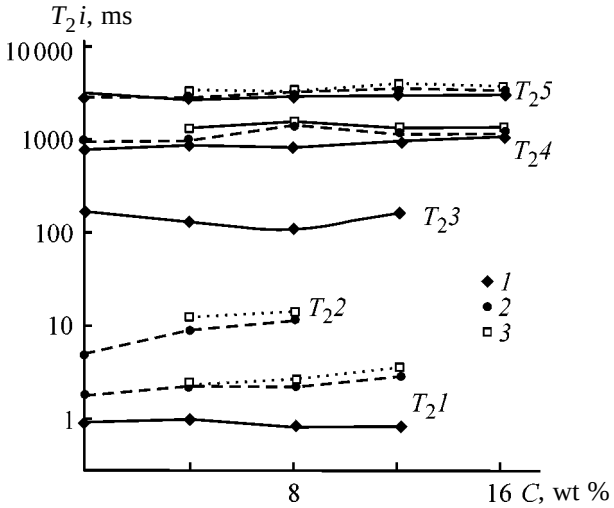

Fig. 4. Relaxation time T_2i of components of solution of fractions and deasphalting product as a function of water content *C*. Temperature, °C: (*1*) 20, (*2*) 30, and (*3*) 40.

number of phases in the system decreases owing to separation of components with the lower molecular mobility. Addition of a new portion of water results in abrupt changes in the structure of the colloidal system, owing to which in precipitation of each fraction the corresponding phase with the relaxation time T_2i is redistributed and disappears. For fraction 2 this is phase *2*; separation of fraction 3 is accompanied by redistribution and disappearance of phase *3*.

Using pulse NMR spectroscopy, we determined the parameters of molecular mobility of the components of fractions obtained at a fractionation temperature of 55°C and the acetone : initial material ratio of 5 after separation of these fractions from acetone and water. With this purpose we studied the temperature dependences of the spin–spin relaxation time of these components, presented in Fig. 5. We determined the physicochemical and structural-group characteristics of the separation products (from the evidence of high-resolution NMR), presented in Table 1.

Analysis of the temperature dependences obtained for the fractions showed that in these fractions, similar to the initial material (Fig. 1), there are three phases corresponding to oils, resins, and asphaltenes. In this case, the relaxation time of the asphaltene phase varies insignificantly for all the fractions, while the relaxation time of the resinous and oil components of the separation products increases with increasing amount of water required for their recovery from the solution of the deasphalting product. Insignificant variations of T_2i values of asphaltenes in the temperature dependence for the fractions may be due to the fact that in the deasphalting product solution to be fractionated

Table 1. Physicochemical characteristics of fractions of Ashal'chinsk NB. Solvent : initial material ratio 5, temperature of deasphalting and fractionation 55°C

Fraction	Yield based on NB, wt %	M*	ρ_4^{20}, g cm^{-3}	C_s, wt %	C_{arom}	CH_2/CH_3	n_D^{20}
Asphalt	36.6	593	1.0407	4.2	6.1	2.78	–
1	14.2	446	0.9615	3.0	5.4	3.29	–
2	21.0	354	0.9618	3.1	4.8	2.55	1.5296
3	10.2	333	0.9619	3.1	5.7	1.89	1.5320
4	6.9	251	0.9705	3.5	6.6	1.56	1.5384
5	7.2	210	1.0486	4.9	11.3	1.4	1.5600

* Molecular weight.

only finely dispersed asphaltenes are retained, having no complicated three-dimensional structure similar to NB and solvated mainly by acetone and water molecules. These associates still remain in the solution with increasing its polarity by adding water, since, as mentioned above, asphaltenes have the highest values of the average molecular polarization in this system and are most strongly retained in a solution of the polar solvent. With increasing water content, coarse less polar components having long aliphatic radicals adjacent to condensed aromatic structures are mainly separated from the deasphalting product. As a result, the most polar, most polarizable, and smallest-size components of the initial material, such as low-molecular-weight heteroatomic and aromatic compounds, are accumulated in the last fraction. This is confirmed by the NMR and IR spectra. In high-resolution NMR spectra of asphalt and all fractions (fractionation temperature 55°C) there are signals with the chemical shifts identified on the basis of published data [10, 11].

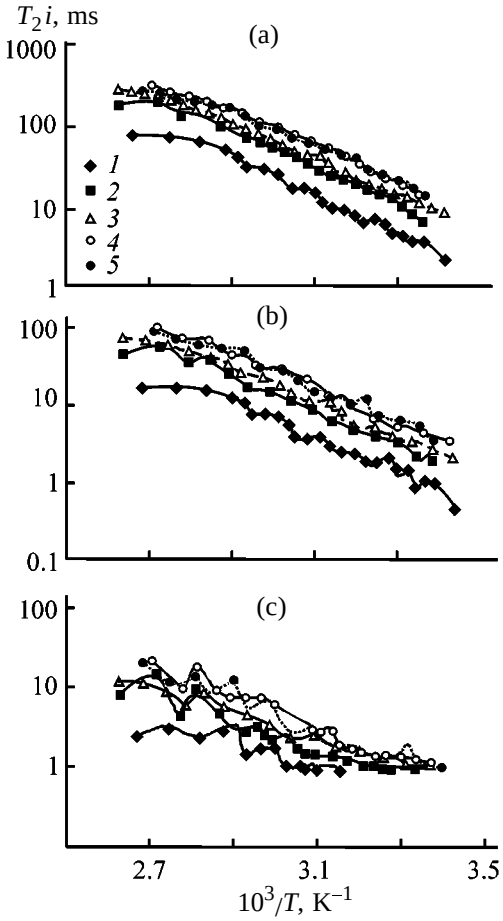

Fig. 5. Relaxation time T_2i of (a) oils, (b) resins, and (c) asphaltenes in fractions 1–5 as a function of temperature T. Fractions: (*1*) 1, (*2*) 2, (*3*) 3, (*4*) 4, and (*5*) 5.

From the ratio of the integral intensities of the signals corresponding to aromatic structures and the total aliphatics in the NMR spectra of separation products and also the ratio of the intensities of the signals of methylene and methyl protons, we obtained the averaged molecular characteristics of the fraction components, such as aromaticity C_{arom} and the length of aliphatic substituents [3, 11] (Table 1, Fig. 6).

Based on the IR data, we determined the parameters described in [12] and characterizing the structure of averaged molecule of separation products: (1) aromaticity C1, (2) degree of branching of aliphatic fragments C2, (3) content of sulfoxide groups in aromatic fragments S1, (4) content of sulfoxide groups in aliphatic fragments S2, and (5) total content of unsubstituted hydrogen atoms in aromatic fragments B1.

Presumably, the increase in the relaxation time of the phases corresponding to resinous and oil components of fractions with increasing water content is due to a decrease in the degree of condensation of molecules in fractions 1–4. The increase in aromaticity of fraction 5 (Fig. 6) is due to accumulation of mono- and bicyclic aromatic compounds.

Variation in the degree of branching of aliphatic fragments C2 in fractions is also characterized by the presence of a maximum. Low degree of branching in asphalt is due to the presence of highly condensed components low-substituted with short aliphatic radicals, which is suggested by the high value of the coefficient B1 and low value of the CH_2/CH_3 ratio. The increase in the coefficient C2 in passing to fractions 1–4 is due to an increase in the solvent polarity, which results in retention of components with a higher polarizability in the solution, namely, of components with shorter carbon chains at the same number of carbon atoms and hence with a greater degree of branching of aliphatic substituents at aromatic rings and a greater number of substituents (Table 2, coefficient B1).

The features of distribution of heteroatomic compounds can be followed for distribution of sulfur-containing compounds among fractions as an example. The character of variation of coefficients S1 and S2 is similar and shows the increase in the amount of sulfoxide groups in passing from asphalt to the last fraction owing to their high polarity and ability to form hydrogen bonds with proton-donor compounds. This results in retention of sulfoxide-containing compounds in aqueous solution of acetone.

An increase in the water content in the deasphalting product solution results in increased role of dipole–dipole interactions and formation of new hydrogen bonds, which facilitates separation of molecules of oil components with the paraffin–naphthene structure, having no tendency to participate in these interactions, from the solution. The presence of more polar water in the solution apparently results in formation of more compact associates with polarizable oil and resinous components with certain molar volume, having short aliphatic substituents at the aromatic ring. In this case, the deasphalting product components having shorter aliphatic fragments and lower degree of condensation as compared to the above components are separated from the solution, which is manifested in longer spin–spin relaxation time of oils and resins in fractions. This assumption is confirmed by data on variation of the molecular weight, aromaticity, and the length of aliphatic chains of fractionation products (Tables 1, 2).

The characteristic feature of the obtained temperature dependences is the presence of an inflection in the curves corresponding to phases of oils and resins (Fig. 5), while for the phase of asphaltenes the jumpwise variations of the molecular mobility, similar to those in the initial material but less pronounced, can be observed (Fig. 2). These jumpwise variations for the asphaltene phase will be studied in the future. The temperature corresponding to the inflection point in the plots for the phases with the lower molecular mobility decreases from 81 to 74°C with increasing water content in the deasphalting product solution, required for separation of the corresponding fraction. The inflection in the curve can originate from the fact that the major part of structural variations in the corresponding phases proceeds up to a certain temperature and further increase in temperature affects insignificantly the molecular mobility of the components.

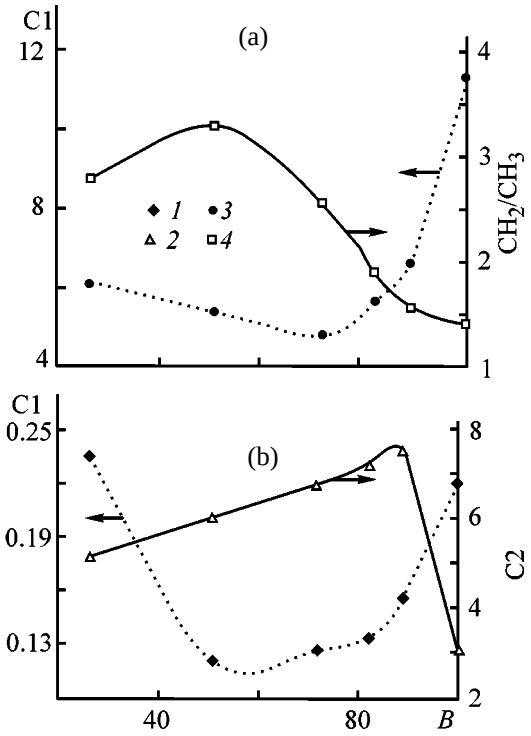

Fig. 6. Structural-group composition of fractions as a function of their yield based on the initial materials: (C1) aromaticity, (C2) degree of branching of aliphatic fragments, (CH_2/CH_3) length of aliphatic chain, and (*B*) total yield of fraction (wt %). Data: (a) NMR and (b) IR spectroscopy.

Table 2. Coefficients characterizing structural-group composition of fractionation products

Fraction	Coefficient				
	C1	C2	S1	S2	B1
Asphalt	0.234	5.158	0.424	0.100	3.674
1	0.120	6.075	0.667	0.080	2.123
2	0.126	6.776	0.708	0.089	2.417
3	0.133	7.230	0.649	0.086	2.579
4	0.155	7.532	0.774	0.122	2.935
5	0.220	3.08	0.688	0.147	3.811

CONCLUSIONS

(1) The mechanism of distribution of components of Ashal'chinsk natural bitumen in its deasphalting and fractionation with acetone was studied by pulse NMR. The restructurization processes occurring in acetone solutions in natural bitumens were studied at various temperatures and solvent ratios and at addition of water in portions.

(2) In the products of deasphalting and fractionation there are three fractions with different molecular mobilities. In deasphalting, the asphaltene phase is concentrated in asphalt. With increasing water amount required for separation of the corresponding fraction the molecular mobility of its oil and resinous components increases.

REFERENCES

1. Khusnutdinov, I.Sh., Kozin, V.G., and Kopylov, A.Yu., *Zh. Prikl. Khim.*, 1998, vol. 71, no. 8, pp. 1019–1023.
2. RF Patent 2 055 858.
3. Rozental', D.A., Posadov, I.A., Popov, O.G., and Paukku, A.N., *Metody opredeleniya i rascheta strukturnykh parametrov fraktsii tyazhelykh neftyanykh ostatkov: Uchebnoe posobie* (Methods for Determination and Evaluation of Structural Parameters of Fractions of Heavy Petroleum Residues: A Textbook), Leningrad: Leningr. Tekhnol. Inst., 1981.
4. Farrar, T.G. and Becker, E.D., *Pulse and Fourier Transform NMR: Introduction to Theory and Methods*, New York: Academic, 1971.
5. Vashman, A.A. and Pronin, I.S., *Yadernaya magnitnaya relaksatsiya i ee primenenie v khimicheskoi fizike* (Nuclear Magnetic Relaxation and Its Application to Chemical Physics), Moscow: Nauka, 1979.
6. Kashaev, R.S., Tarasov, V.F., Idiyatullin, Z.Sh., *et al.*, *Prib. Tekh. Eksp.*, 1993, no. 1, pp. 242–243.
7. Kashaev, R.S., *Zh. Fiz. Khim.*, 1999, vol. 73, no. 1, pp. 1972–1977.
8. USSR Inventor's Certificate no. 1 583 823.
9. Kazakova, L.P. and Krein, S.E., *Fiziko-khimicheskie osnovy proizvodstva neftyanykh masel* (Physicochemical Principles of Production of Petroleum Oils), Moscow: Khimiya, 1978.
10. Pople, J.A., Schneider, W.G., and Bernstein, H.J., *High-Resolution Nuclear Magnetic Resonance*, New York: McGraw-Hill, 1959.
11. Kalabin, G.A., Polonov, V.M., Smirnov, M.B., *et al.*, *Neftekhimiya*, 1986, vol. 26, no. 4, pp. 435–463.
12. Botneva, T.A., Il'ina, A.A., Terskoi, Ya.A., *et al.*, *Metodicheskoe rukovodstvo po lyuminestsentno-bituminologicheskim i spektral'nym metodam issledovaniya organicheskogo veshchestva porod i neftei* (A Guide for Bitumen-Luminescence and Spectral Methods for Studying Organic Substances of Rocks and Crude Oils), Moscow: Nedra, 1979.

Russian Journal of Applied Chemistry, Vol. 74, No. 5, 2001, pp. 877–880. Translated from Zhurnal Prikladnoi Khimii, Vol. 74, No. 5, 2001, pp. 850–853.

CHEMISTRY OF FOSSIL FUEL

Thermal and Molecular Characteristics of Asphalt–Resin Oligomers

I. F. Gladkikh, V. A. Kraikin, N. N. Sigaeva, I. A. Ionova, and Yu. B. Monakov

Poisk Research Center, Ufa, Bashkortostan, Russia
Institute of Organic Chemistry, Ufa Scientific Center, Ufa, Bashkortostan, Russsia

Received April 27, 2000

Abstract—Formation of asphalt–resin oligomers by reaction of petroleum vacuum residues and bitumens with the oligoisoprene fraction from the dimethylformamide distillation bottoms (isoprene production waste) was studied by thermomechanical and thermogravimetric analyses. The number-average molecular weights of the final product and initial components were determined.

Utilization of industrial wastes and by-products, along with solution of environmental problems, will decrease the cost of commercial products and extend the range of raw materials. Among the largest-tonnage wastes of oil-refining and petrochemical industries are pyrolysis tars and bottoms [1], in particular, petroleum asphalts and bitumens. Their condensation with dimethylformamide distillation bottoms (KORD resin, isoprene production waste) containing the oligoisoprene fraction yields asphalt–resin oligomers (ASMOL) [2].

Both ASMOL and formulations thereof are widely used as high-performance corrosion-resistant and waterproofing materials and coatings [3]. In the main service parameters (plasticity, corrosion-resistance power, adhesion) ASMOL surpasses the protective formulations based on petroleum bitumens and high-molecular-weight elastomers [4].

In this work we attempted to reveal factors responsible for the unique properties of this product and, primarily, to find whether ASMOL is merely a mixture of sulfonated products of condensation (or polymerization) of the initial components (bitumen and oligomeric fraction of isoprene) or its formation involves chemical reactions between the components. This is necessary for optimizing the process of ASMOL production and important from the scientific viewpoint, as study of the reactivity of oil cracking residues is one of the major research lines in petrochemistry.

As seen from the table, ASMO contains high-molecular-weight fractions whose molecular weight M exceeds several times that of the initial components, KORD resin and bitumen.

Since ASMOL is produced in the presence of concentrated sulfuric acid, formation of the high-molecular-weight fraction can be associated with condensation of bitumen resins (on heating or acid treatment, neutral resins as components of petroleum bitumens undergo condensation to give asphaltenes, the highest-molecular-weight components of oil [5]). High-molecular-weight compounds can also form by condensation of KORD resin and bitumen, since both the initial and intermediate substances of ASMOL production contain reactive functional groups such as –COOH, –OH, $–HSO_4$, and $–NH_2$. To take into account the contribution of these reactions to the increase in the molecular weight of the final product, we performed separate sulfonation of ASMOL components (bitumen and KORD resin).

As seen from Fig. 1, the thermomechanical curves of ASMOL, KORD resin, bitumen (sulfonated and nonsulfonated), and their mechanical mixtures have a shape characteristic of oligomeric products, with one temperature transition corresponding to the flow point T_f. The resin (low-molecular-weight fraction of isoprene oligomers) and bitumen have the lowest flow points. Introduction into bitumen of 10 wt % resin increases T_f of the mixture, which suggests formation of products with a higher molecular weight. Probably, in the course of ASMOL formation the chemical interaction between the components starts even in the stage of mixing and homogenization. Comparison of the thermomechanical curves of the initial (and separately sulfonated) bitumens and resin shows that sulfonation in both cases increases T_f, with the shift of the total flow branch along the temperature axis for the resin being by a factor of 3 larger than for the bitumen.

1070-4272/01/7405-0877$25.00

Number-average molecular weights M_n of ASMOL and initial components

Sample	M_n			
	before sulfonation	after sulfonation	fraction 2	fraction 1
ASMOL:				
laboratory sample	–	1000	2200	815
batch 2	–	700	6000	690
batch 3	–	760	9450	740
Bitumen:				
no. 1	580	860	–	–
no. 2	470	–	–	–
no. 3, batch 1	620	790	–	–
no. 3, batch 2	–	770	–	–
Resin:				
no. 1	270	–	–	–
no. 2	350	1250	–	–
no. 3	140	990	–	–

The flow of the sulfonated resin is characterized by slow gworth of the deformation in the course of heating. The polydispersity of the sample (presence of fractions with different *M*) can be indirectly judged from the shape of the initial section of the thermomechanical curve [6] (sharp or gradual inflection), and the shift of the branch characterizing the flow of the sample is primarily determined by its molecular weight. In view of these facts, our results suggest that in the course of joint sulfonation of the resin and bitumen (as it is done in production of ASMOL) the growth of the molecular weight of the final product is mainly due to cationic polymerization of oligoisoprene catalyzed with sulfuric acid, rather than to condensation processes involving bitumen. The resulting sulfooligoisoprene apparently has a wide molecular-weight distribution, as indicated by a slow growth of the deformation in the thermomechanical curve. At the same time, the fact that the flow point of a mechanical mixture of sulfonated initial components differs from that of ASMOL is an indirect evidence of interaction of the bitumen and resin components.

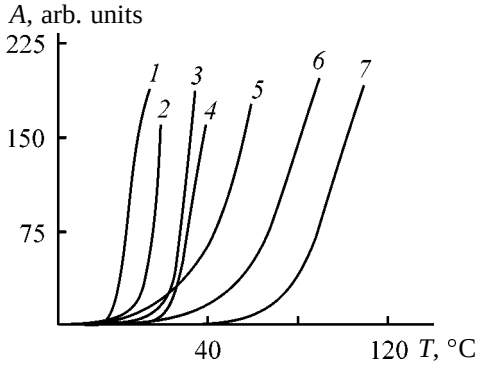

Fig. 1. Thermomechanical curves of (*1*) resin, (*2*) bitumen, (*3*) bitumen–resin mixture, (*4*) sulfonated bitumen, (*5*) sulfonated resin, (*6*) ASMOL, and (*7*) mixture of sulfonated bitumen with sulfonated resin: (*A*) deformation and (*T*) temperature.

This assumption is confirmed by direct determination of the molecular weight of the initial and final products (sulfonated and nonsulfonated). As seen from the table, sulfonation of KORD resin appreciably increases its number-average molecular weight. Sulfonation of oligoisoprenes at double bonds cannot cause such an increase in the molecular weight of the reaction products. Calculations show that addition of two sulfo groups to the initial dimeric isoprene molecule increases its molecular weight by 160 units, whereas actually it increases by 880 units. Such an increase in M_n may be due both to further polymerization of oligoisoprene catalyzed with sulfuric acid and to condensation involving sulfo groups of the oligoisoprene and amino groups of dimethylformamide, always present in a certain amount in the bottoms.

The molecular weights of the bitumen sulfonation products also increase the initial M_n values, but not so significantly. Apparently, with respect to bitumens sulfuric acid mainly acts as a sulfonating agent.

By extraction with heptane (procedure for deasphalting of petroleum bitumens), we separated ASMOL into two fractions: soluble (fraction 1) and insoluble (fraction 2) in toluene and determined their number-average molecular weights in toluene by measuring the thermal effects of condensation; the M_n values obtained are listed in the table. As expected,

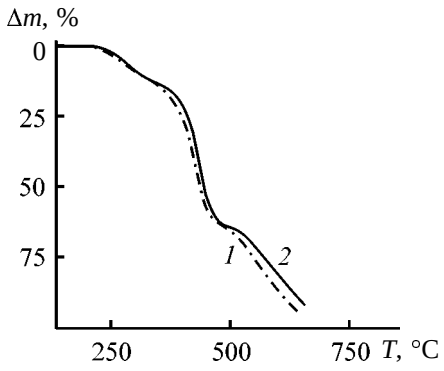

Fig. 2. TG curves of (*1*) commercial and (*2*) laboratory samples of ASMOL in air: (Δ*m*) weight loss and (*T*) temperature; the same for Figs. 4 and 5.

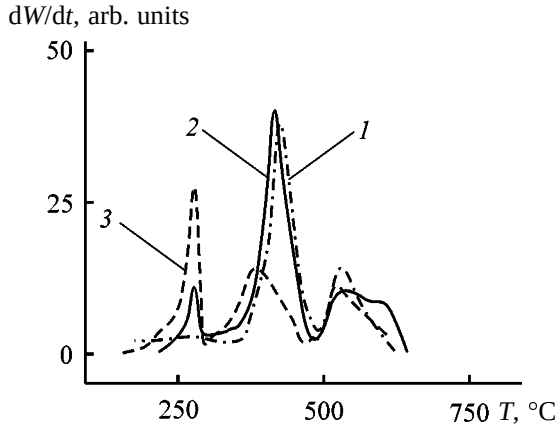

Fig. 3. DTG curves (d*W*/d*t*, rate of weight loss) of (*1*) sulfonated bitumen, (*2*) ASMOL, and (*3*) sulfonated resin in air: (*T*) temperature; the same for Fig. 6.

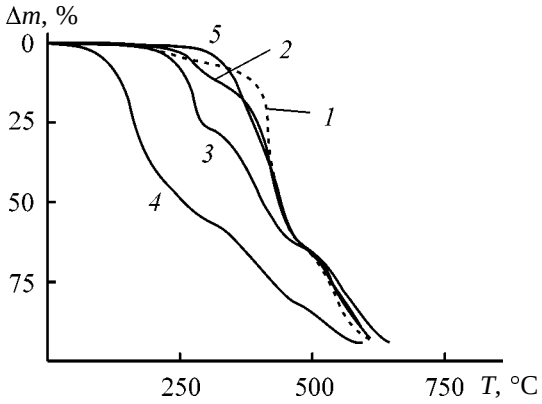

Fig. 4. TG curves of (*1*) sulfonated bitumen, (*2*) ASMOL, (*3*) sulfonated resin, (*4*) resin, and (*5*) bitumen in air.

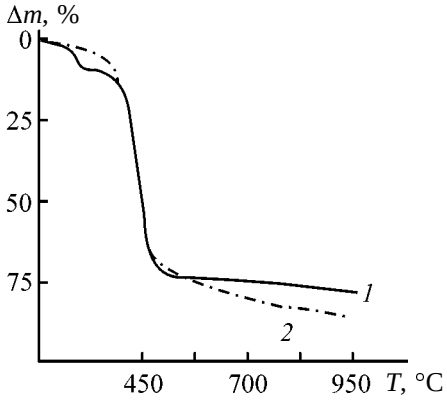

Fig. 5. TG curves of (*1*) ASMOL and (*2*) mixture of sulfonated bitumen and sulfonated resin in argon.

M_n of the heptane-insoluble fraction is considerably higher than that of the heptane-soluble product.

Owing to the presence in ASMOL of components of different molecular weights and different chemical structures, thermal and thermal oxidative degradation of ASMOL is multistage.

According to dynamic TGA data, ASMOL decomposes in air in several stages. In the integral TG curves of laboratory and commercial samples (Fig. 2), we can distinguish three stages, with the corresponding DTG peaks at 280, 420, and 550°C (Fig. 3). To assign these peaks, we performed thermogravimetric analysis of the bitumen and resin (nonsulfonated and separately sulfonated samples) and of two mechanical mixtures prepared, respectively, from the nonsulfonated and sulfonated components. Figures 3 and 4 show that in the TG curves of the sulfonated resin and bitumen a low-temperature decomposition stage appears, and the second decomposition stage shifts toward higher temperatures. Comparison of the TG (Fig. 4) and DTG (Fig. 3) curves of ASMOL and sulfonated initial components suggests that the first decomposition stage and the corresponding DTG peak are due to decomposition of the sulfo groups. Since the weight loss in this stage for the resin is greater than for the bitumen, the extent of sulfonation of the isoprene oligomers is apparently greater as compared to the bitumen. The second degradation stage (about 400°C), apparently, involves decomposition of the bitumen component: The weight loss in this stage is proportional to the bitumen content. Finally, in the range 500–600°C the cross-linked carbon residue is burned out.

Thermogravimetric analysis in an inert atmosphere gave results indirectly suggesting occurrence of condensation of oligoisoprene with bitumene. The TG curves (Figs. 5, 6) show that the course of degradation of ASMOL differs from that of a mechanical mixture of the separately sulfonated bitumen and resin. Whereas with ASMOL there is a sharp step at 280°C, the weight of the mixture sample gradually decreases in

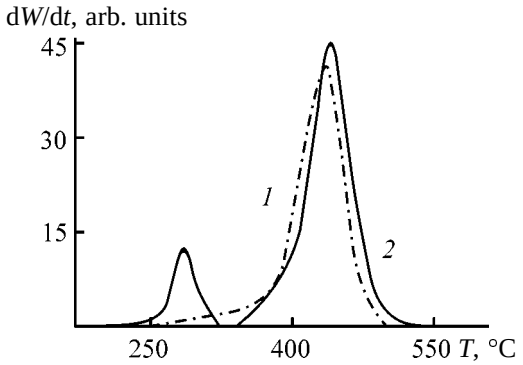

Fig. 6. DTG curves of (*1*) mixture of sulfonated bitumen and sulfonated resin and (*2*) ASMOL in argon.

a wide temperature range. Sharp steps are typical of selective decomposition of specific functional groups and cleavage of specific bonds (with subsequent elimination of low-molecular-weight decomposition products) within relatively high-molecular-weight macromolecules, whereas gradual weight loss, as a rule, suggests gradual evaporation of volatile oligomeric products.

EXPERIMENTAL

Under both industrial and laboratory conditions, ASMOL was prepared in three stages: (1) the initial components (resin and bitumen) were mixed at 90°C; (2) concentrated sulfuric acid was slowly added dropwise, so as to avoid boiling and rise of the reaction temperature (due to exothermic reaction) above 125°C; and (3) the final product was stabilized by heating at 150–160°C for 4 h.

Separate sulfonation of the bitumen and resin and preparation of the mixtures of the initial components (sulfonated and nonsulfonated) were performed similarly.

The flow point was determined on a thermomechanical installation at a load of 3.5 g mm^{-2} and a heating rate of 3 deg min^{-1}.

Dynamic thermogravimetric analysis was performed with an MOM Q-1000 derivatograph in air or argon; the heating rate was 5 deg min^{-1}, and the sample weight, 100 mg.

The number-average molecular weights M_n were determined by measuring the thermal effects of condensation [7]. The device was calibrated using polyethylene glycol samples of various molecular weights as references; the concentrations of solutions of the reference and test samples in benzene was 0.05± 0.01 g ml^{-1}. The measurements were performed at 40±0.01°C. For each sample, five parallel measurements were performed, and the mean M_n value was taken.

CONCLUSION

Our results suggest that formation of asphalt–resin oligomers involves both separate sulfonation and condensation of the initial components and their reaction with each other to give the higher-molecular-weight product. Sulfuric acid plays a dual role: firstly, it catalyzes further polymerization of the initial oligoisoprenes and their condensation with petroleum bitumen components (and also condensation of neutral bitumen resins), and, secondly, it participates in sulfonation of these products.

REFERENCES

1. Nikulin, S.S., Shein, V.S., Zlotskii, S.I., *et al.*, *Otkhody i pobochnye produkty neftekhimicheskikh proizvodstv – syr'e dlya organicheskogo sinteza* (Wastes and By-Products of Petrochemical Industry as a Raw Material for Organic Synthesis), Moscow: Khimiya, 1969.
2. RF Patent 2074224.
3. Gladkikh, I.F., Cherkasov, N.M., Alekseev, A.V., *et al.*, in *Problemy zashchity okruzhayushchei sredy na predpriyatiyakh neftepererabotki i neftekhimii* (Environmental Protection Problems in Oil-Refining and Petrochemical Plants), Ufa: Inst. Problem Neftepererabotki, Akad. Nauk Respubliki Bashkortostan, 1997, pp. 179–182.
4. Gladkikh, I.F., Cherkasov, N.M., Ibragimov, M.Sh., and Petrov, A.P., *Truboprovodn. Transp. Nefti*, 1998, no. 12, pp. 10–11.
5. Rafikov, S.R., Budtov, V.P., and Monakov, Yu.B., *Vvedenie v fizikokhimiyu rastvorov polimerov* (Introduction to Physical Chemistry of Polymer Solutions), Moscow: Nauka, 1978.
6. *Khimicheskaya entsiklopediya* (Chemical Encyclopedia), Moscow: Sov. Entsiklopediya, 1988, vol. 1.
7. Ol'khov, Yu.A. and Irzhak, I.M., *Vysokomol. Soedin., Ser. B*, 1998, vol. 40, no. 10, pp. 1706–1714.

Russian Journal of Applied Chemistry, Vol. 74, No. 5, 2001, pp. 881–884. Translated from Zhurnal Prikladnoi Khimii, Vol. 74, No. 5, 2001, pp. 854–857.

CHEMISTRY OF FOSSIL FUEL

Estimation of Quality of Petroleum Bitumens by NMR Spectroscopy and X-ray Diffraction

O. Yu. Begak and A. M. Syroezhko

St. Petersburg State Technological Institute, St. Petersburg, Russia
Mendeleev Russian Research Institute of Metrology, St. Petersburg, Russia

Received December 4, 2000

Abstract—Certified and substandard paving bituments of Kirishi Petroleum Processing Plant were studied by ^{1}H and ^{13}C NMR spectroscopy and X-ray diffraction. The differences in the aromaticity degree of asphaltenes and malthenes of these bitumens were revealed. The parameters of layered-block stacks of the asphaltenes were measured.

Previously we studied [1] certified and substandard BDUS 70/100 and BDUS 100/130 bitumens by a number of chemical and physicochemical methods. It was found than these bitumens have close chemical compositions of the organic constituents and different content of ash, sulfur, oxygen, alkaline-earth metals (Mg, Ca, Sr, and Ba), 3*d* metals (Cu, Co, and Zn), aluminum, boron, lead and arsenic. During aging of bitumens, their composition and structure, first of all at the associative level, change.

The aim of this work was to determine quantitative parameters of association of bitumen alsphaltenes and differences in the aromaticity degree of malthenes and asphaltenes of certified and substandard bitumens produced at the Kirishinefteorgsintez Joint-Stock Production Association.

EXPERIMENTAL

We used the certified and substandard bitumens characterized in our previous work [1]. Asphaltenes were recovered from the bitumens by exhaustive precipitation with hot pentane in a Soxhlet apparatus. The NMR spectra of certified and substandard bitumens were recorded in $CDCl_3$ solutions at 22°C on a Bruker AM-500 spectrometer (500 MHz, ^{1}H and 125 MHz, ^{13}C) with a 5-mm proton–carbon detector. The ^{13}C NMR spectra were recorded at inverse strobe proton decoupling. The X-ray diffraction analysis of the asphaltenes was performed on a DRON-2 diffractometer in the range $2\theta = 3°–60°$ (CuK_α radiation). The samples were powdered and placed in a cell 25 mm in diameter and 2 mm thick.

The ^{1}H signal of the residual protons of the $CDCl_3$ solvent appears as a sharp signal with a low integral intensity at 7.25 ppm against a background of the broad and strong signal of the bitumen aromatic protons. In the ^{13}C NMR spectra the solvent is manifested as a triplet at 77 ppm (Figs. 1, 2). As seen from Figs. 1 and 2, the bitumen spectra contain two groups of signals: (1) aromatic signals centered at about 7.5 and 135 ppm in the ^{1}H and ^{13}C spectra, respectively, and (2) aliphatic signals with the strongest peaks at 1.3 and 300 ppm in the ^{1}H and ^{13}C spectra, respectively. The aliphatic region of the carbon spectrum consists of five signals at 32.0, 29.8, 29.5, 22.8, and 14.2 ppm. The H_{ar}/H_{al} and C_{ar}/C_{al} ratios in the tested samples, determined by ^{1}H and ^{13}C NMR spectroscopy, are presented in Table 1.

Table 1. Comparative results of ^{1}H and ^{13}C NMR study of certified and substandard bitumens

Bitumen	H_{ar}/H_{al} (^{1}H NMR)	C_{ar}/C_{al} (^{13}C NMR)
BDUS 100/130: certified, produced 5/15/2000, certificate no. 24	0.066	0.441
substandard bitumen, produced 5/10/2000	0.0616	0.420
BDUS 70/100: certified, produced 5/6/2000, certificate no. 14	0.0595	0.425
substandard bitumen, produced 5/10/2000	0.052	0.365

1070-4272/01/7405-0881$25.00

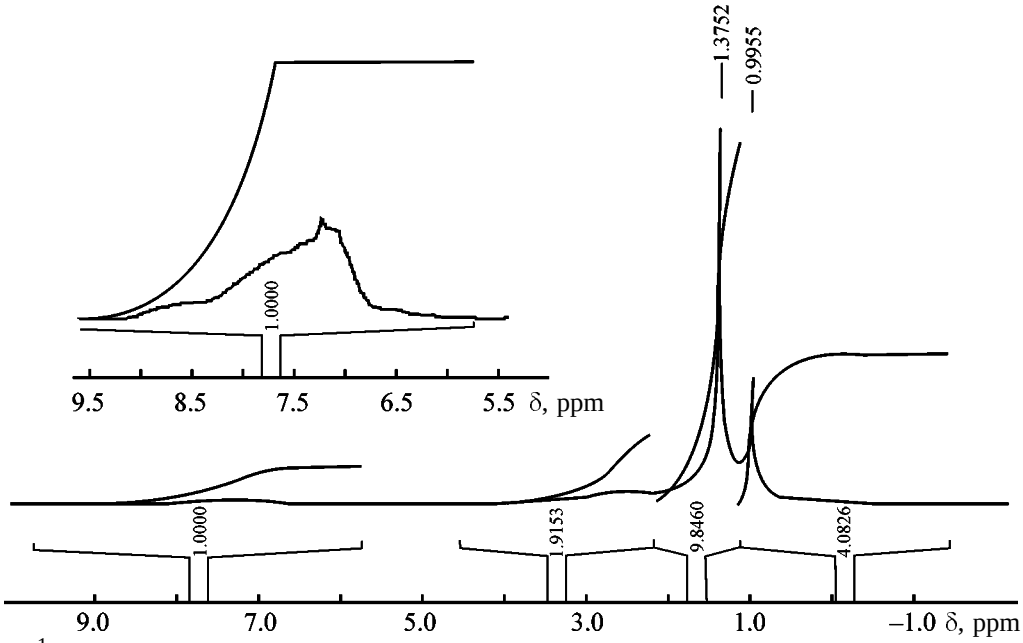

Fig. 1. ^{1}H NMR spectra of certified BDUS 100/130 bitumen. (δ) Chemical shift; the same for Fig. 2.

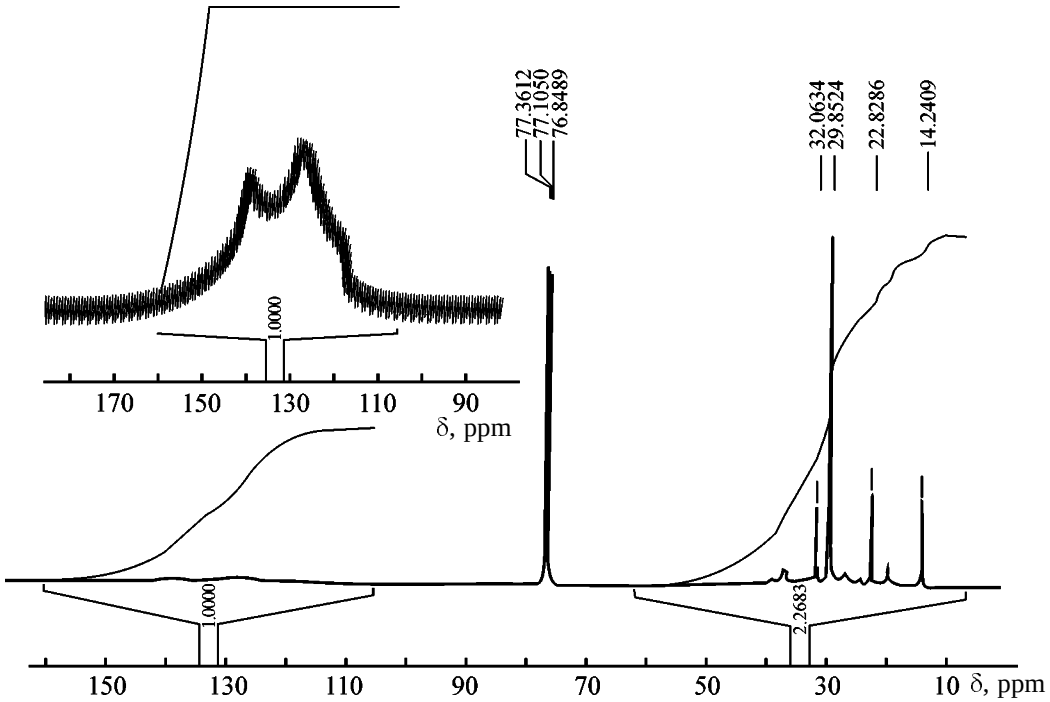

Fig. 2. ^{13}C NMR spectra of certified BDUS 100/130 bitumen.

As seen from Table 1, the H_{ar}/H_{al} and C_{ar}/C_{al} ratios in the both certified bitumens are higher than in the substandard samples (as a whole, these parameters for BDUS 100/130 bitumens are higher than those for BDUS 70/100 bitumens). For example, the H_{ar}/H_{al} ratio in the certified and substandard BDUS 100/130 bitumen is 0.066 and 0.0616, respectively (Table 1).

The H_{ar}/H_{al} ratio in the certified and substandard BDUS 70/100 bitumen is 0.0595 and 0.052, respectively. The C_{ar}/C_{al} ratio in the certified and substandard BDUS 100/130 bitumen is 0.441 and 0.42, respectively (Table 1). In the certified BDUS 70/100 bitumen this ratio is 0.425, whereas in the substandard sample it is 0.365. Thus, the NMR spectroscopic

Table 2. Calculated structural parameters of the asphaltenes

Bitumen	d_m, Å	A_{10}	A_{002}	A_γ	$A_{10}/\Sigma(A_{002}+A_\gamma)$	$B_{1/2(10)}$	$B_{1/2(002)}$	L_a	L_c	M	f_{ar}
		cm^2				deg					
BDUS 100/130: certified, certificate no. 24	3.71	3.5	28.8	31.3	0.035	3.5	3.2	23.6	12.5	4.37	0.48
substandard bitumen, produced 5/10/2000	4.15	10.5	38.5	44	0.130	7.0	4.0	11.8	10	3.4	0.45
BDUS 70/100: certified, certificate no. 14	3.89	7.2	28.7	33.6	0.123	4.5	3.8	18.4	10.5	3.7	0.46
substandard bitumen, produced 5/10/2000	3.94	11.05	40.75	50	0.119	6.5	4.5	12.6	9	3.3	0.45

study, as well as ICP-MS and HPLC [1], reveals differences between BDUS 100/130 and BDUS 70/100 certified and substandard bitumens.

Asphaltene powders recovered from certified and substandard bitumens of the both types were studied by X-ray diffraction at room temperature without using solvent, i.e., under conditions providing maximal degree of association of their molecules in supramolecular structures.

The X-ray pattern of sample no. 1 contains the following reflections. The γ reflection with the maximum at $2\theta_\gamma = 18°$ is due to diffraction on randomly distributed carbon atoms and heteroatoms (the reflection of amorphous carbon). The stack associates are manifested as a weak reflection from the (10) plane at $2\theta_{10} = 42°$ and a reflection form the (002) plane of the stacks with a maximum at $2\theta_{002} = 24°$. In the X-ray patterns of sample nos. 2, 3, and 4 the (002) reflection appears at $2\theta_{002} = 22°$, 21.5, and 22.5°, respectively.

The first step of the treatment of X-ray patterns is subtraction of the background (Fig. 3). To separate the (002) and γ reflections, they were assumed [2] to be symmetrical relative to $\theta = \theta_{002}$ and $\theta = \theta_\gamma$ axis and to be described by the Gaussian distribution function. The interlayer spacings in the stacks $d_m = 0.5\lambda/\sin\theta_{002}$ and the repeated spacings between the saturated molecular fragments $d_\gamma = 0.625\lambda/\sin\theta_\lambda$ (where λ is the wavelength of the radiation used, Å) were calculated from θ_{002} and θ_γ angles after normalization. The average diameter of flat molecular fragments in the stacks $L_a = 0.92/B_{1/2(10)}$ and the average stack thickness $L_c = 0.45/B_{1/2(002)}$ were calculated by the Scherrer equation form the halfwidths of the (10) and (002) reflections $B_{1/2(10)}$ and $B_{1/2(002)}$ measured in the $\sin\theta/\lambda$ units. The average number of layers in a stack was calculated by the equation

$$M = (L_c/d_m) + 1.$$

In addition, the areas of the separated peaks (002) and γ (A_{002} and A_γ, respectively) were measured and the aromaticity factor f_{ar} was calculated as the quotient of division of the area of the (002) reflection by the sum of the areas of (002) and γ reflections:

$$f_{ar} = A_{002}/(A_{002} + A_\gamma).$$

The results of these calculations are presented in Table 2.

The structural parameters of the asphaltene stacks in all samples differ considerably. The most ordered are sample nos. 1 and 2. They have the maximal cohesion which is manifested during the ductility measurement.

It should be noted that the aromaticity degree determined by X-ray diffraction agree well with the results of NMR spectroscopy. The higher the structural ordering of bitumens (the most ordered the

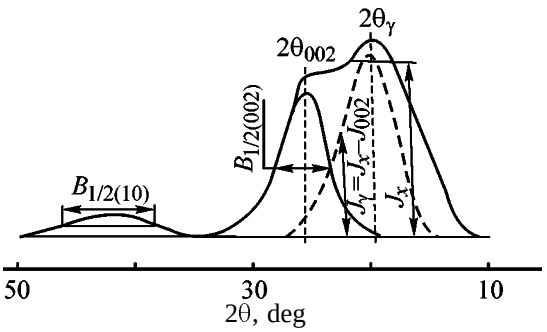

Fig. 3. Scheme for transformation of the normalized X-ray diffraction pattern and measurement of the reflection parameters. (2θ) Bragg angle.

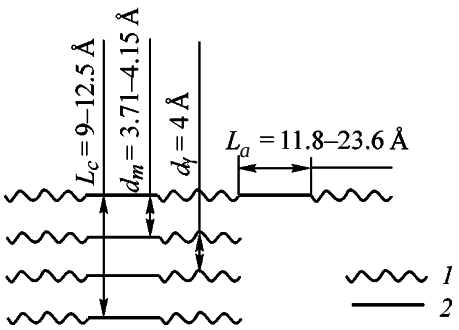

Fig. 4. Schematic structure of asphaltenes in layered-block stacks: (d_m) distance between aromatic layers, (d_γ) intrachain distance ($d_\gamma \sim 4$Å), (L_c) diameter of bunch of condensed layers, and (L_a) the diameter of the condensed aromatic planes. (*1*) Alkyl chains or free naphthene rings and (*2*) section of plates of condensed aromatic rings.

dispersed asphaltene phase), the denser is the packing of malthenes around asphaltene stacks. This affects the service parameters of bitumens (ductility).

Based on the results of the X-ray diffraction study, we suggest that asphaltene molecules are associated in the layered-block stacks (Fig. 4). Thus, X-ray diffraction, along with ICP-MS, HPLC [1], and NMR spectroscopy, can be used to determine meaningful differences between certified and substandard paving bitumens.

CONCLUSION

As compared to substandard bitumens, the layered-block stacks of asphaltene molecules of more structurally ordered (certified) bitumens are denser, and the packing of malthenes around the asphaltene nuclei is more ordered owing to their higher aromaticity. This results in higher thermal stability and, as a consequence, higher ductility of certified paving bitumens.

REFERENCES

1. Begak, O.Yu. and Syroezhko, A.M., *Zh. Prikl. Khim.*, 2001, vol. 74, no. 4, pp. 675–678.
2. Kam'yanov, V.F., Macromolecular Heteroatomic Petroleum Components, *Doctoral Dissertation*, Moscow, 1992.

Russian Journal of Applied Chemistry, Vol. 74, No. 5, 2001, pp. 885–889. Translated from Zhurnal Prikladnoi Khimii, Vol. 74, No. 5, 2001, pp. 858–862.

CHEMISTRY OF FOSSIL FUEL

Pyrolysis of Asphaltenes of G6 Coal Semicoking Tar

V. V. Platonov, V. A. Proskuryakov, D. A. Rozental', S. V. Ryl'tsova, Yu. N. Popova, and O. S. Polovetskaya

Lev Tolstoi State Pedagogical University, Tula, Russia
St. Petersburg State Technological Institute, St. Petersburg, Russia

Received December 21, 2000

Abstract—Homogeneous pyrolysis of asphaltenes of G6 coal semicoking tar at 750–900°C was studied.

Optimization of destructive hydrogenation, high-rate pyrolysis, and high-temperature coking requires primarily detailed information on the chemical composition of the organic matter of coals (OMC), fractional, group, and structural-group compositions of the liquid products of "mild" thermal degradation of OMC, and directions and types of high-temperature transformations of "primary" products. Such data can be obtained by studying various coal extracts and separate groups of compounds of semicoking tars under conditions minimizing high-temperature transformations of primary products, which in this case can be considered with confidence as corresponding to native fragments of the coal macromolecule, and also by revealing the features of high-temperature pyrolysis of these products.

In this work we studied the high-temperature pyrolysis of asphaltenes of the semicoking tar of G6 coal (Kuznetsk Coal Fields).

The content of asphaltenes in the coal semicoking tar reaches 30 wt %; therefore, their contribution to formation of high-temperature liquid products and coke structure will be significant.

The combination of elemental, quantitative functional, structural-group, and emission spectrum analyses, cryoscopy, IR, UV, and ^{1}H NMR spectroscopy, and adsorption liquid, capillary gas–liquid, and preparative thin-layer chromatography showed that the asphaltenes of G6 coal semicoking tar are a complex mixture of high-molecular-weight polycyclic compounds of the alicyclic, hydroaromatic, aromatic, and heterocyclic nature, substituted with various functional groups and alkyl chains [1].

Pyrolysis of asphaltenes was performed in a setup consisting of a quartz pyrolyzer (d = 20 mm, l = 500 mm), a three-sectional oven, and systems for feeding the initial substance and condensing and trapping the pyrolysis products [2]. The vapor–emulsion mixture of asphaltenes fed to the pyrolyzer was diluted with argon in a ratio (1 : 25 by volume) close to that of dilution of resin vapor with coke oven gas in the course of high-temperature coking. Also, dilution with argon allowed accurate measurement and fine control of the residence time of the vapor in the pyrolysis zone.

To determine the contribution of asphaltenes to formation of other classes of compounds, we performed the chemical group analysis of the tars [3] followed by study of the qualitative and quantitative composition of separate groups of components by elemental, functional, and structural-group analyses, cryoscopy, capillary gas–liquid chromatography, and IR and UV spectroscopy.

Pyrolysis of coal asphaltenes was performed at 750, 800, and 900°C; the residence time of the vapor in the heated zone was 0.5, 1.5, 3.0, and 6.0 s.

The material balance data for asphaltene pyrolysis and the results of chemical group analysis of the liquid products are listed in Table 1.

It is seen that asphaltenes of G6 coal semicoking tar undergo extensive transformations whose extent is determined by temperature and residence time of the asphaltene vapor in the pyrolyzer.

Within the first 0.5 s at 750, 800, and 900°C the yield of pyrocarbon (a highly condensed product of the carbon black type) was 11.2, 13.4, and 16.5 wt %, the yield of liquid products, 81.3, 70.1, and 61.3 wt %, and the yield of gaseous products, 7.5, 16.5, and 22.2 wt %, respectively. The rate of asphaltene degradation in the next second at 750°C is somewhat lower, as suggested by small changes in the yields of pyro-

1070-4272/01/7405-0885$25.00

Table 1. Material balance of pyrolysis of G6 coal asphaltenes

Pyrolysis product	Yield of pyrolysis products, wt % based on initial asphaltenes, at indicated contact time, h										
	0.5	1.5	3.0	6.0	0.5	1.5	3.0	6.0	0.5	1.5	3.0
	750°C				800°C				900°C		
Pyrocarbon	11.20	19.10	31.80	53.70	13.40	29.00	50.00	61.70	16.50	48.00	70.00
Liquid products, wt % of dry tar including:	81.30	73.00	57.00	26.60	70.10	52.10	26.60	17.85	61.30	25.20	15.00
organic bases	2.37	3.28	3.82	7.86	3.20	3.83	5.62	5.95	3.00	3.93	3.27
carboxylic acids	0.20	0.30	0.41	0.77	0.30	0.47	0.33	0.26	0.48	0.25	0.20
phenols	1.69	2.33	4.13	0.90	3.00	2.22	0.95	0.52	1.51	2.00	0.60
hydrocarbons	6.37	7.90	8.52	12.25	9.80	11.75	13.85	16.10	12.20	16.35	20.00
neutral oxygen compounds	4.15	5.70	3.93	3.23	4.40	5.70	6.28	5.15	4.88	5.20	4.26
"secondary" asphaltenes	49.80	53.20	59.80	72.30	60.10	53.90	64.00	50.30	49.50	52.00	53.50
Gas	7.50	8.90	11.20	19.70	16.50	18.90	23.40	20.45	22.20	26.80	15.00

carbon, tar, and gaseous products (Table 1). However, at 800 and 900°C the decomposition rate in this period is high: The yield of pyrocarbon increases by 15.6 and 31.5 wt %, and that of the tar decreases by 18.0 and 36.1 wt %, respectively. Thus, at higher temperatures the thermal degradation of asphaltenes is intensified.

As the pyrolysis conditions are made more rigorous, the yield of products varies differently. For example, in the period between 1.5 and 3.0 s additional amounts of pyrocarbon are formed (12.7, 21.0, and 22.0 wt % at 750, 800, and 900°C, respectively), and the yield of the tars sharply decreases. In the subsequent 3 s (between 3.0 and 6.0 s) at 750 and 800°C pyrolysis decelerates, which may be due to intermediate formation of thermally stable highly aromatized polycyclic products. The high yield of pyrocarbon suggests predominant occurrence of condensation in the course of asphaltene pyrolysis; it also suggests that asphaltenes are not responsible for formation of liquid products.

The course of asphaltene pyrolysis with several extrema reflects the features of their chemical composition. Subject to degradation is a complex mixture of compounds differing in the thermal stability, with the stability increasing as the degrees of aromaticity and condensation increase. The least stable structures decompose first, after which the degradation rate decreases. Then, as the heat is supplied, other structures of asphaltenes start to degrade. At a sufficiently long reaction time, pyrolysis can occur in steps, as the products of thermochemical transformations of the initial asphaltenes, exhibiting higher aromaticity and higher thermal stability, undergo further degradation but under more rigorous conditions; as a result, a new maximum appears in formation of pyrocarbon and a minimum, in formation of liquid products. It should be noted that in almost all cases the increase in the yield of pyrocarbon is accompanied by a decrease in the yield of the liquid products, with no appreciable changes in the yield of the gaseous products.

The results of chemical group analysis of liquid products show that, as the conditions of asphaltene pyrolysis are made more rigorous, the content of organic bases, hydrocarbons, and neutral oxygen compounds in the tars grows, whereas the content of phenols decreases. The yield of secondary asphaltenes changes significantly; in the first 0.5 s of pyrolysis these compounds rapidly decompose, which is followed by their accumulation as compared to the other groups of compounds. The yield of secondary asphaltenes correlates with formation of pyrocarbon, which is fully consistent with the concept [4, 5] that pyrocarbon is formed via asphaltenes.

The content of organic bases in liquid products at the pyrolysis time of 3.0 s increases from 3.83 wt % at 750°C to 5.62 wt % at 800°C but then decreases to 3.27 wt % at 900°C. The organic bases are formed most actively in the first 0.5 s; their yield at 750, 800, and 900°C is 2.37, 3.20, and 3.00 wt %, respectively.

The influence of pyrolysis time is different at different temperatures. For example, the yield of organic bases in the first 3.0 s is 3.83 and 5.62 wt % at 750 and 800°C, respectively, whereas in the period from 3.0 to 6.0 s their amount increases by 4.0 (750°C) and 0.33 wt % (800°C) (Table 1).

The highest yield of phenols is observed in the first 0.5 s at 800°C. As the pyrolysis conditions are made more rigorous, the yield of phenols decreases, which may be due to prevalence of degradation and condensation of phenols over their formation in thermal degradation of asphaltenes [6–9].

The amount of hydrocarbons in liquid pyrolysis products of asphaltenes increases with time and especially with temperature. For example, as the temperature is increased from 800 to 900°C at a time of 3.0 s, the content of hydrocarbons increases by 6.15 wt %, and as the time is increased from 3.0 to 6.0 s at a temperature of 800°C, their content increases by 2.25 wt %. Similar to organic bases and phenols, accumulation of hydrocarbons is the most significant in the first 0.5 s: 6.37, 9.80, and 12.20 wt % at 750, 800, and 900°C, respectively. The low content of hydrocarbons in liquid pyrolysis products suggests that asphaltenes are not the major source of hydrocarbons in high-temperature tars formed by cracking of vapor–gas products in coke ovens (Table 1).

The content of neutral oxygen compounds considerably exceeds that of phenols (Table 1). For example, at 800°C (6.0 s) the content of phenols is 0.52 wt %, and that of neutral oxygen compounds, 5.15 wt %. Whereas the yield of phenols drastically decreases as the pyrolysis conditions are made more rigorous, the content of neutral oxygen compounds grows. This may be due to features of oxygen incorporation in the initial asphaltene structures, with the thermally stable furan heterocycles prevailing, and to condensation of phenols with formation of furan rings between aromatic rings.

The results of capillary gas–liquid chromatographic analysis of organic bases, phenols, and hydrocarbons isolated from liquid products of asphaltene pyrolysis are listed in Table 2.

It is seen that in the course of pyrolysis the compositions of the considered groups of compounds change significantly. Among organic bases, the content of quinoline, methylquinolines, and quinaldine appreciably increases. For example, at 800°C the yields of quinoline and quinaldine are 0.48 and 0.21 wt % in the first 0.5 s, increasing to 8.52 and 2.68 wt %, respectively, in 3.0 s.

Table 2 shows that under any pyrolysis conditions except 750°C/0.5 s the content of phenol and isomeric cresols among phenols is higher than that of xylenols. This can be readily explained by the higher thermal stability of the former compounds and by hydrodealkylation of the intermediate xylenols and polyalkylphenols. At 750°C and 0.5 s, the phenolic fraction contains 2.29 wt % phenol, 5.84 wt % cresols, and 13.81 wt % xylenols. As the reaction time is increased from 0.5 to 3.0 s, the content of phenol and cresols appreciably grows, with simultaneous decrease in the content of xylenols. Further increase in the pyrolysis time from 3.0 to 6.0 s (at 750°C) favors accumulation in the liquid products of phenol, *m*-cresol, 3,5-xylenol, and also higher-molecular-weight components: naphthols, anthrols, phenanthrols, pyrenols, and chrysenols. The yield of phenol is maximal in 3.0 s at 800°C and in 0.5 s at 900°C.

The phenolic fractions of pyrolysis tars at 800 and 900°C are enriched in phenol, *m*-cresol, and 2,4- and 3,5-xylenols, but the total content of low-boiling products tends to decrease as the pyrolysis conditions are made more rigorous.

Table 2 shows that, as the pyrolysis of asphaltenes is intensified, the hydrocarbon fraction becomes richer in naphthalene, its methyl and dimethyl homologs, and polycyclic aromatics: fluorene, phenanthrene, fluoranthene, pyrene, and chrysene. The content of polycyclic aromatics increases especially significantly at 900°C. As the reaction time is increased from 3.0 to 6.0 s, the developing dealkylation reactions decrease the content of alkylnaphthalenes.

The yield of naphthalene as the major component of high-temperature tars strongly depends on the pyrolysis temperature. For example, at 750, 800, and 900°C the yield of naphthalene in 1.5 s is 8.75, 12.30, and 27.10 wt %, respectively. As the residence time of asphaltene vapor in the heated zone (750°C) is increased from 0.5 to 6.0 s, the content of naphthalene increases from 4.92 to 30.20 wt %. It should be noted that the influence of reaction time on formation of naphthalenes is different depending on temperature. For example, whereas at 750°C the yield of naphthalene is higher at longer reaction times, with increasing time to 6.0 s at 800°C and to 3.0 s at 900°C the yield of naphthalene drastically decreases, with simultaneous increase in the yields of phenanthrene, anthracene, pyrene, chrysene, and other highly condensed aromatic hydrocarbons [10]. For example, at 750, 800, and 900°C the yield of phenanthrene is, respectively, 1.35, 2.20, and 3.10 wt % in 0.5 s and 4.20, 6.70, and 11.60 wt % in 3.0 s. The respective yields of chrysene are 0.19, 0.60, and 1.07 wt % in 0.5 s and 0.94, 1.94, and 1.07 wt % in 3.0 s (Table 2). This fact suggests that, as the temperature and time of pyrolysis are increased, condensations of low-molecular-weight hy-

Table 2. Component composition of organic bases, phenols, and hydrocarbons

Pyrolysis product	Yield, wt % of fraction, at indicated contact time, s										
	0.5	1.5	3.0	6.0	0.5	1.5	3.0	6.0	0.5	1.5	3.0
	750°C				800°C				900°C		
Organic bases											
2,4,6-Collidine	0.45	0.85	2.05	2.86	0.60	1.04	0.85	0.42	0.50	1.00	0.66
4-Ethylpyridine	0.30	0.60	1.20	1.63	0.45	0.80	0.65	0.20	0.80	1.60	0.45
Quinoline	0.40	1.14	2.46	5.78	0.48	3.51	8.52	5.68	2.16	6.45	4.82
Isoquinoline	0.20	0.39	1.20	2.10	0.21	1.30	2.68	1.77	0.68	2.19	1.70
Quinaldine	0.70	0.94	1.47	2.53	0.94	1.81	1.96	1.06	1.20	1.66	1.45
6-Methylquinoline	0.50	0.70	1.40	2.24	0.74	1.50	1.81	0.90	0.80	1.50	0.40
4-Methylquinoline	0.40	0.70	1.39	1.90	0.55	1.13	1.53	0.40	0.60	0.37	0.20
2,4-Dimethylquinoline	0.60	0.77	1.10	1.50	0.77	0.82	0.60	0.50	0.90	1.30	2.52
Sum of components	3.55	6.09	12.26	20.24	4.70	11.91	18.60	10.93	7.64	16.07	12.20
Phenols											
Phenol	2.29	3.32	7.22	10.10		3.80	4.64	2.80	4.84	2.95	0.40
o-Cresol	2.06	2.43	6.59	4.10		1.82	1.55	0.32	3.49	1.93	0.33
2,6-Xylenol	1.43	0.66	0.50	0.30		0.35	0.25	0.10	0.88	0.33	0.06
p-Cresol	2.06	2.48	4.66	4.36		2.57	1.68	0.93	3.76	2.32	0.44
m-Cresol	1.72	2.13	4.01	5.60		2.51	3.03	1.40	2.54	2.00	1.05
2,4-Xylenol + *o*-ethylphenol	6.04	3.10	1.74	1.31		4.09	2.09	0.80	5.80	2.13	0.51
2,5-Xylenol	1.87	1.26	1.17	0.53		1.46	0.76	0.36	1.31	0.71	0.26
2,3-Xylenol + *p*-ethylphenol	2.24	1.20	0.42	0.20		3.62	0.79	0.20	1.93	0.60	0.24
3,5-Xylenol + *m*-ethylphenol	0.92	1.21	1.91	3.67		1.48	2.40	3.10	2.03	1.11	0.20
3,4-Xylenol	1.31	1.45	0.63	0.48		1.03	0.83	0.20	1.58	0.40	0.37
m-Propylphenol	1.61	0.40	0.20	0.05		0.45	0.20	0.03	0.54	0.10	0.06
p-Propylphenol	2.99	1.95	0.98	0.60		1.70	1.00	0.85	2.10	0.54	0.27
Hydrocarbons											
Naphthalene	4.92	8.75	11.70	30.20	5.33	12.30	16.55	11.40	14.10	27.10	13.20
β-Methylnaphthalene	0.71	1.86	2.02	1.86	1.85	1.95	2.33	2.21	1.31	3.13	0.86
α-Methylnaphthalene	0.44	1.47	1.62	1.22	0.92	1.70	1.79	1.22	0.79	1.54	0.43
Diphenyl	0.22	0.48	0.71	0.40	0.91	0.65	1.01	0.56	0.55	1.05	0.54
2,6-Dimethylnaphthalene	0.13	0.76	0.59	0.19	0.21	0.45	0.21	0.16	0.15	0.19	0.13
2,7-, 1,3-, 1,7-Dimethylnaphthalenes	0.50	2.11	1.72	0.68	0.61	1.60	0.60	0.60	0.50	0.85	0.52
1,2-, 1,4-Dimethylnaphthalenes	0.17	0.36	0.41	0.48	0.30	0.40	0.85	0.51	0.18	0.16	0.10
Acenaphthene	0.17	0.27	0.41	0.22	0.30	0.40	0.85	0.30	0.16	0.20	0.25
Fluorene	0.49	1.42	1.82	2.38	1.10	1.60	2.17	2.30	1.28	1.91	2.29
Phenanthrene	1.35	3.54	4.20	6.92	2.20	4.40	6.90	7.55	3.10	8.90	11.60
Anthracene	1.28	2.92	3.44	2.83	1.60	3.60	3.03	2.54	1.87	4.10	4.78
Fluoranthene	1.33	1.92	2.00	2.19	1.70	2.30	2.60	3.50	2.55	3.90	5.17
Pyrene	0.42	0.86	1.40	2.15	0.90	1.70	2.36	3.00	1.22	2.22	3.38
Chrysene	0.19	0.64	0.94	1.67	0.60	1.30	1.94	3.20	1.07	1.60	3.08
2,3-, 1,5-Dimethylnaphthalenes	0.46	1.36	1.66	2.13	0.80	1.40	1.77	0.87	1.67	2.89	2.49
Sum of components	12.78	28.72	34.64	55.52	19.33	35.75	44.82	39.92	30.50	59.74	48.82

drocarbons are intensified, yielding polycyclic aromatic hydrocarbons with prevalence of angular structures (phenanthrene, pyrene, chrysene).

The total content of hydrocarbons lower-boiling than chrysene in 0.5 s at 750, 800, and 900°C is 12.78, 19.33, and 30.50 wt %. In the subsequent 2.5 s at these temperatures their content increases, respectively, to 34.64, 44.62, and 48.82 wt %. With the pyrolysis time of asphaltenes increasing further, the content of these hydrocarbons decreases (Table 2).

The high content in tars of naphthalene, phenanthrene, anthracene, pyrene, fluoranthene, and chrysene and the low content of methyl- and dimethylnaphthalenes apparently reflects the structural features of the initial coal asphaltenes.

CONCLUSION

Study of high-temperature pyrolysis of asphaltenes of G6 coal semicoking tar showed that asphaltenes show a strong tendency to condensation with formation of large amounts of pyrocarbon and are not responsible for the yield of liquid products which are enriched in secondary asphaltenes and hydrocarbons.

REFERENCES

1. Platonov, V.V., Klyavina, O.A., Prokof'ev, E.E., *et al.*, *Khim. Tverd. Topl.*, 1983, no. 6, pp. 75–85.
2. Bunkina, N.A., Makarov, G.N., Bronshtein, A.P., and Platonov, V.V., *Koks Khim.*, 1975, no. 8, pp. 26–30.
3. Kamneva, A.I. and Korolev, Yu.G., *Laboratornyi praktikum po khimii topliva* (Practical Laboratory Course of Fuel Chemistry), Moscow: Mosk. Khimiko-Tekhnol. Inst. im. D.I. Mendeleeva, 1976.
4. Platonov, V.V., Klyavina, O.A., Prokof'ev, E.E., and Ivleva, L.N., *Khim. Tverd. Topl.*, 1981, no. 6, pp. 96–103.
5. Platonov, V.V., Klyavina, O.A., Ivleva, L.N., and Prokof'ev, E.E., *Khim. Tverd. Topl.*, 1983, no. 2, pp. 138–144.
6. Platonov, V.V., Ivleva, L.N., and Prokof'ev, E.E., *Khim. Tverd. Topl.*, 1980, no. 2, pp. 138–147.
7. Platonov, V.V., Ivleva, L.N., Klyavina, O.A., and Prokof'ev, E.E., *Khim. Tverd. Topl.*, 1981, no. 5, pp. 84–94.
8. Platonov, V.V., Ivleva, L.N., Klyavina, O.A., and Prokof'ev, E.E., *Khim. Tverd. Topl.*, 1982, no. 5, pp. 89–99.
9. Platonov, V.V., Ivleva, L.N., and Klyavina, O.A., *Khim. Tverd. Topl.*, 1984, no. 3, pp. 105–114.
10. Platonov, V.V., Klyavina, O.A., Ivleva, L.N., *et al.*, *Khim. Tverd. Topl.*, 1986, no. 5, pp. 75–84.

Russian Journal of Applied Chemistry, Vol. 74, No. 5, 2001, pp. 890–891. Translated from Zhurnal Prikladnoi Khimii, Vol. 74, No. 5, 2001, pp. 863–864.

BRIEF COMMUNICATIONS

Synthesis of Garnets by Coprecipitation from Aqueous Solutions

T. N. Bokovikova and M. V. Dvadnenko

Kuban State Technical University, Krasnodar, Russia

Received July 13, 2000; in final form, March 2001

Abstract—Conditions for the coprecipitation of hydroxides of aluminum and rare-earth elements from the $Al(NO_3)_3$–$Ln(NO_3)_3$–NH_4OH–H_2O system (Ln = La, Sm) by $NH_3 \cdot H_2O$ solutions at 25°C were studied. The resulting precipitates were investigated by thermal analysis, IR spectroscopy, and X-ray phase analysis.

A wide application of aluminum garnets of rare-earth elements (REE) to quantum electronics promoted the synthesis and study of garnet-structure compounds. Yttrium aluminum garnet, which is one of the best solid-state laser materials, has been the most studied.

The garnet-structure compounds can be obtained by solid-phase synthesis from a mixture of oxides and also by coprecipitation of hydroxides from salt solutions. One of the shortcomings of the solid-phase synthesis is high temperature (higher than 1600°C). The coprecipitation technique makes it possible to obtain compounds with required structures as well crystallized and finely dispersed products even at 1000–1200°C. The data on this technique are contradictory and few in number [1], thus its application to the synthesis of REE aluminum garnets requires its further more extended study.

The aim of this work was to study the dehydration and interaction of hydroxides of aluminum and lanthanides, coprecipitated from aqueous solutions of their salts by an ammonia aqueous solution, and to demonstrate a possibility of obtaining lanthanum and samarium garnets by calcination of coprecipitated hydroxides at 965–1050°C. The experimental methods in use were differential thermal analysis (DTA), IR spectroscopy, and X-ray analysis.

EXPERIMENTAL

The hydroxides were precipitated from the $Al(NO_3)_3$–$Ln(NO_3)_3$–NH_4OH–H_2O system by a 4% solution of $NH_3 \cdot H_2O$ with permanent stirring of the suspension. The concentrations of aluminum and rare-earth nitrates were kept constant (1.66 and 1.00 N, respectively), and pH was maintained at 9.5–10. The thermal analysis of precipitates was carried out on a D derivatograph at a heating rate of 10 deg min^{-1}. The IR spectra were recorded on a Specord 75-IR spectrometer in the range 400–4000 cm^{-1} at room temperature from Nujol mulls. Phase compositions was analyzed on a DRON-1 diffractometer (FeK_α radiation).

As the $NH_3 \cdot H_2O$ content in the starting mixtures increased, the following reaction stages occurred sequentially: the formation of poorly filterable colloidal precipitates, quantitative precipitation of aluminum and REE hydroxides with an impurity of basic salts, and, finally, the coprecipitation of aluminum and REE hydroxides. The resulting precipitates were washed with distilled water until nitrate ions disappeared and dried at 25°C for 12 h [2].

A number of endo- and exothermic effects were observed upon heating (Fig. 1). The endothermic ef-

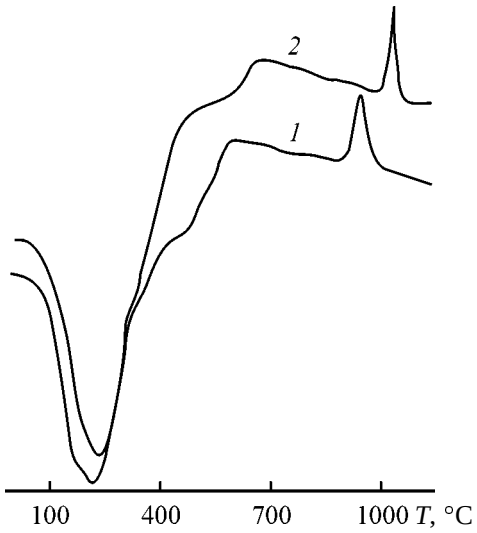

Fig. 1. DTA curves of coprecipitated aluminum and REE hydroxides. (*T*) Temperature. (*1*) $La(OH)_3$ and (*2*) $Sm(OH)_3$.

1070-4272/01/7405-0890$25.00 © 2001 MAIK "Nauka/Interperiodica"

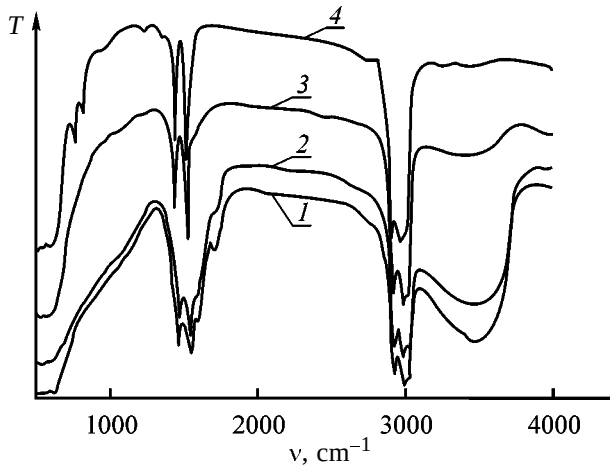

Fig. 2. IR absorption spectra of (*1*) aluminum and REE hydroxides coprecipitated at 25°C and (*2–4*) products of their thermolysis: (*T*) transmission and (ν) wave number. Heating temperature (°C): (*2*) 250, (*3*) 500, and (*4*) 1100.

fects in the range 90–400°C correspond to the removal of adsorbed and structural water, which was proved by the IR spectra.

The IR spectra of coprecipitated hydroxides dried at 25 and 90°C are essentially similar (Fig. 2). Broad bands in the range 3100–3800 cm^{-1} corresponding to the OH stretching vibrations are observed in the both spectra, a wide range of absorption frequencies being typical for bridging OH groups coordinated by metal atoms [3]. Additional bands at 3000–2800 and 1460–1380 cm^{-1} originate from Nujol. A broad strong band caused by the vibrations of –O–M–O– groups in the range 400–850 cm^{-1} is present in the IR spectra of all the precipitates [3]. Thus, all the precipitates have a polymeric structure.

Figure 2 shows that appreciable changes occur in the solid phase in the range 250–1000°C. At 250°C structural water is partially removed (the band of H_2O stretching vibrations decreases) and OH groups are partially lost (a sharp decrease in the intensity of the band in the range 1600 cm^{-1}. Correspondingly, the intensity of the bands of –O–M–O– groups increases, as compared with the IR spectra of the solid phase obtained at 25–90°C. Structural water is almost completely removed at 500°C (Fig. 2), since the bending band at 1630 cm^{-1} practically disappears and the weak band of vibrations of hydroxide groups at 1500 cm^{-1} remains. After heating the precipitates at 1000–1100°C, two bands at 620 and 680 cm^{-1} typical for $Ln_3Al_5O_{12}$ (Ln = La, Sm) garnets are observed in the IR spectrum (Fig. 2), which correspond to the Ln–O stretching vibrations in a tetrahedron [3]. According to X-ray diffraction data, the samples calcined at 950–1050°C have the garnet structure and are free of other phases.

The spectral data agree with the DTA data. For example, the DTA curves contain two exothermic peaks at 1020 and 965°C corresponding to the crystallization and reaction of, respectively, Sm_2O_3 and La_2O_3 with Al_2O_3 [4].

CONCLUSION

Polymeric hydroxo compounds were coprecipitated from solutions of salts of aluminum and rare-earth elements. Their thermal analysis was carried out, and their IR spectra were studied. The calcination at 1050°C of the coprecipitated aluminum and REE hydroxides (5 : 3) results in the crystallization of garnet-structure compounds.

REFERENCES

1. Glushkova, V.B., Zinov'ev, S.Yu., Krzhizhanovskaya, V.A., and Kuznetsov, A.K., *Izv. Akad. Nauk SSSR, Neorg. Mater.*, 1986, vol. 22, no. 7, pp. 1219–1222.
2. Ezhova, Zh.A., Orlovskii, V.P., and Koval', E.M., *Zh. Neorg. Khim.*, 1994, vol. 39, no. 12, pp. 1955–1957.
3. Nakamoto, K., *Infrared Spectra of Inorganic and Coordination Compounds*, New York: Wiley, 1963.
4. Zinov'ev, S.Yu., *Zh. Neorg. Khim.*, 1992, vol. 37, no. 9, pp. 1970–1975.

Russian Journal of Applied Chemistry, Vol. 74, No. 5, 2001, pp. 892–894. Translated from Zhurnal Prikladnoi Khimii, Vol. 74, No. 5, 2001, pp. 265–266.

BRIEF COMMUNICATIONS

Simulation of Kinetics of Stabilizer Migration from Polyolefins to Air and Water

A. V. Dedov and V. G. Nazarov

Military Academy of Radiation, Chemical, and Biological Defense, Moscow, Russia

Received April 6, 1999; in final form, July 2000

Abstract—The applicability of the model for prediction of the kinetics of stabilizer migration from polyolefins to air and water was analyzed.

Simulation of the kinetics of stabilizer migration from polyolefins is the urgent problem caused by the dependence of polymer properties on THE initial composition [1] and by toxicity of many ingredients [2].

Analysis revealed that the model [1] developed further in [3–6] is advantageous for calculation of the migration kinetics of various low-molecular-weight ingredients [3–6]. The rate of stabilizer migration from polyolefins to air and water is mainly controlled by diffusion of the ingredients in the polymer [4, 7]. The calculation equation in this case has the form

$$\tau_i = a_i l^2/D, \quad (1)$$

where τ_i is the migration time of a given amount of stabilizer, l is the parameter relating the conditions of contact of a material with environment to its thickness t ($l = d/2$ for a two-side contact and $l = d$ for a one-side contact), D is the coefficient of stabilizer diffusion in polymer, and a_i is the coefficient calculated from Eq. (1).

$$\frac{M_i}{M_0} = 1 - \sum \frac{2L^2 \exp(-\beta_n^2 T)}{\beta_n^2(\beta_n^2 + L^2 + L)}, \quad (2)$$

M_τ is the amount of the ingredient migrating from the polymer in time τ, M_0 is the initial content of the ingredient in the polymer, L is dimensionless parameter reflecting the ratio of the fluxes of the ingredients in the bulk of a polymer and from its surface as influenced by the aggregate state of the environment, and β is the positive root of the equation $\beta_n \tan\beta_n = L$; $T = D\tau/l^2$.

The solution of Eq. (2) at an M_τ/M_0 ratio from 0 to 1 is obtained in the form of the dependence $\log L = f(\log T)$. The dependence has three regions, one of which describes the kinetics of ingredient migration from polymers in the diffusion-controlled stage [1]. The region itself is described by the equation $\log T = A_i$. The A_i value is determined by the given ratio M_τ/M_0. The solution of the equation $\log T = A_i$ leads to expression (1) and allows determination of the numerical value of a_i in this equation.

The values of the other variables in Eq. (2), as well as the possible methods of its solution, are presented in [1, 5]. Note that the a_i coefficient, which only implicitly enters Eq. (2), is determined by the M_τ/M_0 ratio specified in solving this equation.

The goal of the work is to analyze the applicability of the model [1] for prediction of the kinetics of stabilizer desorption from polyolefins to air and water.

The model [1] was used for prediction of the migration kinetics of stabilizers based on benzophenone derivatives [4] from isotactic polypropylene to air at 25°C and of various polyethylene stabilizers from polyethylenes of different brands to water at 25°C and within 45–70°C [7]. The D values were taken from tables or derived from their dependences on the molecular weight in the homologous series of the ingredients [8]. The compositions of polymer materials and the migration conditions essentially differed from those accepted in development of model [1] and analyzed in [4–6]. The model was corrected at the expense of the a_i coefficient after comparing the calculated and experimental data for the kinetics of stabilizer migration (table).

The table shows that the correctness of the calculation increases in passing to contact with water instead of air and this increase is even more pronounced at increased water temperature.

1070-4272/01/7405-0892$25.00

The necessity for increasing the migration rate, especially significant in the initial stage, arises from the nonuniform distribution of the ingredient in the bulk of real polymeric materials.

Introduction of stabilizers into polyolefins results in their preferable distribution in the amorphous regions [8]. The stabilizer amounts used in this work are far above their equilibrium solubility in polyolefins [2, 3]. As a result, the stabilizer concentrates on the polymer surface and within its surface layer.

Apparently, owing to accumulation of the stabilizer on the polymer surface, the migration rate in the initial stage is controlled by the flux of the ingredient to environment, which exceeds the mass transfer in its bulk. As the stabilizer is removed from the surface of a polymer and its surface layer, the migration process becomes controlled by flux in the bulk of a polymer. In this stage, the time of which is determined by the phase state and nature of the environment in contact, calculated and experimental data on the migration kinetics are in good agreement (see table).

The proposed mechanism of the ingredient migration is characteristic of contact between polymer and air, when the flux from the surface of a material is limited by the stabilizer volatility. Owing to the low vapor pressure of stabilizers [8], the removal of ingredients from the polymer surface is extended in time compared to the case of contact between polymer and water. At higher water temperatures the model even better predicts real migration process, which is reflected in the value of the correctional coefficient a_i. The necessity for correcting a_i over the entire migration time at 25°C arises from elimination of the another assumption accepted in development of model [1], namely, that ingredients are removed from the polymer surface into the environment immediately. This assumption is fulfilled to a higher degree at higher water temperatures.

The complex mechanism of the stabilizer migration in the case of contact between polymer and air necessitates correction of L used to determine the limiting stage of the process [1, 4–6]. The L values are derived from the equation

$$L = IV/(SD), \quad (3)$$

where V is the stabilizer volatility and S, the equilibrium solubility of the ingredient in the polymer.

At $L > 10$ the limiting stage of the migration of ingredients from a polymer is controlled by their flux in the bulk of a material, and Eq. (1) is used for calculating the process kinetics. At $L < 0.6$ migration is limited by the flux from the polymer surface to the environment in contact, and another equation is used for calculating the kinetics [1]. For $10 > L > 0.6$ no equations exists for calculating the kinetics of the ingredient migration.

Calculated and corrected values of the coefficient a_i

M_τ/M_0	a_i^{cal}	a_i^{cor} for migration at indicated temperature, °C		
		25, air	25, H_2O	45–70, H_2O
0.1	0.004	0.12	0.006	0.005
0.2	0.015	0.15	0.023	0.020
0.3	0.038	0.38	0.055	0.045
0.4	0.063	0.42	0.10	0.070
0.5	0.15	0.63	0.24	0.16
0.6	0.30	0.70	0.45	+
0.7	0.80	+	1.2	+
0.8	0.95	+	1.5	+
0.9	1.2	+	1.8	+

Note: The plus sign denotes cases when the experimental and calculated data coincide and no correction coefficient a_i is required.

The analysis of Eq. (3) shows that the complexity of the determination of the limiting stage of migration is due to the fact that in calculation of L the real distribution of ingredient in the bulk of a polymer is not taken into account under equal other conditions.

CONCLUSIONS

(1) The model considered predicts correctly the migration of ingredients in the case of contact between the polymer and water at temperatures from 45 to 70°C. In the case of contact between polyolefins and air it is reasonable to apply the model to prediction of the migration kinetics in the final stages (at $M_\tau/M_0 > 0.7$).

(2) Under equal other conditions, the accuracy of the model is determined by the stabilizer concentration and by the rate of its transfer from the surface to the environment in contact.

REFERENCES

1. Calvert, P. and Billingham, N., *J. Appl. Polym. Sci*., 1979, vol. 24, no. 3, pp. 357–370.
2. Maslova, I.P., Zolotareva, K.A., and Glazunova, N.A.,

Khimicheskie dobavki k polimeram: Spravochnik (Chemical Additives to Polymers: A Handbook), Moscow: Khimiya, 1973.

3. Shlyapnikov, Yu.A., Kiryushkin, S.G., and Mar'in, A.P., *Antiokislitel'naya stabilizatsiya polimerov* (Antioxidant Stabilization of Polymers), Moscow: Khimiya, 1986.
4. Nazarov, V.G., Dedov, A.V., and Klitnyi, F.F., *Vysokomol. Soedin., Ser. B*, 1991, vol. 32, no. 4, pp. 283–286.
5. Rudoi, V.M., *Dokl. Akad. Nauk SSSR*, 1980, vol. 280, no. 3, pp. 669–673.
6. Dedov, A.V., Bablyuk, E.B., and Nazarov, V.G., *Kauchuk Rezina*, 1998, no. 5, pp. 39–41.
7. Nazarov, V.G. and Dedov, A.V., *Zh. Prikl. Khim.*, 1998, vol. 71, no. 2, pp. 316–319.
8. Scott, G., *Developments in Polymer Stabilization*, London: Applied Science, 1980, vol. 1, ch. 5, pp. 185–244.

Russian Journal of Applied Chemistry, Vol. 74, No. 5, 2001, pp. 895–896. Translated from Zhurnal Prikladnoi Khimii, Vol. 74, No. 5, 2001, pp. 867–868.

BRIEF COMMUNICATIONS

Barbiturates of Aromatic Hydroxy Aldehydes as Components of Inhibiting Systems for Thermal Polymerization of Styrene

A. F. Gogotov, M. V. Parilova, and A. K. Khaliullin

Angarsk Petrochemical Company, Joint-Stock Company, Angarsk, Irkutsk oblast, Russia
Institute of Chemistry, Siberian Division, Russian Academy of Sciences, Irkutsk, Russia

Received January 16, 2001

Abstract—Products of condensation of aromatic hydroxy aldehydes with barbituric acid were tested as coinhibitors in inhibiting systems for thermal polymerization of styrene, based on *p*-quinone dioxime.

Modern production of styrene is impossible without using inhibitors [1]. In practice, the majority of Russian plants use as the main inhibitor in distillation of styrene *p*-quinone dioxime (QDO) which is the most effective [2]. However, QDO is insoluble in hydrocarbons and should therefore be used as a fine suspension. As a result, QDO is often deposited in pipelines and dead zones of the process equipment. Attempts were made to use both a soluble derivative of QDO [3] and cosolvents for QDO (e.g., dimethyl sulfoxide [4]). One of the main ways to improve the inhibition is search for QDO-based systems that would be more effective than straight QDO or development of formulations with a decreased consumption of QDO. For example, an inhibiting system consisting of QDO and *p*-nitrophenol (PNP) is widely used in production [5]. Recently an inhibiting system coinsisting of a *p*-phenylenediamine derivative and eugenol (4-allylguaiacol) was suggested for distillation of ethylene compounds [6]. Experiments showed that an effective alternative to this inhibitor system can be a mixture of QDO with barbiturates of aromatic hydroxy aldehydes: *p*-hydroxybenzaldehyde, vanillin [7], or syringaldehyde. The synthesis procedure and properties of vanillin barbiturate (VB) are described elsewhere [8, 9].

The inhibiting power of the known and newly suggested systems was evaluated by determining the yield of polymerized styrene at heating of the monomer at 120°C for 2–7 h with sampling every hour and distillation of the unchanged monomer on a boiling water bath at a residual pressure of 20 mm Hg.

The table shows that addition of PNP as coinhibitor somewhat decreases formation of the polymer on heating of styrene (run nos. 1, 2, 3–5), with addition of the coinhibitor 2 h after the start of the process being more efficient than its addition simultaneously with the main inhibitor. At a lower amount of the inhibitor the yield of the polymer somewhat increases (run nos. 1–4). The use of eugenol (suggested in [6]) instead of PNP, with the same amount of QDO (run nos. 5, 6) decreases formation of the polymer by an order of magnitude, demonstrating the advantages of methoxylated phenols. Replacement of eugenol, which is in a short supply, by more readily available vanillin (run no. 7) shows that vanillin as coinhibitor is somewhat inferior to eugenol but is considerably more effective than PNP. With vanillin barbiturate, which is prepared by condensation of vanillin with a known methylene-active compound, barbituric acid, at the same amount of the coinhibitor with respect to methoxyphenol (run no. 8), we attained almost the same inhibiting effect as with QDO + eugenol. Experiments with various orders of adding the coinhibitor (run nos. 8–11) showed that addition of VB 2 h after the start of the process is the best. Among derivatives of isomeric vanillins (*o*-, *m*-, and *p*-, run nos. 8, 12, 13), the derivative of the most abundant *p*-vanillin showed the highest performance. Experiments with varied amount of the VB added (run nos. 8, 14, 15) showed that the greatest inhibiting effect is attained at an inhibitor content of 0.017 wt % based on styrene. A blank experiment (run no. 16) showed that, when taken separately (without QDO), VB is not effective as inhibitor. The thio derivative, vanillin thiobarbiturate (VTB, run no. 17), shows poor performance under equal other conditions, which is consistent wiht the known fact that thiobarbituric acid initiates polymerization of styrene [10]. Comparison of the performances of barbiturates of vanillin homologs (nonmethoxylated *p*-hydroxybenzaldehyde, run no. 18; vanillin,

1070-4272/01/7405-0895$25.00 © 2001 MAIK "Nauka/Interperiodica"

Influence of the inhibiting system composition on the polymer yield on heating of styrene (120°C)

Run no.	Component of inhibiting system,* wt % based on styrene			Polymer yield, %, in indicated time, h, after adding inhibitor		Order of adding components
	QDO	PNP	AHAB	2	7	
1	0.03	–	–	0.31	14.6	
2	0.03	0.03	–	0.27	12.1	Simultaneously
3	0.017	–	–	0.42	19.9	
4	0.017	0.017	–	0.35	18.7	Simultaneously
5	0.017	0.017	–	0.42	17.1	PNP 2 h after QDO
6	0.017	–	Eugenol, 0.009	0.42	1.02	Eugenol 2 h after QDO
7	0.017	–	Vanillin, 0.009	0.42	4.54	Vanillin 2 h after QDO
8	0.017	–	*p*-VB, 0.017	0.42	1.56	VB 2 h after QDO
9	0.017	–	*p*-VB, 0.017	0.32	8.36	Simultaneously
10	0.017	–	*p*-VB, 0.017	0.38	9.60	VB 1 h after QDO
11	0.017	–	*p*-VB, 0.017	0.61	17.1	VB 3 h after QDO
12	0.017	–	*o*-VB, 0.017	0.42	6.92	*o*-VB 2 h after QDO
13	0.017	–	*m*-VB, 0.017	0.42	5.23	*m*-VB 2 h after QDO
14	0.017	–	*p*-VB, 0.034	0.42	2.60	VB 2 h after QDO
15	0.017	–	*p*-VB, 0.009	0.42	2.27	″
16	–	–	*p*-VB, 0.017	17.4	–	
17	0.017	–	*p*-VTB, 0.017	0.42	30.51	VTB 2 h after QDO
18	0.017	–	pHBAB, 0.017	0.42	5.00	pHBAB 2 h after QDO
19	0.017	–	SAB, 0.017	0.42	1.27	SAB 2 h after QDO

* (AHAB) Aromatic hydroxy aldehyde barbiturates, (VB) vanillin barbiturate, (pHBAB) *p*-hydroxybenzaldehyde barbiturate, and (SAB) syringaldehyde barbiturate.

run no. 8; dimethoxy derivative, syringaldehyde, run no. 19) showed that methoxylation of the aromatic ring enhances the inhibiting power of the coinhibitor. The mechanism of interaction of barbiturates of aromatic hydroxybenzaldehydes with QDO responsible for prolongation of the inhibiting power of the main inhibitor apparently coincides with the previously described [11] mechanism of interaction of QDO with sterically hindered phenols.

Thus, we have found a new class of coinhibitors of quinone dioxime effective in inhibition of thermal polymerization of styrene and studied the inhibiting properties of barbiturates of hydroxybenzaldehydes.

REFERENCES

1. Jones, C., *Chem. Week*, 1996, vol. 158, no. 49, p. 32.
2. Nikulin, S.S., Shein, V.S., Zlotskii, S.S., *et al.*, *Otkhody i pobochnye produkty neftekhimicheskikh proizvodstv – syr'e dlya organicheskogo sinteza* (Wastes and By-Products of Petrochemical Plants as a Raw Material for Organic Synthesis), Moscow: Khimiya, 1989.
3. JPN Patent Appl. 53-103427.
4. USSR Inventor's Certificate no. 1786016.
5. USSR Inventor's Certificate no. 441263.
6. US Patent 5396005.
7. RF Patent 2138473.
8. Gogotov, A.F., Zakazov, A.N., and Babkin, V.A., *Khim. Drev.*, 1992, nos. 2–3, pp. 44–46.
9. Gavrilova, G.A., Chipanina, N.N., Gogotov, A.F., and Turchaninov, V.K., *Izv. Ross. Akad. Nauk, Ser. Khim.*, 1997, no. 4, pp. 769–775.
10. Levina, R.Ya. and Velichko, F.K., *Usp. Khim.*, 1960, vol. 29, no. 8, pp. 929–971.
11. Klyuchnikov, O.R., Brylyakov, K.P., and Poplaukhin, P.V., *Izv. Vyssh. Uchebn. Zaved., Khim. Khim. Tekhnol.*, 1996, vol. 39, nos. 1–2, pp. 98–99.

Russian Journal of Applied Chemistry, Vol. 74, No. 5, 2001, pp. 897–899. Translated from Zhurnal Prikladnoi Khimii, Vol. 74, No. 5, 2001, pp. 869–871.

BRIEF COMMUNICATIONS

Sorption Immobilization of Glucoamylase on Nonionic Sorbent Styrosorb

I. V. Shkutina, O. F. Stoyanova, and V. F. Selemenev

Voronezh State University, Voronezh, Russia

Received January 30, 2001

Abstract—Glucoamylase was immobilized on super-cross-linked nonionic sorbent Styrosorb by the sorption procedure. The features of native and immobilized glucoamylase are compared.

Glucoamylase catalyzes hydrolytic cleavage of starch. This enzymatic reaction is widely used in alcohol industry and in glucose production. Immobilized enzymes are characterized by several advantages as compared to native enzymes: possibility of repeated and continuous use, stability to denaturing agents, and simplicity of preparation of high-purity product [1].

In this work was studied the possibility of sorption immobilization of glucoamylase on super-cross-linked nonionic sorbent Styrosorb used as the efficient sorbent of large biomolecules [2–4].

EXPERIMENTAL

In our experiments we used the enzymic preparation of glucoamylase precipitated with ethanol from an extract of the surface culture *Aspergillus awamori*. Two samples of Styrosorb (Styrosorb-1 with a specific surface area of 440 $m^2 g^{-1}$ and Styrosorb-2 with a specific surface area of 260 $m^2 g^{-1}$) were used as the supports. These sorbents containing no ion-exchange groups were prepared from super-cross-linked polystyrene. Their structure contains certain amount of hydrophobic pockets capable of binding large organic molecules [5]. Glucoamylase was immobilized by sorption from its solution in a 0.1 M acetate buffer under static conditions at 18–20°C for 24 h. The enzyme amount associated with the support was determined as the difference between the protein amount in the solution before and after sorption. The concentration of immobilized protein was expressed as mg of protein per 1 g of the support. The protein concentration in solution was determined by the Lowry method [6], and the glucoamylase activity, by the glucoseoxidase method [7]. The enzyme amount producing 1 μmol of glucose per minute in catalytic hydrolysis of starch at 30°C was accepted as the unit of the enzyme activity.

Glucoamylase molecule consists of the amino acid units which, depending on pH, form various ionic species. Therefore, the hydrogen ion concentration in the enzyme solution can significantly affect the enzyme sorption. We found that the maximal amount of the protein is sorbed at pH 4.7–5.0, i.e., at the isoelectric point of glucoamylase in the solution (Fig. 1).

Figure 2 shows that the curves of glucoamylase sorption on Styrosorb-1 and Styrosorb-2 within the pH range of the maximal sorption rate differ in shape. In passing from Styrosorb-2 to Styrosorb-1 having a larger specific surface area the sorption curve becomes S-shaped, indicating the change in the sorption mechanism. In the first stage of sorption the monomolecular layer of glucoamylase is formed owing to the sorbent–sorbate interactions. Further sorption of enzyme occurs by the mechanism of the sorbate–sorbate interactions. Due to intermolecular association of the enzyme molecules, a polymolecular layers on the sor-

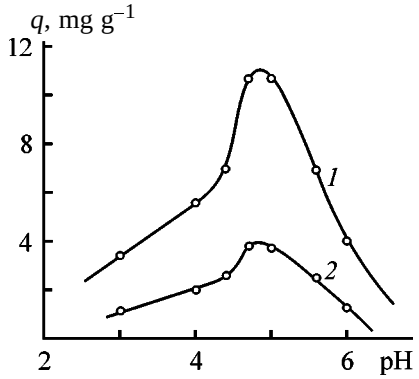

Fig. 1. Dependence of glucoamylase sorption q on pH of the equilibrium solution. (*1*) Styrosorb-1 and (*2*) Styrosorb-2; the same for Figs. 2 and 3.

1070-4272/01/7405-0897$25.00

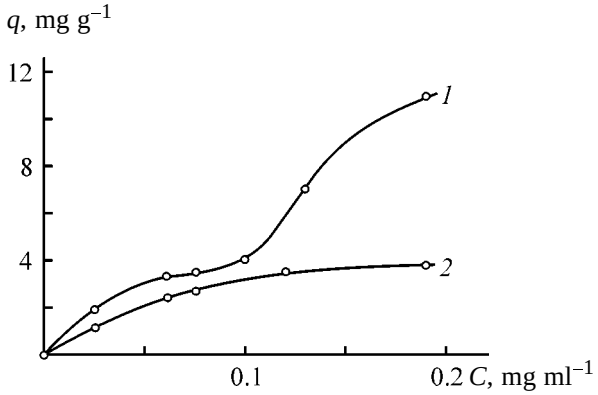

Fig. 2. Curve of glucoamylase sorption at pH 4.7: (*q*) enzyme amount sorbed; (*C*) initial content in solution.

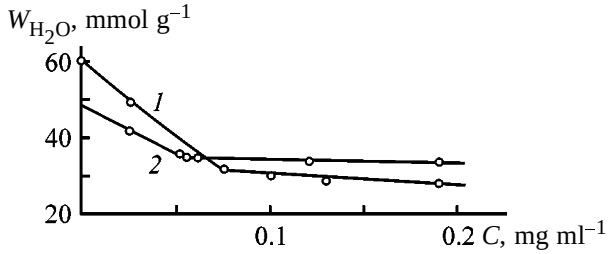

Fig. 3. Variation of the water content in Styrosorb in the course of glucoamylase sorption: (W_{H_2O}) water content in the sorbent; (*C*) initial glucoamylase content in solution.

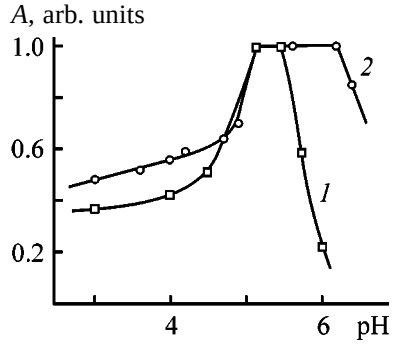

Fig. 4. Enzyme activity *A* of (*1*) native and (*2*) immobilized glucoamylase as influenced by pH of substarte solution.

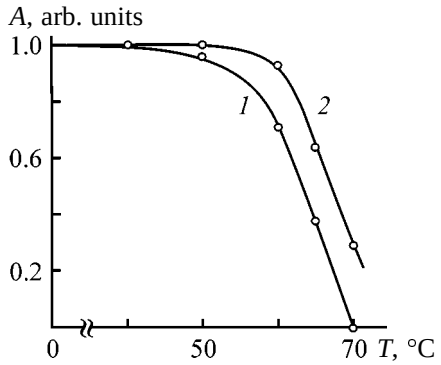

Fig. 5. Thermal stability of (*1*) native and (*2*) immobilized glucoamylase: (*A*) Residual enzymic activity of glucoamylase after incubation at pH 4.7 for 1 h; (*T*) temperature.

bent surface are formed. Completion of the monolyer formation is manifested as the inflection point in the sorption curve. Thus, the first sorption layer is formed owing to interactions of hydrophobic fragments of glucoamylase molecule with hydrophobic walls of the sorbent pores. It is known [8] that glucoamylase molecule contains numerous amino acid units with alkyl side chains (Ala, Val, Met, Ile) playing the important role in protein stabilization. Styrosorb contains also several amount of unpolymerized carbonyl and chloromethyl groups capable of forming hydrogen bonds between the enzyme and support. After completion of formation of the monomolecular enzyme layer the sorbent modified by enzyme molecules is formed. Further sorption of the enzyme occurs by the mechanism of interaction between hydrophilic and hydrophobic parts of glucoamylase molecules. The shape of the curve of glucoamylase sorption on Styrosorb-2 is typical for the monolayer sorption.

Our assumption about the mechanism of glucoamylase interaction with Styrosorb was confirmed by gravimetric monitoring of water content within the sorbent (Fig. 3). Removal of the water from the sorbent increases the amount of sorption sites. Figure 3 shows that at small degree of the sorbent exhaustion the water content in the sorbent decreases more sharply than in the range of prevalence of the enzyme–enzyme interactions. It is possible that these processes occur by the mechanism of the interfacial lubrication suggested in [2].

In further experiments we studied several features of the biocatalyst prepared by us. It is known that pH of a substrate significantly affects the enzymic activity since variation of the hydrogen ion content changes the conformational state of protein and, therefore, can affect both the local and the general structure of polypeptide chains. To find the optimal conditions for the enzyme functioning, the activity of both the native and immobilized glucoamylase was studied as influenced by pH of a substarte (Fig. 4). These studies showed that the immobilized and native enzymes exhibit the maximal activity within pH ranges 4.7–6.2 and 4.7–5.0, respectively. Thus, immobilized glucoamylase is characterized by the more extended range of high activity.

One of the main consequences of enzyme immobilization is increase in their stability to the denaturing effect of medium and, as a result, manifold increase in performance of enzymic transformation of a substrate. Figure 5 shows the temperature dependence of the enzimic activity of glucoamylase in incubation for 1 h. It was found that the immobilized glucoamylase

exhibits higher thermal stability than its native form. For example, on heating at 70°C for 20 min native glucoamylase is completely inactivated. At the same time, under the similar conditions the immobilized enzymes do not loss enzymic activity for 2 h. The immobilized enzyme acquires more rigid conformation providing higher stability to changes and inactivation.

CONCLUSIONS

(1) Styrosorb with a specific surface area of 440 $m^2 g^{-1}$ exhibits the highest sorption capacity for glucoamylase.

(2) Immoblized glucoamylase, as compared to the native enzyme, is characterized by the more extended pH range of the highest enzymic activity and enhanced thermal stability.

(3) Styrosorb is a suitable support for immobilization of glucoamylase.

REFERENCES

1. Trevan, M., *Immobilized Enzymes. An Introduction and Applications in Biotechnology*, Chichester: Wiley, 1980.
2. Oros, G.Yu., Selemenev, G.F., Khokhlov, V.Yu., *et al*., *Zh. Fiz. Khim*., 1998, vol. 72, no. 5, pp. 926–932.
3. Brezhneva, T.A., Selemenev, V.F., Oros, G.Yu., *et al*., *Teor. Prakt. Sorbts. Prots.* (Voronezh), 1999, issue 24, p. 40.
4. Tsarenko, O.V., Chromatographic Purification of Pancreas Enzymes, *Cand. Sci. Dissertation*, St. Petersburg, 2000.
5. Tsyurupa, M.P., Maslova, L.A., Mrachkovskaya, T.A., and Davankov, V. A., *Vysokomol. Soedin*., 1991, vol. 23, no. 12, pp. 2645–2651.
6. Lowry, O.M., Rosenbrough, N.J., Lewis, A.F., and Randall, R.F., *J. Biol. Chem*., 1951, vol. 193, no. 1, pp. 265–275.
7. Lloyd, J.B. and Whelan, W.J., *Anal. Biochem*., 1969, vol. 30, no. 5, pp. 470–473.
8. Aleshin, A.E., Hoffman, C., Firsov, L.M., and Honzatko, R.B., *J. Mol. Biol*., 1994, vol. 238, pp. 575–591.

Russian Journal of Applied Chemistry, Vol. 74, No. 5, 2001, p. 900. Translated from Zhurnal Prikladnoi Khimii, Vol. 74, No. 5, 2001, p. 872.

BOOK REVIEWS

Denisov, V.M., Belousova, N.V., Moiseev, G.K., Bakhvalov, S.G., Istomin, S.A., and Pastukhov, E.A., *Vismutsoderzhashchie materialy: stroenie i fiziko-khimicheskie svoistva* (Bismuth-Containing Materials: Structure and Physicochemical Properties), Yekaterinburg: Ural'sk. Otd. Ross. Akad. Nauk, 2000

This original monograph analyzing and generalizing experimental data on the structure and properties of metallic and oxide bismuth-containing materials in liquid and crystalline states has been published by the initiative of the Institute of Metallurgy, Ural Division, Russian Academy of Sciences, with participation of a number of leading staff members of the institute. The book gives much attention to the structure and properties of liquid bismuth alloys and also considers bismuth-containing oxide systems.

The monograph comprises an introduction and six chapters. The comprehensive and informative bibliography of the book gives references to 769 works.

The brief introduction (pp. 3–6) substantiates the expediency and utility of generalizing the information about the structure and physicochemical properties of bismuth-containing materials and indicates fields of their application.

The first chapter (pp. 7–78) considers the structure of bismuth-based melts. In fact, investigations of liquid metallic bismuth alloys by means of diffraction experiments are dealt with in the chapter and the results obtained are interpreted. Atomic radial distribution functions, structural factors, and the relationship between the structural features of melts and their physicochemical properties are analyzed.

The second chapter (pp. 79–177) describes the thermodynamic properties of bismuth alloys. The analysis is made rather thoroughly with sufficiently complete coverage of the relevant literature, with emphasis placed on works of Russian authors. Some publications in foreign journals remained unnoticed by the authors, which is not surprising in view of the extent to which libraries are presently provided with foreign publications.

The third chapter (pp. 178–228) discusses the surface and bulk properties of liquid bismuth alloys. Theoretical questions arising in calculating and analytically expressing the surface tension isotherms of binary alloys are considered and ample body of reference data for both metallic and oxide systems is provided. Wetting phenomena are discussed.

The spacious fourth chapter (pp. 251–381) is mainly concerned with the electrical properties (electrical conductivity, charge transport, thermoelectric power, electron work function) of bismuth-containing systems. Also given are data on the speed of sound, viscosity, and diffusion.

The fifth chapter (pp. 381–416) is concerned with oxidation of bismuth-based liquid alloys.

The final, sixth chapter (pp. 417–483) makes a thermodynamic analysis of the bismuth–oxygen system and considers bismuth oxides and their thermochemical characteristics. The systems $SrO–Bi_2O_3$ and $CuO–Bi_2O_3$ are discussed.

In assessing the monograph as a whole, mention should be made of the high value of the work done by the authors in systematization of published data on the physicochemical properties of metallic and oxide bismuth-containing systems. However, no impression is created that the joint consideration of such dissimilar objects as metallic and oxide systems offers some advantages. It seems that, if the monograph were divided, with its total volume preserved, into two parts concerned separately with metallic and oxide systems, the book would be simpler in use and more logically consistent. In the first five chapters, the data on oxide systems "dissolve" in a vaster information concerning metallic systems. And only the sixth chapter, dealing exclusively with oxides and oxide systems, occupies a particular position.

The book is of interest to a wide audience of specialists in inorganic materials science and can serve as reference for masters and post-graduate students specialized in chemical technology and metallurgy.

A. G. Morachevskii

1070-4272/01/7405-0900$25.00 © 2000 MAIK "Nauka/Interperiodica"

Russian Journal of Applied Chemistry, Vol. 74, No. 6, 2001, pp. 901–906. Translated from Zhurnal Prikladnoi Khimii, Vol. 74, No. 6, 2001, pp. 881–885.

INORGANIC SYNTHESIS AND INDUSTRIAL INORGANIC CHEMISTRY

A Study of Evaporation in the TiO_2–Nb_2O_5 Oxide System by High-Temperature Mass-Spectrometry

G. A. Semenov and S. I. Lopatin

Research Institute of Chemistry, St. Petersburg State University, St. Petersburg, Russia

Received July 5, 2000; in final form, November 2000

Abstract—High-temperature mass-spectrometry was applied to study the vapor phase composition and dynamics of its variation in evaporation of oxide materials of the system TiO_2–Nb_2O_5. The incongruent nature of evaporation processes is established.

Thin films based on titanium and niobium oxides have rather long been used as optical interference coatings [1]. The main technique used to deposit such coatings is vacuum evaporation of an oxide material of appropriate composition with subsequent oxidizing annealing of the obtained film. However, the actual molecular composition of the vapor phase and the dynamics of its variation in the course of evaporation have not been studied until recently. In the only study concerned with this subject [2], an attempt was made to prognosticate theoretically the vapor composition over a hypothetical two-phase mixture of titanium and niobium oxides with account of dissociative evaporation. Having assumed that the oxygen pressure over the system is determined by the dissociation pressure of Nb_2O_5, the authors calculated for T = 2200 K the following partial pressures of the components (mm Hg): $p(O_2) = 3.45 \times 10^{-2}$, $p(NbO_2) = 1.66 \times 10^{-1}$, $p(TiO_2) = 4.8 \times 10^{-3}$. According to their estimate, the NbO and TiO vapor pressure must be no less than three orders of magnitude lower than the vapor pressures of the corresponding dioxides.

The phase diagram of the system TiO_2–Nb_2O_5 has been studied repeatedly [3–6]. Existence of at least two congruently melting compounds with Nb_2O_5 : TiO_2 ratios of 5 : 2 and 1 : 1 has been reliably established. At T > 2100 K all the compositions of the system will be molten. A mass-spectrometric study of the vapor phase composition over titanium and niobium oxides demonstrated that only $NbO_{2.00}$ and $TiO_{0.67}$ (Ti_3O_5) are congruently sublimating [7]. When heated in a vacuum, the compounds Nb_2O_5 and TiO_2 dissociate, even before the onset of evaporation, into NbO_{2+x} and TiO_{2-y} (with $x \approx 0.1$ and $y \approx 0.13$). The presence of NbO_2, NbO, TiO_2, TiO, and oxygen molecules in the vapor phase over individual oxides was established. The relative content of these molecular species varies, depending on temperature and evaporation time, as the condensed phase compositions approach the above-mentioned congruently melting compositions. Solutions with isomorphic substitution are formed in the oxide system NbO_2–TiO_2 [8, 9]. It has also been noted that the formal oxidation state partly increases from +4 to +5 upon calcination of compacted mixtures of dioxides at 1400°C in a neutral atmosphere [10]. All the aforesaid suggests that, because of the thermal dissociation in a vacuum, the evaporation of systems based on TiO_2 and Nb_2O_5 oxides will become incongruent with the composition of the condensed phase approaching NbO_{2+x}–TiO_{2-y}, in which the indices will depend on temperature and oxygen pressure over the system.

The aim of this study was to confirm experimentally the above assumptions by analyzing how the molecular composition of the vapor changes in the course of evaporation of samples with varied initial relative content of titanium and niobium oxides.

EXPERIMENTAL

High-temperature thermodynamic studies were performed using an MS-1301 mass spectrometer [11]. Samples (mixtures of TiO_2 and Nb_2O_5 containing 10, 40, 50, 67, 75, and 90 mol % TiO_2, calcined in air) were evaporated from electron beam–heated twin molybdenum effusion chambers [12]; the chamber temperature was measured with an EOP-66 optical pyrometer. The pyrometer readings were periodically corrected for radiation absorption by the glass win-

1070-4272/01/7406-0901 $25.00 © 2001 MAIK "Nauka/Interperiodica"

Table 1. Mass spectrum of vapor over NbO_2 and Ti_3O_5

NbO_2				Ti_3O_5			
ion	AE, eV	ion current (rel. units) at indicated E, eV		ion	AE, eV	ion current (rel. units) at indicated E, eV	
		25	AE + 3			25	AE + 3
NbO_2^+	8.2 ± 0.3	1.0	1.0	TiO_2^+	10.3 ± 0.4	0.32 ± 0.02	0.15 ± 0.01
NbO^+	7.4 ± 0.3 14 ± 1	0.18 ± 0.02	0.12 ± 0.01	TiO^+	7.0 ± 0.3 14.5 ± 1	1.0	1.0
Nb^+	18 ± 1	0.02 ± 0.01	–	Ti^+	15 ± 1	0.03 ± 0.01	–

dow, using an SI-10-300 temperature lamp. To calibrate the apparatus, the vapor pressure of gold was measured by the method of complete thermal evaporation of a sample [11, 13]. The obtained data were, on the average, different from published data [14] by no more than ±15%, which corresponds to a temperature measurement error of ±8 K at 1580 K. The ions in the mass spectrum were identified by their mass number, isotope composition, and appearance energy (AE) measured by the method of disappearance of the ion current. The energy scale of ionizing electrons was calibrated with $AE(Au^+)$ = 9.226 eV [15]. The partial pressures of vapor components were measured by differential mass spectrometry [11, 13], with the sample and pressure standard placed in separate compartments of the twin effusion chamber. The measured ion currents are related to the partial pressures of a substance under study (i) and the standard (s) by

$$p_i = a\,\frac{p_s I_i T_i \sigma_s \gamma_s}{I_s T_s \sigma_i \gamma_i}, \qquad (1)$$

where p is the partial pressure, I the ion current intensity, T temperature (K), σ the effective cross-section of electron-impact ionization, and γ the sensitivity coefficient of the secondary-electron multiplier.

The factor a (conductivity ratio of effusion apertures) can be determined experimentally by evaporating the standard substance from both compartments of the effusion chamber simultaneously. Implicitly, the factor a also accounts for the possible temperature gradient between separate parts of the effusion unit. The identical conditions of evaporation from both the compartments are achieved by carefully machining the effusion apertures and selecting the diameter and position of the annular cathodes of the evaporator.

As pressure standard [p_s in formula (1)] can, in principle, serve any suitable simple substance or chemical compound with vapor pressure measured with sufficient accuracy. In this case, the relative ionization cross-sections $\sigma_{i,s}$ are found from the atomic element ionization cross-sections [16], with the use of the additivity rule [11, 13] in calculating the molecule ionization cross-sections. The error appearing in this case may be substantial. The accuracy of pressure measurements can be markedly improved if the vapor pressures of the pure components of the system are used as standards. In this case, the coefficients σ and γ in formula (1) are cancelled and there is no need to make corrections to the ion current intensities $I_{i,s}$ for the mass spectrum coefficients and the isotope composition of ions. As standards were chosen congruently sublimating oxides, NbO_2 and Ti_3O_5. In preliminary experiments, the NbO_2 vapor pressure was again measured by the method of complete isothermal evaporation over a sample of composition $NbO_{2.008}$. The obtained results virtually coincided with the data of Matsiu and Naito [7] for the composition $NbO_{2.011}$. Further, the standard NbO_2 vapor pressures p_s (mm Hg) were calculated using the equation

$$\log p = -28\,640/T + 11.15 \quad (2012\text{–}2155\ \text{K}). \qquad (2)$$

The sample fraction evaporated in the form of NbO was calculated from the ratio $I(NbO_2^+)/I(NbO^+)$ in mass spectra obtained at electron energy E = (AE + 3) eV on the assumption of a negligible fragmentation of molecular ions in this operation mode of the ion source. Table 1 presents a mass spectrum of a vapor over NbO_2 at 2200 K and two electron energies.

Previously, some fundamentally important recent observations have been discussed [12, 13], concerning the ionization cross-sections of MO_2 and MO molecules for which the postulate of additivity of the cross-sections of the constituent atoms is seemingly not observed. Experimental data, although being rather diverse, indicate that the ionization cross-section ratio

$\sigma(MO_2)/\sigma(MO) \approx 0.35$–$0.45$ for Ti, V, Th, and U oxides. The same result was obtained in an earlier study [17]: the $\sigma(NbO_2)/\sigma(NbO)$ ratio was found to be close to 0.5 at 11 eV. If this concept is adopted, the partial pressure of NbO in a saturated pressure over NbO_2 must be not higher than 5–6% of the NbO_2 pressure. Similar reasoning was done when analyzing the results obtained in studying the evaporation of Ti_3O_5. Table 1 presents a typical mass spectrum of the vapor over Ti_3O_5 at 2200 K and ion appearance energy of 25 eV and (AE + 3) eV.

AE measurements show that TiO_2^+ ions have molecular, TiO^+ partially "fragmentary," and Ti^+ completely fragmentary origin. At electron energy (AE + 3) eV, only molecular ions are recorded; however, the ratio of their intensities apparently does not correspond to the ratio of partial pressures (the intensity of the TiO_2^+ current is strongly underestimated, probably because of the different slopes of the ionization efficiency curves for the TiO^+ and TiO_2^+ ions. If the difference in the mass spectra obtained at 25 and (AE + 3) eV were accounted for solely by fragmentation under electron impact, then, the content of TiO_2^+ ions in the mass spectrum should have been higher in the second case in the absence of fragmentation than that at 25 eV, which is not the case. As a result, it was accepted, as before [12], in calculating the partial pressures of TiO_2 and TiO that the content of ions-fragments at 25 eV does not exceed 5% of the content of molecular ions, and no correction for fragmentation was introduced. The method of complete isothermal evaporation of samples was applied to measure the effective Ti_3O_5 vapor pressure and the result was compared with similar data of Wahlbeck and Gilles [18], obtained by the effusion Knudsen method (in both studies the pressure was calculated without taking into account the real vapor composition for M = 223.7, i.e., for the molecular weight of Ti_3O_5). Taking $T_m(Ti_3O_5)$ = 2050 K and enthalpy of melting $\Delta_m H^0(Ti_3O_5)$ = 1669 kJ mol^{-1}, the straight line describing the dependence $\log p_{eff}(Ti_3O_5) = f(1/T)$ was extrapolated to the temperature range analyzed in the present study (Fig. 1). It can be seen that the obtained data lie somewhat higher than this extrapolated line, at good reproducibility. The reliability of the measurements performed was confirmed by satisfactory results of a calibration against the international standard–gold, as discussed above. Therefore, a decision was made to use these data in calculating the TiO_2 and TiO vapor pressures over Ti_3O_5 standard. The ionization cross-section ratio $\sigma(TiO_2)/\sigma(TiO)$ = 0.5 and temperature dependences of the TiO^+ and TiO_2^+ ion currents [12] were used to find the equilibrium TiO and TiO_2 vapor pressures (mm Hg, 2500–2300 K):

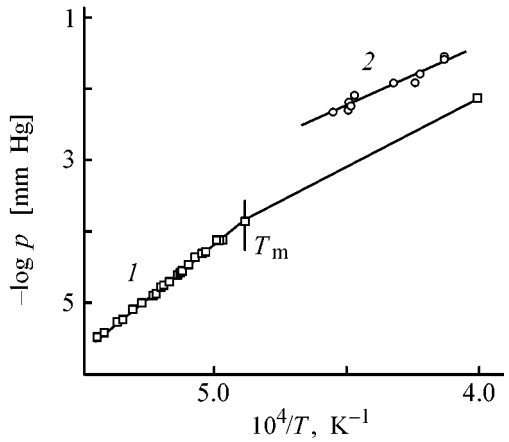

Fig. 1. Ti_3O_5 vapor pressure p_{eff} vs. temperature T. Data: (*1*) [18] and (*2*) present study.

$$\log p(TiO) = -25\,450/T + 9.008, \quad (3)$$

$$\log p(TiO_2) = -25\,120/T + 8.681. \quad (4)$$

The evaporation of all compositions of the system under consideration was studied in the isothermal mode at a temperature close to 2200 K. Figure 2 presents a typical time dependence of the main ion currents in the mass spectrum of vapor over a composition containing 50 mol % TiO_2 (standard Ti_3O_5).

The mass spectrum shows the same ions as the mass spectra of vapors over individual oxides—components of the system; NbO_2^+ and TiO_2^+ ions are molecular, the NbO^+ and TiO^+ ion currents contain 5–6% fragmentary ions. A thorough search for more complex ions, which could be formed in the intermolecular interaction (e.g., of the $TiNbO_3^+$ type), has been unsuccessful: their detection limit can be estimated at less than 0.01% of the NbO_2^+ intensity. It can be clearly seen that the evaporation process has incongruent nature: (a) a more volatile oxide NbO_2 is evaporated and (b) the TiO_2^+/TiO^+ ion current ratio, i.e. the ratio of partial pressures of TiO_2 and TiO, varies continuously.

At the chosen temperature of 2200 ± 30 K, no azeotrope formation was observed for any compositions, including those TiO_2-rich. The TiO_2^+/TiO^+ ratio at the end of an experiment virtually coincides with that for the Ti_3O_5 standard (as seen from Fig. 2). The incongruent nature of evaporation gives rise to well-defined difficulties in calculating the partial pressures of vapor components, since the condensed phase

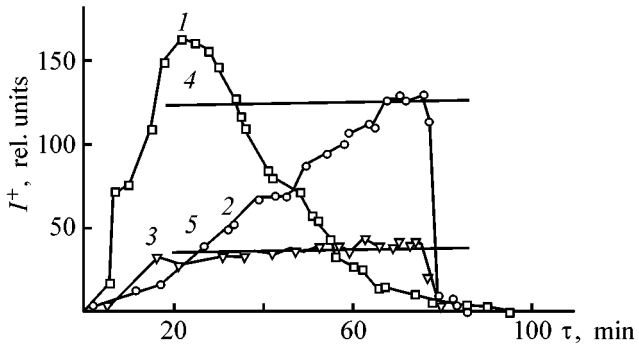

Fig. 2. Ion current intensities I^+ vs. time τ for a sample containing 50 mol % TiO_2. (*1*) NbO_2^+, (*2*) TiO^+, (*3*) TiO_2^+, (*4*) TiO^+ (standard), and (*5*) TiO_2^+ (standard).

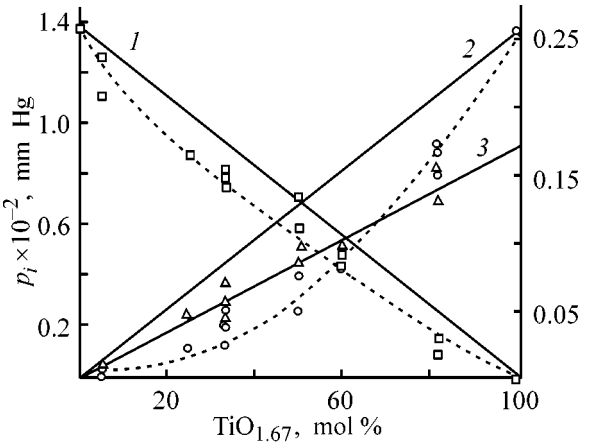

Fig. 3. Diagram partial pressure p_i–condensed phase composition. (*1*) NbO_2, (*2*) TiO, and (*3*) TiO_2.

composition is not invariable, with the loss of oxygen occurring to a substantial extent even before the onset of oxide evaporation in the range of temperature rise to the working temperature of 2200 K. The effusion chamber temperature was rapidly raised from approximately 1700 K (temperature of preliminary keeping at which no evaporation is observed) to the working temperature in order to preclude any substantial distillation of the system by the beginning of measurements; the Ti : Nb ratio in the melt at this instant of time was taken to be equal to that in the sample of the initial composition. However, dissociation of oxides with oxygen loss did occur and the true index by oxygen could not be established. Nevertheless, an attempt was made to characterize quantitatively the evaporation processes in the oxide system under study by constructing a partial pressure–condensed phase composition diagram, with the following conditions introduced.

(1) As a result of thermal dissociation in a vacuum and loss of oxygen with preserved Nb : Ti ratio, all the compositions of the starting system TiO_2–Nb_2O_5 can be interpreted within the new system $TiO_{1.67}(Ti_3O_5)$–NbO_2, in which the pure components are dissociation products—congruently sublimable niobium and titanium oxides. Then, to the starting samples correspond compositions with 5.6, 25.0, 33.3, 50.0, 60.0, and 82 mol % Ti_3O_5 in the new system. The experimental points in the diagram (Fig. 3) reflect the partial pressures of NbO_2, TiO, and TiO_2 over the above compositions. Since the temperature was somewhat different (within 30 K) from 2200 K in some experiments, the experimental partial pressures were recalculated to 2200 K using the equations describing the temperature dependence of the vapor pressure for pure oxides [Eqs. (2)–(4)].

(2) Since the samples were evaporated from effusion chambers in which the thermodynamic equilibrium vapor–condensed phase was maintained during the experiment, it was considered possible to plot in the diagram (Fig. 3) straight lines representing the dependence of the partial pressures on the composition of the condensed phase in accordance with the Raoult law and to analyze the position of the experimental points relative to these straight lines (lines *1*–*3*). Despite the assumptions made, the diagram yields quantitative information about the order of magnitude and relative values of the partial pressures of the vapor components over the system under study. It can be seen that the NbO_2 vapor pressure is only slightly underestimated, and the TiO_2 vapor pressures coincide, to within data scatter, with the values corresponding to evaporation by the Raoult law, which points to a weak interaction of niobium and titanium oxides in the melt. By contrast, the TiO vapor pressure (measured in the initial stage of an experiment, when the O_2 vapor pressure over the system being evaporated is higher than that over TiO_{2-y}, at least for NbO_2-rich compositions) is strongly underestimated and increases only after a pronounced evaporation of NbO_2 (Fig. 2). The dashed lines and in Fig. 3 represent the real averaged positions of points for the partial pressures of NbO_2 and TiO. The experimentally measured NbO_2 and TiO_2 pressures over system are much lower (5–8-fold) than the estimates by Yudin *et al*. [2], whereas the pressures of NbO, and especially TiO, exceed the estimated values by more than an order of magnitude.

Several samples of the system were studied on a UELI–MASS laboratory mass-spectrometric installation with an electron-beam evaporator [20], operating in a mode reproducing the technological condi-

Table 2. Mass spectrum of vapor over a composition 50 mol %TiO_2–50 mol %Nb_2O_3

Ion	Intensity, rel. units		Ion	Intensity, rel. units		Ion	Intensity, rel. units	
	a*	b*		a*	b*		a*	b*
NbO_2^+	1.0	1.0	Nb^+	0.015	0.016	TiO_2^+	0.07	0.24
NbO^+	0.16	0.21	TiO^+	0.38	0.05	Ti^+	0.03	0.015

* Evaporation: (a) fron Knudsen chamber and (b) by electron beam.

tions of film deposition by evaporation. Table 2 presents a mass spectrum of vapor over a sample containing 50 mol % TiO_2, with the mass spectrum obtained in evaporation of a sample of the same composition from a Knudsen effusion chamber given for comparison. The spectra are normalized to the highest ion current of NbO_2^+. Differences in the vapor composition are well seen: in the case of electron-beam evaporation the vapor phase is strongly enriched in TiO_2. Probably, in evaporation from the crater surface, the degree of dissociation of the oxides is lower than in the case of evaporation from the effusion chamber because of the greater sample mass, convection agitation of the melt, and arrival of fresh portions of the material from the boundary between the crater and the unmelted bulk of the sample. Nevertheless, even under conditions of intensive evaporation of the material by the electron beam, the more volatile oxide NbO_2 continues to evaporate. Thus, the results obtained in direct mass-spectrometric studies of the real molecular composition of the vapor over the TiO_2–Nb_2O_5 system demonstrate that the incongruent nature of evaporation must lead to a nonuniformity of the TiO_2/Nb_2O_5 ratio across the layer thickness, smoothed out only in the course of thermal annealing of the film.

CONCLUSIONS

(1) The assumption of the vapor phase composition and incongruent nature of vacuum evaporation of oxides of the system TiO_2–Nb_2O_5 was confirmed experimentally.

(2) The partial vapor pressures of titanium and niobium oxides were measured and vapor pressure–condensed phase composition diagrams at 2200 K were constructed.

(3) The vapor composition is qualitatively the same in thermal and electron-beam evaporation of the system under study, with the TiO_2 content somewhat higher in the latter case.

REFERENCES

1. *Physics of Thin Films. Advances in Research and Development*, Hass, G. and Thun, R.E., Eds., New York: Academic, 1973.
2. Yudin, B.F., Konopel'ko, M.V., Fedotova, G.V., and Vvedenskii, V.D., *Izv. Vyssh. Uchebn. Zaved., Khim. Khim. Tekhnol.*, 1983, vol. 25, no. 8, pp. 938–941.
3. *Diagrammy sostoyaniya sistem tugoplavkikh oksidov*, issue 5, part 2, *Dvoinye sistemy: Spravochnik* (Phase Diagrams of Systems with High-Melting Oxides, Binary Systems: Reference Book), Galakhov, F.Ya., Ed., Leningrad: Nauka, 1986.
4. Babich, E.G., Zagorodnyk, A.V., Teterin, G.A., *et al.*, *Zh. Neorg. Khim.*, 1988, vol. 33, no. 4, pp. 996–1000.
5. Khodos, M.Ya., Belysheva, G.M., and Krivosheev, N.V., *Zh. Prikl. Khim.*, 1988, vol. 33, no. 4, pp. 1066–1067.
6. Fedorov, N.F., Maslennikova, O.V., Saltykova, V.A., *et al.*, *Zh. Neorg. Khim.*, 1989, vol. 34, no. 5, pp. 1316–1319.
7. Kazenas, E.K. and Tsvetkov, Yu.V., *Isparenie oksidov* (Evaporation of Oxides), Moscow: Nauka, 1997.
8. Goldschmidt, H.J., *Metallurgia*, 1960, vol. 62, no. 373, pp. 211–218.
9. Rudorff, W. and Luginsland, H.-H., *Z. Anorg. Allgem. Chem.*, 1964, vol. 334, no. 3–4, pp. 125–129.
10. Antonio, M.R., Inho Song, and Yamada, H., *J. Solid State Chem.*, 1991, vol. 93, no. 1, pp. 183–192.
11. Semenov, G.A., Nikolaev, E.N., and Frantseva, K.E., *Primenenie mass-spektrometrii v neorganicheskoi khimii* (Application of Mass Spectrometry in Inorganic Chemistry), Leningrad: Khimiya, 1976.
12. Semenov, G.A., Lopatin, S.I., and Kuligina, L.A., *Vestn. SPb. Gos. Univ., Ser. 4, Fiz. Khim.*, 1994, issue 1, pp. 46–54.
13. Semenov, G.A. and Stolyarova, V.L., *Mass-spektrometricheskoe issledovanie ispareniya oksidnykh sistem* (A Mass-Spectrometric Study of the Evaporation of Oxide Systems), Leningrad: Nauka, 1990.

14. Paule, R.C. and Mandel, J., *Pure Appl. Chem.*, 1972, vol. 31, no. 3, pp. 371–394.
15. *Energii razryva khimicheskikh svyazei: Potentsialy ionizatsii i srodstvo k elektronu: Spravochnik* (Chemical Bond Rupture Energies: Ionization Potentials and Electron Affinity: Reference Book), Kondrat'ev, V.N., Ed., Moscow: Nauka, 1974.
16. Mann, J.B., *Recent Developments in Mass Spectroscopy*, Ogata, K. and Hayakawa, T., Eds., Baltimore: University Park, 1970, pp. 814–819.
17. Frantseva, K.E., A Thermodynamic Study of the Evaporation of Vanadium and Niobium Oxides, *Cand. Sci. Dissertation*, Leningrad, 1968.
18. Wahlbeck, P.G. and Gilles, P.W., *J. Chem. Phys.*, 1967, vol. 46, no. 7, pp. 2465–2473.
19. *Termodinamicheskie svoistva individual'nykh veshchestv: Spravochnik* (Thermodynamic Properties of Individual Substances: Reference Book), Glushko, V.P., Ed., Moscow: Nauka, 1982, vol. 4, book 2.
20. Semenov, G.A., Lopatin, S.I., and Misharev, A.D., *Prib. Tekh. Eksp.*, 1993, no. 3, pp. 219–223.

Russian Journal of Applied Chemistry, Vol. 74, No. 6, 2001, pp. 907–911. Translated from Zhurnal Prikladnoi Khimii, Vol. 74, No. 6, 2001, pp. 886–890.

INORGANIC SYNTHESIS AND INDUSTRIAL INORGANIC CHEMISTRY

A Study of Stability of Potassium Fluoride Peroxosolvates $KF \cdot nH_2O_2$ (n = 1, 2) in Solid State and in Aqueous Solutions

K. V. Titova, V. P. Nikol'skaya, V. V. Buyanov, and I. P. Suprun

Institute for Problems of Chemical Physics, Russian Academy of Sciences, Chernogolovka, Moscow oblast, Russia
GosNII Biologicheskogo Priborostroeniya State Scientific Center, Moscow, Russia

Received July 10, 2000

Abstract—The results obtained in a study of the stability of potassium fluoride peroxosolvates $KF \cdot nH_2O_2$ (n = 1, 2), including that in prolonged storage, are presented. The kinetics of $KF \cdot nH_2O_2$ decomposition in solid state and in aqueous solutions was analyzed. The obtained results characterize potassium fluoride peroxosolvates as the most stable solid carriers of hydrogen peroxide, promising for practical use.

It was shown in [1, 2] that the peroxosolvates $KF \cdot nH_2O_2$ (n = 1, 2) show a wide spectrum of antimicrobial activity. These compounds have been used to create disinfectants possessing a number of essential advantages over other presently used disinfectants, especially those containing chlorine. The developed preparations are ecologically safe in manufacture and use, corrosion-inactive, nontoxic, have no odor, and cause no allergic reactions.

Among important operation characteristics of any disinfectant are such parameters as stability in storage in solid state and in aqueous solutions.

The present communication summarizes results of investigations of the stability of potassium fluoride peroxosolvates. The kinetics of $KF \cdot nH_2O_2$ decomposition in solid state and in aqueous solutions was studied and the stability of the solvates in prolonged storage was determined.

Potassium fluoride peroxosolvates were synthesized as described in [3]. Samples of composition $KF \cdot H_2O_2$ and $KF \cdot 2H_2O_2$ were used, and also an equimolar mixture of these, with bulk chemical composition $KF \cdot 1.5H_2O_2$.

The content of hydrogen peroxide in the samples, found by permanganatometric titration, corresponded to that calculated for $KF \cdot H_2O_2$ and $KF \cdot 2H_2O_2$. The content of H_2O_2 in equimolar mixtures of these solvates was in the range from 40 to 44 wt % (41.6 wt % calculated for $KF \cdot 1.5H_2O_2$).

The stability of solid samples and aqueous solutions of the solvates in prolonged storage was studied at 20 ± 4°C in closed glass and polymer vessels. The degree of decomposition of hydrogen peroxide was judged from changes in its content with time. The stability was calculated in the form of a coefficient β equal to percentage of decomposition in unit time. In comparing the stabilities of different objects under study, the β values were taken for equal exposures.

The kinetics of decomposition of solid $KF \cdot H_2O_2$ samples was studied under isothermal conditions in the temperature range 90–125°C. A device for decomposition comprised a gas burette and a thermostated 15-cm^3 glass vessel, in which a 0.15–0.25-g portion of a sample was placed. The liberated water was absorbed by a layer of anhydrone in the upper part of the vessel. The volume of evolved oxygen was measured using a gas burette with an accuracy of 0.05 cm^3. The degree of decomposition was determined as the volume ratio of oxygen evolved by instant of time τ to oxygen contained in the weighed portion of a sample.

Solutions prepared in studying the kinetics of solvate decomposition in aqueous solutions contained approximately 7 wt % H_2O_2. The solutions were placed in a device comprising a vessel (Pyrex glass) equipped with a reflux condenser, control thermometer, and aperture for agitation and sampling in order to make analysis for the content of hydrogen peroxide. The solution volume was 40 ml. The device was placed in a furnace thermostated to within ±0.5°C. The study

1070-4272/01/7406-0907 $25.00 © 2001 MAIK "Nauka/Interperiodica"

Table 1. Stability of $KF \cdot 1.5H_2O_2$ solvate at different temperatures

T, °C	β, % day^{-1}	Annual loss of H_2O_2, %
–18	0.0039	1.4
20	0.0052	1.9
37	0.0217	7.8

was performed in the temperature range 75–95°C. Prior to the beginning of the main set of experiments, the assembled device was filled with a solvate solution and kept at 75°C for 6–7 h. Reproducible kinetic data were obtained after performing several preliminary passivating operations of this kind. Special experiments demonstrated that the water loss associated with incomplete condensation was less than 1% in the temperature range 75–90°C and as high as 3% at 95°C.

Mono- and diperoxosolvates are rather stable in solid state. The results obtained in studying the decomposition kinetics were used to find, by extrapolating the degrees of decomposition to low temperatures, that $KF \cdot H_2O_2$ loses 4×10^{-2}% H_2O_2 per year at 25°C [4]. Under real conditions, $KF \cdot H_2O_2$ obtained under laboratory conditions from high-grade components and stored in a polymer vessel at 20 ± 2°C for five years retains the initial content of H_2O_2. However, the stability of peroxosolvates strongly depends on the presence of microimpurities of foreign substances brought into the solvate together with the starting reagents and also impurities present on the reaction vessel surface or washed out of it. Therefore, the averaged results obtained for many syntheses give real data characterizing the stability of the solvates. At a storage time of 6 months the β values are as follows

Solvate	β, % day^{-1}	Annual loss of H_2O_2, %
$KF \cdot H_2O_2$	0.0031	1.10
$KF \cdot 1.5H_2O_2$	0.0066	2.40
$KF \cdot 2H_2O_2$	0.0057	2.05

The dependence of the stability of peroxosolvates on their storage temperature is demonstrated for the example of $KF \cdot 1.5H_2O_2$ (Table 1). It can be seen that the annual loss of H_2O_2 is 1.4% at –18°C and as high as 7.8% at 37°C. Thus, even in the case when the solvate is stored at 37°C, the annual loss of H_2O_2 does not exceed 10%.

The kinetics of thermal decomposition of potassium fluoride peroxosolvates was studied for the example of $KF \cdot H_2O_2$. The $KF \cdot H_2O_2$ decomposition curves processed using the Kolmogorov–Erofeev equation

$$[-\log(1 - \eta)]^{1/3} = k(\tau - \tau_0)$$

give two rectilinear portions with deceleration in the second stage. The duration of the initial portion with high rates grows with increasing temperature from $\eta = 0.01$ at 90°C to $\eta = 0.12$ at 125°C. The decomposition rate constants take the following values

T, °C	90.0	95.2	100.2	105.2
$k_1 \times 10^3$, min^{-1}	0.33	0.39	0.46	0.67
$k_2 \times 10^3$, min^{-1}	0.21	0.26	0.37	0.42
T, °C	110.2	115.2	120.2	125.2
$k_1 \times 10^3$, min^{-1}	0.78	1.20	1.40	2.07
$k_2 \times 10^3$, min^{-1}	0.50	0.76	0.80	1.05

Comparison of the kinetic parameters of $KF \cdot H_2O_2$ and other investigated peroxosolvates of salts of inorganic acids (Table 2) shows that potassium fluoride peroxosolvates exhibits the highest thermal stability.

The main reason for the high stability of solid $KF \cdot H_2O_2$ and $KF \cdot 2H_2O_2$ is that no compounds forming strongly alkaline or acid solutions are present among the products of solvate interaction with moisture.

All the known peroxosolvates are hygroscopic. Moisture absorption by peroxosolvates or their insufficient dehydration results in that a solution whose nature depends on the nature of a salt being solvated is formed on the surface of, or within crystallites consti-

Table 2. Kinetic parameters of selected peroxosolvates [5]

Solvate	Initial stage, η	$k_1 \times 10^3$, min^{-1}, 115°C	E_1, kJ mol^{-1}	$k_2 \times 10^3$, min^{-1}, 115°C	E_2, kJ mol^{-1}
$KF \cdot H_2O_2$	0.01–0.12	1.2	69.9	0.8	52.7
$Na_2CO_3 \cdot 1.5H_2O_2$	0.07–0.8	8.2	125.1	9.8	133.9
$NH_4F \cdot H_2O_2$	0.04–0.4	–	56.1	–	16.7
$BaF_2 \cdot 2H_2O_2$	0.04–0.6	–	34.3	–	47.3
$Na_2HPO_4 \cdot 2H_2O_2$	0.1–0.5	12.0	121.3	8.3	56.9
$Na_4P_2O_7 \cdot 3H_2O_2$	0.04–0.06	4.0	123.0	1.1	112.1

tuting the film or the local zone. For example, sodium carbonate peroxosolvate forms a solution with high pH value, which favors catalytic decomposition of coordinated hydrogen peroxide. The stability of $Na_2CO_3 \cdot 1.5H_2O_2$ is much lower than that of $KF \cdot H_2O_2$. For example, in the initial stage, k_1 for $Na_2CO_3 \cdot 1.5H_2O_2$ is 6.8 times k_1 for $KF \cdot H_2O_2$; and in the second stage, k_2 is 12 times higher.

In the case of phosphate peroxosolvates, the stability of the peroxosolvates is affected in opposite directions by the following two factors: a certain stabilizing effect of phosphate ions on hydrogen peroxide and the alkaline medium of the solution. The predominant influence is exerted in this case by the alkalinity of the solution formed in hydrolysis, with the result that the stability of phosphate peroxosolvates is also lower than that of $KF \cdot H_2O_2$.

Neutrality or weak alkalinity of the products formed in reaction of KF with water is the key factor determining the stability of $KF \cdot nH_2O_2$ both in solid state and in aqueous solutions.

The stabilities of aqueous solutions of some peroxosolvates and hydrogen peroxide at exposure of 40 h are compared in Table 3.

It can be seen that the stability of potassium fluoride peroxosolvate in an aqueous solution is two orders of magnitude higher than that of the industrial hydrogen peroxide and nearly five orders of magnitude higher than that of sodium carbonate peroxosolvate.

$KF \cdot H_2O_2$ solutions are also stable at elevated temperatures. For example, when heated at a rate of about 10 deg min^{-1}, solutions virtually retain the initial content of hydrogen peroxide on reaching a prescribed temperature in the range from 30 to 100°C at intervals of 10°C.

Kinetic curves describing the decomposition of aqueous solutions of $KF \cdot H_2O_2$, measured at 20°C within the time range extending to 960 h and processed using the equation $\log C_0/C = k(\tau - \tau_0)$, exhibit two linear portions with acceleration in the later stage. The time τ of changeover is 380 h (see the figure, curve *1*). In the initial stage, $k_1 = 2.5 \times 10^{-6}$ min^{-1}, and in the second, $k_2 = 9.3 \times 10^{-6}$ min^{-1}. The average degree of $KF \cdot H_2O_2$ decomposition during a storage time of 960 h (40 days) is 0.0017 % h^{-1}, or 1.2 % $month^{-1}$. Thus, potassium fluoride monoperoxosolvate solutions can be stored at room temperature and used during no less than 1 month without virtually any loss of H_2O_2.

It seemed important to characterize quantitatively the stability of $KF \cdot H_2O_2$ solutions at as high temperatures as possible, enabling their use for disinfecting. It is known for the example of hydrogen peroxide and other disinfectants that elevating the temperature by 30°C (from 20 to 50°C) raises tenfold the extinction rate of microorganisms.

Table 3. Stability of aqueous solutions of selected peroxosolvates 20°C, 10 wt %, τ = 40 h

Solvate	Average decomposition coefficient, % h^{-1} (in glass)
$KF \cdot H_2O_2$	0.00008 ± 0.00001
$Na_2CO_3 \cdot 1.5H_2O_2$	2.4170 ± 0.011
$(NH_2)_2CO \cdot H_2O_2$	0.0278 ± 0.0002
H_2O_2	0.0048 ± 0.0004

The kinetics of decomposition of aqueous solutions of $KF \cdot H_2O_2$ was studied at the highest possible temperatures (75–95°C) at intervals of 5°C. The typical dependence of $\log C_0/C$ on τ is presented in the figure (curves *2–6*). Table 4 lists the average decomposition rate constants calculated on the basis of 5–7 parallel runs.

As in the case of 20°C, the curves obtained in the range 75–95°C show a bend. The shape of curves with a bend is characteristic of the thermal decomposition of all the presently studied solid peroxides: $Na_2CO_3 \cdot 1.5H_2O_2$, $K_2CO_3 \cdot 3H_2O_2$, $NH_4F \cdot H_2O_2$, $KF \cdot H_2O_2$, $BaF_2 \cdot 2H_2O_2$, $Na_2HPO_4 \cdot 2H_2O_2$, and $Na_4P_2O_7 \cdot 3H_2O_2$ [5]. However, only in a single case $Na_2CO_3 \cdot 1.5H_2O_2$ the process is accelerated in the

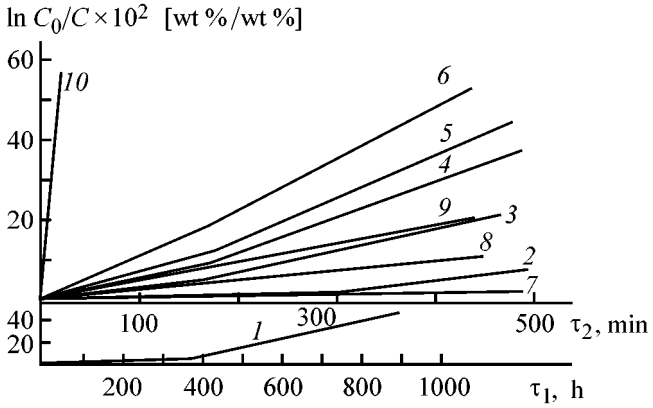

Kinetic curves of $KF \cdot H_2O_2$ decomposition in aqueous solution. (C_0, C) Initial and current concentrations and (τ_1, τ_2) time. Temperature (°C): (*1*) 20, (*2*) 75, (*3*) 80, (*4*, *7–10*) 85, (*5*) 90, and (*6*) 95. Decomposition conditions: (*1–6*) in glass, (*7*) in polyethylene, (*8*) in polyethylene and 1 g of ground glass, (*9*) in polyethylene and 1 g of Fe_2O_3, and (*10*) in polyethylene and 1 g of MnO_2.

Table 4. Kinetic parameters of $KF \cdot H_2O_2$ decomposition in aqueous solutions

Material, *T*, °C	τ range	k_1, min^{-1}	τ range	k_2, min^{-1}
Glass:				
20	0–385 h	2.5×10^{-6}	385–960 h	9.3×10^{-6}
75	0–310 min	$(1.7 \pm 0.8) \times 10^{-4}$	310–700 min	$(5.0 \pm 0.7) \times 10^{-4}$
80	0–160 min	$(4.8 \pm 0.4) \times 10^{-4}$	160–460 min	$(5.5 \pm 0.4) \times 10^{-4}$
85	0–170 min	$(6.1 \pm 0.7) \times 10^{-4}$	170–400 min	$(11.4 \pm 1.1) \times 10^{-4}$
90	0–180 min	$(7.7 \pm 0.6) \times 10^{-4}$	180–400 min	$(12.1 \pm 0.7) \times 10^{-4}$
95	0–170 min	$(11.8 \pm 0.1) \times 10^{-4}$	170–400 min	$(14.5 \pm 3.4) \times 10^{-4}$
Polyethylene, 85	–	1.0×10^{-4}	–	–
Polyethylene + ground glass, 85	–	2.8×10^{-4}	–	–
Polyethylene + Fe_2O_3, 85	–	5.1×10^{-4}	–	–
	E_1 = 72.8 kJ mol^{-1}		E_2 = 60.4 kJ mol^{-1}	

second range. In all other cases, the second stage proceeds with deceleration.

The decelerated decomposition of solid peroxosolvates can be attributed to disrupted contact between the solvate and the catalytically acting surface of the reaction vessel as a result of formation of a solid shell composed of reaction products. Explaining the acceleration of $Na_2CO_3 \cdot 1.5H_2O_2$ decomposition in the later stage without additional studies is difficult.

The similarity of $KF \cdot H_2O_2$ decomposition processes in solid state and in aqueous solution consists, in addition to double-stage nature, also in that the temperature dependence of the rate is stronger in the initial stage, compared with the second one. For example, E_1 = 69.9 and E_2 = 52.7 kJ mol^{-1} for $KF \cdot H_2O_2$, and E_1 = 72.8 and E_2 = 60.4 kJ mol^{-1} for solution. However, decomposition proceeds in the second stage with deceleration for the solid solvate, and is accelerated in aqueous solution.

The acceleration of $KF \cdot H_2O_2$ decomposition in solution at a certain τ value is possibly related to the involvement of an additional homogeneous decomposition of H_2O_2 in the solution bulk, catalyzed by products coming into the solution from the decomposing glass surface, in the process of heterogeneous catalytic decomposition of H_2O_2.

The extent of the catalytic influence exerted by the glass surface on H_2O_2 decomposition in aqueous solutions of $KF \cdot H_2O_2$ is seen from a comparison of the rates of the process in a glass device and in the same device, but with the surface insulated by a thin polymer pocket inserted into the device. The solution was isolated from the glass surface completely, but part of hydrogen peroxide could be decomposed catalytically on the uninsulated members of the device. With account of the low concentration of the solutions under study, this part seems to be insignificant.

At 85°C, decomposition of $KF \cdot H_2O_2$ solutions in a polymer vessel proceeds in the entire time range without acceleration (see the figure, curve *7*). The rate constant $k = 1.0 \times 10^{-4}$ min^{-1} is more than an order of magnitude lower than $k_2 = 11.4 \times 10^{-4}$ min^{-1} for the same temperature and 6 times lower than $k_1 = 6.1 \times 10^{-4}$ min^{-1}. On adding catalysts to the solution, the rate markedly increases immediately after their introduction, and no characteristic process acceleration is observed, either (curves *8–10*). $k = 2.8 \times 10^{-4}$ min^{-1} for ground glass (1 g) and 5.1×10^{-4} min^{-1} for Fe_2O_3, in the presence of MnO_2 the decomposition process is complete in 10–15 min.

The obtained data are in agreement with the assumption that a homogeneous bulk reaction catalyzed by glass disintegration products is additionally included in the heterogeneous process of hydrogen peroxide decomposition catalyzed by the reaction vessel surface. In the given case, this process is manifested most clearly, since fluoride ions are hydrolyzed in water to give HF and HF_2^-. Both of these species exert destructive influence on the glass.

This assumption is supported by the enhanced stability of aqueous solutions of peroxosolvates in glass at lower content of KF. For example, in the case of storage for 120 h at 20°C, β = 0.0012 % h^{-1} for

$KF \cdot H_2O_2$ (63.1% KF), 0.0009 % h^{-1} for $KF \cdot 1.5H_2O_2$ (58.4% KF), and 0.0007 % h^{-1} for $KF \cdot 2H_2O_2$ (46.1% KF).

CONCLUSION

The results obtained in studying the kinetics of decomposition and the stability in prolonged storage of $KF \cdot nH_2O_2$ solvates in solid state and in aqueous solutions demonstrate that potassium fluoride peroxosolvates belong to the most stable solid carriers of hydrogen peroxide. A strong influence of the material of which the vessels used in experiment are made on the stability of $KF \cdot nH_2O_2$ in aqueous solutions is established.

REFERENCES

1. Nikol'skaya, V.P., Titova, K.V., and Korolev, N.I., Abstracts of Papers, *1-aya Vsesoyuznaya konferentsiya po khimii peroksokompleksov i peroksosol'vatov* (1st All-Union Conf. on Chemistry of Peroxocomplexes and Peroxosolvates), Chernogolovka, 1991, p. 22.
2. Pudova, O.B., Nikol'skaya, V.P., Buyanov, V.V., and Titova, K.V., *Dezinf. Delo*, 1999, no. 3, pp. 19.
3. Titova, K.V., Gelyuk, I.P., and Rosolovskii, V.Ya., *Zh. Neorg. Khim.*, 1987, vol. 32, no. 11, pp. 2612–2615.
4. Titova, K.V., Kolmakova, E.I., and Rosolovskii, V.Ya., *Zh. Neorg. Khim.*, 1989, vol. 34, no. 12, pp. 3016–3020.
5. Titova, K.V., *Zh. Neorg. Khim.*, 1999, vol. 44, no. 6, pp. 925–930.

Russian Journal of Applied Chemistry, Vol. 74, No. 6, 2001, pp. 912–915. Translated from Zhurnal Prikladnoi Khimii, Vol. 74, No. 6, 2001, pp. 890–893.

INORGANIC SYNTHESIS AND INDUSTRIAL INORGANIC CHEMISTRY

Synthesis of Lower Oxides of Transition Metals from Chloride Melts

V. V. Lesnyak, D. A. Stratiichuk, N. S. Slobodyanik, and V. S. Sudavtsova

Shevchenko National University, Kiev, Ukraine

Received November 13, 2000; in final form, March 8, 2001

Abstract—Synthesis of transition metal oxides MO_2 (M^{IV} = Mo, W, or Nb) and V_6O_{13} in alkali chloride melts and their crystallographic characteristics are described. The advantages of the proposed technology are demonstrated. The thermodynamic parameters of the proposed reactions are calculated.

Basic and applied studies aimed to develop new energy-saving methods for obtaining oxide materials allow synthesis of materials for electronics, catalysis, automatics, and radio engineering in considerably shorter time at a fundamentally new level. Dioxides of polyvalent metals, e.g., molybdenum and tungsten dioxides, which have found wide application as multifunctional heterogeneous catalysts for oxidation of NO and CO and for selective oxidation of *n*-butane and other hydrocarbons [1, 2], are widely used in solving both industrial and ecological problems. Some metal oxides, e.g., niobium and vanadium oxides, are semiconductors.

Since the known methods for synthesizing polycrystalline compounds involve gross consumption of energy and employ high-cost equipment [3], we developed in this study a method for synthesizing oxides of transition metals (Mo, W, Nb, and V) from fluxes—alkali chloride melts. The method makes it possible to perform the reaction at comparatively low temperature in a short time without use of expensive equipment.

EXPERIMENTAL

The experiment was carried out using mixtures of higher *d*-element oxides and finely dispersed powders of the respective metals, in amounts corresponding to the stoichiometry of the following reactions.

$$2MoO_3 + Mo \rightarrow 3MoO_2, \quad (1)$$

$$2WO_3 + W \rightarrow 3WO_2, \quad (2)$$

$$2Nb_2O_5 + Nb \rightarrow 5NbO_2, \quad (3)$$

$$13V_2O_5 + 4V \rightarrow 5V_6O_{13}. \quad (4)$$

As the reaction medium served a flux of a eutectic composition of the system LiCl–KCl (40 mol % KCl), chosen because of its being readily available and having a low melting point. The eutectic composition of the LiCl–KCl system (T_{mel} = 352°C) is inferior in temperature characteristics solely to the composition LiCl–RbCl (44.5 mol % RbCl; T_{mel} = 312°C).

Thoroughly ground metal oxides, powdered metals, and the eutectic mixture LiCl–KCl (Table 1) were used to prepare formulations in the initial stage of the experiment. Then, the formulations were placed in porcelain crucibles and heated to 400°C. The system was kept under these conditions for 30–40 min until residual oxygen was removed and two separate fractions were obtained: lower layer containing a mixture of oxide and a metal and upper layer composed of the eutectic melt LiCl–KCl and occupying 20–30% of the working volume of the crucible. Then, the temperature was raised to 750–780°C at a rate of 30–40 deg h^{-1}. After being kept at 780°C for 30–40 min, the system was cooled at a rate of 30–40 deg h^{-1}. The melt cooled to approximately 400°C was decanted, with the obtained solid residue washed with hot distilled water and dried at 120°C.

Table 1. Synthesis conditions of polyvalent metal oxides

Reaction	*T*, °C	τ, h	Amount of LiCl–KCl, g per 10 g of mixture
(1)	750	5	35
(2)	650	3	40
(3)	750	5	35
(4)	750	5	35

1070-4272/01/7406-0912 $25.00 © 2001 MAIK "Nauka/Interperiodica"

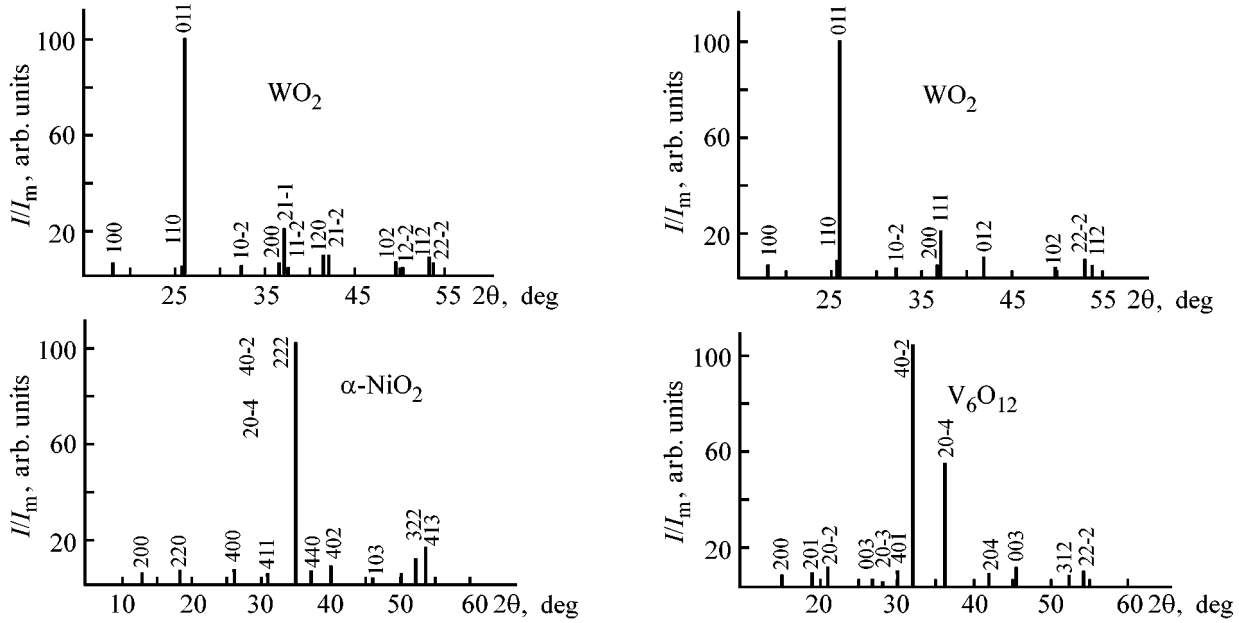

Fig. 1. X-ray powder diffraction patterns of the prepared oxides. (I/I_m) Relative intensity and (2θ) Bragg angle.

The reactions proceeding in these systems yielded finely dispersed brown powders of molybdenum and tungsten dioxides ($\rho_{X\text{-}ray}$ = 6.47 and ρ_{exp} = 5.44 g cm^{-3}). Vanadium and niobium form dark blue oxides ($\rho_{X\text{-}ray}$ = 3.91 and ρ_{exp} = 5.98 g cm^{-3}). It should be noted that, in synthesizing tungsten dioxide WO_2, a 10–15%-excess of metallic tungsten and a temperature not higher than 650°C are the optimal phase formation conditions. This can be attributed to high oxidizability of tungsten and formation of bronzes of variable composition.

Analysis of spent fluxes revealed that the *d*-element compounds are not dissolved in salt melts even in trace amounts, which, in fact, indicates that the process cannot occur via the solvent–solute stage. Most likely, the scheme of the given reaction is as follows: (1) thermal dissociation of an oxide with the formation of MO_x^+ cations, (2) formation of a transition complex with the melted flux, (3) its transfer to the metal surface, and (4) interaction of the complex with the metal to give a lower oxide. This reaction scheme formally occurs in many heterogeneous processes in temperature-reducing fluxes. In addition, the chloride melts strongly activate the metal surface, with oxide films removed and the number of defects increased. It should be noted that, in the case when a direct reaction metal–oxide or oxide–oxide (sintering) is used, the process rate is limited in early stages by the rate of reagent transfer to the reaction region, and later, by reagent diffusion through a layer of the formed products [4].

The phase composition of the reaction products was studied by X-ray phase analysis (XPA). The obtained results are shown in Fig. 1 and listed in Table 2. According to the ASTM Powder Diffraction Data File, the obtained oxides are the monoclinic V_6O_{13}, WO_2, MoO_2 and rhombic α-NbO_2 (Table 2). The amount of metal in the samples, *M* (wt %), was determined by X-ray fluorescence analysis on a Philips-1500 apparatus (Table 3).

Table 2. Calculated XPA data for the obtained compounds

Compound	Sp. gr.	*a*	*b*	*c*	β, deg	*V*, Å^3	$\rho_{X\text{-}ray}$, g cm^{-3}
		Å					
MoO_2	$P2_1/c$	5.61	4.84	5.52	119.26	121.0	6.47
WO_2	$P2_1$	5.65	4.89	5.55	120.42	133.0	5.44
α-NbO_2	$I4_1/a$	13.68	5.97	5.97	–	1118.0	5.98
V_6O_{13}	$C2/m$	11.92	3.68	10.13	100.87	436.0	3.91

Table 3. Data on X-ray fluorescence analysis for the prepared compounds

Compound	*M*, wt %		Compound	*M*, wt %	
	calculated	experimental		calculated	experimental
MoO_2	75.0	74.3	α-NbO_2	74.4	72.1
WO_2	85.32	83.1	V_6O_{13}	66.6	67.3

Table 4. $-\Delta G^0$ values for reactions (1)–(4)

Reaction	$-\Delta G^0$ (kJ mol^{-1}) at indicated temperature, K						
	298	400	600	800	1000	1200	1400
(1)	129.0	142.4	151.6	161.3	168.4	–	–
(2)	38.3	42.5	32.9	28.4	23.2	–	–
(3)	168.0	168.5	165.5	154.0	147.0	–	–
(4)	449.5	449.5	450.0	462.5	463.0	432.0	421.8

To predict the course of the reactions studied, we calculated the standard change in the Gibbs energy of the reactions, ΔG^0, at 298–1000 K from the data reported in [5]. The obtained results are presented in Table 4 and Fig. 2.

To predict the possibility of reactions of metals belonging to subgroups V-B and VI-B with their higher oxides in an oxygen-free atmosphere at 298–1000 K, the change in the Gibbs energy of the reactions

$$2CrO_3 + Cr \rightarrow 3CrO_2, \quad (5)$$

$$2V_2O_5 + V \rightarrow 2.5V_2O_4 \quad (6)$$

was calculated on the basis of the standard thermodynamic functions of the starting and final substances [5]. For reaction (1), the dependence of ΔG^0 on temperature is a nearly linear within 298–1000 K, which indicates that the reaction rate grows with increasing temperature.

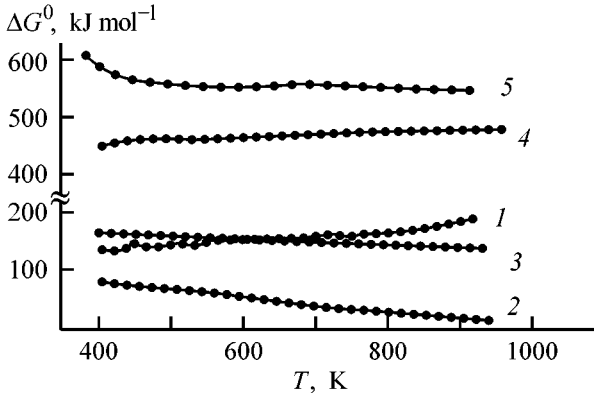

Fig. 2. ΔG^0 vs. temperature T for reactions (1)–(5). (*1*) MoO_2, (*2*) WO_2, (*3*) NbO_2, (*4*) V_6O_{13}, and (*5*) CrO_2.

The experimentally selected conditions of molybdenum dioxide synthesis in chloride melts are the optimal and agree well with the thermodynamic data. The dependence $\Delta G^0 = f(T)$ for reaction (1) is nearly linear within 298–1000 K. The conditions of MoO_2 synthesis in the range 823–1053 K correspond to the maximum absolute value of ΔG^0. This means that such a temperature interval is necessary for reaction (1) to occur, in which the diffusion coefficients of the reagents are high enough and the reagent surfaces are sufficiently active. In this case, the rate of the presented reaction will be high [6].

Reaction (2) is characterized by low Gibbs energy and, according to the ΔG^0 values, its optimal temperature is 600 K. The temperature of interaction in chloride melts approaches 923 K, which is due to the necessity for a higher rate of back diffusion of components. According to the thermodynamic data, reaction (3) must occur at 800 K, which is in agreement with the experimental results. To compare the ΔG^0 values for reactions (4) and (6), we performed a thermodynamic calculation of the interaction for 1 mol of vanadium(V) oxide. ΔG^0 is –135.6 and –89.9 kJ mol^{-1} for, respectively, reactions (4) and (6). Thus, it is evident that reaction (4) is more probable from the standpoint of thermodynamics and will occur in the first place.

A calculation of ΔG^0 for reaction (5) showed that the tendency toward interaction decreases with increasing temperature (Fig. 2). At the same time, ΔG^0 of this process is rather high (in absolute value). The fact that chromium dioxide cannot be obtained is mainly related to the very high thermodynamic stability of chromium(III) oxide Cr_2O_3 in comparison with other oxides.

CONCLUSIONS

(1) Based on the thermodynamic calculations and experimental results, the optimal conditions were determined for the interaction of higher oxides of *d*-metals (V, Nb, Mo, and W) with the respective metals in alkali chloride melts.

(2) A method for industrial manufacture of lower oxides of *d*-metals was developed.

REFERENCES

1. *Kataliticheskie svoistva veshchestv: Spravochnik* (Catalytic Properties of Substances: Reference Book), Roiter, G., Ed., Kiev: Naukova Dumka, 1968.
2. Nacomoto, Y. and Sano, T., *Catalytic Properties of Oxides Materials*, Osaka: Inter. Sci., 1991.
3. *Handbuch der preparativen anorganischen Chemie*, Baudler, M., Brauer, G., Feher, F., *et al.*, Eds., Stuttgart, 1975.
4. Barer, R.M., *Diffusion in and through solids*, Cambridge, 1941.
5. *Fiziko-khimicheskie svoistva oksidov: Spravochnik* (Physicochemical Properties of Oxides: Reference Book), Samsonov, G.V., Ed., Moscow: Metallurgiya, 1978.
6. Hauffe, K., *Reaktionen in und an festen Stoffen*, Berlin: Springer, 1955.

Russian Journal of Applied Chemistry, Vol. 74, No. 6, 2001, pp. 916–920. Translated from Zhurnal Prikladnoi Khimii, Vol. 74, No. 6, 2001, pp. 894–897.

INORGANIC SYNTHESIS AND INDUSTRIAL INORGANIC CHEMISTRY

A Study of Crystallization in the System $TiO_2(Al_2O_3)$–H_2SO_4–$(NH_4)_2SO_4$–H_2O in Obtaining Titanium–Aluminum Tanning Agent

M. V. Maslova, D. L. Motov, and L. G. Gerasimova

Tananaev Institute of Chemistry and Technology of Rare Elements and Mineral Raw Materials, Kola Scientific Center, Russian Academy of Sciences, Apatity, Russia

Received December 7, 2000

Abstract—The conditions under which a titanium–aluminum tanning agent is obtained from sulfuric acid solutions were studied. The composition was established and the properties were studied of the forming phases.

Recently, the manufacture and use of multicomponent tanning agents making it possible to do without toxic chromium(III) compounds at tanneries have been studied intensively[1–4]. A combination of positive properties inherent in the components of such a tanning agent enables its use in tanning of supple and stiff leather.

The technology for manufacture of tanning agents of this kind is based on the so-called salting-out of a crystalline salt from a mono- or polycomponent sulfate solution. Mainly technological aspects of synthesis of tanning materials have been described in the literature [5, 6].

The aim of the present study was to analyze the influence exerted by the salting-out conditions in the system $TiO_2(Al_2O_3)$–H_2SO_4–$(NH_4)_2SO_4$–H_2O on the composition and properties of the forming solid phases. Data of this kind are necessary for substantiating a new technology for manufacture of a complex titanium–aluminum tanning agent possessing versatile properties [7].

EXPERIMENTAL

The salting-out was done from a sulfate titanium–aluminum solution containing (g l^{-1}): TiO_2 92.6, Al_2O_3 25.9, and H_2SO_4 175, prepared by dissolving oxotitanium monohydrate in water with subsequent addition of a necessary amount of aluminum sulfate.

The crystallization was performed by introducing crystalline ammonium sulfate and concentrated sulfuric acid into this solution, with their excess (free) concentration in the reaction mass varied between 50 and 500 g l^{-1}.

The experimental procedure was as follows. A titanium–aluminum solution with prescribed concentration of free sulfuric acid was introduced into a suspension of ammonium sulfate [1000–1200 g l^{-1} $(NH_4)_2SO_4$] in the course of 1 h at a temperature not exceeding 25°C. The mixture was kept with stirring for 2 h and then allowed to stand without stirring for 1 h for crystals to be formed. The precipitate was separated from the liquid phase, washed with an ammonium sulfate solution [450 g l^{-1} $(NH_4)_2SO_4$] with s : l = 1 : 0.5, dried in air, and analyzed for the content of salt components. The phase composition of the precipitates was determined by the crystal-optical method. In doing so, the basicity of a salt (ratio of titanium and aluminum ions bound to OH^- groups to the total amount of titanium and aluminum ions in the tanning agent, expressed in percent), characterizing the quality of a tanning agent, was calculated.

The choice of the end points with respect to salt mass components is due to technological features of the process. At a content of free sulfuric acid exceeding 500 g l^{-1}, $Al_2(SO_4)_3 \cdot 18H_2O$ precipitates, in agreement with the solubility data for the system H_2SO_4–$Al_2(SO_4)_3$–H_2O at 25°C [8]. It is known that ammonium sulfate is a weaker salting-out agent than H_2SO_4, and making its concentration higher than 500 g l^{-1} is unpractical, since it will exert no essential influence of the degree of salting-out of the tanning salt.

In the concentration range studied there occurs crystallization of the monohydrate salt $(NH_4)_2TiO(SO_4)_2 \cdot H_2O$ [titanium(IV) ammonium sulfate, TAS], $NH_4Al(SO_4)_2$

1070-4272/01/7406-0916 $25.00 © 2001 MAIK "Nauka/Interperiodica"

(ammonium aluminum alum, AAA), titanium–aluminum salt, and, at some points of the system, anhydrous TAS as impurity phase. The degree of salting-out and the dispersity of the titanium salt depend on the concentration in solution of free sulfuric acid and ammonium sulfate. At H_2SO_{4exc} content of up to 100 g l^{-1} the degree of TAS precipitation does not exceed 40% over the entire range of $(NH_4)_2SO_{4exc}$ concentrations. The crystallizing titanium salt is finely disperse, with particle size of 1–2 μm.

With increasing concentration of salting-out agents, the extent of TAS precipitation grows, and, at a total concentration of free H_2SO_4 and $(NH_4)_2SO_4$ exceeding 550 g l^{-1}, more than 95% of the titanium salt is precipitated at 1 : (0.8–1) mass ratio of free H_2SO_4 to $(NH_4)_2SO_4$. In this case, TAS crystals grow in size to 7–9 μm.

Substantially raising the ammonium sulfate concentration at low content of H_2SO_{4exc} leads to a minor change in the solubility of the double salt. Raising the content of ammonium sulfate at high free sulfuric acid concentrations causes a more dramatic decrease in the solubility of TAS and the corresponding increase in the degree of its precipitation.

At H_2SO_{4exc} concentration exceeding 400 g l^{-1}, an anhydrous product impairing the quality of the tanning agent is formed together with TAS monohydrate. Under these conditions, a finely crystalline salt with particle size of 2–5 μm is formed, with a large amount of the mother liquor in inclusions.

The degree of AAA precipitation under the chosen conditions depends only slightly on the concentration of salting-out agents and constitutes 94–98%. The alum is in the form of coarse crystals 15–30 μm in size.

A comparison of the obtained data with those for the quaternary system TiO_2–H_2SO_4–$(NH_4)_2SO_4$–H_2O [9] demonstrated that, at low concentrations of salting-out agents, aluminum(III) has little effect on the TAS solubility, whereas at a total concentration of free H_2SO_4 and $(NH_4)_2SO_4$ exceeding 300 g l^{-1} the solubility of the titanium salt increases in the presence of aluminum(III).

The obtained experimental data were used to construct composition–property diagrams in the Cartesian coordinate system in relation to the content of free sulfuric acid and ammonium sulfate not bound to titanium(IV) in the form of a salt. For convenience of technological use of the diagrams, the concentrations of salting-out components are given in grams per liter. The presented curves are horizontal projections of the basicity and solubility surfaces.

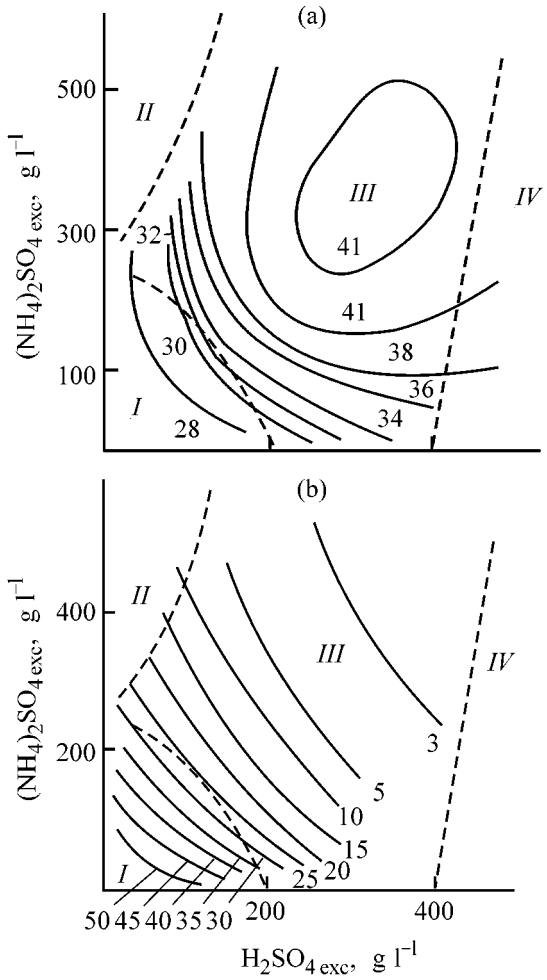

Fig. 1. (a) Basicity of titanium–aluminum product obtained along the section of the system $TiO_2(Al_2O_3)$–H_2SO_4–$(NH_4)_2SO_4$–H_2O (TiO_2 92.3, Al_2O_3 26.5 g l^{-1}) and (b) TiO_2 content of the mother liquor after salting-out of the titanium–aluminum product. [$(NH_4)_2SO_{4exc}$, H_2SO_{4exc}] Content. Isolines: (a) basicity (%) and (b) TiO_2 concentration (g l^{-1}).

Figure 1a shows the surface formed by basicity isolines. With this method of presentation, the surface is stretched in the direction toward the ordinate axis. This means that the H_2SO_{4exc} concentration affects the basicity of the tanning agent to a greater extent than that of $(NH_4)_2SO_{4exc}$. Low basicity (28%) corresponds to a tanning agent obtained at a total concentration of salting-out agents of 100–200 g l^{-1}. In such a product, the mass ratio TiO_2 : Al_2O_3 = (0.8–1) : 1. Low content of Ti(IV) in the tanning agent gives no way of using it in the main process and it can only serve as a pre- or post-tanning agent.

With the concentration of salting-out agents increasing to their total content of 400 g l^{-1}, the basicity of

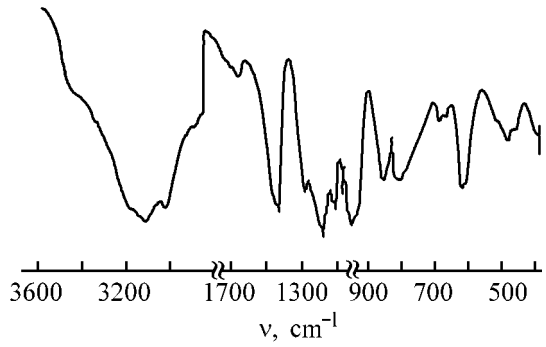

Fig. 2. IR spectrum of the titanium–aluminum product. (ν) Wave number.

the tanning agent grows from 30 to 38%, with the change in basicity to a greater extent depending on the H_2SO_{4exc} concentration. The tanning salts contain 9–14 TiO_2 and 7–4.5% Al_2O_3 and can be used as tanning agents for supple leather.

Products with basicity of 40–41% were obtained at H_2SO_{4exc} and $(NH_4)_2SO_{4exc}$ concentrations of 200–400 and 160–500 g l^{-1}, respectively. Tests with the Ti–Al tanning agent demonstrated that the highest temperature of leather cooking is achieved with tanning agents having a basicity of about 41%. Salts with the required basicity were obtained at a total concentration of H_2SO_{4exc} and $(NH_4)_2SO_{4exc}$ of 540–860 g l^{-1} and mass ration H_2SO_{4exc} : $(NH_4)_2SO_{4exc}$ = 1 : (0.8–1).

One of characteristics of the crystallization process is the degree of precipitation of tanning components, which should be no less than 90%. To determine the optimal range of the salting-out agent concentration for obtaining a high-quality tanning agent, lines of TiO_2 content (g l^{-1}) in the mother liquor after salting-out, which are horizontal projections of the conventional solubility surface in the three-dimensional coordinate system, were plotted (Fig. 1b).

The surface is gently inclined toward the increasing content of the salting-out agents. At a content of free sulfuric acid higher than 300 g l^{-1}, the residual content of TAS in the mother liquor does not exceed 5 g l^{-1} in terms of TiO_2.

By superimposing the projections of the surfaces of basicity and TiO_2 content in the mother liquor, the region in which high-quality product is obtained was determined, limited to concentrations of 250–300 g l^{-1} for free sulfuric acid and 280–400 g l^{-1} for free ammonium sulfate at a total content of salting-out agents of 550–700 g l^{-1} and H_2SO_{4exc} : $(NH_4)_2SO_{4exc}$ = 1 : (1–0.8).

Four characteristic zones can be distinguished in the diagrams, differing in the concentration of salting-out agents, dispersity of the forming solid phase, and, correspondingly, its basicity. In zone *I*, a finely disperse salt is formed in salting-out from solutions, the tanning agent has low basicity, and up to 40 g l^{-1} of TiO_2 remains in the mother liquor. The unsatisfactory technological characteristics indicate that high-quality products cannot be obtained in this region.

In zone *II*, where the content of free ammonium sulfate much exceeds that of free sulfuric acid, the degree of salting-out and the basicity of the tanning agent approach the required values with increasing total content of salting-out components, but the product is finely disperse, which affects adversely the technological regime of the process.

In zone *III*, a product is formed with varied basicity depending on the concentration of salting-out agents, with an increase in the content of free sulfuric acid affecting the basicity and degree of TAS salting-out to a greater extent than that in the content of free ammonium sulfate.

In zone *IV*, where the content of free sulfuric acid in solution exceeds 400 g l^{-1}, anhydrous TAS crystallizes in the solid phase together with TAS monohydrate. The higher the content of H_2SO_{4exc}, the greater amount of anhydrous TAS, inapplicable as tanning agent, is formed.

The composition and properties of titanium–aluminum phases obtained in studying the system $TiO_2(Al_2O_3)$–H_2SO_4–$(NH_4)_2SO_4$–H_2O were investigated by means of X-ray phase analysis (XPA) and IR spectroscopy. For this purpose, precipitates were washed with alcohol to remove the mother liquor and dried in air for 2 h. It was found that, at high $(NH_4)_2SO_{4exc}$ concentrations and low acidity, crystalline ammonium sulfate is present in the product together with TAS and AAA.

According to XPA, the precipitates contain, together with TAS and AAA, a phase characterized as individual (see the table). Significant changes in the X-ray diffraction patterns of the synthesized titanium–aluminum phase, compared with TAS and AAA, may point to a distortion of the crystal lattice of TAS through incorporation of aluminum. According to crystal-optical data, the content of this phase fluctuates between 5 and 15% over the volume.

IR spectra of the precipitate are complex (Fig. 2). They reflect the presence of H_2O, and SO_4^{2-}, NH_4^+, O–M–O, and M–OH groups.

Comparison of X-ray diffraction patterns of TAS, AAA, and Ti–Al product

TAS		AAA		Ti–Al product		TAS		AAA		Ti–Al product	
d, Å	I_{rel}	*d*, Å	I_{rel}	*d*, Å	I_{rel}	*d*, Å	I_{rel}	*d*, Å	I_{rel}	*d*, Å	I_{rel}
10.50	23	–	–	–	–	3.59	31	–	–	3.57	22
9.65	100	–	–	9.70	6.7	–	–	–	–	3.50	17
9.15	46	–	–	9.30	30	3.40	59	–	–	3.42	24
8.20	10	–	–	–	–	–	–	3.39	6	3.38	39
7.90	14	–	–	–	–	3.32	56	–	–	–	–
7.65	27	–	–	7.60	18	3.30	39	–	–	–	–
7.05	8	7.10	55	7.01	27	3.27	37	3.27	75	3.27	100
6.30	14	–	–	–	–	3.16	29	–	–	3.14	44
–	–	6.05	13	6.10	12	3.06	31	3.06	30	3.06	78
5.50	20	5.50	55	5.50	50	–	–	–	–	3.0	36
–	–	–	–	5.20	16	–	–	2.97	20	–	–
–	–	5.0	35	–	–	–	–	2.88	11	2.89	17
4.96	40	–	–	4.99	43	2.80	19	2.82	30	2.81	35
4.91	43	–	–	–	–	–	–	2.67	1.4	2.67	24
–	–	–	–	4.87	34	–	–	2.61	12	2.61	22
–	–	–	–	4.75	23	–	–	–	–	2.48	15
4.65	23	–	–	4.62	16	–	–	–	–	2.32	15
4.59	30	–	–	–	–	–	–	–	–	2.17	15
–	–	4.33	100	4.36	100	–	–	2.04	10	2.04	7
4.10	23	4.08	80	4.09	53	–	–	1.98	16	1.98	10
3.91	26	–	–	3.90	39	–	–	1.93	13	1.94	20
–	–	3.70	40	3.69	35						

Crystal water manifests itself at 3700–3200 (symmetric stretching vibrations of O–H) and 1630–1600 cm^{-1} (deformation vibrations of H–O–H). The absorption band at 1440 cm^{-1} is associated with δ-NH [10].

It is known that the sulfate group gives rise to a great number of absorption bands in an IR spectrum at 500–700 and 1000–1250 cm^{-1}, corresponding to stretching, deformation, and other vibrations of this group [10].

The spectra of the precipitate indicate that its structure is characterized by two types of symmetry of SO_4^{2-} groups. Noteworthy is the strong splitting of the ν_3 and ν_4 bands of SO_4^{2-}, which is due to the presence of bi- and polydentate groups. Compared with those in the spectrum of TAS [11], these bands are narrower and have lower intensity, which can be attributed to a change in the bond strength under the influence of the aluminum ion. The presence of ν_1 and ν_2 bands of medium intensity confirms the symmetry lowering to C_{2v} and the presence of a bidentate complex. The absorption band at 800 cm^{-1} is associated with stretching vibrations of bound Al–OH [12].

The IR spectral data confirmed that the precipitates under study are composed of a mixture of compounds, including TAS, AAA, and a titanium–aluminum phase in which titanium(IV) is bound to aluminum(III) via an OH^- group.

CONCLUSIONS

(1) The results obtained in studying the system $TiO_2(Al_2O_3)$–H_2SO_4–$(NH_4)_2SO_4$–H_2O were used to construct composition–property diagrams. The employed presentation technique can be conveniently used for technological purposes.

(2) In studying the salting-out process along a section of the system $TiO_2(Al_2O_3)$–H_2SO_4–$(NH_4)_2SO_4$–H_2O, the solution concentration range was established, in which the degrees of titanium(IV) and aluminum(II) precipitation are, respectively, 94–96 and 97–98%.

(3) A region with the optimal concentrations of free ammonium sulfate (280–400 g l^{-1}) and sulfuric acid (250–300 g l^{-1}) was chosen in the system under study, in which the technological process yields a tanning agent of required quality.

(4) Salting-out from sulfuric acid titanium–aluminum solutions yields, in addition to $(NH_4)_2TiO(SO_4)_2 \times H_2O$ and ammonium aluminum alum, a complex titanium–aluminum compound whose existence is confirmed by IR spectral and XPA data.

REFERENCES

1. USSR Inventor's Certificate, no. 340 703.
2. Kolpachkova, N.M., Maiskaya, T.Z., and Nekhamkin, L.G., *Zh. Neorg. Khim.*, 1975, vol. 20, no. 1, pp. 97–100.
3. Madiev, U.K., *Kozhev.-Obuvnaya Prom–st.*, 1979, no. 5, pp. 4–6.
4. Covington, A.P. and Sykes, R.L., *JACA*, 1978, vol. 82, pp. 1369–1373.
5. USSR Inventor's Certificate, no. 1 068 480.
6. RF Patent 2 057 184.
7. RF Patent 2 096 331.
8. *Spravochnik po rastvorimosti* (Reference Book of Solubilities), Kafarov, V.V., Ed., Moscow: Akad. Nauk SSSR, 1951, vol. 3, book 1.
9. Motov, D.L., *Zh. Neorg. Khim.*, 1957, vol. 2, no. 12, pp. 2797–2806.
10. Nakamoto, K., *Infrared Spectra of Inorganic and Coordination Compounds*, New York: John Wiley & Sons, 1963.
11. Godieva, M.M., Motov, D.L., Nikitina, S.D., and Metelkin, A.I., *Kozhev.-Obuvnaya Prom–st.*, 1975, no. 6, pp. 38–41.
12. Farmer, V.C., *The Infra-red Spectra of Minerals*, London: Bartholomew, 1974.

Russian Journal of Applied Chemistry, Vol. 74, No. 6, 2001, pp. 921–924. Translated from Zhurnal Prikladnoi Khimii, Vol. 74, No. 6, 2001, pp. 898–900.

INORGANIC SYNTHESIS AND INDUSTRIAL INORGANIC CHEMISTRY

Geometric Photoisomerization of Chiral Platinum(II) Sulfoxide Compounds

V. N. Spevak, D. A. de Vekki, and N. K. Skvortsov

St. Petersburg State Technological Institute, St. Petersburg, Russia

Received January 17, 2001

Abstract—Photochemical behavior of platinum(II) sulfoxide-containing complexes in methyl chloride was studied by polarimetry and ^{1}H NMR spectroscopy.

Effective catalysts for hydrosilylation of unsaturated compounds [1, 2] and antitumor preparations [3] were found among platinum(II) aminosulfoxide compounds [Pt(RR'SOAmCl_2] (Am is amine; R and R' are Alk or Ar). Their catalytic properties and biological activity depend on the arrangement of ligands in the inner coordination spheres of Pt(II) square-planar complexes. For example, diamino derivatives are biologicaly active if they have *cis*-arrangement of neutral ligands, whereas in the case of [Pt(RR'SO)AmCl_2] the *trans*-isomer is the most active [3].

cis-Aminosulfoxide complexes appeared to be more active in catalytic hydrosilylation, and diamino coordination compounds were completely catalytically inactive in this reaction.

In this work, we made an attempt to study photoinduced isomerization of the complex [Pt(RR'SOAmCl_2]. The photoinduced effect is known [4–8] to change in some cases the geometry of certain coordination compounds, which may be useful for photoactivated catalytic hydrosilylation.

As subjects for this study we chose geometrical isomers of (–)[Pt(Me-*p*-TolSO)(Py)Cl_2], investigated earlier [9, 10] by X-ray diffraction analysis, ^{1}H and ^{13}C NMR and IR spectroscopy, and the method of optical rotation dispersion (ORD), enabled by the presence of a chiral sulfoxide. Along with NMR spectroscopy, the ORD method provides valuable information, for example, in analyzing the ligand exchange in platinum(II) coordination compounds [2, 11–13] or for determining kinetic and thermodynamic parameters of changes in the inner coordination sphere of complexes in solution [11].

Chiral sulfoxides in the complex compounds under consideration are coordinated via a sulfur atom {specific rotation of (–)*trans*-[Pt(Me-*p*-TolSO)(Py)Cl_2] measured in methyl chloride is –22° in contrast to –117° for the *cis*-isomer}, which makes it possible to readily monitor any processes involving a sulfoxide ligand in both the resulting geometrical isomers by means of polarimetry. In this case, the isolation of a free sulfoxide [specific rotation (+)Me-*p*-TolSO is +142°] results in a sharp change in the observed angle of rotation for the reaction mixture, to the point of a full inversion of the sign of rotation.

A kinetic ORD monitoring by the change in the observed rotation angle of the chiral farmulation de-

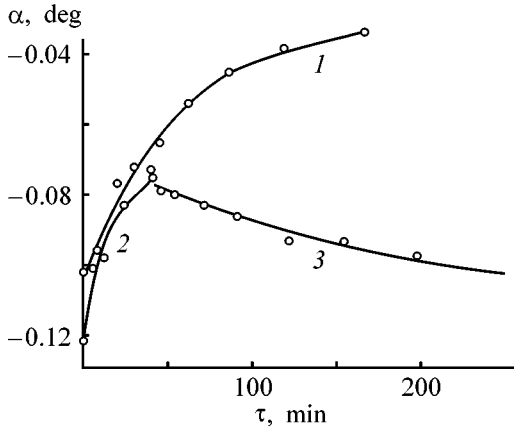

Rotation angle α of the chiral composition in methyl chloride vs. time τ. (*1*) Photolysis of (–)*cis*-[Pt(Me-*p*-TolSO)PyCl$_2$] (20°C, $c_0 = 1.7 \times 10^{-4}$ M, irradiation time 166 min); (*2*) irradiation of (–)*cis*-[Pt(Me-*p*-TolSO)$_2$Cl$_2$] (25°C, $c_0 = 1.1 \times 10^{-4}$ M, irradiation time 41 min); (*3*) dark relaxation of (–)*cis*-[Pt(Me-*p*-TolSO)$_2$Cl$_2$] after irradiation (25°C, $c_0 = 1.1 \times 10^{-4}$ M).

1070-4272/01/7406-0921 $25.00 © 2001 MAIK "Nauka/Interperiodica"

monstrated that platinum(II) *trans*-pyridinesulfoxide complexes are inert when irradiated with near UV light, whereas *cis*-compounds rather easily transform to *trans*-products (Figure, curve *1*). Prolonged photolysis of a solution of (–)*cis*-dichloropyridine-(methyl-*para*-tolylsulfoxide)platinum(II) in methylene chloride gives solely the chiral complex (–)*trans*-[Pt(Me-*p*-TolSO)(Py)Cl_2]. When the solvent is gradually removed, 100% conversion into the desired product is reached in 1.5 h.

Reverse slow dark isomerization of the *trans*-compound occurs in a toluene solution at higher temperature (boiling water bath, yield of the *cis*-complex in several days 15%). Thus, the quantitative photoisomerization is attributable in this case to the absence of a fast spontaneous interconversion of such compounds in uncoordinated solvents, in contrast to solutions in dimethyl sulfoxide [14], where isomerization is catalyzed by sulfoxide:

$$\textit{cis}\text{-[Pt(Me-}p\text{-TolSO)PyCl}_2\text{]} \underset{\Delta}{\overset{h\nu}{\rightleftarrows}} \textit{cis}\text{-[Pt(Me-}p\text{-TolSO)PyCl}_2\text{].}$$

Additional monitoring by the intensity of the ^{1}H NMR signal of the methyl group in *cis*- ($CDCl_3$; δ, ppm: 3.59 t, $J_{Pt–H}$ 23 Hz) and *trans*-complexes ($CDCl_3$; δ, ppm: 3.47 t, $J_{Pt–H}$ 20 Hz) demonstrated that, along with both the geometrical isomers, up to 1% uncoordinated (+)methyl-*para*-tolylsulfoxide ($CDCl_3$; δ, ppm: 2.70 s) is present in the reaction solution; the signal from this compound disappears upon complete conversion of the starting compound. The photolysis of such *cis*-complexes seems to give rise to dissociation of sulfoxide, leading to a coordinatively unsaturated intermediate, stabilized via formation of a thermodynamically unstable chiral *trans*-product, which is not photoactivated:

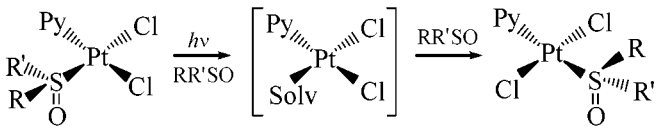

The photolysis of bissulfoxide complexes is known [8] to result also in *cis*- → *trans*-isomerizations; however, attempts to isolate the *trans*-product in pure state were unsuccessful. A study of the photochemical behavior of (–)*cis*-dichlorobis(methyl*para*-tolylsulfoxide)platinum(II) in methylene chloride {the specific rotation of (–)*cis*-[Pt(Me-*p*-TolSO)$_2Cl_2$] measured in acetone is –220°C [12]} demonstrated that side processes occur along with photoisomerization (figure, curve *2*). These are fast reverse dark isomerization (curve *3*), and, on prolonged photolysis (60 min and more), formation of colloidal platinum, which is not characteristic of pyridine-sulfoxide compounds.

This phenomenon can be explained on the basis of X-ray data [9, 10, 12]. For example, the length of the Pt–S bond is 2.214 Å in (–)*cis*-[Pt(Me-*p*-TolSO)-(Py)Cl_2] and 2.249 Å in (–)*cis*-[Pt(Me-*p*-TolSO)$_2Cl_2$] (length of the Pt–N bond in the pyridine-sulfoxide complex is 2.032 Å), which makes the isomerization and destruction of the metal complex easier and, therefore, is responsible for the high mobility of sulfoxide in platinum(II) bissulfoxide complexes.

The aforementioned researches show that platinum(II) pyridine-coordination compounds, catalyzing hydrosilylation, can be further photoactivated with the homogeneous metal-complex center preserved.

It is necessary to note in conclusion that the photolysis of optically active geometrical isomers of (–)[Pt(Me-*p*-TolSO)(Py)Cl_2] does not result in loss of chirality of both the complexes themselves and the coordinated sulfoxide, as opposed to the data of [15], indicating that free (+)Me-*p*-TolSO undergoes photoracemization. However, this process requires high-energy irradiation for several hours, whereas in our case the reaction occurs under mild conditions in the course of 1.5–2 h.

The whole set of the obtained data allows photoirradiation to be recommended as a method for synthesizing thermodynamically unstable Pt(II) sulfoxide *trans*-compounds, which at the same time do not isomerize spontaneously.

EXPERIMENTAL

The ^{1}H NMR spectra were recorded in $CDCl_3$ on a Bruker AC-200 instrument with spectrum accumulation, operating at 200 MHz.

Optical rotation dispersion was measured on a Perkin Elmer 241MC polarimeter in methyl chloride in temperature-controlled quartz cells of length 10 cm in the range 450–610 nm. The concentration of the complex was varied in the range 1×10^{-4}–1×10^{-5} M.

The IR spectra were taken on a Perkin Elmer Spektrum-1000 spectrometer (4000–400 cm^{-1}) in chloroform, l = 0.135 mm, 1% solution; the FIR spectrum was recorded on a Hitachi FIS-3 spectrometer (400–100 cm^{-1}) in KBr pellets.

Photolysis of metal complexes was carried out in a polarimeter cell in methylene chloride solution under the action of broadband UV light (DRL-400 lamp, quartz or pyrex filter) passing through a water layer of 40 mm thickness.

Methylene chloride of "Merk" production was used in the experiments. (–)*cis*-Dichlorobis(methyl-*para*-tolylsulfoxide)platinum(II), potassium (–)trichloro-(methyl-*para*-tolylsulfoxide)platinite(II), and (+)methyl-*para*-tolylsulfoxide were obtained as described in, respectively, [12], [16], and [17].

(–)*cis*-Dichloropyridine(methyl-*para*-tolylsulfoxide)platinum(II). Potassium (–)trichloropyridineplatinite(II) (79.6 mg, i.e., 0.190 mmol) was dissolved in 4 ml of water in a beaker. Then 29.3 mg (0.190 mmol) of (+)methyl-*para*-tolylsulfoxide was added slowly with stirring. The reaction mixture was kept at room temperature for 1 day, then the resulting white flocculent precipitate was filtered off and dried in a thermostat at 50°C to give 85.6 mg (0.171 mmol, yield 90.4%) of (–)*cis*-[Pt(Me-*p*-TolSO)$PyCl_2$]. $[\alpha]_{589}$ = –117°C (5 g in 100 ml of CH_2Cl_2). ^{1}H NMR spectrum (δ, ppm): 2.46 s (3H, Ph–CH_3); 3.59 t ($J_{Pt–H}$ 23 Hz, 3H, S–CH_3); 7.30 t ($J_{Pt–H}$ 6 Hz, 2H, Py); 7.37 d ($J_{H–H}$ 8 Hz, 2H, Ph); 7.82 t ($J_{Pt–H}$ 15 Hz, 1H, Py); 7.96 d ($J_{H–H}$ 8 Hz, 2H, Ph); 8.61 t ($J_{Pt–H}$ 41 Hz, 1H, Py); 8.64 t ($J_{Pt–H}$ 40 Hz, 1H, Py). IR spectrum (cm^{-1}): ν(Py) 1612; δ (CH, Me) 1454; ν(S=O) 1150, 1116; δ(CH, Py) 1075, 1059; τ(Me) 970; δ(CH, Ph) 810. FIR spectrum (cm^{-1}): γ(CSO) 391; ν(Pt–Cl) 339, 324, 318; ν(Pt–Py) 277.

(–)*trans*-Dichloropyridine(methyl-*para*-tolylsulfoxide)platinum(II). Potassium (–)trichloro(methyl-*para*-tolylsulfoxide)platinite(II) (81.3 mg, i.e., 0.164 mmol) was dissolved in 3 ml of water in a beaker. Then 1 ml of 0.163 M aqueous solution of pyridine was added slowly with stirring at 15°C, which immediately resulted in the formation of a finely dispersed precipitate. The reaction mixture was stirred for 20 min more, then the precipitate was filtered off and dried in a thermostat at 50°C to give 72.7 mg (0.145 mmol, yield 88.6%) of the light yellow precipitate of (–)*trans*-[Pt(Me-*p*-TolSO)$PyCl_2$]. $[\alpha]_{589}$ = –22°C (5 g in 100 mls CH_2Cl_2). ^{1}H NMR spectrum (δ, ppm): 2.48 s (3H, Ph–CH_3), 3.47 t ($J_{Pt–H}$ 20 Hz, 3H, S–CH_3), 7.40 d ($J_{H–H}$ 8 Hz, 2H, Ph), 7.43 t ($J_{Pt–H}$ 18 Hz, 2H, Py), 7.88 t ($J_{Pt–H}$ 16 Hz, 1H, Py); 7.97 d ($J_{H–H}$ 8 Hz, 2H, Ph); 8.78 t ($J_{Pt–H}$ 33 Hz, 1H, Py), 8.81 t ($J_{Pt–H}$ 32 Hz, 1H, Py). IR spectrum (cm^{-1}): ν(Py) 1612; δ(CH, Me) 1455; ν(S=O) 1145, δ(CH, Py) 1077; τ(Me) 969; δ(CH, Ph) 813. FIR spectrum (cm^{-1}): ν(Pt–Cl) 353.

CONCLUSION

Irradiation of a solution of (–)*cis*-[Pt(Me-*p*-TolSO)$PyCl_2$] with broadband light results in the isomerization of the complex into the *trans*-complex, which is photochemically inert. Platinum(II) *cis*-bissulfoxide coordination compounds are more sensitive to irradiation, decomposing to colloidal platinum. Coordinated chiral sulfoxides in the systems under study are not racemated under the action of light. Thermal activation of (–)*trans*-[Pt(Me-*p*-TolSO)$PyCl_2$] leads to its conversion to the *cis*-form.

ACKNOWLEDGMENTS

This work was financially supported by the Russian Foundation for Basic Research (grants nos. 00-03-32 670a and 01-03-32598) and the Ministry of Education (grant № E00-5.0-373).

REFERENCES

1. Trofimov, A.E., Skvortsov, N.K., Spevak, V.N., *et al.*, *Zh. Obshch. Khim.*, 1990, vol. 60, no. 2, pp. 276–279.
2. De Vekki, D.A., Skvortsov, N.K., Fedotova, G.P., *et al.*, Abstracts of Papers, *Vserossiiskoe soveshchanie "Kremniiorganicheskie soedineniya: sintez, svoistva, primenenie"* (All-Russia Conf. "Organic Silicon Compounds: Synthesis, Properties, Application"), Moscow, 2000, p. 183.
3. Farrell, N., Kinley, D.M., Schmidt, W., and Hacker, M.P., *Inorg. Chem.*, 1990, vol. 29, no. 2, pp. 383–397.
4. Lifschitz, I. and Froentjes, W., *Z. Anorg. Allg. Chem.*, 1937, vol. 233, pp. 1–34.
5. Mastin, S.H. and Haake P., *Chem. Commun.*, 1970, no. 4, p. 202.
6. Balzani, V., Carassiti, V., Moggi, L., and Scandola, F., *Inorg. Chem.*, 1965, vol. 27, no. 4, pp. 1243–1244.
7. Haake, P. and Hylton, T.A., *J. Am. Chem. Soc.*, 1962, vol. 84, no. 19, pp. 3774–3775.
8. Price, J.H., Birk, J.P., and Wayland, B.B., *Inorg. Chem.*, 1978, vol. 17, no. 8, pp. 2245–2250.
9. De Vekki, D.A., Skvortsov, N.K., and Spevak, V.N., Abstracts of Papers, *II Natsional'naya kristallokhimicheskaya konf.* (II National Crystal-Chemical Conf.), Chernogolovka, 2000, pp. 147–148.

10. Skvortsov, A.N., de Vekki, D.A., Belsky, V.K., *et al.*, Abstracts of Papers, *34th Int. Conf. on Coordination Chemistry*, Edinburgh, 2000, p. P0684.
11. de Vekki, D.A., Spevak, V.N., and Skvortsov, N.K., *Zh. Obshch. Khim.*, 2000, vol. 70, no. 8, pp. 1323–1325.
12. Spevak, V.N., Skvortsov, N.K., Bel'skii, V.K., *et al.*, *Zh. Obshch. Khim.*, 1992, vol. 62, no. 12, pp. 2646–2652.
13. Lobadyuk, V.I., Spevak, V.N., and Skvortsov, N.K., *Zh. Obshch. Khim.*, 1996, vol. 66, no. 5, p. 871.
14. Kong, P.-C., Iyamuremye, D., and Rochon, F.D., *Canad. J. Chem.*, 1976, vol. 54, no. 19, pp. 3224–3226.
15. Mislow, K., Axelrod, M., Rayner, D.R., *et al.*, *J. Am. Chem. Soc.*, 1965, vol. 87, no. 21, pp. 4958–4959.
16. Spevak, V.N., Lobadyuk, V.I., Skvortsov, N.K., *et al.*, *Zh. Obshch. Khim.*, 1999, vol. 69, no. 5, pp. 745–750.
17. Drabowics, J., Bujnicki, B., and Mikolajczyk, M., *J. Org. Chem.*, 1982, vol. 47, no. 17, pp. 3325.

Russian Journal of Applied Chemistry, Vol. 74, No. 6, 2001, pp. 925–929. Translated from Zhurnal Prikladnoi Khimii, Vol. 74, No. 6, 2001, pp. 901–904.

INORGANIC SYNTHESIS AND INDUSTRIAL INORGANIC CHEMISTRY

Solubility of Carbon in Sulfide Melts of the System Fe–Ni–S

L. B. Tsymbulov and L. Sh. Tsemekhman

Institut Gipronikel' OAO, St. Petersburg, Russia

Received February 20, 2001

Abstract—The solubility of carbon in iron-nickel sulfide melts at 1673 K was studied in the entire range of compositions of the Fe–FeS–Ni_3S_2–Ni tetragon. The boundaries of the stratification area were determined in this system upon its being saturated with carbon. Lines of carbon isosolubility are plotted in the tetragon field outside the stratification area.

To reduce oxides of non-ferrous metals, various carbon-containing materials are added to blends when nickel and cooper-nickel raw materials are smelted to produce a matte (an alloy of iron, copper, nickel and cobalt sulfides), with slag depleted of these non-ferrous metals. These manufacturing processes were described in detail in [1–7].

Carbon dissolves in the sulfide phase formed upon smelting. Its concentration is determined not only by the amount of a reducing agent added to a blend, but also by the content of sulfur in the matte, relative content of metal components in it, and temperature.

The available published data on the solubility of carbon in matte melts are extremely scarce and mainly concern the Fe–S system [8, 9].

The scantiness of the published data is related, on the one hand, to the absence, until recently, of reliable procedures for determining the carbon content in sulfide products with sufficiently high content of sulfur, and, on the other, to the conventional opinion that admixtures (of which the main are oxygen and carbon) insignificantly affect both the distribution of metals in a matte–slag system and the physicochemical processes occurring in further processing of the matte. However, a trend has appeared recently toward smelting to obtain mattes with greater metal content, which is known to make lower the loss of non-ferrous metals with slag [10].

It is natural to assume that the carbon content in such mattes will be higher, and, therefore, its effect will be stronger. Furthermore, data on carbon solubility can be also useful for gaining deeper insight into the structure of sulfide melts.

The initial object of our research was the system Fe–S–C [11]. It is known from the literature that it is characterized by separation into the sulfide and metallic phases [8, 9]. We confirmed this once more, our data on the carbon solubility in both phases being in good agreement with the data of [8]. This fact proved the correctness of the selected experimental technique, which was as follows.[1]

A 30-g portion of powdered iron, nickel, and sulfides of these metals was placed in a graphite crucible, and 5 g of graphite powder was poured above. The crucible with the blend was placed in an alundum reactor mounted in a furnace with a graphite heater. The reactor was heated to 1673 K in an argon atmosphere, and the melt was kept at this temperature for a specified time (this time was 5 h for stratifying compositions and 2 h for homogeneous melts). On completion of experiment, the crucible was taken out of the furnace and cooled in an argon flow. The thus cooled sample was analyzed for the content of iron, nickel, sulfur, and carbon.

The content of metals and sulfur in the sulfide phase was determined by chemical methods, that of sulfur and carbon in the metallic phase—on a CS-444 analyzer ("LECO" production), and that of carbon in the sulfide phase—on an analyzer of the same make but upgraded for determining the carbon content at high sulfur content. The inaccuracy of carbon determination in the sulfide phase was as follows (wt %): ±0.014 for concentrations 0.05–0.10, ±0.018 for 0.10–0.20, ±0.025 for 0.20–0.50, ±0.09 for 0.50–1.00,

[1] The experimental technique is described in more detail in [11].

1070-4272/01/7406-0925 $25.00 © 2001 MAIK "Nauka/Interperiodica"

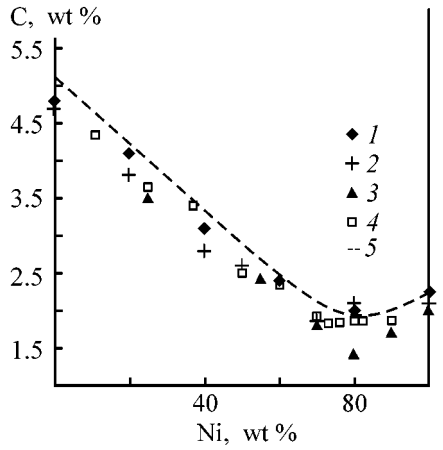

Fig. 1. Solubility of carbon in Fe–Ni melts according to the data of various authors. (C, Ni) Contents. Data: (*1*) [14], (*2*) [12], (*3*) [13], (*4*) [15]; (*5*) present work. Temperature (K): (*1*) 1680, (*2–4*) 1623, and (*5*) 1673.

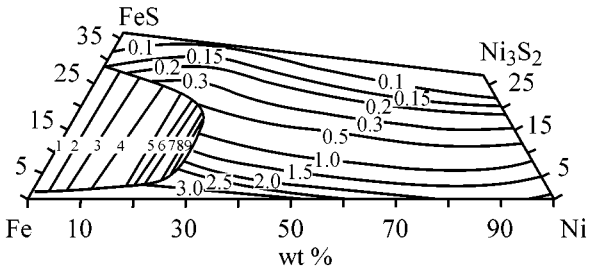

Fig. 2. Diagram of carbon isosolubility in the Fe–FeS–Ni_3S_2–Ni system at 1673 K. *Numbers at conodes in the stratification area* correspond to the numbers of experiments in the table. *Numbers at isosolubility curves* denote carbon concentration.

and ±0.11 for 1.0–3.0. The inaccuracy of carbon determination in the metallic phase was ±0.015% for concentrations of 1.0–5.0 wt %.

The following stage of our work was to study the carbon solubility in the system Fe–Ni. The solubility of carbon in this system, both in the solid and in the molten states, has been repeatedly studied. Among the publications dedicated to the carbon solubility in Fe–Ni at temperatures close to our experimental temperature of 1673 K, [12–15] are noteworthy.

Figure 1 presents the results of various authors together with the data of the present work, which are in good agreement with [14]. The smaller solubility of carbon, reported in other publications, seems to result from a lower (by 50 K) temperature of the experiment.

Therefore, our data on the carbon solubility may well be considered reliable. Furthermore, they additionally confirm the reliability of the chosen experimental technique.

It is evident from Fig. 1 that all the authors have found that carbon is the least soluble in melts containing about 80 wt % nickel.

This phenomenon, which is abnormal at first sight, is also observed in studying the solubility of other components in Fe–Ni melts. For example, H.A. Wriedt and J. Chipman observed a minimum in the oxygen solubility at nickel content of about 90 wt % [13]. They attributed this minimum to an increase in the oxygen potential of the slag, enriched with nickel oxide when the nickel content in the alloy in contact with the slag is greater than 90 wt %, i.e., these authors were not inclined to see any anomalies in Fe–Ni alloys.

However, the reasoning on this problem in [15] seems to be the most convincing. The authors of this work studied the carbon solubility in Fe–Ni melts (Fig. 1) and came to a conclusion that the minimum in the solubility at nickel content of about 80 wt % is attributable to the existence of short-range order in the melts of $FeNi_3$ composition.

We started studying the carbon solubility in sulfide melts of the system Fe–Ni–S from the stratification area by adding various amounts of nickel to melts of the system Fe–FeS.

As a result, we determined the boundaries of the stratification area, shown in the Fe–FeS–Ni_3S_2–Ni diagram (Fig. 2). Compositions of the stratified phases are given in the table.

As already noted, melts of the system Fe–S separate into sulfide and metallic phases on addition of carbon. It is necessary to note that the separation takes place if the initial content of sulfide sulfur is in the range from 1.94 to 28.7 wt %.

The stratification results from positive deviations from ideality in the Fe–S system [16, 17]. The deviations increase upon addition of carbon, which points to mutual repulsion of carbon and sulfur atoms in the melt [18].

The following takes place upon addition of nickel to the system Fe–S. The increase in the nickel content in the metallic phase lowers the solubility of carbon in it and increases the solubility of sulfur. The content of sulfur in the sulfide phase is lowered correspondingly, i.e., it becomes more metallized, and, therefore, the solubility of carbon in it increases. Gradually, with increasing amount of added nickel, the metallized phase becomes more and more sul-

fidized, and the sulfide phase—more metallized. The contents of sulfur in these phases approach each other, and the melt becomes homogeneous at nickel concentrations greater than 25%.

To confirm the boundary of the stratification area at nickel content of about 25%, we replicated experiments nos. 9 and 11 with fast quenching of a melt. In these experiments, a melt was poured out onto a copper disk rotated at a speed of 25 000 rpm, which ensured a quenching rate of approximately 1000 deg s^{-1}. The quenched samples were studied by scanning electron microscopy and X-ray fluorescence microanalysis (Fig. 3).

The morphology of microstructures (Fig. 3) indicates beyond any doubt that the melt with the composition of experiment no. 11 is homogeneous (Fig. 3a), and the melt with the composition of experiment no. 9 consists of two phases arranged in layers on pouring the melt onto the disk. The boundary between the layers is well pronounced (Fig. 3b).

After determining the boundaries of the stratification area, we studied the solubility of carbon throughout the remaining range of compositions of the system Fe–FeS–Ni_3S_2–Ni. Using the obtained data, we plotted isosolubility lines of carbon (Fig. 2) on the phase diagram. The arrangement of these lines points to a rather complicated nature of the variation of the carbon concentration in this metal–sulfide system.

The minimum carbon solubility in metallic melts, at nickel concentration of about 80%, also takes place in strongly metallized mattes containing up to 15% sulfur (Fig. 2). It is necessary to note that the minimum is somewhat shifted to greater Ni : Fe ratios with increasing content of sulfur. This fact agrees well with the data of Vaisburd [16] on the system Fe–Ni–S. Examining the activity of components in melts of

Compositions of carbon-saturated sulfide and metallic phases in the stratification area

Experiment no.	Content, wt %					
	in metallic phase			in sulfide phase		
	Ni	S	C	Ni	S	C
1	–	1.94	4.25	–	28.7	0.17
2	3.5	1.63	4.06	4.4	27.5	0.20
3	7.3	1.80	3.88	8.7	26.3	0.21
4	11.5	2.16	3.54	13.0	24.6	0.31
5	17.2	3.48	3.08	17.6	22.6	0.37
6	18.5	3.67	3.06	20.2	21.7	0.46
7	21.4	3.60	2.95	22.0	21.0	0.52
8	24.4	4.41	2.93	24.2	19.6	0.64
9	24.5	4.27	2.81	24.9	19.0	0.69
10	No stratification			25.1	12.9	1.21
11	〃			26.3	13.5	1.11

Note: Iron content was determined as difference.

the system Fe–Ni–S, Vaisburd concluded that, in the melt, the bonds of nickel with sulfur are stronger than those of iron. It follows from his theory of microheterogeneous structure of sulfide melts that nickel in a melt is predominantly surrounded by sulfur, and iron is concentrated in more metallized areas. Therefore, if sulfur is added to a metal alloy with Ni : Fe ratio of 80 : 20, this ratio will be less than 80 : 20 in metallized microareas of the sulfide melt (where, most likely, the main body of carbon dissolves). Such a ratio of metal contents will also take place in melts lying to the right of the line connecting the 80 : 20 Ni–Fe alloy with the vertex corresponding to pure sulfur (Fig. 2).

The next feature of the solubility of carbon in metal-sulfide melts of the system Fe–FeS–Ni_3S_2–Ni is

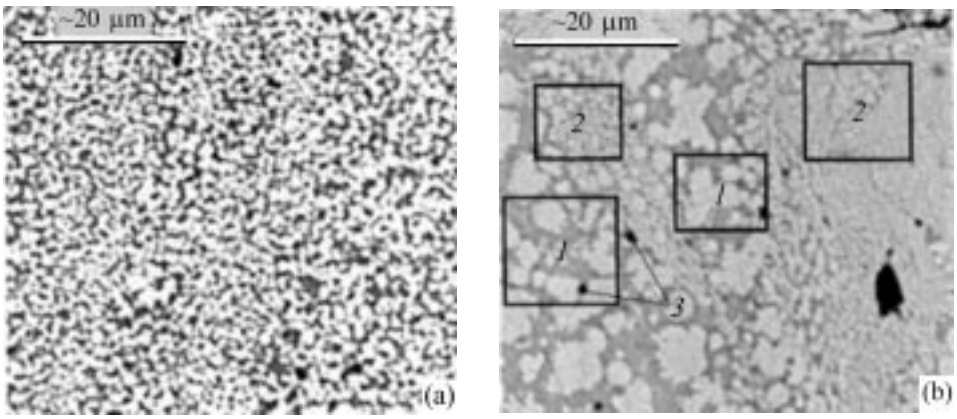

Fig. 3. Microstructures of (a) homogeneous sulfide melt saturated with carbon and (b) melt separated into sulfide and metallic phases. Quenching on a fast-rotating copper disk. (*1*) Sulfide phase, (*2*) metallic phase, and (*3*) carbon precipitated upon crystallization.

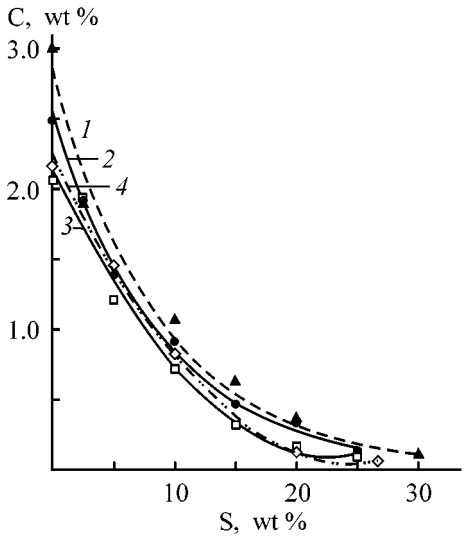

Fig. 4. Solubility of carbon C vs. the content of sulfur in a melt, S, at 1673 K. Fe : Ni ratio: (*1*) 50 : 50, (*2*) 40 : 60, (*3*) 10 : 90, and (*4*) 0 : 100.

its nonlinear change upon addition of sulfur to the metallic melt (Fig. 4). It is evident from the plots that the solubility of carbon sharply decreases upon addition of minor amounts of sulfur, with its decrease becoming insignificant further.

The irregular change in the solubility of carbon is attributable to the change in the nature of bonds in the melt from metallic to ionic-covalent on addition of sulfur to the metallic melt [19, 20].

The authors of [20] came to a conclusion that sulfur atoms form multicenter ionic-covalent bonds with metals. Therefore, addition of even minor amounts of sulfur results in a rather sharp decrease in the number of metal–metal bonds, which seems to be responsible for the dependences given in Fig. 4.

We point out that the initial decrease in the solubility is sharper for melts with large content of iron. This is attributable to the difference in electronic configuration between iron and nickel atoms. Iron has two electrons less than nickel on its *d*-level, and, therefore, it involves a greater number of centers participating in the formation of multicentered metal–sulfur bonds [20].

It is also necessary to pay attention to a number of carbon solubility maxima at high concentrations of sulfur and Fe : Ni = 70 : 30 (Fig. 2).

The increase in the carbon concentration with growing content of iron in a melt (at constant content of sulfur) in the region of compositions to the right from the maxima is quite natural, since the metal–metal groups are also enriched in iron dissolving a greater amount of carbon than nickel does.

At the same time, with the content of iron in a melt increasing at constant content of sulfur, the number of multicentered ion-covalent bonds between metal and sulfur grows, because iron forms a greater number of such bonds, compared with nickel. Certainly, this should result in decreasing solubility of carbon.

The presence of two opposite tendencies seems to be the reason for the occurrence of maxima in the isosolubility lines.

REFERENCES

1. Reznik, I.D., *Sovershenstvovanie shakhtnoi plavki okislennykh nikelevykh rud* (Perfecting of Blast Smelting of Oxidized Nickel Ores), Moscow: Metallurgiya, 1983.
2. Serebryanyi, Ya.L., *Elektroplavka medno-nikelevykh rud i koncentratov* (Electrosmelting of Copper-Nickel Ores and Concentrates), Moscow: Metallurgiya, 1974.
3. Brovkin, V.G. and Piotrovskii, V.K., *Pererabotka zhidkikh konvertornykh shlakov* (Processing of Liquid Converter Slags), Moscow: Metallurgiya, 1978.
4. Rusakov, M.P., *Tsvet. Metally*, 1985, no. 3, pp. 40–42.
5. Tsymbulov, L.B., Development of New Non-polluting Technology for Processing of Oxidized Nickel Ores with the Use of Coke-free Smelting, *Cand. Sci. Dissertation*, St. Petersburg, 1995.
6. Tsymbulov, L.B., Tsemekhman, L.Sh., Vigdorchik, E.M., *et al.*, *Nickel–Cobalt 97: Pyrometallurgy Fundamentals and Process Development*, 1997, vol. 2, pp. 145–151.
7. Abramov, N.P., Govorov, A.V., Tsemekhman, L.Sh., *et al.*, Environment and Innovation in Mining and Mineral Technology, *Proc. IV Int. Conf. on Clean Technologies for Mining Industry*, Santiago, Chile, 1998, vol. 2, pp. 795–802.
8. Wang, C., Hirama, I., Nagasaka, T., and Ban-Ya, S., *ISIJ International*, 1991, vol. 31, no. 11, pp. 1292–1299.
9. Turkdogan, E.T. and Hancock, R.A., *J. Iron Steel. Inst.*, 1955, vol. 179, pp. 155–159.
10. Lomagin, F.E., Lipin, B.V., and Mechev, V.V., *Izv. Vyssh. Uchebn. Zaved., Tsvetn. Metall.*, 1973, no. 6, pp. 23–26.
11. Tsymbulov, L.B., Gavrilov, P.V., and Tsemekhman, L.Sh., *Metally*, 2000, no. 2, pp. 29–31.
12. Gabriel, A., Gustafson, P., and Ansara, I., *Calphad.*, 1984, vol. 11, no. 2, pp. 203–218.

13. Turkdogan, E.T., Hancock, R.A., Heritz, S.I., and Dentan, J., *J. Iron Steel. Inst.*, 1956, vol. 183, pp. 69–72.
14. Miller, K.O. and Elliott, J.F. *Trans. Soc. Am. Inst. Met. Eng.*, 1960, vol. 218, no. 5, pp. 900–910.
15. Ward, R.G. and Wright, J.A., *J. Iron Steel. Inst.*, 1960, vol. 194, March, pp. 304–306.
16. Vaisburd, S.E., *Fiziko-khimicheskie svoistva i osobennosti stroeniya sul'fidnykh rasplavov* (Physicochemical Properties and Structural Features of Sulfide Melts), Moscow: Metallurgiya, 1996.
17. Burylev, B.P., *Termodinamika metallicheskikh rastvorov vnedreniya* (Thermodynamics of Metallic Intercalation Solutions), Rostov-na-Donu: Rostov. Univ., 1984.
18. Burylev, B.P., *Izv. Vyssh. Uchebn. Zaved., Chern. Metall.*, 1960, no. 6, pp. 5–14.
19. Vaughan, D.J. and Craig, J.R., *Mineral Chemistry of Metal Sulfides*, Cambridge: Cambridge Univ., 1978.
20. Kapustin, O.A. and Bryukvin, V.A., *Rasplavy*, 1988, vol. 2, no. 4, pp. 35–40.

Russian Journal of Applied Chemistry, Vol. 74, No. 6, 2001, pp. 930–932. Translated from Zhurnal Prikladnoi Khimii, Vol. 74, No. 6, 2001, pp. 905–907.

PHYSICOCHEMICAL STUDIES OF SYSTEMS AND PROCESSES

Modeling of Thermodynamic Properties of Liquid Alloys in the System Magnesium–Tin

A. G. Morachavskii and K. B. Erofeev

St. Petersburg State Technical University, St. Petersburg, Russia

Received April 3, 2001

Abstract—The results obtained in studying experimentally the thermodynamic properties of liquid alloys in the system magnesium–tin are analyzed. The concentration dependences of the excess molar Gibbs energy and the enthalpy of mixing of the magnesium–tin system in the liquid state are described in terms of the ideal and regular solution models, using modified software.

The phase diagram of the system magnesium–tin is characterized by the formation of only a single congruently melting compound Mg_2Sn (mp 1043.7 K) forming eutectic mixtures both with magnesium (mp 834.4 K, $x_{Sn} = 0.107$, x_{Sn} is the mole fraction of tin in the alloy) and tin (mp 505.0 K, $x_{Sn} = 0.904$) [1, 2].

The thermodynamic properties of liquid alloys of the system Mg–Sn have been repeatedly studied by various methods [3–13]. These include measuring the saturated vapor pressure under isopiestic conditions [3, 6] and the emf in concentration cells with liquid electrolyte [4, 7, 10–13], the emf method with CaF_2 solid electrolyte [9], quantitative thermography [8], high-temperature calorimetry of mixing [10], and calculations based on the phase diagram [5]. The isotherms of component activity in the system show significant negative deviations from the ideal behavior, the enthalpy of mixing is negative, with its minimum value close to a composition corresponding to Mg_2Sn. The agreement between the data obtained in different studies can be assessed by considering a number of examples. According to the first systematic study of thermodynamic properties of the Mg–Sn liquid alloys (773–1123 K, $0.10 \le x_{Mg} \le 0.90$, x_{Mg} is the mole fraction of magnesium in the alloy), the maximum enthalpy of mixing, as obtained by the emf method, is –14.06 kJ mol^{-1} over the given temperature range [4]. In the same range of compositions, calorimetric measurements [11] yield the following ΔH values (kJ mol^{-1}): –14.8 (1073 K), –14.3 (1133 K), and –13.4 (1213 K), in sufficiently good agreement with the results of [4]. According to the data of [7], the minimum value of ΔH in the temperature range 973–1173 K is –14.31 kJ mol^{-1}.

Mozer *et al.* [13] pointed to a good agreement between the partial molar Gibbs energies of magnesium, ΔG_{Mg}, obtained in [4, 6, 7, 9–13] at comparable temperatures. Only the activity coefficients of magnesium and tin obtained in [8] are markedly different from the results of other researchers. All these circumstances make the system Mg–Sn a convenient object for verifying the reliability of various models or polynomial expressions for describing the dependence of the thermodynamic functions on concentration.

The interaction in liquid alloys of the system Mg–Sn was analyzed in detail in terms of the associated solution models in [14–25]. The model of the ideal associated solution requires taking into account both the compound Mg_2Sn and the product of its partial dissociation, MgSn. With the model of the regular associated solution, it suffices to take into account only the compound Mg_2Sn.

Eckert *et al.* [17] proposed a somewhat different approach to determining the composition of associates in liquid alloys of magnesium with tin. Based on the similarity of properties of the systems Mg–Sn and Ca–Sn, the authors postulated for liquid magnesium–tin alloys the existence of three associates (Mg_2Sn, MgSn, and $MgSn_3$), for which the following constants: 306.4, 41.3, and 84.7, respectively, were found at 1073 K. In this approach, too, Mg_2Sn remains the dominating associate. Only the compound Mg_2Sn is revealed in the curve describing the dependence of the structural factor on composition for magnesium–tin liquid alloys [14].

1070-4272/01/7406-0930 $25.00 © 2001 MAIK "Nauka/Interperiodica"

Integral molar excess Gibbs energies and enthalpies of mixing in the system magnesium–tin at 1073 K

x_{Mg}, mole fraction	$-\Delta G^{exc}$, kJ mol^{-1}						$-\Delta H$, kJ mol^{-1}					
	[12]	IAS	RAS	[18]	IAS	RAS	[11]	IAS	RAS	[18]	IAS	RAS
0.10	4.09	3.98	3.98	3.57	3.52	3.54	2.30	2.32	2.22	3.31	3.26	3.27
0.20	7.53	7.57	7.57	7.00	6.98	7.01	4.80	4.88	4.73	6.61	6.55	6.59
0.30	10.2	10.2	10.3	10.1	9.99	10.1	8.00	8.02	7.94	9.67	9.59	9.59
0.40	12.2	12.3	12.2	12.6	12.6	12.6	11.1	10.6	10.8	12.2	12.3	12.2
0.50	13.6	13.7	13.7	14.2	14.2	14.2	13.3	13.1	13.2	13.9	13.9	13.9
0.60	14.2	14.2	14.2	14.7	14.7	14.7	14.8	14.7	14.7	14.5	14.5	14.5
0.70	13.0	12.9	12.9	13.8	13.7	13.8	14.0	13.8	14.1	13.6	13.6	13.6
0.80	9.50	9.45	9.42	11.2	11.2	11.2	9.90	9.84	9.94	11.1	11.0	11.1
0.90	5.05	5.00	5.00	6.72	6.65	6.68	4.85	4.89	4.91	6.69	6.73	6.68

Note: [11], [12], and [18] are references from which experimental data were taken. IAS and RAS stand for the results of approximation in terms of ideal and regular associated solution models, respectively.

The dissociation of the complex via the pathway $Mg_2Sn \rightleftarrows 2Mg + Sn$ at 1073 K was described in terms of the regular associated solution model in [18]. The K_{dis} value is 0.0854, and the characteristic parameters of the model, ω_{12}, ω_{13}, and ω_{23}, are equal to (kJ mol^{-1}): –35.33, –53.44, and –63.61, respectively. The enthalpy of complex formation is –22.76 kJ mol^{-1}.

Sommer [19, 20] described, using the equations of the regular associated solution model, the excess heat capacity and the enthalpy of mixing of the magnesium–tin liquid alloys as functions of temperature. As follows from the ΔH^0 and ΔS^0 values reported by the author for the associate Mg_2Sn at 1073 K, the equilibrium constant of compound formation from pure components is 329.8. It should be noted that in [19, 20] the energies of interaction of pure components with the associate were assumed to be zero.

In [21], the possibility of extrapolating the thermodynamic data on liquid alloys to lower temperature was discussed and a new model of chemical interaction between the components was proposed. According to the data obtained by the authors, the degree of association near the composition Mg_2Sn is higher than that reported in earlier studies. In [26], the dependences of the enthalpy of mixing on temperature and composition were described in terms of algebraic polynomials.

Analysis of the literature suggests that, despite the fact that the polynomial dependences based on associated solution models describe experimental data satisfactorily in all the works cited, the sets of constants playing the role of fitting parameters are different. To determine the parameters of the associate models used to describe the concentration dependence of the thermodynamic functions of liquid metal systems with strong interaction between the components, thermodynamic properties of a model system, magnesium–tin, at 1073 K are described here, using the most reliable experimental data. For this purpose we

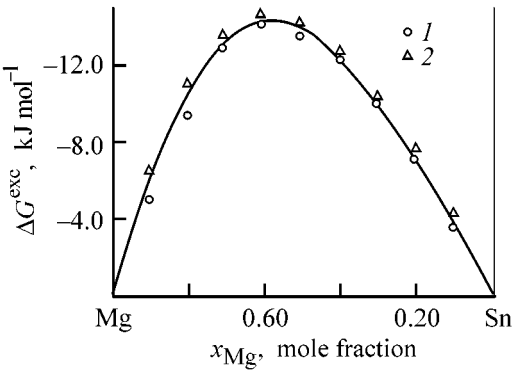

Fig. 1. Integral molar excess Gibbs energy ΔG^{exc} vs. composition x_{Mg} for the magnesium–tin system at 1073 K. Reference: (*1*) [12] and (*2*) [18].

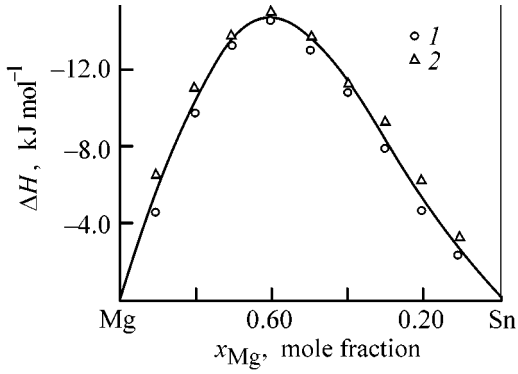

Fig. 2. Integral molar enthalpy of mixing ΔH, vs. composition x_{Mg} for the system magnesium–tin at 1073 K. Reference: (*1*) [11] and (*2*) [18].

used modified software whose main parameters were described previously in [27]. The calculations were done using the ΔG^{exc} value obtained by the emf method in [12], ΔH obtained calorimetrically in [11], and ΔG^{exc} and ΔH taken in modeling the Mg–Sn system in [18]. The input data and the results of approximation are given in the table. The maximum in the concentration dependences of ΔG^{exc} and ΔH at 1073 K (Figs. 1, 2) is shifted somewhat from the composition Mg_2Sn (x_{Mg} = 0.667) toward the tin-richer region (x_{Mg} of about 0.60).

In applying the model of an ideal associated solution in this study, the formation of the Mg_2Sn and MgSn groups in liquid alloys was taken into account. To compare the calculation results for the dependences $\Delta G^{exc} = f(x_{Mg})$ and $\Delta H = f(x_{Mg})$, we used the formation constants of both the associates. In the case of the model of a regular associated solution, the formation of only a single compound, Mg_2Sn, was taken into account. The following values of the formation constants at 1073 K were obtained by processing the above data in terms of both the models:

Input data	Ideal solution model		Regular solution model
	K_{Mg_2Sn}	K_{MgSn}	K_{Mg_2Sn}
ΔG^{exc} [12]	261.0	65.3	237.0
ΔG^{exc} [18]	252.8	53.9	249.7
ΔH [11]	263.0	55.2	239.0
ΔH [18]	254.0	55.6	250.3

The associate formation constants determined with different input data agree sufficiently well with one another and with the results of other authors [11, 12, 14, 22]. This confirms the applicability of the associated solution models for describing the concentration dependence of thermodynamic functions in the Mg–Sn system, the objectivity of the assessment of the complexation processes in it, and the reliability of the employed software.

REFERENCES

1. Nayeb-Hashemi, A.A. and Clark, J.B., *Bull. Alloy Phase Diagrams*, 1984, vol. 5, no. 5, pp. 486–489.
2. *Diagrammy sostoyaniya dvoinykh metallicheskikh sistem: Spravochnik* (Phase Diagrams of Binary Metal Systems: Reference Book), Lyakishev, N.P., Ed., Moscow: Mashinostroenie, 1999, vol. 3, book 1.
3. Ashtakala, S. and Pidgeon, L.M., *Canad. J. Chem.*, 1962, vol. 40, pp. 718–728.
4. Eremenko, V.N. and Lukashenko, G.M., *Fiziko-khimicheskie osnovy metallurgicheskikh protsessov* (Physicochemical Foundations of Metallurgical Processes), Moscow: Metallurgiya, 1964, pp. 179–189.
5. Steiner, A., Miller, E., and Komarek, K.L., *Trans. Met. Soc. AIME*, 1964, vol. 230, October, pp. 1361–1367.
6. Eldridge, J.M., Miller, E., and Komarek, K.L., *Trans. Met. Soc. AIME*, 1966, vol. 236, January, pp. 114–127.
7. Sharma, R.A., *J. Chem. Thermodyn.*, 1970, vol. 2. pp. 373–389.
8. Nayak, A.K. and Oelsen, W., *Trans. Indian Inst. Metals*, 1971, June, pp. 22–28, 66–73.
9. Egan, J.J., *J. Nucl. Mater.*, 1974, vol. 51, no 1, pp. 30–35.
10. Mozer, Z. and Fitzner, K., *Thermodynamics of Nuclear Materials*, Vienna: Int. Atomic Energy Agency, 1975, vol. 2, pp. 379–391.
11. Sommer, F., Lee, J.-J., and Predel, B., *Z. Metallkunde*, 1980, vol. 71, no. 12, pp. 818–821.
12. Eckert, C.A., Irwin, R.B., and Smith, J.S., *Met. Trans. B.*, 1983, vol. 14B, September, pp. 451–458.
13. Mozer, Z., Zakulski, W., Panek Z., *et al.*, *Met. Trans B.*, 1990, vol. 21B, August, pp. 707–714.
14. Glazov, V.M., *Metallurgiya i materialovedenie tsvetnykh splavov* (Metallurgy and Materials Science of Non-Ferrous Alloys), Moscow: Nauka, 1982, pp. 24–31.
15. Morachevskii, A.G. and Kozin, L.F., *Termodinamika i materialovedenie poluprovodnikov* (Thermodynamics and Materials Science of Semiconductors), Glazov, V.M., Ed., Moscow: Metallurgiya, 1992, pp. 53–75.
16. Glazov, V.M., and Pavlova, L.P., *Khimicheskaya termodinamika i fazovye ravnovesiya* (Chemical Thermodynamics and Phase Equilibria), Moscow: Metallurgiya, 1988.
17. Eckert, C.A., Smith, J.S., Irwin R.B., and Cox, K.P., *Am. Inst. Chem. Eng. J.*, 1982, vol. 28, no. 2, pp. 325–333.
18. Lele, S. and Ramachandrarao, P., *Met. Trans. B.*, 1981, vol. 12B, December, pp. 659–666.
19. Sommer, F., *Ber. Bunsengesell. Phys. Chem.*, 1983, vol. 87, no. 9, pp. 749–756.
20. Sommer, F., *Diagrammy faz v splavakh* (Phase Diagrams of Alloys), Moscow: Mir, 1986, pp. 128–141.
21. Jonsson, B. and Agren J., *Met. Trans. A.*, 1986, vol. 17A, April, pp. 607–615.
22. Kaschin, V.I., Katsnelson, A.M., and Krylov A.S., *Z. Metallkunde*, 1990, vol. 81, no. 7, pp. 516–520.
23. Qin, J., Lin, R., Schaefers, K., and Frohberg M.G., *Z. Metallkunde*, 1993, vol. 84, no. 10, pp. 675–681.
24. Singh, R.N., Jha, I.S., and Pandey, D.K., *Condens. Matter*, 1993, vol. 5, pp. 2469–2478.
25. Fries, S.G. and Lukas, H.L., *J. Chem. Phys.*, 1993, vol. 90, pp. 181–187.
26. Tomiska, J., Luck, R., and Predel, B., *Z. Metallkunde*, 1991, vol. 82, no. 12, pp. 935–943.
27. Morachevskii, A.G. and Erofeev, K.B., *Zh. Prikl. Khim.*, 1999, vol. 72, no. 11, pp. 1913–1914.

Russian Journal of Applied Chemistry, Vol. 74, No. 6, 2001, pp. 933–938. Translated from Zhurnal Prikladnoi Khimii, Vol. 74, No. 6, 2001, pp. 908–913.

PHYSICOCHEMICAL STUDIES OF SYSTEMS AND PROCESSES

Comparative Analysis of Open Evaporation and Pervaporation in the Ternary System Water–Ethanol–Isopropanol

A. M. Toikka, E. L. Aksenova, and Yu. P. Kuznetsov

St. Petersburg State University, St. Petersburg, Russia
Institute of Macromolecular Compounds, Russian Academy of Sciences, St. Petersburg, Russia

Received April 24, 2000; in final form, February 2001

Abstract—A comparative analysis is made of pervaporation and equilibrium open evaporation. The possibilities are considered of using data on the liquid–vapor equilibrium for analyzing the pervaporation process. Some specific features of the structure of diagrams for pervaporation and open evaporation of a ternary system are discussed for the example of the water–ethanol–isopropanol system.

The interest in membrane separation processes is largely associated with technological issues. In particular, the efficiency of pervaporation–evaporation through a membrane, compared with distillation, initiated quite a number of studies aimed to search for highly selective high-throughput membranes. Theoretical investigations in this field include analysis of the mechanisms of the process and its modeling [1–6]. At the same time, such traditional problem of thermodynamics as the topology of diagrams has been little studied. The present communication discusses some aspects of the thermodynamic approach and makes a comparative analysis of pervaporation and distillation in a ternary system.

Let us compare of the equilibrium open evaporation and the evaporation through a membrane. As in the case of equilibrium evaporation, the pervaporation process is described by balance equations of the type

$$\frac{\mathrm{d}x_i^{(1)}}{\mathrm{d}\ln m^{(1)}} = x_i^{(2)} - x_i^{(1)} \quad (i = 1, 2, ..., n), \qquad (1)$$

where $x_i^{(1)}$ and $x_i^{(2)}$ are the concentrations (mole or weight fraction) of i-th substance in the feed liquid mixture and in the permeate (vapor); $m^{(1)}$ is the amount of liquid phase (moles or kg); and n is the number of substances.

Equations (1) allow calculation of the permeate composition or verification of the relation between the solution and permeate compositions and the amount of evaporated solution.

The use of Eqs. (1) is limited to the following: in most of experiments the solution composition is maintained constant by means of the flow of the feed mixture, and the system as a whole is in a steady state. At constant composition, it is convenient to determine the separation or enrichment factor and the flux at a given solution concentration. At the same time, in solving practical problems, e.g., substance purification by pervaporation, information is necessary on composition changes in the retentate (liquid outflowing from the membrane unit). A typical process of this kind is the dehydration of organic solvents [2], which, in contrast to conventional rectification, enables separation of azeotropic mixtures. According to [7], at manufacture rates not exceeding 5000 $\mathrm{l\,h^{-1}}$, pervaporation is undoubtedly preferable in economical regard, too. In laboratory practice, changes in composition are possible when installations are used operating in a nonstationary mode, in the absence of feed flow. To a shift of composition corresponds a trajectory in an $(n - 1)$-dimensional concentration space described by equations of the type

$$\left(\frac{\mathrm{d}x_i}{\mathrm{d}x_n}\right)^{(1)} = \frac{x_i^{(2)} - x_i^{(1)}}{x_n^{(2)} - x_n^{(1)}} \quad (i = 1, 2, ..., n - 1). \qquad (2)$$

It should be noted that relations (1) and (2) are merely mass balance equations and, strictly speaking, are not thermodynamic.

Even though the theory of pervaporation relies upon notions closely related to the theory of liquid–

1070-4272/01/7406-0933 $25.00 © 2001 MAIK "Nauka/Interperiodica"

vapor equilibrium (e.g., that of the separation factor α analogous to the relative volatility), the thermodynamics of pervaporation cannot be constructed on the basis of the equilibrium theory. For example, the pervaporation diagrams may have points corresponding to the condition $x_i^{(1)} = x_i^{(2)}$, or $\alpha = 1$ ("permazeotropic point"), but this circumstance is not related to pressure or temperature extremum conditions, as in the case of equilibrium phases. At the same time, data on the liquid–vapor equilibrium are necessary for determining the thermodynamic characteristics of the feed mixture and permeate, in particular, the chemical potentials.

Commonly, it is mentioned that the chemical potential gradients $\nabla\mu_i$ are the driving force of the transfer across a membrane [1–4]. This corresponds to the notions of flows and forces in nonequilibrium thermodynamics (diffusion vectors J_i and gradients of chemical potentials). However, the theory of pervaporation is based, as also the majority of diffusion studies, not on the phenomenological Onsager equations, but on Fick laws relating the mass flux to concentration gradients ∇c_i, rather than to $\nabla\mu_i$. This leads to analysis of problems concerning the dependence of the diffusion coefficients on composition along the membrane profile. In the case of pervaporation, this dependence can be calculated, e.g., in terms of the known Rautenbach–Albrecht model [8].

When written correctly, the phenomenological equations of thermodynamics must include as forces $\nabla\mu_i$, rather than ∇c_i. Then the relation between the fluxes and forces is represented as the dependence of the component transfer rates on the gradients of chemical potentials and pressure:

$$J_i = J(\nabla\mu_1, \nabla\mu_2, ..., \nabla P).$$

The corresponding phenomenological equations make it possible to obtain the relations for fluxes across the membrane in terms of linear nonequilibrium thermodynamics, with the ratios of the transfer rates of different components directly characterizing the selectivity. At the same time, it should be noted that these quantities—fluxes and selectivity, are the parameters commonly determined in experiment. Therefore, an alternative (recursion) form of the equations, defining the thermodynamic forces as functions of fluxes, can also be effective in describing the pervaporation. In both cases, data on the liquid–vapor equilibrium can be used for verification and correlation.

Data on the liquid–vapor equilibrium allow calculation of the component activities a_i (and also μ_i) in the feed mixture. However, determining the a_i values in the permeate requires refining of the very notion "permeate." Since separation occurs in the case of pervaporation only within the membrane (dissolution–diffusion) and on its surfaces (sorption–desorption), the aggregative state of substances cannot be unambiguously determined even in the final stage (desorption). However, it is for this stage (for already separated substances) that the activities should be determined in calculating the driving force. It is noteworthy that vaporization is in fact only permeate sampling.

If the following conditions are met in the final stage: (a) the aggregative state corresponds to a liquid, (b) the entire amount of liquid is vaporized, and (c) the interaction with the membrane surface has no effect on the activity coefficients, then the activities can be calculated from data on the liquid–vapor equilibrium. On the assumption of vapor ideality and possibility of neglecting the effect of pressure P on μ_i in the liquid, the a_i and μ_i values are calculated by

$$a_i = \frac{Px_i^{(2)}}{P_i^0}, \quad \mu_i^{(1)} = \mu_i^0(T, P) + RT\ln a_i, \qquad (3)$$

where $x_i^{(2)}$ and P are determined from data on the equilibrium with the solution whose composition $x_i^{(1)}$ is the same as that of the permeate, P_i^0 is the vapor pressure of i-th pure component at a given temperature T, and $\mu_i^0(T, P)$ is the standard chemical potential.

If, however, the separated substance is in the vapor state at the membrane surface, then the μ_i^0 values in the permeate are to be found using the formula

$$\mu_i^{(2)} = \mu_i^0(T) + RT\ln p_i, \qquad (4)$$

where $p_i = Px_i^{(2)}$ is the partial pressure of i-th component.

In this case, the driving force of the transmembrane transfer of a component is determined not only by the composition of the solution and permeate, but also by pressure, with its value not corresponding to the condensation pressure, as in the case of formula (3). The P value may correspond to the permeate pressure, as indicated indirectly by data on the pressure dependence of selectivity [4]. At the same time, such an interpretation of formula (4) seems to be ambiguous if, as already mentioned, the created rarefaction serves for permeate sampling—this must have no effect on its composition A similar situation occurs in equilibrium evaporation: the rate of the process

has no effect on the vapor composition. The evaporation rate may exceed by hundreds of times the rate of diffusion of the forming vapor through the gas layer adjacent to the surface [9]. Therefore, diffusion is the rate-determining stage of the process. In the case of vapor removal (rarefaction, flux), the evaporation rate grows, but this does not affect the composition.

Relations (1) and (2) can serve as a basis for a thermodynamic-topological analysis of the pervaporation diagrams, as also equations describing the open evaporation curves can be used for analyzing the liquid–vapor equilibrium diagrams. Let us consider the results obtained in an experimental study of pervaporation in the water–ethanol–isopropanol ternary system at 303.15 K. The method used for experimental study of pervaporation in ternary and binary systems was described in [10]. It is noteworthy that the type of membrane was chosen so that the experimental conditions should be reproducible, which is, in the first place, determined by the insignificant change in the properties of the membrane in the course of experiments. The selectivity was unimportant for the present investigation; in studying the entire range of compositions in the concentration triangle, one could expect occurrence of not only a quantitative, but also a fundamental change in how the enrichment factor depends on concentration. The composite membrane made of SILAR-M polymer (polyacrylatesiloxane on polysulfoneamide/phenylone substrate), used in the study, shows organophilic behavior in ethanol–water solutions up to ethanol concentration of 0.65 (mol fraction). With increasing content of ethanol, the membrane mainly passes water, i.e., exhibits organophobic properties (Table 1). It should also be noted that no direct experimental study of pervaporation in the ethanol–isopropanol system was performed in the present investigation because of the high hygroscopicity of ethanol, requiring special experimental conditions. In data processing and discussion, "ternary" data were extrapolated to zero water concentration; the obtained results were used as "binary" data in analyzing the pervaporation diagrams.

Table 2 lists the differences (gradients) of the chemical potentials of the components, calculated using formula (3) for 36 compositions of ternary feed solutions and permeate and also the fluxes J across the membrane.

Despite the quite natural correlation between the differences of the component concentrations in the permeate and feed mixture, on the one hand, and differences of the chemical potential, $\nabla\mu_i$ (having the same sign in most cases), the quantities $\nabla\mu_i$ cannot be substituted in the linear relations (phenomenological equations of nonequilibrium thermodynamics) as thermodynamic forces related to substance fluxes. This would lead to a fundamentally erroneous result: the direction of the flow across the membrane would correspond to permeate transfer into the feed solution.

Table 1. Experimental data on pervaporation in the ethanol–water and isopropanol–water systems (Feed solution temperature 303.15 K, permeate pressure 15 mm Hg)

Ethanol, mol %		Isopropanol, mol %	
feed mixture	permeate	feed mixture	permeate
2.0	14.2	10.0	30.8
7.0	31.5	20.0	39.5
10.0	33.0	30.0	43.2
20.0	47.0	40.0	47.9
25.0	49.3	50.0	58.4
30.0	52.4	60.0	62.0
40.0	57.6	70.0	65.2
50.0	61.4	80.0	72.7
60.0	67.0	90.0	87.1
70.0	70.1		
80.0	80.0		
89.4	87.8		

If, however, the thermodynamic forces are defined on the basis of the component activities in the permeate, with account of the pressure at the back side of the membrane (0–20 mm Hg), then, by virtue of the low P values, $\mu_i^p \to -\infty$. In this case the corresponding differences of the chemical potentials are approximately the same. This gives no way of evaluating even the relative fluxes of different substances across the membrane. At the same time, data on $\nabla\mu_i$ (Table 2) enable characterization of the departure of the system from the equilibrium liquid–vapor state ($\nabla\mu_i = 0$). The J values (Table 2) indicate that the fluxes grow somewhat with increasing total content of alcohols in water.

The positions of the points representing the compositions of the starting solutions and the corresponding permeate compositions are shown in the concentration triangle in Fig. 1. The arrow-heads of the lines connecting these compositions are directed toward the points representing the feed solution compositions. Also presented are some solution–permeate tie lines for binary systems. The arrangement of the tie lines (feed mixture–permeate) corresponds to the direction

Table 2. Experimental data on pervaporation in the system water(1)–ethanol(2)–isopropanol(3) (Feed solution temperature 303.15 K, pressure 20 mm Hg)

Composition no.	Solution (L), mol %			Permeate (P), mol %			Difference $\nabla\mu_i = \mu_i^P - \mu_i^L$, 1×10^3 J mol^{-1}			J, kg m^{-2} h^{-1}
	x_1	x_2	x_3	x_1	x_2	x_3	$\nabla\mu_1$	$\nabla\mu_2$	$\nabla\mu_3$	
1	10.0	10.0	80.0	17.1	10.0	72.9	1.036	0.013	–0.179	3.2
2	20.0	10.0	70.0	25.5	10.4	63.9	1.787	–1.441	–0.110	4.9
3	30.0	10.0	60.0	39.8	9.0	51.2	2.413	–2.801	0.012	3.8
4	40.0	10.0	50.0	42.2	10.6	47.2	2.529	–3.000	0.322	3.4
5	50.0	10.0	40.0	47.7	12.0	40.3	2.727	–3.241	0.669	2.8
6	60.0	10.0	30.0	48.9	13.4	37.7	2.828	–3.488	1.297	2.1
7	70.0	10.0	20.0	55.6	14.3	30.1	3.009	–3.522	2.029	2.0
8	80.0	10.0	10.0	57.8	21.5	20.7	3.070	–2.644	2.969	1.7
9	70.0	20.0	10.0	65.0	22.7	12.3	1.228	3.009	–2.724	1.8
10	60.0	20.0	20.0	56.3	22.7	21.0	1.203	0.921	–1.542	2.0
11	50.0	20.0	30.0	46.9	22.4	30.7	1.156	–0.459	–0.563	2.3
12	40.0	20.0	40.0	42.5	20.7	36.8	1.166	–1.391	0.193	4.7
13	30.0	20.0	50.0	38.5	19.5	42.0	1.165	–2.159	1.083	3.9
14	20.0	20.0	60.0	31.5	19.1	49.4	1.038	–2.856	2.342	4.8
15	10.0	20.0	70.0	18.4	19.5	62.1	0.249	–3.234	4.428	6.0
16	10.0	30.0	60.0	18.0	30.5	51.5	–0.932	2.756	–0.534	*
17	20.0	30.0	50.0	28.0	29.9	42.1	–0.165	1.006	–0.436	4.6
18	30.0	30.0	40.0	37.1	29.6	33.3	0.254	0.087	–0.303	3.7
19	40.0	30.0	30.0	41.9	29.4	28.7	0.472	–0.662	0.200	3.4
20	50.0	30.0	20.0	48.6	31.1	20.3	0.677	–0.919	0.542	2.9
21	60.0	30.0	10.0	51.6	35.9	12.5	0.775	–0.919	1.164	2.8
22	50.0	40.0	10.0	43.4	44.4	12.2	–0.193	3.849	–3.012	*
23	40.0	40.0	20.0	41.1	40.0	18.9	–0.135	1.818	–1.687	4.0
24	30.0	40.0	30.0	35.4	37.9	26.7	–0.200	0.537	–0.376	*
25	20.0	40.0	40.0	27.1	39.2	33.7	–0.464	–0.235	0.931	4.5
26	10.0	40.0	50.0	23.9	34.4	41.7	–0.507	–1.241	3.061	7.2
27	10.0	50.0	40.0	23.3	44.1	32.6	–1.175	3.369	–1.032	8.0
28	20.0	50.0	30.0	27.2	46.0	26.8	–0.884	1.781	–0.821	7.8
29	30.0	50.0	20.0	35.5	45.8	18.7	–0.442	0.846	–0.682	7.0
30	40.0	50.0	10.0	49.5	36.7	13.8	0.296	–0.205	0.229	5.9
31	30.0	60.0	10.0	36.2	53.8	10.0	–0.772	3.770	–3.213	6.5
32	20.0	60.0	20.0	28.3	53.9	17.8	–1.023	1.917	–1.278	6.8
33	10.0	60.0	30.0	18.6	54.0	27.4	–1.546	0.737	1.104	7.9
34	10.0	70.0	20.0	20.2	59.8	20.0	–1.745	3.485	–1.676	9.3
35	20.0	70.0	10.0	20.0	67.8	12.2	–1.752	1.995	–1.446	7.4
36	10.0	80.0	10.0	19.2	69.0	11.8	–1.941	3.240	–2.202	8.4

* Flux not determined for a given composition.

of run of the curves for pervaporation in the ternary system, describing the shift of the solution composition in the course of pervaporation. The direction of the process is shown schematically in Fig. 2.

One of characteristic features of the structure of the pervaporation diagram is the presence of a triple point at which the permeate and the feed mixture have the same composition. This is indicated by the arrangement and direction of the solution–permeate tie lines. Such a phenomenon has been observed previously in experimental studies of pervaporation in binary systems [11] in which this point was named permazeotropic (by analogy with azeotrope). An analysis of the literature demonstrated that a diagram with a triple permazeotropic point was obtained for the first time in the present study.

The curves in question are similar to those of open evaporation, with the direction of the process indicated by the arrangement of liquid–vapor nodes. Since no direct experimental data on the liquid–vapor equilibrium can be found in the literature for the given system at 303.15 K, the equilibrium was calculated

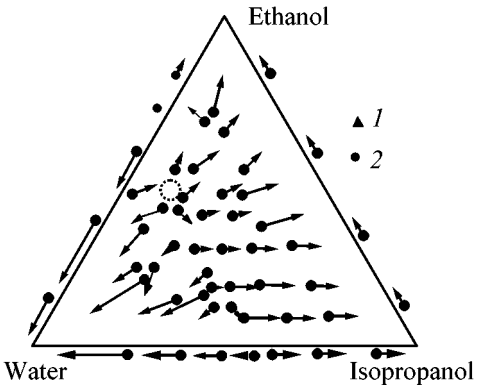

Fig. 1. Points corresponding to the compositions of (*1*) feed solutions and (*2*) permeate, and also permeate–solution tie lines (*2–1*), in the system water–ethanol–isopropanol at 303.15 K. *Dashed circle*: denotes triple permazeotropic point. Lines *2–1* outside the concentration triangle indicate the direction of pervaporation lines in binary systems.

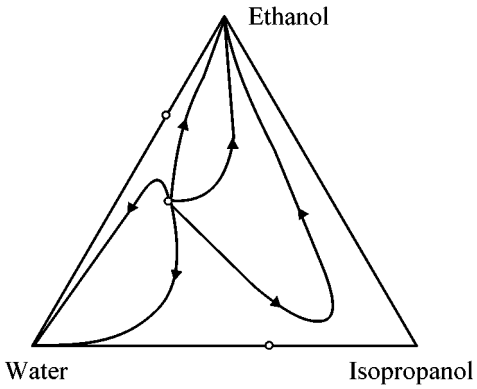

Fig. 2. Qualitative diagram of pervaporation curves in the system water–ethanol–isopropanol at 303.15 K. *Circles*: two double and one triple points.

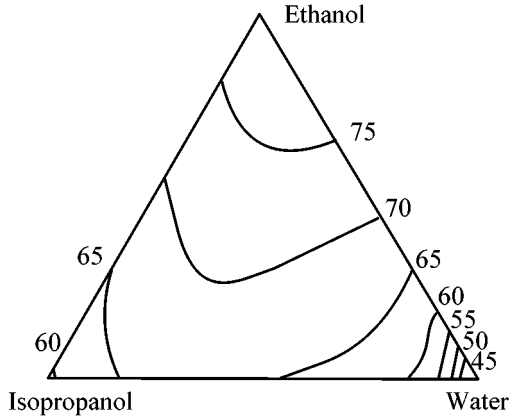

Fig. 3. Projections of the isotherms-isobars of the solution in the system water–ethanol–isopropanol at 303.15 K (calculation by the NRTL equation). Vapor pressures are given in mm Hg.

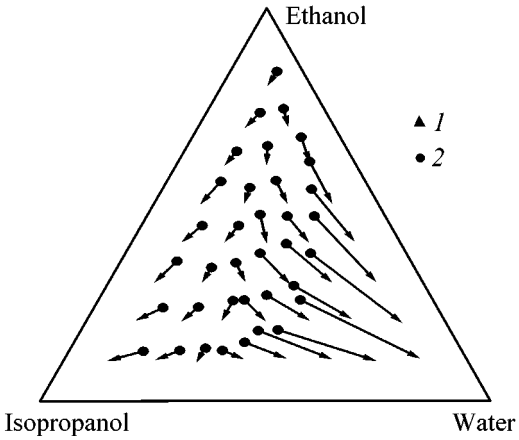

Fig. 4. Liquid–vapor nodes in the ternary system water–ethanol–isopropanol at 303.15 K (calculation by the NRTL equation). Points: (*1*) liquid compositions (lying at nodes of the coordinate grid of the composition triangle), (*2*) vapor compositions.

in the present study by means of the NRTL equation which, as a rule, adequately describes systems of this kind. The equilibrium in the system ethanol–isopropanol was calculated on the assumption that the given binary system exhibits ideal behavior. The isotherms-isobars of the solution, nodes, and a schematic diagram of open evaporation are presented in Figs. 3–5. At 303.15 K the ternary system has only a single (binary) azeotropic point (water–isopropanol); according to a reference book [12], there is no azeotrope in the water–ethanol system at the given temperature. The arrangement of liquid–vapor nodes is strongly different from the corresponding tie lines in the case of the pervaporation diagram.

Comparison of the diagrams in Figs. 2 and 5 shows that they belong to fundamentally different topological types. The pervaporation diagram includes two double and one triple singular points. The diagram of open evaporation includes only one double singular point and belongs to class 3.1.0, type 2 by Serafimov's classification.

To conclude, it should be noted that the behavior of the pervaporation curves in the vicinity of singular points requires additional theoretical analysis, which may be complicated (compared with the case of equilibrium open evaporation) by the lack of equilibrium between the solution and permeate. Correspondingly, the existence is possible of topological types of diagrams thermodynamically forbidden in the case of a liquid–vapor equilibrium. These problems invite separate investigation with the use of methods of nonequilibrium thermodynamics.

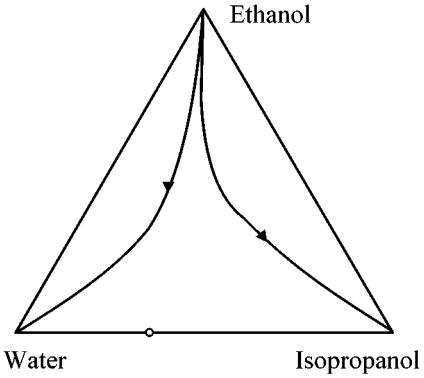

Fig. 5. Qualitative diagram of open evaporation curves in the system water–ethanol–isopropanol at 303.15 K. *Circle*: bynary azeotropic point.

CONCLUSION

Experimental data are presented on the process of pervaporation in the ternary system water–ethanol–isopropanol at 303.15 K. The possibilities are considered of using data on the liquid–vapor equilibrium in studying the pervaporation. Comparative analysis of the diagrams of open evaporation and pervaporation shows the existence of a triple permazeotropic point.

REFERENCES

1. Feng, X. and Huang, R.Y.M., *Ind. Eng. Chem. Res.*, 1997, vol. 36, pp. 1048–1066.
2. Baker, R.W., *Membrane Technology and Applications*, New York: McGraw-Hill, 2000.
3. Volkov, V.V., *Izv. Ross. Akad. Nauk., Ser. Khim.*, 1994, no. 2, pp. 208–219.
4. Staudt-Bickel, C. and Lichtenthaler, R.N., *Vysokomol. Soedin., Ser. B*, 1994, vol. 36, no. 11, pp. 1924–1945.
5. Dytnerskii, Yu.I., Bykov, I.R., Akobyan, A.A., *et al.*, *Razdelenie zhidkikh smesei ispareniem cherez membranu i membrannoi distillyatsiei* (Separation of Liquid Mixtures by Evaporation through Membrane and Membrane Distillation), Moscow: NIITEKhIM, 1989.
6. Hwang, S.-T. and Kammermeyer, K., *Membranes in Separations*, New York: John Wiley and Sons, 1975.
7. Bergdorf, J., *Proc. Fifth Int. Conf. on Pervaporation Processes in the Chemical Industry, Heidelberg, Germany, 20–25 Aug., 1991*, Heidelberg, 1991, pp. 234–235.
8. Rautenbach, R. and Albrecht, R., *J. Membr. Sci.*, 1980, vol. 7, pp. 203–215.
9. Nicolis, G and Prigogine, I., *Self-Organisation in Nonequilibrium Systems: From Dissipative Structures to Order Through Fluctiations*, New York: Wiley, 1977.
10. Aksenova, E.L., Kuznetsov, V.M., Kuznetsov, Yu.P., and Toikka, A.M., *Vestn. SPb. Gos. Univ., Ser. 4*, 2000, issue 4, no. 25, pp. 89–93.
11. Yamasaki, A., Iwatsubo, T., Masuoka, T., and Mizoguchi, K., *J. Membr. Sci.*, 1994, vol. 89, pp. 111–117.
12. Lyudomirskaya, G.S., Barsukova, T.A., and Bogomol'nyi, A.M., *Ravnovesie zhidkost'–par* (Liquid–Vapor Equilibrium), Leningrad: Khimiya, 1987.

Russian Journal of Applied Chemistry, Vol. 74, No. 6, 2001, pp. 939–944. Translated from Zhurnal Prikladnoi Khimii, Vol. 74, No. 6, 2001, pp. 914–919.

PHYSICOCHEMICAL STUDIES OF SYSTEMS AND PROCESSES

Thermodynamic Analysis of Combustible Formulations Forming Gaseous Metals in Combustion Products

D. B. Lempert, G. N. Nechiporenko, G. P. Dolganova, and S. I. Soglasnova

Institute for Problems of Chemical Physics, Russian Academy of Sciences, Chernogolovka, Moscow oblast, Russia

Received July 5, 1999; in final form, May 2000

Abstract—A thermodynamic analysis of the burning temperatures and products formed in combustion of formulations containing zinc or lead was made in relation to the elemental composition and total enthalpy of formation of the starting mixture in order to develop programs searching in the existing database for such formulations whose combustion will produce a prescribed fraction of a metal in gaseous state.

A study of the thermodynamics of combustion of metal-containing solid rocket propellants and blasting powders demonstrated that, under certain conditions, the combustion products contain much more than trace amounts of gaseous metals even in the case of aluminum—an element with high affinity for oxygen. When the energetics of blasting powders and rocket propellants is discussed, presence of gaseous metals in products of their combustion is highly undesirable, but this phenomenon may prove rather useful in a totally different field—in developing special fast-burning formulations aimed to deposit metal coatings or create surface layers doped with specially selected metals. This way to create a gas flow of metal could find application for resolving a number of technological problems, similarly to the known technique in which the reaction of acetylene combustion in oxygen is the source of energy and the concurrent gas flow, and a wire or plate, the source of metal [1].

In developing metal-containing combustible formulations—sources of a high-temperature flow of metal vapor, it is necessary to achieve a combustion temperature sufficient for the metal to be in the gas phase and the equilibria

$$M_xO_y + CO \rightleftarrows M + CO_2, \quad \text{(a)}$$

$$M_xO_y + H_2 \rightleftarrows M + H_2O \quad \text{(b)}$$

to be shifted to the right. In addition, the share of oxygen (or, more precisely, the ratio of the amount of oxygen to the total amount of carbon and hydrogen) in a formulation should not be too high in order that the equilibrium of the reaction $CO_2 + H_2O \rightleftarrows H_2 + CO + O_2$ and, consequently, that of reactions (a) and (b) be strongly shifted to the right. At the same time, the share of oxygen should be sufficient for achieving a combustion heat that is necessary for combustion products to be heated to temperatures ensuring a high fraction of evaporated metal. Therefore, it is apparent that it is immeasurably easier to solve the given problem for metals with high volatility and low chemical activity, e.g., cadmium, compared with more active and higher-boiling metals, e.g., aluminum and chromium. To achieve a relatively high share of gaseous aluminum, it is necessary to use rather specific components, as discussed below, whereas the share of gaseous cadmium (relative to its total content) in combustion products of even the simplest combustible mixture containing 23% cadmium oxide + 8% polyethylene + ammonium nitrate is close to 100%, despite that metal oxide, rather than free metal, is contained in the formulation. In the combustion of a mixture of the above composition (here, a mixture of ammonium nitrate and saturated hydrocarbons is meant) with zinc or lead, the temperature sufficient for lead evaporation is not reached and lead is liberated in liquid state. The combustion temperature reached in the case of zinc is sufficient for its complete evaporation, but insufficient for shifting the equilibria $Zn + CO_2 \rightleftarrows ZnO + CO$, $Zn + H_2O \rightleftarrows ZnO + H_2$, and even $Zn + CO \rightleftarrows ZnO + C$ to the left because of the higher activity of zinc, with mainly zinc oxide formed as a result.

The present study was devoted to a detailed analysis of formulations with zinc and lead, i.e., metals whose physical and chemical properties conform to

1070-4272/01/7406-0939 $25.00 © 2001 MAIK "Nauka/Interperiodica"

the greatest extent to the purposes of development of combustible formulations—sources of a high-temperature flow of metal vapor.

EXPERIMENTAL

As model compositions were considered metal (20 wt %) + C + H + N + O system with widely varied overall enthalpy of formation and relative contents of C, H, N, and O in the organic part of formulations. To determine the chemical composition of a formulation, the following parameters were introduced: $R_1 = (O - C)/(C + 0.5H)$ and $R_2 = 2C/(2C + 0.5H)$, where O, C, and H are the atomic compositions in a formulation, and N_p is the mass fraction of nitrogen.

The R_2 value determines the share of carbon in the sum of carbon and hydrogen (g-equiv). Of interest in the context of the formulated problem are only those formulations in which the content of oxygen is not lower than that necessary to oxidize the entire amount of carbon to CO and not higher than that necessary for complete oxidation of carbon and hydrogen to CO_2 and water (making R_1 higher than unity does not lead to any increase in the combustion heat of the components C, H, N, and O, with the probability of oxidation of free metal by excess oxygen increasing dramatically). In this connection, compositions with R_1 equal to 0, 0.2, 0.4, 0.6, and 0.8 were studied, with the lowest value corresponding to an amount of oxygen strictly equivalent to that of carbon, and the highest is somewhat lower than the amount of oxygen necessary for complete oxidation of carbon and hydrogen. The R_2 values were 0, 0.5, 0.67, 0.8, 0.89, 0.95, and 1.0 (which approximately corresponds to C : H atomic ratios of 0 : 1, 1 : 4, 1 : 2, 1 : 1, 2 : 1, 4 : 1, 1 : 0). The N_p value was in the range from 0 to 0.4 with a step of 0.1 (i.e., from 0 to 40 wt % in a composition). At known metal content, these three quantities (R_1, R_2, and N_p) uniquely determine the elemental composition of a formulation.

Calculation requires setting additionally the enthalpy of formulation formation, ΔH_f^0. This parameter was varied between –750 and +750 kcal kg^{-1} with a step of 250 kcal kg^{-1}. Thus, the chosen interval covers virtually any conceivable formulations with preset limitations on the R_1 value. All thermodynamic studies for calculating the temperatures T_c (K) in the combustion chamber and T_a (K) at the nozzle exit and the product composition were done on Pentium-133 PC with standard software Astra-4 [2] at preset pressures in the chamber and at the nozzle exit of, respectively, 1 MPa (10 atm) and 0.1 MPa (atmospheric). The process of combustion product expansion through the nozzle was considered to be isoentropic.

For each of the metals under study, a thermodynamic calculation of an array of more than 1200 compositions (7 ΔH_f^0 values, 7 R_2 values, 5 R_1 values, and 5 N_p values) gave the temperatures and shares of gaseous metal in the chamber and at the nozzle exit. The difference of temperatures and product concentrations in the chamber and at the nozzle exit depends on the nozzle shape, being the largest for the so-called Laval nozzle in which the maximum fraction of the energy of the chemical reaction is converted into mechanical work. With account of a practical application of the present study (possibility of surface coating with metal present in gaseous state in combustion products of a combustible formulation and condensed from the gas phase directly on a surface being treated), a case is deliberately considered, which is the least favorable as regards the content of gaseous metal at the nozzle exit, namely, the expansion of combustion products in the Laval nozzle, i.e., isoentropic expansion. Mainly the dependence of the fraction of gaseous metal at the nozzle exit, rather than in the combustion chamber, is analyzed.

It should be noted that in the case of zinc the main metal-containing combustion products are condensed zinc oxide and gaseous zinc and other gaseous compounds, e.g., ZnH. Gaseous zinc oxides are present in trace amounts, and condensed (liquid) zinc, only at a very low temperature at the nozzle exit. In the case of lead, a condensed metal is present, together with gaseous Pb and Pb_2 (the fraction of Pb_2 does not exceed 1% of Pb), condensed and gaseous PbO, and gaseous Pb_2O_2, PbO_2, and PbH (the fraction of the last three is very low).

Thus, a practical task is to be set, concerning the development of compositions with a combustion temperature sufficiently high for a free metal to be present in the gas phase having such a composition that the overwhelming fraction of the metal be ejected in the form of a gas (Zn, Pb_x), producing the minimum amount of condensed compounds. The obtained data were analyzed as a dependence of T_c, T_a, and [Me(g)] on ΔH_f^0, R_1, R_2, and N_p, characterizing a combustible formulation. $[Me(g)]_c$ and $[Me(g)]_a$ are the atomic fractions of gaseous free metal in the combustion products, related to, respectively, the total initial amount of metal in the combustion chamber and at the nozzle exit.

The main relationships were analyzed for the example of zinc-containing formulations. Naturally,

an increase in ΔH_f^0 (Figs. 1a and 1b) or decrease in N_p leads to higher T_c and T_a. In this case, the $\partial T_c/\partial \Delta H_f^0$ value is negative because of the progressively deep extent of H_2O and CO_2 dissociation with increasing T_c and T_a. An increase in the oxygen balance R_1 within the interval studied leads to higher combustion heat and, consequently, higher T_c and T_a (Fig. 2). The $\partial T_c/\partial R_1$ value is also negative for the same reason as $\partial T_c/\partial H_f^0$. Variation of R_2 affects the T_c value to a much lesser extent (Fig. 3). It should be noted that raising R_2 from 0 to 1 (transition from a composition with predominance of hydrogen to that with prevalence of carbon) at small R_1 (0.2) leads to a pronounced rise in T_c (by approximately 700 K), whereas at $R_1 = 1$ an increase in R_2 has virtually no effect on T_c. This is a consequence of the physical meaning of R_1—at low R_1 only a minor part of hydrogen is oxidized and, with both R_2 and R_1 approaching zero, the amount of oxygen in a formulation tends to zero, i.e., there is no energy release via oxidation and energy can be only liberated owing to the contribution from ΔH_f^0 in the case of its being positive.

In developing applied software for performing a search for formulations ensuring a share of gaseous zinc at the nozzle exit that would not be lower than a prescribed value, it is necessary to obtain empirical relations between the share of gaseous zinc $[Zn(g)]_a$ and the parameters characterizing the starting combustible mixture. Studying the dependence of $[Zn(g)]_a$ on T_c (Fig. 4a) proved useful for this purpose. It can be seen that the curve describing the dependence $[Zn(g)]_a = f(T_c)$ shows a steep rise in $[Zn(g)]_a$ from 0 to 1 in a rather narrow temperature range (1500–1900 K), with the curves with a certain R_1 value appearing separately. At higher R_1 values, the prescribed $[Zn(g)]_a$ values are achieved at higher temperatures. This a consequence of the fact that a decrease in the share of reducing gases (CO, H_2) in the combustion products shifts to the right the equilibrium of the reactions $Zn + CO_2 \rightleftarrows ZnO + CO$ and $Zn + H_2O \rightleftarrows ZnO + H_2$. At the same time, The difference in R_2 and N_p values between the compositions affects the dependence $[Zn(g)]_a = f(T_c)$ only slightly (R_2, N_p directly affect T_c, similarly to ΔH_f^0 and R_1), and an approximate empirical formula can be found for the dependence of the minimum admissible T_c for reaching the prescribed $[Zn(g)]_a$ value:

$$T_c = A + BR_1. \quad (1)$$

Thus, an estimate was made that $A = 1827$ and $B = 302$ for $[Zn(g)]_a = 0.8$ and $A = 1725$ and $B = 322$

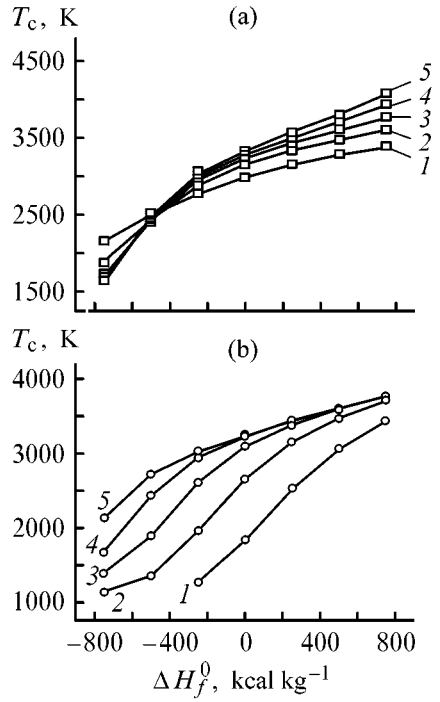

Fig. 1. Temperature T_c in the combustion chamber vs. enthalpy of formation of the formulation, ΔH_f^0. Composition with 20% zinc, $N_p = 20\%$, $R_1 = 0.6$ (a), $R_2 = 0.8$ (b). (a) R_2: (*1*) 0, (*2*) 0.5, (*3*) 0.8, (*4*) 0.95, and (*5*) 1.0. (b) R_1: (*1*) 0, (*2*) 0.2, (*3*) 0.4, (*4*) 0.6, and (*5*) 0.8.

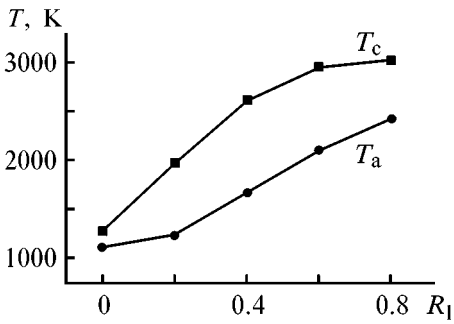

Fig. 2. T_c and T_a vs. R_1 for formulations with 20% zinc. $R_2 = 0.8$, $N_p = 20\%$, $\Delta H_f^0 = -250$ kcal kg^{-1}.

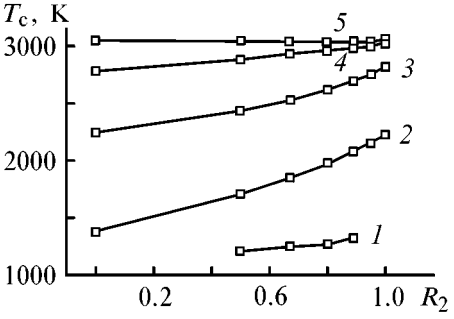

Fig. 3. T_c vs. R_2 for formulations with 20% zinc. $\Delta H_f^0 = -250$ kcal kg^{-1}, $N_p = 20\%$. R_1: (*1*) 0, (*2*) 0.2, (*3*) 0.4, (*4*) 0.6, and (*5*) 0.8.

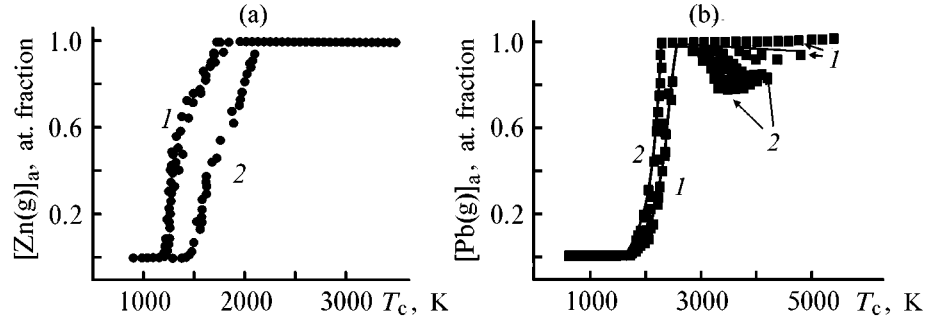

Fig. 4. (a) $[Zn(g)]_a$ and (b) $[Pb(g)]_a$ vs. temperature T for formulations with 20% (a) zinc and (b) lead. R_2 = 0.5–1.0, N_p = 0–40%, ΔH_f^0 = –750 … +750 kcal kg^{-1}. R_1: (*1*) 0 and (*2*) 0.6.

for $[Zn(g)]_a$ = 0.7. As for the T_c value as a function of chemical composition and enthalpy of formation of the starting formulation, it was possible to relate it, with much poorer accuracy, by an empirical formula to R_1, R_2, ΔH_f^0, and N_p. For this purpose, it was necessary to make the interval under study somewhat narrower: only formulations with T_c in the range from 1000 to 3000 K were considered, with the formulations with zero R_1 and R_2 values excluded. However, even after imposing this restriction the array remained rather huge, including more than 350 out of the 1200 calculated compositions. The following empirical formula relating the system parameters was chosen:

$$\Delta H_f^0 = p_0 + p_1 N_p + p_2 N_p^2 + p_3 R_1 + p_4 R_1^2 + p_5 R_2 + p_6 R_2^2 + p_7 T_c + p_8 T_c^2, \quad (2)$$

where ΔH_f^0 is the enthalpy of formation of the overall formulation (kcal kg^{-1}) and N_p is the mass fraction of nitrogen in the formulation.

Parameters of the empirical equation (2) for formulations containing zinc and lead and the average error of ΔH_f^0 calculation by Eq. (2)

Parameter	Parameter value	
	Zn	Pb
T_c, K	1500–2400	1500–3000
p_0	–1120	–511
p_1	1003	1060
p_2	471.6	270.4
p_3	–1595	–1829
p_4	720	934
p_5	–413	–513
p_6	185.2	208
p_7	0.717	0.219
p_8	-6.84×10^{-5}	3.75×10^{-5}
Average error in V, ΔH_f^0, kcal kg^{-1}	60	50

At the above limitations ($1000 < T_c < 3000$ K, $0.2 < R_1 < 0.8$, $0.5 < R_2 < 1$), the parameters of Eq. (2) are presented in the table, with the mean deviation for ΔH_f^0 constituting about 60 kcal kg^{-1}, which is equivalent to an error in T_c of ~130 K in the T_c range 1500–2400 K.

A similar calculation performed for T_a, i.e.,

$$\Delta H_f^0 = P_0 + P_1 N_p + P_2 N_p^2 + P_3 R_1 + P_4 R_1^2 + P_5 R_2 + P_6 R_2^2 + P_7 T_a + P_8 T_a^2, \quad (3)$$

gives the following parameters of Eq. (3): P_0 = –1877, P_1 = 925, P_2 = 829, P_3 = –1652, P_4 = 635, P_5 = –565, P_6 = 260, P_7 = 2.11, and P_8 = –0.0005 with virtually the same deviation.

The obtained parameters of Eq. (2) and the fact that, in a search for compositions with prescribed $[Zn(g)]_a$, T_c can be replaced by the expression $A + BR_1$ {A and B are functions of the sought-for quantity $[Zn(g)]_a$} were used to develop a program executing a computer search for suitable compositions on the basis of the available components. On setting by the user of a required $[Zn(g)]_a$ value, e.g., 0.8, it only remains to bring into operation the system of cyclic pairwise sorting of components present in the database and solve an equation with a single unknown x—the content of the first component, with all the parameters of Eqs. (1) and (2) either already known (p_0–p_8, A, B) or being functions of x and characteristics (chemical composition, ΔH_f^0) of a considered pair of components. If the obtained analytical solution x lies in the interval 0–80% and R_1 is less than unity, then the solution has physical meaning and is acceptable. In this case, the solution is delivered to the output and the program proceeds to considering a next pair of components. The program covers compositions containing not only a free metal, but also its oxide

(provided that the total content of metal is 20%); a correction for the known ΔH_f^0 of the oxide and additional amount of oxygen contained in the oxide is made for this purpose.

The program allows for introduction into a formulation of a preset number of components necessary for ensuring various operation properties, with the search for a formulation composition remaining virtually unchanged. The program can be modified to enable a search for a composition with contents of three components varied. In this case, if a solution exists, it may be multiple since there is a single equation for two unknowns, but in some cases this may be useful for preliminary analysis. In addition, various restrictions can be introduced into the program. It is to be specified that the use of the described application software should only be a first step for preliminary search, and it is necessary to further finally refine the composition of the formulation by means of a standard program for thermodynamic calculations and to test real formulations.

As an example, a search for compositions with $[Zn(g)]_a$ of 80% was performed among formulations containing 20% free zinc. The numerous output formulations included the following formulations containing (%): (a) 14.5–17 polyethylene + ammonium salt of dinitramide (ADNA, a new oxidant for solid propellants [3], (b) 7–19 acetylene + ammonium nitrate (AN), (c) 17.5 carbon + ADNA, (d) 30 trinitrocellulose (TNC) + 50 mononitrocellulose (MNC), (e) 30 TNC + 11 water + 39 dinitrocellulose (DNC), (f) 30 TNC + 47 NA + 3 polyethylene, (g) 48 TNC + 32 trinitrotoluene (TNT), and (h) 67 DNC + 13 TNT.

A calculation by the standard technique gives the following content of components in the compositions studied (%): (a) 14 polyethylene, (b) 5 or 12 acetylene at acetylene content between 5 and 12%, $[Zn(g)]_a$ exceeds 80%}, (c) 17 carbon, (d) 31.5 TNC + 48.5 MNC, (e) 14.5 water + 35.5 DNC + 30 TNC, (f) 7 polyethylene + 43 AN + 30 TNC, (g) 50 TNC + 30 TNT, and (h) 69 DNC + 11 TNT, i.e., the developed algorithm of the program gives quite satisfactory results as a basis for tentative choice of the most acceptable target compositions.

A search gave no compositions containing 25% ZnO (amount corresponding to 20% Zn) and ammonium nitrate for any of the combustibles present in the database. Indeed, in a formulation with free zinc and ammonium nitrate, only introduction of such a high-enthalpy combustible as acetylene allows creation of the desired formulation; at the same time, on lowering the initial enthalpy of formation of a formulation (by approximately 250 kcal kg^{-1}) by replacing zinc with its oxide, even use of acetylene as combustible has no positive effect. The engineering problem of practical use of a gaseous product as a component of formulation is not considered in the present study; it should only be mentioned that this is quite technically possible. A special-purpose calculation confirmed that the maximum achievable $[Zn(g)]_a$ value in the formulation containing 25% ZnO + AN + acetylene is at the level of 0.55–0.60 at acetylene content of 8–9%. However, if such widely used compounds as nitrocellulose or trinitrotoluene are allowed as combustibles in the case of AN, then the program gives a wide variety of compositions, e.g., 25% MNC + 15% AN + 35% TNC, or 25% MNC + 3% water + 47% TNC, or 21% TNT + 54% TNC, even though nitro compounds, rather than AN, form the basis of such formulations, with AN only diluting somewhat the main formulation.

A study of a similar system with lead demonstrated the only basic difference between the systems with zinc and lead. In a system with zinc, with the combustion temperature increasing at any of the studied R_1 and R_2 values, the $[Zn(g)]_a$ value reaches unity an then remains virtually unchanged (Fig. 4a). At the same time, when a $[Pb(g)]_a$ value of ~1 is reached in a system with lead, further increase in T_c (at $R_1 \geq 0.2$) leads to a decrease in $[Pb(g)]_a$ because of the growing share of gaseous PbO at the output. In this case, the higher R_1, the more pronounced this effect (Fig. 4b). S-shaped portions of the curve describing the dependence $[Me(g)]_a = f(T_c)$ are qualitatively the same for both the metals, with the quantitative difference consisting only in the T_c of the onset and completion of a rise in $[Me(g)]_a$—in the case of zinc, T_c is approximately 250°C lower. It should be noted that this value (250°C) is much smaller than the difference between the boiling points of the two metals (1186 and 2025 K). This is due to the fact that, as a result of the higher (compared with lead) affinity of zinc to oxygen, compositions with zinc require higher overheating to achieve the equal shares of gaseous metal at the output. The parameters of Eq. (2) were found for $1500 < T_c < 3000$ K, $0.2 < R_1 < 0.8$, and $0.5 < R_2 < 1$ (see the table).

The same method as in the case of zinc-containing compositions gave the following results: the $[Pb(g)]_a$ value is as high as 0.8 at $T_c = 2417 - 247R_1$ and 0.7 at $T_c = 2330 - 165R_1$. It is noteworthy that, in zinc-containing compositions, the coefficient B at R_1 [Eq. (1)] is positive, whereas in the case of lead it is negative. The positive sign of the coefficient B in the case of zinc is readily accounted for by the fact

that, in contrast to a temperature rise, an increase in R_1 shifts to the right the equilibria of the reactions $2CO + O_2 \rightleftarrows 2CO_2$, $2H_2 + O_2 \rightleftarrows 2H_2O$, $Zn(g) + CO_2 \rightleftarrows ZnO(cond) + CO$, and $Zn(g) + H_2O \rightleftarrows ZnO(cond) + H_2$, and, therefore, at higher R_1 in zinc-containing compositions it is necessary to raise the temperature to preserve the high share of zinc vapor. In the case of lead, however, gaseous PbO is formed, by contrast, just at elevated temperatures and higher R_1 values, i.e., the equilibria of the reactions $Pb(g) + CO_2 \rightleftarrows PbO(g) + CO$ and $Pb(g) + H_2O \rightleftarrows PbO(g) + H_2$ are shifted to the right with increasing temperature or R_1. At 1700–2400 K {S-shaped portion of the curve describing the dependence $[Pb(g)]_a = f(T_c)$}, virtually no oxide is formed yet and nearly the entire amount of lead is present in free state in equilibrium between the liquid and gas phases.

Replacing in the above-described program searching for compositions with 20% zinc the parameters of Eqs. (1) and (2) for the respective parameters obtained for compositions with lead allows a search for suitable compositions in the same way as it was described for the case of zinc.

A similar analysis can be performed for many other metals: theoretically, a formulation can always be obtained with extremely high ΔH_f^0 value to raise the combustion temperature at low R_1. For example, even if a combustible formulation with elemental composition $C_xH_{2x}N_xO_{2x}$ or $C_xH_{2x}N_xO_{3x}$ with extremely high (ΔH_f^0 = +3000 kcal kg^{-1}, which is absolutely unrealistic) enthalpy of formation could be created in a mixture with aluminum, this would give a content of gaseous metal not exceeding 30%. However, if high-enthalpy compositions with extremely low, or even zero content of oxygen are used, e.g., dicyanoacetylene {N≡C–C≡C–C≡N, $\Delta H_{f(l)}^0$ = +119.6 kcal mol^{-1} = 1574 kcal kg^{-1} [4]}, for which the nozzle exit temperature of about 3000 K is achieved, the share of gaseous aluminum may exceed 60–70%.

In addition to the considered zinc and lead, the described scheme can well be used for bismuth. This was done in the same volume as in the case of zinc and lead to give the results close to those for lead. There is no need to consider these results in more detail since, in our opinion, the case of bismuth is of no practical value. Solving the problem for copper is a somewhat more complicated task since, because of the lower volatility of copper, higher combustion temperatures are necessary to make higher the yield of gaseous metal. A composition containing 10% metallic copper mixed with TNC gives in combustion under the above-described conditions 67% of the metal in the form of gas. Introduction of MNC, DNC, octogen, or even acetylene into the composition fails to raise the output of gaseous metal. However, use of a more powerful oxidant—ADNA, with acetylene as combustible, raises to 95% the content of gaseous copper. If liquid acetylene-containing compounds with empirical formula C_nH_n with $\Delta H_f^0 \approx +1000$ kcal kg^{-1} (quite a number of such compounds are known) are used as a combustible in combination with ADNA, then yields of gaseous copper of up to 76% are achieved. As for compositions with iron, nickel, and especially chromium, i.e., metals less volatile than copper and having higher oxygen affinity, the problem of creating such formulations is rather difficult to solve.

CONCLUSIONS

(1) Combustible formulations can be composed on the basis of readily available components, ensuring nearly 100% content of gaseous cadmium, zinc, lead, or bismuth in combustion products.

(2) An analysis of how the yield of gaseous metal (Zn, Pb, Bi) in isoentropic burning of a combustible formulation depends on its elemental composition and enthalpy of formation gave: (a) empirical equations relating the chemical composition of a starting combustible formulation, its enthalpy of formation, temperatures in the chamber and the nozzle exit, and the yield of gaseous metal; and (b) programs for finding satisfactory combustible formulations, with their components chosen from the available component database.

(3) A thermodynamic calculation established that a combustible formulation containing 10% copper and trinitrocellulose can be created, whose combustion gives about 67% of the metal in the gaseous form.

REFERENCES

1. Matting, A., British Weld. J., 1966, *Sept.*, pp. 526–532.
2. Sinyarev, G.B., Vatolin, N.A., Trusov, B.G., and Moiseev, G.K., *Primenenie EVM dlya termodinamicheskikh raschetov metallurgicheskikh protsessov* (Use of Computers in Thermodynamic Calculations of Metallurgical Processes), Moscow: Nauka, 1982.
3. Luk'yanov, O.A. and Tartakovskii, V.A., *Ross. Khim. Zh.*, 1997, vol. 41, no. 2, part 1, pp. 5–13.
4. Armstrong, G.T. and Maratz, S., *J. Phys. Chem.*, 1963, vol. 67, no. 12, pp. 2888–2890.

Russian Journal of Applied Chemistry, Vol. 74, No. 6, 2001, pp. 945–949. Translated from Zhurnal Prikladnoi Khimii, Vol. 74, No. 6, 2001, pp. 920–923.

SORPTION AND ION-EXCHANGE PROCESSES

Extractive Recovery of Tantalum(V) and Niobium(V) with Octanol from Hydrofluoric Acid Solutions Containing Large Amounts of Titanium(IV)

V. G. Maiorov, A. I. Nikolaev, L. I. Sklokin, and I. V. Baklanova

Tananaev Institute of Chemistry and Technology of Rare Elements and Mineral Raw Materials, Kola Scientific Center, Russian Academy of Sciences, Apatity, Murmansk oblast, Russia

Received April 11, 2000

Abstract—Extractive recovery with *n*-octanol of tantalum(V) and niobium(V) from hydrofluoric acid solutions containing large amounts of titanium (up to 2–3 M) was studied. The conditions were found for separation of tantalum(V) and niobium(V) from titanium(IV), allowing recovery of 95.7 and 84.1% of tantalum and niobium fluoride complexes, respectively, in one extraction cycle, with 2.6% recovery of titanium.

Extractive recovery of tantalum(V) and niobium(V) is performed under industrial conditions with methyl isobutyl ketone and, more seldom, with tributyl phosphate [1]. These extractants have several substantial drawbacks: methyl isobutyl ketone is dangerously explosive and is highly soluble in the aqueous phase; tributyl phosphate is toxic and is readily converted to other phosphorus-containing compounds contaminating the final product. Alcohols are characterized by extraction features close to those of methyl isobutyl ketone. Extraction of tantalum(V) and niobium(V) with alcohols has been studied insufficiently [1]. Several reports concerning extraction processing of relatively pure niobium-tantalum raw material with the use of octanol as extractant have been published recently [2–4]. No data on extractive recovery of tantalum(V) and niobium(V) from solutions containing large amounts of foreign metals are known.

In this work, tantalum(V) and niobium(V) were extracted with *n*-octyl alcohol (OCL). This extractant is free of the above-noted drawbacks of methyl isobutyl ketone and tributyl phosphate and is commercially produced in Russia. Tantalum(V) and niobium(V) were recovered from titanium fluoride solutions in hydrofluoric acid containing no other mineral acids. These solutions are formed in processing loparite with hydrofluoric acid [5, 6]. They contain small amounts of tantalum(V) and niobium(V), ~0.0045 and ~0.11 M, respectively, and a large amount of titanium (up to 2–3 M). It has been reported previously [7-11] that the effect of fluorotitanic acid on the extraction of tantalum(V) fluoride is close to that of sulfuric acid.

The aim of this work was to study the possibility of preparing pure compounds of tantalum(V) and niobium(V) by their extraction from solutions containing large amounts of titanium(IV) without introduction of additional mineral acids hindering HF recovery from spent process solutions [5, 6]. Extraction of tantalum(V) and niobium(V) from hydrofluoric-sulfuric acid solutions was reported in [2–4].

Procedures for preparing solutions, performing experiments, analysing target metals, and safely handling chemically aggressive hydrofluoric acid solutions have been reported in detail previously [1]. Characteristics of octyl alcohol used in our experiments were as follows: main substance content about 98% (content of 3-octanol as an impurity was less then 0.5%), solubility in water 0.05 wt %, density 0.824 g cm^{-3}, mp 15–16°C, bp 195°C, and flash point 81°C. The extraction was performed in the course of 5 min. Preliminary experiments showed that the extraction equilibrium is attained at a contact time of no more than 3 min.

The data on the effect exerted by the solution composition and ratio of the organic and aqueous phases $V_o : V_a$ on the distribution of the main components are listed in the table, where HF_{free} is the HF concentration calculated as the difference between the total HF concentration and the HF amount in the main complexes $HTa(Nb)F_6$, H_2TiOF_4, and H_2SiF_6 formed in the systems [1, 11–13].

Since the degree of tantalum(V) recovery exceeds 90% throughout its concentration range, the main goal was to search for conditions for extraction

1070-4272/01/7406-0945 $25.00 © 2001 MAIK "Nauka/Interperiodica"

Extraction of tantalum(V), niobium(V) and titanium(IV) from hydrofluoric acid aqueous solutions

Run no.	HF_{free}, M	$V_o : V_a$	Concentration, M				Recovery, %		
			Ti(IV)	Ta(V)	Nb(V)	Si(IV)	Ta(V)	Nb(V)	Ti(IV)
1	4.5	1 : 1	1.88	0.0068	0.15	0.20	95.8	36.5	0.23
2	4.5	1 : 1	3.12	0.0034	0.075	0.10	>93	50.7	12.8
3	4.5	2 : 1	1.88	0.0034	0.075	0.10	>93	49.3	0.46
4	4.5	2 : 1	3.12	0.0068	0.15	0.20	>97	71.3	23.8
5	4.0	1.6 : 1	2.50	0.0045	0.11	0.15	>90	57.5	9.11
6	4.0	2 : 1	2.50	0.0045	0.11	0.15	>90	61.7	10.6
7	4.5	2 : 1	2.50	0.0045	0.11	0.15	>90	66.1	–
8	5.0	1.8 : 1	2.50	0.0045	0.11	0.15	>90	73.0	8.95
10	6.0	2 : 1	2.50	0.0045	0.11	0.15	>90	83.5	7.13
11	9.0	1 : 1	2.50	0.0045	0.11	0.15	97.3	81.8	3.05

of niobium(V), with minimum amount of titanium(IV) passing into the organic phase. This is particularly important because of a high molar ratio of titanium(IV) and niobium(V) in the aqueous phase (up to 40 : 1).

At low HF_{free} content (run nos. 1–4), the extraction of niobium(V) and especially titanium(IV) is most strongly influenced by the concentration of titanium(IV), occurring in the form of fluorotitanic acid, as a source of protons. With the titanium(IV) content increasing from 1.88 to 3.12 M, the extraction of niobium(V) (depending on the ratio $V_o : V_a$) grows from 36.5–49.3 to 50.7–71.3%, and that of titanium(IV), from 0.23–0.46 to 12.8–23.8%. Introduction into the system of additional HF (run nos. 5–10) improves the recovery of niobium(V) to the acceptable level of about 80%. Such conditions also ensure lower recovery of titanium(IV). Variation of the HF concentration affects the niobium(V) distribution to a greater extent than does the variation of the $V_o : V_a$ ratio. Under the optimal conditions (run no. 11), exhaustive extraction of tantalum(V) and niobium(V) is readily reached in continuous countercurrent extraction at relatively low recovery of titanium(IV) (about 3%).

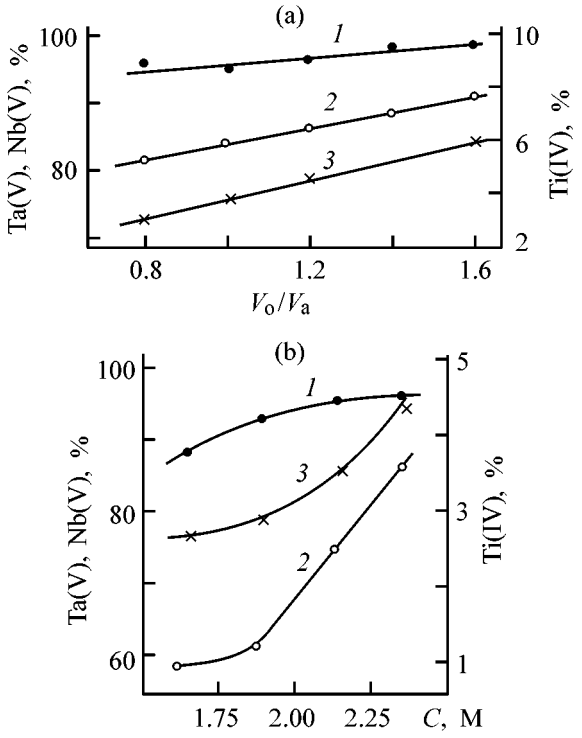

Fig. 1. Effect of (a) volume ratio of the organic and aqueous phases (V_o/V_a) and (b) titanium(IV) concentration C on distribution of (*1*) tantalum(V), (*2*) niobium(V), and (*3*) titanium(IV). *Ordinate*: recovery of indicated elements.

Figure 1a shows the effect of variation of the $V_o : V_a$ ratio on the distribution of the main metals. The extraction was performed from aqueous solutions of the following composition (M): Ta(V) 0.0047, Nb(V) 0.11, Ti(IV) 2.34, Si(IV) 0.14, and HF_{free} 8. With decreasing $V_o : V_a$, the recovery of Ta(V), Nb(V), and Ti(IV) decreases. The recovery of these metals varies in direct proportion to $V_o : V_a$. The slopes of the straight lines increase in the order tantalum(V) < niobium(V) < titanium(IV), which correlates with the order of increasing extractability of fluoride complexes of the elements in question: tantalum(V) > niobium(V) > titanium(IV) [1].

Figure 1 shows that, with the $V_o : V_a$ ratio decreasing by a factor of two, the amount of titanium passing into the organic phase decreases to the same extent, and only a minor amount of niobium(V) passes into the organic phase. However, owing to the high titanium(IV) concentration in the initial solution, the molar ratio Ti(IV) : Nb(V) in the organic phase in exhaustive recovery of niobium(V) by means of continuous countercurrent extraction is considerable: about 0.67 : 1

even at $V_o : V_a = 0.8$. This ratio is lower than that in the initial solution (21 : 1) by a factor of approximately 30, but, nevertheless, this indicates that the organic phase should be washed effectively to remove titanium(IV) impurities.

The trends in extraction of metals (Fig. 1a) suggest that the $V_o : V_a$ ratio can be decreased further, which must make lower the coextraction of titanium(IV) with niobium(V) and tantalum(V).

The distribution of the target metals is shown in Fig. 1b as influenced by the titanium concentration. In these experiments, the composition of the initial solution was the same as in Fig. 1a. It should be noted that lowering the titanium(IV) concentration to less than 2.3 M results in a sharp decrease in extraction of both titanium(IV) (positive effect) and niobium(V). At titanium(IV) concentrations lower than 1.6 M, the distribution of titanium(IV) and niobium(V) fluoride complexes weakly depends on the titanium(IV) amount because the extraction of the metals is apparently controlled by the HF content under these conditions.

In our extraction system, both niobium(V) and titanium(IV) are extracted in the form of fluorometallic acids by the hydrate-solvate mechanism [1, 14]. If no additional mineral acids are introduced into the system, then fluorotitanic acid, predominantly H_2TiOF_4, becomes the main source of protons. Therefore, with decreasing titanium(IV) content in the system, the recovery of niobium(V) and tantalum(V) diminishes. It is evident that the above-noted critical titanium(IV) concentration, equal to 2.3 M, is virtually the concentration of dibasic H_2TiOF_4 acid present in this solution, which is equivalent, in terms of proton content in the system, to 2.3 M H_2SO_4 (approximately 230 g l^{-1}). According to the data reported in [1] for approximately the same concentration, the dependence of niobium(V) recovery with oxygen-containing organic extractants on the H_2SO_4 concentration, as a rule, starts to change. This fact shows that both titanium(IV) and H_2SO_4 affect the distribution of niobium(V) fluoride complexes by the identical mechanisms.

Our experimental results show also that, with increasing HF concentration facilitating the formation of the readily extractable complex $HNbF_6$ [1, 14], the recovery of niobium(V) grows. The dependence of the extraction of titanium(IV) on the HF content, or, more precisely, on the ratio HF : Ti(IV), is more complicated. Titanium(IV) forms fluorotitanic complexes of various compositions exhibiting different extractability. According to the data reported in [1, 14], the recovery of titanium(IV) increases in the order $H_2TiOF_4 < H_2TiF_6 < HTiF_5$. It was noted above that the complex H_2TiOF_4 is predominantly formed in the system under consideration. Therefore, the fraction of titanium passing into the organic phase is relatively low and its variations are mainly caused by variations in the contributions of H_2TiF_6 and $HTiF_5$ complexes to the total content of the fluorotitanic acids in the aqueous phase. Therefore, with increasing HF concentration, first the recovery of titanium can be expected to grow owing to the formation of a readily extractable monobasic acid $HTiF_5$ and then to decrease through an increase in the concentration of the less extractable acid H_2TiF_6. This complicated extraction system deserves separate study.

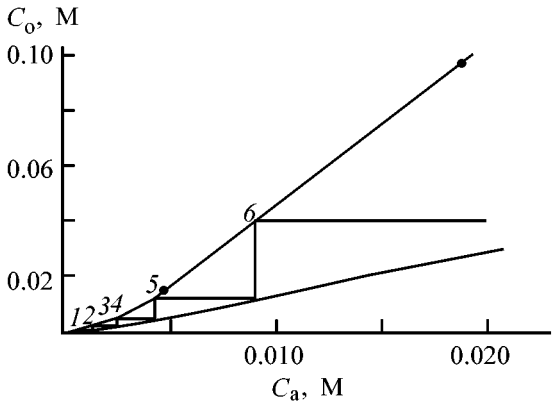

Fig. 2. Extraction isotherm of niobium(V) at HF_{free} concentration of 8.2 M and $V_o/V_a = 1 : 1$. (C_o, C_a) niobium(V) concentration in the organic and aqueous phases, respectively. (*1*–*6*) For comments, see text.

Figure 2 shows an extraction isotherm of niobium(V) obtained by the "exhaustion" technique. According to this technique, the metals were successively extracted four times from aqueous solution with the initial composition close to that given in Fig. 2. In the first extraction, the recovery was 95.7% for tantalum(V), 84.1% for niobium(V), and 2.6% for titanium(IV). In each subsequent extraction with OCL, the recovery of niobium falls owing to a decrease in the titanium(IV) and HF_{free} concentrations. This is one of the main drawbacks of the exhaustion technique.

The plot in Fig. 2 shows that, for the working line corresponding to $V_a : V_w = 1 : 0.7$ (slope of the working line) and a residual niobium(V) concentration of 0.00058 M [99.5% recovery of niobium(V)], six successive equilibrium stages are necessary for continuous countercurrent extraction. Since the recovery of niobium(V) is deteriorated in the course of the "exhaustion" extraction, the actual number of the extraction stages should be lower. A calculation by the well-known Kremers equation [15] showed that

General flowsheet for preparation of pure niobium(V) and tantalum(V) compounds by extraction from hydrofluoric acid solutions with OCL.

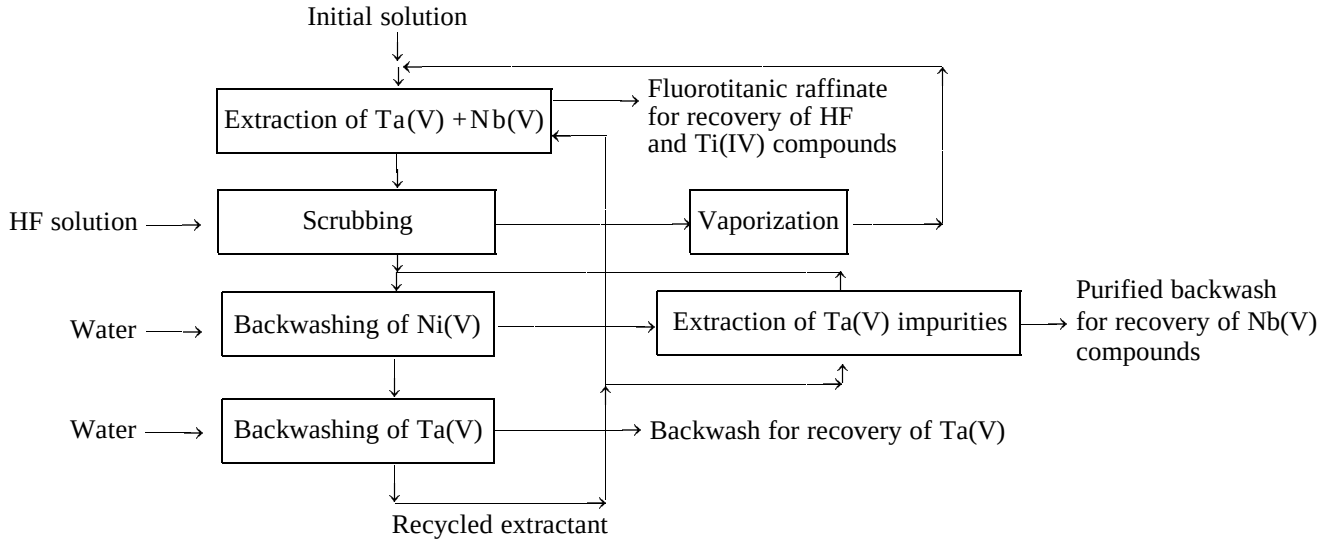

at a constant degree of niobium(V) recovery equal to 84% (in the first extraction stage) the niobium(V) recovery by 99.9% is reached with only four stages of continuous countercurrent extraction.

We also performed preliminary studies of scrubbing of the organic phase containing tantalum(V) and niobium(V) to remove titanium(IV) impurities. It was found that, with 25 M HF ($V_a : V_o$ = 0.088 : 1), 72% of titanium and approximately 10% of niobium(V) and tantalum(V) pass from the organic phase in a single scrubbing into the hydrofluoric acid solution containing 0.0046 M Ta(V), 0.095 M Nb(V) and 0.062 M Ti(IV). With increasing volume of the scrubbing solution ($V_a : V_o$ = 0.17 : 1), the amount of titanium(IV) passing into the aqueous phase slightly increases (to 77%). However, under these conditions, the amount of titanium(IV) and niobium(V) passing into the scrubbing solution grows, too.

Further processing of washed extract can be done by successive backwashing of niobium(V) and tantalum(V) with water, similarly to processing of the loparite solutions with methyl isobutyl ketone as extractant with basicity close to that of OCL [1, 2].

In this paper, we present a general flowsheet for treatment of solutions formed in hydrofluoric acid processing of loparite [5, 6]. This flowsheet is based both on our experimental results and on published data [1, 2–4, 14]. Processing of dilute niobium–tantalum solutions containing up to 2–3 M titanium by this technique allows preparation of pure niobium(V) and tantalum(V) compounds.

CONCLUSIONS

(1) The influence exerted by the composition of aqueous solutions and ratio of the organic and aqueous phases $V_o : V_a$ on the distribution of tantalum(V) and titanium(IV) in their extraction from hydrofluoric acid aqueous solutions containing large amounts of titanium(IV) with *n*-octanol was studied.

(2) Within the concentration range studied the recovery of tantalum exceeds 90%, the recovery of niobium(V) is high, at a concentration of HF_{free} and titanium(IV) of no less than 8 and 2.3 M, respectively.

(3) Conditions for separation of tantalum(V) and niobium(V) from titanium(IV) were found at which no more than 3% of titanium(IV) passes into the organic phase.

(4) Continuous countercurrent extraction of tantalum(V) and niobium(V) allows complete recovery of these metals in 4–6 extraction stages.

(5) General flowsheet for preparation of pure niobium(V) and tantalum(V) compounds by extraction from fluorotitanic solutions with OCL was developed.

REFERENCES

1. Babkin, A.G., Maiorov, V.G., and Nikolaev, A.I., *Ekstraktsiya niobiya, tantala i drugikh elementov iz ftoridnykh rastvorov* (Extraction of Niobium, Tantalum and Other Elements from Fluoride Solutions), Leningrad, Nauka, 1988.

2. *Hydrometallurgical Extraction of Tantalum and Niobium in China*. Tantalum–Niobium International Study Center (T.I.C.), 1988, Bull. no. 93, pp. 1–5.
3. Travkin, V.F., Agulyanskii, A.I., Glubokov, Yu.M., and Karamushko, E.V., *Tsvetn. Metall.*, 1998, nos. 8–9, pp. 18–22.
4. Travkin, V.F., Agulyanskii, A.I., Glubokov, Yu.M., and Karamushko, E.V., *Tsvetn. Metall.*, 1999, no. 4, pp. 19–22.
5. Sklokin, L.I., Abstracts of Papers, *Khimiya i tekhnologiya pererabotki kompleksnogo syr'ya Kol'skogo poluostrova* (Chemistry and Technology of Processing of Multicomponent Raw Materials of the Kola Peninsula) Scientific Conf., Apatity, April 12–24, 1996, pp. 12–15.
6. Kalinnikov, V.T., *Zh. Prikl. Khim.*, 1997, vol. 70, no. 5, pp. 705–712.
7. Nikolaev, A.I., Maiorov, V.G., Shevyreva, E.V., and Il'in, E.G., Abstracts of Papers, *Int. Solvent Extraction Conf. (ISEC'90), Kyoto, July 16–21*, 1990, p. 165.
8. Nikolaev, A.I., Maiorov, V.G., Shevyreva, E.V., *et al.*, *Zh. Neorg. Khim.*, 1992, vol. 37, no. 6, pp. 1403–1407.
9. Maiorov, V.G., Nikolaev, A.I., Shevyreva, E.V., and Zalkind, L.M., *Zh. Neorg. Khim.*, 1992, vol. 37, no. 6, pp. 1414–1418.
10. Mayorov, V.G. and Nikolaev, A.I., *Hydrometallurgy*, 1996, vol. 41, no. 1, pp. 71–78.
11. Mayorov, V.G., Nikolaev, A.I., and Kopkov, V.K., *Zh. Prikl. Khim.*, 1999, vol. 72, no. 6, pp. 929–932.
12. Ryss, I.G., *Khimiya ftora i ego neorganicheskikh soedinenii* (Chemistry of Fluorine and Its Inorganic Compounds), Moscow: Goskhimizdat, 1956, p. 718.
13. Buslaev, Yu.A., Nikolaev, A.I., Ilyin, E.G., and Mayorov, V.G., *J. Fluorine Chem.*, 1985, vol. 29, nos. 1–2, p. 51.
14. Zolotov, Yu,A., Iofa, B.Z., and Chuchalin, P.K., *Ekstratsiya galogenidnykh kompleksov metallov* (Extraction of Metal Halide Complexes), Moscow: Nauka, 1973.
15. Al'ders, L., *Zhidkostnaya ekstraktsiya* (Liquid Extraction), Moscow: Inostrannaya Literatura, 1962.

Russian Journal of Applied Chemistry, Vol. 74, No. 6, 2001, pp. 950–953. Translated from Zhurnal Prikladnoi Khimii, Vol. 74, No. 6, 2001, pp. 924–927.

SORPTION AND ION-EXCHANGE PROCESSES

Vanadium(V) Sorption by Organosilicon Polymers

A. I. Kirillov, E. V. Panezhda, N. N. Vlasova, Yu. N. Pozhidaev, O. A. Minchenko, L. I. Belousova, and M. G. Voronkov

Irkutsk State University, Irkutsk, Russia

Irkutsk Institute of Chemistry, Siberian Division, Russian Academy of Sciences, Irkutsk, Russia

Received July 13, 2000; in final form, January 2001

Abstract—Features of vanadium(V) sorption by cross-linked organosilicon polymers—polyorganylsilsesquioxanes containing acetamide, phthalamide, malondiamide, and thiourea dioxide functional substituents, were studied.

Polymers studied in this work contain carbofunctional substituents with nitrogen, oxygen, and sulfur atoms and can exhibit complex-forming and ion-exchange properties with respect to many elements. The cross-linked organosilicon polymers poly[*N*-(3-silsesquioxanylpropyl)acetamide] (PSMA-3) and poly[bis-*N*,*N*'-(3-silsesquioxanylpropyl)phthalamide] (PSF-3) are efficient sorbents of rare-earth elements [1]. In [2], sorption of gold, silver, and platinum by poly[bis-*N*,*N*'-(3-silsesquioxanylpropyl)thiourea dioxide] (PSOT-3) was studied. It is known that vanadium(V) is also recovered with sorbents containing oxygen and nitrogen atoms in the functional groups [3–5]. Therefore, a study of the sorption power of PSOT-3, PSF-3, PSMA-3, and poly[bis-*N*,*N*'-(3-silsesquioxanylpropyl)-malonamide] (PSMD-3) with respect to vanadium(V) ions is of interest:

$[O_{1.5}Si(CH_2)_3NH–C(SO_2)–NH–(CH_2)_3SiO_{1.5}]_n$,
PSOT-3

$\{[O_{1.5}Si(CH_2)_3NHC(O)]_2C_6H_4\}_n$,
PSF-3

$[O_{1.5}Si(CH_2)_3NHC(O)CH_3]_n$,
PSMA-3

$[O_{1.5}Si(CH_2)_3NH–CO–CH_2–NH–CO(CH_2)_3–SiO_{1.5}]_n$.
PSMD-3

EXPERIMENTAL

The static sorption of V(V) by the above polymers was studied. A sorbent sample was vigorously agitated with V(V) solution for the optimal time. Then the sorbent was separated from the liquid phase by filtration. The residual amount of V(V) in the solution was monitored spectrophotometrically [6] and by the atomic-absorption method. Chemically pure reagents were used. A stock V(V) solution (1 g l^{-1}) was prepared from NH_4VO_3. Less concentrated solutions were prepared by dilution of the stock solution.

The most important factors affecting the sorption are the V(V) concentration and pH. At V(V) concentration less than 1×10^{-4} g-ion l^{-1}, the following monomeric species exist in equilibrum in the solution:

$$VO_2^+ \overset{+OH^-}{\rightleftarrows} HVO_3 \overset{-H^+}{\rightleftarrows} VO_3^- \overset{+OH^-}{\rightleftarrows} HVO_4^{2-} \overset{-H^+}{\rightleftarrows} VO_4^{3-}.$$

VO_2^+, VO_3^-, HVO_4^{2-}, and VO_4^{3-} species prevail at pH 0–3, 3.5–8, 8.0–12.0, and 12–14, respectively. At vanadium concentrations higher than 1×10^{-4} and pH 0–3, VO_2^+ species remain prevalent. With decreasing acidity (pH > 3), these species react with OH^- ions to form vanadium polyions. For instance, at pH 5.0–8.0 the $V_3O_9^{3-}$ and $V_4O_{12}^{4-}$ ions and at pH 10–12, the $H_2V_2O_7^{2-}$ ions exist in the solution. Condensation of these ions yields more complex polyions [7, 8]. Our experimental data confirm the above pattern. As seen from the figure, the V(V) sorption starts at pH 1, reaches a maximum at pH 3, and then decreases with pH growing further.

The polymers PSF-3, PSMA-3, and PSMD-3 have similar structures as polymeric derivatives of carboxylic acid amides. It is known that the amide group **I** exhibits prototropy and can react in the tautomeric isoamide form **II**:

1070-4272/01/7406-0950 $25.00 © 2001 MAIK "Nauka/Interperiodica"

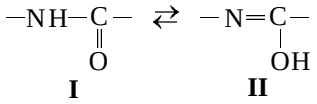

I **II**

Thus, V(V) can be sorbed by the ion-exchange mechanism in accordance with the scheme

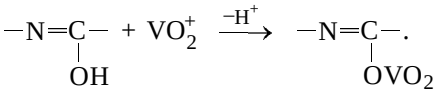

However, the VO_2^+ reaction by the donor–acceptor mechanism with the formation of chelate complexes is also possible:

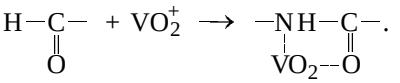

A specific feature of PSOT-3 is that it efficiently recovers V(V) within the pH range 2–9. This is probably due to reaction of V(V) with thiourea dioxide group of the polymer, having the zwitterionic structure.

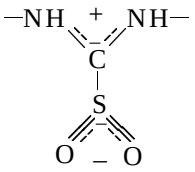

As a result, PSOT-3 is able to bind both cationic VO_2^+ and anionic VO_3^- vanadium species.

A study of the degree of recovery as a function of the phase contact time showed that the sorption equilibrium in V(V) solutions is reached in 60 min, and the main part of the metal is recovered in 10–20 min with all the sorbents (Table 1).

The effect of the ionic strength μ of solution was studied for the example of NaCl. It was found that with the ionic strength increasing to 0.25 (C_{NaCl} > 15 g l^{-1}) the V(V) recovery decreases, and, within the $0.25 < \mu < 1$ range, the metal sorption is sharply suppressed. The PSMA-3 polymer does not recover V(V) from solutions with μ exceeding 0.25. Probably, this is due to competitive interaction of VO_2^+ species with chloride ions to form negatively charged complexes. To determine the sorption capacity, the V(V) recovery from solutions was studied as a function of metal concentration, the sorption isotherms were obtained, and then the static sorption capacities SSC (mg g^{-1}) and distribution coefficients D (cm^3 g^{-1}) were calculated (Table 2). The sorption capacities of PSOT-3 and PSMD-3 and the distribution coefficients show that these sorbents can be used for recovery and concentration of V(V) trace amounts from solutions of both artificial and natural origin.

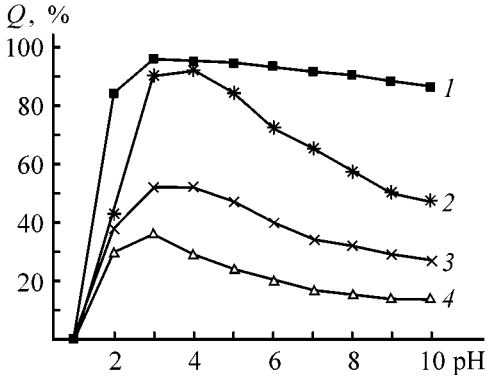

Degree of V(V) recovery Q vs. pH. Sorbent: (*1*) PSOT-3, (*2*) PSMD-3, (*3*) PSF-3, and (*4*) PSMA-3.

To determine the possibility of vanadium recovery from multicomponent solutions, the V(V) sorption in the presence of Co(II), Cd(II), Cu(II), Ni(II), Zn(II), Mo(VI), and U(VI) was studied (Table 3). It was found that 100-fold excess of Co(II), Cd(II), Cu(II), Ni(II), and Zn(II) does not hinder vanadium(V) sorption by PSOT-3 and PSMD-3, and their 10-fold excess, V(V) sorption by PSF-3. Mo(VI) and U(VI) do not hinder V(V) sorption by PSOT-3 at V : M ratio of 1 : 1.

Table 1. Degree of vanadium(V) recovery (m_{sorb} 20 mg, $C_{V(V)}$ 30 mg l^{-1}, V 20 ml, pH 3)

τ, min	Recovery, %			
	PSOT-3	PSF-3	PSMA-3	PSMD-3
5	35	30	10	31
10	54	40	17	50
20	72	47	25	76
30	82	53	31	85
60	91	63	39	92
90	91	66	36	93
120	90	64	35	92

Table 2. Sorption capacities and distribution coefficients of V(V) (m_{sorb} 20 mg, V 20 ml, pH 3)

Sorbent	SSC, mg g^{-1}	D, cm^3 g^{-1}
PSOT-3	400	2.2×10^4
PSMD-3	408	3.5×10^4
PSF-3	120	1.0×10^4
PSMA-3	50	9.2×10^3

Table 3. Degree of V(V) recovery in the presence of various elements ($C_{V(V)}$ 30 mg l^{-1}, V 20 ml, pH 3, τ 2 h)

M, mg	V(V) : M	Recovery, %			M, mg	V(V) : M	Recovery, %		
		PSMD-3	PSOT-3	PSF-3			PSMD-3	PSOT-3	PSF-3
Not added	–	92	95	67	Cd(II):				
Ni(II):					0.6	1 : 1	90	95	65
0.6	1 : 1	91	94	69	6	1 : 10	94	97	66
6	1 : 10	93	94	66	60	1 : 100	84	93	33
60	1 : 100	79	94	58	600	1 : 1000	70	73	38
600	1 : 1000	59	80	42	Cu(II):				
Co(II):					0.6	1 : 1	90	96	64
0.6	1 : 1	90	95	67	6	1 : 10	93	93	66
6	1 : 10	92	96	68	60	1 : 100	91	87	49
60	1 : 100	85	94	45	600	1 : 1000	53	63	39
600	1 : 1000	38	46	37	Mo(VI):				
Zn(II):					0.6	1 : 1	–	95	–
0.6	1 : 1	92	95	65	6	1 : 10	–	60	–
6	1 : 10	91	95.9	64	U(VI):				
60	1 : 100	87	94	39	0.6	1 : 1	–	96	–
600	1 : 1000	60	70	30	6	1 : 10	–	79	–

Table 4. Effect of desorbent nature on the degree of vanadium desorption

Desorbing agent	Desorption, %			
	PSOT-3	PSMA-3	PSF-3	PSMD-3
HCl 3 M	89	70	88	95
NaOH 10%	96	98	98	97
H_2O_2 5%	12	10	0	14
NH_4OH (1 : 4)	96	98	99	97
Na_2CO_3 10%	99	100	98	97

Table 5. Sorption–extraction–photometric determination of V(V) in artificial mixtures (m_{sorb} 0.2 g, V 200 ml, pH 3, n 4, P 0.95)

Introduced,* mg l^{-1}	Found, mg l^{-1}	S_r
0.05	0.06 ± 0.01	0.15
0.1	0.08 ± 0.02	0.14
0.5	0.5 ± 0.1	0.14
0.9	0.8 ± 0.2	0.13
2.0	1.9 ± 0.3	0.13

* Solution composition, mg l^{-1}: Cu(II), Cd(II), Zn(II), Co(II), and Ni(II) 15; Mo(VI) and U(VI) 1; NaCl 15.

For repeated use of the above sorbents, we studied the V(V) desorption from the surface of PSOT-3, PSMD-3, PSMA-3, and PSF-3 sorbents. The choice of desorbing agents was governed by their complexing properties with respect to V(V). It follows from Table 4 that V(V) desorption is virtually completely effected by hydrochloric acid, ammonium hydroxide, and sodium carbonate. They do not produce any substantial changes in the sorbent structures. The polymers preserve their sorption properties and can be used repeatedly.

Using the above data, we performed recovery and concentration of V(V) from model solutions with PSOT-3 and found that vanadium is recovered from solutions completely (Table 5).

A statistical treatment of sorption data demonstrated their good reproducibility. For instance, at a V(V) concentration of 0.05–30.0 mg l^{-1} the relative standard deviation S_r was 0.13–0.15.

CONCLUSION

Organosilicon polymers poly[bis-*N*,*N*'-(3-silsesquioxanylpropyl)thiourea dioxide] and poly[bis-*N*,*N*'-(3-silsesquioxanylpropyl)malonamide] are rather efficient sorbents of V(V) and can be recommended for concentration, separation, and determination of this element in multicomponent solutions.

REFERENCES

1. Vlasova, N.N., Kirillov, A.I., Pozhidaev, Yu.N., *et al.*, *Dokl. Ross. Akad. Nauk*, 1999, vol. 364, no. 4, pp. 492–494.
2. Vlasova, N.N., Pozhidaev, Yu.N., Raspopina, O.Yu. *et al.*, *Zh. Obshch. Khim.*, 1999, vol. 69, no. 9, pp. 1446–1449.
3. Vernon, F., *Pure Appl. Chem.*, 1982, vol. 54, no. 11, pp. 2151–2158.
4. Sadikova, Z.A., Tikhomirova, T.I., and Lapukh, A.V., *Zh. Anal. Khim.*, 1997, vol. 52, no. 3, pp. 234–236.
5. Liu Chuen-Ging and Sun Peng-Young, *Talanta*, 1984, vol. 31, no. 5, pp. 353–356.
6. Marczenko, Z., *Kolorymetryczne oznaczanie pierwiastkow*, Warszawa: Wydawnictwa Naukowa-techniczne, 1968.
7. Luzin, V.N., Khamzina, L.B., Zolotavin, V.L., *et al.*, *Analiticheskaya khimiya vanadiya* (Analytical Chemistry of Vanadium), Moscow: Nauka, 1981.
8. Morachevskii, Yu.V. and Tserkovnitskaya, I.A., *Osnovy analiticheskoi khimii redkikh elementov* (Fundamentals of Analytical Chemistry of Rare Elements), Leningrad: Leningr. Gos. Univ., 1980,
9. Mathieu, J. and Panico, R., *Mécanismes réactionnels en chimie organique*, Paris: Hermann, 1972.

Russian Journal of Applied Chemistry, Vol. 74, No. 6, 2001, pp. 954–957. Translated from Zhurnal Prikladnoi Khimii, Vol. 74, No. 6, 2001, pp. 927–930.

SORPTION AND ION-EXCHANGE PROCESSES

Precipitation Recovery of Rhenium(VII) from Aqueous Solutions with Coagulating Cationic Polyelectrolyte

D. G. Petrov, I. D. Troshkina, A. M. Chekmarev, and A. B. Maiboroda

Mendeleev Russian University of Chemical Engineering, Moscow, Russia

Received January 31, 2001

Abstract—Rhenium(VII) recovery from dilute aqueous solutions by coprecipitation with VA-212 cationic polyelectrolyte in the presence of nitrate ions was studied.

In industry, rhenium (one of the least abundant chemical elements) is recovered from dilute but, as a rule, highly saline solutions [1, 2]. Sorption methods are the most frequently used in this case, but their use is restricted by low sorbent exchange capacity and slow metal sorption at its low concentrations.

The aim of this work was to study the use of water-soluble polyelectrolytes (PEs) for rhenium(VII) recovery from dilute mineralized solutions.

EXPERIMENTAL

A commercial cationic polyelectrolyte VA-212, polybisdimethylaminoisopropyl methacrylate alkylated with benzyl chloride and containing 3.4 mg-equiv g^{-1} of tertiary ammonium groups, was used.

Preliminarily, we studied the aggregation stability of VA-212 in solutions of various salts. It was found that this polyelectrolyte starts to coagulate in the presence of low-molecular-weight electrolytes (LME) when the LME concentration exceeds a certain limit C_t (coagulation threshold) depending on the LME nature. The concentration C_t was determined by the method based on variation of the optical properties of the disperse system during coagulation. Raising the LME concentration in the PE–LME system decreases the thermodynamic stability of the polyelectrolyte solution, and, on attaining C_t, spontaneous aggregation of polyelectrolyte macromolecules (coagulation) starts. The growth of aggregates increases the turbidity of the system because of the increasing light scattering and absorption [3]. The C_t value was experimentally determined from a jump discontinuity in the curve of the solution optical density vs. LME concentration.

The rhenium(VII) recovery was performed by PE precipitation from nitrate-containing solutions. A 2% solution of PE in distilled water was introduced into a solution containing sodium nitrate and ammonium perrhenate with agitation. The change in the rhenium(VII) concentration was monitored with the use of ^{188}Re tracer ($T_{1/2}$ = 16.7 h) [4]. The concentrations of the polyelectrolyte, nitrate ion, and rhenium were varied within 1.0–2.0 g dm^{-3}, 0.1–0.5 g-equiv dm^{-3}, and 0.5–10 mg dm^{-3}, respectively. The solution with the PE precipitate was agitated for 20 min and then filtered. After precipitate separation, the Re(VII) concentration was determined from the residual radioactivity of the solution. To determine the time in which thermodynamic equilibrium is attained between the precipitated PE and solution, a solution with the PE precipitate was stored with stirring for a week, and then the Re(VII) content was determined by the kinetic method with sulfonitrazo R [5]. The Re(VII) concentration in this solution was the same (within the analysis error) as in the solution contacting with PE for 20 min. Thus, we showed that this time is enough for equilibrium in the PE precipitate–solution system to be attained.

We studied the influence exerted by the nature of cations and anions of low-molecular-weight electrolyte on the coagulation threshold. Below are presented the threshold concentrations of sodium, potassium, ammonium, calcium, and nitric acid, causing precipitation of VA-212 polyelectrolyte at its concentration of 1 g dm^{-3}:

Nitrate of	Na^+	K^+	NH_4^+	Ca^{2+}	H^+
$C_t \times 10^2$, M	4.82	4.89	4.84	4.79	4.77

As seen, the coagulation threshold is practically independent of the nature of the low-molecular-weight

1070-4272/01/7406-0954 $25.00 © 2001 MAIK "Nauka/Interperiodica"

Table 1. Threshold of VA-212 polyelectrolyte coagulation for various salting-out agents

Agent	C_t (g-equiv dm^{-3}) at indicated PE concentration, g dm^{-3}					
	0.01	0.05	0.10	0.50	1.00	5.00
$HClO_4$	2.09×10^{-4}	1.98×10^{-4}	1.82×10^{-4}	1.77×10^{-4}	1.75×10^{-4}	1.76×10^{-4}
HI	9.81×10^{-4}	9.77×10^{-4}	9.78×10^{-4}	9.77×10^{-4}	9.76×10^{-4}	9.77×10^{-4}
HBr	4.05×10^{-2}	3.42×10^{-2}	3.35×10^{-2}	3.33×10^{-2}	3.31×10^{-2}	3.31×10^{-2}
NH_4NO_3	5.03×10^{-2}	4.91×10^{-2}	4.84×10^{-2}	4.82×10^{-2}	4.84×10^{-2}	4.84×10^{-2}
NaCl	1.94×10^{-1}	1.92×10^{-1}	1.90×10^{-1}	1.91×10^{-1}	1.91×10^{-1}	1.90×10^{-1}
$(NH_4)_2SO_4$	1.17	1.15	1.15	1.15	1.14	1.15
$NaNO_2$	3.21	3.07	3.06	3.06	3.07	3.06

electrolyte. Therefore, in further studies C_t was regarded as the limiting concentration of the anion causing coagulation.

In Table 1, the C_t values are listed for various LMEs as a function of the polyelectrolyte concentration. As seen, the coagulation threshold depends on the anion nature and remains constant for the given anion at polyelectrolyte concentration of 0.1 g dm^{-3}.

The distribution of ions in an electric double layer around the polyelectrolyte molecule depends on their polarizability. More polarizable ions can make closer approach to the macromolecular counterion. As a result, the charge of the macromolecule is shielded more effectively, and the coagulation threshold efficiency is lowered [6]. The molar refraction R_0 is the physical constant characterizing the polarizability of a molecule or an ion. It is a function of the refractive index and substance density and, to a first approximation, is proportional to polarizability. The coagulation thresholds found for VA-212 (at polyelectrolyte concentration of 1.0 g dm^{-3}) were compared with the ionic refractions of anions as saltingout agents [7]. Table 2 shows a linear $\log C_t$–R_0 dependence. The efficiency of oxygen-containing anions as precipitants of cationic polyelectrolytes substantially depends on the strength of the conjugated acids [6]. For the oxygen-containing anions studied (Table 2), it was found that $\log C_t$ is a linear function of pK_a, where K_a is the acid dissociation constant.

To predict the aggregative stability of polyelectrolytes in multicomponent solutions (containing several LME anions), we determined the coagulation thresholds in the VA-212–NO_3^-–SO_4^{2-} and VA-212–NO_3^-–Cl^- systems at varied ratio of anions. The choice of these anions was due to their high abundance in rhenium-containing process solutions (mine water, wastewater, and solutions of underground leaching). Table 3 and Figs. 1a and 1b show that sulfate and nitrate ions affect the VA-212 coagulation additively, and synergism of the anions is observed for the VA-212–NO_3^-–Cl^- system.

Table 2. $\log C_t$ of VA-212 polyelectrolyte, ionic refraction R_0, and pK_a of the conjugated acids for various anions ([PE] = 1.0 g dm^{-3})

Anion	$\log C_t$	$R_0 \times 10^6$, m^3 mol^{-1}	pK_a
ClO_4^-	–3.757	–	–8.0
I^-	–3.010	17.53	–11.0
Br^-	–1.480	11.60	–9.0
NO_3^-	–1.315	10.10	–1.6
Cl^-	–0.719	8.22	–7.0
SO_4^{2-}	0.059	–	1.9
NO_2^-	0.486	–	3.2

Table 3. Effect of nitrate ion concentration on sulfate and chloride concentrations required for VA-212 polyelectrolyte precipitation

$C^{NO_3^-}$, g-equiv dm^{-3}	$C^{NO_3^-}/C_t^{NO_3^-}$	$C^{SO_4^{2-}}/C^{Cl^-}$	$C^{SO_4^{2-}}/C_t^{SO_4^{2-}}$ ($C^{Cl^-}/C_t^{Cl^-}$)
Sulfate ions			
9.68×10^{-3}	0.2	0.87	0.76
1.94×10^{-2}	0.4	0.66	0.58
2.90×10^{-2}	0.6	0.42	0.34
3.39×10^{-2}	0.8	0.25	0.22
Chloride ions			
9.68×10^{-3}	0.2	0.13	0.66
1.94×10^{-2}	0.4	0.08	0.42
2.90×10^{-2}	0.6	0.052	0.27
3.39×10^{-2}	0.8	0.031	0.16

Table 4. Effect of VA-212 and nitrate ion concentrations on rhenium recovery ($[Re]_i = 1.07 \times 10^{-5}$ M)

$[NO_3^-]_i$, M	$[Re]_f \times 10^5$, M	Degree of rhenium recovery, %	K	$[NO_3^-]_i$, M	$[Re]_f \times 10^5$, M	Degree of rhenium recovery, %	K
[PE] = 1.0 g dm^{-3}				[PE] = 2.0 g dm^{-3}			
0.1	0.401	62.5	47.4	0.1	0.218	79.6	53.6
0.2	0.641	40.1	38.7	0.2	0.423	60.5	43.5
0.3	0.779	27.2	32.6	0.3	0.555	48.1	40.0
0.5	0.852	20.4	29.9	0.5	0.657	38.6	36.4

We also studied the effect of PE and nitrate ion concentrations on Re(VII) distribution between the precipitate and solution at coagulation of VA-212 (Table 4). The polyelectrolyte is precipitated in the form of nitrate. The precipitate captures trace amounts of ReO_4^- ions. The equation of the reversible exchange of the perrhenate ions between the solution and the precipitated (as nitrate) polyelectrolyte is as follows:

$$\underset{\text{Solution}}{ReO_4^-} + \underset{\text{Precipitate}}{[R_4N]NO_3} \rightleftarrows \underset{\text{Precipitate}}{[R_4N]ReO_4} + \underset{\text{Solution}}{NO_3^-}, \quad (1)$$

where R is the hydrocarbon skeleton of PE.

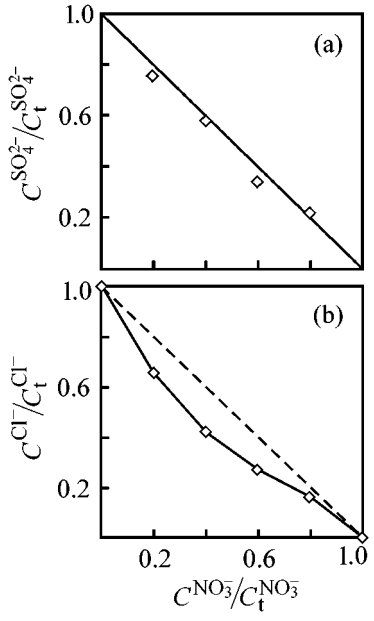

Fig. 1. Correlations of (a) $C^{SO_4^{2-}}/C_t^{SO_4^{2-}}$ and (b) $C^{Cl^-}/C_t^{Cl^-}$ with $C^{NO_3^-}/C_t^{NO_3^-}$.

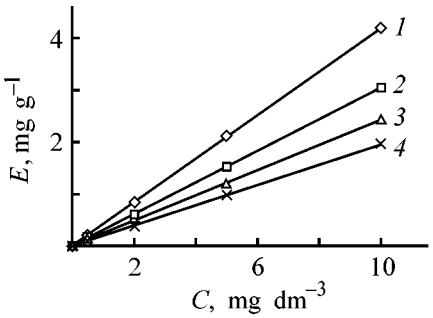

Fig. 2. VA-212 capacity E for rhenium(VII) vs. the Re(VII) concentration in the solution C. [PE] = 2 g dm^{-3}. Concentration of nitrate ions (M): (*1*) 0.1, (*2*) 0.2, (*3*) 0.3, and (*4*) 0.5.

The concentration equilibrium constant for reaction (1) can be presented as follows:

$$K = \frac{[ReO_4^-]_{PE}[NO_3^-]_f}{[ReO_4^-]_f[NO_3^-]_{PE}}, \quad (2)$$

where $[ReO_4^-]_f$ and $[NO_3^-]_f$ are the concentrations of the perrhenate and nitrate ions in the solution after separation of the PE precipitate (M) and $[ReO_4^-]_{PE}$, and $[NO_3^-]_{PE}$ are the concentrations of the perrhenate and nitrate ions in the phase of the PE precipitate (mol g^{-1}).

Assuming that the coagulated polyelectrolyte captures anions from the solution in amounts corresponding to the number of PE quatertiary ammonium groups (C_q = 3.4 mg-equiv g^{-1}), we can transform Eq. (2) into

$$K = \frac{[ReO_4^-]_i - [ReO_4^-]_f}{[ReO_4^-]_c} \cdot \frac{[NO_3^-]_i - C_q[PE]}{C_q[PE]}, \quad (3)$$

where $[ReO_4]_i$ and $[NO_3^-]_i$ are the concentrations of the perrhenate and nitrate ion in the solution before introduction of PE (M), and [PE] is the concentration of PE introduced into the solution (g dm^{-3}).

The degree of Re(VII) recovery and ion-exchange constants are listed in Table 4 in relation to the concentrations of PE and nitrate ions. The K values calculated by Eq. (3) are of the same order of magnitude. A small decrease in K with increasing NO_3^- concentration and decreasing PE concentration is probably due to a change in the activity coefficients of ions involved in the ion-exchange reaction both in

solution and in the PE precipitate phase. The average concentration constant of ion exchange $K = 40.3 \pm 7.3$ shows that the recovery of ReO_4^- by coagulation of VA-212 cationic polyelectrolyte under the action of nitrate ions is highly selective.

We obtained isotherms of Re(VII) sorption by the precipitated PE. Figure 2 shows the dependences of PE exchange capacity with respect to rhenium E on the Re(VII) concentration at different concentrations of NO_3^- ions. They are linear within the range of Re(VII) concentrations studied (0.5–10 mg dm^{-3}). The obtained exchange capacities show that rhenium is concentrated by a factor of 200–400 in recovery of perrhenate ions with VA-212 polyelectrolyte, depending on the nitrate ion concentration.

CONCLUSION

The possibility of selective concentration of Re(VII) from nitrate-containing solutions with VA-212 water-soluble cationic polyelectrolyte was demonstrated.

REFERENCES

1. Lebedev, K.B., *Renii* (Rhenium), Moscow: Metallurgizdat, 1963.
2. *Khimiya i tekhnologiya redkikh i rasseyannykh elementov* (Chemistry and Technology of Rare and Trace Elements), Bol'shakov, K.A. Ed., Moscow: Vysshaya Shkola, 1976, part 3.
3. Vasil'ev, V.P., *Analiticheskaya khimiya* (Analytical Chemistry), Moscow: Vysshaya Shkola, 1989, part 2.
4. Kodina, G.E., Tulskaya, T.A., and Gureev, E.V., in *Technetium and Rhenium in Chemistry and Nuclear Medicine*, New York: Raven, 1989, pp. 641–645.
5. Demin, Yu.V., Borisova, L.V., and Gatinskaya, N.G., *Zh. Anal. Khim.*, 1996, vol. 51, no. 6, pp. 638–641.
6. Burkhardt, C.W., Parazak, D.P., McCarthny, K.J., and Jackson, G.J., *J. Appl. Polym. Sci.*, 1986, vol. 32, no. 4, pp. 4701–4708.
7. *Kratkii spravochnik fiziko-khimicheskikh velichin* (Concise Handbook of Physicochemical Quantities), Mishchenko, K.P. and Ravdel', A.A., Eds., Leningrad: Khimiya, 1974, p. 144.

Russian Journal of Applied Chemistry, Vol. 74, No. 6, 2001, pp. 958–960. Translated from Zhurnal Prikladnoi Khimii, Vol. 74, No. 6, 2001, pp. 931–933.

SORPTION AND ION-EXCHANGE PROCESSES

Combined Activation of Anthracite

V. V. Strelko, N. V. Gerasimenko, and N. T. Kartel'

Institute of Sorption and Endoecological Problems, Ukrainian National Academy of Sciences, Kiev, Ukraine

Received September 12, 2000; in final form, March 2001

Abstract—The effect of anthracite pretreatment on the production of activated carbons and increase in the specific porosity of the resulting adsorbent was studied.

Production of new types of activated carbons is an urgent problem owing to the growing demand for carbon adsorbents for water treatment, purification of drinking water, recovery of solvents, and decontamination of gases released by chemical, metallurgical, and fuel-producing plants. Among starting materials used for production of activated carbons, anthracite shows much promise owing to the inexhaustible resources, low cost, high carbon content, and low content.

However, it should be noted that anthracite has low reactivity, which is due to the high degree of metamorphism of this type of coal (fairly well arranged supramolecular structure with the short- and, partially, long-range order of the carbon lattice). This is the reason why all attempts to develop fairly efficiently its porous structure and to produce adsorbents with high specific characteristics of porosity by direct activation have, as a rule, failed.

A number of treatments preceding steam-gas activation of anthracite have been proposed for the development of porosity of the final product. For example, Bessant and Walker [1] and Walker and Almargo [2] proposed a two-stage process including prepyrolysis of anthracite in an N_2 flow at 850–950°C and then activation proper with carbon dioxide. This procedure yields samples with fairly high specific surface area, reaching 1800 $m^2 g^{-1}$.

It is believed that the porosity of activated carbons is governed to a large extent by their pretreatment preceding the activation. For example, Parra and coworkers [3, 4] showed that preoxidation of carbons with atmospheric oxygen is one of the most important pathways for producing high-quality sorption materials. In this oxidation, a transport porous structure is formed, which facilitates the activation [5, 6].

A procedure including treatment of anthracite with chemical activators is also known [7]. For example, anthracite was activated with steam at 850–900°C up to combustion loss of 10–20%, and an intermediate product with a specific surface area of 770 $m^2 g^{-1}$ was obtained. Then, carbon was impregnated with aqueous solution of NaOH, Na_2CO_3, or Na_2SO_4, dried, and calcined at 850–910°C. The residue was washed with water and dilute sulfuric acid. The remaining carbon was additionally activated with steam at 750°C, and mesoporous activated carbon with specific pore surface area of 900 $m^2 g^{-1}$ was obtained.

Based on the above procedures of anthracite activation, it was appropriate to carry out a pretreatment of the initial raw material, including combination of the above procedures.

The aim of this work was to study the effect of anthracite pretreatment on its activation with steam, with the aim to raise the reactivity of highly metamorphozed material with respect to oxidizing gases in gasification.

As a starting material we used anthracite of brand A.[1] The chemical composition of the main components of the initial raw material was as follows: A^c = 4–5%, V^{dat} = 6–7%, and C^{daf} = 95%. The particle size of anthracite was 0.25–1.0 mm; the initial volume of sorption pores with respect to benzene, less than 0.01 $cm^3 g^{-1}$; and the bulk density, 0.9 g cm^{-3}.

The pretreatment included a series of operations. Initially, the starting material was activated with steam at 900°C up to combustion loss of 30%. Then, the samples were oxidized with moistened air at 270–

[1] Dolzhenskaya Kapital'naya Mine, Sverdlovantratsit Production Association, Donetsk Field.

1070-4272/01/7406-0958 $25.00 © 2001 MAIK "Nauka/Interperiodica"

300°C until a static exchange capacity (SEC) of 0.5–1.0 mg-equiv g^{-1} was reached. It was assumed that this oxidation of anthracite surface must facilitate the subsequent pretreatment process involving incorporation of "wedging" ions into the anthracite structure by the ion exchange [8]. Oxidized anthracite was impregnated with a solution of chemical activator (sodium nitrate) and dried at 120–130°C for 2–3 h. The anthracite samples impregnated with a solution of alkali metal compound were repeatedly activated with steam at 900°C up to combustion loss of 80%. The steam flow rate was 0.1 l h^{-1}, which provided a 8–9-fold excess with respect to the reaction stoichiometry.

To confirm the effect of anthracite pretreatment on the activation process, we directly activated in parallel the initial (untreated) sample at the same temperature and the same steam flow rate.

At all stages of the study we carried out porometric monitoring of the samples by measuring the volume of sorption pores with respect to benzene W_s [9]. At the oxidation stage, we also determined the static exchange capacity SEC from the sorption of 0.1 N NaOH. At the preliminary and final stages of activation, we determined the weight and volume yields of the sample (R_m and R_v), bulk density Δ, and the combustion loss ω. The errors did not exceed 2 rel. %.

The specific surface area was measured with a Quantochrome Autosorb Automated Gas Adsorption System (United Kingdom).

The activation of anthracite by the above procedure produced microporous carbons. This is suggested by the isotherm of nitrogen adsorption on activated carbons subjected to thermochemical treatment. This isotherm has a shape typical of microporous adsorbents (Fig. 1). The calculated specific surface area reaches 820 $m^2 g^{-1}$.

A kinetic study of the combustion loss for the anthracite samples showed that the pretreatment considerably accelerates gasification of the samples (see table). It is seen from the data listed in the table that

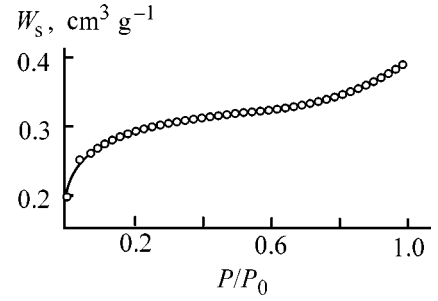

Fig. 1. Isotherm of nitrogen adsorption on activated carbon produced from anthracite subjected to thermochemical treatment. (W_s) Pore volume, and (P/P_0) relative pressure.

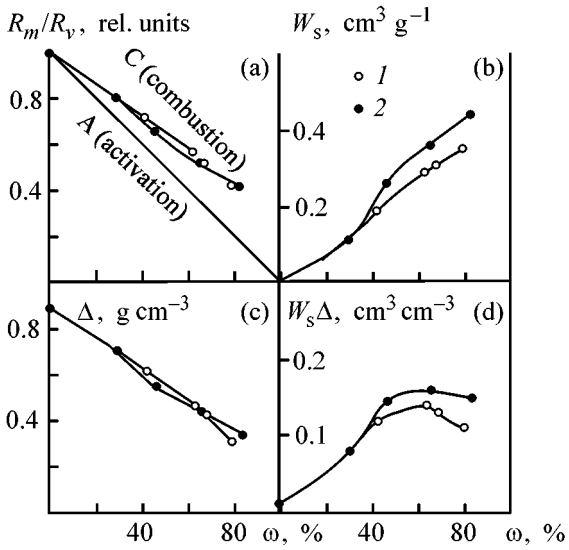

Fig. 2. Parameters of activated carbons produced from anthracite by (*1*) the standard scheme and (*2*) the modified scheme vs. combustion loss ω. (R_m/R_v) Activation index, (W_s) volume of sorption pores with respect to benzene, (Δ) bulk density, and ($W_s\Delta$) bulk porosity.

the maximum of combustion loss is reached in 6.5 h with direct activation and in 3 h with the thermochemical pretreatment, which is important from the standpoint of processing, since it allows the maximum pore formation to be achieved in a shorter time interval.

Figure 2 shows how the parameters of carbon sorbents produced by activation of the initial anthracite

Combustion loss for samples obtained at various activations of the initial anthracite

Activation	τ, h	ω, %	Activation	τ, h	ω, %
Direct	0	0	With thermochemical treatment	0	0
	2	29.7		2	29.7
	3	41.7		2.25	46
	5	62.7		2.5	60.7
	6	67.5		3	82.4
	6.5	79.4			

with pretreatment and by direct activation depend on the combustion loss. The dependence of the activation index R_m/R_v on the combustion loss (Fig. 2a) shows that thermochemical treatment of anthracite samples does not complicate the activation process. The gasification process is the same as that in direct activation. In both cases, the process occurs smoothly and is practically optimal, with strong prevalence of pore formation (line A) over combustion (line C).

Of some interest are data presented in Fig. 2b, in which the dependence of the sorption pore volume with respect to benzene W_s on combustion loss is shown. The curves coincide up to a combustion loss of 29.7%, since for both samples the initial process is direct activation. Then, one of the samples is subjected to thermochemical treatment, and the activation is continued. This action affects the subsequent second stage of activation, so that higher values of W_s at the same combustion loss are attained (curve *2*). At maximum combustion loss equal to 80% in direct activation, the largest attainable sorption pore volume with respect to benzene is 0.35 $cm^3\ g^{-1}$; in this case, the bulk density reaches 0.32 $g\ cm^{-3}$. In activation of anthracite samples subjected to thermochemical pretreatment, the largest attainable value of W_s is 0.44 $cm^3\ g^{-1}$ at the same bulk density.

The dependence of the bulk density Δ on the combustion loss is linear in both cases (Fig. 2c), and the lines practically coincide. Taking into account that the dependences of the activation index on the combustion loss completely coincide for both samples, we can conclude that this coincidence is not occasional.

The dependences of the bulk porosity $W_s\Delta$ on the combustion loss (Fig. 2d) are somewhat different for the samples subjected to direct activation with thermochemical pretreatment. Such a modified sample has a great resource of capacity to form the "sorption potential." In other words, it is likely that pretreatment of anthracite affects not only the activation rate but also the development of porous structure, presumably owing to an increase in the number of meso- and micropores.

CONCLUSIONS

(1) Combined anthracite activation by thermochemical treatment somewhat improves the porous structure of the matrix.

(2) The main advantage of the improved procedure of anthracite activation is the intensification of the final stage; in this case, the activation rate considerably increases (by a factor of 2).

(3) Our study reveals new potentialities for production of carbon adsorbents even from such highly metamorphozed material as anthracite.

REFERENCES

1. Bessart, G.A.R. and Walker, P.L., *Jr., Carbon*, 1994, vol. 32, p. 1171.
2. Walker, P.L., Jr. and Almargo, A., *Carbon*, 1995, vol. 33, p. 239.
3. Parra, J.B., Pis, J.J., Sousa, J.C. de, *et al.*, *Carbon*, 1996, vol. 34, p. 783.
4. Parra, J.B., Sousa, J.C. de, Pis, J.J., *et al.*, *Carbon*, 1995, vol. 33, p. 801.
5. Munoz-Guillena, M.J., Illan-Gomes, M.J., Martin-Martinez, J.M., *et al.*, *Energy Fuels*, 1992, vol. 6, p. 9.
6. Gergova, K., Eser, S., Shobert, H.H., *et al.*, *Fuel*, 1995, vo. 74, p. 1042.
7. Hassler, S., *Chem. Eng. Progr.*, 1956, vol. 12, no. 52, pp. 56–58.
8. Strelko, V.V., Gerasimenko, N.V., and Kartel', N.T., *Teor. Eksp. Khim.*, 1999, vol. 35, no. 5, pp. 306–310.
9. Kel'tsev, N.K., *Osnovy adsorbtsionnoi tekhniki* (Principles of Adsorption Engineering), Moscow: Khimiya, 1984.
10. Kolyshkin, D.A. and Mikhailova, K.K., *Aktivnye ugli: Spravochnik* (Activated Carbons: A Handbook), Leningrad: Khimiya, 1972.

Russian Journal of Applied Chemistry, Vol. 74, No. 6, 2001, pp. 961–965. Translated from Zhurnal Prikladnoi Khimii, Vol. 74, No. 6, 2001, pp. 934–938.

APPLIED ELECTROCHEMISTRY AND CORROSION PROTECTION OF METALS

Electrocrystallization of Molybdenum Carbide in Oxide Melts and the Influence of Electrolysis Parameters on Grain Size and Quality of Deposits

V. V. Malyshev, Kh. B. Kushkhov, and V. I. Shapoval

Vernadskii Institute of General and Inorganic Chemistry, National Academy of Sciences of Ukraine, Kiev, Ukraine
Kabardino-Balkar State University, Nalchik, Kabardino-Balkariya, Russia

Received October 16, 2000

Abstract—The influence of current density and temperature on crystal grain size in electroplating of molybdenum carbide from tungstate–molybdate–carbonate melts was studied. The initial stages of molybdenum carbide electrocrystallization from tungstate–molybdate–carbonate melts at 750–900° on different substrates were studied by the method of galvanostatic switch-on curves and *in situ* microstructural analysis.

Electrodeposition of molybdenum carbide coatings from tungstate–molybdate–carbonate melts [1, 2] is a more advanced method than plating from halide–oxide electrolytes [3, 4]. Pure oxide melts allow use of a wider variety of substrates than halide–oxide melts do (in this case, steels of various brands can be used in addition to graphite, copper, nickel, molybdenum, and tungsten). They do not require any protective atmosphere, open up possibilities of using open electrolytic baths, and give much thicker coatings (up to 200 μm).

It has been established [5] that in a wide range of cathode current densities the phase overvoltage depends on current density logarithmically, similarly to the Tafel dependence:

$$\eta = a + b\log i. \qquad (1)$$

Analysis of the data reported in [6–13] shows that the values of the coefficients a and b vary widely between different electrode–deposited metal–electrolyte systems: a = 40–230 mV and b = 10–85 mV. The coefficient a decreases with increasing temperature or concentration of the deposited metal in the melt. These dependences are accounted for by the fact that the interaction between the metal and the substrate becomes stronger at higher temperatures.

In the case when dilute solutions of a salt of the metal being deposited are subjected to electrolysis in a melt, the growth rate of a crystal nucleus is determined by diffusion of discharging ions to its surface. The number of crystals being formed was determined by the authors of [5] by calculating in a quasi-stationary approximation the rate of substance transfer to the growing nucleus with the use of the equation of transient diffusion toward a continuously expanding semi-sphere:

$$Z = \frac{2.3 \times 10^{12} K_3^{1/2} T^{3/2} i^{3/2}}{z^{5/2} V^{1/2} D^{3/2} C_0^{3/2} C_c^{1/2} \eta^3} = K \frac{T^{3/2} i^{3/2}}{\eta^3}, \qquad (2)$$

where $K_3 = W^* \eta^2 / KT$ is a parameter independent of the overvoltage (W is the work of nucleus formation), T the melt temperature, i the cathode current density, z the ion charge of the metal being plated, V the molar volume of the metal being deposited, D the diffusion coefficient of an ion being discharged, C_0 the concentration of discharging ions in the melt volume, C_c the cathode capacitance, and η the maximum overvoltage.

As seen from Eq. (2), the number of crystals is affected by the crystallization overvoltage, temperature, and cathode current density. Analysis of experimental studies [6–13] shows that in the galvanostatic mode the number of forming nuclei as a function of the cathode current density can be found using the empirical equation

$$Z = K i^{\nu}, \qquad (3)$$

where ν is within 1–1.25.

1070-4272/01/7406-0961 $25.00 © 2001 MAIK "Nauka/Interperiodica"

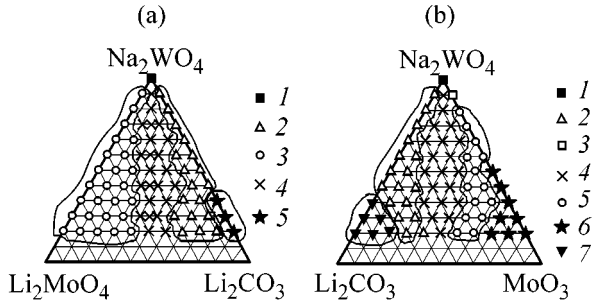

Fig. 1. Composition diagrams of the cathodic products of the systems (a) Na_2WO_4–Li_2MoO_4–Li_2CO_3 and (b) Na_2WO_4–MoO_3–$LiCO_3$. *T* 1173 K; cathode–C, Ni, and Cu; anode–graphite; i_c = (5.0–7.5) × 10^{-2} A cm^{-2}. (a) (*1*) No deposit, (*2*) C powder, (*3*) Mo coating, (*4*) Mo_2C coating, and (*5*) WC powder. (b) (*1*) No deposit, (*2*) C powder, (*3*) Mo coating, (*4*) Mo_2C coating, (*5*) Mo_2O coating, (*6*) Na_2MoO_3 bronzes, and (*7*) WC powder.

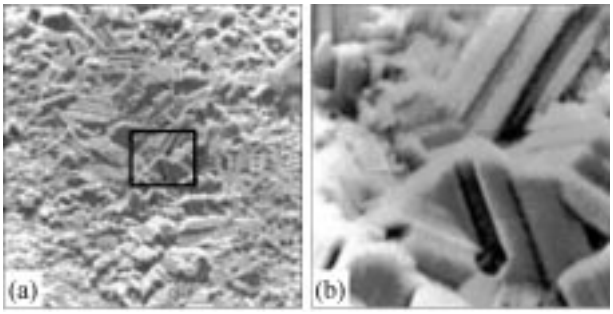

Fig. 2. (a) SEM microgram of the surface of molybdenum carbide coating electrodeposited from the melt Na_2WO_4–5 mol % Li_2MoO_4–5 mol % Li_2CO_3 and (b) its enlarged fragment. *T* = 1173 K, i_c = 0.075 A cm^{-2}. Magnification 3410.

This is in good agreement with the theoretical Eq. (2). The decrease in the amount of forming nuclei leads to increasing crystal size [5]:

$$L = Z^{-1/2}. \quad (4)$$

Thus, the amount of the nuclei grows with increasing cathode current density. All the coefficients of Eq. (2), combined into the constant *K*, are temperature-dependent. However, the effect of temperature on the coefficients of ion diffusion in the melt is the strongest, and the number of the nuclei decreases with increasing temperature. The amount of deposited nuclei is larger and the crystal sizes are smaller at lower temperatures and higher cathode current densities.

EXPERIMENTAL

It was reported in [1, 2] that plated coatings of molybdenum carbide can be, in principle, electrodeposited from oxide melts. The results obtained in studying the cathodic products of tungstate–molybdate–carbonate melts are represented in more detail in composition diagrams of the cathodic products (Figs. 1a and 1b). Molybdenum carbide coatings are deposited from the Na_2WO_4–Li_2MoO_4–Li_2CO_3 electrolyte when the concentrations of lithium molybdate and lithium carbonate are equal (to within 2.5 mol %) and do not exceed 20–25 mol %. The deposit contains carbon, molybdenum, and carbide at lower lithium molybdate concentrations, and molybdenum oxides at higher concentrations. At lower concentrations of lithium carbonate, the deposit mainly contains molybdenum, with free carbon predominantly deposited at higher concentrations. A more accessible industrial reagent—source of molybdenum, is its oxide. With molybdenum oxide used as a source of molybdenum, an approximately two times higher amount of lithium carbonate is needed as compared with the case of lithium molybdate.

Continuous molybdenum carbide coatings were obtained at 1073–1223 K and current densities of up to 0.5 A cm^{-2}. At temperatures below 1073 K and current densities exceeding 0.5 A cm^{-2}, a finely dispersed molybdenum carbide powder was obtained with specific surface area of up to 30 $m^2 g^{-1}$. Uniform and absolutely non-porous coatings with good adherence were deposited from the Na_2WO_4–5 mol % MoO_3–10 mol % Li_2CO_3 electrolyte at current densities ranging from 0.01 to 0.10 A cm^{-2} at 1173 K. In the current density range under study, the deposition rate is 5–25 μm h^{-1}, the current efficiency by molybdenum carbide in the form of a coating reaches 80%, and the coating are as thick as 100 μm. The effect of temperature and cathode current density on the crystal grain size in electroplating of molybdenum carbide was studied in the melt Na_2WO_4–5 mol % Li_2MoO_4–5 mol % Li_2CO_3 at 800–950°C and cathode current densities of 0.02–0.15 A cm^{-2}. The amount of electricity remained constant in all the runs (0.075 A h). After being washed with distilled water under identical conditions, the deposits were studied on a Stereoscan S-4 scanning electron microscope. The grain size was determined as the arithmetic mean of 50–100 grains. The outward appearance of a coating is presented in Fig. 2.

With the temperature raised from 800 to 950°C, the average grain size grows from 11.3 to 17.8 μm at the same cathode current density (0.075 A cm^{-2}).

The influence of temperature and cathode current density is demonstrated in Fig. 3. The average grain size increases from 13.5 μm at a current density of 0.15 A cm^{-2} to 19.6 μm at 0.02 A cm^{-2}).

It has been shown that epitaxial deposition of molybdenum carbide onto a substrate occurs in electrodeposition of the carbide from tungstate–carbonate melts [14]. The grain size can be reduced by applying a current pulse at the beginning of electrolysis or by using the reverse electrolysis mode. The pulsed current was produced by a special generator of rectangular pulses. The dc current density at the cathode was 7.5×10^{-2} A cm^{-2} in all the runs.

Application of a cathodic pulse at the beginning of electrolysis makes the deposit grains finer. For example, when a pulse with amplitude of 30 A cm^{-2} and 40–50-ms duration is applied, the grain size changes from 10–14 to 3–5 μm. Presumably, a slight, from 1860 to 1990 kgs mm^{-2}, increase in microhardness can be attributed to the finer grain structure of the deposit. An X-ray study showed that the initial pulses with amplitude of up to 30 A cm^{-2} have no effect on the deposit orientation. Irrespective of an initial pulse, the molybdenum carbide deposit has a (110) structure. In this case, only the layer defectiveness grows on applying pulses of this amplitude because of the formation of new metal nuclei on each grain of the deposit. When the pulse amplitude exceeds 50 A cm^{-2}, the deposits become spongy and weakly adherent to the surface. Presumably, this means that the near-cathode layer of the electrolyte is virtually completely depleted of bimolybdate and carbonate ions. In this case, the deposit properties can be explained by secondary reduction of $Mo_2O_7^{2-}$ and CO_3^{2-} ions by sodium atoms deposited on the cathode by the primary reaction and diffusing away from it.

Use of the reverse electrolysis mode yielded coatings with less coarsely crystalline structure and thickness increased up to 200 μm. The optimal parameters are as follows: $\tau_c/\tau_a = 20-40$, the anodic period duration 0.5–2.0 s, and the anode current density 0.15–0.50 A cm^{-2}. The main features of metal electrocrystallization from molten salts, including nucleation at the cathode, kinetics of electrode processes, microdistribution of the current, and structure of cathodic deposits, were established in [5, 10, 11]. The electrocrystallization in electrochemical synthesis has been studied to a considerably lesser extent. The electrocrystallization of tungsten oxide and molybdenum oxide bronzes was studied in [15, 16]. Published data on the electrocrystallization of molybdenum carbide are virtually lacking. This problem was investigated

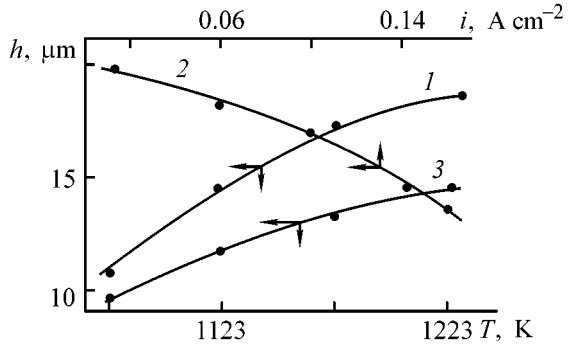

Fig. 3. Crystal grain size *h* vs. temperature *T* and cathode current density *i* for electrodeposition of molybdenum carbide in (*1*, *2*) conventional galvanostatic and (*3*) reverse modes.

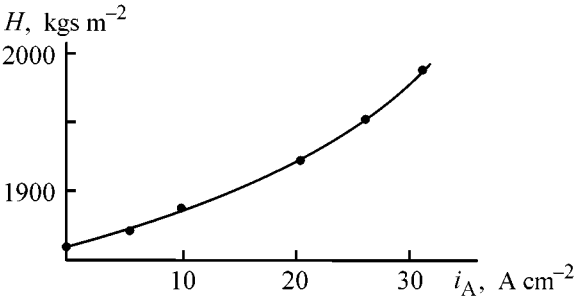

Fig. 4. Microhardness *H* vs. cathodic pulse amplitude i_A.

by means of electrochemical methods for studying phase formation, combined with a simultaneous microstructural analysis of the substrate surface and electrolysis products being formed.

The employed experimental setup included an electric-resistance crucible furnace with a platinum heater, a complex for measuring galvanostatic switch-on potential–time curves, and a microstructure analyzer based on an MBS-9 microscope. The measurements were performed in a three-electrode cell. A platinum crucible served as the anode and melt reservoir. As the working electrode was used platinum, molybdenum, or glassy carbon microelectrode 0.5–1.0 mm in diameter sealed in quartz glass. A platinum–oxygen electrode Pt, $O_2 | Na_2WO_4$–0.2 WO_3 in air served as reference. The reversibility of such an electrode in oxide melts was demonstrated in [17–19].

The shape of the upper part of the oscillogram describing the variation of the platinum electrode potential on switching-on dc current indicates (by the presence of a characteristic peak) that crystallization overvoltage exists at the onset of molybdenum carbide formation. A quantitative estimate of the phase overvoltage yields a value of 8–40 mV for silver electrodes at 1023–1123 K.

Microstructural analysis of the dynamics of growth of the new phase shows that a great number of crystallization centers are formed at the beginning of the process. Then, separate crystals grow and merge into a continuous layer with the formation of a plane crystallization front. Slight depolarization is observed in the switch-on curve. To ascertain its origin, we studied the electrocrystallization of individual components of the compound being synthesized.

Comparison of the molybdenum phase formation from a Na_2WO_4–K_2WO_4(1 : 1)–Li_2MoO_4(5 mol %) melt and of molybdenum carbide from a similar melt with addition of lithium carbide shows similarity of their *E*–*t* curves. A slight depolarization preceding the main process can be attributed to the formation of platinum and molybdenum intermetallides [20, 21]. This result is indirectly confirmed by the change in the substrate color, observed visually at the beginning of polarization. The nucleation of molybdenum crystals occurs similarly to electrocrystallization of metals from molten salts. The crystallization centers appear solely at the beginning of the process, which corresponds to the peak in the switch-on curve, and then grow [5]. The phase overvoltages and the intervals of time in which the maximum nucleation overvoltage is reached under the identical plating conditions are well comparable for molybdenum and its carbide. However, the duration of the metastable state (i.e., the width of the overvoltage peak) is two times longer in the case of carbide formation, compared with that when the metal phase is formed.

No pure carbon is deposited from the tungstate–molybdate melt at 900°C owing to the formation of carbides. Carbon powders badly adherent to the electrode surface can be obtained on lowering the temperature to 750°C. No overvoltage peaks were observed in the *E*–*t* curve upon carbon deposition. This experimental fact suggests that there is no crystallization overvoltage in carbon deposition.

Thus, to a first approximation, the electrocrystallization of molybdenum carbide resembles crystallization of both molybdenum and carbon. On the one hand, similarly to electrodeposition of elementary carbon, nucleation of a great number of crystallization centers of molybdenum carbide occurs virtually over the entire substrate surface. On the other hand, formation of the Mo_2C phase requires a certain supersaturation, which corresponds to the phase overvoltage in electrocrystallization of pure molybdenum.

We studied the influence of the current density and temperature on the initial stages of electrocrystallization of molybdenum carbide. For example, changing the current density from 5×10^{-3} to 0.10 A cm^{-2} alters not only the phase composition of the obtained product, but also the nature of electrocrystallization in the initial stage. With the current density raised further, formation of lithium oxide also occurs along with the growth of Mo_2C layers. When the Li_2O solubility in the near-electrode region reaches the limiting value, the surface of the carbide deposit is passivated via blocking by lithium oxide. This affects the stability of the plane crystallization front and results in the deposition of a carbide powder, especially at lower temperatures. The performed study demonstrated that the temperature of electrodeposition is the most important parameter determining whether or not molybdenum carbide crystallizes as a continuous deposit.

Interesting results were obtained in studying the nucleation of the molybdenum carbide phase on glassy carbon. In equilibrium conditions, the following redox processes occur at the glassy carbon|melt interface:

$$C + CO_3^{2-} = 2CO + O^{2-}, \quad (5)$$

$$C + CO_2 = 2CO. \quad (6)$$

Gaseous carbon oxides are well sorbed by the substrate. The shape of the switch-on curves shows that electrochemical synthesis is unstable immediately after the dc current is switched on. It is interesting to note that synthesis of molybdenum carbide occurs on the surface of CO and CO_2 bubbles sorbed by the electrode and acting as a source of carbon.

In conclusion, we present some considerations concerning the mechanisms of electrochemical synthesis of molybdenum carbide. In the bulk of the Na_2WO_4–K_2WO_4 melts containing Li_2CO_3 and Li_2MoO_4, there occur the following equilibria [1, 2]:

$$CO_3^{2-} + xLi^+ = (Li_x^+CO_3^{2-})^{x-2} = Li_xO^{x-2} + CO_2, \quad (7)$$

$$MoO_4^{2-} + xLi^+ = (Li_x^+MoO_4^{2-})^{x-2}. \quad (8)$$

On switching on the electrode current, carbon dioxide and molybdate ion discharge simultaneously with the deposition of carbon and molybdenum atoms.

$$2CO_2 + 4e = C + 2CO_3^{2-}, \quad (9)$$

$$(Li_x^+MoO_4^{2-})^{x-2} + 6e = Mo + x/2Li_2O + (4 - x/2)O^{2-}. \quad (10)$$

Then, carbon and molybdenum atoms interact at the electrode to form Mo_2C.

CONCLUSION

A study of the influence exerted by the current density and temperature on the crystal grain size in electrodeposition of molybdenum carbide from tungstate–molybdate–carbonate melts revealed the existence of a crystallization overvoltage in nucleation of molybdenum carbide.

REFERENCES

1. Malyshev, V.V., *Fiz. Khim. Mekhanika Mater.*, 1998, vol. 64, no. 6. pp. 96–102.
2. Malyshev, V.V., Novoselova, I.A., Kushkhov, Kh.B., and Shapoval, V.I., *Zh. Neorg. Khim.*, 1997, vol. 42, no. 4, pp. 540–547.
3. Stern, K.H., Singer, J.L., and Geffries, R.A., *Thin Solid Films*, 1983, vol. 108, no. 1, pp. 103–107.
4. Kushkhov, Kh.B., Malyshev, V.V., and Shapoval, V.I., *Zashch. Met.*, 1990, vol.26, no.6, pp. 1019–1021.
5. Baraboshkin, A.N., *Elekrtokristallizatsiya metallov iz rasplavlennykh solei* (Electrocrystallization of Metals from Molten Salts), Moscow: Nauka, 1976.
6. Baraboshkin, A.N., Kosikhin, L.T, and Saltykova, N.A., *Trudy Inst. Elektrokhim. Acad. Nauk SSSR, Ukr. Fil.*, 1964, issue 5, pp. 89–94.
7. Baraboshkin, A.N., Kosikhin, L.T, and Saltykova, N.A., *Trudy Inst. Elektrokhim. Acad. Nauk SSSR, Ukr. Fil.*, 1965, issue 7, pp. 47–51.
8. Baimakov, Yu.V., and Vetyukov,M.M., *Elektroliz rasplavlennykh solei* (Electrolysis of Molten Salts), Moscow: Metallurgiya, 1966.
9. Baraboshkin, A.N., Kaliev, K.A, Ksenofontova, T.B., and Tarasova, K.P., *Trudy Inst. Elektrokhim. Acad. Nauk SSSR, Ukr. Fil.*, 1970, issue 15, pp. 74–79.
10. Grilikhes, S.Ya., *Ellektrokhimicheskoe i khimicheskoe polirovanie. Teoriya i praktika* (Electrochemical and Chemical Polishing. Theory and Practice), Leningrad: Khimiya, 1990.
11. Kabanov, B.N., *Elektrokhimiya metallov i adsorptsiya* (Electrochemistry of Metals and Adsorption), Moscow: Nauka, 1966.
12. Chukreev, N.Ya., Polishchuk, V.A., and Shapoval, V.I., *Ukr. Khim. Zh.*, 1986, vol. 52, no. 3, pp. 282–287.
13. Chukreev, N.Ya., Shapoval, V.I., and Polishchuk, V.A., *Elektrokhimiya*, 1984, vol. 20, no. 4, pp. 520–524.
14. Malyshev, V.V., Kushkhov, Kh.B., Novoselova, I.A., and Shapoval, V.I., *Kristallografiya*, 1996, vol. 41, no. 1, pp. 188–190.
15. Zakhar'yash, S.M., Kaliev, K.A., and Bugrimov, V.V., *Fizicheskaya khimiya i elektrokhimiya rasplavlennykh i tverdykh elektrolitov* (Physical Chemistry and Electrochemistry of Liquid and Solid Electrolytes), Sverdlovsk: Akad. Nauk SSSR, Ukr. Otd., 1979, part 2, pp. 4–5.
16. Zakhar'yash, S.M., Kaliev, K.A., and Baraboshkin, A.N., *Fizicheskaya khimiya i elektrokhimiya rasplavlennykh i tverdykh elektrolitov* (Physical Chemistry and Electrochemistry of Liquid and Solid Electrolytes), Sverdlovsk: Akad. Nauk SSSR, Ukr. Otd., 1981, p. 31.
17. Malyshev, V.V., and Kushkhov, Kh.B., *Elektrokhimicheskoe povedenie platino-kislorodnogo elektroda v volframatno–molibdatno–karbonatnykh rasplavakh* (Electrochemical Behavior of the Platinum–Oxygen Electrode in Tungstate–Molybdate–Carbonate Melts), Available from VINITI, 1988, Moscow, no. 23/9B.
18. Afonichkin, V.K., Leont'ev, V.N., and Komarov, V.E., *Elektrokhimiya*, 1993, vol. 29, no. 3, pp. 341–347.
19. Mittals, S., and Eliott, J.F., *J. Electrochem. Soc.*, 1987, vol. 134, no. 2. pp. 44–249.
20. Shapoval, V.I., Baraboshkin, A.N., Kushkhov, Kh.B., and Malyshev, V.V., *Elektrokhimiya*, 1987, vol. 23, no. 7, pp. 942–946.
21. Komarov, V.E., Afonichkin, V.K., and Zyryanov, V.G., *Elektrokhimiya*, 1981, vol. 17, no. 11, pp. 1739–1743.

Russian Journal of Applied Chemistry, Vol. 74, No. 6, 2001, pp. 966–969. Translated from Zhurnal Prikladnoi Khimii, Vol. 74, No. 6, 2001, pp. 939–942.

CATALYSIS

Synthesis of Catalyst for Hydrorefining with Domestic Raw Materials

G. Sh. Artukova, E. A. Ibragimov, O. A. Eshmuradov, M. P. Yunusov, and G. Sh. Talipov

Sultanov Research Chemical-Pharmaceutical Institute, Tashkent, Uzbekistan

Received May 12, 2000; in final form, March 2001

Abstract—Basic requirements to the physicochemical and texture properties of supports for hydrorefining catalysts are formulated. Methods have been developed for synthesizing supports and hydrorefining catalysts with the use of kaolin, bentonite, and regenerated zeolites.

Aluminocobalt- or aluminonickel–molybdenum catalysts are widely used in the world practice as hydrorefining catalysts [1, 2]. These catalysts are synthesized by coprecipitation of the components or impregnation of a pretreated support with solutions of salts of the active components. However, in virtually all technologies of oil refining and gas processing, the main kinds of the employed catalysts are imported. The possibility of large-tonnage manufacture of these catalysts is limited in the first place by the lack of domestic aluminum hydroxide or oxide, whose content in finished catalysts may be as high as 85%. In this connection, the aim of the present study was to analyze the possibility of preparing nickel–molybdenum catalysts for hydrodesulfirization of natural gas and hydrorefining of various fuel fractions on a support produced with the use of domestic raw materials: Angren kaolin, Keles bentonite, and spent zeolite—a waste formed in natural gas purification to remove hydrogen sulfide.

EXPERIMENTAL

The supports were produced as follows: a thoroughly ground raw material was used to prepare a homogeneous paste formed into cylinders 5 mm in diameter and 5–7 mm long. The obtained granules were successively dried and calcined at 550–600°C. Catalyst samples were obtained by successive impregnation of the supports with solutions of nickel nitrate and ammonium paramolybdate $(NH_4)_6Mo_7O_{24}$. The catalyst activity was tested on flow-through laboratory and pilot installations, with, respectively, 2.0 and 50.0 cm^3 of catalyst charged. Diffuse reflection (DR) spectra were measured on a HITACHI-330 instrument with a DR attachment.

It should be noted that, in replacing aluminum oxide or hydroxide, the raw material used must possess the necessary set of physicomechanical properties: hydrophilicity and properties ensuring production of a homogeneous and well-formable paste. Moreover, the granules of the obtained support must have, upon calcination, the required strength and low wearability. In addition, for catalyst preparation by impregnation, these granules must also have a total porosity enabling introduction of the necessary amount of impregnating solutions. No less important are the acid–base properties of the surface structures of a support. The obtained supports must not have too high acidity. Otherwise, cracking of the hydrocarbon raw material will proceed concurrently with the hydrogenolysis of sulfur-containing compounds, making lower the production output and leading to catalyst caking. The performed analysis allowed formulation of the basic requirements to how new supports for hydrorefining catalysts are to be chosen. The hydromechanical characteristics of the synthesized catalyst samples are presented in Table 1.

As indicated by the obtained data, supports prepared from pure kaolin and bentonite have the highest mechanical strength, but relatively low specific surface area and water absorption capacity. The highest values of these latter were obtained for a sample of regenerated zeolite and its mixture with aluminum hydroxide. At the same time, the introduction of aluminum hydroxide into the bentonite and kaolin supports in a 1 : 1 ratio led to an increase in the specific surface area from 39.5 and 46.2 to 65.6 and 100.4 $m^2 g^{-1}$ and in water absorption capacity from 21.4 and 23.1 to 63.6 and 63.0%, respectively.

It can be seen from the presented results that physicomechanical characteristics of support samples N-4,

1070-4272/01/7406-0966 $25.00 © 2001 MAIK "Nauka/Interperiodica"

Table 1. Physicomechanical properties of the obtained support samples*

Support	Raw material used	Peptizing agent	T_c, °C	P, kg/granule	ρ, kg dm^{-3}	S_{sp}, m^2 g^{-1}	W, %
N-1	Al $(OH)_3$	NH_4OH	600	4.85	0.467	184	93.0
N-2	Kaolin	HNO_3	600	5.3	0.917	6.2	23.1
N-3	Bentonite	HNO_3	600	8.2	0.863	39.5	21.4
N-4	Kaolin + $Al(OH)_3$	NH_4OH HNO_3	600	4.73	0.575	100.4	63.0
N-5	Bentonite + $Al(OH)_3$	NH_4OH NHO_3	600	3.00	0.520	65.6	63.6
N-6	Regenerated zeolite RK-38	HNO_3	500	3.9	0.71	482.0	47.0
N-7	Regenerated zeolite RK+$Al(OH)_3$	HNO_3	500	5.50	0.490	286.0	79.4
N-8	Regenerated zeolite RK + kaolin	HNO_3	500	3.7	0.560	240.1	45.5

* T_c is the calcination temperature, P the mechanical strength against crushing along the generatrix, ρ the bulk density, S_{sp} the specific surface area, and W the water absorption capacity.

Table 2. Activity of nickel–molybdenum catalyst samples in AMC hydrogenolysis (G 5000 h^{-1})

Support	AMC conversion (%) at indicated temperature, °C					
	200	225	250	300	350	380
N-4	45.7	80.5	97.8	98.4	99.5	99.8
N-6	–	58.9	67.1	98.3	98.3	99.3
N-7	33.6	74.4	87.5	97.6	99.8	99.8
N-8	–	63.7	70.2	98.3	99.6	99.8
KND-46	80.5	90.9	96.0	99.3	99.4	99.5
Rhone-Poulenc	88.6	96.5	96.5	99.5	99.6	99.8
ACM catalyst	26.3	78.0	88.0	98.9	99.3	99.6

N-6, N-7, and N-8 satisfy requirements to catalyst supports. Therefore, the obtained supports were used to prepare by impregnation nickel–molybdenum catalysts containing (%): 14 active components, 10.5 MoO_3, and 3.5 NiO. For comparison, catalysts were also synthesized on imported supports KND-46 (Japan) and Rhone-Poulenc (France). The activities of the synthesized catalysts were tested on a flow-through laboratory installation in a model reaction of amylmercaptan (AMC) hydrogenolysis. The obtained results are presented in Table 2.

As seen from the data in Table 2, at temperatures higher than 300°C all the synthesized catalysts differ in activity only slightly and compare well with the catalysts obtained on imported supports and with the aluminocobalt–molybdenum catalyst AKM (Russia). Differences in activity start to appear at process temperatures lower than 300°C. In this case, the highest activity is observed for catalyst samples synthesized on Rhone-Poulenc and KND-46 supports. The lowest activity is exhibited by catalyst samples prepared using regenerated zeolite RK-38 (N-6) or its mixture with kaolin (N-7) or bentonite (N-8). Comparison of the data in Tables 1 and 2 shows that the zeolite much exceeds in specific surface area the Rhone-Poulenc (210 m^2 g^{-1}) and KND-46 (195 m^2 g^{-1}) supports. Therefore, this parameter cannot account for the observed low activity of the catalyst on the zeolite support. In this connection, an assumption was made that this fact may be related to formation of active centers in catalysts based on γ-Al_2O_3 and highly crystalline Al–Si zeolite.

It is known that a number of nickel-aluminum structures are not revealed by X-ray analysis owing to the low temperature of their calcination (450–550°C) and the nonstoichiometric NiO/Al_2O_3 ratio. Spinel

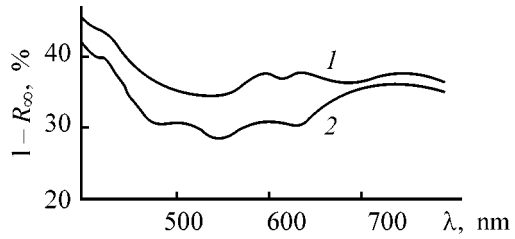

Spectra of diffuse reflection, $1 - R_\infty$, from nickel–molybdenum catalysts on different supports. (λ) Wavelength. (*1*) Al_2O_3 and (*2*) RK-38 zeolite.

structures formed through incorporation of nickel ions into tetrahedral voids in γ-Al_2O_3 are commonly identified using DR spectra [3–5]. The DR spectra of the catalyst samples, measured in this connection in the range 400–750 nm, are presented in the figure. It can be seen that the spectra of the synthesized samples contain the following sets of bands (nm): zeolite catalyst, 430, 490, and 720; catalysts with Rhone-Poulenc and KND-46 supports, 430, 550, 600, 635, and 730. Both sets of bands have been identified in the literature. The bands at 550, 600, and 635 nm are the most characteristic of a nickel-aluminum spinel, and those at 430, 490, and 720 nm, of nickel molybdate.

Table 3. Activity of a sample from the pilot batch of the ANM-2/1-1 catalyst (G 7500 h^{-1})

T, °C	AMC conversion (%) on indicated catalyst		
	ANM-2/1-1	AKM	TK-550
250	58.3	57.0	59.1
275	68.6	67.3	70.8
300	87.1	85.9	86.8
350	91.5	90.3	90.9
400	99.6	99.8	99.7

Table 4. Activity of catalysts in hydrorefining of high-sulfur gas condensate (P = 2.0 MPa, C = 0.79 wt %, V_{cat} = 50.0 cm^3, G = 2.0 h^{-1})

Parameter	Catalyst		
	ANM-2/1-1	AKM	TK-550
Granule diameter, mm	3–4	3–4	4–5
Bulk density, kg m^{-3}	750–860	700–800	700–800
Chemical composition, wt %:			
NiO	3.5	–	–
CoO	–	4.5	4.0
MoO_3	10.5	12.4	16.0
Degree of raw material desulfurization (%) at indicated temperature, °C:			
300	65.0	67.0	70.0
325	67.3	68.8	71.2
350	69.6	72.0	80.0
375	80.5	81.3	88.7
400	89.3	90.0	92.5

Thus, the use of supports with varied chemical nature leads to different surface and bulk structures of nickel and molybdenum compounds. On the zeolite and a mixture of the zeolite with kaolin predominates reaction between the active components to give $NiMoO_4$. On aluminum oxide or hydroxide supports, nickel-aluminum spinel is present together with $NiMoO_4$. This circumstance can presumably account for the different activities of the catalysts synthesized at low temperature.

Previously [4, 5], it has been shown that the reduction of the Ni–Al system strongly depends on the calcination temperature of a catalyst.

Samples calcined at 450–500°C show maximum hydrogen absorption at 400–500°C, which virtually coincides with the catalyst testing temperature and indicates nickel reduction under these conditions.

In addition, it should be kept in mind that the small sizes of micropores and their openings can make the sufficiently large surface area of the catalyst prepared with the use of the zeolite, found from low-temperature nitrogen adsorption, inaccessible to organosulfur compounds whose molecules are larger than the pore openings in the CaA zeolite.

The obtained data served as a basis for selecting a catalyst sample on a support composed of aluminum hydroxide and kaolin in a 1 : 1 ratio (N-4) for further tests. A technology was developed for preparing nickel–molybdenum catalyst ANM-2/1-1 on the given support, and its pilot batch was manufactured. The results obtained in testing the activity of this catalyst in a model reaction of AMC hydrogenolysis and in gas-condensate purification are presented in Tables 3 and 4. It can be seen that the activity of a sample from the pilot batch of the synthesized catalyst in hydrodesulfurization of natural gas and hydrorefining of highsulfur gas condensate compares well with the activities of the known commercial catalysts TK-550 (Holdor Topsoe) and AKM (Russia).

Thus, the performed investigations allowed formulation of the basic requirements to the physicochemical and texture properties of supports for hy-

drorefining catalysts. Methods were developed for synthesizing hydrorefining catalyst supports with the use of domestic raw materials: Keles bentonite, Angren kaolin, and regenerated zeolites.

CONCLUSIONS

(1) The specific surface area and total porosity (water absorption capacity) should be not lower than 50 $m^2 g^{-1}$ and 50%, respectively; and the mechanical strength, not lower than 4.0 kg/granule.

(2) The aluminonickel–molybdenum catalyst ANM-2/1-1 on a support composed of Angrene kaolin and aluminum hydroxide in a 1 : 1 ratio compares well in activity in hydrorefining of natural gas and high-sulfur gas condensate with the known commercial catalysts.

REFERENCES

1. Radchenko, E.D., Nefedov, B.K., and Aliev, R.R., *Promyshlennye katalizatory gidrogenizatsionnykh protsessov neftepererabotki* (Commercial Catalysts for Hydrogenization Processes in Oil Refining), Moscow: Khimiya, 1987.
2. Vail', Yu.K., Sukhorukov, A.M., Nikolaichuk, V.A., *et al.*, *Khim. Tekhnol. Topl. Masel*, 1998, no. 1, pp. 25–27.
3. Vorob''ev, V.N., Nurseitova, T.E., Martirosov, A.E., and Talipov, G.Sh., *Zh. Obshch. Khim.*, 1975, vol. 45, no. 12, pp. 2573–2578.
4. Sharipov, A.Kh., Kalinevich, A.Yu., Ismailov, I.S., and Talipov, G.Sh., *Zh. Obshch. Khim.*, 1977, vol. 47, no. 3, pp. 545–550.
5. Khasanov, F.N., Vorob''ev, V.N., Sventsitskii, E.S., and Talipov, G.Sh., *Zh. Prikl. Khim.*, 1978, vol. 60, no. 4, pp. 784–789.

Russian Journal of Applied Chemistry, Vol. 74, No. 6, 2001, pp. 970–975. Translated from Zhurnal Prikladnoi Khimii, Vol. 74, No. 6, 2001, pp. 943–948.

PRODUCTION AND USE OF NEW MATERIALS

Anomalous Behavior of Some Third Derivatives of the Gibbs Potential of the Liquid Phase near Liquidus, Analyzed in Connection with Phase Formation Processes

V. V. Golubkov, B. A. Shakhmatkin, A. A. Pronkin, N. A. Charykov, S. V. Ruzaev, B. A. Aksel'rod, and O. Kh. Chakhal'yan

Institute of Silicate Chemistry, Russian Academy of Sciences, St. Petersburg, Russia
St. Petersburg State Technological Institute, St. Petersburg, Russia
St. Petersburg Institute of Mechanical Engineering, St. Petersburg, Russia

Received March 14, 2001

Abstract—The method of small-angle X-ray scattering was applied to study the Na_2O–B_2O_3 glass-forming system at Na_2O concentrations of up to 33 mol % at 400–1000°C. The temperature-concentration intervals close to binodal curves (at liquidus temperatures corresponding to stable formation of first crystals of the solid phase on cooling the system) were analyzed in most detail.

Previously, the method of small-angle X-ray scattering (SAXS) has been applied to study the structure of melts and glasses in a number of borate systems [1–5], in the concentration range with relatively low content of alkali metal oxide (Na_2O), Li_2O, K_2O) [1–4], and, additionally, in regions with higher content of Na_2O and K_2O (up to 33 and 20 mol %, respectively) [5]. In all cases, the plotted temperature dependences of the SAXS intensity [$I_{SAXS} = f(T)$] exhibited bends in close vicinity of the liquidus temperature (near the binodal curve corresponding to a stable phase equilibrium between the melt and the solid phase). In [1, 2], an assumption was made that the existence of such bends is associated with the transition of the liquid phase from the stable into a metastable, supercooled state.

Simultaneously, in crossing a binodal curve, it is impossible to detect precipitation of a new phase in crystalline form by direct experimental methods [by measuring the specific heat C_p, density ρ, or volume V of the system (Fig. 1)]. In other words, it is impossible to reveal any anomalous behavior of the first and second derivatives of the Gibbs potential of the liquid phase. From the thermodynamic standpoint, this result is quite expected, since, when the fluid transforms into a metastable state without precipitation of a new phase and, thus, with the homogeneous state of the system preserved, the thermodynamic potentials must exhibit a continuous dependence on the state parameters, determined by the partial equation of phase in terms of van der Waals–Storonkin [6]. Appearance of discontinuities in any-order derivatives of the Gibbs potential G would be inexplicable in the case under consideration.

The aim of the present study was to provide a possible explanation for the obtained experimental fact, based on the assumption that an infinitesimal amount of a "new" phase that differs to an infinitely small extent from the "old" phase is formed on crossing the binodal curve (passing from the stable liquid phase to

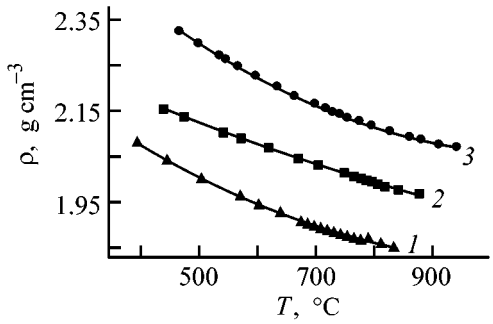

Fig. 1. Liquid phase density ρ vs. temperature T in the Na_2O–B_2O_3 system at constant composition. Na_2O content (mol %): (*1*) 12.5, (*2*) 20.0, and (*3*) 33.0.

1070-4272/01/7406-0970 $25.00 © 2001 MAIK "Nauka/Interperiodica"

a metastable one), i.e., nuclei (microdrops) of a new liquid phase, from which crystals of the solid phase are further formed, appear in the matrix of the old liquid phase. To accomplish this task, the Na_2O–B_2O_3 glass-forming system was studied most thoroughly in the composition range up to 23 mol % Na_2O in the temperature interval 400–1000°C, with primary attention given to the temperature–concentration ranges in close vicinity to the binodal curves (at liquidus temperatures corresponding to stable formation of first crystals of the solid phase upon cooling). As a result, the anomalous behavior of some third mixed derivatives of the Gibbs potential of the liquid phase, the most pronouncedly manifested in the temperature and concentration dependences of the derivatives of the isothermal compressibility β_T with respect to temperature T and concentration X at, respectively, constant concentration and temperature, was confirmed experimentally.

The experimental procedure was described in detail in [1–5]. Typical experimental temperature dependences of the SAXS intensity I_{SAXS} at constant melt composition X in the Na_2O–B_2O_3 system are presented in Fig. 2 together with the liquidus temperatures (binodal temperatures) for the melt composition studied, found from the data of [7]. It can be seen from Fig. 2 that the temperatures of discontinuities of II kind (bends) in the I_{SAXS}–T curves coincide within the experimental error (±5 deg) with the liquidus temperature. This phenomenon is observed for all melt compositions except $0.2Na_2O \cdot 0.8B_2O_3$ corresponding to the stoichiometry of the compound $Na_2O \cdot 4B_2O_3$ crystallizing to give a solid phase in this composition range [7]. It is for this composition that virtually no bend is observed (Fig. 2).

Typical temperature dependences of the isothermal compressibility of the liquid phase, $\beta_T(T)_X$, in the system Na_2O–B_2O_3 are presented in Fig. 3. Naturally, in this case, too, discontinuities of II kind are observed in the functions $\beta_T(T)_X$, coinciding with high precision with the liquidus temperature for all compositions except $0.2Na_2O \cdot 0.8B_2O_3$.

To evaluate the relative discontinuity in the derivative in passing through the liquidus temperature, the function $I_{SAXS}(T)$ was approximated mathematically and the obtained approximation was used to calculate the functions $\beta_T(T)_X$ and $(d\beta_T/dT)_X$. A typical result of approximation for the composition $0.33Na_2O \cdot 0.67B_2O_3$ is presented in Fig. 4. It can be seen that the function $\beta_T(T)_X$ is virtually linear before and after the liquidus temperature, and the function $(d\beta_T/dT)_X$ shows a discontinuity which is relatively significant

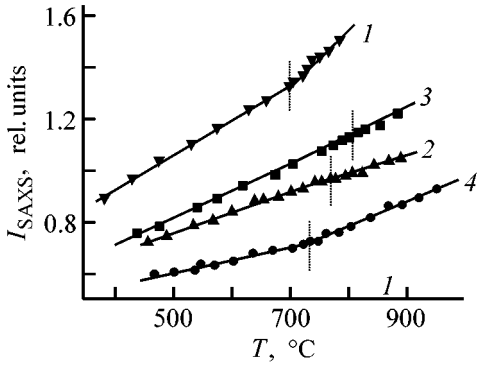

Fig. 2. Intensity of small-angle X-ray scattering by the liquid phase, I_{SAXS}, vs. temperature T in the Na_2O–B_2O_3 system at constant composition. Na_2O content (mol %): (*1*) 10.0, (*2*) 15.0, (*3*) 20.0, and (*4*) 33.0; the same for Fig. 3. *Dotted lines* show the liquidus temperatures according to [5, 7]; the same for Figs. 3 and 4.

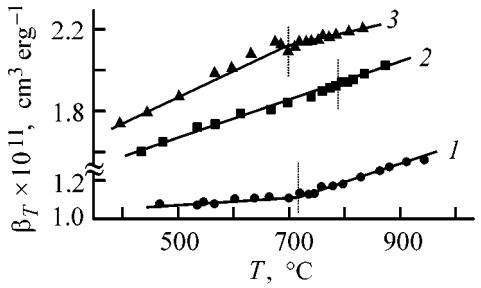

Fig. 3. Isothermal compressibility of the liquid phase, β_T, vs. temperature T in the Na_2O–B_2O_3 system at constant composition.

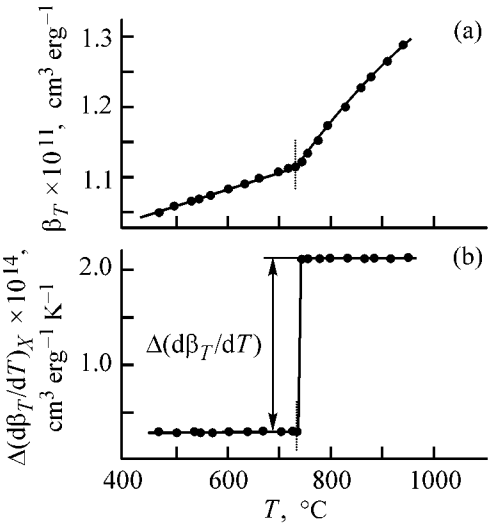

Fig. 4. Approximation of (a) isothermal compressibility β_T and (b) its temperature derivative $(d\beta_T/dT)_X$ for the liquid phase in the system Na_2O–B_2O_3 for the composition $0.33Na_2O \cdot 0.67B_2O_3$. ($T$) Temperature.

and constitutes hundreds of relative percent [in terms of the $(d\beta_T/dT)_X$ function value]. A similar pattern is observed for other compositions studied in the Na_2O–B_2O_3 system, with the discontinuity in the $(d\beta_T/dT)_X$ function also varying between tens and hundreds of relative percent.

An exception is the composition $0.2Na_2O \cdot 0.8B_2O_3$ corresponding to the composition $Na_2O \cdot 4B_2O_3$ which should have crystallized in the solid phase. For this composition, $(d\beta_T/dT)_X \approx$ const and there is no discontinuity in the corresponding derivative.

A similar pattern is observed in considering isothermal concentration dependences of the functions $I_{SAXS}(T)$. In [5], this kind of behavior was observed in a number of other systems, in particular, silicate and borate, containing potassium and lithium oxides. It follows from elementary considerations that a similar pattern must be observed in the behavior of other temperature- or concentration-related baric or volume functions—coefficients of volume and linear thermal expansion, compressibility factors, etc.

It can be seen from experimental data that, in crossing a binodal curve, part of third mixed Gibbs derivatives, e.g., $(d\beta_T/dT)_T$ and $(d\beta_T/dT)_X$, suffers a discontinuity, with the lower-order derivatives, e.g., $\beta_T(X)_T$, $\beta_T(T)_X$, $\rho(X)_T$, $\rho(T)_X$, ... (ρ is density), exhibiting no discontinuities of this kind. Indeed, we are dealing with specific features of just third mixed derivatives, since, e.g.,

$$(d\beta_T/dT)_X = (\partial V/\partial T)(\partial^2 G/\partial P^2)/V^2 - (1/V)(\partial^3 G/\partial P^2 \partial T) \quad (1)$$

and it apparently follows that $(\partial^3 G/\partial P^2 \partial T) = \pm\infty$ from the fact that the derivative $(d\beta_T/dT)_X = \pm\infty$ and, according to the experimental data, $(\partial V/\partial T) \neq \pm\infty$ and $(\partial^2 G/\partial P^2)/V^2 \neq \pm\infty$.

Let us consider crossing a binodal (curve or liquidus surface) as a result of some infinitesimal perturbation—change in temperature, dT, at constant composition $\mathbf{X}$ and pressure P, or upon a change in the concentration of one of the components in the system, dX_i, at constant T, P, and concentrations of all other components $X_{j\neq i,n}$ (the number of components in the system has no effect on the following reasoning). In the case of such a perturbation in the old liquid phase, the following phase processes may, in principle, occur.

(1) Let us assume that a finite mass is formed of a phase differing from the old phase to a finite extent. Such a situation occurs, e.g., when the binodal curve is crossed at the melting point of a component or congruently melting compound, or at the extremum of the melting point of the solid solution. From the system of differential equations describing the process of phase formation, e.g., crystallization, follows, in the case of the only variable intensive parameter of the heterogeneous complex, e.g., temperature ($n \geq 2$) [8, 9], that

$$(\mathbf{X}^{(s)} - \mathbf{X}^{(l)})\hat{G}^{(l)} d\mathbf{X}^{(l)} = (Q^{(ls)}/T)\,dT, \quad (2)$$

$$d\mathbf{X}^{(l)} = (\mathbf{X}^{(s)} - \mathbf{X}^{(l)})\,dm^{(s)}, \quad (3)$$

where $\mathbf{X}^{(s)}$, $\mathbf{X}^{(l)}$, and $d\mathbf{X}^{(l)}$ are vectors representing, respectively, the compositions of the solid phase and the melt and the shift in melt composition upon formation (e.g., crystallization) of $dm^{(s)}$ moles of the new phase s (e.g., solid) from 1 mol of the melt; $\hat{G}^{(l)}$ is the operator corresponding to the matrix of second derivatives of the Gibbs potential of the melt with elements $G_{ij}^{(l)} = (\partial^2 G/\partial X_i \partial X_j)^{(l)}_{TPX_{k\neq j,n}}$—the differential molar heat effect of crystallization.

The vectors $\mathbf{X}^{(j)}$ originate in the Cartesian space of independent variables—mole fractions of the components, $X_i^{(j)}$ [8, 9]. From the system of Eqs. (2) and (3) follows that

$$(\mathbf{X}^{(s)} - \mathbf{X}^{(l)})\hat{G}^{(l)}(\mathbf{X}^{(s)} - \mathbf{X}^{(l)})T/Q^{(ls)} = dT/dm^{(s)}. \quad (4)$$

Since in the case in question the node vectors are zero and the phase effect of crystallization is nonzero, the corresponding derivative of temperature with respect to the mass of the crystallizing phase is zero and the derivative of the mass of the crystallizing phase with respect to temperature is infinite. Indeed, to an infinitesimal change in temperature must correspond a finite change in mass:

$$\mathbf{X}^{(s)} - \mathbf{X}^{(l)} = 0, \quad Q^{(ls)} \neq 0, \quad dm^{(s)}/dT = \pm\infty. \quad (5)$$

This kind of consideration disagrees with the experiment, since, according to the thermodynamic theory of first-order phase transitions [6], the Gibbs potential G of a heterogeneous system suffers in this case a discontinuity of second kind, and the first, second, and other derivatives of the Gibbs potential (V, S, β_T, ...) suffer a discontinuity of the first kind, which is not observed in the experiment under consideration. The discontinuity is determined by the difference of these derivatives in the liquid (l) and solid (s) states.

(2) Let us assume that no new phase is formed, i.e., the state of the metastable liquid is in this case in no way distinguishable from the state of the stable liquid.

This variant of preservation of the homogeneous state of the system is also impossible since in this case the thermodynamic potentials of the system and any of their derivatives must exhibit a continuous dependence on the state parameters, determined by the partial equation of phase.

(3) Let us assume that a finite amount of a phase differing from the old phase to an infinitely small extent. Such a situation occurs, e.g., when critical phases are formed from a homogeneous melt. It is noteworthy that the solid and liquid phases cannot, in principle, form a critical phase [6] since they are described by fundamentally different equations of phase. This means that in this case two or more new liquid phases must form from a homogeneous melt.

In this case, the node vectors in Eq. (4) are again zero, with, however, the phase effect being zero, too (by definition of the critical phase); the operator $\hat{G}^{(l)}$ corresponds to a matrix with zero determinant; the corresponding indeterminate form in Eq. (4) is evaluated as zero [6], the derivative of the mass of the crystallizing phase with respect to temperature is infinite, and to an infinitesimal change in temperature must correspond a finite change in mass:

$$\mathbf{X}^{(s)} - \mathbf{X}^{(l)} = 0, \quad Q^{(ls)} = 0, \quad dm^{(s)}/dT = \pm\infty. \quad (6)$$

Let us demonstrate that this variant is also impossible in principle. Let (h), (s), and (l) be the indices of a heterogeneous complex of new (e.g., solid) and old (e.g., liquid) phases; Par is some arbitrary intensive state parameter: T, P, X_i, ... (we take derivatives with respect to only one parameter, a similar situation will be in considering mixed derivatives); $m^{(s)}$ is the mass of the new phase appearing at the points where the binodal curve is crossed; ΔG is the difference of the molar Gibbs potentials of phases l and s; $G^{(l)}$ and $G^{(s)}$ are the molar Gibbs potentials of the respective phases; and the index α characterizes the corresponding parameter fixing in differentiation. Then

$$G^{(h)} = G^{(l)} + m^{(s)}\Delta G, \quad (7)$$

$$(\partial G^{(h)}/\partial \mathrm{Par})_\alpha = (\partial G^{(l)}/\partial \mathrm{Par})_\alpha + (\partial \Delta G/\partial \mathrm{Par})_\alpha m^{(s)} + \Delta G(\partial m^{(s)}/\partial \mathrm{Par})_\alpha, \quad (8)$$

$$(\partial^2 G^{(h)}/\partial \mathrm{Par}^2)_\alpha = (\partial^2 G^{(l)}/\partial \mathrm{Par}^2)_\alpha + (\partial^2 m^{(s)}/\partial \mathrm{Par}^2)_\alpha \Delta G + (\partial^2 \Delta G/\partial \mathrm{Par}^2)_\alpha m^{(s)} + 2(\partial \Delta G/\partial \mathrm{Par})_\alpha (\partial m^{(s)}/\partial \mathrm{Par})_\alpha, \quad (9)$$

where $(d\mathrm{Par})_\alpha$ is a first-order infinitesimal, $(\partial G^{(l)}/\partial \mathrm{Par})_\alpha$ is finite, and $(\partial^2 G^{(l)}/\partial \mathrm{Par}^2)_\alpha$ is infinite physically, all these parameters being taken for a homogeneous (stable or metastable) phase α; $m^{(s)}$ is finite at the given perturbation according to the starting assumption 3; ΔG is infinitesimal according to phase equilibrium conditions; $(\partial \Delta G/\partial \mathrm{Par})_\alpha$ and $(\partial^2 \Delta G/\partial \mathrm{Par}^2)_\alpha$ are infinitesimal according to the critical phase properties; $(\partial m^{(s)}/\partial \mathrm{Par})_\alpha = \pm\infty$ also in accordance with assumption 3 and Eq. (6); the corresponding indeterminate form $\Delta G(\partial m^{(s)}/\partial \mathrm{Par})_\alpha$ is evaluated as finite and, consequently, $(\partial G^{(h)}/\partial \mathrm{Par})_\alpha$ is also finite, in agreement with the experiment.

Let us now consider the behavior of $(\partial^2 G^{(h)}/\partial \mathrm{Par}^2)_\alpha$. All the terms in Eq. (9) are finite with the exception of the product $\Delta G(\partial^2 m^{(s)}/\partial \mathrm{Par}^2)_\alpha$, an indeterminate form evaluated as $\pm\infty$. Therefore, $(\partial^2 G^{(h)}/\partial \mathrm{Par}^2)_\alpha = \pm\infty$, which contradicts the experiment.

(4) Let us assume that an infinitesimal amount is formed of a phase differing to a finite extent from the old phase. Such a situation occurs when the binodal curve is crossed at a "nonsingular" point of a multicomponent system, with the new phase formed but formation of infinitesimal amounts of the solid phase always corresponding to an infinitesimal change in temperature. In this case, the node vectors in Eq. (4) are nonzero, the phase effect of crystallization is other than zero, the derivative of the mass of the crystallizing phase with respect to temperature is finite, and to an infinitesimal change in temperature must correspond an infinitesimal change in mass:

$$\mathbf{X}^{(s)} - \mathbf{X}^{(l)} \neq 0, \quad Q^{(ls)} \neq 0, \quad dm^{(s)}/dT \text{ is finite.} \quad (10)$$

This case is similar to the already considered case 3, i.e., $(\partial G^{(h)}/\partial \mathrm{Par})_\alpha$ is finite and $(\partial^2 G^{(h)}/\partial \mathrm{Par}^2)_\alpha = \pm\infty$, which again contradicts the experiment.

(5) Let us, finally, consider the case not analyzed previously [6], namely, the formation of an infinitesimal amount of a new phase differing from the old phase to an infinitely small extent. This case is close to variant 3; however, by virtue of the fact that the node vectors are zero the corresponding indefinite form in Eq. (4) is evaluated as finite and the derivative of the mass of the forming phase with respect to temperature is also finite:

$$\mathbf{X}^{(s)} - \mathbf{X}^{(l)} = 0, \quad Q^{(ls)} = 0, \quad dm^{(s)}/dT \text{ is finite.} \quad (11)$$

In this case, both the derivatives $(\partial G^{(h)}/\partial \mathrm{Par})_\alpha$ and $(\partial^2 G^{(h)}/\partial \mathrm{Par}^2)_\alpha$ are finite, in agreement with the experiment.

Let us again use relation (7), differentiating it once more:

$$(\partial^3 G^{(h)}/\partial \mathrm{Par}^3)_\alpha = (\partial^3 G^{(l)}/\partial \mathrm{Par}^3)_\alpha + 3(\partial^2 m^{(s)}/\partial \mathrm{Par}^2)_\alpha(\partial \Delta G/\partial \mathrm{Par})_\alpha + 3(\partial^2 \Delta G/\partial \mathrm{Par}^2)_\alpha(\partial m^{(s)}/\partial \mathrm{Par})_\alpha + (\partial^3 G/\partial \mathrm{Par}^3)_\alpha m^{(s)} + (\partial^3 m^{(s)}/\partial \mathrm{Par}^3)\Delta G, \quad (12)$$

where $(\partial^3 G^{(h)}/\partial \mathrm{Par}^3)_\alpha$ is finite and $(\partial^n G^{(h)}/\partial \mathrm{Par}^n)_\alpha$ ($n = 1, 2$) are infinitesimal physically.

In their turn, $(\partial^2 m^{(s)}/\partial \mathrm{Par}^2)_\alpha$ and $(\partial^3 m^{(s)}/\partial \mathrm{Par}^3)_\alpha$ are equal to $\pm\infty$. This means that $(\partial^3 G^{(h)}/\partial \mathrm{Par}^3)_\alpha = \pm\infty$ and the third derivative of the Gibbs potential suffers a discontinuity of I kind, in good agreement with the experiment.

Of the variants considered, assumption 5 is the only one that does not contradict the experiment. Naturally, this assumption is a sufficient, but in no way necessary condition.

Thus, in crossing the binodal curve, an infinitesimal amount (micronuclei) of a new liquid phase originally differing to an infinitely small extent from the old phase is formed in the matrix of the old liquid phase. From these nuclei, the solid phase is further formed. Let us make several additional remarks.

(1) The given crystallization mechanism (always going via preliminary segregation) has not been, to our knowledge, proposed so far. The liquid phase seemingly "prepares" to form from itself a solid phase. It is noteworthy that in this case there is virtually no interface between the old liquid phase-matrix and the new liquid phase differing to an infinitely small extent from the old one. Therefore, no essentially positive surface energy appears in the system, i.e., the nuclei are not limited in their growth by the surface tension.

(2) This mechanism describes the onset of crystallization in systems tending to form metastable states (supercooled, oversaturated, etc.). If a system does not tend to form metastable states (to be supercooled or oversaturated), then the "distance" between the binodal and spinodal curves in a variable parameter (temperature or, e.g., concentration) is relatively small and the effect under consideration may be not actually observed in the experiment.

(3) Let us elucidate the wording "infinitesimal amount of new phase." This means the amounts conforming to the concept of phase as such ($>10^{10-12}$ particles per mole of old phase). The seeming contradiction is eliminated if we assume in our reasoning that the mass of the formed phase $m^{(s)}$ and the perturbation d Par are mathematically quantities of the same order of smallness (simply infinitesimals).

(4) Let us now elucidate the wording "phase differing to infinitely small extent from old phase." The difference may be associated with dissimilarity in properties (as a result of, e.g., the appearance of long- or medium-range order) or, simultaneously, with that in composition. We assume that in the given case we have an infinitesimally small difference in composition. This is indicated by the absence of any effects for the composition corresponding to the stoichiometry of the equilibrium solid phase ($Na_2O \cdot 4B_2O_3$ in the case in question). Indeed, if a new liquid phase emerges, shifting its composition toward that of the solid phase, then such a shift will be always observed except in the case when the compositions of the liquid and solid phases coincide. However, this explanation cannot be exhaustive since the compound $Na_2O \cdot 2B_2O_3$ (also melting congruently) does show the corresponding effect.

(5) If we adopt the mentioned postulate, then, under the conditions in question, the third derivatives of the Gibbs potential of a heterogeneous system with respect to extensive state parameters (S, V, ...) must pass through zero, or second derivatives of the intensive parameters (T, P, X, ...) with respect to extensive parameters (S, V, m_i) must pass through zero, or second derivatives of the extensive parameters with respect to intensive parameters must be infinite or suffer a discontinuity of I kind, and its own state parameter fixing in differentiation should be performed for each derivative.

(6) Other mixed second or third derivatives can be considered in a similar way. Noteworthy are some fundamental functions which (in terms of the proposed mechanism) must suffer a discontinuity of I kind in crossing the binodal curve: first derivatives of the isothermal compressibility, thermal expansion coefficients, and compressibility factors, etc. with respect to temperature and concentration; first derivatives of the isobaric or isochoric specific heat with respect to temperature and concentration; second derivatives of the chemical potentials of the components with respect to temperature and second mixed derivatives of the same parameter with respect to temperature–concentration or concentration–concentration, etc.

(7) In a real experiment, the discontinuities in derivatives of this kind may be unobservable because of the relatively poor precision of the experiments performed: the accuracy of determining the third derivatives of the Gibbs potential is incomparably poorer than that with which the second, and the more so the first, derivatives are found, and the jumps of I(II) kind themselves may be relatively weak, especially in sys-

tems that do not tend to form metastable states (see remark 2). In particular, even data on G_p are determined in a thermodynamic calorimetric experiment indirectly, by measuring the corresponding heats (temperatures). In this regard, the experiment on determining the isothermal compressibility holds a distinctive position, since this parameter is measured in experiment virtually directly with rather high accuracy, which gives reason to believe that jumps in derivatives of just this function will be revealed in the simplest way.

CONCLUSION

A plausible and consistent explanation for the experimental fact that the derivatives of the isothermal compressibility of the liquid phase with respect to concentration and temperature suffer discontinuities of I kind in crossing the binodal curve is the assumption that nuclei of a new liquid phase (microdrops) are formed in this case in the matrix of the old liquid phase, with crystals of the solid phase further formed from these nuclei.

ACKNOWLEDGMENTS

The study was supported by the Russian Foundation for Basic Research and the Council of the Presidium of the Russian Federation for grants (projects nos. 00-03-32 220 and 00-15-99 334).

REFERENCES

1. Golubkov, V.V., *Fiz. Khim. Stekla*, 1992, vol. 18, no. 2, pp. 14–19.
2. Golubkov, V.V., Titov, A.P., and Porai-Koshits, E.A., *Fiz. Khim. Stekla*, 1992, vol. 18, no. 2, pp. 46–52.
3. Golubkov, V.V., *J. Non-Cryst. Solids*, 1995, vols. 192–193, pp. 463–466.
4. Golubkov, V.V., *Fiz. Khim. Stekla*, 1998, vol. 24, no. 3, pp. 289–294.
5. Golubkov, V.V. and Shakhmatkin, B.A., *Fiz. Khim. Stekla*, 1999, vol. 25, no. 4, pp. 444–449.
6. Storonkin, A.V. *Termodinamika geterogennykh sistem* (Thermodynamics of Heterogeneous Systems), Leningrad: Len. Gos. Univ., 1967, part 1.
7. Levin, E.M. and McMurdic, H.T., *Phase Diagrams for Ceramics*, Reser, M.K., Ed., Columbus, Ohio: Am. Chem. Soc., 1975, vol. 3.
8. Charykov, N.A., Rumyantsev, A.V., and Charykova, M.V., *Zh. Fiz. Khim.*, 1998, vol. 72, no. 1, pp. 39–44.
9. Charykov, N.A., Rumyantsev, A.V., and Charykova, M.V., *Zh. Fiz. Khim.*, 1998, vol. 72, no. 2, pp. 277–281.

Russian Journal of Applied Chemistry, Vol. 74, No. 6, 2001, pp. 976–980. Translated from Zhurnal Prikladnoi Khimii, Vol. 74, No. 6, 2001, pp. 949–953.

ENVIRONMENTAL PROBLEMS OF CHEMISTRY AND TECHNOLOGY

Flow-Through Conductometric Analysis for Microconcentrations of Ammonia in Natural Water with Chromatomembrane Separation into Deionized Water

L. N. Moskvin, G. L. Grigor'ev, and A. G. Papsueva

St. Petersburg State University, St. Petersburg, Russia

Received October 19, 2000

Abstract—A new scheme is considered of flow-through conductometric analysis for ammonium ions in natural water, based on chromatomembrane separation of ammonia into deionized water. The proposed scheme is compared in efficiency with that based on dialytic separation of ammonia.

Determining the content of ammonia is an important task in monitoring the quality of natural water, since these ions belong to biogens promoting development of phytoplankton. At concentrations in water exceeding 0.2 mg l^{-1}, ammonia is toxic for quite a number of aquatic organisms [1]. Presently, the following maximum permissible concentrations of ammonium nitrogen in water are established (mg l^{-1}): 0.4 for fishing reservoirs and 2.0 for those with water used for technological and drinking purposes. Thus, on-line monitoring of the quality of natural water regarding the ammonia content requires procedures for determining ammonia in the concentration range 0.2–(3–5) mg l^{-1}.

Ammonia is most frequently determined in aqueous solutions photometrically, using the Nessler reagent and the Berthelot reaction. Both variants of the photometric method for ammonia determination are well known and are used both in classical and in flow-through schemes of analysis: flow-injection (FIA) and continuous flow-through analysis (CFTA). The possibilities of different variants of flow-through analysis for ammonia were compared in [2, 3]. Photometric methods generally enable ammonia determination in the required range of concentrations, but have a common shortcoming associated with the use highly toxic reagents.

This shortcoming can be eliminated in the case of the Berthelot reaction by replacing the toxic phenol with sodium salicylate [4]. However, the most efficient solution for overcoming this disadvantage of the photometric techniques was the idea to include into the scheme of flow-injection determination of ammonia a stage of its preliminary dialytic separation [5, 6]. According to this scheme, an alkali solution is introduced into water being analyzed. The ammonia formed in the process diffuses through pores of the hydrophobic membrane of the dialyzer into a flow of deionized water circulating in a closed circuit including a flow-through conductometric detector. The advantage of this scheme of analysis consists, in addition to ruling out use of highly toxic components, in a high selectivity and possibility of achieving low ammonia detection limits because of the high sensitivity of the conductometric sensor in deionized water. With a specially developed flow-through conductometric cell and slit dialyzer (slit depth 100 μm) and a 50-μm-thick poly(ethylene terephthalate) membrane, the calibration plot is linear within the range 0.03–0.5 mg l^{-1}) NH_3 [6].

Apparently, the range of determinable concentrations and the possibility of adjusting its limits are governed in the given scheme of analysis in the first place by the efficiency of operation of the membrane mass-exchange device—narrow-slit dialyzer. The flow of a substance being isolated is limited in the course of dialysis by the diffusion coefficient and membrane thickness. Correspondingly, all other conditions being the same, the range of determinable concentrations can be only changed by varying the thickness of the membranes used. In gas-diffusion processes, the diffusion coefficient is not, as a rule, the rate-determining factor in the case of sufficiently thin membranes (less than 100 μm thick). However, this gives rise to a technical problem associated with the easy de-

1070-4272/01/7406-0976 $25.00 © 2001 MAIK "Nauka/Interperiodica"

formability of such membranes. For reproducible operation of dialyzes with thin gas-diffusion membranes, the pressures in the feed and receiving chambers of the dialyzer should be maintained strictly equal. This is difficult to achieve in the FIA scheme with mixed flows of aqueous media, created by peristaltic pumps, switched at the inlet of the feed chamber.

In order to extend the limits of the range of determinable concentrations and possibilities of control over these limits, and to simplify the conditions under which reproducible results can be obtained, it is proposed to use the chromatomembrane way to perform mass-exchange processes in the liquid–gas system [7] as an alternative to the dialytic separation of ammonia with its subsequent conductometric determination in the FIA and CFTA schemes.

The aim of the present study was to develop a scheme and procedure for flow-through conductometric determination of ammonia ions in natural water, based on chromatomembrane separation of ammonia into deionized water, and to compare the efficiency of the developed scheme with that of the known scheme of analysis with dialytic separation of ammonia under the same conditions of conductometric measurements.

EXPERIMENTAL

To perform chromatomembrane separation of ammonia, a special cell was designed with two identical mass-exchange chambers having separate inlets and outlets for the aqueous solution and gas phase. The mass-exchange chambers are filled with biporous polytetrafluoroethylene with micro- and macropores 05–1.0 μm and 1–2 mm in size, respectively. The inlet and outlet collectors are separated from the biporous mass-exchange layers in the chambers and from each other by a microporous (0.2 mm) polytetrafluoroethylene membrane (Fig. 1). The geometric dimensions of the mass-exchange chambers in the chromatomembrane cell (CMC)—length, width, and height along the liquid flow direction—are 2, 1, and 1 cm, respectively. At the chosen chamber dimensions and porous structure of mass-exchange layers, the flows of the aqueous phase in both CMC chambers can be varied independently within the limits from 0 to 15 ml min^{-1}, and the carrier gas flow rate, from 0 to 20 ml min^{-1}.

The comparison dialyzer has the form of a mass-exchange cell with two chambers separated by a polytetrafluoroethylene membrane identical to those used in the CMC. To reduce the probability of membrane deformation in the case of the possible pressure surges in the dialyzer chambers, the chambers are designed as labyrinths. The depth of channels forming the labyrinths is 0.5 mm, i.e., corresponds to the minimum radius of macropores in the mass-exchange layer of the CMC.

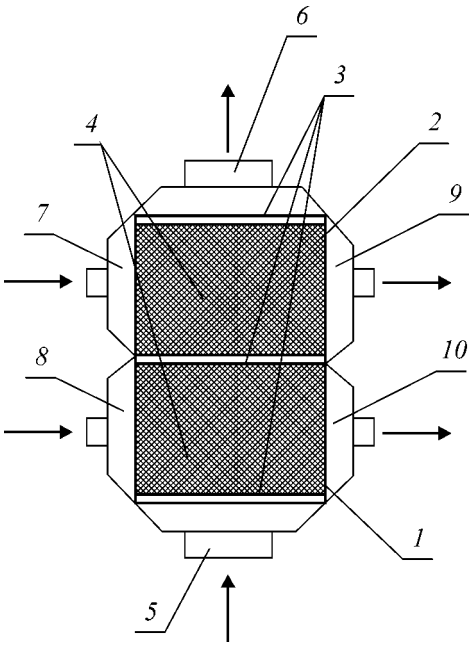

Fig. 1. Schematic of a two-chamber chromatomembrane cell. (*1*) Feed chamber; (*2*) receiving chamber; (*3*) membranes; (*4*) mass-exchange layer; (*5*, *6*) inlet and outlet gas phase collectors, respectively; and (*7–10*) inlet and outlet collectors of the receiving and feed chambers, respectively, in order of enumeration.

The area of the membrane separating the feed and receiving solutions in the dialyzer is 10 times the area of the interface between the mass-exchange chambers in the CMC, or 20 cm^2.

The hydraulic scheme of FIA for ammonium ions in natural water (Fig. 2) was assembled on the basis of standard units of a PIA-ION[1] commercial flow-through analyzer. The scheme variants A and B differ solely in the type of a mass-exchange device (CMC and dialyzer, respectively). The analyzer allows work in two modes: FIA and CFTA. The electrical conductivity of the receiving solution was measured on the standard flowthrough conductometric detector of a TsVET-3006 ion chromatograph.

Irrespective of the analysis mode, the receiving chambers of the mass-exchange devices were included into the closed circuit with deionized water. To maintain constant the composition of deionized water at

[1] Granit-IEMP, St. Petersburg, Russia.

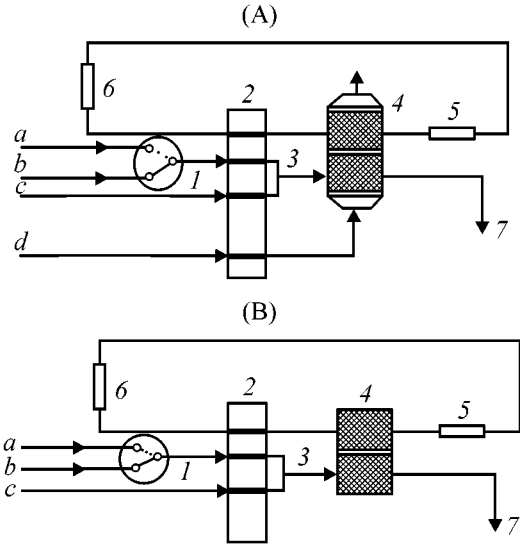

Fig. 2. Schematic of flow-through analyzers for conductometric determination of ammonia in aqueous solution with (A) chromatomembrane and (B) dialytic separation. (*a*) Deionized water, (*b*) sample, (*c*) NaOH + Na_2H_2EDTA solution, and (*d*) air. (*1*) Switching cock; (*2*) peristaltic pump; (*3*) mixing helix; (*4*) CMC or dialyzer, respectively; (*5*) conductometric detector; (*6*) column for deionized water; and (*7*) discharge line for aqueous phase.

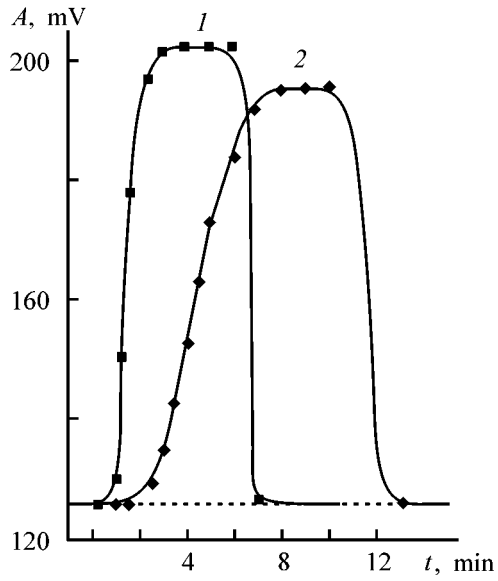

Fig. 3. Kinetic curves demonstrating how the analytical signal *A* from a conductometric detector is formed in ammonia separation from an aqueous solution into deionized water with the use of (*1*) CMC and (*2*) dialyzer. Ammonia concentration in the feed solution 0.54 mg l^{-1}; flow rates of the carrier gas and the feed and receiving solutions 12, 6, and 1.5 ml min^{-1}, respectively. (*t*) Time in which the detector signal reaches a stationary value.

the inlet of the mass-exchange device, a column with mixed ion-exchange stock of KU-2×8 cation-exchange resin and AB-17×6 anion exchange resin. In the CFTA mode, either analyzed or deionized water was alternately fed, using a switching cock, at a rate of 4 ml min^{-1} into the feed chambers of the mass-exchange cells. In calibrating the analyzer, standard solutions of ammonium ions of known concentration were fed instead of water to be analyzed. The standard solutions of ammonia ions were prepared by diluting the starting solution obtained by dissolving a precisely weighed portion of ammonium chloride (chemically pure) predried at 110°C for 12 h [8].

Before being fed into the mass-exchange cells, the flows of water to be analyzed or a standard solution were mixed with a solution of Trilon B (0.1%) in 0.3 M NaOH (flow rate 2 ml min^{-1}). Addition of Trilon B to the alkali is necessary to prevent precipitation in the form of hydroxides of metals contained in natural water. Gaseous ammonia formed in mixing of flows of a sample (standard solution), and the adjusting solution came, driven by the concentration gradient (scheme B) or carrier gas flow (scheme A), into the receiving chamber of the mass-exchange cell, included into a closed circuit with a flow-through conductometric detector. Water was circulated through the closed circuit mainly through stainless steel pipes. The length of sections formed by silicone hoses in the peristaltic pump and connections between metallic pipes was made as short as possible to reduce the diffusion supply of atmospheric carbon dioxide into the deionized water. CO_2 was removed from air used for mass-transfer of ammonia from the feed into the receiving chamber in the CMC by passing air through a flow of alkaline solution in the feed chamber.

To compare the response times of the chromatomembrane and dialytic schemes of ammonia separation, the background value of the analytical signal was recorded in the switching cock position corresponding to delivery of a sample of deionized water into the feed chambers of the CMC and dialyzer through the input line. After a stationary value of the analytical signal was reached, the cock was switched into the position for feeding-in a sample in the form of a standard solution with ammonium ion concentration of 0.54 mg l^{-1}.

Figure 3 presents kinetic curves demonstrating how the signal from the conductometric detector reaches its stationary value for schemes A and B after such flow switching. The analytical signal *A* was measured

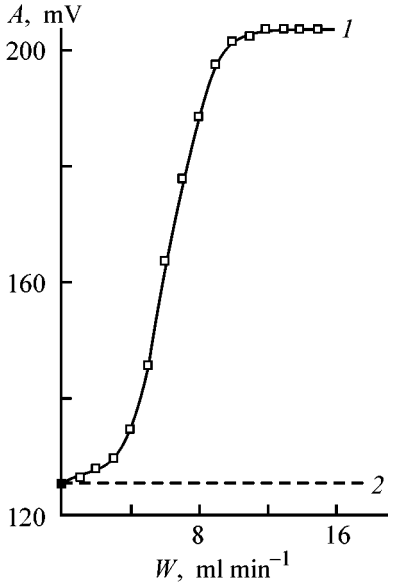

Fig. 4. Detector signal *A* vs. carrier gas flow rate *W*. Ammonia concentration in the feed solution 0.54 mg l^{-1}; flow rates of the feed and receiving solutions 6 and 1.5 ml min^{-1}, respectively. (*1*) Solution of ammonia ions and (*2*) deionized water.

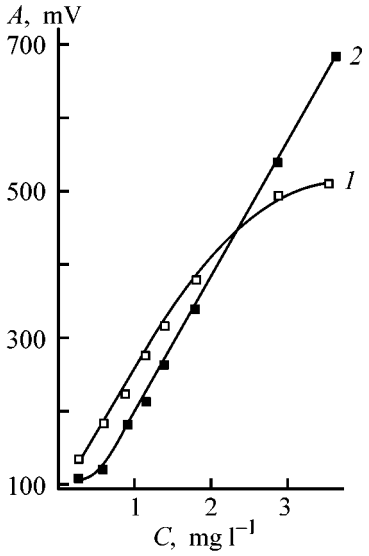

Fig. 5. Detector signal *A* vs. ammonium ion concentration *C* in the aqueous solution in chromatomembrane separation of ammonia into deionized water. Flow rates of carrier gas and feed solution 12 and 6 ml min^{-1}, respectively. Flow rate of receiving solution (ml min^{-1}): (*1*) 1.5 and (*2*) 5.

in millivolts on the scale of the conductometric detector of an ion chromatograph. In view of the relative nature of the measurements, no calibration against standard solutions in electrical conductivity units was done. It can be seen that the analytical signal is formed in a scheme with chromatomembrane separation and substance transfer from a sample into the receiving chamber induced by the carrier gas flow, much (3 times) faster than in the case of dialytic separation with diffusion mass transfer of ammonia from the feed into the receiving solution, despite the fact that in the former case the interface area in the mass-exchange chambers is 10 times that in the latter.

A similar pattern of slowed-down operation of the dialytic scheme is also observed in the following FIA stage—washing of the sample passage line in the hydraulic system with deionized water to bring the detector signal to the background value. With scheme A, the duration of this stage is virtually independent of the concentration of the substance to be determined over the entire concentration range studied (0.15–3.5 mg l^{-1}), being equal to approximately 1.2 min. For scheme B, this time is 3 min at a NH_4^+ concentration in a sample of 0.54 mg l^{-1} and grows with increasing concentration of the component to be determined.

The decrease in the response time of the analytical signal on passing from the dialytic scheme to a chromatomembrane one depends on the flow rate of the carrier gas (Fig. 4). All other conditions being the same, the detector signal grows with increasing carrier gas flow rate, to reach a maximum at 12–15 ml min^{-1}, which corresponds to a linear velocity in pores of about 1 cm s^{-1}. The contribution from the purely diffusion component to the overall mass transfer can be evaluated by comparing the detector signals in those cases when a solution of ammonium ions (Fig. 4, curve *1*) and pure deionized water (Fig. 4, straight line *2*) are used as feed solutions. The fact that the initial portions of the curves virtually merge indicates that, at a carrier gas flow rate $W \to 0$, this contribution is no more than several percent. It is the exceedingly low contribution of the purely diffusion component to the overall mass transfer that accounts for the fast response of the analytical system with chromatomembrane separation of ammonia. Hence follows one important practical consequence: in view of its fast response, the chromatomembrane method of sample processing can be effectively used not only in FIA, but also in CFTA. This is indicated by the shape of the analytical signals (Fig. 3) corresponding to the response to a change in the ammonium ion concentration in a solution being analyzed in the continuous mode. An important factor in this case is the high stability of the background signal, ensured by the invariable quality of deionized water in the closed circuit with an ion-exchange column.

The implementation in the chromatomembrane process of an advantage of the membrane methods of separation—the possibility of varying the flow rates of the feed and receiving solutions, makes it possible to solve one more practically important problem: enable control over the range of determinable concentrations within the same scheme of analysis. It can be seen from Fig. 5 that the calibration plot is linear at a receiving solution flow rate of 1.5 ml min^{-1} and ammonium ion content in the range from 0.15 to 1.4 mg l^{-1}. However, since ammonia concentrations on the order of 2 mg l^{-1} are of interest in monitoring the quality of some kinds of water, e.g., water for technological and drinking purposes, a necessity arises for expanding the range of determinable concentrations.

The investigations performed with the use of the chromatomembrane method of ammonia separation in its flow-injection conductometric determination demonstrated that, all other conditions being the same, raising the flow rate of the receiving solution makes the upper limit of determinable ammonia concentrations higher. For example, at a flow rate of the receiving solution of 1.5 ml min^{-1}, the calibration plot is linear up to ammonia concentrations of 3.5 mg l^{-1}, with the slope of the curve independent of the flow rate.

The obtained data suggest that the scheme of conductometric determination of ammonium ions in natural water, based on chromatomembrane separation of ammonia into deionized water, is preferable to the dialytic scheme. The proposed scheme of analysis can be used for any kind of natural water on making an appropriate choice of the range of determinable concentrations by fixing the corresponding flow rate of the receiving solution.

CONCLUSIONS

(1) A new scheme and a procedure for flow-injection and continuous flow-through analyses for ammonium ions in natural water is proposed, based on chromatomembrane separation of ammonia. The method makes it possible to determine ammonium ions in water at concentrations in the range from 0.15 to 1.4–3.5 mg l^{-1}, depending on the flow rates of a sample, absorbing solution, and gas inducing the mass transfer of ammonia.

(2) The efficiency of the developed scheme is compared with that of the analytical scheme with dialytic separation of ammonia under identical conditions of conductometric measurements. It is shown that the chromatomembrane scheme ensures faster response of the analytical signal and, correspondingly, the possibility of on-line continuous flow-through analysis.

ACKNOWLEDGMENTS

The authors are grateful to the Russian Foundation for Basic Research (grant no. 99-03-32-654).

REFERENCES

1. Przybylko, A.R.M., Thomas, C.L.P., Anstice, P.J., *et al.*, *Anal. Chim. Acta*, 1995, no. 311, pp. 77–83.
2. Hussein, M.T., *Anal. Lett.*, 1988, vol. 21, no. 7, pp. 1285–1296.
3. Schulze, G., Liu, C.Y., Brodowski, M., *et al.*, *Anal. Chim. Acta*, 1988, no. 214, pp. 121–136.
4. Gibb, S.W., Mautoura, R.C., and Liss, P.S., *Anal. Chim. Acta*, 1995, no. 316, pp. 291–304.
5. Andrew, K.N., Worsfold, P.J., and Comber, M., *Anal. Chim. Acta*, 1995, no. 314, pp. 33–43.
6. Cardoso de Faria, L. and Pasquini, C., *Anal. Chim. Acta*, 1991, no. 245, pp. 183–190.
7. Moskvin, L.N., *Zh. Anal. Khim.*, 1996, vol. 51, no. 11, pp. 1125–1129.
8. Pasquini, C. and Cardoso de Faria, L., *Anal. Chim. Acta*, 1987, no. 193, pp. 19–27.

Russian Journal of Applied Chemistry, Vol. 74, No. 6, 2001, pp. 981–985. Translated from Zhurnal Prikladnoi Khimii, Vol. 74, No. 6, 2001, pp. 954–958.

PROCESSES AND EQUIPMENT OF CHEMICAL INDUSTRY

Calculation of Capillary Disintegration of Fluid Jet into Drops in Terms of Linear Theory

Yu. G. Chesnokov

St. Petersburg State Technological Institute, St. Petersburg, Russia

Received May 23, 2000; in final form, February 2001

Abstract—A formula is derived for calculating the wave number at which the highest rate of perturbation build-up is observed in relation to the Reynolds number. The diameter of drops appearing in spontaneous disintegration of a fluid jet into drops and the time elapsed from the appearance of a perturbation till the fluid jet disintegration into drops are plotted as functions of the Reynolds number.

A fluid jet outflowing from a nozzle into a gaseous medium may spontaneously disintegrate into drops. This phenomenon occurs as a result of instability of the fluid flow in the jet against minor perturbations. The reason for flow instability is the action of surface tension forces at the jet surface. When there occurs a local decrease in the jet radius, the capillary forces cause a local increase in pressure. Contrariwise, in the case of a local increase in the jet radius, the pressure decreases. As a result, the fluid flows from regions with higher pressure to those with lower pressure, and the perturbation is enhanced. The phenomenon of capillary disintegration of a fluid jet into drops finds numerous applications in chemical engineering and other fields of technology [1]. For this reason capillary waves on the fluid jet surface have long been studied both experimentally and theoretically. A review of the literature on this issue was given in [1, 2].

As long ago as in Rayleigh's works it was shown that, in the presence of a sinusoidal perturbation, the flow is unstable when the perturbation wavelength exceeds the perimeter of a circle delimiting the jet cross-section. Rayleigh used linearized equations of hydrodynamics and boundary conditions at the jet surface, assuming that the amplitudes of perturbations of fluid velocity and pressure and jet radius are small. He obtained an algebraic equation relating the perturbation wavelength and the rate of perturbation amplitude build-up. The Rayleigh theory is applicable, generally speaking, only to description of the initial stage of perturbation development. In the course of time, the perturbation amplitude grows and the linearized equations, only valid for small-amplitude perturbations, become inapplicable. That is why further development of the theory has been aimed at describing the nonlinear interaction of perturbations.

The nonlinear stage of perturbation evolution has been described using different approaches. In [3–7], a solution to the problem of nonlinear development of capillary waves on the surface of a jet of ideal fluid was constructed in the form of expansions in terms of a small parameter—perturbation amplitude. In [8–12], the process of fluid jet disintegration into drops was subjected to direct numerical modeling, involving a huge expenditure of computing time. Therefore, it is difficult to use such calculations for a systematic study of the influence exerted by various factors on the capillary disintegration of a jet.

As shown by the experimental data obtained in [13, 14], the linear theory well describes the experimentally measured rate of perturbation build-up. This theory can be used to calculate the interval of time between the onset of a perturbation and the jet disintegration into drops. In the case when perturbations arise spontaneously, perturbations with different wavelengths are possible. Since a perturbation with a certain wavelength has the highest build-up rate, the fluid jet may disintegrate into drops through build-up of perturbations with just this wavelength. The wavelength of the perturbation with the highest build-up rate can be calculated using a relation obtained by Rayleigh. However, calculations of this kind are rather labor-consuming, since they require multiple solution of a transcendent equation involving Bessel functions.

1070-4272/01/7406-0981 $25.00 © 2001 MAIK "Nauka/Interperiodica"

The aim of this study was to construct simple calculational expressions for determining the wavelength of the perturbation having the highest build-up rate and to find the build-up rate of this perturbation.

Let as consider the development with time of a small perturbation on the surface of a cylindrical jet of a Newtonian viscous fluid outflowing into a gaseous medium. It is assumed that fluid flow is laminar. If the fluid velocity in the jet is high enough, the gravity force will have no significant influence on the fluid motion in the jet. Also, at not-too-high fluid velocities the interaction of the fluid with the ambient can be disregarded. Both these conditions are considered to be fulfilled. As far back as in Rayleigh's works it was established that the fluid flow in a jet may be unstable only with respect to perturbations possessing axial symmetry. Therefore, the fluid motion in the jet is assumed to be axially symmetric.

When writing down equations describing the fluid flow and boundary conditions for these equations, we use dimensionless variables. Let us introduce the following designations: a, the jet radius which can be used as the characteristic linear scale of the problem; ρ, the fluid density; and σ, the surface tension at the fluid–ambient interface. As is known, in the case of a jet of ideal fluid, the interval of time between the instant of perturbation appearance and that of jet disintegration into drops is proportional to a quantity having dimensionality of time, $t_0 = (\rho a^3/\sigma)^{1/2}$. We use this quantity as the characteristic time scale for the problem under consideration. Then, $u_0 = a/t_0 = (\sigma/\rho a)^{1/2}$ can be used as velocity scale. As pressure scale we introduce $p_0 = \sigma/a$.

Let us introduce into consideration a cylindrical system of coordinates (r, ϑ, z) whose z-axis coincides with the jet axis. We denote time by t; the axial and radial components of the fluid flow velocity by, respectively, u and ν; and the fluid pressure by p. All these quantities are assumed to be dimensionless. The equations describing the fluid flow in a jet are the continuity equation and the axial and radial components of the Navier–Stokes equation. In dimensionless form, these equations are as follows:

$$\nu_r + \nu/r + u_z = 0,$$

$$u_t + \nu u_r + u u_z = -p_z + \frac{1}{\mathrm{Re}}\left[\frac{1}{r}(r u_r)_r + u_{zz}\right],$$

$$\nu_t + \nu\nu_r + u\nu_z = -p_r + \frac{1}{\mathrm{Re}}\left[\frac{1}{r}(r\nu_r)_r - \frac{\nu}{r^2} + \nu_{zz}\right].$$

The Reynolds number Re, appearing in these equations, is defined by

$$\mathrm{Re} = (\rho a \sigma)^{1/2}/\mu,$$

where μ is the fluid viscosity.

In writing the equations, the subscripts of the variables denote differentiation with respect to the corresponding variable, i.e., $\nu_r = \partial\nu/\partial r$ etc.

We now consider the boundary conditions at the fluid surface. Let the equation of the free surface have the form

$$r = \eta(z, t).$$

Then we have kinematic boundary condition

$$r = \eta: \quad \eta_t + u\eta_z = \nu$$

and two dynamic boundary conditions

$$r = \eta: \quad 2\nu_r\eta_z + (u_r + \nu_z)(1 - \eta_z^2) - 2u_z\eta_z = 0,$$

$$p - \frac{1}{\mathrm{Re}}\left[2\nu_r - (u_r + \nu_z)\eta_z\right] = p_a + \frac{1}{\eta(1 + \eta_z^2)^{1/2}} - \frac{\eta_{zz}}{(1 + \eta_z^2)^{3/2}},$$

where p_a is the ambient pressure.

In a coordinate system moving together with the fluid, the formulated problem has the following solution

$$\eta = 1, \quad u = \nu = 0, \quad p = p_a.$$

This solution describes the unperturbed motion of the fluid jet in a coordinate system moving together with the fluid.

Let us assume that at the initial instant of time there exists a sinusoidal perturbation of the jet surface

$$t = 0: \quad \eta = 1 + \varepsilon\cos(kz),$$

where ε is the initial amplitude of the perturbation, and k is the wave number.

The equations of hydromechanics and the boundary conditions, written in the dimensionless form, contain a single dimensionless parameter—Reynolds number. Therefore, the process of fluid jet disintegration into drops will be entirely defined by setting three quantities: Reynolds number Re, initial perturbation amplitude ε, and wave number k. The development of

this perturbation with time can be described as follows. The quantities η, u, v, and p can be sought for as power series in small parameter ε:

$$\eta = 1 + \varepsilon\delta\eta + ..., \quad p = p_a + \varepsilon\delta p + ...,$$
$$u = \varepsilon\delta u + ..., \quad v = \varepsilon\delta v...$$

Substituting these expansions into the equations of hydromechanics and the boundary conditions and neglecting terms quadratic in ε, we obtain linearized equations and boundary conditions for determining $\delta\eta$, δu, δv, and δp. These equations allow a solution of the following type

$$\delta\eta = \eta_0 e^{\omega t}\cos(kz), \quad \delta p = q(r)e^{\omega t}\cos(kz),$$
$$\delta u = f(r)e^{\omega t}\cos(kz), \quad \delta v = g(r)e^{\omega t}\sin(kz).$$

The quantity ω in these formulas should be found by solving the problem. It depends on the wave number k and Reynolds number Re and determines the rate of perturbation amplitude build-up. Rayleigh obtained a relation between the wave number k and ω, which can be written as [15]:

$$F(k)\omega^2 + \frac{k^2}{\mathrm{Re}}[4F(k) - 1]\omega = \frac{k^2}{2}(1 - k^2) + \frac{4k^4}{\mathrm{Re}^2}[F(k_1) - F(k)], \quad (1)$$

$$k_1^2 = k^2 + \omega\mathrm{Re}, \quad F(x) = \frac{xI_0(x)}{2I_1(x)},$$

where $I_0(x)$ and $I_1(x)$ are, respectively, modified zero- and first-order Bessel functions.

At prescribed values of the Reynolds number Re and wave number k, Eq. (1) can be solved for ω. At $k < 1$, Eq. (1) has two real roots, one of which is positive. Therefore, the perturbation amplitude will increase in this case in the course of time, which will lead to jet disintegration into drops. Equation (1) was used to plot the dependences $\omega = f(k)$ at varied Re, shown in Fig. 1. It can be seen that at a certain wave number k, depending on Re, we have a maximum value of ω. Let us denote these values by, respectively, k_m and ω_m. In order to have a possibility to find fast k_m for a given Re, we construct an approximate formula for calculating this value. As shown by calculations, in the case of the ideal fluid ($\mathrm{Re} \to \infty$), $k_m = 0.697019$ and $\omega_m = 0.343339$. As seen from Fig. 1, k_m falls with decreasing Re. Figure 2 shows the dependence of $\ln k_m$ on $\ln \mathrm{Re}$. This dependence was determined by solving numerically Eq. (1) at varied Re and k. It can be seen that, at small Re, the k_m value is also small. Therefore, an approximate

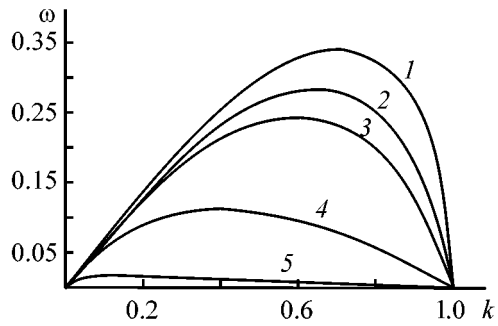

Fig. 1. Effect of wave number k on the rate ω of perturbation amplitude build-up. Reynolds number: *(1)* ∞, *(2)* 10, *(3)* 5, *(4)* 1, and *(5)* 0.1.

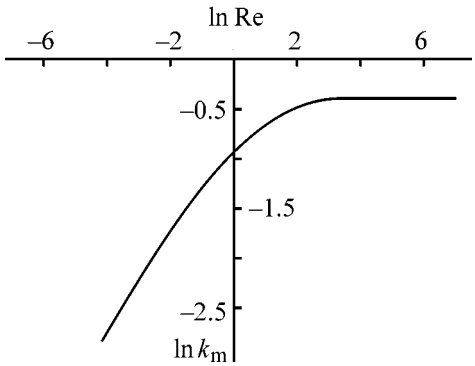

Fig. 2. Effect of Reynolds number on the wave number k_m at which the rate of perturbation build-up is at a maximum.

formula can be obtained at small Re by expanding the Bessel functions appearing in the left- and right-hand sides of Eq. (1) in power series in small parameter k. As a result, we have for long-wavelength perturbations, instead of (1), the following approximate equation

$$\left(\frac{2}{k} + \frac{k}{4}\right)\omega^2 + \frac{6k}{\mathrm{Re}}\omega = k(1 - k^2). \quad (2)$$

It is necessary to find such a wave number value k_m at which the function $\omega(k)$ has a maximum. At the extremum point the derivative $d\omega/dk$ vanishes. Differentiating Eq. (2) with respect to k and assuming that $d\omega/dk = 0$ in the obtained relation, we have

$$\left(\frac{1}{4} - \frac{2}{k^2}\right)\omega^2 + \frac{6\omega}{\mathrm{Re}} = 1 - 3k^2. \quad (3)$$

From Eqs. (2) and (3) follows that at small Re the k_m and ω_m values are related by

$$\omega_m = k_m^2/\sqrt{2}. \quad (4)$$

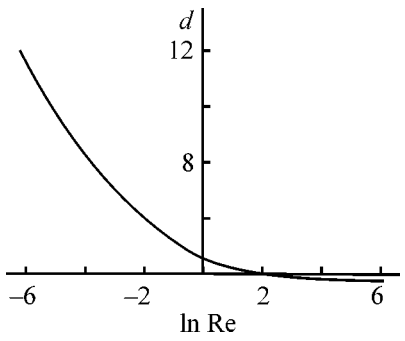

Fig. 3. Dimensionless diameter d of drops into which the jet disintegrates in spontaneous disintegration vs. the Reynolds number Re.

Substituting (4) into Eq. (2), we obtain

$$\frac{k_m^4}{8} + \frac{6k_m^2}{\sqrt{2\mathrm{Re}}} = 1 - 2k_m^2.$$

Since k_m is small at small Re, the first term in the left-hand side of this formula can be dropped. Therefore, the approximate formula for calculating k_m, valid at $\mathrm{Re} \to 0$, will have the form

$$k_m = \frac{1}{\sqrt{\dfrac{6}{\mathrm{Re}\sqrt{2}} + 2}}. \quad (5)$$

Let us modify formula (5) in such a way that at $\mathrm{Re} \to 0$ its asymptotic form should coincide with (5), and at $\mathrm{Re} \to \infty$ it give a correct limiting value of 0.697. Such a procedure for constructing approximate formulas was named by Polyanin and Dil'man [16–18] the method of asymptotic interpolation. As a result, we have

$$k_m = \frac{1}{\sqrt{\dfrac{6}{\mathrm{Re}\sqrt{2}} + \dfrac{2 + \mathrm{Re}}{1 + 0.697^2\mathrm{Re}}}} = \frac{1}{\sqrt{\dfrac{4.24264}{\mathrm{Re}} + \dfrac{2 + \mathrm{Re}}{1 + 0.48584\mathrm{Re}}}}. \quad (6)$$

The obtained formula is applicable over the entire range of Re variation. Comparison with results of numerical calculations by Eq. (1) shows that the maximum relative error of calculation by Eq. (6) does not exceed 0.25%.

In a similar way can be obtained a formula for calculating ω_m as a function of Re. At small Reynolds numbers, formula (4) is valid. Using relations (4) and (5), we obtain a formula valid at small Re ($\mathrm{Re} \to 0$)

$$\omega_m = \frac{1}{6/\mathrm{Re} + 2\sqrt{2}}. \quad (7)$$

Let us modify this relation so that it would give the correct limiting value of 0.343 at $\mathrm{Re} \to \infty$. As a result, we have

$$\omega_m = \frac{1}{\sqrt{\dfrac{6}{\mathrm{Re}} + \dfrac{2\sqrt{2} + \mathrm{Re}}{1 + 0.343\mathrm{Re}}}}. \quad (8)$$

Having formulas (6) and (8) for k_m and ω_m, we can calculate in relation to the Reynolds number the diameter of drops formed in spontaneous disintegration of a fluid jet into drops and also the interval of time between the instant at which a perturbation appears and that when the fluid jet disintegrates into drops. Since the amplitude of the perturbation with wave number k_m increases at the fastest rate, it can be considered that the jet will disintegrate into drops because of the increasing amplitude of the perturbation with this wave number. The wavelength λ of a perturbation is related to its wave number k by

$$\lambda = 2\pi/k.$$

Therefore, in dimensionless variables, the diameter of drops formed in jet disintegration can be found using the formula

$$d = (12\pi/k_m)^{1/3}.$$

The dependence of the drop diameter on the Reynolds number is shown in Fig. 3. It should be noted that, in fluid jet disintegration into drops, comparatively small drops, the so-called drops-satellites, can be formed in addition to the comparatively large drops of the predominant size. The formation of drops-satellites cannot be described in terms of the linear theory. This phenomenon appears as a result of a nonlinear interaction of capillary waves on the fluid jet surface [6, 11]. Whether or not the drops-satellites appear depends on the Reynolds number and the initial perturbation amplitude. Even if the drops-satellites do appear, their volume is comparatively small. Therefore, in this case, too, the diameter of drops with the predominant diameter can be approximately determined from Fig. 3 or using the above formulas.

The interval of time t_1 between the instant of perturbation appearance and that of jet disintegration into drops can be found as follows. At $k < 1$, Eq. (1) has

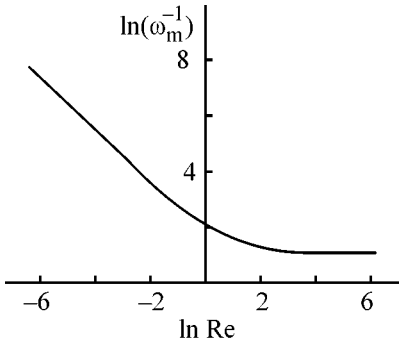

Fig. 4. ω_m^{-1} vs. Reynolds number Re.

two real roots, one positive and the other negative. Therefore, the expression for the amplitude of jet radius perturbation will contain terms exponentially increasing and exponentially decreasing with time. The exponentially decreasing term can be neglected and the t_1 value found from the condition

$$\varepsilon e^{\omega_m t_1} = 1, \text{ i.g., } t_1 = -(\ln \varepsilon)/\omega_m. \quad (9)$$

This condition means that, at the instant of disintegration, the amplitude of jet radius perturbation becomes equal to unperturbed radius, so that the jet radius becomes zero in the narrowest cross-section of the jet. Naturally, the perturbation amplitude cannot be considered small as compared with radius at the point of jet disintegration. Therefore, the linear theory, generally speaking, breaks down. Nevertheless, the available experimental data [13, 14] indicate that calculation of t_1 in terms of the linear theory is in satisfactory agreement with experiment. In dimensionless variables, the fluid velocity in the jet is unity and the length of the nondisintegrated part of the jet can be calculated using formula (9). The effect of the Reynolds number on the interval of time elapsed till jet disintegration into drops and on the length of the nodisintegrated part of the jet is illustrated in Fig. 4.

CONCLUSION

The obtained approximate formulas for calculating the wavelength of a perturbation whose amplitude increases at the highest rate and the ω_m value governing the build-up rate of the perturbation with this wavelength are applicable at any Reynolds numbers, being in good agreement with the results of an exact solution of the problem. These formulas can be applied to find the diameter of drops formed in spontaneous jet disintegration and the length of the nondisintegrated part of the jet.

REFERENCES

1. Ametistov, E.V., Blazhenkov, V.V., Gorodov, A.K., *et al., Monodispergirovanie veshchestva: printsipy i primenenie* (Monodispersion of Substances: Principles and Application), Moscow: Energoatomizdat, 1991.
2. Bogy, D.B., *Ann. Rev., Fluid Mech.*, 1979, vol. 11, pp. 207–228.
3. Yuen, M.-C., *J. Fluid. Mech.*, 1968, vol. 33, no. 1, pp. 151–163.
4. Nayfeh, A.H., *Phys. Fluids*, 1970, vol. 13, no. 4, pp. 841–847.
5. Markova, M.P. and Shkadov, V.Ya., *Izv. Akad. Nauk SSSR, Mekh. Zhidk. Gaza*, 1972, no. 3, pp. 30–37.
6. Lafrance, P., *Phys. Fluids*, 1975, vol. 18, no. 4, pp. 428–432.
7. Chaudhary, K.C. and Redekopp, L.G., *J. Fluid Mech.*, 1980, vol. 96, no. 2, pp. 257–274.
8. Bousfield, D.W., Keunings, R., Marrucci, G., and Denn, M.M., *J. Non-Newt. Fluid Mech.*, 1986, vol. 21, no. 1, pp. 79–97.
9. Shokouhi, F. and Elrod, H.G., *J. Comput. Phys.*, 1987, vol. 71, pp. 324–342.
10. Mansour, N.N. and Lundgren, T.S., *Phys. Fluids*, 1990, vol. A2, no. 7, pp. 1141–1144.
11. Ashgriz, N. and Mashayek, F., *J. Fluid Mech.*, 1995, vol. 291, pp. 163–190.
12. Huynh, H., Ashgriz, N., and Mashayek, F., *J. Fluid Mech.*, 1996, vol. 320, pp. 185–210.
13. Donnelly, R.J. and Glaberson, W., *Proc. R. Soc. London, Ser. A*, 1966, vol. A290, no. 1423, pp. 547–556.
14. Goedde, E.F. and Yuen, M.C., *J. Fluid Mech.*, 1970, vol. 40, no. 3, pp. 495–511.
15. Bechtel, S.E., Karlson, C.D., and Forest, M.G., *Phys. Fluids*, 1995, vol. 7, no. 12, pp. 2956–2971.
16. Polyanin, A.D. and Dil'man, V.V., *Teor. Osn. Khim. Tekhnol.*, 1985, vol. 19, no. 1, pp. 3–11.
17. Polyanin, A.D. and Dil'man, V.V., *Int. J. Heat Mass Transfer*, 1985, vol. 28, no. 1, pp. 45–48.
18. Dil'man, V.V. and Polyanin, A.D., *Metody model'nykh uravnenii i analogii v khimicheskoi tekhnologii* (Methods of Model Equations and Analogies in Chemical Technology), Moscow: Khimiya, 1988.

Russian Journal of Applied Chemistry, Vol. 74, No. 6, 2001, pp. 986–989. Translated from Zhurnal Prikladnoi Khimii, Vol. 74, No. 6, 2001, pp. 959–962.

PROCESSES AND EQUIPMENT OF CHEMICAL INDUSTRY

A Study of Sorption Processes in Transient Mode

R. I. Zeinalov, F. V. Yusubov, Ch. Sh. Ibragimov, and R. K. Babaev

Azerbajan State Oil Academy, Baku, Azerbaijan

Received February 28, 2001

Abstract—A mathematical description is presented of the duration of separate stages and the whole cycle of adsorption dearomatization of liquid paraffins from the 200–320°C fraction in a fixed bed of an aluminosilicate adsorbent.

Of particular importance in optimal design, calculations of the economical efficiency, and control over sorption processes is a mathematical description of the duration of a cycle and separate stages of adsorber operation [1, 2]. The present study describes mathematically the duration of separate stages and the whole cycle of adsorption dearomatization of liquid paraffins of the 200–320°C fraction in a fixed bed of an aluminosilicate adsorbent.

In sorption processes, the possibility of prognostication of how the product composition changes with time is rather important. It is known that under transient conditions the process is more intensive. Therefore, it is more economically efficient to withdraw a product from a column before equilibrium is attained. Moreover, it is also known that the extent of departure from equilibrium determines the cycle duration of a diffusion process [1, 2].

To ensure the continuity of the adsorption dearomatization of liquid paraffins as regards the raw material and finished product flows, four adsorbers are present in the installation, with one stage of the process performed in each of these during a certain time interval [2]. The technological scheme of the process is shown in the figure. At the considered instant of time, adsorber A-1 is in the adsorption stage; A-2, in the stage of discharge of the raw material and desorption of aromatic hydrocarbons; A-3, in the stage of purging and adsorbent dehydration; and A-4, in the stage of cooling (see the figure). The operation schedule of the adsorbers is given in Table 1.

The process of adsorption dearomatization of liquid paraffins comprises the following stages: (1) adsorption of aromatic hydrocarbons from the raw material in the liquid phase by the adsorbent, with pure paraffins obtained; (2) removal of raw material residues from the adsorber volume and desorption of aromatic hydrocarbons from adsorbent pores with the use of isopropanol; (3) adsorber purging with a mixture of overheated steam and purge gas to remove the alcohol, dehydration of the adsorbent bed; and (4) cooling of the adsorbent bed to the adsorption temperature with a circulating purge gas.

In performing practical calculations for optimal design of the adsorption dearomatization of liquid paraffins, it is necessary to determine correctly the duration of each stage and the cycle as a whole [3, 4]. The previously developed mathematical model of the adsorption dearomatization of liquid paraffins in a fixed bed [5] makes it possible to determine the duration of the adsorption cycle. The mathematical model has the form of a system of second-order partial differential equations. The system was solved with the use of the Laplace–Karson transforms. On performing some mathematical operations with this system, the following system of equations was derived [6, 7]:

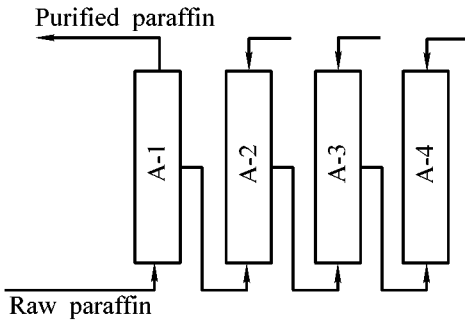

Technological diagram of adsorbers.

1070-4272/01/7406-0986 $25.00 © 2001 MAIK "Nauka/Interperiodica"

Table 1. Cyclogram of adsorber operation

Adsorber	Process stage, h			
	1–7	8–14	15–21	22–28
A-1	Adsorption	Discharge and desorption	Purging and dehydration	Cooling
A-2	Discharge and desorption	Purging and dehydration	Cooling	Adsorption
A-3	Purging and dehydration	Cooling	Adsorption	Discharge and desorption
A-4	Cooling	Adsorption	Discharge and desorption	Purging and dehydration

$$a_* = 2K_a D_a \frac{1}{r_*}\tau_a, \quad (1)$$

$$a = D_a 4\pi r_0^2 N' K_a \tau_a, \quad (2)$$

$$C_c = 2K_c D_c \frac{1}{r}\tau_a - a, \quad (3)$$

$$K_c = \frac{C}{R}, \quad (4)$$

$$K_a = \frac{a}{r_0}, \quad (5)$$

$$C_c = \frac{a}{[b(a_\infty - a)]}, \quad (6)$$

$$C = 0.9[-C_S(S_1) + \frac{16}{3}C_S(S_2) - \frac{16}{5}C_S(S_3)], \quad (7)$$

$$C_S = f(D_{eff}), \quad (8)$$

$$S_1 = \frac{1}{(2.89r_a)}, \; S_2 = \frac{3}{(2.89r_a)}, \; S_3 = \frac{5}{(2.89r_a)}, \quad (9)$$

where a_* is the concentration of the substance being adsorbed in microporous formations, C the adsorbate concentration, D_a the diffusion coefficient of the substance being adsorbed in the microporous formations, τ_a the adsorption time, r_* the running radius of microporous formations, r_0 the radius of the macroporous formations, D_c the diffusion coefficient of the substance being adsorbed in transport pores, R the adsorbent grain radius, r the running adsorbent grain radius, N' the number of microporous formations per unit volume, b constant in the Langmuir equation, D_{eff} the effective diffusion coefficient, K_a and K_c coefficients, and a_∞ the limiting adsorbate concentration.

The adsorption time is found with the use of Eqs. (1)–(9) by the random search method [7] on the basis of the criterion

$$F = (\tau_a^{calc} - \tau_a^{exp}) \le \varepsilon, \quad (10)$$

where τ_a^{calc} and τ_a^{exp} are, respectively, the calculated and experimental adsorption times; and ε is a certain prescribed error, $\varepsilon = 0.01$.

It should be noted that the time of desorption of aromatic hydrocarbons from the aluminosilicate adsorbent can also be calculated using the system of equations (1)–(9) with account of the changing signs of some terms of the equations.

To determine the time of drying of the aluminosilicate adsorbent, let us write the equation for the rate of drying [3] as follows

$$\nu = -\frac{M}{S}\frac{dx}{d\tau_{dr}}, \quad (11)$$

where ν is the rate of drying, M the amount of adsorbent in terms of dry residue, x the moisture content of the adsorbent, S the area of drying, and τ_{dr} the time of drying. Integrating Eq. (11) between the limits from x_1 to x_2, we obtain an expression for the quantity τ_{dr}:

$$\tau_{dr} = \frac{M}{S}\int_{x_2}^{x_1}\frac{dx}{\nu}. \quad (12)$$

It is known that the dependence of the adsorbate drying rate on x is linear. Then, Eq. (12) can be written in the form

$$\tau_{dr} = \frac{M}{S}\frac{x_1 - x_2}{\nu_n}, \; \nu_n = a_1 x + a_2, \quad (13)$$

where a_1 is the slope of the straight line, and a_2 is a constant.

Taking into account the drying rate ν in Eq. (12), we obtain

$$\tau_{dr} = \frac{M}{S}\int_{x_2}^{x_1}\frac{dx}{a_1 x + a_2} = \frac{M}{a_1 S}\ln\frac{a_1 x_1 + a_2}{a_1 x_2 + a_2}, \quad (14)$$

where $a_1 x_1 + a_2 = \nu_1$, $a_1 x_2 + a_2 = \nu_2$, and $a_1 = (\nu_1 - \nu_2)/(x_1 - x_2)$.

Then we have

$$\tau_{dr} = \frac{M}{a_1 S}\ln\frac{\nu_1}{\nu_2}. \quad (15)$$

It is known that an infinitely small quantity of heat dQ released by a solid during an infinitely short pe-

Table 2. Material balance of the adsorption purification of paraffins

Parameter	Amount	
	thousand tons/year	wt %
Taken: fresh raw material	80.0	80.0
Obtained: purified paraffins	75.6	94.5
Desorbate	3.9	4.9
Loss	0.5	0.6
Total	80.0	100.0

Table 4. Diffusion coefficient D in relation to concentration of adsorbate C and substance being adsorbed a at 298 K

τ, min	C	a	D_a	D_c	D_{eff}
	g/100 g		$cm^2\ min^{-1}$		
15	0.005	0.1703	4.630	6.010	234
30	0.028	0.8758	2.310	2.820	129
45	0.038	1.1434	1.540	1.830	93
60	0.055	1.3623	1.160	1.140	75.5
75	0.074	1.6056	0.925	0.818	65.1
90	0.118	1.8245	0.771	0.498	59.7
105	0.165	2.0191	0.661	0.350	56.4
120	0.235	2.1894	0.578	0.244	56.2
135	0.380	2.1966	0.514	0.135	69.6
150	0.490	2.2218	0.463	0.096	122
165	0.530	2.2215	0.421	0.081	337

Table 3. Characterization of aluminosilicate adsorbent (crumb) of brand A

Parameter	Value
Bulk density, $g\ cm^{-3}$	0.6–0.7
Granulometric composition, %, fraction	
> 0.8 mm	5
0.28–0.8	95
0.2–0.8	–
Specific humidity at 800°C, %	No more than 4
Impurity content, wt %	
Fe oxide	No more than 0.2
V oxide	No more than 0.5
Specific surface area, $m^2\ kg^{-1}$	22
Specific pore volume, $m^3\ g^{-1}$	0.4884

Table 5. Optimal technological and design parameters of the process

Parameter	Value
Adsorption temperature T_a, K	313
Desorption temperature T_d, K	368
Purge temperature T_p, K	623
Working bed height L_w, m	0.73
Condensation temperature T_c, K	288
Adsorbent charge M, kg	13700
Adsorber diameter D, m	1.86
Adsorber height L, m	7.78
Linear velocity of raw material feed flow into adsorbers, ω, $m\ s^{-1}$	1.33×10^{-3}

riod of time $d\tau_0$ is proportional to the temperature difference between the solid and the ambient:

$$dQ = -K(t_2 - t_1)d\tau_0, \quad (16)$$

where t_1 is the temperature of the ambient, t_2 the temperature of the solid (adsorbent), K a constant, and τ_0 the duration of the adsorbent cooling stage.

The amount of heat released by the adsorbent in cooling is given by the equation

$$Q = cm(t_2 - t_1),$$

where m is the mass, and c the specific heat of the adsorbent.

The quantity c will be considered constant:

$$dQ = cmdt.$$

With account of this relation, formula (16) takes the form

$$cmdt = -K(t_2 - t_1)d\tau_0. \quad (17)$$

Hence

$$d\tau_0 = -\frac{cm}{K(t_2 - t_1)}dt. \quad (18)$$

Integrating Eq. (9), we obtain

$$d\tau_0 + C = -\frac{cm}{K}\ln(t_2 - t_1). \quad (19)$$

If $\tau = 0$, then $t_3 = t_2$ and we have

$$C = -\frac{cm}{K}\ln(t_3 - t_1). \quad (20)$$

Subtracting Eq. (20) from (19), we obtain

$$\tau_0 = cm\frac{1}{K}\ln\frac{t_2 - t_1}{t_3 - t_1}. \quad (21)$$

The optimal values of τ_a, τ_d, τ_{dr}, and τ_0 were calculated by the method of dynamic programming on the basis of Eqs. (7), (15), and (21) with the use of the data from Tables 2–5.

The following optimal values of the process parameters were obtained (h): $\tau_a = \tau_d = 6.34$, $\tau_{dr} = 6.29$, and $\tau_0 = 6.32$. The complete cycle duration is 25.29 h. It should be noted that prior to optimization the duration of the adsorption cycle was 28 h. The possible improvement of the adsorption technology is largely associated with the creation of more perfect schedules of adsorption apparatus operation. Here, the following tendencies can be distinguished: making shorter the total duration of the adsorption cycle and raising the intensity of operation of an adsorption installation, and, consequently, reducing the capital outlays.

Thus, Eqs. (7), (9), (15), and (21), describing the duration of separate stages, can serve as a basis for developing the algorithm and system of optimal control over the sorption process.

CONCLUSIONS

(1) A mathematical description of the duration of separate stages of liquid-phase adsorption in a fixed bed was developed.

(2) The optimal duration of separate stages of the adsorption dearomatization of liquid paraffins was determined, making the total duration of the process shorter and the process intensity higher.

REFERENCES

1. Kel'tsev, N.V., *Osnovy adsorbtsionnoi tekhniki* (Fundamentals of the Adsorption Technology), Moscow: Khimiya, 1984.
2. Taganov, I.N., *Modelirovanie protsessov mass- i energoperenosa* (Modeling of Mass and Energy Transfer Processes), Leningrad: Khimiya, 1979.
3. Mironenko, V.A., *Izv. Vyssh. Uchebn. Zaeved., Geol. Razvedka*, 1972, no. 11, pp. 72–79.
4. Zhilinskas, A. and Shaltyanis, V., *Poisk optimuma: komp'yuter rasshiryaet vozmozhnosti* (In Search of Optimum: Computer Opens up New Possibilities), Moscow: Nauka, 1989.
5. Yusubov, F.V., Zeinalov, R.I., and Ibragimov Ch.Sh., *Zh. Prikl. Khim.*, 1994, vol. 67, no. 5, pp. 861–863.
6. Zeinalov, R.I., Ibragimov, Ch.Sh., and Yusubov, F.V., *Zh. Prikl. Khim.*, 1993, vol. 66, no. 3, pp. 694–696.
7. Yusubov, F.V., Zeinalov, R.I., and Ibragimov, Ch.Sh., *Zh. Prikl. Khim.*, 1994, vol. 67, no. 7, pp. 1121–1123.

Russian Journal of Applied Chemistry, Vol. 74, No. 6, 2001, pp. 990–992. Translated from Zhurnal Prikladnoi Khimii, Vol. 74, No. 6, 2001, pp. 963–965.

ORGANIC SYNTHESIS AND INDUSTRIAL ORGANIC CHEMISTRY

Synthesis of *N*-(*o*- and *p*-Alkenylphenyl)-Substituted Quinazolin-4-ones

R. R. Gataullin, M. F. Nasyrov, E. M. Vyrypaev, O. V. Shitikova, and I. B. Abdrakhmanov

Institute of Organic Chemistry, Ufa Scientific Center, Russian Academy of Sciences, Ufa, Bashkortostan, Russia

Ufa State Petroleum Technical University, Ufa, Bashkortostan, Russia

Received February 8, 2001

Abstract—Alkenylphenyl-substituted quinazolinones were prepared by reactions of 2-methyl-4*H*-3,1-benzoxazin-4-one with *o*- and *p*-alkenylanilines.

The interest in quinazoline derivatives is largely due to their high biological activity; intensive studies have been performed in this field recently [1–10]. A traditional line of synthetic studies is preparation of numerous derivatives of N^3-substituted quinazolinones. The spectrum of biological effect of these derivatives is wide; their preparations are used in neurology, microbiology, endocrinology, cardiology, and gerontology. Synthetic routes to quinazolin-4-ones are mostly based on the use of anthranilic acid and 3,1-benzoxazin-4-one derivatives [1–5].

Previously synthesized [11] alkenyl- and cycloalkenylanilines were used for preparing 3-alkenylphenylated heterocycles of the quinazoline series with the aim of subsequent functionalization at the alkenyl moiety.

For example, fusion of benzoxazine **I** with amines **II**–**XVII** at 140°C gives quinazolines **XVIII**–**XXXIII** (the analytical data are given in Table 1) in good yields (Table 2).

Condensation of benzoxazine **I** with *p*- or *m*-alkenylanilines yields a single reaction product (Table 2):

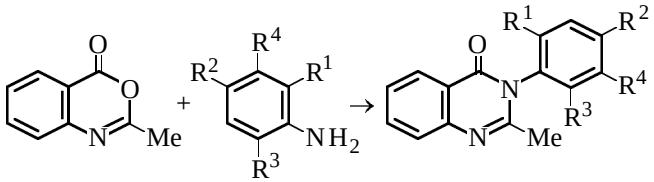

I **II**–**XVII** **XVIII**–**XXXIII**

R^1 = $CH_2(CH_3)CH{=}CHCH_3$, R^2 = R^3 = R^4 = H (**II**), (**XVIII**)*; R^2 = R^4 = H, R^3 = CH_3 (**VII**), (**XXIII**)*; R^2 = R^3 = CH_3, R^4 = H (**XV**), (**XXXI**)*; R^2 = $CH_2(CH_3)CH{=}CHCH_3$, R^1 = R^3 = R^4 = H (**III**), (**XIX**); R^1 = R^4 = H, R^3 = CH_3 (**VIII**), (**XXIV**), R^3 = R^1 = H, R^4 = CH_3 (**XIV**), (**XXX**); R^3 = $CH_2(CH_3)CH{=}CHCH_3$, R^2 = R^1 = H, R^4 = CH_3 (**XIII**), (**XXIX**); R^1 = 2-cyclopenten-1-yl, R^2 = R^3 = R^4 = H (**IV**), (**XX**)*; R^2 = R^4 = H, R^3 = CH_3 (**IX**), (**XXV**)*; R^2 = R^3 = CH_3, R^4 = H (**XVI**), (**XXXII**)*; R^1 = 2-cyclohexen-1-yl, R^2 = R^3 = R^4 = H (**V**), (**XXI**)*; R^2 = R^4 = H, R^3 = CH_3 (**X**), (**XXVI**)*; R^1 = 1-cyclopenten-1-yl, R^2 = R^4 = H, R^3 = CH_3 (**XI**), (**XXVII**); R^2 = R^3 = CH_3, R^4 = H (**XVII**), (**XXXIII**)*; R^1 = 1-cyclohexen-1-yl, R^2 = R^3 = R^4 = H (**VI**), (**XXII**); R^2 = R^4 = H, R^3 = CH_3 (**XII**), (**XXVIII**) (the compounds in which some of the signals in the ^{13}C NMR spectra are doubled are marked with an asterisk).

At the same time, a similar reaction with *o*-alkenylanilines yields two isomers. We believe that this is due to the sterically hindered state of the alkenyl unit. This can be clearly seen from the ^{13}C NMR spectra in which some carbon atoms in compounds **XVIII**, **XX**, **XXI**, **XXIII**, **XXV**, **XXVI**, and **XXXI**–**XXXIII** give double signals. When a substituent with the vinyl double bond is present in the *o*-position, doubling of signals is observed only in 1-cyclopent-1-enyl-containing quinazoline **XVII**.

The mass spectra of **XVIII** and **XIX** contain strong molecular peaks $[M]^+$, which are base peaks or are close to base peaks in intensity, in contrast to the previously studied structurally related quinazoline alkaloids [12–14]. The loss of the hydrogen atom ($[M - H]^+$ ions) or methyl radical ($[M - CH_3]^+$ ions)

1070-4272/01/7406-0990 $25.00 © 2001 MAIK "Nauka/Interperiodica"

Table 1. Analytical data for **XVIII**–**XXXIII**

Compound no.	Found (%)/Calculated (%)			Formula	Compound no.	Found (%)/Calculated (%)			Formula
	C	H	N			C	H	N	
XVIII	79.21	6.42	9.11	$C_{20}H_{20}N_2O$	**XXVI**	79.87	6.66	8.35	$C_{22}H_{22}N_2O$
	78.92	6.62	9.20			79.97	6.71	8.48	
XIX	78.33	6.53	8.57	$C_{20}H_{20}N_2O$	**XXVII**	79.45	6.36	8.70	$C_{21}H_{20}N_2O$
	78.92	6.62	9.20			79.72	6.37	8.85	
XX	79.32	6.01	9.15	$C_{20}H_{18}N_2O$	**XXVIII**	79.90	6.67	8.37	$C_{22}H_{22}N_2O$
	79.44	6.00	9.26			79.97	6.71	8.48	
XXI	79.68	6.31	8.67	$C_{21}H_{20}N_2O$	**XXIX**	79.17	7.03	9.01	$C_{21}H_{22}N_2O$
	79.72	6.37	8.85			79.21	6.96	8.80	
XXII	79.45	6.33	8.71	$C_{21}H_{20}N_2O$	**XXX**	78.35	6.90	8.48	$C_{21}H_{22}N_2O$
	79.72	6.37	8.85			79.21	6.96	8.80	
XXIII	79.01	7.12	8.78	$C_{21}H_{22}N_2O$	**XXXI**	79.57	7.35	8.37	$C_{22}H_{24}N_2O$
	79.21	6.96	8.80			79.48	7.28	8.43	
XXIV	78.99	6.90	8.73	$C_{21}H_{22}N_2O$	**XXXII**	79.34	6.69	8.52	$C_{22}H_{22}N_2O$
	79.21	6.96	8.80			79.97	6.71	8.48	
XXV	79.37	6.30	8.77	$C_{21}H_{20}N_2O$	**XXXIII**	80.11	6.55	8.20	$C_{22}H_{22}N_2O$
	79.72	6.37	8.85			79.97	6.71	8.48	

Table 2. Yields, R_f values, and IR spectra of quinazolin-4-ones **XVIII**–**XXXIII**

Compound no.	Yield, %	R_f	IR spectrum, ν, cm^{-1}		Compound no.	Yield, %	R_f	IR spectrum, ν, cm^{-1}	
			C=O	C=N				C=O	C=N
XVIII	78	0.3	1660	1616	**XXVI**	70	0.4	1684	1604
XIX	80	0.3	1660	1616	**XXVII**	81	0.5	1680	1600
XX	80	0.3	1664	1612	**XXVIII**	77	0.5	1684	1600
XXI	75	0.4	1684	1604	**XXIX**	74	0.3	1688	1600
XXII	81	0.4	1684	1600	**XXX**	80	0.4	1676	1596
XXIII	73	0.5	1692	1604	**XXXI**	68	0.4	1660	1616
XXIV	85	0.5	1692	1600	**XXXII**	70	0.5	1672	1596
XXV	74	0.5	1660	1616	**XXXIII**	76	0.4	1684	1608

was observed in all cases. The first process is characteristic of all aromatic compounds [15]. We also detected numerous double-charged ions, characteristic of binuclear aromatic compounds. The methyl radical is probably lost from the 3-aryl substituent to a greater extent than from the 2-methylquinazoline core [16]. In the mass spectrum of compound **XVIII** containing an *o*-pentenyl group in the *N*-aryl substituent, we observed strong fragment peaks $[M - 29]^+$, $[M - 41]^+$, $[M - 43]^+$, $[M - 55]^+$, $[M - 56]^+$, $[M - 57]^+$, and $[M - 69]^+$, which may be due to the following ions: $[M - H - CO]^+$, $[M - CH_3CN]^+$, $[M - CH_3CO]^+$, $[M - H - CO - C_2H_2]^+$, $[M - CH_3 - CH_3CN]^+$, $[M - H - CH_3CN - CH_3]^+$, and $[M - C_5H_9]^+$. The loss of HCN, CH_3CN, and CO molecules is characteristic of quinazoline alkaloids [12, 13], and the loss of C_2H_2 and H, of aromatic compounds [15].

The ions $[M - C_5H_9]^+$ deserve special consideration. Their formation seems to be improbable as involving disadvantageous cleavage of the bond at the phenyl ring. Previously, Ramana and Kantharaj [17] stuidied the mass spectra of 2-substituted 3-(2-methylphenyl)-4(3*H*)-quinazolinones and their analogs. A strong intermolecular interaction of the C=O and C=S groups with the *o*-substituent in the 3-phenyl ring resulted in the formation of stable cyclic fragment ions formed through the loss of both the *o*-substituent and the $OH^{\cdot}$ or $SH^{\cdot}$ radical. Also observed were the ions $[M - ArO]^+$ and $[M - ArS]^+$ forming through migration of the aryl substituent from the nitrogen atom to

the oxygen or sulfur atom. Our results are fairly consistent with the data in [17]. For example, in the mass spectra of structural isomers **XVIII** and **XIX** with the *o*- and *p*-positions of the alkenyl substituent, the relative intensities (%) of certain fragment peaks differed significantly: $[M - C_5H_9]^+$, m/z = 235, 100 (**XVIII**), 9.5 (**XIX**); and $[M - CH_3]^+$, m/z = 289, 57 (**XVIII**), 100 (**XIX**). The major fragmentation pathway of **XVIII** is the loss of the pentenyl radical due to anchimeric assistance of the C=O group [18], with *ortho* cyclization to form ion **A**.

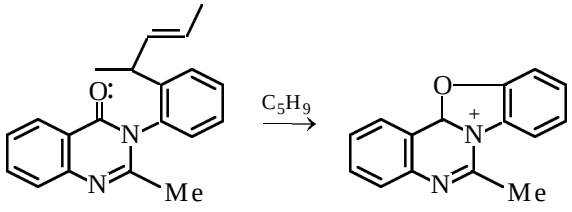

A

$[M]^+$ = 304 (69.6) 235 (100)

The major fragmentation pathway of **XIX** is the loss of the methyl group. The high stability of ion B is due to the conjugated system of double bonds and the formation of the quinoid structure [15].

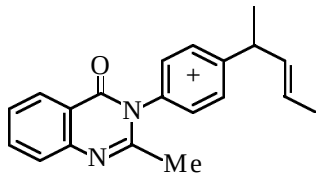

$[M]^+$ = 304 (93.9)

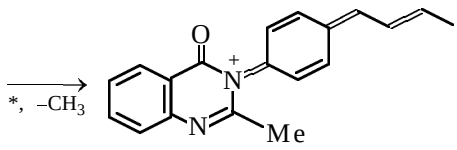

289 (100)

EXPERIMENTAL

The ^1H and ^{13}C NMR spectra were taken on a Bruker AM-300 spectrometer (working frequencies 300.13 and 75.47 MHz, respectively); internal reference TMS. The IR spectra were recorded with a Specord M-80 spectrophotometer. The product purity was checked with a Chrom 5 chromatograph (Chromaton N-AW, 5% SE-30, 1200 × 3-mm column, carrier gas He, heating rate 12 deg min^{-1}) and by TLC on Silufol UV-254 plates (eluent hexane–ethyl acetate, 6 : 1). The mass spectra were taken on an MKh-1320 spectrometer (70 eV).

Quinazolin-4-ones were prepared by fusion of 3.1 mmol of appropriate amine with 3.1 mmol of 2-methyl-4H-3,1-benzoxazin-4-one at 140°C for 5 h. If required, the product was passed through a column packed with alumina (eluent pentane).

REFERENCES

1. Mitskyavichyus, V.Yu. and Baltrutis, R.S., *Khim. Geterotsikl. Soedin.*, 1992, no. 10, pp. 1391–1394.
2. Abdel-Alim, A.-A.M., El-Shorbagi, A.-B.A., El-Gendy, M.A., and El-Shareif, A.H.H., *Coll. Czech. Chem. Commun.*, 1993, vol. 58, no. 8, pp. 1963–1968.
3. Vassin, F.A., Eissa, A.M.F., and Wasfy, A.A.F., *Indian J. Chem. B*, 1994, vol. 33, no. 12, pp. 1193–1196.
4. Kumar, P.R. and Reddy, M.S., *Indian J. Chem. B*, 1994, vol. 33, no. 9, pp. 883–884.
5. Ukrainets, I.V., Taran, S.G., Gorokhova, O.V., *et al.*, *Khim. Geterotsikl. Soedin.*, 1994, no. 2, pp. 225–228.
6. Akazome, M.A., Kondo, T., and Watanabe, Y., *J. Org. Chem.*, 1993, vol. 58, no. 2, pp. 310–312.
7. Savel'ev, V.A. and Loskutov, V.A., *Khim. Geterotsikl. Soedin.*, 1991, no. 6, pp. 791–793.
8. Molina, P., Aller, E., and Lorenzo, A., *Synthesis* (FRG), 1998, no. 3, p. 283.
9. US Patent 5214144.
10. Heinicke, G., Hung, T.V., Prager, R.H., and Ward, A.D., *Aust. J. Chem.*, 1984, vol. 37, no. 4, pp. 831–844.
11. Abdrakhmanov, I.B., Sharafutdinov, V.M., and Tolstikov, G.A., *Izv. Akad. Nauk SSSR, Ser. Khim.*, 1982, no. 9, pp. 2160–2162.
12. *Mass-spektrometricheskie kharakteristiki organicheskikh i elementoorganicheskikh soedinenii* (Mass-Spectrometric Characteristics of Organic and Organometallic Compounds), Tolstikov, G.A., Ed., Ufa: Bashkir. Filial Akad. Nauk SSSR, 1987.
13. Schidknecht, H. and Wenneis, W.F., *Z. Naturforsch.*, 1966, vol. 21, no. 6, pp. 552–556.
14. Telezhnetskaya, M.V. and Yunusov, S.Yu., *Khim. Prirodn. Soedin.*, 1977, no. 6, pp. 731–743.
15. Terent'ev, P.B. and Stankyavichus, A.P., *Mass-spektrometricheskii analiz biologicheski aktivnykh azotistykh osnovanii* (Mass-Spectrometric Analysis of Biologicaly Active Nitrogen Bases), Vilnius: Moklas, 1987.
16. Kirmani, M.Z., Kanta Sethi, and Ahmed, S.R., *Indian J. Chem.*, 1979, vol. 18, no. 5, pp. 432–435.
17. Ramana, D.V. and Kantharaj, E., *J. Mass. Spectrom.*, 1995, vol. 30, no. 2, pp. 262–268.
18. Takhistov, V.V., *Prakticheskaya mass-spektrometriya* (Practical Mass Spectrometry), Leningrad: Leningr. Gos. Univ., 1977.

Russian Journal of Applied Chemistry, Vol. 74, No. 6, 2001, pp. 993–997. Translated from Zhurnal Prikladnoi Khimii, Vol. 74, No. 6, 2001, pp. 966–970.

ORGANIC SYNTHESIS AND INDUSTRIAL ORGANIC CHEMISTRY

Color Characteristics of Aqueous Solutions of Synthetic Food Dyes

A. V. Gerasimov

Russian Research Institute of Food Aromatizers, Acids, and Dyes, St. Petersburg, Russia

Received October 20, 2000; in final form, March 2001

Abstract—The color characteristics of aqueous solutions of synthetic food dyes Azo Rubine, tartrazine, Indigo Carmine, Ponceau 4R, Sunset Yellow, and Brilliant Blue were studied. A formula is proposed for determining the hue of dye solutions.

The color of solutions of both individual and mixed dyes is determined by sensor methods. Usually the solution color is visually compared with that of solutions of references dyes or with a special color scale on paper or on plastic cards [1]. Despite the apparent roughness, this method is widely used up to now, because it does not require any special analytical equipment. In our previous studies we developed a procedure for determining the color characteristics of colored compounds, based on scanning and subsequent computer processing of the image. This method was successfully used for interpreting the results of separation of food dyes, in a thin sorbent layer [2, 3].

In this work we studied the color parameters of synthetic food dyes using the previously developed procedure.

EXPERIMENTAL

We chose six synthetic food dyes: Azo Rubine (**I**), Brilliant Blue (**II**), Sunset Yellow (**III**), Indigo Carmine (**IV**), Ponceau 4R (**V**), and tartrazine (**VI**), produced by Warner Jenkinson and Flevo Chemie (the Netherlands). These dyes are widely used as components of foodstuffs and belong to different classes of substances (azo, indigoid, and triphenylmethane dyes). The characteristics of the dyes are listed in Table 1.

Aqueous solutions of dyes were placed in cells for a photoelectric colorimeter and then scanned on a Mustek Scan Express 6000P scanner (True Color mode, 24 bit/pixel or 16.7×10^6 colors, optical resolution 100 dpi). Since the scanner detects reflected light and solutions of food dyes are transparent liquids, we placed a white paper sheet behind the cell. The color characteristics were determined with the Adobe Photoshop 5.0 package by the procedure described in [3], in the color modes CMYK [cyan (blue)–magenta (red)–yellow–black] and HBS (hue–saturation–brightness).

Typical color spectra of 100 g t^{-1} aqueous solutions of dyes, obtained in the CMYK mode, are shown in Fig. 1. The CMYK mode allows operation with three main colors: red, yellow, and blue. The dye solutions exhibit pronounced peaks in each of the color bands in accordance with the dye color. Sunset Yellow (imparts orange color to solutions) absorbs in both yellow and red ranges, and dyes of the red group (Azo Rubine and Ponceau 4R) exhibit absorption in the yellow range, more pronounced with Ponceau 4R.

Table 1. Characteristics of synthetic food dyes

Dye	EC index	INCI(CTFA) nomenclature	Color index
I	E 122	C.I.14720 Acid Red 14	14720
II	E 133	C.I.42090	42090
III	E 110	Sunset Yellow	15985
IV	E 132	C.I.73015 Acid Blue 74	13015
V	E 124	C.I.16255	16255
VI	E 102	C.I.191140 Acid Yellow 23	19140

1070-4272/01/7406-0993 $25.00 © 2001 MAIK "Nauka/Interperiodica"

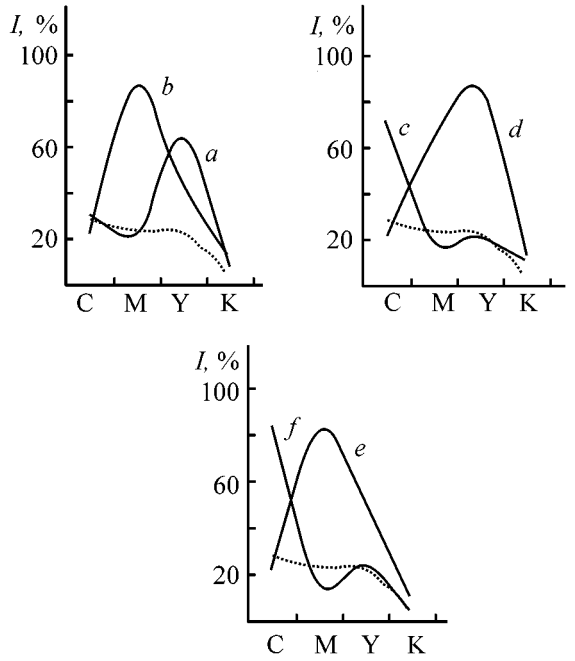

Fig. 1. Color spectra of aqueous solutions (100 g t^{-1}) of synthetic food dyes: (*a*) tartrazine, (*b*) Azo Rubine, (*c*) Indigo Carmine, (*d*) Sunset Yellow, (*e*) Ponceau 4R, and (*f*) Brilliant Blue. (*I*) Color intensity: (C) cyan (blue), (M) magenta (red), (Y) yellow, and (K) black; the same for Figs. 2 and 4. The *dotted line* shows the background absorption (water).

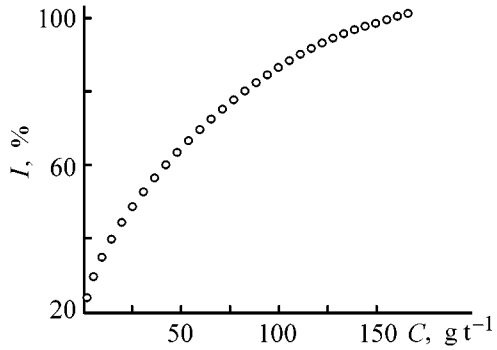

Fig. 3. Solution color intensity *I* in the red range vs. dye content *C*, by the example of calibration solutions of Azo Rubine.

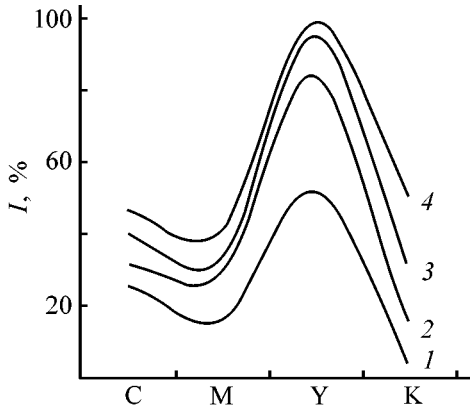

Fig. 2. Tartrazine color intensity as influenced by layer thickness, mm: (*1*) 1, (*2*) 3, (*3*) 5, and (*4*) 10.

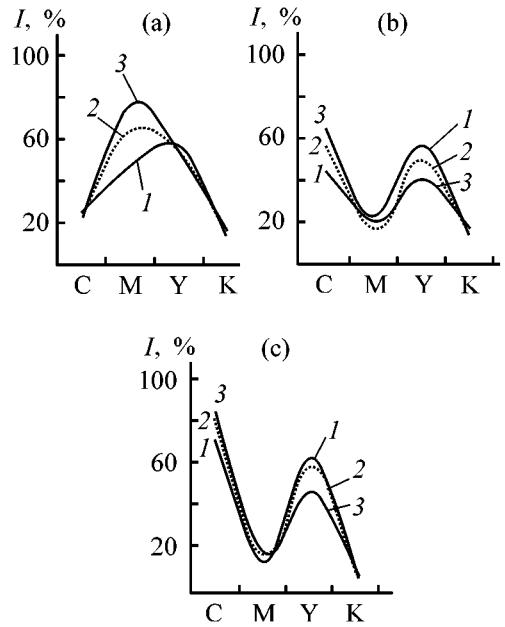

Fig. 4. Color spectra of binary solutions of synthetic food dyes. Dye mixture: (a) Azo Rubine + tartrazine, (b) Indigo Carmine + tartrazine, and (c) Brilliant Blue + tartrazine. Mixture composition (g t^{-1}): (*1*) 25 : 75, (*2*) 50 : 50, and (*3*) 75 : 25.

The influence of layer thickness on absorption is demonstrated for the example of tartrazine solutions. Figure 2 shows that, with increasing layer thickness, the color intensity grows in all ranges. Since it is appropriate to use lower color intensities for analytical purposes, we employed 1-mm cells for determining the color characterstics of dye solutions. Furthermore, capillary forces prevent outflow of solution from such thin cells, which facilitates scanning with a common flatbed scanner.

It was interesting to find how the color intensity depends on the dye content in solution. This was done for Azo Rubine as an example. We found that the concentration dependence of the solution color intensity is nonlinear (Fig. 3). It is known that the linear Bouguer–Lambert–Beer law is valid for the transmission mode only. In the reflection mode, used in scanning, the concentration dependence of the color intensity is described by nonlinear equations based on the Kubelka–Munk theory [4, 5].

In the food industry, preference is usually given to mixed dyes. The possibility of combining dyes, makes feasible any hue. As a rule, only two components are combined, since taking more components would complicate the process and lead to higher the product cost. We studied the color characteristics of some binary solutions of synthetic food dyes. With the relative content of the components varied, the color maximum shifts from one color range into another, as illustrated in Fig. 4.

As already noted, the color intensity evaluated in the CMYK mode nonlinearly depends on the concentration, which complicates analysis of dye mixtures in the CMYK mode. To characterize solutions, we chose hue as a parameter (H function in the HSB mode). This parameter (for more detail, see [3]) denotes the angle on the color circle (Fig. 5); it is independent of the dye concentration in solution. We found that the solution hue varies by approximately linear law, depending on the concentration ratio of the dissolved dyes. Examples of such dependences are given in Figs. 6a and 6b. The dependences (for calculation scheme, see Fig. 6c) are described by the formula

$$H_x = H_1 + \frac{H_2 - H_1}{100}\omega_2, \quad (1)$$

where H_x is the hue of a binary solution, H_1 and H_2 are the hues of the solutions of the individual dyes, and ω_2 is the relative content (rel.%) of component 2:

$$\omega_2 = \frac{C_2}{(C_1 + C_2)} \times 100, \quad (2)$$

provided that H_2 is located to the left (clockwise) relative to H_1, and H_1 takes the values

$$H_1 = \begin{cases} H_1 \text{ at } |H_1 - H_2| < 180, \\ (360 - H_1) \text{ at } |H_1 - H_2| \geq 180. \end{cases} \quad (3)$$

The second alternative in conditions (2) reflects the situation when, as the concentration of one of the components is varied, the hue passes through the point 0, 360 on the color circle (see, e.g., Fig. 6b).

The proposed procedure for calculating the hue of binary solutions was tested with mixed dyes (Table 2). The method gives fairly good results (the correlation factor of the calculated and true hue values is r = 0.974). At the same time, in some cases, the calculated and true hue values differ by more than 50°. Our further studies showed that the difference between the true and calculated hue values depends on the differ-

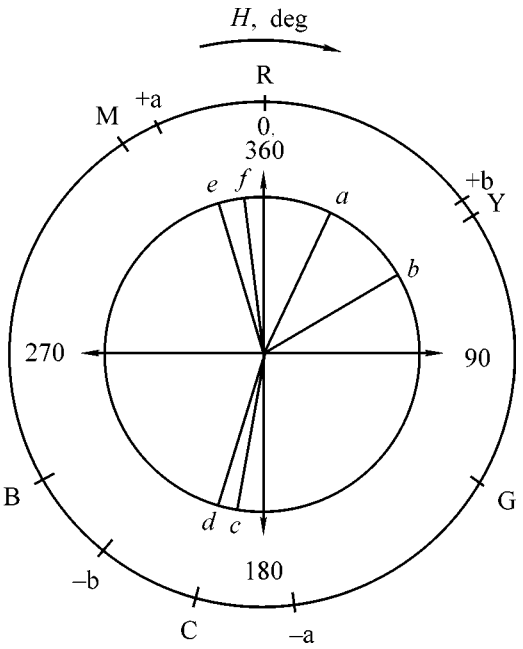

Fig. 5. Location on the color circle of solutions of (*a*) Sunset Yellow, (*b*) tartrazine, (*c*) Brilliant Blue, (*d*) Indigo Carmine, (*e*) Azo Rubine, and (*f*) Ponceau 4R. (*H*) Hue. For comparison is shown the location of "pure" colors: CMYK scale, (C) cyan (blue), (M) magenta (red), and (Y) yellow; RGB scale, (R) red, (G) green, and (B) blue; and Lab (CIE Lab) scale, (+a) red, (–a) green, (+b) yellow, and (–b) blue.

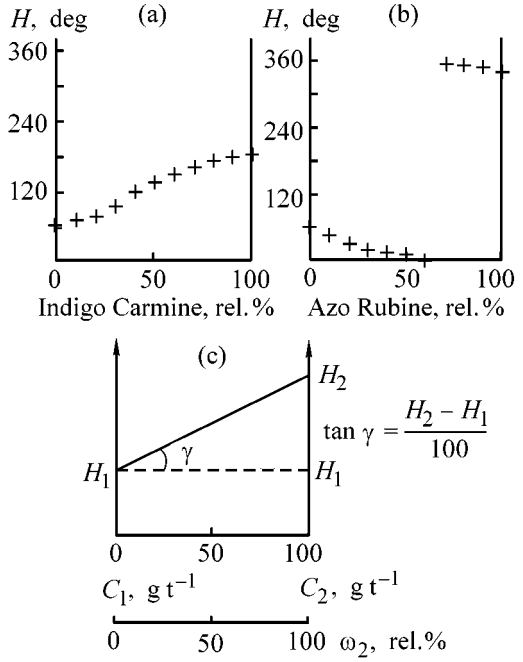

Fig. 6. Hues of binary solutions of tartrazine with (a) Indigo Carmine and (b) Azo Rubine; (c) scheme for calculating the parameters of linear equation. (*H*) Hue; (C_1, C_2) content of dyes 1 and 2, respectively, in solution; (ω_2) relative content of component 2 [formula (2)]. Total content of dyes 100 g t^{-1}.

Table 2. Hue values of binary solutions of synthetic food dyes

Mixture no.	Component	Dye	Component content in mixture, g t^{-1}	H, deg			
				of dye, H_i	of mixture		
					calculated, H_x	true, H_s	$\Delta = \lvert H_s - H_x \rvert$
1	1	**I**	20	344	350	349	1
	2	**V**	80	352			
2	1	**I**	45	344	7	8	1
	2	**III**	55	25			
3	1	**I**	60	344	284	312	28
	2	**IV**	40	195			
4	1	**I**	80	344	313	259	54
	2	**II**	20	189			
5	1	**IV**	65	195	136	159	23
	2	**III**	35	25			
6	1	**V**	60	352	289	323	34
	2	**IV**	40	195			
7	1	**V**	20	352	18	19	1
	2	**III**	80	25			
8	1	**V**	55	352	22	11	11
	2	**VI**	45	59			
9	1	**VI**	50	59	42	32	10
	2	**III**	50	25			
10	1	**VI**	75	59	91	155	64
	2	**II**	25	189			

ence between the hues of the individual substances (correlation factor $r = 0.81$):

$$\Delta_i = 0.304[(H_1 - H_2)_i] - 5.107. \quad (4)$$

It was noted that this parameter also depends on the dye nature. The difference between the calculated and true hue values was the largest with solutions containing Brilliant Blue (Table 2).

Table 3. Formulation of dye mixtures with preset hue ($H = 142°$)

A	Component	Dye	H_i, deg	C_i, g t^{-1}	H_s, deg
1	1	**VI**	59	36.15	165
	2	**II**	189	63.85	
2	1	**VI**	59	38.97	150
	2	**IV**	195	61.03	
3	1	**III**	25	28.66	168
	2	**II**	189	71.34	
4	1	**III**	25	31.18	158
	2	**IV**	195	68.82	

Note: (A) Alternative, (H_i) dye hue, (C_i) dye content in solution, (H_s) hue of mixed dye solution.

Nevertheless, mathematical prediction of the hue value of binary solutions of food dyes can be used in formulating dye mixtures, since the difference of ±10°–15° affects the hue only slightly and is not always detectable visually (especially in the finished product). Thus, calculation by formula (1) can be used for rough estimation of the hue value of a mixed dye solution.

A better approach is, apparently, to find the relative content of components of a mixed dye, required to obtain the desired hue (or hue range) of the solution. In this case, using practically any graphics editor, it is possible to obtain the desired hue on the computer monitor and evaluate it visually, to determine the color characteristics of the chosen hue, and then to estimate the formula of the mixed dye. However, in this case it is desirable to choose dyes with the following characteristics: (1) their hues must be as close as possible to the desired hue, (2) the condition $H_1 < H < H_2$ must be met (H is the desired hue, and H_1 and H_2 are the hues of the individual

dyes), and (3) the colors of the dyes must be as close as possible to the main colors, i.e., to colors that cannot be obtained by mixing other colors: red, yellow, and blue.

With these conditions met, the binary dye mixture can be preliminarily formulated by Eq. (1) (with the exception of mixtures including Brilliant Blue).

Let us consider as an example the formulation of a green mixed dye. For convenience, we fixed the total dye concentration at 100 g t^{-1}. The results are listed in Table 3. We selected two yellow (tartrazine and Sunset Yellow) and two blue (Indigo Carmine and Brilliant Blue) dyes.

Table 3 shows that the experimental hue values of the binary solution are close to the prescribed values. The best results are obtained with the mixtures containing tartrazine. This fact agrees with the recommendations in [5], as the tartrazine hue (H = 59) is closer to the hue of the resulting solution (142) than the hue of Sunset Yellow (H = 25). Thus, it is possible to formulate binary dye mixtures on the basis of the prescribed hue of the finished solution, which can be useful in food industry.

CONCLUSIONS

(1) The correlation between the hues of binary dye solutions and their components was revealed and described mathematically.

(2) For binary solutions, the hue is a function of the relative content of dyes in solution.

(3) A method is proposed for formulating dye mixtures to obtain a prescribed hue.

REFERENCES

1. Wallace, G.M., *Food Technol. N.Z.*, 1966, vol. 1, pp. 227–234.
2. Gerasimov, A.V., Krasikov, V.D., and Malakhova, I.I., Abstracts of Papers, *Seminar "Sovremennye problemy planarnoi khromatografii"* (Seminar "Modern Problems of Planar Chromatography"), Moscow, 2000, pp. 5–6.
3. Gerasimov, A.V., *Zh. Anal. Khim.*, 2000, vol. 55, pp. 1292–1297.
4. Kubelka, P. and Munk, F., *Z. Tech. Phys.*, 1931, vol. 12, pp. 593–601.
5. Kubelka, P., *J. Opt. Soc. Am.*, 1948, vol. 38, pp. 448–457.

Russian Journal of Applied Chemistry, Vol. 74, No. 6, 2001, pp. 998–1001. Translated from Zhurnal Prikladnoi Khimii, Vol. 74, No. 6, 2001, pp. 971–974.

ORGANIC SYNTHESIS AND INDUSTRIAL ORGANIC CHEMISTRY

Biocidal and Anticorrosive Effect of 2-Aminothiazole Derivatives Used as Additives to Jet Fuels

K. A. Karpov, A. V. Nazarenko, B. V. Pekarevskii, and V. M. Potekhin

St. Petersburg State Technological Institute, St. Petersburg, Russia

Received April 16, 2001

Abstract—The effect of 2-aminothiazole derivatives on the biological resistance and corrosion activity of jet fuels was studied under conditions of water condensation.

2-Aminothiazole derivatives are widely used in pharmacology [1]. Aminothiazoles exhibit antimicrobial [1–3] and antioxidant [4] activity. Some disubstituted aminothiazole derivatives are used as antioxidant additives to hydrocarbon fuels, mineral and synthetic lubricating oils, solid paraffins, polyolefins, and animal and vegetable fats [5]. *sym*-Triazine derivatives containing substituents with 2-aminothiazole fragments are effective anticorrosive, antiwear, and antiscuff additives to lubricating oils [6].

With the aim to look for high-performance additives of polyfunctional effect among 2-aminothiazole derivatives, we studied the compounds of the general formula

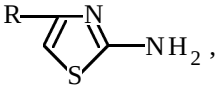

where R = H (**I**), Me (**II**), Ph (**III**), and 1-naphthyl (**IV**).

In this work, we studied the biocidal and anticorrosive properties of 2-aminothiazole derivatives **I**–**IV** when used as additives to jet fuels.

Biocidal additives to fuels are used to suppress the biological damage by microorganisms, impairing the service properties of fuels [7–9]. The effect of these additives is based on inhibiting the activity of microorganisms contaminating the fuel and living in hydrocarbon medium. Biocidal additives are active in concentrations that do not exceed the level prescribed for additives serving for other purposes. In any processes of fuel purification, the danger of fuel deterioration by microorganisms is decreased. However, these measures can only diminish, but not prevent the possibility of fuel contamination [7]; it can be fully precluded only by using special additives.

EXPERIMENTAL

Compounds **I**–**IV** were prepared by the Hansch procedure, namely, by reactions of thiourea with α,β-dichlorodiethyl ether (**I**) [10], with iodine and acetone (**II**) [11, 12], with iodine and acetophenone (**III**) [10, 11], and with iodine and 1'-acetonaphthone (**IV**). The purity and structures of **I**–**IV** were proved by TLC and by IR and NMR spectroscopy. The relevant physicochemical data are listed in Table 1.

The biological resistance of jet fuels RT anbd TS-1 [GOST (State Standard) 10227–86, intended for use in different climatic zones] protected with biocidal additives was determined according to GOST 9.023–74 within the framework of a common system of measures for corrosion and aging protection. The procedure involves incubation of fuels with additives in contact with an aqueous-mineral medium containing test microorganisms which actively grow in the fuel with no additive. Incubation was performed for 15

Table 1. Yields, melting points, and retention factors of 2-aminothiazole derivatives **I**–**IV**

Compound no.	Yield, %	mp, °C	R_f^*
I	90	88 ± 1, 90 [10]	0.44
II	60	40–41, 42 [11]	0.49
III	80	152–153, 151–152 [11]	0.61
IV	80	165 ± 1	0.68

* Eluent 2-propanol–octane, 1 : 1.

1070-4272/01/7406-0998 $25.00 © 2001 MAIK "Nauka/Interperiodica"

Table 2. Microbial resistance of jet fuels in the presence of 2-aminothiazole derivatives **I**–**IV*** (1×10^{-3} M)

Test culture	Unprotected fuel	4-Substituent in aminothiazole				Ionol
		H	Me	Ph	1-naphthyl	
RT jet fuel						
Pseudomonas aeruginosa	++	+	+	+	+	++
Candida utilis	++	–	+	+	+	++
Cladosporium resinae	+	+	–	+	–	+
TS-1 jet fuel						
Pseudomonas aeruginosa	++	–	–	+	+	++
Candida utilis	++	–	–	–	+	++
Cladosporium resinae	+	–	–	–	–	+

* (–) No growth, (+) slight pigmentation and/or turbidization of the medium, and (++) turbid medium and/or formation of a flaky suspension.

Table 3. Sensitivity of test microorganisms to 2-aminothiazole derivatives **I**–**IV** (4×10^{-4} M), evaluated by diffusion into agar

Test culture	Diameter of the spot of microorganism growth delay, mm				
	4-substituent in aminothiazole				Ionol
	H	Me	Ph	1-naphthyl	
Staphylococcus aureus	0	8	0	0	0
Escherichia coli	2	4	0	0	0
Bacillus cereus	4	8	2	0	0
Pseudomonas aeruginosa	1	2	0	0	0
Candida utilis	0	0	0	0	0
Penicillium aurantiogriseum	0	6	0	0	0
Aspergillus niger	0	8	0	0	0

days under conditions optimal for the microbial growth. The extent of fuel protection with a biocidal additive was evaluated by comparing the samples with unprotected fuel (control). The results of the tests are listed in Table 2.

Our results show that 2-aminothiazole derivatives **I**–**IV** are fairly effective biocidal additives. In this connection, it is of interest to compare the microbial resistance of jet fuels containing additives **I**–**IV** and commercial additive Ionol (2,6-di-*tert*-butyl-4-methylphenol). As seen from Table 2, this additive shows no biocidal properties, and the microbial impact tests give results identical with those for the control sample.

To obtain quantitative characteristics of the biocidal effect of **I**–**IV**, we evaluated the sensitivity of test microorganisms to 2-aminothiazole derivatives by the method of duffusion into agar [13]. For the tests we used the standard culture media: Czapek agar and meat–peptone agar.

Table 3 shows how 2-aminothiazole derivatives affect the microbial growth. With respect to the efficiency of the bactericidal effect the compounds can be ranked in the order **II** > **I** > **III**.

According to our results, the structure of the 4-substituent in 2-aminothiazole derivatives affects the activity toward test microorganisms. Compound **II**, containing the methyl substituent, is characterized by the largest diameters of growth delay spots. Aromatic substituents drastically decrease the biocidal effect of the additives. Compound **IV** showed no biocidal properties under the experimental conditions.

The biological activity of 2-aminothiazole derivatives **I**–**IV** correlates with the electron-donor and electron-acceptor power of substituents. According to [14], compounds containing heteroatoms and multiple bonds can enter into donor–acceptor interactions with biopolymers, disturbing the normal vital activity of a microorganism. In our case, compound **II** containing

Table 4. Corrosion resistance of St.3 steel in hydrated RT jet fuel in the presence of 2-aminothiazole derivatives **I**–**IV** (98°C, additive concentration 5×10^{-4} M)

Additive	K, g m^{-2}	γ
–	1.71	–
I	1.32	0.30
II	1.24	0.38
III	0.78	1.19
IV	0.57	2.00
Ionol	1.36	0.26

an electron-donor methyl substituent exhibits the strongest biocidal effect, whereas compounds **III** and **IV**, containing aromatic substituents lowering the electron density in the thiazole ring, show a weak biological activity.

It is believed that antioxidants mainly behave as biocides [15]. However, as shown in Table 3, commercial oxidation inhibitor Ionol shows no biocidal effect at all.

As biocidal additives are used ammonia and amine derivatives, potassium permanganate, copper sulfate, zinc chloride, and a number of organic compounds [16]. However, many of them stimulate corrosion [17]. The corrosion activity of hydrocarbon media toward metal surfaces is, in particular, due to acids [18] formed by oxidation. 2-Aminothiazole derivatives, inhibiting oxidation of hydrocarbons [5], decrease the probability of corrosion. To evaluate unambiguously the anticorrosive effect of **I**–**IV**, we determined the corrosive activity of RT fuel in the presence of test compounds according to GOST 18597–73. It was evaluated by the weight loss of a metallic plate (St.3 steel) immersed in a fuel for 4 h under conditions of fuel saturation with water and its condensation on the plate. The corrosion activity of fuels under conditions of water condensation, K (g m^{-2}), was calculated by the formula

$$K = \frac{(m - m_1) - h}{S}, \quad (1)$$

where m is the plate weight before the test (g), m_1 is the plate weight after the test (g), h is the etching constant (g), S is the area of the top and side surfaces of the plate (m^2; the bottom surface is in contact with the vessel bottom and does not participate in corrosion).

The corrosion inhibition factor γ was calculated by the formula

$$\gamma = \frac{K - K'}{K'}, \quad (2)$$

where K' is the corrosion activity of the fuel containing an additive (g m^{-2}).

The corrosion activities and corrosion inhibition factors are listed in Table 4.

Thus, 2-aminothiazole derivatives show high anticorrosive power and surpass commercial inhibitor Ionol in performance. Along with the already noted inhibition of acid formation in fuel, the mechanism of the anticorrosive effect of 2-aminothiazole derivatives may also involve formation of a monomolecular layer of compounds (as a rule, coordination compounds) on the metal surface, insulating it from the hydrocarbon medium [19].

CONCLUSIONS

(1) 2-Aminothiazole derivatives exhibit biocidal properties and can be used as additives to RT and TS-1 jet fuels.

(2) The biocidal properties of **I**–**IV** depend on the nature of a 4-substituent.

(3) Aminothiazoles **I**–**IV** exhibit anticorrosive activity in RT fuel under conditions of water condensation.

REFERENCES

1. Manian, A.K., Khadse, B.G., Kirtikar, P.A., and Sengupta, S.R., *Indian J. Pharm. Sci.*, 1991, vol. 53, no. 3, pp. 102–103.
2. US Patent 5856347.
3. FRG Patent Appl. 19719053.
4. Uchikawa, O., Fukatsu, K., Suno, M., *et al.*, *Chem. Pharm. Bull.*, 1996, vol. 44, no. 11, pp. 2070–2077.
5. US Patent 3201409.
6. Kelarev, V.I., Gracheva, O.G., Silin, M.A., *et al.*, *Nefte pererab. Neftekhim.* (Moscow), 1997, no. 12, pp. 29–32.
7. Sablina, Z.A. and Gureev, A.A., *Prisadki k motornym toplivam* (Additives to Motor Fuels), Moscow: Khimiya, 1977.
8. Koval', E.Z. and Sidorenko, L.P., *Mikodestruktory promyshlennykh materialov* (Fungi Decomposing Industrial Materials), Kiev: Naukova Dumka, 1989.
9. Hedrick, H., Carroll, M.T., Owen, H.P., and Pritchard, D.J., *Appl. Microbiol.*, 1963, vol. 11, no. 6, pp. 472–478.
10. *Oganicheskie reaktsii*, Kochetkov, N.K. and Volodina, V.S, Eds., Moscow: Mir, 1953, vol. 6.

11. Dodson, R.M. and King, L.C., *J. Am. Chem. Soc.*, 1945, vol. 67, no. 12, pp. 2242–2243.
12. Baiers, J., Dikki, J., *Organic Synthesis*, coll. vol. 2, Adams, R., Clark, H.T., Conant, J.B. *et al.*, Eds., New York: Wiley, 1946, 2nd ed. Translated under the title *Sintezy organicheskikh preparatov*, Moscow: Inostrannaya Literatura, 1949, coll. 2, pp. 40 – 41.
13. *Meditsinskaya mikrobiologiya* (Medical Microbiology), Korolyuk, A.M. and Boichakov, V.B., St. Petersburg: Elbi, 1999, part 1.
14. Zachinyaev, Ya.V., Chemistry of Perfluorionated Carboxylic Acid Fluorides, *Doctoral Dissertation*, St. Petersburg, 1998.
15. Allen, F., *J. Inst. Petrol.*, 1945, vol. 31, no. 253, pp. 9–17.
16. Yones, D.G., Limaye, S.H., and Young, B.B., *J. Inst. Petrol.*, 1972, vol. 58, no. 563, pp. 268–271.
17. Sherwood, P.W., *Corros. Technol.*, 1962, vol. 9, no. 8, pp. 211–214.
18. Denisov, E.T. and Kovalev, G.I., *Okislenie i stabilizatsiya reaktivnykh topliv* (Oxidation and Stabilization of Jet Fuels), Moscow: Khimiya, 1983.
19. Kuzharov, A.S. and Suchkov, V.V., *Zh. Fiz. Khim.*, 1980, vol. 56, no. 12, pp. 3114 –3117.

Russian Journal of Applied Chemistry, Vol. 74, No. 6, 2001, pp. 1002–1006. Translated from Zhurnal Prikladnoi Khimii, Vol. 74, No. 6, 2001, pp. 975–979.

MACROMOLECULAR CHEMISTRY AND POLYMERIC MATERIALS

Synthesis, Structure, and Characteristics of Ultra-High-Molecular-Weight Poly-*N*-methacryloyloxyethyl-*N*,*N*,*N*-Trimethylammonium Methyl Sulfate

V. A. Molotkov, V. I. Kurlyankina, S. I. Klenin, N. A. Matveeva, G. V. Shishkina, A. I. Kipper, E. N. Khlebosolova, L. D. Ostrovskaya, N. V. Rumyantseva, and S. V. Valueva

Institute of Macromolecular Compounds, Russian Academy of Sciences, St. Petersburg, Russia

Received July 19, 2000; in final form, March 2001

Abstract—Two procedures for synthesis of water-soluble poly-*N*-methacryloyloxyethyl-*N*,*N*,*N*-trimethylammonium methyl sulfate are compared. Synthesis occurred by the radical mechanism with the Co(III)–glycine system and with acid catalytic initiation. The effect of the initiator nature and the reaction conditions on the course of polymerization was studied.

This work is devoted to synthesis of poly-*N*-methacryloyloxyethyl-*N*,*N*,*N*-trimethylammonium methyl sulfate, widely used for solving environmental problems. Previously, two fundamentally different procedures for radical polymerization, resulting in the formation of water-soluble polymers with molecular weights of $(10–30) \times 10^6$, were developed. One of these is based on the use of the redox system Co(III)–glycine as initiator [1], and the other is based on generation of polymerization centers by catalytic decomposition of monomer molecules [2].

In this report, we compare these processes with the aim to elucidate the features of the reactions allowing production of polymers with ultra-high molecular weights and to establish factors governing the structure and characteristics of the resulting polymers. The developed procedures of synthesis have been patented [3, 4] and served as the basis for production of ultra-high-molecular-weight flocculant Akromidan LK used for purification of drinking water and wastewaters.

EXPERIMENTAL

Poly-*N*-methacryloyloxyethyl-*N*,*N*,*N*-trimethylammonium methyl sulfate was synthesized as follows. In polymerization by the redox system Co(III)–glycine, solutions of the initiator and monomer were prepared separately. To obtain a solution of the initiator, a calculated amount of $Co_2(SO_4)_3 \cdot 18H_2O$ was added to an aqueous solution with a given concentration of glycine, cooled to 0°C; then argon was bubbled-through to remove dissolved oxygen. The solution with the required monomer concentration and acidity was bubbled with argon, cooled to 0°C, and added to the reaction mixture. The reaction was carried out in an inert medium. After the process was complete, the polymer was dissolved in distilled water and purified by dialysis to remove the residual monomer and low-molecular-weight impurities with the use of a cellulose membrane. The conversion was determined from the concentration of the resulting polymer solution by weighing the dry residue.

In polymerization by the acid-catalytic procedure, the working solution with required pH and monomer concentration was blown-through with argon and placed in a thermostat with a given temperature. The reaction was carried out in an argon medium. After the reaction was complete, the polymer was dissolved and the conversion determined as described above.

The intrinsic viscosity of the resulting polymers was measured in a 1 M aqueous solution of $NaNO_3$ in an Ostwald viscometer at 20°C. The molecular weight of polymers M was determined by the light-scattering technique (M_w) on a Fica-50 photodiffusimeter [5] and by the sedimentation-diffusion technique (M_{sd}) [6]. In the light-scattering technique,

1070-4272/01/7406-1002 $25.00 © 2001 MAIK "Nauka/Interperiodica"

the wavelength of the incident vertically polarized light was 546 nm. The increment of the refractive index d*n*/d*c* was determined on an IRF-23 refractometer to be 0.154. The experimental data were processed by the Zimm double extrapolation technique.

The initiation methods have the following features. It was shown by NMR that, in initiation of polymerization with the redox system Co(III)–glycine [1], the reaction proceeds to form intermediate complex **I** and chelate **II**:

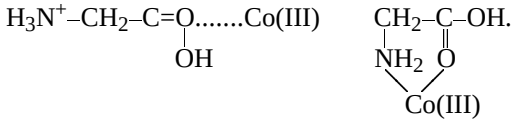

I **II**

Chelate **II**, in turn, decomposes to form free radical **III**:

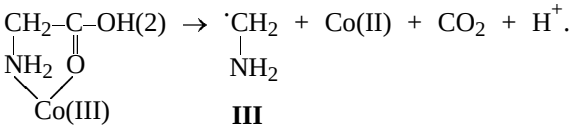

III

The $^{\cdot}CH_2$–NH_2 radical initiates polymerization. The equilibrium constant of formation of the linear complex is $\beta_1 = 0.91 \pm 0.16$, and that of the chelate, $\beta_2 = 0.31 \pm 0.07$ M. Cobalt(III) is a strong oxidizing agent [7], but the chelate is fairly stable in dilute aqueous solutions and at a Co(III) concentration of 0.3–0.6 mg-equiv l^{-1} provides active development of polymerization in the course of 7–10 h at 20–40°C.

The initiation by the acid-catalytic procedure occurs via decomposition of monomer molecules under the action of protons [2]. The reaction proceeds by the radical mechanism. The initiation rate $V_{OR\cdot}$ is expressed by the equation

$$V_{OR\cdot} = K_{pr}\, x K_{OR\cdot}\, x\,[M]\, x\,[H^+],$$

where K_{pr} is the protonation constant of the monomer, $K_{OR\cdot}$ is the decomposition constant of the protonated species with formation of free radicals, and [M] and $[H^+]$ are the concentrations of monomer and protons in the reaction mixture, respectively.

The optimum conditions of synthesis of macromolecular polymers by this procedure are at concentrations of radicals in the range $(0.7–0.8) \times 10^{-8}$ M [2].

Studies showed that, to synthesire high-molecular-weight polymers, a monomer concentration of no less than 50–70% and stable concentration of the radicals on the order of 10^{-8} M are required in both cases [1, 2]. The use of kinetic methods for monitoring the polymerization course is hindered under these conditions; therefore, as the main parameters of monitoring we selected the yield of the polymer, its molecular weight, and the average number of macromolecules formed [8], which gives insight into the overall course of the reaction.

Table 1. Yield and molecular weight of polymer *M* at various initiator concentrations for the system Co(III)–glycine*

τ, h	[Co(III)] = 0.3 mg-equiv l^{-1}, [gl] = 3.0 mM		[Co(III) = 0.6 mg-equiv l^{-1}, [gl] = 3.0 mM	
	Polymer yield, %	$M \times 10^{-6}$	Polymer yield, %	$M \times 10^{-6}$
1	5.5	–	48.4	–
2	12.5	11.2	69.0	9.9
3	22.0	13.5	82.1	11.2
4	35.0	15.6	88.3	12.4
5	48.0	17.8	90.2	13.1
6	67.5	19.8	93.0	14.3
7	81.0	22.0	97.3	15.4

* [M] = 50 wt %, pH 2.5, T = 30°C.

A study of polymerization of methacryloyloxyethyl-*N*,*N*,*N*-trimethylammonium methyl sulfate with the use of the redox system Co(III)–glycine showed that the key factor of its development is generation of free radicals via decomposition of chelate **II**. We found that the optimum concentrations of reagents are in the following ranges: Co(III), 0.3–0.6 mg-equiv l^{-1} and glycine, 3.0–6.0 mM. Taking into account the high redox potential of Co(III), we selected the upper temperature limit of 40°C to provide stable operation of the initiator.

The dependences of the yield of poly-*N*-methacryloyloxyethyl-*N*,*N*,*N*-trimethylammonium methyl sulfate and its molecular weight on the initiator concentration in the case of the system Co(III)–glycine are presented in Table 1. With the concentrations of Co(III) and glycine growing by a factor of 2, the polymerization rate increases abruptly. For example, in the first case, the yield of the polymer is 12.5% and 48%, and in the second case, 69.0% and 90.2% in 2 and 5 h, respectively. In this case, an increase in the concentration of Co(III) and glycine results in a decrease in the molecular weight of the polymer, since free radical **III** is not only the polymerization initiator but also a chain-terminating agent.

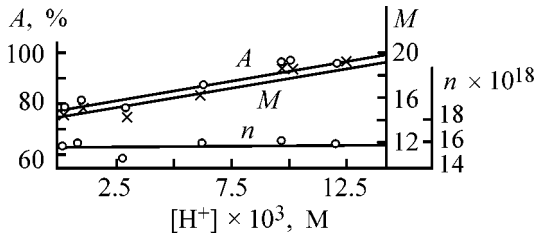

Fig. 1. Effect of the concentration of hydrogen ions $[H^+]$ on the yield of polymer *A*, molecular weight *M*, and the average number of marcomolecules *n* in 1 l of the reaction solution. Initiation with the system Co(III)–glycine. Reaction conditions: [M] = 50 wt %, [Co(III)] = 0.6 mg-equiv l^{-1}, [gl] = 6.0 mM, *T* = 40°C, and reaction time 4 h.

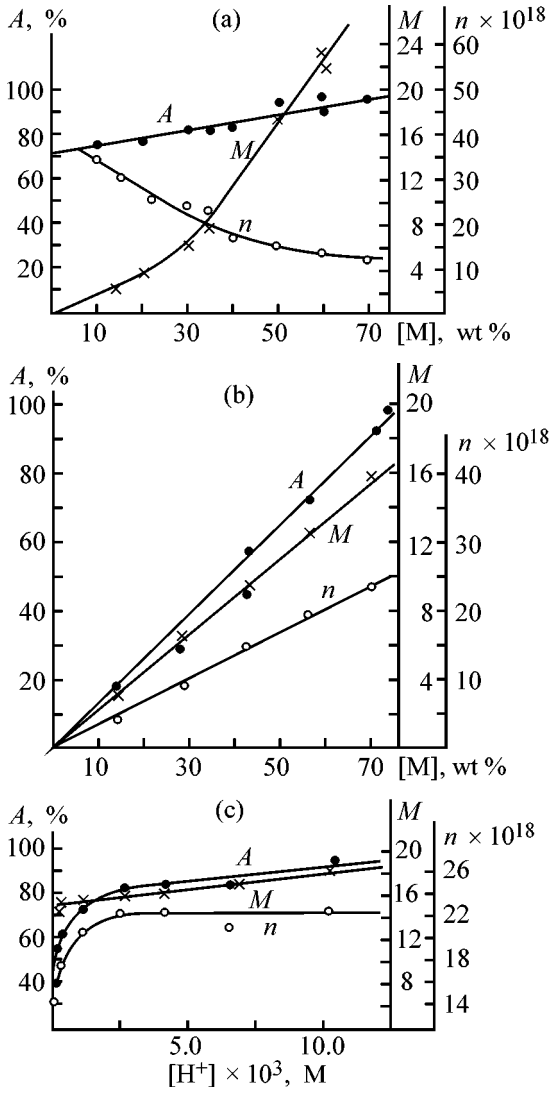

Fig. 2. Effect of concentration of (a, b) monomer [M] and (c) hydrogen ions $[H^+]$ on the yield of polymer *A*, molecular weight *M*, and the average number of macromolecules *n*. (a) Initiation by the system Co(III)–glycine, [Co(III)] = 0.6 mg-equiv l^{-1}, [gl] = 6.0 mM, pH 2.5, *T* = 40°C, and reaction time 4 h; (b) acid-catalytic procedure, *T* = 60°C, reaction time 6 h. (b) [M] = 70 wt % and (c) pH 2.0.

Varying the concentration of hydrogen ions also affects the polymerization process. According to data presented in Fig. 1, the molecular weight and the yield of the polymer grow steadily with increasing concentration of hydrogen ions throughout the studied range of pH at a constant number of formed macromolecules.

The dependences of the polymer yield and its molecular weight on the monomer concentration are presented in Fig. 2a. With increasing concentration of the monomer, the yield of the polymer grows steadily and reaches 88–95%. At the same time, the rate of increase in the molecular weight of the polymer in the range of monomer concentration above 30% grows by a factor of 2, which is apparently caused by changes in the nature of termination of the growing chains. It is seen from Fig. 2a that the number of chains in the second period considerably decreases. It should be noted that gelation begins even at a monomer concentration of approximately 2%.

Three factors affect acid-catalyzed polymerization: monomer concentration, pH of the reaction solution, and temperature [2]. The corresponding dependences are presented in Figs. 2b and 2c and in Table 2.

It is seen from Fig. 2b that the yield of the polymer, its molecular weight, and the number of the resulting macromolecules increase in direct proportion to the monomer concentration and, with this concentration increasing from 10 to 70%, the yield of the polymer grows from 14 to 93%, *M* increases from 2.4×10^6 to 16×10^6, and the average number of macromolecules *n* in 1 l of the reaction solution increases from 3.5×10^{18} to 24×10^{18}.

It is evident that the initiation by the acid-catalytic procedure proceeds differently: The number of the resulting polymer chains increases progressively, and, hence, the way in which the growing chains are terminated does not change. In this process the monomer is the polymerization initiator; therefore, its initiating power grows in proportion to the increasing concentration of the monomer.

Figure 2c shows the effect of proton concentration on the yield of the resulting polymer, its molecular weight, and the number of polymer chains. The study was carried out in a wide range of proton concentration, 10^{-5}–10^{-2} M. It was found that the polymerization begins at $[H^+] = 10^{-4}$ M; however, the yield reaches only 40%. The optimum conditions of synthesis of high-molecular-weight polymers are in the range $[H^+] = 2.5 \times 10^{-3}$–$1 \times 10^{-2}$ M. At a monomer concentration of 70% the concentration of hydrogen ions

of 2.5×10^{-3} M is sufficiently high for the process of polymer formation to become stable. In this case, the yield of the polymer reaches 83.0–94.2%, M = $(16.3–18.2) \times 10^6$, and the average number of macromolecules n in 1 l of the solution is 22.4×10^{18}.

The yield and molecular weight of the polymer are presented in Table 2 as functions of the temperature and time.

It is evident that the yield of the polymer grows with increasing reaction time. The optimum temperature of synthesis is in the range 60–70°C; in this case, the yield of the polymer reaches 95–98% and the molecular weight decreases insignificantly. However, the reaction at lower temperatures is of interest since it yields a polymer with increased molecular weight. At 50°C and the reaction times of 6 and 20 h we obtained polymers with M = $(18.9–19.2) \times 10^6$, and, at 20°C and 0°C, polymers with M = $(30–35) \times 10^6$.

The molecular weights of poly-*N*-methacryloyloxyethyl-*N*,*N*,*N*-trimethylammonium methyl sulfate were determined by two absolute methods: light scattering (M_w) [5] and sedimentation-diffusion analysis (M_{sd}) [6]. The results of determination by both methods are in good agreement within the experimental error (10–15%). The results obtained show that the samples studied have relatively narrow molecular-weight distribution (MWD), M_w/M_n = 1.5.

Figure 3 shows the dependence $\log[\eta] = f(\log M_w)$ in a wide range of molecular weights (5×10^4–3×10^7) for samples synthesized with the redox system Co(III)–glycine [9, 10]. For samples obtained by the acid-catalytic procedure (Table 3) the intrinsic viscosity [η] and molecular weight M fit in nearly the same dependence, which suggests structural and conformational homology of the macromolecules formed with the system Co(III)–glycine and by the acid-catalytic initiation procedure.

CONCLUSIONS

(1) Two procedures with different ways of initiation were developed for production of ultra-high-molecular-weight water-soluble poly-*N*-methacryloyloxyethyl-*N*,*N*,*N*-trimethylammonium methyl sulfate with molecular weight of $(10–30) \times 10^6$. The first is based on generation of free radicals by decomposition of a complex of Co(III) with glycine, and the second, on generation of polymerization centers in the reaction of the monomer with protons.

Table 2. Yield and molecular weight M of the polymer prepared with acid-catalytic initiation*

τ, h	Yield, %, and $M \times 10^{-6}$ at indicated temperature, °C					
	0	20	50	60	70	80
	Yield of polymer					
0.7	1.0	2.0	8.0	23.5	24.0	23.0
1.5	2.5	5.0	23.0	43.0	47.0	38.0
3.0	5.0	9.0	38.0	63.0	70.0	56.0
4.5	8.0	13.0	53.0	75.0	83.0	69.0
6.0	11.0	18.0	64.0	85.0	96.0	75.0
20.0	16.0	30.0	86.0	95.0	98.0	90.0
	Molecular weight					
6.0	–	–	18.9	16.0	16.3	11.2
20.0	–	30.0	19.2	16.6	16.0	11.2
30.0	35.0	–	–	–	–	–

* [M] = 70 wt %, pH 2.0.

Table 3. Synthesis conditions and molecular characteristics of poly-*N*-methacryloyloxyethyl-*N*,*N*,*N*-trimethylammonium methyl sulfate obtained with acid-catalytic initiation

pH	[M], wt %	T, °C	τ, h	Conversion, %	[η], dl g^{-1}, in 1 N $NaNO_3$	$M_w \times 10^{-6}$
2.0	70	60	6	74.0	7.5	19.6
2.0	70	70	6	81.1	7.0	14.7
3.4	70	70	20	98.3	3.2	7.4
1.6	70	70	2	52.9	5.6	13.6
1.65	70	70	2	25.9	5.0	12.0
2.0	50	50	48	76.0	3.8	6.1
2.5	60	25	24	74.0	9.9	26.0

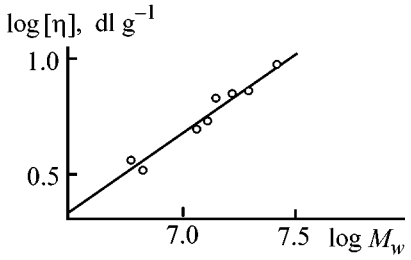

Fig. 3. $\log[\eta]$–$\log M_w$ plot for poly-*N*-methacryloyloxyethyl-*N*,*N*,*N*-trimethylammonium methyl sulfate in 1 N $NaNO_3$. (*Straight line*) polymer obtained with the system Co(III)–glycine [9, 10]; (*points*) polymer samples obtained acid catalysis.

(2) The main characteristics of poly-*N*-methacryloyloxyethyl-*N*,*N*,*N*-trimethylammonium methyl sulfate produced by the two above procedures are similar.

REFERENCES

1. Kurlyankina, V.I., Molotkov, V.A., Antonov, N.G., and Denisov, V.M., *Zh. Obshch. Khim.*, 1996, vol. 66, no. 11, pp. 1841–1846.
2. Kurlyankina, V.I., Molotkov, V.A., Dobrodumov, A.V., *et al.*, *Dokl. Ross. Akad. Nauk*, 1995, vol. 341, no. 3, pp. 358–363.
3. RF Patent 2106370.
4. USSR Inventor's Certificate, no. 1748420.
5. Eskin, V.E., *Rasseyanie sveta rastvorami polimerov i svoistva makromolekul* (Light Scattering in Polymer Solutions and Characteristics of Macromolecules), Leningrad: Nauka, 1986.
6. Tsvetkov, V.N., *Zhestkotsepnye polimernye molekuly* (Rigid-Chain Polymer Molecules), Leningrad: Nauka, 1986.
7. Mironov, V.E., *Usp. Khim.*, 1970, vol. 39, no. 4, pp. 702–726.
8. *Fizicheskaya entsiklopediya* (Physical Encyclopedia), Petrov, A.M., Ed., Moscow: Sov. Entsiklopedia, 1988, vol. 1, p. 151.
9. Bykova, E.N., Klenin, S.I., Petrova, S.F., *et al.*, Abstracs of Papers, *IV Vsesoyuznaya konferentsiya "Vodorastvorimye polimery i ikh primenenie"* (IV All-Union Conf. "Water-Soluble Polymers and Their Application"), Irkutsk: Vost.-Sib. Pravda, 1991, p. 115.
10. Klenin, S.I., Valueva, S.V., Lyubina, S.Ya., *et al.*, *Vysokomol. Soedin., Ser. A*, 1994, vol. 36, no. 7, pp. 1164–1171.

Russian Journal of Applied Chemistry, Vol. 74, No. 6, 2001, pp. 1007–1009. Translated from Zhurnal Prikladnoi Khimii, Vol. 74, No. 6, 2001, pp. 979–981.

MACROMOLECULAR CHEMISTRY AND POLYMERIC MATERIALS

Polymerization of Vinyl Chloride in the Presence of Alcohols

A. G. Kronman, G. L. Groshev, L. V. Leshina, E. F. Sitnikova, and T. V. Sulina

Research Center, Kaprolaktam Joint-Stock Company, Dzerzhinsk, Nizhni Novgorod oblast, Russia

Received November 14, 2000; in final form, March 2001

Abstract—Precipitation polymerization of vinyl chloride in solution in the presence of alcohols was studied. The reaction mechanism was suggested, and the product composition was estimated by IR spectroscopy and selective extraction.

In polymer chemistry, major attention is given to synthesis of modifiers, in particular, telomers, which can be used as plasticizers. Synthesis of vinyl chloride (VC) telomers using such telogens as polychloroalkanes (carbon tetrachloride, chloroform, tetrachloropropane), bromo and iodo derivatives (methyl bromide, bromoform), and esters was described in ample detail in monograph [1]. Initiating systems include iron trichloride, pentacarbonyliron, benzoin, acetonitrile, and dimethylformamide. The telomerization temperature was varied from 90 to 140°C, depending on the nature of a telogen and initiator.

Also, in the case of chloroalkanes (trichloroethane, 1,1,1,3-tetrachloropropane), telomerization of vinyl chloride with cleavage of the C–Cl bond cannot be effected with initiation by azo compounds and peroxides [2].

The use of such monomers as vinyl and vinylidene chloride, characterized by high rate constants of propagation of the intermediate radicals in homopolymerization, is favorable for formation of telomers containing more than three units [1]. However, the molecular weight M of these products is very low (200–1000). It is known [3, 4] that, to prepare low-molecular-weight vinyl chloride polymers, mono- and dihydric alcohols are added to a polymerization formulation, with the process performed in the presence of traditional initiators (peroxides, percarbonates). Therefore, we made an attempt to prepare low-molecular-weight polyvinyl chloride (PVC) in alcohols by precipitation polymerization in solution. The results are reported in this paper.

EXPERIMENTAL

Synthesis of low-molecular-weight PVC in the presence of alcohols was performed in a 3-l steel vessel with a stirrer at 70°C for 36 h. The reaction medium was monohydric isopropyl alcohol (IPA) or polyethylene glycol PEG-400. The vinyl chlolride : alcohol ratio was 1 : 1. The polymerization was initiated with azobis(isobutyronitrile) (AIBN). After polymerization was complete, the product was thoroughly washed with water to remove isopropyl alcohol; the completeness of IPA removal was checked by a procedure based on the reaction of alcohol with *p*-dimethylaminobenzaldehyde in sulfuric acid. Removal of PEG-400 was monitored by means of the Nessler reagent. The polymer was dried at 40–45°C and analyzed to determine the Fickentscher constant K_f and the chlorine content. The molecular weight M of the polymers was calculated by the formula $[\eta] = KM^{\alpha}$, where $[\eta]$ is the intrinsic viscosity, and K and α are the empirical constants equal, respectively, to 2.04×10^{-3} and 0.56 (solvent cyclohexanone). Also, we measured the IR spectra in the range 3800–400 cm^{-1} (Specord M-80 spectrophotometer). Films for IR spectroscopy were prepared from THF solutions on a KBr support.

To compare the properties of the polymers prepared in the presence of alcohols, we synthesized under the same conditions a PVC sample by suspension polymerization.

The table shows that the polymers prepared by precipitation polymerization of vinyl chloride in solution in the presence of alcohols have intermediate molecular weights between the telomers and common PVC. The strong difference between the molecular weights of the polymers prepared in run nos. 1 and 2 and that of the control sample (run no. 3) is due to the high efficiency of termination reactions; in PEG-400 this effect is stronger, which is confirmed by the considerably lower yield (50%, compared with 90%).

1070-4272/01/7406-1007 $25.00 © 2001 MAIK "Nauka/Interperiodica"

Synthesis of PVC in the presence of alcohols

Run no.	Medium	Yield, %	Product composition, wt %			K_f	$[\eta]$, dl g^{-1}	M
			Cl	VC	PEG-400			
1	IPA	90	55.4	96.7	–	28.9	0.197	3500
2	PEG-400	50	49.9	87.8*	12.2	24.1	0.162	2500
3	Water	94	56.6	99.6	–	52.2	0.644	29 000

* Data for the fraction after separation of PVC homopolymer.

The lower content of chlorine in product no. 1, compared with the control PVC sample, is due to the considerably higher relative content of terminal groups (fragments of the initiator and IPA as chain-transfer agent). Analysis of product no. 2 shows that occurrence of chain transfer under conditions of vinyl chloride polymerization results in formation of a chemical bond between PVC and PEG-400, since the reaction product is preliminarily thoroughly washed to remove PEG-400 (checked with the Nessler reagent). However, in this case it was of interest to study the product composition in more detail.

The chain transfer in polymerization of vinyl chloride in the presence of PEG must inevitably result in the formation of a mixture of the homopolymer and a block copolymer of PVC with PEG-400. Since PVC is insoluble in trichloroethylene, we attempted to extract the reaction product with this solvent (4 h at 50°C). Analysis of the insoluble fraction for chlorine showed that this is a homopolymer; its content in the reaction product was about 60%. The block copolymer of PVC with PEG-400 was isolated by precipitation with heptane of the fraction soluble in trichloroethylene.

The figure shows the IR spectra of suspension PVC (control sample) and the polymers prepared in the presence of IPA and PEG-400. Comparison of the spectra of sample nos. 1 and 2 with that of the control sample shows that an additional band appears at 3420 cm^{-1}, belonging to stretching vibrations of the OH groups. Their presence in the polymer is confirmed by the preservation of this band in the reprecipitated product. Thus, polymerization of vinyl chloride in IPA can be represented by the following scheme:

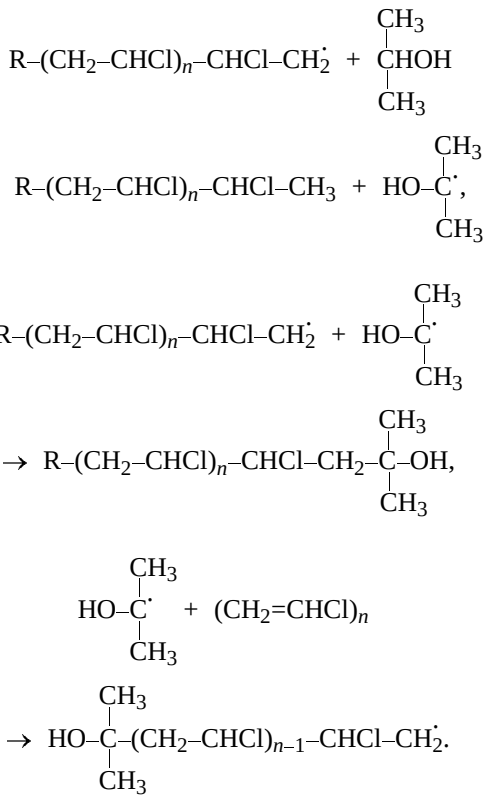

Apparently, in this case the polymerization product will be a mixture of polymers both with and without the hydroxy group; therefore, the intensity of the band at 3420 cm^{-1} is relatively low.

The IR spectrum of PVC prepared in the polyethylene glycol medium contains a strong absorption band of OH stretching vibrations at 3420 cm^{-1} and a new band at 1104 cm^{-1}, belonging to vibrations of the ether

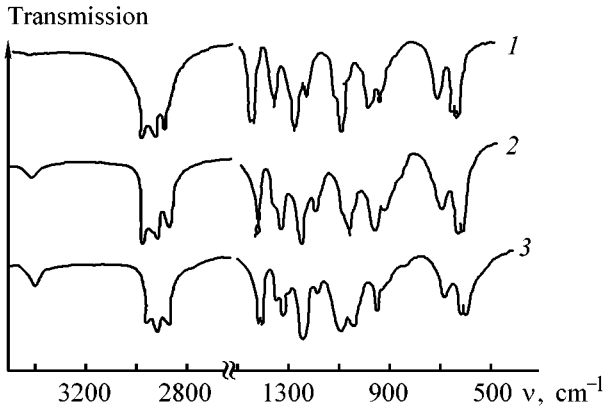

IR spectra of PVC samples prepared (*1*) by suspension polymerization, (*2*) in the presence of IPA, and (*3*) in the presence of PEG-400. (ν) Wave number.

bond C–O–C. Also, the bands at 2910 and 1350 cm^{-1}, belonging, respectively, to the stretching and bending vibrations of methylene groups, become stronger. The structure of the block copolymer formed in the process can be represented as follows:

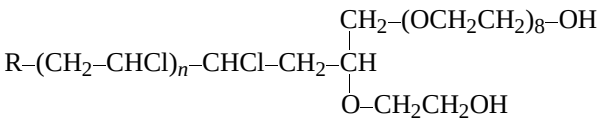

The suggested structure of the polymers prepared in the presence of IPA and PEG-400 can be confirmed by the fact that alcohols are among telogens reacting in radical polymerization with cleavage of the C–H bond. Since the C–H and O–H bond energies are 85.5 and 110 kcal mol^{-1}, respectively [5], it can be stated that the hydroxy groups will occur in the main polymer chain in both cases.

CONCLUSIONS

(1) Based on the results of precipitation polymerization of vinyl chloride in alcoholic solutions (isopropyl alcohol and polyethylene glycol PEG-400), the mechanism was suggested in which the alcohols act as effective chain-terminating agents with respect to polyvinyl chloride.

(2) According to the IR spectra, the polymer prepared in the presence of isopropyl alcohol contains, in contrast to traditional polyvinyl chloride, hydroxy groups, and the polymer prepared with PEG-400 contains hydroxy, methylene, and ether groups.

REFERENCES

1. Freidlina, R.Kh., Velichko, F.K., Zlotskii, S.S., *et al.*, *Radikal'naya telomerizatsiya* (Radical Telomerization), Moscow: Khimiya, 1988.
2. Kamyshova, A.A., Osipov, B.N., and Freidlina, R.Kh., *Izv. Akad. Nauk SSSR, Ser. Khim.*, 1972, no. 1, pp. 60–65.
3. GDR Patent 232 282.
4. GDR Patent 240 550.
5. Temnikova, T.I., *Kurs teoreticheskikh osnov organicheskoi khimii* (Course of Theoretical Principles of Organic Chemistry), Leningrad: Goskhimizdat, 1962.

Russian Journal of Applied Chemistry, Vol. 74, No. 6, 2001, pp. 1010–1015. Translated from Zhurnal Prikladnoi Khimii, Vol. 74, No. 6, 2001, pp. 982–988.

MACROMOLECULAR CHEMISTRY AND POLYMERIC MATERIALS

Process for Preparation and Modification of Formulations for Medicine, Based on Blends of Ultra-High-Molecular-Weight Polyethylene and Polysiloxane

O. O. Nikolaev, V. P. Britov, and V. V. Bogdanov

St. Petersburg State Technological Unstitute, St. Petersburg, Russia

Received December 21, 2000

Abstract—A process is proposed for preparing formulations based on ultra-high-molecular-weight polyethylene and polysiloxane, yielding materials with the required adhesion between the phases. Procedures are developed for physicochemical modification of the compositions with the aim to prepare items for medical purposes with various properties on working surfaces.

The range of polymeric materials used in such a specific field of medicine as endoprosthetics is very limited. Among such materials are ultra-high-molecular-weight polyethylene (UHMWPE) and polysiloxanes (PSNs).

Thanks to a combination of biological inertness, high levels of strength, wear, and creep resistance, and low friction coefficient [1], UHMWPE is widely used in endoprosthetics, in particular, in fabrication of inserts for coxa prostheses. However, a significant disadvantage of UHMWPE from the standpoint of functional performance of prostheses is the lack of elasticity. The natural human joints could be imitated more adequately by inserts with the required combination of rigidity and elasticity in different sections of the item in the direction perpendicular to the load. Thus, items with property gradients are required. Such prostheses of a new generation can be fabricated only from composites; however, among potentially suitable polymers, only PSNs, along with UHMWPE, are permitted for use in endoprosthetics.

A number of properties of polysiloxanes are quite opposite to those of UHMWPE. Along with such positive characteristics as elasticity in a wide temperature range, high resistance to heat, thermal oxidative degradation, and hydrolysis, biological inertness, low adhesion to living tissues, and high gas permeability, they have such drawbacks as poor strength and low hardness [2].

Formulations based on UHMWPE and PSNs could eliminate the drawbacks inherent in both polymers and form be a new class of medical materials exhibiting, along with bioinertness, a set of controllable physicomechanical and service characteristics. By varying the component ratio, preparation conditions, and modification procedure, one could produce materials with a property gradient and to control within wide limits their elasticity and strength. This, in turn, would allow development of prostheses imitating human organs more closely than the existing polymeric items.

The chemical composition and structure of UHMWPE and PSNs rule out the possibility of their reaction to form a chemical compound; the most suitable procedure for preparing formulations from them is, apparently, mechanical blending. However, traditional blending procedures are unsuitable for this polymeric system, because the viscosity of PSNs is considerably lower than that of UHMWPE. Thus, new procedures for preparing formulations are to be developed.

The working surfaces of items used in endoprosthesis, as a rule, play different roles and should have different and in some cases quite opposite properties: hardness and density close to that of soft human tissues; rigidity in combination with wear resistance and elasticity. Such a combination of properties can be ensured by physicochemical modification of separate phases of a UHMWPE–PSN blend, which opens broader possibilities than modification of a homogeneous material. In this case it is necessary to develop procedures for modification of both the formulations and the surfaces of items fabricated from these materi-

1070-4272/01/7406-1010 $25.00 © 2001 MAIK "Nauka/Interperiodica"

als. Such materials, owing to their unique properties, can be used in various fields of engineering.

The goal of this work was to develop composite materials based on UHMWPE–PSN blends and items from them for medical purposes. The study involved (1) development of a process for preparing UHMWPE–PSN formulations, (2) comprehensive study of the physicochemical, rheological, and service properties of the formulations, and (3) development of procedures for physicochemical modification of the formulations and finished items.

In our study we used siloxane rubbers SKTV-Shch1 (Russia) and LSR 2050 (Bayer, Germany) and UHMWPE produced in Gur'ev (Kazakhstan) and by Hostalen Gur (Germany).

The formulations were prepared by a common mechanical blending procedure (rollers, rubber mixer). Since specific features of the initial components do not allow high-quality blending by a common procedure, we developed a new procedure involving additional heat treatment of PSN.

Although the chemical composition and structure of the components do not suggest the possibility of chemical reactions between them, we analyzed both the separate components and the composition by IR spectroscopy, taking into account the intended use of the materials in endoprosthetics.

Thermal analysis under dynamic conditions was performed on an MOM derivatograph (Hungary). Vulcanization measurements were done according to GOST (State Standard) 12535–84 (ISO 3417–77).

The structure of uncured formulations was studied with an optical microscope (×150 magnification), and that of the cured (vulcanized) formulations, with REM-100 [×(1000–10000) magnification] and BS-500 [with a microtome, ×(4000–16000) magnification] scanning electron microscopes.

The physicomechanical properties (density, hardness, elasticity, strength) were determined by standard procedures. The durability tests were performed as recommended by Zhurkov and Tomashevskii [3].

The radiation treatment was performed by irradiation with fast electrons generated with an ILU-6 pulse electron accelerator (Institute of Nuclear Physics, Siberian Division, Russian Academy of Sciences). This installation generated an electron beam with energy of up to 2.2 MeV, pulse frequency of up to 50 Hz, and beam power of up to 25 kW. In irradiation runs, the electron beam parameters were as follows: electron energy 1.0–2.0 MeV, pulse frequency 50 Hz, and dose rate 0.2–0.6 Gy min^{-1}. The absorbed dose was varied from 0.2 to 0.6 MGy.

Traditional blending procedures do not ensure high interphase adhesion in UHMWPE–PSN formulations. Therefore, the physicomechanical parameters of the material are poor. We suggested that the problem can be solved by modifying the process characteristics of the formulations in the stage of blending. In this case, it would be possible to use the existing blending procedure without developing special equipment. Therefore, we analyzed possible ways to ensure strong adhesion of the couple.

In the existing theories, the adhesion strength is considered a function of many variables; as applied to the polymer system in hand, only the temperature, molecular weight (viscosity), pressure, and time can affect the adhesion in the course of formulation preparation.

The adhesion strength, as a rule, increases with increasing blending temperature. However, UHMWPE does not pass to the viscous-flow state with increasing temperature, and the effect of temperature on the viscosity of PSN, is very weak. To blend the components more efficiently, high shear stresses are required, which can be provided by increasing viscosity; however, with PSN, this cannot be attained by decreasing temperature. The viscosity can be increased by partial scorching of PSN; in this case, the role of temperature will be decisive.

The necessity for increasing the shear stress in the course of component blending also follows from the results of an optical study of UHMWPE and its blends with PSN. Despite the fact that UHMWPE particles have a relatively developed surface, cavities are formed preventing flowing-in of PSN.

Based on these views, a procedure was developed for preparing UHMWPE–PSN formulations [4], consisting in the following. The PSN phase is subjected to partial scorching (the conversion should not exceed 25–50%), which increases the viscosity by a factor of 2–10. At the same time, it is necessary to choose the scorching conditions so as to ensure development of the required shear stress at any component ratio; the scorching temperature (range 120–150°C) is chosen according to the scheme shown in Fig. 1. The figure contains two curves. Curve *1* shows the viscosity of the blend η_b as a function of the UHMWPE content: $\eta_b = F(x)$; curve *2* shows the viscosity as a function of the scorching temperature T_{sc} and time τ_{sc}. If the degree of filling is known, we find the corresponding point *1* in the curve $\eta_b = F(x)$. Then we find the

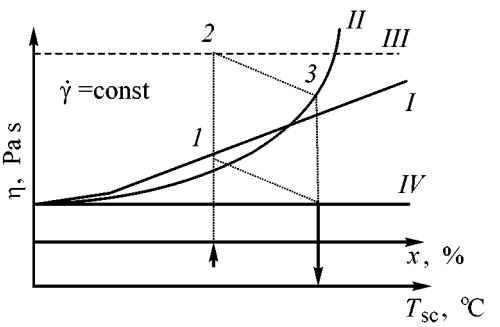

Fig. 1. Scheme for choosing the scorching conditions: (η) viscosity, (*x*) degree of filling, and (T_{sc}) scorching temperature. (*I*) $\eta_b = F(x)$, (*II*) $\eta = F(\eta_0, T_{sc}, \tau_{sc})$, (*III*) $\eta = \tau_{req}/\dot{\gamma}$, and (*IV*) η_0. (*1–3*) For explanation, see text.

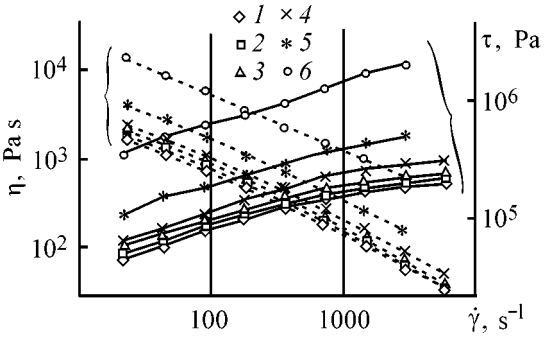

Fig. 2. Viscosity η and shear stress τ of formulations with SKTV and UHMWPE (Gur'ev) vs. shear rate $\dot{\gamma}$. UHMWPE content (wt %): (*1*) 0, (*2*) 20, (*3*) 40, (*4*) 60, (*5*) 70, and (*6*) 100.

extent η_0 to which the viscosity of the initial system should be increased (segment 1–2). In the curve $T = f(\eta_0, T_{sc}, \tau_{sc})$ we find point *3* corresponding to this additional viscosity and then determine the scorching temperature.

Of no less importance than determination of the scorching time is the choice of conditions for preparing a formulation. Traditional views on the shear strain are unsuitable as criteria of efficiency of the external action on the system, since they do not take into account the shear stress, which is one of the major factors in obtaining a couple with strong adhesion. We have chosen a criterion which is, in the physical sense, the strain energy density and is a product of the shear stress and shear strain $\tau\gamma$ ($\gamma = \dot{\gamma}t$, where $\dot{\gamma}$ is the shear rate and *t* is the action time). This criterion takes into account the main parameters required to obtain a high-quality blend and is a function of the processing conditions. Knowing the required strain energy density (depending on the UHMWPE content, it varies from 950 to 600 000 mJ m^{-3}), it is possible to determine the process parameters for any type of the mixer.

Comparison of the traditional blending procedure with that developed by us shows that the strength of the formulation can be increased by 10 to 100%, depending on the UHMWPE content.

To evaluate the applicability of the formulations in medical items, we should analyze the components and consider the possibility of chemical transformations in the system. The IR data confirmed the absence of chemical interactions between UHMWPE and PSN in the stage of formulation preparation by our procedure (the spectrum of the unvulcanized stock is the superposition of the spectra of the components); the vulcanization procedure used is traditional for medical items.

Thus, we can tentatively conclude that the composites developed are suitable for medicine and, in particular, for endoprosthetics.

A study by electron and optical microscopy showed that the formulations have a macroheterogeneous structure consisting of the PSN matrix, UHMWPE phase, and developed interphase layer. The size of the polyethylene particles is about $(5–7) \times 10^{-2}$ (Hostalen Gur) and $(1–2) \times 10^{-2}$ mm (Gur'ev), being essentially the same as in the starting polyethylene. However, the interphase layer on the polyethylene surface is fairly developed. This fact shows that the shear stresses arising in the course of blending by the developed procedure are sufficient for "unrolling" of PSN molecules on the UHMWPE surface and, at the same time, do not exceed the level at which the polyethylene grains are broken down.

Rheological tests were performed with formulations based on two UHMWPE brands: from Gur'ev (Kazakhstan) and Germany. The plots of the viscosity and shear stress vs. shear rate for the Gur'ev sample are shown in Fig. 2.

Irrespective of the UHMWPE type, the rheological behavior of the formulations with the polyethylene content from 0 to 60% is described by the equation

$$\eta / \eta_m = 1 + (A/B)x,$$

where η_m and η are the viscosities of the matrix (polysiloxane phase) and blends, respectively (Pa s); *A* and *B* are coefficients; and *x* is the weight fraction of polyethylene.

The equation is similar in form to the Einstein and Gut equations for solid particles in a viscous medium (with particle size small as compared with the vessel

size and large as compared with the size of liquid molecules). However, the A/B ratio is in the range 0.6–0.7, i.e., is a factor of 2–3 lower than in these equations. This may be due to a certain plasticity of polyethylene particles at the vulcanization temperature.

The strength, relative elongation at break, and hardness of the formulations, depend, as expected, on the type and content of UHMWPE. For UHMWPE samples with more developed surface, these characteristics are approximately additive.

Analysis of the physicomechanical properties of the formulations shows that, by varying the component ratio, it is possible to attain the required combination of hardness, strength, and elasticity. However, in medical practice, items with so-called property gradient are required; for example, the working surfaces playing different roles must have different characteristics (in particular, hardness). The developed polymeric formulations open up new possibilities for creating such materials. These materials are, as shown above, heterogeneous systems; therefore, both UHMWPE and PSN can be, in principle, subject to modification. The possibilities of modifying UHMWPE by procedures acceptable for medical formulations are very limited, whereas modification of PSN allows variation of its properties in a wide range. Therefore, we initially examined the possibility of modifying PSN.

We suggested that materials with controllable properties can be produced by combining thermochemical and radiation vulcanization of PSN. A detailed study of thermochemical vulcanization and radiation crosslinking showed that the scorching temperature should be in the range 125–145°C, and the dose of electron irradiation should not exceed 0.4 MGy. Combination of the two types of vulcanization allows the strength of PSN samples to be raised to 14.0 MPa, and relative elongation, to 100%; the hardness of the item surfaces being treated and the treatment depth can be varied in a wide range.

Based on the results of this study, a procedure [5] was developed for preparing PSN items with gradient of properties on different surfaces. The procedure involves preliminary scorching of a PSN item at a temperature depending on the required hardness of the "soft" surface of the item ($T \approx H_{B,\,soft} + 125$), after which the other surface is subjected to radiation vulcanization in the dose range 0.1–0.6 MGy to attain the required hardness ($\alpha \approx 0.88H_{B,\,hard}$, where α is the radiation dose). Thus, it is possible to obtain items in which one side is similar in hardness to human tissues and the other has increased hardness and wear resistance.

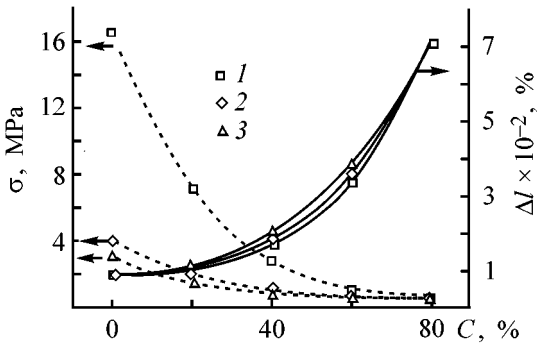

Fig. 3. Strength σ and relative elongation at break Δl of vulcanized UHMWPE (Gur'ev)–PSN formulations vs. UHMWPE content C. Irradiation dose, MGy: (*1*) 0, (*2*) 0.2, and (*3*) 0.4.

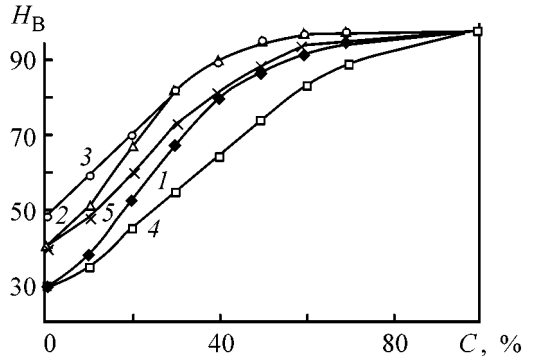

Fig. 4. Shore hardness H_B of SKTV–UHMWPE formulations irradiated with fast electrons as a function of the UHMWPE content C. UHMWPE sample: (*1–3*) Gur'ev and (*4, 5*) Hostalen Gur. Irradiation dose, MGy: (*1, 4*) 0, (*2, 5*) 0.2, and (*3*) 0.4.

This procedure can also be applied to UHMWPE–PSN formulations. Experimental studies showed an increase in the sample hardness by up to 30% (Figs. 3 and 4), with a slight increase in strength and drastic decrease (by up to 80%) in the relative elongation at break. The degree of variation of the physicomechanical properties strongly depends on the component ratio. This is due to the fact that the radiation resistance of UHMWPE is considerably higher than that of PSN. As a result, the physicomechanical properties of polyethylene vary to a lesser extent than those of PSN. For example, the hardness as a function of the radiation dose varies the more strongly, the higher the content of PSN in a formulation.

The procedure for preparing and modifying the formulations was used as the basis for developing new materials and items based on UHMWPE, PSN, and their blends, including those with the property gradient. An extreme case of items with property gradient are multilayer composites. The developed UHMWPE–

Materials and items based on UHMWPE, PSN, and their composites

Material type	Treatment		
	thermochemical vulcanization (T)	radiation vulcanization (R)	combained
Individual polymers			
	2 σ, H_B, Δl, τ_d	1 H_{B1}, H_{B2} 3 H_B, ρ	4 H_{B1}, H_{B2}, ρ
UHMWPE–PSN composition			
5 Δl, σ	6 H_B, Δl, τ_d	7 H_B, Δl, τ_d, ρ	8 H_B, Δl, τ_d
Composites (binary system)			
9 Δl, σ	10 H_B, Δl, τ_d	11 H_B, ρ, Δl, τ_d	12 H_B, ρ, Δl, τ_d
13 Δl, σ	14 H_B, Δl, τ_d	15 H_B, ρ, Δl, τ_d	16 H_B, ρ, Δl, τ_d
17 Δl, σ	18 H_B, Δl, τ_d	19 H_B, ρ, Δl, τ_d	20 H_B, ρ, Δl, τ_d
Composites (two-component ternary systems)			
21 Δ	22 Δ	23 Δ	24 Δ
25 Δ	26 Δ	27 Δ	28 Δ
29 Δ	30 Δ	31 Δ	32 Δ
33 Δ	34 Δ	35 Δ	36 Δ
37 Δ	38 Δ	39 Δ	40 Δ
41 Δ	42 Δ	43 Δ	44 Δ
Composites (three-component ternary systems)			
45 Δ	46 Δ	47 Δ	48 Δ
49 Δ	50 Δ	51 Δ	52 Δ
53 Δ	54 Δ	55 Δ	56 Δ

Note: (H_B) Hardness, (σ) strength, (Δl) relative elongation (elasticity), τ_d durability (resistance to cracking), (ρ) density, and (Δ) all parameters are controllable; ( ) PSN, ( ) UHMWPE, and ( ) UHMWPE + PSN.

PSN formulation allows, owing to its structure and properties of the components, fabrication of multilayer items. In such items, PSN can be covulcanized with the elastomer phase of the formulation, and UHMWPE can be sintered in the plastic phase. Experiments showed that the strength of both types of couples is determined by the intrinsic strength of the layers.

Possible variants of such items are shown in the table: (1) UHMWPE item in which one or both surfaces were subjected to radiation treatment; the surface hardness and wear resistance of the items depend on the absorbed dose; (2) semifinished or finished PSN item; thermochemical vulcanization of PSN in the range 140–150°C allows fabrication of materials

with controllable elasticity and hardness and with increased durability (lower probability of cracking); (3) semifinished of finished item with controllable hardness and density; (4) semifinished or finished PSN item whose hardness and elasticity can be varied in wider limits than those of variant 3 and differing from item 1 by the presence of elastic properties; (5) semifinished or finished item with a combination of strength and elasticity controllable by varying the component ratio (prepared using the developed blending procedure); (6–8) semifinished or finished item with a combination of strength and elasticity and with controllable hardness, elasticity, and durability; (9) elastic material on a rigid support; rigid material on an elastic support; (10) the same as 9, but with controllable elasticity of the PSN support; (11) the same as 9, but with controllable surface hardness of the rigid support and controllable density, elasticity, and hardness of the elastic support; (12) the same as 9, but with combination of variants 10 and 11; (13–16) similar to 9–12, but in another range of properties of the elastic support; (17–20) similar to 9–12, but in another range of properties of the elastic and rigid supports; (21) elastic material with two-sided hard coating; (22) similar to 21, but with controllable elasticity; (23) similar to 21, but with controllable coating hardness; (24) similar to 21, but with combination of variants 22 and 23; (25–28) similar to 21–24, but with another range of properties of the elastic component; (29) hard material with two-sided elastic coating; (30–32) similar to 29, with controllable properties of elastic coatings; (33–36) similar to 29–32, but with another range of properties of the rigid component; (37–40) similar to 21–24, but with another range of coating properties; combines hardness and elasticity; (41–44), similar to 29–32, but with another range of coating properties; combines hardness and elasticity; (45) material with properties smoothly varying from rigid, hard to soft, elastic; (46–48) similar to 45, but with component properties varying in a wider range; (49–52) similar to 21–24, but with properties of one of the coatings varying in a wider range, from hard, rigid to elastic; (53–56) similar to 29–32, but with properties of one of the coatings varying in a wider range, from hard, rigid to elastic.

CONCLUSIONS

(1) Preliminary heat treatment of polysiloxane yields partially cross-linked three-dimensional network modified with the low-molecular-weight component; subsequent mixing with ultra-high-molecular-weight polyethylene at a prescribed strain energy density ensures formation of a material with the required adhesion between the phases.

(2) In the range of ultra-high-molecular-weight polyethylene concentrations from 0 to 60 wt %, the formulation has a macroheterogeneous structure consisting of the polysiloxane matrix and a phase of ultra-high-molecular-weight polyethylene with the same particle size as in the initial polyethylene and developed interphase layer; the rheological behavior of the formulation is described by the Gut law. In the range of ultra-high-molecular-weight polyethylene concentrations from 60 to 70 wt %, phase inversion occurs in the course of blending, and the flow mode changes from shear to boundary slipping. At higher content of polyethylene, the continuity of the formulation is broken.

(3) Combination of the thermochemical scorching of polysiloxane with the subsequent radiation treatment of the surfaces allows preparation of items with different properties on the working surfaces.

(4) Owing to their structure, formulations of ultra-high-molecular-weight polyethylene with polysiloxane allow covulcanization with polysiloxane and sintering with ultra-high-molecular-weight polyethylene, with the adhesion equal to the cohesion of the components. This allows fabrication of binary, two-component ternary, three-component ternary, and multicomponent composites.

REFERENCES

1. Andreeva, I.N., Veselovskaya, E.V., Nalivaiko, E.I., *et al.*, *Sverkhvysokomolekulyarnyi polietilen* (Ultra-High-Molecular-Weight Polyethylene), Leningrad: Khimiya, 1981.
2. Yuzhelevskii, Yu.A. and Sokolov, S.V., *Zh. Vses. Khim. O–va im. D.I. Mendeleeva*, 1982, vol. 27, no. 4, pp. 12–18.
3. Bartenev, G.M., *Prochnost' i mekhanizm razrusheniya polimerov* (Strength of Polymers and Mechanism of Their Breakdown), Moscow: Khimiya, 1984.
4. RF Patent 2119429.
5. RF Patent 2147517.

Russian Journal of Applied Chemistry, Vol. 74, No. 6, 2001, pp. 1016–1020. Translated from Zhurnal Prikladnoi Khimii, Vol. 74, No. 6, 2001, pp. 988–992.

MACROMOLECULAR CHEMISTRY AND POLYMERIC MATERIALS

Reactivity of Polysaccharide Aldehydes toward *N*-Nucleophiles

O. B. Suvorova, A. A. Iozep, and B. V. Passet

St. Petersburg State Academy of Pharmaceutical Chemistry, St. Peterbsurg, Russia

Received October 16, 2000; in final form, March 2001

Abstract—The conversion of aldehyde groups in polysaccharide aldehydes to azomethine groups in reactions with amines and hydrazine derivatives was studied in relation to the structure of polysaccharide aldehyde and reaction conditions.

Chemically modified polysaccharides are used in medicine, biotechnology, and food and cosmetic industry, in particular, to develop new and improve the existing drugs. One of methods for activation of neutral polysaccharides is periodate oxidation allowing introduction of a required amount of aldehyde groups into the polymer. Polysaccharide aldehydes react with amine and hydrazine derivatives to give azomethines and hydrazones. This reaction occurs under mild conditions and is used for fixation of antibiotics, enzymes and other protein compounds, and biologically active hydrazides on polysaccharide matrix with the aim to develop new and improve the existing drugs.

Published data refer mainly to reactions of *N*-nucleophiles with polyaldehydes derived from cellulose and dextran. Furthermore, there is no common approach to choosing conditions for modification of polysaccharide aldehydes with biologically active substances. Therefore, the goal of this study was to determine the optimal conditions for reaction of polysaccharide aldehydes with amines and hydrazides for the example of dextran polyaldehyde (DPA) and to compare the reactivities of polyaldehydes with different structures toward aniline, benzylamine, and isonicotinic acid hydrazide, taken as model compounds.

In this study we used extracellular microbial polysaccharides: aubasidan (branched β-1,3-β-1,6-α-1,4-glucan produced by yeastlike fungus *Aureobasidium pullulans*), rhodexman (β-1,3-β-1,4-mannan, produced by *Rhodotorula rubra*), rhonasan (sulfated rhodexman), and also dextran commercially produced in Russia.

The chemical modification of the polysaccharides was performed by the scheme

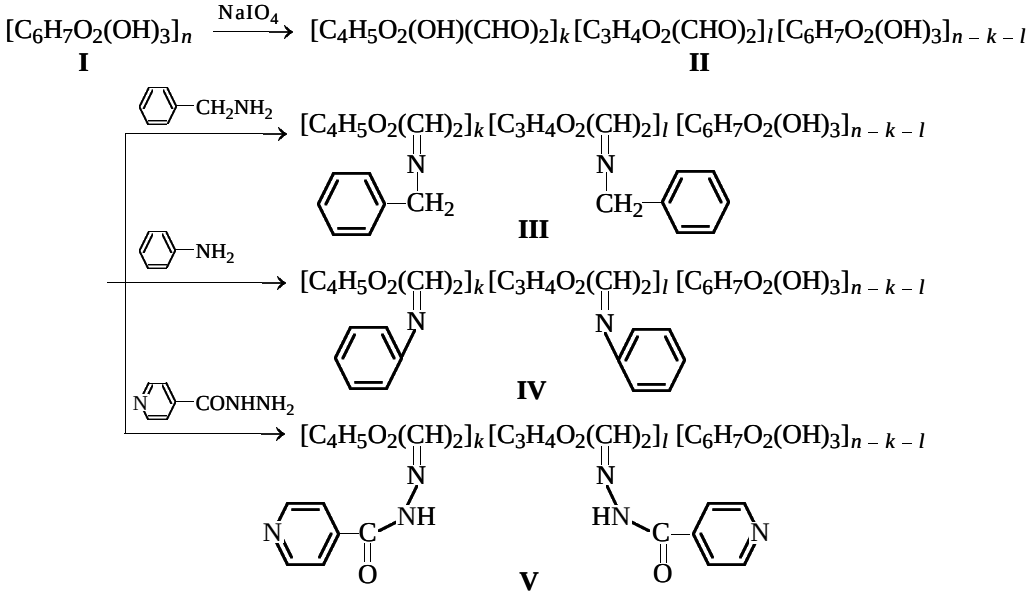

1070-4272/01/7406-1016 $25.00 © 2001 MAIK "Nauka/Interperiodica"

Polysaccharides **I** were activated by periodate oxidation [1] in an acetate buffer solution (pH 4.1). The consumption of sodium metaperiodate was monitored spectrophotometrically at 222.5 nm [1]; the amount of released formic acid was determined by volumetric titration. Water-soluble polyaldehydes **II** derived from dextran (DPA), rhodexman, and rhonasan were isolated from the reaction mixture by dialysis (to remove low-molecular-weight substances), followed by concentration in a vacuum at 60°C and precipitation with ethanol. Water-insoluble aubasidan polyaldehyde (APA) was filtered off, washed successively with distilled water, alcohol, and ether, and dried under reduced pressure (20–25 mm Hg) at 60°C.

Reactions of polyaldehydes with *N*-nucleophiles were performed in water at 20–60°C in the course of 15–180 min at pH 2–12; the molar ratio of *N*-nucleophile to aldehyde groups of the polysaccharide was (1–5) : 1. The reaction with isonicotinic acid hydrazide (INAH), which is soluble in weakly acidic solutions, was performed in a buffer solution at pH 5. After the reaction was completie, the products were filtered off, washed with alcohol and acetone, and dried under reduced pressure (20–25 mm Hg) at 60°C. In the case of rhonasan, the reaction products were precipitated with alcohol and reprecipitated from aqueous alkali to remove ionically bound *N*-nucleophiles. The product purity was checked by thin-layer chromatography.

The products are amorphous colorless (**V**), light beige (**III**), or yellow (**IV**) powders, insoluble in water (except azomethines and acylhydrazones derived from rhonasan), alcohol, ether, and most of other organic solvents.

The products were characterized by IR and UV spectroscopy, elemental analysis, and conductometric titration after hydrolysis of the azomethine bond with 0.1 N HCl.

The IR spectra of the derivatives of the polysaccharide aldehydes with aniline and benzylamine contain absorption bands at 690 and 730 cm^{-1}, characteristic of monosubstituted benzene, at 1500 and 1580–1600 cm^{-1} ($\nu_{C=C(arom)}$), and at 1640–1660 cm^{-1} ($\nu_{C=N}$). The IR spectra of acylhydrazones contain absorption bands in the range 1650–1670 cm^{-1} characteristic of the stretching vibrations of the C=N and C=O (amide **I**) bonds, and also the bands at 1510 and 1400 cm^{-1}, absent in the spectra of the polyaldehyde and characteristic of INAH.

The UV spectra of the products formed in reactions of rhonasan polyaldehyde with *N*-nucleophiles exhibit absorption peaks absent in the spectrum of the initial polyaldehyde and characteristic of the initial *N*-nucleophiles: 275 (**III**), 238 and 276 (**IV**), and 262 nm (**V**). UV spectra of the other reaction products were not taken because of their poor solubility in water and organic solvents.

Table 1. Influence of reaction conditions on the amount of *N*-nucleophile incorporated into DPA in 2 h

Reaction conditions		C_{ca}, %
T, °C	amount of *N*-nucleophile, mol mol^{-1} monomeric unit	
Benzylamine		
20	2	75
40	2	77
60	2	78
20	3	73
20	4	73
20	5	69
Aniline		
20	2	45
40	2	69
60	2	70
20	3	60
20	4	65
20	5	72
Isonicotinic acid hydrazide		
20	2	54
40	2	59
60	2	61
20	1	53*
20	3	80*
20	4	90*
20	5	90*

* Reaction time 2.5 h.

The derivatives of polyaldehydes with *N*-nucleophiles were characterized by the degree of substitution C_s (number of low-molecular-weight fragments per monosaccharide unit), which was calculated from the data of elemental analysis, conductometric titration, and UV spectroscopy. The reactions of polyaldehydes with *N*-nucleophiles were characterized by the degree of conversion of aldehyde groups $C_{ca} = [C_s/C_{sa}] \times 100\%$, where C_{sa} is the number of aldehyde groups in the initial polymer per monomeric unit.

To determine the conditions for introducing into the polyaldehyde molecule the required amount of *N*-nucleophile, we studied the influence of temperature, reaction time, reactant ratio, and pH on the degree of conversion of the aldehyde groups in dextran polyaldehyde.

Table 1 shows that the major fraction of aldehyde groups in DPA react with benzylamine even at room

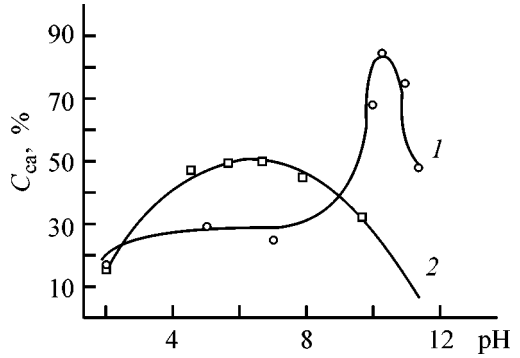

Fig. 1. Degree of conversion of DPA aldehyde groups, C_{ca}, in reactions with (*1*) benzylamine and (*2*) aniline vs. pH (20°C, 1 h, 2 mol of amine per mole of aldehyde groups).

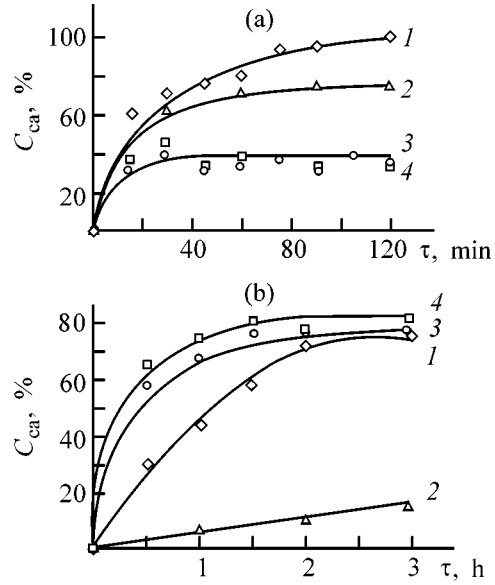

Fig. 2. Dynamics of azomethine formation in reactions of (a) benzylamine and (b) aniline with the polyaldehydes derived from (*1*) dextran, (*2*) aubasidan, (*3*) rhodexman, and (*4*) rhonasan. (C_{ca}) Degree of conversion of aldehyde groups and (τ) time. 20°C; molar ratio of amine to aldehyde groups: (a) 2 and (b) 3; pH: (a) 10 and (b) 6.0.

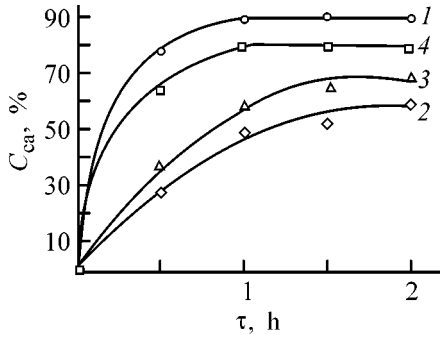

Fig. 3. Dynamics of the reaction of isonicotinic acid hydrazide with the polyaldehydes derived from (*1*) dextran, (*2*) aubasidan, (*3*) rhodexman, and (*4*) rhonasan. 20°C, 5 mol of INAH per mole of aldehyde groups, pH 5. (τ) Time.

temperature in 2 h. When the reaction temperature is raised to 60°C, the degree of substitution does not increase appreciably; the conversion of the aldehyde groups in the polysaccharide does not exceed 80%. With aniline, as expected, DPA reacts more slowly; the amount of azomethine fragments incorporated into the polymer grows with temperature, but C_{ca} remains less than 80%. With increasing molar ratio of aniline to aldehyde groups, the degree of substitution increases considerably; at a fivefold molar excess of the amine the result is similar to that attained by heating to 60°C. In view of this fact, and taking into account that many biologically active amines (enzymes, antibiotics) are labile, subsequent syntheses of azomethines were performed at room temperature.

In the reaction of DPA with benzylamine, the degree of conversion of the aldehyde groups varies with the reactant ratio in a more complex fashion: At a larger excess of the amine, C_{ca} slightly decreases rather than increases. This may be due to higher pH of the reaction medium, provided by excess amine.

In the reaction with INAH, the amount of the nucleophile also affects the completeness of transformation of the aldehyde DPA groups into hydrazones more strongly than the temperature does. The C_{ca} values at 20 and 60°C are practically equal, whereas at the equimolar ratio of the reactants the conversion of the DPA aldehyde groups is about 55%, and at a 4–5-fold excess, about 90%. Therefore, subsequent syntheses were performed at room temperature with a fivefold excess of the nucleophile. Under these conditions the reaction is fast, being virtually complete in 2 h.

As expected, the greatest effect on the conversion of the aldehyde groups is exerted by pH of the medium; this reaction is catalyzed by both acids and bases, but the highest degree of substitution with benzylamine is attained at pH 10, and with aniline, in the range pH 4–7 (Fig. 1).

Having determined the temperatures of the reactions of DPA with *N*-nucleophiles, molar ratios of reactants, and pH values ensuring the highest degrees of substitution, we studied the dependence of the reactivity of DPA and other polysaccharide aldehydes under these conditions on the reaction time. The results are presented in Figs. 2 and 3.

We found that under these conditions the aldehyde groups of DPA react with benzylamine to practically 100% in 2 h. Aubasidan polyaldehyde is also highly reactive toward benzylamine. The maximal degree of

substitution of its aldehyde groups (C_{ca} = 70%) is attained still faster, in 1 h; however, in further reaction it remains virtually unchanged. The smallest amount of the azomethine groups is formed in reactions of benzylamine with rhodexman and rhonasan polyaldehydes. In these polymers, the maximal C_{ca} values (less than 40%) are attained in 20–30 min and then do not increase further.

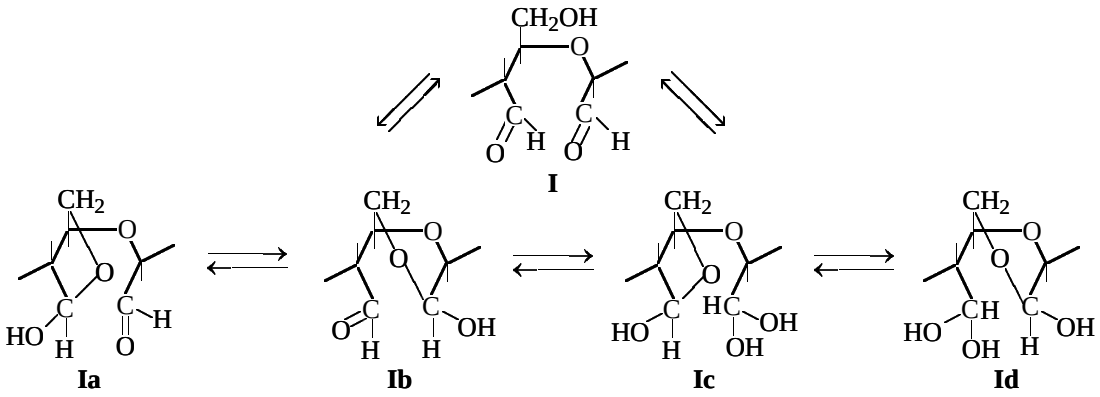

Such a variation of the reactivity of polyaldehydes is probably associated with the presence in them of various amounts of 2,3-oxidized fragments able to form three types of structures: dialdehyde (**I**) and its hemiacetal (**Ia**, **Ib**) and hemiacetal–hydrate (**Ic**, **Id**) forms existing in equilibrium [2]. In alkaline solutions, the equilibrium is shifted toward formation of structures **Ic** and **Id**; the reactivity of the aldehyde groups thus decreases, and, to ensure more complete reaction, it becomes necessary to take the nucleophile in a larger excess than in the case of DPA and APA (Table 2).

In dextran and aubasidan polyaldehydes, 2,4-oxidized fragments prevail. Such fragments can exist in form **I** only; therefore, high degrees of substitution are attained.

In contrast to benzylamine, aniline is poorly soluble in water; hence, the conversion of the aldehyde groups is largely influenced in this case by the solubility of the polysaccharide aldehydes in water. Indeed, the highest degrees of substitution are attained in reactions of aniline with the polyaldehydes derived from rhodexman and rhonasan, readily soluble in water. The poorly soluble DPA reacts more slowly, and approximately the same C_s values are attained in a longer time. With insoluble aubasidan polyaldehyde, only 16% of the aldehyde groups are converted, probably because the APA reaction centers are inaccessible to the amine.

To make higher the conversion of the aldehyde groups of rhodexman and aubasidan polyaldehydes in reactions with benzylamine and aniline, we varied the reaction time, temperature, and reactant ratio. In each particular case the goal is reached in a different way (Table 2). With rhodexman, raising the amount of benzylamine by a factor of 1.5 increased C_{ca} from 34 to 77% (by a factor of 2.5), in reactions of APA with a tenfold excess of aniline C_{ca} increased to only 37%. At the same time, with temperature raised to 60°C, more than 90% of APA aldehyde groups reacted with the amine.

In reactions with INAH, all the polysaccharide aldehydes show high reactivity. However, as in the reactions with amines, the reactivity depends on the

Table 2. Influence exerted by conditions of reactions between polyaldehydes and amines (2 h) on the conversion of the aldehyde groups into azomethine groups

T, °C	Amount of amine, mol mol^{-1} monosaccharide unit	C_s	C_{ca}, %
Rhodexman–benzylamine, pH 10.3			
20	2	0.22	34
20	3	0.57	77
20	5	0.57	77
20	10	0.55	75
Aubasidan–aniline, pH 6			
20	3	0.17*	28*
20	3	0.1	16
20	5	0.11	17
20	10	0.23	37
40	3	0.4	69
60	3	0.53	91
80	3	0.53	91

* Reaction time 24 h.

structural and conformational features of the polyaldehyde molecules (Fig. 3).

In the reactions with INAH, the highest C_{ca} values of the polyaldehydes derived from aubasidan, rhodexman, rhonasan, and dextran (60, 70, 80, and 90%, respectively) vary practically in the same order as in the reactions with aniline, which may be due to different primary and secondary structures of the polysaccharides. For example, rhonasan polyaldehyde is more reactive than rhodexman polyaldehyde, probably because introduction of sulfate groups into the rhodexman polyaldehyde molecule somewhat unrolls it, facilitating the access of the nucleophile to the aldehyde groups [3].

CONCLUSIONS

(1) Aubasidan, rhodexman, and rhonasan polyaldehydes react, similarly to dextran polyaldehyde, with *N*-nucleophiles and can be used for developing new and improving the known biologically active substances.

(2) When choosing conditions for chemical modification of polyaldehydes, account should be taken of their structure, solubility, and other factors. In reactions with *N*-nucleophiles, the polyaldehydes derived from aubasidan, rhodexman, and rhonasan are, in some cases, more active, and in other cases, less active than dextran polyaldehyde.

(3) Water-soluble polymeric azomethines can be prepared by reactions of amines with polyaldehydes derived from sulfated polysaccharides.

REFERENCES

1. *Methods in Carbohydrate Chemistry,* Whistler, R.L. and Wolfrom, M.L., Eds., New York: Academic, 1962–1965.
2. Drobchenko, S.N., Isaeva-Ivanova, L.S., Grachev, S.A., and Bondarev, S.N., *Vysokomol. Soedin., Ser. B,* 1990, vol. 32, no. 4, pp. 254–258.
3. Panov, V.P. and Zhbankov, R.G., *Vnutri- i mezhmolekulyarnye vzaimodeistviya v uglevodakh* (Intra- and Intermolecular Interactions in Carbohydrates), Minsk: Nauka i Tekhnika, 1988.

Russian Journal of Applied Chemistry, Vol. 74, No. 6, 2001, pp. 1021–1026. Translated from Zhurnal Prikladnoi Khimii, Vol. 74, No. 6, 2001, pp. 993–998.

MACROMOLECULAR CHEMISTRY AND POLYMERIC MATERIALS

Influence of Organoiron Compounds on Properties of Polyacetylenes Prepared by Phase-Transfer Dehydrochlorination of Polyvinyl Chloride

V. N. Salimgareeva, N. S. Sannikova, Yu. A. Prochukhan, and Z. Kh. Kuvatov

Institute of Organic Chemistry, Ufa Research Center, Russian Academy of Sciences, Ufa, Bashkortostan, Russia

Received February 8, 2001

Abstract—The influence of ferrocene and iron acetylacetonate additives on the chemical, magnetic, and electrophysical properties of thermolyzed and nonthermolyzed polyacetylenes prepared by phase-transfer dehydrochlorination of polyvinyl chloride was studied.

Properties of polymers containing conjugated double bonds appreciably change upon introduction of iron compounds. For example, partial oxidation of polyacetylene doped with trivalent iron compounds (chloride, perchlorate, phosphate, acetate, etc.) raises the conductivity from 10^{-8} to 10^{2} Ω^{-1} cm^{-1} and improves the polymer stability [1, 2].

Iron compounds can be incorporated in the polymeric chain, e.g., during synthesis of polyferrocenevinylenes. Pendant ferrocene groups have virtually no effect on the polyvinylene conductivity. The electrical conductivity $\sigma_{50°}$ of this polymer is 2.85×10^{-10} Ω^{-1} cm^{-1} [3]. When the polyvinylene chains are cross-linked with ferrocene groups, the conductivity at 50°C decreases to 9.2×10^{-13} Ω^{-1} cm^{-1} [3]. The electrical conductivity of polyferrocenevinylenes calcined at 300°C is $(1.0–1.15) \times 10^{-9}$ Ω^{-1} cm^{-1}.

Ferrocene-containing polymers are highly paramagnetic compounds: their specific static magnetic susceptibility is $(400–500) \times 10^{-6}$ g^{-1} at magnetic field intensity of 3.0–3.5 kOe, whereas polyvinylenes containing no ferrocene groups have negative susceptibility not exceeding $-(0.5–1.5) \times 10^{-6}$ g^{-1} in the same magnetic field [4].

In this work, we studied the influence of biscyclopentadienyliron (ferrocene) and iron acetylacetonate [Fe(acac)$_3$] on chemical, magnetic, and semiconducting properties of polyacetylenes whose thermolysis products contain ferromagnetic compounds [5].

Polyacetylenes were prepared by phase-transfer dehydrochlorination of polyvinyl chloride and had different supramolecular structures. Another aim of this work was to find a new dopant raising sharply the electrical conductivity of polymers.

EXPERIMENTAL

Amorphous and polycrystalline polyacetylene samples were prepared by dehydrochlorination of polyvinyl chloride with an aqueous potassium hydroxide solution; those with mixed structure, by dehydrochlorination with granulated potassium oxide in the presence of phase-transfer catalysts [6]. Purified polymers were dried at 100°C in a vacuum. The size of perfect polyacetylene crystals in the polycrystalline sample is larger than the known values and reaches 1.0×10^{3} μm. Traces of an amorphous phase are present in the sample. The sample with mixed structure is amorphous polyacetylene containing 20% crystalline phase.

Commercial dicyclopentadienyliron $Fe(C_5H_5)_2$ (ferrocene) and iron acetylacetonate $Fe(C_5H_7O_2)_3$ [Fe(acac)$_3$] of chemically pure grade were used. The melting points of these compounds are 173 and 184°C, respectively, which agrees with published data [7]. Since the iron complexes are readily soluble in various solvents and have low sublimation temperatures (~100°C), their excess can be readily removed during washing and drying of polyacetylene.

The iron complexes were introduced into the polymer by two procedures. The first is treatment of polyacetylene with a 1.5% Fe(acac)$_3$ solution in absolute ethanol, with subsequent washing of the product with ethanol until the solution becomes colorless. The sec-

1070-4272/01/7406–1021 $25.00

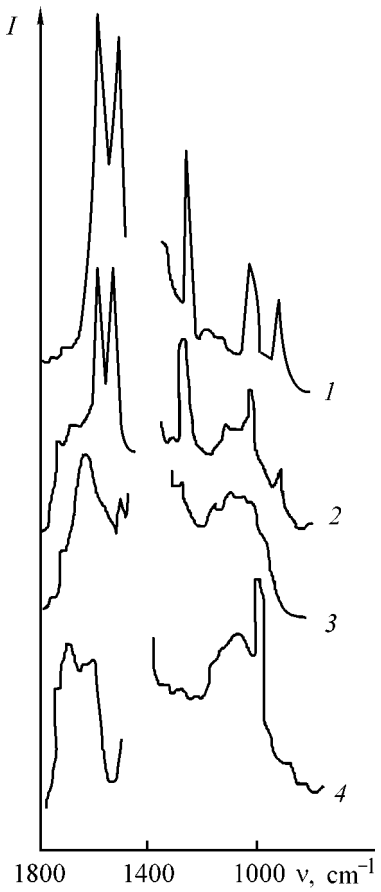

Fig. 1. IR spectra of (*1*) $Fe(acac)_3$, (*2*) mixture of polyacetylene with $Fe(acac)_3$, and polyacetylene prepared (*3*) in the presence and (*4*) in the absence of $Fe(acac)_3$. (*I*) Intensity and (ν) wave number.

ond is synthesis of polyacetylene in the presence of the iron compounds in amounts of 40 wt % with respect to polyvinyl chloride.

The samples were heated at a 1.5 deg min^{-1} rate in a quartz tube in a vacuum (residual pressure about 10^{-3} mm Hg) and then kept at required temperature for 2 h. The loading and unloading of the samples were performed in an argon atmosphere. The iron content in the polymer was determined by chemical analysis.

Atmospheric oxygen dried over P_2O_5 was used as the oxidizing agent. The thermal stability was studied on an MOM derivatograph. The heating rate was 0.08 deg min^{-1}. The weighed portion of the sample was 0.1×10^{-3} kg.

The structure of polyacetylenes prepared without iron additives was studied by optical and electronic microscopy.

The resistivity was measured in a cell with stainless steel electrodes by the four-probe method using an E 7-8 ac bridge operating at 1 kHz. The design of the measuring cell allowed preparation of polymer pellets 50–300 μm thick.

The magnetic susceptibility of polyacetylene powders was measured by Faraday's procedure [8] in magnetic field with intensity ranging from 2 to 15 kOe and at temperature from 20 to 100°C.

Incorporation of iron compounds into the polymer is determined by its structure. The iron content in polyacetylene treated with an alcoholic solution of $Fe(acac)_3$ and a ferrocene solution is 1–2 and 0.03–0.20 wt %, respectively. The iron content in the polymer prepared by phase-transfer dehydrochlorination of polyvinyl chloride in the presence of $Fe(acac)_3$ and ferrocene is 5–9 and 0.03–0.035%, respectively. As indicated by IR spectroscopy, the resulting polymer is not a mechanical mixture and its structure differs from that of pure polyacetylene. The IR spectrum of polyacetylene containing and not containing $Fe(acac)_3$ is shown in Fig. 1 as an example. The spectrum of the polymer prepared in the presence of $Fe(acac)_3$ contains no bands of acetylacetonate group coordinated to the metal ($\nu_{C=O}$ 1570 cm^{-1} and $\nu_{C=C}$ 1530 cm^{-1} [9]), typical for $Fe(acac)_3$ (curves *1, 3*). The spectrum of a mechanical mixture of the polymer with $Fe(acac)_3$ in amounts similar to that in the iron-doped polymer contains these bands (curve *2*). The out-of-plane bending vibrations of the *trans*-=C–H fragments of the polyacetylene chain (curve *4*) are manifested as a weak band at 1000–1015 cm^{-1} in the spectrum of the sample containing $Fe(acac)_3$ additive (curve *3*).

Similarly, the ferrocene bands (1002 and 1107 cm^{-1} [10]) are absent in the IR spectrum of polyacetylene doped with ferrocene. This indicates the absence of a free cyclopentadienyl ring in the sample. Hence, the organoiron compounds react with polyvinyl chloride during polymer synthesis.

Semiconducting and magnetic properties of polyacetylene due to the presence of delocalized π electrons in the macromoleclues change considerably upon introduction of the iron compounds into the polymer.

Polyacetylene is a weakly magnetic material, since its magnetic susceptibility χ, characterizing magnetization of a substance in a magnetic field, does not exceed 10^{-6} g^{-1}. Both amorphous and crystalline samples are diamagnetic: $\chi < 0$. The amorphous polymer containing 20% crystalline modification is paramagnetic, since its $\chi > 0$. The dependence of the static

magnetic susceptibility of the amorphous sample on the magnetic field intensity differs from that of the crystalline sample. With increasing magnetic field intensity, the susceptibility of crystalline polyacetylene grows and that of amorphous and amorphous-crystalline structure decreases (Fig. 2). In a weak field (2–8 kOe) the diamagnetism of the crystalline sample is higher than that of the amorphous sample: the curves for the dependence of χ of the crystalline polyacetylene on the magnetic field intensity H lie below those of the amorphous samples (Fig. 2, curves *1* and *2*).

As determined by chemical and X-ray fluorescence analysis, the transition metal content in thermolyzed polymers does not exceed 10^{-3} wt %. Even traces of ferromagnetic impurities can change the actual magnetic susceptibility. However, the influence of the structure of the polymer and products of its thermolysis on the magnetic properties of the polymer can be determined by comparing changes in χ of the solid samples at two or more magnetic field intensities H. The influence of the structure was revealed by studying the magnetic properties of structurally different polyacetylenes treated with an alcoholic solution of $Fe(acac)_3$. As seen from Fig. 2, diamagnetic polyacetylene is converted into the paramagnetic state (χ becomes positive) upon treatment with diamagnetic [11] $Fe(acac)_3$. The magnetic susceptibility of the polymer does not correlate with the iron content, but depends on the polymer structure. The magnetic susceptibility of the polymer with mixed structure, containing 1.12% Fe, exceeds by and order of magnitude that of amorphous and crystalline samples containing 2.03 and 0.98% Fe, respectively.

The electrical conductivity of polyacetylene is low (10^{-9}-10^{-11} Ω^{-1} cm^{-1}). Introduction of ferrocene or $Fe(acac)_3$ during polymer synthesis or by treating polymer isolated from the reaction mixture decreases the conductivity to 10^{-13} Ω^{-1} cm^{-1}, probably owing to loosening of the polymer structure by bulky molecules of the iron compounds.

Uniaxial compression slightly (by a factor of 1.1–1.26) increases the electrical conductivity of all the structural modifications of polyacetylene. Clearly, this is due to an increase in the charge carrier mobility owing to shortening of the distance between the macromolecules and hence a decrease in the energy barrier between the polyconjugated fragments. The pressure dependence of the electrical conductivity of polyacetylene flattens out at a pressure of 0.2 GPa (Fig. 3, curves *1–3*). In this region the electrical conductivities of structurally different samples are almost the same. The conductivity of polyacetylene samples modified with the organoiron compounds grows from 10^{-13} to 10^{-12} Ω^{-1} cm^{-1} with increasing pressure (curve *4*).

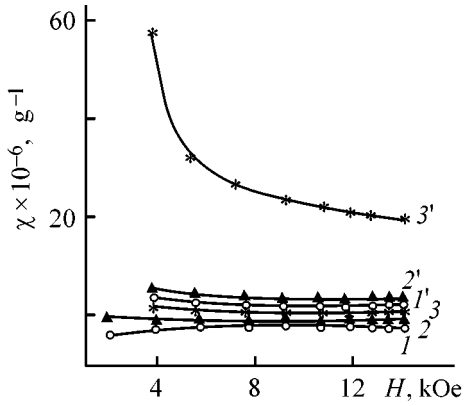

Fig. 2. Static magnetic susceptibility χ of (*1, 1*') crystalline, (*2, 2*') amorphous, and (*3, 3*') crystalline-amorphous polyacetylene, (*1–3*) initial and (*1*'–*3*') treated with $Fe(acac)_3$, vs. the magnetic field intensity H. Iron content (wt %): (*1–3*) *0*, (*1*') 0.98, (*2*') 2.03, and (*3*') 1.12.

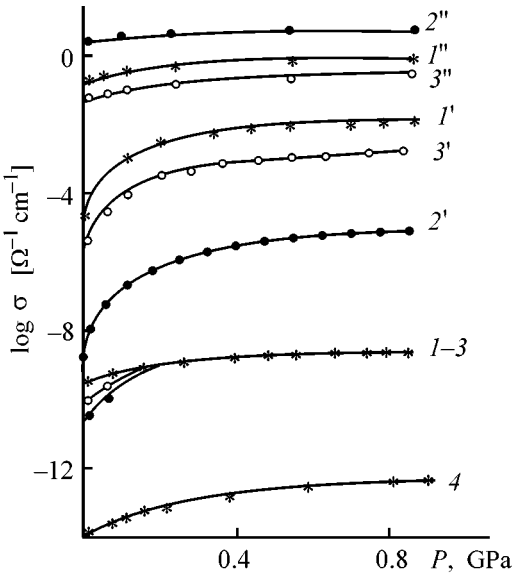

Fig. 3. Electrical conductivity σ of (*1–4*) initial polyacetylenes and (*1*'–*3*', *1*"–*3*") polyacetylenes thermolyzed at 600°C vs. pressure P. The samples have (*1, 1*', *1*", *4*) crystalline, (*2, 2, 2*", *4*) amorphous and (*3, 3*', *3*", *4*) amorphous-crystalline structure. Polyacetylene was prepared in the presence of (*1*"–*3*", *4*) $Fe(acac)_3$, (*4*) ferrocene or ferrocene–$Fe(acac)_3$ mixture and (*1–3, 1*'–*3*') in the absence of the iron compounds. Iron content (wt %): (*1–3, 1*'–*3*') 0, (*4*) from 0.035 to 9.4, (*1*") 10.6, (*2*") 15.7, and (*3*") 8.16.

The probability of electron exchange, i.e., the charge carrier mobility, must increase with shorten-

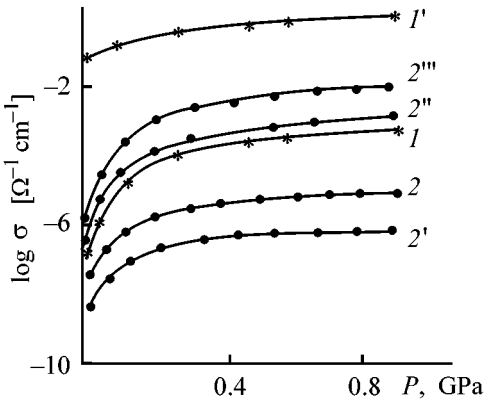

Fig. 4. Electrical conductivity σ of the products of pyrolysis at 500°C of polyacetylene with (*1*, *1*') crystalline and (*2*, *2*', *2*'', *2*''') amorphous-crystalline structure and (*1*, *2*) undoped and doped with (*1*', *2*') $Fe(acac)_3$, (*2*'') ferrocene, and (*2*''') $Fe(acac)_3$–ferrocene mixture vs. pressure *P*. Iron content (wt %): (*1*, *2*) 0, (*1*') 7.80, (*2*') 7.76, (*2*'') 0.03, and (*2*''') 9.6.

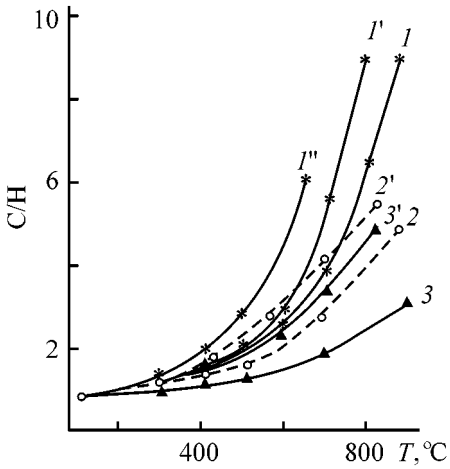

Fig. 5. C/H ratio in (*1*, *1*', *1*'') crystalline, (*2*, *2*') amorphous-crystalline, and (*3*, *3*') amorphous polyacetylenes (*1*–*3*) undoped and doped with (*1*'–*3*') $Fe(acac)_3$, and (*1*'') $Fe(acac)_3$–ferrocene mixture vs. temperature *T*. Iron content (wt %): (*1*–*3*) 0, (*1*') 4.9, (*1*'') 6.6, (*2*') 5.3, and (*3*') 9.4.

ing of the distance between conjugated sections of the macromolecules, which occurs during heat treatment [3]. As a result, the electrical conductivity of the polymers containing and not containing the organoiron compounds increases upon heat treatment. The electrical conductivity of the thermolysis products depends on the history of a sample. The conductivity of pyrolized crystalline samples is higher than that of amorphous samples throughout the tested pressure range (Fig. 3, curves *1*' and *2*'). The influence of the supramolecular structure of polyacetylene is preserved in products of pyrolysis at temperatures <500°C of samples containing ferrocene and $Fe(acac)_3$. Despite the high iron content in the product of pyrolysis at 500°C of amorphous-crystalline polyacetylene prepared in the presence of $Fe(acac)_3$, the curves of the pressure dependence of its electrical conductivity lie lower than those for the pyrolysis products of the amorphous-crystalline polymer containing no iron additive (Fig. 4, curves *2*, *2*'). The curve for the thermolysis product of crystalline polyacetylene doped with $Fe(acac)_3$ runs higher than that of the polymer with mixed structure, although the iron content in these samples is virtually the same (7.80 and 7.6%, respectively).

The influence of the dopant nature on the conductivity was studied for amorphous-crystalline polyacetylene thermolyzed at 500°C (Fig. 4). The electrical conductivity of the polymer prepared in the presence of $Fe(acac)_3$ and containing 6.6–7.8% Fe is lower upon the heat treatment, and the electrical conductivity of the polymer doped with ferrocene and containing 0.03% Fe after thermolysis, higher than that of the thermolysis product of undoped polymer. The electrical conductivity of the pyrolysis product of polyacetylene prepared by dehydrochlorination of polyvinyl chloride in the presence of an $Fe(acac)_3$–ferrocene mixture exceeds that of the sample prepared in the presence of ferrocene only. No correlations between the iron content in the pyrolysis products and their conductivity were revealed. The electrical conductivity of the iron-containing samples thermolyzed at temperatures higher than 500°C depends mainly on the iron concentration. For example, the conductivity of polyacetylenes with different supramolecular structures, thermolyzed at 600°C, correlates with the iron content in the samples (Fig. 3, curves *1*''–*3*'').

Clearly, the electrical conductivity of pyrolyzed polyacetylenes depends on their history (supramolecular structure), the polymer structure formed during heat treatment in the presence of additives and their transformation products, and the nature of the iron additives.

The polyacetylene structure undergoes pronounced changes during thermolysis. Dehydrogenation of the crystalline polymer starts at 250–300°C to form completely carbonized products at 1200–1300°C via a number of intermediates. The temperature dependence of the C/H ratio characterizing the degree of sample dehydrogenation (Fig. 5) indicates that dehydrogenation of crystalline polyacetylene (curve *1*) is faster than that of the amorphous sample (curve *3*). Dehydrogena-

tion of the amorphous sample is complete at temperatures higher than 2000°C. The organoiron compounds sensitize this process: dehydrogenation of doped polymers is faster and occurs at lower temperatures (Fig. 5). In the presence of both the additives, a synergistic effect is observed: dehydrogenation of polyacetylene doped with a ferrocene–$Fe(acac)_3$ mixture is faster than that of a polymer doped with any one of the components (curves *1*, *1*', *1*"). Probably, the organoiron compounds loosen the polymeric structure and increase its porosity, thus promoting hydrogen elimination from closed pores.

Thermal degradation of crystalline polyacetylene, occurring with appreciable weight loss, is more difficult as compared with that in the amorphous sample. The weight loss curves are shifted to higher temperatures in going from amorphous polymer containing 20% crystalline phase to a crystalline sample (Fig. 6, curves *1* and *2*). The iron compounds catalyze thermal degradation of the macromolecules. The thermal degradation curves of polyacetyeles prepared in the presence of ferrocene, $Fe(acac)_3$, and their mixture are shifted to lower temperatures (Fig. 6). The synergistic effect was observed for a sample doped with a ferrocene–$Fe(acac)_3$ mixture: thermal degradation of the polymer is faster than that of the polymers doped with either ferrocene or $Fe(acac)_3$.

We found that the organoiron compounds affect the nucleophilic properties of polyacetylenes. High reactivity of this polymer in reactions with electrophilic agents, for example with oxygen, is due to the nucleophilic properties of polyacetylene. The stability of polyacetylenes against atmospheric oxygen depends on their supramolecular structure. The rate of oxygen uptake, corresponding to the oxidation rate, decreases in going from amorphous to crystalline structure: the weight gain in 24 h is 2.3 and 1.1 wt %, respectively. Probably, the oxidation is controlled by oxygen diffusion which is slower in dense crystalline samples as compared with amorphous polyacetylene. The oxidation of Fe-containing polyacetyelenes is faster as compared with the undoped samples.

The weight gain in 24 h for amorphous and crystalline polymer prepared in the presence of $Fe(acac)_3$ is 2.7 and 2.5%, respectively. The stronger influence of the iron-containing additive on the oxidation of crystalline polymer, compared with the amorphous sample, is probably due to stronger structural loosening of the crystalline sample. Upon doping, the porosity of the crystalline sample becomes equal to that of amorphous polyacetylene and the samples take up equal amounts of oxygen.

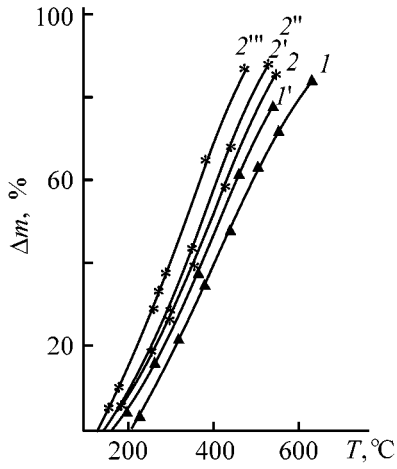

Fig. 6. Weight loss Δm from (*1*, *1*') crystalline and (*2*, *2*', *2*", 2''') amorphous-crystalline polyacetylenes prepared (*1*, *2*) in the absence and in the presence of (*1*', *2*') $Fe(acac)_3$, (*2*") ferrocene, and (*2*''') $Fe(acac)_3$–ferrocene mixture vs. temperature *T*. Iron content (wt %): (*1*, *2*) 0, (*1*') 6.03, (*2*') 5.34, (*2*") 0.03, and (2''') 8.16.

Thus, the organoiron compounds affect the chemical, magnetic, and electrophysical properties of polyacetylene.

CONCLUSIONS

(1) A sensitizing effect of ferrocene and iron acetylacetonate both on oxidation by oxygen of polyacetylenes prepared by phase-transfer dehydrochlorination of polyvinyl chloride and on high temperature dehydrognetation and degradation of these polymers was revealed.

(2) Introduction of ferrocene and iron acetylacetonate into polyacetylene decreases the electrical conductivity of both nonthermolyzed and thermolyzed samples and promotes transformation of the diamagnetic polymer to the paramagnetic state.

REFERENCES

1. Lee, M., Tzeng, J.-S., and Chen, J.-S., *Synth. Met.*, 1989, vol. 31, no. 2, pp. 191–198.
2. Pron, A., Bernier, P., Billand, D., and Letfrant, S., *Solid State Commun.*, 1983, vol. 46, no. 8, pp. 587–590.
3. Paushkin, Ya.M., Vishnyakova, T.P., Lunin, A.F., and Nizova, S.A., *Organicheskie polimernye poluprovodniki* (Organic Macromolecular Semiconductors), Moscow: Khimiya, 1971.

4. Dulov, A.A., Slinkin, A.A., and Rubinshtein, A.M., *Vysokomol. Soedin.*, 1963, vol. 5, no. 10, pp. 1441–1445.
5. Chuvyrov, A.N., Leplyanin, G.V., Kosykh, L.A., and Salimgareeva, V.N., *Fiz. Tverd. Tela*, 1989, vol. 31, no. 3, pp. 1–7.
6. Leplyanin, G.V. and Salimgareeva, V.N., *Izv. Ross. Akad. Nauk, Ser. Khim.*, 1995, no. 10, pp. 1886–1893.
7. Ripan, R. and Ceteanu, I., *Chemia Metalelor*, Bucuresti: Editura Didactica si Pedagogica, 1968, vol. II.
8. Vonsovskii, S.V., *Magnetizm* (Magnetism), Moscow: Nauka, 1972.
9. Nesmeyanov, A.N., *Khimiya σ- and π-kompleksov zheleza, margantsa i reniya* (Chemistry of σ and π Complexes of Iron, Manganese, and Rhenium), Moscow: Nauka, 1980.
10. Nesmeyanov, A.N., Kazitsina, L.A., and Lokshin, B.V., *Dokl. Akad. Nauk SSSR*, 1957, vol. 117, no. 3, pp. 433–436.
11. Hemeda, O.M., *Appl. Phys. Commun.*, 1994, vol. 13, no. 2, pp. 113–127.

Russian Journal of Applied Chemistry, Vol. 74, No. 6, 2001, pp. 1027–1030. Translated from Zhurnal Prikladnoi Khimii, Vol. 74, No. 6, 2001, pp. 998–1002.

MACROMOLECULAR CHEMISTRY AND POLYMERIC MATERIALS

Metal Transfer in Polyethylene Films Oxidized on Copper Supports

D. G. Lin and E. V. Vorob'eva

Skorina State University, Gomel, Belarus

Received February 19, 2001

Abstract—Contact oxidation of polyethylene films on copper was studied as influenced by their thickness. An oxidation mechanism is proposed.

Contact oxidation of polyethylene films on copper is accompanied by diffusion of copper compounds—products of contact reactions, in the bulk of the film [1–3]. At low concentrations, these compounds catalyze oxidation, and at high concentrations they inhibit it [4, 5]. In this connection, we suggest [1] that the catalytic oxidation of polyethylene (PE) on copper is a homogeneous process catalyzed by transferred copper compounds.

Transfer of copper (copper compounds) strongly depends on the thickness of a polymeric film. With increasing thickness, the oxygen uptake grows. As a result, the region of intensive polymer oxidation is shifted from the near-support layer to the film surface [1], and two-stage copper accumulation is observed not only in the boundary PE layer, but also in the bulk of the film [6]. However, the nature of copper transfer in the bulk of PE being oxidized is not understood. To gain insight into these processes, systematic studies are required. In this work, we studied PE oxidation and copper transfer in a PE film as influenced by the film thickness.

EXPERIMENTAL

We used nonstabilized high-density PE prepared at low pressure using complex organometallic catalysts [GOST (State Standard) 163338–85, brand 20306-005]. Two types of samples, supported and filled polymeric films, were prepared from a polymer powder by hot pressing. The support and filler were, respectively, M1 copper foil and M1 copper powder with grain size ranging from 50 to 70 μm. Filled PE was prepared by mechanical mixing of the polymer and copper powders. Unfilled and copper-filled polymers were applied to copper supports by hot pressing at 150°C for up to 5 min. The resulting samples were oxidized in ovens in air and cooled under natural conditions. Then a copper support was separated, and the obtained polymeric film was studied.

The degree of PE oxidation was estimated by IR transmission and MATIR spectroscopy. We suggested that the degree of oxidation is proportional to the optical density of the band at 1720 cm^{-1} assigned to the carbonyl groups, or to the extinction coefficient K calculated as the ratio of the optical density to the film thickness expressed in centimeters. The IR spectra were recorded on a Specord 75-IR spectrophotometer. The MATIR spectra were recorded with a KRS-5 element (θ = 45°C, n = 2, 4; N = 14).

The amount of copper compounds accumulated in a PE film was evaluated by separating it from the support and ashing by two-stage thermal treatment in air [7]. The residue was dissolved in water. The copper content in these solution was determined by polarography. The procedure was described in detail in our previous communication [8].

The time dependences of the extinction coefficient and the copper concentration in 30- and 500-μm PE films oxidized on copper are shown in Fig. 1. These specific parameters characterize, respectively, the average number of carbonyl groups and copper in a unit volume of the polymer. As seen from Fig. 1, these dependences for the films with the same thickness flatten out after almost the same oxidation time (curves *2*, *4*), i.e., PE oxidation and copper transfer are interrelated processes. As noted above, copper compounds both catalyze (at low concentration) and inhibit (at high concentration) the PE oxidation. The

1070-4272/01/7406-1027 $25.00

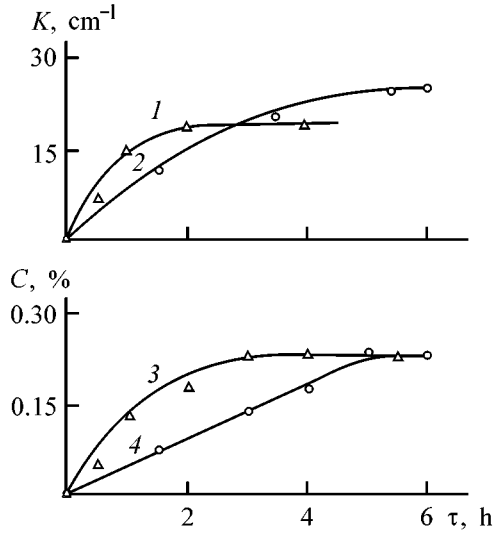

Fig. 1. (*1*, *2*) Extinction coefficient K for the band at 1720 cm^{-1} and (*3*, *4*) copper concentration C in PE films vs. time τ of oxidation at 150°C of films on a copper support. Film thickness (μm): (*1*, *3*) 30 and (*2*, *4*) 50.

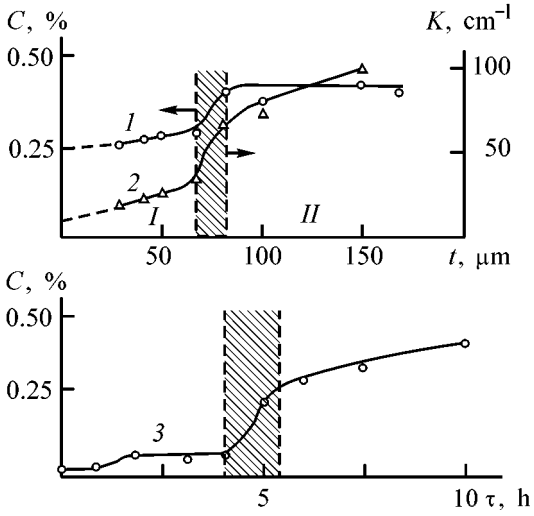

Fig. 2. (*1*, *3*) Copper concentration C in PE films and (*2*) extinction coefficient K for the band at 1720 cm^{-1} in IR spectra vs. (*1*, *2*) film thickness t and (*3*) time τ of oxidation on a copper support. Oxidation temperature 150°C. (*1*, *2*) Oxidation time 9 h; (*3*) film thickness 300 μm.

inhibition of oxidation (plateau in the kinetic curves of accumulation of carbonyl groups) is due to the accumulation of copper compounds in the polymer in amounts sufficient for suppression of oxidation.

The time required for accumulation of the critical concentration of copper compounds in PE grows with increasing film thickness (Fig. 1, curves *3*, *4*). Correspondingly more time is required for the extinction coefficient curve to flatten out (Fig. 1, curves *1*, *2*).

The dependences of the limiting extinction coefficient and the limiting metal concentration in the film on the film thickness are presented in Fig. 2. The oxidation time was enough for complete stabilization of the oxidation processes in the sample. As seen from Fig. 2, the region of tested thicknesses can be divided in two sections: *I* from 0 to 70 and *II* from 80 to 170 μm, in which the extinction coefficient changes relatively slowly (Fig. 2, curve *2*). In the narrow region between these sections (the hatched section in Fig. 2) the content of carbonyl groups increases abruptly. The dependence of the limiting concentration of copper compounds transferred in the film is similar (Fig. 2, curve *1*). The minimum copper concentration required to inhibit PE oxidation can be determined by extrapolating curve *1* (Fig. 2) to zero thickness. This concentration is about 0.25 wt %. In this case, the degree of polymer oxidation is very low. The extinction coefficient determined by extrapolation of curve *2* (Fig. 2) is 5–10 cm^{-1}.

Similar results were obtained for PE filled with copper powder. The dependence of the limiting extinction coefficient K of the band at 1720 cm^{-1} in the IR spectra of PE films on the filler content C in the films (oxidation temperature 150°C, film thickness 100 μm) is presented below.

C, vol %	0.2	0.5	1.5	3	5	7
K, cm^{-1}	60	39	23	11	5	4

These data show that oxidation of films with copper content of 5 vol % and higher is inhibited at low degree of polymer oxidation (extinction coefficient is about 5 cm^{-1}). This is due to thinning of the polymer layer surrounding filler particles with increasing copper concentration in PE. Hence, the influence of thinning of the unfilled copper-supported PE films on PE oxidation is similar to that of an increase in the filler concentration in the film at constant film thickness.

To elucidate the reasons for the observed complex influence of the film thickness (Fig. 2, curves *1*, *2*), we studied the oxidation kinetics in different layers of a copper-supported PE film. The kinetic curves of accumulation of carbonyl groups in the surface and near-support layers of a PE film (thickness of analyzed layer about 2 μm) were obtained by means of MATIR spectroscopy [9]. The results of a study of both thin (50 μm, curves *1*, *2*) and thick (150 μm, curves *3*, *4*) films are presented in Fig. 3.

Polyethylene film is not uniformly oxidized across its thickness. Carbonyl groups start to form in the near-support layer (Fig. 3, curves *2*, *4*). Then PE oxidation in the surface layer is accelerated, and the optical density of this layer increases (Fig. 3, curves *1*, *3*). The kinetic curves of accumulation of carbonyl groups in the surface and near-support layers of PE film flatten out irrespective of the film thickness. On the plateau, the degree of oxidation of the surface layer of polymer is always higher than that of the near-support layer, the film thickness being constant.

The film thickness affects the following parameters of the inhibition stage: the optical density corresponding to the saturation of the kinetic curves, D_0, and the oxidation time required for the optical density to reach saturation, τ_0. These parameters are indicated in Fig. 3, curve *3*. The parameters grow with increasing film thickness.

It should be noted that the ratio of τ_0 values for the surface and near-support layer depends on the film thickness. In thin films, the oxidation is stabilized faster in the near-support layer: τ_0 for this layer is lower (Fig. 3, curves *1*, *2*). This parameter for the near-support layer of thick films is higher than that for the surface layer. We believe that this difference in oxidation of thin and thick films (Fig. 3, curves *3*, *4*) is mainly responsible for the appearance of two ranges of film thickness in Fig. 2. It should be noted that thestabilization of the concentration of carbonyl groups in the surface layer of thick films does not mean that oxidation is complete in this layer (Fig. 3, curves *3*, *4*). Presumably, dynamic equilibrium is attained between the carbonyl groups formed in the surface layer and carbonyl groups of the low-molecular weight oxidation products diffusing from this layer of the sample inwards. Polymer oxidation is completely inhibited when the content of the carbonyl groups is stabilized across the whole thickness of the film.

We propose the following scheme for PE oxidation on a copper support. In the first stage, the oxidation is localized in the near-support layer. Copper compounds diffusing in a PE film catalyze PE oxidation to form low-molecular-weight products of thermal oxidative degradation. These products, in turn, react with the support to form copper compounds which again diffuse in the bulk of the film. As a result, a concentration of copper compounds that is enough to inhibit the oxidation is attained in the neat-support layer. As determined by MATIR spectroscopy, a layer of inhibited polymer is formed at the film–support interface after approximately 15 min of oxidation

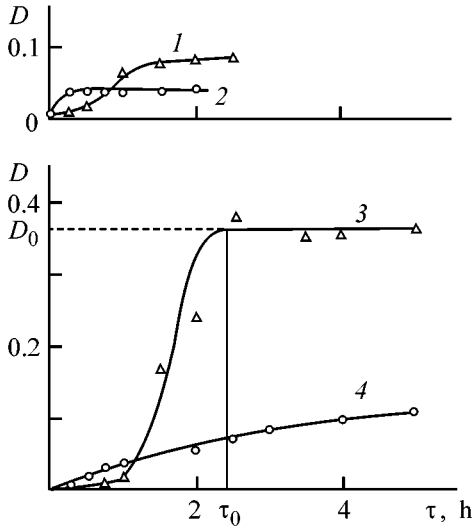

Fig. 3. Optical density D for the absorption band at 1720 cm^{-1} in IR MATIR spectra of (*1*, *3*) surface layer of PE film and (*2*, *4*) film layer adjacent to the support, vs. time τ of oxidation at 150°C on a copper support. Film thickness, μm: (*1*, *2*) 50 and (*3*, *4*) 150.

(Fig. 3, curve *2*). During further oxidation, this layer becomes thicker owing to diffusion of copper compounds through it. In the course of time, the entire polymeric film must be inhibited, with the oxidation stopped.

However, displacement of the zone of intensive oxidation from the near-support layer to the surface layer of the coating should also be taken into account [6]. In the course of oxidation, the oxygen uptake by the surface layer increases (which is promoted by diffusion of small amounts of copper compounds in this layer), thus decreasing oxygen penetration into the film. As a result, the oxidation is localized in the surface layer of the polymeric film and is suppressed deeper inside the film owing to oxygen deficiency. The metal transfer into the film is correspondingly decelerated. Low-molecular-weight products of thermal degradation, formed in large amounts in the surface layer diffuse through the film to the neat-support layer. These products react with the support to form copper compounds. In terms of our previous work [6], the second stage of metal transfer to PE being oxidized begins with diffusion of these compounds into the polymeric film. The metal transfer in this stage will continue until stabilization of oxidation in all layers of a film.

Thus, oxidation of a copper–supported PE film can be inhibited by both single- and two-stage-mechanism. The single-stage inhibition is only possible in thin films. In this case, the thickness of the inhibited

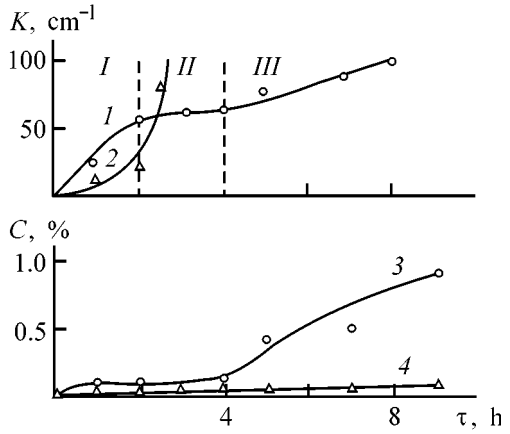

Fig. 4. (*1, 2*) Extinction coefficient K for the band at 1720 cm^{-1} in IR spectra and copper concentration C in (*3, 4*) surface and (*2, 4*) near-support layers of a 300-μm PE film vs. time τ of film oxidation at 150°C on a copper support.

layer gradually grows from the near-support layers toward the surface layer of the sample. Copper transfer into polymer is continuous. The two-stage inhibition of PE is typical of thicker films. In this case, the thickening of the layer of the inhibited polymer is interrupted owing to localization of the oxidation in the surface layer of the film. The metal transfer is interrupted simultaneously. However, it is resumed after diffusion of the oxidation products from the surface layer to the near-support layer. In this stage, the conversion of the polymer to the inhibited state is completed.

Kinetic studies of copper transfer in a 300-μm polymeric film (Fig. 4, curves *3*, *4*; Fig. 2, curves *3*) confirmed the proposed scheme of PE oxidation on copper support. The dependence of copper accumulation in the near-support layer (thickness of the analyzed layer is 10–15 μm) is characterized by two stage of metal transfer, which are separated by an interval of time. During this time, the metal content in a tested layer remains virtually constant (Fig. 4, curve *3*). The dependence of accumulation of carbonyl groups is similar (Fig. 4, curve *1*). The oxidation is stabilized when the degree of PE oxidation in the surface layer is low (extinction coefficient is about 20 cm^{-1}), but traces of transferred copper are clearly detected in it (Fig. 4, curve *4*). If the material of the near-support layer, oxidized for a time sufficient for stabilization, is heated with is free access of oxygen, the content of carbonyl groups increases slowly, i.e., PE oxidation in this layer is inhibited. The second stage of accumulation of carbonyl groups in the near-support PE layer is due to diffusion of low-molecular-weight products of thermal oxidation from the surface layer of the film, which by this time is characterized by high degree of oxidation (extinction coefficient exceeds 100 cm^{-1}). The second stage of copper transfer into PE films begins almost simultaneously with the onset of diffusion of the oxidation products in the near-support layer.

The two-stage mechanism of copper accumulation is typical of not only the near-support polymer layer, but also the film as a whole. The shape of the corresponding kinetic curves (Fig. 2, curve *3*) is similar to that of the dependence of the limiting copper concentration on the film thickness (Fig. 2, curve *1*). This similarity is due to features of copper diffusion in PE film. The initial portions of the curves (Fig. 2, curves *1*, *3*) correspond to the first stage of copper transfer without involvement of the thermal oxidation products formed in the surface layer. The next portion reflects the overall copper transfer in the first and second stages.

CONCLUSION

The area of intensive accumulation of the products of thermal oxidation of copper-supported polyethylene films shifts from the near-support layer to the surface layer of the polymer. This is the main reason for the change in the mechanism of metal diffusion in the film. As the film becomes thicker, the single-stage mechanism gives way to a two-stage mechanism. The mechanism changeover, in its turn, alters the parameters responsible for inhibition of oxidation processes in the polymer.

REFERENCES

1. Lin, D.G., *Cand. Sci. Dissertation*, Gomel, 1993.
2. Egorenkov, N.I., Kuzavkov, A.I., and Lin, D.G., *Modifikatsiya polimernykh materialov* (Modification of Polymeric Materials), Riga: Rizhskii Politekhnicheskii Inst., 1985, pp. 41–48.
3. Kin, D.G., *J. Appl. Polym. Sci.*, 1994, vol. 54, pp. 1789–1793.
4. Egorenkov, N.I., Lin, D.G., and Belyi, V.A., *Dokl. Akad. Nauk SSSR*, 1974, vol. 214, no. 6, pp. 1376–1379.
5. Egorenkov, N.I., Lin, D.G., and Belyi, V.A., *J. Polym. Sci. Polym. Chem. Ed.*, 1975, vol. 13, pp. 1493–1498.
6. Lin, D.G., Kapshai, M.N., Kachamin, A.N., *et al.*, *Zh. Prikl. Khim.*, 1983, vol. 56, no. 8, pp. 1836–1839.
7. USSR Inventor's Certificate, no. 1226119.
8. Sviridenko, V.G., Lin, D.G., and Eliseeva, I.M., *Zh. Anal. Khim.*, 1987, vol. 42, no. 8, pp. 1525–1527.
9. Egornkov, N.I., Kuzavkov, A.I., and Lin, D.G., *Kompozits. Polimer. Mater.*, 1982, no. 13, pp. 46–53.

Russian Journal of Applied Chemistry, Vol. 74, No. 6, 2001, pp. 1031–1033. Translated from Zhurnal Prikladnoi Khimii, Vol. 74, No. 6, 2001, pp. 1002–1005.

MACROMOLECULAR CHEMISTRY AND POLYMERIC MATERIALS

Effect of Modifying Reagents on Rheological Characteristics of Magnetite Dispersions in Transformer Oil

T. G. Lazareva, E. V. Shinkareva, and S. A. Prodan

Institute of General and Inorganic Chemistry, Belarussian National Academy of Sciences, Minsk, Belarus

Received December 18, 2000

Abstract—Rheological properties of magnetite dispersions in transformer oil were studied in relation to the conditions of modification of the magnetite surface with water vapor and water-soluble polymers such as polyvinyl alcohol and carboxymethyl cellulose. Various modification modes are considered.

Directed preparation of various structures with prescribed mechanical properties is among the most important tasks of the modern physical chemistry of dispersed systems [1]. The commonly accepted approach is the optimal combination of mechanical dispersion with modification of the dispersed phase surface by, e.g., introduction of such modifying reagents as water-soluble polymers able to affect the strength of interparticle interactions and to be readily cross-linked in the presence of metal cations. The performance characteristics of such systems are largely controlled by their rheological parameters such as the viscoelastic, strength, and hyperelastic indices of solutions. In turn, these parameters are governed by the strength of macromolecular interaction responsible for the formation of a three-dimensional network structure. The basic factors controlling the viscosity of a structured suspension are the concentrations of the polymer and dispersed phase and temperature.

In this work, we studied the effect of sorption of water vapor and water-soluble polymers by magnetite particles on the structural and rheological characteristics of magnetite dispersions in transformer oil.

EXPERIMENTAL

Rheological measurements were carried out with a Rheotest-2 rotary viscometer for determining the dynamic viscosity of both Newtonian and non-Newtonian fluids over a wide range of the shear rates from 3 to 1312 s^{-1} at a temperature of 30–70°C.

As the continuous phase served transformer oil, and as the dispersed phase, magnetite Fe_3O_4 (pure grade), finely ground and dried at 105°C prior to use. The magnetite concentration in the oil dispersions varied from 5 to 25%. Sorption of water vapor on magnetite was studied as follows. A sample was placed in a desiccator and allowed to stand over saturated salt solutions at room temperature for 20 days at a fixed relative humidity of 30, 60, 80, and 100%. To obtain modified magnetite, it was brought in contact with solutions of water-soluble polymers such as 0.5% carboxymethyl cellulose (Na-CMC, 70/300) or 5% polyvinyl alcohol (PVA, 16/1). The liquor ratios were, respectively, Na-CMC/Fe_3O_4 = 2.5 and PVA/Fe_3O_4 = 5. The resulting mixtures were then allowed to stand at 105°C for 5 h and ground in an agate mortar.

The temperature and concentration dependences of the dynamic viscosity η of magnetite in transformer oil at 30, 40, 60, and 70°C and a shear rate of 81 s^{-1} are given in Fig. 1. With increasing temperature, η decreases from 16 to 3, from 22 to 7, from 32 to 16, from 50 to 30, and from 130 to 54 mPa s^{-1} in 5, 10, 15, 20, and 25% magnetite suspensions, respectively. With increasing magnetite concentration, η grows, which is due to the increasing number of contacting dispersed phase particles in unit volume, leading to intensive structurization and higher dynamic viscosity.

The fact that η strongly depends on the shear stress or rate (Fig. 2) indicates that magnetite dispersions in transformer oil are non-Newtonian fluids. In a 5% magnetite dispersion, η initially decreases rapidly with increasing shear stress (portion *I* of the curve), and then a uniform flow of a fluid anisotropically oriented in the field is established (portion *II*). Therefore, the system demonstrates the property of plasticity as a result of particle structuration and formation of a structure anisotropically oriented in the mechanical field. Sorption of water on magnetite

1070-4272/01/7406-1031 $25.00 © 2001 MAIK "Nauka/Interperiodica"

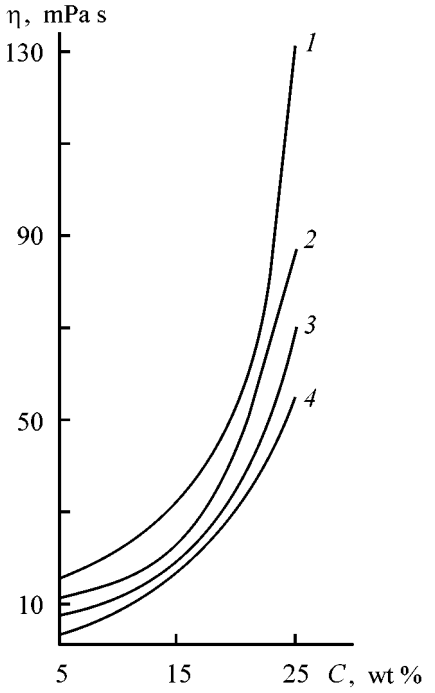

Fig. 1. Dynamic viscosity η of magnetite dispersion in transformer oil vs. the magnetite concentration *C*. Temperature (°C): (*1*) 30, (*2*) 40, (*3*) 60, and (*4*) 70.

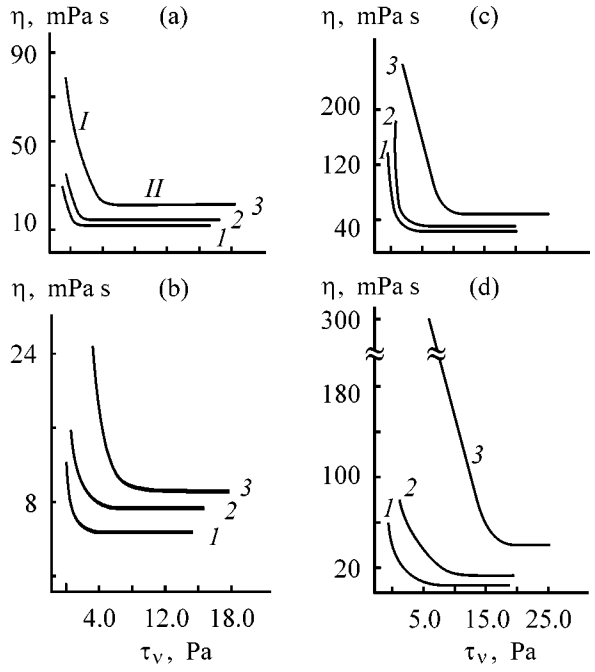

Fig. 2. Dynamic viscosity η of (a, b) 5 and (c, d) 15% magnetite dispersion in transformer oil vs. the shear stress τ_v. Temperature (°C): (a, c) 30 and (b, d) 70; the same for Fig. 3. Moisture content and relative humidity (%): (*1*) dried Fe_3O_4; (*2*) 0.7, 60 and (*3*) 5, 100.

leads to higher viscosity and shifs the viscosity curves toward higher shear stress (Fig. 2a, curves *2, 3*). With increasing temperature, the viscosity curves are shifted to higher shear stress, too. The effect of anisotropic structurization is observed in the 5% magnetite dispersion at 2.5 Pa, and in the dispersions containing 0.7 and 5% water, at 4.0 and 7.5 Pa, respectively.

In the presence of adsorbed water, the dynamic viscosity grows with increasing magnetite content. For example, in a 15% magnetite dispersion containing 0.7% water, η is 180 and 80 mPa s^{-1} at 30 and 70°C, respectively. At a moisture content of 5% the corresponding values are 250 and 300 mPa s^{-1} (Figs. 2c, 2d). In this case, the structurization is complete at higher shear stress as compared with the 5% magnetite dispersion (in dispersions with dried Fe_3O_4 this occurs at a shear stress of 2.5 and 5.0 Pa at 30 and 70°C, respectively; and in magnetite dispersions containing 5% water, at 9.0 and 19.0 Pa).

Therefore, the structurization of the magnetite dispersions can be controlled by varying the amount of sorbed water in the system.

Figure 3 shows the dependence of the dynamic viscosity on the shear stress in a 5% dispersion of magnetite modified with 0.5% Na-CMC and 5% PVA. Both the modifying reagents change the shape of the viscosity curves considerably: initially the viscosity increases and then levels off (Figs. 3a, 3b; curves *1*). The medium acquires the properties of a dilatant fluid [2]. Additional introduction of water into magnetite modified with a water-soluble polymer makes the dynamic viscosity higher (Figs. 3a, 3b; curves *3*). In this case the nature of flow changes, with both the plastic and dilatant types of behavior exhibited, which is manifested in the appearance of a maximum in the viscosity curves. For example, modification of magnetite with 5% PVA, followed by sorption of 8.1% water, results in an increase in η to 55 and 24.8 mPa s^{-1} at 30 and 70°C, respectively. Modification of magnetite with 0.5% Na-CMC, followed by sorption of 8.8% water, raises η to 550 and 240 mPa s^{-1} at 30 and 70°C, respectively.

Evidently, these effects are associated with a change, in the mechanical field, in the nature of the intermolecular interaction in magnetite containing sorbed water. In this case, water molecules strengthen the network of hydrogen bonds between the hydroxy groups of the polymers. Water sorption by the modified dispersions favors formation of a more developed network structure in the bulk of the dispersion, as demonstrated by a dramatic increase in the dynamic viscosity. With the shear stress increasing further (Fig. 3a, curve *3*,

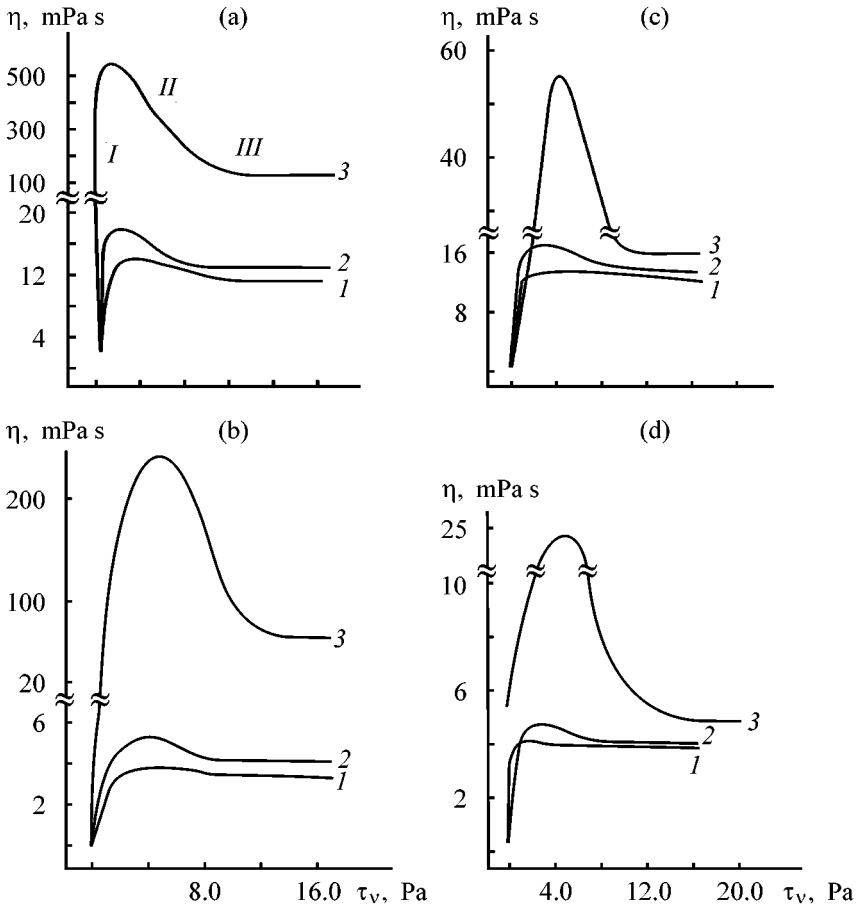

Fig. 3. Dynamic viscosity η of a 5% dispersion of magnetite modified with (a, b) 0.5% Na-CMC and (c, d) 5% PVA vs. the shear stress τ_v. Moisture content and relative humidity (%): (*1*) Dried Fe_3O_4; (*2*) (a, b) 0.6, 60 and (c, d) 0.4, 60; and (*3*) (a, b) 8.8, 100 and (c, d) 8.1, 100.

portion *II*), the binder undergoes structurization in the mechanical field, which results in the formation of anisotropically oriented magnetite particles (Fig. 3a, curve *3*, portion *III*).

CONCLUSIONS

(1) Modification of magnetite with water affects the nature of flow of magnetite dispersions in transformer oil in the mechanical field.

(2) Additional introduction of water into magnetite modified with water-soluble polymers results in the formation of media showing both dilatant and plastic properties, which is associated with the formation in the mechanical field of a network of hydrogen bonds and subsequent structurization of the disperse system with increasing shear stress through anisotropic orientation of magnetite particles.

(3) Depending on the modification conditions, fluid magnetite dispersions demonstrate both plastic and dilatant properties.

(4) The obtained results allow modification of binders of fluid formulations to be regarded as a method for preparing of media sensitive to mechanical fields.

REFERENCES

1. Skorokhod, V.V., Solonin, Yu.N., and Uvarova, I.V., *Khimicheskie diffuzionnye i reologicheskie protsessy v tekhnologii poroshkovykh materialov* (Chemichal, Diffusion, and Rheological Processes in Powder Technology), Kiev: Naukova Dumka, 1990.
2. Schramm, G., *A Practical Approach to Rheology and Rheometry*, Karlsruhe: Gmbh, 1994.

Russian Journal of Applied Chemistry, Vol. 74, No. 6, 2001, pp. 1034–1035. Translated from Zhurnal Prikladnoi Khimii, Vol. 74, No. 6, 2001, pp. 1005–1010.

MACROMOLECULAR CHEMISTRY AND POLYMERIC MATERIALS

Quantitative Refractometric-Spectrophotometric Analysis of Oil Solutions of Vitamins A and E

I. G. Zenkevich, V. M. Kosman, V. G. Makarov, and Yu. V. Dadali

Adaptogen Inter-Regional Center, Close Corporation, St. Petersburg, Russia

Received November 23, 2000, in final form, February 2001

Abstract—A refractometric–spectrophotometric method is proposed for routine analyses for vitamins A and E in oil solutions, which is 3–4 times less time-consuming than HPLC. The determination procedure includes measurements of the refractive index n_D^{20} of samples and optical density of their solutions in hexane at 325 nm.

Modern requirements to routine analytical procedures, especially those used in industry, refer not only to the adequacy of analysis, but also cover such criteria as the time consumption, labor intensiveness, reagent consumption, cost, etc. [1, 2].

Solutions of vitamins E (α-tocopherol acetate **I**) and A (retinol palmitate **II**) in vegetable oils are commercially produced as drugs, including Aevit polyvitamin {FS (Pharmacopoeia Item) 42-1699–95 [3]}, and food supplements [4]. The difficulties arising in quantitative determination of such mixtures are caused by high hydrophobicity of all components, high viscosity of the samples, and variability of the properties of the matrix (like most natural products, it is a mixture of variable composition).

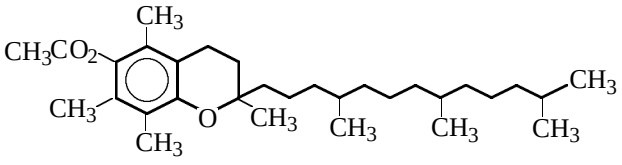

I

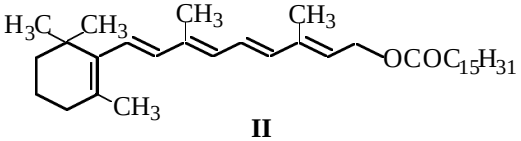

II

According to the modern views, the most accurate method of quantitative determination of compounds **I** and **II** in oil soilutions is HPLC with UV detection and external references. In this method, sample preparation includes preparation of test solutions and reference samples with concentrations of about 1 mg ml^{-1}. Each of these should be then analyzed at least twice. The intercalibration tests of this method for the example of analysis for vitamin A showed that the results may vary within 10–27 rel.% (about 15% on the average) [5]. Despite its simplicity, this technique appears to be non-optimal judging by the time consumption criterion (time required for analysis may be as long as 2–3 h and more). Therefore, a search for more rapid methods is an urgent task.

Oil solutions of individual vitamins A and E may be regarded formally as two-component mixtures, whose analysis requires measurement of only a single analytical parameter, e.g., the refractive index n_D^{20} [6]. The use of the refractometric method for determination of vitamin E in oil made it possible to cut the analysis time to 3–5 min, i.e., by a factor of 25–60 at absolute accuracy of $(+0.1 \pm 0.6\%)$, which is better than that in the case of HPLC. Since n_D^{20} of **II** is higher than that of **I** (1.555 ± 0.002 and 1.497 ± 0.001, respectively), and, e.g., this parameter varies from 1.467 [7] to 1.475 (data of the authors) between various lots of soybean oil, the expected accuracy of refractometric determination of vitamin A must be considerably higher.

Simultaneous determination of **I** and **II** in an oil solution, i.e., in a three-component mixture, requires measurement of one more independent parameter in addition to n_D^{20} [6]. However, none of the presently used combinations of analytical characteristics of ternary systems is suitable for accomplishing the task. For example, measuring the density as a second parameter is unsuitable because of the close similarity of this value for **I** and **II** and the need in large samples for analysis; measuring the refractive index at sev-

1070-4272/01/7406-1034 $25.00 © 2001 MAIK "Nauka/Interperiodica"

eral wavelengths [8] is difficult because of the lack of commercial instruments for this purpose; selective extraction of the one of the components [8] cannot be used because of the similarity of the physicochemical characteristics (including the hydrophilicity) of the target components and the matrix; and, finally, the refractometric–chromatographic method [6] has no advantages in time consumption over the ordinary chromatographic method.

Therefore, optimizing the procedure for quantitative determination of vitamins A and E in oil solutions requires, in fact, that new modifications of the refractometric analysis of ternary systems should be developed. In this work, we examine the potentialities of the refractometric–spectrophotometric method.

EXPERIMENTAL

As objects of study served model mixtures of vitamins E (**I**) and A (**II**), prepared by dissolving weighed portions of the corresponding concentrates in soybean oil, commercial samples of Aevit polyvitamin (rated concentrations of **I** and **II** are 50 and 30 wt %, respectively), and some other technological samples.

For comparison, the concentrations of **I** and **II** in the test samples were determined by HPLC on a Beckman Gold System liquid chromatograph with a Luna C_{18} column (4.6 × 150 mm; sorbent particle size 5 μm), a precolumn (4.6 × 20 mm) packed with the same sorbent, and a UV detector. As eluent served an 85 : 15 mixture of acetonitrile (HPLC grade) and dichloromethane (chemically pure grade). Elution was carried out in the isocratic mode at a rate of 1.0 ml min^{-1}. The target components were detected at 285 nm (18 min after the introduction of a sample) and then at 325 nm. The total time of analysis was 35–40 min; the retention time of **I** was about 12 min, and that of **II**, about 30 min. Samples for analysis were prepared by dissolution of weighed portions (40–100 mg) in 50 ml of isopropyl alcohol (chemically pure grade). Standard solutions were prepared gravimetrically from both the model samples (soybean solutions) and concentrates of vitamins A and E. No less than two chromatograms were recorded for each solution until the peak areas were reproducible within 3%. Data processing was performed using GOLDV402 program pack. The concentrations of **I** and **II** in samples C (wt %) were estimated by the external-reference method, using the relation

$$C = (kS_s m_{ref})/(S_{ref} m_s),$$

where S_s and S_{ref} are the peak areas (arb. units) for the test and standard solutions, respectively; m_s and m_{ref} are the weights of the test and reference samples (g), respectively; and k is a formally dimensionless coefficient accounting for the degree of dilution of all the samples and the recalculation of the concentrations from g ml^{-1} to %.

The refractive indices n_D^{20} were measured with an IRF 454B2M refractometer at room temperature (20 ± 1°C).

Spectrophotometric determination of **II** was carried out with SF-26 and SF-46 instruments in 1-cm quartz cells at 325 nm. Solutions of the samples in hexane (chemically pure grade) were prepared so that their optical density D was in the range 0.1–0.6. A weighed portion of a sample (about 25 mg) was dissolved in 50 ml of hexane, and the resulting stock solution was then diluted 50-fold with the same solvent. As reference solutions were used similarly prepared soybean oil solutions or hexane. In both cases, we obtained similar results, but sample preparation with hexane should be recommended as being simpler.

The working wavelengths were selected from analysis of the general UV spectra (Specord M40). The spectra showed peaks at 325.4 and 286.6 nm for **II** and **I**, respectively, which is well consistent with the reference data (324–326 and 285 nm). We also demonstrated that absorption of soybean oil at $\lambda >$ 322 nm is negligible.

The solutions prepared from individual samples of **I** and **II** were used to estimate (from D/C) the mass and molar extinction coefficients of **I** and **II** and also the specific extinction coefficient of **II**. The mass extinction coefficients ε_{mas} of **I** and **II** were found to be 98.0 ± 4.7 and (94.4 ± 6.6) × 10^3, and the molar extinction coefficients ε_{mol}, 46.0 ± 2.0 and (49.4 ± 3.5) × 10^3, respectively. The specific extinction coefficient of **II** at 325 nm $E_{1cm}^{1\%}$ = 949.4 ± 30.3. To estimate ε_{mas}, ε_{mol}, and $E_{1cm}^{1\%}$, the component concentrations in the solutions were expressed in g ml^{-1}, M, and %, respectively. Published data for retinol: ε_{mol} = 52.48 × 10^3 [9].

The retinol palmitate concentration C (wt %) in the model mixtures and Aevit polyvitamin was estimated by the relationships

$$C = (100kD)/(\varepsilon_{mas} m_s), \quad C = (kDM_r)/(10\varepsilon_{mol} m_s),$$

$$C = (100Dk)/(E_{1cm}^{1\%} m_s),$$

where D is the optical density of the test solution; ε_{mas}, ε_{mol}, and $E_{1cm}^{1\%}$ are the extinction coefficients; m_s is the sample weight (g); k is the coefficient reflecting the degree of dilution of the solutions; M_r = 524.87

is the molecular weight of retinol palmitate; 100 and 10 are the factors for recalculation of the concentrations from, respectively, g ml^{-1} and g l^{-1} to %.

To estimate the concentration of vitamin E and the sensitivity of results of its determination to slight variations in the experimental parameters, we used QBasic software.

The prerequisite for selecting just the refractometric method for analyzing the ternary systems under consideration was the fact that the molecules of **I** and **II** contain no active hydrogen atoms. Therefore, one may exclude the possibility of some specific interaction with the matrix components and consider the dependence of the refractive index of the mixtures to be nearly linear. Then, for the binary mixtures, n_D^{20} is proportional to the volume fraction of a component to be determined:

$$C_v(X) = (n_s - n_0)/(n_X - n_0), \quad (1)$$

where n_s, n_0, and n_X are the refractive indices of the sample, matrix (soybean oil), and the component to be determined, respectively (hereinafter the indications of the wavelength and temperature in the symbol for n_D^{20} are omitted for the sake of simplicity).

Passing from the volume to mass fractions requires taking into account the densities of the sample d_s and of the component to be determined d_X:

$$C_m(X) = (d_s/d_X)(n_s - n_0)/(n_X - n_0). \quad (2)$$

Contrary to [6, 8], in this work we were not restricted to calculations by Eq. (2), since estimation of the adequacy of the obtained results requires differentiation of the relationships to determine the random error of analysis. For example, when determining vitamin E in oil solutions, we demonstrated that the relative error of the obtained results depends primarily on $C_m(X)$ itself:

$$\delta C_m(X) \approx 2\Delta n[1 + 1/C_m(X)^2]^{1/2}/(n_X - n_0), \quad (3)$$

where $\Delta n \approx 10^{-4}$ is the limiting accuracy of determining the refractive index with critical-angle refractometers (Abbe refractometers).

For oil solutions of **I**, $(n_X - n_0) \approx 0.024$, so that $\delta C_m(X) \approx 1.9\%$ at $C_m(X) \approx 0.5$, but at $C_m(X) \approx 0.05$ the theoretical random error increases to 16.7%, indicating the inapplicability of the method. In other words, a certain minimum concentration of an analyte exists, which can be determined with a prescribed accuracy. In the case of ternary systems, such an analysis of the errors becomes even more necessary.

Since none of the existing techniques for refractometric analysis of ternary systems is applicable in our case, the required supplementary information about the composition of the samples can be obtained from spectrophotometric data. Because of the fact that the extinction coefficients of retinol palmitate at λ = 325 nm are higher by a factor of about 10^3 than those of α-tocopherol acetate, all the existing spectrophotometric methods for analysis of mixtures with known extinction coefficients (for example, the Fierordt method [10]), based on solving systems of linear equations, appear to be equally unsuitable, especially with account of the requirements to the evaluation of the random error component. Therefore, it is the combination of the refractometric and spectrophotometric data that can provide the required adequacy of analysis.

The refractive index n_s of the investigated ternary system can be written as a function of its composition as

$$n_s = n_A C_{m,A} d_s/d_A + n_E C_{m,E} d_s/d_E + (1 - C_{m,A} d_s/d_A - C_{m,E} d_s/d_E) n_0, \quad (4)$$

where n_A, n_E, and n_0 are the refractive indices of the components A and E and the matrix, respectively. It is noteworthy that this relationship does not include terms of the C_iC_j type, reflecting intermolecular interactions of the components [8].

Preliminary spectrophotometric determinations showed that at λ = 325 nm the absorption of **I** and the matrix can be neglected, i.e., one can directly determine the concentration of vitamin A in the samples (see Experimental). Next, rearranging (4), we obtain for the concentration of **II**

$$C_{m,E} = [(n_s - n_0)(d_E/d_s) - C_{m,A}(n_A - n_0)(d_E/d_A)]/(n_E - n_0). \quad (5)$$

The specific features of calculations by Eq. (5) are as follows. Similarly to the case of two-component mixtures, the necessary initial data, which should be determined preliminarily, are the refractive indices and densities of individual preparations of vitamins A and E and of the matrix (soybean oil). On passing to other batches of these components, the initial data should be rechecked. Five out of the six indicated parameters are known (n_E = 1.4965, d_E = 0.953, n_A = 1.554, n_0 = 1.4745, and d_0 = 0.916). We obtained no experimental data for the density of the concentrates of vitamin A, since its determination requires large samples (reference data could not be

Table 1. Results of determination of vitamins E and A in soybean oil solutions and Aevit commercial polyvitamin by HPLC and combined refractometric–spectrophotometeric method

A/E, wt %/wt %, or sample no.	n_D^{20}	Method of determination				Absolute error	
		refractometry–spectrophotometry		HPLC			
		$C_{m,\,A}$	$C_{m,\,E}$	$C_{m,\,A}$	$C_{m,\,E}$	ΔC_A	ΔC_E
Model samples*							
13.1/14.4	1.4880	12.7 ± 0.6	17.4	–	–	–0.4	+3.0
6.4/18.9	1.4830	6.1 ± 0.3	17.9	6.1 ± 0.4	17.6 ± 1.0	–0.3	–1.0
8.7/31.9	1.4870	8.9 ± 0.4	26.3	8.7 ± 0.5	28.5 ± 1.5	+0.1	–5.6
18.4/0	1.4890	18.4 ± 0.9	1.8	18.3 ± 1.1	0	+0.1	+1.8
0/18.0	1.4781	0.023 ± 0.001	16.8	0	18.1 ± 1.1	+0.2	–1.2
13.6/49.6	1.4955	13.6	47.9	–	–	0	–1.7
Actual samples**							
1	1.5105	31.6 ± 0.4*	50.9	30.6 ± 1.9	51.6 ± 2.7	+1.0	–0.7
2	1.5100	31.1 ± 1.4	50.5	32.0 ± 0.9	47.7 ± 1.7	–0.9	+2.8
3	1.5105	31.7 ± 2.0	50.5	31.6 ± 0.9	50.4 ± 2.1	+0.1	+0.1
4	1.4955	17.5 ± 0.1	34.3	19.4 ± 0.5	33.0 ± 0.3	–1.9	+1.3
5	1.5105	30.2 ± 1.7	55.7	31.0 ± 0.9	51.8	–0.8	+3.9
6	1.5025	23.7 ± 1.3	43.6	23.8 ± 0.9	42.0 ± 1.1	–0.1	+1.6
7	1.5080	29.2 ± 1.8	48.4	30.7 ± 1.1	49.0 ± 1.3	–1.5	–0.6
8	1.5100	30.8 ± 1.7	51.5	33.1 ± 1.6	50.2 ± 1.1	–2.3	+1.3
9	1.5090	30.0 ± 3.1	50.0	32.8 ± 1.6	48.3 ± 1.0	–2.8	+1.7

* Errors are given as estimated relative to fixed concentrations of the components.

** For actual samples all the $C_{m,\,A}$ values are estimated by averaging the results of two determinations; as the errors are given the differences of the results obtained by the two methods.

found, either). Theoretically, it is possible to estimate the density of any compound from the relationship for the molar refraction MR_D: $d = (M_r/MR_D)(n^2 - 1)/(n^2 + 2)$, where M_r is the molecular weight of the compound. However, for retinol palmitate, the thus determined density appears to be substantially overestimated ($d_A = 0.995$) as a result of the presence of the system of five conjugated bonds in the molecule and the impossibility of taking account into correctly the optical exaltation. By contrast, estimation of this value using ACD software gives a clearly underestimated result ($d_A = 0.920 \pm 0.060$). In this case, d_A should be considered a conditional parameter allowing variation within certain limits in the course of the optimization procedure. As a first approximation, we adopted the average of the two above-mentioned estimates ($d_{A,\,arb} = 0.958$, which is close to d_E), since the sensitivity of the results to this parameter is rather low.

Similarly, one can consider the density of the test samples to be experimentally inaccessible, since their determination requires considerably larger samples, compared with those needed for measuring n_A only, and much longer analysis time. Therefore, it is preferable to use a modified algorithm of data processing. In this case, to obtain the initial value of n_E, one can take any (!) conditional value of d_s as a first approximation (e.g., 0.938, which is the average over all the samples studied). In the next step (after calculating the initial value of $C_{m,\,E}$) the indicated conditional value of d_s can be ascertained using the following linear relation

$$d_s = d_A C_{m,\,A} + d_E C_{m,\,E} + d_0(1 - C_{m,\,A} - C_{m,\,E}). \quad (6)$$

Then, the refined value of d_s is substituted into Eq. (5), and the calculation procedure is repeated to obtain reproducible results for $C_{m,\,E}$. Such iteration algorithms are typical of data processing in refractometric analysis of ternary systems, particularly in the case of uncertainty in some of initial parameters

Table 2. Sensitivity of results of vitamin E determination to slight variations in the experimental parameters*

Parameter	Variation of parameter	Effect on $C_{m,\,E}$
n_A	+0.0001	–0.1
	–0.0001	+0.1
n_E	+0.0001	–0.2
	–0.0001	+0.2
n_0	+0.0001	–0.1
	–0.0001	+0.1
n_s	+0.0001	+0.4
	–0.0001	–0.3
d_A	+0.001	+0.1
	–0.001	–0.1
d_E	+0.001	<+0.1
	–0.001	<–0.1
d_0	+0.001	≈0
	–0.001	≈0
$C_{m,\,A}$	+0.1	+0.4
	–0.1	–0.3

* Obtained with a model sample containing vitamins E and A in amounts of 50 and 30 wt %, respectively.

[8]. To attain constant $C_{m,\,E}$, it is mostly sufficient to make one iteration cycle using the simplest computation programs.

Table 1 presents a data sample characterizing the accuracy of determination of vitamins A and E in soybean oil, using HPLC and the technique proposed in this work. The mean deviation of the results of refractometric determinations from the fixed concentrations is $-0.8 \pm 3.0\%$ (the value of 3% characterizes the random component of the determination error, which exceeds the absolute value of the systematic error, 0.8%) and from the HPLC results, $-0.4 \pm 1.8\%$ (the same relation between the components of the total error). Table 2 also lists the results obtained in analyzing actual industrial samples of Aevit polyvitamin and intermediates used in its production. In this case, the mean deviation of the refractometric–spectrophotometric data from the reference data is $+1.1 \pm 1.7\%$, i.e., again we observe an excess of the random component over the systematic error.

Possible errors in determining vitamin A by the proposed method depend only on the errors of spectrophotometric analysis [usually $\delta(D) < \delta(\varepsilon)$], being no less than 3%. Differentiation of Eq. (5), to estimate the error of vitamin E determination, gives cumbersome relations inconvenient for practical use. It seems more preferable to estimate the sensitivity of analytical results to variation of all the experimental parameters by a method like numerical differentiation. The estimates given in Table 2 indicate that the errors in determining d_0 have the minimum effect on the accuracy of $C_{m,\,E}$ determination. Variations in d_A within 0.10 (experimental values are inaccessible) can change the error of $C_{m,\,E}$ determination by no more than 1%, which is quite acceptable on the background of the estimated accuracy of analysis. The strongest effects are obtained for n_s and results of spectrophotometric determination of vitamin A. The relative error $\delta C_{m,\,A}$ is about 3% (at $C_{m,\,A} \approx 50\%$ this corresponds to $\Delta C_{m,\,A} \approx 1.5\%$), whereas the theoretically expected random error of $C_{m,\,E}$ determination may amount to ±6%. In fact, deviations of the parameters for all the samples studied varied from –6 to +2% (Table 1), suggesting high reliability of the proposed method. The proposed refractometric-spectrophotometric method for determining vitamins A and E in oil solutions is 3–4 times less time-consuming than HPLC. However, as in refractometric analysis of two-component systems [6], acceptable accuracy can only be attained when the concentrations of the components being analyzed exceed a certain critical value. To the greatest extent this refers to vitamin E (critical concentration is about 10%), since the difference between the refractive indices of vitamins E (1.4965) and the matrix (1.467–1.475) is considerably lower than in the case of vitamin A (1.554).

CONCLUSION

A refractometric–spectrophotometric method for determinig simultaneously vitamins A and E in oil solutions is proposed. The determination procedure includes measurements of the refractive index n_D^{20} of sample and the optical density of their solutions in hexane at 325 nm. The method meets the requirements to the accuracy of analysis of industrial samples, and the systematic error does not exceed the random error.

REFERENCES

1. Jennings, W.G. and Rapp, A., *Sample Preparation for Gas Chromatographic Analysis*, Heidelberg: Hüthig, 1983.
2. Zenkevich, I.G., Korolenko, L.I., and Khralenkova, N.B., *Zh. Anal. Khim.*, 1995, vol. 50, no. 10, pp. 1027–1034.
3. Mashkovskii, M.D., *Lekarstvennye sredstva* (Phar-

maceutical Substances), Moscow: Meditsina, 1986, 10th ed., vol. 2.

4. Buldakov, A.S., *Pishchevye dobavki: Spravochnik* (Food Supplements: A Handbook), St. Petersburg, 1996.
5. *Determination of Vitamin A in Animal Feedingstuffs by HPLC: Rep. Anal. Methods Committee, Analyst*, 1985, vol. 10, no. 8, pp. 1019–1026.
6. Ioffe, B.V., *Refraktometricheskie metody khimii* (Refractometric Methods in Chemistry, Leningrad: Khimiya, 1974, 2nd ed.
7. *Khimicheskaya entsiklopediya* (Chemical Encyclopedia), Moscow: BRE, 1995, vol. 4, pp. 192–196.
8. Ioffe, B.V. and Morachevskii, A.G., *Zh. Anal. Khim.*, 1955, vol. 10, no. 1, pp. 3–13.
9. Dawson, R.M.C., Elliot, D.C., Elliot, W.H., and Jones, K.M., *Data for Biochemical Research*, Oxford: Clarendon, 1986.
10. Bernshtein, I.Ya. and Kaminskii, Yu.L., *Spektrofotometricheskii analiz v organicheskoi khimii* (Spectrophotometric Analysis in Organic Chemistry), Leningrad; Khimiya, 1986, 2nd ed.

Russian Journal of Applied Chemistry, Vol. 74, No. 6, 2001, pp. 1040–1043. Translated from Zhurnal Prikladnoi Khimii, Vol. 74, No. 6, 2001, pp. 1011–1014.

MACROMOLECULAR CHEMISTRY AND POLYMERIC MATERIALS

Influence of the Type of Oligoisocyanate on the Properties of Thiourethane Compounds

A. D. Elchueva, I. V. Bortnikov, and A. A. Tabachkov

Kazan State Technological University, Kazan, Tatarstan, Russia

Received October 5, 2000; in final form, February 2001

Abstract—Thiourethane sealants were developed on the basis of various ester and ether prepolymers. The possibility of replacing in sealants thiokol, whose production is ecologically unsafe, by thiopolyether was examined.

Thiourethane compounds, compared with thiokol materials, exhibit enhanced strength, elasticity, and adhesion; they have good low-temperature properties and are resistant to corrosive media. They can be prepared from a wide range of initial components by means of diverse curing procedures.

Among the drawbacks of composites based on oligothiols are low tensile strength, high residual deformation, and its fast accumulation under the action of a constant load. The adhesion of thiokol sealants to metals, glass, wood, plastics, and rubbers is 0.1–0.5 kN m^{-1}. At the same time, production of thiokol (polysulfide oligomer, PSO) is restricted by the short supply of the starting organic dichlorides and environmental problems in production of the initial monomers and thiokol itself (release of hydrogen sulfide and sulfur-containing gases into the atmosphere).

At present, the most promising way is chemical modification with preparation of a new generation of sealing compounds (SCs) surpassing in properties the commercial thiokol sealants. The best studied modifiers are reactive oligomers. The thiol group of PSO, reacting with the other functional groups of the oligomers, acts most frequently as a nucleophilic agent.

A prominent place among modified PSO-based compounds is occupied by polythiocarbamate materials, the so-called thiourethane compounds. In Russia, such elastomers have been prepared from polyfunctional polydiethylen glycol adipate, toluene 2,4-diisocyanate, and PSO [1]. This reaction can be regarded as primary extension of the oligomer chain, followed by cross-linking.

Of particular interest is modification of thiopolyether based on polyoxyalkylene [2]. Its composites exhibit a satisfactory set of physicomechanical properties but have a substantial drawback: strong swelling in water (800–1600 wt %) at 1–2°C, which makes them unsuitable as components of sealants to be used in outdoor building works. It was found that the swelling is mainly due to the presence in the polymer structure of the ethylene oxide block and dihydroxydisulfide groups formed in the course of curing. Therefore, it was proposed to modifyt the thiopolyether with macroisocyanates based on polyoxypropylenepolyol. The choice of this polyether was governed by such factors as the absence of the ethylene oxide block in the backbone polyol chain and the number-average content of hydroxy groups in the thiopolyether higher than 2, and that of thiol groups lower than 2, which excludes formation of disulfide bonds in the course of curing. It was noted that isocyanate groups react not only with hydroxy groups but also with thiol groups of thiopolyethers to give thiourethanes; therefore, dibutyltin dilaurate, mainly catalyzing the reaction of isocyanate and hydroxy groups, was chosen as catalyst. It is significant that the synthesis conditions (temperature, amount of catalyst) do not affect noticeably the viscosity of the final products. The activation energy of viscous flow is 9.2–11.1 kcal mol^{-1}.

As a rule, modification of thiokol SCs with oligoisocyanates increases the adhesion to 2–3 kN m^{-1} and improves the castability and processing properties of sealants [3]; hence, it shows considerable promise.

At present, the major problem is development of formulations of filled sealants with the use of cata-

1070-4272/01/7406-1040 $25.00 © 2001 MAIK "Nauka/Interperiodica"

lytic systems of the amine type for interaction of the reactive oligomers; a new approach to forming interpenetrating polymer networks is implemented [4].

For cross-linking of oligothiols through terminal mercaptan groups, we used urethane prepolymers with terminal isocyanate groups, based on ether, ester, and oligodiene polyols.

EXPERIMENTAL

As oligothiols were used grade 1 thiokol [GOST (State Standard) 12 812–80] and thiopolyether [TU (Technical Specifications) 38.403 431–82]. As catalysts served products of amine interchange in phenolic Mannich bases, ethylenediaminomethylphenols (EDAMPs) (TU 6.05.1663–74).

As oligoisocyanates were used commercial prepolymers: oligoesters of SKU-F-E4 brand (TU 38.403 506–84), based on oligoethylene butylene glycol adipate, and of OEDGA-50T brand (TU 38.103 446–79), based on oligoethylene diethylene glycol adipate, and oligoethers of SKU-PFL brand (TU 38.103 137–78), based on oligooxytetramethylene glycol (polyfurite), and of SKU-DF-2 brand (TU 38.103 451–79), based on oligobutadienepolyol.

As fillers served industrial carbon of P-803 brand (GOST 7885–77) and chalk (GOST 842–52).

To determine the deformation and strength properties, samples were prepared as plates of thickness 2 mm and width 25 mm. Tests were performed on an RMI-250 tensile testing machine in conformity with GOST 21 751–76.

It has been reported previously [5] that SCs prepared at the equimolar ratio of the reactive oligomers have the best physicomechanical properties. This fact indicates that in the systems under consideration the polymer network is formed by reaction of the oligomers through the terminal functional groups, with the homocuring of one or another oligomer being of minor or no importance, since even insignificant deviation from the equimolar ratio in any direction results in simultaneous decrease both in the nominal tensile strength and in the relative elongation of the composites.

For the formulations PSO + SKU-F-E4, the best properties are attained with 0.3 wt part of the catalyst per 100 wt parts of the oligothiol. In this case, the maximal nominal strength is as high as 5.6 MPa. The relative elongation of the composites at a catalyst content of 0.5 wt part is 680%. With the thiopolyether, the strength is 4.5 MPa, and the relative elongation, 480%.

With the OEDGA-50T prepolymer, the plots of the physicomechanical characteristics against catalyst content pass through extrema corresponding to the content of ethylenediaminomethylphenol of 0.3 wt part per 10 wt parts of oligothiol. With thiokol and thiopolyether, the optimal characteristics are as follows: strength 3.5 and 2.8 MPa; relative elongation 480 and 400%, respectively.

The thiourethane sealant based on SKU-PFL exhibits enhanced adhesion and elasticity but has a high deformation set (20–28%). The strength of the composites reaches 2.8 MPa, the elasticity is as high as 800%, and the adhesion at break is about 7.5 kN m^{-1}.

With the ether prepolymer SKU-DF-2, the best physicomechanical parameters are attained at EDAMP content of 0.5 wt part. These composites well compete with SCs based on OEDGA-50T.

The physicomechanical characteristics of the composites get worse on deviation from the optimal catalyst dosage, irrespective of the nature of the oligothiol and oligoisocyanate. This is due to the fact that, when present in large amounts, ethylenediaminomethylphenol causes cyclization of the prepolymer through isocyanate groups, along with activation of the mercapto groups of the oligothiol [6]. Formation of isocyanurate structures affects the ratio of the reactive groups of the oligomers in the sealant formulation, which has negative effect on the set of properties of the composites. Experiments proved that the mercapto groups form no disulfide bonds in the presence of isocyanurates.

Thus, with respect to the physicomechanical characteristics of sealants, oligoisocyanates can be ranked in the following order: SKU-F-E4 > OEDGA-50T > SKU-PFL > SKU-DF-2.

Also, the use of more polar thiokol for cocuring with prepolymers based on polyesters is more appropriate as compared to that of thiopolyether. The higher the polarity of the prepolymer (SKU-F-E4 compared with OEDGA-50T), the better the properties of SC.

Irrespective of the type of the oligothiol and oligoisocyanate, the properties of the composites as functions of the content of the active filler—industrial carbon—pass through extrema. With a mineral filler, chalk, the nominal strength increases and the relative elongation decreases with growing filler content (Table 1).

As objects for studying the chemical resistance we chose thiourethane sealants of the optimal composition. It is known [7] that urethane rubbers based on polyesters are less resistant to hydrolysis than rub-

Table 1. Physicomechanical characteristics of composites*

Prepolymer	Industrial carbon, wt parts						Chalk, wt parts					
	30		40		50		80		100		120	
	σ, MPa	α, %	σ, MPa	α, %	σ, MPa	α, %	σ, MPa	α, %	σ, MPa	α, %	σ, MPa	α, %
Based on thiokol												
SKU-F-E4	5.0	600	6.0	680	4.5	550	2.1	550	2.2	450	2.4	350
OEDGA-50T	3.0	450	3.5	480	2.8	360	1.7	450	2.0	420	2.3	400
SKU-PFL	2.0	500	2.8	650	2.5	550	1.8	280	1.9	250	2.1	230
SKU-DF-2	1.9	480	2.5	620	1.8	450	1.6	250	1.7	200	1.9	180
Based on thiopolyether												
SKU-F-E4	2.8	300	3.8	450	2.6	360	2.0	300	2.2	280	2.4	250
OEDGA-50T	1.9	300	2.2	400	1.6	320	1.6	310	1.8	300	2.2	270
SKU-DF-2	2.0	280	2.2	400	1.7	350	1.8	320	2.0	280	2.6	200

* (σ) Nominal tensile strength and (α) relative elongation at break.

Table 2. Swelling of thiokol-based prepolymer-containing thiourethane sealants in aggressive media

Prepolymer	Swelling, wt %, 900 h			Swelling, wt %, 250 h			
	in water			in 20% solutions		in 3 : 1 benzine : benzene mixture	in toluene
	distilled	tap	sea	H_2SO_4	KOH		
SKU-F-E4	44.0	42.3	29.0	4.72	5.8	8.0	46.95
OEDGA-50T	43.5	39.7	30.9	5.97	4.38	8.1	50.94
SKU-PFL	32.8	31.2	27.3	7.3	3.69	16.8	85.4
SKU-DF-2	13.5	11.5	9.7	–	–	40.7	148.1
U-30 M (commercial)	22.7	21.5	21.8	5.79	4.57	8.5	56.95

bers based on polyethers. This is manifested in the behavior of thiourethane sealants in aggressive media (Table 2).

According to published data [8], swelling of thiokol sealants in seawater and tap water is somewhat lower than that in distilled water. Thiourethane sealants show the same trend, but, compared with thiokol sealants, their swelling is considerably stronger, which is probably due to hydrolysis of the ether and ester groups. With respect to water resistance, urethane prepolymers can be ranked in the order SKU-DF-2 > SKU-PFL > OEDGA-50T > SKU-F-E4.

Table 3. Thermomechanical properties of thiokol-based thiourethane sealants

Sealant	T_g	T_f
	°C	
SKU-PFL	–51	115
SKU-DF-2	–52	166
OEDGA-50T	–32	136
SKU-F-E4	–38	119
U-30 M (commercial)	–60	120

The behavior of both thiokol and thiourethane sealants in solutions of acids and alkalis is the same: Samples relatively weakly swell in 20% solutions of KOH and H_2SO_4. The composites prepared from ester prepolymers are resistant to organic solvents and show the same swelling in benzine–benzene mixture and in toluene as the thiokol sealant U-30 M. The materials prepared from oligoethers are less resistant owing to enhanced swelling of the urethane block.

Thus, sealants based on SKU-PFL and SKU-DF-2 can be used instead of the thiokol material under conditions of contact with seawater and solutions of acids and alkalis, whereas the sealants based on poly-

esters show lower hydrolysis resistance but can be used as benzine-and-oil-resistant coatings.

It is known that the capability of elastomers to preserve at low temperatures their service properties, mainly elasticity, can be characterized by the glass transition point T_g. The glass transition point does not change significantly in going from thiokol to the developed oligoether-based materials (Table 3), but introduction of ester blocks strongly impairs the low-temperature properties of the sealants. The flow point T_f noticeably depends on the chemical structure of the urethane constituent. This parameter determines the limiting working temperature of the material under constant load; for the sealants based on oligobutadiene urethane T_f is as high as 170°C.

CONCLUSIONS

(1) The physicomechanical properties of sealant compounds prepared by catalytic reaction of oligothiols and oligoisocyanates were studied. As catalyst for curing the composites was used ethylenediaminomethyl phenol, the product of amine interchange in phenolic Mannich bases. The content of thiokol, whose production is ecologically unsafe, in the sealant formulation can be decreased by 37–42%; furthermore, thiokol can be completely replaced with thiopolyether.

(2) The influence of the chemical nature of oligoisocyanates on the properties of thiourethane sealants was studied. The main physicomechanical parameters and the resistance to benzine and oil grow in going from ether to ester prepolymers, whereas the composites prepared from oligoethers exhibit higher water resistance.

(3) In thiourethane sealants, oligothiol and urethane prepolymer are present in equimolar amounts; the output of thiokol-based sealing compounds can be thus increased by a factor of 2 and more. Such sealants can be used instead of thiokol sealants in virtually all cases. The process for sealant production is made simpler because of using oligoisocyanate as separate component. The traditional equipment used for production of thiokol sealants is suitable for commercial production of the developed compounds.

REFERENCES

1. Apukhtina, N.P., Novoselok, F.B., Kurovskaya, L.S., and Ternavskaya, G.K., *Sint. Fizikokhim. Polim.*, 1970, no. 6, pp. 141–143.
2. Chernyi, A.Kh., Sinaiskii, A.T., Ivanova, T.L., and Gurari, V.E., in *Sintez i svoistva poliefiruretanovykh elastomerov: Sbornik nauchnykh trudov VNIISK* (Synthesis and Properties of Oligoether Urethane Elastomers: Coll. of Scientific Works of the All-Union Research Inst. of Chemical Rubber), Moscow: TsNIITEneftekhim, 1987, pp. 134–136.
3. Shakhbazov, G.M., Modification of Thiokol Sealants, *Cand. Sci. Dissertation*, Kazan, 1986.
4. Elchueva, A.D., Sealants Based on Reactive Oligothiols: *Cand. Sci. Dissertation*, Kazan, 1989.
5. Elchueva, A.D., Kalabina, I.M., and Averko-Antonovich, L.A., Kauchuk Rezina, 1989, no. 6, pp. 29–30.
6. Elchueva, A.D., Sukhanov, P.P., Dzhanbekova, L.R., and Averko-Antonovich, L.A., *Kauchuk Rezina*, 1996, no. 3, pp. 28–32.
7. Apukhtina, N.P., Mozzhukhina, L.V., and Morozov, Yu.L., *Proizvodstvo uretanovykh elastomerov* (Production of Urethane Elastomers), Moscow: TsNIITEneftekhim, 1969.
8. Averko-Antonovich, L.A., Kirpichnikov, P.A., and Smyslova, R.A., *Polisul'fidnye oligomery i germetiki na ikh osnove* (Polysulfide Oligomers and Sealants Based on Them), Leningrad: Khimiya, 1983.

Russian Journal of Applied Chemistry, Vol. 74, No. 6, 2001, pp. 1044–1046. Translated from Zhurnal Prikladnoi Khimii, Vol. 74, No. 6, 2001, pp. 1015–1017.

MACROMOLECULAR CHEMISTRY AND POLYMERIC MATERIALS

Photosensitivity and Physicochemical Properties of the Two-Layer Photoresist Based on Naphthoquinone Diazide and Cyclorubber

E. N. Gudymovich

Tomsk State University, Tomsk, Russia

Received April 25, 2000; in final form, February 2001

Abstract—The possibility was examined of preparing a model of a two-layer photoresist based on a photosensitive layer of naphthoquinone diazide (FP-383) and a planarizing layer of cyclorubber (FN-11) and enhancing the photosensitivity and physicochemical resistance of FN-11 films after irradiation through the naphthoquinone diazide layer and its removal by development in KOH.

The loss of the structure planarity in fabrication of integrated circuits requires preparation of multilayer resistive coatings eliminating many drawbacks of the single-layer systems. Also, with a multilayer structure of a resist it is possible to meet a set of mutually contradicting requirements: high resolving power at sufficient thickness of the planarizing layer, low film defectiveness at small thickness of the sensitive layer, etc. The common drawback of all masks based on multilayer resist films is more complex forming process involving numerous operations, in which the advantages of the idea of forming topological structures are lost in numerous process stages [1, 2].

The model of a two-layer photoresist based on naphthoquinone diazide (NQD) and cyclorubber (FN-11), proposed in this work, eliminates many labor-consuming operations of the lithographic process and provides a sharp pattern in the SiO_2 layer; the system needs no separating layer.

All experiments were performed on polished silicon wafers with 0.9-μm-thick SiO_2 layer. Wafers were degreased in acetone and ethanol. The two-layer resist was formed as follows. A planarizing layer of FN-11 was applied to a silicon wafer by centrifuging at 2600 rpm for 30 s. The film was dried in an oven at 90°C for 30 to 120 min. After cooling, a photosensitive layer of FP-383 was applied under the same conditions as for FN-11 and dried at 80°C for 20 to 60 min. Then FN-11 was hardened at 135°C for 20 min. The sample was exposed to the light of a DRL-250 mercury-arc luminescent lamp (continuous emission spectrum). Working phototemplates with element size from 5 to 1.5 μm were used. The openings in the FP-383 layer were made by treatment with 0.3% KOH, and those in FN-11, by treatment with xylene. The resist removal was monitored with an MMU-3 microscope (magnification from ×80 to ×476) and its being complete was judged from the disappearance of the characteristic supramolecular structure of FP-383. The transmission coefficient A was measured with an SF-46 spectrophotometer with an absolute error of ±1% at 365 nm. The IR spectra were obtained on a Specord-40 spectrophotometer (photometric accuracy ±0.2% A).

The use as planarizing layer of the negative photoresist FN-11 is due to its good physicochemical and physical properties [adhesion, viscosity, low polar constituent of the resist (χ^p = 2 dyne cm^{-1})], and also by the higher drying temperature (90–95°C) at which the FP-383 layer can partially lose the photosensitivity if used as the lower planarizing layer in drying the upper FN-11 layer.

Dioxane used as solvent for NQD causes cracking of a dried FN-11 film. The developers (KOH for NQD and xylene for FN-11) are inert toward dried films. Raising the film drying time to 60 min made both layers stable; the IR spectra of a purely FN-11 film were fully identical to those of the FN-11 film after removal of the upper photosensitive layer (Fig. 1). The spectrum of the latter contains no bands characteristic of FP-383. All the characteristic bands belong to FN-11 [3, 4] (cm^{-1}): 2940 and 2870,

1070-4272/01/7406-1044 $25.00

stretching vibrations of the C–H bond in the CH_3 and CH_2 groups of rubber; 2160–2120, asymmetric stretching vibrations of the $-N_3$ group of the bisazide; 1660–1650, vibrations of the C=O bond in the 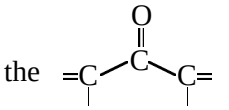 group of bisazide; 1460, inplane vibrations of the C=C bond in the benzene ring of bisazide; 1375, bending vibrations of the C–C bond in the $C–CH_3$ group of rubber; and 615, vibrations in benzene derivatives.

The characteristic curves plotted for FN-11 in the coordinates film thickness–minimal irradiation time required for complete cross-linking (judged from the resistance of the films to development for more than 10 min) shows that the photosensitivity of the FN-11 film increases after application of naphthoquinone diazide. The irradiation dose for cross-linking of FN-11 through the upper sensitive layer of naphthoquinone diazide is considerably lower than the energy required for cross-linking of a single FN-11 layer (Fig. 2, curve *1*).

The times t_1 and t_2 corresponding to the ends of the intervals of proportional image transmission correspond to the same thickness of the cross-linked polymer, after which in both cases the rate of relief formation decreases steeply as the exposure energy increases. The identity of the transmission bands in the IR spectra of the single- and two-layer structures (Fig. 1) shows that these two layers do not react chemically under experimental conditions (simple physical contact of dried films 3 to 9 μm thick, with short UV irradiation). Probably, the photochemical activity of cyclorubber is initiated owing to multiple reflection from the layer boundaries upon completion of the photolysis in the upper sensitive layer of naphthoquinone diazide.

Since the absorption maxima of naphthoquinone diazide and cyclorubber coincide (365 nm) [5] and there is no separating layer, irradiation of the photosensitive layer through a phototemplate produces an image in the lower planarizing layer, too, after development (with 0.3% KOH and xylene, respectively). To describe the photochemical aspect of the photosensitivity of the FN-11 layer, we measured the transmission coefficient *A* as a function of irradiation time for various types of films (Fig. 3). Figure 3 shows that the FP-383 layer transmits a significant fraction of the incident radiation, sufficient to produce image also in the lower layer also.

The physicochemical aspect of the photosensitivity is characterized in the table by the irradiation dose

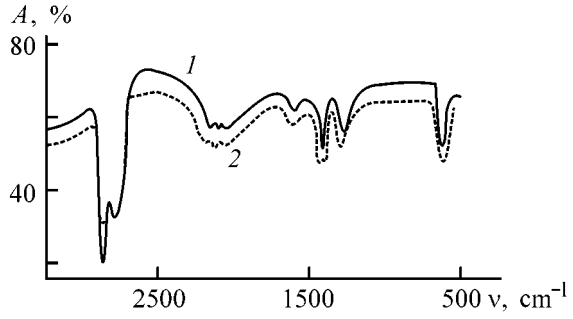

Fig. 1. IR spectra of (*1*) purely FN-11 film and (*2*) FN-11 film after removal of the naphthoquionone diazide layer. (*A*) Transmission coefficient and (ν) wave number.

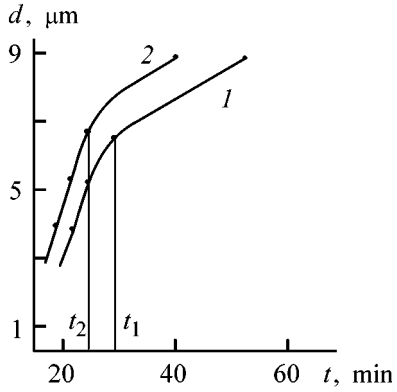

Fig. 2. Characteristic curves for the (*1*) purely FN-11 layer and (*2*) FN-11 layer irradiated through a layer of naphthoquinone diazide. (*d*) Film thickness and (*t*) minimal irradiation time.

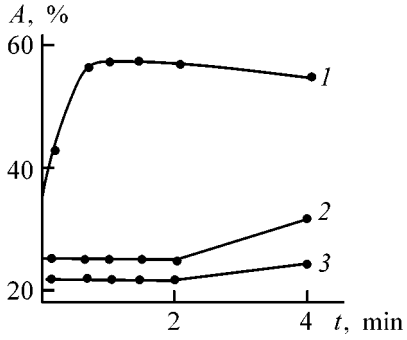

Fig. 3. Transmission coefficient *A* vs. the irradiation time *t* for (*1*) FP-383 film, (*2*) FN-11 film, and (*3*) FN-11 irradiated through a layer of FP-383, after removal of this layer.

required to make the film resistant to the developer. It is seen that the resistance of the FN-11 film appreciably increases when the image in this film is formed through a layer of FP-383, after removal of the latter in KOH solution. These results are fully consistent with the characteristic curves (Fig. 2).

Resistance of FN-11 films to the developer as influenced by the irradiation dose

t, s	Resistance of FN-11 films, s		*t*, s	Resistance of FN-11 films, s	
	single-layer	after removal of FP-383 layer		single-layer	after removal of FP-383 layer
40	15	20	120	25	> 600
60	20	25	150	> 600	> 600
90	25	> 600	300	> 600	> 600

Since the FN-11 photoresist is resistant to plasma, it is possible to obtain in this system an image using as planarizing layer a hardened (in the course of FN-11 drying) FP-383 layer, which can be subsequently broken down by plasmochemical etching. In this case a sharp image is formed in the FN-11 layer.

CONCLUSION

In the system FP-383–FN-11, it is possible to form a two-layer photoresist exhibiting significant advantages over other systems: the absence of a separating layer and the same radiation source for the planarizing and sensitive layers (UV, 365 nm); elimination of such operations as matching, repeated irradiation, and breakdown of the sensitive layers to make windows. FP-383 enhances the photosensitivity of the FN-11 layer and its physicochemical resistance to the developer.

REFERENCES

1. Moreau, W.M., *Semiconductor Lithography. Principles, Practices, and Materials*, New York: Plenum, 1988, part 2.
2. Bokov, Yu.S. and Frolov, V.M., *Elektronn. Tekh.*, 1985, Ser. 3, issue 3.
3. Kazitsyna, L.A. and Kupletskaya, N.B., *Primenenie UF-, IK-, YaMR- i mass-spektroskopii v organicheskoi khimii* (Use of UV, IR, NMR, and Mass Spectroscopy in Organic Chemistry), Moscow: Mosk. Gos. Univ., 1979.
4. Dechant, J., Danz, R., Kimmer, W., *et al.*, *Ultrarotspektroskopische Untersuchungen and Polymerene*, Berlin: Akademie, 1972.
5. Treushnikov, V.M., Pomerantseva, L.L., and Frolova, N.V., *Zh. Nauchn. Prikl. Fotogr. Kinematogr.*, 1979, vol. 24, issue 1, pp. 40–42.

Russian Journal of Applied Chemistry, Vol. 74, No. 6, 2001, pp. 1047–1052. Translated from Zhurnal Prikladnoi Khimii, Vol. 74, No. 6, 2001, pp. 1018–1023.

CHEMISTRY OF FOSSIL FUEL

Homogeneous Pyrolysis of Anisole

V. V. Platonov, V. A. Proskuryakov, S. V. Ryl'tsova, and Yu. N. Popova

St. Petersburg State Technological Institute, St. Petersburg, Russia

Tolstoy State Pedagogical University, Tula, Russia

Received December 21, 2000

Abstract—Homogeneous pyrolysis of anisole in argon (1 : 25 volume ratio) at 750–900°C and contact time of 1.5–4.5 s was studied. The conversion and group composition of the tar and component composition of the gaseous pyrolysis products, phenols, and hydrocarbons were determined; asphaltenes and neutral oxygen-containing compounds were characterized. The kinetic parameters of formation of methane, hydrogen, and carbon monoxide and dioxide were calculated; mechanisms of their formation are proposed.

Intensifying high-rate pyrolysis of mineral oils and raising the yield of tars of prescribed qualitative and quantitative composition require detailed information on high-temperature conversion of the primary degradation products.

Since the primary tar and even its separate fractions are complex multicomponent mixtures of compounds of various classes, studying their high-temperature conversion is rather difficult. Therefore, analysis of the pyrolysis of groups of similar compounds and especially of individual components making the most pronounced contribution to the composition of liquid products is the best way to attack the problem.

Based on the latter approach, we can determine the mechanism and main pathways of the occurring reactions, together with their order and activation energies. The kinetic equations obtained in this case can be used to simulate the behavior of separate fractions of primary tars and the resulting tar as a whole in the course of pyrolysis.

Pyrolysis of individual compounds has been studied extensively [1–22], but in some cases data on the composition of secondary products are lacking [1–8]. Moreover, owing to different apparatus and experimental procedures used in these works, their results are difficult to compare.

The goal of this work was to study the homogeneous pyrolysis of anisole, to determine the composition of phenols, hydrocarbons, asphaltenes, and oxygen-containing compounds (NOCs), and to evaluate the kinetic parameters of formation of separate components of the gaseous pyrolysis products.

Pyrolysis of anisole was performed in a setup described in [23]; the tar composition was analyzed by the procedure described elsewhere [24].

The material balance of anisole pyrolysis, the group composition of liquid products, and the component composition of the gaseous pyrolysis products are given in Table 1. As seen, anisole decomposes to a significant extent at the temperatures and contact times used in the experiments.

Gases and tar are the main pyrolysis products at 750–800°C, whereas at 850–900°C the yield of pyrographite increases simultaneously with the yield of the gaseous pyrolysis products. For example, at a contact time of 1.5 s and 800°C the yield of gaseous pyrolysis products, tar, and pyrographite is 20.00, 52.00, and 18.80 wt %, whereas at 900°C it is 37.50, 24.90, and 32.80 wt %, respectively, based on anisole.

The yield of crude benzene, containing up to 90% benzene, is the highest at 800°C and contact time of 1.5 s (9.20 wt % based on anisole); under more severe conditions, the yield of benzene decreases.

The results of group analysis (Table 1) show that up to 850°C (1.5 s) phenols are the main component of the tar; their content varies from 63.50 wt % (750°C) to 29.50 wt % (850°C) at contact times of 4.5 and 1.5 s, respectively. Raising the temperature and contact time further strongly decreases the content of phenols. At 850°C and 3.0 s their content is 5.40 wt %, and at 900°C and 3.0 s the content of phenols in the tar decreases to 1.5 wt %. This is probably due to the degradation of phenols and to a certain change in the direction of pyrolysis reactions.

1070-4272/01/7406-1047 $25.00 © 2001 MAIK "Nauka/Interperiodica"

Table 1. Material balance of anisole pyrolysis

Pyrolysis products	Yield of pyrolysis products (wt % based on initial anisole) at indicated contact time, s								
	4.5	1.5	3.0	4.5	1.5	3.0	4.5	1.5	3.0
	750°C	800°C			850°C			900°C	
"Crude benzene"	7.20	9.20	4.00	2.70	5.90	2.60	2.00	4.80	2.00
Pyrographite	23.80	18.80	25.60	3.60	24.90	31.80	36.40	32.80	40.40
Tar, including (wt %):	48.20	52.00	39.80	29.00	38.20	26.60	18.20	24.90	12.90
phenols	63.50	65.20	37.50	31.50	29.50	5.40	2.90	1.90	1.50
hydrocarbons	17.50	52.30	34.50	39.20	36.40	45.70	51.50	42.80	50.30
neutral oxygen-containing compounds	1.50	1.80	2.20	2.50	2.20	2.70	3.30	2.50	2.00
asphaltenes	9.40	4.30	10.30	13.30	21.50	30.40	39.10	38.90	43.10
resins	8.10	3.40	15.20	13.50	10.40	15.80	3.20	13.90	3.10
Gaseous pyrolysis products + losses, including (wt %) of gaseous pyrolysis products:	20.80	20.00	30.60	37.70	31.00	39.00	43.40	37.50	44.70
H_2	30.50	25.30	29.90	33.70	30.80	38.30	43.10	35.30	46.20
CH_4	27.10	24.80	22.60	20.70	23.20	18.50	17.80	21.10	16.20
CO	37.80	41.50	36.30	35.80	38.20	34.20	33.80	37.30	32.90
CO_2	4.60	8.40	11.20	9.80	7.80	9.00	5.30	6.30	4.70

Table 2. Component composition of phenols

Component	Yield of pyrolysis products (wt % based on initial anisole) at indicated contact time, s								
	4.5	1.5	3.0	4.5	1.5	3.0	4.5	1.5	3.0
	750°C	800°C			850°C			900°C	
Phenol	14.632	14.170	6.823	4.702	5.410	0.776	0.310	0.239	0.085
o-Cresol	0.520	0.373	0.060	0.018	0.045	0.010	0.008	0.016	0.002
p-Cresol	0.398	0.542	0.119	0.037	0.045	0.013	0.015	0.016	0.004
m-Cresol	0.122	0.271	0.090	0.046	0.056	0.010	0.016	0.006	0.004

Note: Only trace amounts of xylenols are found in the phenol fraction.

Simultaneously with the decrease in the yield of phenols, the content of hydrocarbons and asphaltenes in the tar increases. At 750°C (4.5 s) the content of hydrocarbons in the tar is 17.50 wt %, and at 900°C (3.0 s) it grows to 50.30 wt %, and the content of asphaltenes increases from 9.40 to 43.10 wt % owing to intensification of the condensation processes. The content of NOCs varies insignificantly.

The main components of the gaseous pyrolysis products (Table 1) are hydrogen, methane, and carbon monoxide and dioxide. With increasing temperature and contact time, the yield of hydrogen steadily increases from 25.30 to 46.20 vol %, based on total gaseous products, at 800°C (1.5 s) and 900°C (3.0 s), respectively. Simultaneously the yield of methane and carbon monoxide decreases from 24.80 and 41.50 to 16.20 and 32.90 vol %, respectively.

To obtain a clearer pattern of thermochemical transformations of anisole, we studied the chemical composition of phenols, hydrocarbons, asphaltenes, and neutral oxygen-containing compounds.

The data obtained by means of capillary gas-liquid chromatography (CGLC) of phenols (Table 2) show that the main component of the tar is phenol, whose content changes from 14.632 to 0.085 wt %, based on anisole, upon heating from 750°C (4.5 s) to 900°C (3 s). The decrease in the phenol yield under more severe conditions of pyrolysis is due to intensification of the secondary processes of dehydration and condensation. The content of cresols is the highest at 750°C (4.5 s) and 800°C (1.5 s); the content of xylenols is insignificant.

Table 3. Component composition of hydrocarbons

Component	Yield of pyrolysis products (wt % × 10^{-3} based on initial anisole) at indicated contact time, s								
	4.5	1.5	3.0	4.5	1.5	3.0	4.5	1.5	3.0
	750°C	800°C			850°C			900°C	
Naphthalene	1502.32	2171.40	2540.05	2694.69	3099.70	3222.40	2867.22	2643.68	1356.41
β-Methylnaphthalene	50.64	92.12	96.11	68.22	139.00	97.28	65.59	63.96	38.94
α-Methylnaphthalene	59.08	184.24	151.03	102.33	166.80	109.44	74.96	63.96	32.45
Diphenyl	531.72	881.72	1070.94	727.68	1000.80	960.64	590.31	735.54	480.26
2,6-, 2,7-Dimethylnaphthalene	25.32	65.80	54.92	45.48	55.60	24.32	18.74	21.32	6.49
2,3-Dimethylnaphthalene	75.96	78.96	137.30	159.18	180.70	267.52	402.91	234.52	45.43
Diphenyl ether	1755.52	2368.80	2746.00	1955.64	1765.30	1653.76	1405.50	1279.20	778.80
Fluorene	151.92	381.64	672.77	602.61	597.70	583.68	534.09	245.18	240.13
Phenathrene	202.56	473.76	810.07	898.23	1209.30	1544.32	1424.24	1492.40	843.70
Anthracene	227.88	618.52	1057.21	932.34	903.50	1203.84	974.48	938.08	441.32
Fluoranthene	50.64	92.12	233.41	238.77	208.50	352.64	299.84	266.50	305.03
Pyrene	67.52	118.44	178.49	181.92	222.40	231.04	243.62	309.14	311.52
Benzophenanthrene	67.52	184.24	288.33	318.36	417.00	413.44	356.06	479.70	389.40

Table 4. Properties of asphaltenes and neutral oxygen-containing compounds

Parameter	Contact time, s								
	4.5	1.5	3.0	4.5	1.5	3.0	4.5	1.5	3.0
	750°C	800°C			850°C			900°C	
Asphaltenes									
Molecular weight	233	236	264	287	279	292	304	336	360
Content of functional groups, g-equiv mol^{-1}:									
quinoid	0.143	0.266	0.072	0	0.206	0	0	0.178	0
phenol	0.110	0.335	0.117	0.084	0.163	0.088	0.072	0.107	0
alkoxy	0.775	0.994	1.690	1.195	0.249	0	0	0.224	0
oxygen in heterocycles	0.054	0	0	0.409	0	0	0.495	0.192	0.415
Iodine number, g-equiv mol^{-1}	0.412	0.420	0.417	0.413	0.608	0.531	0.499	0.625	0.598
Neutral oxygen-containing compounds									
Molecular weight	189	195	211	219	215	228	226	215	221
Content of functional groups, g-equiv mol^{-1}:									
quinoid	0.352	0.505	0.289	0.217	0.310	0.097	0	0	0
alkoxy	1.890	0.565	0.632	1.340	2.150	1.120	1.030	0.885	0.790
oxygen in heterocycles	0	0.203	0.464	0.550	0.494	0.966	0.508	0.853	0.669
Iodine number, g-equiv mol^{-1}	0.106	0.195	0.230	0.272	0.309	0.218	0.113	0.236	0.137

The component composition and yield of individual hydrocarbons are listed in Table 3. The main components of the hydrocarbon fraction are naphthalene, diphenyl ether, phenanthrene, and anthracene. The yield of naphthalene is the highest at 850°C (3.0 s) and the lowest at 900°C (3.0 s): 3222.40×10^{-3} and 1356.41×10^{-3} wt %, based on anisole, respectively. The yield of phenanthrene and anthracene is the highest under the same conditions. It should be noted that the above compounds are accumulated in the tar at temperatures up to 850°C and contact time of 1.5 s; under more severe conditions of pyrolysis these compounds are converted into more condensed hydrocarbons. This is confirmed by the steady increase in

the content of pyrene, benzophenanthrene, and fluoranthene in the tar.

Detailed data on the composition of NOCs and asphaltenes are necessary to study the most important stages of anisole degradation and to determine the fields of efficient utilization of the degradation products.

The molecular structure of asphaltenes and NOCs was studied by cryoscopy [25] and quantitative functional analysis [26–30]; the results are given in Table 4.

As seen, asphaltenes and NOCs differ in molecular weight and content of functional groups. For example, NOCs contain almost no phenolic hydroxy groups, which occur in asphaltenes where their content is the highest at 800°C and contact time of 1.5 s (0.335 g-equiv mol^{-1}). As the pyrolysis conditions are made more severe, the content of these groups decreases to zero through their complete degradation. The appearance of phenolic groups in asphaltenes is due to the large size of asphaltene molecules, which hinders attack of the reaction centers. By contrast, quinoid groups are concentrated in NOCs (0.505 and 0.266 g-equiv mol^{-1} in, respectively, NOCs and asphaltenes at 800°C and contact time of 1.5 s). With increasing temperature and contact time, the content of quinoid groups decreases, probably because of their higher lability as compared with that of other functional groups. The appearance of these groups in the products of anisole pyrolysis suggests the intermediate formation of quinoid or related structures in the course of pyrolysis. The alkoxy groups occur in the initial compound and can be formed by the attack of the radical fragments of ring degradation on the phenolic and quinoid groups; as a result, they are predominant in the NOC structures. Heterocyclic oxygen is the most thermodynamically stable form, and it is found in the asphaltenes under more severe conditions of pyrolysis at 900°C or at more prolonged contact. In the case of NOCs, heterocyclic oxygen is not formed only at 750°C (4.5 s), which suggests increased lability of heterocyclic fragments in oxygen-containing compounds as compared with asphaltenes. The degree of unsaturation of asphaltenes, which is characterized by the iodine number, is several times greater than that of the neutral oxygen-containing compounds.

To evaluate the overall thermal stability of anisole, we calculated the kinetic parameters of formation of components of gaseous pyrolysis products.

The formation of carbon monoxide is described by a 1.5-order kinetic equation with activation energy of 345.00 kJ mol^{-1}, which is of particular importance, since for most of the compounds studied this is a first-order process and the whole body of experimental data suggests intramolecular mechanism of CO liberation. In our case, the order of 1.5 is due to a more complex mechanism of formation, whereas the higher activation energy, compared with that in radical reactions, suggests their insignificant contribution.

The close activation energies of CO formation from anisole and phenols [21, 22] suggest that the structures of their activated complexes are similar. Since the activated complex of phenols has a quinoid structure, it would probably have a pseudoquinoid nature in the case of anisole. Then, the cleavage of CO from anisole can be described by the following reaction:

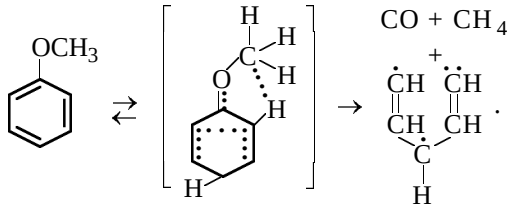

Based on the additivity of the bond energies in the activated complex [31], we calculated the activation energies for the above process. The resulting activation energy (368.30 kJ mol^{-1}) is close to the experimental value, which is slightly lower, probably owing to the contribution of secondary radical reactions.

Also, another mechanism of CO formation is possible:

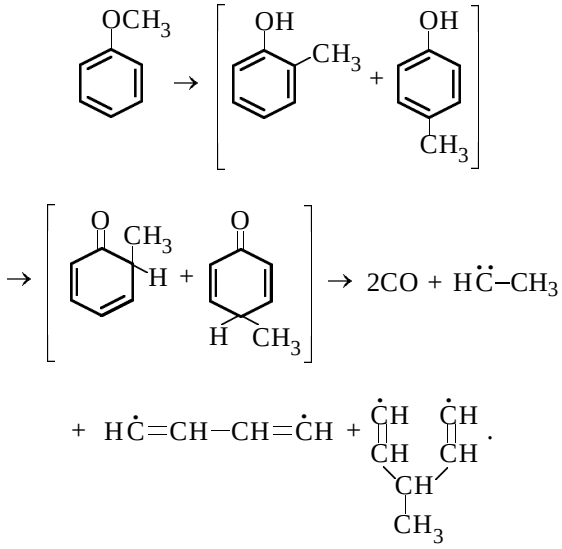

The calculated activation energy of this process is 404.75 kJ mol^{-1}, and this mechanism accounts for the formation of cresols in the phenol fraction of the tar.

The formation of carbon dioxide is described by a second-order kinetic equation; at 850°C and contact time of 3.0 s the mechanism changes. At 800–850°C the activation energy is 92.18 kJ mol^{-1}, being as high as 206.15 kJ mol^{-1} at 850–900°C. Such small activation energies suggest the radical mechanism of the process, which can be described as follows: CO^* molecules formed by cleavage of the activated complex attack either the anisole molecules at the methoxy group (1) or the methoxy radicals in the gas phase (2):

$$CO^* + CH_3OC_6H_5 \rightarrow CO_2 + C_6H_5CH_3, \quad (1)$$

$$CO^* + CH_3O^{\cdot} \rightarrow CO_2 + {}^{\cdot}CH_3. \quad (2)$$

It is also possible that formation of CO_2 is accompanied by reactions catalyzed with pyrographite.

Methane can be formed simultaneously with carbon monoxide and also from methyl radicals in the course of formation of carbon dioxide. At equal contributions of these mechanisms the activation energy calculated by the Moin procedure [31] is 272.35 kJ mol^{-1}, in agreement with the experiment (256.43 kJ mol^{-1}). The smaller experimental value probably suggests occurrence of a less energy-consuming process. The accumulation of methane is described by a second-order equation.

Hydrogen is formed in anisole pyrolysis through condensation, degradation, and recombination reactions; its accumulation is described by a 1.5-order equation with activation energy of 98.88 kJ mol^{-1}.

The kinetic equations of formation of the gaseous pyrolysis products components are given in Table 5.

Table 5. Kinetic equations of formation of the gaseous pyrolysis products

Component	Reaction order	Kinetic equation
CO	1.5	$k_{ck} = 4.0 \times 10^{18}\exp(345000/RT)$
CH_4	2.0	$k_{ck} = 1.1 \times 10^{15}\exp(-256428/RT)$
H_2	1.5	$k_{ck} = 3.3 \times 10^{6}\exp(-98884/RT)$
CO_2	2.0	$k_{ck} = 8.3 \times 10^{7}\exp(-92180/RT)$ (800–850°C)
		$k_{ck} = 4.1 \times 10^{14}\exp(-206148/RT)$ (850–900°C)

CONCLUSIONS

(1) A study of homogenous pyrolysis of anisole showed that anisole is thermally unstable even at relatively low temperatures. The predominant liquid products obtained at 750–800°C and contact times of 1.5–4.5 s are phenols and hydrocarbons, and at 850–900°C, hydrocarbons and asphaltenes. Methane, hydrogen, and carbon monoxide and dioxide are the main components of the gaseous pyrolysis products.

(2) The phenol fraction of the liquid products consists of phenol, cresols, and trace amounts of xylenols; naphthalene and diphenyl ether are the main components of the hydrocarbon fraction. Asphaltenes and neutral oxygen-containing compounds are complex mixtures of predominantly aromatic compounds with various functional groups and alkyl chains.

(3) The kinetic parameters of formation of the gaseous pyrolysis products were calculated, and the mechanisms of their formation are proposed.

REFERENCES

1. Telichev, M.D., *Zh. Prikl. Khim.*, 1939, vol. 12, no. 5, pp. 739–758.
2. Magaril, R.Z., *Mekhanizm i kinetika gomogennykh termicheskikh prevrashchenii uglevodorodov* (Mechanism and Kinetics of Homogenous Thermal Transformations of Hydrocarbons), Moscow: Khimiya, 1970.
3. Badger, G.M. and Novotny, J., *J. Chem. Soc.*, 1961, no. 8, pp. 3400–3402.
4. Cypers, R., *Ann. Mines Belg.*, 1965, nos. 7–8, pp. 1091–1109.
5. Fields, E.K. and Meyerson, S., *J. Am. Chem. Soc.*, 1966, vol. 88, no. 1, pp. 2286–2290.
6. Burova, L.G., Kokurin, A.D., and Emchenko, G.I., *Zh. Prikl. Khim.*, 1972, vol. 45, no. 10, pp. 2286–2290.
7. Dobryanskii, A.F. and Saprykin, A.P., *Zh. Obshch. Khim.*, 1939, vol. 9, no. 14, pp. 1313–1314.
8. Makoto, T., *Bull. Chem. Soc. Jpn.*, 1960, vol. 33, no. 6, pp. 801–808.
9. Makoto, T., *Bull. Chem. Soc. Jpn.*, 1960, vol. 33, no. 6, pp. 808–813.
10. Hund, C.D. and Macon, A.R., *J. Am. Chem. Soc.*, 1962, vol. 84, no. 23, p. 1524.
11. Hund, C.D., *The Pyrolysis of Carbon Compounds*, New York: Am. Chem. Soc., 1929.
12. Platonov, V.V., Klyavina, O.A., Ivleva, L.N., *et al.*, *Khim. Tverd. Topl.*, 1986, no. 5, pp. 57–84.
13. Platonov, V.V. and Ivleva, L.N., *Khim. Tverd. Topl.*, 1979, no. 1, pp. 96–103.

14. Platonov, V.V., Klyavina, O.A., Ivleva, L.N., *et al.*, *Khim. Tverd. Topl.*, 1985, no. 1, pp. 86–92.
15. Platonov, V.V., Klyavina, O.A., Ivleva, L.N., *et al.*, *Khim. Tverd. Topl.*, 1985, no. 2, pp. 73–79.
16. Platonov, V.V., Klyavina, O.A., and Ivleva, L.N., *Izv. Akad. Nauk Est. SSR*, 1984, vol. 33, no. 1, pp. 15–21.
17. Platonov, V.V., Klyavina, O.A., and Ivleva, L.N., *Izv. Akad. Nauk Est. SSR*, 1985, vol. 34, no. 2, pp. 98–104.
18. Platonov, V.V., Tabolenko, N.V., Klyavina, O.A., and Ivleva, L.N., *Izv. Akad. Nauk Est. SSR*, 1984, vol. 33, no. 2, pp. 102–109.
19. Platonov, V.V., Tabolenko, N. V., Klyavina, O.A., and Ivleva, L.N., *Izv. Akad. Nauk Est. SSR*, 1985, vol. 34, no. 1, pp. 11–16.
20. Platonov, V.V., Klyavina, O.A., Prokof'ev, E.E., *et al.*, *Khim. Tverd. Topl.*, 1983, no. 6, pp. 75–85.
21. Platonov, V.V., Ivleva, L.N., and Prokof'ev, E.E., *Khim. Tverd. Topl.*, 1980, no. 2, pp. 138–147.
22. Platonov, V.V., Ivleva, L.N., and Klyavina, O.A., *Khim. Tverd. Topl.*, 1984, no. 3, pp. 105–114.
23. Bunkina, N.A., Makarov, G.N., Bronshtein, A.P., and Platonov, V.V., *Koks Khim.*, 1975, no. 8, pp. 26–30.
24. Kamneva, A.I. and Korolev, Yu.G., *Laboratornyi praktikum po khimii topliva* (Laboratory Course of Fuel Chemistry), Moscow: Mosk. Khimiko-Tekhn. Inst. im. D.I. Mendeleeva, 1976.
25. Rybak, B.M., *Analiz nefti i nefteproduktov* (Analysis of Petroleum and Petroleum Products), Moscow: Gostoptekhizdat, 1962.
26. Meyer, W., *Die Bestimmung funktioneller Gruppen an Huminsubstanzen aus Boden*, Zurich: Juris, 1962.
27. Glebko, L.I., Determination of Functional Groups in Humic Acids, *Cand. Sci. Dissertation*, Moscow, 1971.
28. *Novye metody issledovaniya guminovykh kislot: Sbornik statei* (New Methods of Analysis of Humic Acids: Coll. of Papers), Elyakov, G.B., Ed., Vladivostok: Dal'nevost. Nauchn. Tsentr, 1972.
29. Veibel, S., *The Identification of Organic Compounds. A Manual of Qualitative and Quantitative Methods*, Copenhagen: Gad, 1954.
30. Rudolf, E. von, *Flav. Fragr.*, 1985, vol. 1, pp. 33–35.
31. Moin, F.B., *Usp. Khim.*, 1967, vol. 36, no. 7, pp. 1223–1243.

Russian Journal of Applied Chemistry, Vol. 74, No. 6, 2001, pp. 1053–1057. Translated from Zhurnal Prikladnoi Khimii, Vol. 74, No. 6, 2001, pp. 1024–1028.

CHEMISTRY OF FOSSIL FUEL

Homogeneous Pyrolysis of α-Naphthol

V. V. Platonov, V. A. Proskuryakov, S. V. Ryl'tsova, and Yu. N. Popova

Tolstoy State Pedagogical University, Tula, Russia

St. Petersburg State Technological Institute, St. Petersburg, Russia

Received December 21, 2000

Abstract—Homogeneous pyrolysis of α-naphthol in argon (1 : 25 volume ratio) at 750–900°C and contact time of 1.5–4.5 s was studied. The conversion and group composition of the liquid products, and component composition of the gaseous pyrolysis products and hydrocarbons were determined; the asphaltenes formed were characterized. The kinetic parameters of α-naphthol degradation and formation of methane, hydrogen, and carbon monoxide were calculated; the possible mechanisms of these processes are proposed.

Phenols are significant component of the tars formed in semicoking (low-temperature carbonization) and high-rate pyrolysis of caustobioliths, and their content in the tar may be as high as 30–35 wt %. In high-temperature pyrolysis, the fraction of phenols in the tar decreases to 1.5 wt %, with the yield of neutral oxygen-containing compounds, hydrocarbons, and asphaltenes increasing simultaneously. Optimization of pyrolysis conditions to prepare products of prescribed composition requires detailed information on the behavior of various phenols, including naphthols, and on how high-temperature tars are formed.

It has been found [1–12] that the temperature and contact time strongly affect the yield and composition of the degradation products of phenols. However, owing to the lack of systematic data, small range of phenols studied, and significant differences in the experimental conditions, evaluation of the thermal stability in the phenol series is still difficult. Moreover, the kinetic parameters of pyrolysis and data on the group and component composition of liquid products are lacking. In [13–18], data on high-temperature conversion of phenol, cresols, xylenols, and dihydric phenols were presented, the group composition of the tars and the component composition of the gaseous pyrolysis products determined, the kinetic parameters of degradation of the initial raw material and of formation of the tar and gaseous pyrolysis products components calculated, and the reaction mechanisms proposed.

The aim of this work was to study the features of homogeneous pyrolysis of α-naphthol, determine the qualitative and quantitative composition of hydrocarbons and asphaltenes, and evaluate the kinetic parameters of formation of the gaseous pyrolysis products components.

Pyrolysis of α-naphthol was performed on a setup described in [19]; the tar composition was analyzed by the procedure described elsewhere [20].

The material balance for α-naphthol pyrolysis is given in Table 1 indicating a significant transformations of the initial compound at temperatures of 750–900°C and contact time of 1.5–4.5 s. Under the above conditions, the tar fraction decreases from 89.00 to 26.30 wt %, with the yield of gaseous pyrolysis products and pyrographite increasing from 6.50 to 26.50 and from 3.30 to 45.20 wt %, respectively. The content of benzene fraction remains almost constant and at 850°C (4.5 s) it does not exceed 2.55 wt % relative to α-naphthol. This is probably due to a rather complex pathway of formation of mononuclear aromatic hydrocarbons from the system of two fused aromatic naphthalene rings.

The result of group analysis of the liquid products and the component composition of the gaseous pyrolysis products are also listed in Table 1.

As seen, the content of the phenol fraction in the tar decreases, because the hydroxy group in phenol is the first to degrade. For example, the content of phenols in the tar is 58.5 wt % at 800°C (1.5 s) and only 5.3 wt % at 900°C (3.0 s). Simultaneously, asphaltenes and hydrocarbons are accumulated in liquid degradation products. The yield of hydrocarbons

1070-4272/01/7406-1053 $25.00 © 2001 MAIK "Nauka/Interperiodica"

Table 1. Material balance of α-naphthol pyrolysis

Pyrolysis products	Yield of pyrolysis products (wt % based on initial α-naphthol) at indicated contact time, s								
	4.5	1.5	3.0	4.5	1.5	3.0	4.5	1.5	3.0
	750°C	800°C			850°C			900°C	
Benzene hydrocarbons	1.20	1.00	1.55	2.00	2.10	2.30	2.55	2.45	2.00
Tar, including (wt %):	89.90	85.50	74.50	61.90	73.05	51.90	39.85	37.30	26.30
phenols	48.20	58.50	43.20	20.80	36.10	16.40	8.20	12.20	5.30
hydrocarbons	17.20	15.00	22.20	19.00	25.40	43.40	50.30	28.90	36.50
neutral oxygen-containing compounds	0.40	1.60	2.00	0.80	1.30	1.10	0.60	0.80	0.60
asphaltenes	22.00	15.70	22.30	18.57	22.80	31.00	35.00	40.00	50.00
resins	12.20	9.20	10.30	2.73	14.40	9.10	5.90	18.30	7.60
Gaseous pyrolysis products + losses, including (wt %):	6.50	7.20	12.95	18.30	13.00	17.70	20.50	24.95	26.50
H_2	32.50	24.80	46.10	42.50	41.30	49.40	57.70	52.90	58.30
CH_4	4.60	3.50	5.70	5.80	5.90	7.10	7.50	6.70	7.30
CO	62.90	71.70	48.20	51.60	52.80	43.50	34.80	40.40	34.40
Pyrographite	3.30	6.30	11.00	17.80	12.85	28.10	37.10	35.50	45.20

strongly depends on the contact time. This is probably due to the prolonged period of their formation from hydrocarbon fragments generated in degradation. The content of neutral oxygen-containing compounds (NOCs) is insignificant. Their highest content in the tar (2.00 wt %) is attained at 800°C (3.0 s); further decrease in the NOCs content is due to instability of the resulting structures and their degradation on heating.

Simultaneously, with decreasing yield of phenols, the content of asphaltenes in the tar increases to become 15.70 wt % at 800°C (1.5 s) and 50.00 wt % at 900°C (3.0 s). This is due to the structure of α-naphthol, containing two aromatic rings whose condensation gives macromolecular compounds.

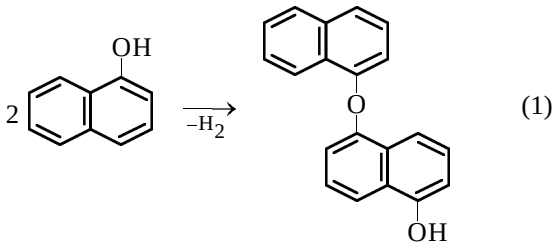

(1)

The main component of the gaseous products formed at 750–800°C is carbon monoxide yielded by the following reactions:

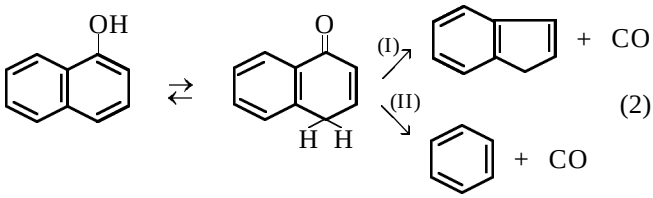

(2)

$$+ H\dot{C}{=}\dot{C}H + \ddot{C}H_2$$

$$\ddot{C}H_2 + 2\dot{H} \rightarrow CH_4$$

With increasing temperature and contact time, the content of hydrogen and methane in the gaseous pyrolysis products grows, with the yield of carbon monoxide decreasing simultaneously. This is probably due to the fact that CO is formed by mechanism (I) in the initial stages of pyrolysis and by mechanism (II) under more severe conditions, with the formation of radical fragments.

To determine the contribution of α-naphthol to the formation of individual phenols, hydrocarbons, and neutral oxygen-containing compounds, the phenol and hydrocarbon fractions were studied by the capillary gas-liquid chromatography (CGLC). The phenol fraction consists of unchanged α-naphthol; other low-boiling components are almost absent.

The component composition of hydrocarbon fraction of the tar formed in α-naphthol pyrolysis is shown in Table 2. This fraction contains naphtha-

Table 2. Component composition of hydrocarbons

Component	Yield of pyrolysis products (wt % × 10^2, based on initial α-naphthol) at indicated contact time, s								
	4.5	1.5	3.0	4.5	1.5	3.0	4.5	1.5	3.0
	750°C	800°C			850°C			900°C	
Naphthalene	519.01	250.19	476.35	715.30	593.60	900.80	947.89	452.76	526.08
β-Methylnaphthalene	2.30	1.67	4.14	5.70	7.42	6.76	5.01	3.23	1.92
α-Methylnaphthalene	5.36	3.85	6.62	9.50	10.20	6.76	3.01	3.77	2.40
Diphenyl	1.53	0.77	1.49	2.85	3.71	3.38	2.00	3.77	1.44
2,7-Dimethylnaphthalene	0.77	3.21	1.65	1.52	1.48	1.13	0.80	0.86	0.58
2,3-Dimethylnaphthalene	3.83	4.36	7.44	13.30	10.20	16.89	18.04	14.55	9.60
Acenaphthene	0.77	0.51	0.99	2.28	1.48	3.38	3.81	1.62	0.96
Fluorene	1.53	1.92	3.64	4.75	4.64	9.01	11.02	5.39	2.88
Phenathrene	1.53	1.28	2.65	5.70	5.57	10.13	17.03	10.24	15.74
Anthracene	1.22	0.77	3.31	4.75	6.49	9.01	10.02	7.55	11.52
Fluoranthene	3.83	7.06	11.58	19.00	19.48	52.92	61.12	28.57	43.20
Pyrene	4.59	3.21	5.79	12.35	8.16	15.76	19.04	7.55	7.68
X_1	64.91	48.75	81.05	104.20	76.98	127.24	79.16	60.91	27.84
X_2	79.61	71.21	103.38	123.20	75.13	104.71	104.21	81.93	46.08
Benzophenanthrene	137.02	142.41	277.87	493.00	253.21	355.81	386.77	185.42	205.44
High-boiling hydrocarbons	703.19	741.83	666.05	382.60	777.25	628.31	335.07	209.88	56.64

lene, its methyl and dimethyl homologs, acenaphthene, fluorene, phenanthrene, anthracene, fluoranthene, pyrene, benzophenanthrene, and high-boiling hydrocarbons. The main components of the hydrocarbon fraction are naphthalene and benzophenanthrene. Under more severe conditions, the yield of these compounds increases. For example, the yield of naphthalene grows from 250.19×10^{-2} at 800°C (1.5 s) to 526.08×10^{-2} wt % at 900°C (3.0 s); under the same conditions, the yield of benzophenanthrene increases from 142.41×10^{-2} to 205.44×10^{-2} wt %, respectively.

The content of hydrocarbons boiling out after benzophenanthrene is rather significant at 800– 850°C and contact time of 1.5 s (741.83×10^{-2} and 777.25×10^{-2} wt %) and rapidly decreases on heating to 900°C at a contact time of 3.0 s (56.64×10^{-2} wt %). These high-boiling hydrocarbons can be used to prepare low-molecular-weight hydrocarbons and asphaltenes, whose yield grows with increasing temperature and contact time.

Detailed data on the structure of asphaltenes are necessary to analyze the most important stages of α-naphthol degradation and to determine the contribution of these compounds to the formation of the qualitative and quantitative composition of the "secondary" tars.

The molecular structure of asphaltenes was studied by cryoscopy [21] and quantitative functional analysis [22–26]; the obtained results are given in Table 3.

The content of phenol groups is the highest at 800°C and contact time of 3.0 s (1.47 mg-equiv g^{-1}); under more severe conditions their content decreases, which is due to the degradation of phenol hydoxy groups of both α-naphthol and the resulting asphaltenes.

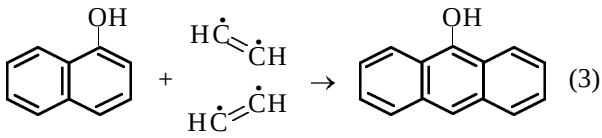

(3)

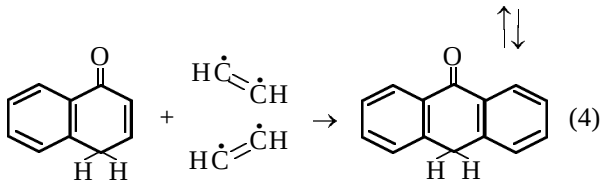

(4)

The possibility of mechanism (4) is confirmed by the presence of quinoid groups in the asphaltene structures; their content is the highest at 800°C and contact time of 3.0 s and decreases under more severe conditions.

A significant fraction of oxygen is contained in heterocycles; its content increases at 800 and 850°C

Table 3. Properties of asphaltenes

T, °C	Contact time, s	Molecular weight	Content of functional groups, mg-equiv g^{-1}				Iodine number, mg-equiv g^{-1}
			phenol	quinoid	alkoxy	oxygen in heterocycles	
750	4.5	291	1.26	0.93	0.21	1.01	0.18
800	1.5	273	0.48	2.68	0.51	1.62	0.19
	3.0	293	1.47	4.46	1.06	1.98	0.23
	4.5	300	1.04	1.24	0.67	2.13	0.25
850	1.5	282	1.26	2.42	0.59	1.91	0.26
	3.0	303	0.86	3.08	1.40	2.09	1.65
	4.5	313	0.81	1.18	0.55	2.01	2.82
900	1.5	290	0.64	0.76	0.71	1.82	0.45
	3.0	312	0.50	0.42	0.50	1.49	0.91

Table 4. Kinetic equations of degradation of α-naphthol and formation of components of gaseous pyrolysis products

Process	Reaction order	Kinetic equation
Degradation of α-naphthol	1.5	$k_{ck} = 1.96 \times 10^{14}\exp(-233\,800/RT)$
Formation of:		
CO	1.0	$k_{ck} = 7.34 \times 10^{17}\exp(-319\,280/RT)$
CH_4	1.5–2.0	$k_{ck} = 2.12 \times 10^{10}\exp(-256\,850/RT)$
H_2	1.5–2.0	$k_{ck} = 5.30 \times 10^{11}\exp(-270\,260/RT)$

and decreases at 900°C, which may be due to limited thermal stability of the resulting rings.

The content of alkoxy groups is small because of the low concentration of the fragments able to attack the phenol hydroxyl or quinoid group:

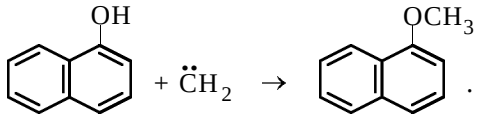

(5)

At 850°C and contact time of 3.0–4.5 s, formation of unsaturated fragments is the most intensive; under more severe conditions, high concentration of hydrogen (Table 1) promotes hydrogenation of unsaturated bonds. This is confirmed by the variation of the iodine number (mg-equiv g^{-1}) 0.25 at 800°C (4.5 s), 2.82 at 850°C (4.5 s), and 0.91 at 900°C (3.0 s).

To evaluate the total thermal stability of α-naphthol, the kinetic parameters of formation of gaseous pyrolysis products were calculated.

The degradation of α-naphthol is described by a 1.5-order kinetic equation with activation energy of 233.80 kJ mol^{-1}, a 20% higher value as compared with phenol [13], which may be due to a stronger stabilizing effect of two more rigid condensed naphthalene rings. The energy barrier of this process is two times lower than the energy of any bond in the α-naphthol molecule, which suggests a significant contribution of rapid radical processes with low activation energies. Moreover, similarly to phenols [13–18], pyrolysis of α-naphthol probably proceeds through an intermediate labile quinoid form [scheme (2)]. However, owing to the lower mobility of the phenolic hydrogen in α-naphthol, formation of the quinoid structures requires much more energy.

Formation of carbon monoxide is described by a first-order equation with activation energy of 319.28 kJ mol^{-1}; this process is primary and determines the pyrolysis rate.

The activation energies of methane and hydrogen formation are 256.85 and 270.26 kJ mol^{-1}, respectively; their lower values are due to the contribution of the secondary radical reactions proceeding with almost zero activation energy:

$$:CH_2 + 2H\cdot \rightarrow CH_4,$$

$$\cdot H + \cdot H \rightarrow H_2.$$

The reaction order varies within 1.5–2.0.

The kinetic equations of α-naphthol degradation and formation of the components of the gaseous pyrolysis products are listed in Table 4.

To test the proposed mechanism describing the formation of carbon monoxide, we calculated the activation energy by a procedure based on the additivity of bond energies in the activated complex [27].

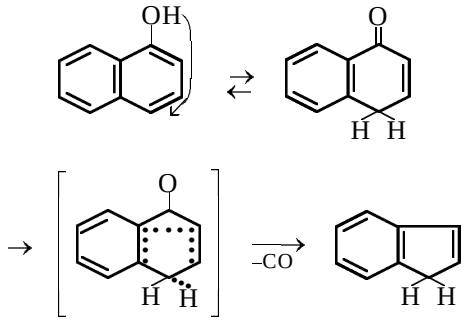

The theoretical activation energy of 322.63 kJ mol^{-1} is in good agreement with the experimental results and confirms the proposed mechanism.

CONCLUSIONS

(1) Homogeneous pyrolysis of α-naphthol undergoes significant changes in the temperature range studied. With increasing temperature and contact time, the content of hydrocarbons and asphaltenes in the liquid products grows, whereas the content of phenols decreases. Hydrogen and carbon monoxide are the main components of the gaseous pyrolysis products.

(2) The hydrocarbon fraction contains mostly naphthalene and benzophenanthrene; asphaltenes are complex mixtures of predominantly aromatic compounds with various functional groups and alkyl chains.

(3) The kinetic parameters of α-naphthol degradation and formation of components of gaseous pyrolysis products are calculated, and mechanisms of their formation are proposed.

REFERENCES

1. Wolle, G., *Ind. Eng. Chem., Process Des. Develop.*, 1962, vol. 1, no. 1, pp. 73–79.
2. Mulcahy, M.F.R., Tucker, B.G., Williams, D.J., and Wilmhurst, J.R., *Aust. J. Chem.*, 1965, vol. 23, pp. 609–610.
3. Raudsepp, Kh.T. and Raudsepp, Kh.E., *Tr. Tallinsk. Politekhn. Inst., Ser. A*, 1968, issue 18, no. 262, pp. 13–20.
4. Raudsepp, Kh.T. and Raudsepp, Kh.E., *Izv. Akad. Nauk Est. SSR, Ser. Geol.*, 1968, vol. 17, no. 2, pp. 149–153.
5. Raudsepp, Kh.T. and Raudsepp, Kh.E., *Khim. Tverd. Topl.*, 1971, no. 3, pp. 139–141.
6. Raudsepp, Kh.T., *Goryuch. Slantsy. Khim. Tekhnol.* (Tallin), 1956, issue 2, pp. 107–116.
7. Hagemann, A. and Neyhaus, M., *Braunkohle*, 1931, no. 45, pp. 876–891.
8. Yamasaki, Y., Kamai, T., and Higuchi, T., *J. Jpn. Petrol. Inst.*, 1971, vol. 14, no. 8, pp. 594–600.
9. Braekmann-Danheux, C. and Heyvaert, A., *Ann. Mines Belg.*, 1972, no. 1, pp. 37–44.
10. Cypres, R. and Bettens, B., *Tetrahedron*, 1974, vol. 30, no. 10, pp. 1253–1260.
11. Delaunois, C. and Bettens, B., *Ann. Mines Belg.*, 1968, no. 5, pp. 633–641.
12. Kawese, T., Arai, H., Tominaga, H., and Kunugi, T., *J. Chem. Soc. Jpn., Ind. Chem. Sect.*, 1970, vol. 73, no. 5, pp. 959–964.
13. Platonov, V.V., Ivleva, L.N., and Prokof'ev, E.E., *Khim. Tverd. Topl.*, 1980, no. 2, pp. 138–147.
14. Platonov, V.V., Ivleva, L.N., Klyavina, O.A., and Prokof'ev, E.E., *Khim. Tverd. Topl.*, 1982, no. 5, pp. 89–99.
15. Platonov, V.V., Klyavina, O.A., Ivleva, L.N., and Prokof'ev, E.E., *Khim. Tverd. Topl.*, 1982, no. 2, pp. 138–144.
16. Platonov, V.V., Ivleva, L.N., Klyavina, O.A., and Prokof'ev, E.E., *Khim. Tverd. Topl.*, 1981, no. 5, pp. 84–94.
17. Platonov, V.V., Klyavina, O.A., Prokof'ev, E.E., and Ivleva, L.N., *Khim. Tverd. Topl.*, 1981, no. 6, pp. 96–103.
18. Platonov, V.V., Ivleva, L.N., and Klyavina, O.A., *Khim. Tverd. Topl.*, 1984, no. 3, pp. 105–114.
19. Bunkina, N.A., Makarov. G.N., Bronshtein, A.P., and Platonov, V.V., *Koks Khim.*, 1975, no. 8, pp. 26–30.
20. Kamneva, A.I. and Korolev, Yu.G., *Laboratornyi praktikum po khimii topliva* (Laboratory Course of Fuel Chemistry), Moscow: Mosk. Khimiko-Tekhnol. Inst. im. D.I. Mendeleeva, 1976.
21. Rybak, B.M., *Analiz nefti i nefteproduktov* (Analysis of Petroleum and Petroleum Products), Moscow: Gostoptekhizdat, 1962.
22. Meyer, W., *Die Bestimmung funktioneller Gruppen an Huminsubstanzen aus Boden*, Zurich: Juris, 1962.
23. Glebko, L.I., Determination of Functional Groups in Humic Acids, *Cand. Sci. Dissertation*, Moscow, 1971.
24. Glebko, L.M. and Maksimov, O.B., *Novye metody issledovaniya guminovykh kislot: Sbornik statei* (New Methods for Analysis of Humic Acids: Coll. of Papers), Vladivostok, 1972.
25. Veibel, S., *The Identification of Organic Compounds. A Manual of Qualitative and Quantitative Methods*, Copenhagen: Gad, 1954.
26. Rudolf, E. von, *Flav. Fragr.*, 1985, vol. 1, pp. 33–35.
27. Moin, F.B., *Usp. Khim.*, 1967, vol. 36, no. 7, pp. 1223–1243.

Russian Journal of Applied Chemistry, Vol. 74, No. 6, 2001, pp. 1058–1060. Translated from Zhurnal Prikladnoi Khimii, Vol. 74, No. 6, 2001, pp. 1029–1031.

BRIEF COMMUNICATIONS

Some Characteristics of Synthetic Hydroxyapatite

E. B. Yarosh, B. A. Dmitrevskii, V. P. Naryzhnyi, and S. K. Tsvetkov

St. Petersburg State Technological Institute, St. Petersburg, Russia

Received January 30, 2001

Abstract—Physicochemical, morphological, and crystal-chemical characteristics of several calcium phosphates are given. The effect of various parameters of manufacturing process on the product quality is described.

Hydroxyapatite $Ca_{10}(PO_4)_6(OH)_2$ is identical in composition to the bone tissue of living organisms and has similar physical, mechanical, and other properties. It shows high biocompatibility, does not give rise to inflammatory phenomena, and is non-toxic. Therefore, articles made from synthetic $Ca_{10}(PO_4)_6(OH)_2$ are used in stomatology, traumatology, orthopedy, and cosmetology for regeneration of bone tissues [1].

$Ca_{10}(PO_4)_6(OH)_2$ exhibits no tendency toward destabilization in an organism; by contrast, it promotes aggregation and absorption of substances from the medium of the organism. Bioactive materials stimulate bone formation and restore bone tissues of a human body. Therefore, implants made of calcium phosphates are the most promising. It is known that $Ca_{10}(PO_4)_6(OH)_2$ samples with the same initial stoichiometric composition may differ in both the biological stability and the tendency toward biodegradation [1]. Samples of nonstoichiometric $Ca_{10}(PO_4)_6(OH)_2$ form a biologically stable phase in a living organism. An ion-exchange equilibrium can take place between a living tissue and $Ca_{10}(PO_4)_6(OH)_2$. To reduce the induction period required for binding between articles made of $Ca_{10}(PO_4)_6(OH)_2$ and a living tissue, nonstoichiometric $Ca_{10}(PO_4)_6(OH)_2$ can be used as a material for artificial bones [2].

When calcium phosphates are synthesized from solutions, the kinetics of the process and the microstructure of the crystalline material depend on the process parameters. The synthesis of $Ca_{10}(PO_4)_6(OH)_2$ crystals is complicated by the formation of intermediate and attendant phases—pseudo-apatites with the ratio $Ca/P \le 1.5$ [3] or calcium phosphates of varied composition [4]. Therefore, we studied the effect exerted by the amount of a calcium-containing reagent, the concentration of working solutions, pH (degree of neutralization), and temperature on the chemical and crystalline characteristics of the resulting salts. The experiments were carried out over a wide range of parameters of the manufacturing process.

Quite a number of researchers have synthesized $Ca_{10}(PO_4)_6(OH)_2$ from aqueous solutions [5–16]. Physicochemical properties [5–8] of $Ca_{10}(PO_4)_6(OH)_2$ and precursor salts and also conditions for their precipitation from $CaCl_2$ and NaH_2PO_4 solutions at low [9, 10], medium [11], and high [12] oversaturation and constant composition of liquid phase [13–16] have been studied. In this work, we used solutions of calcium nitrate and chloride and orthophosphoric acid. To maintain a specified value of pH, we applied solutions of ammonium and sodium hydroxides. The synthesis temperature was varied from 25 to 75°C. Liquid and solid phases were identified by standard procedures [17]. The solid phase was identified by X-ray phase analysis and IR spectroscopy.

The experiments were carried out at constant pH. The size of crystals and the amount of forming $Ca_{10}(PO_4)_6(OH)_2$ grow with increasing duration of syntheses (Fig. 1). It is necessary to note that an amorphous product is formed first, then it is converted to crystalline $Ca_8(HPO_4)_2(PO_4)_4 \cdot 5H_2O$ and(or) $Ca_{10}(PO_4)_6(OH)_2$ (Fig. 2). With increasing pH, the du-

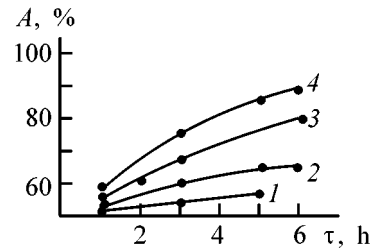

Fig. 1. Effect of synthesis duration τ on the yield *A* of $Ca_{10}(PO_4)_6(OH)_2$. Temperature 25°C, concentration of reagents 0.25 wt %. pH: (*1*) 6, (*2*) 8, (*3*) 10, and (*4*) 11.

1070-4272/01/7406-1058 $25.00 © 2001 MAIK "Nauka/Interperiodica"

ration of $Ca_{10}(PO_4)_6(OH)_2$ synthesis decreases (Fig. 1). If ammonium hydroxide is used, the amorphous phase is only formed at pH 6 and 8. In the presence of sodium hydroxide, amorphous $Ca_{10}(PO_4)_6(OH)_2$ is precipitated as a solid phase up to pH ~ 10. Small crystals up to 1 μm in size are formed on its recrystallization, whereas 3–5 μm crystals are formed when ammonium hydroxide (10% solution) is used.

Characteristics of calcium phosphates precipitated from initial solutions with various compositions are given in Fig. 3. These products were dried at 80°C. It was found that the product obtained from dilute solutions (CaO and P_2O_5 concentrations in initial reagents ranging from 0.25 to 1 wt %) is crystalline $Ca_{10}(PO_4)_6(OH)_2$ (Fig. 3, *a*), with crystal formation becoming slower at higher concentrations. Raising the initial concentration of solutions to 5 wt % CaO and 5 wt % P_2O_5 (stoichiometric ratio of the reagents) in a synthesis at constant pH 6 results in the formation of calcium-deficient $Ca_{10}(PO_4)_6(OH)_2$. The IR spectrum of this salt is given in Fig. 2b. Raising the pH to 8–10 gives poorly crystallized $Ca_{10}(PO_4)_6(OH)_2$. Raising the concentration of the initial solutions yields a finely crystalline product with crystal size of up to 1 μm. Thermal treatment of the products obtained at 800°C results in recrystallization of finely crystalline $Ca_{10}(PO_4)_6(OH)_2$ to give a macrocrystalline product (with crystal size increasing by a factor of 1.5–3). Calcium-deficient $Ca_{10}(PO_4)_6(OH)_2$ is converted into a mixture of calcium β-phosphate and diphosphate. Thermal treatment of the precipitates allows formation a crystalline salt. The IR spectra of the calcined products are more clear-cut, with the intensity of peaks increasing dramatically as compared with the spectra of dry salts. An X-ray phase analysis confirmed that the quality of crystals depends on the conditions of thermal treatment. The diffraction lines of a dry $Ca_{10}(PO_4)_6(OH)_2$ salt (3.44, 2.81, 2.77, 1.92, 1.84, and 1.74 Å), are broadened, their peaks are indistinct. In the X-ray diffraction patterns of calcined samples, the height of peaks grows and they become narrower, i.e., the diffraction lines become better pronounced.

A thermal analysis of salts synthesized at pH 8–10 demonstrated that, with increasing pH, a more stable salt is formed. The endothermic effect (125–135°C) is related to loss of water. At 295–320°C, CO_3^{2-} ions adsorbed by the salt from air are removed. The salt obtained at constant pH 8 is converted to β-$Ca_3(PO_4)_2$ on heat treatment (820°C). Raising the pH to 10 yields a product stable up to 850°C. Synthesis at pH ~ 11 favors formation of a salt stable up to T ~ 1000°C.

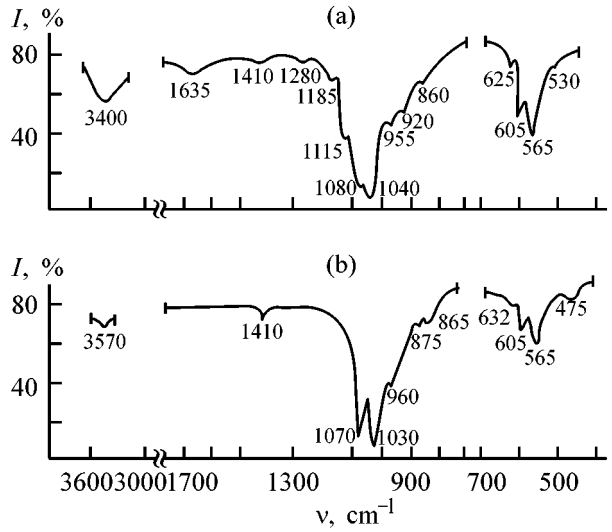

Fig. 2. IR spectra of (a) $Ca_8(HPO_4)_2(PO_4)_4 \cdot 5H_2O$ and (b) calcium-deficient $Ca_{10}(PO_4)_6(OH)_2$. (*I*) intensity and (ν) wave number.

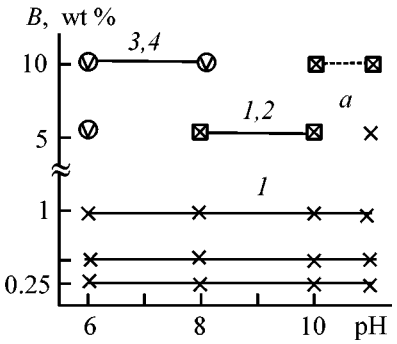

Fig. 3. Characteristics of calcium phosphates precipitated from solutions with various concentrations. (*B*) Initial concentration of CaO and P_2O_5. (*1*) $Ca_{10}(PO_4)_6(OH)_2$, (*2*) poorly crystallized $Ca_{10}(PO_4)_6(OH)_2$, (*3*) calcium-deficient $Ca_{10}(PO_4)_6(OH)_2$, and (*4*) mixture of calcium β-phosphate and diphosphate. (*2*) and (*3*) are only characteristic of an uncalcined material; (*4*) only calcined material.

The synthesis temperature essentially affects the crystallization of salts. We found that stoichiometric $Ca_{10}(PO_4)_6(OH)_2$ is formed in the range 25–75°C at pH 10–11. As temperature increases, the crystal size decreases from 3–5 to less than 1 μm. However, the salt is better crystallized in this case. The IR absorption bands of salts obtained at 75°C are more intensive than those of salts obtained at 25°C. The products have a clear X-ray diffraction pattern with reflections characteristic of $Ca_{10}(PO_4)_6(OH)_2$. According to thermal analysis, salts obtained at a higher temperature are less stable.

CONCLUSION

(1) The obtained data make it possible to forecast conditions for synthesis of calcium phosphates with specified chemical and crystalline structure.

(2) Lowering the concentration of initial solutions and raising the pH and synthesis duration within the limits under study give larger crystals of the products. Thermal treatment of the precipitates results in their structuring and improves the product quality.

REFERENCES

1. Iarcho, M., *J. Mater. Sci.*, 1976, vol. 11, no. 1, pp. 20–27.
2. Groot, K., *Absorption and Surface Chemistry of Hydroxyapatite*, K. de Croot, Ed., CRC Press, BoCa Ration, F.L., 1984, pp. 97–100.
3. Lemure, A., *Phosph. Sulfur. Silicon Relat. Elem.*, 1993, vol. 77, no. 1–4, pp. 288–290.
4. Boskey, A.L. and Posner, A.S., *J. Phys. Chem.*, 1993, vol. 77, no. 19, pp. 2313–2315.
5. Termine, I.D. and Eanes, E.D., *Calc. Tiss. Res.*, 1972, vol. 10, no. 2, pp. 171–175.
6. LeGeros, R.Z. and Le Geros, J.P., *Phosphate Minerals*, Nriagu, J.O. and Moore, P.B., Eds., Berlin: Springer, 1984, pp. 351–385.
7. Brown, W.E. and Chow, L.C., *Ann. Rev. Mater. Sci.*, 1976, vol. 6, no. 6, pp. 213–236.
8. Nancollas, G.H., *Biological Mineralization and Demineralization*, Nancollas, G.H., Ed., Berlin: Springer, 1982, pp. 79–100.
9. Bowsky, A.L. and Posner, A.S., *J. Phys. Chem.*, 1976, vol. 80, no. 1, pp. 40–41.
10. Moreno, E.C. and Varughesi, K., *J. Cryst. Growth.*, 1981, vol. 53, no. 1, pp. 20–30.
11. Feenstra, T.P. and de Bruyn, P.L., *J. Phys. Chem.*, 1979, vol. 83, no. 5, pp. 475–479.
12. Brecevic, L. and Furedi-Milhofer, H., *Calc. Tiss. Res.*, 1972, vol. 10, no. 1, pp. 82–90.
13. Amjad, Z., Koutsoukos, P., Tomson, M.B., and Nancollas, G.H., *J. Dent. Res.*, 1978, vol. 57, no. 1, pp. 9–10.
14. Koutsoukos, P., Amjad, Z., Tomson, M.B., and Nancollas, G.H., *J. Am. Chem. Soc.*, 1980, vol. 102, no. 5, pp. 1553–1557.
15. Dmitrievskii, B.A., Ponomarev, D.V., and Tsvetkov, S.K., *Zh. Prikl. Khim.*, 1996, vol. 69, no. 4, pp. 562–565.
16. Iretskaya, S.N., Yarosh, E.B., Dmitrievskii, B.A., and Ponomarev, D.V., *O vliyanii uslovii sinteza na svoistva gidroksidapatita* (Effect of Synthesis Conditions on the Properties of Hydroxyapatite), Available from VINITI, 1997, no. 808-B97.
17. *Gosudarstvennye standarty SSSR. Udobreniya mineral'nye. Metody analiza* (USSR State Standards. Mineral Fertilizers. Methods of Analysis), *GOST* (State Standards) *20851.1–75–GOST 20851.4–75*, Moscow: Izd. Standartov, 1975.

Russian Journal of Applied Chemistry, Vol. 74, No. 6, 2001, pp. 1061–1063. Translated from Zhurnal Prikladnoi Khimii, Vol. 74, No. 6, 2001, pp. 1031–1033.

BRIEF COMMUNICATIONS

Reactions of Lower Titanium Chlorides with Molten Magnesium-containing Chlorides of Alkaline Metals

V. A. Oleinikova and N. A. Loginov

Institute of High-Temperature Electrochemistry, Ural Division, Russian Academy of Sciences, Yekaterinburg, Russia

Received February 19, 2001

Abstract—Conditional equilibrium constants K_n^* of reactions between titanium chlorides and molten magnesium were calculated.

Various admixtures, particularly metallic magnesium, are removed from chloride wastes of titanium-magnesium industry in the course of their electrochemical processing.

Chloride wastes have various compositions: these may be salts from a titanium chlorinator or waste electrolyte from the carnallite technique for magnesium production with composition (wt %): KCl 78, NaCl 14, $MgCl_2$ 6, and $CaCl_2$ 2, containing magnesium chloride upon reduction of titanium tetrachloride with solidified drops and regulus of metallic magnesium, and also slams from continuous refining furnaces containing more than 15 wt % magnesium [1, 2].

It was of practical interest to calculate the conditional equilibrium constants for the reactions of $TiCl_2$, $TiCl_3$, and $TiCl_4$ with magnesium in molten chlorides of alkaline metals (mp 650°C) in the range 1000–1250 K.

The aim of the calculations was to show that metallic magnesium can react chemically with titanium chlorides in addition to its electrochemical recovery from titanium-magnesium industry wastes.

We calculated temperature dependences of the conditional standard electrode potentials Ti(II)/Ti, Ti(III)/Ti and Ti(IV)/Ti, using equilibrium redox potentials of titanium in alkaline metal melts. The conditional standard electrode potential Mg(II)/Mg was taken from [3].

Equations for $E^*_{M^{n+}/M}$ (V) are shown in Table 1. The conditional equilibrium constants were calculated for the following reactions

Table 1. Temperature dependence of $E_{M^{n+}/M}$ in molten chlorides of alkaline metals (chlorine reference electrode)

Salt medium	$E^*_{M^{n+}/M}$, V	Reference	Salt medium	$E^*_{M^{n+}/M}$, V	Reference
	$E^*_{Ti(II)/Ti}$			$E^*_{Ti(IV)/Ti}$	
NaCl–KCl	$-2.51 + 5.6 \times 10^{-4}T \pm 0.006$	[4]	NaCl–KCl	$-2.05 + 3.5 \times 10^{-4}T \pm 0.02$	[4]
KCl	$-2.60 + 6.0 \times 10^{-4}T \pm 0.006$		KCl	$-2.09 + 3.8 \times 10^{-4}T \pm 0.02$	
CsCl	$-2.67 + 6.2 \times 10^{-4}T \pm 0.006$		CsCl	$-2.12 + 3.5 \times 10^{-4}T \pm 0.02$	
	$E^*_{Ti(III)/Ti}$			$E^*_{Mg(II)/Mg}$	
NaCl–KCl	$-2.24 + 3.5 \times 10^{-4}T \pm 0.006$	[4]	NaCl–KCl	$-3.26 + 5.63 \times 10^{-4}T \pm 0.01$	[3]
KCl	$-2.33 + 3.7 \times 10^{-4}T \pm 0.006$		KCl	$-3.32 + 5.7 \times 10^{-4}T \pm 0.01$	
CsCl	$-2.43 + 3.9 \times 10^{-4}T \pm 0.006$		CsCl	$-3.412 + 6.07 \times 10^{-4}T \pm 0.01$	

1070-4272/01/7406-1061 $25.00 © 2001 MAIK "Nauka/Interperiodica"

Table 2. Temperature dependence of conditional equilibrium constants K_n^* of reactions (1)–(3)

Salt melt	T, K	$\log K_1^*$	$\log K_2^*$	$\log K_3^*$
NaCl–KCl	1000–1200	–0.030 + 7561/T	–6.442 + 30847/T	–4.294 + 24395/T
KCl	1100–1250	0.302 + 7258/T	–6.048 + 29940/T	–3.831 + 24798/T
CsCl	1000–1200	0.131 + 7480/T	–6.563 + 29698/T	–5.182 + 26048/T

Table 3. Characteristics of reactions (1)–(3) in molten chlorides of alkaline metals

T, K	K_1^*	$-\Delta G_p^*$	K_2^*	$-\Delta G_p^*$	K_3^*	$-\Delta G_p^*$
	reaction (1)		reaction (2)		reaction (3)	
	Equimolar mixture NaCl–KCl					
1000	3.4×10^7	144.2	2.5×10^{24}	467.3	1.3×10^{20}	384.9
1050	1.48×10^7	144.2	8.6×10^{22}	461.1	8.7×10^{18}	380.7
1100	6.98×10^6	144.1	4.0×10^{21}	454.9	7.6×10^{17}	376.6
1150	3.51×10^6	144.1	2.4×10^{20}	448.8	8.3×10^{16}	372.5
1200	1.87×10^6	144.0	1.8×10^{19}	442.6	1.1×10^{16}	368.4
	Potassium chloride					
1100	7.95×10^6	145.3	1.5×10^{21}	445.9	5.2×10^{18}	394.1
1150	4.10×10^6	145.6	9.7×10^{19}	440.1	5.4×10^{17}	390.4
1200	2.24×10^6	145.9	8.0×10^{18}	434.3	6.8×10^{16}	386.8
1250	1.28×10^6	146.2	8.0×10^{17}	428.5	1.0×10^{16}	383.1
	Cesium chloride					
1000	4.08×10^7	145.7	1.4×10^{23}	442.9	7.3×10^{20}	399.5
1050	1.80×10^7	145.9	5.3×10^{21}	436.6	4.2×10^{19}	394.5
1100	8.53×10^6	146.0	2.7×10^{20}	430.4	3.1×10^{18}	389.6
1150	4.32×10^6	146.1	1.8×10^{19}	424.1	2.9×10^{17}	384.6
1200	2.31×10^6	146.2	1.5×10^{18}	417.8	3.3×10^{16}	379.7

$$TiCl_{2(melt)} + Mg_{(l)} = MgCl_{2(melt)} + Ti_{(s)}, \quad (1)$$

$$\log K_1^* = \frac{2 \times 10^4}{1.984\,T}\,(E^*_{Ti(II)/Ti} - E^*_{Mg(II)/Mg});$$

$$TiCl_{3(melt)} + 3Mg_{(l)} = 3MgCl_{2(melt)} + 2Ti_{(s)}, \quad (2)$$

$$\log K_2^* = \frac{6 \times 10^4}{1.984\,T}(E^*_{Ti(III)/Ti} - E^*_{Mg(II)/Mg});$$

$$TiCl_{4(melt)} + 2Mg_{(l)} = 2MgCl_{2(melt)} + Ti_{(s)}, \quad (3)$$

$$\log K_3^* = \frac{4 \times 10^4}{1.984\,T}(E^*_{Ti(IV)/Ti} - E^*_{Mg(II)/Mg}).$$

The calculated data for various salt systems are shown in Table 2 and, in more detail, for reactions (1) and (2), in Table 3, where the changes in Gibbs energy (J mol^{-1}) are also given, as calculated by the expression:

$$\Delta G_r^* = -4.576 \times 4.184\,T \log K_n^*.$$

Values of K_n^* for reactions (1), (2), and (3) decrease with temperature. For the series (NaCl–KCl)–KCl–CsCl the values of K_1^* at 1100 K are 6.98×10^6, 7.95×10^6, 8.53×10^6, and those of K_2^* are 4.0×10^{21}, 1.5×10^{21}, and 2.7×10^{20}, respectively, K_2^* being greater than K_1^* by 14–15 orders of magnitude.

The value of K_3^* for a NaCl–KCl melt in the range 1000–1200K varies from 1.3×10^{20} to 1.1×10^{16}, for a KCl melt at 1100–1250 K—from 5.2×10^{18} to 1.0×10^{16}, and for a CsCl melt at 1000–1200 K—from 7.3×10^{20} to 3.3×10^{16}, i.e., the process may occur to a rather great extent (Table 3).

The interactions of the components are rather complicated, the above equations of reactions are only stoichiometric relationships. The melt contains complex ions (MCl_4^{3-}, $TiCl_3^-$, $TiCl_4^{2-}$, $TiCl_5^{2-}$, $TiCl_6^{3-}$, $TiCl_5^-$, $TiCl_6^{2-}$, $MgCl_4^{2-}$, etc.), which can variously affect each other and react with each other. These com-

plex ions have different bonding energies Ti^{4+}–Cl^-, Ti^{3+}–Cl^-, and Ti^{2+}–Cl^- and vibrational frequencies.

CONCLUSIONS

(1) The conditional equilibrium constants for the reactions of titanium chlorides with magnesium in various salt media were calculated using experimental and published data on conditional standard electrode potentials $E^*_{M^{n+}/M}$.

(2) The reactions are rather complicated and depend on a number of factors such as concentrations of components, temperature, nature of salt-solvent, etc.

REFERENCES

1. Sushenkov, V.P., Olesov, Yu.G., and Devyatkin, V.N., *Rasplavy*, 1992, no. 2, pp. 76–78.
2. Sushenkov, V.P., Ryabukhin, Yu.M., Zabelin, I.V., and Olesov, Yu.G., Abstracts of Papers, *VII Vsesoyuznaya konferentsiya po elektrokhimii* (VII All-Union Conference on Electrochemistry), Chernovtsy, 1988, vol. 3, p. 131.
3. Lebedev, V.A., *Izbiratel'nost' zhidkometallicheskikh elektrodov v rasplavlennykh galogenidakh* (Selectivity of Liquid-Metal Electrodes in Molten Halides), Chelyabinsk: Metallurgiya, 1993.
4. Smirnov, M.V., *Elektrodnye potentsialy v rasplavlennykh khloridakh* (Electrode Potentials in Molten Chlorides), Moscow: Nauka, 1973.

Russian Journal of Applied Chemistry, Vol. 74, No. 6, 2001, pp. 1064–1065. Translated from Zhurnal Prikladnoi Khimii, Vol. 74, No. 6, 2001, pp. 1034–1035.

BRIEF COMMUNICATIONS

High-Performance Gas Diffusion Electrode

A. Gawdzik, S. Gaida, N. M. Yurchuk, and A. N. Sofronkov

University of Opole, Poland
Odessa State Academy of Food Technology, Odessa, Ukraine

Received May 17, 1999; in final form, January 2000

Abstract—A high-performance gas diffusion electrode is fabricated by hot pressing with an asbestos laying used to provide uniform load in the process. The electrode was studied in cathodic reduction of oxygen in acidic electrolyte at various temperatures.

In fabrication of high-performance gas diffusion electrodes, the necessary condition is to ensure the maximal efficiency of a supported catalyst, particularly in the cases when electrocatalysis proceeds at a low rate. It is known [1–3] that the polarization can be diminished and the rate of an electrochemical reaction raised by making larger the surface of the catalyst–gas–electrolyte interface.

To raise the activity of oxygen reduction electrodes, we fabricated a composite with a porous structure, including two types of pores: hydrophilic pores formed by a carbon-supported catalyst and hydrophobic pores formed by a mixture of carbon black and fluoroplastic. As a carbonaceous support we used acetylene carbon black with a specific surface area of 200 $m^2 g^{-1}$. The electrodes were tested in sulfuric and phosphoric acid solutions. Carbon black was pretreated by roasting at 873°C, followed by boiling for 3 h in nitric acid for hydrophilization. Hydrophobization of acetylene carbon black was performed by mixing with a suspension of fluoroplastic in Sintanol (Sintanol-10 : fluoroplastic = 3 : 1). After intimate mixing, the surfactant Sintanol-10 was removed by heating. The catalyst was applied by impregnation of the electrode with a soluble salt of a metal of variable oxidation state, followed by treatment with an alkaline solution (pH ~13.0) of sodium borohydride [4].

The electrode was formed by hot pressing of the hydrophobic and hydrophilic layers at 773°C under a pressure of 5 kg cm^{-2}, using an asbestos laying to ensure uniform load over the entire electrode area. A currentcollecting copper grid (annealed in hydrogen) was arranged within the hydrophilic layer. The catalyst surface density in the reaction zone was 0.5 mg cm^{-2}.

The polarization curves of cathodic oxygen reduction were recorded in the potentiostatic mode at 298 and 333°C under atmospheric pressure. Typical polarization curves are presented in the figure. For all of the tested electrodes we observed a linear dependence of φ on *i* over the entire polarization range.

The effective surface area *S* (μF m^{-2}) of the catalyst and the number of active sites *n* were estimated from the charging curves [5] as

$$n = \frac{Q}{96\,500} \times 6.023 \times 10^{23}, \quad S = \frac{C}{C_S} = \frac{C}{1120},$$

where *C* is the capacitance of the working electrode.

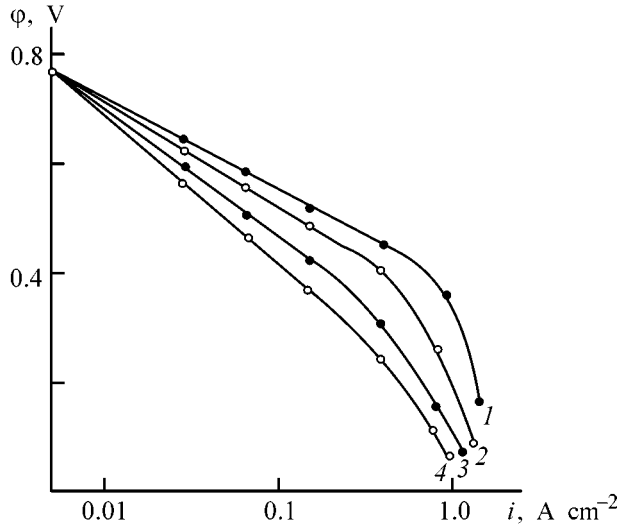

Polarization curves of cathodic oxygen reduction in sulfuric acid. (φ) Polarization and (*i*) current density. Hydrophilic to hydrophobic constituent ratio: (*1*) 2 : 3, (*2*) 7 : 3, (*3*) 5 : 5, and (*4*) 3 : 7.

1070-4272/01/7406-1064 $25.00 © 2001 MAIK "Nauka/Interperiodica"

The catalyst efficiency was defined by

$$\Pi = S/S^0,$$

where S is the effective surface area of the catalyst and S^0 is the total catalyst surface area obtained either for the supported electrode (1 : 1) or for a carbon-supported electrode hydrophobized with fluoroplastic (9 : 1), in which all the clusters are wetted by the electrolyte.

The amount of the electrolyte in the reaction zone of the electrode was estimated from the electrode weight before and after testing.

The electrodes fabricated using the proposed technique are formed of a mixture of the supported catalyst and fluoroplastic in which individual pores are not wetted by the electrolyte because of their high hydrophobicity. As a result, catalytic clusters are formed that are not involved in the reaction (their content may be up to 30% of the total). The proposed electrode fabrication technique ensures easy access of the electrolyte to the catalyst. In this case, the degree of filling with the electrolyte is well consistent with the experimental Π. The shares of the hydrophobic and hydrophilic structures of the active layer were chosen so as to ensure the minimum thickness of the reaction zone to minimize the diffusion component of the polarization. The figure shows that the electrode efficiency strongly depends on the hydrophilic to hydrophobic layer thickness ratio, reaching the maximum at the ratio of 2 : 3.

Cathodic oxygen reduction in a sulfuric acid electrolyte has been extensively studied previously [6–8]. Two portions were found in the Tafel curves. The first is described by the dependence $d\varphi/d\log i = -2.3RT/F$, and the second (for more positive potentials), by $2(-2.3RT)/F$. The transition point is at $\varphi = 0.85$ V, which corresponds to a changeover of the adsorption isotherm type from that described by the Temkin equation to the Langmuir isotherm [9].

For the electrodes under study the slope of the polarization curves is about 0.65 V at $\varphi > 0.85$ V. If oxygen reduction is kinetic- and diffusion-controlled, the slope is higher by a factor of 2.0–2.5 as compared to the purely kinetic mode.

To conclude, the maximum electrode efficiency is attained by minimizing the thickness of the reaction zone at the gas–electrolyte interface. This is ensured by the structure of the active layer containing a carbon-supported catalyst and hydrophobic pores formed in a mixture of carbon black and fluoroplastic taken at certain ratios.

REFERENCES

1. Vielstich, W., *Brennstoffelemente*, Weinheim: Chemie, 1965.
2. Justi, E.W. and Winsel, A.W., *Kalte Verbrennung Fuel Cells*, Wiesbaden: Steiner, 1962.
3. *Fuel Cells*, Mitchell, W., Ed., New York: Academic, 1963.
4. Labunets, V.F., Voloshin, L.G., and Kindrachuk, M.V., *Iznosostoikie boridnye pokrytiya* (Durable Boride Coatings), Kiev: Tekhnika, 1989.
5. Vetter, K.J., *Electrochemische Kinetik*, Berlin: Springer, 1961.
6. Nekrasov, L.N., *Toplivnye elementy: Kinetika elektrodnykh protsessov* (Fuel Cells: Kinetics of Electrode Processes), Moscow: Nauka, 1968, p. 121.
7. Podzhlovchenko, B.I., *Itogi Nauki Tekh., Ser.: Elektrokhimiya*, 1981, no. 18.
8. Newman, J.S., *Electrochemical Systems*, Englewood Cliffs (NJ): Prentice-Hall, 1973.
9. Boreskov, K., *Geterogennyi kataliz* (Heterogeneous Catalysis), Moscow: Nauka, 1986.

Russian Journal of Applied Chemistry, Vol. 74, No. 6, 2001, pp. 1066–1067. Translated from Zhurnal Prikladnoi Khimii, Vol. 74, No. 6, 2001, pp. 1035–1037.

BRIEF COMMUNICATIONS

7-Aminoheptanoic and 8-Aminooctanoic Acid Esters

A. Hrabálek, P. Doležal, and M. Mahacek

Pharmaceutical Faculty, Karlov University, Gradec Kralowe, Czechia

Received April 6, 2001

Abstract—A procedure was developed for preparing esters of secondary alcohols with 7-aminoheptanoic and 8-aminooctanoic acids.

Esters of primary alcohols with 7-aminoheptanoic and 8-aminooctanoic acids raise the permeability of skin [1, 2]. Also, such compounds are of interest as starting substances in synthesis of dendrimers by the convergence scheme when the dendrimer branches (dendrons) are prepared first and are then linked to the dendrimer core [3].

Proceeding with studies of compounds of this class, we developed a simple route to esters of secondary alcohols with 7-aminoheptanoic and 8-aminooctanoic acids, involving treatment of appropriate alcohols with amino acid chloride hydrochlorides in dry chloroform, followed by conversion of the resulting hydrochlorides to free amino esters by treatment with triethylamine:

$$\bar{Cl} \cdot H_3\overset{+}{N}(CH_2)_nCOOH + SOCl_2 \rightarrow \bar{Cl} \cdot H_3\overset{+}{N}(CH_2)_nCOCl$$

$$\xrightarrow[2.\,(C_2H_5)_3N]{1.\,CH_3(CH_2)_mCHOHCH_3} H_2N(CH_2)_nCOOCH(CH_2)_mCH_3,\ \ CH_3$$

I–VIII

where $n = 6$, $m = 4$ (**I**), $m = 5$ (**II**), $m = 6$ (**III**), $m = 7$ (**IV**); $n = 7$, $m = 4$ (**V**), $m = 5$ (**VI**), $m = 6$ (**VII**), $m = 7$ (**VIII**).

The required acid chlorides were prepared from the corresponding amino acid hydrochlorides, since conversion to the hydrochloride is the simplest and the most efficient way to protect the N–H bond [4]. The amino acid hydrochlorides were treated with thionyl chloride at 30–35°C (at higher temperatures the reaction is accompanied by polymerization). Esters of 7-tetradecanol with 7-aminoheptanoic (**IX**) and 8-aminooctanoic (**X**) acids were prepared similarly.

After being purified by column chromatography, all the esters are colorless highly viscous oils; yield 55–75%.

Tests performed according to [5] showed that amino esters **I**–**X** are less active, compared with the corresponding esters of isomeric primary alcohols, as agents raising the permeability of skin.

EXPERIMENTAL

The starting hydrochlorides of 7-aminoheptanoic and 8-aminooctanoic acids were prepared by acid hydrolysis of the corresponding lactams [6]. The IR spectra were taken on a Nicolet Impact 400 IR spectrophotometer in $CDCl_3$, and the ^1H NMR spectra, on a Tesla BS 497 spectrometer in $CDCl_3$ (internal reference TMS).

7-Tetradecyl 8-aminooctanoate (X). A solution of 1.96 g (0.01 mol) of 8-aminooctanoic acid hydrochloride in 15 ml of thionyl chloride was stirred for 0.5 h at 30–35°C. Excess thionyl chloride was removed in a vacuum, and the residue was treated with absolute toluene (30 ml). After removal of toluene, 2.14 g (0.01 mol) of 7-tetradecanol in 40 ml of absolute chloroform was added, the mixture was refluxed for 3 h with stirring, the solvent was removed, and the residue was dried in a vacuum desiccator over KOH. The crude amino ester hydrochloride was dissolved in 50 ml of water, and the aqueous phase was washed with diethyl ether (3 × 20 ml) and treated with 20 ml of triethylamine. Amino ester **X** was extracted with diethyl ether (3 × 20 ml), the combined extract was dried over magnesium sulfate, the solvent was removed, and the residue was purified chromatographically on crystalline cellulose (0.02–0.05 mm, 50 g); eluent diethyl ether. Yield of amino ester **X** 2.21 g

1070-4272/01/7406-1066 $25.00 © 2001 MAIK "Nauka/Interperiodica"

(62%). IR spectrum, ν, cm^{-1}: 1378, 1464, 1720, 2820, 2850, 2920, 2958. ^1H NMR spectrum, δ, ppm: 0.89 t (6H, $2CH_3$, *J* 6.5 Hz), 1.20–1.80 m (34H, $6CH_2$ + $5CH_2$ + $5CH_2$ + NH_2), 2.31 t (2H, CH_2CO, *J* 6.5 Hz), 2.73 br.s (2H, CH_2N), 4.91 m (1H, OCH).

Found, %: C 74.56, 74.60; H 13.01, 13.20; N 3.64, 3.75.

$C_{22}H_{45}NO_2$.

Calculated, %: C 74.37, H 12.68, N 3.94.

Compounds **I**–**X** were prepared similarly.

2-Heptyl 7-aminoheptanoate (I). IR spectrum, ν, cm^{-1}: 1378, 1468, 1720, 2820, 2850, 2920, 2958. ^1H NMR spectrum, δ, ppm: 0.88 t (3H, CH_3, *J* 6.5 Hz), 1.20 d (3H, CH_3, *J* 6.5 Hz), 1.27 m (8H, $4CH_2$), 1.46 m (8H, $4CH_2$), 1.80 br.s (2H, NH_2), 2.31 t (2H, CH_2CO, *J* 6.5 Hz), 2.72 br.s (2H, CH_2N), 4.90 m (1H, OCH).

2-Octyl 7-aminoheptanoate (II). IR spectrum, ν, cm^{-1}: 1377, 1468, 1720, 2818, 2850, 2922, 2958. ^1H NMR spectrum, δ, ppm: 0.88 t (3H, CH_3, *J* 6.5 Hz), 1.21 d (3H, CH_3, *J* 6.5 Hz), 1.28 m (10H, $5CH_2$), 1.46 m (8H, $4CH_2$), 1.85 br.s (2H, NH_2), 2.31 t (2H, CH_2CO, *J* 6.5 Hz), 2.72 br.s (2H, CH_2N), 4.91 m (1H, OCH).

2-Nonyl 7-aminoheptanoate (III). IR spectrum, ν, cm^{-1}: 1378, 1467, 1719, 2820, 2855, 2924, 2962. ^1H NMR spectrum, δ, ppm: 0.89 t (3H, CH_3, *J* 6.5 Hz), 1.20 d (3H, CH_3, *J* 6.5 Hz), 1.29 m (12H, $6CH_2$), 1.46 m (8H, $4CH_2$), 1.80 br.s (2H, NH_2), 2.32 t (2H, CH_2CO, *J* 6.5 Hz), 2.74 br.s (2H, CH_2N), 4.92 m (1H, OCH).

2-Decyl 7-aminoheptanoate (IV). IR spectrum, ν, cm^{-1}: 1378, 1468, 1726, 2820, 2848, 2920, 2954. ^1H NMR spectrum, δ, ppm: 0.89 t (3H, CH_3, *J* 6.5 Hz), 1.21 d (3H, CH_3, *J* 6.5 Hz), 1.29 m (14H, $7CH_2$), 1.46 m (8H, $4CH_2$), 1.77 br.s (2H, NH_2), 2.31 t (2H, CH_2CO, *J* 6.5 Hz), 2.72 br.s (2H, CH_2N), 4.92 m (1H, OCH).

7-Tetradecyl 7-aminoheptanoate (IX). IR spectrum, ν, cm^{-1}: 1375, 1466, 1720, 2820, 2850, 2918, 2958. ^1H NMR spectrum, δ, ppm: 0.89 t (6H, $2CH_3$, *J* 6.5 Hz), 1.20–1.80 m (32H, $6CH_2$ + $5CH_2$ + $4CH_2$ + NH_2), 2.32 t (2H, CH_2CO, *J* 6.5 Hz), 1.80 br.s (2H, NH_2), 2.73 br.s (2H, CH_2N), 4.90 m (1H, OCH).

2-Heptyl 8-aminooctanoate (V). IR spectrum, ν, cm^{-1}: 1378, 1468, 1720, 2819, 2850, 2920, 2956. ^1H NMR spectrum, δ, ppm: 0.89 t (3H, CH_3, *J* 6.0 Hz), 1.20 d (3H, CH_3, *J* 6.0 Hz), 1.28 m (10H, 5 CH_2), 1.46 m (8H, $4CH_2$), 1.80 br.s (2H, NH_2), 2.32 t (2H, CH_2CO, *J* 6.5 Hz), 2.72 br.s (2H, CH_2N), 4.90 m (1H, OCH).

2-Octyl 8-aminooctanoate (VI). IR spectrum, ν, cm^{-1}: 1378, 1465, 1720, 2826, 2854, 2922, 2955. ^1H NMR spectrum, δ, ppm: 0.88 t (3H, CH_3, *J* 6.0 Hz), 1.20 d (3H, CH_3, *J* 6.0 Hz), 1.28 m (10H, 5 CH_2), 1.46 m (10H, $5CH_2$), 1.85 br.s (2H, NH_2), 2.32 t (2H, CH_2CO, *J* 6.5 Hz), 2.73 br.s (2H, CH_2N), 4.91 m (1H, OCH).

2-Nonyl-8-aminooctanoate (VII). IR spectrum, ν, cm^{-1}: 1378, 1468, 1720, 2825, 2852, 2920, 2954. ^1H NMR spectrum, δ, ppm: 0.88 t (3H, CH_3, *J* 6.5 Hz), 1.20 d (3H, CH_3, *J* 6.5 Hz), 1.29 m (12H, $6CH_2$), 1.46 m (10H, $5CH_2$), 1.85 br.s (2H, NH_2), 2.30 t (2H, CH_2CO, *J* 6.5 Hz), 2.73 br.s (2H, CH_2N), 4.92 m (1H, OCH).

2-Decyl 8-aminooctanoate (VIII). IR spectrum, ν, cm^{-1}: 1378, 1470, 1722, 2821, 2853, 2925, 2936. ^1H NMR spectrum, δ, ppm: 0.89 t (3H, CH_3, *J* 6.5 Hz), 1.20 d (3H, CH_3, *J* 6.5 Hz), 1.28 m (14H, $7CH_2$), 1.46 m (10H, $5CH_2$), 1.80 br.s (2H, NH_2), 2.32 t (2H, CH_2CO, *J* 6.5 Hz), 2.74 br.s (2H, CH_2N), 4.92 m (1H, OCH).

ACKNOWLEDGMENTS

The authors are grateful to Dr. P. Mericka, Mrs. J. Zizkova, and Mrs. J. Fendrichova for assistance in the work and to the Scientific Foundation of the Karlov University (grant no. 24/1999/B CH/FaF) and Ministry of Education of the Czech Republic (grant no. 111 600 001) for financial support.

REFERENCES

1. Doležal, P., Hrabálek, A., and Semecký, V., *Pharm. Res.*, 1993, vol. 10, no. 7, pp. 1015–1019.
2. Hrabálek, A., Doležal, P., Roman, M., *et al.*, *Pharmazie*, 1994, vol. 49, no. 5, pp. 325–328.
3. Beletskaya, I.P. and Chuchuryukin, A.V., *Usp. Khim.*, 2000, vol. 69, no. 8, pp. 699–720.
4. Greene, T.W. and Wuts, P.G.M., *Protective Groups in Organic Synthesis*, New York: Wiley, 1999.
5. Franz, T.J., *Invest. Dermatol.*, 1975, vol. 64, pp. 190–195.
6. Ruzicka, L., Kobelt, M., Höflinger, O., and Prelog, V., *Helv. Chim. Acta*, 1949, vol. 32, pp. 544–552.

Russian Journal of Applied Chemistry, Vol. 74, No. 7, 2001, pp. 1069–1075. Translated from Zhurnal Prikladnoi Khimii, Vol. 74, No. 7, 2001, pp. 1041–1047.

INORGANIC SYNTHESIS AND INDUSTRIAL INORGANIC CHEMISTRY

Production of High-Purity Potassium by Vacuum Distillation with Dephlegmation

E. P. Lokshin

Tananaev Institute of Rare Element and Mineral Chemistry and Technology, Kola Research Center, Russian Academy of Sciences, Apatity, Murmansk oblast, Russia

Received January 31, 2000; in final form, May 2001

Abstract—A procedure was developed for evaluating the efficiency of substance purification by vacuum distillation with vapor dephlegmation in a heated condenser. A technology and apparatus are proposed for obtaining high-purity potassium by this method. The potassium quality is assessed using a set of chemical and physical techniques.

High-purity potassium is necessary for manufacture of photoelectric devices, illuminating lamps, high-temperature heat pipes, and low-melting heat carriers. The quality of technical-grade potassium, produced in conformity with GOST (State Standard) 10588–75 and containing up to 2 wt % Na and 0.8 wt % heavy metals (in terms of lead), gives no way of using it in manufacture of some kinds of materials and apparatus and performing precision scientific investigations. In addition to the controlled impurities, technical-grade potassium contains oxides, carbonates, calcium, organic impurities, chloride and hydroxide ions, and a number of other impurities.

For purifying potassium to remove oxygen, hydrogen, calcium, magnesium, iron, titanium, and other impurities, it has been proposed to make impurities pass into metallic lithium, which is poorly soluble in potassium [1, 2]. However, the achieved purification level (Ca 0.003, Mg 0.003, Fe 0.0005 wt %) was insufficient, and the consumption of lithium (in volume ratio of 1 : 1 to potassium to be purified), high, with its content in the purified potassium not determined. Zone smelting was found to be inefficient for deep purification of potassium [3].

Although the distillation methods are more versatile, equilibrium distillation cannot ensure, judging from the separation coefficients calculated with account of component activities of sodium–potassium alloys [4], deep purification of potassium to remove sodium impurity. Introduction of oxygen into technical-grade potassium in an amount no less than that stoichiometrically necessary for sodium oxidation makes higher the degree of potassium purification to remove sodium in subsequent distillation; however, the residual content of sodium is in this case more than 0.01 wt % [5].

It has been reported that distillation in a column was used to obtain potassium with Na impurity content less than 1%, from which 99.99% purity potassium was produced by further purification. However, no information about the employed technology of deep purification and analytical procedures was given. For the potassium manufactured abroad, its guaranteed content is at the level of 99.95 wt % (see catalogs of Aldrich, US; Fluka, Switzerland, etc.) Distillation of potassium containing 0.3–1.0 wt % sodium at residual gas pressure of 100 Pa in a column filled to a height of 1000 mm with steel ring packing gave a product containing (wt %) Na 0.015–0.05, Fe $\geq$0.002, SO_4^{2-} $\geq$0.004, and Cl 0.0013–0.0064 [7].

The aim of this study was to develop an industrial technology for manufacture of high-purity potassium with content of sodium impurity not exceeding 0.01 wt % at the minimum possible amount of other impurities. As starting materials were used technical-grade potassium and potassium–sodium alloys obtained as wastes in distillation of cesium–rubidium–potassium–sodium alloys of varied composition [8]. The possibilities of the previously proposed method of vacuum distillation with equilibrium dephlegmation of vapor in a heated condenser were studied. In this process, the temperature and vapor pressure of the substance being purified markedly vary between different apparatus zones. Since the procedure for evaluating the efficiency of component separation in this process has not been reported previously, it is

1070-4272/01/7407-1069$25.00

described here for the example of potassium–sodium alloys.

EXPERIMENTAL

The composition of the initial vapor in the equilibrium distillation process is determined by the composition of the starting alloy and the process temperature. In condensation of an infinitely small amount of vapor, the material balance equation has the form [10]

$$yG = (G - dL)(y + dy) + x dL,$$

whence follows

$$dy = dL(y - x)/G. \quad (1)$$

Equation (1) allows evaluation of the content of the low-boiling component (LBC) in the vapor at varied fraction of the condensed product on the basis of the known analytical dependence $f(x)$. This equation has been used previously in the cases when vapor dephlegmation was performed at constant pressure, since in this case it can be solved using the graphical dependence $y = f(x)$. If the distillation process with dephlegmation is performed in a vacuum, with the vapor temperature and pressure steadily decreasing, this way of solving Eq. (1) is inapplicable.

Let us assume that the initial vapor contains an insignificant amount of impurity. Then it may be considered that the molecular weight of the vapor after dephlegmation is equal to that of the initial vapor, and the vapor pressure is determined by the vapor pressure of the basic component of the alloy. The vapor pressure of pure alkali metals is described with high precision by the equation

$$\ln P = A - B/T. \quad (2)$$

The amount of vapor coming in unit time to dephlegmation is given by the Langmuir equation

$$G = \alpha SP(M/2\pi RT)^{1/2}, \quad (3)$$

where M is the molecular weight of vapor, S is the evaporation (condensation) surface area, P is the vapor pressure at temperature T, R is the universal gas constant, and α is the coefficient of evaporation (condensation). Eliminating T from expression (3) with the use of relation (2), we obtain

$$G = \alpha SP[M(A - \ln P)/2\pi RB]^{1/2}, \quad (4)$$

whence follows

$$dL = -dG = \alpha SP(M/2\pi RB)^{1/2} \times [(A - \ln P) - 0.5](A - \ln P)^{-1/2} dP. \quad (5)$$

Substituting (4) and (5) into Eq. (1), we have

$$dy = \frac{-(A - 0.5) + \ln P}{P(A - \ln P)}(y - x)dP. \quad (6)$$

At low impurity contents, the Henry law is valid, and, consequently, in the case of LBC purification to remove a high-boiling component (HBC),

$$y = \beta x + (1 - \beta),\ 0 < \beta < 1; \quad (7)$$

and in the case of HBC purification to remove LBC,

$$y = \beta x,\ \beta > 1. \quad (8)$$

In Eqs. (7) and (8), $\beta = f(P)$.

With x eliminated from Eq. (6) with the use of relations (7) and (8), the equation

$$\ln\frac{1 - y_2}{1 - y_1} = -\int_{P_1}^{P_2} \frac{(A - 0.5) - \ln P}{P(A - \ln P)} \frac{1 - \beta}{\beta} dP \quad (9)$$

is valid for the case of LBC purification to remove HBC, and

$$\ln\frac{y_2}{y_1} = -\int_{P_1}^{P_2} \frac{(A - 0.5) - \ln P}{P(A - \ln P)} \frac{\beta - 1}{\beta} dP, \quad (10)$$

for the case of HBC purification to remove LBC. Indices 1 and 2 denote, respectively, the initial and final stages.

Equation (9) makes it possible to calculate by how many times decreases the HBC content in the vapor $[(1 - y_2)/(1 - y_1) = 1/K]$, and Eq. (10), by how many times the vapor is enriched with LBC. $y_2/y_1 = K$, depending on the dephlegmation process parameters.

Equations (9) and (10) were applied to evaluate the efficiency of sodium purification to remove potassium impurity and potassium purification to remove sodium impurity.

The temperature dependences of the vapor pressure, obtained by processing of the recommended experi-

Table 1. Coefficients in Eq. (2)*

Metal	Coefficient		*T*, K
	A	*B*	
Na	8.1526	2331	583–943
K	7.9451	1891	553–943

* Pressure given in pascals.

mental values [11] and used in our calculations, are presented in Table 1.

The approximate interpolation equations $\beta = f(P)$ (Table 2) were obtained from the $y = f(x)$ diagrams calculated for the sodium–potassium system with account of the component activities in the melt.

The equations obtained upon substitution of the dependences $\beta = f(P)$ into formulas (9) and (10) were integrated approximately, using the method of trapezoids.

The results of calculations are presented in Figs. 1a and 1b. Figure 1a shows how grows the logarithm of the content of potassium impurity in sodium, and Fig. 1b, how decreases the logarithm of the content of sodium impurity in potassium, in equilibrium dephlegmation of saturated vapor in the case of cooling of a saturated vapor in a prescribed temperature range. For this purpose, it suffices to subtract from the ordinate corresponding to the higher temperature that corresponding to the lower temperature.

As seen from Figs. 1a and 1b, the purification efficiency depends on the degree of dephlegmation. In cooling a vapor by a certain temperature difference, it also depends on the initial vapor temperature: the lower the initial temperature, the more efficient the separation (concentration) of the impurity in dephlegmation. However, on lowering the initial temperature of the vapor, its amount decreases, as also does, consequently, the process productivity.

With the content of impurity in the starting metal increasing beyond the limits in Table 2, the process efficiency must decrease because of the unfavorable change in the coefficients *K* in Eqs. (9) and (10). Indeed, in the case of LBC purification to remove HBC, β grows with the impurity content increasing beyond the limiting value, and, consequently, falls the factor $(1 - \beta)/\beta$ in Eq. (9), i.e., the numerator decreases remaining positive and the denominator increases. In a similar way decreases the factor $(\beta - 1)/\beta$ in Eq. (10) with increasing LBC content, because of the decrease in the β value in this case.

With a knowledge of how the impurity content varies with (or, in fact, the separation coefficients depend on) the conditions under which the equilibrium dephlegmation is performed, we can find the composition of the products formed in the process. Let us denote by x the mole fraction of LBC in the metal being distilled, by y the mole fraction of LBC in the vapor remaining after dephlegmation, and by W the amount of the metal being distilled.

Let dW of vapor be removed from the process in an infinitely short time. If the amount of metal present in the dephlegmator in the form of vapor and reflux is neglected, then the material balance equation has the form

$$xW = (W - dW)(x - dx) + y dW,$$

whence follows

$$dW/W = dx/(y - x). \quad (11)$$

Equation (11) is virtually identical to the Rayleigh equation [10] for equilibrium distillation, differing only in the type of the $y = f(x)$ dependence. In calculations, the purification in the metal evaporation stage was disregarded since the efficiency of equilibrium distillation is low at high temperatures.

It was shown above that the change in the impurity content in the course of vapor dephlegmation is only

Table 2. $\beta = f(P)$ dependences

Metal		Applicability limits			$\beta = f(P)$	rms deviation of $\beta = f(P)$ values from reference points, %
base	impurity	*P*, Pa	limiting impurity content			
			at. %	wt %		
Na	K	0.66–130	2.5	4.18	$e^{2.2192} - 28.37P$	5.74
Na	K	130–13 000	2.5	4.18	$e^{2.2192} - 19.33P$	3.2
K	Na	0.66–13 000	25	16.4	$e^{2.0026} + 23.61P$	4.67

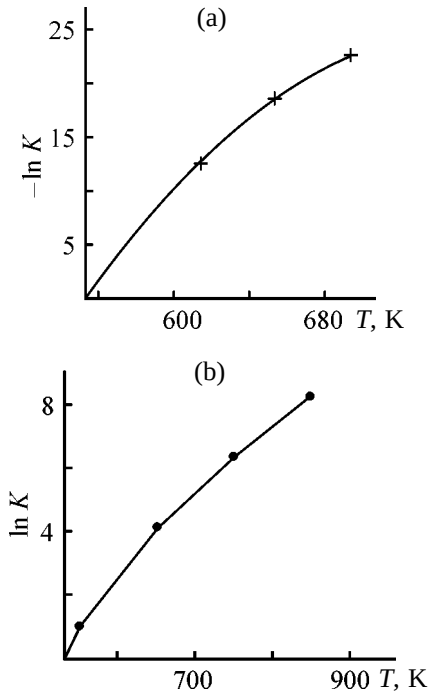

Fig. 1. Concentrations of (a) sodium impurity in potassium and (b) potassium impurity in sodium upon vapor cooling from temperature T to 553 K. (K) Separation coefficient.

determined by the initial and final temperatures of the vapor, but is independent of its composition in a wide range of impurity concentrations, which makes it possible to solve Eq. (11). Let us consider these solutions separately for the cases of LBC purification to remove HBC impurity and HBC purification to remove LBC impurity.

In the case of LBC purification to remove HBC impurity, we obtain, assuming that the composition of the vapor coming to dephlegmation is identical to the composition of the metal being purified and disregarding the purification in the evaporation stage, that

$$1 - x = K(1 - y). \quad (12)$$

If the initial amount of metal is W_0, and its impurity content, $1 - \varphi$ (φ, mole fraction), then, substituting (12) into (11) and solving the obtained equation, we find

$$\ln(W/W_0) = -\frac{K}{K-1}\ln\frac{1-y}{1-\varphi}$$

or

$$1 - y = \frac{1-\varphi}{K}(W/W_0)^{(K-1)/K}. \quad (13)$$

Equation (13) makes it possible to find the content of impurity in the condensate formed at the given instant of time. If Q is the fraction of metal that passed into the distillate, then the average content of impurity in it is given by

$$(1 - y)_{av} = Q^{-1}\int_0^Q (1 - y)\,dQ.$$

Since $W/W_0 = 1 - Q$,

$$1 - y = \frac{1-\varphi}{K}(1 - Q), \quad (14)$$

$$(1 - y)_{av} = Q^{-1}\int_0^Q (1 - \varphi)K^{-1}(1 - Q)^{(1-K)/K}\,dQ$$

$$= (1 - \varphi)[1 - (1 - Q)^{1/K}]Q^{-1}, \quad (15)$$

Equation (15) can be used to determine the average content of impurity in the distillate in relation to the impurity content of the starting metal, process conditions, and fraction of evaporated metal.

The composition of the first, purest vapor portion can be calculated using Eq. (13), provided that $W = W_0$:

$$(1 - y)_0 = \frac{1-\varphi}{K}, \quad (16)$$

In LBC evaporation in a still, the LBC impurity accumulates. As seen from Table 2, Eq. (13) and other equations obtained on its base are applicable if the content of HBC in the still does not exceed the limiting values listed in Table 2. The corresponding limiting impurity concentration in the distillate is given by

$$(1 - y)_{lim} = \frac{(1 - x)_{lim}}{K}, \quad (17)$$

Substituting (17) into (14), we obtain

$$\ln(1 - Q)_{lim} = \frac{K[\ln(1 - y)_{lim} - \ln(1 - \varphi) + \ln K]}{K}. \quad (18)$$

Equation (18) enables calculation of the extent of alloy evaporation at which the impurity content in the bottoms does not exceed the maximum permissible value.

To obtain potassium containing no more than 0.001 wt % sodium (0.0017 at. %) at a sodium content in the bottom alloy of 25 at. %, a coefficient is necessary $K \geq 25/1.7 \times 10^{-3} \approx 1.5 \times 10^4$, which, as seen from Fig. 1a, must not pose any difficulties. Below are given Q_{lim} values in relation to the content of sodium in the starting alloy, calculated at $K = 1.5 \times 10^4$ by Eq. (18) (the content of sodium in the purified metal does not exceed 0.001 wt %):

Content of sodium in the starting potassium, wt %	Q_{lim}, % relative to the initial value
0.05	99.7
0.5	96.95
1.0	93.9
1.5	91.5
2.0	88.8

In HBC purification to remove a low-boiling impurity, the impurity concentrations in the distillate and the starting metal are related by

$$y = Kx. \quad (19)$$

If the initial amount of metal is W_0, and the content of impurity in it is φ, then, substituting (19) into (11), we obtain

$$\ln(W/W_0) = (K - 1)^{-1} \ln(x/\varphi) \text{ or } x = \varphi(W/W_0)^{K-1}. \quad (20)$$

Equation (20) can be used to find the content of impurity in purified metal, which, as in the preceding case, depends on the impurity content in the starting metal, process conditions, and amount of unevaporated metal. Equation (20) is applicable at $x \leq x_{lim}$ (Table 2). At these x values, Eq. (19) is also applicable. We assume that, at $x > x_{lim}$, an alloy is evaporated containing y_{lim} of LBC. Then we have from the material balance equation

$$y_{lim} Q'_{lim} + x_{lim}(1 - Q'_{lim}) = \varphi,$$

$$Q'_{lim} = \frac{\varphi - x_{lim}}{y_{lim} - x_{lim}} - \frac{\varphi - x_{lim}}{x_{lim} - (K - 1)}, \quad (21)$$

where Q'_{lim} is the fraction of metal which is to be evaporated in order that Eq. (20) should be applicable to the remaining metal.

After evaporation of Q'_{lim}, Eq. (20) is applicable to the remaining metal, which makes it possible to determine what part of it, Q_{lim}, can be obtained under the given process conditions with a prescribed impurity content x:

$$Q'_{lim} = (x/x_{lim})^{1/K-1}. \quad (22)$$

The total yield of metal of prescribed purity is given by the product

$$Q_{lim} = Q_{lim}(1 - Q'_{lim}) \times 100. \quad (23)$$

Table 3. Expected minimum yield of products in purification of technical-grade sodium (potassium content 0.25 wt %) by distillation with vacuum dephlegmation

K	Yield of sodium, %, at indicated content of potassium in purified product, wt %		
	10^{-2}	10^{-3}	10^{-4}
27	88.43	80.98	74.17
220	98.56	97.54	96.54
1170	99.68	99.48	99.28

The obtained equations were used to evaluate the efficiency of sodium purification in vapor cooling from temperature T (653, 753, and 853 K) to 553 K. As seen from Fig. 2, the respective values of $K = y_2/y_1$ are 27, 220, and 1170.

As seen from Table 3, sodium can also be thoroughly purified to remove potassium impurity, since the temperatures at which the K values used in calculations can be achieved are quite practicable.

Thus, the calculations demonstrated that the method of vacuum distillation with equilibrium dephlegmation of vapor can be used to obtain pure metals in sufficiently high yield from technical-grade sodium and potassium. The process is the most efficient in purification of LBC to remove HBC impurity and it was used for purifying technical-grade potassium to remove sodium impurity.

The investigations were carried out on an installation shown schematically in Fig. 2. It comprises a still *1*, dephlegmator *2* with a pouring-in extension *3*, cover *4*, still heating furnace *5*, melting device *6*, container *7* for collecting the metal being distilled from condenser *8*, and the main *9* and auxiliary *10* vacuum lines. The still could be charged with 15 kg of potassium. Pockets *11–15* accommodating Chromel–Alumel thermocouples were welded to the bottom, middle, and top parts of the dephlegmator, and in the cover and bottom of the still. The dephlegmator case was heat-insulated with a layer of a clay-chamotte mixture, and the upper third and the cover of the

Table 4. Conditions and results of experiment on potassium purification

Metal, fraction	Temperature, °C						Mass, g	Sodium content, wt %	*K*	Evaporation rate	
	cover	dephlegmator section				still				kg day^{-1}	g dm^{-2} h^{-1}
		1	2	3	4						
Initial							5010	1.98			
Fraction:											
1	270	280	300	310	415	460	3500	0.0007	10 000	8.45	112.1
2	400	400	400	450	500	550	1450	0.2	–	–	–

dephlegmator, with an additional layer of Sovelite. A steel crosspiece was mounted in the bottom part of the dephlegmator on a specially designed annular shoulder *16*, and packing *17* in the form of briquettes of cuttings was placed on the crosspiece. The packing bed height was 530 mm. Separate units of the installation could be shut-off by means of liquid–metal (*18–21*) or vacuum (*22*, *23*) valves. The main vacuum line was used for continuous evacuation of the distiller during the process, and the auxiliary line, for evacuating containers during their replacement.

Fractions of distilled metal were collected into specially designed metallic containers equipped with three level gages. The rate of metal evaporation was continuously monitored with batch meter *24* connected to the discharge extension and container.

To heat the installation in the course of distillation and in its final stage for complete removal of the metal from the dephlegmator packing, additional removable heaters were mounted onto the dephlegmator case. The metal poured in the still was heated by an electric furnace.

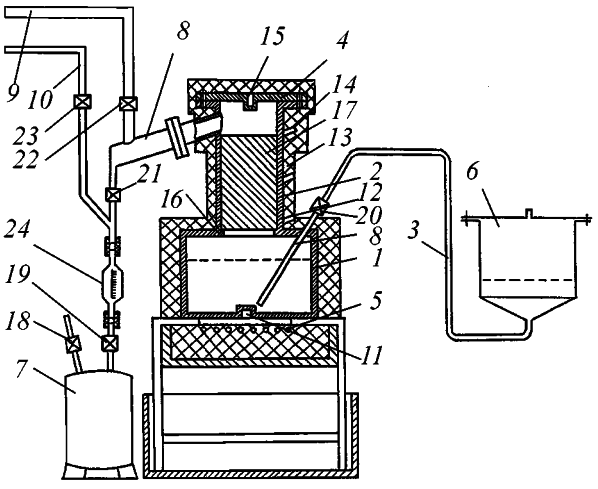

Fig. 2. Schematic of installation for potassium purification by distillation with dephlegmation. For explanations, see text.

To preclude the possible influence of oxygen [5] on the experimental results, technical-grade potassium was preliminarily distilled in a vacuum and then an additional amount of sodium metal was introduced to bring the impurity content to the required level.

The experiment was carried out as follows. An assembled installation was evacuated, tested for leaks, and heated. Potassium was charged through the pouring-in extension, and the valve in the pouring-in extension was closed. The metal poured in the still was heated to a prescribed temperature, with the evaporating metal gradually heating the dephlegmator to a certain temperature. The evaporated metal was collected in the condenser extension and discharged through the batch meter into the receiving container. The rate of metal evaporation was continuously monitored, together with the temperature regime. When filled with metal, the containers were replaced. For this purpose, the valves in the discharge extension of the distiller, auxiliary vacuum line, and container were closed and a filled container was disconnected. Then, the next container was connected, the valves in the container and auxiliary vacuum line were opened, the container was evacuated, and the valve in the discharge extension of the distiller was opened.

The exhaustion of metal in the still was inferred from a decrease in the apparatus cover temperature and in the rate of metal evaporation at invariable power consumed by the still-heating furnace. Then, additional heating furnaces were mounted on the dephlegmator, the apparatus was heated to 400–500°C to completely remove the metal from the packing, and the installation was cooled. The conditions and results of an experiment on potassium purification by vacuum distillation with partial dephlegmation in a heated condenser are listed in Table 4. It can be seen that the metal was obtained in about 70% yield, with the sodi-

um impurity content in the metal at the sensitivity limit of the available analytical methods. The main part of sodium did not find its way into the condenser, being "smeared" over the installation parts. Even though the efficiency of separation (K value) was less than expected (possible reasons: higher temperature of the central part of the vapor flow arriving at the condenser; poor metal agitation in the still, leading to enrichment of the surface layer of the melt with sodium; insufficient accuracy of determination of minor amounts of sodium because of sample contamination from the ambient), it was sufficiently high for practical purposes. Fraction 2, contaminated with sodium, was obtained in evaporating the metal from the packing.

Further, the charge was raised to 15 kg. After evaporation of 60–70% of the charged metal, 10–12 kg of technical-grade potassium was twice introduced additionally. At the end of the process, 0.4–0.5-kg fractions were obtained. With this experimental procedure, the yield of potassium into the pure fraction (sodium content 0.0005–0.002 wt %) was made as high as 98.2%, with sodium concentrated at the end of the process in an alloy containing 40–60% sodium.

The developed technologies and apparatus also allow successful separation of potassium–sodium alloys. For example, distillation of 12.35 kg of an alloy of this kind, containing 48.93 wt % sodium, gave in 99.78% yield potassium with sodium impurity content of 0.001 wt %. The evaporated sodium contained 0.03 wt % potassium, which is presumably due to contamination of distilled sodium in the condenser containing residual potassium.

The finishing purification of potassium was done by repeated distillation at 250–270°C and residual gas pressure of no more than 6.7×10^{-3} Pa. The purified metal was analyzed by atomic-absorption and spectral methods with preliminary chemical enrichment with impurities. The quality of potassium purified by the developed technology is characterized below (impurity; content, wt %): Na $<5 \times 10^{-4}$, Rb $<1 \times 10^{-3}$, Cs $<1 \times 10^{-3}$, Cu $<1 \times 10^{-6}$, Ag $<8 \times 10^{-7}$, Mg $<2 \times 10^{-5}$, Ca $<1.5 \times 10^{-4}$, Zn $<2.5 \times 10^{-5}$, Al $<1 \times 10^{-5}$, Ga $<2 \times 10^{-6}$, In $<2 \times 10^{-6}$, Tl $<4 \times 10^{-6}$, Ti $<5 \times 10^{-6}$, Sn $<5 \times 10^{-6}$, Pb $<5 \times 10^{-6}$, Sb $<1 \times 10^{-5}$, Bi $<2 \times 10^{-6}$, V $<1 \times 10^{-6}$, Cr $<5 \times 10^{-6}$, Mo $<5 \times 10^{-6}$, Mn $<1 \times 10^{-6}$, Fe $<1.4 \times 10^{-5}$, Co $<3 \times 10^{-6}$, and Ni $<1 \times 10^{-6}$.

The ratio of the residual electrical resistance ρ_0 (at $T \to 0$) of high-purity potassium to the resistance[1] at 293 K was 1.5×10^{-4}, which corresponds to a total content of impurities of about 0.001%.

CONCLUSIONS

(1) A procedure is proposed for calculating the efficiency of component separation by vacuum distillation with partial dephlegmation of vapor in a heated condenser. It is shown that this process must ensure effective purification of potassium to remove sodium impurity and sodium to remove potassium impurity.

(2) Apparatus designs and process regime ensuring efficient potassium purification to remove sodium impurity were developed.

(3) Additional purification by high-vacuum distillation gives potassium surpassing in quality the best of the available foreign commercial samples.

(4) The developed technology and apparatus made it possible to set up industrial manufacture of high-purity potassium in conformity with TU (Technical Specifications) 48-4-476–86.

REFERENCES

1. US Patent 3243280.
2. US Patent 4721525.
3. Foster, H.J. and Meier, P.H.E., *J. Res. Nat. Bur. Stand.*, 1967, vol. A71, no. 2, pp. 127–132.
4. Lokshin, E.P. and Ignat'ev, O.S., *Teplofiz. Vys. Temp.*, 1971, vol. 9, no. 1, pp. 94–100.
5. USSR Inventor's Certificate no. 389166.
6. Borgstedt, H.U. and Mathews, Ch.K., *Applied Chemistry of the Alkali Metals*, New York: Plenum, 1987.
7. Zaretskii, S.A., Busse-Machukas, V.B., and Malyusov, V.A., *Sb. Izobr. Ratspredl., NIITEKhIM* (Cherkassy), 1960, no. 1, p. 14.
8. Lokshin, E.P., *Zh. Prikl. Khim.*, 1996, vol. 69, no. 4, pp. 555–561.
9. Lokshin, E.P., *Izv. Akad. Nauk SSSR, Metally*, 1987, no. 1, pp. 12–17.
10. Gel'perin, N.I., *Distillyatsiya i rektifikatsiya* (Distillation and Rectification), Moscow: Goskhimizdat, 1947, vol. 1.
11. Shpil'rain, E.E., Yakimovich, K.A., Totskii, E.E., *et al.*, *Teplofizicheskie svoistva shchelochnykh metallov* (Thermal and Physical Properties of Alkali Metals), Moscow: Izd. Standartov, 1970.

[1] Measured at FTINT, National Academy of Sciences of Ukraine (Kharkov) under supervision of B.N. Aleksandrov.

Russian Journal of Applied Chemistry, Vol. 74, No. 7, 2001, pp. 1076–1078. Translated from Zhurnal Prikladnoi Khimii, Vol. 74, No. 7, 2001, pp. 1048–1050.

INORGANIC SYNTHESIS AND INDUSTRIAL INORGANIC CHEMISTRY

Refractoriness and Phase Composition of ZrB_2–Si Materials

G. N. Gorbatova, I. B. Ban'kovskaya, N. S. Yuritsyn, and I. S. Malygina

Grebenshchikov Institute of Silicate Chemistry, Russian Academy of Sciences, St. Petersburg, Russia

Received December 21, 2000; in final form, March 2001

Abstract—The influence of silicon concentration and of the mode and time of heat treatment in air on the refractoriness and phase composition of ZrB_2–Si materials was studied. Recommendations are given for preparing refractory coatings on graphite in air using the given materials.

Coatings of ZrB_2 on a carbon material have been obtained in argon at 1900°C [1].

In this work we studied the feasibility of using ZrB_2–Si materials for obtaining refractory coatings on graphite in air at lower temperature. We studied how the silicon concentration and the mode and time of heat treatment influence the refractoriness and phase composition of the material.

Oxidation of ZrB_2 has been described in the literature [2–4]. Up to 1000°C ZrB_2 is oxidized only slightly, but at higher temperatures the oxidation accelerates sharply. The primary components of the oxide film are zirconium dioxide and hydrated boron(III) oxide, which evaporates at high temperatures. A scale formed on zirconium diboride shows no protective properties, because, owing to porosity, it does not impede oxygen diffusion into the sample. Zirconium diboride is used as refractory material. It is incorporated in a number of the composite alloys operating at high temperatures in an oxidizing medium. Also, it is a coating component. Thus, it is necessary to enhance its resistance to oxidants.

This is provided by addition of silicon-containing compounds [5–7]. Doping of the boride alloys with silicon or metal silicides yielding volatile oxides results in the formation of the oxide film that mainly consists of borosilicate glass and reliably protects the alloy from oxidation. According to the published data, boride materials with addition of silicon-containing compounds are prepared by hot pressing or sintering of the appropriate mixtures in inert medium. In this work, samples in the form of slip castings were used without additional heat treatment. The samples were dried to constant weight at room temperature.

The samples for studying refractoriness were heated in an electric furnace with silicon carbide heaters in air under the static conditions at 1400°C for 5, 15, 30, and 60 min. Three samples were heated for each time. The heat resistance was judged from the weight change (mg cm^{-2}) of the sample heated for the given time.

The open porosity of the samples was determined by water absorption. The phase composition of the surface after heating was studied on a DRON-2.0 diffractometer (CuK_α radiation, Ni filter). The microstructure of the samples was studied on an MIM-8M metallographic horizontal microscope. Zirconium diboride (pure grade) and silicon (KR-1 grade) were finely dispersed powders with particles no larger than 63 μm. The materials studied are presented in Table 1.

Each charge was mixed for 20 min. Then, slip casting was used for preparing the samples as castings. The binder was a 2% solution of carboxymethyl cellulose. The samples were $1.5 \times 1.5 \times 0.5$ cm in size. The samples were dried in air for 2–3 days.

We studied how the silicon concentration and the mode and time of heat treatment affect the refractoriness and composition of the ZrB_2–Si samples. The obtained results are plotted in the figure and given in Tables 1 and 2.

The figure shows the weight change of the samples heated in air at 1400°C as a function of the heating time. As seen, the silicon-containing samples are oxidized less intensely than zirconium diboride. Heating of the samples is accompanied by complex processes including oxidation of the initial components with atmospheric oxygen, interaction of the resulting compounds with each other, formation of borosilicate glass, volatilization of boron(III) oxide, and partial evaporation of silicon from the sample surface. The total contribution of all the occurring processes is reflected in the figure.

1070-4272/01/7407-1076$25.00

Table 1. Crystalline phases on the surface of the ZrB_2–Si samples heat-treated at 1400°C in air

Material no.	Composition, wt %		Phase composition* after heating for indicated time, min					
	ZrB_2	Si	5	15	30	60	300	600
1	100		ZrB_2, ZrO_2	ZrB_2, ZrO_2	ZrB_2, ZrO_2	ZrB_2, ZrO_2	ZrB_2 (traces), ZrO_2	ZrB_2 (traces), ZrO_2
2	95	5	ZrB_2, ZrO_2	ZrB_2, ZrO_2	ZrB_2, ZrO_2	ZrB_2, ZrO_2	ZrB_2 (traces), ZrO_2, $ZrSiO_4$	ZrB_2 (traces), ZrO_2, $ZrSiO_4$
3	90	10	ZrB_2, ZrO_2	ZrB_2, ZrO_2	ZrB_2, ZrO_2	ZrB_2, ZrO_2, $ZrSiO_4$	ZrB_2, ZrO_2, $ZrSiO_4$	ZrB_2, ZrO_2, $ZrSiO_4$
4	80	20	ZrB_2, ZrO_2	ZrB_2, ZrO_2	ZrB_2, ZrO_2	ZrB_2 (traces), $ZrSiO_4$	ZrO_2, $ZrSiO_4$	ZrO_2, $ZrSiO_4$
5	70	30	ZrB_2, ZrO_2	ZrB_2, ZrO_2	ZrO_2, $ZrSiO_4$	ZrO_2, $ZrSiO_4$	ZrO_2, $ZrSiO_4$	ZrO_2, $ZrSiO_4$
6	60	40	ZrB_2, ZrO_2	ZrB_2, ZrO_2	ZrO_2, $ZrSiO_4$	$ZrSiO_4$		
7	50	50	ZrB_2, ZrO_2	ZrB_2, ZrO_2,	ZrB_2, ZrO_2, $ZrSiO_4$	ZrB_2, ZrO_2, $ZrSiO_4$		

* Monoclinic ZrO_2.

Table 2. X-ray phase analysis of the surface of the heat-treated ZrB_2–Si samples

Material no.	Phase composition* after heating in indicated mode		
	I	II	III
1	ZrB_2, ZrO_2	ZrB_2, ZrO_2	ZrO_2
2	ZrB_2, ZrO_2	ZrO_2	ZrO_2
3	ZrB_2, ZrO_2, $ZrSiO_4$	ZrO_2, $ZrSiO_4$	ZrO_2, $ZrSiO_4$
4	ZrB_2, ZrO_2, $ZrSiO_4$	ZrO_2, $ZrSiO_4$	ZrO_2, $ZrSiO_4$
5	ZrO_2, $ZrSiO_4$	ZrB_2, ZrO_2, $ZrSiO_4$ $ZrSiO_4$	ZrB_2, ZrO_2, $ZrSiO_4$ $ZrSiO_{4c}$, α-cristobalite
6	$ZrSiO_4$	ZrO_2, $ZrSiO_4$	ZrO_2, $ZrSiO_{4c}$, α-cristobalite
7	ZrB_2, ZrO_2, $ZrSiO_4$	ZrO_2, $ZrSiO_{4c}$, α-cristobalite	ZrO_2, $ZrSiO_{4c}$, α-cristobalite

* Monoclinic ZrO_2.

The new phases, ZrO_2 (monoclinic) and $ZrSiO_4$, are revealed on the surface of the ZrB_2–Si samples in the course of heat treatment (Table 1). In samples with 5 wt % silicon, zirconium silicate is formed after 5 h. At higher silicon concentrations the time of zirconium silicate formation is shorter: 1 h at 10–20% and even 30 min at 30%.

The open porosity of the heat-treated samples decreases with increasing silicon concentration and heating time. The porosity of the zirconium diboride samples kept for 5 min at 1400°C is 40%, and the porosity of those kept for 10 h, 29%. As the silicon concentration increases, the porosity of the samples kept for 5 min decreases to 26% and of those kept for 10 h at the same temperature, to 16%. Table 2 shows how the heat treatment mode affects the phase com-

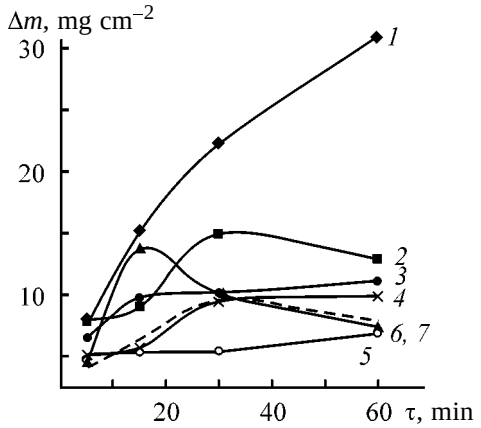

Weight change Δm of ZrB_2–Si samples heated in air at 1400°C vs. heating time τ. The curve numbers are the same as the material numbers in Table 1.

position of the sample surface. Three modes were used for heating samples: (I) samples placed into the furnace preheated to 1400°C were kept there for 1 h, (II) samples placed into a furnace at room temperature were heated to 1400°C (with a rate of 10 deg min^{-1}), and (III) samples were placed into the furnace at room temperature, heated there to 1400°C, and then they were kept at this temperature for 1 h. In all cases, the heat-treated samples were withdrawn from the furnace and cooled in air.

Table 2 shows that modes II and III yield α-cristobalite having a high expansion coefficient, which is undesirable in preparing coatings on graphite.

The results of studying the material in air were used for preparing refractory coatings on graphite. The coatings are nonporous and strongly adherent to graphite. Their microstructure is heterogeneous. Crystalline grains of the initial zirconium diboride and new phases formed during heat treatment are distributed uniformly throughout the glassy matrix.

The coatings obtained can be recommended for use at up to 1600°C. The X-ray phase analysis of the coating surface revealed the crystalline phases of zirconium silicate and zirconium diboride.

CONCLUSIONS

(1) With increasing silicon concentration the refractoriness of the compound increases owing to formation of new crystalline phases and of the encapsulating matrix of borosilicate glass.

(2) The X-ray phase analysis of the samples heated at 1400°C revealed the crystalline phases of ZrB_2, ZrO_2, $ZrSiO_4$, and α-cristobalite on the surface.

(3) With the silicon concentration increased to 30%, zirconium silicate is formed on the surface even within 30 min.

ACKNOWLEDGMENTS

The work was supported by the Russian Foundation for Basic Research (project no. 01-03-32318).

REFERENCES

1. Ban'kovskaya, I.B., Gorbatova, G.N., Sazonova, M.F., and Filipovich, V.N., *Zh. Prikl. Khim.*, 1997, vol. 70, no. 11, pp. 1907–1910.
2. Samsonov, G.V., Serebryakova, T.I., and Neronov, V.A., *Boridy* (Borides), Moscow: Atomizdat, 1975.
3. Voitovich, R.F., and Pugach, Z.A., *Poroshk. Metall.*, 1974, no. 3, pp. 86–91.
4. Voitovich, R.F., *Tugoplavkie soedineniya* (Refractory Compounds), Kiev: Naukova Dumka, 1971.
5. Portnoi, K.I., Samsonov, G.V., and Frolov, K.I., *Izv. Akad. Nauk SSSR, Metall. Topl.*, 1959, no. 2, pp. 117–121.
6. Portnoi, K.I., and Samsonov, G.V., *Izv. Akad. Nauk SSSR, Otd. Tekh. Nauk*, 1958, no. 7, pp. 140–141.
7. Kuzenkova, M.A., and Kislyi, P.S., *Poroshk. Metall.*, 1965, no. 10, pp. 75–79.

Russian Journal of Applied Chemistry, Vol. 74, No. 7, 2001, pp. 1079–1081. Translated from Zhurnal Prikladnoi Khimii, Vol. 74, No. 7, 2001, pp. 1051–1053.

INORGANIC SYNTHESIS AND INDUSTRIAL INORGANIC CHEMISTRY

Oxidation of Polycrystalline Zinc Selenide with Atmospheric Oxygen

E. L. Khlopochkina, P. E. Gaivoronskii, E. M. Gavrishchuk, Yu. E. Elliev, and E. V. Yashina

Lobachevskii State University, Nizhni Novgorod, Russia
Institute of Chemistry of High-Purity Substances, Russian of Academy of Sciences, Nizhni Novgorod, Russia

Received June 16, 2000; in final form, February 2001

Abstract—Oxidation of granulated polycrystalline zinc selenide (grain size 0.2–6.5 mm) with atmospheric oxygen at 430–700°C was studied. The optimal conditions for the oxidation were found. An installation for the oxidation of kilogram amounts of zinc selenide was designed and fabricated.

Published data on the oxidation of zinc selenide as single crystals, polished plates, and powders include estimates of the oxidation rate at 300–950°C, composition of the reaction products, and suggested equations for the oxidation [1–5]. However, there are a number of contradictions in the determination of composition of the nonvolatile oxidation products. For instance, according to [1–3], zinc oxide is the only nonvolatile product, but in [4] significant amounts (up to 18%) of zinc selenite were found in the range 490–560°C along with zinc oxide. According to [5], zinc selenite is the main product of the oxidation at 300°C; as the temperature increases, its fraction appreciably decreases as compared to zinc oxide. Volatile oxidation products either were not investigated at all [1, 2, 5] or only their qualitative composition as a mixture of selenium and selenium dioxide [3, 4] was established. The effect of the grain size of the initial zinc selenide on the rate of its oxidation is still obscure, and probable oxidation mechanisms were not discussed.

In this work the study was concerned with waste polycrystalline zinc selenide of various grain size, formed from production of optical parts for IR technique [6]. One of the ways of processing waste products is their oxidizing calcination. In this connection, the aims of this work were to study the oxidation kinetics of granulometric zinc selenide samples of various grain size, to identify the products of the oxidation at 430–700°C, and also to study the mechanism of the oxidation with atmospheric oxygen.

EXPERIMENTAL

First we carried out a thermodynamic analysis of the system zinc selenide–air. Though the oxidation conditions were far from equilibrium, the thermodynamic analysis is important for the estimation of the relative contents of products both in gas and condensed phases. The calculation was carried out at various stoichiometric ratios of the initial reactants. The calculated equilibrium concentrations of components (in moles per total number of moles of atoms in the initial substances) for the system zinc selenide–air in excess oxidant (molar ratio zinc selenide–oxygen in the experiments was 1 : 4.5) are given in Fig. 1. Apparently, within the whole temperature

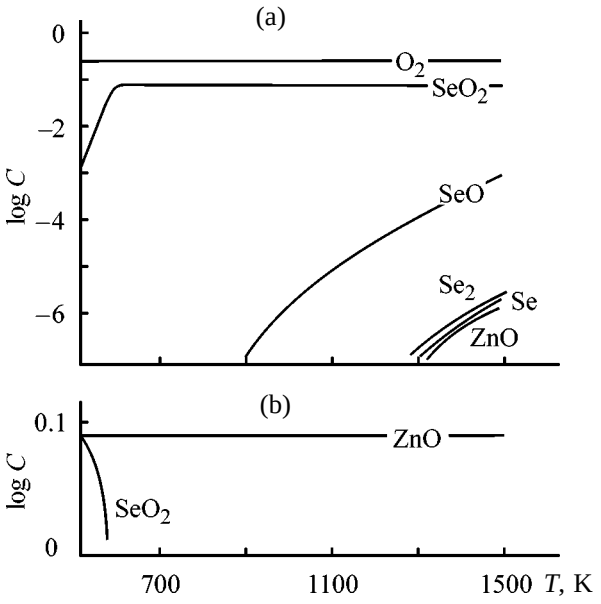

Fig. 1. Temperature dependence of the equilibrium composition of the system zinc selenide–oxygen. (*C*) Equilibrium concentration [mol (mol of atoms)$^{-1}$]. Phase: (a) gas and (b) condensed.

1070-4272/01/7407-1079$25.00 © 2001 MAIK "Nauka/Interperiodica"

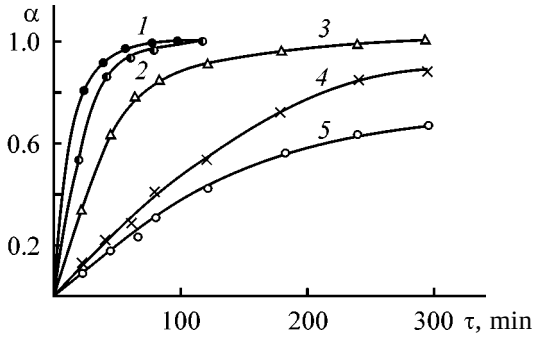

Fig. 2. Kinetic curves of zinc selenide oxidation: (α) conversion and (τ) time. Temperature (°C): (*1*) 700, (*2*) 600, (*3*) 550, (*4*) 500, and (*5*) 430.

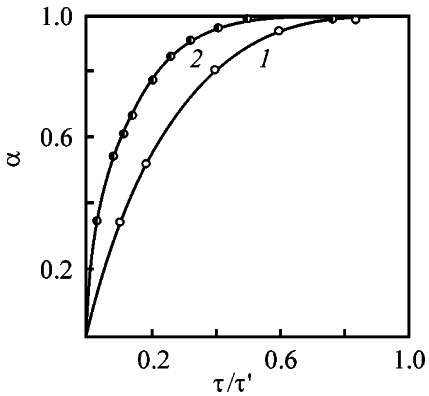

Fig. 3. Variation with relative oxidation time τ/τ' of the zinc selenide conversion α. Temperature (°C): (*1*) 550 and (*2*) 700.

range (500–1500 K) the main reaction product in the gas phase is selenium dioxide. The content of the other selenium species (Se, Se_2, Se_3, etc.) is lower by several orders of magnitude. In the condensed phase selenium dioxide exists only within a narrow temperature range.

The installation for oxidation consisted of an inclined quartz reactor (30 mm in diameter and 400 mm in length) and a condenser for volatile oxidation products. When the reactor is heated in a tubular electric furnace, a steady-state convection air stream arises. The temperature in the oxidation zone was varied from 430 to 700°C during experiments. The accuracy of temperature determination did not exceed 3%. The granulometric compositions of powders were determined by sieving. The particle size of zinc selenide varied from 0.20 to 6.50 mm. Samples of powders (18.00 ± 0.01 g) were placed in quartz boats ($60 \times 25 \times 15$ mm). The composition of the nonvolatile products remaining in the decomposition zone was determined by X-ray phase analysis. The qualitative composition of the volatile products condensed in the receiver was determined by chemical methods based on reactions with sodium thiosulfate, thiourea, and a mixture of concentrated potassium iodide and hydrochloric acid [7].

We found that the main nonvolatile product in the temperature range under study is zinc oxide, with the total content of zinc selenide, selenite, and selenate being lower than 5%. The volatile product is a mixture of selenium and its dioxide. To determine the amounts of individual components, the volatile products were dissolved in distilled water, the solution was filtered, and the precipitated selenium was dried and weighed. We found that the proportion of selenium and its dioxide in volatile products varies in the course of reaction [8]. This allowed us to offer the following equation for oxidation of zinc selenide:

$$ZnSe + (0.5 + y)O_2 \longrightarrow ZnO + xSe + ySeO_2,$$

In this equation factors *x* and *y* change in the course of the process, but the sum of them is equal to unity [9].

The variation of the molar ratio selenium : selenium dioxide in volatile oxidation products requires an independent study and was not considered in this work. To estimate the kinetic features, we studied only the nonvolatile oxidation products. The prevalence of zinc oxide in these products allowed us to estimate the degree of conversion of the initial zinc selenide by the gravimetric analysis. The time dependence of the zinc selenide conversion at 430–700°C is shown in Fig. 2.

To reveal the kinetic features of the oxidation, we examined the variation of the zinc selenide conversion (α) with the relative oxidation time τ/τ' (τ is current time and τ' is time of complete conversion). The dependences for 0.6–1.5-mm particles at 550 and 700°C are shown in Fig. 3. When studying the kinetics of processes in gas–solid systems, in particular of calcination of solid materials, it is common to take the model of a spherical particle with unreacted nucleus [10] as a basic model. According to this model, the limiting stage is characterized by the dependence of the conversion on the contact time, particle size, and temperature. The comparison of theoretical curves and our experimental data (Fig. 3) suggests that the oxidation process under consideration is controlled by internal diffusion [10].

The dependence of the time of 90% oxidation of zinc selenide (i.e., the reciprocal of the oxidation rate) on the particle size of the initial zinc selenide is plotted in Fig. 4. Particle sizes correspond to the mean values within the ranges (mm) 0.2–0.3, 0.3–0.4, 0.4–0.6, 0.6–1.5, 1.5–2.5, 2.5–3.5, 3.5–4.5, and 4.5–5.5.

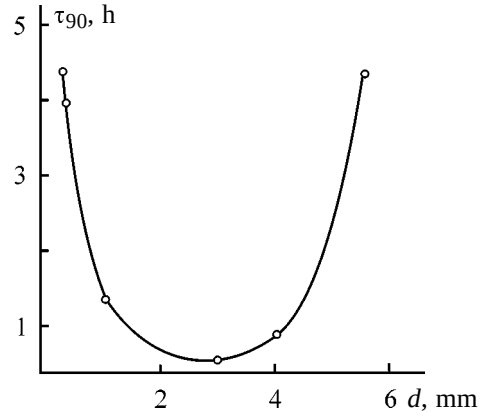

Fig. 4. Rate of zinc selenide oxidation as a function of its particle size *d*: (τ_{90}) time of 90% conversion.

It is evident that the reaction rate grows considerably with decreasing particle size (the right branch of the curve), which also confirms the assumption on the internal diffusion control of the process.

At the particle size decreased further (the left branch of the curve), the oxidation rate decreases, which seems to be due to the effect of another limiting stage, namely, diffusion of oxygen through a bed of the solid product [10]. This mechanism was discussed in the literature as applied to oxidation of FeS_2 in the industrial production of sulfuric acid [11].

From our experimental data we plotted the temperature dependence of the reaction time in the coordinates $\log(1/\tau)$–$1/T$ and determined the apparent activation energy of 83 kJ mol^{-1} for the range 430–700°C. It follows from the theory of diffusion kinetics of gas–solid phase interactions that the activation energy of processes controlled by internal diffusion is approximately a half of the activation energy of a chemical reaction [10]. The activation energy for the oxidation of polycrystalline plates of zinc selenide is known to be 170 kJ mol^{-1} [2]. In this case the activation barrier seems to be caused by the proper reaction between zinc selenide and oxygen, i.e., the reaction is kinetically controlled. The obtained apparent activation energy is approximately half of the value given in [2], which supports the assumption on the internal diffusion mode of the process.

The kinetic features allowed us to find optimal conditions for the oxidation of polycrystalline zinc selenide. This made it possible to design and fabricate an installation for the oxidation of kilogram amounts (0.6–1.5 kg) of zinc selenide [8].

CONCLUSION

Zinc oxide was found to be the main nonvolatile product of zinc selenide oxidation at 430–700°C. The oxidation is apparently controlled by internal diffusion. The temperature of 600°C and the particle size of 1.5–4.5 mm are the optimal for the oxidation of powdered polycrystalline zinc selenide by atmospheric oxygen.

REFERENCES

1. Korneeva, I.V. and Novoselova, A.V., *Zh. Neorg. Khim.*, 1960, vol. 5, no. 10, pp. 2265–2268.
2. Gunchenko, N.N., Dronova, G.N., Maksimova, I.A., *et al.*, *Izv. Akad. Nauk SSSR, Neorg. Mater.*, 1988, vol. 24, no. 1, pp. 36–40.
3. Pinaev, G.F., Murashkevich, A.N., and Goryachev, V.M., *Izv. Akad. Nauk SSSR, Neorg. Mater.*, 1976, vol. 12, no. 7, pp. 1301–1304.
4. Stepanova, N.D., Kalinkin, I.P., and Sokolov, V.A., *Izv. Akad. Nauk SSSR, Neorg. Mater.*, 1975, vol. 11, no. 6, pp. 1030–1034.
5. Kulakov, M.P. and Fadeev, A.V., *Izv. Akad. Nauk SSSR, Neorg. Mater.*, 1983, vol. 19, no. 3, pp. 347–351.
6. Gaivoronskii, P.E., Khlopochkina, E.L., Elliev, Yu.E., and Gavrishchuk, E.M., *Vestn. Nizhegorod. Gos. Univ., Khim.*, 1998, no. 1, pp. 3–6.
7. Nazarenko, I.I., and Ermakova, A.N., *Analiticheskaya khimiya selena i tellura* (Analytical Chemistry of Selenium and Tellurium), Moscow: Nauka, 1971.
8. Gaivoronskii, P.E., Khlopochkina E.L., Elliev, Yu.E., *et al.*, *Vestn. Nizhegorod. Gos. Univ., Khim.*, 1998, no. 1, pp. 7–9.
9. Gaivoronskii, P.E., Khlopochkina, E.L., Elliev, Yu.E., *et al.*, Abstracts of Papers, *X Konferentsiya po khimii vysokochistykh veshchestv* (X Conf. on the Chemistry of High-Purity Substances), Nizhni Novgorod, May 2000, pp. 53–54.
10. Kiperman, S.L., *Osnovy khimicheskoi kinetiki v geterogennom katalize* (Principles of Chemical Kinetics in Heterogeneous Catalysis), Moscow: Khimiya, 1979.
11. Mukhlenov, I.P., Averbukh, A.Ya., Tumarkina, E.S., and Furmer, I.E., *Obshchaya khimicheskaya tekhnologiya* (General Chemical Technology), Moscow: Vysshaya Shkola, 1977, part 1.

Russian Journal of Applied Chemistry, Vol. 74, No. 7, 2001, pp. 1082–1084. Translated from Zhurnal Prikladnoi Khimii, Vol. 74, No. 7, 2001, pp. 1054–1056.

INORGANIC SYNTHESIS AND INDUSTRIAL INORGANIC CHEMISTRY

Solubility in the Ternary System Water–Cadmium Bromide–Copper(II) Bromide

M. Yu. Skripkin, I. V. Zamyatin, and L. V. Chernykh

St. Petersburg State University, St. Petersburg, Russia

Received January 16, 2001

Abstract—Solubility in the system $CuBr_2$–$CdBr_2$–H_2O at 25°C was determined by the method of isothermal saturation. The obtained data were examined from the viewpoint of competitive formation of acido complexes in aqueous solutions.

Revealing relations between types of interparticle interactions in solutions and the corresponding solid phase is one of the most important problems of inorganic chemistry. Regular trends in these relations should form a basis for predicting types and properties of solid-phase compounds crystallizing in water–salt systems. These trends are useful for the development and improvement of hydrometallurgical processes and methods for concentrating mineral raw materials and separating elements. They can also form a basis for the development of procedures for directed synthesis of compounds with specified properties from solutions.

Previously we considered the formation of solid compounds in systems with dominating processes of association, hydration, and complex formation. The revealed regular trends were described in [1–3]. In this work we considered the solution–solid phase equilibrium in systems containing two complex-forming cations. Systems containing copper(II) and cadmium halides were selected as objects of the research. Solubility in the system $CuBr_2$–$CdBr_2$–H_2O was not studied previously. Data for the system $CuCl_2$–$CdCl_2$–H_2O were taken from [4].

The solubility was determined by the isothermal saturation method.

The systems were kept at prescribed temperature (±0.2°C) for 1 day. The copper content was determined by iodometric titration, and the total content of copper and cadmium, by EDTA titration. The cadmium content was calculated as the difference. The solid phase composition was determined by the Schreinemakers method. The results are given in the table and in Fig. 1.

The interactions occurring in solution can be judged from the presence or absence of crystallization branches of complex compounds in the solubility isotherm and from the lengths of the crystallization branches of initial compounds, the salting-in or salting-out effects; also, the interactions can be manifested as dehydration of the initial compounds.

Particular manifestations of the interactions depend on the contributions of their types, i.e., on the competition between them. In the systems under consideration the shape of the solubility isotherms is determined first of all by the competition between the complex formation processes.

Figure 1 shows that the solubility isotherms of the bromide and chloride systems differ considerably. The main principal distinction is the absence of the crystallization branch of a double halide in the bromide

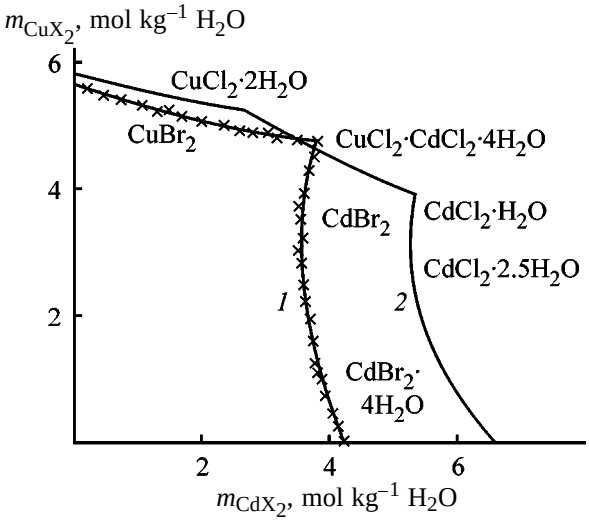

Fig. 1. Solubility in the systems (*1*) $CuBr_2$–$CdBr_2$–H_2O and (*2*) $CuCl_2$–$CdCl_2$–H_2O at 25°C. (m_{CuX_2}, m_{CdX_2}) Solubilities of CuX_2 and CdX_2, respectively.

1070-4272/01/7407-1082$25.00

system. According to the X-ray diffraction and spectral (Raman and IR) data, the compound $CuCl_2 \cdot CdCl_2 \cdot 4H_2O$ is a solid-phase heteronuclear complex of copper and cadmium with bridging chloride ligands. The copper and cadmium chloride complexes exhibit similar stability (the logarithm of the first-step stability constant $\log K_1$ is 1.55 for $CdCl^+$ and 0.98 for $CuCl^+$ [5]). This fact favors formation of precursors of the heteronuclear complexes in concentrated solutions (the similarity in the chemical species in saturated solution and solid phase was confirmed by Raman spectroscopy) and their further transition to the solid phase. The high stability of cadmium chloride complexes determines the uniformity of their coordination sphere in the solid compound, whereas copper ions are surrounded with both chloride and aqua ligans. As for the bromide system, the much greater stability of cadmium bromide complexes, as compared to copper(II) complexes {$\log K_1$ 0.32 ($CuBr^+$) and 2.30 ($CdBr^+$) [5]}, makes formation of heteronuclear bridged complexes unfavorable.

The different stability of copper and cadmium complexes in chloride and bromide systems also affects the length of the crystallization branches and the salting-in and salting-out of the initial compounds. In the system $CuCl_2$–$CdCl_2$–H_2O only salting-out of the components is observed, whereas in the system $CuBr_2$–$CdBr_2$–H_2O a clear transition from salting-out to salting-in takes place. The ratio of salting-out and salting-in of the components in the systems under consideration (Fig. 2) is determined by the hydration of ions and by the stability of acido complexes and fully corresponds to the ratio that could be predicted from the ratio of stability constants of the halide complexes.

The addition of the second electrolyte to a saturated solution of cadmium or copper halide is accompanied by two interdependent oppositely directed effects. On the one hand, the presence of an additional amount of halide ions will enhance the complex formation, which is accompanied by the detachment of water from the hydration spheres of the ions and increases the solubility [6]. On the other hand, the increase in the total concentration of ions results in greater binding of water and in decreasing solubility of the salt in the forming ternary solution, as compared to the binary solution. It should be expected that the first effect would make a greater contribution in the case of systems with stronger acido complex formation. In fact, the salting-out of copper chloride is weaker than that of copper bromide [$K_{st}(CuCl_n^{2-n}) > K_{st}(CuBr_n^{2-n})$]. In the case of cadmium halides, which are characterzed by even stronger acido complex formation, the salting-out of cadmium chloride is replaced by salting-out–salting-in of cadmium bromide [$K_{st}(CdCl_n^{2-n}) < K_{st}(CdBr_n^{2-n})$].

Solubility in the system $CdBr_2$–$CuBr_2$–H_2O at 25°C

Liquid phase				Solid phase composition
$CdBr_2$	$CuBr_2$	$CdBr_2$	$CuBr_2$	
wt %		m, mol kg^{-1} H_2O		
0	55.79	0	5.65	$CuBr_2$
1.06	54.89	0.09	5.58	″
2.21	53.83	0.18	5.48	″
3.27	53.08	0.27	5.44	″
4.57	52.21	0.39	5.41	″
8.51	49.12	0.74	5.19	″
18.01	42.80	1.69	4.89	″
22.06	39.83	2.13	4.68	″
23.57	39.07	2.32	4.68	″
29.82	35.50	3.16	4.58	″
30.10	35.21	3.19	4.54	″
30.76	35.11	3.31	4.61	″
31.30	34.65	3.38	4.56	″
31.39	34.48	3.38	4.52	″
32.40	34.49	3.59	4.66	″
33.37	34.37	3.80	4.77	$CuBr_2$ + $CdBr_2$
33.50	34.33	3.83	4.78	″
33.07	34.16	3.71	4.67	$CdBr_2$
32.45	33.84	3.54	4.49	″
32.09	32.63	3.34	4.14	″
32.48	31.48	3.31	3.91	″
32.97	29.73	3.25	3.57	″
33.92	27.83	3.26	3.36	″
34.33	27.36	3.29	3.20	″
36.06	25.50	3.45	2.97	″
37.61	22.62	3.47	2.55	″
39.24	19.73	3.51	2.15	″
41.32	17.87	3.72	1.96	$CdBr_2$ + $CdBr_2 \cdot 4H_2O$
41.18	17.72	3.68	1.93	″
41.86	15.71	3.62	1.66	$CdBr_2 \cdot 4H_2O$
42.21	15.26	3.65	1.61	″
42.58	15.09	3.70	1.60	″
45.13	8.57	3.58	0.83	″
45.84	7.36	3.60	0.70	″
46.98	5.39	3.62	0.51	″
47.44	4.44	3.62	0.41	″
52.86	0	4.12	0	″

The greater stability of cadmium complexes, as compared to copper(II) complexes, results in a redistribution of ligands from copper to cadmium. “Vacant

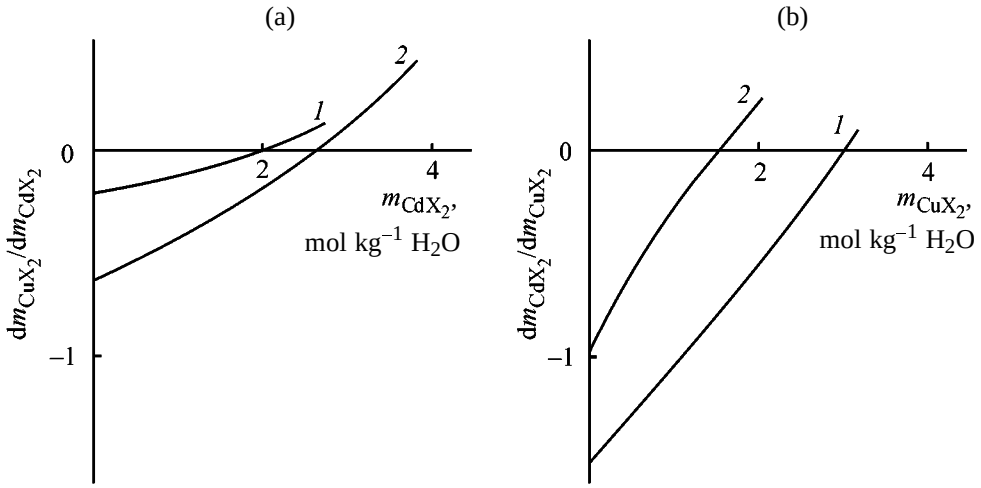

Fig. 2. Salting-out–salting-in of (a) CuX_2 and (b) CdX_2 in CuX_2–CdX_2–H_2O systems. X^-: (*1*) Cl^- and (*2*) Br^-.

positions" in the coordination sphere of copper ions are filled with water molecules, which results in decreasing content of "free" water in solution and in salting-out of the copper halide. In the bromide system this effect is stronger owing to the large difference in the complex formation of cadmium and copper. At the same time, because of the competition of copper and cadmium complex formation, the salting-out in the systems under consideration is stronger than in the ternary solutions CuX_2–MX_2–H_2O and CdX_2–MX_2–H_2O (M^{2+} is Mg^{2+}, Ba^{2+}) [7, 8].

The difference in the complex formation of cadmium halides also affects conditions of the dehydration of hydrates of these salts in the solid phases. The observed dehydration can be considered as a result of the replacement of water molecules in cadmium aqua halide complexes in solution by halide ions. This process should be more pronounced in the bromide system, as compared to the chloride system, which is observed experimentally. In this case the competition with copper(II) complex formation is manifested in that the point of the transition from the tetrahydrate to the anhydrous salt is displaced to larger concentrations of the second component, as compared to the systems containing double-charged noncomplexing cations.

Thus, solubility in the systems containing cadmium and copper(II) halides is determined by the competition of cadmium and copper complex formation. In the chloride system the similar contributions of these processes favor formation of solid heteronuclear complexes with chloride bridges and weaker salting-out of copper chloride dihydrate and stronger (compared to the bromide system) salting-out of cadmium chloride hydrate. Considerable redistribution of bromide ions in favor of cadmium bromide results in a change of the solid phase from the terahydrate to the anhydrous salt at relatively low concentrations of the second component.

REFERENCES

1. Skripkin, M.Yu. and Chernykh, L.V., *Zh. Neorg. Khim.*, 1994, vol. 39, no. 10, pp. 1747–1751.
2. Chernykh, L.V. and Skripkin, M.Yu., *Zh. Obshch. Khim.*, 1996, vol. 66, no. 1, pp. 26–30.
3. Chernykh, L.V. and Skripkin, M.Yu., *Koord. Khim.*, 1996, vol. 22, no. 5, pp. 413–416.
4. Bassett, H. and Strain, R.N.C., *J. Chem. Soc.*, 1952, no. 5, pp. 1795–1802.
5. Sillen, L.G. and Martell, A., *Stability Constants of Metal–Ion Complexes*, New York: Pergamon, 1976.
6. Kumok, V.N., Kuleshova, O.M., and Karabin, L.A., *Proizvedeniya rastvorimosti* (Solubility Products), Novosibirsk: Nauka, 1983.
7. Schreinemakers, F.A.H. and Baat, W.C. de., *Z. Phys. Chem.*, 1908–1909, vol. 65, pp. 555–559.
8. Benrath, A. and Lechner, K., *Z. Anorg. Chem.*, 1940, vol. 244, pp. 359–365.

Russian Journal of Applied Chemistry, Vol. 74, No. 7, 2001, pp. 1085–1087. Translated from Zhurnal Prikladnoi Khimii, Vol. 74, No. 7, 2001, pp. 1057–1059.

INORGANIC SYNTHESIS AND INDUSTRIAL INORGANIC CHEMISTRY

Composite Silver Bromide Based T-Crystals of Epitaxial Type

B. A. Sechkarev, E. V. Prosvirkina, T. A. Larichev, A. N. Utekhin, and A. A. Kol'miller

Kemerovo State University, Kemerovo, Russia

Received December 7, 2000

Abstract—The process was studied in which heterocontact microcrystals based on silver bromide are obtained in bulk crystallization. The influence exerted by parameters of the crystallization process on the epitaxial growth was revealed. The conditions were determined for obtaining the AgBr/AgCl and AgBr/AgSCN epitaxial systems with the use of substrate-type tabular AgBr microcrystals (T-crystals of AgBr).

Epitaxial crystals constitute an extremely interesting system as regards both carrying out fundamental studies of the mechanism of microcrystal growth in bulk crystallization and solving practical problems of interaction between photographically active (sensitizing, stabilizing, antifogging, developing, etc. agents) substances with the surface of a heterophase microcrystal. That is why these crystals attract close attention of researchers all over the world [1–3]. Recently, numerous attempts have been made to create a material based on epitaxial microcrystals. Quite a number of rather unexpected effects have been revealed, with no scientific explanation provided so far [4, 5].

Here we made an attempt to reveal basic mechanisms and driving forces of the processes in which heterocontact microcrystals of epitaxial type are formed in bulk crystallization. Heterocontact systems were studied in bulk crystallization of AgBr/AgCl and AgBr/AgSCN epitaxial microcrystals. Simultaneously, we made an attempt to determine the possibilities opened up by the use of epitaxial systems in studying the fundamental problems of modern photographic chemistry.

EXPERIMENTAL

As substrate were used tabular AgBr crystals (T-crystals of AgBr) with average equivalent diameter $d = 2.0 \pm 0.2$ μm, coefficient of size variation C_v = 40%, and crystallographic uniformity S_T = 90%. The epitaxial systems were grown in the absence of any growth modifiers or organic dyes.

It is known from the literature that an important parameter of the epitaxial growth is the structural-geometric similarity of the planes growing together [6]. Thus, epitaxy of silver chloride and bromide is seemingly possible because of the isomorphism of these compounds and their close lattice constants.

However, it was found that no epitaxial growth is observed upon addition of a fine-grained emulsion (FGE) of AgCl to the substrate and subsequent co-crystallization at T = 60°C and pAg 7.6. Alternate introduction of $AgNO_3$ and KCl into an aqueous gelatin solution with substrate-type T-crystals of AgBr does not lead to epitaxial system growth, either.

It was established that addition of potassium iodide to the AgBr matrix and subsequent alternate introduction of $AgNO_3$ and KCl leads to growth of silver chloride epitaxial microcrystals on substrate-type T-crystals of AgBr. In the course of the experiment, the concentrations of the delivered reagent solutions were varied between 0.01 and 0.1 M. It was demonstrated that angular epitaxy of silver chloride is observed even at reagent solution concentrations of 0.02 M (Fig. 1).

Also noteworthy is the fact that, at high concentrations of the supplied reagent solutions, nonepitaxial growth of the chloride phase is observed over the

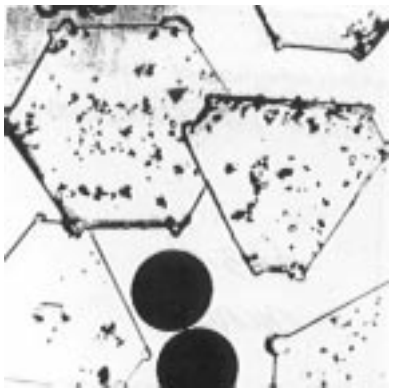

Fig. 1. Electron micrograph of a carbon replica of T-AgBr with AgCl epitaxial microcrystals. Internal reference latex; d = 0.914 μm; C_v = 5%.

1070-4272/01/7407-1085$25.00

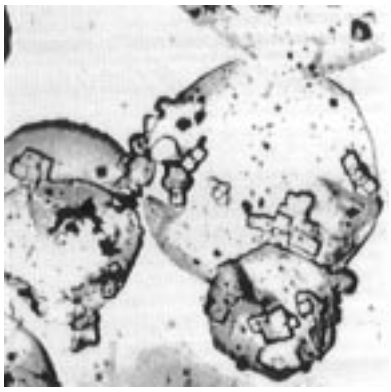

Fig. 2. Electron micrograph of a carbon replica of T-AgBr with nonepitaxial AgCl regions.

entire AgBr T-crystal surface that is not defect-free (Fig. 2). On separate parts of the surface of AgBr T-crystals, relatively large pyramidal structures are discernible, smoothly adjoining the surface of the substrate microcrystal. Possibly, this is due to the nonuniform deposition of silver iodide over the substrate surface. It may be assumed that those parts of the AgBr T-crystal surface which are covered with a layer of silver iodide serve as effective crystallization centers for AgCl epitaxial microcrystals. In this case, deposition of excess silver bromide from solution onto the silver iodide free parts of the surface and growth of the base microcrystal in the direction perpendicular to the {111} plane to form a pyramidal structure are possible when pAg increases steeply. Such a behavior of the system can, in our opinion, be accounted for by the fact that ion exchange occurs in cocrystallization of silver chloride and bromide: chlorine ions are introduced into the AgBr crystal lattice, whereas silver ions cannot form nuclei with chlorine ions because of the Coulomb repulsion from silver ions belonging to the substrate lattice.

Under the chosen crystallization conditions, iodide ions cannot penetrate inside the AgBr lattice because of the large difference between the solubilities of silver iodide and bromide. Therefore, they are adsorbed on the crystal lattice surface and serve as crystallization centers for silver chloride epitaxial microcrystals.

In this set of experiments, the optimal rate of reagent solution supply in crystallization was found to be 0.002 mmol min^{-1}.

Rather unexpected was the observed strong influence exerted by the crystallization process conditions (temperature, concentration of reagent solutions, and their delivery rate) on the epitaxial growth of AgSCN. It is known that silver thiocyanate is a good solvent for any silver halide [7] and, therefore, no significant dependence of the epitaxial growth on crystallization conditions would be expected. The observed dependence can be understood on making the following assumptions. It is known that formation of epitaxial microcrystals is preceded by the stage of solute adsorption on the substrate [6]. Therefore, differences in adsorption may lead to difference in epitaxial growth. In its turn, the adsorption is strongly affected by conditions in the sorption system (temperature, concentration of sorbates, etc.). In particular, the surface concentration of the adsorbate strongly depends on temperature and the solute concentration. It may be assumed that, on raising the concentration of silver thiocyanate in solution at 50°C, the adsorption of silver on the surface of AgBr T-crystals is unhindered. Naturally, the adsorption primarily proceeds in those areas where the surface energy is reduced to the maximum extent by adsorption. These places of preferential adsorption are the active elements of the AgBr T-crystal surface: edges and vertices. However, adsorption also occurs on the surface of basal (large) and lateral faces of the AgBr T-crystal because of the higher activity of {111} planes, compared with {100}. The edges and vertices are degenerate fast-growing faces of the crystal and, by the virtue of this fact, they are places of the most intensive mass exchange with the sorption medium. Local egress of ions may give rise to a surface with even higher effectiveness of silver thiocyanate adsorption.

In this case, the new surface becomes thermodynamically stable upon thiocyanate adsorption. Therefore, an effect similar to crystal etching is observed on repeatedly performing the given process (Fig. 3a). Silver bromide cannot fill the forming etching pits since the surface is protected by firmly adsorbed silver thiocyanate. In this case, deposition of silver bromide occurs in some other place of the crystal, in all probability on its basal planes, since under the crystallization conditions the growth of the {111} surface is rather effective. In the absence of silver thiocyanate, physical ripening of substrate crystals under the same conditions does not lead to formation of etching pits since there exists no hindrance to their being filled with silver bromide and the difference between the surface energies of the {111} and {100} faces is insufficient for effective mass transfer to occur. With increasing temperature, the situation changes. At 60°C, adsorption on the surface of the basal planes of the T-crystal becomes less effective. In this case, the edges and vertices of the T-crystal (where the matching of the AgBr and AgSCN lattices is the best) may primarily act as places of effective adsorption. Therefore, silver thiocyanate is accumu-

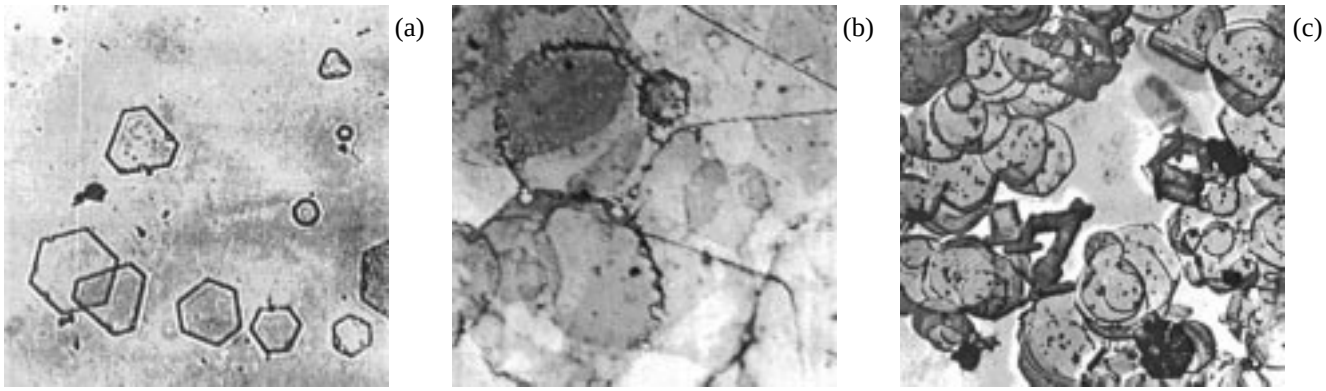

Fig. 3. Electron micrographs of carbon replicas of T-AgBr/AgSCN, obtained at different temperatures. Temperature (°C): (a) 50, (b) 60, and (c) 70.

lated in solution in the course of crystallization (supersaturation grows fast), which leads in the end to heterogeneous nucleation on the surface of the existing monolayer of AgSCN. In this way grows the epitaxial microcrystal, with the region of epitaxy limited to that of the effective adsorption of silver thiocyanate under the given conditions (Fig. 3b). However, in the case of a very low degree of supersaturation (low rate of reagent solution introduction), the adsorption on the surface of AgBr T-crystals becomes a more effective channel of silver thiocyanate consumption and the situation at 50°C is reproduced (Fig. 4). Finally, at 70°C, adsorption becomes ineffective even at vertices and edges. In this case, silver thiocyanate is accumulated in solution (supersaturation grows) until the critical level of homogeneous nucleation is reached. Under these conditions, AgSCN microcrystals nucleate and grow in the form of a separate independent phase (Fig. 3c).

A study of the influence exerted by epitaxial microcrystals of the indicated composition on the chemical sensitization of heterocontact systems AgBr T-crystal/AgCl revealed the following general features: for epitaxial systems, the time of chemical sensitization, i.e., the time in which the maximum light sensitivity is achieved, is shorter than that for the conventional emulsion-type AgBr T-crystals. When the maximum light sensitivity is achieved, the optical density of the fog of the epitaxial systems much exceeds that for the reference. It is shown that a smaller amount of a sensitizing agent is required for achieving the highest sensitivity of the epitaxial systems, and, therefore, photographic materials based on AgBr T-crystals with epitaxial microcrystals must be more stable in storage.

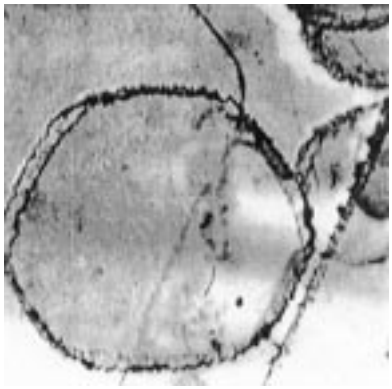

Fig. 4. Electron micrograph of a carbon replica of T-AgBr/AgSCN.

CONCLUSIONS

(1) A study of how heterocontact silver bromide based microcrystals are obtained in bulk crystallization revealed the influence of parameters of the crystallization process on the epitaxial growth.

(2) The effectiveness of epitaxial growth is determined by the possibility of adsorption of the material constituting the epitaxial microcrystals on the matrix of the AgBr T-crystal and by conditions in the sorption system.

REFERENCES

1. Maskasky, J.E., *Photogr. Sci. Eng.*, 1981, vol. 25, no. 3, pp. 96–101.
2. Maskasky, J.E., *J. Imag. Sci.*, 1988, vol. 32, no. 4, pp. 160–168.
3. Stepanov, A.L., Burda, A.V., and Stolov, A.L., *Zh. Nauchn. Prikl. Fotogr. Kinematogr.*, 1989, vol. 34, no. 6, pp. 468–472.
4. US Patent 4435501.
5. US Patent 5631126.
6. Chernov, A.E., Givargizov, E.I., Bagdasarov, Kh.S., *et al.*, *Sovremennaya kristallografiya* (Modern Crystallography), vol. 3: *Obrazovanie kristallov* (Formation of Crystals), Moscow: Nauka, 1980.
7. *The Theory of the Photographic Process*, James, T.H., Ed., New York: Macmillan, 1977.

Russian Journal of Applied Chemistry, Vol. 74, No. 7, 2001, pp. 1088–1092. Translated from Zhurnal Prikladnoi Khimii, Vol. 74, No. 7, 2001, pp. 1060–1064.

INORGANIC SYNTHESIS AND INDUSTRIAL INORGANIC CHEMISTRY

Synthesis of Ultradisperse Corundum from Industrial Waste

A. A. Khanamirova

Institute of General and Inorganic Chemistry, National Academy of Sciences of Armenia, Yerevan, Armenia

Received October 30, 2000

Abstract—The method is developed for fabrication of nonaggregated submicrocrystalline chemically active corundum from the production waste of capacitor aluminum foil. Such corundum is practically free of alkali metal impurities and has good rheological properties.

Many up-to-date technologies use corundum ceramics, which is hard, chemically inactive, and corrosion-resistant, has high compression strength and low friction coefficient, and is compatible with biological objects [1, 2]. Potentialities of corundum ceramics are highly appreciated [3]. However, the dynamic friability and low tensile strength limit its applicability. Studies showed that the properties of the ceramics could be appreciably improved by increasing diffusion coefficient and decreasing particle size. A universal route for preparing ceramics with prescribed properties is taking the components in the ultradisperse state (with no more than 100–150-nm particles). In such ultradisperse ceramics a unique combination of mechanical properties can be attained, including high hardness and superelasticity [2, 4–7].

To prepare such corundum ceramics, it is necessary to use α-Al_2O_3 as pure, nonaggregated powder with submicrorystalline (100–40 nm) or nanocrystalline (40–1 nm) particles. Its high dispersity and the minimal content of impurities facilitate mineralization in the course of formation of the ceramic structure, decrease the sintering temperature, retard particle growth, and increase the mechanical strength and heat resistance [1]. The necessity of disaggregating corundum powders is dictated by the fact that aggregated particles are sintered first, whereas between the aggregates coarse pores are formed, remaining in the ceramics, which decreases its density and results in nonuniform crystallization [8].

Ultradisperse monofractional powders can be obtained by various methods [2, 6–11]. Among them are the chemical and physical procedures, thermal decomposition of disperse chemical compounds with modifiers [12], and mechanical disintegration [13, 14]. Certain physicochemical methods allow attainment of a 100–10-nm dispersity. At the same time, they have a number of disadvantages, including complexity, high cost, and specificity. Mechanochemical treatment allows ceramic materials with the similar dispersity to be synthesized under milder conditions, provides control of their structure and properties, and intensifies sintering [15]. However, after the limiting particle size is attained, the disintegration ceases, and ultradisperse particles start to interact via van der Waals forces to form dense molecular aggregates [16, 17].

The final stage of high-temperature sintering of ceramic materials, when open (intergranular) porosity is mainly removed, is recrystallization [1, 18]. The studies showed that the original corundum crystals 1–3 μm in size start growing at 7.5–10% porosity. At a porosity of 2.5 and 0.5–1% their size increases to 6 and 18–8 μm, respectively [1]. Evidently, for preparing nonporous corundum, it is necessary to retard crystal growth till complete removal of pores from the cake.

To intensify sintering, decrease its temperature, and retain small ceramic grains, it is recommended to perform sintering in the presence of dopants protecting the crystals of the growing phase and retarding their fast growth [12, 19]. The sintering temperature of corundum can be decreased by mechanical activation [20]. For fabricating nanocrystalline nonaggregated corundum, a method has been developed including mechanical activation of α-Al_2O_3 at 40*g* load in the presence of disaggregating substance, removal of the latter by boiling of disintegrated corundum with hydrochloric acid, and sintering of purified corundum at 1270°C to obtain submicrocrystalline ceramics [21].

Fabrication of ultradisperse (0.5–1.0 μm) α-Al_2O_3 with a low content of alkali impurity (0.02–0.06 wt % Na_2O) in hydrochemical, thermochemical, mechanochemical, and radiation-thermal reprocessing

1070-4272/01/7407-1088$25.00

of aluminum hydroxides and oxides of different origin in the presence of dispersing and disaggregating inorganic and organic substances has been studied previously.

In this work, a method involving sequential thermochemical and mechanochemical activation was developed for preparing nonaggregated submicrocrystalline high-purity α-Al_2O_3 from cheap disperse industrial aluminum hydroxide.

EXPERIMENTAL

Anodic sludge, a large-tonnage residue of the production of capacitor foil by electrolytic pickling of aluminum, was the raw material. The composition of the initial anodic sludge was (wt %) 6.25 Na_2O, 0.056 SiO_2, and 0.006 Fe_2O_3 at a 60% moisture content. The aggregate size was 3–10 μm. and the size of the aggregate single crystals, 0.5–3 μm. The sludge was washed with distilled water and treated hydrochemically [22]. The resulting anodic aluminum hydroxide (AAH) had the bayerite structure and contained (wt %) 0.04 Na_2O, 0.053 SiO_2, and 0.006 Fe_2O_3 (based on Al_2O_3). The main part (~80%) consisted of individual single crystals (0.5–1 μm) and ~20%, of loose friable aggregates (3–5 μm).

The thermochemical activation of AAH was performed in the presence of ultradisperse mineralizers (ammonium fluoride, aluminum acetate, and aluminum citrate) and modifiers (manganese acetate tetrahydrate and manganese citrate hydrate). The mineralizers and modifiers were added to AAH as saturated solutions at pH 3–3.5. The mixture was thoroughly agitated and dried in air. Such a procedure assists the uniform distribution of the additive particles in the bulk of $Al(OH)_3$, which is preserved on further heating of the mixture, thus intensifying interaction of its components and decreasing the temperature of polymorphous transitions. The thermal decomposition of AAH containing additives was performed in an electric furnace with Silit heaters at 1000–1200°C (heating rate 7 deg min^{-1}) for 0.5–5 h.

The α-Al_2O_3 powder formed under the optimal conditions of the thermochemical treatment of bayerite was subjected to mechanical treatment for a short time (1–10 min) in the presence of microadditives (0.01–0.07 wt %) of OP-7 nonionic surfactant in a planetary mill at comparatively low centrifugal load, (8–15)*g*.

To confirm the feasibility of fabricating ultradisperse corundum ceramics from mechanochemically treated submicrocrystalline corundum, the latter was sintered at 1000–1350°C for 1–5 h in single tests with addition of magnesium acetate (0.2 wt % in terms of MgO) and citric acid (0.05 wt %) into the charge.

Content of mineralizers and modifiers for fabricating ultradisperse corundum with a low content of alkali impurities by thermochemical treatment of AAH (1025°C, 2 h)

Formulation*	Content, wt %		
	1	2	3
I	3.3	4.2	0.9
	3.5	3.6	0.8
	3.9	3.0	0.8
II	3.5	3.9	0.9
	3.8	3.3	0.8
	4.2	2.8	0.8

* Components: (I) (1) aluminum acetate, (2) manganese acetate tetrahydrate, and (3) ammonium fluoride; (II) (1) aluminum citrate, (2) manganese citrate hydrate, and (3) ammonium fluoride.

The content of impurities in the samples was determined by standard methods of analysis [23]. The phase composition and the size of the single crystals and aggregates were determined by the crystal optical method on a POLAM P-112 polarization microscope [23]. The size of submicrocrystallites was determined by X-ray diffraction on a DRON-4 apparatus from broadening of the reflection maxima *hkl* [24].

Based on the results obtained, we determined the optimal content of mineralizers and modifiers (see table) and the optimal conditions of thermochemical treatment of AAH (1025°C, 2 h). α-Al_2O_3 formed under these conditions contains about 0.008 wt % Na_2O and consists mainly (90%) of separate single crystals 0.200–0.003 μm in size, with the remainder (~10%) being unstable aggregates of 3–5 single crystals.

Such ultradisperse corundum subjected to mechanochemical treatment under the optimal conditions (centrifugal load 15*g*, 5 min, 0.07 wt % OP-7) contains virtually no aggregates and alkali impurities and consists of separate single crystals 0.080–0.085 μm in size. It is chemically active, shows good rheological properties, and forms dense submicrocrystalline corundum ceramics when sintered with the modifier and dispersant at 1350°C for 3 h.

Numerous studies showed that the solid phase formed in a multistep topochemical process inherits the structure of the preceding solid phase [25]. This suggests that the properties of the resulting submicro-

crystalline corundum were established in the stage of formation of the anodic sludge and AAH.

Because the anodic sludge was formed at electrochemical activation of aluminum, its particles have excess energy. They are colloid-polymeric discrete formations in the form of aggregates of aluminum hydroxide with the electrolyte (NaCl). The majority of electrolyte ions in the anodic sludge is physically sorbed in pores, and the remaining ions are incorporated into $Al(OH)_3$ micelles instead of the hydroxide ions and protons and are held there owing to chemical affinity [26]. After the hydrochemical treatment [22] with the dispersant, the activity and dispersity of AAH grow.

The thermochemical activation is caused by the presence of dispersing, disaggregating, and mineralizing thermally unstable chemical substances upon AAH decomposition. The organometallic compounds of aluminum and manganese decompose in the temperature interval of the bayerite–boehmite transformation when their most finely dispersed and active state is realized owing to formation of anionic vacancies upon water removal. In the process are formed nanometric particles of hydroxides and oxides of aluminum and manganese [27], which in the bulk of bayerite become centers of crystallization of ultradisperse α-Al_2O_3 and facilitate dispersion and disaggregation of its crystals. Manganese(II) oxide formed by transformation of the Mn^{2+} salt has enhanced reactivity (the Headwall effect), which favors formation of aluminum–manganese spinel $MnAl_2O_4$ above 1000°C [25]. With addition of Mn^{2+} ion whose radius (0.91 Å) is larger than that of Al^{3+} (0.57 Å), the γ-Al_2O_3 phase becomes less stable, and new vacancies are formed owing to tensile stresses [28]. As a result, diffusion is facilitated, which leads to the decrease in the apparent activation energy and temperature of the γ-Al_2O_3–α-Al_2O_3 transition and to the increase in the corundum dispersity.

The gases evolved upon decomposition of NH_4F and organometallic compounds are sorbed by $Al(OH)_3$, AlOOH, and γ-Al_2O_3 and diffuse into the space free from crystals and aggregates, which increases the γ-Al_2O_3 dispersity and accelerates its transformation into α-Al_2O_3 at lower temperatures. The gases react with the alkali metal ions migrated onto the surface of the bayerite and boehmite crystals with the formation of salts evaporating upon calcination.

The positive technological effect of the mechanical treatment of ultradisperse corundum subjected to thermochemical activation is attained owing to the change in its physicochemical properties [13, 14, 29, 30] resulted from the stress field relaxation after mechanical action. Due to mechanochemical activation, centers, predominantly of radical origin, are formed on the surface [31], and the near-surface layers of the particles undergo elastic deformation to form dense molecular aggregates. For the formation of nonaggregated α-Al_2O_3, apart from the mechanical action, the surface physicochemical phenomena responsible for the aggregation also play the important role [16]. Such physicochemical phenomena may be provided by introduction of surfactants [32]. The surfactant as monomolecular layer wets the whole surface of ground and activated α-Al_2O_3 grains and diffuses along the steric structural defects, thus facilitating disintegration under the action of capillary forces, preventing α-Al_2O_3 aggregation and assisting disaggregation of the initial powders [33]. The mechamism of such mechanosorption effect involves mechanical cracking of the sorbed surfactant molecules onto more active unsaturated free radicals [14, 29, 34, 35], their chemical interaction with active centers on the α-Al_2O_3 surface, diffusion along the structural defects, and formation of dense molecular aggregates from dispersed particles. The mechanosorption effect assisting corundum disintegration can attain 600–800% [17]. The mechanochemical activation in the presence of OP-7 assisted not only disintegration and disaggregation of α-Al_2O_3 particles, but also their passage into the nonequilibrium state characterized by enhanced reactivity, better plasticity, lower sintering temperature, and slower grain growth.

The submicrocrystalline corundum activated by mechanochemical treatment was sintered with the modifier (Mg) and dispersant (citric acid). Magnesium acetate added to the charge decomposes above 400°C with formation of nanosized highly reactive MgO [27]. The latter is distributed throughout the boundary of the α-Al_2O_3 phase as thin layer, and above 1000°C it forms aluminum–magnesium spinel $MgAl_2O_4$ impeding uncontrollable recrystallization of the corundum grains up to formation of a practically nonporous cake.

Like $MgAl_2O_4$, aluminum–manganese spinel $MnAl_2O_4$ entering the charge along with α-Al_2O_3 is the structural modifier of corundum ceramics. The presence of manganese(II) in the slip ensures formation of the melt wetting well α-Al_2O_3 crystals, decreases the sintering temperature, facilitates formation of the finely crystalline ceramic structure, and enhances the strength, plasticity, and endurance of the ceramics [36, 37]. Small amounts of citric acid control rheological properties of the molded masses on the basis of ultradisperse α-Al_2O_3 having the high surface

and bulk energy and high surface tension [38]. The citric acid molecules, being adsorbed on the corundum grain boundaries and diffusing into the intercrystal space, assist spontaneous disintegration of grains, facilitate disaggregation owing to break of intermolecular interactions, stabilize aqueous corundum dispersion, and decrease the sintering temperature.

CONCLUSIONS

(1) Submicrocrystalline corundum with high purity, low tendency to aggregation, good rheological properties, and high sinterability was prepared from the capacitor foil production waste sequentially subjected to hydrochemical treatment under mild conditions, low-temperature thermochemical activation, and low-intensity mechanochemical activation in the presence of dispersants and disaggregators (without additional operations for their removal).

(2) In reprocessing into submicrocrystalline corundum, anodic sludge and anodic aluminum hydroxide have undoubted advantages over technical-grade aluminum hydroxide and aluminum oxide, because anodic sludge is a cheap and ultradisperse material (3–10-μm grains against 20–150 μm in technical-grade aluminum hydroxide) from which alkali metal impurities can be almost completely washed out (95–98% against 20–50% in technical-grade aluminum hydroxide).

REFERENCES

1. Kainarskii, I.S., Degtyareva, E.V., and Orlova, I.G., *Korundovye ogneupory i keramika* (Corundum Refractory Materials and Ceramics) Moscow: Metallurgiya, 1981.
2. Maslennikova, G.N., Mamaladze, R.A., Mudzita, S., and Koumoto, K., *Keramicheskie materialy* (Ceramic Materials), Moscow: Stroiizdat, 1991.
3. Partner for Success, *Ceram. Ind. Int.*, 1991, vol. 101, no. 1087, pp. 8–9.
4. Morokhov, I.D., Trusov, L.I., and Lapovok, V.N., *Fizicheskie yavleniya v ultradispersnykh sredakh* (Physical Phenomena in Ultradisperse Media), Moscow: Energoatomizdat, 1984.
5. Gleiter, H., *Nanostr. Mater.*, 1992, vol. 1, no. 1, pp. 1–30.
6. Andrievskii, R.A., *Usp. Khim.*, 1994, vol. 63, no. 5, pp. 431–444.
7. Gusev, A.I., *Usp. Fiz. Nauk*, 1998, vol. 168, no. 1, pp. 55–83.
8. Lukin, E.S., *Tr. Mosk. Khim.-Tekhnol. Inst. im. D.I. Mendeleeva*, 1982, no. 123, pp. 5–13.
9. Vlasov, A.S., *Ross. Khim. Zh.*, 1998, vol. 42, no. 6, pp. 152–156.
10. Vasserman, I.M., *Khimicheskoe osazhdenie iz rastvorov* (Chemical Deposition from Solutions), Leningrad: Khimiya, 1980.
11. Nano-primed, *Chem. Eng*. (USA), 1999, vol. 106, no. 4, pp. 39–40.
12. Lukin, E.S., *Ogneupory Tekh. Keram.*, 1996, no. 4, pp. 2–13.
13. Avvakumov, E.G., *Mekhanokhimicheskie metody aktivatsii khimicheskikh protsessov* (Mechanochemical Activation of Chemical Processes), Novosibirsk: Nauka, 1986.
14. Heinicke, G., *Tribochemistry*, Berlin: Akademie, 1984.
15. Zyryanov, V.V., in *Mekhanokhimicheskii sintez v neorganicheskoi khimii* (Mechanochemical Synthesis in Inorganic Chemistry), Novosibirsk: Nauka, 1991, pp. 102–125.
16. Rebinder, P.A., *Fiziko-khimicheskaya mekhanika: Novaya oblast' nauki* (Physicochemical Mechanics: A Novel Field of Science), Moscow: Znanie, 1958, ser. 4, nos. 39–40, pp. 3–20.
17. Khodakov, G.S. and Rebinder, P.A., *Kolloidn. Zh.*, 1960, vol. 22, no. 3, pp. 365–372.
18. Geguzin, Ya.E., *Fizika spekaniya* (Physics of Sintering), Moscow: Nauka, 1984.
19. *Khimicheskaya tekhnologiya keramiki i ogneuporov* (Chemical Technology of Ceramic and Refractory Materials), Budnikov, P.P., Ed., Moscow: Stroiizdat, 1972.
20. Kieffer, R., Heimke, G., Wruss, W., and Vendi, A., *Tonind-Ztg.*, 1972, vol. 96, no. 2, pp. 317–332.
21. Karagedov, G.P., and Lyakhov, N.Z., *Khim. Inter. Ustoich. Razv.*, 1999, vol. 7, no. 3, pp. 229–238.
22. USSR Inventor's Certificate no. 908747.
23. *GOSTs* (State Standards) *13583.5–97, 25733–97, and 25734–97: Alumina. Technical Specifications*.
24. Aleksandrov, I.V., and Valiev, R.Z., *Fiz. Met. Metalloved.*, 1994, vol. 77, no. 6, pp. 77–87.
25. Tret'yakov, Yu.D., *Tverdofaznye reaktsii* (Solid-Phase Reactions), Moscow: Khimiya, 1978.
26. Bogoyavlenskii, A.F., *Zh. Prikl. Khim.*, 1972, vol. 45, no. 3, pp. 682–687.
27. Gribov, B.T., Domrachev, G.A., Zhuk, B.V., *et al.*, *Osazhdenie plenok i pokrytii razlozheniem metalloorganicheskikh soedinenii* (Deposition of Films and Coatings by Decomposition of Organometallic Compounds), Moscow: Nauka, 1981.
28. Balkevich, V.L., Belyakov, A.V., Men'kova, E.P., and

Safronova, T.A., *Tr. Mosk. Khim.-Tekhnol. Inst. im. D.I. Mendeleeva*, 1985, no. 137, pp. 77–87.

29. Butyagin, P.Yu., *Usp. Khim.*, 1971, vol. 40, no. 11, pp. 1935–1954.
30. Boldyrev, V.V., *Eksperimental'nye metody mekhanokhimii tverdykh neorganicheskikh veshchestv* (Experimental Methods of Mechanochemistry of Solid Inorganic Substances), Novosibirsk: Nauka, 1983.
31. Butyagin, P.Yu., *Usp. Khim.*, 1984, vol. 53, no. 11, pp. 1769–1789.
32. Khodakov, G.S., *Fizika izmel'cheniya* (Physics of Disintegration), Moscow: Nauka, 1972.
33. Khodakov, G.S., *Kolloidn. Zh.*, 1998, vol. 60, no. 5, pp. 684–697.
34. Baramboim, N.K., *Mekhanokhimiya vysokomolekulyarnykh soedinenii* (Mechanochemistry of Macromolecular Compounds), Moscow: Khimiya, 1978.
35. Butyagin, P.Yu., *Usp. Khim.*, 1994, vol. 63, no. 12, pp. 1031–1043.
36. Kukolev, G.V., *Zh. Vses. Khim. O–va. im. D.I. Mendeleeva*, 1960, vol. 5, no. 2, pp. 134–140.
37. Ozawa, M., Kato, O., Suzuki, S., *et al.*, *J. Mater. Sci. Lett.*, 1996, vol. 15, no. 7, pp. 564–567.
38. Hidber, P.C., Glaule, T.J., *et al.*, *J. Am. Ceram. Soc.*, 1996, vol. 79, no. 7, pp. 1893–1897.

Russian Journal of Applied Chemistry, Vol. 74, No. 7, 2001, pp. 1093–1097. Translated from Zhurnal Prikladnoi Khimii, Vol. 74, No. 7, 2001, pp. 1065–1069.

INORGANIC SYNTHESIS AND INDUSTRIAL INORGANIC CHEMISTRY

Improvement of the Iodine and Bromine Production Processes

G. A. Vlasov, N. D. Bushina, G. I. Buravtseva, and L. V. Mukhametshina

Perm Branch, Prikladnaya Khimiya Russian Scientific Center, Perm, Russia

Received May 17, 1999; in final form, October 2000

Abstract—Ways to improve the existing process for iodine and bromine production from iodine-containing drill waters were studied.

Various types of mineral raw materials, such as seawater, brine of salt lakes, solutions from processing potassium-containing minerals, and underground waters and brines, are used in the iodine and bromine production. Depending on the type and characteristics of the raw materials, various methods and flowsheets are used, including highly expensive and obsolete. Therefore, it is urgent to improve the existing technology for processing of iodine- and bromine-containing raw materials and to develop new high-performance processes increasing the economic efficiency and environmental safety of the iodine and bromine production.

In the existing process [1] of treatment of drill water containing 9–10 mg l^{-1} of iodide ions and up to 750 mg l^{-1} of bromide ions as salts, first extracted is bromine and then iodine. The drill water after removal of bromine is directed to iodine extraction. It contains up to 60 mg l^{-1} of oxidants, including elemental bromine and chlorine and also iodate ions. For iodine adsorption on coal, iodate ions should be preliminarily reduced with sodium sulfite. Simultaneously, redox reactions of sodium sulfite with chlorine and bromine proceed in drill water, and the consumption of sodium sulfite in side reactions exceeds its amount required for the reduction of iodate ions.

The necessity of reducing iodate ions rises the cost of the iodine extraction from raw materials and makes the process of iodine production insufficiently profitable. Therefore, the development of efficient processes for treatment of drill water with primary extraction of iodine is of practical interest.

Conventional oxidants (compounds of active chlorine) failed to solve the problem of selective oxidation of iodide ions in drill water containing considerable amounts of bromide ions (compared to iodide ions), because of simultaneous oxidation of bromide ions (to elemental bromine). The use of sodium nitrite and nitrosylsulfuric acid, which selectively oxidize iodide ions in a weakly acid medium, results in the liberation of highly toxic nitrogen oxides, which should be recovered for reuse [1, 2].

A procedure was published [3] for the isolation of iodine from drill waters by oxidation of iodide ions to iodate ions in a part of drill waters with ozone at pH 7–8, subsequent acidification of this part of waters by sulfuric acid, and mixing with 4–5 parts of the initial drill water. The yield of iodine in this case reaches 96%. The drawbacks of this procedure are the formation of a precipitate on alkalization of the initially weakly acidic drill waters and also the liberation of elemental bromine in water oxidized with ozone due to partial oxidation of bromide ions.

Of interest are the data [4] on oxidation of iodide ions in a liquid medium containing up to 150 g of NH_4I per 100 g of water with oxygen or an oxygen-containing gas in the presence of compounds of transition metals [Fe(III), Co(II), Ni(II), Cu(II), etc.] and a weak acid or hydrophosphates. The oxidation is carried out at 20–100°C and oxygen partial pressure of 0.2–10 kg cm^{-2}. The yield of iodine is 50–82%.

Taking into account the goal of the study and the above-discussed processes, we examined selective oxidation of iodide ions to iodine in iodine- and bromine-containing drill water by atmospheric oxygen with ozone added to initiate oxidation, and also with iron(II) salt added to prevent the accumulation of bromine released from the oxidation of bromide ions in the drill water. As a reducing agent we used iron(II) chloride, which was obtained from 30% solution of $FeCl_3$ (a waste of bromine production) and iron shavings. Drill water was acidified with hydrochloric acid and oxidized with an ozone–air mixture containing 0.5–0.8 mg l^{-1} of ozone.

1070-4272/01/7407-1093$25.00

Table 1. Oxidation of iodide and bromide ions in drill water by an ozone–air mixture

Run no.	Acidity of drill water, mequiv l^{-1}	Specific consumption of ozone–air mixture, $l\ l^{-1}\ min^{-1}$	Weight ratio Fe^{2+}/I^- in water	Concentration of I_2				Concentration of Br_2			
				mg l^{-1}, in oxidized water at indicated ozonation time, min							
				1	2	3	5	1	2	3	5
1	0.15	0.1	–	2.25	2.58	5.07	6.63	2.1	1.4	2.4	1.9
2	0.50	0.1	–	3.92	7.72	9.16	9.29	0.6	0.2	0.5	0.6
3	1.00	0.1	–	6.54	7.27	7.80	7.59	0	0.6	0.1	1.0
4	3.00	0.1	–	5.77	5.91	9.57	9.67	0	1.8	1.3	0.7
5	0.50	0.1	0.66	2.23	3.00	7.39	8.37	0	0	0	0
6	1.00	0.1	3.9	6.26	7.69	8.11	7.71	0	0	0	0
7	1.50	0.1	0.66	6.09	6.97	8.11	9.37	0	0	0	0
8	3.00	0.1	11.6	2.13	6.63	9.05	10.0	0	0	0	0
9	0.50	0.17	0.66	4.72	4.84	8.76	8.76	0	0	0	0
10	1.00	0.17	3.9	7.85	7.98	9.16	8.76	0	0	0	0
11	1.00	0.17	–	7.00	6.80	9.00	7.71	0	0.2	0.4	0.7
12	3.00	0.17	11.6	5.27	7.91	9.89	10.0	0	0	0	0
13	3.00	0.17*	9.6	0	0	0	0	0	0	0	0

* In run no. 13 drill water with $FeCl_3$ added and air without ozone were used.

We oxidized drill water from iodine–bromine production containing 750 mg l^{-1} of bromide ions and 10 mg l^{-1} of iodide ions as salts, and also prepared on its basis water samples containing 50 mg l^{-1} of I^- and 150 mg l^{-1} of Br^-. The experimental data are given in Table 1.

Table 1 shows that iodide ions are not oxidized in acidified drill water in air without ozone even in the presence of an iron(III) salt (Table 1, run no. 13), which is probably due to the extremely low reaction rate at low concentrations of iodide ions. Iodine appears in the drill water only after air bubbling for 1 h, which is unacceptable for processing large volumes of waters under production conditions.

When preliminarily acidified drill water is treated with ozone–air mixture, iodide ions are oxidized fairly actively at the rate of the mixture feeding of 0.1–0.17 $l\ l^{-1}\ min^{-1}$. Depending on the oxidation time τ, the yield of iodine reaches 80 (τ = 2 min) and 90–100% (τ = 3–5 min), which allows the process to be performed in the continuous mode. The consumption of ozone for the oxidation of iodide ions was much less than the stoichiometric amount required for the reaction

$$2I^- + O_3 + 2H^+ \rightarrow I_2 + O_2 + H_2O.$$

This fact suggests that iodide ions are oxidized with atmospheric oxygen, and ozone acts only as the oxidation initiator.

Table 1 shows that the addition of iron(II) chloride in the amount of 0.66 wt parts of Fe^{2+} per 1 wt part of I^- to drill water prevents the formation of elemental bromine, which suggests the occurrence of the fairly fast redox reaction

$$2Fe^{2+} + Br_2 \rightarrow 2Fe^{3+} + 2Br^-.$$

Without iron(II) chloride addition, free bromine appears in the oxidized drill water in the amount of 1–2 mg l^{-1}, which is not allowed by the existing technology of iodine sorption on coal.

Thus, our experiments proved that iodide ions can be selectively oxidized in drill water, and the process is quite suitable for the existing iodine–bromine production.

In bromine production gaseous bromine is absorbed from a bromine–air mixture by iron shavings periodically sprayed with water or solutions of iron bromides. A feature of this process consists in binding of bromine into iron(II) or (III) bromide. To liberate bromine from them, chlorine is used in the subsequent production stage, which results in the formation of a solution of iron(III) chloride as a liquid waste product simultaneously with the main product formation.

The drawbacks of using iron shavings as a bromine chemisorbent are the formation of the difficult-to-utilize by-product and also the accumulation of bromine-containing slimes in vessels for bromine chemisorption, which should be disposed of at regular intervals.

Table 2. Sorption of bromine from a bromine–air mixture (BAM) by aqueous solutions of *N*-(*n*-pentyl)pyridinium bromide (**I**) in a bubbling mode (time of gas–liquid contact about 1 s)

Initial concentration of **I** in absorbing solution		Averaged concentration of bromine in BAM, mg l^{-1}		Degree of bromine removal from BAM, %	Characteristics of resulting polybromide complex		
M	wt %	before reactor	after reactor		color	bromine content, wt %	density at 18°C, kg dm^{-3}
1	21.95	10.3	1.05×10^{-2}	99.9	Light cherry	40.5	1.659
2	42.05	9.5	9.8×10^{-3}	99.7	Cherry	53.7	1.907
3	60.69	11.8	1.02×10^{-2}	99.2	Dark cherry	66.0	2.136
4	78.23	7.7	8.3×10^{-3}	99.0	″	74.1	2.283

The application of soluble bromine sorbents is free of these drawbacks. Quarternary ammonium salts are of a special interest for the process of bromine production. They are safe in handling (nonvolatile, low-toxic, fire- and explosion-proof) and are not steam-distilled. They can be used as aqueous solutions binding bromine into polybromide complexes on contact with a bromine–air mixture. Bromine is readily desorbed from such complexes at moderate heating, and then it can be blown off with air or steam.

The preparation of quarternary ammonium salts by quaternization of tertiary amines with alkyl halides in polar solvents was studied in sufficient detail [5–9], and their application as bromine absorbents has been described in [10, 11].

Comparative examination of the data on the operation of liquid absorbents in bromine sorption–desorption showed that *N*-alkylpyridinium bromides show the most promise for bromine production [12–14].

In view of the aforesaid, we studied the absorbing properties of solutions of *N*-(*n*-pentyl)pyridinium bromide with respect to bromine in bromine–air mixtures under conditions close to those of bromine manufacturing. The choice of the salt was governed by the fact of production of *n*-pentyl bromide at the iodine–bromine plant.

N-(*n*-Pentyl)pyridinium bromide was prepared from equimolar amounts of pyridine and *n*-pentyl bromide in the presence of water (5–10 wt %) [5] in a quartz round-bottomed reactor with a reflux condenser at 90–95°C by the reaction

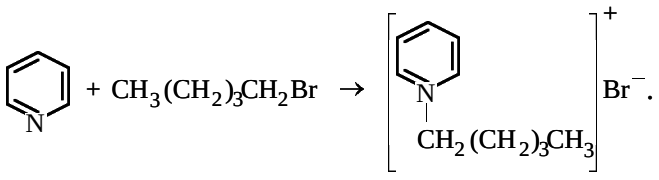

At the 2–3 h synthesis time the yield of the salt was 95%. The unchanged initial components were removed from the salt using a separatory funnel.

For the sorption of bromine from a bromine–air mixture we used 20–80% aqueous solutions of *N*-(*n*-pentyl)pyridinium bromide. The sorption was carried out in a quartz round-bottomed reactor at room temperature and the phase contact time of about 1 s. A polybromide complex formed from the bromine sorption was accumulated on the reactor bottom as a separate layer of a cherry-colored heavy oily liquid immiscible with the absorbing solution. The sorption of bromine vapor was terminated on complete saturation of the *N*-(*n*-pentyl)pyridinium salt in the absorbing solution. The data on the sorption of bromine vapor by *N*-(*n*-pentyl)pyridinium bromide solutions are given in Table 2.

Our experiment showed that the bromine content in the polybromide complex increases with increasing initial concentration of *N*-(*n*-pentyl)pyridinium bromide in the absorbing solution and reaches 40–75 wt % at the degree of bromine sorption from the bromine–air mixture equal to or greater than 99%. As the concentration of bromine in the polybromide complex increases, the color of the complex changes from light cherry through red-brown to dark cherry, and its density increases from 1.659 to 2.283 kg dm^{-3}.

Bromine was desorbed from the polybromide complex by heated air or steam in the same reactor in which bromine was sorbed from a bromine–air mixture. The bromine–air mixture (or a mixture of bromine vapor and steam) formed from the decomposition of the complex was directed to a reflux condenser with the aim to return water completely or partially (when steam was used) into the reactor, so as to keep a high rate of bromine desorption. The results of the experiments on the bromine desorption from the polybromide complex are given in Table 3.

Table 3. Desorption of bromine from the polybromide complex (initial concentration of bromine in the complex 49.81 wt %)

Weight ratio complex/water, m_{com}/m_w	Rate of air feeding for bromine desorption,* l min^{-1} g^{-1}	τ, min	Temperature, °C		Average concentration of bromine in BAM, mg l^{-1}	Degree of bromine desorption, %
			in reactor still	in dephlegmator		
1.66	1.50×10^{-2}	165	95–105	22–45	189	93.8
2.50	1.25×10^{-2}	150	96–105	22.45	232	87.2
1.66	1.80×10^{-2}	180	110–118	48–83	56	36.3
0.50	1.50×10^{-2}	180	96–105	21.24	222	40.1
1.66	2.30×10^{-2}	180	85–92	29–45	47	38.9

* In calculations of the rate of air feeding, m_{com} was expressed in grams.

Table 3 shows that the efficiency of bromine distillation from the polybromide complex depends on a number of factors: temperature in the still and in the dephlegmator, amount of solvent (water) for pyrydinium salt in the reaction mass, and space velocity of air (or steam) fed for the bromine desorption.

Our experiments showed that the maximal rate of bromine desorption, and also a high bromine concentration in a bromine–air flow, are observed at the beginning of bromine distillation when the content of polybromide complexes is high. As their concentration decreases in the course of bromine distillation, the rate of bromine desorption from the complex and the concentration of Br_2 vapor in the bromine–air flow decrease.

The optimal temperature of the complex decomposition is 95–105°C. Below this temperature the rate of bromine desorption starts to decrease, whereas at higher temperatures water is actively boiled off and removed through the dephlegmator, which results in the dehydration of the reaction mass and drastic deceleration of the bromine desorption rate.

The optimal temperature of the dephlegmator, intended for the complete (or partial) return of the condensed water into the reactor, is determined by the surface area of the dephlegmator and the space velocity of air (or steam) fed for bromine desorption.

The optimal weight ratio polybromide complex : water in the reactor approaches 1 : 1.5. The higher ratio (e.g., 1 : 0.5) results in decreased rate of bromine desorption, whereas at the lower ratio (1 : 2.5) the desorption rate does not increase further.

An optimal specific consumption of air or steam for the bromine desorption approximately corresponds to the ranges 1.25–1.75 m^3 (air) and 2–2.5 kg (steam) per kilogram of the polybromide complex and depends on the reactor design and also on the dephlegmator operation mode.

The 85–90% degree of bromine desorption from the complex was reached in 2.5–3 h of heat treatment of the complex. The bottom residue is a solution of pyridinium bromide containing 5–10 wt % bromine. It can be repeatedly directed to the sorption of bromine vapor from a bromine–air mixture.

To obtain liquid bromine, bromine vapor was blown off from the complex with steam. The resulting steam–bromine mixture was fed from the steam distillation column to a heat exchanger. Its condensation at 20–25°C gave crude bromine and bromine water containing about 3 wt % bromine. After separation of liquid bromine, the bromine water was fed to single-stage bromine extraction by the initial organic bromide. As a result, the bromine content in the bromine water sharply decreased (to 0.003 wt %).

In the case of air desorption of bromine from the complex, the content of bromine in the bromine–air flow gradually decreases from 1000–1200 (at the start of the process) to 100–150 g m^{-3} (at the end of desorption). Such a flow with a variable bromine content can be used for "mild" bromination in syntheses of various bromine-containing products (salts, certain organic compounds, etc.).

CONCLUSIONS

(1) The feasibility was confirmed for selective oxidation of iodide ions in the presence of bromide ions in acidified drill water by atmospheric oxygen with ozone added to initiate the oxidation of iodide ions and with an iron(II) salt added to prevent bromine liberation. The conditions eliminating bromine formation in the solution and simultaneously ensuring the yield of iodine in the range 70–100% were determined.

(2) The sorption of bromine from a bromine–air mixture by aqueous solutions of *N*-(*n*-pentyl)pyridinium bromide with the formation of a polybromide complex containing up to 75 wt % bromine was studied. The conditions of bromine desorption from the polybromide complex providing the yield of bromine in a gaseous or liquid product of no less than 85–90% was determined.

REFERENCES

1. Ksenzenko, V.I. and Stasinevich, D.S., *Khimiya i tekhnologiya broma, ioda i ikh soedinenii* (Chemistry and Technology of Bromine, Iodine, and Their Compounds), Moscow: Khimiya, 1995.
2. USSR Inventor's Certificate no. 162115.
3. USSR Inventor's Certificate no. 66684.
4. US Patent 4487752.
5. Weygand–Hilgetag, *Organisch-Chemische Experimentierkunst*, Leipzig: Johann Ambrosius Barth, 1964, 3rd ed.
6. USSR Inventor's Certificate no. 539867.
7. FRG Patent 2723120.
8. UK Patent 1583932.
9. JPN Patent Pending 54-41567.
10. US Patent 4124693.
11. Gabrielyan, G.L., Babayan, L.A., and Babayan, A.T., *Izucheie kompleksoobrazuyushchikh svoistv solei ammoniya s bromom* (Complexation of Ammonium Salts with Bromine), Available from VINITI, 1986, Moscow, no. 4889-V86.
12. USSR Inventor's Certificate no. 1143689.
13. Babayan, A.T., Gabrielyan, G.L., Babayan, L.A., *et al.*, *Arm. Khim. Zh.*, 1988, vol. 41, no. 3, pp. 166–168.
14. USSR Inventor's Certificate no. 1386556.

Russian Journal of Applied Chemistry, Vol. 74, No. 7, 2001, pp. 1098–1102. Translated from Zhurnal Prikladnoi Khimii, Vol. 74, No. 7, 2001, pp. 1070–1074.

INORGANIC SYNTHESIS AND INDUSTRIAL INORGANIC CHEMISTRY

Extraction of Palladium(II) and Platinum(IV) from Hydrogen Chloride Solutions with 3,7-Dimethyl-5-thianonane-2,8-dione and Complexation of This Reagent with the Platinum Metals

V. V. Potapov, R. A. Khisamutdinov, Yu. I. Murinov, L. A. Baeva, A. D. Ulendeeva, and N. K. Lyapina

Institute of Organic Chemistry, Ufa Scientific Center, Russian Academy of Sciences, Ufa, Bashkortostan, Russia

Received December 26, 2001

Abstract—Extraction of palladium(II) and platinum(IV) from acidic chloride solutions with solutions of 3,7-dimethyl-5-thianonane-2,8-dione in toluene and chloroform and complexation of this reagent with platinum metals in aqueous acetone were studied by ^1H and ^{13}C NMR and IR spectroscopy. The possibility of extractive separation of palladium(II) from platinum(IV) and their separation from Cu(II), Ni(II), Co(II), Mn(II) and Fe(III) with solutions of 3,7-dimethyl-5-thianonane-2,8-dione in organic solvents was studied. The apparent concentration constants of extraction of palladium(II) and platinum(VI) with 3,7-dimethyl-5-thianonane-2,8-dione and the corresponding thermodynamic parameters were determined.

It is known that γ-oxo sufides are efficient and selective extractants for palladium(II), gold(III), and silver(I) [1]. For example, the reagents of this type allow selective separation of palladium(II) from platinum(IV) by extraction from acidic chloride solutions. A major portion of the works devoted both to synthesis of γ-oxo and γ,γ-dioxo sulfides by alkylthiomethylation of ketones and to study of their extraction power toward metals was performed at the Institute of Organic Chemistry, Ufa Scientific Center, Russian Academy of Sciences. However, extraction of platinum metals with γ,γ-dioxo sulfides practically was not studied. In this work we synthesized 3,7-dimethyl-5-thianonane-2,8-dione (DTD) and studied extraction of palladium(II) and platinum(IV) from acidic chloride solutions with this reagent and its complexation with the platinum metals.

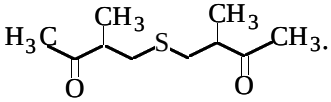

3,7-Dimethyl-5-thianonane-2,8-dione can be readily prepared by thiomethylation of butanone with a mixture consisting of formaldehide and sulfur-containing reagents. Suitable sulfur-containing reagents are not only pure potassium hydrosulfide [2] and sodium sulfide and hydrosulfide [3], but also spent sulfite alkaline solutions from the gas- and petroleum-processing plants [4] containing various amounts of these compounds.

In this work DTD was prepared with the use of solutions containing 8.25 and 5.62 wt % sulfur in the sulfide and hydrosulfide forms, respectively, formed by treatment of the gas flow with 10–20% NaOH to remove hydrogen sulfide in production of additives to lubricating oils.

Synthesis of 3,7-dimethyl-5-thianonane-2,8-dione. 0.82 mol of formaldehyde (35% aqueous solution) and 0.82 mol of butanone (78 ml) were added to 100 g of a sulfite alkaline solution containing 13.87 wt % (0.82 mol) of sulfide and hydrosulfide (recalculated on S^{2-}). This mixture was stirred at room temperature for 1 h. The reaction progress was monitored by determination of the sulfide content by potentiometric titration with an $[Ag(NH_3)_2]NO_3$ aqueous solution [5]. After reaction completion the organic phase was separated and the aqueous phase was treated by contacting with chloroform. The chloroform extract was combined with the organic phase, washed successively with 10% HCl and water, and dried with magnesium sulfate. Thereafter chloroform was evaporated and the residue was distilled in a vacuum. The yield of DTD was 78% (68 g).

We studied extraction of palladium(II) and platinum(IV) chloride complexes from aqueous hydrogen chloride solutions of required concentration with the solutions of DTD in toluene and chloroform. The palladium and platinum chloride solutions were

1070-4272/01/7407-1098$25.00

prepared from palladium(II) chloride and hexachloroplatinic acid hexahydrate, respectively. The working concentrations of the platinum metals and the extractant were varied within the range 0.002–0.2 M and 0.01–0.1 M, respectively. The concentration of palladium(II) and platinum(IV) in both the initial solutions and raffinates was determined on a Hitachi 508 atomic-absorption spectrophotometer equipped with lamps with a hollow cathode made from the metal to be determined. The samples were sprayed into an acetylene–air flame.

The extraction was performed in temperature-controlled separatory funnels at 25±1°C. The constant volume ratio of the aqueous and organic phases was 1 : 1. After the stirring was stopped, the phases was separated within several seconds, and a sharp stable phase boundary was formed. In the course of the extraction no second organic phase was formed. The extracted complexes were precipitated from the extract by addition of hexane.

The extractable complexes of palladium(II) and platinum(IV) were prepared also by the direct reaction between the corresponding reagents. Potassium tetrachloropalladate(II) and potassium hexachloroplatinate(IV) were used as the initial platinum metal compounds. The calculated weighed portions of the disulfide and the platinum metal salts were fully dissolved in acetone and water, respectively. These solutions were combined and kept with stirring with a magnetic stirrer at room temperature until the complexation was completed, as judged from the solution decolorization and precipitation of poorly soluble compounds. These compounds were filtered off, successively washed with water and hexane, and dried. The ^{1}H and ^{13}C NMR spectra of DTD and its complexes with the platinum metals in deuterochloroform were registered on a Bruker AM300 NMR spectrometer (300 MHz, stabilization by the residual signals of chloroform). The IR spectra were recorded on an Specord 80 spectrophotometer (mull in Vaseline oil, KRS-5 windows).

In preliminary experiments we found that the time of contacting the aqueous and organic phases required for attainment of the extraction equilibrium was 15 min for palladium(II) and 2 h for platinum(IV). The real contacting time was 20 min and 2 h, respectively. The distribution of palladium(II) and platinum(IV) between the aqueous solution and the extractant was also studied in relation to acidity. Figure 1 shows that the platinum metals are most efficiently extracted from low acidic solutions (C_{HCl} < 0.5 M). It is known [6] that in the 0.1–0.5 M hydrogen chloride solutions Pd(II) and Pt(IV) predominantly exist in the form of anionic complexes $[PdCl_4]^{2-}$ and $[PtCl_6]^{2-}$, respectively. Therefore, we studied the extraction of palladium(II) and platinum(IV) from 0.5 and 0.1 M HCl solutions, respectively. Comparison of the isotherms of palladium(II) and platinum(IV) extraction with dioxo sufide (Fig. 2) shows that this reagent more efficiently extracts palladium(II) than platinum(IV). At the phase contact time τ = 20 min palladium and platinum are separated with a factor of ~10^4. In extraction of palladium(II) and platinum(IV) with DTD from hydrogen chloride solution containing Cu(II), Ni(II), Co(II), Mn(II), and Fe(III), these metals

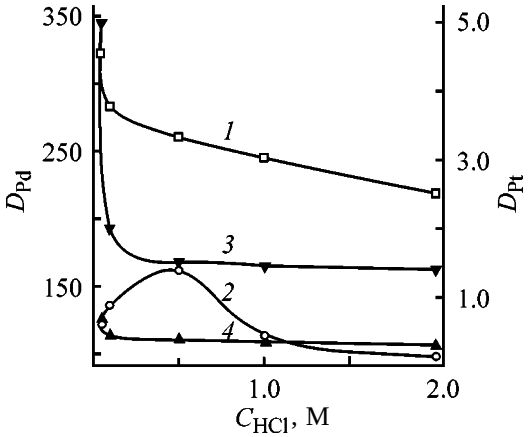

Fig. 1. Distribution factors of palladium(II) and platinum(IV) D in their extraction with DTD as influenced by HCl concentration in aqueous phase (C_{HCl}). C_{DTD} = 0.1 M; the same for Fig. 3. (*1*) C_{Pd} = 0.02 M, chloroform; (*2*) C_{Pd} = 0.02 M, toluene; (*3*) C_{Pt} = 0.025 M, toluene; and (*4*) C_{Pt} = 0.025 M, chloroform; the same for Fig. 3.

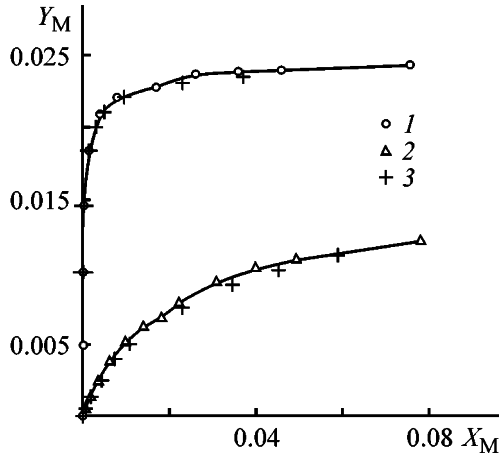

Fig. 2. Isotherms of (*1*) palladium(II) and (*2*) platinum(IV) extraction from 0.1 and 0.05 M aqueous hydrogen chloride solutions, respectively, with DTD solution in chloroform at 25°C. (X_M, Y_M) Equilibrium concentrations of the platinum metals in the raffinate and extract, respectively; (*3*) Calculated values.

Table 1. Elemental composition and several physicochemical characteristics of DTD and its complexes with Pd(II) and Pt(IV) prepared by (E) extraction technique and (D) direct synthesis

Medium	Preparation technique	M : DTD	Composition	Calculated/found, %					Appearance	mp, °C
				C	H	S	M	Cl		
		–	DTD	49.6/49.5	8.3/8.5	14.5/14.8	–	–	Mobile yellow liquid	114–115*
Neutral, water–acetone	D	1 : 2, 2 : 1	$PdCl_2(DTD)_2$	41.3/41.7	6.2/6.5	11.0/10.5	18.3/19.0	12.2/12.7	Bright yellow powder	117–119
0.5 M HCl–chloroform	E	1 : 2, 2 : 1	″							
0.5 M HCl–toluene	D	1 : 2, 2 : 1	″							
Neutral, water–acetone	D	1 : 2, 2 : 1	$PtCl_4(DTD)_2$	32.4/32.1	4.9/4.9	8.6/8.2	26.3/26.7	19.1/18.9	Yellow powder	(290)**
0.5 M HCl–chloroform	E	1 : 2, 2 : 1	″	32.4/32.2	4.9/4.9	8.6/9.0	26.3/26.7	19.1/18.8	Yellow-brown powder	125–127
0.5 M HCl–toluene	E	1 : 2, 2 : 1	″							125–127

* Boiling point at 133.32 Pa.
** Decomposition point.

do not noticeably pass to the organic phase. Using the techniques of saturation and shift of the extraction equilibrium, we determined that the solvation number *q* in the extractable complexes of platinum metals in question is two. Elemental analysis of the extractable complexes (Table 1) showed that palladium(II) and platinum(IV) are extracted with DTD in the form of compounds with the M : Cl : DTD ratio of 1 : 2 : 2 and 1 : 4 : 2, respectively.

To elucidate the mechanism of extraction of palladium(II) and platinum(IV) with DTD, their complexes with DTD were prepared in neutral aqueous acetone. The results of elemental analysis and several physicochemical characteristics of the prepared complexes are listed in Table 1. These data show that palladium(II) and platinum(IV) react with DTD to form the complexes $PdCl_2(DTD)_2$ and $PtCl_4(DTD)_2$, irrespective of both the ratio between the metals and reagent and the experimental conditions.

In Tables 2 and 3 are given the parameters of the ^1H and ^{13}C NMR spectra of DTD and its complexes with the platinum metals. These data show that in passing from DTD to the complexes the maximal additional downfield shift occurs for the protons (δ = 0.3–0.6 ppm) and the carbon atoms (δ ~4 ppm) of the methylene groups (d) in the α-position to the sulfur atom. The signal of the carbon atoms of the oxo groups (b) is shifted upfield by 1.5–1.7 ppm. At the same time, the position of the proton and carbon atom signals of the methyl groups (a) closest to the oxo groups remains virtually unchanged. These results show that complexation of DTD with palladium(II) and platinum(IV) involves coordination of the platinum metals to the sulfur atom. This conclusion was confirmed by the results of IR spectroscopic studies.

In passing from DTD to its complexes with Pd(II) and Pt(IV) the strong absorption bands in the IR spectra at 1710 and 1358 cm^{-1} due to ν(C=O) and δ_s(CH) vibrations in the –C(=O)–CH_3 group of DTD molecule are slightly shifted toward higher frequencies. This spectroscopic effect shows that the oxygen atoms do not participate in complex formation. At the same time, as a result of complexation, the weak absorption band at 720 cm^{-1} due to ν(C–S) vibrations is shifted toward low frequencies by 20–50 cm^{-1}. The position and intensity of the other absorption bands remain virtually unchanged. A series of the absoption bands in the long-wave region of IR spectrum of the Pd(II) complexes, observed irrespective of their preparation technique, includes a strong absorption band ν(PdCl) at 358 cm^{-1} and a medium-intensity band ν(Pd–S) at 292 cm^{-1}, indicating the

trans configuration of the coordination center [7]. A strong absorption band at 345 cm^{-1} and a weak absorption band at 320 cm^{-1} in the spectrum of $PtCl_4(DTD)_2$ prepared by the direct synthesis can be assigned to ν(Pt–Cl) and ν(Pt–S) vibrations, respectively, in the complex with the *trans* configuration [8]. At the same time, in the spectrum of the identical complex prepared by the extractive technique a broad absorption band of the medium intensity with a maximum near 311 cm^{-1} is observed. It is possible that this band is due to superposition of the close-lying absorption bands corresponding to the stretching vibrations Pt–Cl and Pt–S in *cis*-$PtCl_4(DTD)_2$ [8]. Thus, as opposed to palladium(II) complex, the structure of the $PtCl_4(DTD)_2$ coordination sphere depends on the synthesis technique.

Thus, extraction of palladium(II) and platinum(IV) from hydrogen chloride aqueous solutions with DTD involves formation of *trans*-$PdCl_2(DTD)_2$ and *cis*-$PtCl_4(DTD)$:

$$[PdCl_4]^{2-} + 2DTD \rightleftarrows PdCl_2(DTD)_2 + 2Cl^-,$$

$$[PtCl_6]^{2-} + 2DTD \rightleftarrows PtCl_4(DTD)_2 + 2Cl^-.$$

The apparent concentration extraction constants $\tilde{K}_{Pd}$ and $\tilde{K}_{Pt}$ were calculated by the equations

$$\tilde{K}_{Pd} = \frac{[PdCl_2(DTD)_2][Cl^-]^2}{[PdCl_4^{2-}][DTD]^2} \frac{y(2y + C_H)^2}{x(S_0 - 2y)^2},$$

$$\tilde{K}_{Pt} = \frac{[PtCl_4(DTD)_2][Cl^-]^2}{[PtCl_6^{2-}][DTD]^2} \frac{y(2y + C_H)^2}{x(S_0 - 2y)^2},$$

where x and y are the equilibrium metal concentrations in the aqueous and organic phases, respectively (M), S_0 is the initial extractant concentration (M), and C_H is the hydrogen chloride concentration equal to 0.5 M.

The apparent concentration constants of palladium(II) and platinum(IV) extraction with DTD solution in chloroform are $18\,400 \pm 400$ and 3.55 ± 0.30, respectively. From these values we calculated the equilibrium concentrations of palladium(II) and platinum(IV) in the aqueous and organic phases. Figure 2 shows that the calculated and experimental values are in good agreement.

It is known that effect of diluent on the efficiency of metal extraction is determined by the difference in its solvating power with respect to the extractable complex and extractant. Figure 1 shows that the use of toluene as the diluent ensures the more efficient recovery of platinum(IV). At the same time, palladium(II) is more efficiently extracted with solution of DTD in chloroform. This fact is consistent with the

Table 2. Proton chemical shifts δ and additional chemical shifts (Δδ, in parenteses) in the ^1H NMR spectra of DTD and its metal complexes

$$(\overset{a}{C}H_3\text{–}\overset{b}{\underset{\underset{O}{\|}}{C}}\text{–}\overset{c}{\underset{\underset{\overset{e}{C}H_3}{|}}{C}}H\text{–}\overset{d}{C}H_2)_2S$$

Compound	Proton chemical shifts, ppm			
	e	a	c	d
DTD	1.18 d	2.19 s	2.51 sex	2.79 t
$PdCl_2(DTD)_2$:				
D, E	1.22 (0.04)	2.19 (0.00)	2.75 (0.24)	3.12 (0.33)
$PtCl_4(DTD)_2$:				
D	1.25 (0.07)	2.22 (0.03)	2.80 (0.29)	3.18 (0.39)
E	1.19 (0.01)	2.19 (0.00)	2.53 (0.07)	3.00 (0.21)

* (D, E) Direct and extraction synthesis.

Table 3. ^{13}C chemical shifts δ and the additional chemical shifts (Δδ, in parenteses) in the ^{13}C NMR spectra of DTD and its extractable complexes

Compound	^{13}C chemical shifts, ppm				
	a	b	c	d	e
DTD	16.37	210.47	46.35	35.09	28.63
$PdCl_2(DTD)_2$	16.73 (0.36)	208.76 (–1.71)	46.85 (0.50)	38.88 (3.79)	28.69 (0.06)
$PtCl_4(DTD)_2$	16.97 (0.60)	209.02 (1.45)	45.62 (–0.73)	39.14 (4.05)	28.80 (0.17)

Table 4. Thermodynamic functions of extraction of palladium(II) and platinum(IV) from hydrogen chloride solutions with DTD organic solutions at 25°C

Extracted metal and organic diluent	C_{HCl}, M	ΔH	ΔG	ΔS, J mol^{-1} K^{-1}
		kJ mol^{-1}		
Pd(II), toluene	0.5	16	–	–
Pd(II), chloroform		–11	–24	44
Pt(IV), toluene	0.1	77	–	–
Pt(IV), chloroform		10	–3	44

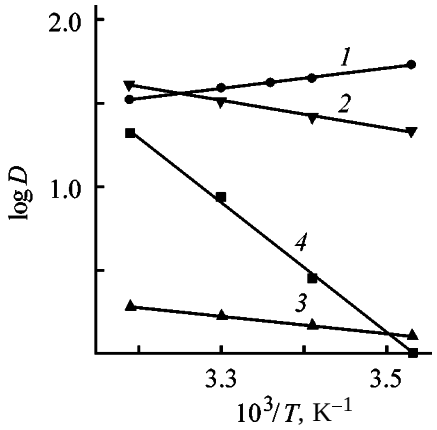

Fig. 3. Temperature dependence of log *D* in extraction of palladium(II) from 0.5 M and platinum(IV) from 0.1 M hydrogen chloride aqueous solutions with DTD solution in toluene.

order in which the extractive recovery of Pd(II) from hydrogen chloride solution with solution of octylthiomethylacetophenone in organic solvents decreases: chloroform > dichloroethane > benzene > carbon tetrachloride, this order correlates with the decrease in the negative nonideality in the extractant–diluent systems [1]. Deviation from this order in the case of extraction of platinum(IV) with DTD is apparently due to the difference in the chemical features of platinum metals concerned and their extractable complexes.

The thermodynamic functions of extraction of palladium(II) and platinum(IV) with DTD were evaluated from the temperature dependence of the distribution factors (Fig. 3). The extraction enthalpy was determined graphically [9]. The calculated values of the thermodynamic functions of the extraction are listed in Table 4. Figure 3 (curves *2*, *3*) shows that with increasing temperature the recovery of palladium(II) and platinum(IV) with DTD solution in toluene increases. The mutual arrangement of curves *2* and *3* is indicative of the larger heat absorption in extraction of platinum(IV), as compared to palladium(II), with solution of DTD in toluene. The heat absorption in extraction of platinum(IV) with DTD solution in chloroform is considerably lower than that in extraction with DTD solution in toluene. In contrast to the other extraction systems concerned, recovery of palladium(II) with DTD solution in chloroform is accompanied by heat liberation. Thus, the enthalpy characteristics of extraction of palladium(II) and platinum(IV) with DTD solutions in organic diluents are consistent with the correlation between the diluent nature and the extraction efficiency.

CONCLUSIONS

(1) The optimal conditions were found for extraction of palladium(II) from hydrogen chloride solutions with 3,7-dimethyl-5-thianonane-2,8-dione (DTD), and thermodynamic parameters of extraction and the apparent concentration constants were determined. DTD can be used as a highly efficient selective extractant for recovery of palladium(II) from aqueous solutions containing along with platinum(IV) several nonferrous metals and iron.

(2) Palladium(II) is more efficiently extracted from hydrogen chloride aqueous solutions with 3,7-dimethyl-5-thianonane-2,8-dione solution in chloroform, whereas in extraction of platinum(IV) the better diluent is toluene.

(3) Palladium(II) and platinum(IV) are bound to the sulfur atom of DTD to form *trans*-$PdCl_2(DTD)_2$ (irrespective of preparation technique), *cis*-$PtCl_4(DTD)_2$ (extraction technique), and *trans*-$PtCl_4(DTD)_2$ (direct synthesis).

REFERENCES

1. Murinov, Yu.I., Maistrenko, V.N., and Afzaletdinova, N.G., *Ekstraktsiya metallov S,N-organicheskimi soedineniyami* (Extraction of Metals with S,N-Organic Compounds), Moscow: Nauka, 1993.
2. Dronov, V.I., Nigmatullina, R.F., Khalilov, L.M., and Nikitin, Yu.E., *Zh. Org. Khim.*, 1980, vol. 16, no. 7, pp. 1392–1396.
3. Ulendeeva, A.D., Baeva, L.A., Lyapina, N.K., *et al.*, *Neftekhimiya*, 1997, vol. 37, no. 2, pp. 180–188.
4. Ulendeeva, A.D., Baeva, L.A., Vasil'eva, E.V., and Lyapina, N.K., *Neftekhimiya*, 1996, vol. 36, no. 3, pp. 266–273.
5. Rubinshtein, I.A., Kleimenova, Z.A., and Sobolev, E.P., in *Metody analiza organicheskikh soedinenii nefti, ikh smesei i proizvodnykh* (Methods of Analysis of Oil Organic Compounds, Their Mixtures, and Derivatives), Moscow, 1960, pp. 74–100.
6. Buslaeva, T.M. and Simanova, S.A., *Koord. Khim.*, 1999, vol. 25, no. 3, pp. 165–176.
7. Adams, D.M., *Metal–Ligand and Related Vibrations: A Critical Survey of the Infrared and Raman Spectra of Metallic and Organometallic Compounds*, London: Edward Arnold, 1967.
8. Ferraro, J.R., *Low-Frequency Vibrations of Inorganic and Coordination Compounds*, New York: Plenum, 1971.
9. Korenman, I.M., *Ekstraktsiya v analize organicheskikh veshchestv* (Extraction in Organic Analysis), Moscow: Khimiya, 1977.

Russian Journal of Applied Chemistry, Vol. 74, No. 7, 2001, pp. 1103–1105. Translated from Zhurnal Prikladnoi Khimii, Vol. 74, No. 7, 2001, pp. 1075–1077.

INORGANIC SYNTHESIS AND INDUSTRIAL INORGANIC CHEMISTRY

Removal of Sulfur from the Active Mass of Lead Battery Scrap

A. G. Morachevskii, Z. I. Vaisgant, A. I. Rusin, and M. N. Khabachev

St. Petersburg State Technical University, St. Petersburg, Russia

Received March 13, 2001

Abstract—Process parameters of sulfur removal from the active mass of lead battery scrap, the main type of lead-containing secondary raw materials, were discussed.

Modern technology of processing lead battery scrap involves sulfur removal from the active mass (desulfurization), which is the most important from the environmental viewpoint [1–4]. The process consists in the conversion of lead(II) sulfate from the active mass to lead(II) carbonate, hydroxocarbonate, or hydroxide, i.e., to compounds which are readily reduced by carbon reagents at relatively low temperature without evolution of noxious gaseous products. At the same time, sulfur passes to the aqueous phase and is thus totally utilized. Aqueous solutions of sodium hydroxide and sodium carbonate are the most appropriate reagents for the sulfur removal [2, 3]. The reaction is based on significantly lower solubility products of lead hydroxide or carbonate compared to $PbSO_4$. For example, in the case of lead(II) sulfate pL_{PbSO_4} is 7.80, and it changes slightly as temperature increases, whereas $pL_{Pb(OH)_2}$ and pL_{PbCO_3} are 15.3 (20°C) and 13.1 (25°C), respectively.

Certain preliminary conclusions on the desulfurization with both sodium hydroxide and carbonate can be made on the basis of our previous studies [5–8] and published data [9–13]. In the case of desulfurization with sodium hydroxide, the preferable concentration range is 20–40 g l^{-1}, and the preferable temperature is 50°C. For the stoichiometric ratio $[OH^-] : [SO_4^{2-}]$ of 2 : 1 the desulfurization degree is 94–96%. A 10–20% excess of alkali with respect to the stoichiometry of the reaction

$$PbSO_4(s) + 2NaOH(aq) = Pb(OH)_2(s) + Na_2SO_4(aq) \quad (1)$$

is required to increase the conversion of lead(II) sulfate. However, at excess of alkali a minor amount of Pb(II) ions pass into solution, and addition of sulfuric acid is required to precipitate them. After solution evaporation, sodium sulfate meeting the standards with respect to the content of heavy metals and other impurities can be obtained [8].

Antimony, which enters the active material of positive and negative plates owing to corrosion electrochemical processes during battery operation, does not pass to the aqueous phase upon desulfurization with sodium hydroxide [7, 14].

Desulfurization of the active mass by sodium carbonate, which was studied in a greater detail, has received wider acceptance [2, 3]. In this case, an excess of the reagents relative to reaction (2) is also required.

$$PbSO_4(s) + Na_2CO_3(aq) = PbCO_3(s) + Na_2SO_4(s). \quad (2)$$

In contrast to desulfurization with sodium hydroxide, lead(II) ions are not detected in solution in excess of Na_2CO_3, but in this case up to 6% of the total antimony content in the active material passes into the aqueous phase [7, 14]. According to [15], the solid phase consists mainly of lead carbonate, but in other publications [9, 10] it was found that, depending on solution pH, Na_2SO_4 concentration, and other process conditions, hydrocerussite $Pb_3(CO_3)_2(OH)_2$ or the double salt $NaPb_2(CO_3)_2OH$ can form by the following reactions:

$$3PbSO_4(s) + 4Na_2CO_3 + 2H_2O = Pb_3(CO_3)_2(OH)_2(s) + 3Na_2SO_4 + 2NaHCO_3(aq), \quad (3)$$

$$2PbSO_4(s) + 3Na_2CO_3 + H_2O = NaPb_2(CO_3)_2OH(s) + 2Na_2SO_4 + NaHCO_3(aq). \quad (4)$$

The occurrence, to certain extent, of reactions (3) and (4) affects the actual consumption of sodium carbonate, which can be determined by reaction (2). The rate of $PbSO_4$ conversion is controlled, irrespective of

1070-4272/01/7407-1103$25.00

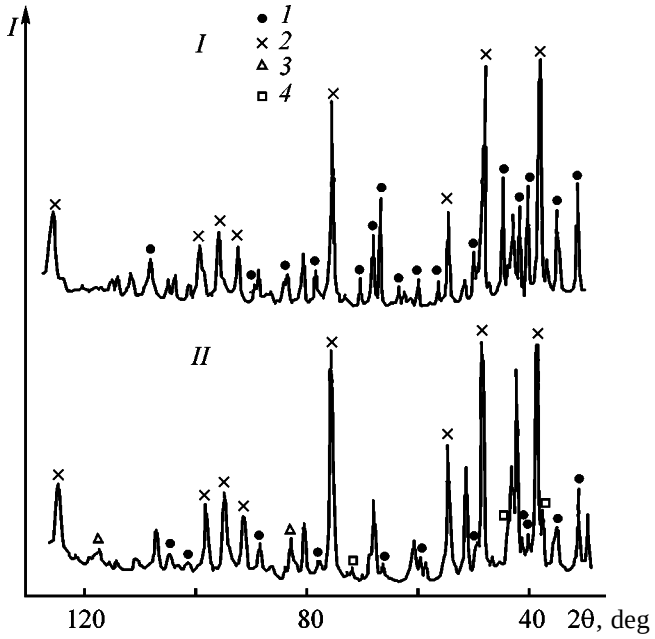

Fig. 1. Diffraction patterns of the (*I*) initial active mass and (*II*) active mass after desulfurization. (*I*) Intensity of reflection lines and (2θ) Bragg angle. Phase: (*1*) $PbSO_4$, (*2*) PbO_2, (*3*) $Pb_3(CO_3)_2(OH)_2$, and (*4*) $PbCO_3$.

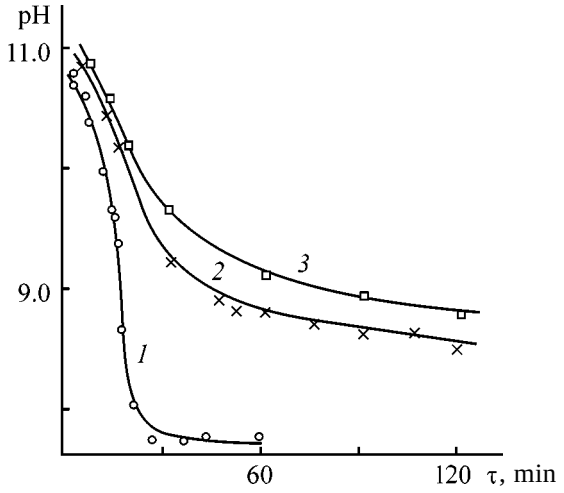

Fig. 2. Variation of pH in the course of desulfurization (for explanations, see text). (τ) Time.

the process mechanism, by the diffusion of CO_3^{2-} ions through the bed of reaction products. Changes in the composition and porosity of the solid phase caused by changes in the composition and temperature of the solution are factors primarily controlling the process rate. For the most part the reaction between pure lead sulfate and Na_2CO_3 solution is complete within 30 min at 20°C and 15 min at 50°C [3]. The experiments [3, 6, 7] show that a 10–20% excess of sodium carbonate over its amount required for reaction (2) is necessary for complete desulfurization of the active mass. The concentration of solution must provide the weight ratio of the solid and liquid phases (s : l) in the range from 1 : 5 to 1 : 3. According to the experimental data, the optimal temperature range is 40–60°C; however, there are indications that the process can be performed at a lower temperature but for a longer time. For example, Lyakov *et al*. [12] carried out the desulfurization at 23°C for 5 h.

At 40–60°C, with sufficient agitation, the recovery of SO_4^{2-} ions into solution reaches 80–85% in the first minutes and 90% within 30 min. Subsequent accumulation of Na_2SO_4 in the solution retards the process. It was of interest to obtain additional data on the permissible content of accumulated SO_4^{2-} ions and on their effect on the solution pH.

The main components of the active mass of lead batteries are $PbSO_4$ and PbO_2. Among other possible components are Pb_2OSO_4, Pb_2O_3, metallic lead, and small amounts of certain impurities. According to [16], more complex compounds like $3PbO \cdot 3PbSO_4 \cdot H_2O$, $4PbO \cdot PbSO_4$ can also be present in the active mass. In [11] the following average chemical composition of the dried active mass was reported (wt %): Pb 73.5, Sb 0.3, As ≤0.04, Ca 0.1, Fe 0.05, and SO_4^{2-} 16.7.

In our experiments the dried active mass containing 47 wt % $PbSO_4$ was subjected to desulfurization. The X-ray diffraction patterns of the active mass before and after desulfurization are shown in Fig. 1. The data were obtained using CrK_α radiation on a BGO diffractometer equipped with an HZG-4 goniometer. There are two major phases, PbO_2 and $PbSO_4$, in the starting sample. After desulfurization the content of $PbSO_4$ abruptly decreases, and the $PbCO_3$ and $Pb_3(CO_3)_2(OH)_2$ phases are present. Several intense peaks are also observed in the diffraction pattern of the sample after desulfurization, but, unfortunately, we failed to identify them with the use of the available database.

Desulfurization experiments were carried out at 50°C under continuous stirring. Crushed active mass (80 g) was added in small portions to the solution (240 ml) which contained Na_2CO_3 in the amount calculated for the complete desulfurization of the active material. The solution pH was controlled during the experiments. After the experiments the desulfurized active mass was washed, dried at 90–100°C for 5–6 h, crushed, and analyzed for the $PbSO_4$ content. The concentrations of Na_2CO_3 and $NaHCO_3$ were determined in the mother liquor. The fact that

the starting solution in addition to Na_2CO_3 contained sodium sulfate with a concentration of 150 g l^{-1} was a specific feature of the experiments. In addition to the active mass of various grain size, a synthetic mixture of finely divided crystalline powders of $PbSO_4$ and PbO_2 with the same content of lead sulfate as in the active mass was subjected to desulfurization. The time dependence of pH for these experiments is shown in Fig. 2. In the case of the synthetic mixture (curve *1*) even within 30 min a constant value of pH is attained, and the $PbSO_4$ content in the solid phase is reduced to 1 wt %. In the case of the active mass with the particle size less than 0.15 mm (curve *2*) desulfurization is slower, and after 2 h the $PbSO_4$ content is 2 wt %. In the case of the active mass with the particle size less than 0.50 mm (curve *3*) even after 2 h the $PbSO_4$ content decreases only to 7 wt %. The experiments also showed that $NaHCO_3$ is accumulated in the solution owing to possible reactions (3) and (4). For example, after a single desulfurization experiment the solution contains 7 g l^{-1} of $NaHCO_3$ and 67 g l^{-1} of Na_2SO_4 (solution density 1.07 g cm^{-3}), and after repeated use, 19 and 138 g l^{-1}, respectively (density 1.13 g cm^{-3}). After the third cycle the $NaHCO_3$ content in the solution attains 35, and that of Na_2SO_4, 208 g l^{-1} (1.19 g cm^{-3}). The time of complete desulfurization (to obtain the residual content of $PbSO_4$ in the active mass less than 3 wt %) increases from 60 to 120 min, and for the third cycle, to 150 min.

It was shown in special experiments that the use of $NaHCO_3$ as a reagent for desulfurization instead of Na_2CO_3 accelerates the process. Thus, the accumulation of Na_2CO_3 is the factor which retards the desulfurization at repeated use of the mother liquor.

Our experiments and earlier studies [5–14] allow the following conclusions. The most important factor affecting the extent of desulfurization is crushing of the active mass. At appropriate particle size and temperature, the accumulation of sodium sulfate strongly affects the desulfurization rate and the possibility of reusing the mother liquor. At the same time, the accumulation of HCO_3^- ions does not inhibit the process. Monitoring of the desulfurization completeness by pH variation is appropriate only in the case of a single-pass desulfurization without recirculation of the mother liquor.

REFERENCES

1. Morachevskii, A.G., Vaisgant, Z.I., and Demidov, A.I., *Pererabotka vtorichnogo svintsovogo syr'ya* (Reprocessing of Secondary Lead Raw Material), St. Petersburg: Khimiya, 1993.
2. Morachevskii, A.G., *Zh. Prikl. Khim.*, 1997, vol. 70, no. 1, pp. 3–15.
3. Morachevskii, A.G., *Zh. Prikl. Khim.*, 1998, vol. 71, no. 6, pp. 881–890.
4. Morachevskii, A.G., Vaisgant, Z.I., and Korelyakov, A.V., *Zh. Prikl. Khim.*, 2000, vol. 73, no. 7, pp. 1125–1130.
5. Morachevskii, A.G., Kogan, M.S., Demidov, A.I., and Vaisgant, Z.I., *Zh. Prikl. Khim.*, 1993, vol. 66, no. 8, pp. 1871–1874.
6. Morachevskii, A.G., Kogan, M.S., Demidov, A.I., and Vaisgant, Z.I., *Zh. Prikl. Khim.*, 1993, vol. 66, no. 9, pp. 2099–2100.
7. Morachevskii, A.G., Kal'ko, O.A., and Vaisgant, Z.I., *Zh. Prikl. Khim.*, 1995, vol. 68, no. 1, pp. 127–128.
8. Morachevskii, A.G., Vaisgant, Z.I., Kal'ko, O.A., *et al.*, *Zh. Prikl. Khim.*, 1997, vol. 70, no. 1, pp. 167–168.
9. Gong, Y., Dutrizac, J.E., and Chen, T.T., *Hydrometallurgy*, 1992, vol. 28, pp. 399–421.
10. Gong, Y., Dutrizac, J.E., and Chen, T.T., *Hydrometallurgy*, 1992, vol. 31, pp. 175–199.
11. Chen, T.T. and Dutrizac, J.E., *Hydrometallurgy*, 1996, vol. 40, pp. 223–245.
12. Lyakov, N., Tsaneva, M., Kharlampiev, G., and Girdzhev, N., *God. Vissh. Khim.-Tekhnol. Inst.* (Sofia), 1992–1993, vol. 31, book 3, pp. 31–33.
13. Prengman, R.D., *J. Metals (JOM)*, 1995, January, pp. 31–33.
14. Kal'ko, O.A., Behavior of Antimony in the Course of Reprocessing of Active Mass of Lead Battery Scrap, *Cand. Sci. Dissertation*, St. Petersburg, 1996.
15. Arai, K. and Togury, J.M., *Hydrometallurgy*, 1984, vol. 12, pp. 49–59.
16. Rusin, A.I. and Dasoyan, M.A., *Zh. Prikl. Khim.*, 1973, vol. 46, no. 12, pp. 2643–2646.

Russian Journal of Applied Chemistry, Vol. 74, No. 7, 2001, pp. 1106–1111. Translated from Zhurnal Prikladnoi Khimii, Vol. 74, No. 7, 2001, pp. 1078–1083.

PHYSICOCHEMICAL STUDIES OF SYSTEMS AND PROCESSES

Kinetics of Bulk Crystallization of Salts from Aqueous Solutions of Ethanol

O. D. Linnikov

Institute of Solid-State Chemistry, Ural Division, Russian Academy of Sciences, Yekaterinburg, Russia

Received July 6, 1998; in final form, November 2000

Abstract—The kinetics of crystallization of a number of salts from aqueous solutions of ethanol was studied under isothermal conditions on a setup enabling simultaneous automated recording of the electrical conductivity, optical transmission, and light scattering (at an angle of 90° to the incident light beam) of a supersaturated solution in salt crystallization. The rate coefficients of crystal growth were determined.

Control over processes of industrial bulk crystallization requires a knowledge of their mechanism. However, despite the great number of studies carried out in this direction, the question is far from being clear. Recent investigations have shown that crystallization is frequently accompanied by aggregation of crystals [1–5]. Coarse crystals can be formed not only through growth, but also as a result of aggregation of fine, submicroscopic crystals [1–4]. The existing theoretical concepts and methods for processing of experimental data on crystallization do not always take this factor into account. It is unclear whether bulk crystallization is invariably accompanied by aggregation of the forming crystals. In [1, 2], crystal aggregation was observed at solution supersaturation of 5 and more. Crystal aggregation was also observed in studying the spontaneous crystallization of potassium and sodium chlorides from aqueous and aqueous-alcoholic solutions, but at much lower supersaturations [6, 7].

The aim of the present work was to study further the kinetics and mechanism of salt crystallization from aqueous-alcoholic solutions. Since the supersaturation in a solution was created by introducing into it ethanol, it was of interest to reveal the possible influence of ethanol on the kinetic parameters of crystal growth.

The advantage of the method chosen for creating supersaturation consists in the ease of control over crystallization processes and in the possibility of obtaining in some cases compounds that cannot be isolated in the conventional way from aqueous solutions [8, 9]. Therefore, the given method of crystallization has found increasing industrial application recently.

EXPERIMENTAL

Salts with different solubilities and properties were taken for study. The experiments were carried out on a setup that enabled simultaneous automated recording of the electrical conductivity, optical transmission, and light scattering (at an angle of 90° to the incident light beam) of a supersaturated solution in salt crystallization. The salt concentration was determined from the electrical conductivity of a solution with the use of calibration curves. The supersaturation was created by introducing diluted ethanol into an unsaturated solution of a salt. To prevent formation of local supersaturations, ethanol was poured-in in the form of a thin jet, with vigorous agitation of the solution with a magnetic stirrer. Spontaneous crystallization started in a supersaturated aqueous-alcoholic solution of a salt after a certain time (induction period). After the crystallization was complete, the stirrer was switched off and the variation of the optical transmission of the solution in sedimentation of the formed crystals was recorded. The obtained curve was used to calculate the granulometric composition of the crystalline product and the optical absorption constant K_s of the salt [10].

In the process of supersaturation lifting, the solutions in the crystallization cell were thermostated with water flow from a UT-15 thermostat to within ±0.05°C. The error in measuring the light scattering intensity and optical transmission of solutions constituted ±1.5%, the rms deviation of the measured electrical conductivities was 0.2%. The crystalline product formed in each run was subjected to X-ray phase analysis, which demonstrated that the phase composition of the product remained unchanged and corresponded to the composition of the starting salts.

1070-4272/01/7407-1106$25.00

Further processing of the experimental data was done using the formulas

$$W = a + bC, \quad (1)$$

$$-\frac{dC}{d\tau} = \frac{KS}{V}(C - C_{sat})^n, \quad (2)$$

$$D = \log(I_0/I) = K_s S, \quad (3)$$

$$N = (D/4.84K_s)^3\left[\frac{\rho_s}{(C_{in} - C)MV}\right]^2, \quad (4)$$

$$\bar{d} = \left[\frac{6(C_{in} - C)MV}{\pi N\rho_s}\right]^{1/3}, \quad (5)$$

where W is the electrical conductivity of a salt solution (S); a, b are regression coefficients; C_{sat}, C_{in}, and C are the concentrations of a saturated salt solution, initial supersaturated salt solution, and that at instant of time τ, respectively (M); K is the rate coefficient of crystal growth (m s^{-1}); S is the total surface area of the crystals formed in a solution (m^2); $V = 25 \times 10^{-6}$ m^3 is the solution volume in the crystallization cell; D is the optical density of the salt solution in the course of its crystallization; I_0, I is the optical transmission of the salt solution at the initial instant of time and at instant of time τ (%): M is the molar weight of the salt (g mol^{-1}); N is the total number of salt crystals formed in the solution; $\bar{d}$ is the average crystal diameter (m); and ρ_s is the density of salt crystals (kg m^{-3}).

Equation (1) describes the electrical conductivity of salt solutions in the concentration range studied, Eq. (2) gives the rate of supersaturation lifting in a solution in the course of crystallization, and formula (3) represents Wagner's law [10], according to which the optical density of a suspension with a minor amount of the solid phase is directly proportional to the total surface area of solid particles contained in solution. The range of supersaturations of the salts under study was chosen in such a way that Wagner's law was always observed in their crystallization, i.e., the optical density of the forming suspensions was directly proportional to the total surface area of the precipitating crystals. This was verified in special experiments. Formulas (4) and (5) make it possible to calculate the number and average diameter of the crystals formed in crystallization.

If the average volume of salt crystals is v, then, under the assumption that the shape of the crystals is nearly spherical, their average diameter is given by

$$\bar{d} = (6v/\pi)^{1/3}, \quad (6)$$

and the average surface area of a crystal, by

$$\bar{S}_c = \pi d = \pi(6v/\pi)^{2/3} \approx 4.84v^{2/3}. \quad (7)$$

Expressing v in terms of a change in the solution concentration in crystallization and the total number N of formed salt crystals, we obtain formula (5). In a similar manner, with account of the fact that $S = NS_c$, we derive Eq. (4) from (3), (6), and (7). It can be shown that the calculation of the number of crystals formed in solution by means of formula (4) is sufficiently correct if the crystals have nearly spherical shape.

The order n of Eq. (2) describing the rate of salt crystallization is commonly equal to 1 or 2 [11, 12]. Joint solution of Eqs. (1)–(3) gives the rate coefficient of crystal growth and the order n of the crystallization equation. In the simplest case of $n = 1$ this solution has the form

$$K = -\frac{K_s V}{D(\tau - \tau_0)}\ln\frac{W - W_{sat}}{W_{in} - W_{sat}}, \quad (8)$$

where W_{sat} is the electrical conductivity of a saturated salt solution (S); W_{in} is the electrical conductivity of a supersaturated salt solution at the initial instant of time (S); and τ_0 is the duration of the induction period of crystallization, found from measurements of the electrical conductivity of solutions (s).

Basic data on crystallization of the salts under study are listed in Table 1. Figure 1 presents the experimental curves describing the variation of light scattering intensity I_s, optical transmission I, and electrical conductivity W of a solution in the course of KNO_3 crystallization (recording of I, I_s, and W was started immediately after ethanol was introduced into the salt solution). At the initial instant of crystallization, the electrical conductivity of the solution starts to change somewhat, whereas the intensity of light scattering and the optical transmission remain unchanged for a certain time. This corresponds to the induction period of salt crystallization, with the duration of the induction period for I, I_s, and W being not the same, which reflects the different sensitivities of the employed measurement techniques. For example, in KNO_3 crystallization, the induction period duration is zero judging from electrical conductivity measure-

Table 1. Kinetics of crystallization of the salts studied*

Salt	Run no.	C_{alc}, vol %	T, °C	C_{in}, M	C_{sat}, M	n_c, min^{-1}	$K \times 10^6$, m s^{-1}	$S_n \times 10^6$, m s^{-1}	n_n
$NaNO_3$	4	29.72	20.0	4.058	3.905	400	7.86	0.19	6
$CaSO_4 \cdot 2H_2O$	2	17.83	21.0	0.0113	0.0037	400	4.65	0.27	9
	10	17.83	20.5	0.0106	0.0037	500	6.26	0.27	9
KNO_3	2	12.85	18.0	2.053	1.568	400	30.98	1.37	13
	3	7.73	18.0	2.259	1.978	400	42.45	1.55	7
$NaNO_2$	7	29.72	18.0	5.114	5.029	400	25.02	5.02	4
	9	32.20	18.0	5.114	4.733	400	14.74	3.97	13
K_2SO_4	1	5.15	21.0	0.628	0.450	400	14.18	0.17	14
	5	10.31	20.5	0.573	0.316	400	11.80	0.34	17
$Ba(NO_3)_2$	1	14.85	19.5	0.271	0.177	400	33.13	1.74	16
	2	5.94	19.0	0.311	0.262	400	56.95	1.29	15

Salt	Run no.	$N_0 \times 10^{-5}$	$K_2 \times 10^{10}$, s^{-1}	$N_\infty \times 10^{-5}$	$S_k \times 10^{10}$, s^{-1}	n_k	$\bar{d}_n \times 10^6$, m	$\bar{d}_f$, m
$NaNO_3$	4	1820.1	3.28	89.3	0.22	7	5.73	31.3
$CaSO_4 \cdot 2H_2O$	2	571.2	0.175	114.7	0.021	13	4.38	13.3
	10	121.3	0.153	79.1	0.039	17	7.60	14.5
KNO_3	2	6.96	839.6	0.223	117.9	15	37.8	368.1
	3	0.84	1807.4	0.107	181.3	11	87.1	391.7
$NaNO_2$	7	49.3	78.9	4.32	11.6	5	18.3	66.8
	9	4136.2	25.1	14.8	2.4	14	3.63	73.2
K_2SO_4	1	65.6	244.8	0.376	27.67	17	15.9	245.2
	5	60.0	55.1	2.58	8.70	18	17.3	146.1
$Ba(NO_3)_2$	1	151.8	55.6	3.90	7.2	17	9.70	97.5
	2	76.0	164.3	1.45	11.9	17	9.51	109.7

* C_{alc} is the volume fraction of alcohol in solution; n_s, the rotation frequency of the stirrer; S_n, n_n, the standard deviation and number of K measurements; K_2, the rate coefficient of crystal aggregation; S_k, n_k, the standard deviation and number of K_2 measurements; d_{in}, d_f, the average diameter of the forming crystals immediately after the end of the induction period of crystallization and at the end of experiment, respectively; N_0, N_∞, the total number of salt crystals in solution immediately after the end of the induction period of crystallization and at the end of experiment, respectively; and T, the solution temperature.

ments, 28 s for I_s, and 24 s for I (Fig. 1). With the salt precipitating from the solution, I_s, I, and W first change and then level off, indicating the completion of crystallization. Similar dependences were observed in crystallization of other salts.

Experimental data processing demonstrated that the kinetics of crystallization of the salts studied is described by Eq. (2) with $n = 1$. Typical kinetic curves in the coordinates of the integral form of this equation are presented in Fig. 2, whence follows that at the end of the crystallization period, when the total surface area of the formed crystals is virtually constant, the dependence becomes linear. A calculation of the rate coefficients of crystal growth by formula (8) demonstrated that the K value remains constant during the entire period of salt crystallization. This also indicates that $n = 1$. Examples of experimental data processing by means of formulas (1)–(5) and (8) are given in Table 2.

For some of the salts, higher K values were observed in the initial stage of crystallization (e.g., KNO_3; Table 2), which was due to the high transparence of the crystals and the influence of light diffraction (owing to the small size of salt crystals at the beginning of crystallization). This gave underestimated optical densities of the solutions during this

period [10], which is confirmed by calculation of the diameters of formed crystals by means of formula (5). As seen from the data in Table 2, the diameter of KNO_3 crystals formed in solution, calculated using formula (5), is larger at the beginning of crystallization, compared with the diameter at its end. The crystal size varies nonmonotonically with time: first decreases and then starts to increase. This contradicts the available published data. Therefore, "true" values of D, $\bar{d}$, and N were calculated for the initial stage of crystallization with the use of average rate coefficients of crystal growth (Table 1). The calculated true values of D, $\bar{d}$, and N are given in parentheses under the experimental values (Table 2).

It can be seen from Table 2 that no phenomena of this kind are observed in $NaNO_3$ crystallization. The optical density of the solution from the very beginning corresponded to its true value, the rate coefficient of crystal growth remained approximately constant during the entire crystallization period, and the diameter of the formed crystals steadily increased.

The rate coefficients K (average values) of crystal growth for other salts are listed in Table 1. The obtained values indicate the kinetic mode of crystal growth under the experimental conditions. For example, in the diffusion mode of the process

$$K \approx D_1/\delta, \quad (9)$$

where D_1 is the diffusion coefficient of the salt in solution ($m^2\ s^{-1}$) and δ is the thickness of the diffusion layer around a crystal (m).

If account is taken of the fact that, for aqueous salt solutions, $D_1 \approx 10^{-9}\ m^2\ s^{-1}$, $\delta \approx 10^{-6}$–10^{-5} m [6, 7], then the rate coefficients of crystal growth can be evaluated in the diffusion mode of the process as $K \approx 10^{-4}$–$10^{-3}\ m\ s^{-1}$. This value much exceeds the determined values (Table 1).

The obtained results are in agreement with the data of [6, 7, 13] and indicate that the rate coefficients of salt crystal growth decrease with increasing volume fraction of alcohol. This can be attributed to a decrease in the solvent permittivity, resulting in a stronger interaction between the salt molecules and ions in solution with their hydrate shells, and also to a change in the solution structure upon introduction of alcohol.

It should be noted that the crystal diameter is 3.63–87.1 μm after the completion of the induction period of crystallization and increases 3–10-fold by the end of the process (Table 1).

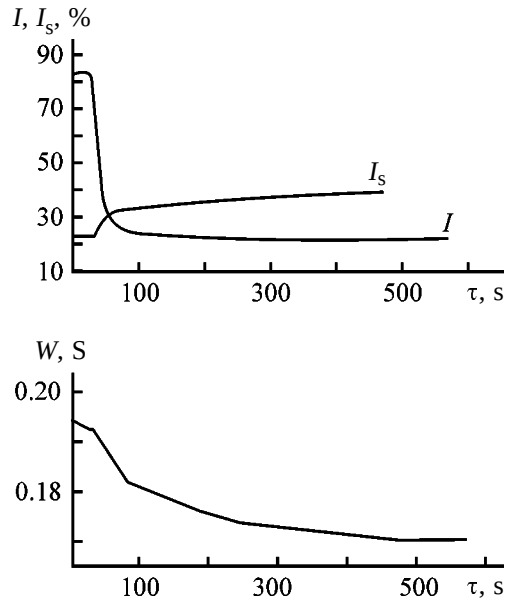

Fig. 1. Light scattering intensity I_s, optical transmission I, and electrical conductivity W of solution in KNO_3 crystallization (run no. 3) vs. time τ.

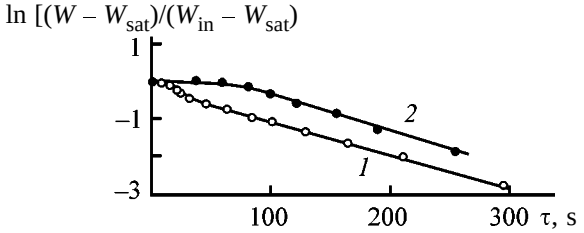

Fig. 2. Kinetic curves of crystallization, plotted in the coordinates of the integral form of Eq. (2) (n = 1). (τ) Time; the same for Fig. 3. (*1*) KNO_3, run no. 2; (*2*) $NaNO_3$, run no. 4.

Calculations by means of formula (4) demonstrated (Table 2) that in the course of crystallization the total number N of salt crystals formed in solution decreases, i.e., there occurs aggregation of the crystals. This phenomenon accompanies crystallization of any of the salts studied, irrespective of its nature, properties, and initial supersaturation of a solution. N is the largest at the initial instant of crystallization (immediately after the completion of the induction period).

Assuming [6, 7] that the kinetics of aggregation of crystals obeys the same laws as the coagulation of colloid particles, we transform the known Smoluchowski formula [14] describing the coagulation of colloid particles

$$\nu = \nu_0(1 + K_1\nu_0\tau)^{-1} \quad (10)$$

to a form convenient for our calculations

$$N = N_0[1 + K_2N_0(\tau - \tau_0)]^{-1}, \quad (11)$$

Table 2. Calculation by formulas (1)–(5) and (8) of the parameters of bulk crystallization of KNO_3 (run no. 3) and $NaNO_3$ (run no. 4)

τ, s	*W*, S	*C*, M	$\ln [(W - W_{sat})/(W_{in} - W_{sat}]$	*D*	$K \times 10^{-6}$, m s^{-1}	$\bar{d} \times 10^5$, m	$N \times 10^{-3}$
KNO_3 crystallization K_c = 114 m^{-2}, τ_0 = 0 s, ρ_s = 2110 kg m^{-3}, *M* = 101.1 g mol^{-1}							
0	0.1942	2.259	0	0	–	–	–
24.7	0.1923	2.235	–0.083	0.0021 (0.226)*	4571	937.8 (8.71)*	0.0001 (83.7)*
29.6	0.1923	2.235	–0.083	0.0235 (0.189)*	340.88	83.80 (10.44)*	0.093 (48.2)*
38.5	0.1908	2.217	–0.154	0.2052 (0.269)*	55.61	16.80 (13.73)*	20.30 (45.7)*
49.5	0.1883	2.178	–0.285	0.4027	40.73**	16.51	41.25
61.3	0.1852	2.155	–0.475	0.4818	45.84**	17.17	42.86
80.0	0.1818	2.109	–0.736	0.5232	50.12**	23.53	26.38
106.7	0.1805	2.095	–0.857	0.5446	42.04**	24.70	24.89
136.4	0.1786	2.074	–1.066	0.5594	39.80**	27.14	21.20
181.8	0.1761	2.043	–1.429	0.5729	39.11**	30.94	16.70
239.1	0.1739	2.019	–1.917	0.5787	39.48**	34.03	13.95
474.3	0.1704	1.978	–	0.5887	–	39.17	10.71
$NaNO_3$ crystallization K_c = 34.07 m^{-2}, τ_0 = 57.3 s, ρ_s = 2257 kg m^{-3}, *M* = 85 g mol^{-1}							
0	0.1253	4.058	0	0	–	–	–
37.5	0.1253	4.058	0	0	–	–	–
57.3	0.1253	4.058	0	0	–	–	–
80.0	0.1246	4.039	–0.131	0.6392	7.69**	0.573	18.20×10^4
99.8	0.1238	4.017	–0.305	0.8559	7.15**	0.923	9.38×10^4
120.6	0.1229	3.994	–0.547	0.9280	7.93**	1.329	4.91×10^4
154.2	0.1221	3.972	–0.824	0.9402	7.71**	1.762	2.83×10^4
189.7	0.1212	3.948	–1.271	0.9590	8.52**	2.209	1.84×10^4
254.9	0.1205	3.929	–1.846	0.9720	8.18**	2.556	1.39×10^4
411.1	0.1196	3.905	–	0.9402	–	3.135	0.89×10^4

* The true values are given in parentheses.
** The *K* values used to calculate the average rate coefficient of salt crystal growth (Table 1).

where ν, ν_0 are the concentrations of colloid particles at the initial instant of time and at a time τ; *N*, N_0 is the total number of salt crystals in solution at the initial instant of crystallization (immediately after the completion of the induction period) and at instant of time τ.

The coagulation constant of colloid particles, K_1, in Eq. (10) is related to the aggregation rate coefficient K_2 by the expression $K_2 = K_1 V^{-1}$. An example of experimental data processing by means of formula (11) is given in Fig. 3. It can be seen that during the initial period of crystallization the dependences are linear. This confirms the validity of formula (11). However, as the equilibrium state is approached, a certain departure from linearity is observed, presumably due to the fact that the aggregation rate coefficient K_2 decreases as the supersaturation in solution is lifted, this making lower the probability of crystal coalescence [15, 16]. Nevertheless, Eq. (11) can be used to describe approximately the kinetics of aggregation of crystals (correlation coefficient 0.60–0.99).

The results obtained in calculations by formula (11) are presented in Table 1. It can be seen that the N_0 and K_2 values may differ by several orders of magnitude in crystallization of different salts. For example, in crystallization of $NaNO_3$, $N_0 = 1820.1 \times 10^5$, $K = 3.28 \times 10^{-10}$ s^{-1}, whereas in the case of KNO_3 crystallization (run no. 3), $N_0 = 0.84 \times 10^5$, $K_2 = 1807.4 \times 10^{-10}$ s^{-1}. With increasing alcohol concentration in

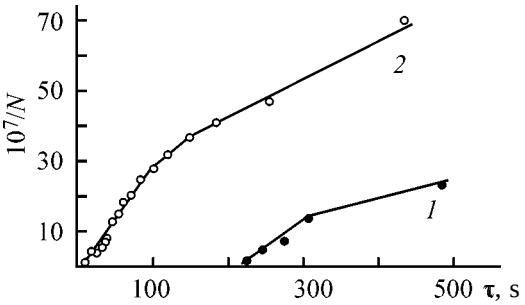

Fig. 3. Kinetic curves of crystal aggregation, plotted in the coordinates of Eq. (11). (N) Total number of crystals in solution by instant of time τ. (*1*) $NaNO_2$, run no. 7; (*2*) $Ba(NO_3)_2$, run no. 3.

solution, K_2 decreases and N_0 grows. This is observed in crystallization of nearly all of the salts studied, being presumably associated with the increasing viscosity of the solution and its growing supersaturation. The latter is supported by data on $CaSO_4 \cdot 2H_2O$ crystallization, according to which the N_0 value grows with increasing supersaturation at the same alcohol concentration in solution. The K_2 value is largely determined by the hydrodynamic state of a solution and, therefore, must decrease with its viscosity increasing upon introduction of alcohol. As known, the number of originally formed crystals, N_0, depends on the initial solution supersaturation and must increase with growing supersaturation, which does occur in crystallization of $CaSO_4 \cdot 2H_2O$. Unfortunately, it was impossible to analyze, as before [6, 7], the granulometric composition of crystals upon crystallization, the relevant data being lost.

CONCLUSION

A study of bulk crystallization of a number of salts from aqueous solutions of ethanol revealed that, irrespective of the nature of a salt and the initial supersaturation in solution, spontaneous crystallization is always accompanied by aggregation of the forming crystals. The greatest number of crystals is formed at the initial instant of crystallization (immediately after the completion of the induction period). Their further aggregation is approximately described by Smoluchowski's coagulation equation. With increasing alcohol concentration in solution, the rate coefficients of salt crystal growth and aggregation decrease. The growth of the forming crystals of the salts studied is described by a reaction equation of first order with respect to supersaturation.

REFERENCES

1. Melikhov, I.V. and Kelebeev, A.S., *Kristallografiya*, 1979, vol. 24, no. 2, pp. 410–412.
2. Melikhov, I.V., Mikheeva, I.E., and Rudin, V.N., *Teor. Osn. Khim. Tekhnol.*, 1985, vol. 19, no. 6, pp. 742–748.
3. Tkhai Ba Kau and Torocheshnikov, N.S., *Teor. Osn. Khim. Tekhnol.*, 1980, vol. 14, no. 4, pp. 501–508.
4. Ryall, R.G., Ryall, R.L., and Marshall, V.R., *J. Cryst. Growth*, 1986, vol. 76, no. 2, pp. 290–298.
5. El Moussaouiti, M., Boistelle, R., Bouhaouss, A., and Klein, J.P., *J. Cryst. Growth*, 1996, vol. 169, no. 1, pp. 118–123.
6. Linnikov, O.D., *Zh. Prikl. Khim.*, 1989, vol. 62, no. 5, pp. 1042–1048.
7. Linnikov, O.D., *Zh. Prikl. Khim.*, 1990, vol. 63, no. 2, pp. 297–302.
8. Nyvlt, J., *Chem. Prum.*, 1983, vol. 33, no. 8, pp. 402–405.
9. Chivate, M.R., Palwe, B.G., and Tavare, N.S., *Chem. Eng. Commun.*, 1979, vol. 3, no. 3, pp. 127–133.
10. Kouzov, P.A., *Osnovy analiza dispersnogo sostava promyshlennykh pylei i izmel'chennykh materialov* (Fundamentals of Analysis of the Dispersion Composition of Industrial Dusts and Powdered Materials), Leningrad: Khimiya, 1971.
11. Matusevich, L.N., *Kristallizatsiya iz rastvorov v khimicheskoi promyshlennosti* (Crystallization from Solutions in Chemical Industry), Moscow: Khimiya, 1968.
12. Konak, A.R., *J. Cryst. Growth*, 1973, vol. 19, no. 4, pp. 247–252.
13. Treivus, E.B., *Kristallografiya*, 1982, vol. 27, no. 1, pp. 165–169.
14. Smoluchowski, M., in *Koagulyatsiya kolloidov* (Coagulation of Colloids), Moscow: ONTI, 1936, pp. 7–39.
15. Shchukin, E.D., Amelina, E.A., Yusupov, R.K., *et al.*, *Dokl. Akad. Nauk SSSR*, 1973, vol. 213, no. 1, pp. 155–158.
16. Melikhov, I.V., Kuleshova, O.V., Berdonosov, D.G., and Burlakova, E.V., *Kolloidn. Zh.*, 1991, vol. 53, no. 1, pp. 375–378.

Russian Journal of Applied Chemistry, Vol. 74, No. 7, 2001, pp. 1112–1117. Translated from Zhurnal Prikladnoi Khimii, Vol. 74, No. 7, 2001, pp. 1084–1090.

SORPTION AND ION-EXCHANGE PROCESSES

Composite Sorbents Based on Inorganic Adsorbents and Binders

V. V. Samonin, L. V. Grigor'eva, and V. V. Dalidovich

St. Petersburg State Technological Institute, St. Petersburg, Russia

Received October 9, 2000; in final form, March 2001

Abstract—The routes of fabricating and the main properties of composite sorbents based on mineral adsorbents as fillers and inorganic binders are considered.

The possibilities and methods of fabricating and the properties of composite sorbents (CSs) based on mineral adsorbents as fillers and organic polymers as binders were considered in [1–5]. In many cases, such CSs were unsuitable for repeated exploitation, because the temperatures for regeneration of sorbents incorporated into CSs exceed the range of stability of organic polymeric matrices.

Synthesis of such CSs and their possible structure have been reported previously [4]. The polymeric nature of some inorganic compounds of silicon and aluminum [6, 7] suggests that interaction of the initial sorbent with the inorganic polymer should occur similarly as with organic binder.

In this work we prepared and stuided CSs based on inorganic sorbents and polymeric binders of various origins and structures.

EXPERIMENTAL

Inorganic sorbents were silica gel (KSMG grade), NaX zeolite, AOA-1 grade active aluminum oxide (AAO), and coarse-pore water-resistant silica gel (OSG grade) impregnated with lithium and calcium chlorides.

Silicic acid sol (SAS), aqueous sodium silicate solution (water glass, WG), and potassium tetrasilicate (PTS) based cement were inorganic binders. They are readily available and have the enhanced thermal stability as compared to organic materials, which is essential in view of necessity of recovering inorganic sorbents at high temperatures (from 180–200°C for silica gel to 350–400°C for zeolite). Moreover, the different structure of these polymeric systems allows the mechanism of the formation of CSs based on inorganic polymers to be analyzed in more detail.

The CS as consolidated mixture was prepared in the shell of the adsorber, which is the main part of its body.

The filler used with a WG binder was NaX zeolite mixed with active aluminum oxide (AOA-1 grade) in the 1 : 1 ratio. The mixture of this composition is optimal for synthesizing, for example, mineral filters intended for complex purification of freons to remove moisture and degradation products of freon oils. After vibration packing of granules, the aqueous binder solution was poured through the mixture and then the fabricated CS was dried for 4–6 h at 200–350°C depending on the initial sorbent. The WG had the ratio $m = 2.2$ of the number of SiO_2 and R_2O groups in sodium silicate and contained 40 wt % sodium silicate. The coagulants (aqueous solutions containing 5–25 wt % H_3PO_4, NH_4OH, or $CaCl_2$) were added to it preliminarily. The coagulant fraction was varied within 10–65 wt % of WG, the latter amounting to 20 wt % of CS.

CS as consolidated mixture with SAS binder was prepared similarly. SAS with a density of 2.5 g cm^{-3}, containing 20 wt % substance, with micelle size of 25 nm and pH 10.5, was used in the experiments. The initial SAS was diluted by a factor of 2 or 3, if necessary. The SAS aqueous solution in an amount of 50% of the volume of the initial sorbent was poured through the mixture.

CS with PTS binder in the form of consolidated mixture was also prepared in the shell of the adsorber. The binder used in this work was the calcination product of the K_2O–SiO_2 (30 mol % K_2O) system ensuring the best strength characteristics of cement stone upon tempering and solidification [8]. According to X-ray phase analysis, PTS is a mixture of potassium tetrasilicate (monoclinic crystal system, density

1070-4272/01/7407-1112$25.00

Table 1. Static a and dynamic a_d sorption capacities for water vapor of CSs fabricated with WG

Coagulant, wt %	Weight ratio of coagulant and binder	P/P_s = 0.85		P/P_s = 0.13		a_d, g g^{-1}	k
		a, cm^3 g^{-1}	$D_a \times 10^{11}$, m^2 s^{-1}	a, cm^3 g^{-1}	$D_a \times 10^{11}$, m^2 s^{-1}		
NH_4OH, 25.0	0.65	0.26	10.8	0.20	4.1	0.20	0.81
$CaCl_2$, 5.0	0.50	0.26	7.2	0.20	2.3	0.19	0.70
H_3PO_4, 7.0	0.10	0.28	7.8	0.22	3.1	0.18	0.70
CS without coagulant		0.15	1.5	0.13	–	–	–
Starting stock NaX + AOA-1		0.28	29.0	0.25	17.0	0.25	0.90

* (k) Utilization factor of the equilibrium dynamic capacity, and (D_a) apparent diffusion coefficient.

2.335 g cm^{-3}, mp 765°C) and potassium disilicate (PDS) (rhombic crystal system, density 1.538 g cm^{-3}, mp 1045°C) [8]. The PTS : PDS molar ratio is 60 : 40, as determined by the initial stock composition of the K_2O–SiO_2 system. The grain size of the PTS powder (about 1 μm) was calculated from its specific surface area [9]. The initial sorbent was mixed with PTS, formed as layer in the shell of the adsorber, kept for 6 days at room temperature, and heat-treated for 3–4 h at 350–400°C. The PTS amount was varied from 1 to 30 wt % CS.

The sorption properties and pore structure of CSs were studied using the methods described in [10, 11]. Dynamic study was performed at a 60–65% relative humidity of the initial water vapor–air flow, its temperature of 20°C, and the flow velocity of 0.5 l min^{-1} cm^{-2}, with a 20-mm CS bed. The specific surface area of samples was determined from low-temperature desorption of argon [12]. The hydraulic resistance R was measured as in [13] and the crushing strength, as in [14].

CSs prepared by different procedures were a blown-through mixture consolidated in the shell of the adsorber. The hydraulic resistance of the sorbing bed to humid air flow upon formation of the consolidated mixture increased from 50 in the starting stock to 250–300 Pa in the CSs synthesized with sodium silicate solution. The crushing strength of the article formed outside the shell of the adsorber was (1–2) × 10^5 Pa.

The main sorptive properties and the degree of blocking of sorbent pores with binder were studied on both composite and initial sorbents. The properties with respect to water vapor under static and dynamic experimental conditions for CSs with WG are given in Table 1.

Table 1 shows that the sorption capacity of CSs with WG is somewhat lower (by 7–20%) than that of the initial sorbents. Also, the apparent diffusion coefficient D_a calculated from the kinetic sorption curves obtained on single grains decreases considerably (3–5-fold) compared to the initial stock. The similar phenomenon is observed for both values (0.13 and 0.85) of the relative water vapor pressure P/P_s. However, the deterioration of CS sorption properties compared to the properties of the initial stock was more pronounced for P/P_s = 0.13 than for P/P_s = 0.85.

Most likely, this is due to the fact that the silicon–oxygen xerogel matrix formed at alkaline pH values has coarse-grain structure and, consequently, considerable sorption capacity only at high relative water vapor pressures. The formed matrix partially blocks fine pores of the sorbents, thus decreasing the sorption capacity at low pressures (P/P_s = 0.13). At higher pressures the coarse-pore structure of the forming matrix makes certain positive contribution to the CS sorption capacity. Along with this, the dynamic capacity a_d of CSs decreases by 20–28% in comparison with the initial sorbent (Table 1). The utilization factor of the equilibrium dynamic capacity $k = a_d/a_{eq}$ decreases by 15%, i.e., the kinetic characteristics of the water vapor absorption by the consolidated mixture are satisfactory (a_d is the dynamic capacity of the sorbent corresponding to 10% breakthrough of the water vapor and a_{eq} is its equilibrium capacity corresponding to the moment when the water vapor concentration behind the stock becomes equal to the initial concentration).

Hence, the study performed shows that the use of WG with a coagulant allows preparation of sufficiently active CSs. When WG is used without coagulant, the absorption capacity of the initial stock sharply decreases because of the blocking of the sorbent pores with sodium silicate impermeable film formed on the surface of the initial sorbent. The formation of a permeable silicate film appeared to be possible only with coagulants (Table 1), which, affecting the

sodium silicate solution, cause gelation of silicic acid in its volume. The latter forms xerogels with open porosity. However, some decrease in the sorption capacity and a more considerable decrease in the equilibrium capacity D_{eq} of CS for water vapor shows that the initial sorbent pores are partially blocked with the matrix.

From this standpoint, it is more reasonable to use SAS binder, which is a coarser disperson system than sodium silicate solution. The fact that the molecules in SAS are initially rolled up favors formation of a permeable system upon drying. The lower viscosity of SAS as compared to WG solution is also the positive factor facilitating its penetration into pores of the initial stock and ensuring efficiency of the CS fabrication. Comparatively coarse sol macromolecules may block pores of the initial sorbent if it contains even coarser pores (as in coarse-pore silica gel and AAO). For zeolite sorbent this process is improbable. It should be noted that successful approbation of SAS for preparation of granulated sorbents from silica gel powders and AAO has been described in the literature [3, 5], and we can expect the positive result when using SAS for the fabrication of CSs from granulated commercial sorbents. Therefore, in the next stage we studied the feasible routes of fabrication and the main properties of CSs based on various inorganic granulated sorbents and SAS, as well as the behavior of SAS upon CS synthesis.

The process parameters and properties of CSs are given in Table 2. The presented data show that CSs synthesized with SAS binder have the sorption characteristics virtually identical to those of the initial sorbent. The main characteristics (W_s and S_{sp}) of the initial sorbent surpass by no more than 5% the analogous characteristics of CSs fabricated with sol binder. The D_e and k values of CSs differ from those of the initial sorbents by less than 10%. The R values of CSs exceed those of the initial sorbent only slightly (by no more than 10%), with the exception of those with OSG. For CS with the latter sorbent R increases 13-fold, which may be due to some other mechanisms of the process and to the formation of a voluminous loose film of silicic acid xerogel upon interaction of SAS with calcium and lithium chlorides.

In this work, along with the analysis of the changes in the sorption and hydraulic characteristics of the materials, the variation of pH of the initial sol on the surface of the initial sorbent was also estimated from measurements of the pH value with test paper. For example, for AAO and zeolite pH of the sol decreases insignificantly (Table 2) as compared to silica gel and OSG (silica gel impregnated with potassium and lithium chlorides). Compared to the initial sorbent, the S_{sp} value of CSs slightly decreases in the first case, whereas in the second case it slightly increases.

This difference is presumably due to different mechanisms of the film formation on the surface of granules of the initial sorbent depending on its origin. As known [15], the sorption surface of silica gels exhibits acid properties arising from partially polarized hydroxy groups, whereas that of AAO and zeolite exhibits amphoteric and base properties, respectively, owing to specific chemical nature of alumogels and aluminosilicates [16]. The experimental pH values of the silica gel aqueous extracts and SAS lie within 5–6. At the same time, for AAO and zeolite, they are 7 and 8, respectively. The necessary amount of SAS was added by pouring it through the initial sorbent. Owing to its low viscosity, the process is fast and practically no excess sol requiring removal is formed. A thin SAS film formed on the surface of AAO and zeolite granules undergoes no significant chemical transformations, which is confirmed by a small decrease in the SAS pH (Table 2). At the same time, S_{sp} of CSs obtained by interaction of SAS with AAO decreases by 10% as compared with the initial AAO, which shows that some macromolecules of the initial sol penetrate into the sorbent pores, blocking the active surface. Then, on the surface of sorbent granules a strong porous SAS film is formed upon drying.

When the silica gel sorbent (with and without impregnation) is used for CS fabrication, pH of the initial sol in contact with the initial sorbent decreases from 10.5 to 6–7 (Table 2) and S_{sp} increases by 6–7%. Most likely, this effect may be due to another mechanism of the film formation on the silica surface. Silica gels, including impregnated ones, initiate recondensation of SAS followed by its gelation when coming in contact with the sorbent. At the same time, AAOs and zeolites with the base properties of the surface do not behave as pronounced SAS destabilizers. The effect of sol destabilization is the most pronounced under the action of impregnating additives (Table 2, OSG + SAS) yielding hydroxides and silicates, which are not sufficiently soluble under the conditions considered. As a result, a voluminous film is formed, which, along with amorphous silica, contains potassium silicates and hydroxides. This film blocks CS pores and considerably enhances the hydraulic resistance of the article.

The PTS cement is another representative of silicate binders considered in this work. The character-

Table 2. Properties of PSs fabricated with mineral sorbents and SAS

Sorbent	Degree of sol dilution	Sol to sorbent volume ratio	S_{sp}, $m^2\ g^{-1}$	P/P_s = 0.85		k	R, Pa	pH variation
				a, $cm^3\ g^{-1}$	$D_a \times 10^{11}$, $m^2\ s^{-1}$			
AAO	–	–	163	0.60	18.4	0.78	49	–
AAO + SAS	1 : 3	0.8 : 1	141	0.58	19.5	0.72	51	0.5
Zeolite	–	–	–	0.25	38.0	0.90	51	–
Zeolite + SAS	–	1.0 : 1	–	0.25	35.0	0.81	59	0.5
Silica gel	–	–	904	0.42	13.0	0.28	74	–
SG + SAS	1 : 2	5.0 : 1	967	0.40	12.1	0.32	85	3.0
OSG	–	–	94	–	41.7	–	49	–
OSG + SAS	1 : 1.5	1.0 : 1	132	–	39.1	–	640	4.0

Table 3. Properties of CSs from PTS and shaped spherical zeolite NaX

Sorbent	a, $cm^3\ g^{-1}$ at indicated P/P_s (H_2O)		$D_a \times 10^{11}$, $m^2\ s^{-1}$ at indicated P/P_s (H_2O)		a_d (H_2O), $cm\ g^{-1}$	k	W_s (C_6H_6) $cm^3\ g^{-1}$	V_Σ $cm^3\ g^{-1}$	P_{cr}, MPa	R, Pa
	0.13	0.85	0.13	0.85						
PTS	0.13	0.55	13.0	15.0	–	–	0.08	0.15	0.12	–
NaX + PTS*										
70 : 30	0.17	0.35	24.0	35.0	0.12	0.48	0.14	0.20	3.0	290
80 : 20	0.19	0.30	28.0	60.0	0.21	0.84	0.20	0.35	2.5	200
90 : 10	0.20	0.27	35.0	62.0	0.22	0.82	0.25	0.49	Low strength	–
NaX	0.24	0.26	45.0	65.0	0.23	0.90	0.25	0.60	–	49

* Weight ratio.

istics of the CSs obtained with this binder are given in Table 3.

Study of the fabricated articles show that, as the binder amount increases, the properties of the resulting CSs change regularly. The equilibrium adsorption of water vapor at its relative pressure of 0.13 decreases. In this case, the limiting volume of the sorption space W_s of CSs with respect to benzene, as determined at a relative pressure of benzene vapor P/P_s = 1, and its total pore volume V_Σ, as calculated from the difference in the reciprocal values of the apparent and pycnometric densities of the sorbents, decrease relative to the initial zeolite [10]. Most probably, owing to formation of polymeric crystal hydrates [17], the binder forms a dense film, impeding sorbate diffusion into zeolite pores upon formation of the cement matrix. Nevertheless, the D_e values suggest that the PTS film covering granules of the initial sorbent is sufficiently permeable, which is in line with the published data. At the high relative water vapor pressure (P/P_s = 0.85) the sorption capacity of CSs grows with increasing PTS concentration, which is due to the formation of crystal hydrates of the polymeric matrix under these conditions. The same was not observed at P/P_s = 0.13.

The study of the routes of high-temperature regeneration show that multiple regeneration of the articles obtained with the inorganic polymeric binder of the PTS type does not deteriorate the CS sorption (Table 4). The dynamic sorption capacity a_d and the utilization factor of the dynamic sorption capacity k remain virtually unchanged.

The analysis of the CS characteristics obtained with the use of various polymeric inorganic systems shows that articles with PTS considerably surpass in strength (P_{cr} = 2.5–3.0 MPa) those with sodium silicate and sol binders (P_{cr} = 0.1–0.2 MPa, Tables 1 and 2, respectively). However, their hydraulic resistance R to the air flow is considerably higher (5–6-fold) than that of CS with SAS and is virtually the same as that of SC with WG.

Also, Tables 1–3 evidently show that for articles fabricated with the binder in various dispersion states

Table 4. Sorptive characteristics of NaX + PTS articles after regeneration

NaX : PTS weight ratio	a_d, $cm^3\ g^{-1}$	k
First regeneration		
80 : 20	0.21	0.84
70 : 30	0.12	0.48
Second regeneration		
80 : 20	0.20	0.80
70 : 30	0.12	0.50
Third regeneration		
80 : 20	0.21	0.80
70 : 30	0.12	0.50

the D_e value (as determined at P/P_s = 0.85 for the close values of the binder concentration in CSs) differs from the analogous characteristic of the initial sorbent. With molecular solution (WG) D_e decreases by a factor of 2.7–3.7, whereas with sol binder (SAS), by 6–9%, and with coarsely dispersed binder (PTS), by 5–8%. This indicates that the binder forms films of different structure on the sorbent surface. Thus, the articles fabricated from CSs with sols and coarsely dispersed silicate systems as binders have enhanced kinetic parameters as compared to those fabricated from CSs with solutions, even in the case when coagulants favoring formation of porous and more permeable film are added into the system.

Table 5 shows how the state of the polymeric silicate system correlates with the CS structure and properties. The binders used for preparing CSs were polymeric systems differing in the degree of dispersity. Sodium silicate solution was a molecular solution of the polymer, silicic acid sol was an inorganic colloid, and PTS was a coarsely dispersed system.

The set of the obtained data allows a conclusion that, with binder used as molecular solution, dense weakly permeable film of sodium silicate is formed on the sorbent surface. The materials obtained have considerable strength and equilibrium sorption capacity. At the same time, they have poor kinetic characteristics and considerable hydraulic resistance. This is due to the fact that the binder film formed upon interaction of sorbent with viscous WG solution has considerable thickness. It is appropriate to fabricate articles based on molecular solutions of inorganic polymers in the form of structural elements intended for operation under static conditions.

The film formed on the surface of sorbent granules upon interaction with sol is nonuniform, ensuring free access of adsorbate molecules inside the article. Owing to permeability of the binder film, the capacity and kinetic characteristics of the articles are retained at a level of those of the initial sorbent. The low viscosity of the sol ensures the low residual amount of the binder in the article at the hydraulic resistance close to that of the initial sorbent. At the same time, this produces the negative effect on the strength of sol-bound CSs. It is preferable to prepare the latter CSs in the form of consolidated mixture in the shell of the adsorber and to use them under conditions of a flow-type reactor.

The combination of the initial sorbent with coarsely dispersed binders allows fabrication of articles in the form of both consolidated mixture and single structural element. The strength of a CS is determined by the number of sorbent and binder particles in contact per unit volume of the article, and its sorptive properties, by the binder amount in the article. When

Table 5. Correlation between the state of the polymeric silicate system and the CS structure and properties

State of polymeric structure	Molecular solution (WG)	Colloid (SAS)	Coarsely dispersed system (PTS)
CS structure	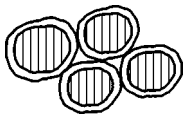	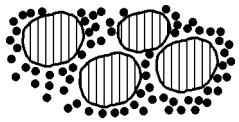	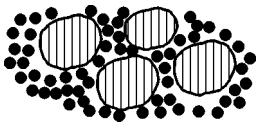
Physical shape of article	CM *SE*	*CM* SE	*CM* *SE*
Field of CSs application	Dynamic conditions *Static conditions*	*Dynamic conditions* Static conditions	*Dynamic conditions* *Static conditions*

* (CM) Consolidated mixture and (SE) structural element.

the binder amount is 20% of the article weight, strong materials are formed, characterized by high hydraulic resistance and low kinetic parameters. It is appropriate to use such materials under static conditions and at high mechanical loads. The CSs with less than 10% binder content allow fabrication of articles as a mixture consolidated in the absorber. Such articles have low hydraulic resistance, high kinetic factors, and are suitable for operating in the dynamic mode.

By analogy with the classification of organic polymeric systems [4], the correlation between the state of the polymeric system used for CS fabrication and the structure and properties of the fabricated articles and areas of their application is demonstrated in Table 5. The preferable modes of application of CSs fabricated by different methods are printed italic. The structural elements formed with solution are the most suitable for operation under static conditions. For a flow-type reactor we can recommend a consolidated mixture prepared by interaction of the initial sorbent with sol. Coarsely dispersed systems allow fabrication of both types of CSs, i.e., for static and dynamic conditions.

CONCLUSIONS

(1) Strong composite sorbents in the form of block articles or a mixture consolidated in the absorber can be fabricated on the basis of inorganic granulated sorbents and silica matrices. The optimal process parameters are determined, providing high strength and considerable sorption capacity of the articles. The materials of this type exhibit high sorption characteristics inferior to those of the initial sorbent by no more than 5–20%. They have sufficiently high strength and low hydraulic resistance to water vapor–air flow when operating under dynamic conditions.

(2) Use of silicic acid sol and coarsely dispersed binder like potassium silicate cement allows the pore structure of the initial granulated sorbents to be preserved in the course of formation of block articles. At the same time, with sodium silicate solutions the active sorbents can be fabricated only with coagulants.

REFERENCES

1. Moskvin, L.N., Mel'nikov, V.A., Besedin, A.A., *et al*., *Zh. Prikl. Khim*., 1983, vol. 56, no. 3, pp. 516–520.
2. Belotserkovskii, G.M., Ivakhnyuk, G.K., Fedorov, N.F., and Babkin, O.E., *Zh. Prikl. Khim*., 1993, vol. 66, no. 2, pp. 283–287.
3. Ivakhnyuk, G.K., Babkin, O.E., Belotserkovskii, G.M., and Fedorov, N.F., *Zh. Prikl. Khim*., 1993, vol. 66, no. 2, pp. 462–464.
4. Fedorov, N.F., Ivakhnyuk, G.K., Samonin, V.V., *et al*., *Zh. Prikl. Khim*., 1991, vol. 64, no. 4, pp. 610–616.
5. USSR Inventor's Certificate no. 1818142.
6. Sychev, M.M., *Neorganicheskie klei* (Inorganic Adhesives), Leningrad: Khimiya, 1974.
7. Cherkinskii, Yu.S., *Khimiya polimernykh vyazhushchikh veshchestv* (Chemistry of Polymeric Binders), Leningrad: Khimiya, 1974.
8. Mikhailova, A.I., Synthesis and Study of Novel Binders Based on the K_2O–SiO_2–R_2O_3 Systems, where R is Al^{3+}, Fe^{3+}, Cr^{3+}, and B^{3+}, *Cand. Sci. Dissertation*, Leningrad, 1973.
9. Morokhov, I.D., Trusov, L.I., and Chizhin, S.P., *Ultradispersnye metallicheskie sistemy* (Ultradisperse Metallic Systems), Moscow: Atomizdat, 1977.
10. Cherepov, A.G., Yurkevich, A.A., Vorozhbitova, L.N., and Sevryugov, L.B., *Opredelenie piknometricheskoi, kazhushcheisya i gravimetricheskoi plotnostei vysokodispersnykh poristykh tel: Metodicheskie ukazaniya* (Determination of Pycnometric, Apparent, and Gravimetric Densities of Ultradisperse Porous Substances. Methodical Guidelines), Leningrad: Leningr. Tekhnol. Inst. im. Lensoveta, 1983.
11. Dalidovich, V.V. and Samonin, V.V., *Issledovanie adsorbtsii parov vody: Kinetika vodopogloshcheniya: Metodicheskie ukazaniya* (Study of Water Vapor Adsorption: Kinetics of Moisture Absorption. Methodical Guidelines), St. Petersburg: Sintez, 1996.
12. Vorozhbitova, L.N., Ivakhnyuk, G.K., Samonin, V.V., *et al*., *Opredelenie udel'noi poverkhnosti tverdykh tel gazokhromatograficheskim metodom: Metodicheskie ukazaniya* (Gas Chromatographic Determination of the Specific Surface Area: Methodical Guidelines), Leningrad: Leningr. Tekhnol. Inst. im. Lensoveta, 1988.
13. Keier, B.R., and Cherepov, A.G., *Rekuperatsiya parov letuchikh rastvoritelei: Issledovanie kinetiki adsorbtsii v potoke gaza-nositelya: Metodicheskie ukazaniya* (Recuperation of Vapors of Volatile Solvents in a Flow of Carrier Gas: Methodical Guidelines), Leningrad: Leningr. Tekhnol. Inst. im. Lensoveta, 1990, pp. 3–13.
14. Kolosentsev, S.D., Belotserkovskii, G.M., and Sevryugov, L.B., *Opredelenie prochnostnykh svoistv sorbentov i katalizatorov: Metodicheskie ukazaniya* (Determination of the Strength Properties of Sorbents and Catalysts: Methodical Guidelines), Leningrad: Lening. Tekhnol. Inst. im. Lensoveta, 1979.
15. Neimark, I.E., and Sheinfain, R.Yu., *Silikagel', ego poluchenie, svoistva, primenenie* (Silica Gel: Synthesis, Properties, and Application), Kiev: Naukova Dumka, 1973.
16. Kel'tsev, N.V., *Osnovy adsorbtsionnoi tekhniki* (Principles of Adsorption Technology), Moscow: Khimiya, 1984.
17. Pashchenko, A.A., *Teoriya tsementa* (Theory of Cement), Kiev: Budivel'nik, 1991.

Russian Journal of Applied Chemistry, Vol. 74, No. 7, 2001, pp. 1118–1121. Translated from Zhurnal Prikladnoi Khimii, Vol. 74, No. 7, 2001, pp. 1091–1094.

APPLIED ELECTROCHEMISTRY AND CORROSION PROTECTION OF METALS

Electrochemical Behavior of Lithium in Aqueous Solutions of Alkali Metal Hydroxides

A. I. Demidov, V. K. Domanskii, and A. G. Morachevskii

St. Petersburg State Technical University, St. Petersburg, Russia

Received March 6, 2001

Abstract—Published data on the interaction of lithium with aqueous solutions of alkali metal hydroxides are discussed. The behavior of lithium in aqueous solutions of LiOH and KOH was studied experimentally.

One of promising chemical power cells is that based on the lithium–water system [1, 2]. Use of lithium in water-activated chemical power cells is enabled by the formation of a passivating film of complex structure on the lithium surface brought in contact with an electrolyte. Presumably, this film consists of an outer porous layer of hydrated lithium hydroxide impregnated with electrolyte and an inner porous layer of lithium oxides of indeterminate composition, adjacent to the metal [3]. This film is stable in an electrolyte with the LiOH concentration exceeding 1.5 m, where m is molality unit (mol/1000 g H_2O) [4]. The film has pores $1–10^3$ nm in size [5]. The total surface area of the pores constitutes approximately 5–25% of the total surface area of the film at a lithium hydroxide concentration in the electrolyte of 5.0–3.5 m [6, 7].

The rate of interaction between the alkali metal and the electrolyte (rate of lithium corrosion) depends on the solution composition and temperature. For example, the rate of lithium corrosion in solutions of the system LiOH–H_2O ($3.1 < m < 4.8$) decreases from 9.8×10^{-4} to 3.9×10^{-4} kg m^{-2} s^{-1} with the lithium hydroxide concentration in solution increasing from 3.1 to 4.0 m [8]. Raising the content of LiOH in solution further has little effect on the amount of corrosion losses. At the same concentration of an alkali metal hydroxide in the electrolyte, the rate of corrosion increases in going from LiOH solutions to solutions of NaOH, KOH, and CsOH (Fig. 1) [8, 9], although the activity of water decreases in this series of electrolytes [10, 11]. Such a discrepancy is possibly due to occurrence of reactions between lithium and alkali metal ions in solution:

$$Li + Na^+ = Li^+ + Na, \quad (1)$$

$$Li + K^+ = Li^+ + K, \quad (2)$$

$$Li + Cs^+ = Li^+ + Cs. \quad (3)$$

The changes in the Gibbs energy for reactions (1)–(3) at 298 K are, respectively, –30, –10, and –0.8 kJ. Since the intensity of interaction between alkali metals and water increases in going from lithium to sodium, potassium, and cesium, the occurrence of reactions (1)–(3) may lead to lithium corrosion rate increasing in the following order of electrolyte solutions: LiOH < NaOH < KOH < CsOH.

The temperature dependence of the rate of lithium corrosion in aqueous solutions of alkali metal hydroxides is well described by the Arrhenius equation [3, 9, 12, 13]. As seen from the table, the activation energies of lithium interaction with water decrease in going from the system LiOH–H_2O to KOH–H_2O.

Lithium corrosion in aqueous electrolyte solutions is a spontaneous electrochemical process which can be represented, in the case of solutions of the system LiOH–H_2O, as conjugated electrochemical reactions

$$Li = Li^+ + e, \quad (4)$$

$$H_2O + e = OH^- + 1/2H_2, \quad (5)$$

$$Li + H_2O = LiOH + H_2. \quad (6)$$

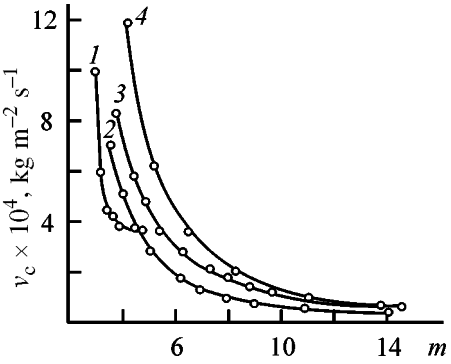

Fig. 1. Lithium corrosion rate v_c vs. molal concentration m of alkali metal hydroxide in solutions: (*1*) LiOH, (*2*) NaOH, (*3*) KOH, and (*4*) CsOH.

1070-4272/01/7407-1118$25.00

The state of the system lithium–aqueous solution of lithium hydroxide can be characterized by the stationary potential of the lithium electrode in this solution. The stationary potential E of the lithium electrode in solutions of the system LiOH–H_2O ($3.1 < m < 4.8$) is virtually independent of the solution concentration, being equal to -2.76 ± 0.01 V relative to the standard hydrogen electrode (s.h.e.) [8]. In solutions of the systems NaOH–H_2O, KOH–H_2O, and CsOH–H_2O, the stationary potential of the lithium electrode $-2.84 < E < -2.79$ V is affected by the occurrence of not only reaction (6), but also reactions (1)–(3). Since hydrogen reduction on lithium by reaction (5) is characterized by a higher overvoltage of about 2 V [3, 14, 15], then, as believed by Littauer and Tsai [3], it is the rate of this electrochemical reaction that determines the overall rate of corrosion.

Anodic dissolution of lithium in aqueous solutions of alkali metal hydroxides

$$Li + OH^- = LiOH + e \qquad (7)$$

proceeds at pore bases through the inner protective layer with thickness of, in all probability, only several molecular layers [3].

Presently, there exists no unified standpoint on what stage is rate-determining in anodic dissolution of lithium in aqueous solutions of alkali metal hydroxides. Cooper *et al*. [16] believe that the anodic dissolution of lithium is controlled by dissolution of the forming lithium hydroxide in the aqueous solution. According to [17], the anodic dissolution of lithium is limited by water diffusion in the film formed on the metal. In [13], it was assumed that the rate-determining stages of the electrochemical process are both water transfer from the solution bulk to the electrode surface and removal of the products formed in the electrochemical reaction. According to our previous study [18], the rate-determining stage of the anodic dissolution of lithium in aqueous solutions of alkali metal hydroxides is LiOH diffusion from the anode surface into the solution bulk.

In anodic polarization of the lithium electrode in aqueous solutions of alkali metal hydroxides from the stationary potential to values $-2.5 < E < -2.3$ V relative to s.h.e., the rate of metal corrosion decreases and the current of anodic dissolution of lithium increases, approaching its limiting value (Fig. 2) [15]. The limiting current decreases with increasing concentration of alkali metal hydroxide in solution [18–22]. In Fig. 2, the rate of lithium corrosion is expressed in electrical units in the form of the current density for the equivalent process of hydrogen reduction, j_{H_2}. With the electrode potential shifted to positive values, the rate of electrochemical lithium oxidation [reaction (4)] increases and that of electrochemical hydrogen reduction [reaction (5)] decreases, which leads to lower corrosion loss and, consequently, to higher efficiency of utilization of the active paste of the anode. As seen from Fig. 2, the highest values of the lithium utilization efficiency in the alkali metal hydroxide solutions studied at 298 K are $81 < \eta < 88\%$. According to [23], the efficiency of lithium utilization in a 4.5 m LiOH solution at $291 < T < 328$ K may be as high as $98 < \eta < 99\%$. At $T > 328$ K, the efficiency of utilization of the active paste of the anode decreases substantially because of the dramatic increase in the rate of lithium corrosion.

Activation energies E_a of lithium reaction with water in electrolytes of various compositions

Electrolyte concentration m, mol/1000 g H_2O	E_a, kJ mol^{-1}	T, K	References
	LiOH–H_2O		
4.0, 4.5	64.9	277–333	[3]
	NaOH–H_2O		
4.9, 6.8, 9.4	52.4	293–313	[12]
6.0	56.5 ± 2.5	293–313	[9]
	KOH–H_2O		
5.9	43.4–50.7	278–298	[13]
7.7	52.4 ± 1.7	298–313	[9]
10.0	58.2 ± 2.5	298–313	[9]

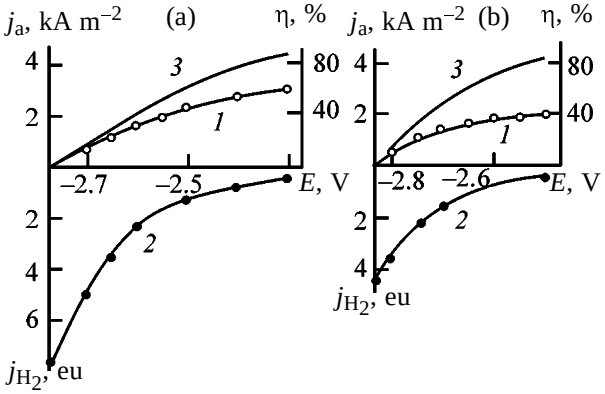

Fig. 2. (*1*) Discharge current density j_a, (*2*) corrosion rate j_{H_2}, and (*3*) lithium utilization efficiency η vs. potential E in solutions of systems MOH–H_2O. (a) 3.2 m LiOH and (b) 6.2 m KOH1.

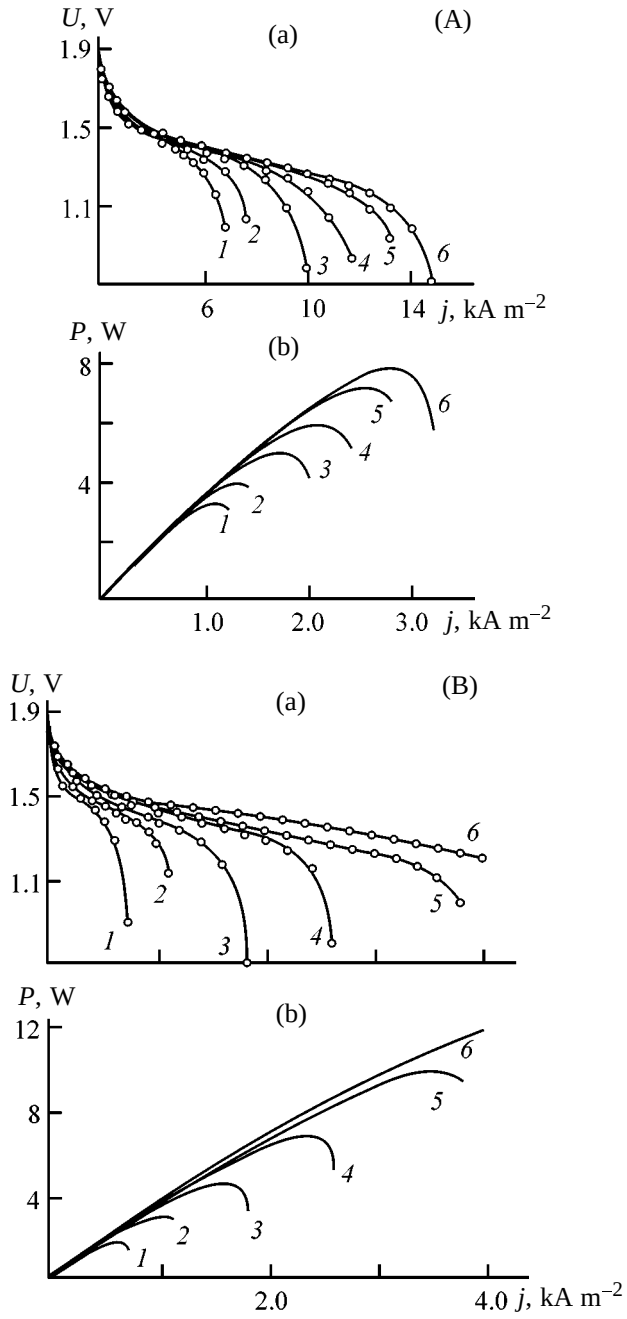

Fig. 3. (a) Discharge voltage U and (b) power P vs. discharge current density j for chemical power cells with (A) $LiOH–H_2O$ and (B) $KOH–H_2O$ electrolytes with varied molal concentration. m: (A) (*1*) 4.5, (*2*) 4.3, (*3*) 4.1, (*4*) 3.9, (*5*) 3.7, and (*6*) 3.5; (B) (*1*) 11.4, (*2*) 10.0, (*3*) 9.0, (*4*) 8.0, (*5*) 7.0, and (*6*) 6.0.

It should be noted that the efficiency of lithium utilization largely depends on the chemical power cell design, and, therefore, the results obtained in an electrochemical cell can only serve as guidelines in choosing the power cell operation mode.

Current–voltage characteristics of chemical power cells with pressure electrodes and electrolytes based on aqueous solutions of the systems $LiOH–H_2O$ and $KOH–H_2O$ were measured at 291 ± 1 K and power values at certain current densities were calculated. As seen from Figs. 3A and 3B, the power of a chemical power cell decreases with increasing content of alkali metal hydroxide in solution. With aqueous solutions of potassium hydroxide used as electrolyte, higher power of chemical power cells can be achieved, compared with the case of the conventional electrolytes of the system $LiOH–H_2O$. In discharge of chemical power cells with 3.5 m LiOH and 6 m KOH as electrolytes in constant-current mode (discharge current density 0.2 and 0.3 A cm^{-2}), lithium utilization efficiencies η = 51 and 50%, respectively, were obtained.

Thus, the obtained results indicate the advisability of using solutions of the system $KOH–H_2O$ in chemical power cells with lithium anode and aqueous electrolyte.

REFERENCES

1. Kedrinskii, I.A., Dmitrenko, V.E., and Grudyanov, I.I., *Litievye istochniki toka* (Lithium Power Cells), Moscow: Energoatomizdat, 1992.
2. Demidov, A.I., Domanskii, V.K., and Morachevskii, A.G., *Zh. Prikl. Khim.*, 1997, vol. 70, no. 8, pp. 1384–1385.
3. Littauer, E.L. and Tsai, K.C., *J. Electrochem. Soc.*, 1977, vol. 124, no. 6, pp. 850–855.
4. Littauer, E.L. and Tsai, K.C., *26th Power Source Symp. Proc.*, New York: Red Bank, 1974, pp. 56–60.
5. Korovin, N.V. and Smirnov, S.E., *Elektrokhimiya*, 1982, vol. 18, no. 11, pp. 1510–1512.
6. Littauer, E.L., Tsai, K.C., and Hollandsworth, R.P., *J. Electrochem. Soc.*, 1978, vol. 125, no. 6, pp. 845–852.
7. Littauer, E.L., *Glasn. Khem. Drush.* (Belgrade), 1983, vol. 48, pp. 49–81.
8. Demidov, A.I., Konstantinova, M.V., Morachevskii, A.G., and Gerasimenko, L.N., *Zh. Prikl. Khim.*, 1984, vol. 57, no. 10, pp. 2373–2374.
9. Konstantinova, M.V., Gerasimenko, L.N., Demidov, A.I., and Morachevskii, A.G., *Zh. Prikl. Khim.*, 1985, vol. 58, no. 2, pp. 412–414.
10. *Voprosy fizicheskoi khimii rastvorov elektrolitov* (Physical Chemistry of Electrolyte Solutions), Mikulin, G.I., Ed., Leningrad: Khimiya, 1968.
11. Kirgintsev, A.N., *Ocherki o termodinamike vodno-solevykh sistem* (Essays on Thermodynamics of Aqueous-Salt Systems), Novosibirsk: Nauka, 1976.

12. Dmitrenko, V.E., Dolinin, E.A., Astakhova, G.F., and Kassyura, V.P., *Elektrotekh. Prom–st., Khim. Fiz. Ist. Toka*, 1981, no. 1(76), p. 1.
13. Ivanov, E.G., Kozhevnikov, A.N., Khimanin, Yu.I., and Pospelov, A.V., in *Sbornik rabot po khimicheskim istochnikam toka* (Coll. of Works on Chemical Power Cells), Leningrad: Energiya, 1971, pp. 118–122.
14. Dmitrenko, V.E., Dolinin, E.A., Astakhova, G.F., and Kassyura, V.P., *Elektrotekh. Prom–st., Khim. Fiz. Ist. Toka*, 1980, no. 6(75), pp. 7–8.
15. Konstantinova, M.V., Demidov, A.I., Morachevskii, A.G., and Gerasimenko, L.N., in *Khimicheskie istochniki toka: Mezhvuzovskii sbornik* (Chemical Power Cells: Intercollegiate Coll. of Works), Novocherkassk: Novocherk. Politekh. Inst., 1985, pp. 13–20.
16. Cooper, J.F., Hosmer, P.K., and Homsy, R.V., *J. Electrochem. Soc.*, 1978, vol. 125, no. 1, pp. 1–7.
17. Korovin, N.V. and Smirnov, S.E., *Elektrokhimiya*, 1984, vol. 20, no. 2, pp. 246–248.
18. Demidov, A.I., Konstantinova, M.V., Morachevskii, A.G., *et al.*, *Zh. Prikl. Khim.*, 1988, vol. 61, no. 7, pp. 1610–1613.
19. Littauer, E.L. and Tsai, K.C., *J. Electrochem. Soc.*, 1976, vol. 123, no. 6, pp. 771–776.
20. Littauer, E.L. and Tsai, K.C., *J. Electrochem. Soc.*, 1976, vol. 123, no. 7, pp. 964–969.
21. Ovanes'yan, K.K., Anodic Oxidation of Lithium in Aqueous Electrolyte Solutions, *Cand. Sci. Dissertation*, Leningrad, 1976.
22. Ovanes'yan, K.K., Egorov, I.M., and Smirnova, E.N., Anodic Oxidation of Lithium in Solutions of Potassium and Lithium Hydroxides, *Available from VINITI*, 1981, Leningrad, no. 4750-81 Dep.
23. Littauer, E.L. and Tsai, K.C., *J. Electrochem. Soc.*, 1980, vol. 127, no. 3, pp. 521–524.

Russian Journal of Applied Chemistry, Vol. 74, No. 7, 2001, pp. 1122–1125. Translated from Zhurnal Prikladnoi Khimii, Vol. 74, No. 7, 2001, pp. 1094–1097.

APPLIED ELECTROCHEMISTRY AND CORROSION PROTECTION OF METALS

Development of Ways To Diminish Corrosion of Zinc Electrode

T. I. Devyatkina, Yu. L. Gun'ko, and M. G. Mikhalenko

Nizhni Novgorod State Technical University, Nizhni Novgorod, Russia

Received November 13, 2000; in final form, March 2001

Abstract—The influence exerted by addition of α-hydroxynaphthoic acid and combined additive Hg + Pb + α-hydroxynaphthoic acid on the corrosion and self-discharge of a porous zinc electrode in alkali solution was studied.

One of disadvantages of nickel–zinc (NZ) power cells is the poor corrosion resistance of the zinc electrode in alkaline solution. As is known, the corrosion rate of the zinc anode depends on the hydrogen overvoltage on zinc in a given electrolyte. To diminish the corrosion of the zinc electrode, it is recommended that metals with high hydrogen evolution overvoltage (Hg, Pb, Cd) should be introduced into the active paste of the electrode [1]. However, all these additives are rather toxic.

An important task is a search for zinc corrosion inhibitors that can simultaneously serve to make lower the content of toxic compounds of mercury, lead, and cadmium. One of ways to lower the corrosion activity of zinc in an alkali solution is to select surfactants that can adsorb onto the zinc electrode and make higher the hydrogen evolution overvoltage. However, the selection of such additives is limited because of the weak adsorption of surfactants on the electrode as a result of competing adsorption of OH^- ions.

In [2], mention was made of the inhibiting action of polyoxyethylene ether on the corrosion of the Zn–In alloy. It was found that this additive has no effect on the rate of zinc corrosion and inhibits the corrosion of the alloy. The inhibition efficiency grows with increasing inhibitor concentration.

Wei Jie *et al.* [3] studied the effect of suppression of zinc corrosion by introduction of oleic and linoleic acids into a 40% KOH solution. Both the acids hinder the corrosion of zinc by forming on the metal a film of chemisorbed molecules of a fatty acid. However, the authors did not demonstrate the effect of these acids on the anodic dissolution of zinc and capacity characteristics of the zinc electrode.

Introduction into electrolyte of potassium salts of perfluorinated aliphatic carboxylic acids makes higher the hydrogen evolution overvoltage in alkaline solutions [4]. Shi Lian-zhen *et al.* [4] found that introduction of both Pb and surfactant lowers the discharge rate of H_2O molecules. Particularly effective is combining the given additives. However, even though the proposed surfactant additive is effective, it is difficultly available for manufacture of power cells with zinc anode. Therefore, it was necessary to search for a surfactant exerting the same effect, but simultaneously readily available and nontoxic. α-Hydroxynaphthoic acid (α-HONA) was chosen as an additive of this kind.

With account of the fact that mercury and lead are introduced into the active paste of the zinc electrode, an attempt was made to introduce into the electrolyte, to diminish corrosion, an α-HONA additive used in manufacture of acid batteries for hindering the corrosion of lead [1].

EXPERIMENTAL

Since α-HONA has been recommended for diminishing lead corrosion proceeding with hydrogen depolarization in acid medium, it was of interest to study its influence on hydrogen evolution on zinc in alkali. Investigations were carried out in concentrated alkali (10 M). This is due to the fact that, with increasing concentration of the working electrolyte, the self-discharge of the positive electrode becomes much weaker [5], which is exceedingly important for designing cells and lowering the corrosion of zinc through a shift of the potential of the hydrogen electrode to more negative values.

The potentiodynamic method was applied to study the effect of α-HONA and deposited Pb (Pb_d) on hydrogen evolution on the zinc electrode from an alkali electrolyte.

1070-4272/01/7407-1122$25.00

It was found that introduction of α-HONA additive into alkali solution has virtually no effect on the hydrogen evolution on zinc. A strong inhibited influence on the corrosion process with hydrogen depolarization on zinc is exerted by a combined additive composed of lead and α-HONA. In this case, a stronger, compared with that in the presence of only lead, decrease in the hydrogen evolution rate was observed (Fig. 1a).

The hindrance to hydrogen evolution on the zinc electrode may be due to adsorption of α-HONA onto lead.

The ability of α-HONA to adsorb on zinc was studied by the Rebinder method. It was found that deposition of lead onto zinc shifts the zero-charge potential to negative values by approximately 20 mV. In the presence of α-HONA in solution, the peak in the curve is shifted to the positive side, which is due to the formation of chelate complexes between lead and α-HONA [6]. No α-HONA adsorption was observed in the absence of lead.

It was also found that these additives hinder somewhat the anodic dissolution of zinc (Fig. 1b). The lowered anodic activity of zinc is presumably due to blocking of active centers of zinc dissolution by chelate complexes formed between Pb and α-HONA.

The decrease in the rate of zinc corrosion in the galvanic couple Zn–Pb (Fig. 2) in the presence of α-HONA in alkali solution is confirmed by the polarization diagram.

In the presence of the α-HONA additive, the corrosion current I_{cor} decreases from 9.7 to 6.7 mA, and the rate of zinc dissolution, from 4.9 to 3.39 g m^{-2} h^{-1}. The efficiency of α-HONA action (%) can be calculated by the formula

$$Z = \frac{K_1 - K_0}{K_1} \times 100, \qquad (1)$$

where K_1, K_2 are the rates of zinc dissolution when in contact with lead without and with α-HONA, respectively.

The protective effect Z of the additional introduction of α-HONA is 30.8%.

As already noted, mercury is one of the most effective corrosion inhibitors. An active paste is known of a porous zinc electrode of a power cell, containing 13% mercury and 0.1–2.0% lead. However, when electrodes with so high mercury content are used, the amount of active paste per unit capacity of a power cell also increases. In addition, since the mercury content exceeds its solubility in zinc (2.5 wt %), it may aggregate into drops short-circuiting the power cell. With account also taken of the high toxicity of mercury, its use in so high amounts is undesirable [7].

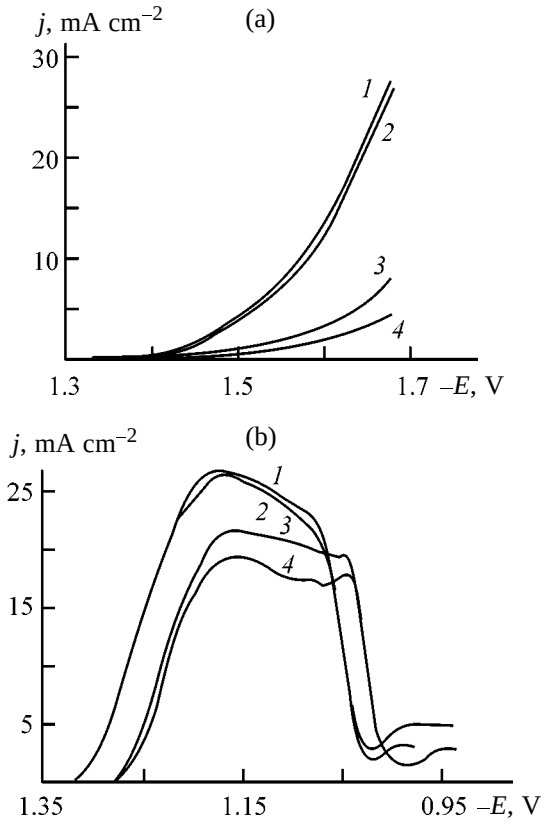

Fig. 1. (a) Cathodic and (b) anodic polarization curves measured on zinc with additives. Sweep rate 4 mV s^{-1}, alkali concentration 10 M. (*j*) Current density and (*E*) potential (vs. s.h.e.). Sample: (*1*) control, (*2*) with addition of α-HONA (in solution), (*3*) Pb_d, and (*4*) Pb_d + α-HONA (in solution).

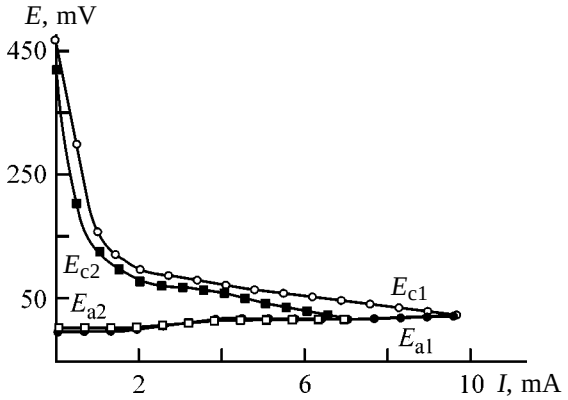

Fig. 2. Corrosion diagram for the galvanic couple Zn–Pb. (*E*) Potential vs. zinc reference electrode and (*I*) current. Cathode, lead; anode, zinc. Alkali concentration 10 M; (*1*) no additive and (*2*) with α-HONA additive.

Effect of α-HONA on the capacity and self-discharge of zinc electrode containing 3% Pb and varied amount of mercury Storage time 300 h at 50°C; electrolyte: 10 M KOH + 15 g l^{-1} $LiOH \cdot H_2O$; j_d = 4 mA cm^{-2}

Additive content		Capacity, A h g^{-1}		Self-discharge, %
in electrode, %	α-HONA in electrolyte, g l^{-1}	before storage	after storage	
6	–	0.629	0.535	14.9
3	–	0.634	0.496	22
3	0.7–1.2	0.629	0.514	18.3
1	–	0.596	0.522	12.4
1	0.7–1.2	0.757	0.707	6.6
0	0.7–1.2	0.447	0.368	17.6

In accordance with the existing technology [5], zinc electrodes are amalgamated to diminish corrosion by introducing 2–10% metallic mercury relative to zinc mass. The authors of [8] recommend introducing mercury in amounts of 1.65–4.5%, noting that making the content of mercury even higher virtually fails to further decrease the hydrogen evolution rate.

To decrease the content of mercury in the active paste of the zinc electrode to improve the environmental safety of manufacture, it is of particular practical interest to search for ways to make lower the content of toxic additives in the negative electrode without impairing the corrosion resistance of zinc. Introduction of α-HONA into the active paste of the zinc electrode or into the electrolyte makes it possible to lower the content of mercury in the electrode from 3–6 to 1% and simultaneously diminish its self-discharge (see table).

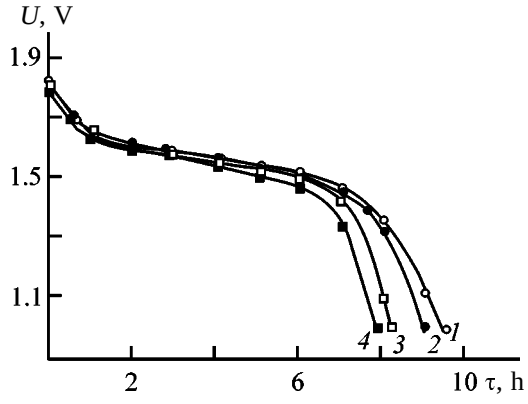

Fig. 3. Effect of additive on the discharge voltage *U* and discharge time τ of a nickel–zinc cell. J_d = 4 mA cm^{-2}, alkali concentration 10 M. Sample: (*1, 3*) control, (*2, 4*) with α-HONA additive in electrolyte, and (*3, 4*) after storage (300 h at 50 ± 1°C).

It can be seen from the obtained data that lowering the content of mercury from 6 to 3% enhances the self-discharge of the zinc electrode. With the content of mercury decreased further (to 1%), the amount of self-discharge decreases substantially, presumably as a result of increased electrochemical activity of zinc. If no mercury is contained in the active paste of the zinc electrode, it is impossible to achieve the required decrease in its self-discharge.

As revealed in the study, the presence of α-HONA exerts a positive influence on the preservation of the zinc electrode. However, one of conditions for possible use of this additive in an NZ cell is the absence of a negative influence on the counterelectrode. It was found in the study that the additive has no effect on the discharge voltage and time of an NZ cell and, consequently, does not impair the working capacity of the nickel oxide electrode (NOE) both before and after its storage at 50°C (Fig. 3). Therefore, it can be recommended for use in NZ cells.

Thus, introduction of α-HONA into the electrolyte of primary alkali–zinc power cells makes it possible to substantially reduce the content of mercury in the active paste of the zinc electrode and to diminish its self-discharge.

CONCLUSIONS

(1) A study of the influence exerted by α-HONA additive, Pb, and combined additive Pb + α-HONA on the rate of hydrogen evolution on the zinc electrode revealed that introduction of the combined additive markedly hinders hydrogen evolution on zinc in alkaline electrolyte.

(2) The α-HONA additive is only adsorbed onto the zinc surface in the presence of lead, which is presumably due to formation of chelate complexes between lead and the acid. The anodic activity of zinc decreases in the presence of this additive.

(3) Introduction of α-HONA additive into the active paste of the zinc electrode or into the electrolyte of alkali–zinc power cells allows a 3–6-fold decrease in the content of mercury in the negative electrode containing mercury and lead additives, with its self-discharge diminished simultaneously.

(4) The recommended additive exerts no negative influence on the counterelectrode (nickel oxide electrode) in the nickel–zinc cell, which demonstrates the possibility of its use in primary power cells of the given system.

REFERENCES

1. Varypaev, V.N., Dasoyan, M.A., and Nikol'skii, V.A., *Khimicheskie istochniki toka* (Chemical Power Cells), Moscow: Vysshaya Shkola, 1990.
2. Wang, J.M., Lu, Y., Zhang, J., and Cao, C., *Corros. Sci*., 1998, vol. 40, no. 7, pp. 1161–1168.
3. Wei Jie, Zhang Wenly, Zhou Ding, and Zhou Derui, *High Technol. Lett*., 1998, vol. 4, no. 2, pp. 91–94.
4. Shi Lian-zhen, Zhou Yun-hong, and Gao Gui-ging, *Extended Abstracts, 46th Int. Soc. Electrochem. Annual Meet*. (Xiamen, August 27–September 1, 1995), Xiamen, 1995, vol. 1, pp. 1–14.
5. Dam'e, V.N. and Rysukhin, N.F., *Proizvodstvo pervichnykh khimicheskikh istochnikov toka* (Manufacture of Primary Chemical Power Cells), Moscow: Vysshaya Shkola, 1980.
6. Shekhter, Yu.N. and Krein, S.E., *Poverkhnostno-aktivnye veshchestva iz neftyanogo syr'ya* (Surfactants Produced from Oil Raw Materials), Moscow: Khimiya, 1971.
7. Arkhangel'skaya, Z.P., Afanas'eva, P.A., and Reshetova, G.N., in *Sbornik rabot po khimicheskim istochnikam toka* (Coll. of Works on Chemical Power Cells), 1967, issue 2, pp. 86–92.
8. USSR Inventor's Certificate no. 664248.

Russian Journal of Applied Chemistry, Vol. 74, No. 7, 2001, pp. 1126–1128. Translated from Zhurnal Prikladnoi Khimii, Vol. 74, No. 7, 2001, pp. 1097–1099.

APPLIED ELECTROCHEMISTRY AND CORROSION PROTECTION OF METALS

Purification of Rhodium-Plating Electrolytes To Remove Nonferrous Metal Impurities

L. B. Khar'kova, S. V. Volkov, and V. I. Pekhn'o

Vernadsky Institute of General and Inorganic Chemistry, National Academy of Sciences of Ukraine, Kiev, Ukraine

Received February 28, 2001

Abstract—Optimal conditions were determined for purification of sulfate rhodium-plating electrolyte to remove ions of iron(III) and nonferrous metals. Electrochemical and chemical purification techniques were developed.

The sulfate rhodium-plating electrolyte used to deposit anticorrosive coatings in radio engineering and instrument-making is commonly prepared from rhodium trichloride $RhCl_3 \cdot 4H_2O$ of pure grade [1]. This salt contains minor impurities of nonprecious metals, in the first place iron(II) etc. Therefore, a freshly prepared rhodium-plating electrolyte with an Rh content of about 5–10 g l^{-1} commonly contains nonferrous metal ions in the following concentration (mg l^{-1}): Fe^{3+} < 10; Cu^{2+}, Zn^{2+}, Sn^{2+} ≤ 2. Such an impurity content exerts no significant influence on the kinetics of rhodium reduction.

In the course of rhodium plating, ions of nonferrous metals (copper, zinc, and tin) are gradually accumulated in the sulfate electrolyte used for this purpose. The reduction potentials of these impurities being close to the reduction potential of rhodium (Rh^{3+}/Rh +0.27, Cu^{2+}/Cu +0.34, Sn^{2+}/Sn –0.14 V), they can strongly affect the cathodic process at concentrations C_M > 0.20 mg l^{-1}, impairing the quality of the plated coatings.

The method presently used in industry to purify rhodium-plating electrolytes is based on extraction with CCl_4 of diethyldithiocarbamates of nonprecious metals, formed in the electrolyte upon addition of sodium diethyldithiocarbamate [1]. A shortcoming of this method consists in the low limiting concentration of extracted complexes in CCl_4, requiring use of large solvent volumes and additional purification of the electrolyte to remove organic impurities.

The aim of this study was to determine the optimal conditions for recovery of iron and nonferrous metals from sulfate rhodium-plating electrolytes.

EXPERIMENTAL

As objects of study were chosen two rhodium-plating electrolytes: (I) prepared from $RhCl_3 \cdot 4H_2O$ and contaminated in use with Fe^{3+}, Cu^{2+}, Zn^{2+}, and Sn^{2+} ions and (II) prepared from rhodium-containing industrial waste.

Electrolysis was carried out in a 0.5-l glass electrolyzer. Platinum foil served as anode, and preliminarily rhodium-plated (h_{Rh} = 2 μm) copper foil of area 2 cm^2, as cathode. Table 1 presents the composition of the electrolytes under study.

Two purification techniques were studied: electrochemical and chemical.

The optimal electrolysis conditions ensuring deposition of nonferrous metals at the cathode were determined on the basis of the fact that the current density of rhodium reduction is directly proportional to the concentration of rhodium in the electrolyte. At rhodium concentrations of 4–10 g l^{-1}, the optimal current density was in the range 0.4–1.0 A dm^{-2}. Voltammetric studies of sulfate rhodium-plating electrolytes have shown that at cathode current densities i_c <

Table 1. Concentrations of rhodium C_{Rh} and impurity metals C_M in electrolytes under study ($C_{H_2SO_4}$ = 0.1 M)

Electrolyte	C_{Rh}, g l^{-1}	C_M, mg l^{-1}			
		Fe	Cu	Zn	Sn
(I)	6.37	293.5	384.0	118.5	36.5
(II)	5.85	80.0	108.0	32.0	10.0

1070-4272/01/7407-1126$25.00

0.2 A dm^{-2} ($C_{Rh} \geq 4$ g l^{-1}) the current efficiency by metal was less than or equal to 10% [2]. Therefore, for purifying the rhodium-plating electrolyte to remove nonferrous metal impurities, electrolysis was carried out at i_c = 0.1–0.2 A dm^{-2}.

Table 2 and the figure present the concentrations of rhodium and impurity metals in relation to the amount of electricity passed through electrolytes (I) and (II). In both cases, i_c = 0.2 A dm^{-2}. It can be seen from Table 2 that, on passing 0.105 A h l^{-1} of electricity through the electrolyte, the concentration of copper in solution decreases by a factor of 7.3, reaching a value acceptable for the rhodium-plating electrolyte. The concentrations of zinc and tin remain virtually the same and that of iron decreases only slightly. Despite this fact, the electrochemical purification technique can find application in plating since rhodium-plating electrolytes are mainly contaminated with copper ions when in use.

The chemical method for purification of rhodium-plating electrolyte to remove impurity metals is based on the ability of rhodium hydroxide $Rh(OH)_3 \cdot 2H_2O$ to lose crystallization water at 200°C. On further heating it decomposes with oxidation of Rh(III) to Rh(IV) and formation of rhodium dioxide RhO_2 (200–450°C), which is, in turn, reduced to α-Rh_2O_3 at 750°C [3]. Rhodium oxides are insoluble in any of the known acids or mixtures of these.

Hydroxide compounds of rhodium and nonferrous metals were precipitated from the rhodium-plating electrolyte with a 40% KOH solution. After filtration and washing with distilled water, metal hydroxides were calcined at 500°C for 5 h. Iron and nonferrous metals were separated from the obtained mixture of oxides by boiling in HCl (1 : 1). To synthesize rhodium-plating electrolyte, rhodium in the form of filtered-off and washed mixture of oxides was converted into a water-soluble form by fusion with $Na_2S_2O_7$. Metal hydroxide was precipitated from a rhodium sulfate solution and dissolved in a calculated amount of concentrated H_2SO_4 to obtain the rhodium-plating electrolyte.

Table 3 presents the composition of the initial electrolyte (I) and that after purification by the chemical method (Ia). It can be seen that the concentration of impurity metals decreases 2.5–22-fold, reaching values acceptable for rhodium-plating electrolytes.

The loss of rhodium is 2.5–2.8 and 3.5–3.7% in, respectively, electrochemical and chemical purification.

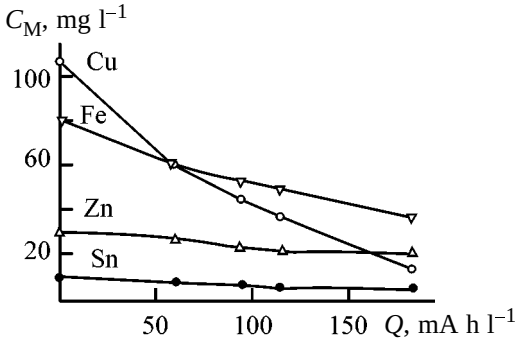

Concentration of impurity metals in rhodium-plating electrolyte C_M vs. amount of electricity Q passed through electrolyte.

CONCLUSIONS

(1) The optimal conditions for purification of sulfate rhodium-plating electrolyte to remove impurities of iron and nonferrous metals were determined.

(2) An electrochemical purification technique based on electrolysis at i_c = 0.1–0.2 A dm^{-2} was developed, lowering the concentration of copper in the electrolyte approximately sevenfold.

(3) A chemical purification technique based on

Table 2. Concentrations of rhodium C_{Rh} and impurity metals C_M in relation to the amount of electricity Q passed through electrolyte

Q, A h l^{-1}	C_{Rh}, g l^{-1}	C_M, mg l^{-1}			
		Cu	Zn	Sn	Fe
0	6.37	384.0	118.5	36.5	293.5
0.080	6.34	349.5	112.5	36.5	291.0
0.083	6.31	301.0	106.8	36.7	280.0
0.087	6.29	257.5	108.8	36.2	271.5
0.091	6.22	200.5	107.6	34.1	273.0
0.095	6.21	156.4	107.9	34.0	271.9
0.100	6.20	104.8	108.1	39.9	272.3
0.105	6.19	52.4	107.8	38.5	270.4

Table 3. Concentrations of rhodium C_{Rh} and impurity metals C_M before and after chemical purification

Electrolyte	C_{Rh}, g l^{-1}	C_M, mg l^{-1}			
		Fe	Cu	Zn	Sn
(I)	6.37	384.0	118.5	36.5	293.5
(Ia)	6.14	17.6	49.0	11.30	13.34

precipitation of hydroxides of all metals with their subsequent calcination at 500°C and washing with hydrochloric acid was developed, making it possible to decrease the concentration of iron, copper, zinc, and tin in rhodium-plating electrolytes 2.5–22-fold.

ACKNOWLEDGMENTS

The study was financially supported by the Ukrainian Center for Science and Technology (project no. Gr-32J).

REFERENCES

1. *Gal'vanicheskie pokrytiya v mashinostroenii* (Electroplated Coatings in Machine-Building), Shluger, M.A., Ed., Moscow: Mashinostroenie, 1985, vol. 1.
2. Gorodyskii, A.V., Nechaeva, N.E., and Khar'kova, L.B., Abstracts of Papers, *XII Vsesoyuznoe Chernyaevskoe soveshchanie po khimii, analizu i tekhnologii platinovykh metallov* (XII All-Union Meet. on Chemistry, Analysis, and Technology of Platinum Metals), Moscow: Nauka, 1982, p. 102.
3. Shorikov, Yu.S., Muzychuk, R.V., Sbitnev, V.L., *et al*., *Zh. Neorg. Khim.*, 1989, vol. 34, no. 3, pp. 596–601.

Russian Journal of Applied Chemistry, Vol. 74, No. 7, 2001, pp. 1129–1131. Translated from Zhurnal Prikladnoi Khimii, Vol. 74, No. 7, 2001, pp. 1100–1102.

CATALYSIS

Determining the Activity of Supported Vanadium Catalyst for Sulfur Dioxide Oxidation from Data Furnished by Flow-Through Method

E. I. Dobkina, S. M. Kuznetsova, L. A. Nefedova, and S. A. Lavrishcheva

St. Petersburg State Technological Institute, St. Petersburg, Russia

Received March 26, 2001

Abstract—The rate of sulfur dioxide oxidation on a supported vanadium catalyst and the influence exerted by the chemical composition of the catalyst on its activity were studied.

The main service characteristic of any catalyst is its activity. As characteristics of activity can serve both the conversion and the rate constant at an appropriate temperature. The most effective procedure for determining the rate constant and directly the reaction rate is the differential flow-through-circulation conversion of sulfur dioxide [1]. However, implementing this technique requires rather complex kinetic installations, which are frequently difficult to assemble, particularly under industrial conditions of catalyst manufacture and at plants where catalysts are used. Also, reliable data on the activity of the manufactured catalysts are, as a rule, necessary together with monitoring for assessment of the stability of catalyst operation in industrial reactors. In this case, it is advisable to use flow-through installations [1, 2] which make it possible to determine the conversion in a wide temperature range and then to calculate, by means of a chosen kinetic equation, the reaction rate constant.

As is known, sulfur dioxide is oxidized using vanadium catalysts of various kinds. All of these contain vanadium(V) oxide as the main active component, alkaline promoters, and support. The composition of the active component of the catalyst can be expressed as $V_2O_5 \cdot mK_2O \cdot nSO_3$ [1–3]. As a catalyst works, the ratio of the oxides in it changes, depending on temperature, initial concentrations of gas phase components, and the extent of SO_2 oxidation into SO_3. The m value is determined by synthesis conditions, whereas n varies, depending on reaction conditions, between $2m$ and $4m$.

EXPERIMENTAL

A spherical supported vanadium catalyst was chosen for the study. In chemical composition the catalyst is close to the industrial SVD catalyst [1]. The catalyst grain size was 1.5 or 0.75 mm. The dependence of the degree of sulfur dioxide oxidation, x, on temperature and space velocity V is shown for the chosen samples in Figs. 1a and 1b. The experiments were done on a flow-through kinetic setup under the standard conditions specified by Boreskov [1–3]. The virtually complete coincidence of the results for particles 1.5 and 0.75 mm in size guarantees the kinetic control of the process. The curves in Fig. 1 exhibit a characteristic peak determined by the relative rates of the forward and reverse reactions, with the optimal temperature mode corresponding to the maximum x value. With increasing space velocity, the maximum conversions decrease and the optimal temperatures, correspondingly, increase.

The obtained experimental relationships can be used to calculate the reaction rate constant using various kinetic equations [1, 4], e.g.,

$$dx/d\tau = k/a(x_{eq} - x)^{0.8}/x^{0.8}(b - ax/2) \times 273/T\beta, \quad (1)$$

where a is the initial sulfur dioxide concentration; b is the initial concentration of oxygen; τ is the time of contact under normal conditions; x is the conversion; x_{eq} is the equilibrium conversion under given conditions; and β is the correction factor defining the increase in concentration, caused by a decrease in the total volume of the gas mixture as a result of the reaction; in the experiments it was close to unity and, therefore, is not taken into account in what follows.

Equation (1) was used in calculations, with conversions taken from Fig. 1b, and $dx/d\tau$ values, from Fig. 2. The equilibrium conversions (for a gas phase

1070-4272/01/7407-1129$25.00

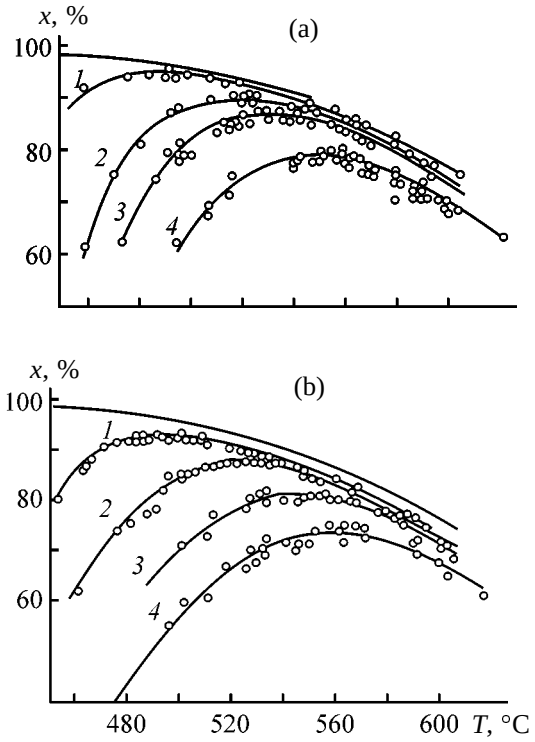

Fig. 1. Effect of temperature T on the conversion x of sulfur dioxide. V (h^{-1}): (*1*) 3750, (*2*) 7500, (*3*) 11270, and (*4*) 14670. Catalyst grain size (mm): (a) 0.75 and (b) 1.5.

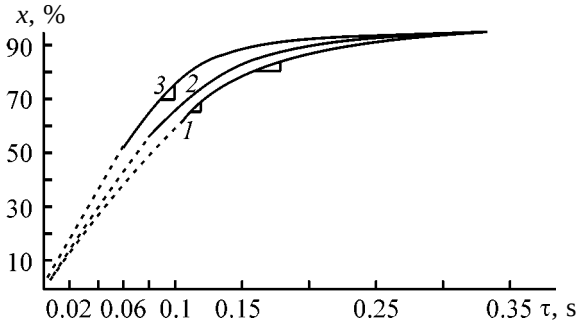

Fig. 2. Extent of SO_2 oxidation x vs. time of contact τ at different temperatures. Temperature (°C): (*1*) 490, (*2*) 500, and (*3*) 520.

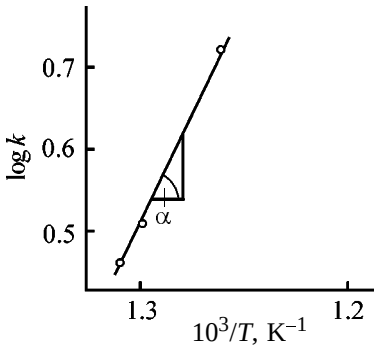

Fig. 3. Reaction rate constant k vs. temperature T.

composition 7% SO_2 + air) were taken from the literature.

The rate constants calculated by means of Eq. (1) were 5.45, 3.25, and 2.86 at, respectively, 520, 500, and 485°C.

The rate constants obtained in calculations by Eq. (1) for a crushed industrial vanadium catalyst SVD virtually coincide with the above values. The closeness of the activities of the catalysts in question is also indicated by their close activation energies.

Vanadium catalysts have different activities at low and high temperatures [1, 2, 4]. The activity changes in the temperature range 400–470°C, which is due to chemical transformations of the active component of the catalyst. The authors were primarily interested in the working range of high temperatures, for which the activation energy was calculated. According to the Arrhenius equation, the dependence of the reaction rate constant k on temperature is as follows:

$$\ln k = -E/RT + \ln k_0,$$

where E is the apparent activation energy, k is the reaction rate constant, and k_0 is the pre-exponential factor in the Arrhenius equation.

The slope of the straight line in the coordinates $\log(k - 1)/T$ is $-E/R$, which makes it possible to determine E. The slope $\tan\alpha$ is found from Fig. 3 and then the activation energy is determined:

$$E = 2.303R\tan\alpha, \quad (2)$$

where $R = 8.31$ J mol^{-1} deg^{-1}, $\tan\alpha = 5 \times 10^3$.

Consequently, $E = 2.303 \times 8.31 \times 5 \times 10^3 = 95.5 \times 10^3$ J mol^{-1}.

Calculation of the activation energy for the SVD catalyst by Eq. (2) gives virtually the same value [1, 4].

CONCLUSION

Analysis of the presented data on rate constants and activation energies confirms once again the Boreskov's concept that the chemical composition, and in the first place the content of the main active component and promoter, rather than the preparation method, determine the primary service characteristic of a catalyst, its activity (the first catalyst of those

studied is supported and the second is of mixed type). It is highly important that the samples should have similar pore structures ensuring a sufficient reaction surface area and "free" mass transfer.

REFERENCES

1. Mukhlenov, I.P., Dobkina, E.I., Deryuzhkina, V.I., and Soroko, V.E., *Tekhnologiya katalizatorov* (Technology of Catalysts), Leningrad: Khimiya, 1989.
2. Boreskov, G.K., *Geterogennyi kataliz* (Heterogeneous Catalysis), Moscow: Nauka, 1986.
3. Boreskov, G.K., *Kataliz* (Catalysis), Novosibirsk: Nauka, 1987.
4. Boreskov, G.K., *Kataliz v proizvodstve sernoi kisloty* (Catalysis in Manufacture of Sulfuric Acid), Moscow: Goskhimizdat, 1954.

Russian Journal of Applied Chemistry, Vol. 74, No. 7, 2001, pp. 1132–1136. Translated from Zhurnal Prikladnoi Khimii, Vol. 74, No. 7, 2001, pp. 1102–1106.

CATALYSIS

Effect of Pore Structure of Al–Co–Mo Catalyst on the Rate of Various Pathways of Hydrofining of Oil Residues

M. A. Lur'e, L. P. Milova, L. N. Storozheva, I. Z. Kurets, and F. K. Shmidt

Irkutsk State University, Irkutsk, Russia
Boreskov Institute of Catalysis, Siberian Division, Russian Academy of Sciences, Novosibirsk, Russia

Received February 28, 2001

Abstract—Evolution in the activity and texture of the Al–Co–Mo catalyst in hydrofining of black oil is studied. The catalyst efficiency in desulfurization, deasphalting, and demineralization of black oil is estimated as dependent on the catalyst pore structure and process conditions.

The steadily growing demands for the quality of petroleum products, on the one hand, and production of motor fuels by thorough-going processes, on the other hand, make the development of processes of hydrofining of heavy oil cuts particularly important. Furthermore, the growing shear of sulfur-bearing and sour oils in petroleum production [1] makes this problem even more pressing. A thorough-going method for production of low-sulfur fuel oil and raw materials for manufacture of pollution-free motor fuel is hydrofining of petroleum residues, primarily, black oil. However, such processes find no wide applications in industry yet, because their implementation is a rather difficult problem, first of all due to the nature of heavy oil cuts, which represent a complex colloid system in which asphaltenes are dispersed in mutually soluble oil resins and polycyclic hydrocarbons. In other words, the petroleum residues represent a multicomponent heterogeneous system whose constituents are characterized by variable elemental composition, structures, and physicochemical characteristics.

About 60–80% of the total sulfur remains in residues after oil distillation at atmospheric pressure [2], and about 20% is contained in resins and asphaltenes [3]. The fraction of asphaltenes (the most complex and difficultly decomposable component of oil) includes a part of metals contained in oil.

Asphaltenes have a strong decelerating effect on hydrodesulfurization of petroleum residues [4]. This is probably due to the fact that, owing to the low diffusion rate in the liquid phase and catalyst pores, they hinder the access of hydrogen and sulfurous compounds to the inner surface of the catalyst, thus decreasing the desulfurizing activity. Another possible reason is irreversible sorption of asphaltenes on the catalyst surface with formation of condensation products (CPs) of them. It should be pointed out also that sulfur contained in asphaltenes is the most difficultly removable. All these facts require giving particular attention to the catalyst activity in the course of decomposition of the asphaltic-resinous components of the raw material.

The specific features of hydrofining of heavy oil cuts place a series of constraints on the catalyst, among them the presence of a zone of coarse pores, which reduce the diffusion hindrance and increase the coverage of the catalyst surface. The available relevant information is rather contradictory, which may be due to a wide variety of the compositions of the raw materials studied. Thus, the problem of optimization of the catalyst texture should be solved individually for each particular raw material and required product quality [5].

Previously we demonstrated [6] how the pore structure of the Al–Co–Mo catalyst controls its activity in hydrodesulfurization of black oil produced from West-Siberian oil. The goal of this work is to clarify the nature of evolutions in the activity and size of particular zones of the pore structure of the Al–Co–Mo catalyst in hydrofining of black oil, and also the effect of the size of macropores (more than 100 nm in diameter) on the catalyst performance in various process pathways.

EXPERIMENTAL

In the work we studied test samples of varied pore structure, having various concentrations of active sites. The γ-Al_2O_3 support was synthesized by the nitrate technique, and its pore structure was controlled

1070-4272/01/7407-1132$25.00

by introducing varied amounts of a 25% $NH_3 \cdot H_2O$ solution into the aluminum hydroxide paste being formed. The catalysts were prepared by successive impregnation with solutions of ammonium paramolybdate and cobalt nitrate of the support calcined at 550°C. The resulting catalyst mass was allowed to stand in air for 24 h and dried at 60–70°C for 2–3 h under an IR lamp with intermittent stirring and then in an oven at 120°C for 4 h. The dried samples were calcined in air at 450–550°C for 6 h. The specific surface area of the oxide catalyst S_{sp} thus obtained was determined from nitrogen thermal desorption data obtained by the dynamic method. The pore structure was studied by mercury porosimetry.

The catalyst activity was tested in a high-pressure flow-through (no recycling) setup. Prior to testing the samples were sulfidized at 400°C. The testing time was 24–110 h, temperature 380–420°C, pressure 5–10 MPa, and hydrogen consumption at normal conditions 1000 nl l^{-1}. The catalyst grain size was 0.4–3 mm. The space velocity of black oil across the catalyst bed was 1–30 h^{-1}.

In special-purpose experiments we demonstrated that there is no external-diffusion hindrance of the process under the experimental conditions.

The initial black oil contained sulfur, asphaltenes, resins, and the fraction distilled below 360°C in amounts of 1.7, 2.0, 25, and 9 wt %, respectively. The V and Ni contents were 27 and 18 ppm, respectively. As a raw material we used also such model compounds as benzene and cyclohexane. In addition to the desulfurizing activity we also assessed the catalyst activity with respect to deasphalting, demineralization, cracking, hydrogenation, and isomerization. To characterize all the indicated types of the catalyst activity and their evolution during the tests, hydrogenizate samples were periodically taken and analyzed. Sulfur in the initial black oil and hydrogenizates was determined by the burning method [7], asphaltenes, by precipitation with *n*-heptane, and V and Ni, by the atomic absorption method on Saturn and AAS-1N spectrometers using white spirit as a solvent [8]. To determine the fraction distilled below 360°C in the initial black oil and hydrogenizates, they were distilled. The composition of benzene and cyclohexane hydrogenizates was determined chromatographically. As the measures of the catalyst activity we used the conversion α and the average apparent rate of the process *W*.

After the raw material feed was terminated, the reactor was cooled under hydrogen, the pressure was relieved, and the spent catalyst was washed with

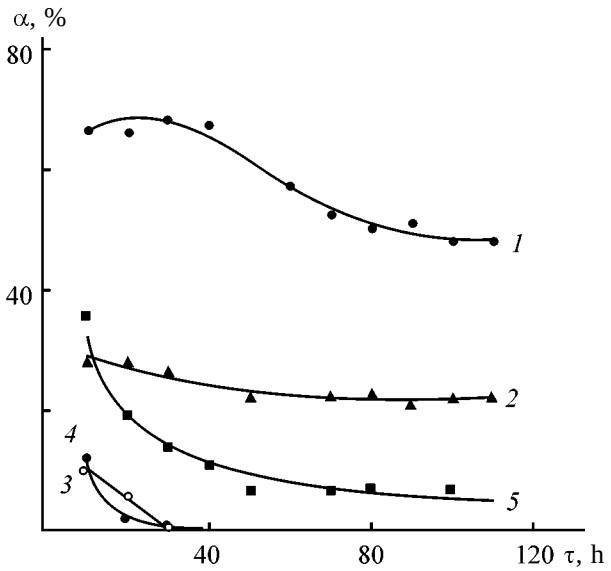

Fig. 1. Activity α of the catalyst as a function of time τ in hydrofining of black oil. Temperature 420°C, hydrogen pressure 10 MPa, space velocity of black oil 1 h^{-1}, catalyst grain size 3 mm; the same for Fig. 2. Reaction: (*1*) desulfurization, (*2*) deasphalting, (*3*) cracking of the fraction boiling above 360°C, (*4*) conversion of cyclohexane to methylcyclopentane, and (*5*) hydrogenation of benzene.

diesel fraction. Prior to study of the pore structure and determination of S_{sp} and the degree of coking, the catalyst was vacuum-treated at 100°C and 2–3 mm Hg. The amount of condensation products deposited on the catalyst surface was determined by burning.

Figure 1 demonstrates evolution in the activity of the catalyst sample (Mo 9 and Co 3.6 wt %) in a 100-h experiment on hydrofining of black oil. The experiment was carried out in the cyclic mode at 420°C and 10 MPa. Every 10 h throughout the experiment benzene and cyclohexane were passed in turn (for 2 h each) instead of black oil, to characterize the hydrogenizing and isomerizing activity of the catalyst. The hydrogenizates were sampled for analysis in each cycle. The samples were collected in the last 4 and 0.25 h of passing black oil and the model hydrocarbons, respectively.

In the first 40 h of catalyst operation the desulfurization level was practically unchanged, and then the catalyst activity gradually decreased (Fig. 1, curve *1*). The deasphalting level (Fig. 1, curve *2*) remained practically unchanged throughout the experiment (only in the first hours it slightly declined). Similar trends were observed for demineralization. The benzene hydrogenation level drastically decreases in the first hours from 37 to 7%, and then the activity stabilizes (Fig. 1, curve *5*). The cracking and isomerizing

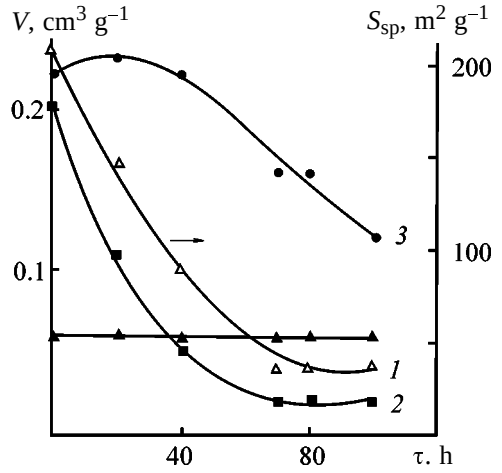

Fig. 2. Evolution of (*1*) S_{sp} and (*2–4*) pore volume V of the catalyst in black oil hydrofining. (τ) Time. Pore radius (nm): (*2*) 4–10, (*3*) 10–100, and (*4*) >100.

activities totally decay in the first 30 h of the catalyst operation (Fig. 1, curves *3, 4*), which is probably due to rapid poisoning of the acidic sites on the catalyst surface. Such a strong difference in the nature of evolution of the two latter types of activity and the desulfurization activity in time indirectly suggests the lack of a close correlation between the desulfurization activity and acidity of the catalyst.

The observed dissimilarity in the dynamics of the catalyst activity with respect to desulfurization, hydrogenation, and cracking (Fig. 1, curves *1, 5, 3*) is consistent with the existing views of the hydrocracking mechanism of sulfur-containing compounds [9], according to which cleavage of the C–S bond of a thiophene ring and hydrogenation of the hydrocarbon fragment proceed by the concerted mechanism on specific active sites of layered MoS_2-like structures.

Refining of such a heavy raw material as black oil is accompanied by vigorous coking of the catalyst surface. In this work we demonstrated that the amount of condensation products in the sample operated for 110 h as a catalyst in black oil refining was about 21 wt %. Concentration of such amounts of CPs should initiate considerable transformation of the catalyst texture and decrease in the catalyst effective area, which can be one of the most significant causes of deterioration of the efficiency and selectivity of hydrofining. Let us consider how the pore structure and S_{sp} of the test sample change in the course of black oil hydrofining (Fig. 2).

Even in the initial stage of hydrofining S_{sp} starts to decrease. It continues to decrease for about 70 h, then remaining practically unchanged. In the initial 50 h we also observed an abrupt reduction in the volume of fine pores (radius 4–10 nm), suggesting that these pores contribute significantly to S_{sp}. The volume of pores with a radius of 10–100 nm starts to gradually decrease even only 40 h of the catalyst operation. We observed no noticeable blocking of macropores (>100 nm) throughout the experiment.

The results show a clear correlation between evolution of the degree of desulfurization and the volume of pores with a volume of 10–100 nm (Figs. 1, 2). Evidently, hydrogenolysis of sulfur-containing compounds contained in black oil occurs primarily on the surface of pores of this size, while fine pores (4–10 nm) do not contribute significantly to desulfurization, as being blocked because of coking of the catalyst. In this process the macropores (>100 nm) fulfil only the transport function.

On the contrary, the observed direct correlation between the volume of fine pores (4–10 nm) and the degree of hydrogenation of benzene suggests that the process occurs essentially on the surface of these pores, which is consistent with small size of benzene molecules and also with considerable contribution of the fine pores to S_{sp}.

The invariability of the volume of macropores (>100 nm) in the course of the process as well as of the catalyst activity with respect to deasphalting suggest that only these pores are accessible for bulky asphaltene macromolecules. Analogous conclusion may be expanded to metal-containing structures either.

Figures 1 and 2 demonstrate that it is the pores over 10 nm in radius that mainly provide the transport and catalytic functions in hydrogenolysis of sulfur-containing compounds and in cracking of the highest-molecular-weight components of black oil. In this case the macropores (>100 nm) are, evidently, of primary importance in transportation of the raw material to the inner surface of the catalyst.

To study in more detail the role of the macropores (>100 nm) in hydrofining, let us consider how their volume influences the coverage of the catalyst surface (catalyst efficiency index) in various hydrofining processes. Therefore, we tested a series of Al–Co–Mo catalysts with variable volume of macropores, Mo concentration (4.8–9.0 wt %), Co/Mo weight ratio (0.3–0.5), and S_{sp} (120–180 $m^2\ g^{-1}$). In the series the volume of pores 10–100 nm in radius was 0.3–0.05 $cm^3\ g^{-1}$. The test time was 24 h. The desulfurization level was maintained to be rather low (25–35%), which was realized by varying the raw material feed rate, depending on the sample activity. The tests

were performed with catalyst samples with coarse (3 mm) and fine (0.4 mm) grains at 380°C and 10 MPa. Grinding to 0.4 mm ensures the reaction to proceed practically in the kinetic control mode, as was demonstrated in a series of experiments with the catalysts with various grain sizes.

The catalyst efficiency index was estimated relating the average apparent reaction rate on coarse grains to that on the fine grains. The results are given in Fig. 3. The observed data scattering can be attributed to the spread in values of the Mo and Co concentrations and, therefore, of the catalyst activity and the diffusion to reaction rate ratios. Despite this fact the results clearly demonstrate that the pore structure of the catalyst has different effects on various hydrofining pathways. The coverage of the catalyst surface in cracking of asphaltenes drastically increases with increasing volume of the macropores. Under conditions of thermal motion in hydrocarbon medium, the asphaltene micelles have a sufficiently long free path. Estimated from the molecular kinetic data on motion of colloid particles in solution (asphaltene concentration 2 wt %; molecular size 5–10 nm), the free path (up to 60 nm [10]) exceeds the size of certain fraction of the pores in the catalyst structure. With increasing fraction of macropores the contribution of molecular diffusion should increase relative to the Knudsen component, facilitating the transport of asphaltenes to the inner surface of the catalyst and increasing its coverage. Previously we observed such a drastic increase in the catalyst efficiency factor with increasing volume of macropores in demineralization of black oil [11].

In the case of hydrodesulfurization (Fig. 3, curve *1*) the effect of the amount of macropores is considerably lower. However, the trend to increasing effective surface area of the catalyst with increasing volume of macropores is observed in this case also. Evidently, in transportation and conversion of sulfur-containing compounds fine pores (10–100 nm) play a crucial role.

Let us consider next how the pore structure of the catalyst influences the desulfurization and deasphalting of black oil at various process conditions.

Figure 4 demonstrates the effect of the volume of macropores on the amounts of sulfur removed and condensation products (V + Ni) in 100 h of the catalyst operation at 380°C and various hydrogen pressures (Mo and Co concentrations in the catalyst 7–8 and 2.5 wt %, respectively). The initial process level was 35–70%. Increase in one of the varied parameters (P, V_{mp}) results in decreasing sensitivity of the process to variation of the other parameter. The higher V_{mp}, the weaker the effect of the hydrogen pressure on the catalyst performance, and vice versa, the effect of macropores decreases with increasing pressure. Evidently, with increasing P and, therefore, decreasing free path and diffusion coefficient [12, 13], the contribution of macropores decreases. The pressure has a considerable effect only at sufficiently strong diffusion hindrances, i.e., at a small fraction of macropores.

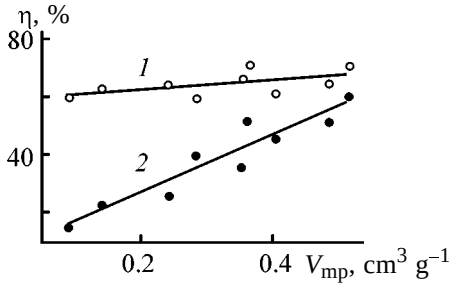

Fig. 3. Effect of the volume of macropores V_{mp} on the coverage of the catalyst surface η (grain size 3 mm) in (*1*) desulfurization and (*2*) cracking of asphaltenes at 380°C and 10 MPa.

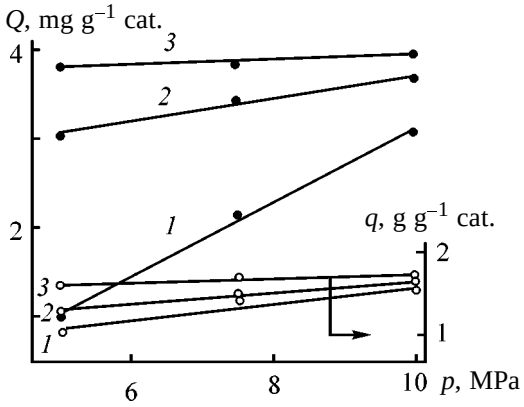

Fig. 4. Effect of the hydrogen pressure p on the amount of sulfur removed q and the total amount Q of V + Ni deposited in 100 h at 380°C. Catalyst grain size 3 mm. Volume of macropores (cm^3 g^{-1}): (*1*) 0.1, (*2*) 0.2, and (*3*) 0.3.

Note that deposition of V and Ni considered separately is described by similar dependence as deposition of their sum (V + Ni, Fig. 4). The degree of removal of V from black oil is higher by a factor of 1.5–2.0 than that of Ni.

Cracking of asphaltenes is sensitive to P and V_{mp} to similar extent as demineralization.

With respect to desulfurization the indicated trends are less pronounced (Fig. 4), additionally confirming the lower contribution of the diffusion factor to this

process. Furthermore, it is worth noting that the desulfurization efficiency only slightly depends on the hydrogen pressure. According to the existing views of the hydrogenolysis mechanism of thiophene as a model compound [9], desulfurization proceeds via concerted electron and hydrogen transfer across the system of chemical bonds of the sulfide bimetallic catalyst, and the first step (adsorption of the sulfur-containing electron-donor molecule) occurs on a Co cation (it acquires acidic properties as a result of oxidative addition of hydrogen with formation of a strongly bound occluded form in the catalyst matrix). The amount of this form of hydrogen is controlled by the number of atoms of the active component of the catalyst; therefore, apparently, the effect of the total hydrogen concentration in the system on the desulfurization efficiency is insignificant.

CONCLUSION

The cracking and isomerizing functions of the Al–Co–Mo catalyst totally decay in the first hours of operation in hydrofining of black oil under the experimental conditions. The reduction in the efficiency of desulfurization, deasphalting, and demineralization of black oil is caused to a considerable extent by changing texture of the catalyst. The relative decrease in the volume of particular fractions of pores in the catalyst structure in the course of the process was found to be 90, 45, and 0% for pores 4–10, 10–100, and >100 nm in radius, respectively, i.e., this parameter decreased with increasing pore size. Desulfurization of black oil proceeds essentially on the surface of pores 10–100 nm in radius. The catalyst efficiency in deasphalting and demineralization as well as the coverage of the catalyst surface in these processes are controlled by the volume of coarse pores (>100 nm).

REFERENCES

1. Sweeney, B.N.C., *Oil Gas J.*, 1993, vol. 91, no. 29, pp. 30–43.
2. Eigenson, A.S., Ezhov, B.M., Berg, G.A., *et al.*, *Khim. Tekhnol. Topl. Masel*, 1977, no. 7, pp. 21–26.
3. Kosugi, M., *J. Jpn. Petrol. Inst.*, 1978, vol. 21, no. 5, pp. 302–311.
4. Eigenson, A.S., Berg, G.A., Khabibullin, S.G., *et al.*, *Khim. Tekhnol. Topl. Masel*, 1974, no. 1, pp. 1–3.
5. Berg, G.A. and Khabibullin, S.G., *Kataliticheskoe gidrooblagorazhivanie neftyanykh ostatkov* (Catalytic Hydrofining of Oil Residues), Leningrad: Khimiya, 1986.
6. Lur'e, M.A., Milova, L.P., Chenets, V.V., *et al.*, *Zh. Prikl. Khim.*, 2001, vol. 74, no. 1, pp. 64–68.
7. Zhestkov, D.K., *Metody analiza organicheskikh soedinenii nefti, ikh smesei i proizvodnykh* (Methods for Analysis of Petroleum Organic Compounds, Their Mixtures, and Derivatives), Moscow: Nauka, 1969.
8. Kholodnaya, G.S., Goncharova, N.K., and Dorogova, I.V., *Available from TsNIITEneftekhim*, January 16, 1989, no. 118-NKh89.
9. Startsev, A.N., *Kinet. Katal.*, 1999, vol. 40, no. 6, pp. 898–905.
10. Sergienko, S.R., Taimova, B.A., and Talalaev, E.I., *Vysokomolekulyarnye neuglevodorodnye soedineniya nefti: smoly and asfal'teny* (High-Molecular-Weight Nonhydrocarbon Petroleum Compounds: Resins and Asphaltenes), Leningrad: Leningr. Gos. Univ., 1980.
11. Lur'e, M.A., Milova, L.P., Zaidman, N.M., *et al.*, *Kinet. Katal.*, 1985, vol. 26, no. 3, pp. 650–653.
12. Boreskov, G.K., *Poristaya struktura katalizatorov i protsessy perenosa v geterogennom katalize* (Pore Structure of Catalysts and Transport Phenomena in Heterogeneous Catalysis), Novosibirsk: Nauka, 1970.
13. Kiperman, S.O., *Osnovy khimicheskoi kinetiki v geterogennom katalize* (Principles of Chemical Kinetics as Applied to Heterogeneous Catalysis), Moscow: Khimiya, 1979.

Russian Journal of Applied Chemistry, Vol. 74, No. 7, 2001, pp. 1137–1140. Translated from Zhurnal Prikladnoi Khimii, Vol. 74, No. 7, 2001, pp. 1107–1110.

CATALYSIS

Effect of Composition of Al–Co–Mo Catalyst on Its Desulfurizing, Deasphalting, and Demineralizing Activity in Hydrofining of Oil Residues

M. A. Lur'e, L. P. Milova, L. N. Storozheva, I. Z. Kurets, and F. K. Shmidt

Irkutsk State University, Irkutsk, Russia
Boreskov Institute of Catalysis, Siberian Division, Russian Academy of Sciences, Novosibirsk, Russia

Received March 22, 2001

Abstract—Effect of the composition of Al–Co–Mo catalysts on their desulfurizing, deasphalting, and demineralizing activities in hydrofining of black oil and interrelation of these activities with coking and deactivation of the catalyst are studied.

Study of physicochemical and catalytic characteristics of catalysts for hydrofining of heavy oil cuts is important in view of growing spread of this process. Thus, in the United States the annual output capacity of heavy cut hydrofining installations in refineries increased by 33 million tons in the period from 1980 to 1996 [1, 2]. This tendency is initiated primarily by steadily increasing atmospheric pollution with SO_2 (about 160 million tons of SO_2 is annually released all over the world to the atmosphere as a result of black oil and coal combustion), so that the steadily growing demand for environmentally clean motor fuels should be satisfied by hydrofining of heavy cuts.

In this connection optimization of the composition of catalysts is one of the most important problem.

Here we report on the effect of the concentration of the active component of the Al–Co–Mo catalyst on its desulfurizing, deasphalting, and demineralizing activities and formation of condensation products (CPs) on the catalyst surface in hydrofining of black oil produced from West-Siberian crude oil.

EXPERIMENTAL

In experiments we used samples with various concentrations of the active components and phase compositions. The γ-Al_2O_3 support for the catalysts was prepared by the nitrate method. The catalysts of fixed composition were prepared by impregnation of the support calcined at 550°C with solutions of ammonium paramolybdate and cobalt nitrate. The resulting catalyst mass was air-dried for 24 h, dried at 60–70°C under an IR lamp with intermittent stirring, and in an oven at 120°C for 4 h. The dried samples were then calcined in air for 6 h at a fixed temperature from the range 450–550°C.

The samples thus obtained varied not only in the Mo and Co concentrations, but also in the relative content of crystallized Co and Al molybdates and the degree of their crystallinity. The phase composition was varied as in [3, 4] using data on the effects of the sequence of application of Mo and Co to Al_2O_3 and the mode of oxidative thermal treatment of the catalyst mass. The Co/Mo atomic ratio in the samples was 0.40 ± 0.03. The phase composition of the catalysts was studied by X-ray diffraction analysis on a DRON-1.5 diffractometer (CuK_α radiation, graphite monochromator for reflected beam). In data processing we used the external reference method. As reference mixtures we used γ-Al_2O_3 + MoO_3, γ-Al_2O_3 + $Al_2(MoO_4)_3$, and γ-Al_2O_3 + $CoMoO_4$.

The catalyst activity was tested in a high-pressure flow-through (no recycling) setup. Prior to testing the samples were sulfidized at 400°C. The testing time was 24–110 h, temperature 380–420°C, pressure 10 MPa, and hydrogen consumption at normal conditions 1000 nl l^{-1}. The experimental space velocity of black oil across the catalyst bed provided the desulfurization level of 25–35%.

In special-purpose experiments we demonstrated that there is no external-diffusion hindrance of the process under the experimental conditions. Furthermore, at a grain size of 0.4 mm internal-diffusion hindrance is not manifested also, which allows an adequate estimation of the effect of the chemical composition of the catalyst on its activity.

1070-4272/01/7407-1137$25.00

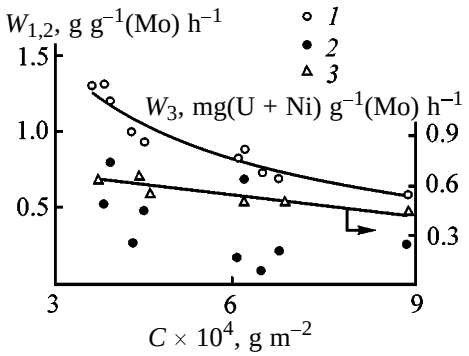

Fig. 1. Average apparent rates of (*1*) desulfurization, (*2*) deasphalting, and (*3*) demineralization as functions of the Mo concentration *C* in the catalyst. Temperature 380°C, hydrogen pressure 10 MPa, catalyst grain size 3 mm; the same for Figs. 2 and 3. ($W_{1,2}$) Desulfurization and deasphalting rates and (W_3) demineralization rate.

The initial black oil contained sulfur, asphaltenes, tars, and the fraction boiling point of below 360°C in amounts of 1.7, 2.0, 25, and 9 wt %, respectively. The V and Ni contents were 27 and 18 ppm, respectively. To characterize the catalyst activity with respect to desulfurization, deasphalting, and demineralization, hydrogenizate samples were periodically taken and analyzed. Sulfur in the initial black oil and hydrogenizates was determined by burning [5], asphaltenes, by precipitation with *n*-heptane, and V and Ni, by the atomic absorption method on Saturn and AAS-1N spectrometers using white spirit as a solvent [6]. As the measures of the catalyst activity we used the average apparent rate of the process *W* at the indicated process level.

After the raw material feed was terminated, the reactor was cooled under hydrogen, the pressure was relieved, and the spent catalyst was washed with diesel fraction. Prior to determination of the degree of coking, the catalyst was vacuum-treated at 100°C and 2–3 mm Hg. The amount of condensation products deposited on the catalyst surface was determined by burning.

The Mo concentration differently influences the rates of desulfurization, deasphalting, and demineralization (Fig. 1). The catalyst activity (estimated per Mo unit mass) in hydrogenolysis of sulfur-containing compounds decreases with increasing Mo content; in demineralization the effect is only slightly pronounced; and as for deasphalting, no clear correlation is observed, suggesting that the indicated processes demonstrate different sensitivity to the composition and structure of the effective catalyst layer.

The observed decrease in the specific desulfurizing activity with increasing Mo concentration irrespective of the phase composition of the catalyst can be attributed to increasing aggregation of Mo species and, hence, decreasing fraction of Mo accessible for sulfur-containing components of black oil.

In deasphalting the highest activity is demonstrated by the catalysts whose oxide precursors contain more cobalt molybdate as compared to aluminum molybdate. In this case the specific activity (per Mo unit mass) increases with increasing crystallinity of the former. The possible reason is that catalytic cracking of an asphaltene micelle requires simultaneous breakdown of a large amount of bonds. Therefore, in this case an active catalytic center should be much greater in size than in hydrogenolysis of ordinary sulfur-containing molecules.

The fact that the activity of the sulfide form of the catalyst depends on the dispersity of Mo in the oxide precursor is consistent with data of [7, 8] demonstrating that this dependence is maintained on passing of the Al–Co–Mo system from the oxide to the sulfide form.

Demineralization of black oil is practically insensitive to variations in the chemical and phase compositions of the catalyst (Fig. 1).

Hydrofining of heavy oil cuts is accompanied by a considerable coking of the catalyst surface, which is the major factor responsible for decreasing catalyst activity. Since the raw material has a complex composition, questions arise as to what components of the reaction mixture are the principal monomers in formation of the condensation products and how the latter process is associated with the other reactions occurring in hydrofining. In [9, 10] it was suggested that asphaltenes having high adsorption capacity and tending to coking are, most likely, precursors of the condensation products. However, it was demonstrated that decreasing asphaltene content in oil residues by a factor of 9 reduces the amount of CPs by a factor of 1.4 only [11], and that introduction of asphaltenes in the cracked distillate even somewhat decelerates formation of CPs [12], which has cast some doubt on the determining role of asphaltenes in coking of the catalysts.

Figure 2 demonstrates the dependence of the amount of CPs deposited on the catalyst surface on the Mo concentration. Figures 1 and 2 show that decreases in the desulfurization activity and amount of deposited CPs with increasing Mo concentration are correlated processes, which is consistent with results obtained in [13] for a series of catalysts with vari-

ous chemical compositions and desulfurizing activities, demonstrating a direct correlation between the amounts of sulfur removed and CPs deposited in 24-h runs. Thus, one may suggest occurrence of a rather close relation between hydrogenolysis of sulfur-containing compounds and formation of CPs. For cracking of asphaltenes such a relation is not found (Figs. 1, 2).

As for metal-containing components of black oil, their concentration is too low to contribute significantly to formation of CPs.

Evidently, CPs are formed primarily from strongly coke-forming unsaturated products of hydrogenolysis of sulfur-containing compounds. This conclusion is confirmed by data on contributions of model organic compounds (with benzene and thiophene) to coking of the Al–Co–Mo catalyst using a radioactive tracer [13]. The contribution of thiophene was demonstrated to be higher by more than two orders of magnitude as compared to benzene. Such a close relation between hydrogenolysis of sulfur-containing compounds and coking of the catalyst suggests that the degree of catalyst deactivation directly depends on the desulfurization level.

It was demonstrated with an example of the simplest model reaction [14] that the deactivation of catalysts can decrease when internal-diffusion hindrance occurs. It is advisable to check this result for consistency in the case of hydrofining of oil residues. Note that comparison of the degree of reduction of the desulfurizing activity of the catalysts should be made taking into account the presence in the raw material of a broad spectrum of sulfur-containing compounds differing in the molecular weight, reactivity, structure, and coke-forming capacity of hydrogenolysis products as precursors of CPs. Changing desulfurization level is not an extensive phenomenon. It results in different qualitative composition of the major monomers of CPs, i.e., it changes the coke-forming capacity of the reaction mixture. Therefore, comparison of deactivation of any catalysts of hydrodesulfurization (including the kinetically and diffusion-controlled zones of the reaction) can provide adequate results only at close desulfurization levels. In this work the experiments were carried out at a desulfurization level of $30 \pm 5\%$, i.e., the above condition was met. We tested the catalysts with fine (0.4 mm) and coarse (3 mm) grains. The results showed that in the former case the initial desulfurization rate was higher by a factor of 1.1–1.2, and the amount of CPs was higher by a factor of 1.3–1.5. In estimating the degree of deactivation it should be taken into account that in the case of the fine-grain catalyst, in order to obtain the desulfurization level close to that for the coarse-grain catalyst, we were forced to use a higher space velocity. Therefore, the catalyst efficiency (amount of sulfur removed) is higher with fine grain also. To take this factor into account in comparison of the deactivation of the catalysts, the difference between the initial and final (after a 24-h run) desulfurization rates was related to the amount of sulfur removed in this time per unit weight of the catalyst. The results show (Fig. 3) that the differential change in the activity of the catalytic system is practically independent of the conditions of mass transfer, but is controlled by the amount of sulfur removed. Thus, we experimentally confirmed that deactivation of the catalysts for hydrofining of oil residues is caused essentially by coking with products of hydrogenolysis of sulfur-containing components of the raw material.

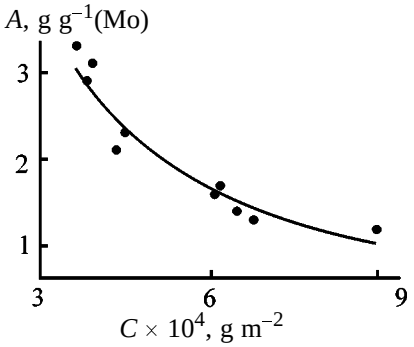

Fig. 2. Amount of CPs A as a function of the Mo concentration in the catalyst C.

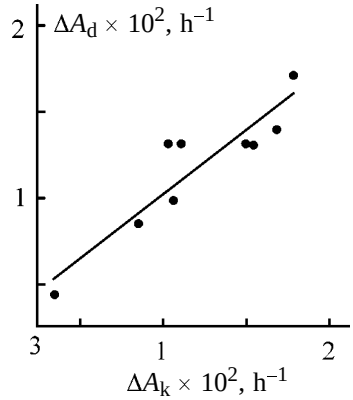

Fig. 3. Correlation between the differential changes in the desulfurization rate on coarse (ΔA_d) and fine (ΔA_k) grains.

CONCLUSION

The rates of desulfurization, deasphalting, and demineralization differently depend on the composition of the Al–Co–Mo catalyst. The specific (per unit

weight of Mo) desulfurizing activity decreases with decreasing Mo content. The deasphalting activity is controlled by the amount of crystallized cobalt molybdate. Demineralization is practically insensitive to changing phase composition of the catalyst as well as the Mo content over the experimental range of its variation. The degree of coking of the catalyst and its deactivation increase with increasing extent of desulfurization.

REFERENCES

1. Wisdom, L., Peer, E., and Bonnitay, P., *Oil Gas J*., 1998, vol. 96, no. 6, pp. 58–60.
2. Bagrii, E.I. and Nekhaev, A.I., *Neftekhimiya*, 1999, vol. 39, no. 2, pp. 83–97.
3. Milova, L.P., Plyasova, L.M., Zaidman, N.M., *et al*., *Izv. Akad. Nauk SSSR, Neorg. Mater*., 1981, vol. 17, no. 1, pp. 148–152.
4. Milova, L.P., Zaidman, N.M., Plyasova, L.M., *et al*., *Kinet. Katal*., 1982, vol. 23, no. 1, pp. 150–154.
5. Zhestkov, D.K., *Metody analiza organicheskikh soedinenii nefti, ikh smesei i proizvodnykh* (Methods for Analysis of Petroleum Organic Compounds, Their Mixtures, and Derivatives), Moscow: Nauka, 1969.
6. Kholodnaya, G.S., Goncharova, N.K., and Dorogova, I.V., *Available from TsNIITEneftekhim*, January 16, 1989, no. 118-NKh89.
7. Topsoe, N., *J. Catal*., 1980, vol. 64, no. 2, pp. 235–237.
8. Okamoto, Y., Imanaka, T., and Teranishi, S., *J. Catal*., 1980, vol. 65, no. 2, pp. 448–460.
9. Absi-Halabi, M., Stanislays, A., and Trimm, D.L., *Appl. Catal*., 1991, vol. 72, no. 2, pp. 193–215.
10. Furimsky, E., *Erdol Kohle*, 1979, vol. 32, no. 8, pp. 383–390.
11. Eigenson, A.S., Berg, G.A., Khabibullin, S.G., *et al*., *Khim. Tekhnol. Topl. Masel*, 1974, no. 1, pp. 1–3.
12. Kapustin, V.M., Matveeva, N.K., and Smidovich, E.V., *Khim. Tekhnol. Topl. Masel*, 1990, no. 5, pp. 13–15.
13. Lur'e, M.A., Storozheva, L.N., Kurets, I.Z., and Lipovich, V.G., *Kinet. Katal*., 1993, vol. 34, no. 3, pp. 572–576.
14. Kumbilieva, K., Kiperman, S.L., and Petrov, L., *Kinet. Katal*., 1995, vol. 36, no. 1, pp. 82–88.

Russian Journal of Applied Chemistry, Vol. 74, No. 7, 2001, pp. 1141–1146. Translated from Zhurnal Prikladnoi Khimii, Vol. 74, No. 7, 2001, pp. 1110–1115.

CATALYSIS

Effect of Organoaluminum Compound on Kinetic Nonuniformity and Structure of Active Centers of Neodymium Catalytic Systems in Butadiene Polymerization

N. N. Sigaeva, T. S. Usmanov, V. P. Budtov, and Yu. B. Monakov

Institute of Organic Chemistry, Ufa Scientific Center, Russian Academy of Sciences, Ufa, Bashkortostan, Russia

Received September 12, 2000; in final form, March 2001

Abstract—The effect of organoaluminum compound nature on the kinetic nonuniformity of the active centers of neodymium-containing catalytic systems at butadiene polymerization was studied. The concentrations of each type of active centers were calculated.

Previously [1, 2] we used the Tikhonov's regularization method [3, 4] to characterize the activity of the lanthanide-containing systems in diene polymerization and found that, irrespective of the diene nature and polymerization conditions, macromolecules are synthesized on lanthanide catalysts with participation of four types of active centers (AC). In this work, we studied the effect of the nature of organoaluminum compound (OAC) on the kinetic nonuniformity and structure of the active centers of neodymium catalytic systems in butadiene polymerization.

Using the Tikhonov's regularization method and experimental curves of molecular-weight distribution (MWD) of 1,4-*cis*-polybutadiene (PB) [3–6] (Figs. 1, 2), we characterized the activity of the $NdCl_3 \cdot 3TBP$–OAC catalytic systems in butadiene polymerization as a function of the molecular weight of the polymer formed. Here TBP is tributyl phosphate and OACs are $Al(i\text{-}C_4H_9)_3$ (TIBA), $Al(C_2H_5)_3$ (TEA), $Al(C_6H_{13})_3$ (THA), and $Al(C_8H_{17})_3$ (TOA).

Irrespective of the nature of OAC used, all the curves of the kinetic activity are characterized by a polymodal form and have four maxima. Each point on the curve characterizes the fraction of ACs generating macromolecules with the molecular weight M_i with the probability of the chain termination equal to ψ_i. The function $\pi(\ln\beta)$ shows the kinetic nonuniformity of the catalytic systems, and four maxima of this function indicate the existence of at least four AC types differing in their structure.

As seen, the multimodality of the $\psi(\ln\beta)$ curves is observed even at the lowest butadiene conversions (Fig. 1). This shows that ACs of all the four types arise in the initial stage of the process. Thus, the catalytic system is initially nonuniform.

The curve of the kinetic activity of the $NdCl_3 \cdot 3TBP$–TEA catalytic system differs from the $\psi(\ln\beta)$ curves for the systems with TIBA, THA, and TOA (Fig. 2). For the system with TEA, two pronounced maxima corresponding to ACs forming the lowest-molecular-weight (M_w 10^3–10^4) and highest-molecular-weight ($M_w \sim 10^6$) polymer fractions are typical. ACs of these two types generate the major fraction of the polymer, while the part of ACs giving macro-

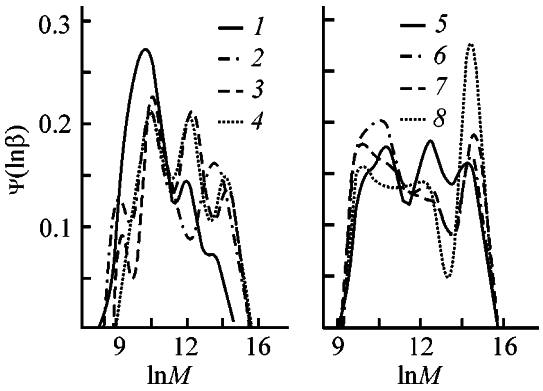

Fig. 1. Kinetic activity of the $NdCl_3 \cdot 3TBP$–TIBA catalytic systems in butadiene polymerization. Polymerization conditions: toluene; $C_m = 1.5$ and $C_{Al} = 3 \times 10^{-2}$ M; Al/Nd = 30; $T = 25$°C; the same for Figs. 3 and 4. (β) Polymerization statistical parameter equal to the ratio of the total rate of the chain termination W_t to the rate of the chain propagation W_p: $\beta = (1/m)(W_t/W_p)$ (m is the monomer molecular weight); (M) molecular weight; the same for Fig. 2. Conversion (%): (*1*) 3.61, (*2*) 11.1, (*3*) 17.4, (*4*) 25.6, (*5*) 55.6, (*6*) 67.8, (*7*) 87.9, and (*8*) 88.8.

1070-4272/01/7407-1141$25.00

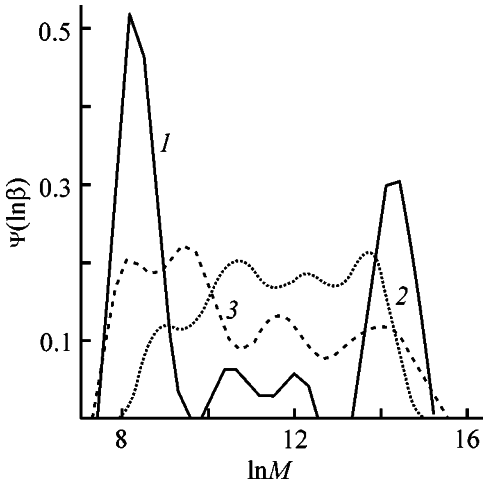

Fig. 2. Kinetic activity of the $NdCl_3 \cdot 3TBP$–OAC catalytic systems in butadiene polymerization. Conversion ~40%. OAC: (*1*) TEA, (*2*) THA, and (*3*) TOA.

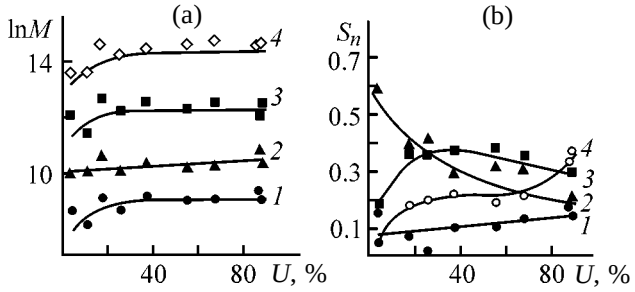

Fig. 3. Position of the maxima of (a) ln*M* and (b) kinetic activity S_n of centers of butadiene polymerization as a function of the monomer conversion *U*. Catalytic system $NdCl_3 \cdot 3TBP$–TIBA.

molecules with intermediate weights is small. Probably, specifically due to such a feature of the $NdCl_3 \cdot 3TBP$–TEA catalytic system the resulting PB has bimodal MWD [7].

Assuming random character of activity deviations from the maxima, we presented the experimental curves as a sum of Gaussian functions. The area under each Gaussian component corresponds to the fraction of the polymer generated on AC of the given type. Such a consideration allows estimation of the contribution of each AC type and its variation.

Figure 3a shows the position of such Gaussian peaks for the $NdCl_3 \cdot 3TBP$–TIBA catalytic system as a function of the degree of the monomer conversion. The changes in the position are small, i.e., each AC synthesizes macromolecules of the definite length.

The active centers of the neodymium catalytic systems with TIBA, THA, and TOA produce polymer fractions with the same molecular weight. For the system with TEA, the position of the first (low-molecular-weight) peak somewhat differs, and the corresponding AC produces polymer with slightly lower molecular weight as compared to the systems with TIBA, THA, and TOA.

The activity of each AC presented as the corresponding peak area changes during polymerization. Figure 3b illustrates this for the $NdCl_3 \cdot 3TBP$–TIBA catalytic system. As seen, ACs corresponding to the first maximum on the distribution curve (generation of low-molecular-weight polymers) are characterized by low activity, which slightly increases during polymerization. For the second AC type, the activity decreases. For the third type, the increase with saturation, and for the fourth, the steady increase are observed during polymerization. Certain scattering in data is explained by the random nature of the polymerization. Nevertheless, the trend in the activity of various ACs can be estimated.

In Fig. 4A, curves of the activity of the $NdCl_3 \cdot 3TBP$–OAC catalytic systems are grouped together for each type of ACs. The figure reveals the trend in the kinetic nonuniformity of the catalytic systems with various OACs. As seen, with TIBA, THA, and TOA the activities of all four types of ACs vary similarly with increasing monomer conversion (though to a different extent). ACs generating low-molecular-weight fraction increase their activity during polymerization (for the catalytic system with TEA the activity of this center decreases). The activities of the centers corresponding to the second and third peaks decrease for all the catalytic systems studied. For the fourth AC type, the activity steadily grows with all OACs.

For all the four AC types, we measured their activities at various Al/Nd ratios. As in the case of conversion curves, with TIBA, THA, and TOA the dependences of the kinetic activity on the Al/Nd ratio are similar. For the $NdCl_3 \cdot 3TBP$–TEA catalytic system, the first maximum, in contrast to the other catalysts, is high. It slightly decreases with increasing Al/Nd ratio. The behavior of the fourth maximum also differs from that for the other catalytic systems: with increasing the TEA content its intensity increases.

We found that the kinetic activity of ACs of the $NdCl_3 \cdot 3TBP$–OAC catalytic systems is practically independent of the catalyst concentration at the constant OAC content.

Figure 4B shows the effect of the polymerization temperature on the activity of the catalytic systems studied. As seen, the intensities of the first and the

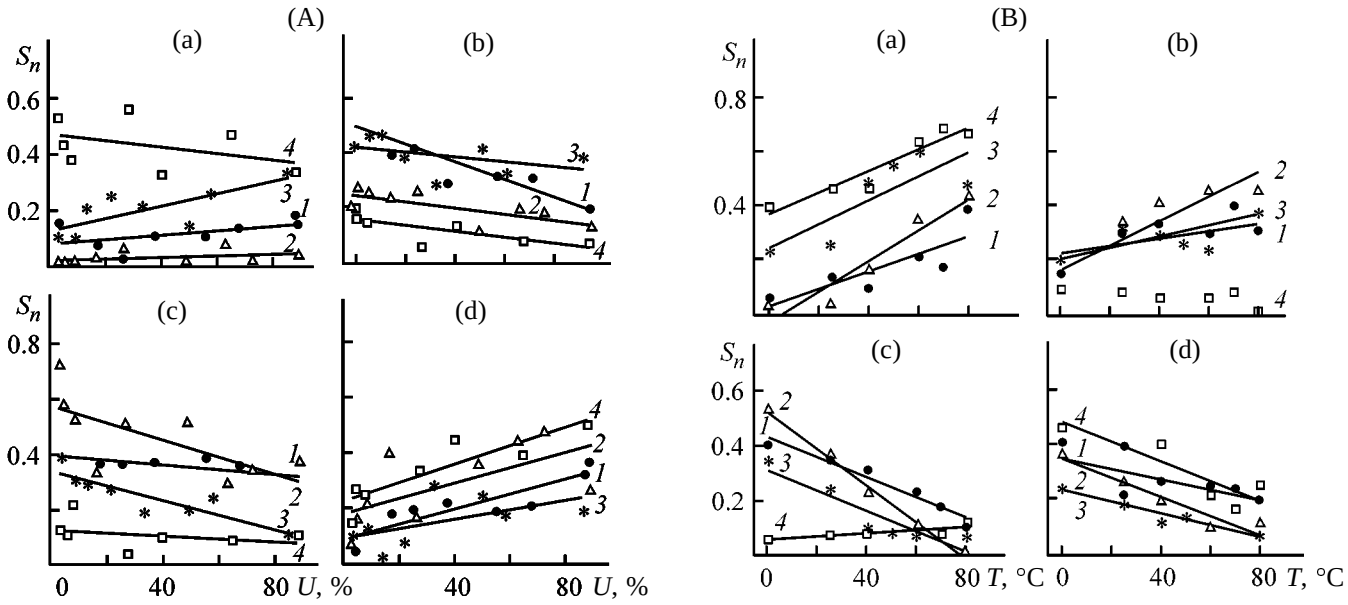

Fig. 4. Kinetic activity S_n of the centers of butadiene polymerization as a function of the (A) monomer conversion U and (B) temperature T. Catalytic systems $NdCl_3 \cdot 3TBP$–OAC. OAC: (*1*) TIBA, (*2*) THA, (*3*) TOA, and (*4*) TEA. Peak: (a) no. 1, (b) no. 2, (c) no. 3, and (d) no. 4.

second peaks corresponding to ACs forming low-molecular-weight polymers increase with temperature. On the other hand, the third and fourth peaks (generation of high-molecular-weight polymers) decrease. This shows that the ACs forming high-molecular-weight fractions are less stable as compared to the ACs forming low-molecular-weight polymers. Similarly to conversion dependences, the activities of ACs corresponding to the second and third peaks are very low for the catalytic system with TEA.

Sharp difference between the system with TEA, on the one hand, and systems with TIBA, THA, and TOA, on the other hand, can be explained by the difference in the association degree of free OAC molecules in the polymerization system. Association sharply increases with decreasing length of the hydrocarbon radical (TIBA is not capable of association because of branching of its hydrocarbon radicals) [8]. Probably, it is the greater tendency of TEA molecules to association in comparison with TIBA, THA, and TOA that is responsible for the observed differences in the activity of ACs.

As mentioned above, the peak area of the separate Gaussian components of the activity curve S_i characterizes the fraction of the chains formed on *i*th AC and is equal to the ratio of the number of these chains Q_{0i} to the total chain number Q_0:

$$S_i = Q_{0i} / Q_0. \qquad (1)$$

Let us assume that

$$\mu = C_{m0} C_{ai} x / \Sigma C_{ai} \qquad (2)$$

is the fraction of the monomer consumed on the *i*th AC by the time corresponding to conversion x, where C_{ai} is the concentration of the *i*th center and C_{m0} is the initial concentration of the monomer.

Then, the quantity

$$\frac{k_{mi} C_m + k_{Ali} C_{Al}}{k_{pi} C_m} \mu \qquad (3)$$

determines the amount of the "dead" chains formed on the *i*th center by transfer to the monomer and OAC by the time corresponding to conversion x, where k_{mi} and k_{Ali} are the rate constants of transfer to the monomer and OAC, respectively, and k_{pi} is the rate constant of the chain propagation on *i*th AC.

The total number of macromolecules formed on the *i*th center is

$$Q_{0i} = C_{ai} + \frac{k_{mi} C_m + k_{Ali} C_{Al}}{k_{pi} C_m} \frac{C_{m0} C_{ai}}{\Sigma C_{ai}} x, \qquad (4)$$

where the first term C_{ai} characterizes the number of "living" chains.

The total number of chains Q_0 is the ratio of the

Concentrations of various types of ACs of the $NdCl_3 \cdot 3TBP$–OAC catalytic systems in butadiene polymerization

OAC	$C_{ai} \times 10^5$, M				$\Sigma C_{ai} \times 10^5$	$\langle C_a \rangle \times 10^5$
	C_{a1}	C_{a2}	C_{a3}	C_{a4}	M	
TIBA	3.9	21.7	7.5	5.7	38.8	40.1
THA	0.05	0.9	1.5	0.8	3.3	3.0
TOA	23.9	6.2	6.9	28.7	65.6	65.0
TEA	6.8	3.9	3.0	6.8	20.5	25.0

amount of the converted monomer to the number-average degree of polymerization P_n:

$$Q_0 = C_{m0} x / P_n. \quad (5)$$

Taking into account Eqs. (8) and (9), Eq. (5) can be transformed after simple operations into

$$\frac{S_i C_{m0} x}{P_n} = C_{ai}\left(1 + \frac{C_{m0} k_{mi}}{k_{p\,i} \Sigma C_{ai}} x + \frac{C_{Al} k_{Ali} C_{m0}}{C_m k_{p\,i} \Sigma C_{ai}} x\right). \quad (6)$$

Let us assume that

$$S_i C_{m0} x / P_n \equiv A_i.$$

The position of the maximum on the kinetic activity curve characterizes the degree of polymerization P_{ni} of the polymer fraction formed on the corresponding ACs, which, in turn, is defined as the ratio of the amount of the monomer μ converted on the *i*th center to the number of chains Q_{0i} formed on it. Using (6), we obtain

$$P_{ni} = \frac{C_{m0} C_{ai}}{Q_{0i} \Sigma C_{ai}} x. \quad (7)$$

For the initial instant of polymerization ($\tau \to 0$), taking into account that the conversion is determined as $x = 1 - e^{-\tau \Sigma k_{pi} C_{ai}}$, we can assume

$$x \approx \tau \Sigma k_{pi} C_{ai} = \tau \langle k_p \rangle \Sigma C_{ai}, \quad (8)$$

where $\langle k_p \rangle$ is the overall rate constant of the chain propagation. Then, taking into account (8), we can write Eq. (7) as

$$P_{ni} = C_{m0} \langle k_p \rangle \tau. \quad (9)$$

It is follows from Eq. (9) that the slope of the $P_{ni}(\tau)$ curves at $\tau \to 0$ is constant for all the ACs and characterizes the given catalytic system. Thus, the shift of the maxima in Fig. 3a in the initial stage of polymerization is the regular phenomenon.

By substitution of Eq. (4) into (7) we obtain the following equation for analysis of P_{ni}:

$$B_i \equiv \frac{C_{m0} C_{ai} x}{P_{n\,i} \Sigma C_{ai}}$$

$$= C_{ai} + \frac{k_{m\,i} C_m + k_{Ali} C_{Al}}{k_{p\,i} C_m} \frac{C_{m0} C_{ai}}{\Sigma C_{ai}} x. \quad (10)$$

Extrapolation of the dependence of A_i or B_i on the monomer conversion x to zero conversion in accordance with Eqs. (6) and (10) allows determination of C_{ai}, which is the concentration of each type of AC, and of the total concentration of all ACs ΣC_{ai}.

The concentrations of the separate ACs in butadiene polymerization on the catalytic systems studied are listed in the table. $\langle C_a \rangle$ is also the total AC concentration, but it is determined from the analysis of the polymerization kinetics by the equation $W_p = k_p C_m / \langle C_a \rangle$. As seen, a good agreement is observed for results calculated by both methods. This confirms the adequacy of the model used.

Introduction of OAC into the polymerization system initiates processes yielding ACs. The soluble complex of neodymium chloride with TBP reacts with OAC molecules, which initially abstract TBP molecule, and desolvated neodymium chloride starts to precipitate as the coordination polymer $(NdCl_3)_n$ with chloride bridges. Simultaneously $NdCl_3$ is alkylated with formation of $NdCl_2R$. As shown in [9], TBP is practically removed from the catalytic complex. The excess AlR_3 (Al/Nd ~ 30) can give complexes

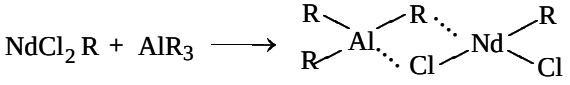

It should be noted that the above processes can occur simultaneously, affecting each other.

The catalytic systems containing no organoaluminum compound are known [10, 11]. Hence, OAC is not the necessary component of the catalytic complex controlling *cis* stereoregulation, although the presence of OAC makes the catalyst substantially more active. This means that ACs do not necessarily contain OAC fragments.

It was shown in [10, 11] that centers forming *cis* units are the compounds with the formula LnX_2R (X is electronegative group), when individual lanthanide organic compounds are used as catalysts of diene polymerization; triorganolanthanides LnR_3 are the catalysts of *trans* polymerization, and the compounds $LnXR_2$ are inactive in polymerization.

Taking into account these facts, we can assume the existence of ACs differing in the degree of alkylation of neodymium chloride and in the content of the organoalunimum component. Structure *a* is formed by alkylation of one Nd–Cl bond (see scheme). Structure **b** arises when, in addition to alkylation, complexation with OAC molecule occurs. When two Nd–Cl bonds are alkylated, active centers **c** and **d** are formed.

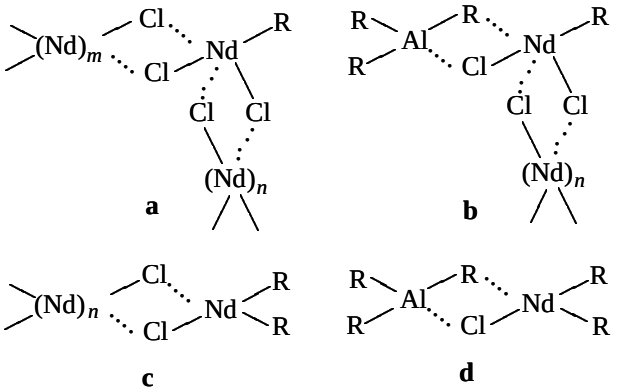

EXPERIMENTAL

Butadiene polymerization was performed at 25°C in the presence of the $NdCl_3 \cdot 3TBP$–OAC catalytic systems (OAC = TIBA, TEA, THA, and TOA). The $NdCl_3 \cdot 3TBP$ complex was synthesized according to [9]. The catalyst was prepared *in situ*, i.e., in the solution of the monomer in toluene (C_m = 1.5 M) initially OAC ($C_{Al} = 3 \times 10^{-2}$ M) and then $NdCl_3 \cdot 3TBP$ were introduced. The Al/Nd ratio was 30.

The content of 1,4-*cis* units in polybutadiene was 90–95% and that of 1,2 units was less than 1%, the remainder being 1,4-*trans* units.

The molecular weights and MWD of polybutadiene were determined on a KhZh-1302 gel chromatograph; four columns packed by Waters styrogel with a pore size of 3×10^2–5×10^6 A were used. The separation temperature was 25°C. Chloroform was used as an eluent. The column system was calibrated against polystyrene references with narrow MWD ($M_w/M_n \leq 1.2$) using the universal Benoit dependence [12] and the equation correlating the polybutadiene molecular weight with the intrinsic viscosity [13].

The chromatograms and molecular weights were corrected with regard to device broadening by the special method [14]. The approximation method of solving the Tung equation [15, 16] was taken as a "testing" method.

The distribution with respect to the kinetic nonuniformity of the $NdCl_3 \cdot 3TBP$–OAC catalytic system was calculated by the Tikhonov's regularization method [3, 4]. The minimum of the Tikhonov's functional was attained at the regularization parameter α equal to 9.4×10^{-5} with the root-mean-square error δ^2 0.0001. The unbalance was 1.07×10^{-4}. The method used and the IUPR procedure allow variation of the error in the choice of the integral equation core. However, because the core, which is the Schultz–Flory function, was selected as a model, the error was taken to be $h \to 0$.

CONCLUSIONS

(1) Irrespective of the nature of organoaluminum compound used in the neodymium catalytic system and conditions of the process, butadiene polymerization proceeds on four types of active centers formed at the start of polymerization and generating polymers with different molecular weight.

(2) The method was developed for determination of the concentrations of each type of active centers in the neodymium catalytic systems, and these concentrations were calculated.

(3) The possible structures of the active centers in the neodymium catalytic systems differing by the content of organoaluminum compound in the catalytic complex were proposed.

REFERENCES

1. Sigaeva, N.N., Usmanov, T.S., Shirokova, E.A., *et al*., *Dokl. Ross. Akad. Nauk*, 1999, vol. 365, no. 2, pp. 221–224.
2. Sigaeva, N.N., Usmanov, T.S., Budtov, V.P., *et al*., *Vysokomol. Soedin*., 2000, vol. 42, no. 1, pp. 112–117.
3. Tikhonov, A.N., Goncharskii, A.V., Stepanov, V.V.,

and Yagola, A.G., *Chislennye metody resheniya nekorrektnykh zadach* (Numrical Methods of Solving Incorrect Problems), Moscow: Nauka, 1990.

4. Usmanov, S.M., *Relaksatsionnaya polyarizatsiya dielektrikov. Raschet spektrov dielektricheskoi relaksatsii* (Relaxation Polarization of Dielectrics. Calculation of Dielectric Relaxation Spectra), Moscow: Nauka, 1996.
5. Kozlov, V.G., Nefed'ev, K.V., Marina, N.G., *et al*., *Dokl. Akad. Nauk SSSR*, 1988, vol. 299, no. 3, pp. 652–656.
6. Sigaeva, N.N., Kozlov, V.G., Savel'eva, I.G., *et al*., *Bashk. Khim. Zh.*, 1998, vol. 5, no. 4, pp. 31–36.
7. Kozlov, V.G., Nefed'ev, K.V., Marina, N.G., *et al.*, *Dokl. Akad. Nauk SSSR*, 1988, vol. 299, no. 3, pp. 652–656.
8. Korneev, N.N., Popov, A.F., and Krentsel', B.A., *Kompleksnye metalloorganicheskie katalizatory* (Complex Organometallic Catalysts), Leningrad: Khimiya, 1969.
9. Murinov, Yu.I., Monakov, Yu.B., Shamaeva, Z.G., *et al*., *Izv. Akad. Nauk SSSR, Ser. Khim.*, 1977, no. 12, pp. 2990–2992.
10. Vollershtein, E.L., Glebova, N.N., Gol'shtein, S.B., *et al*., *Dokl. Akad. Nauk SSSR*, 1985, vol. 284, no. 1, pp. 140–142.
11. Dolgoplosk, B.A., Tinyakova, E.I., Yakovlev, V.A., *et al*., *Vysokomol. Soedin*., 1996, vol. 38, no. 3, pp. 442–446.
12. Benoit, H., Crubisic, L., and Rempp, P.A., *J. Polym. Sci., B*, 1967, vol. 5, no. 9, pp. 753–759.
13. Berg, A.A., Kozlov, V.G., Budtov, V.P., *et al*., *Vysokomol. Soedin*., 1980, vol. 22, no. 3, pp. 543–550.
14. Usmanov, T.S., Nabiullin, A.R., Sigaeva, N.N., *et al*., Abstracts of Papers, *V Mezhdunarodnaya Konferentsiya "Neftekhimiya-99"* (V Int. Conf. "Petrochemistry-99"), Nizhnekamsk, September 14–17, 1999, vol. 2, pp. 227–229.
15. Tung, L.H., *J. Appl. Polym. Sci*., 1966, vol. 10, pp. 375–385.
16. Kislov, E.N., Zotikov, E.G., Podosenova, N.G., *et al*., *Vysokomol. Soedin., Ser. A*, 1978, vol. 20, no. 8, pp. 1910–1912.

Russian Journal of Applied Chemistry, Vol. 74, No. 7, 2001, pp. 1147–1150. Translated from Zhurnal Prikladnoi Khimii, Vol. 74, No. 7, 2001, pp. 1116–1119.

CATALYSIS

Cobalt(III)–*d*-Metal Triethanolamine Complexes as Catalysts of Electrochemical Reduction of Oxygen

V. S. Kublanovskii and Yu. K. Pirskii

Vernadsky Institute of General and Inorganic Chemistry, National Academy of Sciences of Ukraine, Kiev, Ukraine

Received September 12, 2000; in final form, April 2001

Abstract—Carbon-supported oxide catalysts of oxygen electroreduction were prepared from Co(III)–M(II) ethanolamine complexes. The electrochemical properties of these catalysts were studied. The apparent activation energies of the reduction were measured.

Development of new electrocatalysts free from noble metals and electrodes on their base for chemical current sources is an urgent problem [1]. One of the most promising catalysts for oxygen electroreduction in metal–air chemical current sources and electrochemical generators are *d*-metal N_4 complexes [2–5]. Catalysts with required properties can be prepared by variation of the ligands and the central metal. Thermal treatment of carbon materials modified with organometallic N_4 complexes enhances their catalytic activity in electrochemical reduction of oxygen and increases the discharge voltage and capacity of voltaic cells. The structure of catalytically active centers depends on the ligand nature and on the temperature and atmosphere of pyrolysis. For example, the active centers of the catalysts prepared by thermolysis of cobalt(II) and iron(II) polyacrylonitrile complexes at 800–900°C are anchored to the carbon support via nitrogen atoms [2]. When a carbon material modified with products of condensation of ethylenediamine and formaldehyde with *d*-metals are used as the precursors, the most active catalysts are formed at 500–600°C [3]. Effective catalysts of oxygen electrochemical reduction were prepared by heat treatment of polymeric cobalt(III) complexes with *p*-phenylenediamine and 2,6-diaminopyridine at 923–1123°C in a vacuum, with the catalytic activity increasing with the temperature of the heat treatment. Tarasevich and Radyushkina [5] showed that effective catalysts based on cobalt(II) and iron(II) porphyrin and phthalocyanine complexes can be prepared by calcination at 800–900°C. Among the best catalysts are 3*d*-metal oxides with the spinel structure [6]. However, the electrical conductivity of these oxides is low, and preparation of catalysts with high surface conductivity by application of these oxides to carbon support is rather complex problem. The electrocatalytic activity of oxides is known [1, 7] to depend mainly on the nature of surface cations and structural defects. The aim of this work was to prepare catalysts of electrochemical oxygen reduction by pyrolysis of cobalt(III)–*d*-metal(II) triethanolamine complexes on carbon support to form metal oxides with the spinel structure.

EXPERIMENTAL

Catalysts of electrochemical reduction of oxygen were prepared by treatment of AG-3 activated carbon with methanolic or aqueous-methanolic solutions of $[Co(HTEA)H_2TEA]_2 \cdot M(OOCCH_3)_2$ (where H_3TEA is triethanolamine and M is Mn^{2+}, Ni^{2+}, Cu^{2+}, or Zn^{2+}).

The initial complexes were prepared by addition of a 0.2 M methanolic or aqueous methanolic solution (10 ml) of appropriate *d*-metal (Mn^{2+}, Ni^{2+}, Cu^{2+}, or Zn^{2+}) acetates to 0.004 M methanolic solution (5 ml) of cobalt aminoalcoholate $[Co(HTEA)H_2TEA]_2$ prepared by the procedure in [8]. Methanol was used as the solvent of nickel acetate and zinc acetate and water–methanol mixture (1 : 1), as the solvent for manganese acetate and copper acetate. Manganese(II) acetate was prepared by dissolving metallic manganese in glacial acetic acid, followed by recrystallization from water. The other acetates were of analytically pure grade. AG-3 activated carbon (1 g) with particles smaller than 50 μm and the BET specific surface area of 850 $m^2 g^{-1}$ was added to a solution of appropriate metal acetate. The mixture was allowed to stand for 12 h. Then 80% of the solvent was distilled off. The impregnated carbon was filtered off, washed with a small amount of isopropanol and then with

1070-4272/01/7407-1147$25.00

ether, and dried at 120°C to constant weight. The weight gain of the activated carbon after sorption of $[Co(HTEA)H_2TEA]_2 \cdot Mn(OOCCH_3)_2$, $[Co(HTEA)H_2 \cdot TEA]_2 \cdot Cu(OOCCH_3)_2$, $[Co(HTEA)H_2TEA]_2 \cdot Zn \cdot (OOCCH_3)_2$, and $[Co(HTEA)H_2TEA]_2 \cdot Ni(OOCCH_3)_2$ was 51, 55, 20, and 64%, respectively.

The currents passed through the catalysts were adjusted depending on the weight of the complex applied to the carbon.

The triethanolamine complexes have the following structure:

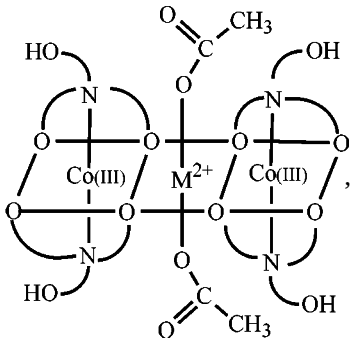

where curve segments denote the $–C_2H_4–$ fragments.

As seen from this figure, the double-charged metal located in the equatorial plane is bound via oxygen bridges to the triple-charged cobalt ions. There are reasons to believe that this fragment in the form of spinel or substoichiometric mixed oxides can be retained on the carbon surface after pyrolysis of the complexes at definite temperatures. Thermal degradation of the complexes of this type in a carbon matrix is known [5] to start from elimination of the terminal groups. The products are incorporated into the structure of the carbon matrix.

A weighed portion of carbon-supported metal complexes (200 mg) was placed in a quartz tube furnace. The sample was gradually heated in an argon counterflow to the required temperature, kept at this temperature for 1 h, and cooled to room temperature. The heat treatment was performed at temperatures from 200 to 800°C with a 100°C increment. The catalytic activity of the resulting samples in electrochemical reduction of oxygen was studied.

The electroreduction of oxygen was performed at room temperature in 1 M KOH on a floating gas-diffusion electrode [11] in an electrochemical cell with separated cathodic and anodic compartments. The electrochemical measurements were performed in a PI-50-1.1 potentiostat using an Ag/AgCl reference electrode. The partial pressure of oxygen before and after bubbling of oxygen through the electrolyte was measured by an OP-210/3 microanalyzer [12].

The working floating gas-diffusion electrode was prepared by the following procedure. A nickel wire was pressed at a pressure of 50–70 kg cm^{-2} in acetylene black (400 mg) hydrophobized with 30% polytetrafluoroethylene. A thin layer of finely divided catalyst (<20 μm) was applied to the surface of the resulting single-layer porous electrode (d = 10.15 mm, density 0.95 g cm^{-3}, thickness ~1 mm). The composite was pressed at 50–60 kg cm^{-2}. The amount of applied catalysts was determined by weighing the electrode before and after pressing of the catalyst powder. To determine the state of the catalyst surface before and after the electrochemical reduction, polarization curves were recorded in an argon atmosphere with a sweeping rate of 2 mV s^{-1}. The potentiostatic polarization curves were constructed from the current densities measured at constant potentials adjusted with a 10 mV increment by a PI-50-1.1 potentiostat. The current was registered with an M-104 milliammeter with extrapolation to $t \to \infty$.

Since the thermal treatment was performed in an inert atmosphere, we suggest that centers active in the oxygen reduction are metal atoms or their oxides dispersed in AG-3 activated carbon. As seen from the kinetic parameters of oxygen electroreduction on the tested catalysts (see table), the active catalysts are formed after calcination of the cobalt triethanolamine complexes on the carbon support at 300–500°C.

The influence of the calcination temperature on the properties of catalysts based on Co(III)–M(II) triethanolamine complexes is seen from the results presented in the table. The maximal exchange currents are observed for the catalysts prepared at 400°C, which is probably due to formation of active centers. With increasing calcination temperature to 800°C, the currents decrease owing to degradation of these centers to form inactive species. The slopes of the stationary polarization curves lie in the following ranges (mV): b_1 = 44–64 and b_2 = 100–127. The dependence of oxygen electroreduction at a constant potential E = –0.125 V (vs. silver chloride electrode) on the calcination temperature is shown in Fig. 1. The maximal current was observed with the catalysts calcined at 400°C. This is the best temperature for preparing active catalysts from cobalt(III)–*d*-metal triethanolamine complexes. The activity of the tested catalysts decreases in the following order: Co–Mn > Co–Zn > Co–Cu > Co–Ni.

The most active catalysts were prepared from Co–Mn triethanolamine complexes. We suggested that

Kinetic parameters of oxygen electroreduction in 1 M KOH at 20°C on catalysts prepared by pyrolysis of the Co(III)–Mn(II) triethanolamine complexes

Catalyst	T, °C	E_{st}, V	$j_0 \times 10^3$, mA cm^{-2}	$\partial E/\partial \log j$, V		W_{app}, kJ mol^{-1}
				b_1	b_2	
AG-3	–	–0.007	11.35	0.058	0.116	60.1
Co–Mn(AG-3)	–	–0.053	4.78	0.061	0.117	56.7
	200	–0.098	5.68	0.046	0.124	56.0
	300	–0.007	5.31	0.049	0.119	55.6
	400	–0.003	12.32	0.064	0.126	54.0
	800	–0.100	4.54	0.048	0.123	59.1
Co–Ni(AG-3)	–	–0.084	2.59	0.052	0.115	60.2
	300	–0.092	1.97	0.056	0.109	59.5
	400	–0.073	2.84	0.048	0.103	58.8
	800	–0.097	1.60	0.060	0.118	60.5
Co–Zn(AG-3)	–	–0.065	5.38	0.060	0.116	60.6
	200	–0.102	3.81	0.057	0.127	60.4
	300	–0.090	4.69	0.055	0.126	59.5
	400	–0.044	10.0	0.047	0.120	59.0
	800	–0.105	3.09	0.054	0.128	60.4
Co–Cu(AG-3)	–	–0.072	3.21	0.047	0.106	60.8
	200	–0.100	1.60	0.047	0.105	60.4
	300	–0.098	1.98	0.044	0.100	60.2
	400	–0.061	2.74	0.046	0.105	59.1
	800	–0.111	0.99	0.046	0.104	60.3

* j_0 is the exchange current density; b_1 and b_2 are the slopes of stationary polarization curves.

the Co–Ni catalysts would be the next in the sequence of the catalytic activity. However, this was not the case. The X-ray diffraction study showed the absence of the crystalline phase. Since the complexes contain oxygen and metal atoms, we suggest that in this case double metal oxides with spinel or nonstoichiometric oxide structure are formed. The catalytically active centers of this catalyst are formed on structural defects [1, 7] containing excess oxygen. The defects promote formation of cationic vacancies and increase the electrical conductivity. As a result, the electrochemical properties of the catalysts are improved.

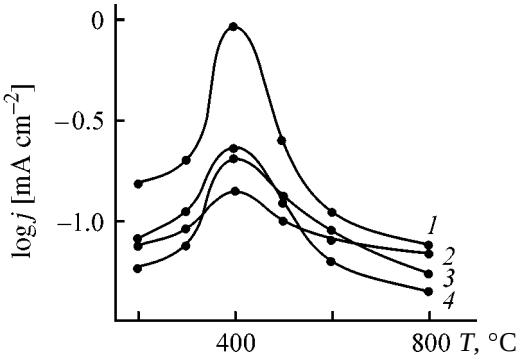

Fig. 1. Rate of oxygen electroreduction in 1 M KOH at 20°C on catalysts prepared by pyrolysis of Co(III)–M(II) triethanolamine complexes on AG-3 activated carbon as a function of the pyrolysis temperature T. Potential E = –0.125 V vs. silver chloride electrode. (j) Current density. Catalyst: (*1*) Co–Mn, (*2*) Co–Ni, (*3*) Co–Cu, and (*4*) Co–Zn.

These data agree with the results of [13] where spinel and nonstoichiometric oxides prepared also at 300–400°C were used as catalysts.

The ponetiostatic polarization curves of oxygen electroreduction on the catalyst prepared from Co–Mn triethanolamine complexes supported on AG-3 activated carbon, AG-3 activated carbon without supported metal, and hydrophobized carbon black substrate are shown in Fig. 2. As seen from Fig. 2, the activity of the catalysts is higher than that of AG-3 carbon. The stationary polarization curve of the catalysts is shifted by 50 mV to the positive potentials. We also calculated the apparent activation energy of oxygen electroreduction on the catalysts prepared from Co(III)–M(II) triethanolamine complexes supported by AG-3 activated carbon. For this purpose the potentiostatic polarization curves of Co(III)–M(II) electrocatalysts were measured in an oxygen at-

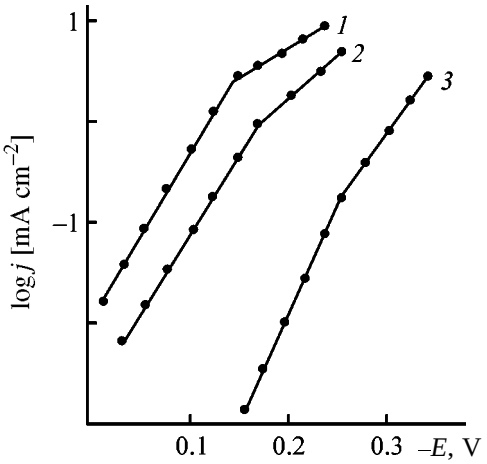

Fig. 2. Potentiostatic polarization curves of oxygen electroreduction measured in 1 M KOH at 20°C on a hydrofibized carbon black substrate. (*j*) Current density and (*E*) electrode poetical. (*1*) Co–Mn triethanolamine complex on AG-3 (400°C, Ar), (*2*) AG-3, and (*3*) hydrophibized carbon black.

mosphere at 20, 30, 40, and 50°C to determine the exchange currents. Then the dependences of the exchange currents of oxygen electroreduction on the reciprocal temperature were plotted. The apparent activation energy was calculated by the following equation [14]:

$$W_{app} = -2.303R\frac{\partial \ln j_0}{\partial(T^{-1})},$$

where W_{app} is the apparent activation energy of oxygen electroreduction, j_0 is the exchange current density, and T is the temperature.

The calculated apparent activation energies of oxygen electroreduction agree with those for the catalysts supported by carbon materials and spinels. The activation energy for the Co–Mn catalysts and AG-3 activated carbon is 54.0 and 60.1 kJ mol^{-1}, respectively. Our results show that the apparent activation energy of oxygen electroreduction decreases with an increase in the catalytic activity. The values of the apparent activation energies and the kinetic data show that the electrochemical reduction is kinetically controlled.

CONCLUSIONS

(1) The best pyrolysis temperature of cobalt–*d*-metal triethanolamine complexes in an inert atmosphere is 300–400°C. Under these conditions the catalysts of oxygen electroreduction were prepared. The spinel and nonstoichiometric oxide structure of the catalysts was suggested.

(2) The most active catalyst was prepared by calcination of Co(III)–Mn(II) triethanolamine complex on AG-3 carbon support at 400°C in an inert atmosphere.

ACKNOWLEDGMENTS

This work was financially supported by the State Foundation for Basic Research of Ukraine.

REFERENCES

1. *Problemy elektrokataliza* (Problems of Electrocatalysis), Bagotskii, V.S., Ed., Moscow: Nauka, 1980.
2. Gupta, S., Tryk, D., Bae, J., *et al*., *J. Appl. Electrochem*., 1989, vol. 19, no. 1, pp. 19–27.
3. Kublanovskii, V.S., Pirskii, Yu.K., and Yakimenko, N.G., *Zh. Fiz. Khim*., 1997, vol. 71, no. 1, pp. 54–59.
4. Bazanov, M.I., Siling, S.A., Smirnov, R.P., *et al*., *Elektrokhimiya*, 1996, vol. 32, no. 9, pp. 1120–1124.
5. Tarasevich, M.R. and Radyushkina, K.A., *Kataliz i elektrokataliz metalloporfirinami* (Catalysis and Electrocatalysis with Metal Porphyrins), Moscow: Nauka, 1982.
6. Razina, N.F., *Okisnye elektrody v vodnykh rastvorakh* (Oxide Electrodes in Aqueous Solutions), Alma-Ata: Nauka, 1982.
7. *Elektrokataliz i elektrokataliticheskie protsessy: Sbornik nauchnykh trudov* (Electrocatalysis and Electrocatalytic Processes: Collection of Works), Kublanovskii, V.S., Ed., Kiev: Naukova Dumka, 1986.
8. Udovenko, V.V., Stepanenko, O.N., and Eroshok, B.G., *Zh. Neorg. Khim*., 1974, vol. 19, no. 9, pp. 2455–2459.
9. Stepanenko, O.N. and Reiter, L.G., *Ukr. Khim. Zh*., 1992, vol. 58, no. 12, pp. 1047–1053.
10. Kapanadze, T.Sh., Gulya, A.P., Novotortsev, A.I., *et al*., *Koord. Khim*., 1991, vol. 17, no. 7, pp. 934–940.
11. Shteinberg, G.V., Kukushkina, I.A., Bagotskii, V.S., and Tarasevich, M.R., *Elektrokhimiya*, 1979, vol. 15, no. 4, pp. 527–532.
12. Kublanovskii, V.S., Belinskii, V.N., Pirskii, Yu.K., and Yakimenko, N.G., *Ukr. Khim. Zh*., 1988, vol. 54, no. 1, pp. 43–46.
13. Ivanova, N.D., Filatov, K.V., Boldyrev, E.I., *et al*., *Dopov. Akad. Nauk Ukr*., 1992, no. 11, pp. 136–139.
14. Tomilov, B.I. and Loshkarev, I.A., *Dokl. Akad. Nauk SSSR*, 1963, vol. 151, no. 4, pp. 894–897.

Russian Journal of Applied Chemistry, Vol. 74, No. 7, 2001, pp. 1151–1155. Translated from Zhurnal Prikladnoi Khimii, Vol. 74, No. 7, 2001, pp. 1120–1124.

ORGANIC SYNTHESIS AND INDUSTRIAL ORGANIC CHEMISTRY

Gas-Phase Fluorination of Fluoroethanes with Elemental Fluorine

D. S. Pashkevich, D. A. Mukhortov, Yu. I. Alekseev, V. S. Asovich, and O. V. Rozhdestvenskaya

Prikladnaya Khimiya Russian Scientific Center, St. Petersburg, Russia

Received May 22, 2000; in final form, February 2001

Abstract—Scientific basis for industrial gas-phase fluorination of fluoroethanes with elemental fluorine allowing production of higher-fluorinated fluoroethanes from lower-fluorinated compounds is developed.

Fluorine is extremely reactive and its reactions are highly exothermic. Therefore, at present preparation of fluorinated organic compounds using fluorine has almost no industrial application.

Fluorine is commercially available, and its utilization for production of valuable fluorinated products is rather urgent. These products include a series of fluoroethanes, e.g., 1,1-difluoroethane (DFE, R152a), 1,1,2-trifluoroethane (R143a), 1,1,1,2-tetrafluoroethane (TFE, R134a), pentafluoroethane (PFE, R125), and hexafluoroethane (HFE, R116), which are widely used as refrigerants, propellants, fire extinguishers, reagents for plasmochemical production of superlarge integrated circuits, gas dielectrics, etc. [1]. The world's consumption of these compounds reaches tens thousands tons per year.

The modern industrial process for production of fluoroethanes is based on catalytic fluorination of fluorochloroethanes and ethylenes with hydrogen fluoride. The initial chlorinated materials used in this case are ozone-dangerous, and, in accordance with the Montreal Protocol, their production should be terminated. Moreover, this process yields significant amounts of hydrogen chloride (by-product) and requires periodical replacement and utilization of the spent chromium–manganese fluoride catalyst. Thus, development of alternative procedures for synthesis of fluoroethanes is urgent. One of such procedures can be synthesis of higher-fluorinated ethanes by gas-phase fluorination of lower-fluorinated compounds with elemental fluorine.

The first data on the gas-phase fluorination are given in [2–5]. In particular, the gas-phase fluorination of ethane with fluorine was studied and the possibility of preparing HFE was confirmed. However, the corresponding industrial procedures still are not developed.

The kinetics of 1,1,1,2-TFE fluorination was studied in [6]; it was found that industrial synthesis in the steady-state thermal mode is unsuitable. As shown in [7], industrial fluorination of fluoroethanes should be carried out in the nonstationary thermal mode (wave or combustion modes). In this case fluoromethanes are not formed in noticeable amounts at the initial concentration of fluorine lower than 30 vol %.

Development of the industrial process for fluorination of fluoroethanes requires understanding of the principles of scaling the reactor for gas-phase fluorination operating in the wave mode.

One of the features of combustion is that the reaction profile in a laminar torch comprises tenth fractions of millimeter. In tunnel jets conversion of compounds in the turbulent torch reaches 80% within the length of five diameters of the crater [8]. Such a structure of the turbulent torch suggests that, if the thermal radiation of the gas is negligible, the main conversion of compounds proceeds at temperature fairly close to adiabatic. In this case the composition of the products of 1,1,1,2-TFE gas-phase fluorination in the mode of a steady-state self-propagating wave should be independent of the diameter of the reaction unit and of the gas flow mode (without taking into account thermal decomposition of fluoroethanes outside the fluorination zone). To verify this assumption, we performed a series of tests with reactors of various diameters.

The tests we carried out using changeable tubes with an internal diameter of 10, 4, 3, and 2 mm at flow rates of the cold reaction mixture providing constant velocities of the gas flow. To eliminate the

1070-4272/01/7407-1151$25.00

Table 1. Experimental parameters and the composition of the reaction products after fluorination of 1,1,1,2-TFE in the mode of self-propagating thermal wave using reactors of various diameters

Experimental parameters				Product composition			
d, mm	u_m, m s^{-1}	Re	α, W m^{-2} K^{-1}	$C_2H_2F_4$	C_2HF_5	C_2F_6	FM*
10	1.0	572	25.6	62.4	31.0	5.5	1.1
4	1.5	368	64.1	64.1	30.1	4.9	0.9
3	1.4	140	85.6	64.1	30.0	5.1	0.8
2	1.2	147	128.2	63.8	30.2	5.2	0.8

* FM is total content of fluoromethanes in the reaction products.

breakthrough of the reaction front up with a gas flow into a mixer, the internal diameter of the latter was 0.8 mm. The parameters of these tests (reactor diameter d, gas velocity u_m, Re number, and convection coefficient of the heat exchange from the reaction zone to the reactor wall α) and the composition of the reaction products are listed in Table 1; the fluorine concentration was 30 vol %.

The composition of products formed in the wave process is independent of the convection coefficient of the heat exchange α in the 25–130 W m^{-2} K^{-1} range, which confirms our assumption that there is no heat exchange in the reaction zone of fluorine and 1,1,1,2-TFE and allows extrapolation of these results to larger reactors at a constant initial concentration of fluorine.

Thus, the fluorine concentration is a unique parameter affecting the composition of the products of the wave synthesis, which simplifies design and operation of the reactor.

The kinetic study of the gas-phase fluorination of 1,1,1,2-TFE revealed the autocatalytic character of this process. To explain this feature, we studied the effect of the formed hydrogen fluoride on the reaction rate [6].

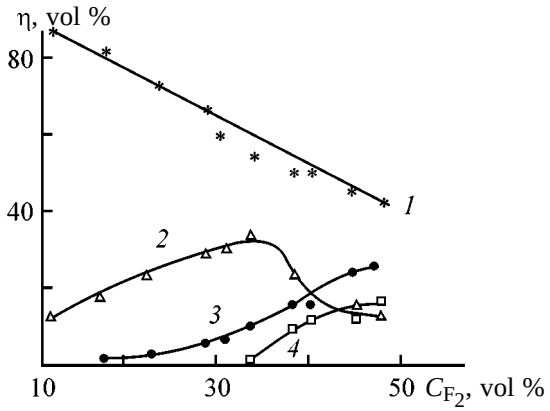

Fig. 1. Composition η of the products of 1,1,1,2-TFE fluorination in the wave mode as influenced by fluorine concentration C_{F_2} in the presence of 5–10 vol % of hydrogen fluoride: (*1*) 1,1,1,2-TFE, (*2*) PFE, (*3*) HFE, and (*4*) total content of fluoromethanes; the same for Fig. 2.

As-produced fluorine always contains hydrogen fluoride [1]. Special treatment is required to remove HF, which increases the cost of its production. Thus, investigation of the effect of small amounts of hydrogen fluoride in the initial mixture on the composition of the reaction products in the mode of self-propagating thermal wave is urgent.

The procedure and experimental setup used were described previously in [7]. Fluorine was mixed with 5–10% of hydrogen fluoride, the fluorine concentration was 11–47 vol %, and the flow rate of the cold reaction mixture was 50–75 cm^3 s^{-1}.

As in the case of pure fluorine [7], we observed the dependences typical for the wave modes. The composition of the reaction products as influenced by the fluorine concentration is shown in Fig. 1. Comparison of these results with those determined for pure fluorine [7] shows that the composition of the reaction products obtained in the wave mode of PFE synthesis is almost independent of the concentration of hydrogen fluoride (5–10 vol %) in the reaction mixture in the entire range of fluorine concentrations.

This fact allows utilization in the wave synthesis mode of the electrolysis gas of fluorine production without additional treatment.

The disadvantage of the wave mode is the requirement to perform the reaction at the substoichiometric concentration of one of the components. In the gas-phase fluorination of fluoroethanes the maximum permissible concentration of fluorine is about 30 vol %. At higher concentrations and thus at higher adiabatic temperature of the wave process the degradation of fluoroethanes becomes pronounced, and significant amounts of fluoromethanes appear in the reaction products.

Table 2. Composition of the fluorination products of the mixture of 1,1-DFE (14 vol %) and HFE (85 vol %) in the wave mode as influenced by the fluorine concentration C_{F_2} (vol %)

C_{F_2}, vol %	Product composition, vol %									
	CHF_2–CH_3	CHF_2–CH_2F	CF_3–CH_3	CHF_2–CHF_2	CF_3–CH_2F	C_2HF_5	C_2F_6	CF_4	CHF_3	CH_2F_2
15.4	6.7	3.2	3.2	1.3	1.0	0.20	83.8	–	0.47	0.15
18.8	4.6	2.8	3.0	1.2	1.3	0.71	85.8	–	0.41	0.08
19.4	4.8	3.7	3.3	1.2	1.8	1.08	83.1	–	0.36	0.12
22.1	4.4	3.4	3.3	1.6	1.7	1.11	83.3	0.64	0.44	0.13
23.0	4.1	3.5	3.1	2.0	2.0	1.48	82.6	0.78	0.36	0.17
23.6	4.1	2.2	2.4	1.2	1.3	1.21	85.5	1.37	0.41	0.31
24.3	3.3	2.1	2.0	1.1	1.3	1.08	86.7	1.46	0.41	0.36
28.6	2.9	2.0	1.7	1.2	1.3	1.32	86.0	2.17	0.47	0.69
31.7	2.1	1.4	1.3	0.8	1.0	1.34	86.4	2.88	0.72	1.42

Table 3. Experimental parameters and composition of the products in fluorination of 1,1,1,2-TFE to HFE using dilution with argon

Initial mixture, vol %			Composition of the reaction gas, vol %					
Ar	F_2	$C_2H_2F_4$	$C_2H_2F_4$	C_2HF_5	C_2F_6	CF_4	CHF_3	CH_2F_2
84.4	13.9	1.72	–	1.1	97.6	–	0.4	0.9
88.1	10.1	1.80	0.5	0.9	97.3	–	–	1.3
90.7	7.4	1.85	3.9	6.0	88.0	–	–	3.2
90.6	6.6	2.79	3.8	14.6	76.6	–	2.1	2.8

Tetrafluoromethane (TFM) boils at –128°C, which causes the loss of the desired product during distillation. According to the calculations of the distillation column, the content of TFM should not exceed 0.5 vol %.

At fluorine concentrations lower than 30 vol % distillation of the reaction products becomes simpler, but the conversion of the initial material is relatively low. The following ways to increase conversion are used. (1) A certain fraction of the material to be fluorinated can be replaced by HFE, which does not participate in the reaction at a fluorine concentration <30 vol %, or by another inert compound. (2) Fluorination can be performed using several series-connected wave reactors with intermediate cooling of the reaction mixture. (3) The reaction mixture can be recycled, with recovery of the unchanged material from the products of the wave process and its addition to the initial reaction mixture.

To illustrate the first way, we studied the wave fluorination of 1,1-DFE to prepare trifluoroethanes (Table 2); HFE was used as inert diluent, which increases the conversion of the initial material. The initial 1,1-DFE (14 vol % concentration) contained 0.35% CHF_3 and 0.49% CF_3CH_3. The conversion of 1,1-DFE reached 80%, and the selectivity with respect to trifluoroethanes was 50%. However, at the concentration of fluorine >20 vol % the content of TFM became significant. This is probably due to the fact that at such fluorine concentrations HFE is not absolutely inert to fluorine under the wave synthesis conditions.

We studied preparation of HFE from 1,1,1,2-TFE using dilution with argon. The process parameters and the reaction product composition are given in Table 3. With excess fluorine, the dilution with argon provides almost complete conversion of the initial material, and the selectivity with respect to HFE reaches 97%. The degradation of fluoroethanes under such conditions is insignificant. It should be noted that the reaction was carried out at a temperature of the reaction wall of 200–250°C. At a temperature of the reaction wall of 10°C the gas flow blew off the thermal wave from the reactor.

A series of tests with a mixture containing 32 vol % PFE and 68 vol % 1,1,1,2-TFE was carried out to

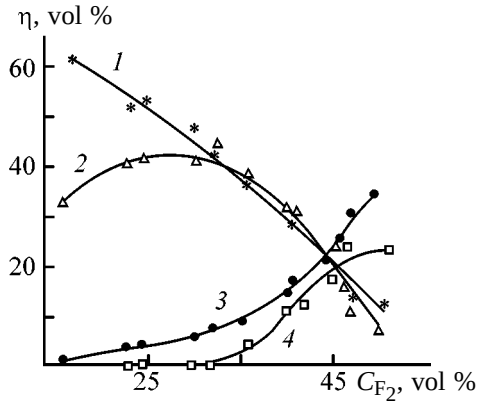

Fig. 2. Composition η of the fluorination products of the mixture of PFE (32 vol %) and 1,1,1,2-TFE (68 vol %) in the wave mode as influenced by the fluorine concentration C_{F_2}.

simulate two-step conversion of 1,1,1,2-TFE into pentafluoroethane. The results are shown in Fig. 2.

In the course of fluorination the content of PFE in the reaction products passes a maximum (43 vol %) corresponding to the fluorine concentration of 27 vol %. In this case the content of HFE is 6 vol %, and fluoromethanes are almost absent. The results given in Fig. 2 allow estimation of the ratio of the fluorination rate constants of 1,1,1,2-TFE and PFE. Assuming that fluorination of 1,1,1,2-TFE and PFE yields only PFE and HFE, respectively, we obtained that at a fluorine concentration of 25 vol % (1000 K adiabatic temperature in the reaction zone) the rate constant of 1,1,1,2-TFE fluorination is 1.5 times greater.

The activation energy of PFE fluorination of 53 kJ mol^{-1} was evaluated from the data given in Fig. 2; the activation energy of 1,1,1,2-TFE fluorination was taken as 50 kJ mol^{-1} [6].

The activation energy of high-temperature fluorination of 1,1-DFE of 44 kJ mol^{-1} was calculated from experimental data (Table 2 in [7]), also assuming that the activation energy of 1,1,1,2-TFE fluorination E = 50 kJ mol^{-1}. In the course of calculations we assumed that fluorination of 1,1-DFE yields 1,1,1-TFE, 1,1,2-TFE, 1,1,1,2-TFE, and 1,1,2,2-TFE, whereas in the case of 1,1,1,2-TFE only PFE and HFE are obtained.

Table 4. Simulated data on the composition of the inlet, outlet, and recycling gas flows in conversion of 1,1,1,2-TFE into HFE on a single-stage wave reactor with recycling of incompletely fluorinated products

Flow	Composition of the gas mixture, kg h^{-1}				
	$C_2H_2F_4$	C_2HF_5	C_2F_6	CF_4	HF
Inlet	11.91	3.59	31.88	0.14	0.40
Outlet	0.83	3.59	46.84	0.21	4.43
Recycling	0.83	3.59	31.88	0.14	0.36

Based on the experimental data on fluorination of 1,1,1,2-TFE, PFE, and their mixtures in the wave mode, the kinetic model of the process was constructed, which involves two main fluorination reactions: hydrogen substitution and cleavage of the C–C bond with formation of fluoromethanes. Based on published data on the bond energies in the corresponding molecules [9, 10], we determined the ratio of the activation energies of these reactions. The ratio of the rate constants was refined using experimental data. The composition of the reaction mixture at the inlet and outlet of the single-stage wave reactor with recycling of incompletely fluorinated products and HFE was simulated by the PC treatment of the system of the corresponding equations. The data on the composition of the inlet, outlet, and recycling reaction mixtures at fluorine concentration in the inlet flow of 25 vol % are listed in Table 4 for the reactor with a capacity of 100 tons per year.

This PC program was improved using the experimental data on fluorination of 1,1-DFE, and fluorination of 1,1-DFE to prepare PFE and HFE using two- and three-stage wave reactors at fluorine concentration of 23 vol % was simulated. The results are shown in Table 5. The intermediate incompletely fluorinated products are recycled. The flow compositions are given for the capacities with respect to PFE and HFE of 954 and 250 tons per year, respectively.

As seen from Table 5, in the case of three-stage wave reactor and recycling of incompletely fluorinated products the 1,1-DFE conversion reaches 90%.

CONCLUSIONS

(1) The gas-phase fluorination of fluoroethanes with fluorine in the mode of self-propagating thermal wave was studied.

(2) The principles for scaling of the wave gas-phase reactor were developed.

(3) In the wave mode the composition of the fluorination products of fluoroethanes is not noticeably influenced by the presence of hydrogen fluoride.

(4) Based on experimental and theoretical data, the ways to improve conversion of the initial raw material

Table 5. Simulated data on the composition of the inlet and outlet gas flows in conversion of 1,1,1,2-TFE into PFE and HFE on single-, two-, and three-stage wave reactors

Flow	Composition of the gas mixture, kg h^{-1}							
	CHF_2–CH_3	CHF_2–CH_2F	CF_3–CH_3	CHF_2CHF_2–CF_3CH_2F	C_2HF_5	C_2F_6	FM	HF
First stage inlet	90.0	11.5	7.6	300.1	–	–	–	–
First stage outlet, second stage intlet	48.6	26.3	10.6	303.3	38.9	2.7	–	27.5
Second stage outlet, third stage intlet	19.4	25.7	9.0	303.0	91.1	16.6	0.9	56.8
Third stage outlet	9.0	11.5	7.7	302.5	120.4	31.6	1.6	84.0

and selectivity with respect to the desired product are proposed, which involve dilution of the initial gas mixture with an inert compound, recycling of incompletely fluorinated products, and utilization of two- and three-stage wave reactors.

REFERENCES

1. *Promyshlennye ftororganicheskie produkty: Spravochnik* (Industrial Organofluorine Compounds: Handbook), Maksimov, Yu.N., Barabanov, V.G., Serushkin, I.L., *et al*., Eds., St. Petersburg: Khimiya, 1996.
2. Fukuhara, N. and Bigelow, L.A., *J. Am. Chem. Soc*., 1941, vol. 63, pp. 2792–2796.
3. Gilbert, A. and Bigelow, L.A., *J. Am. Chem. Soc*., 1950, vol. 72, pp. 4879–4882.
4. Robson, P., McLoughlin, V.C.R., Hynes, J.B., and Bigelow, L.A., *J. Am. Chem. Soc*., 1961, vol. 83, pp. 5010–5014.
5. Tyszkowski, E.A. and Bigelow, L.A., *J. Am. Chem. Soc*., 1955, vol. 77, pp. 3007–3012.
6. Pashkevich, D.S., Muhortov, D.A., Podpalkina, E.A., and Baranov, V.G., *J. Fluorine Chem*., 1999, no. 6, pp. 3–5.
7. Pashkevich, D.S., Alekseev, Yu.I., and Mukhortov, D.A., *Zh. Prikl. Khim*., 1999, vol. 72, no. 12, pp. 2000–2007.
8. Khitrin, L.N., *Fizika goreniya i vzryva* (Physics of Combustion and Explosion), Moscow: Mosk. Gos. Univ., 1957.
9. Millward, G.E. and Tschuikow-roux, E., *J. Phys. Chem*., 1972, vol. 76, no. 3, pp. 292–295.
10. Tschuikow-roux, E., *J. Phys. Chem*., 1971, vol. 75, no. 3, pp. 295–300.

Russian Journal of Applied Chemistry, Vol. 74, No. 7, 2001, pp. 1156–1163. Translated from Zhurnal Prikladnoi Khimii, Vol. 74, No. 7, 2001, pp. 1125–1132.

ORGANIC SYNTHESIS AND INDUSTRIAL ORGANIC CHEMISTRY

Alkylation of 5-Aminotetrazole with Dihalo-Substituted Compounds in Dimethylformamide

M. I. Barmin, S. A. Gromova, and V. V. Mel'nikov

St. Petersburg State University of Technology and Design, St. Petersburg, Russia

Received June 19, 2000; in final form, April 2001

Abstract—Possible pathways of alkylation of 5-aminotetrazole with dihalo-substituted compounds and the alkylation products were studied.

Tetrazoles are widely used in organic and coordination chemistry, medicine, biology, and agriculture [1–5]. At the same time, because of the lack of systematic data on alkylation of 5-aminotetrazole (5-AT) with dihalo derivatives, the pattern of its reactivity was incomplete. The enthalpy of formation, the thermal and chemical stability, the solubility in water and alkaline solutions, and the nitrogen content are higher in bis derivatives of 5-AT described previously [6]. In this context, we prepared bis(5-aminotetrazolyl) derivatives, studied their structure and properties, and examined the feasibility of using them as fungicides.

The selectivity of alkylation of 5-substituted tetrazoles is largely determined by the electronic structure of the substituent at the cyclic carbon atom. Electron-donor substituents at the 5-position of the tetrazolate ion favor alkylation at the N^1 atom, and electron-acceptor substituents, at the N^2 atom [2, 7]. The ratio of the alkylation products in an alkaline solution depends on the nature of the alkylating agent insignificantly [8]. However, with diazomethane (in ether) as alkylating agent, the N^2-alkylated product is formed irrespective of the nature of the 5-substituent [8]. The selective alkylation at N^2 in the reaction with diazomethane and the insensitivity to the electronic effect of 5-substituents may be due to the nonpolar transition state in this reaction. Alkylation of 5-substituted tetrazoles with *tert*-butyl, isopropyl, or cyclohexyl alcohol in a strongly acidic medium ensuring virtually total protonation of the tetrazole ring and excluding existence of tetrazoles in the anionic and neutral forms yields exclusively N^2-substituted tetrazoles [9], irrespective of the nature of the 5-substituent. Thus, the substituent effect is the most significant in reactions involving the tetrazolate anion.

Study of the influence of cation on the ratio of the reaction products in alkylation of 5-phenyltetrazole salts with dimethyl sulfate in acetonitrile showed [10] that at substrate concentrations of 10^{-5}–10^{-4} M, at which its dissociation is practically complete irrespective of the cation, the reactive species is the 5-phenyltetrazolate anion. The cation in these reactions, however, affects the ratio of the resulting isomeric tetrazoles. With decreasing cationic radius, the degree of cation coordination in the intermediate increases, and the fraction of the N^1-substituted isomer decreases. The high selectivity of alkylation of triethylammonium 5-aryltetrazolates with vinyl methyl ketone in aprotic dipolar solvents (only the N^2-substituted products are formed) is due to steric shielding of the N^1 atom of the tetrazole ring with the bulky triethylammonium cation [8, 10], which forms a hydrogen bond with the ring. The individual products were isolated from isomer mixtures by fractional crystallization [11–13], chromatography [14], and selective extraction [9, 15]. The reactions of 1,1'-bis(chloromethyl)-ferrocene with sodium tetrazolate, 5-methyltetrazolate, and 5-nitrotetrazolate in acetone or dimethylformamide (DMF) yielded the corresponding alkylation products, heteroannular bis(heterylmethyl) ferrocene derivatives [16]. Analysis of the isomeric composition of the products by ^{1}H NMR spectroscopy showed that with 5-methyltetrazole alkylation occurs at the N^1 positions of both rings, and with 5-nitrotetrazole, at the N^2 position. Alkylation of sodium tetrazolate gave two reaction products identified as 1,2'- and 2,2'-alkylated derivatives. The third possible isomer, 1,1'-alkylated product, was not isolated, probably because of its low yield. The melting point of the 1,2' isomer (101–103°C) is lower than that of the 2,2' isomer (107–108°C) [16].

Reaction of potassium 5-phenyltetrazolate with 1,2-dibromoethane gave 1-(5-phenyltetrazol-1-yl)-2-

1070-4272/01/7407-1156$25.00

(5-phenyltetrazol-2-yl)- and 1,2-bis(5-phenyltetrazol-2-yl)ethanes. Their structure was proved by ^{1}H NMR spectroscopy. The yields of the 1,2' and 2,2' isomers are 8 and 29%, respectively. 5-Aryl(heteryl)tetrazoles in the presence of excess K_2CO_3 at 130°C in DMF give the 1,2' and 2,2' bistetrazole derivatives [18], with the 2,2' isomer prevailing; the content of the 1,2' isomer increases in the presence of electron-donor substituents and decreases in the presence of electron-acceptor substituents at the 5-position of the tetrazole ring. The melting points of the 1,2' isomers are lower than those of the 2,2' isomers.

Different reactivity of the exocyclic amino group and hydrogen atom at N^1 in 5-AT is obvious. This fact, and also the occurrence of 5-AT in solution in the imino form [19–21] imparted abnormal properties to the monomeric units and ultimately led to chain termination in polycondensation and to formation of oligomers [22]. Therefore, our next task was preparation of monomers based on 5-AT in which two amino groups would exhibit similar reactivity. To this end, we performed alkylation of potassium 5-aminotetrazolate (K-5-AT) with dihalo-substituted compounds in DMF.

The choice of the potassium cation was governed by conclusions made in [23]. For comparison, we performed experiments also with sodium 5-aminotetrazolate. Under equal other conditions, the yield of the target product was lower than with K-5-AT by 25–30%. As reaction medium we also tested acetone. However, attempted synthesis of 1,1'-bis(5-aminotetrazolyl)methane in acetone failed. No target product was isolated after heating the reaction mixture for 32–36 h at 55–56°C. As alkylating agents we used dibromomethane, 1,2-dibromoethane, 1,3-dibromopropane, and 1,4-dibromobutane.

Let us consider the reactivity of these agents in nucleophilic substitutions. It is known that in S_N1 reactions 1,2-dibromoethane is more reactive than dibromomethane, whereas in S_N2 reactions dibromomethane is more reactive. Since in dialkylation the limiting stage is S_N2, dibromomethane will be more active. When considering the effect of methylene groups on the reactivity of the compounds, it should be taken into account that these groups exhibit a $+\gamma$ effect and will favor displacement of halogen from the molecule. In the series $F^- < Cl^- < Br^- < I^-$, the stability of the anion increases, and hence the R–Hlg bond will be cleaved more readily in the reaction with dibromomethane. When comparing the reactivities of such compounds as β,β'-dichlorodiethyl ether (Chlorex) and γ,γ'-dichlorodipropyl ether, it should be taken into account that the electronic effect of the ether group in the latter compound is weaker. Thus, all the alkylating agents can be ranked with respect to decreasing reactivity in the order indicated above. Thus, we predicted the conditions of 5-aminotetrazole alkylation.

According to the ^{1}H NMR spectra of reaction mixtures, alkylation of 5-AT with dibromoalkanes yields three isomers, irrespective of the nature of the solvent and counterion. The characteristics of the isolated alkylation products, previously unknown bis(aminotetrazolyl)alkane **I**–**IX**, are listed in Table 1. In alkylation of 5-AT salts with bis(chloroalkyl) ethers, two isomers were detected by ^{1}H NMR in the reaction mixtures, identified as 1,1' and 1,2' isomers. Pure isomeric bis(aminotetrazolyl)alkanes were isolated and characterized [3]. The influence of solvents and cations on the reaction selectivity was studied with alkylation of 5-AT by 1,2-dibromoethane as example. In the range δ 4.5–4.9 ppm in which the ^{1}H NMR signals of the NCH_2 protons are detected, neither the initial compounds nor the reaction by-products have signals, and all the three isomers give well-resolved signals with the difference in the chemical shifts of about 0.15 ppm. Thus, the isomer ration can be determined from the ratio of the integral intensities of these signals.

Monoalkylation of tetrazoles via tetrazolate anions usually involves two stages: deprotonation of the substrate and nucleophilic substitution [24, 25]. However, not always the solvent suitable for the first stage is appropriate for the second one, and vice versa. The following conditions should be met [24]: The base should deprotonate the substrate; the base and/or substrate should be sufficiently soluble in the solvent to ensure deprotonation; the substrate anion and/or electrophile should be sufficiently soluble in the solvent to ensure the reaction; the base should not decompose the substrate or solvent; the solvent should increase the nucleophilicity of the substrate anion.

It was shown [3] that, irrespective of the solvent and counterion, 5-AT anion in the reaction with 1,2-dibromoethane gives all the three isomeric products: 1,2-bis(5-aminotetrazol-1-yl)ethane (**I**), 1-(5-aminotetrazol-1-yl)-2-(5-aminotetrazol-2-yl)ethane (**II**), and 1,2-bis(5-aminotetrazol-2-yl)ethane (**III**). The isomer ratio depends on the reaction conditions. Ethanes **I**–**III** were isolated by selective extraction followed by fractional recrystallization (Table 1). In all cases the major product was the 1,2' isomer.

The ^{1}H NMR spectra of reaction products in the range of the chemical shifts of the methylene protons

Table 1. Characteristics of **I**–**XIII**

Compound no.	Yield, %	mp, °C	R_f	μ, D (MNDO)	^{1}H NMR spectrum, δ, ppm	Found, %			Formula	Calculated, %		
						C	H	N		C	H	N
I	70–75	210–212	0.08	3.85	4.51 s (4H, N^1CH_2), 6.75 br.s (4H, NH_2)	24.81, 24.74	4.53, 4.58	71.49, 71.62	$C_4H_8N_{10}$	24.49	4.08	71.43
II	76–78	220–222	0.14	3.12	4.60 t (2H, N^1CH_2), 4.79 t (2H, NCH_2), 6.04 br.s (2H, NH_2), 6.77 br.s (2H, NH_2)	24.30, 24.34	4.11, 4.18	71.57, 71.40	$C_4H_8N_{10}$	24.49	4.08	71.43
III	72–74	234–236	0.34	2.28	4.90 s (4H, N^2CH_2), 6.06 br.s (4H, NH_2)	25.34, 25.16	4.33, 4.50	71.17, 71.43	$C_4H_8N_{10}$	24.49	4.08	71.43
IV	21	220–221	0.10	5.55	2.22 m (2H, CH_2), 4.13 t (4H, N^1CH_2), 6.75 br.s (4H, NH_2)	29.02, 28.87	4.36, 4.44	66.21, 66.39	$C_5H_{10}N_{10}$	28.57	4.76	66.67
V	47	117–118	0.18	5.08	2.42 m (2H, CH_2), 4.47 t (4H, N^1CH_2), 6.05 br.s (4H, NH_2)	28.51, 28.58	4.77, 4.45	66.60, 66.75	$C_5H_{10}N_{10}$	28.57	4.76	66.67
VI	16	152–153	0.39	2.24	2.42 m (2H, CH_2), 4.47 t (4H, N^1CH_2), 6.05 br.s (4H, NH_2)	28.51, 28.58	4.26, 4.50	66.07, 66.25	$C_5H_{10}N_{10}$	28.57	4.76	66.67
VII	27	195–196	0.11	5.87	1.71 m (4H, CH_2), 4.11 t (4H, N^1CH_2), 6.65 br.s (4H, NH_2)	31.78, 31.95	5.23, 5.29	62.14, 62.30	$C_6H_{12}N_{10}$	32.14	5.36	62.50
VIII	42	108–109	0.21	4.39	1.74 m (2H, CH_2), 1.79 m (2H, CH_2), 4.13 t (2H, N^1CH_2), 4.40 t (2H, N^2CH_2), 5.93 br.s (2H, NH_2), 6.63 br.s (2H, NH_2)	32.02, 32.06	4.98, 5.27	62.51, 62.54	$C_6H_{12}N_{10}$	32.14	5.36	62.50
IX	15	147–148	0.45	2.25	1.83 m (4H, CH_2), 4.41 t (4H, N^1CH_2), 5.91 br.s (4H, NH_2)	32.18, 32.34	5.00, 5.17	62.45, 62.32	$C_6H_{12}N_{10}$	32.14	5.36	62.50
X	38	–	0.20	4.71	4.65 s (4H, N^1CH_2), 6.68 br.s (4H, NH_2)	–	–	–	$C_4H_8N_{10}O$	22.64	3.77	66.04
XI	10	–	0.52	3.66	4.72 s (2H, N^1CH_2), 4.88 s (2H, N^2CH_2), 6.08 br.s (2H, NH_2)	–	–	–	$C_4H_8N_{10}O$	22.64	3.77	66.04
XII	48	210–212	0.24	8.02	3.72 t (4H, CH_2), 4.23 t (4H, N^1CH_2), 6.59 br.s (4H, NH_2)	29.89, 29.92	5.63, 5.41	58.05, 58.16	$C_6H_{12}N_{10}O$	30.00	5.00	58.33
XIII	8	232–239	0.60	5.58	3.80 m (4H, CH_2), 4.40 m (4H, NCH_2), 5.98 br.s (2H, NH_2), 6.61 br.s (4H, NH_2)	–	–	–	$C_6H_{12}N_{10}O$	30.00	5.00	58.33

contain three groups of signals: a singlet at 4.51 ppm, two triplets centered at 4.60 and 4.79 ppm, and a singlet at 4.90 ppm, belonging to the NCH_2 protons in **I**–**III**. The signals were assigned taking into account the trend observed with alkylated tetrazole derivatives: The methylene signals of the N^2 isomers are shifted downfield relative to the N^1 isomers [16, 26–28]. Furthermore, the molecular structure can be judged from the signal shape: The unsymmetrical 1,2' isomer gives a multiplet of NCH_2 protons [17] which at a high resolution is resolved into two triplets, whereas the signals of the symmetrical 1,1' and 2,2' isomers are singlets [28, 29]. In reaction of K-5-AT with 1,2-dibromoethane, the ratio of the isomers 1,1', 1,2', and 2,2' is 1.5 : 2.5 : 1, and with the triethylammonium salt of 5-AT, 1 : 3 : 1. An additional factor in favor of the given assignment is the trend observed with the melting points (Table 1): It is known that the melting point of the 1,1' isomer is the highest, and that of the 1,2' isomer, the lowest [17].

To identify compounds **I**–**III**, we compared their dipole moments. In the series of monoalkylated 5-R-tetrazoles, 1,5-disubstituted products have higher dipole moments than the corresponding 2,5 derivatives [22, 24]. For tetrazoles **I**–**III**, no data on dipole moments is available. For comparison with the monosubstituted derivatives, we calculated by the MNDO method the dipole moments of **I**–**III** (Table 1). The dipole moments decrease in the order 1,1' > 1,2' > 2,2'. Our conclusions are indirectly confirmed by the R_f values (Table 1). The 2,2' isomer **III** has the highest R_f value in the system benzene–acetone (1 : 1), as it is the least polar and is most readily eluted with benzene, whereas R_f of the most polar 1,1' isomer **I** is the lowest. Reactions of the triethylammonium salt of 5-AT with 1,3-dibromopropane and 1,4-dibromobutane yield three isomers each, **IV**–**VI** and **VII**–**IX**, respectively; however, accurate determination of the isomer ratio was impossible because of the overlap of the proton signals of the isomers. Nevertheless, experiments on isolation of the products showed that in both cases, similar to the reaction with 1,2-dibromoethane, the 1,2' isomers [1-(5-aminotetrazol-1-yl)-3-(5-aminotetrazol-2-yl)propane (**V**) and [1-(5-aminotetrazol-1-yl)-4-(5-aminotetrazol-2-yl)butane (**VIII**), respectively] are the major products (Table 1).

The structures of the products were proved by IR and ^{1}H NMR spectroscopy, and also by correlation of the calculated dipole moments with the TLC data and by comparison of the melting points. Previous calculations of the normal vibrational modes and frequencies in tetrazole and its derivatives [30], and also recent data [4] allowed assignment of the vibrational frequencies of the tetrazole ring in the IR spectra of our compounds. To the stretching vibrations of the tetrazole ring in 5-AT belong the bands at 1605, 1460, 1445, and 1298 cm^{-1} [30]. As in the spectra of monosubstituted tetrazoles, in the IR spectra of **IV**–**IX** we can distinguish three groups of the ring stretching vibrations at 1600, 1470 and 1450, and 1265 cm^{-1}. An interesting feature is the low-frequency shift of the latter band, originating mainly from the C–N and N–N vibrations of the ring, as compared to 5-AT (1298 cm^{-1}), 1-methyltetrazole (1279 cm^{-1}), and 2-methyltetrazole (1352 cm^{-1}). Apparently, this band is the most sensitive to substituents in the ring. The stretching–bending vibrations of the ring lie at 1160–995 cm^{-1} (in the case of **IV**–**IX**, at 1000–1140 cm^{-1}). The out-of-plane bending vibrations of the ring lie below 700 cm^{-1}. In the range 3400–3200 cm^{-1}, there are two well-resolved medium-intensity and strong bands, assigned to the stretching vibrations of the amino group. In the ^{1}H NMR spectra of bistetrazoles **IV**–**IX**, the proton signals of similar groups (NCH_2, CH_2, NH_2) in the isomers differ by 0.05–0.1 ppm. Alkylation of K-5-AT with bis(chloromethyl) and β,β'-dichlorodiethyl ethers yielded 1,1' and 1,2' isomers **X**–**XIII**. From the reaction mixture we were able to isolate only the 1,1' isomer, 1,5-bis(5-aminotetrazol-1-yl)-3-oxapentane (**XII**) (Table 1). In the reaction with dichlorodimethyl ether, formation of two isomers was proved only by ^{1}H NMR spectroscopy and chromatography, as the reaction products undergo tarring in air at attempted isolation. In reactions of 5-AT with the dihalo derivatives, the major reaction products are the 1,2' isomers.

It is known that the thermodynamic stability of isomers can be evaluated by semiempirical quantum-chemical calculations. Since in these cases the structurally related molecules are compared, the errors inherent in calculation procedures are mutually compensated. The enthalpies of formation ΔH_f of **I**–**XIII** were calculated by the PM3 method (Table 2).

In the gas phase, for all the compounds, the 1,1' isomer is the most favorable, and the 2,2' isomer, the least stable. However, the products isolated from the reaction mixture show a different trend: In the reaction with dibromoalkanes the major product is the 1,2' isomer. Only in the reactions with dichloro ethers the isomer ratio is consistent with the ΔH_f values. In S_N2 reactions, of major importance are steric factors, namely, hindrance of formation of the transition state at increasing size of the nucleophile and substrate. Hence, along with thermodynamics there are

Table 2. Enthalpies of formation of bis(aminotetrazolyl) derivatives **I**–**XIII**

Compound	ΔH_f, kJ mol^{-1}, for indicated isomer		
	1,1'-	1,2'-	2,2'-
Bistetrazolylethanes **I**–**III**	717.5	728.8	736.6
Bistetrazolylpropanes **IV**–**VI**	695.3	704.1	715.7
Bistetrazolylbutanes **VII**–**IX**	683.1	684.9	688.8
Bistetrazolyl-2-oxapropanes **X**, **XI**	574.0	578.6	590.2
Bistetrazolyl-3-oxapentanes **XII**, **XIII**	553.2	560.1	567.9

some other factors affecting the isomer ratio. Since the reaction was performed in solution at initial reactant concentrations of about 1 M, and dissociation of tetrazole salts is complete at concentrations of about 10^{-3} M [8], actually the reacting species were ion pairs, and hence the alkylation site should depend on the counterion. It is known [29] that the MNDO method is unsuitable for systems with hydrogen bonds, and hence it cannot be used for calculating triethylammonium salt of 5-AT. Therefore, we used the AM1 semiempirical method [29]. To reduce the calculation time and improve the convergence of the molecular geometry of the triethylammonium salts, we preliminarily characterized by molecular mechanics [30] the 5-AT anion and structures **A**–**D**:

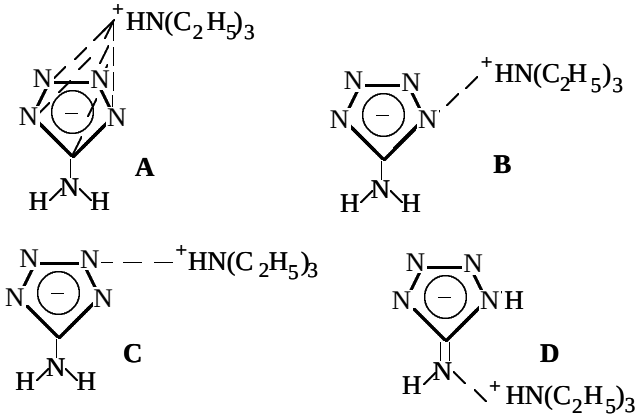

In such solvents as acetone or DMF, ammonium or triethylammonium ions form with organic anions H-bonded complexes [31]. For tetrazolate anions, various structures are possible. X-ray diffraction study of 5-AT monohydrate [32], 5-AT hydrazinate [33], and guanidinium salt of 5-AT [34] showed that hydrogen bonds can be formed not only through the ring hydrogen atom but also through those of the amino group. For triethylammonium tetrazolate, Bryden [34] concluded that the most energetically favorable is the planar structure with the hydrogen bond with the N^1 atom of the ring. For triethylammonium salt of 5-aminotetrazole were calculated the structures in which the cation was located over the ring plane and was hydrogen-bnded with the ring. In the first stage the steric hindrance in formation of the transition state is less important than the electron density distribution in the ring, and the reaction mainly goes at the N^1 position, which is characteristic of monoalkylation of 5-AT salts. In this case, with K-5-AT, the yield of the N^1 isomer should be higher than in alklylation of the triethylammonium salt in which, despite large difference in the charge densities between the N^1, N^4 and N^2, N^3 atoms (Table 3), the bulky triethylammonium cation prevents approach to the N^1 atom.

In going to the second stage, the steric hindrance in formation of the transition state of 5-AT salts with bromoalkanes containing a bulky heteryl substituent become decisive, and the reaction mainly occurs at the N^2 atom. The change in the attack direction in going from the first to the second stage explains predominant formation of the 1,2' isomer in alkylation with dibromoalkanes. In alkylation of K-5-AT with dichloro ethers, the isomer ratio is different, which is probably due to the fact that increase in the length of the alkyl chain (reaction with Chlorex) and introduction into the alkyl chain of the ether oxygen atom, which is less bulky than the CH_2 group, decrease the steric hindrance in the transition state, so that the 1,1' isomer becomes the major product. Based on these data, we can predict the behavior of 5-substituted tetrazoles in alkylations with dihaloalkanes. When the 5-position is occupied by an electron-withdrawing group, the 2,2' isomer is the major product, since the steric and electronic effects act in the same direction, favoring alkylation at N^2. When the 5-substituent is an electron donor, a mixture of all the three isomers (1,1', 2,2', and 3,3') can be obtained, with the isomer ratio varying depending on the reaction conditions. In alkylation with dibromoalkanes, the thermodynamically favorable 1,2' isomer is the major product.

The ^{1}H NMR spectra were taken on a Bruker WP-80 spectrometer (80 MHz) in DMSO-d_6, internal reference TMS. The IR spectra were taken on an IKS-29 spectrometer (KBr pellets). The reaction progress was monitored and the isomeric purity checked by TLC on Silufol UV-254 plates with UV development.

Bis(5-aminotetrazolyl)alkanes I–VI. (a) To a solution of 7.38 g (0.06 mol) of K-5-AT in 20 ml of DMF we added dropwise 4.7 g (0.025 mol) of 1,2-di-

Table 3. Atomic charges, dipole moments, and enthalpies of formation of triethylammonium salt of 5-AT

Structure	Charge on indicated atom, e							μ, D	ΔH_f^0, kJ mol^{-1}
	N^1	N^2	N^3	N^4	C^5	N^6	H_{ring}		
5-AT anion	–0.302	–0.183	–0.183	–0.302	0.02	–0.381			
A	–0.220	–0.178	–0.168	–0.208	–0.250	–0.268	0.293	12.76	466
B	–0.242	–0.045	–0.039	–0.160	0.049	–0.293	0.295	7.51	365
C	–0.208	–0.168	–0.178	–0.220	–0.249	–0.293	0.293	12.76	465
D	–0.245	–0.046	–0.039	–0.162	0.053	–0.300	0.294	7.53	375

bromoethane. The mixture was stirred at 118–120°C for 16 h. The reaction completion was determined by the Beilstein's test for bromine. Th KBr precipitate was filtered off, and the solvent was distilled off. Total yield of the crude reaction products 4.16 g (85%). The dry residue was treated with dioxane. From the dioxane solution, 0.38 g (9% of total yield) of 1,2-bis(5-aminotetrazol-2-yl)ethane (**III**) was isolated, mp 163–164°C (from benzene). After treatment of the residue with ethanol, 2.26 g (54% of total yield) of 1-(5-aminotetrazol-1-yl)-2-(5-aminotetrazol-2-yl)ethane (**II**) was isolated from the ethanol solution, mp 135–136°C. By crystallizatiuon of the residue from distilled water, 1.08 g (26% of total yield) of 1,2-bis(5-aminotetrazol-1-yl)ethane (**I**) was isolated, mp 226–227°C. IR spectrum, ν, cm^{-1}: 3410, 3340, 1630, 825 (NH_2), 1585, 1565, 1530, 1515, 1460, 1425, 1300, 1110, 1095, 1025, 1080, 1065, 1040 (ring), 2920, 1390, 1360 (CH_2).

(b) A solution of 4.7 g (0.025 mol) of 1,2-dibromoethane in 25 ml of acetone was added to a mixture of 6.18 g (0.06 mol) of 5-AT monohydrate and 6.06 g (0.06 mol) of triethylamine in 25 ml of acetone. On stirring with reflux for 1 h, the mixture became homogeneous. The stirring and refluxing were continued for an additional 2 h. After cooling, the mixture of **I**–**III** was filtered to remove triethylammonium bromide, and the solvent was evaporated. Total yield of the crude products 4.27 g (87%). The isomers were separated and purified similarly. Yields, g (% of total): **I**, 0.76 (18); **II**, 2.43 (57); **III**, 0.70 (16).

A solution of 5.05 g (0.025 mol) of 1,3-dibromopropane in 25 ml of acetone was added to a mixture of 6.18 g (0.06 mol) of 5-AT monohydrate and 6.06 g (0.06 mol) of triethylamine in 25 ml of acetone. On stirring with reflux for 1 h, the mixture became homogeneous. The stirring and refluxing were continued for an additional 2.5 h. After cooling, the mixture of **IV**–**VI** was filtered to remove triethylammonium bromide, and the solvent was evaporated. Total yield of the crude products 4.41 g (84%). The dry residue was treated with dioxane. From the dioxane solution, 0.71 g (16% of total yield) of 1,3-bis(5-aminotetrazol-2-yl)propane (**VI**) was isolated, mp 152–153°C (from benzene). After treatment of the residue with ethanol, 2.07 g (47% of total yield) of 1-(5-aminotetrazol-1-yl)-3-(5-aminotetrazol-2-yl)propane (**V**) was isolated from the ethanol solution, mp 117–118°C (from acetone). By crystallization of the residue from distilled water, 0.93 g (21% of total yield) of 1,3-bis(5-aminotetrazol-1-yl)propane (**IV**) was obtained, mp 220–221°C (from water). IR spectrum, ν, cm^{-1}: 3420, 3350, 1640, 835 (NH_2), 1595, 1575, 1540, 1525, 1450, 1415, 1290, 1100, 1085, 1015, 1070, 1055, 1030 (ring), 2910, 2870, 1380, 1350 (CH_2).

Bis(5-aminotetrazolyl)alkanes VII–IX. A solution of 5.4 g (0.035 ml) of 1,4-dibromobutane in 25 ml of acetone was added to a mixture of 6.18 g (0.06 mol) of 5-AT monohydrate and 6.06 g (0.06 mol) of triethylamine in 25 ml of acetone. On stirring with reflux for 2 h, the mixture became homogeneous. The stirring and refluxing were continued for an additional 3 h. After cooling, the mixture of **VII**–**IX** was filtered to remove triethylammonium bromide, and the solvent was evaporated. Total yield of the crude products 4.87 g (87%). The dry residue was treated with dioxane. From the dioxane solution, 0.73 g (15% of the total yield) of butane **IX** was isolated, mp 147–148°C (from benzene). After treatment of the residue with ethanol, 2.05 g (42% of the total yield) of butane **VIII** was isolated from the ethanol solution, mp 108–109°C (from acetone). By crystallization of the residue from distilled water, 1.31 g (27% of the total yield) of 1,4-bis(5-aminotetrazol-1-yl)butane (**VII**) was isolated, mp 195–196°C (from water). IR spectrum, ν, cm^{-1}: 3415, 3370, 1650, 810 (NH_2), 1600, 1580, 1555, 1540, 1485, 1470, 1460, 1280, 1110, 1090, 1070, 995 (ring), 2940, 2910, 1355 (CH_2).

Bis(5-aminotetrazolyl)alkanes X and XI. To a solution of 7.38 g (0.06 mol) of K-5-AT in 20 ml of

DMF we added dropwise 5.4 g of dichlorodimethyl ether (0.025 mol). The mixture was stirred at 110°C for 30 h. The reaction completion was determined from the Beilstein's test for bromine. The KCl precipitate was filtered off, the solvent was distilled off, and the residue was analyzed. Total yield of crude reaction products **X** and **XI** 2.3 g (44%). IR spectrum, ν, cm^{-1}: 3450, 3340, 1660 (NH_2), 1620, 1440, 1260, 1130 (ring), 1100 (C–O–C).

Bis(5-aminotetrazolyl)oxapentanes XII and XIII. Total yield of crude products 3.66 g (61%). After twofold crystallization from acetone, 3.18 g (87% of the total yield) of oxapentane **XII** was obtained, mp 210–212°C. IR spectrum, ν, cm^{-1}: 3420, 3330 (NH_2), 1605, 1500, 1545, 1470, 1440, 1290, 1160, 1120, 1045, 1005 (C–O–C), 995 (ring), 1270, 1380, 1360 (CH_2).

CONCLUSIONS

(1) The pathway of alkylation of 5-aminotetrazole with dihaloalkanes changes from the first to the second stage. The first stage predominantly yields the N^1 isomers, whereas in the second stage the steric hindrance to formation of the transition complex between the 5-aminotetrazole salt and bromoalkane becomes decisive, and the reaction occurs at the N^2 atom. As a result, the 1,2' isomer becomes the major alkylation product.

(2) The number of isomers increases with increasing electrophilicity of the radical in bis(aminotetrazolyl) derivatives. In alkylation, the number of isomers increases with increasing polarity of the aminoazole molecule.

(3) Alkylated 5-aminotetrazoles exhibit a high-frequency shift of the absorption bands of the tetrazole ring in the IR spectra; in the ^1H NMR spectra, the signals of the 1,1' isomer are shifted upfield relative to the 1,2' and 2,2' isomers.

REFERENCES

1. Koldobskii, G.I. and Ostrovskii, V.A., *Usp. Khim.*, 1994, vol. 63, no. 10, pp. 847–865.
2. Barmin, M.I., Gromova, S.A., Lebedintseva, O.V., *et al.*, *Zh. Prikl. Khim.*, 1995, vol. 68, no. 8, pp. 1333–1338.
3. Gromova, S.A., Alkylation of Aminoazoles with Dihaloalkanes, *Cand. Sci. Dissertation*, St. Petersburg, 1997.
4. Shchipanov, V.P., Tautomerism of 5-Aminotetrazole, *Cand. Sci. Dissertation*, Yekaterinburg, 1996.
5. Butler, R.N., *Comprehens. Heterocycl. Chem.*, 1984, vol. 5, no. 2, pp. 817–819.
6. Barmin, M.I., Shemyakin, A.I., and Mel'nikov, V.V., *Sintez i svoistva bis-(5-aminotetrazolil)alkanov* (Synthesis and Properties of Bis(5-aminotetrazolyl)alkanes), Available from ONIITEKhIM, Cherkassy, June 26, 1984, no. 1009-khp-84.
7. Poplavskii, V.S., Titova, I.E., Ostrovskii, V.A., *et al.*, *Zh. Org. Khim.*, 1989, vol. 25, no. 10, pp. 2182–2186.
8. Shirobokov, I.Yu., Ostrovskii, V.A., and Koldobskii, G.I., *Zh. Org. Khim.*, 1980, vol. 16, no. 4, pp. 788–792.
9. Shirobokov, I.Yu., Ostrovskii, V.A., and Koldobskii, G.I., *Zh. Org. Khim.*, 1979, vol. 45, no. 4, pp. 839–844.
10. Titova, I.E., Poplavskii, V.S., Ostrovskii, V.A., *et al.*, *Zh. Org. Khim.*, 1987, vol. 23, no. 10, pp. 1082–1085.
11. Raap, R. and Howard, J., *Can. J. Chem.*, 1969, vol. 47, no. 5, pp. 813–817.
12. Einberg, F., *J. Org. Chem.*, 1970, vol. 35, no. 11, pp. 3978–3984.
13. Hattori, K., Lieber, F., and Horwitz, J.P., *J. Am. Chem. Soc.*, 1956, vol. 78, no. 3, pp. 411–414.
14. Buzilova, S.R., Vrekhov, Yu.V., Afonin, A.V., *et al.*, *Zh. Org. Khim.*, 1989, vol. 25, no. 7, pp. 1524–1528.
15. Scott, F.L. and Tobin, J.C., *J. Chem. Soc. (C)*, 1971, vol. 52, no. 3, pp. 703–709.
16. Tverdokhlebov, V.P., Tselinskii, I.V., Vasil'eva, N.Yu., *et al.*, *Zh. Org. Khim.*, 1980, vol. 16, no. 1, pp. 218–222.
17. Schwartz, N.V., *Appl. Polym. Sci.*, 1972, vol. 16, no. 11, pp. 2715–2720.
18. Kitaeva, V.G., Beresnev, D.G., Ishmetova, R.I., *et al.*, *Zh. Org. Khim.*, 1995, vol. 31, no. 4, pp. 620–623.
19. Barmin, M.I., Shemyakin, A.I., Karaulova, I.B., *et al.*, *Issledovanie amino-iminnoi tautomerii 5-aminotetrazola IK i PMR spektroskopiei* (IR and ^1H NMR Study of Amine–Imine Tautomerism of 5-Aminotetrazole), Available from ONIITEKhIM, Cherkassy, March 22, 1985, no. 64-khp-85.
20. Barmin, M.I., Shemyakin, A.I., Karaulova, I.B., *et al.*, *Khim. Geterotsikl. Soedin.*, 1985, no. 12, pp. 1690–1691.
21. Barmin, M.I., Gromova, S.A., Kasatikova, E.L., *et al.*, *Zh. Org. Khim.*, 1992, vol. 28, no. 8, pp. 1767–1768.
22. Ostrovskii, V.A., Poplavskii, V.S., and Koldobskii, G.I., *Perspektivnye napravleniya khimii i khimicheskoi tekhnologii* (Promising Research Lines in Chemistry and Chemical Technology), Dudyrev, A.S., Ed., Leningrad: Khimiya, 1991, pp. 103–112.
23. Begtrup, M. and Larsen, P., *Acta Chem. Scand.*, 1990, vol. 44, no. 6, pp. 1050–1057.
24. Reichardt, Ch., *Lösungsmittel-Effekte in der organischen Chemie*, Weinheim: Chemie, 1969.

25. Schofield, K., Grimmett, M.R., and Keene, B.R.T., *Heteroaromatic Nitrogen Compounds: The Azoles*, Cambridge: Cambridge Univ. Press, 1976.
26. Scott, F.L. and Butler, R.N., *J. Chem. Soc. (B)*, 1967, vol. 6, no. 5, pp. 919–920.
27. Polya, J.B., *Comprehens. Heterocycl. Chem.*, 1984, vol. 5, no. 3, pp. 734–790.
28. Shpak, M.L., Ostrovskii, V.A., Shirobokov, I.Yu., *et al.*, *Zh. Org. Khim.*, 1978, vol. 14, no. 11, pp. 2444–2446.
29. Simkin, B.Ya. and Sheikhet, Ya.I., *Kvantovo-khimicheskaya i statisticheskaya teoriya rastvorov: Vychislitel'nye metody i ikh primenenie* (Quantum-Chemical and Statistical Solution Theory: Computational Procedures and Their Use), Moscow: Khimiya, 1989.
30. Burkert, U. and Allinger, N.L., *Molecular Mechanics*, Washington, DC: Am. Chem. Soc., 1982.
31. Bryden, J.H., *Acta Crystallogr.*, 1951, vol. 11, no. 1, pp. 32–37.
32. Paoloni, L., La Manna, G., and Gamilletti, F., *J. Mol. Struct.*, 1974, vol. 20, no. 1, pp. 135–139.
33. Bryden, J.H., *Acta Crystallogr.*, 1958, vol. 11, no. 1, pp. 31–37.
34. Bryden, J.H., *Acta Crystallogr.*, 1953, vol. 6, no. 4, pp. 669–670.

Russian Journal of Applied Chemistry, Vol. 74, No. 7, 2001, pp. 1164–1168. Translated from Zhurnal Prikladnoi Khimii, Vol. 74, No. 7, 2001, pp. 1132–1136.

ORGANIC SYNTHESIS AND INDUSTRIAL ORGANIC CHEMISTRY

Identification and Quantitative Determination of 5-(Hydroxymethyl)furfural in Sugar Color

I. G. Zenkevich, A. I. Pimenov, L. I. Sokolova, and V. G. Makarov

Adaptogen Interregional Center, Private Company, St. Petersburg, Russia

Received March 1, 2001

Abstract—The possibility was examined for quantitative determination of 5-(hydroxymethyl)furfural without reference samples by chromatographic analysis with several internal references whose molar extinction coefficients are known.

Sugar color (SC, E150a) is a concentrated aqueous solution of saccharose caramelized at 160–180°C. It is widely used in food industry as coloring agent for confectioneries and numerous drinks. Therefore, it is necessary to develop efficient procedures for both standardization of sugar color and its determination in various samples [1–3]. Among substances formed by caramelization of carbohydrates, the volatile components have been studied most comprehensively; they can be identified by gas chromatography and GC–MS. The volatile components include numerous compounds belonging to the main "sequence" of hexose dehydration, $C_6H_{12}O_6 \rightarrow C_6H_{10}O_5 \rightarrow C_6H_8O_4 \rightarrow C_6H_6O_3$, and also partially reduced compounds such as $C_6H_8O_3$, $C_6H_8O_2$, and some other products, in particular, and derivatives of furan [furfural, 5-(hydroxymethyl)furfural, 2-acetylfuran, 2-acetyl-3-hydroxyfuran (isomaltol), substituted 3-hydroxy-2-(5*H*)- and 4-hydroxy-3(2*H*)-furanones], 4-pyrone (maltol), etc. Among diverse carbohydrate oligocondensation products, SC presumably contains caramelan ($C_{24}H_{36}O_{18}$), caramelene ($C_{36}H_{50}O_{25}$), and still more complex compounds (caramelin). Maltol exhibits a bactericidal effect and is used as a special additive (E636) to enhance the taste and odor of foodstuffs [2]. Also, aldehydes of the furan series present in SC impart to it certain antioxidant effect.

The diversity of components of different chemical nature and the variability of SC composition complicate its standardization and determination in various objects. One of ways to solve the problem is to choose a specific compound among the main products of thermal degradation of hexoses [4] whose chromatographic parameters would be sufficiently specific for its separation from concomitant components by gas and reversed-phase high-performance liquid (HPLC) chromatography. In the latter case, the presence of a chromophore for UV detection is necessary. As such component in HPLC analysis we can suggest 5-(hydroxymethyl)furfural. This work is devoted to identification of this compound by HPLC and to evaluation of its content in commercial SC samples without using reference samples of this product.

EXPERIMENTAL

Commercial SC samples (Meligen Private Company, Leningrad oblast) were prepared by thermal treatment of saccharose at 160–180°C for 4 h, followed by addition of 50 wt % water.

Analysis by reversed-phase HPLC was performed with a Beckman System Gold chromatograph [UV detector, Gold V-402 software, Luna C_{18} column (150 × 4.6 mm, sorbent particle size 5 μm), 20 × 4.6-mm precolumn packed with the same sorbent]. Elution was performed in a step mode with a mixture of acetonitrile (Kriokhrom Scientific and Production Complex, St. Petersburg) with 0.05% aqueous trifluoroacetic acid (pH ~2.0). Isocratic elution (5% acetonitrile, 5 min) was followed by gradient elution with the acetonitrile content varied from 5 to 100% over a period of 95 or 40 min. Detection was performed at 220, 229, 254, 284, and 320 nm. Prior to analysis, SC samples were dissolved in water (1 : 100 ratio); the dosage was 10 μl. To determine the retention indices (RIs), we measured in parallel the retention times of reference alkyl phenyl ketones $C_6H_5COC_nH_{2n+1}$ (n = 1–3). The RIs of the compounds eluted before the first reference component (acetophenone) were determined by extrapolation in the scale of the retention times squared [5].

1070-4272/01/7407-1164$25.00

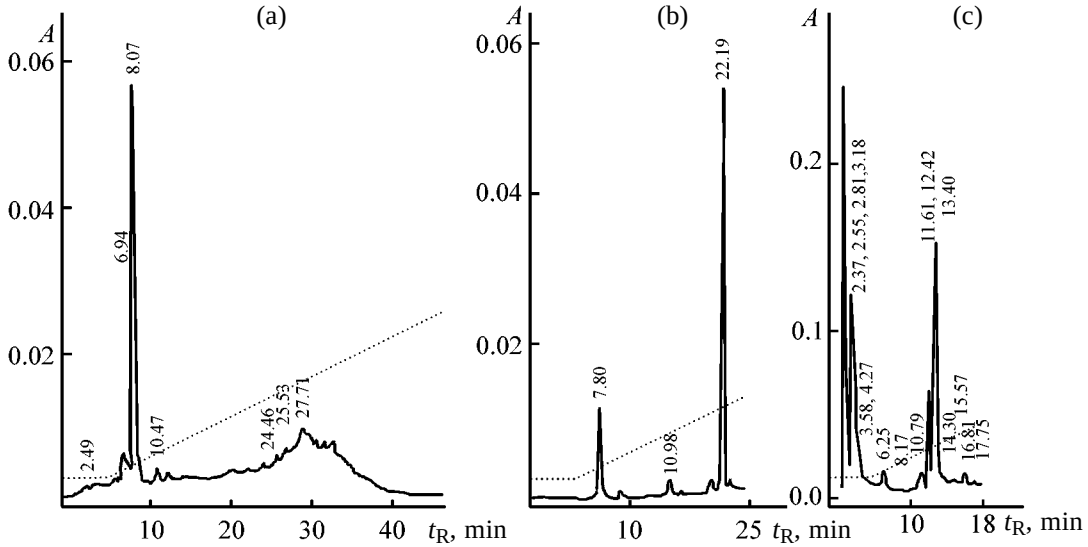

Fig. 1. Chromatograms of sugar color: (a) initial aqueous solution, (b) after acetylation, and (c) after treatment with hydroxylamine. HPLC analysis UV detection at 254 nm. (*A*) Optical density and (t_R) retention time.

To prepare acetyl derivatives, 0.5 ml of SC was treated with 0.5 ml of acetic anhydride containing catalytic amounts of sulfuric acid, and an additional 0.5 ml of the anhydride was added 1 min after the mixture warmed up. To prepare oximes, to a solution of 0.5 ml of SC in 2 ml of 50% ethanol we added 0.5 g of hydroxylamine hydrochloride and 0.3 g of NaOH and stirred the mixture for 3 min. Both samples before chromatographing were dissolved in 50% ethanol (1 : 100 ratio). For quantitative determinations, samples of SC and internal references (10–25 mg) were dissolved in 50 ml of water or 80% ethanol, depending on their hydrophobicity.

Statistical treatment of the data was performed using the software for a CASIO PB 10 programmable calculator; the hydrophobicity parameters of organic compounds ($\log P$) were estimated with ACD software.

A typical total chromatogram of SC (HPLC, detection wavelength 254 nm) is shown in Fig. 1. Under the chosen conditions of gradient elution, only a single predominant signal of an individual component (retention time 8.0 ± 0.2 min, RI 619 ± 3) is detected. The remaining compounds absorbing in the near-UV range are eluted as a broad band of unresolved peaks with the retention times in the range 20–35 min; the available columns do not ensure their separation. Specifically this group of peaks is mainly responsible for the interfering effect of SC in analysis of SC-containing samples. The only detected individual chromatographic peak is thus the most characteristic manifestation of SC. Therefore, we can formulate the goal of this work as identification and quantitative determination of the corresponding component. As already noted, both problems can be solved without using reference samples.

Identification of substances by HPLC is based on the use of chromatographic retention parameters, UV data, and derivatization reactions. The principal element of the logical scheme is transforming the problem from exploring analysis (identification of an unknown compound without any additional available data) to confirming determinations (the nature of the analytes is assumed *a priori*). In our case, the hypothesis to be verified is the structure of 5-(hydroxymethyl)furfural, the expected main product of thermal degradation of hexoses [4]. To confirm this assumption unambiguously, it is necessary to prove the presence of two functional groups (CH_2OH and CHO) and to determine the chromophore type.

One of the simplest ways of derivatization of compounds containing active hydrogen, including that in aliphatic hydroxy groups, is preparation of their acyl (in particular, acetyl) derivatives [6, 7]:

$$X\text{–}OH + Ac_2O \rightarrow X\text{–}OAc + AcOH.$$

The general chromatographic (including HPLC) feature of monoacetyl derivatives is the difference between the RIs of the reaction products and initial substances, amounting to 126 ± 16 according to [7] (provided that the molecule contains no intramolecular hydrogen bonds). Treatment of an SC sample with excess acetic anhydride yields a single reaction product

with the retention time of about 22 min and RI 717 ± 3 (Fig. 1b); the RI difference, $(717 \pm 3) - (619 \pm 3) = 98 \pm 5$, is close to the above-indicated range. This unambiguous result makes it unnecessary to use more complex derivatization procedures (e.g., treatment with a mixture of two reagents to determine the number of functional groups [8]).

The structure of the detected reaction product can be additionally confirmed by independent evaluation of the RI of the acetyl derivative of 5-(hydroxymethyl)furfural using a well-known correlation between the retention indices of organic compounds in HPLC and their hydrophobicity parameters, namely, logarithms of the distribution factors in the system 1-octanol–water $\log P$ [9]. To the retention index of 5-(hydroxymethyl)furfural (RI 619 ± 3) corresponds the calculated value of $\log P$ of -0.45 ± 0.35; as a second component we can choose acetophenone [$\log P$ 1.73 (experimental value); RI 800 (by definition)]. For the acetate, the calculated value of $\log P$ is 0.44 ± 0.36; linear interpolation gives the expected value of RI of 693 ± 31, which agrees with the experimental value of 717 ± 3.

To confirm the presence of the formyl group, we can use oximation:

$$\text{Y–CHO} + \text{NH}_2\text{OH}\cdot\text{HCl} + \text{NaOH} \rightarrow \text{Y–CH=NOH} + 2\text{H}_2\text{O} + \text{NaCl}.$$

The chromatogram of the reaction mixture after treatment of an SC sample with hydroxylamine contains two product peaks with the intensity ratio of 1 : 2.2 (irrespective of the detection wavelength), belonging to the *syn* and *anti* isomers of 5-(hydroxymethyl)furfural oxime (Fig. 1c); their retention times are 11.6 and 12.4 min, and retention indices, 648 ± 2 and 653 ± 2, respectively. Thus, the qualitative reactions with HPLC monitoring of the reaction mixtures confirm the presence of the expected functional groups.

The simplest way to confirm the type of the chromophore in a molecule under conditions of HPLC analysis is comparison of the experimental relative optical densities $A_{rel} = A(\lambda_1)/A(\lambda_2)$ with reference data [10]. However, total tabulated UV spectra [11] are not available for 5-(hydroxymethyl)furfural, and the molar extinction coefficients are only given for the peak maxima ($\lambda_1 = 229 \pm 1$ nm, $\log \varepsilon_1 = 3.46 \pm 0.12$; $\lambda_2 = 284 \pm 1$ nm, $\log \varepsilon_2 = 4.22 \pm 0.01$). This means that for identification of the chromophore it is necessary to compare the areas of the chromatographic peaks, measured specifically at these detection wavelengths, since $A_{rel} = S_1/S_2$. The experimental value of $A_{rel}(284/229)$ for different SC samples is 5.9 ± 1.9, which is consistent with the ratio of the molar extinction coefficients, $10^{4.22-3.46} = 5.6 \pm 0.5$. This ratio is also close to the relative optical density for unsubstituted furfural [$\lambda_1 = 229 \pm 1$ nm, $\log \varepsilon_1 = 3.51 \pm 0.11$; $\lambda_2 = 277 \pm 1$ nm, $\log \varepsilon_2 = 4.14 \pm 0.05$; $A_{rel}(227/229) = 4.3 \pm 0.3$], which also proves the nature of the chromophore in the molecule. In addition to the quantity $A_{rel}(284/229)$, we determined for 5-(hydroxymethyl)-furfural two similar quantities, $A_{rel}(254/220) = 0.43$ and $A_{rel}(320/254) = 2.2$, which, if necessary, can also be used for identification of this compound.

The main methods for quantitative chromatographic analysis (absolute calibration, external and internal references, standard addition) imply the availability of reference samples of a compound to be determined. However, if such samples are lacking, this does not mean that quantitative determination is impossible. Furthermore, development of new analytical procedures without using reference samples is one of the most urgent problems of modern organic analytical chemistry [13, 14].

The problems with quantitative determinations in such a case are the greatest specifically in HPLC analysis, since the relative sensitivity coefficients of UV detectors to different compounds, depending on the chromophore type, can vary within several orders of magnitude. However, in this case it is possible to use as internal references any available compounds with known quantitative characteristics of the UV spectra [13, 14]. The weight m or concentration a of an analyte in the sample is given by

$$m_X(c_X) = m_{ref}(c_{ref})[(M_X/M_{ref})(\varepsilon_{ref}/\varepsilon_X)](S_X/S_{ref}), \quad (1)$$

where the subscripts X and ref refer to parameters of the compound to be determined and chosen reference, M is the molecular weight, ε is the molar extinction coefficient, and S is the chromatographic peak area; the absolute values of ε and S depend on the chosen detection wavelength.

The expression in brackets is the coefficient of relative sensitivity of a UV detector to the compound being determined relative to the chosen internal reference:

$$f(\text{X/ref}) = (M_X/M_{ref})(\varepsilon_{ref}/\varepsilon_X). \quad (2)$$

In our case, among the simplest available substances we chose four compounds with the known molar extinction coefficients at 229 and 284 nm [11].

Initial analytical data and results of evaluating the content of 5-(hydroxymethyl)furfural (**I**) (M = 126) in an SC sample without a reference sample of the compound to be determined

Internal reference	c_{SC}, mg ml^{-1}	λ, nm	M_{ref}	c_{ref}, mg ml^{-1}	$\varepsilon_{ref} \times 10^{-3}$	$\varepsilon_X \times 10^{-3}$	f(X/ref)	S_X (arb. units)	S_{ref} (arb. units)	c_X, mg ml^{-1}	Concentration of **I** in SC sample, wt %*
Nitrobenzene	10.04	284	123	0.46	5.43	16.6	0.34	50.8	157.3	0.050	0.50
Acetol	10.04	229	148	0.35	7.69	2.88	2.3	13.8	59.6	0.051	0.51
Benzoic acid	10.98	284	122	0.28	0.479	16.6	0.030	132.7	32.1	0.034	0.31
	5.27	284	122	0.24	0.479	16.6	0.030	70.7	23.2	0.022	0.42
Coumarin	5.27	284	146	0.20	8.02	16.6	0.42	70.7	209.7	0.028	0.53

* Average 0.45 ± 0.09.

According to [14], the set of such internal references can be arbitrary:

Compound (in the order of chromatographic elution)	$\varepsilon(229) \times 10^{-3}$	$\varepsilon(284) \times 10^{-3}$
5-(Hydroxymethyl)furfural (compound to be determined)	2.88	16.6
Benzoic acid	14.6	0.479
Coumarin	32.0	8.02
Nitrobenzene	2.26	5.43
Acetol	7.69	6.38

In the table are given the initial experimental data and the results of quantitative determination of 5-(hydroxymethyl)furfural in one of typical commercial SC samples, using all the four above-named substances as internal references. The mean weight fraction of 5-(hydroxymethyl)furfural is 0.45 ± 0.9 (variation coefficient 20%). Since the published values of ε used as reference data were measured under conditions differing from those of HPLC analysis (for solutions in ethanol; for nitrobenzene, in aqueous solution), the reproducibility of the results may be different depending on the particular reference and detection wavelength. Indeed, the scatter of the c_X values determined at 229 nm (0.44 ± 0.28) considerably exceeds the scatter at 284 nm (0.45 ± 0.09). However, the mean concentrations themselves coincide, which confirms the reliability of our approach. Along with difference between the conditions of UV measurements in reference literature and UV detection in HPLC, another significant source of the random error, as noted in [14], is the error of peak integration. Nevertheless, the content of 5-(hydroxymethyl)furfural (see table) was determined with the relative standard deviation as low as 20%, which does not exceed variations in its concentration in different SC samples due to specific features of the production process.

In SC prepared by the other (not used in Russia) procedures, including sulfite (E150b), ammonia (E150c), and ammonia–sulfite (E150d) procedures [2], the content of 5-(hydroxymethyl)furfural should be lower owing both to a different major pathway of carbohydrate degradation in basic media [4] and to reaction of aldehydes with sulfites [15]:

$$Y\text{–}CHO + HSO_3^- \rightarrow YCH(OH)SO_2O^-.$$

The resulting hydrosulfite derivatives are considerably more hydrophilic and exhibit different UV characteristics.

CONCLUSIONS

(1) 5-(Hydroxymethyl)furfural is one of the most characteristic components of sugar color (E150a food additive) in analysis of samples containing sugar color by reversed-phase HPLC.

(2) A combination of chemical derivatization procedures with UV examination was suggested for identification of this compound, and a version of the internal reference method using several reference compounds with known molar extinction coefficients at different wavelengths was suggested for its quantitative determination for the case when the reference sample is not available.

REFERENCES

1. Buldakov, A.S., *Pishchevye dobavki: Spravochnik* (Food Additives: Handbook), St. Petersburg, 1996.
2. *SanPiN* (Sanitation Rules and Regulations) *2.3.2.560–96: Hygienic Requirements to the Quality and Safety of Raw Materials for Food Industry and Foodstuffs. 2.3.2. Raw Materials for Food Industry and Foodstuffs*, Moscow: Goskomsanepidnadzor Rossii, 1997.
3. *Eliksiry* (Elixirs), Makarov, V.G., Ed., St. Petersburg:

Mezhregional'nyi Tsentr "Adaptogen," 1999.

4. Stepanenko, B.N., *Khimiya i biokhimiya uglevodov* (Chemistry and Biochemistry of Carbohydrates), Moscow: Vysshaya Shkola, 1977.
5. Zenkevich, I.G., *Zh. Prikl. Khim.*, 1995, vol. 68, no. 8, pp. 1321–1327.
6. *Encyclopedia of Chromatography*, Cazes, J., Ed., New York: Marcel Dekker, 2001, vol. 1, pp. 228–231, 237–240.
7. Zenkevich, I.G. and Kosman, V.M., *Zh. Fiz. Khim.*, 1997, vol. 71, no. 7, pp. 1293–1297.
8. Zenkevich, I.G., *Fresenius' J. Anal. Chem.*, 1999, vol. 365, no. 4, pp. 305–309.
9. *J. Chromatogr. Library*, vol. 57: *Retention and Selectivity in Liquid Chromatography*, Smith, R.M., Ed., Amsterdam: Elsevier, 1995.
10. Zenkevich, I.G. and Kosman, V.M., *Zh. Prikl. Khim.*, 1997, vol. 70, no. 11, pp. 1861–1869.
11. Lang, L., *Absorption Spectra in the UV and Visible Region*, Budapest: Akad. Kiado, 1966, vols. 1–24.
12. *Organic Electronic Spectral Data*, Kamlet, M.J., Ed., New York: Interscience, 1956, vols. 1, 2.
13. Zenkevich, I.G. and Kosman, V.M., Abstracts of Papers, *Vserossiiskaya konferentsiya "Khimicheskii analiz veshchestv i materialov"* (Russian Conf. "Chemical Analysis of Substances and Materials"), Moscow, April 25–28, 2000, pp. 283–284.
14. Zenkevich, I.G. and Kosman, V.M., *Zh. Anal. Khim.*, 2001, vol. 56, no. 3, pp. 298–307.
15. Becker, H., Berge, W., Domschke, G., *et al.*, *Organikum. Organisch-chemisches Grundpraktikum*, Berlin: Wissenschaften, 1976.

Russian Journal of Applied Chemistry, Vol. 74, No. 7, 2001, pp. 1169–1172. Translated from Zhurnal Prikladnoi Khimii, Vol. 74, No. 7, 2001, pp. 1137–1141.

ORGANIC SYNTHESIS AND INDUSTRIAL ORGANIC CHEMISTRY

Thermal Transformations of Polymetallosiloxanes Prepared by the Sol–Gel Procedure

V. A. Sviderskii, M. G. Voronkov, S. V. Klimenko, and V. S. Klimenko

Kiev Polytechnic Institute, National Technical University of Ukraine, Kiev, Ukraine
Institute of Organic Chemistry, Siberian Division, Russian Academy of Sciences, Irkutsk, Russia

Received October 30, 2000; in final form, April 2001

Abstract—Thermal stability and crystal structure transformations of polyalkoxymetallosiloxanes (metallosilicas) prepared by the sol–gel procedure involving hydrolytic polycondensation of tetraethoxysilane with salts and oxides of Group I, II, and IV metals (Cu, Zn, Hg, Sn, and Pb) were studied.

Incorporation of metal atoms (M) into polysiloxane structure to form Si–O–M–O–Si groups strongly affects thermal and hydrolytic stability, adhesion, and cohesion of the initial silicon polymers and imparts to them biological activity and some other important properties [1–3]. This is due to changes in the steric and stereoelectronic structure of their crystal lattice and changes in the nature of the intramolecular interactions. The strength of the Si–O–M fragments appreciably depends on the nature of the heteroatom M and its ability to form M ← O coordination bonds [1].

Although the structure and properties of heterosiloxanes are extensively studied, precise prediction of their thermal and chemical transformations is difficult and requires special investigation. This is, in particular, due to the fact that the structure and properties of polymetallosiloxanes depend on the preparation procedure and can strongly differ even at almost identical composition [1, 4].

Taking into account theoretical and practical importance of this problem, we studied thermal transformations of polymetallosiloxanes prepared previously by the sol–gel procedure [5].

EXPERIMENTAL

Heterosiloxanes (polyalkoxymetallosiloxanes or metallosilicas) were prepared by hydrolytic polycondensation of partially hydrolyzed tetraethoxysilane (Etilsilikat-40) with Group I, II, and IV metal compounds in the presence of NH_4OH as a catalyst. The products were dried at 120 ± 0.5°C to the xerogel state.

The initial metal compounds were CuO, $CuSO_4 \cdot 5H_2O$, $CuCl_2 \cdot 2H_2O$, $Cu(OH)_2$, $Cu(NO_3)_2 \cdot 3H_2O$, $Hg_2(NO_3)_2 \cdot 2H_2O$, $Hg(NO_3)_2 \cdot 0.5H_2O$, Pb_3O_4, $Pb(OCOCH_3)_2 \cdot 3H_2O$, $SnCl_2 \cdot 2H_2O$, $Zn(NO_3)_2 \cdot 6H_2O$, and finely dispersed zinc powder.

We studied thermal transformations of the metallosiloxanes during programmed heating in air with a 10 deg min^{-1} rate (MOM derivatograph, Hungary). The structural transformations were studied by powder X-ray diffraction (DRON-3 diffractometer).

Incorporation of metal atoms into the siloxane lattice appreciably enhances the thermal stability of silica xerogels. The DTA curves of ethoxylated xerogel contain a weak exothermic peak at 265°C, whereas several exothermic effects are observed at higher temperatures in the DTA curves of the tested metallosiloxanes (Table 1). This is likely due to shielding of the residual ethoxy groups by the Si–O–M–O–Si fragments and indicates higher thermooxidative stability of the heterosiloxanes.

The exothermic peaks in the DTA curves of the metallosilica xerogels containing copper, zinc, and mercury(II) heteroatoms are usually broad (diffuse) with the main maxima at 700°C. These peaks are probably due to several parallel and consecutive processes.

(1) Thermal degradation of residual ethoxy groups shielded by the Si–O–Si and Si–O–M bonds. This is confirmed by the weight loss at 200 – 600°C (Table 2).

(2) Formation of additional Si–O–M–O–Si groups in this temperature range by the following condensation:

$$\equiv SiOEt + XM- \rightarrow \equiv Si-O-M + EtX,$$

$$\equiv SiOH + XM- \rightarrow \equiv Si-O-M + HX,$$

1070-4272/01/7407-1169$25.00

Table 1. Thermal analysis of metallosilica xerogels

Initial metal compound	T_{max},* °C
CuO	300 w, 720 s
$CuSO_4$	260 w, 730 s
$CuCl_2$	285 w, 750 s
$Cu(OH)_2$	390 s, 490 w, 790 s
$Cu(NO_3)_2$	280 w, 355 w, 710 s
$Hg_2(NO_3)_2$	260 w, 400 s
$Hg(NO_3)_2$	445 w, 735 s
Pb_3O_4	300 w, 420 w, 560 w, 620 w
$Pb(OCOCH_3)_2$	250 w, 350 w, 510 w
$SnCl_2$	240 w, 400 s
$Zn(NO_3)_2$	350 w, 530 w, 740 w
Zn (powder)	300 w, 405 w
Silica xerogel	265 w

* Temperature of a maximum of exothermic peaks on the DTA curves; peaks: (w) weak and (s) strong.

Table 2. Thermogravimetric analysis of metallosilica xerogels

Initial metal compound	Weight loss, wt %, at indicated temperature, °C		
	20–200	200–600	600–1000
CuO	4.00	0.66	+1.67*
$CuSO_4$	7.24	4.13	1.38
$CuCl_2$	12.34	5.14	1.03
$Cu(OH)_2$	3.76	7.52	1.03
$Cu(NO_3)_2$	5.34	5.34	1.00
$Hg_2(NO_3)_2$	5.34	5.67	1.00
$Hg(NO_3)_2$	2.04	14.29	4.08
Pb_3O_4	12.09	4.03	3.02
$Pb(OCOCH_3)_2$	3.34	2.67	0.33
$SnCl_2$	3.43	3.43	0.69
$Zn(NO_3)_2$	8.36	4.70	1.57
Zn (powder)	7.69	4.10	+2.05*
Silica xerogel	3.64	3.15	1.45

* Weight gain.

where M is the bivalent metal; X is the acid anion or OH^-.

(3) Crystallization of the resulting metallosilicas, confirmed by X-ray diffraction (Figs. 1a–1j).

(4) Structural transformations at elevated temperatures [6] of amorphous silica prepared by the sol–gel procedure, increasing the porosity of the metallosilica structure (swelling); this, in turn, affects the heat capacity of the samples.

The exothermic effects in the DTA curves of metallosilica xerogels prepared from $CuSO_4$, $Hg_2(NO_3)_2$, $PbOCOCH_3$, and $SnCl_2$ are observed at lower temperatures as compared to the silica xerogel. This can be due to catalysis of thermal degradation of ethoxy groups by the heteroatoms. It is also possible that the resulting highly dispersed polymetallosiloxanes are compositions of macromolecular structures with various condensation degree (exothermic peaks at 300°C and higher temperatures) and low-molecular-weight powders with weak intermolecular interactions (exothermic peaks at temperatures lower than 300°C).

The metals are incorporated into the siloxane structure not only by hydrolytic polycondensation to form endo- and exoskeleton heterosiloxane structures but also by parallel sorption of the initial metal compounds on the resulting highly porous silica and metallosilica matrices. This is confirmed by the fact that the X-ray patterns of the majority of thoroughly washed metallosilica xerogels dried at 120 ± 0.5°C contain sharp and strong reflections superimposing on the diffuse "halo" and coinciding with those of the initial metal compounds.

The presence of these reflections indicates sorption of the initial compounds on the surface of silica and metallosilica matrices. The sorption layer should be thicker than 10 nm, since reflections from thinner layers are blurred and cannot be observed against the background. This is the case, for example, for the metallosilicas prepared from $Cu(NO_3)_2$, $CuCl_2$, $CuSO_4$, $Zn(NO_3)_2$, and $Pb(OCOCH_3)_2$.

As seen from Fig. 1, the X-ray diffraction patterns of the majority of the metallosilicas heated to 900°C with a rate of 10 deg min^{-1} contains sharp and strong refections assigned to metal oxides formed probably by the following reaction:

$$\equiv Si–O–M–O–Si\equiv \rightarrow \equiv Si–O–Si\equiv + MO.$$

The X-ray diffraction patterns of the metallosilicas contain reflections of CuO (*d* 0.254, 0.233, 0.187, 0.171, and 0.158 nm). Along with copper oxide, traces of unidentified phase were also detected (*d* 0.276, 0.198, 0.196 nm). The X-ray diffraction patterns of metallosilicas prepared form zinc powder and zinc nitrate contain sharp strong reflections of β-cristobalite [7] (*d* 0.405, 0.283, 0.251, 0.248, 0.213, 0.203, and 0.191 nm) formed by crystallization of amorphous silica. Zinc oxide (*d* 0.247, 0.191, and 0.162 nm) and appreciable amounts of willemite Zn_2SiO_4 (*d* 0.350, 0.263, 0.261, 0.232, 0.203 nm) formed by reaction of ZnO with SiO_2 were also detected.

The weight gain of polymetallosiloxanes prepared

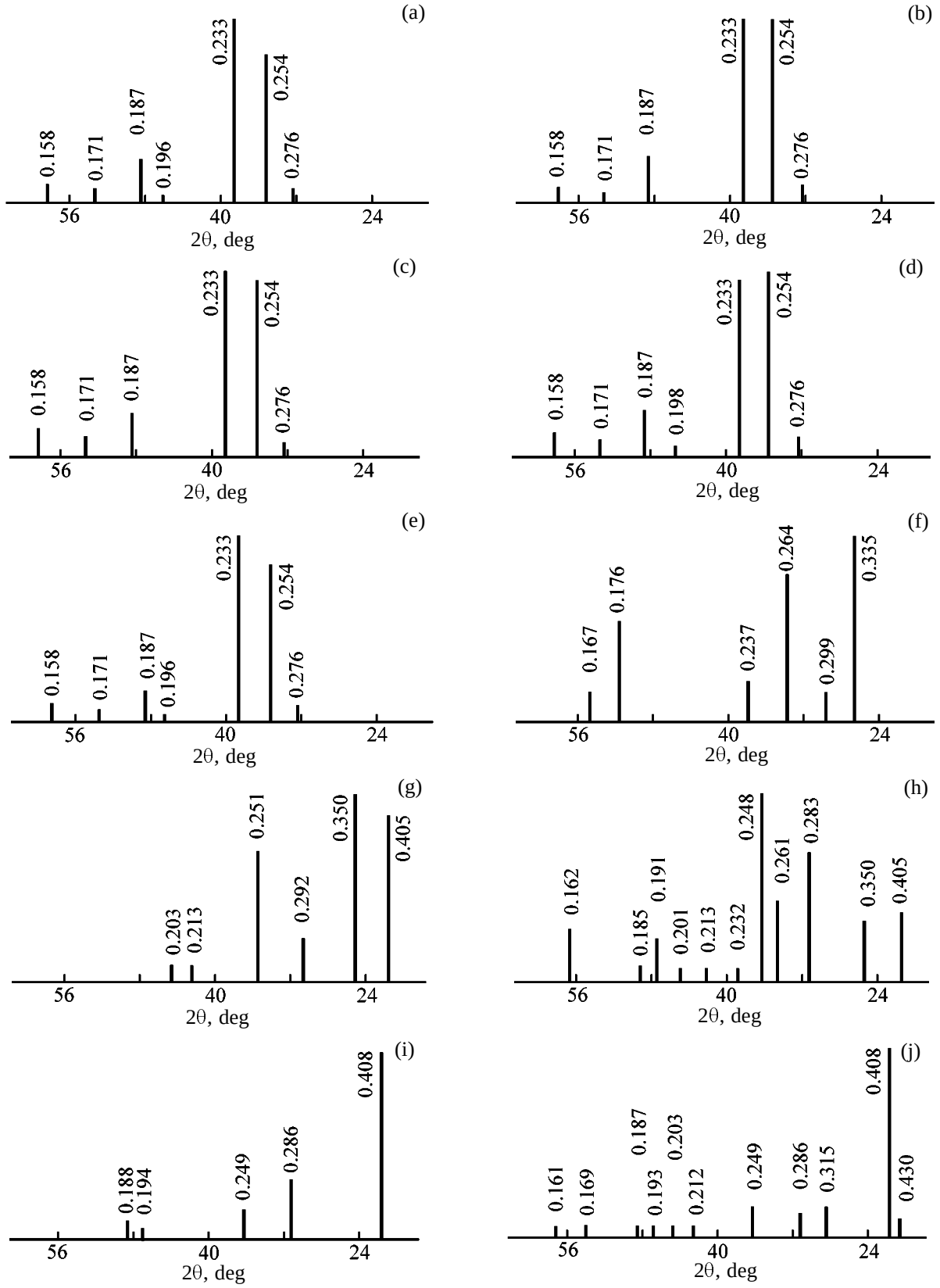

X-ray diffraction patterns of metallosilicas prepared from (a) CuO, (b) $Cu(NO_3)_2$, (c) $CuCl_2$, (d) $CuSO_4$, (e) $Cu(OH)_2$, (f) $SnCl_2$, (g) $Zn(NO_3)_2$, (h) Zn powder, (i) Pb_3O_4, and (j) $Pb(OCOCH_3)_2$ and heated at 900°C.

from CuO and ZnO (up to 1.67 and 2.05 wt %, respectively) at temperatures from 600 to 1000°C is due to high-temperature genesis of metal oxides. For example, copper formed at lower temperature by reduction of CuO with eliminated ethanol is oxidized with atmospheric oxygen to CuO even at 400–500°C:

$$CuO + CH_3CH_2OH \rightarrow Cu + CH_3CHO + H_2O,$$

$$Cu + 0.5O_2 \rightarrow CuO.$$

The X-ray patterns of metallosilicas prepared from $SnCl_2$ and heated at 900°C contain reflections of SnO_2 and SnO.

As determined by X-ray diffraction, two crystalline phases, β-cristobalite and PbO, are present in the lead-containing silicas. Lead oxide is formed only in the metallosilica prepared from $Pb(OCOCH_3)_2$. Weaker and broader reflections in the X-ray pattern of the metallosilica prepared from Pb_3O_4 indicate smaller amount and lower degree of crystallizaton of β-cristoballite in this material.

The X-ray diffraction patterns of mercurosilicas heated at 900°C contain no reflections of crystalline phases. This indicates degradation of the mercurosilica matrix with mercury liberation:

$$\equiv Si–O–Hg–O–Si\equiv \xrightarrow{T_1} \equiv Si–O–Si\equiv + HgO,$$

$$2HgO \xrightarrow{T_2\ (>T_1)} 2Hg + O_2.$$

The silica xerogel heated at 120 or 900°C is also X-ray amorphous.

We suggest that Zn and Pb atoms present in the siloxane structure as ≡Si–O–M–O–Si≡ fragments and salts and oxides of these metals sorbed on the metallosilica matrix catalyze β-cristobalite formation from amorphous SiO_2 even at temperatures lower than 900°C. This is primarily due to both the nature of the metal atom M and high molecular uniformity of the polyheterosiloxane systems. The catalytically active species are mainly ZnO and PbO formed from xerogel thermolysis (except for the system with Pb_3O_4). The catalytic action of these oxides can be also explained by the Headwall's effect, i.e., increased reactivity of highly dispersed substances with disordered crystal lattice, formed in the course of phase transformations.

Amorphous SiO_2 prepared by the sol–gel procedure from tetraethoxysilane was previously shown to crystallize into β-cristobalite at 1300°C. This process can be controlled by the synthesis conditions [6, 8].

Thus, zinc and lead atoms incorporated into the polysiloxane structure effectively catalyze silica crystallization.

CONCLUSION

Incorporation of copper, zinc, tin, and lead atoms into the siloxane skeleton of silica strongly enhances the thermal stability of the initial xerogel. The lead and zinc atoms catalyze crystallization of amorphous silica in the corresponding metallosiloxanes.

REFERENCES

1. Voronkov, M.G., Maletina, E.A., and Roman, V.K., *Geterosiloksany* (Heterosiloxanes), Novosibirsk: Nauka, 1984.
2. Voronkov, M.G., Kukharskaya, E.V., and Voronkova, V.M., *Zh. Prikl. Khim.*, 1983, vol. 56, no. 4, pp. 868–873.
3. Voronkov, M.G., Kukharskaya, E.V., and Voronkova, V.M., *Zh. Prikl. Khim.*, 1984, vol. 57, no. 7, pp. 1671–1672.
4. Iler, R.K., *The Chemistry of Silica*, New York: Wiley–Interscience, 1979.
5. Sviderskii, V.A., Voronkov, M.G., Klimenko, V.S., and Klimenko, S.V., *Zh. Prikl. Khim.*, 1997, vol. 70, no. 10, pp. 1698–1703.
6. Sviderskii, V.A., Voronkov, M.G., Klimenko, V.S., and Klimenko, S.V., *Zh. Prikl. Khim.*, 1999, vol. 72, no. 10, pp. 1600–1607.
7. Gorshkov, V.S., Timashev, V.V., and Savel'ev, V.G., *Metody fiziko-khimicheskogo analiza vyazhushchikh veshchestv* (Procedures for Physicochemical Analysis of Binders), Moscow: Vysshaya Shkola, 1981.
8. Sviderskii, V., Klimenko, S., and Klimenko, V., *Main Group Met. Chem.*, 1998, vol. 21, no. 2, pp. 85–87.

Russian Journal of Applied Chemistry, Vol. 74, No. 7, 2001, pp. 1173–1177. Translated from Zhurnal Prikladnoi Khimii, Vol. 74, No. 7, 2001, pp. 1142–1147.

MACROMOLECULAR CHEMISTRY AND POLYMERIC MATERIALS

Segregation of Polymers in the Course of Film Formation from a Mixture of Latexes

V. N. Pavlyuchenko, O. N. Primachenko, S. Ya. Khaikin, S. S. Ivanchev, and M. E. Jones

St. Petersburg Branch, Institute of Catalysis, Siberian Division, Russian Academy of Sciences, St. Petersburg, Russia
Dow Chemical, the United States

Received February 8, 2001

Abstract—Film formation from binary mixtures of latexes of thermodynamically incompatible polymers was studied. Partial segregation of the polymers in the course of latex film formation, causing asymmetry of the resulting films, was proved by IR Fourier spectroscopy. The influence of various factors on the segregation of polymers was examined.

Film preparation from a mixture of two latexes of thermodynamically incompatible polymers can result in formation of various structures. The extreme cases of such structures are (1) uniform distribution of particles of one polymer in the matrix of the other polymer and (2) total segregation of the two polymers. It is clear that both these cases are idealized. Nevertheless, even a tendency to predominant formation of one or another structure creates prerequisites for solution of many applied problems.

Of particular interest are latex films in which the polymeric components undergo segregation in the course of film formation from a mixture of two latexes. Such films, often termed asymmetric films, owing to different chemical composition of the surfaces can find diverse applications: films with an adhesive layer, films with increased surface hardness and high adhesion to the substrate, films with increased surface electrical conductivity, films with increased hydrophobicity or hydrophilicity, etc. Usually latex films of such kind are prepared by successive immersion of a substrate in two different latexes, with intermediate drying of the film after each immersion [1]. Preparation of an asymmetric film from a mixture of latexes by a single immersion cycle is a more promising process.

Numerous studies [2–5] showed that the polymers are distributed nonuniformly across the film prepared from a mixture of latexes. Okubo *et al.* [2, 3] suggest that formation of asymmetric films may be due to different sedimentation rate of particles of different size.

Sedimentation stability of latexes is only one of the factors affecting preparation of asymmetric films. In this study we attempted to reveal the role of other factors, such as, e.g., aggregative stability of latexes and the capability of polymers for specific interactions with a substrate on which the film is formed.

EXPERIMENTAL

Two types of latexes, poly-*n*-butyl acrylate and styrene–*n*-butyl acrylate (ST–BA) copolymer, were prepared with the aim to examine the influence of various factors on the film formation from latex mixtures. Usually synthesis was performed in two stages. In stage 1 we prepared a seeding latex by charging to the reactor a small amount of the monomers and (co)polymerizing them to complete conversion. In stage 2 the monomers were added gradually, and the process was performed in the semicontinuous mode.

Emulsion copolymerization was performed in 250- or 500-ml flasks equipped with a reflux condenser, a stirrer, a dropping funnel for adding monomers, and a nipple for feeding nitrogen. The following chemicals were used.

Monomers, styrene (ST) and *n*-butyl acrylate (BA), were vacuum-distilled; their characteristics agreed with the reference data.

Initiators [potassium persulfate (PP), azobis(isobutyronitrile (AIBN), and 2,2'-azobis(2-amidinopropane) dichloride (AAPDC)] were used without additional purification.

1070-4272/01/7407-1173$25.00

Table 1. Conditions of latex preparation and their characteristics*

Latex***	Synthesis conditions**						Latex dry residue, wt %	*d*, nm	σ, mN m^{-1}	ρ g cm^{-3}
	ST : BA weight ratio	initiator (wt %)	surfactant (wt %)	monomer : water weight ratio	*T*, °C	τ, h				
(BA)-A$^-$	0 : 100	PP, 0.50	SAS, 2.0	1.0 : 1.5	80	3.5	39.7	84	49	1.14
(ST–BA)-A$^-$	47.5 : 52.5	PP, 0.50	SAS, 2.0	1.0 : 1.5	80	5.5	40.5	83	52	1.10
(BA)-0$^-$	0 : 100	PP, 0.67		1.0 : 2.34	80	10.5	29.7	337	54	1.14
(ST–BA)-0$^-$	47.5 : 52.5	AAPDC, 0.67		1.0 : 1.60	80	13.0	19.5	312	59	1.10
(BA)-C$^+$	0 : 100	AAPDC, 0.75	TMDAC, 2.0	1.0 : 1.22	70–75	6.5	41.0	300	41	1.14
(BA)-0$^+$	0 : 100	AIBN, 0.75		1.0 : 2.33	70–75	6.0	29.2	1180	59	1.14
(ST–BA)-N	48.2 : 51.8	AIBN, 0.78	OS-20, 4.0	1.0 : 3.33	65	7.0	23.5	119	50	1.10
(SKF-32)-A$^-$							44.9	200	62.1	1.84

* (*T*) Polymerization temperature, (*d*) particle diameter, (σ) surface tension of the latex, and (ρ) polymer density.

** Concentrations of the initiators and surfactants are given relative to the weight of the monomers.

*** Designations of the latexes include the chemical composition of the polymer or copolymer, type of surfactant [(A) anionic, (C) cationic, (N) nonionic, and (0) no surfactant], and particle charge [(+) positive and (–) negative; no sign means no charge]; into (BA)-A$^-$ and (ST–BA)-A$^-$ latexes after synthesis completion we introduced an additional portion of SAS (4% relative to the polymer weight.

Surfactants [sodium alkylsulfonate C_{14}–C_{16} (SAS), cationic surfactant trimethyldodecylammonium chloride (TMDAC), and nonionic surfactant OS-20, a mixture of oxyethylated aliphatic alcohols $C_{14-16}H_{29-31}\cdot(OCH_2CH_2)_{20}OH$] were used without additional purification. To prepare thermosensitive latexes, we used modified oxyethylated alkylphenols $C_{8-10}H_{17-21}C_6\cdot H_4O(CH_2CH_2O)_{8-10}CH_2N^+(CH_3)(C_2H_5)_2\ C_6H_5SO_3^-$ (leveling agent A) and $C_{8-10}H_{17-21}C_6H_4O(CH_2CH_2\cdot O)_{10-12}SO_3^-\,Na^+$ (S-10). Latexes were prepared in distilled water. The synthesis conditions and characteristics of latexes, and also, for comparison, the characteristics of SKF-32 fluororubber latex (copolymer of trifluorochloroethylene and vinylidene fluoride) are listed in Table 1.

The latex dry residue was determined by drying the latex samples under an IR lamp to constant weight. The size of the latex particles was determined from the turbidity spectra, namely, from the dependences of the optical density of the diluted latex on the incident light wavelength [6]. The surface tension of latexes, measured by the du Nouy (ring detachment) method, qualitatively characterizes their adsorption saturation. Lower surface tension and hence higher adsorption saturation are characteristic of latexes prepared in the presence of surfactants of any type.

Several mixtures containing various types of latexes were prepared to study the effect of various factors on formation of films from latex mixtures. It should be noted that in each system at least two factors act simultaneously, which makes it difficult to distinguish the effects of particular factors. However, we chose the compositions of latex mixtures so as to make the effect of one of the factors predominant.

Films from latex mixtures were cast on different supports: those from glass, Teflon, and siliconized paper (SP). In experiments on ionic deposition of latexes, we used as support an ion-exchange membrane of the Nafion type (copolymer of tetrafluoroethylene with a fluoromonomer containing a sulfonyl fluoride group which was converted to the sulfonic acid form by hydrolysis in an NaOH solution followed by treatment with boiling nitric acid). For studying thermal coagulation, we used a heavy glass support heated to 100°C. For experiments we prepared 100-μm-thick films, unless otherwise stated. The films were used 24 h after preparation.

The extent of polymer segregation in latex films was evaluated from the composition of the polymer compound on the polymer–air (P–A) and polymer–support (P–S) boundaries. The composition was determined by IR Fourier ATIR spectroscopy using an HTR-25 attachment to a Perkin–Elmer (model 1750) Fourier spectrometer. With a KRS-5 prism (45°), the effective penetration depth of the light wave was 2.0 ± 0.8 μm depending on the position of the analytical wavelength and refractive index of the compound. The wavelength dependence of the penetration depth was corrected with a special program.

The ST : BA weight ratio was determined from the

intensity ratio of the bands at 700 (phenyl group of styrene) and 1729 cm^{-1} (carbonyl group of *n*-butyl acrylate). Coatings prepared from ST–BA/SKF-32 latex mixtures were characterized by the intensity ratio of the bands at 700 and 509 cm^{-1} belonging, respectively, to the styrene unit and SKF-32 polymer.

As an example, the figure shows the spectra of two surfaces of a film prepared on a heated support from a mixture of (ST–BA)-A^- and (BA)-0^+ + S-10 latexes. Comparison of the intensity of the band at 700 cm^{-1} for these two phase boundaries shows that the P–A surface is strongly enriched in the ST–BA copolymer.

The role of the sedimentation stability of latexes was studied with a mixture of (ST–BA)-0^- and (SKF-32)-A^- latexes strongly differing in the particle density (Table 1). Films were prepared on different supports and at different temperatures. As seen from Table 2, in this system the factor of the polymer density remains decisive. Despite smaller size of SKF-32 particles and low aggregative stability of particles of the ST–BA copolymer prepared in the absence of surfactants, in all cases the P–S surface is enriched in SKF-32. The effect is more pronounced with the Teflon support exhibiting a higher affinity for the fluoropolymer.

With decreasing temperature, i.e., with increasing time of film formation, the effect of polymer segregation, as expected, is enhanced irrespective of the type of support. The polymer composition on the P–A surface fully corresponds to the polymer ratio in the latex mixture. The lack of balance between the polymer ratios on the P–A and P–S surfaces may be due to complex distribution of polymers in the inner layers of the film.

The influence of the aggregative stability of the latexes, as opposed to the sedimentation stability, was examined with mixtures of latexes of chemically similar polymers, namely, with two pairs of latexes: (ST–BA)-A^-–(BA)-0^- and (ST–BA)-0^-–(BA)-A^-. This factor was studied with SP in order to eliminate possible specific interaction of polymers with the support.

Table 3 shows that in both systems the P–A surface is depleted of, and the P–S surface, enriched in the polymers synthesized in the absence of surfactants, i.e., polymers with lower aggregative stability of the particles.

The effect of specific interactions of polymers with the support was studied with a mixture of latexes (ST–BA)-N and (ST–BA)-C^+, with a Nafion ion-exchange membrane in the acid form as support. The process is essentially similar to coagulative immersion of the substrate in the latex, with the polymeric electrolyte used as coagulant. In the process, we used a mixture of latexes one of which was stabilized with a cationic surfactant, and the other, with a nonionic surfactant. In this case we analyzed only the P–A surface, because it was difficult to separate the formed film from the support.

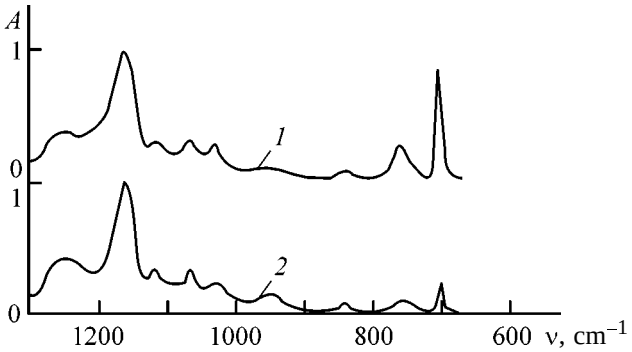

IR Fourier ATIR spectra of the (*1*) P–A and (*2*) P–S surfaces of the latex film prepared from the latex mixture (ST–BA)-A^-–[(BA)-0^+ + S-10] on a glass support at 100°C. (*A*) Normalized absorption and (ν) wave number.

Table 4 shows that the P–A surface is enriched in the ST–BA copolymer whose particles are stabilized with the nonionic surfactant. The difference between the polymer ratios in the latex mixture and on the P–A boundary is maximal in the film formed immediately after preparing the latex mixture. If the latex mixture was used 24 h after its preparation, the difference between the polymer ratios was minimal. Probably, this is due to redistribution in time of the cationic and nonionic surfactants between particles of different latexes.

When a film is formed on a hot support from a mixture of latexes one of which is thermosensitive,

Table 2. Polymer ratios on the P–A and P–S boundaries in films prepared from the latex mixtures (SKF-32)-A^-–(ST–BA)-0^-*

Support	Film formation temperature, °C	Weight ratio SKF-32/(ST–BA)	
		P–A	P–S
Teflon	12	1.0	2.70
	65	1.0	2.20
Glass	12	1.0	1.77
	65	1.0	1.26

* The weight ratio of the polymers in the latex mixture was 1.0 : 1.0.

Table 3. Polymer ratios on the P–A and P–S boundaries of films formed from mixtures of latexes with different aggregative stability*

Latex mixture	Weight ratio of the polymers (ST–BA)BA		
	latex mixture	P–A	P–S
(ST–BA)-A^-	1.82	5.60	1.18
(ST–BA)-A^-	0.50	0.44	1.03
(BA)-A^-	1.00	0.64	1.72

* Temperature of film formation 20°C; SP support.

Table 4. Polymer ratios in the film prepared on an ion-exchange membrane from the latex mixture (ST–BA)-N–(BA)-C^+*

Polymer weight ratio (ST–BA) : BA on P–A	Film formation conditions
1.32	Support (ion-exchange membrane) is kept for 1 min in latex mixture immediately after mixture preparation
1.26	Support is kept for 15 min in latex mixture 30 min after mixture preparation
1.09	Support is kept for 15 min in latex mixture 24 h after mixture preparation

* (ST–BA)/BA ratio in the latex mixture 0.97, film formation temperature 18°C.

segregation of the polymers can be expected. The capability of latexes for thermal coagulation was realized by introducing thermosensitive additives: leveling agent A and S-10. The effect of such additives is based on complete neutralization of the electric charge of latex particles with the corresponding ionic groups of the surfactant. The steric stabilization of particles due to the presence in the surfactant molecules of ethylene oxide units under ambient conditions prevents coagulation of the latexes. However, it is known that at elevated temperatures nonionic surfactants at certain values of the hydrophilic-hydrophobic balance can become water-insoluble owing to dehydration [7]. Thus, latexes for which the steric factor is the only stabilizing factor can coagulate on heating.

When preparing a thermosensitive latex, it is important to properly choose the sensitizing additive. At very low concentrations neutralization of the electric charge of the latex particles is incomplete. On the contrary, high concentrations can cause particle recharging. In both cases the thermal sensitivity of the latex will be insufficient or lacking at all.

To find the optimal concentration of the additive, we determined the coagulation temperature T_c of the latex depending on the additive concentration. We used latexes prepared in the absence of surfactants, because we expected that the thermal sensitivity could be imparted to such latexes at relatively low concentrations of the additives. We tested the following combinations latex–additive: (BA)-0^- + leveling agent A and (BA)-0^+ + S-10. The influence of the concentration of the thermosensitizing additive on the latex coagulation temperature is illustrated below:

[Leveling agent A], % of polymer weight	0.20	0.33	1.00	1.66	2.33	3.00	3.66
T_c, °C	*	*	*	55	60	*	*
[S-10], % of polymer weight	1.80	2.23	2.43	2.66	2.90	3.33	
T_c, °C	82–84	70	71	75	75.5	95–96	

* No coagulation at 100°C.

Our results show that in the first system coagulation occurs only in a narrow range of concentrations of the additive (1.66–2.33 wt %). At other concentrations, no coagulation is observed even on heating the latex to 100°C. In the second system, coagulation occurs in the entire range of S-10 concentrations. However, the coagulation temperature is the lowest at the S-10 content within 2.33–2.90 wt %.

In agreement with our results, thermosensitive latexes were obtained at concentrations of leveling agent A of 1.66 and of S-10 of 2.43 wt %, ensuring the lowest coagulation temperature. The additives were introduced as 5% aqueous solutions. The resulting thermosensitive latexes were mixed with the anionic latex at room temperature. Thus, we studied the thermal coagulation of the following latex mixtures: (ST–BA)-A^-–[(BA)-0^- + leveling agent A] and (ST–BA)-A^-–[(BA)-0^+ + S-10].

The films were prepared on glass supports at 100°C and also, for comparison, at 20°C. Table 5 shows that in all cases the P–A surface is depleted of the thermosensitive polymer even when the films are formed at 20°C. This result could be expected, since the latexes prepared in the absence of surfactants, owing to large particle size, have decreased sedimentation stability. Preparation of films on heated supports appreciably

Table 5. Influence of thermal coagulation on film formation from latex mixtures

Latex mixture	Film formation temperature, °C	Weight ratio (ST–BA) : BA		
		latex mixture	P–A	P–S
(ST–BA)-A^-–[(BA)-0^- + leveling agent A]	20	3.12	4.59	3.22
	100	3.12	5.56	3.03
(ST–BA)-A^-–[(BA)-0^+ + S-10]	20	1.00	2.80	1.04
	100	1.00	9.23	0.51

enhances the effect of polymer segregation, especially in the system (ST–BA)-A^-–[(BA)-0^- + S-10], which may be due to simultaneous action of several factors, i.e., to the difference between the latexes not only in thermal sensitivity but also in sedimentation and aggregative stability.

The influence of the film thickness on the segregation of polymers was studied with the system (ST–BA)-A^-–[(BA)-0^+ + S-10]. The films were formed on SP at 21°C. The results listed in Table 6 show that the polymer segregation is enhanced with increasing film thickness. Presumably, this effect is due to longer time of formation of thicker films. Similar trends related to slower film formation at lower temperatures were discussed above (Table 2). These results seem to be quite obvious, since the differences in the sedimentation stability of latexes and in their capability for specific interaction with the support should be manifested to a greater extent at longer process times.

CONCLUSIONS

(1) Study of films prepared from mixtures of latexes of thermodynamically incompatible polymers demonstrated the principal possibility of polymer segregation in the course of film formation. The result of the segregation is formation of asymmetric films in which the film–air and film–support surfaces differ in the chemical composition.

(2) The main factors affecting the polymer segregation were considered: sedimentation and aggregative stability of latexes, capability of one of the latexes for specific interactions with the support substance or for thermal coagulation, and film formation time. The polymer segregation in the course of film formation occurs to the greatest extent when several factors act simultaneously.

Table 6. Influence of the film thickness *h* on film formation from a mixture of latexes (ST–BA)-A^-–[(BA)-0^+ + S-10]

h, μm	Weight ratio (ST–BA) : BA		
	latex mixture	P–A	P–S
50	1.00	1.72	1.10
100	1.00	2.44	0.81
235	1.00	3.45	0.77

ACKNOWLEDGMENTS

The authors are greatful to Dow Chemical (the United States) for financial support of this work.

REFERENCES

1. US Patent 58 227 612.
2. Okubo, M. and He, J., *J. Appl. Polym. Sci.*, 1991, vol. 42, no. 8, pp. 2205–2208.
3. Okubo, M., Ando, M., and Matsumoto, T., *Kobunshu Ronbunshu*, 1983, vol. 40, no. 2, pp. 79–85.
4. Tebelius, L.K., Stets, E.M., and Urban, M.W., *J. Appl. Polym. Sci.*, 1996, vol. 62, no. 11, pp. 1887–1892.
5. Urban, M.W., Allison, C.L., Johnson, G.L., and Di Stefano, F., *Appl. Spectrosc.*, 1999, vol. 53, no. 12, pp. 1520–1527.
6. Klenin, V.I., Shchegolev, S.Yu., and Lavrushin, V.I., *Kharakteristicheskie funktsii svetorasseyaniya dispersnykh sistem* (Characteristic Light Scattering Functions of Disperse Systems), Saratov: Saratov. Univ., 1977.
7. Schönfeldt, N., *Grenzflachenaktive Äthylenoxid-Addukte*, Stuttgart: Wissenschaftliche, 1976.

Russian Journal of Applied Chemistry, Vol. 74, No. 7, 2001, pp. 1178–1182. Translated from Zhurnal Prikladnoi Khimii, Vol. 74, No. 7, 2001, pp. 1147–1151.

MACROMOLECULAR CHEMISTRY AND POLYMERIC MATERIALS

Influence of the Chemical Structure of Diarylpenta-1,4-dien-3-one Chromophores on the Nonlinear Optical Properties of Their Polymeric Complexes with Poly-1,10-decamethyleneacetamidine

A. V. Ten'kovtsev, A. E. Trofimov, V. N. Lukoshkin, M. M. Dudkina, F. Boehme, and L. Hessler

Institute of Macromolecular Compounds, Russian Academy of Sciences, St. Petersburg, Russia
Ioffe Physicotechnical Institute, Russian Academy of Sciences, St. Petersburg, Russia
Institute for Polymer Studies, Dresden, Germany

Received March 6, 2001

Abstract—A study was made of the ability of the ionic complexes formed by diarylalkadienone chromophores with poly-1,10-decamethyleneacetamidine to exhibit third-order nonlinear-optical effects. The chemical structure of the chromophores was correlated with the third harmonic generation efficiency.

In recent decades, materials exhibiting nonlinear optical (NLO) properties have attracted ever growing researchers' attention [1]. This is due above all to the promise offered by materials able of second and third harmonic generation (SHG and THG, respectively) in creation of the next generation of computers, so-called "optical computers" with photons instead of electrons as working element. At present, NLO-active devices utilize primarily inorganic materials such as potassium niobate [2], barium β-borate [2], etc. It is generally recognized, however, that the most promising for this purpose are organic, especially polymeric NLO-active substances. In contrast to inorganic materials, the chemical structures of organic and polymeric compounds and, correspondingly, the NLO properties can be widely varied. Also, the film-forming ability of polymeric NLOs significantly facilitates fabrication of optical devices thereof.

Within a large class of materials exhibiting pronounced NLO response, of greatest importance become those characterized by a refractive index widely varying with the light intensity, i.e., those able of THG. As known, practically suitable susceptibilities $\chi^{(3)}$ are exhibited by compounds containing a fairly long π-conjugation system, e.g., β-carotene, polyacetylene, polythiophene, etc. [3]. Despite significant success achieved in this sphere, preparation of this type of macromolecular compounds able of film formation or of the guest–host type composite materials is a complex problem. The reason is the low solubility and difficulties posed by synthesis of polyconjugated polymers in the former case and thermodynamic incompatibility of the polymer and the low-molecular-weight substance in the latter.

In [4], we proposed an alternative procedure of preparing polymeric systems able of THG. It consists in preparation of ionic complexes between low-molecular-weight NLO chromophores and polymer carriers [4], in particular, complexes of di(4-hydroxyaryl)alkadienones and poly-1,10-decamethyleneacetamidine. It was shown that the polymeric complexes with the quinoid structures yielded by ionization of chromophores by highly basic poly-1,10-decamethyleneacetamidine are heat-resistant and stable for more than a year, are capable of film formation, and are able of efficiently generating third harmonic.

In this work, we study the THG efficiency of the ionic complexes of 1-(4-hydroxyphenyl)-5-(aryl)penta-1,4-dien-3-one chromophores with poly-1,10-decamethyleneacetamidine as influenced by the chemical structure of the chromophores.

Synthesis of 1-(4-hydroxyphenyl)-5(aryl)penta-1,4-dien-3-ones followed the scheme

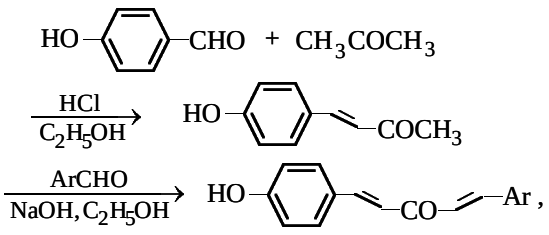

1070-4272/01/7407-1178$25.00

where Ar = C_6H_5 (**I**), 4-FC_6H_4 (**II**), 4-CH_3O–C_6H_4 (**III**), 4-$NO_2C_6H_4$ (**IV**), 4-$N(CH_3)_2C_6H_4$ (**V**), 1-naphthyl (**IV**), 9-anthryl (**VII**), $CH{=}CHC_6H_5$ (**VIII**), $CH{=}CH{-}C_6H_4$-4-NO_2 (**IX**), and CH_3CONH (**X**).

4-(4-Hydroxyphenyl)but-3-en-2-one was prepared by condensing 4-hydroxybenzaldehyde with acetone as described in [5]. Attempts to condense 4-(4-hydroxyphenyl)but-3-en-2-one with substituted aromatic aldehydes under the same conditions failed. However, the desired products were obtained in a 40–50% yield by acid-catalyzed crotonic condensation.

Poly-1,10-decamethyleneacetamidine was synthesized by the method described previously in [6], according to the scheme

$$NH_2(CH_2)_{10}NH_2 + CH_3C(OC_2H_5)_3$$

$$\xrightarrow[150^\circ C]{CH_3COOH} -(CH_2)_{10}N{=}\underset{CH_3}{\overset{}{C}}{-}\overset{H}{N}- .$$

A gel-permeation chromatographic (GPC) study showed that the sample of poly-1,10-methyleneacetamidine used in this work had the molecular weight of 5000 amd the polydispersity coefficient of 2.6.

Complexes of poly-1,10-methyleneacetamidine with chromophores were prepared by mixing saturated ethanol solutions of the polymer and chromophore, followed by removing the solvent.

The thermal-analytical data suggest that the resulting complexes are individual polymeric species rather than mechanical mixtures of the polymer with the low-molecular-weight compound. Whereas the DSC curves for poly-1,10-decamethyleneacetamidine exhibit a transition only at 5°C (T_g), those for all the complexes exhibit only a glass transition in the range 25–75°C, depending on the polymer–chromophore ratio (Fig. 1).

The thermogravimetric curves evidence the onset of thermal degradation (1% mass loss) of the resulting complexes at 195–200°C. This suggests the lack of thermal degradation of the samples during measuring the NLO characteristics. The $\chi^{(3)}$ values obtained refer specifically to the complexes of interest, rather than to the products of thermal degradation under irradiation during measurements (the samples warm up to 150°C).

It should be noted that the films of the complexes under study do not change their physical and spectral characteristics for a long time (no less than a year) under normal conditions; they are resistant to most solvents (toluene, ethanol, acetone, ethyl acetate) and exhibit good adhesion to glass, quartz, and mica.

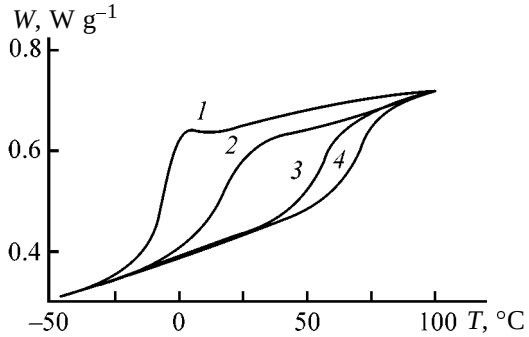

Fig. 1. DCS curves of complexes of **III** with poly-1,10-decamethyleneacetamidine at different content of the chromophore in the complex. (*W*) Heat flux and (*T*) temperature. Polymer : chromophore molar ratio: (*1*) 1 : 0.2; (*2*) 1 : 0.25, (*3*) 1 : 0.5, and (*4*) 1 : 0.75.

High basicity of poly-1,10-decamethyleneacetamidine (pK_a 10.9) is responsible for deprotonation of the chromophore and, thereby, affects their spectral characteristics. As seen from the table, formation of the complexes is accompanied by a bathochromic shift of the long-wave absorption band by more than 100 nm. These changes are evidently due to extension of the π-conjugation system owing to formation of the quinoid species

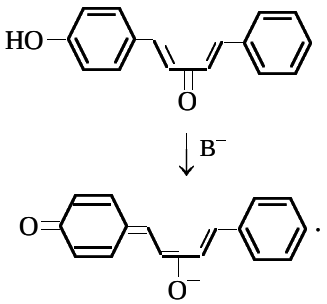

We showed earlier [4] that such a change in the conjugation type, namely, a transition from cross-conjugated to linear π system, is necessary for arising of the third-order NLO effect in the systems under study. It should be noted that this idea was exploited in development of guest–host-type NLO-active systems from derivatives of squaric acid and polymethyl methacrylate [7]. Figure 2 presents the UV absorption spectra of the complexes of poly-1,10-decamethyleneacetamidine with 1-(4-hydroxyphenyl)-5-(4-methoxyphenyl)penta-1,4-dien-3-one at different molar ratios between the monomer unit of the polymer and the chromophore. It is seen that with decreasing content of the chromophore the peak corresponding to the quinoid species grows in intensity (λ_{max} = 456 nm), and at a ratio close to 1 : 0.25 the peak corresponding to the nondeprotonated chromophore (λ_{max} = 377 nm)

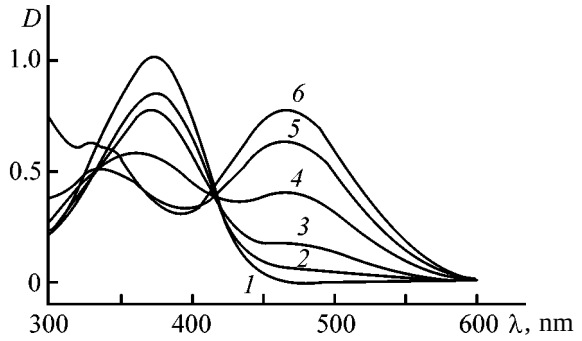

Fig. 2. Absorption spectra of the complexes of **III** with poly-1,10-decamethyleneacetamidine at different content of the chromophore in the complex. (*D*) Optical density and (λ) wavelength. Polymer : chromophore molar ratio: (*1*) 0 : 1, (*2*) 0.5 : 1, (*3*) 1 : 1, (*4*) 1 : 0.75, (*5*) 1 : 0.5, and (*6*) 1 : 0.25.

virtually disappears. For this reason, specifically this ratio was chosen for studying the NLO properties of the complexes.

In this work we studied the NLO properties of the synthesized materials by the GTH method. In view of the difficulties involved in determining the absolute values of the exciting radiation intensity for a sample, the NLO succeptibilities of the materials under study were determined by the relative procedure, by comparison with a reference sample under the same conditions. The reference sample was a 0.5-mm thick melted quartz plate adjusted to the first maximum of the third Maker's beat harmonic intensity [8].

In this case, $\chi^{(3)}$ can be determined by a simple expression, by comparing the intensities of the signals of the third harmonic from the sample and reference:

$$\chi^{(3)} = \chi_s^{(3)}[I^{1/2}(3\varphi)/I_c]/[I_s^{1/2}(3\varphi)/l_{c,s}],$$

Here, $I(3\omega)$ and $I_s(3\omega)$ are the THG intensities for the sample and reference, respectively; I_c and $I_{c,s}$ are the respective coherence lengths; $\chi_s^{(3)} = 3.11 \times 10^{-14}$ cgs units for SiO_2 at $\lambda = 1063$ nm.

Long-wave absorption maxima and THG efficiencies of the complexes

Chromophore	λ_{max}, nm	$\chi^{(3)}$, cgs units
I	451	4.9
II	463	3.8
III	456	7.1
IV	487	3.5
V	471	6.5
VI	465	4.7
VII	464	0.7
VIII	467	7.7
IX	483	2.3
X	455	5.6

The $\chi^{(3)}$ values obtained are presented in the table. It is seen that the majority of the complexes have $\chi^{(3)}$ of the order of 10^{-12} cgs units. This is close to the corresponding values for polyphenylvinylenes [9] and polythiophenes [10] which are considered by the majority of investigators as the class of polymers most suitable as NLO-active media.

The above-said suggests the following. The two-dimensional growing of the π-conjugation system, namely, the change from the phenyl to 1-naphthyl moiety in the chromophore, does not significantly affect the THG efficiency. This is most probably due to steric hindrance and increase in the dihedral angle formed by the naphthyl group and the double bond, which decreases the degree of conjugation. This assumption is substantiated by the fact that with 9-anthryl instead of 1-naphthyl moiety $\chi^{(3)}$ decreases by almost an order of magnitude. This is undoubtedly due to the sterically hindered rotation about the C–C bond between the 9-anthryl and ethylene moieties. One-dimensional growing of the π-conjugation system, namely, the change from the phenyl to styrene moiety, affects $\chi^{(3)}$ only insignificantly. It can be assumed that this minor increase is due to steric factors. Whereas 1,5-diphenylpenta-1,4-dien-3-ones exist as planar conformers, introduction of an additional double bond, evidently, disturbs the coplanar π system and causes the degree of conjugation to increase out of proportion. This follows from the fact that the dihedral angle φ of the C–C bond in butadiene moieties is known to be equal to 40°–50° on the average and the degree of conjugation, to change proportionally to $\cos^2\varphi$.

The tabulated data show that auxochromic substituents introduced in the *para* position of the phenyl ring significantly affect the NLO activity of the complexes. One of the most convenient methods of semiquantitative assessment of the influence exerted by substituents on the conjugated system is that based on the Hammett correlation approach [12]. Figure 3 shows the NLO response of a series of complexes as dependent on the σ constants of the substituents. The parameter $\chi^{(3)}$ correlates well with the electronic effect of the substituent. As known, $\chi^{(3)}$ depends on the polarizability of the electron cloud of the chromophore and on the difference in the dipole moments of the chromophore in the ground and excited states [2]. As a rule, the molecule in the ground state should have a sufficiently large dipole moment. In our case,

the effect of increase in the polarizability prevails, as indicated by increase in $\chi^{(3)}$ with enhancing donor effect of the substituent. The same is indicated by the lack of correlation between $\chi^{(3)}$ and Hammett constants σ_1 which, unlike σ constants, take into account only the inductive effect of the substituent.

EXPERIMENTAL

1-(4-Hydroxyphenyl)-5-(4-methoxyphenyl)penta-1,4-dien-3-one (III). To a stirred solution of 1.6 g (0.01 mol) of 4-(4-hydroxyphenyl)but-3-en-2-one and 1.45 (0.011 mol) of 4-methoxybenzaldehyde in 15 ml of ethanol, a solution of 0.8 g (0.02 mol) of NaOH was added in the form of 40% aqueous solution. The resulting mixture was heated at 50°C for 1 h and left overnight at room temperature. Then the mixture was diluted with a tenfold volume of water, filtered, and neutralized with 5 ml of dilute acetic acid. The resulting precipitate was separated and recrystallized from ethanol. Yield 1.7 g (65%), mp 169°C. Elemental analysis:

Found, %: C 76.89, H 5.70.
Calculated, %: C 77.12, H 5.75.

^{1}H NMR (Bruker DRX 500; CD_3OD; 25°C; δ, ppm): 3.85 (s, 3H, OCH_3), 6.84 (d, 2H, H_{ar}), 6.98 (d, 2H, H_{ar}), 7.06 (d, 1H, –CH=), 7.10 (d, 1H, –CH=), 7.58 (d, 2H, H_{ar}), 7.66 (d, 2H, H_{ar}), 7.71 (d, 1H, –CH=), 7.72 (d, 1H, –CH=).

The other chromophores **I**–**X** were prepared similarly. The elemental analysis data and the spectral characteristics corresponded to the expected structures.

Solutions of the complexes were prepared by mixing at room temperature solutions of the chromophore and poly-1,10-decamethyleneacetamidine in ethanol at the polymer : chromophore ratio of 1 : 0.25 (molar ratio between the polymer units and the low-molecular-weight compound). The samples for optical studies were prepared by casting the ethanol solutions of the complexes onto a rotating glass substrate followed by evaporating the solvent at room temperature and atmospheric pressure. The resulting films were dried in a vacuum (0.1 torr) to a constant weight before measurements.

The calorimetric measurements were carried out on a DSC 7 Perkin–Elmer calorimeter in the range from –50 to 250°C at a rate of 10 deg min^{-1}. The UV spectra were recorded on a Varian Cary 100 spectrophotometer from ethanol solutions and thin films for measuring the NLO characteristics. Thermogravimetric measurements were carried out on a Perkin–Elmer TGA-7 instrument, in the 30–700°C temperature range, at the heating rate of 10 deg min^{-1}.

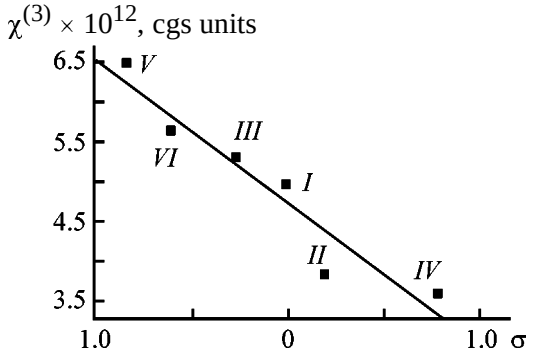

Fig. 3. Correlation of the efficiency $\chi^{(3)}$ of THG genetation by the complexes under investigation with the Hammett constants σ of substituents in chromophores: (*I*) H, (*II*) F, (*III*) OCH_3, (*IV*) NO_2, (*V*) $N(CH_3)_2$, and (*VI*) CH_3CONH.

The samples were excited by a pulse neodymium–garnet laser; the radiation wavelength was 1063 nm. The laser operated in the modulated *Q*-factor regime; pusle duration was 15 ns. The energy of radiation in the pulse was varied within 1–30 MJ.

CONCLUSION

The influence of the chemical structure of the chromophores on the nonlinear-optical properties of polymeric complexes between diarylpenta-1,4-dien-3-ones and poly-1,10-decamethyleneacetamidine was elucidated. The influence exerted by the substituents on the efficiency of generation by the complexes of the third-order nonlinear-optical effects can be described semiquantitatively using Hammett σ constants.

ACKNOWLEDGMENTS

The work was financially supported by the Russian Foundation for Basic Research (project no. 01-03-32 394).

REFERENCES

1. Bredas, J.L., Adant, G., Tackx, P., and Persoons, A., *Chem. Rev*., 1994, vol. 94, no. 1, pp. 243–264.
2. Zyss, J., *Molecular Nonlinear Optics: Materials, Physics, and Devices*, Boston: Academic, 1993.
3. *Nonlinear Optics Molecules and Polymers*, Nalwa, H.S. and Miyata, S., Eds., Boca Raton, FL: CRC, 1997.

4. Ten'kovtsev, A.V., Yakimanskii, A.V., Lukoshkin, V.N., *et al.*, *Fiz. Tverd. Tela*, 2000, vol. 42, no. 11, pp. 2099–2102.
5. Buck, J.S. and Heilborn, I.M., *J. Chem. Soc*., 1922, no. 7, pp. 1085–1101.
6. Boehme, F., Klinger, C., Komber, H., *et al*., *J. Polym. Sci., Polym. Chem.*, 1998, vol. 36, no. 6, pp. 929–934.
7. Mathis, K.S., Kuzyk, M.G., Dirk, C.W., *et al*., *J. Opt. Soc. Am*., 1998, vol. 158B, no. 1, pp. 71–79.
8. Kubodera, K. and Kobayaschi, H., *Mol. Cryst. Liquid Cryst.*, 1990, vol. 182A, pp. 103–121.
9. Bradley, D.D.C., *Macromol. Chem., Macromol. Symp*., 1990, vol. 37, pp. 247–256.
10. Torruellas, W.E., Neher, D., Zanoni, R., *et al*., *Chem. Phys. Lett*., 1990. vol. 175, nos. 1–2. pp. 11–16.
11. Potapov, V.M., *Stereokhimiya* (Stereochemistry), Moscow: Khimiya, 1988.
12. Palm, V.A., *Osnovy kolichestvennoi teorii organicheskikh reaktsii* (Basics of the Quntitative Theory of Organic Reactions), Leningrad: Khimiya, 1977.

Russian Journal of Applied Chemistry, Vol. 74, No. 7, 2001, pp. 1183–1189. Translated from Zhurnal Prikladnoi Khimii, Vol. 74, No. 7, 2001, pp. 1151–1157.

MACROMOLECULAR CHEMISTRY AND POLYMERIC MATERIALS

Features of the Crystal Structure of the Polyimide Derived from 3,3'-Diaminobenzophenone and 3,3',4,4'-Benzophenonetetracarboxylic Dianhydride

V. E. Yudin, A. G. Kalbin, T. K. Meleshko, A. I. Grigor'ev, G. N. Gubanova, N. N. Bogorad, Yu. N. Panov, O. F. Pozdnyakov, B. P. Redkov, A. O. Pozdnyakov, and V. V. Kudryavtsev

Institute of Macromolecular Compounds, Russian Academy of Sciences, St. Petersburg, Russia
Ioffe Physicotechnical Institute, Russian Academy of Sciences, St. Petersburg, Russia
Institute of Machine Science Problems, Russian Academy of Sciences, St. Petersburg, Russia

Received March 26, 2001

Abstract—Changes occurring in the structural organization of the thermoplastic polyimide derived from 3,3'-diaminobenzophenone and 3,3',4,4'-benzophenonetetracarboxylic dianhydride on heat treatment at temperatures in the range 250–350°C were studied, and the influence of these changes on the rheological behavior of the polymer was examined.

Polyimides (PIs) show considerable promise as polymeric binders for preparing fibrous composites with high heat resistance, high softening point, and enhanced crack resistance. It is well known that these polymers, on the one hand, withstand heating up to 500°C and, on the other hand, preserve elastic properties down to the liquid nitrogen temperature [1]. However, the factors making PIs the most heat-resistant among the known polymers (rigidity of the polymer chain and high level of intermolecular interactions) also make them difficultly processable, which significantly limits their use as a matrix in composites.

At present, active efforts are made to solve this problem by developing crystallizing fusible PIs combining the positive properties of thermoplastics (namely, increased viscosity of the matrix failure) with enhanced heat resistance due to crystallization [2, 3].

Such PIs are particularly attractive owing to their excellent resistance to heat and to thermal oxidative degradation, high mechanical and adhesion characteristics, and resistance to solvents, especially to water and alkalis:

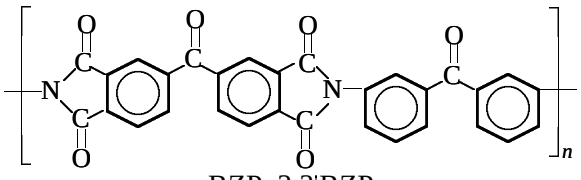

BZP–3,3'BZP

As shown in [4], the structure of this PI in its native state is largely determined by the conditions of its chemical synthesis. In particular, the BZP–3,3'BZP polyimide prepared under conditions of low-temperature chemical imidization in amide solvents is a partially crystalline substance with a low melting point (270–290°C). The same polyimide prepared by thermal imidization, depending on the reaction conditions, can be either amorphous or partially crystalline, with an appreciably higher melting point (340–350°C).

In this work we studied the features of the crystal structure of the BZP–3,3'BZP polyimide and the influence of changes in its structural organization on its rheological behavior. These data are useful for improving the procedures for PI processing to obtain a matrix of a composite.

EXPERIMENTAL

The initial prepolymer (polyamido acid, PAA) was prepared as a 25 wt % solution in *N*,*N*-dimethylacetamide (DMA) from BZP dianhydride (mp 225–226°C) recrystallized from dry acetic anhydride and diamine 3,3'BZP (for preparation procedure, see [4]), taken in a stoichiometric ratio. To prepare the oligoimide (OI), the amount of the dianhydride was decreased to 0.75 mol per mole diamine, and the reactive terminal amine groups were converted at the end of the syn-

1070-4272/01/7407-1183$25.00

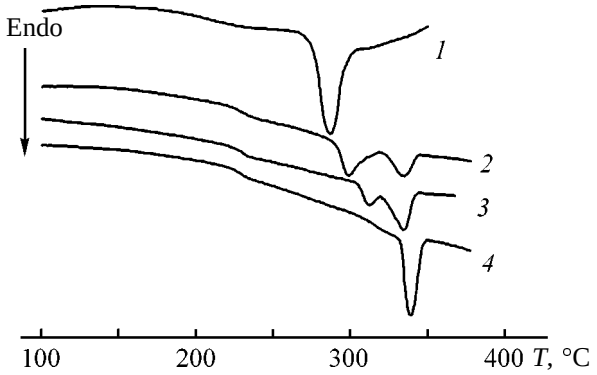

Fig. 1. DSC thermograms of BZP–3,3'BZP CPI samples: (*1*) initial and (*2*–*4*) additionally heated (*2*) at 250°C for 40 min, (*3*) at 300°C for 10 min, and (*4*) at 300°C for 60 min. (*T*) Temperature; the same for Figs. 3 and 4.

thesis by reaction with 0.5 mol of phthalic dianhydride.

Powdered PI and OI samples were prepared by chemical imidization in DMA solution [4]. To exhaustively remove residual solvents and agents of the imidizing mixture, the resulting samples were treated with diethyl ether in a Soxhlet apparatus for 5 h and dried under reduced pressure (50 mm Hg) at 140–150°C.

To prepare carbon-reinforced plastics, an ELUR-P-01 carbon tape was impregnated with a solution of BZP–3,3'BZP PAA, dried at 150°C to remove the solvent, and heated for 15 min at 230°C for thermal imidization of PAA. From the carbon fabric with the supported polymer, we prepared a 24-layer prepreg and pressed at 0.2 MPa under the following conditions: 300°C, 30 min; 350°C, 30 min. When powdered BZP–3,3'BZP PI (OI) was used as binder, it was added to the initial PAA solution in a 1 : 1 ratio, and the carbon tape was impregnated with the resulting suspension. Subsequent preparation and pressing of prepregs were performed similarly.

The IR spectra of PI (or OI) powder (KBr pellets) were taken on a Specord M-80 spectrophotometer. The degree of imidization was determined from the intensity of the imide absorption band at 1780 cm^{-1} [1].

The viscosity of melts of oligoimide powders was measured with a PIRSP rheogoniometer (Russia) with a cone–plane working unit (cone angle 1°, diameter 40 mm) at a constant shear rate of 1×10^{-2} s^{-1} at a given temperature.

The DSC curves of PIs were recorded on a Mettler microcalorimeter at a scanning rate of 10 deg min^{-1}.

The TGA curves were taken with a modified C derivatograph (MOM, Hungary) in air at a heating rate of 10 deg min^{-1}.

X-ray diffraction studies were performed on a DRON-5 diffractometer and an ARS-5 installation with a KRON-1 camera. The Ni-filtered CuK_α radiation was used. For measurements, polyimide powder was pelletized at room temperature and a pressure of 2 atm.

The mass-spectrometric thermal analysis (MTA) was performed with a device based on a magnetic sector mass spectrometer of the MKh-1320 type. The field ionization unit of a standard MKh-1320 device was modified with the aim to provide heating of thin polymer layers on a metallic support-heater with the welded thermocouple (support: oxidized 200-μm-thick Ta foil; thermocouple: Chromel–Alumel, 100 μm in diameter) in the vacuum chamber in the vicinity of the ion source. A thin layer of the polyimide powder was applied directly to the support surface with a putty knife. The sample weight was 10 mg. The area of the sample layer was about 20 mm^2. The heating rate was 10 deg s^{-1}. The rate of release of volatiles from the sample was judged from the intensity of the corresponding molecular peaks (e.g., 87 for DMA and 18 for water). For each PI sample five runs were performed to measure the rate of release of each volatile product.

The bending strength of carbon-reinforced plastics was determined by three-point bending with a 1958U-10-1 breaking machine at a loading rate of 5 mm min^{-1}. The shear moduli of elasticity G'_c and loss G''_c of carbon-reinforced plastics were determined with a torsion pendulum [5] in the range 20–400°C. The glass transition point of the composite T_{gc}, close to T_g of the matrix resin, was determined as the temperature at which G''_c reaches a maximum.

The interlaminar failure viscosity G_{IC} (start of the cleavage crack) of ~3-mm-thick carbon-reinforced plastics was determined by the double cantilever method [6, 7] using the calculation procedure from [7].

BZP–3,3'BZP polyimide prepared by chemical imidization (CPI) in DMA solution is partially crystalline and has a low melting point, T_{m1} = 295°C (Fig. 1, curve *1*). As CPI is additionally heated to 300°C, the melting peak T_{m1} gradually disappears from the DSC curves (Fig. 1, curves *2*–*4*), and a new melting peak, T_{m2}, appears at about 340°C. This fact suggests transition from one crystalline modification, CM1, of the CPI polymer to another, CM2, in the course of heating in the range 250–300°C. In the process, T_{m1} somewhat increases: from 295 to approximately

Table 1. Interplanar spacings *d* of PZB–3,3'BZP CPI samples prepared under various conditions of heat treatment

Sample no.	Treatment	*d*, A									Modification
1	Initial sample	10.5				4.73	4.43		3.90	3.23	CM1
2	250°C/40 min	10.3			5.30	4.70	4.40	4.08	3.94	3.30	CM1 + CM2
3	300°C/60 min		10.3	6.52	5.66	5.21	5.03	4.65	4.03		CM2
4	>350°C	Halo ~4.8									Isotropic

310°C. Heating of CPI above 350°C makes it amorphous (isotropic). The amorphous polymer is characterized only by the glass transition point T_g = 245°C, which becomes clearly detectable in the DSC curves only after heating of the initial CPI to 250°C and higher (Fig. 1, curves *2–4*).

Indeed, according to X-ray diffraction analysis, heating of CPI at 250 and 300°C is accompanied by transition from the structural modification CM1 characteristic of the initial CPI to the modification CM2 (Fig. 2, Table 1). Note that in the polymer heated at 250°C the CM1 and CM2 modifications apparently coexist (Table 1, sample no. 2).

The IR spectra show that the degree of imidization of the initial native CPI does not exceed 85%, and on heating to 300°C it increases to practically 100%. The weight loss (≤2%) of CPI samples on heating in the range 200–300°C, detected by TGA, may be due specifically to imidization of the residual amido acid units in the initial CPI on additional heating (so-called afterimidization) with release of water.

To examine in more detail the changes occurring in CPI in this temperature range, we studied by MTA [9] the kinetics of release of low-molecular-weight substances from the polymer. According to the mass spectra (Fig. 3), water release has a maximum at 293°C (Table 2). At the same time, approximately in the same temperature range the residual solvent DMA in which CPI was prepared is released also (Fig. 3, Table 2). Both water and the solvent, according to the mass spectra, are released in a narrow temperature range close to the melting point T_{m1} of the sample (Table 2). Presumably, afterimidization occurs after melting of CPI accompanied by release of DMA. A striking feature is that DMA is released at a very high temperature, exceeding by almost 140°C its boiling point.

It is known [10] that the amido acid units of PAA form with molecules of an amide solvent like DMA stable complexes decomposing in the course of PAA heating in the range 100–200°C. In our case the solvent molecules, probably involved in complexation with the residual amido acid units of CPI, are retained up to nearly 300°C (Table 2). Presumably, these solvent molecules are incorporated into the ordered CPI structure and are therefore released from the polymer only on melting. Apparently, melting of native CPI at T_{m1} "defrosts" the mobility of the polymer macromolecules and thus facilitates its afterimidization. The water release observed in this temperature range directly confirms this assumption (Fig. 3, Table 2).

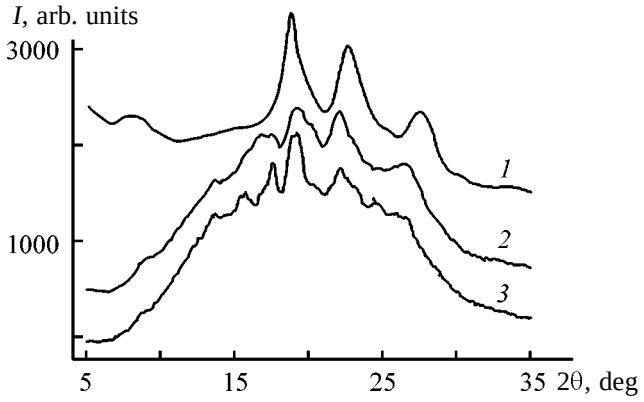

Fig. 2. X-ray diffraction patterns of BZP–3,3'BZP CPI samples: (*1*) initial and (*2*, *3*) heated at 250°C for 40 min and at 300°C for 60 min, respectively. (*I*) Intensity and (2θ) Bragg angle.

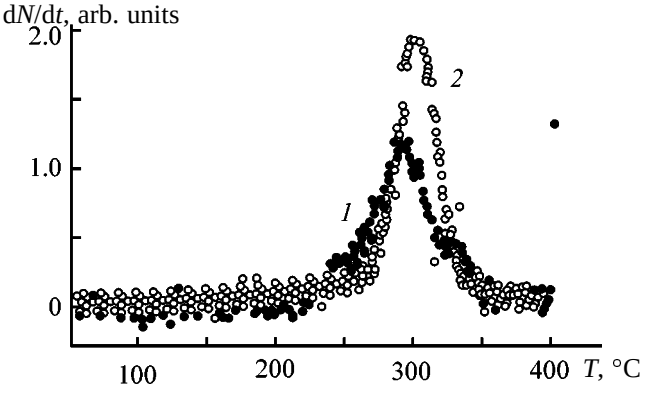

Fig. 3. Temperature dependences of the release rate d*N*/d*t* of (*1*) water and (*2*) solvent (DMA) from CPI samples, monitored by the corresponding peaks in the mass spectra.

Table 2. Melting points T_{m1} and mean values of T_{max} of the release of the solvent and water from BZP–3,3'BZP PI and OI samples

Sample	T_{max} of DMA	T_{max} of H_2O	T_{m1}
	°C		
CPI	303	293	295
OI	252	268	275

Thus, the initial native CPI is characterized by the presence of the crystalline modification CM1 whose melting point T_{m1} (290–310°C) is abnormally close to the glass transition point of the polymer (245°C). The ratio of these temperatures (converted to the Kelvin scale) is considerably lower than the ratios commonly observed for PI: T_m/T_g = 1.25 [3] or 1.3 [1]. Strictly speaking, the initial CPI is not a 100% imide, as indicated by the IR data. The MTA data show that the peaks of release of the solvent and water, accompanying afterimidization of CPI, are observed specifically in the range of CM1 melting. This fact suggests that the CM1 modification is characteristic of the incompletely imidized CPI sample only. In the course of heating and afterimidization, CM1 transforms into the high-melting modification CM2 typical of the completely imidized CPI sample. At the same time, Wang *et al.* show that native partially crystalline CPI that was rendered amorphous by heat treatment at 310°C and then kept in *N*-methyl-2-pyrrolidone at 160°C shows a melting peak in the DSC curve at abnormally low T_m = 300°C [11]. However, X-ray diffraction data that could prove the CM1 modification of the sample with T_m = 300°C are lacking in [11]. Therefore, the possibility of formation of the CM1 modification in the sample completely imidized at 310°C is still the matter of discussion and requires further studies.

Nevertheless, the existence of the CM1 modification in the initial BZP–3,3'BZP CPI is extremely important from the processing viewpoint, because this thermoplastic at moderate temperatures (300–350°C) can pass to the viscous-flow state required for its processing to a matrix of a composite. For more detailed study of the rheological behavior of CPI as influenced by structural rearrangements in the polymer, we studied OI of the following structure:

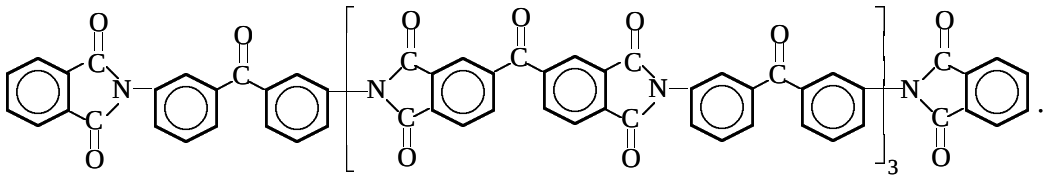

The oligoimide was also prepared by chemical imidization in the DMA solution.

Figure 4 shows the DSC curves of the initial native OI (curve *1*) and of that additionally heated at 250°C for 40 min (curve *2*). Two melting points are detected for OI: T_{m1} = 272–276°C with ΔH = 35–36 J g^{-1} and T_{m2} = 324°C with a low ΔH = 2–8 J g^{-1}, i.e., for OI, similar to CPI, the low-melting (about 275°C) crystalline modification exists also. According to the X-ray diffraction data (Table 3), this low-melting crystalline modification of OI is practically identical to the crystalline modification of CM1 detected in CPI (Table 1).

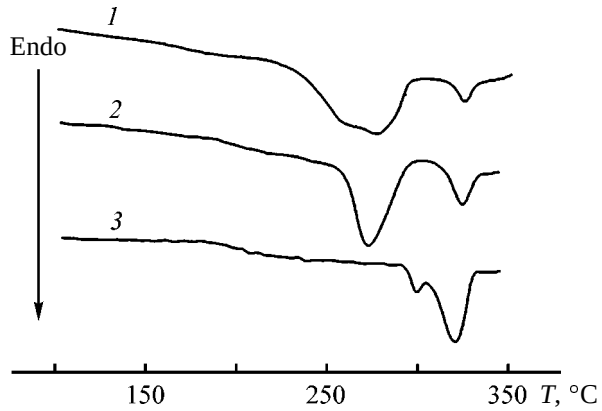

Fig. 4. DSC thermograms of BZP–3,3'BZP OI samples: (*1*) initial and (*2*, *3*) additionally heated at 250°C for 40 min and at 320°C for 60 min, respectively.

According to IR spectroscopic analysis, the degree of imidization of OI is no less than 90%. The TGA data show that the main weight loss, which does not exceed 1.5%, occurs in the range 200–270°C and is probably due to afterimidization of the OI samples. The MTA data (Table 2) show that, similar to CPI, the solvent and water are released from the OI sample in essentially the same temperature range close to the melting point of OI T_{m1}. The whole set of our data shows that, similar to CPI, the melting of OI at T_{m1} is followed by cyclization of the residual amido acid

Table 3. Interplanar spacings *d* of BZP–3,3'BZP OI samples after various heat treatments

Sample no.	Treatment	*d*, Å										Modification
1	Initial sample				5.20	4.70	4.40		3.90		3.30	CM1
2	250°C/40 min	9.94			5.28	4.73	4.42	4.10	3.96		3.32	CM1 + CM2
3	290°C/60 min	10.1	6.50	5.69	5.19	4.95	4.59	3.96	3.79	3.58	3.31	CM2
4	300°C/60 min					4.69		3.93	against background of halo ~4.7			*m*-Phase
5	≥330°C					Halo ~4.7						Isotropic
6	Annealing of sample no. 4 at 290°C/120 min	10.3	6.59	5.69	5.23	4.98	4.62	3.99				CM2

units and, strictly speaking, the low melting point T_{m1} is characteristic of the incompletely imidized sample.

It seemed interesting to compare how the viscosity of the melt of the initial OI varies in time under isothermal conditions at temperatures between T_{m1} and T_{m2} and above T_{m2}, since carbon-reinforced plastics are pressed specifically at these temperatures. The rheological behavior of OI at 330°C (Fig. 5, curve *4*), i.e., above T_{m2}, is typical of thermoplastic PI melts and suggests the possibility of obtaining stable flow of the OI melt for at least 1.5 h. Certain increase in the viscosity in the first minutes of the experiment is apparently due to increase in the oligomer rigidity owing to afterimidization. The DSC and X-ray diffraction data show that in this temperature range (above 330°C) OI passes to the fully amorphous state which is preserved on cooling the melt to room temperature at a rate of 10 deg min^{-1}.

At 280 (Fig. 5, curve *1*) and 290°C (curve *2*), the viscosity of OI fairly rapidly (within 10–20 min) increases to 10^6 Pa s. As follows from the DSC (Fig. 4, curve *3*) and X-ray diffraction (Table 3, sample no. 3) data, at 290°C OI undergoes the transition from the crystalline modification CM1 to CM2 (T_{m2} = 322°C), i.e., the increase in the viscosity at 280–290°C is primarily due to the structural transition of OI from CM1 to CM2.

At 300°C, the OI viscosity gradually (over a period of 20–40 min) increases from 10^3 to almost 10^5 Pa s (Fig. 5, curve *3*). Examination with a polarization microscope shows that the OI melt passes from the fully isotropic state to a mesophase. X-ray diffraction data (Table 3, sample no. 4) confirm that upon annealing for 1 h at 300°C the first crystalline modification CM1 transforms into a mesophase characterized by the presence of two clear reflections against the background of a halo. Subsequent cooling to 290°C and annealing at this temperature for 120 min convert this oligomer from the mesomorphic to fully crystalline (CM2 modification) state (Table 3, sample no. 6).

The whole set of X-ray diffraction and DSC data suggest the following scheme of the structural behavior of OI on melting above T_{m1} = 272°C.

Scheme of structural transitions in BZP–3,3'BZP at various heat treatments

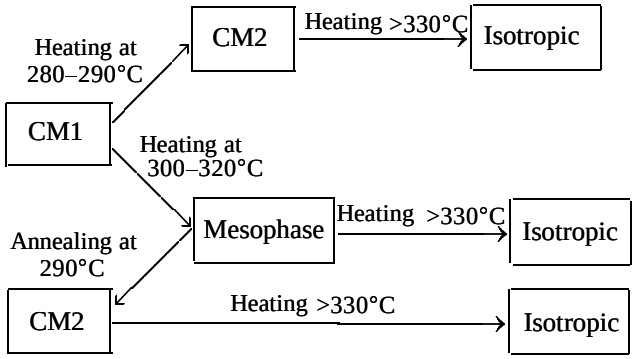

At 280–290°C, OI passes from the first (CM1) to the second (CM2) crystalline modification within a relatively short time (10–20 min). At 300–320°C, the crystalline modification CM1 transforms into a

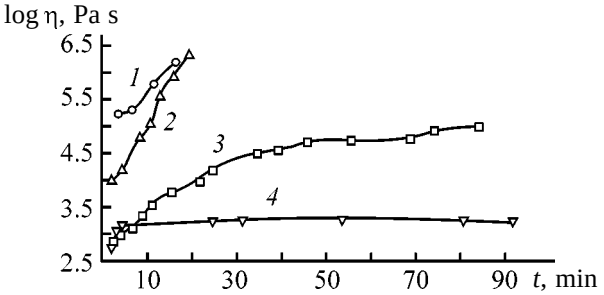

Fig. 5. Viscosity η of BZP–3,3'BZP OI melt as a function of time *t*. Temperature, °C: (*1*) 280, (*2*) 290, (*3*) 300, and (*4*) 330.

Table 4. Thermomechanical properties of carbon-reinforced plastics based on BZP–3,3'BZP PI

Sample no.	Polymer	V_f, %	σ_b, 20°C	σ_b, 200°C	G'_c, 20°C	T_{gc}, °C	G_{1C}, J m^{-2}
			GPa				
1	PI	48	0.9	0.84	3.7	250	470
2	PI + 50 wt % OI	55	1.0	0.94	4.2	231	620
3	PI + 50 wt % CPI	50	0.96	0.90	3.7	250	–

mesophase, which can be converted to the crystalline modification CM2 by annealing at 290°C for 2 h (Table 3, sample no. 6). Above 330°C, OI transforms into the fully isotropic state.

From BZP–3,3'BZP we prepared carbon-reinforced plastics and determined some of their thermomechanical characteristics: the volume fraction of fiber V_f, bending strength σ_b (at 20 and 200°C), shear modulus of elasticity G'_c, and glass transition point T_{gc} of the polymeric matrix of the composite. In Table 4 these characteristics are given for carbon-reinforced plastics based on the pure thermally imidized binder BZP–3,3'BZP PI and on the same binder with addition of 50 wt % OI (sample no. 2) or CPI (sample no. 3).

Addition of CPI and especially OI to the matrix of the carbon-reinforced plastic somewhat increases the volume fraction of fiber in the composite, probably owing to a decrease in the melt viscosity on pressing, which, in turn, increases σ_b and G'_c at room temperature. The bending strength of the carbon-reinforced plastics decreases insignificantly as the temperature is increased from 20 to 200°C, which is due to their sufficiently high glass transition points. However, a noticeable decrease in the glass transition point of the polymeric matrix of the composite prepared with OI (Table 4, sample no. 2) suggests lower softening point of the carbon-reinforced plastic in this case.

Table 4 also contains data on the interlaminar failure viscosity G_{IC} characterizing the crack resistance of the carbon-reinforced plastics. It is seen that addition of partially crystalline powdered OI to the binder noticeably increases G_{IC}.

Also, we prepared carbon-reinforced plastics using as prepregs the layers of carbon fabric with the CPI powder applied by electrostatic spraying. Such a procedure allowed us to abandon the use of a polyamido acid solution for impregnation of the carbon fabric and to prepare the composite on the basis of powdered partially crystalline CPI only. Samples of thus prepared carbon-reinforced plastic are characterized by high G_{IC}, at a level of 730–750 J cm^{-2}.

As noted above, native partially crystalline OI and CPI are rendered amorphous by heat treatment at temperatures above T_{m2}. Therefore, according to DSC, the polymeric matrix is amorphous in all the carbon-reinforced plastics under consideration (the final pressing temperature was 350°C).

Optimization of the pressing temperature and composition of the initial matrix, with the aim to attain simultaneously high values of strength, softening point, and failure viscosity of the resulting material, requires further study of fine structural rearrangements in the crystallizing fusible polyimide binder under conditions of temperature and force fields.

CONCLUSIONS

(1) BZP–3,3'BZP polyimide can exist in two crystalline modifications: CM1 with T_{m1} = 275–290 and CM2 with T_{m2} = 330–350°C. Appearance of the crystalline modification CM1 in the initial native polyimide prepared by chemical imidization in an amide solvent impedes complete imidization of the polymer, which is complete only on melting of the crystallites. Above 350°C the polymer passes into a fully isotropic state, and restoration of its crystalline state on cooling is practically impossible.

(2) It was shown by the example of the corresponding oligoimide that at temperature close to T_{m1} an increase in the viscosity of the oligoimide melt is due to structural transition from the low-melting crystalline modification CM1 to the high-melting modification CM2. The partially crystalline BZP–3,3'BZP polyimide in CM1 modification undergoes a similar structural transition in this temperature range. In the range between T_{m1} and T_{m2}, the oligoimide melt can pass to the mesomorphic state, with increase in the melt viscosity to 10^5 Pa s. Annealing of the mesophase at 290°C results in crystallization of the oligoimide in the CM2 modification.

(3) The partially crystalline BZP–3,3'BZP polyimide is a thermoplastic with a unique property:

Thanks to formation in the chemically imidized polymer of the low-melting crystalline modification CM1, it can be processed into a matrix of a carbon-reinforced composite at temperatures of 300–350°C close to T_g. The resulting carbon-reinforced plastics exhibit fairly high softening points (T_{gc} = 250°C), with high levels of strength (1 GPa) and failure viscosity (G_{IC} = 750 J m^{-2}).

REFERENCES

1. Bessonov, M.I., Koton, M.M., Kudryavtsev, V.V., and Laius, L.A., *Poliimidy – klass termostoikikh polimerov* (Polyimides: A Class of Heat-Resistant Polymers), Leningrad: Nauka, 1983.
2. Sroog, C.E., *Progr. Polym. Sci.*, 1991, vol. 16, pp. 561–694.
3. Sroog, C.E., *Proc. 4th European Technical Symp. on Polyimides and High Performance Polymers*, Montpellier (France), May 13–15, 1996, pp. 266–297.
4. Kudryavtsev, V.V., Meleshko, T.K., Kalbin, A.G., *et al.*, *Zh. Prikl. Khim.*, 1998, vol. 71, no. 12, pp. 2035–2040.
5. Yudin, V.E., Leksovskii, A.M., Sukhanova, N.A., *et al.*, *Mekh. Kompoz. Mater.*, 1989, no. 1, pp. 166–170.
6. *Interlaminar Response of Composite Materials*, Pagano, N.J., Ed., Amsterdam: Elsevier, 1989.
7. Friedrich, K., Walter, R., Carlsson, L.A., *et al.*, *J. Mater. Sci.*, 1989, vol. 29, pp. 3387–3398.
8. Cheng, S.Z.D., Mittleman, M.L., Janimak, J.J., *et al.*, *Polym. Prepr. Am. Chem. Soc., Polym. Chem. Ed.*, 1992, vol. 33, pp. 449–450.
9. Pozdnyakov, O.F., Redkov, B.N., Ginzburg, B.M., and Pozdnyakov, A.O., *Pis'ma Zh. Tekh. Fiz.*, 1998, vol. 24, no. 23, pp. 23–29.
10. Brekner, M.-J. and Feger, C., *J. Polym. Sci., Polym. Chem. Ed.*, 1987, vol. 25, no. 9, pp. 2479–2491.
11. Wang, J., DiBeneditto, A.T., Johnson, J.E., and Huang, S.J., *Polymer*, 1989, vol. 30, no. 4, pp. 718–721.

Russian Journal of Applied Chemistry, Vol. 74, No. 7, 2001, pp. 1190–1193. Translated from Zhurnal Prikladnoi Khimii, Vol. 74, No. 7, 2001, pp. 1158–1161.

MACROMOLECULAR CHEMISTRY AND POLYMERIC MATERIALS

Recombination Chemiluminescence in Photoirradiation of Epoxy Acrylate Polymer Compositions and Its Use for Monitoring of the Network Structure Development

O. L. Kramer, E. M. Battalov, A. I. Voloshin, and Yu. A. Prochukhan

Institute of Organic Chemistry, Ufa Scientific Center, Russian Academy of Sciences, Ufa, Bashkortostan, Russia

Received October 8, 2000; in final form, April 2001

Abstract—Photoinduced recombination chemiluminescence was applied for monitoring of the network structure formation under UV exposure of films prepared by esterification with acrylic acid of oligomers such as UP-612, ED-16, and Oksilin commercial epoxy resins. The chemiluminescence decay was described in terms of the fractal kinetics model. The spectral dimension parameter, apparent luminescence activation energies, and glass transition temperatures of the polymers were calculated.

Epoxy–acrylate resins polymerizing under UV irradiation find application as protective coatings for quartz fibers intended for fiber-optics systems and printed-circuit boards in radioelectronics [1]. Such protective coatings must satisfy a number of requirements which for the most part determine the properties of the articles, in particular, resistance to temperature and mechanical changes and the environment, tensile strength, etc. [2]. The properties of such polymers are mainly determined by the degree of cross-linking. There is a number of classic methods for estimating the latter parameter, of which we will mentioned that based on determining the degree of swelling of polymer in appropriate solvent [3]. In recent years, methods based on the use of luminophores [4], measurement of the post-polymerization reaction heats, UV spectroscopy, etc. have received development [5]. However, studies of cross-linked polymers still lack a uniform experimental approach. This makes urgent the search for new methods of determining, e.g., the degree of cross-linking of polymers, the active chain length, and the radical curing kinetics for such systems.

One of the methods for studying polymer properties that recently have found wide application is recombination luminescence [6]. Recombination luminescence is recorded as a weak light emission arising on UV exposure of organic glasses, resins, and other materials; it depends on the physical properties of the material, radiation energy, and the polarity of the medium. Irradiation can initiate ionization of molecular groups characterized by low electron affinity and photooxidation [7–9]. In the latter case, the luminescence is due to recombination of the leading radical oxidation chain and is treated as recombination chemiluminescence (CL).

In this work we applied recombination CL to monitoring of the network structure formation under UV exposure of films obtained from oligomers such as acrylated UP-612, ED-16, and Oksilin commercial epoxy resins.

EXPERIMENTAL

Epoxy–acrylate resins were synthesized by esterification with acrylic acid (AA) of equimolar amounts of epoxy oligomers in the presence of polymerization inhibitors at 120°C according to the scheme

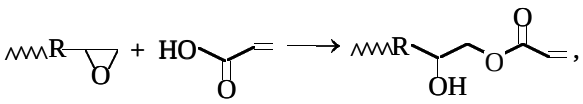

where R is the oligomeric block of epoxy oligomer.

The reaction was monitored by variation of the refractive index. As epoxy oligomers served UP-612, Oksilin, and ERD-16. Acrylic acid was purified by distillation. The resulting oligomer contians (according to epoxy numbers) both acrylates (<75%) and epoxy–acrylates. The assumed structural formulas of these oligomers can be presented as

1070-4272/01/7407-1190$25.00

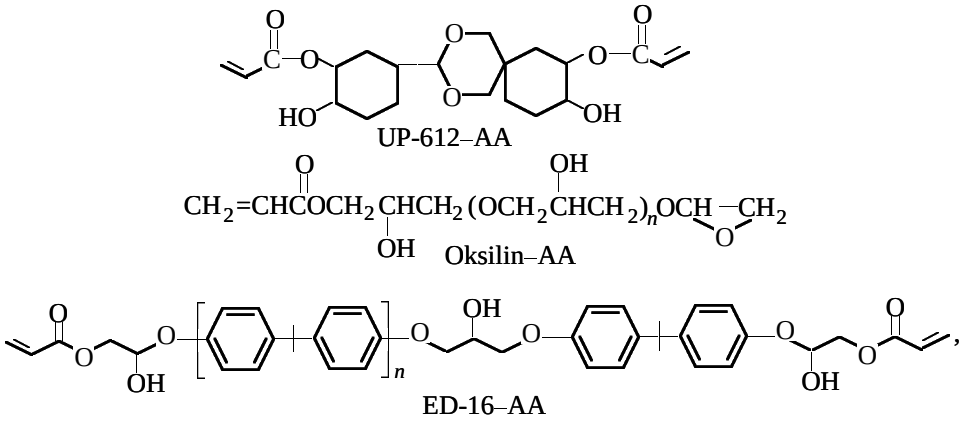

The CL kinetics after photoirradiation were studied using UP-612–AA, Oksilin–AA, and ED-16–AA films prepared from acetone solutions of the initial oligomers with $M_w \times 10^{-3}$ of 3.5, 3.6, and 3.7, respectively, containing 5% of benzophenone (BP) as photoinitiator. Films were ~10 μm thick; they were cut into 0.5 cm^2 squares and exposed to light with the wavelength of 313 nm cut by ZhS-3 and UFS-2 light filters from the spectra of two SVD-120 lamps (VIO-2 illuminator). The patterns of variation of the CL characteristics with the wavelength of the irradiating light were obtained using DKSSh-1000 xenon lamp and MZD-2M wide-aperture monochromator. The irradiating light intensity was determined with a ferrioxalate actinometer [10]. Chemiluminescence was recorded on a photometric setup equipped with a low-inertia temperature-control unit.

Upon exposure to the light with a wavelength of 313 nm, the preliminarily cured epoxyacrylate films that were kept for several days exhibit CL whose typical intensity decay curve is presented in Fig. 1.

The CL decay was described in terms of the fractal kinetics model proposed by Postnikov *et al.* [8, 11, 12]. According to this model, the observed rate constant k_1 of radical recombination varies with time as

$$k_t = k_0 t^{d_s/2 - 1},$$

Here, k_0 is a constant; $t > 1$ (or $t \approx 1$); and d is the "spectral dimension" parameter which is physically related to the diffusion-controlled aggregate [8].

The CL decay is described by the equation [8]

$$I_{cl} = I_1(1 + t/t_1)^{d_s/2 - 1} \alpha^{-2},$$

where I_{cl} is the CL intensity, rel. units; I_1 is the CL intensity at the moment t_1 of taking the first reading; and α is the parameter describing the part of the CL decay due to radical concentration decrease proper. The contribution from the parameter α is significant only at fairly long times.

Figure 2 presents, as an example, a set of curves characterizing the CL decay kinetics for ED-16–AA films cured at different irradiation doses, with the measurement delay time taken into account. The data obtained by processing these curves are presented in the table.

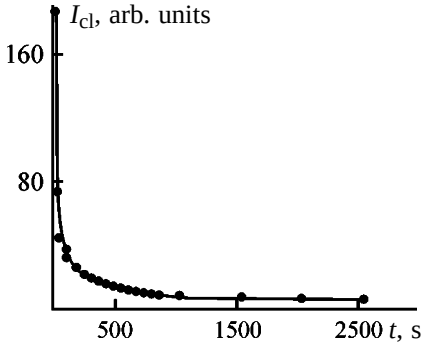

Fig. 1. CL decay curve of cured ED-16–AA film at the dose of 1.1×10^{19} photon cm^{-2}. (I_{cl}) CL intensity and (t) luminescence time; the same for Fig. 2.

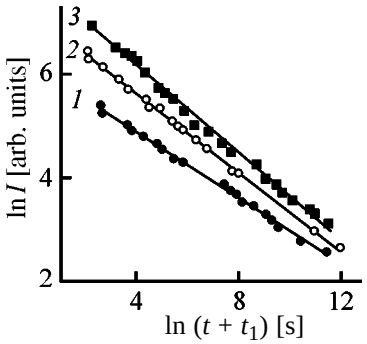

Fig. 2. Kinetic curves of CL decay for ED-16–AA samples cured by irradiation at λ = 313 nm. Irradiation dose $Q \times 10^{-19}$, photon cm^{-2}: (*1*) 1.1, (*2*) 6.4, and (*3*) 24.

Influence of the irradiation dose Q for polymer films on the spectral dimension parameter d_s

Oligomer	$Q \times 10^{-19}$, photon cm^{-2}	d_s
ED-16–AA	1.1	1.36
	6.4	1.26
	24.0	1.16
Oxilin–AA	1.2	1.37
	5.8	1.22
	26.0	1.14
UP-612–AA	0.9	1.32
	6.6	1.20
	24.3	1.18

Note: Spectral dimension is calculated accurately to within 15%.

The spectral dimension d_s determined by the type of inhomogeneous distribution of the reacting particles tends to decrease with increasing irradiation dose. This trend can be interpreted with taking into account formation of interpolymer bonds and three-dimensional structure under irradiation. The parameter d_s determines the space for random motion of peroxy radicals.

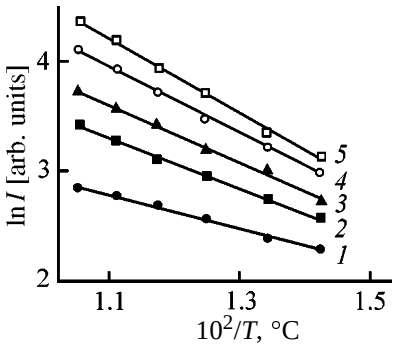

Fig. 3. Steady-state CL intensity I of the ED-16–AA film as a function of the temperature T in the Arrhenius equation coordinates. Irradiation dose Q, photon cm^{-2}: (*1*) 1.4×10^{16}, (*2*) 8.3×10^{16}, (*3*) 2.4×10^{17}, (*4*) 7.9×10^{17}, and (*5*) 1.2×10^{18}.

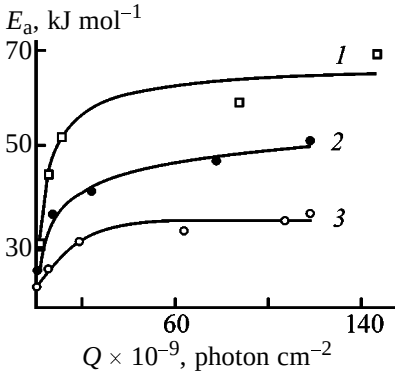

Fig. 4. Apparent activation energy E_a of steady-state CL as a function of the irradiation dose D of polymers (*1*) UP-612–AA, (*2*) ED-16–AA, and (*3*) Oksilin–AA.

Within fairly long time (2–3 h after recording the first point) the CL kinetics become virtually steady-state, with the CL intensity decreasing by less than 1% per hour even at 70°C. The steady-state character of the CL is, evidently, due to major diffusion-related restrictions posed on the reacting particles.

Temperature changes take the system out of the steady state, but under isothermal conditions the system comes to a new steady state. Evidently, under such conditions the response of the system to the temperature change is due to the structural changes in the matrix. Thus, the activation energy calculated from the temperature dependence of the steady-state CL intensity can be considered as a characteristic of the polymer matrix and its evolution during irradiation. The Arrhenius plots, similar to those shown in Fig. 3 for ED-16–AA, allowed calculation of E_a. Figure 4 shows how E_a varies with the irradiation dose. It is seen that under actual conditions formation of the polymer and its network structure is complete at irradiation doses of $(50–70) \times 10^{19}$ photon cm^{-2}. For example, for UPK-612–AA, ED-16–AA, and Oksilin–AA systems E_{max} is equal to 60.7, 48.1, and 34.8 kJ mol^{-1}, respectively. This parameter is, evidently, a function of the rigidity of the polymer network and, probably, reflects in an implicit way the degree of development of the polymer network. Also, account should be taken of the reactivity of the oligomers with triplet BP. The role of the latter as photoinitiator is confined to initiating the reaction of homolytic hydrogen detachment from the OH group of the secondary and tertiary C–H bonds and generating alkoxy- and carbon-centered radicals.

However, under conditions of long-term stationary irradiation, on the one hand, and relatively high rate of hydrogen detachment ($k = 10^5–10^6$ l mol^{-1} s^{-1} [13]), on the other, the reactivity of oligomers with BP in these systems is insignificant. At the same time, at low irradiation doses the reactivity of the oligomers is significant and essentially determines the network formation rate.

Under linear heating at a rate of about 10 deg min^{-1}, the plot of the CL intensity for the films prepared from ED-16–AA passes through a maximum in the temperature range 100–140°C. This suggests a glass–gel transition characterized by the glass transition temperature T_g in the temperature range indicated (Fig. 5). Plots for sample cured and kept for several

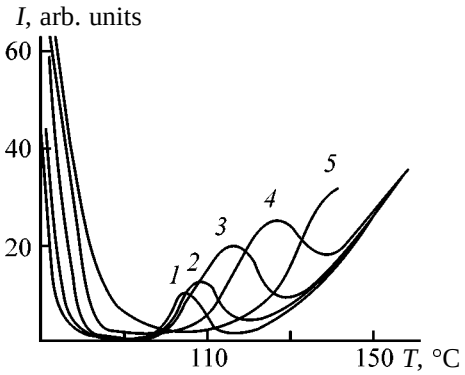

Fig. 5. Temperature dependence of the CL intensity for the polymer based on ED-16–AA. Film thickness 10 μm, λ = 313 nm. (*I*) Irradiation intensity. Irradiation dose *Q*, photon cm^{-2}: (*1*) 1.4×10^{16}, (*2*) 8.3×10^{16}, (*3*) 2.4×10^{17}, (*4*) 7.9×10^{17}, and (*5*) 3.3×10^{18}.

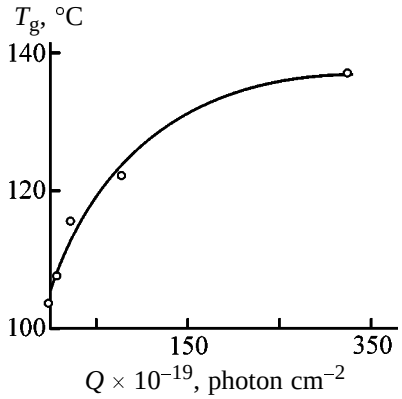

Fig. 6. Dependence of the glass transition temperature T_g, for ED-16–AA epoxy–acrylate polymer on the UV irradiation dose *Q*.

days but not subjected to subsequent photooxidation do not exhibit maximum in this temperature range under linear heating conditions. With increasing irradiation dose in the course of curing, the maxima of the luminescence curves shift to higher temperatures. Figure 6 shows how the parameter T_g varies with irradiation dose. Evidently, T_g, similar to E_a, describes the network formation during UV curing of epoxy–acrylate oligomers.

The data in Figs. 4 and 6 show that the irradiation doses at which the plots flatten out are of the same order of magnitude. The fact that the plots of the glass transition temperatures T_g and the activation energies E_a vs. irradiation dose attain saturation, i.e., that these parameters become independent of the amount of the photons taken up during further irradiation, evidences the maximal possible cross-linking of the polymers under the actual conditions.

CONCLUSION

Activation energy and glass transition temperature determined by the recombination luminescence method characterize the degree of cross-linking of UV-cured polymers. The spectral dimension decreases with increasing irradiation dose, while the apparent luminescence activation energies and glass transition temperatures for the polymers studied tend to increase.

REFERENCES

1. Zadontsev, B.G., Baranovskii, L.A., and Baranovskaya, N.F., *Epoksiakrilovye smoly: Obzornaya informatsiya. Khimicheskaya promyshlennost'. Epoksidnye smoly i materialy na ikh osnove*. (Epoxy–Acrylic Resins: Review. Chemical Industry. Epoxy Resins and Materials Thereof), Moscow: NIITEKhIM, 1981.
2. USSR Inventor's Certiicate no. 1 649 774.
3. Rafikov, S.R., Budtov, V.P., and Monakov, Yu.B., *Vvedenie v fizikokhimiyu rastvorov polimerov* (Introduction to Physical Chemistry of Polymer Solutions), Moscow: Nauka, 1978.
4. US Patent 5 598 005.
5. Lecamp, L., Yousset, B., Bunel, C., and Lebaudy, P., *Polymer*, 1999, vol. 40, no. 26, pp. 6313–6320.
6. Lange, J., Ekelof, R., and George, G.A., *Polymer*, 1998, vol. 39, no. 1, pp. 149–155.
7. Lewis, G.N. and Lipkin, D., *J. Am. Chem. Soc*., 1942, vol. 64, no. 12, pp. 2801–2807.
8. Postnikov, L.M. and Vinogradov, A.V., *Vysokomol. Soedin., Ser. B*., 1999, vol. 41, no. 4, pp. 706–711.
9. Korobeinikova, V.N., Kazakov, V.P., Aleev, R.S., and Chuvylin, Yu.N., *Vysokomol. Soedin., Ser. A*, 1974, vol. 16, no. 12, pp. 2717–2725.
10. Rabek, J.F., *Experimental Methods in Polymer Chemistry. Physical Principles and Applications*, Chichester, Wiley, 1980.
11. Postnikov, L.M. and Vinogradov, A.V., *Vysokomol. Soedin., Ser. A*, 1996, vol. 38, no. 6, pp. 950–958.
12. Postnikov, L.M. and Vinogradov, A.V., *Vysokomol. Soedin., Ser. A*, 1998, vol. 40, no. 4, pp. 643–648.
13. Guillet, J., *Polymer Photophysics and Photochemistry. An Introduction to the Study of Photoprocesses in Macromolecules*, Cambridge: Cambridge Univ. Press, 1985.

Russian Journal of Applied Chemistry, Vol. 74, No. 7, 2001, pp. 1194–1197. Translated from Zhurnal Prikladnoi Khimii, Vol. 74, No. 7, 2001, pp. 1162–1165.

MACROMOLECULAR CHEMISTRY AND POLYMERIC MATERIALS

Correction of Gel Chromatograms for Instrumental Broadening

T. S. Usmanov, A. R. Nabiullin, N. N. Sigaeva, V. P. Budtov, S. M. Usmanov, S. I. Spivak, and Yu. B. Monakov

Institute of Organic Chemistry, Ufa Scientific Center, Russian Academy of Sciences, Ufa, Bashkortostan, Russia

Received October 2, 2000; in final form, March 2001

Abstract—The Tikhonov regularization method was proposed for correction of gel chromatograms for instrumental broadening. The results obtained in solving the Tung equation by approximation and regularization methods and also in using the Gauss and Pearson distributions as a function of instrumental broadening were compared.

At present the gel-permeation chromatography (GPC) is a well-developed method of analysis of molecular characteristics and molecular-weight distribution (MWD) of polymers.

However, owing to nonideality and irregularity of chromatographic separation the chromatograms are smeared and, as a result, the MWD diagrams are broadened. The necessity of considering the smearing effect in processing of the experimental chromatograms causes significant complications in passing from gel chromatogram to MWD. A correction of chromatograms is essential when the MWD characteristics serve as the initial data for further calculations, e.g., for identification of the kinetic models of polymerization on the basis of the total MWD of a polymer [1–4].

In the general case the procedure of correction of chromatograms is reduced to solving the Tung equation [5, 6]

$$F(\nu) = \int_{\nu_2}^{\nu_2} W(y)\, G(\nu - y)\mathrm{d}y, \qquad (1)$$

where $F(\nu)$ is the experimental chromatogram; $W(y)$ is the required MWD; and $G(\nu - y)$ is the nucleus of the integral equation which describes the diffusion, concentration, and other effects resulting in a deviation of $F(\nu)$ from $W(y)$.

In the limiting case, when the diffusion is absent, $G(\nu - y) = 1$ and the function $W(y)$ becomes indentical to $F(\nu)$.

Numerous procedures for correction of chromatograms with the use of the Tung equation (1) were suggested [6–11]. All these procedures are generally based on various methods of numerical solution of the Fredholm integral equation of the first kind [1, 6, 12] and are associated with the incorrectly formulated problem. The latter is caused by the fact that, first, in numeral solution of Eq. (1) "oscillations" appear at the ends of the function $W(y)$, and, second, small variations in the slope of $F(\nu)$ result in significant variations in the shape of the resulting function $W(y)$.

When $F(\nu)$ is determined from an experiment with the highest accuracy and the function $G(\nu - y)$ is chosen correctly, the solution for $W(y)$ can be obtained by any procedures proposed in [6–11]. However, actually none of these two conditions can be realized: the analytical form of integral equation (1), which describes the smearing of the bands of polymer homologs in the chromatographic system, is unknown *a priori*, and a certain error δ occurs in all experimental results.

As a rule, this uncertainity of the functions $F(\nu)$ and $G(\nu - y)$ transforms into oscillations of $W(y)$, which is clearly pronounced at the ends of chromatograms, where the function $F(\nu)$ is determined with the lowest accuracy. The problem becomes still more complicated in the case of a large smearing or when the sample contains very narrow peaks.

To avoid these difficulties, the experimental chromatograms are usually presmoothed. In the procedures used in practice this smoothing was carried out in an explicit or implicit form, and the choice of the correction procedure was governed by the success of this operation rather than by the mathematical approach used [1, 6]. In this case, it should be noted that, when

1070-4272/01/7407-1194$25.00

the smoothing is rough, a part of characteristics of the chromatographic curve reflecting the true MWD of polymer can be lost, and when the smoothing has not been performed to completion, the oscillations inevitably appear in the solution of Eq. (1).

Thus, the practical experience of using the above methods shows that at present there is no procedure eliminating the effect of instrumental broadening in evaluation of MWD from the results of gel-chromatographic analysis with fair efficiency and minimum expenditure of time.

The Tung equation is a Fredholm equation of the first kind. Solving Eq. (1) gives the reverse problem of $W(y)$ reduction from the approximate values of $F_\delta(\nu)$, which is a feature of incorrectly formulated problem [13]. The Tikhonov regularization method is the most developed and efficient method of solving of the Fredholm integral equation of the first kind (1) [13, 14]. Therefore, in this work we attempt to use the Tikhonov regularization method for correction of chromatograms for instrumental broadening.

The regularizated solution $W_\alpha = R[\alpha, F_\delta(\nu)]$, i.e., the function $W_\alpha(y)$ at which the minimum of smoothing Tikhonov functional is reached, was selected as an approximated solution

$$M_\alpha(W) = \int_{-\infty}^{\infty} \left[\int_{-\infty}^{\infty} G(\nu - y)\, W(y)\mathrm{d}y - F_\delta(\nu) \right] + \alpha \int_{-\infty}^{\infty} \left[W^2 + (\mathrm{d}W/\mathrm{d}y)^2 \right] \mathrm{d}y, \quad (2)$$

where α is the numerical parameter of regularization, $\alpha > 0$.

We used the standard software IUPR for solving Fredholm single-dimension operator equation. The software realizes the Tikhonov regularizing algorithm [15–17] with selection of the regularization parameter by the generalized discrepancy principle [14, 18].

The regularization procedure gives the approximated solution $W(y)$ on the basis of *a priori* data, e.g., on the errors in the initial data and nucleus $G(\nu - y)$. Therefore, the proximity of the found solution to the true solution is governed by the choice of the nucleus $G(\nu - y)$, which is the function of the instrumental broadening. The selection of the function $G(\nu - y)$ depends on the model in hand, and for various levels of approximation to the instrumental broadening determined experimentally this function has its own form.

In solving Eq. (1) some researchers [5, 8, 9, 12] assume that the diffusion obeys the Gauss law; in this case, $G(\nu, y)$ is approximated by the Gaussian

$$G(\nu, y) = \frac{1}{\sigma(2\pi)^{1/2}} \exp[-(\nu - y)^2/2\sigma^2]. \quad (3)$$

However, in this case the "slopeness" of the instrumental broadening curves is not considered. The method of moments, considering the curve asymmetry [19], requires a great deal of preliminary experiments; in so doing, these experiments should be repeated with variation of the chromatographic conditions. Hence it follows that the choice of the instrumental broadening function should be not random but should follow from the features of chromatographic analysis.

We used the approximation of experimental data on the narrow-dispersion polymeric reference by the system of the Pearson density functions [20]:

$$G(x) = A^2 \frac{2m^{1/2}\Gamma(2^{1/m} - 1)}{\pi\Gamma(m - 1/2)w} \left[1 + 4\frac{2^{1/m} - 1}{w^2}(x - x_c)^2 \right]^{-m}, \quad (4)$$

where $x = (\nu - y)$; the parameters of Eq. (4) were determined from the correlation of the experimental chromatogram of the polystyrene reference sample and the calculated curve by the least-squares technique to be $A = 1.610$, $w = 1.474$, $m = 4.695$, and $x_c = 11.265$; $\Gamma(z)$ is the gamma function

$$\Gamma(z) = \int_{-\infty}^{\infty} t^{z-1} \exp(-t)\mathrm{d}t. \quad (5)$$

Previously [1, 19] it was shown that distributions of this type well approximate both the solution of the system of differential equations describing GPC process and the shape of the chromatogram of individual components.

Figure 1 presents the results of approximation of the experimental chromatogram (curve *1*) of narrow-disperse polystyrene reference sample by the Gaussian (curve *3*) and Pearson (curve *2*) distribution. As seen, the smearing in the chromatographic system in hand is asymmetric and is "sloped" to the range of high eluent volumes. The use of the Pearson distribution gives a higher approximation for description of the smearing of polymer homologs.

As a testing procedure we used the approximation method of solving the Tung equation [12], in which

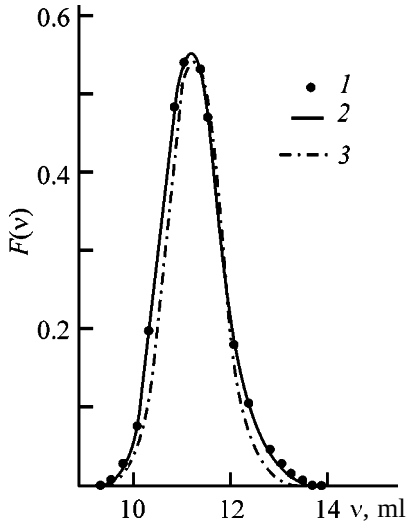

Fig. 1. Approximation of the experimental chromatogram of narrow-disperse polystyrene reference sample. (ν) Eluent volume; the same for Fig. 2. (*1*) Experimental curve, (*2*) Pearson distribution, and (*3*) Gauss distribution.

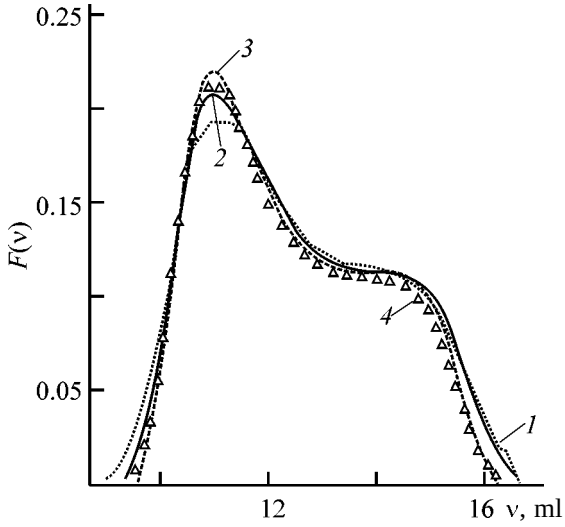

Fig. 2. Results of processing of (*1*) experimental chromatogram of polyisoprene sample by (*2, 3*) regularization technique with the use of the (*2*) Gauss and (*3*) Pearson distributions and (*4*) by the approximation method.

the nucleus of the integral equation and the sought-for solution are approximated by the following function:

$$Q(x) = \begin{cases} C_1 \exp(C_2 x), & x < x_1, \\ P_n(x), & x_1 \le x \le x_2, \\ C_3 \exp(C_4 x), & x < x_2, \end{cases} \qquad (6)$$

where $x = y - \nu$; $P_n(x)$ is a polynomial of the degree n; coefficients C_1–C_4 and also the polynomial coefficients and change-over points x_1 and x_2 are determined by least-squares fitting.

The function $Q(x)$ is butted end-to-end at the interval boundaries. The required solution of $W(y)$ is selected by the least-squares method with optimization of the functional

$$\Phi(z) = \sum_{i=1}^{N} [F(\nu_i) - \int_{y_2}^{y_1} W(y)\, G(y - \nu_i)\mathrm{d}y]^2, \qquad (7)$$

where the elements of vector z are the variables given in Eq. (6): C_1–C_4, change-over points x_1 and x_2, and the polynomial coefficients.

This method has some drawbacks. First, the search for the solution in the form of function (6) can result in some cases in the loss of information at the tails of the chromatograms. In other words, the exponential form of the function $W(y)$ at the ends of the curve, on the one hand, allows elimination of oscillations and, on the other hand, smoothes all data in these portions which can contain additional information. Second, the use of this method for calculation of the true MWD is time-consuming. In correction of multimodal distributions there is a need to increase the polynomial dimension in Eq. (6), which abruptly decreases the rate of processing even with the use of modern computers.

Nevertheless, in spite of these drawbacks, as shown in [12], this method gives data adequate to the true distribution. In so doing, there are no excessive maxima common under these conditions, since the oscillations appearing at the ends of the interval are suppressed by the form of the chosen function. Therefore, this procedure of processing of chromatograms was used for testing the calculations performed by the method proposed in this work.

The results of correction of chromatograms by the regularization technique are presented in Fig. 2. For comparison, we performed evaluations in which both the Pearson and Gauss distributions were used as a nucleus of Eq. (1).

Despite the fact that smearing of the sample in the chromatographic system in hand is insignificant, there are some differences between the experimental and corrected chromatograms. The maxima in the "corrected" distributions are more clearly pronounced, and these distrubutions become somewhat narrower. This fact has no dramatic effect on studying the molecular characteristics of a polymer but affects the determination of the kinetic parameters and also the shape of distributions of polymerization centers with respect to the kinetic activity [2, 3].

Curve *3* in Fig. 2, obtained with the use of the Pearson distribution as a nucleus of the integral equation, is closer to the solution obtained by the approximation method (curve *4*), especially in the range of large eluent volumes, in comparison with the symmetrical Gaussian (curve *2*). This is one more argument in favor of the chosen instrumental broadening function.

This procedure also takes into account the possible errors in choice of the nucleus of the integral equation $G(v - y)$. A quick-operating software allows the use of this procedure in automated processing of chromatographic experiments.

EXPERIMENTAL

The chromatograms of polymers were measured on a KhZh-1302 gel chromatograph. Four columns packed with styrogel (Waters) with the pore size of 3×10^2–5×10^6 Å were used. Chloroform was used as an eluent; the flow rate of the eluent was 2 ml min^{-1}. The system of columns was calibrated from polystyrene references with narrow MWD ($M_w/M_n \cong 1.2$) using the Benoit universal dependence [21] and the relation between the molecular weight of polydiene and the intrinsic viscosity [22]. All calculations were carried out using a specially developed software in the Turbo Pascal environment.

CONCLUSION

A procedure of correction of gel chromatograms was developed, based on the Tikhonov regularization method and approximation of the nucleus of the integral equation by the Pearson distribution. The proposed procedure allows correction of chromatograms without presmoothing and with consideration of asymmetry of the instrumental broadening function.

ACKNOWLEDGMENTS

The study was financially supported by the Russian Foundation for Basic Research (project no. 99-03-33437).

REFERENCES

1. Belen'kii, B.G. and Vilenchik, L.Z., *Khromatografiya polimerov* (Chromatography of Polymers), Moscow: Khimiya, 1978.
2. Sigaeva, N.N., Usmanov, T.S., Shirokova, E.A., *et al.*, *Dokl. Ross. Akad. Nauk.*, 1999, vol. 365, no. 2, pp. 221–224.
3. Sigaeva, N.N., Usmanov, T.S., Budtov, V.P., *et al.*, *Vysokomol. Soedin.*, 2000, vol. 42, no. 1, pp. 112–117.
4. Sigaeva, N.N., Usmanov, T.S., Spivak, S.I., *et al.*, *Bashk. Khim. Zh.*, 2000, vol. 7, no. 2, pp. 36–41.
5. Tung, L.H., *J. Appl. Polym. Sci.*, 1966, vol. 10, pp. 375–385.
6. Tung, L.H., *Sep. Sci.*, 1970, vol. 5, no. 4, pp. 429–436.
7. Provder, T. and Rozen, E.M., *Sep. Sci.*, 1970, vol. 5, no. 4, pp. 437–484.
8. Pierce, P.E. and Armonas, J.E., *J. Polym. Sci., Ser. C*, 1968, no. 21, pp. 23–29.
9. Balke, S.T. and Hamielec, A.E., *J. Appl. Polym. Sci.*, 1969, vol. 13, pp. 1381–1420.
10. Rozen, E.M. and Provder, T., *Sep. Sci.*, 1970, vol. 5, no. 4, pp. 485–521.
11. Rozen, E.M. and Provder, T., *J. Appl. Polym. Sci.*, 1971, vol. 15, pp. 1687–1702.
12. Kislov, E.N., Zotikov, E.N., Podosenova, N.G., *et al.*, *Vysokomol. Soedin., Ser. A*, 1978, vol. 20, no. 8, pp. 1910–1912.
13. Tikhonov, A.N. and Arsenin, V.Ya., *Metody resheniya nekorrektnykh zadach* (Methods of Solving Incorrect Problems), Moscow: Nauka, 1986.
14. Tikhonov, A.N., Goncharskii, A.V., Stepanov, V.V., and Yagola, A.G., *Chislennye metody resheniya nekorrektnykh zadach* (Numerical Methods of Solving Incorrect Problems), Moscow: Nauka, 1990.
15. Usmanov, S.M., *Izv. Vyssh. Uchebn. Zaved., Ser. Fiz.*, 1991, no. 10, pp. 102–107.
16. Usmanov, S.M., *Chislennye metody resheniya nekorrektno postavlennykh zadach i avtomatizirovannaya matematicheskaya obrabotka dannykh relaksatsionnoi spektroskopii* (Numerical Methods of Solving Incorrect Problems and Automated Processing of Data of Relaxation Spectroscopy), Ufa: Bashk. Gos. Univ., 1992.
17. Usmanov, S.M., *Relaksatsionnaya polyarizatsiya dielektrikov. Raschet spektrov vremen dielektricheskoi relaksatsii* (Relaxation Polarization of Dielectrics. Evaluation of Spectra of Dielectric Relaxation Times), Moscow: Nauka, 1996.
18. Tikhonov, A.N., Leonov, A.S., and Yagola, A.G., *Nelineinye nekorrektnye zadachi* (Nonlinear Incorrect Problems), Moscow: Nauka, 1995.
19. Vilenchik, L.Z., Belen'kii, B.G., Aleksandrov, M.L., and Reifman, L.S., *Vysokomol. Soedin., Ser. A*, 1976, vol. 18, no. 4, pp. 946–948.
20. Pollard, J.H., *A Handbook of Numerical and Statistical Techniques*, Cambridge: Cambridge Univ. Press, 1977.
21. Benoit, H., Crubisic, L., and Rempp, P.A., *J. Polym. Sci., Part B*, 1967, vol. 5, no. 9, pp. 753–759.
22. Berg, A.A., Kozlov, V.G., Budtov, V.P., *et al.*, *Vysokomol. Soedin.*, 1980, vol. 22, no. 3, pp. 543–550.

Russian Journal of Applied Chemistry, Vol. 74, No. 7, 2001, pp. 1198–1202. Translated from Zhurnal Prikladnoi Khimii, Vol. 74, No. 7, 2001, pp. 1166 1169.

MACROMOLECULAR CHEMISTRY AND POLYMERIC MATERIALS

Influence of the Phase Distribution of Filler on the Viscosity of Heterogeneous Polymer Blends

A. E. Zaikin and V. V. Molokin

Kazan State Technological Institute, Kazan, Tatarstan, Russia

Received December 14, 2000; in final form, May 2001

Abstract—The influence of the distribution of carbon black between phases of binary heterogeneous blends of polyethylene with elastomers on the viscosity of their melts was studied.

Materials based on polymer blends containing disperse fillers find increasing use [1–3]. However, the rheological properties of such materials are studied poorly. Furthermore, it is known that particles of finely dispersed fillers are usually distributed nonuniformly between the phases of heterogeneous polymer blends and that changes in their distribution can significantly affect the properties of the blends [1, 4–6]. However, in most cases the influence of this distribution on the rheological properties of polymer blends was not taken into account. Only a few works consider this problem [7–10]. However, no general trend was revealed in the influence of the phase distribution of filler particles on the rheological properties of polymer blends [4]. Revealing such trends is of scientific and practical interest and is particularly urgent for blends used in industry.

EXPERIMENTAL

In this work we studied blends of polyethylene with various elastomers, filled with carbon black (CB). We used low-density polyethylene (LDPE) of 15 803-020 brand with the viscosity-average molecular weight M_η = 37 000 and the melt flow index (MFI) of 2.4 g/10 min (at 190°C and a load of 2.16 kg) and high-density polyethylene (HDPE) of 273 brand with $M_w = 2.6 \times 10^5$ and MFI 0.55 g/10 min (190°C, 5 kg). Polyurethane thermoelastoplastic (PU) of Urelan brand, prepared from polyfurite, diphenylmethane-4,4'-diyl diisocyanate, and 1,4-butanediol in the molar ratio 1 : 2 : 1, had the molecular weight of 3.5×10^4 and MFI 60 g/10 min (190°C, 5 kg). Isoprene–styrene block copolymer of the styrene–isoprene–styrene type of IST-30 brand, containing 30 wt % styrene, had $M_w = 7.3 \times 10^4$ and MFI 4.5 g/10 min (190°C, 5 kg). Butadiene–acrylonitrile rubber of SKN-40m brand, containing 39.5 wt % acrylonitrile, had $M_\eta = 2.2 \times 10^5$ and the Mooney viscosity of 54. As disperse filler we used N 254 carbon black with the mean size of primary aggregates of 28 nm and specific adsorption surface area of 225 $m^2 g^{-1}$.

The components were blended on rollers at 130–140°C for the materials containing LDPE and at 145–155°C for those containing HDPE. To control the CB distribution between the phases of polymer blends, the sequence of mixing was varied [1, 5]. According to one procedure, CB was preliminarily dispersed in a melt of one of the polymers, after which the second polymer was added. According to another procedure, CB was added to a melt of the polymer blend prepared in advance. The mixing time was 5 min in each stage. Hereinafter, the sequence of mixing is indicated by placing in parentheses the components mixed in advance. All polymers contained 0.2 wt % Irganox 1010 stabilizer to prevent thermal oxidative degradation.

In all the HDPE + SKN blends the SKN phase was subjected to "dynamic" vulcanization directly on rollers in the course of mixing. To do this, we added to the ready mixture on the tenth minute of mixing 4 wt % of the standard sulfur vulcanizing mixture of the composition (wt %) ZnO 50, stearic acid 15, 2-mercaptobenzothiazole 15, and sulfur 20 [11], after which the mixing was continued for an additional 10 min.

The viscosities of the melts of the polymers and their blends were measured with an IIRT capillary viscometer at a constant pressure by a known procedure [12]. To take into account the pressure loss at the inlet of the melt into the capillary, we used two capillaries of different length [12].

1070-4272/01/7407-1198$25.00

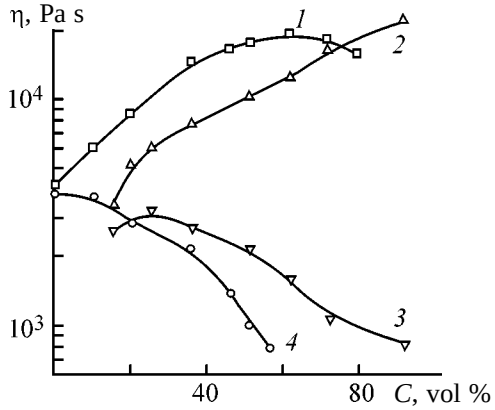

Fig. 1. Apparent viscosity η of LDPE + PU + CB blends as a function of the PU content *C*. CB content 5.4 vol %. Sequence of component mixing: (*1*, *4*) (PE + CB) + PU and (*2*, *3*) (PU + CB) + PE. Measurement conditions: (*1*, *2*) 130°C, shear stress $\tau = 1.25 \times 10^5$ Pa; (*3*, *4*) 190°C, $\tau = 39 \times 10^4$ Pa.

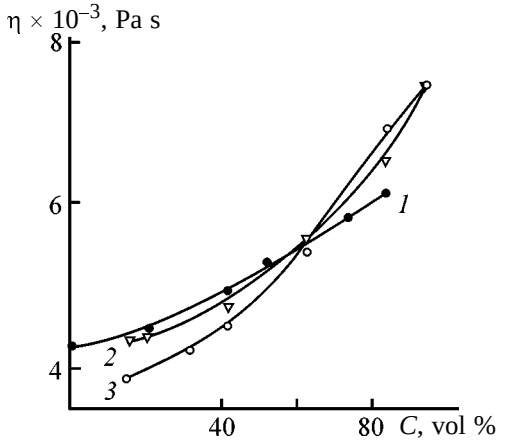

Fig. 3. Apparent viscosity η of the LDPE + IST + CB blend at 190°C at 190°C and $\tau = 3.9 \times 10^4$ Pa as influenced by the IST content *C*. CB content 5.3 vol %. Sequence of component mixing: (*1*) (PE + CB) + IST, (*2*) (PE + IST) + CB, and (*3*) (IST + CB) + PE.

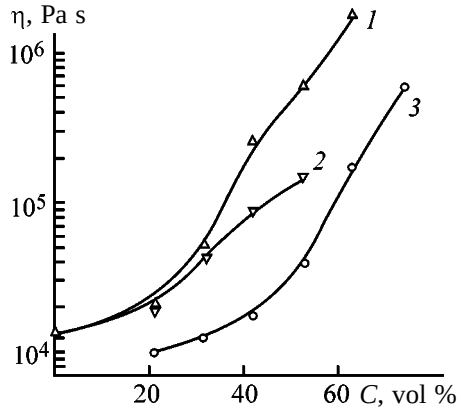

Fig. 2. Apparent viscosity η of HDPE + SKN + CB blends at 190°C and $\tau = 1.8 \times 10^5$ Pa as a function of the SKN content *C*. CB content 8.4 wt %. Sequence of component mixing: (*1*) (PE + CB) + SKN, (*2*) (PE + SKN) + CB, and (*3*) (SKN + CB) + PE.

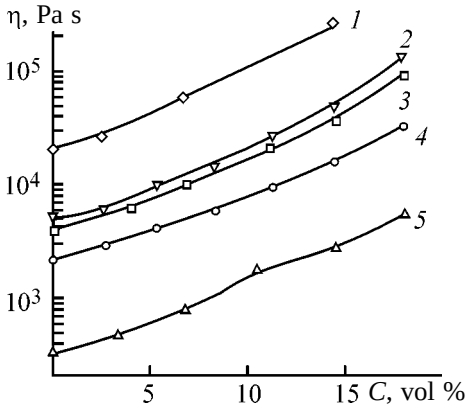

Fig. 4. Apparent viscosity η of polymers at $\tau = 3.9 \times 10^4$ Pa as a function of the CB content *C*. (*1*, *5*) PU, (*2*, *4*) LDPE, and (*3*) IST. Measurement temperature, °C: (*1*, *2*) 130 and (*3*–*5*) 190.

It is known that the mutual solubility of the components of sufficiently high molecular weight in the systems PE + PU, PE + SKN-40, and PE + IST-30 in a wide temperature range does not exceed 1% [13–15].

Finely dispersed filler practically fully remains in that phase of the heterogeneous polymer blend into which it was preliminarily introduced [1, 4, 5]. This fact was used to control the filler distribution between the phases of polymer blends.

Studies showed that the viscosity η of the melt of the filled polymer blend depends on the phase distribution of the filler. This dependence is the more pronounced, the larger the difference between the polymer components in viscosity (Figs. 1–3). For example, the viscosities of LDPE and IST-30 at 190°C are close (Fig. 4); therefore, the viscosity η of their blend only slightly depends on the phase distribution of CB (Fig. 3). In the system LDPE–PU, the difference in η (Fig. 4) is larger, and hence the effect of the sequence of mixing is stronger (Fig. 1). The strongest effect of the sequence of mixing on η is observed with HDPE + SKN blends (Fig. 2) in which SKN shows no flowability because its phase is vulcanized under dynamic conditions on mixing [2, 3].

The experimental data (Figs. 1–3) allow us to reveal the following regular trends in variation of the viscosity of the polymer blends as influenced by the phase distribution of the filler. All the systems in a wide range of the component ratios have the lowest η in the case of localization of CB in the more viscous

component and the highest η in the opposite case. This relationship is observed when the relative contents of the polymers are comparable or when the low-viscous polymer prevails. However, at high concentrations of the more viscous component the influence of the phase distribution of CB on the flowability of the blend is quite opposite (Figs. 1–3). Hence, as the polymer ratio is changed, the influence of the sequence of component mixing on the viscosity of the blend changes. This trend is observed with PE + PU and PE + IST blends. The stronger the difference between the polymer components in viscosity, the narrower the range of relative concentrations in which the highest viscosity is observed when CB is localized in the phase of the low-viscosity polymer. No such trend is observed with HDPE + SKN blends in which the elastomer phase shows no flowability (Fig. 2).

The compositions prepared by adding CB to the polymer blend prepared in advance have intermediate viscosity in the entire composition range (Figs. 2, 3).

It is important that the revealed trends in the influence of the mixing sequence on the viscosity of the blends are related neither to features of polymer–CB interactions nor to different degree of degradation of the polymer components in the course of filling; these trends are governed exclusively by the ratio of the polymer viscosities. This follows from variation of the viscosity of the same composition LDPE + PU + CB at different temperatures (Fig. 1). At 190°C the blends prepared by the scheme (PE + CB) + PU show the highest flowability, whereas at 130°C the system (PU + CB) + PE is the least viscous (Fig. 1). This difference is due to the fact that at 190 and 130°C the less viscous components are PU and LDPE, respectively (Fig. 4). Hence, at both temperatures the viscosity of the blend in a wide composition range is lower if CB is localized in the phase of the more viscous polymer.

The simplest explanation of the observed influence of the phase distribution of CB on the viscosity of polymer blends involves an assumption that the viscosity of blends at filling varies in accordance with variation of the viscosities of the phases. Such explanation was already made in [9, 10]. According to this assumption, the blend viscosity will be the highest if all CB is localized in the phase of the polymer whose viscosity increases on filling to a greater extent.

To reveal the effect of filler on the polymer viscosity, it is appropriate to use well-known expressions fairly adequately describing the experimental dependences $\eta = f(\varphi)$ [16], e.g., the Mooney equation $\ln(\eta/\eta_0) = K_E\varphi(1 - \varphi/\varphi_m)$ or the equation $\eta/\eta_0 = (1 - \varphi/\varphi_m)^{-2.5}$, where η is the viscosity of the composition, η_0 is the viscosity of the initial polymer, φ is the volume fraction of the filler in the polymer, φ_m is the volume fraction of the filler at its maximally close packing, and k_E is the Einstein's coefficient.

These equations and experimental data (Fig. 4) show that, the higher the polymer viscosity, the larger its absolute increase on filling. Then, according to the above assumption, the viscosity of the blend will be the highest when the filler is localized in the phase of the more viscous polymer. However, in the major part of the range of polymer ratios the trend is opposite (Figs. 1–3). Hence, this assumption is incorrect.

The revealed trends can be explained by considering the structure and behavior of polymer blends in a flow. It is known that the rheological properties of heterogeneous polymer blends are not additive. The viscosity of a two-phase polymer blend is mainly determined by the viscosity of the dispersion medium [1, 17, 18]. Under conditions of flow, in the major part of the range of the component ratios, the low-viscous polymer forms the continuous phase, and it is this polymer that determines the viscosity of the blend. When both phases are continuous, the low-viscosity phase will experience larger shear strains. Hence, in this composition range also the rheology of the blend will be mostly determined by the rheology of the low-viscosity polymer. Therefore, in a wide range of polymer ratios filling of the low-viscosity phase increases the viscosity of the blend to a greater extent than filling of the high-viscosity phase (Figs. 1–3).

However, at a low content of the low-viscosity component the pattern changes. In this case, even under the flow conditions, the dispersion medium is formed by a high-viscosity polymer which mainly determines the viscosity of the system. Therefore, in this composition range introduction of the filler into the more viscous dispersion medium decreases the melt flowability to a greater extent than filling of the less viscous dispersed phase. Hence, the change in the influence of the phase distribution of CB on the blend viscosity at variation of the polymer ratio is due to the fact that the low-viscosity polymer, which initially was the dispersion medium, becomes the dispersed phase. It is known that, the larger the difference between the polymeric components in viscosity, the narrower the composition range in which the high-viscosity polymer can form a continuous phase [1, 17–19] and hence the narrower the range in which the highest viscosity is observed with the blend in which

CB is localized in the more viscous polymer. In the PE + SKN blend prepared under conditions of dynamic vulcanization, the continuous phase is always PE. With this blend, the above-discussed change in the influence of the sequence of the component mixing on the viscosity is not observed (Fig. 2).

The feature of the PE + SKN blend is that at a low content of the elastomer (up to 30 vol %) the flowability of the system PE + CB is lower than that of the system (SKN + CB) + PE (Fig. 2) at equal CB content. From the viewpoint of composition, this relationship seems abnormal. Indeed, addition to the system PE + CB of the nonflowing vulcanized elastomer decreases its viscosity. However, when taking into account the CB distribution, the pattern becomes quite logical. Actually we compare the viscosity of PE containing finely dispersed CB with that of PE containing relatively coarsely dispersed rubber particles incorporating the same CB. It is known that the viscosity of any fluid increases as the degree of dispersion and specific surface area of the filler increase [20]. It is quite reasonable that relatively coarsely dispersed (5–20 μm) rubber particles present in PE in an amount of up to 20–30 vol % do not increase the PE viscosity to the same extent as finely dispersed (specific surface area 225 $m^2 g^{-1}$) CB in an amount of 5–8 vol %. Indeed, CB in the PE phase binds by its very developed surface a large number of PE macromolecules [20], considerably increasing the melt viscosity. When CB is localized in the coarse particles of the added elastomer phase, it does not exert such an effect on PE, and the viscosity of the system becomes lower.

When CB is added to a polymer blend prepared in advance, it is mainly localized in the less viscous polymer [1, 5]. Therefore, the flowability of the blend is relatively low and close to that of the system prepared by adding CB in advance to the less viscous polymeric component (Figs. 1–3). If the fraction of the low-viscosity polymer is low, a significant fraction of CB is localized in the continuous high-viscosity phase. As a result, the viscosity of such a blend is intermediate between the two extreme cases of the phase distribution of CB.

CONCLUSIONS

(1) Distribution of filler particles between the phases of heterogeneous polymer blends considerably affects their viscosity, because the contribution of the polymeric phases to the rheological properties of the blend is out of proportion.

(2) The lowest viscosity is observed when all the filler is localized in the dispersed phase; in the range in which both polymeric phases are continuous, the viscosity is the lowest when the filler is localized in the more viscous polymeric component.

REFERENCES

1. Kuleznev, V.N., *Smesi polimerov* (Polymer Blends), Moscow: Khimiya, 1980.
2. Kresge, E.N., *Polymer Blends*, Paul, D.R. and Newman, S., Eds., New York: Academic, 1978, vol. 2. Translated under the title *Polimernye smesi*, Moscow: Mir, 1981, pp. 312–338.
3. Kanauzova, A.A., Yumashev, M.A., and Dontsov, A.A., *Poluchenie termoplastichnykh rezin metodom "dinamicheskoi vulkanizatsii" i ikh svoistva: Tematicheskii obzor* (Preparation of Thermoplastic Rubbers by "Dynamic Vulcanization" and Their Properties: Topical Review), Moscow: TsNIITEIneftekhim, 1985.
4. McDonel, E.C., Baranwal, K.C., and Andries, J.C., *Polymer Blends*, Paul, D.R. and Newman, S., Eds., New York: Academic, 1978, vol. 2. Translated under the title *Polimernye smesi*, Moscow: Mir, 1981, pp. 280–311.
5. Hess, W.M. and Wiedenhaefer, J., *Rubber World*, 1982, vol. 186, no. 6, pp. 9–27.
6. Pavlii, V.G., Zaikin, A.E., and Kuznetsov, E.V., *Vysokomol. Soedin., Ser. A*, 1987, vol. 29, no. 3, pp. 447–450.
7. Skok, V.I., Kornev, A.E., Vostrokrutov, E.G., *et al.*, *Tr. Mosk. Inst. Tonk. Khim. Tekhnol.*, 1973, vol. 3, no. 2, pp. 219–225.
8. Sircar, A.K., Lamond, T.G., and Pinter, P.E., *Rubber Chem. Technol.*, 1974, vol. 47, no. 1, pp. 48–56.
9. Pavlii, V.G., Zaikin, A.E., and Kuznetsov, E.V., *Plast. Massy*, 1985, no. 9, pp. 25–26.
10. Savel'ev, A.V., Kiselev, V.Ya., and Tutorskii, I.A., *Plast. Massy*, 1992, no. 1, pp. 36–38.
11. Zakharchenko, P.I., Yashunskaya, F.I., Evstratov, V.F., and Orlovskii, P.N., *Spravochnik rezinshchika: Materialy rezinovogo proizvodstva* (Handbook of Rubber Manufacturer: Materials of Rubber Production), Moscow: Khimiya, 1971.
12. Kalinchev, E.L. and Sakovtseva, M.B., *Svoistva i pererabotka termoplastov* (Properties and Processing of Thermoplastics), Leningrad: Khimiya, 1983.
13. Nesterov, A.E. and Lipatov, Yu.S., *Fazovoe sostoyanie rastvorov i smesei polimerov: Spravochnik* (Phase State of Polymer Solutions and Blends: Handbook), Kiev: Naukova Dumka, 1987.
14. Chalykh, A.E., Gerasimov, V.K., and Mikhai-

lov, Yu.M., *Diagrammy fazovogo sostoyaniya polimernykh smesei* (Phase Diagrams of Polymer Blends), Moscow: Yanus-K, 1998.

15. Krause, S., *Polymer Blends*, Paul, D.R. and Newman, S., Eds., New York: Academic, 1978, vol. 2. Translated under the title *Polimernye smesi*, Moscow: Mir, 1981, pp. 26–138.
16. Nielsen, L.E., *Mechanical Properties of Polymers and Composites*, New York: Marcel Dekker, 1974.
17. Han, C.D. and Kim, Y.W., *J. Appl. Polym. Sci.*, 1975, vol. 19, no. 10, pp. 2831–2843.
18. Kuleznev, V.N., Konyukh, I.V., Vinogradov, G.V., *et al.*, *Kolloidn. Zh.*, 1965, vol. 27, no. 4, pp. 540–545.
19. Oene, H. van, *Polymer Blends*, Paul, D.R. and Newman, S., Eds., New York: Academic, 1978, vol. 2. Translated under the title *Polimernye smesi*, Moscow: Mir, 1981, pp. 337–396.
20. Verhelst, W.F., Walthuis, K.G., and Voet, A., *Rubber Chem. Technol.*, 1977, vol. 50, no. 4, pp. 735–746.

Russian Journal of Applied Chemistry, Vol. 74, No. 7, 2001, pp. 1203–1206. Translated from Zhurnal Prikladnoi Khimii, Vol. 74, No. 7, 2001, pp. 1170–1173.

MACROMOLECULAR CHEMISTRY AND POLYMERIC MATERIALS

Behavior of Tetrazole-containing Acrylic Hydrogels in Electrolyte Solutions

A. V. Igrunova, N. V. Sirotinkin, and M. V. Uspenskaya

St. Petersburg State Technological Institute, St. Petersburg, Russia

Received March 16, 2001

Abstract—The influence of temperature, pH, and chemical composition of the medium on the equilibrium swelling of polymeric polyelectrolytic tetrazole-containing acrylic hydrogels was examined.

Interaction of hydrogels with electrolyte solutions, resulting in limited swelling, is actively studied for a long time. Polyelectrolytic hydrogels are of interest from the viewpoint of both modeling of bioinformation systems and various practical applications: agricultural gels, gels for sanitation purposes used for water treatment, etc. Wide prospects are opened by the possibility of varying the phase state of polymeric gels, i.e., of performing transitions between the swollen and collapsed states, under the action of minor changes in the medium. In the past decade major attention has been given to hydrogel systems sensitive to fluctuations of temperature, pH, and ionic strength of solution [1, 2].

Complexation of polymers with metal ions can both increase and decrease the degree of swelling [3]. Modification of the chemical structure of acrylic hydrogel with various comonomers can also affect the degree of swelling in salt solutions.

In this work we studied the features of behavior of polymeric hydrogels of acrylic acid (AA), 2-methyl-5-vinyltetrazole (MVT), and methylenebisacrylamide in various electrolyte solutions and the influence of temperature on the water absorption of the polymers.

EXPERIMENTAL

Hydrogels based on AA and MVT or methylenebisacrylamide (MBAA) as a cross-linking agent were prepared by polymerization in aqueous solution at 60°C in the presence of the initiating system ammonium persulfate (AP)–tetramethylethylenediamine (TMED). The content of the components was as follows (wt %): monomers 30, cross-linking agent 0.1–0.9, and MVT 15–70. The features of synthesis and gelation are described elsewhere [4].

The degree of equilibrium swelling was measured by the standard gravimetric procedure and calculated by the equation

$$Q = (m_s - m_d)/m_d,$$

where m_s is the weight of the swollen sample and m_d is that of the dried sample (g).

In calculations, we averaged the results for five similar samples. The solution pH was monitored with a pH-150 digital pH meter.

The influence of the swelling–drying cycles on the absorption capacity of the hydrogels was studied as follows. Samples of dry hydrogels were placed in an excess of distilled water and kept at 50°C to attain the equilibrium swelling. After separation from the nonabsorbed water, the gel was dried at 50°C to constant weight. The cycles were repeated until the gel either dissolved or lost the absorbing power because of the collapse.

The behavior of acrylic hydrogels modified with MVT in electrolyte solutions has certain specific features. The major advantage of new hydrogels is the high degree of equilibrium swelling in $<10^{-2}$ M solutions of polyvalent metal salts. Under these conditions, the degree of equilibrium swelling of hydrogels in solutions of cobalt, nickel, and copper salts was more than 200 g g^{-1}. In some cases at a low salt concentration (10^{-5}–10^{-4} M) the degree of equilibrium swelling of the gel was higher than in distilled water [5]. Figure 1 shows how the degree of equilibrium swelling of the gel containing 43.5 wt % MVT and 0.1 wt % MBAA (in the monomeric mixture) depends on the concentrations of NaCl and $CoCl_2$ and on the solution pH. The degree of swelling of tetrazole-

1070-4272/01/7407-1203$25.00

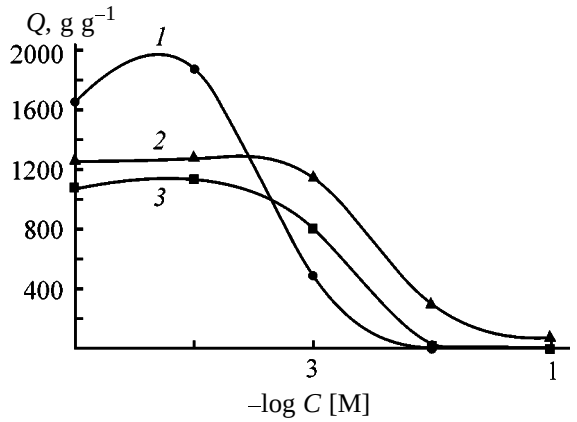

Fig. 1. Degree of equilibrium swelling Q of hydrogels based on AA, MVT, and MBAA as a function of the concentration of external electrolyte C in solution: (*1*) $CoCl_2$, (*2*) NaCl, and (*3*) HCl. Concentration (wt %): MVT 43.5 and MBAA 0.1.

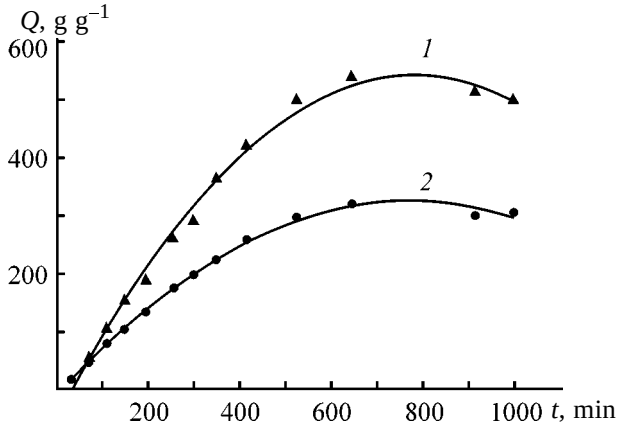

Fig. 2. Degree of equilibrium swelling Q of hydrogel as a function of time t in 0.001 M $CoCl_2$ solution. MBAA concentration 0.1 wt %. MVT concentration (wt %): (*1*) 43.5 and (*2*) 27.0.

containing gels is due to the capability of tetrazole for complexation and its structure-making effect on water [6]. Within the first day, the degree of swelling can exceed the equilibrium value by a factor of 1.5–2.

Table 1. Influence of the cross-linking agent concentration on the rate of hydrogel swelling in 10^{-3} M $NiCl_2$ solution. MVT concentration 27.0 wt %

Content of MBAA in monomer mixture, wt %	Degree of swelling, g g^{-1}	
	in 2 h, $Q_{2\,h}$	equilibrium, Q
0.05	49	643
0.1	78	302
0.2	130	171
0.5	124	142

Swelling of the gels containing 33.3–43.5 wt % MVT is characterized by two successive stages: sharp increase in the degree of swelling and subsequent decrease in the rate of water binding.

At the electrolyte concentration $C_s = 10^{-3}$ M and initial concentration ratio (mol : mol) of the salt and polymer (C_p) C_s/C_p = 1.5–3, the swelling of the gels passes through a maximum in time. The swelling kinetics in a 10^{-3} M solution of $CoCl_2$ is shown in Fig. 2. In the first 2 h the gel absorbs pure water, then absorption of metal ions starts, with $C_s \cong C_p$. Then the degree of equilibrium swelling increases over the course of 6–8 h irrespective of the gel composition, after which it gradually decreases to the equilibrium value, which is as high as 200–500 g g^{-1}. The salt solution is concentrated inside the gel, as indirectly indicated by the intensity of the gel color, as compared to the color of the initial solution.

The pattern of the variation of the swelling degree in time (Fig. 2) shows that before attainment of the equilibrium the curves are adequately described by the equation of a straight line $dQ/dt = k$, or $Q_i = kt_i$, where Q_i is the degree of swelling in time t_i; k is the coefficient determined by the nature of the salt and polymer. As seen from Fig. 2, as the content of MVT in the copolymer is increased, the swelling rate increases; this is due to the complexing power of the tetrazole ring.

The swelling rate of the tetrazole-containing gels is described by the equation $k = \alpha$[MVT], where [MVT] is the weight fraction of MVT in the monomer mixture. The equation describes the swelling rate in the range 13.5–43.5 wt % MVT, and α is determined by the nature of the salt and experimental conditions. In our case $\alpha \cong 1$. The dependence of the swelling rate on the content of the cross-linking agent in the polymer is given in Table 1.

Table 1 shows that, as the cross-linking density is increased, the swelling rate in solutions of metal salts increases, which is due to the high osmotic pressure of swelling. Statistical treatment of the kinetic data on swelling of gels in solutions of different salts, with the same content of MVT in the monomer mixture, gives the correlation $k = \beta$[MBAA], where β is the coefficient depending on the nature of the salt and on swelling conditions. This relationship holds for the range of MBAA concentrations in the monomer mixture 0.05–0.2 wt %; however, it is not valid for MBAA concentrations higher than 0.5 wt % or for the samples containing 70 wt % MVT. This is probably due to the defective structure of the network,

presence of interweavings, engagements, free loops, and strong intermolecular interactions [4]. These factors are responsible for the decrease in the degree of equilibrium swelling in the range of MVT concentrations 40–70 wt % (Fig. 3).

Our studies show that below 11°C or at $C_s/C_p > 5$ the metal ions in the course of swelling are taken up faster than water, which results in gradual contraction of the initially swollen gel to 70–150 g g^{-1} and its subsequent collapse. High degrees of equilibrium swelling of the tetrazole-containing acrylic hydrogels are due to complexation of both tetrazole rings and acrylate groups with metal ions, with presumable formation of chelates [7]. The arising additional bonds act as "intermolecular cross-links" in weakly cross-linked gels and increase the effective density of the network. Coordination of water molecules increases the effective volume and degree of equilibrium swelling.

The effect of complexation at swelling in solutions of polyvalent metal salts is indicated, along with the step course of swelling at $C_s = 10^{-3}$ M, also by a change in the gel color (in some cases, at swelling in a 10^{-2} M $CoCl_2$ solution). Initially the gel becomes blue, which indirectly suggests a change in the number of coordinated water molecules in the inner sphere of the cobalt aqua complex [7].

The hydrogels under consideration, at a content of the cross-linking agent in the monomer mixture of 0.1–0.2 wt %, show a high degree of equilibrium swelling in physiological solution (as compared to copolymeric hydrogels of AA and acrylamide prepared at cross-linking agent concentrations less than 0.06% [2]). The degrees of equilibrium swelling in physiological solution and water at 16°C of the gels prepared at the concentrations of MBAA and MVT in the monomer mixture of 0.1–0.5 and 0–70 wt %, respectively, are listed in Table 2.

Table 2 shows that, as the MVT content is increased, the degree of equilibrium swelling increases. As the content of the cross-linking agent is increased, this quantity decreases. At the MVT concentration less than 40 and that of MBAA in the range 0.05–0.5 wt %, the gels preserve their shape in the swollen state, i.e., exhibit sufficient elasticity.

The gels under consideration show high values of equilibrium swelling in the practically important range pH 3–7. At pH 1.7–2.5 the tetrazole-containing gels collapse, and at pH 2.25 the swelling passes through a maximum. This is probably due to the fact that the ion exchange H^+/Na^+ in the carboxylate groups of the gel is preceded by the phase transition coil–globule of the polymer chains.

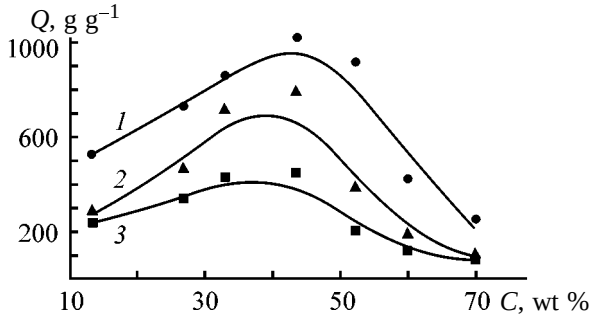

Fig. 3. Degree of equilibrium swelling Q of hydrogels in 0.001 M electrolyte solutions as a function of MVT concentration C. Electrolyte: (*1*) NaCl, (*2*) HCl (pH 3.24), and (*3*) $CuCl_2$.

In various electrolytic media, the influence of the incorporated MVT units on the degree of equilibrium swelling of the hydrogel is characterized by a curve with a maximum at MVT concentrations in the range 27.0–43.5 wt %. Such a shape is characteristic of solutions of both mono- and polyvalent metal salts and acids. At a salt concentration of 10^{-4} M the equilibrium degree of swelling in solutions of polyvalent metal salts is higher than in solution of NaCl, which is due to complexation (Figs. 1, 3).

The hydrogels containing MVT exhibit a high heat resistance. The activation energy of thermal oxidative degradation of the tetrazole-containing copolymers, according to DTA, is E_a = 420 kJ mol^{-1}. The influ-

Table 2. Characteristics of swelling of tetrazole-containing hydrogels in physiological solution at 16°C

Gel composition, wt %		Degree of equilibrium swelling Q, g g^{-1}	
MVT	MBAA	in physiological solution	in distilled water
0	0.1	37	648
13.5	0.1	123	864
27.0	0.1	136	978
33.3	0.1	155	1102
43.5	0.1	164	1189
52.3	0.1	148	1152
70.0	0.1	68	305
27.0	0.05	127	1489
27.0	0.2	92	470
27.0	0.5	66	197

Table 3. Thermal sensitivity of tetrazole-containing hydrogels at swelling in distilled water

T, °C	Degree of equilibrium swelling *Q*, g g^{-1}, at indicated concentrations of MVT and MBAA (wt %, separated by colon)								
	13.5 : 0.1	27.0 : 0.1	33.3 : 0.1	43.5 : 0.1	52.3 : 0.1	70.0 : 0.1	27.0 : 0.2	27.0 : 0.5	27.0 : 0.05
15	691	782	1037	1171	1152	288	440	196	1422
21	925	1071	1293	1264	1280	368	458	253	1758
32	884	1165	1093	1412	1420	515	408	260	2577
40	718	1014	855	1563	1614	590	509	263	1864
51	738	1236	932	1021	1487	462	566	216	1685
65	526	789	805	873	1343	89	396	115	1199

ence of the content of MVT and MBAA in the gels on their thermal sensitivity is illustrated in Table 3.

The hydrogels studied exhibit a high degree of equilibrium swelling below 60°C [8], whereas above 60°C the degree of swelling decreases. At high temperatures the compaction of the gel structure can occur along with dissolution. Compaction is characteristic of gels prepared at a high content of tetrazole (up to 70 wt %) or MBAA (up to 0.9 wt %) in the monomer mixture.

Results of experiments on cyclic swelling–drying of the tetrazole-containing gels at 50°C allow them to be recommended for use in recirculation processes at elevated temperatures, e.g., for agricultural purposes. The highest performance is shown by hydrogels containing 27.0 wt % MVT and 0.1–0.5 wt % MBAA; these hydrogels withstand more than eight cycles without appreciable changes in the absorption power. The gels containing 0.05 wt % cross-linking agent show poor thermal stability at cycling and withstand up to three cycles. When the content of the cross-linking agent exceeds 0.9 wt %, after five cycles the structure undergoes compaction, and the degree of equilibrium swelling noticeably decreases. In the gels with the MBAA concentration higher than 0.1 wt %, the degree of swelling increases after the sixth cycle, suggesting the onset of degradation, but the swollen samples preserve elasticity.

CONCLUSIONS

(1) Tetrazole-containing acrylic hydrogels exhibit a high degree of equilibrium swelling in electrolyte solution in the practically significant concentration range (10^{-3}–10^{-5} M for polyvalent metal salts, 10^{-2}–10^{-5} M for univalent metal salts; pH 3–7).

(2) The water-absorbing power of the hydrogels in salt solutions of concentrations less than 10^{-2} M is 500–1800 g g^{-1}, which is due to chelate formation. The tetrazole-containing gels exhibit a high degree of equilibrium swelling at pH 3–7 and high thermal stability in the swollen state.

(3) The thermal sensitivity of the gels allows their use for treating water and concentrating aqueous solutions of polyvalent metals.

(4) The stability of gels in cyclic swelling–drying processes at elevated temperatures (up to 50°C) allows them to be recommended for agricultural use.

REFERENCES

1. Budtova, T.V., Suleimenov, I.E., and Frenkel', S.Ya., *Zh. Prikl. Khim.*, 1997, vol. 70, no. 4, pp. 529–539.
2. Samchenko, Yu.M., Ul'berg, Z.R., and Komarskii, S.A., *Kolloidn. Zh.*, 1998, vol. 60, pp. 821–825.
3. Budtova, T.V., Bichutskii, D.F., Kuranov, A.L., and Suleimenov, I.E., *Zh. Prikl. Khim.*, 1997, vol. 70, no. 3, pp. 511–513.
4. Igrunova, A.V., Sirotinkin, N.V., and Uspenskaya, M.V., *Zh. Prikl. Khim.*, 2001, vol. 74, no. 5, pp. 793–797.
5. Ricka, J. and Tanaka, T., *Macromolecules*, 1984, vol. 17, no. 12, pp. 2916–2921.
6. Kruglova, V.A., Annenkov, V.V., Saraev, V.V., *et al.*, *Vysokomol. Soedin., Ser. B*, 1997, vol. 39, no. 7, pp. 1257–1259.
7. Rivas, B.L. and Seguel, G.H., *Polyhedron*, 1999, vol. 18, no. 19, pp. 2511–2518.
8. Mun, G.A., Suleimenov, I.E., Nurkeeva, Z.S., *et al.*, *Vysokomol. Soedin., Ser. A*, 1998, vol. 40, no. 3, pp. 433–440.

Russian Journal of Applied Chemistry, Vol. 74, No. 7, 2001, pp. 1207–1210. Translated from Zhurnal Prikladnoi Khimii, Vol. 74, No. 7, 2001, pp. 1174–1177.

MACROMOLECULAR CHEMISTRY AND POLYMERIC MATERIALS

IR Spectroscopic Study of the Chemical Structure of Ethylene–Vinyl Acetate Compolymers Modified with Saturated Alkoxysilane

O. V. Stoyanov, S. N. Rusanova, O. G. Petukhova, and A. B. Remizov

Kazan State Technological University, Kazan, Tatarstan, Russia

Received March 30, 2000; in final form, March 2001

Abstract—The transformations of chemical structure of ethylene–vinyl acetate copolymer after modification with ethyl silicate were studied by IR spectroscopy.

One of effective procedures for modifying polyolefines is introduction of organosilicon compounds into their structure. For this purpose unsaturated silanes are grafted to macromolecules in the presence of radical initiators. Then cross-linked polymers are formed by catalytic hydrolysis and polycondensation of silane functional groups.

However, these are other methods of chemical modification of polyolefins with silanes. Kreshkov *et al*. [1, 2] showed that alkoxysilanes enter ester interchange with carboxylic acid esters to form the corresponding orthosilicates. We suggest that modification of ethylene–vinyl acetate copolymers with saturated alkoxysilanes will change their properties owing to formation of cross-linked polymers with grafted siloxane chains.

Previously we found [3] that physicomechanical properties of polyolefines can be improved by modification with saturated orthosilicates. The resulting material retain the flowability of the initial polymer and can be prossessed by conventional procedures.

In this work the transformation of the chemical structure of some polyolefins modified with saturated alkoxysilanes was studied in detail by IR spectroscopy.

EXPERIMENTAL

We studied industrial ethylene–vinyl acetate copolymer (EVC) [TU (Technical Specifications) 6-05-1636–78, 301-05-56–90] of grades 11104-030, 11306-075, 12508-150, 11708-1250, 11808-240 with different content of ester groups (EVC-7, EVC-14, EVC-30) and low-density polyethylene (PE) of grade 15803-020 [GOST (State Standard) 16337–77). The properties of these materials are presented in the table.

ETS-32 ethyl orthosilicate (tetraethoxysilane, TES) [TU (Technical Specifications) 6-02-895–78], light yellow low-viscous low-freezing transparent liquid, was used as modifier. The silicon content recalculated to silica and tetraethoxysilane content are 30–34 and 50–65%, respectively; the density is 1062 kg m^{-3}; the viscosity is 1.6×10^{-3} Pa s.

The initial EVC-30, EVC-14 and EVC-7 copolymers were modified by mixing with ethyl silicate on laboratory microrollers for 10 min at 80, 120, and 140°C, respectively. Polymer films were prepared by pressing or casting a 2% toluene solution on a KBr support. The IR spectra in the 400–4000 cm^{-1} range were recorded on Specord 75-IR and M-80 spectrophotometers.

The band at 610 cm^{-1} assigned to the bending vibrations of the C–O bond of the ester group of EVC and the band at 1306 cm^{-1} assigned to $\gamma(-CH_2-)$ bending vibrations in PE were used as the references. To separate overlapping bands, the spectra recorded in *D* (optical density)–ν (wave number) coordinates were treated by appropriate computer program.

Alkoxysilanes are known to enter ester interchange with carboxylic acid esters to form the corresponding orthosilicates:

$$4R^1OOC^2 + Si(OR^3)_4 \rightarrow Si(OR^1)_4 + 4R^3OOC^2,$$

$$4R^1CH(OR^2)(CH_2)COOR^2 + Si(OR^3)_4$$

$$\rightarrow [R^2OOC(CH_2)CHR^1O]_4Si + 4R^2OR^3.$$

1070-4272/01/7407-1207$25.00

Properties of tested polymers

Property	EVC-7	EVC-14	EVC-30	LDPE
Vinyl acetate content, %:				
saponification	7.1	14.0	30.1	–
IR spectroscopy	6.8	13.8	29.7	–
Density, kg m^{-3}	929	935	955	920
Degree of crystallinity, %	25.5	16.6	5.3	35.6
Maximal melting point, °C	103	97	74	113
Melt flow index (190°C), g/10 min	0.6	6.5	12.2	2.0
Breaking tensile stress, MPa	19.3	12.8	9.1	11.8
Relative elongation at break, %	670	670	650	550

We suggest that similar reaction is possible between alkoxysilanes and polymers containing ester groups.

Polyolefins containing ester groups, in particular, polyvinyl acetate and vinyl acetate copolymers, relatively readily undergo saponification with alkalis. Determination of the ester number and preparation of polyvinyl alcohol and its copolymers are based on this reaction. Copolymers of esters can react under appropriate conditions with alcohols, acids, and salts of organic acids [5]. Alkoxysilanes and products of their partial hydrolysis with H_2SO_4 were used as cross-linkers for hydroxylated polymers [partially saponified vinyl chloride–vinyl acetate copolymers containing up to 50% of polyvinyl alcohol and copolymers of hydroxyalkyl (meth)acrylate and polyetherpolyols] [6].

Based on the above consideration, we suggested that EVCs can be modified with saturated orthosilicates. In addition, since the Si–OR bond is highly reactive, silanol chain branches and cross-links can be formed during thermochemical modification.

Reaction of EVC with tetraethoxysilane as well as reaction of silane with low-molecular-weight esters occur probably by the ester interchange mechanism:

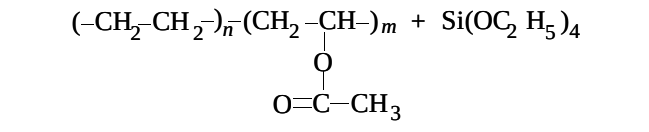

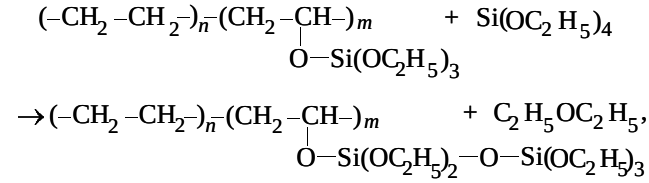

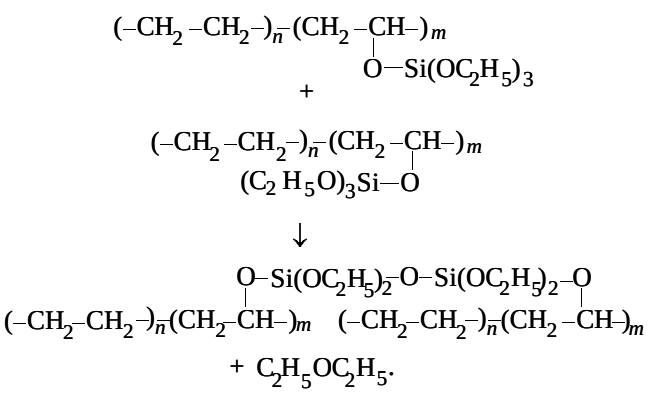

Acetic acid formed by degradation of ester groups during thermomechnaical treatment catalyzes silanol condensation, i.e., is "internal catalyst."

Ethylene–vinyl acetate copolymer reacts with ethyl silicate to form new functional groups in the polymer. The bands in the regions 1110–1180, 1020–1090, and 780–830 cm^{-1}, assigned to stretching vibrations of the Si–O, Si–O–Si, and Si–O–C bonds, appear in the IR spectra of modified EVCs. The optical density of the bands at 1050–1100 and 760–830 cm^{-1} increases and the bands typical for Si–O and Si–O–Si bonds in the open siloxane chains and three-dimensionally cross-linked structures appear with increasing content of the organosilicon additive.

During ester interchange the acetyl fragment of vinyl acetate is substituted by the residue of the organosilicon modifier, which is confirmed by splitting of the C–O stretching band of the ester groups at 1240 cm^{-1} in the IR spectra of modified EVC (Fig. 1). A simultaneous decrease in the intensity of the characteristic band of the CH_3 bending vibrations of vinyl acetate at 1462 cm^{-1} (Fig. 2) also indicates that the acetyl fragment of the copolymer is involved in the reaction.

Since EVC is modified in a melt, reaction of ester

groups of the polymer with ethoxy groups of ethyl silicate is sterically hindered. Our data show that introduction of alkoxysilane in the amount of up to 1% sharply increases (to 30%) the fraction of vinyl acetate groups involved in the ester interchange. On further increase in the modifier concentration the fraction of these groups increases to 35% (Fig. 3). This is probably due to the fact that alkoxysilane reacts mainly with the grafted organosilicon fragment, increasing the length of the siloxane chain owing to higher reactivity of the Si–OR bond as compared to the C–OR bond. An increase in the intensity of the absorption bands of the Si–O–Si bonds in siloxane chains (830 cm^{-1}) and three-dimensionally cross-linked structures (450 cm^{-1}) confirms formation of these fragments in modified EVCs (Fig. 4a, 4b).

We found that the change in the optical density of these characteristic absorption bands during EVC modification strongly depends on the content of ester groups in the copolymer. This is probably due to the fact that the amount of the modifier directly reacting with acetyl fragments of EVC increases with an increase in the content of vinyl acetate groups in the copolymer. In this connection, the increase in the reduced optical densities characterizing the mole fraction of vinyl acetate groups in the copolymer ($D_i^{red} = D_i^{rel}/C_{va}$, where $D_i^{red} = D_i/D_{610}$ and C_{va} is the molar content of vinyl acetate), is faster for EVC-7 having the lower content of ester groups (Fig. 4a, 4b). The differences in the shape of the optical density–modifier concentration dependences confirm the assumption that the amounts of the grafted siloxane chains and three-dimensionally cross-linked organosilicon fragments are different owing to steric hindrance and competition of branching and cross-linking reactions.

The absence of chemical reaction between ethylene fragments of EVC and ETS-32 is confirmed by the fact that the characteristic bands at 720 and 731 cm^{-1} assigned to the bending vibrations of the CH_2 groups do not change. Similar results were obtained for PE modified with hydroxylated methyldiethoxychlorosilane [7]. No broadening or coalescence (as in the case of amorphization) of this split narrow doublet typical for crystalline polyolefins was observed [7].

The IR bands assigned to vibrations of the Si–O, Si–O–C, and Si–O–Si groups also appear in the IR spectra of modified polyolefins free from ester groups (PE) (Fig. 5). The fact that the intensity of the bands of vinyl and vinylidene groups at 909 and 888 cm^{-1} remains the same after modification of PE indicates that the double bonds in the polyolefins are not in-

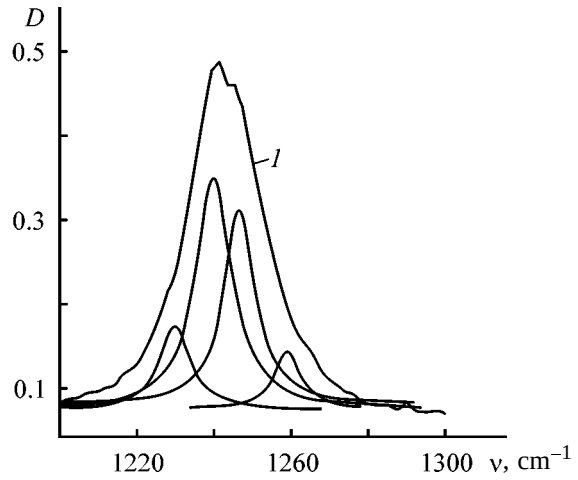

Fig. 1. Range of stretching bands of the ester C–O bonds of EVC modified with tetraethoxysilane: (*1*) experimental spectrum and (*2–5*) computer decomposition of the spectrum into separate bands. (*D*) Optical density and (ν) wave number; the same for Fig. 5.

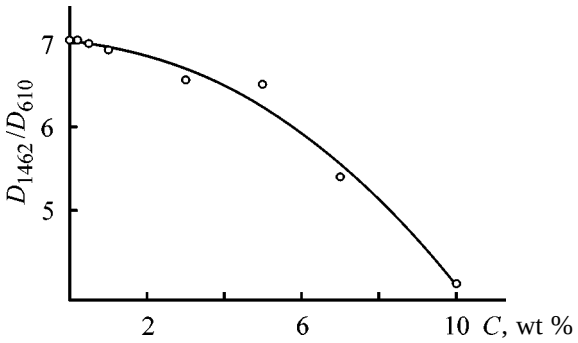

Fig. 2. Optical density of the characteristic absorption band at 1462 cm^{-1} of methyl groups of EVC D_{1462}/D_{610} as a function of the ETS-32 content *C*.

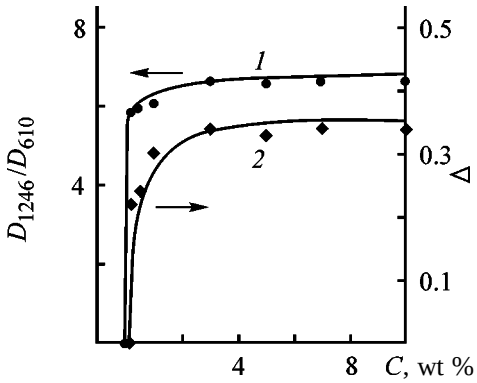

Fig. 3. (*1*) Optical density of the absorption band of vinyl acetate groups of EVC, subjected to ester interchange, D_{1246}/D_{610} and (*2*) the fraction of these groups $\Delta = 1 - (D_{1240}^{rel}/D_{1240}^{0rel})$ as a function of the ETS-32 content *C*.

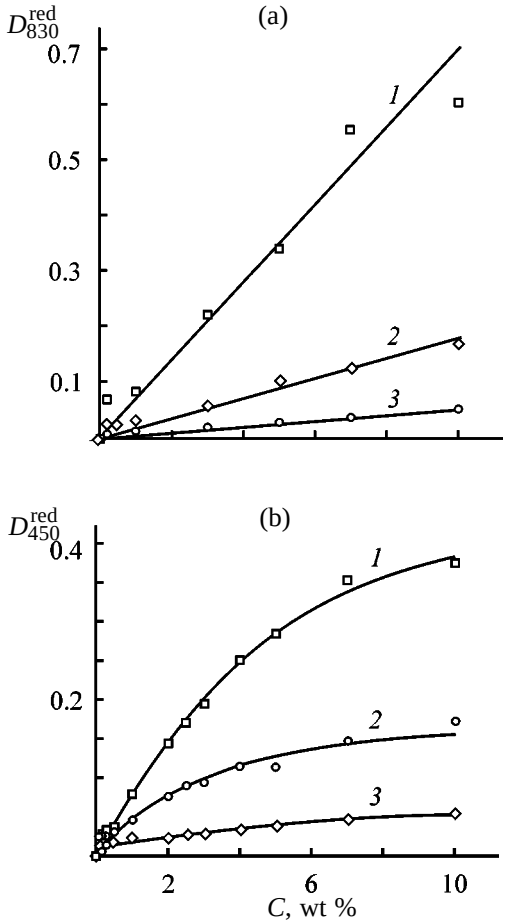

Fig. 4. Optical density of the Si–O–Si absorption band of (a) siloxane fragments D_{830}^{red} and (b) cross-linked structures D_{450}^{red} as functions of the ETS-32 content *C* in (*1*) EVC-7, (*2*) EVC-14, and (*3*) EVC-30.

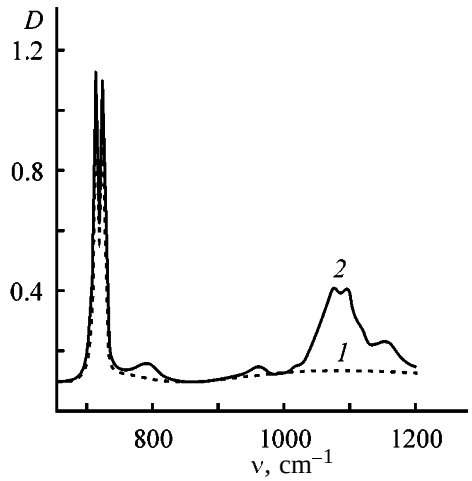

Fig. 5. IR spectra of (*1*) initial PE and (*2*) PE modified with tetraethoxysilane.

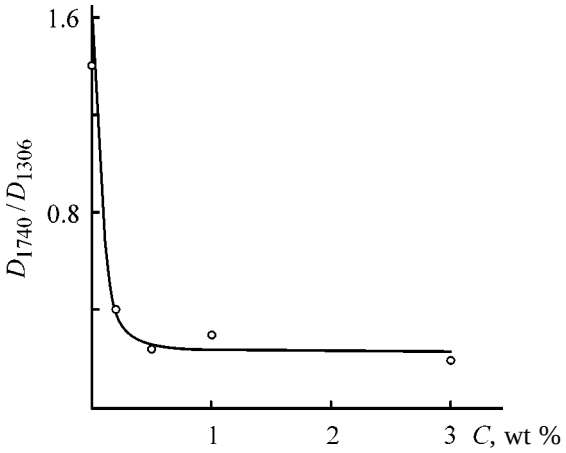

Fig. 6. Relative optical density of the characteristic band of carbonyl groups of PE at 1740 cm^{-1} D_{1740}/D_{1306} as a function of the ETS-32 content *C*.

volved in the reaction. However, the optical density of the characteristic band at 1740 cm^{-1} assigned to stretching vibrations of the C=O bond sharply decreases after modification of PE with ETS-32 (Fig. 6). This is probably due to reaction of tetraethoxysilane with oxygen-containing free radicals formed by thermomechanical degradation of polyolefins. The data agree with the results of the study of thermochemical modification of polyolefins with polyorganosiloxanes.

REFERENCES

1. Konoval, I.V., Konovalenko, N.G., and Ivanchev, S.S., *Usp. Khim.*, 1988, vol. 57, no. 1, pp. 134–148.
2. Dolgov, B.N., *Khimiya kremniiorganicheskikh soedinenii* (Chemistry of Organosilicon Compounds), Moscow: Goskhimizdat, 1933.
3. Rusanova, S.N., Petukhova, O.G., Stoyanov, O.V., and Khuzakhanov, R.M., *Svositva promyshlennykh sevilenov, modifitsirovannykh efirami ortokremnievoi kisloty* (Properties of Industrial Sevilens Modified with Orthosilicic Acid Esters), Available from VINITI, Moscow, September 14, 1999, no. 2836-B99.
4. Andriyanov, K.A., *Kremniiorganicheskie soedineniya* (Organosilicon Compounds), Moscow: Goskhimizdat, 1955.
5. Lambla, M., Druz, J., and Bouilloux, A., *Polym. Eng. Sci.*, 1987, vol. 27, no. 16, pp. 1221–1228.
6. US Patent 4480072.
7. Bogatyrev, V.L., Maksakova, G.A., Villeval'd, G.V., and Logvinenko, V.A., *Izv. Sib. Otd. Akad. Nauk SSSR, Ser. Khim. Nauk*, 1986, no. 2, issue 1, pp. 104–105.
8. Andrianov, K.A., Gul', V.E., Khananashvili, L.M., and Bulgakov, V.Ya., *Izv. Akad. Nauk SSSR, Ser. Khim.*, 1973, no. 4, pp. 797–801.

Russian Journal of Applied Chemistry, Vol. 74, No. 7, 2001, pp. 1211–1214. Translated from Zhurnal Prikladnoi Khimii, Vol. 74, No. 7, 2001, pp. 1178–1181.

MACROMOLECULAR CHEMISTRY AND POLYMERIC MATERIALS

Composite Fibers Based on Chitin

G. M. Mikhailov, M. F. Lebedeva, L. A. Nud'ga, V. A. Petrova, and Yu. G. Baklagina

Institute of Macromolecular Compounds, Russian Academy of Sciences, St. Petersburg, Russia

Received January 30, 2001

Abstract—Composite fibers containing chitin and cellulose ethers (methyl, hydroxyethyl, and hydroxypropyl cellulose) and also chitin and polyvinylpyrrolidone were prepared. The effect of the ratio of system components and also the molecular weight of polyvinylpyrrolidone on the deformation-strength characteristics of the composite fibers and their supramolecular organization was studied.

Chitin is nitrogen-containing derivative of cellulose in which one hydroxy group of the pyranose ring is substituted by the acetamide group. Similar to cellulose, chitin is capable of forming fibers. However, high friability of chitin fibers restricts their use; therefore, chitin fibers are not produced commercially throughout the world. Chitin is well crystallized, and brittle failure of chitin fibers is caused by precisely this feature [1]. Partial heterogeneous deacetylation of chitin results in an increase in its structural nonuniformity and complicates crystallization of macromolecules in production of fibers, which increases their elasticity [2]. At the degree of deacetylation of chitin equal to or lower than 0.30 the fiber is tied and retains up to 40% of the initial strength. However, the use of additional heterogeneous base deacetylation in the production of chitin fiber, decreasing its fiber-forming ability, is not appropriate.

It is well known that the structural nonuniformity of the systems used for production of polysaccharide fibers hampers crystallization of macromolecules. This results in an increase in the elasticity of the fibers. The structural nonuniformity of oriented chitin can be reached by both its chemical modification and incorporation of modifying additives into the fiber.

The method of improvement of physicomechanical characteristics of fibers by their production from a polymer blend has attracted considerable attention [3, 4]. For example, on addition of only 0.1–1.0% of copolymer of acrylonitrile with methyl acrylate (95 : 5) to polyamidobenzimidazole the strength of the fiber increases by 5–13% [5].

Polymers can be blended by mixing their melts or solutions. Since the temperature of degradation of polysaccharides (180–200°C) is lower than their melting point (450–500°C), blends of polysaccharides with various polymers can be obtained only by mixing their solutions. In choosing polymer additives to chitin solutions it is important that these additives should be compatible with chitin in the solution. These additives can be cellulose ethers: methyl, hydroxyethyl, and hydroxypropyl cellulose, having the similar structure and different side substituents, and also polyvinylpyrrolidone (PVP).

Polyvinylpyrrolidone is a unique polymer widely used in industry and medicine. The main features of this polymer are ability to complex formation and solubility in water and organic solvents. It is well known that grafting of PVP to cellulose fibers improves their elasticity, increases hygroscopicity and dyeing ability, decreases shrinkage, and increases laundering resistance of clothes. Addition of PVP as a modifier to fibers produced from polymers able to form hydrogen bonds also improves their deformation-strength characteristics. For example, in modification of poly-*p*-phenylene terephthalamide fibers by addition of PVP to the spinning solution the fiber elongation at break, strength, aging resistance, fire resistance, etc. significantly increase [6]. In addition, prolonged boiling of the fibers modified with PVP does not result in its removal; the characteristics of fibers remain the same.

Methyl cellulose, converted to gel at 80°C, and hydroxypropyl cellulose, coagulating at 60°C, must remain in fibers and hamper crystallization of chitin in fiber formation.

Therefore, it seemed appropriate to modify chitin fibers by both above cellulose ethers and PVP and also to establish the effect of modifying additives on the structure and characteristics of the composite fibers.

1070-4272/01/7407-1211$25.00

EXPERIMENTAL

We used dimethylacetamide (DMAA) dehydrated by boiling with P_2O_5 and distilled in a vacuum, fraction with bp 42°C (7 mm Hg); *N*-methylpyrrolidone (*N*-MP) dehydrated by storage over NaOH and distilled in vacuum, fraction with bp 81°C (12 mm Hg); lithium chloride crystal hydrate dehydrated at 400°C; chitin produced from North Sea shrimp[1] with an ash content of 0.03%, protein-free, degree of polymerization (DP) 1350, molecular weight *M* 275 000; methyl cellulose (MC) with DP of 980 and degree of substitution 0.94; hydroxyethyl cellulose (HOEC) with DP 1220 and the substitution modulus (SM) 1.98; and hydroxypropyl cellulose[2] (HOPC) with DP 1050 and SM 3.0.

Polyvinylpyrrolidone with M_w 8×10^3, 12×10^3, 35×10^3, 8×10^5, and 15×10^5 was produced by radiation-induced polymerization.

The fiber was formed under the standard conditions on a PIFV-01 setup using a dosing syringe and a spinneret (1/0.4). The precipitation bath was a mixture of ethanol and ethylene glycol at the volume ratio of 50 : 50, T = 20°C. The plasticization bath was a mixture of 2-propanol and water at the volume ratio of 80 : 20, T = 50°C.

The fiber was washed to remove lithium chloride to a total absence of chloride ion in the wash water. The fiber was dried at 105°C.

The mechanical tests were carried out on an Instron-110 universal tearing machine. The stress–strain diagrams were obtained for a 50-mm sample at the loading rate of 5 mm min^{-1}. Before testing the samples were kept in a desiccator for 24 h at a relative humidity of 65%.

Chitin and modifying polymer additive were dissolved separately. The solvent was a mixture of DMAA and *N*-MP at the ratio of 50 : 50, containing 5% of lithium chloride. The polymer concentration in the solution (both chitin and modifier) was 3%. To obtain the required solutions, a calculated amount of the modifier was added to the chitin solution. The mixture was thoroughly mixed, degassed in a vacuum, and used in forming of the fiber.

The X-ray studies were carried out on a DRON-2 diffractometer and in an RKV-86 camera using CuK_α radiation filtered with Ni.

[1] Sevtekhrybprom Research and Production Association.
[2] Polimersintez (Vladimir).

Studying the dependence of the intrinsic viscosity of chitin on the DMAA : *N*-MP ratio and the content of lithium chloride in the solvent showed [2] that at the ratio of 50 : 50 and 5% LiCl the intrinsic viscosity has a minimum, and a 3% solution of chitin in this solvent has the optimum rheological characteristics for forming the fiber. Therefore, in the study we used this composition of the solvent. All types of the modifiers in hand are readily soluble in this solvent, and their solutions form transparent mixtures with equiconcentration solutions of chitin.

The cellulose ethers used in the study are nontoxic, have close DPs, but differ in the structure of substituents. At the degree of substitution of 0.94 methyl cellulose contains, on the average, two unsubstituted hydroxyls in each pyranose ring; therefore, the ether is structurally uniform. At SM 2 hydroxyethyl cellulose contains substituents of various length, since in production of HOEC ethylene oxide forms short side chains with DP 2–3. In this case, the number of hydroxyls in the substituted pyranose unit remains equal to 3, since each hydroxyethyl substituent contains one hydroxyl. Therefore, HOEC is structurally nonuniform and able to form hydrogen bonds with both the atom of the acetamide group of chitin and the hydroxy group of the pyranose fragment. The latter conclusion refers all the more to HOPC since hydroxypropyl group is longer and propylene oxide tends to polymerize to a greater extent in etherification of cellulose. We believed that these features of the structure of cellulose ethers would allow control of the elastic characteristics of the composite fibers.

It should be noted that the fibers produced from nonmodified solutions of chitin are characterized by the tensile strength of 300 MPa and the elongation at break of 1.9%.

Figures 1a and 1b present the dependences of the strength and deformation characteristics of composite fibers produced from chitin and cellulose ethers on their composition. It is seen that the largest modifying effect is observed for MC. For example, addition of MC to chitin solution in the amount of up to 1.0% increases the fiber strength to 834 MPa and its elongation to 4.5%. Throughout the studied range of compositions (from 0.5 to 10% of MC) the strength of the modified fiber and the elongation at break are noticeably higher than those of the initial fiber. It is likely that the presence of methyl group, unable to form hydrogen bonds, in MC considerably hinders packing of macromolecules in the crystals, which increases the elongation at break and also favors orientation strengthening of the fiber.

Substitution of hydroxyethyl group for methyl group in the modifier and an increase in its content somewhat decrease the strength characteristics of the resulting fibers. The structural nonuniformity typical for HOEC results in appearance of defective supramolecular structure. The fibers have lower strength but at a low content of HOEC are characterized by a higher elasticity. The elongation at break of the fiber at a 2.5% content of HOEC exceeds that of the initial fiber by a factor of 2.

Addition of HOPC as a modifier, in which substituents vary in the unit length to a greater extent than in HOEC, increases the fiber strength to 450 MPa and the elongation at break to 4%. With the use of this modifier, variation of its content in the systems does not noticeably affect the strength characteristics of the modified fibers. It seems likely that the presence of substituents of various length hampers ordering of the fiber structure even at the minimum addition of HOPC, which acts as interfibrillar plasticizer at the microlevels of the supramolecular organization of system 2.

The results of testing of composite fibers produced from chitin–PVP blends are presented in Figs. 2a and 2b. It is seen that addition of PVP improves the deformation and strength characteristics of chitin fibers. Small (1–2.5%) additions of PVP provide the greatest effect on the mechanical characteristics of the fiber. On addition of 2.5% of PVP with M = 12 000 to the spinning solution the tensile strength increases by a factor of 2, the modulus of elasticity, by 40%, and the relative elongation, by a factor of 3.5 in comparison with the fiber produced from straight chitin. At the PVP concentration in the spinning solution above 2.5% all mechanical characteristics of the fiber are impaired. This trend is observed for PVP of any studied molecular weight.

Considering the effect of molecular weight of PVP at the same concentration in the spinning solution (Fig. 3), the optimum molecular weight is 12.0×10^3, at which the strength is maximal and the deformation of modified fibers is high. The modulus of elasticity of the fibers in the range of the molecular weights of PVP from 12.0×10^3 to 8.0×10^5 does not noticeably vary and is in the range 3–4 GPa. At the extreme values of M (8.0×10^3 and 1.5×10^6) the modulus of elasticity decreases to 1.5–2.5 GPa. This dependence of the mechanical characteristics of the fiber on the molecular weight of PVP is apparently caused by formation of microheterogeneous supramolecular structures even in the spinning solution of chitin with PVP of low and moderate molecular weights. It does not form an individual phase, is uniformly distributed along the solution bulk, exhibits the plasticizing effect, and hampers crystallization of chitin macromolecules in formation of fiber. It is apparent that macromolecular PVP, having a similar effect, favors to a greater extent amorphization of the fiber structure,

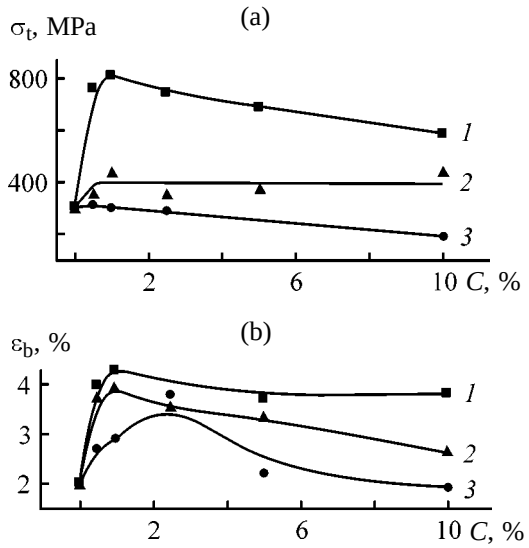

Fig. 1. (a) Tensile strength σ_t and (b) elongation at break ε_b of chitin fibers as functions of modifier concentration C. (*1*) MC, (*2*) HOPC, and (*3*) HOEC.

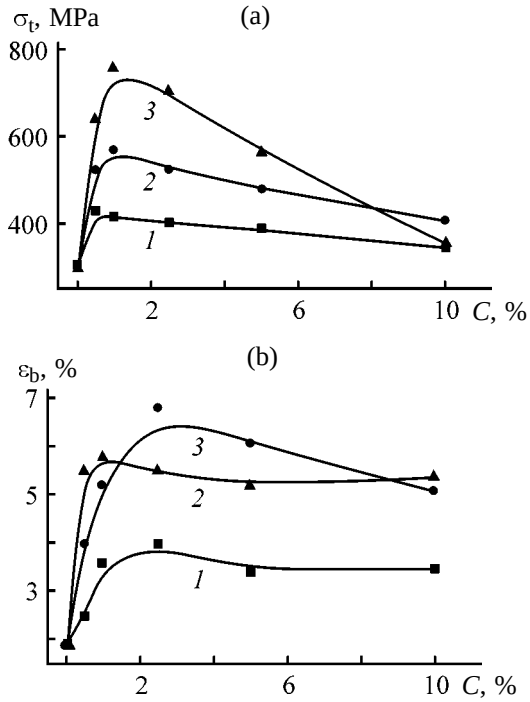

Fig. 2. (a) Tensile strength σ_t and (b) relative elongation at break ε_b of chitin fiber as functions of concentration C of PVP with various molecular weights. Molecular weight: (*1*) 800 000, (*2*) 35 000, and (*3*) 12 000.

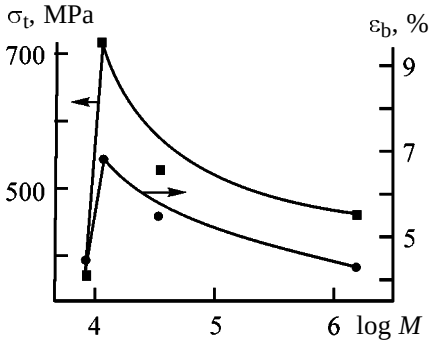

Fig. 3. Tensile strength σ_t and relative elongation at break ε_b of chitin fiber as functions of PVP molecular weight *M*. PVP concentration 2.5%.

which results in deterioration of mechanical characteristics of modified fibers.

The X-ray studies of the fiber produced from straight chitin and composite fibers with addition of cellulose ethers and PVP in the amount of 0.5–2.5% (PVP with molecular weight of 12.0×10^3 and 35.0×10^3) show that the fiber retains its highly ordered structure characteristic for nonmodified chitin fibers. In the diffraction patterns recorded along the fiber axis (meridian) there are reflections at $2\theta = 17°$ and 26° caused by the interplanar spacings of 5.02 and 3.36 Å, respectively. In the diffraction patterns of the fibers containing PVP and MC the reflection at $2\theta = 9°$ is somewhat blurred. In the diffraction patterns recorded across the fiber (equator) there are sharp reflections at $2\theta = 9°$ and $2\theta = 19°36'$ caused by the interplanar spacings of 9.8 and 4.45 Å, characteristic for the initial chitin fiber.

The results of these X-ray studies show that the modifiers do not form individual phases at a concentration of up to 2.5%. It is apparent that addition of this amount of the modifier only weakly affects the crystal packing of chitin in the fiber. The improvement of deformation and strength characteristics of the composite fibers may be due to plasticization of the system on the interfibrillar level.

The electron-microscopic studies of the composite fibers revealed distinctions in the surface morphology. The composite fibers have a smoother and denser surface than the fiber from straight chitin. In shelling of these fibers we found no pores and cavities.

CONCLUSIONS

(1) The composite fibers of chitin with cellulose ethers and polyvinylpyrrolidone were produced. It was shown that the amount of the modifier, molecular weight of polyvinylpyrrolidone, and also the degree of substitution and chemical structure of the substituent in cellulose ethers affect the deformation-strength characteristics of the composite fibers.

(2) The largest positive effect is observed at a 1.0–2.5% content of the modifier.

(3) Methyl cellulose and polyvinylpyrrolidone with $M = 12\,000$ are the best modifiers.

ACKNOWLEDGMENTS

We are grateful to V.N. Ushakova for the samples of polyvinylpyrrolidone and also to O.V. Kudasheva for the electron-microscopic studies.

REFERENCES

1. Sukhanova, T.E., Sidorovich, A.V., Goryainov, G.I., *et al.*, *Vysokomol. Soedin., Ser. B*, 1989, vol. 31, no. 5, pp. 381–384.
2. Nud'ga, L.A., Baklagina, Yu.G., Petropavlovskii, G.A., *et al.*, *Vysokomol. Soedin., Ser. B*, 1991, vol. 33, no. 11, pp. 864–869.
3. Nikitina, O.A., Fedorova, R.G., Kuznetsova, L.K., *et al.*, *Khim. Volokna*, 1978, no. 2, pp. 19–21.
4. Manson, J.A. and Sperling, L.H., *Polymer Blends and Composites*, New York: Plenum, 1976.
5. Nikitina, O.A., Fedorova, R.G., Kudryavtsev, G.I., and Shablygin, M.V., *Khim. Volokna*, 1987, no. 6, pp. 24–26.
6. US Patent 5135687.

Russian Journal of Applied Chemistry, Vol. 74, No. 7, 2001, pp. 1215–1219. Translated from Zhurnal Prikladnoi Khimii, Vol. 74, No. 7, 2001, pp. 1182–1185.

MACROMOLECULAR CHEMISTRY AND POLYMERIC MATERIALS

Copolymerization of Acrylamido Sulfonic Acids with Acrylamide and Acrylonitrile in Concentrated Neutral Aqueous Solutions

Yu. E. Budanova, O. K. Shvetsov, and Zh. A. Maer

Yaroslavl State Technical University, Yaroslavl, Russia
KhEMEKS DOR Research and Production Enterprise, Private Company, Yaroslavl, Russia

Received October 25, 2000; in final form, April 2001

Abstract—Copolymerization of alkali metal salts of acrylamido sulfonic acids with acrylamide and acrylonitrile in concentrated aqueous solutions was studied. The influence of the chemical nature, ratio, and physical interactions of monomers on polymerization and on the intrinsic viscosity of the copolymers was examined.

Water-soluble sulfonic acid copolymers show considerable promise for various branches of engineering, in particular, for water treatment, paper production, and other processes involving changes in the viscosity, structure (thixotropy), and stability of water-based colloidal systems. Functional sulfo groups in the copolymers ensure stability of their performance at high temperatures in the presence of cations of various valences, virtually in the entire pH range.

Recently new interesting procedures were developed for preparing various acrylamido sulfonic acids such as 2-acrylamido-2-methylpropanesulfonic acid and 4-acrylamido-4-methylsulfolane-3-sulfonic acid (AMPSA and ASA, respectively) [1, 2]. However, their copolymerization with such water-soluble monomers as acrylonitrile (AN), acrylamide (AA), and others is studied insufficiently. (Co)polymerization is usually studied at low monomer concentrations, whereas from the practical viewpoint it is more interesting to study relatively concentrated systems. Such systems often show deviations from the classical theory, which are due to strong intermolecular interactions, occlusion, and gel effect, often making the process diffusion-controlled even in the early stages of the reaction.

In this work we studied the features of copolymerization of potassium salts of AMPSA and ASA with AA and AN in concentrated aqueous solutions.

EXPERIMENTAL

In synthesis of polyelectrolytes we followed a typical protocol of radical polymerization in aqueous solution, initiated with $K_2S_2O_8$ [TU (Technical Specifications) 38.103270–87] at 60°C. For the synthesis we used a 30% aqueous solution of AA (TU 2433-004-07507802) prepared by biocatalytic hydration of acrylonitrile and containing no impurities of other monomers; AN [GOST (State Standard) 11097–86]), main substance content 99.9%; laboratory samples of AMPSA (Chair of Technology of Polymeric Materials, Yaroslavl State Technical University), main substance content 97.8% (2.2% *tert*-butylacrylamide); ASA (Chair of Technology of Organic Substances, Dzerzhinsk Branch, Nizhni Novgorod State Technical University), main substance content 96.9%, sulfuric acid content 1.8%; as chain-terminating agent we used diisopropylxanthogen disulfide (diproxyd, TU 6-14-21–75); the other chemicals were of analytically pure grade.

Polymerization was performed in an inert gas atmosphere in a temperature-controlled glass reactor equipped with a thermometer, an electric power-driven stirrer, an inlet for feeding nitrogen, and a sampler. The reactor was charged with an aqueous phase containing AA and amido sulfonic acid preliminarily neutralized with KOH to pH 7.0–7.2 (in a neutral medium polymerization of sulfonic acids, which is too fast in acidic solutions [3], occurs with a controllable rate, and a labor- and time-consuming stage of neutralization of the polymerization product is avoided). AN with dissolved diproxyd was fed in a nitrogen flow. After the required temperature was attained, $K_2S_2O_8$ was added, and this moment was considered as the start of the reaction. Samples were taken at regular intervals, transferred into ampules,

1070-4272/01/7407-1215$25.00

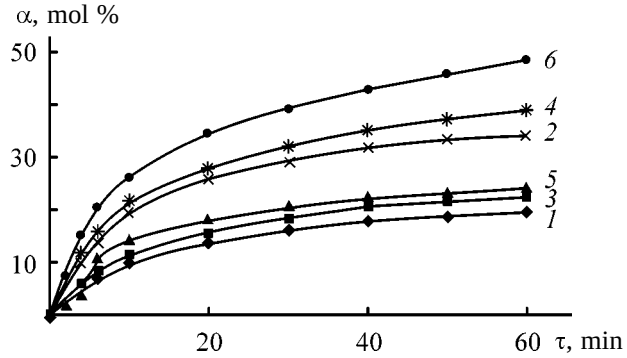

Fig. 1. Kinetics of synthesis of sulfo amide polymers at 60°C. Initial concentration of the monomers 20 wt %; the same for Figs. 2 and 3. (α) Conversion and (τ) time. Monomers and their mixtures: (*1*) AMPSA; (*2*) ASA (monomer concentration 14 wt %, limited by solubility); (*3*) AMPSA, AA; (*4*) ASA, AA; (*5*) AMPSA, AA, AN; and (*6*) ASA, AA, AN; the same for Fig. 3.

and stabilized with hydroquinone. The total conversion of the monomers was determined by the procedure in [4], based on determination of bromine that added to the double bonds of the unchanged monomers; the content of unchanged monomers was also monitored chromatographically. Polymerization was performed to a ≥98% conversion. (Co)polymers of the general formula

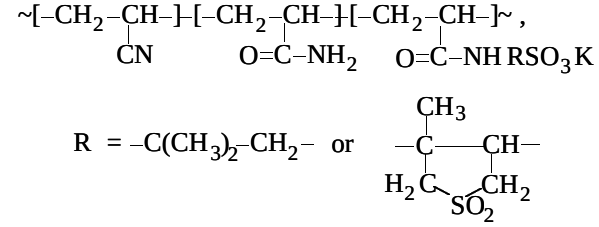

were obtained.

The intrinsic viscosity of the (co)polymers was determined with a Ubbelohde viscometer in a phosphate buffer solution of pH 6.86 (GOST 8.135–74) at 25°C.

Table 1. Apparent rate constants k'_{app} of polymerization, reaction orders with respect to monomers *m*, and reliability of approximation by the logarithmic equation R^2

Initial monomers*	k'_{app}, $l^{m-1}\ mol^{1-m}\ s^{-1}$	*m*	R^2
AMPSA	4.60×10^{-4}	13.1	0.955
AA–AMPSA	2.50×10^{-8}	11.7	0.952
AA–AN–AMPSA	1.19×10^{-7}	9.1	0.759
ASA	8.36×10^{-2}	7.8	0.940
AA–ASA	8.59×10^{-6}	6.8	0.958
AA–AN–ASA	3.52×10^{-5}	5.1	0.960

* Amido sulfonic acids, being strong acids, at pH 7 totally exist in the form of K salts.

To efficiently control the polymer synthesis at high concentrations of the initial mixture, we studied the kinetics of copolymerization of amido sulfonic acids (in the form of K salts) with AA and AN. The kinetic curves are shown in Fig. 1. To estimate the variation of the kinetic parameters, we performed the mathematical treatment of the dependences using the simplified equation for the polymerization rate

$$V_p = k'_{app}[M]^m,$$

where $k'_{app} = k_{app}[I]^n$ at [I] = const.

By taking the logarithms we obtain a linear regression with the slope equal to the reaction order with respect to the monomers; this straight line intercepts the ordinate in the point $\log k'_{app}$. The regression parameters calculated by the least-squares procedure using the MS Excel program are listed in Table 1. It is seen that the values of k'_{app} for all the monomeric mixtures with ASA are higher by a factor of 10^2 than those for the mixtures with AMPSA. This fact is apparently due to the capability of AMPSA for chain transfer to the monomer [5]. With a good, on the whole, approximation of the experimental data (Table 1) by a linear function (Fig. 2 shows an example of regression for the ASA–AA mixture; for the other mixtures the pattern is similar), high reaction orders with respect to the monomers show that the reaction is very sensitive to their concentration and to the nature of the monomer mixture, since polymerization of these monomers in concentrated solutions does not fit in the classical scheme [notably, under these conditions, attempts to choose the required amount of the inhibitor (sodium nitrite, hexachloroquinone, stable iminoxyl radical) to study the reaction kinetics with a scanning calorimeter led either to immediate occurrence of the gel effect or to total inhibition of the reaction]. Apparently, polymerization occurs with the gel effect practically from the very beginning. It is known that under such conditions all the kinetic parameters are variable [6], especially the rate constants of chain termination (and "apparent" values of the reaction orders can be relatively high).

According to published data [7, 8], the reaction order of radical (co)polymerization in dilute systems with respect to AMPSA, AA, and many other acrylic monomers is close to 1.5. This value was used to calculate the apparent rate constants of copolymerization from the experimental data. However, the resulting values did not agree with the real distribution of the

reaction mixtures with respect to the initial reaction rate (Fig. 3).

Figure 3 shows the dependences of the reduced polymerization rate V_r on the monomer conversion for the studied compositions of the monomer mixtures. The growth of V_r and the maxima in the curves at 5–15% conversions suggest occurrence of the gel effect practically from the very beginning of the polymerization. Early occurrence of the gel effect may be due to strong intermolecular interactions of the monomers at their high concentration; most probably, copolymerization involves formation of charge-transfer complexes (CTCs). In homopolymerization, dimerization of sulfonic acids (similar to dimerization of unsaturated carboxylic acids [9]) may play a certain role. Thus, at the chosen concentrations of the monomer and initiator the (co)polymerization of the potassium salts of AMPSA and AA even at low monomer conversions is not described by the classical scheme, and the kinetic parameters (Table 1) merely reflect the strong effect of the concentration and ratio of the monomers. Notably, copolymerization of the potassium salts of AMPSA and ASA with AA and especially AN is fast, with a high intensity of the gel effect. An increase in the reaction rate is due to high cross propagation constants and probably to high constant of AA homopolymerization, not complicated by the electrostatic effects in contrast to polymerization of ionized amido sulfonates. At the same time, copolymerization with AN is still faster, although AN is known to be a less reactive monomer. For example, with AA and AN the copolymerization constants are 1.357 and 1.875, respectively [10]. Increased elementary rate constants of addition of monomers to the "foreign" radical may be due to formation of a CTC between sulfo anions and AA or AN, with stronger intermolecular interactions as compared to sulfonic acid dimers. Amide and nitrile groups can undergo protonation in acidic (and neutral) media to form $-(O)C-NH_3^+$ and $-C\overset{+}{\cdots}NH$ moieties [11] acting as Lewis acids toward RSO_3^- (it is known that carboxylate copolymers of AA and AN form strong bonds via these units with negatively charged particles of mineral dispersions [12]). Such reaction mechanism is supported by the total lack of blocks of amido sulfonate units in the microstructure of the polymers [13], whereas their homopolymerization is not fully hindered by electrostatic factors.

Along with increase in the overall reaction rate in copolymerization of amido sulfonates with protonated monomers, the contribution of the chain termination reactions probably decreases owing to decrease in the

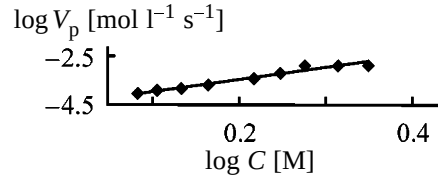

Fig. 2. Polymerization rate V_p as a function of the current concentration of monomers in the reaction mixture C. Molar ratio of monomers: ASA : AA = 11.0 : 89.0.

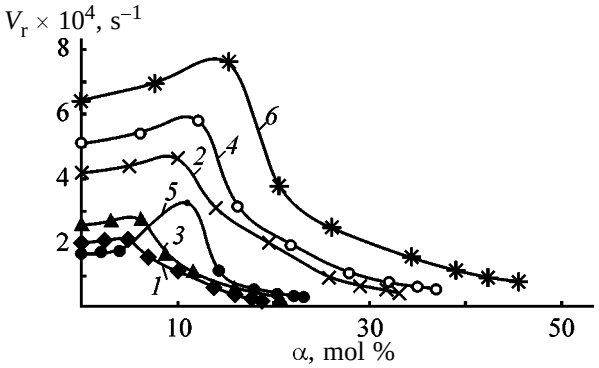

Fig. 3. Reduced rate V_r of (co)polymerization as a function of monomer conversion α.

chain transfer to AMPSA bound in a complex with AA or AN, or to decrease in the AMPSA content. It is known [5] that chain transfer to the monomer plays an important role in radical polymerization of AMPSA, limiting the growth of the molecular weight of the polymer, as clearly seen from the intrinsic viscosities [η] of AMPSA–AN copolymers (Table 2). In the series of AMPSA–AN copolymers, [η] decreases with increasing content of the sulfo monomer in the mixture, despite increase in the content of the ionic groups and decrease in the content of AN units in the copolymer, resulting in compaction of the macromolecular coils in solution. Thus, presumably, the molecular weight of AMPSA copolymers is considerably higher than that of the homopolymers prepared under the same conditions.

The copolymerization rate, k'_{app}, and the intensity of the gel effect in synthesis of ASA (co)polymers are appreciably higher, i.e., with ASA the chain transfer to the monomer does not occur or occurs to a considerably lesser extent than with AMPSA. This conclusion is confirmed by the dependence of the intrinsic viscosity of the synthesized ASA copolymers on the composition of the monomer mixture (at 100% conversion).

For AMPSA–AA–AN terpolymers, at a constant content of AMPSA units, [η] decreases with increasing content of AN. For AMPSA–AA copolymers in a broader composition range [η] passes through a max-

Table 2. Intrinsic viscosity of (co)polymers of AMPSA and ASA with AA and AN. 25°C, phosphate buffer solution, pH 6.86 (GOST 8.135–74)

Copolymer composition, mol %				$[\eta]$, $\times 0.1$ m^3 kg^{-1}
AMPSA	ASA	AA	AN	
32.0	–	–	68.0	1.1
45.0	–	–	55.0	0.9
61.0	–	–	39.0	0.6
71.0	–	–	29.0	0.3
8.0	–	92.0	–	0.9
19.0	–	81.0	–	1.4
26.0	–	74.0	–	1.5
34.0	–	66.0	–	1.6
58.0	–	42.0	–	0.4
7.5	–	75.0	17.5	0.9
7.3	–	64.1	28.6	0.7
7.2	–	57.6	35.2	0.7
7.0	–	44.0	49.0	0.5
–	11.0	89.0	–	0.6
–	16.0	84.0	–	1.8
–	7.5	69.6	22.9	0.9
–	11.0	71.5	17.5	1.0

imum, which is due to the simultaneous effect of several factors (decrease in the molecular weight and increase in the polyelectrolytic effect with increasing content of sulfo groups). For binary and ternary ASA copolymers, in the examined composition range, the intrinsic viscosity increases with increasing content of sulfo groups.

CONCLUSIONS

(1) Radical copolymerization of potassium salts of 2-acrylamido-2-methylpropanesulfonic and 4-acrylamido-4-methylsulfolane-3-sulfonic acids with acrylamide and acrylonitrile at initial concentrations of the monomer mixtures exceeding 0.2 M occurs with an intense gel effect, which is confirmed by the copolymerization kinetics and by the intrinsic viscosity of the resulting polymers.

(2) The intensity of the gel effect depends on the concentration and composition of the monomer mixture; for the case of copolymerization of alkali metal salts of amido sulfonic acids with acrylamide and acrylonitrile, it was explained in terms of formation of complexes with strong intermolecular interactions (charge-transfer complexes of sulfonate anions with protonated monomers).

(3) 4-Acrylamido-4-methylsulfolane-3-sulfonic acid is a more active monomer than 2-acrylamido-2-methylpropanesulfonic acid, which may be due to the low constant of chain transfer to the monomer and increased tendency to complexation with protonated monomers (acrylamide and acrylonitrile) due to the presence in the former of the second center of strong intermolecular interactions ($-SO_2-$).

ACKNOWLEDGMENTS

The study was financially supported by the grants of the Education Ministry of the Russian Federation for basic research in the field of chemical technologies and geology (mining science).

REFERENCES

1. Kazantsev, O.A., Shirshin, K.V., Kazakov, S.A., and Papukova, K.P., Abstracts of Papers, *Mezhdunarodnyi Simpozium IYuPAK "Novye dostizheniya v polimernom sinteze i formirovanii makromolekul"* (Int. Symp. of IUPAC "New Advances in Polymer Synthesis and Formation of Macromolecules"), St. Petersburg: IUPAC, 1997, p. 107.
2. Podgornova, V.A., Khalistova, I.D., and Ustavshchikov, B.F., *Zh. Prikl. Khim.*, 1996, vol. 69, no. 1, pp. 127–131.
3. Lisovtsev, V.V., Rostokin, G.A., and Kulikova, A.E., *(So)polimery na osnove 2-akrilamido-2-metilpropansul'fokisloty: Obzornaya informatsiya* ((Co)polymers Based on 2-Acrylamido-2-methylpropanesulfonic Acid: Review), Moscow: NIITEKhIM, 1984.
4. Kalinina, L.S., Motorina, M.A., Nikitina, N.I., and Khachapuridze, N.A., *Analiz kondensatsionnykh polimerov* (Analysis of Condensation Polymers), Moscow: Khimiya, 1984.
5. Lisovtsev, V.V., Radical (Co)polymerization of 2-Acrylamido-2-methylpropanesulfonic Acid in Solvents and Viscosity Characteristics of Solutions of the Resulting (Co)polymers, *Cand. Sci. Dissertation*, Dzerzhinsk, 1989.
6. Gladyshev, G.P. and Popov, V.A., *Radikal'naya polimerizatsiya pri glubokikh stepenyakh prevrashcheniya* (Radical Polymerization at High Conversions), Moscow: Nauka, 1974.
7. Kurenkov, V.F., Safin, A.G., and Almazova, E.I., *Zh. Prikl. Khim.*, 1998, vol. 71, no. 10, pp. 1704–1708.

8. *Vinyl Polymerization*, Ham, G.E., Ed., New York: Marcel Dekker, 1969.
9. Kabanov, V.A. and Topchiev, D.A., *Polimerizatsiya ionizuyushchikhsya monomerov* (Polymerization of Ionizable Monomers), Moscow: Nauka, 1975.
10. *Copolymerization*, Ham, G.E., Ed., New York: Interscience, 1964.
11. Reid, K.F., *Properties and Reactions of Bonds in Organic Molecules*, London: Longmans, 1968.
12. Shveikina, Yu.E., Synthesis of Anion-Active Polyelectrolytes by Hydrolysis and Sulfomethylation of Copolymers of Acrylamide and Acrylonitrile in Aqueous Medium and Some Fields of Application of the Synthesized Monomers, *Cand. Sci. Dissertation*, Yaroslavl, 1999.
13. Maer, Zh.A., Synthesis and Properties of Copolymers of Amido Sulfonic Acids with Acrylamide and Acrylonitrile as Versatile Stabilizers of Bentonite Dispersions, *Cand. Sci. Dissertation*, Yaroslavl, 1998.

Russian Journal of Applied Chemistry, Vol. 74, No. 7, 2001, pp. 1220–1224. Translated from Zhurnal Prikladnoi Khimii, Vol. 74, No. 7, 2001, pp. 1186–1190.

MACROMOLECULAR CHEMISTRY AND POLYMERIC MATERIALS

Variation of Functional Composition of SKEPT Rubber in the Course of Ozonolysis

E. A. Khazova, N. N. Shugurova, E. I. Grigor'ev, I. S. Dokuchaeva, A. G. Liakumovich, and Ya. D. Samuilov

Kazan State Technical University, Kazan, Tatarstan, Russia

Received March 13, 2001

Abstract—Ozonolysis in hexane of ternary ethylene–propylene rubber (SKEPT), accompanied by formation of oxygen-containing groups and intermolecular cross-linking, was studied. These processes become more pronounced when ozonolysis is performed in hexane containing pyridine.

Ternary ethylene–propylene rubbers (SKEPTs), owing to the chemical inertness of their backbone chain, find growing use in production of articles with enhanced resistance to various kinds of degradation. The favorable properties of SKEPT rubbers could be enhanced if their macromolecules contained polar groups. Such groups would enhance the adhesion and cohesion properties of these rubbers and furnish an opportunity for additional modification via these functional groups and hence for significant modification of the properties of the resulting materials.

SKEPT rubbers contain double bonds in pendant chains. Ozonolysis of double bonds and subsequent transformations can principally be regarded as a route of chemical modification of the pendant fragments. The major advantage of such an approach is that ozonolysis does not require catalysts and high temperatures and pressures; furthermore, no waste to be utilized is formed.

Ozonolysis of double bonds involves a sequence of transformations: 1,3-dipolar addition of ozone to double bonds to form 1,2,3-trioxolanes, their decomposition to carbonyl compounds and carbonyl oxides, and 1,3-dipolar cycloaddition of carbonyl oxides to give 1,2,4-trioxolanes [1–3]:

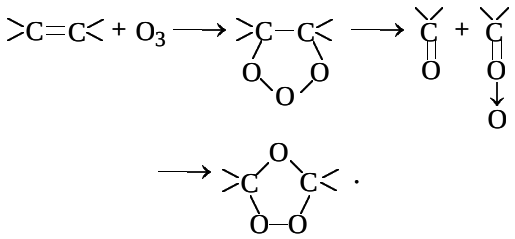

The synthetic advantage of ozonolysis is that the reaction intermediates, carbonyl oxides and carbonyl compounds, can be scavenged by various chemical agents, which allows direct transformation of a C=C double bond into complex functional groups. These possibilities were demonstrated in [4] for ozonolysis of rubbers containing double bonds in the backbone chain as example.

In this work we studied the functional composition of SKEPT rubber prepared with participation of the third monomer, dicyclopentadiene, and subjected to ozonolysis under various conditions.

Initially we performed ozonolysis of SKEPT rubber in a chemically inert solvent, hexane. We expected that ozonolysis in this case would involve no side processes and yield 1,2,4-trioxolanes as final products:

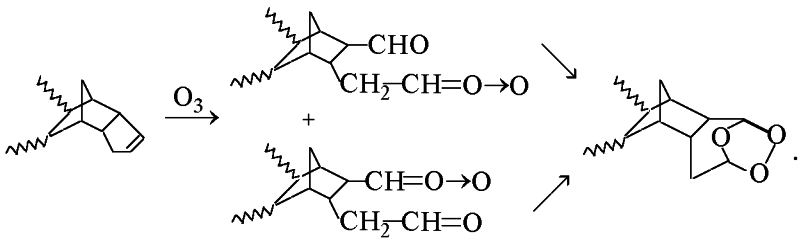

1070-4272/01/7407-1220$25.00 © 2001 MAIK "Nauka/Interperiodica"

However, actually the above transformation was not the sole process. In the course of ozonolysis the solution viscosity increased, suggesting occurrence of intermolecular reactions. Probably, carbonyl oxide (or aldehyde) groups of one macromolecule react with aldehyde (or carbonyl oxide) of another. Such reactions were observed previously in ozonolysis of SKEPT rubber prepared with ethylidenenorbornene as the third monomer [5]. However, in our case changes in the functional composition were more complex. We found that ozonolysis was accompanied by formation of carboxy groups (Fig. 1). This fact suggests that the intermediate carbonyl oxides undergo one more transformation, namely, isomerize into dioxiranes which subsequently either transform into carboxy groups [1, 2] or oxidize the adjacent aldehyde group into carboxy group [6]:

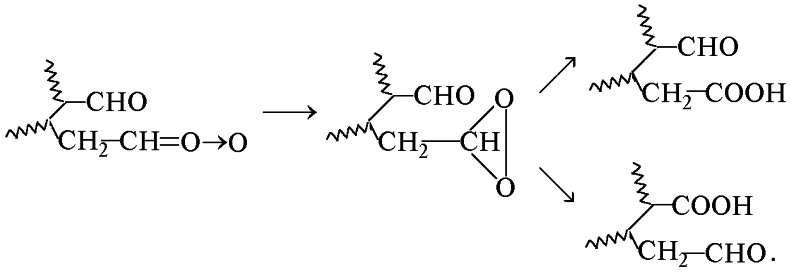

The factor favoring such transformation is that formation of 1,2,4-trioxolane requires a turn of the aldehyde and carbonyl oxide groups formed from decomposition of the primary ozonide by 180° relative to each other, which is impeded by the conformational rigidity of the norbornene moiety. The increased lifetime of carbonyl oxides facilitates side reactions involving them. Isomerization of the dioxirane moiety into the carboxy group and oxidation of the aldehyde group with the dioxirane probably occur by the latent radical mechanism ensuring high product yield [7].

The amount of carboxy groups formed in the course of ozonolysis of SKEPT rubber initially grows and then decreases with time (Fig. 1). It is known [1–3] that carboxylic acids readily react with carbonyl oxide groups to form acyloxy hydroperoxides:

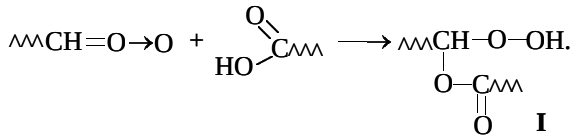

Experimentally we did detect the hydroperoxide groups, but they disappeared already within 15 min after the start of the ozonolysis.The increased basicity of the hydroperoxy group due to α effect [8] results in its relatively facile acid-catalyzed cleavage:

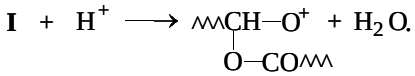

The resulting O-centered electron-deficient intermediates usually undergo deprotonation to form acid anhydrides. Note that ozonolysis of SKD butadiene rubber in the presence of acetic acid allows quantitative preparation of succinic acis [9].

It was already noted that ozonolysis of SKEPT rubber is accompanied by increase in the solution viscosity. The gel remaining after removal of the solvent shows unique properties: It remains unchanged after prolonged storage in chlorinated, aromatic, and saturated hydrocarbons, and also in concentrated nitric and sulfuric acids. The latter fact gives insight into the nature of intermolecular bonds formed in the course of ozonolysis of SKEPT rubber. If these bonds were formed solely by intermolecular reactions of carbonyl oxide and carbonyl groups, i.e., if the structures like

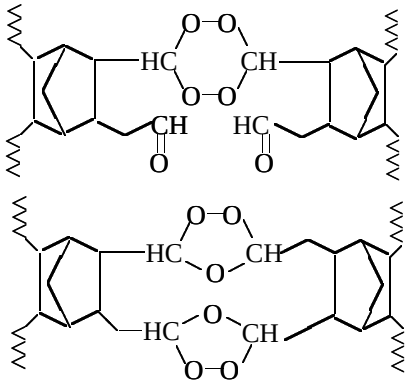

were formed, the ozonolysis product would hardly be resistant to concentrated acids, since acetal derivatives are unstable in acid solutions [10]. The high acid resistance of the ozonolysis products suggests partial

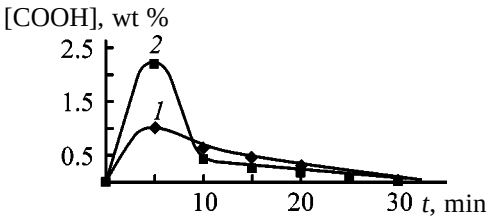

Fig. 1. Content of carboxy groups [COOH] as a function of time *t* in ozonolysis of a 1% solution of SKEPT rubber in (*1*) straight hexane and (*2*) hexane containing an equimolar amount of pyridine relative to the multiple bonds.

formation of intermolecular bonds by reaction of the carbonyl oxide group of one molecule with the C=C double bond of another, occurring as 1,3-dipolar cycloaddition:

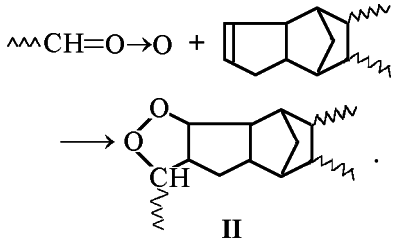

II

The acid-catalyzed transformations of the resulting functional groups should not be accompanied by cleavage of links between separate macromolecules

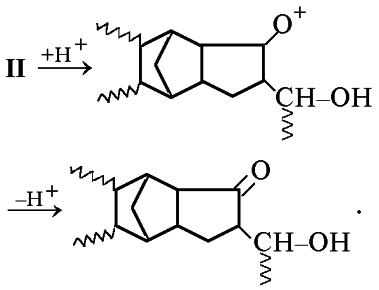

Thus, ozonolysis of SKEPT rubber in an inert solvent, hexane, involves a complex reaction pattern with formation and disappearance of carboxy and hydroperoxy groups; the reaction yields a vulcanization product with a high chemical stability. This fact is of practical interest, since surface treatment with ozone of rubber articles fabricated using SKEPT rubber may enhance their performance. However, ozone vulcanization prevents purposeful use of functional groups generated by ozonolysis in the subsequent modification of SKEPT rubber.

To prevent ozone vulcanization, in subsequent experiments we performed ozonolysis of SKEPT rubber in hexane in the presence of pyridine, since it is known [1–4] that pyridine is an effective agent for transformation of carbonyl oxides into carbonyl compounds. Since in such transformation the carbonyl oxide groups disappear, we could expect that the presence of pyridine would prevent cross-linking of macromolecules.

However, our experiments on ozonolysis of SKEPT rubber in hexane in the presence of pyridine gave a quite opposite result. In the presence of pyridine, carboxy groups are formed at a higher rate (Fig. 1), and their maximal concentration reaches a high level. The rate of formation of hydroperoxy groups in the first stage also increases, and subsequently these groups disappear. Ozonolysis in the presence of pyridine is accompanied by more intense gelation.

Formation of pyridine *N*-oxide in reaction of pyridine with carbonyl oxides can be represented as decomposition of the intermediate bipolar ion via a strained four-membered transition state:

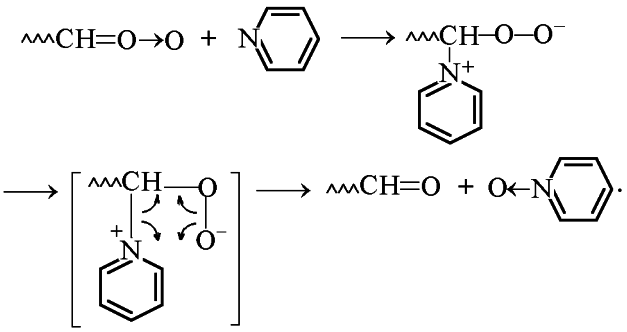

A specific feature of these systems is that the carbon atom of the adjacent carbonyl group becomes accessible for attack by the anionic center of the bipolar ion, which can result in formation of a weakly strained seven-membered ring:

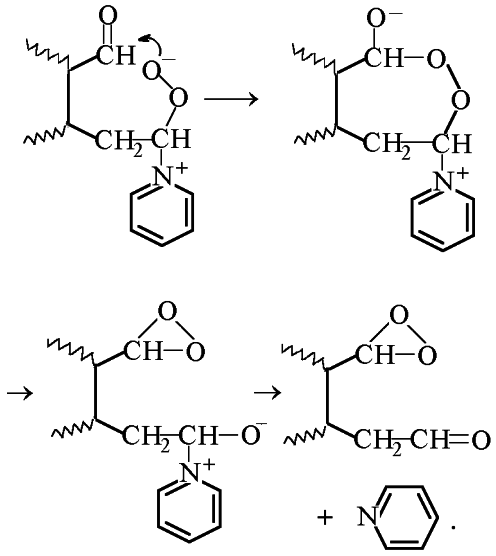

Decomposition of the seven-membered bipolar ion can yield aldehydodioxiranes. The dioxirane group can subsequently transform into the carboxy group. Pyridine in this process is the catalyst. Pyridine *N*-oxide exhibiting strong nucleophilic properties [11–13] can behave similarly.

For the above transformations to occur, the carbonyl and aldehyde groups in the initial molecule should be located close to each other. In cases when in the course of ozonolysis the carbonyl oxide and carbonyl groups are separated in space (e.g., in ozonolysis of SKI and SKD rubbers, and also of SKEPT rubber with ethylidenenorbornene), pyridine practically quantitatively transforms the carbonyl oxide groups into carbonyl groups [4].

Ozonolysis of SKEPT in hexane in the presence of pyridine resulted in formation of the vulcanization product, so that further transformations of the arising functional groups were impossible.

With the aim to obtain soluble ozonolysis products of SKEPT rubber, we attempted ozonolysis in the presence of ethanol. Alcohols are known to scavenge carbonyl oxides [1–4] with formation of alkoxy hydroperoxides:

$$\sim\!\!\sim CH{=}O{\rightarrow}O + HOR \longrightarrow \sim\!\!\sim \underset{\displaystyle OR}{\overset{\displaystyle |}{C}}H{-}OOH.$$

The interest in such ozonolysis conditions was due to the fact that the reaction of carbonyl oxides with alcohols can occur by the molecular mechanism. Figure 2 schematically illustrates interaction of the frontier orbitals of the carbonyl oxide and hydroxy groups. It is seen that the concerted process is allowed by the orbital symmetry rules.

Indeed, ozonolysis of SKEPT rubber in the presence of alcohol occurs with no signs of intermolecular cross-linking. Figure 3 shows how the intrinsic viscosity of SKEPT rubber solutions varies in the course of ozonolysis in the presence of ethanol. The intrinsic viscosity remains constant for a long time. After exhaustion of all the double bonds, the intrinsic viscosity starts to slowly decrease; we believe that this is due to ozone-initiated oxidation of the saturated chain of the rubber. The radical centers arising in saturated fragments should inevitably initiate radical β-decomposition reactions involving carbon–carbon bonds, with the resulting decrease in the molecular weight of the rubber and in the intrinsic viscosity.

Ozonolysis in the presence of alcohol is accompanied by gradual increase in the amount of hydroperoxy and carboxy groups (Fig. 4); their content does not decrease up to complete exhaustion of the C=C double bonds. Oxidative degradation of the rubber is accompanied by active accumulation of carboxy groups. Simultaneously, the content of hydroperoxy groups decreases. The observed trend is consistent with the acid-catalyzed mechanism of their decomposition.

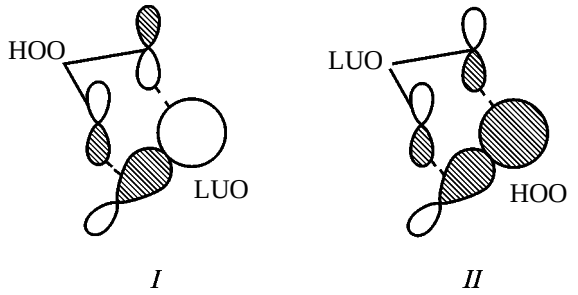

Fig. 2. Scheme of interaction (*I*) of the highest occupied orbital (HOO) of carbonyl oxide with the lowest unoccupied orbital (LUO) of the OH bond and (*II*) of LUO of carbonyl oxide with HOO of OH bond.

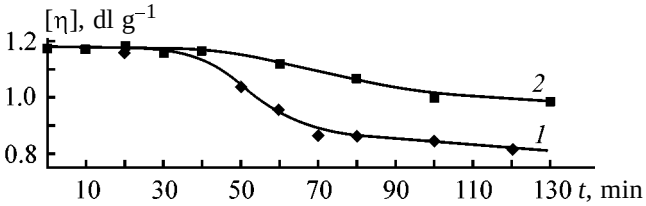

Fig. 3. Intrinsic viscosity [η] as a function of time *t* in the course of ozonation of (*1*) 1% and (*2*) 2% solutions of SKEPT rubber in hexane with addition of ethanol. Molar ratio of double bonds and alcohol 1 : 1; the same for Fig. 4.

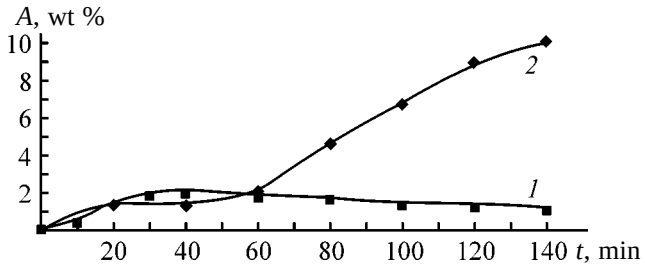

Fig. 4. Accumulation *A* of (*1*) hydroperoxy and (*2*) carboxy groups in ozonolysis of 1% solution of SKEPT rubber in hexane with addition of ethanol. (*t*) Time.

The advantage of the ozonolysis of SKEPT rubber in the presence of alcohol is formation of a large amount of hydroperoxy groups. Hence, a possibility arises of performing radical transformations with their participation (e.g., of preparing block copolymers of SKEPT rubber with various monomers).

The following bands appear in the IR spectra of SKEPT rubber ozonized in the presence of ethanol:

a broad band at 3350–3550 cm^{-1} corresponding to associated OH groups; a band at 1718 cm^{-1} ($\nu_{C=O}$); and bands at 1005, 1040, 1069, and 1100 cm^{-1} assignable to the O–O stretching vibrations. These data confirm the above-discussed reaction patterns.

Thus, it is possible, using ozonolysis, to introduce into the structure of SKEPT rubber alkoxyhydroperoxy, carboxy, and aldehyde groups. We hope that such a substantial change in the functional composition of the rubber will allow development of new routes of its modification.

EXPERIMENTAL

SKEPT rubber (Nizhnekamskneftekhim Joint-Stock Company) contained 35% propylene and 5.8% dicyclopentadiene. Low-molecular-weight impurities and antioxidants were removed by reprecipitation in acetone.

Ozonolysis was performed in a glass bubbler with a porous bottom, charged with a rubber solution in hexane. The process was performed at 15°C. An ozone–air mixture [ozone concentration $(1.5–2.4) \times 10^{-5}$ M] was fed at a rate of 14 $l\,h^{-1}$.

The reaction progress was monitored by variation of the viscosity. Ozonolysis was performed directly in the reservoir of a modified Ubbelohde viscometer with a sealed-in tube for feeding the ozone–air mixture. The intrinsic viscosity $[\eta]$ ($dl\,g^{-1}$) was determined by the Schultz–Blaschke empirical equation [14]

$$[\eta] = (\eta_{sp}/C)/(1 + 0.28\eta_{sp}).$$

In control points, we took samples and calculated $[\eta]$ as $\lim_{C \to 0} \eta_{sp}$. The results of different determinations agreed within 1%.

In the course of ozonolysis we took samples and determined in them the content of carboxy [15] and hydroperoxy [16] groups. The content of available oxygen in the ozonation products was determined by iodometric titration [16].

The IR spectra were taken on a 16 PC FT-IR spectrometer. Samples were prepared as films on KBr.

CONCLUSIONS

(1) Ozonolysis in hexane of SKEPT rubber containing dicyclopentadiene is accompanied by gelation, which is not eliminated by adding pyridine.

(2) Ozonolysis of SKEPT rubber in the presence of alcohol prevents formation of intermolecular bonds. The process is accompanied by formation of ethoxyhydroperoxy, carboxy, and aldehyde groups.

REFERENCES

1. Razumovskii, S.D. and Zaikov, G.E., *Ozon i ego reaktsii s organicheskimi soedineniyami (kinetika i mekhanizm)* (Ozone and Its Reactions with Organic Compounds (Kinetics and Mechanism)), Moscow: Nauka, 1974.
2. Razumovskii, S.D. and Zaikov, G.E., *Usp. Khim.*, 1980, vol. 49, no. 12, p. 2344.
3. Menyailo, A.T. and Pospelov, M.V., *Usp. Khim.*, 1967, vol. 36, no. 4, p. 662.
4. Grigor'ev, E.I. and Beresnev, V.V., *Kauchuk Rezina*, 1999, no. 6, p. 35.
5. Razumovskii, S.D., Anachkov, M.P., Kafeli, A.A., and Zaikov, G.E., *Vysokomol. Soedin., Ser. B*, 1981, vol. 23, no. 5, p. 336.
6. Baumstark, A.L., Beeson, M., and Vasquez, P.C., *Tetrahedron Lett.*, 1989, vol. 30, no. 41, p. 5567.
7. Khursan, S.L., Grabovskii, S.A., Kabal'nova, N.N., *et al.*, *Izv. Ross. Akad. Nauk, Ser. Khim.*, 2000, no. 8, p. 1344.
8. Grekov, A.P. and Veselov, V.Ya., *Usp. Khim.*, 1978, vol. 47, no. 7, p. 1200.
9. RF Patent 2 036 895.
10. *Protective Groups in Organic Chemistry*, McOmie, J.F.W., Ed., New York: Plenum, 1973.
11. Bassindale, A.R. and Stout, T., *Tetrahedron Lett.*, 1985, vol. 26, no. 28, p. 3403.
12. Fife, W.K. and Xin, Y., *J. Am. Chem. Soc.*, 1987, vol. 109, no. 4, p. 1278.
13. Savelova, V.A., Belousova, I.A., Simanenko, Yu.S., and Prokop'eva, T.M., *Zh. Org. Khim.*, 1989, vol. 25, no. 4, p. 671.
14. Braun, D., Cherdron, H., and Kern, W., *Praktikum der makromolekularen organischen Chemie*, Heidelberg: Alfred Huthig, 1971.
15. Toroptseva, A.M., Belogorodskaya, K.V., and Bondarenko, V.M., *Laboratornyi praktikum po khimii i tekhnologii VMS* (Practical Laboratory Course of Chemistry and Technology of Macromolecular Compounds), Leningrad: Khimiya, 1972.
16. Antonovskii, V.L. and Buzlanova, M.M., *Analiticheskaya khimiya organicheskikh peroksidnykh soedinenii* (Analytical Chemistry of Organic Peroxy Compounds), Moscow: Khimiya, 1978.

Russian Journal of Applied Chemistry, Vol. 74, No. 7, 2001, pp. 1225–1229. Translated from Zhurnal Prikladnoi Khimii, Vol. 74, No. 7, 2001, pp. 1191–1194.

MACROMOLECULAR CHEMISTRY AND POLYMERIC MATERIALS

Separation of Styrene–Butadiene Rubbers from Latexes Using Dimethyldiallylammonium Chloride–SO_2 Copolymer

V. N. Verezhnikov, S. S. Nikulin, T. N. Poyarkova, and V. M. Misin

Voronezh State University, Voronezh, Russia

Received March 6, 2001

Abstract—The suitability of *N*,*N*-dimethyl-*N*,*N*-diallylammonium chloride–SO_2 copolymer as coagulant for isolating rubber from synthetic latexes was investigated.

Emulsion rubbers are traditionally separated from latexes using inorganic salts under acidification of the system being coagulated with a mineral acid [1]. Though highly efficient, this procedure does not satisfy the environmental requirements because the wastewater generated by emulsion latex production is heavily polluted with mineral salts. They are not degraded at wastewater treatment facilities and are discharged into natural water reservoirs, which results in environmental pollution and salinization of soils and potable water sources. Environmentally promising are salt-free coagulation methods using proteins of different origin [2] and synthetic cationic polyelectrolytes [3] as coagulants. For separation of butadiene–(α-methyl)styrene latexes, a coagulant based on poly-*N*,*N*-dimethyl-*N*,*N*-diallylammonium chloride (PDMDAAC) was proposed [4, 5]. With this cationic polyelectrolyte, coagulant can be used in a small amount of 1.7–5.0 against 180–250 kg t^{-1} of rubber in the case of sodium chloride. This significantly decreases the pollution of production wastewater with mineral salts. Also, PDMDAAC reacts with anionic components of the latex and bounds them chemically, thus decreasing the level of pollution of wastewater with surfactants, as the resulting poorly soluble complexes are deposited onto the rubber crumb being separated from the latex [6].

However, the presence in the rubber of PDMDAAC and/or the products of its reactions with the emulsion system components accelerates vulcanization of rubber stocks [7]. Wide application of PDMDAAC as coagulant on commercial scales will require correction of the rubber stock composition.

Extension of the spectrum of polyelectrolyte-type cationic coagulants and comparative assessment of the efficiency of their coagulation action and the influence on the properties of rubbers separated and vulcanizates thereof are of scientific and practical interest.

In this context, copolymers of *N*,*N*-dimethyl-*N*,*N*-diallylammonium chloride (DMDAAC), in particular, with sulfur(IV) oxide [8, 9]

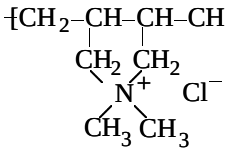

seem promising. In this work we studied the flocculation effect of the copolymer of DMDAAC with SO_2 (PDMDAAC–SO) in separation of rubber from SKS-30 ARK styrene–butadiene latex and the EPB emulsion polybutadiene latex, as well as the influence of the flocculant on the properties of the rubbers separated and vulcanizates thereof.

We used commercial latex samples. The initial solution of PDMDAAC–SO (44 wt %) was a yellow viscous liquid exhibiting a strongly acid reaction (pH 0.11), evidently, owing to incomplete neutralization of hydrochloric acid formed during synthesis [8, 9].

The intrinsic viscosity [η] (measured in the presence of 2 M sodium chloride suppressing the electrolytic swelling) was equal to 0.056 dl g^{-1}. This small [η] value suggests relatively low average molecular weight of the copolymer.

Separation of rubber was studied as follows. Latex (50 ml) was placed into a coagulation setup and kept at appropriate temperature for 10–15 min, whereupon an aqueous solution of PDMDAAC–SO was introduced under permanent stirring. The resulting crumb was separated from the aqueous fraction (serum), washed with warm (30–40°C) distilled water, and

1070-4272/01/7407-1225$25.00

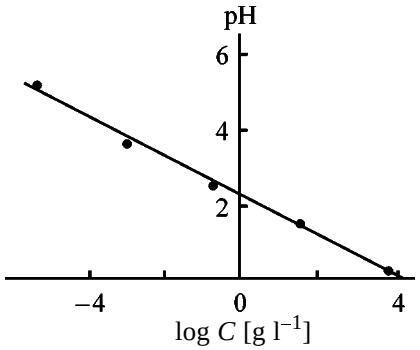

Fig. 1. Influence of dilution on the pH of aqueous solutions of PDMDAAC–SO. (*C*) PDMDAAC–SO content, g l^{-1}.

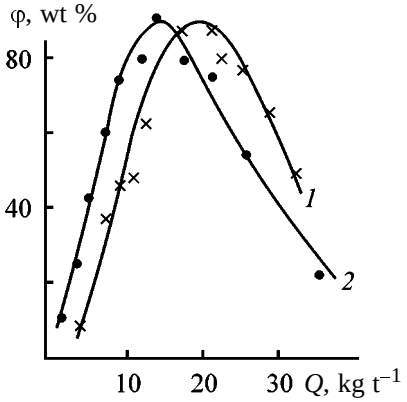

Fig. 2. Fraction φ of rubber separated from latex as a function of the amount *Q* of PDMDAAC–SO. Latex: (*1*) SKS-30 ARK and (*2*) EPB.

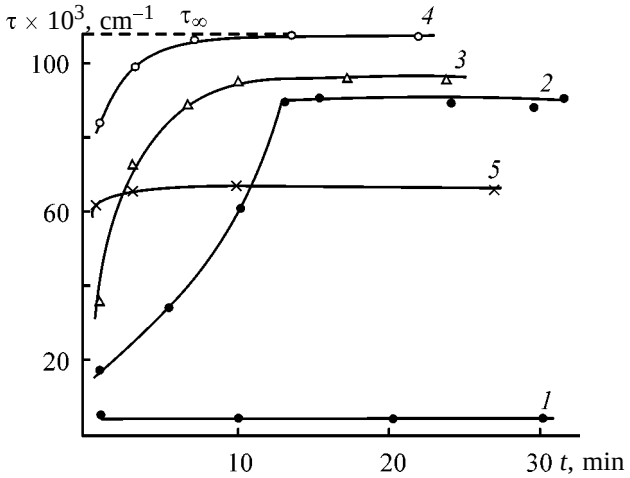

Fig. 3. Kinetic curves of flocculation of SKS-30 ARK latex with PDMDAAC–SO solutions of different concentrations. (τ) Turbidity and (*t*) time. PDMDAAC–SO concentration $C \times 10^4$, g l^{-1}: (*1*) 1, (*2*) 2, (*3*) 3, (*4*) 4, and (*5*) 4.5.

dried in an oven at 75–80°C. The degree of coagulation was estimated visually, from the transparency of the serum, and gravimetrically, from the amount of the rubber separated from the latex. Complete coagulation in some cases required certain keeping time.

In view of the high acidity of the initial PDMDAAC–SO solution, it was reasonable to elucidate how pH varies with the degree of dilution of the solution so as to decide whether it is necessary to additionally acidify the system to be coagulated, in view of the fact that rubbers are separated in an acid medium [1]. We found (Fig. 1) that pH tends to decrease with decreasing content of PDMDAAC–SO in solutions. The log *C*–pH dependence is linear, which suggests the presence of a free acid in solution. Therefore, the subsequent experiments on separation of rubber were run both with and without additional acidification of the system being coagulated with sulfuric acid.

Our experiments showed that the plot of the fraction of the rubber separated from latex vs. the specific amount of the consumed PDMDAAC–SO passed through a maximum (flocculation optimum, Fig. 2). The same pattern of variation was also observed earlier in flocculation of styrene–butadiene latexes by PDMDAAC homopolymer [10]. Complete separation of the rubber from SKS-30 ARK latex is achieved at the amount of PDMDAAC–SO of 18–20, and from EPB latex, of 14–15 kg t^{-1} of rubber.

Addition of sulfuric acid as acidifying agent at the optimal amount of PDMDAAC–SO did not significantly affect the amount of the resulting coagulum. However, at reduced amounts of the flocculant the amount of the added sulfuric acid exerted a major influence. For example, at the amount of PDMDAAC–SO of 9.0 kg t^{-1} of rubber complete separation of the SKS-30 ARK rubber from the latex was achieved at the amount of sulfuric acid of 8.0 kg t^{-1} of rubber. Similar effect was observed for EPB coagulation as well: At the amount of PDMDAAC–SO of 10.8 kg t^{-1} complete coagulation was achieved with sulfuric acid in the amount of 6.0 kg t^{-1} of rubber.

The kinetic relationships in the latex flocculation were studied using the plots of the turbidity τ of dilute ($1 : 10^4$) SKS-30 ARK latex vs. time (Fig. 3). As in the case of the other cationic agents (PDMDAAC [4, 11], 2-methylimidazole [12], and 2,2,4-trimethyl-1,2-dihydroquinoline [13]), the turbidity initially tends to increase and then flattens out, reaching a maximum τ corresponding to formation of large, not degrading in time, floccules. The plots of 1-min turbidity τ_1 characterizing the initial flocculation rate and of the limiting turbidity τ vs. PDMDAAC–SO concentration pass through a maximum (flocculation optimum, Fig. 4). The occurrence of the flocculation optimum established from the kinetic data and the polymer separation curves (Fig. 2) suggest that upon complete

neutralization of particles the subsequent adsorption of the excess polyelectrolyte molecules results in recharging of the particles and restabilization of the dispersion. Similar situation was observed in the case of flocculation of polystyrene [11, 14, 15], styrene–butadiene, and nitrile–butadiene latexes [10] by PDMDAAC–SO, and the recharging was confirmed in all the cases by measurements of the electrokinetic potential of the latex particles.

Chemical analysis of the serum formed after coagulation of SKS-30 ARK latex with PDMDAAC–SO copolymer showed (Table 1) that the dry residues of serum are by a factor of 10–20 smaller than those in the case of separation of rubber with coagulant (sodium chloride). This suggests that the content of soaps of synthetic fatty acids (SFAs), tall oil rosin soap, Leukanol, and other components of the emulsion system in the reference serum significantly exceeds that in the test sample. Reactions of PDMDAAC–SO with emulsifiers can be described by exchange reactions occurring during coagulation of the latex

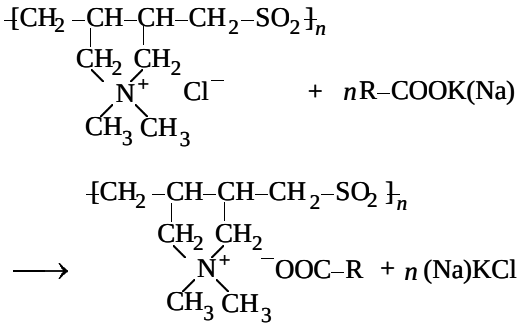

Under acidification, the resulting product can react with sulfuric acid with elimination of free acids by the following scheme:

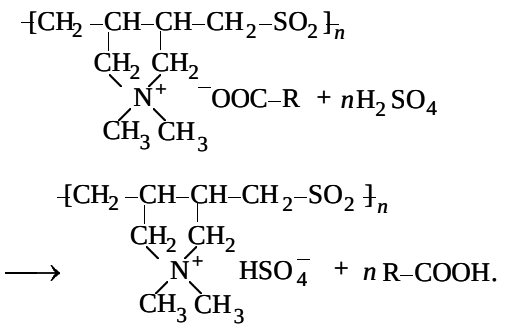

The physicomechanical properties of the rubber stocks and vulcanizates based on SKS-30 ARK rubber separated from latex with the use of PDMDAAC–SO and sodium chloride as coagulants are presented in Tables 2 and 3.

The vilcanization kinetic curves (Fig. 5) show that vulcanization of rubber stocks based on SKS-30 ARK rubber separated from latex with PDMDAAC–SO coagulant begins within a shorter period compared to the reference sample separated with sodium chloride. The optimal times of vulcanization for the reference and test samples are close. However, rubber stocks based on rubber separated from latex with PDMDAAC–SO under acidification attain the vulcanization optimum within a shorter period. In the former case, vulcanization can be accelerated either by PDMDAAC–SO cationic coagulant proper or by the products of its reaction with the emulsion system components. Similar relationships were observed for PDMDAAC as coagulant [14]. Physicomechanical tests (Table 3) showed slight improvement of the strength characteristics of vulcanizates based on the

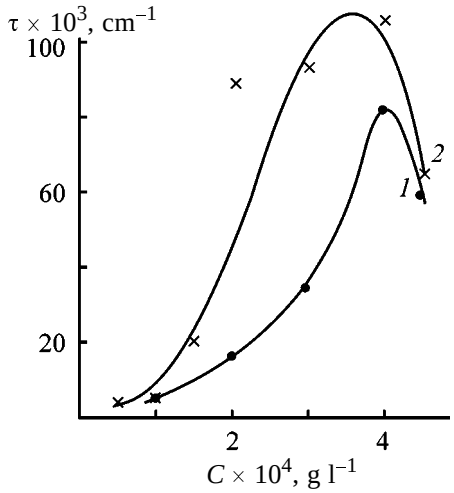

Fig. 4. Variation of (*1*) 1-min and (*2*) limiting turbidity τ with the PDMDAAC–SO concentration *C*.

Table 1. Chemical analysis of the serum formed from coagulation of SKS-30 ARK latex

Parameter*	Coagulant		
	NaCl	PDMDAAC–SO	
		with acidification	without acidification
pH	3.2	7.7	8.2
Content, %			
CO	3.75	0.19	0.21
Cl^-	2.01	0.37	0.36
L	0.012	0.0073	0.007
OAs	0.028	0.008	0.01
OASs	0.019	0.008	0.02

* DR is dry residue, L is Leukanol, OAs is organic acids, and OASs is organic acid soaps.

Table 2. Vulcanization characteristics of standard rubber stocks based on SKS-30 ARK rubber

Parameter*	Coagulant		
	NaCl	PDMDAAC–SO	
		with acidification	without acidification
M_L, N m	0.91	0.8	0.95
M_H, N m	4.66	4.52	4.58
t_S, min	2.2	1.85	1.80
$t_{S(50)}$, min	4.65	3.4	3.82
t, min	7.3	6.0	7.7
R_V, min^{-1}	19.6	24.1	16.9

* M_L is the minimal torque, M_H is the maximal torque, t_S is the vulcanization onset time, $t_{S(50)}$ is the time of attaining 50% degree of vulcanization, t is the optimal vulcanization time, and R_V is the vulcanization rate.

Table 3. Physicomechanical characteristics of vulcanizates based on SKS-30 ARK rubber

Parameter*	Coagulant		
	NaCl	PDMDAAC–SO	
		with acidification	without acidification
U_{nom}, MPa	12.7	13.1	12.7
P_{nom}, MPa	19.6	23.0	25.5
L_{rel}, %	420	460	3.82
D_{rel}, %	8	10	10

* U_{nom} is the nominal stress at 300% elongation, P_{nom} is the nominal tensile strength, L_{rel} is the relative elongation at break, and D_{rel} is the relative deformation set after break.

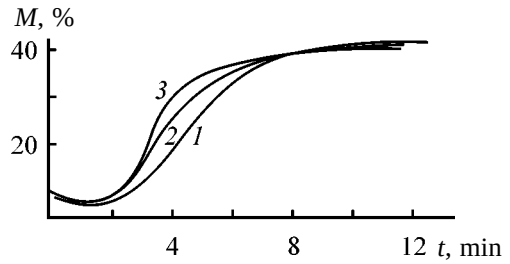

Fig. 5. Characterization of vulcanization of rubber stocks based on SKS-30 ARK rubber separated from latex with (*1*) NaCl, (*2*) PDMDAAC–SO without acidification, and (*3*) PDMDAAC–SO with acidification. (*M*) Vulcanization and (*t*) time.

rubber separated from latex with PDMDAAC–SO compared to the reference sample separated with sodium chloride.

CONCLUSIONS

(1) Rubbers are satisfactorily separated from latexes by the copolymer of poly-*N*,*N*-dimethyl-*N*,*N*-diallylammonium chloride with SO_2 both with and without acidification. Additional acidification of the system being coagulated with aqueous sulfuric acid makes it possible to reduce the coagulant consumption.

(2) The plot of the fraction of the polymer separated, as well as of the kinetic parameters of flocculation, vs. coagulant concentration pass through a maximum (flocculation optimum). Restabilization of the system can be due to recharging of the particle surface after introducing excess flocculant.

(3) Poly-*N*,*N*-dimethyl-*N*,*N*-diallylammonium chloride and the products of its interaction with the emulsion system components accelerate vulcanization.

REFERENCES

1. Kirpichnikov, P.A., Averko-Antonovich, L.A., and Averko-Antonovich, Yu.O., *Khimiya i tekhnologiya sinteticheskogo kauchuka* (Chemistry and Technology of Synthetic Rubber), Leningrad: Khimiya, 1987.
2. Moiseev, V.V., Popova, O.K., Kosovtsev, V.V., and Evdokimova, O.A., *Primenenie belkov pri poluchenii elastomerov: obzor* (Use of Proteins in Elastomer Production: Review), Moscow: TsNIITEneftekhim, 1985.
3. Verezhnikov, V.N., Nikulin, S.S., Poyarkova, T.N., and Garshin, A.P., *Vestn. Tambov. Univ.*, 1997, vol. 2, issue 1, pp. 47–52.
4. Garshin, A.P., Nikulin, S.S., Shapovalova, N.N., *et al.*, *Proizv. Ispol'z. Elastom.*, 1994, no. 11, pp. 2–6.
5. Garshin, A.P., Nikulin, S.S., Shapovalova, N.N., *et al.*, *Proizv. Ispol'z. Elastom.*, 1994, no. 12, pp. 9–14.
6. Garshin, A.P., Nikulin, S.S., Naumova, Yu.M., *et al.*, *Proizv. Ispol'z. Elastomer.*, 1996, no. 5, pp. 8–10.
7. Garshin, A.P., Nikulin, S.S., Slukina, Z.D., *et al.*, *Proizv. Ispol'z. Elastom.*, 1994, vol. 9, pp. 14–19.
8. Leplyanin, G.V., Abstracts of Papers, *18-ya konferentsiya "Khimiya i tekhnologiya organicheskikh soedinenii sery"* (18th Conf. "Chemistry and Technology of Organic Sulfur Compounds"), Kazan, 1992, part 3, p. 184.
9. Vorob'eva, A.I., Vasil'eva, E.V., Gaisina, Kh.A.,

et al., *Vysokomol. Soedin., Ser. A*, 1996, vol. 38, no. 10, pp. 1663–1667.

10. Verezhnikov, V.N., Nikulin, S.S., Poyarkova, T.N., *et al.*, *Zh. Prikl. Khim.*, 2000, vol. 73, no. 10, pp. 1720–1724.
11. Verezhnikov, V.N., Nukulin, S.S., Misin, B.M., and Poyarkova, T.N., *Russ. Polym. News*, 1999, vol. 4, no. 4, pp. 36–41.
12. Verezhnikov, V.N., Nikulin, S.S., and Garshin, A.P., *Zh. Prikl. Khim.*, 1997, vol. 70, no. 12, pp. 2052–2055.
13. Nikulin, S.S., Verezhnikov, V.N., Poyarkova, T.N., and Shmyreva, Zh.V., *Zh. Prikl. Khim.*, 2000, vol. 73, no. 1, pp. 144–148.
14. Verezhnikov, V.N., Nikulin, S.S., Krutikov, M.Yu., and Poyarkova, T.N., *Kolloidn. Zh.*, 1999, vol. 61, no. 1, pp. 37–40.
15. Verezhnikov, V.N., Poyarkova, T.N., Nikulin, S.S., and Kurbatova, N.A., *Kolloidn. Zh.*, 2000, vol. 62, no. 1, pp. 26–30.

Russian Journal of Applied Chemistry, Vol. 74, No. 7, 2001, pp. 1230–1234. Translated from Zhurnal Prikladnoi Khimii, Vol. 74, No. 7, 2001, pp. 1195–1199.

CHEMISTRY OF FOSSIL FUEL

Analysis of Impurities in Mixtures of West-Siberian Crude Oils

O. Yu. Begak and A. M. Syroezhko

Mendeleev Russian Research Institute of Metrology, St. Petersburg, Russia
St. Petersburg State Technological Institute, St. Petersburg, Russia

Received April 5, 2001

Abstract—The content of B, Mg, Na, Al, P, V, Mn, Cu, Cr, Fe, Ni, Zn, Ag, Br, Sn, I, Ba, W, Pb, and Bi in 24 samples of industrial mixtures of West-Siberian oils was studied using the method of inductively coupled plasma with mass spectrometric registration.

At present the contribution of difficultly extractable oils to the total balance of the oil production of the FSU countries increases significantly, which requires special procedures to improve the oil field efficiency [1]. In most cases such treatment of the oil layer involves the use of corrosion-active compounds, which along with native heteroatomic compounds (S–, O–, N–) and impurities accumulated in the oil cause local and systematic failure of the metallic equipment (tubes, process apparatus, and engines using motor fuels) in the course of the oil production and recovery [2]; therefore, monitoring of such impurities is an urgent problem. In this work we analyzed impurities, including corrosion-active organic and inorganic compounds, in industrial mixtures of the West-Siberian oils processed at the Kirishinefteorgsintez Joint-Stock Company.

EXPERIMENTAL

The initial oil samples (a total of 27) were taken from the Yaroslavl–Kirishi pipeline in July–October 2000. The total content of sulfur in the samples was determined by X-ray fluorescence analysis using a Spectroscan L-F spectrometer with an accuracy of ±0.07–0.09%. The procedure was certified at the Mendeleev Russian Research Institute of Metrology.

The elemental composition of the oils and impurities (metals and nonmetals) was analyzed by mass spectrometry with inductively coupled plasma (ICP-MS) on a VG Plasma Quad PQ mass spectrometer under the standard conditions using imported reference samples.

The content of sulfur in 19 of 27 studied oil samples varies within 1.2–1.67 wt %, whereas in the other eight samples its content is 0.3–1.18 wt %. Such difference in the sulfur content (5.56 times) suggests that the Kirishinefteorgsintez Joint-Stock Company is supplied with crude oil not only by the Surgutneftegaz Joint-Stock Company but also from the other oil fields (with higher and lower content of sulfur as compared with standard oil). Due to technical reasons, the Kirishi Oil-Refining Plant does not process the purchased crude oil separately. As a result, the quality of the light petroleum products, mazut, and asphalt varies in wide ranges, even when the process conditions on the AT and AVT units are strictly followed. This significantly affects operation of the bitumen and reforming units. Moreover, special procedures are necessary to obtain the required quality of the boiler fuel.

The content of 20 impurity elements (ppm) in the oil samples is listed in the table. Only the iodine, chlorine, bismuth, and tungsten ions are detected in all the samples. The other impurities are distributed nonuniformly. Let us analyze the experimental results.

Elements of the main and secondary subgroups of Group I of the periodic system (sodium, copper, and silver). The content of sodium in the oil samples differs significantly from its almost total absence (sample nos. 21, 22, 459) to 450–530 ppm (sample nos. 453 and 463). The highest content of sodium (1200 ppm) was observed for sample no. 17, which is also characterized by abnormal content of the other impurity elements.

As known, significant content of impurity sodium and magnesium ions is typical for the stratal water of the oil fields, and these ions, due to the ion exchange, easily pass into the oil phase forming organic salts. In this case carboxylic acids, phenols, thiophenols, and complex molecules of resins and asphaltenes containing acid groups can act as counterions [3]. These

1070-4272/01/7407-1230$25.00

Content of impurities in crude oil samples determined by ICP-MS

Element	Content, ppm, in sample no.											
	1	2	16	17	18	19	20	21	22	23	24	25
B	**128**	**49**	**33**	**706**	**380**	–	–	–	**90**	–	7.1	–
Mg	**12**	5.4	–	**6.6**	–	–	**30**	–	–	–	–	–
Na	**125**	**61**	**180**	**1200**	**130**	**103**	**75**	–	6.6	**66**	**18**	**66**
Al	**33**	3.3	5.2	**180**	45	–	–	–	–	1.5	–	–
P	1.2	–	3.5	–	4.4	–	–	1.1	–	0.3	–	–
V	**15**	**14**	**18**	–	0.4	–	1.0	1.2	–	–	2.1	1.2
Mn	1.2	2.1	0.4	–	0.6	0.7	–	–	–	–	–	–
Cu	**12**	–	7.5	0.6	2.4	–	–	–	–	–	–	–
Cr	1.1	0.7	0.07	0.12	1.0	–	–	–	–	2.2	–	–
Fe	2	1.5	–	**850**	5.4	–	–	–	–	–	–	–
Ni	9	**12**	**36**	–	6.2	–	**24**	–	–	–	–	6.3
Zn	–	3.6	–	2.7	6.6	–	2.1	–	**12**	–	–	–
Ag	0.3	0.04	0.04	3.7	**11**	–	–	0.1	–	–	–	–
Br	–	5.6	**12**	–	6.7	–	3.6	–	–	–	–	–
Sn	–	**13**	–	–	–	4.9	–	–	–	–	–	–
I	**30**	**14**	**22**	**82**	**26**	**14**	**36**	**23**	**56**	**62**	**27**	**22**
Ba	1.2	8	5.5	**11**	–	1.0	–	–	2.2	0.9	1.5	1.1
W	2.2	0.5	6.1	3.5	**10**	2.1	1.0	1.9	**15**	0.12	6.0	0.5
Pb	0.12	–	0.2	0.3	0.9	0.03	1.5	0.5	**11**	3.2	2.2	–
Bi	1.2	1.3	0.8	1.1	1.1	0.11	1.3	2.0	1.3	3.4	0.7	1.1

Element	Content, ppm, in sample no.											
	26	419	421	433	437	441	445	427	453	459	463	467
B	–	–	**69**	**159**	–	**140**	–	**250**	–	–	**244**	**72**
Mg	–	**24**	–	–	–	–	–	–	–	**143**	**54**	**15**
Na	**45**	**75**	**150**	**24**	**13**	**63**	**15**	**130**	**450**	0.4	**530**	**66**
Al	–	–	–	–	–	–		**12**	–	–	**15**	–
P	–	–	2.6	–	5.2	**26**	1.8	**18**	–	**11**	**16**	**24**
V	1.8	1.8	1.3	–	1.5	6.1	–	–	2.1	1.4	1.8	**14**
Mn	–	0.9	–	0.7	2.1	–	–	–	–	–	2.4	–
Cu	–	–	–	6.3	–	–	–	**27**	–	–	–	–
Cr	–	–	–	–	–	2.1	–	**12**	–	–	–	–
Fe	–	7.5	–	–	–	–	–	–	–	**21**	**15**	–
Ni	–	–	–	**15**	2.8	–	–	–	–	–	2.4	–
Zn	–	3.6	–	–	–	1.3	–	**1.3**	–	–	–	–
Ag	–	–	–	0.7	–	–	3.8	–	–	–	0.2	–
Br	–	**14**	1.6	–	2.5	–	–	–	–	–	2.0	–
Sn	–	–	–	–	–	–	–	–	2.2	–	–	–
I	**16**	**33**	**16**	**43**	**25**	**42**	**24**	**32**	**43**	**31**	**16**	**25**
Ba	1.0	**16**	6.1	6.1	–	–	**11**	–	**10**	–	0.6	1.4
W	1.8	2.3	0.8	4.9	5.4	1.5	**12**	**23**	6.4	9.3	2.1	0.6
Pb	1.1	**31**	3.2	1.5	**10**	1.3	**21**	6	2.2	7	1.2	4.3
Bi	0.6	2.4	0.6	1.1	2.3	1.0	5	3	1.1	2.2	0.6	1.0

salts are highly corrosion-active, and their content in the oils supplied to the Oil-Refining Plant should by thoroughly controlled and restricted.

The copper ions were observed only in six samples, and only in sample nos. 1 and 427 its content is significant (12 and 27 ppm, respectively).

Silver was found in nine oil samples, and its content varies from 0.04 (sample nos. 2 and 16) to 11 ppm (sample no. 18).

Elements of the main subgroup of Group II of

the periodic system (magnesium and barium). Only six samples (nos. 1, 20, 419, 459, 463, and 467) contain large amounts of magnesium, and its content varies by an order of magnitude from 12–15 (sample nos. 1 and 467) to 143 ppm (sample no. 459).

Barium was found in 17 samples; its content varies from 0.6–0.9 (sample nos. 463 and 23) to 16 ppm (sample no. 419).

Elements of the main subgroup of Group III of the periodic system (boron and aluminum). Boron compounds were found in sample nos. 1, 2, 16–18, 22, 421, 427, 433, 441, 463, and 467, and its content varies from 33 (sample no. 16) to 706 ppm (sample no. 17).

Significant content of aluminum is typical for sample nos. 1, 17, 18, 427, and 463; the Al(III) content ranges from 12–15 (sample nos. 427 and 463) to 180 ppm (sample no. 17).

Elements of the main subgroup of Group IV of the periodic system (tin and lead). Tin compounds were observed only in sample nos. 2, 19, and 453, and the tin content varies from 2.2 (sample no. 453) to 13 ppm (sample no. 2).

Lead is present in almost all the samples, and its content varies from 0.003 (sample no. 19) to 31 ppm (sample no. 419). The presence of organometallic tin compounds in oils was first found in [4]. It is known that tin and lead form compounds with one or several alkyl or aryl groups [4, 5].

Elements of the main subgroup of Group V of the periodic system (phosphorus and bismuth). Phosphorus compounds were observed in 13 of 24 oil samples. The content of phosphorus varies from 1.1–1.2 (sample nos. 21 and 1) and 0.3 (sample no. 23) to 24–26 ppm (sample nos. 467 and 441). As seen from the published data, in oils phosphorus forms heteroorganic compounds in which it is bound to relatively small hydrocarbon radicals.

It should be noted that phosphorus compounds activate corrosive hydrogenation and failure of steels (increase amount of hydrogen penetrating into the steel), which increases hydrogen corrosion and accelerates failure of the process equipment [6]. Phosphorus ion exhibits the highest activation affect on the hydrogen corrosion of steels: P > S > As > Se > Sb > Te > Bi [7].

Bismuth ions were found in all the samples, and its content varies from 0.11 (sample no. 19) to 5 ppm (sample no. 445).

Elements of the secondary subgroup of Group VI of the periodic system (chromium and tungsten). Chromium compounds were detected only in eight oil samples, its content changes from 0.07 (sample no. 16) to 12 ppm (sample no. 427).

Tungsten was observed in all the samples, its content ranges from 0.12 (sample no. 23) to 23 ppm (sample no. 427).

Elements of the main and secondary subgroups of Group VII of the periodic system (bromine, iodine, and manganese). Bromine ions were found in only eight of 24 oil samples; its content ranges from 1.6–2.0 (sample nos. 421 and 463) to 12–14 ppm (sample nos. 16 and 419).

As known, bromine compounds significantly accelerate the equipment corrosion, and their corrosion activity strongly increases with heating [8]. Bromine can be present in all classes of petroleum compounds, but, as compared with the other halogens, it prefers more complex asphaltene structures [9].

Large amounts of iodine were observed in all the samples studied, which indicates that the crude oils supplied to the Oil-Refining Plant contain significant amounts of corrosion-active iodine compounds. The content of iodide ions in the samples varies from 14 (sample nos. 2 and 19) to 82 ppm (sample no. 17).

Iodine compounds, similarly to bromine and chlorine, strongly accelerate corrosion of petroleum processing equipment, in particular pipelines, especially in the presence of water. It should be noted that iodide ions are the most corrosion-active under other equal conditions. As known [8], aluminum and its alloys even at room temperature react with 0.13% HI (corrosion rate >72 g cm^{-2} day^{-1}), whereas in hydrochloric acid these alloys are considered as materials with decreased stability but suitable for operation (corrosion rate ≤24 g cm^{-2} day^{-1}). Armco iron, cast iron, and carbon steels, which are also the materials with decreased stability but suitable for operation in hydrochloric acid at room temperature, cannot be used in HI because their corrosion rate exceeds 72 g cm^{-2} day^{-1}.

Manganese ions were observed in only 9 of 24 oil samples, and its content varies from 0.4 (sample no. 16) to 2.4 ppm (sample no. 463). It is often considered that the manganese and iron ions, occurring in the oil, substitute the protons in some compounds, especially multifunctional resin molecules.

3*d* transition elements (vanadium, nickel, iron, and zinc). Significant amounts of vanadium compounds were found in sample nos. 1, 2, 16, and 467,

and its content varies within 14–18 ppm. Vanadium compounds are corrosion-active [7, 10]. It was found that about a half of this element in the oil occurs in porphyrin complexes [11].

High content of nickel is typical only for sample nos. 16, 20, and 433. The nickel content varies by a factor of 15: from 2.4 (sample no. 463) to 36 ppm (sample no. 16). Similarly to vanadium, 5–50% of nickel occurs in the oil as porphyrin complexes [12].

Iron was found in seven oil samples, but only in sample nos. 17, 459, and 463 its content is significant and varies from 15 (sample no. 463) to 850 ppm (sample no. 17).

Zinc was determined in only 8 of 24 oil samples, and its content ranges from 1.3 (sample no. 441) to 12–13 ppm (sample nos. 22 and 427).

Significant content of metal and nonmetal impurities in the oil samples can be due to the fact that the stratal water impurity occurring as emulsion in crude oil includes significant amounts of dissolved salts and suspended mineral particles. Moreover, some fraction of metals occurs in the oil proper as complex compounds (chromatography–mass spectrometry data), and certain fraction of impurities appears in the oil with the corrosion products of oil-extraction equipment. Pretreatment of the oil does not ensure complete removal of such impurities, and oil often contains finely dispersed water and colloidal particles. These factors can significantly affect the composition and concentration of impurities in the oil, increasing, in particular, the content of the main rock-forming elements (cations and anions) such as Al, Fe, P, Na, Mg, and Ba and Br and I and thus increasing the corrosion activity of the oil supplied to the Oil-Refining Plant [9].

There are no general trends in the distribution of impurities in the samples studied. At the same time, all the samples studied can be subdivided into three main groups.

The first group (12 oil samples) includes the samples with the highest content of sodium ions (sample nos. 2, 16, 17, 19, 20, 23, 25, 26, 419, 421, 453, and 463). The second most abundant element in the majority (7 of 12) of the samples is iodine, and its content in all the samples is significant. The sodium : iodine ratio in this group does not, as a rule, exceed 10 (in 9 of 12 samples), but in sample no. 463 this ratio is 33, whereas for sample no. 17 with abnormal content of impurities the Na/I ratio reaches 146.

The second group (7 oil samples) includes the samples containing significant amounts of boron (sample nos. 1, 18, 22, 427, 433, 441, and 467), and the next most abundant in this group are sodium or iodine. As a rule, the boron : iodine ratio does not exceed 10, except sample no. 18 (B/I = 14.6).

The third group includes four oil samples (sample nos. 21, 24, 437, and 445); the iodide ions are the main impurity in these samples.

Only sample no. 459 contains magnesium as the main impurity.

The lack of regular trends in the impurity distribution and significant difference in the total content of sulfur in the oil samples studied indicate that the Kirishinefteorgsintez Joint-Stock Company is supplied with crude oil from oil fields of various regions or with mixture of crude oils from different oil fields.

It is obvious that the oil samples with the higher content of sodium, magnesium, iodide, chloride, and bromide ions exhibit a higher corrosion activity as compared with the other samples.

CONCLUSIONS

(1) The total content of sulfur in 27 oil samples supplied for processing varies within 0.3–1.67 wt %.

(2) The content of B, Mg, Na, Al, P, V, Mn, Cu, Cr, Fe, Ni, Zn, Ag, Br, Sn, I, Ba, W, Pb, and Bi in 24 samples of industrial oil mixtures was studied. Their concentration varies within a wide range, and only tungsten, bismuth, and iodine were observed in all the samples studied.

(3) The oil samples for processing can be subdivided into three groups by the content of the main impurities (sodium, boron, and iodine) determined by the method of inductively coupled plasma with mass-spectrometric registration.

(4) Variation in the content of sulfur and 20 impurity elements in the oil samples indicates that in different periods the Kirishinefteorgsintez Joint-Stock Company is supplied with crude oil not only by the Surgutneftegaz Joint-Stock Company but also from the other oil fields.

(5) In the oil samples studied the sulfur compounds and impurities of iodine, bromine, chlorine, sodium, phosphorus, magnesium, and vanadium are highly corrosion-active.

REFERENCES

1. Negreev, V.F., *Korroziya oborudovaniya neftyanykh promyslov* (Corrosion of the Oil Field Equipment), Baku: Aznefteizdat, 1969.

2. Gonik, A.A., *Korroziya neftepromyslovogo oborudovaniya i mery ego preduprezhdeniya* (Corrosion of the Oil Field Equipment and Prevention Measures), Moscow: Nedra, 1976.
3. Saumin, A.Z., Tokunov, V.I., Polyakov, G.A., *et al*., *Neft. Khoz*., 2000, no. 7, pp. 16–18.
4. Yen, T.P., *Ann. Arbor Sci. Publ. USA: Ann. Arbor Mich*, 1975, pp. 1–30.
5. Melikadze, L.D., Goderdzishvili, K.G., and Zul'fugarly, Dzh.I., *K izucheniyu mikroelementov neftei Gruzii* (Study of Microelements in Georgian Oils), Tbilisi: Metsniereba, 1976.
6. Shreider, A.V., Shparber, I.S., and Archakov, Yu.I., *Vliyanie vodoroda na neftyanoe i khimicheskoe oborudovanie* (Effect of Hydrogen of Petroleum and Chemical Equipment), Moscow: Mashinostroenie, 1976.
7. Tumanovskii, A.G. and Zel'kind, M.E., *Neftepererab. Neftekhim*., 1972, no. 3, pp. 9–12.
8. Rachev, KhD. and Stefanova, S.T., *Spravochnik po koroziya* (Corrosion Handbook), Sofia, 1977.
9. Kam'yanov, V.F., Aksenov, V.S., and Titov, V.I., *Geteroatomnye komponenty neftei* (Heteroatomic Oil Components), Moscow: Nauka, 1981.
10. Mashireva, L.G. and Shakhbazyan, G.I., *Khim. Tekhnol. Topl. Masel*, 1972, no. 1, pp. 58–61.
11. Dunning, H.N., Moore, J.W., Bieber, H., and Williams, R.B., *J. Chem. Eng. Data*, 1960, vol. 5, p. 546.
12. Sugihara, J.M., *J. Chem. Eng. Data*, 1962, vol. 7, p. 269.

Russian Journal of Applied Chemistry, Vol. 74, No. 7, 2001, pp. 1235–1239. Translated from Zhurnal Prikladnoi Khimii, Vol. 74, No. 7, 2001, pp. 1200–1204.

CHEMISTRY OF FOSSIL FUEL

Softeners for Rubber and Corrosion-Resistant Coatings Based on Shale and Petroleum Raw Materials

A. M. Syroezhko, V. A. Proskuryakov, O. Yu. Begak, V. V. Fedorov, S. N. Korchemkin, Yu. V. Sokolova, and O. Yu. Kuznetsova

St. Petersburg State Technological Institute, St. Petersburg, Russia

Received March 6, 2001

Abstract—A broad spectrum of softeners for vulcanized rubber and corrosion-resistant materials are obtained by mechanical mixing of kerogen shale (Kerogen-70[1]) with commercial products of petroleum refining and shale chemistry such as oil tar, bitumens BND 90/130 and G, softener A-10, residue of atmospheric distillation of crude shale oil boiling above 350°C, and also by thermal treatment of the indicated mixtures at 360–400°C.

Selection of the type and concentration of plasticizers (softeners) in rubber compounds is made depending on the destination of a product. Softener B (residue of atmospheric distillation of crude shale oil) finds wide application in reclaiming of tire rubber. However, the quality of this softener is not sufficiently high. One of the most important factors controlling the quality of a softener is its polarity. High polarity provides strong interaction of a softener with the polymer and high strength of the reclaimed rubber. The performance of shale softeners of various fraction and chemical compositions in reclaiming of rubber of various types was studied at the Research Institute for Tire Industry (Moscow, Russia). The best performance was demonstrated by the softeners containing phenols in the high-boiling fraction of shale oil and also thermal polycondensation products obtained by thermal treatment at about 400°C of high-boiling fractions from atmospheric distillation of crude producer shale oil. Such softeners are characterized by a softening point of about 80–100°C (determined by the ring-and-ball method). High reclaiming characteristics of these softeners were confirmed by production test results. Rubraxes were demonstrated to be high-quality softeners also. They facilitate dispersion of carbon black in a rubber compound and improve the moisture resistance of the products, their hardness and modulus of rupture, but somewhat decrease the elasticity. Rubraxes have diverse effects on vulcanized rubber, since they tends to oxidation, condensation, interaction with sulfur, and antiscorching.

The purpose of this work was development of modified softeners based on kerogen shale (Kerogen-70) and the product of thermal treatment of high-boiling residue from atmospheric distillation of producer shale oil boiling above 350°C [1, 2], and also of those based on Kerogen-70 and oil tar. Additionally, to obtain the softeners we used mechanical mixing of commercial products from the Ukhta refinery (bitumen G or BND 90/130; softener A-10) with Kerogen-70. The softeners obtained in the work were compared with the ordinary softeners (Rubraxes) [3].

[1] Contains 70% organics.

EXPERIMENTAL

The characteristics of the initial products used in this work were as follows. Kerogen-70. Working moisture content 1.1% and ash content 27.2%. Elemental composition of the organic (kerogen) fraction (%): C 77.4, H 9.65, O 9.75, N 0.6, and S 2.6.

Crude producer shale oil. Density 1010 kg m^{-3}. Fraction composition, °C (%): <200 (8), 200–250 (10), and 300–350 (14). Elemental composition (%): C 83, H 8.8, S 1.1, N 0.3, and O 6.8.

Softener A-10 is produced at the Ukhta refinery from a mixture of asphalt of Yarega oil (25%), heavy cuts from motor oil production (50%), and residue from distillation of Usinsk oil (25%). Softening point 126°C and penetration at 25°C 11×0.1 mm. Elemental composition (%): C 84.31, H 10.68, N 0.49, S 0.71, and O 3.81.

Bitumen G (Ukhta refinery). Softening point 126°C and penetration at 25°C 5×0.1 mm.

Bitumen BND 90/130 (Kirishi refinery). Softening point 46°C and penetration at 25°C 100×0.1 mm, ductility 60 cm (25°C), and brittle point –23°C.

1070-4272/01/7407-1235$25.00 © 2001 MAIK "Nauka/Interperiodica"

Table 1. Composition of stock blend no. 2711

Material	Consumption per 100 wt parts of rubber	Component content in compound, %
Synthetic rubber SKMS-30 ARK P	100	19.19
Tire thermochemical reclaim	169.75	32.39
Ground natural crude sulfur M 9950	3.021	0.58
2-Mercaptobenzothiazole	3.021	0.58
Zinc white	2.917	0.56
Cleaned natural chalk	68.75	13.19
Kaolin	100	19.1
Crude furnace black P-803	43.75	8.4
Naftoplast oil	10.625	2.04
Rubrax (high-melting oxidized oil asphalt)	20.208	3.88

Rubrax (granulated oil asphalt oxidized in the presence of alkali). Softening point 137°C and penetration at 25°C 32×0.1 mm.

Mixtures of Kerogen-70 with asphalt from AVT-6 plant of the Kirishi refinery and leavings of distillation of producer shale oil were thermally treated in a Fischer converter controlling the treatment temperature and time and the softening temperature of the resulting softener.

The resulting softeners were characterized by the volatile matter and ash contents, determined according to GOSTs (State Standards) 6383–91 and 1102–75, respectively. The softening point of the samples was determined by the ring-and-ball method in accordance with GOST 9950–83 and the penetration (needle penetration depth), with GOST 11508–78. The elastomechanical characteristics in load tension were measured in accordance with GOST 270–75 and the Shore hardness, with GOST 263–75. The vulcanization characteristics were determined with a Mooney viscometer (GOSTs 10722–64, 12536–67) and the rebound elesticity, with a UMR-2 pendulum elastometer (GOST 6950–54). The tear resistance was measured in accordance with GOST 262–73.

As a reference material we selected rubber compound no. 2711 used at the Treugol'nik Joint-Stock Company (St. Petersburg, Russia) for rubber covering of textile materials in footwear manufacture. The compound includes 20 parts of Rubrax (by weight), which makes it a convenient object for comparison with the products prepared using modified plasticizers proposed in this work. Therefore, we prepared rubber compounds with the composition similar to mother batch no. 2711 (Table 1), but containing various amounts of Rubrax and the modified softeners.

Rubber compounds were prepared in two steps with an AG 320 160/160 laboratory roller mixer. Initially a stock blend containing synthetic rubber and all other ingredients (except for a softener) was prepared. In the second step a fixed amount of Rubrax or a modified softener was introduced. The resulting blend was vulcanized at 150°C for 15 min with an electric hydraulic press.

In the initial stage of this work we examined the possibility of changing Rubrax for bitumens modified with Kerogen-70. A fused bitumen (or a softener) was rapidly mixed with Kerogen-70 (25–50 wt %). Introduction of Kerogen-70 (25 wt %) increased the softening point of bitumen G or softener A-10 by 11%, i.e., to that of Rubrax (137°C). Introduction of Kerogen-70 (50 wt %) in bitumen BND 90/130 increased the softening point from 46 to 78°C.

Figures 1a-1h demonstrate the effect of softener on the mechanical properties of vulcanized rubber. The strength, modulus ε, relative elongation, and tear resistance of vulcanized rubber containing 20–40 wt % Rubrax (relative to rubber) are higher than those of vulcanized rubber with the test softeners (A-10, bitumens G and BND 90/130). However, the hardness, elasticity, Mooney viscosity, and moisture content of vulcanized rubber with the test softeners are higher than with Rubrax.

In the second stage of the work a mixture of Kerogen-70 (25%) with leavings of distillation of crude shale oil boiling above 350°C or oil tar was thermally treated at 350°C for 60 min in a Fischer converter.

The products of thermodissolution of Kerogen-70 in crude shale oil and oil tar (Table 2, sample nos. 1 and 2, respectively) provide a lower stickiness of rubber compounds and easier distribution throughout the polymer matrix as compared to Rubrax.

Rubber compounds were vulcanized in the com-

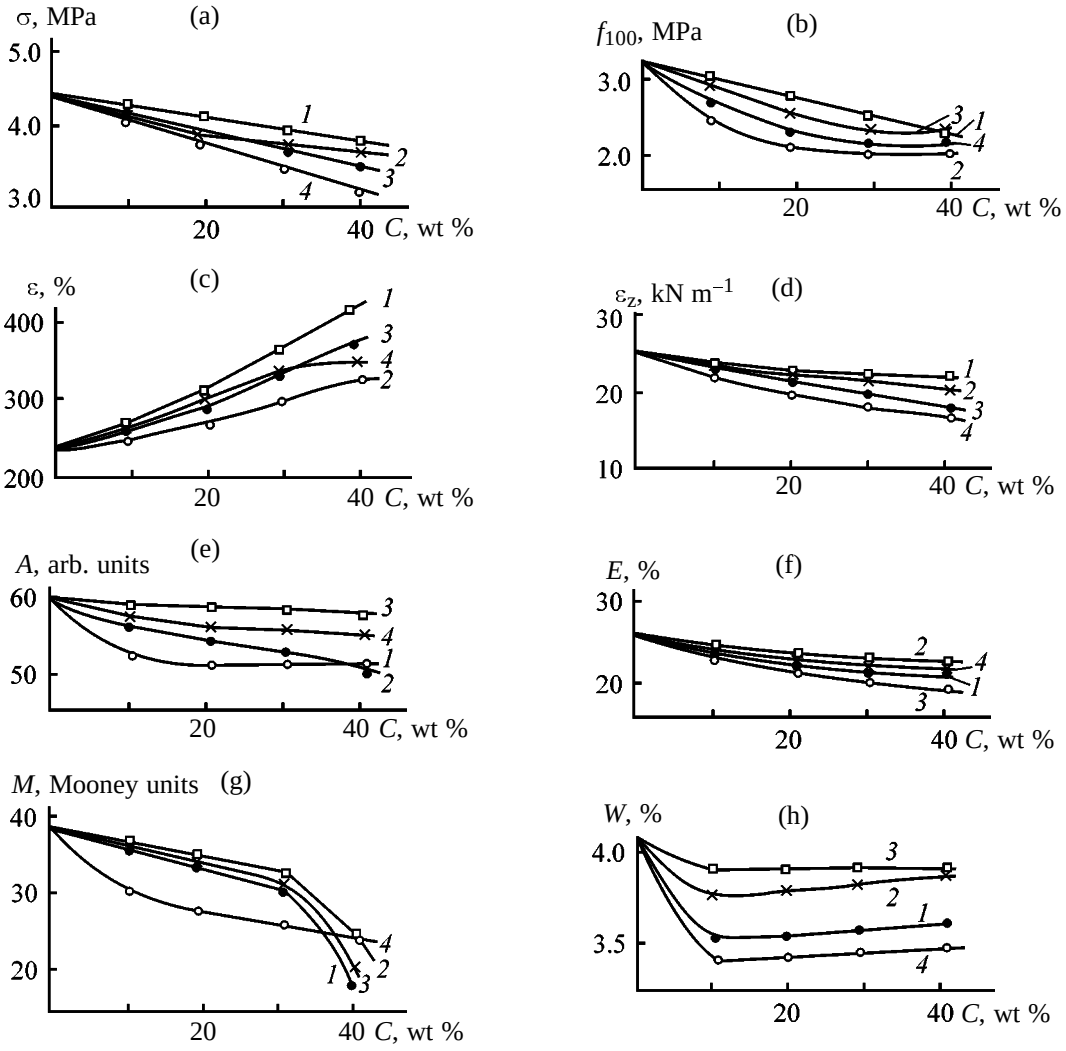

Fig. 1. (a) Strength σ, (b) nominal strength at 100% elongation (modulus *f*100), (c) relative elongation ε, (d) tear resistance ε_Z, (e) hardness *A*, (f) elasticity *E*, (g) Mooney viscosity of the mother blend *M* (Mooney units), and (h) swellability (moisture content) *W* as functions of the softener content *C*. (*1*) Rubrax, (*2*) bitumen *G*, (*3*) softener A-10, and (*4*) bitumen BND 90/130.

monly accepted mode. The performance characteristics of vulcanized rubbers with the modified shale oil and oil tar softeners are summarized in Table 2. Sample no. 1 was obtained by thermal dissolution of Kerogen-70 (25 wt %) in leavings after distillation of crude producer shale oil at 360°C, and sample no. 2 (softening point 108°C), in oil tar (AVT-6 plant; Kirishinefteorgsintez Production Association, Joint-Stock Company) at 360°C for 90 min.

The results show that the mechanical properties (strength, modulus α, tear resistance, hardness, elasticity, and relative elongation) of vulcanized rubber with these softeners compare well with those containing Rubrax.

In further experiments we tested the method for preparation of corrosion-resistant materials by thermal dissolution of ordinary or enriched shale in a reactor with a mechanical stirrer. Ordinary or enriched shale (70–90% enrichment) was dissolved in commercial shale oil (products of thermal treatment of shale) or in high-boiling oil fractions (black oil, vacuum gas oil, oil tar), or in bitumen at 350–400°C at continuous removal, cooling, and condensation of hot-vapor products, to obtain a homogenous solution. The solvent to shale weight ratio was varied from 0.33–1.0 to 2.0, and the process time, from 0.25 to 3 h.

Characteristics of the solid products thus obtained are given in Table 3. Then they were applied to steel (St. 3) plates and immersed in water containing 3 wt % NaCl and allowed to stand for 6 months. The coatings

Table 2. Mechanical characteristics of vulcanized rubbers with ordinary (Rubrax) and modified softeners

Characteristics	Content, wt % (relative to rubber)		
	modified softener		Rubrax
	sample no. 1	sample no. 2	
Strength, MPa	4.25 (20)*, 4.1 (40)	4.2 (20), 4.0 (40)	4.2 (20), 4.1 (40)
Modulus $f100$, %	2.8 (20), 2.3 (40)	2.75 (20), 2.4 (40)	2.8 (20), 2.3 (40)
Tear resistance, kN m^{-1}	22.5 (20), 22.5 (40)	22 (20), 20.8 (40)	24.3 (20), 22.5 (40)
Hardness, arb. units	53 (20), 51 (40)	52 (20), 50 (40)	53 (20), 52 (40)
Elasticity, %	21 (20), 17 (40)	19.5 (20), 16.5 (40)	21 (20), 19 (40)
Relative elongation at break, %	330 (20), 390 (40)	400 (20), 500 (40)	345 (20), 420 (40)
Viscosity, Mooney units	32 (20), 27.5 (40)	27 (20), 25 (40)	29 (20), 26.5 (40)
Moisture content of vulcanizate, %	3.5 (20), 3.55 (40)	3.2 (20), 3.6 (40)	3.6 (20), 3.7 (40)

* In the parentheses is given the softener content (wt % relative to rubber).

Table 3. Characteristics of solid products of thermal dissolution of Kerogen-70, tested as corrosion-resistant coatings

T_s, °C	P, mm	W, %	Adhesion to metal, kg cm^{-2}		Toluene-insoluble fraction, %
			shear	break	
25.6	263	0.29			7.06
34.8	142	0.036			9.03
50.9	53	0.4			19.7
60.8	3	0.44			21.5
36.2	220	0.07			10.4
26.2	230	–			1.4
58.9	26	1.19	3.4		17.4
64.5	19	0.53	8.5		19.8
62.9	17	3.1	6.5	5	18
130	1	0.8		10.6	26
56.9	21	0.08	2		18.8
63.3	11	0.06	11.7		21.1
44	140	0.05			10.4
42.8	217	1.67	6.7	1	22
55.1	42	0.75			16.6
64.6	34	2.4	10.6		16.6
61.7	19	4.41	2.2	2	15.7
110	1	2.36			33.3

Notes: (T_s) Softening point (ring-and-ball method); (P) penetration at 25°C, 0.1 mm; and (W) moisture content.

remained unchanged after the experiment, and we found no indications of corrosion of the metal.

Table 3 demonstrates that we were able to obtain a broad spectrum of solid products of thermal dissolution with the performance characteristics varied in a wide range. Thus, the softening point varies from 26.2 to 130°C, the penetration at 25°C, from 1×0.1 to 230×0.1 mm, and the moisture content, from 0.036 to 4.41%. The samples demonstrate fairly high shear (2–11.7 kg cm^{-2}) and breaking adhesion ($2 \times$ 10.6 kg cm^{-2}). The content of toluene-insoluble fraction, which correlates indirectly with the ash content, varies from 1.4 to 33.3%.

Study of the corrosion resistance of the samples in 5% H_2SO_4 and 5% NaOH revealed that the metal is fairly reliably protected in the alkali solution, but rapidly corrodes in the acid solution, which can be attributed to the presence of carbonate in the mineral fraction.

CONCLUSIONS

(1) Low-temperature modification by mechanical mixing of Kerogen-70 with oil tar, bitumens G and BND 90/130, and softener A-10 only slightly increases (by 10–11°C) the softening point. Therefore, these composites cannot be regarded as a full-value alternative to Rubrax in rubber compounds.

(2) High-temperature (360–370°C) treatment of a mixture of Kerogen-70 (25%) and heavy leavings after distillation of crude producer shale oil boiling above 350°C for 60 min in a Fischer converter produces softeners with the softening point of 100–108°C, whose performance characteristics compare well with Rubrax.

(3) Products of thermal dissolution of ordinary or enriched shale in shale oils (light-middle, overall, and heavy) or in heavy leavings (black oil, vacuum gas oil, oil tar, and bitumens) are effective corrosion-resistant coatings.

REFERENCES

1. Zelenin, N.I., Fainberg, V.S., and Chernysheva, K.V., *Khimiya i tekhnologiya slantsevoi smoly* (Chemistry and Technology of Shale Oil), Leningrad: Khimiya, 1968.
2. *Spravochnik po khimii i tekhnologii tverdykh goryuchikh iskopaemykh* (A Handbook of Chemistry and Technology of Solid Fossil Fuels), Chistyakov, A.N., Ed., St. Petersburg: Khimiya, 1996.
3. Alekperov, K.A., Study of Petroleum Refining Products as Softeners for Rubber Compounds, *Cand. Sci. Dissertation,* Leningrad, 1966.

Russian Journal of Applied Chemistry, Vol. 74, No. 7, 2001, pp. 1240–1245. Translated from Zhurnal Prikladnoi Khimii, Vol. 74, No. 7, 2001, pp. 1205–1210.

HISTORY OF CHEMISTRY AND CHEMICAL TECHNOLOGY

To Centennial Anniversary of Awarding the First Nobel Prize in Chemistry (1901–2001)

International prizes have been awarded annually, beginning in 1901, in accordance with Alfred Nobel's will, for outstanding discoveries in physics, chemistry, physiology, and medicine, and also for creation of the most prominent literary work and valuable contribution to fraternity among nations and promotion of peace. During the last century, Nobel Prizes in chemistry were not awarded, for various reasons, only in 1916, 1917, 1919, 1924, 1933, and 1940–1942 [1, 2].

Vast literature is devoted to A. Nobel's life and activities and his will [2–8]. Nevertheless, there are essentially different opinions on some important issues associated with A. Nobel's scientific and engineering activities. Detailed biographic evidence can be found in E. Bergengren's book [2] and also in memoirs of A. Sohlmann (1870–1948) [5], A. Nobel's close friend and assistant and one of the two executors of his last wishes, named in his will. The memoirs were written in the late 1940s, shortly before the author's death.

Alfred Bernhard Nobel was born on October 21, 1833, into the family of Immanuel Nobel (1801–1872), an architect and inventor engaged in various business activities. In view of severe economic grievances, I. Nobel, having left his family in Sweden, moved to Turku (Finland) in 1837, and thence went to St. Petersburg, where he later managed to found a large, by that time, plant *Liteinye zavody i mekhanicheskie masterskie. Emmanuel' Nobel' i ego synov'ya* (Casting Yard and Machine Shop. Immanuel Nobel & Sons). In the autumn of 1842, when Alfred was 9, the whole family moved to his father to Russia. During the Crimean War (1853–1856), Nobel's plants had particular numerous delivery orders, manufactured underwater mines and other kinds of armament for the Russian Navy.

In 1841–1842, A. Nobel attended school in Stockholm; later he was educated at home and, in addition to Swedish, spoke fluent Russian, German, French, and English, well knew the world history, was deeply interested in literature, and possessed profound knowledge in chemistry. According to some of his biographers, A. Nobel was instructed in chemistry by

A. Nobel.

Professor N.N. Zinin (1802–1880), later an academician of the St. Petersburg Academy of Sciences and one of founders of the Russian Chemical Society and its first President (1868–1877). The founder of the Kazan school of organic chemists, Zinin moved to St. Petersburg in the end of 1847, and was elected there an ordinary professor at the Chair of Chemistry and Physics of the St. Petersburg Medical-Surgical Academy (Military Medical Academy since 1881) [9]. However, there is also some evidence [10, 11] that A. Nobel became acquainted with Zinin and his works on explosives only in 1855.

In 1850, A. Nobel went to the United States to complete his education and then visited France and other European countries. Little is known about his stay in New York, it has only been mentioned that A. Nobel met there J. Ericsson (1803–1889), a Swedish engineer working in the field of steam engines. In 1851–1852, A. Nobel worked in Paris at the laboratory of Professor T.J. Pelouze (1807–1867), a promi-

1070-4272/01/7407-1240$25.00

nent scientist and foreign corresponding member of the St. Petersburg Academy of Sciences (since 1856). There he became acquainted with A. Sobrero (1812–1873), an Italian chemist and the inventor of nitroglycerin, who was a pupil of Pelouze and J. Liebig (1803–1873), an outstanding German chemist.

A. Nobel returned to St. Petersburg and resumed his work at his father's plant only in the autumn of 1854. However, already in 1859, in view of the diminishing military orders and the resulting unfavorable economic situation, Immanuel Nobel went to Sweden together with his wife and younger son. Alfred Nobel and two his elder brothers, Robert (1829–1896) and Ludwig (1831–1888), continued business in Russia.

A. Nobel's attention was increasingly attracted by the manufacture of explosives, which were in steadily high demand for building and mining purposes. In 1863, A. Nobel returned to Sweden, and in 1865, started there manufacture of nitroglycerin and also founded "Alfred Nobel and Co." for production of nitroglycerin in some other countries. Accidents occurring in manufacture, transportation, storage, and use of nitroglycerin forced A. Nobel to work hard in order to develop safer explosives. Dynamite patented by A. Nobel in a number of countries in the end of 1867 proved to be the most successful invention. The manufacture and use of dynamite were started already in the late 1860s.

Also insufficiently clear is the question as to what extent A. Nobel's engineering and scientific activities were affected by his acquaintance with works in the field of explosives, carried out in St. Petersburg by Zinin and military engineer V.F. Petrushevskii (major-general since 1871 and lieutenant-general since 1881; 1829–1891) [10–13]. To keep state secrets, Russian scientists did not patent their designs, although they undoubtedly have priority in the technology of large-scale manufacture of nitroglycerin and its practical use in blasting and defense technology.

In 1879, A. Nobel invested heavily in *Tovarishchestvo neftyanogo proizvodstva brat'ev Nobel'* company (Nobel Brothers' Oil Production Company) [14].

Alfred Nobel died of heart attack on December 10, 1896, at the age of 63, in San Remo (Italy). The last will and testament, signed by him in Paris on November 27, 1895, was made public in early January 1897. The will, in particular, stated that "the whole of my remaining realizable estate shall be dealt with in the following way. The capital shall be invested by my executors in safe securities and shall constitute a fund,

J.H. van't Hoff.

the interest on which shall be annually distributed in the form of prizes to those who, during the preceding year, shall have conferred the greatest benefit on mankind. The said interest shall be divided into five equal parts, which shall be apportioned as follows: one part to the person who shall have made the most important discovery or invention within the field of physics; one part to the person who shall have made the most important chemical discovery or improvements; one part to the person who shall have made the most important discovery within the domain of physiology or medicine; one part to the person who shall have produced in the field of literature the most outstanding work of an idealistic tendency; and one part to the person who shall have done the most or best work for fraternity among nations, for the abolition or reduction of standing armies and for the holding and promotion of peace congresses... It is my express wish that in awarding the prizes no consideration whatever shall be given to the nationality of the candidates, so that the most worthy shall receive the prize..." [2, 5].

By the time of A. Nobel's death, his property was worth more than 31 billion Swedish crowns by that time's rate. The commonly accepted date of foundation of the Nobel Foundation is December 10, 1896, the day of Alfred Nobel's death. This foundation acquired official status after the statute of the Nobel Foundation was approved by a royal decree on June 20, 1900, together with special rules regulating the

activities of Swedish committees awarding the prizes. In accordance with A. Nobel's will, the Prizes in physics and chemistry were to be awarded by the Swedish Royal Academy of Sciences.

The first Nobel Prize in chemistry was awarded to Jacobus Henricus van't Hoff, prominent Dutch scientist of the late XIX–early XX century, a founder of the modern physical chemistry.

He was awarded Nobel Prize on December 10, 1901, for "his pioneering work on chemical dynamics and osmotic pressure in solutions."

A great number of studies, including those performed in Russia, have been concerned with van't Hoff's life and scientific activities. Among active supporters and advocates of van't Hoff's ideas in Russia in the late XIX century were such well-known scientists as I.A. Kablukov (1857–1942), professor of the Moscow University, and V.A. Kistyakovskii (1865–1952), professor of the St. Petersburg Polytechnic Institute. They published voluminous works explaining approaches of van't Hoff and S. Arrhenius (1859–1927) to the understanding of solution properties [15–17]. The most complete biographic evidence was presented by Cohen [18], van't Hoff's pupil and close friend.

In the domestic literature, van't Hoff's life and main directions of his scientific activities were first considered by D. Dobroserdov [19] in connection with scientist's death. In more detail, these issues were discussed by Professor M.A. Blokh, a known historian of chemistry [20, 21]. A biographic essay about van't Hoff, written by Blokh, was also included in the Russian edition of the most important scientific work of the Dutch scientist [22]. Later Russian publications about van't Hoff [23–26] are largely based on Blokh's works. Van't Hoff's contribution to investigation of solutions and to other branches of physical chemistry was considered in ample detail in Yu.I. Solov'ev's monographs [27, 28] and a book concerned with the theory of the chemical process [29]. In 1984, the series *Klassiki nauki* (Classics of Science) published selected van't Hoff's works on chemistry [30] including as supplement a scientific-biographical essay about the scientist's life, compiled by N.A. Figurovskii. An essay about van't Hoff was included in the biographies of great scientists [31].

J.H. van't Hoff was born on August 30, 1852, in Rotterdam (The Netherlands) into a family of an ancient Dutch kin. His father was a known physician and had sufficient means to provide good education and upbringing for his children. Beginning with his early youth, van't Hoff exhibited disposition to natural sciences and figurative thinking. He had his primary education in a splendid private school and, having finished in 1867, passed examinations to enter the fourth form of a five-year municipal school, where he made his first acquaintance with chemistry. In 1869, the scientist-to-be entered the Polytechnic School in Delft, where much attention was given to teaching of chemistry, physics, and mathematics. He completed a three-years' course in two years and obtained a technology diploma in 1871.

Aiming to deepen his knowledge of mathematics, van't Hoff entered Leiden University; however, a year after, he makes final decision to devote himself entirely to studying chemistry. Van't Hoff moved to Bonn (Germany) and, in the autumn of 1872, started his work at the laboratory of Professor F.A. Kekule (1829–1896) at the university of that town. Kekule's interests were mainly centered in the field of theoretical organic chemistry and synthesis of organic compounds. In 1865, Kekule suggested the cyclic structural formula of benzene. A known scientist, he was repeatedly elected president of the German Chemical Society and was a foreign corresponding member of the St. Petersburg Academy of Sciences (since 1887). By Kekule's advice, and having his recommendations, van't Hoff went to Paris already in June 1883 to work at the laboratory of another prominent chemist of that time, Professor A. Wurtz (1817–1884), reiterated president of the French Chemical Society, member of the Paris Academy of Sciences, foreign corresponding member of the St. Petersburg Academy of Sciences. Undoubtedly, the work at the laboratories of such outstanding scientists as Kekule and Wurtz had positive effect on the subsequent van't Hoff's scientific activities. In October 1874, he returned to his homeland and completed his education by backing his doctoral dissertation *Contribution to the Knowledge of Cyanoacetic Acids and Malonic Acid*. Virtually at that same time van't Hoff published in Dutch a small, but meaningful article on the spatial arrangement of atoms in molecules of organic compounds. In 1875, this paper was published in French (*La chimie dans l'espase*), and in 1887, in German (*Lagerung der Atome im Raume*). Nearly simultaneously, and independently of van't Hoff, a similar paper was published by French chemist J.A. Le Bel (1847–1930). According to the concepts developed by these scientists, the affinity units of the carbon atom are directed along axes of a tetrahedron; also, mention was made of the existence of two stereoisomers of compounds containing carbon atoms with four different substituents. The results obtained by

van't Hoff and Le Bel were compared, and these studies were related to earlier concepts of L. Pasteur (1822–1895) concerning the spatial arrangement of atoms, by L.A. Tschugaeff (1873–1922) [32]. Van't Hoff's works laid foundation for a prominent branch of modern science, stereochemistry.

Despite all these investigations, the young scientist could obtain lecturer's position only in March 1876: he was elected a docent of Veterinary College at Utrecht. In 1877, a prominent change occurred in van't Hoff's scientific career: he became professor of chemistry, mineralogy, and geology at the University of Amsterdam. Van't Hoff occupied this position during 18 years despite numerous proposals from higher school institutions of quite a number of countries. Together with delivering lectures, he performed, during this time, fundamental investigations in chemical thermodynamics, kinetics, and theory of solutions. In 1881, van't Hoff published a book *Principles of Organic Chemistry* in which he made an attempt to correlate the molecular structure of substances with their physical and chemical properties. But fame was brought to the author by *Etudes de dynamique chimique* [22, 30] published in 1884, in which he for the first time presented strictly and logically, with the use of the necessary mathematical apparatus, quite a number of problems underlying the understanding of chemical processes. Already in 1885, Arrhenius wrote in a review of these essays that van't Hoff "provided explanation of the mathematical laws of chemical transformations... Although the author has already attained fame owing to his ability to disclose secrets of nature, all his previous works are entirely outshone by this paper..." [33]. A detailed analysis of the essays was made in a study of Blokh [20], in the already mentioned article of Figurovskii, and in other studies of van't Hoff's creative work [18, 26] and history of modern physical chemistry [27, 28].

A further development of van't Hoff's physicochemical investigations was the article *Chemical Equilibrium in Systems of Gases and Dilute Solutions*, published in 1886. The author demonstrated theoretically and experimentally the applicability of the laws of gas state to describing the osmotic pressure in dilute solutions. The value of the universal gas constant, obtained by him from osmotic pressure measurements, was virtually the same as that for ideal gases. However, in the case of mineral acids and salts van't Hoff had to introduce a factor whose physical meaning was unclear. At the same time, this factor could be found by means of a number of independent methods. An explanation of this factor was provided already in 1887 by Arrhenius in his theory of electrolytic dissociation [15, 33]. In 1903, he was awarded Nobel Prize in Chemistry as "acknowledgment of the particular importance of his theory of electrolytic dissociation for the development of chemistry." A prominent Swedish scientist, Arrhenius was elected for his scientific achievements a member of academies and scientific societies of a number of countries. He was a foreign corresponding member of the St. Petersburg Academy of Sciences (since 1903) and honorary member of the Academy of Sciences of the USSR (since 1926). In 1887, van't Hoff took active part in the foundation of the first world's journal devoted to physical chemistry (*Zeitschrift für Physikalische Chemie*). The Editor-in-Chief of the journal was W. Ostwald (1853–1932), a professor of the Leipzig University. In 1909, he was also awarded Nobel Prize in chemistry as "acknowledgment of his works on catalysis and also investigation of the basic principles of control over chemical equilibrium and rates of reactions." Ostwald was a foreign corresponding member of the St. Petersburg Academy of Sciences (since 1896). Van't Hoff's investigations gained universal acceptance by the late 1880s. He was elected an honorary member of the German Chemical Society in 1889; the Royal Society of London awarded him, together with Le Bel, the Davy medal in 1893; he also received a Legion of Honor from the President of France in 1894. In 1895, the Dutch scientist was elected a foreign corresponding member of the St. Petersburg Academy of Sciences and a honorary member of a number of scientific societies in Russia and other countries. On January 30, 1896, van't Hoff was elected a member of the Prussian Academy of Sciences. Simultaneously he occupied a position of a professor of the Berlin University with minimum pedagogical obligations. In accordance with his own wishes, he delivered a course of physical chemistry during four semesters, one hour a week. Van't Hoff's lectures on theoretical and physical chemistry were published in 1898–1900 in three parts. The last of these, concerned with solutions, was translated into Russian under the editorship of Kistyakovskii.[1]

In 1901, van't Hoff was invited to the Chicago University (USA) and delivered eight lectures on physical chemistry. These lectures were also published in Russia in 1903 under the editorship of Academician P.I. Val'den (1863–1957) with his preface. The structure and specific features of the lectures was analyzed in detail by R.B. Dobrotin and Solov'ev

[1] A list of van't Hoff's books published in Russian was given in [26]. A complete bibliographic index of published works of the Dutch scientist in chronological order can be found in the supplement to his Selected Works [30].

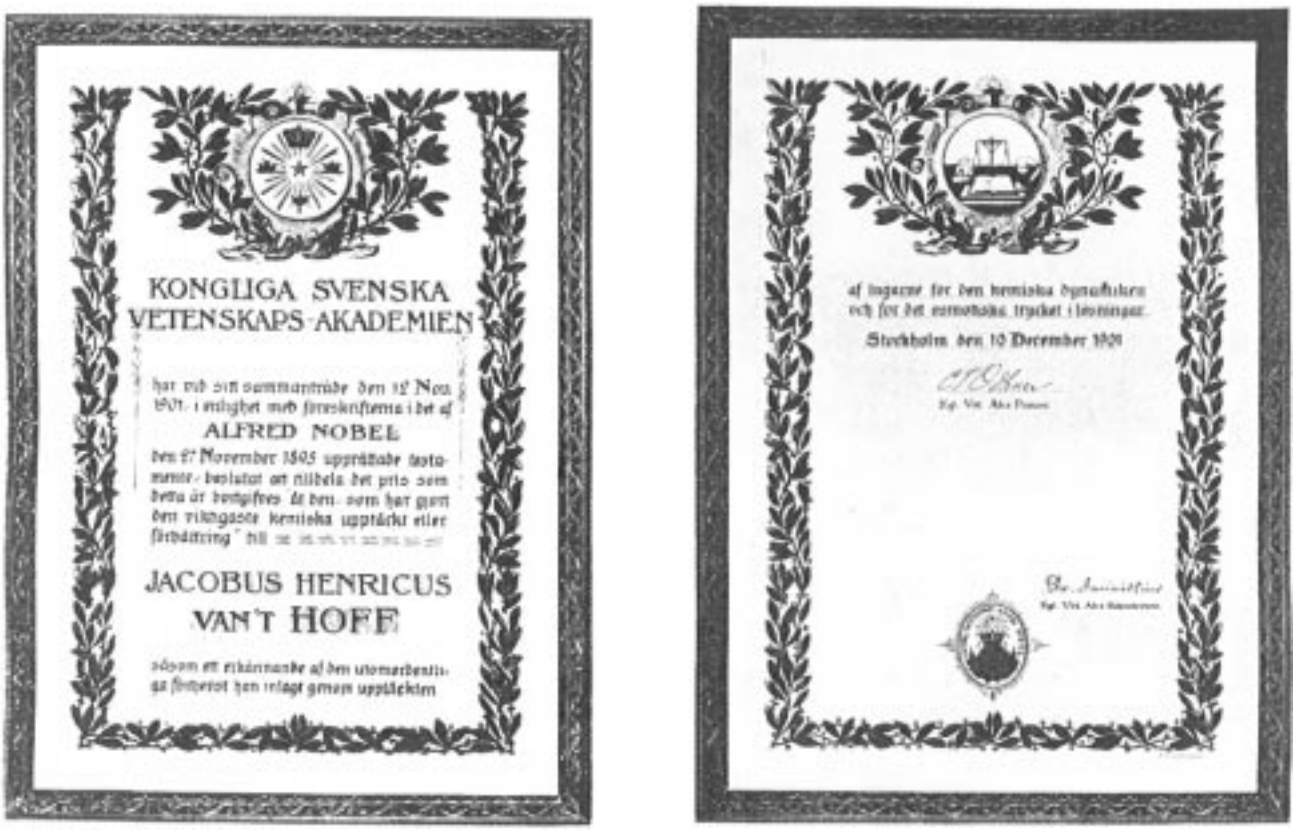

J.H. van't Hoff's Nobel diploma.

[26]. The singularity of the lectures consists in the particular attention to the presentation of those problems of physical chemistry which were studied by the author.

In his introductory statement at the Academy of Sciences in Berlin on July 2, 1886, van't Hoff explained in which direction he would continue his investigations: "In the first place I am going to devote my efforts to that branch of physical chemistry which is concerned with transformations and formation of double-decomposition salts... Of particular importance is the idea of its possible application in Stassfurt industry and geology" [20, 26]. Here are meant large deposits of potassium salts in Saxony near Stassfurt.

Already before moving to Berlin, van't Hoff started experimental investigations of heterogeneous equilibria in various condensed systems. However, large-scale studies of salt equilibria began during the Berlin period of the scientist's life. Beginning in 1897, and till 1908, van't Hoff and coworkers published a series of 52 communications under the common title *A Study of the Conditions of Formation of Oceanic Salt Deposits and, in Particular, Salt Deposits at Stassfurt.* Basic data were obtained on the behavior of Na^+, Mg^{2+}, K^+, SO_4^{2-}, and Cl^- in brines, mainly at 25°C. Some systems were studied at higher temperatures.

The principal van't Hoff's co-worker in these large-scale investigations was W. Meierhoffer (1864–1906), his pupil and friend. The investigations were conducted at a small private laboratory created by the scientists. The obtained results were summarized in a book by van't Hoff, Meierhoffer, *et al*., *Zur Bildung der okeanischen Salzablagerungen*, which was published in two parts (part 1, 1905; part 2, 1909). In 1936, the book was translated into Russian. The scientists established that the key factor in salt formation is temperature. In some cases, a major role is played by time. Studies of the conditions of formation of oceanic salt deposits and the obtained results are rather important for geology, halurgy, and chemistry. Among Russian scientists, F.Yu. Levinson-Lessing (1861–1939) [34] and I.A. Kablukov [35] were those who highly appreciated these investigations.

Beginning in 1905, van't Hoff was strongly interested in biochemical problems; it seemed of importance to him to reveal in the first place the action of enzymes in plants, from photosynthesis to formation of glucosides. However, his illness interfered

with these intentions. Van't Hoff died of pulmonary tuberculosis on March 1, 1911, in Berlin.

The outstanding van't Hoff's scientific merits gained the widest recognition. Numerous academies of sciences all over the world, scientific societies, and universities elected him a member and awarded him honorary medals and titles.

In 1936, opening a meeting of the Moscow branch of the Mendeleev All-Union Chemical Society, devoted to 25th anniversary of van't Hoff's death, Academician N.S. Kurnakov named the Dutch scientist "one of the most prominent chemists and thinkers of the present epoch" [36]. The first winner of the Nobel Prize in chemistry went down in history as a founder of stereochemistry, the theory of chemical equilibrium and chemical kinetics, osmotic theory of solutions, and chemical geology.

REFERENCES

1. Farber, E., *Nobel Prize Winners in Chemistry 1901–1961*, London: Adelard–Schuman, 1963.
2. *Nobel Prize Winners*, Wasson, T., Ed., New York: H.W. Wilson, 1987.
3. Bergengren, E., *Alfred Nobel: Eine Biographie*, Munich: Bechtle, 1965.
4. Kant, H., *Alfred Nobel*. Leipzig: B.C. Teubner, 1983.
5. Sohlman, R., *The Legacy of Alfred Nobel*, London: The Bodley Head, 1983.
6. Rudder, O. de, *Alfred Nobel*, Denoel, 1997.
7. D'yakonova, I.A., *Vopr. Ist*., 1975, no. 9, pp. 127–141.
8. Lishevskii, V.P., *Vestn. Ross. Akad. Nauk*, 1995, vol. 65, no. 9, pp. 820–825.
9. Figurovskii, N.A. and Solov'ev, Yu.I., *Nikolai Nikolaevich Zinin*, Moscow: Akad. Nauk SSSR, 1957.
10. Averbukh, A.Ya., *Zh. Prikl. Khim*., 1966, vol. 39, no. 11, pp. 2613–2614.
11. Averbukh, A.Ya., *Vopr. Ist. Estestvozn. Tekh*., 1965, issue 19, pp. 128–131.
12. Averbukh, A.Ya., *Vasilii Fomich Petrushevskii*, Leningrad: Nauka, 1976.
13. Radivanovskii, N., *Porokh, piroksilin, dinamit i drugie vzryvchatye veshchestva* (Gunpowder, Pyroxylin, Dynamite, and Other Explosives), St. Petersburg, 1881, part 1.
14. *Dvadtsatipyatiletie tovarishchestva neftyanogo proizvodstva Br. Nobel', 1879–1904* (Twenty-Fifth Anniversary of Noble Brothers' Oil Production Company, 1879–1904), St. Petersburg, 1904.
15. Kablukov, I.A., *Sovremennaya teoriya rastvorov Vant-Goffa i Arreniusa v svyazi s ucheniyami o khimicheskom ravnovesii* (Modern Theory of Solutions by van't Hoff and Arrhenius in Connection with the Concept of Chemical Equilibrium), Moscow, 1891.
16. Kistyakovskii, V.A., *Zh. Ross. Fiz.-Khim. O–va., Chast' Khim*., 1897, vol. 29, sect. I, no. 4, pp. 286–287.
17. Kistyakovskii, V.A., *Izv. SPb. Politekh. Inst., Otd. Tekh., Estestvozn. Matem*., 1911, vol. 15, no. 2, pp. 831–834.
18. Cohen, E., *Jakobus Henricus Van't-Hoff, sein Leben und Werken*, Leipzig, 1912.
19. Dobroserdov, D., *Gendrik Vant-Goff, Ego zhizn' i trudy* (Henricus van't Hoff, His Life and Works), Kazan: Imperat. Univ., 1912.
20. Blokh, M.A., *Zhizn' i tvorchestvo Vant-Goffa* (Van't Hoff's Life and Creative Activities), Petrograd: Nauchnoe Khimiko-Tekh., 1923.
21. Blokh, M.A., *Priroda*, 1936, no. 11, pp. 118–127.
22. Van't Hoff, J.H., *Etudes de dynamique chimique*, Amsterdam: Frederik Muller, 1884.
23. Parmenov, K.Ya., *Biol. Khim. Shkole*, 1936, no. 2, pp. 50–61.
24. Stepanov, B.I., *Nauka Zhizn'*, 1941, no. 2, pp. 51–54.
25. Musabekov, Yu.S. and Chernyak, A.Ya., *Vydayushchiesya khimiki mira: Bibliograficheskii ukazatel'* (Outstanding Chemists of the World: Biographical Index), Moscow: Kniga, 1971.
26. Dobrotin, R.B. and Solov'ev, Yu.I., *Vant-Goff* (Van't Hoff), Moscow: Nauka, 1977.
27. Solov'ev, Yu.I., *Istoriya ucheniya o rastvorakh* (History of the Theory of Solutions), Moscow: Akad. Nauk SSSR, 1959.
28. Solov'ev, Yu.I., *Ocherki po istorii fizicheskoi khimii* (Essays on the History of Physical Chemistry), Moscow: Nauka, 1964.
29. *Istoriya ucheniya o khimicheskom protsesse, Vseobshchaya istoriya khimii* (History of the Theory of Chemical Process, General History of Chemistry), Moscow: Nauka, 1981.
30. Van't Hoff, J.H., *Izbrannye trudy po khimii* (Selected Works in Chemistry), Moscow: Nauka, 1984.
31. Tuchs, G., Heinig, K., Kertscher, G. *et al., Biographien bedeutender Chemiker*, Berlin: Volk und Wissen Volkseigener, 1977.
32. Tschugaeff, L.A., in *Novye idei v khimii, Sbornik no. 1* (New Ideas in Chemistry, Collection no. 1), St. Petersburg: Obrazovanie, 1912, pp. 9–32.
33. Solov'ev, Yu.I. and Figurovskii, N.A., *Svante Arrenius* (Svante Arrhenius), Moscow: Akad. Nauk SSSR, 1959.
34. Levinson-Lessing, F.Yu., in *Novye idei v khimii, Sbornik no. 1* (New Ideas in Chemistry, Collection no. 1), St. Petersburg: Obrazovanie, 1912, pp. 33–44.
35. Kablukov, I.A., *Izv. Inst. Fiz.-Khim. Anal*., 1927, vol. 23, no. 2, pp. 760–841.
36. Kurnakov, N.S., *Usp. Khim*., 1937, vol. 6, no. 1, pp. 121–123.

A. G. Morachevski

Russian Journal of Applied Chemistry, Vol. 74, No. 7, 2001, pp. 1246–1247. Translated from Zhurnal Prikladnoi Khimii, Vol. 74, No. 7, 2001, pp. 1211–1212.

BOOK REVIEWS

Reznik, I.D., Ermakov, G.P., and Shneerson, Ya.M., *Nikel'* (Nickel),

Moscow: OOO Nauka i Tekhnologiya, 2001, vol. 2, 468 pp.

The first volume of the three-volume monograph by I.D. Reznik and co-authors[1] was devoted to general problems of the development of nickel industry in the Soviet Union in 1945–1991 (part I, chapters 1 and 2), preparation of nickel ores for metallurgical processing (part II, chapters 3–9), and concentration of oxidized nickel ores (part III, chapter 10). The second volume (parts IV–VII, chapters 11–26) presents exclusively evidence concerning oxidized nickel ores: their deposits and processing features, theory and technology of pyro- and hydrometallurgical processing of oxidized ores.

The authors characterize in sufficient detail deposits of oxidized nickel ores, give their mineralogical composition (ch. 11), and present data on the world resources of these ores (ch. 12). It is noted that the world's land stock of nickel ores is estimated to be 135 million tons in terms of nickel, including proven resources of 49 million tones by the beginning of 1998. Of the proven resources, 40 to 66% of nickel is contained in oxidized ores; 33%, in sulfide ores; and 0.7% in others. The reserves of nickel ores proven to industrial extent will last 50 years at the modern level of mining and processing. The largest deposits of oxidized nickel ores are possessed by Cuba, New Caledonia, Indonesia, and some other countries. At present, processing is, as a rule, done with ores containing more than 1.4% nickel, although a tendency have emerged toward use of lower-grade ores. According to the estimates presented in the book, out of 30 nickel-producing plants of the world (as of 1997), 17 plants processed oxidized nickel ores to produce about 300 thousand tons of nickel, i.e., 40% of the world output of this metal. The authors point out specific features of flowsheets used at plants processing oxidized nickel ores (ch. 13).

A separate part of the monograph (part V) is devoted to theoretical foundations of the pyrometallurgical processing of oxidized ores. Fusibility curves of a number of metallic, oxide, and more complex systems, which are important for analysis of pyrometallurgical processes (ch. 14), and physical characteristics of some oxide and oxide–sulfide melts (ch. 15) are discussed. Much attention is given by the authors to the distribution of nickel and cobalt among smelting products (ch. 16). The presentation is mainly descriptive, without any detailed physicochemical or thermodynamic analysis of the occurring processes. Also considered is the influence of various factors on the rate of reduction of iron oxides by solid carbon in melts (ch. 17). Introduction of calcium oxide in silicate-ferriferous slags markedly accelerates the carbothermic reduction of iron oxides to metal, which gives nickel- and cobalt-leaner slags.

The central place in the second volume (part VI) is occupied by a description of pyrometallurgical methods used to process oxidized nickel ores. Production of ferronickel by electrosmelting, presently the most widely accepted technology, is considered in detail (ch. 18). The technology of manufacture of ferronickel at the Russian Pobuzh ferronickel plant and a number of plants in other countries is discussed. Also considered are other techniques for smelting of oxidized nickel ores to give ferronickel (ch. 19). Of interest are the methods for processing of secondary nickel-containing raw materials: spent iron–nickel alkaline batteries, waste alloyed steels from metal-working industry, and other kinds of raw materials, described by the authors. An electrothermic shop for processing of secondary raw materials to produce ferronickel was put into practice at the Rezh nickel plant in 1970 (ch. 20). Joint smelting of oxidized nickel ores and phosphorites is also described (ch. 21).

Much attention was paid by the authors to blast smelting of oxidized nickel ores to produce matte (ch. 22). Designs of shaft furnaces and specific features of the process are considered in detail. It should, however, be kept in mind that the blast smelting to produce matte has been preserved mainly in Russia.

The final part of the second volume is concerned with the present state of hydrometallurgical techniques

[1] For review, see *Zh. Prikl. Khim.*, 2001, vol. 74, no. 4, p. 691.

1070-4272/01/7407-1246$25.00 © 2001 MAIK "Nauka/Interperiodica"

for processing of oxidized nickel ores (part VII). It discusses autoclave sulfuric acid leaching (ch. 24), ammonia-carbonate leaching of ores upon their reduction (ch. 25), and methods for recovery of nonferrous metals from solutions and sludges obtained in ammonia–carbonate leaching (ch. 26). The authors point out that autoclave sulfuric acid leaching is the lowest-cost technology allowing recovery of both nickel and cobalt to give high-quality products.

The information value of the material included in the second volume is rather high, much attention is given to a detailed description of flowsheets used at a number of plants beyond Russia. The second volume gives reference to 383 works, mainly of Soviet and Russian authors. Of much interest is the evidence concerning the history of development of the nickel industry.

A. G. Morachevskii and I. N. Beloglazov

Russian Journal of Applied Chemistry, Vol. 74, No. 7, 2001, pp. 1248–1249. Translated from Zhurnal Prikladnoi Khimii, Vol. 74, No. 7, 2001, pp. 1212–1213.

BOOK REVIEWS

Fedorov, P.I. and Akchurin, R.Kh., *Indii* (Indium),

Moscow: Nauka–MAIK "Nauka/Interperiodica," 2000, 276 pp.

The monograph by P.I. Fedorov and R.Kh. Akchurin considers a wide variety of problems concerning the chemical properties, manufacturing technology, and some fields of application of indium and some of its most important compounds. The material presented in the book well supplements the previously published monograph by S.P. Yatsenko: *Indii, Svoistva i primeneneie* (Indium, Properties and Use), published in 1987 and mainly concerned with indium alloys.[1]

The book comprises nine chapters and a vast bibliographic list including 574 references to papers by domestic and foreign authors.

A small introductory chapter (pp. 7–11) mentions the most important fields of application of indium and its alloys and compounds and gives brief evidence concerning the scale of manufacture and consumption of indium in a number of countries and indium prices on the world market. The authors present requirements to the purity of various domestic brands of indium.

The second chapter (pp. 12–22) is devoted to the physical and chemical properties of metallic indium. Also discussed are the possible oxidation states and coordination numbers of indium in various compounds.

The third, and the largest, chapter summarizes data on properties of indium compounds: oxides, hydroxides, hydroxoindates, indates, indium salts of oxygen-containing salts, indium halides and oxohalides, indium cyanide and related compounds, chalcogenides, compounds of indium with Group V elements (nitrogen, phosphorus, arsenic, antimony), other nonmetals, and organic compounds. The presentation is rather detailed; particular attention is given to indium halides and systems containing these compounds. A large number of investigations of the properties of indium compounds have been carried out by one of the authors of the monograph, Professor Fedorov, and his co-workers.

The fourth chapter (pp. 134–141) considers the state of indium in aqueous solutions. It mainly presents published evidence concerning the nature of complexation processes involving indium(III) and (I) ions in various media.

The fifth chapter (pp. 142–153) discusses types of indium deposits and industrial sources of indium in relation to its behavior in processing of zinc, lead, and copper concentrates, and tin or iron ores.

The sixth chapter (pp. 154–196) contains evidence concerning the technology of indium recovery from various materials. The authors mention that no specific chemical processes are known for indium, which could allow its separation from large amounts of associated elements. In this connection, flowsheets for indium recovery from one or another raw material are rather complex and include multiple stages. As examples are briefly considered general principles of direct recovery of indium from zinc ores and its recovery from zinc-containing sublimates and material produced in processing of lead ores. Much attention is paid by the authors to describing separate procedures used for concentrating and purifying indium-containing solutions. To procedures of this kind belong hydrolytic precipitation, cementation with pure metals and amalgams, extraction with organic solvents, sorption and ion exchange, ionic flotation. The same chapter considers production of metallic indium from various raw materials and processing of secondary indium-containing materials.

The seventh chapter (pp. 197–215) is devoted to indium refining. It considers both chemical (successive cementation, chloride method) and electrochemical techniques (chloride, chloride–sulfate aqueous electrolytes), amalgam refining, distillation, and crystallization techniques. Examples are given of flowsheets for manufacture of high-purity indium.

The eighth chapter (pp. 216–252) contains data on indium-based semiconductor materials. The basic properties and methods of preparation of III–V compounds (InSb, InAs, InP) and solid solutions on their base are discussed. The solid solutions are commonly

[1] For review, see *Zh. Prikl. Khim.*, 1987, vol. 60, no. 12, pp. 2748–2749.

1070-4272/01/7407-1248$25.00 © 2001 MAIK "Nauka/Interperiodica"

produced through isovalent substitution of elements in the cation or anion sublattices of indium compounds with Group V elements.

The final, ninth chapter (pp. 253–254) points to the toxicity of some indium compounds.

Monitoring of scientific information shows that the second half of the XX century was characterized all over the world by a dramatic rise in the amount of chemical information (on the territory of the Former Soviet Union this process slowed down only in the last decade). Any adequate systematization of this information seems to be rather valuable. The monograph by Fedorov and Akchurin contains in the first place a systematical presentation of chemical properties of widely different classes of indium-containing compounds. Much less attention is given to industrial problems. Unfortunately, the entire information about manufacture of indium in Russia is limited to the following. "Russia occupies one of the leading places in the world in manufacture of indium. Large quantities of indium are exported." This seems to be insufficient. It would be of interest to find in such a summarizing monograph at least historic evidence concerning the development of indium industry in the Soviet Union. The material of the eighth chapter could be enlivened by description of how the semiconducting properties of III–V compounds were discovered.

The utility and high quality of Fedorov and Akchurin's monograph are beyond any doubt. The book is of interest for a wide variety of specialists in chemistry and chemical technology of rare elements, inorganic materials science, and technology of materials for electronics.

A. G. Morachevskii

Russian Journal of Applied Chemistry, Vol. 74, No. 7, 2001, p. 1250. Translated from Zhurnal Prikladnoi Khimii, Vol. 74, No. 7, 2001, p. 1214.

INFORMATION

IX Enikolopov Symposium

IX Enikolopov Symposium (March 13, 2001, Moscow) was held at the Enikolopov Institute of Synthetic Polymeric Materials, Russian Academy of Sciences (RAS). The symposium was organized by RAS (Department of General and Technical Chemistry together with Scientific Council on Macromolecular Compounds) with active participation of the Enikolopov Institute of Synthetic Polymeric Materials, RAS; Semenov Institute of Chemical Physics, RAS; Institute of Problems of Chemical Physics, RAS; and Moscow Physicotechnical Institute.

The advisory board of the symposium included such distinguished scientists as S.M. Aldoshin, N.F. Bakeev, A.A. Berlin, A.L. Buchachenko, V.A. Kabanov, N.N. Kudryavtsev, A.G. Merzhanov, A.N. Ozerin, and N.A. Plate. The symposium program included four plenary lectures which were presented by Academician N.S. Enikolopov' disciples.

S.L. Blazhenov in his plenary lecture examined degradation of unidirectional fiber plastics. The macrokinetic problems, as applied to design of turbulent tube reactors, were reported in a lecture given by A.A. Berlin. A.N. Ozerin gave a lecture on the modern status of the problem of the structure of dendritic molecules. The lecture held by B.I. Zapadinskii on photocurable composites for direct forming using laser stereolithography has evoked a considerable interest.

The lectures presented at the symposium revealed a close relation between the modern theoretical concepts and current practical problems. IX Enikolopov Symposium has demonstrated that Enikolopov's ideas stated in the period from 1980 to early 1990s are being successfully developed by his disciples, being, without question, of considerable theoretical and practical interest.

The next X Symposium will be held in March 2002.

G. E. Zaikov and A. Ya. Polishchuk

1070-4272/01/7407-1250$25.00 © 2001 MAIK "Nauka/Interperiodica"

Russian Journal of Applied Chemistry, Vol. 74, No. 7, 2001, pp. 1251–1252. Translated from Zhurnal Prikladnoi Khimii, Vol. 74, No. 7, 2001, pp. 1214–1215.

INFORMATION

Polymeric Materials 2000

The 1st International Conference "Polymeric Materials 2000" was held from September 25 to 27, 2000 in Halle (Germany). The conference was organized on the basis of the Martin Luther University (Halle–Wittenberg) under scientific coordination of W. Grellmann and J. Kressler. Sixteen German organizations and research centers were sponsors of the conference. The conference participants were more than 400 scientists from 24 countries (Austria, Azerbaijan, Belarus Republic, Brasilia, Bulgaria, China, Czech Republic, Egypt, France, Germany, Greece, Hungary, Italy, Japan, Poland, Portugal, Romania, Russia, Slovak Republic, Spain, Switzerland, Ukraine, the United Kingdom, and the United States). The conference topics covered a broad spectrum of problems of the chemistry and physics of polymers and composite materials, including synthesis, characterization, and applications.

In the opening ceremony professors W. Grellmann and J. Kressler outlined the topicality of the problems to be discussed, and their importance from the theoretical and practical standpoints. Then Prof. W. Grecksch (Rector of the Martin Luther University) and W. Fichler (Culture Minister of the Sachsen-Anhalt Land) told about the contribution of scientists of the Martin Luther University and other research institutions of the Sachsen-Anhalt to the progress of the polymer science.

There were presented 9 plenary lectures on the basic topics of the conference, including colloid systems and new polymeric materials [M. Antonietti (Golm, Germany)], new advancements in Dow polyolefins technology [Che-I Kao (Dow Chemical, Middland, Michigan, the United States)], polymer melts in chemical technology [H.M. Laun (BASF AG, Ludwigshaften, Germany)], innovations in polymer engineering [P. Eyrer, Stuttgart, Germany)], investigation on polymer lasers [F.E. Karasz (University of Massachusetts, Amherst, the United States)], polymers for medical use [E. Wintermantel (Schlieren, Switzerland)], biosynthesis of polyesters and polyamides [A. Steinbuchel (Munster, Germany)], fatigue crack growth in engineering plastics [R.W. Lang, (Leoben, Austria)], and structure in thin polymer blend films [M. Stamm (Mainz)].

Then the Conference was held as nine sections. The main lecture of Section A (New Materials) was devoted to the effect of laser light on polymer films [J. Feldman (Munich)]. The section included 15 oral presentations on applications of polymers in optics, polymers as lubricant additives, development of liquid-crystal systems for use in electrooptical displays, etc. Section B (Biopolymers and Medical Applications). G.E. Zaikov (Institute of Biochemical Physics, Russian Academy of Sciences, Moscow, Russia) in his main lecture told about the kinetic aspects of biodegradation and biocompatibility of polymers. Then various aspects of biodegradation of polymers and of medical applications of polymers (biomimetics, polymer materials for surgery, polymer implants of temporary and continuous action, polymeric forms of drugs, etc., were examined in 15 lectures).

Section C (Functionalized Polymers and Surface Modification). The main lecture [K. Lunkwitz, H.-M. Buchhammer, M. Muller, U. Oertel, G. Petzold, and S. Schwarz (Dresden, Gernany)] was devoted to modification of polyelectrolytes and polyelectrolyte complexes. Section D (Polymer Testing and Diagnostics). The main lecture on the topic was given by G. Busse (Stuttgart, Germany). The section included 15 oral presentations on various aspects of polymer structure and evolution of the polymer morphology in time. A special section (Section E) was devoted to the morphology and characterization of polymers. The main lecture on the topic (Applications of Block Polymers in Polymer Blends) was given by V. Altstadt, H. Ott, A. Mantey, and V. Abetz (Hamburg, Germany). The section included 15 oral presentations on various aspects of the topic.

Section F (Modelling and Simulation) included a main lecture and 5 oral presentations. The main lecture [B. Michel (Berlin, Germany)] was devoted to modeling and prediction of the thermomechanical behavior of polymers of various structures. Section G (Polymer Processing and Innovative Products) included a main lecture and 5 oral presentations. G. Menning (Chemnitz, Germany) in his main lecture told about the advances in processing of thermoplastics.

Section H (Sustainable Development, Recycling, and Ageing) included 9 oral presentations. The main

1070-4272/01/7407-1251$25.00 © 2001 MAIK "Nauka/Interperiodica"

lecture was prepared by B. Bohlmann, P. Eyrer, Th. Hirth, S. Kroner, and K. Worsing (Pfinzthal-Berghausen, Germany). All oral presentations including the main lecture were devoted primarily to practical problems.

Finally, Section I (Elastomers, Networks, and Foams) included 9 oral presentations and a main lecture. In the main lecture G. Heinrich (Hannover, Germany) told about high-performance elestomers (synthesis, characterization, and applications). Also the conference included the corresponding poster sessions (a total of more than 100 poster contributions).

As a censorious remark, a drawback of the conference organization was that the most of the plenary and main lectures were given by German scientists, although many distinguished researchers from other countries were among the conference participants. For instance, among the Russian participants one may say about Yu.K. Godovskii (Karpov Physicochemical Institute, Moscow) and Yu.Ya. Gotlib (Institute of Macromolecular Compounds, Russian Academy of Sciences, St. Petersburg), who could give very interesting lectures on such topics as Morphology and Phase Transitions and Elastomers and Networks. This may be related also to V. Privalko (Kiev Institute of Macromolecular Compounds, Ukrainian National Academy of Sciences). Generally, the Conference has demonstrated a high theoretical and experimental research level and a good potentiality of such meetings where lectures are combined with discussions and living contacts of a large number of scientists. The 2nd International Conference "Polymeric Materials 2002" will be held in the same place. Russian scientists are already invited.

G. E. Zaikov and M. I. Artsis

Russian Journal of Applied Chemistry, Vol. 74, No. 8, 2001, pp. 1253–1259. Translated from Zhurnal Prikladnoi Khimii, Vol. 74, No. 8, 2001, pp. 1217–1234.

REVIEWS

Applied Significance of Polyimides

Yu. N. Sazanov

Institute of Macromolecular Compounds, Russiam Academy of Sciences, St. Petersburg, Russia

Received April 18, 2001

Abstract—The review is devoted to the use of polyimides in various fields of science and technology. Polyimide materials as films, fibers, foams, membranes, plastics, composites, glues, adhesives, and coatings are widely used for fabrication and coating of various structures, units, and parts operating under extreme temperature conditions. The progress of modern science and technology is impossible without polyimide materials.

The history of the search for heat-resistant materials exhibiting, along with thermal stability, also a number of other valuable, often mutually excluding properties reflects the history of the scientific and technological progress in the second half of the XX century as a whole. Since the 1950s, scientists, engineers, technologists, and businessmen throughout the world became involved in the race for new scientific and technical achievements. With the development of space engineering, the speeds increased by several orders of magnitude, and problems arose related to protection of objects operating under extreme conditions. By protection was meant the whole complex of materials and measures related to developing, testing, and bringing into practice various kinds of insulation from extreme thermal, biological, radiation (with broad spectrum), mechanical, and acoustic impacts.

Initially, the problems were not solved comprehensively, and all stringent requirements to insulation were satisfied on the basis of the trial-and-error method. However, one of the major goals of science and technology was significant extension of the operating temperature range of objects. With respect to many parameters, the available heat-resistant materials (mainly inorganic) appeared to be fully unsuitable, primarily because of the poor mechanical properties, high density of inorganic insulators, sophisticated production processes, shortage of required raw materials, etc. Therefore, the search for new heat-resistant insulators was focused on the development of synthetic materials based on macromolecular compounds. Polymeric substances, often in combination with inorganic materials, were already known and used at that time as electrical and thermal insulators. However, they showed stable service characteristics only at temperatures below 100°C. The search for more heat-resistant polymers started with studies of organic compounds resistant to high temperatures. Under the guidance of such prominent organic and polymer chemists as V.V. Korshak, M.M. Koton, and A.N. Pravednikov in the former Soviet Union; J. Marwell in the UK; D. Stille in the US; and N. Iwakura in Japan, works were initiated on preparation of new polymers containing various aromatic and heterocyclic fragments, because, as shown for low-molecular-weight model compounds, just fragments of this kind exhibit the highest thermal stability both in air and in inert atmosphere. The cyclic fragments should be linked in polymer molecules in such sequences that would ensure, along with the high heat resistance, good service characteristics of the material. Polyoxazoles, polyoxadiazoles, polythiadiazoles, polytriazines, and related materials were prepared. Of particular interest were polymers with condensed rings, e.g., those formed by combination of benzene rings with five- and six-membered heterocycles. It was found that a combination of two condensed cyclic structures in such polymers as polybenzimidazoles, polyquinoxalines, etc. extends the range of thermal stability of the macromolecule to 300°C. However, it was difficult to pass from laboratory samples to commercial production, because it was necessary to ensure not only high heat resistance of the new polymers but also their resistance to thermal shocks in the range from –190 to +400°C. Also, these polymers should exhibit sufficient strength, flexibility, and elasticity. Further search for organic structures meeting these requirements revealed structures withstanding brief heating to 600°C without noticeable decomposition; furthermore, when incorporated into a polymer chain, these structures appeared to

1070-4272/01/7408-1253 $25.00 © 2001 MAIK "Nauka/Interperiodica"

appreciably surpass the low-molecular-weight analogs in the heat resistance. The entire history of the search for heat-resistant polymers showed that the best properties are exhibited by a rigid structure consisting of a benzene ring tightly linked to two five-membered nitrogen-containing rings (pyromellitdiimide). Such polymers were termed aromatic polyimides.

For already 40 years the polymers of these class remain the most versatile heat-resistant polymers; their unique characteristics ensure their leading position among polymeric materials used in various branches of science and technology. Polyimides are subjects of numerous monographs and regularly published reviews [1–6]. Various polyimide-based materials such as films, fibers, coatings, varnishes, plastics, composites, binders, and foam and vapor materials can operate under extreme temperature conditions.

During the 1990s, there has been a considerable progress in applications of these materials. Economical problems (competition of polyimides with other polymeric materials) stimulated the solution of some problems that were "bottlenecks" of the first- and second-generation polyimides.

Modification of the chemical structure (preparing fluorinated polyimides and polyimides containing bulky and asymmetric groups in side substituents; making macromolecules more flexible by introducing various "hinge" links; preparing random and block copolymers) made polyimides soluble in common organic solvents [7–12]. The use of polyamido acid esters allowed solvent-free synthesis of polyimides and preparation of a series of fusible polyimides [8, 12–14]. These achievements extended the temperature range of nondestructive processing of polyimides, which simplified and made cheaper forming of ready items from them. It appeared feasible to apply to a wide range of polyimides common procedures for processing plastics such as powder pressing, pressure casting, extrusion, solution processes, etc.

FILMS

Polyimide films were the first commercial material used for production of highly heat-resistant dielectrics [15]. At present, annual production of polyimide films in the world amounts to 1000 t. The first place is occupied by PM films (based on pyromellitic dianhydride and diaminodiphenyl ether) [16]. Recently, there has been a certain functional redistribution in the total production balance of polyimide film materials.

As previously, polyimide films are used as insulators of electrotechnical items: cables, generators, electric motors, and other units and parts operating at elevated temperatures. Polyimide insulation in electrotechnical items is used not only for insulating materials of the highest grade of heat resistance (H and C) but also for items operating at lower temperatures, which considerably extends their service life and ensures reliable protection in the case of emergency overheatings.

In some electrotechnical items used in cable industry, various polyimides combine well with other insulation materials. For example, Du Pont mastered production of multilayer insulation for aviation wire by combining Kapton polyimide with fluoroplastic. The junction of both the materials is tight, and the insulation characteristics are acceptable even with the insulation thickness decreased by a factor of 2–3, which saves 25 and 50% of weight and space, respectively. The service life of such wires exceeds 2000 h at 250°C.

The service life can be considerably prolonged by using, in combination with polyimide, heat-resistant graphitic carbon fillers. A particular attention is given to chemically resistant polyimide coatings which successfully operate in deep-well electric engines used in oil extraction [17]. In some cases Upilex polyimide film is used for these purposes, as well as for enhancing the hydrolytic resistance of insulating electrotechnical materials. This film has an adhesive layer and is prepared from diphenyltetracarboxylic acid and diaminodiphenyl ether or *p*-phenylenediamine [18]. The high stability of the surface layers of polyimide films determines their predominant use in production of resistors. The scatter of the surface resistivity of such films is a factor of 2–3 smaller than that of devitrified glass supports, owing to the different surface roughness [19].

Further improvement of the electrical insulation based on polyimide films resulted in the production of films heat-weldable from two-layer polyimido-fluoroplastic films (PMF) (Plastik Research and Production Association, Joint-Stock Company) which well compare with the imported analog, Kapton HV [20] (Table 1). This film is widely applied as insulation of PPI-U wires for motors used in deep boring units. Subsequently, the PMF film was improved by replacing the fluoroplastic layer by layers of thermoplastic polyimide, which soften at high temperatures and retain high radiation resistance. Single- and double-layer films were developed, weldable by electric-current contact welding at 300–350°C under a pressure of 0.15–1.0 kg cm^{-2}. The adhesion strength of the weld is 200–250 N m^{-1}. The nonshrinking polyimide film produced by Plastik Re-

Table 1. Comparative characteristics of 50-μm polyimide films [20]

Characteristic	PM nonshrinking	Kapton HV	PMF	Kapton HF
Tensile strength, kg cm^{-2}	1600–1800	1800	900–1200	1000
Relative elongation at break, %	70–90	70–80	75–95	75–95
Modulus of elasticity, kg cm^{-2}	25000–30000	30000–35000	–	–
Density, g cm^{-3}	1.4–1.42	1.4–1.42	–	–
Electrical strength, kV m^{-1}	220–240	220–240	180–220	160–180
Volume resistivity, Ω m	1×10^{16}	1×10^{16}	–	–
Dielectric constant	3.0–3.5	3.0–3.5	–	–
Tangent of dielectric loss angle	0.0025	0.0025	–	–
Thermal conductivity coefficient at 25°C, W μm^{-1}	0.14	0.12	–	–
Thermal expansion coefficient at 20–250°C, deg^{-1}	$(20–30) \times 10^{-6}$	31×10^{-6}	–	–
Glass transition point, °C	Does not soften	Does not soften	–	–
Melting point, °C	Does not melt	Does not melt	–	–
Flammability, °C	Self-extinguishes	Self-extinguishes	–	–
Shrinkage after keeping for 1 h at 200°C, %	0.03–0.05	0.03–0.05	–	–
Resistance to acids and alkalis	Resistant	Resistant	–	–
Water absorption in 1 day at 23°C, %	1.8–2.2	2.5	–	–
Exfoliation resistance, g cm^{-1}	–	–	500–800	300–400

search and Production Association is used for fabricating cables and flexible and flexible-rigid printed-circuit boards of precision grade IV–V. The properties of this film are compared in Table 1 with those of the analog produced by Du Pont. The film exhibits high dielectric stability at elevated temperatures close to thermal breakdown [21]. Such films of the PMK type with a coating containing industrial carbon are intended for production of heating elements, heat-resistant coatings of printed-circuit boards, wires, and cables. Another modification is a protective film with an adhesive coating, protecting the conducting pattern of flexible printed-circuit boards from corrosion and preventing shorting and accidental contact of conductors with metallic surfaces of the equipment.

Instead of fluoroplastic coatings of the polyimide films, thermoplastic copolyimide layers can be used [22], or fluoirine can be introduced into the polyimide structure [23]. Such modifications simplify the production of compound cables [24] and enhance the flexibility of wire circuits in items that are subject to prolonged sign-variable loads.

The demand for heat-resistant film coatings for microelectronics has considerably increased during the recent decades; with particular attention given to ultrathin films with low dielectric constant ε. Process regulations for production of printed-circuit boards and microcircuits for various devices require combination of high thermal and mechanical characteristics with low coefficients of thermal expansion and minimal shrinkage. In addition to these characteristics, which are presently met by polyimides, some of these materials have ε in the range 2–3, whereas the dielectric constant of silicon oxide widely used in integrated circuits is 4–10, depending on the moisture content. When passing to polymeric materials, particular attention should be given to the stability of this parameter. Numerous studies in this field have shown that the set of characteristics of polyimide film materials make them suitable for production of some parts and units of electronic devices [25, 26], but for high-precision units it is often necessary to strictly ensure the low moisture content, which cannot be provided by common polyimide films like PM or Kapton whose moisture absorption varies within 2.5–3.5%.

A good way to make polyimide films with low ε hydrophobic is synthesis of fluorinated polyimides [7]. According to [7], membranes based on fluorinated polyimides are promising dielectrics; their ε is within 2.3–3.0, and moisture absorption, within 0.5–0.85%. As the temperature is raised to 300°C, ε increases by no more than 1–1.5%. It should be noted that replacement of hydrogen atoms in polyimide by fluorine extends the range of solvents in which these polymers are soluble, which simplifies production of various parts for microelectronics. Also, global computerization brings about many problems related to the cost of computers. One of the ways to decrease the costs or preserve their level with extension of the potential of computers and other microelectronic devices is to

Table 2. Comparative characteristics of some fluorinated polyimide of the general formula [7]

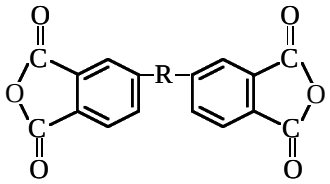

Polyimide	F content	Moisture absorption	ε at indicated moisture content, %	
	%		0	~55
R1	32.0	0.79	2.71	3.04
R2	24.6	0.85	2.72	3.02
R3	28.9	0.71	2.74	2.99
PM	0	2.77	3.10	3.71

Note: R1 =

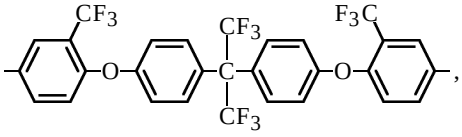

R2 =

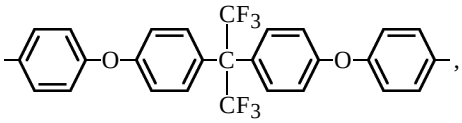

R3 =

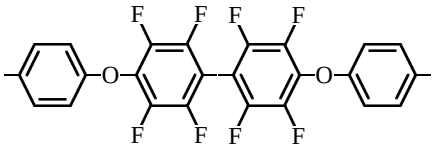

decrease the size of the parts used. Although minicomputerization is not a new topic, its urgency stimulates development of suitable polymeric materials. The increased solubility of fluorinated polyimides and their good capability to soften allowed the temperature range of their processing to be extended to 150–200°C. Various combinations of fluorinated segments of the polyimide chain with bulky substituents in the side chains and at the ends of oligomeric constituents, and also blends of fluorinated polyimides and copolyimides (Table 2) considerably expanded the assortment of heat-resistant materials for fabrication of mini- and microparts of electronic devices [7, 8, 27].

Detailed studies of fluorinated polyimides showed that fully fluorinated films based on (diphenyl oxide)-resorcinoltetracarboxylic dianhydride and *m*-phenylenediamine, and on cyclobutanetetracarboxylic dianhydride exhibit high optical transparency in the visible and UV ranges [8]. This allows their use in optical telecommunications technology. Since the mid-1990s, the body of data on the use of these polyimides for microelectronics started to increase. This concerns light guides and microfilters made of fluorinated polyimides [28], thin (0.035 mm) flexible polyimide films for forming components of electronic curcuits [29], planar orientation for optoelectronics [30], polyimide films with fullerene and a dye as laser radiation power limiters [31], and an exclusively transparent polyimide film [32]. From the viewpoint of production automation, it appeared convenient to use the polyimide based on benzophenonetetracarboxylic dianhydride and *p*-phenylenediamine; this polymer is used for ensuring high size precision in automated assembling of integrated circuits on a tape support and in semiconductors and multilayer microchips [16].

A number of polyimide films and film coatings are used in liquid-crystal (LC) systems of various displays. As structural layer, polyimide films are capable of orienting LC molecule in the support plane [33]. These films were also tested for negative compensation of birefringence for white nematic LC displays [34]. A combinatiuon of LC with polyimide films operates in acceleration of reversible recording processes in holographic arrays [35]. Polyimide supports in LC displays show induction reorientation of signals [36]. Noticeable alignment of the LC layer of indicator cells was reported in [37–40].

A prominent place in wireless communication systems and in production of various resistors and capacitors is occupied by metal-coated polyimide films. The field of their application extends beyond conducting structures and includes, in particular, the areas where strong, flexible, and heat-resistant supports are required for mirrors, screens, and reflectors of broad-spectrum energy flows. Polyimide films can be joined, using an adhesive, with a metal foil, or a metal can be sputtered directly on the film surface [1, 15]. To improve the adhesion, the film surface is modified by corona discharge, plasma or laser treatment, chemical etching, or application of a silicone binder [12, 27, 41, 42]. In some cases the metal is introduced into the polyimide film in the prepolymer stage. For example, certain amounts of gold and silver are introduced as a fine dispersion into a polyamido acid solution. Its imidization and surface treatment yield a film with uniform distribution of metal throughout the film bulk [43–46]. As for surface metallization, such polyimide films are used in space engineering, in mirror coatings of solar battery parts and heliotechnical equipment, and in multilayer protective clothes for astronauts, firemen, and emergency

Table 3. Ultimate thermomechanical properties of main heat-resistant fibers* [1]

Initial polymers	T_d, °C	Strength parameters at 20°C			σ (% of value) under indicated conditions					
					without thermal aging			after thermal aging		
		σ, sN tex^{-1}	ε	E, GPa	300°C	400°C	500°C	250 h, 300°C	100 h, 400°C	10 h, 500°C
Aromatic polyamides	<360	350	3–20	150	60	40	10	50	25	–
Aromatic polyamides with heterocycles in chain	<300	400	3–10	120	50	30	–	55	40	25
Polyheteroarylenes	<350	80	10–16	50	60	50	40	70	40	–
Aromatic polyimides	≈400	200	8–10	130	60	45	30	70	60	30
Half-ladder polymers	>300	50	3–5	20	80	50	25	70	40	–
Ladder polymers	>400	40	3–5	50	95	70	50	80	50	40

* (T_d) Degradation temperature, (σ) tensile strength, (ε) relative elongation at break, and (E) modulus of elasticity.

teams of hot shops and nuclear power plants [47–49]. One of the main application fields of polyimide films in electronics is fabrication of heat-resistant photosensitive coatings. Depending on the destination and design features of photoconducting systems, polyimides of various chemical structures are used, from common PM polyimide to fully fluorinated polymers based on aromatic dianhydrides and diamines.

Particular attention is given now to ultrathin Langmuir–Blodgett films (LBFs) whose preparation, properties, and use are described in [50]. It is also emphasized in [50] that polyimide LBFs, thanks to their unique characteristics, have found use in production of various parts for photonics and molecular electronics. Preparation of polyimide LBFs with a monolayer thickness of 4 Å allowed forming of multilayer structures with which many photoelectric processes can be controlled on the electronic and molecular level, e.g., photoinduced molecular direct and reverse current switching in LBF monolayers [50, 51]. Polyimide LBFs are widely used in structures of a three-layer photodiode, in positive resists [52], in photolithography [53], and for stabilization of sign-variable voltages in commutation memory systems [54, 55]. As a rule, soluble polyimides are used as photosensitive components of both negative and positive types [56–61].

It should be noted that in the past 5–7 years there has been considerable interest in carbonization of polyimides from the scientific standpoint and in view of applications of carbonized polyimide materials. It was reported in [6] that high-temperature treatment of polyimides yields cross-linked carbo- and heteroaromatic structures with reasonable yield (up to 50–70%), which exhibit new interesting characteristics making these new materials promising for practice. Subsequent studies [62–66] showed that the properties of carbonized polyimides depend on the chemical structure of the initial polymer, its supramolecular structure, process parameters of heat treatment, and shape and size of the materials and items thereof. The major application field of carbonized polyimides is production of various composite materials [67, 68].

FIBERS

In the period of active search for new heat-resistant fiber-forming polymers, theoretical foundations were laid in Russia for production of polyimide fibers, and these processes were commercially implemented [15]. Arimid T polypyromellitimide fiber still remains the most heat-resistant synthetic fiber with the operation range from –270 to +450°C. This fiber is fire-resistant; Arimid T fabric placed for 2 min in a gas burner flame preserves its structure and is destroyed only after an external action. Polyimide fibers fully preserve the elasticity and strength [breaking elongation 6–10%, strength (70–78) × 10^3 kg cm^{-2}] at the liquid nitrogen temperature. These are the only fibers that withstand without noticeable damage total doses of nuclear and UV radiation of up to 10–30 MGy. Polyimide fibers and fabrics virtually completely restore upon elastic deformations at elevated temperatures. The main thermochemical characteristics of polyimide fibers are compared in Table 3 with those of the other heat-resistant fibers. A combination of unique properties allows the polyimide fibers to be used in equipment operating for a long time at increased levels

of radiation and temperature; for reinforcing rubber items, fiber glass materials, thermoplastics, and multilayer structural materials; for production of work outfits for hot shop and nuclear plant workers; and for production of volume filters for treatment of hot gases and corrosive liquids.

During the past decade, the interest in further search for new polyimide materials for fiber production has decreased somewhat. This is due to a number of factors, one of which is the sophisticated production process as compared with production of other heat-resistant fibers (polyamides, copolyimides, other polyheteroarylenes). Improvement and simplification of the production process, effective stabilizers and modifiers—all these factors allowed such fibers as Fenilon, Nomex, Kevlar, Kermel, etc. to compete well with pure polyimide fibers. Furthermore, analysis of reviews concerning synthetic fibers [69] reveals a world's trend toward a decrease in the share of synthetic fibers and items thereof in production of artificial fibers. For example, in 1998, the rise in the world's production of synthetic fibers and yarns was smaller than that in 1997 by almost a factor of 10. The production of synthetic fibers in South-East Asia slightly increased, whereas in developed countries (the US, ASEAN, Japan, West Europe) it decreased by approximately 5%. The demand for polyimide fibers noticeably decreased, which is confirmed by the lack of surveys of new developments in recent reviews [69–71]. Only in [72, 73] mention is made of the relative heat resistance and other mechanical characteristics of Arimid T, Aramos, SVM, Pogllen, and some other fibers produced beyond Russia (Nomex, Conex, Kermel, PBI, P-84). In the subsequent papers one can find only consideration of the results of the past decade, summary of procedures for manufacturing of Kapton fiber [74], and main principles of construction of aromatic homopolyimides [75] and copolyimides [76]. To conclude, we can mention polyimide fibers prepared by a process that considerably differs from the traditional technology used for forming polyimide-based fibers for fiber optics. Defect-free hollow fibers of asymmetric structure were prepared from polyimides based on hexafluoropropane derivatives. These fibers are suitable for membrane technology [77, 78]. The forming process and particular properties of fluorinated polyimides allowed preparation from them of light guides for fiber optics [28, 79–81].

POLYIMIDE FOAMS

Foamed plastics. Foamed plastics have long been studied as materials for insulation of various apparatus, devices, units, and mechanisms from external impacts [82]. However, every decade (and now even every year) the requirements to such insulation become more and more stringent. In this connection, unique properties of polyimides attracted particular attention of researchers working on development of protective structures for high-speed apparatus, primarily for air- and spacecrafts. The ways to protect the crew and the scientific apparatus in drone air- and spacecrafts were sought for long before flights at speeds of thousands and tens thousand kilometers per hour became real. The main requirements to such protection are enhanced heat and fire resistance, low density of the inner casing of cockpits, flexibility and elasticity of various components of the insulation, and the possibility of using multilayer insulation with jointless junction of parts. In the case of emergencies, the foam insulation should not burn or release toxic degradation products or smoke. Comparison of various properties of foamed polyimides (according to ASTM standards) with those of the well-known and widely used foamed polyurethanes revealed an undoubted advantage of polyimide foams. For example, the weight loss of foamed polyimide and polyurethane in fire tests is 11 and 84%, respectively; the smoking is zero from polyimide and 100% from polyurethane; the release of HCN and CO toxic gases from polyimides is a factor of 10–30 lower than that from polyurethanes. Furthermore, with respect to a number of electrical, acoustic, and deformation-strength properties, foamed polyimides surpass foamed polyurethanes. One of the main tests passed only by foamed polyimide is the test for crew insulation under extreme conditions. Namely, the material should withstand, together with the cockpit material, the fire impact for no less than 5 min without release of toxic products, with increase in the internal temperature to 200°C and strong acoustic overloads. Laboratory tests showed that the polyimide foam withstands for 5 min the action of the gas burner flame (about 1500°C) without losing shape. The most suitable polymers meeting these requirements are polyimides for which a number of procedures have been developed for production of foam materials. These procedures are based on various chemical reactions causing foaming during formation of the polyimide structure [83–86]. All these reactions involve formation of low-molecular-weight volatile products whose release from a viscous melt of the intermediate and final imidization products results in foaming of the reaction mixture, followed by solidification. With account of specific parameters of ready items, foamed polyimide materials can exhibit a wide range of various characteristics (density; heat, fire, and acoustic resistance; deformation-strength characteristics; environmental safety). These proper-

ties can be controlled not only by varying the synthetic procedures but also by using various procedures for preparing foamed materials. For example, with air-circulation furnaces, cells of irregular structure are formed in the bulk of the polymer, with a large scatter of the foam density throughout the bulk of the material. This drawback can be eliminated by using high-frequency (or microwave) heating. This procedure allowed preparation from polyimide prepolymers of the best grades of foamed materials with cells of similar structure and with the minimal content of cavities and other defects, which is especially important in production of insulation materials for casing of cockpits in supersonic aircraft and manned spacecraft [87]. However, in some cases, despite the fact that the principal parameters determining the suitability of foamed polyimides for aerospace engineering are met, additional problems arise requiring further modification of foamed materials. One of such "particular" examples is the development of special hydrolysis-resistant foamed polyimides for seats and arm rests. Despite the flexibility and elasticity of seats made of common foamed polyimides, these materials caused discomfort of the crew and passengers because of the insufficient hydrolysis resistance. This problem was solved by preparing special copolyimides and abandoning surfactants in foaming.

Of particular significance is foamed polyimide insulation in medicobiological tests under conditions of prolonged space flight. The tests revealed the reliability of fixation of various medical glassware at high G-factors, increased vibration, and lack of gravity. In unmanned spacecraft, the application sphere of foamed polyimides is not restricted to biological shielding, and the service range of foamed polyimides with respect to thermal, mechanical, acoustic, and radiation characteristics is considerably extended. For example, the service temperatures on satellites cover the range from –60 to +180°C, the mechanical overloads exceed by a factor of 2–3 those acceptable in manned spacecraft, and the radiation background depends on specific operation conditions of a satellite. Foamed polyimide protection ensures uninterrupted tele- and radiocommunication, reliable preservation of scientific data, and coordinated work of the electrical, electronic, and optical equipment of space laboratories [87].

Depending on design features and functions of specific units and parts of a spacecraft, the density of foamed polyimides varies in a wide range: from 6.5 to 950 $kg\,m^{-3}$. This is achieved by proper choice of the chemical structure of the initial polyimide components and of the foaming process and by the use of additives ensuring the required flexibility, elasticity, or rigidity of foamed materials used for manufacturing walls, floors, seats, ceilings, and other elements of not only air- and spacecraft, but also ships, submarines, high-speed trains and cars, and also certain units of pipelines, compressors, and other parts for transporting corrosive gases and liquids [88, 89]. In some cases, to enhance the rigidity and impact strength, foamed polyimides are formed in combination with reinforcing materials such as fiber glass, fibrous carbon, spherical fillers, honeycomb cells, semirigid segments with addition of boron nitrides, etc. It seems quite realistic to construct in the outer space large structures of high strength and low weight, using reinforced hollow carbon fibers connected with ultrathin semiconducting polyimide hybrid films. This will allow construction of high-power solar batteries for spacecraft.

Analysis of the literature published in the late 1990s shows that the major attention in the field of development and modification of foamed polyimides was given to the development of new polyimide nanostructures [8, 12, 89–92] with simplified and cheap process for production of foamed materials. Major attention was paid to powder technology. For example, Dutruch *et al.* [93] reported a very simple process for production of foamed polyimide by heating a mixture of oligoimide containing nadic and benzhydroxy groups (97%) and a silicone elastomer (3%). The resulting foamed polyimide exhibits high insulating power and preserves its mechanical characteristics up to temperatures as high as 300°C. Also of interest are foamed polyimides with glass sphere fillers; these materials surpass in strength and acoustic resistance the analogous materials based on epoxy resins [94]. Recently, production of foamed polyimides from various mixed formulations was initiated; in these formulations, polyimides are combined with copolyimides and other aromatic polymers and their derivatives. A light and strong material with high softening point (260°C), stable up to 570°C, was prepared from such mixtures (IPO-2) in combination with carbon and synthetic felts fabricated from such fibers as SVM, Arimid, Arimid VM, Oksalon, or Terlon [95–99]. The initial material for the IPO-2 binder is a powder soluble in methanol, ethanol, and acetone. The powder melts at 120–130°C, and the melt viscosity is 0.8–1 Pa s. When IPO-2 is used in combination with a surfactant, an elastic polyimide is obtained with density, mechanical strength, and cell size adjustable in a wide range. It is feasible to add reinforcing components into the same formulation and to obtain materials used as finishing and insulating materials in aviation, automobile construction, and ship building. The density

Table 4. Properties of multilayer foamed composites based on polyimide binders, H complexes of benzophenonetetracarboxylic acid and aromatic diamines [97]

Characteristic*	Carbon	Fiber			
		Arimid T			Oksalon
Number of layers in composite	7	8 (pressure)	8	4	4
Density, kg dm^{-3}	0.5	1.1	0.45	0.28	0.41
Components, vol %:					
filler	5	38	7	6	8
binder	31	39	25	14	21
air	64	23	68	80	71
Bending strength, MPa	24 ± 3	125 ± 11	31 ± 5	9.4 ± 0.2	20 ± 2
Compression modulus of elasticity, MPa	210	–	150	12	140
Shear modulus of elasticity, GPa	1.6	4	1.4	–	0.9

* Oxygen index 45–50%.

of such materials varies within 0.1–1.2 g cm^{-3}; they are heat-resistant up to approximately 400°C and have an oxygen index of 45–50%. Some characteristics of composites based on these materials are listed in Table 4 [97].

Foamed polyimides are widely used in microelectronics as dielectrics with a very low dielectric constant (ε = 1–1.5) [100], protective sensor coatings, and stress buffers for compensation of vibration loads on integrated curcuit components under extreme conditions [27].

Membranes. The unique properties of polyimides allowed development and putting into practice, within the past 20 years, of a new generation of membranes for separation of gases, vapors, and liquids. Polyimide membranes exhibit exceedingly high resistance to almost all chemical agents. Their heat resistance allows separations to be performed for a long time at elevated temperatures, and the high selectivity is very important for gas separation. The possibility of obtaining membranes that would be highly selective and, at the same time, permeable for water and organic substances is due to specific molecular design of polyimides. This problem can be solved on the macromolecular level if methods are available for preparing structures with reliable articulation of rigid backbone segments providing, in their turn, calibrated interchain packing with very narrow free volume distribution. In polyimides, this possibility is fully implemented owing to the well mastered methods for adjusting the polymer structure by varying the chemical structure of the diamine and dianhydride components of the polyimide. Basic theoretical studies and rich experience in synthesis of polyimides by various polycondensation procedures allowed fabrication of diverse membranes from more than hundred polyimides of various chemical structures [1, 2, 27, 101–107]. A conglomerate of rigid oriented polyimide structures with a definite polarization, the possibility of their interaction with the surrounding substrate via hydrogen bonds and other weak short-range forces give polyimides undisputable advantages over other polymers, and their unique heat resistance and chemical stability considerably extend the possibility of using these polymers for purification, separation, and ultra- and microfiltration of numerous chemical and biological products.

Fifteen years after the synthesis of the first high-molecular-weight polyimide from pyromellitic dianhydride and aromatic diamine, Du Pont developed the first commercial polyimide membrane, Permasep, for treatment and desalination of water. Since that time, there has been enormous progress in commercial production of polyimide membranes. As judged from the patent literature, by the end of the XX century the total number of the developed commercial procedures for preparation and use of polyimide membranes exceeded that in the 1970s by three orders of magnitude. At present, the leading place in the polyimide membrane industry is occupied by the United States and Japan.

Polyimide membranes showed the best performance in treatment and separation of gas mixtures, especially "simple" gases such as hydrogen, helium, carbon dioxide, and some other gases from petrochemical industry. In this field, there is a practically unlimited market for separation devices with polymeric filters exhibiting high heat resistance, resistance to high pressures, low solubility, stability toward corrosive

gases, and high separation factors and permeability. At present, hydrogen, the demand for which grows year by year, is isolated, purified, and concentrated with polyimide membranes. The main sources of hydrogen are gases from refining of hydrocarbon raw materials; synthetic gas mixtures used in various chemical, coal-chemical, and metallurgical processes; gaseous wastes from production of ammonia; and electrolysis by-products. Each of these sources has its specific features related to the technology of the main product. The limiting temperature and pressure, their drops, gas flow rate, chemical composition of the gases to be separated, the corrosiveness under process conditions, catalysts, structural materials of the reactors and communications—all these factors impose requirements, often very stringent, on the material of separators for hydrogen recovery. Practical experience has shown [2, 101, 108] that polyimides are the best materials among other polymers and inorganic products used for hydrogen membranes. For example, polyimide membranes used by Ube (Japan) for separation and purification of hydrogen operate at 150°C and a pressure of 15 MPa; the pressure drop is 14 MPa, and the H_2/CH_4 separation factor, 200–250. The membrane material is resistant under these conditions to ammonia, hydrogen sulfide, carbon dioxide, and vapors of water and some organic substances (Table 5). In a number of parameters, polyimide membranes considerably surpass membranes made of cellulose acetate, polysulfonesilicone elastomer, and polyaramides. Polyimide membranes are also advantageous as compared with glass membranes (Table 6). These examples show that the considerable progress in mastering of polyimides as materials for hydrogen purification membranes leads to significant quantitative results. As the separation factor is raised from 50 to 200, the yield of hydrogen from a hydrocarbon mixture with methane increases from 65 to 98%. The increase in the permeability coefficient allowed the production capacity to be raised to $(7.5–10) \times 10^3$ $m^3 h^{-1}$. High physicomechanical parameters of polyimide membranes eliminate the problem of "utilization" of hydrogen from gas flares, typical of fuel technology. With polyimide membranes, it is now possible to solve the problem of production of ultrapure hydrogen widely used in semiconductor industry, refining of some metals, and chemical reactions involving fine catalytic processes. Ohya *et al.* [2] described installations operating on by-products of ammonia production at a flow rate of 120 $m^3 h^{-1}$, ensuring recovery with polyimide filters of 99.9996% pure hydrogen containing as impurities no more than $(1–2) \times 10^{-6}$% nitrogen, argon, and methane.

Table 5. Chemical resistance of polyimide fibers produced by Ube Industries [2]

Impurity	Resistance at indicated impurity content, vol%					
	0.01	0.1	1	3	5	10
H_2	++	++	++	++	++	++
H_2S	++	++	++	++	+	+
HCl	++	++	++	++	+	+
NH_3	++	+	–	–	–	–
CH_3OH	++	++	++	++	++	+
CH_3OCH_3	++	++	++	++	++	+
CH_3CHO	++	++	++	++	+	+
Benzine	++	++	++	++	++	+

Note: (++) Resistant for a long time, (+) resistant for a short time, and (–) nonresistant.

Table 6. Comparison of the parameters of polyimide and glass membranes based on hollow fibers

Characteristic	Glass	Polyimide
Permeability for hydrogen, $m^3 s^{-1} m^{-2} Pa^{-1}$	1.5×10^{-8}	1.5×10^{-9}
H_2/CO permeability ratio	2.3	50
Outer diameter of fiber, mm	2	0.4
Membrane area in a standard unit, m^2	94	470

Another gas equally well purified on polyimide membranes is helium. Helium is recovered both from mixtures of natural gases and from artificial mixtures containing air and industrial gases. A two-step installation for recovery of helium from mixtures with nitrogen, ensuring an increase in the helium concentration in the gas flow from 6 to 93%, have operated for approximately 10 years. Removal from helium of impurities of air and other gases allows production of 99.7% pure helium. One of the most interesting problems solved with polyimide membranes is recovery of helium from spent deep-sea respiration gas mixtures [109]. Combination in a single unit of several membranes and step compressors allowed recovery of 90 to 95% of helium from a ternary gas mixture consisting of oxygen, nitrogen, and helium.

Of no less urgency is the problem of CO_2 recovery from various gas mixtures for its subsequent use in chemical technology or for its removal from gases (as well as the problem of removal of other so-called acidic gases). Thanks to unique properties of polyimide membranes, there has been an impressive suc-

cess in recovery of CO_2 from various gas mixtures in gas and oil-refining industry. For example, it is well known that the output of worked-out wells can be increased by elevating the pressure in depleted oil-bearing strata. This can be achieved, e.g., by pumping gas mixtures containing CO_2 into the strata. When returning to the surface, the spent gases become enriched in methane. Carbon dioxide is separated from methane with various membrane separators. In this field, the advantage of polyimide membranes is also beyond any doubt, since they ensure a CO_2/CH_4 separation factor as high as 40–60, whereas with the other membranes this factor does not exceed 20–25. The high heat resistance of polyimide membranes was used for treatment of gases from electrolysis of carbonate melts; the initial temperature of these gases (H_2 + CO_2) is 650°C.

At present, an important problem is treatment of natural gas. Its composition strongly depends on a particular gas field. As a rule, natural gas is a mixture consisting mainly of methane and CO_2. The content of methane varies from 40 to 60%. For using this mixture as a fuel, it should be enriched in methane, which is mainly provided today by the membrane technology. Comparison of the efficiency of various polymeric membranes shows that polyimide membranes allow production of a concentrate containing up to 94% methane and no more than 1% CO_2. This process allows solution of still more important environmental problems related to utilization of biologically active wastes accumulated in municipal dumps. The experience of using a process line consisting of a cascade of separators with polyimide membranes [2] showed not only the economical efficiency of recovery and concentrating of methane from gaseous decomposition products but also a significant environmental effect due to removal and utilization of such gaseous products as CO, CO_2, H_2S, etc. There also has been a considerable success in Japan in using polyimide membranes for treatment of natural gas to remove CO_2. It was shown that, even at an initial CO_2 content of about 20%, the content of CO_2 in the gas lines was as low as 1.7% in the course of a 2-year service. Certain advantages of the membrane process, compared with liquid treatment with diglycol ammonia, were revealed. These advantages are manifested in the absence of corrosion of compressor units and considerable simplification of maintenance, which now actually consists in measuring weekly the CO_2 concentration and replacing every year the filters [2].

Successful use of polyimide membranes for treatment of low-boiling gases stimulated research works in the field of use of these materials for separation and treatment of gas flows to remove various vapors of organic and inorganic substances, primarily for dehydration of gases. It was found [110, 111] that the permeability of polyimide membranes to water vapor is a factor of 200–500 higher than that to air and that permeation of vapors of organic compounds through these membranes is an exponential function of their normal boiling points. Two types of water vapor separators are produced, using various arrangements of compressors and separators and packing of polyimide materials used as membranes (mainly hollow fibers): membrane driers and filters for conditioners. Their design and operation are described in [112–114]. Along with household purposes, polyimide membranes are used in chemical industry for vapor-phase dehydration of organic solvents. Owing to the high thermal and chemical stability of polyimides, these processes can be performed at temperatures of up to 120°C and the optimal pressure of 0.1–0.2 MPa (economic mode). Installations for dehydration of ethanol, purification of isopropanol, and synthesis of catechol esters, equipped with polyimide membranes, have operated for more than 10 years [110–115]. Effective treatment of gas–air flows containing various solvents (alcohols, ketones, ethers, esters, aromatic and halogenated compounds) can be ensured by proper design of the apparatus and combination of membrane units with different separation factors. Such systems are used for trapping environmentally hazardous hydrocarbon vapors from off-gases of oil refineries, oil tanks, pipes, and terminals for fuel pumping. Furthermore, recovery of fuel from tanks brings a certain economic effect corresponding to thousands tons of naphtha, gasoline, hexane, and other fuel components [116]. During the past decade, a success was acheived in industrial use of polyimide membranes for purification, separation, and concentating of organic liquids. Along with ultrafiltration treatment of some high-boiling organic solvents, polyimide membranes were used [117, 118] for quantitative recovery from paint-and-varnish wastes and machine oil of such solvents as toluene, xylene, methyl ethyl ketone, ethyl acetate, etc. Thanks to the high stability of polyimide membranes and their chemical inertness, first attempts were made to use them in food and medical industry for treatment of vegetable oils and development of artificial organs. For example, membranes from fluorinated polyimides were tested in an artificial lung apparatus. As compared with silicone coatings, this material for vascular oxygenation shows considerably better gas exchange with respect to oxygen (by a factor of 3) and carbon dioxide (by a factor of 4) and good compatibility with blood components [119].

PLASTICS

Syntheses and studies of polyimides of varied chemical and supramolecular structure showed the feasibility of preparing novel materials whose processing to finished items became so simple that the well-known and mastered procedures used in production of common plastics appeared to be quite suitable without significant changes. The solubility, fusibility, and good rheological properties of melts and thermoplastics, characteristics of polyimides of the third and fourth generations, lifted many limitations in polyimide processing. In the mid 1980s polyimide plastics, binders, and press powders were mainly produced from PM-67 and PM-69 materials in the former Soviet Union and from Vespel and Skybond plastics [1] in other countries, whereas at present from 350 to 500 diverse materials and articles containing from 5 to 100% polyimides and their derivatives are patented annually.

Since the formation of stable solvation complexes between polyamido acids and various solvents [120–122] and interpolymeric complexes between polyimides and other polymers [123–127] was proved, polyimides and their prepolymers came into use for preparation of diverse composite materials with wide application fields. To ensure the process efficiency, it is appropriate to use plasticization of polyimide prepolymers or oligoimides in the stage of thermoplastic curing. It is proposed to use SKN-type rubbers for this purpose, and reactive solvents based on furan derivatives [128, 129] for lowering the curing point of API-type oligoimides. These procedures allowed preparation of a series of imido plastics, a base for strong and heat-resistant composite materials with working temperatures of 300–450°C. Such composite imido plastics are used in aerospace parts, such as tips of nose cones and front edges of wings of space shuttles, control surfaces, nozzle linings, and parts of gas pipes of rocket and aviation engines [130]. Some polyimide materials and blends are processed by extrusion [131], pressing [132], and other methods known for thermoplastics [133].

Thermoplastic polyimide Aurum was developed by Mitsui Toatsu (Japan) on the basis of pyromellitic dianhydride and 3,3'-diphenyldioxydiphenylmethane [134]. This polymer belongs to superstructural plastics; its glass transition point is 250°C, and melting point, 388°C; it is stable without weight loss to approximately 500°C, radiation-resistant, and inert to acids, oils, organic solvents, and other chemicals. Aurum is used in various modifications in both crystalline and amorphous forms; it is also used in the form of composites reinforced with fiber glass or carbon fibers (Table 7). These composites surpass in a number of strength parameters such thermoplastic polymers as Torlon, Ultem, LARC-TPI, PES, PEEK, and PEN. The main application fields of Aurum are structural elements and sliding parts. For example, in supporting structures designed for cyclic loads, Aurum with carbon fiber replaced aluminum in parts of new V2500 aircraft engine, which resulted in decreased (by half) weight and increased strength of the parts; no deformation at 300°C was observed. Owing to its thermal plasticity, Aurum is used in friction units for direct molding of precision high-strength and heat-resistant sliding parts of complex shape (detachable cams for duplicators, thrust collars for various machines, gears, disks, supporting cantilevers of electronic equipment, cog wheels, valves, bearings for various mechanisms in automobile construction, hydraulics, oil-and-gas equipment) [135–138]. For antifriction parts, polyimides with Teflon or graphite filler are used [139–142]. Such units operate for a long time at 280°C and for a short time at temperatures of up to 480°C; they show minimal creep and high impact strength. The same materials are used to mold rods, sticks, sheets, tubes, or gaskets [143, 144]. Polyimide materials are suitable in engine construction for carburetors, high-strength motor parts, reducers, and other parts [145–147]. Among plastics in which polyimides are essential components, laminated plastics and especially carbon-reinforced plastics should be mentioned. For structural elements, of particular promise are imido plastics with reinforcing elements from fiber glass in the form of honeycomb materials [125, 140, 148, 149], laminates for electronics [150], and various printed-circuit boards made from polyimides in combination with epoxy resins and aramide nonwoven materials [151]. Recently, the use of polyimides and their prepolymers and derivatives considerably improved the service parameters of carbon-reinforced plastics, especially their heat and fire resistance and strength. Studies of the features of polyimide carbonization [65, 66, 141, 152–158] made it possible to develop, test, and put into practice in Russia a series of polyimide binders based on di- and tetraacetyl derivatives of aromatic diamines and dianhydrides of aromatic tetracarboxylic acids (ITA binders, Table 8) [13, 159–162] and oligoimides based on one or several aromatic diamines and acidic diesters of aromatic tetracarboxylic acids with terminal nadic groups (IPO binders) [12, 163–165]. The processability of carbon-reinforced plastics by melting can be improved by using thermoplastic polyimide binders based on polyesterimides prepared from polynuclear sulfur-containing diamines (PEI binders) [166, 167].

Table 7. Characteristics of Aurum polyimide thermoplastic and Aurum-based composites [134]

Characteristic	Aurum	Aurum-based composite*					
		G1a	G2a	G2c	C1a	C2a	C2c
Density, g cm^{-3}	1.33	1.56	1.57	1.59	1.43	1.42	1.44
Moisture absorption, %	0.34	0.10	0.09	0.07	0.10	0.10	0.08
Shrinkage, %	0.83	0.44	0.44	–	0.21	0.21	–
Tensile strength, kg cm^{-2}:							
at 23°C	940	1680	1770	2070	2330	2540	2890
at 150°C	590	1080	–	1400	1440	–	2160
Breaking elongation, %							
at 23°C	90	3	3	3	3	2	2
at 150°C	90	4	–	3	4	–	3
Bending strength, kg cm^{-2}							
at 23°C	400	2460	2580	2990	3260	3630	4030
at 150°C	900	1760	1700	2050	2200	0	3200
Bending modulus of elasticity $\sigma \times 10^{-3}$, kg cm^{-2}:							
at 23°C	30	97	95	106	194	208	223
at 150°C	20	82	71	95	171	–	202
Shear strength, kg cm^{-2}							
at 23°C	830	830	–	–	930	–	–
at 150°C	800	780	–	–	620	–	–
Izod impact strength, integer units	9	12	13	9	11	12	9
Glass transition point, °C	250	250	250	–	>260	–	>260
Heat capacity at 23°C, cal g^{-1} deg^{-1}	0.24	0.23	–	–	0.22	–	–
Heat transfer coefficient, kcal m^{-1} h^{-1} deg^{-1}	0.15	0.30	0.30	–	0.42	–	–
Linear expansion coefficient at 23°C, deg^{-1}	5.5	5.3	–	–	–	–	–
Temperature of 5% weight loss, °C	570	–	–	–	–	–	–

* Composite: (G1, G2) with fiber glass (30 and 60% fiber, respectively); (C1, C2) with carbon fiber (30 and 60% fiber, respectively); (a) amorphous and (c) crystalline.

Table 8. Properties of carbon-reinforced plastics based on ELUR fiber and ITA polyimide binder [159–161] (volume content of the fiber 60 – 65%)

Characteristic	Value	Characteristic	Value
Breaking bending stress, MPa:		Onset of thermal degradation, °C:	
at 20°C	1150	in air	550
at 200°C	1130	in vacuum	600
at 300°C	1090	Coke residue of binder after vacuum thermolysis at 1000°C, %	75–80
at 370°C	930		
Shear modulus of elasticity, GPa:		Density,* g cm^{-3}	1.4
at 20°C	4.5–5.0	Porosity,* %	13
at 370°C	3.0–4.0	Breaking bending stress,* MPa	350
Breaking interlayer viscosity, J m^{-2}	200	Tensile modulus of elasticity,* GPa	95
Softening point, °C	400	Shear modulus of elasticity,* GPa	7.5
		Breaking interlayer viscosity,* J m^{-2}	35

* Characteristics of carbon–carbon composites based on ITS thermolysis products and ELUR fiber.

From the same polymers and their derivatives, binders were prepared whose structure is a semi-interpenetrating polymer network (SIPN). SIPN binders contain oligoimides with maleinimide and nadic groups. To the same group of PEI binders belong thermoplastic partially crystalline polyimides [168–174].

Carbon-reinforced polyimide plastics surpass in crack and heat resistance the carbon composites prepared on another polymer base [175]. These materials are of particular interest for development of reliable spacecraft and hypersonic aircraft (M > 2). Along with aviation, these materials can be successfully used in military and civil ship building in bellow compensators with reinforcing rings fabricated from carbon-reinforced imide plastics, in shock absorbers for ship equipment, in vibration-absorbing coatings, in fireproof shields, in structural elements for air-cushion ships, and in casings for high-power electric motors on ships. As substitutes of aluminum and titanium alloys, imide plastics with carbon fillers are competitive in automobile construction for manufacturing parts and mechanisms operating at high speeds, temperatures, and loads, in power engineering for reactor insulation, and in equipment for chemical industry [176].

VARNISHES, ADHESIVES, AND COATINGS

Polyimide varnishes, adhesives, and coatings are still the major kinds of polyimide materials. The development of soluble and fusible polyimides and new polyimide prepolymers allowed successful use of previously mastered processes of plastics technology, with application of coatings to parts of any shape and subsequent curing under mild conditions.

Polyimide varnishes are successfully used, both as solutions and as adhesive formulations, for preparing enameled copper, aluminum, and steel wires. Russian varnish PAK-1 and its American analog Pyre-ML considerably surpass in service characteristics, especially in heat and crack resistance, varnishes based on other polymers [1, 15] and are still used, along with polyamidoimide varnishes, in electrotechnical industry [177]. The same is true for adhesives such as Skybond, Pyralin, Nodimide NR-150, LARC-15, etc. [1, 168], which are in some cases still indispensable for joining polyimide films with each other and with metallic articles [178, 179]. As for advances of the recent decade, the development of new varnishes is undoubtedly associated with microelectronics. This field requires readily soluble materials forming elastic, flexible, hydrophobic, low-shrinking, and transparent coatings. These requirements are met by partially or fully fluorinated polyimides [7, 8, 27]. In polygraphic fabrication of various semiconductor curcuits, these polyimides are used as photosensitive layers. Many process parameters and characteristics, such as photosensitivity, resolving power, exposure time, and irradiation intensity, depend on the chemical structure of a polyimide, thickness of applied layer, and concentration of sensitizers and photosensitive groups in the polymer [27, 180–183].

Along with fluorinated imides, siloxane-containing polyimides are used as adhesives in electronics [184, 185]. Owing to methylsiloxane substituents in the polyimide, they exhibit very low dielectric constant as compared with other polyimides (0.33–0.35) and low hygroscopicity. Good adhesion and high heat resistance allow their use as adhesive varnishes and films or as special sealants in automated assembling of integrated curcuits on a tape support. Also, these materials are equally useful in flexible and rigid multilayer printed-circuit boards. The assortment of adhesives has been recently supplemented with polyimides and oligoimides with reactive groups in the chain (malimide, hydroxy, cyanurate, epoxy, acrylate). An example of such polyimides is bisallylnadicimide [186] used in various adhesives in combination with epoxy and other resins for plastics, electric insulation coatings, coatings for magnets, etc. Polyamides containing sulfur in the backbone, aliphatic substituents in pendant chains, and also polyhydroxy imides with diazonaphthoquinone in combination with other soluble adhesive polyimides are used for assembling devices in microelectronics and luminescence engineering [187–189].

CONCLUSION

Analysis of publications of the past decade shows that advances in synthesis of new polyimides made it possible to overcome certain bottlenecks in the technology for producing materials based on them. Preparation of soluble, fusible, and readily processable polyimides strengthened their leading role in advanced branches of industry. High heat resistance, combined with other unique characteristics (strength, radiation and chemical resistance), allows use of films, fibers, plastics, composites, foams, membranes, adhesives, and other materials in diverse structures, apparatus, units, and parts operating under extreme conditions of high speeds in any media (surface, underground, air, underwater, space).

REFERENCES

1. Bessonov, M.I., Koton, M.M., Kudryavtsev, V.V., and Laius, L.A., *Poliimidy – klass termostoikikh poli-*

merov (Polyimides: A Class of Heat-Resistant Polymers), Leningrad: Nauka, 1983.

2. Ohya, H., Kudryavtsev, V.V., and Semenova, S.I., *Polyimide Membrans—Applications, Fabrications and Properties*, Kodanasha: Gordon and Breach, 1996.
3. Sroog, C.E., *Prog. Polym. Sci.*, 1991, vol. 16, pp. 561–694.
4. Koton, M.M., *Zh. Prikl. Khim.*, 1995, vol. 68, no. 5, pp. 822–826.
5. Sroog, C.E., Endrey, A.L., Abramo, S.V., *et al.*, *J. Polym. Sci. A*, 1996, vol. 34, no. 11, pp. 2069–2086.
6. Gribanov, A.V. and Sazanov, Yu.N., *Zh. Prikl. Khim.*, 1997, vol. 70, no. 6, pp. 881–902.
7. Rusanov, A.L., Stadnik, T.A., and Müllen, K., *Usp. Khim.*, 1999, vol. 68, no. 8, pp. 760–772.
8. *Advances in Polyimides and Low Dielectric Polymers: Proc. 6th Int. Conf. on Polyimides (October 8–10, 1997)*, Sachdev, H.S., Khojasteh, M.M., and Feger, C., Eds., Meatel, NJ: Soc. Plast. Eng., 1999.
9. Lau, K.Y., *Chem. Rev.*, 1993, vol. 93, no. 1, pp. 449–462.
10. Rusanov, A.L., Elshina, L.B., Bulycheva, E.G., and Müllen, K., *Vysokomol. Soedin.*, 1999, vol. 41, no. 1, pp. 7–27.
11. Hatani, H., *Kogyo Zairyo*, 1997, vol. 45, no. 13, pp. 42–45.
12. *Polyimides: Trends in Materials and Applications: Proc. 5th Int. Conf. on Polyimides (November 2–4, 1994)*, Feger, C., Khojasteh, M.M., and Molis, S.E., Eds., Ellenville, New York: Soc. Plast. Eng., 1996.
13. Goikhman, M.Ya., Svetlichnyi, V.M., Kudryavtsev, V.V., *et al.*, *Zh. Prikl. Khim.*, 1990, vol. 63, no. 1, pp. 168–172.
14. Rumyantseva, N.V., Yudin, V.E., Goikhman, M.Ya., *et al.*, *Mekh. Kompoz. Mater.*, 1991, no. 1, pp. 170–172.
15. Koton, M.M. and Sazanov, Yu.N., *Nauka Chelov.: Mezhdunar. Ezhegod.*, 1986, pp. 278–290.
16. Inone, H., *Kobunshi*, 1997, vol. 46, no. 8, pp. 556–559.
17. Abramov, V.G., *Neft. Khoz.*, 1994, no. 9, pp. 23–24.
18. Mohri, Y., *Fiber* (Japan), 1994, vol. 50, no. 3, pp. 96–101.
19. Zhukov, A.A., Ostroukhov, N.N., Nikolaev, A.I., *et al.*, *Elektrotekh. Prom–st.*, 1995, no. 3, pp. 28–29.
20. Zimin, Yu.B., Berezina, A.B., Dontsova, E.P., *et al.*, *Plast. Massy*, 1999, no. 10, pp. 13–15.
21. Borisova, M.E. and Marchenko, M.S., *Elektrotekhnika*, 1998, no. 5, pp. 4–6.
22. US Patent 5411765.
23. Simpson, J.O. and Claiz, A.K.St., *Polym. Prepr. Am. Chem. Soc.*, 1996, vol. 37, no. 1, pp. 715–716.
24. RF Patent 2100859.
25. Denton, D.D., Day, D.R., Prior, D.F., *et al.*, *J. Electr. Mater.*, 1985, vol. 14, pp. 119–123.
26. Kimura, F., Matsuura, T., and Sasaki, S., *J. Colloid Interface Sci.*, 1988, vol. 124, no. 2, pp. 290–299.
27. Extended Abstracts, *7th Int. Conf. on Polymer in Electronic Packing (October 18–20, 2000)*, Feger, C., Khojasteh, M.M., and Molis, S.E., Eds., Mid. Hudson Sec: Soc. Plast. Eng., 2000.
28. Sasaki, S., *Fiber* (Japan), 1994, vol. 50, no. 3, pp. 102–105.
29. Poliimiden für elektronische Kettelen, *Galvanoplastik*, 1997, no. 1, pp. 283–284.
30. Functional and High Performance Polymers: *Preprints, Taipei*, November 14–16, 1994.
31. Kamanina, N.V. and Kaporskii, L.N., *Pis'ma Zh. Tekh. Fiz.*, 1999, vol. 25, no. 14, pp. 46–50.
32. Fujita, K., *Nitto Giho*, 1991, vol. 29, no. 1, pp. 20–22.
33. Agapov, O.A., Kurchatkin, S.P., Murav'eva, N.A., and Sevast'yanov, V.T., *Elektron. Prom–st.*, 1995, no. 8, pp. 25–26.
34. Li, F.M., Harris, F.W., and Cheng, S.Z.D., *Polymer*, 1996, vol. 37, no. 23, pp. 5321–5325.
35. Kamanin, N.V., *Opt. Zh.*, 1990, vol. 64, no. 5, pp. 107–115.
36. US Patent 5856430.
37. US Patent 5856432.
38. US Patent 5856431.
39. US Patent 5969055.
40. US Patent 5969088.
41. Wang, J., Ye, Yu., Cui, Q., *et al.*, *J. Fudan Univ. Nat. Sci.*, 1998, vol. 37, no. 3, pp. 242–252.
42. US Patent 5906886.
43. Caplan, M.L., Stoaklay, D.M., and Clair, A.K.St., *J. Appl. Polym. Sci.*, 1995, vol. 56, no. 8, pp. 995–1006.
44. Soutward, R.E., Thompson, D.W., and Clair, A.K.St., *Chem. Mater.*, 1997, vol. 9, no. 2, pp. 501–510.
45. US Patent 5677418.
46. Levin, K.L., Frolov, V.I., Boyarchuk, Yu.M., *et al.*, *Vysokomol. Soedin.*, 1999, vol. 41, no. 2, pp. 363–367.
47. *Entsiklopediya polimerov* (Polymer Encyclopedia), Kabanov, V.A., Ed., Moscow: Sov. Entsiklopediya, 1974, vol. 2.
48. Polyimidy dza suponeċ pożaravy, *Plasty Kauc.*, 1998, vol. 35, no. 9, pp. 280–281.
49. Mettalpolyide insrlatians, *Ind. Anz.*, 1998, vol. 120, no. 9, p. 25.
50. Arslanov, V.V., *Usp. Khim.*, 1994, vol. 63, no. 1, pp. 3–42.
51. Hoh, E. and Iwamto, M., *Trans. Inst. Electr. Eng. Jpn.*, 1998, vol. 118A, no. 12, pp. 1412–1417.
52. US Patent 5336925.

53. Hou Haoqing, Li Yuesheng, and Ding Mengxian, Chin. *J. Appl.*, 1998, vol. 15, no. 2, pp. 100–102.
54. Kamijama, K. and Nakazawa, E., *Res. Repts. Kogakuin Univ.*, 1997, no. 83, p. 7379.
55. Nogouchi, M., Saito, S., Mochida, T., and Nakazawa, E., *Res. Repts. Kogakuin Univ.*, 1995, no. 79, pp. 59–63.
56. Berrada, M., Carriere, F., Coutin, B., *et al.*, *Chem. Mater.*, 1996, vol. 8, no. 5, pp. 1029–1034.
57. Onciu, M. and Chiriac, C., *Acad. Rom.*, 1997, no. 18, pp. 197–218.
58. RF Patent 2124530.
59. RF Patent 2120652.
60. USSR Inventor's Certificate, no. 1324476.
61. USSR Inventor's Certificate, no. 1210584.
62. Suhng, Y., Hashhizume, K., Kaneko, T., *et al.*, *Synth. Met.*, 1997, vol. 86, nos. 1–3, pp. 2285–2286.
63. Gribanov, A.V., Sazanov, Yu.N., Beloborodova, E.V., and Fedorova, G.N., *Zh. Prikl. Khim.*, 1999, vol. 72, no. 3, pp. 467–473.
64. Gribanov, A.V. and Sazanov, Yu.N., *Zh. Prikl. Khim.*, 2000, vol. 73, no. 3, pp. 465–469.
65. Gribanov, A.V. and Sazanov, Yu.N., *Zh. Prikl. Khim.*, 2000, vol. 73, no. 6, pp. 987–991.
66. Gribanov, A.V. and Sazanov, Yu.N., *Zh. Prikl. Khim.*, 2000, vol. 73, no. 10, pp. 1705–1709.
67. Wyun, C.H., *J. Electrochem. Soc.*, 1997, vol. 144, no. 11, pp. 3769–3771.
68. Fink, D., Vacik, J., Orünwald, R., *et al.*, *Fullerene Sci. Technol.*, 1997, vol. 5, no. 1, pp. 267–274.
69. Aizenshtein, E.M., *Khim. Volokna*, 1999, no. 5, pp. 3–12.
70. Perepechkin, L.P. and Perepechkina, N.P., *Khim. Volokna*, 1999, no. 6, pp. 3–11.
71. Tatsuya, H. and Phillips, G.O., *New Fibers*, Cambridge: Woodhead, 1997.
72. Volokhina, A.V. and Shchetinin, D.M., *Khim. Volokna*, 1998, no. 2, pp. 3–7.
73. Perepelkin, K.E., Gurova, E.Yu., Baranova, A.S., and Kynin, A.T., *Khim. Volokna*, 1993, no. 6, pp. 43–47.
74. Kunugi, T., *Sen'i Gakkaishi*, 1998, vol. 54, no. 4, pp. 134–137.
75. Mikhailov, G.M., Korzhavin, L.N., Lebedeva, M.F., and Baklagina, Yu.G., *Zh. Prikl. Khim.*, 1998, vol. 71, no. 12, pp. 2040–2050.
76. Mikhailov, G.M., Lebedeva, M.F., Baklagina, Yu.B., and Maricheva, T.A., *Zh. Prikl. Khim.*, 1999, vol. 72, no. 3, pp. 472–480.
77. Chung, T.S., Katchinski, E.R., and Vora, R., *J. Membr. Sci.*, 1994, vol. 88, no. 1, pp. 21–36.
78. US Patent 5413852.
79. Qiul, X., Shen, Q., Cao, Z., *et al.*, *J. Shanghai Jiaotong Univ.*, 1997, vol. 31, no. 10, pp. 39–41.
80. Matsuuza, T., Kobajashi, J., Ando, S., *et al.*, *Appl. Opt.*, 1997, vol. 38, no. 6, pp. 966–971.
81. Han, K., Lee, H.J., and Rhee, T.H., *J. Appl. Polym. Sci.*, 1999, vol. 74, no. 1, pp. 107–112.
82. Berlin, A.A. and Shutov, F.A., *Penopolimaterialy na osnove reaktsionnosposobnykh oligomerov* (Foamed Polymeric Materials Based on Reactive Oligomers), Moscow: Khimiya, 1978.
83. RF Patent 1828649.
84. RF Patent 1824885.
85. Artem'eva, V.N., Kudryavtsev, V.V., Kukarkin, E.N., *et al.*, *Plast. Massy*, 1990, no. 4, pp. 32–34.
86. *Advances in Polyimide Science and Technology: Proc. 4th Int. Conf. on Polyimides*, Feger, C., Khojasteh, M.M., and Hoto, S.M., Eds., Ellenville, New York (USA): Soc. Plast. Eng., 1991.
87. Gagliani, J. and Supkis, D.E., *Acta Astronaut.*, 1980, vol. 7, pp. 653–683.
88. McGath, J.E., Jayarman, S.K., Lakshman, P., *et al.*, *Polym. Prepr. Am. Chem. Soc.*, 1996, vol. 37, no. 1, pp. 136–137.
89. Carter, K.R., DiPietro, R.A., Sancher, M., and Russell, T.P., *Chem. Mater.*, 1997, vol. 9, no. 1, pp. 105–118.
90. RF Patent 2081134.
91. Yudin, V.E., Artemyeva, V.N., Kudryavtsev, V.V., *et al.*, *Proc. 15th Int. Conf. "Plastics High Performance Packing Dusseldorf,"* Dusseldorf (Germany): Soc. Plast. Eng., 1994.
92. Artem'eva, V.N., Chupans, P.I., Kudryavtsev, V.V., *et al.*, *Plast. Massy*, 1995, no. 2, pp. 11–13.
93. Dutruch, L., Senneran, M., Bartholin, M., *et al.*, *Polymeric Foams*, Khemani, K.C., Ed., Washington: ACS Symp. Ser., 1997, pp. 37–53.
94. Kenig, S., *Polymer Powder Technology*, Narkis, M. and Rosenzweig, N., Eds., New York: J. Wiley and Sons, 1995, pp. 531–539.
95. Yudin, V.E., Otaigbe, J.U., and Artemieva, V.N., *Polym. Comp.*, 1999, vol. 20, no. 3, pp. 337–345.
96. Yudin, V.E., Artemieva, V.N., and Gubanova, G.N., in *New Polyimides for Advanced Compounds: Proc. 2nd East Asian Conf. on Polymers for Advanced Technologies*, Seoul (Korea), August 11–16, 1999, pp. 59–60.
97. Yudin, V.E., Otaigbe, J.U., and Artemjeva, V.N., in *Technical Papers of Conf. SPEANTEC "Plastic Bridging the Millennia,"* San Francisco (USA), April 4–6, 1999, pp. 2027–2031.
98. Kostereva, T.A., Artem'eva, V.N., Kudryavtsev, V.V., *et al.*, Abstracts of Papers, *XX Simpozium po reologii* (XX Symp. on Rheology), Karacharovo (Russia), June 11–14, 2000, p. 213.
99. Yudin, V.E., Otaigbe, J.U., and Artemyeva, V.N., Extended Abstracts, *7th Int. Conf. on Polymers in*

Electronic Packaging, USA: Electr. Div., 2000, no. 7, p. 5.

100. *High-Temperature Properties and Applications of Polymeric Materials*, Tant, M.R., Ed., Washington DC, ACS Symp. Ser., 1995, vol. 603.
101. US Patent 5320650.
102. Ohya, H., Futamura, H., Ichihara, T., *et al.*, *Membrane*, 1990, vol. 15, no. 3, pp. 139–143.
103. Polotskaya, G.A., Kuznetsov, Yu.P., Romashkova, K.A., *et al.*, *Vysokomol. Soedin., Ser. A*, 1992, vol. 34, no. 10, pp. 167–173.
104. Polotskaya, G.A., Kostereva, T.A., Stepanov, N.G., *et al.*, *Vysokomol. Soedin., Ser. B*, 1996, vol. 38, no. 7, pp. 1234–1238.
105. Polotskaya, G.A., Martynenkov, A.A., Trofimov, A.E., *et al.*, *Zh. Prikl. Khim.*, 1997, vol. 70, no. 2, pp. 321–326.
106. Polotskaya, G.A., Kostereva, T.A., and Elyashevich, G.K., *J. Sep. Pur.*, 1998, vol. 14, pp. 13–18.
107. Polotskaya, G.A., Sklizkova, V.P., Kozhurnikova, N.D., *et al.*, *J. Appl. Polym. Sci.*, 2000, vol. 75, pp. 1026–1032.
108. H-High Quality Membranes, *Chem. Eng.*, 1997, no. 642, p. 15.
109. Kim, H.T., Koros, W.J., Husk, J.R., and O'Brien, K.C., *J. Membr. Sci.*, 1998, vol. 37, pp. 45–62.
110. Nakamura, A. and Makino, H., *Membrane*, 1987, vol. 12, no. 5, pp. 289–292.
111. Ohya, H., Ichihara, T., Higasigima, T., and Negishi, Y., *Membrane*, 1992, vol. 17, no. 1, pp. 27–42.
112. Kukuchi, M., Asano, S., and Ninomiya, H., *Kagaku Kougaku*, 1989, vol. 53, no. 1, pp. 51–53.
113. Tsunemi, K., *Sulfuric Acid Ind.*, 1989, vol. 41, no. 12, pp. 212–218.
114. Ono, S., *Dye Ind.*, 1989, vol. 37, no. 4, pp. 185–190.
115. Nakamura, A., Ono, S., and Ninomiya, H., *Kagaku Kougaku*, 1987, vol. 51, no. 9, pp. 695–698.
116. Inoue, K., Ishii, K., Kawashima, T., *et al.*, *Tech. Rep. Nitto Electr.*, 1993, vol. 31, no. 1, pp. 25–34.
117. Iwana, A. and Kazuse, Y., *J. Membr. Sci.*, 1992, no. 11, pp. 297–309.
118. US Patent 5264166.
119. Polyimide Membranes for Biological Purpose, *High Polym. Jpn.*, 1996, vol. 45, no. 9, p. 672.
120. Sazanov, Yu.N., Daungauer, S.A., Shibaev, L.A., *et al.*, *J. Thermal Anal.*, 1982, vol. 25, no. 3, pp. 441–447.
121. Sazanov, Yu.N., Shibaev, L.A., Daungauer, S.A., *et al.*, *Acta Polym.*, 1984, vol. 35, no. 4, pp. 291–209.
122. Magamedova, N.S., Chetkina, L.A., Bel'skii, V.K., *et al.*, *Zh. Strukt. Khim.*, 1986, vol. 27, no. 4, pp. 135–139.
123. Sazanov, Yu.N., Szekely, T., Antonova, T.A., *et al.*, *Thermochim. Acta*, 1986, vol. 102, pp. 223–238.
124. Sazanov, Y.N., Shibaev, L.A., Stepanov, N.G., and Boiko, A.A., *J. Thermal Anal.*, 1989, vol. 35, no. 3, pp. 947–955.
125. Sazanov, Y.N., Spirina, T.N., Shibaev, L.A., *et al.*, *J. Thermal Anal.*, 1990, vol. 36, no. 12, pp. 2329–2338.
126. Sazanov, Yu.N., Kostereva, T.A., Stepanov, N.A., *et al.*, *Vysokomol. Soedin., Ser. B*, 1994, vol. 36, no. 9, pp. 1563–1567.
127. Gribanov, A.V. and Sazanov, Yu.N., *Zh. Prikl. Khim.*, 1999, vol. 72, no. 11, pp. 1896–1900.
128. Miichenko, I.P. and Mikhailin, Yu.A., *Plast. Massy*, 1993, no. 1, pp. 27–33.
129. Miichenko, I.P. and Mikhailin, Yu.A., *Tekhnol. Konstr. Kompoz. Mater.*, 1994, no. 2, pp. 9–17.
130. Kostyuchenko, V.N., Abstracts of Papers, *22-e Gagarinskie chteniya: Molodezhnaya nauchnaya konferentsiya* (22nd Gagarin Readings: Conf. of Young Scientists), Moscow: TsAGI, 1996, part 3, pp. 106–107.
131. US Patent 5069848.
132. Kataoka, S., *Purasuchikkusu*, 1995, vol. 46, no. 1, pp. 49–51.
133. Tamai, S., Yamaguchi, A., and Ohta, M., *Polymer*, 1996, vol. 37, no. 16, pp. 3683–3692.
134. Yasunori, Y., *Kogyo Zairyo*, 1997, vol. 45, no. 4, pp. 99–102.
135. Gabriele, M.C., *Plast. Technol.*, 1995, vol. 41, no. 8, pp. 28, 30–31.
136. Koba, T., *Plast. Age*, 1993, vol. 39, no. 8, pp. 131–136.
137. Hok, A., *Mach. Des.*, 1994, vol. 66, no. 19, pp. 107, 109–110.
138. USSR Inventor's Certificate, no. 1508551.
139. Avdeev, D.T., Vasil'ev, B.N., and Pleshakova, T.D., in *Osnovy konstruirovaniya mashin* (Machine Design Philosophy), Novocherkassk: Gos. Tekh. Univ., 1994, pp. 42–46.
140. Shobesberger, M., *Osterr. Kunstst. Z.*, 1995, vol. 26, nos. 5–6, pp. 93–96.
141. RF Patent 2072373.
142. US Patent 5466737.
143. Polyimides for Construction Parts, *Polym. News*, 1997, vol. 22, no. 6, pp. 214–215.
144. Polyimidovy sčtučny, *Plasty Kauč.*, 1996, vol. 33, no. 7, p. 216.
145. Plasty materialy do motoruv, *Plasty Kauč.*, 1998, vol. 35, no. 7, pp. 215–216.
146. Leaveersuch, R.D., *Mod. Plast. Int.*, 1998, vol. 28, no. 8, pp. 33–34.

147. *Die Maschienenplastik konstruktionen, Maschinenmarkt*, 1998, vol. 104, no. 16, p. 167.
148. US Patent 5 260 117.
149. Grabil'nikov, A.S. and Zinevich, O.M., *Mekh. Kompoz. Mater.*, 1994, vol. 30, no. 6, pp. 848–852.
150. US Patent 5 334 698.
151. Thrmount and Azbon, *Galvanotechnik*, 1998, vol. 89, no. 5, p. 1725.
152. Gribanov, A.V. and Sazanov, Y.N., *Prepr. 11th Conf. Ital. Disc. Technol. Macromol.*, Dicenza, Torino, 1993, pp. 152–154.
153. Gribanov, A.V., Kol'tsov, A.I., and Sazanov, Yu.N., in *Sovremennye aspekty YaMR spektroskopii polimerov: Sbornik nauchnykh trudov VNIISK* (Modern Aspects of NMR Spectroscopy of Polymers: Collection of Scientific Works of the Russian Research Inst. of Synthetic Rubber), St. Petersburg, 1994, pp. 13–18.
154. Inagaki, M., Ibuki, T., and Takeichi, T., *J. Appl. Polym. Sci.*, 1992, vol. 44, no. 3, pp. 521–525.
155. Gribanov, A.V., Sazanov, Yu.N., Beloborodova, E.V., *et al., Zh. Prikl. Khim.*, 1999, vol. 72, no. 3, pp. 467–473.
156. Gribanov, A.V., Sazanov, Yu.N., Goikhman, M.Ya., *et al., Zh. Prikl. Khim.*, 2000, vol. 73, no. 12, pp. 2002–2006.
157. Hishiyama, Y., Nakamura, M., Nagata, Y., *et al., Carbon*, 1994, vol. 32, no. 4, pp. 645–650.
158. Laius, L.A., Dolotova, N.A., and Gofman, I.V., *Plast. Massy*, 1999, no. 4, pp. 44–46.
159. Goykhman, M.Ya., Svetlichnyi, V.M., Kudryavtsev, V.V., *et al., Polym. Eng. Sci.*, 1997, vol. 37, no. 8, pp. 1381–1386.
160. Rumyantseva, N.V., Yudin, V.E., Goikhman, M.Ya., *et al., Mekh. Kompoz. Mater.*, 1991, no. 1, pp. 170–172.
161. USSR Appl. no. 4 871 847/05.
162. Goykhman, M.Ya., Svetlichnyi, V.M., Kudryavtsev, V.V., *et al., Acta Montana, Ser. B*, 1997, no. 7 (105), pp. 9–19.
163. Artem'eva, V.N., Bolotnikova, L.S., Glumova, T.D., *et al., Zh. Prikl. Khim.*, 1991, vol. 64, no. 11, pp. 2405–2410.
164. Artem'eva, V.N., Baklagina, Yu.G., Kudryavtsev, V.V., *et al., Zh. Prikl. Khim.*, 1993, vol. 66, no. 8, pp. 1826–1831.
165. Artem'eva, V.N., Yudin, V.E., Kudryavtsev, V.V., *et al., Plast. Massy*, 1996, no. 5, pp. 3–5.
166. Svetlichnyi, V.M., Zhukova, T.I., Kudryavtsev, V.V., *et al., Polym. Sci.*, 1995, vol. 35, no. 16, pp. 1321–1324.
167. Yudin, V.E., Goykhman, M.Ya., Kudryavtsev, V.V., *et al., Acta Montana, Ser. B*, 1997, no. 7 (105), pp. 73–81.
168. Yudin, V.E., Svetlichnyi, V.M., Gubanova, G.N., *et al.*, in *Proc. 4th Eur. Technical Symp. on Polyimides and High Performance Polymers*, Montpellier: LEMP/MAO, Univ. Montpellier 2, May 12–18, 1996, pp. 25–35.
169. Myagnova, L.A., Svetlichnyi, V.M., Kudryavtsev, V.V., *et al., Proc. 4th. Eur. Technical Symp. on Polyimides and High Perfomance Polymers*, Montpellier: LEMP/MAO, Univ. Montpellier 2, May 12–18, 1996, pp. 33–40.
170. Wang, J., Ye, Yu., Cui, Q., *et al., High Technol. Lett.*, 1996, vol. 6, no. 3, pp. 9–11.
171. Dugger, T. and Hirt, D.E., *Polym. Comp.*, 1996, vol. 17, no. 3, pp. 492–496.
172. Harris, F.W., Cheng, S.Z.D., and Li, F.M., *J. Adv. Mater.*, 1994, vol. 26, no. 1, pp. 23–32.
173. Kim, Dae S. and Lee, Sac R., *J. Mater. Res.*, 1995, vol. 53, no. 6, pp. 711–716.
174. Shimokawa, T., Hamaguchi, Ya., and Kamon, H., *J. Comp. Mater.*, 1996, vol. 33, no. 18, pp. 1685–1698.
175. Miichenko, I.P., Mikhailin, Yu.A., and Kostyuchenko, V.N., *Tekhnol. Konstr. Kompoz. Mater.*, 2000, no. 1, pp. 30–35.
176. Yudin, V.E., Viscoelasticity of a Polymer Matrix and Failure of Heat-Resistant Fibrous Composites, *Doctoral Dissertation*, St. Petersburg, 2000.
177. Zhubanov, B.A., Kravtsova, V.D., Bekmagambetova, K.Kh., and Akhmettaev, D.A., *Elektrotekhnika*, 1998, no. 11, pp. 57–60.
178. JPN Patent Appl. 450 279.
179. US Patent 5 346 982.
180. Photosensitive Plastics, *Galvanotechnik*, 1997, vol. 88, no. 10, p. 3503.
181. US Patent 5 539 080.
182. US Patent 5 868 968.
183. US Patent 5 858 518.
184. Yamada, Y., Furukawa, V., and Kimura, Y., *Mitsubisy Kako*, 1997, vol. 46, no. 2, pp. 50–59.
185. US Patent 5 959 068.
186. Hutaesaki, N. and Kudo, M., *Plast. Age*, 1998, vol. 44, no. 9, pp. 120–125.
187. US Patent 5 480 965.
188. Nakayama, T., Mochizuki, A., and Ueda, M., *React. Funct. Polym.*, 1996, vol. 30, nos. 1–3, pp. 109–115.
189. Marek, M. and Bednař, B., *Plasty Kauč.*, 1996, vol. 33, no. 1, pp. 9–14.

Russian Journal of Applied Chemistry, Vol. 74, No. 8, 2001, pp. 1270–1273. Translated from Zhurnal Prikladnoi Khimii, Vol. 74, No. 8, 2001, pp. 1235–1238.

INORGANIC SYNTHESIS AND INDUSTRIAL INORGANIC CHEMISTRY

Phase Equilibria in the System $CaSiO_3$–$BaGeO_3$

G. A. Mikirticheva, V. I. Shitova, S. A. Petrov, L. Yu. Grabovenko, S. K. Kuchaeva, and P. G. Grebenshchikov

Grebenshchikov Institute of Silicate Chemistry, Russian Academy of Sciences, St. Petersburg, Russia

Received January 30, 2001

Abstract—The phase relationships in the system $CaSiO_3$–$BaGeO_3$ were studied and its phase diagram was constructed.

Proceeding with investigations of phase equilibria and isomorphism in partial sections of a ternary mutual system CaO, BaO || SiO_2, GeO_2 [1–5], we studied the system $CaSiO_3$–$BaGeO_3$, which is a diagonal section of the concentration quadrangle $CaSiO_3$–$CaGeO_3$–$BaGeO_3$–$BaSiO_3$.

The chemical composition of the simplest pyroxenoids is expressed by the general formula $M_n[SiO_3]_n$, where M represents a group of cations with large ionic radius (Ca^{2+}, Sr^{2+}, and Ba^{2+}) in various integral and fractional ratios [6].

Extending the range of chemical compositions of pyroxenoid silicates, studying the phase relationships between them, and establishing the concentration regions of homogeneity in these systems constitute one of necessary stages in the development of new materials.

According to previous studies [4, 7, 8], potassium metasilicate $CaSiO_3$ crystallizes in two polymorphic modifications: low-temperature β-form with chain-like structure of anionic radicals and high-temperature pseudowollastonite α-form with ring-like structure of anionic groups. The temperature of the β→α transition is 1180°C; the given polymorphic transformation is monotropic under atmospheric pressure.

Barium metagermanate $BaGeO_3$ also exists in two polymorphic modifications. Its low-temperature pseudowollastonite α-form transforms at 1225°C into a high-temperature β-form with chain-like structure of anionic radicals. The latter form differs from β-$CaSiO_3$ in the arrangement of tetrahedral chains. In β-$CaSiO_3$, the anionic chains with identity period of three tetrahedrons consist of diortho groups alternating with separate tetrahedrons. In the structure of barium metagermanate (β-form), the anionic chains with identity period of two tetrahedrons are formed solely by diortho groups [8, 9].

In the present study, samples for analyzing phase equilibria in the $CaSiO_3$–$BaGeO_3$ system were prepared by solid-phase synthesis. As starting components of the stock served $CaCO_3$ (special purity), $BaCO_3$ (chemically pure), GeO_2 (special purity), and SiO_2 (99.99% pure). Prior to synthesis, a stock of prescribed composition was thoroughly ground in distilled water, compressed into pellets, and then subjected to high-temperature calcination for a time varied between 3 and 50 h, depending on sample composition. The temperature of the initial calcination was 1180°C. Samples of intermediate compositions were synthesized both from oxide mixtures and from the end members of the section, β-$CaSiO_3$ and α-$BaGeO_3$, synthesized in advance. The system was studied in the temperature range 1000–1450°C, using a set of physicochemical methods, including X-ray phase (XPA, Cu_{K_α}-radiation) differential thermal (DTA, MOM derivatograph, Hungary), and crystal optical (immersion) analyses, and the method of annealing and quenching.

The phase diagram of the $CaSiO_3$–$BaGeO_3$ system was constructed on the basis of the results obtained in the experiment performed (Fig. 1). The phase relationships in the subsolidus region are characterized by a certain complexity and diversity of the crystallizing structural types. Optical and X-ray characterization of the phases existing in the system are presented in Figs. 2 and 3. Five regions of homogeneity are distinguished in the diagram, differing in their dimensions along the concentration and temperature axes. A region with the broadest concentration range is occupied by the $Ca_{1-x}Ba_x(Si_{1-x}Ge_x)O_3$ ($0.18 < x < 0.56$,

1070-4272/01/7408-1270 $25.00 © 2001 MAIK "Nauka/Interperiodica"

at T = 1060°C) solid solution having a walstromite-like structure according to XPA [10]. The given phase is stable over the entire temperature range studied, up to its melting point. The existence of a broad homogeneity region in the central part of the system is confirmed by a steady change in the refractive indices of the crystals and by monotonic change in the interplanar spacings d/n. In all probability, the walstromite-like solid solution $Ca_{1-x}Ba_x(Si_{1-x}Ge_x)O_3$ is formed from a compound similar in nature to double salts with 2 : 1 stoichiometric ratio of the starting components.

To the end members of the system, $CaSiO_3$ and $BaGeO_3$, are adjacent narrow homogeneity fields (2 to 10 mol %) based on their α- and β-polymorphic modifications. The boundary lines in the phase diagram were plotted on the basis of DTA and XPA data and the results obtained using the method of annealing and quenching. The concentration region of homogeneity of the α-$CaSiO_3$ solid solution is narrow, its boundary is plotted conventionally.

As follows from the phase diagram, the conjugate isomorphism $Ca^{2+}Si^{4+} \rightleftarrows Ba^{2+}Ge^{4+}$ affects differently the thermal stability of different structural types of the metasilicates–metagermanates studied. For example, simultaneous substitution of Ba^{2+} for Ca^{2+} and Ge^{4+} for Si^{4+} raises the thermal stability limit of a solid solution based on the low-temperature modification of $CaSiO_3$ from 1180 to 1300°C (i.e., to the temperature of its incongruent melting). With Ba^{2+} and Ge^{4+} in the α-$BaGeO_3$ lattice replaced by, respectively, Ca^{2+} Si^{4+}, the temperature range of stability of this solid solution is markedly narrowed and that of its high-temperature modification (β-form) considerably broadened. For the phase of variable composition, $Ca_{1-x}Ba_x(Si_{1-x}Ge_x)O_3$, the homogeneity region becomes only slightly narrower with increasing temperature for $CaSiO_3$-richer compositions.

The optical characteristics of the phases crystallizing in the system (Fig. 2) differ in the refractive indices n_g, n_p and birefringence $\Delta = n_g - n_p$. The largest birefringence is observed for crystals of the α-$CaSiO_3$ and α-$BaGeO_3$ solid solutions, and the smallest, for the $Ca_{1-x}Ba_x(Si_{1-x}Ge_x)O_3$ solid solution. The X-ray diffraction patterns of the α-forms of the $CaSiO_3$ and $BaGeO_3$ solid solutions are similar (Fig. 3). The only difference is that the diffraction peaks are shifted to smaller angles and the relative intensities of the reflections are redistributed in the case when calcium ion is replaced in this structural type by the larger barium ion. Figure 3 also clearly shows that the X-ray diffraction patterns of two solid solutions, β-$CaSiO_3$

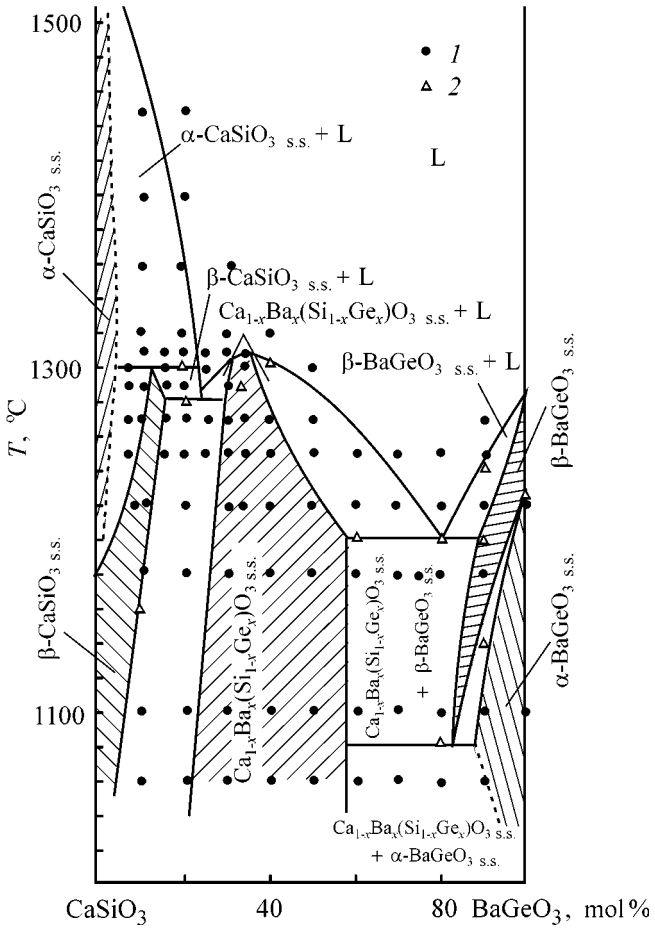

Fig. 1. Phase diagram of the system $CaSiO_3$–$BaGeO_3$. (T) Temperature. Method: (*1*) annealing and quenching and (*2*) DTA.

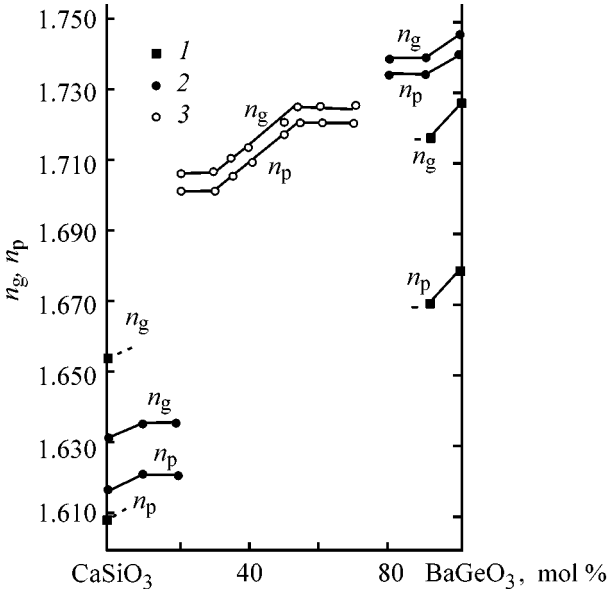

Fig. 2. n_g and n_p of solid solutions in the system $CaSiO_3$–$BaGeO_3$. (*1*) α-$CaSiO_3$ and α-$BaGeO_3$, (*2*) β-$CaSiO_3$ and β-$BaGeO_3$, and (*3*) $Ca_{1-x}Ba_x(Si_{1-x}Ge_x)O_3$ ($0.2 < x < 0.56$).

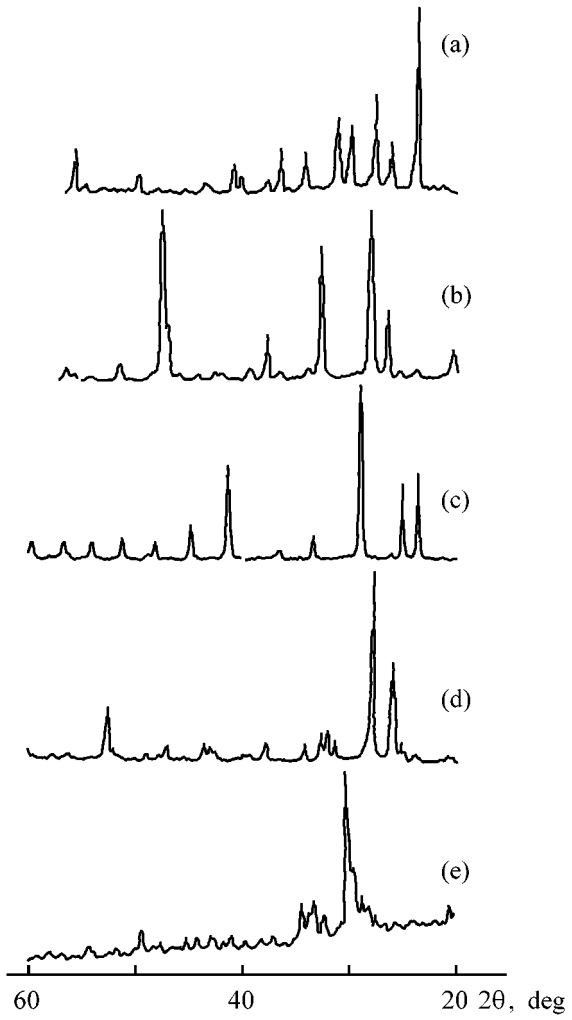

Fig. 3. X-ray diffraction patterns of solid solutions in the system $CaSiO_3$–$BaGeO_3$. (2θ) Bragg angle. (a) β-$CaSiO_3$, (b) α-$CaSiO_3$, (c) α-$BaGeO_3$, (d) β-$BaGeO_3$, and (e) $Ca_{1-x}Ba_x(Si_{1-x}Ge_x)O_3$ ($0.2 < x < 0.56$) (walstromite structural type).

and β-$BaGeO_3$, are markedly different. This is due to the difference in the identity periods of their chains and, correspondingly, in the configurations of the tetrahedral chains in their structure. The X-ray diffraction pattern of the $Ca_{1-x}Ba_x(Si_{1-x}Ge_x)O_3$ solid solution is typical of the structural type of walstromite $Ca_2BaSi_3O_9$.

In the concentration range 56–87 mol % $BaGeO_3$, the system is represented by two-phase fields based on one of the two polymorphic modifications of $BaGeO_3$ (α- or β-form) and by the $Ca_{1-x}Ba_x(Si_{1-x}Ge_x)O_3$ solid solution (Fig. 1). In the given concentration range at 1080°C, eutectoid decomposition of the β-$BaGeO_3$ solid solution into the solid solutions α-$BaGeO_3$ and $Ca_{1-x}Ba_x(Si_{1-x}Ge_x)O_3$ occurs in the system. In all probability, the revealed eutectoid decomposition of β-$BaGeO_3$ into α-$BaGeO_3$ and the limiting composition of the walstromite solid solution ($x = 0.56$) reflects a kinetically nonequilibrium process, which is responsible for the slope of the limiting solubility boundaries untypical of the given case of phase decomposition.

The results of DTA and XPA and a crystal optical study of samples quenched from different temperatures confirm the eutectic nature of the interaction between the β-$BaGeO_3$ solid solution and the walstromite-like phase.

The liquidus and solidus curves of the system were plotted on the basis of data furnished by DTA and the visual-polythermal method, using the results of crystal optical studies of samples quenched from different temperatures.

Establishing the liquidus and solidus relationships in the concentration range from 10 to 40 mol % $BaGeO_3$ was made difficult by the fact that the fields of equilibrium coexistence of the liquid and solid solution phases are narrow. The close phase transition temperatures (1280–1300°C) in the given concentration range required an additional study to elucidate the nature of melting (eutectic or peritectic) of the $Ca_{1-x}Ba_x(Si_{1-x}Ge_x)O_3$ solid solution and to detail its interaction with the β-$CaSiO_3$ solid solution.

In this case, the key factor were the results obtained in studying quenched samples successively annealed within the 1250–1340°C range with a step of 10–20°C. Four samples with compositions differing by 5 mol % were simultaneously annealed in a platinum crucible. The visual-polythermal and crystal optical analyses of these samples showed that the most readily fusible composition in the concentration range studied is $Ca_{0.75}Ba_{0.25}(Si_{0.75}Ge_{0.25})O_3$. Liquid phases appeared in the sample at a calcination temperature of 1280°C. At higher temperatures (1290–1300°C) their phase composition changed. In the samples enriched in calcium metasilicate, compared with the boundary composition $Ca_{0.75}Ba_{0.25}(Si_{0.75}Ge_{0.25})O_3$, only prismatic crystals whose refractive indices n_g and n_p were similar to those of the β-$CaSiO_3$ solid solution were in equilibrium with the liquid. For $BaGeO_3$-enriched samples, only isometric grains with considerably higher values of n_g and n_p were clearly revealed in an immersion preparation along with the liquid phase, which is characteristic of a walstromite-like solid solution (Fig. 2). Analysis of the obtained experimental data confirms unambiguously that the interaction between

the $Ca_{1-x}Ba_x(Si_{1-x}Ge_x)O_3$ and β-$CaSiO_3$ solid solutions is eutectic. The eutectic composition is 75 mol % $CaSiO_3$ + 25 mol % $BaGeO_3$, and T_{eut} = 1280°C. The β-$CaSiO_3$ solid solution melts peritectically at 1300°C to give the α-$CaSiO_3$ solid solution and a liquid.

The performed study of the phase relationships in the system $CaSiO_3$–$BaGeO_3$ (Fig. 1) demonstrated that the given system belongs to those with limited mutual solubility of the solid-state components to give the $Ca_{1-x}Ba_x(Si_{1-x}Ge_x)O_3$ berthollide phase of variable composition. In the concentration region in which this phase exists, the liquidus curve has a clearly resolved irrational peak at 1310°C for the composition corresponding to $CaSiO_3$: $BaGeO_3$ = 2 : 1. However, the refractive index curves show no inflection point for this solid solution composition. This means that there is no pronounced singularity point in the phase diagram owing to the high degree of dissociation of the compound and, correspondingly, confirms that this phase has berthollide physicochemical origin (Fig. 1).

Taking into account that Ca and Ba, and Si and Ge are similar in chemical nature, one would expect that extensive regions of homogeneity exist in the system considered on basis of its end members. However, according to the data obtained, nothing of this kind is actually observed. By contrast, a rather broad region of the $Ca_{1-x}Ba_x(Si_{1-x}Ge_x)O_3$ berthollide-like solid solution isostructural with walstromite is formed in its central part. The given structure is in fact a distorted pseudowollastonite form [10]. When the conjugate isomorphous substitution $Ca^{2+}Si^{4+} \rightleftarrows Ba^{2+}Ge^{4+}$ occurs in the cationic and anionic sublattices of the system, the appearance of a walstromite-like phase seems to be reasonable because of the significantly different types of behavior exhibited by the end members of the system. Probably, the walstromite structural type allows more substantial variation of the size of large cations constituting the distorted pseudowollastonite lattice, compared with the pyroxenoid structure.

CONCLUSIONS

(1) The phase relationships in the $CaSiO_3$–$BaGeO_3$ system were studied and its phase diagram was constructed.

(2) The system in question is polymorphic and belongs to systems characterized by limited solubility of components in solid state and formation of the $Ca_{1-x}Ba_x(Si_{1-x}Ge_x)O_3$ berthollide phase of variable composition ($0.2 < x < 0.56$ at T ~1050°C).

(3) The liquidus–solidus relationships in the system are characterized by the existence of eutectic and peritectic equilibria.

(4) Correlations were established between the temperature and concentration boundaries of isomorphous substitutions in the solid solutions of the given system.

REFERENCES

1. Brisi, C., and Appendino, P., *Ann. Chim. (Rome)*, 1965, vol. 55, no. 5, pp. 461–468.
2. De Vries, R.C., *J. Am. Ceram. Soc.*, 1988, vol. 71, no. 10, pp. 416–417.
3. Grebenshchikov, R.G., Shirvinskaya, A.K., and Parfenenkov, V. N., *Izv. Akad. Nauk SSSR, Neorg. Mater.*, 1970, vol. 6, no. 2, pp. 323–326.
4. Shirvinskaya, A.K., Grebenshchikov, R.G., Shitova, V.I., and Toropov, N.A., *Izv. Akad. Nauk SSSR, Neorg. Mater.*, 1966, vol. 11, no. 10, pp. 1900–1904.
5. Grebenshchikov, R.G., and Shitova, V.I., *Izv. Akad. Nauk SSSR, Neorg. Mater.*, 1976, vol. 12, no. 4, pp. 674–678.
6. Zussman, J., *Earth. Sci. Rev.*, 1968, vol. 4, no. 1, pp. 39–67.
7. Petrov, S.A., Mikirticheva, G.A., and Shitova, V.I., *Zh. Prikl. Khim.*, 2000, vol. 73, no. 11, pp. 1758–1762.
8. Belov, N.V., *Ocherki po strukturnoi mineralogii* (Essays on Structural Mineralogy), Moscow: Nedra, 1976.
9. Hilmer, W., *Acta Crystallogr.*, 1962, vol. 15, nos. 10–12, pp. 1101–1105.
10. Dent Glasser, L.S., and Glasser, F.P., *Am. Mineralogist*, 1968, vol. 53, no. 1, pp. 9–13.

Russian Journal of Applied Chemistry, Vol. 74, No. 8, 2001, pp. 1274–1277. Translated from Zhurnal Prikladnoi Khimii, Vol. 74, No. 8, 2001, pp. 1239–1241.

INORGANIC SYNTHESIS AND INDUSTRIAL INORGANIC CHEMISTRY

Preparation of Al, Cr, Nb, Mo, and W Monophosphides from a Lithium Metaphosphate Melt

V. V. Lesnyak, D. A. Stratiichuk, V. S. Sudavtsova, and M. S. Slobodyanik

Shevchenko National University, Kiev, Ukraine

Received November 13, 2000; in final form, March 2001

Abstract—Synthesis of a series of phosphides (AlP, CrP, NbP, MoP, and WP) by reactions of powdered metals with a melt of lithium metaphosphate $LiPO_3$ was studied. Thermodynamic parameters (ΔH^0_{298}, ΔS^0_{298}, ΔG^0_{298}, and ΔG^0_{1273}) of the reactions were calculated and their temperature modes were optimized on the basis of the standard thermodynamic characteristics of the initial substances and the reaction products. X-ray patterns of the powders of the obtained compounds are presented.

The main method for synthesizing phosphides of *d* and *p* elements consists in direct reactions of metal powders with red phosphorus [1]. The reactions are carried out in evacuated quartz ampules at 1073–1473 K. Hydrogen or carbon dioxide is often used as carrier gas for phosphorus vapors. Certain phosphides are prepared in industry by immersing white phosphorus in a bath with molten metal. Thermally unstable higher phosphides are obtained by the "Faraday method," which consists in heating metal powders with an excess amount of red phosphorus. In this case, the temperature does not exceed 1373 K, and excess phosphorus is condensed in the coldest part of the apparatus. When the reaction is carried out at temperatures exceeding the boiling point of red phosphorus, its vapor pressure in the system increases considerably. This procedure for synthesizing higher phosphides is called "process under pressure" [2]. The majority of lower phosphides are obtained by sintering higher phosphides with stoichiometric amounts of metals. For example, V_3P was obtained by heating metallic vanadium with vanadium monophosphide VP, which, in its turn, was prepared by thermal decomposition of the diphosphide VP_2 [3].

The high-temperature electrolysis of sodium metaphosphate melts containing oxides or salts of heavy metals (vanadium, titanium, chromium, etc.) is the most promising industrial method of synthesis, which widely uses phosphates of alkaline and alkaline-earth metals as a source of phosphorus. Controlling the melt composition, synthesis temperature, and current density allows directional synthesis of various types of phosphides of a metal. Tungsten phosphide W_4P was obtained in such a way, whereas all other methods were unsuccessful [4].

In chemistry of solids, particularly in the preparative chemistry, the problem of directional synthesis of phosphides of *p* and *d* elements under specified conditions often arises. In most cases, it is possible to obtain mixtures consisting of lower and higher phosphides, the reaction products often containing unreacted starting substances or by-products.

In this work, we made thermodynamic calculations for certain redox reactions and, on this basis, carried out directional syntheses of a number of phosphides of *p* and *d* elements with the use of high-temperature melts of lithium metaphosphate.

EXPERIMENTAL

The following reagents were used in the work: Li_2CO_3, $(NH_4)_2HPO_4$, both of chemically pure grade; powders of Cr, Al, Nb, Mo, and W metals, all of chemically pure grade, with grain size of 4–8 μm; and also a glass based on lithium metaphosphate. The glass was obtained by the following technique. Stoichiometric amounts of lithium carbonate Li_2CO_3 and ammonium hydroorthophosphate $(NH_4)_2HPO_4$ were heated in a platinum ware (973 K) to complete removal of carbon dioxide, water, and ammonia:

$$Li_2CO_3 + 2(NH_4)_2HPO_4 \rightarrow 2LiPO_3 + CO_2\uparrow + 3H_2O\uparrow + 4NH_3\uparrow.$$

1070-4272/01/7408-1274 $25.00 © 2001 MAIK "Nauka/Interperiodica"

As a result, we obtained a transparent metaphosphate glass with fixed ratio $Li_2O : P_2O_5 = 1 : 1$. Phosphides were synthesized in the range 298–1273 K in the setup shown in the figure. Temperature was controlled with accuracy of ±1–2 deg. Phosphides of metals were obtained from a high-temperature melt of lithium metaphosphate by the following reactions:

$$3LiPO_3 + 13/3Al \rightarrow 5/3Al_2O_3 + Li_3PO_4 + 1/4P_4 + AlP, \quad (1)$$

$$3LiPO_3 + 13/3Cr \rightarrow 5/3Cr_2O_3 + Li_3PO_4 + 1/4P_4 + CrP, \quad (2)$$

$$3LiPO_3 + 7/2Nb \rightarrow 5/2NbO_2 + Li_3PO_4 + 1/4P_4 + NbP, \quad (3)$$

$$3LPO_3 + 7/2Mo \rightarrow 5/2Mo_2O_3 + L_3PO_4 + 1/4P_4 + MoP, \quad (4)$$

$$3LiPO_3 + 7/2W \rightarrow 5/2WO_2 + Li_3PO_4 + 1/4P_4 + WP. \quad (5)$$

A mixture of powders of a metal and an excess amount (15–20% wt %) of lithium metaphosphate were thoroughly ground in an agate mortar and placed in a corundum crucible to fill its volume by 15–20%. Then the system was evacuated to residual partial oxygen pressure of 1–10 Pa. The system was heated at a rate of 20–30 deg h^{-1} up to 1253–1273 K, kept under these conditions for 5–6 h, and then cooled at a rate of 10–15 deg h^{-1} to room temperature. We found that metal phosphides were crystallized as needle-like crystallites in the colder part of the reactor (~923–1023 K) as a result of a gas-transport reaction. The transport agent in these reactions is phosphorus vapor formed as a by-product in the reaction between a metal and a melt. The main reactions result in the formation of metal oxides, which enter in the composition of the obtained orthophosphate melt.

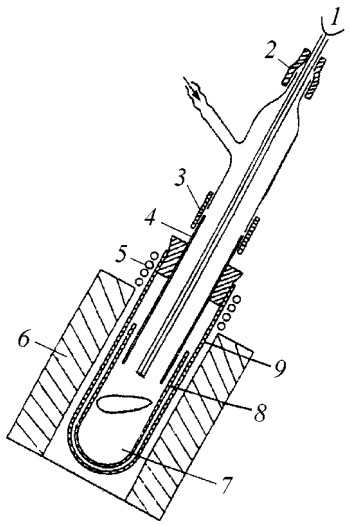

Setup for synthesis of metal phosphides: (*1*) thermocouple, (*2*) Teflon sealant, (*3*) sealing titanium foil, (*4*) stainless steel tube, (*5*) cooling jacket, zone of condensation of phosphides (~923–1023 K), (*6*) SShOL-1-2 shaft furnace, working zone (~1253–1273 K), (*7*) starting mixture of metal powder and lithium-metaphosphate glass, (*8*) corundum crucible, (*9*) sintered corundum tube.

Table 1. X-ray data for synthesized phosphide powders*

hkl	*d*, Å	I/I_m	*hkl*	*d*, Å	I/I_m	*hkl*	*d*, Å	I/I_m
	AlP			MoP			WP	
002	5.688	30	001	3.191	25	101	4.215	25
101	3.199	100	100	2.790	100	011	2.880	100
004	2.844	10	101	2.100	50	200	2.866	15
103	2.504	15		CrP		102	2.734	20
112	2.178	45				201	2.603	20
105	1.879	8	100	6.108	50	111	2.573	83
	NbP		110	4.028	50	210	2.149	15
			200	3.054	12	112	2.092	25
002	5.688	20	020	2.680	50	211	2.031	20
101	3.199	100	210	2.655	25			
103	2.503	25	111	2.461	100			
112	2.178	30	120	2.450	25			
105	1.880	5	021	2.30	10			
			211	2.18	10			

* Crystallographic parameter, Å: AlP a_{exp} = 5.49; NbP a_{exp} = 3.39, c_{exp} = 11.39; MoP a_{exp} = 3.29, c_{exp} = 3.21; WP a_{exp} = 5.78, b_{exp} = 3.24, c_{exp} = 6.29; CrP a_{exp} = 6.11, b_{exp} = 5.39, c_{exp} = 3.10.

Table 2. Crystallographic parameters of unit cells of monophosphides

Compound	Space group	a_{theor}	b_{theor}	c_{theor}	V_{exp}, Å	Z_{theor}	ρ_{theor}, g cm^{-3}
		Å					
AlP	F43*m*	5.467	–	–	163.40	4	2.194
NbP	$I4_1md$	3.334	–	11.377	126.46	4	6.668
MoP	P6*m*2	3.222	–	3.191	120.00	1	1.756
WP	P*nma*	5.732	3.249	6.222	115.87	4	12.43
CrP	P*bcm*	6.108	5.36	3.11	101.82	4	5.45

The contents of metals and phosphorus in the resulting crystalline phases were determined by X-ray fluorescent analysis on a VRA-20 instrument. According to this analysis, we assigned the following empirical formulas to the obtained crystalline phases: AlP (Al 42.59 and P 56.81 wt %), CrP (Cr 64.96 and P 35.83 wt %), NbP (Nb 75.05 and P 24.5 wt %), MoP (Mo 75.59 and P 23.91 wt %), and WP (W 85.58 and P 13.52 wt %). The X-ray patterns of the powders were recorded on a DRON-3 instrument using Cu_{K_α} radiation (λ = 1.54178 Å) and processed using the LATEX program and the ASTM structural database. The obtained results are given in Table 1.

The calculated crystallographic unit cell parameters a_{exp}, b_{exp}, and c_{exp} for the obtained phosphides agree with the data of the ASTM file (a_{theor}, b_{theor}, and c_{theor}) (Table 2). To optimize the synthesis conditions and to substantiate theoretically the data obtained, we calculated ΔH^0_{298}, ΔS^0_{298}, ΔG^0_{298}, and ΔG^0_{1273} for reactions (1)–(5) on the basis of standard thermodynamic functions [5–7] of the starting substances and reaction products. The calculations proved that these reactions are possible in the temperature range 298–1273 K (Table 3). The thermodynamic functions ΔS^0_{298} for the phosphides were calculated according to the additivity law.

Table 3. Thermodynamic parameters of reactions (1)–(5)

Reaction	ΔS^0_{298}, J mol^{-1} K^{-1}	ΔH^0_{298}	ΔG^0_{298}	ΔG^0_{1273}
		kJ mol^{-1} of phosphide		
(1)	–76.0	–1188.5	–1165.6	–1101.2
(2)	37.4	–1411.9	–1019.5	–1047.6
(3)	14.3	–653.3	–657.6	–671.5
(4)	13.0	–9.1	–13.1	–22.1
(5)	14.3	9.8	5.5	–8.4

In the case of reaction (1), (preparation of aluminum phosphide AlP), despite the negative ΔS^0_{298} value (–76 J mol^{-1} K^{-1}), the value of $\Delta_f H^0_{298}$ for the resulting aluminum oxide (–1676.81 kJ mol^{-1}) strongly affects the ΔG^0 of the reaction, which becomes negative at both 298 and 1273 K.

Theoretically, reaction (2) (synthesis of chromium monophosphide), which yields thermally stable chromium(III) oxide, is possible even at room temperature: ΔG^0_{298} = –1019.5 kJ mol^{-1} of the phosphide. To prepare M_2O_3 oxides by reactions (1) and (2), the values $\Delta_f H^0_{298}$ for their formation must be about –1 MJ mol^{-1}. In the case of formation of MO_2 oxides, the reaction would be intensive only when $\Delta_f H^0_{298}$ is within the limits –0.8…–1 MJ mol^{-1}. Greater negative values of both ΔG^0_{298} and ΔG^0_{1273} K for reaction (4) (synthesis of molybdenum phosphide), compared with reaction (5) (synthesis of tungsten phosphide), are attributable to the negative value of ΔH^0_T for reaction (4). This means that molybdenum has greater affinity to phosphorus than tungsten and also confirms the empirical rule which states that the stability of phosphides in subgroups of *d* metals decreases with increasing atomic weight of metal.

CONCLUSIONS

(1) The conditions of monophosphide syntheses (1)–(5) were optimized in accordance with thermodynamic calculations.

(2) It was shown that niobium, aluminum, chromium, tungsten, and molybdenum monophosphides can be synthesized by gas-transport reactions in M–$LiPO_3$ systems.

REFERENCES

1. *Handbuch der Praparativen Anorganischen Chemie*, Brauer, G., Ed., Stuttgart: Stuttgart Enke, 1960
2. Van Wazer, J.R., *Phosphorus and its compounds*, New York, 1958–1961.
3. Zumbusch, M. and Blitz, W., *Z. Anorg. Allgem. Chem.*, 1941, vol. 249, pp. 30–37.
4. Hartmann, H. and Orban, J., *Z. Anorg. Allgem. Chem.*, 1936, vol. 226, p. 257.
5. *Fiziko-khimicheskie svoistva oksidov: Spravochnik* (Physicochemical Properties of Oxides: Reference Book), Samsonov, G.V., Ed., Moscow: Metallurgiya, 1978.
6. *Termodinamicheskie svoistva neorganicheskikh veshchestv: Spravochnik* (Thermodynamic Properties of Inorganic Substances: Reference Book), Zefirov, A.P., Ed., Moscow: Atomizdat, 1965.
7. Gordienko, S.P., *Termodinamicheskie kharakteristiki tverdykh binarnykh fosfidov* (Thermodynamic Characteristics of Solid Binary Phosphides), Kiev: Izd. Inst. Problem Mater., 1987.

Russian Journal of Applied Chemistry, Vol. 74, No. 8, 2001, pp. 1278–1284. Translated from Zhurnal Prikladnoi Khimii, Vol. 74, No. 8, 2001, pp. 1242–1248.

INORGANIC SYNTHESIS AND INDUSTRIAL INORGANIC CHEMISTRY

Optimization of Sodium Sulfite Production on the Basis of Graphical Analysis of Solubility Diagrams for Systems $Na^+, NH_4^+//Cl^-, SO_3^{2-}–H_2O$ and $Na^+, NH_4^+//Cl^-, HSO_3^-–H_2O$

O. B. Dormeshkin, A. F. Minakovskii, and N. I. Vorob'ev

Belorussian State Technological University, Minsk, Belarus

Received April 16, 2001

Abstract—The solubility was studied in the systems Na_2SO_3–NaCl–NH_4Cl–$(NH_4)_2SO_3$–H_2O at 20 and 40°C and NH_4HSO_3–$NaHSO_3$–NaCl–NH_4Cl–H_2O at 40°C by the graphic-analytical method. The obtained results were used to choose the most efficient method for obtaining sodium sulfite by conversion and to substantiate the optimal temperature condition of the process. The data obtained in studying stages of conversion of ammonium sulfate solution with sodium chloride and crystallization of a by-product—ammonium chloride, made it possible to find the optimal technology of the closed cyclic process.

The conversion technologies for inorganic salt production are widely used because of their simplicity, high intensity, and efficiency. They are among the main techniques employed to manufacture chlorine-free potassium fertilizers. The conversion technology also underlies methods for obtaining potassium sulfite from ammonium sulfate and sodium chloride. The practical use of this technique obviates the necessity for soda ash, thereby reducing the cost of the target product. There have been reports that sodium chloride can be used to obtain sodium sulfite [1]; however, they cannot serve as a basis for practical implementation of the given method, being scanty. In particular, the optimal pathway of the conversion and the choice of the temperature conditions have not been substantiated to a sufficient extent. The problems associated with water balances and with the possibility of performing a closed cyclic process have not been considered in the literature at all.

The conversion method for obtaining sodium sulfite is based on processes occurring in aqueous mutual salt systems Na_2SO_3–NaCl–NH_4Cl–$(NH_4)_2SO_3$–H_2O (sulfite system) and NH_4HSO_3–$NaHSO_3$–NaCl–NH_4Cl–H_2O (hydrosulfite system) at temperatures ranging from 20 to 85°C. Since there are no published data on solubility in these systems in a sufficiently wide temperature range, prognosticating how the composition of solutions of the sulfite and hydrosulfite systems varies with temperature and optimizing the technological cycle seems to be rather complicated and problematic task.

To solve this problem, the solubility in the sulfite and hydrosulfite systems has been studied and new data have been obtained for the solubility in the sulfite system at 20 and 30°C and in the hydrosulfite system at 40°C [2]. The obtained results were used to plot solubility isotherms and their water projections at 20–85°C for the sulfite system and 25–60°C for the hydrosulfite one. This served as a theoretical basis for optimizing the conversion of sodium chloride to give sodium sulfite.

Three most feasible variants of the given technological process were chosen (see the scheme). These variants were analyzed using the graphic-analytical method for studying solubility diagrams in the sulfite and hydrosulfite systems at various temperatures [3]. The obtained results made it possible to determine the optimal variant and to substantiate some technological parameters of the process.

As the main criterion for choosing the optimal variant of the process served the maximum yield of the target process at the minimum power consumption. In addition to establishing the optimal pathway of the process, the graphic-analytical analysis of solubility diagrams was used to determine the optimal temperature conditions of crystallization stages of the target product and by-product.

1070-4272/01/7408-1278 $25.00 © 2001 MAIK "Nauka/Interperiodica"

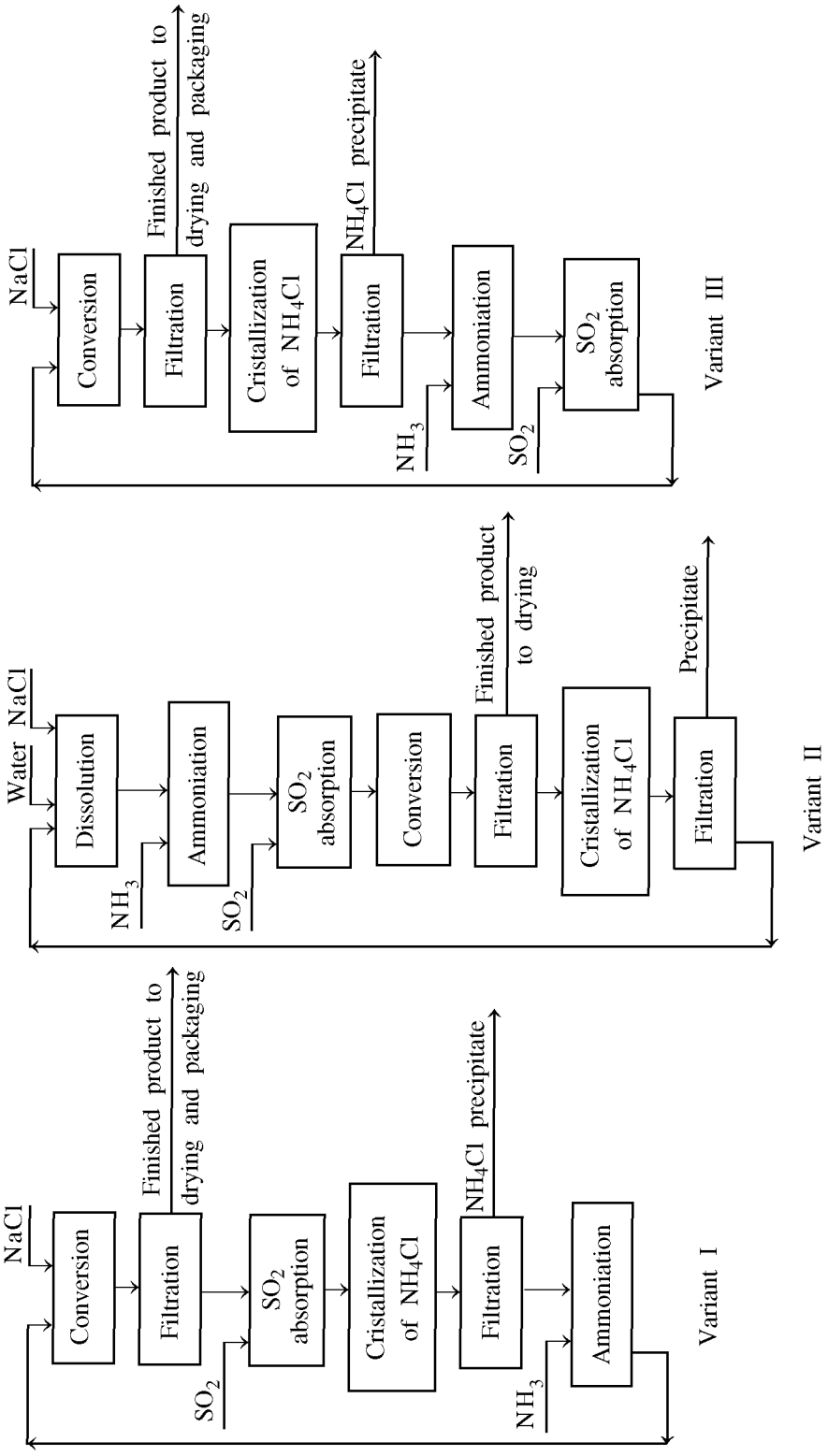
NaCl
Conversion
Filtration
Finished product to drying and packaging
Cristallization of NH_4Cl
Filtration
NH_4Cl precipitate
Ammoniation
NH_3
SO_2
SO_2 absorption
Variant III
Water
NaCl
Dissolution
NH_3
Ammoniation
SO_2
SO_2 absorption
Conversion
Filtration
Finished product to drying
Cristallization of NH_4Cl
Filtration
Precipitate
Variant II
NaCl
Conversion
Filtration
Finished product to drying and packaging
SO_2
SO_2 absorption
Cristallization of NH_4Cl
Filtration
NH_4Cl precipitate
NH_3
Ammoniation
Variant I

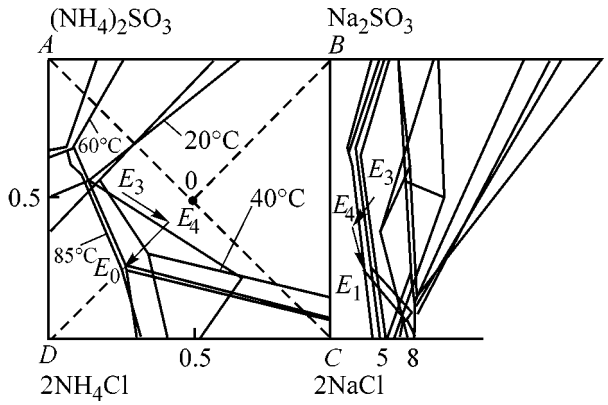

Fig. 1. Solubility diagram for the system Na_2SO_3–NaCl–NH_4Cl–$(NH_4)_2SO_3$–H_2O (sulfite diagram).

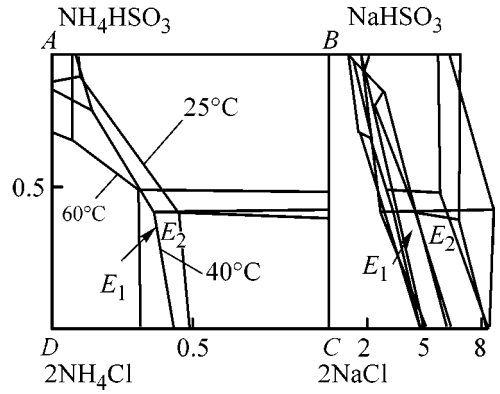

Fig. 2. Solubility diagram for the system NH_4HSO_3–$NaHSO_3$–NaCl–NH_4Cl–H_2O (hydrosulfite diagram).

Variant I, chosen for comparison, was described in [1], but its detailed analysis based on graphic-analytical method for studying the solubility in the corresponding aqueous-salt systems have not been performed so far. In the general form, this is a cyclic process whose initial stage is production of an ammonium sulfite solution via absorption of sulfur dioxide by ammonia solution by the reaction

$$2NH_3 + H_2O + SO_2 = (NH_4)_2SO_3. \quad (1)$$

Further, an equimolar amount of sodium chloride is introduced into the resulting solution

$$(NH_4)_2SO_3 + 2NaCl = Na_2SO_3 + 2NH_4Cl. \quad (2)$$

The figurative point of the salt system formed upon introduction of an equimolar amount of sodium chloride lies at the intersection of diagonals (point 0) of the solubility diagram of the sulfite system (Fig. 1). In the temperature range 20–80°C, point 0 lies within the crystallization field of Na_2SO_3. Therefore, the salt system is a suspension whose solid phase consists of sodium sulfite which crystallizes along ray *B*0 from point 0 to the intersection with the crystallization field of ammonium chloride (point E_0). Further, ammonium chloride (by-product) should be isolated into the solid phase from the mother liquor (point E_0). Otherwise, the finished product will be strongly contaminated with ammonium chloride in the case of a closed, with respect to the liquid phase, process (recycling of the mother liquor). For this purpose, the mother liquor is saturated with sulfur dioxide in the proposed variant to convert sulfite into hydrosulfite by the reaction

$$Na_2SO_3 + SO_2 + H_2O = 2NaHSO_3. \quad (3)$$

The composition of the system formed in this case will be represented by a figurative point E_1 in the solubility diagram of the hydrosulfite system NH_4HSO_3–$NaHSO_3$–NaCl–NH_4Cl–H_2O (Fig. 2). As it can be seen from the diagram, the figurative point E_1 lies within the crystallization field of ammonium chloride at below 60°C. Consequently, a sufficient amount of the by-product can be isolated into the solid phase by cooling the solution of the above-mentioned composition. (point E_1). However, it should be mentioned that intermediate isolation of NH_4Cl can be achieved in both the hydrosulfite and sulfite systems. The main criterion for selecting a system in which intermediate isolation of ammonium chloride is feasible is the parameter "optimal yield of ammonium chloride."

As seen from reaction (2), two moles of NH_4Cl are to be removed from the system per every mole of the forming sodium sulfite in accordance with the stoichiometric equation. That yield of ammonium chloride is to be considered optimal for which a stoichiometric, or a somewhat greater amount of NH_4Cl is isolated into the solid phase. If the actual amount of isolated ammonium chloride much exceeds the optimal value, then the ammonia consumption will be much greater. Otherwise, the excess amount of ammonium chloride will pass into the solid phase in the stage of crystallization of the target product, contaminating it.

Thus, to find the most efficient technological way to isolate ammonium chloride (sulfite or hydrosulfite system), it is necessary to determine the theoretical optimal yield of ammonium chloride and further compare the actual yields for the sulfite and hydrosulfite systems. This can be done in graphical analysis of the crystallization stages of ammonium chloride in the systems under consideration.

After separating ammonium chloride by the given procedure, ammonia is introduced into the solution to obtain ammonium sulfate and convert the hydrosulfite system into the sulfite one

$$2NaHSO_3 + 2NH_3 = Na_2SO_3 + (NH_4)_2SO_3. \quad (4)$$

The composition of the system upon ammoniation is represented in the sulfite diagram by a figurative point E_3 lying within the crystallization field of sodium sulfite. The obtained solution is recycled into the stage of conversion with sodium chloride. Graphically, the course of sodium sulfite formation is represented by a broken line $E_3E_4E_0$ (Fig. 1), where segment E_3E_4 corresponds to dissolution of sodium chloride, and segment E_4E_0 of the crystallization conode B_0E, directly to crystallization of sodium sulfite.

The results obtained in studying the solubility isotherms in the systems Na_2SO_3–NaCl–NH_4Cl–$(NH_4)_2SO_3$–H_2O and NH_4HSO_3–$NaHSO_3$–NaCl–NH_4Cl–H_2O served as a basis for calculating theoretically the optimal pathway of the process and substantiating graphically the temperatures of separate stages. With this aim in view, the compositions of the starting and intermediate solutions at varied temperature were first calculated. Then the optimal temperature conditions of conversion of ammonium sulfate with sodium chloride and isolation of the by-product were determined by means of graphical analysis. For this purpose, the yields of sodium sulfite and ammonium chloride were calculated at varied temperature [4]. The yield of crystalline Na_2SO_3, $W_{Na_2SO_3}$, was calculated with respect to the total content of Na_2SO_3 in the starting solution.

A preliminary calculation based on the solubility diagrams of the sulfite system (water projections) demonstrated that the concentration of the initial ammonia solution should be 14.8 wt % NH_3. Saturation with gaseous sulfur dioxide of an ammonia solution with this concentration yields an ammonia sulfite solution containing 39.4 wt % $(NH_4)_2SO_3$. After mixing this solution with sodium chloride and separating the precipitating sodium sulfite, the composition of the mother liquor is represented by the figurative point E_0 corresponding to a triple eutonics of the sulfite system. According to a calculation based on published data on the solubility at 85°C, the eutonic solution E_0 contains 32.6 wt % NH_4Cl and 13.4 wt % Na_2SO_3 (85°C). The calculated theoretical yields of sodium sulfite into the solid phase are presented below in relation to the conversion temperature of ammonia solution, T_{cn}:

T_{cn}, °C	$W_{Na_2SO_3}$, %
40	52.4
60	62.4
85	65.1

The yield of sodium sulfite was not calculated at temperatures below 40°C since at < 33.4°C the precipitate is only composed of sodium sulfite heptahydrate $Na_2SO_3 \cdot 7H_2O$, which is not the target product in the technology being developed.

The highest yield of crystalline sodium sulfite is observed at the temperature of ammonium sulfite conversion and, correspondingly, at the temperature of crystallization of sodium sulfite, equal to 85°C. Consequently, the optimal temperature of the stage of Na_2SO_3 crystallization is 80–85°C. This is also indicated by the configuration of the diagrams (Fig. 1), according to which the working solutions are 1.7–2 times more dilute at 40°C, compared with similar solutions at 60 and 85°C.

However, the most important problem in obtaining sodium sulfite by a process of this kind is mother liquor utilization. This solution should be either discharged into a slurry pond or processed in a cyclic manufacture of sodium sulfite, envisaging its intermediate discharge as a by-product. Since the solubility of NH_4Cl decreases as temperature is lowered, isolation of the by-product into the solid phase will occur on cooling a saturated ammonium chloride solution.

The yield of the NH_4Cl precipitate into the solid phase was calculated with respect to the total content of ammonium chloride in the starting solution. Calculations of the theoretical yield of ammonium chloride, W_{NH_4Cl}, into the solid phase upon cooling of solutions with composition corresponding to the composition of the system at the eutonic points E_0 and E_1 in the hydrosulfite system at different crystallization temperatures T_{cr} give the following results

T_{cr} NH_4Cl, °C	W_{NH_4Cl}, %
60	23.3
40	40.2
25	58.7

The stoichiometric yield of ammonium chloride, calculated for reaction (2), is 34.9% relative to its content in solution. Consequently, that yield of crystalline ammonium chloride is to be considered optimal, which is the closest to the stoichiometric value, but is no less than 34.9%.

Table 1. Physicomechanical properties of NH_4Cl crystals in relation to crystallization temperature*

T_{cr}, °C	H, wt %	L, μm	$K_f \times 10^5$, cm s^{-1}
40	11.4	24.3	1.1
30	32.75	28.9	0.89
25	43.33	35.6	0.78

* H is humidity, L crystal fragment size, and K_f filtration coefficient.

To verify the theoretical data, experiments were carried out to determine the actual yield of ammonium chloride into the solid phase on cooling to different temperatures a solution corresponding to point E_1 of the hydrosulfite system. The obtained results are presented below.

T_{cr} NH_4Cl, °C	W_{NH_4Cl}, %
50	28.1
40	39.3
30	52.4
25	58.7

As seen from the obtained results, the practical yield of ammonium chloride, equal to 39.3%, is the closest to the theoretical (calculated) value at 40°C. It should be mentioned for comparison that at a temperature of 25°C, recommended in [1], the yield of ammonium chloride into the solid phase is 58.7%, which is nearly 50% higher than the optimal value. Moreover, lowering the crystallization temperature to 20–25°C involves additional consumption of energy for cooling and the subsequent heating of the reaction mixture. Cooling the solution to 40°C leads, in addition to lower consumption of ammonia, to much lower energy expenditure and shorter process duration, and, consequently, to a higher intensity of sodium sulfite manufacture.

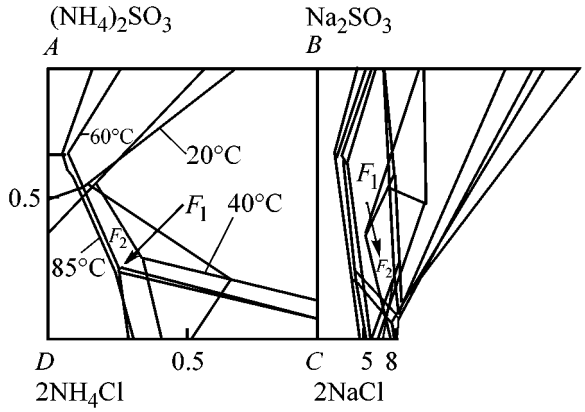

Fig. 3. Solubility diagram for the system Na_2SO_3–NaCl–NH_4Cl–$(NH_4)_2SO_3$–H_2O (variant II).

Also, as shown by additional investigations (Table 1), lowering the crystallization temperature entails a significant deterioration of the physicomechanical properties of ammonium chloride (the humidity of the precipitate becomes much higher and its filterability is impaired). Judging from data furnished by optical microscopy, the present case involves accreted dendrite composed of spherical ammonium chloride fragments, rather than individual crystals.

It is the formation of dendrites that accounts for the lack of correlation between the physicomechanical properties of the NH_4Cl precipitate formed at different temperatures and the size of its fragments.

It should be kept in mind that moisture contained in the humid cake is nothing other than mother liquor saturated at this temperature. In drying of a precipitate, the ingredients of the mother liquor pass into the product, contaminating it. This is confirmed by the results of an X-ray phase analysis of ammonium chloride precipitates for different crystallization temperatures. For example, an X-ray diffraction pattern of a precipitate obtained by cooling the starting solution to 25°C contains additional peaks corresponding to sodium chloride. At the same time, there are no such peaks in the X-ray pattern of the precipitate obtained on cooling the solution to 40°C.

The studies performed suggest that 40°C should be considered the optimal temperature in the stage of by-product isolation—crystallization of ammonium chloride. This conclusion is confirmed by a comparative calculation of material and heat balances of the cyclic process at cooling temperatures in the crystallization stage of 25 and 40°C. Comparison of the results obtained in calculating the heat balance shows that performing the crystallization at 40°C lowers the consumption of circulating water by 18.7% (by 1628.9 m^3 per 1000 kg of Na_2SO_3) as compared with the cooling of the starting solution in this stage to 25°C.

Another possible way to obtain sodium sulfite is conversion of a saturated sodium chloride solution after its preliminary ammoniation, with subsequent neutralization of ammonia with gaseous sulfur dioxide. The course of this variant of the process is described by the functional scheme. At a NaCl : $(NH_4)_2SO_3$ molar ratio of 2 : 1, the figurative point of the system, F_1, lies at intersection of the diagonals of the sulfite diagram (Fig. 3), and crystallization of sodium sulfite will occur at a temperature of 60–85°C in the resulting system Na_2SO_3–NaCl–NH_4Cl–$(NH_4)_2SO_3$–H_2O. It may be assumed that, since diffusion processes at

the phase boundary (dissolution of sodium chloride) are ruled out with the process carried out in this way, high-purity sodium sulfite can be obtained.

A graphical analysis of the given process demonstrated that, to obtain as a result of conversion a eutonic solution of composition corresponding to point E_0 (13.4 wt % Na_2SO_3, 32.6 wt % NH_4Cl; Fig. 4), at which the yield of sodium sulfite is at a maximum, the starting sodium chloride solution must have a concentration of 37.3 wt %. However, such a solution cannot be prepared in principle, since the solubility of sodium chloride at 80°C is 27.6 wt %. With a 27.6% solution of sodium chloride used as a basis, the solution after introduction of an equivalent amount of ammonium sulfite will be described by point F_1 (Fig. 3), corresponding to the intersection of diagonals of the sulfite diagram, with water coordinate I = 5.35 mole H_2O/1 mole of a sum of dry salts. After crystallization and separation of sodium sulfate, the mother liquor contains 14.8 wt % Na_2SO_3 and 23.1 wt % NH_4Cl, has a water coordinate I = 6.28 mole H_2O/1 mole of a sum of dry salts, and is represented in the sulfite diagram by point F_2 (Fig. 3). Consequently, the position of the segment F_1F_2 in the diagram indicates a substantial dilution of the working solution, much impairing the efficiency of the process. The theoretical yield of sodium sulfite into the solid phase does not exceed 45.6% of its total content in the starting solution, which is 20% lower than the value in the case of a process employing sodium chloride in crystalline form. Therefore, the given variant of the process cannot be considered optimal and recommended for practical use.

Variant III of obtaining sodium sulfite by conversion consists in that the process is only performed in the sulfite system. The functional scheme of such a process is presented in Fig. 4. The process is carried out in a closed technological cycle. The base solution is the mother liquor with removed sodium sulfite, containing 13.4 wt % Na_2SO_3 and 32.6 wt % NH_4Cl, which corresponds to the composition of the system at the figurative point E_0. The ammonium chloride byproduct is isolated by cooling the base solution, with the subsequent filtration of the resulting suspension (segment E_0X_2 of the crystallization ray DX_2). Thus, under the optimal conditions, the course of the cyclic process for obtaining sodium sulfite by the given variant is described in the sulfite diagram (Fig. 4) by the broken line $E_0X_2E_3E_4E_0$.

The results obtained in a graphical calculation of the yield of ammonium chloride in cooling a solution

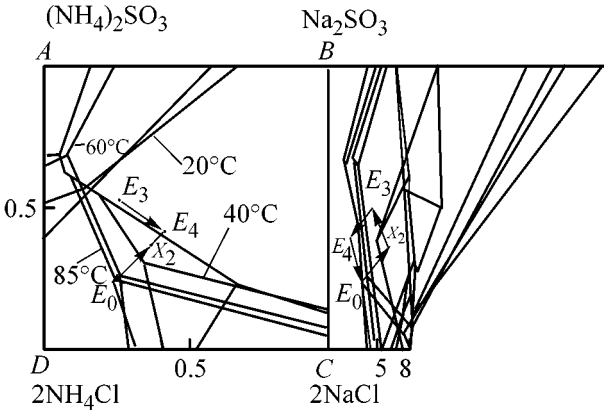

Fig. 4. Solubility diagram for the system Na_2SO_3–NaCl–NH_4Cl–$(NH_4)_2SO_3$–H_2O (variant III).

in the sulfite system to different crystallization temperatures are presented below.

T_{cr} NH_4Cl, °C	W_{NH_4Cl}, %
60	2.7
40	26.7
20	54

Analysis of the obtained data shows that the yield of ammonium chloride in the sulfite system is much lower than that in the hydrosulfite system at about the same temperatures. For example, in cooling a eutonic solution (point E_0) to 60°C in the sulfite system, the yield of crystalline NH_4Cl is 2.7%, and the yield in the hydrosulfite system at the same temperature, 25.2%. To isolate in the crystallization stage the optimal, stoichiometric amount of ammonium chloride (34.9%) when carrying out the given process in the sulfite system, the base solution is to be cooled to below 30°C, whereas in the hydrosulfite system the theoretical yield is 40.2% even at 40°C (actual yield 39.3%). Consequently, performing the stage of ammonium chloride isolation in the sulfite system at 40°C will fail to ensure isolation of the amount of ammonium chloride required by stoichiometric calculations and will lead to its accumulation in the system, with the yield of the target product lowered and the product contaminated. At the same time, crystallizing ammonium chloride at lower temperatures (below 30°C) will lead to much higher energy consumption as compared with carrying the process out in the hydrosulfite system (by variant I).

Thus, the performed graphical analysis of the possible ways to obtain sodium sulfite by conversion, based on the solubility diagrams for the systems Na_2SO_3–NaCl–NH_4Cl–$(NH_4)_2SO_3$–H_2O and NH_4HSO_3–$NaHSO_3$–NaCl–NH_4Cl–H_2O, made it possible to select the optimal variant of such a process and substantiate its optimal temperature conditions.

Table 2. Compositions of solutions used in a cyclic process for production of sodium sulfite*

Solution	Composition, wt %		
	SO_3^{2-}	Cl^-	NH_4^+
Mother liquor after separation of Ns_2SO_3	6.8 / 6.57, 6.7, 6.38	21.63 / 21.7, 19.4, 21.8	10.97 / 9.3, 9.7, 11.3
After absorption of SO_2	12.74 / 12.9, 12.8, 12.4	20.25 / 19.4, 21.9, 20.8	10.27 / 10.0, 9.6, 10.0
Mother liquor after separation of NH_4Cl	14.28 / 12.0, 15.1, 14.0	14.46 / 16.8, 16.4, 15.8	7.48 / 6.6, 7.5, 8.1
Ammoniated	13.74 / 11.1, 11.3, 11.3	14.2 / 15.5, 14.8, 14.5	11.2 / 12.2, 11.4, 11.1

* Numerator: theoretically calculated content of particles; denominator: actual content of particles in solution.

Variant I should be regarded as the optimal since it ensures the highest yield of the target product (65.2%) at the lowest energy expenditure for isolation of the by-product. In this case, crystalline sodium chloride is used as sodium-containing raw material without preliminary dissolution, and the target product (NH_4Cl) is isolated in the hydrosulfite system on cooling the solution to 40°C.

To confirm the validity of the conclusions made in the graphic-analytical study, a set of experiments was carried out in order to obtain sodium sulfite in a closed technological cycle in accordance with the theoretically substantiated optimal technological parameters. Three successive cycles were performed in the experiments. The working solution compositions are presented in Table 2.

The obtained data suggest that the process of sodium sulfite production is stable since the solution compositions in the same stages, but different cycles are identical. The actual solution compositions are close in content of the basic ions to the solution compositions calculated from the theoretically substantiated optimal parameters of the process.

CONCLUSION

As a result of the investigations performed, the most efficient pathway and the optimal technological parameters of sodium sulfite production in conversion with sodium chloride were substantiated theoretically and verified experimentally. The obtained data can serve as a basis for developing a full-scale technological installation and setting-up industrial manufacture of the given product.

REFERENCES

1. Pozin, M.E., *Tekhnologiya mineral'nykh solei* (Technology of Mineral Salts), Leningrad: Khimiya, 1970, part 1.
2. Vorob'ev, N.I., Dormeshkin, O.B., and Minakovskii, A.F., *Vestsi Nats. Akad. Nauk Belarusi, Ser. Khim. Navuki*, 1999, no. 2, pp. 114–117.
3. Viktorov, M.M., *Graficheskie raschety v tekhnologii neorganicheskikh veshchestv* (Graphical Calculations in Technology of Inorganic Substances), Leningrad: Khimiya, 1972.
4. Sokolovskii, A.A., *Zh. Prikl. Khim.*, 1956, vol. 29, no. 5, pp. 743–752.

Russian Journal of Applied Chemistry, Vol. 74, No. 8, 2001, pp. 1285–1288. Translated from Zhurnal Prikladnoi Khimii, Vol. 74, No. 8, 2001, pp. 1249–1252.

PHYSICOCHEMICAL STUDIES OF SYSTEMS AND PROCESSES

A Study of Liquid–Vapor Phase Equilibrium in Binary Organic Mixtures

N. N. Gorlova, T. M. Gredneva, S. A. Vasil'eva, L. V. Polyakova, and L. F. Komarova

Polzunov Altai State Technical University, Barnaul, Russia

Received July 5, 1999; in final form, September 2000

Abstract—The liquid–vapor equilibrium was studied experimentally in the following binary systems: ethyl cellosolve–toluene, acetone–ethyl cellosolve, butanol–ethyl cellosolve, and butyl acetate–toluene. The obtained experimental data are described mathematically in terms of the Wilson equation, and parameters characterizing the concentration dependence of the component activity coefficients are calculated.

In plants of various branches of industry, where organic solvents are used, spent mixtures form a flow of toxic liquid wastes whose discharge into the environment is unacceptable. This makes necessary the development of technologies for recovering the starting solvents from the wastes and recycling them, and just this is the goal of the present study. Spent mixtures containing alcohols, ethers and esters, ketones, and aromatic hydrocarbons frequently undergo thermal destruction, which accounts for 26 to 35% of the total loss in the technological process [1].

As a mixture for study was chosen a 646 solvent widely used in the national economy. In addition, its three-, four- and five-component constituents are independent commercial products with their own brand names (647, 648, 650, and KR-36 solvents). The mixture under study contains (wt %): acetone (AC) 7, ethanol (E) 15, butanol (B) 10 toluene (T) 50, butyl acetate (BA) 10 and ethyl cellosolve (EC) 8. Spent solvents contain varied amount of water.

The components of the mixture under study belong to different classes of organic compounds and, depending on their functional groups, differ in polarity, density, boiling point, viscosity, vapor pressure, etc. The components of a number of binary and ternary constituents have close boiling points, which suggests possible formation of azeotropes with different numbers of components.

The most common methods for processing of liquid wastes in order to recycle the valuable components are various distillation and rectification techniques [2]. The choice of one of the possible variants is governed by the requirements to the quality of recovered products, by the physicochemical properties of the components being separated, and by a number of other requirements. Since the composition and volume of spent solvents vary widely, the following requirements to the technology were formulated: it must be versatile, the processing technique must uniform, the apparatus employed sufficiently simple, and the cost of mixture processing low. These requirements are met by the batch rectification methods, chosen as the basis in the present study.

The development of a technique for separating a mixture under study assumes that data are available on the vapor–liquid equilibrium in a certain range of temperatures and pressures, corresponding to the industrial conditions. Published data on the vapor–liquid equilibrium could be found for the following systems: acetone with butyl acetate, toluene, butanol, ethanol, or water; butyl acetate with butanol, water or ethyl cellosolve; butanol with water, toluene, ethanol, or butyl acetate; and ethanol with ethyl cellosolve, toluene, or water [3, 4]. Data for the binary constituents toluene–butyl acetate, ethyl cellosolve–acetone, and butanol–toluene could not be found in the literature and were obtained experimentally using the known methods [3] at a pressure of 760 mm Hg.

In the first stage of the study, the starting substances were purified [5]. The achieved purity was evaluated by the boiling point, refractive index, and results of a chromatographic analysis on a commer-

1070-4272/01/7408-1285 $25.00 © 2001 MAIK "Nauka/Interperiodica"

Table 1. Parameters of liquid–vapor equilibria in binary systems

System	Content of components, mol %		bp, °C
	in liquid X_1	in vapor Y_1	
AC(1)–EC(2)	0.1548	0.5306	115.2
	0.2357	0.6750	106.3
	0.4931	0.8853	86.0
	0.7400	0.9679	70.3
	0.9010	0.9989	60.1
B(1)–EC(2)	0.1100	0.3006	126.9
	0.1200	0.3200	125.8
	0.3210	0.5300	122.2
	0.5500	0.6300	119.2
	0.6300	0.7109	117.9
	0.8400	0.8600	117.6
T(1)–BA(2)	0.1046	0.1627	123.9
	0.2870	0.3917	119.9
	0.3993	0.5109	118.4
	0.4999	0.6082	117.3
	0.6528	0.7422	115.0
T(1)–EC(2)	0.2100	0.3250	120.4
	0.3500	0.4750	115.6
	0.4000	0.5500	114.6
	0.5500	0.6760	113.0
	0.6750	0.7500	111.6
	0.8500	0.8600	110.7
	0.8900	0.8900	110.2
	0.9500	0.9400	110.5

Table 2. Constants of the Antoine equation

Component	Constant		
	A	*B*	*C*
AC	7.05860	1162.88	222.105
B	7.42530	1425.13	196.033
T	6.98010	1358.85	220.840
BA	7.13180	1435.13	211.377
EC	7.81910	1801.90	230.000
E	8.714631	1927.839	252.0518
H_2O	8.101019	1748.83	235.0123

cial LKhM-80 chromatograph, version 1, with heat conductivity detector and programmed temperature control units. Individual substances and aqueous–organic mixtures were analyzed using combined gas-liquid and gas-adsorption chromatography. The content of water was determined using SEPARON porous polymer as adsorbent. Tests with various fixed phases demonstrated satisfactory results in analysis of the organic constituents of the solvent on a XROMATON-N-AW-DMCS phases modified with polyethylene glycol with molecular weight of 1500. The obtained chromatograms were processed using an I-02 integrator. The composition of the mixtures being analyzed was calculated by the method of normalization of peak areas with account of correction coefficients [6].

The liquid–vapor equilibrium was studied by analyzing the dependences of the boiling point and vapor phase composition on the composition of the liquid phase (*X*–*Y*–*T*) under isobaric conditions (*P* = 760 mm Hg) with the use of a Jillespi circulation device [3]. The binary systems under study were prepared by means of gravimetry. The boiling point was measured with a mercury thermometer to within 0.1°C, with account taken of the corrections for pressure and the projecting mercury column [5]. The obtained experimental data on the liquid–vapor equilibrium in the systems studied are presented in Table 1.

The experimental and published data on the liquid–vapor equilibrium in binary systems were described using the Wilson equation [7].

To model the liquid–vapor equilibrium in n-component systems and calculate the rectification process, it is necessary to determine the temperature dependence of the vapor pressures of individual substances, given by the Antoine equation

$$\log P_0 = A - B/(C + T),$$

where P_0 is pressure (mm Hg); T temperature (K); A, B, and C the constants of the Antoine equation.

The constants listed in Table 2 were further used to describe mathematically the liquid–vapor equilibrium in terms of the Wilson equation.

The obtained binary interaction parameters for two-component constituents of a mixture under study, λ_{12} and λ_{21}, are presented in Table 3 together with average and maximum deviations of the boiling point.

As reliability criterion for the obtained parameters may serve modeling of the liquid–vapor equilibrium in ternary systems and comparison of the results of modeling with experiment. Data on the liquid–vapor equilibrium in ternary subsystems, acetone–toluene–ethyl cellosolve, acetone–butanol–ethyl cellosolve, and toluene–butyl acetate ethyl cellosolve could not be found in the literature and were obtained experimentally.

Table 3. Parameters of the Wilson equation, average and maximum deviations of the boiling point

System	Wilson parameter		Deviation, °C	
	λ_{12}	λ_{21}	ΔT_{av}	ΔT_{max}
AC–EC*	3.8420	0.2608	0.500	0.90
B–EC*	0.3099	1.0860	0.380	0.64
T–BA*	0.5870	1.4170	0.180	0.49
T–B?*	0.8668	0.0379	0.350	0.42
E–BA	1.2820	0.3896	0.014	0.16
BA–EC	1.2860	0.4937	0.016	0.36
E–T	0.2385	0.3450	0.040	0.36
AC–T	0.7094	0.8165	0.011	0.28
AC–E	0.6116	0.8754	0.022	0.41
E–B	1.9310	0.3615	0.090	0.14
AC–B	0.6673	0.7416	0.090	0.56
AC–BA	1.4230	0.4443	0.040	0.60
B–BA	0.8262	0.6274	0.070	0.27
T–B	0.5713	0.4089	0.062	0.14
E–EC	0.8440	1.1850	0.051	0.24
AC–H_2O	0.1657	0.4407	0.011	0.17
H_2O–B	0.5473	0.0146	0.021	0.74
H_2O–EC	1.1120	0.1325	0.030	0.39
H_2O–BA	0.1291	0.0416	0.050	0.70
H_2O–T	0.0162	0.0143	0.071	0.30

* Systems studied experimentally.

For a limited number of points in the concentration field, the dependences of the boiling points on the liquid phase composition were determined as described above. The results obtained in an experimental study of the liquid–vapor equilibrium are presented in Table 4.

The liquid–vapor equilibrium in ternary systems was modeled using the set of binary interaction parameters of the Wilson equation, presented in Table 3. The average and maximum absolute deviations of the calculated and experimental boiling points are presented for ternary systems in Table 5.

Table 5 shows a satisfactory agreement between the calculated and experimental values, suggesting that the binary interaction parameters are reliable.

With the use of the experimental and available published data [8], the existence of azeotropes in the binary and ternary constituents of the solvent under study were established, which markedly hinders the isolation of individual components.

Table 4. Characteristics of liquid–vapor phase equilibria in ternary systems

System	Content of components in liquid, mol %			bp, °C
	X_1	X_2	X_3	
AC(1)–T(2)–EC(3)	9.910	80.07	10.02	94.5
	19.89	59.94	20.17	85.0
	29.61	29.53	40.86	77.4
	55.87	10.50	33.63	65.5
	75.17	2.45	22.38	61.6
AC(1)–B(2)–EC(3)	9.990	80.00	10.01	88.8
	19.62	58.46	21.92	75.2
	40.93	33.75	25.32	66.1
	51.54	17.54	30.92	64.0
	69.99	10.00	20.01	60.8
T(1)–BA(2)–EC(3)	10.12	79.99	9.99	120.0
	20.01	59.99	20.00	118.2
	30.60	23.73	39.67	116.4
	50.00	20.00	30.00	115.1
	70.02	9.99	19.99	112.5

Table 5. Average and maximum deviations of boiling points in ternary systems

System	T_{av}	T_{max}
	°C	
AC–T–EC	0.32	0.61
AC–B–EC	0.28	0.44
T–BA–EC	0.42	0.64

The modeling of the liquid–vapor equilibrium in the ternary constituents revealed an azeotrope—H_2O–toluene–butanol, whose properties were determined with more precision experimentally. Boiling point (°C): H_2O 100, toluene 110.6, butanol 117.3, azeotrope 84.5; concentration (wt %): water 55.0, toluene 42.1; heterogeneous azeotrope.

CONCLUSIONS

(1) The liquid–vapor equilibrium was studied experimentally in the following binary systems: acetone–ethyl cellosolve, butanol–ethyl cellosolve, toluene–butyl acetate, and toluene–ethyl cellosolve.

(2) The Antoine equation parameters were determined for calculating the temperature dependence of the vapor pressure of pure substances.

(3) The obtained experimental data were described mathematically to give a set of binary interaction parameters for the components of the system under

study. This set can be used to model the liquid–vapor equilibrium in multicomponent systems.

(4) The reliability of the binary interaction parameters was confirmed by comparing the calculated and experimental values characterizing the equilibrium in ternary systems.

(5) The modeling of the liquid–vapor equilibrium in the ternary constituents of the system under study revealed a ternary azeotrope—H_2O–toluene–butanol.

REFERENCES

1. Stekol'shchikov, M.N., *Uglevodorodnye rastvoriteli* (Hydrocarbon Solvents), Moscow: Khimiya, 1971.
2. Zharov, V.T. and Serafimov, L.A., *Fiziko-khimicheskie osnovy distillyatsii i rektifikatsii* (Physicochemical Foundations of Distillation and Rectification), Leningrad: Khimiya, 1975.
3. Kogan, V.B., Fridman, V.M., and Kafarov, V.V., *Ravnovesie mezhdu zhidkost'yu i parom* (Liquid–Vapor Equilibrium), Moscow: Nauka, 1966, vols. 1 and 2.
4. Lyudmirskaya, G.S., Barsukova, T.A., and Bogomol'nyi, A.M., *Ravnovesie zhidkost'–par: Spravochnik* (Liquid–Vapor Equilibrium: Reference Book), Bogomol'nyi, A.M., Ed., Leningrad: Khimiya, 1987.
5. Weissberger, A. and Proskauer, E.S., *Organic Solvents. Physical properties and methods of purification,* Riddig, J.A. and Toops, E.E., Eds., New York: Interscience, 1955.
6. Vyakhirev, D.A. and Shushunov, A.F., *Rukovodstvo po gazovoi khromatografii* (Manual of Gas Chromatography), Moscow: Khimiya, 1971.
7. Davydov, A.G., Batch Rectification in Columns of Various Types, *Cand. Sci. Dissertation*, Moscow, 1991.
8. Ogorodnikov, S.K., Lesteva, E.M., and Kogan, I.B., *Azeotropnye smesi: Spravochnik* (Azeotropes: Reference Book), Kogan, V.B., Ed., Leningrad: Khimiya, 1971.

Russian Journal of Applied Chemistry, Vol. 74, No. 8, 2001, pp. 1289–1294. Translated from Zhurnal Prikladnoi Khimii, Vol. 74, No. 8, 2001, pp. 1252–1257.

PHYSICOCHEMICAL STUDIES OF SYSTEMS AND PROCESSES

Dissolving and Selective Properties of Morpholine-based Mixed Solvents

V. G. Kozin and A. A. Mukhamadiev

Kazan State Technological University, Kazan, Tatarstan, Russia

Received December 19, 2000; in final form, April 2001

Abstract—Liquid–liquid phase equilibria were studied in the systems morpholine–monoethanolamine–hexane–benzene, morpholine–mono(ethylene glycol)–hexane–benzene, morpholine–monoethanolamine–heptane–toluene, and morpholine–mono(ethylene glycol)–heptane–toluene at 40, 50, and 60°C. A mathematical description of the phase equilibria in the systems studied was obtained.

A number of requirements, the most important among which are selectivity and dissolving ability, are imposed upon extracting agents used to recover individual aromatic hydrocarbons from reforming catalyzates by liquid extraction techniques. Various solvents have acquired industrial importance [1–4]; however, no solvent has been found up to now, satisfying all the requirements. The main extracting agents used in domestic industry still are tri(ethylene glycol) (TEG) and di(ethylene glycol) (DEG) possessing low selectivity and dissolving ability. In this connection, extraction is commonly performed at a temperature of 150°C and high solvent to raw material mass ratio [(8–15) : 1], which leads to high operation costs. The most promising way to solve this problem is to pass to use of extracting agents of mixed type, whose application will improve the performance characteristics in manufacture of monocyclic aromatic hydrocarbons.

This study is concerned with phase equilibria in liquid–liquid systems formed from hexane–benzene and heptane–toluene model mixtures and morpholine-based binary solvents of varied composition.

EXPERIMENTAL

Liquid–liquid phase equilibria were studied in four-component systems morpholine–monoethanolamine (MEA)–benzene–hexane (**I**), morpholine–mono(ethylene glycol) (MEG)–benzene–hexane (**II**), morpholine–MEA–toluene–heptane (**III**), and morpholine–MEG–toluene–heptane (**IV**). The physicochemical properties of the solvents and hydrocarbons—density and refractive index after purification and drying by known techniques [5]—were in agreement with published data. The content of the second component in morpholine was varied within 35–100 wt % for MEG and 40–100 wt % for MEA. Experiments were performed in sealed thermostated 15-ml test-tubes at 40, 50, and 60°C. The thermostating of the systems under study was done with a UT 2/77 laboratory thermostat to within 0.2°C. The composition of equilibrium phases was determined by gas-liquid chromatography on a Tsvet-500M chromatograph. For each binodal curve, 6 or 7 equilibrium compositions were determined at fixed composition of a binary extracting agent. The sampling of coexisting phases after the attainment of equilibrium was done with a 1-μl chromatographic syringe preliminarily heated to the temperature of experiment. Each solution was analyzed three times under the following conditions: flame ionization detector; flow rates (ml min^{-1}): hydrogen 30, air 300, carrier gas (nitrogen) 30; temperature (°C): column thermostat 140, evaporator and detector 160. A 3-m chromatographic column with 3-mm inner diameter was used, as immobile liquid phase served PEG-20M on Chromaton. The component concentrations were calculated by the internal normalization method, the calibration coefficients for the compounds being analyzed were found by the known procedures [6].

The obtained experimental data on the composition of the coexisting phases for systems (**I**) and (**II**) at 40°C are presented in Tables 1 and 2.

Analysis of the experimental data shows that addition of a second component to morpholine makes the heterogeneous region wider, and at MEA and MEG content exceeding, respectively, 60 and 50 wt %, bi-

1070-4272/01/7408-1289 $25.00 © 2001 MAIK "Nauka/Interperiodica"

Table 1. Composition of equilibrium phases in the system morpholine–ethanolamine–benzene–hexane at varied mixed solvent composition at 40°C

Extract phase, wt %				Raffinate phase, wt %			
hexane	benzene	morpholine	ethanolamine	hexane	benzene	morpholine	ethanolamine
Ethanolamine, 100%							
0.54	0.00	0.00	99.46	99.95	0.00	0.00	0.05
0.56	1.89	0.00	97.55	83.97	15.93	0.00	0.10
0.56	4.08	0.00	95.36	67.74	32.13	0.00	0.13
0.53	6.50	0.00	92.97	54.27	45.51	0.00	0.22
0.49	9.41	0.00	90.10	40.43	59.06	0.00	0.51
0.37	14.0	0.00	85.63	19.53	79.25	0.00	1.22
0.00	20.35	0.00	79.65	0.00	97.50	0.00	2.50
Ethanolamine, 70%–morpholine, 30%							
1.60	0.00	25.65	72.75	88.50	0.00	11.25	0.25
1.55	3.30	23.70	71.45	77.50	10.75	11.45	0.30
1.42	7.24	22.22	69.12	63.87	23.61	12.10	0.42
1.29	10.84	21.01	66.86	51.16	35.44	12.25	1.15
1.17	14.61	21.97	62.25	36.18	47.56	13.14	3.12
0.90	21.00	17.76	60.34	18.04	61.26	16.27	4.43
0.00	32.70	14.99	52.31	0.00	71.93	20.95	7.12
Ethanolamine, 60%–morpholine, 40%							
2.26	0.00	33.63	64.11	86.43	0.00	12.76	0.81
2.21	3.02	31.42	63.35	75.01	9.65	14.39	0.95
2.14	7.04	26.11	64.71	62.65	21.63	14.61	1.11
2.09	11.72	21.89	64.30	49.39	33.12	13.98	3.51
2.02	16.41	19.04	62.53	34.74	42.52	16.46	6.28
1.96	24.50	13.61	59.93	20.46	49.48	20.93	9.13
1.70	32.18	26.59	39.53	8.76	54.16	25.74	11.34
Ethanolamine, 50%–morpholine,50%							
3.07	0.00	43.82	53.11	82.79	0.00	16.86	0.35
3.12	2.08	42.54	52.26	76.39	5.18	17.95	0.48
3.18	4.61	40.97	51.24	70.13	11.01	18.18	0.68
3.22	7.61	38.56	50.61	63.57	17.45	17.98	1.00
3.33	12.72	35.05	48.90	51.03	27.55	18.57	2.85
3.48	20.47	29.68	46.37	35.60	38.30	21.44	4.66
3.71	26.33	29.41	40.55	14.81	45.87	33.39	5.93

nodal opening occurs, enabling production of highly concentrated extracts. With increasing content of the second component in a binary extracting agent, the slope of chords steadily grows. At equal contents of MEA and MEG in morpholine, higher heterogeneity is observed for system (**II**). A common property of systems (**I**)–(**IV**) is the rather high solubility of the extracting agents in the raffinate phase, becoming higher with decreasing content of the second component in the solvent, which is due to the pronounced mutual solubility of morpholine and paraffin hydrocarbons [4]. A similar behavior was observed for the rest of the systems studied at 40, 50, and 60°C.

The phase equilibria in the four-component systems studied were described using complete third-order polynomials of the type

$$Y_i = B_0 + B_1X_1 + B_2X_2 + B_{11}X_1^2 + B_{22}X_2^2 + B_{111}X_1^3 + B_{222}X_2^3 + B_{12}X_1X_2 + B_{122}X_1X_2^2 + B_{112}X_1^2X_2, \quad (1)$$

where B_i are the regression equation coefficients; X_1 the mass fraction of the second component (MEA or MEG) in the extracting agent; X_2 the mass fraction of aromatic hydrocarbon in the extract phase; Y_i the mass fractions of hexane or heptane, and MEA or

Table 2. Composition of equilibrium phases in the system morpholine–ethylene glycol–benzene–hexane at varied mixed solvent composition at 40°C

Extract phase, wt %				Raffinate phase, wt %			
hexane	benzene	morpholine	ethylene glycol	hexane	benzene	morpholine	ethylene glycol
Ethylene glycol, 100%							
0.26	0.00	0.00	99.74	99.90	0.00	0.00	0.10
0.26	1.08	0.00	98.66	82.78	14.12	0.00	0.10
0.24	2.52	0.00	97.24	63.23	36.45	0.00	0.32
0.21	3.51	0.00	96.28	50.93	48.70	0.00	0.37
0.18	4.20	0.00	95.62	46.19	53.32	0.00	0.49
0.10	6.20	0.00	93.70	22.60	74.92	0.00	2.48
0.00	7.11	0.00	92.89	0.10	92.23	0.00	7.67
Ethylene glycol, 75%–morpholine, 25%							
0.63	0.00	23.81	75.56	93.68	0.00	6.14	0.18
0.62	1.94	22.36	75.08	80.39	13.20	6.21	0.20
0.62	3.80	20.29	75.29	66.32	27.21	6.25	0.22
0.61	6.11	18.54	74.74	53.19	39.80	6.58	0.43
0.54	8.45	17.09	73.92	40.10	51.40	7.22	1.28
0.32	11.50	18.92	69.26	22.98	63.55	7.45	6.02
0.00	15.26	21.88	62.86	0.00	78.37	11.41	10.22
Ethylene glycol, 50%–morpholine, 50%							
1.62	0.00	42.68	55.70	86.49	0.00	13.31	0.20
1.82	4.64	40.41	53.13	73.55	12.80	13.33	0.32
1.97	9.40	37.67	50.96	59.78	26.32	12.98	0.92
2.01	16.45	34.21	47.33	43.49	41.23	13.30	1.98
1.85	23.23	30.92	44.00	27.45	52.74	13.48	6.33
1.56	28.60	30.69	39.15	14.52	57.35	18.39	9.74
1.30	38.41	25.25	35.04	6.09	57.80	20.99	15.12
Ethylene glycol, 25%–morpholine, 75%							
4.37	0.00	61.14	34.49	73.99	0.00	24.49	1.52
5.27	3.94	61.05	29.74	66.41	7.09	24.36	2.14
6.54	9.51	59.31	24.64	55.07	17.13	25.24	2.56
8.05	16.16	54.66	21.13	45.65	24.51	26.24	3.60
9.19	21.16	49.55	20.10	35.90	30.95	26.57	6.58
10.57	27.20	42.17	10.06	20.81	32.39	35.59	11.21

MEG, in the extract and raffinate phases, and mass fraction of benzene or toluene in the raffinate phase.

The concentration of morpholine in the extract and raffinate phases was found from the condition $\Sigma Y_i = 1$. The coefficients of Eq. (1) were calculated by the least-squares method. These equations make it possible to determine for each system at an appropriate temperature the content of all the components in coexisting phases, i.e. the family of binodal curves within the region studied. The boundaries of this region are defined by the minimum and maximum concentrations of the second component (MEA or MEG) in the mixed solvent. For example, for systems (**I**) and (**II**) at 40°C these intervals are, respectively, 50–100 and 25–100 wt % (Tables 1 and 2).

The significance of the coefficients of Eq. (1) was evaluated using Students criterion at a significance level of 0.95 and a number of degrees of freedom $f = 2$ for three parallel runs for each Y_i. Discarding of the insignificant coefficients and recalculation gave coefficients of Eq. (1). The coefficients for systems (**I**) and (**II**) at 40°C are presented as an example in Table 3, in which S^2_{ad} and S^2_{rep} are, respectively, the adequacy and reproducibility variances calculated by methods described in [7]. Other coefficient tables are not given here because of their vast volume. The

Table 3. Coefficients of regression equation (1) describing the phase equilibrium in systems (**I**) and (**II**) at 40°C

Coefficient	Extract phase		Raffinate phase		
	hexane	MEA	benzene	hexane	MEA
	Morpholine–MEA–benzene–hexane				
B_0	0.090	–3.201	–	0.672	–
B_1	–0.155	15.216	–	0.314	–
B_2	0.436	–	–1.306	2.480	–
B_{11}	0.071	–20.031	–	–	–
B_{22}	–	–	–	–12.250	0.986
B_{111}	–	8.997	–	–	–
B_{222}	–	–3.419	–	–	–
B_{12}	–1.151	–	8.185	–9.957	–
B_{122}	–0.107	–	–9.815	25.404	–
B_{112}	0.710	–0.762	–	–	–
S^2_{ad}	3.95×10^{-7}	5.77×10^{-4}	8.35×10^{-4}	5.62×10^{-4}	1.87×10^{-4}
S^2_{rep}	5.12×10^{-7}	2.65×10^{-4}	1.05×10^{-3}	6.22×10^{-4}	5.12×10^{-7}
F	0.8	2.2	0.9	0.8	0.09
F_{tab}	19.5	19.5	19.5	19.5	19.5
Coefficient	Extract phase		Raffinate phase		
	hexane	MEG	benzene	hexane	MEG
	Morpholine–MEG–benzene–hexane				
B_0	0.106	0.155	–	0.570	–
B_1	–0.340	0.761	–	0.754	–
B_2	0.613	–3.022	2.827	–2.865	–
B_{11}	0.425	–	–	–0.340	–
B_{22}	–	5.416	–	–4.105	–
B_{111}	–0.189	0.078	0.048	–	–
B_{222}	–	3.746	–	–	–
B_{12}	–1.874	8.822	–8.292	9.873	0.700
B_{122}	–	–15.577	–8.006	13.162	–
B_{112}	1.277	–6.162	17.43	–20.614	–
S^2_{ad}	3.47×10^{-6}	6.59×10^{-5}	8.83×10^{-4}	6.4×10^{-4}	4.72×10^{-4}
S^2_{rep}	5.23×10^{-6}	8.13×10^{-6}	1.19×10^{-4}	7.81×10^{-5}	6.34×10^{-4}
F	0.7	8.1	7.4	8.2	0.8
F_{tab}	19.4	19.4	19.4	19.4	19.4

adequacy of the obtained equations was verified using Fisher's test $F = S^2_{ad}/S^2_{rep}$.

As it can be seen from Table 3, all the equations adequately describe phase equilibria in the system studied at the adopted significance level of 0.95. The correctness of the obtained experimental data was verified using Hand's correlation method [8], with the four-component system regarded as a pseudoternary system in which the concentration of the extracting agent was equated to the sum of concentrations of the constituents of the mixed extracting agent. The high correlation coefficient $R > 0.98$ indicates the correctness of the obtained experimental data.

The obtained experimental data on phase equilibria were used to determine, using the method of graphical interpolation after Sherwood [8], the compositions of the coexisting phases under conditions of single-stage extraction of model mixtures hexane–benzene and heptane–toluene. The content of the aromatic hydrocarbon in the raw material was chosen to be 35 wt %, and the mass ratio of the solvent to the raw material, 2 : 1. The obtained data were used to calculate the coefficients of distribution of the aromatic hydrocarbon among the phases, $K_a = X_{ae}/X_{ar}$ and the separation coefficients $\beta = K_a/K_{na}$ characterizing the selectivity of the given process [9], where K_a and K_{na} are the

Table 4. Results obtained in single-stage extraction of model mixtures with different solvents*. Extracting agent to raw material mass ratio 2 : 1, content of aromatic hydrocarbon in raw material 35 wt %

Solvent	Raw material	T, °C	C	α	K	Reference
			wt %			
Morpholine + 70% MEA)	Benzene–hexane	40	82.9	39.76	0.31	This study
Morpholine + 50% MEG	"	40	79.8	43.28	0.34	"
DEG + 7% H_2O	"	150	75.0	23.8	0.13	[10]
TEG	Toluene–heptane	50	82.3	29.6	0.17	[11]
N-MP + 20% H_2O	"	20	93.7	30.0	0.18	[12]
N-MP + 40% MEG	"	50	69.9	57.7	0.42	[13]

* C is the content of aromatic hydrocarbon in the extract, α the degree of extraction of the aromatic hydrocarbon, and K the distribution coefficient for the aromatic hydrocarbon.

coefficients of distribution of the aromatic and nonaromatic hydrocarbons, respectively, between the extract and raffinate phases; X_{ae} and X_{ar} are the mass concentrations of an aromatic hydrocarbon (benzene or toluene) in the extract and raffinate phases.

The experiments demonstrated that, with increasing content of the second component in a binary solvent, the separation coefficient grows, whereas the distribution coefficient of the aromatic hydrocarbon decreases. For example, making the MEG content higher than 75 wt % for systems (**I**) and (**III**) is inexpedient in view of the substantial decrease in the dissolving ability; the corresponding values for systems (**II**) and (**IV**) are 50 and 60 wt %, respectively. At equal contents of the second component, adding MEG to morpholine leads to lower distribution coefficients and wider stratification region. A similar behavior was observed for all of the systems studied.

The content of the second component in the extracting agent, which ensures the best combination of selectivity and dissolving ability, is about 70 wt % for MEA and 50 wt % for MEG. The results obtained in calculating the basic parameters in the case of a single-stage extraction with binary solvents of composition morpholine + 70% MEA and morpholine + 50% MEG are listed in Table 4, presenting in addition the corresponding parameters for some commercial extracting agents. The basic parameters of single-stage extraction were calculated by means of the conventional formulas [8, 9] with the use of compositions of coexisting phases, found by Sherwood's correlation method. Content of aromatic hydrocarbon in the raw material 35 wt %, solvent to raw material mass ratio 2 : 1. The correlation line was plotted using equilibrium data for binodals corresponding to 70% MEA and 50% MEG in the binary extracting agent (Tables 1 and 2).

As seen from Table 4, the proposed extracting agents surpass DEG and TEG in both selectivity and dissolving ability. Compared with the extracting agent Arosolvan [*N*-methylpyrrolidone (*N*-MP) + 40% MEP], the extracting agents studied have lower dissolving ability, but higher selectivity.

Thus, the analysis of the experimental data obtained with model mixtures suggests that the binary solvents studied, morpholine–MEA and morpholine–MEG, exhibit sufficiently high dissolving and selective properties and can be recommended as extracting agents for recovery of aromatic hydrocarbons from reforming catalyzates. However, final assessment should be made after optimization and calculation of performance parameters.

CONCLUSIONS

(1) Equations adequately describing phase equilibria in the systems morpholine–monoethanolamine–hexane–benzene, morpholine–mono(ethylene glycol)–hexane–benzene, morpholine–monoethanolamine–heptane–toluene, and morpholine–mono(ethylene glycol)–heptane–toluene at 40, 50, and 60°C were obtained.

(2) The extracting properties of binary solvents were studied in relation to their composition. It is shown that morpholine-based binary extracting agents with addition of monoethanolamine or mono(ethylene glycol) show good extracting properties and surpass tri(ethylene glycol) and di(ethylene glycol) in both selectivity and dissolving ability.

REFERENCES

1. Bittrikh, G.-I., Gaile, A.A., Lempe, D., *et al.*, *Razdelenie uglevodorodov s ispol'zovaniem selektivnykh rastvoritelei* (Separation of Hydrocarbons with Selective Solvents), Leningrad: Khimiya, 1987.

2. Marusina, N.B., Gaile, A.A., and Semenov, L.V., *Zh. Prikl. Khim.*, 1994, vol. 67, no. 8, pp. 1311–1315.
3. Sharifullin, A.V. and Kozin, V.G., *Neftekhimiya*, 1996, vol. 36, no. 5, pp. 464–468.
4. Tsisun, E.L., Lipkin, G.M., and Sardanashvili, A.G., *Khim. Tekhnol. Topliv Masel*, 1977, no. 5, pp. 22–23.
5. Gordon, A.J. and Ford, R.A., *The Chemist's Companion. A Handbook of Practical Data, Techniques and References*, New York: John Wiley & Sons, 1972.
6. McNair, H.M. and Bonelli, E.J., *Basic Gas Chromatography, Walnut Creek*, Calif.: Varian Aerograph, 1967.
7. Akhnazarova, S.L. and Kafarov, V.V., *Metody optimizatsii eksperimenta v khimicheskoi tekhnologii* (Methods for Experiment Optimization in Chemical Technology), Moscow: Vysshaya Shkola, 1985.
8. Treybal, R.E., *Liquid Extraction*, New York: McGraw Hill, 1963.
9. Alders, L., *Liquid-liquid Exration. Theory and Laboratory Practice*, Amsterdam: Elsevier, 1959.
10. Grishchenko, N.P., Pokorskii, V.N., and Yablochkina, M.N., *Protsessy zhidkostnoi ekstraktsii i khemosorbtsii* (Liquid Extraction and Chemisorption Processes), Moscow: Khimiya, 1966, p. 319.
11. USSR Inventor's Certificate, no. 455080.
12. USSR Inventor's Certificate, no. 509573.
13. USSR Inventor's Certificate, no. 620470.

Russian Journal of Applied Chemistry, Vol. 74, No. 8, 2001, pp. 1295–1300. Translated from Zhurnal Prikladnoi Khimii, Vol. 74, No. 8, 2001, pp. 1258–1264.

SORPTION AND ION-EXCHANGE PROCESSES

Adsorption and Desorption of Ni(II) in Quartz–Aqueous Solution Systems at Various pHs

K. P. Tikhomolova, Yu. V. Kufman, and I. N. Urakova

St. Petersburg State University, St. Petersburg, Russia

Received October 25, 2000; in final form, May 2001

Abstract—Adsorption of Ni(II) onto quartz from aqueous solution with pH 3–7 and its subsequent desorption are studied. The desorption was done by three procedures with different extents of action on adsorbed metal ion.

This study is one of a series of works on adsorption of metal cations capable, in principle, of forming chemical bonds with active sites on the adsorbent surface [1–4]. Our selection of the subject matter was determined by the possibility of donor–acceptor bonding, with account of the electronic structure of the ion and the lability of the resulting adsorption complex. In this connection, transition metal cations (as possible acceptors of unshared electron pairs) and oxides whose surface groups are potential donors of such pairs are chosen to constitute an adsorbate–adsorbent pair. The coordination properties of surface groups of an oxide can be judged from the general concepts of the coordination chemistry, including those of the structure of electronic shells and the mutual effect of the constituents of the complexes formed in the solution bulk [5–8]. Therefore, those oxides should be selected in which an adsorbed metal does not enter the crystal lattice, i.e., oxides nonisomorphous with a given metal.

Of course, electrostatic (Coulombic) forces also contribute to the interaction between the cation and negatively charged sites on the adsorbent surface. The range of these forces is much longer than the length of the donor–acceptor bonds. Adsorption controlled by these forces is totally reversible, and the adsorption equilibrium (controlled by cation diffusion) is established rapidly. The role of the Coulombic interaction is restricted to concentration of the cations in the diffusion layer at the interface; the higher the surface potential, the higher the metal concentration.

The adsorption of ionic and molecular species is only one type of possible interactions. At sufficiently high pH values, hydroxide particles (colloids in many cases) form a new phase. In this case, the sorption mechanism changes fundamentally, and adsorption gives way to interaction of species of varied nature and size, which will be further be treated in terms of adhesion.[1]

It is known that in most of actual systems the species are considerably more tightly associated than in the case of a simple coagulation contact, when no chemical interaction between active centers of the species is realized (this case is treated in the classical version of the DLFO theory). Our thought is that the presence of $-O^-$ and –OH groups on the surfaces of the hydroxide adsorbate and oxide adsorbent and the larger size of the colloidal particles as compared to ionic and molecular species may result in that hydrogen bonding plays the determining role in fixation of the adsorbate species on the adsorbent surface [4]. Donor-acceptor bonding can contribute to adhesion also, but, probably, to a lesser extent, as follows from the known strict steric limitations.

In this work we studied Ni(II) as an adsorbate. Being a *d* metal ($3d^8$), Ni can serve as an acceptor of the electron pair in complexation with oxygen-containing ligands. According to coordination chemical views, Ni(II) forms more or less stable, depending on the ligand nature, and relatively inert complexes in the bulk of aqueous solutions. From the practical standpoint the selection of Ni is due to the fact that it is a component of waste of many industries.

[1] In the cases when coagulation in dispersions with species having different nature and size is the subject matter, the term heteroadagulation is sometimes used. We prefer to use the term adhesion for the indicated process, as emphasizing the point of sticking of hydroxide species to the adsorbent surface.

1070-4272/01/7408-1295 $25.00 © 2001 MAIK "Nauka/Interperiodica"

As in the previous studies, we used quartz as adsorbent. In the adsorption–desorption experiments, we employed powdered quartz with equivalent particle diameter of <120 μm (the powder contained a relatively large amount of small particles). In the electrophoretic experiments, we used quartz with particle size of several micrometers.

The selection of quartz is due primarily to the fact that it is nonisomorphous to Ni(II) compounds, and, in contact with aqueous solutions at pH 3–7, its surface is charged negatively (on the average over the surface); the zero-charge point of quartz varies from 1.5 to 2.0. The slope of the pH dependence of the electrokinetic potential of quartz is rather high [2, 3]. The ionic centers of the negatively charged quartz surface are $[\equiv SiO]^-$ and $[\equiv SiOH]^0$, both being potential surface ligands. Note that the siloxane groups [=Si=O] can be surface ligands, too. The indicated fraction of quartz was selected to follow the effect of electroosmosis without applying concentration polarization [9].

Finally, the selection of quartz as adsorbent appears to be relevant, since quartz sand and other Si- and O-containing compounds are among the basic components of the soil. By virtue of its relatively low cost, quartz sand may appear rather efficient adsorbent for *d* metals under certain conditions.

The main goal of this work was to study the kinetics of adsorption (adhesion) of Ni(II) onto quartz and of its desorption. The processes were monitored by the Ni(II) concentration in the solution bulk, *C*, and the amount of metal on the adsorbent surface, *X* (recalculated to 1 g of adsorbent). Nickel(II) was determined in solution spectrophotometrically with a Specol-10 instrument using 0.01% ethanolic solution of PAN [1-(2-pyridylazo)-2-naphthol] as indicator [10].

Adsorption (adhesion) was studied by the static method. Quartz after adsorption (adhesion) is called modified.

Desorption was studied by the static, dynamic, and electroosmotic displacement methods differing in the effect exerted on the adsorption layer. Among these methods, the static method is the mildest, and the electroosmotic method, the most vigorous. In all cases, we used in the desorption stage Ni-free solutions (supporting solutions) having the same composition by the other components as the Ni(II) solution used in the adsorption stage (working solution). In static desorption experiments, modified quartz was placed in weighing bottles, and the supporting solution was refreshed at fixed intervals. In the dynamic and electroosmotic modes, the supporting solution was passed through a membrane of modified quartz, under the action of a pressure gradient and dc field, respectively.

To compare the efficiencies of desorption by the dynamic and electroosmotic methods, experiments were carried out at the same flow rates of the supporting solution. In the electroosmotic experiments, the dc field strength was 10 V cm^{-1}. The pressure gradient in the dynamic desorption experiments was estimated by the formula for the maximal electroosmotic rise [11], derived with the Darcy equation [9] substituted for Poiseuille's equation.

The static and dynamic techniques are widely used in desorption experiments. Hereinafter these methods are called conventional. Studies devoted to the potentialities of the electroosmotic technique for this purpose are scarce. The main concern of these works is mostly soil compaction or consolidation grouting [12].

The working solutions were prepared from a 10^{-4} M $Ni(NO_3)_2$ stock solution (total ionic strength 10^{-3}) at pH 3.0, 5.0, 7.2–7.4, and 9.4 (system nos. 1–4, respectively). The Ni(II) concentration in the working solutions was chosen for studying the adsorption efficiency in view of the fact that the commonly used wastewater treatment processes can reduce the metallic pollutant concentration to 10^{-3}–10^{-4} M, which is much higher than the maximal admissible concentration.

To evaluate the effect of aging of the working solution through Ni(II) hydrolysis, the solutions were potentiometrically titrated 1 and 24 h after preparation.

The results obtained with the freshly prepared solutions are consistent with those reported in [13] for pH < 9.5. At the same time, the results clearly demonstrated that Ni(II) speciation substantially changes with time, especially at pH > 8. For example, at pH 9.4 and short contact time, the amount of the hydroxide was determined to be 80% of the total; such ionic species as $[Ni(H_2O)_5(OH)]^+$, $[Ni(H_2O)_3(OH)_3]^-$, and $[Ni(OH)_4]^{2-}$ were present in nearly equal amounts (6–7%). With longer contact time, the amount of the hydroxide decreased to 48%, and the content of ionic species increased. Therefore, we used in our experiments fresh working solutions (age 1–2 h). In these solutions, about 97% of the total Ni(II) exists at pH 7.2–7.4 as $[Ni(H_2O)_6]^{2+}$. However, it is known that Ni(II) exists essentially in hydroxo forms at pH 8.3. Therefore, the difference between pH 7.2–7.4 of the working solution and pH 8.3 of hydroxide precipitation is too small to eliminate the possibility of occurrence of a minor amount of the hydrolyzed form $[Ni(H_2O)_5(OH)]^+$ in the working solutions. Note also that Farley *et al*. [14] suggested that at pH only

slightly lower than that corresponding to the onset of hydroxide formation in the bulk of the liquid phase, formation of hydroxides and their further association may occur in the surface layer.

The ionic strength and pH of the working solutions were adjusted by adding KNO_3, HNO_3, or KOH. It is known that at the experimental pH values the quartz surface is charged negatively, i.e., Ni(II) aqua cations must be attracted to the surface by electrostatic forces. To characterize the electrostatic interaction and the evolution of the relative amounts of the surface groups $[\equiv SiO]^-$ and $[SiOH]^0$ with increasing pH, we measured in the working systems, and also in the system with pH 10.5, the electrokinetic potential ζ by the microelectrophoretic method. The initial ζ values ($t_{ad} = 0$) of the working systems were –7, –35, –50, –70, and –100 mV. These values and their evolution with increasing pH and t_{ad} suggest that, in all the cases, the quartz surface has active sites $[\equiv SiO]^-$. In the systems with pH 3, the amount of these groups is small; and most of the sites exist in the $[\equiv SiOH]^0$ form. Naturally, the amount of the $[\equiv SiO]^-$ groups increased with growing pH at the expense of the $[\equiv SiOH]^0$ form, and it is most likely that $[\equiv SiO]^-$ is the dominant form in the system with pH 10.5. Thus, in all of the working systems the quartz surface possesses surface sites of both types.

The above working pH values were chosen on the basis of the speciation data for fresh Ni(II) solutions, solubility product of $Ni(OH)_2$, and relative amounts of the indicated two forms of the surface sites.

Both in the case of adsorption (adhesion) and in desorption, the metal concentration in the liquid phase C was monitored. Then we estimated the amount X of Ni(II) on quartz in adsorbed (adhering) state per gram of the adsorbent. The adsorption (adhesion) efficiency was characterized by the amount of adsorbed (adhering) Ni(II) related to its total amount in the system, X_{ad} (%). The desorption efficiency is characterized by the decrease in the amount of adsorbed (adhering) Ni(II) related to its total amount in the system, X_{des} (%), by the same decrease but related to the limiting adsorption in the preceding adsorption stage, X^{∞}_{des} (%), and by the increase in the metal ion concentration related to the limiting adsorption in the preadsorption stage C^{∞}_{des} (%):

$$X^0_{ad} = \frac{C_0 - C_{ad}}{C_0} \times 100,$$

$$X^0_{des} = \frac{(C_0 - C_{ad})V_{ad} - C_{des}V_{des}}{C_0V_{ad}} \times 100,$$

$$X^{\infty}_{des} = \frac{(C_0 - C_{ad})V_{ad} - C_{des}V_{des}}{C^{\infty}_{ad}V_{ad}} \times 100,$$

$$C^{\infty}_{des} = \frac{C_{des}V_{des}}{C^{\infty}_{ad}V_{ad}} \times 100,$$

where the lower indices ad and des refer to the adsorption and desorption, respectively; C_0 is the Ni(II) concentration in the aqueous phase before adsorption; and V is the volume of the liquid phase (time-independent in adsorption and depending on the number of refreshments of the supporting solution in static desorption and the desorption time in dynamic and electroosmotic desorption).

The error of spectrophotometric determination of Ni(II) was within 0.5–3.0%. Within these limits the error increased with increasing pH. The reason is that the Ni(II) concentration in the solutions after adsorption and after desorption by the conventional methods was very low (close to the determination limit by the method used). The error of determination of pH was no more than 0.05 pH units in the acidic region and 0.1 pH units in the alkaline region. The error of determination of the ζ potential ranged from 3 to 15%; in the neutral and alkaline regions the standard deviation was below 3% for seven parallel runs, and in the acidic region it was 8–15%.

The major trends in the adsorption–desorption behavior of Ni(II) in the investigated system are demonstrated in Figs. 1 and 2. The dependences $X_{ad} = f(t_{ad})$, $X_{des} = f(t_{des})$, and $C^{\infty}_{des} = f(t_{des})$ are given in Figs. 1a, 1b–1d, and 2, respectively. Additionally, some X_{des} values are given in the text.

Figure 1a shows that, in all the systems, Ni(II) is intensively adsorbed from the liquid phase but in different amounts. The most clearly pronounced differences are observed with increasing pH in the systems with Ni(II) in the form $[Ni(H_2O)_6]^{2+}$. The limiting adsorption of Ni is 36, 60, and 90% of the total at pH 3, 5, and 7.2, respectively. At pH 9.4, i.e., in the case of hydroxide adhesion, Ni is virtually totally removed from the liquid phase.

The time of attainment of the adsorption equilibrium (limiting adsorption) was found to be about 4 h in the systems in which ionic species of Ni(II) are adsorbed; in the case of adhesion of the hydroxide species, the major part of the metal was already adsorbed during the first hour, and then the process slowly approached saturation in several days.

Let us consider data on desorption in the systems in which Ni(II) was adsorbed as the ionic species $[Ni(H_2O)_6]^{2+}$. Note, first, that in this case the efficiency of desorption by the conventional methods

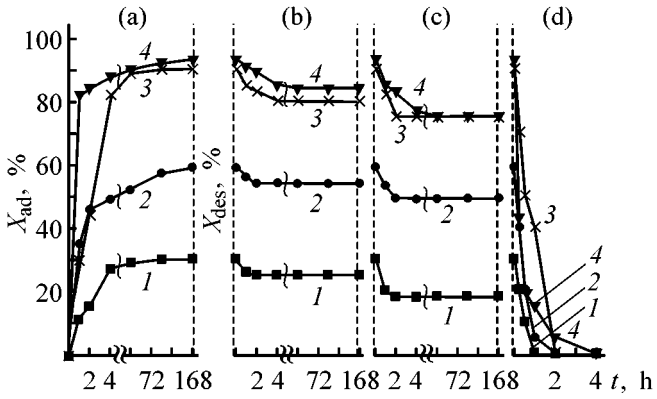

Fig. 1. Adsorption X_{ad} of Ni(II) on quartz and its desorption X_{des} vs. contact time *t*. Solution pH: (*1*) 3.0, (*2*) 5.0, (*3*) 7.2–7.4, and (*4*) 9.5. (a) Adsorption and 7-day desorption in (b) static, (c) dynamic, and (d) electroosmotic modes.

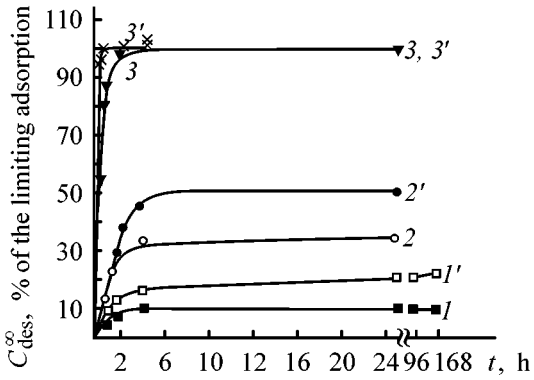

Fig. 2. Gain in the Ni(II) concentration in solution C^{∞}_{des} vs. the desorption time *t* at pH 3. Adsorption time (h): (*1*′–*3*′) 1 and (*1*–*3*) 24. Desorption technique: (*1, 1*′) static, (*2, 2*′) dynamic, and (*3, 3*′) electroosmotic.

strongly depends on the adsorption time: the longer the adsorption time, the lower the desorption rate and the limiting desorption. The effect was observed even at adsorption time longer than that in which equilibrium was attained in the adsorption stage. In electroosmotic desorption, we observed the effect of t_{ad} too, but, first, to a much lower extent and, second, for the desorption rate only.

The effect of t_{ad} is shown in Fig. 2 for system no. 1 at the shortest and the longest experimental adsorption times and for all the three desorption techniques used.

To illustrate the effects of pH, t_{des}, and the desorption technique on the desorption behavior, desorption data for all of the systems studied are given in Figs. 1b–1d for one and the same, and the longest experimental adsorption time (t_{ad} = 7 days), since this time was demonstrated to be sufficient for saturation of all interactions and surface processes occurring in the investigated systems.

Let us consider first the conventional desorption techniques. At pH 3 the efficiency of desorption by both the conventional methods is low, as clearly demonstrated by Figs. 1b, 1c, and 2. Also this fact is clearly pronounced in X^{∞}_{des}. Recalculation of X^{0}_{ad} to X^{∞}_{des} gives 73 and 45% at t_{ad} = 1 h and 90 and 70% at t_{ad} = 7 days for the static and dynamic desorption, respectively. Such a low desorption efficiency even at pH 3 is a clear indication of the occurrence of specific adsorption. According to our concept [1, 3], the crucial role in realization of specific adsorption is played by donor–acceptor interactions. When discussing data on adsorption of metals other than Ni, we suggested that donor–acceptor binding to active sites of the SiO_2 surface may initiate various chemical reactions in the adsorbate layer, thus favoring stronger fixation of the metal species. Also, we suggested that olic or oxolic bonds may be formed between the adhering species, as well as protonation and deprotonation of the adsorbate [2, 3]. In Ni(II) adsorption, these processes are unlikely. Furthermore, at small t_{ad} (about 1 h) the initiated reactions, even if occurring, could provide very low yields. It follows from these considerations that the adsorbate–adsorbent surface complex is strongly fixed on the surface by the donor–acceptor forces. The observed low efficiency of Ni(II) desorption by the conventional methods in the systems with pH 3 suggests that in this case not only $[\equiv SiO]^-$, but also $[\equiv SiOH]^0$ may by a surface ligand.

Let us now consider the desorption data obtained by the traditional methods in the systems with pH 5.0 and 7.2–7.4. In this case, we observed a stronger adsorption and a higher fraction of undesorbable Ni(II) as compared with the systems having pH 3, and also an increase in adsorption efficiency and decrease in desorption efficiency with increasing pH. In terms of our concept, these data can be attributed to the fact that, among the indicated surface ligands, $[\equiv SiO]^-$ is more likely to substitute water molecules of the aqua cation $[\equiv SiOH]^0$. It is not improbable that latter can also replace water, but an ultimate answer can be obtained only experimentally. It follows from published and our data on the electrokinetic potential of the initial quartz that the relative amount of the $[\equiv SiO]^-$ groups substantially grows in passing from pH 3 to pH 5.0 and then to pH 7.2–7.4, at the expense of $[\equiv SiOH]^0$. At the same time, as noted above, a minor amount of the hydroxo cation $[Ni(H_2O)_5(OH)]^+$ can be formed in the systems at pH 7.2–7.4. Association of such species may result in the appearance of polyhydroxo forms in the surface layer. However, we have no direct confirmation of the occurrence of these sur-

face processes. Our thought is that the conclusion about the increasing relative content of $[\equiv SiO]^-$ groups, and decreasing content of $[\equiv SiOH]^0$ groups, is sufficient for adequately interpreting the experimental data.

The electroosmotic displacement technique provides rapid total desorption of Ni(II) (in 4 h in the extreme cases) (Figs. 1d, 2). Also, the results clearly demonstrate the advantage of the electroosmotic technique over the conventional desorption methods (Figs. 1b–1d, 2). These results are well consistent with the theoretical views of the structure of electroosmotic and pressure filtration flows [9].

Let us now consider data on system no. 4. The contribution of chemical bonding to adhesion of Ni hydroxide species to the quartz surface was the most clearly pronounced in the static desorption experiments. It should be pointed out first that in the adsorption stage ζ reaches its limiting value quite rapidly, suggesting that all the transformations occurring in bond formation are localized in the interparticle contact zone only (rather than in the bulk of an adhering hydroxide species) [4, 15]. The absence of chemical transformations is probably due to the fact that the interacting dispersed species are nonisomorphous to one another. Furthermore, one may suggest on the basis of the results obtained that the contact between a $Ni(OH)_2$ particle and SiO_2 is stronger than a simple coagulation contact. To estimate the coagulation contact energy in the investigated systems, we used the method employed more than once previously in treating other systems [16, 17], relying upon the classical version of DLFO calculation. In calculations, we accepted $\zeta(SiO_2) = -70$ mV and $\zeta[Ni(OH)_2)] = -12$ mV [4]; at particle size of $Ni(OH)_2$ and quartz of 1 and 10 μm, respectively; and the Hamacker constant $A_{120} = 1 \times 10^{-20}$ J.[2] The probability of formation of a coagulation contact is controlled by $U_{max}/U_{max.crit.}$, where U_{max} is the energy barrier estimated by DLFO for the actual values of ζ of the interacting particles and $U_{max.crit.}$ is that estimated at $\zeta(SiO_2) = \zeta[Ni(OH)_2)] = -30$ mV. This procedure is based on the well-known empirical observation that, regardless of the sign of the potential, the value 30 mV is critical in the sense that at higher (or lower) absolute values of the potential coagulation does not occur (or occurs). According to our estimates, $U_{max}/U_{max.crit.}$ is somewhat above 1 for the pair SiO_2–SiO_2, below zero for $Ni(OH)_2$–$Ni(OH)_2$, and about 1.5 for SiO_2–$Ni(OH)_2$. These results show that in the framework of the classical version of the DLFO theory, aggregates consisting of only quartz particles cannot be formed in the investigated systems; nickel hydroxide particles must be strongly associated, and the $Ni(OH)_2$–quartz interaction is on the verge of probability. At the same time the equilibrium $|\zeta|$ in system no. 4 was found to be 20 mV, which is lower by 50 mV than that of the initial quartz. Such a high $\Delta|\zeta|$ clearly indicates that SiO_2 interacts with $Ni(OH)_2$ in this system. Thus, as in the case of adsorption of cationic forms of Ni(II), the experimental results for system no. 4 are inconsistent with the theoretical predictions obtained with no allowance for chemical interaction between the active interfacial centers.

Note also that the measured equilibrium ζ in system no. 4 (–20 mV) is much closer to the potential of the $Ni(OH)_2$ surface than to that of SiO_2. We estimated the coverage of the surface of the SiO_2–$Ni(OH)_2$ aggregate with $Ni(OH)_2$ particles by the equation relating the mean ζ of a two-component solid surface to ζ of the components and to the fractions of the surface occupied by them. The coverage of SiO_2 with $Ni(OH)_2$ was estimated to be 0.80–0.85. According to the microscopic data, the hydroxide species are at least 1 μm in size. The particles of this size may cover only 3–4% of the quartz surface (in this case the mean ζ would be close to that typical of quartz). The results can be accounted for on the assumption that the observed 1-μm hydroxide species are aggregates of much smaller particles and that, when approaching the surface layer, these aggregates disintegrate to give a large amount of primary particles. Such interpretation is consistent with our concept of the existence of high-energy bonds between metal hydroxide species and SiO_2 [16].

The rather low-efficient desorption by the static method in the systems with pH 9.4 can be attributed, as in our previous studies, to a significant effect of hydrogen bonding between the oxygen-containing groups on the quartz surface and the hydroxy groups of the Ni(II) hydroxide particle surface (such bonds ensure fairly strong fixation of an adsorbate on the adsorbent surface). Furthermore, accumulation of a great amount of very small hydroxide particles at the adsorbent surface could initiate their association in the surface layer, thus favoring fixation of Ni(II). Note that in many cases hydrogen bonding causes significant undesired problems in regeneration of the adsorbent surface.

As in desorption of ionic species, in the case of initial adhesion of $Ni(OH)_2$ particles, electroosmotic displacement technique provides high desorption efficiency.

[2] The Hamacker constant of $Ni(OH)_2$ was estimated by the method proposed in [18]: the Lorentz–Lorenz equation, relating the electronic polarizability to the refractive characteristics, is substituted in the relationship for the London constant.

Since in the case of dynamic desorption it is not improbable that the complex pore structure of the membranes affects the particle motion in the liquid, induced by the liquid flow, one cannot attribute the observed low efficiency of Ni(II) desorption only to the effect of hydrogen bonding. Theoretically, motion of small colloidal species within the membrane pores can be initiated by electroosmotic flow [9]. Such a strong difference between the efficiency of desorption of adhered colloidal species of Ni hydroxide, obtained in the dynamic and electroosmotic desorption experiments, provides an additional evidence in favor of the employment of electroosmotic regeneration of modified quartz.

CONCLUSIONS

(1) Quartz intensively adsorbs Ni(II); the adsorption considerably grows with ingreasing pH of the aqueous phase. The adsorption equilibrium is established in several hours (4 h and more).

(2) Desorption of Ni(II) from quartz depends on the desorption procedure used. The desorption efficiency in the conventional methods (static and dynamic) is rather low even at a desorption time as long as many days; the desorption efficiency in the dynamic mode is somewhat higher. In electroosmotic replacement, Ni(II) is totally desorbed quite rapidly (in 0.5–1 h).

(3) In the conventional desorption modes the desorption efficiency significantly depends on the adsorption time, but only slightly on the pH of the Ni-containing working solution. In the electroosmotic displacement method, the desorption efficiency is independent of these parameters.

(4) In 7 days, about 95% of Ni(II) adheres to the quartz surface. Adhesion occurs throughout the experiment; however, the main part of the hydroxide (>80%) adheres in the first hour.

(5) The trends observed in desorption of adhering Ni(II) hydroxide are quite similar to those for the case of adsorbed ionic species. The desorption efficiency is rather low in desorption by the conventional methods, while electroosmotic displacement provides rapid and total desorption.

(6) The adsorption, adhesion, and desorption behaviors of Ni(II) in quartz dispersions may be interpreted in terms of the formation of donor–acceptor bonds between Ni(II) and active centers of the quartz surface in the case of adsorption, and of hydrogen bonding between Ni hydroxide species and the active sites in the case of adhesion.

ASKNOWLEDGMENTS

The work was financially supported by the Russian Foundation for Basic Research (project no. 00-15-97 357).

REFERENCES

1. Tikhomolova, K.P. and Aleksandrova, L.K., *Kolloidn. Zh.*, 1988, vol. 50, no. 1, pp. 100–104.
2. Tikhomolova, K.P. and Demin, S.A., *Fiz.-Khim. Mekh. Liofil'n. Dispersn. Sist.*, 1991, issue 22, pp. 77–89.
3. Tikhomolova, K.P. and Tsukanova, V.M., *Zh. Prikl. Khim.*, 1997, vol. 70, no. 3, pp. 353–370.
4. Tikhomolova, K.P., Ivanova, M.V., and Tsukanova, V.M., *Zh. Prikl. Khim.*, 1997, vol. 70, no. 7, pp. 1078–1085.
5. Cotton, F.A. and Wilkinson, G., *Basic Inorganic Chemistry*, New York: Wiley, 1976.
6. Kukushkin, Yu.N., *Khimiya koordinatsionnykh soedinenii* (Chemistry of Coordination Compounds), Moscow: Vysshaya Shkola, 1985.
7. Kostromina, N.A., Kumok, V.N., and Skorik, N.L., *Khimiya koordinatsionnykh soedinenii* (Chemistry of Coordination Compounds), Moscow: Vysshaya Shkola, 1990.
8. Glikina, F.B. and Klyuchnikov, N.G., *Khimiya kompleksnykh soedinenii* (Chemistry of Complex Compounds), Moscow: Prosveshchenie, 1982.
9. Tikhomolova, K.P., *Elektroosmos* (Electroosmosis), Leningrad: Khimiya, 1989.
10. Přibil, R., *Komplexony v chemické analyse*, Praha: Nakl. Československé akad., 1957.
11. Grigorov, O.N., Koz'mina, Z.P., Markovich, A.V., and Fridrikhsberg, D.A., *Elektrokineticheskie svoistva kapillyarnykh sistem* (Electrokinetic Properties of Capillary Systems), Moscow: Akad. Nauk SSSR, 1956, pp. 91–92.
12. Zhinkin, G.N., *Elektroosmoticheskoe zakreplenie gruntov v stroitel'stve* (Electroosmotic Consolidation Grouting in Building), Leningrad: Stroiizdat, 1966.
13. Baes, C.F. and Mesmer, R.E., *The Hydrolysis of Cations*, New York: Wiley, 1976.
14. Farley, K.J., Dzomak, D.A., and Morel, F.M., *J. Colloid Interface Sci.*, 1985, vol. 106, no. 1, pp. 226–242.
15. Tikhomolova, K.P., Vasil'eva, E.O., and Ivanova, M.V., *Kolloidn. Zh.*, 1995, vol. 57, no. 6, pp. 868–872.
16. Tsukanova, V.M. and Tikhomolova, K.P., *Kolloidn. Zh.*, 1995, vol. 57, no. 6, pp. 878–883.
17. Tsukanova, V.M. and Tikhomolova, K.P., *Kolloidn. Zh.*, 1996, vol. 58, no. 5, pp. 697–703.
18. Malov, V.A. and Eron'ko, O.N., *Teoreticheskie osnovy nekotorykh metodov pererabotki dispersnykh sistem* (Theoretical Principles of Some Methods for Processing of Dispersed Systems), St. Petersburg: Sankt-Peterburg. Tekhnol. Inst., 1994.

Russian Journal of Applied Chemistry, Vol. 74, No. 8, 2001, pp. 1301–1304. Translated from Zhurnal Prikladnoi Khimii, Vol. 74, No. 8, 2001, pp. 1265–1268.

SORPTION AND ION-EXCHANGE PROCESSES

Kinetics of Heterogeneous Reduction of Red-Brown Zh Vat Dye with Rongalite in the Absence of Diffusion Hindrance

Yu. V. Polenov, V. A. Pushkina, V. V. Budanov, and O. S. Khilinskaya

Ivanovo State University of Chemical Engineering, Ivanovo, Russia

Received November 17, 2000

Abstract—The kinetics of heterogeneous reduction of red-brown Zh vat dye with formaldehyde sodium sulfoxylate (rongalite) was studied. The dye was reduced in the form of nonporous disk, which eliminates the effect of mass transfer on the reaction rate. The stages of the reduction mechanism and the reaction rate equations are proposed.

Due to wide assortment and high lightfastness and resistance to wet treatment, vat dyes are widely used in the textile industry. The main stage in the textile finishing is conversion of a water-insoluble dye into a soluble leuco compound. This reaction proceeds in the presence of sulfur- and oxygen-containing reducing agents: formaldehyde sodium sulfoxylate (FSS) or sodium dithionite [1]. The conversion of the vat dye in the leuco form is a heterogeneous reaction whose rate is determined by chemical structures of the dye and reducing agent and by reaction conditions: temperature, solution pH, reactant concentrations, and dispersion of the initial dye.

In general, the above process may involve the following stages: diffusion of molecules of the reducing agent to the surface of dye particles, sorption of the reducing agent, chemical reaction between the dye and reducing agent on the dye surface with the formation of a leuco compound, desorption of the leuco compound and oxidation products from the surface into the solution, and reverse diffusion of the oxidation products into the solution bulk.

In some works [2, 3], diffusion was suggested to be the main factor controlling the reduction rate. However, the effect of dye surface modification [4] and formaldehyde additives on the reaction rate and its nonlinear dependence on the reducing agent concentration [5, 6] suggest that the chemical stage significantly affects the total rate of the process. Since investigation of a multistage process is a rather difficult problem, the development of an adecuate kinetic model requires elimination of some stages in order to study the others.

To study the reduction kinetics, the dye was pressed in the form of a nonporous disk, which is common for electrochemical studies [7].

EXPERIMENTAL

In this study, we used red-brown thioindigo Zh dye, which was prepared from a pigment treated to remove lyophilizing and stabilizing additives. The pigment was thoroughly washed with distilled water at 80°C. The impurities were extracted with ethanol in a Soxhlet apparatus, then the dye was dried at 60°C and analyzed for the content of the pure pigment [8]. The content of the main product was 96.4%. As reducing agent we used formaldehyde sodium sulfoxylate $HOCH_2SO_2Na \cdot 2H_2O$ prepared by double recrystallization of the crude product from water. According to iodometric titration data, the content of the main compound in the recrystallized product was no less than 97.6%.

The dye was pressed at 50 kg cm^{-2} in a metallic mold as a planar nonporous disk with one open side and placed in a reaction vessel. The disk was rotated at 100–1430 rpm in an aqueous solution of the reducing agent (C_{FSS} = 0.05–0.24 M) and chemically pure grade sodium hydroxide (2.5×10^{-2}–6.25×10^{-3} M).

To prevent the oxidation of the leuco compound formed, the reduction of the vat dye was performed in

1070-4272/01/7408-1301 $25.00 © 2001 MAIK "Nauka/Interperiodica"

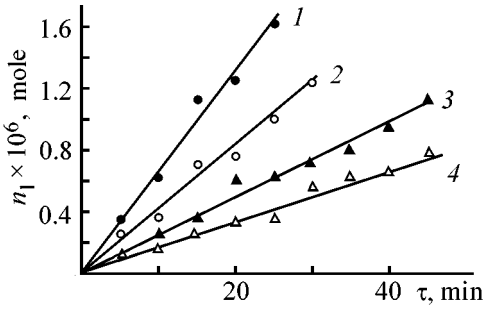

Fig. 1. Accumulation of the dye leuco form n_l vs. time τ. T 363 K, C_{FSS} 0.2, C_{NaOH} 0.025 M; N 800 rpm. Formaldehyde concentration $C_{CH_2(OH)_2} \times 10^4$ (M): (*1*) 0, (*2*) 1.15, (*3*) 3.45, and (*4*) 5.75.

a thermostated cell (±0.5 K) in an argon atmosphere. The solution volume in the cell was 100 ml. In the course of the reaction, 3.5-ml samples were taken to determine the concentration of the resulting leuco form of the dye.

The concentration of the leuco form was measured spectrophotometrically (λ_{max} = 425 nm) on an SF-46 spectrophotometer. Preliminary tests showed that the dependence of the optical density of the solution on the concentration of the dye leuco form obeys the Lambert–Bouguer–Beer law.

To determine the reaction rates from the kinetic curves, we calculated the concentration of the forming leuco compound from the following equation:

$$n_{i,l} = C_{i,l}V/1000 + n_{(i-1),l}, \quad (1)$$

where $n_{i,l}$ is the amount of the dye (mole) formed by the time of measurement (i is the measurement number); $C_{i,l}$ is the concentration of the dye determined in ith measurement (M); V is the solution volume at the instant of measurement (ml); $n_{(i-1),l}$ is the amount of dye (mole) formed by the time of the preceding measurement ($n_{0,l}$ = 0).

The typical kinetic curves of accumulation of the resulting leuco form are shown in Fig. 1. Since each curve has a linear portion, the reaction rate constant k_{app} (mol min^{-1}) was determined from the slopes, using the least-squares procedure.

To reveal the regions of the kinetic and diffusion control, we studied the dependences of the reaction rate k_{app} on the disk rotation speed N (C_{NaOH} = 0.025, C_{FSS} = 0.2 M; T = 363 K):

N, rpm	$k_{app} \times 10^8$, mol min^{-1}
100	1.6 ± 0.2
200	4.1 ± 0.2
400	4.9 ± 0.1

The above data suggest that the speed of disk rotation affects the reaction rate up to N = 400 rpm. Similar dependence is typical of heterogeneous reactions [9] and reveals regions of the kinetic and diffusion control. Our further tests were performed at a constant rotation speed N = 800 rpm, which corresponds to the kinetic control of the process in question.

It is known that the majority of reactions with FSS proceed with cleavage of the C–S bond by the following reversible reaction

$$HOCH_2SO_2^- + OH^- \underset{k_2}{\overset{k_1}{\rightleftarrows}} SO_2^{2-} + CH_2(OH)_2 \quad (I)$$

with the formation of intermediate anions of sulfoxylic acid [10]. This is confirmed by the deceleration of the reaction rate in the presence of formaldehyde, which binds the active intermediates [reaction (I)].

As seen from Fig. 1, with increasing concentration of CH_2O, which in the alkali medium occurs as $CH_2(OH)_2$, the rate of vat dye reduction decreases. This indicates that the stages of formation of SO_2^{2-} anions and their further interaction with dye should be taken into account in performing reduction of the vat dye.

Our data suggest that the reduction of the vat dye (pressed as a planar nonporous disk) in the absence of diffusion hindrance involves the following stages.

(1) Formation of active species of the reducing agent (chemical stage in solution)

$$r_1 = dC_{SO_2^{2-}}/d\tau = k_1 C_{FSS} C_{OH^-} - k_2 C_{SO_2^{2-}} C_{CH_2(OH)_2}, \quad (2)$$

where C_{FSS} is the concentration of formaldehyde sodium sulfoxylate ($HOCH_2SO_2^-$ ions) (M), C_{OH^-} is the concentration of OH^- ions or NaOH (M), $C_{SO_2^{2-}}$ is the concentration of SO_2^{2-} ions in solution (M), and $C_{CH_2(OH)_2}$ is the concentration of formaldehyde (M).

(2) Sorption of SO_2^{2-} ions onto the dye surface

$$r_2 = dZ_{SO_2^{2-}}/d\tau = k_s Z C_{SO_2^{2-}} Sf - k_d Z_{SO_2^{2-}} Sf, \quad (3)$$

where k_s and k_d are the rate constants of sorption and desorption of SO_2^{2-} anions; Z is the number of free sorption centers on the dye surface (mol m^{-2}); $Z_{SO_2^{2-}}$ is the number of sorption centers on the surface, occupied by SO_2^{2-} anions (mol m^{-2}); S is the surface area (m^2); and f is the roughness coefficient.

(3) Chemical reaction of SO_2^{2-} anions sorbed on the surface with the dye

$$r_3 = dn_l/d\tau = k_c Z_{SO_2^{2-}} Sf, \quad (4)$$

where k_c is the rate constant of chemical reaction (II).

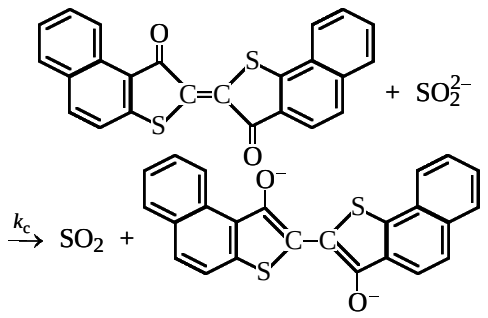

(II)

The kinetic equation was deduced on the following assumptions: the process occurs in the steady-state mode, which is attained in a relatively short period; the reducing intermediates SO_2^{2-} (I) in solutions are formed with attainment of quasi-equilibrium characterized by equilibrium constant

$$K_e = k_1/k_2;$$

the equilibrium is attained rapidly in the stage of sorption–desorption of SO_2^{2-} anions; and the desorption of the resulting leuco compound and of the products of FSS oxidation is fast and their further sorption is insignificant.

At sorption equilibrium the following equations are valid

$$k_s Z C_{SO_2^{2-}} = k_d Z_{SO_2^{2-}}, \quad (5)$$

$$Z = Z_\infty - Z_{SO_2^{2-}}, \quad (6)$$

where Z_∞ is the total amount of sorption centers on the dye surface (mol m^{-2}).

From Eqs. (5) and (6) follows that

$$Z_{SO_2^{2-}} = Z_\infty K C_{SO_2^{2-}}/(1 + K C_{SO_2^{2-}}), \quad (7)$$

where $K = k_s/k_d$ is the sorption equilibrium constant (mol^{-1}).

Now, substituting (7) into Eq. (4), we determine the formation rate of the dye leuco form passing into the solution:

$$dn_l/d\tau = [k_c Z_\infty K C_{SO_2^{2-}}/(1 + K C_{SO_2^{2-}})] S f. \quad (8)$$

The quasi-equilibrium conditions of stage (I) suggest that

$$C_{SO_2^{2-}} = K_e C_{FSS} C_{OH^-}/C_{CH_2(OH)_2}. \quad (9)$$

Substituting (9) into (8) and integrating it at excess of FSS and NaOH and constant content of formaldehyde [quasi-equilibrium (I)], and taking into account that $n_l = 0$ in the initial moment $\tau = 0$, we obtain the following equation:

$$n_l = A[K K_e C_{FSS} C_{OH^-}/(C_{CH_2(OH)_2} + K K_e C_{FSS} C_{OH^-})]\tau, \quad (10)$$

where $A = k_c Z_\infty S f$.

As seen from Eq. (10), the reaction rate is independent of the leuco compound concentration, which is confirmed by experimental data [Fig. 1, linear portion of the dependences $n_l = f(\tau)$]. The k_{app} value determined from the kinetic curves can be represented as

$$k_{app} = A K K_e C_{FSS} C_{OH^-}/(C_{CH_2(OH)_2} + K K_e C_{FSS} C_{OH^-}). \quad (11)$$

The linear form of Eq. (11) is given by

$$1/k_{app} = C_{CH_2(OH)_2}/A K K_e C_{FSS} C_{OH^-} + 1/A. \quad (12)$$

The experimental rate constants as functions of the concentration of some reagents (FSS, NaOH, and formaldehyde) at constant concentrations of the other components are shown in Figs. 2a–2c.

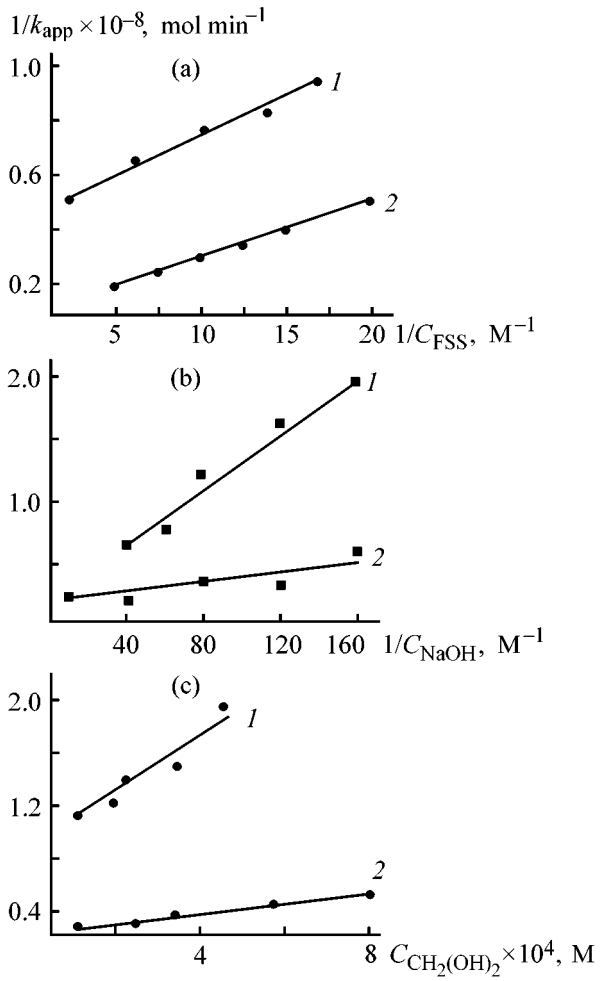

Fig. 2. Reaction rate constants k_{app} in relation to the concentration of (a) FSS C_{FSS}, (b) NaOH C_{NaOH}, and (c) formaldehyde $C_{CH_2(OH)_2}$. Concentration, M: (a) 0.025 NaOH, (b) 0.2 FSS, and (c) 0.025 NaOH and 0.2 FSS. Temperature, K: (*1*) 353 and (*2*) 363.

Parameters of kinetic equation (12) (N = 800 rpm; concentration, M: (I) 0.025 NaOH; (II) 0.2 FSS, and (III) 0.025 NaOH and 0.2 FSS)

T, K	$1/k_{app} = f(1/C_{FSS})$ (I)		$1/k_{app} = f(1/C_{NaOH})$ (II)		$1/k_{app} = f(1/C_{CH_2(OH)_2})$ (III)	
	$A \times 10^8$, mol min^{-1}	$C_{CH_2(OH)_2}/KK_e \times 10^3$, mol^2 l^{-1}	$A \times 10^8$, mol min^{-1}	$C_{CH_2(OH)_2}/KK_e \times 10^3$, mol^2 l^{-1}	$A \times 10^8$, mol min^{-1}	$1/KK_e$, mol
363	10.9 ± 1.1	6.8 ± 2.2	7.4 ± 1.5	3.7 ± 1.3	4.2 ± 1.5	7 ± 2
353	2.2 ± 0.8	1.6 ± 0.9	2.5 ± 0.6	5.2 ± 1.4	1.2 ± 0.7	14 ± 4

The linear dependences obtained in the coordinates of Eq. (12) and the close values of the parameters, calculated from these data (see table), indicate that our model adequately describes the experimental results.

The parameter A includes the rate constant of the chemical reduction of the dye by SO_2^{2-} anions on the dye surface. Therefore, using known values of A at different temperatures, we can evaluate the activation energy of this stage. According to the Arrhenius equation, the activation energy is 185 ± 10 kJ mol^{-1}.

Using the equilibrium rate constants K_e [9] for cleavage of formaldehyde sodium sulfoxylate molecules and parameters $1/KK_e$ given in the table, we calculated the sorption equilibrium constants K to be 2.73×10^4 and 4.06×10^4 mol^{-1} at 80 and 90°C, respectively.

A slight rise in K with increasing temperature indicates that the sorption is endothermic, probably owing to desolvation of the reducing agent molecules and the dye surface in the course of sorption.

CONCLUSIONS

(1) The kinetics of heterogeneous reduction of the vat dye by formaldehyde sodium sulfoxylate under kinetic control conditions was studied.

(2) Based on dependences of the reduction rates on temperature and on concentrations of the reducing agent, alkali, and formaldehyde, the mechanism of this process was proposed and the kinetic equation describing their effect on the process rate was evaluated.

(3) Experimental verification of this equation showed scheme the proposed described adequately to kinetic data.

REFERENCES

1. Yakimchuk, R.P., Mishchenko, A.V., and Bulusheva, N.E., *Primenenie kubovykh krasitelei* (Use of Vat Dyes), Moscow: Legprombytizdat, 1985.
2. Baumgarte, U., *Textilveredlung*, 1969, vol. 4, no. 11, pp. 821–832.
3. Porter, J.J., *Text. Res. J.*, 1966, vol. 36, no. 3, pp. 289–290.
4. Fox, M.R., *J. Soc. Dyers Color.*, 1962, vol. 78, no. 8, pp. 393–404.
5. Astaf'eva, I.V., Polenov, Yu.V., Fain, E.Ya., and Budanov, V.V., *Zh. Prikl. Khim.*, 1991, vol. 64, no. 3, pp. 697–701.
6. Astaf'eva, I.V., Polenov, Yu.V., Zorenko, I.B., and Budanov, V.V., *Mezhvuzovskii sbornik nauchnykh trudov "Luchshie raboty studentov – narodnomu khozyaistvu strany"* (Intercollegiate Coll. of Scientific Works "The Best Students' Studies for National Economy"), Moscow, 1990, pp. 44–46.
7. Pleskov, Yu.V. and Filinovskii, V.Yu., *Vrashchayushchiisya diskovyi elektrod* (Rotating Disk Electrode), Moscow: Nauka, 1972.
8. Golomb, L.M. and Shalimova, G.V., *Tekstil. Prom–st.*, 1962, no. 5, pp. 67–80.
9. Delmon, B., *Introduction á la Cinétique Hétérogene*, Paris: Technip, 1969.
10. Budanov, V.V. and Makarov, S.V., *Khimiya serosoderzhashchikh vosstanovitelei* (Chemistry of Sulfur-Containing Reducing Agents), Moscow: Khimiya, 1994.

Russian Journal of Applied Chemistry, Vol. 74, No. 8, 2001, pp. 1305–1309. Translated from Zhurnal Prikladnoi Khimii, Vol. 74, No. 8, 2001, pp. 1269–1273.

SORPTION AND ION-EXCHANGE PROCESSES

Gallium(III) Extraction from Alkaline Solutions with 5-Amylthio-8-quinolinol

A. N. Turanov, N. K. Evseeva, and B. G. Karepov

Institute of Physics of Solids, Russian Academy of Sciences, Chernogolovka, Moscow oblast, Russia

Received November 27, 2000

Abstract—Equilibrium extraction of gallium(III) from alkaline solutions with 5-amylthio-8-quinolinol was studied.

The main source of gallium are alkaline solutions of alumina production. A promising procedure for gallium recovery from these solution is extraction [1]. The best extractants of gallium(III) from alkaline solutions are chelating agents [2, 3]. Gallium extraction with 8-quinolinol derivatives, and particularly with 7-(5,5,7,7-tetramethyl-1-octen-3-yl)-8-quinolinol produced under the trade name Kelex 100, was studied in detail in [4–8]. Extraction properties of 8-quinolinols substituted at the position 5 have been studied to a lesser extent [9, 10]. Bankovskii *et al*. prepared 5-alkylthio derivatives of 8-quinolinol [11] and studied physicochemical properties of chelates of this compounds with a number of metals [12]. It was noted that these chelates are readily soluble in low-polar organic solvents, which makes these extractants promising for application in hydrometallurgy, including gallium(III) recovery from aqueous alkaline solutions.

In this work, we studied the extraction equilibrium attained during Ga(III) recovery from aqueous alkaline solution into an organic phase containing 5-amylthio-8-quinolinol (HL) or into a phase of macroporous polymeric sorbent impregnated with 5-amylthio-8-quinolinol.

EXPERIMENTAL

As extractant was used 5-amylthio-8-quinolinol [TU (Technical Specifications) 6-09-16-1300–82, Biokhimreactiv Scientific and Production Association]. Chloroform, 1,2-dichloroethane, CCl_4, toluene, *m*-xylene, *n*-decane of chemically pure or analytically pure grade and lamp kerosene were used as solvents as received. When kerosene was used as a solvent, the organic phase was solubilized by adding 10% *n*-decanol [8].

Impregnated sorbent was prepared from nonionic macroporous styrene-divinylbenzene copolymer, Wofatit EP-60 (Bitterfeld Chemical Plant, Germany). The properties of this copolymer, presented in [13], are close to those of similar materials produced in Russia—Polisorbs [14]. The copolymer was impregnated with 5-amylthio-8-quinolinol by the procedure described in [15].

The starting Ga(III) solutions were prepared by dissolving gallium oxide of pure grade in 1 M NaOH, with subsequent dilution with water. The required pH or NaOH concentration was adjusted by adding HCl or NaOH solutions prepared from chemically pure grade chemicals. The Ga(III) content in the starting solutions was 1×10^{-3} M.

Extraction and sorption were performed under static conditions at $18 \pm 2°C$. The aqueous phase was mixed with an extractant solution or with impregnated sorbent in a mixing apparatus with stirrer rotating at 60 rpm for 3 h. Under these conditions, a constant distribution coefficient of gallium D_{Ga} was attained. The phase volume ratio in extraction and in sorption was $V_a : V_o = 11 : 1$ and $V_a : m_{sol} = 20 : 1$, respectively.

The gallium(III) content in aqueous solutions before and after extraction or sorption was determined photocolorimetrically with PAR [16] on a KFK-2MP photocolorimeter. The NaOH concentration in the aqueous solutions was determined by potentiometric titration; the pH was measured with a pH-150 pH meter.

Gallium(III) extraction with chelating extractants depends on the pH of the aqueous phase (Fig. 1, curve *6*), since the concentration of H^+ (or OH^-) ions affects both the protolytic equilibrium of the extractants and the speciation of Ga(III) in the aqueous

1070-4272/01/7408-1305 $25.00 © 2001 MAIK "Nauka/Interperiodica"

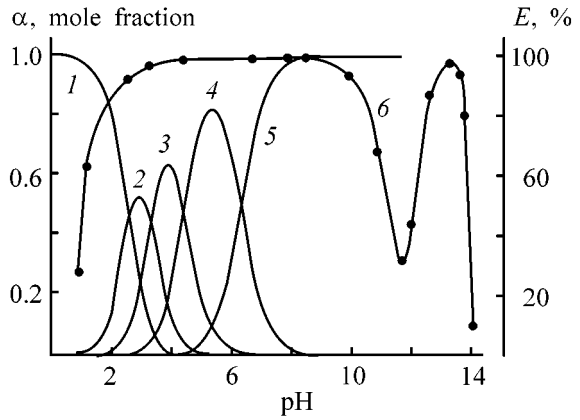

Fig. 1. Mole fraction of (*1*) Ga^{3+}, (*2*) $Ga(OH)_2^+$, (*3*) $Ga(OH)_2^+$, (*4*) $Ga(OH)_3$, and (*5*) $Ga(OH)_4^-$ in the aqueous phase, and (*6*) extraction *E* of gallium with 0.05 M solution of HL in kerosene containing 10% decanol vs. pH of the aqueous phase.

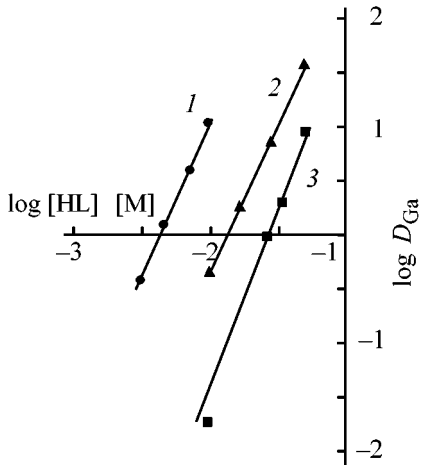

Fig. 2. Gallium(III) distribution coefficient of D_{Ga} vs. the HL content in (*1, 2*) chloroform and (*3*) kerosene containing 10% decanol in extraction of gallium from NaOH solution. C_{NaOH}, M: (*1*) 1.0, (*2*) 0.067, and (*3*) 0.3.

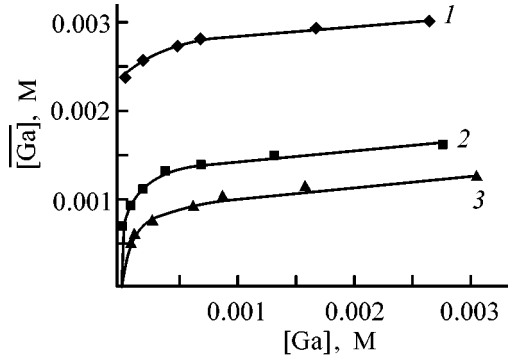

Fig. 3. Gallium(III) distribution between 1 m NaOH and a solution of HL in chloroform. ([$\overline{Ga}$], [Ga]) Equilibrium gallium(III) concentrations in organic and aqueous phases, respectively. Initial HL concentration in theorganic phase: (*1*) 0.01, (*2*) 0.006, and (*3*) 0.005.

phase in the form of Ga^{3+} ion or hydroxo complexes $Ga(OH)_i^{(3-i)+}$, where i = 1–4.

Since the distribution factor of 5-amylthio-8-hydroxyquinolquinoline in the tested extraction system is $P_{HL} = 3.8 \times 10^5$ [12], it is present mainly in the organic phase.

The mole fraction of Ga(III) species α_i at a certain pH can be calculated from the stability constant of gallium hydroxo complexes β_i by the equation

$$\alpha_i = \frac{\beta_i [OH^-]^i}{1 + \sum_{1}^{i=4} \beta_i [OH^-]^i}. \quad (1)$$

The values $\log \beta_1 = 11.4$, $\log \beta_2 = 22.1$, $\log \beta_3 = 31.7$, and $\log \beta_4 = 39.4$ were taken from the handbook [17]. Comparison of the dependence of the gallium(III) extraction on the pH of the aqueous phase (Fig. 1, curve *6*) and diagrams of distribution of Ga(III) hydroxo complexes as a function of pH (Fig. 1, curves *1–5*) indicates that the maximum gallium(III) extraction corresponds to formation of gallium(III) hydroxo complexes in the aqueous phase.

Gindin *et al*. [18] showed that the extraction constants of metal carboxylates depend on the solubility product of the extracted metal hydroxide, i.e., extraction can be regarded as hydrolytic recovery of metal compounds into the organic phase. In terms of this assumption, gallium(III) extraction can be described by reaction of Ga(III) hydroxides with undissociated HL molecules, i.e., by neutralization reaction, as proposed in [19]:

$$Ga(OH)_i^{(3-i)+} + (3 - i)OH^- + 3\overline{HR} \rightleftarrows \overline{GaL}_3 + 3H_2O \quad (2)$$

(i = 0–4, the components of the organic phase are marked with overline).

The Ga : L ratio in the extracted complexes, determined by the equilibrium shift method [20] is 1 : 3 (Fig. 2), which is consistent with the data on saturation of an HL solution with gallium(III) (Fig. 3) and agrees with the results of [12].

The constants of Ga(III) extraction described by reaction (2) are expressed by

$$K_i = \frac{[\overline{GaL}_3]}{[Ga(OH)_i][OH^-]^{(3-i)}\,[\overline{HL}]^3}, \quad (3)$$

where the total concentration of Ga(III) in the organic phase is calculated as

$$[\overline{GaL}_3] = [\overline{HL}]^3 \Sigma K_i [Ga(OH)_i][OH^-]^{(3-i)}. \quad (4)$$

Hence, the dependence of the experimental distribution coefficient of gallium(III) on the extractant concentration in the organic phase and the OH^- concentration in the aqueous phase can be described by the equation

$$D_{Ga} = \frac{[\overline{GaL_3}]}{[Ga(III)]_a} = \frac{[\overline{HL}]^3\,[Ga^{3+}][OH^-]^3\Sigma K_i\beta_i}{[Ga^{3+}](1 + \Sigma\beta_i\,[OH^-]^i)}$$

$$= \frac{[OH^-]^3\,[\overline{HL}]^3 K'}{(1 + \Sigma\beta_i\,[OH^-]^i)} \quad (5)$$

or

$$D_{Ga} = \frac{\alpha_3 K'[\overline{HL}]^3}{\beta_3} = \alpha_3[\overline{HL}]^3 K'_{ex}, \quad (6)$$

where $[\overline{HL}] = C_{HL} - 3[\overline{Ga}]$, C_{HL} is the initial concentration of HL in the organic phase, and K'_{ex} is the extraction constant.

The distribution coefficient D_{Ga} is proportional to the mole fraction of gallium hydroxide in the aqueous phase. This indicates that the maximum extraction of gallium(III) from weakly acidic and neutral solutions is provided by chemical reaction of the extractant with gallium hydroxide. The results of a study of gallium(III) extraction with oligomeric phenolic extractant [19] confirm this assumption.

The logarithm of the equilibrium extraction constant $\log K^e_{ex}$, calculated by Eq. (6) on the basis of the data shown in Fig. 1 is 9.15 ± 0.03 and remains constant at pH ranging from 1.7 to 11.5. This fact confirms the scheme proposed for gallium(III) extraction.

We suggest that, since the HL content in the aqueous phase is low owing to the high P_{HL}, gallium(III) extraction involves (i) formation of gallium(III) hydroxide hydrated to a lesser extent as compared with ionic forms of Ga(III) and (ii) transition of gallium hydroxide from the aqueous phase to the interface. Gallium complex GaL_3 formed via neutralization of $Ga(OH)_3$ by HL at the interface passes into the organic phase. The occurrence of reaction (2) is confirmed by the fact that solid gallium oxide and hydroxide are dissolved in organic solutions of 5-amylthio-8-quinolinol to form GaL_3.

Equation (6) describes well a decrease in D_{Ga} with the concentration of OH^- ions in the aqueous phase increasing to pH 11.5 (Fig. 1). Since Ga(III) in alkaline solutions is mainly in the form of tetrahydroxogallate anion, gallium(III) extraction from alkaline solution can be described by the reaction

$$Ga(OH)_4^- + 3\overline{HL} \overset{K_4}{\rightleftarrows} \overline{GaL_3} + 3H_2O + OH^-. \quad (7)$$

With increasing OH^- concentration, the equilibrium (7) is shifted to the left, i.e., D_{Ga} decreases.

At pH > 11.5, D_{Ga} grows with increasing pH (Fig. 1). This may be due to the fact that OH^- ions formed at pH > 11.5 by reaction (7) are neutralized by HL molecules by the reaction

$$\overline{HL} + Na^+ + OH^- \overset{K_{NaOH}}{\rightleftarrows} \overline{NaL} + H_2O. \quad (8)$$

As a result, equilibrium (7) is shifted to the right, i.e., D_{Ga} increases. At excess amount of HL in the system with respect to Ga(III), the distribution coefficient D_{Ga} grows while $[\overline{NaL}] \le [\overline{Ga}]$. Then D_{Ga} decreases with pH increasing above 13.3, owing to the lowering of the HL concentration in the organic phase because of the NaL formation. In this case, the dependence of D_{Ga} on the activity of the components of the aqueous phase a and the initial concentration of the extractant in the organic phase can be expressed by the equation

$$D_{Ga} = \frac{K_4(C_{HL} - 3[\overline{GaL_3}])^3}{(1 + K_{NaOH}a^2_{OH^-})^3 a_{OH^-}\,a^3_{H_2O}}. \quad (9)$$

Thus, appreciable coextraction of sodium cations results in that gallium(III) extraction decreases dramatically with increasing NaOH concentration in the aqueous phase (Fig. 4). D_{Ga} Cannot be made higher by raising the extractant concentration in the organic phase at NaOH concentrations exeeding 1 M, owing to the low solubility of the sodium salt of the extractant (not exceeding 0.02 M) in the chosen organic solvents.

Gallium(III) extraction from alkaline solutions strongly depends on the nature of the organic diluent. The distribution coefficients D_{Ga} between 0.004 M solution of 5-amylthio-8-quinolinol and 1 M NaOH are presented below:

Diluent	D_{Ga}
Chloroform	2.72
1,2-Dichloroethane	1.12
Toluene	0.41
m-Xylene	0.28
CCl_4	0.29
n-Decane	0.04

Similar dependences were observed in Ga(III) extraction with 8-quinolinol from weakly acidic solutions [21].

Gallium(III) extraction from alkaline solutions with solutions of HL in nonpolar diluents, commonly used in extraction, is very low owing to the formation of sodium salt of the extractant, which is difficultly

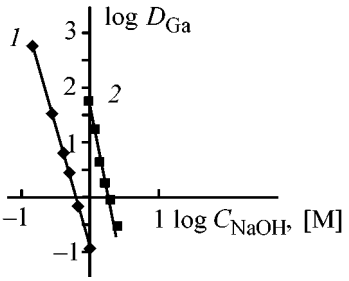

Fig. 4. Gallium(III) distribution coefficient D_{Ga} vs. the NaOH concentration C_{NaOH} in the aqueous phase in extraction with (*1*) 0.05 M solution of HL in kerosene containing 10% decanol and (2) 0.01 M solution of HL in chloroform.

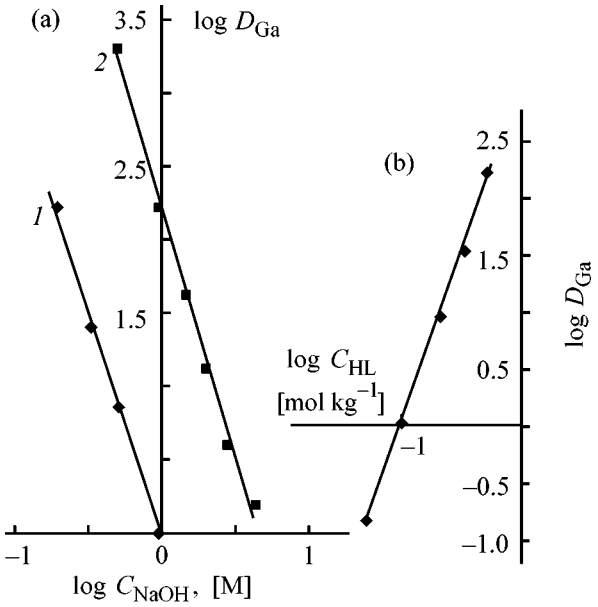

Fig. 5. Gallium(III) distribution coefficient D_{Ga} vs. (a) NaOH concentration C_{NaOH} in the aqueous phase and (b) the HL concentration C_{HL} in the sorbent phase. in sorption by impregnated sorbent. (a) C_{HL}: (*1*) 0.1, and (*2*) 0.5; (b) C_{NaOH} = 1.0 M.

soluble in the organic phase and precipitates at the interface. Addition of decanol to kerosene makes D_{Ga} higher. However, at decanol concentration higher than 10%, D_{Ga} decreases, probably owing to the formation of hydrogen bonds between the alcohol and phenol groups of the extractant.

Sato *et al*. [5] observed a similar decrease in D_{Ga} when studying Ga(III) extraction from alkaline solutions with Kelex 100 extractant in the presence of 2-ethylhexanol. It should be noted that Kelex 100 in kerosene, unlike 5-amylthio-8-quinolinol, extracts Ga(III) from concentrated NaOH solutions. This can be accounteg for by lower coextraction of sodium ions with Kelex 100, which is appreciable only at NaOH concentrations higher than 5 M, when D_{Ga} sharply decreases [6].

As seen from the dependence of D_{Ga} on the composition of equilibrium phases [Eq. (9)], to enhance Ga(III) extraction with the chelating agent from alkaline solutions, i.e., to shift the D_{Ga}–C_{NaOH} curve to higher NaOH concentrations, the structure of the extractant must change so as to decrease the stability of the sodium complex at the interface. In particular, extraction of sodium ions with phenol derivatives strongly depends on the dissociation of the extractant, which usually decreases with lengthening of the hydrocarbon radical in the extractant molecule. This probably leads to higher D_{Ga} in the system 1 M NaOH–0.01 M solution of 8-quinolinol (HOq) derivatives with increasing length of the hydrocarbon radical of the extractants in going from HOq (0.16) to 5-propylthio-8-quinolinol (2.1) and 5-amylthio-8-quinolinol (70.8). Thus, 5-amylthio-8-quinolinol derivatives with long alkyl radical are more promising for liquid extraction of Ga(III) from alkaline solutions.

We also studied Ga(III) extraction from aqueous solutions with NaOH concentrations higher than 1 M by a macroporous sorbent impregnated with 5-amylthio-8-quinolinol. The sodium salt of HL formed in alkaline solution [Eq. (8)] is fixed in the polymeric matrix. In this case, in contrast to liquid extraction, the extractant concentration in the initial impregnated sorbent can be raised to 0.5 mol kg^{-1} of dry sorbent. Since the complex of 5-amylthio-8-quinolinol with Ga(III) is appreciably stronger than that with Na(I), the following exchange reaction can occur at the aqueous phase–solid sorbent interface

$$3\overline{\mathrm{NaL}} + \mathrm{Ga(OH)_4^-} \rightarrow \overline{\mathrm{GaL}}_3 + 3\mathrm{Na^+} + 4\mathrm{OH^-}. \quad (10)$$

It should be noted that Eq. (10) is thermodynamically equivalent to Eq. (7), i.e., the dependences of D_{Ga} on the HL concentration in the solid phase (Fig. 5b) and on the NaOH concentration in the aqueous phase (Fig. 5a) in the case of sorption are similar to those in the case of liquid extraction. As seen from Fig. 5b, Ga(III) is effectively extracted from concentrated NaOH solutions at sufficiently high concentrations of HL in the solid phase.

It is known [4–6] that, in extraction of Ga(III) from alkaline solutions with Kelex 100 extractant, equilibrium is attained slowly. This process is accelerated by adding surfactants to the organic phase [22, 23]. In the case of extraction with 5-amylthio-8-quinolinol, the equilibrium is attained within 3 h. At the same time, with Ga(III) recovered with an impregnated

sorbent, D_{Ga} attains constant value after stirring the phases for 30 min. This is presumably due to the fact that hydrophilic functional groups of 5-amylthio-8-quinolinol sorbed on the polymeric matrix are oriented toward the aqueous phase [24], which strongly facilitates the ion exchange at the interface.

Thus, macroporous styrene-divinylbenzene copolymer impregnated with 5-amylthio-8-quinolinol can be used for gallium(III) recovery and concentration from aqueous alkaline solutions.

CONCLUSIONS

(1) Gallium(III) can be extracted from aqueous solutions with 5-amylthio-8-quinolinol (HL) into the organic phase or into the phase of nonionic macroporous styrene-divinylbenzene copolymer in the form of a GaL_3 complex. The extent of extraction is the highest in the pH range in which Ga(III) is present in the equilibrium aqueous phase in the form of gallium hygroxide.

(2) 5-Amylthio-8-quinolinol applied to a polymeric matrix allows effective extraction and concentration of gallium from 1–3.5 M NaOH solutions.

REFERENCES

1. Reznik, A.M., Ponomareva, E.I., Silaev, Yu.N., *et al.*, *Protsessy ekstraktsii i sorbtsii v khimicheskoi tekhnologii galliya* (Extraction and Sorption in Chemical Technology of Gallium), Alma-Ata: Nauka, 1985.
2. Bukin, V.I., Zhukovskii, P.V., and Reznik, A.M., *Tsvetn. Met.*, 1984, no. 8, pp. 59–62.
3. Apanasenko, V.V., Bukin, V.I., Zhukovskii, P.V., and Reznik, A.M., *Tsvetn. Met.*, 1987, no. 2, pp. 55–57.
4. Leveque, A. and Helgorsky, J., *Proc. Int. Solvent Extraction Conf.*, Toronto, 1977, vol. 2, pp. 439–442.
5. Sato, T., Nakamura, T., Yabuta, M., and Oishi, H., *Chem. Lett.*, 1982, no. 4, pp. 591–592.
6. Sato, T., Nakamura, T., and Oishi, H., *Solvent Extr. Ion Exch.*, 1984, vol. 2, no. 1, pp. 45–60.
7. Sato, T., *J. Jpn. Inst. Light Met.*, 1986, vol. 36, no. 3, pp. 137–142.
8. Sato, T. and Oishi, H., *Hydrometallurgy*, 1986, vol. 16, pp. 315–324.
9. Pescher-Cluzeau, Y., Desbarres, J., and Bauer, D., *Solvent Extr. Ion Exch.*, 1986, vol. 4, no. 2, pp. 301–315.
10. Bauer, D. and Pescher-Cluzeau, Y., *Hydrometallurgy*, 1987, vol. 18, pp. 243–253.
11. Bankovskii, Yu.A., Tsirule, M.A., Brusilovskii, P.I., and Tsilinskaya, I.A., *Khim. Geterotsikl. Soedin.*, 1979, no. 11, pp. 1501–1504.
12. Bankovskii, Yu.A., Zaruma, D.E., Efimenko, I.A., *et al.*, *Zh. Neorg. Khim.*, 1994, vol. 39, no. 5, pp. 797–798.
13. Kremenskaya, I.N., Turanov, A.N., Muhl, P., and Gle, K., *Zh. Prikl. Khim.*, 1984, vol. 57, no. 1, pp. 72–76.
14. Polyakova, V.V. and Levchenko, T.M., *Khim. Tekhnol. Vody*, 1981, vol. 3, no. 4, pp. 327–331.
15. Turanov, A.N., Reznik, A.M., Popandopulo, N.V., and Kremenskaya, I.N., *Zh. Neorg. Khim.*, 1984, vol. 29, no. 8, pp. 2075–2079.
16. Dymov, A.M. and Savostin, A.P., *Analiticheskaya khimiya galliya* (Analytical Chemistry of Gallium), Moscow: Nauka, 1968.
17. Lur'e, Yu.Yu., *Spravochnik po analiticheskoi khimii* (Handbook of Analytical Chemistry), Moscow: Khimiya, 1989.
18. Gindin, L.M., Bobikov, P.I., Patyukov, G.M., and Rozen, A.M., in *Ekstraktsiya* (Extraction), Moscow: Goskhimizdat, 1962, issue 2, pp. 87–111.
19. Zhukovskii, P.V., Bukin, V.I., and Reznik, A.M., *Zh. Neorg. Khim.*, 1985, vol. 30, no. 11, pp. 2888–2890.
20. Gindin, L.M., *Ekstraktsionnye protsessy i ikh primenenie* (Extraction Processes and Their Application), Moscow: Nauka, 1984.
21. Vinogradov, A.V. and Elinson, S.V., *Oksikhinolin* (8-Quinolinol), Moscow: Nauka, 1979.
22. Fourre, P. and Bauer, D., *Anal. Chem.*, 1983, vol. 55, no. 4, pp. 662–667.
23. Fourre, P. and Bauer, D., *Solvent Extr. Ion Exch.*, 1983, vol. 1, no. 1, pp. 465–483.
24. Gustafson, R.L., Albright, R.L., Heisler, J., *et al.*, *JEC Res. Devel.*, 1968, vol. 7, no. 2, pp. 107–115.

Russian Journal of Applied Chemistry, Vol. 74, No. 8, 2001, pp. 1310–1317. Translated from Zhurnal Prikladnoi Khimii, Vol. 74, No. 8, 2001, pp. 1274–1281.

APPLIED ELECTROCHEMISTRY AND CORROSION PROTECTION OF METALS

Voltammetric Determination of Cobalt(II) in Zinc Sulfate Solution

G. A. Borovkov and V. I. Monastyrskaya

North-Ossetian State University, Vladikavkaz, North Ossetia, Russia

Received January 16, 2001; in final form, April 2001

Abstract—A method for automated polarographic analysis for Co(II) ions in technological solutions of zinc production was developed. The influence exerted by the components of a supporting electrolyte on the sensitivity and selectivity of measurements was studied. The method is intended for determining the content of cobalt(II) in purification of a zinc sulfate solution to remove impurities and for ecological monitoring of wastewater produced at nonferrous metallurgy plants.

Thorough purification of technological solutions to remove impurities adversely affecting the process of electrolysis is the necessary condition for achieving high performance in hydrometallurgical manufacture of zinc. The impurities whose concentration in a zinc-containing electrolyte is strictly regulated include cobalt(II). At Co(II) ion content in a purified zinc sulfate solution exceeding 2 mg l^{-1}, the cathode sheet is corroded, the current efficiency markedly decreases, and energy consumption grows [1]. Use of new hi-tech purification processes makes it possible to reduce the content of Co(II) in a neutral zinc-containing electrolyte to 0.5 mg l^{-1}. In particular, a new purification method has been put into practice, based on oxidation of Co(II) to Co(III) with potassium permanganate, with subsequent removal of cobalt(III) ions from the process in the form of a poorly soluble $Co(OH)_3$.[1]

Effective purification of zinc production solutions to remove impurities is impossible without continuous or discrete monitoring of the ionic composition at the input and output of separate stages of the technological process [2]. The most complicated is the problem of selective monitoring of low concentrations of Cu(II), Cd(II), Sb(III), Pb(II), Ni(II), and Co(II) ions in purified zinc sulfate solutions.

Among physicochemical analysis methods that have found wide use in automated or proximate analysis of the ionic composition of zinc-containing solutions is differential pulse polarography (DPP) [3–5]. The problem of polarographic determination of Co(II) in zinc sulfate solutions has remained unsolved until recently because of the closeness of the reduction potentials of Co(II) and Zn(II) ions found in the overwhelming majority of supporting electrolytes employed in analytical practice.

The highest resolution of the DPP method in determining Co(II) in concentrated zinc solutions was achieved in [6], where measurements were done in a supporting electrolyte of composition 0.1 M sodium citrate $Na_3C_6H_5O_7$ + 0.1 M NH_4Cl + 0.08% dimethylglyoxime $C_4H_8O_2N_2$ (DMG). The difference of the reduction potentials of Co(II) and Zn(II) ions at the dropping mercury electrode is 240 mV (φ_p^{Co} = –1.02, φ_p^{Zn} = –1.26 V), which enables monitoring of Co(II) in the presence of a 50×10^4-fold excess of Zn(II), with lower detection limit of 2.5 mg l^{-1}. However, such selectivity and sensitivity of DPP are insufficient for determining 0.5 mg l^{-1} Co(II) in neutral solutions containing up to 150 g l^{-1} Zn(II), i.e., under the conditions of a modern high-efficiency zinc production.

In addition to Zn(II), adverse influence on voltammetric determination of Co(II) in supporting solution of composition 0.1 M $Na_3C_6H_5O_7$ + 0.1 M NH_4Cl + 0.08% DMG is also exerted by Mn(VII) and Ni(II) whose DPP peak potentials are, according to the authors' data, –0.98 and –0.97 V, respectively. It should be mentioned that the concentrations of Ni(II) and Co(II) ions in a purified zinc-containing solution are, as a rule, comparable, whereas the content of Mn(VII) exceeds that of Co(II) more than 1000-fold [7]. The cathodic voltammetric curves of Mn(VII) and Ni(II) mask the DPP peak of Co(II), and, already at concentration (mg l^{-1}) ratios [Ni] : [Co] = 4 : 1 and [Mn] : [Co] = 5 : 1, polarographic determination of Co(II) in the given supporting electrolyte becomes impossible.

[1] Elektrotsink Plant (Vladikavkaz).

1070-4272/01/7408-1310 $25.00 © 2001 MAIK "Nauka/Interperiodica"

A significant shortcoming of the technique proposed in [6] is that the slope of the calibration plot for Co(II) depends on the content of Zn(II) in a solution being analyzed, which inevitably impairs the accuracy of measurements. Moreover, the necessity for blowing nitrogen, for deoxygenation purposes, through a solution being analyzed markedly hinders automation of polarographic analysis under industrial conditions.

The present study established the possibility of substantially increasing the selectivity, sensitivity, and accuracy of Co(II) determination in a purified zinc solution when performing a polarographic analysis in a supporting electrolyte containing DMG and hydroxylamine hydrochloride.

The ion concentration in solutions was monitored by DPP on an AZhE-11 voltammetric analyzer equipped with a transducer with stationary dropping mercury electrode (SDME) of the valve type [8]. A three-electrode electrochemical cell was used (working electrode of the "hanging mercury drop" type, silver chloride reference electrode, glassy carbon auxiliary electrode). Rectangular 40-ms pulses with repetition period of 80 ms were applied.

The chloride-ammonia supporting electrolyte is widely used in analytical practice for determining cobalt(II) in various objects. The Co(II) half-wave potential on the background of 1 M NH_4Cl + 1 M NH_4OH is –1.3 V [9]. The sensitivity of analysis is improved dramatically upon introducing into the supporting electrolyte an alcoholic or ammonia solution of DMG [10, 11]. The height of the cathodic peak of Co(II) strongly depends on the DMG concentration and the pH of the medium. For example, in [11], a solution being analyzed was titrated with an ammonia solution to pH 9.0, prior to being subjected to polarography, in order to raise the sensitivity. A new electrochemically active complex, reduced at mercury electrode in a more positive range of potentials, is formed in a DMG-containing chloride–ammonia supporting electrolyte. It has been established that a catalytic wave, which can be used for analytical purposes, is recorded in an ammonia solution of DMG in the presence of Co(II) [12, 13]. In [14], a mechanism was proposed, describing the appearance of a catalytic current of hydrogen in an ammonia buffer solution in the presence of cobalt(II) and nickel(II) dimethylglyoximates.

It was pointed out in monograph [15] that none of DMG complexes gives a polarographic wave similar to the catalytic wave of a complex with cobalt(II). Presumably this occurs because the hydrogen ion in the complex, which is involved in the hydrogen bond,

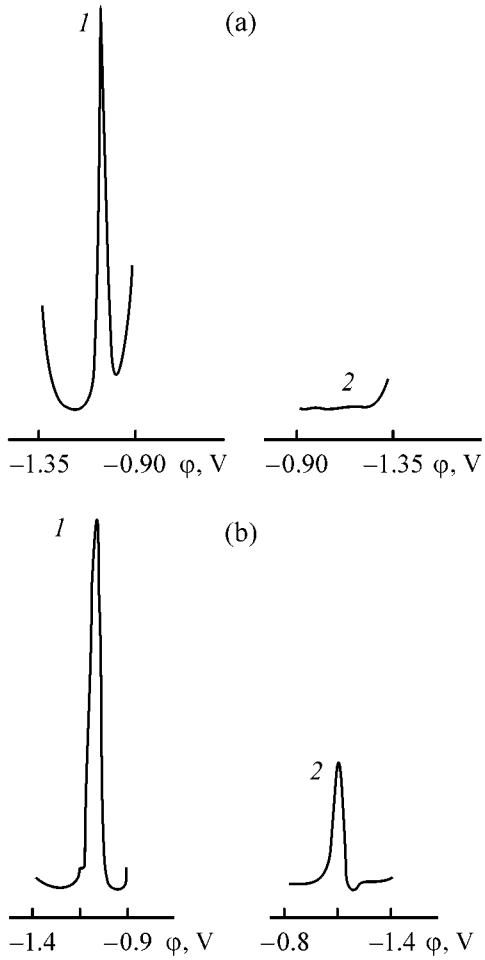

Fig. 1. DPP curves of cobalt(II). (φ) Potential; the same for Figs. 2, 3, and 6. Co(II) concentration (mg l^{-1}): (a) 0.5 and (b) 0.1. Buffer solution: (a) I and (b) II; the same for Fig. 3. Curve: (*1*) cathodic and (*2*) anodic.

is reduced, and this process is responsible for the catalytic action of the molecule of the complex. According to IR spectral analysis, the weakest hydrogen bonds are found in complexes of cobalt(II) with DMG, compared with other doubly charged transition metals. The experimental data obtained in [10] indicate that Co(II) dimethylglyoximates much exceed Cu(II) and Ni(II) dimethylglyoximates in catalytic effect.

The authors of [6] noticed that the voltammetric curves of Co(II) in the presence of 0.1 M $Na_3C_6H_5O_7$ + 0.1 M NH_4Cl + 0.08% DMG, recorded using cyclic voltammetry with triangular wave, reveal no anodic peak. This shows that reduction of Co(II) chelate with DMG is totally irreversible. A similar result was obtained in the present study in recording cathodic and anodic voltammetric curves of Co(II) with a DMG-containing chloride-ammonia supporting electrolyte

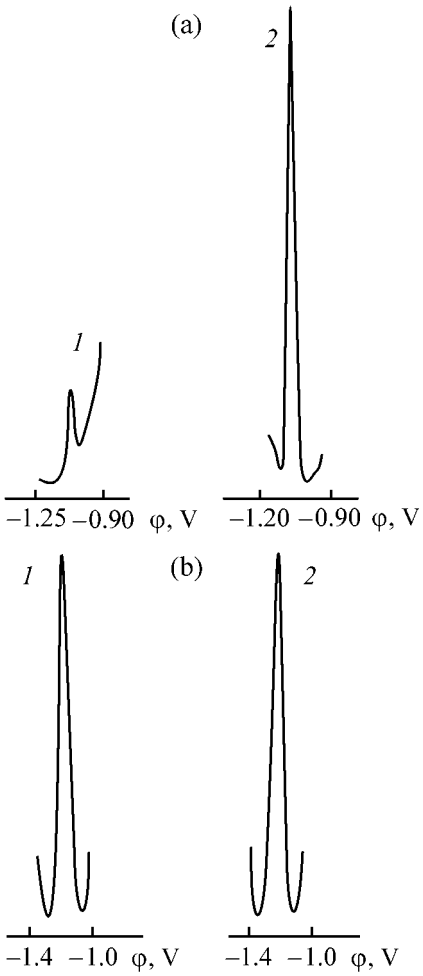

Fig. 2. Effect of $NH_2OH \cdot HCl$ on polarographic determination of (a) cobalt(II) and (b) zinc. Ion concentration (mg l^{-1}): (a) Co(II): (*1*) 0.05 and (*2*) 0.005; (b) Zn(II) 20.2. Buffer solution: (*1*) I and (*2*) II.

by DPP on SDME. The buffer solution of composition 1 M NH_4Cl + 1 M NH_4OH + 1×10^{-3} M DMG (pH 9) (I) was prepared in accordance with the methodological recommendations of [10, 11].

It can be seen from Fig. 1a that Co(II) is irreversibly reduced at SDME in solution I at a DPP peak potential of –1.04 V (curve *1*), whereas anodic curve in this range of potentials reveals no DPP peak (curve *2*). Introduction of 0.2 M of hydroxylamine hydrochloride (Fig. 1b, curve *1*) shifts the DPP peak potential of Co(II) by 60 mV into the negative range of voltages (φ_p = –1.10 V), which indicates the formation in the solution, and electroreduction at SDME, of a new complex compound. In the process, the cathodic peak height increases more than 50-fold, and a peak at –1.09 V is recorded in the anodic voltammogram (Fig. 1b, curve *2*).

An assumption can be made on the basis of the data of [16] that introduction of hydroxylamine into a DMG-containing chloride-ammonia buffer leads to formation of a complex compound of cobalt(II) with two ligands (hydroxylamine and DMG). The cathodic DPP peak of the mixed complex is characterized by the appearance of a catalytic current which much exceeds that of the complex of cobalt(II) with DMG (Fig. 2a) and, even the more so, the limiting diffusion current of the cobalt(II) ion [10]. The higher sensitivity in the case of polarography of catalytic currents of coordination compounds and the reversibility of their waves correspond to catalysis by the metal ion–ligand complex which can be formed both in the solution bulk and in the adsorption layer [17, 18]. Of fundamental importance for selectively determining Co(II) ions in zinc solutions is the fact that addition of hydroxylamine hydrochloride to a DMG-containing chloride-ammonia supporting electrolyte has virtually no effect on the height and shape of the voltammetric curve for reduction of Zn(II) ions (Fig. 2b).

In considering the mechanism of action of $NH_2OH \cdot HCl$ in polarographic determination of cobalt(II) on SDME, an assumption can be made that, in the presence of hydroxylamine, the formation of the new polarographically active complex involves DMG adsorbed onto the surface of the mercury electrode (the chemical stage preceding the reduction is of surface-heterogeneous nature). The system electrode–DMG–cobalt(II)–hydroxylamine is electrically conducting, and the reduction of the mixed complex occurs via "bridge" transfer of electron. It is assumed that electrochemically active complexes with two or more ligands (with account of the ammonia buffer in the given case), adsorbed onto the electrode surface, have a more distorted symmetry than similar complexes in the solution bulk, which must, in turn, lead to faster charge transfer rate [17] and, correspondingly, to higher catalytic current and better sensitivity of polarographic analysis.

The possibility of polarographic determination of Co(II) with supporting solution I is strongly limited by the hindering action of Mn(VII) and Zn(II) ions (Fig. 3a), similarly to the case when 0.1 M $Na_3C_6H_5O_7$ + 0.1 M NH_4Cl + 0.08% DMG is used as supporting electrolyte [6]. In the presence of manganese (VII) in a solution being analyzed, the right-hand branch of the DPP peak of cobalt(II) is distorted (curve *2*). Presence of Zn(II) ions in a solution being monitored distorts the left-hand branch of the DPP peak of cobalt (curve *3*). At a 100-fold excess of Mn(VII) and Zn(II), polarographic determination of Co(II) ions in solution I becomes virtually impos-

sible (curve *4*). When zinc(II) ions are present in a solution being analyzed, the slope of the calibration plot for cobalt(II) changes, which inevitably impairs the measurement accuracy. The masking action of Mn(VII) and Zn(II) ions in polarographic determination of Co(II) is eliminated by introduction of hydroxylamine hydrochloride into a solution being analyzed.

Redox reactions of $NH_2OH \cdot HCl$ with $KMnO_4$ were considered in [19]. In alkaline medium, hydroxylamine reduces Mn(VII) to Mn(II); the reaction rate is high since the forming Mn(II) ions catalyze the oxidation of $NH_2OH \cdot HCl$. A visual sign of the occurrence of the reaction is the virtually instantaneous decolorization of a solution of permanganate ions into which hydroxylamine is introduced.

In an ammonia-chloride electrolyte, Mn(II) is electrochemically reduced in a more negative range of potentials, compared with Co(II), and does not interfere with its polarographic determination [20]. In supporting solution I, the DPP peak potential of Mn(II) is –1.5 V. When a voltammetric curve is measured with supporting solution I containing 0.2 M $NH_2OH \cdot HCl$, no cathodic DPP peak of Mn(II) is recorded. It can be seen from the polarograms presented in Fig. 3b that the interference of excess concentrations of Mn(VII) and Zn(II) is much weakened on introduction of 0.2 M of $NH_2OH \cdot HCl$ into the supporting solution I.

The investigations performed demonstrated that, in contrast to [10, 11], polarographic determination of Co(II) in a chloride-ammonia supporting solution makes unnecessary maintaining the pH value at a strictly prescribed optimal level. The acid solution of hydroxylamine was neutralized and an alkaline medium, necessary for polarographic determination of Co(II) in the presence of DMF, was created with the use of a buffer solution containing equal molar concentrations of ammonium hydroxide and chloride.

The sensitivity and selectivity of the polarographic determination of Co(II) ions in zinc production solutions strongly depend on the concentrations of the supporting electrolyte, DMG, and hydroxylamine. With decreasing concentration of the chloride-ammonia buffer, the height of the DPP peak of Co(II) markedly grows (Fig. 4, curve *1*). However, in this case, the selectivity of cobalt(II) determination in the presence of excess amounts of zinc(II) markedly decreases. It can be seen from Fig. 4 (curve *2*) that the difference of the potentials of the cathodic DPP peaks of Co(II) and Zn(II) grows with increasing concentration of the supporting solution. Thus, high re-

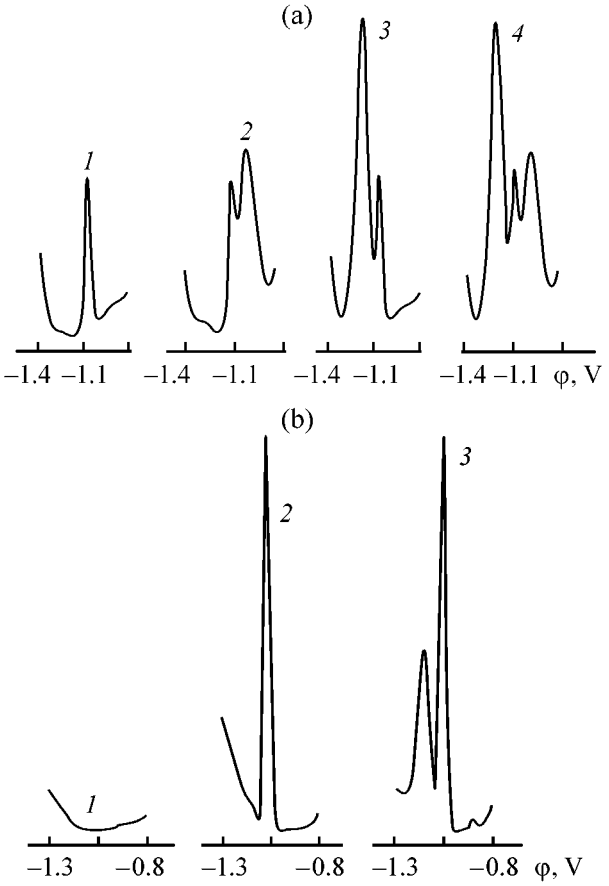

Fig. 3. Effect of accompanying ions on polarographic determination of cobalt(II). Ion concentration (mg l^{-1}): (a) (*1*) Co(II) 0.2, Zn(II), Mn(VII) 0; (*2*) Co(II) 0.2, Mn(VII) 20, Zn(II) 0; (*3*) Co(II) 0.2, Zn(II) 20, Mn(VII) 0; and (*4*) Co(II) 0.2, Mn(VII), Zn(II) 20; (b) (*2*) Co(II) 0.005, Zn(II), Mn(VII) 0; and (*3*) Co(II) 0.005, Zn(II) 100, Mn(VII) 20; (*1*) buffer.

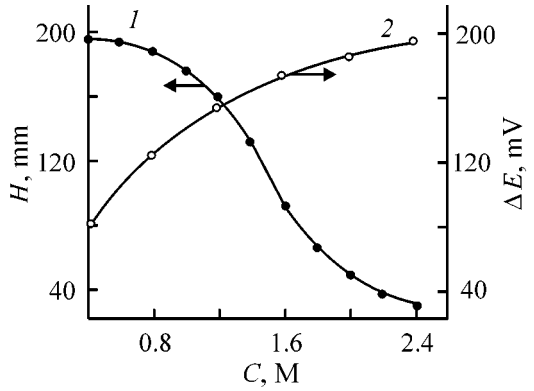

Fig. 4. Sensitivity and selectivity of polarographic determination of cobalt(II) vs. concentration *C* of chloride-ammonia supporting solution $NH_4Cl + NH_4OH$. Concentration of components of the supporting electrolyte (M): DMG 2×10^{-3}, $NH_2OH \cdot HCl$ 0.2. (*1*) (*H*) Height of the DPP peak of cobalt(II) and (*2*) (ΔE) difference of the potentials of DPP peaks of cobalt(II) and zinc(II). Concentration (mg l^{-1}): (*1*) Co(II) 0.005; (*2*) Co(II) 0.025, Zn(II) 6.

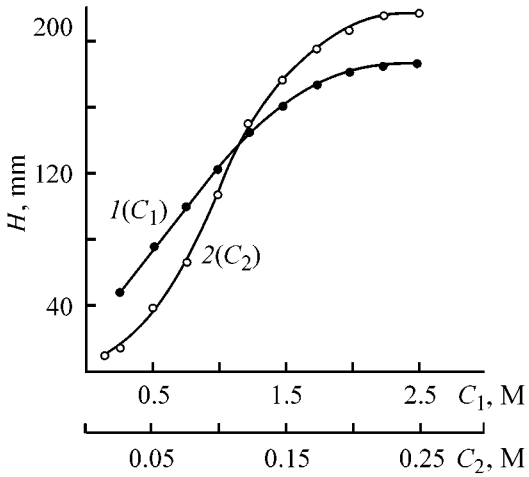

Fig. 5. Sensitivity of polarographic determination of cobalt(II) in a supporting electrolyte 2 M NH_4Cl + 2 M NH_4OH vs. concentrations of DMG, C_1, and hydroxylamine, C_2. Cobalt(II) concentration in solution 0.01 mg l^{-1}. (H) Height of DPP peak of cobalt(II). Concentration (M): (*1*) $NH_2OH \cdot HCl$ 0.2 and (*2*) DMG 2×10^{-3}.

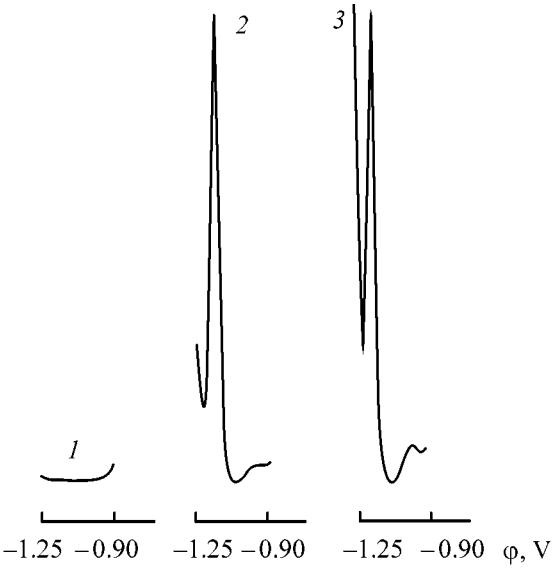

Fig. 6. DPP curves of cobalt(II) in supporting solution II. (*1*) Supporting solution; ion concentration (mg l^{-1}): (*2*) Co(II) 0.005 and Zn(II), Mn(VII) 0; (*3*) Co(II) 0.005, Zn(II) 1500, and Mn(VII) 200.

solution of the polarographic method in determining low contents of cobalt(II) in a zinc sulfate solution can only be achieved with the use of sufficiently concentrated supporting electrolytes. It was found that the optimal buffer solution is that containing 2 M NH_4Cl + 2 M NH_4OH, which enables, at appropriate choice of the DMG and hydroxylamine concentrations, polarographic determination of microscopic amounts of cobalt(II) in zinc electrolytes containing up to 150 g l^{-1} of Zn(II).

It can be seen from Fig. 5 that the sensitivity of cobalt(II) determination in a supporting solution 2 M NH_4Cl + 2 M NH_4OH markedly grows with increasing concentration of DMG (curve *1*) and hydroxylamine (curve *2*). A simultaneous increase in the concentrations of DMG and hydroxylamine improves the selectivity of voltammetric determination of cobalt(II) because of the selective rise in the height of the cathodic (catalytic) peak of Co(II) at unchanged heights of the DPP peaks of the majority of accompanying compounds. With a supporting electrolyte of composition 2 M NH_4Cl + 2 M NH_4OH + 2×10^{-3} M DMG + 0.2 M $NH_2OH \cdot HCl$ (II), direct polarographic determination of Co(II) is possible, with a lower detection limit of 0.0025 mg l^{-1} at a concentration ratio (mg l^{-1}) [Zn] : [Co] = 300 000 : 1. Raising further the concentrations of the components of the supporting electrolyte fails to offer any noticeable advantages, being, therefore, inexpedient.

The sensitivity of polarographic determination of cobalt(II) strongly depends on the rate V_s of potential sweep. With the sweep rate increasing from 0.5 to 10 mV s^{-1}, the height of the cathodic DPP peak of Co(II) varies linearly. Raising the V_s further, to 40 mV s^{-1}, exerts no noticeable influence on the sensitivity of voltammetric analysis, but may affect adversely the reproducibility of measurement results.

Based on the results of the performed experimental investigation, the following optimal conditions of polarographic determination of cobalt(II) in zinc sulfate solutions were chosen: supporting electrolyte II, initial voltage –1.05 V, cathodic potential sweep rate 10 mV s^{-1}, potential sweep 0.25 V. It can be seen from the DPP curves presented in Fig. 6 that this mode of voltammetric analysis ensures high sensitivity and selectivity of Co(II) monitoring in the presence of excess concentrations of Zn(II) and Mn(VII) ions. In a supporting electrolyte of composition 2 M NH_4Cl + 2 M NH_4OH + 2×10^{-3} M DMG, the lower detection limit of Co(II) ions by DPP on SDME is 0.4 mg l^{-1} at admissible concentration (mg l^{-1}) ratios [Zn] : [Co] = 10 000 : 1 and [Mn[: [Co] = 200 : 1, which indicates a significant decrease in the sensitivity and selectivity of analysis in the case when there is no $NH_2OH \cdot HCl$ in the supporting electrolyte.

The calibration plots for Co(II) with supporting solution (II) are linear in the concentration range 0–2.5 mg l^{-1}. Introduction of Zn(II) ions into a solution being analyzed has no effect on the slope of the calibration plot. This makes it possible to achieve a high sensitivity of polarographic determination of Co(II) irrespective of the zinc sulfate concentration in the technological solutions being monitored.

Polarographic determination of Co(II) with supporting solution II in the presence of accompanying substances

Ion	C, mg l^{-1}	E, V (silver chloride electrode)	ΔE, mV	$\alpha_{M/Co}$
Cu(II)	0.1–0.5	–0.43	720	No interference
Cd(II)	1–2	–0.75	400	"
Ge(IV)	≤0.01	–0.96	190	100 : 1
Fe(II)	30–50	–0.98	170	4000 : 1
Ni(II)	0.2–1.0	–1.00	150	400 : 1
Co(II)	0.5–2.0	–1.15	–	–
Zn(II)	(120–150) × 10^3	–1.43	280	300 000 : 1

* C is the content of ions in purified zinc-containing solution, E the DPP peak potential, ΔE the difference between the DPP peak potentials of Co(II) and accompanying ion, $\alpha_{M/Co}$ the maximum admissible ratio of concentrations (mg l^{-1}) of the accompanying impurity and Co(II).

Also, the influence of ion components that are characteristic of technological solutions used in zinc manufacture and can be electrochemically reduced at the mercury electrode in solution II: Cu(II), Cd(II), Ni(II), Fe(II), and Ge(IV) on the polarographic determination of Co(II) was studied.

It can be seen from the data presented in the table that the developed technique ensures high selectivity of Co(II) determination in the presence of the above-mentioned ions and can be used for analyzing purified zinc-containing solutions of complex composition. Microscopic amounts of Sb(III) present in a zinc-containing electrolyte are precipitated in ammonia medium [21]. Fe(III) ions are reduced to Fe(II) by hydroxylamine contained in the supporting electrolyte [19]. Arsenic(III) is reduced at mercury electrode in chloride-ammonia supporting electrolytes at a potential of –1.7 V and does not interfere with polarographic determination of cobalt(II) [22].

The developed technique for voltammetric monitoring of Co(II) ions in zinc sulfate solutions served as a basis for a Kobalt-1 automated analyzer.[2] Raw materials (concentrates) processed at the plant contain considerable amounts of water-soluble compounds of cobalt(II) affecting adversely the electrolysis of zinc.

Previously, technological solutions produced in permanganate purification at the leaching shop were analyzed photocolorimetrically with the use of a nitroso-R salt, forming in aqueous solutions a red complex salt with Co(II) ions at pH 5.5, as a selective complexing agent [23]. The photometric determination of cobalt(II) assumes a complicated procedure for preprocessing of zinc solution samples, including treatment with aggressive reagents, boiling, and cooling, which makes analysis substantially longer and virtually rules out its automation. Photocolorimetric analysis for cobalt(II) in the express laboratory of the leaching shop was made no more than three or four times per shift, which hindered purification in the optimal mode and led to over-expenditure of potassium permanganate.

The analyzer was tested on industrial samples taken from tanks for purified zinc sulfate solution. The concentration of ion components in the solutions being analyzed varied during the tests within the following ranges (mg l^{-1}): Zn(II) (130–140) × 10^3, Mn(VII) 500–1500, Ni(II) 0.2–1.0, Cu(II) 0.1–0.2, Cd(II) 0.5–1.0, Fe(II) 30–50, Co(II) 0.3–2.8, Sb(III) 0.2–0.3; As(III) 0.01–0.05.[3]

A total of 35 zinc solution samples with Co(II) ion concentration varying between 0.48 and 2.36 mg l^{-1} were analyzed. As a control was used the photocolorimetric method of analysis. The reduced rms error of Co(II) determination in the concentration range 0–2.5 mg l^{-1} did not exceed 1.7%. The maximum reduced rms deviation from the results of main and control analyses for cobalt(II) ions in a sample, characterizing the reproducibility of measurements, was 0.5%.

Automation of analysis for Co(II) ions on the basis of the developed voltammetric technique will make it possible to optimize the permanganate purification of technological solutions to remove cobalt(II) impurities and, in the end, to improve the performance in cathode zinc manufacture. The technique can be used for ecological monitoring of Co(II) in industrial wastewater discharged by plants of nonferrous metallurgy.

[2] Put in practice at the Elektrotsink plant.

[3] Data of the production control department of the Elektrotsink plant.

EXPERIMENTAL

Standard solutions of Co(II), Cu(II), Cd(II), Ni(II), Fe(II), Mn(VII), Ge(IV), and Zn(II), prepared by procedures described in [24], were used in the study. The model solutions were prepared using distilled water.

To determine Co(II) in a purified zinc sulfate solution, 0.5 ml of a sample of the zinc-containing electrolyte being analyzed was introduced in a 50-ml volumetric flask, 25 ml of a supporting electrolyte of composition 4 M NH_4Cl + 4 M NH_4OH + 4×10^3 M DMG + 0.4 M $NH_2OH \cdot HCl$ was added, and the solution was brought to the mark with distilled water. The obtained mixture was poured into an electrochemical cell and a cathodic DPP curve was measured in the potential range –1.05…–1.30 V. The potential sweeping was done at a rate of 10 mV s^{-1}, with a set of 3–5 curves obtained and height of cathodic peaks measured at a potential of –1.15 V, and the content of Co(II) in the solution was determined using a calibration plot constructed with account of a 100-fold dilution of the sample. The total duration of analysis of a sample for the content of cobalt(II) is not longer than 5–7 min with manual sample preparation.

In the case of automated analysis, dilution of a sample with water, its mixing with a supporting electrolyte, and delivery of a solution being analyzed into the flow-through voltammetric cell were done with the use of DZZh-4 three-chamber dosing devices made of chemically stable materials [8]. After the sample preparation was complete, commands of the control unit were successively executed in accordance with the preset program to discharge a spent, and form a new mercury drop and to switch-on the potential sweep and the chart strip drive. Each voltammetric curve was recorded with a newly formed mercury drop. After the computing unit calculated the parameters of the voltammetric curve, the output signal of the analyzer, proportional to the concentration of Co(II) ions in a solution being analyzed, was recorded.

CONCLUSIONS

(1) A highly selective method was developed for voltammetric determination of Co(II) ions in zinc manufacture solutions of complex composition with chloride-ammonia buffer solution containing dimethylglyoxime and hydroxylamine as supporting electrolyte.

(2) Introduction of $NH_2OH \cdot HCl$ into the supporting electrolyte improves dramatically the sensitivity and selectivity of polarographic determination of cobalt(II) in the presence of excess concentrations of zinc(II) and completely eliminates the adverse influence of permanganate ions.

(3) The developed method for voltammetric determination of Co(II) ions is easily automated and can be used for on-line monitoring of technological solutions and wastewater of plants of nonferrous metallurgy.

REFERENCES

1. Snurnikov, A.P., *Gidrometallurgiya tsinka* (Hydrometallurgy of Zinc), Moscow: Metallurgiya, 1981.
2. Rannev, G.G. and Salin, A.A., *Metody i pribory avtomaticheskogo kontrolya kachestva rastvorov* (Methods and Instruments for Automated Monitoring of Solution Quality), Tashkent: Fan, 1968.
3. Bond, A.M. and Knight, R.W., *Analyt. Chem.*, 1988, vol. 60, no. 21, pp. 2445–2448.
4. Zaretskii, L.S., Varnovskii, B.I., and Pidorich, M.I., *Zavod. Lab.*, 1982, vol. 48, no. 10, pp. 6–7.
5. Borovkov, G.A. and Dzhioeva, E.A., *Tsvetn. Met.*, 1991, no. 7, pp. 67–70.
6. Geibler, M. and Maia, R.D., Fresenius Z. *Anal. Chem.*, 1988, vol. 330, no. 7, pp. 624–626.
7. Lakernik, M.M. and Pakhomova, G.N., *Metallurgiya tsinka i kadmiya* (Metallurgy of Zinc and Cadmium), Moscow: Metallurgiya, 1969.
8. Borovkov, G.A., Zaretskii, L.S., and Babitskii, L.B., *Tsvetn. Met.*, 1987, no. 1, pp. 49–51.
9. Dolezal, J. and Musil, J., *Polarografická Analyza Nerostných Surovin*, Praha: SNTL, 1977.
10. Astaf'eva, V.V., Prokhorova, G.V., and Salikhdzhanova, R.M.-F., *Zh. Anal. Khim.*, 1976, vol. 31, no. 2, pp. 260–264.
11. Manita, M.D., Salikhdzhanova, R.M.-F., and Yavorskaya, S.F., *Sovremennye metody opredeleniya atmosfernykh zagryaznenii naselennykh mest* (Modern Methods for Determining Atmospheric Contamination of Habitats, Moscow: Meditsina, 1980.
12. Stromberg, A.G. and Zemlyanskaya, A.I., *Zh. Obshch. Khim.*, 1945, vol. 15, no. 2, pp. 303–305.
13. Burger, K., Syrek, G., and Farsang, Gy., *Acta Chim. Acad. Sci. Hung.*, 1966, vol. 49, pp. 113–116.
14. Vinogradova, E.N. and Prokhorova, G.V., *Zh. Anal. Khim.*, 1968, vol. 23, no. 11, pp. 1666–1668.
15. Burger, K., *Organicheskie reagenty v neorganicheskom analize* (Organic Reagents in Inorganic Analysis), Moscow: Mir, 1975.
16. Kharitonov, Yu.A. and Sarukhanov, M.A., *Khimiya kompleksov metallov s gidroksilaminom* (Chemistry of Metal Complexes with Hydroxylamine), Moscow: Nauka, 1977.

17. Ruvinskii, O.E., *Polyarografiya: Problemy i perspektivy* (Polarography: Problems and Prospects), Riga: Zinatne, 1977, pp. 189–215.
18. Tur'yan, Ya.I., *Usp. Khim.*, 1973, vol. 42, no. 6, pp. 969–986.
19. Brikun, I.K., Kozlovskii, M.T., and Nikitina, L.V., *Gidrazin i gidroksilamin i ikh primenenie v analiticheskoi khimii* (Hydrazine and Hydroxylamine and Their Use in Analytical Chemistry), Alma-Ata: Nauka, 1967.
20. Kryukova, T.A., Sinyakova, S.I., and Aref'eva, T.V., *Polyarograficheskii analiz* (Polarographic Analysis), Moscow: Goskhimizdat, 1959.
21. Pats, R.G. and Vasil'eva, L.N., *Metody analiza s ispol'zovaniem polyarografii peremennogo toka* (Methods of Analysis with the Use of AC Polarography), Moscow: Metallurgiya, 1967.
22. Nemodruk, A.A., *Analiticheskaya khimiya mysh'yaka* (Analytical Chemistry of Arsenic), Moscow: Nauka, 1976.
23. *Rukovodstvo: Metody analiticheskogo kontrolya v tsvetnoi metallurgii, tom 2. Proizvodstvo svintsa i tsinka. Chast' 2. Metody analiticheskogo kontrolya v proizvodstve tsinka* (Methods of Analytical Monitoring in Nonferrous Metallurgy, vol. 2, Manufacture of Lead and Zinc, part 2, Methods of Analytical Monitoring in Manufacture of Zinc), Moscow: Tsvetmetinformatsiya, 1977.
24. Lazarev, A.I., Kharlamov, I.P., Yakovlev, P.A., and Yakovleva, E.F., *Spravochnik khimika-analitika* (Handbook of Chemist-Analyst), Moscow: Metallurgiya, 1976.

Russian Journal of Applied Chemistry, Vol. 74, No. 8, 2001, pp. 1318–1320. Translated from Zhurnal Prikladnoi Khimii, Vol. 74, No. 8, 2001, pp. 1281–1284.

SORPTION AND ION-EXCHANGE PROCESSES

Electrochemical Methoxylation of Styrene with Gas-Lift in Continuous Mode

I. B. Il'chibaeva, E. Sh. Kagan, and A. P. Tomilov

Southern-Russia State Technical University, Novocherkassk, Russia

State Research Institute of Organic Chemistry and Technology, Moscow, Russia

Received February 14, 2001

Abstract—Anodic oxidation of styrene in methanol was performed in an electrolyzer with gas-lift. The possibility of carrying this process out in continuous mode with the use of technical-grade methanol was studied.

Recently, the reaction of styrene methoxylation, making possible manufacture of a number of important organic preparations, e.g., benzaldehyde and anisaldehyde, has been studied intensively. Electrochemical methoxylation of styrene (**I**) leads to formation of 1,2-dimethoxyethylbenzene (**II**) with subsequent splitting of the C–C bond and conversion of **II** into dimethylacetal of benzaldehyde (**III**):

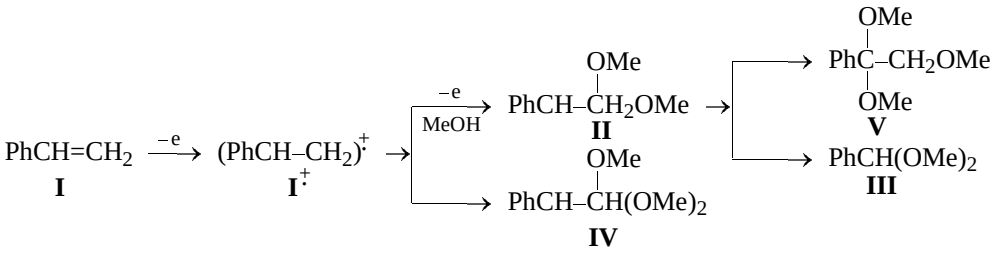

A number of studies have been concerned with the effect of a supporting electrolyte, anode material, and other factors on the yield of the reaction products [1–5]. It was established that conversion of styrene **I** into 1,2-dimethoxyethylbenzene **II** is the most efficient in electrolysis with a platinum anode and potassium fluoride solution as supporting electrolyte. The conditions were described under which the yield of compound **III** is as high as 66%, and the current efficiency, 33%, after passing 8 F of electricity per 1 mol of styrene.

All the experiments described in the literature have been performed in a diaphragmless glass electrolyzer equipped with magnetic stirrer for solution agitation. Such an electrolyzer cannot serve as a prototype of an industrial apparatus.

In the industry, the best-developed design is the electrolyzer of filter-press type in which the electrolyte circulation is effected by gases formed in electrolysis—the gas-lift system [6]. Electrolyzers of this kind exhibit good performance in electrolysis of water. It has been shown that cathodic hydrodimerization of acetone can be performed in an electrolyzer with gas-lift system [7].

Electrochemical synthesis of compound **III** is of practical importance. In view of this fact, the present study was aimed at verifying the possibility of carrying out the given reaction in a prototype industrial electrolyzer. In order to create conditions as close as possible to those used in the industry, the process was performed in continuous mode with the use of technical-grade methanol [GOST (State Standard) 2222–95] as solvent.

EXPERIMENTAL

The experiments were carried in electrolyzer *1* (see figure) in the form of a glass cylinder 55 mm in diameter and 140 mm high. An electrode pack compris-

1070-4272/01/7408-1318 $25.00 © 2001 MAIK "Nauka/Interperiodica"

ing alternating anode and cathode plates was placed inside the electrolyzer. Two platinum plates of size 15×80 mm were used as anode, and three stainless steel plates of the same size, as cathode. The interelectrode spacing of 3 mm was ensured by fluoroplastic spacers placed at electrode edges. The installation is shown schematically in the figure. The ascending pipe of the gas-lift system had inner diameter of 6 mm and height of 1650 mm. The capacity of the whole system was 420 ml. The current density was calculated on the assumption of the uniform distribution of current over the entire surface of the cathodes.

A 20.8-g portion of styrene (0.2 mol), 1.4 g (0.02 mol) of KF, and 397 ml of methanol was placed in the system, so that it was filled to the level shown in the figure. The electrolysis was carried out at a current density of 0.1 A cm^{-2} (current strength 4.8 A), with 8 F of electricity passed per 1 mol of styrene **I** and no fresh electrolyte added. The voltage across the electrolyzer was 10 V.

After the electrolysis was complete, methanol was evaporated under a water-jet pump vacuum at a temperature of 40°C, still bottoms were extracted with hexane (20×3), and the solvent was evaporated from the extract. The still bottoms were weighed and analyzed by liquid-gas chromatography on an LKhM-8MD chromatograph (detector catharometer, carrier-gas helium, column length 1.5 m, column diameter 3 mm, support Chromaton-N-AW, immobile phase PEG-4000, flow rate 4 ml s^{-1}, sensitivity 1 : 3, column temperature 130°C, evaporator temperature 250°C).

For comparison, experiments were performed in an electrolyzer with magnetic stirrer, with design close to that described in [1–5].

Table 1 presents data on the accumulation of electrolysis products both in an electrolyzer with gas-lift and in that with mechanical stirring. It can be seen that the yield of benzaldehyde dimethylacetal **III** is nearly 14% higher in the electrolyzer with a gas-lift system, compared with that equipped with mechanical stirrer.

Further experiments were carried out in order to verify the possibility of performing the process in the continuous mode. A certain amount of electrolyte solution was removed from the electrolyzer every hour and a fresh portion of the same volume was added. Two sets of experiments were carried out with fresh electrolyte supplied at a rate of 25 ml h^{-1}.

The yield of the reaction products was found not to change substantially on passing from batch to continuous mode (Table 2). Also, the possibility was verified of conversion of the intermediate electrolysis product—1,2-dimethoxyethylbenzene, in an electrolyzer of continuous type with gas-lift. In this case, one more product of the reaction of electrochemical methoxylation of styrene—1,1,2-trimethoxyethylben-

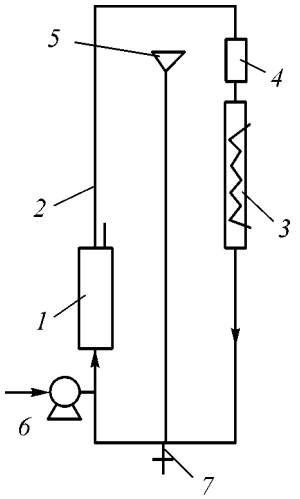

Electrolyzer with gas-lift system. (*1*) Electrolyzer, (*2*) glass tube, (*3*) condenser, (*4*) separator, (*5*) system filling level, (*6*) dosing pump, and (*7*) discharge cock.

Table 1. Electrooxidation of styrene in methanol in batch mode in electrolyzers with (A) mechanical stirring and (B) gas-lift

Quantity of electricity, F mol^{-1}	Composition of electrolysis products, %				
	(I)	**(II)**	**(III)**	**(IV)**	BA
Electrolyzer (A)*					
1	20	73.2	4.4	1.9	1
2	12	76.5	7.4	2.3	2
3	–	87.5	7.9	2.6	2
4	–	74.2	16.8	7	2
5	–	67.7	20.9	8.4	3
6	–	59.5	29.1	8.5	3
7	–	54.7	33.6	8.7	3
8	–	39	42.8	13	5
Electrolyzer (B)					
1	25	65.5	6.9	1.6	1
2	18.3	68.9	7.6	3.2	2
3	9.7	70.7	11.1	5.5	3
4	–	71	20	6	3
5	–	66.7	29.8	6.5	3
6	–	56	32	8	4
7	–	45.3	41.8	8.9	4
8	–	30	57	9	4

* Electrolysis conditions: 10.4 g (0.06 mol) styrene, 0.7 g (0.01 mol) KF, and 185 ml methanol; T = 60°C; BA, benzaldehyde.

Table 2. Electrooxidation of styrenes in electrolyzer with gas-lift system in continuous mode (fresh solution supplied at a rate of 25 ml h^{-1})

τ, h	Composition of electrolysis products, %									
	II	**III**	**IV**	**V**	BA	**II**	**III**	**IV**	**V**	BA
	Styrene					1,2-Dimethoxyethylbenzene**				
9	30	56	10	–	4	30	57	10	–	4
17*	31	55	10	–	5	10	57	10	18	5
25*	30	55	10	–	5	8	56	10	21	5
33*	31	54	10	–	5	8	56	10	21	5
41*	30	55	10	–	5	7	56	10	22	5

* Addition of fresh electrolyte (styrene) was started after passing 8 F of electricity per 1 mol of styrene.

** Fresh electrolyte: 12 g (0.06 mol) of 1,2-dimethoxyethylbenzene, 0.7 g of KF, and 200 ml of methanol.

Table 3. Electrooxidation of styrene in methanol in continuous mode (fresh electrolyte supplied at a rate of 50 ml h^{-1})

τ, h	Composition of electrolysis products, %				τ, h	Composition of electrolysis products, %			
	II	**III**	**IV**	BA		**II**	**III**	**IV**	BA
	i = 0.1 A cm^{-2}					i = 0.2 A cm^{-2}			
9	30	55	10	5	4.5	30	56	10	4
17*	44	39	11	6	12.5*	40	45	10	5
25*	46	38	10	6	20.5*	40	44	10	6
33*	46	37	11	6	28.5*	39.5	43.5	11	6
41*	44	39	11	6	36.5*	39	44	11	6

* Addition of fresh electrolyte (styrene) was started after passing 8 F of electricity per 1 mol of styrene.

zene (**V**), is formed in yield of up to 18–22% in a continuous-type electrolyzer with gas-lift and 10% in an electrolyzer with mechanical stirring [5].

A set of experiments carried out with varied current density at a supply rate of fresh electrolyte of 50 ml h^{-1} demonstrated that the yield of the target product grows with the current density increasing to 0.2 A cm^{-2} (Table 3).

Tables 1–3 present the results averaged over three measurements. The relative error of the average is 1.6% at confidence probability α = 0.95.

The obtained data indicate that in an electrolyzer with gas-lift system, operating in the continuous mode, the process course is stable, with lower electrolyte supply rate ensuring higher yield of product **III**, virtually coinciding with that achieved in the batch mode.

CONCLUSION

Methoxylation of styrene to obtain benzaldehyde dimethylacetal can be carried out in continuous mode in an electrolyzer with electrolyte circulation effected by gas-lift.

REFERENCES

1. Plzak V., Schneider, H., and Wendt, H., *Ber. Bunsengesell. Phys. Chem.*, 1974, vol. 78, no. 12, pp. 1373–1379.
2. Ogibin, Yu.N., Elinson, M.N., Sokolov, A.V., and Nikishin, G.I., *Izv. Akad. Nauk SSSR, Ser. Khim.*, 1990, no. 2, pp. 494–495.
3. Ogibin, Yu.N., Ilovaiskii, A.N., and Nikishin, G.I., *Izv. Ross. Akad. Nauk, Ser. Khim.*, 1991, no. 3, pp. 644–649.
4. Ogibin, Yu.N., Ilovaiskii, A.N., and Nikishin, G.I., *Izv. Ross. Akad. Nauk, Ser. Khim.*, 1993, no. 1, pp. 140–143.
5. Ogibin, Yu.N., Ilovaiskii, A.N., and Nikishin, G.I., *Izv. Ross. Akad. Nauk, Ser. Khim.*, 1994, no. 9, pp. 1624–1627.
6. *Prikladnaya elektrokhimiya* (Applied Electrochemistry), Tomilov, A.P., Ed.,. Moscow: Khimiya, 1984.
7. Stepnova, N.P., Makarochkina, S.M., and Tomilov, A.P., *Zh. Prikl. Khim.*, 2000, vol. 73, no. 2, pp. 227–230.

Russian Journal of Applied Chemistry, Vol. 74, No. 8, 2001, pp. 1321–1324. Translated from Zhurnal Prikladnoi Khimii, Vol. 74, No. 8, 2001, pp. 1285–1289.

ENVIRONMENTAL PROBLEMS OF CHEMISTRY AND TECHNOLOGY

Measurement of Electrical Conductivity of Wastewater for Fast Determination of Metal Ion Concentration

F. Prieto, E. Barrado, M. Vega, and L. Deban

University Autonoma del Estado de Idalgo, Mexico;
University Vagliadolida, Spain

Received May 15, 2000

Abstract—The possibility of determining the content of 15 toxic elements in wastewater from their electrical conductivity was studied in order to evaluate the amount of iron(II) ions required for precipitation of these toxic elements.

Treatment of wastewater to remove metal ions requires data on their total content. Convenient express method for determining the solution mineralization and concentration of metal ions is based on measuring the electrical conductivity of solutions. To determine the weight fraction of certain particles in solution, the total content of solid substance, and the content of ionized solid substance, the electrical conductivity ($\mu S\ cm^{-1}$) is multiplied by an empirical factor varying from 0.55 to 0.99, depending on the nature of dissolved components and temperature [1]. Electrical conductivity measurements are often used to determine the salinity of natural and waste waters [2]. For this purpose, various empirical equations have been obtained and salinity scales developed [3], which can be used for a wide variety of samples. For example, scales of the seawater salinity [4] including a scale for low-salinity solutions [5] have been developed.

Highly efficient treatment of wastewater containing metal ions is based on addition of Fe(II) ions to a solution under study in alkali medium in the presence of oxidants, which results in precipitation of metal ions in the form of ferrites possessing magnetic properties [6, 7]. It has been found that the highest purification efficiency and the greatest magnetic moments of the precipitates are attained when the weight concentration of Fe(II) is 15 times the total concentration of the metal ions to be removed [8, 9]. Thus, evaluation of the total content of Fe(II) that should be added to wastewater to maintain the optimal 15 : 1 ratio requires that the concentration of all metal ions in solution should be determined. However, common analytical procedures used in this case are rather laborious. Thus, development of a new fast and cheap procedure for determining metal ions in wastewater, based on measurement of its certain physicochemical properties, is rather urgent. Electrical measurements are rather simple, and the electrical conductivity correlates with the concentration of metal ions in solution. The aim of this study was to determine the empirical dependence between the electrical conductivity and the concentration of metal ions in solution and thus to evaluate the total content of metal ions and, consequently, the amount of Fe(II) necessary for *in situ* treatment of wastewater via precipitation of metal ferrites.

Previously, it has been found that compounds able to form complexes with metal ions affect the precipitation of the corresponding metal ferrites from solutions [10]. Moreover, complex formation changes the charge and size of metal-containing ions in a solution and thus affects its electrical conductivity. Hence, evaluating the effect of complex formation on how the electrical conductivity depends on the content of metal ions in solution, with the aim to determine the general empirical correlation, is equally urgent.

EXPERIMENTAL

To determine the specific electrical conductivity χ, the electrolyte solution is placed in a measurement cell (length L and cross-section A). Then the resistance R of this cell is determined and the electrical conductivity is calculated using the following expression

$$\chi = \frac{L/A}{R}. \quad (1)$$

1070-4272/01/7408-1321 $25.00 © 2001 MAIK "Nauka/Interperiodica"

Although the electrical conductivity is measured in the SI system in $S\ m^{-1}$, results are mostly given in $\mu S\ cm^{-1}$ because of the low conductivities of the systems in question.

The size of the measurement cell is fixed, and for a given cell the L/A ratio (cell constant K_c) is invariable. This constant is determined experimentally by measuring R for a solution with known χ:

$$\chi = K_c/R. \quad (2)$$

The electrical conductance G is a characteristic not only of the electrolyte solution with given concentration and temperature, but also of the cell geometry:

$$G = 1/R. \quad (3)$$

The molar electrolytical conductivity Λ ($S\ m^2\ mol^{-1}$) is a measure of the capability of a given electrolyte to carry electric current:

$$\Lambda = \chi/C \times 10^{-3}, \quad (4)$$

where $\chi = \chi(\text{solution}) - \chi(\text{solvent})$ ($S\ m^{-1}$) and C is the electrolyte molar concentration (M). The molar electrical conductivity of electrolyte is determined by the contributions of all the present ions:

$$\Lambda = \Sigma \nu_i \lambda_i, \quad (5)$$

where λ_i is the ionic molar conductivity ($S\ m^2\ mol^{-1}$) and ν_i is the number of ions (cations and anions) formed by one electrolyte molecule. The ionic molar conductivity gives quantitative information on the contribution of a given ion type to the solution conductivity. Its value depends on the total concentration of ions ($\Sigma z_i c_i$) in the solution and grows with its dilution. With increasing concentration of a strong electrolyte, χ grows because a greater amount of ions participate in the current transport. In weak electrolytes, χ also grows with increasing concentration, but Λ decreases because of the decreasing dissociation. At very high ion concentrations, Λ may decrease because of ion pair formation and increasing solution viscosity.

The electrical conductivity depends on temperature. With increasing temperature, the Brownian motion becomes more pronounced, leading to a rise in χ. The accuracy of the χ measurement is determined by the stability of temperature in the course of the tests. The temperature coefficient α of electrolyte conductivity can be expressed as follows:

$$\alpha = \frac{d\chi/dt}{\chi} \quad (6)$$

and thus

$$\chi_i = \chi_{25}[1 + \alpha(t - 25)]. \quad (7)$$

The content of metal ions in solution was determined by atomic-emission spectrometry with inductively coupled plasma (AES-ICP) on a Philips 7000 atomic-emission inductively coupled plasma spectrometer (Philips, Netherlands).

The electrical conductivity was measured with an accuracy of no less than 0.20% in the entire conductivity range, using a Crison 522 conductometric unit (Crison, Spain) with a platinum cell (K_c 1.280 cm^{-1}).

The solution pH was measured with a Crison micro-pH 2002 unit (Crison, Spain) equipped with a combination glass electrode and a temperature compensation probe.

In all the tests, analytically pure chemical reagents were used. The test solutions were prepared using deionized water (conductivity 17.2 $\mu S\ cm^{-1}$). The electrical conductivity of water was subtracted from all experimental results.

Nineteen wastewater samples were collected at laboratories of the Analytical Chemistry Department of the University Vagliodolida within one academic year. The ion concentrations of 15 toxic elements [As(V), Ba(II), Cd(II), Co(II), Cu(II), Cr(VI), Fe(III), Hg(II), Mn(II), Mo(II), Ni(II), Pb(II), Sr(II), V(V), and Zn(II)] were determined by AEP-ICP method using solutions diluted to an appropriate degree. The measurements were performed 3 times and the average concentrations of the above elements were calculated.

To determine the electrical conductivity, an aliquot (1 ml) of acidic wastewater was diluted to 50 ml with deionized water, and its pH was adjusted to 3.0 with sodium hydroxide. The measurements were carried out at a constant temperature of $20.0 \pm 0.2°C$. The tests were performed 5 times for each solution under these conditions.

The average electrical conductivities and corresponding rms errors for 19 samples in question (5 parallel tests) and the total concentrations of metal ions (3 parallel tests for each of 15 elements) are listed in the table. The total concentration of metal ions was calculated as a sum of concentrations of 15 elements studied and its rms error was evaluated. Then, using experimental concentrations, the total content of metal ions in diluted solutions was determined and the concentration dependence of the electrical conductivity was plotted (Fig. 1). For the samples in question this dependence is linear and is described by the following equation obtained by least-squares procedure ($R^2 = 0.9970$):

$$\chi = 25.104C + 909.85. \quad (8)$$

The adequacy of empirical equation (8) for determining the concentration of metal ions in wastewater from its electrical conductivity was analyzed using a model sample containing 15 above elements present in all 19 wastewater samples (the total average concentration of metal ions was 3232 mg l^{-1}, see table). The model solution was prepared by dissolving the required amounts of Cd(II), Co(II), Cr(III), Cu(II), Fe(III), Hg(II), Ni(II), Pb(II), Sr(II), and Zn(II) nitrates, Ba(II) and Mn(II) chlorides, and sodium molybdates, vanadates, and arsenates in deionized water. Then 5 aliquots of the model solution were diluted (1 : 50), the solution pH was adjusted to 3.0 using sodium hydroxide, and the electrical conductivity of the resulting solutions was measured (n = 5). The average conductivity was 2866 μS cm^{-1}. Substitution of this value in Eq. (8) gives the total concentration of metal ions of 77.9 mg l^{-1}, which corresponds to the concentration of the initial model solution (3895 mg l^{-1}). Thus, the deviation from the average concentration (3232 mg l^{-1}) is 20%. This error is rather large but positive, and thus Eq. (8) can be used to calculate the amount of Fe(II) which should be added to the wastewater to remove no less than 99% of heavy metals [Fe(II) concentration should exceed the total concentration of these metals by a factor of 15]. This equation guarantees that an excess amount of Fe(II) is added to the solution, sufficient for effective precipitation of metal ions.

Oxidants and organic compounds, which can interact with metal ions and thus hinder their precipitation as ferrites because of competitive reactions modifying the species in solutions, can strongly affect the efficiency of wastewater treatment to remove metal ions via formation of ferrites [8, 10]. It would be expected that presence of these compounds also affects the electrical conductivity and thus the feasibility of using its values to determine the total concentration of metal ions and the amount of Fe(II) required for effective wastewater treatment.

Previously [10], we simulated the effect of complexing organic compounds for the example of ethylenediaminetetraacetate ions (EDTA), which were taken because they form stable complexes with metal ions and can be analyzed as a model of the other natural ligands with similar complexing properties. To study the effect of organic ligands on the electrical conductivity of a wastewater containing metal ions, aliquots of the model solution were diluted (1 : 50), and appropriate amounts of EDTA disodium salt (from 10^{-8} to 0.5 M) were added. The solution pH was adjusted to 3.0 with NaOH, and the electrical conductivity was measured.

Electrical conductivity (n = 5) and total concentration of metal ions (n = 3) for wastewater samples diluted in 1 : 50 ratio

Sample no.	χ, μS cm^{-1}		Σ[Me^{n+}], mg l^{-1}	
	average value	rms error	average value	rms error
1	1058	9	445	5
2	2005	11	2356	20
3	2933	10	4072	33
4	4210	12	6575	30
5	3485	16	5050	33
6	4048	16	6245	30
7	2188	13	2541	16
8	1598	8	1253	8
9	2593	16	3296	19
10	2118	13	2356	18
11	1670	9	1401	11
12	1105	8	451	6
13	2455	16	2973	11
14	2220	15	2608	10
15	3443	16	5034	21
16	3663	16	5284	24
17	3933	16	6009	32
18	2368	16	2879	10
19	1350	11	574	8

The logarithmic dependence of the electrical conductivity of the wastewater (n = 5) on the EDTA concentration is shown in Fig. 2. As seen, the electrical conductivity is nearly constant at EDTA concentrations lower than 5×10^{-5} M, then it sharply decreases and becomes constant at concentrations higher than 10^{-2} M. This fact can be accounted for as follows. At pH 3, EDTA participates in the competitive reactions with protons (H_3EDTA^- and H_2EDTA^{2-} are predominant) and thus the concentration of EDTA required for complexation increases. At low EDTA concentrations, only metal ions forming the strongest chelates with the organic ligand participate in complexation and the electrical conductivity remains nearly constant because the ionic composition of the solutions changes insignificantly. At higher EDTA concentrations (>10^{-2} M), almost all metal ions participate in complexation and, as a result, further increase in the ligand concentration does not affect the conductivity, because EDTA is a weak electrolyte only slightly changing the ionic composition of the solution.

At the maximum EDTA concentration studied (0.5 M), the electrical conductivity was 2631 μS cm^{-1}, which is 8% smaller than that in the absence of the complexing additive. The total concentration of metal ions in the initial model solution, calculated from

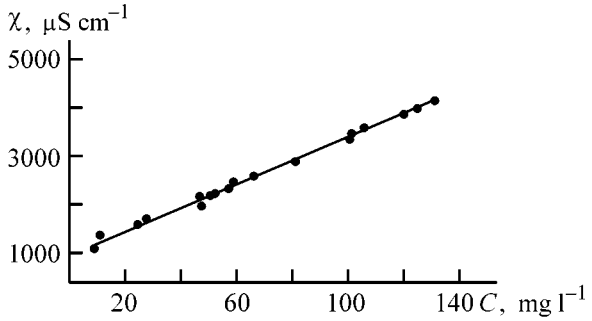

Fig. 1. Electrical conductivity χ of model wastewater vs. the total concentration of metal ions *C* in wastewater strongly contaminated with ions of 15 heavy metals. Samples diluted to 1 : 50 ratio; the same for Fig. 2.

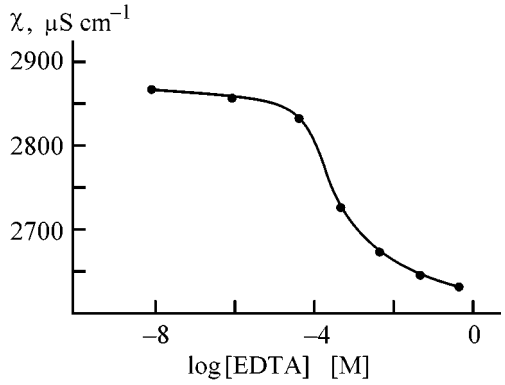

Fig. 2. Electrical conductivity χ of model wastewater containing ions of 15 heavy metals vs. EDTA concentration.

is 3428 mg l^{-1}, which is 6% greater than the real concentration (3232 mg l^{-1}). Since the possible concentration of organic ligands in wastewater is significantly smaller, such calculations give the overestimated total concentration of metal ions and thus of the amount of Fe(II) ions required for their recovery as metal ferrites, which guarantees the maximal efficiency of the treatment process.

To evaluate the applicability of the above empirical expression relating the electrical conductivity to the total concentration of metal ions in wastewater, a new sample containing the same ions (1990 mg l^{-1}) was taken in the academic laboratories. This sample was divided in two aliquots, which were diluted in 1:50 ratio for conductivity measurements. Then EDTA was added to one aliquot (5×10^{-2} M or 10^{-3} M after dilution), and the conductivity of these samples was measured. The total content of metal ions in solutions with organic ligand and without it were calculated by means of Eq. (8) to be 2231 and 2365 mg ml^{-1}. These results were used to determine the amount of Fe(II) required for water treatment, taking into account the optimal Fe/total metal content ratio of 15 : 1 [8]. Then the treatment was performed under the optimized conditions [8, 10], and its efficiency was evaluated from the content of metal ions (AES-ICP method) remaining in the solution after treatment. In both cases the purification efficiency was greater than 99%, which confirms the possibility of using the electrical conductivity measurements to determine the amount of iron(II) required for wastewater treatment to remove metal ions in the form of their ferrites.

CONCLUSIONS

(1) A linear dependence between the electrical conductivity and the total content of metal ions in solutions was established.

(2) Addition of EDTA forming complexes with metal ions decreases the electrical conductivity, but evaluation of the total content of metal ions and thus of the amount of iron(II) ions from the electrical conductivity of wastewater remains acceptable for practical use.

ACKNOWLEDGMENTS

The work was financially supported by C.I.C.Y.T (project no. AMB94-0938). F. Prieto is grateful to ITEGMA for the financial support and AECI for the grant received after backing his dissertation.

REFERENCES

1. APHA-AWWA-WPCF: *Standard Methods for the Examination of Water and Wastewater*, United States: Am. Health Assoc., 16th ed., 1985, pp. 76–80.
2. Lewis, E.L., *J. Geophys. Res.*, 1978, vol. 83, pp. 466–470.
3. Lewis, E.L., *IEEE J. Oceanic Eng.*, 1980, vol. 5, pp. 3–11.
4. Bradshaw, A.L. and Schleicher, K.E., *IEEE J. Oceanic Eng.*, 1980, vol. 5, pp. 50–56.
5. Hill, K.D., Dauphinee, T.M., and Woods, D.J., *IEEE J. Oceanic Eng.*, 1986, vol. 11, pp. 109–113.
6. Katsura, T., Tamaura, Y., and Terada, H., *Ind. Water*, 1977, vol. 233, pp. 16–21.
7. Tamaura, Y., Katsura, T., Rojarayanont, S., *et al.*, *Water Sci. Technol.*, 1991, vol. 23, pp. 1893–1900.
8. Barrado, E., Vega, M., Pardo, R., *et al.*, *Water Res., Ser. A*, 1996, vol. 30, pp. 2309–2314.
9. Barrado, E., Vega, M., Pardo, R., *et al.*, *J. Anal. Lett., Ser. B*, 1996, vol. 29, pp. 613–633.
10. Barrado, E., Prieto, F., Vega, M., and Fernandez-Polanco, F., *Water Res., Ser. A*, 1998, vol. 32, pp. 3055–3062.

Russian Journal of Applied Chemistry, Vol. 74, No. 8, 2001, pp. 1325–1328. Translated from Zhurnal Prikladnoi Khimii, Vol. 74, No. 8, 2001, pp. 1289–1292.

ENVIRONMENTAL PROBLEMS OF CHEMISTRY AND TECHNOLOGY

Effect of pH on the Flocculation of Aqueous Ocher Suspension in the Presence of Ionic Copolymers of Acrylamide

V. A. Myagchenkov and V. E. Proskurina

Kazan State Technological University, Kazan, Tatarstan, Russia

Received February 12, 2001

Abstract—The effect of pH on the kinetics of flocculation of an aqueous ocher suspension in the presence of ionic polyacrylamide flocculants was studied and their flocculation properties were compared.

Ionic and nonionic copolymers of acrylamide find increasing use as flocculants at various stages of water treatment and in other industrial processes, owing to their high performance, availability, low toxicity, and relative cheapness [1, 2]. The performance of polyacrylamide flocculants (PAAFs) is controlled not only by their chemical nature, molecular parameters, structure, and thermodynamic and kinetic flexibility of the macromolecules of acrylamide (co)polymers, but also by the properties of the particles (especially surface) of the disperse phase (DP) and dispersion medium [3]. The presence of relatively small amounts of the surfactants, electrolytes, and compounds with various functional groups able to modify the surface of the DP particles can also affect the flocculation properties of PAAFs [4, 5]. These compounds control the aggregation and sedimentation stability of the disperse system (DS) and, taking into account their effect on the conformation of macromolecules, affect the flocculation properties of PAAFs.

Although the effect of pH of the dispersion medium is important, it has been poorly studied. In this work, we studied, using a model ocher suspension in water, the effect of pH of the dispersion medium on the flocculation properties of macromolecular ionic (anionic and cationic) PAAFs.

EXPERIMENTAL

In our work, we used the ocher suspension ["golden" brand, TU (Technical Specifications) 301-10-019–90] with average particle radius $\bar{R} = 9.25 \times 10^{-6}$ m. The following ionic PAAFs were used in the tests: anionic (**A**) random copolymer of acrylamide and sodium acrylate (viscosity-average molecular weight $\bar{M}_\eta$ 5.4×10^6, content of ionic groups β 17.4%) and cationic (**C**) random copolymer of acrylamide and dimethylaminoethyl methacrylate hydrochloride ($\bar{M}_\eta$ 2.3×10^6, β 16.3%). The sedimentation kinetics of the ocher particles was studied in the mode of free (unhindered) sedimentation (the concentration of the disperse phase was C 0.8%) using a VT-500 torsion balance in a 400-ml cylinder at different pH adjusted by adding 0.1 M HCl and KOH solutions. Before tests the ocher suspensions were clarified for 1 day at each given pH. The required copolymer (0.02% aqueous solutions of **A** and **C** copolymers) was added to a supernatant volume directly before mixing of the ocher suspension by means of a perforated disk stirrer, which was slowly shifted in the cylinder 10 times in the vertical direction.

The viscosity of copolymers **A** and **C** in water was measured on an Ostwald viscometer (0.54 mm capillary diameter). The correction for the kinetic flow energy was lower than 2% and was neglected in the calculations of the reduced viscosity η_{sp}/C.

The electrophoretic mobility of the ocher particles at various pH was determined on an PARMOQUANT (Carl Zeiss, Jena) automated measuring microscope at 20°C and 10 mA current; 0.01 M KCl served as supporting electrolyte.

The kinetic curves of ocher sedimentation in solutions with various pH values are given in Fig. 1. The sedimentation kinetics was monitored using a dimensionless parameter $m(t)/m_{max}$, where $m(t)$ and m_{max} are the current and maximal weight of the pre-

1070-4272/01/7408-1325 $25.00 © 2001 MAIK "Nauka/Interperiodica"

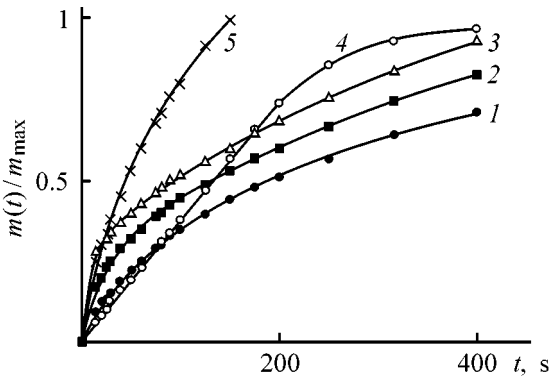

Fig. 1. Kinetic curves of sedimentation of the ocher suspension $m(t)/m_{max}$ in water at various pH. (*t*) Time; the same for Fig. 3. pH: (*1*) 7.0, (*2*) 4.7, (*3*) 10.9, (*4*) 3.0, and (*5*) 11.7.

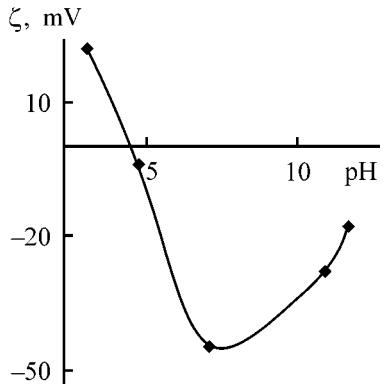

Fig. 2. Electrokinetic potential ζ of the ocher particles vs. pH.

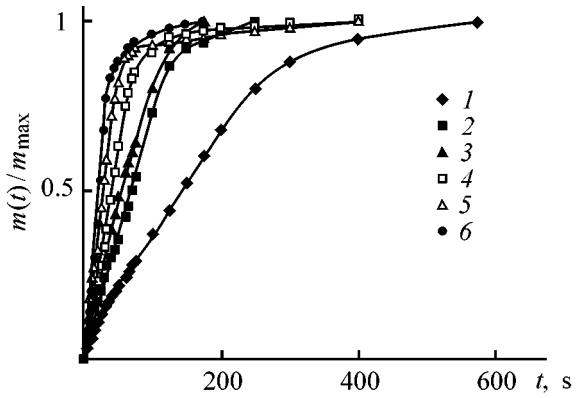

Fig. 3. Kinetic curves of sedimentation of the ocher suspension $m(t)/m_{max}$ at pH 3.0 in the presence of ionic PAAFs; [**A**] 2.25×10^{-5} and [**C**] 0.75×10^{-5}%. Additive: (*1*) no, (*2*) {**A** + **C**}, (*3*) **C**, (*4*) **A**, (*5*) (**C** + **A**), and (*6*) (**A** + **C**).

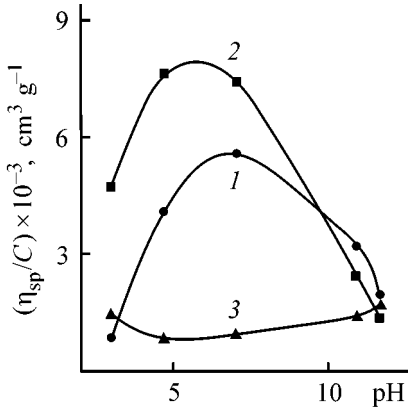

Fig. 4. Reduced viscosity η_{sp}/C vs. the solution pH for (*1*) copolymer **A**, (*2*) copolymer **C**, and (*3*) their mixture, [**A**]/([**A**] + [**C**]) 0.75; [PAAF] = 0.05%.

cipitate on the torsion balance [5]. Ocher sedimentation significantly accelerates with pH deviation from the neutral to basic or acidic values. This is obviously due to the effect of pH on the aggregation and thus on the sedimentation stability of the DP particles, related to the changes in the structure of the electrical double layer (its size and electrokinetic potential ζ) around the DP particles. As seen from Fig. 2, this potential strongly depends on the solution pH and a certain decrease in the absolute value of the ζ potential in alkaline and acidic media well agrees with the decreasing sedimentation stability of the system at given pH (Fig. 1).

We expected that this effect of pH on the sedimentation stability of the ocher would *a priori* appear upon addition of ionic PAAFs in the system. For example, the effect of **A** and **C** PAAFs and their binary mixture on the flocculating parameters of the system at pH 3.0 is illustrated in Fig. 3. For binary PAAF mixtures, three modes of addition were used: (**A** + **C**), (**C** + **A**), and {**A** + **C**}; in the first case we initially added copolymer **A** and then copolymer **C**; in the second case, vice versa, we first added copolymer **C** and then copolymer **A**; and in the last case copolymers **A** and **C** were added simultaneously.

As seen from Fig. 3, the mode of flocculant addition affects the flocculation rate. This is probably due to the almost complete irreversibility of the PAAF sorption [6] and selective interaction between negatively (**A**) and positively (**C**) charged macroions.

Selective interaction between macroions **A** and **C** was suggested previously on the basis of viscometric and conductometric data. The data in Fig. 4 show that the experimental reduced viscosities of mixtures of **A** and **C** are significantly smaller as compared with the initial copolymers **A** and **C** (Fig. 4, curves *1, 2,* and *3*), which indicates the "contraction"

(decrease in the rms size) of macroions **A** in the presence of macroions **C** with opposite charge. It should be noted that pH significantly affects the solution viscosity of copolymers **A** and **C** and thus the effective size of the macromolecular globules, because these parameters vary in parallel [7]. To obtain the qualitative characteristics of the flocculation kinetics, we calculated the parameters of flocculation effect D and flocculation activity λ [3, 5]:

$$D = v/v_0 - 1, \quad (1)$$

$$\lambda = (v/v_0 - 1)/C, \quad (2)$$

where v and v_0 are the average rates of ocher sedimentation at $m(t)/m_{max}$ 0.7 in the presence of polymer flocculant (concentration C) and without it, respectively.

The correlated dependences $\lambda = f(\text{pH})$ for copolymers **A** and **C** and $D = f(\text{pH})$ for binary mixture of ionic PAAFs for all three modes of their addition are shown in Fig. 5. As seen, the experimental dependences $D = f(\text{pH})$ and $\lambda = f(\text{pH})$ are extremal, because the conformation of macromolecule, electric double layer parameters, and the "energy pattern" of the dispersion particle surface depends on the solution pH [3]. Naturally, the mode of copolymer addition and solution pH must also affect the adsorption interaction of macromolecule with one or several particles of the disperse phase [8]. The real mechanism of the adsorption of ionic copolymer macromolecules on the DP particles is rather complex owing to the presence of both negatively and positively charged areas on the particle surface, produced predominantly by silanol groups and Fe^{3+} cations, respectively. With account taken of the relatively low content of the ionic units in the copolymers in question, uncharged acrylamide fragments of macromolecules undoubtedly affect the adsorption interaction with one or several ocher particles [9–11]. The anionic and cationic copolymers differ significantly nature of adsorption and flocculation, which is indirectly confirmed by the difference in flocculating activity between copolymers **A** and **C**; namely $\lambda_{\mathbf{A}} > \lambda_{\mathbf{C}}$. This fact unambiguously indicates the predominantly bridging (and not neutralization) nature of the flocculation effect of copolymers **A** and **C**, because the DP particles are negatively charged in the entire pH range studied, i.e., similarly with respect to macroions **A** and oppositely with respect to macroions **C**. These data also suggest that the fraction of the effective bridging bonds for copolymer **A** is significantly greater as compared with copolymer **C**. Thus, it is apparent that the conformation state of macromolecules **A** and **C** cannot be regarded as a unique

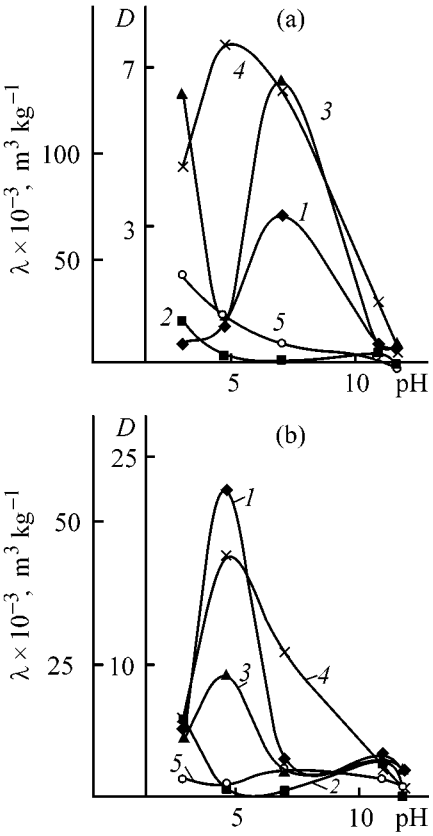

Fig. 5. Flocculation parameters (*1*, *2*) λ and (*3*–*5*) D vs. the solution pH; [PAAF] 3×10^{-5}%; [**A**]/([**A**] + [**C**]) (a) 0.25 and (b) 0.75. PAAF: (*1*) **A**, (*2*) **C**, (*3*–*5*) first, second, and third modes of copolymer addition, respectively.

parameter of the flocculation activity of PAAFs. As seen from Fig. 5, in the case of anionic PAAFs, the dependences $\lambda = f(\text{pH})$ and $D = f(\text{pH})$ are nearly parallel, whereas in the case of cationic copolymers such trends are absent. Taking into account the selective interaction of macroions **A** and **C**, we can account for the effect of how the copolymer is added to the system, namely, the fact that the parameter D is the smallest in the case of third addition mode in the entire pH range studied. It is apparent that, upon simultaneous addition of copolymers **A** and **C**, the "contraction" effect for macromolecular globules of the binary copolymer mixtures is the strongest, which was shown already by means of viscometry (Fig. 4).

Now, omitting the analysis of the rather complex mechanisms of adsorption and flocculation in the systems in question, we consider the significant effect of pH on the flocculating parameters of anionic and cationic PAAFs and compositions on their basis. Despite the predominantly correlation nature of the observed dependences $D = f(\text{pH})$ and $\lambda = f(\text{pH})$, they may be promising for optimization of the flocculation

processes not only in the model systems, but also in complex multicomponent disperse systems with varied pH.

CONCLUSIONS

(1) The kinetic parameters of flocculation of the ocher suspension in the free (unhindered) sedimentation mode in the presence of anionic and cationic copolymers of acrylamide and their mixtures (3 : 1 and 1 : 3) in solutions with various pH were studied.

(2) The flocculation parameters of polyacrylamide flocculants with respect to the ocher suspension in water strongly depends on the solution pH, which is predominantly due to the dependence of the electrochemical properties of the ocher particles and conformation of copolymer macromolecules on the pH.

ACKNOWLEDGMENTS

The authors are grateful to G.V. Bulidorova for performing the electrophoretic study.

REFERENCES

1. Babenkov, E.D., *Ochstka vody koagulyantami* (Water Treatment with Coagulants), Moscow: Nauka, 1977.
2. Veitser, Yu.I. and Mints, D.M., *Vysokomolekulyarnye flokulyanty v protsessakh ochistki prirodnykh i stochnykh vod* (Macromolecular Flocculants in Treatment of Natural and Waste Waters), Moscow: Stroiizdat, 1984.
3. Myagchenkov, V.A., Baran, A.A., Bekturov, V.A., and Bulidorova, G.V., *Poliakrilamidnye flokulyanty* (Polyacrylamide Flocculants), Kazan: Kazan Tekhnol. Univ., 1998.
4. Abramson, A.A., *Poverhnostno-aktivnye veshchestva* (Surfactants), Leningrad: Khimiya, 1981.
5. Myagchenkov, V.A. and Proskurina, V.E., *Zh. Prikl. Khim.*, 2000, vol. 73, no. 6, pp. 1007–1010.
6. Lipatov, Yu.S. and Sergeeva, L.M., *Adsorbtsiya polimerov* (Adsorption of Polymers), Kiev: Naukova Dumka, 1984.
7. de Gennes P.-G., *Scaling Concepts in Polymer Physics*, Ithaca: Cornell University Press, 1979.
8. Baran, A.A., *Polimersoderzhashchie dispersnye sistemy* (Polymer-Containing Dispersed Systems), Kiev: Naukova Dumka, 1986.
9. Li, D., Zha, S., Pelton, R.H., and Spafford, M., *Colloid Polym. Sci.*, 1999, vol. 277, pp. 108–114.
10. Ma, M. and Zha, S., *Colloid Polym. Sci.*, 1999, vol. 277, pp. 115–122.
11. Proskurina, V.E. and Myagchenkov, V.A., *Zh. Prikl. Khim.*, 2000, vol. 73, no. 12, pp. 2030–2035.

Russian Journal of Applied Chemistry, Vol. 74, No. 8, 2001, pp. 1329–1337. Translated from Zhurnal Prikladnoi Khimii, Vol. 74, No. 8, 2001, pp. 1293–1302.

MACROMOLECULAR CHEMISTRY AND POLYMERIC MATERIALS

Effect of Fullerene C_{60} on Thermal Oxidative Degradation of Polymethyl Methacrylate Prepared by Radical Polymerization

B. M. Ginzburg, L. A. Shibaev, and V. L. Ugolkov

Institute of Machine Science Problems, Russian Academy of Sciences, St. Petersburg, Russia
Institute of Macromolecular Compounds, Russian Academy of Sciences, St. Petersburg, Russia

Received June 8, 2001

Abstract—The influence of small C_{60} additions on thermal and thermal oxidative degradation of polymethyl methacrylate prepared by radical polymerization was studied by differential scanning calorimetry, thermogravimetric analysis, differential thermogravimetric analysis, and mass spectrometry.

Kashiwagi *et al.* [1], applied differential thermogravimetric analysis (DTG) to study weak bonds in molecules of atactic polymethyl methacrylate (PMMA) prepared by radical polymerization and the influence of these bonds on the thermal degradation of the polymer. In the course of heating in an inert atmosphere (N_2), they detected three peaks (Fig. 1a). Peak *I* (~165°C) was assigned to degradation initiated by head-to-head chain defects (or H–H bonds); peak *II* (~270°C), to degradation involving unsaturated terminal groups; and peak *III* (~360°C), to degradation of the main chains. In [2, 3], we studied the influence of fullerene C_{60} on thermal degradation of PMMA, using mass-spectrometric thermal analysis (MTA). In PMMA without additives we observed the same three peaks as in [1], at approximately the same temperatures (Fig. 1b). Addition of small amounts of C_{60} to PMMA led to considerable changes in the MTA patterns: Peak *I* disappeared almost completely, and peak *II* noticeably decreased in height. It was concluded from these results that C_{60} retains the products of thermal degradation, i.e., it acts as a scavenger of free radicals released in degradation. At the same time, peak *III* grew in relative intensity and shifted toward higher temperatures by approximately 15°C, which corresponds to an increase in the energy of the cleaved bonds by approximately 4 kJ mol^{-1} [3]. Thus, C_{60} stabilizes PMMA both at low and at elevated temperatures.

Note that peaks *I* and *II*, related to cleavage of specific weak bonds, were appreciably narrower than peak *III* related to random bond cleavage. Addition of C_{60} also makes the peaks narrower. Apparently, degradation pathways become more definite in the presence of C_{60}; they involve addition of PMMA radicals to C_{60}, followed by cleavage of the CC and CO bonds in the vicinity of the addition site.

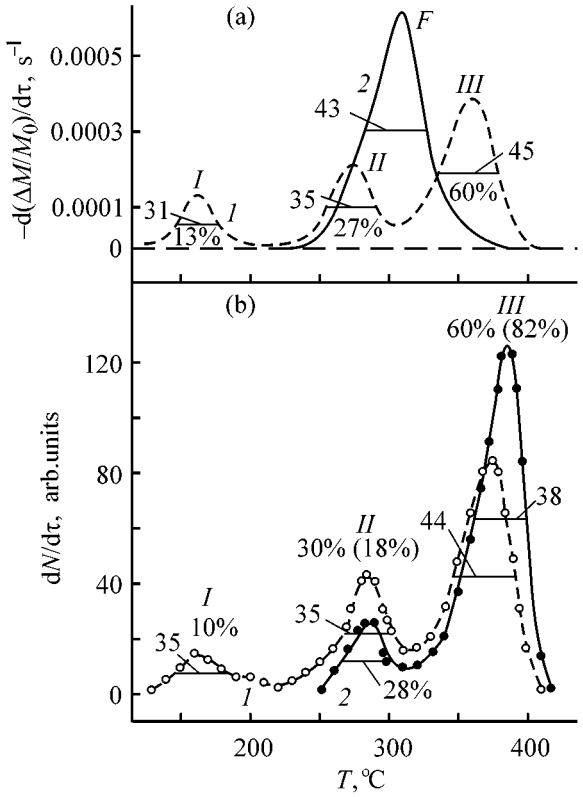

Fig. 1. Yield of products of PMMA thermal degradation vs. temperature *T*. [$-d(\Delta M/M_0)/d\tau$] rate of relative weight loss and ($dN/d\tau$) rate of monomer release. (a) DTG data [1], heating of PMMA (*1*) in N_2 and (*2*) in air; (b) MTA data [2], heating in a vacuum of (*1*) PMMA and (*2*) mixture of PMMA with C_{60}. *Figures at curves* denote the relative peak areas in % (in parentheses, after addition of C_{60}) and the half-widths (°C).

1070-4272/01/7408-1329 $25.00 © 2001 MAIK "Nauka/Interperiodica"

Numerical estimation shows that the unit weight of a sample at 1% C_{60} concentration contains approximately equal the numbers of C_{60} molecules and PMMA macromolecules (at M = 85000). Since each C_{60} molecule can add up to 6–10 radicals, the C_{60} concentration is quite sufficient to add all the arising radicals.

The relative areas of peaks *I–III* in Fig. 1a are S_I = 0.13, S_{II} = 0.27, and S_{III} = 0.60 of the total peak area S_0. Estimation of the MTA peak areas before addition of C_{60} (Fig. 1b) gives close values: S_I = 0.10, S_{II} = 0.30, and S_{III} = 0.60. Similar estimations made after addition of C_{60} allowed determination of the fraction of PMMA molecules "trapped" by fullerene: S_{Fu} = = S_I + (S_{II} – S_{II}'), where S_{II}' is the relative area of peak *II* after addition of C_{60}. We found that $S_{Fu} \approx 20$, i.e., only about 20% of C_{60} molecules take up two PMMA radicals arising from chain cleavage, or 40% of C_{60} molecules take up one radical. Apparently, the true fraction of bound C_{60} molecules is closer to 20%, since, in cleavage of a PMMA chain, the resulting radical centers are localized practically at the same place, and the C_{60} molecule, if occurring in the vicinity of this place, takes up both radicals. Thus, at least two different types of C_{60} molecules are formed in the system: free and bound to PMMA.

The described studies of thermal degradation were mainly performed in an inert atmosphere or in a vacuum. Of no less interest, especially from the practical viewpoint, is thermal oxidative degradation in air. The presence of oxygen also results in disappearance of peak *I* (Fig. 1a) [1]. The DTG curve taken in the presence of O_2 exhibits a new strong peak at ~300°C, whose position lies between peaks *II* and *III* obtained in a nitrogen atmosphere. Kashiwagi *et al.* [1] believe that the experimentally observed peak is actually a sum of a new peak *F* and peaks *II* and *III*, with major contribution made by peak *F*. However, it is difficult, in our opinion, to reveal any contributions from peaks *II* and *III* in the curves reported in [1]. Nevertheless, a conclusion can be made that oxygen plays a dual role: It enhances the stability of the system at low temperatures but decreases it at high temperatures [1].

Naturally, the chain degradation detected by DTG and MTA can be accompanied by thermal effects which can also arise without weight loss. Thus, thermogravimetric and calorimetric methods supplement each other in studies of thermal degradation and, when used in combination, can furnish essentially new information. This is especially important when studying such complex processes as thermal oxidative degradation of PMMA which, in our opinion, must be, in the case of an open system, a superposition of at least three processes accompanied by thermal effects:

$$Q_\Sigma = -Q_D + Q_O - Q_S, \quad (1)$$

where Q_Σ is the total thermal effect, Q_D the endothermic effect due to chain degradation, Q_O the exothermic effect due to oxidation of the chains and thermal degradation products, and Q_S the endothermic effect of sublimation or vaporization of degradation products.

Addition of C_{60} to the polymer can affect these processes differently, so that it may be possible to reveal their separate manifestations. Presumably, C_{60} will compete with oxygen for free radicals and thus stabilize the system. However, since fullerene and oxygen affect high-temperature degradation differently, it was unclear whether stabilization would be observed in the entire temperature range of degradation.

The main goal of this study was to examine the influence of C_{60} on thermal oxidative degradation of PMMA using a combination of thermogravimetric analysis (TG) and differential scanning calorimetry (DSC).

The processes of thermal and thermal oxidative degradation of PMMA and polystyrene (PS) in the presence of fullerenes were studied by DSC in [4, 5], and it was concluded that fullerenes play a stabilizing role. However, with PMMA this conclusion is consistent with the results of [2, 3], whereas with PS it contradicts previous data [6]. Probably, this is due to differences in the experimental methods, molecular structure of the polymers in hand, and procedures for evaluating the thermal stability. Therefore, we gave in this work a particular attention to the methodological aspects of evaluating the thermal stability and to correlation of the TG, MTA, and DSC data.

EXPERIMENTAL

The initial fullerene C_{60} (99.7% purity) was prepared by the Huffman–Krätschmer procedure [7]. Polymethyl methacrylate with the viscosity-average molecular weight of 8.5×10^4 was prepared by radical polymerization. To introduce C_{60} into PMMAs, their toluene solutions were combined in a ratio required for ensuring the desired concentration of fullerene. Samples were prepared by casting films from these solutions. Thermal degradation of the materials was studied with an STA 429 Netzsch thermal analyzer (Germany) in air at linear heating rates of 5 and 10 deg min^{-1} in the range 20–700°C. In the course of heating, the temperature, weight variation, and ther-

mal effects were recorded simultaneously. We studied the samples of the starting powdered PMMA, films of PMMA without additives, and films of PMMA with 1 and 10% C_{60}. The sample weight was 120 mg at a heating rate of 10 deg min^{-1} (10-10 series) and 1 or 5 mg at a heating rate of 5 deg min^{-1} (5-1 and 5-5 series, respectively). From numerous experiments, we chose the 5-5 series as basic. The smaller sample weight (1 mg) and its grinding and uniform distribution over the bottom of the measuring cell, at a relatively low heating rate, allowed minimization of the possible effects of slow diffusion, low thermal conductivity, and variation of the gaseous medium in the cell due to release of degradation products; however, the intensity of the useful signals decreased simultaneously, and "weak" processes could not be revealed. In the 10-10 series, the testing conditions were the most rigorous. In this case, it is possible to "amplify" weak processes, but the results can be disturbed because of changes in the gaseous medium, especially in the range of active release of degradation products. With increasing heating rate, most of the characteristic effects shift toward higher temperatures, but, on the whole, the results remain similar. In what follows, we consider in most detail the results obtained with the 5-5 series, and other results will only be discussed when certain processes will be manifested more clearly or to confirm the results of the main series.

The baselines were plotted using the results of experiments performed under the same conditions with samples of sapphire which undergoes neither weight loss nor phase transitions in the temperature range under consideration. For all the samples, the TG curves in the range from 20 to approximately 150°C showed an apparent weight gain due to convective air flows along the vertical axis of the furnace [8]. This gain amounted to no more than 2.5% for 10-mg samples but was significant for 1-mg samples. In DSC measurements, the baseline was parabolic. However, in the temperature range of interest, its curvature was the smallest and did not distort significantly the position and shape of the peaks; therefore, in many cases the qualitative effects were revealed without "straightening" the baseline.

To characterize the thermal degradation products, we used the temperature positions of peaks, T_m, in the DTG, DSC, and MTA curves. The T_m values were determined to within ±5°C. An important characteristic of the thermal stability of a substance is the onset temperature of thermal degradation, T_0. This temperature was determined from the deviation of the weight loss from zero by a conventional value of 0.3% (method 1). The determination error was also about 5°C. Frequently, T_0 is also determined by extrapolation of the main branch of the TG curve to intersection with the baseline parallel to the abscissa (method 2). However, in this case T_0 strongly depends on the curvature of the TG curve, which can give rise to considerable systematic errors. Therefore, in what follows we determined T_0 by method 1 only.

Comparison of characteristic temperatures of thermal oxidative degradation of PMMA, determined by various procedures*

Sample	TG, range of weight loss	DTG		DSC		
		T_m of peaks	T_m^{av}	T_0	$T_{m,II}$	$T_{m,III}$
	°C					
5-5 series						
5-5-0**	252–390	313, 333	315	?	–	364
5-5-1	276–390	353	353	?	–	380
5-5-10	260–390	348, 365	350	?	–	392
5-1 series						
5-1-0	*230*–380	266, 309	270	*230*	245	335
5-1-1	290–380	323, 344	325	255	–	–
5-1-10	270–370	337	337	220	–	–
10-10 series						
10-10-0	*233*–400	300, 390	300	*233*	255	?
10-10-1	286–423	370	370	?	–	387
10-10-10	275–418	360	360	340	–	391

* In sample notation, the third figure gives the C_{60} concentration in %; the "?" sign means that unambiguous determination of the peak position is impossible; the coinciding values of T_0 obtained by TG and DSC are printed italic.

** Sample of PMMA film cast from a toluene solution. In the other series, the initial powders were used as samples of PMMA without additives.

The temperatures characterizing thermal oxidative degradation of PMMA, and determined by different methods, are listed in the table.

Endothermic DSC peak and its interpretation. The DSC thermograms of all the samples exhibit a common striking feature: Approximately in the middle of the thermal oxidative degradation range, a sharp transition occurs from the heat release to heat absorption (sharp endothermic peak), which is followed by new exothermic processes and their gradual decay until

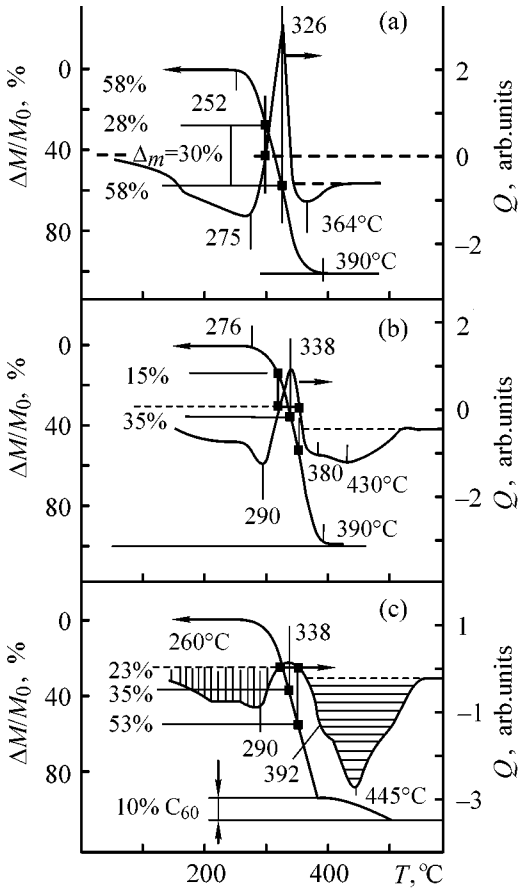

Fig. 2. Patterns of thermal oxidative degradation of PMMA in air, 5-5 series: ($\Delta M/M_0$) relative weight loss, (Q) heat flow, and (T) temperature; the same for Fig. 3. (a) PMMA film, (b) PMMA + 1% C_{60}, and (c) PMMA + 10% C_{60}. *Figures at curves* denote characteristic temperatures (°C); the same for Fig. 3. *Dashed lines* denote baselines.

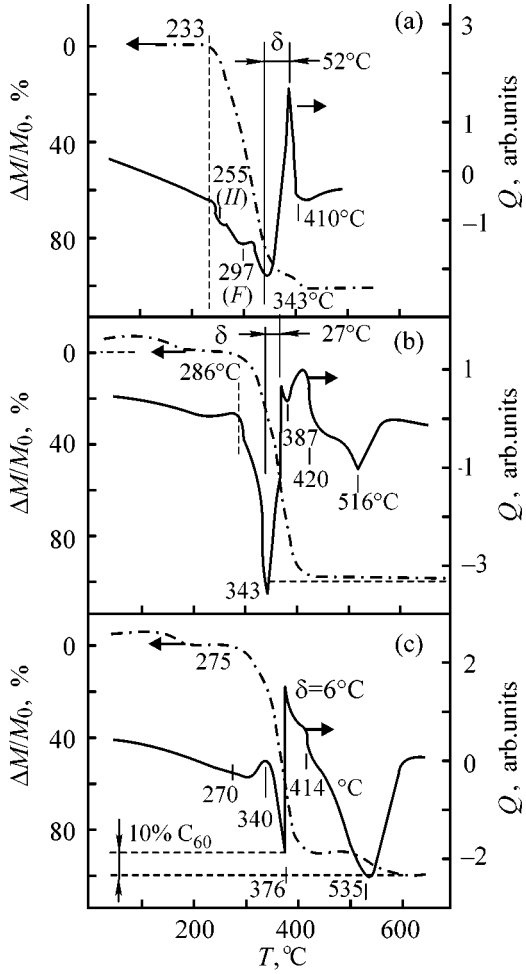

Fig. 3. Patterns of thermal oxidative degradation of PMMA in air, 10-10 series: (a) PMMA powder, (b) PMMA + 1% C_{60} film, and (c) PMMA + 10% C_{60}. The baselines were not straightened.

the degradation products are fully removed from the experimental cell. Let us consider a combination of the TG and DSC curves for PMMA films without additives (Fig. 2). An endothermic peak is observed at about 326°C. On its low-temperature side, practically from the very beginning of the experiment there is a fairly smooth increase in heat release up to 275°C. The peak at 275°C seems to correspond to peak *II*; however, we believe that its another interpretation (see below) is more probable. On the high-temperature side of the endothermic peak, there is a peak at about 364°C, i.e., in the region of peak *III*. With the temperature increasing from that of the endothermic peak to ~364°C, the major fraction of the material (the least defective and the most thermostable) is, apparently, oxidized as the polymer decomposes to the monomer, with a part of the polymer that does not decompose to the monomer (5–8% according to published estimates), and probably forms cross-linked structures, being oxidized too. This part of PMMA is revealed more clearly at higher heating rates and larger sample weight (Fig. 3a). In this case, the TG curves show gradual weight loss (up to 94%) in the range from ~230 to 360°C. Then, from 360 to 400°C, there is a step corresponding to additional 6% weight loss, and the DSC curve exhibits an exothermic peak at about 410°C. Also, three exothermic peaks at 255, 297, and 343°C are clearly seen in the DSC curves. The first peak can be related to peak *II*, and the second, to peak *F*. In the 5-5 series, peak *F* was observed in the same temperature range as the strong endothermic peak and, therefore, was not always revealed. At the same time, the exothermic peak at 343°C can hardly be related to peak *III* (~360°C), because it is observed at an appreciably lower temperature. Presumably, according to Eq. (1), competition of the endothermic effect due to sublimation of the degradation products and thermal degradation of the already oxidized products with

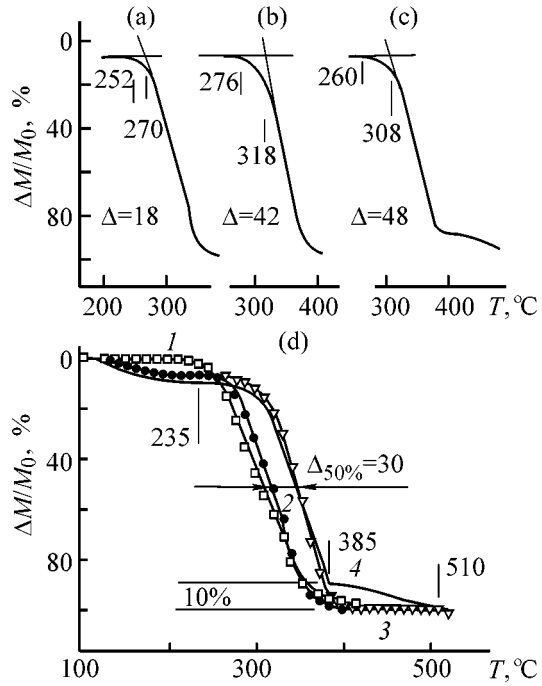

Fig. 4. Weight loss of PMMA (5-5 series) vs. temperature T. ($\Delta M/M_0$) Relative weight loss. (a) PMMA films, (b) PMMA + 1% C_{60}, and (c) PMMA + 10% C_{60}; (d) similar dependences for (*1*) PMMA powder, (*2*) PMMA film, (*3*) PMMA + 1% C_{60}, and (*4*) PMMA + 10% C_{60}. ($\Delta_{50\%}$) Shift of TG curves at the level of 50% weight loss; the same for Fig. 5. *Figures at curves* denote the degradation onset temperatures T_0 determined by methods 1 and 2 and the difference Δ between these values (°C).

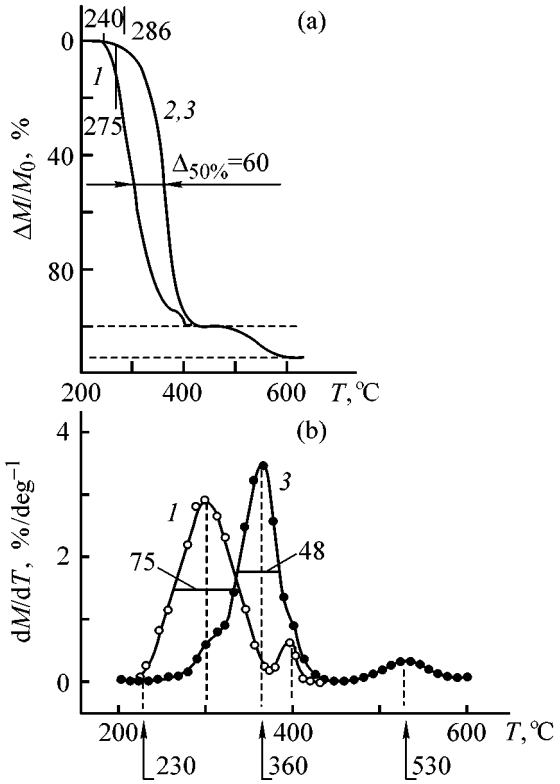

Fig. 5. (a) TG and (b) DTG curves of samples of the 10-10 series: ($\Delta M/M_0$) relative weight loss of the sample and [d($\Delta M/M_0$)dT] its derivative with respect to temperature. (*1*) PMMA powder, (*2*) PMMA + 1% C_{60} film, and (*3*) PMMA + 10% C_{60}. *Figures at curves*: (a) T_0 (°C) for PMMA powder (240), PMMA + 1% C_{60} film (286), and PMMA + 10% C_{60} film (275); (b) peak half-widths (°C).

the exothermic effect due to oxidation (Q_O sharply decreases) gives rise to an apparent peak and sharp change in the sign of the overall thermal effect. The apparent peak at 275°C in Fig. 2a has probably the same origin.

The occurrence of an endothermic effect allows us to distinguish arbitrarily three stages of thermal oxidative degradation with increasing temperature: with heat release (before the endothermic peak), with heat absorption, and again with heat release. We will analyze these stages and give quantitative estimates for them by comparing the straight samples and those containing C_{60}.

Effect of C_{60} on the temperature shift of the oxidative degradation. Figure 4 shows the temperature dependences of the weight loss. It is seen that, with increasing C_{60} concentration, the slope of the initial section of the dependences decreases. Correspondingly, T_0 determined by method 2 changes more strongly. The difference between the T_0 values determined by procedures 1 and 2 for the samples containing 0, 1, and 10% C_{60} is 18, 42, and 48°C, respectively. Variation of the curvature of the initial section of the plots is naturally due to an increase in the concentration of C_{60} retaining the degradation products. Note that, on adding 1% C_{60}, T_0 shifts to higher temperatures (from 252 to 276°C), whereas a reverse shift (to 260°C) is observed on adding 10% C_{60}. This effect is small, but it is reproduced in all the sample series (see table). It can be accounted for by assuming that, in the initial stages of degradation, C_{60} interacts with oxygen and prevents, to some extent, oxidation of the arising polymer radicals. However, degradation in the whole temperature range is not significantly affected by raising the fullerene concentration from 1 to 10%. The TG curves for the samples containing C_{60} coincide (Fig. 4d) in virtually the entire temperature range, except in the above-mentioned initial range and at temperatures above ~385°C where the C_{60} weight loss becomes appreciable. Therefore, we believe that the shift of the curves along the abscissa

axis (e.g., $\Delta_{50\%}$ at 50% weight loss) characterizes the variation of the thermal stability of the system more adequately than T_0 does. The high-temperature shift of the TG curves in going from a PMMA film without additives to the samples containing C_{60} is about 30°C, which is consistent with the MTA data [2]. Similar results were obtained with the 10-10 series. Figure 5a shows that the TG curves obtained at different C_{60} concentrations coincide, but the above-noted qualitative differences in the initial and final sections of the TG curves are preserved. Figure 3 shows particularly clearly a decrease in the slope of the initial TG front with increasing C_{60} concentration and a clear step corresponding to the release of 10% C_{60} at the end of the process. However, Fig. 5a additionally confirms the fact that the C_{60} concentration in the range above 1% has no significant effect on the thermal stability and that the temperature shift of the TG curves is a more convenient characteristic of the relative thermal stability than T_0. In the DTG curves (Fig. 5b) taken in the presence of C_{60}, the main peak shifts toward higher temperatures and becomes narrower by a factor of ~1.5; the latter fact is apparently due to addition of PMMA radical chains to C_{60}, followed by cleavage of CC or CO bonds between C_{60} and PMMA.

Three stages of thermal oxidative degradation and effect of C_{60} on them. Let us consider three stages of thermal oxidative degradation for samples of the 5-5 series as an example. Stage 1 involves oxidation of degradation products originating from the cleavage of weak bonds in the chains. The onset of the endothermic peak for PMMA without additives corresponds to approximately 28% weight loss (Fig. 2a). This value is noticeably smaller than the fraction of products formed by cleavage of weak bonds in the course of thermal degradation (~40%), as estimated from the thermograms in Fig. 1. Thus, not all the products formed by degradation of PMMA without additives via cleavage of weak bonds undergo oxidation. The fraction of oxidized products in the samples containing C_{60} decreases to 15–23% (Figs. 2b, 2c). Simultaneously decreases the heat release in the range corresponding to this weight loss: The area of the exothermic peaks in Figs. 2b and 2c decreases by 15 and 34%, respectively. This fact suggests that C_{60} prevents oxidation of PMMA, competing with oxygen for the polymer or directly interacting with oxygen. Assume as a rough estimate that about 20% of the polymer has been oxidized. This is half the weight corresponding to peaks *I* and *II*. The other half has apparently combined with C_{60}, which is consistent with the MTA estimates for the fraction of the polymer captured by C_{60}. In stage 2, the degradation products volatilize with heat absorption, rather than heat release (we arbitrarily regard as the beginning of this stage the temperature corresponding to the first intersection of the endothermic peak with the baseline, and as the end, the temperature corresponding to the endothermic minimum). These may be both unoxidized degradation products (the remaining 10–13% in the case of straight PMMA) and the products of degradation of previously oxidized chains or radicals, which undergo in this stage only thermal degradation without further oxidation. In PMMA without additives, the content of these products is about 30% of the total sample weight, and in samples containing 1 and 10% C_{60}, ~20 and ~12%, respectively, i.e., the "retaining" role of C_{60} is clearly manifested here. At the same time, these estimates show that about 20% of products formed by random chain cleavage are released from straight PMMA without oxidation. The decrease in the intensity of the endothermic peak with increasing C_{60} content also indicates that the total heat of decomposition and sublimation of the degradation products in this stage is considerably lower for the C_{60}-containing samples.

In PMMA without additives, oxidation starts again (stage 3) at about 326°C (endothermic minimum), whereas the products linked to C_{60} do not undergo oxidation up to ~338°C (Figs. 2b, 2c). In the latter case, subsequent degradation is accompanied by release of less heat than degradation of C_{60}-free PMMA. The heat is released in two stages, with peaks at 380 and 430°C for the sample with ~1% C_{60} and at 392 and 445°C for the sample with 10% C_{60}. This fact suggests the presence of two types of C_{60} molecules, those bonded and not bonded with the PMMA chains. This conclusion is consistent with MTA data. The noticeable heat release corresponding to degradation of C_{60} even at its 1% content indicates that the calorific value of C_{60} is very high. The heat released after the endothermic effect increases by a factor of approximately 5 as compared with the heat released in this range in the case of PMMA without additives. At the same time, with the C_{60} concentration raised tenfold, the heat release increases by only a factor of 3.3. This means that the evaporated products of thermal oxidative degradation of free C_{60} can also be subdivided in two groups: products that have actually underwent oxidation and degradation with heat release and C_{60} molecules volatilizing without oxidation (no less than half of their initial amount, as estimated from the thermal effects). Note also that after the endothermic peak the baseline shifts (an abrupt change in the heat capacity): the higher the C_{60} concentration, the smaller the shift.

Comparison of data obtained by different methods. The major (92 to 95%) gaseous product of PMMA thermal degradation is the monomer. This fact predetermines the good agreement between the DTG and MTA data. Naturally, the DTG curves are directly related to the TG curves. However, the run of the DTG curves may be fairly complex, so that no accurate quantitative conclusions can be made on how the thermal stability of the system changes. We believe that more adequate conclusions can be made by "aligning" the TG curves and determining their shift at 50% or any other arbitrarily chosen level of weight loss.

The T_0 values determined from the DSC and TG data (see table) coincide only in rare cases, mainly with PMMA powders without additives. In the presence of C_{60}, on the one hand, the slope of the thermograms decreases, complicating determination of T_0; on the other hand, if rough estimation of T_0 is still possible, the T_0 values obtained by DSC are always appreciably lower than those given by TG. Apparently, DSC detects the starting degradation and subsequent oxidation or "fullerenization" of PMMA degradation products (latent degradation), but C_{60} prevents the degradation products from leaving the system.

Mechanisms of chemical reactions in thermal oxidation of PMMA. The following elementary steps, determining the specific features of degradation, can be distinguished in thermal oxidation of PMMA.

(1) Cleavage of H–H bonds, formation of macroradicals [scheme (2)], and their stabilization in the presence of oxygen [scheme (3)] [1]:

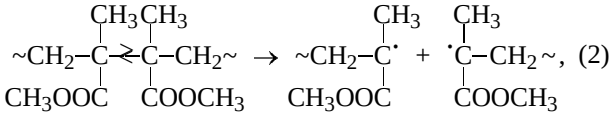

(2)

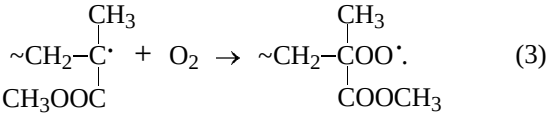

(3)

The stabilization mechanism (3) can be described by a series of reactions:

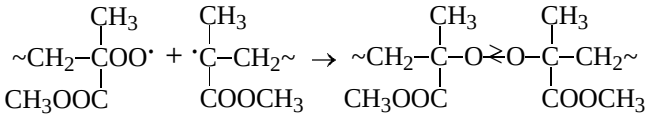

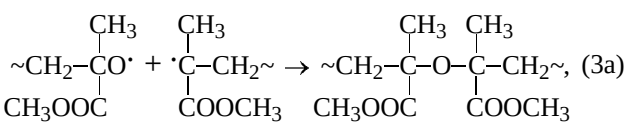

(3a)

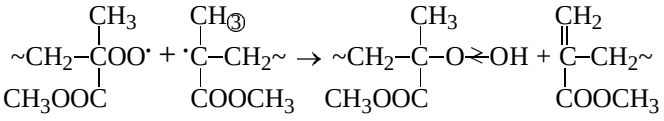

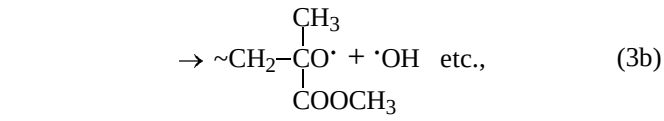

(3b)

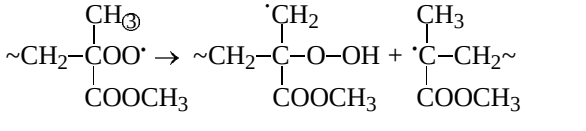

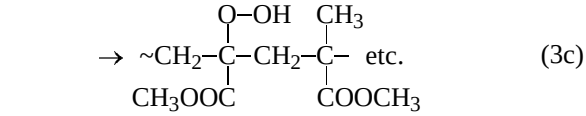

(3c)

Thus, the arising products of macroradical oxidation prevent depolymerization of PMMA. In the process, there is no weight loss, but heat is released. At higher temperatures, the products of macroradical oxidation undergo thermal degradation with heat absorption.

(2) Cleavage of β-bonds at unsaturated ends of polymer chains. Thermal degradation in the range 240–300°C, initiated by unsaturated terminal groups of the polymer chains, is apparently somewhat stabilized in the case of thermal oxidation (the peak *F* shifts toward high temperatures relative to peak *II*; see Fig. 1a). This fact can be accounted for by reactions of the arising macroradicals with oxygen, similar to reactions (3). As in the previous case, oxidation of macroradicals is apparently accompanied by heat release, and their thermal decomposition, by heat absorption. Since peak *II* lies at higher temperatures than peak *I*, oxidized macroradicals formed in the region of peak *II* (as also macroradicals added to C_{60}) undergo thermal decomposition to a greater extent as the temperature is raised further (stage 2), and peak *II* does not fully disappear from the DTG and MTA curves in the presence of oxygen and/or C_{60}.

(3) Thermal oxidation of "defect-free" PMMA molecules. At sufficiently high temperatures, defect-free sections of PMMA chains become subject to thermal oxidation [scheme (4)]. This is accompanied by weight loss and exothermic processes of stage 3:

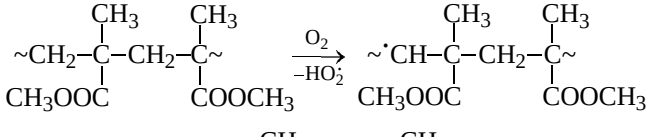

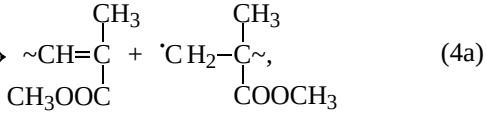

(4a)

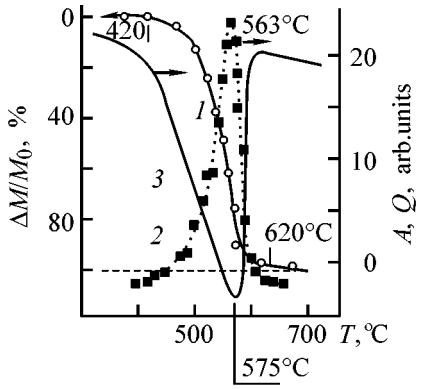

Fig. 6. (*1*) TG, (*2*) DTG, and (*3*) DSC curves of the initial fullerene C_{60}: ($\Delta M/M_0$) relative weight loss, [$A \equiv d(\Delta M/M_0)dT$] its derivative with respect to temperature, (*Q*) heat flow, and (*T*) temperature.

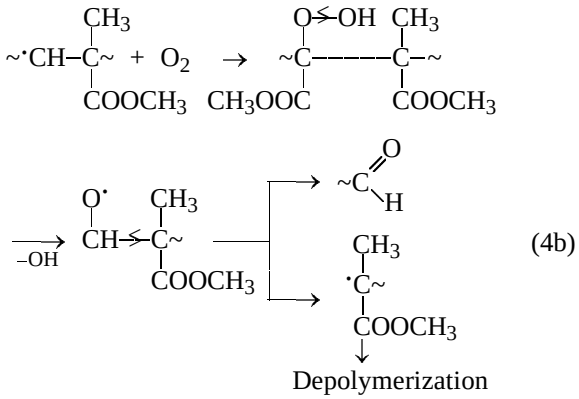

(4b)

The products of thermal oxidative degradation are the monomer, oligomers, aldehydes, ketones, CH_3OH, H_2O, CO, CO_2, etc.

(4) Thermal degradation of oxygen-stabilized chains and defect-free PMMA macromolecules [scheme (5)]. Stage 3 involves random thermal decomposition of oxygen-stabilized and main (defect-free) PMMA chains or chain sections:

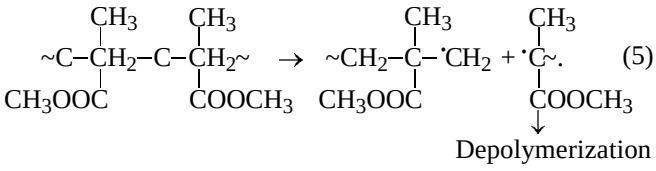

(5)

As in the two preceding cases, weight loss is observed. Owing to such a diversity of reactions, the DTG curve for oxidative degradation of PMMA has a broad half-width and a somewhat unusual shape, strongly differing from the Gaussian shape; furthermore, an additional small peak is observed at about 400°C.

Let us discuss the changes in the mechanism of thermal oxidation of PMMA in the presence of C_{60}. The cleavage of the H–H bonds, the presumably, undergoes no changes. Along with stabilization of macroradicals with oxygen, they are captured by C_{60} molecules with the formation of fullerene-containing polymers (FCPs):

$$C_{60} + R^{\cdot} \rightarrow {}^{\cdot}C_{60}R + R^{\cdot} \rightarrow RC_{60}R. \qquad (6)$$

Similarly, C_{60} adds to oxygen-containing macroradicals formed by oxidation of macroradicals in any stage of thermal oxidative degradation:

$$C_{60} + R^{\cdot} + {}^{\cdot}RO \rightarrow ROC_{60}R. \qquad (7)$$

The fullerene molecule with added macroradicals $R^{\cdot}$ and $RO^{\cdot}$ becomes more susceptible to thermal oxidation because of the distortion of the conjugation system; as a result, thermal oxidation of PMMA chains (both bonded to C_{60} and free) is inhibited by the extra-chain mechanism, and the thermal oxidation of defect-free PMMA chains considerably decreases. At 300°C, the release of thermal oxidation products in the presence of C_{60} is insignificant, whereas without fullerene the rate of release of the degradation products is highest at this temperature (Fig. 5b). An alternative explanation of the inhibiting effect of fullerene on thermal oxidation of PMMA is passivation of oxygen in the presence of fullerene.

Above 300°C, thermal degradation of PMMA chains starts in both fullerene-bonded and free PMMA macromolecules. Therefore, the curve of PMMA thermal oxidation in the presence of C_{60} is close to the curve of thermal degradation in a vacuum or in an inert medium with respect to both the position (365°C) and the half-width (48°C) of the peak in the DTG curve.

Thus, the inhibiting effect of C_{60} is mainly due to FCP formation and extra-chain inhibition of thermal oxidation.

Effect of PMMA on thermal oxidative degradation of C_{60}. Figure 6 illustrates the thermal behavior of pure C_{60}. It is seen that the heat release and weight loss occur at temperatures considerably exceeding those of the peaks observed with C_{60}–PMMA mixtures. Apparently, the polymeric matrix also affects the thermal behavior of C_{60}. The influence of the polymer on the thermal behavior of C_{60} was observed in [3, 9, 10]. It was shown that, in the case of strong interactions with the polymer, C_{60} acts as a kind of microprobe and volatilizes from the system at tem-

peratures close to those at which the polymer degradation products are released. For example, in the case of covalent binding of C_{60} with polystyrene, the bimodal MTA thermograms for C_{60} resemble the bimodal thermograms of styrene monomer release [3, 9]. In reactions with halogens in the trifluorochloroethylene–vinylidene fluoride copolymer, the C_{60} thermograms reproduce the bimodal thermograms of the release of hydrogen halides formed by thermal degradation [10]. These examples give additional grounds to believe that, in the case of mixtures of C_{60} with PMMA, the two peaks in the DSC curves observed after the endothermic peak are due to sequential release of free and PMMA-bonded C_{60}.

The peak at 380°C in Fig. 2c should be assigned to degradation of C_{60}-bonded PMMA chains on the basis of its position and dome-like shape. A certain contribution to this peak is, apparently, also made by fullerene, but its weight fraction is too low (~0.2%) to significantly affect the peak shape. At higher C_{60} concentrations, the peak transforms into a well-defined shoulder of the main peak at 445°C. Thus, in this series of experiments we failed to distinguish the manifestations of PMMA and PMMA-bonded C_{60} in this series of experiments. This can possibly be done in Fig. 3b where a peak at 387°C and a shoulder at 420°C can be assigned to, respectively, PMMA and PMMA-bonded C_{60}.

CONCLUSIONS

(1) The thermal stability of polymethyl methacrylate is most adequately characterized by the temperature shift of the TG curves in the entire range of thermal oxidative degradation.

(2) Thermal oxidative degradation of polymethyl methacrylate involves three stages. In the first stage, the thermal degradation products formed by cleavage of the chains across weak bonds are oxidized with major heat release. In the second stage, the thermal degradation of the already oxidized products continues, with the overall heat consumption. In the third stage, the least defective chains of the polymer undergo oxidation and thermal degradation. Small amounts of C_{60} added to the polymer displace oxygen or partially prevent oxidation; as a result, in the first stage, the extent of oxidation and the amount of the formed degradation products decrease, whereas in the third stage, the amounts of the formed degradation products and released heat grow.

(3) Thermal oxidative degradation of polymethyl methacrylate, especially in the presence of C_{60}, involves latent degradation. Small additions of C_{60} enhance the thermal stability of the polymer and make the DTG and MTA peaks narrower because the feasible degradation pathways become fewer.

(4) A part of C_{60} introduced into the polymer is partially bound by its radicals (~20%), another part is oxidized in the course of degradation, and the remaining part volatilizes without oxidation and degradation.

(5) The inhibiting effect of C_{60} consists in the formation of C_{60}-containing polymer chains and extrachain inhibition of its thermal oxidation.

(6) The polymethyl methacrylate matrix noticeably affects the thermal behavior of C_{60}: the heat release in oxidative thermal degradation of C_{60} and the corresponding weight loss are observed at considerably lower temperatures than with pure powdered C_{60}.

REFERENCES

1. Kashiwagi, T., Inaba, A., Brown, J.E., *et al., Macromolecules*, 1986, vol. 19, no. 8, pp. 2160–2168.
2. Shibaev, L.A., Antonova, T.A., Vinogradova, L.V., *et al., Pis'ma Zh. Tekh. Fiz.*, 1997, vol. 23, no. 18, pp. 81–86.
3. Shibaev, L.A., Antonova, T.A., Vinogradova, L.V., *et al., Zh. Prikl. Khim.*, 1998, vol. 71, no. 5, pp. 835–841.
4. Troitskii, B.B., Troitskaya, L.S., Yakhnov, A.S., *et al., Dokl. Ross. Akad. Nauk*, 1998, vol. 363, no. 1, pp. 79–81.
5. Troitskii, B.B., Troitskaya, L.S., Yakhnov, A.S., *et al., Int. J. Polym. Mater.*, 2000, vol. 46, no. 2, pp. 301–314.
6. Ginzburg, B.M., Pozdnyakov, A.O., Zgonnik, V.N., *et al., Pis'ma Zh. Tekh. Fiz.*, 1996, vol. 22, no. 4, pp. 73–77.
7. Krätschmer, W. and Huffman, D.R., *Phil. Trans. R. Soc. London, Ser. A*, 1993, vol. 343, no. 1667, pp. 33–38.
8. Wendlandt, W.Wm., *Thermal Methods of Analysis*, New York: Wiley–Interscience, 1974.
9. Pozdnyakov, A.O., Pozdnyakov, O.F., Redkov, B.P., *et al., Pis'ma Zh. Tekh. Fiz.*, 1996, vol. 22, no. 18, pp. 57–60.
10. Pozdnyakov, A.O., Ginzburg, B.M., Pozdnyakov, O.F., *et al., Zh. Prikl. Khim.*, 2000, vol. 73, no. 1, pp. 134–136.

Russian Journal of Applied Chemistry, Vol. 74, No. 8, 2001, pp. 1338–1342. Translated from Zhurnal Prikladnoi Khimii, Vol. 74, No. 8, 2001, pp. 1302–1307.

MACROMOLECULAR CHEMISTRY AND POLYMERIC MATERIALS

Pervaporation Membranes for Separating Mixtures of Methanol and Methyl *tert*-Butyl Ether

Yu. P. Kuznetsov, S. V. Kononova, E. V. Kruchinina, K. A. Romashkova, V. M. Svetlichnyi, and V. A. Molotkov

Institute of Macromolecular Compounds, Russian Academy of Sciences, St. Petersburg, Russia

Received March 20, 2001

Abstract—Transport characteristics of new types of bi- and multilayer composite polymer pervaporation membranes and asymmetrical membranes in separating mixtures of methanol and methyl *tert*-butyl ether were studied. The principles of design of the membranes and their mass-exchange characteristics are treated in terms of the Henis–Tripodi resistance model.

One of the most important goals of the chemical industry is to minimize the energy intensity of technological processes. In some cases, the target products form azeotropic mixtures with components of the reaction mixture, which leads to additional expenses for their separation. In particular, this is the case in synthesis of methyl *tert*-butyl ether (MTBE), which finds wide application as a pollution-free gasoline additive [1]. For example, MTBE forms azeotropic mixtures with the starting products (methanol, isobutylene), whose separation by the conventional methods requires two distillation columns. Another possible way is to use a hybrid process in which a distillation column is combined with a pervaporation unit. Such a scheme makes it possible to decrease the energy intensity in a closed separation cycle by 20% (provided that the membranes combine high permeability with high selectivity with respect to methanol [2]).

Therefore, development of new types of polymer membranes with optimal transport characteristics for pervaporation separations is an urgent problem. It is known from the available literature and patents that pervaporation membranes can be prepared for the indicated purpose on the basis of various polymers [3–5]. As a rule, the known types of membranes demonstrate high selectivity in separating methanol–MTBE mixtures, but relatively low permeability.

Previously we reported a method for preparation of a multilayer composite membrane (MCM) demonstrating high selectivity and permeability in separating mixtures of polar (methanol) and weakly polar (cyclohexane, benzene, toluene, etc.) organic liquids [6]. Such a membrane consists of a microporous support [ultrafilter fabricated from an aromatic polyamidoimide (PAI)] to whose surface is applied a two-layer coating of quaternized poly(2-dimethylaminoethyl)methacrylate (PDMA) and a ladder polyorganosiloxane (LP) as interlayer and coating diffusion layers, respectively.

In this work, we studied the transport characteristics of a multilayer composite membrane and its constituents in separating methanol–MTBE mixtures. Of particular interest was to consider in terms of the Henis–Tripodi resistance model [7] the possibility of fabricating for this purpose a high-performance MCM, using a commercial polyacrylonitrile (PAN) ultrafilter as the support.

EXPERIMENTAL

The procedures for preparing PAI supports, fabricating MCMs with PDMA and LP layers, and also carrying out pervaporation separation experiments were described elsewhere [6]. To prepare bilayer membranes and MCMs, we also used a microporous support of an HV3/T PAI ultrafilter [GKSS (Germany)] with mean pore size in the skin layer of 67 Å.

The separation factor α and permeability $\prod$ of the multilayer membrane are plotted in Fig. 1 as functions of the methanol concentration in the feed mixture. As in the case of methanol–cyclohexane mixtures [6], in our case methanol is a more penetrable component. As a result, the permeability of MCM

1070-4272/01/7408-1338 $25.00 © 2001 MAIK "Nauka/Interperiodica"

grows steadily with increasing methanol concentration in the feed mixture (curve *1*). The dependence of α on the feed composition (curve *2*) shows a maximum (α = 473) corresponding to the initial feed composition close to that of the azeotropic mixture with 14.5 wt % MTBE. It is worth noting that MCM has high permeability in general, including the case of azeotropic mixture (Π = 5.9 kg m^{-2} h^{-1}). In this parameter MCM considerably surpasses the existing membrane intended for similar purposes (see below). The reason for the observed high permeability lies in morphological features of MCM as a whole and its elements and, first of all, in the morphology of the PAI support having, according to electron microscopic data [8], finger-shaped pores in the base cross section, low thickness of the skin layer (0.1 μm), and mean pore size in this layer of about 50–60 Å. The thickness of the PDMA interlayer was demonstrated to be very small, too (0.04 μm). Furthermore, the fact that the polymer has very high molecular weight (M_w 2 × 10^6) and segment size larger than the pore size in the skin layer of the support hinders penetration of PDMA into the skin layer in the stage of interlayer formation. It is demonstrated below that this considerably decreases the resistance to mass transfer in the case of PDMA/PAI two-layer system. To conclude the analysis of the high permeability of MCM, it should be pointed out that LP, even taken as a homogenous 60-μm film, demonstrates very low resistance, i.e., very high permeability in the case of methanol–MTBE mixtures, especially at low methanol concentrations (Fig. 2, curve *1*). At the same time, the obtained results show (Fig. 2, curve *2*) that LP cannot serve as a selective polymer in separating methanol–MTBE mixtures, even when being an element of MCM, with the thickness of its layer being about 1–2 μm.

It was of interest to estimate the selectivity of other polymer layers of MCM. Figure 3 shows the dependences of α and Π on the composition of the methanol–MTBE feed for PAI homogenous asymmetric pervaporation membrane [9]. It should be noted that the permeability of the PAI membrane (Fig. 3, curve *1*) is lower than that of MCM (Fig. 1, curve *1*). The reason is the higher resistance of the diffusion skin layer (0.2 μm thick) of the PAI membrane to mass transfer of vapors and gases, which is typical of diffusion-type membranes based on polymers from the class of aromatic polyimides or PAI [10]. As for MCM, α increases with decreasing methanol concentration in the feed mixture (Fig. 3, curve *2*), but the dependence has no extremum. Comparison of α values of multilayer composite and PAI membranes in

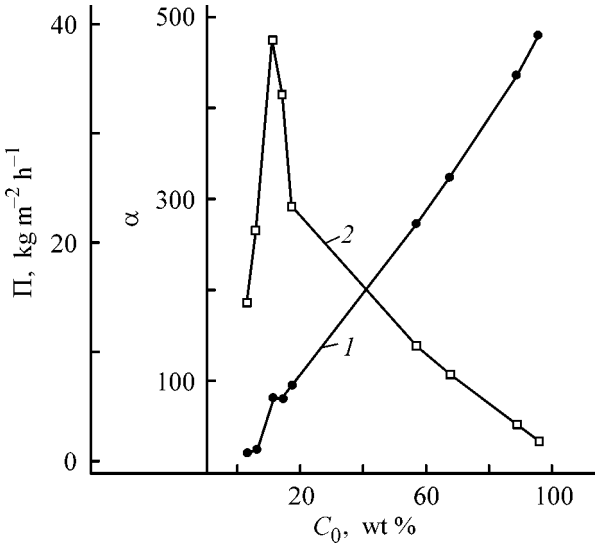

Fig. 1. (*1*) Permeability Π and (*2*) separation factor α of multilayer LP/PDMA/PAI membrane vs. the methanol concentration in the methanol–MTBE feed mixture, C_0, at 50°C.

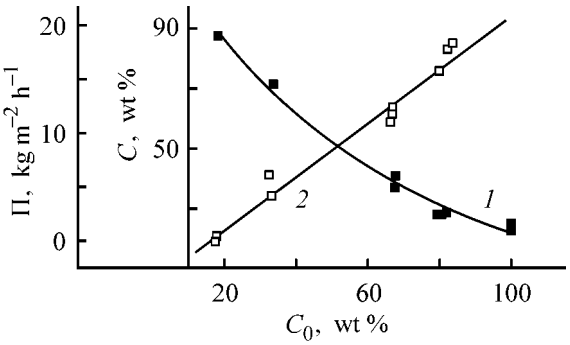

Fig. 2. (*1*) Permeability Π and (*2*) methanol concentration in the permeate, *C*, vs. the methanol concentration in the methanol–MTBE feed mixture, C_0, at 50°C for a 60-μm LP membrane.

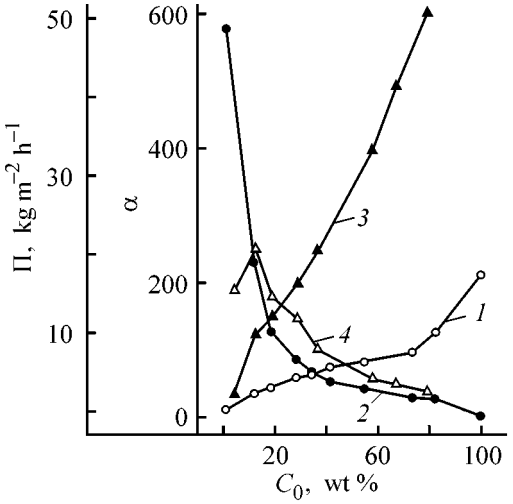

Fig. 3. (*1, 3*) Permeability Π and (*2, 4*) separation factor α vs. the methanol concentration in the methanol–MTBE feed mixture C_0. Membrane: (*1, 2*) asymmetric, PAI and (*3, 4*) bilayer, PDMA/PAI.

Data on pervaporation separation of azeotropic methanol–MTBE mixture at 50°C

Membrane no.	Membrane	Π, kg m^{-2} h^{-1}	α_{MeOH}	$\alpha\Pi$, kg m^{-2} h^{-1}	References
1	PAI (asymmetric)	2.3	164	506	This work
2	PDMA/PAI	9.6	248	2390	″
3	LP/PDMA/PAI	5.9	412	2440	″
4	PDMA/PAN	6.4	15	96	″
5	LP/PDMA/PAN	6.4	3.5	22.4	″
6	PEI/PDMA/PAN	1.7	2940	5000	″
7	PAN (a film)	–	0.696	–	[13]
8	PI* (asymmetric)	0.7	1500	1050	[3]
9	Pervap. 137	1.5	562	843	[4]
10	Polyelectrolyte complex	1.75	396	693	[5]

* Aromatic polyimide.

separation of methanol–MTBE mixture of the azeotropic composition (α 412 and 164, respectively) suggests that PDMA contributes significantly to selective mass transfer across MCM. We failed to determine the mass-exchange characteristics of the PDMA interlayer, since sufficiently thick films of this polymer cannot be obtained. The contribution of PDMA to the total selectivity of MCM was estimated with the use of a composite prepared by multiple impregnation of a support of an inert cermet microfilter with 0.3% PDMA, thus eliminating the effect of the support on selective mass transfer. In separation of a model methanol–cyclohexane mixture (10 : 90 by weight) on this composite, methanol appears to be a more penetrating component at α = 9080. This value is well comparable with that obtained previously in separation of this mixture on MCM [6].

The results show that the MCM elements determining the selectivity in methanol–MTBE separation are the PDMA interlayer and the nonporous PAI support surface, while LP is not a selective polymer, but serves to cure the defects of the PDMA interlayer. The occurrence of such defects is demonstrated by the fact that a PDMA/PAI membrane is nonselective at the same thickness of the DPMA layer as in MCM. Thus, the curing effect favors the selective properties of PDMA and PAI in MCM. The mechanism of participation of LP in mass transfer across MCM is similar to that in a gas-separation composite membrane (Monsanto), where the polydimethylsiloxane coating layer support serves to cure the defects of the selective layer [11]. Therefore, in these membranes, formation of thin coating layers of a low-selective siloxane polymer (but thick enough to provide a diffusion barrier on the support surface) raises the total selectivity of the composite membrane to a value close to the inherent selectivity of the support polymer.

With the thickness of the PDMA interlayer increasing from 0.04 (in MCM) to 0.125 μm, i.e., with the formation of a defect-free skin layer, we obtained a high-performance PDMA/PAI bilayer membrane [12] in which both the polymers are selective with respect to methanol transport. The transport characteristics of this membrane in separation of methanol–MTBE mixtures are given in Fig. 3.

This bilayer membrane demonstrates very high permeability (Fig. 3, curve *3*). In separation of a mixture of the azeotropic composition, this parameter is 9.64 kg m^{-2} h^{-1}. As in the case of MCM, the dependence of α on the feed composition (Fig. 3, curve *4*) passes through a maximum (α = 248) corresponding to the azeotropic mixture.

It was of interest to compare the transport characteristics of all the PAI-based membranes studied. These data are given in the table for the case of separation of a methanol–MTBE azeotropic mixture. As an additional parameter useful in optimization of the transport characteristics (selectivity to permeability relationship) we introduced the membrane efficiency factor defined as the product $\alpha\Pi$.

Comparison of data for membrane nos. 1–3 reveals that the MCM and bilayer membranes have considerably higher efficiency. It should be pointed out also that the maximal selectivity of MCM and PAI-based bilayer membranes is observed in the case of a mixture of the azeotropic composition, which is important for practical use of such membranes.

In large-scale production of gas-separation or pervaporation composite membranes, commercial ultrafilters are mostly used as supports. In this connection, one of the tasks of this work was to fabricate analogs of the PAI-based bilayer and MCM membranes using a commercial PAN ultrafilter as a support. The prob-

lem was to obtain a skin layer with morphology close to that in PAI-based membranes. We fabricated several kinds of PAN-based bilayer and multilayer composite membranes with coating layer thickness corresponding to that of the PAI-based membranes. The selectivity of these membranes (see table, membrane nos. 4, 5) appeared to be very low, which may be due only to the negative effect (in contrast to PAI) of the PAN support on the total selectivity. This is supported by data of [12] on a homogeneous PAN film membrane (22 μm thick) with $\alpha = 0.696$ with respect to methanol in separation of a methanol–MTBE azeotropic mixture (for a PAI asymmetrical membrane the corresponding value is 164). Thus, in separation of a methanol–MTBE mixture, the PAI and PAN supports of composite membranes have opposite effects on the total selectivity, being selective with respect to methanol and MTBE, respectively.

The conclusion that the nature of a polymer of the support is important is consistent with the basic principles of the Henis–Tripodi resistance model developed for composite membranes of diffusion type [7]. According to this model, the nonporous part of the support surface also contributed to selective mass transfer. This contribution is controlled to a considerable extent by the thickness of the diffusion coating layer, as demonstrated in [11] for the example of a polysulfone/polydimethylsiloxane gas-separation composite membrane. For such a membrane the selectivity of separation of a gas mixture approaches that of a low-selective coating polymer with increasing thickness of the polydimethylsiloxane coating layer. In PAI-based pervaporation composite membranes the situation is more favorable, since both PAI and PDMA in these membranes are selective polymers with respect to methanol. Making the PDMA diffusion layer thicker can decrease only the permeability, but not the selectivity of PAI-based bilayer of multilayer composite membranes. The reverse is the case with a PAN-based bilayer membrane, and especially with a PAN-based MCM. Two elements of a PAN-based MCM (PAN and LP) are nonselective, and a thin PDMA interlayer cannot provide an acceptable selectivity. Furthermore, it is seen from the table (membrane nos. 4, 5) that α grows with increasing thickness of the PDMA layer, suggesting the need to make thicker of the PDMA coating layer in a PAN-based MCM. However, owing to the fact that this coating polymer is highly viscous, this can only be done by using such a time-consuming method as multiple layer-by-layer coating. The alternative is changing the nonselective LP coating layer for some polymer selective with respect to methanol, for example, a polyetherimide (PEI) based on dianhydride of 1,3-bis(3,4-dicarboxyphenoxy)benzene and 4,4'-bis(4''-aminophenoxy)diphenyl sulfone. A thus obtained multilayer PEI/PDMA/PAN composite membrane consists of two selective coating polymer layers formed on the support surface, which compensate the small thickness of the PDMA layer in MCM. Thus, the efficiency of PAN-based membrane no. 6 (see table) is considerably higher (5000 $kg\ m^{-2}\ h^{-1}$) as compared with the PAI-based bi- and multilayer membranes. Such a high membrane efficiency is possible in the case of a very high selectivity ($\alpha = 2940$ for a methanol–MTBE mixture of azeotropic composition). In this case, the methanol concentration in the permeate (flux passed through a membrane) is 99.8 wt %.

For comparison, the transport characteristics of known membranes intended for similar purposes are also given in the table (membrane nos. 8–10). It is seen that among them the best performance is shown by an asymmetrical aromatic polyimide membrane [3]. It is seen from the table that the permeation characteristics of bilayer and multilayer composite membranes with PAI support and of multilayer composite membranes with PAN support are superior to those of other membranes by virtue of the higher permeability and separation selectivity, respectively.

Analysis of the transport characteristics of all the investigated membranes with PAI support suggests that, to obtain a high-performance composite pervaporation membranes, it is advisable to form the membrane on a support of a polymer selective to a target component of a mixture to be separated. In this case the problem of selecting a polymer for the coating layer becomes much simpler, since even a nonselective polymer (LP) can be used for this purpose, as serving to cure the defects of the underlying two layer of the selective polymers (PAI and PDMA).

At the same time, the inverted selectivity of PAN in separating methanol–MTBE mixtures requires that the coating diffusion layer on the PAN support should be thicker, which can be attained by using a combination of two polymers (PDMA and PEI) selective with respect to methanol.

Finally, application of a thin interlayer of PDMA, having ultrahigh molecular weight, to a PAI or PAN support appears to be quite significant. This affects not only the selectivity, but also permeability of the composite membrane, as demonstrated for the example of a DPMA/PAI membrane.

To conclude, the results confirm the possibility of obtaining a series of high-performance composite membranes for pervaporation separation of methanol–

MTBE mixtures, whose transport characteristics are consistent with the Henis–Tripodi model.

CONCLUSIONS

(1) Novel types of composite membranes combining high permeability and selectivity in separation of methanol–methyl *tert*-butyl ether were prepared.

(2) The polyamidoimide and polyacrylonitrile supports of the multilayer membranes have opposite effects on the total selectivity.

(3) Introduction of an active polyamidoimide support allows use of a nonselective (with respect to methanol transport) ladder polyorganosiloxane as a coating polymer.

(4) The inert polyacrylonitrile support requires that a combination of two selective coating polymers, poly(2-dimethylaminoethyl) methacrylate and polyetherimide, shoud be used.

(5) High membrane permeability of the multilayer membranes is attained by virtue of the low thickness of the interlayer or coating diffusion layer of poly(2-dimethylaminoethyl) methacrylate, having ultrahigh molecular weight.

ACKNOWLEDGMENTS

The authors are grateful to D. Paul and H.-H. Schwarz (Institute of Chemistry, Teltow, Germany) for furnishing an opportunity to perform pervaporation experiments.

REFERENCES

1. Danilov, A.M., *Prisadki i dobavki* (Additives), Moscow: Khimiya, 1996.
2. Rautenbach, R., *Proc. 3rd Int. Symp. Euromembrane'97*, Univ. of Twente (Netherlands), 1997, p. 356.
3. UK Patent Appl. no. 224 229.
4. Rautenbach, R., *Proc. Membrane Colloquium*, Aachen (Germany), 1995, p. 263.
5. Schwarz, H.-H., Richau, K., and Apostel, R., *Macromol. Symp.*, 1997, vol. 126, p. 95.
6. Kononova, S.V., Kuznetsov, Yu.P., *et al.*, *Zh. Prikl. Khim.*, 1995, vol. 68, no. 8, pp. 1361–1366.
7. Henis, J.M.S. and Tripidi, M., *J. Membrane Sci.*, 1981, vol. 8, no. 2, pp. 233–246.
8. Sukhanova, T.E., Kuznetsov, Yu.P., *et al.*, *Vysokomol. Soedin., Ser. A*, 1989, vol. 31, no. 12, pp. 2501–2506.
9. RF Patent no. 2 126 291.
10. Ohya, H., Kudryavtsev, V.V., and Semenova, S.I., *Polyimide Membranes*, Tokyo: Gordon and Breach, 1996, pp. 120, 157.
11. Chen, Y., Miyano, T., and Matsura, T., *J. Membrane Sci.*, 1990, vol. 48, pp. 203–219.
12. RF Patent no. 2 129 910.
13. Renxiang, X., Guixiang, L., and Xiangyang, H., *Proc. ICOM'96*, Iokohama (Japan), 1996, p. 1088.

Russian Journal of Applied Chemistry, Vol. 74, No. 8, 2001, pp. 1343–1347. Translated from Zhurnal Prikladnoi Khimii, Vol. 74, No. 8, 2001, pp. 1307–1311.

MACROMOLECULAR CHEMISTRY AND POLYMERIC MATERIALS

Thin-Layer Chromatography of Neutral Sugars as Influenced by the Nature of the Cation of Impregnating Salt

K. B. Kalinina and L. S. Litvinova

State Hermitage, St. Petersburg, Russia;

Institute of Macromolecular Compounds, Russian Academy of Sciences, St. Petersburg, Russia

Received March 6, 2001; in final form, April 2001

Abstract—Thin-layer chromatography of neutral sugars contained in water-soluble binders (gum and honey) was studied on silica gel plates impregnated with solutions of alkali, alkaline-earth, and transition metal sulfates at different pH and concentrations.

Impregnation is one of the simplest ways to impart required properties to sorbents. Silica gel impregnated with salt solutions is used for thin-layer chromatographic (TLC) separation of sugars [1]. The major attention is given to influence of the anion nature on the properties of impregnated sorbents. The effect of the cation has not been virtually studied in this respect. However, sugars are known [2–6] to form complexes with alkali, alkaline-earth, and transition metal cations. Formation of Ca^{2+} complexes with sugars has been used in separation of sugars by column chromatography [7, 8].

Previously we found [9] that sugar sorption on plates impregnated with potassium phosphate buffer is higher, irrespective of the pH value, than that on plates impregnated with sodium phosphate buffer.

In this work, chromatographic behavior of natural sugars contained in gums and honey was studied on silica gel plates impregnated with solutions of alkali, alkaline-earth, and transition metal sulfates. The sugar retention was studied as influenced by pH, concentration of impregnating solutions, and the salt cation. We propose that the impregnation mechanism is based on specific sorption of metal cations from solution by solid oxides and on the ability of sugars to form coordination bonds with metal cations and hydrogen bonds with anions.

EXPERIMENTAL

All chemicals and solvents were of chemically pure and analytically pure grades. The following sugars were used: fucose (biochemical grade, Merck, Darmstadt, Germany), galactose, glucose, mannose, fructose, arabinose, xylose, rhamnose, and saccharose (chemically pure grade, Reakhim, Shostka, Ukraine).

Silica gel plates were impregnated with solutions of alkali, alkaline-earth, and transition metal sulfates (Na_2SO_4, K_2SO_4, $MgSO_4$, $CuSO_4$, $ZnSO_4$, $MnSO_4$, $CoSO_4$, and $NiSO_4$) with different pH values: (a) at the initial pH_{in} determined by the salt nature and its concentration in the solution; (b) at pH 3.5; (c) at pH close to pH of precipitation of the corresponding metal hydroxides (see table). Solutions with pH 3.5 were prepared by acidification with 95% H_2SO_4. Alkaline solutions were prepared by addition of 1.0 M NaOH. pH was measured with an HI-8314 pH-meter (Hanna Instrument, Germany).

Sugars were separated by ascending TLC in an N-chamber [10] saturated with eluent vapor. We used 10 × 10-cm commercial (Løene Kadeer, Estonia) glass plates with KSKG silica gel fixed by silica sol binder [11]. Prior to use, the plates were kept for 10 min in a solution of $K_2Cr_2O_7$ in H_2SO_4, washed with water to neutral reaction of wash water, and kept for 24 in a solution of appropriate salt. Then the plates were immersed in water, kept there for 2 s, and then dried and activated by heating at 120°C for 1 h in an oven.

A 0.5% sugar aqueous solution (0.5 μl) or a solution of sugar mixture (1.0 μl) containing 0.5% of each sugar was applied to a plate at a distance of 10 mm from the lower edge. The plates were eluted three times to a height of 4, 6, and 8 cm with a mixture *n*-PrOH : $CHCl_3$: H_2O = 14 : 8 : 2 vol.

1070-4272/01/7408-1343 $25.00 © 2001 MAIK "Nauka/Interperiodica"

Properties of tested cations and their salts [17–19]

Cation	Electronic configuration	Rate constant of exchange, k_{ex}	pH of hydroxide precipitation		pH of initial solutions		
			at indicated concentration, M				
			0.01	1.00	0.067	0.100	0.150
Na^+	$3s^0$	4×10^8	–	–	6.4	6.1	5.5
K^+	$4s^0$	9×10^8	–	–	6.4	6.0	5.4
Mg^{2+}	$3s^04p^0$	7×10^6	9.4	10.4	6.3	5.9	5.3
Mn^{2+}	$3d^54s^0$	2×10^7	7.8	8.8	5.1	3.9	3.8
Co^{2+}	$3d^74s^0$	3×10^5	6.6	7.6	5.8	5.4	5.2
Ni^{2+}	$3d^84d^0$	3×10^4	6.7	7.7	5.5	5.4	5.3
Cu^{2+}	$3d^94s^0$	3×10^6	5.0	6.0	4.3	4.1	3.9
Zn^{2+}	$3d^{10}4s^0$	1×10^7	5.4	6.4	5.8	5.4	5.2

The apparent retention factor $R_f(R_{f,i})$ after the third elution was calculated as the ratio between the distance from the starting line to spot center and that from the starting line to the front line.

The chromatograms of the sugars (where $R_{f,i}$ is the average of three parallel measurements) are shown schematically in Fig. 1. The relative determination error of $R_{f,i}$ did not exceed 6%. The sugar chromatograms were developed by the procedure described in [9].

Silica gel plates with silica sol binder are readily impregnated, which offers unrestricted possibilities of sorbent modification. The plates can be repeatedly used after washing with a solution of $K_2Cr_2O_7$ in H_2SO_4 and can be kept in salt solutions for a long time.

Previously we showed [9] that the retention factor of sugars on the plates with the H form of sorbent prepared by washing with solution of $K_2Cr_2O_7$ in H_2SO_4 or treatment with 0.1 M HCl is higher than that of the initial sorbent, which drastically deteriorates sugar separation. Impregnation of the plates with salt solutions yields surface groups other than ≡Si–OH (irrespective of the salt nature) and alters the chromatographic behavior of sugars. To study the influence of the cation of the impregnating salt on sugar retention, plates with the H form of the sorbent were impregnated with solutions of salts containing different cations and the same anion.

The influence of impregnation is determined by two factors: (1) specific features of interaction of new sorption centers with sugars and (2) surface concentration of these centers. The surface concentration of new centers depends on both the concentration of impregnating solution and the strength of sorption bonds between the salt and the sorbent, which, in turn, is determined by the specific sorption of the cation on the silica gel surface and the formation of hydrogen bonds between the anion and the surface groups. In the course of impregnation, metal cations are adsorbed onto the sorbent surface by electrostatic interaction and then form donor–acceptor bonds with the surface ≡Si–O^- (≡Si–OH) groups which are involved, along with ligands from the solution bulk, in substitution reactions. The possibility of formation of such a bond and its parameters depend on the following factors: (1) structure of valence orbitals of the acceptor (metal cation); (2) donor power of the competing ligands (≡Si–O^- and ≡Si–OH); and (3) lability of both the surface and unsupported complexes [12].

The surface interaction of cations having vacant *d* and *p* orbitals [13] and cations capable of hybridization (Cu^{2+}) [14, 15] is the strongest. The interaction of K^+ and Na^+ with the surface is electrostatic and hence the specific sorption of these cations is low [12, 16].

Taking into account the above considerations, the following cations, exhibiting different capacities for specific sorption, were used for impregnation: Cu^{2+}, Co^{2+}, Mn^{2+}, Ni^{2+}, Zn^{2+}, Mg^{2+}, K^+, and Na^+. Some properties of these cations and their salts are summarized in the table [17–19]. We chose SO_4^{2-} anions since they are strongly sorbed on the silica surface owing to the formation of hydrogen bonds with silica surface groups. Coordination of SO_4^{2-} promotes substitution of water in the *trans* position in the unsupported complex owing to the *trans* effect [20], which favors formation of the surface complex. In addition, sugars are known [3] to form hydrogen bonds with SO_4^{2-} anion.

Both the concentrations and the pH values of the impregnating solutions were varied, in, respectively, the ranges from 0.067 to 0.150 M and from 3.5 to

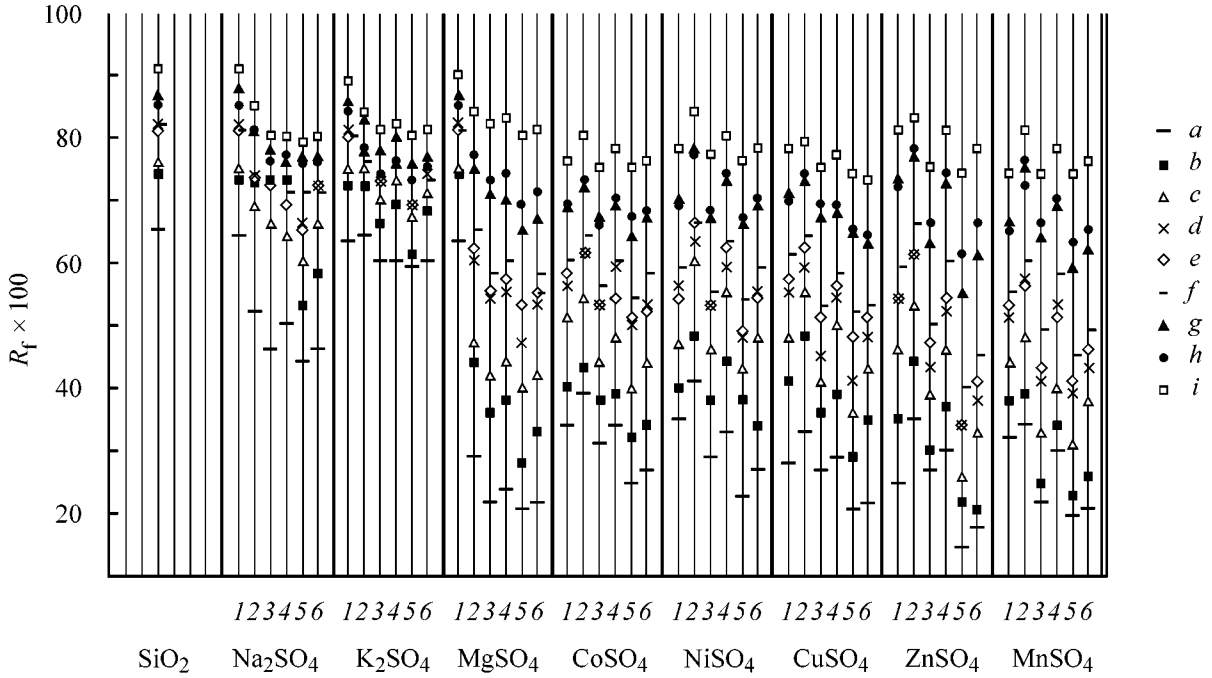

Fig. 1. Scheme of sugar chromatograms on plates with the H form of SiO_2 and plates impregnated with metal sulfates at different salt concentrations and pH values. (R_f) retention factor; the same for Fig. 2. Concentration (M), pH: (*1*) 0.067, pH_{in}; (*2*) 0.067, 3.5; (*3*) 0.100, pH_{in}; (*4*) 0.100, 3.5; (*5*) 0.150, pH_{in}; (*6*) 0.150, 3.5; the same for Fig. 2. (*a*) saccharose, (*b*) galactose, (*c*) glucose, (*d*) mannose, (*e*) fructose, (*f*) arabinose, (*g*) xylose, (*h*) fucose, and (*i*) rhamnose.

the pH of precipitation of the corresponding hydroxide. The change in the sorbent properties after impregnation and, hence, the influence of the cation nature on the sugar retention were estimated from the difference (ΔR_f) between the retention factor of sugars on the plates with the H form of the sorbent and that on a plate impregnated with appropriate salt. The arithmetic mean ΔR_f^* for all sugars at similar salt concentrations and pH was calculated by the equation

$$\Delta R_f^* = \Sigma \Delta R_{f,i}/9, \quad (1)$$

or the arithmetic mean ΔR_f^{**} for nine sugars at three concentrations and two pH values was calculated by the equation

$$\Delta R_f^{**} = \Sigma \Delta R_{f,i}/(9 \times 3 \times 2). \quad (2)$$

We found that impregnation with alkaline-earth and transition metal sulfates strongly increases the sugar retention and hence improves sugar separation, except for 0.067 M magnesium sulfates with the initial pH. Impregnation with alkali metal sulfate has virtually no effect on R_f. The chromatograms of sugars on plates impregnated with metal sulfate solutions are shown schematically in Fig. 1.

The sugar separation depends on the cation nature and concentration and on the pH of the impregnating solution. For example, at C = 0.067 M the best separation was observed on a plate impregnated with copper sulfate (pH 4.3). At C = 0.100 M, a positive result was obtained with zinc sulfate (pH 4.1) and manganese sulfate (pH 3.9). The separation on a plate impregnated with magnesium sulfate (pH 3.5) was slightly worse owing to spot smearing. At C = 0.150 M, the best separation was observed on plates impregnated with manganese sulfate (pH 3.5 and 3.8) and zinc sulfate (pH 3.5). A less successful result was obtained with magnesium sulfate (pH 3.5), and still worse result with cobalt and nickel sulfates. Sugar separation on plates impregnated with potassium and sodium sulfates was the worst at any of the tested concentrations.

The dependences of ΔR_f^* on pH and concentration of sulfate solutions are shown in Fig. 2 as a histogram. It can be seen that ΔR_f^* grows with increasing concentration and pH of the impregnating salt. After impregnation with sodium and potassium sulfates, the surface properties of the sorbent change to the least extent. This is due to lower specific sorption of K^+ and Na^+ as compared with Ni^{2+}, Co^{2+}, Mg^{2+}, Cu^{2+}, Zn^{2+}, and Mn^{2+}. The weak influence of potassium and sodium sulfates on R_f is also due to the formation of weak complexes of these cations with SO_4^{2-} [17], which can be easily confirmed by calculations.

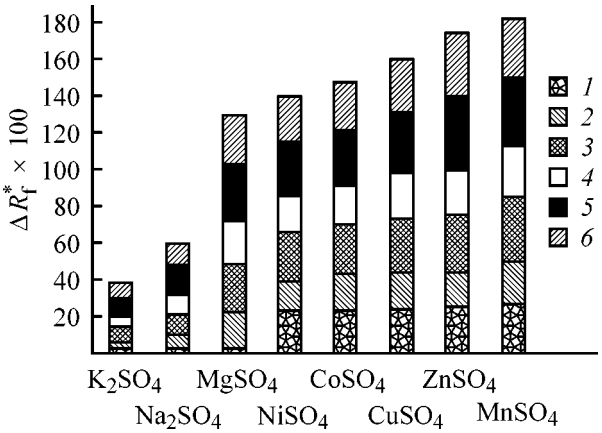

Fig. 2. ΔR_f^* as influenced by the cation nature.

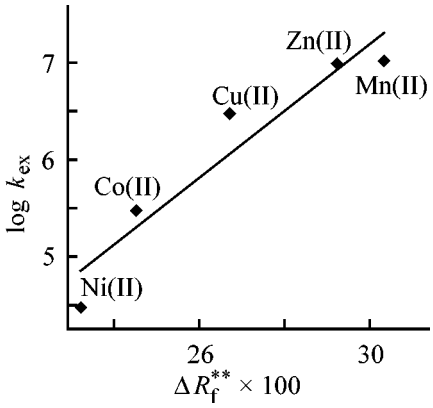

Fig. 3. Correlation between log k_{ex} and ΔR_f^{**} $y = 0.348x - 3.2351$, $R^2 = 0.9116$.

Metal ions M^{n+} in solutions are hydrated to form aqua complexes $[M(H_2O)_{6(4)}]^{n+}$ and complexes like $[MSO_4(H_2O)_{6(4)-1}]^{(4+)-2}$, with the fraction of these species in a solution depending on the salt concentration and pH. The probability of formation of stable surface complex grows with increasing content of $[MSO_4(H_2O)_{6(4)-1}]^{(4+)-2}$ owing to the *trans* effect. The relative content of the aqua and sulfate complexes in solution can be easily calculated from the stability constant of these complex ions [17]. For transition metal cations and Mg^{2+} the [aqua ion] : [sulfate complex] percent ratio is ≅ 20 : 80 within the limits of the tested concentrations and pH. For Na^+ and K^+ this ratio is inverse: [aqua ion] : [sulfate complex] ≅ 80 : 20.

A decrease in R_f with increasing pH is caused by an increase in the fraction of the ≡Si–O^- groups which are stronger donors as compared with ≡SiOH [12]. This makes larger the amount of the surface complexes, such as $[\equiv Si–O–M(H_2O)_5]^{(n+)-1}$ and $[\equiv Si–O–MSO_4(H_2O)_4]^{(n+)-3}$, affecting the separation power of silica gel.

On the basis of ΔR_f^* calculated by Eq. (2), the influence of metal cations can be arranged in order of increasing effect on the retention factor of sugar as follows: $K^+ < Na^+ < Ni^{2+} < Co^{2+} < Mg^{2+} < Cu^{2+} < Cu^{2+} < Zn^{2+} < Mn^{2+}$.

The influence of metal cations on the retention factor of sugars cannot be completely understood on the basis of data on specific sorption of the cations [12] and stability constants of sulfate complexes of these cations. Probably, direct interaction between sugars and metal cations contained in the surface complexes should be taken into account.

A coordination bond between a metal cation and a monosaccharide molecule can be formed by substitution of aqua ligand in the inner coordination sphere by monosaccharide. The probability of formation of this bond depends on the lifetime of water molecule in the hydration shell of the surface complex of the metal cation. Indeed, ΔR_f^{**} on the plates impregnated with transition metal sulfates changes in parallel with the rate constants of the inner-sphere water exchange (see table) [18, 19], described by the equation

$$[M(H_2O)_m]^{n+} + H_2O \rightarrow [M(H_2O)_{m-1}H_2O]^{n+} + H_2O.$$

The correlation between log k_{ex} and ΔR_f^{**} for the transition metals is shown in Fig. 3. This dependence indicates that the probability of interaction between metal cations and sugars grows with increasing rate constant of exchange of inner-sphere water.

Rendelman [3] showed that hydrogen bonds of sugars with OH^- groups are appreciably stronger than those with SO_4^{2-} groups. At low pH, the influence of the ≡Si–O–MOH groups can be neglected, whereas at the pH of precipitation of metal hydroxides, the presence of the above surface complex results in strong smearing of spots. Indeed, sugar separation on the plates impregnated with salt solutions with pH close to the pH of precipitation of the corresponding hydroxides is drastically deteriorated by strong longitudinal smearing of the spots. This is due to the formation of hydroxides by the majority of the tested metals at pH 6.0–10.0 on the sorbent surface.

CONCLUSIONS

(1) Retention and separation of gum and honey sugars on silica gel plates impregnated with solutions of alkali, alkaline-earth, and transition metal sulfates were studied. The influence of an impregnating salt on sugar separation depends on the ability of its cation and anion to form strong surface complexes and complexes in the solution bulk.

Sugar separation is improved after impregnation of the plates with solutions of alkaline-earth and transition metal sulfates. At low salt concentration (C = 0.067 M), the best separation is observed after impregnation with a $CuSO_4$ solution. At higher salt concentration (C = 0.150 M) the best results were obtained after impregnation with solutions of $ZnSO_4$, $MnSO_4$, and $MgSO_4$.

(2) The influence of metal cation of the retention factor increases in the following order $K^+ < Na^+ < Mg^{2+} < Ni^{2+} < Co^{2+} < Cu^{2+} < Zn^{2+} < Mn^{2+}$.

(3) A correlation was revealed between the rate constants of inner-sphere exchange of water in hydration shell of the cation (k_{ex}) and ΔR_f^{**} determined on the silica gel plates impregnated with solutions of transition metal sulfates.

REFERENCES

1. Kirchner, J.G., *Thin-Layer Chromatography*, New York: Wiley, 1978. 2d ed.
2. *Biologicheskie aspekty koordinatsionnoi khimii* (Biological Aspects of Coordination Chemistry), Yatsimirskii, K.B., Ed., Kiev: Naukova Dumka, 1979.
3. Rendelman, I.A., *Adv. Carbohydr. Chem.*, 1966, vol. 21, pp. 209–271.
4. Angyal, S.I. and Davies, K.P., *Carbohydr. Res.*, 1974, vol. 35, no. 1, pp. 165–173.
5. Angyal, S.I., *Pure Appl. Chem.*, 1973, vol. 3, no. 2, pp. 131–146.
6. Zhdanov, Yu.A., Osipov, O.A., and Grigor'ev, V.P., *Koord. Khim.*, 1977, vol. 3, no. 1, pp. 3–11.
7. Kuptsevich, Yu.E., Goryacheva, N.A., Kuligina, N.V., *et al.*, *Zh. Fiz. Khim.*, 1991, vol. 65, no. 2, pp. 464–468.
8. Kuptsevich, Yu.E. and Goryacheva, N.A., *Zh. Fiz. Khim.*, 1993, vol. 67, no. 3, pp. 532–534.
9. Litvinova. L.S. and Kalinina, K.B., *Zh. Anal. Khim.*, 1997, vol. 52, no. 9, pp. 987–992.
10. Geiss, F., *Fundamentals of Thin-Layer Chromatography (Planar Chromatography)*, Heidelberg: Hüthig, 1987.
11. Belen'kii, B.G., Gankina, E.S., Litvinova, L.S., *et al.*, *Bioorg. Khim.*, 1984, vol. 1, no. 1, pp. 244–250.
12. Tikhomolova, K.P., and Tsukanova, V.M., *Zh. Prikl. Khim.*, 1997, vol. 70, no. 3, pp. 353–370.
13. Tikhomolova, K.P. and Demin, S.A., *Fiz. Khim. Mekh. Liofil'n. Dispersn. Sist.*, 1991, no. 22, pp. 77–89.
14. Tsukanova, V.M. and Tikhomolova, K.P., *Kolloidn. Zh.*, 1995, vol. 57, no. 6, pp. 878–886.
15. Tsukanova, V.M. and Tikhomolova, K.P., *Kolloid. Zh.*, 1996, vol. 58, no. 5, pp. 726–732.
16. Suvorov, A.B. and Nikol'skii, A.B., *Obshchaya khimiya* (General Chemistry), St. Petersburg: Khimiya, 1995.
17. Lur'e, Yu.Yu., *Spravochnik po analiticheskoi khimii* (Handbook on Analytical Chemistry), Moscow: Khimiya, 1979.
18. Akbarova, A.B., *Koordin. Khim.*, 1989, vol. 15, no. 1, pp. 3–25.
19. Kostromina, N.A., Kumok, V.N., and Skorik, N.A., *Khimiya koordinatsionnykh soedinenii* (Coordination Chemistry), Moscow: Vysshaya Shkola, 1990.
20. Lilich, L.S. and Khripun, M.K., *Rastvory kak khimicheskie sistemy* (Solutions as Chemical Systems), St. Petersburg: Sankt-Peterb. Gos. Univ., 1994.

Russian Journal of Applied Chemistry, Vol. 74, No. 8, 2001, pp. 1348–1352. Translated from Zhurnal Prikladnoi Khimii, Vol. 74, No. 8, 2001, pp. 1312–1316.

MACROMOLECULAR CHEMISTRY AND POLYMERIC MATERIALS

Solid Macrosupports for Immunoassay, Modified with Polysaccharides

V. V. Shmanai and A. A. Litoshko

Institute of Physical Organic Chemistry, Belarussian National Academy of Sciences, Minsk, Belarus

Received March 28, 2001

Abstract—A series of water-soluble derivatives of natural and synthetic polysaccharides (dextran, pectins, Phycoll, pullulan, hydroxyethyl starch) containing aldehyde, hydrazide, sulfonate, and hydrazine groups were prepared.

The best supports for biologically active macromolecules are natural hydrophilic polysaccharides (mainly agarose) used as microparticles and gels. Immunosorbents based on such polysuccharides are widely used in affinity chromatography, and enzymes immobilized on them are used in enzymology [1]. Covalent immobilization of proteins can be performed after preliminary chemical activation of polysaccharides. Numerous activation pathways are known [1], but the most widely used is activation of hydroxy groups by reaction with cyanogen bromide [2]. Biological macromolecules preserve their functional activity to the greatest extent when immobilized through long hydrophilic spacers [3]; the physical sorption on such matrices is considerably weaker [4], which makes it necessary to bind the reagents chemically.

Nevertheless, the most widely used material for the solid phase in immunoassay is hydrophobic polystyrene on which proteins are immobilized by passive adsorption. As a rule, pressure-cast items (macrosupports) of various shapes are used: test tubes, base tables, star-shaped articles, or spheres. The mechanism of hydrophobic sorption of proteins on such articles is not fully understood, although this has been the subject of numerous studies [5]. It is known that the process is accompanied by significant rearrangement of the protein molecule, which sometimes leads to strong denaturation of antibodies, especially those of monoclonal type [6].

The continuing use of the seemingly not quite suitable system is due, in particular, to problems with handling of microparticles (dosing accuracy, complete separation of the support from the liquid phase) and with manufacturing of molded items from polysaccharides.

Thus, it seems promising to develop new polymeric matrices with surface modified with hydrophilic polysaccharide spacers. In this case, the advantages of molded polystyrene matrices (transparency, ease and accuracy of dosing) could be combined with the functional advantages of polysaccharides (high capacity, strong binding, minimal inactivation of proteins, low level of nonspecific sorption, feasibility of oriented immobilization of reagents), and achievements in immobilization of proteins for enzymology and affinity chromatography [1, 7] could be applied to immunochemical diagnostic procedures and, in particular, to enzyme-mediated immunoassay (EMI).

The demand for molded supports for chemical immunoassay is well known and has been repeatedly stated [8, 9]. The drawbacks of hydrophobic polystyrene call for development of new approaches to preparation of solid supports for immunoreagents. The previously developed supports in the form of chemically modified polystyrene spheres (FPSSs) [10] open up wide possibilities for subsequent modification by reactions of aldehyde groups, with the aim to impart the required properties to the active surface layer of the support. Here we report on the procedures and results of preparation of polysaccharide functional derivatives and modification of FPSSs with them.

Numerous natural and synthetic polysaccharides are known; they are readily subjected to chemical transformations to obtain active derivatives. Taking into account the demands of the biochemical studies, we used in this work several substances of different structures, since the structure of polysaccharide molecules can significantly affect the properties of immobilized immunoreagents.

1070-4272/01/7408-1348 $25.00 © 2001 MAIK "Nauka/Interperiodica"

Water-soluble polysaccharides were functionalized by oxidation of a part of carbohydrate rings with sodium periodate. Further polymer-analogous transformations allow easy modification with such polymer of surfaces containing hydrazide or amino groups, e.g., polystyrene spheres [11, 12]. The electrophilic aldehyde function of a polysaccharide can be converted into a nucleophilic function by reaction with diamines, di- or polyhydrazides, or hydrazine hydrate. Furthermore, pectins containing ester groups readily react with hydrazine to form hydrazide derivatives. Finally, hydroxy groups of the polymer can be subjected to sulfonate activation without cleavage of pyranose rings.

Periodate oxidation was performed with Phycoll (synthetic sucrose polymer with a branched structure, molecular weight 400 kDa), hydroxyethyl starch (product of chemical modification of a natural polysaccharide, molecular weight 120 kDa), pullulan (linear glucose polymer prepared by microbiological synthesis, with units linked by 1→4 and 1→6 bonds, molecular weight 60 kDa), and dextran (microbiological polyglucan with 1→6 bonds).

Polysaccharides were oxidized in 0.1 M phosphate buffer solution (pH 5) at room temperature for 1 day; the molar ratio carbohydrate : periodate was 2 : 1. Hydrazide-containing polymers were prepared in a 0.1 M phosphate buffer solution by reaction of oxidized polysaccharide with an excess amount of dihydrazide, as shown below for hydroxyethyl starch.

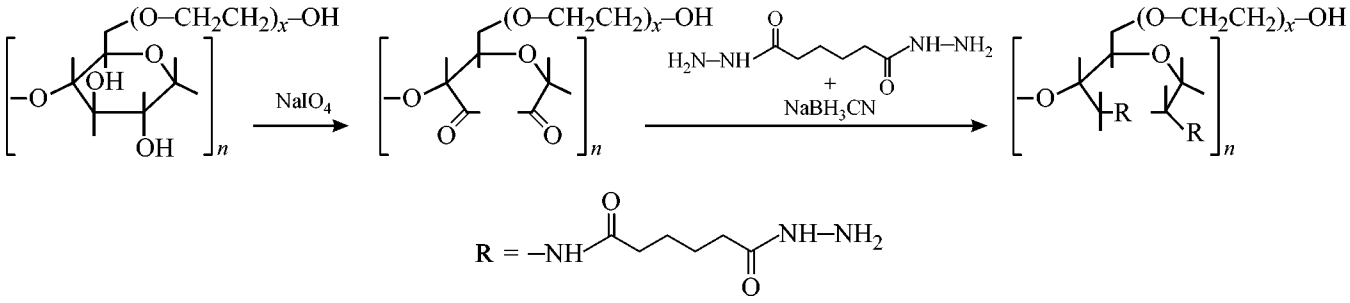

The resulting hydrazones were reduced to substituted hydrazides with sodium borohydride or cyanoborohydride. Low-molecular-weight compounds (excess hydrazide, sodium borohydride and its oxidation products, ions of buffer solution) were removed by ultrafiltration. The reaction products were lyophilically dried and stored at 4°C.

The absence of hydrazide in the filtrate and the presence of hydrazide groups in the polymer were judged from the by formation of an intensely colored product in the reaction with trinitrobenzenesulfonic acid (TNBS) in an alkaline buffer solution [11]:

$$R–NH–NH_2 + NaO_3S–C_6H_2(NO_2)_3 \rightarrow R–NH–NH–C_6H_2(NO_2)_3,$$

where R is the residue of a hydrazide of hydrazide-containing polymer.

All the synthesized polymers showed high activity in a qualitative reaction, indicating the presence of functional groups. A large excess of the hydrazide prevented cross-linking of the polymer molecules and allowed preparation of water-soluble products.

Sulfonate activation differs from the periodate activation in that the pyranose rings of the polysaccharides are not cleaved. Thus, activated products containing the same functional groups may considerably differ in the structure of their macromolecules. We studied sulfonate activation of polysaccharides for the example of reaction of dextran with tosyl chloride followed by substitution of sulfonate groups with hydrazide and hydrazine:

$$\text{Polysaccharide–OH} + CH_3C_6H_4–SO_2Cl \rightarrow \text{Polysaccharide–O–}SO_2–C_6H_4CH_3 + H_2N–NH–CO(CH_2)_4CO–NH–NH_2 \rightarrow \text{Polysaccharide–HN–NH–CO}(CH_2)_4CO–NH–NH_2.$$

By reaction of pectin with hydrazine hydrate we prepared hydrazide-containing apple and citrus pectins. The degree of substitution of ester groups, determined by elemental analysis for nitrogen, was 65–75%. The structural formulas of the monomeric units of the resulting products are as follows:

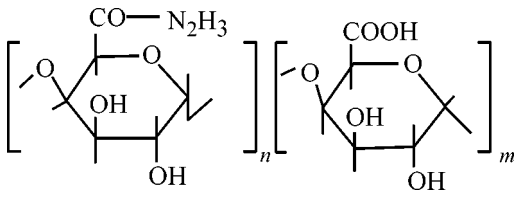

hydrazides of pectins: $n : m = 2 : 1$, citrus; $n : m = 3 : 1$, apple; content of active groups on the support surface 0.51 μmol cm^{-2};

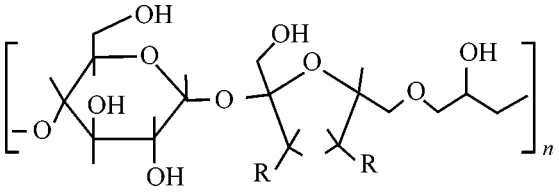

Phycoll hydrazide derivative; 0.20 μmol cm^{-2};

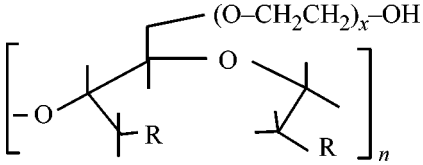

hydroxyethyl starch hydrazide derivative; 0.27 μmol cm^{-2};

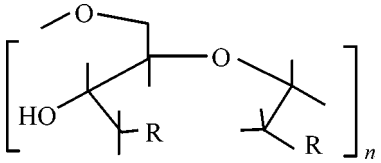

hydrazide derivatives of dextran and pullulan; 0.3–0.5 μmol cm^{-2};

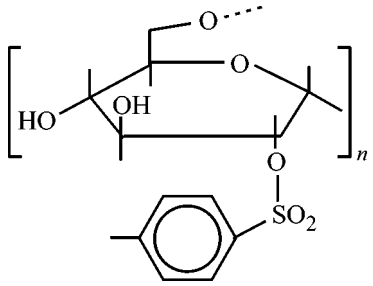

dextran sulfonate derivative

(R = NH–NH–CO–$(CH_2)_4$–CO–NH–NH_2).

By treating FPSSs with polysaccharide hydrazides, we obtained matrices containing 0.05–0.5 μmol cm^{-2} active hydrazide groups. The structures shown above are tentative. To avoid complete degradation of the polymer molecule, oxidation was performed with the periodate taken in deficiency. In Phycoll, both pentose and hexose units are subject to oxidation. The position of sulfonate groups in the structure of activated dextran was not studied and apparently was random (taking into account relative activities of hydroxy groups in different positions of the polymeric molecule).

To optimize the conditions for the reactions of hydrazide-containing polysaccharides with FPSSs, we studied, for the example hydrazide derivatives of pectin and Phycoll, how the activity of the resulting matrices depends on the solution pH and polymer concentration. We found that the highest concentration of the active groups on the support surface is attained in weakly acidic buffer solutions (phosphate or acetate) at pH 5 for Phycoll and in weakly alkaline solutions (pH 8–9) for substituted pectin.

We revealed a strong dependence of the activity of the hydrazide matrices on the polymer concentration in solution: The supports obtained at a polysaccharide concentration less than 10 mg ml^{-1} showed insignificant coloration in a qualitative reaction with sodium trinitrobenzenesulfonate tetrahydrate (TNBS; active group content less than 0.1 μmol cm^{-2}). At a polysaccharide concentration higher than 50 mg ml^{-1}, the content of active groups on the support reached 0.5 μmol cm^{-2}. Thus, the best conditions for synthesis of the hydrazide-containing matrices are as follows: 0.1 M buffer solution, pH 5, polysaccharide concentration no less than 50 mg ml^{-1}.

Preliminary experiments showed that the interaction of the prepared supports with antibodies oxidized with periodate and containing aldehyde groups results in their covalent immobilization.

EXPERIMENTAL

In our study we used general-purpose polystyrene of PSM-115 grade [GOST (State Standard) 20282–86]; polystyrene spheres 0.63 ± 0.01 cm in diameter, prepared by pressure casting followed by abrasive treatment of the surface; membranes for micro- and ultrafiltration (MIFIL, Belarus); gels for chromatography (Pharmacia, Sweden); Dowex 21-K anion-exchange resin (Serva, Germany); sodium azide, sodium borohydride, Timerosal, 3,3',5,5'-tetramethylbenzidine (TMB), glutaraldehyde (25% aqueous solution) (Serva, Germany); sodium metaperiodate (Reanal, Hungary); Tween-20 (Biorad, the United States); TRIS (chemically pure grade, Biolar, Latvia); hydrazine hydrate (pure grade), hydrogen peroxide (chemically pure grade), sulfuric acid (chemically pure grade), adipic acid (pure grade), 2,4-dinitrophenylhydrazine (DNPH, pure grade), sodium trinitro-

benzenesulfonate tetrahydrate (TNBS, pure grade) (Reakhim, Russia); polysaccharides: hydroxyethyl starch (molecular weight 120 kDa); pullulan and dextran (molecular weight 60 kDa); apple pectin (degree of esterification 60%); citrus pectin (molecular weight 150–300 kDa, ICN, the US); Phycoll 400 000 (Pharmacia, Sweden); bovine serum albumin (J.T. Baker, the Netherlands); human immunoglobulin IgG (Belarussian Republican Station for Blood Transfusion, Minsk); and horse radish peroxidase (HRP, A grade, spectral purity parameter RZ = 2.7, Biolar, Latvia).

To remove picric acid from TNBS, 1 M aqueous solution (as judged from the weighed portion) was cooled to 0°C and filtered. The TNBS concentration was determined using the mean molar extinction coefficient of the products of TNBS reaction with amino acids. Hydrazine hydrate was titrated with 0.1 M HCl with methyl orange indicator, and sulfuric acid, with 0.1 M NaOH. The concentration of hydrogen peroxide was determined by iodometric titration.

Adipic acid hydrazide was prepared by refluxing diethyl adipate with 80% hydrazine hydrate in ethanol for 3 h. After cooling, the crystals were filtered off, and the product was recrystallized from aqueous alcohol.

Buffer solutions were prepared from appropriate salts, acids, and bases of chemically pure or ultrapure grade (Reakhim). The concentrate of the phosphate–salt buffer solution (PSB) was prepared by dissolving in distilled water 80.0 g of NaCl, 2.0 g of KH_2PO_4, 13.9 g of $Na_2HPO_4 \cdot 2H_2O$, and 2.0 g of KCl. The solution volume was brought to 1 l. The PSB with pH 7.4 was prepared by tenfold dilution of the concentrate.

Phosphate buffer solutions were prepared by dilution of 1 M phosphoric acid and pH adjustment with 4 M NaOH. The carbonate buffer solution (pH 9.5) was prepared by mixing 0.1 M solutions of sodium carbonate and hydrocarbonate in a 3 : 7 ratio. Buffer solutions containing NaCl were prepared by dissolving the required amount of NaCl. In all experiments we used distilled water, and in the experiments with HRP, double-distilled water.

Immunoglobulin was isolated by ion-exchange chromatography with a 2×10-cm column packed with Sephadex G-50 equilibrated with 0.01 M phosphate buffer solution (pH 6.5), and then purified by gel filtration. The edge fractions were discarded, and the remaining fractions were combined, concentrated to 20 mg ml^{-1} with a PA-100 membrane, and filtered through a capron membrane with pore diameter of 0.22 μm. The solution was stored at 4°C. A 0.1% solution of purified IgG in PSB containing 1% glucose was used for immunization of a rabbit. As adjuvant was used a mixture of 15% lanolin and 85% Vaseline oil [13].

Immunization of a rabbit by human immunoglobulin G was performed by a standard procedure [13]. The activity of antibodies was determined by simple and double immunodiffusion and by direct EMI [13]. The antiserum was separated from the coagulum and diluted twofold with PSB, after which a saturated solution of ammonium sulfate, pH 7.0, was added with continuous stirring to 40% saturation. The stirring was continued for additional 30 min. Then the mixture was centrifuged at 6000 rpm for 15 min, the solution was removed, and the precipitate was dissolved in water. The procedure was repeated twice. All experiments were performed at 4°C. The isolated globulin fraction was purified by gel filtration and stored under the same conditions as IgG.

The IG–HRP conjugate was prepared by the periodate procedure developed by Nakane and Kawaoi [14] and modified by Wilson and Nakane [15]. Gel filtration was performed in a column packed with Sephacryl S-200 equilibrated with 0.1 M borate buffer solution, pH 7.4.

As indicator reaction in EMI we used oxidation of TMB with hydrogen peroxide, catalyzed by HRP. The reaction was stopped with 0.5 M sulfuric acid. The activity of immunosorbents was estimated from the optical density of the substrate solution at a wavelength of 450 nm and layer thickness of 1 cm.

Preparation of polysaccharide functional derivatives. Apple pectin (1.07 g; 1.0 g of the main substance) was suspended in 20 ml of 89% hydrazine hydrate; the mixture was stirred for 3 h at room temperature and for 3 h at 60°C. The solvent was removed in a vacuum, 10 ml of water was added, the mixture was again evaporated to dryness, 10 ml of water was added, and the mixture was acidified to pH 1.5–2 (the reaction product is soluble in acidic and alkaline solutions owing to the formation of salts by hydrazide and carboxy groups, respectively), and precipitated into 100 ml of alcohol; the product was centrifuged and vacuum-dried. Yield of the hydrazide derivative of apple pectin 0.63 g (65% substituted carboxy groups, according to elemental analysis for nitrogen). Hydrazide of citrus pectin was prepared similarly; yield 0.86 g, 72% substitution.

Phycoll (0.649 g; 2×10^{-4} mol of monomer units) was stirred for 3 h in 4 ml of 0.1 M phosphate buffer solution (pH 5) containing 0.214 g (1×10^{-4} mol) of

$NaIO_4$ and left overnight. To remove anions (iodate, periodate, iodide), the solution was passed through a column packed with Dowex 21-K anion-exchange resin equilibrated with the same buffer solution; 0.5-ml fractions were collected. The presence of the oxidized product was checked by the reaction with DNPH (formation of intensely colored hydrazones). The absence of periodate and iodate ions was verified by the reaction with iodide ion (formation of free iodine) in acid solution.

To prepare hydrazide-containing Phycoll, 160 mg of the oxidized polysaccharide was added to a solution of 300 mg of adipic acid dihydrazide in 0.1 M phosphate buffer solution (pH 8.5). The mixture was stirred for 3 h and left overnight. After that, 15 mg of sodium borohydride was added in three portions over a period of 3 h, the mixture was stirred for an additional 1 h, and low-molecular-weight substances were removed by threefold concentrating on a PA-100 membrane. The resulting solution was lyophilically dried and stored at 4°C. Aldehyde and hydrazide derivatives of hydroxyethyl starch (molecular weight 120 kDa) and dextran (molecular weight 20 and 60 kDa) were prepared similarly. To prepare the hydrazine-containing polysaccharide, dextran was activated by transformation of hydroxy groups into sulfonate groups, after which the polymer was treated with hydrazine hydrate [16, 17].

The reaction of FPSSs with hydrazide-containing polymers (5–50 mg ml^{-1}) was performed in 0.1 M phosphate buffer solution (pH 5.0) for 4 h with continuous shaking. The spheres were washed and analyzed for the content of the hydrazide groups on the support, as described previously [11].

CONCLUSION

A series of aldehyde-, hydrazide-, and hydrazine-containing water-soluble polysaccharide derivatives of various structures were prepared. Reactions of hydrazide- and hydrazine-containing polysaccharides with formylated polystyrene spheres yielded solid supports for immunoassay, containing up to 0.5 μmol cm^{-2} of active groups and suitable for covalent immobilization of immunoreagents, including directed immobilization of antibodies.

ACKNOWLEDGMENTS

The study was supported by the Belarussian Republican Foundation for Basic Research (project no. Kh98M-079). The authors are grateful to S.E. Bandarik for providing the possibility for immunization and for assistance in preparing the antiserum.

REFERENCES

1. *Immobilization of Enzymes and Cells*, Bickerstaff, G.F., Ed., Totowa: Humana, 1997.
2. March, S.C., Parikh, I., and Cuatrecasas, P., *Anal. Biochem.*, 1974, vol. 60, no. 1, pp. 149–152.
3. JPN Patent 05 345 022 [93 345 022].
4. Buijs, J., Lichtenbelt, J.W.T., Norde, W., and Lyklema, J., *Colloids Surf.*, 1995, vol. 5B, no. 1/2, pp. 11–23.
5. Van Regenmortel, M.H.V., *Clin. Chem. Lab. Med.*, 1998, vol. 36, no. 6, pp. 353–354.
6. Butler, J.E., Ni, L., Nessler, R., *et al.*, *Mol. Immunol.*, 1993, vol. 30, no. 13, pp. 1165–1175.
7. *Affinity Chromatography*, Dean, P.D.G., Johnson, W.S., and Middle, F.A., Eds., Oxford: IRL Press, 1985.
8. Bulter, J.E., *Immunoassay*, Diamandis, E. and Christopoulus, T., Eds., San Diego: Academic, 1996, pp. 205–225.
9. *Complementary Immunoassays*, Collins, W.P., Ed., Chichester: Wiley and Sons, 1988.
10. Bylina, G.S., Vinokurova, L.G., and Shmanai, V.V., *Zh. Prikl. Khim.*, 1996, vol. 69, no. 3, pp. 493–496.
11. Shmanai, V.V., Nikolaeva, T.A., and Vinokurova, L.N., *Biotekhnologiya*, 1999, no. 2, pp. 59–64.
12. Bylina, G.S., Vinokurova, L.G., and Shmanai, V.V., *Zh. Prikl. Khim.*, 1998, vol. 71, no. 4, pp. 658–661.
13. *Immunologische Arbeitsmethoden*, Friemel, H., Ed., Jena: Fisher, 1984.
14. Nakane, P.K. and Kawaoi, A., *J. Histochem. Cytochem.*, 1974, vol. 22, no. 12, pp. 1084–1091.
15. Wilson, M.B. and Nakane, P.K., *Immunofluorescence and Related Staining Techniques*, Knapp, W., Holubar, K., and Wick, G.N., Eds., Amsterdam: Elsevier, 1978, pp. 215–244.
16. Scouten, W.H., Tweel, W.V.D., Delhaes, *et al.*, *J. Chromatogr.*, 1986, vol. 376, pp. 289–298.
17. Nilsson, K. and Mosbash, K., *Biochem. Biophys. Res. Commun.*, 1981, vol. 102, no. 1, pp. 449–457.

Russian Journal of Applied Chemistry, Vol. 74, No. 8, 2001, pp. 1353–1357. Translated from Zhurnal Prikladnoi Khimii, Vol. 74, No. 8, 2001, pp. 1317–1321.

MACROMOLECULAR CHEMISTRY AND POLYMERIC MATERIALS

Copolymerization of Vinyl Monomers with Different Water Solubilities in the Presence of Manganese Sulfonate Complexes

V. G. Shibalovich, S. A. Khokhrin, and A. F. Nikolaev

St. Petersburg State Technological Institute, St. Petersburg, Russia

Received March 5, 2001

Abstract—Mixed-ligand Mn(III) complexes were prepared from manganese tris(acetylacetonate) and alkylbenzenesulfonic acid, and their surface activity and initiating power with respect to polymerization of vinyl monomers differing in reactivity and water solubility were studied.

Copolymerization of vinyl monomers differing in the polarity and solubility in water attracts considerable attention of researchers, which is due to extensive use of these copolymers in various branches of engineering and national economy [1–4]. Therefore, it is important to study the features and mechanism of formation of such polymerization systems for which, in contrast to the classical Smith–Ewart theory of emulsion polymerization, the colloidal behavior of the system and hence the polymerization kinetics are determined by the solubility of a monomer in water, its polarity, and the nature of the interphase surface formed in the process [1, 2].

It is known that, with mixed-ligand Mn(III) complexes based on acetylacetone and (in)organic acids used as water-soluble redox initiators of radical processes, it becomes feasible to perform low-temperature processes (0–30°C) at a high rate to obtain polymers of high molecular weight [5].

In this work, we prepared a mixed-ligand Mn(III) complex (MMC) from manganese tris(acetylacetonate) (MTA) and alkylbenzenesulfonic acid (ABSA) and studied its reactivity in radical copolymerization of acrylamide (AA) with oil-soluble vinyl monomers differing in reactivity and solubility in water (Table 1); the rate constant of chain propagation K_p varies within 5–18000 l mol^{-1} s^{-1}.

The MMC was prepared by mixing equimolar amounts of MTA and ABSA at 10–30°C in organic solvent (benzene, acetone) in air [6]:

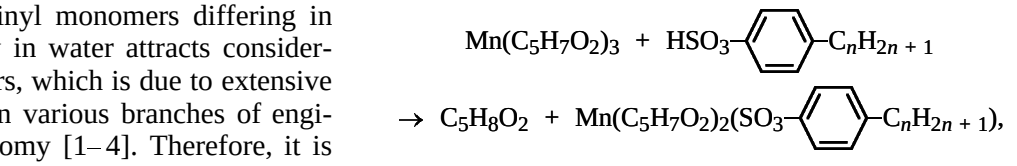

where n = 10–14.

The ligand exchange occurs within 5–10 min, and green crystalline precipitates are formed in 70–90% yields.

We performed elemental microanalysis, measured the IR and UV–Vis absorption spectra of MMC, and determined its molecular weight and manganese val-

Table 1. Characteristics of monomers*

Monomer	Water solubility, g/100 g H_2O	Parameters of Q–e scheme		K_p at 25°C, l mol^{-1} s^{-1}
		Q	e	
AA	204	1.18	1.3	18000
VA	2.5	0.026	–0.22	1000
BA	0.2	0.5	1.06	13
ST	0.0125	1.00	–0.8	5

* Structural formulas of the monomers: 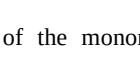 , Acrylamide (AA)

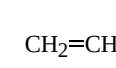 , Vinyl acetate (VA)

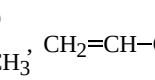 , Butyl acrylate (BA)

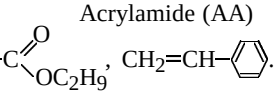 . Styrene (ST)

1070-4272/01/7408-1353 $25.00 © 2001 MAIK "Nauka/Interperiodica"

Table 2. Rate constant of MMC decomposition K_d

Complex	Solvent	$K_d \times 10^4$ (s^{-1}) at indicated temperature, °C					E_d,** kJ mol^{-1}
		10	20	50	80	100	
MABS*	Water	2.9	7.1	–	–	–	32.2
	Water–toluene	–	7.4	–	–	–	–
	Water–ST	–	9.7	–	–	–	–
	Water–BA	–	12.0	–	–	–	–
	Dioxane	–	2.5	–	–	–	–
MTA*	Water	–	0.43	–	–	–	–
	Dioxane	–	–	–	0.15	1.0	106.8
$K_2S_2O_8$	Water	–	–	0.1	–	–	–

* Because of the hydrolysis of Mn(III) compounds, decomposition was performed in 0.1 M aqueous CH_3COOH (pH 5) and monitored by iodometric titration.

** (E_d) Activation energy of thermal decomposition.

Table 3. Surface tension σ at 20°C

Phase boundary	Surface tension σ, mN m^{-1}	
	without MABS	in the presence of 0.05% MABS
Water–air	72.8	31.4
Water–toluene	33.6	2.0
Water–VA (1 : 1)	10.0	1.3
Water–BA (1 : 1)	18.5	1.8
Water–ST (1 : 1)	28.0	2.2

ence [6]. These data show that the prepared compound is monosubstituted Mn(III) complex containing two acetylacetonate and one aromatic sulfonate ligands, i.e., it is manganese alkylbenzenesulfonatobisacetylacetonate (MABS). The product is readily soluble in water and polar organic solvents (acetone, alcohol, tetrahydrofuran, dimethylformamide, etc.), partially soluble in esters, and insoluble in aliphatic and aromatic hydrocarbons. On dissolution in water, the complex undergoes hydrolysis, typical of Mn(III) sulfonate complexes, which is suppressed at pH ≤4.0.

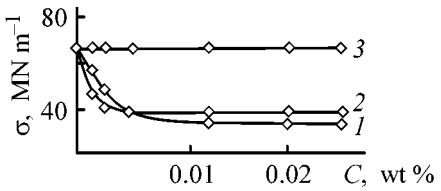

Fig. 1. Isotherms of surface tension σ at the water–air interface. (*C*) Concentration. (*1*) ABSA, (*2*) MABS, and (*3*) MTA.

Thermal decomposition of MABS in the solid phase under argon was studied by DTA/TGA in the range 20–600°C. Examination by elemental microanalysis of the stable intermediates formed in the first stage shows that thermal decomposition involves elimination of one acetylacetonate ligand and reduction of Mn(III) to Mn(II):

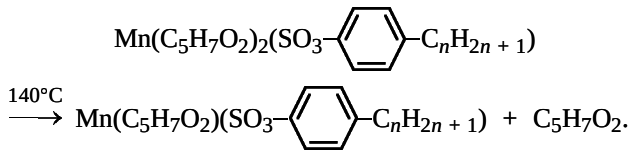

Kinetic study of MABS decomposition in aqueous and organic solutions showed that the decomposition rate is determined by the nature of the coordinated ligand and solvent (monomer). The presence of the sulfonate ligand facilitates the inner-sphere redox reaction, apparently owing to a distortion of the "pseudoaromatic" character of the inner sphere; this circumstance determines the higher initiating activity of MABS as compared with MTA (Table 2).

Significant acceleration of MABS decomposition in water is probably due to specific properties of water as solvent and to specific hydration of the complex.

A study of the surface-active properties of MABS by measuring the surface tension of its aqueous solutions (ring detachment method, Fig. 1) showed that this complex exhibits high surface activity: The surface tension at the water–air interface at the critical micelle concentration (CMC) of 0.7×10^{-3} M decreases by more than a factor of 2, and that at the water–monomer interface falls to 1–2.0 mN m^{-1} (Table 3).

Manganese trisacetylacetonate shows no surface activity under similar conditions. The high surface activity of MABS is due to the presence of the aromatic sulfonate ligand with a long alkyl chain.

Thus, a combination of the high initiating power and surface activity of MABS allows its use in (co)polymerization of vinyl monomers as initiator and emulsifier simultaneously.

The kinetics of AA copolymerization with oil-soluble monomers (VA, BA, ST) was studied in aqueous solution in the presence of 0.1 wt % MABS under argon at 10–20°C and stirring rate of 2.5 rps. The copolymerization kinetics was monitored gravimetrically: Samples of the reaction mixture were precipitated into acetone in the presence of hydroquinone. In all experiments, the conversion did not exceed 10%. The composition of the copolymers was determined by elemental analysis.

A study of the copolymerization of the above-indicated monomers showed that the reaction is heterogeneous and is accompanied by an increase in the viscosity of the reaction medium and formation of fine and fairly stable dispersions which are not settled within 24 h to several days, depending on the reaction conditions.

The colloid properties of the dispersions of AA copolymers with hydrophobic monomers in the presence of MABS were studied by microscopy; the phases were colored with water- and fat-soluble dyes. We found that the systems uner study are direct oil-in-water emulsions.

The plots of conversion against time (Fig. 2) and copolymerization rate against concentration of hydrophobic monomer (M_2, Fig. 3) for the case of AA copolymerization with vinyl monomers show that both the reaction rate and the copolymer yield are the highest (curves *3*) with VA, which is the most hydrophilic.

Determination of the copolymer compositions as influenced by the composition of the initial monomeric mixture and calculation of the constants of AA (M_1) copolymerization with VA, BA, and ST by the Fineman–Ross, Mayo–Lewis, and universal methods (Table 4) allowed a conclusion that in all cases AA is more reactive than the vinyl comonomers, and the copolymers, irrespective of the composition of the initial monomer mixture, are always enriched in the more active AA.

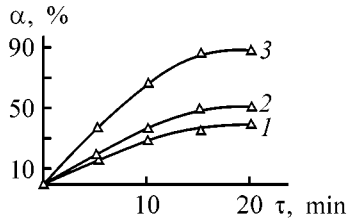

Fig. 2. Monomer conversion α vs. time τ at 20°C. Water : oil = 2 : 1; concentrations (M): monomers 1 and MABS 3×10^{-3}; the same for Fig. 3. Copolymerization of AA with (*1*) ST, (*2*) BA, and (*3*) VA; the same for Fig. 3.

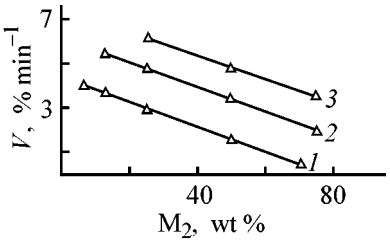

Fig. 3. Copolymerization rate *V* vs. concentration of the oil-soluble monomer M_2 at 20°C.

Table 4 shows that the copolymers with VA exhibit the greatest tendency toward alternation of units in the polymer chain, whereas in the copolymers of AA with BA and ST this tendency is weak. Nevertheless, comparison of our data on the relative activity for the system AA–ST with published data [7] shows that with MABS the reactivity of hydrophobic ST toward

Table 4. Constants of AA (M_1) copolymerization with hydrophobic monomers in aqueous solution

M_2	Initiator	*T*, °C	r_1	r_2	r_1r_2	M_2	Initiator	*T*, °C	r_1	r_2	r_1r_2
VA	MABS	20	5.6	0.14	0.784	ST	MABS	20	2.16	0.8	1.73
BA	〃	20	1.9	0.6	1.14		$K_2S_2O_8$ [7]	70	12.5	0.25	3.13

Table 5. Probability of diad formation in copolymers of AA (M_1) with VA and ST (M_2) at various copolymer compositions

Copolymer composition, wt%		Probability of diad formation				Number of monomeric units in block	
m_1	m_2	F_{11}	F_{12}	F_{21}	F_{22}	$\bar{L}_{M_1}$	$\bar{L}_{M_2}$
Acrylamide–vinyl acetate							
94	6	0.892	0.053	0.053	0.002	17.8	1.04
86	14	0.723	0.130	0.130	0.017	6.56	1.13
70	30	0.435	0.233	0.233	0.099	2.87	1.42
45	65	0.160	0.258	0.258	0.324	1.62	2.26
Acrylamide–styrene							
96.6	3.4	0.96	0.02	0.02	0.001	49.0	1.04
95.0	5.0	0.92	0.04	0.04	0.003	24.0	1.08
90.5	9.5	0.85	0.07	0.07	0.01	13.4	1.14
78.5	21.5	0.73	0.12	0.12	0.03	7.08	1.25

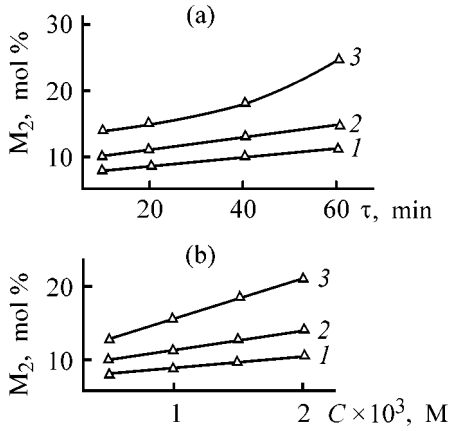

Fig. 4. Compositions (M_2 content) of copolymers (*1*) AA–ST, (*2*) AA–BA, and (*3*) AA–VA vs. (a) copolymerization time τ and (b) concentration of MABS initiator *C* at 20°C. Concentration of monomers in water 1 M. (a) MABS concentration 1×10^{-3} M; (b) reaction time 10 min.

acrylamide radical increases by more than a factor of 5. This fact is apparently due to the possible complexation of ST with MABS, which significantly affects its reactivity and copolymerization activity. Detailed comparative analysis for AA–VA and AA–BA copolymers is impossible because of the lack of published data.

Calculation of the intramolecular distribution of monomeric units in AA–VA and AA–ST copolymers (Table 5) according to [8] confirms the major contribution of the AA–AA diad to the copolymer composition, because both types of the arising polymeric radicals react preferably with AA than with VA or ST.

At AA content in the initial monomer mixture within 10–50 mol %, the AA–VA copolymers show the most ordered structure: The AA blocks consisting of 1–6 monomeric units are separated by 1–2 VA units. With the content of VA increasing above 50%, the tendency toward alternation becomes more pronounced increases. In AA–ST copolymers, even at a large excess of hydrophobic ST in the reaction mixture (initial monomer ratio 3 : 7),there are seven AA units per ST unit.

We studied(at equimolar ratio of the monomers in the initial mixture) how the copolymer compositions depend on the process parameters: reaction time and temperature, concentrations of initiator and comonomers. We found (Figs. 4a, 4b) that, as the reaction time and MABS concentration are increased, the content of hydrophobic monomers in the copolymer grows. This fact suggests predominant polymerization of AA; as AA is exhausted, the copolymer starts to incorporate growing amounts of the hydrophobic monomer. Also, it is seen that MABS enhances the activity of hydrophobic monomers, probably owing to donor–acceptor interaction, which is typical of Mn(III) compounds and vinyl monomers [5].

Variation of the total concentration of the monomers in aqueous solution has virtually no effect on the copolymer composition. As the reaction temperature is raised from 5 to 20°C (at monomer and MABS concentration 1×10^{-3} M), the content of vinyl acetate units in the AA–VA copolymer increases from 8 to 14 mol %, and that of ST units in the AA–ST copolymer, from 4 to 9.5 mol %.

A study of the solubility of AA copolymers with the hydrophobic monomers showed that all the copolymers (except AA–VA with VA content less than, or equal to 20 mol %) are virtually insoluble in water and in most of organic solvents. The precipitation curves for AA–VA, AA–BA, and AA–ST copolymers, obtained by fractional precipitation in the acetic acid–acetone system, are typical of copolymer precipitation, rather than of precipitation of homopolymer mixtures.

Thus, based on the results obtained, we suggest the following copolymerization mechanism: Owing to high solubility of AA and MABS in water and the possibility of their donor–acceptor interaction, initiation and the initial period of chain propagation occur mainly in the aqueous phase:

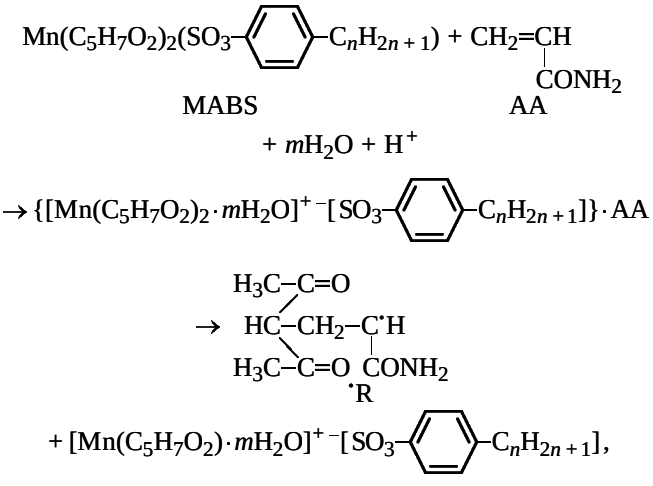

$$R^{\bullet} + M_1 \xrightarrow{k_i} RM_1^{\bullet},$$

$$RM_1^{\bullet} + nM_1 \xrightarrow{k_{11}} R(M_1)_n^{\bullet},$$

$$R(M_1)_n^{\bullet} + M_2 \xrightarrow{k_{12}} R(M_1)_nM_2^{\bullet}.$$

The oil-soluble monomer (VA, BA, ST) occurs in the form of monomer drops from which it diffuses into the aqueous phase. Owing to the high surface activity of MABS and decreased surface tension at the oil–water interface, the hydrophobic monomer molecules diffuse more readily to the active polymerization centers. As the AA concentration in water decreases, the fraction of the oil-soluble monomer in the growing radicals increases, and at a certain critical length of the oligomeric chain the growing radicals start to precipitate; thus, the process becomes heterogeneous, and polymerization continues in latex particles, following the pattern of emulsion polymerization and yielding nucleus-in-shell particles.

EXPERIMENTAL

MABS was prepared by ligand substitution: Equimolar amounts of MTA and ABSA were mixed in an organic solvent in air at 10–30°C [6].

Mixed-ligand Mn(III) complexes were studied by DTA with a Q-1500D derivatograph (MOM).

The rate constant of liquid-phase thermolysis of MABS was determined in 0.1 M aqueous CH_3COOH (pH 5) in the range 10–20°C, and that of MTA, in the range 80–100°C; the thermolysis was monitored by iodometric titration.

The surface-active properties of MABS in water were evaluated by the ring detachment method with a du Nouy device [9].

Copolymerization of vinyl monomers with different water solubilities was performed in aqueous medium in the presence of MABS under argon at temperatures of 10–20°C with stirring at 2.5 rps. The copolymerization kinetics was monitored gravimetrically. The constants of AA copolymerization with hydrophobic monomers and the intramolecular distribution of units were calculated by the Fineman–Ross and Mayo–Lewis methods [8].

CONCLUSIONS

(1) The initiating power and surface-active properties of a mixed-ligand Mn(III) complex prepared from manganese tris(acetylacetonate) and alkylbenzenesulfonic acid were studied. This complex shows high surface activity and high reactivity in copolymerization of vinyl monomers with different water solubilities.

(2) A mechanism of copolymerization of vinyl monomers with different water solubilities in the presence of manganese alkylbenzenesulfonatobisacetylacetonate is proposed. The process follows the emulsion polymerization pattern and yields nucleusin-shell particles.

REFERENCES

1. Eliseeva, V.I., *Polimernye dispersii* (Polymer Dispersions), Moscow: Khimiya, 1980.
2. Eliseeva, V.I., Ivanchev, S.S., Kuchanov, S.I., and Lebedeva, A.V., *Emul'sionnaya polimerizatsiya* (Emulsion Polymerization), Moscow: Khimiya, 1976.
3. Nikolaev, A.F. and Okhrimenko, G.A., *Vodorastvorimye polimery* (Water-Soluble Polymers), Leningrad: Khimiya, 1979.
4. Glubish, P.A., *Primenenie polimerov akrilovoi kisloty i ee proizvodnykh v tekstil'noi i legkoi promyshlennosti* (Use of Polymers of Acrylic Acid and Its Derivatives in Textile and Light Industry), Moscow: Legkaya industriya, 1975.
5. Nikolaev, A.F., Belogorodskaya, K.V., and Shibalovich, V.G., Abstracts of Papers, *IV Mezhdunarodnyi simpozium po gomogennomu katalizu* (IV Int. Symp. on Homogeneous Catalysis), Leningrad, 1984, vol. 3, pp. 165–166.
6. USSR Inventor's Certificate, no. 1011654.
7. Otshuka, Y., Kowaguchi, H., and Sugi, Y., *J. Appl. Polym. Sci.*, 1981, vol. 26, no. 5, pp. 1637–1647.
8. Gindin, L.A., Abkin, A.D., and Medvedev, S.S., *Dokl. Akad. Nauk SSSR*, 1947, vol. 56, no. 2, pp. 177–180.
9. Aivazov, V.V., *Praktikum po khimii poverkhnostnykh yavlenii i adsorbtsii* (Practical Course of Surface Chemistry and Adsorption), Moscow: Vysshaya Shkola, 1973.

Russian Journal of Applied Chemistry, Vol. 74, No. 8, 2001, pp. 1358–1363. Translated from Zhurnal Prikladnoi Khimii, Vol. 74, No. 8, 2001, pp. 1322–1327.

MACROMOLECULAR CHEMISTRY AND POLYMERIC MATERIALS

Formation of Physical Thermally Reversible Gels in Solutions of Methyl Cellulose in Water and Dimethylacetamide and Properties of Films Thereof

A. M. Bochek, N. M. Zabivalova, V. K. Lavrent'ev, M. F. Lebedeva, T. E. Sukhanova, and G. A. Petropavlovskii[†]

Institute of Macromolecular Compounds, Russian Academy of Sciences, St. Petersburg, Russia

Received April 25, 2001

Abstract—Gelation conditions in solutions of methyl cellulose in water and dimethylacetamide were studied. The gelation mechanisms were studied by X-ray diffraction and photocolorimetry, and their differences in the two systems were revealed. The physicomechanical properties of methyl cellulose films prepared from solutions with preliminary gelation were determined.

Recently there has been increased interest in self-associated polymer systems based on natural polymers, which are environmentally safe and biodegradable. It is known that a number of cellulose derivatives, in particular, methyl cellulose (MC), hydroxypropyl cellulose (HPC), hydroxypropyl methyl cellulose (HPMC), and methyl ethyl cellulose (MEC), form physical thermally reversible gels in aqueous solutions. These cellulose derivatives are widely used as gelating agents, thickeners, stabilizers, and emulsifiers in food industry, cosmetics, and perfumery [1]. The most widely used compound is MC.

The gelation mechanism in aqueous solutions of MC was studied in detail by various methods. It was found that gelation conditions depend on many factors, such as molecular weight and degree of substitution (DS) of MC, concentration of the polymer in solution, and uniformity of the substituent distribution in anhydroglucose units and along the macrochain [1–5]. There are several viewpoints on the gelation mechanism in aqueous solutions of MC. Some authors believe that gelation in aqueous solutions of MC is due to local crystallization of macrochain fragments containing predominantly trisubstituted MC units [1–4]. In other papers, it is assumed that incompletely dissolved residual crystallites of the polymer (weakly substituted or unsubstituted sections of cellulose macrochains) may exist in aqueous solutions of MC at low temperatures and initiate gelation on heating [6].

At present, it is generally believed, on the basis of numerous experimental data, that gelation in aqueous solutions of MC occurs in two stages. At low temperatures, water molecules solvate methoxy and hydroxy groups of MC, forming specific structures in solution. On heating, the H bonds between water molecules and methoxy groups are broken; as a result, hydrophobic interactions (association) are enhanced, and the size and shape of associates (clusters) in solution change (stage I). Further heating induces gelation accompanied by phase separation (stage II) [1, 6–9]. The two-stage gelation mechanism was described theoretically by Tanaka and Ishida [10].

It should be noted that gelation on heating is observed in aqueous solutions of MC only with polymer samples in which the distribution of substituents in the anhydroglucose units and along the macrochain is nonuiform, i.e., with MC prepared by a heterogeneous procedure. Methyl cellulose with uniform distribution of substituents in macromolecules does not undergo gelation in aqueous solutions (the polymer precipitates) [5]. Therefore, commercial MC prepared under heterogeneous conditions can be considered a multiblock copolymer consisting of randomly alternating blocks of unsubstituted, mono-, di-, and trisubstituted units. The diffraction patterns of the MC samples with various molecular weights and degrees of substitution in gel form are similar to those of trisubstituted MC. This fact suggests that the centers of local crystallization (formation of a new phase) are trisubstituted MC units [1, 4].

[†] Deceased.

1070-4272/01/7408-1358 $25.00 © 2001 MAIK "Nauka/Interperiodica"

Depending on the DS and preparation procedure, MC can dissolve in other solvents, e.g., in aqueous alkalis, aqueous dimethyl sulfoxide (DMSO), aqueous dimethylacetamide (DMAA), chloroform, or acetone [1, 11–15]. In solutions of MC in DMAA, physical thermally reversible gels are also formed, but only on cooling [12–15]. Thus, it is possible to prepare physical thermally reversible gels in aqueous solutions of MC on heating (system with lower critical solution point, LCSP) and in solutions of MC in DMAA on cooling (system with upper critical solution point, UCSP). The conditions of MC dissolution in H_2O and DMAA reflect the differences between the mechanisms of solvation of polymer macromolecules and formation of physical thermally reversible gels in the above solvents. Presumably, directional variation of the structural organization of moderately concentrated solutions (heating, cooling) must affect the physicomechanical properties of films prepared from MC solutions with preliminary gelation in solutions and subsequent evaporation of solvents.

The goal of this work was to perform a comparative study of the gelation mechanisms in solutions of MC in H_2O and DMAA and examine the influence of gelation on the physicomechanical properties of films prepared from these systems. In our study, we used X-ray diffraction and photocolorimetry.

EXPERIMENTAL

As solvents we used double-distilled water and DMAA distilled in a vacuum from P_2O_5. The starting material was commercial MC (MTs-100 grade, DS 1.62). Methyl cellulose was dissolved in water, and the solutions were filtered under pressure and then centrifuged. MC was recovered from aqueous solutions by lyophilic drying. The molecular weight of purified MC was determined viscometrically from the viscosity of its aqueous solutions at 20°C, using the equation [4] $[\eta] = 2.8 \times 10^{-3} M^{0.63}$. Purified MC had M_η = 154000 (DP 830). Films were prepared from 1.5% solutions of MC in H_2O and DMAA, and the turbidity was studied with 0.5 and 2.0% solutions.

Aqueous solutions of MC were prepared by swelling of the polymer in hot water (80–90°C) followed by dissolution with cooling to 5°C and stirring for 6 h. Solutions of MC in DMAA were prepared by stirring at 90°C. Dissolution was complete in 2 h. The resulting MC solutions were filtered under pressure (aqueous solutions, at 20°C; solutions of MC in DMAA, at 60–70°C) and then deaerated for 1 h.

Films were prepared at 20°C from aqueous solutions of MC by casting onto Teflon plates through a laboratory die with adjustable clearance, with subsequent drying at 20°C. The solvent evaporated within 4 days.

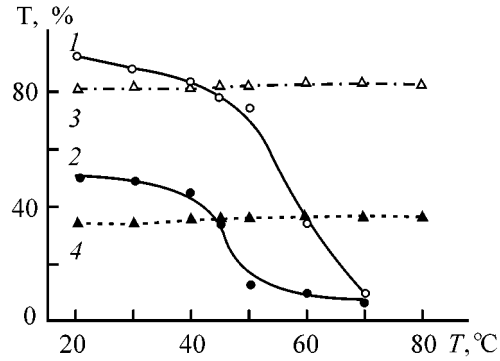

Fig. 1. Absorption spectra of (*1*) 0.5 and (*2*) 2.0% solutions of MC in H_2O and (*3*) 0.5 and (*4*) 2.0% solutions of MC in DMAA. (T) Transmission and (*T*) temperature.

Samples of films with preliminary gelation were prepared by applying the solution at 20°C onto Teflon plates, after which the plates were heated to 60°C. The film formation was complete in 4 h.

Films from solutions of MC in DMAA were prepared by applying a heated solution (70°C) to preheated plates (70°C), which was followed by evaporation of DMAA at 70°C. The film formation was complete in 6 h. Films with preliminary gelation were prepared as follows: A solution at 70°C was applied onto plates preheated to the same temperature, after which the plates were cooled to room temperature. The resulting gel was dried a 20°C for 14 days. In all the experiments, the plates were placed on a temperature-controlled table.

The resulting samples were studied by X-ray diffraction analysis on a DRON-2.0 diffractometer (CuK_α radiation, Ni filter). Samples were prepared as 1–2-mm-thick stacks of films. The diffraction patterns of thermally reversible gels were obtained in a temperature-controlled cell.

The turbidity of 0.5 and 2% solutions of MC was studied photocolorimetrically in the course of varying the temperature from the state of solution to that of gel, i.e., from 20 to 60°C for aqueous solutions of MC and from 90 to 20°C for solutions of MC in DMAA. The samples were kept at each temperature for 20 min before measurement. The measurements were performed with a KFK-2 concentration photocolorimeter with temperature-controlled cells at λ = 590 nm.

The physicomechanical properties of films were studied under uniaxial stretching with an Instron TM-SM universal tensile-testing machine at a rate of 5 mm min^{-1}.

Figure 1 shows the transmission spectra of the solutions as influenced by temperature. For a 2.0%

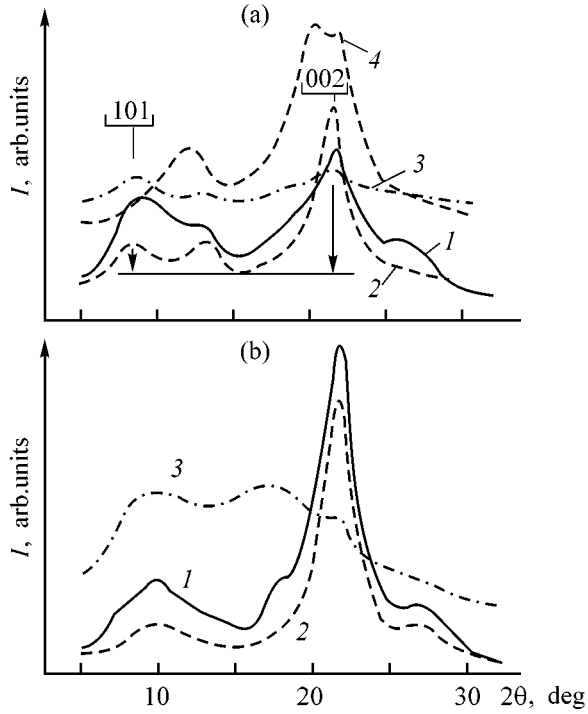

Fig. 2. Diffraction patterns of MC films prepared (a) from aqueous solutions: (*1*) without gelation, (*2*) with preliminary gelation, and (*3*) from gel at 50°C; (b) from solution of MC in DMAA: (*1*) without gelation, (*2*) with preliminary gelation, and (*3*) from gel at 20°C. (a) (*4*) Diffraction pattern of the hydrated cellulose (C II) film. (*I*) Relative intensity and (2θ) Bragg angle.

aqueous solution of MC, the transmission sharply decreases (the turbidity increases) in the temperature range 45–50°C. As the solution concentration is decreased, the cloud point T_{cl} (or the phase separation point) of the aqueous solution shifts toward higher temperatures, which agrees with data in [3]. In contrast to aqueous MC solution, the system MC–DMAA shows no turbidization on cooling. The gel forming in the cell remains fully transparent and elastic. The gels formed in the systems under consideration undergo syneresis when kept for more than 2 h. The aqueous solution of MC exhibits a hysteresis loop for the transition sequence solution–gel–solution, whereas for the solution of MC in DMAA, no hysteresis is observed owing to the absence of noticeable turbidization. The absence of turbidization of the solution of MC in DMAA on transition from solution to gel may be due to at least two factors: (1) different mechanisms of MC dissolution in water and DMAA and different gelation mechanisms, and (2) smaller difference between the refractive indices of DMAA and MC, compared with the MC–H_2O system.

It was shown in [14] that the intrinsic viscosities [η] of MC in water and DMAA are close, but the viscosity of a 1.5% solution of MC in DMAA is an order of magnitude lower than that of the 1.5% aqueous solution. Such a difference in the viscosities of the moderately concentrated solutions is due to different mechanisms of solvation of the polymer macrochains with water and DMAA molecules. Water molecules can form several hydrogen bonds: with functional groups of MC (two H bonds with hydroxy groups and H bond with a methoxy group) and with other water molecules in solution, thus forming a three-dimensional (3D) system of H bonds and structurizing the solutions as a whole. DMAA molecules can form one H bond with OH groups and can interact with methoxy groups of the polymer by the dipole–dipole mechanism. In concentrated solutions of MC in DMAA, dipole–dipole and dispersion interactions between solvated macromolecules are possible. These differences between the mechanisms of solvation of MC macromolecules in water and DMAA may be responsible for different mechanisms of gelation in these systems.

It is known that, when aqueous solutions of MC are heated, the weakest H bonds between the methoxyl oxygen atoms and water molecules are broken first. As a result, the hydrophobic interactions between the solvated macromolecules are enhanced, and separate blocks of the macrochains containing predominantly trisubstituted units form a separate new phase. Dimethylacetamide is a strongly polar associated aprotic solvent, and the mechanism of H bonding between the OH group of MC and a DMAA molecule may be similar to the mechanism of solvation and dissolution of cellulose in aprotic solvents like tertiary amine *N*-oxides [16]. Self-association of solvent molecules occurs via dipole–dipole interactions. Although the H bonding is an exothermic process, it is necessary to raise the temperature (to a certain extent) for decreasing the interactions between the solvent molecules, after which H bonds with the hydroxy groups of the polymer can be formed [17, 18]. In solutions of cellulose with tertiary amine *N*-oxides, the solvent molecules separate out with decreasing temperature to form a new phase (to the point of solvent crystallization). A similar pattern (i.e., separation of solvent molecules in the form of a liquid phase) can be observed in the MC–DMAA system.

It should be noted that, although no turbidization is observed at the gelation temperature in the MC–DMAA system (as judged from the optical density of the solution), the method of polarized light scattering does detect changes in the intensity of scattered light at the solution–gel transition [15]. As the gelation temperature in the systems MC–H_2O and MC–DMAA is approached, the fluctuations of the concen-

tration of the dissolved polymer, the anisotropy of the scattering elements of the solution volume, and the mutual ordering of the anisotropic elements increase.

To elucidate the differences between the gelation mechanisms in the systems MC–H_2O and MC–DMAA, we measured X-ray diffraction patterns of the gels and films cast from solutions and prepared by preliminary gelation in solutions. For comparison, Fig. 2a shows a diffraction pattern of a hydrated cellulose (C II) film. The diffraction patterns of the films prepared by the two different procedures and of the gel (for the MC–H_2O system) are similar to those obtained in [1, 4]. The reflections at 2θ 13.1° and 26.8° correspond to water molecules retained in the films [4]. The reflections at 2θ 8.2° and 21.8° suggest that gelation is accompanied by separation into a new phase and local crystallization (ordering) of the segments of MC macrochains containing predominantly trisubstituted units, which agrees well with data in [4].

A different pattern is observed with the system MC–DMAA (Fig. 2b). The reflections at 2θ 17.5° and 27.0° belong to DMAA molecules. The position of the reflection corresponding to the 101 plane at 2θ 10.0° suggests that gelation is accompanied in this system by separation from solution into a new phase of partially substituted (and probably unsubstituted) units of MC macrochains, followed by their crystallization (ordering). This conclusion is supported by data in Table 1, illustrating the variation of the spacing in the 101 plane for MC samples with different DSs. The angle 2θ 10.0° corresponds to the medium degree of substitution, 1.0. The reflection at 2θ 21.8°–22.0° corresponds to the 002 plane. The reflections from the 002 plane for MC films obtained from aqueous solutions and from DMAA differ insignificantly and lie close to 002 reflections for C II (2θ 22.4°).

The differences in the mechanisms of solvation and desolvation of MC macromolecules with water and DMAA molecules and the differences in the gelation mechanisms must be manifested in the physicomechanical properties of films prepared directly from solution and with preliminary gelation. Table 2 shows that MC films prepared from DMAA solutions exhibit better physicomechanical properties as compared with MC films prepared from aqueous solutions. It is known that, in moderately concentrated solutions of MC in H_2O and DMAA, solvated MC macromolecules form associates of definite size, showing mutual ordering [15]. Presumably, the supramolecular organization of solutions must affect to a certain extent the structural organization of the forming films.

Table 1. Influence of the degree MC of substitution on the interplanar spacing d_{101}

DS	Position of the (101) maximum, 2θ, deg	*d*, Å
0*	12.0	7.12
0.36	11.3	7.55
0.77	10.8	7.90
1.06	10.0	5.54
1.76	8.3	10.27
3.00	8.0	11.03

* Hydrated cellulose.

Table 2. Physicomechanical properties of MC films prepared under different conditions

Sample	Film preparation conditions	σ, MPa	ε, %	*E*, GPa
MC–H_2O	From solution	79.0	9.3	1.8
	From gel	101.0	17.6	2.6
MC–DMAA	From solution	91.0	10.2	2.3
	From gel	123.0	19.3	3.3

* (σ) Breaking stress, (ε) elongation at break, and (*E*) modulus of elasticity.

As the polymer concentration in solution increases in the course of solvent evaporation, separate fragments of MC macromolecules undergo ordering. The mechanism of local crystallization of separate fragments is similar to the mechanisms of formation of crystallites in preliminary gelation, as indicated by the positions of the 101 and 002 reflections (Figs. 2a, 2b). In the course of film formation, the crystallites formed in solution are arranged in a certain order relative to each other, and a 3D network of intermolecular H bonds is formed.

In aqueous solutions, MC forms crystallites consisting predominantly of the trisubstituted units, but less substituted, or more hydrophilic, units also participate in the system of H bonds when a film is formed [4]. Thus, in MC films prepared from aqueous solutions, crystallites are formed via hydrophobic interactions, and fragments of MC macromolecules containing more hydrophilic units are arranged between them, forming a 3D network of H bonds which also fix the mutual arrangement of these crystallites in the films.

In a solution of MC in DMAA with increasing polymer concentration, crystallites are formed from mono- and unsubstituted units owing to the forma-

tion of H bonds via unsubstituted OH groups in anhydroglucose units of MC. In the course of film formation, the macrochain fragments containing more hydrophobic polymer units, remaining in solution, participate in formation of a 3D H-bond system. Thus, in films prepared from solutions of MC in DMAA, crystallites are formed from weakly substituted units having a specific structure and mutual ordering, and these crystallites are stabilized in the polymeric film matrix by more hydrophobic fragments of MC macromolecules forming a 3D network of H bonds and hydrophobic interactions.

The physicomechanical properties of the films are also influenced by the molecular weight of the polymer, degree of ordering (or crystallinity), and the system of intermolecular interactions in the films (H bonds, dipole–dipole, dispersion interactions). The size, shape, and content of crystallites and their mutual arrangement in the polymer matrix may also vary. Since solutions of MC in water and DMAA were prepared from the same polymer sample, the effect of the molecular weight and molecular-weight distribution can be ruled out. The films differ in the nature of the crystallite zones and in the systems of intermolecular 3D interactions in films. Plasticization orientation of MC films prepared from aqueous solutions is accompanied by an increase in the degree of polymer crystallinity and simultaneously by increase in the ordering of crystallites in the films [1]. These processes are accompanied by an increase in the tensile strength σ and modulus of elasticity E of the films, whereas the breaking elongation ε drastically decreases. Presumably, the higher values of σ and E for the MC films prepared from solution in DMAA, compared with the films from aqueous solution, are due to the differences between the nature of crystallites formed in the films and between the systems of intermolecular interactions in the films. The ε values of the films differ insignificantly.

It should be noted that, in both systems, films prepared with preliminary transformation of the solutions into gels and subsequent evaporation of the solvents exhibit considerably better level of all the mechanical properties. This trend is independent of the solvent, which suggests a general nature of the physical process responsible for the increase in σ and E with simultaneous significant increase in the elasticity (parameter ε). The stage of preliminary gelation accelerates formation of crystallites in the systems (Figs. 2a, 2b). With increasing crystallinity of the films (or with increasing content of crystallites in them), σ and E must increase, which is actually the case. The increase in the breaking elongation ε suggests the influence of an additional factor, characteristic of gels only. The suggested differences in the film formation from solution with and without preliminary gelation are illustrated in the scheme.

Scheme of film formation from gel and solution

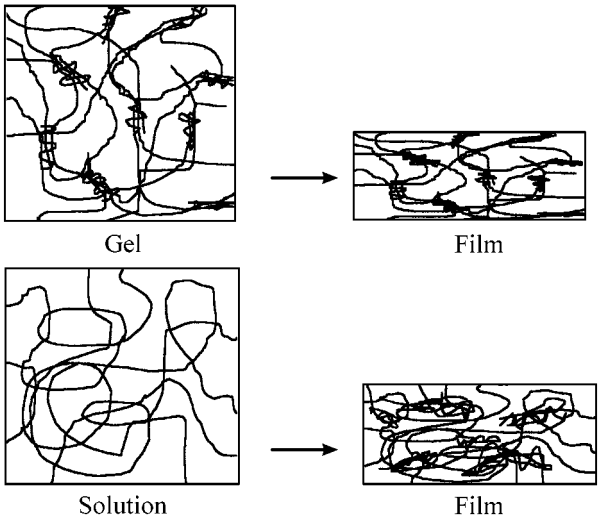

Formation of films from solutions involves ordering of the forming crystallites relative to each other. In films, the orientation increases in the 101 plane and in the surface layers parallel to the support plane. Such an orientation occurs both on the film surface and on support sides [1]. With preliminary gelation, the 3D skeleton of the gel, consisting of crystallites, considerably inhibits mutual ordering of crystallites and their orientation relative to the surface of the forming film and the support. The films prepared from gels contain crystallites which are less ordered relative to each other and to the film planes as compared with the films prepared from solutions (see scheme). Therefore, in the case of tension, a major contribution to strain is made by mutual ordering of the crystallites, which accounts for the significantly higher elasticity of the films prepared with preliminary gelation.

Indeed, Figures 2a and 2b show that the formation of films from solutions of MC in H_2O and DMAA involves ordering, or crystallization, of separate fragments of MC macrochains in two planes: 101 (2θ = 8°–10°) and 002 (2θ = 20°–22°). The highest ordering occurs in the 002 plane, as indicated by the higher intensity of the reflection at 2θ = 20°–22°. The films formed with preliminary gelation show a common trend: higher ordering in the 002 plane as compared with 101. To evaluate this effect quantitatively, we measured the intensities of the peaks observed in the diffraction patterns relative to the baseline at 2θ = 15°, which was proposed as reference in determining the

crystallinity index for C II [19]. The intensity ratios I_{002}/I_{101} for the MC films prepared from aqueous solutions and gels are 1.93 and 6.14, respectively. For the films prepared in the system MC–DMAA from solution and gel, the intensity ratios are 6.48 and 11.9, respectively. This trend confirms our assumption that the skeleton of the forming gel inhibits or "freezes" mutual ordering of the crystallites in the course of film formation.

Thus, preliminary gelation in solutions has a dual effect on the physicomechanical properties of the MC films. On the one hand, gelation accelerates crystallization in solution, which increases the tensile strength and the modulus of elasticity. On the other hand, gelation prevents mutual ordering of the crystallites in the course of film formation, which considerably increases the breaking elongation of the films, i.e., preliminary gelation enhances the strength properties of MC films with simultaneous increase in their elasticity. It should be noted that the physicomechanical properties of the films can also be influenced by the type of the forming gel skeleton and by the gel morphology, which may differ significantly [20].

CONCLUSIONS

(1) Conditions were studied under which physical thermally reversible are formed gels in the systems with the lower (methyl cellulose–H_2O) and upper (methyl cellulose–dimethylacetamide) critical solution points. In contrast to aqueous solutions of methyl cellulose, gelation in dimethylacetamide solutions occurs with decreasing temperature.

(2) The gelation mechanism in the system methyl cellulose–dimethylacetamide was studied for the first time. Gelation is accompaied by separation into a new phase of partially substituted (and possibly unsubstituted) units, followed by their crystallization. Formation of thermally reversible gels is not accompanied by noticeable turbidization of solutions of methyl cellulose in dimethylacetamide.

(3) Preliminary gelation enhances the strength and elasticity of methyl cellulose films prepared in both the systems studied, which is due to a dual effect of gelation on the formation of the supramolecular structure of the films.

REFERENCES

1. Petropavlovskii, G.A., *Gidrofil'nye chastichno zameshchennye efiry tsellyulozy i ikh modifikatsiya putem khimicheskogo sshivaniya* (Hydrophilic Partially Substituted Cellulose Ethers and Esters and Their Modification by Chemical Cross-Linking), Leningrad: Nauka, 1988.
2. Petropavlovkii, G.A., Krunchak, M.M., and Vasil'eva, G.G., *Cellulose Chem. Technol.*, 1972, vol. 6, no. 2, pp. 135–144.
3. Sarkar, N., *J. Appl. Polym. Sci.*, 1979, vol. 24, no. 4, pp. 1073–1079.
4. Kato, T., Yokoyama, M., and Takabashi, A., *Colloid Polym. Sci.*, 1978, vol. 256, no. 1, pp. 15–21.
5. Takahashi, S.-I., Fujimoto, T., Miyamoto, T., and Inagaki, H., *J. Polym. Sci., Part A: Polym. Chem.*, 1987, vol. 25, no. 4, pp. 987–994.
6. Haque, A. and Morris, E.R., *Carbohydr. Polym.*, 1993, vol. 22, pp. 161–169.
7. Sarkar, N., *Carbohydr. Polym.*, 1993, vol. 22, pp. 195–201.
8. Kobayashi, K., Huag, Ch., and Lodge, T.P., *Macromolecules*, 1999, vol. 32, no. 2, pp. 7070–7077.
9. Nishinari, K., Hofman, K.E., Moritaka, H., *et al., Macromol. Chem. Phys.*, 1997, vol. 198, pp. 1217–1226.
10. Tanaka, F. and Ishida, M., *J. Chem. Soc., Faraday Trans.*, 1995, vol. 91, no. 16, pp. 2663–2670.
11. Kondo, T., *J. Polym. Sci., Part B: Polym. Phys.*, 1997, vol. 35, no. 4, pp. 717–723.
12. Bochek, A.M., Petropavlovsky, G.A., Kallistov, O.V., *et al.*, Programme and Abstracts, *Int. Symp. "Molecular Mobility and Order in Polymer Systems,"* St. Petersburg (Russia), October 3–6, 1994, p. 111.
13. Bochek, A.M., Petropavlovsky, G.A., Kallistov, O.V., *et al., Preprints*, A Post Symp. of ISF'94 "Kyoto Conf. on Cellulosics", Kyoto (Japan), October 31–November 1, 1994, p. 106.
14. Bochek, A.M. and Petropavlovsky, G.A., *Cellulose Chem. Technol.*, 1995, vol. 29, no. 5, pp. 567–574.
15. Bochek, A.M., Petropavlovskii, G.A., and Kallistov, O.V., *Zh. Prikl. Khim.*, 1996, vol. 69, no. 8, pp. 1363–1368.
16. Petropavlovskii, G.A., Bochek, A.M., and Shek, V.M., *Khim. Drev.*, 1987, no. 2, pp. 3–21.
17. Bochek, A.M., Petropavlosky, G.A., and Yakimansky, A.V., *Cellulose and Cellulose Derivatives: Physicochemical Aspects and Industrial Applications*, Kennedy, J.F., Phillips, G.O., Williams, P.O., and Picullel, L., Eds., Abington (England): Woodhead, 1985, pp. 131–137.
18. Novoselov, N.P., Sashina, E.S., Tager, E., *et al., Zh. Prikl. Khim.*, 1999, vol. 72, no. 7, pp. 1192–1194.
19. *Cellulose and cellulose derivatives*, Bikales, N.M. and Segal, L., Eds., New York: Wiley-Interscience, 1971.
20. Papkov, S.P., *Studneobraznoe sostoyanie polimerov* (Gelatinous State of Polymers), Moscow: Khimiya, 1974.

Russian Journal of Applied Chemistry, Vol. 74, No. 8, 2001, pp. 1364–1367. Translated from Zhurnal Prikladnoi Khimii, Vol. 74, No. 8, 2001, pp. 1328–1331.

MACROMOLECULAR CHEMISTRY AND POLYMERIC MATERIALS

Optical Adhesives Based on Phosphorus-containing Epoxy Polymers

L. M. Amirova, I. K. Shageeva, and V. F. Stroganov

Tupolev State Technical University, Kazan, Tatarstan, Russia

Kazan Architectural and Building Academy, Kazan, Tatarstan, Russia

Received April 16, 2001

Abstract—The refractive indices, transmission coefficients, and other service characteristics of binary and amine-cured mixtures epoxy oligomer–glycidyl esters of phosphorus acids, proposed as optical adhesives, were measured.

Development of new polymeric optical materials, including adhesives, is an urgent problem [1]. Optical adhesives must meet specific requirements [2]: they must be highly transparent and colorless in the required wavelength range, their refractive index must fall in a definite range, the optical properties must be preserved in the working temperature range; these materials must also exhibit acceptable viscosity, high strength of adhesive joints, etc. Among the versatile adhesives are epoxy adhesives (EAs) ensuring enhanced mechanical strength of adhesive joints of optical parts [3].

Polymers with refractive index adjustable in a wide range can be prepared by copolymerization of two monomers with different n_D^{20} [4]. In the case of epoxy polymers (EPs), this is possible owing to the use of active diluents: epichlorohydrin (OK-50) and phenyl glycidyl ether (OK-72FT$_5$, OK-72FT$_{15}$) [2]. These adhesives exhibit low viscosity, high transmittance (99% at λ = 400–2700 nm), and high frost resistance. However, these formulations also have certain drawbacks: poor physicomechanical characteristics and very narrow range of refractive index variation (1.578–1.582). The authors of [5] proposed an optical adhesive with n_D^{20} 1.493–1.501, consisting of ED-20 epoxy–4,4'-isopropylidenediphenol resin modified with silanol SEDM-3, condensation product of 1,1-dihydroxymethyl-3-cyclohexane with epichlorohydrin, UP-650D agent, and diglycidyl camphorate. As a curing agent was used a mixture of 1,3-bis(aminoalkyl)-adamantane and the product of the reaction of butyl glycidyl ether with an equimolar amount of adamantanediamine. Apparent drawbacks of this compound are the multicomponent formula, complex preparation procedure, difficult availability of some components, and relatively narrow range of variation of the refractive index.

It was shown previously [6] that glycidyl esters of phosphorus acids (GEPs) are effective modifiers of epoxy oligomers (EOs), enhancing the heat and fire resistance and mechanical strength of epoxy polymers. At the same time, the refractive indices of GEPs and EOs differ significantly. Therefore, we examined in this work the possibility of preparing optical adhesives from epoxy polymers modified with GEPs.

EXPERIMENTAL

As investigation objects we chose ED-20 epoxy–4,4'-isopropylidenediphenol oligomer [GOST (State Standard) 10587–84]; curing agents diethylenetriamine (DETA) and monocyanoethyldiethylenetriamine (UP-0633M); and glycidyl esters of phosphorus acids of the general formula $RP(O)(OCH_2{-}CH{-}CH_2)_2$ (O) where R = $-OCH_2{-}CH{-}CH_2$ (O) [triglycidyl phosphate (**I**)], $-OCH_3$ [diglycidyl methyl phosphate (**II**)], and $-CH_3$ [diglycidyl methylphosphonate (**III**)]. The synthesis and properties of GEPs are described elsewhere [7].

The compounds were prepared by mixing ED-20 epoxy oligomer with various amounts of GEP and then adding a stoichiometric amount of the curing agent. The refractive index n_D^{20} was determined by the interference method [8] using IRF-22 and

1070-4272/01/7408-1364 $25.00 © 2001 MAIK "Nauka/Interperiodica"

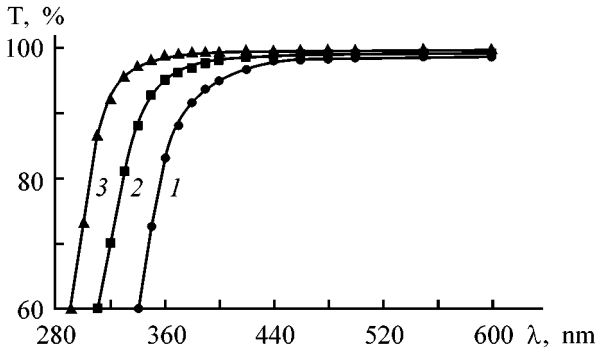

Fig. 1. Transmission spectrum of cured samples based on ED-20–UP-0833M–**III** compounds: (T) transmission and (λ) wavelength. Content of **III**, wt %: (*1*) 0, (*2*) 20, and (*3*) 30.

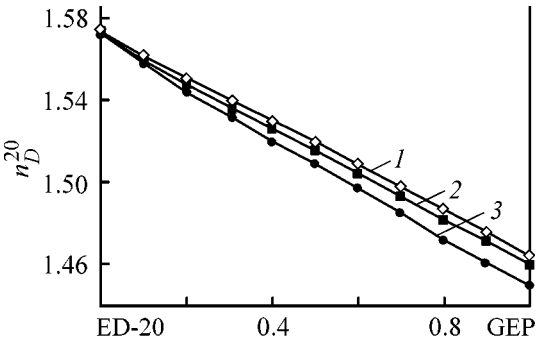

Fig. 2. Refractive index n_D^{20} of ED-20–GEP mixtures vs. the GEP mole fraction. GEP: (*1*) **III**, (*2*) **I**, and (*3*) **II**.

IRM-1 devices for liquid and cured samples, respectively.

The electronic spectra of oligomeric samples (in quartz cells of varied thickness) and cured polymers (as ≥10-μm-thick films) were recorded on an SF-26 spectrophotometer relative to air in the range 200–1000 nm.

Figure 1 shows the transmittance of cured compounds modified with **III**. It is seen that, on adding GEP, the transmission range of the compound is extended toward shorter wavelengths, and the transmittance increases in the entire wavelength range.

It is known [9] that the refractive index n_D^{20} of optical materials can be adjusted by using glycidyl ethers or esters with appropriate refractive indices. For example, n_D^{20} can be reduced by adding butyl glycidyl ether (n_D^{20} = 1.417), butanediol diglycidyl ether (n_D^{20} = 1.459), etc. The refractive indices of the chosen glycidyl esters of phosphorus acids fall in the same range. Figure 2 shows the refractive index of EO–GEP mixtures as a function of the mixture composition. The virtually linear dependence of n_D^{20} on C_{GEP} allows fairly accurate prediction of the refractive index of the obtained polymers. The refractive indices of cured ED-20–GEP–DETA compounds are listed in Table 1. The refractive indices of the cross-linked samples were calculated using the approach suggested in [10, 11] and based on the Lorentz–Lorenz equation, on the additive principle of determination of the molecular refraction and the volume of the repeating fragment of the epoxy polymer network, and on the assumption that the molecular packing coefficient *k* is constant. However, calculation of *k* by the relation proposed in [12] showed that this coefficient may vary with the GEP content. The calculated values of the molecular packing coefficient *k* and refractive index of epoxy polymers with varied GEP content are given in Table 2. As seen, the measured and calculated values of n_D^{20} virtually coincide. Thus, by varying the GEP content, it is possible to adjust the refractive indices of optical epoxy adhesives.

Table 1. Optical characteristics of epoxy polymers based on ED-20–GEP–DETA compounds

Composition, wt %				n_D^{20}	A^*
ED-20	**III**	**II**	**I**		
100	–	–	–	1.574	97
95	5	–	–	1.572	98
91	9	–	–	1.570	99
67	33	–	–	1.551	99
50	50	–	–	1.535	99
33.3	66.7	–	–	1.517	99
9	91	–	–	1.509	99
0	100	–	–	1.499	99
95	–	5	–	1.570	98
91	–	9	–	1.567	99
67	–	33	–	1.549	99
50	–	50	–	1.530	99
33.3	–	66.7	–	1.513	99
9	–	91	–	1.501	99
0	–	100	–	1.491	99
95	–	–	5	1.571	98
91	–	–	9	1.569	99
67	–	–	33	1.552	99
50	–	–	50	1.533	99
33.3	–	–	66.7	1.515	99
9	–	–	91	1.506	99
0	–	–	100	1.497	99

* (*A*) Spectral transmission coefficient of the adhesive layer at λ = 400–1000 nm.

Table 2. Calculated molecular packing coefficients and refractive indices n_D^{20} of EPs prepared from ED-20–GEP–DETA compounds

Mole fraction of GEP*	I		II		III		Mole fraction of GEP*	I		II		III	
	k	n_D^{20}	k	n_D^{20}	k	n_D^{20}		k	n_D^{20}	k	n_D^{20}	k	n_D^{20}
0	0.701	1.574	0.701	1.574	0.701	1.574	0.3	0.708	1.551	0.702	1.548	0.702	1.550
0.1	0.701	1.566	0.701	1.565	0.701	1.566	0.8	0.713	1.514	0.704	1.507	0.703	1.511
0.15	0.701	1.562	0.701	1.560	0.701	1.561	0.9	0.716	1.506	0.706	1.499	0.702	1.503
0.2	0.703	1.558	0.701	1.556	0.701	1.557	1	0.703	1.499	0.706	1.491	0.702	1.497

* Without considering curing agent.

Table 3. Properties of optical adhesives based on ED-20–GEP–UP-0633M compounds

Composition, wt %				n_D^{20}	X,* MPa	Composition, wt %				n_D^{20}	X,* MPa
ED-20	I	II	III			ED-20	I	II	III		
4.8	0.1	95.1	–	1.490	34.8	49.5	0.99	49.5	–	1.530	32.7
4.8	0.1	–	95.1	1.499	33.1	100	9.1	30.3	–	1.544	36.0
9.1	0.2	90.7	–	1.501	34.2	100	1.3	–	32.9	1.551	31.0
16.3	2.4	81.3	–	1.505	36.1	100	1.9	–	2.9	1.572	30.1
9.1	0.2	–	90.7	1.509	32.7	100	1.9	–	1.9	1.573	30.0
16.6	0.3	–	83.1	1.512	32.2						

* (X) Adhesion strength for the sapphire–sapphire joint.

Table 4. Service properties of various optical adhesives based on epoxy–4,4'-isopropylidenediphenol oligomers

Parameter	Developed optical adhesive [13]	Known optical adhesives	
		[5]	OK-72FT$_5$
Transmission coefficient in the wavelength range 400–2700 nm, %	99	98	99
Refractive index n_D^{20}, 20°C	1.490–1.573	1.493–1.501	1.553–1.557
Heat resistance of the adhesive layer (°C) no lower than	150	150	140
Frost resistance of the adhesive layer (°C) no higher than	–170	–170	–170
Adhesive strength for a sapphire–sapphire joint (MPa) no less than	30	30	9.8
Moisture resistance (%) without failure of adhesive layer at 40°C and 98% relative humidity, no less than	56	56	70
Thermal shock resistance in the range from +60 to –60°C, number of cycles, no less than	100	100	65

When developing an optical adhesive, we took into account preliminary data on physicomechanical properties of GEP-modified EPs, according to which the high mechanical strength of the cured compounds is due to the presence of the trifunctional modifier **I**, and the required elasticity, to the presence of diglycidyl esters **II** and **III**. Therefore, to attain the best characteristics, we added simultaneously in various ratios two modifiers differing in functionality. Some properties of cured adhesives and formulas of compounds in the system ED-20–GEP–UP-0633M are given as example in Table 3.

Comparative analysis of the properties of known optical adhesives with those of the developed compounds [13] reveals advantages of the new formulations. The main distinctive feature of GEP-containing adhesives is the possibility of varying the refractive index in a relatively wide range, between 1.490 and 1.573. This was achieved by varying the ratio of modifiers with different refractive indices. The developed compounds show relatively low initial viscosity (0.05–2.1 Pa s) and satisfactory working life (30–40 min). Also, these GEP-containing adhesives exhibit high heat and fire resistance characteristic of phosphorus-containing polymers [6].

CONCLUSION

Optical adhesives were developed on the basis of epoxy oligomer–glycidyl esters of phosphorus acids–amine compounds, with the refractive index adjustable in a wide range. The materials exhibit high transmittance, resistance to heating and thermal shock, and adhesion strength.

REFERENCES

1. *GOST* (State Standard) *14887–87: Optical Adhesives. Types and Main Parameters.*
2. *Uspekhi v oblasti sinteza elementorganicheskikh polimerov* (Advances in Synthesis of Heteroorganic Polymers), Korshak, V.V., Ed., Moscow: Nauka, 1980.
3. Ishmuratova, M.S., Sergeev, L.V., and Gerasimova, L.A., *Opt.-Mekh. Prom–st.*, 1972, no. 3, pp. 30–31.
4. Shepurev, E.I., *Opt.-Mekh. Prom–st.*, 1986, no. 1, pp. 51–55.
5. USSR Inventor's Certificate, no. 1665685.
6. Sakhabieva, E.V. and Amirova, L.M., in *Struktura i molekulyarnaya dinamika sistem* (Structure and Molecular Dynamics of Systems), Ioshkar-Ola: Mariisk. Gos. Tekh. Univ., 1995, part 2, pp. 178–180.
7. Rizpolozhenskii, N.I., Boiko, L.V., and Zvereva, M.A., *Dokl. Akad. Nauk SSSR*, 1964, vol. 155, no. 5, pp. 1137–1139.
8. *GOST* (State Standard) *28869–90: Optical Materials. Methods for Measuring Refractive Index.*
9. Lee, H., Nevill, K., *Handbook of Epoxy Resins*, New York: McGraw-Hill, 1967.
10. Zuev, B.M., Utei, B.I., Chistyakov, E.V., *et al.*, *Vysokomol. Soedin., Ser. A*, 1980, vol. 22, no. 7, pp. 1523–1528.
11. Fridman, Yu.B. and Shchurov, A.F., *Vysokomol. Soedin., Ser. A*, 1983, vol. 25, no. 7, pp. 1474–1477.
12. Askadskii, A.A., *Usp. Khim.*, 1998, vol. 67, no. 8, pp. 755–787.
13. RF Patent 2141989.

Russian Journal of Applied Chemistry, Vol. 74, No. 8, 2001, pp. 1368–1373. Translated from Zhurnal Prikladnoi Khimii, Vol. 74, No. 8, 2001, pp. 1332–1337.

CHEMISTRY OF FOSSIL FUEL

Influence of the Products of Chemical Modification of Atactic Polypropylene on Properties of Bitumen Binders

V. P. Nekhoroshev, A. V. Nekhorosheva, E. A. Popov, and L. P. Gossen

Tomsk State University, Tomsk, Russia

Received January 30, 2001

Abstract—The influence of low- and highly oxidized atactic polypropylene on the properties of paving and building bitumens was studied experimentally. The possibilities of commercial production of bitumen–polymer binders are discussed.

Bitumen materials used in building are mainly produced at Russian enterprises by deep oxidative dehydrogenation of vacuum residue with atmospheric oxygen. As estimated by specialists of Russian and foreign companies using bitumens in building, oxidized bitumens have low viscosity and insufficient deformability and resistance to oxidative aging; although such bitumens show better frost resistance, residual bitumens are, on the whole, preferable. It has been shown experimentally that the quality of paving bitumens prepared by the oxidation process leaves much to be desired, and the longevity of roads built with such bitumens is apparently insufficient [1]. The major line of research aimed at prolonging the service life of articles is to modify the properties of bitumen binders with the aim to increase their deformability and heat resistance, enhance the resistance to aging and cracking, and improve adhesion properties with respect to polar mineral fillers. The last property is of particular importance, since, according to the strength theory, the failure of all composite materials starts at the binder–filler interface. Enhancement of the adhesion strength of bitumen binders with fillers prolongs the service life of composite materials and articles thereof. Highly filled bitumen composites containing up to 95% inorganic fillers (e.g., asphalt concretes) should be prepared using special dressing additives enhancing the adhesion of the binder to the filler. The use of low-molecular-weight dressings is undesirable because of their tendency toward gradual diffusion to the article surface, followed by evaporation and washout with water [2].

As reported previously [3], bitumen–polymer binders (BPBs) containing oxidized atactic polypropylene (APP) exhibit enhanced resistance to thermal oxidative aging. Bitumens prepared by oxidation of vacuum residue contain graphitic crystalline structures with conduction electrons detected by ESR spectroscopy [4]. There is a direct correlation between the concentration of conduction electrons and the rate of thermal oxidative aging of bitumen binders. Addition of a small amount of oxidized APP (about 2.0%) results in disappearance of the conduction electrons (as judged from the ESR spectra), and articles prepared from such bitumen–polymer binders have a prolonged service life.

In this work we examined the effect of oxidized APP on the structure and physicomechanical and adhesion properties of bitumen binders.

EXPERIMENTAL

Atactic polypropylene (Tomsk Petrochemical Plant, Joint-Stock Company) was oxidized by bubbling of atmospheric oxygen through a polymer melt at 180 and 250°C for 2 and 6 h. Low- and highly oxidized APP was prepared. The oxidation procedure and the structure and properties of the resulting polymers are described elsewhere [5]. The moisture absorption of oxidized APP was determined gravimetrically from the weight gain of the polymer kept in water for 72 h. In our work, we used paving and building bitumens [Achinsk Oil Refinery, GOSTs (State Standards) 22 245–90 and 6617–90] prepared by high-temperature oxidation of vacuum residues of commercial West-Siberian oil. Bitumen–polymer compounds were prepared in a heated metallic reactor equipped with a stirrer and a temperature-control unit. The polymer was added to the bitumen melt at 140°C, and the mixture was stirred at this temperature for 40 min.

1070-4272/01/7408-1368 $25.00 © 2001 MAIK "Nauka/Interperiodica"

Oxidized APP completely dissolved in bitumen within 15 min, whereas the initial APP dissolved only partially because of the increased molecular weight and the presence of isotactic fraction as impurity. To record the IR spectra of BPBs, compounds were prepared without heating, by mixing at 20°C benzene solutions of bitumen and polymer of known concentrations. The IR spectra were measured on an Impact 410 Nicolet Fourier spectrometer by the multiple attenuated total internal reflection technique on a zinc selenide crystal [6]. Benzene solutions of BPB were applied to a crystal which was then kept in a desiccator under vacuum for 48 h until the solvent evaporated completely. Melts were applied to a crystal as films at 20°C and then kept for 48 h at room temperature. The measurement conditions were as follows: number of scans 36, resolution 4 cm^{-1}, amplification 4, scan frequency 0.6329, aperture 35, DTGS KBr detector, scanning range 4000 – 650 cm^{-1}. The optical density of IR absorption bands was determned from the ratio of the integral intensity of these bands to that of the C–H bending vibrations band at 1375 cm^{-1}.

The physicomechanical properties of BPBs were determined by standard procedures according to GOST 22245–90; the resistance of BPBs to thermal oxidative aging was evaluated from variation of the softening point of the binder after heating in a thermal chamber a 2-mm layer of its melt for 5 and 10 h [2, 7]. The heat resistance of BPBs was characterized by their softening point which corresponds to the upper limit of their working temperature. The adhesion of BPB to concrete and steel at normal break was determined with mushroom-shaped devices at adhesive layer thickness of 30 – 45 μm [8]. The ultimate adhesion strength was determined with an Instron 1122 tensile-testing machine at a clamp velocity of 10 mm min^{-1}. The dynamic viscosity of BPB melts was measured at 60 – 200°C with a Rheotest-2 rotary viscometer equipped with a temperature-control unit. Bitumen–polymer binders containing 3.0–5.0% polymer were used for preparing asphalt concrete of the following composition (wt %): crushed stone (5–10 mm fraction) 33.0, siftings (<5 mm fraction) 18.9, sand (<5 mm fraction) 23.5, fine mineral powder 18.9, and BPB based on BND 90/130 bitumen 5.7. Asphalt concrete compounds were prepared at 120–130°C, which corresponds to the conditions of the industrial process. The physicomechanical and strength properties of asphalt concrete compounds were determined on standard equipment according to GOST 9128–84.

Appearance of polar carbonyl and hydroxy groups does not affect the water resistance of oxidized APP, since the water absorption is the same for the initial and oxidized polymers. Oxidized APP is readily compatible in the melt with the bitumens of the examined grades. No additional dissolution of the polymer in oil cuts of petroleum is required, which simplifies the process, reduces the cost of BPB, decreases the fire hazard, and improves the service properties of BPB. In the course of prolonged storage (3 years) at temperatures ranging from –30 to +50°C, BPBs undergo no cracking or separation into ingredients.

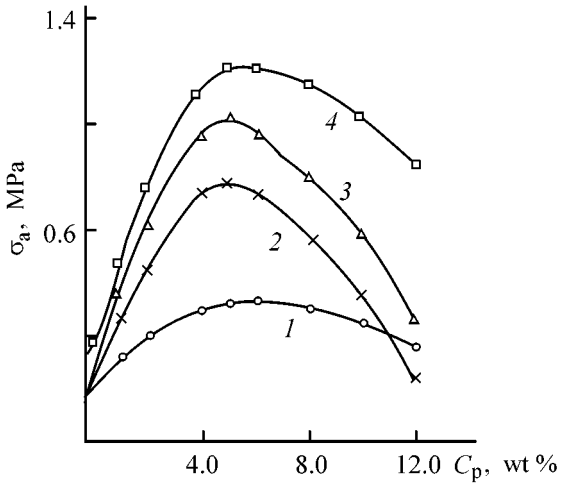

Fig. 1. Ultimate adhesion strength σ_a vs. the polymer content C_p. Support: (*1–3*) concrete and (*4*) St.3 steel. BPB: (*1–3*) BND 90/130 bitumen + APP, highly oxidized APP, and low-oxidized APP, respectively; (*4*) BN 70/30 bitumen + low-oxidized APP.

With increasing concentration of the polymer, the adhesion power of BPB (Fig. 1) is considerably enhanced, reaching a maximum in the polymer content range 4.0 – 6.0 wt %. Compounds containing oxidized APP exhibit higher adhesion to polar materials, which is due to chemical interactions of hydroxy groups of the polymer with carboxy groups of the asphaltogenic acids of bitumens, probably to give esters.

The IR spectra of BPBs, compared with the initial bitumen, contain two new bands peaked at 3280 and 1696 cm^{-1} (Table 1). The relative intensity of the broad band at 3280 cm^{-1} grows with increasing polymer concentration, which confirms the formation of hydrogen bonds between the hydroxy group of oxidized APP and carbonyl group of acids or esters. The stretching vibration band at 1696 cm^{-1} associated with the carbonyl group of the polymer, conjugated with the olefin double bond, is observed in BPB containing APP, suggesting slight oxidation of the polymer in the course of compounding in air. Cross-linking of BPB is accompanied by increase in strength,

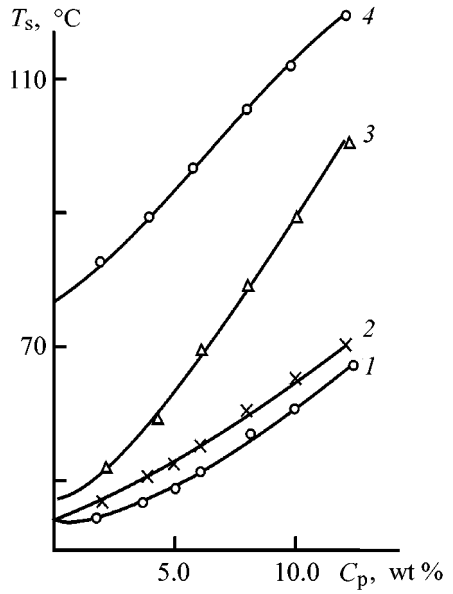

Fig. 2. Softening point T_s vs. polymer content C_p. BPB: (*1*, *2*) BND 60/90 bitumen + APP or highly oxidized APP, respectively; (*3*) BND 90/130 bitumen + low-oxidized APP; and (*4*) BN 70/30 bitumen + low-oxidized APP.

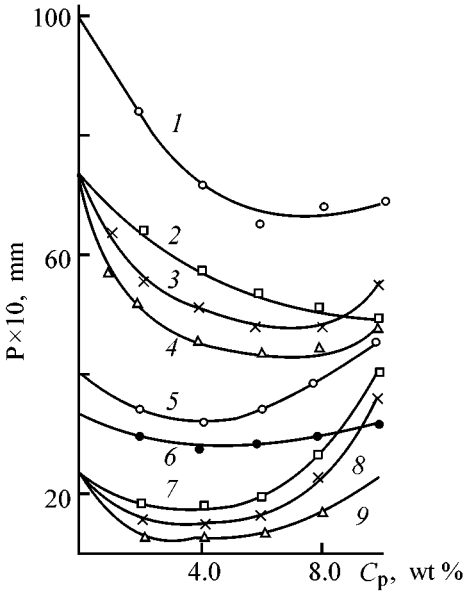

Fig. 3. Depth of needle penetration P at (*1–4*, *6*) 25 and (*5*, *7–9*) 0°C vs. the polymer content C_p. BPB: (*1*, *5*) BND 90/130 bitumen + low-oxidized APP; (*2*, *7*) BND 60/90 bitumen + APP; (*3*, *8*) BND 60/90 bitumen + low-oxidized APP; (*4*, *9*) BND 60/90 bitumen + highly oxidized APP; and (*6*) BN 70/30 bitumen + low-oxidized APP.

hardness, and melt viscosity and decrease in the stretchability of BPB. Similar changes in physicomechanical properties are observed in cross-linking of rubbers and polyethylene with peroxy initiators [9], which suggests that the features of BPB cross-linking are similar. The softening point of BPB significantly deviates from the additive value calculated from the formula without taking into account the chemical interaction of oxidized APP with bitumen components (Fig. 2). Increased softening points of BPBs (i.e., their higher heat resistance) are especially important for use of these compounds in roofings and asphalt concretes, since in summer these materials warm up above the softening point of bitumen. Unoxidized APP has a Fraas brittle point of –15°C; therefore, addition of more than 2.0% polymer increases the brittle point of BPB. For example, a BPB compound containing 95.0% BND 90/130 bitumen and 5.0% low-oxidized APP has a brittle point of –15°C, which is 2°C higher than the prescribed level. The plasticity range of BPB, increases compared with the initial bitumen, by 15°C.

Table 1. Relative intensity *I* of absorption bands in the IR spectra of BPBs

Polymer for bitumen modification	Polymer content in BPB, wt %	*I* (rel. units) of band with indicated maximum, cm^{-1}		
		3280	1696	1600
APP	2.0	0.00	0.52	0.72
	4.0	0.01	0.53	0.65
	6.0	0.02	0.50	0.51
	10.0	0.04	0.32	0.42
Low-oxidized APP	2.0	0.02	0.59	2.11
	4.0	0.04	0.53	1.97
	6.0	0.09	0.52	1.75
	10.0	0.11	0.26	0.75
Highly oxidized APP	2.0	0.01	0.55	1.48
	4.0	0.02	0.56	1.33
	6.0	0.06	0.32	1.18
	10.0	0.07	0.31	0.55

The cross-linking effect of oxidized APP decreases the penetration (P) of BPB. Changes in this parameter for compounds prepared from paving bitumens are more significant than those compounds prepared from building bitumens (Fig. 3, curve *6*). Highly oxidized APP with high content of functional groups in the macromolecule exerts a stronger effect on the BPB penetration owing to chemical interaction of the ingredients in the course of compounding. The P0/P25 ratio characterizing the heat resistance of the binder first slightly decreases and then, on adding 4.0% polymer and more, starts to rapidly increase. The most

sensitive parameter, strongly depending on the content of the polymer in BPB, is the stretchability (Fig. 4), which decreases particularly sharply at 25°C. The use of low-oxidized APP in BPB has virtually no effect on the dynamic viscosity of the binder at temperatures used in industry (120–140°C) for preparing hot asphalt concretes (Fig. 5). Owing to a considerable increase in the BPB viscosity at service temperatures below 100°C, diffusion syneresis is decelerated, and the aging of bitumens is inhibited. The resistance to thermal oxidative degradation of BPB containing 3.0–5.0 wt % low-oxidized APP increases as compared with the initial bitumen by more than a factor of 2, which may be due to chemical interaction of α,β-unsaturated conjugated keto group of the polymer with paramagnetic polyconjugated structural fragments of asphaltenes, carbenes, and carboids in bitumens. Conjugated polymeric α,β-unsaturated ketones are active dienophiles in the Diels–Alder reaction, and linearly and peri-annelated polycyclic compounds of bitumens (anthracene, dibenzanthracene, tetracene, 3,4-benzotetracene, pentaphene, perylene, benzanthrene, and their heterocyclic analogs) readily react as dienes at elevated temperatures [10]. As a result of cycloaddition, the size of the polyconjugated structural fragments decreases, which is manifested in the ESR spectra as disappearance of signals from conduction electrons in BPBs modified with oxidized APP (P is a polymeric radical).

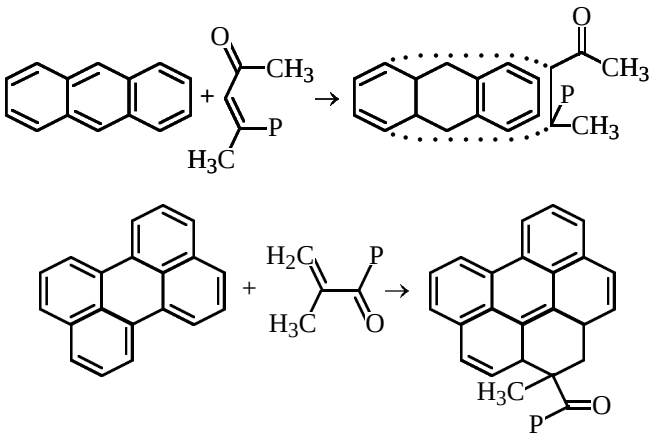

In view of the high reactivity of oxidized APP toward polyconjugated systems, further progress of the Diels–Alder reaction is possible. The adduct of perylene with oxidized APP contains three dienophilic double bonds that are not involved in the aromatic system; they can enter a dominoes-type reaction [11] which occurs between the surface layers of colloidal bitumen particles containing conduction electrons and leads to breakdown of the polyconjugated structural fragments [12]. Distortion of the conjugated chain is accompanied by disappearance of the signals from

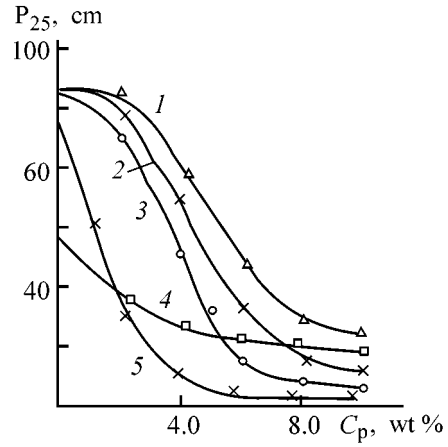

Fig. 4. Stretchability of BPB at 25°C, P_{25}, vs. the polymer content C_p. BPB: (*1–3*) BND 60/90 bitumen + highly oxidized, low-oxidized, and initial APP, respectively; (*4, 5*) low-oxidized APP + BN 70/30 and BND 90/130 bitumens, respectively.

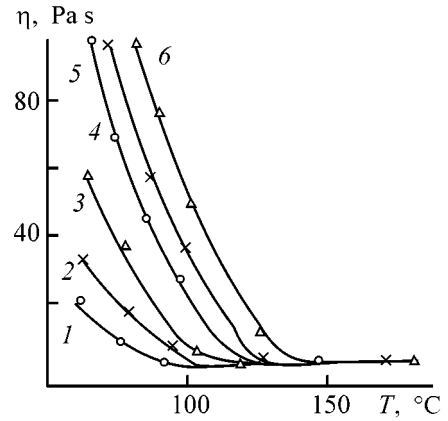

Fig. 5. Dynamic viscosity η of BPB with low-oxidized APP vs. temperature *T*. Bitumen–polymer binder with 5 wt % polymer + bitumen: (*1, 4*) BND 90/130, (*2, 5*) BND 60/90, and (*3, 6*) BN 70/30.

conduction electrons in the ESR spectra, which is experimentally shown in [3]. The proposed mechanism of reaction of oxidized APP with some bitumen components is confirmed by the IR spectra (Table 1). The relative intensity of the vibration band of the conjugated carbonyl group at 1696 cm^{-1} gradually decreases in all the samples, whereas a new band of the nonconjugated carbonyl group appears at about 1712 cm^{-1} with increasing amount of the polymer in BPB, which is consistent with the suggested reaction pattern. The decrease in the intensity of the 1600 cm^{-1} band is due to shortening of the conjugation chain involving aromatic structures. It should be noted that oxidized APP is a more effective bitumen modifier than the initial APP. In BPBs containing oxidized APP, the relative intensity of the 1600 cm^{-1} band

Table 2. Composition and properties of hot asphalt–concrete compounds*

Parameter	APP content in BPB, %			BND 90/130 bitumen
	3.0**	5.0**	3.0	
Water saturation, %	2.6	2.4	3.5	3.8
Swelling, vol %	0.30	0.30	0.65	0.90
Ultimate compression strength, MPa, at temperature, °C:				
50	1.1	1.1	1.0	1.0
20	4.5	4.6	3.8	3.5
20 (after water saturation)	4.4	4.5	3.5	3.1
0	8.3	8.5	9.7	10.0
Temperature sensitivity coefficient	7.5	7.7	9.7	10.0
Water resistance factor	0.98	0.98	0.92	0.88

* All samples show adhesion of the binder to the mineral fraction; mean density 2.3 g cm^{-3}, porosity of the mineral fraction 18.0 vol %, residual porosity 5.0 vol %.

** Low-oxidized APP.

decreases by a factor of 2.8, and in those containing the initial APP, by a factor of 1.7. Similar changes are observed with the bands at 1696 and 3280 cm^{-1}. The proposed mechanism of chemical interaction, though being a matter of discussion, accounts for plains the modifying effect of oxidized APP in bitumens prepared by oxidation of vacuum residue. Oxidized APP stabilizes the colloidal structure of bitumens and simultaneously inhibits BPB aging. Under service conditions, the thermal oxidative aging of bitumen and that of APP occur in opposite directions. Chemical transformations of bitumens involve formation of more condensed molecules and low-molecular-weight substances [2], whereas APP macromolecules are gradually oxidized under these conditions and undergo degradation to give macromolecules of lower molecular weight [5], reacting with polyconjugated bitumen structures.

The properties of hot asphalt concrete compounds are listed in Table 2. Asphalt concrete compounds with low-oxidized APP exhibit lower water saturation, lower swelling in water, enhanced strength at 20 and 50°C, and high water resistance factor. A decrease in the temperature sensitivity coefficient enhances the deformation resistance of road pavements in seasonal variations of the ambient temperature, and the low strength level at 0°C suggests enhanced crack resistance of asphalt concrete at low temperature. Complex improvement of the properties of BPBs modified with oxidized APP allows these materials to be recommended for manufacture asphalt concretes and roofing, corrosion-protecting and waterproofing materials. Oxidized APP is readily compatible in melts and solutions with styrene copolymers, polyethylene, and polyisobutylene, which are widely used for preparing BPBs.

CONCLUSIONS

(1) Oxidized atactic polypropylene is an effective modifier of bitumens prepared by high-temperature oxidation of vacuum residue.

(2) Bitumen–polymer binders containing 2.0–5.0 wt % oxidized atactic polypropylene exhibit enhanced resistance to thermal oxidative degradation and aging and high levels of adhesion, hardness, and heat resistance.

(3) A mechanism of reaction between oxidized atactic polypropylene and polyconjugated polycyclic bitumen compounds is proposed and confirmed by spectroscopic studies.

REFERENCES

1. Kut'in, Yu.A., Khairudinov, I.R., Biktimirova, T.G., *et al., Bashkir. Khim. Zh.*, 1996, vol. 3, no. 3, pp. 27–32.
2. Pechenyi, B.G., *Bitumy i bitumnye kompozitsii* (Bitumens and Bitumen Compounds), Moscow: Khimiya, 1990.
3. Unger, F.G., Efa, A.K., Tsyro, L.V., *et al., Avtomob. Dorogi*, 1998, no. 11, pp. 22–23.
4. Unger, F.G. and Andreeva, L.N., *Fundamental'nye aspekty khimii nefti. Priroda smol i asfal'tenov* (Principles of Petrochemistry. Nature of Resins and Asphaltenes), Novosibirsk: Nauka, 1995.

5. Nekhoroshev, V.P., Nekhorosheva, A.V., Gossen, L.P., *et al., Zh. Prikl. Khim.*, 2000, vol. 73, no. 6, pp. 996–999.
6. Smith, A.L., *Applied Infrared Spectroscopy: Fundamentals, Techniques, and Analytical Problem-Solving*, New York: Wiley & Sons, 1979.
7. Grudnikov, I.B., *Proizvodstvo neftyanykh bitumov* (Production of Petroleum Bitumens), Moscow: Khimiya, 1983.
8. Karyakina, M.I., *Ispytanie lakokrasochnykh materialov i pokrytii* (Testing of Paint-and-Varnish Materials and Coatings), Moscow: Khimiya, 1988.
9. Aksenenko, I.V., Balakhonov, E.G., Nekhoroshev, V.P., *et al., Plast. Massy*, 1986, no. 5, pp. 39–41.
10. Weigand-Hilgetag, *Organisch-chemische Experimentierkunst*, Leipzig: Johann Ambrosius Barth, 1964, 3rd ed.
11. *Khimicheskaya entsiklopediya* (Chemical Encyclopedia), Moscow: Sov. Entsiklopediya, 1990, vol. 2.
12. Bogomolov, A.I., Gaile, A.A., Gromova, V.V., *et al., Khimiya nefti i gaza* (Oil and Gas Chemistry), Leningrad: Khimiya, 1989.

Russian Journal of Applied Chemistry, Vol. 74, No. 8, 2001, pp. 1374–1379. Translated from Zhurnal Prikladnoi Khimii, Vol. 74, No. 8, 2001, pp. 1337–1342.

MACROMOLECULAR CHEMISTRY AND POLYMERIC MATERIALS

Quantitative Relationship between the Capability of Brown Coals for Destructive Hydrogenation and Presence of Functional Groups in Them

F. N. Grigor'ev and E. N. Grigor'eva

Institute of Data Transfer Problems, Russian Academy of Sciences, Moscow, Russia
Institute of High Temperatures, Russian Academy of Sciences, Moscow, Russia

Received February 8, 2001

Abstract—Quantitative relationship between the structure of organic matter of coals and composition of functional groups in semicoking tars, on the one hand, and the capability of coals for destructive hydrogenation, on the other, was studied.

Long-term researchers' efforts have led to considerable progress in the techniques for thermal transformation of coals, but no processes economically competitive with oil refining have been developed [1–3]. This is largely due to the fact that the structure of these natural polymers is extremely complex. The reasons for high reactivity of coal on heating and for thermal transformations of the coal substance are still unclear [1].

Traditional combustion of coals for power generation [3], though remaining the major pathway of coal utilization throughout the world in the first half of the XXI century, is not already the major line in modern coal chemistry [2, 3]. Much attention is given to qualified processing of coals into carbon materials, fuels, and chemical products, and also to environmental protection. Along with the traditional methods of analysis of physical, chemical, and petrographic characteristics of coals, study of their structure in relation to reactivity has become a separate research line. These lines are prevailing in coal chemistry.

At present, there is a growing trend toward correlating the high reactivity of coals with the presence in their organic matter (OMC) of functional groups, primarily oxygen-containing groups. It is known that the content of oxygen in coals reaches 28% of OMC [4–6]. Since the nitrogen content in brown coals, as a rule, does not exceed 1%, its role is believed to be secondary and is not taken into account in most cases.

The major fraction of oxygen in brown coals (from 60 to 95 [7] or from 70 to 95% [8]) is in the form of reactive functional groups. However, a significant part of oxygen (up to 47%) is in the so-called "unaccounted for" form, i.e., in the form of functional groups and heteroaromatic fragments that are inaccessible for determination by common coal-chemical procedures [4, 7, 8].

The concentrations of various oxygen-containing functional groups in brown coals vary widely. According to [9], the content of functional groups for various deposits of the Kansk–Achinsk basin is as follows (%): –OH 5–11, –CO 3–10, –COOR 1–7, and –COOH 1–3. No ethers were detected. In contrast, according to [10], half of oxygen in the Borodinskoe deposit occurs in carboxylic acid derivatives, including $12 \pm 1\%$ free acids and $13 \pm 3\%$ calcium carboxylate; from 1 to 13% of oxygen is in ethers. The estimate of the ester and lactone content ($21 \pm 1\%$) coincides with that in [9]. The differences between data of various authors are often due to different analytical procedures.

Some researchers assess quite oppositely the influence of oxygen in coals on their transformation into final products. The only fact that is beyond any doubt is that both reactive oxygen-containing groups in coals [11–13] and oxygen in the unaccounted for form [8–11] affect the conversion of coals and the quality of the resulting products. It has been shown [8] that coals with identical main technical parameters show varied reactivity in destructive hydrogenation and that brown coals with increased content of ester and acid groups are more reactive. Conversion of coal in hydrogenation is the higher, the lower the content

1070-4272/01/7408-1374 $25.00

of the unaccounted for oxygen in its organic matter; however, the amount of the forming liquid products decreases in proportion [9]. It was found [11] that oxygen in the cyclic structures makes higher the extent of coal transformation into liquid products. The positive effect of OH [2, 14] and COOH [8, 9] groups on the degree of destructive hydrogenation of coals has been noted. The role of oxygen-containing compounds in coals is significant. They can appreciably affect the rate of coal transformations and, probably, determine the pathways of the main reactions.

The majority of researchers assess qualitatively the influence of particular oxygen-containing groups on thermal transformation of coals. Experiments performed under different conditions and with different coal samples do not allow the data to be combined and even particular oxygen-containing groups to be ranked with respect to their significance in the course of processing. It is impossible to construct quantitative correlations on the basis of these data.

Platonov *et al.* [15–21] made an attempt to assess the diversity of structural features of the OMC carbon skeleton and, in particular, of functional groups, using a large dataset and similar analytical procedures, with the aim of constructing quantitative relationships between the concentrations of particular types of OMC fragments and functional groups and elucidating their correlation with the degree of destructive hydrogenation of coal. Using IR, UV, and NMR spectroscopies, cryoscopy, elemental, quantitative chemical, and structural-group analyses, and capillary GLC, Platonov *et al.* elucidated the structure of a large number of compounds isolated from OMC [19–21] and obtained partial and general linear correlations between the degree of destructive hydrogenation and chemical composition of OMC [19].

The problem was solved in [19] in two steps. First, using data on the group chemical composition and degree of destructive hydrogenation for 27 representative samples taken from various mines, sections, and open pits of the Near-Moscow Coal Fields, for which these characteristics varied widely, Platonov *et al.* obtained separate linear correlations for each parameter (hereinafter, factor) and degree of OMC destructive hydrogenation [20]. Then, the partial dependences were used to evaluate the influence of the whole set of factors on the degree of OMC destructive hydrogenation.

The quantitative results obtained in [19] are contradictory. For example, for the effect of phenol ethers on the yield of liquid products both positive (9) and negative (–0.02) coefficients were obtained. *A* similar pattern is observed with the other factors. Therefore, it is necessary to additionally consider the available large body of experimental data and make substantiated conclusions.

For clearer presentation, let us introduce vector and matrix notations. Vector Y denotes the first column of Table 1 in [19], namely, the experimental degrees of destructive hydrogenation of coal, wt %. The vector consists of 27 components $Y = (87.4, ..., 21.0)^m$. Matrix X denotes the factor concentrations in the coals under consideration, $X \times 10^2$, wt % (Table 1 in [19]) Matrix X has 27 rows and 28 columns. In [20], Platonov *et al.* chose for the polydimensional linear regression problem the model (1) describing the yield of the products of destructive hydrogenation Y as a function of factors:

$$XA = Y. \quad (1)$$

The solution of the problem consists in finding an unknown vector A with 28 components and satisfying the system of linear equations (1). In our case, Eq. (1) has a set of solutions of the form

$$A = A_0 + tA_1, \quad (2)$$

where 28-dimensional vectors A_0 and A_1 are as follows:

A_0 = (–0.3144, –0.0435, 13.4250, 0.1931, –1.2474, 2.4186, 4.7132, 0.6225, –1.2095, –11.8149, 7.6594, –2.1403, –5.3642, –11.4610, 0.7710, –0.2677, –1.2562, –1.1687, 8.6950, –60.5206, –6.8589, –13.6322, 0.1812, 0.3123, 13.6757, 5.3166, 22.7809, 0.0000)^t,

A_1 = (0.1059, 0.1133, –1.0495, –0.0636, 0.0676, –0.1589, –0.4069, 0.1583, –0.0255, 0.7972, –0.5951, 0.3133, 0.3901, 0.7299, –0.0114, 0.0380, 0.1198, 0.0935, –0.4078, 5.6846, 0.0764, –1.7826, –0.0108, –0.1558, –0.1352, –0.4925, –2.9380, 1.0000)^t,

where t is any real number, $-\infty < t < +\infty$.

In a geometric representation, expression (2) sets a straight line in a 28-dimensional space. Each solution of system (1) is a point lying on straight line (2), and, vice versa, each point of straight line (2) is a solution of system (1). It is, however, unclear what solution from the set of possible solutions should be taken for practical use. It has been proved in the evaluation theory that the best solution in such cases is that obtained with the Moore–Penrose pseudo-inverse matrix [22].

Since the set of coefficients given in the regression equation in [19] has not been obtained with the pseudo-inverse matrix and, furthermore, it does not belong to solution (2), we determined the distance in a 28-

dimensional Euclidean space between the point with the coordinates equal to the set of coefficients in [19] and straight line (2). The square of this distance is 385.6, which by no means can be attributed to coefficient rounding in the regression equations. Therefore, the polydimensional regression equation obtained in [19] does not correspond to the initial data, and its use, in contrast to the authors' viewpoint, cannot be useful for optimizing the industrial process.

Data in [19] show that the factors (typical fragments and functional groups of OMC) affect the industrial process to varied extent, with only some of the factors exerting significant influence on the target quantity and the others being less significantly. The problem is to reveal and identify, using appropriate methods, the significant, dominating factors against the "noise" of the other factors.

To solve this problem, we first found the mean values of the yield of destructive hydrogenation products $\overline{Y}$ and the factors $\overline{X}$ by the formulas

$$\overline{Y} = \frac{1}{27}\sum_{i=1}^{27} Y_i \text{ and } \overline{X_j} = \frac{1}{27}\sum_{i=1}^{27} X_{i,j},\ j = 1, 2, \ldots, 28.$$

In the next calculation step, we determined deviations of the yields from the mean value and normalized deviations from the mean values of factors

$$\tilde{Y} = Y - \overline{Y}E,\ X = [\tilde{X} - I\mathrm{diag}(\overline{X_j})]\mathrm{diag}(1/D_j),$$

where E is a 27-dimensional unit vector; I is a 27×28 matrix consisting of unities; $\mathrm{diag}(\overline{X_j})$ is a 28×28 diagonal matrix in which the jth element on the diagonal is equal to $\overline{X_j}$;

$$D_j = \frac{1}{2}(\max X_{i,j} - \min X_{i,j}).$$

Then we found the vector of coefficients A as a pseudosolution to the system

$$\tilde{X}A = \tilde{Y},$$

i.e., $A = \tilde{X}^{+}\tilde{Y}$, where $\tilde{X}^{+}$ is the pseudo-inverse matrix to the matrix.

It should be noted that system (3) describes variation of the yield of coal destructive hydrogenation in the vicinity of mean values, variations of the factors are dimensionless, and the range of variation of each factor is close to (–1, 1). This procedure is extremely useful, since it becomes possible to directly compare the effect of various factors as dimensionless quantities on the yield of liquid products in destructive hydrogenation of coal.

The dimensionless values a of the coordinates of the vector of coefficients A obtained by solution of system (3) are listed in the table. For comparison, we

Calculated regression coefficients a, their rms deviations da, and absolute values of the ratios $\mathrm{d}a/|a|$

Factor no.	Group of compounds [19]	a [19]	a	Factor no.	Group of compounds [19]	a [19]	a
1	Dihydric phenols	1.9	14.78	17	Terpenes	0.4	5.93
2	Trihydric phenols	0.8	3.53	18	Tri- and polycyclic aromatic hydrocarbons	–0.4	–4.21
3	Phenol ethers	–0.02	1.56				
4	Indanols	–1.4	–2.94	19	Asphaltenes	4.0	10.98
5	Cresols	–0.3	–2.53	20	Benzene–ethanol extract	10.8	4.71
6	Xylenols	0.3	2.31	21	Humic acids	–6.0	–15.48
7	Alicyclic ketones	1.5	1.96	22	Organic sulfur in asphaltenes	–54.5	–3.62
8	Esters	3.9	5.17	23	Organic sulfur in benzene–ethanol extract	0.1	–0.34
9	Benzofurans	–1.7	–3.53				
10	Dibenzofurans	–3.4	–7.17	24	Phenolic groups of humic acids	–5.0	–6.22
11	Lactones	0.3	1.3				
12	Organosulfur compounds	4.87	15.05	25	Quinoid groups of humic acids	13.2	21.35
13	Terpene derivatives	–0.3	0.016	26	Carboxy groups of humic acids	2.1	–1.41
14	Metal porphyrins	–2.7	–10.26	27	Keto groups of humic acids	–15.5	–12.40
15	Cycloalkanes	0.5	9.29				
16	Hydroaromatic hydrocarbons	0.1	1.01	28	Iodine number	19.1	16.40

Table. (Contd.)

Factor no.	a_1	da_1	$da_1/\lvert a_1\rvert$	a_2	da_2	$da_2/\lvert a_2\rvert$	a_3	da_3	$da_3/\lvert a_3\rvert$
1	10.95	2.38	0.28	9.66	2.14	0.22	10.57	2.06	0.19
2	4.46	1.73	0.39	2.34	1.55	0.66			
3									
4									
5									
6									
7									
8	4.46	1.82	0.41	6.49	1.27	0.20	6.38	1.33	0.21
9	–3.71	2.14	0.58	–2.97	1.79	0.60			
10	–3.05	1.76	0.58	–3.07	1.38	0.45			
11	3.29	2.06	0.63	2.02	1.96	0.97			
12	8.44	4.47	0.53	7.99	2.59	0.32	4.95	2.36	0.38
13									
14	–10.21	1.82	0.18	–8.09	1.63	0.20	–6.44	1.73	0.27
15	11.41	2.19	0.19	13.42	2.14	0.16	12.67	2.07	0.16
16									
17	1.74	2.15	1.23						
18	3.16	3.91	1.24						
19	9.89	1.93	0.20	10.76	1.68	0.16	9.64	1.54	0.16
20	1.46	2.15	1.47						
21	–14.18	2.77	0.20	–12.79	2.47	0.19	–11.15	2.10	0.19
22	1.08	2.85	2.63						
23									
24	–5.82	2.77	0.4758	–8.11	2.20	0.27	–8.71	1.69	0.19
25	21.58	4.20	0.1948	21.90	3.47	0.16	19.72	3.23	0.16
26									
27	–13.18	3.30	0.25	–12.29	2.93	0.24	–12.12	2.59	0.21
28	11.41	2.50	0.22	10.72	1.75	0.16	10.07	1.92	0.19

also present the coefficients a_1 of the linear regression equation obtained in [19]. The coefficients have different dimensions and, therefore, cannot be compared directly.

Comparative analysis of the coordinates of vector A shows that factor nos. 3–7, 13, 16, 23, and 26 affect the yield of the liquid products insignificantly. Therefore, in further consideration they were disregarded. With the number of factors decreased from 28 to 19 and the number of destructive hydrogenation experiments remaining the same (27), it became possible to use the least-squares procedure for subsequent analysis and calculate both the estimates of the coefficients a_i, $i = 1, 2, 3$, and the estimates of their rms deviations da_i, $i = 1, 2, 3$.

Then the problem was solved successively using the least-squares procedure with the LSCOV function (least-squares procedure in the presence of noise) of the MATLAB 5.2 software. The factors with large ratios $da_i/\lvert a_i\rvert$ were rejected three times. As a result, from we determined 11, out of 28 initial, factors that significantly affect the destructive hydrogenation and found the linear regression equation

$$Y = 10.57(X_1 - 22.05)/10.2 + 6.38(X_8 - 4.01)/2.9 + 4.95(X_{12} - 10.32)/4.6 - 6.44(X_{14} - 3.21)/2.8 + 12.67(X_{15} - 21.58)/22.4 + 9.64(X_{19} - 10.02)/5.1 - 11.15(X_{21} - 7.16)/2.9 - 8.71(X_{24} - 6.28)/3.2 + 19.72(X_{25} - 3.86)/2.6 - 12.12(X_{27} - 1.49)/1.0 + 10.06(X_{28} - 1.16)/0.8 + 49.04.$$

The estimates of the rms deviations of the regression coefficients are given in the table.

Our results considerably differ from the conclusions made in [19]. Determination of the coefficients

for the normalized factors revealed three groups of OMC fragments: those positively, negatively, and insignificantly (the largest group) affecting the destructive hydrogenation.

The positive influence, in decreasing order, is exerted by the following fragments: quinoid groups of humic acids > cycloalkanes > dihydric phenols ≈ iodine number ≈ asphaltenes > esters > organosulfur compounds.

The negative influence, in decreasing order, is exerted by the following fragments: keto groups of humic acids ≈ humic acids ≥ phenolic groups of humic acids > metal porphyrins.

The group of components that affect the process insignificantly includes phenol ethers, indanols, cresols, xylenols, alicyclic ketones, terpene derivatives, hydroaromatic hydrocarbons, carboxy groups of humic acids, and organosulfur compounds present in the benzene–ethanol extract.

A quantitative analysis also showed that, when all the factors are taken into account simultaneously, as in the general dependence in [19], the experimental data are reproduced more adequately than in the case when the estimation is made by a single parameter. Indeed, coals are "living" metastable organized systems in which any change can cause a response of the system as a whole. In this case, partial dependences are too rough and cannot describe adequately the structure–reactivity relationship for coals. Apparently, only examination of the whole set of the factors will allow solution of this problem.

The results obtained with our mathematical model suggest that it is desirable to use in destructive hydrogenation brown coals with high content of alkane and cycloalkane fragments containing double bonds, and also ester groups and oxygen-containing fragments.

A striking feature is the extremely high level of the positive effect of quinoid groups of humic acids on the destructive hydrogenation, whereas other functional groups of humic acids exert a pronounced negative effect. In combination with the positive effect of organosulfur compounds and negative effect of metal porphyrins, this fact suggests the leading role of radical processes in destructive hydrogenation of coal.

The data obtained are, of course, estimates, and they require further mathematical study and experimental confirmation, since some factors may in part duplicate each other, e.g., cycloalkanes and asphaltenes (fraction of aliphatic compounds).

CONCLUSIONS

(1) A linear quantitative correlation was found between the chemical structure parameters of brown coal and the yield of liquid products of destructive thermal hydrogenation. Confidence intervals were found for the parameters of this model.

(2) Among a large set of experimentally determined factors, the groups of significant and "noise" factors were distinguished, which allowed simplification of the general dependence.

(3) Structural parameters of the organic matter of coals, positively and negatively affecting formation of liquid products, were revealed, which allows prediction of the capability of coals for destructive hydrogenation.

(4) The functional groups and typical fragments of the organic matter of coal were ranked with respect to the extent of their effect on destructive hydrogenation of coal.

ACKNOWLEDGMENTS

The study was financially supported by the Russian Foundation for Basic Research, project nos. 00-01-00571 and 00-15-96116, in the framework of the Russian–Polish Program for Scientific and Technical Cooperation in 2000–2001.

REFERENCES

1. Krichko, A.A., Abstracts of Papers, *III Mezhdunarodnyi simpozium "Kataliz v prevrashcheniyakh uglya"* (III Int. Symp. "Catalysis in Transformations of Coals), Novosibirsk, July 10–13, 1997, part 1, pp. 40–42.
2. *Proc. Conf. ICCS'97*, Ziegler, A., Heek, K.H. van, Klein, J., and Wanzl, W., Eds., Essen (Germany): DGMK Tagungsbericht, 1997.
3. *Prospects for Coal Science in the 21th Century (ICCS'99)*, Bao Qing Li and Zhen Yu Liu, Eds., Taiyuan (China): Shanxi Science and Technology, 1999.
4. Aronov, S.G. and Nesterenko, L.L., *Khimiya tverdykh goryuchikh iskopaemykh* (Chemistry of Solid Fossil Fuels), Kharkov: Khar'k. Gos. Univ., 1960.
5. Jurkiewicz, A., Marzec, A., and Idziak, S., *Fuel*, 1981, vol. 60, pp. 1167–1172.
6. Maloletnev, A.S., Krichko, A.A., and Garkusha, A.A., *Poluchenie sinteticheskogo zhidkogo topliva gidrogenizatsiei uglei* (Production of Synthetic Liquid Fuel by Hydrogenation of Coals), Moscow: Nedra, 1992.
7. Kukharenko, T.A., *Okislennye v plastakh burye i kamennye ugli* (Lignites and Coals Oxidized in Strata), Moscow: Nedra, 1972.

8. Lesnikova, E.B., Characteristic Chemical Bonds in Brown Coals of the Kansk–Achinsk Basin, Affecting the Behavior of These Coals in Hydrogenation, *Cand. Sci. Dissertation*, Moscow, 1985.
9. Grigor'eva, E.A., Lesnikova, E.B., Gagarin, S.G., *et al.*, *Khim. Tverd. Topl.*, 1990, no. 5, pp. 64–70.
10. Kuznetsov, P.N., *Khim. Tverd. Topl.*, 1998, no. 3, pp. 53–68.
11. Grigor'eva, E.A., Zharova, M.N., Zimina, E.S., *et al.*, *Khim. Tverd. Topl.*, 1983, no. 1, pp. 114–120.
12. Baryshnikov, S.V., Sharypov, V.I., Emel'yanova, G.I., *et al.*, Abstracts of Papers, *III Mezhdunarodnyi simpozium "Kataliz v prevrashcheniyakh uglya"* (III Int. Symp. "Catalysis in Transformations of Coals), Novosibirsk, July 10–13, 1997, part 1, pp. 202–208.
13. Baryshnikov, S.V., Influence of Ozonation and Thermal Modification of Kansk–Achinsk Brown Coal on Its Reactivity in Thermal Dissolution and Hydrogenation, *Cand. Sci. Dissertation*, Krasnoyarsk, 1999.
14. Kamia, I., Sato, H., and Jao, T., *Fuel*, 1978, vol. 57, no. 11, pp. 681–685.
15. Platonov, V.V., Proskuryakov, V.A., Alfonso, M., and Nechaeva, E.A., *Zh. Prikl. Khim.*, 1998, vol. 71, no. 10, pp. 1725–1729.
16. Platonov, V.V., Proskuryakov, V.A., Ryl'tsova, S.V., *et al.*, *Zh. Prikl. Khim.*, 1998, vol. 71, no. 10, pp. 1729–1736.
17. Platonov, V.V., Proskuryakov, V.A., Teka, Zh.A., *et al.*, *Zh. Prikl. Khim.*, 1999, vol. 72, no. 2, pp. 303–314.
18. Platonov, V.V., Proskuryakov, V.A., and Polovetskaya, O.S., *Zh. Prikl. Khim.*, 1999, vol. 72, no. 2, pp. 314–318.
19. Platonov, V.V., Dobrovol'skii, N.M., Proskuryakov, V.A., *et al.*, *Zh. Prikl. Khim.*, 1998, vol. 71, no. 2, pp. 336–343.
20. Platonov, V.V., Proskuryakov, V.A., Savchenkov, V.E., and Pipchenko, I.A., *Zh. Prikl. Khim.*, 1998, vol. 71, no. 2, pp. 343–346.
21. Platonov, V.V., Proskuryakov, V.A., Savchenkov, V.E., *et al.*, *Zh. Prikl. Khim.*, 1997, vol. 70, no. 11, pp. 1890–1892.
22. Strang, G., *Linear Algebra and its Applications*, New York: Academic, 1980.

Russian Journal of Applied Chemistry, Vol. 74, No. 8, 2001, pp. 1380–1384. Translated from Zhurnal Prikladnoi Khimii, Vol. 74, No. 8, 2001, pp. 1343–1347.

CHEMISTRY OF FOSSIL FUEL

Elemental Content and Functional Group Analysis of Humic Acids in Fossilized Soils of Different Ages

V. D. Tikhova, M. M. Shakirov, V. P. Fadeeva, M. I. Dergacheva, E. V. Kallas, and L. A. Orlova

Institute of Organic Chemistry, Siberian Division, Russian Academy of Sciences, Novosibirsk, Russia
Institute of Soil Science and Agrochemistry, Siberian Division, Russian Academy of Sciences, Novosibirsk, Russia
Tomsk State University, Tomsk, Russia
Geolological Institute, Siberian Division, Russian Academy of Sciences, Novosibirsk, Russia

Received March 23, 2001

Abstract—A comparative study of elemental composition, thermal characteristics, and IR and NMR spectra of humic acids recovered from modern and fossilized soils was made. The results obtained allow reconstruction of trends in variation of the environmental conditions in the course of soil formation at lake depressions in the Khakassia over a period from 3400 to 850 years before present day.

Soil is natural matter accumulating the results of a combined action of diverse soil-forming factors, such as climate, plant and animal organisms, soil-forming rocks, relief, and time. Therefore, soil features are a peculiar memory about environmental factors controlling soil formation over periods of geological scale.

One of soil substances exhibiting the structural environmental memory is humic acid (HA) [1].

Humic acids are dark gray or reddish-brown nitrogen-containing macromolecular hydroxycarboxylic acids of variable composition. These acids are recovered from soils by treatment with alkaline aqueous solution. Dergacheva *et al*. [1–4] showed that HAs can be used for retrospective analysis of the paleoenvironment evolution.

Bioclimatic conditions that existed in the period of formation of HA macromolecules are mainly responsible for features of this soil substance, such as the ratio of unhydrolyzable and hydrolyzable parts, optical characteristics, ratio of aromatic and aliphatic fragments, degree of aromaticity, polydispersity, capability of forming organomineral complexes, etc. The aim of this work was to reconstruct the features of environmental conditions that existed in the region of lake depressions in Khakassiya during formation of fossilized soils of different ages. To solve this problem, we used previously obtained data on elemental composition, thermal characteristics, and IR and NMR spectra of HAs of well-studied soils [5].

EXPERIMENTAL

In this work, we studied humic acids recovered from soil samples taken from lake depressions located in the Khakassian steppe region (Table 1). The absolute age of these soils varies from 850 ± 45 to 3370 ± 85 years [6]. In passing from the oldest to more recent soils, the content of the total organic carbon (C_{org}) and the ratio of humic and fulvic acids (C_{HA}/C_{FA}) gradually increase. The elemental composition (C, H, N, P) and thermochemical characteristics of HA samples were studied, and the IR and ^{13}C and ^{31}P NMR spectra were recorded. To reconstruct the variation with time of the environmental features via corresponding changes in humic acid characteristics, we used previously obtained data reported in [5].

The carbon, hydrogen, and nitrogen content of humic acids was determined on a 1106 Carlo Erba elemental analyzer. The C and H content was also determined by the technique commonly used in elemental analysis of organic compounds. The total phosphorus was determined spectrophotometrically in the form of a colored complex with a vanadium-molybdenum reagent. Prior to determining phosphorus,

1070-4272/01/7408-1380 $25.00 © 2001 MAIK "Nauka/Interperiodica"

Table 1. Characteristics of fossilized soils

Sample* no., cm	Profile	Soil type**	C_{org}, %	C_{HA}/C_{FA}	Age, year (dating by ^{14}C)
5–15	16–96, Lake Utich'e	Ordinary chernozem	4.28	1.80	850 ± 45
7–17	4–96, Lake Shunet	〃	6.00	2.03	940 ± 45
20–27	2–96, Lake Shunet	Meadow-marsh-humus with buried peaty horizon	4.28	1.70	1940 ± 35
32–37	25–96, Lake Utich'e	Meadow-chernozem	1.52	1.11	2800 ± 90
45–59	4–96, Lake Shunet	Ordinary chernozem	0.93	0.82	3370 ± 85

* Depth of soil deposition.

** All the soils have sandy loam composition.

Table 2. Elemental composition of humic acids of soils

Humic acid sources	Elemental composition (at. %) in terms of weighed portion of benzene					H/C	O/C	C/N
	C	H	N	O	P			
Soils of various climatic zones								
Southern chernozem	43.17	29.70	2.38	24.65	0.39	0.69	0.57	18.14
Chestnut	47.60	26.95	2.20	23.17	0.04	0.56	0.49	21.64
Grey forest	30.62	46.74	1.40	20.79	0.31	1.53	0.68	21.87
Tundra podzolic gley 3	25.64	57.68	1.94	13.69	0.50	2.25	0.53	13.21
Tundra podzolic gley 4	27.20	52.94	2.56	16.15	0.62	1.95	0.59	10.63
Tundra podzolic gley 5	24.69	45.19	0.82	28.21	0.66	1.83	1.14	30.11
Tundra surface gley 2	30.20	47.55	1.45	20.18	0.38	1.57	0.69	20.83
Paleosoils								
Sample, cm:								
5–15	29.97	40.97	2.17	26.59	0.29	1.37	0.89	13.84
7–17	35.66	35.66	1.84	26.53	0.22	1.00	0.74	19.35
20–27	34.07	36.11	2.23	26.83	0.77	1.06	0.79	15.29
32–37	34.17	36.12	2.13	27.13	0.44	1.06	0.79	16.04
45–59	19.72	44.49	1.29	34.20	0.31	2.26	1.73	15.33

the humic acid samples were burned in a flask filled with oxygen and the resulting residue was dissolved.

The HA NMR spectra was recorded in a solution prepared by dissolving a weighed HA sample in 0.5 M NaOH–D_2O mixture. This solution was placed in a 5-ml cylindrical tube of external diameter 5 mm. The ^{13}C and ^{31}P NMR spectra were recorded on an DRX-500 Bruker NMR spectrometer at frequencies of 125.76 and 202.46 MHz, respectively. The Overhauser effect was eliminated by proton decoupling using the INVGATE technique. The ^{31}P NMR spectra were recorded under monoresonance conditions. In recording ^{13}C and ^{31}P NMR spectra, TMS and H_3PO_4 (85%), respectively, were used as external references. The NMR spectra were recorded with 1-s delay between pulses.

The IR spectra (KBr pellets, HA/KBr = 1 : 50) were recorded on an IR Fourier spectrometer in the 400–4000 cm^{-1} range.

Thermal analysis of HA sample placed in a platinum crucible was carried out on an MOM derivatograph (Hungary) in air with heating from 20 to 1000°C at a rate of 5 deg min^{-1}. The measurement sensitivity was as follows: TG 100 mg, DTG 1/3, and DTA 1/3.

It was found that the elemental composition of HAs recovered from fossilized soils of different ages is consistent with the HA classification proposed by Orlov [7]. It is known [2] that the chemical composition of HA depends not only on the soil type, but also on the bioclimatic conditions of soil formation. The elemental composition of HAs reflects the genet-

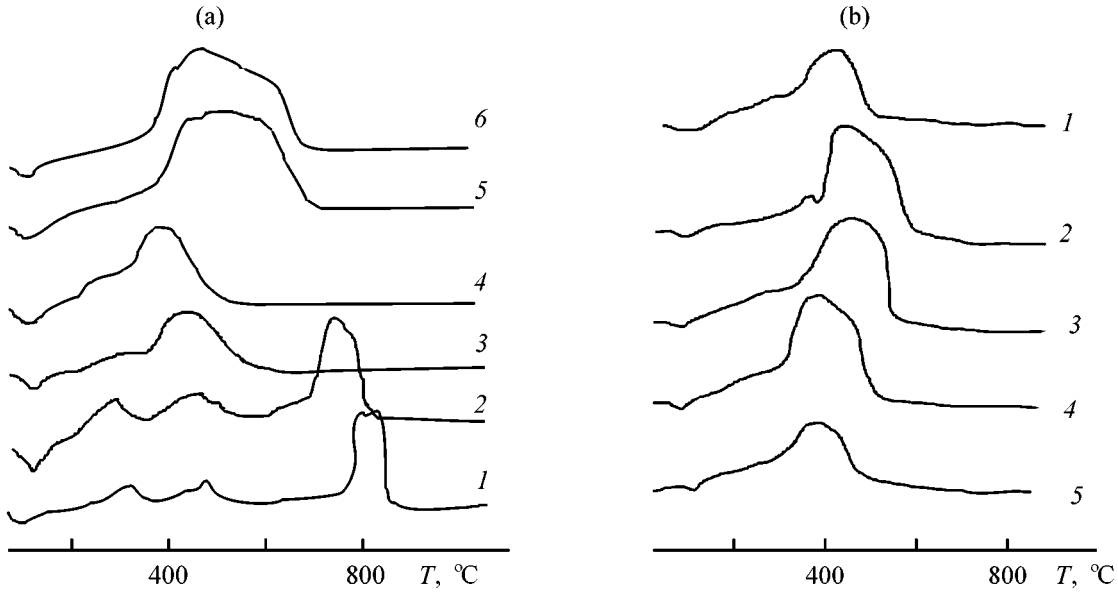

Fig. 1. DTA curves of HAs of (a) modern soils of different climatic zones and (b) fossilized soils. (*T*) Temperature. (a) Soil: (*1*) tundra 1, (*2*) tundra 2, (*3*) tundra 4, (*4*) gray-forest, (*5*) chestnut, and (*6*) south chernozem. (b) Fossilized soils (cm): (*1*) 5–15, (*2*) 7–17, (*3*) 20–27, (*4*) 32–37, and (*5*) 45–49; the same for Figs. 2 and 3.

ic features of soil and is one of the main parameters allowing reconstruction of paleoenvironmental conditions. Humic acids recovered by means of identical techniques from soil samples taken at a step of 5–10 cm from different horizons of the soil profile can be used for time reconstruction of changes in the environmental conditions in a given geographical zone.

We found (Table 2) that the elemental composition of fossilized soils is intermediate between the compositions of steppe and tundra soils. This fact shows that the paleosoils were formed under conditions differing from those for the modern soils. Table 2 shows that in passing from chernozem to tundra surface gley soil, as well as from a top to deeper horizons in a series of the paleosoils, the total carbon content decreases and both H/C ratio and the extent of carbon oxidation O/C increases. The features of paleosoil samples taken from the oldest horizon (45–49 cm) are close to those of tundra soils. The C/N ratio in a series of the humic acids exhibits irregular deviations. Elucidation of the relationship between the C/N ratio and the environmental conditions of HA formation requires further study.

There is a great body of data on HA thermochemical characteristics. These data were analyzed in detail and generalized by Orlov [8]. Thermal analysis is an efficient technique for HA identification. This technique is also promising for elucidation of the effect of artificial and environmental factors on HA composition and properties.

Figure 1a shows that the shape of the DTA curves of HAs of dry-steppe soils significantly differs from those of tundra soils. All the DTA curves show a low-temperature (100°C) endothermic effect. Figure 1 shows also that for HAs of tundra soil the heat evolution is characterized by two pronounced maxima separated by some temperature interval, whereas for HAs of chernozem the exothermic effect extends over a range from 370–400 to 700°C. We believe that this difference is due to the following factors. Decomposition of the aromatic core of HA from dry-steppe soil is accompanied by so pronounced heat evolution that the exothermic effect due to decomposition of small amounts of the aliphatic groups becomes unnoticeable. At the same time, in decomposition of HAs from tundra soil with small aromatic content, the exothermic effects due to decomposition of both the aliphatic and aromatic constituents become well resolved.

As seen from Fig. 1b, for HAs of paleo- and dry-steppe soils the exothermic effects due to decomposition of the aliphatic groups and aromatic core are not clearly resolved. Only one paleosoil sample taken from the 7–17 cm horizon exhibits a distinct exothermic effect at 360°C. We believe that this soil was formed at the middle of intermittently waterlogged flat slope. The DTA curves show also that, with increasing soil age, the temperature of complete HA decomposition decreases, and the peak in the DTA curve shifts toward lower temperatures

corresponding to less thermostable humic acids. However, the behavior of the exothermic peac for HAs from the paleosoil taken from the 5–15 horizon is an exception. It is possible that a shift of the environmental conditions toward cooling and wetting occurred within a period of 940–850 years to present day. This assumption is confirmed by analysis of these soil samples by other techniques.

The IR spectra of both the paleo- and modern soils (Fig. 2) contain a diverse set of absorption bands due due to vibrations of various atomic groups in the HA macromolecule. These spectra are characterized by several features allowing elucidation of the environmental changes over periods on the geological scale. With increasing soil age, the total intensity of the HA absorption bands gradually decreases. The IR spectra of HA of the oldest soils are close to those of the tundra soil.

The ^{13}C NMR spectra (Fig. 3) allow determination of the following functional groups in HA macromolecules: alkyl radicals (0–65 ppm), carbohydrates, alcohols and acetals (65–100 ppm), aromatic core (110–160 ppm), and carboxy groups (160–200 ppm). The above-noted ranges of the ^{13}C chemical shifts of different functional groups are commonly used in analyzing the ^{13}C NMR spectra of humic acids. However, these intervals may differ by 5–10 ppm in a number of cases.

It is known that for low-molecular-weight compounds the integrated intensity of the ^{13}C NMR spectra allows only qualitative determination of carbon atoms of different types. This limitation is caused by the significant effect of the chemical environment on the relaxation rate of the ^{13}C nucleus. However, for humic acids the difference between the relaxation parameters of ^{13}C nucleus with different kinds of environment decreases so that a 1-s delay between pulses is sufficient to ensure their quantitative determination. This is due to low mobility of humic acid molecules and presence in their composition of paramagnetic centers (mainly semiquinones and Fe^{3+} ions).

The content of various functional groups in humic acids from both the modern soils of different climatic zones and paleosoils, determined from the ^{13}C NMR spectra, is given in Table 3. These results show that, with increasing paleosoil age, the content of alkyl groups in HA macromolecule increases from 14.4 to 27.2% and the content of the aromatic core decreases from 44.7 to 25.9%. In HA from paleosoil of 850-year age, the content of alkyl groups is abnormally high (34.2%). With increasing paleosoil age, the content of polysaccharides in the humic acid increases from 10.6 to 29.8%, and the content of the carboxy groups decreases from 14.8 to 6.8%.

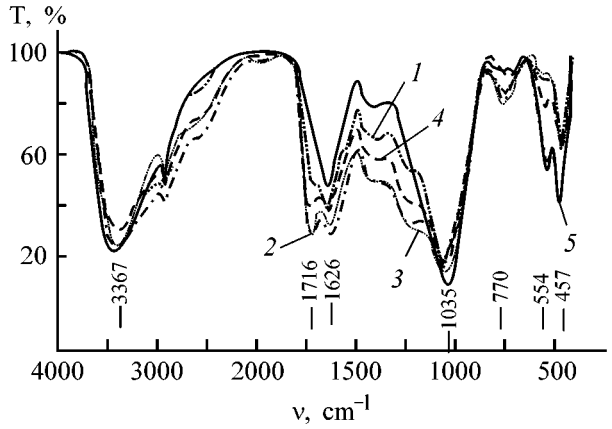

Fig. 2. IR spectra of HAs recovered from fossilized soils: (*T*) light transmission and (ν) wave number.

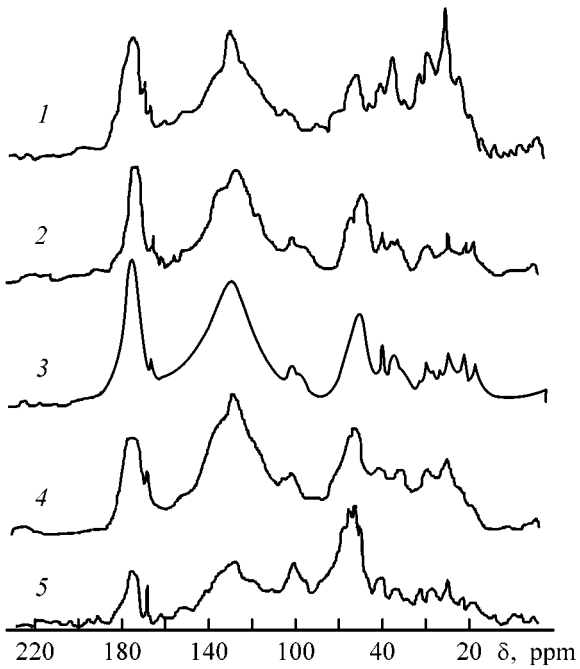

Fig. 3. ^{13}C NMR spectra of HAs of fossilized soils. (δ) Chemical shift.

The ^{31}P NMR spectra of HAs of paleosoils exhibit a broad signal of the phosphorus atoms of phosphate monoesters at about 5 ppm. All the spectra, except that of HAs of the soil sample of 850 ± 45-year age, show the presence of small amounts of diester groups. We found that, on the whole, the humic acids of modern soils contain phosphorus in smaller amounts than humic acids of older soils do.

CONCLUSION

As compared with humic acids of fossilized soils, humic acids of the modern soils are characterized by larger aromatic core, reduced aliphatic component, and modified relative contents of its separate constituents. Since fossilized and modern humic acids were recovered from soils of the same territory, we believe that the above-noted differences between their features are due to gradual warming within a period from 3000–1000 years to present day. The specific features of humic acids of the youngest fossilized soils formed about 850 years ago may indicate cooling and waterlogging that occured during the preceding 100-year period.

REFERENCES

1. Dergacheva, M.I., *Arkheologicheskoe pochvovedenie* (Archaeological Soil Science), Novosibirsk: Sib. Otd. Ross. Akad. Nauk, 1997.
2. Dergacheva, M.I. and Zykina, V.S., *Organicheskoe veshchestvo iskopaemykh pochv* (Organic Substance of Fossilized Soils), Novosibirsk: Nauka, 1988.
3. Dergacheva, M.I., *Organicheskoe veshchestvo pochv: statika i dinamika (na primere Zapadnoi Sibiri)* [Organic Substance of Soils: Statics and Dynamics (for the Example of West Siberia)], Novosibirsk: Nauka, 1984.
4. Dergacheva, M.I., Vashukevich, N.V., and Granina N.I., *Gumus i golotsen-pliotsenovoe pochvoobrazovanie v Predbaikal'e* (Humus and Holocene-Pliocene Soil Formation in the Baikal Region), Novosibirsk: Sib. Otd. Ross. Akad. Nauk, Filial "Geo", 1997.
5. Tikhova, V.D., Shakirov, M.M., Fadeeva, V.P., and Dergacheva, M.I., *Zh. Prikl. Khim.*, 1998, vol. 71, no. 7, pp. 1173–1176.
6. Dergacheva, M.I., Kallas, E.V., Orlova, L.A., and Solov'eva, T.P., Rate of Upwards Soil Growth under Conditions of Dry Khakassian Steppes, *Preprint of the Inst. of Soil Science and Agrochemistry*, Novosibirsk, 1999.
7. Orlov, D.S., *Gumusovye kisloty pochv i obshchaya teoriya gumifikatsii* (Humic Acids of Soils and General Theory of Humification), Moscow: Mosk. Gos. Univ., 1990.
8. Orlov, D.S., *Gumusovye kisloty pochv* (Humus acids of Soils): Moscow: Mosk. Gos. Univ., 1974.
9. Preston, C.M. and Blackwell, B.A., *Soil. Sci.*, 1985, vol. 139, p. 88.

Russian Journal of Applied Chemistry, Vol. 74, No. 8, 2001, pp. 1385–1389. Translated from Zhurnal Prikladnoi Khimii, Vol. 74, No. 8, 2001, pp. 1348–1353.

CHEMISTRY OF FOSSIL FUEL

Chemical Composition of Shale Kerogen (Kerogen-70) from Leningrad Oblast

V. V. Platonov, V. A. Proskuryakov, I. L. Novikova, O. A. Shavyrina, and A. V. Glybina

Tolstoy State Pedagogical University, Tula, Russia

St. Petersburg State Technological Institute, St. Petersburg, Russia

Received December 21, 2000

Abstract—The chemical composition of various extracts from oil shale (kerogen-70) was studied in detail.

The composition of oil shale is a subject of numerous studies [1–10]. However, there are no generally accepted views about the origin of the mother substance of kerogen (and shale in general), genetic relationship of its composition with the initial vegetable and animal material and biogeochemical transformations of this material in the course of dia- and catagenesis. There are also no common procedures for studying oil shales, which is primarily due to the complex chemical composition of their organic matter (OM).

This work is devoted to detailed and comprehensive study from the organic matter of oil shale (kerogen-70) from Leningrad oblast. This shale is a competitor formed in the lower Ordovician period and having a purely sapropelite origin. The moisture content of this shale is 25.0, and the ash content, 30.0%. The elemental composition (wt % daf) is as follows: C 69.9, H 8.1, N 0.3, and O + S 21.7. The functional composition (mg-equiv g^{-1}) is as follows: phenolic groups 0.91, keto groups 10.40, quinoid groups 5.90, carboxy groups 0.20, and iodine number 0.36.

To characterize the molecular structure of shale compounds, we used extraction, adsorption-liquid and capillary gas–liquid chromatography (CGLC); elemental, emission spectrum, X-ray fluorescence, quantitative functional, and structural-group analyses; cryoscopy; and IR and UV/Vis spectroscopy.

Extraction of oil shale was performed in a Soxhlet apparatus at the boiling points of the solvents in the sequence shown in the scheme. The yields of separate extracts, their molecular weights, and elemental compositions are given in Table 1.

In the IR spectra of the extracts, we identified the absorption bands of the following structural fragments ($\bar{\nu}$, cm^{-1}):

– aromatic rings [3000–3100, 3030–3070, doublet at 1500–1600 with higher intensity of the low-frequency component, especially for toluene and acetone extracts, which suggests prevalence of monocyclic structures (1450, 675–900)] in these extracts;

Scheme of comprehensive study of shale kerogen.

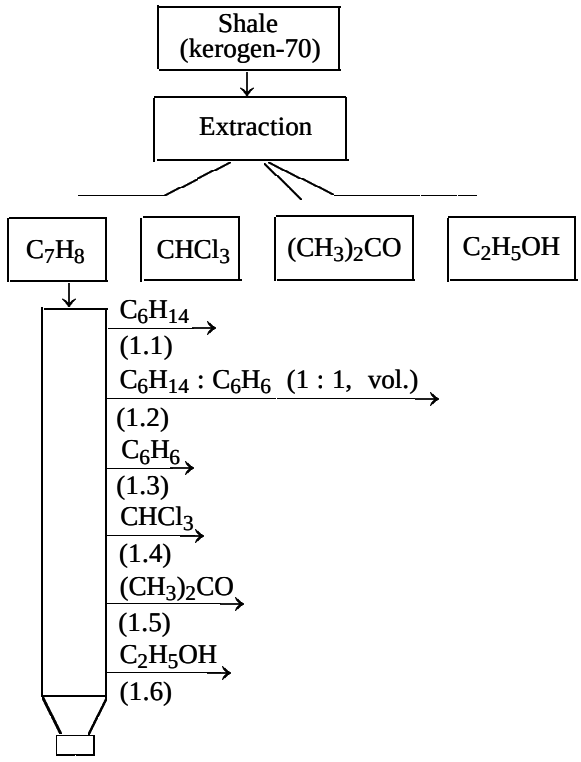

1070-4272/01/7408-1385 $25.00 © 2001 MAIK "Nauka/Interperiodica"

Table 1. Yield and structural parameters of extracts and eluates of kerogen-70

Extract	Yield, wt % of OMS	Structural parameters*
Toluene (1), including eluates:	20.0	*M* 254; C 85.8; H 11.4; N 0.4; O, S 2.4; H/C 1.59; C_a 0.09; C_n 0.20; C_{as} 0.71
hexane (1.1)	13.0	*M* 200; C 84.8; H 12.1; N 0.2; O, S 2.9; H/C 1.71; C_a 0.05; C_n 0.14; C_{as} 0.81
benzene–hexane (1.2)	2.4	*M* 265; C 84.2; H 10.5; N 0.8; O, S 4.5; H/C 1.49; C_a 0.2; C_n 0.12; C_{as} 0.68
benzene (1.3)	1.0	*M* 328; C 77.8; H 9.1; N 0.6; O, S 12.5; H/C 1.40; C_a 0.19; C_n 0.36; C_{as} 0.45
chloroform (1.4)	2.7	*M* 372; C 82.3; H 11.8; N 0.7; O, S 5.2; H/C 1.72; C_a 0.13; C_n 0.47; C_{as} 0.40
acetone (1.5)	0.3	*M* 390; C 79.9; H 10.5; N 0.7; O, S 8.9; H/C 1.58; C_a 0.24; C_n 0.38; C_{as} 0.38
ethanol (1.6)	0.6	*M* 425; C 65.5; H 6.5; N 0.5; O, S 27.5; H/C 1.19; C_a 0.30; C_n 0.28; C_{as} 0.42
Chloroform (2)	0.2	*M* 342; C 74.4; H 8.4; N 0.6; O, S 16.6; H/C 1.35; C_a 0.21
Acetone (3)	6.2	*M* 410; C 69.9; H 7.5; N 2.6; O, S 20.0; H/C 1.29; C_a 0.33
Ethanol (4)	8.6	*M* 445; C 62.2; H 5.0; N 3.9; H/C 0.96; C_a 0.50

* (OMS) Organic matter of shale; (M) molecular weight, amu; (C, H, N, O, S) content of carbon, hydrogen, nitrogen, oxygen, and sulfur, wt % daf; (H/C) atomic ratio; (C_a, C_n, C_{as}) degrees of aromaticity, naphthenicity, and alkyl substitution, respectively.

mononuclear aromatic structures give rise to bands at 735 and 710. The chloroform and ethanol extracts contain bi- and tricyclic fragments;

– CH_3, CH_2, and CH groups of alkyl chains and cycloalkane rings (2926–2980, 2860, 2880, 2925, 2960, 1455, 1460, 1470, 1440, 1380, 1375, 1270, 970, 728); long-chain alkanes prevail in the toluene extract, and cycloalkanes, in the chloroform and acetone extracts;

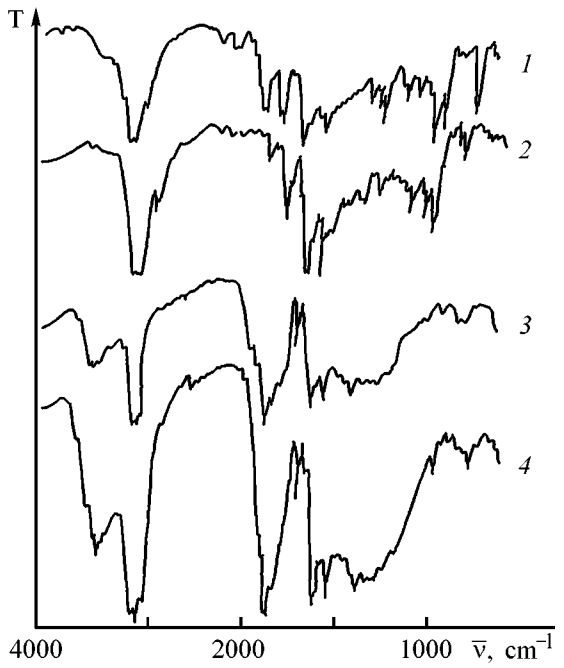

Fig. 1. IR spectra of extracts from shale kerogen: (T) transmission and ($\bar{\nu}$) wave number; the same for Fig. 3. (*1*) C_7H_8, (*2*) $CHCl_3$, (*3*) $(CH_3)_2CO$, and (*4*) C_2H_5OH.

– hydroxy groups of phenols and alcohols (3570, 3300, 1310–1410, 1360, 1330–1420, 1215, 1220, 635–660) prevailing in the acetone and ethanol extracts;

– keto groups (1695, 1705, 1715); aliphatic and alicyclic ketones prevail in the toluene, chloroform, and, especially, acetone extracts, and the ethanol extract contains mainly aliphatic ketones. The major amount of ketones is contained in the acetone extract;

– carboxy groups (2500–3000, 1705, 1715, 1410, 1200–1300, 925), mainly present in the ethanol extract containing aliphatic and alicyclic carboxylic acids. The chloroform extract contains virtually no acids;

– alkoxy groups (2900, 1200–1225, 1085, 1020–1075, 814); ester and lactone groups (1735–1750, 1000–1300, 1163), including methyl esters of long-chain fatty acids (1250, 1205, 1175);

– cyclic anhydrides and amides (1770, 1850, 3400–3450, 1690) prevailing in the acetone and ethanol extracts;

– furan (3125–3165, 1565, 1500, 1030, 885–870, 800–740), thiophene (3050–3125, 1520, 1050, 690–750, 850), and pyrrole heterocycles, amines, pyridine, quinoline, and piperidine fragments (3300–3370, 3440, 3450–3460, 1490, 1250–1350, 745); disulfides (420, 460). The content of furan heterocycles is the highest in the acetone extract; that of thiophene derivatives, in the acetone and ethanol extracts; and that of pyrrole derivatives, in the chloroform extract which also contains significant amounts of amines and various nitrogen-containing heterocyclic compounds.

The IR spectra of the extracts are shown in Fig. 1.

According to the obtained UV/Vis data, the extracts contain (band peak position, nm) unsaturated acids and their derivatives (200), flavonols (250, 370), carotenoid pigments (450, 480–494, 500–550), chlorophylls (380, 418, 428, 464, 510, 580, 675, 700), steroid diketones (280), α-diketones (466), and chromones (625).

Emission-spectral and X-ray fluorescence analyses showed that the mineral fraction of the shale contains Al, Si, S, Cl, Ca, K, Fe, Cu, Ti, Zn, Br, Sr, Pb, Mn, Ni, and V (some of these in the form of organometallic complexes).

Thus, we can conclude that the chemical composition of OMS is very nonuniform; the extracts differ considerably in elemental and functional composition, molecular weight, and nature and content of metals.

In view of the high yield of the toluene extract (Table 1), for obtaining more detailed data on the OMS composition it is appropriate to further separate this extract by adsorption liquid chromatography, with subsequent characterization of the resulting extracts by means of a set of physicochemical methods (see scheme). The yields, molecular weights, and elemental compositions of the eluates of the toluene extract are listed in Table 1.

The major fraction (76.7 wt %) of the toluene extract is eluted with hexane and benzene–hexane (1 : 1); the yield of the chloroform eluate is also rather significant (13.5 wt %, Table 1).

The hexane eluate is characterized by increased H/C ratio and presence in the IR spectrum of strong bands (cm^{-1}) of the CH, CH_2, and CH_3 groups of long alkyl chains and cycloalkane fragments (2950, 2909, 2850, 1450, 1460, 1470, 1378, 1270, 1260, 965, 728). The band at 780 indicates the presence of C_2H_5 groups. Among aromatic compounds, monocyclic compounds prevail (3030–3050, doublet at 1510–1605 with higher intensity of the low-frequency component; series of bands at 1595, 900–1200). Also detected are carotenoids (780, split band at 965, 880), double bonds (1580–1650), minor amounts of long-chain alkanoic acids (1700–1710, 1720), esters, and lactones (1795, 1745, 1760, 1790). The IR data are confirmed by the UV/Vis data. The major absorption peaks (nm) belong to λ-diketones and carotenoids (432, 598, 650), nickel porphyrins (515, 550), unsaturated acids and their derivatives (220), and enones (220, 310).

Using CGLC, we identified in the alkane fraction of the hexane eluate *n*- and *iso*-alkanes C_{11}–C_{37} with maximum at C_{16} (Table 2). The even homologs clearly prevail, and the content of C_{16}–C_{31} components is high. The coefficient characterizing the content of odd homologs is 0.52. The whole chromatogram of the alkane fraction of the hexane eluate is shown in Fig. 2.

Table 2. Content of *n*- and *iso*-alkanes in the hexane eluate

Content, wt % of fraction			
n-alkanes		*iso*-alkanes	
n-$C_{11}H_{24}$	0.06	*i*-$C_{11}H_{24}$	0.02
n-$C_{12}H_{26}$	0.08	*i*-$C_{12}H_{26}$	0.20
n-$C_{13}H_{28}$	0.08	*i*-$C_{13}H_{28}$	0.04
n-$C_{14}H_{30}$	0.33	*i*-$C_{14}H_{30}$	0.10
n-$C_{15}H_{32}$	0.89	*i*-$C_{15}H_{32}$	0.35
n-$C_{16}H_{34}$	22.03	*i*-$C_{16}H_{34}$	0.66
n-$C_{17}H_{36}$	1.73	*i*-$C_{17}H_{36}$	0.20
n-$C_{18}H_{38}$	1.24	*i*-$C_{18}H_{38}$	0.23
n-$C_{19}H_{40}$	1.73	*i*-$C_{19}H_{40}$	0.15
n-$C_{20}H_{42}$	2.18	*i*-$C_{20}H_{42}$	0.13
n-$C_{21}H_{44}$	2.54	*i*-$C_{21}H_{44}$	0.11
n-$C_{22}H_{46}$	2.60	*i*-$C_{22}H_{46}$	0.28
n-$C_{23}H_{48}$	3.58	*i*-$C_{23}H_{48}$	–
n-$C_{24}H_{50}$	3.43	*i*-$C_{24}H_{50}$	–
n-$C_{25}H_{52}$	2.97	*i*-$C_{25}H_{52}$	0.33
n-$C_{26}H_{54}$	2.96	*i*-$C_{26}H_{54}$	0.37
n-$C_{27}H_{56}$	2.54	*i*-$C_{27}H_{56}$	0.23
n-$C_{28}H_{58}$	2.56	*i*-$C_{28}H_{58}$	0.19
n-$C_{29}H_{60}$	2.24	*i*-$C_{29}H_{60}$	0.009
n-$C_{30}H_{62}$	1.81	*i*-$C_{30}H_{62}$	0.26
n-$C_{31}H_{64}$	1.54	*i*-$C_{31}H_{64}$	0.23
n-$C_{32}H_{66}$	1.29	*i*-$C_{32}H_{66}$	0.21
n-$C_{33}H_{68}$	1.02	*i*-$C_{33}H_{68}$	0.19
n-$C_{34}H_{70}$	0.84	*i*-$C_{34}H_{70}$	0.31
n-$C_{35}H_{72}$	0.56	*i*-$C_{35}H_{72}$	0.23
n-$C_{36}H_{74}$	0.55	*i*-$C_{36}H_{74}$	0.19
n-$C_{37}H_{76}$	0.33	*i*-$C_{37}H_{76}$	0.23

The benzene–hexane eluate, compared with the hexane eluate, is characterized by lower H/C ratio

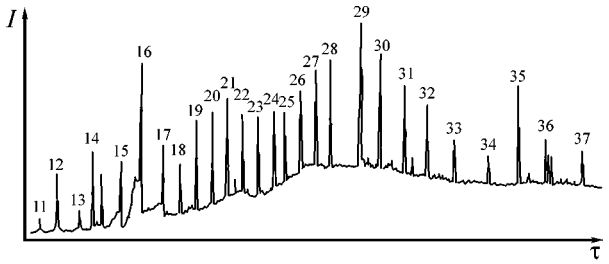

Fig. 2. Chromatogram of the alkane fraction of the hexane eluate of the toluene extract: (*I*) relative intensity and (τ) retention time.

and lower oxygen content. This fact suggests prevalence of weakly polar saturated compounds.

In the IR spectrum of the eluate, we identified the following fragments and bands ($\bar{\nu}$, cm^{-1}):

– aromatic rings, nonconjugated or characterized by low degree of conjugation (C–H stretching vibrations at 3030–3050, C=C in-plane vibrations at 1574–1606, 1480–1510);

– CH_3 and CH_2 groups of long alkyl chains and cycloalkanes (2908, 2950, 2850, 1470, 1460, 1450, 1380, 1270, 1260, 965, 720);

– unsaturated bonds in long alkyl chains; terpenes and carotenoids may also be present (3050–2970, 1850–1800, 1870–1625, 1320–1270, 968, 860, 780);

– keto groups of aliphatic ketonbes (1715, 1705);

– C=O stretching vibrations in esters and lactones (1770, 1745, 1735) and quinones (1675, 1645);

– C–O stretching vibrations and O–H in-plane bending vibrations in primary and secondary alcohols (1075–1000, 1350–1260 and 1120–1030, 1350–1260, respectively); O–H stretching vibrations in alcohols (3400 with shoulders at 3480 and 3450) involved in inter- and intramolecular hydrogen bonds.

By UV/Vis spectroscopy we detected in this eluate the following compounds (band peak position, nm): unsaturated compounds (200), naphthalene rings (200, 281, 314), steroid derivatives (284, 338), carotenoids (338, 428, 440.5); chlorophyll b (428, 465, 675), and chlorophyll (380, 418, 428, 510, 580, 700).

According to elemental analysis (Table 1), the benzene eluate, has the lowest carbon content and a significant content of oxygen and sulfur. This fact suggests that this eluate mainly consists of polar and unsaturated compounds.

According to the IR spectra, the following fragments prevail in the eluate ($\bar{\nu}$, cm^{-1}): CH, CH_2, and CH_3 groups of alkanes and cycloalkanes (2960, 2925, 2880, 1460–1470, 1475, 1380; the broad band is split, suggesting the presence of isopropyl and *gem*-dimethyl groups); band at 770–780 is characteristic of ethyl groups, and that at 735, of *n*-propyl groups; aromatic rings (3040–3045, doublet at 1500–1600, 1610, a series of bands at 900–700); aliphatic ketones (1715, 1100); ester groups (1735), three bands at 1000–1300, 1300–1310, 1000–1065; four-membered cyclic ketones (1780). The presence of the thiophene ring is confirmed by bands at 700, 1040, 1520, 3050–3125. The UV/Vis spectra (λ, nm) suggest the presence in the benzene eluate of meso-chlorins (619), chlorophyll b (442, 578, 628), carotenoids (440), cisoid cyclic diene (262) of the λ-terpinene type, flavonols (279, 380), chlorophyll b (728, 464, 675), and compounds with a thiophene ring (302).

The chloroform eluate is characterized by relatively high yield and increased H/C atomic ratio (Table 1), suggesting the presence of large amounts of aliphatic and hydroaromatic structures.

In the IR spectra, we identified ($\bar{\nu}$, cm^{-1}) alkane and cycloalkane structures (2960, 2925, 2860, 1470–1455, 1380 sharp, 1260, 970), aromatic rings (3010–3080, doublet at 1500–1600, 1580), mainly condensed, possibly with admixture of hydroaromatic rings; alkoxy (2850, 2815–2830, 1070–1150, 1070–1020), quinoid (1676, 1638), keto (1720, 1710, 1695) groups; pyridine, quinoline, pyrrole, and indole rings (3490, 3100–3125, doublet at 1500–1600, 1010–1035, 740–770, 770–830).

By UV/Vis spectroscopy, we detected in this eluate (λ, nm) steroid diketones (280), chromones (625), porphyrin rings (520, 560), carotenoids (440.5), chlorophyll a (380, 418, 428, 510, 580, 700), and chlorophyll b (428, 465, 675).

The acetone eluate is characterized by high content of oxygen and sulfur and medium H/C atomic ratio (Table 1); hence, it mainly consists of strongly polar aromatic compounds. According to the IR spectra, the content of alkyl groups is insignificant; we detected aromatic rings (3000–3060, a doublet at 1500–1600, 1200–900), including phenanthrene structures (890, 812, 800, 760). The major oxygen compounds ($\bar{\nu}$, cm^{-1}) are cyclic ethers (broad band at 1180–1290), steroid alcohols [3390, 3200, 1612, 1585, 1500, 1435–1415 (O–H groups in steroids-17), 1054, 870, 815], and ketones (1725, 1715, 1690).

According to the UV/Vis spectra, the acetone eluate contains (λ, nm) alkylbenzenes (263.5, 202); cyclic α-diketones (263.5, 323); chlorins (696); presumably, derivatives of flavonols, anthocyan (510–550), and anthocyanidins (404, 449, 346); carotenoids (440.5); chlorophyll a (388, 418, 428, 510, 580, 700); chlorophyll b (428, 465, 675).

The ethanol extract has rather high content of oxygen and sulfur and low H/C ratio, which suggests the presence of strongly polar compounds (Table 1).

According to the IR spectra, the prevailing components of this eluate ($\bar{\nu}$, cm^{-1}) are long-chain carboxylic acids, esters, ketones, lactones (2960, 2925, 2860, 1755–1770, 1715, 1720, 1730, 1740, 1780 broad,

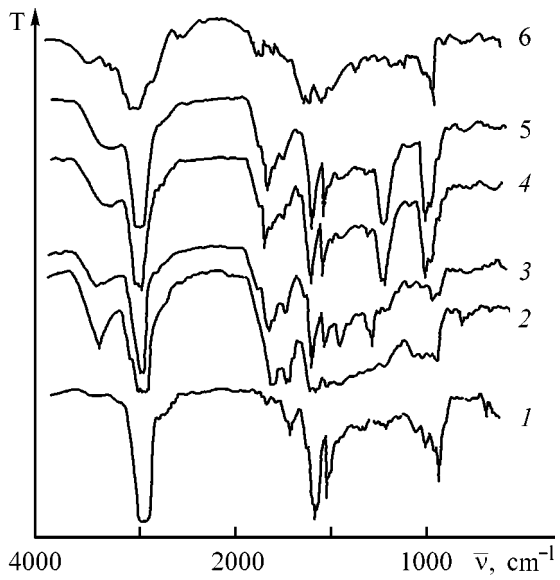

Fig. 3. IR spectra of separate eluates of the toluene extract.

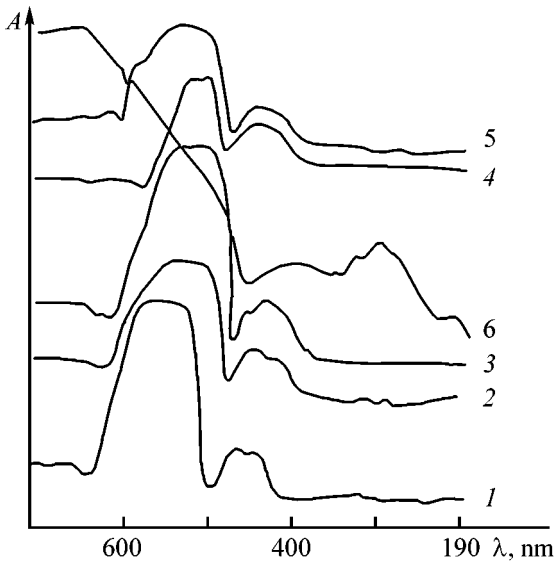

Fig. 4. UV/Vis spectra of separate eluates of the toluene extract: (*A*) absorption and (λ) wavelength. (*1*) C_6H_{14}, (*2*) $C_6H_{14} : C_6H_6$, (*3*) C_6H_6, (*4*) $CHCl_3$, (*5*) $(CH_3)_2CO$, and (*6*) C_2H_5OH.

1460, 1470, 1480, 1375–1380, 1260, 970, 720) and alcohols (3170, 3420, 3620, 1310–1410, 1155). By UV-Vis spectroscopy we detected (λ, nm) chlorins (698), in particular, meso-pyrroetiochlorins (642); diketones of the diterpene series (311); coumarone derivatives (shoulder at 240 and peak at 283); flavonols (251, 371, 510–540); chromone derivatives (622); pyrrole rings (214); chlorophyll b (428, 465, 675).

The IR and UV/Vis spectra of separate eluates of the toluene extract are shown in Figs. 3 and 4.

CONCLUSIONS

(1) The chemical composition of the toluene extract from oil shale (kerogen-70) was studied for the first time by using a combination of extraction, adsorption-liquid and capillary gas–liquid chromatography; elemental, emission spectrum, X-ray fluorescence, quantitative functional, and structural-group analyses; cryoscopy; and IR and UV/Vis spectroscopy.

(2) A procedure including extraction and adsorption liquid chromatography was developed for separating oil shale into fractions differing in molecular weight, elemental and functional composition, degree of aromaticity, and type of condensation.

(3) The formation of the organic matter of shale involved not only an algal material, but also a terrigenic material of higher plants, bacterial bioproduction, animal bodies, and fungi.

REFERENCES

1. Lapo, A.V. and Mikhailova, N.S., *Goryuch. Slantsy*, 1988, vol. 5, no. 4, pp. 349–355.
2. Zhmur, S.I., Serova, N.B., and Melamedova, V.S., *Goryuch. Slantsy*, 1986, vol. 3, no. 4, pp. 365–375.
3. Yurkevich, E.A., Luk'yanova, Z.K., Makeeva, E.P., and Drozdovskaya, S.V., *Goryuch. Slantsy*, 1986, no. 1, pp. 270–275.
4. Silverstein, R.M., Clayton, G.C., and Morrill, T.C., *Spectrometric Identification of Organic Compounds*, New York: Wiley, 1974.
5. *Elucidation of Structures by Physical and Chemical Methods*, Bentley, K.W., Ed., New York: Wiley Interscience, 1963.
6. Isagulyants, V.I. and Egorova, G.M., *Khimiya nefti* (Petrochemistry), Moscow: Khimiya, 1965.
7. Koltanets, V.A. and Butuzova, L.R., *Vopr. Khim. Khim. Tekhnol.*, 1977, issue 47, pp. 96–100.
8. Gulyaeva, N.D., Aref'eva, O.A., and Petrov, A.A., *Khim. Tverd. Topl.*, 1976, no. 4, pp. 3–7.
9. Cheronis, N.D. and Ma, T.S., *Organic Functional Group Analysis by Micro and Semimicro Methods*, New York: Interscience, 1964.
10. Dunning, H.N., *Organic Geochemistry: Monograph, Symp. Pull. Div. Earth Sci. Ser.*, Breger, J.A., Ed., Oxford: Pergamon, 1963, no. 16, pp. 367–430.

Russian Journal of Applied Chemistry, Vol. 74, No. 8, 2001, pp. 1390–1391. Translated from Zhurnal Prikladnoi Khimii, Vol. 74, No. 8, 2001, pp. 1354–1355.

BRIEF COMMUNICATIONS

Refining the Phase Diagram of the System $3Al_2O_3 \cdot 2SiO_2$–ZrO_2

S. S. Ordan'yan, P. S. Gudovskikh, and O. V. Pozhidaeva

St. Petersburg State Technological Institute, St. Petersburg, Russia

Received February 19, 2001

Abstract—The quasi-binary section mullite–zirconium dioxide in the ternary system Al_2O_3–SiO_2–ZrO_2, described by an eutectic phase diagram with T_{eut} = 1750°C, was studied experimentally.

Published ternary phase diagrams of the system Al_2O_3–ZrO_2–SiO_2 are constructed on the assumption that the section mullite–ZrO_2 is a quasi-binary system of a simple eutectic type [1]. Tentatively constructed phase diagrams [2, 3] contain no experimental data on the true composition and melting point of the eutectic in the $3Al_2O_3 \cdot 2SiO_2$–ZrO_2 quasi-binary system. Moreover, this section was not, probably for technical reasons, among the seven sections studied in detail in [4]. This made it necessary to specify the position of the eutectic point in the $3Al_2O_3 \cdot 2SiO_2$–ZrO_2 quasi-binary system, which is of great importance for fabricating refractory structural materials.

Initially, the phase diagram of this system was calculated in terms of the ideal solution approximation [5] relying upon the Schroder–Le-Chatelier equation for determining the liquidus temperatures.

According to the calculations, the eutectic contains 12 wt % ZrO_2 and its melting point is 1870°C; however, the calculated values were found to be in disagreement with experiment. For this reason, the system was studied by differential thermal (DTA), metallographic, and X-ray phase (XPA) analyses. Compositions with various weight contents of mullite and zirconium dioxide were prepared by mixing powdered starting components in isopropyl alcohol.

The differential thermal analysis was performed in molybdenum crucibles in an atmosphere of helium, using a VTA-980 high-temperature analyzer. Heating was performed to 2200°C at a rate of 10–80 deg min^{-1}.

The DTA curves of samples containing 10–70 wt % ZrO_2 showed clearly resolved peak at 1750°C ± 15°C (Fig. 1), attributable to an irreversible endothermic effect. This temperature was taken to be the eutectic melting point.

For a number of the compositions studied, another endothermic effect attributable to liquidus line crossing was recorded (see the table). This endothermic effect was not recorded for the composition containing 70 wt % ZrO_2. Thus, we can conclude that the liquidus temperature for this composition is above 2200°C. The lack of the second effect in heating the mixtures containing 30 and 35 wt % ZrO_2 can be accounted for by the impossibility of resolving by means of thermal analysis the liquidus and solidus temperatures for compositions close to the eutectic.

Thus, the performed analysis of the DTA data suggests that the eutectic in the $3Al_2O_3 \cdot 2SiO_2$–ZrO_2 system has a melting point of 1750 ± 15°C and contains 30–35 wt % ZrO_2.

The structure of samples formed upon melting and crystallization of the mixtures in the course of DTA was studied by optical microscopy. A typical eutectic structure was observed for a composition containing 30 wt % ZrO_2. In addition to the characteristic eutectic structure, excess grains of mullite could be

Thermal analysis data

ZrO_2 content, wt %	The onset temperature (°C) of the indicated endothermic effect	
	first	second
10	1750	1850
20	1750	1810
25	1750	1780
30	1750	–
35	1760	–
40	1765	1810
50	1740	1950
70	1745	–

1070-4272/01/7408-1390 $25.00 © 2001 MAIK "Nauka/Interperiodica"

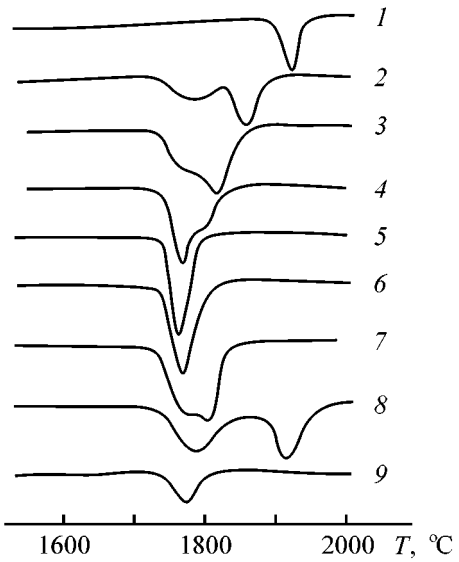

Fig. 1. DTA curves of samples of the $3Al_2O_3 \times 2SiO_2$–ZrO_2 system. (*T*) Temperature; the same for Fig. 2. ZrO_2 content (wt %): (*1*) 0, (*2*) 10, (*3*) 20, (*4*) 25, (*5*) 30, (*6*) 35, (*7*) 40, (*8*) 50, and (*9*) 70.

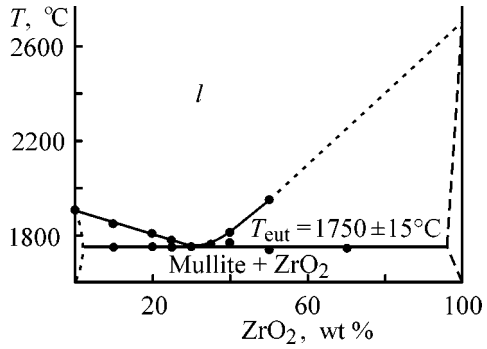

Fig. 2. Experimental phase diagram of the system mullite–zirconium dioxide.

seen in polished sections of samples containing 10, 20, and 25 wt % ZrO_2; and excess ZrO_2, in sections of samples containing 35 wt % and more ZrO_2.

According to XPA, all the samples studied are two-phase and contain only *m*-ZrO_2 and mullite, which confirms the assumed quasi-binary character of the section studied.

In constructing the phase diagram, the melting point of pure ZrO_2 was taken to be 2700°C [6, 7]. The evidence on the character and temperature of melting of pure mullite is contradictory [8]. A DTA curve of mullite preliminary obtained by solid-phase synthesis at 1600°C demonstrated another endothermic peak at 1910°C (Fig. 1a). Just this temperature was accepted as the melting point of pure mullite in constructing the phase diagram, in agreement with [9].

An experimental phase diagram of the quasi-binary system $3Al_2O_3 \cdot 2SiO_2$–ZrO_2 is presented in Fig. 2; the mutual solubility of components was not studied.

The whole set of data furnished by the differential thermal, metallographic, and X-ray phase analyses suggests that the system $3Al_2O_3 \cdot 2SiO_2$–ZrO_2 is indeed a quasi-binary eutectic system. The eutectic contains 30 wt % ZrO_2 and 70 wt % $3Al_2O_3 \cdot 2SiO_2$ and its melting point is 1750°C.

The obtained data may serve as a basis for developing high-temperature ceramic composites.

REFERENCES

1. *Diagrammy sostoyaniya sistem tugoplavkikh oksidov: Spravochnik* (Phase Diagrams of Refractory Oxide Systems: Handbook), Galakhov, F.Ya., Ed., Leningrad: Nauka, 1972, issue 3.
2. Budnikov, P.P. and Litvakovskii, A.A., *Dokl. Akad. Nauk SSSR*, 1956, vol. 106, no. 2, pp. 267–269.
3. Litvakovskii, A.A., *Steklo. Keramika*, 1956, no. 11, pp. 11–13.
4. Quercshi, M.H., and Brett N.H., *Trans. Brit. Ceram. Soc.*, 1968, vol. 67, no. 11, pp. 569–578.
5. Udalov, Yu.P. and Ordan'yan, S.S., *Raschet diagramm plavkosti binarnykh i troinykh sistem s uchastiem tugoplavkikh soedinenii. Uchebnoe posobie* (Calculation of Fusion Diagrams of Binary and Ternary Systems Involving Refractory Compounds. Textbook), St. Petersburg: Sankt-Peter. Tekhnol. Inst., 1994.
6. Toropov, N.A., Barzakovskii, V.P., Bondar', I.A., and Udalov, Yu.P., *Diagrammy sostoyaniya silikatnykh sistem. Metall-kislorodnye soedineniya. Spravochnik* (Phase Diagrams of Silicate Systems. Metal-Oxygen Compounds. Handbook), Leningrad: Nauka, 1970, issue 2.
7. Rutman, D.S., Toropov, Yu.S., and Pliner, S.Yu., *Vysokoogneupornye materialy iz dioksida tsirkoniya* (Highly Refractory Zirconium Dioxide Materials), Moscow: Metallurgiya, 1985.
8. Strelov, K.K., and Kashcheeev, I.D., *Ogneupory*, 1995, no. 8, pp. 2–8.
9. Toropov, N.A., and Galakhov, F.Ya., *Dokl. Akad. Nauk SSSR*, 1951, vol. 78, no. 2, pp. 299–302.

Russian Journal of Applied Chemistry, Vol. 74, No. 8, 2001, pp. 1392–1394. Translated from Zhurnal Prikladnoi Khimii, Vol. 74, No. 8, 2001, pp. 1356–1358.

BRIEF COMMUNICATIONS

Processing of Aluminum Sulfates into Alumina

Sh. B. Nazarov, Kh. Sh. Gulakhmadov, M. M. Khakdodov, and Sh. G. Aminov

Nikitin Institute of Chemistry, Academy of Sciences of Tajikistan, Dushanbe, Tajikistan

Received June 21, 2000; in final form, May 2001

Abstract—The possibility of processing aluminum sulfates into alumina with the use of calcium carbonate was studied.

Production of alumina from aluminum sulfates in processing of high-silica aluminum ores (alunites, nephelines, clays, poor-quality bauxites, siallites, etc.) is of great practical interest. The known methods to obtain alumina from aluminum sulfates have a number of shortcomings: cumbersome technological schemes, difficult deferrization of solutions, necessity for high-temperature heating of salts containing a great amount of crystallization water, evaporation of large amounts of mother liquors, and high energy expenditure for thermal decomposition of aluminum sulfates.

For example, according to the Kalunit scheme [1], dehydrated alunite ore is leached with reused sulfuric acid containing potassium sulfate. Fe(III) is removed from the sulfate solutions with dehydrated alunite ore. A more thorough removal of iron(III) from solutions can be achieved in the scheme by recrystallization of alum calcined at 1000°C. SO_2 and SO_3 gases obtained in calcination are used in production of sulfuric acid. The product of alum decomposition is leached with water, with sulfates of alkali metals dissolved and alumina remaining in a sediment.

In another method [2], clay is treated to remove Fe(III) with a weak solution of sulfuric acid, calcined, and decomposed with sulfuric acid. Aluminum and iron(III) hydroxides isolated from the sulfate solution by adding Na_2CO_3 are dissolved in alkali, and $Al(OH)_3$ is isolated by carbonization. Aluminum hydroxide is then used to obtain alumina by calcination.

Much attention has been given by researchers to processing of alunite ores [3]. Alunites are sulfated aluminates of alkali metals—$MAl_3(OH)_6(SO_4)_2$, where M = Na, K. The sulfate products obtained in ore processing are used to obtain alumina by various methods. However, all of these require improvement and simplification of their technological schemes.

The present study is concerned with the possibility of processing of aluminum sulfates with the use of calcium carbonate to obtain alumina without solution evaporation or crystallization and thermal decomposition of salts, which much simplifies the technology.

An aluminum sulfate solution to be used in the experiments was obtained by processing an alunite ore of the following chemical composition (wt %): Al_2O_3 27.5, K_2O 7.2, Na_2O 0.15, SO_3 26.3, Fe_2O_3 1.3, CaO 1.08, SiO_2 24.1, and calcination loss 12.37. The ore was sintered at 400–650°C and the resulting mass was treated with 10–20% sulfuric acid at 100°C in the reactor. The resulting suspension (sludge) was filtered to remove the solid phase (SiO_2 and its compounds). The filtrate contained sulfates of aluminum, iron(III), potassium, sodium, etc.

To the filtrate was added calcium carbonate for aluminum(III) and iron(III) to be precipitated in the form of their hydroxides by the reactions

$$Al_2(SO_4)_3 + 3CaCO_3 + 3H_2O \rightarrow 2Al(OH)_3\downarrow + 3CaSO_4 + 3CO_2\uparrow, \quad (1)$$

$$Fe_2(SO_4)_3 + 3CaCO_3 + 3H_2O \rightarrow 2Fe(OH)_3\downarrow + 3CaSO_4 + 3CO_2\uparrow. \quad (2)$$

The obtained mass was agitated in the reactor with a stirrer at 20–30°C for 10–30 min. Then the liquid and solid phases of the suspension were separated. The filtrate was composed of potassium, sodium, and other sulfates; the residue contained $Al(OH)_3$, $Fe(OH)_3$,

1070-4272/01/7408-1392 $25.00 © 2001 MAIK "Nauka/Interperiodica"

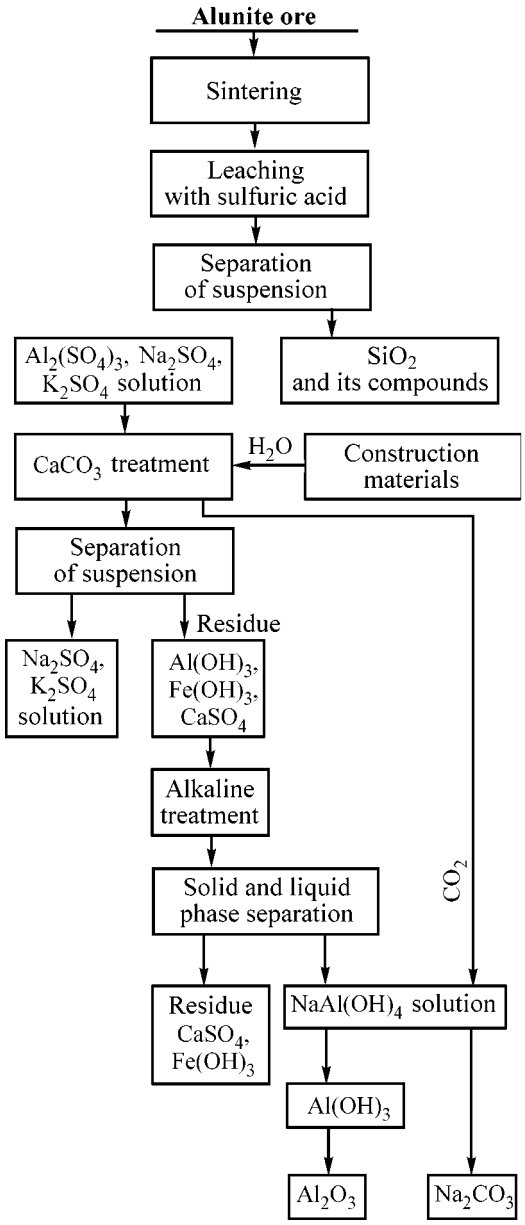

and $CaSO_4$. $MgCO_3$ or $CaMg(CO_3)_2$ (dolomite) could be used for the above purposes instead of $CaCO_3$.

To obtain alumina, the mixture of aluminum and iron(III) hydroxides and calcium sulfate was subjected to alkaline treatment, and then $Fe(OH)_3$ and $CaSO_4$ were separated from the aluminate solution by filtration. The sodium aluminate solution was carbonized to give $Al(OH)_3$ transformed into alumina upon dehydration at 650°C.

In the present study, the influence exerted by various factors: treatment temperature T, process duration τ, amount (dosage) of $CaCO_3$ (relative to stoichiometry) C_{CaCO_3}, mass ratio of liquid and solid phases l : s, on the degree α of $Al(OH)_3$ and $Fe(OH)_3$ precipitation from sulfate solution was studied (Table 1).

Table 1. Effect of various factors on the degree of precipitation of $Al(OH)_3$ and $Fe(OH)_3$ from their sulfates

T, °C	τ, min	l : s, by weight	C_{CaCO_3}, % relative to stoichiometry	α, %	
				$Al(OH)_3$	$Fe(OH)_3$
20	60	10 : 1	100	90.1	86.7
60	60	10 : 1	100	96.3	91.9
100	60	10 : 1	100	99.8	99.7
100	5	10 : 1	100	62.3	51.6
100	20	10 : 1	100	88.5	86.4
100	40	10 : 1	100	98.8	97.9
90	50	1 : 1	100	98.8	97.9
90	50	4 : 1	100	74.9	70.3
90	50	8 : 1	100	97.8	95.4
90	50	12 : 1	100	99.6	99.2
100	60	9 : 1	90	87.4	85.6
100	60	9 : 1	95	96.1	95.2
100	60	9 : 1	100	99.6	99.7
100	60	9 : 1	105	95.7	93.1

Table 2. Effect of various factors on recovery of aluminum(II) from solid residue in its alkaline treatment

T, °C	C_{NaOH}, g l^{-1}	Al_2O_3 recovery, %
20	250	85.4
60	250	95.7
90	250	98.9
100	50	89.4
100	100	92.8
100	200	100.0

The obtained results suggest that the optimal process conditions are as follows: T = 50–100°C, τ = 40–60 min, stoichiometric dosage of $CaCO_3$, l : s = 6 : 1–10 : 1.

Further, the process of alkaline treatment of the obtained residue, containing $Al(OH)_3$, $Fe(OH)_3$, and $CaSO_4$, was studied in order to separate the residue into components and make these marketable. For this part of the technological process, the effect of various factors on the extraction of residue components, namely, aluminum and iron, into solution was studied. The basic results for recovery of aluminum in the form of Al_2O_3 from a mixture of $Al(OH)_3$, $Fe(OH)_3$, and $CaSO_4$ in alkaline treatment are presented in Table 2.

When a mixture of $Al(OH)_3$, $Fe(OH)_3$, and $CaSO_4$ is treated with alkali, $Al(OH)_3$ dissolves in accordance with the equation

$$Al(OH)_3 + NaOH \rightarrow Na[Al(OH)_4]. \quad (3)$$

The obtained mixture is filtered, with the solid phase composed of a mixture of $Fe(OH)_3$ and $CaSO_4$, processed into a pigment (Fe_2O_3) and alabaster ($CaSO_4 \cdot 0.5\ H_2O$). The liquid phase consists of sodium aluminate. The filtrate is treated with carbon(IV) oxide formed in accordance with Eqs. (1) and (2). As a result of this treatment, $Al(OH)_3$ precipitates:

$$2Na[Al(OH)_4] + CO_2 \rightarrow Na_2CO_3 + 2Al(OH)_3\downarrow + H_2O. \quad (4)$$

Calcination of aluminum hydroxide at 550–600°C gives alumina (see the scheme).

The method also enables processing into alumina of basic aluminum sulfates, with the consumption of $CaCO_3$ markedly reduced in this case. It should also be noted that the chemical composition of potassium and sodium sulfates in the starting sludge remains unchanged. These salts are isolated from the mother liquor by crystallization.

CONCLUSIONS

(1) The optimal mode of $Al(OH)_3$ formation from $Al_2(SO_4)_3$ with the use of calcium carbonate is as follows: treatment temperature 50–100°C, process duration 40–60 min, stoichiometric dosage of $CaCO_3$, l : s = 6 : 1–10 : 1.

(2) A technique was developed for obtaining alumina from poor-quality aluminum ores.

REFERENCES

1. Fleisher, A., *Trans. Am. Inst. Mining Met. Eng.*, 1944, no. 159, pp. 267–279.
2. Dadonov, Ya.Ya., Medoks, G.V., and Soshestvenskaya, E.M., *Zh. Prikl. Khim.*, 1947, vol. 20, no.9, pp. 870–874.
3. Zapol'skii, A.K., *Sernokislotnaya pererabotka vysoko kremnistogo alyuminievogo syr'ya* (Sulfuric Acid Processing of High-Silica Aluminum Raw Materials), Kiev: Naukova Dumka, 1981.

Russian Journal of Applied Chemistry, Vol. 74, No. 8, 2001, pp. 1395–1396. Translated from Zhurnal Prikladnoi Khimii, Vol. 74, No. 8, 2001, pp. 1358–1359.

BRIEF COMMUNICATIONS

Independent Method for Determining the Anisotropic Component of the Energy of Intermolecular Interactions in Strongly Polar Liquids

A. N. Bykov and S. M. Karabanov

OAO Ryazanskii Zavod Metallokeramicheskikh Priborov, Ryazan, Russia

Received April 26, 2001

Abstract—A simple method is proposed for determining the anisotropic component of the energy of intermolecular interactions in strongly polar liquids.

It is known [1] that the anisotropic component of the field of molecular forces affects virtually all of the thermodynamic properties of polar liquids, and, therefore, determining its value is of particular practical importance. According to the commonly accepted approach to description of the energetics of intermolecular interactions (IMI) in liquid insulators [2, 3], the IMI energy is operationally separated into the anisotropic and isotropic components—ΔU_{an} and ΔU_{is}, respectively. Then the total energy of a molecule, ΔU_s, is given by

$$\Delta U_s = \Delta U_{is} + \Delta U_{an}.$$

By ΔU_{an} and ΔU_{is} are understood the ΔU_s components which are, respectively, dependent on, and independent of the orientation of the polar molecule. This communication proposes an unsophisticated independent method for evaluation of ΔU_{an} for simple unassociated strongly polar liquids in which ΔU_{an} is determined by the orientation of dipole molecules in local molecular fields. As shown in [4], the extent of mutual compensation of dipole moments B of molecules within a sample of polar liquid, taken in a vacuum, is determined by the average strength of the local molecular field **F** created by all other particles of the system at the center of an arbitrarily chosen molecule:

$$B = \frac{\langle M_d^2 \rangle_0}{N\mu^2} = 1 - L(\alpha), \quad (1)$$

where $\langle M_d^2 \rangle_0$ is the average squared spontaneous electric moment of a macroscopic sphere in a vacuum, N the number of molecules within the sphere, μ the di-

Values of the anisotropic part of IMI in polar liquids, obtained in two independent ways

Compound	n_D	μ_0, D	ε	$\langle M_d^2 \rangle_0$	$N\mu^2$	U_{an}' *	U_{an} **
				10^{-14}, D^2 mol^{-1}		kJ mol^{-1}	
Nitrobenzene	1.553	4.22	35.25	265	2345	20.9	18.4
Acetonitrile	1.342	3.91	35.95	140	1510	25.7	23.3
Propionitrile	1.366	3.56	27.5	181	1285	16.5	18.0
Nitromethane	1.380	3.50	35.8	142	1276	21.3	23.4
Dimethyl sulfoxide	1.477	3.96	46.7	191	1878	23.3	25.2
Dimethylformamide	1.427	3.86	36.71	203	1700	19.7	21.4
Acetone	1.359	2.88	20.7	180	864	10.8	13.6
Pyridine	1.507	2.20	12.3	164	556	7.20	6.6
Acetophenone	1.534	3.02	17.4	265	1125	9.4	9.5

* Given by (8).

** Independent estimate [3].

1070-4272/01/7408-1395 $25.00 © 2001 MAIK "Nauka/Interperiodica"

pole moment of molecules in liquid, $L(\alpha)$ the Langevin function of α, and

$$\alpha = \frac{\mu\langle|\mathbf{F}|\rangle}{kT}. \quad (2)$$

The $\langle M_d^2\rangle_0$ value is determined by Fröhlich's strict thermodynamic relation [5]

$$\frac{\varepsilon - \varepsilon_\infty}{\varepsilon + 2} V = \frac{4\pi}{3}\frac{\langle M_d^2\rangle}{3kT}. \quad (3)$$

The μ value is given by the conventional approximation

$$\mu = \mu_0 \frac{\varepsilon_\infty + 2}{3}\,\frac{2\varepsilon + 1}{2\varepsilon + \varepsilon_\infty}, \quad (4)$$

where $\varepsilon_\infty \cong 1.05 n_D$, and n_D is the refractive index.

In the case of strongly polar liquids ($\alpha >> 1$), it can be written with sufficient accuracy that

$$L(\alpha) \cong 1 - \alpha^{-1}.$$

Then, using Eq.(1), we have

$$\alpha^{-2} - 2\alpha^{-1} + B = 0, \quad (5)$$

whence

$$\alpha = [1 - \sqrt{1 - B}\,]^{-1}. \quad (6)$$

Using Eqs. (1) and (6) for the average energy of anisotropic interaction of polar molecules in a mole of liquid, we obtain [4]

$$U_{an} = \frac{1}{2} N\langle \mu\mathbf{F}\rangle \cong \frac{1}{2} N\mu L(\alpha)\langle|\mathbf{F}|\rangle = \frac{1}{2} L(\alpha)\alpha RT$$

$$= \frac{RT}{2}\,\frac{\sqrt{1 - B}}{1 - \sqrt{1 - B}}. \quad (7)$$

At $B << 1$ we have

$$U'_{an} \cong \frac{2 - B}{2B} RT. \quad (8)$$

As shows comparison of the $\Delta U'_{an}$ values calculated using relation (8) with the result obtained in determining ΔU_{an} by another independent method [2, 3], whose efficiency was convincingly confirmed in describing quantitatively numerous processes in liquids, there is satisfactory agreement between $\Delta U'_{an}$ and ΔU_{an}. The average deviation for the nine considered liquids was about 10% (see table).

REFERENCES

1. Reid, R.G., Prausnitz, J.M., and Sherwood, T.K., *The Properties of Gases and Liquids*, New York: McGraw-Hill Book Company, 1977.
2. Sol'vatokhromiya: *Problemy i metody* (Solvatochromy: Problems and Methods), Bakhshiev, N.G., Ed., Leningrad: Len. Gos. Univ., 1989.
3. Gorodyskii, V.A. and Moskvicheva, L.A., *Vestn. SPb. Gos. Univ., Ser. 4*, 1994, no. 1, pp. 55–65.
4. Bykov, A.N., *Khim. Fiz.*, 1993, vol. 12, no. 8, pp. 1106–1121.
5. Fröhlich, H., *Theory of Dielectrics, Dielectric Constants and Dielectric Loss*, Oxford: Clarendon Press, 1958.

Russian Journal of Applied Chemistry, Vol. 74, No. 8, 2001, pp. 1397–1399. Translated from Zhurnal Prikladnoi Khimii, Vol. 74, No. 8, 2001, pp. 1360–1362.

BRIEF COMMUNICATIONS

Structuring in Interphase Layer of Extraction System

N. F. Kizim, O. P. Nesterova, and V. A. Malyukova

Novomoskovsk Institute, Mendeleev Russian University of Chemical Technology, Novomoskovsk, Russia

Received December 26, 2000; in final form, April 2000

Abstract—The results of a study of the rheological properties of the interphase layer formed when an aqueous phase containing HCl and $PrCl_3$ is brought in contact with a solution of an extracting agent (nonoxymethylphosphonic acid) in toluene at varied content of the components in the system are presented.

In extraction of metal ions with organophosphorus acids, an important role is played by interphase layers within which chemical reactions between the components of the extraction system, giving rise to two-dimensional structures, can be localized [1].

The influence exerted by the content of components on the rheological properties of an interphase layer formed on bringing in contact the $PrCl_3$–H_2O–HCl system with a solution of nonoxymethylphosphonic acid (NMPA) in toluene was investigated.

The rheological parameters were found from kinetic deformation curves [2] obtained by the method of tangential displacement of a plate at 298 K and from flow curves. A 0.1-mm-thick plate 3 mm in diameter, made of a ferromagnetic material and platinum plated to improve its corrosion resistance, was used in the study.

The method consists in that the displacement of plate 1 at the phase boundary under the action of an electromagnet driven by voltage U (V) from a dc power supply was measured with a microscope at certain intervals of time t. Preliminary experiments demonstrated that the shear stress is proportional to the electric voltage across the electromagnet terminals. The measurements were done until the displacement of 1 became larger than 1 mm. The measurement error did not exceed 10%. The experimental technique was described in detail in [3].

Typical flow curves obtained at varied content of the components $PrCl_3$ and HCl and the extracting agent NMPA are presented in Fig. 1. An analysis of the rheological curves demonstrated that, under the conditions studied, the adsorption layers can be classed as systems of three types [4–6]: approximately Newtonian, Newtonian-dilatant, and weakly structured.

With increasing solution acidity, there occurs a transition from an approximately Newtonian system in a 10^{-4} M solution of HCl to a weakly structured system, disintegrating in the course of time in a 10^{-4}–10^{-3} M solution of HCl and becoming more stable at $C > 10^{-3}$ M HCl.

When the NMPA content is varied (0.2–0.4 M), weakly structured layers are formed, mainly with a structure becoming stronger with time.

The structure strengthening is presumably due to hindered diffusion and orientation of the extracting agent molecules being adsorbed, which can both dissociate at low HCl concentrations and form a polymeric structure at higher HCl concentrations.

Raising the concentration of the extracting agent makes weaker the contact interaction and leads to higher flowability and longer time of the elastic aftereffect.

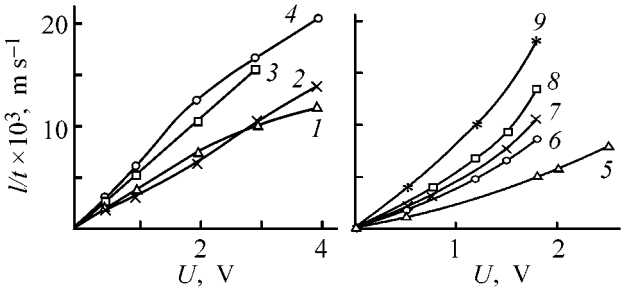

Fig. 1. Rheological flow curves for interphase layers. (l/t) Flow velocity and (U) voltage across electromagnet terminals. Time of contact between phases (h): (*1*) 9, (*2, 4*) 0.5, (*3, 9*) 4.5, (*5*) 10, (*6*) 5, (*7*) 1, and (*8*) 2.5. Concentration (M): HCl: (*1, 4–7*) 10^{-2}, (*2, 3*) 10^{-4}, and (*8, 9*) 10^{-3}; $PrCl_3$: (*1, 4*) 0.05 and (*2, 3, 5–9*) 0.75; extracting agent: (*1, 4*) 0.2 and (*2, 3, 5-9*) 0.4.

1070-4272/01/7408-1397 $25.00 © 2001 MAIK "Nauka/Interperiodica"

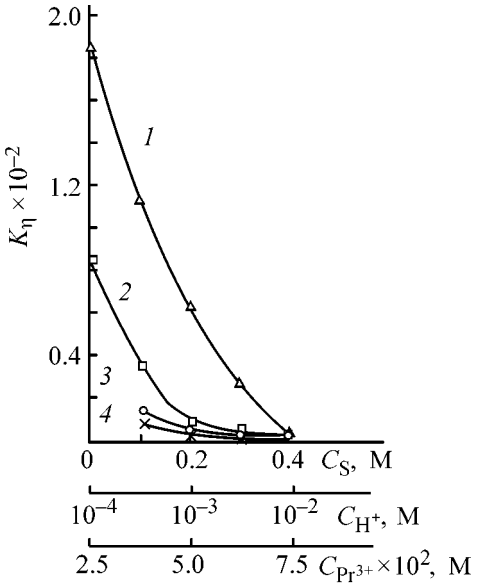

Fig. 2. Structuring factor K_η vs. the concentrations of the system's components: (*1, 2*) HCl, C_{H^+}; (*3*) extracting agent, C_S; and (*4*) $PrCl_3$, $C_{Pr^{3+}}$. Time of contact between phases (h): (*1*) 1 and (*2–4*) 4.

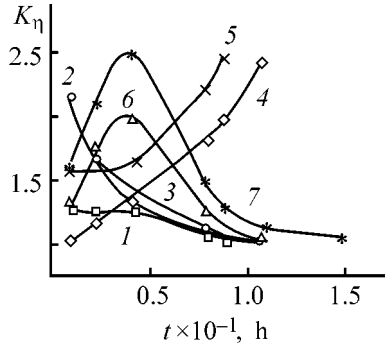

Fig. 3. Structuring factor K_η vs. the time of contact between phases *t*. Concentration (M): HCl: (*1, 4–7*) 10^{-2}, (*2*) 10^{-4}, and (*3*) 10^{-2}; $PrCl_3$: (*1*) 0.025, (*2–4, 6, 7*) 0.075, and (5) 0.05; extracting agent: (*1, 5–7*) 0.2 and (*2–4*) 0.4.

The broadest spectrum of interphase layer states is manifested when varying the salt concentration in the range $(2.5–7.5) \times 10^{-2}$ M $PrCl_3$: approximately Newtonian, Newtonian-dilatant, and weakly structured kinds of systems. In the $PrCl_3$ concentration range $(2.5–5.0) \times 10^{-2}$, slowed-down formation of the interphase layer is observed, taking 8 h. A transition to dilatant systems occurs, as shown by [5, 6], when stabilization is enhanced and nearly monodisperse systems are formed. The maximum layer flowability is observed at a $PrCl_3$ content of 5.0×10^{-2} M. At higher concentrations of the salt, the interphase layers can be regarded as weakly structured systems. Modification of the adsorption layers—"stretching"— causes irreversible disintegration of contacts, upon which the surface layer becomes a Newtonian system as regards its rheological parameters.

Viscosity is a rheological parameter that is the most sensitive to the influence of the factors under study. An estimate was made of the structuring factor K_η in relation to the concentration of the components of the system (Fig. 2).

The concentration dependence of the structuring factor indicates that introduction of acid and extracting agent makes the structuring factor lower. The dominating influence is exerted by hydrochloric acid: the K_η value decreases by nearly two orders of magnitude in the interval 10^{-4}–10^{-2} M HCl 1 h after the formation of the adsorption layer. The extracting agent also strongly affects the K_η value. In the course of time, the steep decrease in K_η slows down and the influence domain is shifted to lower HCl concentrations.

The whole set of results obtained in studying the structuring kinetics at varied content of components reveals three types of the $K_\eta = f(t)$ dependence (Fig. 3): decreasing structuring factor K_η, increasing K_η, and K_η passing through a maximum.

The decrease in K_η is observed in systems with HCl content in the range 10^{-4}–10^{-3} M HCl, with the rate of K_η variation decreasing after 4 h. An antibate run of the dependence is observed at 10^{-2} M HCl. The kinetic curves $K_\eta = f(t)$ pass through a maximum in systems containing 0.075 M $PrCl_3$ and 0.2 NMPA.

The decrease in the strength of interphase layers is presumably favored by increasing degree of dissociation of the extracting agent and the large thickness of the electric double layer at low HCl concentrations. With the content of the acid and, correspondingly, the ionic strength of the solution increasing further, the electric double layer contracts, the thickness of the diffusion layer decreases, the number of contacts between particles grows, and the structuring is enhanced.

Interphase layers possess pronounced elasticity. The degree of elasticity, calculated from kinetic deformation curves, changes with time from 90 to 70% in a system with 10^{-2} M HCl, the time of elastic aftereffect θ_2 in this system is 30–40 s, which exceeds nearly twofold that in other systems, thus confirming the development of a structure.

The obtained results may be helpful in choosing optimal conditions of formation of interphase layers with prescribed rheological properties in order to control the rate of mass exchange in combined processing of raw materials and industrial wastes.

CONCLUSIONS

(1) The interphase layers formed when a salt solution $PrCl_3$–H_2O–HCl is brought in contact with a solution of nonoxymethylphosphonic acid in toluene under the conditions studied can be classed as systems of three types: approximately Newtonian, Newtonian-dilatant, and weakly structured.

(2) From the standpoint of structuring, the optimal conditions of extraction are created in the concentration range 10^{-4}–10^{-3} M HCl, since the interphase layers disintegrate in the course of time.

REFERENCES

1. Dupal, A.Ya., Tarasov, V.V., Yagodin, G.A., and Arutyunyan, V.A., *Kolloid. Zh.*, 1988, vol. 50, no. 2, pp. 355–358.
2. Izmailova, V.N. and Rebinder, P.A., *Strukturoobrazovanie v belkovykh sistemakh* (Structuring in Protein Systems), Moscow: Nauka, 1974.
3. Tarasov, V.V., Yagodin, G.A., and Pichugin, A.A., *Kinetika ekstraktsii neorganicheskikh veshchestv. Itogi nauki i tekhniki. Neorganicheskaya khimiya* (Kinetics of Extraction. Advances of Science and Technology. Inorganic Chemistry), Moscow: VINITI Akad. Nauk SSSR, 1984, vol. 11, pp. 38–39.
4. Merinov, Yu.A., Trapeznikov, A.A., Kartashova, N.A., and Kirillov, A.I., *Kolloid. Zh.*, 1982, vol. 44, no. 6, pp. 1077–1082.
5. Merinov, Yu.A. and Ryabov, V.V., *Kolloid. Zh.*, 1994, vol. 56, no. 2, pp. 214–219.
6. Merinov, Yu.A., Trapeznikov, A.A., Zakharova, Z.S., and Shvarev, E.P., *Kolloid. Zh.*, 1984, vol. 46, no. 5, pp. 917–926.

Russian Journal of Applied Chemistry, Vol. 74, No. 8, 2001, pp. 1400–1402. Translated from Zhurnal Prikladnoi Khimii, Vol. 74, No. 8, 2001, pp. 1362–1364.

BRIEF COMMUNICATIONS

Electrodeposition of Tin–Antomony–Copper Alloy from Sulfate Electrolytes with Organic Additives

G. I. Medvedev and N. A. Makrushin

Novomoskovsk Institute, Mendeleev Russian University of Chemical Technology, Novomoskovsk, Russia

Received April 12, 2001

Abstract—The process of electrodeposition of a tin–antimony–copper alloy from a sulfate electrolyte with organic additives was studied.

A Sn–Sb–Cu alloy has been recommended for improving the antiwear properties of metals [1]. This alloy is presently electrodeposited from a fluoroborate electrolyte with organic additives. As additives of this kind are used β-naphthol and joiner's glue. The process is performed at 25°C and current density of 6 A dm^{-2}, with an alloy of the following composition deposited at the cathode (wt %): Sn 88, Sb 5.1 and Cu 6.3 [2].

The present study is concerned with electrodeposition of a Sn–Sb–Cu alloy from a sulfate electrolyte with the following organic additives: 2-butyne-1,4-diol (35% solution), formalin (37% solution), and syntanol DS-10. The electrodeposition was performed in an electrolyte of composition (g l^{-1}): $SnSO_4$ 20–30, $Sb_2(SO_4)_3$ 0.5–0.8, $CuSO_4 \cdot 5H_2O$ 0.5–1.0, H_2SO_4 100–120, syntanol 1–3; 2-butyne-1,4-diol 1–50; formalin 1–10 ml l^{-1}. Antimony sulfate was prepared by dissolving metallic antimony in hot concentrated sulfuric acid. The investigations were carried out in the temperature range 18–25°C.

Polarization curves were measured in potentiodynamic mode with a P-5827 potentiostat. The alloy was analyzed by the method described in [3]. Coatings 9–30 μm thick were deposited onto copper samples.

A study of the outward appearance of the coatings in relation to current density and nature of organic substances demonstrated that poor-quality coatings are obtained in an electrolyte containing 1 to 10 ml l^{-1} of formalin, or 1 to 50 ml l^{-1} of butynediol, or both. Adding formalin or butynediol to an electrolyte with syntanol also yields matte coatings. At the same time, simultaneous presence in an electrolyte of 1 to 3 g l^{-1} of syntanol, 6 to 8 ml l^{-1} of formalin, and 40 to 45 ml l^{-1} of butynediol gives shining finely crystalline coatings. It should be noted that shining coatings are only obtained with electrolyte stirring. Without stirring, matte coatings are produced. A chemical analysis of the coatings obtained from the electrolytes studied demonstrated that a Sn–Sb–Cu alloy is formed in this case. The influence of the $SnSO_4$, $Sb_2(SO_4)_3$, and $CuSO_4$ concentrations on the alloy composition is illustrated in Table 1. It can be seen that the content of Sb and Cu in the alloy decreases with increasing i_c. Raising the concentration of $Sb_2(SO_4)_3$ and $CuSO_4$ trolyte at constant $SnSO_4$ concentration in the elecmakes higher the Sb and Cu content in the alloy. Raising the concentration of $SnSO_4$ [at constant concentration of $Sb_2(SO_4)_3$ and $CuSO_4$] leads to lower content of Sb and Cu in the alloy.

Table 1 also indicates that for the electrolytes studied the content of Sb in the alloy varies within 2.4–13.5 wt %, and that of Cu, within 3.2–28.1 wt %, at i_c = 1–4 A dm^{-2}. At i_c = 3–4 A dm^{-2} and appropriate $SnSO_4$, $Sb_2(SO_4)_3$, and $CuSO_4$ concentrations, tin babbitts can be obtained of the following compositions (wt %): B-88 brand: Sn 90.7–88.7, Sb 7.3–7.8, Cu 2.5–3.5; B-83 brand: Sn 84.5–81.5, Sb 10.0–12.0, Cu 5.5–6.5 [4].

Changing the H_2SO_4 concentration in the electrolyte from 100 to 120 g l^{-1} has not effected on change the outward appearance of the obtained coatings, but makes the Sb and Cu content of the alloy higher by 1–1.5 wt %, depending on the i_c value. The current efficiency by the alloy (CE) was measured in electrolytes that allow fabrication of shining coatings.

1070-4272/01/7408-1400 $25.00 © 2001 MAIK "Nauka/Interperiodica"

Data on how the $Sb_2(SO_4)_3$ and $CuSO_4$ concentrations affect CE at different i_c are presented in Table 2. It can be seen that the CE by the alloy decreases with increasing i_c. With increasing content of $Sb_2(SO_4)_3$ or $CuSO_4$ in the electrolyte, the CE by the alloy decreases or slightly increases, respectively.

Polarization measurements were performed in electrolytes with organic additives in electrodeposition of Sn, Sb, Cu, and Sn–Sb–Cu. As seen from the figure, the cathodic polarization curve of alloy deposition lies in a more electropositive range of potentials, compared with the curves for Sn, Sb, and Cu, i.e., Sn, Sb, and Cu are deposited into the alloy with depolarization. The depolarization in deposition of metals into the alloy is presumably due to a decrease in their partial energy of alloying [5]. To determine the rates of deposition of separate metals into the alloy, partial current densities of Sn, Sb, and Cu deposition were calculated. The calculation was done by the procedure described in [6] with account of alloy composition at different i_c, the CE by the alloy, and electrochemical equivalents of Sn, Sb, Cu, and Sn–Sb–Cu alloy. As it can be seen from the figure (curves *1*'–*3*'), at i_c = 1–4 A dm^{-2} the rate of Sn deposition into the alloy, i'_{Sn}, is higher than i'_{Sb} and i'_{Cu}, which leads to formation of tin-rich alloys. Comparison of the partial current densities of Sb and Cu deposition shows that the share of antimony in the alloy exceeds that of copper in the case of electrodeposition at i_c = 1–4 A dm^{-2} (see the figure, curves *2*' and *3*').

The investigation performed made it possible to develop a sulfate electrolyte for electrodeposition of the Sn–Sb–Cu alloy. Electrolyte composition: H_2SO_4 20–30, $Sb_2(SO_4)_3$ 0.5–0.8, $CuSO_4 \cdot 5H_2O$ 0.5–1.0, syntanol DS-10 2–3 g l^{-1}; butynediol (35% solution) 40–45, formalin (37% solution) 6–8 ml l^{-1}; i_c = 1–4 A dm^{-2}. Content of metal in the alloy (wt %): antimony 2.4–13.5, copper 3.2–28.1. Current efficiency by the alloy 92–98%.

Electrodeposition is to be performed in the temperature range 18–25°C in an agitated electrolyte. The alloy should be deposited onto copper samples. In depositing the alloy onto steel, the substrate should be preliminarily coated with copper. Anodes of pure tin are to be introduced into the electrolyte with voltage already applied to preclude contact deposition of Sb and Cu onto Sn. After the completion of an experiment, the anodes are to be removed from the electrolyte. The adjustment of the electrolyte with respect to $SnSO_4$, $Sb_2(SO_4)_3$, $CuSO_4$, H_2SO_4, formalin, and butynediol is done in accordance with chemical analysis data [7]. The electrolyte adjustment with respect

Table 1. Effect of $SnSO_4$, $Sb_2(SO_4)_3$, and $CuSO_4$ concentrations and current density on the composition of the Sn–Sb–Cu alloy (Electrolyte composition: H_2SO_4 100, syntanol 2 g l^{-1}; butynediol 40, formalin 6 ml l^{-1})

Concentration of sulfates, g l^{-1}			M	M* content in the alloy (wt %) at indicated current density, A dm^{-2}			
Sn	Sb	Cu		1	2	3	4
20	0.5	0.5	Sb	10.1	9.2	8.5	7.4
			Cu	9.7	6.8	4.3	3.2
20	0.5	0.7	Sb	8.3	7.2	5.7	3.8
			Cu	13.1	9.7	7.5	5.4
20	0.5	1.0	Sb	6.9	5.4	3.7	2.8
			Cu	28.1	23.5	18.4	15.5
20	0.8	0.5	Sb	13.5	12.4	11.5	10.5
			Cu	9.8	7.8	6.5	5.5
20	0.8	0.7	Sb	11.4	9.5	7.3	5.8
			Cu	9.8	8.5	5.3	4.5
20	0.8	1.0	Sb	8.3	7.2	6.4	4.8
			Cu	25.4	18.3	16.1	11.4
30	0.5	0.5	Sb	8.2	7.3	6.1	5.3
			Cu	7.0	4.9	3.5	2.5
30	0.5	0.7	Sb	6.7	5.4	4.3	3.2
			Cu	10.7	8.4	6.5	4.6
30	0.5	1.0	Sb	5.6	4.3	3.2	2.4
			Cu	25.3	18.1	14.3	11.2
30	0.8	0.5	Sb	9.3	8.3	7.3	6.4
			Cu	5.1	3.5	2.5	1.7
30	0.8	0.7	Sb	8.1	6.9	5.2	4.5
			Cu	7.9	5.8	4.5	3.8
30	0.8	1.0	Sb	6.5	5.6	4.8	3.5
			Cu	20.0	15.0	11.1	8.2

* M = Sb, Cu.

Table 2. Effect of $Sb_2(SO_4)_3$ and $CuSO_4$ concentrations and current density on the CE by the Sn–Sb–Cu alloy (Electrolyte composition: $SnSO_4$ 30, H_2SO_4 100, syntanol 2 g l^{-1}; butynediol 40, formalin 6 ml l^{-1}; mechanical stirring)

Concentration, g l^{-1}		CE by alloy (%) at indicated current density, A dm^{-2}			
$Sb_2(SO_4)_3$	$CuSO_4$	1	2	3	4
0.5	0.5	96.1	95.3	93.9	92.1
0.5	0.7	97.2	96.1	95.3	93.4
0.5	1.0	97.8	96.8	96.1	94.3
0.8	0.5	93.5	92.9	91.3	90.3
0.8	0.7	94.4	93.5	92.3	91.4
0.8	1.0	95.5	94.6	93.4	92.3

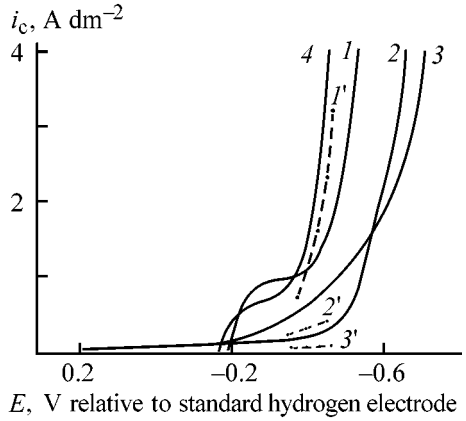

(*1*–*3*) Cathodic and (*1*'–*3*') partial polarization curves of deposition of (*1*, *1*') Sn, (*2*, *2*') Cu, (*3*, *3*') Cu, and (*4*) Sn–Sb–Cu alloy. Electrolyte composition: H_2SO_4 100, syntanol 2 g l^{-1}; butynediol 40, formalin 6 ml l^{-1}; mechanical stirring. (i_c) Current density and (E) potential. Electrolyte + additive (g l^{-1}): (*1*) $SnSO_4$ 30, (*2*) $Sb_2(SO_4)_3$ 0.8, (*3*) $CuSO_4$ 0.5, and (*4*) 1 + 2 + 3.

to syntanol should be made on passing 50 A h l^{-1} of electricity through the electrolyte, by introducing 1 g l^{-1} of additive into the bath.

In contrast to the fluoroborate electrolyte, the developed sulfate electrolyte contains no fluorides, allows deposition in a wider i_c range, and makes it possible to obtain tin babbitts of B-88 and B-83 brands [4].

REFERENCES

1. Bochvar, A.A., *Metallovedenie* (Physical Metallurgy), Moscow: Metallurgiya, 1956.
2. Brenner, A., *Electrodeposition of Alloys. Principles and Practice*, New York: Academie, vol. 11, 1963.
3. Vyacheslavov, P.M., *Novye elektrokhimicheskie pokrytiya* (New Electrochemical Coatings), Leningrad: Lenizdat, 1972.
4. *GOST* (State Standard) *1320–78: Tin and Lead Babbitts. Technical Specifications*, 1978.
5. Bibikov, N.N., Fedot'ev, N.P., and Vyacheslavov, P.M., *Elektroliticheskie splavy* (Electrolytic Alloys), Moscow: Mashgiz, 1962.
6. Kudryavtsev, N.T., *Osnovnye zakonomernosti elektrolitycheskikh protsessov polucheniya metallov i splavov* (Fundamental Aspects of Electrolytic Production of Metals and Alloys), Moscow: Mos. Khim.-Tekhnol. Inst., 1973.
7. Kotik, F.I., *Uskorennyi kontrol' rastvorov i rasplavov: Spravochnik* (Express Analysis of Solutions and Melts), Moscow: Mashinostroenie, 1978.

Russian Journal of Applied Chemistry, Vol. 74, No. 8, 2001, pp. 1403–1404. Translated from Zhurnal Prikladnoi Khimii, Vol. 74, No. 8, 2001, pp. 1365–1366.

BRIEF COMMUNICATIONS

Utilization of *N*,*N*-Dichloro-*p*-chlorobenzenesulfonamide

V. K. Shiryaev

Karpov Institute of Physical Chemistry, State Scientific Center of the Russian Federation, Obninsk Branch, Obninsk, Kaluga oblast, Russia

Received November 23, 2000; in final form, March 2001

Abstract—The kinetic parameters of the reaction of *N*,*N*-dichloro-*p*-chlorobenzenesulfonamide with hydrochloric acid were determined, and the main parameters of the commercial process were estimated.

In the context of elimination of chemical weapons, a problem arises of utilization of agents used for rendering war gases harmless. One of such agents is *N*,*N*-dichloro-*p*-chlorobenzenesulfonamide (**I**, Russian commercial name DTKh-2). Owing to the high reactivity of the N–Cl bond, a promising way of its utilization is replacement of active chlorine atoms by hydrogen atoms with the formation of *p*-chlorobenzenesulfonamide (**II**), which can be used for synthesis of sulfamide drugs, dyes, and effective means for plant protection [1–3]. For this process, a reagent should be chosen that would be cheap and readily available and would give the minimum amount of minor or difficult-to-trap products. One of such agents is hydrochloric acid.

The goals of this study were to determine the kinetic characteristics of the reaction of **I** with HCl and estimate the main parameters of the commercial process.

EXPERIMENTAL

The reaction was performed in a glass vessel equipped with a jacket and a thermometer. The vessel was charged with 10 g of **I**, after which 50 ml of 2 N HCl (equivalent excess 0.34 mmol) was added, and the solution was heated to a required temperature (77 or 92°C) under stirring with a magnetic stirrer.

The experimental conditions should be chosen so as to ensure the most active reaction (i.e., to eliminate possible diffusion hindrance); the optimal temperature and concentration should be determined. Preliminary experiments showed that at a stirrer rotation rate of no less than 700 rpm the conversion is independent of the stirring rate. The suitable reaction temperature is restricted by the thermal stability of the melt of **I** under water (up to 95°C [4]); 2 N HCl is convenient as it is sufficiently concentrated, but does not fume yet. Also, it is known that in more concentrated HCl the solubility of chlorine increases, which complicates its separation.

At appropriate intervals, we sampled the reaction mixture to determine the HCl concentration by alkali titration. Samples of the solid phase were analyzed for available chlorine by iodometric titration [5] after drying to constant weight and dissolution in a 1 : 1 mixture of 1,2-dichloroethane and glacial acetic acid. When calculating the conversion, we took into account the variation of the molecular weight of the solid phase in the course of the reaction.

Amide **II** was identified by the melting point (143 ± 1°C; according to [4], 143–144°C) and IR spectrum. The IR spectra of **I** and **II** in mineral oil were measured on a Specord-80 spectrophotometer. The spectrum of **II** shows two bands (3332 and 3240 cm^{-1}) belonging to antisymmetric and symmetric stretching vibrations of the NH_2 group. Such bands are absent in the spectrum of **I**.

Figure 1 shows as a function of time τ the conversion η with respect to available chlorine (*1*, *3*) and HCl (*2*, *4*), at 92 and 77°C; the conversion with respect to HCl was calculated by the formula

$$\eta = 1 - (C - \bar{C})/(C_0 - \bar{C}), \quad (1)$$

where C, $\bar{C}$, and C_0 are the current, excess, and initial concentrations of HCl, respectively.

It is seen from the figure that the conversion is complete only with respect to dichloramide **I** (with respect to HCl, $\eta < 1$). This means that reversible reaction [4] is shifted to the right (owing to removal

1070-4272/01/7408-1403 $25.00

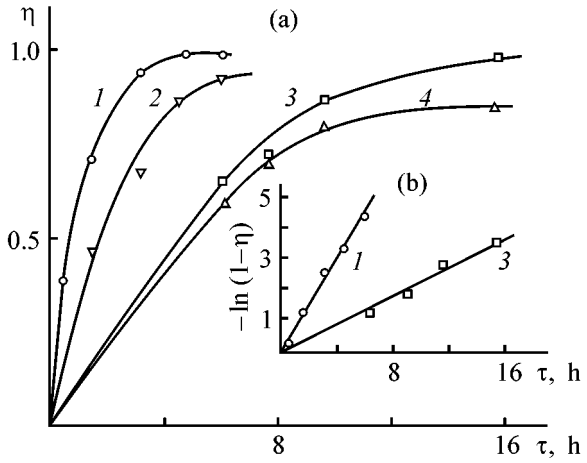

Fig. 1. (a) Conversion η with respect to (*1, 3*) available chlorine and (*2, 4*) HCl vs. time τ; (b) linearization of curves *1* and *3* in the coordinates $\ln(1 - \eta)$–τ. Temperature, °C: (*1, 2*) 92 and (*3, 4*) 77.

of chlorine) and that HCl is not only consumed, but also formed (most probably, by reaction of chlorine with water):

$$p\text{-}ClC_6H_4SO_2NCl_2 + 2HCl \rightleftarrows p\text{-}ClC_6H_4SO_2NH_2 + 2Cl_2. \quad (2)$$

Therefore, the kinetic parameters were calculated only from dependences *1* and *3* linearized in the coordinates $\ln(1 - \eta)$–τ (Fig. 1b).[1] From the slope of the straight lines we determined the rate constants of removal of available chlorine *k*, and from their temperature dependence we estimated the activation energy of the process to be 89.1 kJ mol^{-1}.

Then, in the formula for calculating the conversion of available chlorine

$$\eta = 1 - \exp(-k\tau) \quad (3)$$

the rate constant k (h^{-1}) is

$$k = 3.6 \times 10^{12}\exp(-89\,100/RT). \quad (4)$$

where $R = 8.314$ J mol^{-1} K^{-1}.

[1] Linearization of dependences *1* and *3* in the coordinates of a first-order reaction equation is probably due to the mutual compensation of two opposite processes: acceleration owing to additional formation of HCl and deceleration owing to the reaction reversibility. Therefore, the constants determined in this work should be regarded as apparent.

The experimentally estimated activation energy confirms the assumed kinetic control of the process.

Formulas (3) and (4) allow approximate estimation of the most important parameter of the commercial process, specific output *V* of a reactor of unit volume. If the reaction is performed at 92°C to 98% conversion, then, according to formulas (3) and (4), the residence time will be 5 h; hence, $V = 40$ kg m^{-3} h^{-1}, i.e., the specific output is moderate.

A significant factor in this process is stirring. Calculation of the power of the electric stirrer according to [6] gave a value of 0.65 kW m^{-3}. The heat consumption for heating of the reaction volume (1 m^3) is 0.1 Gcal. It is seen that the power consumption is low. Note also that the released gaseous chlorine can be readily absorbed in a standard alkaline absorber [7] to form a valuable product, hypochlorite.

Thus, the proposed procedure for utilization of I is attractive owing to the low power consumption and low environmental impact.

ACKNOWLEDGMENTS

The author is grateful to V.V. Shapovalov and A.Yu. Ivanov for assistance in the experiments.

REFERENCES

1. Grigorovskii, A.M. and Dykhanov, N.N., *Zh. Prikl. Khim.*, 1957, vol. 30, no. 8, pp. 1215–1230.
2. Stepanov, B.I., *Vvedenie v khimiyu i tekhnologiyu organicheskikh krasitelei* (Introduction to Chemistry and Technology of Organic Dyes), Moscow: Khimiya, 1984.
3. Arbuzov, B.A., *Izv. Akad. Nauk SSSR, Ser. Khim.*, 1990, no. 9, p 2151.
4. *Promyshlennye khlororganicheskie produkty* (Commercial Organochlorine Products), Oshin, L.A., Ed., Moscow: Khimiya, 1978.
5. Charlot, G., *Les methods de la chimie analytique. Analyse quantitative minerale*, Paris: Masson, 1961, 4th ed.
6. Strẹnk F., *Mieszanie i mieszalniki*, Warszawa: Wydawnictwa Naukowo-Techniczne, 1971.
7. Planovskii, A.N. and Gurevich, D.A., *Apparatura promyshlennosti organicheskikh poluproduktov i krasitelei* (Apparatus for Production of Organic Intermediates and Dyes), Moscow: Goskhimizdat, 1961.

Russian Journal of Applied Chemistry, Vol. 74, No. 8, 2001, pp. 1405–1407. Translated from Zhurnal Prikladnoi Khimii, Vol. 74, No. 8, 2001, pp. 1367–1368.

BRIEF COMMUNICATIONS

Use of Ozone in Synthesis of 5-Hydroxy-1,4-naphthoquinone

A. V. Mamchur, L. F. Gorbas, and G. A. Galstyan

Rubezhnoe Branch, East-Ukrainian National University, Rubezhnoe, Lugansk oblast, Ukraine

Received November 28, 2000; in final form, March 2001

Abstract—The feasibility of low-waste production of 5-hydroxy-1,4-naphthoquinone with regeneration of Cr(VI) with the use of ozone was examined. The optimal conditions were found for oxidation of Cr(III) to Cr(VI) in the presence of manganese(II) sulfate.

Oxidation of aromatic compounds with potassium dichromate is widely used in production of food additives, drugs, intermediates, and dyes. Oxidation, as a rule, occurs under mild conditions but is accompanied by the formation of large amounts of highly toxic difficultly utilizable acidic chromium-containing wastewater whose treatment requires large expenditure. A promising way to improve the environmental safety of such processes is to develop low-waste technologies using ozone [1].

In this study, we examined the feasibility of production of 5-hydroxy-1,4-naphthoquinone by a closed-loop process.

5-Hydroxy-1,4-naphthoquinone (juglone) is used as preservative for nonalcoholic drinks. It is prepared in 22.0% yield by the following scheme:

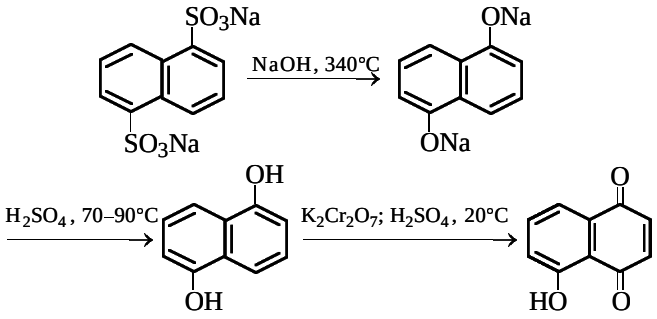

To increase the yield of 5-hydroxy-1,4-naphthoquinone, it is recommended to add 1,5-dihydroxynaphthalene in the oxidation stage without its isolation in the form of an aqueous suspension containing 1,5-dihydroxynaphthalene (1.53 M), Na_2SO_4 (1.72 M), and H_2SO_4 (0.21 M) [2]. The resulting 5-hydroxy-1,4-naphthoquinone is separated, and a mixture of the filtrate with wash water, containing $Cr_2(SO_4)_3$, sulfuric acids, and organic impurities, is subjected to ozonation.

In this study, we examined the possibility of (i) oxidizing Cr(III) to Cr(VI) by ozonation of aqueous acidic solutions of chromium sulfate obtained in filtration of 5-hydroxy-1,4-naphthoquinone suspension and (ii) utilizing the ozonized solutions for oxidation of 1,5-dihydroxynaphthalene.

According to the procedure described in [3], ozonation of wastewater was performed in a 0.4-l glass column equipped with a dispersing glass frit. The column was charged with 50 ml of the solution from the filtration stage, containing 0.127 M $Cr_2(SO_4)_3$, 0.56 M H_2SO_4, and 0.02 M $MnSO_4 \cdot 5H_2O$. The required temperature was adjusted, and an ozone–air mixture was passed through the solution at a rate of 30 l h^{-1} for 8–12 h. The gas mixture contained 1.2–1.6 vol % ozone; the degree of ozone uptake was

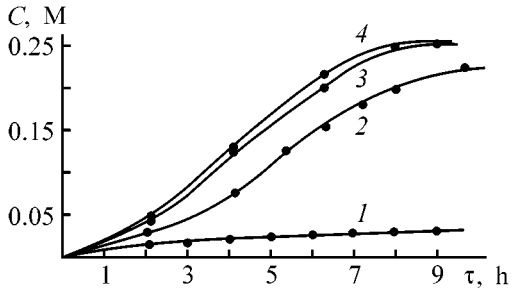

Fig. 1. Influence of the concentration of the $MnSO_4 \cdot 5H_2O$ catalyst on the rate of Cr(VI) accumulation. Solution volume 50 ml, rate of ozone–oxygen mixture feeding 30 l h^{-1}, T = 80°C, $C_{H_2SO_4}$ = 6%, $C_{Cr_2(SO_4)_3}$ = 0.127 M. (*C*) Cr(VI) concentration and (τ) reaction time; the same for Figs. 2 and 3. Catalyst concentration (M): (*1*) 0, (*2*) 0.01, (*3*) 0.02, and (*4*) 0.03.

1070-4272/01/7408-1405 $25.00 © 2001 MAIK "Nauka/Interperiodica"

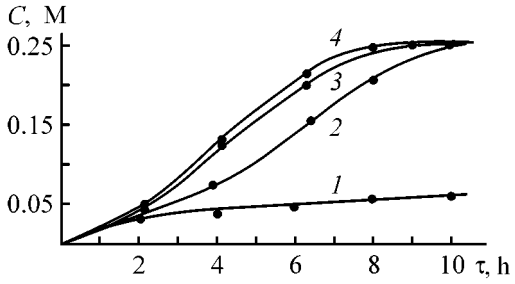

Fig. 2. Influence of temperature on the rate of Cr(VI) accumulation. Solution volume 50 ml, rate of ozone–oxygen mixture feeding 30 l h^{-1}, $C_{H_2SO_4}$ = 6%, $C_{MnSO_4 \cdot 5H_2O}$ = 0.02 M. Temperature, °C: (*1*) 20, (*2*) 60, (*3*) 80, and (*4*) 100.

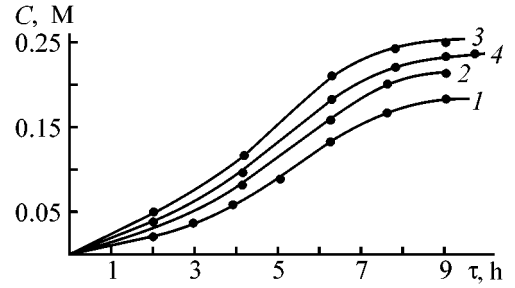

Fig. 3. Influence of the H_2SO_4 concentration on the rate of Cr(VI) accumulation. Solution volume 50 ml, rate of ozone–oxygen mixture feeding 30 l h^{-1}, T = 80°C, $C_{MnSO_4 \cdot 5H_2O}$ = 0.02 M. $C_{H_2SO_4}$, %: (*1*) 3, (*2*) 4.5, (*3*) 6, and (*4*) 9.

90–95% in the first 2–3 h and 40–45% by the end of ozonation; oxidation of Cr(III) to Cr(VI) was quantitative.

To the ozonized solution containing 0.25 M CrO_3 we added oleum to an H_2SO_4 content of 2.38 M. The resulting solution (70 ml, 2.38 M H_2SO_4, 0.25 M CrO_3, 0.02 M $MnSO_4$) was placed in a 0.5-l flask at 20°C, and a suspension of 1,5-dihydroxynaphthalene (75 ml) from the stage of sulfuric acid breakdown of the alkali fusion product was loaded. Oxidation was performed for 4 h, after which the suspension was filtered and the precipitate washed to neutral reaction. The filtrate and wash waters were combined and ozonized.

Results of 1,5-hydroxynaphthalene oxidation in a closed-loop process

Run no.	Cycle	Compensation for $MnSO_4$ loss, M	*A*, %
1	First	0.000	22.18
2	Second	0.000	22.12
3	Third	0.000	18.54
4	Fourth	0.003	23.4
5	Fifth	0.000	22.2
6	Sixth	0.000	19.1
7	Seventh	0.000	17.59
8	Eighth	0.002	23.67
9	Ninth	0.001	22.44

Figure 1 shows that inder the experimental conditions Cr(III) is not noticeably oxidized by ozone (curve *1*). Only in the presence of catalytic amounts of manganese(II) sulfate, transformation of Cr(III) to Cr(VI) is practically quantitative (curves *3, 4*). The following mechanism of the catalytic effect of manganese was suggested [4]:

$$Mn(II) + O_3 \rightarrow Mn(III) + O_3^{\cdot}, \quad (1)$$

$$O_3^{\cdot} + H^+ \rightarrow HO_3^{\cdot}, \quad (2)$$

$$HO_3^{\cdot} \rightarrow HO^{\cdot} + O_2, \quad (3)$$

$$O_3^{\cdot} + H_2O \rightarrow HO^{\cdot} + HO^- + O_2, \quad (4)$$

$$Mn(II) + HO^{\cdot} \rightarrow Mn(III) + HO^-, \quad (5)$$

$$3Mn(III) + Cr(III) \rightarrow 3Mn(II) + Cr(VI). \quad (6)$$

In the presence of manganese(II) sulfate, Cr(III) is oxidized by ozone even at room temperature, but quantitative conversion of Cr(III) to Cr(VI) takes 22–24 h (Fig. 2). Therefore, it is more appropriate to perform oxidation at elevated temperatures. For example, the reaction time is three times shorter at 80°C.

The rate of oxidation of Cr(III) to Cr(VI) also depends on the sulfuric acid concentration in the solution being ozonized, reaching a maximum in 6% acid, which is consistent with the scheme of catalysis.

Thus, oxidation of Cr(III) in chromium(III) sulfate solutions to Cr(VI) is quantitative and fast at 80°C in the presence of 6% H_2SO_4 and catalytic amounts of manganese(II) sulfate.

After being ozonized and concentrated, wastewaters were repeatedly used for oxidation of 1,5-dihydroxynaphthalene (see table). As seen from the table, the yield of 5-hydroxy-1,4-naphthoquinone decreases in run nos. 3 and 7 owing to the loss of $MnSO_4$ in the stage of filtration. Compensation for the catalyst loss in the fourth, eighth, and ninth cycles restores the yield of the target product at a level of 22–24%. The quality of 5-hydroxy-1,4-naphthoquinone met the requirements (mp 145–148°C) in all cases.

CONCLUSION

The feasibility of Cr(VI) regeneration in the course of synthesis of 5-hydroxynaphthoquinone in weakly acidic solutions by ozonation in the presence of catalytic amounts of manganese(II) sulfate was examined. The ozonized chromium and manganese compounds can be used repeatedly for oxidation of 1,5-dihydroxynaphthalene to 5-hydroxy-1,4-naphthoquinone.

REFERENCES

1. Gurevich, D.A., *Pererabotka otkhodov v promyshlennosti poluproduktov i krasitelei* (Waste Processing in Production of Intermediates and Dyes), Moscow: Khimiya, 1980.
2. Mostoslavskii, M.A. and Vlasenko, G.I., *Sposoby polucheniya 5-oksi-1,4-naftokhinona* (Procedures for Synthesis of 5-Hydroxy-1,4-naphthoquinone), Rubezhnoe: Rubezhanskii Filial Nauchno-Issled. Inst. Organicheskikh Poluproduktov i Krasitelei, 1979, no. A-4158.
3. Galstyan, G.A., Yakobi, V.A., and Galstyan, T.M., *Zh. Prikl. Khim.*, 1975, vol. 48, no. 1, pp. 16–19.
4. USSR Inventor's Certificate, no. 1807680.

Russian Journal of Applied Chemistry, Vol. 74, No. 8, 2001, pp. 1408–1409. Translated from Zhurnal Prikladnoi Khimii, Vol. 74, No. 8, 2001, pp. 1369–1370.

BRIEF COMMUNICATIONS

Acetalization of Polyvinyl Alcohol Fiber with Aldehyde-containing Polyvinyl Alcohol Fiber

L. M. Shtyagina, V. M. Vainburg, and L. E. Vinogradova

St. Petersburg State University of Technology and Design, St. Petersburg, Russia

Reveived March 6, 2001; in final form, April 2001

Abstract—A procedure is proposed for preparing polyvinyl alcohol fiber with increased water absorption by acetalization of a freshly formed fiber with dialdehyde-containing polyvinyl alcohol fiber. The fiber characteristics were determined in relation to the acetalization conditions.

One of the ways to render polyvinyl alcohol (PVA) fiber insoluble is acetalization with aldehydes. In the case of acetalization with dialdehydes (glyoxal; maleic, glutaric, phthalic, and isophthalic dialdehydes), the presence of two reactive groups in the molecule makes intermolecular reaction the most probable. However, part of aldehyde groups remain unchanged [1–3]. The resulting fibers exhibit relatively high water-absorbing power and, at the same time, preserve the fibrous structure with active centers required for further modification, i.e., grafting of ionic vinyl polymers and covalent immobilization of proteins, enzymes, and drugs.

Acetalization with low-molecular-weight dialdehydes is performed in aqueous solutions in the presence of mineral salts (sodium sulfate) and sulfuric acid. Salts are added to decrease the swelling of the fiber, and sulfuric acid serves as a process catalyst. Among the negative features of the process are fiber degradation under the action of acid and the necessity for prolonged washing of the fiber to remove excess salt. As a result, the resulting fiber is brittle.

Instead of low-molecular-weight dialdehydes, it is possible to carry out acetalization with freshly formed PVA fiber containing terminal aldehyde groups introduced by periodate oxidation [4]. Oxidation of PVA in solutions to give PVA dialdehyde was performed by Sakurada [5]. With certain corrections, this process can be successfully carried out with freshly formed PVA fiber. Oxidation of freshly formed PVA fiber was performed in aqueous solutions of periodic acid at 20°C and liquid-to-solid ratio of 50. The conditions and results of oxidation are listed in Tables 1 and 2.

The resulting dialdehyde from PVA fiber was used for acetalization of freshly formed PVA fiber. The reaction was performed as follows: Freshly formed PVA fiber was thoroughly mixed with dialdehyde

Table 1. Influence of periodic acid concentration C_a on the characteristics of the dialdehyde from PVA fiber* (reaction time 60 min)

C_a, M	C_{COH}, wt %	SW	W
		%	
0.1	0.67	Gelation	226
0.2	1.48	44	350
0.3	3.12	30	339
0.4	3.60	27	229

* (C_{COH}) Content of free aldehyde groups, (SW) shrinkage of fiber in boiling water, and (W) water absorption [determined in all cases according to GOST (State Standard) 3816–81].

Table 2. Influence of oxidation time on the characteristics of dialdehyde from PVA fiber (periodic acid concentration 0.3 M)

τ, min	C_{COH}, wt %	SW	W
		%	
30	0.06	Gelation	276
60	3.12	30	339
90	3.65	29	326
120	3.92	28	304

1070-4272/01/7408-1408 $25.00 © 2001 MAIK "Nauka/Interperiodica"

from PVA fiber and heated in an oven on a Teflon-coated tray. After the reaction was complete, the characteristics of the fiber were determined (Table 3; the boundary values are given).

With water absorption taken as the main criterion of fiber assessment, we can conclude that, with increasing temperature and concentration of dialdehyde from PVA fiber, the influence of acetalization time decreases considerably (run nos. 1, 8).

Originally, acetalization under these conditions seemed to be improbable. However, there is evidence that the reaction does occur. At the lowest reaction parameters (run no. 1), the fiber undergoes neither dissolution nor gelation on boiling. With increasing reaction parameters, the water absorption steadily increases, suggesting the formation of a fibrous network structure capable of water absorption. In our case this may be due to acetalization.

Fairly good results were obtained when the acetalized PVA fiber was heat-treated with IR radiation. Data on the water absorption of a thus treated fiber are given below:

C_d, %	75	50	33	25	20
W, %	590	780	845	660	510

As expected, at too high dialdehyde concentrations the water absorption decreases because of the high degree of cross-linking.

We failed to prepare by acetalization with low-molecular-weight dialdehydes a fiber with water absorption of 800–900%; the best results obtained, e.g., with maleic dialdehyde were 450–470%.

EXPERIMENTAL

Freshly formed PVA fiber (length 50–60 mm) was placed in flat-bottomed flasks with beads, and the calculated amount of periodic acid was added at 20°C. The mixture was kept for 30–120 min. After that the fiber was thoroughly washed with distilled water (the completeness of acid removal was checked with methyl orange) and dried at 20°C.

The IR treatment was performed at a wavelength of 1.2 μm for 40–80 s; a KG 220-1000-6 lamp was placed at a distance of 80 mm from the fiber surface.

The content of free aldehyde groups was determined by condensation with hydroxylamine hydrochloride [6].

To determine the water absorption, air-dry fiber (weighed with 0.005-g accuracy) was placed in a vessel with distilled water for 0.5 h. Then the sample was placed on a filter paper folded in three layers, covered with three layers of filter paper, and carefully squeezed with constant force. After that the sample was weighed, and the water absorption was calculated.

Table 3. Characteristics of PVA fiber acetylated with dialdehyde from PVA fiber

Run no.	C_d,* %	T, °C	τ, min	C_{COH}, wt %	SW, %	W, %
1	25	50	30	0.79	51	484
2	25	50	150	0.61	50	717
3	25	90	30	0.69	51	671
4	25	90	150	0.58	46	817
5	50	50	30	1.60	58	572
6	50	50	150	1.36	52	732
7	50	90	30	1.24	50	818
8	50	90	150	0.95	38	900

* (C_d) Concentration of dialdehyde from PVA fiber.

The shrinkage in boiling water was determined as follows. Fiber samples (50–60 mm) were measured at 20°C with accuracy of 0.05 cm and placed in a round-bottomed flask equipped with a reflux condenser; then distilled water at 95–98°C was added, and the flask was placed in a boiling water bath for 30 min. After that the fiber was dried at 20°C, and the shrinkage was determined.

CONCLUSION

A procedure was developed for acetalization of freshly formed polyvinyl alcohol fiber with aldehyde-containing polyvinyl alcohol fiber. The water absorption of the resulting fiber considerably exceeds that of the fiber acetalized with low-molecular-weight dialdehyde.

REFERENCES

1. Ushakov, S.N., *Polivinilovyi spirt i ego proizvodnye* (Polyvinyl Alcohol and Its Derivatives) Moscow: Akad. Nauk SSSR, 1960, vol. 1.
2. Maksimov, A.M., Kharit, Ya.A., and Vol'f, L.A., *Zh. Prikl. Khim.*, 1965, vol. 38, no. 7, pp. 1638–1639.
3. JPN Patent Appl. 59-62665.
4. RF Patent 2076157.
5. Sakurada, I., *Kolloid*, 1954, vol. 139, no. 3, pp. 155–163.
6. Kaverzneva, E.D. and Salova, A.S., *Zh. Anal. Khim.*, 1953, vol. 8, no. 6, pp. 365–369.

Russian Journal of Applied Chemistry, Vol. 74, No. 8, 2001, pp. 1410–1412. Translated from Zhurnal Prikladnoi Khimii, Vol. 74, No. 8, 2001, pp. 1371–1373.

BRIEF COMMUNICATIONS

Synthesis of Zinc Dialkyls from Zinc and Alkyl Bromides

I. V. Eremeev, S. M. Danov, V. R. Sakhipov, and A. G. Skudin

Dzerzhinsk Branch, Nizhni Novgorod State Technical University, Dzerzhinsk, Nizhni Novgorod oblast, Russia

Received March 22, 2001

Abstract—Zinc dialkyls with linear radicals were prepared from zinc and alkyl bromides in the presence of stimulating systems based on a transition metal derivative and an organometallic compound capable of reducing the transition metal derivative under the reaction conditions.

Zinc alkyl compounds are widely used in laboratory studies and industry as starting compounds in inorganic, organic, and organometallic synthesis and as catalysts for polymerization of unsaturated compounds [1–7]. However, one of the major application fields of alkyl derivatives of nontransition metals and zinc is preparation of materials for electronics [7–22].

A procedure for preparing diethylzinc in 92% yield, involving reaction of zinc powder with ethyl bromide, was proposed in [23]:

$$Zn + AlkBr \rightarrow AlkZnBr, \quad (1)$$

$$2AlkZnBr \rightarrow Alk_2Zn + ZnBr_2. \quad (2)$$

Stage (1) is performed in the liquid phase under atmospheric pressure without solvent at 38–45°C in the presence of catalytic amounts of stimulating systems whose necessary components are a transition metal derivative and an organometallic compound (OMC). The latter should be capable of reducing the transition metal derivative under the reaction conditions. Disproportionation of alkylzinc bromide (2) with simultaneous distillation of dialkylzinc in a vacuum is performed in the same vessel at elevated temperature under isothermal conditions, or with a more sophisticated temperature schedule. This procedure eliminates the labor-consuming procedure for preparing a zinc–copper couple, the use of relatively expensive ethyl iodide, and the uncontrollable induction period in the first stage. Among a broad range of tested stimulating systems based on a transition metal derivative and an OMC (some of them are listed in patent [23]), the system copper(I) iodide–ethylzinc bromide showed high performance in synthesis of diethylzinc. However, attempts to use this system for preparing dipropyl- and dibutylzinc resulted in low yields of zinc dialkyls. Therefore, we carried out a study aimed at extending the synthetic potential of the procedure for preparing zinc dialkyls.

It is known [2, 3] that organic halides can react with OMCs. This is a complex process, and its mechanism is not still fully understood; the reactions are often accompanied by exchange, hydride reduction, and dehydrohalogenation of the organic halide. As a result, a complex mixture of products is usually formed. The reaction catalysts are commonly transition metals or their derivatives. Hence, it could be expected that the most probable reasons for low yields of dipropyl- and dibutylzinc in the preliminary experiments are side reactions of the initial alkyl bromides with the forming mono- and diorgano derivatives of zinc, yielding a mixture of hydrocarbons and zinc bromide. The other possible side reactions [reduction of copper(I) iodide with organozinc compounds or their thermal decomposition] can hardly be responsible for the poor yields of zinc dialkyls. Indeed, even complete reduction of the catalytic amounts of copper(I) iodide as a component of the stimulating system can decrease the yield of zinc dialkyl only to approximately 93%. The insignificant effect of thermal decomposition of zinc dialkyls on their synthesis follows, e.g., from the approximately equal yields of diethyl-, dipropyl-, and dibutylzinc (78–86%) in their synthesis by Noller's procedure from a zinc–copper couple and equimolar mixtures of the corresponding alkyl iodides and alkyl bromides under conditions similar to those of our experiments [1]. If this is the case, then, if unchanged alkyl bromide or a solid residue containing a transition metal and its derivative is removed from the reaction mixture before thermal disproportionation of alkylzinc bromide, the

1070-4272/01/7408-1410 $25.00 © 2001 MAIK "Nauka/Interperiodica"

selectivity of zinc dialkyl synthesis must increase considerably.

Our experiments showed that the selectivity of synthesis of alkylzinc bromides at $T \le 50°C$ is very high: The reaction mixtures contained only unchanged initial compounds (zinc and alkyl bromide) and alkylzinc bromide. The release of gaseous products was monitored with a gas meter connected to the reactor, and was insignificant. However, the conversion of alkyl halides in 4–8 h was as low as 50–80%. Subsequent thermal disproportionation of alkylzinc bromides with simultaneous vacuum distillation of zinc dialkyls from such reaction mixtures resulted in low yields of zinc dialkyls. The results of two of such experiments (nos. 1 and 3) are listed in the table. Removal of unchanged alkyl bromides from the reaction mixtures by vacuum distillation at temperatures below 50°C prior to thermal decomposition noticeably increased the yield of zinc dialkyls. Also, we found that, in the absence of other components of the reaction mixtures, the alkyl bromides in hand do not react with the corresponding organozinc compounds under the experimental conditions. Therefore, as expected, when the solid residue was removed from the reaction mixture prior to disproportionation, the yield of zinc dialkyls also increased (see table, run nos. 2 and 4). Since 5–15% of the formed organozinc compounds always remains in the reactor after the final stage of synthesis, our results show that, in the absence of alkyl bromides or substances catalyzing reaction of organic halides with OMC, disproportionation of alkylzinc bromides into zinc dialkyls is highly selective.

Thus, our study supports the above assumption concerning the reasons for the low yield of zinc dialkyls in their synthesis from zinc and alkyl halides in the presence of stimulating systems based on a transition metal derivative and an OMC. It should be noted that, to prepare high-purity zinc dialkyls, it is appropriate to use alkylzinc bromide formed in the first stage or the corresponding zinc dialkyl as the organometallic component of the stimulating system.

EXPERIMENTAL

In our experiments, we used PTs-10 zinc powder [TU (Technical Specifications) 48-4015-1/0–81] and pure grade copper(I) iodide (TU 6-09-02-437–87). Pure grade alkyl bromides were dried over calcium chloride and distilled before use. Ethylzinc bromide was prepared from zinc powder and ethyl bromide in the presence of the copper(I) iodide–ethylzinc bromide stimulating system, as described in [23]. The resulting solution of ethylzinc bromide in ethyl bromide was separated from unchanged zinc, and excess ethyl bromide was distilled off in a vacuum. The remaining crystalline ethylzinc bromide was dissolved in an appropriate alkylbromide for subsequent use as a component of the stimulating system.

Synthesis of zinc dialkyls from zinc and alkyl bromides in the presence of the copper(I) iodide–ethylzinc bromide stimulating system

Run no.	Alk_2Zn	τ,* h	Yield, %	
			AlkZnBr by analysis	Alk_2Zn
1	Pr_2Zn	7	75	30
2	Pr_2Zn	7	81	68**
3	Bu_2Zn	4	52	0
4	Bu_2Zn	8	78	66**

* (τ) Time of AlkZnBr synthesis.

** The solid residue was removed from the reaction mixture prior to disproportionation of alkylzinc bromide.

Synthesis of zinc dialkyls. A mixture of 8.76 g (0.046 mol) of copper(I) iodide and 50 g (0.765 mol) of zinc powder was vacuum-treated for 10 min, dry oxygen-free argon was passed, and alkyl bromide and a solution of ethylzinc bromide in the corresponding alkyl bromide were added. The total amount of alkyl bromide and the amount of ethylzinc bromide in the mixture were 0.66 and 0.04–0.05 mol, respectively. In the process, the reactor was protected from atmospheric moisture. Then the system was connected to a gas meter. The first stage was performed with stirring at 50°C. Then the stirring was stopped, the mixture was cooled to room temperature, and thermal disproportionation of alkylzinc bromide formed in the first stage was performed, with simultaneous vacuum distillation of zinc dialkyl. In certain experiments unchanged alkyl bromide was distilled off in a vacuum prior to disproportionation, or unchanged zinc was separated by decanting and washed with several portions of appropriate alkyl bromide. The liquid phase was separated by decanting after each washing. After combining all the liquid phases from washings and the liquid fraction of the reaction mixture, alkyl bromide was distilled off in a vacuum, and alkylzinc bromide was subjected to thermal disproportionation. The constants of the resulting dipropylzinc and dibutylzinc agreed with published data [1]. The yield of zinc dialkyls was determined from the amount of the isolated reaction products. The content of alkyl bromide in the reaction mixture was determined by GLC

on a Tsvet-110 chromatograph after hydrolysis of alkylzinc bromide and extraction of alkyl bromide with toluene [24]. The yield of alkylzinc bromide in the first stage of the synthesis was evaluated from the content of zinc ions (EDTA titration [25]) after hydrolysis of alkylzinc bromide in a solid particle-free sample of the reaction mixture and dissolution of the resulting zinc hydroxide precipitate in aqueous HCl.

CONCLUSIONS

(1) Stimulating systems based on a transition metal derivative and an organometallic compound allow synthesis of zinc dialkyls with linear radicals in high yields from zinc and alkyl halides.

(2) In thermal disproportionation of alkylzinc halides, the reaction mixture should not contain significant amounts of the initial alkyl halides.

REFERENCES

1. *Metody elementoorganicheskoi khimii. Tsink, kadmii* (Methods of Organometallic Chemistry. Zinc, Cadmium), Nesmeyanov, A.N. and Kocheshkov, K.A., Eds., Moscow: Nauka, 1964.
2. Reutov, O.A., Beletskaya, I.P., Artamkina, G.A., and Kashin, A.N., *Reaktsii metalloorganicheskikh soedinenii kak redoks-protsessy* (Reactions of Organometallic Compounds as Redox Processes), Moscow: Nauka, 1981.
3. *Comprehensive Organic Chemistry. The Synthesis and Reactions of Organic Compounds*, Barton, D. and Ollis, W.D., Eds., Oxford: Pergamon, 1979.
4. Collman, J.P., Hegedus, L.S., Norton, J.R., and Finke, R.G., *Principles and Applications of Organotransition Metal Chemistry*, Mill Valley, California, University Science Books, 1987.
5. Erdik, E., *Tetrahedron*, 1987, vol. 43, no. 10, pp. 2203–2212.
6. Bumagin, N.A. and Beletskaya, I.P., *Usp. Khim.*, 1990, vol. 59, no. 12, pp. 2003–2020.
7. Harwuud, J.H., *(Industrial Applications of the Organometallic Compounds*, A Literature Survey, London: Chapman & Hall, 1963.
8. Razuvaev, G.A., Gribov, B.G., Domrachev, G.A., and Salamatin, B.A., *Metalloorganicheskie soedineniya v elektronike* (Organometallic Compounds in Electronics), Moscow: Nauka, 1972.
9. Gribov, B.G., *Usp. Khim.*, 1973, vol. 42, no. 11, pp. 1921–1942.
10. Gribov, B.G., *Gidridy, galidy i metalloorganicheskie soedineniya osoboi chistoty* (Ultrapure Hydrides, Halides, and Organometallic Compounds), Devyatykh, G.G., Ed., Moscow: Nauka, 1976, pp. 97–109.
11. Domrachev, G.A. and Suvorova, O.N., *Usp. Khim.*, 1980, vol. 49, no. 9, pp. 1671–1686.
12. *Osazhdenie plenok i pokrytii razlozheniem metalloorganicheskikh soedinenii* (Deposition of Films and Coatings by Decomposition of Organometallic Compounds), Razuvaev, G.A., Ed., Moscow: Nauka, 1981.
13. Devyatykh, G.G. and Churbanov, M.F., *Zh. Vses. Khim. O–va. im. D.I. Mendeleeva*, 1984, vol. 29, no. 6, pp. 6–14.
14. Efremov, A.A., Blyum, G.Z., and Grinberg, E.E., *Zh. Vses. Khim. O–va. im. D.I. Mendeleeva*, 1984, vol. 29, no. 6, pp. 37–45.
15. Zhuk, B.V., *Usp. Khim.*, 1985, vol. 54, no. 8, pp. 1312–1334.
16. *Primenenie metalloorganicheskikh soedinenii dlya polucheniya neorganicheskikh pokrytii i materialov* (Use of Organometallic Compounds for Preparing Inorganic Coatings and Materials), Razuvaev, G.A., Ed., Moscow: Nauka, 1986.
17. Dyagileva, L.M. and Aleksandrova, Yu.A., *Usp. Khim.*, 1986, vol. 55, no. 11, pp. 1854–1866.
18. Efremov, A.A., Fedorov, V.A., and Grinberg, E.E., *Vysokochist. Veshch.*, 1988, no. 3, pp. 5–43.
19. Bregadze, V.I., Golubinskaya, L.M., and Usyatinskii, A.Ya., *Metalloorg. Khim.*, 1988, vol. 1, no. 3, pp. 517–533.
20. Gas'kov, A.M., *Zh. Vses. Khim. O–va. im. D.I. Mendeleeva*, 1991, vol. 36, no. 3, pp. 32–38.
21. Vorotyntsev, V.M., *Vysokochist. Veshch.*, 1993, no. 2, pp. 21–33.
22. Yablokov, V.A. and Yablokova, N.V., *Usp. Khim.*, 1995, vol. 64, no. 10, pp. 1017–1031.
23. RF Patent 1 775 403.
24. Grishnova, N.D., Moiseev, A.N., Salganskii, Yu.M., and Sorochkina, T.G., *Zh. Anal. Khim.*, 1986, vol. 41, no. 2, pp. 328–335.
25. Charlot, G., *Les methods de la chimie analytique. Analyse quantitative minerale*, Paris: Masson, 1961, 4th ed.

Russian Journal of Applied Chemistry, Vol. 74, No. 8, 2001, pp. 1413–1414. Translated from Zhurnal Prikladnoi Khimii, Vol. 74, No. 8, 2001, pp. 1374–1375.

BRIEF COMMUNICATIONS

Copolymerization of Vinyl Chloride with 1-Vinyl-1,2,4-triazole

O. V. Lebedeva, N. S. Shaglaeva, G. A. Pirogova, S. V. Fedorov, and A. K. Khaliullin

Irkutsk Institute of Chemistry, Siberian Division, Russian Academy of Sciences, Irkutsk, Russia

Received April 16, 2001

Abstract—Copolymerization of vinyl chloride with 1-vinyl-1,2,4-triazole was studied. The copolymerization constants were determined. The chemical structure of the resulting copolymers was studied by NMR and IR spectroscopy.

Polyvinyl chloride is one of the most important and widely used polymers. To modify the properties of polyvinyl chloride (solubility, processability, softening point, physicochemical properties), vinyl chloride is copolymerized with other monomers.

Previously, we have studied radical copolymerization of vinyl chloride (VC) with *N*-vinyl-4,5,6,7-tetrahydroindole [1] and with 2-methyl-5-vinylpyridine and showed that the formation of macromolecules is accompanied by dehydrochlorination, with the degree of dehydrochlorination depending on the nature of the comonomer.

In this work, we studied radical copolymerization of VC with 1-vinyl-1,2,4-triazole (VT). Preliminary experiments showed that, as expected, the degree of dehydrochlorination is lower when copolymerization is performed in solvents. Therefore, experiments on copolymerization of VC with VT were performed in solutions of *N*-methyl-2-pyrrolidone and dimethylformamide (DMF). DMF appeared to be the most suitable solvent, since double-reprecipitated copolymers prepared in *N*-methyl-2-pyrrolidone contained, according to the ^{13}C NMR spectra, fragments originating from reaction of *N*-methyl-2-pyrrolidone with HCl [2]. The copolymers prepared in DMF showed no such signals. Therefore, all further experiments on copolymerization of VC with VT were performed in DMF.

Copolymers are formed at any initial monomer ratio in the examined range (see table). Copolymerization of VC with VT yielded powdered products readily soluble in DMF, dimethyl sulfoxide, and *N*-methyl-2-pyrrolidone.

The VT units introduced into the copolymer affect its solubility: The range of solvents dissolving the copolymers extends as compared with polyvinyl chloride. Hence, new possibilities arise for processing these copolymers.

With increasing content of VT in the initial mixture, the yield of the product and its intrinsic viscosity grow.

For the system VC–VT, we determined the copolymerization constants. Their values, $r_{VC} = 0.30 \pm 0.02$ and $r_{VT} = 1.24 \pm 0.02$, indicate that the rate constant of the reaction of VC radical with VT monomer is much higher than the rate constant of its reaction with VC.

The IR spectra of the copolymers contain no absorption bands characteristic of the *N*-vinyl group (960, 1680 cm^{-1}), whereas the vibration bands of the triazole ring are preserved (1030, 1210, 1560 cm^{-1}), and a band appears at 1640 cm^{-1}, characteristic of

Copolymerization of VC with VT ([AIBN] = 1.57 wt %, 60°C)

VT/VC monomer molar ratio	VT/VC molar ratio in copolymer, calculated from content of		Yield, %	[η], dl g^{-1}
	N	Cl		
20/80	24.91/75.09	28.33/73.67	5.01	0.07
40/60	58.69/41.39	62.77/39.29	6.28	0.09
50/50	65.33/33.67	71.20/30.80	7.32	0.12
60/40	74.47/25.53	79.48/22.52	8.48	0.58
80/20	84.76/15.24	90.73/12.94	9.16	0.75

1070-4272/01/7408-1413 $25.00 © 2001 MAIK "Nauka/Interperiodica"

the CH=CH bonds. The ^{13}C NMR spectrum of the VT–VC copolymer contains broadened resonance signals corresponding to the carbon atoms of the triazole rings (151.91 and 144.38 ppm), a group of signals of the vinyl fragment CH=CH (127.92–127.58 ppm), and signals from the >CHCl carbon atoms (58.49–56.67 ppm), NCH group (54.6 ppm), and $>CH_2$ groups (45.4 – 41.9 ppm).

The CH=CH fragments in the copolymer originate from dehydrochlorination of VC.

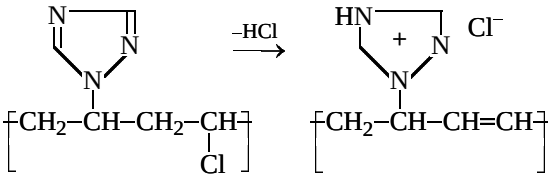

The fact that signals from the CH=CH fragment appear in the ^{13}C NMR spectra directly confirms the occurrence of dehydrochlorination in the course of copolymerization. From the ^{13}C NMR spectra, we calculated the degree of dehydrochlorination Z

$$Z = a/A,$$

where a is the amount of CH=CH groups and A is the total amount of vinyl chloride and CH=CH groups.

Also, the degree of dehydrochlorination was calculated from the difference between the content of VC units in the copolymer, calculated from the chlorine content and from the content of VT units (evaluated from the nitrogen content). These two independent procedures for determining Z give reasonably consistent results. With increasing content of VT in the initial mixture, the degree of dehydrochlorination grows, reaching a maximum (15%) at a VT content of 80 mol %.

Thus, copolymerization of VC with VT in DMF occurs with insignificant dehydrochlorination. In contrast to polyvinyl chloride, the resulting copolymers are soluble in DMF and *N*-methyl-2-pyrrolidone, which extends the possibilities of processing these materials.

EXPERIMENTAL

Copolymerization of the monomers was performed in sealed ampules at 60°C in the presence of azobis(isobutyronitrile) in an argon atmosphere. The reaction mixture was dissolved in DMF, and the copolymer was precipitated with acetone. The copolymers were reprecipitated from solution into acetone and vacuum-dried to constant weight. The intrinsic viscosity was determined in DMF at 20°C by the dilution procedure.

The relative activity constants were calculated by the Fineman–Ross and Kelen–Tudos procedures [3], using the program developed by G.I. Deryabina and the Mortimer–Tidwell experimental design method. In calculations we used the results of experiments performed to no more than 10% conversion. The IR spectra were taken on a Specord 75-IR spectrometer from KBr pellets or mulls in mineral oil.

The proton-noise-decoupled ^{13}C NMR spectra of copolymer samples were recorded on a Varian VXR-500S spectrometer (125.5 MHz) from DMSO-d_6 solutions, with the relaxation delay of 2.5 s and 90° pulse. Chromium tris(acetylacetonate) (0.02 M) was used as relaxant.

The molar ratios of the copolymer components and impurities were calculated by a common procedure: The fraction of a single carbon atom in VT, q_{VT}, was taken equal to one carbon atom, which corresponds to 1 mol of VT, M_{VT}. The numbers of moles of the other components were calculated by the formula

$$M_X = q_X/q_{VT},$$

where q_X is the fraction of the carbon atom in component X; $q_X = I_X/I_{tot}$ (I_X and I_{tot} are the integral intensity of the signal from atom X and the total integral intensity, respectively).

CONCLUSIONS

(1) Radical copolymerization of vinyl chloride with 1-vinyl-1,2,4-triazole is accompanied by insignificant dehydrochlorination; the second comonomer appears to be more reactive.

(2) Introduction of 1-vinyl-1,2,4-triazole units into the copolymer improves the solubility of the polymers in organic solvents.

REFERENCES

1. Shaglaeva, N.S., Mikhaleva, A.I., Lebedeva, O.V., *et al.*, *Izv. Ross. Akad. Nauk, Ser. Khim.*, 1997, no. 12, p. 2267.
2. Marr, D.Y., *Org. Magn. Reson.*, 1980, vol. 13, no. 2, pp. 28–32.
3. Kennedy, K.J.P., Kelen, T., and Tudos, F., *J. Polym. Sci., Polym. Chem. Ed.*, 1975, vol. 13, no. 10, pp. 2277–2289.

Russian Journal of Applied Chemistry, Vol. 74, No. 8, 2001, pp. 1415–1417. Translated from Zhurnal Prikladnoi Khimii, Vol. 74, No. 8, 2001, pp. 1376–1378.

BRIEF COMMUNICATIONS

Synthesis of Glycol Ethers and Their Use for Intensification of Oil Recovery

N. N. Lebedeva, V. V. Mazaev, and N. Yu. Tret'yakov

Tyumen State University, Tyumen, Russia

Received March 27, 2001

Abstract—Monoalkyl ethers of ethylene and triethylene glycols were prepared and tested for intensification of oil recovery. The features of oil displacement with aqueous solutions of glycol ethers from bulk models of strata and the effect of glycol ethers on acid treatment of oil-saturated samples were examined. A correlation between the structure of ether and its performance was revealed. The interphase tension at the boundary between the aqueous solution of the glycol ether and kerosene was determined.

Glycol ethers are widely used as solvents for water–hydrocarbon systems owing to their good compatibility with the aqueous and organic phases, high hydrolytic stability, and low toxicity. In the oil recovery practice, ethylene glycol monobutyl ether (EGMBE) is used as a component of complex acid formulations for treatment of critical zones of oil strata [1]. It is known that dipropylene glycol ethers, e.g., butyl ether used in paint-and-varnish industry [2] or methyl ether used for dissolving oil components [3], surpass cellosolves in performance owing to the higher washing-out power with respect to aliphatic and aromatic hydrocarbons.

The goal of this study was to prepare a series of glycol monoalkyl ethers differing in length of the hydrocarbon radical and number of oxyalkyl units and to choose the best ethers for intensification of oil recovery.

In industry, glycol ethers are prepared by oxyalkylation of alcohols. For their laboratory synthesis, we chose another procedure involving reaction of alkyl halide with glycol in aqueous dioxane in the presence of solid alkali, followed by isolation of the product by vacuum distillation [4]. We prepared ethylene glycol monoheptyl ether (EGMHE) and triethylene glycol monomethyl, monopentyl, and monoheptyl ethers (TEGMME, TEGMPE, and TEGMHE, respectively). Their structures were proved by refractometry and IR spectroscopy (see table).

The synthesized glycol ethers, EGMBE, and ethylene glycol (EG) were tested as additives to acid solutions used in oil recovery for treatment of critical zones of the strata with the aim to improve their filtration properties and capacity. Glycol ethers decrease the interphase tension between oil and water and facilitate removal of fine particles wetted with oil and restoration of the hydrophilic properties of the surface owing to the washing-out effect. The effect of glycol ethers on acid treatment was studied under laboratory conditions using a model of carbonate rock saturated with oil and water. To a weighed portion of the rock we added a solution of HCl and glycol ether and determined the rate of CO_2 evolution. The rate of breakdown of the carbonate rock with HCl (ml CO_2/s) in the presence of various ethers was as follows: no ether, 0.3; EG, 0.26; EGMBE, 0.50; EGMHE, 0.10; TEGMME, 0.37; TEGMPE, 0.56; and TEGMHE, 0.46 (0.01 g of $CaCO_3$, 0.1–0.2 mm fraction, 5 ml of 3% HCl, 10 wt % of glycol ether).

These results show that, in the presence of glycol ethers, the rate of reaction of the acid with the rock

Selected propereties of glycol ethers*

Glycol ether	Yield, %	Published data [5]		Data of this work	
		bp, °C / *P*, mm Hg	n_D^{20}	bp, °C / *P*, mm Hg	n_D^{20}
EGMHE	27	92/3	1.4325	90/3	1.4362
TEGMME	15	122/10	1.4380	95/3	1.4376
TEGMPE	27.5	–	1.4410	200/3	1.4413
TEGMHE	26	–	1.4450	250/3	1.4450

* IR data, cm^{-1}: C–O–C 1360, –OH 3800–3400.

1070-4272/01/7408-1415 $25.00 © 2001 MAIK "Nauka/Interperiodica"

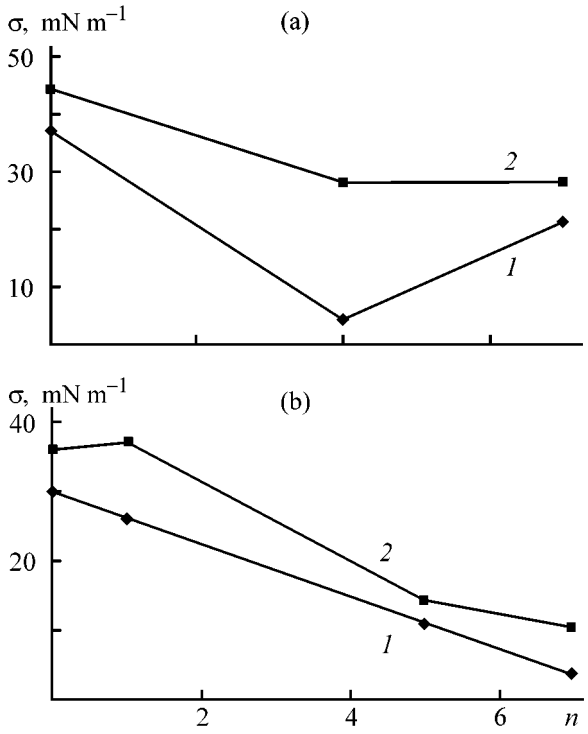

Fig. 1. Influence of the structure of (a) ethylene glycol and (b) triethylene glycol ethers on the interphase tension σ at the water–kerosene boundary. (*n*) Number of atoms in the alkyl group of glycol ether. Concentration of glycol ether, wt %: (*1*) 1 and (*2*) 10.

increases. The performance of an acid formulation depends on the structure of ether, namely, on the length of the hydrocarbon radical and the number of oxyethyl units. The breakdown of the carbonate rock was the fastest with ethers containing 4–5 carbon atoms in the alkyl group. Apparently, glycol ethers with short alkyl group dissolve oil to a lesser extent, and ethers with long alkyl group are worse miscible with the aqueous phase. Owing to their better compatibility with water and oil, triethylene glycol ethers accelerate breakdown of the oil-saturated model rock at any length of the alkyl radical.

Similar trends were obtained in studying the oil-displacing power of ether. A special column modeling an oil stratum was charged with crushed rock and brought to required temperature, after which water, oil, and again water were successively fed until the oil displacement stopped (at a constant rate of filtration of the liquids). From the volume of displaced oil we calculated the oil displacement factor K_o equal to the fraction of oil displaced from the column with water. After that, an aqueous solution of glycol ether was fed. Below are given the values ΔK_o by which the oil displacement factor increased on adding glycol (concentration of glycol ether 10 wt %; reagent volume 15% of the pore volume):

Glycol ether	EGMBE	EGMHE	TEGMME	TEGMPE	TEGMHE
ΔK_o, %	18.0	11.8	2.2	24.8	7.0

It is seen that TEGMPE and EGMBE show the best performance. Apparently, 4–5 carbon atoms in the alkyl group are sufficient to ensure the maximal compatibility of a solution being pumped-in and residual oil in the stratum model and its efficient displacement. With longer alkyl radicals, the solubility of an ether in oil becomes the prevailing factor, which results in retention of oil in the stratum model. On the whole, triethylene glycol ethers show a higher oil-displacing power owing to higher hydrophilicity.

The performance of formulations used for oil recovery is usually associated with a decrease in the interphase tension at the aqueous phase–oil boundary. Using a stalagmometer, we determined the interphase tension at the boundary between aqueous solution of glycol and kerosene. As seen from Figs. 1a and 1b, the interphase tension decreases on adding glycol ethers to water (1 or 10%). However, there is no unambiguous correlation between the interphase tension and performance of ethers in intensification of oil recovery. For example, TEGMHE considerably decreases the interphase tension but shows poor performance in oil displacement. In acid treatment, it is adsorbed on the particle surface and makes it more hydrophobic, decreasing the efficiency of reaction of acid with the rock; in oil displacement, it readily mixes with residual oil, is adsorbed on the rock, and is not displaced by liquid. The minimal interphase tension is observed with a 10% solution of EGMBE, though it is not the best oil-displacing agent. Thus, along with interphase tension, some other factors may be significant, e.g., compatibility of ethers with the aqueous and organic phases.

CONCLUSIONS

(1) Ethylene glycol monoheptyl ether and triethylene glycol monomethyl, monopentyl, and monoheptyl ethers were prepared and tested for intensification of oil recovery.

(2) Glycol ethers accelerate breakdown of oil-saturated calcium carbonate with acid formulations owing to washing-out of oil. The breakdown rate depends on the structure of an ether. The highest performance is shown by glycols containing 4–5 carbon atoms in the alkyl group.

(3) Aqueous solutions of glycol ethers make considerably higher the oil displacement factor and can be used for secondary recovery of oil. Ethylene glycol monobutyl ether and triethylene glycol monopentyl ether raise the oil displacement factor to the greatest extent.

(4) High performance of these ethers in acid treatments and oil displacement is due not only to a decrease in the interphase tension at the water–oil boundary but also to compatibility with the aqueous and oil phases.

REFERENCES

1. Cristian, M., Socol, S., and Constantinescu, A., *Creşterea Productivitatii şi Receptivitătii Sondelor*, Bucuresti: Editura Technică, 1982.
2. Vegh, L. and Spauwen, J., *Spec. Chem.*, 1987, vol. 7, no. 1, pp. 12–14.
3. Spauwen, J., *Oil Colour Chem. Assoc.*, 1988, vol. 71, no. 2, pp. 47–49.
4. USSR Inventor's Certificate, no. 1447809.
5. *Fluka Chemie AG, Buchs* (Switzerland): Sigma–Aldrich, 1997, pp. 675–676.

Russian Journal of Applied Chemistry, Vol. 74, No. 8, 2001, pp. 1418–1421. Translated from Zhurnal Prikladnoi Khimii, Vol. 74, No. 8, 2001, pp. 1378–1381.

BRIEF COMMUNICATIONS

Activity of Nonionic Surfactants

B. R. Fakhrutdinov, O. A. Varnavskaya, L. K. Khvatova, N. A. Lebedev, I. N. Diyarov, and R. Z. Fakhrutdinov

Kazan State Technological University, Kazan, Tatarstan, Russia

Received September 25, 2000; in final form, March 2001

Abstract—The surface activity of block copolymers of ethylene and propylene oxides, based on ethylenediamine, mono(ethylene glycol), and triethanolamine, was studied. Adsorption characteristics of the investigated compounds at the water–air interface are estimated.

At present, nonionic surfactants are widely used as emulsifiers, stabilizers of dispersions, corrosion inhibitors, antistatic agents, and demulsifiers [1, 2].

Both in Russia and abroad, studies of surfactants as demulsifiers revealed that the highest demulsifying effect is provided by nonionic surfactants. Furthermore, it is known that high-molecular-weight compounds of this type are more efficient than low-molecular-weight compounds [3]. However, their adsorption characteristics at the water–air interface have not been studied adequately. Therefore, we studied in this work the surface activity of newly synthesized nonionic surfactants, block copolymers of ethylene oxide (EO) and propylene oxide (PO), based on ethylenediamine (EDA), mono(ethylene glycol) (MEG), and triethanolamine (TEA), and estimated the adsorption characteristics of the investigated compounds at the water–air interface.

In the experiments, we used nonionic surfactants based on EDA (sample nos. 1–9), MEG (sample nos. 10–16), and TEA (sample nos. 17, 18), with different molecular weights M and PO/EO ratios or having the same M, but different degrees of oxyethylation. All the surfactants were developed at the NIInefteprom khim Joint-Stock Company.

EXPERIMENTAL

The surface tension of aqueous solutions of the nonionic surfactants at the water–air interface was determined by the anchor-ring method with a LAUDA tensometer without displacement, using an inductive

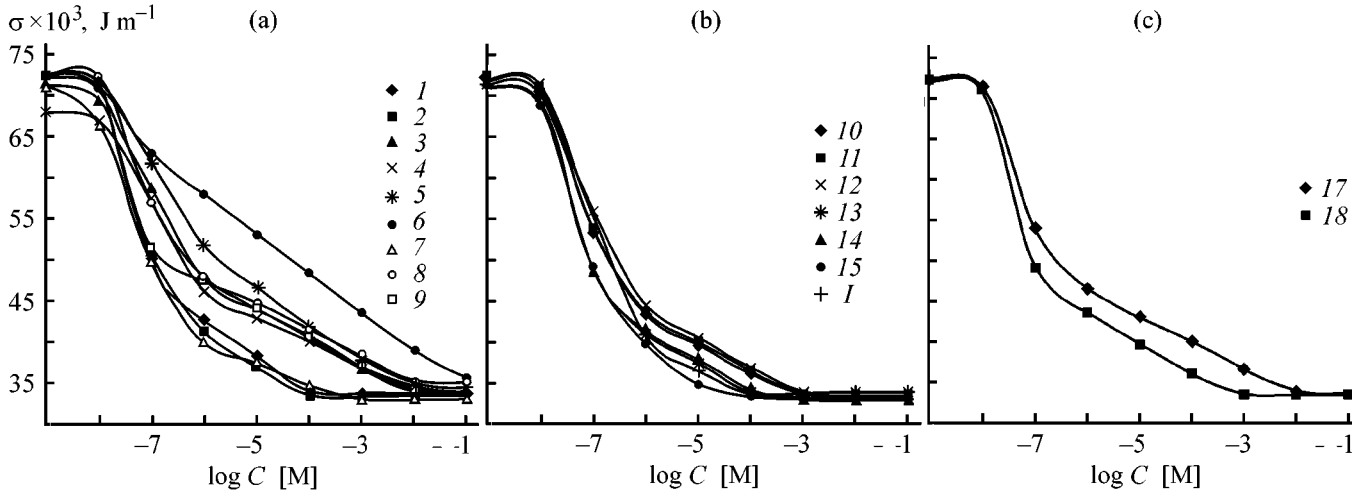

Fig. 1. Surface tension isotherms of aqueous solutions of block copolymers of PO and EO, based on (a) EDA, (b) MEG, and (c) TEA. (σ) Surface tension and (*C*) concentration. The numbers *1–15*, *17*, and *18* correspond to the sample numbers; and *I*, to MEG.

1070-4272/01/7408-1418 $25.00 © 2001 MAIK "Nauka/Interperiodica"

Adsorption characteristics of nonionic surfactants studied

Sample no.	PO : EO, % : %	M	CMC × 10^3, M	$\Gamma \times 10^6$, mol m^{-2}	$S_m \times 10^{17}$, m^2	M_a, kJ mol^{-1}
1	80 : 20	7000	0.1000	0.802	0.208	57.6
2	75 : 25	7000	0.1096	0.613	0.272	49.5
3	70 : 30	7000	7.9430	0.643	0.259	46.4
4	60 : 40	7000	9.1200	0.540	0.309	44.6
5	50 : 50	7000	11.4800	0.580	0.287	43.6
6	30 : 70	7000	50.1200	0.869	0.192	42.0
7	80 : 20	10 000	0.3980	0.476	0.350	49.0
8	50 : 50	10 000	10.0000	0.579	0.288	46.0
9	70 : 30	4500	13.8038	0.618	0.270	46.0
10	80 : 20	6000	0.6025	0.639	0.261	58.0
11	70 : 30	6000	0.7244	0.661	0.252	48.0
12	60 : 40	6000	0.8709	0.660	0.252	45.0
13	80 : 20	7000	0.1047	0.655	0.254	57.0
14	70 : 30	7000	0.2187	0.639	0.261	46.0
15	80 : 20	10 000	0.0209	0.869	0.192	49.0
16	70 : 30	4200	0.0692	0.302	0.552	45.0
17	70 : 30	7500	8.7096	0.593	0.281	52.0
18	70 : 30	7500	0.4365	0.682	0.244	56.0

receiver of an amplifier, embodying the displacement angle concept. The force proportional to the surface tension is converted into electric voltage recorded by a self-recorder. Prior to each measurement, the ring was washed with bichromate and distilled water and then steamed. Each measurement was repeated at least three times at $20 \pm 2°C$.

Figures 1a–1c demonstrate the surface tension isotherms of aqueous solutions of the investigated nonionic surfactants. It should be pointed out that over the concentration range from infinite dilution to critical micelle concentration (CMC) there are two portions of the isotherms, whose position and slope depend, in our opinion, on the PO/EO ratio.

From the experimental surface tension isotherms, we estimated, using data from [4–7], the adsorption Γ, limiting adsorption Γ_m, work of adsorption W_a, molecular site area S_m, and CMC.

The adsorption Γ was estimated from the slopes ($d\sigma/d\log C$) of tangents to the initial portions of the isotherms, by substitution of these slopes in the Gibbs equation:

$$\Gamma = -\frac{1}{2.3RT}\frac{d\sigma}{d\log C}. \quad (1)$$

To determine Γ_m, the slope $d\sigma/d\log C$ of the linear section of the isotherm before CMC was substituted in Eq. (1).

The work of adsorption W_a, characterizing the surface activity, in the energy gain on passing of a mole of the surfactant from the bulk to the surface. This parameter was estimated to be

$$W_a = RT\ln(\Gamma/\delta C),$$

where δ is the thickness of the adsorption layer, determined taking into account the range of intermolecular forces at the interface (9×10^{-10} m for the water–air interface [8]).

We estimated W_a of the investigated nonionic surfactants at various concentrations C, including that at infinite dilution. In discussing the obtained results, we compared W_a values found by extrapolation to zero concentration of a surfactant.

CMC was determined from the adsorption isotherms plotted in the coordinates σ–log C, and S_m was estimated to be

$$S_m = 1/(\Gamma_m N_A).$$

The results are summarized in the table.

It was demonstrated for a series of polymeric homologs of oxyethylated alkylphenols and aliphatic alcohols [9] that S_m depends on the length of the oxyethyl chain. At low degrees of oxyethylation, S_m remains unchanged as a result of straightening of the hydrophilic chains and their vertical orientation in saturated adsorption layers. At high content of the oxyethyl groups, straightening becomes thermodynam-

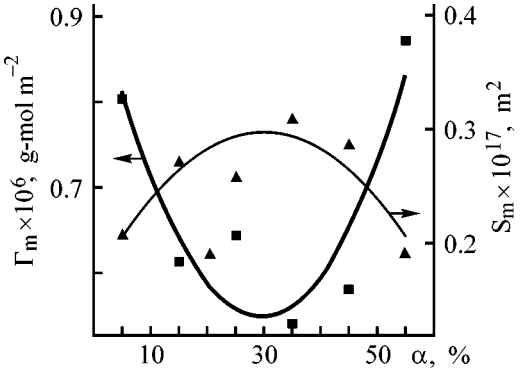

Fig. 2. Limiting adsorption Γ_m and molecular site area S_m vs. the degree of oxyethylation. (α) Degree of oxyethylation expressed as the percentage of EO (see table); the same for Figs. 3 and 4.

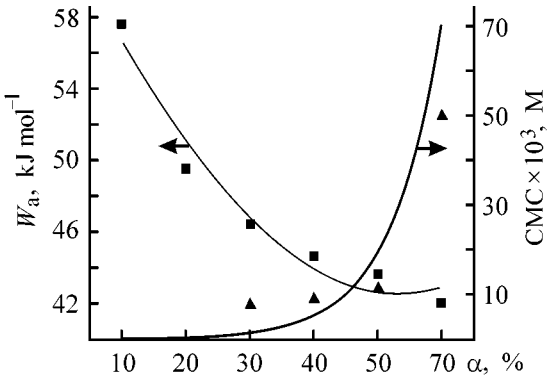

Fig. 3. Work of adsorption W_a and CMC vs. the degree of oxyethylation α.

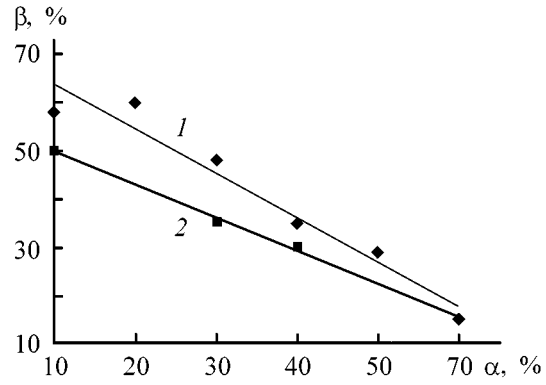

Fig. 4. Demulsifying activity β of block copolymers based on (*1*) EDA and (*2*) MEG vs. the degree of oxyethylation α.

ically unfavorable, and, in this case, S_m is controlled by the size of a convolute oxyethyl chain [9].

We found that S_m is about the same for all the surfactants studied, being only slightly dependent on their molecular weight. For EDA-based PO/EO block copolymers with MW 7000 (sample nos. 1–6), S_m depends on the degree of oxyethylation, reaching the maximum ($S_m = 0.309 \times 10^{-17}$ m^2) at PO/EO = 60/40 (Fig. 2). For MEG-based block copolymers at the same degree of oxyethylation and comparable MW (sample nos. 10–12), S_m remains unchanged, which is probably due to different molecular arrangements of the indicated block copolymers.

It is seen from Fig. 2 and the table that Γ_m shows a minimum at PO/EO = 60/40 for sample nos. 1–6. It is interesting that increased demulsifying activity of similar compounds at the same PO/EO ratio was reported in [3].

The adsorption activity of compounds is mostly characterized by S_m or Γ_m. However, it is more pictorial to express it via such energy parameter as the work of adsorption W_a. Our results showed that W_a monotonically decreases with increasing degree of oxyethylation (Fig. 3), which can be attributed to increasing degree of pulling of the hydrophilic fragment of a molecule into the aqueous phase, which results in decreasing energy gain in adsorption from water. With increasing hydrophilicity of a molecule, CMC increases (see table and Fig. 3). Such a pattern is typical of both EDA- and MEG-based block copolymers.

For the example of nonionic surfactants prepared on the basis of commercial and thoroughly dried TEA (sample nos. 17 and 18, respectively), we demonstrated the effect exerted by the composition of a starting reagent on the surface activity of the resulting block copolymers. It is seen from the table that CMC of sample no. 18 is lower by an order of magnitude than that of sample no. 17, while the other adsorption characteristics are only slightly different. Additionally we studied the demulsifying activity of a series of EDA- and MEG-based copolymers with MW 7000 and 6000, respectively, having various PO/EO ratios. Figure 4 shows the dependences of the demulsifying activity of the block copolymers on the degree of oxyethylation. The demulsifying activity decreases with increasing hydrophilicity of the samples. Finally analysis of the results obtained (Figs. 3, 4) reveals that the work of adsorption decreases together with the demulsifying activity of the block copolymers with increasing degree of oxyethylation.

CONCLUSION

With increasing hydrophilicity of nonionic surfactant molecules, their CMC grows and the work of adsorption and demulsifying activity decrease. The molecular site area and limiting adsorption are dependent on the degree of oxyethylation and steric characteristics of molecules of nonionic surfactants.

REFERENCES

1. Schenfeldt, N., *Surface Active Ethylene Oxide Adducts,* Oxford: Pergamon, 1969.
2. Abramzon, A.A., *Poverkhnostno-aktivnye veshchestva* (Surfactants), Leningrad: Khimiya, 1981.
3. Levchenko, D.N., Bergshtein, N.V., and Nikolaeva, N.M., *Tekhnologiya obessolivaniya neftei na neftepererabatyvayushchikh predpriyaityakh* (Oil Desalination Processes in Refineries), Moscow: Khimiya, 1985.
4. Vyaseleva, G.Ya, Konopleva, A.A., and Barabanov, V.P., *Kolloidn. Zh.*, 1999, vol. 61, no. 4, pp. 481–486.
5. Babak, V.G., Pavlov, A.N., Svitova, T.F., *et al.*, *Kolloidn. Zh.*, 1996, vol. 58, no. 1, pp. 5–12.
6. Makarevich, N.A. and Dikhtievskaya, L.V., *Kolloidn. Zh.*, 1999, vol. 61, no. 3, pp. 357–361.
7. Abramzon, A.A., Zaichenko, L.P., and Petukhova, L.A., *Metodicheskie ukazaniya k raschetnym zanyatiyam po svoistvam i primeneniyu PAV* (Methodological Recommendations to Theoretical Exercises on Properties and Application of Surfactants), Leningrad: Khimiya, 1980.
8. Abramzon, A.A. and Pankratov, V.A., *Zh. Prikl. Khim.*, 1984, vol. 57, no. 2, pp. 293–297.
9. Petrov, A.A. and Pozdnyshev, G.N., *Kolloidn. Zh.*, 1966, vol. 28, no. 6, pp. 858–864.

Russian Journal of Applied Chemistry, Vol. 74, No. 8, 2001, pp. 1422–1425. Translated from Zhurnal Prikladnoi Khimii, Vol. 74, No. 8, 2001, pp. 1382–1385.

Works of Academician B. S. Jacobi in the Field of Applied Chemistry (To B. S. Jacobi's bicentennial birthday anniversary)

The scientific interests of Academician Jacobi were primarily with physics and investigations of electromagnetic phenomena and their practical applications. At the same time, he made an outstanding contribution to the development of applied electrochemistry, studied and improved chemical power sources; he also discovered galvanoplastics and promoted its wide acceptance.

Boris Semenovich Jacobi (Moritz Herman von Jacobi before acquiring Russian citizenship) was born on September 9 (21), 1801, in Potsdam (Germany) into a highly educated merchants' family. He received his primary, very high-grade education at home, studied ancient and European languages, and fundamentals of mathematics. In January 1821, after a year of military service, Jacobi entered Berlin University; however, already in August of the same year he went to Göttingen University. In October 1823, he returned to Potsdam and started working at the Building department of Prussia. In May 1829, he received Göttingen University's diploma in architecture.

Already in those years, Jacobi, dealing with building works, displayed keen interest in investigations in electricity and magnetism and studied works of such known scientists as T.J. Seebeck (1770–1831), A.M. Ampere (1775–1836), H.C. Oersted (1777–1851), and M. Faraday (1791–1867).

In 1883, Moritz Herman Jacobi moved to Königsberg, where his younger brother, Karl Gustav Jacobi (1804–1851), professor, an already known mathematician, one of creators of the theory of elliptic functions, member of the Berlin Academy of Sciences (since 1836), and a corresponding (since 1830) and full member (since 1833) of the St. Petersburg Academy of Sciences, was teaching at the University. In Königsberg, M.H. Jacobi continued working as architect and devoted his entire off-service time and the available means to problems of electrical engineering and electric motor design.

On March 1, 1833, Jacobi became a full member of the Königsberg physico-economical society. In this connection, he delivered at a meeting of the society, in June of the same year, a scientific report "On the Use of Natural Forces for Human Needs," published in the form of a separate brochure. The author appeared before the members of the Society as an excellently educated person and broad-minded engineer well familiar with the latest advances in science [1]. In May 1834, Jacobi demonstrated a prototype electric motor to a group of scientists including A. Humboldt (1769–1859), an outstanding German naturalist. Jacobi sent a report about the electric motor, invented by him, to the Paris Academy of Sciences, and later submitted there a detailed description of the invention. Jacobi's works strongly influenced further research in electric motor design in various countries [2]. In December 1834, by Humboldt's request, the Prussian government provided some funds for financing Jacobi's experiments. However, the scientist's position in Königsberg gave him no way of expanding his studies in the field of practical application of electromagnetic phenomena.

B.S. Jacobi in 1836.

1070-4272/01/7408-1422 $25.00 © 2001 MAIK "Nauka/Interperiodica"

In June 1835, Königsberg University awarded *honoris causa* the doctor of philosophy degree to Jacobi, and already in June of that year he was elected, by recommendation of known Russian scientists K.M. Ber (1792–1876) and V.Ya. Struve (1793–1864), an extraordinary professor at the chair of civil architecture at Derpt (Tartu) University (Estonia). In September 1835, Jacobi moved to Derpt, and his entire scientific and engineering activities proceeded in Russia from that time on. In May 1837, Jacobi reported to the minister of public education and, simultaneously, the president of the St. Petersburg Academy of Scientists Prince S.S. Uvarov (1786–1855) on the possibility of practical application of the electric motor. Already in June, "Committee for Application of Electromagnetism to Machine Motion by Professor Jacobi's Method" was created by the Academy [3]. The Committee included such known scientists as academicians P.N. Fuss (1798–1855), A.Ya. Kupfer (1799–1865), M.V. Ostrogradskii (1801–1861), and E.H. Lenz (1804–1865); P.G. Sobolevskii (1781–1841), a corresponding member of the St. Petersburg Academy of Sciences; and P.L. Shilling (1786–1837), inventor of electromagnetic telegraph. The Committee was headed by Admiral I.F. Krusenstern (1770–1846), an outstanding seafarer and honorary member of the Academy of Sciences.

In August 1837, Jacobi was invited to St. Petersburg to carry out experiments on use aboard ships of the motor designed by him. From that time, and till the end of his life, the scientist lived in St. Petersburg. However, till June 1840 he remained professor of Derpt University, but was relieved of delivering lectures. In November 1839, by initiative of a group of academicians headed by Fuss, Jacobi was elected an adjunct of the St. Petersburg Academy of Sciences in practical mechanics and applied mathematics. In May 1842, at a general meeting of the Academy of Sciences, Jacobi was elected extraordinary academician in applied mathematics. In February 1847, Jacobi was elected ordinary academician in technology and applied chemistry. In October 1865, in view of the opening of a vacancy after Lenz's death, Jacobi was appointed ordinary academician in physics. In April 1848, the scientist acquired Russian citizenship.

Krusenstern's committee was mainly concerned with the assessment of the possibility of applying the electric motor to ship motion; however, with galvanic cells as electric power source, this problem was unsolvable. The activities of the Committee were terminated in 1842, and its final report pointed out that the investigations carried out "aided in explanation of quantitative relations associated with the phenomenon of electromagnetism" [4].

Being very broad-minded scientifically, Jacobi was one of the first in the world to construct cable telegraph lines in St. Petersburg (1841–1846), invented about ten designs of telegraph apparatus, and performed basic research in the field of electromagnetic phenomena [5, 6]. Jacobi dealt with problems of applied chemistry, took active part in studies of ways to machine platinum, and wrote a spacious treatise "On Platinum and Its Use as Coins" (1860). Evidence on scientist's investigations in this field can be found in his correspondence with H. Saint-Claire Deville (1818–1881), a French chemist and a foreign corresponding member of the St. Petersburg Academy of Sciences [7].

The present brief essay covers only Jacobi's works in applied electrochemistry. High-power galvanic cells were necessary for feeding electric motors. The first Jacobi's paper on power sources, published in 1837 (*Pogg. Ann.*, 1837, no. 40, pp. 67–73) was written in Derpt in connection with the dispute on the so-called Becquerel circuit. A.-C. Becquerel (1788–1878), a French scientist, described a galvanic cell comprising two platinum electrodes, one in contact with concentrated nitric acid, and the other, with a concentrated solution of potassium hydroxide. The two liquids were separated by a porous clay diaphragm. According to Becquerel, neutralization was the reaction responsible for current generation. Jacobi confirmed Becquerel's experiments and studied thoroughly the gaseous products evolved on platinum, but made little progress in understanding the mechanism of the occurring electrode reactions. However, somewhat later (1841), Jacobi noted that "As regards galvanic action, platinum in nitric acid is a metal different from platinum immersed in alkali" [5].

Much greater attention was paid by Jacobi to improving the copper–zinc cell proposed in 1836 by British scientist J.F. Daniell (1790–1845). In this cell, amalgamated zinc was immersed in a sulfuric acid solution, and copper, in a copper(II) sulfate solution. The solutions were separated by a porous clay diaphragm well wettable by both the liquids. Jacobi proposed to replace sulfuric acid with an ammonium chloride solution and used in the diaphragm a material with much lower electrical resistance. As noted by W. Ostwald (1853–1932), in the understanding of the mechanism of operation of this cell "Daniell failed to make the final, decisive step, despite that he was very close to doing so... the conclusion that there is no need at all for sulfuric acid was made not by him" [8]. Jacobi improved the copper–zinc cell already in Derpt in the end of 1836 and reported on his achievement in his letter to Academician Lenz in February 1837.

Last portrait of B.S. Jacobi.

In a search for a more powerful current source, Jacobi thoroughly studied the cell proposed by English physicist W.R. Grove (1811–1896). The circuit comprised platinum, concentrated nitric acid, dilute sulfuric acid, and zinc. Grove cells were used by Jacobi in his experiments with a boat driven by electric motor. Having made a detailed theoretical analysis of the possibilities of primary galvanic cells, Jacobi came to a conclusion that their combination with electric motor is noncompetitive with steam machines.

The last Jacobi's works on chemical power sources already referred to secondary cells—batteries. As noted by Academician A.N. Frumkin (1895–1976) [5, 9], Jacobi holds priority on making an attempt to use secondary cells for practical purposes. Originally, Jacobi's battery had only platinum electrodes, which allowed accumulation of a very small amount of electricity. In experiments performed in 1870 at the suggestion of French physicist G. Plante (1834–1889), platinum electrodes were replaced by lead ones immersed in concentrated sulfuric acid. This allowed a substantial increase in the storage capacity of secondary power cells.

Jacobi's studies in the field of chemical power cells led the scientist to the discovery of galvanoplastics, made in February 1937, before moving to St. Petersburg. It is this date of the discovery that was given by Jacobi himself in a letter to M. Faraday of June 21, 1839 [5]. On October 4, 1838, Jacobi reported on his invention in an official letter to the Academy of Sciences and submitted a sample fabricated by him. In 1840, the scientist got a permission of the Russian government to publish the results of his investigations in the form of a detailed manual [10, 11]. The book *Galvanoplastics or a Method to Fabricate Prototype-reproducing Copper Articles from Copper Solutions by Means of Galvanism* was published in Russian and German simultaneously and was at once translated into English and French. Its author stated with pride: "Galvanoplastics belongs exclusively to Russia. Here it originated, and here it was developed." This was confirmed by Academician P.I. Walden (1863–1957) who paid much attention to the history of chemistry [12]. In the manual, Jacobi presented quite a number of conditions for production of good copper deposits. The author was aware of the broadest possibilities of practical application of galvanoplastics. The development of galvanoplastics in Russia during the first years after its discovery was described in detail in I.G. Spasskii's article, included as a supplement in the collection of Jacobi's works [5]. The same supplement contains other materials referring to this discovery (Jacobi's leters to Prince Uvarov, correspondence with A.N. Demidov, comments by press, opinions of scientists.

In April 1840, Jacobi was awarded Demidov Prize for the invention of galvanoplastics, but the scientist handed the entire amount of money to the Academy of Sciences. In summer of 1867, at the World Exhibition in Paris, Jacobi was awarded for his discovery the First Prize and the Major Gold Medal. In 1889, a galvanoplastics exhibition was staged in St. Petersburg, devoted to 50th anniversary of Jacobi's discovery [13].

Already after discovering the galvanoplastics, Jacobi submitted to the Academy of Sciences the results of his investigations of the processes of gilding (1842), brass coating (1844), and electrolytic recovery of iron (1868). This field of applied electrochemistry was named galvanostegy by the scientist.

A major part of Jacobi's electrochemical works was devoted to development of methods for measuring the amount of electricity, electromotive force of galvanic cells, and their internal resistance. All these works were initiated by the need to have more precise evaluation techniques on which depended the possibility of using in practice various kinds of chemical power sources [5, 14].

Jacobi took active part in the activities of the St. Petersburg Academy of Sciences; he was repeatedly elected a member of the managing committee of the Academy, was a member of a great number of various

permanent and temporary committees, and performed various tasks.

As noted by Frumkin [5], the discovery of galvanoplastics, investigation of chemical power sources, and development of methods for measuring electrochemical quantities put Jacobi to one of the first places in the electrochemical science of the XIX century.

Jacobi's merits in various fields of science and technology were highly appreciated in Russia and abroad. A full member of the St. Petersburg Academy of Sciences, he was also elected a foreign corresponding member of the Berlin Academy of Sciences, Göttingen Society of Sciences, scientific societies of Italy, honorary member of the British society for promotion of valuable arts, Scottish society of arts, a member of the Physical society in Frankfurt, Dutch society of sciences in Harlem, and other societies and institutions. By the end of his life, Jacobi had the title of Privy Counselor and had been awarded the highest Orders of Russia and orders of other countries.

Among the vast number of publications devoted to Jacobi, mention should necessarily be made of the book by M.G. Novlyanskaya [15]. The book presents lists of scientist's works (176 items) and publications about Jacobi's life and activities, which appeared during the period from 1834 till 1953 (571 items), and biographic materials covering in chronological order all his life.

Boris Semenovich Jacobi died of heart attack on February 27, 1874, at age of 72. He was buried at Smolenskoe Lutheran cemetery in St. Petersburg. A memorial plaque on an Academy of Sciences building in Vassilievsky island on a Neva embankment reminds descendants that "a famous physicist and electrical engineer Boris Semenovich Jacobi" had lived in this house.

REFERENCES

1. Kravets, T.P., *Usp. Fiz. Nauk*, 1949, vol. 38, no. 3, pp. 4101–4113.
2. Efremov, D.V. and Radovskii, M.I., *Elektrodvigatel' v ego istoricheskom razvitii* (Electric Motor in Its Historical Development), Mitkevich, V.F., Ed., Moscow: Akad. Nauk SSSR, 1936.
3. Radovskii, M.I., *Usp. Fiz. Nauk*, 1948, vol. 35, no. 4, pp. 580–588.
4. Efremov, D.V. and Radovskii, M.I., *Dinamomashina v ee istoricheskom razvitii* (Dynamo in Its Historical Development), Mitkevich, V.F. Ed., Leningrad: Akad. Nauk SSSR, 1934.
5. Jacobi, B.S., *Raboty po elektrokhimii* (Works on Electrochemistry), Frumkin, A.N., Ed., Moscow: Akad. Nauk SSSR, 1957.
6. Vil'd, G.I., *O zhizni i trudakh akademika B.S.Yakobi* (Life and Acivities of Academician B.S. Jacobi), St. Petersburg: Imperat. Akad. Nauk, 1875.
7. Solov'ev, Yu.I., *Voprosy Ist. Estestvozn, Tekhn.*, 1963, no. 14, pp. 82–87.
8. Ostval'd, V., *Istoriya elektrokhimii* (History of Electrochemistry), St. Petersburg: Obrazovanie, 1911.
9. Frumkin, A.N. and Obrucheva, A.D., *Elektrichestvo*, 1953, no. 2, pp. 71–74.
10. Jacobi, M.H., *Gal'vanoplastika, ili sposob po dannym obraztsam proizvodit' mednye izdeliya iz mednykh rastvorov s pomoshch'yu gal'vanizma* (Galvanoplastics—a Method for Fabricating Prototype-reproducing Articles from Copper Solutions by Means of Galvanism), St. Petersburg, 1840.
11. Il'in, A.A., *Boris Semenovich Yakobi. Istoricheskii ocherk izobreteniya gal'vanoplastiki* (Boris Semenovich Jacobi. Historical Essay on the Discovery of Galvanoplastics), St. Petersburg: Izd. K.L. Rikkera, 1889.
12. Val'den, P.I., *Nauka i zhizn'* (Science and Life), Petrograd: Nauch. Tekhn. Izd., part 1, 1922.
13. Deshevov, M.M., *Zap. Imperat. Russkogo Tekhn. O–va*, 1889, vol. 23. April, pp. 1–15.
14. Yarotskii, A.V., *Boris Semenovich Yakobi* (Boris Semenovich Jacobi), Moscow: Nauka, 1988.
15. Novlyanskaya, M.G., *Boris Semenovich Yakobi. Bibliograficheskii ukazatel'* (Boris Semenovich Jacobi. Bibliography), Shafranovskii, K.I., Ed., Moscow: Akad. Nauk SSSR, 1953.

A. G. Morachevskii

Russian Journal of Applied Chemistry, Vol. 74, No. 8, 2001, p. 1426. Translated from Zhurnal Prikladnoi Khimii, Vol. 74, No. 8, 2001, p. 1386.

BOOK REVIEWS

Aleksandrovskii, S.V., Dong Von Li, and Gopienko, V.G., *Novye protsessy polucheniya tugoplavkikh soedinenii titana* (New Processes for Producing High-Melting Titanium Compounds), Moscow: Ruda i Metally Publ. House, 2001, 128 pp.

High-melting titanium compounds—carbides, nitrides, and carbonitrides find wide use in diverse fields of new technology. All the three classes of compounds are characterized by high melting points, hardness, and wear resistance, and serve as a basis for manufacture of alloys and formulations with a required set of properties. In a small monograph by Aleksandrovskii and co-authors, the existing and prospective ways to obtain high-melting compounds belonging to the systems Ti–C, Ti–N, and Ti–C–N are considered.

The book comprises a brief introduction, three chapters, and bibliography containing 101 references to works of domestic and foreign authors. The introduction (pp. 3–5) mainly presents the fields of application of high-melting titanium compounds. The first chapter (pp. 6–25) describes the properties of the compounds under consideration—phase diagrams of the systems Ti–C, Ti–N, and Ti–C–N, wettability of the carbides and nitrides by various metals, and other physicochemical properties are discussed. The second chapter (pp. 26–34) considers the most important methods for obtaining high-melting titanium compounds. To these belong direct synthesis of titanium compounds from components, reduction of titanium dioxide by carbon, reaction of titanium tetrachloride with ammonia to give titanium nitrides, reduction of titanium dioxide by various reducing agents in atmosphere of nitrogen, and synthesis of carbonitrides by nitration of a mixture of titanium dioxide with carbon.

The third chapter, occupying the central place in the monograph (pp. 34–118), is concerned with investigations of ways to obtain high-melting titanium compounds by various new methods. In this group are placed plasmochemical synthesis of titanium carbide, synthesis of high-melting compounds in vapor phase, and self-propagating high-temperature synthesis. However, particular attention is given by the authors to synthesis of high-melting titanium compounds with the use of technologies, apparatus, and half-products of titanium-magnesium production. Manufacture of a wide assortment of various kinds of high-melting titanium compounds with relatively low production cost can be set up on the basis of a titanium-magnesium combine. The technological process can be based on thermal reduction with magnesium of titanium and carbon chlorides on standard equipment used in production of titanium sponge.

The monograph has clearly pronounced technological orientation. Thermodynamic calculations would become more thorough with the use of data presented in a monograph by A.G. Turchanin and M.A. Turchanin [*Termodinamika tugoplavkikh karbidov i karbonitridov* (Thermodynamics of Carbides and Carbonitrides), Moscow: Metallurgiya, 1991].

The book is well published and contains extensive reference material. Unfortunately, insufficient attention was given in editing the book to unity of terminology and measurement units.

Judging from the manner of presentation, the monograph by S.V. Aleksandrovskii and co-workers can be used by wide audience of specialists interested in problems of inorganic materials science.

A. G. Morachevskii

1070-4272/01/7408-1426 $25.00 © 2001 MAIK "Nauka/Interperiodica"

Russian Journal of Applied Chemistry, Vol. 74, No. 8, 2001, p. 1427. Translated from Zhurnal Prikladnoi Khimii, Vol. 74, No. 8, 2001, p. 1387.

========== BOOK REVIEWS ==========

Stiller, W., *Uravnenie Arreniusa i neravnovesnaya kinetika* (Arhenius Equation and Nonequilibrium Kinetics), Translation from English, Moscow: Mir, 2000, 176 pp.

The book is written by a known German physicist and published in English in connection with the centennial jubilee of the Arrhenius equation, celebrated in 1989. In addition to presenting the history of the equation, the book contains a brief, but informative treatise of the modern state of the theoretical foundations of nonequilibrium kinetics.

The author considers theoretically and practically important problems associated with intensively developing fields of chemistry, physics, physical chemistry, and chemical technology. Much attention is paid in the monograph to correct use of concepts and quantities in considering theoretical and practical problems.

In 1889, Svante August Arrhenius (1859–1927), an outstanding physical chemist and, later, a Nobel Prize winner (1903), published a paper "On Rates of Inversion Reaction in Cane-Sugar under the Action of Acids" (*Z. Phys. Chem.*, 1889, vol. 4, pp. 226–248) containing an expression for the reaction rate constant. This expression became widely known as the Arrhenius equation. At that time Arrhenius worked as assistant of W. Ostwald (1853–1932) at the physicochemical laboratory of Leipzig University.

In a brief foreword, the translation editor (L.S. Polak) and translator (A.V. Khachoyan) noted that by now the application domain of the famous equation has expanded considerably. The notion "Arrhenius kinetics" is used in analyzing and describing a wide diversity of processes: from stress relaxation in solids to mass transfer in gas systems.

The book comprises eight chapters, afterword, supplement, and bibliography with 231 references to works of virtually only foreign authors. The first chapter (pp. 9–24) is a historical essay covering three periods of the development of chemical kinetics: prior to Arrhenius's works (before 1889), the time when his basic works were published (1889–1900), and the later time (before 1950). The author gives a brief characterization of the main directions of physicochemical kinetics in the first half of the XX century.

The second chapter (pp. 25–43) is concerned with the present state of the Arrhenius kinetics. Primary attention is given to gas-phase reacting systems. Ion-molecular and radical-molecular reactions are considered. Problems encountered in applying the Arrhenius equation to modeling of complex reactions are discussed, methods for calculating the parameters appearing in the Arrhenius equation are presented, and possible cases of deviation from this law are analyzed.

The third chapter (pp. 44–69) considers specific features of equilibrium gas-phase kinetics for the case of moderately rarefied gases with uniform temperature. The fourth chapter (pp. 70–78) discusses nonequilibrium gas-phase systems with reactants having different temperatures (two-temperature Arrhenius equation). The fifth (pp. 79–92) and sixth (pp. 93–111) chapters present a mathematical description of the nonequilibrium kinetics of chemically reacting gas-phase systems. In the seventh chapter (pp. 112–137), the methods of nonequilibrium kinetics are applied to systems with nonthermally activated reactions (plasmochemistry, radiation chemistry, chemistry of "hot atoms").

The final, eighth chapter (pp. 138–147) is named "Prospects of the Arrhenius equation." The author discusses the possible future applications of the Arrhenius equation and its modifications in various fields of physical chemistry, physics, and biology. In the afterword to the Russian translation (pp. 148–161), the editor and translator supplement some concepts of the monograph, in the first place those concerning open systems interacting with the environment and exhibiting varied degree of departure from equilibrium, and give reference to the relevant literature.

The supplement (pp. 162–166) presents evidence concerning the chronology of Arrhenius's life and activities and a list of his basic works.

In a foreword, the editor and translator, justly note that the book is written in a concise, nearly sketchy manner and is intended for a trained reader. At the same time, regarding the nature of the problems discussed, the monograph may be of interest for a wide audience of scientists, high-school teachers, and postgraduate students specialized in chemistry and physics.

I.N. Beloglazov and A.G. Morachevskii

1070-4272/01/7408-1427 $25.00 © 2001 MAIK "Nauka/Interperiodica"

Russian Journal of Applied Chemistry, Vol. 74, No. 8, 2001, p. 1428. Translated from Zhurnal Prikladnoi Khimii, Vol. 74, No. 8, 2001, p. 1388.

BOOK REVIEWS

Prilutskii, V.S., *Vol'framovyi torirovannyi karbidirovannyi katod* (Carbidized Thoriated Tungsten Cathode), Moscow: Ruda i Metally Publ. House, 2001. 152 pp.

Thoriated tungsten (tungsten wire with ThO_2 additive) was proposed as emitter and material for fabrication of cathodes for electronic valves by Langmuir as far back as 1915. Thorium dioxide additive (1–2%) enables much stronger electron emission as compared with pure tungsten. The cathode performance can be substantially improved further by using cathodes made of thoriated tungsten whose surface layer is converted into tungsten carbide W_2C (carbidized). The monograph by Prilutskii considers from modern standpoint the theory and practice of designing and fabricating carbidized thoriated tungsten cathodes (CTTC). The book comprises introduction, nine chapters, supplement, and bibliography including 171 references to works of domestic and foreign authors.

The first chapter considers properties of tungsten carbides: phase diagram of the system tungsten–carbon, various properties of the carbides, and the nature of chemical bonding in these materials. The second chapter (pp. 21–41) is devoted to the technology of carbidization and activation of CTTCs. Among the methods for obtaining tungsten carbides, the following are discussed: synthesis from elements, reduction of carbides by carbon, chemical isolation from alloys, electrolysis of molten media, and gas-phase deposition. Also considered is the process of CTTC fabrication and optimization. A very brief third chapter (pp. 42–44) contains evidence concerning some properties of carbidized thoriated tungsten (electrical resistivity, thermal and physical and physicomechanical characteristics). The fourth chapter (pp. 45–56) discusses the physical understanding of how the CTTCs operate. Their high emissive ability is ensured by the presence on the cathode surface of a nearly monolayer-thick film of thorium atoms. The fifth chapter (pp. 57–70) is concerned with specific features of the design and calculation of CTTCs, the sixth chapter (pp. 71–81) considers the specific features of their fabrication technology.

The seventh chapter (pp. 82–107) discusses problems associated with the service life of CTTCs, determined by a combination of factors. Ways to make the service life of a cathode longer are discussed. The eighth (pp. 108–119) and ninth (pp. 120–130) chapters contain special evidence concerning the design and calculation of cathodes and their accelerated longevity tests.

The monograph as a whole gives integrated consideration to the theory and practice of CTTC design and fabrication and is largely based on the author's working experience.

In addition to accomplishing strictly specialized purposes, the evidence presented in the monograph may be of interest for specialists in inorganic materials science and technology of electronic materials.

A. G. Morachevskii

1070-4272/01/7408-1428 $25.00 © 2001 MAIK "Nauka/Interperiodica"

Russian Journal of Applied Chemistry, Vol. 74, No. 9, 2001, pp. 1431–1434. Translated from Zhurnal Prikladnoi Khimii, Vol. 74, No. 9, 2001, pp. 1393–1396.

INORGANIC SYNTHESIS AND INDUSTRIAL INORGANIC CHEMISTRY

Anomalous Phenomena in Zirconium, Hafnium, and Titanium Salt Solutions, Studied by Capillary Isotachophoresis

O. V. Oshurkova, A. I. Gorshkov, and V. P. Nesterov

Ioffe Physicotechnical Institute, Russian Academy of Sciences, St. Petersburg, Russia
Sechenov Institute of Evolutionary Physiology and Biochemistry, Russian Academy of Sciences, St. Petersburg, Russia

Received November 29, 2000

Abstract—Capillary isotachophoresis was used to separate mixtures of solutions containing zirconium, hafnium, titanium, and aluminum salts with various anions. Anomalous phenomena occurring in separation of mixtures in solutions with medium and high concentrations are described and analyzed.

The conventional capillary isotachophoresis [1] consists in that bands of pure electrolyte solutions move in a capillary under the action of electric field at the same rate. The bands of pure solutions are formed as a result of separation of their mixture in the course of motion of the constituent ions in a separating column under the action of a dc electric field. Ionic components with only slightly differing mobilities are separated using a hydrodynamic counterflow [2] in order to have an opportunity to make longer the distance traversed by the ions relative to the solvent, without increasing the column length. For example, nearly all rare-earth elements have been separated by means of isotachophoresis under counterflow conditions [3].

The situation is somewhat more complicated in the case of isotachophoretic crystallization [4] considered in [5]. The conventional capillary isotachophoresis uses single-phase systems, liquid solutions. Isotachophoretic crystallization adds a solid phase, crystals, in one or several bands.

EXPERIMENTAL

The aim of this study was to analyze by means of cationic isotachophoresis the conditions of separation of various mixtures of solutions containing zirconium, hafnium, titanium, and aluminum salts.

A single-channel device for capillary isotachophoresis with boundary detection by means of a refraction pattern was used [6]. Experiments were done in glass and quartz capillaries with uncoated inner surface, having outer diameter of 0.2–0.6 mm and channel diameter of 0.1–0.3 mm. The strength of the electric current flowing through the capillary was in the range 0.5–3.0 mA. Isotachophoregrams obtained upon separation were interpreted using the method described in [7].

The separation was done in solutions of chloride and thiocyanate salts. As leading solution (leader), or catholyte, in separation of chlorides commonly served hydrochloric acid of concentration 4.0–8.0 M; as terminating solution (terminator), or anolyte, were used aqueous solutions of cadmium, zinc, and uranyl chlorides. In the case of thiocyanate solutions, 2.0 M solution of ammonium thiocyanate served as leader, and solutions of cadmium and zinc salts as terminators. In the experiments, terminators were acidified to hydrochloric acid concentrations of 0.03–0.2 M to make the pH lower in the bands by creating a through H^+ flow from the anolyte into the catholyte. Such a flow makes bands of pure electrolyte solutions longer owing to the fact that the mobility of H^+ is higher that that of the other ions and the electric current is largely created by motion of hydrogen ions at low pH. In the steady state, the H^+ flow is the same in any section of the column:

$$Q_i = C_i u_i E_i = \text{const},$$

where C_i and u_i are the concentration and mobility of H^+ in ith band; E_i is the electric field strength in the same band.

Lowering the pH value by a through flow of H^+ precludes precipitation of metal hydroxides in the column.

1070-4272/01/7409-1431$25.00

Separation was applied to multicomponent mixtures of substances with widely varying pH of precipitation of their hydroxides. These mixtures contained cations of potassium, sodium, calcium, samarium, magnesium, lithium, cobalt, aluminum, zirconium, hafnium, titanium, copper, and iron in various combinations. To prevent precipitation of hydroxides directly in a mixture under study prior to the experiment, it was strongly acidified to a hydrochloric acid concentration of 2.0–3.0 M. It was found that at weak, less than 0.03 M, acidification of the terminator an attempt to separate a mixture leads to solution column rupture and precipitation of some hydroxides. In the case of terminator acidification in the range 0.1–0.2 M, the mixture separation process goes till band formation, with the zirconium-containing band exhibiting unusual behavior.

Let us describe in more detail one of the experiments and consider the essence of the anomaly. A 5.4 M hydrochloric acid solution served in this experiment as leader, and a 0.9 M solution of zinc chloride acidified to a hydrochloric acid concentration of 0.1 M, as terminator. The strength of the electric current flowing through the capillary was 0.8–2.0 mA. The electric current initiated separation of the mixture and led to adjustment of electrolyte solutions in accordance with the controlling relationship [8]. In the course of separation, a sharp symmetric peak first appeared in the refraction pattern, gradually transforming into a broad zirconium band. The longer the time of mixture separation, the wider the zirconium band in the refraction pattern. The time of mixture separation varied within 3–10 h in different runs. The greater width of the zirconium band in the refraction pattern of the capillary indicates an exceedingly high refractive index of the substance in this band, evaluated as follows. It was shown in [9] that the refractive index of a solution in a band is proportional to the width of its refraction pattern. Among the available relations between the band width in the refraction pattern and the refractive index of the solution, we chose that best fitting the point corresponding to a 5.4 M hydrochloric acid solution. This linear dependence was extrapolated to refractive indices of about 1.5. The width of the refraction pattern of the zirconium band was used to evaluate the refractive index of the substance in this band to be 1.49 ± 0.02. This parameter could not be found in any other way since the volume of the zirconium band was only about 1.5×10^{-5} cm^3 and the contents of the band could not be extracted from the capillary. The refractive index of the substance in the zirconium band is close to that for glasses. Particular emphasis is to be placed on the fact that, in the course of the adjustment, the zirconium band becomes immobile relative to walls of the separation column, and adheres to them. This follows from the fact that the band does not move along the capillary when the solution levels in the electrode vessels are varied widely. The position of the band remains unchanged, either, in varying the strength of the electric current flowing through the capillary. The zirconium band is seen not only in the refraction pattern, but also simply by visual inspection. Its boundaries with neighboring solutions are well visible, whereas the boundary between the zirconium band and the capillary wall (glass or quartz) cannot be seen, apparently because of the closeness of the refractive indices. Despite the already formed gel-like zirconium band, the mixture continues to separate and ions pass through this immobilized band in both directions. In the process, pure solution bands are formed both in front of, and behind the zirconium band, being arranged between the leader and terminator in the order of decreasing mobilities of their ionic components. Raising the current strength causes an increase in the separation rate, and vice versa.

Commonly the concentration of ionic substance in a mixture being separated is chosen to be much lower than the steady-state value. This is due to the fact that at the same current strength the separation is in this case much faster than that in separating a mixture with the concentration higher than the equilibrium value. In the experiment described here the starting mixture was much more diluted than the steady-state bands.

After a mixture is separated and bands are formed, all of them remain immobile relative to the separation capillary. Creating an external pressure difference of 10–20 cm of water column did not cause hydrodynamic flow of the solution in the column and, consequently, left the bands unshifted. The solution flow in the capillary cannot be induced even upon applying a pressure difference of about 1 atm, created by a water-jet pump, to a capillary with separated mixture, extracted from the device. After the zirconium band is formed, raising the strength of the electric current flowing through the capillary to the point of overheating and rupture of the solution column does not shift the bands along the capillary, either. In fact, the formation of a gel-like band rules out any motion

of the solutions as a whole, induced by counterflow and electroosmosis.

The contents of the zirconium band had the form of a gelatinous, glassy mass. This could be ascertained by breaking the capillary at this band.

After the experiment was complete, the zirconium band and all other bands could not be removed from the capillary by conventional methods to enable its repeated use. It was necessary to pass reverse current through the column for a long time or replace the catholyte and anolyte in the electrode vessels with concentrated hydrochloric acid and then also pass current through the capillary.

Occasionally, two, rather than one, zirconium bands separated by solution were formed in separating a zirconium-containing mixture.

Similar anomalous phenomena were observed in separation of hafnium-containing mixtures. With zirconium and hafnium present simultaneously in a sample, they could not be separated, being always concentrated in a single, glassy band. In addition, a glassy band was observed when separating a mixture containing Ti(III) ions in chloride and thiocyanate solutions. The gel-like band of titanium had lower refractive index than the zirconium and hafnium bands; it was transparent, but had a violet tint characteristic of titanium solutions. A very narrow band of glassy gel was also obtained from an aluminum formate solution, but its refractive index was nearly the same as that of the other solutions. A solution of ammonium formate served as leader, and a formic acid solution, as terminator.

Let us make an attempt to explain these phenomena, uncommon for the conventional isotachophoresis, for the example of zirconium. Zirconium is contained in such cation species as Zr^{4+}, ZrO^{2+}, $Zr(OH)^{2+}$, $Zr_2O_3^{2+}$, $Zr_5O_8^{4+}$, and $ZrOOH^+$. At the initial instant of electrolysis in a strongly acidic mixture taken for separation, the equilibrium is shifted toward formation of Zr^{4+} and ZrO^{2+} ions. In further separation, H^+ ions are continuously removed from the mixture into the leading solution, with the pH in the column depending on the through flow of H^+ from the anolyte into the catholyte. This flow may also decrease in intensity, depending on the electrolysis time and other separation conditions. All this results in that the solution pH in the column grows steadily, with the equilibrium between cation species shifted toward $ZrOOH^+$ to give hydrated zirconium dioxide whose formation on raising the solution pH was described in a monograph [10], where the appropriate equations were also given:

$$ZrOCl_2 + H_2O \longrightarrow ZrOOH^+ + H^+ + 2Cl^-,$$

$$ZrOOH^+ + OH^- \longrightarrow ZrO(OH)_2 \xrightarrow{H_2O} ZrO_2 \cdot xH_2O.$$

Hydrated zirconium dioxide is composed of very fine crystals whose accretion forms the crystalline skeleton. An opinion has been reported [10] that, depending on the conditions of $ZrO_2 \cdot xH_2O$ formation (pH, temperature, etc.), there occurs dehydration accompanied by polymerization:

$$Zr(OH)_4 \xrightarrow{H_2O} ZrO(OH)_2 \xrightarrow{H_2O} ZrO_2 \cdot xH_2O.$$

Glassy gels are hydrated compounds in which water and zirconium dioxide are present in nonstoichiometric ratio.

Thus, the appearance of $ZrO_2 \cdot xH_2O$ glassy gel is presumably accounted for by the chemical properties of this amphoteric element, by the process of isotachophoretic concentration adjustment, and by the creation in the column of conditions leading to a slow increase in pH in the formed zirconium band.

The above data on zirconium refer in full measure to hafnium because of the closeness of their chemical properties and mobilities of their cation components. Similarly to zirconium, titanium can form hydrated oxides [10]. Under the conditions when hydrated oxides of zirconium, hafnium, and titanium are formed in chloride and thiocyanate solutions, aluminum concentrates into a common isotachophoretic band. The appearance of a glassy aluminum gel in the form of a narrow band in its band in aqueous formate solutions could not be accounted for as yet.

To conclude, it should be noted that gel-like bands were only observed in amphoteric substances. Probably, formation of a kind of gel-like bands would also be expected for other amphoteric compounds, e.g., organic, of the type of proteins.

CONCLUSION

Depending on the composition of mixtures being separated and separation conditions, isotachophoresis and, in particular, its capillary variety, furnishes an opportunity to obtain bands in the form of pure electrolyte solutions, glassy gels, and saturated solutions with solid crystals. Zirconium and hafnium give an immobilized glassy band in which the substance has

the refractive index close to that of a solid glass. Similar, but less pronounced phenomena are observed in separation of titanium-containing solutions.

REFERENCES

1. Konstantinov, B.P. and Oshurkova, O.V., *Dokl. Akad, Nauk SSSR*, 1963, vol. 148, no. 5, pp. 1110–1113.
2. Brewer, A. and Madorsky, S., *J. Res. Nat. Bur. Stand.*, 1947, vol. 38, no. 1, pp. 132–149.
3. Oshurkova, O.V., Konstantinov, B.P., and Lyadov, N.S., *Zh. Prikl. Khim.*, 1972, vol. 45, no. 5, pp. 963–969.
4. Oshurkova, O.V. and Gorshkov, A.I., *Usp. Khim.*, 1993, vol. 62, no. 8, pp. 775–787.
5. Oshurkova, O.V., Gorshkov, A.I., and Nesterov, V.P., *J. Chromatogr.*, 1996, vol. A752, pp. 251–259.
6. Konstantinov, B.P. and Oshurkova, O.V., *Zh. Tekh. Fiz.*, 1966, vol. 36, no. 5, pp. 942–957.
7. Oshurkova, O.V. and Gorshkov, A.I., *Ukr. Khim. Zh.*, 1992, vol. 58, no. 2, pp. 187–192.
8. Gorshkov, A.I., *Zh. Fiz. Khim.*, 1985, vol. 59, no. 3, pp. 626–629.
9. Konstantinov, B.P., Lyadov, N.S., and Oshurkova, O.V., *Zh. Tekh. Fiz.*, 1968, vol. 38, no. 12, pp. 2117–2118.
10. Blumenthal, W.B., *The Chemical Behavior of Zirconium*, New York: Van Nostrand, 1958.

Russian Journal of Applied Chemistry, Vol. 74, No. 9, 2001, pp. 1435–1438. Translated from Zhurnal Prikladnoi Khimii, Vol. 74, No. 9, 2001, pp. 1397–1400.

PHYSICOCHEMICAL STUDIES OF SYSTEMS AND PROCESSES

Thermodynamic Characteristics of Titanium(IV) Tetrakis(dialkylamide)–Benzene Systems

A. K. Baev and V. E. Mikhailov

Institute of Solution Chemistry, Russian Academy of Sciences, Ivanovo, Russia
Belarussian State Technological University, Minsk, Belarus

Received December 26, 2000; in final form, May 2001

Abstract—The *p–T–x* dependences were measured in the entire concentration range of the systems $Ti[N(CH_3)_2]_4$–C_6H_6 and $Ti[N(C_2H_5)_2]_4$–C_6H_6, the enthalpies and entropies of vaporization were found, the energies of specific interactions in liquid titanium tetrakis(dialkylamides) were evaluated, and a strong intermolecular interaction between the nitrogen atom in $Ti(NR_2)_4$ and a benzene molecule was substantiated.

The developed technique for synthesizing titanium(IV) tetrakis(dialkylamides) with benzene as solvent ensures high yield of the target compounds [1]. Obtaining these compounds in high-purity state for synthesizing titanium nitride films and carbide–nitride coatings requires that the *p–T–x* dependences and thermodynamic properties of solutions containing these components should be determined. Since the observed set of changes in the solutions is associated in a certain way with the energy- and entropy-related (structural) characteristics, the thermodynamic characteristics of the solutions, combined with data on the structure of liquid components, furnish information about the mutual position of species in solution [2]. The present study, proceeding with investigations in this direction, is concerned with the *p–T–x* dependences and thermodynamic properties of solutions in the systems $Ti[N(CH_3)_2]_4$–C_6H_6 and $Ti[N(C_2H_5)_2]_4$–C_6H_6.

For dialkylamide compounds of titanium(IV), the thermodynamic characteristics of vaporization process have been obtained with good accuracy [3, 4], and the existence of monomer molecules in vapor has been substantiated. In [5], the tetrahedral structure of the TiN_4 fragment in the $Ti[N(CH_3)_2]_4$ molecule with strong bonding was established. An NMR study of $Be[N(CH_3)_2]_2$ [6] revealed the structure of the molecule. The NMR spectrum of $Al[N(CH_3)_2]_3$ shows peaks corresponding to terminal and bridging $N(CH_3)_2$ groups [6], with the bridge formation being due to the donor properties of the nitrogen atom in this group: $Al–NR_2\rightarrow Al$. The most favorable structure for liquid $Ti(NR_2)_4$ will be that with two bridging bonds $Ti–N\rightarrow Ti$ and a coordination number of six for the titanium atom:

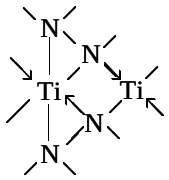

In such a structure, each titanium atom forms two bonds with the terminal amide group and four bridging bonds. This ensures a high enthalpy of vaporization. However, it is the considerable difference in $\Delta_v H^0(T)$ and $\Delta_v S^0(T)$ between $Ti[N(CH_3)_2]_4$ (53.8 ± 3.0 kJ mol^{-1} and 107 ± 0.7 J mol^{-1} K^{-1}) and $Ti[N(C_2H_5)_2]_4$ (94.6 ± 4.0 kJ mol^{-1} and 170.2 ± 9.5 J mol^{-1} K^{-1}) that points to the essential influence of the ethyl group on the enthalpy of vaporization. The value of this parameter reflects the fact that the carbon atom of the methyl group and the terminal methyl group of the ethyl group [7] differently affect the intermolecular interaction [8]. The formation of a dative bond [7] provides for the enhanced donor properties of the methyl carbon atom in the ethyl group and, consequently, for stronger intermolecular interactions:

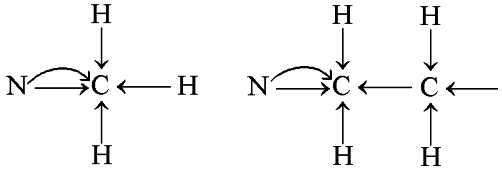

Therefore, at equal numbers of nitrogen atoms in the molecules of titanium(IV) tetrakis(dimethyl- and

1070-4272/01/7409-1435$25.00

Coefficients of the equation $\log p = B - A/T$, enthalpies and entropies of vaporization of solutions of the systems $Ti(NR_2)_4$–C_6H_6

c [$Ti(NR_2)_4$], M	T, K	A	B	$\Delta H^0(T)$, kJ mol^{-1}	$\Delta S^0(T)$, J mol^{-1} K^{-1}
		$Ti[N(CH_3)_2]_4$–C_6H_6			
100	343.1–423.2	2815 ± 144.0	10.60 ± 0.35	53.8 ± 3.0	107.1 ± 7.0
90.51	293.7–339.4	1531 ± 1.0	8.42 ± 0.05	29.32 ± 0.30	65.4 ± 1.0
74.35	293.8–341.8	1554 ± 1.0	8.88 ± 0.04	29.76 ± 0.27	74.2 ± 0.8
49.14	293.9–353.1	1645 ± 1.0	9.35 ± 0.08	31.51 ± 0.29	84.2 ± 0.9
26.85	294.0–360.2	1655 ± 1.0	9.56 ± 0.57	31.61 ± 0.55	87.3 ± 0.8
16.09	281.9–360.4	1645 ± 1.0	9.58 ± 0.07	31.50 ± 0.25	87.7 ± 0.8
0	293.3–334.5	1738 ± 1.0	9.93 ± 0.05	32.28 ± 0.31	94.4 ± 1.0
		$Ti[N(C_2H_5)_2]_4$–C_6H_6			
100	423.1–463.2	4930 ± 176.0	13.89 ± 0.38	94.6 ± 4.0	170.2 ± 9.5
89.66	290.7–351.1	1576 ± 0.1	8.44 ± 0.01	30.19 ± 0.11	66.9 ± 0.3
81.02	297.7–358.9	1549 ± 0.1	8.62 ± 0.01	29.66 ± 0.38	69.3 ± 1.2
60.24	294.3–359.6	1632 ± 1.0	9.18 ± 0.03	31.25 ± 0.18	80.0 ± 0.5
50.98	290.9–354.6	1637 ± 1.0	9.30 ± 0.04	31.35 ± 0.27	82.4 ± 0.8
40.68	293.9–349.9	1616 ± 2.0	9.35 ± 0.55	30.95 ± 0.90	83.3 ± 2.1
19.12	293.8–352.3	1678 ± 1.0	9.65 ± 0.03	32.13 ± 0.23	89.1 ± 0.7

diethylamides) and the same numbers of the Ti←N donor–acceptor bonds in the liquid state and the N←R (R = CH_3, C_2H_5) intermolecular interactions, the difference of 40.8 kJ mol^{-1} in the enthalpies of vaporization qualitatively reflects the influence exerted by the ethyl group on the stabilization of the intermolecular interaction. The question concerning the effect of the ethyl group can be elucidated using the method proposed in [9]. The energy of interaction between the alkyl group (CH_3 or C_2H_5) and the nitrogen atom of a contacting molecule is determined by the half-sum of the energies of interaction in liquid methane or ethane between $Ti(NR_2)_4$ and a similar ligand. Correspondingly, $D_{N\leftarrow CH_3}$ and $D_{N\leftarrow CH_3-CH_2}$ are 3.15 and 4.15 kJ mol^{-1}. The last two digits in the estimates can be disregarded.

With all their tentativeness, these results undoubtedly correctly reflect the behavior of real systems. With account taken of the number of N←R interactions (8) and donor–acceptor bonds (6) in solution, the energies of dissociation of the latter in liquid dimethyl- and diethylamides are 4.8 and 10.2 kJ mol^{-1}, respectively.

These values are limiting because of the unaccounted-for universal interactions. It follows from these data that the less stable dative bond in $N(C_2H_5)_2$ determines the better donor properties of the nitrogen atom and of the carbon atom in the terminal methyl group of the ethyl substituent in the formation of the bonds $D_{Ti\leftarrow N}$ and $(H_2C_2)N\rightarrow(C_2H_5)N$ of the contacting molecules in $Ti[N(C_2H_5)_2]_4$, compared with the corresponding properties of $Ti[N(CH_3)_2]_4$.

The studies were carried by the static method with a membrane null gage. The starting compounds, preliminarily degassed by freezing in a vacuum, were distilled into ampules by means of cooling with liquid nitrogen on a special manifold with ground-glass joints. All measurements were done in all-sealed systems preliminarily dried by heating with a zeolite pump. The membrane chambers were filled in a special device, with successive opening of the ampules and distillation of, first, titanium(IV) tetrakis(dialkylamide) and then benzene. Vapor pressure measurements were done in an air thermostat with a bulky metal block for equalizing the temperature along the entire membrane chamber. The vapor pressure was measured with an MChR-3 gage with a scale interval of 13.3 Pa at strictly fixed temperatures with the accuracy of controlling and measuring temperature of ±1 K.

The results obtained in measuring the total vapor pressure over solutions of varied composition are described by the dependence $\log p = f(1/T)$ in the form of straight lines arranged in a fan-like pattern, lying between the lines corresponding to the vapor pressures of the individual starting components. The experimental vapor pressures are described by the dependence $\log p = B - A/T$ whose coefficients are presented in the table.

The isotherms calculated from data on vapor pressure indicate the occurrence in the system of a positive deviation from the line representing a pressure change in accordance with the Raoult law. The system $Ti[N(CH_3)_2]_4$–C_6H_6 exhibits a stronger deviation from the additive value, increasing with temperature. The enthalpies and entropies of vaporization calculated from data on vapor pressure for various solution compositions (see table) in the form of the dependences $\Delta H^0(T) = f(x)$ and $\Delta S^0(T) = f(x)$ demonstrate a negative deviation from the additive value (Figs. 1a, 1b). Addition of 10–13 mol % benzene to titanium(IV) tetrakis(dialkylamide) leads to a dramatic decrease in the enthalpy of vaporization. The difference between the enthalpies of vaporization and the respective additive values is 24.5 kJ mol^{-1} for the $Ti\cdot[N(CH_3)_2]_4$–C_6H_6 system and 64.5 kJ mol^{-1} for $Ti\cdot[N(C_2H_5)_2]_4$–C_6H_6. The total entropy decreases in this system from 170.2 J mol^{-1} K^{-1} for $Ti[N(C_2H_5)_2]_4$ to 67 J mol^{-1} K^{-1} at 10.34 mol % C_6H_6. The information about specific features of the interaction in systems with benzene is extracted from the fact that the stability of titanium(IV) tetrakis(dialkylamides) falls dramatically upon their dissolution in benzene:

$c\{Ti[N(CH_3)_2]_4\}$, mol %	T, K	$c\{Ti[N(C_2H_5)_2]_4\}$, mol %	T, K
100	423	100	413
90.51	349	89.66	351
74.35	347	81.66	354
49.14	353	60.24	353
26.86	353	50.98	352
16.09	352	40.68	344
		19.12	355

The recorded temperature of the onset of thermal decomposition of titanium(IV) tetrakis(dimethylamide) (423 K) decreases upon its dissolution in benzene by 70–76 K. Correspondingly, the temperature of noticeable thermal decomposition of titanium(IV) tetrakis(diethylamide) (413 K) decreases in this case by 58–69 K. This fact can be accounted for by a significant change in the intramolecular bond $Ti \rightarrow N$ in the molecule of titanium(IV) tetrakis(dialkylamide), caused by the interaction between the nitrogen atom and benzene molecules.

The obtained decomposition temperatures give no way of speaking about any tendency in this influence with increasing content of benzene in solution. However, in the context of the problem considered here, an important result obtained in studying the dependence of the enthalpies of vaporization on the content of components (Figs. 1a, 1b) is that these dependences

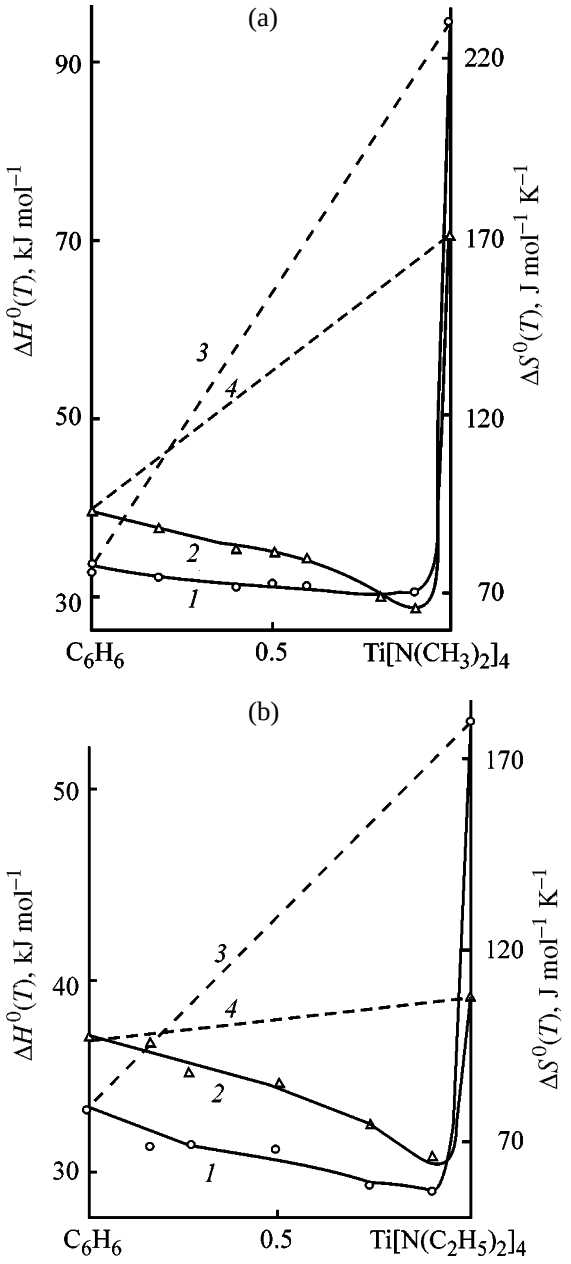

Fig. 1. (*1*) Enthalpy $\Delta H^0(T)$ and (*2*) entropy $\Delta S^0(T)$ of vaporization vs. content of $Ti(NR_2)_4$ in the systems (a) $Ti[N(CH_3)_2]_4$–C_6H_6 and (b) $Ti[N(C_2H_5)_2]_4$–C_6H_6 and (*3*, *4*) the corresponding additive values.

show a minimum at 10–13 mol % benzene, i.e., in the case when titanium(IV) tetrakis(dialkylamide) acts as a solvent. Interpreting the specificity of the interaction between the nitrogen atom and the benzene molecule is a complicated task. However, judging from its energy contribution, it must be insignificant since the minimum in the composition dependence of the enthalpy of vaporization of the solutions is observed at 10–13 mol % C_6H_6 and the contribution from in-

teractions occurring in liquid $Ti(NR_2)_4$ to the enthalpy of vaporization decreases by 24.5 and 64.5 kJ mol^{-1}, compared with the additive values, for $Ti[N(CH_3)_2]_4$ and $Ti[N(C_2H_5)_2]_4$, respectively.

CONCLUSION

The choice of a procedure for purification of titanium(IV) alkylamides is governed by the vapor pressures of the systems $Ti[N(CH_3)_2]_4$–C_6H_6 and $Ti\cdot[N(C_2H_5)_2]_4$–C_6H_6, measured in a wide temperature range, by the calculated thermodynamic characteristics of the vaporization process, and by the established fact of a decrease in the decomposition temperatures of titanium(IV) dialkylamides owing to rather strong specific interactions between benzene and the unshared electron pair of the nitrogen atom.

REFERENCES

1. Mikhailov, V.E., Thermodynamics and Thermal Decomposition of Alkylamide Compounds of Titanium, *Cand. Sci. Dissertation*, Minsk, 1987.
2. Krestov, G.A., Vinogradov, V.I., Kessler, Yu.M., *et al*., *Sovremennye problemy khimii rastvorov* (Modern Problems of Solution Chemistry), Moscow: Nauka, 1998.
3. Baev, A.K., Mikhailov, V.E., and Baev, A.A., *Vestsi Akad. Navuk Bel. SSR, Ser. Khim. Navuk*, 1984, no. 4, pp. 75–77.
4. Baev, A.K., Mikhailov, V.E., and Baev, A.A., *Izv. Vyssh. Uchebn. Zaved., Khim. Khim. Tekhnol.*, 1985, vol. 28, no. 7, pp. 115–116.
5. Burger, H., Stammreich, H., and Texeira Sans, T., *Monatsh. Chem.*, 1966, vol. 97, no. 4, pp. 1276.
6. Pitter, N.R. and Peters, F.M., *Can. J. Chem.*, 1965, vol. 2, no. 6, pp. 1884–1886.
7. Baev, A.K., *Koord. Khim.*, 1996, vol. 22, no. 5, pp. 399–402.
8. Shustorovich, E.M., *Khimicheskaya svyaz' v koordinatsionnykh soedineniyakh* (Chemical Bond in Coordination Compounds), Moscow: Znanie, 1975.
9. Baev, A.K., *Izv. Vyssh. Uchebn. Zaved., Khim. Khim. Tekhnol.*, 1999, vol. 42, no. 6, pp. 3–13.

Russian Journal of Applied Chemistry, Vol. 74, No. 9, 2001, pp. 1439–1445. Translated from Zhurnal Prikladnoi Khimii, Vol. 74, No. 9, 2001, pp. 1401–1406.

SORPTION AND ION-EXCHANGE PROCESSES

Platinum Complexation at Sorption of Hexachloroplatinate(IV) Ion with Fibrous N,S-Containing Sorbents Based on Polyacrylonitrile (of TIOPAN Type)

S. A. Simanova, T. V. Kuznetsova, V. N. Demidov, O. V. Knyaz'kov, and L. V. Konovalov

St. Peterburg State Technological Institute, St. Petersburg, Russia

Received January 16, 2001; in final form, June 18, 2001

Abstract—Sorption properties of fibrous nitrogen-containing sorbents based on polyacrylonitrile containing diethyldithiocarbamate (TIOPAN-2) and 8-mercaptoquinoline groups (TIOPAN-6) with respect to the platinum(IV) chloride complex were studied. The effects of the temperature, platinum concentration, and acidity on the metal recovery were determined. The kinetics of sorption and sorption capacity of sorbents in hydrochloric acid and chloride solutions were established. The most probable mechanism of sorption and the composition of compounds formed in the fiber phase were proposed.

Sorbents with N,S-containing functional groups are promising materials for recovery of platinum metals from solutions [1–4]. The mechanism of sorption is of special interest. It was discussed in [5–16]. A review on sorption recovery of platinum with N,S-containing materials was made in [5].

Materials containing thioamide groups are widely used for recovery of platinum metals [6–12]. MTILON-T fiber, which is a copolymer of polyacrylonitrile (PAN) and cellulose treated with hydrogen sulfide, recovers 0.5 mmol g^{-1} of K_2PtCl_6 from 1 M HCl at 100°C. In the presence of Fe(III) and Cu(II) salts, sorption decreases by 50–70% [6]. The mechanism of platinum recovery with MTILON-T fiber was not considered.

The modified copolymer of polyvinyl alcohol with PAN (MSPVS fiber) containing thioamide groups quantitatively and selectively recovers platinum(II) and (IV) chloro complexes from HCl and NaCl solutions of various concentrations [7–12]. In 2 M HCl, the sorption capacity of the MSPVS fiber with respect to K_2PtCl_4 is 0.48 and 1.50, and with respect to K_2PtCl_6, 0.16 and 0.42 mmol g^{-1} at 20 and 98°C, respectively. It was found that the sorption in both cases proceeds with formation of a $[Pt^{2+}\{R\text{-}C(NH_2)S\}Cl_3]$ type complex, in which thioamide groups are coordinated via sulfur atoms, with the successive hydrolytic conversion of thioamide complexes into sulfides strongly retained in the fiber matrix [7]. To recover Pt(IV) complexes, Ni Cai-Hia and Xu Yu-Wu [13] proposed a chelating ion exchanger containing groups of the CH_2–CH_2–SH–CH_2–$N(C_2H_5)_2$ type, which was prepared by treating polyoxyethylene with diethylaminomethylthiirane. The composition of the sorbed complexes was not determined. Chelating resins containing dithiocarbamate groups quantitatively and very selectively recover precious metals, including Pt(IV), from solutions. The platinum species were not studied [14].

Fibrous sorbent TIOPAN-13 based on PAN with mercaptobenzothiazole functional groups very rapidly recovers Pt(IV) complexes from solutions at pH 0.5–2.0. Large amounts of heavy metals do not interfere with the recovery [15]. The mechanism of the sorption recovery was not studied.

Monivex and Srafion resins, which are styrene–divinylbenzene copolymers containing isothiourea, can recover platinum group metals, including platinum [16]. The chelating resin based on macronetwork styrene–divinylbenzene copolymer with thiosemicarbazide as a functional group quantitatively recovers platinum group metals, including Pt(IV), from hydrochloric acid solutions. The maximal sorption capaccity with respect to Pt(IV) (0.71 mmol g^{-1}) is observed in 1 M HCl, in which platinum group metals form stable complexes. It was found that the metal–thiosemicarbazide ratio in the complex formed in the sorbent phase is close to 1 : 1 [17].

Earlier we studied the sorption properties of

1070-4272/01/7409-1439$25.00

Table 1. Conditions of preparation of TIOPAN-type fibers and their properties [20]

Sorbent	Modifying reagent, wt %	τ, min, at 100°C	C_S, %	SSC_{Ag}, mmol g^{-1}
TIOPAN-1	Thiosemicarbazide, 2	15	10.0	2.04
TIOPAN-2	Sodium diethyldithiocarbamate, 8	30	14.3	1.48
TIOPAN-3	Thioacetamide, 8	60	15.5	2.59
TIOPAN-4	Thiourea, 8	40	8.7	1.48
TIOPAN-5	Ammonium thiocyanate, 4	60	7.8	1.48
TIOPAN-6	Sodium 8-mercaptoquinolinate, 3	20	4.0	1.11

GLIPAN-1 fiber (which is a fibrous sorbent based on PAN modified with thiosemicarbazide) with respect to Pt(IV) chloride complexes and showed that this fiber quantitatively recovers K_2PtCl_6 from HCl and NaCl solutions (C_{Pt} = 1–10 mM) with similar rates [18]. The maximal sorption capacity (1.35 mmol g^{-1}) is observed in 0.5 M HCl. Sorption of Pt(IV) chloride complexes with GLIPAN-1 in all cases is caused by metal complexation with sorbent as a polymeric ligand and metal reduction in the fiber phase. The complex [R–NH–C(NH–NH_2)=SPt(II)Cl_2], in which the thiosemicarbazide group is a bidentate ligand, is the final sorbed species of platinum [18].

For recovery of platinum(II) chloride complexes, we proposed fibrous nitrogen-containing sorbents of the TIOPAN type (copolymers of PAN with grafted polyglycidyl methacrylate PAN–PGMA) modified with various N,S-containing reagents (Table 1) [19–22]. High Pt(II) sorption is observed with TIOPAN-6 at room temperature and with TIOPAN-2, TIOPAN-5, and TIOPAN-6 at elevated temperatures. The static sorption capacity (SSC) of these fibers in 1 M HCl decreases in the order TIOPAN-6 > TIOPAN-5 > TIOPAN-2 at 20°C and TIOPAN-2 > TIOPAN-5 > TIOPAN-6 at 98°C (Table 2). We concluded that in all cases the Pt(II) sorption is caused by complexation with the sorbents as polymeric ligands. In the fiber phase, TIOPAN-2 forms complexes [Pt(SR_2)Cl_2], TIOPAN-5 gives [Pt(SHR)$_2Cl_2$] in which polymeric ligands coordinate via sulfur atoms, and TIOPAN-6 forms *cis*-[Pt(SQuinR)$_2Cl_2$] in which 8-mercaptoquinoline group is a monodentate ligand bonded to Pt(II) via nitrogen atom [19].

Table 2. Recovery of platinum from 1 M HCl with TIOPAN-type sorbents

Sorbent	Recovery, %		
	Pt(IV) at 98°C	Pt(II) at indicated temperature, °C [19]	
		20	98
TIOPAN-1	1	29	47
TIOPAN-2	82	15	100
TIOPAN-3	0	3	8
TIOPAN-4	19	9	25
TIOPAN-5	2	43	82
TIOPAN-6	97	100	96

In this work, we studied the sorption properties of TIOPAN-type N,S-containing fibers with respect to Pt(IV) chloride complexes and the composition of the species formed in the sorbent phase.

EXPERIMENTAL

Sorption was studied under static conditions at the continuous agitation and at 18 and 98°C. The starting Pt(IV) compound, K_2PtCl_6, was synthesized by the method described in [23]. Sorption was performed from freshly prepared 1–20 mM solutions of K_2PtCl_6 in 0.1–4.0 M HCl or 0.1–2 M NaCl. In all cases, the volume of solutions taken was 20 ml, and the sorbent sample was 0.1 g. The platinum content in solutions was determined spectrophotometrically with tin(II) chloride [24]. The amount of the metal sorbed was calculated as the difference between its content in the solution before and after sorption. The IR spectra of fibers within the 400–4000 cm^{-1} range were measured on an IKS-29 spectrophotometer, and within the 140–400 cm^{-1} range, on a Hitachi FIS-3 spectrophotometer. Samples were prepared as in [5]. X-ray photoelectron spectra (XPES) were recorded on a Perkin–Elmer PH 15400 spectrometer with excitation by Mg X-ray radiation. Spectra were treated (quantitative analysis and line separation) using standard programs. The spectra were standardized against C1*s* electron binding energy of 285.0 eV. The binding energy was determined with an error of 0.2 eV. Thermograms of sorbents were recorded on an MOM (Hungary) derivatograph within the 20–800°C range

at a heating rate of 10 deg min^{-1}. Isothermal heating of sorbents was performed on a special device equipped with a system for a qualitative analysis of the liberated gaseous products. Thermal conversion of samples (temperature of the decomposition onset) was visually controlled on a Koeffler stage.

Initially, the sorption power of TIOPAN fibers with respect to Pt(IV) at sorption from solutions of K_2PtCl_6 in 1 M HCl was studied at 98°C (Table 2). The sorption duration was 1 h, the platinum concentration in the initial solution was 1 mM. As seen, Pt(IV) is efficiently recovered with TIOPAN-2 and TIOPAN-6, and Pt(II), also with TIOPAN-5. There is no correlation between the sulfur content in the fiber and the recovery of both Pt(II) and Pt(IV) (Tables 1, 2). TIOPAN-1, TIOPAN-3, TIOPAN-4, and TIOPAN-5 fibers recover Pt(IV) poorly.

TIOPAN-2 and TIOPAN-6 fibers containing diethyldithiocarbamate and 8-mercaptoquinoline groups, respectively, were studied in detail. It was found that the time of attaining the apparent equilibrium τ_{ap} in distribution of Pt(IV) between the fiber and 1 M HCl solution is 2 h at 18°C and 1 h at 98°C for TIOPAN-6 and 2 h at 98°C for TIOPAN-2. The half-sorption time $\tau_{1/2}$ for TIOPAN-6 is 2 and 4 min at 98 and 18°C, respectively. The low rate of Pt(IV) sorption with TIOPAN-2 should be noted: $\tau_{1/2}$ is 25 min even at 98°C (Fig. 1a, Table 3).

For sorption from 0.5 M NaCl, the apparent equilibrium of Pt(IV) between the solution and sorbent in all cases is attained in 2 h, and $\tau_{1/2}$ both at 98 and 18°C is 4 min for TIOPAN-6 and ~23 min for TIOPAN-2 (Fig. 1a, Table 3). At room temperature, TIOPAN-2 recovers Pt(IV) chloride complexes neither from HCl nor from NaCl solutions.

The type of the diffusion kinetics of sorption is commonly determined using the known dependence of the exchange degree F ($F = Q_\tau/Q_\infty$, where Q_τ is sorption in time τ and Q_∞ is the equilibrium sorption) on sorption time τ [25] and the dependence on sorption time of B_τ and $-\ln(1 - F)$, where B_τ is the kinetic coefficient of sorption [$B_\tau = (F/1.08)^2$] [26]. The analysis of the kinetic curves of sorption (Fig. 1) shows mixed diffusion character of the kinetics of Pt(IV) sorption with TIOPAN-6 fiber from acid solutions. The linear sections of $-\ln(1 - F)$–τ curves indicate that the "film diffusion" is the major factor affecting the kinetics of Pt(IV) sorption with TIOPAN-2 fiber [26] (Fig. 1c).

It was found that at platinum sorption with TIOPAN-6 at 18 and 98°C (C_{Pt} = 1 mM) the Pt(IV) recovery decreases with increasing concentration of hydrochloric acid: platinum is practically completely recovered from 0.1–0.5 M HCl and to only 75–80% from 4 M HCl. The effect of HCl concentration on platinum(IV) sorption with TIOPAN-2 is even stronger. At 98°C, platinum recovery decreases from 100 to 45% in going from 0.1 to 4 M HCl.

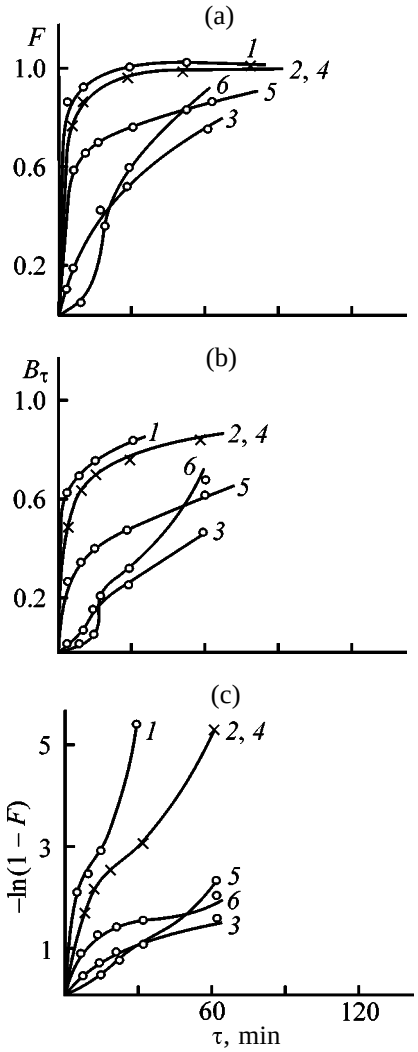

Fig. 1. Dependences of (a) F, (b) B_τ, and (c) $-\ln(1 - F)$ on the time of sorption τ of K_2PtCl_6 from 1 M HCl with (*1, 2*) TIOPAN-6 and (*3*) TIOPAN-2 and from 0.5 M NaCl with (*4, 5*) TIOPAN-6 and (*6*) TIOPAN-2. (*F*) Exchange degree; $F = Q_\tau/Q_\infty$, where Q_τ is Pt sorption in time τ and Q_∞ is equilibrium sorption; (B_τ) kinetic coefficient of sorption, $B_\tau = (F/1.08)^2$. Temperature, °C: (*1*) 3, (*6*) 98, and (*4, 5*) 18.

The dependence of SSE with respect to Pt(IV) on equilibrium metal concentration is shown in Fig. 2. Sharp slope of the isotherms of the Pt(IV) sorption from HCl solutions allows TIOPAN-2 and TIOPAN-6 to be recommended for quantitative recovery of platinum from both dilute and concentrated solutions, the

Table 3. Recovery of platinum(IV) chloride complexes with TIOPAN-2 and TIOPAN-6 fibers

T, °C	Medium, M	SSC, mmol g^{-1}	$\tau_{1/2}$, min	τ_{app}, min	Pt(IV) recovery, %
		TIOPAN-2			
98	HCl, 1	0.75	25	120	82
98	NaCl, 0.5	0.54	23	120	79
		TIOPAN-6			
18	HCl, 1	0.57	4	120	91
18	NaCl, 0.5	0.16	4	120	21
98	HCl, 1	0.80	2	60	97
98	NaCl, 0.05	0.53	4	120	35

former sorbent at heating and the latter, both at room temperature and heating. The data on SSC of fibers are listed in Table 3. The platinum(IV) recovery from NaCl solutions is weaker (Table 3, Fig. 2).

Sorption of Pt(IV) with TIOPAN-2 and TIOPAN-6 is practically irreversible: only 0.6 and 1.0% of Pt is desorbed with 6 M HCl and 22 and 26% of Pt is desorbed with thiourea solution in 10% HCl from TIOPAN-2 and TIOPAN-6, respectively.

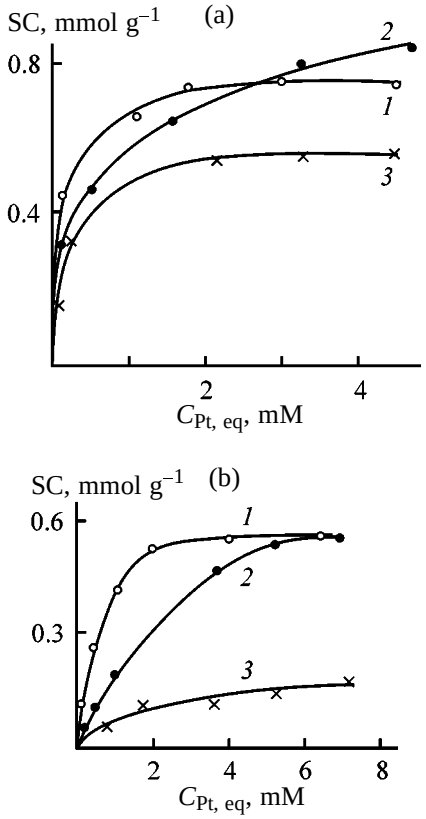

Fig. 2. Isotherms of K_2PtCl_6 sorption from (a) 1 M HCl and (b) 0.5 M NaCl at (*1*, *2*) 98 and (*3*) 18°C. (SC) Sorption capacity; ($C_{Pt,eq}$) equilibrium concentration. Sorbent: (*1*) TIOPAN-2 and (*2*, *3*) TIOPAN-6.

The comparison of the kinetic and capacity characteristics of the fibers shows that in all cases platinum(II) is recovered faster and with greater SSC as compared to Pt(IV). This may be due to two factors: (1) greater charge density on $PtCl_4^{2-}$ as compared to $PtCl_6^{2-}$, which increases electrostatic attraction of the complex anion to the protonated nitrogen atom of the fiber, and (2) greater steric hindrance in interaction of the octahedral $PtCl_6^{2-}$ complex as compared to the square-planar $PtCl_4^{2-}$ ion.

It should be noted that TIOPAN-5 containing thiol groups practically completely recovers K_2PtCl_4 [19] but sorbs K_2PtCl_6 poorly (Table 2).

The analysis of the kinetics and capacity parameters of TIOPAN-2 with respect to K_2PtCl_6 suggests that the platinum recovery from both hydrochloric acid and NaCl solutions proceeds with formation of a Pt(II) compound of the $[Pt(SR)_2Cl_2]$ type in the sorbent phase. The diethyldithiocarbamate group of the polymeric ligand coordinates to Pt(II) via sulfur atom as a monodentate ligand. The low rate of sorption, sharp temperature dependence of sorption, and comparison of the IR and far-IR spectra of fibers after sorption of K_2PtCl_6 (Figs. 3, 4) and K_2PtCl_4 [19] indicate complex formation. In both cases the spectra are similar. A strong change of the IR spectrum in the ν(CS) and ν(CN) range (1200–1600 cm^{-1}) (Fig. 3) shows formation of a covalent bond of platinum with the fiber. XPES indicates reduction of Pt(IV) to Pt(II) during K_2PtCl_6 sorption. The binding energy of the Pt4$f_{7/2}$ electron is 72.7 eV, which agrees with reference data for Pt(II) [27].

For comparison, we performed a reaction of K_2PtCl_4 with the monomeric ligand, sodium diethyldithiocarbamate. To a hot solution of K_2PtCl_4, a hot solution of sodium diethyldithiocarbamate was added gradually with stirring. The resulting pale yellow precipitate was filtered off and washed with ether. As shown by elemental analysis and far-IR and IR spectra, the compound corresponds to the previously described complex $[PtS_2N(C_2H_5)_2]$ [28] in which diethyldithiocarbamate ion coordinates to platinum atom via sulfur atom. In the IR spectra of this compound and of TIOPAN-2 fiber after K_2PtCl_6 sorption the same bands assigned to stretching vibrations of the coordinated diethyldithiocarbamate group are observed in the 1200–1600 cm^{-1} range (Fig. 3). However, their far-IR spectra differ substantially: the spectrum of the fiber after sorption of K_2PtCl_6 from 1 M HCl contains two bands at 310 and 328 cm^{-1} assigned to the stretching vibrations ν(Pt–Cl) of asymmetrical *cis*-$[Pt(SR)_2Cl_2]$. TIOPAN-2 fiber after sorption of K_2PtCl_6 from 0.5 M NaCl has the similar spectrum. In the far-IR spectrum of the chelate with the monomeric ligand such bands are absent [28]. The difference in reaction of K_2PtCl_6 with the monomeric ligand and the fibrous sorbent, both containing diethyldithiocarbamate group, may be due to two factors: (1) one of two sulfur atoms of the polymeric ligand (TIOPAN-2) is bound with the fiber matrix PAN–PGMA and cannot participate in formation of the chelate bond with platinum and (2) steric hindrances arise in interaction of the platinum atom with the bulky diethyldithiocarbamate group bonded with the polymeric matrix of the fiber.

The high rate of recovery of the platinum(IV) chloride complexes with TIOPAN-6 fiber from both acid and neutral media and weak dependence on temperature suggest that in the first stage of sorption the initial complex reacts with protonated fiber

$$2RQuinS \cdot HCl + K_2PtCl_6 \rightarrow (RQuinSH)_2PtCl_6 + 2KCl,$$

$$2RQuinS \cdot H_2O + K_2PtCl_6 \rightarrow (RQuinSH)_2PtCl_6 + 2KOH.$$

The next stage is the partial reduction of the onium platinum(IV) complex to the analogous platinum(II) complex $[(RQuinSH)_2PtCl_4]$ with 8-mercaptoquinoline groups that do not participate in sorption. The XPES data indicate the prevalence of platinum(II) complexes on the fiber. The binding energy of the Pt4$f_{7/2}$ electron of 73.1 eV is in a good agreement with the reference data for Pt4$f_{7/2}$, e.g., in K_2PtCl_4 [27]. We can assume that sorption from NaCl solutions involves in the second stage the Anderson rearrangement with formation of *cis*-$(RQuinSH)_2PtCl_4$ coordinated via the nitrogen atom:

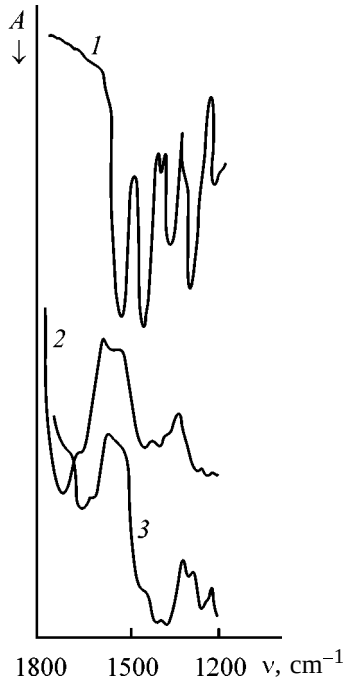

Fig. 3. IR spectra of (*1*) $[Pt(S_2N(C_2H_5)_2]$, (*2*) TIOPAN-2 fiber after K_2PtCl_6 sorption from 1 M HCl, and (*3*) sodium diethyldithiocarbamate. (*A*) Absorption and (ν) wave number; the same for Fig. 4.

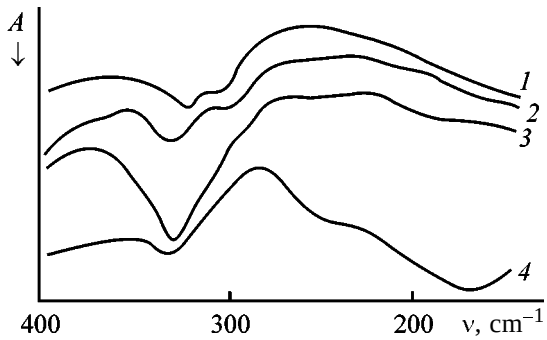

Fig. 4. Far-IR spectra of fibers after K_2PtCl_6 sorption. Sorption temperature 98°C, C_{Pt} = 8 mM. Sorption from (*1–3*) 1 M HCl and (*4*) 0.5 M NaCl. (*2*) Fiber heated at 180°C for 0.5 h. Sorbent: (*1*) TIOPAN-2 and (*2–4*) TIOPAN-6.

$$(RQuinSH)_2PtCl_4 \rightarrow cis\text{-}[Pt(RQuinS)_2Cl_2] + 2HCl.$$

Heating promotes such transformation. To simulate this reaction, we estimated the rearrangement temperature from the termogravimetric data for the fiber. In the far-IR spectrum of TIOPAN-6 fiber after sorption of K_2PtCl_4 from 1 M HCl, subjected to isothermal heating at 180°C for 0.5 h, two bands are

observed at 305 and 329 cm^{-1}, belonging to Pt–Cl stretching vibrations of the asymmetrical *cis*-dichlorodiammine complex. Formation of H bonds between protonated nitrogen of the fiber mercaptoquinoline groups and chloride ions in the inner coordination sphere of the metal complex facilitates such transformation.

It is known that in reactions of platinum complexes with 8-mercaptoquinoline and its derivatives yield the Pt(II) chelates [29]. For instance, reaction of 8-mercaptoquinoline with both K_2PtCl_4 and K_2PtCl_6 produces the compound $[Pt(SNC_9H_6)_2]$ in which the organic ligand coordinates to platinum via N and S atoms [29]. Since, when PAN–PGMA is modified with sodium 8-mercaptoquinolinate [20], the modifying agent is incorporated into the fiber matrix via the sulfur atom. The platinum atom is probably bound with the fiber via the nitrogen atom.

CONCLUSIONS

(1) Sorbents TIOPAN-2 and TIOPAN-6 (copolymers of polyacrylonitrile with grafted polyglycidyl methacrylate modified with sodium diethyldithiocarbamate and 8-mercaptoquinoline, respectively) can quantitatively recover platinum(IV) chloride complexes from acid and neutral solutions. TIOPAN-6 with high rate and quantitatively recovers Pt(IV) at 18 and 98°C, while TIOPAN-2 efficiently sorbs Pt(IV) only at heating.

(2) In all cases, Pt(IV) sorption is caused by complexation with sorbents as polymeric ligands. The platinum(IV) chloride complex reacts with TIOPAN-2 fiber with formation of the $[Pt(SR)_2Cl_2]$-type compound, in which the polymeric ligand coordinates via sulfur atom. At Pt(IV) sorption with TIOPAN-6, the onium compound $(RQuinSH)_2PtCl_4$ is formed. At heating, this compound converts into *cis*-$[Pt\cdot(RQuinS)_2Cl_2]$ in which 8-mercaptoquinoline group coordinates via nitrogen atom.

REFERENCES

1. Simanova, S.A. and Kukushkin, Yu.N., *Izv. Vyssh. Uchebn. Zaved., Khim. Khim. Tekhnol.*, 1985, vol. 28, no. 8, pp. 3–15.
2. Simanova, S.A. and Kukushkin, Yu.N., *Izv. Vyssh. Uchebn. Zaved., Khim. Khim. Tekhnol.*, 1986, vol. 29, no. 5, pp. 3–14.
3. Simanova, S.A. and Kukushkin, Yu.N., *Probl. Sovr. Khim. Koord. Soedin.*, 1992, no. 10, pp. 125–141.
4. Myasoedova, G.V. and Komozin, P.N., *Zh. Neorg. Khim.*, 1994, vol. 39, no. 2, pp. 280–288.
5. Simanova, S.A., Kuznetsova, T.V., Belyaev, A.N., *et al.*, *Zh. Prikl. Khim.*, 1999, vol. 72, no. 8, pp. 1276–1281.
6. Orobinskaya, V.A., Chuikova, N.E., Nazarenko, G.N., *et al.*, in *Analiz i tekhnologiya blagorodnykh metallov* (Analysis and Technology of Precious Metals), Moscow: Metallurgiya, 1971, pp. 91–95.
7. Simanova, S.A., Bobritskaya, L.S., Kukushkin, Yu.N., *et al.*, *Zh. Prikl. Khim.*, 1981, vol. 54, no. 4, pp. 764–771.
8. Simanova, S.A., Bobritskaya, L.S., Kukushkin, Yu.N., *et al.*, *Information Bulletin of NTIP Interbranch Regional Center*, 1979, no. 1393-79.
9. Simanova, S.A., Bobritskaya, L.S., Kukushkin, Yu.N., *et al.*, *Zh. Prikl. Khim.*, 1981, vol. 54, no. 3, pp. 514–517.
10. Simanova, S.A., Bobritskaya, L.S., Kukushkin, Yu.N., *et al.*, *Zh. Prikl. Khim.*, 1986, vol. 59, no. 1, pp. 175–178.
11. Simanova, S.A., Kukushkin, Yu.N., Kolontarov, I.Ya., *et al.*, *Zh. Prikl. Khim.*, 1977, vol. 50, no. 31, pp. 519–522.
12. Simanova, S.A., Bobritskaya, L.S., Kalyamin, A.V., and Kukushkin, Yu.N., *Zh. Prikl. Khim.*, 1984, vol. 57, no. 11, pp. 2470–2476.
13. Ni Cai-Hia and Xu Yu-Wu, *Chem. J. Chin. Univ.*, 1995, vol. 16, no. 4, pp. 657–659.
14. Dong Shihua and Tang Wanxiong, *Acta Polym. Sin.*, 1990, no. 1, pp. 28–34.
15. Tat'yankina, E.M., *Zh. Anal. Khim.*, 1996, vol. 51, no. 5, pp. 498–501.
16. Warshawsky, A., Fieberg, M.B., and Mihalik, P., *Separ. Purif. Meth.*, 1980, vol. 9, no. 2, pp. 209–265.
17. Siddihanta, S. and Dos, H.R., *Talanta*, 1985, vol. 32, no. 6, pp. 457–460.
18. Simanova, S.A., Knyaz'kov, O.V., Belyaev, A.N., *et al.*, *Zh. Prikl. Khim.*, 1998, vol. 71, no. 2, pp. 220–226.
19. Simanova, S.A., Zamorova, I.N., Kazakevich, Yu.E., *et al.*, *Zh. Prikl. Khim.*, 1992, vol. 65, no. 9, pp. 1987–1994.
20. Simanova, S.A., Kazakevich, Yu.E., Danilova, E.Ya., *et al.*, *Zh. Prikl. Khim.*, 1992, vol. 65, no. 3, pp. 686–691.
21. Simanova, S.A., Zamorova, I.N., Kazakevich, Yu.E., *et al.*, *Zh. Prikl. Khim.*, 1992, vol. 65, no. 7, pp. 1619–1630.
22. Simanova, S.A., Zamorova, I.N., Kazakevich, Yu.E., *et al.*, *Zh. Prikl. Khim.*, 1992, vol. 65, no. 10, pp. 2274–2281.

23. *Sintez kompleksnykh soedinenii metallov platinovoi gruppy: Spravochnik* (Synthesis of Platinum Group Metal Complexes: Handbook), Chernyaev, I.I., Ed., Moscow: Nauka, 1964.
24. Ginzburg, S.I., Ezerskaya, N.A., Prokof'eva, I.V., *et al*., *Analiticheskaya khimiya elementov: Platinovye metally* (Analytical Chemistry of Elements: Platinum Metals), Moscow: Nauka, 1972.
25. Polyanskii, N.G., Gorbunov, G.V., and Polyanskaya, N.L., *Metody issledovaniya ionitov* (Methods of Studying Ion Exchangers), Moscow: Khimiya, 1976.
26. Saldadze, K.M. and Kopylova-Valova, V.D., *Kompleksoobrazuyushchie ionity* (Complexing Ion Exchangers), Moscow: Khimiya, 1980.
27. Nefedov, V.I., *Rentgenoelektronnaya spektroskopiya khimicheskikh soedinenii: Spravochnik* (X-ray Photoelectron Spectroscopy of Chemical Compounds: Handbook), Moscow: Khimiya, 1984.
28. Baker, A.T. and Emett, M.T., *Aust. J. Chem.*, 1992, vol. 45, pp. 429–434.
29. Bankovskii, Yu.A., *Khimiya vnutrikompleksnykh soedinenii merkaptokhinolina i ego proizvodnykh* (Chemistry of Chelate Compounds of Mercaptoquinoline and Its Derivatives), Riga: Zinatne, 1978.

Russian Journal of Applied Chemistry, Vol. 74, No. 9, 2001, pp. 1446–1449. Translated from Zhurnal Prikladnoi Khimii, Vol. 74, No. 9, 2001, pp. 1407–1409.

SORPTION AND ION-EXCHANGE PROCESSES

Effect of Cationic Form of a Fibrous Sulfonic Cation-Exchange Resin on Sorption of Tetramminepalladium(II) and Its Cross-Sectional Distribution

V. Z. Radkevich, I. E. Kistanova, V. S. Soldatov, and Yu. G. Egiazarov

Institute of Physical Organic Chemistry, Belarussian National Academy of Sciences, Minsk, Belarus

Received November 17, 2000; in final form, May 2001

Abstract—The effect of the nature of exchangeable cation (Na^+, Mg^{2+}, Ba^{2+}, La^{3+}) in FIBAN K-1 fibrous sulfonic cation-exchange resin on sorption of tetramminepalladium(II) and its cross-sectional distribution in fabrication of Pd catalysts is studied.

Sulfonic cation-exchange resins can be used as supports in fabrication of metal-containing catalysts. For instance, it was demonstrated [1, 2] that the supported Pd catalyst based on FIBAN K-1 fibrous cation-exchange resin in the Ba form shows high activity in oxidation of hydrogen.

In the first stage of preparation of Pd catalysts palladium is incorporated in a polymeric support (fibrous cation-exchange resin) by ion exchange in a tetramminepalladium(II) chloride solution. Then the catalyst is dried, heated in a helium current, and reduced to Pd^0 in a hydrogen stream.

A review of works on sorption of $[Pd(NH_3)_4]^{2+}$ on granulated cation-exchange resins can be found in [3]. However, information on its sorption on fibrous sulfonic cation-exchange resins is lacking in the literature.

Since the catalyst activity depends not only on the Pd content and dispersity, but also on its distribution throughout the bulk of a support, in this work we studied certain features of ion exchange $M^{z+} \rightarrow [Pd(NH_3)_4]^{2+}$ (M^{z+} = Na^+, Mg^{2+}, Ba^{2+}, La^{3+}) in FIBAN K-1 fibrous sulfonic cation-exchange resin and also the effect of the cationic form of this resin on the Pd cross-sectional distribution.

EXPERIMENTAL

FIBAN K-1 fibrous sulfonic cation-exchange resin was prepared by radiation three-dimensional grafting of a copolymer of styrene (98%) and divinylbenzene (2%) to polypropylene staple fiber followed by sulfonation of the resulting matrix with concentrated sulfuric acid [4]. The grafting proceeds quite uniformly (at a 120% degree of grafting the fiber diameter is 40 ± 3 μm).

Totally substituted Na, Mg, Ba, and La forms of K-1 were prepared from the H form (exchange capacity 3.24 mg-equiv g^{-1}) by passing an excess of a 1 N solution of the corresponding metal chloride through a column packed with the resin until pH of the filtrate became equal to that of the initial solution. Then the samples were washed with distilled water to a negative reaction for chloride and air-dried at room temperature. The swellability of the samples was determined by centrifugation [5].

Ion exchange of Na^+, Mg^{2+}, Ba^{2+}, and La^{3+} for $[Pd(NH_3)_4]^{2+}$ was studied by placing a weighed portion of the resin in the corresponding form in 0.01 N tetramminepalladium(II) chloride at $n\mathrm{Pd}_0^{2+}/n\mathrm{Pd}_{max}^{2+} = 0.35$, where $n\mathrm{Pd}_0^{2+}$ is the $[Pd(NH_3)_4]^{2+}$ content in the initial solution and $n\mathrm{Pd}_{max}^{2+}$ is the limiting (estimated from the exchange capacity) content of $[Pd(NH_3)_4]^{2+}$ in the resin phase.

The resin samples (2 g) were preliminarily held in distilled water to attain the limiting swellability, and then the tetramminepalladium(II) chloride solution was added in amount estimated taking into account the exchange capacity of the given cationic form of K-1 resin. The total volume of the aqueous phase was 100 ml. Keeping in mind that the ammine complex $[Pd(NH_3)_4]^{2+}$ is stable at pH ≥ 8 [6], and also to minimize formation of lanthanum hydroxide and basic salts, ion exchange $M^{z+} \rightarrow [Pd(NH_3)_4]^{2+}$ was performed at pH 8–8.5. The experiments were carried out at room temperature with vigorous stirring (magnetic

1070-4272/01/7409-1446$25.00

stirrer). The contact time was 10 min, which was demonstrated to be sufficient for reaching the saturation. Samples (1 ml) of the liquid phase were taken at fixed intervals (10–60 s) and analyzed for Pd and the exchangeable cation. Palladium was determined spectrophotometrically [7], and Mg^{2+}, Ba^{2+}, and La^{3+}, by chelatometric titration with Na_2EDTA (Mg^{2+} and Ba^{2+} with Eriochrome Black T [8] and La^{3+} with Xylenol Orange [9]). The Na^+ concentration was determined indirectly as follows [10]: An aliquot of the solution was acidified with HCl to pH 1, evaporated to dryness, and heated at 120°C to remove HCl. Then the solid residue was dissolved in water, and the sum of chlorides was determined by Mohr titration. From this value we determined the sum of sodium and palladium in the solution. The Na^+ concentration was then estimated as the difference between this value and the Pd concentration determined spectrophotometrically.

Using the data on the M^{z+} and $[Pd(NH_3)_4]^{2+}$ concentrations in the aqueous phase, the selectivity coefficient was estimated as

$$S = \frac{\bar{X}_{Pd} X_M}{X_{Pd} \bar{X}_M}$$

where $\bar{X}$ and X are the equivalent fractions of the cations in the resin phase and solution, respectively. The equivalent fraction of palladium in the resin phase $\bar{X}_{Pd}$ was estimated as

$$\bar{X}_{Pd} = \frac{n\mathrm{Pd}_0^{2+} - n\mathrm{Pd}_{eq}^{2+}}{n\mathrm{Pd}_{max}^{2+}},$$

where $n\mathrm{Pd}_{eq}^{2+}$ is the Pd content in the equilibrium solution.

The degree of exchange with respect to M^{z+} was estimated as the ratio of the amount of the exchangeable cation in the equilibrium solution to its initial amount in the resin.

As an experimental parameter characterizing the ion-exchange rate with various exchangeable cations we selected $t_{0.9}$, i.e., the time required to reach 90% saturation of the resin with respect to $[Pd(NH_3)_4]^{2+}$.

The cross-sectional distribution of Ba^{2+} and $[Pd(NH_3)_4]^{2+}$ was studied by electron micro probe analysis (EPMA) with a Cameca MS-46 instrument. The distribution data were obtained parallelly for no less than 10 fibers of a sample. The reproducibility of the data was sufficiently high (7–8 fibers of 10 had practically the same diameters and demonstrated identical distribution curves).

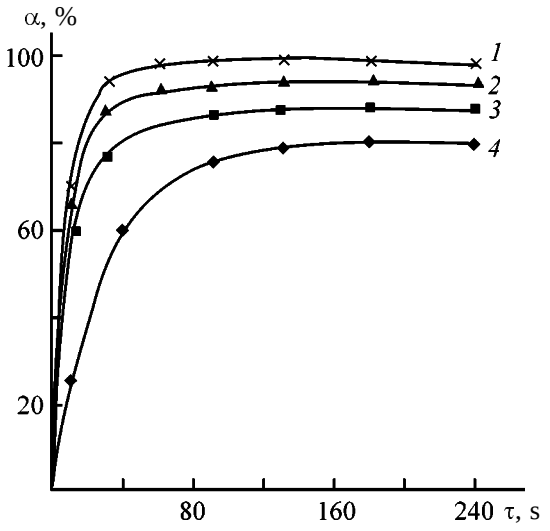

Fig. 1. Degree of sorption of $[Pd(NH_3)_4]^{2+}$ on FIBAN K-1 α as a function of time τ. Cationic form of the resin: (*1*) Na, (*2*) Mg, (*3*) Ba, and (*4*) La.

The Pd content in samples specially prepared for EPMA was about 1%. The catalyst based on the Na form of K-1 was prepared as follows. A weighed portion of the resin (2 g) was poured over with 20 ml of distilled water, allowed to stand until reaching the limiting swelling, and 13.2 ml of 0.025 N tetramminepalladium(II) chloride was added with vigorous stirring. After a 10-min contact the resin was separated from the solution, washed to remove chloride, and air-dried at room temperature. The catalysts based on the Mg and Ba forms were prepared similarly, except that the volume of 0.025 N tetramminepalladium(II) chloride added was 14.0 and 15.2 ml, respectively.

The kinetic curves of cation exchange on various cationic forms of K-1 with $[Pd(NH_3)_4]^{2+}$ are given in Fig. 1. In the case of the Na form tetramminepalladium(II) is practically totally recovered from the aqueous phase. For the Mg, Ba, and La forms the degree of exchange was found to be 95, 89, and 80% of the theoretical value, respectively. The degree of saturation of the resin phase with $[Pd(NH_3)_4]^{2+}$ is 0.35, 0.33, 0.31, and 0.28% for the Na, Mg, Ba, and La forms, respectively. The relative error of determination of the degree of saturation was within 1.5%. The degrees of exchange estimated from the $[Pd(NH_3)_4]^{2+}$ and exchangeable cation contents in the equilibrium solution were well consistent (the difference was within 1%).

Characteristics of FIBAN K-1 in various cationic forms

Cation	Swellability		$t_{0.9}$, s	S
	wt %	mol H_2O equiv^{-1} resin		
H^+	111.0	19.0	–	–
Na^+	97.0	17.8	22	>20
Mg^{2+}	91.0	16.2	25	9.4
Ba^{2+}	54.8	11.4	40	3.1
La^{3+}	54.2	10.7	72	1.5
$[Pd(NH_3)_4]^{2+}$	35.8	7.8	–	–

On passing from the Na form of the resin to the Mg, Ba, or La forms $t_{0.9}$ increased from 22 to 72 s, and the selectivity coefficient decreased (see table).

Previously we demonstrated by EPMA that in a sulfonic cation-exchange resin the cross-sectional distribution of functional groups depends on the synthesis conditions [11]. In this work with an example of the Ba form of K-1 we demonstrated that in FIBAN K-1 fibrous sulfonic cation-exchange resin functional groups are uniformly distributed throughout the cross section of its fibers (Fig. 2a). In the Na form and to a lesser extent in the Mg form the surface layer of the resin grains is enriched with $[Pd(NH_3)_4]^{2+}$ ions (Figs. 2b, 2c). In the Ba form Pd is distributed uniformly throughout the fiber cross section (Fig. 2d). The results obtained suggest that under the experimental conditions the system approaches the ion-exchange equilibrium only in the case of the Ba form. Presumably, the observed rapid exchange of Na^+ and Mg^{2+} for $[Pd(NH_3)_4]^{2+}$ results in formation of slightly swelling surface layer {see data for the $[Pd(NH_3)_4]^{2+}$ form in the table}, impeding further penetration of strongly hydrated Na and Mg cations. For the Na and Ba forms $t_{0.9}$ was found to be 22 and 40 s, respectively. This result is consistent with the conclusion made in [12]. Finally, changing the cationic form of the resin, one may control the rate of ion exchange $M^{z+} \rightarrow [Pd(NH_3)_4]^{2+}$ as well as the Pd cross-sectional distribution, which is important for fabrication of special-purpose Pd catalysts.

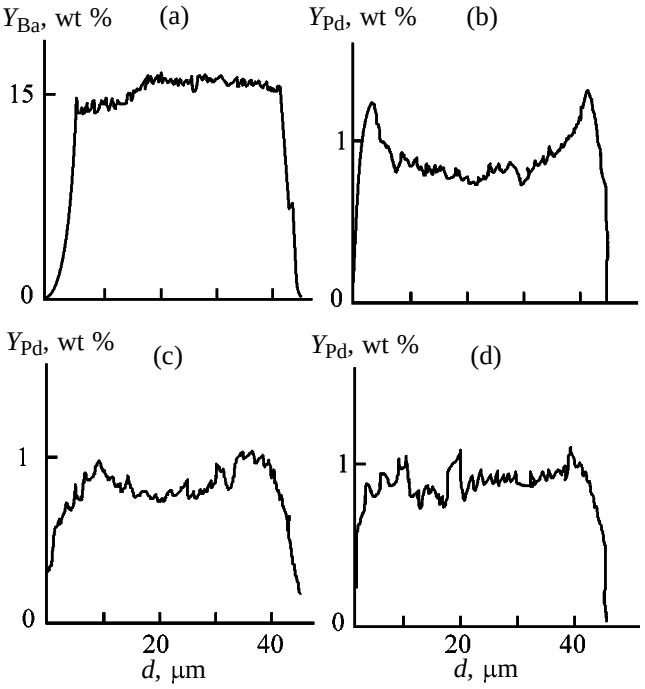

Fig. 2. Cross-sectional distribution of (a) Ba^{2+} and (b–d) $[Pd(NH_3)_4]^{2+}$. (Y_{Ba}, Y_{Pd}) Ba and Pd contents and (d) fiber diameter. Cationic form of the resin: (b) Na, (c) Mg, and (d) Ba.

CONCLUSIONS

(1) The limiting exchange capacity for $[Pd(NH_3)_4]^{2+}$ decreases on passing from the Na form of FIBAN K-1 fibrous sulfonic cation-exchange resin to the Mg, Ba, and La forms.

(2) The cross-sectional distribution of $[Pd(NH_3)_4]^{2+}$ depends on the cationic form of the resin: in the Na form Pd is concentrated in the surface layer, whereas in the Ba form it is uniformly distributed across the fiber. The Mg form takes an intermediate position.

REFERENCES

1. Egiazarov, Yu.G., Soldatov, V.S., Radkevich, V.Z., *et al.*, Abstracts of Papers, *XVI Mendeleevskii s'ezd po obshchei i prikladnoi khimii* (XVI Mendeleev Congr. on General and Applied Chemistry), St. Petersburg, May 25–29, 1998, vol. 2, p. 292.
2. Yegiazarov, Yu.G., Radkevich, V.Z., Jurgen, J., *et al.*, *React. Funct. Polym.*, 2000, vol. 44, pp. 145–152.
3. Ginzburg, E.I., Ezerskaya, N.A., Prokof'eva, I.V., *et al.*, *Analiticheskaya khimiya elementov: Platinovye metally* (Analytical Chemistry of Elements: Platinum Metals), Moscow: Nauka, 1972.
4. Soldatov, V.S., Pokrovskaya, A.I., and Martsinkevich, R.V., *Zh. Prikl. Khim.*, 1984, vol. 57, no. 9, pp. 2030–2034.
5. Potapova, L.L., Shunkevich, A.A., Akulich, Z.I., and Egiazarov, Yu.G., *Zh. Prikl. Khim.*, 2000, vol. 73, no. 5, pp. 780–784.

6. Zamanova, L.P., Aleksandrova, I.L., and Khadzhiev, S.N., Abstracts of Papers, *II Vsesoyuznaya konferentsiya "Primenenie tseolitov v katalize"* (II All-Union Conf. "Applications of Zeolites in Catalysis"), Moscow, October 1981, pp. 277–280.
7. Veshtort, V.Z., Shingel', I.A., Savchits, M.F., and Egiazarov, Yu.G., *Zavod. Lab*., 1989, no. 10, pp. 6–8.
8. Schwarzenbach, G. and Flaschka, H., *Die komplexometrische Titration*, Stuttgart: Ferdinand Enke, 1965.
9. Tereshin, G.S. and Tananaev, I.V., *Zh. Anal. Khim*., 1962, vol. 17, no. 4, pp. 526–527.
10. Soldatov, V.S. and Bychkova, V.A., *Ionoobmennye ravnovesiya v mnogokomponentnykh sistemakh* (Ion-Exchange Equilibria in Multicomponent Systems), Minsk: Nauka i Tekhnika, 1988.
11. Radkevich, V.Z., Shunkevich, A.A., Kistanova, I.E., *et al*., *Zh. Prikl. Khim*., 2000, vol. 73, no. 11, pp. 1861–1864.
12. Kokotov, Yu.A. and Pasechnik, V.A., *Ravnovesie i kinetika ionnogo obmena* (Equilibrium and Kinetics of Ion Exchange), Leningrad: Khimiya, 1970.

Russian Journal of Applied Chemistry, Vol. 74, No. 9, 2001, pp. 1450–1452. Translated from Zhurnal Prikladnoi Khimii, Vol. 74, No. 9, 2001, pp. 1410–1412.

SORPTION AND ION-EXCHANGE PROCESSES

Organomineral Sorbents Based on Clinoptilolite-Containing Tuffs and Polyethylenimime

V. A. Nikashina, P. A. Gembitskii, E. M. Kats, L. F. Boksha, and A. Kh. Galuzinskaya

Vernadsky Institute of Geochemistry and Analytical Chemistry, Russian Academy of Sciences, Moscow, Russia
Topchiev Institute of Petrochemical Synthesis, Russian Academy of Sciences, Moscow, Russia
Institute of Environmental and Technological Problems, Moscow, Russia

Received April 25, 2001

Abstract—Low-swelling sorbent with weakly basic anion-exchange properties was prepared from clinoptilolite-containing tuffs and polyethylenimine using epichlorohydrin cross-linking agent. The properties of this sorbent (total anion-exchange capacity, swellability, etc.) were studied as influenced by the concentrations of the modifying and cross-linking agents, their ratio, period after sorbent preparation, and number of sorption–desorption cycles. The optimal conditions for modifying clinoptilolite-containing tuffs were developed and elemental composition of the resulting sorbent (with respect to C, H, and N) was determined.

At present cheap ion-exchange materials find expanding application in solving various problems in industry and ecology. These sorbents include natural zeolites such as clinoptilolite-containing tuffs (CTs) [1] and new sorbents prepared from CTs modified with amino-containing organic compounds, e.g., cheap and available hexadecyltrimethylammonium, which affects the surface properties and imparts anion-exchange properties to the natural zeolite [2–4]. However, the anion-exchange capacity of such material is rather low (0.02–0.06 mg-equiv g^{-1}). Anion exchangers based on CT were prepared by tuff impregnation with polyhexamethyleneguanidine amine-containing electrolyte (PHMG) followed by cross-linking with epichlorohydrin (ECH) [5, 6]. As a result, we obtained sorbents with a moderate exchange capacity; the anion-exchange capacity of the best samples was 0.15–0.20 mg-equiv ml^{-1}. The selectivity of these sorbents with respect to oxygen-containing anions (e.g., chromate ion [7]) was studied. The resulting sorbents preserve the cation-exchange capacity of the initial CTs [6].

In this work we studied the preparation of organozeolite with weakly basic properties and high anion-exchange capacity.

EXPERIMENTAL

As mineral support we used natural CT, an abundant zeolite. The required material containing 50–60% zeolite was supplied from the Tedzami deposit (Georgia), and its fractional composition was as follows (mm): $-1.0+0.5$ and $-2.5+1.6$ The unit cell of this zeolite can be described by the empirical formula $(K_2, Na_2, Ca)_3(Al_6Si_{30}O_{72})\cdot 24H_2O$.

As modifying agent we used polyethylenimine (PEI), which is a water-soluble polyelectrolyte with weakly basic amine groups [8]. The initial zeolite was modified with PEI by the following procedure. A weighed portion of washed CT with certain grain size was wetted with the appropriate volume of the PEI solution (the PEI concentration was varied from 15 to 33%) and thoroughly mixed. Then the cross-linking agent was added and the resulting composition was mixed. In our work we used ether ECH tetrahydrate or its 25% alcoholic solution. The PEI/ECH molar ratio was varied within 2.0–5.0. The sorbent with the modifying agent after its treatment with ECH was left overnight, and then washed with water to remove soluble and weakly bound polymer from the sorbent [8].

The quality of the resulting sorbent was evaluated using the experimental data on the anion- and cation-exchange capacity and swellability of the modified samples. The anion-exchange capacity of zeolites modified with PEI was studied using the static procedures, which allow determination of the total exchange capacity and its variation as influenced by the solution pH.

The total anion-exchange capacity of the sorbent was determined from the sorption of anions from

1070-4272/01/7409-1450$25.00

acidic solutions by the following procedure. The sorbent was preliminarily converted to the Cl form using a 0.3 M HCl solution under the static conditions (6 ml of sorbent, 90 ml of 0.3 M HCl, 48 h contact time). Then the sorbent was washed with distilled water (5 × 20 ml). The chloride anions were desorbed under the static conditions with 0.2 N H_2SO_4 (100 ml), contact time 48 h. It was found that the additional portion of sulfuric acid did not affect desorption of Cl^- anions. The amount of chloride anions in the regenerate corresponded to the total anion-exchange capacity of the sorbent. The concentration of chloride ions in solution was determined by mercurimetry [9]. The anion-exchange capacity was calculated by the following equation:

$$A_{Cl} = C_{Cl}V/w,$$

where A_{Cl} is the anion-exchange capacity (mg-equiv ml^{-1}), C_{Cl} is the concentration of chloride ions in the regenerate (mg-equiv ml^{-1}), V is the volume of 0.2 M sulfuric acid solution (ml), and w is the sorbent volume (ml).

The anion-exchange capacity at pH 6–7 was evaluated by sorption of sulfate ions at pH 6–7 and their desorption with carbonate ions using the ion chromatography [10].

The cation-exchange capacity of modified CT was measured by sorption of ammonium ions. In this case, 0.5-g sorbent sample was placed in a 0.1 M solution of ammonium chloride (25 ml), stirred for 28 days under the static conditions, and then ammonium cations were desorbed with 2 M sodium chloride solutions (50 ml) for 13 days, also under the static conditions. The content of the desorbed ammonium cations was determined with formaldehyde [11].

The cation-exchange capacity of the modified CT sorbent was calculated from the following equation:

$$A_{NH_4^+} = C_{NH_4^+}V/m,$$

where $A_{NH_4^+}$ is the cation-exchange capacity (mg-equiv g^{-1}), $C_{NH_4^+}$ is the concentration of ammonium ions in the eluate (mg-equiv ml^{-1}), V is the volume of 2 M sodium chloride solution (ml), and m is the sorbent weight (g).

The swellability of the sorbent was determined as the volume (ml) occupied by a 1-g sample of the modified CT after its preliminary swelling in water.

To determine the modification conditions, we studied the anion-exchange capacity and swellability as influenced by the concentrations of the modifying (PEI) and cross-linking (ECH) agents, the PEI/ECH molar ratio, and the time after the sample preparation. The main properties of the resulting samples are listed in Tables 1 and 2.

Table 1. Anion-exchange capacity A_{Cl} (pH 6–7) and swellability of modified CTs as influenced by the preparation conditions

Concentration, %		PEI/ECH molar ratio	Swellability, ml g^{-1}	A_{Cl}, mg-equiv ml^{-1}
PEI	ECH			
25	4	5.0	1.1	0.04
25	4	2.5	1.0	0.16
25	4	2.0	1.2	0.14
15	25	5.0	1.1	0.15
25	25	5.0	1.1	0.24
33	25	5.0	2.4	0.20
25	25	5.0	1.1	0.24
25	25	2.5	1.2	0.30
25	25	2.0	1.5	0.35

Table 2. Anion-exchange capacity A_{Cl} of modified CT as influenced by the time after the sample preparation τ, its granulation, and solution pH

Granulation, mm	τ, days	A_{Cl}, mg-equiv ml^{-1}, at indicated pH	
		2	6
0.5–1.0	6	–	0.34
0.5–1.0	270–540	0.86	0.40
1.6–2.5	4	0.48	–
1.6–2.5	28	0.63	–
1.6–2.5	62	0.67	–

As seen from Table 1, the highest anion-exchange capacity was found for the CT samples modified with 25% PEI solution and 25% ECH solution at PEI/ECH = 2.0. With increasing PEI concentration (>25%) and decreasing PEI/ECH ratio (<2.5) the swellability of the resulting sorbent significantly increases. More detailed study of the anion-exchange properties was performed using the CT samples modified with 25% PEI solution in the presence of 25% ECH solution at PEI/ECH = 2.5 and granulation of 0.5–1.0 and 1.6–2.5 mm. We studied the effect of pH on the working capacity and some other properties of the modified sorbent (time after the sample preparation and number of sorption–desorption cycles under the dynamic conditions). The results are listed in Tables 2 and 3.

Table 3. Anion-exchange capacity A_{Cl} of modified CTs as influenced by the number of sorption–desorption cycles; sorbent granulation 0.5–1.0 mm

Cycle no.	A_{Cl}, mg-equiv ml^{-1}, at indicated pH	
	6–7	2
1	0.27	–
2	0.42	–
3	0.44	–
4	–	0.75
5	–	0.90
6	–	0.86

Table 4. Theoretical (based on the data of elemental analysis) and experimental anion-exchange capacity of modified CTs

Modifying agent	Content, %			α*	A_{Cl}, mg-equiv ml^{-1}	
	H	C	N		theory	experiment
PEI	1.04	6.74	2.52	3/4	1.04	0.6–0.9
PHMG	0.34	2.33	0.96	1/3	0.21	0.15–0.20

* Fraction of nitrogen capable of ion exchange.

Table 5. Cation-exchange capacity of natural and modified CT

Clinoptilolite	PEI/ECH molar ratio	Cation-exchange capacity, mg-equiv g^{-1}
Natural	–	1.10
Modified	7.7	0.70
	2.5	0.79
	2.0	0.80

As seen, our procedure allows preparation of the sorbent with stable properties, almost independent of the time after the sample preparation and of the number of sorption–desorption cycles.

Elemental analysis for carbon, hydrogen, and nitrogen (Table 4) allows evaluation of the theoretical capacity and its comparison with the experimental data.

Our data show that the theoretical values of the anion-exchange capacity of CT modified with PEI or PHMG are fairly close to the experimental results. The anion-exchange capacity of CT modified with PEI exceeds the capacity of CT modified with PHMG by a factor of 3 and 6 in neutral and acidic solutions, respectively.

The sorbent properties listed in Table 5 indicate that the cation-exchange capacity of the modified sorbent is slightly smaller than the cation-exchange capacity of the initial zeolite, which is probably due to partial blocking of the zeolite surface with the modifying agent.

CONCLUSIONS

(1) Modification of clinoptilolite with polyethylenimine followed by cross-linking with epichlorohydrin yields sorbents exhibiting the properties of weakly basic anion exchangers but retaining the cation-exchange properties of the initial clinoptilolite-containing tuffs. The anion-exchange capacity depends on the solution pH, and the highest capacity is attained in a weakly acidic medium.

(2) The total anion-exchange capacity (0.6–0.9 mg-equiv ml^{-1}) of the resulting sorbent is significantly higher than the capacity (0.15–0.20 mg-equiv ml^{-1}) of the sorbent prepared by modification of clinoptilolite-containing tuffs with 15% polyhexamethyleneguanidine solution.

(3) The cation- and anion-exchange capacities of the resulting sorbent are comparable.

REFERENCES

1. Kirov, G.D., Filizova, L.D., Tsitsishvili, G.V., and Andronikashvili, T.G., *Prirodnye tseolity* (Natural Zeolites), Moscow: Khimiya, 1985.
2. Haggerty, G.M. and Bowman, R.S., *Environ. Sci. Technol.*, 1994, vol. 28, pp. 452–460.
3. Li, Zh., Angel, I., and Bowman, R.S., *J. Dispers. Sci. Technol.*, 1998, vol. 19, pp. 843–857.
4. Li, Zh., Roy, St.J., Zou, Y., and Bowman, R.S., *Environ. Sci. Technol.*, 1998, vol. 32, pp. 2628–2632.
5. Nikashina, V.A., Gembitskii, P.A., Kats, E.M., and Boksha, L.F., *Izv. Ross. Akad. Nauk, Ser. Khim.*, 1994, pp. 1550–1553.
6. Nikashina, V.A., Kats, E.M., and Gembitskii, P.A., *Izv. Ross. Akad. Nauk, Ser. Khim.*, 1994, pp. 1554–1556.
7. Katz, E.M. and Nikashina, V.A., Abstracts of Papers, *2nd Int. Congr. "Water: Ecology and Technology," Ecwatech-96*, Moscow, 1966, pp. 155–156.
8. Gembitskii, P.A., Zhuk, D.S., and Kargin, V.A., *Polietilenimin* (Polyethylenimine), Moscow: Khimiya, 1971.
9. *Unifitsirovannye metody analiza vod* (Unified Methods for Water Analysis), Moscow: Khimiya, 1971.
10. Fritz, J.S., Gjerde, D.T., and Pohla, Ch., *Ion Chromatography*, Heidelberg: Hüthing, 1982.
11. Charlot, G., *Les methods de la chimie analytique. Analyse quantitative minerale*, Paris: Masson, 1961.

Russian Journal of Applied Chemistry, Vol. 74, No. 9, 2001, pp. 1453–1457. Translated from Zhurnal Prikladnoi Khimii, Vol. 74, No. 9, 2001, pp. 1413–1416.

SORPTION AND ION-EXCHANGE PROCESSES

Effect of Oxidizing Treatment of Walnut Shell on the Properties of Activated Carbon

A. A. Bagreev, A. P. Broshnik, V. V. Strelko, and Yu. A. Tarasenko

Institute of Sorption and Endoecological Problems, National Academy of Sciences of Ukraine, Kiev, Ukraine

Received July 5, 1999; in final form, December 2000

Abstract—The effect of oxidizing treatment of walnut shell on the yield of activated carbon and on its pore structure was studied.

We have shown recently that active carbons (AC) with acceptable structural and sorption characteristics can be obtained by a traditional procedure (carbonization with subsequent activation) from walnut shell (WS) with the yield of about 10%. At the same time, it is known that fruit kernels and various nut shells are cellulose materials [2], and the procedures conventionally used in their heat treatment can be extended to the technology of obtaining AC [3].

Preliminary oxidation is one of the methods for the treatment of cellulose materials with the aim to improve the pore structure and increase the yield of AC obtained from them [[2]. In this case we must distinguish between the action of oxygen as an external agent, the excess of which will result in complete combustion of a polymer, and the action of oxygen incorporated into elementary units of a polymer and taking part in the material cross-linking on heat treatment. In the latter case oxygen promotes formation of intermediate bridges and intra- and intermolecular cross-links determining the formation of the molecular structure of a carbon material.

Within limited temperature and concentration ranges atmospheric oxygen also can play the same role, but its excess is undesirable, since it decreases the carbon yield at the expense of incontrolled degradation of the polymer and ultimately results in a loss of the AC quality. In view of the aforesaid the method of "sparing" oxidizing heat treatment found use in obtaining carbon fibers [7] and also synthetic AC (SKN and SKS) [8].

In this work we studied the effect of preliminary oxidizing treatment on preparation and properties of AC based on WS.

EXPERIMENTAL

The installation and procedures for oxidizing treatment of WS, the carbonization of the oxidized material, and the activation of the resulting carbonizates were described earlier [1]. WS was preoxidized in air at 150–330°C for 1–10 h and carbonized in flowing argon at a heating rate of 5 deg min^{-1}. The samples were kept at 800°C for 1 h. To obtain AC with various degrees of combustion loss, the activation was carried out in steam under a pressure of 0.1 MPa at 750°C for 0.1–2 h.

In this work after each stage of heat treatment we measured changes in the weight X_m (%) and volume X_V (%) of the samples under study (weight and volume combustion loss), the pore volume with respect to benzene V_s (%) ($cm^3\ g^{-1}$), and also the yield of AC R (%). The parameters of the pore structure of the samples in various stages of the thermolysis: the micropore volume V_{mi} ($cm^3\ g^{-1}$), the sorption pore volume V_s ($cm^3\ g^{-1}$), and the specific surface area S_{BET} ($m^2\ g^{-1}$), were determined from the isotherms of carbon dioxide adsorption at 0°C and of nitrogen adsorption at –196°C. The isotherms were treated by generally accepted procedures of the modern adsorption theory [9, 10].

Structural changes resulting from the heat treatment of the products were studied by X-ray diffraction (a DRON-2 diffractometer), and the interplanar spacings d_{002} (Å) were calculated. The static exchange capacity (mg-equiv g^{-1}) of the materials based on WS was determined by alkali titration. In this work averaged data of 3–5 experiments are given.

Oxidation of WS was accompanied by weight loss and contraction of the material. Figure 1 gives the

1070-4272/01/7409-1453$25.00

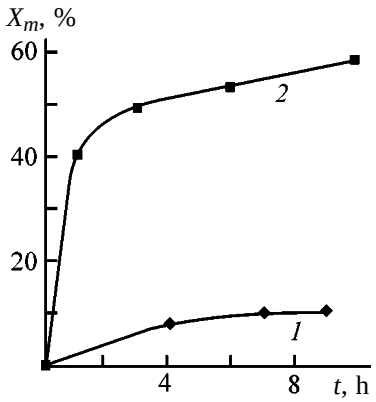

Fig. 1. Kinetic curves of the WS weight loss X_m on its oxidation in air. (*t*) Time. Temperature (°C): (*1*) 150 and (*2*) 200.

Table 1. Properties of the initial and oxidized WS

WS	X_m, %	V_s, $cm^3\ g^{-1}$	d_{002}, Å	SEC, mg-equiv g^{-1}
Initial	–	0.01	4.16	0.23
Oxidized	58.3	0.02	3.52	0.68

Table 2. Properties of carbonizates and activates obtained from WS*

Parameter	Carbonizates	Activates-1	Activates-2
X_m, %	72.3 (69.8)**	25 (23)	58 (60)
R, %	27.7 (30.2)	20.8 (23.3)	11.6 (12.1)
V_s, $cm^3\ g^{-1}$	0.06 (0.15)	0.34 (0.44)	0.60 (0.95)
$V_{mi}(N_2)$, $cm^3\ g^{-1}$	0.03 (0.18)	0.32 (0.37)	0.33 (0.47)
$V_{mi}(CO_2)$, $cm^3\ g^{-1}$	0.19 (0.19)	0.23 (0.19)	0.18 (0.26)
$V_s(N_2)$, $cm^3\ g^{-1}$	0.05 (0.19)	0.50 (0.55)	0.50 (0.85)
$S_{BET}(N_2)$, $m^2\ g^{-1}$	70 (350)	700 (800)	720 (1040)
d_{002}, Å	3.87 (3.93)	– (–)	4.01 (3.99)

* Activates-1 and activates-2 correspond to the AC combustion loss of 23–25 and 58–60%, respectively.

** The values for preoxidized samples are given in parentheses.

data on the kinetics of the weight loss during WS oxidation in air. At 150°C (curve *1*) the weight loss of WS is slow, and even in 10 h less than 10% is lost. At 200°C (curve *2*) the kinetics of the process is sharply changed: in 1 h the WS weight loss is already about 40% and in the subsequent 9 h it attains almost 60%. At 300°C and higher the weight loss in 1 h exceeds 70%. The oxidation is accompanied by contraction of the material, which attains about 30% in 1 h at 200°C.

We emphasize that the heat treatment of the initial WS in argon at 200°C for 10 h [1] results in an increase in the pore volume and in the static exchange capacity (SEC) of the material to 0.04 $cm^3\ g^{-1}$ and 0.45 mg-equiv g^{-1}, respectively. Carbonization decreases the yields to 25% and increases V_s to 0.05 $cm^3\ g^{-1}$. After activating the carbonizate to the combustion loss of 63%, the resulting AC has the pore volume of 0.77 $cm^3\ g^{-1}$, and its yield is 9.3%. These data suggest that the heat treatment of WS in an inert medium results in a decrease in V_s and in the AC yield compared to the AC samples obtained from WS preoxidized at 200°C for 10 h. The characteristics of the initial WS and that oxidized under the above-mentioned condition are given in Table 1. The pore volume by benzene in both initial and oxidized WS samples is 0.01–0.02 $cm^3\ g^{-1}$, i.e., no micro- and mesoporous structure is developed during the WS oxidation.

Preliminary heat treatment of cellulose materials in air allows the structural defects resulting from degradation to be "healed" at the expense of the formation of intermolecular bonds, "oxygen bridges" among them [4]. The degradation of cellulose on heating in air yields oxycellulose [11] containing carboxy groups. Typical of the oxycellulose thermolysis are hampering of depolymerization [5] and intensification of dehydration [12], occurring both intramolecularly to give the >C=O and >C=C< groups and intermolecularly with cross-linking.

In fact, the measurements (Table 1) have shown that the static exchange capacity increases from 0.23 to 0.68 mg-equiv g^{-1} during the WS oxidation, which points to the formation of phenol and carboxy groups on the material surface. Therefore, after oxidation of the initial WS we obtain another material, so-called oxidized WS (Table 1).

On carbonization and activation of the initial and also preoxidized WS samples we obtained materials whose properties are given in Table 2 and Fig. 2. On carbonization of WS a further weight loss occurs: up to 69.8% in oxidized WS and up to 72.3% in the initial WS [1, 13]. Therefore, the yield increases even

in the stage of the carbonization of preoxidized WS, as compared to the carbonization of the unoxidized samples (Table 2).

Table 2 also shows that on the carbonization of the initial and oxidized WS samples their porous structure develops differently. The carbonization of the preoxidized samples, as compared to the initial samples, results in the development of larger micropores, as determined by nitrogen adsorption (0.18 and 0.03 $cm^3 g^{-1}$, respectively). The volumes of smaller micropores, determined by CO_2 adsorption, appear to be approximately the same for the oxidized and unoxidized carbonizates (~0.19 $cm^3 g^{-1}$). At the expense of larger volume of coarse micropores in the carbonizates obtained from oxidized WS, their S_{sp} appears to be higher than in the carbonizates obtained from unoxidized WS (350 $m^2 g^{-1}$ compared to 70). It is known that the volumes and the average size of micropores determined from N_2 adsorption isotherms for carbons with high combustion losses (50–70%) considerably (sometimes twice) exceed the corresponding values calculated from the data on CO_2 adsorption. Such a difference is determined by the formation of large micro- and supermicropores in which the CO_2 adsorption at 0°C occurs partially by the mechanism of superficial and not only volume filling [14].

We emphasize that no mesoporosity develops in the stage of carbonizing materials obtained from both the initial and preoxidized WS. As for V_s, preoxidation of WS results in the increase in the pore volume of the carbonizate from 0.06 for unoxidized samples to 0.15 $cm^3 g^{-1}$ for preoxidized samples (Table 2).

During carbonization of carbon-containing materials the precursors of AC are formed. Their properties largely determine the properties of AC [15]. The yield of carbonizates obtained from the oxidized material somewhat increases (30.2% compared to 27.7%), and a more developed porous structure is formed, as compared to carbonizates based on the initial WS (Table 2).

In the activation stage, the differences in the properties of materials obtained from preoxidized and unoxidized WS become substantial. The yield of activates-1 (Table 2, combustion loss 23–25%) from the oxidized material is 23.3% and from the unoxidized material, only 20.8%. But even when the combustion loss is 58–60% (activates-2), the yield also appears to be higher for preoxidized samples compared to unoxidized ones (12.1 and 11.6%).

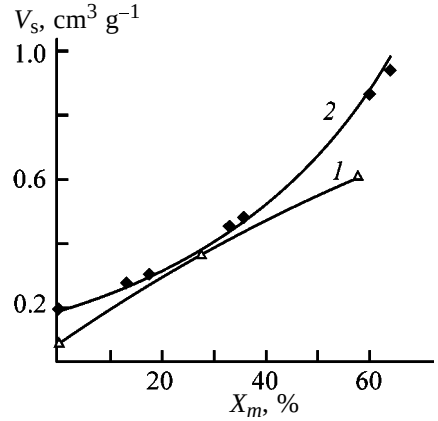

Fig. 2. Plot of pore volume V_s vs. the degree of combustion loss X_m on activation of WS carbonizates. Samples: (*1*) unoxidized and (*2*) oxidized.

Testing activates-1 with the 25% combustion loss for N_2 and CO_2 adsorption (Table 2) showed that the preoxidized samples have a more developed porous structure compared to the samples obtained from unoxidized WS and, as a consequence, a larger specific surface area (800 and 700 $m^2 g^{-1}$, respectively). The distinctive feature of activates obtained from oxidized WS is formation of mesoporosity in them, as demonstrated by the difference between the volumes of sorption pores and micropores (Table 2).

Testing activates-2 for nitrogen adsorption showed a more developed porous structure in them. In the activates obtained from the oxidized WS samples the specific surface area exceeds 1000 $m^2 g^{-1}$, whereas in the activates obtained from the unoxidized materials the specific surface area is 720 $m^2 g^{-1}$. The dependence of the pore volume on the combustion loss in activation (Table 2, Fig. 2) shows that in AC with the combustion loss of 30–40%, obtained from both preoxidized and unoxidized WS, the pore volume is approximately the same (Fig. 2, curves *1, 2*). The differences appear in the samples with the combustion loss more than 40%. For example, when the combustion loss is more than 60%, the AC samples from unoxidized WS have $V_s \sim 0.60$ $cm^3 g^{-1}$, whereas in AC from preoxidized WS $V_s = 0.95$ $cm^3 g^{-1}$.

It is known [16] that the X-ray patterns of cellulose materials, WS among them, are characterized by strong (101) and (002) relfections, which point to a regular structure. The X-ray patterns of heat-treated WS samples (preoxidized WS, carbonizate, and also the activate obtained from it) are shown in Fig. 3. Structural changes in WS occur during both its con-

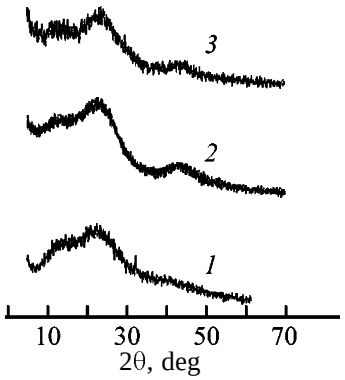

Fig. 3. X-ray diffraction patterns of carbon materials in various stages of WS heat treatment. (2θ) Bragg's angle. (*1*) Oxidized sample, (*2*) carbonizate, and (*3*) activate.

ventional heat treatment [1] and the treatment with preoxidation (Fig. 3).

It is essential that in oxidized WS (Fig. 3, curve *1*) the cellulose structure appears to be preserved; the carbon structure also is not formed, in contrast to WS carbonization in argon at 700°C [1]. The carbon structure is formed in preoxidized WS samples only on their carbonization (Fig. 3, curve *2*). A similar structure of carbonizates is also observed in the samples obtained by the conventional procedure [1]. During carbonizate activation under these conditions no essential structural changes occur in the material (Fig. 3, curves *2*, *3*).

An important characteristic of structural changes in carbon materials is the interplanar spacing. Preoxidation of WS results in a decrease in the interplanar spacings of its crystal lattice from 4.16 to 3.52 Å (Table 1). This occurs at the expense of linking of lattice planes by oxygen bridges. The heat treatment of WS in an inert medium decreases the interplanar spacings only to 4.10 Å [1].

It was shown previously that the WS carbonization results in a decrease in the interplanar spacings: on the carbonization of the initial WS (800°C) the interplanar spacing decreases to 3.87 Å. The carbonization of preoxidized WS results in the increase in the interplanar spacings to 3.93 Å compared to the carbonizates obtained from the initial WS (Table 2), which is due to expansion of the interplanar space of the sample crystal lattice at the expense of the loss of a part of bridging oxygen groups formed during WS oxidation. In this case the carbonizates obtained from both preoxidized and unoxidized WS have close interplanar spacings of ~3.90 Å (Table 2). The activation of carbonizates to high degrees of combustion loss (activates-2), both preoxidized and unoxidized, results in the minor increase in the interplanar spacings, to 4.01 and 3.99 Å (Table 2).

Thus, the cross-linked structural units in the composition of oxidized materials have a considerable effect on the properties of not only carbonizates, but also of activates. The preoxidation of WS allows preparation of AC with a more developed porous structure and with pores of particular size, with retention of structural carbon and increased yield of AC.

CONCLUSION

The effect of oxidizing treatment of the walnut shell on the properties and yield of the resulting activated carbons was studied. The preoxidation promotes the development of micro- and mesoporosity of carbons (the total volume of micro- and mesopores attains 0.9–1.0 $cm^3 g^{-1}$, S_{sp} by BET is within 1000–1100 $m^2 g^{-1}$). The yield of the product is 12%.

REFERENCES

1. Bagreev, A.A., Broshnik, A.P., Srelko, V.V., and Tarasenko, Yu.A., *Zh. Prikl. Khim.*, 1999, vol. 72, no. 6, pp. 942–946.
2. Gribanov, A.V. and Sazanov, Yu.N., *Zh. Prikl. Khim.*, 1997, vol. 70, no. 6, pp. 881–902.
3. Ermolenko, I.N., Lyubliner, I.P., and Gul'ko, N.V., *Elementosoderzhashchie ugol'nye voloknistye materialy* (Element-Containing Fibrous Carbon Materials), Minsk: Nauka i Tekhnika, 1982.
4. Strong, S.L., *J. Mater. Sci.*, 1974, vol. 9, no. 6, pp. 993–1003.
5. Madorsky, S.L., *Thermal Degradation of Organic Polymers*, New York: Interscience, 1964.
6. Aseeva, R.M., Smutkina, Z.S., Berlin, A. A., and Kasatochkin, V.I., *Strukturnaya khimiya ugleroda i uglei* (Structural Chemistry of Carbon and Coals), Kasatochkin, V.I., Ed., Moscow: Nauka, 1969, pp. 161–200.
7. Konkin, A.A., *Uglerodhye i drugie zharostoikhie voloknistye materialy* (Carbon and Other Heat-Resistant Fibrous Materials), Moscow: Khimiya, 1974.
8. Kartel', N.T., Carbon Hemosorbents Based on Synthetic Active Carbons, *Doctoral Dissertation*, Kiev, 1985.
9. Dubinin, M.M., *Usp. Khim.*, 1982, vol. 51, no. 7, pp. 1065–1074.

10. Jankowska, H., Swiatkowski, A., and Choma, J., *Active Carbon*, Ellis Horwood, 1991.
11. Shafizadeh, F., *Adv. Carbohydr. Chem*., 1968, vol. 23, pp. 419–474.
12. Kochergina, T.A., Fedoseev, S.D., Trapeznikov, N.M., *et al.*, in *Konstruktsionnye materialy na osnove ugleroda* (Structural Materials Based on Carbon), Moscow, 1978, no. 13, pp. 100–103.
13. Limonov, N.V., Olontsev, V.F., Glushankov, L.V., and Solntsev, V.V., *Zh. Prikl. Khim*., 1994, vol. 67, no. 10, pp. 1648–1650.
14. Martin-Martinez, J.M. and Torregrosa-Masia, R., *Fuel*, 1995, vol. 74, pp. 111–115.
15. Kinle, H. von and Bader, E., *Aktivkohle und ihre industrielle Anwendung*, Stuttgart: Enke, 1980.
16. Popova, L.G., Burkov, G.L., Piyalkin, V.N., and Slavyanskii, A.K., *Izv. Vyssh. Uchebn. Zaved., Lesn. Zh*., 1973, no. 5, pp. 105–108.

Russian Journal of Applied Chemistry, Vol. 74, No. 9, 2001, pp. 1458–1460. Translated from Zhurnal Prikladnoi Khimii, Vol. 74, No. 9, 2001, pp. 1417–1419.

SORPTION AND ION-EXCHANGE PROCESSES

Adsorption of Chlorobenzene on V_2O_5/γ-Al_2O_3 Catalyst

L. D. Asnin, A. A. Fedorov, Yu. S. Chekryshkin, and R. M. Yakushev

Institute of Technical Chemistry, Ural Division, Russian Academy of Sciences, Perm, Russia

Received December 14, 2000

Abstract—Isotherms of chlorobenzene adsorption on V_2O_5/γ-Al_2O_3 catalyst within the 0.07–18 Pa range of adsorbate partial pressure were measured, and certain thermodynamic characteristics of adsorption were found.

The V_2O_5/γ-Al_2O_3 catalyst can be used for deep oxidation of chlorobenzene (ChB). The kinetics of this process was studied in [1]. Davidenko *et al.* [2, 3] examined the mechanism of ChB adsorption on the above catalyst using IR spectroscopy and temperature-programmed desorption. At the same time, data on ChB equilibrium adsorption on oxide vanadium–aluminum catalyst are lacking. This problem is studied in the present work.

EXPERIMENTAL

Synthesis of γ-Al_2O_3 used as a support is described in [4]. Vanadium(V) oxide (5% of the support weight) was applied to aluminum oxide by impregnation with aqueous solutions of pure grade NH_4VO_3. Then the catalyst was dried at 373 K and annealed in air at 673 K for 5 h. The specific surface area of the catalyst sample found by nitrogen thermal desorption was 115 $m^2\ g^{-1}$.

Adsorption isotherms were measured chromatographically [5] on a Tsvet-500 chromatograph equipped with a flame-ionization detector. Helium additionally dried over aluminum oxide and CaA zeolite was used as a carrier gas; its flow rate was 30 $ml\ min^{-1}$. A 0.200–0.315-mm catalyst fraction and a 35 cm × 4 mm stainless steel column were used. The catalyst sample in the column was 1.183 g. Before the experiment, the column was conditioned at 573 K for 6–8 h.

Chemically pure grade chlorobenzene was additionally distilled and kept in hermetically sealed flasks over freshly calcined NaA zeolite. The samples of the adsorbate vapor were introduced into the column through a heated dosing cock. The vapor–helium mixture was prepared by mixing pure helium and helium saturated with the ChB vapor in a temperature-controlled saturator.

Adsorption isotherms (figure, Table 1) were measured within the 463–513 K range. The error of determination of the adsorbate partial pressure p (Pa) and excess adsorption Γ ($mol\ m^{-2}$) was less than 5%. In the above temperature interval, the chromatograms showed no evidences of chemical conversion of chlorobenzene.

The adsorption isotherms are characterized by slight nonlinearity and are well (determination coefficient $r^2 > 0.999$) approximated by the Freundlich equation of the adsorption isotherm $\Gamma = Cp^{1/n}$, where C and n are coefficients depending on temperature T (K). Within the temperature range studied, the dependence of C on T can be described by the function $C(T) = 5.06 \times 10^{-8} - 5.23 \times 10^{-5}/T + 0.0135T^2$ ($r^2 = 0.997$), and the dependence of n on T, by the function $n(T) = 0.234 + 425/T$ ($r^2 = 0.88$).

The isosteric heats of the ChB adsorption q_{st} calculated from the isotherms obtained are listed in Table 2 for certain Γ values. The q_{st} values for ChB on the

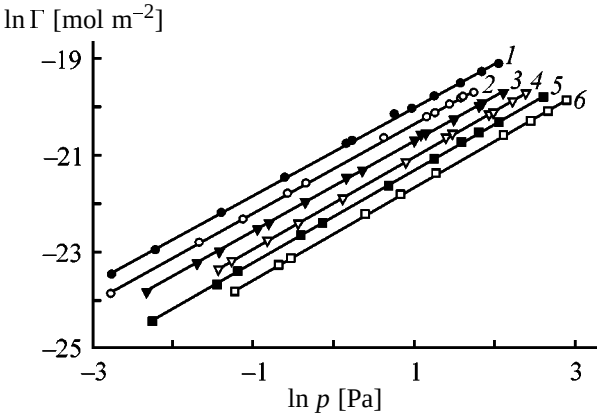

Isotherms of chlorobenzene adsorption on V_2O_5/γ-Al_2O_3 catalyst: (Γ) adsorption of chlorobenzene and (p) chlorobenzene partial pressure. Temperature, K: (*1*) 463, (*2*) 473, (*3*) 483, (*4*) 493, (*5*) 503, and (*6*) 513.

1070-4272/01/7409-1458$25.00

supported catalyst coincide within the experimental error with the heats of ChB adsorption on neat support [4]. Hence, vanadium oxide on the γ-Al_2O_3 surface does not generate more active adsorption centers than those on the surface of the initial support. Spiridonova *et al*. [6] studied pyridine adsorption on V_2O_5/γ-Al_2O_3 catalyst and concluded that vanadium ions do not affect the character of Al_2O_3 acidity: the total number of the acidic centers does not change, but the fraction of weaker (relative to pyridine) centers increases. Taking into account the difference in the nature of adsorbates, we can suggest that the data of [6] are consistent with our results.

The change of the differential excess entropy of adsorption [7] $\Delta\bar{S}^s$ is equal to $-q_{st}/\hat{T}$, where $\hat{T}$ is the average temperature of the interval studied, $\hat{T}$ = 488 K. Transition from the change of the differential entropy to the change of the average molar entropy $\Delta\tilde{S}^s$ for the case when adsorption is described by the Freundlich equation is realized by the equation [8]

$$\Delta\tilde{S}^s = \Delta\bar{S}^s + R[n(\hat{T}) + Tn'(\hat{T})],$$

where $n'(T)$ is the derivative of $n(T)$ function in the point $\hat{T}$; the second term of the equation (right part) amounts to 2 J mol^{-1}K^{-1}.

Certain information on the behavior of ChB molecules in the adsorption layer can be obtained by comparing the experimental $\Delta\tilde{S}^s$ values and those theoretically calculated from the model of ideal two-dimensional gas [4, 9], $\Delta\tilde{S}^s_{calc}$. These values for certain Γ are listed in Table 2. As seen, $|\Delta\tilde{S}^s_{calc}| < |\Delta\tilde{S}^s|$. This inequality can be explained by assuming that the motion of ChB molecules along the surface is not absolutely free, as it is assumed in the model of ideal two-dimensional gas, and hence spaces with elevated adsorption potential exist. They retain the adsorbate molecules for a some time, which is less than the residence time of the molecule on the surface. Changes in the inner (rotational and vibrational) degrees of freedom at adsorption are also possible. However, thermodynamic characteristics are insufficient to make unambiguous conclusion about the redistribution of adsorbate molecules with the respect to the degrees of freedom in the adsorption field. Since the measurements are related to very small values of adsorption, all deviations from ideality are caused by adsorbent–adsorbate interactions.

The difference between the calculated and experimental entropy decreases (in parllel with q_{st}) as the degree of surface filling increases, i.e., the state of the

Table 1. Excess adsorption of chlorobenzene on V_2O_5/γ-Al_2O_3 catalyst

p, Pa	$\Gamma \times 10^{10}$, mol m^{-2}	p, Pa	$\Gamma \times 10^{10}$, mol m^{-2}
463 K		493 K	
0.06	0.64	0.24	0.72
0.11	1.06	0.28	0.86
0.24	2.33	0.43	1.31
0.54	4.77	0.63	1.84
1.16	9.65	1.11	3.07
1.25	10.3	2.43	6.53
2.12	17.9	4.01	10.9
2.63	20.2	3.99	11.2
3.48	25.9	4.35	11.8
4.82	34.2	4.36	12.2
6.29	43.2	6.88	17.9
7.75	50.9	7.27	18.3
		9.23	23.5
		10.8	26.9
		11.0	27.1
473 K		503 K	
0.06	0.43	0.10	0.24
0.19	1.25	0.23	0.52
0.32	2.03	0.30	0.68
0.56	3.44	0.66	1.45
0.70	4.25	0.87	1.87
1.86	10.9	1.96	4.03
3.16	17.0	3.50	6.94
3.52	18.5	4.90	10.0
4.20	22.1	6.06	12.2
4.85	24.9	7.79	15.2
4.97	25.3	13.7	25.1
5.69	28.2		
483 K		513 K	
0.10	0.45	0.29	0.45
0.18	0.81	0.50	0.77
0.24	1.03	0.58	0.91
0.38	1.65	1.46	2.27
0.44	1.88	2.28	3.37
0.69	2.90	3.54	5.27
1.16	4.75	8.19	11.4
1.41	5.55	11.4	15.5
2.71	10.2	14.3	19.1
2.96	11.5	18.0	24.0
3.13	12.0		
4.44	16.0		
6.08	21.5		
6.30	22.2		
8.16	28.3		

Table 2. Thermodynamic characteristics of chlorobenzene adsorption on $V_2O_5/\gamma\text{-}Al_2O_3$ catalyst

$\Gamma \times 10^{10}$, mol m^{-2}	q_{st}, kJ mol^{-1}	$-\Delta\tilde{S}^s$	$-\Delta\tilde{S}^s_{calc}$	$\lvert\Delta\tilde{S}^s\rvert - \lvert\Delta\tilde{S}^s_{calc}\rvert$
		J mol^{-1} K^{-1}		
0.9	80 ± 7	162 ± 15	107	55
8.7	72 ± 3	145 ± 7	105	40
26.1	68 ± 2	137 ± 3	104	33

real adsorption layer approximates the state of the ideal one. This also shows that ChB molecules adsorbed on the active centers from the first adsorbate portions are less mobile than those adsorbed from the successive portions.

CONCLUSIONS

(1) Vanadium oxide on the surface of $\gamma\text{-}Al_2O_3$ generates no adsorption centers more active with respect to chlorobenzene.

(2) Within the studied interval of adsorption values the state of the chlorobenzene adsorption layer differs from that of the ideal two-dimensional gas, but approaches it with increasing degree of filling.

ACKNOWLEDGMENTS

The authors are indebted to N.E. Skryabina (Perm State University) for assistance. The work was performed under financial support of the Integratsiya Foundation (grant 00-06).

REFERENCES

1. Jones, J. and Ross, J.R.H., *Catal. Today*, 1997, vol. 35, pp. 97–105.
2. Davidenko, I.V., Davydov, A.A., Pyatnitskii, Yu.I., *et al.*, *Zh. Fiz. Khim.*, 1991, vol. 65, no. 1, pp. 164–169.
3. Davidenko, I.V., Davydov, A.A., Pyatnitskii, Yu.I., *et al.*, *Teor. Eksperim. Khim.*, 1990, vol. 26, no. 4, pp. 468–473.
4. Asnin, L.D., Fedorov, A.A., , and Chekryshkin, Yu.S., *Izv. Ross. Akad. Nauk., Ser. Khim.*, 2001, no. 1, pp. 65–69.
5. Kiselev, A.V.and Yashin, Ya.I., *Gazo-adsorbtsionnaya khromatografiya* (Gas-Adsorption Chromatography), Moscow: Nauka, 1967.
6. Spiridonova, D.V., Fokina, E.A., Spiridonov, K.N., and Krylov, O.V., *Kinet. Katal.*, 1977, vol. 18, no. 6, pp. 1495–1500.
7. Lopatkin, A.A., *Teoreticheskie osnovy fizicheskoi adsorbtsii* (Theoretical Fundamentals of Physical Adsorption), Moscow: Mosk. Gos. Univ., 1983.
8. Asnin, L.D., Fedorov, A.A., , and Chekryshkin, Yu.S., *Izv. Ross. Akad. Nauk., Ser. Khim.*, 2000, no. 1, pp. 175–178.
9. Lopatkin, A.A., *Zh. Fiz. Khim.*, 1997, vol. 71, no. 5, pp. 916–919.

Russian Journal of Applied Chemistry, Vol. 74, No. 9, 2001, pp. 1461–1464. Translated from Zhurnal Prikladnoi Khimii, Vol. 74, No. 9, 2001, pp. 1420–1423.

APPLIED ELECTROCHEMISTRY AND CORROSION PROTECTION OF METALS

Electrodeposition of Rhenium onto Oriented Rhenium Foils from Salt Melts[1]

N. O. Esina, L. M. Minchenko, A. A. Pankrat'ev, V. A. Isaev, and N. G. Molchanova

Institute of High-Temperature Electrochemistry, Ural Division, Russian Academy of Sciences, Yekaterinburg, Russia

Received April 10, 2001

Abstract—Epitaxial growth of rhenium layer electrodeposited from chloride melts onto single-crystal and polycrystalline rhenium substrates with orientations $(10\bar{1}0)$, $(11\bar{2}0)$, and (0001) was studied. Conditions for epitaxial growth on single-crystal rhenium foil with orientation (0001) were found. The surface morpholgy of rhenium deposits was studied and microhardness of single-crystal and polycrystalline rhenium layers with orientation (0001) was measured.

Previously, a number of experiments have been carried out in order to study the growth of molybdenum and tungsten in deposition from oxide and chloride solutions onto crystalline molybdenum substrates of various orientations. These studies revealed fundamental aspects of the epitaxial growth of metals with body-centered crystal lattice in electrocrystallization from salt melts [6]. It has been shown for molybdenum that the mechanism of transition from epitaxy to growth texture includes two stages. The first stage consists in formation of grains in twinning positions, and the second involves preferential growth of grains in twinning position with their simultaneous gradual and continuous inclination within 15° in the direction of the texture growth axis characteristic of these conditions [3]. This suggested the possibility of epitaxial growth of bent monoface single-crystal coatings of small thickness (up to 1 mm). Coatings of this kind were obtained with molybdenum and tungsten.

It seems of interest to study the influence exerted by the symmetry of a metal being deposited and its physicochemical properties on the mechanism of epitaxial growth. In contrast to molybdenum and tungsten, rhenium crystallizes to give a more complex face-centered close-packed lattice and possesses a unique combination of physicochemical properties: ultrahigh temperature resistance, room-temperature plasticity, and chemical inertness (except toward oxygen).

This study is concerned with the structure, texture, and morphology of the growing surface and the microstructure of epitaxial rhenium layers electrodeposited from chloride melts onto planar and bent single-crystal and polycrystalline substrates of various orientations.

[1] Reported at X Kola Symposium "Electrochemistry of Rare Metals," Apatity, December 4–7, 2000.

EXPERIMENTAL

Experiments were performed in a hermetically sealed quartz cell. A $CsCl–Cs_2[ReCl_6]$ electrolyte was placed in a crucible made of pyrocarbon-densified graphite, with side walls screened by a rhenium ring whose upper edge was above the electrolyte level. The ring served as reference electrode. A rhenium billet was used as anode.

The supporting electrolyte CsCl was dried under vacuum and then remelted in air. The rhenium salt was prepared by chlorination in a melt. The rhenium concentration in the electrolyte was 3–5 wt %, as determined analytically. The difficulty consisted in that cesium hexachlorohenate is poorly soluble in water. A weighed portion of the salt was heated in distilled water until rhenium(IV) hydroxide was formed and then dissolved in hydrogen peroxide [7]. Rhenium was determined by atomic-absorption spectroscopy in an N_2O–acetylene flame on a 403 Perkin–Elmer spectrophotometer (λ = 346.0 nm). The relative determination error did not exceed 3%.

The inert gas (argon) passing over the melt was purified to remove traces of oxygen with a solid-electrolyte electrochemical pump; the gas purity at the cell inlet was monitored with an electrochemical transducer. A weak flow of argon was continuously passed through the cell during its operation.

1070-4272/01/7409-1461$25.00

The studies were carried out in the temperature range 720–920°C at current densities of 0.01–0.20 A cm^{-2}. The deposition was done onto substrates of annealed dense graphite, single-crystal rhenium foil with orientation (0001), and polycrystalline rhenium foils with orientations (0001), $(11\bar{2}0)$, and $(10\bar{1}0)$. The cathode area did not exceed 2 cm^2. Prior to deposition, rhenium substrates were polished in an electrolyte of the composition $K_3[Fe(CN)_6] : CH_3COOH : H_2O$ and then washed in distilled water. A part of rhenium foil substrates was bent, with the bending radius ranging from 3 to 10 mm. The structural perfection and texture of the obtained rhenium layers and their surface morphology were studied by X-ray structural, metallographic, and optical-goniometric methods on DRON-3 and DRON-3M diffractometers, Neophot-32 optical microscope, and Camebax scanning electron microscope. To study the microstructure of deposits and determine their microhardness, metallographic cross sections of the samples studied were prepared by mechanical grinding with abrasive paper and diamond paste and subsequent chemical etching with $K_3[Fe(CN)_6] : NaOH : H_2O$ etchant with the components taken in appropriate proportions.

Polarization curves were measured in the galvanostatic mode with a PI-50 potentiostat, and E–τ curves were recorded with an S9-8 digital storage oscilloscope. The current densities were in the range 0.005–0.100 A cm^{-2} at a pulse duration of 0.1 s. To preserve the electrode surface, an anodic pulse was applied after each cathodic pulse, with the amplitude and duration equal to that of the cathode pulse. The electrode potential, monitored with a digital voltmeter, did not differ from its initial value by more than 2 mV at high current densities.

The investigations performed revealed that rhenium deposits on graphite mainly had growth texture $(10\bar{1}L)$, where $3 \le L \le \infty$. With increasing temperature and decreasing deposition current density, $L \to \infty$ and the texture is transformed into (0001). At low temperatures (720–750°C) and high current densities (0.1 A cm^{-2} and more) a growth texture (1120) was formed in the deposits. If the rhenium substrate orientation coincided with the growth texture direction, epitaxial growth of the deposit was observed till termination of electrolysis (400 μm). The epitaxial growth was disrupted and growth texture formed in a rhenium layer being deposited in the case of misalignment of the substrate orientation and the direction of the growth texture axis. Epitaxial growth on single-crystal rhenium foils with (0001) orientation was observed at 870–920°C and cathodic current densities in the range 0.01–0.10 A cm^{-2}. Similar results were obtained on bent single-crystal substrates with (0001) orientation at any bending radii. In depositing rhenium onto polycrystalline foils with orientations $(11\bar{2}0)$ and $(10\bar{1}0)$ under the above conditions, a (0001) growth texture was formed, as also in the case of graphite substrates [8]. Under the conditions when a $(11\bar{2}0)$ texture was formed, epitaxial growth was observed on the substrates with the same orientation. No rhenium deposits with $(10\bar{1}0)$ growth texture were obtained in the studies, and, therefore, there was no epitaxial growth on foils with $(10\bar{1}0)$ orientation. In this case, rhenium deposits with $(11\bar{2}0)$ and $10\bar{1}L$) textures were obtained.

The morphology of the growing surface of rhenium layers was studied. Growth pyramids faceted with $(10\bar{1}3)$ planes were formed on the surface of polycrystalline deposits obtained under the conditions of (101L) growth texture. In the case of epitaxial growth on a planar or bent single-crystal foil with orientation (0001), growth pits appeared on the surface. They had the form of 6–12-face inverse pyramids faceted with $(10\bar{1}1)$ and $(10\bar{1}2)$ planes. Some of them had blunted vertex (Fig. 1a). Under the conditions when $(11\bar{2}0)$ texture was formed at 750°C and cathodic current densities in the range 0.1–0.2 A cm^{-2}, skeletal growth forms were observed on a $(10\bar{1}0)$ substrate (Fig. 1b). In this case, the rate of the deposit growth in the direction perpendicular to the substrate exceeded that along the substrate. With increasing temperature and decreasing deposition current density, holohedral pyramids appeared, faceted with $(10\bar{1}1)$, $(10\bar{1}2)$, and $(10\bar{1}3)$ planes (Fig. 1c). The inclination of the faceting planes with respect to the substrate plane is dependent on the deposition current density. With increasing cathodic current density, the angle of inclination grows too. The surface morphology of rhenium deposits is the same on planar and bent foils with identical orientations and is independent of the foil bending radius.

Metallographic studies of cross sections and fractures of rhenium deposits demonstrated that, in the case of epitaxial growth, the deposit–substrate boundary was either absent at all, or was observed in the form of a step (Fig. 2a). A clearly visible boundary between the deposited rhenium and the substrate is present in samples having no epitaxial layer (Fig. 2b). The structure of deposits on graphite is columnar, the grain size is 20–30 μm (Fig. 2c, thickness 50 μm). As seen from Figs. 1a and 1c, the types of fracture of rhenium deposits are different. In the case of a single-crystal epitaxial deposit, a pitted relief, characteristic

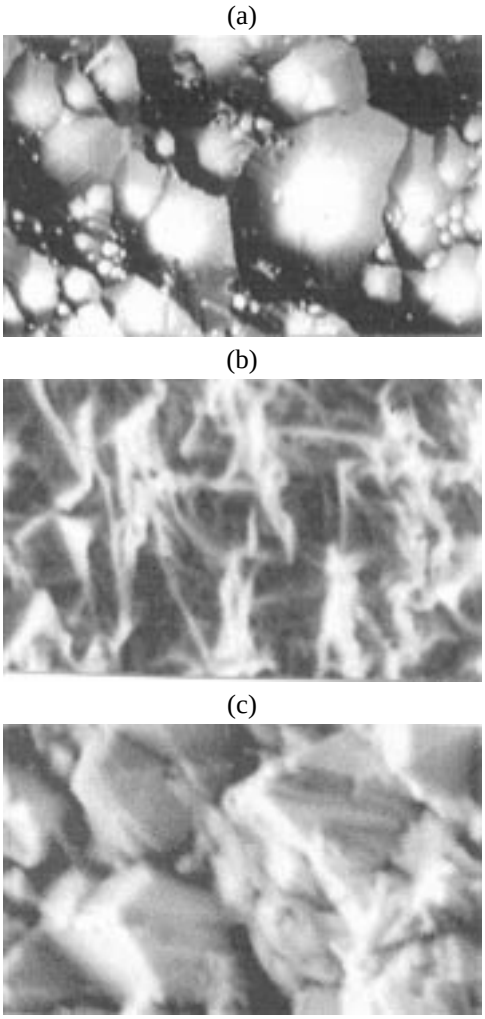

Fig. 1. SEM image of the surface of rhenium deposits obtained on rhenium foils with various orientations. Magnification: (a) 400 and (b, c) 800. Current density i_C, A cm^{-2}: (a) 0.01, (b) 0.17, and (c) 0.10. Temperature, °C: (a, c) 900 and (b) 750. Rhenium substrate: (a) single-crystal (0001), epitaxy; (b) polycrystalline (10$\bar{1}$0); and (c) polycrystalline (11$\bar{2}$0).

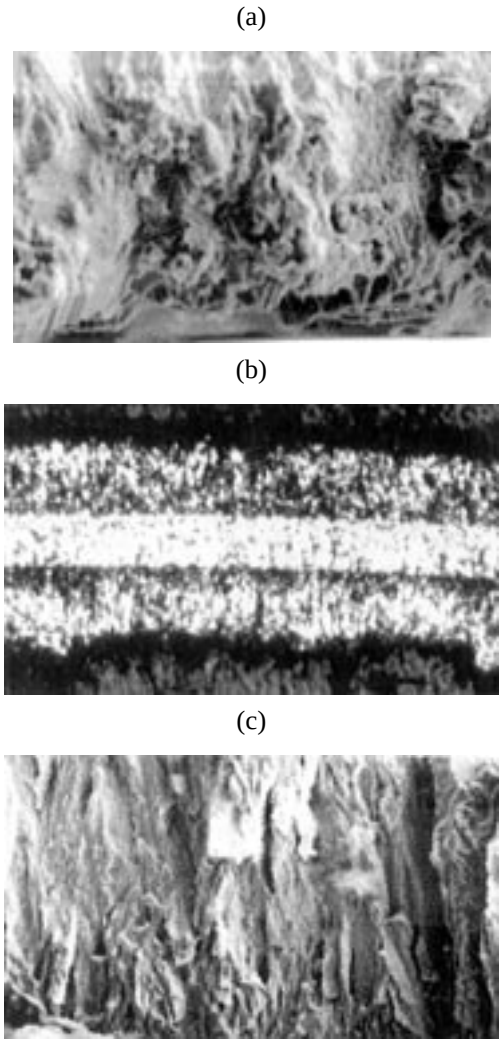

Fig. 2. Cross-sectional micrographs of rhenium deposits. Magnification: (a, c) 400 and (b) 300. (a) Fracture of rhenium deposit on single-crystal (0001) rhenium substrate, (b) metallographic cross section of rhenium deposit on (10$\bar{1}$0) polycrystalline rhenium substrate, and (c) fracture of (11$\bar{2}$0) rhenium deposit on graphite.

of ductile fracture, is observed. For polycrystalline rhenium deposit on graphite, a mixed type of fracture is observed: brittle intergrain fracture with regions of ductile detachment and minor regions of brittle cleavage.

The microhardness was measured on metallographic cross sections of polycrystalline and single-crystal rhenium deposits with (0001) orientation. Its values were in the range 240–270 kg mm^{-2}, which indicates the high purity of the obtained rhenium layers. It has been shown previously that the polarization of the rhenium electrode depends on its orientation and grows in the order (10$\bar{1}$0) → (11$\bar{2}$0) → (0001). The overall polarization also grows with improvement of the (0001) texture to reach the maximum value for the single-crystal electrode of the same orientation [9]. In the present study, anodic and cathodic polarization curves (Fig. 3) were obtained on planar and bent single-crystal electrodes with (0001) orientation. Comparison of the obtained data suggests that the overall polarization is lower on the bent electrode, especially in the anodic region, which may be due to build-up of elastic deformation and increasing number of active sites.

CONCLUSIONS

(1) The possibility is demonstrated of obtaining relatively thick (400 μm) epitaxial single-crystal rhe-

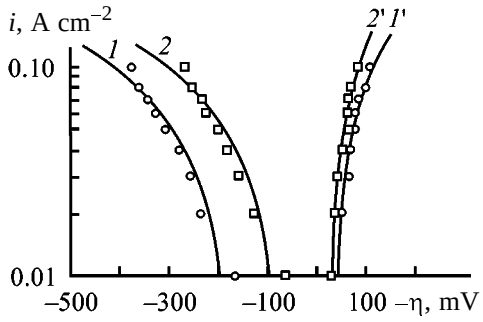

Fig. 3. Polarization curves for rhenium on (*1*, *1*') planar and (*2*, *2*') bent (0001) single-crystal substrates at 780°C. (*i*) Current density and (η) overvoltage. Curves: (*1*, *2*) anodic and (*1*≅ *2*') cathodic.

nium layers by electrodeposition onto single-crystal rhenium foils from salt melts.

(2) The surface morphology of a growing rhenium deposit depends on both the substrate orientation and the electrolysis conditions. For example, with increasing deposition current density, the surface is smoothed and growth pits and pyramids become smaller. However, the deposit structure is independent of the substrate bending radius.

(3) The microhardness of rhenium deposits with (0001) orientation is within the range 240–270 kg mm^{-2}. This indicates that the electrodeposited rhenium is comparable in purity with that of the metal obtained by electron-beam zone melting.

ACKNOWLEDGMENTS

The authors thank the Russian Foundation for Basic Research for the financial support of the study (project no. 00-03-32 024a).

REFERENCES

1. Baraboshkin, A.N., *Elektrokristallizatsiya metallov iz rasplavlennykh solei* (Electrocrystallization of Metals from Molten Salts), Moscow: Nauka, 1976.
2. Esina, N.O., Baraboshkin, A.N., Talanova, M.I., *et al*., *Fiz. Met. Metalloved*., 1981, vol. 52, no. 6, pp. 1314–1317.
3. Baraboshkin, A.N. and Esina, N.O., Extended Abstracts, *30th Meet. of Int. Soc. of Electrochemistry*, Yugoslavia, 1981, pp. 349–352.
4. Esina, N.O., Tarasova, K.P., and Baraboshkin, A.N., *Elektrokhimiya*, 1987, vol. 23, no. 1, pp. 116–120.
5. Plaksin, S.V., Molchanov, A.M., Baraboshkin, A.N., and Korovenkova, E.S., *Elektrokhimiya*, 1997, vol. 33, no. 10, pp. 1236–1240.
6. Esina, N.O., Molchanov, A.M., Valeev, Z.I., and Baraboshkin, A.N., Refractory Metals in Molten Salts: Their Chemistry. Electrochemistry and Technology, *NATO ASI Ser*., 1998, vol. 53, pp. 109–116.
7. USSR Inventor's Certificate no. 1 739 253.
8. Baraboshkin, A.N., Vinogradov-Zhabrov, O.N., Martem'yanova, Z.S., and Esina, N.O., *Tr. Inst. Elektrokhim. Ural. Otd. Akad. Nauk SSSR*, 1975, no. 22, pp. 37–43.
9. Vinogradov-Zhabrov, O.N. and Minchenko, L.M., *Research Conf. on Molten Salts*, Porquerolles (France), June 27–July 3, 1998, poster B44.

Russian Journal of Applied Chemistry, Vol. 74, No. 9, 2001, pp. 1465–1469. Translated from Zhurnal Prikladnoi Khimii, Vol. 74, No. 9, 2001, pp. 1424–1428.

APPLIED ELECTROCHEMISTRY AND CORROSION PROTECTION OF METALS

Electrodeposition of Tin–Antimony Alloy from Sulfate Electrolytes with Organic Additives

G. I. Medvedev, N. A. Makrushin, and N. Yu. Fursova

Novomoskovsk Institute, Mendeleev Russian University of Chemical Engineering, Novomoskovsk, Tula oblast, Russia

Received November 28, 2000; in final form, March 2001

Abstract—Electrodeposition of the tin–antimony alloy from sulfate electrolytes containing $SnSO_4$, $Sb_2(SO_4)_3$, H_2SO_4, syntanol, formalin, and coumarin was studied. The electrolyte composition and electrodeposition conditions allowing deposition of lustrous coatings of tin–antimony alloy of controllable composition were determined.

Previously, the electrodeposition of the Sn–Sb alloy from sulfate electrolytes in the presence of syntanol, formalin, butynediol, and benzyl alcohol has been studied [1–3]. It was shown that syntanol, formalin, butynediol, and benzyl alcohol contained in electrolytes favor formation of lustrous alloy coatings at i_c = 0.5–12 A dm^{-2}. Proceeding with these investigations, we studied the electrodeposition of the Sn–Sb alloy from a sulfate electrolyte in the presence of syntanol, formalin, and coumarin. As is known [4], coumarin is a luster-producing additive to nickel plating electrolytes.

The electrodeposition was performed from an electrolyte of the composition (g l^{-1}): $SnSO_4$ 5–50, $Sb_2(SO_4)_3$ 0.1–0.8, H_2SO_4 100–120, syntanol (DS-10) 1–3, and coumarin 0.1–2; formalin (37% solution) 1–10 ml l^{-1}. The process temperature was 18–20°C. Coatings were deposited onto copper substrates to a thickness of 1–20 μm.

Polarization curves were measured by the potentiostatic method with a P-5827 potentiostat. The alloy composition was analyzed by the technique described in [5]. Antimony(III) sulfate was prepared by dissolving metallic antimony in hot concentrated sulfuric acid.

The leveling power of the electrolytes was found by direct prophilography [6]. The throwing power was determined in Mohler's slit cell [6]. The microhardness of Sn–Sb alloy deposits was measured on a PMT-3 device. The internal stress was measured by the method of deformation of a flexible cathode [7]. The electrical resistance of the coatings was measured in accordance with GOST (State Standard) 9.302–79. The solderability was determined using a soldering iron in accordance with GOST (State Standard) 20-57.406–81. An X-ray diffraction analysis of Sn–Sb alloy deposits was made on DRON-3 X-ray diffractometer in CuK_α radiation.

A study of the influence exerted on the outward appearance of coatings by organic additives in the electrolyte (g l^{-1}): $SnSO_4$ 5–50, $Sb_2(SO_4)_3$ 0.1–0.8, and H_2SO_4 100, demonstrated that high-quality lustrous coatings can only be obtained in the simultaneous presence of 2–3 g l^{-1} of syntanol, 6–8 ml l^{-1} of formalin, and 1.5–2 g l^{-1} of coumarin. Going beyond these concentration limits leads to deposition of silvery matte coatings. It should be noted that 1–20-μm-thick lustrous coatings can be obtained with electrolyte stirring. Without stirring, lustrous coatings are only formed to a thickness of 1–3 μm.

It was found that the i_c range in which lustrous coatings are obtained is determined by the $SnSO_4$ concentration in the electrolyte. At concentrations of $SnSO_4$ 5–20 and $Sb_2(SO_4)_3$ 0.1–0.8 g l^{-1}, lustrous coatings are obtained at i_c = 1–5 A dm^{-2}. Raising the $SnSO_4$ concentration to 30–50 g l^{-1} expands the i_c range in which lustrous coatings are obtained to 2–10 A dm^{-2}. A chemical analysis of the electrolytic deposits obtained from the electrolytes under study demonstrated that an Sn–Sb alloy is formed in this case.

Data on the influence exerted by the concentrations of $SnSO_4$ and $Sb_2(SO_4)_3$ in the electrolyte and the current density on the alloy composition are presented in Table 1. It can be seen that, with increasing $Sb_2(SO_4)_3$ concentration in the electrolyte (at constant

1070-4272/01/7409-1465$25.00

Table. 1. Content of Sb in the alloy and CE by the Sn–Sb alloy in relation to $SnSO_4$ and $Sb_2(SO_4)_3$ concentrations and current density i_c. Electrolyte composition, g l^{-1}: H_2SO_4 100, syntanol, 2, coumarin 2; formalin 6 ml l^{-1}; mechanical stirring

Concentration, g l^{-1}		Sb content, wt %, at indicated i_c, A dm^{-2}									
$SnSO_4$	$Sb(SO_4)_3$	1	2	3	4	5	6	7	8	9	10
5	0.1	19.1	18.8	18.6	17.0	15.8	–	–	–	–	–
	0.3	21.0	20.4	19.5	18.1	16.4	–	–	–	–	–
	0.5	22.7	22.3	21.6	19.9	17.5	–	–	–	–	–
	0.8	24.2	23.9	23.2	21.7	20.0	–	–	–	–	–
10	0.1	17.0	16.1	15.2	14.0	13.0	–	–	–	–	–
	0.3	19.0	18.0	17.2	16.2	14.5	–	–	–	–	–
	0.5	21.0	20.2	19.1	17.8	16.0	–	–	–	–	–
	0.8	23.0	22.1	21.0	19.9	18.5	–	–	–	–	–
20	0.1	13.0	11.7	10.6	9.8	8.8	–	–	–	–	–
	0.3	15.8	14.0	12.9	11.9	11.0	–	–	–	–	–
	0.5	18.0	16.1	15.0	14.0	13.0	–	–	–	–	–
	0.8	20.4	19.0	18.0	17.2	16.9	–	–	–	–	–
30	0.1	–	12.4	10.5	9.3	8.5	7.5	7.2	6.8	–	–
	0.3	–	13.0	11.5	10.2	9.3	8.6	7.9	7.2	–	–
	0.5	–	14.0	12.2	11.0	10.0	9.0	8.6	8.0	–	–
	0.8	–	15.7	14.5	13.7	12.8	12.1	11.7	11.0	–	–
50	0.1	–	–	–	4.7	3.5	2.8	2.5	2.2	2.1	2.0
	0.3	–	–	–	5.2	4.1	3.5	3.2	2.9	2.7	2.5
	0.5	–	–	–	5.7	4.7	4.0	3.6	3.4	3.2	3.0
	0.8	–	–	–	6.3	5.4	4.8	4.5	4.1	4.0	3.9
Concentration, g l^{-1}		CE by the alloy, %, at indicated i_c, A dm^{-2}									
$SnSO_4$	$Sb(SO_4)_3$	1	2	3	4	5	6	7	8	9	10
5	0.1	94.2	83.4	75.6	71.4	69.3	–	–	–	–	–
	0.3	93.2	82.3	74.6	70.1	68.8	–	–	–	–	–
	0.5	92.1	80.3	72.1	69.4	68.2	–	–	–	–	–
	0.8	91.3	77.4	70.2	67.4	65.2	–	–	–	–	–
10	0.1	95.2	88.3	82.4	77.1	73.3	–	–	–	–	–
	0.3	94.3	84.3	80.1	75.2	72.0	–	–	–	–	–
	0.5	93.1	85.4	79.5	74.2	71.3	–	–	–	–	–
	0.8	92.3	84.1	77.2	72.1	68.4	–	–	–	–	–
20	0.1	95.3	93.4	88.3	84.5	80.1	–	–	–	–	–
	0.3	94.5	92.4	87.6	82.8	79.2	–	–	–	–	–
	0.5	94.1	91.3	86.5	91.2	78.3	–	–	–	–	–
	0.8	92.3	88.5	92.1	77.3	73.1	–	–	–	–	–
30	0.1	–	99.2	99.0	98.3	91.8	89.1	84.8	83.4	–	–
	0.3	–	99.1	97.2	94.3	90.0	86.1	82.0	79.2	–	–
	0.5	–	98.1	95.8	92.1	87.0	82.4	79.6	76.2	–	–
	0.8	–	96.1	93.8	89.3	84.0	80.1	76.8	75.3	–	–
50	0.1	–	–	–	99.8	99.7	99.6	98.3	96.2	94.7	93.1
	0.3	–	–	–	99.7	99.6	99.6	97.7	95.3	93.8	91.7
	0.5	–	–	–	99.6	99.4	99.2	96.5	94.3	92.0	90.2
	0.8	–	–	–	99.5	98.0	97.3	94.4	90.3	88.5	87.2

$SnSO_4$ content), the content of antimony in the alloy grows. Raising the concentration of $SnSO_4$ [at constant content of $Sb_2(SO_4)_3$] and the current density leads to lower content of antimony in the alloy.

The effect of the H_2SO_4 concentration on the outward appearance of coatings and the alloy composition was also studied. It was found that raising the H_2SO_4 concentration in the electrolyte from 100 to 120 g l^{-1} does not change the i_c range in which lustrous coatings are obtained, but leads to an increase in the antimony content of the alloy by 0.5–1.0 wt % [depending on the $Sb_2(SO_4)_3$ concentration in the electrolyte and the current density]. Such an influence of the H_2SO_4 concentration on the alloy composition can be accounted for by a change in the ion composition of the electrolyte with increasing H_2SO_4 concentration. In this case, a complex ion, $Sn[Sn(SO_4)_2]$, is probably present in the electrolyte together with Sn(II) and Sb(III) ions [8]. The presence of such a complex in the electrolyte leads to lower activity of tin(II) ions and a shift of its reduction potential to negative values, with kinetic hindrance to Sn(II) discharge enhanced and the alloy enriched in antimony.

The current efficiency (CE) was measured in electrolytes allowing deposition of lustrous Sn–Sb alloy coatings. The data on how the electrolyte composition and current density affect the CE are presented in Table 1. It can be seen that, with the $Sb_2(SO_4)_3$ content of the electrolyte increasing from 0.1 to 0.8 g l^{-1} and growing current density, the CE decreases. With the concentration of $SnSO_4$ increasing from 5 to 50 g l^{-1}, the CE becomes higher.

Raising the concentration of H_2SO_4 from 100 to 120 g l^{-1} lowers the CE by 1–1.5%.

The microhardness of the obtained deposits was measured. It can be seen from Table 2 that the microhardness increases with growing content of $Sb_2(SO_4)_3$ in the electrolyte and decreases with increasing current density. The increase in the microhardness of the alloy is associated with its growing antimony content (Table 1).

As is known [9], for alloys of the type of mechanical mixture, a linear relationship must exist at a constant current density between the logarithms of the ratio of metal contents in the alloy and the ratio of the concentrations of their cations in the electrolyte. In the case of electrodeposition of an intermetallic compound or a solid solution the type of dependence is different.

The dependence $\log([Sn]/[Sb])$–$\log([Sn^{2+}]/[Sb^{3+}])$ for Sn–Sb alloys deposited from the electrolyte under study at an $Sb_2(SO_4)_3$ content ranging from 0.1 to 0.8 g l^{-1} and i_c 2–8 A dm^{-2} is presented in Fig. 1 whence follows that it is nonlinear. These data suggest that an intermetallic compound or a solid solution is formed in the course of Sn–Sb electrodeposition.

Table 2. Alloy microhardness in relation to $Sb_2(SO_4)_3$ concentration C in the electrolyte and current density i_c Electrolyte composition, g l^{-1}: $SnSO_4$ 30, H_2SO_4 100, syntanol 2, coumarin 2; formalin 6 ml l^{-1}; mechanical stirring

C, g l^{-1}	Microhardness, MPa, at indicated i_c, A dm^{-2}			
	1	2	3	4
0.1	588.1	519.4	460.6	431.2
0.3	590.0	550.1	510.0	440.1
0.5	627.2	558.6	519.4	490.0
0.8	656.5	617.4	588.0	558.6

An X-ray diffraction analysis of the alloy composition demonstrated that a solid solution of antimony in tin (α-phase) is, indeed, formed in all of the electrolytes studied at an Sb content of 2–5 wt % in the alloy. At an antimony content of 10–25 wt %, a two-phase system (mechanical mixture), solid solution of antimony in tin and intermetallic compound SnSb ($\alpha + \beta$ phases), is formed, in agreement with the phase diagram of the Sn–Sb system [10].

The dependences in Fig. 1 allow prediction of the composition of the Sn–Sb alloy in relation to the concentration of deposited components in the electrolyte.

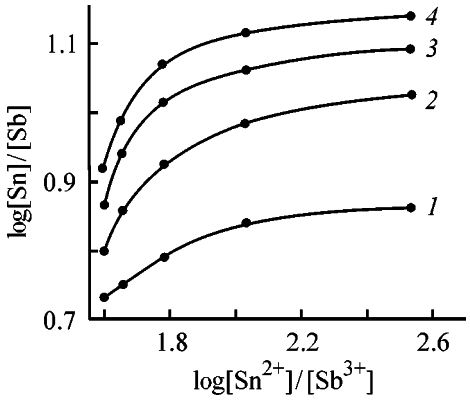

Fig. 1. $\log([Sn]/[Sb])$–$\log([Sn^{2+}]/[Sb^{3+}])$ dependence for Sn–Sb alloys. Electrolyte composition (g l^{-1}): $SnSO_4$ 30, H_2SO_4 100, syntanol 2, coumarin 2; $Sb_2(SO_4)_3$ 0.1, 0.3, 0.5, and 0.8; formalin 6 ml l^{-1}. Mechanical stirring; the same for Fig. 2. Current density (A dm^{-2}): (*1*) 2, (*2*) 4, (*3*) 6, and (*4*) 8.

Table 3. Throwing power of sulfate electrolytes with respect to current (TP_c), metal (TP_m), and thickness (TP_{th}) for electrodeposition of Sn–Sb alloy. Electrolyte composition, g l^{-1}: $Sb_2(SO_4)_3$ 0.8, H_2SO_4 100, syntanol 2, coumarin 2; formalin 6 ml l^{-1}; mechanical stirring

C_{SnSO_4}, g l^{-1}	TP	TP value, %, at indicated i_c, A dm^{-2}							
		1	2	3	4	5	6	7	8
10	TP_c	36.4	34.7	32.8	30.3	25.0	–	–	–
	TP_m	32.8	31.6	29.5	28.0	20.2	–	–	–
	TP_{th}	33.2	32.0	29.9	28.5	20.6	–	–	–
30	TP_c	–	33.0	21.0	16.9	15.5	14.8	13.0	11.4
	TP_m	–	31.7	19.2	15.9	14.5	13.3	12.1	10.8
	TP_{th}	–	32.2	21.0	16.5	14.8	13.9	12.8	11.3

The leveling (LP) and throwing (TP) power values were measured in electrolytes that yield lustrous coatings. It was found that the sulfate electrolytes yielding lustrous coatings possess leveling power. The dependence LP–i_c is presented in Fig. 2. It can be seen that the LP value is determined by the $SnSO_4$ concentration in the electrolyte. At an $SnSO_4$ concentration of 10 g l^{-1} the LP–i_c dependence passes through a maximum (P = 0.8) at i_c = 3 A dm^{-2} (curve *1*). At an $SnSO_4$ concentration of 30 g l^{-1} the leveling power decreases from 0.35 to 0.18 (curve *2*). The different leveling power values of sulfate electrolytes with organic additives at $SnSO_4$ concentrations of 10 and 30 g l^{-1} are possibly due to changing conditions of adsorption–diffusion processes involving the organic additives [11].

Data on the throwing power of the electrolytes studied are presented in Table 3. It can be seen that the TP decreases with increasing cathodic current density and increases with decreasing $SnSO_4$ concentration in the electrolyte.

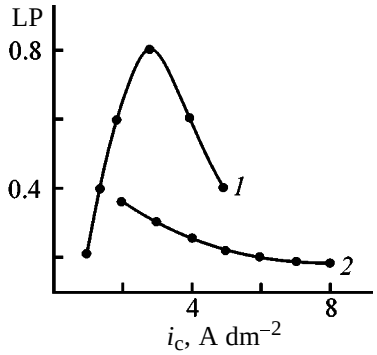

Fig. 2. Leveling power LP of sulfate electrolyte vs. current density i_c for electrodeposition of the Sn–Sb alloy. Electrolyte composition (g l^{-1}): $Sb_2(SO_4)_3$ 0.8, H_2SO_4 100, syntanol 2, coumarin 2; $SnSO_4$ (*1*) 10 and (*2*) 30; formalin 6 ml l^{-1}.

The data in Table 3 indicate that $TP_m < TP_c$, $TP_{th} > TP_m$, although the current efficiency by the alloy decreases with increasing i_c. This is due to the fact that, with increasing i_c, the alloy is enriched in tin having higher electrochemical equivalent and density, compared with antimony.

Lustrous alloy coatings were tested for adhesion strength, porosity, and solderability, and their internal stresses and electrical resistance were measured. It was found that Sn–Sb alloy coatings firmly adhere to the substrate and have no pores at thicknesses exceeding 3 μm. Weak internal compression stresses appear in the alloy deposits, decreasing from 6.6 to 2.8 MPa with increasing i_c. The solderability tests with samples coated with the Sn–Sb alloy demonstrated that coatings with antimony content of 5–10 wt % are well solderable. At an Sb content of 15 and 20 wt %, soldered samples have rough surface, which does not conform to GOST (State Standard) requirements.

The electrical coating resistance R_c of lustrous tin and Sn–Sb alloy coatings was measured. It was found that the R_c of the Sn–Sb alloy is somewhat higher than that of pure tin. R_c grows with increasing content of antimony in the alloy. For example, at antimony content in alloy of 5, 10, and 15 wt % and a load of 10 g at a current of 50 mA the R_c value increases from 6 to 8 mΩ.

The anodic process was studied with tin and antimony as anode. It was found that the anodic dissolution of tin occurs with weak polarization and current efficiency of 100%. The anodic dissolution of antimony proceeds with strong polarization as a result of surface polarization. In view of this fact, it is recommended to use pure tin as anode. The anodic current density should be 1.3 times less than the cathodic current density. To preclude contact deposition of

Table 4. Main characteristics of sulfate electrolytes with organic additives for electrodeposition of the Sn–Sb alloy

Characteristic	TPG electrode	
	no. 1	no. 2
$SnSO_4$, g l^{-1}	5–20	30–50
$Sb_2(SO_4)_3$, g l^{-1}	0.1–0.8	
H_2SO_4, g l^{-1}	100–120	
Syntanol (DS-10), g l^{-1}	2–3	
Formalin (37% solution), ml l^{-1}	6–8	
Coumarin, g l^{-1}	1.5–2.0	
i_c, A dm^{-2}	1.0–5.0	2.0–10.0
Sb, wt %	9.8–24.7	3.0–10.0
CE, %	64.2–93.7	74.3–98.3

antimony, tin anodes are to be introduced into, and removed from the bath with voltage applied. To prevent electrolyte contamination through sludge formation, the anodes are to be placed in sheaths of polypropylene fabric.

Based on our results, we developed sulfate electrolytes with organic additives for electrodeposition of lustrous Sn–Sb alloy coatings. The compositions and the main characteristics of the electrolytes are presented in Table 4.

Sulfate electrolyte no. 1 is more dilute. This reduces the consumption of reagents for its preparation and the loss of tin(II) and antimony(III) with processed articles and their accumulation in washing water, which improves the environmental safety of the process.

Sulfate electrolytes allow preparation of Sn–Sb alloy coatings with an antimony content of 15–30 wt %, exhibiting better physicomechanical characteristics and suitable for use instead of tin coating.

Sn–Sb alloy coatings are to be deposited onto copper substrates or steel substrates with preliminarily deposited 2–3-μm-thick copper layer. The electrolysis is to be carried out at room temperature with electrolyte stirring. The content of $SnSO_4$, $Sb_2(SO_4)_3$, H_2SO_4, formalin, and coumarin in the electrolyte is to be adjusted in accordance with chemical analysis data [12]. The adjustment of the syntanol content is done by introducing into the bath its additional amount of 1 g l^{-1} after passing 80 A h l^{-1} of electricity.

CONCLUSIONS

(1) A study of the electrodeposition of the Sn–Sb alloy from sulfate electrolytes in the presence of organic substances demonstrated that high-quality lustrous coatings are obtained in an electrolyte containing $SnSO_4$, $Sb_2(SO_4)_3$, and H_2SO_4, and also organic additives: syntanol, formalin, and coumarin.

(2) The content of antimony in the alloy grows with increasing concentration of $SnSO_4$ and H_2SO_4 in the electrolyte. Raising the $SnSO_4$ concentration leads to lower content of antimony in the alloy. With increasing current density, the content of antimony in the alloy decreases.

(3) The investigations performed made it possible to develop sulfate electrolytes for electrodeposition of an Sn–Sb alloy with controllable composition.

REFERENCES

1. Medvedev, G.I., Zhuravlev, V.I., and Fursova, N.Yu., *Zh. Prikl. Khim.*, 1998, vol. 71, no. 7, pp. 1113–1120.
2. Medvedev, G.I. and Fursova, N.Yu., *Zh. Prikl. Khim.*, 2000, vol. 73, no. 3, pp. 403–406.
3. Medvedev, G.I., Zhuravlev, V.I., and Fursova, N.Yu., *Zh. Prikl. Khim.*, 2000, vol. 73, no. 4, pp. 673–676.
4. *Blestyashchie elektroliticheskie pokrytiya* (Lustrous Electrolytic Coatings), Vilnius: Mintis, 1969.
5. Vyacheslavov, P.M., *Novye elektrokhimicheskie pokrytiya* (New Electrochemical Coatings), Leningrad: Lenizdat, 1972.
6. Kudryavtsev, N.T., *Elektrokhimicheskie pokrytiya metallami* (Electrolytic Metal Coatings), Moscow: Khimiya, 1979.
7. Vyacheslavov, P.M. and Shmeleva, N.M., *Metody ispytanii elektroliticheskikh pokrytii* (Methods for Testing Electrolytic Coatings), Leningrad: Mashinostroenie, 1977.
8. Dyatkina, S.L., Damaskin, B.B., Kol'tsova, T.N., and Kosmodamianskaya, L.V., *Elektrokhimiya*, 1985, vol. 21, no. 3, pp. 319–323.
9. Bibikov, N.N., Fedot'ev, N.P., and Vyacheslavov, P.M., *Elektroliticheskie splavy* (Electrolytic Alloys), Moscow: Mashgiz, 1962.
10. Gulyaev, A.P., *Metallovedenie* (Physical Metalurgy), Moscow: Metallurgiya, 1977.
11. Kruglikov, S.S., *Itogi Nauki Tekh., Ser.: Elektrokhim.*, 1965, pp. 117–151.
12. Kotik, F.I., *Uskorennyi kontrol' rastvorov i rasplavov: Spravochnik* (Express Analysis of Solutions and Melts): Handbook, Moscow: Mashinostroenie, 1978.

Russian Journal of Applied Chemistry, Vol. 74, No. 9, 2001, pp. 1470–1473. Translated from Zhurnal Prikladnoi Khimii, Vol. 74, No. 9, 2001, pp. 1429–1432.

APPLIED ELECTROCHEMISTRY AND CORROSION PROTECTION OF METALS

Electrolytic Preparation of Vanadium(V) Oxide from Oxovanadium(IV) Sulfate Solutions in the Presence of Sodium Ions

V. M. Nagirnyi, R. D. Apostolova, and E. M. Shembel'

Ukrainian State University of Chemical Engineering, Dnepropetrovsk, Ukraine

Received September 19, 2000; in final form, April 2001

Abstract—Effect of various factors on the character of anodic processes and the properties of vanadium(V) oxide deposits electroplated from oxovanadium(IV) sulfate solutions in the presence of sodium ions was studied.

Because of high electrochemical characteristics, vanadium(V) oxide electroplated from aqueous solutions of oxovanadium sulfate, including that plated in the presence of sodium ions, is efficient cathode material of lithium batteries [1–3]. The preliminary experimental tests showed that compact coatings and dispersed deposits of vanadium(V) oxide can be obtained in a quantitative yield from a 0.15–0.3 M oxovanadium sulfate solutions (pH 1.6–2.0) at 75–85°C and an anodic current density of 7–12.5 mA cm^{-2}. The use of gauze or smooth anodes made of 12Cr18Ni9Ti steel, in contrast to gold and platinum anodes used in [3, 4], make the given conditions of the electrolysis suitable for industry. However, in this case the corrosion resistance of the anode material during electrolysis becomes a factor of particular importance. These data and data on the effect of sodium ions on the character of anodic processes in electroplating of vanadium(V) oxide from vanadium sulfate solutions are lacking. The presence of sodium ions can change not only the nature of the electrode process but the properties of the formed deposits as well.

It was appropriate to study in detail the electrolysis conditions in the above solutions, including those containing sodium ions, taking into account their effect on the properties of anodic deposits and the corrosion of anode material.

Solutions were prepared from an equimolar mixture of crystalline vanadium(V) oxide and oxalic acid sintered at 125–135°C. The resulting dark blue sinter contained vanadium dioxide VO_2 as the main product and vanadium oxide V_2O_3 as the main by-product. Solution of oxovanadium sulfate $VOSO_4$ containing vanadium(III) sulfate impurity $V_2(SO_4)_3$ was prepared by dissolving the sinter in distilled water with added sulfuric acid. To prepare solutions, we used pure and analytically pure grade reagents and distilled water.

The electrolysis was performed in a temperature-controlled glass cell of 0.25 dm^3 volume from the solutions containing 0.15, 0.25, and 0.35 M oxovanadium sulfate at pH 1.6–2.0, 85°C, and I_a = 0.5–35 mA cm^{-1}, and also in the presence of sodium sulfate (0.025–0.4 M). Compact coatings of vanadium(V) oxide were deposited on gauze and smooth two-side anodes made of 12Cr18Ni9Ti steel of 10 × 10 × 0.15 mm size (gauze cell 0.04–0.1 mm), to which thin-plate current leads made of the same steel were welded. Preliminarily, the electrodes were degreased with Vienna lime and activated in concentrated hydrochloric acid. Smooth plates made of the above steel were used as cathodes.

The electrolysis efficiency under the given conditions was determined from the yield of the anodic deposit as a function of current, assuming that the whole efficient current is spent for oxidation of oxovanadium(IV) ions and formation of vanadium(V) oxide (electrochemical equivalent 3.4 g h^{-1}). The current efficiency was measured with a copper coulometer.

The polarization curves were taken in the range I_a = 0.5–3.5 mA cm^{-2} at 85°C and different sodium sulfate concentrations in the solution on the surface of a 12Cr18Ni9Ti steel electrode. The curves were taken with a temperature-controlled glass cell. A plate of VT-1 commercial titanium with a ratio of the anodic and cathodic surfaces of 1 : 2 served as a cathode. The anode potentials were measured relative to silver

1070-4272/01/7409-1470$25.00

chloride reference electrode (φ_{ref} = 0.225 V) using a P3003 voltage comparator and then were recalculated to hydrogen scale. The external appearance of the deposits and the microstructure of the surface of the corresponding thin-film (1.5–2.5 μm thick) oxide coatings were studied with an MBI-1 microscope. The adhesion and mechanical resistance of the deposits were estimated from the weight loss of a 20 × 10 × 0.3-mm sample with an oxide coating at a 180° bending. The phase composition of the deposits was determined by X-ray diffraction (DRON-2 diffractometer).

The current efficiency as a function of the current density, pH, and sodium ion concentration in oxovanadium sulfate solution at its constant concentration and temperature is plotted in Figs. 1 and 2. Irrespective of the presence of sodium ions, the current efficiency in the range pH 1.6–2.0 markedly increases, reaching the limiting value at pH 1.8–2.0 (Fig. 1a). The current efficiency increases jumpwise in the range I_a = 5–15 mA cm^{-2}, passes through a maximum at 7.5 and 10 mA cm^{-2} at the sodium sulfate concentrations below and above 0.1 M, respectively, and then decreases to a certain constant value (Fig. 1b). It should be noted that under the same conditions the rate of the vanadium oxide deposition attains the maximal value at the currant densities of 10–15 and 15–20 mA cm^{-2} (5.5 and 2.5 mg cm^{-2} h^{-1}, respectively). In the range of the oxovanadium sulfate concentrations of 0.15–0.35 M the efficiency of the anodic process is affected slightly. When small amounts of sodium sulfate (up to 0.05 M) are added to a solution with a constant concentration of oxovanadium sulfate (0.25 M), the current efficiency slightly increases as compared to that in the initial solution containing no additive. As the Na_2SO_4 concentration is increased further, to 0.15–0.2 M, the current efficiency decreases nearly twofold and then gradually approaches the lowest value at the supporting electrolyte concentration above 0.4 M (Fig. 2). This result is responsible for the enhanced tendency to corrosion of the anode material during electrolysis, which is due to the longer time from the instant of the current switching on to the formation of a continuous oxide film on the anode. This results in the accumulation of iron, nickel, and other ions in the solution, destabilization of electrolysis, and contamination of anodic deposits by foreign impurities.

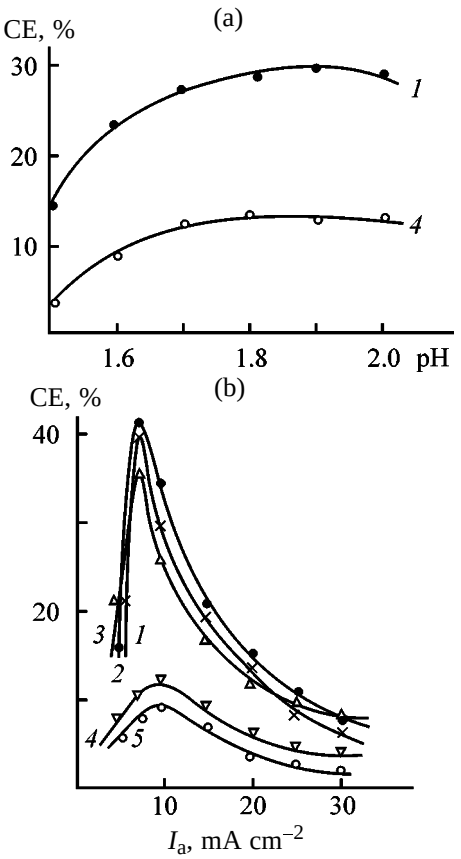

Fig. 1. Current efficiency CE by V_2O_5 vs. (a) pH and (b) anodic current density I_a in electrolysis of 0.25 M $VOSO_4$ solutions. T = 85°C; (a) I_a = 10 mA cm^{-2}; (b) pH 1.8. Na_2SO_4 concentration, M: (*1*) 0, (*2*) 0.05, (*3*) 0.1, (*4*) 0.2, and (*5*) 0.4.

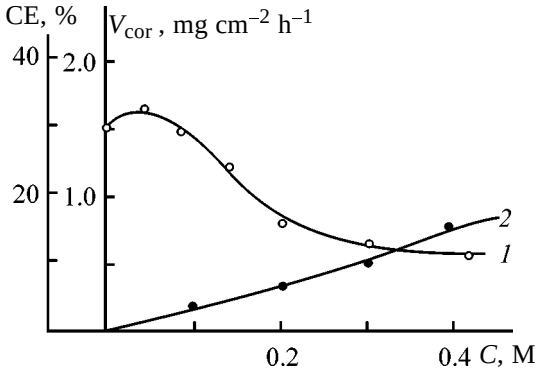

Fig. 2. (*1*) Current efficiency CE by V_2O_5 and (*2*) the dissolution rate V_{cor} of the anode support made of 12Cr18Ni9Ti steel in electrolysis of 0.25 M $VOSO_4$ solutions vs. Na_2SO_4 concentration C. T = 85°C, I_a = 10 mA cm^{-2}, pH 1.8.

Table 1 shows how the rate of the gauze electrode dissolution depends on the electrolysis time in oxovanadium solution containing 0.43 M sodium sulfate at pH 1.8 and 2.0. As seen, the weight loss of the anode mainly occurs in the initial period of the electrolysis and is terminated after a continuous oxide film is formed on the surface. Correspondingly, the shortening of this time at higher pH markedly de-

Table 1. Dissolution of a gauze electrode made of a 12Cr18Ni9Ti steel during anodic deposition of V_2O_5 from a 0.25 M $VOSO_4$ + 0.43 M Na_2SO_4 solution at T = 85°C and I_a = 10 mA cm^{-2}

pH	Weight loss, mg cm^{-2} h^{-1}, in indicated time, min					
	5	10	15	20	25	30
1.8	0.6	0.65	0.70	0.72	0.73	0.73
2.0	0.37	0.43	0.45	0.45	0.45	0.47

Table 2. Current efficiency with respect to V_2O_5 in electrolysis. Solution: (*1*) 0.25 M $VOSO_4$ and (*2*) 0.25 M $VOSO_4$ + 0.20 M Na_2SO_4; T = 85°C, I_a = 10 mA cm^{-2}, pH 1.8

Solution	Current efficiency, wt %, at indicated ratio $S_a : S_c$					
	1 : 1	1 : 2	1 : 3	1 : 4	1 : 5	1 : 7
1	12	13	18	20	30	33
2	3	4	9	10	13	15

creases the corrosion rate. The calcination of the anode support at 300°C for 1–1.5 h increases the corrosion resistance owing to the formation of the protective passivation film. In this case, even in solutions with a high sodium sulfate concentration (0.4 M), the weight loss of the anode decreases to difficultly detectable values (0.1–0.3 mg cm^{-2} h^{-1}). Under the similar electrolysis conditions, the corrosion rate of the smooth platelike anode made of the same steel is two times lower than that of the gauze anode.

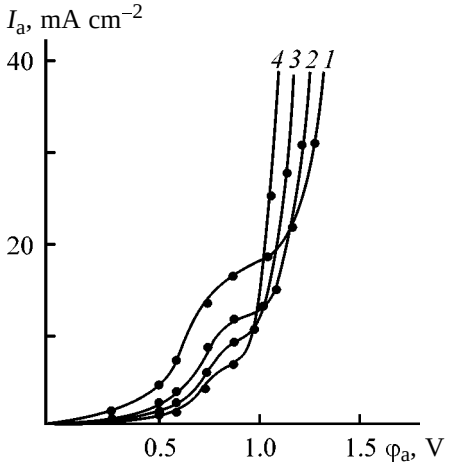

Fig. 3. Voltammetric curves of the anodic process in electrolysis of 0.25 M $VOSO_4$ solutions in the presence of Na_2SO_4. T = 85°C, pH 1.8. (I_a) Anodic current density and (φ_a) potential. Na_2SO_4 concentration, M: (*1*) 0, (*2*) 0.1, (*3*) 0.2, and (*4*) 0.4.

Under similar other conditions, the electrolysis stability is largely determined by the ratio of the anode to cathode surfaces. This is caused by the change in the dynamic equilibrium established in the solution between the vanadium compounds of various oxidation states, depending on the relative rates of electrode reactions. For example, apart from oxovanadium oxidation and the side reaction of oxygen evolution, the following reactions can also occur:

$$V^{3+} + 2H_2O - 2e \rightarrow VO_2^+ + 4H^+, \quad (1)$$

$$V^{3+} + H_2O - e \rightarrow VO^{2+} + 2H^+. \quad (2)$$

Owing to the high concentration of oxovanadium ions in the solution and their directional migration toward the cathode, the occurrence of reverse reaction (2) with a sufficient intensity is also probable on the cathode. Therefore, at $I_a \approx I_c$ the V^{3+} ions accumulate in the solution, which decreases the yield of the anodic products and causes hydrolysis of vanadium sulfate, with the solution becoming turbid. In the presence of sodium ions, the intensity of these processes increases owing to alkalization of the near-cathode space and larger extent of the hydrolytic processes. This is confirmed by the observed decrease in the current efficiency with respect to the anodic deposit at the decreased relative cathode surface (Table 2). The comparison of data in the table shows that the ratio $S_a : S_c = 1 : (\geq 5)$, at which the rate of the side cathodic reactions decreases to minimum, is optimal.

For the identical electrolysis conditions, the dependences considered agree satisfactorily with the corresponding voltammetric curves of the anodic process (Fig. 3). It is notable that the curves have two ascending branches with a transition plateau between them. The anodic current densities corresponding to the extreme points and the relative positions of the upper and lower sections of the curve strictly correlate with the concentration of sodium ions in the solution. The higher the concentration, the lower the limiting transition current and the larger the shift of the lower and upper sections toward higher and lower anode potentials, respectively.

It is quite evident that the nature of the anodic processes in the region of the above sections is different. For example, the lower sections predominantly reflect formation of vanadium(V) oxide at a weakly competing reaction of oxygen discharge. When the diffusion-limited current of this process is attained, the anode potential shifts toward positive region (the limiting plateau) to the values corresponding to oxygen evolution under the given conditions. This process

Table 3. Comparative characteristics of the V_2O_5 anodic deposits plated from the 0.25 M $VOSO_4$ solutions at T = 85°C, I_a = 10 mA cm^{-2}, and pH 1.8

Deposit characteristics	Na_2SO_4 concentration in solution, M		
	–	0.1	0.2
External appearance of deposits ($\delta \geq 10$ μm)	Very rough, with developed surface; marked edge effect	Rough, fairly compact, uniform	Dull, smooth, compact, uniform, slight pitting
Microstructure of the surface of thin-film coatings ($\delta \geq 5$–2.5 μm)	Amorphous, with highly developed microrelief	Crystalline with a random orientation of grains and a marked microrelief	Crystalline, with ordered structure and regular sequence of microprotrusions and concaves
Adhesion and mechanical resistance, as estimated from the weight loss at bending of 15–17 mg cm^{-2} coating, wt %	12–15	7–9	5–7

process becomes potential-determining in the region of the upper sections of curves. Hence, it follows that the retardation of the vanadium(V) oxide formation and the decrease in the limiting transition current density with increasing sodium concentration are governed by the increase in the anodic polarization and by the creation of more favorable conditions for oxygen evolution [5]. This can explain why the lower sections of curves shift toward higher anode potentials. The acceleration of oxygen discharge and the corresponding shift of the upper sections toward lower anode potentials are evidently caused by deceleration of the anodic deposit formation and by weakening of the shielding effect initiated by it.

The vanadium(V) oxide deposits electroplated in the presence of sodium ions have essentially different quality and structure. This is clearly seen from comparison of some characteristics of the deposits plated from the solutions with and without sodium ions (Table 3). In this case, sodium ions actively affect the phase formation process. This is manifested in formation of anodic deposits, which, unlike amorphous deposits formed without additive, are characterized by ordered crystalline structure enhancing their mechanical resistance and adhesion. The phase composition of the deposits which, according to X-ray diffraction analysis, mainly consist of an $Na_xV_2O_5$-type compound (x = 0.22–033), changes simultaneously. The latter compound heat-treated at 500–520°C is clearly identified as sodium–vanadium bronze. At the sodium sulfate concentration above 0.1 M the phase composition of the deposits remains unchanged. This is quite important for preparation of ballastless cathodes of lithium batteries by deposition of oxide coatings of the given phase composition on gauze or smooth stainless steel support, providing enhanced adhesion and mechanical resistance and a highly developed specific surface area of coatings, with the high efficiency of the anodic process being preserved.

The optimal conditions for electrolytic preparation of the corresponding oxide materials are anodic deposition from the solutions containing 0.2–0.25 M oxovanadium sulfate and 0.05–0.1 M sodium sulfate at 80–85°C, I_a = 7.5–12.5 mA cm^{-2}, pH 1.8–2.0, and $S_a : S_c$ = 1 : 5 and subsequent heat treatment at 500–520°C for 5–7 h.

CONCLUSIONS

(1) Upon electrolysis of oxovanadium sulfate solutions in the presence of sodium ions, the deposits qualitatively different from those prepared without additives are formed on the anode.

(2) According to X-ray diffraction analysis, the deposits heat-treated for 5–7 h at 500°C are sodium–vanadium bronzes of the composition $Na_xV_2O_5$ characterized by enhanced electrochemical activity and showing promise as cathode material of lithium batteries.

REFERENCES

1. Shembel, E., Apostolova, R., Nagirny, V., *et al*., *Power Sources*, 1999, vol. 80, pp. 90–97.
2. Apostolova, R.D., Shembel', E.M., and Nagirnyi, V.M., *Elektrokhimiya*, 2000, vol. 36, no. 1, pp. 41–48.
3. Sato, Y., Nomura, T., Tanaka, H., and Kobayakawa, K., *J. Electrochem. Soc*, 1991, vol. 138, no. 1, p. L37.
4. Andrukaitis, E., Jacobs, P.W.M., and Lorimer, J.W., *Solid State Ionics*, 1990, vol. 37, p. 157.
5. Delahay, P., *Double Layer and Electrode Kinetics*, New York: Interscience, 1966.

Russian Journal of Applied Chemistry, Vol. 74, No. 9, 2001, pp. 1474–1478. Translated from Zhurnal Prikladnoi Khimii, Vol. 74, No. 9, 2001, pp. 1433–1437.

APPLIED ELECTROCHEMISTRY AND CORROSION PROTECTION OF METALS

Electrolytic Preparation of Vanadium(V) Oxide from Saturated Solutions of Ammonium Metavanadate

V. M. Nagirnyi, R. D. Apostolova, A. S. Baskevich, P. M. Litvin, and E. M. Shembel'

Ukrainian State University of Chemical Engineering, Dnepropetrovsk, Ukraine

Received February 12, 2001

Abstract—A study was made of the voltammetric characteristics and dependences of the deposition rate and current efficiency on the electrolysis conditions in anodic deposition of vanadium(V) oxide on a stainless steel support from saturated solutions of ammonium vanadate, including those containing active and supporting additives.

Vanadium(V) oxide can be electroplated, preferably in a cyclic mode, from saturated neutral aqueous solutions of ammonium metavanadate in the presence of conducting additives, Na_2SO_4 and K_2SO_4, at 40–60°C and a current density of 1–4 mA cm^{-2} on gold, platinum, and stainless steel supports [1–3]. The resulting product is crystalline vanadium pentoxide containing ammonium ions and water, which are partially removed at 300°C. However, data on the effects of the electrolysis conditions, including current density, temperature, time, active and supporting inorganic additives, on the process stability are lacking. This was the subject of the present work.

Test solutions were prepared from analytically pure and pure grade reagents and distilled water. The electrolysis was performed in a 200-ml temperature-controlled open glass cell with symmetrically arranged cathodes (smooth plates of stainless steel or VT-1 titanium alloy) at 20, 30, 50, and 85°C. The sample to be plated was inserted between them so as to maintain a 15-mm interelectrode spacing and the ratio $S_a : S_c$ = 1 : 5. To prepare the saturated solution, a calculated volume of water with an excess of the salt was heated at 50–55°C for 2.5 h on a water bath. Inorganic additives were added into the solution after preliminary dissolution in a small volume of water with stirring and moderate heating to 30–40°C. The deposition rate V_{dep} (mg cm^{-2} h^{-1}) of vanadium oxide was estimated from the weight gain of the deposit after electrolysis and then recalculated per unit surface and unit time. The current efficiency (CE) was measured with a copper coulometer. The anode potential was measured relative to silver chloride reference electrode (E = +0.225 V) in the range I_a = 0.1–7.0 mA cm^{-2} with a Shch-4315 digital voltmeter. The X-ray structural analysis of the deposits was done on a DRON-2 diffractometer. The microrelief and microstructure of the surface of deposits were studied by a nanoscope.

A specific feature of the electrolytic preparation of anodic vanadium oxide deposits from ammonium metavanadate saturated solutions is the necessity of their preliminary "development" to accelerate deposition. Below we show how the deposition rate V_{dep} and the current efficiency by vanadium(V) oxide vary with electrolysis time τ in a solution freshly prepared for each experiment (pH 6.5, 85°C, I_a = 4 mA cm^{-2}, $S_a : S_c$ = 1 : 5, anode load 1 dm^2 dm^{-3}):

τ, min	V_{dep}, mg cm^{-2} h^{-1}	CE, %
15	1.3	8.7
30	2.1	14.5
45	3.0	21.0
60	3.5	24.5
75	4.3	30.1
90	4.7	33.0
120	5.0	35.0
150	7.1	42.0

The data obtained show that the yield of the anodic product increases with increasing electrolysis time. This results from gradual accumulation in the solution of vanadium ions of the lower oxidation state, among which the oxovanadium ions VO^{2+} formed by cathodic reduction of vanadium(V) are predominant:

$$VO_3^- + 4H^+ + e \rightarrow VO^{2+} + 2H_2O. \quad (1)$$

During 50–60 min of development, the solution

1070-4272/01/7409-1474$25.00

color changes from pale yellow to green. In the developed solution (without taking into account development period) the anodic product yield reaches 60% (V_{dep} = 9.0–9.5 mg cm^{-2} h^{-1}).

The relationships presented can vary depending on various factors, including volume load, current density, cathode material, ratio of electrode surfaces, etc. For example, a twofold increase in the anodic current density and anodic load corresponds to a nearly twofold shortening of the development time. This indicates that the vanadium oxide formation under the conditions considered is mainly limited by oxidation of oxovanadium ions accumulated in the solution by reaction (1):

$$2VO^{2+} + 2H_2O - e \rightarrow 2VO_2^+ + 4H^+, \quad (2)$$

$$2VO_2^+ + H_2O \rightarrow V_2O_5 + 2H^+ \quad (3)$$

$$2VO^{2+} + 3H_2O - 2e \rightarrow V_2O_5 + 6H^+ \quad (4)$$

which agrees with the data of [4]. However, along with these reactions, vanadium oxide(V) can be deposited on the anode owing to the adsorption-molecular interaction of HVO_3 forming in the near-electrode space, by analogy with reaction (3):

$$HVO_3 \rightarrow V_2O_5 + H_2O. \quad (5)$$

The occurrence of this reaction is confirmed to a certain extent in the case of electrolysis with the anode and cathode spaces separated by ceramic partitions. In the process, the current efficiency by the anodic product markedly exceeds that attained in the same time without separation of the electrode spaces, despite the lower rate of delivery of oxovanadium(IV) ions formed on the cathodes and a less intense change in the solution color near the anode. Even after 1 h of electrolysis the corresponding deposition rate reaches a maximum value for the developed solution (9.5 mg cm^{-2} h^{-1}).

The rate of the vanadium oxide(V) deposition V_{dep} from unsaturated solution of NH_4VO_3 (pH 6.5) is a function of the current density I_a and temperature T:

I_a = 4 mA cm^{-2}

T, °C	V_{dep}, mg cm^{-2} h^{-1}
25	0.9
35	2.0
50	3.5
75	8.2
85	9.0
90	8.7

T = 85°C

I_a, mA cm^{-2}	V_{dep}, mg cm^{-2} h^{-1}
0.5	3.0
1.0	5.0
2.0	6.7
3.0	8.5
4.0	9.0
5.0	9.5
7.0	8.6
10	7.3

The data presented show that with increasing temperature and current density the rate of the anodic product formation grows to a certain maximum and then decreases.

The deposition rate is affected by pH insignificuntly in the range pH 6–7 and decreases at higher pH, especially at pH > 7.5. When the solution is adjusted with sulfuric acid to pH < 6.0, the electrolysis is destabilized, which is manifested as formation of flaky particles of vanadium oxide.

Correspondingly, the external appearance and quality of the anodic deposits change. In the range of moderate current densities (2–4 mA cm^{-2}) and high temperatures (>75°C), the vanadium oxide deposits are compact and uniform and have enhanced adhesion, which allows mechanically resistant coatings up to 20–25 μm thick to be deposited onto smooth stainless steel plates. At current densities exceeding 10 mA cm^{-2} the anodic deposits, even thin (10–15 μm), are loose, and their adhesion is considerably worse. Decreasing electrolysis temperature produces the similar effect. The vanadium oxide deposits formed under the conditions have a color from light orange to light brown and are crystalline. These deposits strongly differ from black deposits with a comparatively developed structure, plated from acid solutions [5].

The supporting and active inorganic additives significantly affect electrolysis under the conditions considered.

The rates of vanadium oxide deposition from saturated solution of ammonium metavanadate containing 0.3 and 0.1 M Na_2SO_4 are given in the table. As seen, in the presence of sodium ions the deposition rate is lower than in the initial ammonium vanadate solution, and it decreases with growing concentration of the supporting electrolyte. The highest V_{dep} is attained at comparatively high current densities (5.0 mA cm^{-2}). The appearance of the deposits does not essentially

Rate V_{dep} of vanadium(V) oxide deposition from saturated solutions of NH_4VO_3 containing Na_2SO_4 at 85°C and pH 6.5

I_a, mA cm^{-2}	V_{dep}, mg^2 cm^{-2} h^{-1}, at indicated $C_{Na_2SO_4}$, M	
	0.03	0.10
1.0	1.5	1.0
2.0	2.6	1.9
3.0	5.0	3.8
4.0	6.2	5.9
5.0	7.3	7.0
6.0	7.0	6.7
7.0	6.7	6.2

change in the process. At the same time, the deposits are more fine-grained and more compact and exhibit higher chemical resistance and stronger adhesion to the support than those deposited from the initial solution.

With the nitrate ions added into the solution in the form of 0.1–0.4 M sodium salt, V_{dep} decreases by a factor of nearly 5 compared to the optimal values, but the adhesion and uniformity of the deposits are improved. At the same time, the high oxidizing power of nitrate ions produces the negative effect on electrolysis stability.

The active components under study were manganese, nickel, and cobalt sulfates and cobalt nitrate.

Study of the V–Mn system under various electrolysis conditions, even at a low (0.005–0.01 M) concentration of manganese sulfate, shows that after 7–10 min of switching on the current the solution becomes turbid and the electrolysis destabilizes. In the process, an abundant brown deposit precipitates on the cell bottom. A brown film on the anode is formed at a rate of 1.0–1.5 mg cm^{-2} h^{-1}.

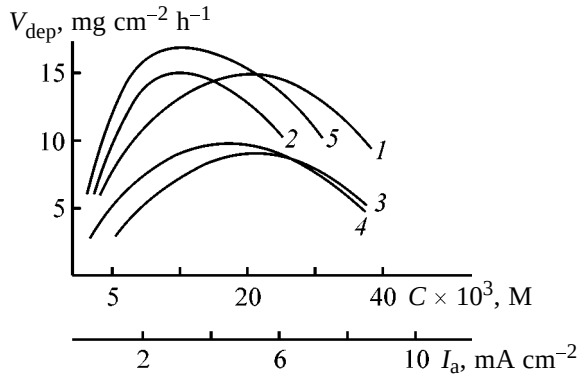

Fig. 1. Deposition rate V_{dep} of vanadium(V) oxide vs. (*1*) $CoSO_4 \cdot 7H_2O$ concentration at I_a = 4 mA cm^{-2} and (*2–5*) current density I_a. (*1, 4*) Saturated NH_4VO_3 solution; additive (M): (*2*) 0.02 $CoSO_4 \cdot 7H_2O$, (*3*) 0.04 $CoSO_4 \cdot 7H_2O$, and (*5*) 0.02 $Co(NO_3)_2 \cdot 6H_2O$. Temperature 85°C, pH 6.5; the same for Figs. 3 and 4.

In the presence of $NiSO_4 \cdot 7H_2O$ (concentration range 0.004–0.02 M), formation of the anodic deposit is fully suppressed. Under the electrolysis conditions optimal for the solution studied, a thin opalescent passivating oxide film is formed on the anode in the presence of nickel ions. In this case, oxygen evolution on the anode is the predominant process.

Among the systems considered, only the system V–Co is electrolytically compatible. When even small amounts (<0.02 M) of cobalt in the form of sulfate or nitrate are added to the solution, the nature of the anodic process and the structure and composition of the anodic product change. Figure 1 shows the rate of the anodic deposit formation in the saturated solution of NH_4VO_3 as a function of the cobalt sulfate concentration (curve *1*) and of the current density for the initial solution (curve *4*) and for those containing cobalt sulfate (curves *2, 3*) and cobalt nitrate (curve *5*). Curves *1* and *2* pass maxima at V_{dep} = 15 mg cm^{-2} h^{-1}, which is by a factor of 1.5 higher than in the initial solution. With the cobalt sulfate concentration increased twofold (curve *3*), V_{dep} decreases to a similar extent, with the maximum shifted toward higher current densities. In the presence of cobalt nitrate in the similar concentration, the maximum in the V_{dep}–I_{an} curve reaches 16 mg cm^{-2} h^{-1}, which confirms the positive effect of nitrate ions on the anodic formation of the corresponding oxides (curve *5*). At the same time, nitrate ions adversely affect the electrolysis stability and the solution performance owing to spontaneous sedimentation of cobalt nitrate crystals and corrosion of the anode support. In the presence of cobalt ions, anodic deposits are always uniform and grayish black with a lusterless smooth surface. The black color becomes more intense at higher cobalt concentrations. At lower concentrations (<0.04 M) fairly uniformly distributed inclusions of orange-brown crystals and spheroidal throwings are clearly revealed on the surface of deposits under a ×100 magnification. At higher concentrations of the additive this effect becomes less pronounced. This shows that at a certain stage of the deposition vanadium oxide is formed before its codeposition with cobalt oxide.

The above-noted character of the deposits forming in saturated ammonium vanadate solutions correlates

with the microstructure of their surface (Figs. 2a–2d). As seen, the structure and formation of the vanadium oxide deposits are strongly affected by the electrolysis conditions. For example, the deposits obtained in acid solutions of oxovanadium sulfate (pH 1.8–2.0) have a highly developed surface and a rather developed microrelief (Fig. 2a) [5]. The deposits obtained in the ammonium vanadate solutions studied have a crystalline structure with well-faced crystals growing in the parallel directions (Fig. 2c). After the deposits are cathodically treated in the same solution for a short time (0.3–5 min, depending on thickness), the edges of the crystal faces become smoother and the surface relief, slightly more developed (Fig. 2b). In the presence of cobalt ions the finely grained anodic deposits with a highly developed microrelief in the form of randomly oriented globular grains are formed (Fig. 2d). Evidently, this is a result of the interaction of anodically codeposited oxide phases, which is manifested, e.g., as suppressed growth of vanadium oxide crystals forming simultaneously with cobalt oxide nuclei. The coexistence of cobalt oxide in the anodic deposit with vanadium oxide V_2O_5 and the compound CoV_2O_5 was confirmed by X-ray diffraction (Fig. 3).

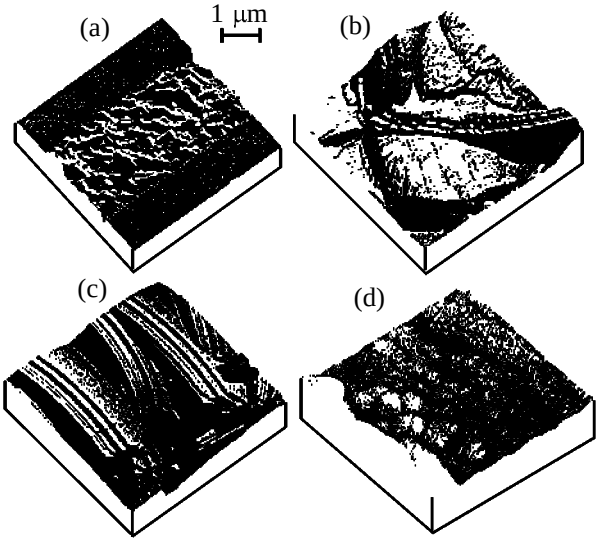

Fig. 2. Microstructure of the surface of vanadium(V) oxide deposits obtained under different conditions: (a) in acid solution of oxovandium sulfate and (b–d) in saturated NH_4VO_3 solution (T = 85°C, I_a = 4 mA cm^{-2}, pH 6.5), with subsequent cathodic treatment for a short time (c) in the same solution and (d) in the solution containing 0.02 M $CoSO_4$.

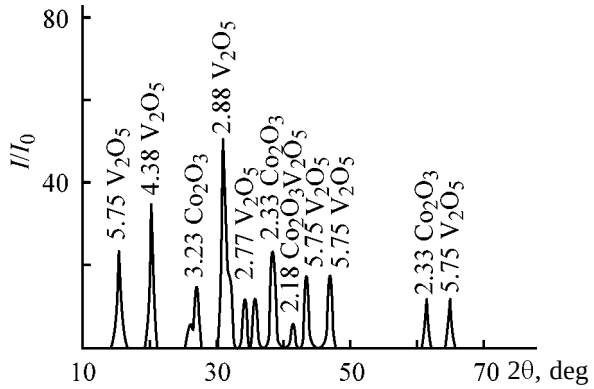

Fig. 3. Diffraction pattern of the anodic deposit obtained from the NH_4VO_3 saturated solution containing 0.02 M $CoSO_4$ at I_a = 4 mA cm^{-2} with subsequent heat treatment at 300°C for 7 h in air. (I/I_0) Relative intensity and (2θ) Bragg angle.

The above data are consistent with the voltammetric characteristics of the processes, taken under similar conditions. The typical I_a–E graphs for the developed solutions are shown in Fig. 4. At the optimal temperature (85°C) the dependence obtained for the initial solution on the initial surface of a stainless steel anode (V7 grade roughness) has two ascending sections separated by a limiting-current plateau (Fig. 4, curve *1*). For the anode surface preliminarily coated with a continuous vanadium oxide film, the similar dependence gradually passes from the lower mildly sloping section to the ascending section without inflections, with the relative shift toward positive values exceeding 200 mV (Fig. 4, curve *2*). Evidently, such a significant difference is caused by the fact that after the potentials of the onset of the vanadium oxide formation and oxygen evolution (the first ascending section) are attained, the anodic process on the initial surface occurs without overvoltage with increasing current (first ascending section), since in this case oxidation of oxovanadium ions to the corresponding oxide is the potential-determining reaction. Owing to diffusion and partial shielding of the anode by an oxide film, a further increase in the current density, after the limiting current of this reaction is attained, is accompanied by the shift of the anode potential (limiting plateau) to the values at which the vanadium oxide deposit is formed with a more intense oxygen evolution. When the passivating film on the anode is continuous, this process occurs without intermediate transitions, with the oxygen evolution additionally hindered. As a result, the anodic polarization increases. The relative decrease in the anode potential on the initial surface of the anode at the temperature decreased to 30°C (Fig. 4, curve *3*) evidently results from the predominant oxygen evolution on a stainless

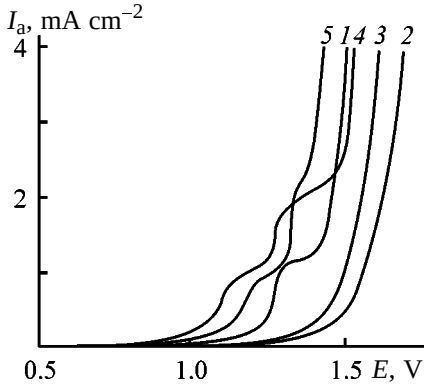

Fig. 4. I_a vs. E curves obtained in saturated NH_4VO_3 solutions on a 12Cr18Ni9Ti steel (*2*) straight and (*1, 3–5*) precoated with a vanadium oxide film. (*3*) T = 30°C. Additive (0.02 M): (*4*) $CoSO_4 \cdot 7H_2O$ and (*5*) $Co(NO_3)_2 \cdot 6H_2O$.

steel support under a weak influence of the concurrent reaction of vanadium(IV) oxidation without formation of a stable oxide film. In the presence of cobalt ions, the corresponding dependences consist of three ascending sections separated by steps (Fig. 4, curves *4, 5*). In a solution containing cobalt nitrate, the lower sections of curve *5* are located in the region of more positive potentials than those in a solution containing cobalt sulfate (Fig. 4, curve *4*). Correspondingly, the upper ascending sections of curves *4* and *5* are arranged in the opposite order with a relative shift of 100 mV, with the anode potentials lower than that in the ascending section of curve *1* for the pure solution. The stepwise character of these dependences confirms the different nature of the anodic processes for different polarizing currents. Apparently, for cobalt-containing solutions, the lower ascending sections of the curves reflect the simultaneous process of vanadium oxide deposition and oxygen evolution. With the limiting current of the oxovanadium(IV) oxidation attained, the polarization increases and the anode potential shifts toward positive values at which the cobalt(II) oxidation, being the main anodic reaction in the second ascending section, becomes feasible. The fact that the lower sections of curve *5* are located at more positive potentials for nitrate- than for sulfate-containing solution is due to the probable effect of nitrate ions. Their high oxidizing power can facilitate accelerated formation of anodic oxide film and inhibit the oxygen discharge even at low polarizing currents. As a result, the anodic polarization increases. The limitation of the cobalt ion transfer and the corresponding redistribution of the rates of simultaneous anodic reactions results in an additional jump of the anode potential (the second step) to the values favorable for accelerated oxygen evolution. In this case, vanadium and cobalt oxides in the upper ascending sections of the curves are formed more intensely owing to minimal diffusion. In this range the anodic process is conrolled by the slowest reaction of cobalt(II) oxidation accelerating in the presence of nitrate ions. This fact is probably responisble for the relative shift to less positive anode potentials of the corresponding section of curve *5*, which is to a certain extent confirmed by comparison of the V_{dep}–I_a plots for solutions containing equal concentrations of cobalt sulfate and cobalt nitrate (Fig. 1, curves *3, 5*).

CONCLUSIONS

(1) Saturated ammonium vanadate solutions show promise in electrolytic synthesis of high-performance cathode materials for lithium batteries. The complex V–Co oxide systems produced by anodic codeposition of vanadium and cobalt oxides from ammonium vanadate solutions in the presence of cobalt ions are of particular interest.

(2) The main electrolysis conditions for the systems studied are as follows: temperature 80–85°C, current density I_a 2–7 mA cm^{-2}, and pH 6–7. To enhance the specific surface area of the pure deposits of vanadium oxide, it is appropriate to use cathodic treatment for a short time (3–5 min) under the same electrolysis conditions.

REFERENCES

1. Goncharenko, A.S., *Elektrokhimiya vanadiya* (Electrochemitry of Vanadium), Moscow: Metallurgiya, 1969.
2. Andrukaitis, E., Jacobs, P.W., and Lorimer, J.W., *Solid State Ionics*, 1990, vol. 37, no. 2, pp. 157–169.
3. Andrukaitis, E., *Proc. 6th Int. Meet. on Lithium Batteries*, Munster (Germany), May 10–15, 1992, pp. 603–610.
4. Potiron, E., Le Gal La Salle, A., Verbaere, A., *et al.*, *Electrochim. Acta*, 1999, vol. 45, pp. 197–214.
5. Shembel' E.M., Nagirnyi, V.M., Apostolova, R.D., and Chaikovskaya, V.M., *Zh. Prikl. Khim.*, 2000, vol. 73, no. 3, pp. 409–412.

Russian Journal of Applied Chemistry, Vol. 74, No. 9, 2001, pp. 1479–1484. Translated from Zhurnal Prikladnoi Khimii, Vol. 74, No. 9, 2001, pp. 1438–1442.

APPLIED ELECTROCHEMISTRY AND CORROSION PROTECTION OF METALS

Effect of Electrolyte Composition on the Performance of Electrodes in Nickel–Zinc Batteries

Z. P. Arkhangel'skaya, R. P. Ivanova, T. B. Kas'yan, and L. B. Raikhel'son

Rigel' Joint-Stock Company, St. Petersburg, Russia

Received December 2, 1999; in final form, March 2001

Abstract—Variations in the electrolyte composition on cycling of nickel–zinc batteries were studied, and ways for its stabilization and service life prolongation were revealed.

The service life of a nickel–zinc (NZ) battery is usually determined by the negative electrode. When it works in combination with a nickel oxide electrode (NOE), its capacity on cycling decreases faster owing to gradual redistribution of its paste on the surface ("shape loss") and to the subsequent progressing local passivation [1, 2].

Therefore, when selecting an electrolyte composition, specific features of its interaction with a zinc electrode are taken into account to decrease inter- and intraelectrode zinc transfer; in particular, solutions are used in which the solubility of zinc oxide compounds is reduced. For example, the service life of batteries was prolonged by using solutions containing 3–5 M KOH and 3–4 M K_2CO_3 [3] instead of 7–8 M KOH solutions [4].

However, the suitability of electrolytes with reduced KOH concentration for NZ batteries is not obvious, as the processes on NOE are accompanied by a considerable change in the concentration of OH^- ions in the reaction zone. The concentration of hydroxide ions in NOE pores is considerably reduced on its anodic polarization even in electrolytes with a high KOH content (7–8 M) [5, 6], which hampers charging of deep layers of the electrode. On cycling the deficiency of the OH^- ions increases, as in NZ batteries the KOH concentration is reduced owing to the formation of CO_3^{2-} ions and to accumulation of potassium carbonate in the electrolyte [7].

NZ-25 batteries were manufactured of standard materials under conditions of industrial production. The negative electrodes 1.4 mm thick were prepared by roll-forming of the paste on a conducting framework. The paste consisted of a mixture of Zn and ZnO, corrosion inhibitors, and also binders and surfactants. The positive electrodes with a cermet base were 1 mm thick and were used in pairs. The ratio of capacities of the negative and positive electrodes was 3 : 1. A set of separators consisted of an alkaliproof paper and a hydrated cellulose film on the negative electrode and of nonwoven polypropylene on the positive electrode.

We studied batteries with three formulations of electrolyte, differing in the KOH and LiOH concentrations (Table 1). The concentration of LiOH corresponded to its maximum solubility in the electrolyte at the corresponding KOH concentration. The concentration of K_2CO_3 (as an impurity) in the starting electrolyte did not exceed 10 g l^{-1}.

We charged the batteries in a three-stage mode, with decreasing current in each subsequent step after attaining a voltage of 1.98 V (Table 1). Such an optimized mode allowed us to reduce substantially the oxygen evolution on NOE and to balance the main and side processes on the positive and negative electrodes. The imparted capacity was limited by the positive electrode, which allowed us to control its performance.

Table 1. Composition of electrolytes and modes of testing NZ-25 batteries

Battery no.	Electrolyte concentration, M		Charging*	
	KOH	LiOH	mode (in steps), A	initial capacity, A h
1	8.5	0.6	3–1.5–0.5	30
2	6.8	1.0	3–1.5–0.5	28
3	5.0	1.2	3–1.5–0.5	27

* Discharge current 5 A.

1070-4272/01/7409-1479$25.00

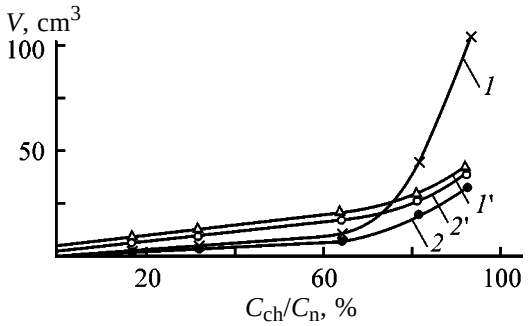

Fig. 1. Volume *V* of (*1*, *2*) oxygen and (*1*', *2*') hydrogen evolved during charging of NZ-25 batteris. (C_{ch}/C_n) Ratio of the charging and nominal capacities. Electrolyte, g-equiv l^{-1}: (*1*, *1*') KOH 8.5 and LiOH 0.6; (*2*, *2*') KOH 6.8 and LiOH 1.0.

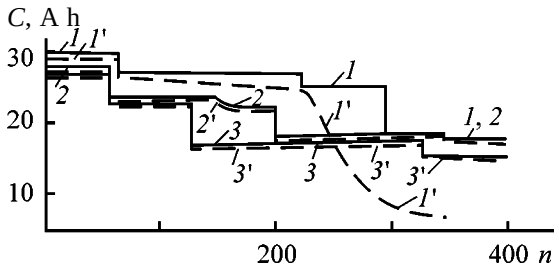

Fig. 2. Variation of the (*1*–*3*) charging and (*1*'–*3*') discharging capacities *C* during cycling of NZ-025 batteries. (*n*) Number of cycles; the same for Fig. 4. Electrolyte, g-equiv l^{-1}: (*1*, *1*') KOH 8.5 and LiOH 0.6; (*2*, *2*') KOH 6.8 and LiOH 1.0; (*3*, *3*') KOH 5.0 and LiOH 1.2.

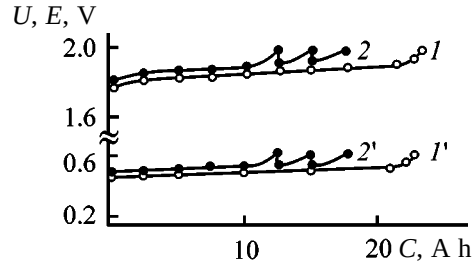

Fig. 3. Variation in the 150th cycle of the (*1*, *2*) voltage *U* and (*1*', *2*') potential *E* of NOE on charging of NZ-25 batteries containing electrolytes of different concentrations. (*C*) Capacity. Electrolyte, g-equiv l^{-1}: (*1*, *1*') KOH 6.8 and LiOH 1.0; (*2*, *2*') KOH 5.0 and LiOH 1.2.

However, even in this charging mode the oxygen evolution was not eliminated completely (Fig. 1). In batteries no. 1, starting from the charging degree of 0.6 of the nominal capacity, oxygen was formed in larger amounts than in batteries no. 2, whereas the volumes of the evolved hydrogen were the same, i.e., the degree of balance of the processes on the positive and negative electrodes increased as the KOH concentration decreased.

This conclusion is also confirmed by the minimal difference between the discharging and charging capacities for batteries nos. 2 and 3 (no more than 1–2%, Fig. 2), which allowed us to maintain an equal degree of charging of the positive and negative electrodes.

The discharging capacity of batteries no. 1 in the initial cycles is lower by 4–5% than the capacity imparted on charging, which points to the consumption of the corresponding current fraction for oxygen evolution on NOE and to the incomplete balance of the main processes on the positive and negative electrodes. The disbalance between the charging and discharging capacities increased to 8–10% to the 200th cycle. Simultaneously the "shape" of the zinc electrode changed, and in further cycles the capacity of the batteries of this type progressively decreased owing to passivation of the zinc electrode.

When charging of batteries nos. 2 and 3, as the number of cycles increases, problems arose, manifested as an increase in the potential of the positive electrode and in the corresponding increase in the voltage in the final stage of charging (Fig. 3). In this connection it was necessary to reduce the charging capacity.

The origin of these problems can be elucidated when comparing Figs. 2 and 4. A decrease in the KOH concentration with increasing K_2CO_3 concentration, which is shown in Fig. 4, is the reason for the increase in the NOE potential in the final charging stage, when a deficiency of hydroxide ions arises in the NOE pores [5, 6].

The main changes in the electrolyte composition occur in the initial cycling stage, and further changes are slower. The first decrease in the charging capacity for all the batteries takes place between the 50th and 60th cycles (Fig. 2). It results from a considerable decrease in the KOH concentration in the electrolyte to this moment (Fig. 4), especially in NOE pores [6].

In the subsequent cycling, batteries no. 3 required a decrease in the capacity on the 120–140th cycle, and batteries no. 2, on the 200th cycle (Fig. 2). The capacity of these batteries was stabilized at the level of 60% of the nominal value at the KOH concentration in the electrolyte of 2.5–3.0 g-equiv l^{-1} (Fig. 4). However, to charge batteries no. 3 to the level of 60% of C_n, it appeared necessary to add concentrated KOH solution to the electrolyte after 140 cycles to maintain its content at the level of 2.5–3 g-equiv l^{-1} (Fig. 4, curve *3*).

In batteries no. 1 the KOH concentration decreased

to 4 g-equiv l^{-1} and the necessity in correcting the charging capacity did not arise in the period from the 60th to the 200th cycle (Fig. 2). However, by the end of this period the battery capacity progressively decreased because of disbalance between the charging and discharging capacities. We have found out that the capacity of the batteries was not stabilized in the case of the initial KOH concentration of 8.5 g-equiv l^{-1} owing to the changes in the state of the negative electrode (shape losses).

Thus, we have revealed a certain relation between the change in the KOH concentration in the electrolyte and the capacity that can be imparted on charging the NZ battery to a feasible voltage when the maximum of the current is spent for the main process and the minimum, for oxygen evolution.

The transfer of impurities of metal carbonates from the paste into the electrolyte and the oxidation of organic substances contained in the battery and of the separator materials is the main factor responsible for the decrease in the KOH concentration in the electrolyte during cycling [7]. The initial content of carbonates in the zinc electrode in terms of CO_3^{2-} was 3%, the content of carbonates in NOE (after forming) was no more than 0.5%, and the K_2CO_3 concentration (as an impurity) in the initial electrolyte did not exceed 10 g l^{-1}.

It was shown earlier [7] that in batteries with the electrolyte containing 8.5 g-equiv l^{-1} KOH about 50% of the total amount of carbonates originates from the electrode paste. Because of their transfer into solution, the K_2CO_3 concentration increased to approximately 2 g-equiv l^{-1}. In the course of the subsequent 100–150 cycles the concentration of carbonates in the electrolyte increased further by a factor of almost 2, after which the content of carbonates in the electrolyte remained practically unchanged, though they were accumulated in the NOE paste.

The study of batteries with electrolytes of different concentrations, on the whole, confirmed these conclusions (Fig. 4), but it showed that the dynamics of K_2CO_3 accumulation and decrease in the KOH content in these batteries differ from each other. In batteries nos. 2 and 3 the carbonate was accumulated more slowly, and its content was about half that in batteries no. 1.

These data can be explained by considering specific features of the K_2CO_3 formation in NZ batteries. The increase in the K_2CO_3 concentration may be due to three processes.

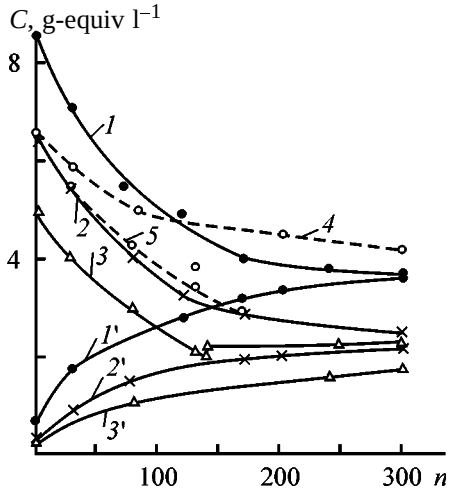

Fig. 4. Change in the concentration *C* of (*1*–*5*) KOH and (*1*'–*3*') K_2CO_3 in the course of cycling of NZ-25 batteries at various initial KOH concentration. Electrolyte, g-equiv l^{-1}: (*1*, *1*') KOH 8.5 and LiOH 0.6; (*2*, *2*', *4*, *5*) KOH 6.8 and LiOH 1.0; (*3*, *3*') KOH 5.0 and LiOH 1.2. (*4*, *5*) Calculated curves [(*4*) according to reaction (1) and (*5*) taking into account reaction (3)].

(1) First dissolves K_2CO_3 formed in the positive electrode from potassium hydroxide that remained in pores (after forming and washing) as a result of its reaction with atmospheric CO_2 before assembling the battery. This process is not accompanied by a decrease in the KOH concentration in the electrolyte.

(2) Further increase in the K_2CO_3 concentration is due to oxidation of organic substances with oxygen evolved on NOE. Thus, the KOH concentration changes in accordance with the reaction

$$2KOH + CO_2 \rightarrow K_2CO_3 + H_2O. \quad (1)$$

The rate of this process was found [7] to increase as the content of the products of separator breakdown in the electrolyte increases. It also depends on the amount of evolved oxygen, which is much less in batteries nos. 2 and 3 than in batteries no. 1 (Figs. 1, 2).

(3) Metal carbonates (basically $ZnCO_3$) contained in the paste of the negative electrode are also a source of K_2CO_3 accumulation. Its amount in the battery under study (in terms of CO_3^{2-}) is about 5 g (0.83 mol).

Zinc carbonate participates in the processes occurring on the zinc electrode [7], and the K_2CO_3 content in the electrolyte of a charged battery is higher than for an uncharged battery. Hence, on charging a battery, along with reaction (2)

$$Zn(OH)_2 + 2e \rightarrow Zn^0 + 2OH^-, \quad (2)$$

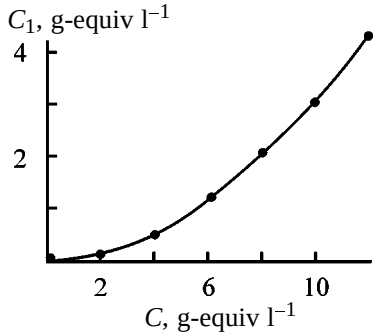

Fig. 5. $Zn(OH)_4^{2-}$ concentration C_1 as a function of the KOH concentration C.

occurs reduction of zinc carbonate by reaction (3):

$$ZnCO_3 + 2e \rightarrow Zn^0 + CO_3^{2-}. \quad (3)$$

The feasibility of reaction (3) is due to higher solubility of $ZnCO_3$ in water (solubility product SP 1.5×10^{-11}) as compared to the solubility of $Zn(OH)_2$ (SP $= 7 \times 10^{-18}$) [8].

A comparison of the amount of carbonates (in terms of CO_3^{2-}) contained in the negative electrodes of the batteries and the amount of K_2CO_3 accumulated in the electrolyte (1.7 g-equiv l^{-1}) of batteries no. 3 suggests that almost all carbonate ions pass into the electrolyte. The participation of the evolved oxygen in the formation of potassium carbonate is insignificant.

The formation of CO_3^{2-} ions in batteries no. 2 is also predominantly associated with the processes on the zinc electrode, and only a small part of them was formed by redox processes.

The K_2CO_3 content in batteries no. 1 is approximately twice that in batteries nos. 2 and 3 (Fig. 4). This fact suggests that in batteries with a high concentration of alkali, formation of about 50% of CO_3^{2-} ions is associated with evolution of a significant amount of oxygen on discharging.

As the cathodic reduction of zinc from $ZnCO_3$ is not accompanied by the formation of OH^- ions in the electrolyte, their concentration in the vicinity of the zinc electrode increases to a lesser extent than at the zinc reduction from $Zn(OH)_2$. Calculations, similar to those carried out in [6] for the zinc electrode, with consideration for the data of Fig. 5, showed that the transfer of CO_3^{2-} ions into the electrolyte results not only in the decreased release of OH^- ions from the electrode, but also in the decreased equilibrium concentration of $Zn(OH)_4^{2-}$ ions owing to a shift of the equilibrium of the chemical reaction accompanying the electrochemical process:

$$Zn(OH)_2 + 2OH^- \rightarrow Zn(OH)_4^{2-}. \quad (4)$$

The decrease in the concentration of OH^-- ions by 2 g-equiv l^{-1} within the range from 10 to 6 M results in a reduction by no less than 1 g-equiv l^{-1} of the content of $Zn(OH)_4^{2-}$ ions formed by the chemical reaction (Fig. 5). Thus, the increase in the K_2CO_3 concentration owing to reaction (3) is accompanied by an almost twofold decrease in the concentration of OH^- ions.

This is confirmed by the data of Table 2 summarizing the effect of reaction (3) on the change in the concentration of OH^- ions in batteries no. 2 in 30 cycles. The initial electrolyte concentration is 6.5 g-equiv l^{-1}. The electrolyte volume in the batteries under study is 100 ml. The volumes of pores of the positive (33 ml) and negative (28.5 ml) electrodes, and also of separators (28.5 ml) correspond to the values found in [6]. The calculations are based on the assumption that all CO_3^{2-} ions accumulated within this period (2.58 g, or 0.086 g-equiv l^{-1}) are formed by reaction (3) and pass into the electrolyte during one charging (Table 2). The charging capacity is 1 F (26.8 A h).

In the calculations we took into account variations in the concentrations of the OH^- and $Zn(OH)_4^{2-}$ ions in pores of electrodes during charging and discharge of the batteries due to electrochemical processes, migration, and also to the dissolution of zinc carbonate and chemical decomposition of $Zn(OH)_4^{2-}$ ions. The amount of forming and decomposing zincate ions was determined from Fig. 5. The transfer number of K^+ ions was taken to be equal to 0.25 [6], that of OH^- ions, to 0.7, and that of $Zn(OH)_4^{2-}$ ions, to 0.05–0.06, taking into account the most probable ratio of the diffusion coefficients of these ions of 4 : 1 and the ratio of their concentrations in the electrolyte (Fig. 5). Diffusion of the ions was not taken into consideration, as its effect in NZ batteries is insignificant [6].

We took into account the contents of components in separators when determining the average KOH concentration in the electrolyte. We assumed that their contents remain unchanged on charging and discharge, as the amount of ions entering the zone on migration and leaving it should be the same. In the calculation of the averaged KOH concentration we also took into account the release of water on charging (1 mol per 1 F) and its similar removal on discharge [5].

Owing to a number of assumptions and also to instability of the zincate complex, we can consider the

Table 2. Change in the content of OH^- ions during charging–discharge of an NZ-25 battery

Area	Content of OH^- ions, g-equiv (g-equiv l^{-1})			
	without account for CO_3^{2-}		with account for CO_3^{2-}	
	ZE	NOE	ZE	NOE
	Charging			
In pores:				
prior to the start of charging	0.25	0.215	0.25	0.215
during charging	+0.15	–0.174	+0.079	–0.201
after charging	0.40	0.041	0.329	0.014
	(10.4)	(1.24)	(8.54)	(0.42)
Average in the battery	0.196	0.168	0.163	0.14
	(5.1)	(5.1)	(4.25)	(4.25)
	Discharge			
In pores:				
during discharge	–0.163	+0.184	–0.154	+0.167
after disharge	0.033	0.352	0.009	0.307
	(0.86)	(10.7)	(0.03)	(9.3)
Average in the battery	(6.55)	(6.55)	(5.4)	(5.4)

* ZE is zinc electrode.

resulting KOH concentrations only as approximate. However, according to Table 2, the difference between the initial KOH concentration and its final value, calculated without taking into account participation of the CO_3^{2-} ions, is approximately 1%, indicating the reliability of the calculations. The arrangement of points in curves *2* (experimental) and *5* (calculated) in the 30th cycle differs insignificantly (Fig. 4). The KOH concentrations in the 80th and 130th cycles were calculated similarly, which allowed us to determine the arrangement of curve *5* up to 170 cycles.

We did not carry out calculations for a larger number of cycles, as this part of curve *2* is parallel to calculated curve *4* (Fig. 4), the slope of which is determined by the formation of CO_3^{2-} according to reaction (1). The slopes of curves *2* and *2'* in this case should be close to each other, but opposite in sign, which is actually observed.

Thus, the dynamics of decrease in the KOH concentration in the electrolyte of the NZ battery is determined by the contributions of reactions (2) and (3).

In batteries no. 1 the passing of CO_3^{2-} ions from the electrode paste makes a smaller contribution, which is due to the preferential and considerable formation of K_2CO_3 by reaction (1).

Thus, our data suggest that the initial KOH concentration of 7 M is optimal for the batteries under study, having a considerable thickness of NOEs (2 mm) and a noticeable content of carbonate impurities in zinc electrodes (up to 3%).

The use of an electrolyte with a higher KOH concentration results in an increase in the oxygen evolution, despite the use of the optimized three-stage charging mode. Furthermore, it is evident from Fig. 2 that the charging capacity should be limited, as in the final period of charging the battery to a specified voltage of 1.98 V the concentration of the OH^- ions in the zinc electrode increases during the initial cycles to 10–11 M, which promotes a change in its shape.

CONCLUSIONS

(1) Hampering of the anodic process on the nickel oxide electrode in the cycling nickel–zinc battery is associated with a decrease in the KOH concentration due to formation of carbonate ions.

(2) A decrease in the KOH concentration in the electrolyte is different depending on its initial content and is determined by the ratio of the rates of oxygen evolution and of passing of carbonates from the electrode pastes into the electrolyte, which is accompanied by breaking of the balance between the arrival of OH^- ions from the electrodes and their consumption in electrochemical processes.

(3) Stabilization of the capacity on prolonged cycling of the batteries under study at a level of about 60% of C_n was provided at the initial KOH concentration of 7 M, which decreased to 3 M by the end of the cycling.

(4) An increase in the initial KOH concentration to compensate for the observed changes is unfavorable for the zinc electrode because of increased loss of its paste and acceleration of processes leading to a progressing decrease in its capacity.

(5) To increase the service life of nickel–zinc batteries, it is necessary to reduce to a minimum the content of carbonates in the electrode paste. This will make narrower the range within which the KOH concentration varies in the electrolyte.

REFERENCES

1. Alekseeva, M.E., Arkhangel'skaya, Z.P., Ivanova, R.P., *et al.*, *Zh. Prikl. Khim.*, 1998, vol. 71, no. 6, pp. 940–946.
2. Alekseeva, M.E., Arkhangel'skaya, Z.P., Ivanova, R.P., *et al.*, *Zh. Prikl. Khim.*, 1998, vol. 71, no. 10, pp. 1653–1656.
3. Adler, T.C., McLarnon, F.R., and Cairns, E.J., *J. Electrochem. Soc.*, 1993, vol. 140, no. 2, pp. 289–294.
4. Plivelich, R.F., McLarnon, F.R., and Cairns, E.J., *J. Appl. Electrochem.*, 1995, vol. 25, no. 5, pp. 433–440.
5. Boldin, R.V., Akbulatova, A.D., and Mel'nikova, T.A., in *Sbornik rabot po khimicheskim istochikam toka* (Coll. of Works on Chemical Current Sources), Leningrad: Energoatomizdat, 1983, pp. 47–51.
6. Arkhangel'skaya, Z.P., Ivanova, R.P., Kas'yan, T.B., and Raikhel'son, L.B., *Zh. Prikl. Khim.*, 2001, vol. 74, no. 4, pp. 589–593.
7. Alekseeva, M.E., Arkhangel'skaya, Z.P., Ivanova, R.P., *et al.*, *Zh. Prikl. Khim.*, 1998, vol. 71, no. 8, pp. 1303–1307.
8. *Spravochnik po analiticheskoi khimii* (Handbook on Analytical Chemistry), Lur'e, Yu.Yu., Ed., Moscow: Goskhimizdat, 1962.

Russian Journal of Applied Chemistry, Vol. 74, No. 9, 2001, pp. 1485–1489. Translated from Zhurnal Prikladnoi Khimii, Vol. 74, No. 9, 2001, pp. 1443–1447.

APPLIED ELECTROCHEMISTRY AND CORROSION PROTECTION OF METALS

Express Voltammetric Control of Permanganate Ions in Process Solutions from Zinc Production

G. A. Borovkov and V. I. Monastyrskaya

North-Ossetian State University, Vladikavkaz, North Ossetia, Russia

Received January 18, 2001

Abstract—Express voltammetric analysis of zinc sulfate solutions for manganese(VII) ions was developed. The influence of the components of the supporting electrolyte on the measurement sensitivity and selectivity was studied. The method is intended for automated control of the permanganate treatment of the zinc electrolyte to remove cobalt(II) ions.

In modern industry, metallic zinc is usually produced by hydrometallurgical method, in which the most important stage is treatment of the solution to remove impurities. Among impurities producing the strongest interfering effect on electrolysis is cobalt(II). At a Co(II) content exceeding 2 mg l^{-1} the current efficiency drastically decreases, and corrosion of a zinc plate is observed [1].

The Co(II) ions from highly concentrated process solutions are removed by the so-called permanganate method involving their oxidation with MnO_4^- and precipitation of the resulting Co(III) ions in the form of the hydroxide $Co(OH)_3$, which can be easily removed from the process solution during concentrating and filtration.

One of the necessary conditions for optimizing permanganate treatment of zinc sulfate solutions to remove cobalt(II) is express control of the residual concentration of MnO_4^- ions. Maintenance of the permanganate concentration at a prescribed level ensures the necessary degree of Co(II) removal from the zinc electrolyte. This procedure can also be used for controlling $KMnO_4$ consumption during purification. For example, in reprocessing of cobalt(II)-rich concentrates, to reduce the Co(II) concentration in the purified zinc solution to 0.5 mg l^{-1}, the residual concentration of Mn(VII) should be maintained at a level of 500–700 mg l^{-1} (hereinafter, the Mn(VII) concentration is in terms of metal).[1]

The main method of express control of the ionic composition of hydrometallurgical solutions is voltammetry [2–4].

Various polarographic procedures are successfully used for the automated control of zinc electrolytes for the content of Cu(II), Cd(II), Pb(II), Co(II), In(III), and Ni(II) ions. However, data on using voltammetric methods for measuring the concentration of permanganate ions in zinc sulfate solutions are lacking.

Polarographic determination of manganese(VII) in aqueous solutions involves certain problems [5–7]. Firstly, several reduction waves are recorded, which are expanded along the potential scale and are hardly suitable for analytical purposes. Secondly, the analysis results are poorly reproducible. As a rule, voltammetric determination of permanganate ions is performed in acid supporting electrolytes on solid indicator electrodes.

In this work we examined the possibility of monitoring by differential pulse polarography (DPP) the manganese(VII) ion in an NH_4Cl + NH_4OH solution on a stationary dropping mercury electrode (SDME). Permanganate ions in an NH_4Cl + NH_4OH solution do not produce a proper polarographic wave, but a readily resolved DPP cathodic peak proportional to the Mn(VII) concentration in the test solution was recorded upon addition of dimethylglyoxime (DMG) into the electrolyte.

In alkaline medium permanganate ion is reduced to manganese dioxide. Presumably, MnO_2 reacts with DMG to form the complex

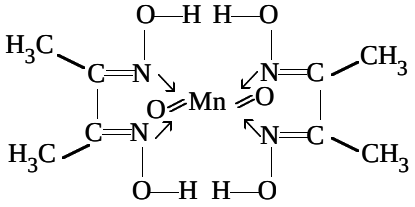

[1] According to data of the pilot shop of the Elektrotsink plant.

1070-4272/01/7409-1485$25.00

Fig. 1. DPP curves of manganese(II) in the 0.8 M NH_4Cl + 0.8 M NH_4OH + 2×10^{-3} M DMG supporting electrolyte. Manganese(VII) concentration 10 mg l^{-1}. (φ) Potential; the same for Fig. 3. Curves: (*1*) cathodic and (*2*) anodic.

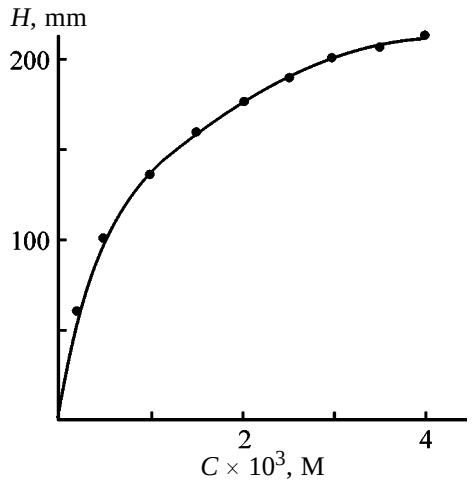

Fig. 2. Height of the DPP peak *H* of manganese(VII) vs. DMG concentration *C* in the 2 M NH_4Cl + 2 M NH_4OH supporting electrolyte.

We found that the complex of manganese dioxide with DMG is reversibly reduced on SDME in an NH_4Cl + NH_4OH solution, whereas Mn(II) does not produce analytical signal under these conditions.

Figure 1 shows the cathodic and anodic DPP curves of Mn(VII) (10 mg l^{-1}) in the 0.8 M NH_4Cl + 0.8 M NH_4OH + 2×10^{-3} M DMG electrolyte, recorded on an AZhE-11 voltammetric analyzer [3]. The potentials of the cathodic and anodic peaks are virtually the same ($\varphi_p^c = -0.98$ V and $\varphi_p^a = -0.97$ V), and the heights of the voltammetric curves differ by a factor of no more than 1.3.

The polarographic analysis of the solutions was performed in a three-electrode electrochemical cell with SDME indicator electrode, silver chloride reference electrode, and carbon glass auxiliary electrode. The DPP peaks were recorded in the automated mode at a potential sweeping rate of 10 mV s^{-1}. The amplitude of the pulsed polarizing voltage was 20 mV. The rectangular pulses of 40 ms length were applied at an 80-ms period.

The DPP cathodic peaks of Mn(VII) (10 mg l^{-1}) in the 2.0 M NH_4Cl + 2.0 M NH_4OH + 2×10^{-3} M DMG electrolyte taken before and after 40 mg l^{-1} of Mn(II) was added into the analyzed solution show that Mn(II) does not interfere with the Mn(VII) determination, making possible selective voltammetric control of permanganate ions in the solutions containing both manganese forms.

The sensitivity of the polarographic determination of MnO_4^- ions is largely dependent on the DMG concentration in the test solution and considerably increases as this concentration increases from 0.2×10^{-3} to 2×10^{-3} M. A further increase in the DMG concentration does not noticeably increase the amplitude of the Mn(VII) peak (Fig. 2). Therefore, the DMG concentration in the solution was maintained at a level of 2×10^{-3} M.

The possibilities of polarographic determination of Mn(VII) in the NH_4Cl + NH_4OH supporting electrolyte containing DMG are limited by the influence of various concomitant elements, firstly, of Zn(II), Co(II), Ni(II), and Fe(II). Therefore, for Mn(VII) monitoring in process solutions of zinc production, the analysis in the presence of excess Zn(II) should be sufficiently selective.

In NH_4Cl + NH_4OH solutions containing surfactants, Zn(II) produces a pronounced wave, which is used for analytical purposes [5]. Despite the fact that in an NH_4Cl + NH_4OH solution Zn(II) is electrochemically reduced at a more negative potential than the Mn(VII) complex with DMG, even a comparatively small excess of zinc(II) results in a drastic deterioration of the selectivity of polarographic determination of permanganate ions. For example, in a 0.1 M NH_4Cl + 0.1 M NH_4OH + 2×10^{-3} M DMG solution the potentials of the Mn(VII) and Zn(II) DPP peaks are –1.014 and –1.142 V, respectively. As seen from Fig. 3a, the DPP peak of manganese is markedly distorted even at equal concentrations of these ions in the test solution (curve *2*), and at a concentration ratio (mg l^{-1}) [Zn] : [Mn] = 10 : 1 the polarographic determination of permanganate ions becomes virtually impossible (curve *3*).

It is known that with increasing ammonia concentration the half-wave potential of zinc shifts toward negative values [5]. Therefore, we examined the possibility of enhancing selectivity of Mn(VII) determination in the presence of Zn(II) by increasing the concentration of the supporting electrolyte. We found that, as the (NH_4Cl + NH_4OH) concentration is increased from 0.25 to 2.0 M, the potential of the DPP peak of Mn(VII) changes from –1.01 to – 0.98 V, and that of Zn(II), from –1.20 to –1.36 V. As seen from Fig. 4, with increasing solution concentration the difference between the reduction potentials of the above ions regularly increases, i.e., the selectivity of determination of Mn(VII) in the presence of Zn(II) increases. We found that the variation of the supporting electrolyte concentration does not noticeably affect the sensitivity of Mn(VII) determination in the presence of Zn(II). For example, as the concentration of the supporting electrolyte components (NH_4Cl + NH_4OH) increases from 0.25 to 2.0 M, the intensity of the DPP peak of Mn(VII) remains unchanged, whereas that of Zn(II) increases by a factor of more than 1.7. Thus, the high resolution of polarographic determination of permanganate ions in zinc-containing solutions can be attained only with the use of sufficiently concentrated supporting electrolytes.

In a 2 M NH_4Cl + 2 M NH_4OH + 2×10^{-3} M DMG solution the direct polarographic determination of Mn(VII) is possible with a detection limit of 0.5 mg l^{-1} at [Zn] : [Mn] = 7500 : 1. Figure 3b shows the DPP peaks of Mn(VII) (92 mg l^{-1}) in a 2 M NH_4Cl + 2 M NH_4OH + 2×10^{-3} M solution before (curve *2*) and after 12 000 and 16 000 mg l^{-1} of zinc(II) is added into the test solution (curves *3* and *4*, respectively).

To concomitant substances appreciably interfering with the polarographic determination of permangante ions in NH_4Cl + NH_4OH solutions containing DMG belong Co(II) and Ni(II). Cobalt(II) and nickel(II) form with DMG stable complexes catalyzing hydrogen evolution on a mercury electrode. The strongest catalytic effect was observed in taking polarographic curves of nickel and cobalt dimethylglyoximates in NH_4Cl + NH_4OH buffer solutions with a sensitivity of the Co(II) and Ni(II) determination at a level of 1×10^{-8} M. The catalytic currents are used in voltammetric control of cobalt and nickel microconcentrations in various natural objects, for example, in the atmosphere [10].

In a supporting electrolyte of the composition 2 M NH_4Cl + 2 M NH_4OH + 2×10^{-3} M DMG, the DPP peak potential of Ni(II), Mn(VII), and Co(II) is –0.95, –0.98, and –1.14 V, respectively. The DPP peaks of Ni(II) and Mn(VII) are summed up, and the left descending branch of the resulting peak is distorted by the presence of cobalt(II) in the solution. This pattern is observed at the concentration ratio (mg l^{-1}) [Mn(VII)] : [Ni(II)] : [Co(II)] = 25 : 5 : 1. Naturally, at further growth of the Ni(II) and Co(II) concentrations their negative effect on the MnO_4^- determination increases.

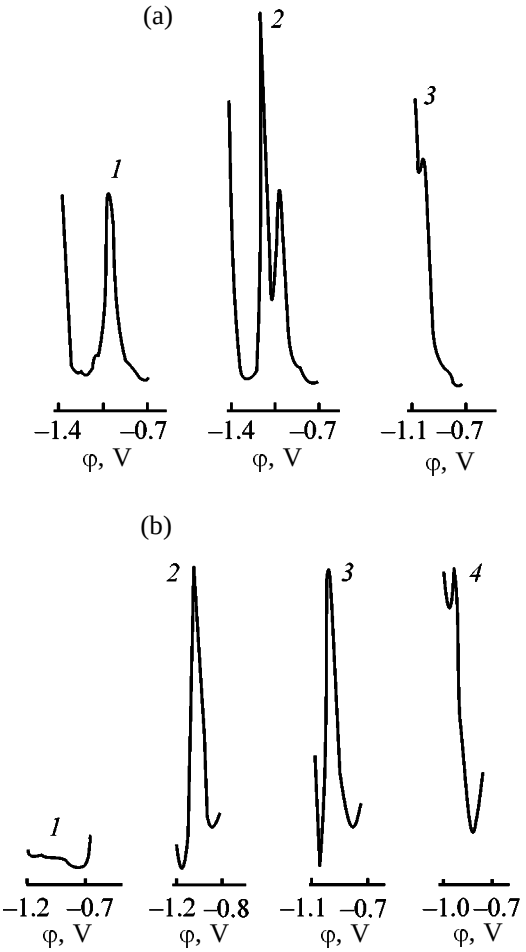

Fig. 3. Effect of Zn(II) concentration $C_{Zn(II)}$ (mg l^{-1}) on the polarographic determination of manganese(VII). (a) Supporting solution 0.1 M NH_4Cl + 0.1 M NH_4OH + 2×10^{-3} M DMG. Ion concentration (mg l^{-1}): (*1*) Mn(VII) 10 and Zn(II) 0; (*2*) Mn(VII) 10 and Zn(II) 10; and (*3*) Mn(VII) 10 and Zn(II) 100. (b) Supporting solution 2 M NH_4Cl + 2 M NH_4OH + 2×10^{-3} M DMG. (*1*) Supporting solution; ion concentration (mg l^{-1}): (*2*) Mn(VII) 2 and Zn(II) 0, (*3*) Mn(VII) 2 and Zn(II) 12 000, and (*4*) Mn(VII) 2 and Zn(II) 16 000.

Our study showed that the interfering effect of nickel(II) and cobalt(II) in polarographic determination of permanganate ions can be eliminated by addition of EDTA, which forms stable elecrtochemically

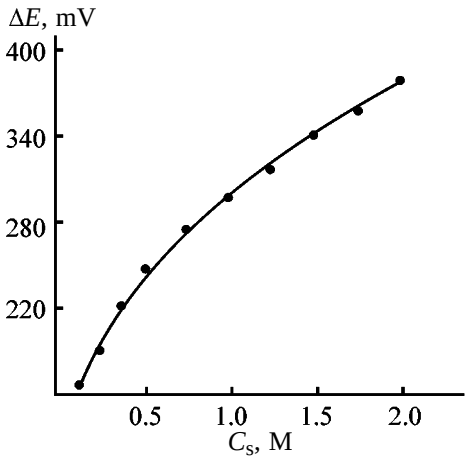

Fig. 4. Difference ΔE between the DPP peak potentials of manganese and zinc as a function of the concentration of the NH_4Cl + NH_4OH supporting electrolyte C_s. Concentration: 10 mg l^{-1} Mn(VII) and Zn(II) and 2×10^{-3} M DMG.

inactive complexes with Ni(II) and Co(II) [8, 11], but does not affect voltammetric determination of Mn(VII). In the case of MnO_4^- ions the effect of Ni(II) and Co(II) is suppressed completely. We found that in the electrolyte of the composition 2 M NH_4Cl + 2 M NH_4OH + 2×10^{-3} M DMG + 2×10^{-3} M EDTA, voltammetric determination of Mn(VII) is feasible at a 5-fold excess of Co(II) and a 50-fold excess of Ni(II).

Moreover, addition of EDTA into the supporting electrolyte made it possible to eliminate a hindering effect of Fe(II) ions. It is known that in an NH_4Cl + NH_4OH solution the Fe(II) ions are reduced electrochemically on a mercury electrode at high negative potentials. For example, the half-wave potential of Fe(II) in the 1 M NH_4Cl + 1 M NH_4OH supporting electrolyte is –1.52 V [12]. We found, however, that in the NH_4Cl + NH_4OH electrolyte containing DMG Fe(II) forms a purple complex which is polarographically reduced at a more positive potential. For example, in the 2 M NH_4Cl + 2 M NH_4OH + 2×10^{-3} M DMG electrolyte, the DPP of Fe(II) on SDME is recorded at a potential of –1.15 V.

The presence of Fe(II) in the test solution causes distortion of the Mn(VII) peak, but this distortion is completely eliminated by addition of EDTA. We found that in the 2 M NH_4Cl + 2 M NH_4OH + 2×10^{-3} M DMG + 2×10^{-3} M EDTA electrolyte a 10-fold excess of Fe(II) does not interfere with determination of permanganate ions and at the EDTA concentration increased to 4×10^{-3} M the Mn(VII) determination becomes possible even at a 20-fold excess of Fe(II).

Typical components of hydrometallurgical solutions of zinc production are also Cu(II), Cd(II), Sb(III), and As(III). In the 2 M NH_4Cl + 2 M NH_4OH + 2×10^{-3} M DMG + 2×10^{-3} M EDTA electrolyte, the DPP peak of cadmium(II) was not recorded experimentally at its concentration of 250 mg l^{-1} (in the purified zinc solution the Cd(II) content does not commonly exceed 1–2 mg l^{-1} [1]). The Sb(III) ions present in the zinc electrolyte are deposited in an ammonia solution [13]. The Sb(III) ions in the NH_4Cl + NH_4OH supporting electrolytes are reduced on a mercury electrode at a potential of –1.7 V [17] and do not interfere with the polarographic determination of Mn(VII).

The calibration curve of Mn(VII) in the 2 M NH_4Cl + 2 M NH_4OH + 2×10^{-3} M DMG + 2×10^{-3} M EDTA electrolyte is linear in the concentration range 0–25 mg l^{-1}. Solutions containing more than 25 mg l^{-1} manganese(VII) require dilution before analysis.

Our results allow development of a procedure for quantitative polarographic determination of permanganate ions in various objects including process solutions and sewage of zinc production.[2]

The method of standard additions served as control. A total of more than 30 test solutions of zinc electrolyte with the Mn(VII) concentration varied from 760 to 1180 mg l^{-1} were analyzed. The test solutions were diluted with water by two orders of magnitude. The measurements were done on an AZhE–11 voltammetric analyzer. The rms error of the Mn(VII) analysis in the concentration range 0–25 mg l^{-1} did not exceed 2.4%. The highest rms deviation of the main and control analyses of the same test solution, characterizing the reproducibility of measurements, was 0.7%.

The method developed can be used for the automated or express analysis of permanganate ions in process solutions and sewage of zinc production, which will enhance the efficiency of their treatment to remove impurities.

EXPERIMENTAL

We used standard solutions of Mn(VII), Co(II), Ni(II), Zn(II), and Fe(II) prepared by methods described previously [15]. The model solutions were prepared in double-distilled water.

The mixture for determining Mn(VII) in purified

[2] The method was tested with industrial zinc sulfate solutions at the Elektrotsink plant.

zinc sulfate solutions was prepared in a 100-ml volumetric flask from a test solution (1 ml) of zinc electrolyte and 50 ml of the supporting electrolyte of the composition 4 M NH_4Cl + 4 M NH_4OH + 4×10^{-3} M DMG + 4×10^{-3} M EDTA, to which distilled water was added to the mark. The mixture was poured into an electrochemical cell, in which cathodic voltammetric curves were taken in the potential range from –0.8 to –1.2 V with a potential sweeping rate of 10 mV s^{-1}. The amplitude of the DPP peaks at a potential of –0.98 V was measured, and the concentration of the Mn(VII) ions in the test solution was determined from the calibration plot. The total time of analysis for manganese(VII) did not exceed 7 min for one test solution.

When analysis was done in the automated mode, dilution of test solution with water, its mixing with the supporting electrolyte, and delivery of the test solution to the cell of a voltammetric sensor were performed with DZZh-4 three-chamber membrane batchers made of corrosion-resistant materials [3]. After the test solution was prepared, the spent mercury drop was dumped, then a new drop was formed, and the potential sweeping mechanism and the diagram tape driver of the secondary device were sequentially switched on by the control unit in accordance with the given program. Each voltammetric curve was recorded on a renewed mercury drop. After the parameters of the voltammetric curve were calculated by a computing device, the output signal of the analyzer, proportional to the Mn(VII) concentration in the test solution, was recorded with a secondary device.

CONCLUSIONS

(1) The possibility of selective polarographic determination of permanganate ions in the presence of Zn(II) in the NH_4Cl + NH_4OH supporting electrolyte containing dimethylglyoxime was established.

(2) The selectivity of the Mn(VII) analysis in the presence of excess Zn(II) ions is enhanced with increasing concentration of the supporting electrolyte. The negative effect of Co(II), Ni(II), and Fe(II) ions is eliminated by their complexation with EDTA to form electrochemically inactive species.

(3) The developed method of voltammetric determination of permanganate ions can be recommended for the automated or express analysis of multicomponent process solutions and sewage of zinc production.

REFERENCES

1. Snurnikov, A.P., *Gidrometallurgiya tsinka* (Hydrometallurgy of Zinc), Moscow: Metallurgiya, 1981.
2. Bond, A.M., and Knight, R.W., *Anal. Chem.*, 1988, vol. 60, no. 21, pp. 2445–2448.
3. Borovkov, G.A., Zaretskii, L.S., and Babitskii, L.B., *Tsvetn. Metall.*, 1987, no. 1, pp. 49–51.
4. Geibler, M., and Maia, R.D., *Fresenius Z. Anal. Chem.*, 1988, vol. 330, no. 7, pp. 624–626.
5. Kryukova, T.A., Sinyakova, S.I., and Aref'eva, T.V., *Polyarograficheskii analiz* (Polarographic Analysis), Moscow: Goskhimizdat, 1959.
6. Lavrukhina, A.K. and Yukina, L.V., *Analiticheskaya khimiya margantsa* (Analytical Chemistry of Manganese), Moscow: Nauka, 1974.
7. Williams, W.J., *Handbook of Anion Determination*, London: Butterworths, 1979.
8. Burger, K., *Organic Reagents in Metal Analysis*, Budapest: Akad. Kiado, 1973.
9. Inczedy, J., *Analytical Applications of Complex Equilibria*, Budapest: Akad. Kiado, 1976.
10. Manita, M.D., Salikhdzhanova, R.M.-F., and Yavorskaya, S.F., *Sovremennye metody opredeleniya atmosfernykh zagryaznenii naselennykh mest* (Modern Methods of Determination of Atmospheric Pollution in Populated Areas), Moscow: Meditsina, 1980.
11. Vydra, F., Stulik, K., and Julakova, E., *Rozpousteci polarografie a voltametrie*, Prague: Nakl. Technicke Literatury, 1977.
12. Vinogradova, E.N., Gallai, Z.A., and Finogenova, Z.M., *Methody polyarograficheskogo i amperometricheskogo analiza* (Methods of Polarographic and Voltammetric Analyses), Moscow: Mosk. Gos. Univ., 1960.
13. Pats, R.G., and Vasil'eva, L.N., *Metody analiza s ispol'zovaniem polyarografii peremennogo toka* (Methods of Analysis Using ac Polarography), Moscow: Metallurgiya, 1967.
14. Nemodruk, A.A., *Analiticheskaya khimiya mysh'yaka* (Analytical Chemistry of Arsenic), Moscow: Nauka, 1976.
15. Lazarev, A.I., Kharlamov, I.P., Yakovlev, P.A., and Yakovleva, E.F., *Spravochnik khimika-analitika* (Handbook of Analytical Chemist), Moscow: Metallurgiya, 1976.

Russian Journal of Applied Chemistry, Vol. 74, No. 9, 2001, pp. 1490–1494. Translated from Zhurnal Prikladnoi Khimii, Vol. 74, No. 9, 2001, pp. 1448–1493.

APPLIED ELECTROCHEMISTRY AND CORROSION PROTECTION OF METALS

Principles Determining the Current Modes of Solid-State Integrator Operation

I. E. Shpak and A. M. Mikhailova

Saratov State Technical University, Saratov, Russia

Received March 2, 2001

Abstract—The polarization resistance of integrator, electrolyte conductivity, electrolyte decomposition voltage, and residual current of integrator were determined in a wide range of temperatures by the method of rectangular pulse and cyclic voltammetry.

Complete removal of silver from the inert electrode of an $Ag\,|\,RbAg_4I_5\,|\,Au$ integrator is accompanied by a steep rise in the electrode potential, which is the output signal of the integrator, used to control external devices. The natural current limits depend on side processes occurring in the integrator. The lower limit is determined by the residual current, and the upper, by the electrolyte decomposition voltage (ca. 670 mV for $RbAg_4I_5$) [1, 2]. These limits are temperature-dependent.

The voltage drop across the integrator, ΔU, is constituted by the voltage drop in the electrolyte and across the electrode|electrolyte boundaries: $\Delta U = IR_e + IR_F$ (here a steady current not affected by charging of non-Faraday capacitances is meant). The polarization resistance R_F is a complex function of charging current, temperature, electrode charge, etc. [3], whereas R_e is independent of charge, but depends on temperature. Determining R_F precisely under flowing current conditions, i.e., the conditions characterized by pronounced departure from equilibrium, poses severe technical difficulties.

EXPERIMENTAL

The most acceptable method for determining the polarization resistance is the rectangular current pulse technique [4]. Using the parameters of the voltage response of an electrochemical system under study to a current pulse passed through it, the polarization resistance of the electrode, R_e, and some other characteristics can be calculated using the equations

$$R_e = \Delta U/(|I_{ch}| + |I_d|), \quad (1)$$

$$R_F = (\Delta U_2/|I_{ch}|) - (\Delta U_1/(|I_{ch}| + |I_d|), \quad (2)$$

$$C_d = |I_d|/|dU/d\tau|_u, \quad (3)$$

where $|dU/d\tau|$ is taken at the instant of time when $\Delta U = \Delta U_2 - \Delta U_1$ is reached.

However, the validity of the results obtained with this method depends on whether it is possible to provide steep leading fronts of the charging and discharge currents, ensure that the equality $|dU/d\tau| = 0$ holds at the instant when the ohmic components ΔU_1 and ΔU_2 are measured, and use sufficiently fast measuring apparatus. The existence of strict limitations imposes stringent requirements on the measurement procedure and equipment used. To meet these requirements, a special apparatus was developed (see figure).

The apparatus was used to study integrator samples in a wide range of currents and temperatures. The results obtained for one of the samples at temperatures of +20 and –50°C are presented in Table 1.

Similar results were obtained for all other temperatures (–20.0 and 50°C). Data on the dependence of the integrator voltage on the charging current in the entire temperature range are presented in Table 2.

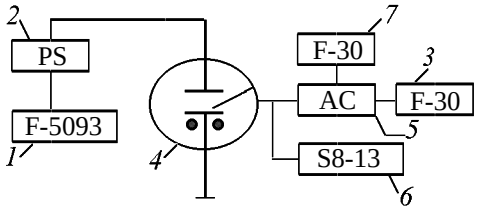

Schematic of the apparatus for measuring the integrator parameters with a single current pulse: (*1*) F-5093 frequency divider, (*2*) power source, (*3, 7*) F-30 digital multimeter, (*4*) electrochemical system under study, (*5*) analog computer, and (*6*) S8-13 versatile digital storage oscilloscope.

1070-4272/01/7409-1490$25.00 © 2001 MAIK "Nauka/Interperiodica"

Table 1. Integrator parameters in charging with different currents. Q_{ch} = 1 μC, I_d = 1 mA

I_{ch}, mA	τ_{ch}, s	ΔU_2	ΔU_1	R_F	R_e	$R_{ext} = R_F + R_e$
		mV		Ω		
			20°C			
20	0.05	200	110	4.8	5.2	10
10	0.10	140	63	8.3	5.7	14
1	1	60	–	–	–	60
0.6	1.67	55	–	–	–	91.7
			–50°C			
20	0.05	550	340	11.3	16.2	27.5
10	0.10	380	190	20.8	17.2	38
1	1	170	50	153	25	170
0.6	1.67	145	30	224	18.7	241
0.1	10	105	10	148	9	165

The *I*–*U* dependence, which is nonlinear at small currents, becomes linear at currents exceeding 5 mA. This means that, at charging current of up to 20 mA, electrolyte decomposition is virtually impossible at any of the temperatures studied. However, with account of the fact that at –50°C the voltage across an integrator being charged with a current of 20 mA becomes as high as 0.55 V, i.e., approaches the upper limiting voltage of the system under study (0.6 V), the maximum admissible, for the temperature range in question, current should presumably be not higher than 20 mA.

To elucidate the mechanism underlying the effect of current and temperature, it is advisable to consider the behavior of separate components of the electrode system with these factors. The results of the experiments performed indicate that the dependence of the charging current on the polarization resistance R_F is well approximated by a linear equation in log–log coordinates. The plots of the dependence $\log I_{ch} = f(\log R_F)$ are presented in Fig. 1. Hence follows that at T = const

$$R_F = K_1 I_{ch}^{-K_2}. \quad (4)$$

Calculation of the coefficients K_1 and K_2 on the basis of the plots in Fig. 1

T, °C	K_1	K_2
50	39.49	0.793
20	54.95	0.800
0	73.00	0.806
–20	98.31	0.805
–50	130.8	0.804

shows that K_2 is virtually temperature-independent and equal to 0.8, whereas the temperature dependence of K_1 is linear in the range from 50 to –20°C in the $\log K_1 - 1/T$ coordinates (Fig. 2). The temperature at which a deviation from the linear run of the dependence is observed coincides with the dew point (ca. –20°C) in the box used to assemble the integrator. Probably, crystallization of trace amounts of atmospheric moisture, which found their way into the sample in assembling the integrator, at the electrode | electrolyte interface can change the activation energy of the electrode reaction on passing to temperatures lower than the dew point. With account taken of the slope of the linear portion in the $\log K_1 - 1/T$ dependence in Fig. 2, the following expression is valid for K_1:

$$K_1 = 0.832 \exp(0.103/KT), \quad (5)$$

where the Boltzmann's constant $K = 8.6 \times 10^{-5}$ eV deg^{-1}.

Table 2. Integrator voltage in charging with different currents in the interval from –50 to 50°C. Q_{ch} = 1 μC

I_{ch}, mA	*U*, mV, at indicated temperature, °C				
	–50	–20	0	20	50
1	170	–	84	60	43
2	210	130	110	76	53
4	260	160	120	92	70
8	340	210	160	125	94
10	380	230	180	140	104
15	460	280	220	175	130
20	550	340	265	200	150

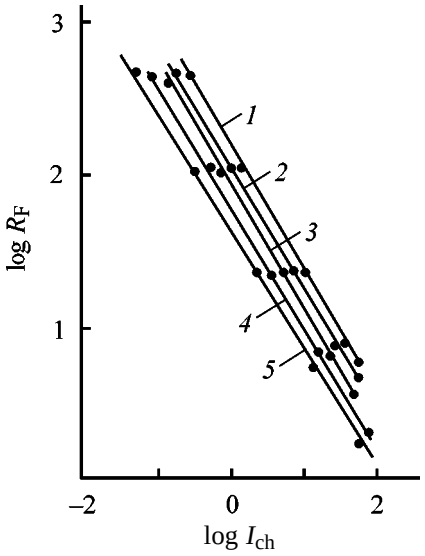

Fig. 1. $\log R_F$–$\log I_{ch}$ dependence in the temperature interval from –50 to 50°C. Temperature, °C: (*1*) –50, (*2*) –20, (*3*) 0, (*4*) 20, and (*5*) 50.

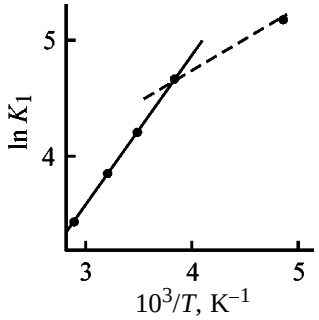

Fig. 2. Temperature dependence of the coefficient K_1 of Eq. (4).

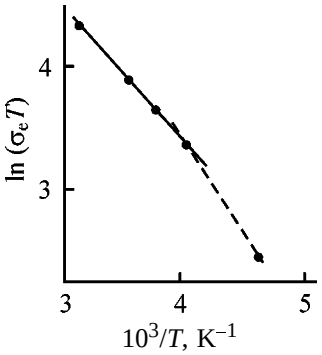

Fig. 3. Temperature dependence of $\sigma_e T$.

The activation energy is in good agreement with the activation energy of conductivity, obtained for $RbAg_4I_5$ in [5]. This suggests that the parameter K_1, determining the behavior of R_F, is related to the nature of the electrolyte.

The temperature dependence of the electrolyte conductivity σ_e in integrators, obtained by measuring the electrolyte resistance by the rectangular pulse method (Table 1), indicates that $\sigma_e \to 0$ at a temperature of about –75°C. This temperature is rather close to the temperature of phase transition of $RbAg_4I_5$ to a virtually nonconducting modification (ca. –65°C according to [6, 7]). Analytically, this dependence is described by the expression

$$\sigma_e = 1/R_e = -0.387 + 1.98 \times 10^{-3} T. \quad (6)$$

In the coordinates $\ln(\sigma_e T)$–$1/T$ (Fig. 3), the plot of the dependence shows two linear portions with a transition point lying at about –20°C, as in Fig. 2. For the linear portion in the temperature interval from 50 to –20°C we have

$$\sigma_e T = 3.3 \times 10^{-3} \exp(-0.1038/KT), \quad (7)$$

i.e., the activation energy of the conductivity of the electrolyte is 0.1038 eV, which virtually coincides with the value found from the dependence of the polarization resistance R_F on current and temperature [Eq. (4) for K_1].

Knowing the behavior of R_F and R_e as functions of current and temperature, we can write the general expression for the voltage drop across the integrator:

$$\Delta U = I(R_F + R_e) = K_1 I^{0.2} + IR_0 \exp(E'/KT). \quad (8)$$

The value of K_1 can be readily found using Eq. (5). Expression (8) not only fully describes the voltage across the system in integrator charging for the entire range of currents and temperatures, but also accounts for the nonlinearity of current–voltage characteristics of the samples at small currents (Table 2). It can be seen that, with the charging current increasing in this range, the polarization resistance R_F of the inert electrode decreases by 4–5 orders of magnitude and, beginning with a current of 5 mA, the electrolyte resistance remains virtually the only factor limiting the rate of the electrode process.

In the general case, the most probable residual current components for a system with solid electrolyte are the current of electronic conduction, Faraday current of minority carriers, and adsorption currents caused by crystal lattice relaxation in the contacting phases on changing the electrode potential and the capacitance of the electrode | electrolyte interface. The flowing of these currents, shunting the main anodic process during formation of a voltage step in readout

of the charge imparted to the integrator, introduces a certain positive error, which is the larger, the closer are the readout and residual currents.

The residual current of the integrators was determined using a method based on analysis of potentiodynamic characteristics of samples at various potential sweep rates. Direct measurement of steady-state residual currents at fixed electrode potentials failed to ensure sufficient reproducibility in view of the indeterminate stationarity conditions for the system under study. A set of potentiodynamic curves measured on one of the samples at 20°C is presented in Fig. 4. Equipotential points in these curves were used to plot the dependence of the current on the potential sweep rate (Fig. 5). Extrapolation to zero sweep rate (steady state) gave the residual current at a given potential.

The residual current depends in a complicated manner on the potential of the gold electrode: at potentials lower than 25 mV it is negative, i.e., silver is deposited at the electrode. At higher potentials the current passes through zero and, at around 50 mV, a first anodic current peak is observed, which is presumably due to dissolution of deposited silver.

In the range 150–200 mV, i.e., in approaching the resting potential of the inert electrode (100 ± 20 mV), the residual current falls virtually to zero. Finally, at potentials exceeding 200 mV the residual current grows following a nearly quadratic law. At a potential of 400 mV the residual current is within 0.2 μA for all of the samples studied.

It should be noted that any set of potentiodynamic curves contains two points (Fig. 4, points *A* and *B*) at which all the curves intersect. Apparently, the current at these points is independent of the sweep rate, and, consequently, corresponds to the residual current at intersection point potentials. Below are given the residual currents at various inert electrode potentials at 20°C (U_A = 31.25, U_B = 417.5 mV; I_A = 0.05, I_B = 0.2 μA):

U, mV	I_{res}, μA
50	0.05
100	0.025
150	0.000
250	0.05
350	0.055
400	0.15
425	0.25

Similar data were obtained for other temperatures within the working interval. A steeper increase in the residual current at $U > 400$ mV makes necessary setting the cutoff level at $U \le 400$ mV.

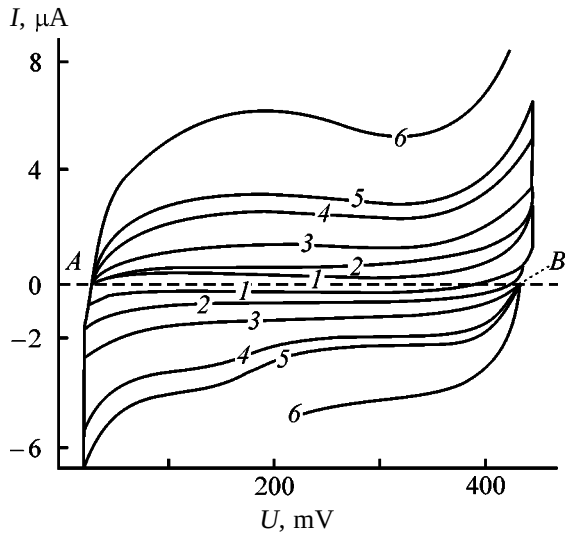

Fig. 4. Potentiodynamic characteristics *I*–*U* of Au | $RbAg_4I_5$ system at 20°C. Potential sweep rate, mV s^{-1}: (*1*) 2.6, (*2*) 5.2, (*3*) 10.4, (*4*) 20.8, (*5*) 26, and (*6*) 52.

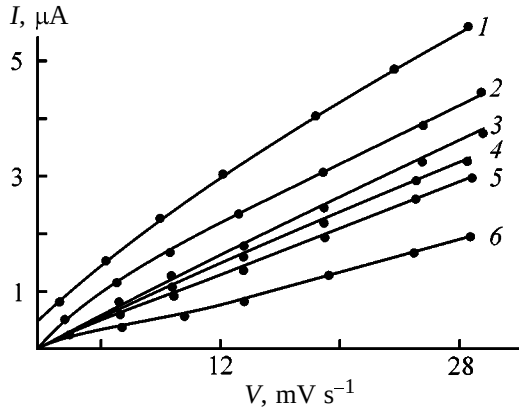

Fig. 5. Anode current *I* vs. potential sweep rate *V*. Inert electrode potential, mV: (*1*) 425, (*2*) 400, (*3*) 300, (*4*) 200, (*5*) 100, and (*6*) 50 (*T* = 20°C).

Extrapolation of potentiodynamic characteristics plotted in the *I*–*V* coordinates (*V* is the potential sweep rate) can be applied to find the residual currents at any working electrode potential. The residual currents of prototype samples of integrators, computed using special linear extrapolation software (at $V \to 0$, U = 350 mV), are the following:

T, °C	I_{res}, μA
–50	0.0102
–20	0.069
20	0.126
50	0.320

In view of the requirements that the minimum

readout current must be, as a rule, an order of magnitude higher than the residual current of integrator, we can take for the minimum acceptable working current a value of 1–2 μA at room temperature, and a higher value of 3–4 μA at 50°C.

CONCLUSIONS

(1) The obtained experimental data indicate that the dependence of the polarization resistance R_F on the charging current can be well approximated with a linear equation in log–log coordinates.

(2) The activation energy of the electrolyte conductivity (0.1038 eV) virtually coincides with the values determined from the dependence of the polarization resistance R_F on current and temperature.

(3) Residual currents, which flow in the system and shunt the main anodic process during the formation of a potential step in readout of the charge imparted to the integrator, introduce a certain positive error, which is the larger, the closer are the readout and residual currents.

REFERENCES

1. Mikhailova, A.M. and Kopchekchi, L.G., *Elektrokhimiya*, 1976, vol. 12, no. 1, pp. 156–157.
2. Gailish, E.A., D'yakonov, M.N., and Kuznetsov, V.P., *Elektron. Prom–st.*, 1975, no. 8, pp. 42–44.
3. Armstrong, R.D., *J. Electroanal. Chem.*, 1974, vol. 52, no. 3, pp. 413–419.
4. *Techniques of Electrochemistry*, Yeager, E. and Salkind, A.J., Eds., New York: Wiley–Interscience, 1972, vol. 1.
5. Ukshe, E.A. and Bukun, N.G., *Tverdye elektrolity* (Solid Electrolytes), Moscow: Nauka, 1977.
6. Geller, S., *Phys. Rev. B*, 1976, vol. 14, no. 10, pp. 4345–4355.
7. Atovmyan, L.O., Tkachev, V.V., and Ukshe, E.A., *Zh. Strukt. Khim.*, 1979, vol. 20, no. 5, pp. 940–942.

Russian Journal of Applied Chemistry, Vol. 74, No. 9, 2001, pp. 1495–1499. Translated from Zhurnal Prikladnoi Khimii, Vol. 74, No. 9, 2001, pp. 1452–1456.

APPLIED ELECTROCHEMISTRY AND CORROSION PROTECTION OF METALS

Diffusion Coating of Nickel with Tantalum in Chloride–Fluorotantalate Melts[1]

V. N. Kolosov, E. S. Matychenko, V. M. Orlov, and A. T. Belyaevskii

Tananaev Institute of Chemistry and Technology of Rare Elements and Mineral Raw Materials, Kola Scientific Center, Russian Academy of Sciences, Apatity, Murmansk oblast, Russia

Received January 30, 2001

Abstract—The effect of temperature and time on the diffusion saturation of nickel with tantalum in molten salt mixture NaCl–14 mol % K_2TaF_7 in the presence of metallic tantalum powder was studied, and characteristics of the obtained diffusion coatings were analyzed.

Owing to its corrosion resistance, nickel is frequently used as structural material in contact with molten salts, including preparation of sodium-reduced tantalum powders for capacitors. The content of nickel in such powders is strictly regulated by technical specifications. In this connection, it is urgent to develop protective diffusion coatings on the nickel surface, which diminish the apparatus corrosion and thereby prevent contamination of tantalum powders with nickel in the course of their manufacture.

Previous analysis of chronopotentiograms of free corrosion [1, 2] demonstrated that the potentials of nickel and tantalum in a chloride–fluorotantalate melt start to come closer 0.5 h after a nickel electrode is brought in contact with the melt, and only after 2 h a solid intermetallic protective layer of Ni_3Ta starts to grow. Such a prolonged contact of nickel with the melt before the beginning of formation of a protective layer leads to contamination of the melt and, consequently, of the obtained metal with nickel.

In this connection, it was necessary to accelerate the formation of surface diffusion-formed alloy coatings in molten salts. This can be achieved by introducing powdered tantalum into the melt [3], because in this case the surface area of tantalum in contact with the melt increases manyfold. This ensures an extremely fast saturation of the melt with tantalum ions in lower oxidation state and eliminates limitations on the overall process rate. Previous investigations confirmed the efficiency of the proposed technique [4].

In this study we examined the effect of temperature, time, and also concentration and dispersity of the tantalum powder introduced into the melt on the diffusion saturation of nickel with tantalum in a molten salt mixture and analyzed the characteristics of the obtained diffusion coatings.

EXPERIMENTAL

Experiments were performed in a hermetically sealed steel retort under helium at 950–1050 K. As containers for the melt served SU-2000 glassy carbon crucibles. Sodium chloride of ultrapure grade was dehydrated in air by heating to 900 K and then fused under pure helium. Working samples were cut from rolled nickel of N0 brand (thickness 0.4 mm, 99% purity), treated with a mixture of acids, washed with alcohol, and dried. As reference electrodes served chemically polished tantalum rods. A PI-50-1.1 potentiostat and a PDA-1A self-recorder were used. The parameters monitored in the experiments included the sample weight before and after the tests, variation of the working electrode potentials with time, and presence of impurities in the melt. X-ray phase analysis (XPA) of the samples and potassium fluorotantalate was made on a DRON-2 diffractometer (CuK_α radiation). The coating structure was studied on metallographic sections of the samples with a Neophot optical microscope and a Hitachi scanning electron microscope. The roughness was measured with a profilograph–profilometer manufactured by the Kalibr plant (model 250). As roughness parameters were chosen the mean-arithmetic profile deviation R_a and roughness profile amplitude at 10 points, R_z. The R_a and R_z values were calculated from the results of 12 measurements done in two perpendicular directions. Element distribution profiles in nickel samples were

[1] Reported at the X Kola Seminar "Electrochemistry of Rare Metals," Apatity, December 4–7, 2000.

1070-4272/01/7409-1495$25.00

Coefficients of Eqs. (1) and (2)

Ta powder fraction (0.8 wt %), μm	T, K	$k_0 \times 10^2$	$\Delta k \times 10^2$	τ, h	$A_0 \times 10^{-2}$	$\Delta A \times 10^{-2}$
		kg m^{-2} h$^{-1/2}$			kg m^{-2}	
–50	950	2.0	0.2	0.25	0.8	0.1
+50–63		2.7	0.3		1.0	0.2
+63		3.1	0.2		1.2	0.1
–50	1000	3.4	0.4	0.5	1.1	0.1
+50–63		4.1	0.4		1.8	0.2
+63		4.6	0.5		2.1	0.2
–50	1050	5.8	0.5	5	2.3	0.3
+50–63		7.8	0.4		2.7	0.4
+63		9.0	0.7		2.9	0.4
–50				10	3.0	0.4
+50–63					4.2	0.5
+63					5.0	0.4

measured on a Cameca X-ray microanalyzer. The microhardness was measured on a PMT-3 microhardness meter (20-g load).

The high-purity tantalum powder used in the experiments was obtained by sodium reduction [5] and contained the following amounts of controlled impurities (wt %): Fe 7×10^{-4}, Si 1.7×10^{-4} , Cr $\leq 2 \times 10^{-4}$, C 6×10^{-4}, Ni 7×10^{-4}, Zr $< 5 \times 10^{-4}$, and Nb 3×10^{-3}. The bulk density m_{sp} and specific surface area S_{sp} of the powder are given below in relation to the fractional composition:

Fraction, μm	m_{sp}, g cm^{-3}	S_{sp}, cm^2 g^{-1}
–50	2.31	1900
+50–63	2.40	1150
+63	2.80	840

The results of experiments on determining how the specific weight gain $P = \Delta m/S$ (Δm is the increase in the weight of a nickel sample as a result of diffusion saturation, S is the sample surface area) depends on the time τ of keeping in a melt with addition of powder of varied fractional composition at different temperatures are presented in Fig. 1. P is related to τ by the equation

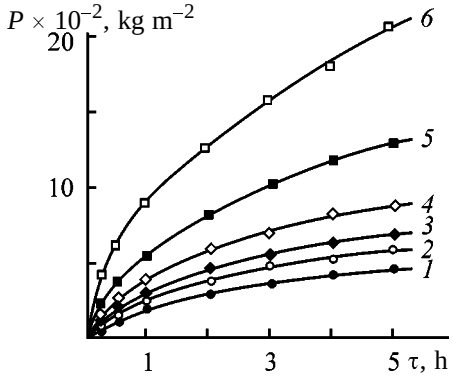

Fig. 1. Specific weight gain P for nickel samples vs. time τ of keeping in NaCl–K_2TaF_7 melt. Temperature, K: (*1–4*) 950 and (*5, 6*) 1050. Initial content of Ta powder in melt, wt %: (*1, 3, 5, 6*) 0.8 and (*2, 4*) 3.0. Ta powder fraction, μm: (*1, 2, 5*) –50 and (*3, 4, 6*) +63.

$$P = k\tau^{1/2}, \quad (1)$$

where $k = k_0 \pm \Delta k$ is an empirical coefficient which depends on the melt temperature and the amount and fractional composition of the powder (in this study the amount of powder introduced into the melt was expressed in weight percent relative to the mass of K_2TaF_7 salt in a melt under study).

Under the conditions studied, the dependence of the specific weight gain on the process temperature can be described by the equation

$$P = A\exp(-E/RT), \quad (2)$$

where R is the universal gas constant, $A = A_0 \pm \Delta A$ is an empirical coefficient which depends on time and the fractional composition of the employed tantalum powder, and $E = 70 \pm 5$ kJ mol^{-1} is an empirical coefficient which has the meaning of the apparent activation energy of diffusion saturation.

The coefficients of Eqs. (1) and (2) are given in the table for different conditions of interaction between nickel and melt.

XPA of the coatings demonstrated that the diffusion layer is composed of two phases (Fig. 2). As

follows from the phase diagram, there are five intermetallic compounds in the system nickel–tantalum: Ni_8Ta, Ni_3Ta, Ni_2Ta, NiTa, and $NiTa_2$ [6]. Among these, the compound Ni_3Ta is the most stable (at 1020 K, $\Delta G = -112 \pm 28$ kJ mol^{-1} [7], maximum growth rate constant $k = 1.3 \times 10^{-12}$ [8]). Previously, with compact metal used as a source of tantalum in NaCl–K_2TaF_7 melt (2.5 mol %), formation of just this compound on the nickel surface was observed [1]. In a melt with a higher content of potassium fluorotantalate (14 mol %), saturated with tantalum powder, Ni_2Ta is formed in addition to Ni_3Ta (Fig. 2).

It should be noted that the formation of coatings under study is based on an electroless transport process that is due to the presence in the melt of ions (in varied oxidation state) of the metal being deposited [9]. Raising the content of K_2TaF_7 and replacing compact tantalum with powdered metal create more favorable conditions for growth of Ni–Ta layers because of the increasing rate of melt saturation with tantalum ions in lower oxidation state. The possible mechanism of coating formation is as follows. After an intermetallic layer, the richest in nickel, is formed, tantalum continuing to be deposited reacts with this layer to form other compounds, which can be represented in a simplified form as the following sequence [2]:

$$2Ni_3Ta + Ta \rightleftarrows 3Ni_2Ta,\ \Delta G = -86.8 \text{ kJ g-at}^{-1}\ Ta,$$

$$Ni_2Ta + Ta \rightleftarrows 2NiTa,\ \Delta G = -21.4 \text{ kJ g-at}^{-1}\ Ta,$$

$$NiTa + Ta \rightleftarrows NiTa_2,\ \Delta G = 27.7 \text{ kJ g-at}^{-1}\ Ta.$$

Formation of Ni_2Ta is more thermodynamically favorable than that of Ni_3Ta, which is confirmed by the experiment (Fig. 2). The growth kinetics of a surface compound is governed by diffusion of nickel as a more mobile component into the surface layer. Nickel atoms have much higher diffusion mobility in Ni_3Ta and Ni_2Ta lattices, compared with heavier tantalum atoms. The results obtained in this study suggest the following: nickel is not subject to corrosive dissolution in tantalum-containing melts with high potassium fluorotantalate content, which are in equilibrium with metallic tantalum. Just the opposite, in the case of electroless deposition of tantalum ions, protective layers composed of Ni_3Ta and Ni_2Ta are formed on the nickel surface.

According to X-ray fluorescence microanalysis of samples with electroless coatings of thickness $\delta \geq 15$ μm, the content of tantalum in these coatings is 51.7–53.7 wt % (Fig. 3), in agreement with XPA data.

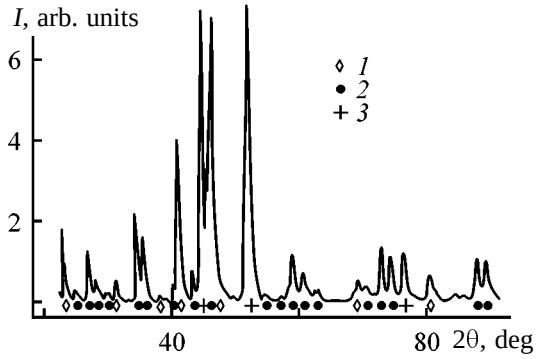

Fig. 2. X-ray diffraction pattern for Ni–Ta coating on nickel. (*I*) Intensity and (2θ) Bragg angle. (*1*) Ni_2Ta, (*2*) Ni_3Ta, and (*3*) nickel base.

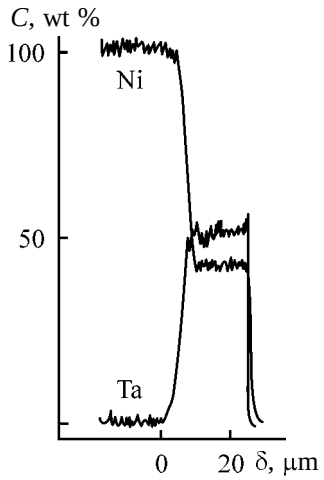

Fig. 3. Element depth profile for an Ni–Ta coating on nickel. (*C*) Concentration and (δ) thickness.

A study of the microstructure of the coatings with an optical microscope demonstrated uniformity of their thickness. Also, the previously established relationship between the sample weight gain and Ni–Ta layer thickness [4] was confirmed:

$$\delta = 1.8\ (\Delta m/S) \times 10^{-4}, \quad (3)$$

where δ is the coating thickness (μm), Δm is the weight gain (kg), and S is the sample surface area (m^2).

The nature of the surface relief was analyzed and the coating microstructure studied in more detail by means of electron microscopy. Figure 4 shows micrographs of (a) nickel substrate and surface of (b) thin and (c) thick diffusion Ni–Ta coatings. It can be seen that the thin coating is fine-grained and possesses a large covering power. The roller traces on the nickel base surface are smoothed out, and, gradually, a low-

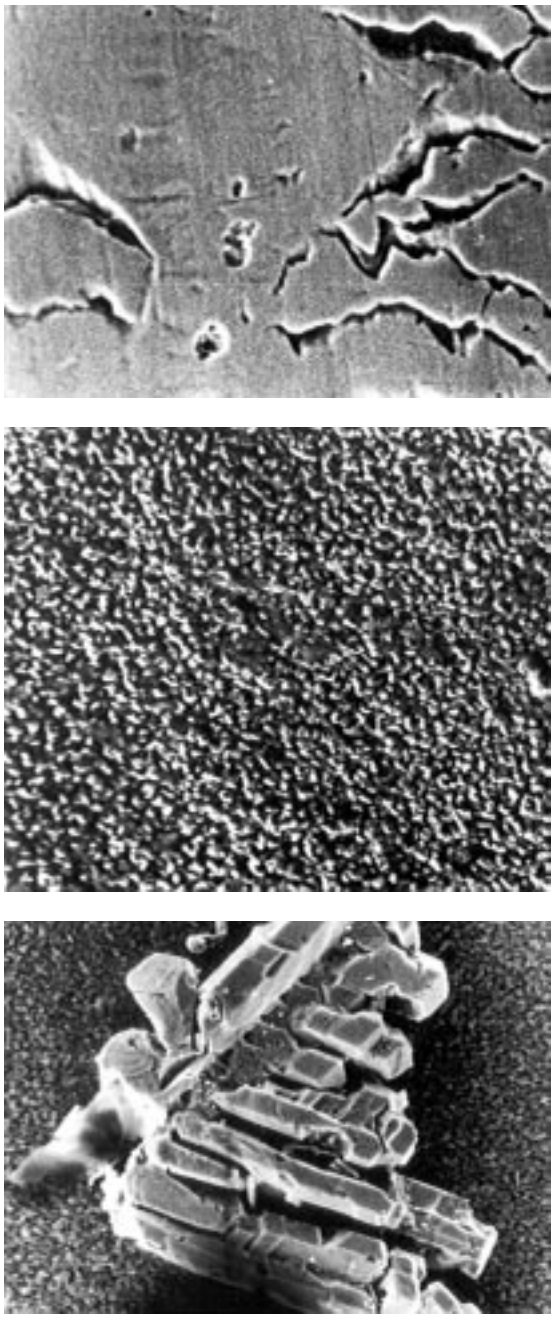

Fig. 4. Micrographs of substrate and Ni–Ta coatings (× 1000 magnification). Surface: (a) nickel substrate, (b) thin coating ($\delta \approx 500$ Å), and (c) thick coating ($\delta \approx 20$ μm).

roughness coating is formed over the entire surface. With increasing thickness of a coating, its roughness becomes more pronounced and formation and growth of separate dendrites are observed (Fig. 4c). The electron-microscopic data are confirmed by roughness measurements with a profilograph-profilometer. It can be readily seen (Fig. 5) that, for samples with coating thickness of less than 4–5 μm, R_a and R_z are much

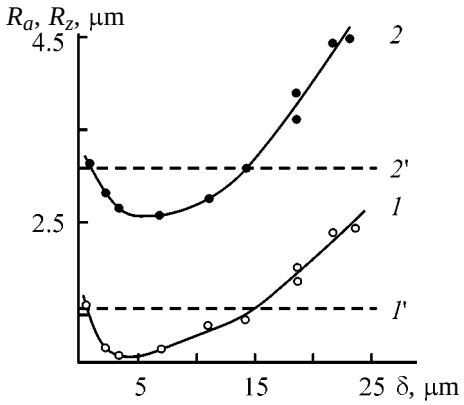

Fig. 5. Surface roughness parameters (*1*) R_a and (*2*) R_z vs. thickness δ. *1'* and *2'* denote, respectively, the R_a and R_z values for the initial substrate.

lower than the values for the initial nickel surface, and only at thicknesses exceeding 15 μm the roughness parameters of the coating become higher than those for the initial substrate.

The microhardness H_μ of the coatings (5100 ± 400 MPa) is independent, within measurement error, of the coating thickness and exceeds more than fourfold the microhardness of the nickel base (H_μ = 1150 ± 50 MPa). The coating microhardness values are in agreement with the results of X-ray fluorescence microanalysis (Fig. 3) which demonstrated that there is no variation, either, of the sample composition across the thickness within the experimental error. Comparison of the data in Figs. 2 and 3 indicates, as also do the results of metallographic studies, that the coating is a mixture of Ni_3Ta and Ni_2Ta phases, rather than a two-layer structure.

CONCLUSIONS

(1) It is shown that a coating containing, together with Ni_3Ta, Ni_2Ta is formed on the nickel surface in chloride–fluorotantalate melts that contain a large amount of potassium fluorotantalate and are in equilibrium with metallic tantalum.

(2) With tantalum used in the form of powder, rather than compact metal, the rate of formation of a diffusion layer can be markedly raised. In this case, the process of coating formation is affected not only by melt temperature, but also by the amount and fractional composition of the powder added to the solution.

(3) The forming coatings exhibit high covering power, which protects nickel from corrosive dissolu-

tion. At coating thicknesses of less than 10–15 μm, a polishing effect is observed, which consists in a decrease in the surface roughness parameters. The microhardness H_μ of the coatings is 5100 ± 400 MPa and does not vary, within the measurement accuracy, across the layer thickness.

(4) The obtained results make it possible to propose a practicable method for corrosion protection of nickel used as structural material in contact with molten salts.

ACKNOWLEDGMENTS

The study was supported by the State R&D Program "New Materials," subprogram "Materials for Electronics" (project no. 07.06.01 000) and in part by the program "Leading Scientific Schools" (project no. 00-15-97 364).

REFERENCES

1. Matychenko, E. and Novichkov, V., in *Refractory Metals in Molten Salts; Their Chemistry, Electrochemistry and Technology*, Dordrecht: Kluwer Academic, 1998, pp. 205–210.
2. Matychenko, E.S. and Novichkov, V.Yu., *Zashch. Met*., 1999, vol. 35, no. 1, pp. 57–60.
3. Ilyushchenko, N.G., Anfinogenov, A.I., and Shurov, N.I., *Vzaimodeistvie metallov v ionnykh rasplavakh* (Interaction of Metals in Ionic Melts), Moscow: Nauka, 1991.
4. Kolosov, V.N., Matychenko, E.S., and Belyaevskii, A.T., *Zashch. Met*., 2000, vol. 36, no. 6, pp. 607–612.
5. Kolosov, V.N. and Orlov, V.M., *Proc. 19th Riso Int. Symp. on Materials Science "Modelling of Structures and Mechanics of Materials from Microscale to Product,"* Carstensen, J.V., Ed., Roskilde (Denmark): Riso National Laboratory, 1998, pp. 319–324.
6. Nash, A. and Nash, P., *Bull. Alloy Phase Diagr*., 1984, vol. 5, no. 3, pp. 259–271.
7. Lyakishev, N.P., Snitko, Yu.P., Alekseev, V.I., and Levshin, G.A., *Dokl. Akad. Nauk SSSR*, 1981, vol. 258, no. 6, pp. 1404–1406.
8. Pimenov, V.N., Ugaste, Yu.E., and Akkushkarova, K.A., *Izv. Akad. Nauk SSSR, Ser. Met*., 1977, no. 1, pp. 184–189.
9. Matychenko, E.S., Zalkind, O.A., Kuznetsov, V.Ya., *et al*., *Zh. Prikl. Khim*., 2001, vol. 74, no. 2, pp. 177–181.

Russian Journal of Applied Chemistry, Vol. 74, No. 9, 2001, pp. 1500–1505. Translated from Zhurnal Prikladnoi Khimii, Vol. 74, No. 9, 2001, pp. 1457–1462.

APPLIED ELECTROCHEMISTRY AND CORROSION PROTECTION OF METALS

Acridine Derivatives as Inhibitors of Copper Dissolution

V. V. Ekilik, A. G. Berezhnaya, and M. N. Svyataya

Rostov State University, Rostov-on-Don, Russia

Received December 8, 2001

Abstract—Copper dissolution in an acidified chloride solution containing or not containing some acridine derivatives and potassium iodide was studied as influenced by the potential, stirring of the solution, time, and temperature.

Acridines inhibit corrosion and anodic dissolution of a number of metals, primarily iron [1] and some alloys [2–5]. The influence of these compounds on particular steps of copper dissolution was not studied.

EXPERIMENTAL

To study copper dissolution, chronoammograms at constant potential E and polarization curves at the potential increasing stepwise were recorded in 1 M NaCl + 0.01 M HCl solutions purged with purified argon or neon. Prior to the measurements, a Teflon-reinforced copper disk electrode with the working surface area of 0.2 cm^2 was trimmed at a rotation rate m = 1050 rpm with an abrasive paper with a grain size decreasing form 2 to 0, polished with an MgO suspension applied on chamois, and polarized at the cathodic potential E lower by 200 mV than the corrosion potential E_{corr}. The measurements were performed on stationary and rotating (m = 270–1050 rpm) electrodes in a three-electrode cell with separated catholyte and anolyte. A saturated silver chloride electrode was used as the reference electrode. The copper oxidation state n was determined by coulometry under galvanostatic conditions with control of E.

10-Methylacridinium iodide (no. 1), acridinium chloride (no. 2), 9-aminoacridinium chloride (no. 3), 9-aminoacridine (no. 4), and, for comparison, 10^{-4} M KI (no. 5) were used as inhibitors. In some cases the concentration dependences were studied.

The inhibitor efficiency was estimated from the deceleration coefficient K, i.e., the factor by which the process is decelerated.

Prior to the study of the inhibitor efficiency, let us consider the kinetics and mechanism of anodic dissolution of copper, which appreciably determines the inhibiting power of the additives. The degree of deceleration of hydrogen depolarization also affects E_{corr} and hence the corrosion resistance of copper.

The anodic polarization curves recorded on a stationary electrode (Fig. 1) can be separated into several characteristic sections. Tafel straight lines with angular coefficient b_a = 60 mV, observed in the potential range from –0.2 to –0.1 V, indicate reversible dissolution to form Cu^+ [6, 7]. Then the curves pass

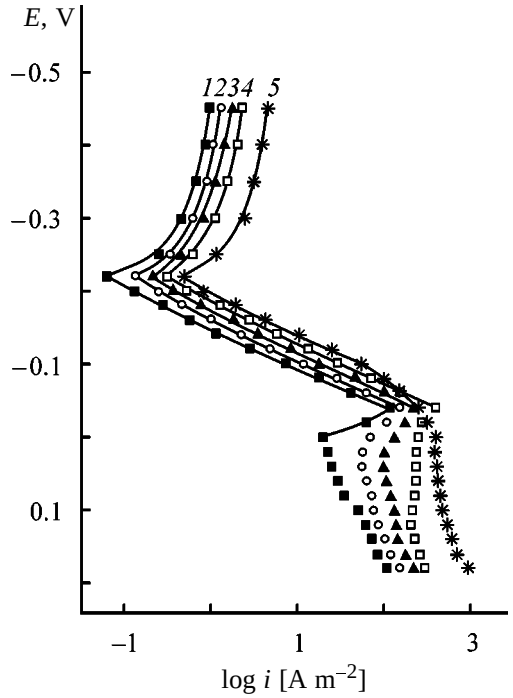

Fig. 1. Polarization curves at (*1*, *5*) 25, (*2*) 35, (*3*) 45, and (*4*) 55°C and a rate of the disk electrode rotation of (1–4) 0 and (*5*) 1050 rpm in the solution free from the inhibitors. (*E*) Potential and (*i*) current density.

1070-4272/01/7409-1500$25.00 © 2001 MAIK "Nauka/Interperiodica"

through a maximum followed by a section of the limiting current at increased temperature T and rotation rate (m > 200 rpm). This indicates the salt passivation. On a stationary electrode, the process is accelerated with further increase of E. This can be explained by the results of the coulometric study: At the potential ($E \le 0.02$ V) lower that that of the current density minimum i, Cu^+ (n = 0.95–1.05) chloride complexes pass into the solution, whereas at $E > 0.02$ V more readily soluble Cu^{2+} (n = 1.9–2.0) compounds are formed. On a rotating disk electrode the current density i increases aslo, but at higher potential E, which is due to different conditions of formation and degradation of the salt film.

The activation energy W calculated from the temperature dependence of i measured on the cathodicaly polarized electrode is 11.4 kJ mol^{-1} and corresponds to slow diffusion into the bulk of the solution. At the anodic polarization, W is approximately two times higher in almost entire potential range, which can be due to hindered diffusion through the film of the forming anodic products.

The anodic chronoammograms of the stationary electrode (Fig. 2) have the sections of nonstationary and stationary diffusion, separated by a small transition section. At the beginning of the process the i vs. $\tau^{-1/2}$ dependence is described by the equation

$$i = nFC_S(D/\pi\tau)^{-1/2} = \gamma\tau^{-1/2} \quad (1)$$

and is extrapolated to the origin. This indicates that the diffusion coefficient D is independent of time τ, since the concentration of anodic products C_S on the electrode surface is constant.

The dependence of the nonstationary currents on E within the i–$\tau^{-1/2}$ straight line range at τ = constant is a Tafel straight line with $b_a \sim 60$ mV, which agrees with the above consideration. The E–logγ straight line in accordance with Eq. (1) has the same slope (Fig. 3a).

The second section of the anodic chronoammogram is a horizontal straight line with stationary i_{st}. The slope of the E–logi_{st} straight line (Fig. 3b) is also $b_a \sim 60$ mV.

Since copper dissolution is controlled by diffusion [6–8], the i–m dependence is described by the equation [9]

$$i = 0.62nFC_S D^{2/3}\nu^{-1/6}\omega^{1/2} = \lambda m^{1/2}, \quad (2)$$

where ν is the kinematic viscosity and $\omega = 2\pi m$.

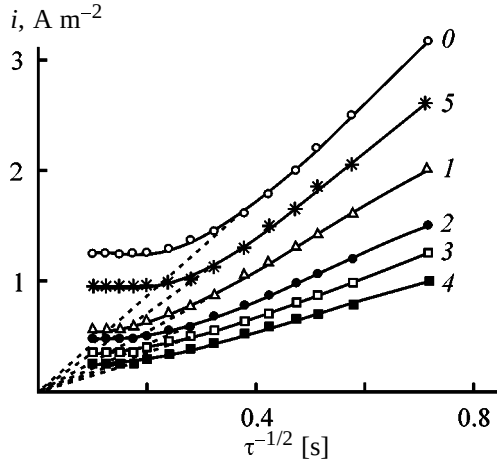

Fig. 2. Anodic chronoammograms recorded on a stationary electrode at –0.15 V in solutions (*0*) with no inhibitor and (*1–5*) containing the respective inhibitor. Inhibitor concentration 10^{-4} M; temperature 25°C; the same for Figs 3, 4. (i) Current density and (τ) time.

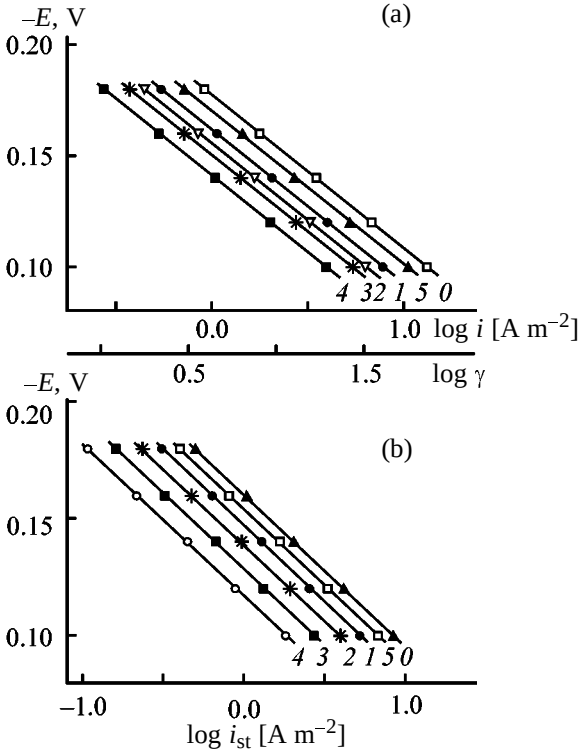

Fig. 3. Polarization curves of stationary electrode, constructed form the anodic chronoammograms recorded in solutions (*0*) with no inhibitor and (*1–5*) containing the respective inhibitor. (E) Potential; (i) Current density in 10 s; (i_{st}) stationary current density.

Parameter λ is 2.9, 157, and 165 A s$^{1/2}$ m^{-2} at E = –0.15, 0.05, and 0.2 V, respectively. The similar dependence was obtained at hydrogen liberation (λ = 0.35 A s$^{1/2}$m^{-2} at E = –0.4 V), which is reasonable

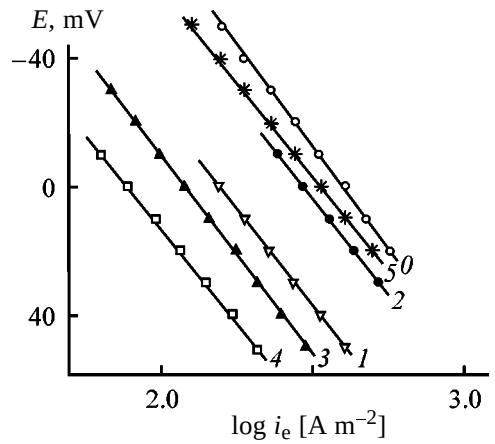

Fig. 4. Polarization curves recorded in the solution (*0*) with no inhibitor and (*1*–*5*) containing the respective inhibitor. (*E*) Potential and (i_e) rate of the electrochemical step.

for weakly acidic solutions. As follows from Eq. (2), the slope of the E–$\log\lambda$ straight line in the Tafel region (E from –0.2 to –0.1 V) is also 60 mV.

Generally, the measured anodic current density distorted by the concentration polarization is related to the diffusion rate i_d and the rate of electrochemical reaction i_e by the approximate equation [10]

$$i = i_e i_d (i_e + i_d)^{-1}. \quad (3)$$

Since $i_e \gg i_d$, in the above cases $i \sim i_d$ and i is appreciably lower than the exchange current density i_0. However, the diffusion control can give way to the electrochemical control with increasing i [11]. It also should be taken into account that b_a in the case of the diffusion control is 2 times lower than that at the electrochemical control. Hence, the factor by which $\log i_d$ increases with increasing anodic polarization ΔE_a is 2 times higher compared to $\log i_e$. In this case the process can be controlled by both the diffusion and the electrochemical reaction. However, whereas i_e steadily increases with increasing ΔE_a, i_d and correspondingly i measured on a rotating disk electrode will reach the limiting values (Fig. 1). The region of the mixed kinetics of $Cu \rightarrow Cu^+$ oxidation should be manifested on the curvilinear section of the polarization curve between the Tafel straight line and the section with the limiting i_d. This agrees with the fact that the i–$m^{1/2}$ dependences in the range of E from –60 to +10 mV are curvilinear. The i_e was determined from the segment intercepted on the ordinate by extrapolation of the i^{-1}–$m^{-1/2}$ straight lines to $m^{-1/2} = 0$. The results confirmed that the examined reaction is of the first order and Eq. (3) describes well the relation between i, i_d, and i_e. As expected, the range of the potentials E corresponding to the mixed kinetics increases with increasing m. The values of i_d and i_e are comparable. As seen from Eq. (2), $i_e = i_d$ at $m_1 = (i_e/\lambda)^2$. m_1 ranges from 210 to 320 rpm and depends on E insignificantly. The slope ($b_a \sim 120$ mV) of the E–$\log i_e$ Tafel straight line (Fig. 4) indicates the one-electron copper ionization.

Thus, effective inhibitors of dissolution of copper electrode should decelerate the diffusion step. Taking into account that $i \sim i_d$ at $m = 0$, to study the diffusion deceleration, the anodic chronoammograms in the Tafel region (E from –0.2 to –0.1 V) and the polarization curves were recorded on stationary and rotating disk electrodes.

The results of the potentiostatic measurements partially presented in Fig. 2 show that the additives inhibit nonstationary and stationary diffusion (Table 1).

As expected, K_d^1 and K_d^2 are independent of E and τ. Generally, the performance of the additives is determined by a change in D and C_S owing to formation of polymolecular films and a change in the nature of diffusing particles. Complexation in the bulk of the solution and on the electrode surface should strongly affect the inhibition. Since $K_d^2 > K_d^1$, the deceleration increases in the transition region of τ. If the additional protecting film is formed on the electrode at these τ values, its microcrystallinity will increase in the presence of the inhibitors owing to their surfactant properties.

When dissolution of a copper anode is decelerated at the potentials of the Tafel section, the additives can affect E_{lim} and i_{lim} of the salt passivation, which correspond to the maximum of the polarization curve at $m = 0$. Indeed, acridinium chloride and 9-aminoacridine increase E_{lim} by 25–80 mV and decrease i_{lim} by 20–60%. In the presence of 9-aminoacridine E_{lim} increases to the greatest extent and falls within the range of Cu^{2+} formation. As a result, the maximum on the anodic curve disappears almost completely, especially at elevated temperatures. The exception is KI which decreases i_{lim} and has virtually no effect on E_{lim}. The additives weakly increase (by 1–2 kJ mol^{-1}) the activation energy of copper dissolution W and increase by a factor of almost 2 that of hydrogen liberation, which can be due to formation of an inhibitor film at the cathodic polarization. As for adsorption inhibitors, the concentration dependence of K is described by the equation

$$\log K = \log K_{C_0} + \beta \log C/C_0, \quad (4)$$

Table 1. Coefficient of deceleration of nonstationary diffusion K_d^1 described by Eq. (1) and stationary diffusion K_d^2 and constants K_{C_0} and β of Eq. (4) at $m = 0$

Additive no.	K_d^1	K_d^2	K_{C_0}			β		
	at indicated E, V							
	from –0.1 to –0.16		–0.4	–0.14	0.06	–0.4	–0.14	0.06
1	1.6	2.1	–	–	–	–	–	–
2	2.1	2.5	1.3	2.1	1.7	0.09	0.13	0.13
3	2.4	3.6	–	–	–	–	–	–
4	3.2	4.6	2.5	3.2	–	0.40	0.47	–
5	1.2	1.3	1.2	2.1	1.6	0.13	0.36	0.31

where C_0 is the standard concentration (10^{-4} M) corresponding to K_{C_0}.

The constants K_{C_0} and β presented in Table 1 show that the effect is the strongest and is the most sensitive to C at the potentials of the Tafel region of the anodic curve. As also seen from Table 1, the protecting effect depends on the conditions of film formation at potentiostatic polarization and step change in the potential. The data for the rotating disk electrode (Table 2) show that the coefficient of the diffusion deceleration K_d depends on the process conditions.

The fact that K_d of copper dissolution (E = –0.15 V) is higher than that of hydrogen liberation (E = –0.4 V) (Table 2) indicates that the protecting film is mainly formed by reaction of the inhibitors with the anodic reaction products. If the influence of electrostatic adsorption were strong, the relation between the K_d values would be inverse, taking into account the zero-charge potential of copper (–0.48 V) [12]. The sharp decrease in K_d in the range of limiting current i_d of salt passivation (E = 0.05 V) indicates hindered inhibition of copper dissolution at intense salt formation. Conversely, K_d slightly increases after partial destruction of the salt film at E = 0.2 V.

The influence of the inhibitors on the diffusion and electrochemical steps of copper dissolution was estimated from i_d and i_e in the mixed kinetic region. The values of $K_d = i_d/i_{d,i} = \lambda/\lambda_i$ and $K_e = i_e/i_{e,i}$ (index i denotes the presence of the inhibitor) are summarized in Table 3.

The coefficients K_d and K_e are comparable, with E = 0 V being approximate boundary between the regions of $K_d > K_e$ and $K_e > K_d$. As follows form Eq. (3), the coefficient of deceleration of copper dissolution $K = i/i_i$, K_d, and K_e are related to each other by the equation

$$K = K_d(1 + \gamma_i)/(1 + \gamma) = K_e(1 + 1/\gamma_i)/(1 + 1/\gamma), \quad (5)$$

where $\gamma = i_d/i_e$, $\gamma_i = i_{d,i}/i_{e,i}$, $\gamma_i/\gamma = K_e/K_d$.

Although K_e, K_d and i_e remain the same with an increase in m, i_d and $i_{e,i}$ increase to a variable extent. As a result, K depends on m. Since i_d and and i_e as well as K_e and K_d are comparable, K, being intermediate between K_e and K_d, should weakly depend on m. The type of the K–m dependence is determined by the ratio between K_e and K_d and hence by the ratio of γ_i and γ. If $K_e < K_d$, K should decrease with an increase in m as i_d increases. At $K_e > K_d$ the K–m dependence is inverse and at $K_e \sim K_d$ $K \neq f(m)$ (Table 4).

Since $K_e \neq f(E)$, the decrease in K with increasing E is due to the diffusion component described above.

Comparison of the performance of potassium iodide (no. 5) with that of 10-methylacridinium iodide (no. 1) (Tables 1–4) reveals the predominant role of the organic cation in inhibition of the copper dissolution. 10-Methylacridinium iodide is a more powerful inhibitor than KI in the ionization step (Fig. 3). This

Table 2. Influence of E and the nature of the additives on K_d at the diffusion control of the process

Additive no.	K_d at indicated E, V			
	–0.40	–0.15	0.05	0.20
1	1.3	2.5	1.2	1.6
2	1.5	3.2	1.2	1.7
3	2.0	7.5	3.0	3.2
4	2.9	14.0	4.1	4.3
5	1.1	1.5	1.1	1.2

Table 3. Influence of E and the nature of the additives on K_d and K_e at the diffusion-kinetic control of the process*

Additive no.	K_e	K_d at indicated E, V								
		–40	–30	–20	–10	0	10	20	30	40
1	2.6	–	–	–	–	1.4	1.3	1.2	1.1	1.1
2	1.4	–	–	1.8	1.5	1.3	1.2	1.2	1.1	1.2
3	4.3	6.0	5.8	5.6	5.0	4.1	3.8	3.5	3.3	3.1
4	5.1	–	9.2	8.8	6.8	5.8	5.2	4.6	4.4	4.2
5	1.2	1.1	1.1	1.1	1.1	1.1	1.1	1.1	1.1	1.1

* A dash corresponds to diffusion control of the process at the indicated potential in solutions containing the inhibitors.

fact can be explained as follows. Both additives decelerate the electrochemical step owing to blocking of the surface active centers. However, the 10-methylacridinium cation additionally decelerates the process owing to an increase in the ψ_1 potential. The I^- anion of the organic salt is a bridge between the cation and the positively charged copper surface. The I^- anion of KI decreases the ψ_1 potential, thus accelerating the process.

An introduction of additional coordination and adsorption center (amino group) in an acridine molecule increases K, K_e, and K_d (additive nos. 2 and 3). The difference in the performance of additive nos. 3 and 4 in freshly prepared solution (Tables 1–4) should also be noted. In acidic chloride solution they should exist in the similar state and provide the same K, K_e, and K_d. We suggest that this difference is due to decelerated protonation of 9-aminoacridine, which is indicated by lower solubility of this compound as compared to that of its hydrochloride. Hence, 9-aminoacridine is more stable in the solution, is more readily salted-out and adsorbed, and is a stronger inhibitor of copper dissolution. The leveling-out of the inhibiting power of additive nos. 3 and 4 after aging of their solution for several days confirms the above assumption.

Table 4. Influence of m, E, and the nature of the additives on K

Additive no.	K at indicated m, rpm				
	270	460	620	860	1050
			E = –20 mV		
1	1.6	1.6	1.6	1.6	1.6
2	1.6	1.6	1.5	1.5	1.5
3	5.1	5.1	5.0	5.0	4.9
4	7.0	6.8	6.8	6.7	6.6
5	1.1	1.1	1.1	1.1	1.1
			E = 0 mV		
1	1.5	1.5	1.5	1.6	1.6
2	1.3	1.3	1.4	1.4	1.3
3	4.2	4.3	4.2	4.1	4.2
4	5.4	5.4	5.3	5.3	5.3
5	1.1	1.2	1.2	1.1	1.1
			E = 20 mV		
1	1.4	1.4	1.5	1.5	1.5
2	1.2	1.2	1.2	1.2	1.3
3	3.8	3.8	3.9	4.0	4.0
4	4.7	4.7	4.8	4.8	4.9
5	1.2	1.1	1.1	1.1	1.1

CONCLUSIONS

(1) Copper dissolution on a stationary copper electrode is controlled by diffusion and is characterized by the maximum of the salt passivation current. Degradation of the protecting layer is due to an increase in the copper oxidation state and formation of more soluble products.

(2) As the potential increases, copper dissolution from a rotating disk electrode is controlled by diffusion, then by diffusion and chemical reaction, and finely by diffusion again, at limiting current of salt passivation.

(3) In the region of the mixed kinetics the acridine derivatives comparably inhibit the ionization and diffusion steps. The ratio between these effects depends on the potential and the nature of the additives but is independent of the rotation rate of the disk electrode.

(4) The inhibiting effect of salt additives, especially with respect to the ionization step, is mainly due to the organic cation.

(5) The inhibiting power of the tested additives increases with time at potentiostatic polarization and

decreases with an increase in the anodic polarization under conditions of salt passivation.

REFERENCES

1. Altsybeeva, A.I. and Levin, S.Z., *Ingibitory korrozii metallov* (Inhibitors of Metal Corrosion), Moscow: Khimiya, 1968.
2. Ekilik, V.V., Komakhidze, M.G., and Berezhnaya, A.G., *Zh. Prikl. Khim*., 1998, vol. 71, no. 9, pp. 1560–1562.
3. Ekilik, V.V., Berezhnaya, A.G., and Komakhidze, M.G., *Izv. Ross. Akad. Nauk, Ser. Khim*., 1998, no. 10, pp. 1950–1954.
4. Ekilik, V.V. and Skvortsova, I.Yu., *Elektrokhimiya*, 2000, vol. 36, no. 1, pp. 23–27.
5. Pevneva, A.V., Khaldeev, G.V., Gimasheva, I.M., and Kuznetsov, V.V., *Zh. Prikl. Khim*., 1984, vol. 57, no. 2, pp. 266–269.
6. Kiss, L. and Farkas, *Acta Chim. Acad. Sci. Hung*., 1970, vol. 66, no. 3, pp. 395–402.
7. Losev, V.V., *Itogi Nauki., Ser: Elektrokhimiya*, 1971, vol. 6, pp. 65–164.
8. Altukhov, V.K., Marshakov, I.K., Vorontsov, E.S., and Klepinina, T.N., *Elektrokhimiya*, 1976, vol. 12, no. 1, pp. 88–91.
9. Pleskov, Yu.V. and Filinovskii, V.Yu., *Vrashchayushchiisya diskovyi elektrod* (Rotating Disk Electrode), Moscow: Nauka, 1972.
10. Damaskin, B.B., *Printsipy sovremennykh metodov izucheniya elektrokhimicheskikh reaktsii* (Principles of Modern Methods for Studying Electrochemical Reactions), Moscow: Mosk. Gos. Univ., 1965.
11. Losev, V.V., Molodov, A.I., and Gordetskii, V.V., *Elektrokhimiya*, 1965, vol. 1, no. 4, pp. 572–578.
12. Antropov, L.I., *Teoreticheskaya elektrokhimiya* (Theoretical Electrochemistry), Moscow: Vysshaya Shkola, 1984.

Russian Journal of Applied Chemistry, Vol. 74, No. 9, 2001, pp. 1506–1508. Translated from Zhurnal Prikladnoi Khimii, Vol. 74, No. 9, 2001, pp. 1463–1465.

CATALYSIS

Temperature-Hysteresis Effects in CO Oxidation on Cement Catalysts with Various CuO Content

A. N. Subbotin, B. S. Gudkov, V. I. Yakerson, S. V. Chertkova, E. Z. Golosman, and G. V. Kozyreva

Zelinsky Institute of Organic Chemistry, Russian Academy of Sciences, Moscow, Russia
Institute of Nitrogen Industry, Novomoskovsk, Tula oblast, Russia

Received February 22, 2001

Abstract—The temperature dependence of the degree of CO oxidation with atmospheric oxygen on copper–cement catalysts was studied.

In a series of previous publications we suggested and substantiated a new concept explaining the origin of temperature-hysteresis effects observed in various heterogeneous catalytic reactions. This concept was described in the most detail in [1]. According to this concept, when an exothermic heterogeneous catalytic reaction reaches a certain rate, the amount of heat liberated on the active reaction center becomes too large to be dissipated in the environment. This is usually due to a low heat conductivity of a porous support or of an inactive catalytic mass in which active centers are disseminated. Therefore, the actual "point" temperature of the reaction on the active center becomes much higher than the average temperature in a catalyst bed, usually measured with a thermocouple and treated as the "reaction temperature." At the expense of local overheating of active centers, the degree of conversion becomes higher than that corresponding to a given measured temperature. It increases the heat evolution even more and, therefore, the temperature of the active center, and as a result, the conversion in a narrow temperature range rapidly increases. After reduction or even full termination of the heat input from the outside (i.e., on cooling a reactor), the excessive heat, which had no time to be dissipated because of a poor heat removal, makes it possible to support a higher actual temperature of the active center than the temperature detected by a thermocouple. In this case the descending branch of the temperature dependence of the conversion degree is displaced to the left on the scale of the measured temperature relative to the ascending branch, i.e., an "anti-clockwise" hysteresis loop is observed.

Ukharskii and Berman [2] have similar views on the causes of the temperature hysteresis in the benzene oxidation on supported platinum catalysts. They have calculated theoretically that platinum particles can be overheated relative to the support by 150–200°C (it is necessary to remember that the thermal effect of benzene oxidation is much higher than that of CO oxidation, 3267 and 283 kJ mol^{-1}, respectively). According to the classic concept of Frank-Kamenetskii [3], the temperature hysteresis in heterogeneous catalysis is a consequence of the macrokinetic transition from the kinetic to the diffusion mode. In this case the whole active surface of a catalyst is considered as an entity. However, we focus our attention on local overheating of active centers containing a restricted number of atoms, which are surrounded by the main inactive mass of a catalyst or support.

According to our concept, the temperature hysteresis phenomenon can be characteristic of only exothermic heterogeneous catalytic reactions, which was confirmed by both our experiments and examination of published data [1].

It follows from this concept that the variation of the catalyst activity depending on the content of an active component should also affect the value of temperature-hysteresis effect. In fact, an increase in the content of an active component is accompanied by an increase in the number of active centers and consequently in the amount of thermal energy evolved in the exothermic reaction. Therefore, we can expect that, if the temperature hysteresis effect took place, it should become stronger.

To check this assumption, we studied the temperature dependences of the degree of carbon monoxide oxidation with atmospheric oxygen on a series of copper-containing catalysts on a cement support. These catalysts are highly stable, and their preparation is a routine practice [4, 5].

1070-4272/01/7409-1506$25.00

EXPERIMENTAL

Three samples of copper–cement catalysts with increasing CuO contents were tested. To prepare them, we used copper and zinc carbonates, talum (a mixture of calcium mono- and dialuminates), and a 25% solution of NH_4OH. According to the X-ray phase analysis, the samples obtained by mixing the components without calcination contained the phases of zinc hydroxoaluminate, calcite, aragonite, and gibbsite [5]. The resulting catalysts had the following composition (wt %):

Sample no.	CuO	ZnO	Al_2O_3	CaO
1	6.3	47.9	33.4	10.8
2	28.3	22.5	32.7	14.6
3	50.5	28.3	13.9	6.9

The specific surface area of all the three samples was within 60–80 $m^2\,g^{-1}$.

The experiments on the CO oxidation with atmospheric oxygen were carried out in a catalytic semiautomatic circulation installation ensuring controllable supply of mixture components into a reactor and smooth inertialess variation of the reactor temperature. The weight of each sample loaded into the reactor was 0.5 g. The molar ratio $CO : O_2$ in the starting reaction mixture was varied in separate experiments from 1 : 5 to 5 : 1 at a total flow rate of 8 l h^{-1}. Before loading in the reactor each sample of the catalyst was treated in an air flow at 300°C for 4 h.

The mixture leaving the reactor was analyzed for the CO content using a gas-chromatographic column packed with Porapak Q.

The temperature dependences of the degree of CO oxidation at various $CO : O_2$ ratios on three studied samples with different copper content are shown in Figs. 1a–1c. Figure 1a corresponds to a large excess of oxygen (~1 : 5, whereas the stoichiometric ratio is 2 : 1), Fig. 1b, to its moderate excess (~1 : 2), and Fig. 1c, to the stoichiometric ratio (~2 : 1, curves *2* and *3*) and even at an overstoichiometric CO content (~5 : 1, curve *1*). It is evident that in all the cases without exception there is a pronounced temperature hysteresis, and at the stoichiometric and higher ratios the process turns to a self-sustained mode, when even the full termination of heating does not result in reaction termination or even in a reduction in the conversion degree. The temperature required for the CO oxidation is supported at the expense of the reaction heat.

On the whole, the observed pattern completely

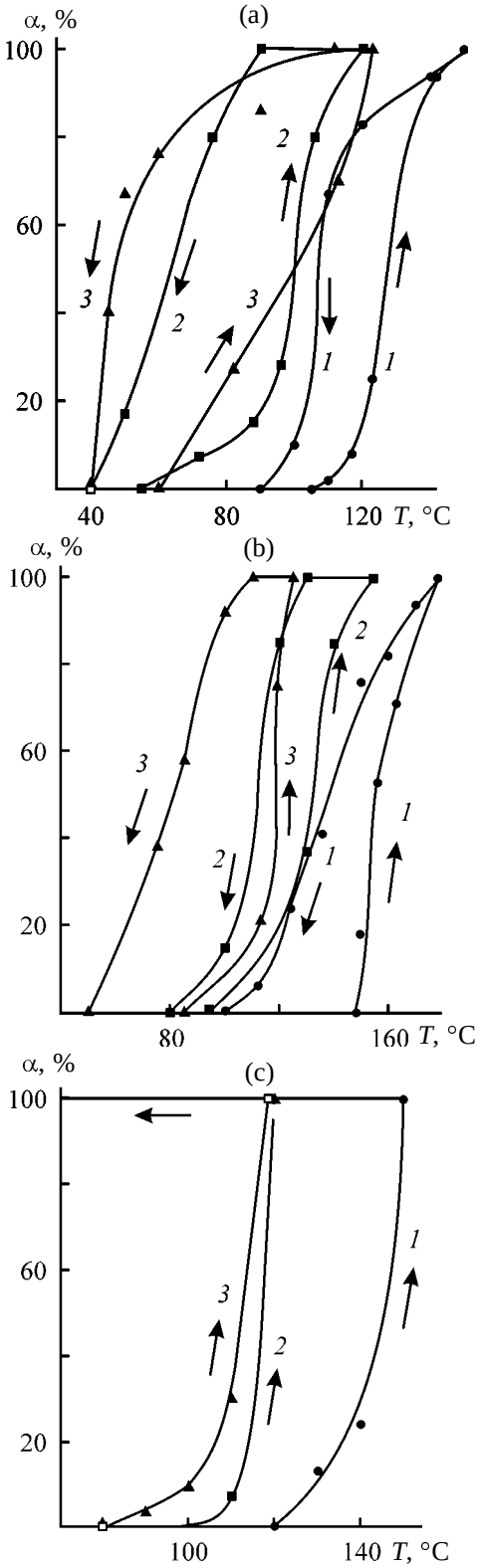

Fig. 1. Degree of CO oxidation α on copper-containing catalysts as a function of temperature *T*. CuO content (%): (*1*) 6.3, (*2*) 28.8, and (*3*) 50.5. $CO : O_2$ ratio: (a) ~1 : 5; (b) (*1*, *2*) ~1 : 2 and (*3*) ~1 : 1.5; (c) (*1*) ~5 : 1 and (*2*, *3*) ~2 : 1.

meets the expectations following from the above-described concept of local overheatings. As the copper(II) content increases, i.e., the number of active centers of the catalyst increases, the area of the reaction occurrence shifts to lower temperatures, and the hysteresis effect somewhat decreases. The extent of the effect can be estimated in various ways, for example, by the width of the hysteresis loop, namely, by the temperature difference ΔT in the ascending and descending branches of the dependence for the same conversion degree. In this case we selected the 50% conversion. With this criterion, the width of the hysteresis loop ΔT_{50} in Fig. 1a is 17, 23 and 35°C for the catalysts with the CuO content of 6.3, 28.8, and 50.5%, respectively, and that in Fig. 1b is 21, 37, and 55°C, respectively. When the ratio $CO : O_2$ approaches the stoichiometric value, this difference levels out, and the estimation of the width of the hysteresis loop in the mode of a self-sustained reaction becomes difficult.

It is most likely that the growth of the copper(II) content accompanied by an increase in the number of active centers results in increased reaction rate and hence in increased heat evolution. This gives rise to a greater local overheating of active centers and, therefore, to a stronger hysteresis effect.

Comparison of Figs. 1a and 1b demonstrates that an increase in the CO fraction in the reaction mixture shifts the area of reaction occurrence on the same catalyst to lower temperatures and promotes an increase in the width ΔT_{50} of the hysteresis loop. This can also be due to an increase in the reaction rate and hence in the amount of evolved energy, as the CO concentration increases. The kinetic data confirm the fact that the rate of CO oxidation on copper-containing catalysts is proportional within certain limits to the partial pressure of CO [6].

Our attention was engaged by a specific "sharp" shape of the temperature dependences obtained on a catalyst with the lowest copper(II) content (Figs. 1a and 1b, curves *1*). These curves contain no horizontal part, which is observed in other curves at the beginning of cooling of the reactor (initial parts of descending branches). This may be due to relatively small local overheating of active centers at their relatively low concentration, though the hysteresis loop itself on this catalyst is quite clearly seen.

On the whole, our data completely agree with the concept of the local overheating of active centers as the main cause of the temperature-hysteresis phenomena in heterogeneous catalysis.

CONCLUSIONS

(1) The value of the temperature hysteresis in CO oxidation on copper–cement catalysts increases with increasing CuO content.

(2) An increase in the CO fraction in the reaction mixture shifts the area of reaction occurrence to lower temperatures and increases the width of the hysteresis loop.

(3) The data obtained support the concept of the local overheating of active centers as the main cause of the temperature hysteresis in heterogeneous catalysis.

ACKNOWLEDGMENTS

The authors are grateful to I.A. Mamaeva (State Institute of Nitrogen Industry) for help in the work.

The work was financially supported by the Russian Foundation for Basic Research (project no. 00-03-32 169).

REFERENCES

1. Subbotin, A.N., Gudkov, B.S., and Yakerson, V.I., *Izv. Ross. Akad. Nauk, Ser. Khim.*, 2000, no. 8, pp. 1379–1385.
2. Ukharskii, A.A. and Berman, A.D., *Kinet. Katal.*, 1992, vol. 33, nos. 5–6, pp. 1107–1112.
3. Frank-Kamenetskii, D.A., *Diffuziya i teploperedacha v khimicheskoi kinetike* (Diffusion and Heat Transfer in Chemical Kinetics), Moscow: Nauka, 1987, 3rd ed.
4. Yakerson, V.I. and Golosman, E.Z., *Usp. Khim.*, 1990, vol. 59, no. 5, pp. 778–806.
5. Yakerson, V.I. and Golosman, E.Z., *Katalizatory i tsementy* (Catalysts and Cements), Moscow: Khimiya, 1992.
6. Sharma, C.S. and Huges, R., *Chem. Eng. Sci.*, 1979, vol. 34, no. 5, pp. 613–624.

Russian Journal of Applied Chemistry, Vol. 74, No. 9, 2001, pp. 1509–1512. Translated from Zhurnal Prikladnoi Khimii, Vol. 74, No. 9, 2001, pp. 1466–1469.

ENVIRONMENTAL PROBLEMS OF CHEMISTRY AND TECHNOLOGY

Detoxication of Aqueous Cyanide Solutions with Oxygen in the Presence of S(IV) and Cu(II) Compounds

D. V. Kharchenko, I. A. Agapov, and N. V. Vorob'ev-Desyatovskii

Navy Engineering Institute, St. Petersburg, Russia

Received June 18, 2001

Abstract—Oxidation of cyanide anions with atmospheric oxygen in aqueous solutions in the presence of Na_2SO_3 and $NaHSO_3$ mixture and $CuSO_4$ as a catalyst was studied. The reaction mechanism was proposed.

Cyanide solutions are widely used in electroplating and mining. Usually they contain from hundreds of milligrams to tens of grams per liter of NaCN and cyanide complexes of transition metals [Cu(I), Zn(II), Cd(II), Ni(II), Fe(II), Fe(III), Cr(III), etc.] and also some impurities like $NH_3 \cdot H_2O$, HCO_3^-, SCN^-, and $HCOO^-$ [1, 2]. Detoxication of these solutions is an important task, which can be solved by numerous ways. In general there are six main approaches to this problem [3, 4].

(1) The passive detoxication is based on the reduction in the concentrations of free and coordinated CN^- ions in solutions upon prolonged staying under natural conditions owing to a combination of photolysis, oxidation (including biological oxidation), precipitation (in the case of complex ions), and hydrolysis caused by gradual pH reduction on the dilution of solutions by rain and water from thawed snow and by salt freeze-out in wintertime.

(2) Distillation of HCN from acidified solutions and its subsequent sorption by alkaline solutions.

(3) Sorption of CN ions and complex cyanide anions on activated carbons in the presence of Cu(II) compounds and on ion-exchange resins.

(4) Electrochemical anodic oxidation of free and bound in relatively weak complexes CN^- ions. The oxidation can be either direct or can accompany anodic oxidation of chloride ions if they are present in the same solution.

(5) Biological transformation (oxidation and hydrolysis) of free and bound cyanides with the use of microbial biocenoses (associations of aerobes and anaerobes in the form of activated sludge), biosorbents, immobilized microorganisms, or specific bacterial enzymes (rhodonase and cyanide hydratase).

(6) Reagent detoxication, which can be subdivided into binding of CN^- ions in nondissociated or difficulty soluble compounds [treatment with CH_2O, Fe(II) salts] and oxidation of free and bound CN^- ions with elemental chlorine in an alkaline medium or with calcium (or sodium) hypochlorite prepared in advance, and also with hydrogen peroxide in the presence of Cu(II), with ozone or atmospheric oxygen in systems containing aqueous solutions of S(IV) and Cu(II) compounds (INCO and Noranda processes).

The use of each of these methods is determined by climatic and economical conditions and also by local legislation regulating wastewater discharge. Recently the detoxication of free and bound cyanide ions by their oxidation with atmospheric oxygen bubbled through aqueous solutions of S(IV) and Cu(II) compounds received growing use in cold-climate countries. However, the information on this method can be found only in patents and special mining literature, and available data [2] give no way of developing the method because they cannot reveal its chemical essence and potential. In this work we studied the detoxication of cyanide solutions obtained after electrochemical deposition of noble metals from agitation cyanide leaching solutions of concentrates of Dukat ore mining and concentrating enterprise. The solution composition is given below.

We tested $Na_2S_2O_5$ and its mixture with Na_2SO_3 as a source of S(IV). Weighed samples of solid salts were placed into a 0.5-l sample to be neutralized, and then 0.11 g of the catalyst $CuSO_4 \cdot 5H_2O$ was added. The flask was closed, and air was blown through it with a rate of 2.5 l min^{-1}. The residual concentrations of CN^- ion and other simple and complex ions were determined 1 h after the start of detoxication.

1070-4272/01/7409-1509$25.00

Table 1. Detoxification of straight aqueous NaCN solution with atmospheric oxygen in the presence of a mixture of Na_2SO_3 and $Na_2S_2O_5$

Concentration, g l^{-1}		Residual CN^- concentration, mg l^{-1}
Na_2SO_3	$Na_2S_2O_5$*	
19.80	3.00	120
24.75	3.75	78
29.70	4.50	70
34.65	5.25	45
39.60	6.00	28
59.40	9.00	15

* With respect to the starting substance, which does not exist in the solution.

The concentrations of CN^- ions above 4 mg l^{-1} were determined by the titration with $AgNO_3$ solution in the presence of KI as an indicator [5]. In the case of lower concentrations of cyanide ions their content was determined by photometry on a KFK-3 instrument using the pyridine–barbiturate reaction [6].

The concentrations of metal and nonmetal ions in solutions before and after neutralization were determined by atomic absorption spectroscopy on Varian AA 110 and AA 220 (Australia) instruments.

Formally the use of pure sodium disulfite is very successful, as it reduces residual NaCN concentrations. However, according to analysis of the gas phase, it contains significant amounts of HCN, which results from a strong acidification of the solution caused by the HSO_3^- formation and its subsequent oxidation.

If pH is reduced to 8, 94% of free cyanide ions are in the form of HCN, which is blown off from the solution by air current [4]. We note in addition that the reactivity of HCN, as compared to CN^- ion itself, with respect to the action of electrophilic reagents is much lower. Therefore, in all subsequent experiments we used a mixture of Na_2SO_3 and $Na_2S_2O_5$, thoroughly keeping pH of 10.0 ± 0.3.

The data on the neutralization of a solution containing 2200 mg l^{-1} of CN^- ions with a mixture of Na_2SO_3 and $Na_2S_2O_5$ at pH 10.0 are shown in Table 1.

A comparison of our data with published data [2] suggests that solutions containing less than 1 g l^{-1} of free CN^- ions are the most suitable for the neutralization. An increase in the CN^- concentration is accompanied by an increase in the S(IV) consumption and leads to relatively high residual CN^- concentrations exceeding its maximum permissible concentration (0.1 mg l^{-1}).

In going to a solution containing cyanide compounds of other elements in addition to NaCN, the situation becomes even more complicated (Table 2).

The solution was treated at pH ~10.0 with a mixture of 59.4 g l^{-1} of Na_2SO_3 and 9 g l^{-1} of $Na_2S_2O_5$ (Table 1).

Tables 1 and 2 show that the residual CN^- concentration is approximately doubled on passing from pure NaCN to a real solution containing significant amounts of impurities. The degree of detoxication with respect to free CN^- ions was 0.987. Furthermore, it follows from Table 2 that the concentrations of Fe(II), Cd(II), Mn(III), Hg(II), Pb(II), As(III), Cr(III), and Se(II) in the solution became several times lower after the neutralization. The Zn(II) concentration decreased by 28%, the concentration Ni(II) remained almost unchanged, whereas the Cu(I) concentration increased, which is indicative of an unjustified excess of the catalyst in the experiment.

Let us consider available information on the process mechanism. Free CN^- ions are known to have significant reducing power [7] and to be oxidized with Cu(II) salts in aqueous solutions. The primary product of the CN^- oxidation is the CN radical, which can dimerize (with further disproportionation in alkaline medium) or react with a water molecule to give finally the CNO^- ion. Complexes of Cu(II) with cyanide ions in the inner sphere have been described in the literature [8], with the cyanide ligands undergoing intramolecular oxidation. This process should not be fast at room temperature. In spite of the fact that this process results in decreasing concentration of free CN^- ions, it cannot form a basis for the detoxication, because with excess cyanide ions copper(I) forms stable $[Cu(CN)_n]^{(n-1)-}$ complexes (n = 2, pK_{inst}^{1-2} ~24; n = 3, pK_{inst}^{1-3} ~28.6; n = 4, pK_{inst}^{1-4} ~30.3). These complexes cannot be oxidized in solution to copper(II) compounds with atmospheric oxygen.

In this work we studied the oxidation of cyanide ion with atmospheric oxygen using the acrylonitrile test for the radical reaction mechanism. We found that acrylonitrile does not noticeably polymerize in air in a solution containing only NaCN, $CuSO_4$, and acrylonitrile. Atmospheric oxygen does not oxidize cyanide ions in the presence of a mixture of SO_3^{2-} and HSO_3^- anions with acrylonitrile either. However, introduction of hydrated Cu^{2+} ions into the mixture almost im-

Table 2. Detoxication of an industrial solution containing free and coordinated CN^- ions

Component	MPC of free anion or central atom of complex, mg l^{-1}	Concentration in solution, mg l^{-1}		
		before treatment with a mixture of S(IV) and Cu(II) compounds	after treatment with a mixture of S(IV) and Cu(II) compounds	after additional treatment with $Cu(OCl)_2$ and $FeSO_4$ solution
CN^-	0.1	2200	28	N/d*
$[Cu(CN)_3]^{2-}$	1.0	250	413	2.3
$[Zn(CN)_4]^{2-}$	1.0	71	51	N/d
$[Fe(CN)_6]^{4-}$	0.3	4.4	8.5	2.7
$[Ni(CN)_4]^{2-}$	0.1	0.73	0.70	0.15
$[Cr(CN)_6]^{3-}$	0.5	0.1	N/d	N/d
$[Mn(CN)_6]^{3-}$	0.1	15.5	3.7	0.11
$[As(OH)_4]^-$	0.05	0.23	N/d	N/d
$[Pb(OH)_4]^{2-}$	0.03	9	N/d	N/d
$[Cd(CN)_4]^{2-}$	0.0001	0.07	0.007	N/d
$[Hg(CN)_4]^{2-}$	0.0005	0.0013	N/d	N/d
$SeCN^-$	0.01	0.83	N/d	N/d

(N/d) Not detected within experimental error.

mediately results in appearance of a white flaky precipitate of polyacrylonitrile.

Its formation is accompanied by a sharp decrease in the NaCN concentration in solution, which suggests that the initiating stage of the process under consideration is the one-electron oxidation of SO_3^{2-} or HSO_3^- ions with Cu^{2+} aqua ions:

$$SO_3^{2-} + Cu^{2+} \rightarrow SO_3^- + Cu^+, \quad (1)$$

$$HSO_3^- + Cu^{2+} \rightarrow HSO_3^- + Cu^+. \quad (2)$$

Such one-electron redox processes have been well studied [9, 10]. The reaction of the above-mentioned radical anions or radicals with oxygen dissolved in water results in the formation of peroxomonosulfate radical anions in alkaline media [11, 12].

$$SO_3^- + O_2 \rightarrow SO_5^-, \quad (3)$$

$$HSO_3^- + O_2 \rightleftarrows HSO_5 \xrightarrow[-H_2O]{+OH^-} SO_5^-. \quad (4)$$

Radical anions of Caro's acid are powerful oxidants in alkaline solutions, capable of converting cyanide anions to cyanate anions:

$$SO_5^- + CN^- \rightarrow CNO + SO_4^{2-}, \quad (5)$$

$$CNO + Cu^+ \rightarrow CNO^- + Cu^{2+}. \quad (6)$$

Furthermore, reaction (6) regenerates Cu^{2+} ions required for the catalytic process. We also point out that, according to the one-electron oxidation potential $E^0_{1e}CNO/CNO^- = 2.66$ V, the cyanate radical CNO is a powerful oxidant [13, 14].

The proposed mechanism of detoxication of cyanide ions allows us to make certain assumptions concercning the optimal pH and the required Cu^{2+} content in solution. The pH must be selected so as to prevent formation of $Cu(OH)_2$, which removes copper(II) ions from the reaction sphere. Furthermore, it is necessary to take into account possible loss of Cu^{2+} due to formation of difficulty soluble salts like $Cu_2[Fe(CN)_6]$, $Cu_3[Cr(CN)_6]_2$, $Cu[Hg(CN)_4]$, etc.

CONCLUSIONS

(1) Atmospheric oxygen was shown to oxidize cyanide ions at pH 10.0 in the presence of SO_3^{2-} ion and catalytic amounts of Cu^{2+}.

(2) Oxidation of cyanide ion was found to occur by the radical mechanism.

REFERENCES

1. Milovanov, L.V. and Krasnov, B.P., *Metody khimicheskoi ochistki stochnykh vod gornorudnykh predpriyatii tsvetnoi metallurgii* (Chemical Treatment of Wastewater from Nonferrous Metallurgy Enterprises), Moscow: Nedra, 1967.
2. Smith, A. and Mudder, T., *The Chemistry and Treat-*

ment of Cyaniding Wastes, London: Mining J. Books, 1991.

3. Ilyaletdinov, A.I. and Alieva, P.M., *Mikrobiologiya i biotekhnologiya ochistki promyshlennykh stochnykh vod* (Microbiology and Biotechnology of Industrial Wastewater Treatment), Alma-Ata: Nauka, 1990.
4. *Kuchnoe vyshchelachivanie blagorodnykh metallov* (Heap Leaching of Noble Metals), Fazlullin, M.I., Ed., Moscow: Akad. Gornykh Nauk, 2001.
5. Zelenov, V.I., *Metodika issledovaniya zoloto- i serebro-soderzhashchikh rud* (Procedure of Investigation of Gold- and Silver-Containing Ores), Moscow: Nedra, 1989.
6. Franke, S., *Lehrbuch der Militarchemie*, Berlin: Deutscher Militarverlag, 1967–1969.
7. Kolthoff, M., Belcher, R., Matsuyama, G. and Stenger, V.A., *Volumetric Analysis*, vol. 3: *Titration Methods: Oxidation–Reduction Reactions*, New York: Interscience, 1957.
8. Nekrasov, B.V., *Osnovy obshchei khimii* (Foundations of General Chemistry), Moscow: Khimiya, 1973, vol. 2.
9. Ozawa, T. and Kwan, T., *Polyhedron*, 1985, vol. 4, no. 11, pp. 1995–1996.
10. Norman, R.O.C. and Storey, P.M., *J. Chem. Soc. (B)*, 1971, no. 3, pp. 1009–1013.
11. Waters, W.A., *The Chemistry of Free Radicals*, Oxford, 1946. Translated under the title *Khimiya svobodnyh radikalov*, Moscow: Inostrannaya Literatura, 1948, pp. 213–215.
12. Zhang, W., Muir, D.M., and Singh, P., *Hydrometallurgy*, 2000, vol. 58, no. 2, pp. 117–125.
13. Stanbury, D.M., *Adv. Inorg. Chem.*, 1989, vol. 33, pp. 69–138.
14. Stanbury, D.M., *Central Aspects of Chemistry of Radicals*, Alfassi, Z.B., Ed., London: John Wiley, 1999, pp. 348–384.

Russian Journal of Applied Chemistry, Vol. 74, No. 9, 2001, pp. 1513–1516. Translated from Zhurnal Prikladnoi Khimii, Vol. 74, No. 9, 2001, pp. 1469–1473.

ENVIRONMENTAL PROBLEMS OF CHEMISTRY AND TECHNOLOGY

Deamination as a Method of Pretreatment of Nitrogen-Containing Wastewater before Biological Treatment

I. L. Glazko, S. V. Levanova, M. G. Pechatnikov, A. B. Sokolov, A. L. Kanaev, and A. S. Krizhanovskii

Samara State Technical University, Samara, Russia

Received April 11, 2001

Abstract—A deamination method was proposed for pretreatment before biological treatment of process nitrogen-containing wastewater from caprolactam production.

Russian enterprises producing nitrogen-containing organic compounds such as caprolactam (CL), acetonitrile, etc. generate large amounts of wastewater to be subjected to biological treatment, involving nitrification and denitrification [1, 2]. Biological treatment has doubtless advantages over thermal methods from both economic and environmental viewpoints, though poses rigid requirements on the chemical composition of the initial wastewater. In many cases, wastewater subjected to treatment does not satisfy modern environmental standards on biological treatment because of increased content of ammonium ions in the wastewater after denitrification. For example, wastewater from caprolactam production contains a total of 36.6 mM of ammonium ions, which exceeds the permissible level by several orders of magnitude. This shifts the living activity balance of microorganisms and affects their species ratio, and thus affects the treatment quality on the whole and increases the content of ammonium ions in the water leaving the treatment works. In this situation enterprises often prefer to burn such wastes.

Experts in chemical and related branches of industry in various countries of the world have convincingly proven the need in and advantage of the approach based on solving industrial environmental problems at their origination site. To this end, combined treatment procedures are finding ever wider application in wastewater treatment. Examples are combinations of biological and physicochemical methods (e.g., treatment in bioadsorbers and filtration tanks) or combinations of biological and chemical methods (chemically modifying the wastewater composition so that the prepared wastes meet the requirements at a given wastewater treatment works).

Zlateva [3] showed that CL when in concentrations over 200 mg l^{-1} and ammonium salts with ammonium ion in concentraitons ranging from 0.6 to 8.3 mM inhibit the activity of nitrifying bacteria. Ammonia and nitrous acid also can exert an inhibiting effect. Laboratory and industrial investigations by Anthonisen and Loehr [4] revealed the concentration ranges within which ammonium and nitrous acid exert an inhibiting effect. When in concentrations within 0.6–8.3 mM, NH_4^+ inhibits nitrite bacteria, and within 0.006–0.06, nitrate bacteria. Nitrous acid exerts an inhibiting effect on nitrate bacteria when in concentrations from 0.22 to 0.28 mg l^{-1}.

In this work, we propose a procedure for pretreatment of nitrogen-containing wastewater to decrease the NH_4^+ ion concentration virtually to zero before biological treatment. The raw material was the wastewater from CL[1] production before burning; it had the following composition, %: CL 1.037, $(NH_4)_2SO_4$ 2.2 (chemical oxygen demand COD 56000 mg l^{-1}). Also, we used nitric acid condensate (NAC) with the total content of acids, as recalculated for HNO_3, of 3.03% and a 3% Na_2CO_3 solution.

The method proposed by us involves treating wastewater with nitric acid or its salts at 150–220°C (the temperature should not exceed 310°C) and elevated pressure ensuring existence of a liquid phase at this temperature.

Deamination of CL-containing wastewaters was studied by chemical and physicochemical methods. Dichromate oxidizability (COD) of waters and the content of ammonium sulfate in solutions were determined by standard procedures. CL was determined in

* Kuibyshevazot Joint-Stock Company (Togliatti).

1070-4272/01/7409-1513$25.00

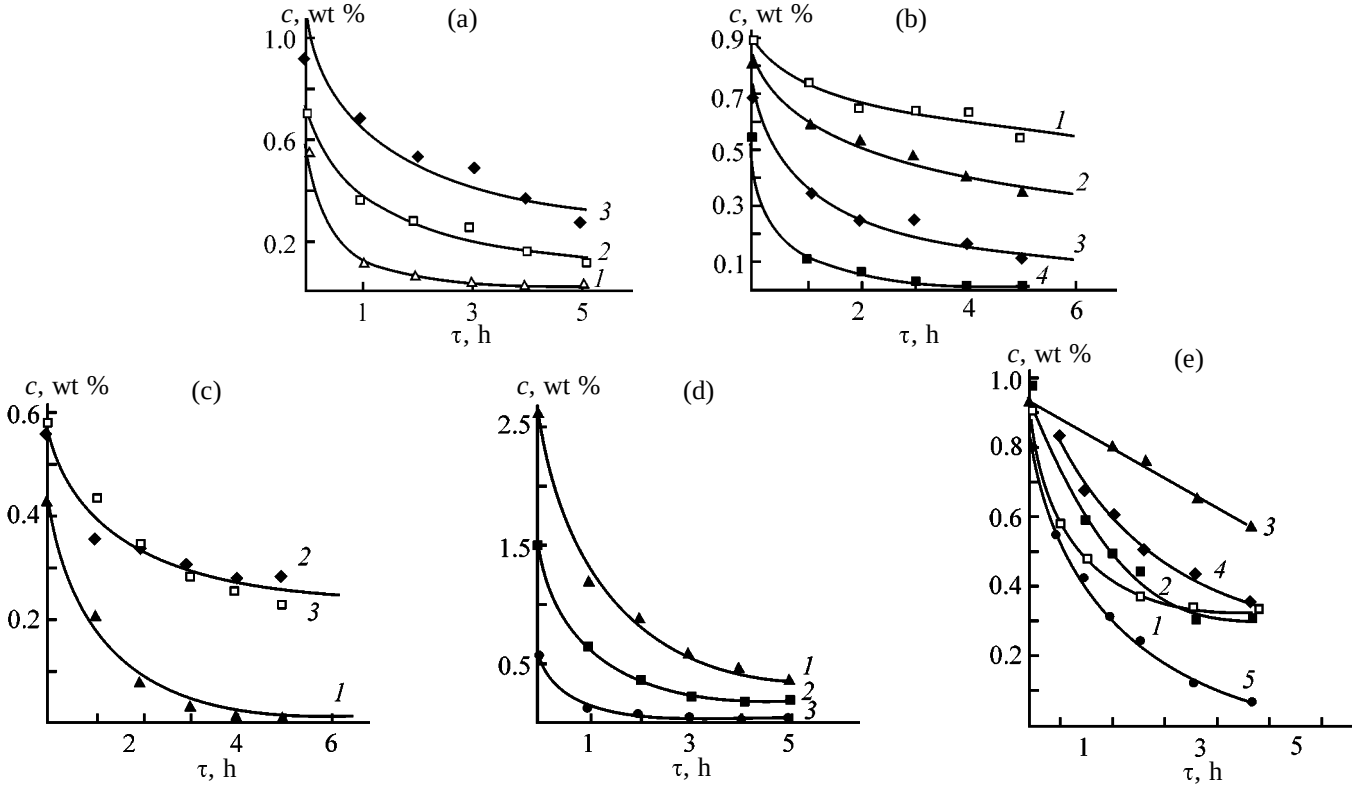

Fig. 1. Variation of the CL concentration c with time τ. Waste deamination with: (a) (*1*, *2*) NAC and (*3*) 0.19 M nitric acid solution; (b–d) NAC. Deaminaiton temperature, °C: (a, b) 100; (c) (*1*) 100, (*2*) 80, and (*3*) 70. (a) Initial concentrations of nitrite and nitrate ions, M: (*1*) 0.38 and (*2*) 0.19. (b) NAC/CL ratio: (*1*) 0.56, (*2*) 1.16, (*3*) 2.23, and (*4*) 4.46. (d) Initial concentration of CL, wt %: (*1*) 3, (*2*) 1.8, and (*3*) 1. (e) Initial concentration of the nitrate and nitrite ions 0.38 M. Sulfate concentration, wt %: (*1*) $(NH_4)_2SO_4$, 1, (*2*) $(NH_4)_2SO_4$, 3; (*3*) $(NH_4)_2SO_4$, 7; (*4*) Na_2SO_4, 3; and (*5*) 0.

aqueous solutions chromatographically. Though well-known, this method is of a limited application as it suffers from two drawbacks: columns fail rapidly and the CL peak is blurred and asymmetric because of high polarity of CL. We developed an improved chromatographic procedure. We tested various supports and liquid phases. The peak was symmetric only with strongly silanized supports when the amount of a liquid nonpolar phase was large. The best results were obtained with a 1-m column, 15% Apiezon-L on a Chromaton N-AW-DMCS; column temperature 170°C, vaporizer temperature 250°C; helium as carrier gas with the flow of 25 ml min^{-1}. The column is stable in 3-month operation. Analysis was carried out on a Tsvet-100 chromatograph with a flame-ionization detector. The chromatographic data were quantitatively calculated by the external reference method. The reaction products were identified by direct introduction of pure authentic components.

Pretreatment of wastewater involves three stages: deamination of wastewater with NAC, neutralization of the reaction mixture by an Na_2CO_3 solution to pH 9–10, air blowing of the ammonia formed and its absorption with water, and neutralization of the pretreated wastewater to pH 7–7.5 with nitric acid or NAC.

We found that deamination proceeds under the action of not only NAC but also 2–3% nitric acid (Fig. 1a). On heating the reaction mixture, nitric acid, possibly, converts to nitrous acid, which is active species in deamination. The transformations in the system HNO_3–HNO_2–H_2O can be represented by the scheme

$$4HNO_3 \rightleftarrows 4NO_2 + 2H_2O + O_2,$$

$$2NO_2 + H_2O \rightleftarrows HNO_3 + HNO_2.$$

Nitrous acid rapidly reacts with CL or its oxidation products. Such reactions occur also on boiling wastewater with NAC, as the COD of the wastewater significantly decreases. For example, after boiling the wastewater (COD 56000) with a twofold (by volume) excess of NAC and subsequent neutralization with one volume of a 3% Na_2CO_3 solution, the COD of the resulting solution was 4000.

Deamination of CL with nitrous acid can be represented as

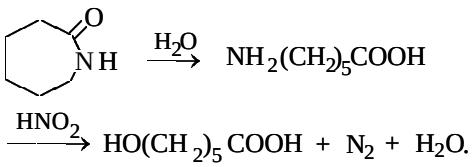

Hydrolysis of CL gives ε-aminocaproic acid which transforms into ε-hydroxycaproic acid by reaction with nitrous acid [5]. Thus, the products of wastewater pretreatment can include sodium salts of ε-aminocaproic and ε-hydroxycaproic acid.

Analysis of the kinetic curves of CL consumption showed that initially (on mixing of CL and NAC solutions) the CL concentration sharply decreases (Figs. 1a, 1b). The magnitude of this decrease depends, above all, on the volume ratio n = NAC/CL solution (ml/ml). For example, with a 2–3-fold excess of NAC, up to 50% of CL is consumed immediately after mixing. Further deamination proceeds at a rate corresponding to the reaction with nitric acid (Fig. 1a). Probably, even at 20–230°C the nitrous acid contained in NAC is exhausted. Further deamination involves conversion of nitric acid.

We also studied how the deamination rate varies with temperature at the atmospheric pressure (Fig. 1c). With decreasing temperature from 100 to 70°C, the reaction rate decreases 10–20-fold. To study how the deamination rate is affected by the CL concentration, we conducted experiments on model solutions with the CL concentration of 1–3% (Fig. 1d). We found that the reaction orders with respect to acid and CL are close to unity.

In view of the fact that the real wastewater contains up to 3 wt% of ammonium sulfate, we performed experiments with introducing ammonium sulfate into CL solutions. We found that ammonium sulfate inhibits deamination: both the initial rate and the secondary reaction rate decrease (Fig, 1e). The equation for the deamination reaction rate has the form

$$r = k_1[\mathrm{CL}][\mathrm{NO_3^-}] - k_2[\mathrm{NO_3^-}][\mathrm{SO_4^{2-}}].$$

The experimental data obtained (Fig. 2) were used for calculating the constants in the equations for the deamination rate of caprolactam-containing wastewater: $k_1 = 1.07 \times 10^{-2}$ and $k_2 = 1.18 \times 10^{-3}$ min^{-1}.

We also performed experiments with additions of other inorganic compounds: ammonium nitrate and sodium sulfate. The former does not affect the deamination rate, and sodium sulfate inhibits the reaction similarly to ammonium sulfate (Fig. 1e). Thus, an inhibiting effect is exerted specifically by the sulfate ions. For treating wastewater containing up to 3–4% ammonium sulfate, the contact time should be increased to 10 h and more.

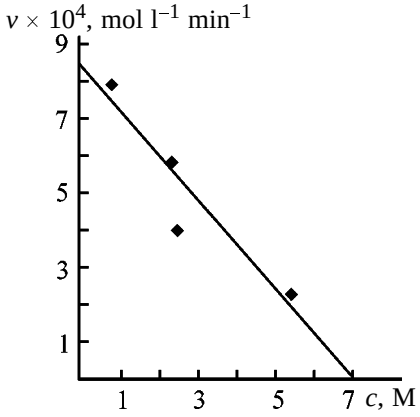

Fig. 2. CL deamination rate v as a function of the total concentration of the nitrate and nitrite ions c.

We checked our results on a laboratory setup under conditions of a continuous process. The setup involved two main reactors (deamination and neutralization reactors), a system for reactor heating, a cooling system, a unit for supply of the initial mixture, and a system for absorption of exhaust gases. A mixture of caprolactam-containing wastewater and NAC was supplied by a pump via feedline to the deamination reactor. The total time of deamination was 10 h. From the deamination reactor the mixture came to the neutralization reactor, into which a 3% Na_2CO_3 solution was added for neutralizing unchanged NAC and removing ammonium salts (1 ml ml^{-1} of wastewater). Also, nitrogen was supplied to the neutralization reactor for removing waste gases. The reaction time was 2–3 h. Waste gases from the reactors passed through reflux condensers and entered the trap system. Wastewater freed from ammonium was subject to biological treatment. The conversion of CL was 98.0–98.5%, and the leaving water contained no NH_4^+ ions.

In industry, the ammonia water yielded by absorption of waste gases can be utilized in an ammonia production shop.

The wastewater freed from ammonia was adjusted to pH 7 with nitric acid. The treated wastewater is characterized in the table.

The table shows that chemical treatment of the wastewater decreased the CL content by a factor of 52 and that of ammonium, virtually to zero.

Characteristization of caprolactam-containing wastewater before and after chemical treatment

Component	Content, mg l^{-1}	
	before treatment	after treatment
Caprolactam	10421	1200
SO_4^{2-}	14764	5500
NO_3^-	0	15000
NH_4^+	5537	0
COD	56000	4000
pH	7–8	7.0

The pretreated wastewater can be subject to biological treatment. When in concentrations of up to 200 mg l^{-1}, caprolactam does not exert an inhibiting action on denitrification. In the course of denitrification the nitriate ions are reduced to molecular nitrogen [6], and this involves oxidation of organic impurities by oxygen contained in NO_2^- and NO_3^- anions. Miyaji and Kato [7] found that nitrates are converted according to the equation

$$2NO_3^- + H_2O = N_2 + 2OH^- + 5O.$$

The following conditions of the above-discussed process were found to be optimal: temperature 100°C, NAC/CL molar ratio 4.5. The sulfate ions present in wastewater inhibit the process, which calls for rigid regimes.

CONCLUSION

An effective and inexpensive procedure was proposed for pretreatment, before biological treatment, of caprolactam-containing wastewater by deamination with nitric acid condensate forming as caprolactam-containing waste.

REFERENCES

1. Karnowsky, F., *Forum Stadte Hyg.*, 1978, vol. 29, no. 8, pp. 199–201.
2. Yasunori, T., *Ferment Ind.*, 1980, vol. 38, no. 1, pp. 31–39.
3. Zlateva, P., *Vodosnabzh., Kanaliz. Sanit. Tekh.*, 1974, vol. 10, no. 2, pp. 175–182.
4. Anthonisen, A.C. and Loehr, R. C., *I. Water Pollut. Contr. Fed.*, 1976, vol. 48, no. 5, pp. 835–852.
5. *Comprehensive Organic Chemistry. The Synthesis and Reactions of Organic Compounds*, Barton, D. and Ollis, W.D., Eds., vol. 2: *Nitrogen Compounds*, Oxford: Pergamon, 1979.
6. JPN Pat. 51-15651.
7. Miyaji, Y. and Kato, K., *Water Res.*, 1975, vol. 9, no. 1, pp. 95–101.

Russian Journal of Applied Chemistry, Vol. 74, No. 9, 2001, pp. 1517–1520. Translated from Zhurnal Prikladnoi Khimii, Vol. 74, No. 9, 2001, pp. 1473–1476.

ENVIRONMENTAL PROBLEMS OF CHEMISTRY AND TECHNOLOGY

Use of Piezoelectric-Crystal Microbalance for Analyzing Phenol and Its Nitro Derivatives in Air

Ya. I. Korenman, Zh. Yu. Kochetova, and T. A. Kuchmenko

Voronezh State Technological Academy, Voronezh, Russia

Received January 15, 2001; in final form, June 2001

Abstract—A piezielectric-crystal resonator was used for analyzing phenol and nitrophenols in air. The resonator electrodes were modified with Triton X-100, beewax, and bee glue (propolis). Sorption conditions ensuing reproducibility of the results were optimized uner static conditions.

Development of sensitive, prompt, and economically feasible procedures for air analysis is an urgent task. In this connection, ever growing researchers' attention is attracted by piezoelectric-crystal microweighing. This method is suitable for determining with high precision microconcentrations of organic substances in air [1–3].

The subjects of investigation were phenol, 2-nitrophenol, and 2,4-, 2,5-, and 2,6-dinitrophenols. These toxic compounds disturb the functions of the nervous, blood-circulation, and respiratory systems and exhibit a cumulative action. The MPCs in the working zone are 0.3, 5.0, and 0.05 mg m^{-3} for phenol, 2-nitrophenol, and dinitrophenols, respectively [4, 5].

One of the methods of determining volatile organic compounds in air with the use of piezoelectric-crystal microbalance is that involving modification of the resonator electrodes with a sorbent solution and thermal removal of solvent, injection of an air sample into the detection cell, and recording of the analytical signal, which is a function of the sorbate concentration [6–8].

The selectivity of sensors is governed primarily by the nature and properties of the coating (modifier) of the piezoelectric-crystal quartz resonator (PQR) [9]. An important requirement to the modifier is a high sorption capacity with respect to individual components or groups of related compounds. In this work, we tested new non-conventional sorbents as PQR electrode modifiers with the aim to selectively determine the phenol content in air in the presence of nitro derivatives.

EXPERIMENTAL

Experiments do not require special expensive equipment. The experimental setup involved a temperature-controlled detection cell manufactured from glass or stainless steel, 20–50 cm^3 in volume, with a polyurethane plug for injection of air samples at the level of resonator electrodes. The temperature of the detection cell was $25 \pm 1°C$. A PQR connected to the excitation scheme was fixed on the cell cover in a holder. The vibrational frequency F, Hz, was measured with a frequency meter whose frequency fixing range was 5 s.

The PQR electrodes were modified by uniformly applying with a microsyringe acetone, chloroform, and ethanol solutions of Triton X-100, beewax, and propolis, respectively (10 mg cm^{-3}). For solvent evaporation, PQR was kept for 30–45 min in a desiccator at $45 \pm 5°C$. The degree of solvent removal was controlled from the time stability of the analytical signal ΔF, Hz (variation of the vibrational frequency within 3 Hz min^{-1}).

The analytical signal is related to the masses of the modifier film and the substance sorbed on PQR electrodes by Sauerbrey equation [10]

$$\Delta F_s = -km,$$

where m is the film (sorbate) mass, μg, and k is the propotionality coefficient taking into account the intrinsic vibrational frequency and the frequency characteristic of quartz, its nature, and electrode area.

A required air volume was sampled with a syringe from flasks containing saturated vapor of chemically

1070-4272/01/7409-1517$25.00

Table 1. Phenol sorption parameters

Parameter*	Triton X-100				Beewax				Propolis			
	at indicated mass of the modifier film, μg											
	2.5	4.6	15.0	35.6	1.0	3.6	10.8	27.0	5.5	8.5	24.2	40.2
ΔF_s, Hz	480	590	700	860	120	200	290	490	200	240	310	400
$a \times 10^3$	143	55	51	50	41	37.7	23.7	18.1	17	21	10	6
$S \times 10^{-3}$, Hz dm^3 mol^{-1}	24.0	29.0	35.0	43.0	6.0	10.0	14.5	22.5	10.0	12.0	15.5	20.0
S_r, %	0.5	1.3	2.3	5.7	2.0	2.8	7.8	12.4	1.0	1.9	6.8	7.8

* ΔF_s is the analytical signal, a is the sorption capacity of the modifier, S is the sensor sensitivity, S_r is the relative standard deviation.

pure preparations and introduced into the detection cell at the level of PQR electrodes. This decreased the phenol loss by adsorption on the cell walls. The piezoelectric-crystal resonator was arranged linearly along the flow of the sample introduced, which decreased the sorption error due to nonuniform distribution of the sorbate in the near-surface air layer and increased the sensor sensitivity and reproducibility of the analytical signal.

The limiting concentration of vapor was calculated by the Mendeleev–Clapeyron equation [11]

$$C_i = 1.22 \times 10^7 P_i M/PT,$$

where P_i is the partial pressure of the sorbate vapor, Pa; M is the molecular weight, g mol^{-1}; P is the external pressure, Pa; and T is the temperature, K.

The initial concentrations of phenols in the detection cell was calculated by the dilution method, taking into account the volumes saturated with sample vapor. The kinetic parameters of sorption were estimated from the time of exhaustive sorption τ and half-sorption $\tau_{1/2}$, s, and the sorption constant k^+, i.e., change in the analytical signal at the initial moment, 5 s, corresponding to the smallest influence of desorption on the total rate of the process. The sorption efficiency of the modifiers is characterized by the sorbent sensitivity

$$S = \Delta F_{si}/C_i,$$

Hz dm^3 mol^{-1}, and sorption capacity a (the sorbate–sorbent mass ratio).

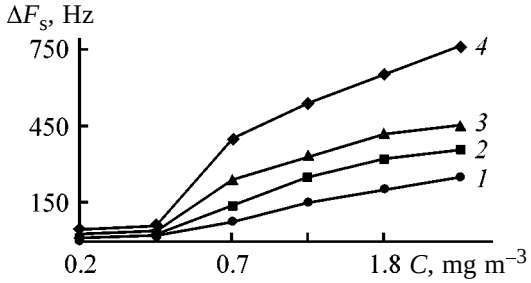

Fig. 1. Isotherms of phenol sorption on Triton X-100 films. (ΔF_s) Analytical signal and (C) phenol concentration. Film mass, μg: (*1*) 2.5, (*2*) 4.6, (*3*) 15.0, and (*4*) 36.5.

A major parameter essential for optimizing phenol detection conditions in air is the sorbent mass determining the regime and stability of the PQR operation (Table 1).

The modifiers studied in this work exhibited a decrease in the sorption capacity with increasing coating mass. This can be explained by the decay of the acoustic wave in the pre-electrode layer of the sorbent and by a decrease in its effective mass at $m > 10$–20 μg. This is consistent with the known data from [12]. Increase in the film mass decreases the reproducibility of the results S_r, %, as only a part of the modifier volume participates in sorption. This increases the contribution from the quenching of the volume-acoustic waves in the preelectrode sorbent layer. For coating with the optimal mass of 5–20 μg the reproducibility of sorption is within 7.8%.

With the phenol–Triton X-100 system as an example, we plotted sorption isotherms for film coatings with different masses (Fig. 1) [13]. With increasing m, the analytical signal (sensor sensitivity) is enhanced. With microamounts of phenols (under these conditions, the analytical signal is indistinguishable), it is necessary to use sorbent films with $m > 20$ μg for obtaining a reliable signal. For determining phenol on the MPC level (0.3 mg m^{-3}), with account of continuous sorption of 2–3 air samples (without sorbent regeneration), the use of a beewax film can be recom-

mended (m = 27.0 μg); in this case the sensor response is reproduced in a reliable way (the average root-mean-square error is ≤2.9%). When sensor further operates in such a regime, the sensor sensitivity gradually decreases. The amount of phenol (contained in air in different amounts) absorbed by a beewax film exceeds approximately twofold the mass of the coating itself (m = 27.0 μg).

Increase in the mass of the sorbed phenol relative to that of the sorbent film, evidently, suggests a layer-by-layer sorption of phenol to form a condensed phase on the sorbent surface. This can be interpreted as additional modification of the film surface. This suggestion is confirmed by phenol sorption not only on Triton X-100, beewax, and propolis, but also on other polar sorbents [14].

The kinetic sorption parameters τ, $\tau^{1/2}$, and k^+ also vary with the nature of the component of the sorbate–sorbent system and the analysis conditions (sorbent mass, sorbate concentration), and with increasing phenol content C_{ph} in the sample they regularly increase (Table 2).

The phenol sorption rate was at a minimum on the Triton X-100 film ($\tau_{1/2max}$ = 90 s) and at a maximum, on the propolis film ($\tau^{1/s}$ < 5 s). The interaction mechanisms differ for these systems: The time and rate of phenol sorption on the propolis film is independent of the analysis conditions, while the kinetic characteristics of sorption on the Triton X-100 film are strongly affected by the film mass and phenol concentration.

Nitrophenols exhibit similar relationships, the sorption affinity for Triton X-100 and propolis being weaker compared to phenol-containing systems. As to beewax, phenol and its nitro derivatives exhibit identical sorption affinities.

Sorption of nitrophenols is affected by the number of NO_2 groups in them, which governs the dipole–dipole interactions between the sorbate and the sorbent (Fig. 2). Phenol exhibits the smallest steric hindrance to sorption on the sorbents studied (one substituent in benzene ring), and dinitrophenols, the greatest. With decreasing polarity of sorbents in the Triton X-100 > propolis ≈ beewax series the influence of the pattern of electron density distribution in the sorbate molecules weakens, and the differences in the sorption efficiency of phenol and its nitro derivatives smoothen.

The sorption relationships established are suitable for qualitatively predicting the features of phenol sorption in systems with other sorbents. It is impossible to

Table 2. Kinetic parameters of the phenol sorption on a beewax film with a mass of 2.0 μg

C_{ph}, mg m^{-3}	ΔF_s, Hz	τ, s	$\tau_{1/2}$, s	k^+
0.1	33	15	<5	7.8
0.3	36	15	<5	7.9
0.4	49	20	<5	10.0
0.7	95	30	5	17.6
1.1	113	45	10	21.0
1.8	125	45	10	22.8
2.7	187	60	15	29.4

a priori estimate quantitatively the sorption efficiency for phenol and mono- and dinitrophenols on test modifiers because of the lack of identical physicochemical characteristics. As test sorbents we chose polyethylene glycol-2000 (PEG-2000), polyethylene glycol succinate (PEGS), and polystyrene (PS) which are similar in polarity to Triton X-100, propolis, and beewax, respectively. With respect to the efficiency of sorption of phenol, the sorbents can be ranked in the following order: PEG-2000 > PEGS > PS. The relationships established were experimentally substantiated (Fig. 2, curves *4*–*6*). Thus, knowing the quantitative criteria of phenol distribution in systems with modifiers of different polarities, it is possible to predict their sorption efficiency on films of other sorbents.

Using the internal reference method, we estimated the selectivities of the sorbents with respect to the phenols under conditions corresponding to the natural concentration of the air pollutants at 20°C (Fig. 3). Propolis is the most efficient sorbent in the case of detecting phenol in a mixture with nitro derivatives (the interference of nitrophenols is at a minimum). In the case of a beewax film selective detection is im-

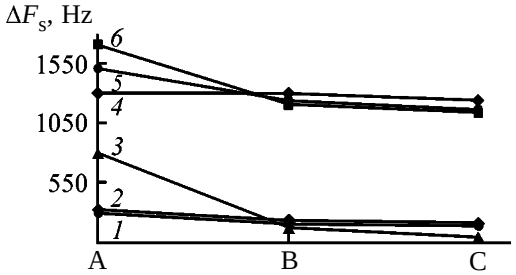

Fig. 2. Analytical signal ΔF_s of phenol sorption as a function of the number of nitro groups. Modifier: (*1*) beewax, (*2*) propolis, (*3*) Triton X-100. Test modifier: (*4*) PS, (*5*) PEGS, and (*6*) PEG-2000. Sorbate: (A) phenol, (B) 2-nitrophenol, and (C) 2,4-dinitrophenol.

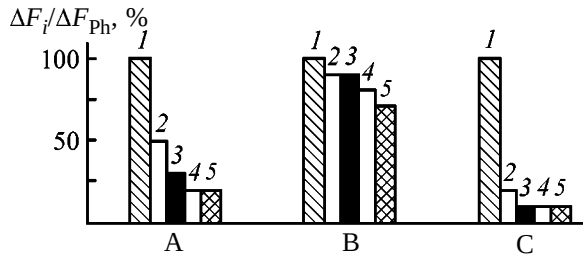

Fig. 3. Sorption histograms for (*1*) phenol, (*2*) 2-nitrophenol, and (*3*–*5*) 2,4-, 2,5-, and 2,6-dinitrophenols, respectively. ΔF_i and ΔF_{ph} are analytical signals of the modifiers and phenol, respectively. Modifier: (A) Triton X-100, (B) beewax, and (C) propolis.

possible, and in the case of a Triton X-100 film, the dinitrophenols virtually do not affect phenol determination.

CONCLUSION

Conditions of analyzing phenol in a mixture with mono- and dinitro derivatives using piezoelectric-crystal microbalance and modifiers of resonator electrodes of different polarities (Triton X-100, beewax, and propolis) were optimized. Phenol can be selectively analyzed in mixtures with nitrophenols on a propolis film.

REFERENCES

1. Prusak-Sochaczewski, E. and Luong J.H., *Anal. Lett.*, 1990, no. 3, pp. 401–424.
2. Dorozhkin, L.M., Doroshenko, V.S., Krasilov, Yu.I., *et al.*, *Zh. Anal. Khim.*, 1995, vol. 50, no. 9, pp. 979–982.
3. Milanko, O.S., Milinkovic, S.A., and Rajakovic, Lj.V., *Anal. Chim. Acta*, 1992, no. 264, pp. 43–52.
4. Murav'eva, S.I., Kazina, N.I., and Prokhorova, E.K., *Normokontrol' veshchestv v vozdukhe* (Monitoring of the Concentrations of Substances in Air), Moscow: Khimiya, 1988.
5. Lazarev, N.V., *Vrednye veshchestva v promyshlennosti* (Harmful Substances in Industry), Leningrad: Khimiya, 1976, vol. 1.
6. Alder, J.F. and McCallum, J.J., *Analyst*, 1983, no. 1291, pp. 123–131.
7. Beitnes, H. and Schroder, K., *Anal. Chim. Acta*, 1984, vol. 158, pp. 57–65.
8. Sanchez-Pedreno, J.A.O., Drew, P.K.P., and Alder, J.F., *Anal. Chim. Acta*, 1986, vol. 182, pp. 285–291.
9. Guilbault, G. and Jordan, Y.M., *Anal. Chem.*, 1988, no. 1, pp. 1–19.
10. Malov, V.V., *P'ezokvartsevye datchiki* (Piezoelectric-Crystal Sensors), Moscow: Energoatomizdat, 1978.
11. Rajakovic, L.V., *J. Serb. Chem. Soc.*, 1991, nos. 8–9, pp. 521–534.
12. Bel'kov, V.M., *Zh. Fiz. Khim.*, 1988, vol. 62, no. 12, pp. 3295–3299.
13. Edmons, T.E. and West, T.S., *Anal. Chim. Acta*, 1980, vol. 17, pp. 147–157.
14. Korenman, Ya.I., Tunikova, S.A., and Kuchmenko, T.A., *Zh. Anal. Khim.*, 1997, vol. 52, no. 7, pp. 763–766.

Russian Journal of Applied Chemistry, Vol. 74, No. 9, 2001, pp. 1521–1524. Translated from Zhurnal Prikladnoi Khimii, Vol. 74, No. 9, 2001, pp. 1477–1480.

ENVIRONMENTAL PROBLEMS OF CHEMISTRY AND TECHNOLOGY

Comparative Study of Water Softening with Granular and Fibrous Ion Exchangers

V. S. Soldatov, A. A. Shunkevich, and V. V. Martsinkevich

Institute of Physical Organic Chemistry, Belarussian National Academy of Sciences, Minsk, Belarus

Received July 26, 2000; in final form, February 2001

Abstract—Comparative study of softening of model hard water with both strongly acidic fibrous FIBAN K-1 and granular KU-2 ion exchangers was carried out. The influence of the filter-bed height, packing density of fibrous ion exchangers, volume sorption capacity, and filtering rate on the efficiency of calcium removal from model hard water was analyzed.

Owing to a favorable combination of features, textile ion exchangers are more preferable in conducting several processes than granular resins. Textile ion exchangers consist of separate thin threads of equal diameter (5–50 μm) forming a material with uniform thickness. These structural features ensure fast ion-exchange and sorption kinetics. Another important advantage of textile ion exchangers is very high stability against osmotic processes. The fibers of fibrous ion exchangers are not noticeably broken after repeated drying–moistening cycles [1]. Data on synthesis and features of the main types of fibrous ion-exchange materials such as weakly and strongly basic anion exchangers, weakly and strongly acidic cation exchangers, polyampholytes, and complexing sorbents were reported in [2–4]. The most available among these sorbents are FIBAN AK-22 weakly basic anion exchanger and FIBAN K-5 and FIBAN K-4 weakly acidic ion exchangers which are used for air treatment to remove impurities and also serve as filter in Akvapor, Mifil and Krinichka filtering units for purification of household and drinking water for individual and collective use [5]. In spite of considerable advantages of fibrous ion exchangers, these sorbents have not found use in industrial water treatment. Currently ion-exchange water softening and demineralization is performed with granular ion exchangers [6, 7].

The fiber diameter of fibrous ion exchangers is comparable with that of microspherical grains of resins commonly used in analytical practice. Both these resins exhibit similar sorption kinetics. Owing to high filter resistance and difficulties in fixation of microspherical sorbent (200–400 mesh) within a column, it is unlikely that microspherical ion exchangers can be used on an industrial scale. Short-cut fibrous ion exchangers are free of these drawbacks. The permeability of the filtering bed prepared from this material can be readily controlled by variation of the packing density so as to satisfy the process requirements [8].

The aim of this work was to study water softening with FIBAN K-1 strongly acidic fibrous ion exchanger and evaluate its sorption efficiency as compared to KU-2 granular resin.

EXPERIMENTAL

The comparative experiments on water softening were performed using FIBAN K-1 fibrous sulfonic cation exchanger based on graft copolymer of polypropylene and polystyrene prepared in a laboratory and standard commercial KU2 × 8 cation exchanger. The characteristics of these resins are given in Table 1.

The model solutions simulating hard water were prepared by addition of $CaCl_2$ and NaCl to distilled water to concentrations of 13.7 and 0.87 mg-equiv dm^{-3}, respectively.

Table 1. Sulfonic cation exchanger characteristics

Characteristic	Ion exchanger	
	KU-2 × 8	FIBAN K-1
Exchange capacity, mg-equiv g^{-1}	5.00	3.10
Swelling, g H_2O g^{-1}	1.17	1.78
Granule and fiber diameter, mm	0.25–0.68	0.034–0.040
Packing density, g cm^{-3}	0.38	0.068–0.27
Volume capacity, mg-equiv cm^{-3}	1.90	0.21–0.92

1070-4272/01/7409-1521$25.00

Table 2. Characteristics of water softening with ion exchangers*

h, mm	v, cm min^{-1}	E_V, mg-equiv cm^{-3}	V_1	V_2	E_1	E_2	λ_1	λ_2
					mg-equiv cm^{-3}			
KU-2 ion exchanger								
10	16.4	1.7	0	4.9	0	0.20	0	0.04
20	16.4	1.9	0	14.3	0	0.51	0	0.10
32	16.4	1.9	5.0	77.0	0.18	2.74	0.07	0.55
40	16.4	1.9	30.0	87.0	1.09	3.13	0.22	0.62
10	4.0	1.7	0	21.0	0	0.85	0	0.17
10	8.0	1.7	0	16.0	0	0.65	0	0.13
10	16.4	1.7	0	4.9	0	0.20	0	0.04
10	37.0	1.7	0	3.2	0	0.13	0	0.03
FIBAN K-1 ion exchanger								
7	16.4	0.92	23.4	46.8	1.05	2.10	0.34	0.68
10	16.4	0.83	27.0	46.0	1.37	2.32	0.44	0.75
20	16.4	0.82	32.7	46.7	1.70	2.40	0.55	0.77
30	16.4	0.83	43.7	51.9	2.20	2.60	0.70	0.84
20	16.4	0.21	4.1	9.8	0.80	1.93	0.26	0.62
20	16.4	0.42	12.3	23.0	1.24	2.32	0.40	0.75
20	16.4	0.83	32.8	46.7	1.70	2.40	0.55	0.78
10	4.0	0.83	32.8	52.4	1.66	2.65	0.53	0.86
10	8.0	0.83	32.8	58.0	1.66	2.32	0.53	0.75
10	16.4	0.83	27.0	46.0	1.37	2.32	0.44	0.75
10	37.0	0.83	19.6	39.3	1.00	1.99	0.32	0.64

* (V_1, V_2) Volumes of softened water related to the column volumes; (E_1, E_2) dynamic sorption capacities by the moment of Ca^{2+} breakthrough.

In our experiments a fibrous ion exchanger sample was placed in a column 12.5 mm in diameter. The fibers were compacted with a perforated piston to reach the required thickness and density of the filtering bed. The solution flow rate was controlled with a peristaltic pump.

The ion exchanger tested was converted to the Na form with 4% NaCl aqueous solution. Thereafter, without washing off excess NaCl, the model hard water was passed through the column. The eluate was analyzed for Ca^{2+} by complexometric titration with Acid Chrome Dark Blue indicator. From these data the output sorption curves were obtained and the following sorption characteristics were calculated: the volumes of softened water per unit of volume of sorbent V_1 and V_2, the sorption capacities of sorbent by the moment of Ca^{2+} breakthrough E_1 and E_2, and the efficiency of the column operation λ_1 and λ_2. The lower index 1 relates to highly softened water containing no more than 0.02 mg-equiv dm^3 Ca^{2+}, which corresponds to the Ca detection limit by complexometric titration. The lower index 2 relates to poorly softened water containing 7 mg-equiv dm^3 of calcium, which corresponds to 5% calcium content relative to the initial hard water. In accordance with recommendations reported in [9], water containing no more than 0.02% mg-equiv dm^3 Ca is considered to be highly softened water. Water of such quality can serve as heat carrier for thermal and nuclear power plants. Water containing from 0.02 to 0.7 mg-equiv dm^3 Ca is hard water suitable for replenishment of cooling systems and for household consumption.

Commercial FIBAN K-1 fabric is nonwoven needle-punched loose material with the bulk density of 0.1 g cm^{-3}. In the use of this sorbent (200–400 mesh) for water softening its performance can be improved by compacting fibers within a column. This procedure increases the volume capacity of the ion exchanger, decreases its free volume, and increases the packing density to 0.27 g cm^{-3}.

The efficiency of Ca removal from the model hard water was studied as a function of variation of the following factors: the ion exchanger bed height (h) from 7 to 40 mm, the packing density E_V from 0.21 to 0.92 mg-equiv cm^{-3}, and the water flow velocity from 4 to 37 cm min^{-1}. The main parameters characterizing the efficiency of water softening are listed in Table 2.

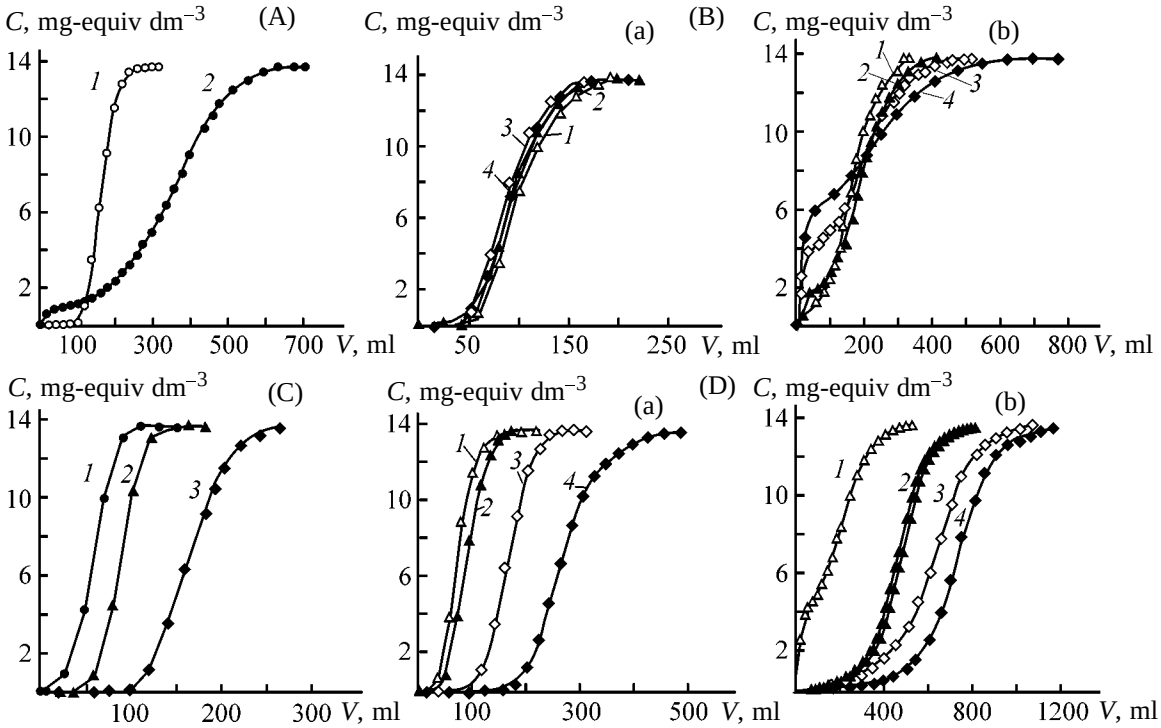

Fig. 1. Output curves of Ca^{2+} sorption: (*C*) Ca^{2+} concentration; (*V*) solution volume passed through column. (A) Thickness of filtering bed h = 20 mm, flow velocity v = 16.4 cm min^{-1}. Ion exchanger: (*1*) FIBAN K-1 and (*2*) KU-2. (B) (a) FIBAN K-1 and (b) KU-2; h = 10 mm. v, cm min^{-1}: (*1*) 4.0, (*2*) 8.0, (*3*) 16.4, and (*4*) 37.0. (C) FIBAN K-1, h = 20 mm. Packing density of sorbent E_V, mg-equiv cm^{-3}: (*1*) 0.21, (*2*) 0.42, and (*3*) 0.83. (D) (a) FIBAN K-1 and (b) KU-2; v = 16.4 cm min^{-1}. h, mm: (a) (*1*) 7, (*2*) 10, (*3*) 20, and (*4*) 30; (b) (*1*) 10, (*2*) 28, (*3*) 32, and (*4*) 40.

These data show that the compacted fibrous ion exchangers ensure efficient water softening even at a filtering bed height as small as 10 cm and high flow velocity v = 37 cm min^{-1}. Under these conditions we prepared a large batch of softened water, a portion of which was highly softened. As seen from Table 2, the efficiency of the column calculated as the ratio of its sorption capacity by a moment of calcium breakthrough to the total sorption capacity was fairly high (λ_1 = 0.32 and λ_2 = 0.64). Our results show that the most favorable conditions for water softening are ensured by a column packed with highly compacted strongly acidic fibrous ion exchanger at the bed height (h) of 20–30 mm and a water flow velocity of 16–37 cm min^{-1}.

With granular strongly acidic ion exchangers calcium breakthrough occurs right after the start of filtration. Therefore, in preparation of deeply softened water the filtering bed of the granular ion exchanger must be higher than 40 mm. This is evident from the shape and mutual arrangement of the output curves of calcium sorption on fibrous and granular ion exchangers at a bed height of 20 mm (Fig. 1A). For example, in the RECOFLO process based on water softening on granular ion exchangers the high efficiency of operation is reached at the filtering bed height no less than 7.5 cm [10].

The dependence of the output curves of calcium sorption on FIBAN K-1 and KU-2 strongly acidic ion exchangers on the flow velocity of water through the 10-cm sorbent bed is shown in Fig. 1. In the case of FIBAN K-1 the output sorption curves are symmetrical, and their initial portion indicates the absence of calcium breakthrough into the eluate. Thus, fibrous sulfonic cation exchanger exhibits excellent kinetic features which allow water softening even in filtration through 10- or 20-mm filtering bed at a high flow velocity.

It was found that a 10-fold variation in the filtration rate insignificantly influences the calcium removal in water softening on fibrous ion exchanger. With increasing the flow velocity from 4 to 37 cm min^{-1} the efficiency of calcium removal decreases from 0.53 to 0.32 at high (λ_1) and from 0.86 to 0.64 at low (λ_2) degrees of water softening.

Filtration of the model hard water through a thin bed (10–20 mm) of the standard KU-2 cation exchanger does not ensure water softening even at minimal flow velocity. The output curves of calcium sorp-

tion lack portion corresponding to the calcium-free eluate. We found that calcium breaks through even in the first eluate fractions.

The effect of the compaction degree of the fibrous ion exchanger on the efficiency of water softening at a sorbent bed height of 20 mm and a flow velocity of 16.4 cm min^{-1} is shown in Fig. 1B.

These results show that even noncompacted fibrous ion exchanger with the volume sorption capacity of 0.21 mg-equiv cm^{-3} exhibits fairly large dynamic sorption capacity E_2. With increasing the packing density of fibrous ion exchanger from 0.21 to 0.83 mg equiv cm^{-3} the efficiency of the column λ_2 increases from 0.62 to 0.78 (Table 2).

The output curves of calcium sorption by fibrous and granular ion exchangers are compared in Fig. 1D for different bed thicknesses at a flow velocity of 16 cm min^{-1}. These curves show that the standard KU-2 granular cation exchanger has higher volume sorption capacity and smaller free volume than the fibrous cation exchanger. The volume sorption capacity of KU-2 is 1.7–1.9 mg-equiv cm^{-3}, which is more than twice that of the close-packed FIBAN K-1 fibrous cation exchanger (0.83 mg-equiv cm^{-3}).

It is possible that the advantages of granular sorbents can be used for water softening at a higher filtering bed. For example, higher volume sorption capacity of granular cation exchanger allows preparation of water of low softening degree containing 0.7 mg-equiv dm^{-3} Ca with a filtering bed higher than 32 mm. In spite of a low efficiency of this process (λ_2 is 0.35 and 0.62 at the filtering bed height of 32 and 40 mm, respectively), it allows preparation of larger volume of softened water than with the fibrous cation exchanger of equal bed height. However, in obtaining deeply softened water, granular cation exchanger exhibits very low efficiency. Filtration of water through 20-mm and thinner bed of the fibrous cation exchanger ensures more efficient removal of calcium from water.

In water softening with the granular ion exchangers under identical conditions calcium breaks through in the first eluate fraction. At the same time, fibrous FIBAN K-1 cation exchanger ensures exhaustive removal of calcium from the first eluate fractions even at a sorbent height as small as 7 mm (Table 2). The efficiency of this process is sufficiently high (λ_2 = 0.34). All the tested fibrous sulfonic cation exchangers, irrespective of the bed height, are more efficient sorbents for preparation of deeply softened water than the granular resin.

Based on experimental results, we evaluated that a filtering unit for water softening equipped with the filtering bed with a surface area of 1 m^2 and 20 mm high ensures preparation of 600 l of deeply softened water within 20 min at the initial water hardness of 14 mg-equiv dm^{-3}.

Our experiments showed that the use of the filtering beds prepared from close-packed thin-fiber ion exchangers can be promising in development of small high-performance filtering units for deep water softening.

CONCLUSIONS

(1) Owing to excellent ion-exchange kinetic characteristics of thin (40 μm) fibers in the fibrous FIBAN K-1 ion exchanger, this sorbent can be used for efficient water softening.

(2) The use of thin-fiber close-packed fibrous ion exchangers considerably simplifies control of the permeability and hydrodynamic resistance of filtering beds to ensure the required conditions for water softening.

REFERENCES

1. Soldatov, V.S., Tsygankova, A.V., Elinson, I.S., *et al*., *Vestsi Akad. Navuk Bel. SSR, Ser. Khim. Navuk*, 1987, no. 2, pp. 78–83.
2. Soldatov, V.S. and Sergeev, G.I., *Zh. Vses. Khim. O–va. im. D.I. Mendeleeva*, 1990, vol. 35, no. 1, pp. 101–106.
3. Shunkevich, A.A., Sergeev, G.I., and Elinson I.S., *Zh. Vses. Khim. O–va. im. D.I. Mendeleeva*, 1990, vol. 35, no. 1, pp. 64–72.
4. Soldatov, V.S., Shunkevich, A.A., and Sergeev, G.I., *React. Polym*., 1988, no. 7, pp. 159–172.
5. Omel'chenko, T.N., Elinson, I.S., and Martinovich, V.I., *Vestsi Akad. Navuk Bel., Ser. Khim. Navuk*, 1999, no. 3, pp. 63–68.
6. Senyavin, M.M., *Ionnyi obmen v tekhnologii i analize neorganicheskikh veshchestv* (Ion Exchange in Technology and Analysis of Inorganic Compounds), Moscow: Khimiya, 1983.
7. Ashirov, A., *Ionoobmennaya ochistka stochnykh vod, rastvorov i gazov* (Ion-Exchange Decontamination of Wastewater, Solutions, and Gases), Leningrad: Khimiya, 1983.
8. Soldatov, V.S., Martsinkevich, R.V., and Pokrovskaya, A.I., *Vestsi Akad. Navuk Bel. SSR, Ser. Khim. Navuk*, 1986, no. 1, pp. 19–22.
9. *Teplotekhnicheskii spravochnik* (Handbook of Thermal Engineering), Gerasimov S.G, Kagan, Ya.A., Lebedev, P.D., *et al*., Eds., Moscow: Gosenergoizdat, 1957, vol. 1.
10. Brown, C.J. and Fletcher, C.J., *Ion Exchange for Industry*, Slater, M., Ed., Chichester: Ellis Horwood, 1992, pp. 392–403.

Russian Journal of Applied Chemistry, Vol. 74, No. 9, 2001, pp. 1525–1528. Translated from Zhurnal Prikladnoi Khimii, Vol. 74, No. 9, 2001, pp. 1481–1484.

ENVIRONMENTAL PROBLEMS OF CHEMISTRY AND TECHNOLOGY

Treatment of the Wastewater of Finishing-and-Dyeing Production Using Polyelectrolyte Flocculants Based on Nitron Fiber Scrap

V. I. Grachek, A. A. Shunkevich, O. P. Popova, and S. E. Radkevich

Institute of Physical Organic Chemistry, National Academy of Sciences of Belarus, Minsk, Belarus

Received April 4, 2001

Abstract—The performance of FK-1 and FK-3 cationic polyelectrolytes and of new AMF-2 amphoteric polyelectrolyte in treatment of the wastewater of finishing-and-dyeing production was studied as influenced by the concentrations of flocculant and coagulant.

Due to the increasing environmental pollution, including pollution of natural waters, development of new effective reagents for treatment of wastewaters is very urgent. Wastewater of the finishing-and-dyeing production of textile industry contains various dyes (up to 40% of the amount used) and concomitant chemicals (such as sodium chloride, soda ash, sodium hydroxide, acetic acid, etc.).

Such wastewaters are often treated with water-soluble polyelectrolytes based on polyacrylonitrile [1, 2]. It is known [3] that dyes are removed from water using aliphatic or aromatic amines.

In this work we studied the performance of new flocculants based on Nitron fiber scrap[1] (NFS) in treatment of the wastewaters from finishing-and-dyeing production[2].

EXPERIMENTAL

In our work we used FK-1 cationic flocculant [4], FK-3 cationic flocculant prepared by amidation of NFS with 3-dimethylaminopropylamine [5], and new AMF-2 amphoteric polyelectrolyte.

The AMF-2 polyelectrolyte was prepared in two stages. In the first stage NFS was aminated with 3-dimethylaminopropylamine to the exchange capacity of 5.0–5.5 mg-equiv g^{-1}. The resulting product was washed with water to remove excess amine and then hydrolyzed with 2–3% alkali at 95–100°C for 2–3 h.

The resulting AMF-2 polyelectrolyte was studied by IR and ^{1}H NMR spectroscopy. The IR spectrum contains a broad band at 3400 cm^{-1} belonging to the stretching vibrations of the NH group and strong bands at 1650 and 1710 cm^{-1} typical of the –C=O vibrations in the amide and carboxy groups, respectively. The bands at 1540 and 1400 cm^{-1} are due to the asymmetric and symmetric vibrations of the $–COO^-$ group.

The ^{1}H NMR spectrum ($CDCl_3$) contains the signals at 7.5 (–NHCO group), 3.20–3.25 (methylene protons in the $–CH_2NHCO$ group), and 2.2 ppm (CH_3 groups). Some properties of the polyelectrolytes are listed in Table 1.

Table 1. Properties of the polyelectrolytes*

Polyelectrolyte	[η], cm^3 g^{-1}	Exchange capacity, mg-equiv g^{-1}
FK-1	42	SEC_{amine} = 7.0
FK-3	48	SEC_{amine} = 5.2
AMF-2	36	SEC_{COOH} = 2.3, SEC_{amine} = 5.0

* Main functional groups:

FK-2

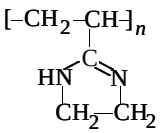

FK-3

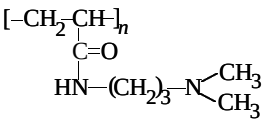

AMF-2

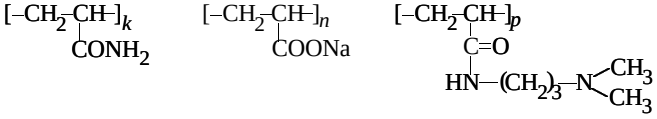

[1] Worsted-and-Dyeing Plant, Slonim, Belorus.

[2] Polimir Production Association, Novopolotsk, Belarus.

1070-4272/01/7409-1525$25.00

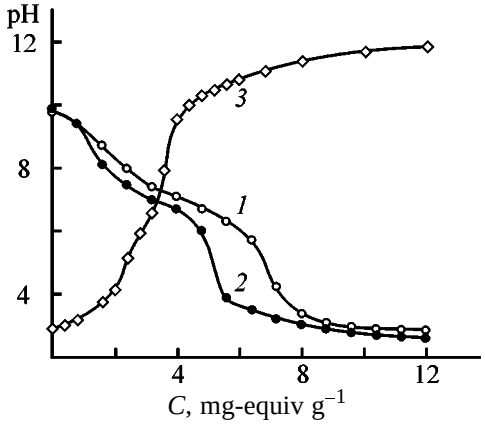

Fig. 1. Potentiometric titration curves of polyelectrolytes. (*C*) Concentration (mg-equiv of titrant per gram of flocculant). Polyelectrolyte: (*1*) FK-2, (*2*) FK-3, and (*3*) AMF-2; the same for Fig. 2.

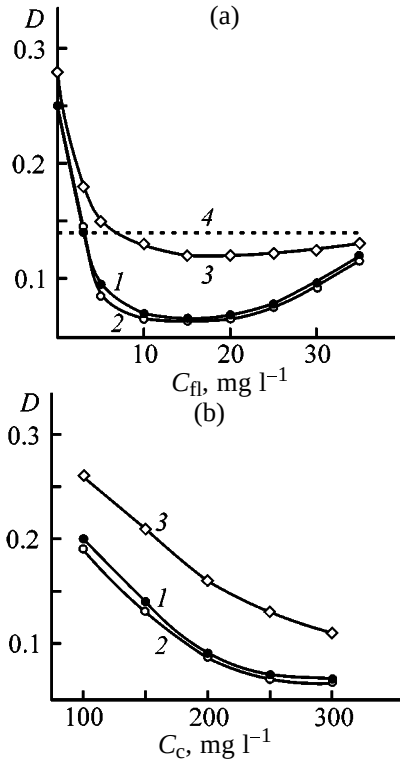

Fig. 2. Degree of wastewater clarification as influenced by concentrations of (a) flocculant C_f and (b) coagulant C_c. (a, *4*) C_c = 200 mg l^{-1}, and (b) C_f = 10 mg l^{-1}. (*D*) Optical density.

The exchange capacity of cationic electrolytes was determined from the inflection in the potentiometric titration curve. A weighed portion of a polyelectrolyte was titrated with a 0.1 M solution of hydrochloric acid in a potentiometric cell [6] equipped with an I-130 M ionometer. The exchange capacity of the amphoteric polyelectrolyte was determined by the procedure given elsewhere [7].

In our work we used pure grade $Al_2(SO_4)_3 \cdot 18H_2O$ and $Ca(OH)_2$, distilled water, and other chemically pure grade reagents. The intrinsic viscosity of the polymer solutions [η] was measured on an Ubbelohde viscometer at 20°C (d_c = 0.56 mm).The optical density was measured on a KFK-2 photocolorimeter (λ = 440 nm); the content of the petroleum products and surfactants was determined on a Flyuorat 02 liquid analyzer.

The chemical oxygen demand (COD) was measured by the bichromate oxidation procedure [8]. The amount of bound chromium (hereinafter chromium) was determined by titration [9]; and the water color index was determined by the procedure used at the plant, which is analogous to the procedure described in [9].

The titration curves of the polyelectrolytes in question are shown in Fig. 1. The FK-2 and FK-3 flocculants are the cationic polyelectrolytes containing weakly basic amino groups. The content of the amino groups per gram of the polymer dried to constant weight at 80°C was calculated from the inflection points in the titration curves.

The inflection points in the titration curve of the amphoteric polyelectrolyte are ill-defined, and thus the content of amino and carboxy groups in this polymer cannot be determined directly from the titration data.

The flocculation activity of polyelectrolytes was evaluated using the real wastewater of the finishing-and-dyeing production. First we determined the flocculation activity as influenced by the nature and concentration of the polyelectrolytes in question. The test mixtures were stored for 1 h before measurements, because previously we found [7] that at simultaneous addition of the flocculant and coagulant nearly 60-min storage is required for efficient purification of the wastewater.

The dependences of the optical density on the concentration of polyelectrolytes at constant concentration of the coagulant C_c = const are shown in Fig. 2a. With the cationic flocculants the degree of water clarification is greater than with the amphoteric polyelectrolyte. At the same time, the clarification degrees for FK-1 and FK-3 flocculants are similar. As seen from Fig. 2a, the highest flocculation efficiency is observed at concentrations of 10–20 and 10–30 mg l^{-1} for cationic and amphoteric polyelectrolytes, respectively. At these concentrations polyelectrolyte macromolecules have the optimal ratio between the sign and density of the charge and the extent of unfolding of the macromolecular chains, providing interaction with

the greatest number of the dispersed particles. With increasing concentration above the optimum the degree of water purification decreases, and this decrease is more abrupt with cationic flocculants as compared with the amphoteric polyelectrolyte.

The effect of the coagulant $Al_2(SO_4)_3$ concentration in the 100–300 mg l^{-1} range was studied at constant flocculant concentration C_f = const (Fig. 2b). As seen, the total flocculation effect for all polyelectrolytes increases with increasing coagulant concentration, which is obviously due to more efficient coagulation of the disperse phase.

The wastewater of the dyeing production contains chromium, which occurs in the oxidation states (3+) and (6+) depending on the nature of the dyes used, petroleum products, and other organic compounds. Therefore, we studied the performance of FK-1, FK-3, and AMF-2 flocculants in treatment of wastewaters to remove these pollutants. The results are summarized in Table 2. As seen, the effect of FK-1 and FK-3 in water treatment is similar, and the chromium concentration in water depends only on the content of the cationic polyelectrolytes added. In the course of treatment the chromium concentration decreases to 0.12–0.11 mg l^{-1} (i.e., by a factor of 2.7) at FK-1 and FK-3 concentrations of 10–15 mg l^{-1}. However, the decrease in the chromium concentration is the most abrupt at the cationic polyelectrolyte concentration of 5 mg l^{-1}, and further increase in the flocculant concentration only slightly affects the chromium content in the solution. At FK-1 and FK-3 concentrations of 10–15 mg l^{-1} the content of petroleum products decreases by a factor of 3.7–4.2 and COD decreases by a factor of 2.5–3.6. In the case of amphoteric polyelectrolyte, the content of chromium and COD decreases by a factor of 1.7 (to 0.18 mg l^{-1}) and 1.9, respectively. The effect of the amphoteric flocculant on the petroleum products is similar to that of the cationic polyelectrolytes.

Based on laboratory tests, FK-3 flocculant was selected as optimal, its pilot batch was prepared, and the industrial trials were carried out.

During industrial trials of the treatment process we studied industrial wastewater containing dyes without chromium. This wastewater was a dark cherry liquid with characteristic odor. In the industrial process of water treatment used at the plant $Al_2(SO_4)_3$ coagulant is added in combination with calcium hydroxide alkalizing agent. In the case of FK-3 flocculant, we used only the coagulant because in the presence of this polyelectrolyte the constant pH of the purified water was attained. The results of industrial trials listed in Table 3 are the averages of 5–6 measurements. As seen from Table 3, simultaneous use of the coagulant and calcium hydroxide did not provide the required quality of purified water, which was determined by the color index and content of organic compounds (COD). At the same time FK-3 flocculant used in combination with the coagulant allowed deodoration,

Table 2. Efficiency of wastewater purification using polyelectrolytes.* Coagulant concentration 250 mg l^{-1}, content in wastewater, mg l^{-1}: petroleum products 14.0 and chromium 0.3; COD 480 mg l^{-1}

C_f, mg l^{-1}	C_{pp}, mg l^{-1}	α_1, %	C_{Cr}, mg l^{-1}	α_2, %	COD, mg O_2/l	α_3, %
			FK-1			
5	4.5	67.8	0.13	56.7	228	52.5
10	3.6	74.3	0.12	60.0	208	56.4
15	3.2	77.2	0.11	63.4	175	63.3
20	2.7	80.7	0.11	63.4	132	72.4
			FK-2			
5	4.4	68.6	0.13	56.7	232	51.7
10	3.7	73.6	0.12	60.0	205	57.1
15	3.3	76.4	0.11	63.4	181	62.3
20	2.6	81.4	0.11	63.4	138	71.3
			AMF-2			
5	4.5	67.8	0.2	33.4	275	42.2
10	3.7	73.6	0.28	40.0	253	47.0
15	3.4	75.8	0.18	40.0	253	47.0
20	2.7	80.7	0.18	40.0	252	47.5

* (C_{pp}) Content of petroleum products; Purification degree with respect to (α_1) petroleum products, (α_2) chromium, and (α_3) COD.

Table 3. Properties of wastewater after its purification* with FK-3 flocculant

C_c	C_f	pH	β	C, mg l^{-1}	COD, mg O_2/l
mg l^{-1}					
190	5	6.6	1 : 12	0.024	160
180	10	6.7**	1 : 10	0.020	115
170	14	6.6	1 : 10	0.020	110
250***	–	6.3	1 : 30	0.025	195

* Characteristics of wastewater before treatment: pH 6.5, dilution factor β = 1 : 55, content of anionic surfactants C = 0.025 mg ml^{-1}, COD = 320 mg O_2/l.

** Before treatment pH 6.6.

*** Treatment was performed in the presence of calcium hydroxide suspension (125 mg l^{-1}).

decolorization (dilution factor decreased from 1 : 55 to 1 : 10–1 : 12), decrease in COD by a factor of 2.0–2.3, and decrease in the amount of the coagulant used in the process.

Thus, FK-3 flocculant provides better purification of the wastewater of the finishing-and-dyeing production as compared with the existing processes.

CONCLUSIONS

(1) The flocculation activity of polyelectrolyte flocculants prepared from Nitron fiber scrap in the treatment of wastewaters of the finishing-and-dyeing production depends on the concentration of the polyelectrolytes and changes in the following order: FK-3 = FK-1 > AMF-2.

(2) Industrial trials showed that the wastewaters of the finishing-and-dyeing production are efficiently purified with FK-3 flocculant at a concentration of 10 mg l^{-1}.

REFERENCES

1. Zapol'skii, A.K. and Baran, A.A., *Koagulyanty i flokulyanty v protsesse ochistki vody* (Coagulants and Flocculants in Water Treatment), Leningrad: Khimiya, 1987.
2. RF Patent Appl. 95 113 393/25.
3. FRG Patent Appl. 4 125 665.
4. Shunkevich, A.A., Grachek, V.I., Popova, O.P., *et al*., in *Resursosberegayushchie i ekologicheski chistye tekhnologii: Sbornik nauchnykh trudov II nauchno-tekhnicheskoi konferentsii* (Resource-Saving and Environmentally Clean Technologies: Collection of Scientific Works of II Scientific and Technical Conf.), Grodno, 1997, part 1, pp. 179–185.
5. Shunkevich, A.A., Grachek, V.I., Akulich, Z.I., *et al*., *Vestn. Nats. Akad. Nauk Belarusi, Ser. Khim. Nauk*, 1999, no. 3, pp. 55–57.
6. Soldatov, V.S., Sergeev, G.I., Martsinkevich, R.V., *et al., Zh. Prikl. Khim*., 1988, vol. 61, no. 1, pp. 46–50.
7. Grachek, V.I., Schunkevich, A.A., and Popova, O.P., *Zh. Prikl. Khim*., 2001, vol. 74, no. 2, pp. 260–265.
8. Novikov, Yu.V., Lastochkina, K.O., and Boldina, Z.N., *Metody opredeleniya vrednykh veshchestv v vode vodoemov* (Analysis of Pollutants in Water Reservoirs), Moscow: Meditsina, 1981.
9. Lur'e, Yu.Yu., *Analiticheskaya khimiya promyshlennykh stochnykh vod* (Analytical Chemistry of Industrial Wastewater), Moscow: Khimiya, 1984.

Russian Journal of Applied Chemistry, Vol. 74, No. 9, 2001, pp. 1529–1533. Translated from Zhurnal Prikladnoi Khimii, Vol. 74, No. 9, 2001, pp. 1485–1488.

PROCESSES AND EQUIPMENT OF CHEMICAL INDUSTRY

Absolute Measurements of the Combustion Heat of Natural Gas

Yu. I. Aleksandrov and V. P. Varganov

Mendeleev Russian Research Institute of Metrology, State Unitary Enterprise, St. Petersburg, Russia

Received April 28, 2000; in final form, July 2001

Abstract—A new isothermal calorimetric method for measuring the combustion heat of gas, relying upon the operation principle of the heat pipe, is considered together with the sequence of thermal processes occurring when this method is used. The functional diagram of the calorimeter is analyzed. Two procedures for measuring the heat effects are presented.

The increasing cost of natural gas has always resulted, and does so now, in that the requirements to the accuracy of measurement of its calorific value tend to become increasingly stringent.[1] At present, only four studies concerned with precision measurement of the combustion heat of methane are known [2–5]. Three of these [2–4] served as a basis for recommendations concerning calculations of the combustion heat of natural gas with an error of 0.12% [6] from results of gas-chromatographic analysis of natural gas composition.[2]

Lowering the error in determining the combustion heat of methane requires that a set of investigations should be carried out, comprising three independent stages: (i) developing a method for absolute measurements of the combustion heat of fuels,[3] (ii) designing a gas calorimeter to be used in this method, and (iii) developing a procedure for measuring the combustion heat of natural gas.

Despite significant differences in design, all the known types of calorimeters possess a common feature: necessity for calibration, either electrically or with the use of appropriate pure gases and gas mixtures. This procedure makes an additional contribution to the total error of determining the combustion heat.

Therefore, developing a combustion heat measurement technique requiring no calorimeter calibration will favor, all other conditions being the same, higher measurement accuracy.

The following requirements to the method of combustion heat measurement and the gas calorimeter to be used in the process were formulated: the combustion heat is to be measured in strict conformity with the regulations, with an error of no more than 0.1%, and absolute measurements (i.e., those without any kind of calibration) are to be done at combustion heats of gaseous fuels in the range 20–50 MJ m^{-3}. The measurement technique operating in the isothermal mode was chosen. As shown by Weber [9], it is preferable to perform in this case direct measurements by the compensation method. Such measurements can be, under certain conditions, rather accurate and well reproducible, especially when the Peltier effect is employed to compensate heat released in exothermic reactions.

The main difficulty encountered in developing an isothermal gas calorimeter is the nonuniform distribution of temperature in the combustion chamber. This problem has been solved by fast and loss-free conversion of the combustion heat into the phase transition heat compensated by means of the Peltier effect [10].

For this purpose, the calorimeter design is based on the principle of operation of the heat pipe characterized, on the one hand, by high heat conductivity and, on the other, by the possibility of collecting heat scattered over a large area and concentrating it in a rather limited prescribed surface [11, 12].

Three zones can be distinguished in the heat pipe: those of evaporation and condensation, and the inter-

[1] In the US, the combustion energy of natural gas is to be established in conformity with the "Gas Act" adopted by the Congress of the United States in 1978 with an error of no more than 0.1% [1].

[2] As far back as 1968, specialists pointed to the necessity for performing new investigations in order to reduce the error in question [7], which is only possible with fundamentally new method and equipment.

[3] To absolute measurement techniques are referred methods in which the property being measured is related to basic units by a known theoretical dependence [8].

1070-4272/01/7409-1529$25.00

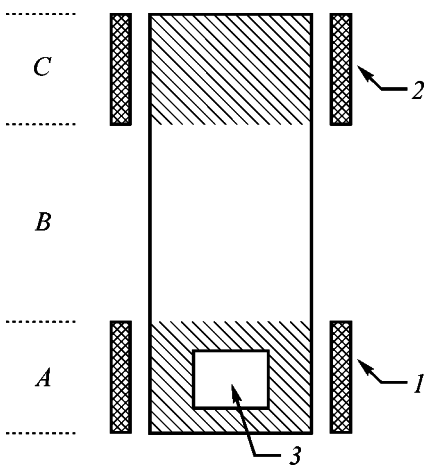

Fig. 1. Schematic of the heat pipe. Zone: (*A*) evaporation, (*B*) transport, and (*C*) condensation. (*1*) Heater, (*2*) Peltier elements, and (*3*) gas burner.

mediate zone. It is this specific feature of the heat tube, and also the possibility of virtually zero-loss and high-rate transfer of heat from the evaporation zone into the condensation zone, that were used to ensure absorption of heat released in gas combustion in the evaporation zone, conversion of this heat into vaporization heat, and transfer of the vapor into the condensation zone, where the condensation heat was compensated by means of the Peltier effect.

Thus, the following sequence of thermal processes occurs when the method in question is used:

$$Q_{comb} \rightarrow Q_{vap}, T_{ph.tr} \rightarrow Q_{cond}, T_{ph.tr} \leftarrow Q_{P.eff}, \quad (1)$$

where Q_{comb} is the heat of combustion of the gas, Q_{vap}, $T_{ph.tr}$ is the heat of vaporization of the working liquid at the phase transition temperature, Q_{cond}, $T_{ph.tr}$ is the heat of condensation of the working liquid at the same phase transition temperature, and $Q_{P.eff}$ the heat absorbed by the Peltier elements.

Taking into account that $|Q_{vap}, T_{ph.tr}| = |Q_{cond}, T_{ph.tr}|$, we have $|Q_{comb}| = |Q_{P.eff}|$. Consequently, the calculation equation for measuring the amount of heat released in gas combustion by the given method is as follows:

$$Q_{comb} = \eta \int_{t_{in}}^{t_{fin}} I(t)dt - Q_{idle}, \quad (2)$$

where η is the Peltier coefficient of the given battery at the boiling point of the working liquid; I is the current fed into the Peltier elements to maintain constant pressure or temperature, corresponding to a prescribed boiling point of the working liquid in the heat pipe; t_{in}, t_{fin} are the instances of current switching on and off in performing compensation; and Q_{idle} is the thermal energy consumed by the heat pipe in the idle mode.

To illustrate the set of operations constituting the given method for measuring the combustion heat, we use the functional scheme of the calorimeter shown in Fig. 1.

The calorimeter design is based on a heat tube with evaporation zone *A*, in which a background heater for heating the working liquid to its boiling point and a gas burner are placed, and transport zone *B* through which the evaporated working liquid is fed into condensation zone *C* and the condensate returns into evaporation zone *A*. Peltier elements are placed in condensation zone *C* in order to remove the heat released in condensation of an excess amount of vaporized working liquid. The vapor spaces of all the three zones are interconnected.

The isothermal conditions are ensured by maintaining prescribed vapor pressure of the working liquid or its prescribed boiling point (condensation temperature). We chose to maintain constant the temperature in one of three zones mentioned above. The control and measurement circuits are shown schematically in Scheme 1, where ATCU is the automated temperature control unit.

Scheme 1.

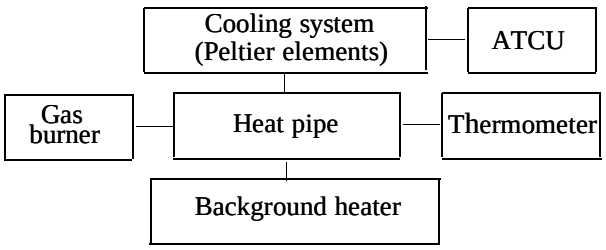

Control circuit of isothermal gas calorimeter.

Initially, the heat pipe is "turned on," with the Peltier current leveling-off at switched-on background heater and working control system, which indicates that the calorimeter has attained thermodynamic equilibrium.

After ignition, the gas combustion heat is utilized in the evaporation zone of the heat tube. As a result, a certain part of the working liquid is vaporized and the vapor passes through transport zone *B* into the con-

densation zone *C*. Simultaneously with evaporation, the vapor pressure of the working liquid and, correspondingly, its boiling point rise, which is compensated for by ATCU. The Peltier current necessary for this purpose is recorded and integrated.

The gas combustion heat can be measured in two gas feed modes: discrete and continuous. In the discrete mode, portions of gas are burnt, whose precise amount, Δm, is determined, e.g., by weighing the gas cylinder before and after an experiment. The combustion heat ΔH is calculated in this case by the equation

$$\Delta H = Q_{comb}/\Delta m.$$

In the continuous mode, it is important to maintain constant, with required accuracy, the flow rate G of all gases fed into the burner. Here, the quantity being measured is thermal power P (W), rather than amount of heat Q (J). The combustion heat is then calculated using the equation

$$\Delta H = P_Q/G_{CH_4}.$$

Thus, the quantity directly measured for maintaining the isothermal conditions in a calorimetric experiment is either the current passed through the Peltier elements (discrete gas feed mode) or power consumed by these elements (continuous gas feed mode).

To achieve the highest possible accuracy in measuring the gas combustion heat, it is necessary to determine sufficiently accurately the Peltier coefficient η, on the one hand, and take into account the dependence of the heat-eliminating power of Peltier elements on the supply current, on the other. This dependence is presented in Fig. 2.

Below are presented the results obtained in measuring the thermal power of the background heater and the current fed to the Peltier elements under the given thermostating conditions (24.800 ± 0.001°C):

I_P, A	$P_{b.h}$, W
1.4918 ± 0.0001	55.554 ± 0.004
1.5912 ± 0.0001	58.505 ± 0.005
1.6907 ± 0.0001	61.378 ± 0.004
1.5912 ± 0.0001	58.517 ± 0.005
1.4917 ± 0.0001	55.568 ± 0.004
1.3926 ± 0.0001	52.531 ± 0.005
1.2932 ± 0.0001	49.399 ± 0.005
1.3926 ± 0.0001	52.531 ± 0.005
1.4918 ± 0.0001	55.569 ± 0.004

Mention should be made here of the rather high reproducibility of measurement results. The maximum deviation of power values obtained under similar measurement conditions was 0.015 W (≤0.03%).

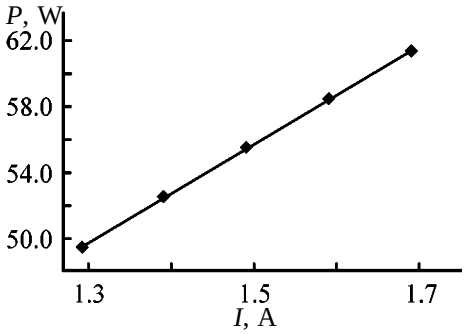

Fig. 2. Thermal power P necessary to maintain the given thermostating level (T = 24.800 ± 0.001°C) vs. current I passed through the Peltier elements.

However, high measurement accuracy can also be achieved in another way: by eliminating the effect of the given dependence on gas combustion heat measurements. This can be done by controlling the power fed into the background heater, provided that constant heat removal is ensured by Peltier elements through which the maximum stable current is passed. Its value is chosen such that the heat pipe should transfer a thermal power exceeding that released in combustion of a gas supplied at the maximum admissible rate. With this method of temperature control, the background heater acquires control functions and, therefore, the control circuit was modified to that shown in Scheme 2.

Scheme 2.

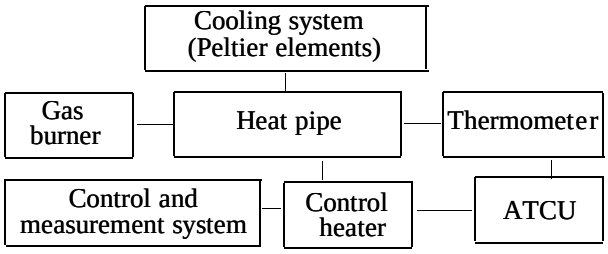

Modified control circuit of isothermal gas calorimeter.

At constant electric power P_{cool} fed into the Peltier elements, a constant power, named initial electric power $P_{in,Ti}$, is to be supplied to the electric heater in order to maintain constant temperature in any zone of the heat pipe.

Let us introduce one more, in addition to the control heater, heat source, gas burner, into the evaporation zone of the heat pipe. Operating burner releases

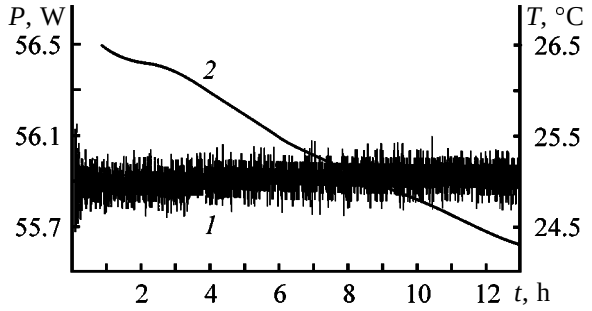

Fig. 3. (*1*) Long-term stability of the initial thermal power P_{in} in idle operation of the heat pipe at room temperature varying within 25 ± 1°C. (*2*) Temperature curve. (*P*) Power, (*T*) temperature, and (*t*) time.

thermal power P_Q. In this case the control system changes the control heater power P_{run} in such a way that the total power released by the two heat sources remains constant and equal to the initial power $P_{in,Ti}$ of the heater:

$$P_{in,Ti} = P_Q + P_{run}. \quad (5)$$

Thus, the thermal power P_Q released in gas combustion is defined as the difference between the initial power of the control heater and the power of the same heater at operating burner:

$$P_Q = P_{in,Ti} - P_{run,Ti}. \quad (6)$$

The main requirement to be met in measuring the thermal power P_Q released by the second thermal power source is long-term stability (constancy) of the total thermal power P_{in} at a given thermostating level.

With all other thermostating conditions preserved, P_{in} must remain constant regardless of whether only the main heater is switched on, or there are additional sources of thermal energy in the evaporation zone of the heat pipe. Whether or not the measurements of the thermal energy released by such sources are correct depends on the extent to which the above requirement is satisfied.

Figure 3 presents as illustration of the long-term stability of $P_{in,Ti}$ the results of measurements in the course of 13 h. It can be seen that measurement fluctuations are randomly distributed, which makes it possible to find the mean value of $P_{in,Ti}$ to be 55.920 ± 0.001 W. The standard deviation from the mean can be regarded as the characteristic of instability of the initial electric power, equal in the given case to 0.002%.

To pass from the heat power P_Q, measured using Eq. (6), to combustion heat of a gas, it is necessary to satisfy some conditions following from the adopted definition of the given quantity [5].

This refers in the first place to the requirement that the temperature of gases at the calorimeter inlet should be equal to that of combustion products at the calorimeter outlet. In addition, it is necessary to diminish the influence of evaporation or condensation (depending on experimental conditions) of part of water formed in combustion and take into account the possible partial loss of this water with combustion products.

CONCLUSION

A new isothermal calorimetric method was suggested for measuring the combustion heat of gases, relying upon the heat pipe principle and operating in both discrete and continuous modes.

ACKNOWLEDGMENTS

The authors are deeply grateful to Harro Bauer and Wolfgang Hemminger, and also to Stefan Sarge (Physicotechnical Institute, Braunschweig, Germany) for the opportinity to perform necessary investigations with the use of the most advanced measuring equipment and helpful discussions in the course of the work that continued for more than five years.

REFERENCES

1. Shapiro, J.C., Burkett, G.R., and Crowley, W.A., *Gas Quality (Groningen, April 22–26, 1986)*, van Rossum, G.J., Ed., Amsterdam: Elsevier, 1986, pp. 739–748.
2. Rossini, F.D., *J. Res. NBS*, 1931, vol. 6, pp. 37–49.
3. Rossini, F.D., *J. Res. NBS*, 1931, vol. 7, pp. 329–330.
4. Pittam, D.A. and Pilcher, G., *J. Chem. Soc., Faraday Trans. 1*, 1972, vol. 68, pp. 2224–2229.
5. Dale, A., Luthall, Ch., Aucott, J., and Sayer, C., *Vor träge des 129, PTB-Seminars am 19–20 März, 1996, PTB-Bericht., PTB-ThEx-1*, Braunschweig, April 1997, pp. 55–67.
6. *ISO DIS 6976:1996, Natural Gas—Calculation of Calorific Value, Density, Relative Density and Wobbe*

Index from Composition, Geneve (Switzerland): Int. Organisation for Standardization, 1996.

7. Garvin, D., Domalski, E.S., Wilhoit, R.C., *et al.*, *Gas Quality (Groningen, April 22–26, 1986)*, van Rossum, G.J., Ed., Amsterdam: Elsevier, 1986, pp. 59–73.
8. *ISO Guide 35 (1989), Certification of Reference Materials—General and Statistical Principles*, Geneve (Switzerland): Int. Organisation for Standardization, 1989.
9. Weber, H., *Thermochim. Acta*, 1974, vol. 9, no. 1, pp. 29–38.
10. RF Patent 2 085 924.
11. Pioro, I.L., Antonenko, V.A., and Pioro, L.S., *Effektivnye teploobmenniki s dvukhfaznymi termosifonami* (Effective Heat Exchangers with Two-Phase Thermosiphons), Kiev: Naukova Dumka, 1991.
12. *Teplovye truby dlya sistem termostabilizatsii* (Heat Pipes for Thermostabilization Systems), Shkriladze, I.G., Ed., Moscow: Energoatomizdat, 1991.

Russian Journal of Applied Chemistry, Vol. 74, No. 9, 2001, pp. 1534–1538. Translated from Zhurnal Prikladnoi Khimii, Vol. 74, No. 9, 2001, pp. 1489–1493.

PROCESSES AND EQUIPMENT OF CHEMICAL INDUSTRY

Design and Study of Gas Calorimeter for Absolute Measurements of the Combustion Heat of Natural Gas

Yu. I. Aleksandrov, V. P. Varganov, and S. Sarge

Mendeleev Russian Research Institute of Metrology, State Unitary Enterprise, St. Petersburg, Russia
Physicotechnical Institute, Braunschweig, Germany

Received April 28, 2000; in final form, June 2001

Abstract—A novel burning calorimeter design based on a heat pipe is presented. A circuit for automated control over operation of the proposed device is considered. The stability of the results is assessed. Several accessory parameters affecting the reproducibility of measurement results are evaluated. One of recent designs of the KTT-7 calorimeter, based on a thermosiphon, is analyzed. The uncertainty in heat power measurements on KTT-7 is evaluated.

A new isothermal method, described in detail in [1], was used in designing a gas calorimeter. It was necessary to design such a heat pipe that could accommodate a gas burner and ensure continuous removal of water formed in gas burning. The desire to diminish the error in measuring the heat energy released in gas combustion to a level not exceeding 0.1% imposed additional requirements to the calorimeter design and choice of measuring equipment. To achieve complete utilization of heat released in gas burning and its transfer with minimum loss to the condensation zone, a heat pipe was developed in the form of a thermosiphon presented in Fig. 1.

Gas burner *1* is situated within heat exchanger *2*. The heat exchanger is close in its design to the known combustion chambers used in industrial gas calorimeters. The heat exchanger is situated in the heating zone of thermosiphon *3* and is submerged in the working liquid, for which freon was chosen.[1]

Control heater *4* is also submerged in freon whose boiling temperature is measured with thermometer *5* placed directly in the bulk of the heat-transfer agent. Battery *6* of Peltier elements is situated at the opposite end of the thermosiphon, with the Peltier elements mounted within a special hollow forming the condensation zone. The temperature of the heat-transfer agent is measured with thermometer *8* whose signal is employed by the control circuit.

All specific design features of the calorimetric unit were aimed (i) to reduce to the maximum possible extent the heat loss both in the heat carrier evaporation zone and in the condensation zone and (ii) to

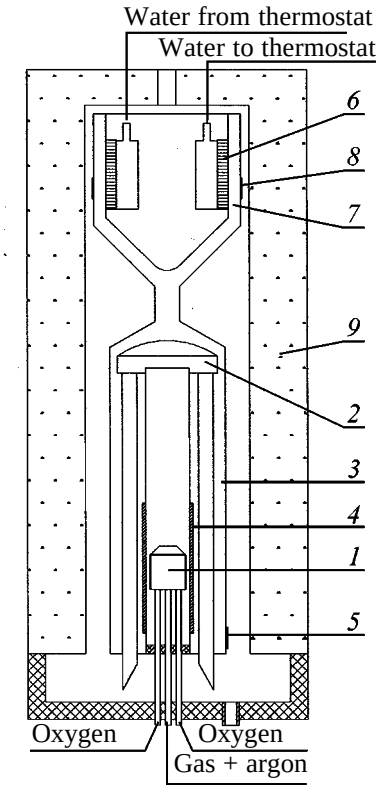

Fig. 1. General view of the calorimetric unit.

[1] The choice of Freon-11 as working liquid was primarily made for the following two reasons. First, it is incombustible, which is of no small importance when employing a gas burner. Second, this substance happily combines a boiling point close to the standardized 25°C and small, compared with that of water, heat of vaporization.

1070-4272/01/7409-1534$25.00

achieve the maximum possible similarity between the heat-transfer agent flows from the evaporation zone to the condensation zone in two operation modes: that with control heater ("idle mode") and that with a switched-on additional heat source.[2]

Water and other combustion products are removed through lateral tubes surrounding the central pipe of the heat exchanger, as this is done in industry. The condensate is collected in a receiver, which is situated below the thermosiphon and serves as a hydroseal, and removed from the calorimeter when accumulated in sufficient amounts. Gaseous combustion products ascend along the outer wall of the thermosiphon in the clearance between the thermosiphon and its casing *9*, which is intended to reduce heat loss, and removed through the upper opening in the casing.

The automated system controlling the operation of the measuring converter in the electric unit is based on a Proterm 100 microprocessor temperature controller with U10-15 power amplifier. As control transducer serves ESP-01 100-Ω platinum resistance thermometer calibrated in the temperature range 0–30°C. To ensure long-term stability of temperature, the thermometer must be, in its turn, sufficiently stable, which was verified. A 24-h variation of the thermometer resistance did not exceed, in terms of temperature, 0.1 mK. The transducer is connected in an arm of a measuring bridge operating on a type 373 power cell with a voltage of 1.5 V. An R4830/1 resistance box is connected in the standard arm of the measuring bridge. The output signal of the bridge is fed into the analog input of the temperature controller. The power amplifier at the output of the temperature controller is a thyristor amplifier with pulse-width modulation.

The control heater operates from a dc voltage varying between 0 and 30 V. This voltage is supplied to the heater through a shunt, reference resistance standard of 0.1 Ω, with a 1 : 100 potential divider comprising two reference resistance standards of 10 and 1000 Ω of 0.01 grade of accuracy connected in parallel to the heater.

The Peltier elements were fed from a B5-47 stabilized dc power source. Four in-series connected Peltier elements (K-1-127-1.4/1.5) were used. The current from the power source was supplied to the elements through a shunt. The current passing through the Peltier elements was determined by measuring the voltage drop across this shunt. The temperature of the hot junctions of the Peltier elements was set to be 25°C and was maintained constant to within 0.005°C by means of thermostating.

[2] As such an additional heat source can serve a gas burner or electric heater used in experiments aimed at checking the correctness of heat power measurements.

Table 1. Stability characteristics of the heat power P_{in} of KTT-7 calorimeter

Time elapsed after switch-on, h	Hour-average P_{in}, W	rms deviation of P_{in}	
		W	%
1			
2	51.220	0.007	0.014
3	51.175	0.009	0.017
4	51.151	0.009	0.017
5	51.167	0.008	0.015
6	51.165	0.007	0.014
7	51.176	0.009	0.017
8	51.177	0.008	0.016
9	51.189	0.007	0.015
10	51.197	0.008	0.016
2–10	51.180	0.003	0.005

The measuring part of the control unit is based on an AK-6.20 (Aksamit) computerized measuring system with IBM PC. The limits of the admissible basic error of voltage measurement by Aksamit were $\pm(100U + 1)$ μV. The power of the control and additional (in verifying the method adequacy) heaters was measured with the same known technique.

Tests of the KTT-7 calorimeter were commenced with determining the long-term stability of the initial heat power P_{in} transferred by the thermosiphon under prescribed conditions (Table 1). In preliminary experiments, the time in which thermal equilibrium is attained was found to be 1 h. Therefore, account was taken of measurements obtained after 1 h, which is reflected in Table 1.

The average (over 9 h) initial heat power ($\bar{P}_{in}$) was calculated from 1-h average values presented in Table 1, rather than from the entire data array whose values were measured at intervals of 1 s. The presented results confirmed high stability of the initial heat power of the KTT-7 calorimeter.

In the next stage, accessory parameters (thermostating temperature T_c; prescribed current passed through the Peltier elements, I_P; and prescribed temperature of hot junctions of the Peltier elements, T_P) were studied in detail.

As prescribed thermostating temperature was chosen, on the basis of preliminary experiments, T_c = 24.900°C. To determine the effect of deviations of T_c

Table 2. Heat power P_{in} transferred by KTT-7 calorimeter at different thermostating levels

T_{in}, °C	P_{in}, W	ΔP, W
25.100	43.410	
		0.346
24.900	43.064	
		0.431
24.700	42.633	

Table 3. Initial heat power P_{in} transferred by KTT-7 in relation to current I_P passed through Peltier elements

I_P, A	P_{in}, W	ΔP, W	$\Delta P/\Delta I$, W A^{-1}
0.800	35.247		
		7.9797	38.98
1.000	43.044		
		7.131	35.66
1.200	50.175		
		10.200	34.00
1.500	60.375		

Table 4. Initial power P_{in} in relation to hot junction temperature

T, K	P_{in}, W	ΔP, W	$\Delta P/\Delta T$, W K^{-1}
26.00	41.627		
		1.417	1.4
25.00	43.044		
		1.642	1.6
24.00	44.686		

within its controlled variation range (±0.001°C) on the stability of P_{in}, a set of measurements was carried out. The change of the thermostating level from the prescribed value was chosen to be 0.200°C. The obtained results are presented in Table 2.

Thus, with T_c maintained constant within ±0.001°C, the heat power varies within ±0.002 W.

The current I_P passed through the Peltier elements was measured with the use of B5-47 high-stability dc power sources. The prescribed current was maintained to within ±0.0001 A. The variation of the $\Delta P/\Delta I$ coefficient with current strength is due to the nonlinear dependence of the Peltier effect on current. Nevertheless, the obtained results allow evaluation of the possible fluctuations of P_{in}, caused by the instability of current passed through the Peltier elements. In the case in question, these fluctuations did not exceed ±0.004 W or 0.008% (Table 3).

The temperature T_P of the hot junctions of the Peltier elements was maintained constant by their thermostating with a water thermostat. To assess the influence exerted by the instability of the hot junction temperature on the possible heat power fluctuations, a set of measurements of the initial heat power P_{in} was performed at different thermostat temperatures.

As follows from Table 4, when the temperature of water thermostating the hot junctions is maintained constant within ±0.005°C, the fluctuations of the heat power transferred by the calorimetric unit will be ±0.008 W.

The estimate of the conversion coefficient and assessment of the influence exerted by the stability of accessory parameters made it possible to formulate requirements to the equipment used in the control and measurement unit of the calorimeter.

The next stage in studying the calorimeter was verification of the adequacy of measurement of the heat power P_Q. For this purpose, the gas burner was replaced with an additional electric heater-simulator. A constant electric power was fed into the heater. Simultaneously, all gases (with the exception of the combustible gas) were supplied into the calorimeter at such rates that their total amount corresponded to the amount of combustion products formed at the maximum flow rate of the combustible gas. In parallel, the electric power fed into the simulator was measured by the known direct method [1].

The set of measurements consisted in alternating operation of the calorimetric unit in the "idle" mode and with switched-on simulator. The duration of work in each mode was 3 h. The data for the last two hours were used for further calculations. The obtained results are presented in Table 5 and Fig. 2.

As P_{in} was taken the average value for the stage preceding the simulator switch-on and that following the simulator switch-off. The electric power supplied to the simulator was taken to be the true value $\bar{P}_{tr}$ = 25.510 ± 0.006 W. The average heat power released at the simulator and transferred by the thermosiphon was found to be $\bar{P}_Q$ = 25.503 ± 0.014 W.

As follows from the performed set of measure-

Table 5. Comparison of measured electric power P_{tr} fed into the simulator with the heat power P_Q transferred by the thermosiphon

P_{in}	P_{run}	$P_Q = P_{in} - P_{run}$	P_{tr}	$\delta = P_{tr} - P_Q$	
W (%)				W	%
52.418 ± 0.015 (0.03%)	26.797 ± 0.019 (0.07%)	25.621 ± 0.024 (0.09%)	25.556 ± 0.005 (0.02%)	–0.065	–0.25
52.325 ± 0.012 (0.02%)	26,803 ± 0.010 (0.04%)	25.522 ± 0.016 (0.06%)	25.529 ± 0.0018 (0.007%)	0.007	0.03
52.362 ± 0.015 (0.03)	26,864 ± 0.017 (0.06)	25.498 ± 0.023 (0.09)	25.510 ± 0.001 (0.004)	0.012	0.05
52.353 ± 0.017 (0.02)	26.855 ± 0.015 (0.06)	25.498 ± 0.023 (0.09)	25.517 ± 0.002 (0.006)	0.019	0.07
52.375 ± 0.031 (0.06)	26.904 ± 0.010 (0.04)	25.471 ± 0.032 (0.12)	25.505 ± 0.0007 (0.003)	0.034	0.13
52.431 ± 0.014 (0.03)	26.930 ± 0.013 (0.05)	25.501 ± 0.019 (0.08)	25.503 ± 0.001 (0.004)	0.002	0.008
52.436 ± 0.013 (0.02)	26.923 ± 0.019 (0.07)	25.513 ± 0.023 (0.09)	25.499 ± 0.001 (0.004)	–0.014	0.06
52.424 ± 0.033 (0.06)	26.948 ± 0.013 (0.05)	25.476 ± 0.035 (0.14)	25.497 ± 0.001 (0.004)	0.021	0.08
52.464 ± 0.013 (0.02)	26.980 ± 0.011 (0.04)	25.484 ± 0.017 (0.07)	25.494 ± 0.0006 (0.003)	0.010	0.04
52.489 ± 0.011 (0.02)	27.047 ± 0.016 (0.06)	25.442 ± 0.019 (0.08)	25.493 ± 0.0007 (0.003)	0.051	0.20

ments, the discrepancy between the electric power P_{tr} fed into the simulator and P_Q established in calorimetric measurements was as low as 0.007 W or 0.03%, which is within a random error. The obtained results point to the absence of any systematic error in measuring the heat power on the given calorimeter. Thereby, prerequisites were created for passing to measurements of the gas combustion heat.

However, before passing directly to the procedure of gas burning it was of interest to evaluate the uncertainty of measurement of the heat power P_Q in the KTT-7 calorimeter [2]. In view of the fact that the random error can be reduced by increasing the number of observations, let us estimate the number of observations [2] necessary for reducing the random error to a desired value. For this purpose, let us use the equation presented in the ISO standard [3]:

$$n^{1/2} = ts/d = 30,$$

where d is the desired value of the random error (0.01 W), n is the number of measurements, s is the standard deviation of a single measurement (≤0.15 W for KTT-7), and t is Student's number (taken to be 2 because of the large number of measurements).

Thus, it suffices to have 900 points in measurements with KTT-7 in order to obtain a random error of measurement not higher than 0.01 W, which constitutes about 0.04% of the value being measured. The duration of measurement should be greater than, or equal to 135 min. In the reported set of measurements, the duration of each stage was 3 h, of which two were used for processing.

In evaluating the measurement uncertainty, it is important to escape "double counting" of uncertainty

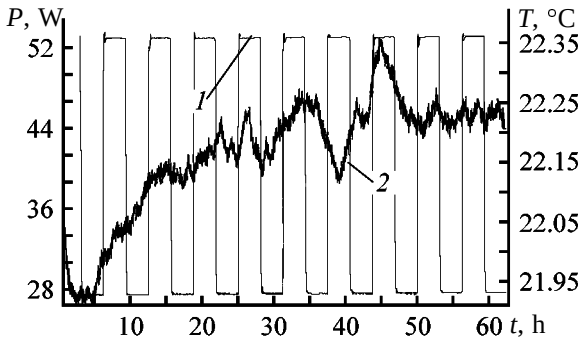

Fig. 2. Variation with time of the (*1*) power of the controlling heater in idle mode and with switched-on additional heater-simulator (P_{tr}) and (*2*) casing temperature. P_{tr} = 25.510 ± 0.006 W. (*P*) Power, (*T*) temperature, and (*t*) time.

components [2]. As applied to the obtained results, this means that the uncertainties due to the accessory parameters considered above should not be taken into account separately in group B, but are part of the uncertainty evaluated in group A in the form of a standard deviation $\bar{U}_A(P_Q) = 0.014$ W or $\tilde{U}_A(\bar{P}_Q) = 0.05\%$.

With account of the metrological characteristics of the equipment used in power measurements, the total standard uncertainty for group B, U_B, was found, using the calculation procedure described in [4], to be $\tilde{U}_B = 0.01\%$.

Thus, the total standard uncertainty in heat power measurement with a KTT-7 calorimeter

$$\tilde{U}_C = (\tilde{U}_A^2 + \tilde{U}_B^2)^{1/2} = 0.05\%.$$

In principle, this is sufficient for passing to development of a procedure for measuring the combustion heat of gases with an error of about 0.1%.

CONCLUSION

As a result of the investigations performed, a calorimeter design was developed, which allows the heat released in gas combustion to be measured by the absolute method with required accuracy ($\pm 0.1\%$).

REFERENCES

1. Aleksandrov, Yu.I. and Varganov, V.P., *Zh. Prikl. Khim.*, 2001, vol. 74, no. 9, pp. 1485–1488.
2. *ISO, Guide to the Expression of Uncertainty in Measurement*, Geneve (Switzerland): Int. Organisation for Standardization, 1993, 1st ed.
3. *ISO 10715:1997(E), Natural Gas-Sampling Guidelines*, Geneve (Switzerland): Int. Organisation for Standardization, 1993, 1st ed.
4. *MI* (Methodical Instructions) *2552–99: Recommendations of the State Measurement Service, Use of the "Guide to the Expression of Uncertainty in Measurement")*, St. Petersburg: Vseross. Nauchno-Issled. Inst. Metrologii im. D.I. Mendeleeva, 1999.

Russian Journal of Applied Chemistry, Vol. 74, No. 9, 2001, pp. 1539–1545. Translated from Zhurnal Prikladnoi Khimii, Vol. 74, No. 9, 2001, pp. 1494–1499.

PROCESSES AND EQUIPMENT OF CHEMICAL INDUSTRY

Method for Measuring the Combustion Heat of Natural Gas with Isothermal Calorimeter

Yu. I. Aleksandrov, V. I. Belyakov, V. P. Varganov, and S. Sarge

Mendeleev Russian Research Institute of Metrology, State Unitary Enterprise, St. Petersburg, Russia
Physicotechnical Institute, Braunschweig, Germany

Received April 28, 2000; in final form, June 2001

Abstract—Factors that are to be taken into account in developing a calorimetric technique are considered. The possible deviations of temperatures at the inlet and outlet of gases in the calorimeter from the nominal values are evaluated and an example of such estimate is given for the case of methane burning in batch and continuous operation modes. The necessity for taking into account the humidity of gases fed into the calorimeter burner is demonstrated. The proposed method was used to perform absolute measurements of the combustion heat of methane.

The proposed technique for measuring the combustion heat of natural gas was developed for an isothermal calorimeter of original design, described in detail previously [1, 2]. Our goal was to make introduction of any corrections unnecessary. In this case, the gas combustion heat can be calculated from the amount of burnt gas and the measured heat power P_Q released in its combustion.

From the existing wide variety of definitions of the notion "combustion heat of a gas" [3–11] follows that, to solve the problem in question, it is necessary (1) to refine the temperature to which the combustion heat is reduced and (2) to ensure, taking into account item 1, that the temperatures of gases fed into the burner and discharged combustion products are equal.

Further, the following standard combustion conditions were used: T_c = 25°C, p_c = 101.325 kPa.

Another important factor to be taken into account in developing a calorimetric technique is the content of water vapor in the gas being burnt. The following variants are distinguished [5]: (1) gas to be burnt is saturated with water vapor prior to being fed into the calorimeter; in this case, combustion heat related to 100% humid gas is measured; (2) gas to be burnt is dried prior to being fed into the calorimeter; the obtained combustion heat is related to dry gas [5]; and (3) gas to be burnt is fed into the calorimeter with the humidity it has; the measured value is the combustion heat of real gas.

Thus, the above circumstance is to be taken into account in comparing gas combustion heat values obtained by different methods. The most logical and promising method is direct measurement of the combustion heat of a real gas.

The measured heat effect in gas burning may be over- or underestimated for internal or external reasons. To internal factors are related effects depending both on the difference of heat capacities of gases fed into the calorimeter and combustion products and on heat of vaporization (condensation) of water vapor arriving at the calorimeter together with feed gases and formed as a combustion product. Therefore, the calorimetric procedure should reduce the effect of internal factors to the maximum possible extent.

External effects are associated with heat exchange between the calorimeter and the environment. Their influence can be substantially reduced by heat insulation, and attention was given to this fact in designing the calorimeter.

Gases fed into the calorimeter were preliminarily thermostated in a water thermostat at 25°C. The temperature maintained in the KTT-7 calorimeter was chosen in such a way that the temperature in the heating zone of the thermosiphon was close to 25°C. The combustion products at the heat-exchanger outlet acquired a temperature close to this value. Below, we estimate possible deviations of the above temperature from the nominal value on condition that the error associated with such a deviation does not exceed 0.01%.

Let us calculate the correction for deviation of the temperature of incoming gases and combustion gases

1070-4272/01/7409-1539$25.00

from 25°C in methane burning

$$CH_4 + 2O_2 \rightarrow CO_2 + 2H_2O. \quad (1)$$

The additional amount of heat entering the calorimeter with each of the incoming gases or absorbed by each of these is given by

$$Q_{in,j} = n_{in,j} C_{P,j} (T_{h.p.} - T_{in}), \quad (2)$$

where $n_{in.j}$ is the number of moles of a gas fed into the calorimeter, $C_{P,j}$ is the molar heat capacity of a given kind of gas, $T_{th.t}$ is the heat pipe thermostating temperature, and T_{in} is the temperature of gas at the inlet of the gas pipe.

The amount of heat removed from the calorimeter with each of the combustion products is

$$Q_{fin.j} = n_{fin,j} C_{P,j} (T_{fin} - T_{h.p.}), \quad (3)$$

where $n_{fin.j}$ is the number of moles of combustion products and T_{fin} is the outlet temperature of the combustion products.

Thus, the total measured amount of heat, which either arrives at the calorimeter or is removed therefrom with each kind of gas, is given by

$$\Delta Q_j = n_{in,j} C_{P,j} (T_{h.p.} - T_h) + n_{fin,j} C_{P,j} (T_{fin} - T_{h.p.})$$
$$= C_{P,j} (n_{in,j} - n_{fin.j}) T_{h.p.} + n_{fin} T_{fin} - n_{in} t_{in},$$
$$\Delta Q_j = C_{P,j} [(V_{in,j} - V_{fin.j}) T_{h.p.} + V_{fin.j} T_{fin} - V_{in,j} T_{in}]/V_0, \quad (4)$$

where V_0 is the true molar volume of a given kind of gas.

The gas volumes at the inlet and outlet may coincide, differ, or even be zero for one of the gases.

Let us evaluate, for the example of methane burning, the effect of deviation from 25°C of the temperature of gas at the calorimeter inlet and that of combustion products at its outlet.

(1) Methane CH_4:

$$V_{CH_4,in} = V_{CH_4}, \quad V_{CH_4,fin} = 0,$$
$$\Delta Q_{CH_4} = [C_P^{CH_4} (T_{h.p.} - T_h) V_{CH_4}]/V_0.$$

(2) Oxygen O_2: (a) oxygen entering into reaction in accordance with the equation

$$V_{O_2,eq.in} = 2V_{CH_4}, \quad V_{O_2,eq.} = 0,$$
$$\Delta Q_{O_2,eq} = [C_P^{O_2} (T_{h.p.} - T_{in}) 2 V_{CH_4}]/V_0.$$

(b) oxygen supplied in excess:

$$V_{O_2,ex} = V_{O_2,\Sigma} - V_{O_2,eq} = V_{O_2,\Sigma} - 2V_{CH_4},$$
$$\Delta Q_{O_2,ex} = [C_P^{O_2} (T_{fin} - T_{in})(V_{O_2,\Sigma} - 2V_{CH_4}).$$

(3) Argon:

$$V_{Ar,in} = V_{Ar,fin} = V_{Ar}.$$

As shown below, the optimal conditions of burning are those with the volume (flow rate) of argon equal to that of methane, and, therefore, we take $V_{Ar} = V_{CH_4}$:

$$\Delta Q_{Ar} = [C_P^{Ar} (T_{fin} - T_{in}) V_{Ar}]/V_0$$
$$= [C_P^{Ar} (T_{fin} - T_{in}) V_{CH_4}]/V_0.$$

(4) Carbon dioxide CO_2:

$$V_{CO_2,in} = 0, \quad V_{CO_2,fin} = V_{CH_4},$$
$$V_{CO_2} = [C_P^{CO_2} (T_{fin} - T_{h.p.}) V_{CH_4}]/V_0.$$

(5) Water H_2O: (a) water formed by oxidation (condensate). Taking into account that $V_{H_2O} = 2V_{CH_4}$, we have for the mass of condensed water

$$m_{H_2O,l}^{con} = M_{H_2O} V_{H_2O}/V_0 = 2M_{H_2O} V_{CH_4}/V_0,$$
$$V_{H_2O} = m_{H_2O,l}^{con} C_{P,l}^{H_2O} (T_{fin} - T_{h.p.}) \quad (5)$$

where $C_{P,l}^{H_2O}$ is the heat capacity of water (J g^{-1} K^{-1}).

(b) Water vapor corresponding to saturated state of gases fed into the calorimeter burner and of combustion products. Assuming that the amount of water vapor fed into the calorimeter with water-saturated oxygen is equal to the amount of water vapor removed from the calorimeter, we have

$$V_{H_2O,vap} = m_{H_2O,}^{vap} C_{P,l}^{H_2O} (T_{fin} - T_{in}) \quad (6)$$

where $m_{H_2O}^{vap} = a V_{O_2,\Sigma}$, and a is the content of water in a saturated gas at a given temperature [12]:

T, °C	20	24	25	26	30
a, g m^{-3}	17.29	21.77	23.04	24.37	30.37

The conditions when this assumption is valid are given below.

In addition, one more assumption is made, consisting in that the saturated vapor pressure of water in

Scheme of gas feed

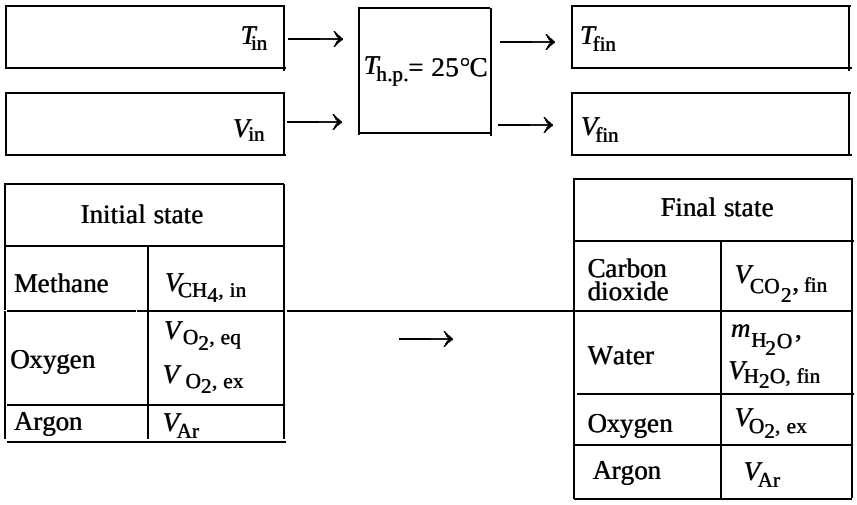

oxygen and combustion products is taken to be constant in the considered range of deviations (~0.1°C) of T_{in} and T_{fin} from 25°C.

(c) Evaporation or condensation of water present in combustion products in the liquid or gas phase as a result of the above deviation of temperature:

$$V_{H_2O}^{ph.tr} = (a_{T_{fin}} - a_{T_{in}}) V_{\Sigma}^{c.pr} q, \quad (7)$$

where q is the specific heat of the liquid←→vapor phase transition, 2.44 kJ g^{-1} at 25°C; and $V_{\Sigma}^{c.pr}$ is the total volume of gaseous combustion products.

The presented formulas for evaluating the effect of deviation of the temperatures of gases fed into the calorimetric cell and combustion products removed from the cell refer to the case of calorimeter operation in the batch mode. However, the continuous mode is preferable under industrial conditions, since it allows permanent control over the calorific value of gases. In this case, heat power P (W) should be substituted in the above equations instead of Q_j (J), and the respective gas flow rates G_j (l h^{-1}), instead of volumes V_j (l).

Let us consider burning of methane in the continuous mode at constant (2, 2.5, or 3.0 l h^{-1}) flow rate G''_{CH_4} of the gas (see scheme).

The flow rates of primary (G'_{O_2}) and secondary (G''_{O_2}) oxygen are chosen in accordance with the recommendations given in [13] and presented Table 1, which also lists the flow rates of the other gases.

To prevent additional condensation of water vapor or condensate evaporation, argon was fed into the burner simultaneously with methane and the whole amount of oxygen was preliminarily saturated with water vapor at 25°C. In methane burning at a flow rate of 2 l h^{-1}, a heat power of 22.13 W is to be released. As a result of the above-considered deviation of temperature (±0.10°C) from T_c = 25°C, a decrease or increase in the measured heat power will be $\pm 1.06 \times 10^{-3}$ W, which corresponds to a relative error of 5×10^{-3}%. The relative error will be the same at other methane flow rates (e.g., 3 l h^{-1}) if the mentioned relations between the flow rates of gases fed into the calorimeter are observed.

Thus, to confine the effect of deviations of the temperatures of gases fed into the calorimeter and combustion products discharged from the calorimeter to within 0.01%, it suffices to maintain this temperature deviation equal to, or less than 0.10°C.

From Tables 2 and 3 follows that about 50% of the correction is accounted for by evaporation or condensation of water, $\Delta P_{H_2O}^{ph.tr}$. And this occurs on the assumption that there is no water condensation due to a decrease in the volume of gaseous combustion products, compared with that of the gases entering the reaction.

Let us consider the conditions under which this assumption is valid. For this purpose, let us revert to the three possible gas burning conditions, but consider only two of these: (1) combustible gas and oxygen are completely saturated with water vapor at T = 25°C and (2) combustible gas and oxygen are completely dried. In doing so, we will take into account not only the humidity of the gas being burned, but also that of oxygen.

Variant 1. Let us take the methane flow rate to be

Table 1. Overall balance of gases and combustion products in relation to methane flow rate

Component	Parameter	Gas flow rate G_j, l h^{-1}		
		Initial state		
Methane	G_{CH_4}	2.00	2.50	3.00
Oxygen	$G_{O_2,eq}$	4.00	5.00	6.00
	$G_{O_2,\Sigma}$	6.00	7.50	9.00
	G'_{O_2}	1.00	1.20	1.50
	G''_{O_2}	5.00	6.30	7.50
Water vapor	$m^{298}_{H_2O,g}$	0.138 g h^{-1}	0.173 g h^{-1}	0.207 g h^{-1}
Argon	G_{Ar}	2.00	2.50	3.00
Total flow rate	$G_{\Sigma,h}$	10.00	12.50	15.00
		Final state		
Carbon dioxide	G_{CO_2}	2.00	2.50	3.00
Water (condensate)	$m^{con}_{H_2O}$	3.223 g h^{-1}	4.028 g h^{-1}	4.834 g h^{-1}
Water vapor	$m^{vap}_{H_2O}$	0.138 g h^{-1}	0.173 g h^{-1}	0.207 g h^{-1}
Oxygen	$G_{O_2,ex}$	2.00	2.50	3.00
Argon	G_{Ar}	2.00	2.50	3.00
Total gaseous combustion products	$G_{\Sigma,fin}$	6.00	7.50	9.00

Table 2. Input data for calculations [3, 14]

Component	Heat capacity C^0_P, J mol^{-1} K^{-1}	Molar volume (true) $V_0 \times 10^{-3}$, m^3	Molar mass M, kg kmol^{-1}
Methane	35.942	22.3600	16.043
Carbon dioxide	37.254	22.2569	44.010
Oxygen	29.307	22.3914	31.9988
Argon	20.704	22.3937	39.948
Water vapor	33.586	21.629	
Water	4.19 J g^{-1} K^{-1}		18.0152

Table 3. Correction for deviation of the temperature of gases fed into the calorimeter and combustion products discharged from it from T_c = 25°C. Methane flow rate 2 l h^{-1}

Heat power P, W	$T_{h.p.} - T_{in} = 0.10$, $T_{fin} - T_{h.p.} = 0.0$°C	$T_{h.p.} - T_{in} = -0.10$, $T_{fin} - T_{h.p.} = 0.0$°C	$T_{h.p.} - T_h = 0.0$, $T_{fin} - T_{h.p.} = 0.10$°C	$T_{h.p.} - T_{in} = 0.0$ $T_{fin} - T_{h.p.} = -0.10$°C
$\Delta P_{O_2,eq.}$	1.45×10^{-4}	-1.45×10^{-4}	0	0
$\Delta P_{O_2,ex}$	0.72×10^{-4}	-0.72×10^{-4}	0	0
ΔP_{CH_4}	0.89×10^{-4}	-0.89×10^{-4}	0	0
ΔP_{Ar}	0.51×10^{-4}	-0.51×10^{-4}	0.51×10^{-4}	-0.51×10^{-4}
$\Delta P^{vap}_{H_2O}$	0.16×10^{-4}	-0.16×10^{-4}	0.16×10^{-4}	-0.16×10^{-4}
ΔP_{CO_2}	0	0	0.93×10^{-4}	-0.93×10^{-4}
$\Delta P^{con}_{H_2O}$	0	0	3.74×10^{-4}	-3.74×10^{-4}
$\Delta P^{ph.tr}_{H_2O}$	0	0	5.29×10^{-4}	-5.29×10^{-4}
$\sum_{j=1}^{j=8} P$	3.73×10^{-4}	-3.73×10^{-4}	10.63×10^{-4}	-10.63×10^{-4}

2.5 l h^{-1} at an excess of oxygen equal to 50%. Both methane (G_{CH_4} = 2.5) and oxygen ($G_{O_2,\Sigma}$ = 7.5 l h^{-1}) are saturated with water vapor at T = 25°C. In this case, a water vapor flow ($G^{vap}_{H_2O}$ = 0.2304 g h^{-1}) is fed into the burner together with the mentioned gases (G_Σ = 10 l h^{-1}). At the same time, a water vapor flow ($G^{vap}_{H_2O}$ = 01152 g h^{-1}) is discharged from the calorimeter together with the combustion products, whose total flow rate is 5 l h^{-1}, including 2.5 l h^{-1} of $O_{2,ex}$ and 2.5 l h^{-1} of CO_2. Thus, the decrease in the combustion product volume leads to continuous condensation of excess water vapor, accompanied by additional heat power release $\Delta P^{ph.tr}_{H_2O}$ = 0.078 W. This additional heat power constitutes 0.28% of the heat power (27.66 W) released in combustion of methane delivered at a rate of 2.5 l h^{-1}. It is by this value that the measured combustion heats will be overestimated when not only methane, but oxygen, too, are completely saturated.

Variant 2. The flow rates of methane and oxygen remain the same. However, neither methane nor oxygen are saturated with water vapor, but are, contrastingly, subjected to complete drying. In this case, no water vapor is delivered to the burner with the given gases. However, we have at the calorimeter outlet, in addition to the formed CO_2 and excess amount of oxygen (with the flow rates of these two remaining equal to 5 l h^{-1}), also a water vapor flow discharged from the calorimeter at the same rate of 0.1152 g h^{-1} owing to saturation of these gases with water formed in methane combustion. It is by this value (0.28%) that the results of methane combustion heat measurements will be lower than its true value.

Variant 3. To eliminate the effect of changes in the volumes of combustion products on the results of combustion heat measurements, the following procedure is proposed: only the flow of oxygen (both primary and secondary) is saturated with water vapor, with the flow rates of methane (2.5 l h^{-1}) and oxygen (taken in 50% excess) remaining unchanged. However, an additional amount of dry argon with the flow rate equal to that of methane is delivered. The last two factors play the key role in the process under consideration.

Thus, the following flows are fed into the burner:

$$G_{\Sigma,\text{inlet}} = G_{CH_4} + G_{\Sigma,O_2,\text{inlet}} + G_{Ar} = 2.5 + 7.5 + 2.5 = 12.5 \text{ l h}^{-1}.$$

Together with these, a water vapor flow is delivered:

$$G_{H_2O,\text{inlet}} = aG_{\Sigma,O_2,\text{inlet}} = 0.02304 \times 7.5 = 0.1728 \text{ g h}^{-1}.$$

The flow of combustion products will be

$$G_{\Sigma,\text{out}} = G_{CO_2} + G_{O_2,ex} + G_{Ar} = 2.5 + 2.5 + 2.5 = 7.5 \text{ l h}^{-1}.$$

Together with this flow, a flow of water vapor is discharged:

$$G_{H_2O,\text{out}} = aG_{\Sigma,\text{out}} = 0.02304 \times 7.5 = 0.1728 \text{ g h}^{-1}.$$

In the proposed variant of gas feed into the burner, both water vapor condensation (as in Variant 1) and evaporation (loss) of water (as in Variant 2) can be completely eliminated.

These conditions served as a basis for a technique of gas burning, and it is these conditions that were taken into account in evaluating the effect of deviation of the temperatures T_{in} and T_{fin} from T_c = 25°C.

Thus, the developed technique for gas burning with the use of the designed isothermal calorimeter (1) enables continuous measurements of the combustion heat; (2) eliminates condensation of water vapor and evaporation of water, both of these resulting from changes in the volume of combustion products; and (3) reduces to a negligible minimum (<0.01%) the effect of differences between the heat capacities of gases at the inlet and outlet of the calorimeter at deviation of the temperatures of these gases and combustion products by less than ±0.10°C from 25.00°C.

Continuous measurements are enabled by using modern electronic units for control over mass flow rates of gases. The most stringent requirements are imposed on the flow rate control unit of the combustible gas. The optimal case is that when the flow rate control units ensure for the combustible gas an error of no more than 0.05% at gas flow rates in the range 1–4 l h^{-1}. It suffices to maintain the flow rates of the other gases constant with an error of no more than 1%.

To implement the proposed technique, the calorimeter was equipped with a unit for gas preparation and processing, which included electronic flow rate controllers for the combustible gas, primary oxygen, secondary oxygen, and argon; vessels for saturation of primary and secondary oxygen with water; and four heat exchangers in a thermostat, used for thermostating at 25°C of each of the above-mentioned four

Table 4. Heat power released in calorimeter in methane combustion. Methane flow rate 2.5009×10^{-3} m^3 h^{-1}

P_{in}	P_{run}	P_Q	Combustion heat H_V^{calc}, kW h m^{-3}
W			
51.348	23.706	27.642	11.053
51.457	23.793	27.664	11.062
52.374	24.713	27.661	11.060
52.276	24.526	27.750	11.096

gases prior to their being delivered to the combustion chamber.

To ensure complete saturation at 25°C, both oxygen flows (primary and secondary) were preliminarily saturated with water vapor at 40–50°C prior to being delivered into the thermostat. The temperature of the combustion products at the calorimeter outlet was maintained constant in such a way that its deviation from 25.00°C did not exceed 0.10°C.

The combustion heat of methane was measured with pure (no worse than 99.95%) methane purchased from Linde Co. in a 40-l cylinder.

The gas flow rate was controlled by electronic control units manufactured by Bronkhorst High-Tech BV. The control unit for methane was additionally calibrated at a single point (50%) using a primary gas flow rate standard. At this point, the mass flow rate was found to be, according to 10 measurements, 4.9844×10^{-4} g s^{-1}, and the volumetric flow rate, calculated with account of the methane density of 0.7175 kg m^{-3} under normal conditions, was 2.5009×10^{-3} m^3 h^{-1}. The calibration uncertainty was 0.17%. The measurement conditions were as follows:

Controlled temperature T_{contr}	24.900 ± 0.001
Current passed through Peltier elements, I_P, A	1.20 ± 0.0001
Temperature of hot junctions of these elements (T_P)	25.00 ± 0.002
Temperature of gases at calorimeter inlet, T_g	25.00 ± 0.002
Temperature of combustion products at outlet, $T_{comb.pr}$	25.0 ± 0.1
Methane flow rate G_{CH_4}, m^3 h^{-1}	2.5009×10^{-3}
Flow rate of primary oxygen, G'_{O_2}, saturated with H_2O, m^3 h^{-1}	1.00×10^{-3}
Flow rate of secondary oxygen, G''_{O_2}, saturated with H_2O, m^3 h^{-1}	5.00×10^{-3}
Flow rate of dry argon, G_{Ar}, m^3 h^{-1}	2.50×10^{-3}

With the data of Table 4 used, the average methane combustion heat H_V^{calc} was found by means of the equation $H_V^{calc} = P_Q/G_{CH_4}$ to be 11.068 kW h m^{-3} with a standard deviation of 0.009 kW h m^{-3}, or 0.08%.

A calculation of the uncertainty of this result, done in conformity with international recommendations [15], demonstrated that (1) the uncertainty u_A, calculated following pattern A and numerically equal to the standard deviation, was 0.009 kW h m^{-3}, or 0.08%; (2) the uncertainty u_B, calculated following pattern B, was 0.011 kW h m^{-3}, or 0.10%; (3) the total standard uncertainty, calculated by the formula $u_C = (u_A^2 + u_B^2)^{1/2}$, was 0.014 kW h m^{-3}, or 0.13%.

The deviation of the obtained combustion heat of methane (11.068 kW h m^{-3}) from the value recommended by ISO 6976:96 (11.064 kW h m^{-3}) was as small as 0.004 kW h m^{-3}, or 0.04%.

CONCLUSIONS

(1) The proposed method does enable absolute measurements of the combustion heat, i.e., those requiring no calibration (electrically or with pure methane).

(2) The developed design of an isothermal gas calorimeter makes it possible to measure the heat power released in gas combustion without any significant systematic errors (≤0.01%).

(3) The developed technique for measuring the gas combustion heat is used with all requirements following from the definition of this quantity satisfied. No corrections are to be introduced into the measured heat power, the determined combustion heat is in agreement with the combustion heat of real gas.

(4) The error in measurement of the combustion heat of methane was 0.04%, and the uncertainty of the measured methane combustion heat, 0.13%. This value can be reduced by improving the accuracy of determining the amount of burnt gas.

REFERENCES

1. Aleksandrov, Yu.I. and Varganov, V.P., *Zh. Prikl. Khim.*, 2001, vol. 74, no. 9, pp. 1484–1488.
2. Aleksandrov, Yu.I., Varganov, V.P., and Sarge, S., *Zh. Prikl. Khim.*, 2001, vol. 74, no. 9, pp. 1488–1493.
3. *ISO/DIS 6976:1996: Natural Gas—Calculation of Calorific Value, Density, Relative Density and Wobbe*

Index from Composition, Geneve (Switzerland): Int. Organisation for Standardization, 1996.

4. *GOST* (State Standard) *30319.0–96: Natural Gas. Methods for Property Calculations*, Moscow: Izd. Standartov, 1997.
5. *ISO/CD 13443:1993: Natural Gas—Standard Reference Conditions*, Geneve (Switzerland): Int. Organisation for Standardization, 1993.
6. *GOST* (State Standard) *21261–75: Petroleum Products. Methods for Determining Specific Heat of Combustion*, Moscow: Izd. Standartov, 1985.
7. *GOST* (State Standard) *147–95 (ISO 1928–76): Solid Mineral Fuel. Determining the Highest and Calculating the Lowest Heat of Combustion*, Minsk: Izd. Standartov, 1995.
8. *GOST* (State Standard) *22667–95: Natural Combustible Gases. Method for Calculation of Combustion Heat, Density, Relative Density, and Wobbe Index from Gas Composition*, Moscow: Izd. Standartov, 1995.
9. *GOST* (State Standard) *27193–86: Natural Combustible Gases. Method for Determining Combustion Heat with Water Calorimeter*, Moscow: Izd. Standartov, 1987.
10. *GOST* (State Standard) *30319.1–96: Natural Gas. Methods for Calculation of Physical Properties. Determining the Physical Properties of Natural Gas, Its Components, and Products of Its Processing*, Moscow: Izd. Standartov, 1997.
11. *DIN 51857–1994: Gasförmige Brennstoffe und sonstige Gase, Berechnung von Brennwert, Heizwert, Dichte, relative Dichte und Wobbeindex von Gasen und Gasgemischen*, 1994.
12. Cerbe, G., *Grundlagen der Gastechnik*, München: Carl Hauser, 1992, 4th ed.
13. Pittam, D.A. and Pilcher, G., *J. Chem. Soc., Faraday Trans. 1*, 1972, vol. 68, pp. 2224–2226.
14. *Physical Properties of Natural Gases*, Geerssen, T.M., Ed., Groningen (Netherlands): N.V. Nederlandse Gasunie, 1988.
15. *MI* (Methodical Instructions) *2552–99: Recommendations of the State Measurement Service. Use of the "Guide to Expression of Uncertainty in Measurements,"* St. Petersburg: Vseross. Nauchno-Issled. Inst. Metrologii im. D.I. Mendeleeva, 1999.

Russian Journal of Applied Chemistry, Vol. 74, No. 9, 2001, pp. 1546–1550. Translated from Zhurnal Prikladnoi Khimii, Vol. 74, No. 9, 2001, pp. 1500–1504.

MACROMOLECULAR CHEMISTRY AND POLYMERIC MATERIALS

Development of Synergistic Stabilizing Compositions for Polyolefins and Evaluation of Their Performance

M. V. Borisova, L. K. Fazlieva, Zh. Fokkho, M. A. Promyshlennikova, E. N. Cherezova, A. D. Khusainov, and N. A. Mukmeneva

Kazan State Technological University, Kazan, Tatarstan, Russia

Received December 18, 2000; in final form, July, 2001

Abstract—A series of new synergistic polyfunctional stabilizing compositions phenol–phosphite for polyolefins were developed. Their performance as antioxidants, color stabilizers, and agents preventing thermomechanical degradation was quantitatively evaluated.

Despite numerous papers published in the field of polymer stabilization [1, 2], search for effective stabilizers remains an urgent problem. Growing attention is given to synergistic mixtures of stabilizers, i.e., to mixtures whose performance under certain conditions exceeds the additive value. Of particular importance are papers aimed at search for synergist intermediates of antioxidation processes, since specifically these processes are most often responsible for preservation of valuable physicochemical properties of polymers [3, 4].

According to the existing theory [5], the most effective compositions inhibiting polymer oxidation are those in which one of the components terminates oxidation chains be decomposing hydroperoxides and the other reacts with peroxy radicals to form inactive products. It is known that phenolic stabilizers inhibit polymer oxidation by decomposing peroxy radicals, and phosphites decompose hydroperoxides [5]. Furthermore, phosphite-containing stabilizing compositions exhibit one more valuable property: they preserve the polymer color in storage, processing, and service, which is very important for production of competitive items [6].

In this work we studied a series of new stabilizing phenol–phosphite mixtures.

EXPERIMENTAL

As phenolic oxidation inhibitors we tested Irganox 1010 (**I**, ester of pentaerythritol and 2,6-di-*tert*-butyl-4-hydroxyphenylpropionic acid, mp 120°C), Agidol 2 [**II**, 2,2-methylenebis(4-methyl-6-*tert*-butylphenol), mp 128–129°C], and Agidol 5 (**III**, 4,4'-dihydroxy-3,3',5,5'-tetra-*tert*-butyldiphenyl, mp 180–181°C).

As organophosphorus component we tested a new stabilizer, Stafor 24 [**IV**, tris(2,4-di-*tert*-butylphenyl) phosphite, mp 175–183°C) [7].[1]

Tests were performed with high-density polyethylene (HDPE) of 289-73 grade [TU (Technical Specifications) 6-05-1870-804) and polypropylene (PP) (TU 2211-015-00203521–95).

The antioxidative performance of the stabilizers was evaluated by the duration of the induction period of oxidation in oxygen [8] under rigorous conditions: 165°C for PP and 195°C for HDPE.

The color stability of the polymers in the course of oxidation in air (PP at 165°C and HDPE at 195°C) was evaluated in a 10-point color scale (white, 1; black, 10).

The efficiency of thermomechanical stabilization was evaluated from variation of the torque M_t in time [9].

The tensile strength of the polymers was evaluated as described in [10]. A polymer sample subjected to thermomechanical degradation was subjected to single sheeting with laboratory rollers (clearance 1.5–2 mm), after which 20–30-mm strips were cut. These strips were subjected to extrusion on the extrusion machine of a Brabender plasticorder with a stock worm diameter of 20 mm and a length-to-diameter ratio of 22 : 1. Samples were formed with a slit head 50 mm wide at a rotation rate of 60 rpm and the following zone tem-

[1] The commercial synthesis procedure was developed at the Kazan State Technological University; the production was mastered at the Kazan'orgsintez Joint-Stock Company.

1070-4272/01/7409-1546$25.00

Table 1. Induction period of oxidation τ, color of PP and HDPE, synergism *S*, and practical synergism S_{pr} in the presence of tested stabilizers (p_{O_2} = 250 mm Hg)

Stabilizer	Content, wt %	τ, min	*S*	S_{pr}	Color, points	
					initial	in 3 h
Polypropylene (165°C)						
–	–	20			1	3
I	0.2				1	2
II	0.2	100			1	7
	0.3	150			1	7
III	0.2	40			2	6
	0.3	100			2	4
IV	0.2	20			1	3
	0.3	30			1	2
I + **IV**:						
2 : 1	0.2	180	0.50	1.80	1	2
1 : 1	0.2	150	0.88	2.50	1	1
1 : 2	0.2	80	0.14	1.60	1	1
3 : 2	0.2	210	1.33	2.92	1	1
2 : 3	0.2	135	0.80	2.45	1	1
II + **IV**:						
2 : 1	0.2	70	0.27	0.92	1	2
1 : 1	0.2	70	0.13	1.16	1	2
1 : 2	0.2	30	0.53	0.68	1	2
II + **IV**:						
2 : 1	0.3	100	0.16	1.00	1	1
1 : 1	0.3	110	0.25	1.65	1	2
1 : 2	0.3	80	0.18	1.74	1	1
III + **IV**:						
2 : 1	0.2	80	0.54	2.50	2	4
1 : 1	0.2	60	0.30	2.31	2	3
1 : 2	0.2	40	0.09	1.66	2	3
2 : 1	0.2	100	0.66	2.50	2	3
1 : 1	0.3	80	0.82	3.30	2	3
1 : 2	0.3	60	0.50	3.00	2	3
High-density polyethylene (195°C)						
–	–	20			1	3
I	0.2	225			1	2
II	0.2	180			1	5
III	0.2	125			2	4
	0.3	–			2	
IV	0.2	40			1	3
I + **IV**:						
2 : 1	0.2	280	0.65	1.86	1	1
1 : 1	0.2	230	1.10	2.50	1	1
1 : 2	0.2	150	0.30	2.00	1	1
3 : 2	0.2	310	0.88	2.30	1	1
2 : 3	0.2	210	0.91	2.30	1	1
II + **IV**:						
2 : 1	0.2	210	0.38	1.59	1	3
1 : 1	0.2	185	0.54	1.80	1	2
1 : 2	0.2	170	0.88	2.50	1	2
III + **IV**:						
2 : 1	0.2	140	0.66	2.19	2	3
1 : 1	0.2	120	1.00	3.00	2	3
1 : 2	0.2	100	1.17	4.16	2	2
3 : 2	0.2	150	1.08	2.08	2	2
2 : 3	0.2	120	0.35	2.19	2	2

Table 2. Torque M_t and temperatures of PP and HDPE 289-73 in the course of processing in a Brabender plasticorder in the presence of various stabilizers (rotor rotation rate 90 rpm)

Stabilizer	Content, wt %	Processing time, min					
		6		12		15	
		M_t, N m	T, °C	M_t, N m	T, °C	M_t, N m	T, °C
Polypropylene (initial processing temperature 180°C)							
–	–	14.0	218	10.0	220	9.0	220
I	0.10	16.50	213	15.0	220	14.50	222
	0.15	15.25	212	13.60	222	13.55	218
	0.20	15.25	210	13.75	217	13.60	218
	0.25	14.50	215	13.10	220	12.75	219
IV	0.10	14.75	219	13.75	222	13.0	222
	0.15	15.25	216	13.25	220	12.90	221
	0.20	14.75	212	13.35	218	13.20	218
	0.25	14.50	217	13.50	220	13.40	220
I + **IV**,	0.10	17.25	210	14.0	218	13.75	215
3 : 2	0.15	16.25	210	13.60	217	13.45	218
	0.20	14.73	212	12.50	219	12.85	219
	0.25	15.0	213	13.55	219	13.25	219
High-density polyethylene (initial processing temperature 190°C)							
–	–	27.0	190	25.50	198	25.0	199
I	0.10	28.50	190	27.80	204	27.0	210
	0.15	28.25	198	29.40	219	29.0	222
	0.20	28.40	198	26.0	205	25.30	207
	0.25	30.60	199	28.90	210	28.0	212
IV	0.10	26.0	184	25.0	200	24.0	210
	0.15	28.85	197	29.40	208	26.0	211
	0.20	26.0	195	25.0	209	25.0	211
	0.25	28.45	197	25.50	207	26.75	211
I + **IV**,	0.10	26.60	199	25.15	208	24.75	210
3 : 2	0.15	30.30	199	27.80	212	26.90	215
	0.20	29.15	199	26.70	209	25.90	214
	0.25	29.65	198	27.05	212	25.80	215

peratures (°C): for PP, feed 170 (T_1), mixing 190 (T_2), plastication 210 (T_3), and head 200 (T_4); for HDPE, T_1 150, T_2 170, T_3 190, and T_4 180. The extruded material was fed to the receiving transporter and pressed with a 2-kg drum. From the resulting strips, blades were cut for strength determination.

We found that, among the individual antioxidants, the longest induction periods of polymer oxidation were obtained with Irganox 1010 (**I**) (Table 1). Agidol 2 (**II**) is somewhat inferior to Irganox 1010. Agidol 5 (**III**) has a high lower critical concentration and does not ensure the required stability at a dosage less than 0.2 wt %. The required stabilizing effect is attained only at an Agidol 5 dosage of 0.3 wt %. The induction periods of polyolefin oxidation appreciably increase when phenol–phosphite mixtures are added (Table 1), i.e., a synergistic effect is observed.

The synergistic effect of inhibitor mixtures [8] was quantitatively characterized by the practical synergism S_{pr} defined as

$$S_{pr} = \tau_m/\tau_1^0,$$

(τ_1^0 is the induction period of polymer oxidation in the presence of the more effective component added in the molar concentration taken for the inhibitor mixture) and by the synergism S defined as

$$S = \frac{\tau_m - (\tau_1 - \tau_2)}{\tau_1 + \tau_2},$$

where τ_m is the induction period of polymer oxidation in the presence of the inhibitor mixture; τ_1 and τ_2 are those in the presence of the respective inhibitors taken separately in the concentrations corresponding to their mole fraction in the mixture.

A combination of synergism and practical synergism allows fairly adequate characterization of the performance of antioxidant mixtures.

In all cases phenol–phosphite mixtures exerted a stabilizing effect on the polymer color in the course of oxidation, although Agidol 5 imparts a yellowish initial color to the polymer (Table 1).

Experimental data clearly demonstrate the high performance of the Irganox 1010–Stafor 24 mixture. The highest synergistic effect is observed at a component ratio of 3 : 2.

This mixture, along with the antioxidative performance, was tested for the capability to prevent thermomechanical degradation of the polymer. The stabilizing effect against thermomechanical degradation was evaluated from the variation of the torque with time, monitored with a Brabender plasticorder. Since the torque, at equal other conditions, is determined by the molecular weight of the polymer [9], there is a direct relationship between the degree of degradation and torque (a sample that is more resistant to thermomechanical degradation will show a higher torque after treatment for a given time) and hence the strength characteristics of the polymer.

In Table 2 are given the torques of PP and HDPE after processing for 6, 12, and 15 min in a Brabender plasticorder in the absence and in the presence of stabilizers. The time at which the torque was recorded was determined by the residence time of polymers in the mixing chamber in production of thermoelastoplastics from the polyolefins in hand.

Addition of Irganox 1010 (**I**), Stafor 24 (**IV**), or their mixtures has no significant effect on the torque at the initial instant of time. As the time of thermomechanical degradation of the polymers is increased (12–15 min), the torque of the stabilized samples becomes significantly different from that of the control sample without stabilizers. Polypropylene and HDPE containing **I** and **IV** are considerably more resistant to thermomechanical degradation, as seen from data on M_t. The temperature in the chamber remains at the same level.

In parallel, we tested these polymers for the tensile strength, since the degree of the polymer degradation directly correlates with the polymer strength. Figures 1a and 1b show that a mixture of **I** and **IV** ensures preservation of the strength of PP and HDPE at higher level as compared to the stabilizers taken separately, which is apparently due to the synergistic effect detected in thermal oxidation. The optimal content of the stabilizing composition is 0.2 wt %.

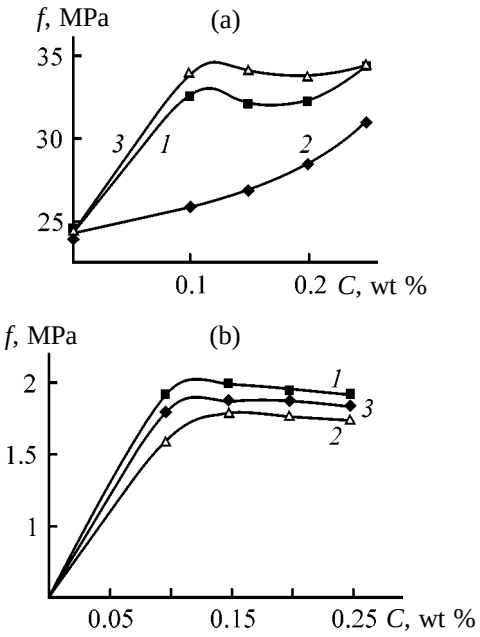

Fig. 1. Tensile strength f of (a) PP and (b) HDPE 289-73 after thermomechanical degradation in a Brabender plasticorder as a function of the stabilizer content C. Stabilizer: (*1*) **I**, (*2*) **IV**, and (*3*) **I** + **IV** (3 : 2).

Thus, new stabilizing compositions phenol–phosphites (Stafor 24) show promise as means to enhance the resistance of polyolefins to oxidative and thermomechanical degradation.

REFERENCES

1. Gurvich, Ya.A., Kumok, S.T., Lopatin, V.V., and Starikova, O.F., *Fenol'nye stabilizatory, sostoyanie i perspektivy: Obzornaya informatsiya* (Phenolic Stabilizers, State and Prospects: Review), Moscow: Tsentr. Nauchno-Issled. Inst. Inform. i Tekhniko-Ekon. Issled. Neftepererab. i Neftekhim. Prom–sti., 1990, no. 5.
2. Moiseev, V.V., Kosovtsev, V.V., Polukhin, A.N., and Poluektov, I.T., *Kauchuk Rezina*, 1991, no. 1, pp. 10–13.
3. Kondratov, S.A. and Maslosh, V.Z., *Zh. Prikl. Khim.*, 1996, vol. 69, no. 3, pp. 470–473.
4. Denisov, E.T. and Azatyan, V.V., *Ingibirovanie tsepnykh reaktsii* (Inhibition of Chain Reactions), Chernogolovka: Ross. Akad. Nauk, 1997.

5. Emanuel', N.M. and Buchachenko, A.L., *Khimicheskaya fizika stareniya i stabilizatsii polimerov* (Chemical Physics of Aging and Stabilization of Polymers), Moscow: Nauka, 1982.
6. Mukmeneva, N.A., Stabilization of Polymer Color with Organic Phosphites, *Doctoral Dissertation*, Kazan, 1980.
7. RF Patent 2 152 396.
8. Piotrovskii, K.B. and Tarasova, Z.N., *Starenie i stabilizatsiya kauchukov i vulkanizatov* (Aging and Stabilization of Rubbers and Vulcanizates), Moscow: Khimiya, 1980.
9. Vol'fson, S.I., Karp, M.G., Gidiyatullin, M.M., and Garifullin, F.A., *Kauchuk Rezina*, 1989, no. 9, pp. 13–16.
10. Okhotina, N.A., *Osnovnye metody fiziko-mekhanicheskikh ispytanii elastomerov: Metodicheskie ukazaniya k laboratornomu praktikumu* (Main Methods for Physicomechanical Tests of Elastomers: Methodical Instructions to Practical Laboratory Course), Kazan: Kazan. Gos. Tekhnol. Univ., 1995.

Russian Journal of Applied Chemistry, Vol. 74, No. 9, 2001, pp. 1551–1553. Translated from Zhurnal Prikladnoi Khimii, Vol. 74, No. 9, 2001, pp. 1505–1507.

MACROMOLECULAR CHEMISTRY AND POLYMERIC MATERIALS

Polyurethane Binders for Condensed High-Energy-Content Systems

V. V. Bestuzheva, N. K. Nalimova, and I. V. Tselinskii

St. Petersburg State Technological Institute, St. Petersburg, Russia

Received May 10, 2001

Abstract—A procedure was developed for preparing poly(ethylene, butylene) glycol adipate urethane plasticized with 1,5-diazido-3-nitrazapentane. The correlation between the conditions of the polymer synthesis and its physicomechanical properties was studied, and the prospects for using the product as a component of condensed high-energy-content systems were evaluated.

Because of the specific features of preparation and use of mixed solid propellants (MSPs), the polymeric combustible binders used as their components should exhibit a wide set of difficultly compatible properties. The most important of them are high levels of energetic and physicomechanical parameters, operation at both positive and negative temperatures, low initial viscosity, and the capability to polymerize at moderate temperatures.

During the progress of rocket engineering, several generations of MSPs have changed. These MSPs were based on polyurethanes [1–3]. An interest in polyurethanes as MSP components is due to the possibility of controlling their characteristics by varying the nature and ratio of the reactants (mainly polyesters and diisocyanates) involved in the elastomer formation [4].

With time, the possibilities of traditional polyurethanes with respect to energetic characteristics became exhausted, and efforts were made for their modification. As a rule, the modification involved introduction of high-energy-content groups (nitro, nitrato, azido) into the polyester moiety of the macromolecule or plasticization of hydrocarbon polyurethane elastomers with high-energy-content compounds, mainly with nitrate esters of polyhydric alcohols [5].

One of the major principles of formulating propellants of a new generation is decreasing the content of toxic and smoke-forming elements in the combustion products. Such elements give rise to environmental problems, reveal the missile on the flight trajectory, and comlicate the use of modern optical, laser, and infrared guidance means. From the viewpoint of the composition of combustion products, of particular interest among high-energy-content compounds are azides. A combination in a binder formulation of the advantages of polyurethanes with the possibilities of azide compounds appreciably improves the principal service characteristics of MSPs based on such binders.

In this work we studied the conditions for preparing poly(ethylene, butylene) glycol adipate urethane plasticized with 1,5-diazido-5-nitrazapentane within a single process by the reaction of urethane formation in a medium of the low-viscosity plasticizer. Improvement of combustible polyurethane binders by their plasticization seems to be one of the most promising routes, because the raw materials are available and the existing production facilities are suitable for the process.

EXPERIMENTAL

The choice of the initial components was governed by their energetic performance, availability, and expected capability to ensure the highest possible level of physicomechanical properties of the products.

As hydroxy component we chose P6-BA linear polyester, which is prepared by reaction of ethylene and butylene glycols with adipic acid, following a common pattern of polycondensation of dihydric alcohols with dibasic acids [6]. We took into account the facts that polyesters, as compared to polyethers, form more robust macromolecules in reactions with diisocyantes; that the molecular weight of the hydroxy component plays a decisive role in formation of elastic properties; and that bifunctional polyesters, as compared to trifunctional compounds, can giver a wider set of three-dimensional structures owing to the use of

1070-4272/01/7409-1551$25.00

Table 1. Properties of plasticized polyurethanes as influenced by the structure and concentration of diisocyanate*

Diisocyanate	NCO/OH ratio	*X*, MPa	ε, %
HMDI	1.1	0.21	1130
	1.2	0.25	1180
	1.3	0.28	1400
	1.4	0.28	1430
TDI	1.1	0.27	690
	1.2	0.45	960
	1.3	0.58	1290
	1.4	0.54	1110
MDI	1.1	0.23	600
	1.2	0.27	610
	1.3	0.34	750
	1.4	0.36	750

* Plasticizer content 50 wt %, triol mole fraction 0.3, catalyst DBTDL (0.3 wt %).

cross-linking additives. The characteristics of P6-BA were as follows: *M* 2000, density 1200 kg m^{-3}, enthalpy of formation –4300 kJ kg^{-1}; prior to reaction with the diisocyanate the oligomer was dried to a moisture content no higher than 0.04 wt %.

The following diisocyanates, purified by distillation, were used: aliphatic hexamethylene diisocyanate (HMDI), aromatic 2,4-toluylene diisocyanate (TDI), and alkylaromatic 4,4'-methylenebis(phenyl isocyanate) (MDI).

As cross-linking agents we used glycerol (Gl) and trimethylolpropane (TMP), which were preliminarily dried over P_2O_5, and as catalyst, dibutyltin dilaurate (DBTDL).

As plasticizer we used 1,5-diazido-3-nitrazapentane (AP) purified chromatographically in a column packed with OU activated carbon of grade A; the properties of the compound were as follows: refractive index at 20°C 1.5260, density 1330 kg m^{-3}. bp 124°C/5 Pa, enthalpy of formation 2490 kJ kg^{-1} [7].

The procedure for preparing plasticized polyurethanes was as follows: A sample of the polyester was heated in a vacuum at 110°C to remove moisture and then cooled to 60°C, after which the required amounts of the diisocyanate, triol, and catalyst were added. After mixing of the components, the plasticizer was added, and the mixture was kept under the same conditions for 15–20 min and then either kept in sealed fluoroplastic molds at 60 ± 2°C for 10 days to obtain polyurethane samples for tests or transferred into a mixer to prepare the fuel compound.

The cured polyurethanes were tested by generally accepted procedures: the ultimate tensile strength and the relative elongation were determined according to GOST (State Standard) 269–66, the glass transition point, according to GOST 12254–66, and the density, according to GOST 267–73. The enthalpy of formation was calculated from the structural formulas of the compounds taking into account thermodynamic corrections for specific groups and bonds [8].

The shock sensitivity was evaluated with a K-44-II impact machine by the lower limit in device no. 2; the friction sensitivity, with a K-44-III pendulum impact machine; and the gas release at static heating, with a Burdon gage.

The goal of this study was to obtain in a single process polymeric plasticized binders with a high level of energetic properties and satisfactory physicomechanical characteristics. For this purpose, it was necessary to reveal the qualitative and quantitative composition of the polymeric component ensuring formation of a maximally strong three-dimensionally cross-linked matrix capable of retaining the maximal amount of the plasticizer.

For tentative quantitative evaluation of the extent of thermodynamic compatibility of the chosen polymer and plasticizer, we prepared a cured polyurethane by reaction of poly(ethylene, butylene) glycol adipate with TDI in the presence of TMP (molar ratio P6-BA : TMP = 70 : 30, NCO : OH = 1 : 1). For this product we determined the limiting content of the plasticizer by equilibrium swelling [9]. We found that the system under consideration preserves its physical stability at 20°C at an azide content of up to 69.8 wt %. Since in what follows we used a procedure involving formation of the macromolecular matrix under conditions when the plasticizer was present in the reaction medium, which ensured more favorable spatial distribution of the solid and liquid phases, we expected that the structure formed in this case would be no less stable thermodynamic ally.

However, before synthesizing compounds with the maximal plasticizer concentration, it was necessary to optimize their physicomechanical parameters depending on the nature and ratio of the reactants forming the polymeric matrix.

To determine how the ultimate tensile strength *X* and relative elongation ε of the plasticized polyurethane are influenced by the nature and amount of the diisocyanate used, we prepared elastomers whose composition and properties are listed in Table 1.

When the ratio of the isocyanate and hydroxy groups in the reaction mixture is less than 1.1, mech-

anically strong samples cannot be prepared under the chosen curing conditions, irrespective of the nature of the diisocyanate. At the molar excess of the diisocyanate increased to 1.3, both the strength and elasticity of polyurethanes increase. Further increase in the NCO : OH ratio have no noticeable positive effect. The best physicomechanical properties, under equal other conditions, are attained with TDI; with HMDI and MDI the results are worse.

Our results show that, to prepare elastomers with the required set of properties, it is appropriate to use toluylene diisocyanate and take it in a 30% molar excess relative to the polyester.

The effect of cross-linking agents on the physicomechanical characteristics of the combustible binders is seen from Table 2.

The polyurethanes prepared with TMP surpass in the strength and elastic parameters the samples prepared with glycerol as the cross-linking additive; the optimal mole fraction of triol relative to a total of hydroxyl-containing agents, when urethane synthesis is performed in the medium of the chosen plasticizer, is 0.30–0.35.

Our next goal was preparation of physically stable elastomers containing an increased amount of the plasticizer. In Table 3 are given data characterizing, along with the strength and elasticity, also the density (ρ), frost resistance (T_g), and enthalpy of formation (ΔH) of polyurethanes containing bound AP (50–75 wt %).

The shock sensitivity of the cured samples (fall of a 10-kg load from a height of 250 mm) is 20–30% depending on the plasticizer content. The gas release at 60°C in 20 days does not exceed 5 $cm^3\ kg^{-1}$.

Thus, the main energetic and service parameters of the plasticized polymers prepared make them promising as MSP components.

CONCLUSIONS

(1) By directed formation of a three-dimensional polymer network, it is feasible to prepare in one process thermodynamically stable poly(ethylene, butylene) glycol adipate urethane modified with 50–75% 1,5-diazido-3-nitrazapentane.

(2) The high-strength elastic matrix ensures the required set of physicomechanical properties, and the azido nitro plasticizer, the high energy content and favorable composition of the combustion products. These factors make the developed compounds promising as combustible binders for mixed solid propellants.

Table 2. Properties of plasticized polyurethanes as influenced by the structure and concentration of triol*

Triol	Triol mole fraction	X, MPa	ε, %
TMP	0.20	0.24	640
	0.30	0.58	1290
	0.35	0.60	1320
	0.40	0.58	1280
Gl	0.20	0.30	650
	0.30	0.39	1210
	0.35	0.45	1250
	0.40	0.40	1250

* Plasticizer content 50 wt %, catalyst DBTDL (0.3 wt %).

Table 3. Properties of polyurethanes as influenced by the plasticizer content*

Content, wt %	X, MPa	ε, %	ρ, kg m^{-3}	T_g, °C	ΔH, kJ kg^{-1}
50	0.60	1320	1260	–71	–64
55	0.57	1360	1270	–77	–328
60	0.36	890	1275	–80	–14
65	0.34	870	1280	–82	+299
70	0.28	820	1290	–82	+612
75	0.15	800	1295	–84	+925

* Mole fraction of triol (TMP) 0.33, catalyst DBTDL (0.3 wt %).

REFERENCES

1. Axelrood, S.L. and Frisch, K.C., *J. Abb. Age*, 1960, vol. 88, no. 3, pp. 465–471.
2. Chi Minn-Shong, *Am. Chem. Soc. Polym. Prepr.*, 1981, vol. 22, no. 2, pp. 191–192.
3. Henke, K., Bonlein-Maub, J., and Schubert, N., *Propellants, Explos., Pyrotech.*, 1996, vol. 21, no. 1, pp. 139–144.
4. Saunders, J.H. and Frish, K.C., *Polyurethanes. Chemistry and Technology*, part 1: *Chemistry*, New York: Interscience, 1962.
5. Chi Minn-Shong, *Am. Chem. Soc. Polym. Prepr.*, 1981, vol. 22, no. 2, pp. 193–194.
6. Losev, I.P. and Trostyanskaya, E.B., *Khimiya sinteticheskikh polimerov* (Chemistry of Synthetic Polymers), Moscow: Khimiya, 1964.
7. Yuxiang Ou, Boren Chen, and Hong Yan, *J. Propul. Power*, 1995, vol. 2, no. 4, pp. 838–847.
8. Avakyan, G.A., *Raschet energeticheskikh i vzryvchatykh kharakteristik VV* (Calculation of Energetic and Explosive Characteristics of Explosives), Moscow: Voenno-Inzh. Akad., 1964.
9. Reikhsfel'd, V.O., Erkova, L.N., and Ruban, V.A., *Laboratornyi praktikum po sinteticheskim kauchukam* (Practical Laboratory Course of Synthetic Rubbers), Moscow: Khimiya, 1967.

Russian Journal of Applied Chemistry, Vol. 74, No. 9, 2001, pp. 1554–1558. Translated from Zhurnal Prikladnoi Khimii, Vol. 74, No. 9, 2001, pp. 1508–1512.

MACROMOLECULAR CHEMISTRY AND POLYMERIC MATERIALS

Regiospecificity of Reactions of Vinyl Chloride–Maleic Anhydride Copolymer with Dimethylformamide

M. S. Safronova, E. M. Berezina, G. A. Terent'eva, E. B. Chernov, and A. G. Filimoshkin

Tomsk State University, Tomsk, Russia

Received January 26, 2001

Abstract—Interaction of macromolecules of vinyl chloride–maleic anhydride copolymer with dimethylformamide molecules was studied by kinetic, thermodynamic, and spectroscopic methods.

Polymers and copolymers of maleic anhydride exhibit a wide spectrum of valuable properties and show much promise. For example, copolymers of maleic anhydride (MA) with vinyl chloride (VC) readily enter into various reactions and are convenient initial substances for synthesis of new copolymers used as carriers for biologically active substances and enzymes, ion exchangers, photographic and pharmaceutical materials, blowing agents, lubricants, etc. [1, 2].

Macromolecules of VC–MA copolymer in organic solvents exhibit cyclic anhydride–enol tautomerism (CAET) with spontaneous formation from VC and anhydride (an) units of enol (en) and dienol (den) units [3, 4]:

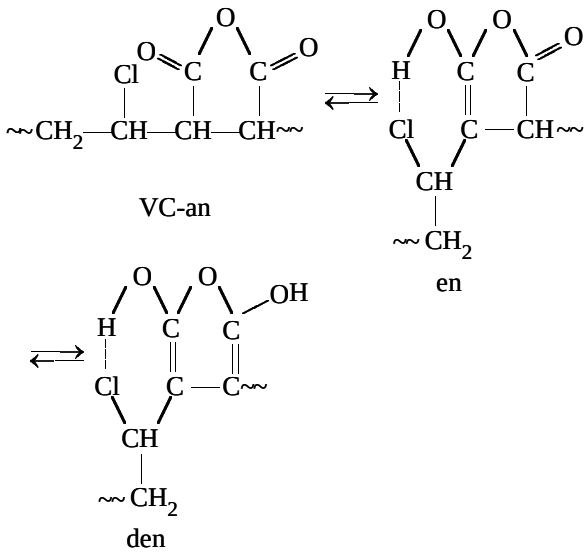

The latter species, for example, instantaneously react with sodium azide in dimethylformamide (DMF) to form structures that immediately decompose, acting as intermediates in dehydrochlorination of VC–MA [5].

Dimethylformamide as bipolar aprotic solvent is widely used in industry, scientific research, and laboratory practice. Interaction of VC–MA with DMF is of scientific and practical interest. VC–MA copolymer readily dissolves in DMF; within 10–15 min, the solution becomes colored, and two new overlapping absorption bands (λ_{max} 530 and 560 nm) appear in the electronic spectra. The optical density of these bands reaches a maximum in several hours and remains constant for 5 days, which suggests formation of stable solvation complexes of DMF molecules and en and den tautomers [6]. At the same time, evolution of HCl is detected throughout the observation period. Comparison of these two facts suggests that, in contrast to reactions with sodium azide, dehydrochlorination and solvation of VC–MA macromolecules with DMF occur concurrently in different units of microstructurally nonuniform VC–MA macromolecules and are regiospecific.

By regiospecificity we mean a definite orientation (among numerous alternatives) of DMF molecules relative to the corresponding units of microstructurally nonuniform VC–MA macromolecules, with subsequent concerted rearrangements of atoms and bonds. Typical regiospecific reactions are, e.g., the Diels–Alder reaction and 1,3-dipolar cycloaddition [7].

In this study we examined qualitatively and quantitatively the regiospecificity of solvation and dehydrochlorination of VC–MA macromolecules in DMF.

1070-4272/01/7409-1554$25.00

EXPERIMENTAL

VC–MA was prepared and identified according to [3]. We used the copolymer with an equimolar ratio of VC and an units. Dimethylformamide was thoroughly purified [8]. The degree of dehydrochlorination was determined by potentiometric titration with an $AgNO_3$ solution (I-120 pH meter, silver electrode).

For kinetic studies, a 0.2200-g sample of the copolymer was dissolved in 22 ml of temperature-controlled DMF. At definite intervals, 2-ml samples were taken, to which 16 ml of water was added, and the solution was quickly titrated with an $AgNO_3$ solution. Experimental points in the kinetic curves were obtained from no less than three runs.

The ^1H NMR spectra of a 1 m solution of VC–MA in DMF-d_7 were taken on a Tesla BS-487 spectrometer (100 MHz, HMDS).

The time dependence of the optical density originating from the accumulated solvation structures [VC–MA·DMF] at a fixed wavelength (λ = 560 nm) was described previously [6].

As already noted, in solutions of VC–MA in DMF the solvates are formed concurrently with dehydrochlorination. An attempt to describe the kinetic curves of HCl accumulation (Fig. 1) by the equation [9]

$$[HCl] = [HCl]_{max}[1 - \exp(-k\tau)]$$

failed, which indicates that HCl is released in several parallel reactions and/or its elimination is preceded by a catalytic process. We suggested that HCl is released both from VC units under the action of DMF, which is known to exhibit a high dehydrochlorinating power, in particular, toward PVC [10], and from the solvates [VC–MA·DMF] (S) when they are decomposed with water prior to titration. Dehydrochlorination of VC–MA could be adequately described with the equation

$$[HCl] = [HCl_{VC}]_{max}[1 - \exp(-k_{HCl}\tau)] + [S]_{max}[1 - \exp(-k_S\tau)],$$

where [HCl] is the concentration of HCl eliminated from VC units (HCl_{VC}) and solvates (HCl_S) under the action of water, assuming that $[HCl]_S = [S]$; k_{HCl} and k_S are the rate constants of dehydrochlorination and solvate formation, respectively; $[HCl]_{max}$ and $[S]_{max}$ are the concentrations of HCl and the solvates, respectively, at $\tau \to \infty$.

Computer decomposition of experimental kinetic curves of HCl elimination (Fig. 1) into the curves corresponding to the two above-mentioned pathways allowed construction of the calculated kinetic curves of HCl_{VC} elimination from VC–an units (Fig. 2) and of the solvate accumulation (Fig. 3).

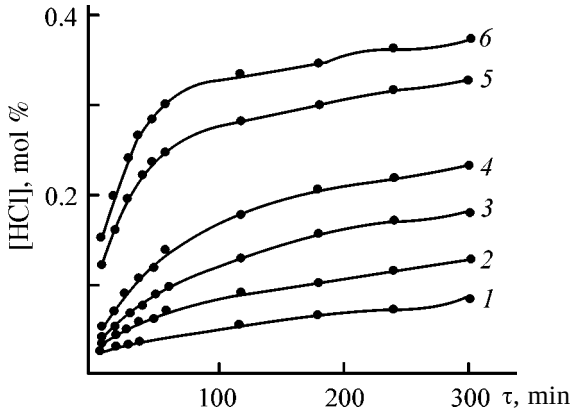

Fig. 1. Concentration of HCl [HCl] released in total from VC–an units and from solvate structures as a function of time τ. Temperature, °C: (*1*) 14, (*2*) 25, (*3*) 34, (*4*) 44, (*5*) 64, and (*6*) 74; the same for Figs. 2 and 3.

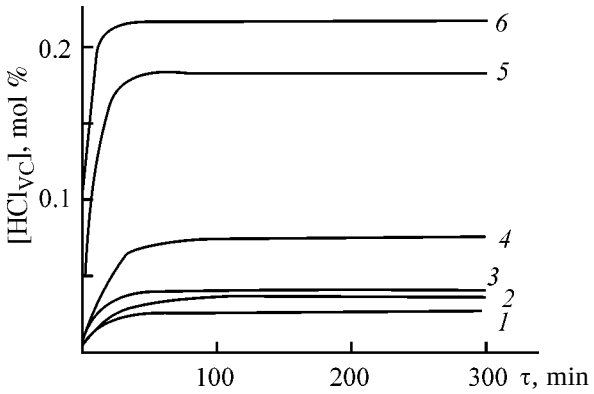

Fig. 2. Concentation of HCl [HCl_{VC}] released from VC–an units as a function of time τ (calculated data).

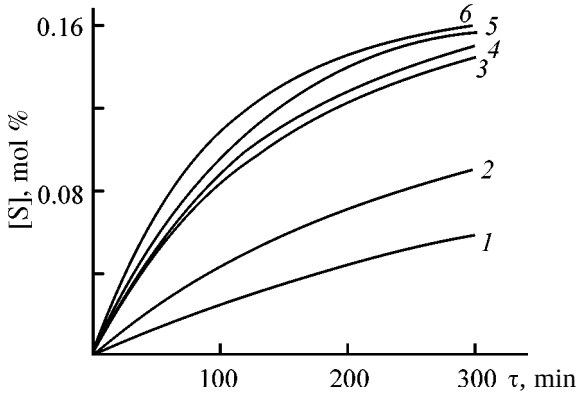

Fig. 3. Accumulation of solvate structures [S] as a function of time τ (calculated data).

The kinetic plots of dehydrochlorination of VC units and accumulation of solvates were processed by

Some characteristics of elementary stages of reactions of VC–MA with DMF according to model (2)

T, °C	$[VC–an]_0$	$[ed]_0$	$k_1 \times 10^4$, s^{-1}	$k_3 \times 10^4$, s^{-1}	$K = k_4/k_5$	ΔG, J mole^{-1}
14.0 ± 1.0	0.62	0.38	25.2	1.05	0.105	5378
25.5 ± 0.1	0.62	0.38	19.0	0.73	0.127	5121
34.4 ± 0.1	0.62	0.38	11.5	1.17	0.197	4153
44.2 ± 0.1	0.62	0.38	6.3	0.85	0.228	3901
64.1 ± 0.1	0.35	0.65	5.0	5.48	0.236	4047
73.9 ± 0.1	0.35	0.65	5.2	6.08	0.256	3963

28 models including elementary stages with participation of VA–an, en, den, and ed units (ed denotes en and den in total). The smallest dispersion between the calculated and experimental data (Fig. 1) was obtained for the model

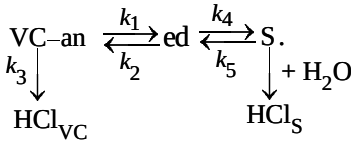

(2)

The mechanism of dehydrochlorination of VC–an units under the action of DMF, by analogy with the mechanism of PVC dehydrochlorination [10], can be represented as follows:

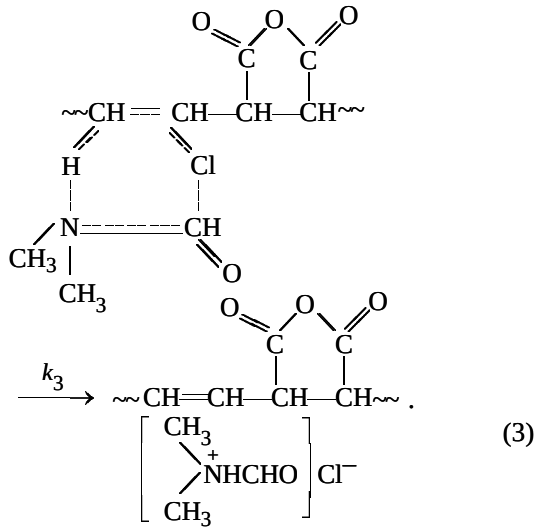

(3)

The kinetic curves (Fig. 1) were processed using a system of differential equations

$$d[VC–an]/d\tau = -(k_1 + k_3)[VC–an] + k_2[ed],$$

$$d[ed]/d\tau = k_1[VC–an] + k_5[S] - (k_2 + k_4)[ed],$$

$$d[HCl]/d\tau = k_3[VC–an],$$

$$d[S]/d\tau = k_4[ed] - k_5[S],$$

which was integrated by the Rosenbrock's implicit method at the initial concentrations $[S]_0 = [HCl]_0 = 0$. The initial concentrations $[VC–an]_0$ and $[ed]_0$ were determined by the optimization procedure [5]. In the range 14–44°C they correspond to $[VC–an]_0$ and $[ed]_0$ in the initial solid sample of the copolymer [11, 12]. A sharp increase in $[ed]_0$ above 44°C at the expense of decrease in $[VC–an]_0$ (see table) may be due to a catalytic effect of DMF on conformational and configuration transitions resulting in additional formation at these temperatures of CAET products, ed tautomers (1), whose content approaches the maximum possible level. Further increase in the content of such fragments is hindered thermodynamically (see table, k_1 values at T = 14–73.9°C).

Calculations showed that formation of ed forms (2) is irreversible, $k_2 \approx 0$. This may be due to formation of a stable six-membered ring with an intramolecular hydrogen bond (IMHB) C–O–H···Cl, ultimately stabilizing the quasiaromatic den structure (1). The high stability of these ensembles may be due both to the cooperative effect of regiospecific interaction of ed tautomers with DMF molecules [6], manifested in the solvates, and to delocalization of the electron density in conjugated five- and six-membered rings (1) [13].

With increasing temperature, the inter- and intramolecular hydrogen bonds become weaker, and k_1, correspondingly, decreases (see table). The constants k_3 remain practically constant up to 44.2°C, being about 1×10^{-4} s^{-1}, and above this temperature the rate of dehydrochlorination by mechanism (2) increases by a factor of approximately 6.

The complex temperature dependence of the order n of solvate formation reaction

T, °C	14.0 ± 1.0	25.5 ± 0.1	34.4 ± 0.1
n	0.28	0.43	0.68
T, °C	44.2 ± 0.1	64.1 ± 0.1	73.9 ± 0.1
n	0.96	0.94	1.44

and of the experimental coefficient of the reaction rate k_e, calculated from the equation

$$d[S]/d\tau = k_e[S]^n,$$

suggests occurrence of an effect apparently related to regiospecific concerted interactions of the reactants, similar to those observed in enzymatic or homogeneous catalytic reactions. For the latter case, Arrhenius dependences are not followed even in a narrow temperature range [14]. Furthermore, on heating the rotation of the dimethylamino [$(CH_3)_2N$] and aldehyde (CHO) groups around the N–C bond in DMF molecules becomes sufficiently fast, and at temperature of about 100°C the shape of the methyl proton signals in the ^{1}H NMR spectrum of neat DMF changes considerably. This fact suggests that at elevated temperatures the molecular structure of DMF changes. The difference between the structures of DMF molecules at low and high temperatures consists in that the conformers become indiscernible in the NMR time scale [15].

The solvates dissociate into the initial components at a rate considerably exceeding the rate of their formation: $K = k_4/k_5 < 1$. The equilibrium constant K slightly increases with temperature (see table); the activation energy E_a of the direct reaction of formation of the solvate structure is as low as 2597 J mol^{-1}, and that of the reverse reaction, 1366 J mol^{-1}. To compare, the activation energy of dehydrochlorination of VC–an units is about 40 000 J mol^{-1}, and that of dehydrochlorination of VC units of PVC in DMF solution, 92 000–97 000 J mol^{-1} [10].

The very low free energies, ΔG_T from 5378 to 3963 J mol^{-1}, of formation of the solvation structures characterize the process as practically equilibrium, with ΔH = 1186 J mol^{-1} and ΔS = 23.54 J mol^{-1} K^{-1}. That is, the solvate formation is entropy-controlled, i.e., it involves a definite favorable ($\Delta S > 0$) orientation of the partners prior to the reaction. It is interesting to compare the reactions of VC–MA with sodium azide, which, despite a phenomenologically similar reaction pattern, show significant quantitative differences. Comparison at similar temperatures of the rate constants and free energies of solvate formation of VC–MA with DMF, on the one hand, and of reactions of VC–MA with NaN_3 [5], on the other hand, shows that the latter reaction is by a factor of almost 3300 faster than solvate formation of VC–MA with DMF: $k_{DMF} = 4.8 \times 10^{-6}$ s^{-1} and ΔG_{DMF} = 5378 J mol^{-1} (see table); $k_{NaN_3} = 1.57 \times 10^{-2}$ s^{-1} and ΔG_{NaN_3} = –19 900 J mol^{-1} [5].

Scheme (2) contains no information about the nature of solvates formed by DMF molecules with ed tautomers containing OH groups. These groups, apparently, play a decisive role in regiospecific interactions with DMF, similar to their role in enzymatic or homogeneous catalytic processes. The ^{1}H NMR monitoring of the interaction of VC–MA with DMF showed that, on storage of the solution for 620 h, the signal of the OH protons is significantly (by 3.76 ppm) shifted downfield, with its integral intensity remaining practically constant:

τ, h	0	6	29	163
δ, ppm	7.74	8.28	9.26	10.70
Δδ, ppm	0	0.54	1.52	2.96
τ, h	285	360	456	620
δ, ppm	11.10	11.26	11.35	11.50
Δδ, ppm	3.44	3.52	3.61	3.76

Computer simulation of the time dependence of Δδ was performed by the equation describing two parallel reactions:

$$\Delta\delta = \Delta\delta_1[1 - \exp(-k_1^{sp}\tau)] + \Delta\delta_2[1 - \exp(-k_2^{sp}\tau)],$$

where $\Delta\delta_1$ and $\Delta\delta_2$ are the changes in the chemical shift at $\tau \to \infty$ due to the first and second reactions, respectively; k_1^{sp} and k_2^{sp} are the rate constants, determined by ^{1}H NMR spectroscopy, of the reactions responsible for the shift of the enol proton signals.

Calculation showed that the chemical shift of the OH protons changes owing to two parallel reactions with the rate constants differing by almost an order of magnitude: $k_1^{sp} = 0.093 \times 10^{-4}$ and $k_2^{sp} = 0.01 \times 10^{-4}$ s^{-1}. A striking feature is coincidence of the rate constants at 25.5°C: $k_4 = 0.1 \times 10^{-4}$ and $k_1^{sp} = 0.093 \times 10^{-4}$ s^{-1}, with the first constant (constant of formation of the solvate structures) being determined from the potentiometric titration data with subsequent mathematical simulation and the second, by ^{1}H NMR spectroscopy. Apparently, solvate formation (2) involves proton transfer from the hydroxy group of the ed forms to the nitrogen atom of DMF. Then this solvate spontaneously, at an order of magnitude lower rate ($k_2^{sp} = 0.01 \times 10^{-4}$ s^{-1}), decomposes to give DMF hydrochloride and the elimination product which is an isomer of the product shown in scheme (3):

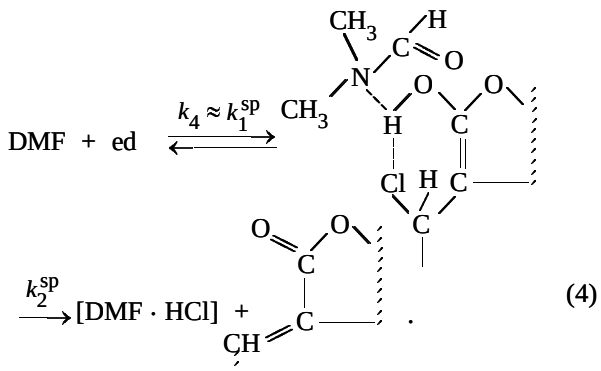

(4)

The regiospecificity of the interaction of VC–MA with DMF at 25.5°C was quantitatively characterized by a higher (by a factor of 7.3) rate of dehydrochlorination of VC units (3) as compared to the rate of solvate formation (4): $k_3 = 0.73 \times 10^{-4}$ and $k_4 = 0.1 \times 10^{-4}$ s^{-1}, respectively. The curve of dehydrochlorination of the VC–an units flattens out within 60 min in the entire temperature range studied (Fig. 2), whereas the curve of the solvate accumulation reaches saturation at 74°C only in 300 min (Fig. 3). It is important that the apparent rate coefficients k_e of formation of the solvation structures, one of which was determined from the potentiometric titration data in this work and the other, by electronic spectroscopy in [6], are close: 0.68×10^{-4} and 0.60×10^{-4} s^{-1}, respectively.

CONCLUSIONS

(1) Cyclic anhydride–enol tautomeric transformations of monomeric units in macromolecules of vinyl chloride–maleic anhydride copolymers in dimethylformamide occur irreversibly with subsequent regiospecific formation of long-lived solvate structures involving dimethylformamide molecules and ed forms of the microstructurally nonuniform macromolecules.

(2) The vinyl chloride–an units that do not participate in prototropic transformations undergo dehydrochlorination in dimethylformamide at 25.5°C by a factor of 7.3 faster as compared to formation of the solvate structures between the ed units and dimethylformamide molecules.

(3) Dehydrochlorination of different segments of the microstructurally nonuniform vinyl chloride–maleic anhydride copolymer yields different isomers.

REFERENCES

1. Fedtke, M., *Reaktionen an Polymeren*, Leipzig: Grundstoffindustrie, 1985.
2. *Entsiklopediya polimerov* (Polymer Encyclopedia), Kabanov, V.A., Ed., Moscow: Sov. Entsiklopediya, 1974, vol. 2, p. 135.
3. Filimoshkin, A.G., Terent'eva, G.A., Berezina, E.M., and Pavlova, T.V., *J. Polym. Chem.*, 1993, vol. 31, pp. 1911–1914.
4. Pavlova, T.V., Terent'eva, G.A., Chernov, E.B., and Filimoshkin, A.G., *Vysokomol. Soedin., Ser. A*, 1994, vol. 36, no. 5, pp. 767–773.
5. Pribytkov, E.G., Berezina, E.M., Eremina, N.S., *et al.*, *Vysokomol. Soedin., Ser. A*, 1997, vol. 39, no. 8, pp. 1365–1369.
6. Filimoshkin, A.G., Chernov, E.B., Terent'eva, G.A., *et al.*, *Vysokomol. Soedin., Ser. A*, 1997, vol. 39, no. 12, pp. 1986–1991.
7. *Khimicheskaya entsiklopediya* (Chemical Encyclopedia), Zefirov, N.S., Ed., Moscow: Bol'shaya Ross. Entsiklopediya, 1995, vol. 4, p. 217.
8. Gordon, A.J. and Ford, R.A., *The Chemist's Companion. A Handbook of Practical Data, Techniques, and References*, New York: Wiley–Interscience, 1972.
9. Emanuel', N.M. and Knorre, D.G., *Kurs khimicheskoi kinetiki* (Course of Chemical Kinetics), Moscow: Vysshaya Shkola, 1974.
10. Evsyukov, S.E., Kudryavtsev, Yu.P., and Korshak, Yu.V., *Usp. Khim.*, 1991, vol. 60, no. 4, pp. 764–798.
11. Filimoshkin, A.G., Chernov, E.B., Terent'eva, G.A., *et al.*, Abstracts of Papers, *Mezhdunarodnaya konferentsiya "Fundamental'nye problemy nauki o polimerakh (k 90-letiyu akademika V.A. Kargina)"* (Int. Conf. "Basic Problems of Polymer Sciences" Dedicated to 90th Birthday of Acad. V.A. Kargin), Moscow, 1997, session 1, p. 78.
12. Filimoshkin, A.G., Chernov, E.B., Terent'eva, G.A., *et al.*, *Zh. Prikl. Khim.*, 2001, vol. 74, no. 2, pp. 292–299.
13. Pavlova, T.V., Terent'eva, G.A., Filimonov, V.D., *et al.*, *Zh. Prikl. Khim.*, 1999, vol. 72, no. 9, pp. 1515–1517.
14. Denisov, E.T., *Kinetika gomogennykh khimicheskikh reaktsii* (Kinetics of Homogeneous Chemical Reactions), Moscow: Vysshaya Shkola, 1978.
15. Bovey, F.A., *High Resolution NMR of Macromolecules*, New York: Academic, 1972.

Russian Journal of Applied Chemistry, Vol. 74, No. 9, 2001, pp. 1559–1562. Translated from Zhurnal Prikladnoi Khimii, Vol. 74, No. 9, 2001, pp. 1513–1516.

MACROMOLECULAR CHEMISTRY AND POLYMERIC MATERIALS

Influence of the Ionic Strength on the Degree of the Form Asymmetry *p* of Poly-2-acrylamido-2-methylpropanesulfonic Acid Macromolecule in Dilute Aqueous-Salt Solutions

S. V. Valueva and A. I. Kipper

Institute of Macromolecular Compounds, Russian Academy of Sciences, St. Petersburg, Russia

Received April 10, 2001

Abstract—Dilute aqueous-salt solutions of macromolecular flexible-chain polyelectrolyte, poly-2-acrylamido-2-methylpropanesulfonic acid, were studied by the method of flow birefringence, viscometry, and light scattering. The degrees of the form asymmetry *p* of poly-2-acrylamido-2-methylpropanesulfonic acid macromolecules determined by this method for ionic strengths I = 1–0.05 M were compared with the main results of theoretical and experimental studies of the *p*–*I* dependence.

The activity of ionic polymers is known to be dependent not only on the properties of their macromolecules (chemical composition, molecular weight, ridigity, conformation, content of ionic groups) but also on the characteristics of the medium (ionic strength I, pH, etc.).

Water-soluble polymers based on acrylic compounds are widely used in diverse branches of economy. High degree of dissociation of poly-2-acrylamido-2-methylpropanesulfonic acid (PAMPS) makes it, e.g., an efficient coagulant able of operating in a wide range of I and pH values [1].

In [2] we studied the degree of form asymmetry *p* of macromolecule of 2-acrylamido-2-methylpropanesulfonic acid copolymer with acrylamide [P(AMPS–AA)] as dependent on the ionic strength. The content of ionic groups amounted to 20%.

The aim of this work is to quantitatively determine by the method of flow birefringence (BR) the degree of the form asymmetry *p* of the PAMPS homopolymer macromolecule (content of ionic groups 100%) at I = 1 M (the case of suppressed electrostatic interactions) and in the region of moderate ionic strengths (0.1 and 0.05 M). As known [3–5], the major role here is played by long-range electrostatic interactions (bulk effects in macromolecules of electrostatic nature), and the percolation effect (changes in the equilibrium rigidity of the polymer chain A) is negligible (A = const).

EXPERIMENTAL

The subject of the study was macromolecular ($M_w = 4.6 \times 10^6$) flexible-chain (A = 2 nm [1]) homopolyelectrolyte PAMPS

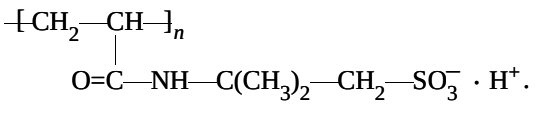

The PAMPS polymer was obtained by a standard procedure [6] by radical polymerization using the Co(III)–glycine system. The residual monomer and other impuruties were removed by dialysis of the resulting product. The polymer was isolated by lyophilic drying.

The flow BR Δn as dependent on the rotor rotation rate gradient g, polymer concentration c, and ionic strength of the medium l was measured by a procedure reported in [7]. We used a titanium dynamooptical caliper with an 4-cm-high internal rotor and the rotor–stator gap of 3×10^{-2} cm. The inaccuracy in measuring the intrinsic flow BR $[n]$ (or optical shift coefficient $[n]/[\eta]$) was about 10%.

The experimental $[n]$ value (in the general case of $dn/dc \neq 0$, where dn/dc is the increment of the refractive index of solution) is composed of three effects: $[n] = [n]_e + [n]_{fs} + [n]_f$, where $[n]_c$ is the intrinsic anisotropy, $[n]_{fs}$ is the micro form effect, and $[n]_f$ is the macro form effect [7]. The full segment anisotropy $[n]_e + [n]_{fs}$ is governed by the parameter A and structure of the monomer unit. The $[n]_f$ parameter is re-

1070-4272/01/7409-1559$25.00

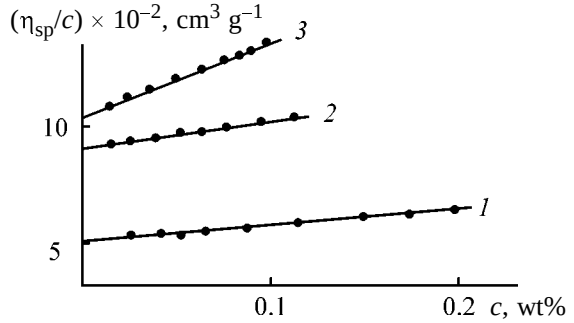

Fig. 1. Reduced viscosity η_{sp}/c as a funciton of the concentration c of the polymer for PAMPS solutions at different ionic strengths. I, M: (*1*) 1, (*2*) 0.1, and (*3*) 0,05; the same for Fig. 3.

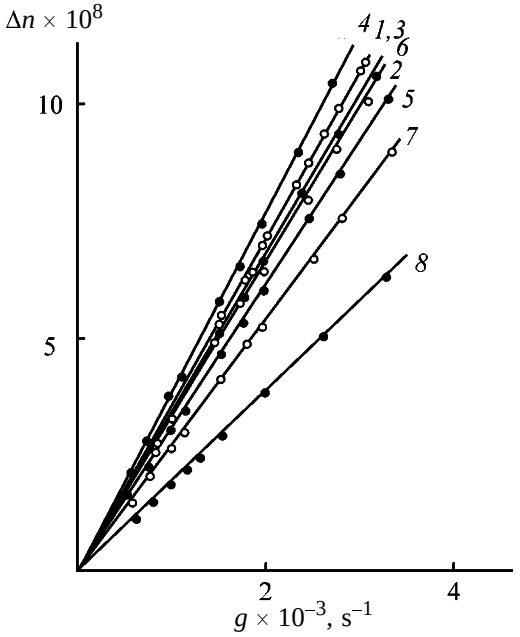

Fig. 2. Flow BR Δn as a function of the rate gradient g for PAMPS solutions at I = 0.05 M. Polymer concentration, wt %: (*1*) 0.102, (*2*) 0.090, (*3*) 0.0832, (*4*) 0.0725, (*5*) 0.065, (*6*) 0.052, (*7*) 0.035, and (*8*) 0.0226.

lated to the degree of asymmetry of the form p of the macromolecule as

$$[n]_f = [(n_s^2 + 2)/3]^2[M(dn/dc)^2 f(p)]/(30\pi RTn_s) = \text{const}\, Mf(p), \quad (1)$$

Molecular and conformation characteristics of PAMPS. $M_w = 4.6 \times 10^6$

I, M	$[\eta] \times 10^{-2}$, cm^3 g^{-1}	$[n]/[\eta] \times 10^{10}$, cm s^2 g^{-1}	$[n] \times 10^8$, cm^4 s^2 g^{-2}	p
1	5.0	24.0	120	2.4
0.1	9.0	78.0	702	5.6
0.05	10.5	90.5	950	6.7

where M is the molecular weight, n_s is the refractive index of the solvent, T is the absolute temperature, R is the universal gas constant, and $f(p)$ is the tabulated function of the relation of the axes of rigid (not flown through by the solvent) ellipsoid approximating the macromolecule [7].

For high-molecular-weight flexible-chain polymers with low weight and insignificant anisotropy of monomer unit, holds $[n]_e \ll [n]_f$, $[n]_{fs} \ll [n]_f$ (or at $[n]_e < 0$ and $[n]_e \approx [n]_{fs}$), the approximate relation $[n] \approx [n]_f$ holds, which allows indirect determination of the parameter p from the experimental data [7].

The molecular weight M_w was determined by the light scattering method [7] using a Fica photogoniodiffusometer at the wavelength of vertically polarized incident light of 546.1 nm in the concentration range $c \sim (0.01–0.1) \times 10^{-2}$ g cm^{-3} (we studied dilute solutions with $c \le c^*$, where c^* is the concentration of units in a polymer globule [8]) and angles (relative to the direction of incident light) θ = 30°–150°. The refractive index increment dn/dc was determined from refractometric measurements on an IRF-23 instrument. The experimental results were proceesed by the Simm's double extrapolation method [9]. The measurements inaccuracy was about 10%.

Viscometric measurements were carried out in an Ostwald capillary viscometer with the water outflow time of 120±0.2 s at 21°C. The intrinsic viscosity $[\eta] = [(\eta_r - 1)/c]_{c\to 0} = (\eta_{sp}/c)_{c\to 0}$ (ν_r is the relative viscosity) was determined accurately to within 3%. We studied dilute solutions only.

Experimental dependences of the reduced viscosity η_{sp}/c on the polymer concentration show that for aqueous-salt solutions of PAMPS at $c \le c^* \sim 1/[\eta]$ and I = 1–0.05 M η_{sp}/c is a linear function of c (Fig. 1). This fact suggests that the size and form of the polyions remain unchanged after dilution of the solution [10–12]. Viscometric data (see table) evidence a fairly strong polyelectrolytic swelling of the polyions with decreeasing I.

PAMPS solutions exhibit positive flow BR over the whole region of c and I studied. The $\Delta n = f(g)$ dependences for $g < g_k$ (g_k is the rate gradient corresponding to flow turbulence) are linear and pass through the origin, whatever the c ($c \le c^*$) and I values. This suggests the molecular dispersity of solutions [7] (e.g., Fig. 2 presents the dependences for PAMPS in 0.05 M $NaNO_3$ solution).

Figure 3 presents the concentration dependences of the reduced anisotropy $\{\Delta n/[g\eta_0(\eta_r - 1)]\}_{g\to 0}$ (η_0 is

the solvent viscosity) for PAMPS at $c \le c^*$ and I = 1–0.05 M. It is seen that the $\{\Delta n/[g\eta_0(\eta_r - 1)]\}_{g\to 0}$ parameter in all cases decreases with increasing polymer concentration. As known [7], such a dependence in the region of relatively small concetrations c ($c \le c^*$) is due to a decrease in the anisotropy of the polymer molecule form (macro form effect) in the solvent with $dn/dc \neq 0$ (for PAMPS dn/dc = 0.133 cm^3 g^{-1}). This is typical for flexible-chain polymers. This phenomenon is due to the fact that enhancement of the "optical interaction" of macromolecules with increasing solution concentration is responsible for a decrease in the effective form anisotropy of the coil Θ_1^* (anisotropy of the macro form at the final value of the solution concentration) [7].

Thus, for solutions studied the macro form effect plays the decisive role.

The table presents the optical coefficient of the shift $[n]/[\eta] = \{\Delta n/[g\eta_0(\eta_r - 1)]\}_{g\to 0}$, as well as the intrinsic flow BR $[n]$ values for different I values. It is seen that the parameter $[n]/[\eta]$ (and especially $[n]$) significantly increase with unfolding of the polyions owing to long-range electrostatic interactions.

In [13], we showed that at I = 1 M for PAMPS $([n]_e + [n]_{fs}) \ll [n]_f$, i.e., the approximation $[n] \approx [n]_f$ holds. The lack of percolation effect ($A \sim$ const) in the I range investigated makes this approximation valid for the ionic strengths of 0.1 and 0.05 M, respectively.

The table and Fig. 4 (curve *1*) present the degrees of the form asymmery p of the macromolecule obtained using relation (1) for PAMPS at different I values. It is seen that p increases by a factor of 2.8 (from 2.4 corresponding to the Gaussian coil to 6.7 corresponding to unfolded asymmetric coil) with the ionic strength decreasing from 1 to 0.05 M. This fact evidences a fairly strong influence of electrostatic interactions on the form of polyions, suggesting that bulk effects in poly ions differ from those in nonionic polymers, where swelling of the polymer coil owing to long-range forces does not markedly change the parameter p [7].

Thus, the conformation of macromolecular flexible polyion in dilute solutions with moderate ionic strengths differs significantly from both that of rigid rod with $p \gg$ 2–2.5 [10, 14–17] and that of Gaussian coil with p = 2–2.5 [18]. Our data confirm the conclusions made in [2, 19, 20] for flexible-chain polymers.

The increase in the parameter p in the region of moderate ionic strengths by a factor of almost 1.5 in

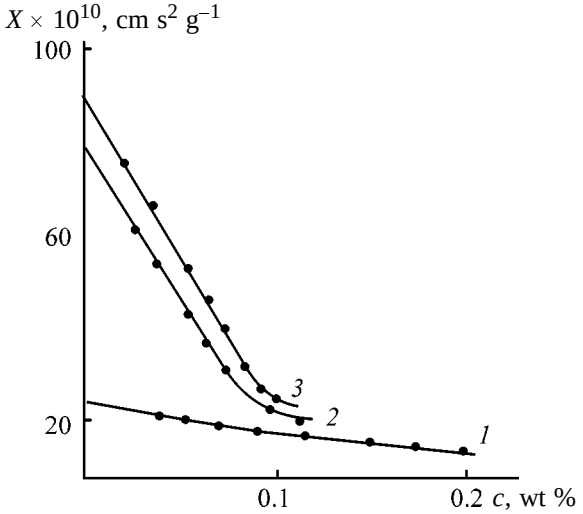

Fig. 3. Reduced anisotropy« $\{\Delta n/[g\eta_0(\eta_r - 1)]\}_{g\to 0} \equiv X$ as a function of polymer concentration c for PAMPS solutions of various ionic strengths.

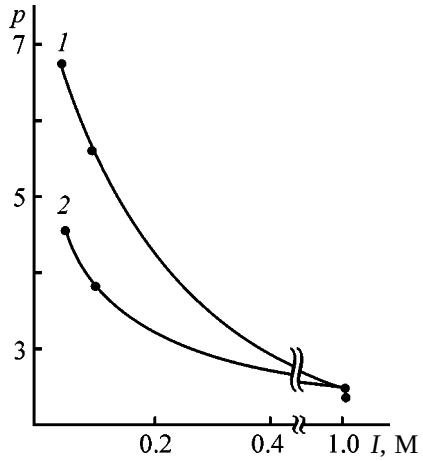

Fig. 4. Degree of form asymmetry p of macromolecules as a function of the ionic strength I for (*1*) PAMPS and (*2*) P(AMPS–AA) [2].

going from P(AMPS–AA) to PAMPS (Fig. 4) is due to increase in the amount of ionic groups (and, consequently, the degree of ionization of macromolecules in solution). As known [14, 21, 22], the number of ionic groups in homopolyelectrolytes of various structures that actually participate in polyelectrolytic swelling (groups with noncondensed counterions) is equal to 30–40%, which exceeds by a factor of 1.5–2 the amount of ionic groups in P(AMPS–AA) copolymer studied by us in [2].

CONCLUSIONS

(1) In the region of ionic strengths I = 1–0.05 M the degree of form asymmetry p of the of poly-2-

acrylamido-2-methylpropanesulfonic acid macromolecules varies from $p = 2.4$ corresponding to suppressed electrostatic interactions (Gaussian coil) to $p = 6.7$ at $I = 0.05$ M (unfolded asymmetric coil).

(2) The change in the parameter p of polyions with decreasing I correlates with the amount of ionic groups that actually participate in polyelectrolytic swelling (groups with noncondensed counterions).

REFERENCES

1. Valueva, S. V., Kipper A. I., Lyublina, S. Ya., *et al*., *Vysokomol. Soedin., Ser. A*, 1992, vol. 34, no. 12, pp. 35–44.
2. Valueva, S. V., Kipper, A.I., Rumyantseva, N.V., *et al*., *Vysokomol. Soedin., Ser. A*, 2000, vol. 42, no. 7, pp. 1152–1157.
3. Alexandrovicz, Z., *J. Chem. Phys*., 1967, vol. 47, no. 11, pp. 4377–4384.
4. Noda, J., Truge, T., and Nagasawa, M., *J. Chem. Phys*., 1970, vol. 74, no. 4, pp. 710–719.
5. Veselkov, A.N., Moroshkin, V.A., Polyakova, P.D., *et al*., *Molek. Biol*., 1976, vol. 10, no. 5, pp. 1050–1060.
6. *Sintez, struktura i svoistva polimerov* (Synthesis, Structure, and Properties of Polymers), Koton, M.M., Ed., Leningrad: Nauka, 1989.
7. Tsvetkov, V.N., Eskin, V.E., and Frenkel, S.Ya., *Struktura makromolekul v rasrvorakh* (Structure of Macromolecules in Solutions), Moscow: Nauka, 1964.
8. Debye, P., *J. Chem. Phys*., 1946, vol. 14, no. 10, pp. 636–639.
9. Eskin, V.E., *Rasseyanie sveta rastvorami polimerov i svoistva makromolekul* (Light Scattering by Polymer Solutions and Properties of Macromolecules), Leningrad: Nauka, 1986.
10. Gennes, P.-G. de, *Scaling Concepts in Polymer Physics*, Ithaca: Cornell Univ. Press, 1979.
11. Pals, D.T.E. and Hermans, J., *J. Polym. Sci*., 1950, vol. 5, no. 6, pp. 733–734.
12. Grosberg, A.Yu. and Khokhlov, A.R., *Statisticheskaya fizika makromolekul* (Statistical Physics of Macromolecules), Moscow: Nauka, 1989.
13. Valueva, S.V., Conformation Properties of Macromolecular Diphilic Polyanions and Polycations in Aqueous-Salt and Aqueous-Acetone Media, *Cand. Sci. Dissertation*, St. Petersburg, 1997.
14. Manning, G.S., *Acc. Chem. Phys*., 1979, vol. 12, pp. 443–449.
15. Scolnick, J. and Fixman, M., *Macromolecules*, 1977, vol. 10, no. 5, pp. 944–948.
16. Odijk, T., *Polymer*, 1978, vol. 19, no. 8, pp. 989–998.
17. Mattoussi, H., Karasz, F.E., and Langley, K.N., *J. Chem. Phys*., 1990, vol. 93, no. 5, pp. 3593–3603.
18. Kron, A.K. and Ptistyn, O.B., *Vysokomol. Soedin., Ser. A*., 1962, vol. 4, no. 8, pp. 1235–1340.
19. Foster, S, and Schmidt, M., *Vysokomol. Soedin., Ser. A*, 1993, vol. 35, no. 11, pp. 1900–1903.
20. Yamanaka, J., Matsuoka, H., Kitano, H., *et al*., *J. Am. Chem. Soc*., 1990, vol. 112, no. 2, pp. 587–592.
21. Tanford, Ch., *Physical Chemistry of Macromolecules*, New York: Wiley, 1963.
22. Morawetz, H., *Macromolecules in Solution*, New York: Wiley, 1965.

Russian Journal of Applied Chemistry, Vol. 74, No. 9, 2001, pp. 1563–1567. Translated from Zhurnal Prikladnoi Khimii, Vol. 74, No. 9, 2001, pp. 1517–1521.

MACROMOLECULAR CHEMISTRY AND POLYMERIC MATERIALS

Structural Transformation of Starch Hydrogels Exposed to Strong Mechanical Field

I. M. Lipatova, A. A. Yusova, S. V. Blokhina, and A. P. Moryganov

Institute of Solution Chemistry, Russian Academy of Sciences, Ivanovo, Russia

Received February 5, 2001; in final form, April 2001

Abstract—Structural transformations of starch hydrogels during mechanical preparation of starch gelatinous materials with a rotary pulse apparatus were studied. Two concentration regions distinguished by the structural transformations of starch hydrogels under high shearing stress were revealed.

Gelatinous materials prepared by cooking of starch dispersions to the required degree of cleavage are widely used in various branches of industry (textile, food, paper, building industry, etc.). One of the procedures for preparing finely dispersed starch gels is treatment of prepasted starch in a rotary pulse apparatus (RPA) operating well under industrial conditions, in particular, in mechanical preparation of starch schlich [1].

Previously we studied the degree of dispersion of starch grains, the size of colloid particles, the content of the water-soluble fraction, and the degree of starch cleavage as influenced by the conditions of mechanical treatment of starch pastes in RPAs. The aim of this work was to study the features of dynamic structurization of starch hydrogels under high shearing stresses and mechanical vibrations generated in RPA.

The behavior of a polymer–solvent system in a mechanical field is extensively studied [3–6]. The majority of works on this point concern conformational transformations of rigid- and flexible-chain polymers in dilute solutions [4, 5]. The influence of the shearing stresses on abnormally viscous polymeric systems was studied to a lesser extent. In particular, one of these works concerns phase transformations of ordered solutions of polymers, initiated by a mechanical field [6].

The influence of a mechanical field on such practically important systems as starch hydrogels was not studied comprehensively. This is likely due to the fact that starch hydrogels are very difficult to study owing to their fractional and phase nonuniformity, ready degradation, and the presence of chemical impurities which cannot be removed.

EXPERIMENTAL

We studied corn starch [GOST (State Standard) 7697–82]. Starch hydrogels (3–8 wt %) to be mechanically treated were prepared by cooking of a starch suspension on a water bath at T = 90°C for 7 min.

The starch hydrogels were mechanically treated at 80°C for 10 s on a laboratory rotary pulse activator (RPA) [2] at the rotor rotation rate of 3500 rpm, providing a 6×10^4 s^{-1} rate gradient.

Starch hydrogels were thermally hydrolyzed in the presence of NaOH and Chloramine B at concentrations of 0.1 and 0.12 g l^{-1}, respectively. The process was performed until Chloramine B was completely consumed.

The content of the water-soluble fraction of starch A (%) was determined by hot extraction [7]. The extract composition was analyzed by absorption of iodine complexes [8]. The content of the water-soluble fraction was expressed as the percent of the total starch concentration. The optical densities of the solutions were measured on a Specord M40 spectrophotometer.

Rheological properties of the starch hydrogels were determined with the aid of a Rheotest-2 rotary viscometer with a coaxial working unit. The rate gradient ranges from 1.5 to 1312 s^{-1}.

The sorption properties of starch before and after mechanical treatment were studied at 60–89°C on a Chrom-5 chromatograph with a flame ionization detector. Starch hydrogel (10.8 wt %) was applied to solid Chromaton N-AW support (0.25–0.31 mm) by evaporation of its solution. We used 1 m × 0.3 mm metal columns. The dead retention time was deter-

1070-4272/01/7409-1563$25.00

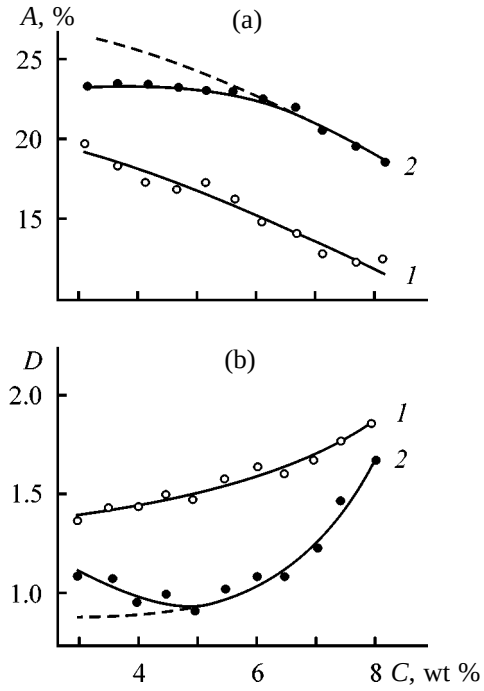

Fig. 1. (a) Content of the water-soluble fraction *A* and (b) optical density of starch hydrogels *D* (λ = 500 nm) as functions of the starch concentration *C* in (*1*) initial and (*2*) mechanically treated hydrogels.

mined with methane. X-ray diffraction study were performed on a DRON-2 diffractometer using CuK_α radiation. The degree of starch crystallinity was 16%.

The surface tension of starch hydrogel at the interface with air was measured with the aid of a Rebinder device [9].

The physicomechanical properties of the films prepared from starch hydrogels were determined on a PM-3-1 tensile-testing machine. Prior to the measurements the films were conditioned at 65% humidity in a hydrostat for 1 day. The film thickness was measured by a Schopper thickness gage.

The reactivity of mechanically activated starch was studied on a model reaction of starch oxidation with potassium permanganate in an acidic solution. The reaction rate was calculated from the decrease in the permanganate concentration measured spectrophotometrically on a Spekol 221 spectrophotometer at λ = 530 nm and *T* = 303 K [10].

The initial starch hydrogels (pastes) are microheterogeneous systems in which swollen starch grains are dispersed in true solution of the water-soluble fraction. Previously we showed [11] that starch grains are completely cleaved to form a new structure within the first 2–3 s of mechnaical treatment of starch hydrogels under definite conditions. We also found [2] that mechanically initiated chemical processes (degradation, cross-linking, oxidation) either do not occur or occur to a negligible extent at the above shearing stresses in the absence of chemical reagents. Thus, strong changes in the properties of starch hydrogels at shearing stress are mainly due to their structural transformations.

Mechanically treated starch hydrogel is also a microheterogeneous system in which the colloid-dispersed phase formed by fragments of starch grains is dispersed in the true solution of the water-soluble fraction. The content of water-soluble amylose in the initial samples monotonically decreases with increasing starch concentration (Fig. 1a, curve *1*) owing to decrease in its solubility. The diffusion of amylose macromolecules in the solution is facilitated and the fraction of the water-soluble polymer increases in the course of breakdown of starch grains during the mechanical treatment (curve *2*). In the absence of phase transformation in the dispersed phase of the hydrogel, curve *2* (Fig. 1a) should pass (dashed line) similarly to curve *1*, since in this case the amylose content in the solutions is determined only by its solubility which increases with decreasing total starch concentration. However, at low starch concentrations the fraction of water-soluble amylose is appreciably lower than the expected value. This fact can be explained as follows. Rigid-chain polymers including starch form aqueous systems with strong particle anisotropy and are readily oriented and associated [3]. At high shearing stresses produced in RPAs, asymmetric particles and separate molecules are ordered to form new supramolecular structures in starch hydrogel. As a rule, mechanically initiated association of polymers in solutions is an irreversible process [12]. Hence, in this concentration range the content of water-soluble amylose determined by the extraction procedure is underestimated.

This assumption is also confirmed by the concentration depenedences of the optical density of the initial and treated starch hydrogels (Fig. 1b). The treated hydrogels are more transparent owing to mechanical breakdown of the primary structure of the initial gels. However, the optical densities of hydrogels with low starch concentrations are lower than the expected values. This also indicates ordering and association processes in this concentration range. An increase in the optical density may be due to formation of solid nucleus. Both in the first and the second cases phase transformations under shearing stress become noticeable at the hydrogel concentrations lower than 5.5 wt %. Curiously, this concentration coincides with

that of the inflection point of the $\log\eta = f(\log C)$ function for the initial starch gels (Fig. 2) at two temperatures. This dependence is graphical interpretation of the Houwink–Klassen equation [13]. The inflection point of the curves shown in Fig. 2 separates two concentration regions with different flow mechanisms. The change in the flow mechanism with increasing starch concentration is due to formation of fluctuation physical network preventing ordering and association of the macromolecules.

Practical application of starch hydrogels (schlich and thickening) involves their drying at high temperatures. It is important to find out whether the structure with increased intermolecular interaction is retained in the dried films. Here we studied this problem by gas–liquid chromatography (GLC).

The main gas-chromatographic parameters are specific retention volumes V_g and differential heat of solution of a volatile standard (*n*-alkanol) in a polymeric amorphous phase ΔH. These parameters were calculated by the equation

$$\log V_g = -\Delta H/RT + B.$$

The contribution of the specific interaction to the total energy of solution was calculated as the difference of ΔH of the standard (*n*-alkanol) and *n*-alkane (which is dissolved without specific interactions) with the same length of the carbon chain or the same polarizability. The experimental and calculated data for the starch–*n*-alkane and starch–*n*-alkanol systems with the starch concentration in the initial and treated hydrogels of 3, 5, and 7 wt % are presented in Table 1.

As seen from Table 1, the mechanical treatment of pasted starch increases its nonspecific interaction with *n*-alkanes. This is due to degradation of the natural structure of starch grains during the mechanical treatment. The less pronounced effect was observed for the gels with the starch concentration of 7 wt %. This is likely due, as noted above, to the decrease in the degree of mechanical degradation of the initial structure with increasing starch concentration. The interaction of starch with aliphatic alcohols can be estimated from the difference $-\Delta\Delta H = \Delta H_2 - \Delta H_1$. The fact that starch retains *n*-alcohols by not only formation of hydrogen bonds with their hydroxy groups but also host–guest complexation with amylose [14] should be taken into account. As determined by the light absorption of iodine–starch complexes, the ability of starch to form inclusion compounds does not change after the mechanical treatment [2]. This indicates that the spiral sections of amylose macromolecules, involved in the complexation, are preserved after conformational transformations caused by shearing stress [8]. Hence, the decrease in the energy of specific interaction of mechanically treated hydrogels with *n*-alkanols is only due to rupture of the hydrogen bonds between the hydroxy groups of starch and the alcohols.

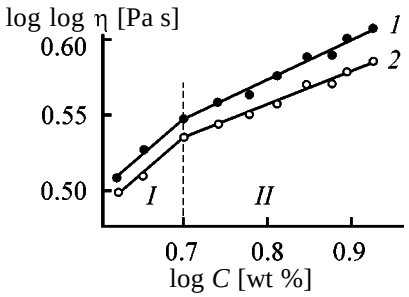

Fig. 2. Viscosity of starch hydrogels at (*1*) 30 and (*2*) 80°C as a function of the starch concentration *C*.

As seen from Table 1, the interaction of 3% gel with *n*-alkanols decreases to the greatest extent after mechanical treatment of the gel. This effect is considerably weaker for 5% gel and is almost absent in

Table 1. Partial enthalpy of solution $-\Delta H$ of *n*-alkanes and *n*-alcohols in amorphous starch structure*

C, wt %	*n*	C_nH_{2n+2}, ΔH_1	$C_nH_{2n+1}OH$, ΔH_2	$-\Delta\Delta H = \Delta H_2 - \Delta H_1$
		kJ mol^{-1}		
3	6	12.4 / 22.4**	48.7 / 43.9	36.3 / 21.5
	7	20.2 / 32.7	53.5 / 47.5	33.3 / 14.8
	8	33.0 / 37.1	54.5 / 56.5	21.5 / 19.4
5	6	40.5 / 51.4	51.7 / 56.7	11.2 / 5.3
	7	43.5 / 55.9	51.6 / 60.1	8.1 / 4.2
	8	45.3 / 51.8	52.3 / 59.1	7.0 / 7.3
7	6	31.8 / 32.5	51.6 / 49.2	14.7 / 12.7
	7	34.3 / 41.7	56.3 / 59.0	22.0 / 17.3
	8	44.9 / 45.3	70.1 / 68.0	25.2 / 22.7

* *C* is the starch concentration in the hydrogel, *n* is the number of carbon atoms is the alkyl chains, and $\Delta\Delta H$ is the difference between the heats of solution of alkane and alcohol with the same length of the alkyl chain.

** Values for the mechanically treated gel are given in the denominator.

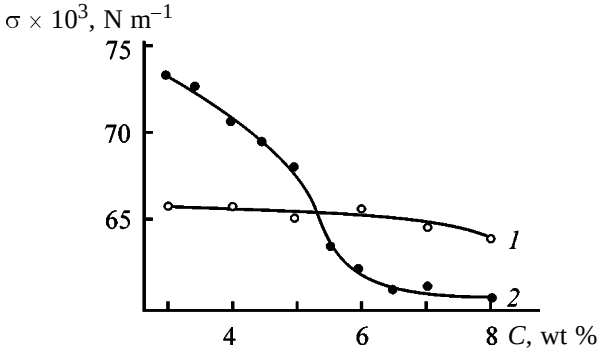

Fig. 3. Surface tension σ of (*1*) thermochemically and (*2*) mechanically cleaved starch hydrogels as a function of the starch concentration *C*.

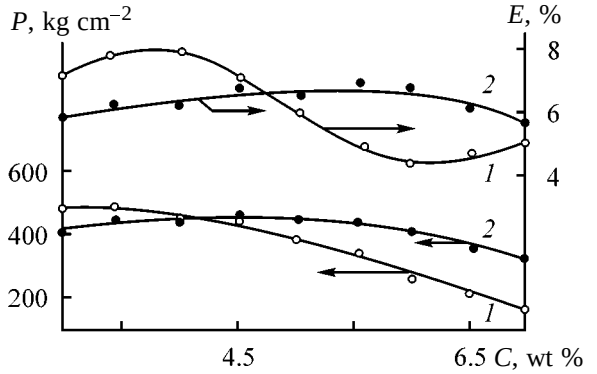

Fig. 4. Ultimate stress *P* and elongation at break *E* of films of cleaved hydrogels as functions of the starch concentration *C*.

the case of 7% gel. Thus, the GLC data suggest that mechanical treatment of starch hydrogels with low starch concentration decreases the number of free hydroxy groups in the starch. This effect decreases with increasing starch concentration.

The most important, from the viewpoint of practical application (in particular, in smoothing), structure-sensitive properties of mechanically cleaved starch gels are surface tension, film-forming ability, and, in some cases, reactivity of the starch. In this work we studied these properties as influenced by the structural transformations of starch hydrogels occurring in RPA.

One of the macroproperties of liquid polymeric systems, determined by intermolecular interaction, is surface tension. The surface tension of starch hydrogels can be higher or lower than that of water (σ^{80} = 6.26×10^{-2} N m^{-1}), depending on the energy of intermolecular interaction and the hydrogel structure. We measured the surface tension of mechanically treated and thermochemically cleaved starch hydrogels with various starch concentrations. The results are presented in Fig. 3. As seen from Fig. 3, there are two concentration regions. In the first region the surface tension of mechanically treated samples with low starch concentration is higher than that of thermochemically cleaved hydrogels. Conversely, at the starch concentration higher than 5.5 wt % the surface tension of mechanically treated hydrogels is lower than that of thermochemically cleaved samples. Thus, in the first concentration region the intermolecular interaction in the polymer–water system increases after the mechanical treatment, whereas in the second region the mechanical treatment weakens the intermolecular interaction.

Profound changes in the structure of starch hydrogels and in the phase composition of the system under strong shearing stress affect the film structure. The mechanical properties of the films are determined by the polymer cohesion. The concentration dependences of the physicomechanical properties of the films cast from mechanically treated starch hydrogels are shown in Fig. 4. The similar dependence for thermochemically cleaved starch is presented for comparison. The strength and elongation at break of the hydrogel with a low starch concentration slightly decrease after the mechanical treatment. We suggest that this is due to residual tension in the structure owing to incomplete relaxation after application of the shearing stresses. As noted above, this concentration region is characterized by the most pronounced conformation transformations.

The influence of mechanical treatment of starch hydrogels on the reactivity of starch hydroxy groups was estimated by starch oxidation with potassium permanganate in an acidic solution. For this purpose the reagents were introduced in a starch hydrogel immediately after its mechanical treatemnt. The results of the kinetic experiments are presented in Table 2.

As seen from Table 2, in the first concentration range (C = 3 wt %) the mechanical activation negatively affects the oxidation; in the boundary region the mechanical treatment has no effect on the starch reactivity; and in the second concentration range the starch reactivity increases after the mechanical pretreatment. One of the factors determining the rate of a chemical reaction is the accessibility of the functional groups, in our case, hydroxy groups. Under strong shearing stress at mechanical treatment, these groups can be released owing to degradation of the old structure and can form hydrogen bonds in the new structure. The decrease in the starch reactivity in the first concentration range can be due to a decrease in the number of accessible OH groups owing to mechanically induced

Table 2. Influence of mechanical pretreatment (MP) on the oxidation of starch with potassium permanganate

C, wt %	*K*	K_{MP}	K_{MP}/K
	l mol^{-1} s^{-1}		
3	2.8 ± 0.3	1.8 ± 0.1	0.64
5	3.2 ± 0.4	3.1 ± 0.2	0.97
7	6.7 ± 0.5	9.3 ± 0.4	1.39

* *C* is the starch concentration; *K* and K_{MP} are the rate constants.

association to form new intermolecular hydrogen bonds. Since the associates formed under shearing stress are impermeable for chemical reagents, which is indicated by a decrease in the starch reactivity, they can be considered as crystallite-like structures.

The presence of three-dimensional fluctuation network in the second concentration region prevents ordering of the macromolecules and formation of new hydrogen bonds between dehydrated OH groups. As a result, the starch reactivity in the preactivated hydrogel increases owing to degradation of the initial structure.

CONCLUSION

Starch hydrogels can be subdivided into two groups by the nature of structural transformations occurring in these gels during treatment in a rotary pulse apparatus. In the first group (starch concentration 3–5 wt %) the surface tension increases, the starch reactivity decreases, and the film-forming properties are deteriorated after the treatment. In the second group (the starch concentration of 5–8 wt %) the surface tension decreases, the starch reactivity increases, and the physicomechanical properties of the films are improved after the treatment.

REFERENCES

1. Lipatova, I.M., Padokhin, V.A., Moryganov, A.P., *et al*., *Tekst. Prom–st.* (Moscow), 1998, no. 5, pp. 32–33.
2. Lipatova, I.M., Yusova, A.A., and Moryganov, A.P., *Zh. Prikl. Khim*., 2000, vol. 73, no. 8, pp. 1372–1376.
3. Vshivkov, S.A., Kulichikhin, S.G., and Rusinova, E.V., *Usp. Khim*., 1998, vol. 67, no. 3, pp. 261–273.
4. Brestkin, Yu.V., D'yakonova, N.E., *et al*., *Vysokomol. Soedin., Ser. A*, 1992, vol. 34, no. 5, pp. 15–23.
5. Povkh, I.L. and Makogon, B.P., *Dopov. Akad. Nauk Ukr. RSR, Ser. B*, 1986, no. 10, pp. 31–33.
6. Vshivkov, S.A. and Safronov, A.P., *Vysokomol. Soedin., Ser. A*, 1986, vol. 28, no. 12, pp. 2516–2520.
7. Shanthy, A.P., *Stärke*, 1980, no. 12, pp. 409–411.
8. Richter, M., Augustat, S., and Schierbaum, F., *Ausgewahlte Methoden der Stärkechemie*, Leipzig: Fachbuchverlag, 1968.
9. Kurilova, V.A. and Volkova, N.V., in *Novye polimernye materialy i materialovedenie v legkoi promyshlennosti* (New Polymeric Materials and Materials Science in Light Industry), Moscow: TsNIITEIlegprom, 1978, vol. 1, pp. 14–17.
10. Lipatova, I.M., Yusova, A.A., Ermolaeva, N.A., and Moryganov, A.P., *Tekst. Khim*., 1995, no. 2(7), pp. 85–89.
11. Lipatova, I.M., Sedova, I.L., Yermolaeva, N.A., *et al*., in *Textile Chemistry*, Nova Science, 1997, pp. 265–271.
12. Lipatova, I.M., Moryganov, A.P., and Yusova, A.A., Abstarcts of Papers, *VI Mezhdunarodnaya konferentsiya "Problemy sol'vatatsii i kompleksoobrazovaniya"* (VI Int. Conf. "Problems of Solvation and Complexation"), Ivanovo, October 10–12, 1995, N-39.
13. Papkov, S.P., *Fiziko-khimicheskie osnovy pererabotki polimerov* (Physicochemical Foundations of Polymer Processing), Moscow: Khimiya, 1971.
14. *Non-Stoichiometric Compounds*, Mandelcorn, L., Ed., New York: Academic, 1964.

Russian Journal of Applied Chemistry, Vol. 74, No. 9, 2001, pp. 1568–1572. Translated from Zhurnal Prikladnoi Khimii, Vol. 74, No. 9, 2001, pp. 1522–1525.

MACROMOLECULAR CHEMISTRY AND POLYMERIC MATERIALS

Structure of Aqueous Methyl and Propyl Methyl Cellulose Solutions in the Initial Stage of Gelation

N. A. Kalinina, A. M. Bochek, I. G. Silinskaya, L. A. Nud'ga, and V. A. Petrova

Institute of Macromolecular Compounds, Russian Academy of Sciences, St. Petersburg, Russia

Received April 25, 2001

Abstract—Evolution of the supramolecular associate structure of moderately concentrated aqueous methyl and propyl methyl cellulose solutions, as dependent on the degree of substitution by propyl groups, is studied by the polarized light scattering using the Debye–Bueche–Stein theory.

Moderately concentrated aqueous solutions of cellulose mixed ethers, classified with self-associated polymeric systems, demonstrate a series of useful properties based on the possibility of forming physical thermally reversible gels. Methyl cellulose (MC) and propyl methyl cellulose (PMC) are gel-forming materials [1, 2]. The gelation temperature in aqueous MC solutions is influenced by such factors as the polymer concentration, degree of substitution, and degree of uniformity of substituent distribution in anhydroglucose units and along the macrochain [3].

Introduction of propyl groups into MC macromolecules decreases the gelation and phase separation temperatures, and increasing degree of substitution by propyl groups (DS_{Pr}) increases the solution viscosity, viscous flow activation enthalpy, and degree of structurization of the solution [2]. In this connection, it appeared interesting to study the effect of DS_{Pr} on the structure of the initial 1.5% aqueous PMC solutions using the polarized light scattering method (PLS).

Treatment of PLS data in terms of the Debye–Bueche–Stein statistical theory allows characterization of the supramolecular correlation in the structure of condensed polymeric systems using structural parameters determined from the experimental indicatrices of the isotropic V_V and anisotropic components (H_V) of light scattering in the range of large scattering angles (40°–140°). It was demonstrated previously [4–6] that data obtained by PLS allow also prediction of the structure of polymer solutions on the basis of the morphological characteristics of the polymer in the condensed state.

Gelation in moderately concentrated aqueous MC solutions is a two-stage process, as demonstrated by viscometry and the dynamic and low-angle neutron scattering methods [7, 8]. In the first stage (T < 45–50°C) hydrophobic supramolecular association occurs, resulting in formation of clusters. In the second stage (T > 45–50°C) a gel is formed. In this stage phase separation of the liquid–liquid type is accompanied by considerable change in the structural parameters of the system. Previously [9] these processes were studied by PLS in 1.5% solutions of MC in water and dimethylacetamide. Thus, the initial stage of gelation may be judged from data on the solution structure in the subgel range at 20°C.

In this work we studied the effect of DS_{Pr} on the structural features of 1.5% aqueous MC and PMC solutions at 20°C.

EXPERIMENTAL

The mixed propyl methyl cellulose ether was prepared from MTs-100 commercial water-soluble methyl cellulose [degree of polymerization (DP) 830; degree of substitution by methoxy groups (DS_{Me}) 1.62] according to the procedure described in [2]. The total degree of substitution was estimated as DS_t = 1.62 + DS_{Pr}. At DS_{Pr} > 0.35 PMC becomes insoluble in water as a result of considerable shift in the hydrophilic–hydrophobic balance of the macromolecules toward higher hydrophobicity. The structure at 20°C of conditioned 1.5% aqueous solutions of MC and PMC with DS_{Pr} of 0.09, 0.13, and 0.30 was studied by PLS with an FPS-3M photoelectric nephelometer. In experiments we used vertically polarized light (λ 546 nm) and measured the angular dependences of the anisotropic (H_V) and isotropic (V_V) components of the scattered light. Calibration was made by scattering in benzene. The Rayleigh ratio for benzene with incident

1070-4272/01/7409-1568$25.00

natural light was found to be 16.4×10^{-6} cm^{-1}. To characterize the supramolecular structure of the solutions, we estimated the parameters of the system in frameworks of the statistical theory [10] as applied to moderately concentrated solutions [11]. From the linear dependence $1/(V_V - 4/3H_V)^{0.5}$ vs. $\sin^2(\theta/2)$ we determined parameters characterizing the isotropic structure: mean squared fluctuation of the polarizability (density) $\langle\eta^2\rangle$ and the radius of the polarizability fluctuation correlation a_V characterizing the degree of inhomogeneity of the system and its correlation size.

From the linear section of the angular dependences of $1/(H_V)^{0.5}$ we determined the parameters characterizing the microanisotropic structure: mean squared density of the optical anisotropy of a scattering element of the bulk $\langle\delta^2\rangle$ and the orientation correlation radius a_H, characterizing the degree of structurization of the system and the dimensions of the oriented domains.

The angular dependences of the V_V component of scattering for 1.5% solutions reveal (Fig. 1a) that introduction of propyl groups changes the position and, to somewhat extent, slope of the curves; in the initial MC and at low DS_{Pr} the slope increases in the low-angle range (40°–90°). Similar data were obtained in [8] by the neutron scattering for moderately concentrated aqueous MC solutions at 20°C, indicating nonuniform spatial distribution of intermolecular interactions in the system. These results suggest that a wide series of associated structures exist in the subgel range. At the same time, dynamic light scattering in dilute solutions of MC reveals two populations of accociated macromolecules [12].

Anisotropic scattering data are given in Fig. 1b. It should be pointed out that the angular dependence of H_V for MC and PMC solutions with small amount of the propyl substituents passes through a maximum in the scattering angle range below 80°. In the high-angle range the intensity of anisotropic scattering H_V abnormally increases, which is not typical of polymeric systems with random fluctuations of the anisotropy. This fact can be attributed to the specific structural features of this MC sample, which contains nuclei of a microcrystalline phase, consisting essentially of trisubstituted MC units, in addition to large ordered associated structures [3. 7, 8]. With increasing fraction of the propyl groups the maximum in the angular dependence degenerates. Nevertheless, the shape of the H_V curve reveals two types of oriented domains in the system [5].

To understand whether such a distinct deviation of the angular dependence of H_V from linearity is associated with the solution structure or this effect is a consequence of incomplete dissolution of the polymer microparticles, all solutions were converted into gels by heating to 70°C and then frozen and allowed to stand for 1 day at –6°C and for 30 days at +5°C, to eliminate hysteresis of characteristics of the system on passing from the solution state to the gel state and backwards [9]. It is known that at low temperatures in solutions of macromolecules containing both hydrophilic and hydrophobic fragments, water molecules form chamber-like structures, surrounding hydrophobic (in our case the methyl and propyl substituents) fragments, thus eliminating the effect of the nonpolar groups on the polar solvent and providing preservation of the hydrophilic–hydrophobic balance [13]. At temperature of about 0°C the solubility of MC and PMC in water increases. On heating the

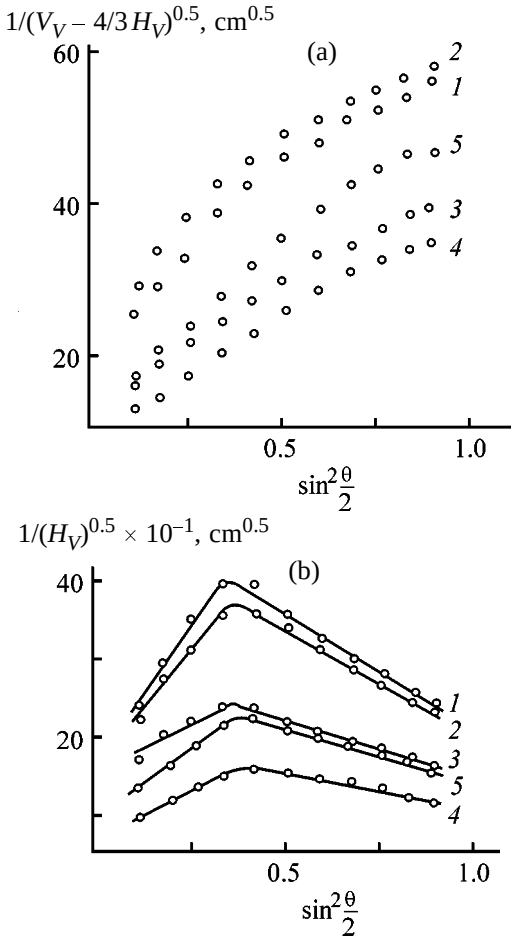

Fig. 1. Angular dependence of the indicatrices of the intensities of (a) isotropic scattering $1/(V_V - 4/3H_V)^{0.5}$ and (b) anisotropic scattering $1/(H_V)^{0.5}$ of 1.5% aqueous cellulose ether solutions after performing the cycle gel–solution–freezing–solution. Solution: (*1*) MC (DS 1.62) and (*2*–*5*) PMC. DS_{Pr}: (*2*) 0.09, (*3*) 0.13, and (*4*, *5*) 0.30.

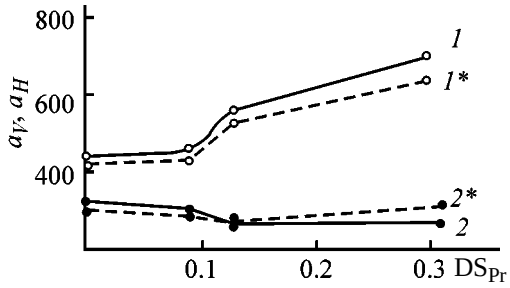

Fig. 2. Statistical parameters (*1*) a_V and (*2*) a_H of the structure of 1.5% aqueous PMC solutions at 20°C as functions of DS_{Pr}. (*1**, *2**) Corresponding parameters after performing the cycle solution–gel–freezing–solution; the same for Fig. 3.

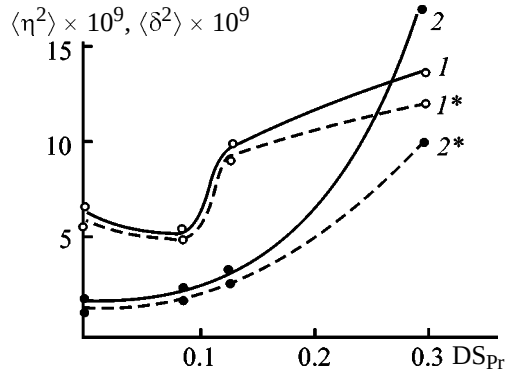

Fig. 3. Statistical parameters (*1*) $\langle\eta^2\rangle$ and (*2*) $\langle\delta^2\rangle$ of the structure of 1.5% aqueous PMC solutions as functions of DS_{Pr}.

weakest H bonds between water molecules and oxygen atoms of the methoxy and propoxy groups break down, which results in strengthening of interactions between the macromolecules by their fragments mainly containing essentially highly substituted units. Thus, hydrophobic self-association of MC and PMC macromolecules occurs, initiating aggregation and phase separation.

The reversibility of the structural transformations in the systems was proved by manifold repetition of the cycle solution–gel–freezing–solution. The angular dependences of the H_V and V_V components of scattering for solutions of PMC with $DS_{Pr} < 0.3$ coincided within the experimental error. For the systems with $DS_{Pr} = 0.3$, i.e., at the critical content of the propyl groups (with regard to the solubility in water), we observed reproducible changes in the scattering intensity (Figs. 1a, 1b; curves *5*). Note that in frozen 1.5% MC and PMC solutions we observed a fine ice texture with well distinguished crystals. On cooling the solutions to 0°C the solubility of MC and PMC increases by virtue of hydration of the polymer macromolecules. At temperature below 0°C H bonds between water molecules and functional groups of the polymers break down, which results in formation of fluctuating domains of displaced structured water serving as nuclei of crystalline phase of ice [13].

The statistical parameters characterizing the effect of substitution of the hydroxy groups of MC by the propyl groups on the structure of the 1.5% aqueous solutions are given in Figs. 2 and 3. The results show that introduction of additional hydrophobic groups provides a three fold increase in $\langle\eta^2\rangle$ (Fig. 3, curve *1*) and increase in a_V from 400 (MC) to 700 Å (PMC; $DS_{Pr} = 0.30$) (Fig. 2, curve *1*). Note that previously we demonstrated that increasing content of the propyl groups in the macromolecules provides increase in the viscosity and degree of structurization of their solutions [2]. These results can be attributed to increasing intermolecular hydrophobic association with increasing DS_{Pr}, which is accompanied by separation of the solvent into particular domains [13]. The domains of intermolecular associates and solvent-rich domains have different polarizabilities, and with increasing a_V of denser domains (due to higher content of propyl groups) the microheterogeneity of the system $\langle\eta^2\rangle$ correspondingly increases. In [14] it was demonstrated that cellulose-based polymers containing critical (for solubility) content of hydrophobic groups are converted into gels at lower temperature, and the resulting gels have lower strength because of relatively higher heterogeneity of the system.

It is known that introduction of bulky alkoxy substituents into the cellulose macromolecule increases its equilibrium rigidity and changes the macrochain conformation, affecting the microanisotropic structure of moderately concentrated polymer solutions. Previously [9] we reported that in moderately concentrated MC solutions fluctuations of the anisotropy and orientation occur, and increasing amount of the propyl groups in the MC macromolecule provides growth in the intensity of anisotropic scattering in the experimental angle range. Thus, over the angle range from 40° to 80° $\langle\delta^2\rangle$ increases by more than an order of magnitude from 1.2×10^{-9} to 1.6×10^{-8} (Fig. 3, curve *2*). As noted above, it follows from the abnormal shape of the angular dependence of the anisotropic H_V component of scattering that the structure of the system can be described by two types of correlations (random and nonrandom) of orientation of optical axes of elementary scattering volumes. The parameters of microanisotropic structure of the first

type ($\langle\delta^2\rangle$ and a_H) were estimated from the initial slope of the H_V curve (Fig. 1b). The estimated values correspond to ordered regions 250–300 Å in size, which, in principle, is consistent with the Kuhn segment length of an individual macromolecule of a cellulose ether (a_H tends to decrease with increasing fraction of the propyl groups). This is caused by hindered orientation of coarser scattering elements (their anisotropy increases with increasing DS_{Pr}) as a result of reorganization of the system of polymer–solvent H bonds. Structures of the second type cannot be quantitatively characterized by PLS. However, X-ray diffraction analysis data for MC gels revealed that there are points of an ordered structure (crystallites) consisting of essentially trisubstituted MC units. The nature of intermolecular interactions of PMC chains in ordered (anisotropic) and amorphous (isotropic) domains can be different [3]. Therefore, it is a valid conclusion that two types of orientation correlation coexist in the solution: one near the nucleation centers of the microcrystalline phase and another in associates formed through hydrophobic association of macromolecular fragments. The experimental data show (Fig. 1b) that the inflection on the angular dependence of the H_V component of scattering becomes less pronounced with increasing fraction of the propyl groups, i.e., the effect of nucleation centers of the microcrystalline phase of MC on the nature of anisotropic scattering somewhat decreases with introduction of an additional hydrophobic substituent.

Turning to the study of the reversibility of the structure of 1.5% solutions of the mixed cellulose ethers, it should be pointed out that the statistical parameters of their structure are practically coincident at low DS_{Pr}.

At $DS_{Pr} = 0.3$ (critical value for solubility) freezing has an effect on both the isotropic and anisotropic structures: $\langle\eta^2\rangle$ and $\langle\delta^2\rangle$ tend to decrease, suggesting that performing the cycle solution–gel–freezing–solution makes the system more homogeneous and the scattering elements, less anisotropic. This is probably due to restoration of hydrogen bonds between OH groups, oxygen atoms of the methoxy and propoxy groups, and clusters of the polar solvent (water) which restores its tetrahedral structure at low temperature also [13]. At lower DS_{Pr} the structure of the polar associated solvent apparently plays a less significant role.

CONCLUSIONS

(1) Treatment of the structure of moderately concentrated methyl and propyl methyl cellulose solutions at 20°C (subgel region) in terms of the statistical theory of polarized light scattering revealed that increasing fraction of propyl groups, introduced as an additional hydrophobic agent, considerably increases the correlation size of microheterogeneity of the solution as a result of hydrophobic association.

(2) The solutions have a microanisotropic structure. The shape of the angular dependence of the H_V component of the light scattering suggests two types of orientation correlation of scattering elements in the bulk. The first type is associated with random fluctuations of orientation at distances of about 200–250 Å corresponding to the length of the rigid part of an individual macromolecule of propyl methyl cellulose in the solution. Ordered regions of the second type may be regarded as nucleation centers formed as a result of hydrophobic interactions of highly substituted polymer units. Increasing fraction of the propyl substituents in the macromolecules results in considerable growth of the mean density of the optical anisotropy in parallel to development of supramolecular structure in the system.

(3) At low content of propyl substituent in mixed propyl methyl cellulose ethers the cycle gel–solution–freezing–solution does not change significantly the structure of their aqueous solutions. The system with the critical content of the propyl groups (with regard to the solubility in water) becomes more homogeneous and less anisotropic after this cycle is performed.

REFERENCES

1. Petropavlovskii, G.A., *Gidrofil'nye chastichno zameshchennye efiry tsellyulozy i ikh modifikatsiya putem khimicheskogo sshivaniya* (Hydrophilic Partially Substituted Cellulose Ethers and Their Modification by Chemical Cross-Linking), Leningrad: Nauka, 1988.
2. Bochek, A.M., Nud'ga, L.A., Petrova, V.A., *et al.*, *Zh. Prikl. Khim.*, 2000, vol. 73, no. 2, pp. 304–308.
3. Kato, T., Yokoyama, V., and Takabashi, A., *Colloid Polym. Sci.*, 1978, vol. 256, no. 1, pp. 15–21.
4. Petropavlovsky, G.A., Kallistov, O.V., Vasil'eva, G.G., *et al.*, *Zh. Prikl. Khim.*, 1983, vol. 56, no. 3, pp. 709–712.
5. Kalinina, N.A., Kallistov, O.V., Kuznetsov, N.P., *et al.*, *Vysokomol. Soedin., Ser. A*, 1990, vol. 32, no. 4, pp. 695–700.
6. Silinskaya, I.G., Kallistov, O.V., Kutsenko, L.I., *et al.*,

Zh. Prikl. Khim., 1992, vol. 65, no. 12, pp. 2770–2774.

7. Tanaka, F. and Ishida, M., *J. Chem. Soc., Faraday Trans.*, 1995, vol. 95, no. 16, pp. 2663–2670.
8. Kobayashi, K., Huang, C., and Lodg, T.P., *Macromolecules*, 1999, vo. 32, pp. 7070–7077.
9. Bochek, A.M., Petropavlovskii, G.A., and Kallistov, O.V., *Zh. Prikl. Khim.*, 1996, vol. 69, no. 8, pp. 1363–1368.
10. Stein, R.S. and Wilson, P.R., *J. Appl. Phys.*, 1962, vol. 33, no. 6, pp. 1914–1922.
11. Kallistov, O.V., Krivobokov, V.V., Kalinina, N.A., *et al.*, *Vysokomol. Soedin., Ser. A*, 1985, vol. 27, no. 5, pp. 968–974.
12. Costeux, S. and Djabourov, M., Abstracts of Papers, *Int. Symp. "Associating Polymers,"* Loen (Norway), 1995, p. 10.
13. Leloux, M.S., *J. Macromol. Sci.*, 1999, vol. 39, no. 1, pp. 3–10.
14. Sarkar, J., *J. Appl. Polym. Sci.*, 1979, vol. 24, no. 4, pp. 1073–1087.

Russian Journal of Applied Chemistry, Vol. 74, No. 9, 2001, pp. 1573–1576. Translated from Zhurnal Prikladnoi Khimii, Vol. 74, No. 9, 2001, pp. 1526–1529.

MACROMOLECULAR CHEMISTRY AND POLYMERIC MATERIALS

Composite Fibers Based on Chitin and Cellulose

G. M. Mikhailov, M. F. Lebedeva, L. A. Nud'ga, and V. A. Petrova

Institute of Macromolecular Compounds, Russian Academy of Sciences, St. Petersburg, Russia

Received March 23, 2001

Abstract—Composite fibers were produced by mixing of chitin and cellulose solutions with subsequent molding from these solutions under standard conditions. The effect of composition of systems on the structural modification and the deformation-strength characteristics of the fibers was studied.

Cellulose and chitin are the most important renewable natural fiber-forming polysaccharides. With the rational use their resourses are unexhaustible. A wide variety of materials based on cellulose and its ethers have been developed and are produced.

At the same time, chitin fibers are not produced commercially anywhere in the world. This is due to the ability of chitin macromolecules to spontaneous crystallization to form fibers of the band-fibrillar morphology characteristic of rigid- or semirigid-chain polymers [1, 2]; therefore, the resulting fibers are highly friable. Contrary to cellulose, chitin is biologically active. This explains the growing researchers' interest in fibers and materials based on chitin.

Polysaccharides can be blended by mixing their solutions. Both chitin and cellulose can be dissolved in a complex solvent such as a solution of lithium chloride in dimethylacetamide (DMAA/LiCl) [3, 4].

Addition of polyvinylpyrrolidone or methyl cellulose to the spinning solution can significantly improve the deformation-strength characteristics of the fibers [5].

It is well known that polymers are well compatible in solutions of cellulose–chitin blends [6]. Therefore, it seems appropriate to study the effect of the composition of blends on the deformation-strength characteristics of fibers based on both chitin modified with cellulose and cellulose modified with chitin.

EXPERIMENTAL

In the study we used dimethylacetamide (DMAA) dehydrated and distilled in a vacuum, bp 42°C/7 mm Hg; lithium chloride crystal hydrate dehydrated at 400°C; chitin produced from crab armor by the SONAT Joint-Stock Company, ash content 0.02%, protein-free, degree of polymerization (DP) 678, molecular weight M 137000 D, $[\eta]$ 8.4 dl g^{-1}; and cellulose produced by the Svetogorsk Pulp and Paper Plant, wood, sulfite, whitened, ash-free, DP 680, M 110000 D, $[\eta]$ 3.36 dl g^{-1}.

The intrinsic viscosity of chitin solution was determined in DMAA + 5% LiCl. The molecular weight was evaluated by the formula [3]

$$[\eta] = 2.4 \times 10^{-3} M^{0.69}.$$

The intrinsic viscosity of cellulose was determined in a solution in cadoxene. The molecular weight M was evaluated by the formula [7]

$$[\eta] = 5.93 \times 10^{-5} M^{0.94}.$$

The fiber was formed on a PIFV-01 setup using a dosing syringe and a 1/04 spinneret. The precipitation bath was a mixture of ethanol and ethylene glycol at the volume ratio of 1 : 1. The plasticization bath was water. The fiber was washed with hot water to remove lithium chloride to a total absence of chloride ion in the wash water (test with silver nitrate). The fiber was air-dried at room temperature.

For more precise estimation of the effect of modifying additives on the mechanical characteristics of the fibers the conditions of fiber production were standardized.

The mechanical tests were carried out on an Instron universal tensile-testing machine. The stress–strain diagrams were obtained with a 50-mm sample at the loading rate of 5 mm min^{-1}. Before testing the samples were kept in a desiccator for 24 h over concentrated aqueous solution of magnesium acetate, i.e., at a relative humidity of 65%.

1070-4272/01/7409-1573$25.00

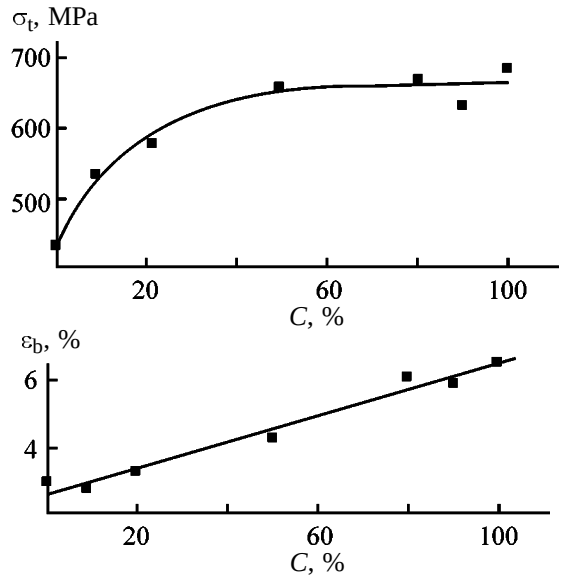

Tensile strength σ_t and elongation at break ε_b of the fibers as functions of the cellulose concentration *C*.

Chitin and cellulose were dissolved by the procedure described in [8]. The content of lithium chloride in the solvent was 9%. Cellulose and chitin were dissolved in a DMAA/LiCl mixture to attain the concentration of each component of 3%. This condition was followed to provide the constant total concentration of the polymers in the spinning solution, 3%, on addition of modifying additives. To obtain the required systems, a calculated amount of the modifier solution was added. The mixture was thoroughly mixed, degassed in a vacuum, and used in forming of the fiber.

To accelerate the dissolution, with the aim to improve the accessibility of the reaction centers, polysaccharides, e.g., cellulose, are commonly treated with water and then methanol; the latter is replaced with DMAA. This procedure allows preparation of a transparent solution of a polysaccharide with a higher concentration of the polymer in a shorter time. The larger the molecular weight of the polymer, the longer the time of solution preparation.

To produce solutions of polysaccharides, the mixture was heated to 150°C [8] and then the transparent solutions were obtained by slow cooling under nitrogen to protect the system from thermal oxidative degradation [8]. In this work we used this procedure to obtain cellulose and chitin solutions from which the fibers were produced.

The figure presents the strength and deformation characteristics of the fibers produced from crab chitin, sulfite cellulose, and their mixtures of various compositions, as functions of the cellulose concentration.

An increase in the strength of the fibers σ_t is usually related to an increase in the total energy of intermolecular interaction. In our case the strength of composite fibers increases with increasing content of cellulose (rigid-chain polymer). Thus, for chitin fibers it increases to 660 MPa with increasing content of cellulose to 50%, after which the curve flattens out (see figure).

The elongation at break ε_b increases practically linearly with increasing concentration of cellulose, and at a 50% cellulose content in the mixture of polymers it is 4.4–4.8% (see figure).

However, in this part of the study of modification of chitin fibers with cellulose and cellulose fibers with chitin at low content of modifiers (no more than 5% of both cellulose in chitin and chitin in cellulose) we observed sharp deviations from the monotonic dependences for the tensile strength and elongation. These deviations are presented in the table.

Characteristics of polysaccharide fibers at low content of modifier

Content, %	σ_t, MPa	ε_b, %
Cellulose in chitin:		
0	436	2.9
0.5	526	2.4
2.5	457	2.2
4.8	482	3.2
9.0	536	2.9
Chitin in cellulose:		
0	651	6.7
0.5	530	11.0
2.5	595	7.7
5.0	617	6.8
10.0	640	6.0

The table shows that on addition of only 0.5% of cellulose to chitin the tensile strength of the fibers increases by 23% and at the modifier content of 2.5% it decreases to almost the initial level. This local maximum of the tensile strength is accompanied by the minimum of the elongation at break.

In modification of cellulose with chitin the situation is opposite: addition of the same amount of modifier (0.5%) results in an abrupt increase in the elongation at break, which reaches 11%, i.e. increases by more than 50%. This abrupt increase is accompanied by the local minimum of the tensile strength.

These extrema in the deformation-strength charac-

teristics of fibers at low content of modifiers can be questioned. However, the studies of the structure of similar solutions of these polysaccharides [10] and unoriented films produced from the similar systems [11] support these results. For example, the study of films preliminarily swollen in heavy-water vapor with various chitin : cellulose ratio showed that the amount of sorbed D_2O vapor decreases on addition of 0.5% of cellulose to chitin and, contrary, increases on addition of 0.5% of chitin to cellulose. The study of these films by the low-angle neutron scattering showed that the minimum size of scattering heterogeneities is typical for the films with a low content of any one of the components. We also observed a sharp local decrease in the size of the scattering heterogeneities. At the content of cellulose in chitin film of 0.5% the size of heterogeneities substantially decreases, their number increases, and the structure of the films becomes more homogeneous. Such homogeneous, though less pronounced, structure of the films takes place at a low (0.5%) content of chitin in cellulose. In [11] we noted that at small additions of chitin and cellulose variations in the structure in both solutions and solids are opposite, and a more heterogeneous structure is formed on addition of chitin to cellulose than on addition of cellulose to chitin.

When considering the chemical structure of chitin and cellulose, we can reveal the driving forces that govern the morphology of modified fibers.

As follows from the presented fragments of cellulose (**A**) and chitin (**B**) macromolecules, the only distinction is that one hydroxy group in the pyranose ring in chitin is replaced by acetamide group:

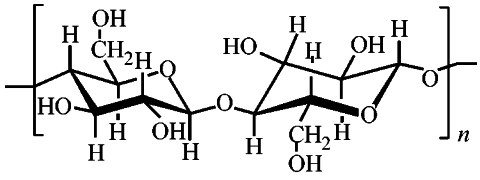

A

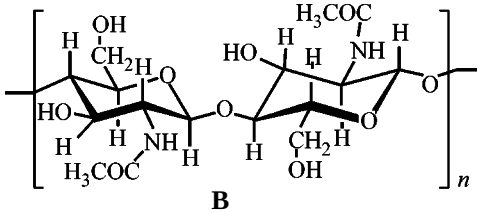

B

These groups will hamper packing of macromolecules in a blend of polysaccharides and affect the characteristics of hydrogen bonds in the system.

Small amounts of cellulose added to chitin can form a layer on the surface of supramolecular structures of chitin, enhancing the interstructure interaction owing to "additional" hydroxy groups. It is just this effect that should result in an increase in the rigidity of the system, which is reflected in decrease in the elongation at break (see table). Thus, small additions of cellulose to chitin act as an antiplasticizer. On the contrary, addition of chitin to cellulose should decrease the intermolecular interaction at the interface of the structural elements, since acetamide groups of chitin will hinder sterically the packing of cellulose macromolecules. Therefore, small additions of chitin will act as a plastizicer. This can explain the increase in the elongation at break of cellulose fibers containing small amounts of the modifier.

Thus, the effect of small additions to the polymer, substantially affecting its characteristics, should be explained by their role in variation of supramolecular ordering of highly arranged polymer systems. It is believed that the origin of these phenomena is as follows. The arrangement of a modifier over the interface of structural supramolecular elements of polymer results in some cases in decrease in the surface energy and thus promotes mobility of its structural elements. In this case, the structural plasticization of the modified system takes place. In other cases, when the energy of interaction of interstructural elements increases, the structural antiplasticization of the polymer with the modifying additive takes place. However, the necessary condition of interpretation of these phenomena is the presence of interfaces of the structural elements of the polymer. This suggests that the system must be heterogeneous, which is in a good agreement with the Papkov's conclusion [12]. These phenomena are manifested in formation of heterogeneous systems with structural elements corresponding to "macroscopic level" of the structure.

The modifier is localized at the interface of macroscopic elements of the supramolecular structure of the polymer. This case can be regarded as formation of a heterogeneous system with the interface at the site of the modifier location. However, probably, for such related polymers as chitin and cellulose having polymeric chains formed by glucopyranose rings we cannot speak of heterogeneity in the generally accepted sense. Actually, the concentration of hydrogen bonds at the surface of micro- and macrofibrils significantly changes. In modification of cellulose with microamounts of chitin this concentration decreases, and in modification of chitin with cellulose, increases.

In this respect we would like to call attention to the specific feature of cellulose satellites, hemicelluloses,

which, being natural structural modifiers, affect the deformation-strength characteristics of plant materials. Therefore, a special attention should be given to the history of the polymer sample subjected to structural modification and procedures of its recovery and pretreatment, which govern its purity and polydispersity and, hence, characteristics of the fibers produced from this polymer.

CONCLUSIONS

(1) The structural modification of chitin fibers with cellulose and cellulose fibers with chitin was carried out.

(2) In modification of chitin fibers with small amounts of cellulose the latter acts as structural antiplasticizer, which forms epitaxial layer at the interface of supramolecular elements and increases the energy of interstructural interaction owing to increase in the density of the network of hydrogen bonds between supramolecular formations.

(3) In modification of cellulose with chitin, small additions of chitin act as structural plasticizer of cellulose fibers. The plasticizing effect is caused by increased energy of hydrogen bonds at the interface of supramolecular structures of cellulose with acetamide groups of chitin.

(4) Addition of cellulose to chitin fibers substantially improves their deformation-strength characteristics.

REFERENCES

1. Sukhanova, T.E., Sidorovich, A.V., Goryainov, G.I., *et al*., *Vysokomol. Soedin., Ser. B*, 1989, vol. 31, no. 5, pp. 381–384.
2. Mikhailov, G.M., Korzhavin, L.N., Lebedeva, M.F., and Baklagina, Yu.G., *Zh. Prikl. Khim*., 1998, vol. 71, no. 12, pp. 2040–2050.
3. Terbojevich, M., Corrado, C., Cosani, A., and Marsano, E., *Carbohydr. Res*., 1988, vol. 180, pp. 73–86.
4. Davsey, T.R. and McCormic, C.L., *J. Macromol. Sci. Rev. Macromol. Phys., Ser. C*, 1990, vol. 30, nos. 1–4, pp. 405–440.
5. Mikhailov, G.M., Lebedeva, M.F., Nud'ga, L.A., *et al*., *Zh. Prikl. Khim*., 2001, vol. 74, no. 7, pp. 1178–1182.
6. Bianchi, E., Marsano, E., Baldini, M., *et al*., *Polym. Adv. Technol*., 1995, vol. 6, no. 12, pp. 727–732.
7. Bolotnikova, L.S. and Samsonova, T.I., *Vysokomol. Soedin*., 1964, vol. 6, no. 3, pp. 533–537.
8. McCormic, C.L., Callais, P.A., and Hutchison, B.N., *Macromolecules*, 1985, vol. 18, no. 12, pp. 2394–2401.
9. McCormic, C.L. and Shen, T.S., in *Macromolecular Solutions*, New York: Pergamon, 1982, pp. 101–107.
10. Bochek, A.M., Nud'ga, L.A., Petrova, V.A., *et al*., *Zh. Prikl. Khim*., 1998, vol. 71, no. 12, pp. 2050–2055.
11. Nud'ga, L.A., Petrova, V.A., Bochek, A.M., *et al*., *Vysokomol. Soedin., Ser. A*, 1999, vol. 41, no. 11, pp. 1786–1792.
12. Papkov, S.P., in *Fiziko-khimicheskie osnovy pererabotki rastvorov polimerov* (Physicochemical Principles of Processing of Polymer Solutions), Moscow: Khimiya, 1971, pp. 345–358.

Russian Journal of Applied Chemistry, Vol. 74, No. 9, 2001, pp. 1577–1580. Translated from Zhurnal Prikladnoi Khimii, Vol. 74, No. 9, 2001, pp. 1530–1532.

MACROMOLECULAR CHEMISTRY AND POLYMERIC MATERIALS

Inhibited Polymerization of *N*,*N*,*N*-Trimethylammonioethyl Methacrylate Methyl Sulfate

F. V. Ermilov, V. G. Shibalovich, and A. F. Nikolaev

St. Petersburg State Technological Institute, St. Petersburg, Russia

Received March 5, 2001

Abstract—The kinetic features of initiation of *N*,*N*,*N*-trimethylammonioethyl methacrylate methyl sulfate polymerization in the presence of manganese(III) bis(acetylacetonate) nitrate and *p*-nitrosoaniline were studied by the inhibited polymerization method. The kinetic parameters of initiation were calculated, and participation of the monomer in the initiation stage was established.

In radical polymerization, the initiation stage is the most energy-consuming and the slowest, as compared to chain propagation and termination, and, as a rule, it determines the overall polymerization rate [1].

A kinetic study of inhibited polymerization of *N*,*N*,*N*-trimethylammonioethyl methacrylate methyl sulfate (TMAEMA–MS) under the action of manganese(III) bis(acetylacetonate) nitrate (MN) was performed in aqueous solution in the temperature range 20–40°C in the presence of radical scavenger, *p*-nitrosoaniline (*p*-NA). The concentrations of the reactants (M) were as follows: inhibitor 6×10^{-7}–5×10^{-5}, initiator 6.3×10^{-4}, and monomer 1.41–2.82.

With *p*-NA added, we observed a clearly pronounced induction period τ_{ind} (Figs. 1a, 1b) within which no polymerization occurred, and after exhaustion of *p*-NA the copolymerization occurred at a constant rate equal to the polymerization rate in the absence of the inhibitor.

The duration of the induction period linearly depends on the inhibitor concentration, which suggests the absence of side reactions between the inhibitor and monomer (Fig. 2).

The constancy of the ratio $[Z]/\tau_{ind}$ ([Z] is the inhibitor concentration) suggests that the inhibitor is consumed only in reactions with primary radicals generated by decomposition of MN.

The facts that the induction period is proportional to the initial inhibitor concentration and that after the end of the induction period no inhibition is observed in the examined concentration range allow us to use the following equation [1] for calculating the initiation constants:

$$v_{in} = [Z_0]/\tau_{ind},$$

where v_{in} is the initiation rate (mol l^{-1} s^{-1}), $[Z_0]$ is the initial *p*-NA concentration (M), and τ_{ind} is the induction period (s). The initiation constant K_{in} (s^{-1}) can be

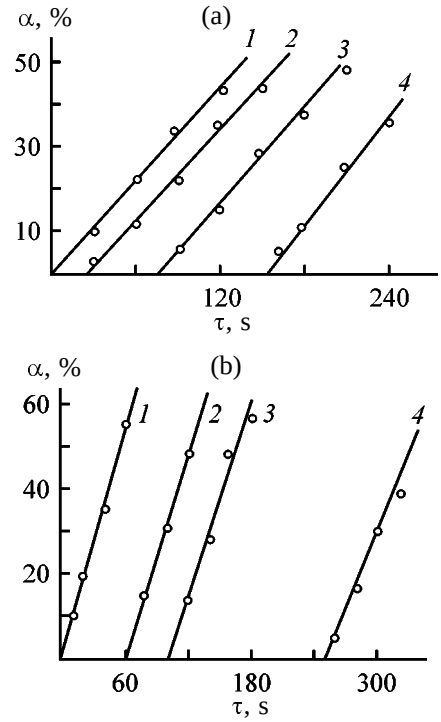

Fig. 1. Kinetic curves of inhibited polymerization of TMAEMA–MS in the presence of *p*-NA at 20°C: (α) conversion and (τ) time. TMAEMA–MS concentration, M: (a) 1.49 and (b) 2.82. *p*-NA concentration $c \times 10^6$, M: (a) (*1*) 0, (*2*) 0.67, (*3*) 1.25, and (*4*) 5.0; (b) (*1*) 0, (*2*) 1.0, (*3*) 2.0, and (*4*) 5.0.

1070-4272/01/7409-1577$25.00

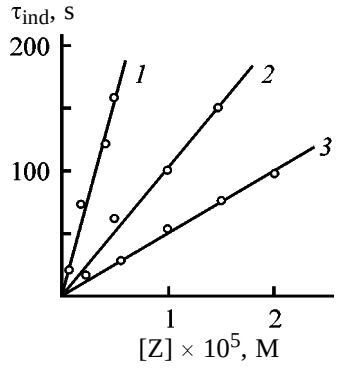

Fig. 2. Induction period τ_{ind} as a function of the inhibitor (*p*-NA) concentration [Z] at (*1*, *3*) 20 and (*2*, *4*) 40°C. Concentration of TMAEMA–MS, M: (*1*, *2*) 1.49 and (*3*, *4*) 2.82.

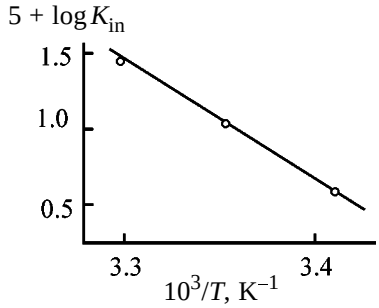

Fig. 3. Rate constant of TMAEMA–MS polymerization initiation K_{in} as a function of temperature *T*. MN concentration 6.3×10^{-4} M.

calculated by the equation

$$K_{in} = v_{in}/[I],$$

where [I] is the initiator (MN) concentration (M).

The initiation efficiency *f* was evaluated by the equation

$$f = v_{in}/K_h[I],$$

where K_h is the rate constant of homolytic decomposition of MN, $K_h = 7.34 \times 10^{-4}$ s^{-1}.

The reactivity of the primary radical in initiation of TMAEMA–MS polymerization in the presence of MN was evaluated by the equation [2]

$$f = v_{in}/(v_{in} + v_{sr}) = [M]/([M] + K_{sr}/K_h),$$

where v_{sr} is the rarte of the side reaction of the primary radical (mol l^{-1} s^{-1}), [M] is the monomer concentration (M), and K_{sr} is the rate constant of the side reaction of the primary radical (s^{-1}).

We found that the calculated initiation constants can be satisfactorily fitted by the Arrhenius equation (Fig. 3). The apparent activation energy of the initiation of TMAEMA–MS polymerization with MN is 40.3 kJ mol^{-1}, which is a typical value for polymerization of such monomers as acrylamide and acrylic acid in the presence of acido derivatives of manganese(III) bis(acetylacetonate) [3].

Experimental data (see table) show that the initiating power of MN, evaluated by K_{in}, *f*, and K_{sr}, significantly depends on the concentration of TMAEMA–MS monomer, which suggests participation of the monomer in the initiation stage.

The initiation efficiency of 0.5, and the high rate constants of the side reaction of the primary radical, comparable with the initiation constants, suggest a high reactivity of the primary radical.

A UV examination of dilute solutions of MN and TMAEMA–MS and of their equimolar mixture (concentration 5×10^{-4} M) showed (Fig. 4) that (1) the band at 47000 cm^{-1} (ε = 19140 l mol^{-1} cm^{-1}), characteristic of TMAEMA–MS in aqueous solutions, shifts to 45100 cm^{-1} (ε = 20100 l mol^{-1} cm^{-1}) in the spectrum of the equimolar mixture of TMAEMA–MS with MN; (2) the *π*–*d* charge-transfer band at 31400 cm^{-1}, characteristic of MN in aqueous solution, shifts to 29800 cm^{-1} upon interaction with TMAEMA–MS; (3) the molar extinction coefficient of the band at 36800 cm^{-1} (ε = 14700 l mol^{-1} cm^{-1}) characteristic of intraligand π–π* transitions in MN decreases upon interaction with TMAEMA–MS by a factor of 2 to 7400 l mol^{-1} cm^{-1}.

The UV data suggest that interaction of TMAEMA–MS with MN involves inner-sphere coordination of the monomer with the complex, which, as shown in numerous papers [6], is possible for such acrylic monomers as acrylamide, acrylic acid, and methyl methacrylate. When considering decomposition of MN in aqueous solutions, account should be taken of the fact that the Mn^{3+} ion has vacant *d* orbitals, which can favor formation of an inner-sphere complex in solution [6]. Thus, interaction of MN with TMAEMA–MS can be described by the following scheme:

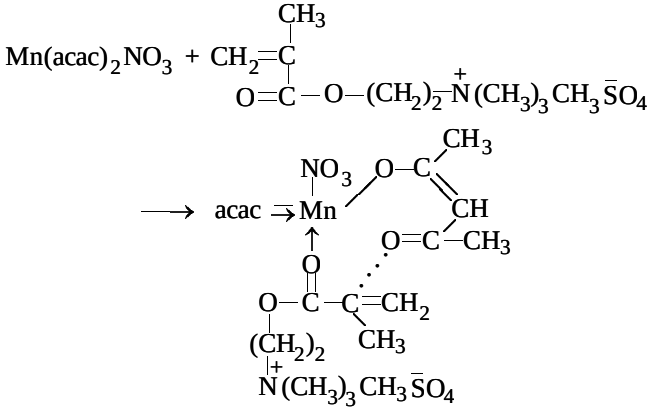

Inhibited polymerization of TMAEMA–MS in the presence of MN and *p*-NA (initiator concentration 6.34×10^{-4} M)

[M], M	*T*, °C	$[Z] \times 10^6$, M	τ_{in}, s	$v_{in} \times 10^{-8}$, mol l^{-1} s^{-1}	$K_{in} \times 10^4$, s^{-1}	*f*	$K_{sr} \times 10^5$, s^{-1}	K_{in}/K_{sr}	E_{in}	E_a	$E_r - 0.5E_0$
									kJ mol^{-1}		
1.49	20	0.62	25	2.48	0.395	0.05	1.56	2.53	40.3	51.8	31.65
	20	1.25	75	2.08							
	20	5.00	100	3.12							
	40	5.00	55	9.10	1.55	0.17	4.68	3.32			
	40	10.00	115	8.70							
	40	20.00	170	10.20							
2.82	20	10.0	60	16.60	3.06	0.41	7.51	4.07	–	47.9	–
	20	20.0	90	22.20							

It should be noted that monomers of the aminoalkyl (meth)acrylate series and their derivatives tend to form intermediate donor–acceptor complexes with initiating systems [7, 8]. This property affects the reactivity of the monomer and initiator and determines the specific features of their behavior in the polymerization medium.

EXPERIMENTAL

The kinetics of the inhibited polymerization of TMAEMA–MS was studied by the inhibition procedure in aqueous solution under oxygen at 20°C in the presence of the mixed-ligand manganese(III) complex MN and the radical scavenger *p*-NA [2].

The UV spectra of the compounds (aqueous solutions, pH 4) were taken on a Specord spectrophotometer.

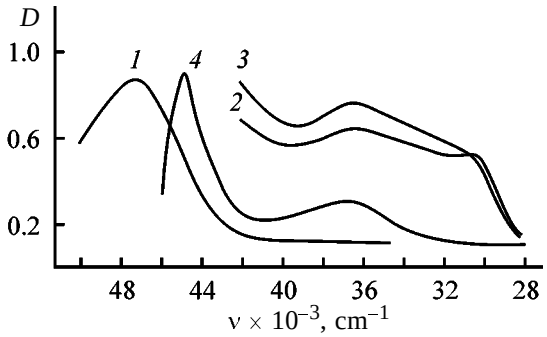

Fig. 4. UV absorption spectra of TMAEMA–MS and MN in aqueous solution (pH 4.0). (*D*) Optical density and (ν) wave number. (*1*) TMAEMA–MS, (*2*) MN, and (*3*, *4*) MN : TMAEMA–MS = 1 : 1 (mol : mol), 1.5 and 10 min after mixing, respectively.

CONCLUSIONS

(1) The kinetic parameters of initiation of *N,N,N*-trimethylammmonioethyl methacrylate methyl sulfate: K_{in}, v_{in}, *f*, and E_{in}, in the presence of manganese(III) bis(acetylacetonate) nitrate and *p*-nitrosoaniline were determined by the method of inhibited polymerization. It was found that manganese(III) bis(acetylacetonate) nitrate exhibits a high initiating activity, which significantly depends on the monomer concentration.

(2) The UV spectra of the compounds and reaction systems show that interaction of *N,N,N*-trimethylammonioethyl methacrylate methyl sulfate with manganese(III) bis(acetylacetonate) nitrate involves formation of a donor–acceptor complex, which determines the specific features of their behavior in the course of polymerization.

REFERENCES

1. Gladyshev, G.N., *Polimerizatsiya vinilovykh monomerov* (Polymerization of Vinyl Monomers), Alma-Ata: Akad. Nauk Kaz. SSR, 1974.
2. Zil'berman, E.N. and Navolokina, R.A., *Primery i zadachi po khimii vysokomolekulyarnykh soedinenii* (Examples and Problems on Chemistry of Macromolecular Compounds), Moscow: Vysshaya Shkola, 1984.
3. Perina, G.P., Polymerization and Copolymerization of Acrylamide and Acrylic Acid in the Presence of Manganese(III) Acidobis(acetylacetonates): *Cand. Sci. Dissertation*, Leningrad, 1982.
4. Ermilov, F.V., Khar'kova, A.M., Shibalovich, V.G., and Nikolaev, A.F., in *Khimicheskaya tekhnologiya, svoistva i primenenie plastmass: Mezhvuzovskii sbornik*

nauchnykh trudov LTI im. Lensoveta (Chemical Technology, Properties, and Use of Plastics: Intercollegiate Collection of Scientific Works of Lensovet Leningrad Technological Institute), Leningrad, 1990, pp. 43–54.

5. Bamford, C.H. and Ferrar, A.N., *J. Chem. Soc., Faraday Trans.*, 1972, vol. 68, pp. 1243–1257.
6. Belogorodskaya, K.V., Polymerization and Copolymerization of Vinyl Compounds in the Presence of Complexes of Variable-Valence Metal Salts and Carboxylic Acids. *Doctoral Dissertation*, Leningrad, 1980.
7. Chulpanov, K.A., Ismailov, I.I., and Dzhalilov, A.T., *Vysokomol. Soedin., Ser. B*, 1983, vol. 25, no. 3, pp. 147–151.
8. Sabirov, B.T., Ismailov, I.I., and Dzhalilov, A.T., *Vysokomol. Soedin., Ser. B*, 1985, vol. 27, no. 7, pp. 523–526.

Russian Journal of Applied Chemistry, Vol. 74, No. 9, 2001, pp. 1581–1584. Translated from Zhurnal Prikladnoi Khimii, Vol. 74, No. 9, 2001, pp. 1533–1536.

MACROMOLECULAR CHEMISTRY AND POLYMERIC MATERIALS

Viscosity and Structure of Melts of H Complexes of Acid Diesters of Aromatic Tetracarboxylic Acids with Aromatic Diamines

T. A. Kostereva, V. N. Artem'eva, N. V. Kukarkina, V. P. Samarin, G. N. Fedorova, V. E. Yudin, Y. N. Panov, and V. V. Kudryavtsev

Institute of Macromolecular Compounds, Russian Academy of Sciences, St. Petersburg, Russia

Received March 27, 2001

Abstract—The viscosity, lifetime, and structure of melts of supramolecular H-bonded complexes of acid diethyl and dimethyl esters of 3,3',4,4'-(diphenyl oxide)tetracarboxylic or 3,3',4,4'-diphenyltetracarboxylic acids with aromatic diamines (diaminodiphenylmethane or *m*-phenylenediamine) are studied.

Polyimide binders for fibrous composite materials are often obtained by acylation of diamines with acid esters of tetracarboxylic acids. In this case the best prepregs can be prepared from powder-like hydrogen-bonded complexes (H complexes) separated in drying of alcoholic solutions of acid esters of tetracarboxylic acids and diamines [1, 2]. In contrast to mechanical mixtures of acid esters of tetracarboxylic acids with diamines, H complexes can be converted to polyimides under mild conditions (at temperature below 220°C) practically without any side reactions [3]. The H complexes are characterized by low melting point (90–130°C) [4], which allows easy impregnation of various reinforcing materials, for example, polyimide felt, and preparation, after further thermal treatment of the resulting prepreg in a die mold (but without applying pressure load), of durable, light, thermostable, heatproof, and cryostable foamed composites, having good sound-proofing properties and applicable as structural materials [5].

Previously, to optimize the conditions of preparation of polyimide foamed composites, we thoroughly studied the viscous characteristic of H complexes based on acid diesters of 3,3',4,4'- benzophenonetetracarboxylic acid (BP) [6]. It was demonstrated that melts of the H complexes have an ordered structure (the exponent in the Ostwald–de-Wille equation

$$\eta \sim \dot{\gamma}^{-n}, \quad (1)$$

where η is the viscosity of the melt of the H complex and $\dot{\gamma}$ is the shear rate, is above 0.7) [7, 8].

The H complexes represent supramolecular structures, which are converted into polyimides by thermal treatment. It is known [9] that the structure of a polyimide is determined primarily by the nature of an acylating fragment of the polyimide chain, and its basis is formed even at the prepolymer stage. The polyimides based on 3,3',4,4'-(diphenyl oxide)tetracarboxylic acid (DPO) are mostly flexible-chain polymers, which is caused by the presence of a hinge oxygen atom between the phenyl radicals. The polyimides based on 3,3',4,4'-diphenyltetracarboxylic (DP) acid are mostly rigid-chain polymers with an ordered supramolecular structure. Therefore, it is interesting to study the effect of the nature of diesters of the indicated tetracarboxylic acids on the supramolecular structure of melts of the H complexes.

In this work we studied the H complexes formed by dimethyl esters of DPO or diethyl esters of DP and 4,4'-diaminodiphenylmethane (DADPM) or *m*-phenylenediamine (MPDA).

EXPERIMENTAL

The H complexes were prepared as follows. The dianhydride of DPO (0.1 mol) or DP (0.05 mol) was dissolved with stirring in the presence of benzimidazole (3 wt %) in 50 ml of methanol or ethanol containing 10–15 vol % water at the boiling temperature of the alcohol. The solution of the acid diester of the tetracarboxylic acid was cooled to room temperature, and the equimolar amount of a diamine was added with stirring (or the two diamines were added one after another). The H complexes formed after homogenization of the solution were isolated as solids by vacuum removal of the solvent at room temperature.

1070-4272/01/7409-1581$25.00

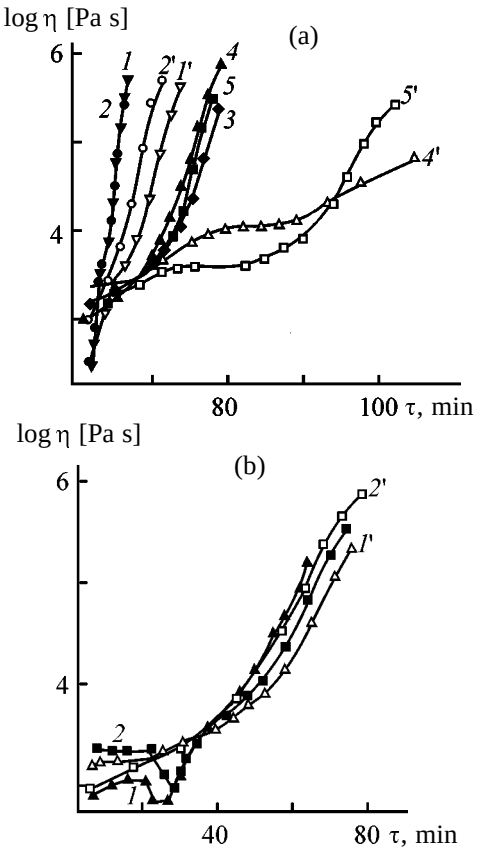

Fig. 1. Viscosity η of melts of H complexes as a function of time τ. $\log\dot{\gamma}$ = –1.88 (s^{-1}); the same for Fig. 4. (a) (*1*, *1*') DPOMe–DADPM, (*2*, *2*') DPOMe–(DADPM + MPDA), (*3*) DPOEt–DADPM, (*4*, *4*') DPOEt–(DADPM + MPDA), and (*5*, *5*') DPOEt–MPDA; (b) (*1*) DPEt–DADPM, (*1*') DPOEt–DADPM, (*2*) DPEt–(DADPM + MPDA), and (*2*') DPOEt–(DADPM + MPDA). Temperature (°C): (a) (*1*–*5*) 105 and (*1*', *2*', *4*', *5*') 95; (b) 105.

The dianhydride of DPO [TU (Technical Specifications) TSR 2159–69; 40 g] was recrystallized from a mixture of *o*-xylene (100 ml) and acetic anhydride (20 ml); mp 226–227°C. The dianhydride of DP was heated at 250°C (4 mm Hg); mp 297–298°C. 4,4'-Diaminodiphenylmethane was purified by vacuum distillation at 1–3 mm Hg (mp 90–92°C), and *m*-phenylenediamine, by vacuum distillation from Zn powder (mp 63°C).

The viscosity of melts of the H complexes was measured at 95 and 105°C with a PIRSP flowmeter with a cone–plane working unit (cone vertex angle 1°; cone diameter 40 mm) [10].

Thermal analysis was carried out with a MOM Model C instrument (Hungary). The sample weight was 50 mg; heating rate 5 deg min^{-1}.

The infrared spectra were registered with a Bruker spectrometer using the KBr technique.

In the molten state the H complexes undergo both physical and chemical transformations caused by such processes as structurization of the melt, imidization, foaming due to the presence of low-molecular-weight imidization products, gelation, and solidification. These processes are interrelated and superimposed. The processes dominating over each fixed time interval can be judged from the time dependences of the viscosity.

We studied the viscosity of melts of the H complexes formed by diethyl ester of DPO or DP with DADPM or (and) MDPA, and also by dimethyl ester of DPO with DADPM or an equimolar mixture of DADPM and MDPA (the indicated H complexes are designated as DPOEt–diamine, DPEt–diamine, and DPOMe–diamine, respectively) at 95 and 105°C. Below the selected temperature range H complexes often do not melt, and above it they form a solid in a short time, i.e., have a short lifetime, which does not permit us to follow the dynamics of the viscosity variation.

Evolution in time of the melt viscosity and lifetime depends to the most extent on the diester used. It was demonstrated with an example of H complexes of DPO diesters with various diamines (DADPM, MPDA, or their mixture) that the lifetime of the H complexes with the dimethyl esters (Fig. 1a, curves *1*, *1*', *2*, *2*') is considerably shorter as compared to those with the diethyl esters (curves *3*, *4*, *4*', *5*, *5*'), which is due to the fact that the imidization rate constant for the former compounds is by several times higher [3].

Changing the acylating fragment in the H complex (DPO diethyl ester for DP diethyl ester) does not affect the viscosity and lifetime of the melt (Fig. 1b, curves *1*, *1*', *2*, *2*'). The only difference is that the kinetic curves at 105°C of the viscosity of the H complexes DPEt–diamine pass through a minimum at 20–40 min. This result can be attributed to more extensive foaming, accompanied by separation of the alcohol and water, as compared to the H complex DPOEt–diamine. It should be pointed out that the viscosity and lifetime of melts of the investigated H complexes differ considerably from those of melts of the BP diesters [6]: the viscosity of the H complexes DPOMe–diamine, DPOEt–diamine, and DPEt–diamine is lower and the melt lifetime is longer than for the H complexes BPMe–diamine and BPEt–diamine.

It is seen from Fig. 1b that at 105°C the viscosity of melts of the H complexes DPOEt–diamine and DPEt–diamine remains practically unchanged in the

first 40 min. The plateau in the viscosity curve is more clearly pronounced at 95°C (Fig. 1a, curves *4'*, *5'*). The processes occurring in various time intervals can be judged from the coefficient *n* in Eq. (1). This parameter, characterizing the supramolecular structure of the melt, was estimated from the dependence of the viscosity on the shear rate at 95°C at fixed times. Such a dependence is presented in Fig. 2 for the H complex DPEt–(DADPM + MPDA).

In Fig. 3 are given the time dependences of the parameter *n* for H complexes of various compositions. Initially the melt had no ordered supramolecular structure ($n < 0.7$). Gradually such a structure was formed, as seen from the evolution of the parameter *n*, and after 30–40 min all the investigated melts got an ordered supramolecular structure ($n > 0.7$). With further time this structure became more and more perfect. The variations in *n* and η for the H complex DPEt–(DADPM + MPDA) are presented in Fig. 3 (curves *3* and *5*, respectively). It follows from the comparison of these curves that the melt gets an ordered structure after reaching the viscosity of about 10^4 Pa s, which is typical of the other investigated H complexes too.

The forward (with increasing shear rate) and backward runs (with decreasing shear rate) of the dependence $\log\eta$–$\log\dot\gamma$ for the H complex DPOEt–(DADPM + MDPA) 30 and 75 min after the beginning of the experiment are given in Fig. 4. Over this time interval the viscosity changes insignificantly. The parameter *n* (determined as the slope of the curve) is relatively high at $\tau = 30$ min, being unchanged for both forward and backward runs of the curve (Fig. 4, curves *1*, *2*). Therefore, the ordered structure of the melt is not changed even at sufficiently high shear rates ($3\log\dot\gamma = 0.5$ s^{-1}). With time the structure of the melt becomes more perfect, as demonstrated by Fig. 3 (*n* increases). Further increasing shear rate provides partial degradation of the supramolecular structure (at $\tau > 75$ min the slope of the backward run of the dependence $\log\eta$–$\log\dot\gamma$ is lower than that of the forward run (Fig. 4, curves *3*, *4*), i.e., *n* decreases ($n_3 = 1.16$, $n_4 = 0.88$).

Therefore, the initial insignificant change in the viscosity of the melt with time is caused by formation of an ordered supramolecular structure and its further perfection.

The rapid final increase in the viscosity (Figs. 1a, 1b) is associated with partial imidization. The time dependences of the viscosity at 95, 105, and 120°C are presented in Fig. 5 for the H complex DPOEt–

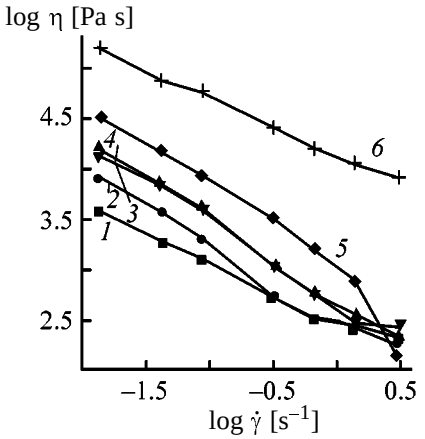

Fig. 2. Viscosity η of the melt of the H complex DPEt–(DADPM + MPDA) as a function of the shear rate $\dot\gamma$ at 95°C. Time (min): (*1*) 20, (*2*) 43, (*3*) 64, (*4*) 84, (*5*) 104, and (*6*) 124.

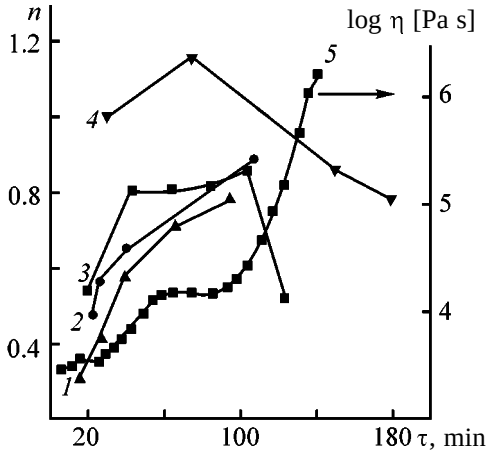

Fig. 3. (*1–4*) Parameter $n = \Delta\log\eta/\Delta\log\dot\gamma$ and (*5*) viscosity η of melts of H complexes as functions of the time τ at 95°C. (*1*) DPEt–DADPM, (*2*) DPOEt–DADPM, (*3*, *5*) DPEt–(DADPM + MPDA), and (*4*) DPOEt–(DADPM + MPDA).

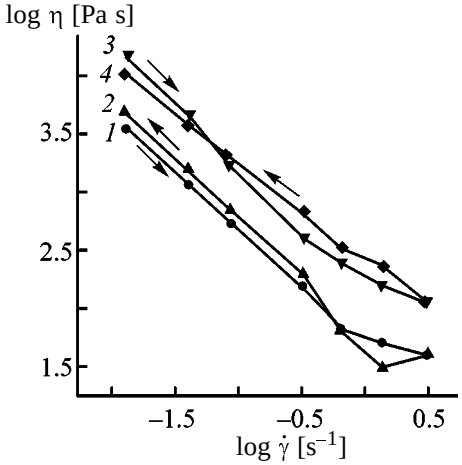

Fig. 4. Viscosity η of the melt of the H complex DPOEt–(DADPM + MPDA) as a function of the shear rate $\dot\gamma$ at 95°C. $n_1 = n_2 = 1$ at $\tau = 30$–40 min; $n_3 = 1.16$; and $n_4 = 0.88$ at $\tau = 75$–88 min.

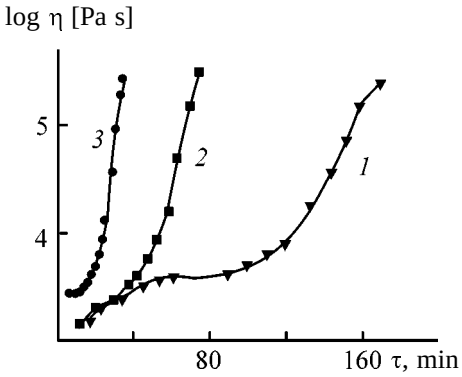

Fig. 5. Viscosity η of melt of H complex DPOEt–MPDA as a function of time τ. Temperature (°C): (*1*) 95, (*2*) 105, and (*3*) 120.

MDPA. As the temperature rises, the lifetime of the melt decreases and the slope of the final section of the curve increases. The samples after the experiment were characterized by TGA. The results showed that the weight loss due to imidization of the initial H complex DPOEt–MDPA corresponds to the theoretical value (see table). From the TGA data we estimated the degree of imidization. The samples after the rheological experiments (heated at 95, 105, and 120°C) appeared to be partially imidized (see table).

The conclusion about partial imidization of the H complexes at the experimental temperatures was confirmed by the IR data. The imidization was monitored by the absorption bands of the carbonyl groups of the imide ring at 725 and 1780 and 1720 cm^{-1} (doublet). In heated samples (95°C, 205 min) we observed the bands at 720 and 1780 cm^{-1}, i.e., the imide rings appear, which were lacking in the initial H complex.

The observed decrease in the parameter *n* in the final section of the time dependence of η (Fig. 3, curves *3*, *5*) reveals that thermal imidization is responsible for degradation of the ordered supramolecular structure ($n < 0.7$).

Degree of imidization α of DPOEt–MDPA samples

T, °C	τ, min	Weight loss due to imidization, %	α
25 (initial sample)	0	24*	0
95	180	18	23
105	75	15	38
120	36	15	38

* The theoretical value is 25%.

CONCLUSIONS

(1) The lifetime of the melt of the H complexes based on dimethyl esters of 3,3',4,4'-(diphenyl oxide)-tetracarboxylic acid is considerably shorter than that of the H complexes based on diethyl esters of this acid and 3,3',4,4'-diphenyltetracarboxylic acid. The viscosity and lifetime of the melts of the H complexes based on acid diesters of 3,3',4,4'-(diphenyl oxide)-tetracarboxylic and 3,3',4,4'-diphenyltetracarboxylic acids are similar.

(2) It is typical for melts of all the H complexes studied that the degree of ordering increases in time until imidization starts.

REFERENCES

1. Yudin, V.E., Otaigbe, J.U., and Artem'eva, V.N., *Polym. Composites*, 1998, vol. 20, no. 3, pp. 337–345.
2. Artem'eva, V.N., Kukarkina, N.V., Samarin, V.P., *et al.*, *Zh. Prikl. Khim.*, 2000, vol. 73, no. 7, pp. 1172–1179.
3. Artem'eva, V.N., Kudryavtsev, V.V., Chupans, P.I., *et al.*, *Izv. Ross. Akad. Nauk, Ser. Khim.*, 1995, no. 6, pp. 1060–1065.
4. Artem'eva, V.N., Chupans, P.I., Kukarkina, N.V., *et al.*, *Zh. Prikl. Khim.*, 2000, vol. 73, no. 5, pp. 810–815.
5. RF Patent 2 081 134, *Compositions for Preparation of Polyimide Foam Materials*.
6. Kostereva, T.A., Artem'eva, V.N., Kukarkina, N.V., *et al.*, *Zh. Prikl. Khim.*, 2001, vol. 74, no. 1, pp. 118–121.
7. Vinogradov, G.V. and Malkin, A.Ya., *Reologiya polimerov* (Rheology of Polymers), Leningrad: Khimiya, 1977.
8. Van Krevelen, D.W., *Properties of Polymers*, New York: Elsevier, 1990.
9. Bessonov, M.I., Koton, M.M., Kudryavtsev, V.V., and Laius, L.A., *Poliimidy – klass termostoikikh polimerov* (Polyimides: A Class of Heat-Resistant Polymers), Leningrad: Nauka, 1983.
10. Vinogradov, G.V., Malkin, A.Ya., Plotnikova, E.P., *et al.*, *Vysokomol. Soedin., Ser. A*, 1978, vol. 20, no. 2, pp. 226–230.

Russian Journal of Applied Chemistry, Vol. 74, No. 9, 2001, pp. 1585–1589. Translated from Zhurnal Prikladnoi Khimii, Vol. 74, No. 9, 2001, pp. 1537–1541.

MACROMOLECULAR CHEMISTRY AND POLYMERIC MATERIALS

Structure of Free Radicals Formed under X-ray Irradiation of Organic Polymeric Acids

V. V. Saraev, I. A. Alsarsur, V. V. Annenkov, and E. N. Danilovtseva

Irkutsk State University, Irkutsk, Russia
Irkutsk Institute of Chemistry, Siberian Division, Russian Academy of Sciences, Irkutsk, Russia

Received December 15, 1999; in final form, May 2001

Abstract—The structure of free radicals formed under X-ray irradiation of polyacrylic and polymetharcylic acids and poly-3-vinyltetrazole was studied by ESR spectroscopy. In polymerization of polymethacrylic acid, the conditions of the polymer recovery from the solution affect the nature of the radiolysis products.

The search for efficient methods preventing spontaneous deterioration of polymers requires exhaustive knowledge of possible reactive species in a solid polymer, free radicals. Under standard conditions the degradation effects initiated by the action of the environment are so small that cannot be detected by the ESR technique. Formation of free radicals in polymers is enhanced by radiolysis [1]. Free radicals formed under these conditions can serve as spin markers, which furnishes valuable information on molecular and supramolecular structure of polymers.

Here we present the results of ESR study of free radicals formed under X-ray irradiation of polyacrylic (PAA) and polymethacrylic (PMAA) acids, poly-5-vinyltetrazole (PVT), and their complexes with Cu^{2+}, Ni^{2+}, and Co^{2+} ions.

After irradiation in an inert atmosphere of PMAA freshly synthesized and dried in air, we recorded intensive asymmetrical ESR signal (Fig. 1a) characteristic of free radicals, in which unpaired electron is localized on the oxygen atom (oxygen radical) [2]. Contrary to PMAA, in PAA and PVT under similar conditions we registered carbon-centered free radicals whose ESR spectra exhibit a resolved hyperfine structure (HFS) due to two equivalent protons (Figs. 1b, 1c). Relatively large linewidth in the triplet suggests the presence of unresolved additional HFS. Spectra in Figs. 1b and 1c did not change for 1–2 h at room temperature. The spectra as a whole also remained practically unchaged. These data strongly suggest that the registered paramagnetic species are stabilized in the bulk of polymers. One of the possible reasons of formation of oxygen radicals can be incorporation of atmospheric oxygen into the polymeric chain in polymerization [3]. However, since the synthesis conditions for PMAA and PAA are the same but the resulting free radicals are essentially different, it can be assumed that oxygen radicals in PMAA originate from carboxy groups. The following structure of the oxygen radical can be suggested:

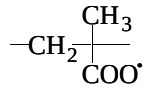

I

The triplet signal in Fig. 1b was observed previously in photopolymerization [3] and polymerization of acrylic acid under hard γ-irradiation [4, 5] and also in PAA subjected to γ-irradiation [5–7]. In [5–8] the

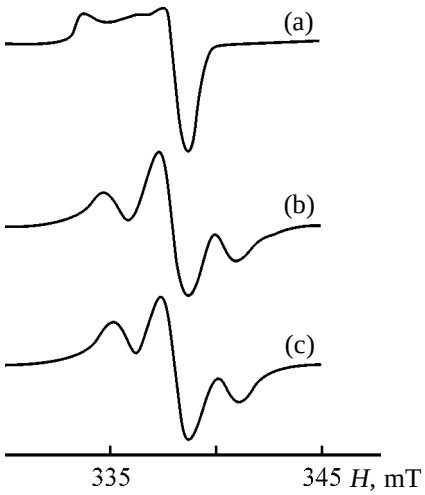

Fig. 1. ESR spectra of irradiated freshly prepared polymers. (*H*) Magnetic induction; the same for Figs. 2, 3. (a) PMAA ($g_{\parallel}$ = 2.034, $g_{\perp}$ = 2.005), (b) PAA [g = 2.003, a(H) = 2.27 mT], and (c) PVT [g = 2.003, a(H) = 2.23 mT].

1070-4272/01/7409-1585$25.00

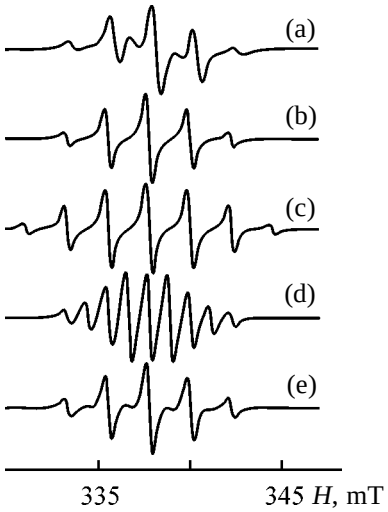

Fig. 2. (a) Experimental ESR spectrum of irradiated PMAA preliminarily dissolved in water and dried in air, (b–d) calculated spectra of conformers, and (e) the total spectrum.

signal shown in Fig. 1b was assigned to free radical of the following type:

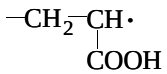

II

The HFS of signal in Fig. 1b is caused by the hyperfine interaction (HFI) of unpaired electron with two protons in α- and β-positions. The second β-proton does not interact with unpaired electron since it is located in the plane of the radical center [3]. The presence of poorly resolved inflections at the ends of signal b (Fig. 1) suggests the anisotropy of the hyperfine interaction with α-proton. For example, the main components of the HFI tensor for α-proton in polyethylene macroradicals are [9] a_x = 1.07, a_y = 1.93, and a_z = 3.42 mT.

Taking into account the similarity in signals b and c (Fig. 1), signal c in PVT can be assigned to macroradical of the following type:

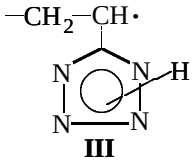

III

The HFS in macroradical **III**, as well as in PAA, is caused by interaction with two protons located in α- and β-positions.

It should be stressed that only secondary radical products of radiolysis, which are stabilized in the bulk of the polymer, are registered under the selected conditions of irradiation (25°C). Significant distinction of PMAA from PAA and PVT is the presence of side methyl groups, which are responsible for distinctions in the structure of macromolecular globules of these polymers. It is evident that in synthesis of PMAA in hydrocarbon medium hydrophilic carboxy groups are concentrated in the inner areas of the globules, which provides the contact of hydrophobic methyl groups with hexane. On the other hand, areas with the increased concentration of oxygen-containing groups, appearing in the polymer, promote formation of oxygen-containing radicals. At the same time, the main chain of PAA is less hydrophobic and less prone to cross-linking.

When PAA and PVT, preliminarily dissolved in water and dried in air, are subjected to irradiation, the same signals b and c are registered again (Fig. 1). In the case of PMAA, instead of asymmetrical signal a (Fig. 1), a symmetrical multiplet appears, which can be considered as a superposition of at least three signals: quintet b with binomial distribution of the intesities 1 : 4 : 6 : 4 : 1 from four equivalent protons with the HFI constant a(H) = 2.23 mT; sextet c with the equidistant lines at 2.23 mT; and weak signal d, whose HFS is registered between the intense lines of signals b and c (Fig. 2). Quintet b was observed previously in photopolymerization of methacrylic acid or methyl methacrylate [8] and also in polymethyl methacrylate subjected to γ-irradiation [3] or mechanochemical treatment [8, 10, 11]. In the series of works [3, 8, 10, 11] quintet b (Fig. 2) is assigned to macroradical of the following type:

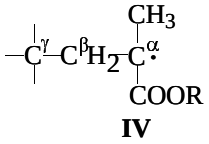

IV

The multiptet consisting of five lines is caused by the interaction of unpaired electron with three equivalent protons of the freely rotating methyl group and one proton of the methylene group. The second proton of the methyl group does not participate in HFI, which suggests its location in the plane of the radical center [3].

Three multiplet signals registered in our case are apparently due to coexistence of three conformers of radical **IV**, differing in the spatial arrangement of protons of the methylene group with respect to the π orbital occupied by the unpaired electron. The limiting structures of conformers corresponding to signals b–d (Fig. 2) can be presented as **A**–**C**, respectively, with the carbon atoms C^{α} and C^{β} aligned with the line

perpendicular to the figure plane:

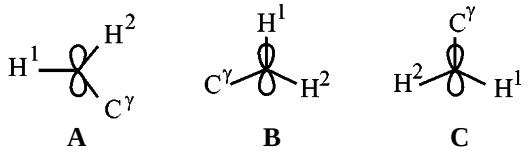

For three selected models we can evaluate the HFI constants for H^1 and H^2 using the well-known relation [12]

$$a(\mathrm{H}) = B\cos^2\varphi,$$

where B is the maximum value of the isotropic constant of HFI with β-proton (5.0 mT), and φ is dihedral angle between the $C^{\alpha}C^{\beta}H$ and $C^{\alpha}C^{\beta}\pi$ planes (π is the symmetry axis of the orbital occupied by unpaired electron).

When the dihedral angle between the $C^{\alpha}C^{\beta}H^1$ and $C^{\alpha}C^{\beta}H^2$ is taken equal to 120°, we obtain (mT) for conformer **A**, $a(H^1) = 0$, $a(H^2) = 3.75$; for conformer **B**, $a(H^1) = 5.0$, $a(H^2) = 1.25$; and for conformer **C**, $a(H^1) = a(H^2) = 1.25$.

Figure 2 presents the calculated ESR spectra of three model structures, which most closely agree with the experimental spectrum, and also the total spectrum e with the weight coefficients b : c : d = 10 : 2 : 1. The calculated HFI constants (mT) are (b) a(3H) = 2.23, a(1H) = 2.23, a(1H) = 0; (c) a(3H) = 2.23, a(1H) = 4.46, a(1H) = 2.23; and (d) a(3H) = 2.23, a(1H) = 1.11, a(1H) = 1.11. The calculation was carried out using the software described in [13]. In all calculations the width of the individual Lorentz line δH = 0.35 mT.

To conclude the studies of the structure of free radicals as influenced by the procedure of sample preparation for analysis, it should be noted that recovery of PMAA from water results in rearrangement of the supramolecular structure of the polymer: the hydrophobic part of the polymer is localized in the inner part of the polymer globule, and the hydrophilic part is localized in the periphery. Contrary to PMAA, recovery of PAA and PVT, containing no hydrophobic radicals, from water does not alter the nature of the stabilized radicals.

When after dissolving in water the polymers are dried lyophilically, the X-ray irradiation gives the same result as after drying of the polymers in air. The only difference was increased intensity of the ESR spectra of the hydrocarbon radicals owing to formation of more friable samples. Hence, supramolecular structure of the polymers is not significantly affected by lyophilic drying.

Fig. 3. ESR spectra of free radical **IV** recorded at 1-min intervals at 343 K. The spectrum with the minimum intensity was obtained after 11 min.

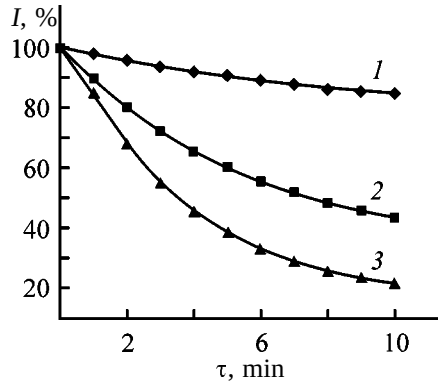

Fig. 4. Reduced intensity I of signal a (Fig. 2) as a function of time τ at (*1*) 343, (*2*) 373, and (*3*) 403 K.

To elucidate the mechanism of recombination of macroradicals **IV**, we studied the process kinetics in the stepwise heating mode [1]. A series of ESR lines recorded after 1 min at 343 K is presented in Fig. 3. Figure 4 shows variation with time of the total intensity of signals a (Fig. 2) reduced to 100% at the initial instant of time for each temperature. Analysis of the initial recombination rates allowed evaluation of the reaction order and activation energy. It was

found that the order of recombination is more than 1 and less than 2, which suggests more complicated mechanism of the process than mechanisms of monomolecular or bimolecular reactions. The activation energy is 44 kJ mol^{-1}, which is close to the activation energy of recombination of alkyl radicals in irradiated polyethylene [1, 14], in which the contact of free radicals is realized by migration of the free valence by the chain reaction

$$\dot{R} + H_2 \rightarrow RH + \dot{H},$$

$$\dot{H} + RH \rightarrow \dot{R} + H_2.$$

Apparently, the same mechanism forms the basis for recombination of radicals **IV** in the case of PMAA.

When PMAA with preliminarily incorporated Cu^{2+} ions in the ratio Cu : Ac ≥ 1 : 10, where Ac is the acyl group of PMAA, is subjected to irradiation, free-radical ESR signals are not registered and only the characteristic signal of the Cu^{2+} carboxylate complex is observed [15]. Weak free-radical signal a (Fig. 2) (10^{16} spin g^{-1}, two orders of magnitude lower than that of the initial polymer) can be registered only with decreased concentration of Cu^{2+} ions in PMAA (Cu : Ac < 1 : 10). It should be noted that under these conditions individual signal c without superposition of signals b and d is registered (Fig. 2). In addition, irradiation results in insignificant decrease in the intensity of the signal from Cu^{2+}, which is apparently caused by partial reduction of Cu^{2+} ion to diamagnetic Cu^{+}. Hence, Cu^{2+} ions in PMAA play a role of a radioprotector significantly decreasing the radiation yield of free radicals owing to redox processes, which results in variation of the oxidation state of the transition metal, e.g., by the scheme

$$\dot{H} + Cu^{2+} \rightarrow R^{+} + Cu^{+}.$$

Contrary to Cu^{2+} ions, Co^{2+} and Ni^{2+} ions incorporated into PMAA in the same amounts do not decrease noticeably the radiation yield of free radicals, but also signal c is mainly registered (Fig. 2). In addition, some broadening of the HFS lines of signal c (Fig. 2) is observed at high concentrations of ions (M^{2+} : Ac > 1 : 10), which suggests magnetic interaction between free radicals and ions of transition metals. Hence, Co^{2+} and Ni^{2+} ions in PMAA do not enter into redox reactions with free radicals, at least at room temperature.

EXPERIMENTAL

We used PAA and PMAA synthesized by polymerization of acrylic and methacrylic acids in hexane at 343 K for 2 h with azobis(isobutyronitrile) (AIBN) as initiator. The concentration of methacrylic and acrylic acids was 10%, and that of AIBN, 0.5% of the polymer weight.

Poly-5-vinyltetrazole was produced by the reaction of polyacrylonitrile with sodium azide at the Sibreaktiv Joint-Stock Company (Angarsk). The commercial sample was purified by double reprecipitation from alkaline solution (2 g l^{-1} PVT and 0.5 g l^{-1} NaOH) into a twofold excess of hydrochloric acid solution (50 g l^{-1}). PVT recovered by this procedure is insoluble in water. To produce water-soluble PVT, it was dissolved in water with addition of NaOH (10% of the amount of tetrazole units) and neutralized by slow addition of 0.1 N HCl. The solution was purified to remove the impurity of sodium chloride by dialysis through a cellophane membrane and subjected to lyophilic drying.

Metal nitrates of chemically pure grade were recrystallized from aqueous solutions before use.

Complexes were synthesized by mixing PMAA, PAA, and PVT solutions with solutions of Cu^{2+}, Co^{2+}, and Ni^{2+} nitrates. The concentration of PMAA, PAA, and PVT was 0.05 M, and the concentration of nitrates was 0.04 M. The resulting soutions of polymers and their complexes were subjected to lyophilic drying and dried in air.

Ampules with samples were evacuated at 10^{-3} mm Hg, bubbled with an inert gas, sealed, and then subjected to radiolysis with X-rays at room temperature for 10 min with an FRA-20 Carl Zeiss X-ray spectrometer equipped with W anode at a voltage of 40 kV and a current of 20 mA; the exposure dose was 10^{5} Gy.

The ESR spectra of solid polymers and their complexes were recorded on a PS-100X spectrometer (operation frequency 9.6 GHz) at room temperature. Mn^{2+} in MgO and diphenylpicrylhydrazyl were used as references. The concentration of free radicals in the irradiated polymers was 10^{18} spin g^{-1}.

CONCLUSIONS

(1) Irradiation of polyacrylic acid and poly-5-vinyltetrazole results in the rupture of the main polymer chain and generation of hydrocarbon radicals which are stabilized in the polymer bulk.

(2) The behavior of polymethacrylic acid in radiollysis is governed by the conformational features of its macromolecules. The polymer synthesized in hexane (hydrophilic carboxy groups are concentrated in the inner areas of globules) gives oxygen radicals. In recovery of polymethacrylic acid from aqueous solutions the association of hydrophobic methyl groups is preserved in the solid sample. After irradiation the resulting radicals are localized at the α-carbon atom of the methacrylic acid unit.

(3) Complex formation of polymeric acids with Cu(II) ions results in inhibition of radiolysis owing to oxidation of the resulting radicals with metal ions.

ACKNOWLEDGMENTS

The study was financially supported by the Russian Foundation for Basic Research (project no. 99-03-32102a) and the Ministry of Education of Russian Federation (project no. 97-0-9.3-29).

REFERENCES

1. Roth, H.-K., Keller, F., and Schneider, H., *Hochfrequenzspektroskopie in der Polymerforschung*, Berlin: Akademie, 1984.
2. Atkins, P.W. and Symon, M.C.R., *The Structure of Inorganic Radicals. An Application of Electron Spin Resonance to the Study of Molecular Structure*, Amsterdam: Elsevier, 1967.
3. Ingram, D.J.E., Symons, M.C.R., and Townsend, M.G., *Trans. Faraday Soc*., 1958, vol. 54, no. 3, pp. 409–413.
4. Ormerod, M.G. and Charlesby, A., *Polymer*, 1965, vol. 5, no. 1, pp. 67–72.
5. Clay, M.R. and Charlesby, A., *Eur. Polym. J*., 1975, vol. 11, no. 1, pp. 187–193.
6. Shioji, S., Ohinishi, S., and Nitta, I., *J. Polym. Sci., Ser. A-1*, 1963, vol. 3, no. 2, pp. 373–381.
7. Sanjeeva Rao, B. and Ramakrishna Murthy, M., *J. Polym. Sci., Polym. Phys. Ed*., 1989, vol. 27, no. 5, pp. 1187–1194.
8. Bresler, S.E., Kazbekov, E.N., and Saminskii, E.M., *Vysokomol. Soedin*., 1959, vol. 1, no. 9, pp. 1374–1382.
9. Tomashevskii, E.N. and Kvachadze, N.G., *Vysokomol. Soedin., Ser. B*, 1995, vol. 37, no. 10, pp. 1788–1792.
10. Tatar, L. and Kaptan, Y., *J. Polym. Sci., Polym. Phys. Ed*., 1997, vol. 35, no. 9, pp. 2195–2200.
11. Iwasaki, M. and Sakai, Y., *J. Polym. Sci., Ser. A-1*, 1969, vol. 7, no. 6, pp. 1532–1544.
12. Carrington, A. and McLachlan, A.D., *Introduction to Magnetic Resonsnce with Applications to Chemistry and Chemical Physics*, London: Chapman, 1979.
13. Saraev, V.V., Kraikivskii, P.B., Lazarov, P.G., *et al*., *Koord. Khim*., 1996, vol. 22, no. 9, pp. 648–654.
14. Voevodskii, V.V., *Fizika i khimiya elementarnykh khimicheskikh protsessov* (Physics and Chemistry of Elementary Chemical Processes), Moscow: Nauka, 1969.
15. Saraev, V.V., Alsarsur, I.A., Annenkov, V.V., and Shchipunov, D.V., *Koord. Khim*., 1999, vol. 25, no. 12, pp. 919–922.

Russian Journal of Applied Chemistry, Vol. 74, No. 9, 2001, pp. 1590–1593. Translated from Zhurnal Prikladnoi Khimii, Vol. 74, No. 9, 2001, pp. 1542–1545.

MACROMOLECULAR CHEMISTRY AND POLYMERIC MATERIALS

Production of High-Purity Dicyclopentadiene from the C_5 Fraction of Hydrocarbon Pyrolysis

E. V. Nurullina, N. B. Solov'eva, A. G. Liakumovich, and Ya. D. Samuilov

Kazan State Technological University, Kazan, Tatarstan, Russia

Received April 26, 2001

Abstract—A process was developed for production of dicyclopentadiene from the C_5 fraction of hydrocarbon pyrolysis. Conditions were found ensuring production of high-purity dicyclopentadiene.

Cyclopentadiene (CPD) and dicyclopentadiene (DCPD) are important monomers in polymer chemistry. Dicyclopentadiene and ethylidenenorbornene produced from CPD are widely used as comonomers in production of SKEPT rubbers [1], which are named rubbers of XXI century. Metathesis of DCPD allows production of materials with high physicomechanical properties [2–6]. Copolymerization of ethylene with norbornene derivatives prepared by the Diels–Alder reaction with CPD allows production of unique polymers exhibiting high transparency and impact resistance [7–14]. Norbornenedicarboxylic anhydride prepared by the Diels–Alder reaction from CPD and maleic anhydride is used in synthesis of norbornene polyester resins which exhibit enhanced physicomechanical properties as compared to phthalate resins [15–17].

CPD and DCPD used in these syntheses should exhibit a high (≥99 wt %) purity. Preparation of DCPD of so high purity is a difficult problem for industrial organic chemistry. Although some approaches to this problem have been outlined [18, 19], there is still no complete solution.

This work concerns production of high-purity DCPD. The major source of DCPD is the C_5 fraction of hydrocarbon pyrolysis.[1] Its quantitative composition depends on the nature of the raw material and processing features, but the qualitative composition remains the same. Below is given the approximate composition of the C_5 fraction used for recovery of DCPD [19].

The main problem related to recovery of DCPD from the C_5 fraction is that common separation procedures do not allow preparation of the high-purity target product. Therefore, additional chemical processes should be performed. The main principles of our approach are as follows.

Component	Content, wt %
3-Methyl-1-butene	0.09
1,4-Pentadiene	1.30
Isopentane	12.94
n-Pentane	24.81
1-Pentene	4.08
2-Methyl-1-butene	8.70
trans-2-Pentene	3.59
cis-2-Pentene	2.48
2-Methyl-2-butene	1.87
Piperylene (*cis* and *trans*)	11.91
Isoprene	12.58
Cyclopentadiene	13.14
Cyclopentene	2.51

(1) Cyclopentadiene in the C_5 fraction is dimerized into DCPD. The boiling points of DCPD and the remaining components of the C_5 fraction differ considerably, and DCPD can be readily separated by distillation. However, DCPD formed by primary dimerization is contaminated with Diels–Alder adducts of CPD with isoprene and piperylene. Therefore, further procedures with "crude" DCPD should involve separation of these impurities.

(2) The crude DCPD formed by primary dimerization is subjected to retrodiene syntheses (monomerization). Adducts of CPD with isoprene and piperylene are more stable than DCPD. Therefore, pure CPD can be recovered by incomplete conversion of crude DCPD. The low boiling point of CPD allows its separation from the high-boiling components.

(3) Dimerization–monomerization of CPD and

[1] We used the C_5 fraction of hydrocarbon pyrolysis from the Nizhnekamskneftekhim Joint-Stock Company.

1070-4272/01/7409-1590$25.00

DCPD should be repeated until the required purity is attained. The optimal conditions for each stage can be chosen on the basis of kinetic and thermodynamic parameters of the transformations. Below are given the Arrhenius parameters for direct and reverse Diels–Alder reactions [19] involved in the process for production of high-purity DCPD.

(1) Dimerization–monomerization of CPD and DCPD

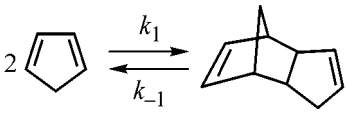

$$k_1 = 1.2 \times 10^6 \exp(-16\,400/RT),$$
$$k_{-1} = 2.6 \times 10^{13} \exp(-34\,000/RT).$$

(2) Reactin of CPD with piperylene

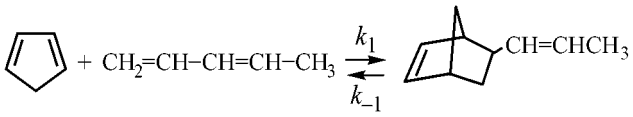

$$k_1 = 2.2 \times 10^4 \exp(-19\,000/RT),$$
$$k_{-1} = 2.6 \times 10^{13} \exp(-38\,900/RT).$$

(3) Reaction of CPD with isoprene

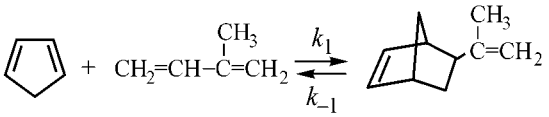

$$k_1 = 3.2 \times 10^5 \exp(-18\,800/RT),$$
$$k_{-1} = 1.02 \times 10^{13} \exp(-39\,400/RT).$$

These data show that the rate constants of CPD dimerization are higher than those of reactions of CPD with isoprene and piperylene; isoprene in the reaction with CPD is more active than piperylene; the difference between the rate constants of CPD dimerization K_{CPD} and of the competing Diels–Alder reactions of CPD with isoprene K_{isop} and piperylene K_{pip} increases with decreasing temperature. Quantitative data on the rate constant ratios are given below:

T, °C	K_{CPD}/K_{isop}	K_{CPD}/K_{pip}
100	95.7	1820
50	159	3150
0	316	6670

These data show that the first stage in the synthesis of high-purity DCPD, dimerization of CPD in the C_5 fraction, should not be performed to full exhaustion. Initially, while the CPD concentration is high, the resulting dimerizate will be enriched in DCPD. As the CPD concentration will decrease, the rate of CPD dimerization, in accordance with the law of mass action, will decrease, whereas the rate of reaction of CPD with isoprene and piperylene will remain relatively high (as the concentration product of the reactants is high). To prepare pure DCPD, low temperatures are preferable.

As already noted, further purification of DCPD can be performed in the course of monomerization of crude DCPD. This process also should not be performed to 100% conversion, lest the impurities present in DCPD would pass to CPD. The above kinetic data show that DCPD decomposes to give CPD more readily than adducts of CPD with isoprene and piperylene. The lower the temperature of the retrodiene synthesis, the larger the difference between the rate constants of these reactions. In retrodiene transformations, the adduct of CPD with isoprene is more stable than that with piperylene. This is a favorable fact, since in the dimerization stage the adduct of CPD with isoprene is the major impurity. Thus, limited conversion and low temperature are prerequisites for increasing the content of CPD in monomerization of crude DCPD.

In the course of the second dimerization, it becomes possible to prepare DCPD with the main substance content of 99.8–99.9 wt %. In this stage DCPD can be separated from low-boiling hydrocarbons by distillation.

The suggested process for production of high-purity DCPD from the C_5 fraction involves the following stages: (1) dimerization of CPD in the C_5 fraction, (2) distillation of crude DCPD to separate low-boiling hydrocarbons of the C_5 fraction, (3) monomerization of crude DCPD, (4) second dimerization of CPD, and (5) distillation.

To confirm our suggestions, we chose the optimal conditions for each stage of the process to obtain 99.5 wt % pure DCPD.

First we studied how the temperature, time, and conversion in dimerization of CPD in the C_5 fraction affect the composition of the resulting product. The results are listed in Table 1.

The experimental data show that the content of CPD adducts with isoprene and piperylene increases with temperature, dimerization time, and conversion of CPD to DCPD. GLC shows that the major impurity

Table 1. Influence of the conditions of CPD dimerization in the C_5 fraction on the DCPD quality

Dimerization conditions		Conversion	DCPD content	Content of impurities	Yield of crude DCPD	DCPD sample no.
T, °C	τ, h	wt %				
50	110	95	88.8	11.2	90.9	1
110	3.5	92	85.8	14.2	84.6	2
110	5	95	83.8	16.2	93.5	3

Table 2. Influence of the conditions of crude DCPD monomerization on the CPD quality

DCPD sample no.	*T*, °C	Conversion	Content of CPD + DCPD	Content of impurities	Yield of CPD	CPD sample no.
		wt %				
1	165–200	90	99.26 + 0.44	0.304	83	1'
	240–250	90–95	82.21 + 2.89	14.90	–	
2	165–200	90	94.07 + 2.84	3.09	86	2'
	240–250	90–95	78.54 + 2.34	19.12	–	
3	165–200	90	86.44 + 3.48	9.96	88	3'

in crude DCPD is the adduct of CPD with isoprene. The experimental results confirmed our assumptions.

Samples of crude DCPD (nos. 1–3) were subjected to monomerization. A fraction of CPD boiling in the range 41.5–42.5°C was taken. The results are listed in Table 2.

As seen from Table 2, the monomerization conditions largely affect the CPD quality. As the monomerization temperature and conversion of DCPD to CPD are increased, the content of impurities in the monomerization products decreases. The best results were obtained in monomerization of sample no. 1: At the monomerization temperature of 165–200°C and conversion of DCPD to CPD to 90% the main substance content was 99.7%. Because of dimerization under ambient conditions, CPD always contains DCPD. Therefore, in Table 2 is given the total content of CPD and DCPD.

Table 2 shows that from 88–89% pure DCPD it is feasible to obtain CPD with the main substance content after monomerization exceeding 99.7%. To this end, dimerization of CPD in the C_5 fraction should be performed at 50°C for 110 h. However, long reaction time prevents to a certain extent commercial implementation of this procedure. In view of the high content of DCPD in sample nos. 2 and 3, it is more appropriate to perform dimerization at 110°C for 3.5–5 h. The purity of CPD after monomerization of these samples is considerably lower than in the case of sample no. 1. Therefore, to prepare DCPD with the main substance content exceeding 99%, it is necessary to perform the second dimerization of CPD at lower temperatures.

The second dimerization of CPD was performed at 50°C for 14–18 h. The conversion of CPD to DCPD was maintained in the range 95–99%. The results are listed in Table 3.

After the second dimerization, the product contains an isoprene impurity. Distillation of the dimerizate in all the three cases yields DCPD with the main substance content of 99.5–99.9%, according to the GLC and NMR data. The total yield of DCPD from the C_5 fraction in our process was 65–70%.

In production of high-purity DCPD, formation of high-molecular-weight polymers (bottoms) in the monomerization stage gives rise to serious problems which have not yet been solved. In the existing commercial processes the amount of bottoms in the monomerization stage reaches 50%. The extent of side processes in monomerization largely depends on the DCPD concentration in the reaction mixture. Therefore, monomerization was performed in a high-boiling inert solvent, heptadecane, in an inert atmosphere in the presence of radical scavengers. As a result, the amount of by-products formed in the monomerization stage was considerably reduced, and their total content did not exceed 10–15%.

The developed process allows production of DCPD

Table 3. Influence of conditions of the second dimerization of CPD on the DCPD quality

CPD sample no.	Dimerization conditions		Conversion	Content of DCPD + CPD	Content of impurities	Yield of DCPD
	T, °C	τ, h	wt %			
1'	50	18	99	98.84 + 1.16	–	94
2'	50	14	99	92.26 + 3.07	4.67	97
3'	50	14	95	96.21 + 3.36	0.33	97

from the C_5 fraction of hydrocarbon pyrolysis with the main substance content exceeding 99.5%.

EXPERIMENTAL

In our study we used laboratory installations for dimerization of the C_5 fraction, monomerization, and distillation of DCPD. Monomerization was performed in a high-boiling solvent, heptadecane, in the presence of hydroquinone under argon. The C_5 fraction, CPD, and DCPD were analyzed with a complex consisting of a Kristall-2000 M chromatograph (30 000 × 0.32-mm capillary column coated with SE-54, 0.5 μm), a Pentium III-500 computer (Chromatec-Analytic software for processing chromatograms, measurement error 0.2%), a Hitachi mass spectrometer, and a Gemini-200 high-resolution NMR spectrometer.

CONCLUSION

A procedure was developed for production of dicyclopentadiene in a 65–70% yield with a purity higher than 99.5% from the C_5 fraction of hydrocarbon pyrolysis. Proper choice of the dicyclopentadiene monomerization conditions allows the amount of bottoms to be reduced to 10–15%.

REFERENCES

1. Dogadkin, B.A., Dontsov, A.A., and Shershnev, V.A., *Khimiya elastomerov* (Elastomer Chemistry), Moscow: Khimiya, 1981.
2. Balcar, H., Doseldova, A., and Petrusova, L., *J. Mol. Catal.*, 1993, vol. 77, no. 3, pp. 289–295.
3. Wagener, K.B. and Priddy, D.B., *Macromolecules*, 1996, vol. 29, no. 2, pp. 786–788.
4. Junji, K. and Tadao, N., *Polym. J.*, 1995, vol. 27, no. 12, pp. 1167–1172.
5. Hafner, A., Muhlebach, A., and Schaaf, P. van der, *Angew. Chem. Int. Ed. Engl.*, 1997, vol. 36, no. 19, pp. 2121–2124.
6. Li, H., Wang, Z., Wang, Y.Q., and He, B.L., *React. Funct. Polym.*, 1997, vol. 33, nos. 2–3, pp. 193–200.
7. EP Patent 0 447 072 A2.
8. EP Patent 0 532 337 A2.
9. EP Patent 0 661 308 A2.
10. EP Patent 0 692 502 A1.
11. EP Patent 0 719 803 A2.
12. EP Patent 0 692 503 A1.
13. EP Patent 0 719 806 A2.
14. EP Patent 0 726 291 A1.
15. Budkin, V.A., Nurullina, E.V., Solov'eva, N.B., *et al.*, *Zh. Prikl. Khim.*, 1995, vol. 68, no. 12, pp. 2065–2067.
16. Budkin, V.A., Solov'eva, N.B., Nurullina, E.V., *et al.*, *Zh. Prikl. Khim.*, 1996, vol. 69, no. 4, pp. 657–661.
17. Budkin, V.A., Nurullina, E.V., Samuilov, Ya.D., *et al.*, *Zh. Prikl. Khim.*, 1996, vol. 69, no. 4, pp. 662–665.
18. *Novye protsessy organicheskogo sinteza* (New Processes of Organic Synthesis), Chernykh, S.P., Ed., Moscow: Khimiya, 1989.
19. Vostrikova, V.N., Chernykh, S.P., and Grigor'ev, A.A., *Neftekhimicheskie tsiklopentadien i ditsiklopentadien – perspektivnoe syr'e dlya organicheskogo sinteza* (Petrochemical Cyclopentadiene and Dicyclopentadiene: Promising Raw Materials for Organic Synthesis), Moscow: TsNIITEneftekhim, 1984.

Russian Journal of Applied Chemistry, Vol. 74, No. 9, 2001, pp. 1594–1599. Translated from Zhurnal Prikladnoi Khimii, Vol. 74, No. 9, 2001, pp. 1546–1550.

MACROMOLECULAR CHEMISTRY AND POLYMERIC MATERIALS

Features of Radical Polymerization of Vinyl Chloride in the Presence of Nitroxyl Radicals

D. F. Grishin, L. L. Semenycheva, M. V. Pavlovskaya, and K. V. Sokolov

Research Institute of Chemistry, Nizhni Novgorod State University, Nizhni Novgorod, Russia

Received April 25, 2001

Abstract—Radical polymerization of vinyl chloride in the presence of *C*-phenyl-*N*-*tert*-butylnitrone, 2-methyl-2-nitrosopropane, and 1-*tert*-butyl-3-phenyl-1-oxytriazene as potential sources of free radicals was studied.

Radical polymerization is one of the major procedures for preparing polyvinyl chloride (PVC). It is known that the main drawback of radical polymerization is that the kinetic parameters of the process and the molecular-weight characteristics of the resulting polymers are difficult to control because of the high reactivity of radical species. One of the ways to solve the problem is based on the new concept, which is being actively developed, of controllable "pseudoliving" radical polymerization. By performing radical polymerization in the "living" chain mode, it is feasible to prepare polymers of definite structure and molecular weight and hence with the preset properties [1–3]. The known chain-terminating agents, stable radicals and iniferters [2,2,4,4-tetramethyl-1-piperidyloxyl (TEMPO), alkoxyamines, alkylthiocarbamates, etc.], are effective only at relatively high temperatures (100–130°C) and are unsuitable for the gaseous monomer vinyl chloride (VC).

Previously, to prepare polymethyl methacrylate with a relatively narrow molecular-weight distribution (MWD), it was suggested to use *C*-phenyl-*N*-*tert*-butylnitrone (PBN), 2-methyl-2-nitrosopropane (MNP), and 1-*tert*-butyl-3-phenyl-1-oxytriazene (BPT) [4–6], which act as chain-terminating agents at lower temperatures (50–70°C). It is known [7] that MNP and PBN react with radicals, including polymeric radicals, to give nitroxyl spin adducts containing a macromolecular tail. Such sterically hindered stable radicals allow control of the radical polymerization of (meth)acrylic monomers at lower temperatures compared to TEMPO.

Therefore, it seemed promising to study polymerization of VC in the presence of MNP and PBN as potential sources of free radicals, and also of BFT which was successfully used previously as iniferter in low-temperature (50°C) controlled radical polymerization of (meth)acrylic monomers [6].

EXPERIMENTAL

Purification and dosage of vinyl chloride were based on standard procedures [8]. The initiators and solvents were purified by common procedures. Postpolymerization was performed as follows: An ampule at a definite conversion of VC was frozen and attached to a vacuum unit, the residual VC was distilled into the trap, and a new VC portion was added (equal to the initial portion), after which the ampule was again sealed and placed in a thermostat. PBN, MNP, and PBT were prepared by the procedures described in [9–11]. The kinetics of VC bulk polymerization was monitored gravimetrically, dilatometrically [12], and calorimetrically [13]. The Fickentscher constant K_F and the intrinsic viscosity [η] were determined visometrically [14]. The MWD of polyvinyl chloride was analyzed by GPC on an installation equipped with a set of five Styrogel columns with the pore diameter of 1×10^5, 3×10^4, 1×10^4, 1×10^3, and 250 Å (Waters, the United States). As detector was used an R-403 differential refractometer (Waters). The eluent was tetrahydrofuran. The device was calibrated with narrow-disperse polystyrene references [15]. The syndiotacticity index was determined by IR spectroscopy from the ratio of the integral intensities D_{635}/D_{693} [16].

We found that PBN efficiently controls the chain propagation in VC polymerization in the presence of dicyclohexyl peroxydicarbonate (CPC).

Polymerization of VC in the presence of PBN additives (0.01 and 0.05 mol %) occurs with a short induction period (5–15 min); the initial rate is 3.0 and

1070-4272/01/7409-1594$25.00

0.7 mol l^{-1} s^{-1}, respectively, which is lower than in the absence of the additive (9.1 mol l^{-1} s^{-1}). This is apparently due to reaction of oligomeric and polymeric PVC radicals with nitrone as radical scavenger. The differential kinetic curves of VC polymerization, obtained by the calorimetric procedure in the presence and in the absence of PBN (Fig. 1), show that addition of 0.005 mol % PBN results in slight deceleration of the polymerization and noticeable decrease in the gel effect (Fig. 1, curve *2*), as compared to the process performed in the absence of PBN (Fig. 1, curve *1*) in which a pronounced gel effect is observed at a 60–80% conversion. As the PBN concentration is increased to 0.01 mol %, the reaction rate slightly decreases also (Fig. 1, curve *3*), the gel effect is practically fully suppressed, and the process, similar to that with CPC, occurs to high conversions (~90%). The calorimetric data were confirmed by gravimetric monitoring of the polymerization kinetics.

Thus, in polymerization of VC PBN suppresses undesirable autoacceleration. Apparently, similar to the system with MMA [4], in the first stage PBN reacts with the propagating macroradical to form the stable nitroxyl radical [reaction (1)]; then the nitroxyl spin adduct reacts with the propagating radical to form a labile bond [reaction (2)] into which the next monomer molecule can be inserted [reaction (3)]:

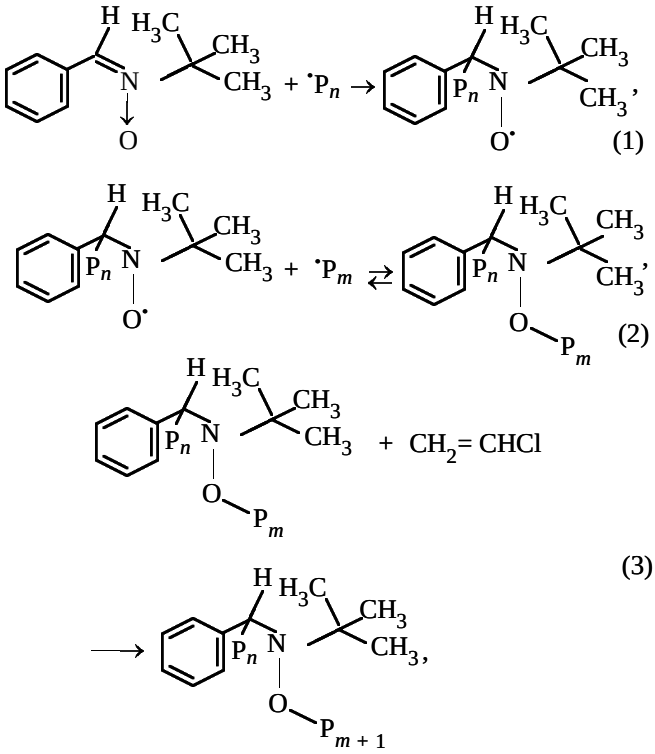

where P_n, P_m, and P_{m+1} is the propagating macroradical.

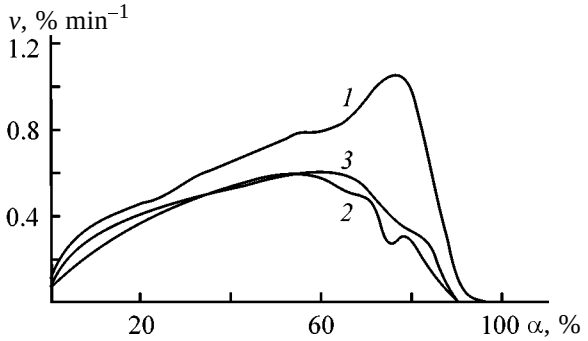

Fig. 1. Differential kinetic curves of VC polymerization in the presence of PBN at 50°C. Initiator CPC, 0.1 mol %; the same for Figs. 2 and 3. (*v*) Polymerization rate and (α) conversion. [PBN], mol %: (*1*) 0, (*2*) 0.005, and (*3*) 0.01.

The reinitiation of polymer chains by reaction (2) is the most significant feature of pseudoliving radical polymerization.

It is known that in pseudoliving polymerization the molecular weight of the polymeric products linearly depends on the conversion, and the polydispersity coefficients of the resulting samples are low. However, it should be noted that a well-known feature of radical polymerization of VC, in contrast to acrylic and some other vinyl monomers, is the high constant of chain transfer to the monomer (K_{ct} ~1×10^3), which ultimately determines the molecular weight of the resulting PVC [16]. Therefore, in radical polymerization of VC the molecular weight of the polymer remains the same irrespective of conversion [16, 17], in contrast to polymerization of acrylic monomers whose molecular weight sharply increases in the stage of the gel effect [18]. The rate constant of the reaction of PBN with secondary alkyl radicals, including the polyvinyl chloride macroradical, is 6.8×10^4 l mol^{-1} s^{-1} [17]. It is almost two orders of magnitude higher than the constant of chain transfer to the monomer. Therefore, if the controllable chain propagation by the mechanism of pseudoliving polymerization actually takes place, in the case of VC the molecular weight should also linearly increase with conversion.

The molecular-weight characteristics of PVC synthesized in the presence of PBN were studied viscometrically and by GPC. It is known [16] that the molecular-weight characteristics of PVC are usually evaluated from the viscosity data using the Fickentscher constant K_F, which is determined from the relative viscosity of a PVC solution of a standard concentration [16], rather than from the Mark–Kuhn–Houwink equation, because of problems with calculation of K and α. The dependence of the number-average molecular weight M_n on conversion for poly-

Table 1. Molecular-weight characteristics of PVC prepared in the presence of PBN. [CPC] = 0.1 mol %, T = 50°C

Sample no.	Conversion, %	[η]	$M_n \times 10^{-3}$	$M_w \times 10^{-3}$	M_w/M_n	D_{635}/D_{693}
[PBN] = 0.01 mol %						
1	4	0.4	19	33	1.7	–
2	13	0.6	28	53	1.9	–
3	23	0.7	32	60	1.9	1.9
4	48	0.8	40	71	1.8	–
5	62	0.8	41	81	2.0	1.9
6	89	0.9	44	97	2.2	1.9
7	94*	1.1	49	114	2.3	–
8	114*	1.1	48	108	2.3	–
[PBN] = 0.05 mol %						
9	6	0.2	8	15	2.0	–
10	12	0.5	18	40	2.3	–
11	31	0.6	19	49	2.6	–
12	41	0.7	30	62	2.0	–
13	63	0.8	35	74	2.1	–

* Samples were prepared by postpolymerization; the new portion of the monomer was added at 58% (sample no. 7) and 52% (sample no. 8) conversion.

merization of VC in the presence of PBN is plotted in Fig. 2. The intrinsic viscosities [η] and the molecular-weight characteristics determined from GPC data are listed in Table 1. These data show that the molecular weight of PVC synthesized in the presence of PBN uniformly grows with increasing VC conversion. The changes in the molecular weight are more pronounced at increased content of PBN in the polymerization products.

Figure 3 shows the MWD curves of polyvinyl chloride prepared in the presence of 0.01 (Fig. 3a, curves *1*–*6*) and 0.05 mol % PBN (Fig. 3b) at various conversions. It is seen that all the curves are unimodal and that with increasing conversion of VC the mode successively shifts to the higher molecular weights. Such a dependence is also one of the evidences of

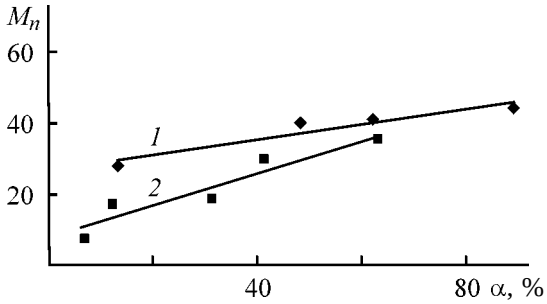

Fig. 2. Number-average molecular weight M_n of PVC prepared in the presence of PBN as a function of conversion α. [PBN], mol %: (*1*) 0.01 and (*2*) 0.05.

pseudoliving polymerization. In the case of a common radical polymerization of VC, no similar shift of the mode of the MWD curves is observed [16, 17].

Table 1 shows that the polydispersity M_n/M_w, where M_w is the weight-average molecular weight, of the polymer prepared in the presence of 0.01 mol % PBN does not change significantly in the range of conversions 4–48%, being in the range 1.7–1.8. With the conversion increasing further, the polydispersity of PVC increases but remains considerably lower than in common radical polymerization (3.7 at high conversion) [17, 19]. In our case, at 89% conversion M_w/M_n = 2.2 (Table 1). Similar trends are observed at a PBN concentration of 0.05 mol %. Such an increase in the polydispersity of the polymers at >50% conversion was observed in polymerization of acrylic monomers by the mechanism of pseudoliving chains in the presence of triphenylmethyl radicals [20, 21]; it suggests decreased contribution of pseudoliving polymerization at high conversions.

Thus, the kinetic data on VC polymerization in the presence of PBN and the molecular-weight characteristics of the resulting PVC show that in the presence of PBN VC polymerizes by the mechanism of pseudoliving chains.

Our results open the possibility for controlling the chain propagation and the molecular weight of PVC in the course of its synthesis. It is known [2] that

postpolymerization and syntheses of block copolymers, star copolymers, etc. are performed by living cationic and anionic polymerization. The possibility of radical polymerization of VC by the mechanism of pseudoliving chains (it is known [16] that vinyl chloride polymerizes only by the radical mechanism) can extend the field of practical applications of PVC, as the polymer with the molecular weight controllable in a wide range will become available. In this context, it seemed interesting to perform postpolymerization of VC in the presence of PBN. For this purpose, to the VC polymer prepared in the presence of PBN we added a new portion of VC. For the polymer samples obtained by postpolymerization, we determined the molecular-weight characteristics by viscometry and GPC. The MWD curves of these samples, similar to those of the polymer obtained in the presence of PBN, are unimodal (Fig. 3a, curves *7*, *8*), and with increasing conversion of VC the mode successively shifts to higher molecular weights. Table 1 shows that the molecular weight of the polymer in this case increases, and the polydispersity M_w/M_n of the polymer prepared by postpolymerization in the presence of 0.01 mol % PBN (sample nos. 7, 8) is comparable with that of PVC at high conversions of PBN (sample no. 6). The M_n values for PVC fall on the extension of the linear dependence of M_n on conversion for PVC prepared in the presence of PBN. These data also support the pseudoliving mechanism of postpolymerization.

An important experimental characteristic of PVC is the syndiotacticity index, i.e., the ratio of the optical densities of the absorption bands of the C–Cl stretching vibrations at 635 and 693 cm^{-1}, D_{635}/D_{693}. This index correlates with such characteristics of PVC as crystallinity, heat resistance, and softening point [16]. From the IR spectra of PVC samples of various conversions, prepared with additions of PBN, we calculated the syndiotacticity indices (Table 1). As seen from these data, the syndiotacticity indices are essentially the same for various PVC samples prepared in the presence of PBN and without additives. This fact shows that the presence of PBN has no effect on formation of syndio- and isotactic fragments in the polymer, as it takes place, e.g., in polymerization in the presence of organometallic compounds [22].

Experiments on the VC polymerization initiated with dicetyl peroxydicarbonate (DPC) with addition of MNP and BPT showed that, in contrast to PBN, in the presence of catalytic amounts of MNP (0.01–0.1 mol %) and BPT (0.01–0.05 mol %) the controllable chain propagation is not realized. According to the kinetic data (Fig. 4), MNP acts as a common

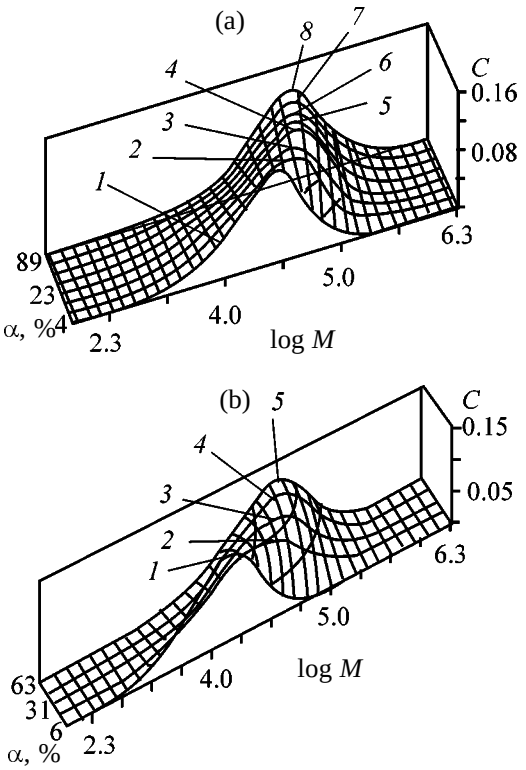

Fig. 3. GPC curves of PVC samples prepared at 50°C in the presence of CPC and PBN. (α) Conversion, (*C*) weight fraction, and (*M*) molecular weight. [PBN], mol %: (a) 0.1 and (b) 0.5. Conversion, %: (a) (*1*) 4, (*2*) 7, (*3*) 23, (*4*) 48, (*5*) 62, (*6*) 89, (*7*) 94, and (*8*) 114 (samples corresponding to curves *7*, *8* were prepared by postpolymerization); (b) (*1*) 6, (*2*) 12, (*3*) 31, (*4*) 41, and (*5*) 63.

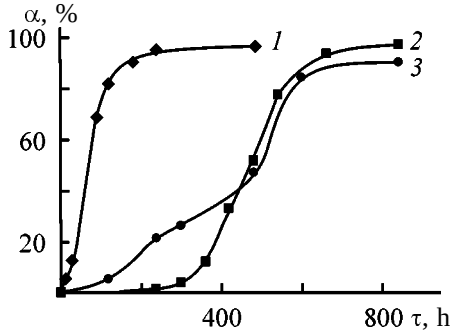

Fig. 4. Kinetic curves of VC polymerization in the presence of MNP and BPT at 50°C. Initiator DPC, 0.1 mol %. (α) Conversion and (τ) time. Additive (0.03 mol %): (*1*) none, (*2*) MNP, and (*3*) BPT.

inhibitor: At the beginning of the process an induction period is observed, after which the process kinetics, up to high conversions, becomes similar to that in the absence of the additive (Fig. 4, curves *2*, *1*, respectively; the kinetic curve of VC polymerization in the presence of DPC and hexane coincides with that in the

Table 2. Intrinsic viscosity of PVC prepared in the presence of MNP. [DPC] = 0.1 mol %, T = 50°C

Conversion	[η]	K_F
[MNP] = 0.03%		
12	0.7	55
33	0.9	58
52	0.8	55
77	0.7	58
79	0.9	58
82	0.8	57
91	0.7	58
97	0.9	57
99	0.9	55
[BPT] = 0.03%		
26	0.7	62
33	0.8	62
46	0.8	62
47	0.8	62
71	0.8	63
84	0.9	64

absence of hexane). The induction period increases from 2 to 4 and 15 h on adding, respectively, 0.01, 0.03, and 0.05 mol % MNP. On adding 0.03 mol % BPT the induction period is 1 h. The polymerization rate slowly increases, and after reaching a 30% conversion the pattern becomes identical to that in the presence of MNP. This may be due to the fact that MNP is formed in the course of polymerization by the scheme suggested in [4, 5]. As a result, the process slightly decelerates.

The molecular weight data for the polymer prepared in the presence of MNP and BPT are well consistent with the kinetic data: The molecular weight of PVC characterized by the intrinsic viscosity and K_F (Table 2) is the same irrespective of the VC conversion, which is typical of common polymerization of VC [16].

The different effects of MNP and PBN on the kinetic and molecular-weight characteristics of the PVC synthesis are probably due to essentially different constants of acception of secondary radicals (in this case, VC propagation radical) by MNP and PBN: For MNP they are higher than for PBN by two orders of magnitude [7]. Therefore, in polymerization of VC MNP acts exclusively as inhibitor.

CONCLUSIONS

(1) Studies of the polymerization kinetics of vinyl chloride, molecular-weight characteristics of the resulting polymer, and postpolymerization of vinyl chloride in the presence of *C*-phenyl-*N*-*tert*-butylnitrone show that in these systems the reaction occurs by the mechanism of pseudoliving chains. It should be noted that the revealed possibility of controlling the chain propagation and molecular weight in the course of synthesis of polyvinyl chloride is the first example of realization of the pseudoliving chain mechanism in polymerization of vinyl chloride.

(2) Our results allow *C*-phenyl-*N*-*tert*-butylnitrone to be considered as agent controlling the propagation and lifetime of the polymeric chain under energetically favorable conditions; they can serve as a basis for development of efficient procedures for preparing polyvinyl chloride with a wide range of molecular weights.

(3) In contrast to *C*-phenyl-*N*-*tert*-butylnitrone, catalytic amounts of 2-methyl-2-nitrosopropane and 1-*tert*-butyl-3-phenyl-1-oxytriazene do not control the propagation of the polymeric chain in polymerization of vinyl chloride under radical initiation conditions.

ACKNOWLEDGMENTS

The study was financially supported by the Russian Foundation for Basic Research.

REFERENCES

1. Smirnov, B.R., *Vysokomol. Soedin., Ser. A*, 1990, vol. 32, no. 3, pp. 583–589.
2. Matyjaszewski, K., *Controlled Radical Polymerization*, Oxford: Oxford Univ. Press, 1998.
3. Korolev, G.V. and Marchenko, A.P., *Usp. Khim.*, 2000, vol. 69, pp. 447–475.
4. Grishin, D.F., Semenycheva, L.L., and Kolyakina, E.V., *Dokl. Ross. Akad. Nauk*, 1998, vol. 362, no. 45, pp. 634–638.
5. Grishin, D.F., Semionicheva, L.L., and Koliakina, E.V., *Mendeleev Commun.*, 1999, no. 6, pp. 609–614.
6. Grishin, D.F., Moykin, A.A., Smirnova, E.P., *et al.*, *Mendeleev Commun.*, 2000, no. 4, pp. 152–154.
7. Zubarev, V.E., *Metod spinovykh lovushek* (Method of Spin Traps), Moscow: Mosk. Gos. Univ., 1984.
8. Tkachenko, G.V., Khomikovskii, P.M., and Medvedev, S.S., *Zh. Fiz. Khim.*, 1951, vol. 25, no. 7, pp. 823–828.
9. Emmons, W.D., *J. Am. Chem. Soc.*, 1967, vol. 79, no. 5, pp. 6522–6529.
10. Dugar, S.M. and Sogani, N.C., *J. Indian Chem. Soc.*, 1966, vol. 43, no. 4, pp. 289–294.

11. Terabe, S. and Konaka, R., *J. Chem. Soc., Perkin Trans. 2*, 1972, no. 14, pp. 2163–2170.
12. *Praktikum po khimii i fizike polimerov* (Practical Course of Polymer Chemistry and Physics), Moscow: Khimiya, 1990.
13. Arulin, V.I. and Efimov, L.I., *Tr. Khim. Khim. Tekhnol.* (Gor'kii), 1970, vol. 2, pp. 74–80.
14. Rafikov, S.R., Pavlov, S.A., and Tverdokhledova, I.I., *Metody opredeleniya molekulyarnykh vesov i polidispersnosti vysokomolekulyarnykh soedinenii* (Methods for Determining Molecular Weights and Polydispersity of Macromolecular Compounds), Moscow: Khimiya, 1963.
15. Moris, S., *J. Liq. Chromatogr.*, 1990, vol. 13, no. 9, pp. 1719–1724.
16. *Poluchenie i svoistva polivinilkhlorida* (Synthesis and Properties of Polyvinyl Chloride), Zil'berman, E.N., Ed., Moscow: Khimiya, 1968.
17. Kolegov, V.I., *Plast. Massy*, 1978, no. 5, pp. 31–34.
18. *Entsiklopediya polimerov* (Polymer Encyclopedia), Moscow: Sov. Entsiklopediya, 1972, vol. 1.
19. Kolegov, V.I., Potapov, V.N., Sorokina, T.M., *et al.*, *Plast. Massy*, 1982, no. 12, pp. 36–38.
20. Chernikova, E.V., Pokataeva, Z.A., Garina, E.S., *et al.*, *Vysokomol. Soedin., Ser. A*, 1995, vol. 37, pp. 1638–1643.
21. Chernikova, E.V., Pokataeva, Z.A., and Garina, E.S., *Vysokomol. Soedin., Ser. B*, 2000, vol. 42, pp. 1530–1533.
22. Razuvaev, G.A., Dodonov, V.A., and Ivanova, Yu.A., *Dokl. Akad. Nauk SSSR*, 1980, vol. 250, no. 1, pp. 119–121.

Russian Journal of Applied Chemistry, Vol. 74, No. 9, 2001, pp. 1600–1603. Translated from Zhurnal Prikladnoi Khimii, Vol. 74, No. 9, 2001, pp. 1551–1554.

MACROMOLECULAR CHEMISTRY AND POLYMERIC MATERIALS

Effect of Praestol Cationic and Anionic Flocculants on the Efficiency of Water Pretreatment at Heat and Electric Power Plants

V. F. Kurenkov, E. L. Gogolashvili, R. R. Saifutdinov, S. V. Snigirev, and A. A. Isakov

Kazan State Technological University, Kazan, Tatarstan, Russia
Energoprogress Engineering Center, Kazan, Tatarstan, Russia

Received May 10, 2001

Abstract—The efficiency of water purification at simultaneous use of Praestol macromolecular flocculants, iron(II) sulfate coagulant, and calcium hydroxide alkalizing agent was studied as influenced by the nature (cationic and anionic), chemical composition, and conformational state of the flocculant macromolecules in solution and by the concentrations of the flocculant and coagulant.

Only highly purified water can be used for feeding of boilers at heat and electric power plants (HEPPs). The treatment of natural waters often involves preliminary reagent purification and several stages of demineralization with ion-exchange resins. During preliminary purification water is alkalized to decrease its hardness and treated most commonly with iron(II) sulfate to promote coagulation. Precipitate forming in the treated water by hydrolysis of the coagulant and subsequent interaction of hydrolysis products with suspended and colloidal dispersed particles is removed using clarifiers and filters. Thus, in the first stage water is treated to remove coarse and colloidal particles, iron compounds, and organic admixtures, which poison ion-exchange resins in the course of further water treatment and promote corrosion and damage of the boilers and pipelines. Preliminary water treatment can be intensified by simultaneous use of coagulants and flocculants [1]. Among polyacrylamide flocculants widely used in water treatment, macromolecular Praestols[1] are the most promising [2, 3]. It was found [4, 5] that the Praestol anionic flocculant used simultaneously with aluminum sulfate at the water-treatment plants provides efficient purification of natural water for drinking water supply.

In this work we studied the performance of Praestol anionic and cationic flocculants at their simultaneous use with iron(II) sulfate (coagulant) and calcium hydroxide (alkalizing agent) in the water treatment at HEPP.

[1] Produced by Moscow–Stockhausen–Perm Russian–German Joint-Stock Company.

EXPERIMENTAL

In the tests we used commercial iron(II) sulfate [GOST (State Standard) 6981–75], saturated solution of construction lime (GOST 9179–77), and commercial Praestols: anionic [copolymers of acrylamide (AA) with sodium acrylate (Na-AA)] and cationic [copolymers of AA with trimethylammoniopropylacrylamide chloride (TMAPAC)]. The properties of these polymers are listed in the table. Solutions were prepared in distilled water; all other reagents were of analytically pure or chemically pure grade. The reagent water pretreatment was studied using river water from the process cycle of the Kazan HEPP-2 (total hardness 4.1 mg-equiv l^{-1}, alkalinity 2.85 mg-equiv l^{-1}, pH 8.34, SiO_2 content 6.05 mg l^{-1}). The samples of natural water were clarified in a 250-ml cylinder. For this purpose natural water was successively treated with lime solution (235.2 mg l^{-1}), iron(II) sulfate (66.9 mg l^{-1}), and Praestol flocculant (0.4 mg l^{-1}); the reagent concentrations given above provide the most efficient water purification and were used in all the tests. Then the cylinder was turned over 10 times, and the variations in the optical density of clarified natural water were registered on an LAM-1 device (λ 670 nm, l 35.2 mm). The measurements were carried out in the same cylinder (at the depth of 90 mm from the surface) after its installation in the

1070-4272/01/7409-1600$25.00 © 2001 MAIK "Nauka/Interperiodica"

Properties of Praestol anionic and cationic flocculants*

Praestol	$\overline{M}_\eta \times 10^{-6}$	$[\eta]$, $cm^3\ g^{-1}$	Content of ionic fragments in copolymer, mol %		
			Na-AA	TMAPAC	AA
A-1	8.7	1550	3	–	97
A-2	4.6	1500	11	–	89
A-3	4.4	1800	20	–	80
A-4	4.5	1600	28	–	72
C-1	–	920	–	9	91
C-2	–	620	–	27	73
C-3	–	690	–	20	80
C-4	–	555	–	33	67

* Structures of macromolecules:

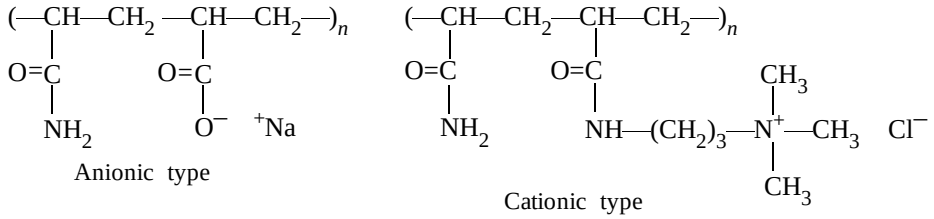

device. After sedimentation the precipitate was filtered off on a paper filter, and the resulting filtrate was analyzed for the iron content and permanganate oxidizability according to the procedures given elsewhere [6]. The reduced viscosity of the Praestol solutions η_{sp}/C_p was measured using a VPZh-3 viscometer (d_c = 0.54 mm) at C_p 0.002% and 25°C.

First we evaluated the effect of the chemical composition of the cationic and anionic Praestols on the sedimentation of the dispersed phase in natural water. The tests were carried out at constant concentrations of the alkalizing agent, coagulant, and flocculant. Typical kinetic curves of the variations in the water turbidity in the presence and absence of flocculant, registered by the turbidimetric procedure, are shown in Fig. 1. As seen, anionic Praestol flocculant being added to water significantly decreases its turbidity, accelerating sedimentation of the dispersed particles. Hydrolysis of iron(II) sulfate after its addition into the alkalized water yields positively charged colloidal aquahydroxy complexes of iron, which neutralize negatively charged particles of colloidal humus and dispersed mineral particles in natural water. As a result, the neurtralized colloidal particles form coarse aggregates and fall down. Further flocculant addition results in formation of large aggregates, which increases the precipitate density and accelerates water clarification. The flocculation factor D used as a criterion of the flocculation effect is defined as follows:

$$D = (V - V_0)/V_0,$$

where V_0 and V are the rates of the 50% change in the water turbidity in the absence and in the presence of Praestol.

The dependences of the flocculating factor D on the content of ionic units α in the macromolecules of anionic and cationic Praestols are shown in Fig. 2. As seen, the $D = f(\alpha)$ dependence passes a maximum for both anionic and cationic flocculants. This is probably due to the similar dependence of the effective size of macromolecular globules $(r^2)^{1/2}$ on α, which is confirmed by the dependence of the reduced viscosity η_{sp}/C_p (determined in water at C_p = const) [7, 8] on

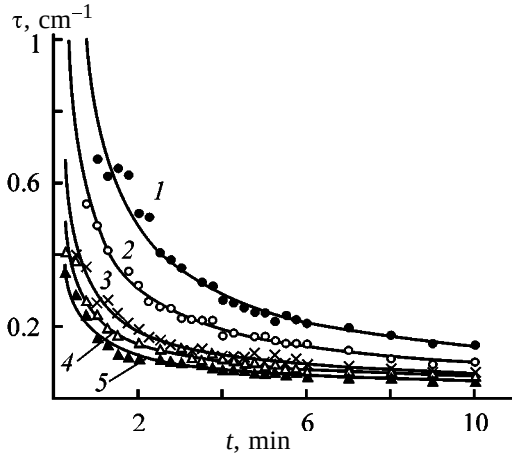

Fig. 1. Water turbidity τ as a function of the sedimentation time t in the course of liming with coagulation of natural water in the (*1*) absence and (*2*–*5*) presence of anionic Praestols. Sample: (*2*) A-1, (*3*) A-2, (*4*) A-3, and (*5*) A-4.

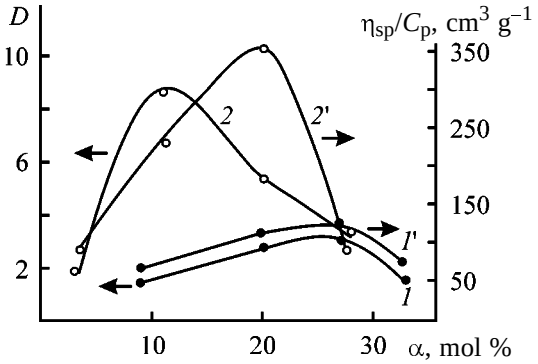

Fig. 2. (*1*, *2*) Flocculation factor *D* and (*1'*, *2'*) reduced viscosity η_{sp}/C_p of flocculant solutions as functions of the content of the ionic fragments α for (*1*, *1'*) anionic and (*2*, *2'*) cationic Praestols.

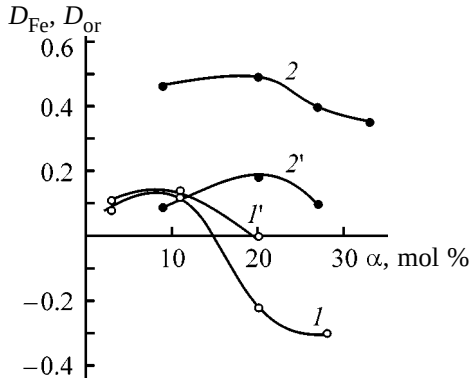

Fig. 3. Recovery of (*1*, *2*) iron D_{Fe} and (*1'*, *2'*) organic compounds D_{or} as a function of the content of ionic fragments α in (*1*, *1'*) anionic and (*2*, *2'*) cationic Praestols; η_{sp}/C_p was determined in water at C_p 0.002% and 25°C.

α for anionic (Fig. 2, curve *1'*) and cationic (curve *2'*) Praestols. The highest flocculation effect *D* (Fig. 2) is observed for anionic Praestol with α 11 mol % (A-2 sample) and for cationic Praestol with α 20 mol % (C-3). Apparently, such composition of macromolecules provides the optimal ratio between the charge density and chain flexibility, which ensure the highest $\langle \bar{r}^2 \rangle^{1/2}$. As a result, a macromolecule with the largest $\langle \bar{r}^2 \rangle^{1/2}$ interacts with a larger number of the dispersed particles causing aggregate coarsening and accelerating their precipitation.

Comparison of the experimental data for the same α (Fig. 2) shows that anionic Praestols provide the greater flocculating effect as compared with the cationic flocculants. This is due to the larger [η] for anionic Praestols (see table) and thus to higher molecular weights *M*, because, according to the Mark–Houwink–Kuhn equation, [η] ~ *M*. With increasing *M* $\langle \bar{r}^2 \rangle^{1/2}$ increases, which promotes interaction of the flocculant with a larger number of particles of the dispersed phase in water and thus enhances the flocculation effect.

We also studied the effect of Praestol flocculants on the recovery of iron compounds and organic impurities from treated water. The tests were performed at a fixed concentrations of the alkalizing agent, coagulant, and flocculant. The efficiency of the iron recovery was evaluated from the following equation:

$$D_{Fe} = (C^0_{Fe} - C_{Fe})/C^0_{Fe},$$

where C_{Fe} and C^0_{Fe} are the contents of iron in water after coagulation in the presence and absence of Praestol as compared with the initial water (%).

The recovery of organic compounds was evaluated by the following parameter:

$$D_{or} = (C^0_{ox} - C_{ox})/C^0_{ox},$$

where C_{ox} and C^0_{ox} are the permanganate oxidizability of water in the presence and absence of Praestol as compared with the initial water (%).

The dependences of D_{Fe} and D_{or} on α for anionic and cationic Praestols are shown in Fig. 3. As seen, the highest D_{Fe} and D_{or} for anionic and cationic Praestols are observed with samples A-2 and C-3 with α = 11 and 20 mol %, respectively. Though the trends in Fig. 3 are weakly pronounced, they agree well with the data presented in Fig. 2, and therefore they can be explained by the same reasons. Moreover, cationic flocculants more efficiently remove iron and organic compounds from water as compared with anionic Praestols (Fig. 3). This is obviously due to the formation of interpolymeric complexes [9] between the positively charged macromolecules of cationic Praestol and negatively charged macromolecules of the humic and fulvic acids and their complexes with iron present in natural water alkalized to pH 11.

Figures 2 and 3 show that the Praestol cationic flocculant with α 20 mol % (C-3 sample) is the most promising for preliminary purification of natural water. For this sample we studied the efficiency of the recovery of iron compounds and organic impurities as influenced by the concentrations of the coagulant (Fig. 4) and flocculant (Fig. 5). As seen from Fig. 4, at fixed concentrations of the flocculant and alkalizing agent the efficiency of recovery of iron compounds and organic impurities decreases with decreasing flocculant concentration from 67 to 15 mg l^{-1}. Figure 5 shows that, at fixed concentrations of the coagulant and alkalizing agent, with decreasing concentration of the Praestol cationic flocculant in the 1.0–0.2 mg l^{-1}

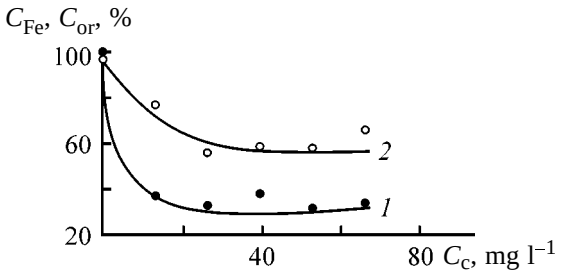

Fig. 4. (*1*) Concentration of iron C_{Fe} (%, with respect to initial) and (*2*) organic compounds C_{or} (%, with respect to initial) as a function of iron(II) sulfate coagulant concentration C_c. Lime concentration 232.5 mg l^{-1}, flocculant concentration 0.4 mg l^{-1}; initial water: iron concentration 194 μg l^{-1}, oxidizability 7.6 mg O per liter.

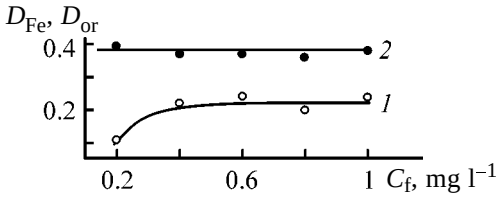

Fig. 5. Recovery of (*1*) iron D_{Fe} and (*2*) organic compounds D_{or} as a function of Praestol cationic flocculant concentration C_f; sample C-3. Lime concentration 232.5 mg l^{-1}, coagulant concentration 66.9 mg l^{-1}.

range the efficiency of recovery of iron compounds decreases at low flocculant concentrations, whereas the content of organic impurities remains almost unchanged. The above data show that under the experimental conditions with cationic Praestol (α 20 mol %) the lower limits of the coagulant and flocculant concentrations ensuring efficient purification of water are 15 and 0.4 mg l^{-1}, respectively.

CONCLUSIONS

(1) In the course of water treatment with Praestol flocculants at constant concentrations of alkalizing agent (calcium hydroxide) and coagulant [iron(II) sulfate] the dependences of D, D_{Fe}, D_{or}, and η_{sp}/C_p (at C_p const) on the content of the ionic fragments are due to the change in the effective size of macromolecules in solutions and pass a maximum at α 11 and 20 mol % for anionic and cationic Praestols, respectively.

(2) The values of D increase on passing from the cationic to anionic flocculants, whereas D_{Fe} and D_{or} decrease.

(3) In the presence of cationic Praestol (α 20 mol %) the lower limits of the coagulant and flocculant concentrations ensuring efficient purification of water are 15 and 0.4 mg l^{-1}, respectively.

REFERENCES

1. Zapol'skii, A.K. and Baran, A.A., *Koagulyanty i flokulyanty v protsessakh ochistki vody: Svoistva. Poluchenie. Primenenie* (Coagulants and Flocculants in Water Treatment: Properties, Preparation, Use), Leningrad: Khimiya, 1987.
2. Kurenkov, V.F., in *Handbook of Engineering Polymeric Materials*, New Jersey: Dekker, 1997, ch. 3, pp. 61–72.
3. Kurenkov, V. F., *Soros. Obrazov. Zh.*, 1997, no. 7, pp. 57–63.
4. Kurenkov, V.F., Churikov, F.I., and Snigirev, S.V., *Zh. Prikl. Khim.*, 1999, vol. 72, no. 9, pp. 1485–1489.
5. Kurenkov, V.F., Snigirev, S.V., Churikov, F.I., *et al*., *Zh. Prikl. Khim.*, 2001, vol. 74, no. 3, pp. 435–439.
6. *Unifitsirovannye metody analiza vod* (Standard Methods of Water Analysis), Lur'e, Yu.Yu., Ed., Moscow: Khimiya, 1973.
7. Kargin, V.A., Mirlina, S.Ya., and Antipina, A.D., *Vysokomol. Soedin.*, 1959, vol. 1, no. 9, pp. 1428–1437.
8. Fernandez, P.L. and Lagos, A.E., *J. Polym. Sci, Part A*, 1964, vol. 2, pp. 2917–2928.
9. Bekturov, E.A. and Bimendina, L.A., *Interpolimernye kompleksy* (Interpolymeric Complexes), Alma-Ata: Nauka, 1977.

Russian Journal of Applied Chemistry, Vol. 74, No. 9, 2001, pp. 1604–1605. Translated from Zhurnal Prikladnoi Khimii, Vol. 74, No. 9, 2001, pp. 1555–1556.

BRIEF COMMUNICATIONS

Alkylation of Crystalline Salts of 1,3-Thiazolidine-2,4-diones with Alkyl Halide Vapors

A. I. Ginak, E. B. Aronova, and M. V. Rutto

St. Petersburg State Technological Institute, St. Petersburg, Russia

Received April 9, 2001

Abstract—Alkylation of 1,3-thiazolidine-2,4-diones with alkyl halide vapors was performed. The composition of the reaction mixtures was determined by thin-layer chromatography.

Alkylated derivatives of 1,3-thiazolidine-2,4-diones are promising compounds exhibiting antibiotic, acaricidal, herbicidal, and other useful properties. However, the traditional procedure of their synthesis by alkylation of alkali metal and ammonium salts of 1,3-thiazolid-4-ones yields a mixture of isomers originating from addition of the alkyl radical to the heterocyclic nitrogen atom and exocyclic oxygen atom at the 2-position. The latter reaction yields 2-alkoxy-Δ^2-1,3-thiazolin-4-ones, unstable by-products decomposing in the course of the reaction, which results in decreased yield and contamination of the target products. The side addition of the alkyl radical to the exocyclic oxygen atom is quite natural, since 1,3-thiazolidine-2,4-diones are ambifunctional compounds showing dual reactivity in nucleophilic substitutions in solutions [1]. Attempts to affect the isomer ratio by varying the nucleophilicity of the substrate, polarizability of the reagent, and polarity of the medium have not improved the situation; in all the cases either an isomer mixture was formed or the alkylation rate drastically decreased; therefore, alkylation in solutions was considered to have no practical significance [2].

A successful attempt of selective synthesis of alkyl derivatives of 1,3-thiazolin-4-ones by a solid-phase reaction [3–5] creates a prerequisite for purposeful synthesis of 3-alkyl-substituted 1,3-thiazolidine-2,4-diones by solid-phase synthesis. 1,3-Thiazolidine-2,4-diones form a close-packed crystal lattice with the space group *Pbca* in which the molecules are packed in the form of planar hydrogen-bonded (N^3–H···O^2–C^2) dimers [6]. In their alkali metal salts, the counterion is equidistant from the O^2 and N^3 reaction centers [7], which makes the nitrogen atom accessible for the electrophilic attack by an alkyl group, whereas shielding of the O^2 atom prevents formation of by-products.

To confirm this assumption, we alkylated the crystalline alkali metal salts with ethyl iodide vapor:

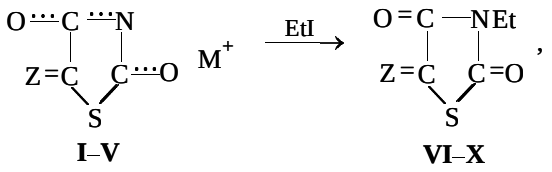

I–V **VI–X**

where Z = H_2 (**I**, **VI**), PhCH (**II**, **VII**), 4-$NO_2C_6H_4CH$ (**III**, **VIII**), 4-$(CH_3)_2C_6H_4CH$ (**IV**, **IX**), 4-$CH_3C_6H_4$·CH (**V**, **X**); M = Li, Na, K.

Crystals of **I**–**V** were treated with ethyl iodide vapor. Special experiments showed that the result is independent of the amount of the alkylating agent and reaction conditions.

The composition of the reaction mixture was determined by quantitative thin-layer chromatography (TLC). We found that the reaction yields only the products of addition of the alkyl group at the N^3 atom (see table). Quantitative analysis shows that the material balance is well kept throughout the experiment, i.e., the "initial" concentration calculated from the weight of the salt sample is equal to the sum of the running concentrations of the salt and reaction product. These concentrations were measured with an error of $\leq$5%.

We also examined the effect of the counterion in the substrate on its reactivity and revealed no difference in the reaction pathway between the Li^+, Na^+, K^+, and Cs^+ salts.

EXPERIMENTAL

1,3-Thiazolidinedione and its 5-arylmethylene derivatives were prepared according to [8]. The compounds were recrystallized from ethanol and identified

1070-4272/01/7409-1604$25.00

Composition of the reaction mixture according to TLC

Compound	R_f	IR spectrum, cm^{-1}		Found, %/Calculated, %	
		$\nu(C^2=O)$	$\nu(C^4=O)$	N	S
VI	0.80	1724	1688	10.8/10.84	24.6/24.82
VII	0.86	1741	1710	6.0/6.00	12.8/13.74
VIII	0.65	1745	1715	11.5/11.38	13.4/13.02
IX	0.69	1741	1711	10.3/10.13	12.0/11.60
X	0.75	1738	1708	6.1/5.66	3.1/12.96

by the melting points, which differed from published data [8] by no more than 1°C. The substance purity was checked by chromatography on alumina modified with oxalic acid, in the system acetone–hexane–acetic acid, 1 : 2 : 0.01. In static solid-phase alkylation, a 0.01-g sample of salt **I**–**V** was kept in an atmosphere of the alkylating agent vapor at room temperature. In the dynamic mode, alkylating agent vapor was passed through a salt sample at room temperature and a residual pressure of 10–200 mm Hg at which condensation of the alkylating agent on the solid phase surface was excluded. After evacuation to remove the alkylating agent vapor, the concentration of the reaction products was determined by quantitative TLC [9] and spectrophotometrically [10], with an accuracy of 5%.

REFERENCES

1. V'yunov, K.A., Ginak, A.I., and Sochilin, E.G., *Zh. Org. Khim.*, 1978, vol. 14, no. 5, pp. 1075–1078.
2. V'yunov, K.A., Ginak, A.I., and Ramsh, S.M., *Zh. Org. Khim.*, 1983, vol. 19, no. 1, pp. 212–215.
3. Basova, Yu.G., Ramsh, S.M., and Ginak, A.I., *Zh. Org. Khim.*, 1981, vol. 17, no. 5, pp. 986–990.
4. V'yunov, K.A., Ginak, A.I., and Ramsh, S.M., *Zh. Org. Khim.*, 1983, vol. 19, no. 1, pp. 209–212.
5. Ginak, A.I., Dymshits, V.A., V'yunov, K.A., *et al.*, *Kinet. Katal.*, 1989, vol. 30, no. 1, pp. 458–461.
6. Form, G.R. and Raper, E.S., *Acta Crystallogr.*, 1975, vol. 31, no. 8, pp. 2183–2187.
7. Matthews, B.W., *Acta Crystallogr.*, 1964, vol. 17, no. 6, pp. 1413–1420.
8. Ginak, A.I., V'yunov, K.A., and Sochilin, E.G., *Khim. Geterotsikl. Soedin.*, 1971, no. 6, pp. 858–859.
9. Bolliger, H.R., Brenner, M., and Gänshirt, H., *Dünschicht Chromatographie. Ein Laboratoriumshandbuch*, Stahl, E., Ed., Berlin: Springer, 1982. Translated under the title *Khromatografiya v tonkikh sloyakh*, Moscow: Mir, 1965, p. 52.
10. Bershtein, I.Ya. and Kaminskii, Yu.L., *Spektrofotometricheskii analiz v organicheskoi khimii* (Spectrophotometric Analysis in Organic Chemistry), Leningrad: Khimiya, 1975, p. 84.

Russian Journal of Applied Chemistry, Vol. 74, No. 9, 2001, pp. 1606–1607. Translated from Zhurnal Prikladnoi Khimii, Vol. 74, No. 9, 2001, pp. 1557–1558.

BRIEF COMMUNICATIONS

^{13}C NMR Study of the Structure of Vinyl Chloride–1-Vinyl-1,2,4-triazole Copolymer

O. V. Lebedeva, L. V. Kanitskaya, G. A. Pirogova, N. S. Shaglaeva, S. V. Fedorov, and A. K. Khaliullin

Irkutsk Institute of Chemistry, Siberian Division, Russian Academy of Sciences, Irkutsk, Russia

Received June 6, 2000; in final form, April 2001

Abstract—The structure of the copolymer prepared by radical copolymerization of vinyl chloride with 1-vinyl-1,2,4-triazole was studied by quantitative ^{13}C NMR spectroscopy. The structural unit of the copolymer consists of the units of vinyltriazole and quaternized vinyltriazole, vinyl group, and four vinyl chloride units.

The most widely used procedure for preparing modified polyvinyl chloride is copolymerization of vinyl chloride (VC) wirth various monomers. It was shown previously that radical copolymerization of VC with *N*-vinyl-4,5,6,7-tetrahydroindole is accompanied by dehydrochlorination [1].

In this work we studied by ^{13}C NMR spectroscopy the structure of the copolymer prepared by radical copolymerization of VC with 1-vinyl-1,2,4-triazole (VT).

Copolymerization of VC with VT was performed in *N*-methylpyrrolidone with azobis(isobutyronitrile) initiator.

The IR spectra of the resulting copolymers contain no bands characteristic of the *N*-vinyl group (960, 1680 cm^{-1}), but the vibration bands of the triazole ring (1030, 1210, 1560 cm^{-1}) are preserved, and a band characteristic of C=C bonds appears at 1640 cm^{-1}. The ^{13}C NMR spectrum of the VC–VT copolymer contains broadened signals of the carbon atoms of the triazole ring (151.91, 144.38 ppm), a group of signals of the vinyl moiety –CH=CH– (128.03–127.58 ppm), and carbon signals of the >CHCl (58.49–56.57 ppm), –N–CH– (54.6), and >CH_2 (45.4 – 41.9 ppm) groups. Along with the above signals, the spectrum contains narrow signals corresponding to the carbon atoms of *N*-methylpyrrolidone (17.21, 27.03, 30.73, 48.56, 173.90 ppm), probably chemisorbed on the copolymer surface. It should be noted that the polymer was reprecipitated two times and vacuum-dried to constant weight.

The vinyl fragments incorporated into the copolymer are formed by elimination of hydrogen chloride from VC in the course of its copolymerization with VT. Hydrogen chloride can be bound by the triazole ring:

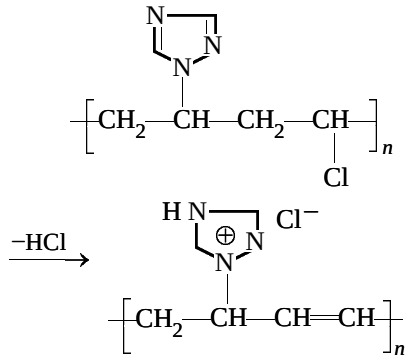

The quantitative analysis of the ^{13}C NMR spectrum showed that the molar ratio of the VC and VT units, vinyl groups, and *N*-methylpyrrolidone is 1.00 : 2.67 : 0.619 : 0.254. The elemental composition and content of each component (wt %) were calculated from the ^{13}C NMR spectra assuming that (1) VT does not bind hydrogen chloride, (2) all VT rings bind hydrogen chloride, and (3) only 0.619 mol of VT binds hydrogen chloride. The results are listed in the table.

The results of chemical analysis are consistent with the composition calculated from the ^{13}C NMR spectrum with assumption 3 (data are printed bold in the table). When calculating the copolymer composition from the elemental analysis data, we took into account the total content of chlorine (both organic and ionic) in the final product; therefore, the content of VC units calculated from the ^{13}C NMR spectrum differs from that calculated from the analytical data.

From the results of quantitative analysis we calcu-

1070-4272/01/7409-1606$25.00

Elemental composition of VC–VT copolymer; relative content of comonomers, vinyl group, and *N*-vinylpyrrolidone in the sample

Element, fragment	Composition, wt %			
	^{13}C NMR spectrum			chemical methods
C	46.91	41.86	**43.65**	43.40
H	5.45	5.16	**5.27**	5.76
N	15.03	13.41	**13.99**	14.81
O	1.34	1.20	**1.25**	1.26 (from difference)
Cl	31.27	38.36	**36.04**	34.77
VT	31.34	27.97	**29.17**	29.42 (by chlorine) 24.91 (by nitrogen)
VC	55.05	49.14	**51.23**	70.58 (by chlorine) 75.09 (by nitrogen)
–CH=CH–	5.31	4.74	**4.94**	4.51 (from difference between copolymer compositions calculated by chlorine and nitrogen)
N-Methyl-pyrrolidone	8.30	7.40	**7.72**	–

lated the structural unit of the copolymer consisting of the VT unit, quaternized VT unit, vinyl group, and four VC units:

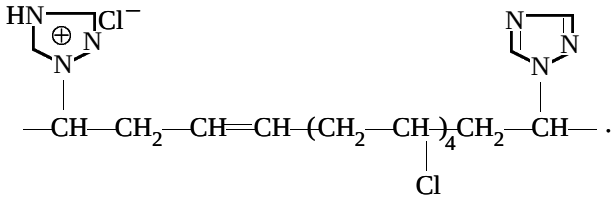

The elemental composition of the structural unit of the copolymer (wt %) is as follows: C 42.99, H 4.98, N 16.71, and Cl 35.32; the content of fragments in the structural unit of the copolymer is as follows (wt %): VC 49.75, VT18.90, quaternized VT 26.17, and CH=CH 5.18.

EXPERIMENTAL

Copolymerization was performed in sealed ampules at 60°C in the presence of azobis(isobutyronitrile) (1.5 wt % relative to comonomers) under argon. The reaction mixture was dissolved in dimethylformamide (DMF), and the copolymer was precipitated with acetone. Then the copolymer was reprecipitated two times from solution in DMF into acetone and vacuum-dried to constant weight. The copolymer composition was determined by elemental analysis following the standard procedure [2]. The content of the –CH=CH– was calculated from the difference between the compositions calculated by nitrogen and chlorine (e.g., 75.09 – 70.58 = 4.51 and 29.42 – 24.91 = 4.51).

The IR spectra were taken on a Specord IR-75 spectrometer (KBr pellets or mulls in mineral oil).

The ^{13}C NMR spectrum of the copolymer sample was taken on a Varian VXR-500S spectrometer (working frequency 125.5 MHz) in DMSO-d_6 at a relaxation delay of 2.5 s and 90° pulse. As relaxant was used chromium tris(acetylacetonate) (0.02 M). The molar ratios of the copolymer components and *N*-methylpyrrolidone were calculated by a common procedure: The fraction of one carbon atom of VT q_{VT} was taken equal to one carbon atom, which corresponds to 1 mol of VT, M_{VT}. The number of moles of the other components was calculated by the formula

$$M_x = q_x / q_{VT},$$

where q_x is the fraction of the carbon atom of component x, $q_x = I_x/I_{tot}$ (where I_x and I_{tot} are the integral intensity of the signal of atom x and the total integral intensity, respectively).

The relative error of the quantitative determination of the relative content of comonomers (wt %) and elemental composition of the copolymers does not exceed 6.7%.

CONCLUSIONS

(1) Radical copolymerization of vinyl chloride with 1-vinyl-1,2,4-triazole in *N*-methylpyrrolidone is accompanied by dehydrochlorination.

(2) The composition of the copolymer, calculated from the ^{13}C NMR spectrum and from elemental analysis data, shows that the released hydrogen chloride protonates approximately each second triazole ring.

REFERENCES

1. Shaglaeva, N.S., Mikhaleva, A.I., Sarapulova, G.I., *et al.*, *Izv. Ross. Akad. Nauk, Ser. Khim.*, 1997, no. 12, pp. 2267–2268.
2. Toroptseva, A.M., Belogorodskaya, K.V., and Bondarenko, V.M., *Laboratornyi praktikum po khimii i tekhnologii vysokomolekulyarnykh soedinenii* (Practical Laboratory Course of Chemistry and Technology of Macromolecular Compounds), Leningrad: Khimiya, 1972.

Russian Journal of Applied Chemistry, Vol. 74, No. 9, 2001, pp. 1608–1609. Translated from Zhurnal Prikladnoi Khimii, Vol. 74, No. 9, 2001, pp. 1559–1560.

BRIEF COMMUNICATIONS

Synthesis of *N*-Vinylpyrrolidone–Vinyltrimethoxysilane Copolymers

M. N. Gorbunova, V. D. Surkov, and M. S. Fedoseev

Institute of Technical Chemistry, Ural Division, Russian Academy of Sciences, Perm, Russia

Received March 6, 2001; in final form, April 2001

Abstract—*N*-Vinylpyrrolidone–vinyltrimethoxysilane copolymers were prepared by radical copolymerization. The composition of the copolymer was studied in relation to the reaction temperature and composition of the initial mixture. The kinetic parameters of the monomer activity were calculated.

Unique properties of polyvinylpyrrolidone (PVP) such as good solubility in water and organic solvents, high complexing power with respect to a wide range of inorganic, organic, and biological objects, and the lack of toxicity allow wide use of PVP in engineering, medicine, pharmacy, and agriculture [1–3]. Therefore, there is a growing interest in syntheses of new polymers based on *N*-vinylpyrrolidone (VP) by copolymerization with other polyfunctional monomers. Of particular interest in this respect are copolymers with a labile organosilicon moiety, capable of further polymer-analogous transformations.

It is known that alkenylsilanes show poor activity in radical polymerization because of the steric and electronic effect of the silicon atom, but they relatively readily copolymerize with acetonitrile, styrene, vinyl acetate, and vinyl chloride [4–6].

This study is aimed at synthesis of VP–vinyltrimethoxysilane (VTMS) copolymers, which practically have not been studied previously.

EXPERIMENTAL

The initial monomers VTMS and VP (commercial products) were vacuum-distilled before use. VTMS: bp 122°C, n_D^{20} 1.390 (cf. bp 52.9°C/49 mm Hg n_D^{20} 1.390 [7]); VP: bp 65°C/1.5 mm Hg, n_D^{20} 1.5117 (cf. bp 71–72°C/2.5 mm Hg, n_D^{20} 1.5117 [1]). Azobis(isobutyronitrile) (AIBN) of cp grade was used without additional purification.

The copolymers were prepared by radical copolymerization in the bulk by heating with AIBN in sealed glass tubes in the presence of atmospheric oxygen. The copolymer was dissolved in acetone and reprecipitated into diethyl ether. After filtration and drying with diethyl ether, the copolymers were dried in an oven at 45°C to constant weight.

Table 1. VP–VTMS copolymers [initiator AIBN (0.05%), reaction time 3 h]

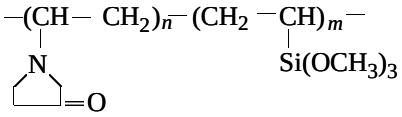

Content of monomers, mol %		*T*, °C	Yield, %	Found N, %	Copolymer composition, mol %	
VP	VTMS				VP	VTMS
84.21	15.79	60	74.0	12.10	97.01	2.99
75.00	25.00	60	51.7	11.13	91.50	8.50
66.67	33.33	60	71.0	9.39	79.58	20.42
25.00	75.00	60	30.7	6.79	60.91	39.09
84.21	15.79	80	82.9	9.73	81.88	18.12
84.21	15.79	100	80.9	8.95	76.57	23.43

1070-4272/01/7409-1608$25.00

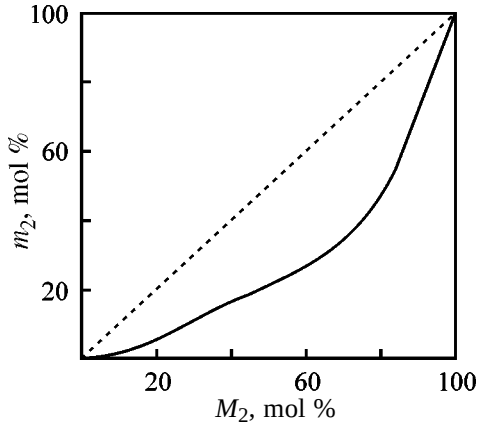

Composition of VP–VTMS copolymers as a function of the monomer ratio. Reaction temperature 60°C, reaction time 3 h. (m_2) Content of VTMS in copolymer and (M_2) content of VTMS in the initial mixture.

The IR spectra were taken on a UR-20 spectrometer. Samples were prepared as mulls in mineral oil. The copolymer composition was calculated from data of elemental analysis for nitrogen.

The copolymers are gelatinous substances soluble in acetone, ethanol, and chloroform; after reprecipitation with diethyl ether and drying in an oven they transform into a white powder. After reprecipitation and drying, the solubility in organic solvents is lost, probably owing to formation of siloxane cross-links. The characteristics of the copolymers are listed in Table 1. The formation of the copolymers was confirmed by the IR spectra, which contain absorption bands at 1680 (VP C=O bonds) and 1094 cm^{-1} (VTMS Si–O bonds).

The bands at 1600 and 1628 cm^{-1}, characteristic of the double bonds in VTMS and VP, respectively, are lacking in the spectra of the copolymers, which confirms occurrence of the radical copolymerization through the double bonds.

Table 2. Parameters of monomer activity*

Calculation method	r_1	r_2	Q_2	e_2
FR	3.64 ± 0.07	0.21 ± 0.02	0.02 ± 0.002	–0.62 ± 0.06
KT	1.44 ± 0.14	0.16 ± 0.02	0.02 ± 0.002	+0.07 ± 0.007

* Q_1 = 0.14, e_1 = –1.14 [9].

The composition of the copolymers as a function of the composition of the initial mixture is shown in the figure.

As seen from the composition diagram, VP forms with VTMS random copolymers enriched in VP units. The copolymerization constants r_1 and r_2 calculated by the Fineman–Ross (FR) and Kelen–Tudos (KT) methods are listed in Table 2. These data were obtained at monomer conversions not exceeding 50%, which is acceptable in calculations of r_1 and r_2 by the Kelen–Tudos method [8].

In this case, the Alfrey–Price *Q*–*e* reactivity parameters of VTMS were as follows: Q_2 = 0.02 and e_2 = 0.07; the published values for VP are Q_1 = 0.14 and e_1 = –1.14 [9].

Thus, we prepared VP–VTMS copolymers and determined the activity parameters of the monomers in radical copolymerization.

REFERENCES

1. Sidel'kovskaya, F.P., *Khimiya N-vinilpirrolidona i ego polimerov* (Chemistry of *N*-Vinylpyrrolidone and Its Polymers), Moscow: Nauka, 1970.
2. Kirsh, Yu.E., *Poli-N-vinilpirrolidon i drugie poli-N-vinilamidy* (Poly-*N*-vinylpyrrolidone and Other Poly-*N*-vinylamides), Moscow: Nauka, 1998.
3. *Sintez, svoistva i primenenie polimerov na osnove N-vinillaktamov* (Synthesis, Properties, and Use of Polymers Based on *N*-Vinyllactams), Tashkent: Fan, 1990.
4. US Patent 2 820 798.
5. Thompson, B.R., *J. Polym. Sci.*, 1956, vol. 19, pp. 373–377.
6. Mixer, R.Y. and Bailey, D.L., *J. Polym. Sci.*, 1955, vol. 18, pp. 573–582.
7. Nagel, R. and Tamborski, C., *J. Org. Chem.*, 1951, vol. 16, p. 1768.
8. Ivanchev, S.S., *Radikal'naya polimerizatsiya* (Radical Polymerization), Leningrad: Khimiya, 1985, p. 148.
9. Spirin, Yu.L., *Reaktsii polimerizatsii* (Polymerization Reactions), Kiev: Naukova Dumka, 1977, p. 42.

Russian Journal of Applied Chemistry, Vol. 74, No. 9, 2001, pp. 1610–1615. Translated from Zhurnal Prikladnoi Khimii, Vol. 74, No. 9, 2001, pp. 1561–1566.

HISTORY OF CHEMISTRY AND CHEMICAL TECHNOLOGY

Professor Gustav Tammann (To 140th Birthday Anniversary)

Similarly to a number of his contemporaries, prominent chemists of the late XIX century–early XX century, Gustav Tammann had rather wide scientific interests. He made an outstanding contribution to investigations of solutions, heterogeneous equilibria, and crystallization processes and studies of metal systems, glassy state, and solid solutions.

Gustav Heinrich Johann Tammann was born on May 28, 1861, in Jamburg, St. Petersburg Province (now Kingisepp, Leningrad oblast). His father, Heinrich Tammann (1833–1864) was of Estonian peasant origin. He graduated from the faculty of medicine of Derpt (Yuryev, Tartu)[1] University in 1857 and worked as a physician first in Jamburg and then at Gorki, Mogilev Province (now Gorki, Mogilev oblast, Belarus). At the same place, Heinrich Tammann taught applied medicine at Gorigoretskii Agricultural Institute [1, 2]. Gustav Tammann's mother, Matilda Schünmann, was of German origin. After Heinrich Tammann's death, his family moved to Derpt. Despite the more than modest means at family's disposal, Gustav Tammann successfully finished gymnasium and entered the physicomathematical faculty of Derpt University in 1879. One of the oldest in Russia, the University was opened in April 1802 (the history of this educational institution dates from 1632, but later its functioning was interrupted for a long time). In 1802–1850, the University did not train specialists in chemistry. The chair of chemistry, formed in 1804, mainly satisfied the demand of medicine and pharmacology [3, 4]. In 1850 the physicomathematical faculty including a chemical department was created, and training of specialists in chemistry was commenced. According to the available data [5], 58% of those studying at the chemical department during the period from 1850 till 1917 were from Baltics, 41% from other provinces of Russia, and 1% from abroad. About 60% of those graduated from the chemical department received a degree of candidate of science.

[1] In 1893, the town of Derpt (Dorpat) was given its previous (1030–1224) name of Yuryev; in 1919, it became Tartu. Correspondingly changed the name of the University.

During G. Tammann's education at the University, all chemical disciplines were taught by professor Carl Schmidt (1822–1894), a known scientist of that time, educated at German universities.[2] Schmidt was a representative of the scientific school created by such prominent chemists of the XIX century as J. Liebig (1803–1873) and F. Wöhler (1800–1882). C. Schmidt became extraodinary professor at the chair of pharmacology in 1850, and ordinary professor of chemistry and head of chemical laboratory in 1852. In 1873, C. Schmidt was elected a corresponding member of the St. Petersburg Academy of Sciences for his works in the field of hydrochemistry.

The main Schmidt's investigations were done in the field of physiological chemistry and also analytical chemistry, hydrochemistry, and agricultural chemistry. Among his widely known works were, in particular, his studies of the chemical composition of chernozem soils of the European Russia. Schmidt's

[2] A major contribution to studies of the life and activities of chemists from Tartu University of the XIX century, C. Schmidt, G. Tammann, W. Ostwald, and others, was made by Ugo Vol'demarovich Palm (1933–1989), professor of the same university, known electrochemist and historian of chemistry.

1070-4272/01/7409-1610$25.00 © 2001 MAIK "Nauka/Interperiodica"

laboratory at Derpt University was a recognized center of the most precise chemical analyses of a wide variety of natural objects: clays, minerals, soils, fertilizers, and water.

At the time of G. Tammann's education at the University, laboratory works with students were conducted at the chair of chemistry by young teachers, among whom mention should be made of J. Lemberg (1842–1902) and W. Ostwald (1853–1932), Derpt University graduates and Schmidt's pupils. Lemberg taught applied chemistry and soil science and exerted a profound influence on the development at the chair of physicochemical investigations, which became the leading direction in the scientific work of the chair beginning in the 1880s. In 1888, Lemberg was elected a professor of the chair of mineralogy and petrography and was the first in Russia to carry out experimental studies in this field, having laid foundations of "chemical geology." Lemberg's works were highly appreciated by F.Yu. Levinson-Lessing (1861–1939) and V.I. Vernadsky (1863–1945) [9].

Ostwald graduated from Derpt University in 1875 and worked at the chair of physical chemistry till 1881, when he became professor of chemistry at Riga Polytechnic Institute. In 1887, he became a university professor in Leipzig (Germany) where he founded the first world's chair of physical chemistry. Ostwald was among those who founded the first journal of physical chemistry (*Zeitschrift für physikalische Chemie*). He was awarded Nobel Prize in 1909.

The development of G. Tammann's scientific interests was also much affected by A. von Oettingen (1836–1920), professor of physics, well educated and all-round scientist. In 1883, G. Tammann received a diploma of a candidate of chemistry and started working at the laboratory of his teacher, Schmidt, as laboratory assistant; he became a privat-docent in 1887 and docent in 1889. In 1890, G. Tammann backed his doctoral dissertation *Über Metamerie der Metaphosphate* (On Metamerism of Metaphosphates). Upon Schmidt's retirement in 1892, G. Tammann took his position of a director of the chemical laboratory at Derpt University and was elected extraordinary professor. In 1894, he became an ordinary professor. G. Tamman's promotion was favored by recommendations of leading Russian scientists N.N. Beketov (1827–1911) and D.I. Mendeleev (1834–1907). G. Tammann delivered all the main courses of lectures on analytical, inorganic, organic, and physical chemistry. The transition of the educational process from German to Russian posed certain difficulties to G. Tammann and some other lecturers, but he got through in the course of time. Frequent trips to St. Petersburg and meetings with colleagues allowed him to master Russian. Nevertheless, the volume of his pedagogical activities was so large that he could not give sufficient attention to scientific studies. Probably, this was the main reason why G. Tammann accepted in December 1902 invitation to head the Institute of Inorganic Chemistry at Göttingen University (Germany). Among those who recommended G. Tammann was W. Nernst (1864–1941), a professor of the same university, physicist and physical chemist, Nober Prize winner (1920), member of many academies, including the Academy of Sciences of the USSR (since 1926). In 1905, Nernst moved to Berlin, and G. Tammann headed in 1907 the Institute of Physical Chemistry of Göttingen University. G. Tammann worked at that university till his retirement in 1930.

Having left Russia, the scientist continued to maintain close scientific relations with his Russian colleagues. Already in 1880 he became a member of the chemical department of the Russian Physicochemical Society by recommendation of D.P. Konovalov (1856–1929), N.A. Menshutkin (1842–1907), and V.E. Tishchenko (1861–1941) [10]. In 1908, he was one of very few foreign chemists who were elected honorary members of this society. In December 1901, G. Tammann took part in the XI Congress of Russian naturalists and physicians and presented a report *On the Relationship between the Crystalline and Liquid States* [11]. The report was highly appreciated by Mendeleev. Much attention was given to Tammann's works in *Osnovy khimii* (Foundations of Chemistry). It is known that Mendeleev called Tamman "... my dear friend" and believed that he developed "...extraordinarily interesting fields of physical chemistry" [10]. Correspondence between G. Tammann and Mendeleev commenced in 1887 and was related to the vapor pressure in the system sulfuric acid–water. Tammann's investigations and conclusions were in agreement with the hydrate theory of solutions, developed by Mendeleev [12]. Later, the scientists met more than once, the last time in 1902 in Derpt (Yuryev) at the centennial anniversary of the resumption of the University's functioning. In 1903, Mendeleev was elected honorary member of Yuryev University.

G. Tammann took part in the II Mendeleev Congress on General and Applied Chemistry in St. Petersburg in December 1911. He reported the results obtained in determining the molecular weight of crystalline substances. There is evidence [13] that in 1909 G. Tammann was offered to stand for election as ordinary academician (full member) of the St. Peters-

burg Academy of Sciences, which, however, involved, in the case of his being elected, obligatory moving to St. Petersburg. At the same time, his work at Göttingen University was quite successful and G. Tammann refused. Another known physical chemist, P.I. Walden (1863–1957), professor of Riga Polytechnic Institute, was elected to fill the vacancy in 1910. In December 1912, Tammann was elected, as a foreign scientist, a corresponding member of the St. Petersburg Academy of Sciences, and in December 1927, an honorary member of the Academy of Sciences of the USSR.

Very sympathetic recollections of G. Tammann were written by N.I. Nikitin (1890–1975, corresponding member of the Academy of Sciences of the USSR since 1939) who worked, by recommendation of Academician N.S. Kurnakov (1860–1941), at G. Tammann's laboratory in Göttingen in 1923–1924 and attended his lectures [14].

When still in Russia, G. Tammann maintained most friendly relationships and repeatedly met with the leading Western scientists of that time: J.H. van't-Hoff (1852–1911), S. Arrhenius (1859–1927), W. Nernst, and G.W.B. Rosenboom (1854–1907). Together with Nernst, G. Tammann carried out a joint investigation into the effect of pressure on the displacement of hydrogen from solutions by metals (1891). The most cordial were G. Tammann's relations with Arrhenius and Nernst [13]. In 1900 in Paris, G. Tammann became acquainted with H.-L. Le Chatelier's (1850–1936) works.

As already noted, G. Tammann's scientific activities were exceedingly versatile. The most important directions of research included: dilute and concentrated solutions (depression of the saturated vapor pressure, osmosis, internal pressure in solutions), heterogeneous equilibria (one-component systems, polymorphism, crystallization processes), glassy state, theory of thermal analysis, phase diagrams of metal systems, nature and corrosion behavior of solid solutions, problems of biochemistry, etc. The most comprehensive analysis of G. Tammann's scientific activities can be found in [15, 16]. More concise evidence was given in a scientific-biographical dictionary [1] and numerous publications devoted to jubilees of the scientist or his death [17–19].[3] Separate directions of G. Tammann's scientific activities, mainly those concerned with solutions, were analyzed in domestic monographs devoted to the history of chemistry [20–22]. Tammann's works carried out before his departure from Russia were considered by U. Palm [23, 24] and N. Ryago [25]. The role of Tammann in the development of physical metallurgy in Germany was discussed by U. Dehlinger [26]. To the sixty-fifth birthday of the scientist was devoted a special volume of *Z. anorg. allg. Chem.* (1926, vol. 154, pp. 1–455) presenting works of his colleagues and pupils. Among the authors were known Russian chemists Nikitin, N.A. Tananaev (1878–1959), and G.G. Urazov (1884–1957, academician of the Academy of Sciences of the USSR since 1946). In connection with G. Tammann's seventieth birthday, a series of papers analyzing his works in the field of structure and properties of metals and alloys was published in *Z. Metallkunde* (1931, vol. 23, no. 5, pp. 134–146).

The most complete list of published G. Tammann's works is given in the reference book [27]. Papers published in the early stage of his scientific activities (before 1901) are listed in the biographic dictionary [28]. We now consider only briefly some results of the versatile activities of the scientist during 55 years, from 1883 till 1938.

In the 1880s, one of the main directions of research in physical chemistry was investigation of dilute electrolyte solutions. In those years, Tammann carried out at the chemical laboratory of Derpt University high-precision measurements of the saturated vapor pressure over solutions and hydrates. Already in 1885, before the appearance of basic van't-Hoff's works, Tammann suggested that the molecular depression of the saturated vapor pressures of similar salts is about the same. To the same period of time belongs a series of Tammann's works concerned with osmosis and properties of semipermeable membranes. He made an important conclusion that the saturated vapor pressures of aqueous solutions with equal osmotic pressures are the same.

By the 1890s, a large group of Tammann's pupils was involved in his investigations, among whom mention should be made in the first place of A.D. Bogoyavlenskii (1868–1940), G. Landesen (1867–1935), and, later, R.F. Hollman (1877–1921) and V.A. Borodovskii (1878–1914). Owing to their participation, Tamman could extend the number of physicochemical problems studied. In 1893–1896, a seriers of investigations of concentrated solutions was performed and an original opinion about their nature was voiced. The developed approach was based on the concept of a gain in the internal pressure of a solution as compared with straight solvent.

Together with studying solutions, Tammann and co-workers commenced investigations of phase tran-

[3] A list of papers devoted to G. Tammann's life and scientific activities is given in the Dictionary of Scientific Biography [1].

sitions and phase equilibria in one-component systems (1897–1902). These studies resulted in a book *Kristallisieren und Schmelzen* (Crystallization and Melting) published in Germany in 1903. In a monograph [20], this series of investigations is characterized as "outstanding in both theoretical and experimental regards."

One of important, although not indisputable Tammann's conclusions was that no critical point at which the crystal becomes identical to its own solution can appear in the fusion curve. Tammann's studies concerned with the full phase diagram of water, which led to the discovery of polymorphous modifications of ice, became widely known (1900). These studies were performed on a unique, by that time, high-pressure (up to 4000 atm) installation. It was demonstrated in studying the kinetics of phase transitions that the crystallization rate depends on the rate of nucleation and linear velocity of crystal growth.

The studies of phase diagrams of metal systems, extensively developed already after G. Tammann moved to Göttingen, were also commenced in Russia. The first paper on metal alloys *On the Structure of Alloys*, concerned with the depression of the melting point of mercury and sodium upon introduction of minor amounts of various metals, was published already in 1889 (*Z. Phys. Chem.*, vol. 3, pp. 441–449). The main goal of the author was to reveal the extent to which general laws established for other types of solutions are applicable to solutions of metals in metals. The second paper in this series, devoted to determining the composition of chemical compounds without chemical analysis, was also prepared before departure to Germany (*Z. Anorg. Chem.*, 1903, vol. 37, pp. 303–313). Later, Tammann was the first to propose the term "thermal analysis" and developed its fundamentals (*Z. Anorg. Chem.*, 1905, vol. 45, pp. 24–38). The contribution made by Tammann, together with other scientists, to the development of the thermal analysis technique was considered in detail by B.N. Menshutkin [20]. G. Tammann gave detailed recommendations as to how cooling curves should be studied and phase diagrams be constructed on their base, and proposed a method for determining the composition of eutectic mixtures. During a short time of his work in Göttingen, Tammann and coworkers studied more than 100 binary metal systems. These works in Germany were conducted in parallel with large-scale investigations of Kurnakov and his closest associates (S.F. Zhemchuzhnyi, N.A. Pushin, N.I. Stepanov, *et al.*) in higher school institutions in St. Petersburg. Based on investigations of a wide variety of properties of metal alloys and salt systems, Kurnakov and Zhemchuzhnyi formulated general principles of physicochemical analysis in 1913. It is known that G. Tammann highly appreciated Kurnakov and his works [14]. It seems inappropriate to speak about any kind of priority in comparing these two most prominent scientific schools [30].

When studying the chemical stability of binary metal solid solutions, Tammann established in 1919 an important relationship between the composition of an alloy and its chemical properties. It was shown that the corrosion resistance (limits of action of chemical reagents) changes stepwise at compositions which are multiples of 1/8 mol of the least active component ("Tammann's *n*/8 law"). This law is applicable not only to metal solid solutions, but also to solubility and some chemical properties of salt solid solutions. The Tammann theory relates the existence of limits to chemical action to the arrangement of atoms in the crystal lattice of a solid solution. The action limits are also revealed in studying the anodic behavior of solid solutions. A detailed analysis of the "*n*/8 law" can be found in a paper by V.V. Schorcelletti and A.I. Shultin [31].

In studying the aggregative states of substances and phase transitions, G. Tammann investigated crystallization of glass-forming liquids and melts. He regarded the glass as a supercooled fluid. Particular attention was given to changes in properties of glass in its transition onto a liquid state ("softening range"). The results of these works were summarized in the monograph *Der Glasszustand* (The Glassy State), published in 1933.

After German professor O. Lehman (1855–1922) made quite certain that liquid crystals do exist and published a series of papers on this question, Tammann was the first Russian scientist to became interested in this problem. In a paper *On the So-Called Liquid Crystals* (*Ann. Phys.*, 1901, vol. 4, pp. 524–530), Tammann made quite a number of critical remarks. He insisted that the samples studied by Lehman are heterogeneous and contain impurities. Simultaneously, he entrusted one of his pupils, F.F. Rotarskii (1874–1912),[4] with a task of carrying out experimental studies and purification of compounds forming liquid crystals. It so happened that Rotarskii did most part of this work in St. Petersburg. Rotarskii graduated from the chemical department of the Physicomathematical Faculty at Yuryev (Derpt) University

[4] Tadeusz Rotarskii, of Polish origin, adopted the name Faddei Feliksovich in Russia.

in 1900, having received a candidate of science degree, and, had on-the-job training at Krakow and Göttingen Universities by G. Tammann's recommendation. He became a laboratory assistant at the chair of physiological chemistry of Women's Medical Institute in 1902 and junior laboratory assistant at the chair of analytical and organic chemistry at St. Petersburg Polytechnic Institute in May 1904 [32]. Together with other young teachers (F. Dreier, Zhemchuzhnyi, L.A. Rotinyants), Rotarskii carried out, by Tammann's initiative, quite a number of studies of thoroughly purified liquid crystals and described their specific features. Only during the period of time from 1905 till 1909, 9 papers concerned with liquid crystals were published in *Izvestiya S.-Peterburgskogo Politekhnicheskogo Instituta* (Bulletin of St. Petersburg Polytechnic Institute). Rotarskii started working on a special monograph, but, because of severe illness, had to return home, to Warsaw, already in October 1909. Rotarskii's colleagues prepared for publication and published the first chapter of the intended monograph, where, in particular, Tammann's views on the problem of liquid crystals were presented in ample detail [33]. Rotarskii's works were supported by Kurnakov and V.A. Kistyakovskii (1865–1952), professors of the Polytechnic Institute. Later, this series of investigations was continued at the St. Petersburg Electrotechnical Institute by N.A. Pushin (1875–1947), a closest Kurnakov's associate, and I.V. Grebenshchikov (1887–1953). These studies were commenced in 1912.

The constructive criticism by Tammann of the concept of liquid crystals and his many years' dispute with Lehman favored the development of research in this field [34].

During the initial period of his scientific activities, G. Tammann, following the example of his teacher Schmidt, studied biochemical objects. The mechanism and kinetics of enzymatic processes were interpreted in purely chemical terms, with the use of the Arrhenius equation. Tammann took part in discussions of physiological problems at meetings of the Society of Naturalists at Derpt University, whose member he was since 1890 (honorary member since 1903).

The scientific legacy of G. Tammann is enormous. Science-statistics data and the number of papers published by G. Tammann on one or another research direction are presented in the dictionary of scientific biographies [1]. A number of the most important scientist's works: *Metallography* (1931), *Physical Metallurgy* (1935), *Handbook of Heterogeneous Equilibria* (1935), and *The Glassy State* (1935), have been translated into Russian.

During his entire life, Gustav Tammann received a great number of honorary titles, prizes, and decorations. He was member of numerous Academies all over the world, an honorary member of the Bunsen Society, German Society of Physical Metallurgists, British Institute of Metals, and Royal Chemical Society of Great Britain.

G. Tammann died on December 17, 1938, at the age of 77. Till the last days of his life he retained vivacity and was always available for scientific discussions. Already in the end of the XIX century he made an invaluable contribution to the development of physical chemistry as independent scientific discipline and, together with his pupils, faithfully served to science during his whole life.

REFERENCES

1. Tammann, G.A., *Dictionary of Scientific Biography*, Gillespie, Ch.C., Ed., New York: Charles Scribner's Sons, 1981, pp. 242–248.
2. Palm, U.V., in *Iz istorii estestvoznaniya i tekhniki v Pribaltike* (History of Natural Science and Engineering in the Baltic Region), Riga: Zinatne, 1976, vol. 5, pp. 134–141.
3. Tamman, G., in *Lomonosovskii sbornik* (Lomonosov Coll.), Moscow: Khimicheskoe Otd. O–va. Lyubitelei Estestvoznaniya, 1901, pp. 1–46.
4. Martinson, E.E., *Istoriya osnovaniya Tartuskogo byvsh. Derptskogo–Yur'evskogo universiteta* (History of Foundation of Tartu, Former Derpt–Yuryev, University), Leningrad: Leningr. Gos. Univ., 1954.
5. Martinson, Kh.R. and Martinson, K.A., *Khimiki – vospitanniki Tartuskogo universiteta do 1917 g.* (Chemists Educated at the Tartu University before 1917), Tallinn: Akad. Nauk Est. SSR, 1978.
6. Palm, U.V., in *Iz istorii estestvoznaniya i tekhniki Pribaltiki* (History of Natural Science and Engineering in the Baltic Region), Riga: Zinatne, 1970, vol. 2(8), pp. 169–178.
7. Palm, U. and Past, V., *Uch. Zap. Tartusk. Gos. Univ.*, 1968, no. 219, pp. 251–262.
8. Arbuzov, A.E., *Izbrannye raboty po istorii khimii* (Selected Works on the History of Chemistry), Moscow: Nauka, 1975.
9. Romanova, M.M., Abstracts of Papers, *Istoriya nauki i naukovedenie: X Pribaltiiskaya konferentsiya po istorii khimii* (History of Science and the Science of Science: X Baltic Conf. on the Histiory of Chemistry), Riga: Zinatne, pp. 67–70.

10. Makarenya, A.A. and Palm, U.V., in *Iz istorii estestvonaniya i tekhniki Pribaltiki* (History of Natural Science and Engineering in the Baltic Region), Riga: Zinatne, 1980, vol. 6, pp. 156–161.
11. *Dnevnik XI s"ezda russkikh estestvoispytatelei i vrachei* (Daybook of the Xi Congr. of Russian Natural Scientists and Physicians), St. Petersburg, 1901, no. 9, p. 382.
12. Makarenya, A.A. and Pozdasheva, V.A., in *Iz istorii estestvoznaniya i tekhniki Pribaltiki* (History of Natural Science and Engineering in the Baltic Region), Riga: Zinatne, 1972, vol. 4, pp. 123–135.
13. Palm, U.V., in *Iz istorii estestvoznaniya i tekhniki Pribaltiki* (History of Natural Science and Engineering in the Baltic Region), Riga: Zinatne, 1968, vol. 1(7), pp. 25–33.
14. Nikitin, N.I., *Na puti nauchnogo rabotnika – khimika* (On the Chemical Researcher's Way), Leningrad: Nauka, 1969.
15. Biltz, W., *Z. Anorg. Allg. Chem.*, 1931, vol. 198, nos. 1–2, pp. 1–31.
16. Garner, W.F., *J. Chem. Soc.* (London), 1952, pp. 1961–1973.
17. Köster, W., *Z. Metallkunde*, 1961, vol. 52, pp. 379–381.
18. Masing, G., *Z. Elektrochem.*, 1939, vol. 45, no. 2, pp. 121–124.
19. Masing, G., *Ber. Deutsch. Chem. Gesell.*, 1940, vol. 73A, no. 2, pp. 25–30.
20. Kipnis, A.Ya., *Razvitie khimicheskoi termodinamiki v Rossii* (Development of Chemical Thermodynamics in Russia), Moscow: Nauka, 1964.
21. Solov'ev, Yu.I., *Ocherki po istorii fizicheskoi khimii* (Essays on the History of Physical Chemistry), Moscow: Nauka, 1964.
22. Solov'ev, Yu.I., *Istoriya khimii v Rossii* (History of Chemistry in Russia), Moscow: Nauka, 1985.
23. Palm, U.V., in *Iz istorii estestvoznaniya i tekhniki Pribaltiki* (History of Natural Science and Engineering in the Baltic Region), Riga: Zinatne, 1968, vol. 1(7), pp. 25–33.
24. Palm, U., *Uch. Zap. Tartusk. Gos. Univ.*, 1966, no. 193, pp. 182–189.
25. Ryago, N.Ya., *Tr. Inst. Ist. Estestvozn. Tekh.*, 1956, vol. 12, pp. 117–120.
26. Dehlinger, U., *Angew. Chem.*, 1939, vol. 52, no. 12, pp. 229–231.
27. *J.C. Poggendorff's biographisch–literarisches Handwörterbuch*, Leipzig, 1904, vol. IV, p. 1474; 1926, vol. V, pp. 1240–1241; 1936, vol. VI, pp. 2610–2612; 1960, vol. VIIA, pp. 623–625.
28. *Biograficheskii slovar' professorov i prepodavatelei Yur'evskogo, byvshego Derptskogo universiteta za sto let ego sushchestvovaniya (1802–1902)* (Biographical Dictionary of Professors and Instructors of Yuryev (Former Derpt) University over the 100-Year Period of Its Existence (1802–1902)), Levitskii, G., Ed., Yuryev, 1902, vol. 2, pp. 257–259.
29. Menshutkin, B.N., *Izv. Sekt. Fiz.-Khim. Anal.*, 1936, vol. 8, pp. 373–408.
30. Pogodin, S.A., *Usp. Khim.*, 1952, vol. 21, no. 9, pp. 1034–1044.
31. Schorcelletti, V.V. and Shultin, A.I., *Khimicheskoe razrushenie metallov* (Chemical Degradation of Metals), Leningrad: Izd. po Chernoi i Tsvetnoi Metallurgii, 1934.
32. Menshutkin, B.N., *Izv. S.-Peterb. Politekh. Inst., Otd. Tekh., Estestvozn. Matem.*, 1912, vol. 18, no. 1, pp. 1–111.
33. Rotarskii, T., *Izv. S.-Peterb. Politekh. Inst., Otd. Tekh., Estestvozn. Matem.*, 1910, vol. 13, no. 1, pp. 149–166.
34. Sonin, A.S., *Doroga dlinoyu v vek* (A Century-Long Road), Moscow: Nauka, 1988.

A. G. Morachevskii

Russian Journal of Applied Chemistry, Vol. 74, No. 10, 2001, pp. 1617–1620. Translated from Zhurnal Prikladnoi Khimii, Vol. 74, No. 10, 2001, pp. 1569–1572.

INORGANIC SYNTHESIS AND INDUSTRIAL INORGANIC CHEMISTRY

Crystallization of SnO_2 Produced by Sol–Gel Technique from Salts of Tin in Different Oxidation States

L. F. Chepik, E. P. Troshina, T. S. Mashchenko, D. P. Romanov, A. I. Maksimov, and O. F. Lutskaya

Institute of Silicate Chemistry, Russian Academy of Sciences, St. Petersburg, Russia

St. Petersburg State Electrotechnical University LETI, St. Petersburg, Russia

Received December 7, 2000

Abstract—SnO_2 xerogels were obtained by the sol–gel technique from alcoholic solutions of tin(II) and (IV) salts and used as model systems for studying the behavior of SnO_2—the main material of gas sensors, in the course of formation and operation under the action of temperature.

The impact on the environment poses the problems of on-line ecological monitoring ensuring the safety of humans under household and industrial conditions. The problem of obtaining the necessary data on the state of the environment can be solved by using analytical monitoring systems based on sensors for gases and liquids. As primary sensitive elements in these systems are used metal-oxide semiconducting compounds, such as SnO_2, ZnO, Fe_2O_3, etc. [1]. Among the materials mentioned, tin dioxide is the most promising material for creating sensor systems for monitoring of various gas media. By combining tin dioxide with other elements, sensors sensitive to most gases can be obtained (CO, H_2S, etc.) [2]. The gas-sensitive SnO_2 material can be used, depending on the design of the monitoring device, as bulk samples or layers. At present, preference is given to thin tin dioxide layers on various substrates because of their sensitivity, determined to a greater extent by the surface, high speed of response, smaller size, and low energy consumption. The methods used to obtain tin dioxide layers can be divided into two groups. The first group is constituted by techniques relying upon physical growth processes, such as reactive cathode sputtering, rf magnetron sputtering, electron-beam evaporation, thermal oxidation, etc. [3–7]. The mentioned methods for obtaining tin dioxide are far from always involving a simple technological process and require complex equipment. On this background, a less numerous group of chemical methods for tin dioxide deposition, based on sol–gel process, yields, at simpler technology, high quality of the material as regards purity, composition, and structural uniformity. This group of methods includes SnO_2 deposition either from solutions of inorganic tin salts, mostly halides [8–10], or from organic tin derivatives, which have not gained wide recognition because of the complexity of synthesis of substances and their high cost.

Analysis of published data suggests that the main attention is given to the possibility of using tin dioxide obtained by one or another method for particular determinations of dynamic characteristics of gas media without evaluation of changes in physicochemical properties under the influence of temperature conditions, varying in structure formation and in the course of device operation.

In this study, tin dioxide was obtained chemically in the form of thin-layer coatings and powders from the liquid phase by sol–gel process from salts with different tin oxidation states—$SnCl_2 \cdot 2H_2O$ and $SnCl_4 \cdot 5H_2O$. Comparative studies of changes in the properties of oxide materials synthesized from two kinds of salts were performed on gel powder samples in relation to synthesis conditions and subsequent thermal treatments. Studies of powders allow modeling of processes occurring in thin SnO_2 layers whose analysis is commonly hindered by the small mass of a substance under study. Gel powders were subjected to differential-thermal (DTA) and X-ray phase analyses (XPA).

Powders of tin dioxide gels were obtained from homogeneous solutions-sols of $SnCl_2 \cdot 2H_2O$ and $SnCl_4 \cdot 5H_2O$. The salt concentrations in the starting

1070-4272/01/7410-1617 $25.00 © 2001 MAIK "Nauka/Interperiodica"

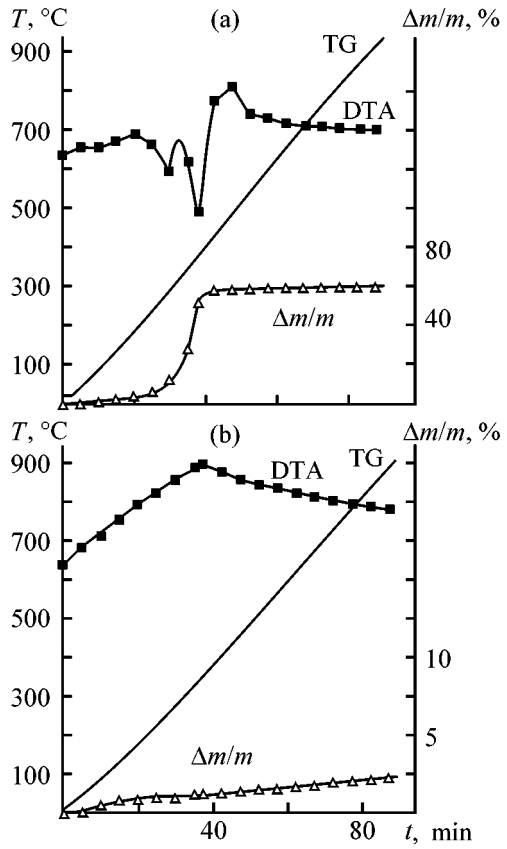

Fig. 1. TG and DTA curves of (a) SnO_2(II) xerogel and (b) that after thermal treatment. (T) Temperature, ($\Delta m/m$) mass loss, and (t) time. Treatment temperature (°C) and time (h): (a) 100, 10; (b) 100, 10; 600, 1.

solutions was 50 g l^{-1}. As solvent served *n*-butyl alcohol. The solutions-sols were homogenized, to ensure complete dissolution of the salts, by vigorous stirring and keeping a solution-sol at room temperature for 10–15 min before its being converted into gel. The medium of the starting solutions was acidic (pH 2–3) without additional introduction of acid. The conversion into gels was done by adding a 1 M aqueous solution of ammonia to the starting solutions-sols of tin salts and adjusting the pH value to 9–10. The obtained humid gels were subjected to two-stage thermal treatment: first, drying at 100°C for 10 h and then keeping in isothermal mode for 1 h at each of the following temperatures—300, 600, and 900°C. The solutions-sols of the $SnCl_2 \cdot 2H_2O$ salt and gels obtained from them were designated SnO_2(II), with $SnCl_4 \cdot 5H_2O$ used as the starting salt the designation was SnO_2(IV).

A DTA of changes occurring in the gels under varied thermal treatment conditions was performed with an MOM derivatograph (Hungary) in the dynamic mode at heating rate of 10 deg min^{-1} in the range from room temperature to 1000°C. As reference served powdered aluminum oxide. An XPA of gel powders was done on a DRON-2 instrument (Cu_{K_α} radiation). The crystalline phases were identified using the ASTM file.

Acid solutions of $SnCl_2 \cdot 2H_2O$ and $SnCl_4 \cdot 5H_2O$ salts in n-butyl alcohol pass into a jelly-like state on pouring-in an aqueous solution of ammonia. In aqueous solution, tin(IV) salts form tin(IV) hydroxide which has clearly pronounced gel nature, with $xSnO_2 \cdot yH_2O$ formula ascribed to it [11]. The gel is based on polymeric formations with ≡Sn–O–Sn≡ bonds appearing as a result of oleation of hydroxo complexes $Sn(OH)_n$, with the subsequent polymerization occurring with splitting-off of water molecules. The increase in the number of bridge bonds, occurring in the gelation stage, is also continued under the action of temperature in the course of thermal treatment. The dehydration process can be described by the scheme [12]

$$2(\equiv Sn\text{–}OH)_n = (\equiv Sn\text{–}O\text{–}Sn\equiv)_n + nH_2O.$$

Being a strong reducing agent, Sn(II) is readily oxidized in acid medium to Sn(IV) [11], with the oxidation process enhanced by atmospheric oxygen and light. In the case of Sn(II) oxidation to Sn(IV), the gelation of $SnCl_2 \cdot 2H_2O$-containing solutions is also accompanied by the formation of ≡Sn–O–Sn≡ bonds, as in the process of gelation with the use of $SnCl_4 \cdot 5H_2O$.

The inorganic network of freshly prepared gels retains a considerable amount of the liquid phase composed of water and organic solvent. In passing from a humid gel to dry xerogel powder in the first stage of drying at 100°C for 10 h, the major part of the liquid phase is removed. However, the TG curves for SnO_2(II) and SnO_2(IV) preheated at 100°C for 10 h show, with increasing temperature, a continuing loss of mass of reaction products retained by the inorganic network of the xerogel. The loss of mass continues for xerogel powders to 440–460°C and constitutes 60.9 wt % for SnO_2(II) (Fig. 1a) and 84.6 wt % for SnO_2(IV). The shape of the DTA curve (Fig. 1) indicates that the enthalpy of the substance under study strongly fluctuates in this temperature interval, which is accompanied by alternation of exo- and endothermic peaks. The endothermic effects in the low-temperature region are most frequently attributed to substance mass loss; however, exothermic processes (T = 320°C) (Fig. 1a) occur simultaneously with the mass loss, which may be due to the onset of crystallization. In xerogels dried at 100°C (100 h) and 600°C (1 h), the mass loss is significantly smaller: 2.41 wt % for SnO_2(II) (Fig. 1b)

and 4.78 wt % for SnO_2(IV). The DTA curve in Fig. 1b shows endothermic processes with a peak at 340°C. DTA curves for SnO_2(IV) are similar to the curves for SnO_2(II), with a shift to higher temperatures by 20°C (not presented here).

The similar nature of thermal effects in the DTA of SnO_2(II) and SnO_2(IV) xerogels indicates that, irrespective of the different oxidation states of tin in the starting salts, xerogels treated under identical temperature conditions have similar nature.

XPA data for SnO_2(II) and SnO_2(IV) xerogels are presented in Figs. 2a and 2b. Analysis shows a strong similarity between the processes of structure formation in xerogel powders obtained from different salts. Upon treatment at 100°C (10 h), X-ray diffraction patterns of SnO_2(II) and SnO_2(IV) show rather strong reflections (Figs. 2a and 2b, curves *1*) (2θ 23.2°, 32.9°, 47.2°) attributed to a crystallized form of NH_4Cl, reaction product formed in reaction of NH_4OH used as precipitating agent with tin chlorides retained by the network structure of the SnO_2 gel. With the xerogel treatment temperature raised to 300°C (1 h), the reflections related to NH_4Cl disappear from the XPA curves of SnO_2(II) and SnO_2(IV) (Figs. 2a and 2b, curves *2*) as a result of its complete removal from the gel structure under the action of temperature. SnO_2(II) and SnO_2(IV) xerogels treated at 100°C (10 h) cannot be considered completely amorphized. The X-ray patterns of both gels (Figs. 2a and 2b curves *1*) show broadened reflections which become, with the xerogel treatment temperature raised to 300, 600, or 900°C, clear narrow reflections characteristic of the crystalline form of SnO_2 in tetragonal modification. The XPA data indicate that, irrespective of the oxidation state of tin in the starting $SnCl_2 \cdot 2H_2O$ and $SnCl_4 \cdot 5H_2O$ salts, thermally treated gels crystallize to form tin dioxide in tetragonal modification, with, however, the process of SnO_2(II) crystallization being more vigorous than that for SnO_2(IV) (Figs. 2a and 2b).

Thin SnO_2 layers were deposited onto semiconducting silicon wafers, glass, and glass ceramics from alcoholic solutions-sols of $SnCl_2 \cdot 2H_2O$ and $SnCl_4 \cdot 5H_2O$ salts. The deposition was done by pouring a solution and subsequent centrifugation at a rate of 2000 rpm. According to ellipsometric data, the obtained films were 50–70 nm thick.

CONCLUSIONS

(1) Irrespective of whether chlorides of doubly or quadruply charged tin are used as starting substances, thermal treatment of xerogel powders leads to formation of SnO_2 of the tetragonal modification.

(2) SnO_2 crystallization in the tetragonal modification in gel powders obtained with the use of tin(II) chloride $SnCl_2 \cdot 2H_2O$ occurs at lower temperatures, compared with the case of $SnCl_4 \cdot 5H_2O$, which allows layer deposition at lower temperatures. This makes simpler the technology of gas sensor fabrication.

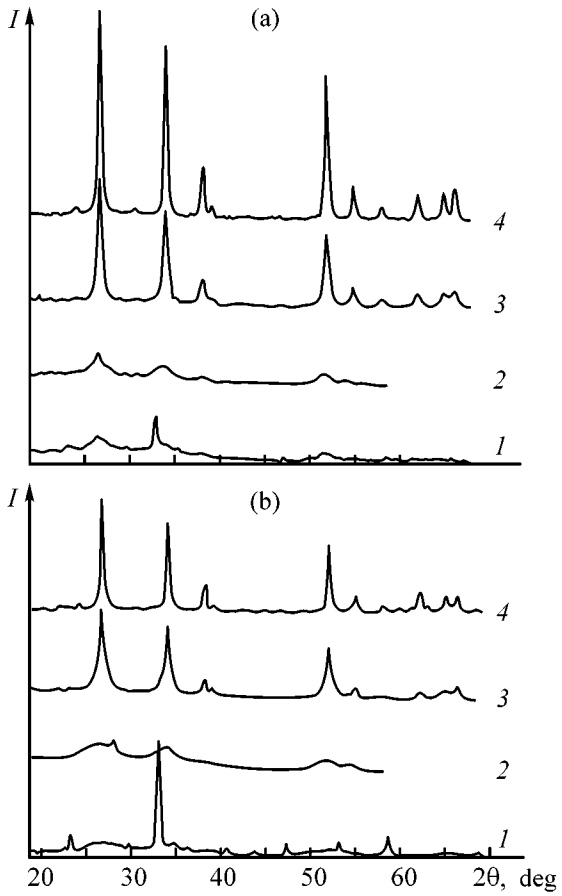

Fig. 2. XPA curves for (a) SnO_2(II) and (b) SnO_2(IV) xerogels subjected to thermal treatment. (*I*) Intensity and (2θ) Bragg angle. Treatment temperature (°C) and time (h): (*1*) 100, 10; (*2*) 100, 10; 300, 1; (*3*) 100, 10; 600, 1; and (*4*) 100, 10; 900, 1.

REFERENCES

1. Morrison, S.R., *Semiconductor Sensors*, Sze, S.M., Ed., New York: Wiley, 1994, pp. 383–413.
2. Vasiliev, R.B., Rumyantseva, M.N., Yakovlev, N.V., and Gaskov, A.M., *Sensors Actuators B*, 1998, vol. 50, pp. 186–193.
3. Masamitsu, N., *J. Cryst. Growth*, 1984, vol. 69, nos. 2–3, pp. 465–468.

4. Goodchild, D.G., Webb, J.B., and Williams, D.T., *J. Appl. Phys.*, 1985, vol. 57, no. 6, pp. 2308–2310.
5. Hubner, H. P. and Obermeier, E., *Sensors Actuators*, 1989, vol. 17, pp. 351–354.
6. Acosta, D.R., Zironi, E.P., Montoya, E., and Estrada, W., *Thin Solid Films*, 1996, vol. 288, pp. 1–7.
7. Kaplan, L., Rusman, I., Boxman, R.L., *et al.*, *Thin Solid Films*, 1996, vol. 290–291, pp. 355–361.
8. Tsukuma, K., Akiyama, T., and Imai, H., *J. Non-Cryst. Solids*, 1997, vol. 210, pp. 48–54.
9. Mesias, F.R., Vega, B.A.V., Scalvi, L.V.A., *et al.*, *J. Non-Cryst. Solids*, 1999, vol. 247, pp. 171–175.
10. Brito, G.E.S., Santilli, C.V., Pulcinelli, S.H., and Craievich, A.F., *J. Non-Cryst. Solids*, 1997, vol. 217, pp. 41–47.
11. Spivakovskii, V.B., *Analiticheskaya khimiya olova* (Analytical Chemistry of Tin), Moscow: Nauka, 1975.
12. Presecatan, R.T., Pulcinelli, S.H., and Santilli, C.V., *J. Non-Cryst. Solids*, 1992, vol.147–148, pp. 340–345.

Russian Journal of Applied Chemistry, Vol. 74, No. 10, 2001, pp. 1621–1626. Translated from Zhurnal Prikladnoi Khimii, Vol. 74, No. 10, 2001, pp. 1573–1577.

INORGANIC SYNTHESIS AND INDUSTRIAL INORGANIC CHEMISTRY

Synthesis and Structural Transformations of Hydrotalcite-like Materials Mg–Al and Zn–Al

R. V. Prikhod'ko, M. V. Sychev, I. M. Astrelin, K. Erdmann, A. Mangel', and R. A. van Santen

Kievskii politekhnicheskii institut National Technical University, Kiev, Ukraine
Kopernik University, Torun, Poland
CI Electronics, Salisbury, UK
Technical University, Eindhoven, the Netherlands

Received January 16, 2001

Abstract—Mg–Al and Zn–Al hydrotalcite-like layered double hydroxides of various compositions were synthesized and characterized. A detailed comparative analysis of the structure and composition of starting and reconstructed layered double hydroxides was made.

Synthetic layered double hydroxides (LDHs), or so-called hydrotalcite-like materials, arouse increased interest as sorbents [1, 2], anion exchangers [3, 4], catalysts [5, 6], and catalyst precursors [7, 8]. The idealized LDH formula is as follows: $[M^{2+}_{1-x}M^{3+}_{x}(OH)_2]^{x+}A^{z-}_{x/z}\cdot mH_2O$, where M^{2+} is Mg^{2+}, Ni^{2+}, Zn^{2+}, ...; M^{3+} is Al^{3+}, Fe^{3+}, Ga^{3+}, ...; and A^{z-} is CO_3^{2-}, NO_3^-, Cl^-, ... [8]. The unit cell is formed by brucite-like layers separated by interlayer gaps. The doubly charged cations, M^{2+}, bound to six oxygen atoms, form primary octahedral fragments joint to form networks [5]. These networks are mutually superimposed in the form of H-bound brucite-like layers. Isomorphic replacement of M^{2+} by differently charged cations, e.g., by Al^{3+}, results in the appearance of a positive charge, which is compensated by the anions localized in the interlayer gaps [5].

Layered double hydroxides are solid bases, which predetermines their use in basic catalysis [4–8]. In most cases, LDHs are used in calcined form [8]. Recently, the feasibility has been shown, however, of using uncalcined LDH catalysts in a number of organic syntheses [4, 6, 7]. At the same time, there is increased interest in materials with reconstructed structure, obtained using the so-called memory effect [4], i.e., the ability of heat-treated LDH to recover the initial hydrotalcite-like structure upon rehydration [5]. In this case, the degree of recovery of the LDH structure depends on the temperature of preliminary heating and the chemical composition of LDH [5]. Despite the fact that the memory effect has been known for more than 20 years and its importance for preparing new catalysts grows [4], the number of works concerned with fundamental aspects of this phenomenon is insufficient [7, 9–12].

In this study, LDHs of different compositions were synthesized and a comparative analysis of their structure before and after transformation was made.

EXPERIMENTAL

As objects of study served Mg–Al and Zn–Al LDHs. Synthesis of these materials with atomic ratios M^{2+}/Al^{3+} of 2, 3, and 5 was described in [7, 13]. The materials prepared are designated as Mg2Al, Mg3Al, and Mg5Al, or Zn2Al, Zn3Al, and Zn5Al, where the digit stands for the atomic ratio Mg/Al or Zn/Al. The residual anions (NO_3^-) were removed by ion exchange for CO_3^{2-} [14].

A part of the LDHs prepared was calcined in thin bed at 673 or 773 K (heating rate 180 deg h^{-1}) for 16 h in a flow of N_2, cooled, and stored in sealed ampules in argon. These materials are designated by index C. The reconstruction of LDHs was performed as described in [15], i.e., 1 g of calcined LDHs was suspended in 100 ml of deionized water, heated to 373 K, kept there for 40 min with stirring, cooled, filtered, and dried at 383 K for 12 h. The materials thus prepared are denoted by index R.

1070-4272/01/7410-1621 $25.00 © 2001 MAIK "Nauka/Interperiodica"

Table 1. Chemical formula, M^{2+}/Al^{3+} atomic ratio, structural parameter *a*, and crystallite size ε of the synthesized LDHs

Sample	Formula	M^{2+}/Al^{3+}	*a*	ε
			nm	
Mg2Al	$[Mg_{0.668}Al_{0.332}(OH)_2](CO_3)_{0.166} \cdot 0.56H_2O$	2.01	0.3042	18.5
Mg3Al	$[Mg_{0.751}Al_{0.249}(OH)_2](CO_3)_{0.125} \cdot 0.62H_2O$	3.02	0.3061	19.9
Mg5Al	$[Mg_{0.833}Al_{0.167}(OH)_2](CO_3)_{0.084} \cdot 0.64H_2O$	4.98	0.3086	20.7
Zn2Al	$[Zn_{0.669}Al_{0.331}(OH)_2](CO_3)_{0.166} \cdot 0.46H_2O$	2.02	0.3071	44.8
Zn3Al	$[Zn_{0.748}Al_{0.252}(OH)_2](CO_3)_{0.126} \cdot 0.45H2O$	2.97	0.3080	40.3
Zn5Al	$[Zn_{0.837}Al_{0.163}(OH)_2](CO_3)_{0.081} \cdot 0.43H_2O$	5.13	0.3088	47.0

X-ray diffraction analysis (XDA) of the materials studied was done on DRON–3 and Philips 1170 diffractometers (Cu_{K_α}-radiation, λ = 0.154178 nm, Ni-filter) with oriented samples. The size of the LDH crystallites along the *a* axis was determined using the Scherrer equation [7], high-purity grade α-SiO_2 served as standard. IR spectra were recorded with a FTIR Perkin–Elmer 2000 spectrophotometer, using samples prepared by compaction of pellets of a material under study with thoroughly dried KBr (1 : 60 ratio). The ^{27}Al NMR spectra were obtained with magic angle rotation on an AMX 300 WB Bruker spectrometer (*H* = 78.20 MHz, $[Al(H_2O)_6]^{3+}$ standard).

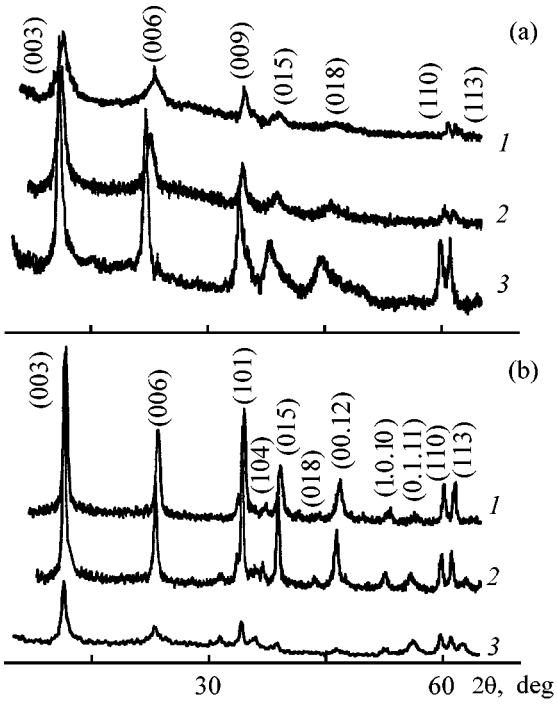

Fig. 1. Diffraction patterns of LDHs synthesized. (2θ) Bragg angle; the same for Figs. 3, 5. (a) (*1*) Mg2Al, (*2*) Mg3Al, and (*3*) Mg5Al; (b) (*1*) Zn2Al, (*2*) Zn3Al, and (*3*) Zn5Al; the same for Figs. 2, 3.

The chemical composition of the materials studied was determined by atomic absorption spectroscopy (AAS) on a Perkin-Elmer 3030 spectrophotometer. The rehydration of calcined LDHs was studied by the method of water absorption on a CIsorp installation (C.I. Electronics Ltd).

The chemical formulas of the materials synthesized (Table 1) show good agreement between the predicted and experimentally found compositions. X-ray diffraction patterns of the obtained LDHs (Fig. 1) contain basal reflections typical of hydrotalcite [5]. As known, the intensity of the (110) reflection is proportional to half the structural parameter *a* of the LDH unit cell, which corresponds to the spacing between the neighboring cations in the brucite-like layer [5]. For the materials studied, this parameter grows with increasing M^{2+}/Al^{3+} atomic ratio (Table 1). Such a dependence was observed on replacing Al^{3+} structural cations with cations of larger ionic radius (Mg^{2+} or Zn^{2+}) [16, 17] and, consequently, confirms their localization in the LDH structure. The crystallite size of these materials along the *a* axis also grows with increasing M^{2+}/Al^{3+} ratio (Table 1).

The IR spectra of the synthesized LDHs in the wave number range 4000–2000 cm^{-1} contain a broad absorption band (AB) peaked at 3600–3650 cm^{-1}, related to OH vibrations in the brucite-like layer [5]. With increasing M^{2+}/Al^{3+} ratio, the position of the band maximum shifts steadily to higher frequencies for Mg–Al and to lower frequencies for Zn–Al. This is reasonable, since a similar absorption band was noted at 3700 and 3620 cm^{-1} for magnesium and zinc hydroxides, respectively. As known, the narrower the full width at half-maximum (FWHM), $I_{1/2}$, of a band, the more ordered is the cation distribution in the LDH structure [5, 18]. For the materials studied, the $I_{1/2}$ parameter grows with increasing Mg^{2+} and Zn^{2+} content. As a result, the distribution of structural cations becomes less ordered. It should be noted that the ab-

sorption band related to $Mg(OH)_2$ impurity is absent. Unfortunately, the similarity of the vibration frequencies of $Zn(OH)_2$ and Zn–Al LDHs makes identification of the zinc hydroxide phase impossible.

In the range 1400–200 cm^{-1}, the IR spectra of LDHs contain a strong band at around 1368–1376 cm^{-1} (Fig. 2), attributed to ν_3 bending vibrations of CO_3^{2-} anions [14, 19]. Weakly resolved shoulders at 1090, 1050–1056, and 860–880 cm^{-1}, attributable to ν_1 and ν_2 vibrations of CO_3^{2-} [12, 19], are also present. The shoulder at 790 cm^{-1} (Al–O– bond vibrations [12]) was noted solely for the Mg2Al sample, evidently indicating the presence of a certain amount of the $Al(OH)_3$ impurity. The absorption band at 760–765 cm^{-1}, attributable to Zn–Al–O vibrations inside the brucite-like layer, is also present in the Zn–Al LDHs IR spectra. In addition, the IR spectra contain absorption bands at 668–624 cm^{-1} (Mg–Al LDH), 612–620 cm^{-1} (Zn–AL LDH; ν_4, bending vibrations of the carbonate bond), and 580–560 cm^{-1}. The last absorption bands are typical of brucite-like layer (stretching and bending vibrations of M–O, M–O–M, and O–M–O bonds) [20]. With increasing content of the M^{2+} cations in LDH, the positions of the 428–396-cm^{-1} bands (vibrations of hydrotalcite octahedral networks [19, 20]) steadily shift to lower frequencies, approaching the value found for brucite (364 cm^{-1}).

The ^{27}Al NMR spectra of the materials studied are similar to those obtained previously for synthetic hydrotalcite [17, 21]. They contain only one strong resonance related to Al^{3+} octahedrons with chemical shift of 7.9 and 14.0 ppm for Mg–Al and Zn–Al, respectively. This implies that, in the LDHs studied, aluminum(III) atoms are localized in octahedral positions of brucite-like layers.

The whole set of the obtained results characterizes the synthesized materials as LDHs with hydrotalcite structure.

As expected, calcination at $T > 573$ K results in amorphization of the LDH crystalline structure. The diffraction patterns of calcined samples contain reflections that can be assigned to MgO or ZnO (Fig. 3). It is quite reasonable that their intensity grows with increasing M^{2+}/Al^{3+} ratio (Fig. 3).

The calcination of Mg–Al and Zn–Al LDHs at 600–773 K yields double oxides, Mg(Al)O or Zn(Al)O, nearly isostructural to MgO or ZnO [7, 12, 21, 22]. Degradation of the Zn–Al LDHs is observed at 573 K, irrespective of the Zn/Al ratio [12]. The presence of the amorphous Al_2O_3 phase or zinc aluminate on the surface of ZnO particles is possible.

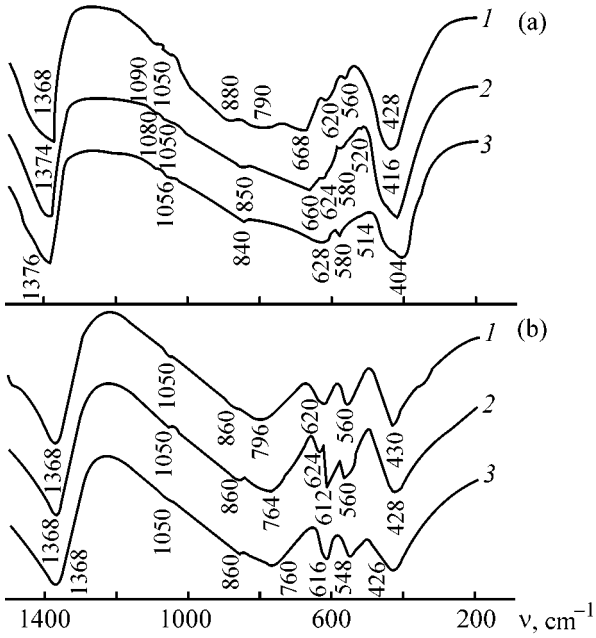

Fig. 2. LDHs IR spectra. (ν) wave number.

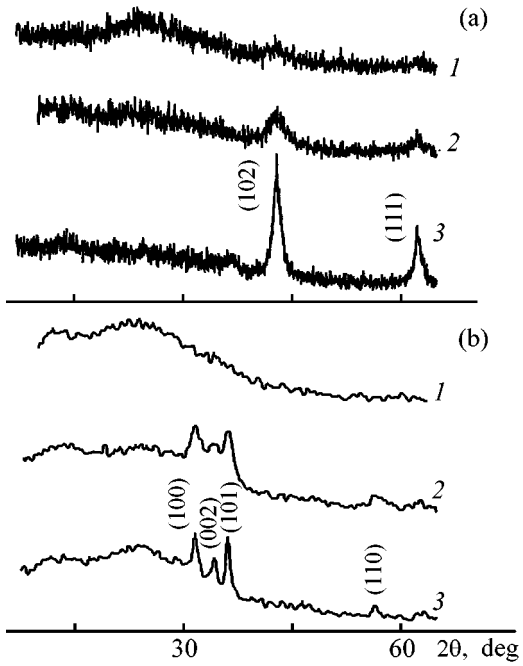

Fig. 3. Diffraction patterns of LDHs calcined at 773 K.

The IR spectra of LDH(C) contain absorption bands characteristic of double oxides [23]. The CO_3^{2-} vibrational bands disappear nearly completely, whereas the weak band around 1370 cm^{-1} is present. This indicates incomplete removal of carbonate anions, which can be occluded in the mixed oxide lattice [24].

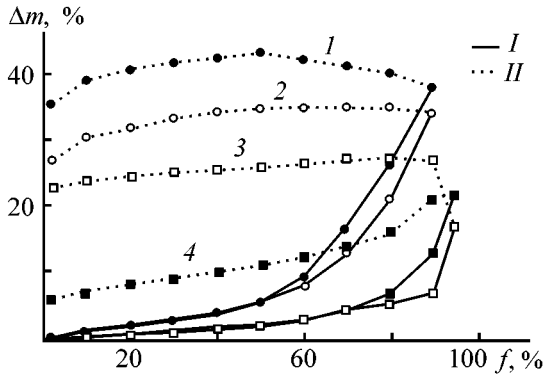

Fig. 4. Adsorption–desorption isotherms of water. (Δm) Change in sample mass and (f) relative humidity. (*I*) Adsorption and (*II*) desorption. (*1*) Mg2Al, (*2*) Mg5Al, (*3*) Zn2Al, and (*4*) Zn5l, all calcined at 773 K.

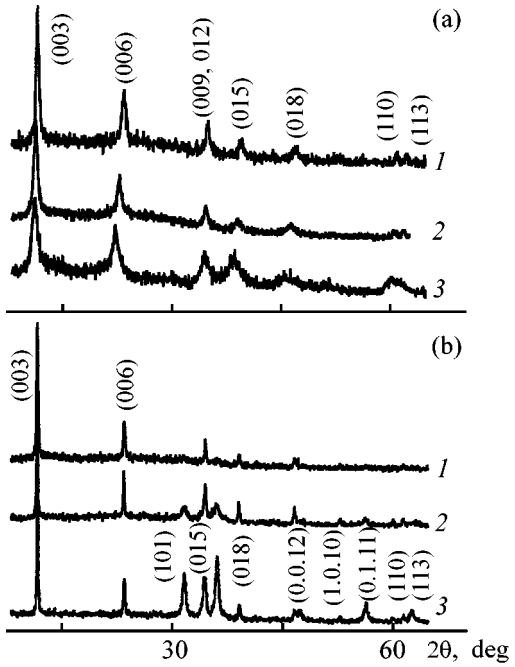

Fig. 5. Diffraction patterns of reconstructed LDHs. (a) (*1*) Mg2Al(R), (*2*) Mg3Al(R), and (*3*) Mg5Al(R); (b) (*1*) Zn2Al(R), (*2*) Zn3Al(R), and (*3*) Zn5Al(R).

The NMR revealed tetrahedrally coordinated Al^{3+} cations, Al^{3+}(tet), in the Mg–Al and Zn–Al LDHs calcined at 673–923 K [7, 17, 22]. For Zn-containing materials, the intensity of the Al^{3+}(tet) resonance is considerably higher than that for Mg–Al LDHs [7]. Double oxides prepared by calcination of Zn–Al LDHs contain Al^{3+} ions mostly in tetrahedral positions [25]. The change in partial coordination of Al^{3+} ions is caused by dehydroxylation of LDHs [17, 21]. With increasing temperature, the coordination environment of Al^{3+}(oct) cations becomes more distorted. This affects neighboring Mg^{2+} or Zn^{2+} ions [7, 21], capable of forming corresponding oxides. An analysis of the parameters of the ^{27}Al NMR line showed that the lowest ordering of Al^{3+} ions and, consequently, the most significant degradation of LDHs occur in the temperature range 723–773 K [7].

The aforesaid suggests that the Mg–Al and Zn–Al LDHs calcined at $T > 923$ K are predominantly the double oxides Mg(O)Al or Zn(O)Al. The most essential disordering of the LDH crystalline structure is observed at 723–773 K. For this reason, materials calcined at 773 K were used to study the structural reconstruction .

Hydration is the driving force of the structural reconstruction of calcined LDHs [5]. This process was studied by the method of adsorption–desorption of water vapor. As expected, it is fundamentally different from physical adsorption. Water absorption is observed even at moderate humidity (less than 40%) (Fig. 4). In the Mg–Al LDHs, the amount of sorbed water grows with increasing M^{2+}/Al^{3+} atomic ratio, whereas for Zn-containing materials, the opposite tendency is observed. The sample mass does not recover to the initial value upon water desorption (Fig. 4), i.e., the hydration is irreversible. The data obtained are consistent with the results of thermogravimetric analysis [5, 18] and show that the amount of water bound with calcined LDHs depends on the origin and concentration of a doubly charged cation. The Zn–Al samples possess lower hydrophilicity.

According to X-ray diffraction analysis, the basal reflections, typical of hydrotalcite, recover after rehydration of these materials (Fig. 5). Except in the case of the Mg5Al(R) sample, the obtained reflections are stronger and narrower than those for unheated LDHs. This result, also obtained by Prinetto *et al.* [4], can be accounted for by the increased crystallinity and (or) a more ordered orientation of LDH(R) crystallites. In the case of Mg5Al(R), in which the Mg^{2+} concentration is the highest, the lower reflection intensities indicate a lower degree of crystallinity and, probably, the presence of the oxide phase, which could not be transformed into LDH completely.

For Mg–Al(R) samples, the structural parameter a increases only slightly, compared with uncalcined LDHs (Table 2). In this case, the relation between the parameter a and the Mg^{2+}/Al^{3+} ratio is virtually similar to that for the starting materials. For Zn–Al(R) LDHs, the effect of the Zn^{2+}/Al^{3+} ratio on a is less pronounced. This may indicate that part of Zn^{2+} cations are not incorporated in brucite-like layers in reconstruction. For Zn–Al(R), the ratio Zn^{2+}/Al^{3+} approaches two, irrespective of the Zn^{2+} content in the

starting LDHs [12]. The validity of this conclusion can be confirmed by the similarity of the average *a* values for Zn–Al(R) and Zn2Al samples (Table 2). The increase in the Zn^{2+}/Al^{3+} ratio differently affects the size of LDH(R) crystallites along the *a* axis. It decreases for Mgn–Al(R) and grows somewhat for Zn–Al(R) (Table 2). This indicates that the morphologies of the reconstructed and starting LDHs are different and are affected by the type of a doubly charged cation.

The ^{27}Al NMR spectra of the reconstructed Mg–Al and Zn–Al LDHs show only a single resonance at 7.8–8.0 ppm, attributable to octahedrally coordinated Al^{3+}. The parameters of this resonance, *W* and $W_{0.1}$ (FWHM and width at one tenth of maximum, respectively), are virtually similar to those of unheated LDHs. For Zn–Al(R) LDHs, the Al^{3+}(oct) resonance is narrower and stronger than that for uncalcined materials. Apparently, in this case, reconstruction facilitates the ordering of the octahedral environment of Al^{3+} cations. It is not improbable that this results from the formation of the $Al(OH)_3$ phase characterized by the most ordered environment of Al^{3+} cations.

As in the case of unheated LDHs, the IR spectra of reconstructed materials contain a strong absorption band at 3650–3500 cm^{-1}, related to OH vibrations of the brucite-like layer [15, 18, 19]. As also in the case of the starting LDHs, the band peak shifts with growing M^{2+}/Al^{3+} ratio.

The FWHM, $I_{1/2}$, of the band in question yields information about the uniformity of the cation distribution in the brucite-like layer of LDHs [18, 19]. The additional absorption bands at around 3700 cm^{-1} indicate the presence of an oxide (hydroxide) impurity. A comparison of the starting and reconstructed LDHs shows that for Mg–Al(R) the $I_{1/2}$ parameter decreases considerably with increasing Mg^{2+}/Al^{3+} atomic ratio (Fig. 6a). Hence follows that reconstruction leads to a more uniform distribution of Mg^{2+} and Al^{3+} ions inside the brucite-like layer. At the same time, the IR spectra of these samples contain a shoulder at 3700 cm^{-1}, whose intensity grows with increasing Mg^{2+} content. Consequently, a part of these cations are not incorporated into brucite-like layers in the course of reconstruction, but form the $Mg(OH)_2$ phase instead. For this reason, Mg–Al(R) LDHs can be regarded as hydrotalcite-like materials with highly ordered structure containing an admixture of brucite.

For Zn–Al(R) samples, raising the Zn^{2+}/Al^{3+} ratio leads to a pronounced increase in the $I_{1/2}$ parameter (Fig. 6b). This indicates the less ordered distribution of Zn^{2+} and Al^{3+} structural cations in the brucite-like layer of reconstructed materials. We cannot exclude that part of them form single phases [$Zn(OH)_2$, $Al(OH)_3$, or oxides], as also indicated by the NMR data.

Table 2. Structural parameter *a* and crystallite size ε of reconstructed LDHs

Sample	*a*	ε
	nm	
Mg2Al(R)	0.3046	34.6
Mg3Al(R)	0.3063	22.7
Mg5Al(R)	0.3088	18.4
Zn2Al(R)	0.3069	21.6
Zn3Al(R)	0.3072	28.9
Zn5Al(R)	0.3075	29.7

In the wave number range 1400–200 cm^{-1}, the LDHs(R) IR spectra contain a strong absorption band near 1360 cm^{-1}, which can be attributed to bending vibrations of interlayer OH^- ions. Weakly resolved shoulders due to ν_1 and ν_2 vibrations of CO_3^{2-} are absent or shifted owing to the replacement of this ion by the hydroxide ion. For the Zn–Al (R) LDHs, the shift to higher wave numbers was observed for the 765–760 cm^{-1} absorption bands (Zn–Al–O vibrations). This can be accounted for by a change in the Zn^{2+}/Al^{3+} ratio in the brucite-like layer. Owing to the exchange

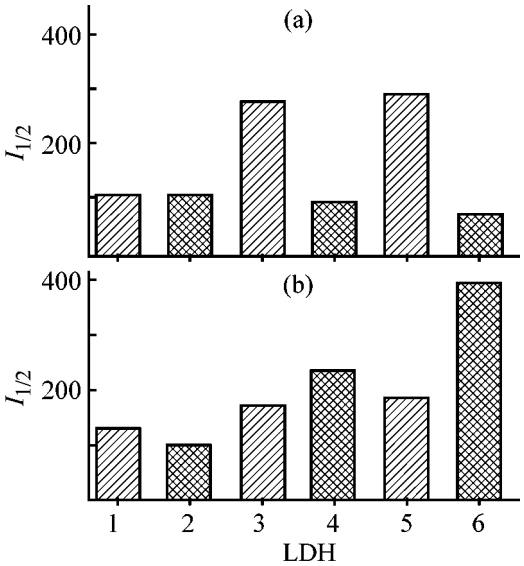

Fig. 6. The FWHM $I_{1/2}$ of the IR band related to OH vibrations (3650–3500 cm^{-1}) in a brucite-like layer for starting and reconstructed LDHs. (a) (*1*) Mg2Al, (*2*) Mg2Al(R), (*3*) Mg3Al; (*4*) Mg3Al(R), (*5*) Mg5Al, and (6) Mg5Al(R). (b) (*1*) Zn2Al, (*2*) Zn2Al(R), (*3*) Zn3Al, (*4*) Zn3Al(R), (*5*) Zn5Al, and (*6) Zn5Al(R).*

of CO_3^{2-} ions for OH^- ions, the intensities of the 688–620 cm^{-1} bands also change as compared with the starting LDHs. The IR spectra of LDH(R) show absorption bands characteristic of brucite layer vibrations at 580–560 cm^{-1} (M–O and M–O–M bonds), which indicates at least a partial reconstruction of the starting hydrotalcite structure.

CONCLUSIONS

(1) Reconstruction of calcined double layered hydroxides by hydration is a complex process resulting in a significant transformation of their structural properties, compared with the starting materials.

(2) The type of doubly charged cation and the M^{2+}/Al^{3+} atomic ratio exert the strongest influence on the extent of reconstruction of layered double hydroxides. The Mg–Al materials possess higher structural reversibility than their Zn–Al analogues.

(3) Full reconstruction of layered microstructure of the Mg–Al and Zn–Al double hydroxides is possible at calcination temperatures not exceeding 723 and 573–623 K, respectively.

(4) An analysis of the IR spectra of layered double hydroxides in the region of OH vibrations of the brucite-like layer (3600–3500 cm^{-1}) yields the most comprehensive information about the uniformity of distribution of the structural cations.

ACKNOWLEDGMENTS

The work was supported by the Ministry of Science and Education of the Ukraine (grant no. 0198 U 001177), Committee of Research of Poland (KBN; grant no. 3 TO9A 04714), and NWO of the Netherlands (Spinoza grant).

REFERENCES

1. Miyata, S., *Clays Clay Miner.*, 1983, vol. 31, pp. 305–311.
2. Kopka, H., Beneke, K., and Lagaly, G., *J. Coll. Interface Sci.*, 1988, vol. 123, pp. 427–436.
3. Rives, V., and Ulibarri, M.A., *Coord. Chem. Rev.*, 1999, vol. 181, pp. 61–120.
4. Prinetto, F., Tichit, D., Teissier, R., and Coq, B., *Catal. Today*, 2000, vol. 55, pp. 103–116.
5. Cavani, F., Trifiro, F., and Vaccari, A., *Catal. Today*, 1991, vol. 11, pp. 173–301.
6. Choudary, B.M., Bhuma, V., and Narender, N., *Indian J. Chem.*, 1997, vol. 36B, pp. 278–280.
7. Sychev, M., Prihod'ko, R., Erdmann K., *et al.*, *Appl. Clay Sci.*, 2001, vol. 18, no. 1–2, pp. 103–110.
8. Sanchez V.J., Figueras, F., Gravelle, M., *et al.*, *J. Catal.*, 2000, vol. 189, pp. 370–381.
9. Reihle, W.T., *CHEMTECH.*, 1986, vol. 1, pp. 58–63.
10. Kelkar, C.P., and Schutz, A.A., *Microporous Mater.*, 1997, vol. 10, pp. 163–172.
11. Chen, Y.Z., Hwang, C.M., and Liaw C.W., *Appl. Catal. A: Gen.*, 1998, vol. 169, pp. 207–214.
12. Kooli, F., Depege, C., Ennaqadi, A., *et al.*, *Clays Clay Miner.*, 1997, vol. 45, pp. 92–98.
13. Velu, S., and Swamy, C.S., *Appl. Catal. A: Gen.*, 1994, vol. 119, pp. 241–252.
14. Aramendia, M.A., Aviles, Y., Benitez, J.A., *et al.*, *Microporous Mesoporous Mater.*, 1999, vol. 29, pp. 319–328.
15. Watanabe, Y., and Tatsumi, T., *Microporous Mesoporous Mater.*, 1998, vol. 22, pp. 399–407.
16. Di Cosimo, J.I., Diez, V.K., Xu, M., *et al.*, *J. Catal.*, 1998, vol. 178, pp. 499–510.
17. Hudson, M.J., Carlino, S., and Apperley, D.C., *J. Mater. Chem.*, 1995, vol. 5, pp. 323–329.
18. Narayanan, S., and Krishna, K., *Appl. Catal. A: Gen.*, 1998, vol. 174, pp. 221–229.
19. Del Arco, M., Rives, V., and Trujillano, R., *Stud. Surf. Sci. Catal.*, 1994, vol. 87, pp. 507–515.
20. Nakamoto, K., *Infrared and Raman Spectra of Inorganic and Coordination Compounds*, ?5th ed., New York: Wiley & Sons, 1997, pp. 132–138.
21. MacKenzie, K.J.D., Meinhold, R.H., Sherriff, B.L., and Xu, Z., *J. Mater. Chem.*, 1993, vol. 3, no. 12, pp. 1263–1269.
22. Kloprogge, J.T., and Frost, R.L., *Phys. Chem. Chem. Phys.*, 1999, vol. 1, pp. 1641–1647.
23. Baird, T., Campbell, K.C., Holliman, P.J., *et al.*, *J. Chem. Soc. Faraday Trans.*, 1995, vol. 91, no. 18, pp. 3219–3230.
24. Rao, K.K., Gravelle, M., Sanchez V.J., and Figueras, F., *J. Catal.*, 1998, vol. 173, pp. 115–121.
25. Soled, S., Levin, D., Miseo, S., and Ying, J., *Stud. Surf. Sci. Catal.*, 1998, vol. 118, pp. 359–367.

Russian Journal of Applied Chemistry, Vol. 74, No. 10, 2001, pp. 1627–1630. Translated from Zhurnal Prikladnoi Khimii, Vol. 74, No. 10, 2001, pp. 1579–1581.

INORGANIC SYNTHESIS AND INDUSTRIAL INORGANIC CHEMISTRY

Ionometric Study of the Kinetics of Acid Decomposition of Fluorapatite

S. V. Dobrydnev, S. A. Pochitalkina, V. V. Bogach, and V. S. Beskov

Novomoskovsk Institute of Mendeleev Russian University of Chemical Technology, Novomoskovsk, Russia

Received September 5, 2000; in final form, April 2001

Abstract—A procedure is proposed for studying acid decomposition of solid materials with the use of ion-selective electrodes, with the experimental data recorded and processed with a personal computer. Variation of the H_3O^+, F^-, and Ca^{2+} concentrations in reaction of fluorapatite concentrate with nitric, sulfuric, and orthophosphoric acids and also the effect of particle size on the rate of solid phase decomposition were studied.

The rate of acid decomposition of mineral raw materials depends on temperature, nature of liquid and solid phases, stirring rate, and some other factors. A number of publications have been devoted to experimental studies of fluorapatite concentrate processing, aimed to reveal factors affecting the process kinetics [1–5]. The influence exerted by the composition of a phosphate substance on the rate of apatite concentrate breakdown was studied by calorimetry [6]. Changes in the density of the filtered-off fraction of nitric-phosphoric solution was found [7, 8] to be proportional to the content of reagents, and, therefore, a densitometric monitoring of the kinetics of this reaction is possible. An equation describing the time dependence of the reaction rate was obtained with the help of conductometric method [9]. However, the techniques considered rely upon the time dependence of only a single physicochemical parameter [6–9], which is apparently insufficient for describing the process mechanism most completely and reliably.

The aim of this work was to study the ionic composition of a reaction mixture in the course of acid decomposition of a fluorapatite concentrate and to develop a procedure for ionometric monitoring with simultaneous use of three ion-selective electrodes.

EXPERIMENTAL

Ionometry [10–12] enables simultaneous determination of several separate ions of starting substances and reaction products. The use of ion-selective electrodes also makes it possible to obtain an analog electric signal proportional to the activities of potential-forming ions. This signal can be recorded and processed with the help of a personal computer.

The principal element of the experimental installation is the measuring cell (reactor) with electrodes connected by means of a high-resistance interface to a personal computer equipped with a device for input and output of analog and digital information (an L-154 board). Separate units, their service characteristics, and principles of operation were described in detail in [13]. As sensors of the ionic composition of the reaction mixture were used fluoride (Kritur 09-107, electrode resistance R_{el} = 1 MΩ), calcium (EM-Ca-01, R_{el} = 0.1–3 MΩ), and glass (ESL43-07, $R_{el} = 50 \pm 40$ MΩ) electrodes. A silver chloride electrode (EVL-1M3) served as reference. Since the input resistance of the high-resistance interface ($R_{in} = 1 \times 10^9$ Ω) appeared to be insufficient in the case of the glass electrode, the input resistance of its measuring channel was raised to $R_{in} = 2 \times 10^{11}$ Ω.

To determine for the system under study the acidity range in which the EM-Ca-01 electrode potential depends linearly on the logarithm of the calcium ion concentration, we studied model systems: HNO_3–$Ca(NO_3)_2$ (I) and HNO_3–HF–$Ca(NO_3)_2$ (II) at concentrations of each component of 0.001, 0.005, 0.01, 0.05, and 0.1 M and temperatures of 298, 303, 308, 313, 318, and 323 K.

The results of potentiometric measurements in the concentration range under study show that the dependences of the potentials of calcium and fluoride

1070-4272/01/7410-1627 $25.00 © 2001 MAIK "Nauka/Interperiodica"

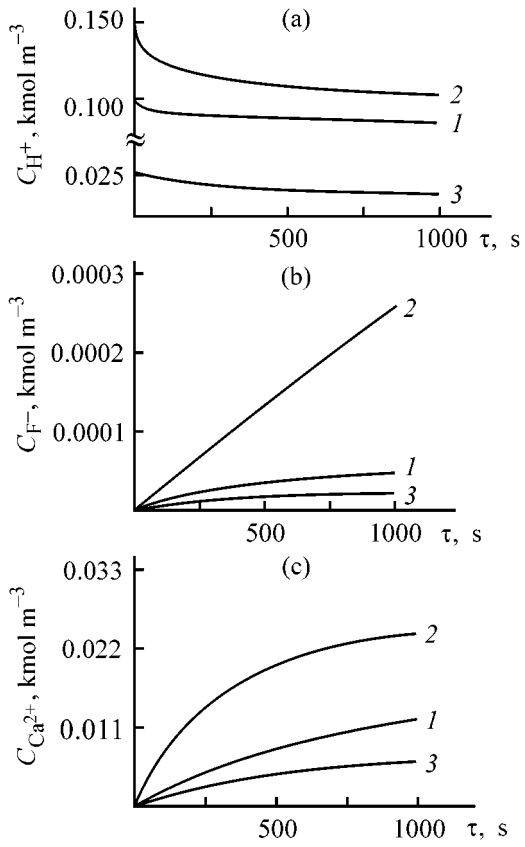

Fig. 1. Variation of concentrations of (a) H_3O^+ ion, C_{H^+}; (b) fluoride ion, C_{F^-}; and (c) Ca^{2+} ion, $C_{Ca^{2+}}$ in the reaction mixture with the time of fluorapatite decomposition τ at 30°C. (*1*) HNO_3, (*2*) H_2SO_4, (*3*) H_3PO_4.

ion-selective electrodes on the logarithm of the analytical concentrations of HF and $Ca(NO_3)_2$ are nonlinear. The reason is that complicated dissociation–association processes occur in solution, which results in a substantial difference between an analytical concentration of the electrolyte and the equilibrium concentration of a potential-determining ion.

To calculate the equilibrium compositions of model systems (I) and (II), we examined reference data [14–16] on the equilibrium constants of all the known reactions between the corresponding ionic and molecular species. The results of previous calculations [17] are in good agreement with the experimental data, which led us to conclude that the procedure used to calculate the equilibrium concentrations of potential-determining ions is reliable.

Studies of model systems (I) and (II) demonstrated that the potentials of ion-selective electrodes depend linearly on the logarithm of the calculated concentrations of ions being determined [18]. Consequently, the obtained calibration curves can be used to determine quantitatively H_3O^+, Ca^{2+}, and F^- ions in the case of their simultaneous presence in solutions with pH 1–3. As shown previously [13], the ionic strength of the reaction mixture can be taken constant during the nitric acid decomposition of a fluorapatite concentrate. Therefore, the data of potentiometric measurements, processed using calibration curves, give analytical concentrations.

We also estimated the response time of the calcium electrode for model systems (I) and (II). The concentrations of the starting solutions (0.001, 0.005, 0.01, 0.05, and 0.1 M) were varied by rapid dilution with stirring (injection procedure [19]). The time of concentration equalization (approximately 0.5 s) was found by conductometry [20]. For a calcium electrode with a solid membrane, the time in which the potential attained a steady value in the Ca^{2+} concentration range under study was from 2 to 6 s, in agreement with the known published data [11, 19]. In the course of heterogeneous reactions of acid decomposition of a fluorapatite concentrate, the content of ions being determined reached no less than 95% of their quasi-equilibrium value in 1000–1200 s. Therefore, the duration of the experiment much exceeds the time in which the potentials of the employed ion-selective electrodes attain a steady value.

Studies of the kinetics of fluorapatite acid decomposition [1–9] showed that this process is diffusion-limited, and, consequently, the rates of dissociation of the products are many times greater than the rate of the decomposition reaction itself. The proposed variant of computerized ionometric monitoring of the kinetics of acid decomposition of solid minerals allows the experiment to be carried out following a prearranged program, with the appearance of ionic forms of reaction products recorded starting from concentrations of 5×10^{-5} kmol m^{-3}.

In this study, we used the fluorapatite concentrate from the Khibiny deposit [GOST (All-Union State Standard) 3277–54], with average particle size of 26.8×10^{-5}, 18.0×10^{-5}, 13.0×10^{-5}, and 8.2×10^{-5} m, and chemically-pure grade acids. To improve the reproducibility of the kinetic data, a weighed portion of apatite was introduced into a temperature-controlled measuring cell containing 100 ml of distilled water, and the required hydrodynamic stirring mode was set. Then we introduced into the reactor 100 ml of a separately thermostated 0.2 M solution of an acid and simultaneously started measurements. The instant of mixing was taken as the reference point for the time of experiment.

The variation of the hydroxonium ion concentration with the time of fluorapatite decomposition by

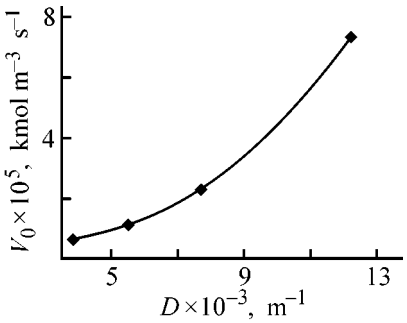

Fig. 2. Initial rate of fluorapatite decomposition, V_0, vs. the dispersity D of solid phase particles at 30°C.

0.1 M HNO_3, H_2SO_4, and H_3PO_4 at 30°C are shown in Fig. 1. It can be seen that the content of H_3O^+ ion in the reaction mixture decreases. This results from the formation of weaker, orthophosphoric and hydrofluoric, acids in the case of the nitric and sulfuric acid decomposition, and of hydrofluoric acid in the case of phosphoric acid decomposition. Experimental data on how the concentrations of F^- and Ca^2 ions vary during the fluorapatite breakdown with 0.1 M HNO_3, H_2SO_4, and H_3PO_4 at 30°C are given in Figs. 1b and 1c, respectively. It can be seen that the concentrations of fluoride anions (Fig. 1b) and calcium cations (Fig. 1c) grow in the course of decomposition. The dependence of the initial rate V_0 of fluorapatite decomposition with 0.1 M HNO_3 at 30°C on the dispersity of solid phase particles is shown in Fig. 2. The rate of heterogeneous reactions is governed by the surface area of contacting phases. Therefore, as the dispersity D (m^{-1}) of solid phase particles (and, consequently, their specific surface area) increases, the reaction rate also becomes higher (Fig. 2).

CONCLUSIONS

(1) The kinetics of fluorapatite decomposition by nitric, sulfuric, and phosphoric acids with initial concentration of 0.1 M was studied by the ionometric method. The obtained experimental data on the content of H_3O^+, Ca^{2+}, and F^- ions in the reaction mixture were interpreted using calibration curves.

(2) The variation of the concentrations of H_3O^+, Ca^{2+}, and F^- ions in decomposition was studied experimentally in relation to time, nature of decomposing agent, and specific surface area of the solid phase particles.

(3) The content of hydroxonium ion was found to decrease in the course of the decomposition, whereas the concentrations of Ca^{2+} and F^- ions increase. The dependences obtained for all the three acids under study are monotonic. Raising the dispersity of fluorapatite makes higher the rate of the acidic decomposition.

REFERENCES

1. Protsenko, A.V., Kosyakov, N.E., Poyarkova, I.F., and Sergienko, I.D., Abstracts of Papers, *6 Nauchno-tekhnicheskii seminar po fosforu (Fosfor Ukrainy–93)* [6th Scientific and Technical Seminar on Phosphorus (Phosphorus of Ukraine–93)], Lviv, 1993, p. 28.
2. Kostyanets, P.V. and Popov, V.M., *Issledovanie protsessa azotnokislotnogo razlozheniya apatitovogo kontsentrata kovdorskogo mestorozhdeniya* (Study of Nitric Acid Decomposition of Apatite Concentrate from Kovdor Deposit), Available from Ukr. NIITI, 1987, Dnepropetrovsk Khimiko-Tekhnol. Inst., no. 2725.
3. RF Patent 2086507.
4. Tishkina, N.S. and Kostyanets, R.V., Tekhnologicheskie issledovaniya protsessa azotnokislogo razlozheniya khibinskogo apatitovogo kontsentrata (Technological Studies of Nitric Acid Decomposition of Khibiny Apatite Concentrate), Available from Ukr. NIITI, 1987, Dnepropetrovsk Khimiko-Tekhnol. Inst., no. 2723.
5. Tishkina, N.S. and Kostyanets, R.V., Kinetika protsessa azotnokislogo razlozheniya khibinskogo apatitovogo kontsentrata (Kinetics of Nitric-Acid Decomposition of Khibiny Apatite Concentrate), Available from Ukr. NIITI, 1987, Dnepropetrovsk Khimiko-Tekhnol. Inst., no. 2721.
6. Bovykin, P.A., Tishkina, N.S., Kostyanets, R.V., and Savchuk, S.N., *Khim. Tekhnol.*, Kiev, 1988, no. 3, pp. 43–47.
7. Tishkina, N.S., Parkhomenko, V.D., Kostyanets, R.V., and Mazurova, L.G., *Khim. Tekhnol., Kiev*, 1985, no. 1, pp. 29–31.
8. Tishkina, N.S., Kostyanets, R.V., and Bondik, I.G., *Khim. Tekhnol., Kiev*, 1990, no. 1, pp. 71–73.
9. Jambor, Y. and Beranek, Y., *Chemicky pramysl.*, 1984, vol. 34/59, no. 6, pp. 289–292.
10. Demina, L.A., Krasnova, N.B., Yurishcheva, B.S., and Chupakhin, M.S., *Ionometriya v neorganicheskom analize* (Ionometry in Inorganic Analysis), Moscow: Khimiya, 1991.
11. Lakshminarayanaiah, N., *Membrane Electrodes*, New York: Academic, 1976.
12. Laboratornye i tekhnologicheskie issledovaniya mineral'nogo syr'ya: Obzor informatsii, Vyp. 1. Primenenie ionometrii v analize mineral'nogo syr'ya (Laboratory and Technological Studies of Mineral Raw Materials: Information Review, issue 1: Use of Ionometry in Analysis of Mineral Resources), 1995.

13. Dobrydnev, S.V., Beskov, V.S., Bogach, V.V., and Pochitalkina, I.A., *Teor. Osn. Khim. Tekhnol.*, 2001, vol. 35, no. 3, pp. 310–315.
14. Vasil'ev, V.P., *Termodinamicheskie svoistva rastvorov elektrolitov* (Thermodynamic Properties of Electrolyte Solutions), Moscow: Vysshaya Shkola, 1982.
15. Ryabin, V.A., Ostroumov, M.A., and Svit, T.F., *Termodinamicheskie svoistva veshchestv: Spravochnik* (Thermodynamic Properties of Substances: Reference Book), Leningrad: Khimiya, 1977.
16. Lur'e, Yu.Yu., *Spravochnik po analiticheskoi khimii* (Handbook of Analytical Chemistry), Moscow: Khimiya, 1979.
17. Dobrydnev, S.V., Bogach, V.V., Pochitalkina, I.A., *et al.*, *Chem. Industry* (Beograd), 2000, vol. 54, no. 7–8, pp. 319–323.
18. Pochitalkina, I.A., Bogach, V.V., Dobrydnev, S.V., and Beskov, V.S. Abstracts of Papers, *Vserossiiskaya konferentsiya "Khimicheskii analiz veshchestv i materialov"* (All-Russia Conf. "Chemical Analysis of Substances and Materials"), Moscow, 2000, pp. 375–376.
19. Nikol'skii, B.P. and Materova, E.A., *Ionoselektivnye elektrody* (Ion-Selective Electrodes), Leningrad: Khimiya, 1980.
20. Caldin, E.F., *Fast Reactions in Solution*, Oxford: Blackwell, 1964.

Russian Journal of Applied Chemistry, Vol. 74, No. 10, 2001, pp. 1631–1635. Translated from Zhurnal Prikladnoi Khimii, Vol. 74, No. 10, 2001, pp. 1582–1586.

INORGANIC SYNTHESIS AND INDUSTRIAL INORGANIC CHEMISTRY

Hydrolysis of Titanium(IV) Sulfate Solutions under Hydrothermal Conditions

A. V. Tolchev, V. Yu. Pervushin, and D. G. Kleshchev

Chelyabinsk State Pedagogical University, Chelyabinsk, Russia

Received September 13, 2000; in final form, June 2001

Abstract—The structure and the phase, granulometric, and chemical composition of hydrated titanium dioxide obtained by hydrolysis of oxotitanium(IV) sulfate and ammonium titanium(IV) oxysulfate solutions under hydrothermal conditions (130–170°C) were studied by X-ray and chemical analyses, electron microscopy, and thermogravimetry. The effect of hydrolysis conditions on the formation of samples with globular shape of particles was studied.

The stage of hydrothermal hydrolysis of titanium(IV) sulfate solutions, in which hydrated titanium dioxide (HTD) is formed with anatase structure, is one of main stages in the production of pigment titanium dioxide by the sulfate method [1, 2]. According to the results of numerous studies of the hydrolysis kinetics, the chemical and granulometric compositions of HTD, including the shape of aggregates, depend on quite a number of synthesis parameters: temperature, titanium(IV) and sulfuric acid concentrations in the starting solution, rate of solution heating to a prescribed temperature, presence of seed crystals and admixtures [2–6], etc. In most of the investigations, the hydrothermal hydrolysis of titanium(IV) sulfate solutions was carried out in open reactors, which imposed limitations on the experimental temperature range (80–110°C). It is known that the hydrolysis rate constant grows with increasing temperature [7].

The aim of this work was to study the fundamental aspects of HTD synthesis by hydrothermal autoclaving of titanium(IV) solutions, which is also important for intensifying this stage in synthesis of pigment titanium dioxide.

EXPERIMENTAL

Solutions of titanium(IV) oxysulfate and ammonium titanium(IV) oxysulfate (both of chemically-pure grade) were prepared by dissolution of reagents in aqueous solutions of sulfuric acid (pure grade) at 80°C. The starting titanium(IV) oxysulfate solutions were characterized by the concentration of Ti(IV) ions (1.25 and 2.5 M) and the ratio of numbers of H_2SO_4 and $TiOSO_4$ moles taken for preparing a solution $\beta = \nu_1/\nu_2$ (1.0, 1.5, 2.0, 2.5, 3.0, and 4.0). In ammonium titanium(IV) oxysulfate solutions, $C_{Ti(IV)}$ was 1.25 M, and β, 1.0, 1.3, and 1.5. In certain experiments, seed crystals with anatase structure were added to the starting solution in amounts ranging from 0.5 to 5 wt % relative to TiO_2 contained in the solution.

We carried out hydrothermal hydrolysis of titanium(IV) sulfate solutions at 130, 150, and 170°C (heat treatment time τ = 1 h) in 0.07-dm^3 steel laboratory autoclaves lined with fluoroplastic from within. The autoclave filling factor was 0.8. Heating and stirring were done with a rotating steel frame placed in a SNOL oven. Six autoclaves were rigidly fixed on the frame and set in rotation at a speed of 50 rpm, using a gearbox. The temperature was monitored with a Chromel–Copel thermocouple connected to a KSP-3 potentiometer. The hot thermocouple junction was placed in a special pocket of an immobile autoclave of similar design, placed in the oven. The time of autoclave heating to a prescribed temperature did not exceed 1 h, the accuracy of the temperature control was ±5°C. To obtain larger samples, we used an enameled steel autoclave with volume of 3 dm^3. The precipitates obtained were separated from the mother liquor by centrifuging or filtration under pressure, washed to remove free sulfuric acid to absence of sulfate ions in the filtrate, dried to constant weight at 40°C, and crushed.

The phase and granulometric compositions of the samples studied were monitored by means of X-ray phase analysis (DRON-3 X-ray apparatus, filtered

1070-4272/01/7410-1631 $25.00 © 2001 MAIK "Nauka/Interperiodica"

Chemical and granulometric composition of HTD samples*

Hydrolysis conditions			Characteristics of HTD samples and suspensions					
T, °C	$C_{Ti(IV)}$, M	β, rel. units	α, %	x	y	v, l m^{-2} h^{-1}	morphology of aggregates	Size of aggregates, μm
130	1.25	2.0	79.7	0.61	0.035	100	gl >> am	0.2–0.4
	1.25	3.0	62.2	0.57	0.039	450	agr	0.1–1
	1.25	4.0	4.8	–	–	–	–	–
	2.5	1.0	86	0.58	0.03	centr	gl	0.2–0.3
	2.5	1.5	66	0.61	0.038	centr	am > gl	~0.5
	2.5	2.5	5.3	–	–	–	–	–
150	1.25	2.0	97.4	0.44	0.028	350	gl	0.3–0.5
	1.25	3.0	99.4	0.45	0.039	centr	gl ≈ am	0.2–0.5
	1.25	4.0	67.5	0.50	0.052	1180	agr ≈ gl	1–2 (agr), 0.2–0.3 (gl)
	2.5	1.0	96	0.48	0.035	30	gl	0.2–0.3
	2.5	1.5	94	0.51	0.042	15	gl >> am	0.5–1 (gl)
	2.5	2.5	49	0.47	0.060	centr	agr ≈ am	–
170	1.25	2.0	99.4	0.28	0.031	310	gl	0.2–0.5
	1.25	3.0	99.4	0.34	0.042	230	″	0.1–1.0
	1.25	4.0	98.5	0.30	0.051	730	″	0.2–2
	2.5	1.0	99.4	0.30	0.032	85	″	0.2–0.3
	2.5	1.5	99.6	0.24	0.044	110	″	0.2–0.5
	2.5	2.5	99	0.27	0.058	720	″	0.5–2

* (α) Degree of hydrolysis, (v) filtration rate; (gl) globules, (am) amorphous phase, (agr) aggregates, (centr) centrifuging.

Cu_{K_α} radiation) and transmission electron microscopy (UEVM-100K electron microscope); the chemical composition was determined by volumetric chemical analysis and thermogravimetry (Q-1000 derivatograph). The average size d of the forming crystals was calculated by Selyakov–Scherer's formula [8] from the physical broadening of diffraction peaks, $\Delta 2\theta$.

According to the X-ray phase analysis of products obtained in hydrothermal hydrolysis of titanium(IV) oxysulfate in solutions, HTD with anatase-type structure is formed in the entire range of temperatures, $C_{Ti(IV)}$ concentrations, and β values used in the study. The average size d of HTD crystals is virtually independent of $C_{Ti(IV)}$ and β, and is largely determined by the heat treatment temperature T, growing linearly with increasing temperature from 15 (T = 130°C) to 20 nm (T = 170°C). The empirical composition of HTD samples, calculated from the data of chemical analysis and thermogravimetry, is described by the formula $TiO_2 \cdot xH_2O \cdot ySO_3$, where x depends on the temperature at which the hydrolysis was carried out (see table), and decreases steadily with increasing T from 0.6 (T = 130°C) to 0.3 (T = 170°C). The y value is affected by temperature and other factors, the main of which seems to be β value. The content of sulfate ions in HTD grows with increasing β (see table). The β value also affects the degree of titanium(IV) oxysulfate hydrolysis in solutions, which decreases steadily with increasing β. Raising the hydrolysis temperature makes this dependence weaker; for example, at 170°C the degree of hydrolysis in all the experiments was no less than 99%.

It follows from the electron microscopic data that HTD samples prepared at 130°C are characterized by different shapes of aggregates, depending on the β value. For example, samples synthesized from titanium(IV) oxysulfate solutions with β = 2 mainly consist of uniform spherical aggregates (globules) (Fig. 1a) with average size D of about 0.3 μm. Comparison of the sizes of HTD aggregates and separate crystals (D >> d) shows that the globular particles contain 10^3 to 10^4 primary crystals randomly oriented relative to one another. Samples of HTD prepared from titanium(IV) oxysulfate solutions with β > 2 consist of dense aggregates of irregular shape with admixture of an amorphous phase (Fig. 1b). With increasing hydrolysis temperature, the range of β values in which HTD globular particles are formed tends to expand

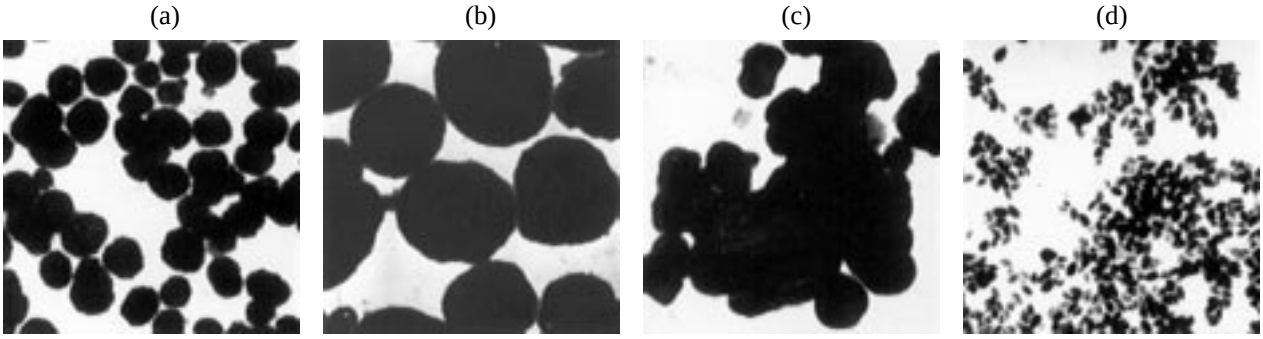

Fig. 1. Microphotographs of products of thermal hydrolysis of (a)–(c) titanium(IV) oxysulfate and (d) ammonium titanium(IV) oxysulfate. Magnification 20000. Content of seed crystals 4 wt % (c). Ti(IV) concentration (M): (a), (b), and (d) 1.25; (c) 2.5. Temperature (°C): (a) and (b) 130; (c) and (d) 150. β: (a) 2, (b) 3; (c) and (d) 1.

(see table), and at β = const their average size also shows a tendency to increase to 2 μm at 170°C.

The effect of seed crystals with anatase-type structure on the HTD formation was studied for the example of hydrolysis of hydrothermal titanium(IV) oxysulfate (T = 150°C) in solutions with $C_{Ti(IV)}$ = 2.5 M and β = 1.0. We found experimentally that the introduction of seed crystals leads to an increase in the degree of titanium(IV) oxysulfate hydrolysis in solution to 99%. At weight fraction of seed crystals less than 3%, separate globular HTD particles are formed; at greater weight fractions of seed crystals, a tendency toward globule aggregation is observed (Fig. 1c).

To determine the generality of the established fundamental aspects of HTD formation in hydrothermal hydrolysis of titanium(IV) oxysulfate, we studied the hydrolysis of ammonium titanium(IV) oxysulfate under similar conditions (T = 150°C). According to X-ray phase analysis data, hydrolysis of ammonium titanium(IV) oxysulfate yields, as also in the case of titanium(IV) oxysulfate hydrolysis, HTD with anatase-type structure, with average size of crystals of about 10 nm. Raising β from 1.0 to 1.5 has only a minor effect on the average size of HTD crystals. It follows from electron-microscopic data that HTD samples obtained at different β values are monodisperse systems consisting of regular-shape aggregates, which include up to 10^3 primary crystals. The shape and size of the HTD aggregates depend on the β value. In particular, an HTD sample obtained at β = 1.0 consisted of lenticular particles with average length of about 100 nm and diameter of 50 nm (Fig. 1d), with the porous structure of these particles seen in the light-contrast areas. Raising β to 1.3 results in the formation of ellipsoidal HTD aggregates, with their average dimensions increasing to 120 and 80 nm, respectively. Spherical HTD particles with average size of about 150 nm are precipitated from ammonium titanium(IV) oxysulfate solutions with β = 1.5. When seed crystals are introduced into the starting ammonium titanium(IV) oxysulfate solution, a tendency toward aggregation of globular HTD particles is observed, which is also the case for titanium(IV) oxysulfate solutions.

Thus, our experimental data suggest that the graining rate and the chemical and granulometric composition of HTD samples formed in hydrothermal hydrolysis of titanium(IV) salts in solutions depend on the following main factors: concentration of sulfuric acid in the starting solution, acid to titanium(IV) salt molar ratio, and temperature. It is known [9] that crystals in solutions grow through incorporation of crystal-forming complexes in a nucleus of the crystalline phase, with both the nucleus and the crystal-forming complexes formed in an interaction between hydroxo aqua complexes of metal ions present in the solution. Owing to the absence of direct methods for studying the structure of such complexes and to the inconsistency of the data on their composition [10], we assume, based on the reaction of hydrolysis of M^{z+} ions in solution

$$M_{aq}^{z+} + iH_2O \rightarrow [M(OH)_i(H_2O)_{k-i}]^{(z-i)+} + iH_{aq}^{+}, \quad (1)$$

that titanium(IV) hydroxo aqua complexes have the composition $[Ti^{4+}(OH)_i(H_2O)_{k-i}]^{(4-i)+}$. Here the quantity i (depth of hydrolysis of Ti^4 ions) is determined by particular conditions of the reaction; k is the coordination number of Ti^{4+} ions in solution.[1]

With decreasing concentration of the acid in the starting solution, the depth of hydrolysis, i, of titanium(IV) ions increases, which yields not only positive-

[1] This assumption is not, on the whole, of fundamental importance and has no effect upon further reasoning.

ly charged hydroxo aqua complexes, but also neutral complexes $[Ti_m(OH)_n(H_2O)_l]^0$ ($m \geq 1$), which are the "construction material" for titanium(IV) oxide compounds [2], including hydrated compounds. The concentration of these complexes grows with increasing temperature and $C_{Ti(IV)}$ in solutions and decreases with increasing acidity of solutions (β value), which accounts for the corresponding dependences of the degree of titanium(IV) hydrolysis (see table) on the above-mentioned conditions of hydrothermal processing.

Let us consider elementary processes occurring in thermohydrolytic precipitation of HTD from titanium(IV) oxysulfate and ammonium titanium(IV) oxysulfate solutions. The whole set of experimental data on the occurrence of a latent period preceding HTD precipitation and a reduction in its duration, accompanied by a dramatic (3–5-fold) increase in the average rate of HTD precipitation, upon introduction of seed crystals into the reaction medium [2, 5] indicates that the limiting stage of HTD precipitation from solutions is the nucleation stage, rather than the hydrolysis reaction (1). Therefore, it may be assumed that by the initial instant of time the concentration of $[Ti_m(OH)_n(H_2O)_l]^0$ complexes in solution reaches the equilibrium value for given thermodynamic conditions.

During the latent period of heat treatment, two opposite processes occur in parallel in local areas of the solution [2]. The first process is the formation of HTD nuclei as a result of polycondensation of titanium(IV) hydroxo aqua complexes, which results in the formation of strong bridging oxo or hydroxo bonds between Ti^{4+} ions in a nucleus

$$p[Ti_m(OH)_n(H_2O)_l]^0 \rightarrow [Ti_{pm}O_q(OH)_{pn-2q}(H_2O)_r]^0 + (q + pl - r)H_2O, \quad (2)$$

The second process is the dissolution of nuclei through their reaction with free sulfuric acid. Nuclei of critical size, not inclined to dissolve, are formed by the end of the latent period as a result of fluctuations in local solution areas. Hydroxo aqua complexes contained in the solution start to be incorporated into these nuclei, thus forming HTD crystals. The small size of primary HTD crystals (no more than 20 nm) suggests that the growth of crystals in thermohydrolytic precipitation of HTD from solution occurs under conditions of strong supersaturation and is accompanied by irregular incorporation of hydroxo aqua complexes into the surface layer of a nucleus. We can assume that all hydroxo aqua complexes located at a distance of a diffusion jump from a critical-size nucleus are incorporated into it almost instantaneously.

This leads to a change in the ratio of activities of hydroxo aqua complexes and other solution components, in particular SO_4^{2-} or HSO_4^- ions, in a local solution region close to a primary crystal. These ions start to react with titanium(IV) ions on the crystal surface to form there a two-dimensional quasi-phase [11], which prevents further crystal growth. This may be a factor responsible for the presence of sulfate ions in HTD samples obtained by thermohydrolytic precipitation from sulfuric acid solutions (see table). The sulfate ions are rather strongly bound to HTD and can be removed on calcination of the samples in air at temperatures above 500°C [2, 11].

In the initial stage of HTD crystal formation, the solutions become heterogeneous, and, owing to an essential reduction in the work of heterogeneous nucleation as compared with homogeneous nucleation [9], nuclei are predominantly formed on the surface of the already existing HTD crystals. Because of the presence of a quasi-phase on their surface, which weakens the effect of the crystal structure of hydrated titanium dioxide on the formation and growth of the nuclei, no epitaxial growth of crystals takes place in aggregates forming in repeated events of nucleation. However, owing to the occurrence of strong chemical bonding between the quasiphase and the formed nucleus, the aggregates are rather strong formations, which retain their configuration in washing HTD to remove water-soluble salts and in mechanical treatment.

The aforesaid furnishes a consistent explanation of the observed dependence of the chemical and granulometric sion composition of HTD formed by thermohydrolytic precipitation from titanium(IV) sulfuric solutions on synthesis conditions. In particular, the increase in the average size of primary HTD crystals and the decrease in the content of crystallization water in these crystals with increasing temperature of heat treatment can be accounted for by the increase in the diffusion mobility of hydroxo aqua complexes, which results in a longer diffusion jump and more ordered incorporation of the complexes into a growing nucleus. The increase in the content of sulfate ions in HTD on raising the concentration of sulfuric acid in solution (molar ratio β) is associated with a rise in the activity of sulfate ions in solution, which results in higher weight fraction of the quasi-phase in the samples. The average size and structure of aggregated primary crystals are determined by the amount of the HTD primary crystals included in the aggregates, which grows with

increasing degree of titanium(IV) hydrolysis in sulfate solutions. Indeed, at high temperatures and α values close to 100%, the maximum concentration of titanium(IV) hydroxo complexes $[Ti_m(OH)_n(H_2O)_l]^0$ in solution is reached, which results in a shorter (down to zero) duration of the latent period of thermohydrolytic HTD precipitation from solution. In this case, the nuclei and titanium(IV) hydroxo aqua complexes are uniformly distributed over the entire volume of the reaction medium, which predetermines equal conditions for the formation of HTD crystals and manifests itself in the formation of monodisperse aggregates with globular structure. Vice versa, at low degrees of hydrolysis of titanium(IV) sulfate compounds ($T \le 150$°C, $\beta > 2$), the latent period becomes longer because of the low concentration of titanium(IV) hydroxo aqua complexes in solution. Therefore, HTD nuclei are formed by a stochastic mechanism [11] at different instants of time and, as a result, are nonuniformly distributed in the reaction medium. This results in local nonuniformity of the concentration of titanium(IV) hydroxo aqua complexes in solution and is responsible for the formation of irregularly shaped polydisperse aggregates.

CONCLUSION

The temperature required for hydrolysis of titanium(IV) in sulfate solutions under hydrothermal conditions was found to be 170°C. In this case, hydrated titanium dioxide with well-pronounced globular structure of aggregates is formed. A possible mechanism of formation of globular particles of hydrated titanium dioxide was considered.

ACKNOWLEDGMENTS

The work was financially supported by the Russian Foundation for Basic Research (grant no. R 2001, 03-03).

REFERENCES

1. Schmid, R., Mronga, N., Radtke, V., and Seeger, O., *Eur. Coat. J.*, 1997, no. 7, pp. 702–705.
2. Dobrovol'skii, I.P., *Khimiya i tekhnologiya oksidnykh soedinenii titana* (Chemistry and Technology of Titanium Oxide Compounds), Sverdlovsk: Ural'sk. Otdel. Akad. Nauk SSSR, 1988.
3. Bonsak, J.P., *J. Coll. Inter. Sci.*, 1973, vol. 44, no. 3, pp. 430–442.
4. Dunkan, J.F. and Richards, R.G., *N. Z. J. Sci.*, 1976, vol. 19, no. 2, pp. 185–194.
5. Gornikova, M.A., Goroshchenko, Ya.G., Zolotarev, A.E., and Svistyur, A.P., *Zh. Prikl. Khim.*, 1983, vol. 56, no. 2, pp. 394–395.
6. Gerasimova, L.G. and Okhramenko, R.F., *Zh. Prikl. Khim.*, 1997, vol. 70, no. 12, pp. 1944–1947.
7. Burkov, K.A., Bus'ko, E.A., and Lilich, L.S., *Khimiya i termodinamika rastvorov* (Chemistry and Thermodynamics of Solutions), 1997, issue 4, pp. 15–43.
8. Kitaigorodskii, A.I., *Rentgenostructurnyi analiz melkokristallicheskikh i amorfnykh tel* (X-ray Structural Analysis of Finely Crystalline and Amorphous Substances), Moscow: GITTL, 1952.
9. Chernov, A.A., Givargizov, E.I, Bagdosarov, Kh.S., *et al.*, *Sovremennaya kristallografiya. T. 3, Obrazovanie kristallov* (Modern Crystallography. Vol. 3: Formation of Crystals), Moscow: Nauka, 1980.
10. Nazarenko, V.A., Antonovich, V.P., and Nevskaya, E.A., *Gidroliz ionov metallov v razbavlennykh rastvorakh* (Hydrolysis of Metal Ions in Dilute Solutions), Moscow: Atomizdat, 1979.
11. Kleshchev, D.G., Sheinkman, A.I., and Pletnev, R.N., Vliyanie sredy na fazovye i khimicheskie prevrashcheniya v dispersnykh Sistemakh (Effect of Medium on Phase and Chemical Transformations in Disperse Systems), Sverdlovsk: Ural'sk. Otdel. Akad. Nauk SSSR, 1990.

Russian Journal of Applied Chemistry, Vol. 74, No. 10, 2001, pp. 1636–1640. Translated from Zhurnal Prikladnoi Khimii, Vol. 74, No. 10, 2001, pp. 1587–1591.

INORGANIC SYNTHESIS AND INDUSTRIAL INORGANIC CHEMISTRY

Film-Forming Capacity of Sn(II), Zr(IV), and Hf(IV) Acetylacetonates

V. V. Dyukov, S. A. Kuznetsova, L. P. Borilo, and V. V. Kozik

Tomsk State University, Tomsk, Russia

Received March 12, 2001

Abstract—$Zr(acac)_4$, $Hf(acac)_4$, and $SnHacacCl_2 \cdot 2H_2O$ were prepared in the solid state and in enthanol solutions. The film-forming capacity and thermal stability of these compounds were studied. Films of ZrO_2, HfO_2, and SnO_2 were prepared from film-forming solutions of the corresponding acetylacetonates.

At present there is demand for thin film materials stable in corrosive media and having good optical properties. The functional and physicochemical properties of these films are mainly determined by their preparation conditions and the nature and composition of the initial film-forming compound (FFC). The promising FFCs are β-diketonates [1]. Data on the thermal stability, volatility, behavior in organic and inorganic solvents, and film-forming capacity of Group IV metal β-diketonates are scarce and often contradictory [2].

In this work, we studied the film-forming capacity of zirconium hafnium, and tin acetylaetonates. For this purpose, we prepared these complexes in the solid phase and in solution, studied their thermal stability in air, and prepared ZrO_2, HfO_2, and SnO_2 films from ethanol solutions of these acetylacetonates.

EXPERIMENTAL

Zirconium and hafnium acetylacetonates $Zr(acac)_4$ and $Hf(acac)_4$ were prepared from aqueous solutions of zirconium and hafnium oxychlorides, respectively, and acetylacetone (molar ratio 1 : 4) at pH 1.9–3.5. The resulting mixture was heated on water bath. The crystalline precipitate was washed with ice-cold water and dried in air. Tin(II) acetylacetonate was prepared from ethanol solution (96 wt % C_2H_5OH) of tin(II) chloride hydrate and acetylacetone (molar ratio 1 : 2).

The zirconium and hafnium content was determined gravimetrically. The actylacetonate ($acac^-$) content was determined by absorption of the iron(III) acetylacetonate complex at λ_{eff} = 550 nm [3].

The qualitative and quantitative composition of $SnHacacCl_2 \cdot 2H_2O$ was determined by means of X-ray spectral microanalysis (XSMA) [4] on a Camebax Microbeam device at accelerating voltage of 20 keV. Metallic tin and single-crystal sodium chloride were used as references. The presence of acetylacetone in the complex was confirmed by qualitative reaction with iron(III) [3].

The compositions of the complexes are presented in Table 1. Acetylacetone in $Zr(acac)_4$ and $Hf(acac)_4$ complexes is in the deprotonated enol form. The tin complex is coordination-unsaturated and contains hydration water and Hacac in the undissociated enol and keto forms, which were previously detected in an ethanol solution acidified with HCl [5].

The solubility of zirconium, hafnium, and tin acetylacetonates in organic and inorganic solvents was studied at room temperature. The solubility of anhydrous zirconium acetylacetonate in chloroform, aceto-

Table 1. Composition of zirconium and hafnium acetylacetonates and dichloro(acetylacetone)tin(II) dihydrate

Composition, wt %	M	$acac^-$	Cl^-
$Zr(acac)_4$:			
found	18.66	80.70	–
calculated	18.72	81.28	
$Hf(acac)_4$:			
found	31.12	66.74	–
calculated	31.07	68.93	
$SnHacacCl_2 \cdot 2H_4O$			
found	35.97	–	26.14
calculated	36.43	–	27.79

1070-4272/01/7410-1636 $25.00 © 2001 MAIK "Nauka/Interperiodica"

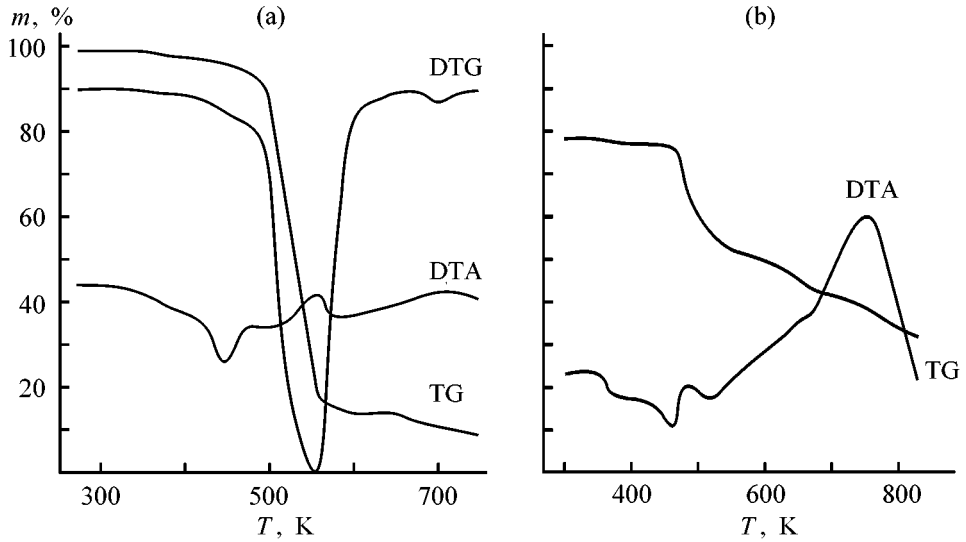

Fig. 1. Thermal analysis curves of (a) $SnHacacCl_2 \cdot 2H_2O$ and (b) $Zr(acac)_4$ decomposition. (*m*) Weight loss and (*T*) temperature; the same for Fig. 3.

nitrile, and acetone is 30, 15, and 4–9 wt %, respectively. The solubility of hafnium acetylacetonate in these solvents is, on the average, 3 wt % lower owing to the more ionic character of the coordination bonds. $SnHacacCl_2 \cdot 2H_2O$ is insoluble in organic solvents and poorly soluble in concentrated mineral acids and water ($\sim 6 \times 10^{-4}$ M) at room and elevated temperatures.

The thermal stability of the complexes in air was studied on a Q-1500 MOM derivatograph (Hungary) in the temperature range 298–1273 K at a heating rate of 10 deg min^{-1}.

Thermal analysis data for $SnHacacCl_2 \cdot 2H_2O$ are shown in Fig. 1a. The first decomposition step is characterized by an exothermic effect in the temperature range 298–473 K and weight loss of up to 4%. As determined by X-ray spectral microanalysis, the remaining product is identical to the initial compound, which indicates that the first effect is due to the sublimation of the compound

Found, wt %: Sn 36.04, Cl 26.98.

$SnHacacCl_2 \cdot 2H_2O$.

Calculated, wt %: Sn 36.43, Cl 27.79.

In the second step (510–563 K) acetylacetone is eliminated and oxidized. As determined by X-ray phase analysis (XPA), the product is $SnCl_2 \cdot 2H_2O$, in agreement with the data of [6]. Weak exothermic peaks in the third step (563–773 K) are assigned to decomposition of $SnCl_2 \cdot 2H_2O$ to give SnO and to oxidation of this product by atmospheric oxygen to SnO_2 (Table 2).

Table 2. X-Ray diffraction patterns of the final decomposition products of metal acetylacetonates and their FFSs

SnO_2 ($SnHacacCl_2 \cdot 2H_2O$)		ZrO_2 [$Zr(acac)_4$]		HfO_2 [$Hf(acac)_4$]	
d, Å	I/I_0	*d*, Å	I/I_0	*d*, Å	I/I_0
3.35(3.34)*	100(100)	3.37(3.63)	20(24)	5.01(5.07)	18(20)
2.64(2.64)	84(63)	3.19(3.19)	100(100)	3.69(3.68)	35(40)
2.37(2.36)	23(18)	2.85(2.85)	78(80)	3.61(3.61)	23(30)
1.76(1.75)	63(63)	2.64(2.63)	30(32)	3.17(3.15)	100(100)
1.67(1.67)	14(10)	2.55(2.55)	18(16)	2.82(2.82)	95(100)
1.59(1.58)	8(5)	2.10(2.09)	23(24)	2.59(2.59)	59(60)
1.49(1.49)	10(14)	1.82(1.81)	44(40)	2.53(2.52)	50(50)
		1.71(1.70)	20(20)	2.33(2.32)	45(50)
		1.49(1.486)	16(16)	2.20(2.196)	60(60)
		1.43(1.426)	14(16)	2.17(2.171)	30(30)
				2.00(2.006)	40(40)
				1.90(1.981)	56(60)

* The data of [8] are given in parentheses.

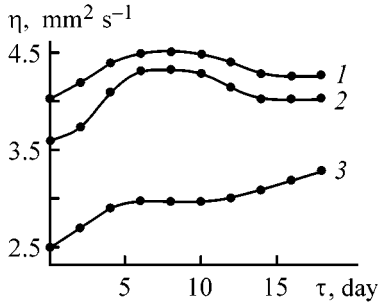

Fig. 2. FFS viscosity η vs. time τ.

The data obtained in thermal analysis of $SnHacacCl_2 \cdot 2H_2O$ and XPA of its decomposition products suggest the following scheme of its decomposition

$$SnHacacCl_2 \cdot 2H_2O \xrightarrow[-\text{Hacac} + O_2 \rightarrow \text{oxidation products}]{} SnCl_2 \cdot 2H_2O \xrightarrow[-H_2O]{} SnCl_2 \cdot H_2O \xrightarrow[-2HCl]{} SnO \xrightarrow{1/2O_2} SnO_2.$$

Decomposition of $Zr(acac)_4$ is also a three-step process (Fig. 1b). In the first step (373–473 K), one acetylacetonate ligand is liberated with an endothermic effect and 18.9% weight loss. The subsequent two steps (473–673 and 673–743 K) are due to exothermic decomposition of the complex to finally form monoclinic ZrO_2 (Table 2).

Thermolysis of $Hf(acac)_4$ is similar to that of $Zr(acac)_4$, with the temperature effects shifted by 30 K to higher temperatures. As determined by XPA, the final thermolysis product is monoclinic HfO_2 (Table 2).

Thus, ZrO_2, HfO_2, and SnO_2 can be prepared from the corresponding metal acetylacetonates at 743, 773, 773 K, respectively.

It is known that oxide films can be conveniently prepared from film-forming solutions in ethanol [8]. Since $Hf(acac)_4$, $Zr(acac)_4$ and $SnHacacCl_2 \cdot 2H_2O$ are poorly soluble in ethanol, we studied preparation of these complexes directly in ethanol without their isolation in the solid state.

Film-forming solutions were prepared from 96% ethanol, acetylacetone and Group IV metal salts [zirconium and hafnium oxychlorides, tin(II) chloride] at Zr^{4+} : acacH, Hf^{4+} : acacH, and Sn^{2+} : acacH ratios of 1 : 4, 1 : 4, and 1 : 2, respectively. The experimental results show that tin(II) acetylacetonate is stable in ethanol solution only at hydrochloric acid concentrations of no less than 0.4 M.

In practice, the stability of FFS can be estimated by their viscosity. The viscosity was measured with VPZh-2 and VPZh-4 viscometers at room temperature. The time dependences of the viscosity of solutions of zirconium and hafnium acetylacetonates are similar (Fig. 2, curves *1*, *2*, respectively). The viscosity reaches a maximum in six days (4.05–4.35 $mm^2 s^{-1}$) and then decreases to constant value by the 15th day. The increase in the viscosity is due to hydrolysis and formation of polymeric associates $-M\leftarrow O=C(CH_3)CH=C(CH_3)OM-$ (M = Zr and Hf) with acetylacetonate bridges [7]. These associates degrade (with a decrease in viscosity) to form mutually oriented coordination-saturated zirconium and hafnium chelates with coordination number of eight.

The time dependence of the viscosity of tin(II) acetylacetonate (Fig. 2, curve *3*) indicates the attainment

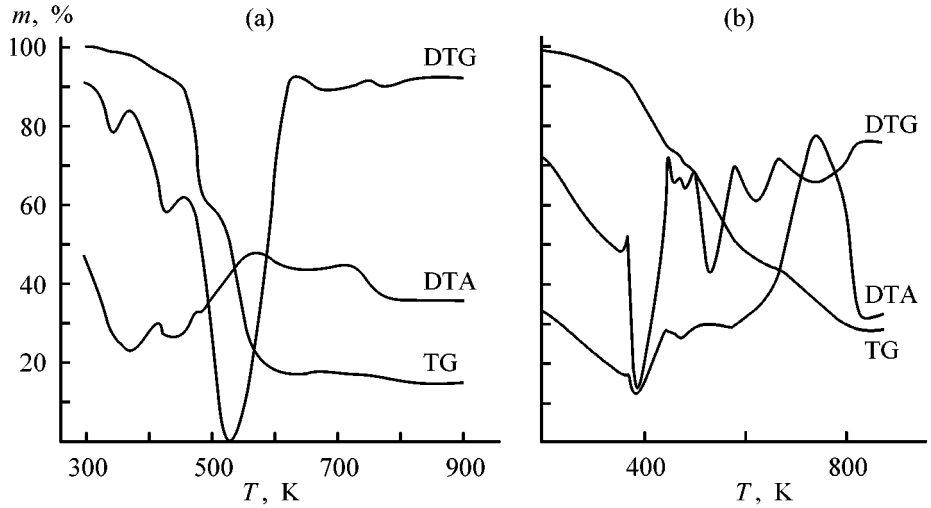

Fig. 3. TG, DTA, and DTG curves of dried FFSs of (a) tin acetylacetonate and (b) zirconium acetylacetonate.

of equilibrium in the solution in four days. The viscosity is constant during the following 6 days. This indicates that equilibrium hydrolysis and complexation of tin(II) are complete. The increase in the viscosity after 10 days is also due to the formation of polymeric associates. Since the viscosity of FFSs does not reach the critical values [8], these solutions can be used during a year after their preparation.

To study the mechanism of oxide film formation, the chemical composition of FFSs dried at 333 K was determined and thermal analysis of these products in the temperature range from 293 to 1073 K was performed.

The chemical composition of an FFS of $SnHacacCl_2 \cdot 2H_2O$ in EtOH, dried at 333 K, was determined by XSMA. The tin and chlorine concentrations in different parts of the sample indicate the presence of $SnCl_2 \cdot 2H_2O$ and $SnHacacCl_2$.

Found in FFS, wt %	Sn	Cl
$SnCl_2 \cdot 2H_2O$	52.49	34.75
$SnHacacCl_2$	43.75	24.16
Calculated, wt %:		
$SnCl_2 \cdot 2H_2O$	52.59	33.46
$SnHacacCl_2$	42.96	24.49

A quantitative XSMA of dried FFS of tin(II) acetylacetonate and $SnHacacCl_2 \cdot 2H_2O$ showed that, during drying of the sample, Hacac is evaporated with ethanol and $SnHacacCl_2 \cdot 2H_2O$ partially decomposing to form $SnCl_2 \cdot 2H_2O$.

The TG, DTA, and DTG curves of an $SnHacacCl_2$–$SnCl_2 \cdot 2H_2O$ mixture (Fig. 3a) somewhat differ from those of $SnHacacCl_2 \cdot 2H_2O$ (Fig. 1a). In the case of dried FFS, the temperature effects are shifted to higher temperatures. The first step is accompanied by two endothermic effects at 323–473 K, associated with sublimation of the complex and desorption of ethanol molecules. In the second step (exothermic effect at 473–593 K), Hacac is liberated from $SnHacacCl_2$ and then oxidized. The third step (593–873 K) involves decomposition of $SnCl_2 \cdot 2H_2O$ to SnO and oxidation of SnO by atmospheric oxygen to give SnO_2 having the rutile structure (according to XPA).

Thermolysis of dried FFS consisting of $ZrOCl_2$, Hacac, and ethanol is a complex process (Fig. 3b). Four endothermic peaks at 370, 388, 448, and 473 K and two exothermic peaks at 531 and 733 K are observed in the DTA curve, with the second exothermic peak being a sum of two effects (DTG). The endothermic effects in the temperature range 321–487 K are probably due to stepwise removal of residual ethanol and water, and to decomposition of zirconium chloride complexes. The exothermic effects in the temperature range 487–873 K are assigned to combustion of the ligand with complete oxidative degradation of FFS to form monoclinic zirconium(IV) oxide (according to XPA).

Table 3. Physicochemical properties of films*

Film composition	n	d, nm	ρ, Ω	F, kg mm^{-2}	ΔE, eV
SnO_2	1.84	41.5	10^6	0.450	3.9
ZrO_2	2.14	65.7	10^8	0.801	–
HfO_2	2.12	58.9	10^7–10^8	0.765	–

* n, F, and ΔE are the refractive index, adhesion, and the optical band gap, respectively.

The DTA curves of dried FFS containing $HfOCl_2$, Hacac, and C_2H_5OH are characterized by three endothermic peaks at 403, 448, 508 K and two exothermic peaks at 693 and 825 K, with the second of these corresponding to two effects. Monoclinic hafnium dioxide is formed at 873 K.

The results of XPA and thermal analysis of dried FFSs indicate that monoclinic zirconium and hafnium dioxides and tin dioxide with rutile stricture are formed at 873 K.

Films of zirconium, hafnium, and tin dioxides were prepared by centrifuging FFSs at 2000–5000 rpm. These films are thermally stable, chemically inert, and have good adhesion to silicon, quartz, glass, and Polikor. The physicochemical properties of high-resistivity semiconducting films of ZrO_2, HfO_2, and SnO_2 on a silicon support are summarized in Table 3. The optical properties of the films were studied with an LEF-3M ellipsometer; the electrical properties, on E7-8 and E7-12 units; and adhesion was measured with a PMT-3 microhardness gage.

CONCLUSION

The complexes $Zr(acac)_4$, $Hf(acac)_4$, $SnHacacCl_2 \cdot 2H_2O$ were prepared in the solid phase and in an ethanol solution. The film-forming capacity and thermal stability in air of these solutions were studied. High-resistivity semiconducting films of ZrO_2, HfO_2, and SnO_2 with high adhesion to different supports were prepared.

REFERENCES

1. Kozyrkin, B.I., in *Primenenie metalloorganicheskikh soedinenii dlya polucheniya neorganicheskikh pokrytii i matarialov* (Preparation of Inorganic Coatings and Materials from Organometallic Compounds), Moscow: Nauka, 1986, pp. 146–151.
2. Tsyganova, S.I. and Dyagileva, L.M., *Usp. Khim.*, 1996, vol. 65, no. 4, pp. 334–349.
3. Kozik, V.V., Skorik, N.A., Borilo, L.P., and Dyukov, V.V., *Zh. Neorg. Khim.*, 1995, vol. 40, no. 10, pp. 1596–1598.
4. Belk, J., *Kolichestvennyi rentgenospektral'nyi mikroanaliz slozhnykh splavov* (Quantitative X-ray Fluorescence Microanalysis of Composite Alloys), Borovskii, I.B., Ed., Moscow: Nauka, 1973.
5. Kuznetsova, S.A., Skorik, N.A., and Kozik, V.V., *Zh. Prikl. Khim.*, 1997, vol. 70, no. 12., pp. 2071–2073.
6. *American Society for Testing Materials, Inorganic Plain Cords.*, Philadelphia, 1946–1969.
7. Peshkov, V.M. and Mel'chakova, N.V., *β-Diketony* (β-Diketones), Moscow: Nauka, 1986.
8. Suikovskaya, N.V., *Khimicheskie metody polucheniya tonkikh plenok* (Chemical Methods for Preparing Thin Films), Leningrad: Khimiya, 1971.

Russian Journal of Applied Chemistry, Vol. 74, No. 10, 2001, pp. 1641–1644. Translated from Zhurnal Prikladnoi Khimii, Vol. 74, No. 10, 2001, pp. 1592–1595.

PHYSICOCHEMICAL STUDIES OF SYSTEMS AND PROCESSES

Solubility and State of Elemental Selenium in Hydrocarbons

E. I. Perov and N. V. Moshchenskaya

Altai State University, Barnaul, Russia

Received February 12, 2001

Abstract—The solubility of metallic and amorphous selenium in *n*-heptane, *n*-octane, *n*-nonane, *n*-decane, *n*-undecane, and *n*-dodecane was determined in the range 298–493 K. The effect of temperature and alkane nature is considered. The average composition of selenium molecules in alkanes was determined from ebullioscopic data.

Our study of the solubility of elemental sulfur in pure *n*-alkanes showed that at 150–200°C "low-molecular-weight" products of thermal dissociation of S_8 rings (down to S_2) exist in solution in noticeable amounts [1]. Also, a saw-tooth dependence of the sulfur solubility on the number of carbon atoms in the hydrocarbon chain was observed for the first time.

Proceeding with studies of synthesis of metal sulfides in organic solvents [2, 3], we proposed an environmentally safe method for preparing metal selenides in liquid *n*-alkanes from elemental selenium and metal carboxylates as initial reagents [4]. Hydrogen selenide formed in the reaction of selenium with hydrocarbons is then converted into a poorly soluble metal selenide. The hydrogen selenide content in the reactor was less than 0.8 mg m^{-3}.

We believe that a study of physicochemical transformations of chalcogens in nonaqueous solutions will allow development of a scientifically substantiated process for preparing semiconductor materials based on metal sulfides and selenides.

The primary stage of the interaction of selenium with *n*-alkanes is its dissolution. The state and solubility of selenium in paraffins have been poorly studied.

In this work, we studied the solubility of two selenium modifications (amorphous and crystalline; the latter is usually termed metallic selenium) in C_7–C_{12} saturated hydrocarbons in the temperature range 25–250°C by the method of immersion filtration [5, 6].

Several conical flasks with preliminarily purified solvent [7] and an immersion filter with selenium were placed in a thermostat equipped with a special vibrator. Samples of saturated solutions were taken with a sampler, and the selenium concen tration was determined gravimetrically after isothermal evaporation of the solvent. The curves of paraffin saturation with metallic and amorphous selenium are shown in Figs. 1 and 2.

The solubility of metallic selenium in *n*-nonane increases from 8.67×10^{-5} M at 298 K to 8.29×10^{-2} M at 418 K (Table 1). The data on solubility of amorphous selenium in *n*-paraffins are listed in Table 2.

Schroeder's equation describing the temperature dependence of the solubility was used for thermodynamic analysis of solubility curves of metallic and

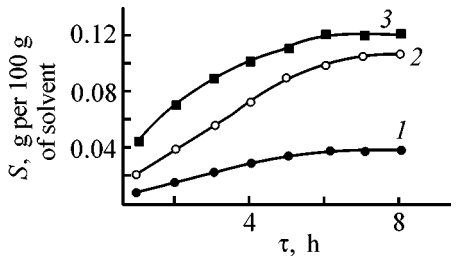

Fig. 1. Curves of solution saturation with metallic selenium at 50°C: (*S*) solubility; (τ) time; the same for Fig. 2. Solvent: (*1*) *n*-heptane, (*2*) *n*-octane, and (*3*) *n*-nonane.

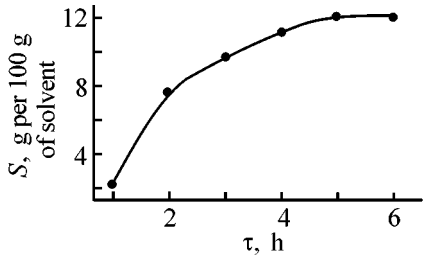

Fig. 2. Curve of saturation of solution in *n*-decane with amorphous selenium at 174°C.

1070-4272/01/7410-1641 $25.00 © 2001 MAIK "Nauka/Interperiodica"

Table 1. Solubility of metallic selenium in hydrocarbons, *S*

T, K	*S*, g per 100 g of solvent			*T*, K	*S*, g per 100 g of solvent		
	n-heptane	*n*-octane	*n*-nonane		*n*-heptane	*n*-octane	*n*-nonane
298	0.009 ± 0.001	0.012 ± 0.001	0.009 ± 0.002	363	0.81 ± 0.01	0.68 ± 0.02	0.75 ± 0.01
323	0.05 ± 0.02	0.11 ± 0.01	0.13 ± 0.01	393	–	0.69 ± 0.01	0.82 ± 0.02
348	0.06 ± 0.02	0.66 ± 0.01	0.69 ± 0.02	418	–	–	0.91 ± 0.01

Table 2. Solubility of amorphous selenium in hydrocarbons, *S*

T, K	*S*, g per 100 g of solvent					
	n-heptane	*n*-octane	*n*-nonane	*n*-decane	*n*-undecane	*n*-dodecane
298	0.12 ± 0.01	0.81 ± 0.02	0.86 ± 0.02	0.92 ± 0.02	3.01 ± 0.02	1.95 ± 0.01
323	1.10 ± 0.01	1.12 ± 0.01	2.53 ± 0.02	2.05 ± 0.01	4.89 ± 0.02	3.87 ± 0.02
348	4.31 ± 0.01	3.79 ± 0.02	5.20 ± 0.02	4.02 ± 0.01	8.03 ± 0.01	6.21 ± 0.01
365	8.48 ± 0.02	5.38 ± 0.02	9.07 ± 0.02	5.79 ± 0.02	12.11 ± 0.01	8.39 ± 0.02
395	–	6.99 ± 0.01	12.44 ± 0.02	7.56 ± 0.01	15.06 ± 0.01	10.24 ± 0.02
421	–	–	15.69 ± 0.02	9.27 ± 0.01	18.12 ± 0.02	13.07 ± 0.02
450	–	–	–	12.89 ± 0.01	21.87 ± 0.02	16.81 ± 0.02
472	–	–	–	–	26.54 ± 0.01	18.02 ± 0.02
493	–	–	–	–	–	20.24 ± 0.01

amorphous selenium in hydrocarbons. The integral form of this equation is as follows:

$$\ln X_{Se}^{sat} = \text{const} - \frac{\Delta H_{m.Se}}{RT},$$

where const is the integration constant, X_{Se}^{sat} is the selenium concentration (mole fraction) in a solution equilibrated with solid selenium, $\Delta H_{m.Se}$ is the heat of selenium melting, T is temperature, and R is the universal gas constant.

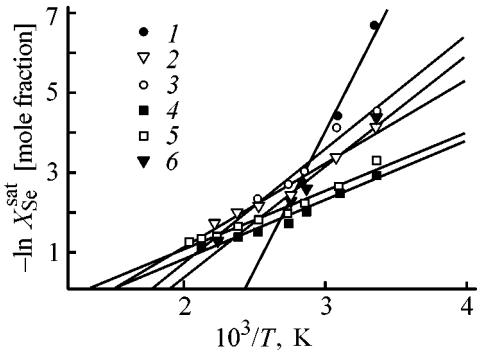

Fig. 3. $\ln X_{Se}^{sat}$–$1/T$ dependence for various solvents: (X_{Se}) concentration of dissolved substance; (T) temperature. Solvent: (*1*) *n*-heptane, (*2*) *n*-octane, (*3*) *n*-nonane, (*4*) *n*-decane, (*5*) *n*-undecane, and (*6*) *n*-dodecane.

The temperature dependences of the solubility of amorphous selenium in *n*-heptane, *n*-octane, *n*-nonane, *n*-decane, *n*-undecane, and *n*-dodecane are shown in Fig. 3. Similar dependences were obtained for metallic selenium.

The melting point of the solute can be found by extrapolation of straight lines in Fig. 3 to intersection with the abscissa ($\ln X_{Se}^{sat} = 0$), and their slope gives the molar heat of melting. However, Schroeder's equation is valid for ideal solutions, and data of Fig. 3 show that such an approximation is unjustified for solutions of selenium in hydrocarbons. A comparison of the reference value of the heat of selenium melting (6.7 kJ per mole of monoatomic selenium) and the values obtained in the experiment showed that Se_n molecules with n = 1–4 prevail in selenium solutions in *n*-alkanes at boiling point. It is usually believed that Se_8 rings are the main selenium species in organic solutions. In the gas phase, Se_8 molecules start to dissociate at 700–2000 K [8]. In this work, we estimated the average molecular composition of selenium in the solution from the temperature dependence of the selenium solubility: $Se_{3.4}$ in *n*-oktane, $Se_{3.4}$ in *n*-nonane, $Se_{2.6}$ in *n*-decane, $Se_{1.8}$ in undecane, and $Se_{1.8}$ in *n*-dodecane. A more precise determination of selenium

Table 3. Average molecular weight of selenium in liquid hydrocarbons (selenium concentration 1 mol per kg of solvent)

Hydrocarbon	$K_{e(calc)}$*	Δt_{boil}, °C	M_{av}
n-C_7H_{16}	3.15	14.3	258.89
n-C_8H_{18}	3.64	18.2	225.60
n-C_9H_{20}	4.80	23.4	224.80

* Ebullioscopic constant.

molecular weight in *n*-alkanes was performed by ebullioscopy.

A statistical processing of the equations $y = b_1x - b_0$ by the least-squares method gave the coefficients b_1 and b_0 of the linear regression equation and sample correlation coefficients r:

$y_1 = -16.56 + 6.82x$, $r = 0.99$, *n*-heptane, 298–365 K,

$y_2 = -5.00 + 2.83x$, $r = 0.98$, *n*-octane, 298–395 K,

$y_3 = -5.19 + 2.75x$, $r = 0.99$, *n*-nonane, 298–421 K,

$y_4 = -3.13 + 2.08x$, $r = 0.98$, *n*-decane, 298–450 K,

$y_5 = -2.14 + 1.45x$, $r = 0.98$, *n*-undecane, 298–472 K,

$y_6 = -1.90 + 1.45x$, $r = 0.98$, *n*-dodecane, 298–493 K.

As noted above, we calculated in [1] for the first time the slopes of the temperature dependence of the solubility of sulfur in various *n*-paraffins. It follows from these data that the temperature dependence of the sulfur solubility is substantially steeper for heptane and nonane, compared with their analogs having even number of carbon atoms in the chain.

This dependence is still more pronounced for the solubility of amorphous selenium in six *n*-paraffins: heptane, octane, nonane, decane, undecane, and dodecane (Table 2). The difference in the temperature dependence of the solubility in paraffins with odd and even number of carbon atoms in the hydrocarbon chain is well seen in Fig. 4. The solubility changes from 1.27 M for octane at 395 K to 3.47 M for dodecane at 493 K. For hydrocarbons of the odd series, the solubility is substantially higher and changes from 1.62 M for heptane (C_7) to 4.59 M for undecane (C_{11}) at 365 and 472 K, respectively.

Ebullioscopic data for selenium solutions in *n*-paraffins and calculated average molecular weights of selenium molecules in the solution are listed in Table 3.

Table 4. Characteristics of thermal dissociation of eight-membered molecular selenium rings

Number of carbon atoms in *n*-alkane chain	M_{av}*	Composition of thermal dissociation products	i	K_{av}
7	258.89	$Se_{3.28}$	2.44	3.24
8	224.80	$Se_{2.85}$	2.81	3.26
9	225.60	$Se_{2.86}$	2.80	4.94

* At maximal selenium solubility.

The low values of these molecular weights experimentally confirm the thermal dissociation of Se_8 rings in liquid alkanes in the range 372–424 K.

A linear correlation was also found between the number i of molecular selenium species formed from the initial Se_8 molecule and the solution dilution $1/C$:

$$i = K_{av} \times 1/C, \quad 1 \le i \le 8.$$

Regression analysis of this equation gives equations relating the empirical quantities x ($\log C$) and y ($\log i$).

$y = 0.510 - 0.703x$, $r = 0.994$, n-C_7H_{16},

$y = 0.513 - 0.586x$, $r = 0.993$, n-C_8H_{18},

$y = 0.510 - 0.582x$, $r = 0.986$, n-C_9H_{20}.

The closeness of the sample correlation coefficient r to unity indicates that the above linear regression $y = a + bx$ is adequate and meaningful.

The molecular weights, composition of products thermal dissociation of eight-membered selenium rings, average number of molecular species in solution, and equilibrium constants are listed in Table 4.

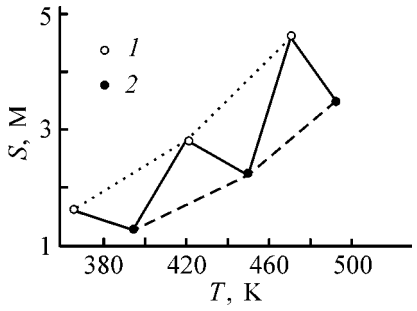

Fig. 4. Temperature trend of solubility S of amorphous selenium in *n*-alkanes with (*1*) odd and (*2*) even numbers of carbon atoms. (T) Temperature.

CONCLUSIONS

(1) The solubility of metallic and amorphous selenium in *n*-C_7–*n*-C_{12} paraffins was determined at 298–493 K by the method of immersion filtration.

(2) It was found from the molar heat of selenium melting, determined as the slope of solubility curves in the $\ln X_{Se}^{sat}$–$1/T$ coordinates (X_{Se}^{sat} is the selenium mole fraction), that Se_n molecules with $n = 1–4$ are the main selenium species in saturated solutions in *n*-paraffins.

(3) A saw-tooth dependence of the solubility of amorphous selenium in *n*-paraffins on the number of carbon atoms in the hydrocarbon chain was revealed.

(4) The average molecular composition of selenium in solutions in *n*-heptane, *n*-octane, and *n*-nonane in a wide concentration range was determined by ebullioscopy. Empirical equations describing the dependence of the average number of Se atoms in molecular selenium species on the selenium concentration in solution were obtained.

REFERENCES

1. Perov, E.I. and Irkhina, E.P., *Zh. Prikl. Khim.*, 1999, vol. 72, no. 1, pp. 48–51.
2. RF Patent 2 112 743.
3. Irkhina, E.P., Environmentally Safe Methods of Synthesis of Metal Sulfides in Liquid Alkanes, *Cand. Sci. Dissertation*, Barnaul, 2000.
4. Moshchenskaya, N.V., Deryabina, I.V., and Perov, E.I., *Izv. Alkaisk. Gos. Univ.*, 2000, no. 3 (17), pp. 19–22.
5. Perov, E.I. and Irkhina, E.P., *Zavod. Lab.*, 2000, vol. 66, no. 4, pp. 37–38.
6. Perov, E.I., Il'ina, E.G., Irkhina, E.P., and Goncharova, I.V., *Koord. Khim.*, 1996, vol. 22, no. 10, pp. 747–748.
7. Becker, H., Berge, W., Domschke, G., *et al.*, *Organikum. Organische-chemisches Grundprakticum*, Berlin; VEB Deutscher Verlag der Wossenschften, 1990, vol. 1.
8. Felz, A.N., *Amorphe und glasartige anorganische Fectkörper*, Berlin: Akad.-Verlag, 1983.

Russian Journal of Applied Chemistry, Vol. 74, No. 10, 2001, pp. 1645–1649. Translated from Zhurnal Prikladnoi Khimii, Vol. 74, No. 10, 2001, pp. 1596–1600.

PHYSICOCHEMICAL STUDIES OF SYSTEMS AND PROCESSES

Physicochemical Properties of Solutions of Sodium Alginate Extracted from Brown Algae *Laminaria Digitata*

I. A. Oberyukhtina, K. G. Bogolitsyn, and N. P. Popova

Arkhangelsk State Technical University, Arkhangelsk, Russia

Severnoe Otdelenie PINRO State Unitary Enterprise, Arkhangelsk, Russia

Received May 28, 2001

Abstract—The rheological properties of sodium alginate solutions were studied as influenced by the concentration of alginic acid, pH of the medium, and temperature. The probable structural and conformational transformations induced on varying these parameters were suggested. The effect of cations and anions of varied nature on the viscous characteristics of these solutions was discussed.

Brown sea algae have recently attracted attention as a source of various substances having wide range of consumer's properties.

Of special value is alginic acid underlying the manufacture of alginates. These are biologically active preparations exhibiting high antiviral, antibacterial, and immunomodulating activities and finding wide application in today's practical medicine [1].

The alginate production procedure is based on alkaline treatment of algae and subsequent separation of this polysaccharide. The drawbacks of this procedure are that the raw material is used ineffectively, as evidenced by production of much waste in the form of algal cellular tissue and large loss of the end product during centrifugation, when the process solution (fugate) is separated from the cellular tissue [2].

This work is a part of the studies of the physicochemical properties of sodium alginate solutions, aimed at gaining deeper insight into processes occurring in various stages of the process and at its further improvement.

In this study, we elucidated how the rheological properties of sodium alginate solutions are affected by the alginic acid concentration c, g dl^{-1}, ionic strength I, M, pH of the medium, and temperature T, °C. Also, we studied how the nature of anions and cations affects the properties of these solutions. The experimental dependences obtained in this study were used for explaining the structural and conformational transformations in these systems.

EXPERIMENTAL

The subjects of investigation were the process solution (fugate) sampled in the stage of centrifugation of algal galert whose main component is sodium alginate and which also contains organic and inorganic substances (chlorides, carbonates, as well as sodium, potassium, magnesium sulfates, etc.) and a sodium alginate solution prepared from the end product, sodium alginate, according to TU (Technical Specifications) 6-09-10-535–76.

The content of alginic acid in the fugate and sodium alginate was estimated by the procedure described in [3] to be 30 and 75% of absolutely anhydrous substance, respectively. The fugate solution yielded by the process had the following characteristics: alginic acid concentration 0.21 g dl^{-1}, pH of solution 10.2, and ionic strength due to Na_2CO_3 introduced in the algae cooking stage 0.053 M.

We measured pH of the solutions on an EV-74 universal ion meter with an ESL-43-07 glass electrode as measuring electrode and an EVL-1M silver chloride electrode as reference. We varied pH of the solutions studied by adding certain amounts of 0.01 M NaOH solution and 0.05 M HCl solution.

We studied the properties of the sodium alginate solutions as influenced by the electrolyte composition by adding inorganic salts; the same salts maintained a constant ionic strength. The influence of the nature of the anions was studied using sodium carbonate, sulfate, orthophosphate, and chloride. The influence of

1070-4272/01/7410-1645 $25.00 © 2001 MAIK "Nauka/Interperiodica"

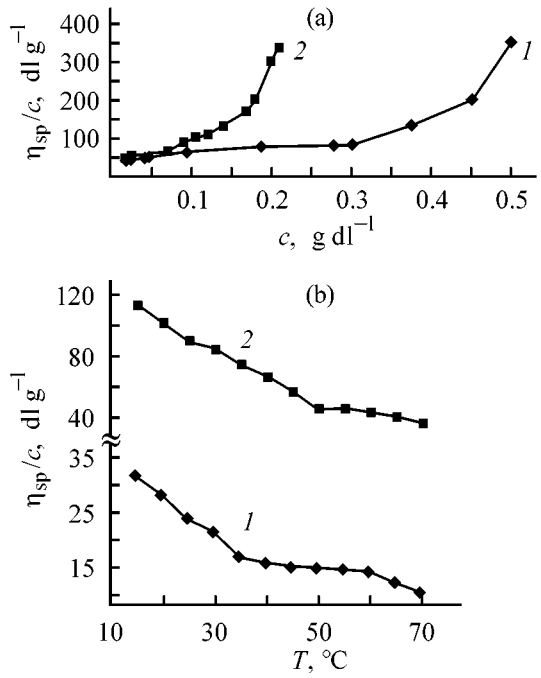

Fig. 1. Reduced viscosity η_{sp}/c, of (*1*) sodium alginate and (*2*) fugate solutions vs. (a) alginic acid concentration c, and (b) temperature T. (a) pH of solution 10.2, I = 0.053 M, T = 25°C and (b) alginic acid concentration in solution c = 0.21 g dl^{-1}.

the nature of the cations was investigated by introducing into sodium alginate solution sodium, potassium, ammonium, and magnesium chlorides. The viscosity was measured on a VPZh-1 glass viscometer with capillary diameter of 1.16, 0.99, and 0.53 mm at T = 25 ± 1°C. The temperature control was provided with a Typ Two thermostat. As the viscosity characteristic served the reduced viscosity η_{sp}/c, dl g^{-1}, which most adequately reflects the structural changes occurring in a system. The measurement error was within 0.5 dl g^{-1}.

To compare the rheological properties of the fugate and sodium alginate solutions, we studied how the concentration of alginic acid affects the reduced viscosity of these solutions (Fig. 1a). The $\eta_{sp}/c = f(c)$ dependence shows that, within the range of relatively low concentrations (c < 0.1 g dl^{-1}), the viscous characteristics of the fugate and sodium alginate solutions are similar. In this concentration range, the solutions are in the micellar state, predominantly in the form of Hartley micelles. With increasing concentration, solutions pass through several equilibrium states characterized by different aggregation numbers, sizes, and shapes of micelles. A sharp increase in the viscosity of solutions (c = 0.17 g dl^{-1} and c = 0.37 g dl^{-1} for the fugate and sodium alginate solutions, respectively) is probably due to the formation of more complex cylindrical or plate-like micelles (McBain micelles) which, in turn, are formed via successive transformations of several mesomorphic phases of different structures [4]. These extended micelles are further arranged into a two-dimensional-hexagonal continuous structure throughout the solution, thus forming a middle mesomorphic phase. With the concentration increasing further, the system converts to a plate-like or lamellar mesomorphic state [5].

The transition of the fugate and sodium alginate solutions from one mesomorphic phase to another at different concentrations can be accounted for by the influence of organic and inorganic impurities occurring in the fugate [2]. The concentration of these impurities is, evidently, sufficient for compressing the electric double layer, thus decreasing the energy barrier preventing the coalescence of colliding particles. Thus, in the fugate solution the interaction of the micellar particles is intensified, which is responsible for a more rapid transition from a less structured to a more structured phase and significantly increases the viscosity of the solution at lower concentrations [6, 7].

We showed that the viscosities of the fugate and sodium alginate solutions are also differently affected by temperature (Fig. 1b). First of all, it should be mentioned that the reduced viscosities of the fugate and sodium alginate solutions with the alginic acid concentration corresponding to that in the process solution (0.21 g dl^{-1}) differ. This suggests that the fugate solution occurs in a more structured (i.e., in one of mesomorphic phases) states than sodium alginate solution. This may be responsible for the different temperature dependences exhibited by these solutions.

For example, the viscosity of the fugate solution decreases with temperature increasing to 50°C; above this temperature a small gradient of the temperature dependence may evidence destruction of a stage in structuring and a transition of the system from micellar to a molecular-micellar state. In sodium alginate solution, an analogous transition occurs at 40°C. The inflection point in the temperature dependence at T = 65°C and the further steeper decrease in the viscosity of sodium alginate solution may be due to a transition of the system to the molecular state, which was not established for the fugate solution in the temperature range of interest.

Although the fugate and sodium alginate solutions markedly differ in the dependences obtained, we can reveal a similar trend in variation of the rheological properties of solutions of these polymers with their concentration and temperature.

To exclude the influence of impurities in the fugate solution, we used in subsequent experiments solutions of sodium alginate as process solution models. The plots of the reduced viscosity of sodium alginate solution against alginic acid concentration suggest that there are two regions of existence of the solutions, namely, the molecular ($c < 0.17 \times 10^{-2}$ g dl^{-1}) and micellar ($c > 0.17 \times 10^{-2}$ g dl^{-1}) regions, throughout the examined pH range (Fig. 2a). The inflection point in the plots discussed corresponds to the critical micelle concentration (CMC), at which micelles formed in solution are in thermodynamic equilibrium with the molecules. This is responsible for a drastic change in a number of properties of solutions and, above all, viscosity.

At close-to-CMC concentrations, the solution contains, for the most part, Hartley micelles, i.e., spherical formations consisting of a hydrocarbon nucleus and an electric double layer. The latter is lined from inside with COO^- ionic groups and from outside, with "bound" and "free" sodium counterions. With increasing concentration of alginic acid in solution the resulting micelles acquire another, namely, plate-like, structure (McBain micelles). Owing to the formation of plate-like micelles, sufficiently concentrated sodium alginate solutions ($c > 0.5$ g dl^{-1}; Fig. 1a, curve *1*) are able to convert into gel.

Our study of how the ionic strength of solution affects the reduced viscosity showed that, with the ionic strength increasing to 0.02 M, the reduced viscosity sharply decreases, while further increase in the ionic strength virtually does not affect the viscous characteristics of the solution (Fig. 2b).

In the case of solutions with alginic acid concentration $c = 0.94 \times 10^{-2}$ g dl^{-1}, corresponding to the micellar region, the influence exerted by sodium chloride taken to create the required ionic strength can be assessed from the viewpoint of the effect on the system of a supporting electrolyte, one of whose ions is identical to the counterions of the colloid particle. Evidently, with increasing content of electrolyte in the system, the electric double layer gets thinner owing to the compression of the diffusion layer. As a result, the ξ potential tends to decrease to zero (at $I = 0.02$ M), which corresponds to the isoelectric state of the system and the minimum reduced viscosity. Further increase in the electrolyte concentration does not affect the reduced viscosity.

The influence exerted by the concentration of the supporting electrolyte on the reduced viscosity of sodium alginate solution with the alginic acid concentration corresponding to the molecular region ($c = 0.15 \times 10^{-2}$ g dl^{-1}) can be accounted for conformational transformations of the alginate macromolecules in the system. The flexible macromolecules of this polymer can take different conformations. The conformations differ in free energy, since the repulsion of the charges of the COO^- groups will result in relatively high free energy for compact conformations, and relatively low, for unfolded conformations. Therefore, at low ionic strengths of solution, the macromolecules are unfolded to the greatest extent, which favors an increase in the viscosity of solutions (Fig. 2a, curve *1*). The increase in the ionic strength of solution, which causes the electric double layer to compress, is responsible for the fact that the shape of the macromolecule approximates the most statistically probable conformations corresponding to the globular state of the system as a whole, which, in turn, decreases the viscosity of solution.

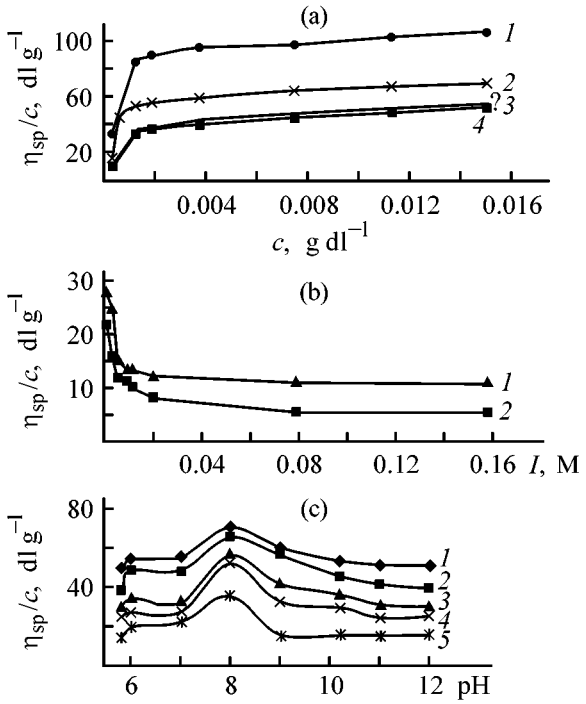

Fig. 2. Reduced viscosity η_{sp}/c of sodium alginate solutions vs. (a) concentration c, (b) ionic strength I, and (c) pH of the medium. (a, c) T = 25°C, I = 0.012 M and (b) pH of solutions 6.5. (a) pH: (*1*) 6.7 (without addition of NaCl electrolyte), (*2*) 8.0, (*3*) 7.0, and (*4*) 10.2. (b) Sodium alginate concentration, g dl^{-1}: (*1*) 0.0094 and (*2*) 0.0015. (c) Alginic acid content, g dl^{-1}: (*1*) 0.0150, (*2*) 0.0075, (*3*) 0.0019, (*4*) 0.0009, and (*5*) 0.0005.

The dependence of the reduced viscosity of sodium alginate solutions on the pH of the medium has a clearly pronounced maximum (Fig. 2c). We varied the pH of solution between 5.8 and 12; the lower boundary of

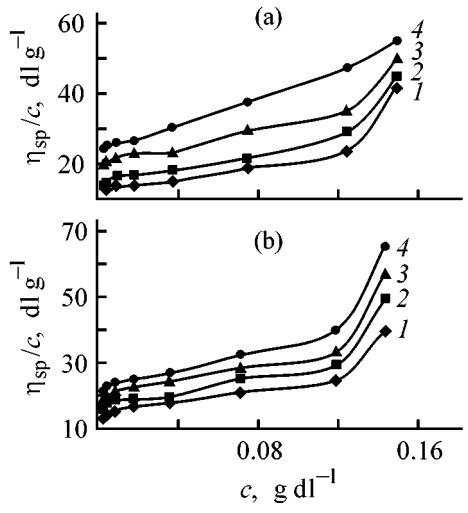

Fig. 3. Reduced viscosity η_{sp}/c of sodium alginate solution vs. the concentration c after introduction of (a) cations and (b) anions of varied nature. (a) Cation: (*1*) Mg^{2+}, (*2*) Na^+, (*3*) NH_4^+, and (*4*) K^+. (b) Anion: (*1*) Cl^-, (*2*) CO_3^{2-} (*3*) SO_4^{2-}, and (*4*) PO_4^{2-}.

this range was chosen in view of the fact that at pH < 5, alginic acid begins to precipitate from solution.

In the molecular concentration region (0.09×10^{-2} and 0.05×10^{-2} g dl^{-1}), the established patterns are quite explicable from the viewpoint of the ability of macromolecules occurring in solution to change their conformation by folding and unfolding.

In the acidic region (5.8 < pH < 6.5), the COO^- groups of sodium alginate molecules react with H^+ ions forming a weak alginic acid. As a result, the electrostatic repulsion forces in the segments of sodium alginate macromolecules weaken, which leads to folding of the macromolecule and, therefore, decreases the solution viscosity.

With increasing pH of sodium alginate solution (6.5 < pH < 8), the degree of dissociation of alginic acid increases, thus enhancing the electrostatic repulsion between the COO^- groups of the molecule. This, in turn, results in unfolding of the macromolecule and, consequently, increases the viscosity of the system. The highest viscosity is observed at pH 8. Further, at 8 < pH < 12 the viscosity of solution tends to decrease because the highly charged sodium counterion in the electrolyte introduced is attracted to the macromolecule surface and strongly shields it, thus decreasing the mutual repulsion of the segments of the molecule carrying negative charges of COO^- group and promoting partial folding of the chain [7].

In the case of micellar solutions (1.5×10^{-2}, 0.75×10^{-2}, and 0.19×10^{-2} g dl^{-1}), the influence of pH is less pronounced and is due to the colloidal-chemical transformations in the system. With increasing pH of the solution, the macromolecules constituting the micelle unfold owing to electrostatic repulsion forces, thus influencing the volume of the aggregate as a whole. Eventually, continuous micellar layers of the McBain micelle type are formed in the system (pH 8), thus increasing the viscosity of solutions.

The pronounced extremum in the plot of the reduced viscosity against pH of the medium in the molecular region is quite explicable by a more prompt response of the system to the state of individual molecules than to that of their aggregates.

We studied how cations of varied nature affect the rheological properties of sodium alginate solutions by introducing NaCl, NH_4Cl, KCl, and $MgCl_2$ salts into these solutions. We found that the reduced viscosity of the sodium alginate solutions tends to decrease in the order $K^+ > NH_4^+ > Na^+ > Mg^{2+}$ (Fig. 3a). The ions of interest form a lyotropic series in which the ion radius tends to decrease from K^+ to Mg^{2+}. This favors formation of less soluble and more compact sodium alginate structures, which, in turn, decreases the solution viscosity.

The same situation was observed with chloride, carbonate, sulfate, and orthophosphate ions introduced into sodium alginate solution. The viscosity of solutions increases in the lyotropic series $Cl^- < CO_3^{2-} < SO_4^{2-} < PO_4^{3-}$ (Fig. 3b). This can be explained in a way analogous to the case of the cations.

Our results can be used in production of alginic acid for regulating and controlling the structure formation processes and intermediate products and products with desired physicochemical properties.

CONCLUSIONS

(1) The molecular ($c < 0.17 \times 10^{-2}$ g dl^{-1}) and micellar ($c > 0.17 \times 10^{-2}$ g dl^{-1}) regions of existence of sodium alginate solutions were revealed.

(2) The influence of the ionic strength and pH of solutions on the viscous characteristics of sodium alginate solutions was established: the reduced viscosity decreases exponentially with increasing ionic strength. The dependence of the reduced viscosity of sodium alginate solutions on the pH of the medium has a maximum at pH 8.

(3) The influence of the cations of anions of different nature is in agreement with the known lyotropic series.

REFERENCES

1. Dobrodeeva, L.K., Belozerov, V. P., Kondakov, N.I., *et al.*, *Pishchevye dobavki vodoroslevogo proiskhozhdeniya dlya profilaktiki i lecheniya immunodefitsitnykh sostoyanii* (Food Additions of Algal Origin in Prevention and Treatment of Immunodeficit States), Arkhangelsk, 1996.
2. Kizevetter, I.V., Gryuner, V.S., and Evtushenko, V.A., *Pererabotka morskikh vodoroslei i drugikh promyslovykh vodnykh rastenii* (Processing of Sea Algae and Other Hydroponics), Moscow: Pishch. Prom–st., 1967.
3. *GOST* (State Standard) *26185–84. Sea Algae, Sea Grass and Their Processing Products. Methods of Analysis*, 1984.
4. Fridrikhsberg, D.A., *Kurs kolloidnoi khimii* (Course of Colloid Chemistry), Leningrad: Khimiya, 1984.
5. Adamson, A.W., *Physical Chemistry of Surfaces*, New York: John Wiley and Sons, 1976.
6. Voyutskii, S.S., *Kurs kolloidnoi khimii* (Course of Colloid Chemistry), Moscow: Khimiya, 1976.
7. Tanford, Ch., *Physical Chemistry of Macromolecules*, New York: Wiley, 1963.

Russian Journal of Applied Chemistry, Vol. 74, No. 10, 2001, pp. 1650–1652. Translated from Zhurnal Prikladnoi Khimii, Vol. 74, No. 10, 2001, pp. 1601–1603.

SORPTION AND ION-EXCHANGE PROCESSES

Effect of Carbonization Temperature and Activation on Structural Formation of Active Lignin Carbons

I. V. Perezdrienko, T. B. Molodozhenyuk, B. E. Shermatov, and M. P. Yunusov

Sultanov Research Chemical Pharmaceutical Institute, Tashkent, Uzbekistan

Received May 12, 2000; in final form, May 2001

Abstract—The effect of thermal and steam treatment on the oxidation state of surface functional groups formed in preparation of granulated carbons from cotton lignin was studied by means of IR spectroscopy and titration with bases of varied strength.

Activated carbons prepared from vegetable raw materials (lignin, fruit kernels, sawdust, peat, nut shells, etc.) are widely used as sorbents. Compared with the known carbons (KAD-iodine, AG-3, and SKT), carbons of this type show higher activity in extraction of precious metals from process solutions after leaching of gravel concentrate.

The formation of the pore structure in active carbons has been studied in sufficient detail, but its chemical origin requires a more thorough study, since the polarity of active carbon surface, determined by surface oxides, and, consequently, the acid–base properties of the surface strongly affect carbon sorption of various substances.

The aim of this study was to analyze by means of IR spectroscopy [1, 2] and titration in various media [3–5] the chemical properties of the surface of activated carbon prepared from cotton hydrolytic lignin.

EXPERIMENTAL

Carbonized carbon samples were prepared at 400–700°C and then activated with superheated steam with addition of 2% oxygen at 800°C. Samples with different combustion losses were obtained by varying the activation time between 15 and 60 min. The total acidity was estimated by back titration with *n*-butylamine [3]. For this purpose, weighed portions (0.5 g) of granulated carbons under study were placed in flasks with ground stoppers, each containing 15 ml of a 0.01 N solution of butylamine in benzene. After periodic shaking for a few hours and clarification, an aliquot portion of the solution was titrated with a 0.005 N solution of acetic acid in benzene. The titration was performed until the Bromophenol Blue indicator changed its color, and then the amount of *n*-butylamine necessary for neutralization of the surface acidic centers was calculated.

It was found experimentally that, when the time of contact between a weighed portion of carbon and a benzene solution of a base is longer than 5 h, no further increase in the neutralization occurs. To differentiate between the acidic surface groups, the interaction of samples with aqueous basic solutions was studied by potentiometric titration. As in [4], we assumed that $NaHCO_3$ neutralizes the strongest acidic centers (H^+), Na_2CO_3 and weaker carboxyls (–COOH), NaOH, and phenolic hydroxyls. In addition to the above groups, C_2H_5ONa also reacts with alcoholic hydroxyls. Using the method of separate weighed portions, we found that under the conditions preventing CO_2 adsorption from air, the highest rise in neutralization is observed during the first 24 h of carbon contact with 0.005 N aqueous solutions of bases. Further, the concentration of acidic centers, especially those determined with $NaHCO_3$ and Na_2CO_3, changes only slightly. Therefore, in this stage of the study, we exposed the test samples to corresponding solutions for 1 day. The IR spectra of the activated carbons in KBr were recorded on a Pay Unicam spectrophotometer.

The IR spectra of the samples carbonized at 400°C contain a set of absorption bands in the interval 3600–430 cm^{-1}; the intensity of these bands markedly decreases with increasing carbonization temperature (see the figure). The absorption bands in the 3500–3330 cm^{-1} range can be assigned to (O–H) stretching vibrations of alcohols, phenols, carboxylic acids, and

1070-4272/01/7410-1650 $25.00 © 2001 MAIK "Nauka/Interperiodica"

Concentration of surface centers of various lignin carbons

Carbonization temperature, °C	Combustion loss, %	Concentration of surface centers, mmol g^{-1}					
		weakly acidic alcoholic (OH^-)	phenolic (OH^-)	carboxylic (–COOH)	strongly acidic (H^+)	total acidity by *n*-butylamine	basic
400	–	0.080	0.070	0.060	0.040	0.090	–
600	–	0.110	0.075	0.045	0.010	0.060	–
700	–	0.130	0.020	0.038	–	0.040	–
700	12*	0.160	0.065	0.040	0.012	0.090	–
700	25*	0.140	0.40	0.050	0.006	0.150	–
700	36.6*	0.130	0.0035	0.061	0.001	0.21	–
700	40*	0.120	0.0025	0.060	–	0.190	0.05
700	60*	0.070	0.001	0.030	–	0.130	0.08
700	80*	0.025	–	0.015	–	0.110	0.10

* Samples activated at 800°C following carbonization.

adsorbed water molecules. However, these frequencies are also a characteristic of stretching vibrations of free and associated (NH_2), (NH), and (C=NH) groups. Therefore, their presence, especially in samples containing up to 2% nitrogen and carbonized within 400–600°C, is rather probable. The weak bands at 2860 and 2800 cm^{-1} unambiguously characterize (C–H) vibrations of the methyl and methylene groups, which, along with a number of (C=O) vibrational bands in the range 1790–1625 cm^{-1}, points to simultaneous presence of compounds containing a carbonyl group in aldehydes and acids. A low-frequency shift of the (C=O) vibrations indicates the formation of intramolecular hydrogen bonds. The presence of oxygen-containing compounds at the surface is also confirmed by the bands at 1413–1440 cm^{-1}, related to bending vibrations of alcoholic hydroxyls, and bands at 1200–1070 cm^{-1} due to (C–O) vibrations of alcohols and phenols. The formation of the surface structures of aromatic type in the course of lignin carbonization can be judged, in particular, from the presence of skeletal vibrations, including (C=C) vibrations at 1600–1585 and 1500–1400 cm^{-1}, and from the out-of-plane bending vibrations of (C–H) in the range 900–675 cm^{-1}.

Analysis of the IR spectra of the carbonized lignin carbons indicates a gradual decrease in the intensity of vibrations of the hydroxyl-containing compounds with the carbonization temperature increasing from 400 to 800°C. This result correlates well with the measured concentration of acidic centers of varied nature (see the table) and confirms their close thermal stabilities. The total acidity of the carbonized samples decreases monotonically with increasing carbonization temperature. Before activation no basic centers are found. The estimate of the amount of surface groups titrated in aqueous media with bases of different strengths shows that high-temperature carbonization raises solely the concentration of the weakest acidic centers formed by alcoholic hydroxyls. At the same time, the number of strong protonic centers and weaker acidic centers decreases.

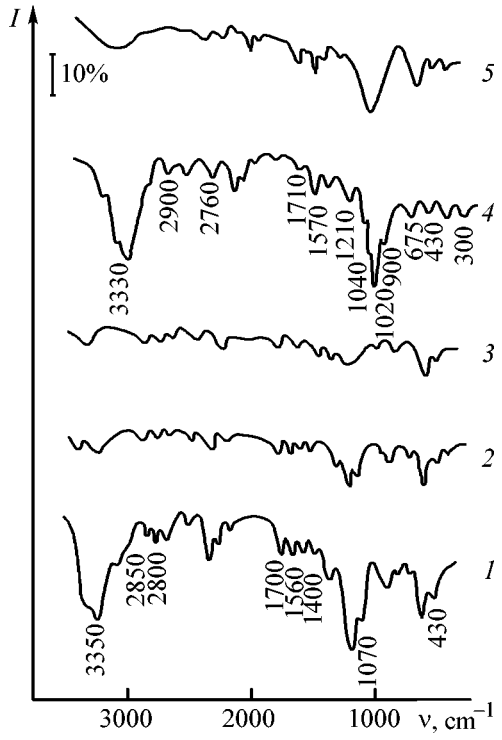

IR spectra of lignin carbons carbonized at (*1*) 400, (*2*) 600, and (*3*) 800°C and those activated at 800°C after carbonization at 700°C with combustion loss of (*4*) 12% and (*5*) 36.6%. (*I*) Absorption intensity and (ν) wave number.

The total acidity of the activated samples is the highest at a 36.5% combustion loss and, on the whole, is lower than that of carbonized samples. In the initial stage of activation, at a 12% combustion loss, a large amount of phenolic and alcoholic hydroxyls is formed. Correspondingly, the intensity of the IR bands at 3330 and 1089–1210 cm^{-1} due to (O–H) and (C–O) stretching vibrations reaches a maximum. It is in this sample that the maximum concentration of strongly acidic COOH and H^+ groups is observed. With increasing activation time, up to a 50% combustion loss, a part of alcoholic hydroxyls undergoes deeper oxidation to carboxyls and aldehydes. This follows from the gradual increase in the intensity of the absorption bands at 1700–1720 cm^{-1}, related to (C=O) stretching vibrations, and a decrease in the intensity of absorption bands at 3330–3350 cm^{-1}, associated with stretching vibrations of the (O–H) bond. Simultaneously, two new bands appear in the IR spectra: strong asymmetric band at 1570 cm^{-1} and a weaker band at 1400 cm^{-1}, due to symmetric stretching vibrations, which is characteristic of carboxylate ions [1].

In our opinion, burning out of organic substances in activation of lignin carbons releases alkali and alkaline-earth metal cations, which, interacting with carboxy groups, block part of strongly acidic centers. Thus, the unexpectedly low acidity of activated samples is due to partial neutralization of the surface carboxy and proton acidic groups by sodium, potassium, magnesium, and calcium ions produced in dissolution of ash particles in adsorbent pores under the action of steam in the course of activation. At higher combustion losses, corresponding to a (8–12%) ash content, the alkali and alkaline–earth metal compounds incorporated into the ash lead to the appearance of basic centers on the background of further decreasing acidity.

In addition to the bands related to various oxygen-containing compounds formed in preparation of active carbons, the IR spectra contain absorption bands whose assignment encounters certain difficulties. For example, a set of bands in the range 2600–2000 cm^{-1} can be attributed to acetylene compounds or to sulfur-containing compounds. The formation of the latter is rather probable in view of the fact that acid lignin containing sulfuric acid is used for preparing the carbons. Thus, the high-frequency bands in the range 2600–2490 cm^{-1} can be attributed to partial reduction of sulfate ions to hydrogen sulfide, present in chemisorbed state in the carbon pores. The strongest bands corresponding to (S–H) bond vibrations are observed at 2636 and 2423 cm^{-1} on a sample carbonized at 400°C. Their intensity falls with increasing carbonization temperature.

Several types of centers with different adsorption activities are formed at the surface in preparing activated carbons [5]. CO, CO_2, and other gaseous products of incomplete oxidation of lignin are physically and chemically adsorbed on the surface of freshly prepared carbon. Owing to the mobility of adsorbed molecules, the most active defect structures are saturated first and form secondary adsorption centers of different nature. According to [1], gaseous CO is characterized by absorption band at 2143 cm^{-1}, associated with stretching vibrations, and gaseous CO_2, by bands at 2349 and 667 cm^{-1} [1]. The surface structures responsible for the higher-frequency bands in the 2200–2140-cm^{-1} range are easily removed from the surface by roomtemperature vacuum treatment, and, consequently, are weakly bound to the surface by Van der Waals forces. Therefore, their appearance in the IR spectra can be attributed to the adsorbed carbon oxides.

CONCLUSIONS

(1) Functional groups whose acidic properties become weaker in going from H^+, to –OOH, and further to –OH groups of phenol-like compounds and alcohols are identified on the surface of active carbons prepared from cotton lignin.

(2) Raising the carbonization temperature from 400 to 800°C makes the concentration of the surface acidic centers lower.

(3) The activation of carbonized carbons with superheated steam at 800°C is accompanied by additional formation of carboxy groups up to 40% combustion loss.

(4) Lignin carbons containing only acidic functional groups, or those containing both acidic and basic centers simultaneously, can be prepared by varying the combustion loss in activation of lignin carbon.

REFRERENCES

1. Little, L.H., *Infrared Spectra of Adsorbed Species*, London: Academic, 1966.
2. Silverstein, R.M., Bassler, G.G., and Morrill, T.C., *Spectrometric Identification of Organic Compounds*, New York: Wiley, 1974.
3. Borodin, V.N., *Zh. Fiz. Khim.*, 1977, vol. 51, no. 4, pp. 928–929.
4. Dubinin, M.M., Nikolaev, K.M., Petukhova, G.A., and Polyakov, N.S., *Izv. Akad. Nauk SSSR*, 1988, no. 1, pp. 35–40.
5. Tarkovskaya, I.A., Goba, V.E., Tomashevskaya, A.N., *et al., Uglerodnye adsorbenty i ikh primenenie v promyshlennosti* (Carbon Sorbents and Their Industrial Application), Moscow: Nauka, 1983, pp. 205–222.

Russian Journal of Applied Chemistry, Vol. 74, No. 10, 2001, pp. 1653–1657. Translated from Zhurnal Prikladnoi Khimii, Vol. 74, No. 10, 2001, pp. 1604–1607.

SORPTION AND ION-EXCHANGE PROCESSES

Depassivation of Ion-Exchange Membranes in Electrodialysis

V. A. Shaposhnik, N. N. Zubets, I. P. Strygina, and B. E. Mill'

Voronezh State University, Voronezh, Russia

Received February 13, 2001

Abstract—Procedures were developed to prevent precipitation on the ion-exchange membrane surface in demineralization of natural hydrocarbonate water by electrodialysis.

Owing to the steadily growing consumption of pure water, its preparation by demineralization of natural water is of interest not only from the scientific and engineering, but also from the social and political standpoints [1]. At present, the most efficient and environmentally safe water treatment procedures are based on membrane processes [2]. In desalination of sea and ocean water, reverse osmosis membranes are the most appropriate. At the same time, in demineralization of the surface and underground brackish water, use of electrodialysis with ion-exchange membranes is preferable. A schematic of a five-compartment electrodialyzer including alternating anion- and cation-permeable membranes is shown in Fig. 1. In commercial electrodialyzers, the number of desalination and concentration compartments may be as large as several tens or even several hundreds. To prevent precipitation at the (anion-exchange membrane)–solution interface, caused by the increasing pH in this zone, the electrodialysis of natural water is performed at current density lower than the limiting diffusion current.

In standard electrodialysis modes, a concentration polarization occurs, resulting in alkalization of the aqueous solution at the boundary between the ion-exchange membrane and the aqueous phase owing to irreversible water dissociation. In particular, when the limiting diffusion current through the boundary layer between the anion-exchange membrane and solution is exceeded, the irreversible water dissociation is caused by selective electromigration of hydroxy anions across the membrane. These hydroxy anions are accumulated in the opposite boundary layer of the anion-exchange membrane in the concentration compartment *3* (Fig. 1). The increased concentration of hydroxy anions in compartment *3* results in the formation of precipitates of poorly soluble calcium carbonate, magnesium hydroxide, and calcium sulfate. According to [3], calcium sulfate does not affect the electrochemical characteristics of the ion-exchange membranes. As opposed to calcium sulfate, calcium carbonate and magnesium hydroxide, precipitating at the interface, shield the transmembrane current in the area of their deposition. At the same time, the current density through free surface increases to a level consider-

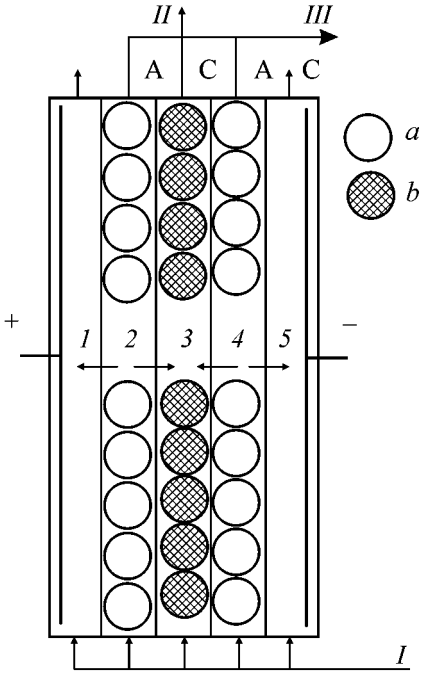

Fig. 1. Electrodialyzer. (*1–5*) Compartment numbers. Membranes: (A) anion-exchange and (C) cation-exchange. Granules: (*a*) anion exchanger and (*b*) cation exchanger. (*I*) Feed, (*II*) concentrate, and (*III*) diluate.

1070-4272/01/7410-1653 $25.00 © 2001 MAIK "Nauka/Interperiodica"

ably exceeding the limiting diffusion current density. These processes passivate the membranes, raise their electrical resistivity, reduce the membrane conductivity, and, finally, suppress the electrodialysis.

Deterioration of electrodialysis can be prevented by decreasing the current density to a level lower than the limiting diffusion current density. However, such a procedure decreases the output of demineralization and, what is more, the irreversible water dissociation can proceed at these current densities, too, owing to the catalytic effect of ionogenic groups of the ion-exchange membranes [4].

There are several ways to prevent precipitation. The passivated membranes can be regenerated by repeated (several times an hour) reversal of current [5]. The membranes can also be depassivated by treatment with a reagent capable of dissolving $CaCO_3$ and $Mg(OH)_2$ precipitates, e.g., by passing a dilute aqueous HCl solution with pH 4.5 through the concentration compartment [6]. One more, widely used technique for membrane depassivation is based on preliminary removal of calcium and magnesium from mineralized water by their precipitation in the form of poorly soluble hydroxides. The alkaline aqueous solution used for magnesium and calcium precipitation is prepared by electrodialysis of a salt solution with bipolar membranes [7], allowing simultaneous preparation of alkaline and acidic solutions. Calcium and magnesium hydroxide precipitates are filtered off, and the filtrate is passed through a column packed with cation exchanger in the H^+ form. This cation exchanger is regenerated by passing aqueous acidic solution prepared by electrodialysis of a salt solution with bipolar membranes. In this work, we developed an electrochemical technique for binding hydroxide and carbonate anions, which prevents formation of poorly soluble calcium carbonate and magnesium hydroxide on the ion-exchange membrane surface in electrodialysis of mineralized water.

In our experiments, we used Voronezh tap water containing 9 mM of magnesium and 1.43 mM of calcium ions. If the product of the concentration of the calcium cations and hydroxide anions exceeds the solubility product, a poorly soluble precipitate of magnesium hydroxide is formed:

$$[Mg^{2+}][OH^-]^2 > K_{s1} = 6.0 \times 10^{-10}. \quad (1)$$

This expression shows that at magnesium hydroxide can precipitate from the tap water at pH > 10.1.

Calcium carbonate precipitation is described by the expression

$$[Ca^{2+}][CO_3^{2-}] > K_{s2} = 3.8 \times 10^{-9}, \quad (2)$$

which shows that this process is more probable than magnesium hydroxide precipitation.

It is known that the carbonate concentration depends on pH (dissociation constant of bicarbonate anion $K_2 = 4.8 \times 10^{-11}$). At a bicarbonate concentration in supply water equal to 2.3 mM, precipitation of calcium carbonate starts at pH > 7.38. Therefore, even upon a small increase in pH of the initial water, calcium carbonate can precipitate in the concentration compartment *3* (Fig. 1).

Our experiments were performed with a five-compartment electrodialyzer with alternating anion- and cation-exchange membranes, platinum anode, and stainless steel cathode. MA-41I anion-exchange heterogeneous membranes were prepared from a composite containing AV-17 strongly basic isoporous anion exchanger (65%) with benzyltrimethylammonium monomeric units and polyethylene matrix.

It was found [8] that, in electrodialysis of carbonate solutions, anion-exchange membranes based on a strongly basic anion exchanger are preferable to membranes containing a resin with weakly basic ionogenic groups. These membranes provide higher current efficiency and smaller consumption of electric power. The commercial MA-40 anion-exchange membranes prepared from EDE-10P medium-basic anion exchanger contain, along with trimethylammonium groups (10–12%), secondary =NH and tertiary ≡N amino groups functioning as ionogenic groups in acidic media only. However, anions of weak acids are protonated in acidic media, and, as a result, the ionic transmembrane transfer decreases. Furthermore, MA-41I resin provides more complete removal of silica derivatives from natural water. Their removal is complete at pH > 12. In the neutral medium the removal of silica derivatives is also sufficiently high. Their transference number for MA-41I membrane is 0.39, which significantly exceeds that for MA-40 membrane (0.09) [9]. These facts were the main arguments in favor of the use of MA-41I membrane.

MK-40 cation-exchange heterogeneous membranes were prepared from a formulation containing KU-2 strongly acidic sulfonic cation exchanger and polyethylene. The electrodialyzer compartments are 120 cm high, 1 cm wide, with intermembrane spacing of 0.09 cm. The desalination compartments *2* and *4* were packed with anion-exchange gauze with granules of the anion exchanger in the cells. The concentration compartment *3* was packed in the same way with cation-exchange gauze and cation-exchange granules.

The way of packing of the intercompartment space with the ion-exchange materials is illustrated in Fig. 2. The ion-exchange gauzes and the corresponding ion-exchange membranes were prepared from the same material. The cells of the anionexchange gauze located in the desalination compartment were packed with AV-17 anion exchange granules. Similarly, the cells of the cation-exchange gauze in the concentration compartment were packed with KU-2 cation exchanger granules. The initial tap water with resistivity of 2 kΩ cm was clarified and then continuously passed through all the compartments at a velocity of 2.2 cm s^{-1}. The resistivity of the initial and desalinated water was determined on a VM-484 semiautomatic bridge in a flow-type conductometric cell with platinum platinized electrodes. A VSA stabilized rectifier was used as direct current source. The current was measured with an M-104 ammeter. The voltage across the electrodialyzer was measured with a V7-15 high-resistance voltmeter. The pH of the medium was measured with an EV-74 ionometer with a glass electrode. Calcium and magnesium were determined complexometrically. Carbonate anions were determined by acidometric titration.

Figure 3 shows the resistivity of desalinated water as a function of the current density. These data show that electrodialysis at current densities within the range $0.25 < i < 0.50$ mA cm^{-2} raises the resistivity from 2 kΩ cm in the initial water to 100–120 kΩ cm in the desalinated product. Electrodialysis at high current density allows preparation of water with characteristics similar to those of double-distilled water. However, to prevent precipitation in prolonged operation of an electrodialyzer, reversal of the water feed is required when the total resistance of the apparatus becomes high. Water demineralized in the first electrodialysis stage can be fed into the second stage of electrodialysis. In this case, the intermembrane space of the desalination compartments should be packed with a mixture of anion and cation exchangers. Such a two-stage treatment of tap water allows preparation of highly desalinated water with resistivity of 20 MΩ cm [10]. This water, with parameters similar to those of the double-distilled water, can be converted into ultrapure water by passing through a mixture of anion and cation exchangers.

Figure 4 illustrates the effect of the current density on the pH of water flowing out from both the desalination and concentration compartments. As seen from curve *2*, the water flowing out of the concentration compartment, where sedimentation is the most probable, has acidic reaction ensuring depassivation of membranes. On packing the desalination compartment with anion exchanger, we did not found any noticeable increase pH. This phenomenon is due to complicated electrochemical processes occurring in the course of electrodialysis with intermembrane space packed with ion exchangers.

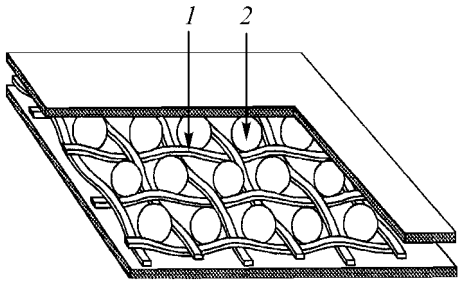

Fig. 2. Packing of the intermembrane space with (*1*) ion-exchange gauze and (*2*) granules.

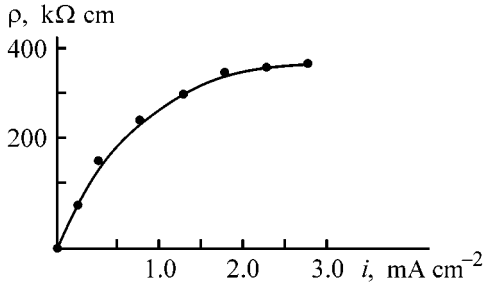

Fig. 3. Resistivity ρ of desalinated water vs. the current density *i* in the electrodialyzer with intermembrane space packed with ion-exchange gauze and granules. Velocity of water feed 2.2 cm s^{-1}.

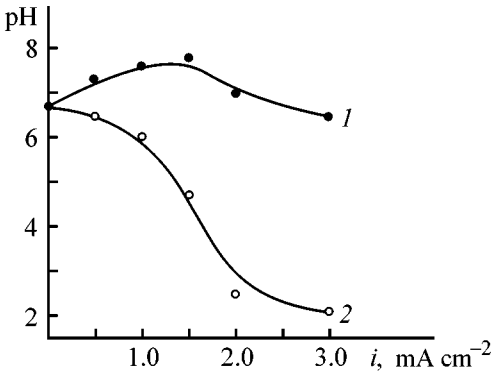

Fig. 4. pH of solutions flowing out of (*1*) desalination and (*2*) concentration compartments vs. the current density *i* in elecrodialysis of weakly mineralized calcium hydrocarbonate water.

The main processes responsible for desalination in electrodialysis occur at the heteropolar boundaries of anion-exchange granules and cation-exchange membranes (Fig. 5). It was established [11] that, in polarization indicated in Fig. 5, the features of the hetero-

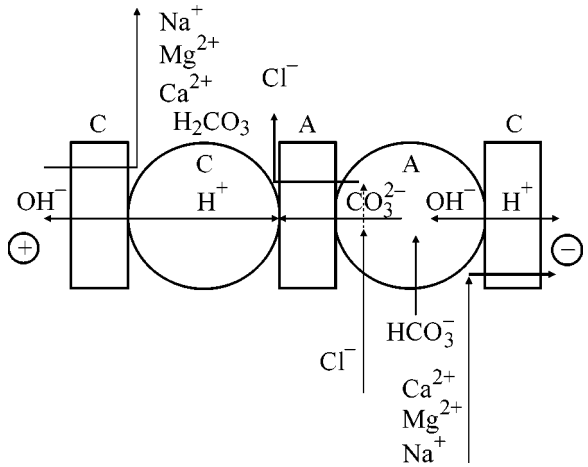

Fig. 5. Scheme of membrane depassivation in two adjacent compartments in electrodialysis of calcium hydrocarbonate water: (C) cation-exchange membranes and granules; (A) anion-exchange membranes and granules.

polar boundaries between the cation-exchange membrane and anion-exchange granules and between the anion-exchange membrane and cation-exchange granules are similar to those of the internal boundary of a bipolar membrane generating hydrogen and hydroxide ions. We believe that the following mechanisms are responsible for this similarity. The exhaustive desalination of water within the capillary heteropolar contact is reached even at very small current densities. Under these conditions, the current is maintained only by irreversible dissociation of water molecules. The high efficiency of this process is ensured by migration of protons and hydroxy anions across the cation-exchange membrane and through anion-exchange granules, respectively (Fig. 5).

In migration through the anion-exchange granule the hydroxy anions react with hydrocarbonate anions sorbed from water. As a result, the hydroxy anion concentration decreases and hydrocarbonate anions are converted into carbonate anions:

$$OH^- + HCO_3^- = CO_3^{2-} + H_2O.$$

Carbonate anions migrate toward the anode through the anion-exchange granules located within the desalination compartments *4* and *2* (Fig. 1) and also across the anion-exchange membranes separating compartments *4* and *3* and *1* and *2* into the concentration compartment *3* and anode compartment *1*, respectively. It was found [12] that the electromigration rate of carbonate anions exceeds that of bicarbonate anions [12].

Hydrogen ions formed by irreversible dissociation of water at the heteropolar contact between the cation-exchange membrane and anion-exchange granule migrate toward the cathode from the desalination compartment to the concentration compartment *3* and then through a cation-exchange granule to the heteropolar contact between the anion-exchange membrane and cation-exchange granule. At polarization indicated in Fig. 5, the following reaction occurs in the capillary space of this heteropolar contact:

$$2H^+ + CO_3^{2-} \rightarrow H_2CO_3 = H_2O + CO_2\uparrow.$$

By this reaction, carbonate anions are converted into weakly dissociating carbonic acid which partially decomposes to give water (target product) and carbon dioxide.

Figure 4 (curve *2*) shows that the pH in the concentration compartment grows with increasing electromigration of hydrogen ions across the cation-exchange membrane. This effect prevents precipitation of calcium carbonate and magnesium hydroxide.

What is more, even when calcium carbonate is precipitated under favorable local conditions, it is converted in any case into soluble calcium bicarbonate by the reaction with active carbon dioxide liberated in carbonic acid decomposition:

$$CO_2 + H_2O + CaCO_3 = Ca(HCO_3)_2.$$

Neutral or weakly alkaline medium in the desalination compartment can facilitate calcium carbonate precipitation. However, this precipitate is continuously dissolved owing to the transfer of calcium and carbonate ions from the saturated solution across the cation and anion-exchange membranes, respectively [13]. This electrochemical process prevents precipitation in the desalination compartment.

CONCLUSIONS

The following factors prevent precipitation in electrodialysis of calcium hydrocarbonate water: (1) conversion of hydroxy anions formed by nonlinear concentration polarization into water molecules by the reaction with hydrocarbonate anions, (2) localization of the reaction of carbonate anions with hydrogen ions within the capillary space of the heteropolar conrtact between the granular ion exchanger and ion-exchange membrane, (3) dissolution of calcium carbonate by the reaction with carbon dioxide, (4) control of pH in the desalination and concentration compartments by packing the intermembrane space with ion exchangers, and (5) electrochemical dissolution of calcium carbonate formed the desalination compartment.

ACKNOWLEDGMENTS

The authors are grateful to the Russian Foundation for Basic Research for supporting this work (project 98-03-32194).

REFERENCES

1. Hauser, H.K.J., *Underwater J.*, 1973, vol. 5, no. 1. pp. 9–17.
2. Shaposhnik, V.A., Mazo, A.A., and Frelikh, P., *Usp. Khim.*, 1991, vol. 60, no. 11, pp. 2469–2483.
3. Bobreshova, O.V., Lapshina, T.E., and Shatalov, A.Ya., *Zh. Prikl. Khim.*, 1980, vol. 53, no. 3, pp. 665–671.
4. Simons, R., *Electrochim. Acta*, 1984, vol. 29, no. 2, pp. 151–159.
5. Valeour, H.C., *Desalination*, 1985, vol. 54, pp. 163–171.
6. Watanabe Tabayuki, Yamamoto Hideo, Akiyama Masao, and Yuri Noriko, *Bull. Soc. Sea Water Sci.*, Jpn, 1972, vol. 26, no. 2, pp. 83–92.
7. Zabolotsky, V.I., Nikonenko, V.V. Pismenskaya, N.D., and Istoshin, A.G., *Desalination*, 1996, vol. 108, pp. 179–182.
8. Smirnova, N.M. and Laskorin, B.N., in *Ionity i ionnyi obmen* (Ion Exchangers and Ion Exchange), Leningrad: Nauka, 1970, pp. 190–196.
9. Shaposhnik, V.A., Strygina, I.P., Reshetnikova, A.K., and Sukhinina, L.N., in *Teoriya i praktika sorbtsionnykh protsessov* (Theory and Practice of Sorption Processes), Voronezh: Voronezh. Gos. Univ.,1986, issue 18, pp. 75–78.
10. Shaposhnik, V.A., Reshetnikova, A.K., Zolotareva, R.I., *et al.*, *Zh. Prikl. Khim.*, 1973, vol. 46, no. 12, pp. 2659–2663.
11. Gluekauf, E., *Brit. Chem. Eng.*, 1959, vol. 4, no. 12, pp. 646–652.
12. Lownis, A. and Gavach, C., *J. Membr. Sci.*, 1990, vol. 54, pp. 63–71.
13. Isaev, N.I. and Shaposhnik. V.A., in *Sintez i svoistva ionoobmennykh materialov* (Synthesis and Properties of Ion-Exchange Materials), Moscow: Nauka, 1968, p. 256.

Russian Journal of Applied Chemistry, Vol. 74, No. 10, 2001, pp. 1658–1663. Translated from Zhurnal Prikladnoi Khimii, Vol. 74, No. 10, 2001, pp. 1608–1613.

SORPTION AND ION-EXCHANGE PROCESSES

Features of Preparation and Properties of FIBAN K-4 Fibrous Sorbents

G. V. Medyak, A. A. Shunkevich, A. P. Polikarpov, and V. S. Soldatov

Institute of Physical Organic Chemistry, Belarussian National Academy of Sciences, Minsk, Belarus

Received February 5, 2001

Abstract—Liquid-phase graft polymerization of acrylic acid on polypropylene fiber after preliminary gamma irradiation was studied as influenced by the ratio of the concentration of peroxides formed during gamma irradiation (^{60}Co) of polypropylene in air to the Fe(II) concentration in the reaction solution. The ion-exchange and mechanical properties of monofunctional carboxylate cation exchanger prepared by the developed procedure were studied.

FIBAN K-4[1] fibrous cation exchanger is a polypropylene (PP) fiber with grafted acrylic acid (AA). Fibrous ion exchangers with carboxy groups are widely used to remove ammonia, amines, and alkali aerosols from air, and cations of nonferrous and heavy metals from water [1–5]. Commercial ion exchangers based on cellulose and polyamides are insufficiently stable in acid solutions, which complicates their regeneration. Fibrous polyacrylonitrile-based anion exchangers have good chemical and mechanical stability, but contain not only carboxy groups but also amidoamine, hydrazide, and ammonium groups. Hence, all technological prescriptions should be strictly followed in production of these ion exchangers and in their use for purification of tap water and also for medical and biological purposes.

From this standpoint, development of a simple and efficient procedure for preparing monofunctional carboxylate cation exchanger based on strong, chemically inert, and nontoxic fiber is an urgent problem. The initial polypropylene fiber chosen for this purpose was functionalized with carboxy groups by graft polymerization of acrylic acid. Granulated acrylic acid–methacrylic acid copolymers cross-linked with divinylbenzene and triacryloyltriazine are widely used in medicine and biology [6].

Several procedures for preparing PP fibers with grafted AA are known [7–9]. Tsetlin *et al.* [10] prepared these fibers by direct irradiation under AA vapor at reduced pressure. This fiber, named KATIOLAN, has good physicomechanical properties and is stable in repeated acid-alkali treatment. This fiber is successfully used in production of protective working outfit. At the same time, maintaining reduced pressure of AA in an installation exposed to gamma radiation is a complicated problem. Furthermore, the problem of efficient removal of the heat of grafting under these conditions has not been solved. This results in nonuniformity of fibers as regards the degree of grafting and exchange capacity. It should also be noted that grafting from an unsaturated AA vapor is a slow process.

EXPERIMENTAL

FIBAN K-4 sorbent was prepared by gamma irradiation of PP fiber with a ^{60}Co source in air, followed by liquid-phase graft polymerization of AA on peroxide groups of the PP in the presence of Fe(II) salts as reducing agents. We used the following starting materials: PP fiber (66-mm staple) with linear density of 0.33 tex, produced at Khimvolokno Kursk Production Association [TU (Technical Specifications) 6-06-535–76]; AA stabilized with Lauroks-9 (Shostka Chemical Plant); $FeSO_4$ and Mohr's salt of pure grade, ferrocene of technical grade; and iron(II) acrylate prepared from FeO and AA.

The starting PP staple was washed with benzene in a Soxhlet apparatus to remove the stabilizer and lubricant. The staple was irradiated on UGU-400 and RKhM γ-20 gamma irradiation units without tempera-

[1] This cation exchanger was developed at the Institute of Physical Organic Chemistry, Belarussian National Academy of Sciences, Minsk, Belarus.

1070-4272/01/7410-1658 $25.00 © 2001 MAIK "Nauka/Interperiodica"

ture control and without using additional equipment in the irradiation zone. The dose rate ranged from 0.5 to 4.7 Gy s^{-1}. The total radiation dose was 114 kGy. The content of peroxy and hydroperoxy groups in irradiated samples was determined by iodometric titration [11] after irradiation, during storage, and just before graft polymerization.

The graft polymerization was done from aqueous solutions of AA under nitrogen in the presence of iron(II) salts. The AA concentration ranged from 7.5 to 80 %. The iron(II) concentration was varied from 0.1 to 6.0 g l^{-1}, which corresponds to 0.05–0.60 g-equiv of iron(II) per 1 g-equiv of peroxy groups. The reaction temperature was varied from 353 K to the boiling point of the solution. The bath ratio (the ratio of liquid and solid phases) ranged from 7 to 100 ml g^{-1}. The degree of grafting was expressed as a percentage of the initial PP weight.

The properties of PP fibers were studied after both irradiation and grafting. The deformation-strength parameters of monofilament were measured on a UMIV-3 universal testing machine [12]. The acidity of the ion exchangers was determined by potentiometric titration [13]. The stability of the ion exchange fiber in aggressive media was characterized by GOST (State Standard) 10899–75 [14].

The synthesis of FIBAN K-4 cation-exchanger was performed as shown below

$$[-CH_2-\underset{\displaystyle CH_3}{\underset{|}{C}}H-]_n + O_2 \xrightarrow{\gamma\text{-ray}} [-CH_2-\underset{\displaystyle OOH}{\underset{|}{\overset{\displaystyle CH_3}{\overset{|}{C}}}}-]_m, \quad (1)$$

$$[-\underset{\displaystyle CH_3}{\underset{|}{C}}H_2-CH-OO-CH_2-]_p + CH_2=\underset{\displaystyle COOH}{\underset{|}{CH}}$$

$$\xrightarrow{Fe^{2+}} [-CH_2-\underset{\displaystyle COOH}{\underset{|}{CH}}-]_q + \text{PP-graft-AA (FIBAN K-4)}. \quad (2)$$

When PP fiber is irradiated with ^{60}Co gamma-rays (1), peroxy and hydroperoxy groups are formed in the sample. Their concentration was determined by iodometric titration on keeping the samples in a solution of sodium iodide in acetic anhydride at $T \geq 333$ K for no less than 10 min. Reaction (2) does not occur after this treatment, i.e., peroxy and hydroperoxy groups initiating this reaction are completely decomposed. After a similar treatment at room temperature for 0.5 h, as recommended in [11], the polymerization is still observed in the system, i.e., the initiating centers are preserved. In addition, the degree of grafting, *P*, and the amount of the homopolymer formed, *H*, are close to those for untreated PP fibers (e.g., *P* is 39 and 37%, and *H*, 1.0 and 0.8%, respectively).

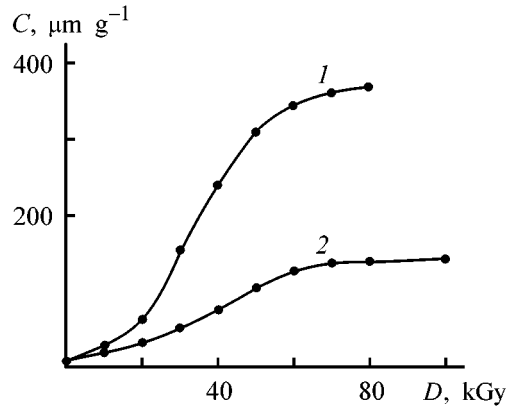

Fig. 1. Accumulation of peroxy and hydroperoxy groups in PP fiber at a dose rate of (*1*) 4.7 and (*2*) 0.5 Gy s^{-1}. (*C*) concentration and (*D*) radiation dose.

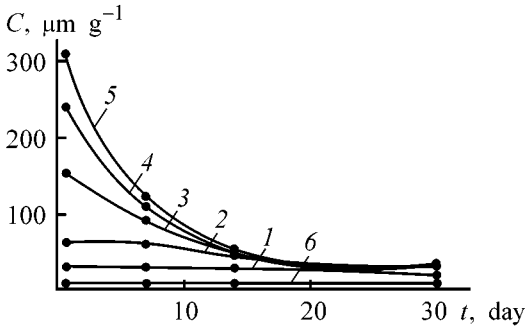

Fig. 2. Total concentration *C* of peroxy and hydroperoxy groups in PP fiber irradiated with (*1*) 10, (*2*) 20, (*3*) 30, (*4*) 40, and (*5*) 50 Gy and (*6*) in the unirradiated sample vs. time *t* of their storage in air at 277–278 K.

As seen from Fig. 1, the concentration of peroxy and hydroperoxy groups grows with increasing total radiation dose until equilibrium between their formation and degradation (individual for each dose rate) is attained. At a dose rate I = 0.5 Gy s^{-1}, the content of peroxy groups in the fiber levels off and reaches 120 μmol g^{-1} at a total radiation dose D = 60 kGy. At I = 4.7 Gy s^{-1}, the content of peroxy groups levels off at a total dose D = 70 kGy and reaches 360 μmol g^{-1}, which suggests the presence of a large number of reaction centers in the PP fiber.

Although peroxy groups are stable at ambient temperature [15], we found that their content in irradiated PP fibers decreases exponentially during their storage even in a refrigerator at 277–278 K (Fig. 2). The composition of irradiated PP fiber stored for 30 days approaches that of unirradiated samples. Hydroperoxy groups present in small amounts in the fiber are

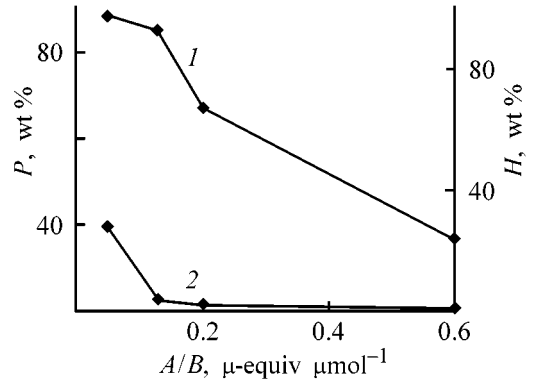

Fig. 3. (*1*) Degree of AA grafting, *P*, and (*2*) the amount of AA homopolymer, H, after polymerization from a 30% AA solution at 373 K for 3 h vs. the ratio of iron(II) concentration *A* to the content of peroxy groups in irradiated PP fiber, *B*.

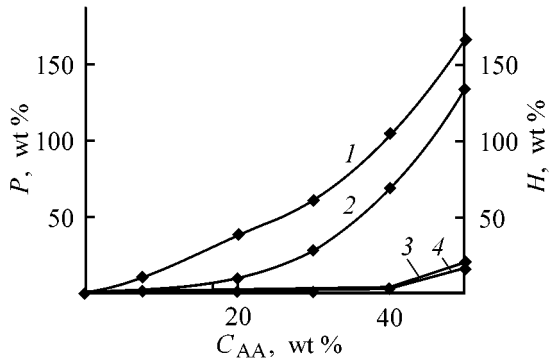

Fig. 4. (*1*, *2*) Degree of AA grafting, *P*, and (*3*, *4*) the amount of AA homopolymer, *H*, after graft polymerization at 373 K for 3 h vs. the AA concentration C_{AA} in the initial solution at a total concentration of peroxy and hydroperoxy groups of (*1*, *3*) 370 and (*2*, *4*) 269 μmol g^{-1}.

unstable even at low temperatures and decompose into radicals:

$$R\text{–}OOH \rightarrow RO^{\cdot} + OH^{\cdot}.$$

These radicals, in their turn, catalyze decomposition of the peroxy groups. To increase the efficiency of AA grafting, graft polymerization (2) should be performed as soon as possible after sample irradiation (1). Hence, the main features of graft polymerization (2) will be determined by the concentration of peroxy and hydroperoxy groups present in the sample by the time of grafting, rather than by the total radiation dose.

The graft polymerization and AA homopolymerization by reaction (2) strongly depend on the molar ratio of Fe(II) concentration in the solution, *A*, to the content of peroxy groups in irradiated PP fiber, *B*, and on the ratio of peroxy and hydroperoxy groups. As seen from Fig. 3, high degrees of AA grafting to PP at negligible formation of AA homopolymer are obtained in a narrow *A*/*B* range 0.1–0.2. If homopolymerization is initiated by OH radicals formed by decomposition of hydroperoxy groups, the content of peroxy groups initiating the graft polymerization should be 4–9 times higher than that of hydroperoxy groups which initiate to the same extent of both the graft polymerization and homopolymerization, even without taking into account the possibility of occurrence of chain-transfer reactions.

When ferrocene and Fe(II) acrylate were used as inhibitors, AA was grafted to PP fiber from an 80% aqueous solution of AA at 353 K [16]. With inorganic Fe(II) salts, the suitable AA concentration was 7.5–50 wt %. The homopolymer formation in the presence of ferrocene is 2–3 times more intensive than that in the presence of other Fe(II) compounds. Taking into account that Fe(II) acrylate is unstable in air, we used $FeSO_4$ and Mohr's salt for preparing experimental batches of grafted fiber.

Since the degree of AA grafting to PP fiber grows exponentially with increasing concentration of peroxy groups in PP, the influence of various factors on the graft polymerization was studied at rather high peroxy concentrations in a preirradiated PP fiber (C = 370 and 269 μg-equiv g^{-1}). The working concentration of AA in the solution ranged from 30 to 40% (Fig. 4). When the AA concentration is lower than 30%, the graft polymerization should be performed at higher content of peroxy groups in the starting fiber (about 400 μg-equiv g^{-1}). In solutions with AA concentration greater than, or equal to 50%, the homopolymer yield increases along with a sharp rise in the degree of grafting. In this case, it is difficult to wash out gelatinous polyacrylic acid (PAA) from the grafted fiber.

The theoretical static exchange capacities (SEC) of carboxylate ion exchangers were calculated from the degree of AA grafting to the PP fiber. The theoretical SECs for cations agree well with the experimental values. The difference between the theoretical and experimental SECs is no higher than 10% (SEC^t = 9.3 and SEC^e = 8.6 mg-equiv g^{-1}) even at high (200 wt %) degree of AA grafting to the PP fiber. This suggests the absence of cross-linking during the grafting and accessibility of all carboxy groups in the grafted fiber.

FIBAN K-4 fibrous carboxylate cation exchanger with SEC of up to 9 mg-equiv g^{-1} was prepared by the above procedure. The acid properties of the cation

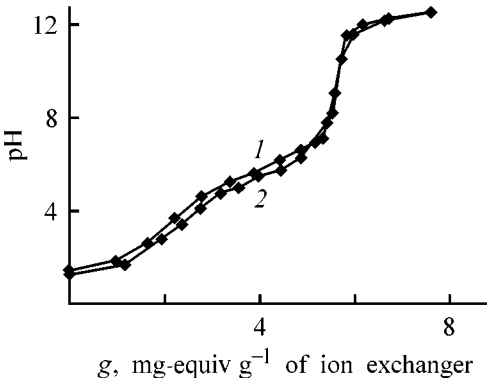

Fig. 5. (*1*) Direct and (*2*) back potentiometric titration of FIBAN K-4 cation exchanger. Supporting electrolyte 1 M KCl; initial excess of HCl 1.85 mg-equiv g^{-1}. (*g*) Amount of the titrating agent. Solid line and points represent calculated and experimental data, respectively.

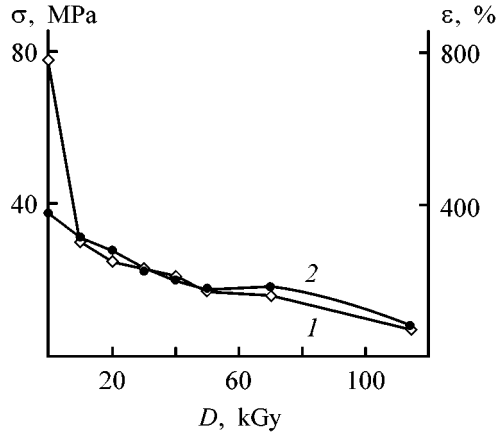

Fig. 6. (*1*) Elongation at break, ε, and (*2*) tensile strength σ of PP fibers vs. the total radiation dose *D*.

exchanger were estimated by theoretical processing of the results of its direct and back potentiometric titration (Fig. 5). Polypropylene fiber with a degree of AA grafting of 98.0% was titrated by the single portion procedure at an initial HCl excess of 1.85 mg-equiv g^{-1} per gram of fiber, using 1 M KCl as the supporting electrolyte. The titrating agent was added at 20-min intervals. The results of calculation of the potentiometric titration curves by Soldatov's procedure [18] allow estimation of the number, quantitative content, and acidity of the functional groups of anion exchanger. This estimation can be performed even when the potentometric titration curve has no pronounced inflection points owing to a large number of functional groups of different kinds in the sorbent and and small difference in their acidities. In this case, it is possible to determine the properties of the functional groups with the same chemical composition but different acidities owing to their different positions or the influence of the adjacent functional groups.

A theoretical processing of the experimental results of potentiometric titration of FIBAN K-4 cation exchanger showed that this fiber is a moderately acidic monofunctional cation exchanger containing carboxy groups with pK 5.3 (ΔpK 2).

The good mechanical properties of FIBAN K-4 ion exchangers and their stable operation in repeated sorption–regeneration cycles and on exposure to aggressive media are of great practical importance. These properties of ion exchangers depend on the conditions of irradiation and grafting, degree of grafting, and nature of reagent.

As seen from Table 1, the deformation strength properties of PP fibers change mainly in the stage of preliminary irradiation. As seen from Fig. 6, the tensile strength σ and elongation at break, ε, of PP monofilaments decrease mainly in the initial stage of irradiation at a total dose D = 30 kGy, which may be due to radiative-chemical oxidation of the strongest chains in the ordered fibers. Further increase in the radiation dose to 70 kGy deteriorates the deformation strength properties of PP fiber only slightly. At a radiation dose of 114 kGy the main parameter of fiber elasticity, the elongation at break, ε, decreases further, to 7%, and the tensile strength, to 80 MPa, which complicates the use of this material as a fiber. Therefore, we used for graft polymerization a PP fiber irradiated at a dose rate of 4 Gy s^{-1} to a total dose of 70 kGy. The content of peroxy groups in the fiber

Table 1. Dependence of the deformation-strength properties* of FIBAN K-4 cation exchangers on the AA concentration in the grafting solution, C_{AA}, and degree of grafting, P

Sample	C_{AA}, vol %	P, wt %	d, μm	F, cN	σ, MPa	ε, %
PP:						
initial	–	0	21	11.7	338	77
irradiated to 70 kGy	–	0	22	6.4	183	16.2
FIBAN K-4	80	98.7	32	7.2	90	22
	30	96.0	31	12.3	168	31
	30	128.0	31	9.8	135	23
	80	56.5	24	6.1	140	18
	80	201.0	33	9.1	102	59
	80	282.9	35	10.3	106	14

* d is the fiber diameter; F, σ, and ε are breaking force, tensile strength, and elongation at break.

Table 2. Resistance of FIBAN K-4 containing 96% PAA to aggressive media

Treatment conditions	SEC, mg-equiv g^{-1}	σ, MPa	ε, %	Treatment conditions	SEC, mg-equiv g^{-1}	σ, MPa	ε, %
Untreated cation exchanger	6.2(100)*	16.8(100)	31(100)	NaOH, 5 g-quiv l^{-1}	5.1(82)	14.6(87)	18(58)
H_2SO_4, 5 g-quiv l^{-1}	5.4(87)	15.8(94)	12(39)	H_2O_2, 10 wt %	3.6(58)	10.9(65)	11(36)

* The percentage relative to the initial value is given in parentheses.

ranges from 200 to 400 μmol g^{-1}, depending on the storage time of the irradiated product.

As seen from Table 1, the diameter *d*, breaking force *F*, and elongation at break of the monofilament grow appreciably with increasing degree of AA grafting to PP fiber (up to a degree of grafting of 201 wt %), i.e., the grafted polymer located in amorphous regions of PP fibers improves their mechanical properties. Thus, although the tensile strength of the fiber containing carboxy groups decreases to 9 MPa, this fiber remains sufficiently strong, elastic, and suitable for processing and practical application. The tensile strength σ and the elongation at break, ε, of the fiber can be raised by using 30%, instead of 80% AA solutions in step (2) (Table 1).

The data on the chemical stability of FIBAN K-4 cation exchanger with 96.0 wt % grafted PAA are presented in Table 2. In accordance with the requirements of GOST (State Standard) 10 899–75, a sample was heated on a boiling water bath with 5 N sulfuric acid or 5 N sodium hydroxide for 30 min and then treated with 10 % hydrogen peroxide for 48 h at room temperature. The SEC and tensile strength σ change in concentrated acids and alkalis only slightly, whereas the elongation at break, ε, significantly decreases, especially after treatment with sulfuric acid and hydrogen peroxide. The low stability of the cation exchanger in 10% hydrogen peroxide may be due to low stability of both the PP matrix and grafted PAA in oxidative media. In an additional experiment, we found that the exchange capacity and deformation-strength parameters of FIBAN K-4 cation exchangers do not change after threefold treatment in regenerating solutions (0.5 N HCl and 0.5 N NaOH) at 293 K. The exchange capacity decreases by a factor of 1.3–2.3 after prolonged operation of the cation exchanger in actual sorptionregeneration processes, e.g., in iron removal from water, involving regeneration with 2 N HCl.

The enhancement of the chemical stability and mechanical strength of FIBAN K-4 fibrous cation exchanger is necessary for prolonged multicycle operation of the fiber in aggressive media. Nevertheless, FIBAN K-4 fibrous cation exchanger can be used for additional treatment of water to remove heavy metal cations.

An experimental batch of FIBAN K-4 fibrous cation exchanger with SEC = 4.5 ± 0.2 mg-equiv g^{-1} was prepared by the above procedure. Nonwoven needle-punched material was prepared from the fiber and used in composition of cartridges for Krynichka and Mifil filters for purification of potable water.

CONCLUSIONS

(1) FIBAN K-4 fibrous monofunctional cation exchanger containing carboxy groups with p*K* 5.3 (Δp*K* 2.0) was prepared.

(2) In graft polymerization of acrylic acid to the fiber at 373 K in inert atmosphere the best molar ratio of Fe(II) to peroxide groups in the irradiated polypropylene fiber is 0.1–0.2.

(3) Preferable inhibitors of acrylic acid homopolymerization are $FeSO_4$ and Mohr's salt.

(4) The ion-exchange and mechanical properties of the cation exchanger allow its use in filters for additional purification of potable water.

REFERENCES

1. Vol'f, L.A., in *Volokna s osobymi svoistvami* (Fibers with Special Properties), Moscow: Khimiya, 1980, pp. 10–114.
2. Zverev, M.P., *Khemosorbtsionnye volokna* (Chemisorption Fibers), Moscow: Khimiya, 1981.
3. Emets, L.V. and Vol'f, L.A., *Ionnyi obmen* (Ion Exchange), Senyavin, M.M., Ed., Moscow: Nauka, 1981, pp. 82–91.
4. Ogorodnikov, V.A., Soldatov, V.S., and Shunkevich, A.A., *Vestsi Nats. Akad. Navuk. Bel., Ser. Khim. Navuk*, 2000, no. 1, pp. 116–119.
5. Soldatov, V.S., Sergeev, G.I., Martsinkevich, R.V., and Shunkevich, A.A., *Zh. Prikl. Khim.*, 1991, vol. 64, no. 12, pp. 2506–2510.
6. Shataeva, L.K., Kuznetsova, N.N., and El'kin, G.E.,

Karboksil'nye kationity v biologii (Carboxylic Cation Exchangers in Biology), Leningrad: Nauka, 1979.

7. U Zhun Zhui, Stasyuk, Kh.A., Kocherginskaya, L.A., *et al.*, *Khim. Volokna*, 1963, no. 5, pp. 12–15.
8. Klein, G.A., Osipova, L.Kh., Tikhomolova, M.P., and Filippov, A.N., *Deistvie yadernykh izluchenii i radiatsionnaya privivka na voloknakn* (Action of Nuclear Radiation and Radiation Grafting on Fibers), Moscow: Legkaya Industriya, 1968.
9. Boldyreva, M.I., Blasov, A.V., Egorov, E.V., *et al.*, *Tr. Inst. Khim. Reakt. Osobochist. Veshch., Khim. Reakt. Prepar.*, 1972, issue 34, pp. 54–59.
10. Malakhova, L.I., Vlasov, A.V., Mikhailov, N.V., and Tsetlin, B.L., *Vysokomol. Soedin., Ser. A*, 1972, vol. 14, no. 4, pp. 751–755.
11. Guben-Veil', *Metody organicheskoi khimii*, (Methods of Organic Chemistry), Moscow: Goskhimizdat, 1963, vol. 2.
12. Popova, O.P., Shunkevich, A.A., Prokopchuk, N.R., and Belotserkovskaya, T.N., *Khim. Volokna*, 1985, no. 4, pp. 28–30.
13. *Fiziko-khimicheskie metody analiza* (Physicochemical Methods of Analysis), Aleskovskii, V.B, and Yatsimirskii, K.B., Eds., Leningrad: Khimiya, 1971.
14. Soldatov, V.S., Tsygankova, A.V., Elinson, I.S., *et al.*, *Vestsi Akad. Navuk Bel. SSR, Ser. Khim. Navuk*, 1986, no. 4, pp. 15–21.
15. Finkel', E.E. and Braginskii, R.P., *Radiatsionnaya khimiya polimerov* (Radiation Chemistry of Polymers), Kargin, V.A., Ed., Moscow: Nauka, 1973, pp. 186–305.
16. Dmitrenko, A.V., Mesh, A.M., and Zamyslov, R.A., *Vysokomol. Soedin., Ser. A*, 1990, vol. 32, no. 3, pp. 542–547.
17. Soldatov, V.S., *Ind. Eng. Chem. Res.*, 1995, vol. 34, no. 8, pp. 2605–2611.
18. Soldatov, V.S., *Dokl. Akad. Nauk Bel.*, 1995, vol. 39, no. 1, pp. 48–52.

Russian Journal of Applied Chemistry, Vol. 74, No. 10, 2001, pp. 1664–1667. Translated from Zhurnal Prikladnoi Khimii, Vol. 74, No. 10, 2001, pp. 1614–1617.

SORPTION AND ION-EXCHANGE PROCESSES

Extraction of Arsenic(V) with Hexabutylphosphoric Triamide

V. F. Travkin, Yu. M. Glubokov, E. V. Mironova, and V. V. Yakshin

Lomonosov Moscow State Academy of Fine Chemical Technology, Moscow, Russia,
State Production Center, Gintsvetmet Institute, Moscow, Russia

Received December, 1999; in final form, May 2001

Abstract—The effects of the concentrations of sulfuric acid and arsenic in the aqueous phase, concentration of the extractant in the organic phase, temperature, and time of phase contact on arsenic(V) extraction with hexabutylphosphoric triamide were studied, and the arsenic(V) extraction constant was calculated.

Liquid extraction is widely used for recovery of arsenic from sulfuric acid solutions [1]. Various compounds, such as tributyl phosphate (TBP) [2, 3], amines [3] and tertiary ammonium [4] salts, trioctylarsine oxide [5], etc., have been proposed as extractants. The extraction of As(V) compounds from copper- and nickel-containing sulfuric acid solutions has been studied is most detail [6, 7], because the extractive purification of copper electrolyte to remove arsenic is performed on the industrial scale. At foreign plants, TBP is used as an extractant [8]. Presumably, other extractants may be more efficient for extractive recovery of arsenic.

In sulfuric acid solutions, arsenic(V) exists in the form of arsenic acid derivatives. The extractive recovery of As(V) can proceed by both anion-exchange and hydrate-solvate mechanisms. In the first case, extraction is performed with amines or substituted ammonium salts, and in the second case, with neutral organophosphorus compounds $X_3P{=}O$ (X = R, RO, R_2N). The stability of the extractable complexes strongly depends on the basicity of the oxygen atom in the phosphoryl group. Usually both the basicity and the extractive power of compounds with active phosphoryl group increase in the order $(RO)_3P{=}O < RP(O)(OR)_2 < R_2P(O)OR < R_3P{=}O$. High-molecular-weight phosphine oxides ($R \geq C_8H_{17}$) are the most efficient extractants of arsenic(V) in this series. The basicity of phosphoryl oxygen becomes even higher when phosphoric acid amides $(R_2N)_3P{=}O$ are used [8, 9]. This effect is due to a decreasing bond order in the phosphoryl fragment, as a result of competition of nitrogen atoms for 3*d* orbitals of the phosphorus atom and appearance of additional electron density at the phosphoryl oxygen. Yakshin *et al.* [8], determined experimentally the basicity of phosphoric acid amides by potentiometric titration with perchloric acid in nitromethane and found that pK_a increases from 8.75 for tributylphosphine oxide to 9.15 for hexabutylphosphoric triamide (HBPTA). Taking this circumstance into account, we can expect a greater extractive power of phosphoric acid amides with respect to As(V).

In this work, the main features of extraction of As(V) from copper-containing sulfuric acid solutions, with HBPTA as an extractant, were studied.

EXPERIMENTAL

The extractant contained no less than 98–99% of the main substance. The extraction was performed from sulfuric acid solutions containing 4–5 g l^{-1} As(V) at 1 : 1 organic to aqueous phase ratio, stirring time of 10 min, and temperature of $20 \pm 1°C$.

The distribution of As(V) between the aqueous phase and 1.1 M HBPTA solution in kerosene as a function of H_2SO_4 concentration is shown in Fig. 1.

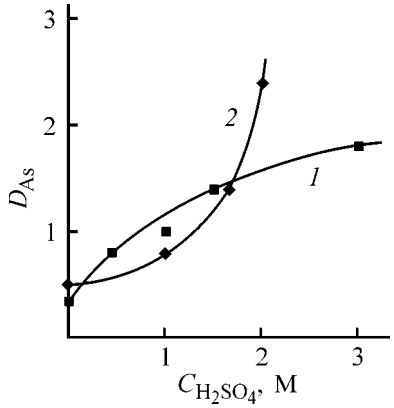

Fig. 1. Effect of sulfuric acid concentration $C_{H_2SO_4}$ on extraction of As(V) with (*1*) TBP and (*2*) 1.1 M HBPTA solution in kerosene. (D_{As}) As(V) distribution coefficient.

1070-4272/01/7410-1664 $25.00 © 2001 MAIK "Nauka/Interperiodica"

As seen, similarly to extraction with TBP, the As(V) recovery grows with increasing H_2SO_4 concentration. The greater basicity of HBPTA ensures As(V) extraction even from weakly acidic solutions. The As(V) recovery with HBPTA from H_2SO_4 aqueous solutions with concentration exceeding 1.5 M is greater than that in the case of TBP.

The dependence of the As(V) distribution coefficients D_{As} on the extractant (HBPTA, TBP) concentration in extraction from 1.7 M H_2SO_4 is shown in Fig. 2. The processing of the experimental data by means of the least-squares method gives the following dependences of D_{As} on the concentration of the unbound extractant:

$$\log D_{As} = 1.90 \log [HBPTA]_{ub} + 0.35, \quad (1)$$

$$\log D_{As} = 2.46 \log [TBP]_{ub} + 0.47, \quad (2)$$

where $[S]_{ub} = [S]_{in} - q[H_3AsO_4]_0 - [H_2SO_4]_0$.

The correlation coefficient for Eqs. (1) and (2) is 0.98.

It follows from Eqs. (1) and (2) that the solvation number q for HBPTA is lower than that for TBP. The obtained solvation numbers suggest that HBPTA recovers arsenic acid mainly in the form of disolvate, while TBP recovers it as a mixture of di- and trisolvates. In the latter case, extraction of a mixture of mono-, di-, and trisolvate is possible. Data of [3] confirm this possibility.

It should be noted that the increase in the As(V) extractive recovery with growing extractant concentration in the organic phase is limited by phase separation.

The reaction of As(V) extraction from sulfuric acid solutions with HBPTA can be represented as follows:

$$m(H^+ + HSO_4^-)_{aq} + nH_3AsO_{4(aq)} + q(HBPTA \cdot hH_2O)_o \rightleftarrows (nH_3AsO_4 \cdot mH_2SO_4 \cdot h_0H_2O \cdot qHBPTA)_o + (h - h_0)H_2O_{aq}. \quad (3)$$

The concentration constants of extraction of arsenic acid with HBPTA and TBP were determined as the slope of the extraction isotherms measured for As(V) dilute solutions at constant H_2SO_4 concentration (Fig. 3). The concentration extraction constants K_{ex} obtained by the least-squares method are listed in Table 1. The correlation coefficient for both extractants is 0.99.

The constant of extraction of arsenic acid from sulfuric acid solutions increases from TBP to HBPTA in parallel with a rise in the extractant basicity.

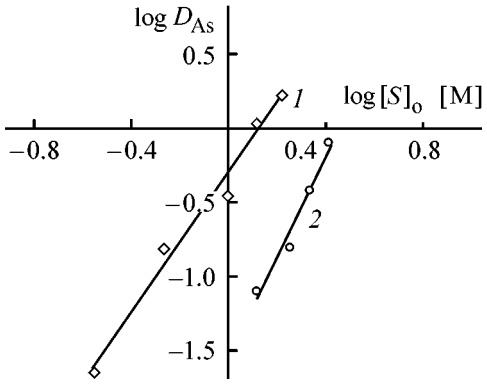

Fig. 2. As(V) distribution coefficient D_{As} vs. extractant concentration in kerosene $[S]_o$: (*1*) HBPTA and (*2*) TBP.

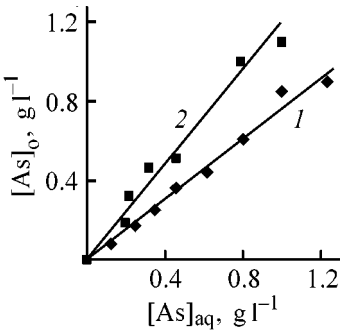

Fig. 3. Isotherms of As(V) extraction from 1.5 M H_2SO_4 with (*1*) TBP and (*2*) 1.1 M HBPTA solution in kerosene. ($[As]_o$, $[As]_{aq}$) As(V) concentrations in the organic and aqueous phases, respectively.

The IR spectrum of HBPTA contains two intense bands ν(P=O) at 1210 cm^{-1} and ν(C–N) at 1180 cm^{-1}. They shift to 1190 and 1170 cm^{-1}, respectively, when arsenic(V) and sulfuric acid are introduced. In addition, new bands characteristic of H-bonded hydroxy groups appear at 1640–1670 cm^{-1}. These changes result from the formation of arsenic acid hydrate-solvates in the organic phase. It is difficult to reveal the ν(As–O) bands because of the superposition of other bands and first of all those of ν(P–N) and ν(C–N). The data obtained show that amide groups hardly participate in coordination with As(V).

Table 1. Characteristics of extraction of arsenic acid ($[As]_o = K_{ex}[As]_{aq} + a$)

Extractant	$[H_2SO_4]_{aq}$	K_{ex}	a
	M		
TBP, 3.66	1.67–1.73	0.76	-7.45×10^{-3}
HBPTA, 1.64 in kerosene	1.73–1.77	1.15	0.07

Table 2. Effect of temperature on extraction of As(V) with 1.1 M HBPTA solution in kerosene*

T, °C	As(V) recovery, %	D_{As}
20	43.2	0.76
35	37.9	0.61
45	32.0	0.47
55	27.1	0.38
64	23.3	0.29

* $C^0_{As} = 0.1$, $C^0_{H_2SO_4} = 2.4$ M.

Table 3. Effect of stirring time τ on extraction of As(V) with 1.1 M HBTA solution in kerosene*

τ, min	Concentration, g l^{-1}				D_{As}
	aqueous phase*		organic phase*		
	As(V)	H_2SO_4	As(V)	H_2SO_4	
1	4.8	227	2.6	9.2	0.54
2	4.5	226	2.9	11.0	0.64
3	4.2	223	3.1	14.0	0.74
5	4.2	226	3.1	10.0	0.74
10	4.2	227	3.2	10.0	0.76
30	4.2	226	3.1	11.0	0.74

* Equilibrium phases.

Table 4. Distribution of components of the initial sulfuric acid solution between raffinate and backwash in extraction of As(V) with HBPTA

Component extracted	Concentration, g l^{-1}		
	initial solution	raffinate	backwash
As(V)	4.10	1.68	1.81
H_2SO_4	209	201	6.9
Cu(II)	29.6	29.8	0.01
Fe(III)	1.10	1.12	0.01
Fe(total)	1.85	1.84	≤0.01
Sb(III)	0.07	0.07	0.001
Ni(II)	11.8	11.7	0.02
Zn(II)	1.50	1.52	0.005
Co(II)	0.60	0.59	0.001

One of important factors influencing the As(V) recovery is the extraction temperature. A special experiment showed that the arsenic distribution coefficient decreases with increasing temperature (Table 2); for instance, in the range from 20 to 60°C it decreases threefold.

The kinetic parameters of As(V) extraction with HBPTA and TBP differ. Extraction with TBP is characterized by faster transfer of As(V) into the organic phase [10] (Table 3) which is probably due to a larger size of the HBPTA molecule as compared with TBP.

Our results show that the equilibrium of extraction with HBPTA is attained within 3 min.

Data on the extraction of concomitant metals present in the copper electrolyte with 1.5 M HBPTA in kerosene are presented in Table 4. Backwashing was performed with 5% aqueous solution of sodium sulfate at 1 : 1 volume ratio of aqueous to organic phase, stirring for 2 min, and 22 ± 1°C.

Thus, HBPTA, similarly to TBP, extracts only As(V) and sulfuric acid. Coextraction of H_2SO_4 does not exceed 3–4% in a single extraction stage. The counter-current regime of extraction ensures a high degree of purification to remove arsenic(V). For instance, in three stages of countercurrent extraction, the As(V) recovery from the aqueous phase under the above conditions amounts to 84%.

The studies performed allow recommendation of the following scheme for extractive purification of copper electrolyte to remove As(V), with HBPTA as extractant (see scheme).

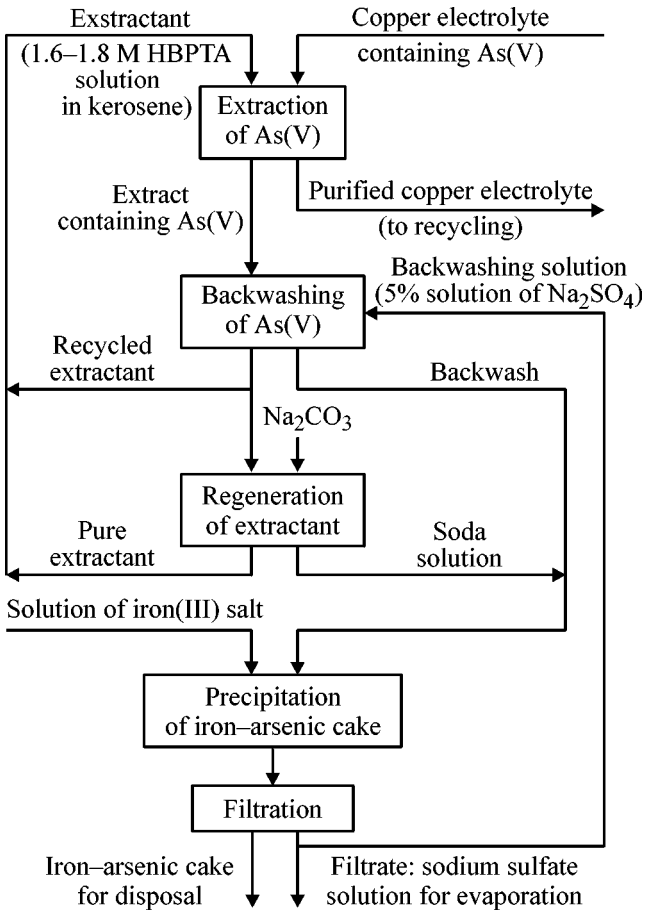

The extraction process includes the following operations: extraction of As(V) with 1.6–1.8 M HBPTA solution in kerosene [3–5 stages of countercurrent extraction, volume ratio of the organic to aqueous phase (1–1.5) : 1, 25–30°C, time of phase contact 3 min], backwashing of As(V) from the organic phase with 5% aqueous solution of Na_2SO_4 [2–3 stages, volume ratio of the organic to aqueous phase (1–2) : 1, 30–40°C, time of phase contact 3 min], and separation of As(V) in the form of a poorly soluble product (e.g., calcium or iron arsenate) followed by its disposal or conversion to a commercial product (copper arsenate).

In this case, the degree of copper electrolyte purification is 80–90%. The electrolyte can be returned to copper electrolysis or directed to copper sulfate production. The optimal concentration of sulfuric acid in the aqueous phase for As(V) extraction with HBPTA is about 2 M.

Laboratory tests of the above process were performed with an electrolyte containing 11.2 g l^{-1} As and 220 g l^{-1} H_2SO_4 to give raffinates containing 1.2 g l^{-1} As(V) and 189 g l^{-1} H_2SO_4. The content of As(V) and H_2SO_4 in the backwash was 14.3 and 37 g l^{-1}, respectively. The recycling organic phase directed to extraction contained 0.3 g l^{-1} As and 1.1 g l^{-1} H_2SO_4. Thus, the process proposed ensures high degree of arsenic removal at small loss of sulfuric acid.

CONCLUSION

Hexabutylphosphoric triamide is more efficient extractant of As(V) than TBP in extraction from aqueous H_2SO_4 solutions with concentrations of 1.5 M and more. Arsenic is extracted with HBPTA solution in kerosene in the form of mixed hydrate-solvate. The degree of As(V) extraction decreases with increasing temperature. A flowsheet is proposed for As(V) extractive recovery from copper electrolyte with HBPTA solution in kerosene, ensuring high degree of arsenic removal from the electrolyte.

ACKNOWLEDGMENTS

The authors thank V.V. Kravchenko and A.N. Kravchenko for assistance.

REFERENCES

1. Ritcey, G.M. and Ashbrook, A.W., *Solvent Extraction. Principles and Applications to Process Metallurgy*, Amsterdam: Elsevier, 1979.
2. Nagai, T., Yamazaki, N., and Kobayashi, V., *J. Mining Met. Inst. Japan*, 1985, vol. 101, no. 11, pp. 537–543.
3. Giganov, G.P., Travkin, V.F., Kravchenko, V.V., *et al.*, *Zh. Neorg. Khim.*, 1988, vol. 33, no. 8, pp. 2073–2079.
4. Cohen, J.M., *Extraction of Metals, 85: Papers of Symp.*, London, September 9–12, 1985, p. 951.
5. Laskorin, B.N., Yakshin, V.V., Travkin, V.F., *et al.*, *Dokl. Akad. Nauk SSSR*, 1985, vol. 281, no. 4, pp. 900–903.
6. Giganov, G.P., Travkin, V.F., Kravchenko, V.V., *et al.*, Abstracts of Papers, *Vsesoyuznoe soveshchanie po primeneniyu ekstraktsii v tekhnologii neorganicheskikh veshchestv* (All-Union Conf. on Use of Extraction in Technology of Inorganic Substances), Apatity, September 23–25, 1986, p. 22.
7. Karimov, E.V., Birkin, K.N., Travkin, V.F., *et al.*, *Tsvetn. Met.*, 1990, no. 7, pp. 55–57.
8. Yakshin, V.V., Tymanyuk, M.N., Sokal'skaya, L.I., *et al.*, *Dokl. Akad. Nauk SSSR*, 1979, vol. 247, no. 1, pp. 128–132.
9. Smirnov, N.P., Lebedev, V.N., Yakshin, V.V., *et al.*, Abstracts of Papers *VII Vsesoyuznaya konferentsiya po khimii ekstraktsii* (VII All-Union Conf. on Extraction Chemistry), Moscow, November 12–14, 1984, Moscow: Nauka, 1984, pp. 63–64.
10. Pushkov, A.A., Lanin, V.P., Travkin, V.F., *et al.*, *Tr. Mosk. Khim.-Tekhnol. Inst. im. D.I. Mendeleeva*, 1986, issue 143, pp. 38–42.

Russian Journal of Applied Chemistry, Vol. 74, No. 10, 2001, pp. 1668–1671. Translated from Zhurnal Prikladnoi Khimii, Vol. 74, No. 10, 2001, pp. 1618–1621.

SORPTION AND ION-EXCHANGE PROCESSES

Extraction of Aromatic Hydrocarbons with Triethylene Glycol–Sulfolane Mixed Extractant

A. A. Gaile, A. S. Erzhenkov, L. V. Semenov, O. M. Varshavskii, G. D. Zalishchevskii, V. E. Somov, and N. B. Marusina

St. Petersburg State Technological Institute, St. Petersburg, Russia

Kirishinefteorgsintez Production Association, Limited Liability Company, Kirishi, Leningrad oblast, Russia

Received May 16, 2001

Abstract—Comparative analysis is made of the operation of an extraction block of the LG 35-8/300B benzene reforming unit (Kirishinefteorgsintez Production Association) before and after its upgrade (with triethylene glycol–sulfolane–water mixed extractant used instead of straight triethylene glycol).

It has been demonstrated previously [1–5] that the use of triethylene glycol–sulfolane–water mixed extractant instead of straight triethylene glycol (TEG) for extraction of aromatic hydrocarbons C_6–C_8 from reforming naphthas allows an increase in both the selectivity and solvency of the extractant. As a result of such a modification, the extractant : feed ratio can be decreased, and the degree of recovery of aromatic hydrocarbons from the reforming naphtha, increased.

In 2000–2001, the indicated mixed extractant was introduced in LG 35-8/300B benzene reforming unit (Kirishinefteorgsintez Production Association). The sulfolane content in the extractant was gradually brought to 15 wt %. In this communication, we report on a comparative analysis of the unit operation before and after upgrade.

Before the upgrade, watered crude TEG was used as an extractant. Its composition was as follows (wt %): water 6.0, ethylene glycol 0.7, diethylene glycol 4.4, TEG 88.4, and tetraethylene glycol 0.5.

The mixed extractant composition, extractant : feed ratio (stable reforming naphtha), and also parameters of extraction of aromatic hydrocarbons before and after upgrade are summarized in Table 1. The tem-

Table 1. Parameters of extraction of aromatic hydrocarbons on LG 35-8/300B benzene reforming unit with TEG and TEG–sulfolane extractants

Parameter	Before upgrade	After upgrade	
		January 2000	March 2001
Extractant composition, wt %:			
crude TEG	94	79	79
sulfolane	–	15	15
water	6	6	6
Extractant : feed (by weight)	8 : 1	6.5 : 1	7.9 : 1
Recycle : feed (by volume)	1 : 1	0.8 : 1	1 : 1
Total degree of recovery of arenes, wt %, including	96.4	96.4	98.5
benzene	99.7	99.7	99.8
toluene	95.9	95.5	98.3
xylenes	72.3	81.6	82.4
Content of target component in commercial products, wt %:			
benzene	99.84	99.78	99.84
toluene	99.94	99.96	99.98
xylenes	99.50	99.50	99.50

1070-4272/01/7410-1668 $25.00 © 2001 MAIK "Nauka/Interperiodica"

Table 2. Parameters of single-step extraction with water of TEG and sulfolane from simulated hydrocarbon mixtures at 45°C (water : feed weight ratio 0.05 : 1)

Hydrocarbon mixture, wt % : wt %	Solvent	Extractant content, wt %			k	α, %
		initial mixture	raffinate	aqueous phase		
Heptane–toluene, 99 : 1	TEG	0.09	–	1.64	–	100
	Sulfolane	0.20	0.007	3.94	563	96.8
Benzene–toluene–*m*-xylene,	TEG	0.36	0.019	6.02	317	94.7
59 : 46.6 : 3.4	Sulfolane	0.15	0.023	2.31	100	85.0

Note: (k) Extractant distribution coefficient and (α) degree of recovery.

perature in the extraction and extractant regeneration columns remained unchanged. The results show that the use of the mixed extractant allowed reduction of the extractant : feed and recycle : feed ratios by about 20%, with the total degree of recovery and the product quality remaining practically unchanged, which is due to increased selectivity and solvency of the mixed extractant with respect to arenes. The possibility of diminishing the recycle consumption is due to a stronger intermolecular interaction of sulfolane with arenes. As a result, the benzene and toluene concentrations in the recycle decrease. The decrease in the extractant and recycle consumption allows an increase in the extractor efficiency with respect to the feed by 20%, and also a decrease in the specific power consumption for recovery of arenes.

In another operation mode of the extraction block (March 2001), when the mixed extractant : feed and recycle : feed ratios were the same as with the use of straight TEG, the total degree of recovery of arenes increased by 2.1 wt %. The most significant increase was achieved with respect to recovery of toluene and xylenes (by 2.4 and 10.1 wt %, respectively), which is due to the lower molecular-weight selectivity of sulfolane and, correspondingly, of the mixed extractant as compared with TEG. For example, at 150°C the molecular-weight selectivity [logarithm of the ratio of the limiting activity coefficients of octane and heptane in the extractant $\log(\gamma^0_{oct}/\gamma^0_{hpt})$] is 0.08 and 0.13 for sulfolane and TEG, respectively [6]. The lower molecular-weight selectivity, along with an increased group selectivity with respect to arenes, allows more efficient extraction with the mixed extractant of not only benzene, but also higher-boiling arenes from fractions with relatively wider boiling ranges. At a potential output of 300 000 t with respect to the feed, an 85–87 wt % yield of stable naphtha, and a 40–45 wt % content of arenes C_6–C_8 in it [7], the unit can additionally produce 2.2–2.4 thousand tons of aromatic hydrocarbons annually.

In the initial period of operation of the unit on the mixed extractant, an increased loss of sulfolane, compared with that of TEG, was found in the raffinate and, to an even higher extent, in the extract, which, unlike the raffinate phase, is not subjected to aqueous washing. The increased sulfolane content in the extract is due to a number of factors. The first among these is the unfortunate flowsheet of the extraction block in the LG 35-8/300B unit, according to which the recycle and extract are steam-distilled not in separate columns (as is done in the process of arene extraction with individual sulfolane), but in a single column with removal of the extract as a sidecut distillate. The second factor is the flatter temperature dependence of the saturated sulfolane vapor pressure: at 150°C (temperature of regeneration of the extractants from the extract phase) the saturated vapor pressure of sulfolane is twice that of TEG, despite the virtually the same standard boiling points [8]. Finally, the third factor is the stronger positive deviation from the Raoult's law in the water–sulfolane system as compared with the water–TEG system (in the first system, the excess Gibbs energy ΔG^E_{max} exceeds 1 kJ mol^{-1} at 30°C [9]).

The efficiency of aqueous stripping of TEG and sulfolane was preliminarily tested on model hydrocarbon mixtures. As a system simulating the composition of the raffinate phase served a heptane–toluene mixture (99 : 1 by weight) containing small amounts of TEG and sulfolane. The extract was simulated with a benzene–toluene–*m*-xylene system with small amounts of the same extractants. The results show (Table 2) that TEG and sulfolane can be virtually totally recovered from the raffinate phase by single-stage stripping. The distribution coefficients of TEG and sulfolane between the simulated extract phase and aqueous phase are considerably lower, which is due to a strong specific interaction of arenes with the mixed extractant components. Correspondingly, the degree of recovery of TEG and, especially, sul-

Table 3. Parameters of aqueous stripping of extractants from the raffinate phase and also from xylenes (weight ratio water : raffinate phase = 0.05 : 1, water : xylenes = 1 : 1)

Solvent	Solvent content, wt %			
	raffinate phase	raffinate	xylenes before stripping	xylenes after stripping
Diethylene glycol	0.001	< 0.001	0.01–0.05	0.001–0.003
TEG	0.015	0.005	0.12–0.13	0.005
Sulfolane	0.09	0.004–0.010	4.3–5.7	0.008–0.02

folane from arene-containing mixtures is insufficiently high.

Since an increase in the water : extract weight ratio is undesirable because of the higher power consumption for the subsequent evaporation of excess water, the aqueous stripping block was upgraded so that it became possible to strip TEG and sulfolane not from the extract phase, but from the toluene column bottoms in which xylene and even higher-boiling TEG and sulfolane are concentrated. Since the xylene fraction in the extract is only 3–6 wt %, the volume of aromatic feed going to aqueous stripping is reduced by a factor of about 15–30. Another advantage is that aqueous stripping of polar solvents from xylene solutions is more efficient than that from mixtures with benzene or toluene, since xylene-containing systems are characterized by higher degree of nonideality. For example, at 35°C the limiting activity coefficients in the system oxylene (1)–sulfolane (2) are $\gamma_1^0 = 6.99$ and $\gamma_2^0 = 13.2$ [10], while the limiting activity coefficient of benzene in sulfolane is 2.4 [11].

In aqueous washing of concentrates of TEG and sulfolane in xylene, instead of those in the extract phase, the tendency of the system to form emulsions decreases as a result of, first, a decrease in the mutual solubility of xylenes, compared with benzene and toluene, in aqueous sulfolane and TEG solutions and, second, an increase in the difference between the phase densities from 130 to 150 kg m^{-3}.

The data on aqueous stripping of TEG and sulfolane after the upgrade of the unit show that, despite high sulfolane concentration in xylenes, their low consumption makes it possible to increase the water : xylenes ratio to 1 : 1 and to achieve a tolerable level of TEG and sulfolane losses (Table 3). Thus, at the rated feed load of the unit, the sulfolane loss with the raffinate and xylenes is estimated at 6–15 and 0.4–0.9 t per year, respectively; and the TEG loss, at 7–8 and 0.2–0.4 t per year. The estimated total loss of the extractants due to insufficiently effective aqueous stripping is 0.14–0.24 kg per ton arene product. A similar level of loss is typical of other arene extraction processes. For example, in the Aromex process with *N*-formylmorpholine, the loss is 0.16 kg extractant per ton of arenes [12]. If aqueous stripping of sulfolane were performed from the overall extract, instead of the xylene fraction, its estimated loss would be as high as 25–35 t per year, and, without aqueous stripping at all, as high as 170–250 t per year. Further reduction in the sulfolane and TEG loss in performing aqueous washing of xylenes with mainly the raffinate is possible by lowering the temperature of the extractant fed into the extractor. Compared with that of aqueous TEG, the increased solvency of the mixed extractant TEG–sulfolane–water with respect to arenes and its lower viscosity make it possible to lower the temperature in the upper section of the reactor from 145–150 to 120°C; in this case, the extractant content in the raffinate phase must decrease.

Further improvement of the efficiency of arene extraction is planned to be achieved by raising the sulfolane fraction in the mixed extractant.

CONCLUSIONS

(1) The extraction of benzene, toluene, and xylenes from the 62–105°C reforming naphtha fraction with mixed triethylene glycol–sulfolane–water extractant containing 15 wt % sulfolane, instead of straight triethylene glycol, at the LG 35-8/300B benzene reforming unit (Kirishinefteorgsintez Production Association) allowed an increase by 2.1 wt % in the total degree of recovery of aromatic hydrocarbons or reduction of the extractant : feed and recycle : feed ratios by 20%.

(2) The loss of sulfolane and TEG with the extract were reduced to a tolerable level as a result of the upgrade of the aqueous washing block, in which provision is made for stripping of TEG and sulfolane not from the extract phase, but from toluene column bottoms.

REFERENCES

1. Marusina, N.B., Gaile, A.A., and Semenov, L.V., *Zh. Prikl. Khim.*, 1994, vol. 67, no. 8, pp. 1311–1315.
2. Marusina, N.B., Gaile, A.A., and Semenov, L.V., *Zh. Prikl. Khim.*, 1996, vol. 69, no. 7, pp. 1163–1169.
3. RF Patent 2 127 718.
4. Gaile, A.A., Somov, V.E., Varshavskii, O.M., and Semenov, L.V., *Sul'folan: svoistva i primenenie v kachestve selektivnogo rastvoritelya* (Sulfolane: Properties and Applications as a Selective Solvent), St. Petersburg: Khimizdat, 1998.
5. Gaile, A.A., Somov, V.E., and Varshavskii, O.M., *Aromaticheskie uglevodorody: vydelenie, primenenie, rynok* (Aromatic Hydrocarbons: Separation, Applications, and Market), St. Petersburg: Khimizdat, 2000.
6. Lanery, L., *Bull. Assoc. Frans. Techn. Petrole*, 1964, no. 164, pp. 165–185.
7. Bannov, P.G., *Protsessy pererabotki nefti* (Oil Refining Processes), Moscow: TsNIITEKhim, 2000.
8. Deal, C.H., Evans, H.D., Oliver, E.D. and Papandopulos, M.N., *V Mezhdunar. neftyanoi kongress* (V International Congress on Petrol), Moscow: Gostoptekhizdat, 1961, vol. 3, pp. 107–124.
9. Benoit, R.L. and Choux, G., *Can. J. Chem.*, 1968, vol. 46, no. 20, pp. 3215–3219.
10. Shcherbina, A.E., Selectivity of Hydrocarbon Separation with Binary Solvents, *Doctoral Dissertation*, Minsk, 1987.
11. Gaile, A.A., Parizheva, N.V., and Proskuryakov, V.A., *Zh. Prikl. Khim.*, 1974, vol. 47, no. 1, pp. 191–194.
12. Stein, M., *Hydrocarbon Process.*, 1973, vol. 52, no. 4, pp. 139–141.

Russian Journal of Applied Chemistry, Vol. 74, No. 10, 2001, pp. 1672–1677. Translated from Zhurnal Prikladnoi Khimii, Vol. 74, No. 10, 2001, pp. 1622–1627.

APPLIED ELECTROCHEMISTRY AND CORROSION PROTECTION OF METALS

Redox Potentials of Samarium and Europium in Molten Cesium Chloride

A. V. Novoselova, V. A. Khokhlov, and V. Yu. Shishkin

Institute of High-Temperature Electrochemistry, Ural Division, Russian Academy of Sciencesd, Yekatirenburg, Russia

Received March 19, 2001

Abstract—The method of direct potentiometry was applied to measure redox potentials of Sm^{3+}/Sm^{2+} and Eu^{3+}/Eu^{2+} in molten cesium chloride relative to chlorine reference electrode in the temperature range 973–1173 K. Changes in the Gibbs energy of the redox reaction $LnCl_{2(l)} + 1/2Cl_{2(g)} \leftrightarrow LnCl_{3(l)}$ were calculated.

Electrochemical methods for processing of rare-earth raw materials in salt melts have been acquiring increasing importance in view of the growing use of rare-earth metals (REM) and their alloys in high technologies. In electrochemical systems based on molten alkali metal halides and containing REM halides, the latter are, as a rule, present, by virtue of their chemical nature, in the form of ions in various oxidation states. There are only scarce published data on redox processes occurring in molten salt electrolytes containing lanthanide halides. As a rule, the available data are only estimates, which results from the use of indirect methods for determining electrochemical parameters [1] or proximate techniques [2] furnishing semiquantitative characteristics applicable only to solution of various technological problems. At the same time, use of methods making it possible to directly determine, e.g., decomposition voltages and redox potentials of halide systems containing rare-earth metals encounters severe difficulties. These are related to the fact that noticeable amounts of alkali metal start to deposit at the decomposition potentials, and the high affinity of lanthanides for oxygen requires an exceedingly clean experimental technique [3]. Meanwhile, successful development of such hi-tech schemes as processing of irradiated fuel [4–6] insistently demands that the occurring processes should be studied more thoroughly and in greater detail, which is impossible without systematic precision studies directly furnishing the required information.

The following most important problems of the electrochemistry of molten alkali metal halides containing lanthanide compounds can be distinguished, which have not been sufficiently well described in the scientific literature. To these belong in the first place the stability and type of REM ions in various oxidation states in these systems; quantitative characteristics of redox reactions (number of electrons involved in a reaction, equilibrium constants, etc.), their dependence on the ionic composition of the salt solvent, concentration of rare-earth halide, and temperature. Analysis of published data [7–9] and the results of previous studies [10, 11], convincingly demonstrates that samarium and europium have only two stable forms, Ln^{3+} and Ln^{2+}, and a reversible redox reaction involving these species is of single-electron type.

It is known that, in molten alkali metal halides, ions of polyvalent metals, including REM, form anionic complex groups whose stability grows on replacing the solvent-salt cation in the following order $Li^+ \rightarrow Na^+ \rightarrow K^+ \rightarrow Rb^+ \rightarrow Cs^+$ [12–14]. Their influence on the equilibrium of the reaction

$$Ln^{3+} + e \rightleftarrows Ln^{2+} \quad (1)$$

is especially strongly manifested in solutions dilute with respect to lanthanide chlorides, since, in this case, ions of rare-earth metals are completely incorporated into $LnCl_6^{3-}$ and $LnCl_4^{2-}$ [7, 13].

In the present study, the potentiometric technique is applied to study the equilibria of the redox reactions

$$SmCl_{2(l)} + 1/2Cl_{2(g)} \rightleftarrows SmCl_{3(l)}, \quad (2)$$

$$EuCl_{2(l)} + 1/2Cl_{2(g)} \rightleftarrows SmCl_{3(l)} \quad (3)$$

in a cesium chloride melt. In this case, by analogy with other salt systems containing polyvalent metals

1070-4272/01/7410-1672 $25.00 © 2001 MAIK "Nauka/Interperiodica"

[12], the stability of complex ions formed by samarium and europium, and their influence of on the equilibrium of trichloride reduction reactions, must be the highest.

EXPERIMENTAL

Cesium chloride of special-purity grade, used in the study, was preliminarily dried, melted, and subjected to zone refining [15]. Anhydrous samarium and europium trichlorides were prepared by chlorination of crystal hydrates by heating in carbon tetrachloride vapor [16]. Crystal hydrates of REM chlorides were obtained by dissolving an oxide in hydrochloric acid to pH 1–1.5 with further evaporation of the resulting solution on water bath. The prepared chlorides were stored, ground, and weighed in a box in an atmosphere of dry nitrogen.

REM chlorides readily decompose at elevated temperature in the presence of atmospheric oxygen and undergo hydrolysis as a result of interaction with moisture to form oxychlorides [17]. With account of this fact, $SmCl_3$ + CsCl and $EuCl_3$ + CsCl fusion cakes of eutectic composition, containing 17 mol % cesium chloride according to fusibility curves [14, 18], were preliminarily synthesized. Since it is known [19–21] that trichlorides of samarium, and especially europium, are thermally unstable at temperatures close to the melting point, the employed technique makes it possible to essentially decelerate the reaction of thermal decomposition of chlorides. The suppression of this process is due to lowering of the melting temperatures of trichloride-containing salt formulations and to occurrence of complexation reactions in the molten solvent-salt. To completely remove trace amounts of rare-earth metal oxychlorides, chlorine with admixture of carbon tetrachloride was bubbled through a melt contained in glassy-carbon or pyrolytic-graphite crucibles. A melt to be studied was prepared directly when carrying out an experiment by fusing a prescribed amount of a preliminarily prepared eutectic with the solvent-salt. In all experiments, the concentration of a rare-earth metal chloride in the salt phase was not higher than 4.5 mol %.

Glassy carbon served as indifferent material for the working electrode. As true values were taken such emf values which remained constant within ±1 mV for 0.5 h at a given temperature. All experimental emf values are given with account of the thermo emf between the platinum and carbon current leads to the cell electrodes.

The design of the experimental cell and experimental procedure were described in detail in [10]. Despite that samarium dichloride is a stable compound, it is exceedingly sensitive to presence of oxidizing agents and, in particular, oxygen in the system [3, 17]. In developing a procedure for measuring the redox potentials of samarium [10], it was shown that reproducible results can only be obtained with special measures taken against presence of oxygen in the gas atmosphere. Otherwise, the slope of experimental isotherms corresponded to a number of electrons much less than unity, and a precipitate was formed in dissolving solidified salt fusion cake in water. As shown by X-ray phase analysis, the chemical composition of the precipitate corresponded to samarium oxychloride, which could be formed in the melt by the reaction

$$SmCl_{2(l)} + 1/2O_{2(g)} = SmOCl_{(s)} + SmCl_{3(l)}. \quad (4)$$

Reaction (4) is even possible in the case of very small admixtures of oxygen in the gas medium or presence of residual amounts of oxygen adsorbed on the surface of crucible and other members of the measurement cell, not removed in thermal treatment. Therefore, special attention was given to argon purification. For this purpose, argon was pumped, during the entire experiment, by an RR 1-05 peristaltic pump through a getter composed of zirconium filings and heated to 1073 K.

The starting salt, containing rare-earth metal trichloride, was electrochemically reduced to a dichloride whose concentration was calculated from the quantity of electricity Q passed through a system under study, measured during the experiment with a copper coulometer.

After an experiment, the salt fusion cake solidified in the inert atmosphere was analyzed for the content of bi- and trivalent samarium or europium ions. The content of samarium dichloride was determined volumetrically from the amount of hydrogen evolved in dissolution of the fusion cake in an acidified aqueous solution, the content of europium dichloride was analyzed by potentiometric titration of its aqueous solution with potassium dichromate. The total content of trivalent ions of rare-earth metals was found by titration with ethylenediamine tetraacetate (EDTA) by the known procedure [22].

The experimental values of redox potentials obtained on an indifferent glassy carbon electrode in molten CsCl are presented in Fig. 1 for the systems Sm^{3+}/Sm^{2+} and Eu^{3+}/Eu^{2+}. In both the systems, the redox potential $E_{Ln^{3+}/Ln^{2+}}$ linearly depends on the logarithm of the trichloride to dichloride concentration ratio $\ln([Ln^{3+}]/[Ln^{2+}])$. The experimental $E_{Ln^{3+}/Ln^{2+}}$ (V) values are described by linear equations at confidence

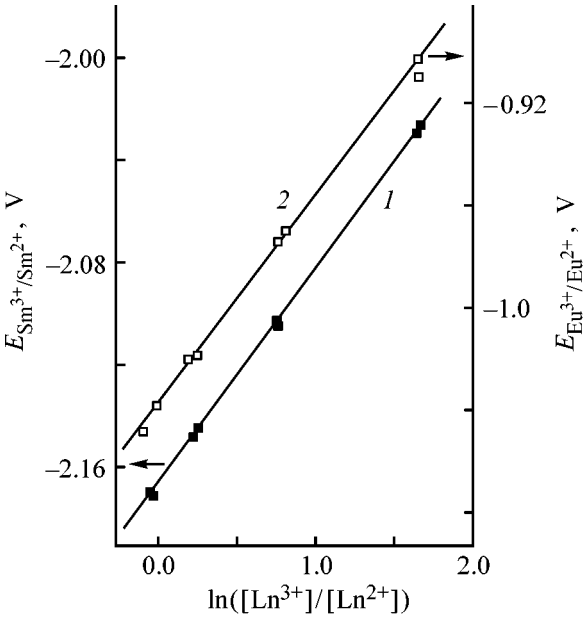

Fig. 1. Redox potentials (*1*) $E_{Sm^{3+}/Sm^{2+}}$ and (*2*) $E_{Eu^{3+}/Eu^{2+}}$ vs. concentration ratio Ln^{3+}/Ln^{2+} at 973 K in CsCl melt. Ln^{3+}/Ln^{2+}: (*1*) Sm^{3+}/Sm^{2+} and (*2*) Eu^{3+}/Eu^{2+}.

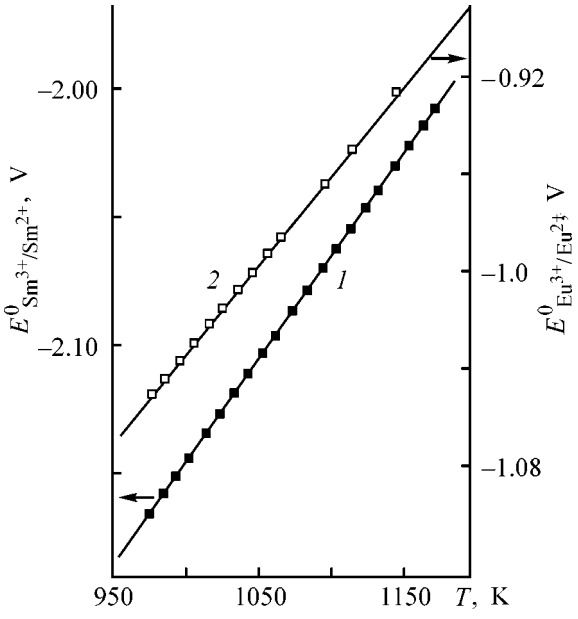

Fig. 2. Conditional standard redox potentials (*1*) $E^0_{Sm^{3+}/Sm^{2+}}$ and (*2*) $E^0_{Eu^{3+}/Eu^{2+}}$ in molten cesium chloride vs. temperature *T*.

probability of 0.95. For 973 K these dependences have the form

$$E_{Sm^{3+}/Sm^{2+}} = -(2.1667 \pm 0.0006) + (0.0833 \pm 0.0006)\ln([Sm^{3+}]/[Sm^{2+}]) \pm 0.001, \quad (5)$$

$$E_{Eu^{3+}/Eu^{2+}} = -(1.036 \pm 0.002) + (0.082 \pm 0.002)\ln([Eu^{3+}]/[Eu^{2+}]) \pm 0.004, \quad (6)$$

where $[Sm^{3+}]$, $[Sm^{2+}]$, $[Eu^{3+}]$, and $[Eu^{2+}]$ are the concentrations of samarium and europium ions in different oxidation states (mol fraction).

The number *n* of electrons involved in the electrochemical reduction of a rare-earth metal trichloride by reaction (1) was determined from the pre-logarithmic coefficients. The *n* value is 1.01 ± 0.01 for samarium and 1.02 ± 0.03 for europium.

A chemical analysis of solidified salt fusion cakes for the content of samarium or europium dichloride, performed after the experiments, confirmed the measurement results. The discrepancies between the coulometric (i.e. that calculated from the quantity of electricity expended for reduction of REM trichloride) and analytical determinations were 2–2.5%. Apparently, the electroreduction reaction in the melt under study proceeds by scheme (1).

The temperature dependence of the conditional standard potential $E^0_{Ln^{3+}/Ln^{2+}}$ (V), obtained on a glassy carbon electrode, is presented in Fig. 2. In the temperature range of the experiment, the dependence is linear for both samarium and europium. The data processed by a least-squares procedure are described in the temperature range 973–1173 K by the equations

$$E^0_{Sm^{3+}/Sm^{2+}} = -(2.943 \pm 0.003) + (79.8 \pm 0.3) \times 10^{-5}T \pm 0.0008, \quad (7)$$

$$E^0_{Eu^{3+}/Eu^{2+}} = -(1.764 \pm 0.003) + (73.0 \pm 0.3) \times 10^{-5}T \pm 0.0009. \quad (8)$$

Equations (5)–(8) involve the rms scatter of the experimental data.

The results obtained in the study indicate that, at one and the same temperature and concentration ratio of electrically active species, the redox potential $E_{Sm^{3+}/Sm^{2+}}$ is more negative than $E_{Eu^{3+}/Eu^{2+}}$, in good agreement with the available data for samarium and europium chloride solutions in a eutectic LiCl–KCl mixture [3] and equimolar NaCl–KCl mixture [2, 10].

Changing the salt solvent strongly affects the conditional standard potentials $E^0_{Ln^{3+}/Ln^{2+}}$. For example, at 1073 K, these potentials were –1.880 and –0.742 V in molten equimolar mixture [10], –1.966 and –0.844 V in molten KCl [17], and –2.087 and –0.981 V in molten CsCl, for samarium and europium, respectively. A linear, within the experimental determination error, dependence of $E^0_{Ln^{3+}/Ln^{2+}}$ on the inverse of the crystal-

chemical cation radii of the solvent-salt is observed (Fig. 3). The radii of the alkali metal cations are taken according to Goldschmidt [23]. For 1073 K this dependence is described by the following empirical equations

$$E^0_{Sm^{3+}/Sm^{2+}} = -(2.57 \pm 0.02) + (0.80 \pm 0.02)/r_R^+ \pm 0.004, \quad (9)$$

$$E^0_{Eu^{3+}/Eu^{2+}} = -(1.54 \pm 0.01) + (0.92 \pm 0.01)/r_R^+ \pm 0.002. \quad (10)$$

The obtained linear dependences of the conditional standard redox potentials on the inverse of the cation radii allow estimation of the $E^0_{Ln^{3+}/Ln^{2+}}$ values for those salt media in the series LiCl–NaCl–KCl–RbCl–CsCl (or mixtures of these) in which these potentials are not determined experimentally.

Table 1 presents conditional standard redox potentials $E^0_{Sm^{3+}/Sm^{2+}}$ and $E^0_{Eu^{3+}/Eu^{2+}}$ for molten NaCl and RbCl and for the LiCl–KCl eutectic mixture at different temperatures.

Johnson and Mackenzie [3] reported redox potentials $E_{Sm^{3+}/Sm^{2+}}$ and $E_{Eu^{3+}/Eu^{2+}}$ for 1 : 1 ratio of oxidized and reduced forms of rare-earth ions, measured on tungsten (for samarium-) and platinum (for europium-containing melts) indicator electrodes in a LiCl–KCl eutectic at 723 K relative to a platinum reference electrode. Recalculated to the chloride reference electrode, these potentials are, respectively, –2.035 and –0.860 V, whereas our data, extrapolated to this temperature, give –1.966 and –0.753 V. With account of the extrapolation error, the results are in satisfactory agreement.

The experimentally determined redox potentials were used to calculate the changes in the conditional standard Gibbs energy, ΔG^0, and the equilibrium constants K_c for the reaction

$$LnCl_{2(l)} + 1/2Cl_{2(g)} \rightleftarrows LnCl_{3(l)}. \quad (11)$$

The ΔG^0 value varies with the cation radius of a solvent-salt and temperature. For the salts studied these dependences are presented in Table 2.

Table 3 lists equilibrium constants for the reaction of samarium and europium trichloride formation in molten NaCl–KCl, KCl, and CsCl at different temperatures. It can be seen that the equilibrium constant decreases with increasing temperature. At equal temperatures, K_c grows with increasing cation radius of the solvent-salt. This indicates that, with decreasing

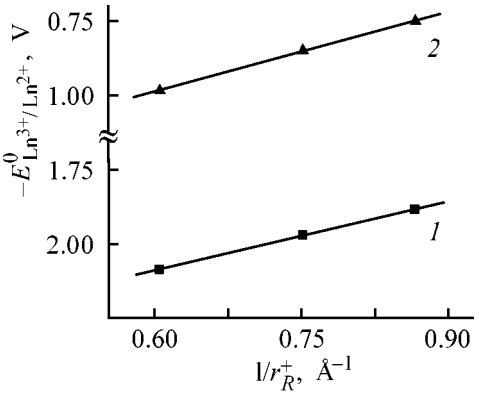

Fig. 3. Conditional standard redox potentials $E^0_{Ln^{3+}/Ln^{2+}}$ vs. cation radii r_R^+ of the solvent-salt at 1073 K in molten alkali metal chlorides. (*1*) $E^0_{Sm^{3+}/Sm^{2+}}$ and (*2*) $E^0_{Eu^{3+}/Eu^{2+}}$.

temperature and increasing cation radius of the solvent-salt, reaction (11) shifts toward formation of rare-earth trichloride.

The shift of the conditional standard potentials $E^0_{Ln^{3+}/Ln^{2+}}$ to more electronegative values and the change in the conventional standard Gibbs energy of the redox reaction in passing from (Na–K)Cl to CsCl are associated with complexation in melts. It is known [7–13] that, in dilute solutions of alkali metal chlorides, rare-earth metal ions Ln^{3+} and Ln^{2+} form complex groups $LnCl_6^{3-}$ and $LnCl_4^{2-}$ whose stability depends both on the ionic potential of the complexing agent [24, 25] and on the size of solvent-salt cations.

Table 1. Calculated conditional standard redox potentials $E^0_{Ln^{3+}/Ln^{2+}}$ in molten NaCl, RbCl, LiCl–KCl

Melt	$E^0_{Sm^{3+}/Sm^{2+}}$			$E^0_{Eu^{3+}/Eu^{2+}}$		
	V, at indicated temperature, K					
	1073	1123	1173	1073	1123	1173
NaCl	–	–1.720	–1.683	–	–0.572	–0.542
RbCl	–2.033	–1.995	–1.956	–0.923	–0.885	–0.850
LiCl–KCl	–1.719	–1.686	–1.649	–0.561	–0.533	–0.504

Table 2. Conditional standard changes in Gibbs energy for reactions (2) and (3) in molten chlorides of alkali metals

Melt	$\Delta G^0_{Sm^{3+}/Sm^{2+}}$	$\Delta G^0_{Eu^{3+}/Eu^{2+}}$
	J mol^{-1}	
NaCl–KCl	–260317 + 73.5T	–136767 + 60.7T
KCl	–265623 + 70.7T	–150131 + 64.1T
CsCl	–283955 + 77.0T	–170200 + 70.4T

Table 3. Constants of equilibrium between di- and trichlorides of samarium, K_c(Sm), and europium, K_c(Eu), in molten alkali metal chlorides

Melt	K_c(Sm)			K_c(Eu)		
	at indicated temperature, K					
	1073	1123	1173	1073	1123	1173
NaCl–KCl	6.81×10^8	1.86×10^8	5.67×10^7	3.07×10^3	1.55×10^3	8.31×10^2
KCl	1.73×10^9	4.60×10^8	1.37×10^8	9.13×10^3	4.32×10^3	2.17×10^3
CsCl	6.33×10^9	1.53×10^9	4.20×10^8	4.06×10^4	1.74×10^4	7.98×10^3

It may be stated, on the basis of the available published data on crystal-chemical radii of doubly and triply charged samarium and europium ions [26, 27], that the stability of the $SmCl_6^{3-}$ and $EuCl_6^{3-}$ complexes much exceeds that of $SmCl_4^{2-}$ and $EuCl_4^{2-}$ groups. At the same time, account should be taken of the influence of the salt-solvent cation, which is the stronger, the smaller its radius. As a result, the relative stability of the complex species $LnCl_6^{3-}$ and $LnCl_4^{2-}$ decreases in order $Cs^+ \rightarrow K^+ \rightarrow (Na–K)^+$. Elevated temperature also favors weakening of interparticle bonds in the complex groups because of the more intensive thermal motion of molten salt particles. As also in other salt systems containing chlorides of polyvalent metals, the decrease in the extent of complexation (weakening of intracomplex interparticle bonds) shifts the redox potentials $E^0_{Sm^{3+}/Sm^{2+}}$ and $E^0_{Eu^{3+}/Eu^{2+}}$ to more positive values.

CONCLUSIONS

(1) Redox potentials of samarium and europium were for the first time measured potentiometrically in molten cesium chloride at 973–1173 K.

(2) The redox potentials $E_{Ln^{3+}/Ln^{2+}}$ depend linearly on $\ln([Ln^{3+}]/[Ln^{2+}])$ in accordance with the Nernst equation. The number of electrons involved in the electrochemical reaction is unity.

(3) The conditional standard potentials $E^0_{Sm^{3+}/Sm^{2+}}$ and $E^0_{Eu^{3+}/Eu^{2+}}$ become more electropositive with decreasing cation radius of the solvent-salt and increasing temperature.

(4) In molten alkali metal chlorides and mixtures of these, the redox potential $E_{Sm^{3+}/Sm^{2+}}$ is more negative than $E_{Eu^{3+}/Eu^{2+}}$ at equal temperatures and concentration ratios of electrically active species.

REFERENCES

1. Mikheev, N.B., Auerman, L.N., and Rumer, I.A., *Elektrokhimiya*, 1987, vol. 23, no. 5, pp. 638–642.
2. Kuznetsov, S.A., and Gaune-Escard, M., *Proc. Int. Papatheodorou Sypm. ICEHT*, Patras, Greece, 1999, pp. 100–104.
3. Johnson, K.E. and Mackenzie, J.R., *J. Electrochem. Soc.*, 1969, vol. 116, no. 12, pp. 1697–1703.
4. Komarov, V.E., Smolenskii, V.V., and Afonichkin, V.K., *Rasplavy*, 2000, no. 2, pp. 59–65.
5. Novikov, V.M., Abstracts of Papers, *Mezhdunarodnyi seminar "Rasplavlennye soli v yadernykh tekhnologiyakh"* (Int. Symp. "Molten Salts in Nuclear Technology"), Dimitrovgrad: GNTs RF NIIAR, 1995.
6. Alekseev, P.N., Ignat'ev, V.V., Men'shikov, L.I., *et al.*, *Mezhdunarodnyi seminar "Rasplavlennye soli v yadernykh tekhnologiyakh"* (Int. Symp. "Molten Salts in Nuclear Technology"), Dimitrovgrad: GNTs RF NIIAR, 1995, pp. 32–34.
7. Novikov, G.I., Polyachenok, O.G., and Frid, S.A., *Zh. Neorg. Khim.*, 1964, vol. 9, no. 2, pp. 472–475.
8. Laptev, D.M., Goryushkin, V.F., Astakhova, I.S., and Polyakova, G.G., *Zh. Neorg. Khim.*, 1979, vol. 24, no. 5, pp. 1311–1316.
9. Laptev, D.M., Kulagin, N.M., Astakhova, I.S., and Tolstoguzov, N.V., *Zh. Neorg. Khim.*, 1981, vol. 26, no. 4, pp. 1023–1028.
10. Novoselova, A.V., Shishkin, V.Yu., and Khokhlov, V.A., *Rasplavy*, 1999, no. 6, pp. 32–39.
11. Novoselova, A.V., Shishkin, V.Yu., and Khokhlov, V.A., *Rasplavy*, 2000, no. 6, pp. 16–21.
12. Smirnov, M.V., *Elektrodnye potentsialy v rasplavlennykh khloridakh* (Electrode Potentials in Molten Chlorides), Moscow: Nauka, 1973.
13. Fukushima, K., Yamoto, H., and Iwadate, Y., *J. Alloys. Compounds*, 1999, vol. 290, no. 1–2, pp. 114–118.
14. Korshunov, B.G., Drobot, D.V., Bukhtiyarov, V.V., and Shevtsova, Z.N., *Zh. Neorg. Khim.*, 1964, vol. 9, no. 6, pp. 1427–1430.
15. Shishkin, V.Yu. and Mityaev, V.S., *Izv. Akad. Nauk SSSR, Neorg. Mater.*, 1982, vol. 18, no. 11, pp. 1917–1918.
16. Revzin, G.E., *Metody polucheniya khimicheskikh reaktivov i preparatov* (Methods for Obtaining Chemical

Reagents and Preparations), Moscow: VNII Khim. Reaktivov Osobo Chist. Veshchestv, 1967, issue 16, pp. 124–129.

17. *Gmelins Handbook of Inorganic Chemistry: Sc, Y, La–Lu, Rare Earth Elements*, Berlin, 1982, Part C 4b, 8th ed.
18. Seifert, H.J. and Sandrock, J., *Z. anorg. allg. Chem.*, 1990, vol. 587, no. 8, pp. 110–118.
19. Polyachenok, O.G. and Novikov, G.I., *Zh. Neorg. Khim.*, 1964, vol. 9, no. 4, pp. 773–777.
20. Laptev, D.M., Kiseleva, T.V., Goryushkin, V.F., *et al.*, Abstracts of Papers, *IV Ural'skaya konferentsiya po vysokotemperaturnoi fizicheskoi khimii i elektrokhimii* (IV Ural Conf. on High-Temperature Physical Chemistry and Electrochemistry), Sverdlovsk, 1985, part 1, pp. 44–45.
21. Laptev, D.M., Kiseleva, T.V., Kulagin, N.M., *et al.*, *Zh. Neorg. Khim.*, 1986, vol. 31, no. 8, pp. 1965–1967.
22. Ryabchikov, D.I. and Ryabukhin, V.A., *Analiticheskaya khimiya redkozemel'nykh elementov i ittriya* (Analytical Chemistry of Rare-Earth Elements and Yttrium), Moscow: Nauka, 1966.
23. *Spravochnik khimika* (Chemist's Handbook), Nikol'skii, B.P., Ed., Leningrad: Khimiya, 1971, vol. 1.
24. Stepanov, V.P. and Smirnov, M.V., *Rasplavy*, 1987, vol. 1, no. 5, pp. 76–80.
25. Smirnov, M.V., Stepanov, V.P., and Khokhlov, V.A., *Rasplavy*, 1987, vol. 1, no. 1, pp. 64–73.
26. Shannon, R.D., *Acta Crystallogr. Sect. A*, 1976, vol. 32, no. 5, pp. 751–767.
27. Ryabukhin, A.G., *Vysokotemperaturn. Rasplavy*, 1997, no. 1, pp. 58–63.

Russian Journal of Applied Chemistry, Vol. 74, No. 10, 2001, pp. 1678–1682. Translated from Zhurnal Prikladnoi Khimii, Vol. 74, No. 10, 2001, pp. 1628–1632.

APPLIED ELECTROCHEMISTRY AND CORROSION PROTECTION OF METALS

Deposition, Structure, and Properties of Electroplated Zinc Coating Alloyed with Cobalt

L. S. Tsybul'skaya, T. V. Gaevskaya, T. V. Byk, and G. N. Klavsut'

Research Institute of Physicochemical Problems, Belarussian State University, Minsk, Belarus

Received February 12, 2001

Abstract—Specific features of deposition, structure, physicomechanical (microhardness, wear resistance), corrosion-protective, and electrical properties of an electrochemical zinc–cobalt coating containing 0.05 to 28 wt % alloying metal.

Electrodeposition of zinc coatings alloyed with other metals is one of methods to improve their service characteristics. Among additives most widely used for alloying are iron subgroup metals: nickel [1–6], cobalt [6–10], and iron [6, 11], and also other metals—manganese [12], molybdenum [13], lead [14], and tin [14]. In alloying, modification of zinc coating properties is achieved both through formation of a finer, more perfect structure of a deposit in joint deposition of zinc and a minor amount of alloying metal and as a result of deposition of more corrosion-resistant phase structures—alloys Zn–Ni, Zn–Fe, Zn–Co, Zn–Mn, Zn–Sn, etc.

Zinc–cobalt coatings are commonly obtained in weakly acid zinc-plating electrolytes with various organic formulations, which yield, even without brightening (chromating), high-quality shining coatings with improved corrosion-protective properties in salt or sea fog. However, the problem of solution composition and deposition conditions of electrolytic Zh–Co deposits with required set of functional properties is for the most part solved empirically. Published data on electrochemical deposition of zinc–cobalt coatings are scarce, especially in what refers to the effect of various factors on the chemical and phase composition, structure, corrosion-protective, and physicomechanical properties.

The aim of this study was to develop a composition of a weakly acid electrolyte and conditions for obtaining a functional zinc–cobalt coating with fine decorative outward appearance and to study the effect of various factors on the chemical and physical composition of the coatings, and also on physicomechanical, electrical, and corrosion-protective properties.

EXPERIMENTAL

Zinc–cobalt coatings were electrodeposited from the developed weakly acid chloride solution onto the copper or steel surface with the use of a B5-49 dc power supply. Zinc of TsO brand was used as anode. The amount of cobalt and zinc in a coating was determined upon its dissolution on a Spectro Flame Modula atomic-emission spectrometer (FRG). The analysis error was not higher than 1%. As brightening additives to the zinc–cobalt plating electrolyte were used formulations of Dipo-tsink and ABC brands. The phase composition and structure of the obtained coatings were studied by means of X-ray diffraction analysis. Xray diffraction patterns were measured on a DRON-3 diffractometer with Co_{K_α} radiation at a recording rate of 1 deg min^{-1} in the angle range $2\theta = 16–110°$. The crystal lattice parameters and sizes of coherent-scattering regions (CSR) were found by the method of Cauchy's approximating function. Auger spectra were recorded from the surface of zinc–cobalt coatings, and also in various stages of ion etching, to study the element distribution across the entire thickness of electroplated coatings. The corrosion tests of the coatings under study (thickness 8.5 ± 0.05 μm) were performed at elevated relative humidity and temperature [GOST (State Standard) 9.308–85] by completely submerging samples in a 3% NaCl solution and subsequent gravimetric determination of the mass loss and also by a method based on measuring polarization curves of anodic dissolution of a coating and cathodic evolution of hydrogen. The polarization curves were measured with a PI-50-1 potentiostat in the potentiodynamic mode at potential sweep rate of 2 mV s^{-1}, with the use of fresh portions of a 3% NaCl

1070-4272/01/7410-1678 $25.00 © 2001 MAIK "Nauka/Interperiodica"

solution (50 ml) and a new working electrode. The potentials are given relative to a saturated silver chloride reference electrode.

The auxiliary electrode was made of platinum; as working electrode served steel plate onto which a zinc–cobalt coating with varied content of the alloying metal was electrodeposited. The measurements were done at 20 ± 1°C with natural aeration (without stirring the solution). The obtained results were presented in the form of a E–log i plot. Extrapolation of linear portions of the anodic and cathodic curves to the stationary metal potential was used to determine the current density and the corrosion potential. The microhardness of a coating about 30 μm thick was measured on a PMT-3 microhardness meter with indenter load of 20 g. The electrical resistance of coatings was measured at dc current of 50 mA under a load of 40 g. The wear resistance was evaluated by the method of reciprocal motion of a sphere (ShKh-15 steel, R = 3 mm) over the surface of a sample under study at a velocity of 25 mm s^{-1} under 50-N load without lubricant, with 1000 cycles executed at a 22-mm path length and the width and depth of the friction track measured, and the volume wear per cycle determined, subsequently.

The study was concerned with the effect of various factors—cathode current density, temperature, pH value, concentrations of the salts of the main metal (zinc chloride) and alloying metal (cobalt chloride) on the coating deposition rate, current efficiency by metal, and chemical composition of electroplated zinc–cobalt coatings. It was found that the deposition rate and the current efficiency are virtually independent of temperature, pH value, and concentration of the alloying metal salt in the zinc plating electrolyte and constitute 30 ± 2 μm h^{-1} and 95 ± 3%, respectively, at i_c = 2 A dm^{-2}. With the temperature increasing from 8 to 50°C, the pH value, from 3.3 to 6.5, and the Co(II) concentration in the electrolyte, from 0.02 to 0.22 M [at constant Zn(II) ion concentration of 0.45 M], the amount of cobalt codeposited with zinc grows, on the average, from 0.05–0.12 to 0.25–0.29 wt % (Fig. 1). The deposition rate, current efficiency by metal and chemical composition of a coating are more strongly affected by the cathode current density. With i_c increasing from 1 to 5 A dm^{-2}, the coating deposition rate grows linearly from 18 to 70 μm h^{-1}, the current efficiency decreases from 98 to 70–75% because of the simultaneously occurring reaction of hydrogen reduction, and the amount of cobalt codeposited with zinc becomes higher. It should be noted that at small current densities (0.5 to 2.0 A dm^{-2}) the mass fraction of cobalt grows at a much lower rate, from 0.12 to 0.18 wt %, than it does at higher current densities (2 to 5 A dm^{-2})—from 0.18 to 0.6 wt % (Fig. 1). The decisive influence on the chemical composition of a zinc–cobalt coating at fixed i_c and Co(II) concentration of 0.15 M is exerted by the ratio of metal salt concentrations in solution. The largest amount of cobalt (up to 28 wt %) is codeposited into a coating at a ratio Zn(II) : Co(II) = 0.3 : 1 [Zn(II) ion concentration 0.05 M] at low alloy deposition rate (~9 μm h^{-1}) and current efficiency (~30%). This is presumably due to the occurrence of concentration polarization: at low zinc salt concentration in the electrolyte and predominant discharge of zinc ions at the cathode, the near-electrode layer is rapidly depleted of Zn(II) ions, and, therefore, the share of cobalt in the coating is rather large. With increasing concentration of Zn(II) ions (to 0.15 M) and decreasing Zn(II) : Co(II) ratio (from 0.3 : 1 to 1 : 1, the amount of cobalt codeposited with zinc decreases dramatically, from 28 to 1.2 wt %, the coating deposition rate grows from 9 to 25 μm h^{-1}, and the current efficiency, from 30 to 85% (Fig. 2). Zn–Co coatings with the finest outward appearance—uniform, dense, and shining, were obtained at Zn(II) : Co(II) ratio in the electrolyte of 2 : 1 and more. The cobalt content in these coatings is 0.18–0.25 wt %, the deposition rate and current efficiency reach their maximum values of 30–32 μm h^{-1} and 98%, respectively (Fig. 2).

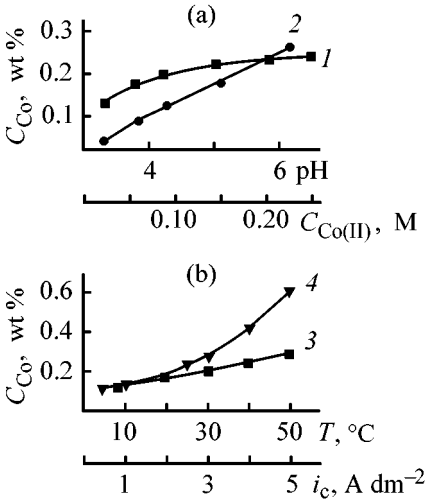

Fig. 1. Amount of cobalt in a Zn–Co coating, C_{Co}, vs. (*1*) pH; (*2*) concentration of Co(II) ions in the electrolyte, $C_{Co(II)}$; (*3*) temperature T; and (*4*) cathode current density i_c. In each curve one parameter varies with the other three remaining constant: T = 20°C, i_c = 2 A dm^{-2}, $C_{Co(II)}$ = 0.15 M, pH 5; the same for Fig. 2.

Thus, the content of cobalt in a coating can be varied in a sufficiently wide range (0.05–28 wt %)

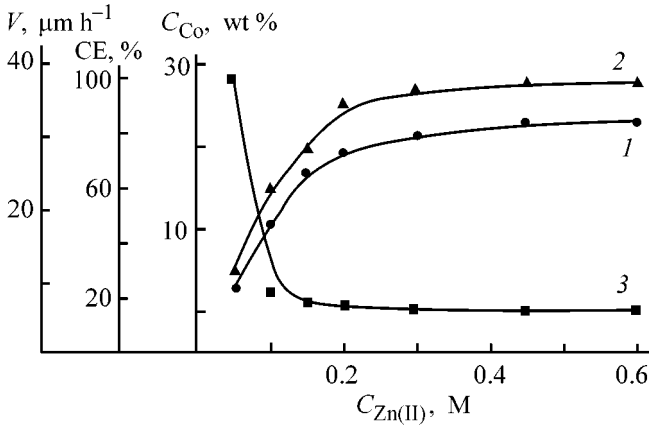

Fig. 2. (*1*) Deposition rate V of a zinc–cobalt coating, (*2*) current efficiency CE, and (*3*) amount of Co in a Zn–Co coating vs. concentration of Zn(II) ions in the electrolyte, $C_{Zn(II)}$.

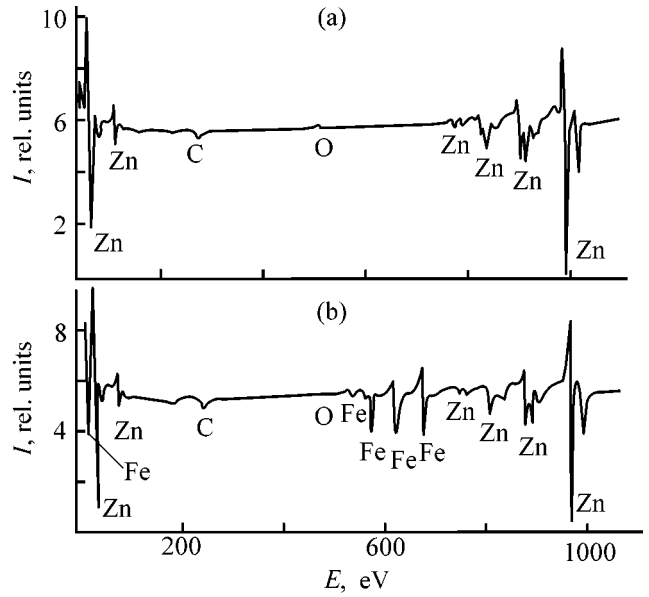

Fig. 3. Auger spectra of a zinc–cobalt coating containing 0.18 wt % cobalt. (*I*) Intensity and (*E*) kinetic energy. Layer: (a) surface and (b) adjacent to the substrate (steel).

by changing the concentration ratio of Zn(II) and Co(II) ions in the electrolyte, and in a much narrower range (0.12 to 0.6 wt %), by changing the electrodeposition conditions—cathode current density, pH value, and temperature.

An X-ray study of electroplated Zn–Co coatings with varied content of cobalt demonstrated that, at small content of the alloying metal (<1.2 wt %), only the phase of crystalline zinc is revealed with a full set of diffraction reflections 002, 100, 101, 102, 103, 110, 112, and 201, and lattice constants $a = b = 0.2665$, $c = 0.4947$ nm, which, according to [15] correspond to hexagonal closest packing. The CSR of the forming grains is 25–30 nm in size (see table). With the content of cobalt in a coating increasing to 2.5 wt %, the intensities of separate reflections change together with the crystal lattice constants: an increase in a and b to 0.2682 and a decrease in c to 0.4920 nm indicate the formation of a solid solution of cobalt in zinc. With the content of cobalt increasing to 28 wt %, no further changes in crystal lattice occur, with only the intensities of some reflections (002, 101, 102, 112) decreasing and that of others (100, 110) increasing, and the CSR size decreasing to 15–17 nm (see table).

Thus, depending on the chemical composition of a Zn–Co coating, either a solid solution of cobalt in zinc can be obtained if the content of the alloying metal exceeds 2.5 wt %, or crystalline zinc, if the content of the alloying metal is less than 1.2 wt %.

Auger spectra of Zn–Co coatings containing 0.18 wt % cobalt indicate that oxygen is incorporated into the coating in very small amounts (<1%) and is uniformly distributed across the entire thickness of the electroplated coatings (Fig. 3). This means that, contrary to the assumptions made in [1], no difficultly soluble hydroxo compounds of Zn(II) and Co(II) ions discharging at the cathode are formed as a result of alkalinization of the near-electrode layer, although the pH grows in the course of electrolysis from 4.5 to 5.0–5.5. At small content of cobalt in a coating, the cobalt phase is observed neither on the outer surface of electroplated Zn–Co deposits, nor on the inner surface adjacent to the iron substrate (Fig. 3). This suggests that cobalt atoms are introduced at defects of the crystal lattice of zinc.

A corrosion-electrochemical study of Zn and Zn–Co coatings with varied content of the alloying metal

Microstructure and phase composition of Zn–Co coating

Co concentration, wt %	Phase composition	CSR size, nm	Crystal lattice constants, nm
<1.2	Crystalline Zn	25–30	$a = b = 0.2665$, $c = 0.4947$*
2.5	Solid solution of Co in Zn	25–30	$a = b = 0.2682$, $c = 0.4920$
28	The same	15–17	$a = b = 0.2682$, $c = 0.4920$

* According to published data [15], $a = b = 0.2665$, $c = 0.4947$ nm.

in a 3% sodium chloride solution demonstrated that alloying of zinc with cobalt improves the corrosion resistance of Zn coatings: in particular, the corrosion current density decreases from 7.4 μA cm^{-2} for zinc coating to 0.7–4.2 μA cm^{-2} for Zn–Co coatings containing from 0.15 to 2.5 wt % cobalt, respectively (Fig. 4). The lowest corrosion current density is observed for coatings containing minor amounts of cobalt: (0.2 ± 0.05 wt %). This is presumably due to the uniform distribution of alloying metal atoms over defect sites in the crystal lattice. The increase in the corrosion current density to 4.2 μA cm^{-2} on raising the amount of the alloying metal in the coating to 2.5 wt % is probably due to the formation of a solid solution of cobalt in zinc. The corrosion potentials of Zn and Zn–Co coatings differ only slightly (–1.05 ± 0.05 V) and correspond to the cathodic steel protection range.

Accelerated corrosion tests of zinc and Zn–Co coatings in a climatic chamber in the course of 30 days (T = 40 ± 2°C, relative humidity 93 ± 3%) demonstrated that, under severe climatic treatment, the zinc coating shows centers of attack on the substrate (red rust) on the background of a white layer of corrosion products having the form of a mixture of ZnO, $6Zn(OH)_2 \cdot ZnCl_2$, and $4Zn(OH)_2 \cdot ZnCl_2$ (white rust) [7]. At the same time, only a very thin film of firmly adhering and difficultly removable corrosion products appeared on coatings containing less than 1 wt % cobalt (the coating became dull), whereas on coatings with 2.5 wt % cobalt the layer of corrosion products was the most pronounced. In both these cases, there were no centers of attack on the base metal.

Tests with samples completely submerged in a 3% NaCl solution with subsequent gravimetric determination of the coating mass demonstrated that zinc coatings alloyed with cobalt have better protective properties than zinc coatings. The average relative loss of mass in 30 days (%) was 5–10 for Zn coating, 2–3 for Zn–Co coatings with 2.5 wt % cobalt and 1–2 for those with 0.18 wt % cobalt.

A study of the physicomechanical (microhardness, wear resistance) and electrical (electrode resistance) properties of zinc and Zn–Co coatings demonstrated that the Zn–Co coatings have higher microhardness, compared with zinc coatings [H_{20}(Zn) = 850 N mm^{-2}]. With the content of cobalt in a coating increasing at low concentrations of the alloying metal (0.05 to 0.25 wt %), the microhardness grows linearly from 900 to 1050 N mm^{-2}. Further increase in the content of cobalt has little effect on the microhardness (1100 N mm^{-2}, Fig. 4). Zn–Co coatings exhibit firm adhesion to the base, with no flaking-off observed on

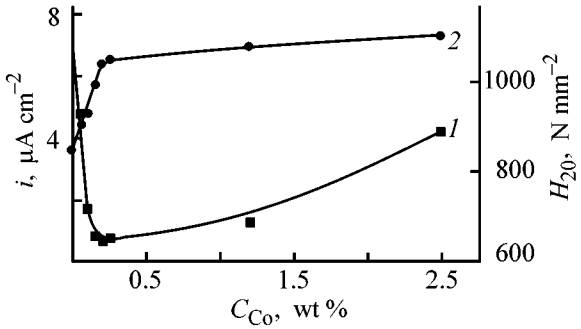

Fig. 4. Effect of the cobalt content C_{Co} of a Zn–Co coating on (*1*) corrosion current density i_c in a 3% sodium chloride solution and (*2*) microhardness H_{20}.

repeated bending of a steel band coated with Zn–Co. When thicker than 3 μm, the zinc coating alloyed with cobalt is nonporous and has a fine, decorative outward appearance—uniform, bright, and shining. It much surpasses the zinc coating in wear resistance. The specific volume wear in 1000 cycles of abrasion under dry friction conditions is (1.8×10^{-7} mm^3 for the Zn–Co coating and 6.5×10^{-7} mm^3 for the zinc coating. In contrast to purely zinc coatings, those alloyed with cobalt require no treatment in chromate solutions, which diminishes the labor-intensity of the process and eliminates the problem of wastewater purification to remove Cr(VI) ions. The resistance of zinc coatings and Zn–Co coatings with small content of cobalt (up to 2.5 wt%) is 4–5 mOhm. With the content of the alloying metal growing to 28 wt %, the resistance increases to 8– 12 mOhm. Presumably, this increase may be due to a twofold decrease in grain size (see table) and growing area of grain boundaries. The intergrain space has higher electrical resistance than the grain bulk, and, therefore, electron transport is hindered in finely crystalline coatings, compared with coarsely crystalline layers.

CONCLUSIONS

(1) A weakly acid (pH 5.0 ± 0.5) chloride solution for electrodeposition of Zn–Co coatings onto a steel or copper substrate was developed, which yields functional Zn–Co coatings with fine, decorative outward appearance in the presence of Dipo-tsink or ABC brand brighteners.

(2) Varying the ratio of Zn(II) and Co(II) ion concentrations in the electrolyte and the electrolysis conditions, one can obtain Zn–Co coatings containing 0.05 to 28 wt % cobalt.

(3) X-ray phase analysis demonstrated that the coating is composed of crystalline zinc at cobalt con-

tent less than 1.2 wt %, with cobalt presumably distributed among defects of the closest hexagonal packing of zinc, and a solid solution of cobalt in zinc at cobalt content exceeding 2.5 wt %.

(4) The best service characteristics: enhanced corrosion resistance and protecting capacity, higher microhardness and wear resistance, and low electrical resistance, are characteristic of zinc–cobalt coatings containing 0.2 ± 0.05 wt % cobalt.

REFERENCES

1. Grigoryan, N.S., Kudryavtsev, V.N., Zhdan, P.A., *et al.*, *Zashch. Met.*, 1989, vol. 25, no. 2, pp. 288–295.
2. Roev, V.G. and Gudin, N.V., *Elektrokhimiya*, 1995, vol. 31, no. 5, pp. 532–534.
3. Skribnaya, O.G., Donchenko, M.I., and Red'ko, R.M., *Zashch. Met.*, 1997, vol. 33, no. 1, pp. 70–72.
4. Shen Muzhao and Hu Zhibin, *Plat. Finish.*, 1994, vol. 16, no. 3, pp. 4–8.
5. Fabri Miranda, F.J. and Barcia, O.E., *J. Electrochem. Soc.*, 1997, vol. 144, no. 10, pp. 3441–3449.
6. Vagramyan, T.A., Kharlamov, V.I., and Kudryavtsev, V.N., *Zash. Met.*, 1996, vol. 32, no. 4, pp. 389–395.
7. Panasenko, S.A., Grishchuk, V.I., and Oleshchenko, N.N., *Zashch. Met.*, 1990, vol. 26, no. 2, pp. 327–330.
8. Gomez, E., Valles, E., and Gorostiza, P., *J. Electrochem. Soc.*, 1995, vol. 142, no. 12, pp. 4091–4096.
9. Gomez, E. and Valles, E., *J. Electroanal. Chem.*, 1997, vol. 421, nos. 1–2, pp. 157–163.
10. Vinogradov, S.N., Mal'tseva, G.N., and Rambergenov, A.K., *Gal'vanotekhn. Obrabotka Poverkhnosti*, 1993, vol. 2, no. 4, pp. 37–43.
11. Titova, V.N., Kazakov, V.A., Yavich, A.A., and Petrova, N.V., *Gal'vanotekhn. Obrabotka Poverkhnosti*, 1998, vol. 6, no. 1, pp. 37–41.
12. Danilov, F.I., Sukhomlin, D.A., Gerasimov, V.V., and Popovich, V.A., *Elektrokhimiya*, 1992, vol. 28, no. 2, pp. 217–223.
13. Korobov, V.I., Trofimenko, V.V., and Loshkarev, Yu.V., *Gal'vanotekhn. Obrabotka Poverkhnosti*, 1992, vol. 1, no. 3–4, pp. 32–35.
14. Kharlamov, V.I., Gorkunenko, G.A., Temkin, S.M., and Vagramyan, T.A., *Elektroosazhdenie metallov i splavov: Sbornik nauchnykh trudov MkhTI* (Electrodeposition of Metals and Alloys: Coll. Sci. Works Mosc. Chem. Technol. Inst.), Moscow, 1991, pp. 52–59.
15. Elliott, R.P., *Constitution of Binary Alloys*, New York: McGraw-Hill, 1965.

Russian Journal of Applied Chemistry, Vol. 74, No. 10, 2001, pp. 1683–1685. Translated from Zhurnal Prikladnoi Khimii, Vol. 74, No. 10, 2001, pp. 1633–1635.

APPLIED ELECTROCHEMISTRY AND CORROSION PROTECTION OF METALS

Electrochemical Polishing of SrM925 Silver Alloy by Means of Pulsed Current

S. I. Galanin, A. V. Chekotin, and M. V. Nikonova

Kostroma State Technological University, Kostroma, Russia

Received March 21, 2001

Abstract—Electrochemical polishing of jewelry silver alloy SrM925 by means of microsecond-pulse current in ammonia-nitrate, thiosulfate, and chromate electrolytes is considered.

Stringent requirements are presently imposed on the outward appearance of jewelry. Manufacture needs effective technological processes for finishing treatment of the surface of composite-profile articles. As a process of this kind can be used electrochemical polishing, which has a number of indisputable advantages over mechanical treatment. The use of electrochemical polishing is hindered by the fact that silver alloys are conventionally polished in hazardous and ecologically unsafe cyanide electrolytes similar to Shpital'skii's electrolyte [1–5]. Also possible is use of non-cyanide electrolytes, e.g., thiosulfate [6], ammonia-nitrate [7], and chromate [5]. However, the quality of the resulting surface gives no way of using electrochemical polishing in these electrolytes as industrial finishing procedure.

According to the theory of electrochemical polishing [5], high quality of the resulting surface is ensured when the rates of anodic dissolution and passivation are comparable and rather high. Investigations have shown that the processes develop at different rates [8], with the difference observed on the microsecond time scale. Therefore, use of pulsed currents with microsecond pulse duration comparable with the time of development of anodic processes allows a certain extent of control over their course at the anode–electrolyte interface in order to achieve high rates of smoothing of the microroughness on a surface being treated [9, 10]. It was recommended in [6] to treat the surface with pulsating current in order to improve the process efficiency.

The aim of the present study was to analyze the possibility of electrochemical polishing of samples cast from SrM925 jewelry silver alloy in non-cyanide electrolytes with the use of microsecond current pulses.

The experiments were carried out using a transistor source of rectangular pulses, with independent control of the output amplitude-and-time parameters [11]. As samples served cast cylinders pressed in fluoroplastic. The cathode was made of 12Kh18N9T steel. The electrolyte in the electrochemical bath was continuously stirred mechanically. The electrolyte temperature was 18–20°C.

The effectiveness of surface microroughness smoothing was judged on the basis of the following criteria: outward appearance of the surface, metal loss Δm, reflectivity factor k_r, relative smoothing ΔR_z, and smoothing efficiency factor λ_{eff}. The coefficient k_r (%) was defined by

$$k_r = (O_{tr}/O_m) \times 100, \quad (1)$$

where O_{tr} and O_m are the intensities of light reflected from a sample under study and a mechanically mirror-polished sample, respectively.

To determine the coefficient k_r, a device was fabricated, measuring the intensity of light reflected perpendicularly to the sample surface. As a source of light served an electric lamp, with the beam of light from the lamp focused onto the sample surface by a lens. The intensity of reflected light was measured with a photographic exposure meter. The relative smoothing of surface microirregularities (the irregularity height R_z was determined with the use of an MII-4 interference microscope) ΔR_z (%) was defined as the ratio of the difference of microirregularity heights before, $R_{z(in)}$, and after treatment, $R_{z(fin)}$ to the value prior to treatment:

$$\Delta R_z = \frac{R_{z(in)} - R_{z(fin)}}{R_{z(in)}} \times 100. \quad (2)$$

1070-4272/01/7410-1683 $25.00 © 2001 MAIK "Nauka/Interperiodica"

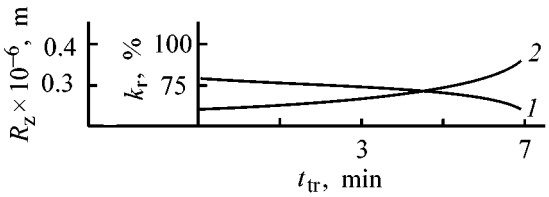

Fig. 1. (*1*) Microirregularity height R_z and (*2*) surface reflectivity factor k_r vs. time t_{tr} of treatment in ammonia-nitrate electrolyte. Electrolysis conditions: i_a = 15 A dm^{-2}, q = 2, t_p = 3000 × 10^{-6} s.

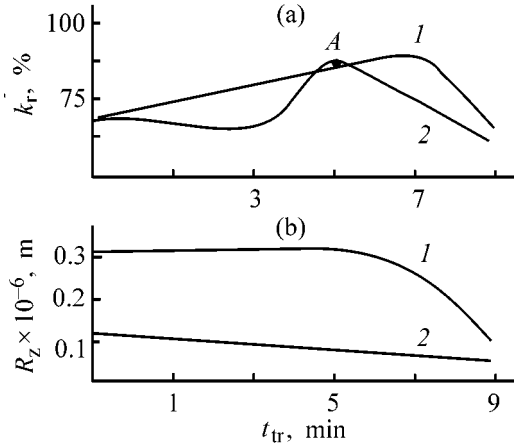

Fig. 2. Effect of the time t_{tr} of treatment in a thiosulfate electrolyte on (a) reflectivity factor k_r and (b) microirregularity height R_z. Electrolysis conditions: (*1*) i_a = 5 A dm^{-2}, q = 4, t_p = 100 × 10^{-6} s; (*2*) i_a = 5 A dm^{-2}, q = 4, t_p = 1000 × 10^{-6} s.

The coefficient λ_{eff} was defined as the ratio of the height of dissolved microprojections to the mass Δm of dissolved metal [5]:

$$\lambda_{eff} = \frac{R_{z\,(in)} - R_{z\,(fin)}}{\Delta m}. \quad (3)$$

The higher λ_{eff}, the more effective the smoothing. A change in reflectivity is a measure of the polishing properties of an electrolyte, whereas the relative smoothing, combined with λ_{eff}, characterizes electrolytes and electrolysis modes from the standpoint of smoothing ability and technological feasibility.

Electrolytes of the following compositions (g l^{-1}) were studied [5–7]: no. 1, ammonia-nitrate (NH_4NO_3, 360; NaOH, 120); no. 2, thiosulfate ($Na_2S_2O_3 \cdot 10H_2O$ 809); and no. 3, chromate (CrO_3, 220; $CaCl_2 \cdot 2H_2O$, 86).

The samples were treated in the following modes: pulse anode current density i_a (A dm^{-2}) (chosen on the basis of recommendations of [5–7] as the most effective for treatment) for electrolyte no. 1: 15, 30, 200; no. 2: 5, 7; no. 3: 5, 10, 15; time of treatment t_{tr}: 1, 3, 5, 7 min; current pulse duration t_p (100, 1000, 3000) × 10^{-6} s; off-duty factor (pulse repetition cycle to pulse duration ratio) q = (2; 4).

Before and after treatment, the microirregularity height, sample mass, and surface reflectivity were measured for each of the above modes.

Let us now consider successively the electrolytes studied.

Electrolyte no. 1. At i_a 30 or 200 A dm^{-2}, the obtained results are unsatisfactory at any pulse lengths and off-duty factors. The surface is subject to pitting etching, with the metal uniformly removed at a rate of 0.003–0.005 g min^{-1}. At i_a = 200 A dm^{-2}, q = 4, the surface is covered with a dense dark brown film, and the sample mass increases by 0.01 g min^{-1}. A shining surface was obtained in the following mode: i_a = 15 A dm^{-2}, q = 2, and t_p = 3000 × 10^{-6} s (Fig. 1), with λ_{eff} = 1.59 × 10^{-6} m g^{-1} and ΔR_z = 22.5%.

Electrolyte no. 2. A shining surface was obtained in the following modes. First mode: i_a = 5 A dm^{-2}, q = 4, and t_p = 100 × 10^{-6} s. The surface acquires mirror shine. At treatment time of 1 to 7 min the reflectivity grows linearly, upon further treatment (up to 9 min) the surface becomes matte (Fig. 2a, curve *1*): λ_{eff} = 2.99 × 10^{-6} m g^{-1}, ΔR_z = 66.7%. Second mode: i_a = 5 A dm^{-2}, q = 4, t_p = 1000 × 10^{-6} s. After treatment for 5 min, the sample surface becomes glossy (as shown by visual inspection; Fig. 2a, curve *2*, point *A*), but the microirregularity height remains unsatisfactory: λ_{eff} = 3.89 × 10^{-6} m g^{-1}, ΔR_z = 35.5%. Thus, a surface is obtained, which possesses rather high reflectivity at considerable microroughness. Such a result is possible in the case of regular surface texture [5].

The smoothing efficiency factor in the second mode is nearly 2 times greater than that in the first one. In any other mode, the surface reflectivity was lower, or pitting etching of the surface was observed and dense dark films were formed.

Electrolyte no. 3. Surface polishing could not be achieved in any mode. Pitting etching and formation of solid gray, brown, yellow, or black films were observed. The films could not be removed by washing with water or acetone. Raising the temperature to 80°C and use of dc current failed to improve the results.

CONCLUSIONS

(1) The surface of silver is not polished in the chromate and ammonia-nitrate electrolytes. The most

promising is the thiosulfate electrolyte used in the optimal electrolysis mode (pulse current density i_a = 5 A dm^{-2}, off-duty factor q = 4, pulse duration t_p = 100×10^{-6} s).

(2) High reflectivity can be obtained not only with a substantially smoothed surface, but also with a surface characterized by regular texture.

(3) Exceeding the optimal treatment duration leads to surface etching. Therefore, a thorough mechanical pretreatment of the surface is necessary to make shorter the final stage of electrochemical polishing.

REFERENCES

1. Lainer, V.I., *Elektroliticheskaya polirovka i travlenie metallov* (Electrochemical Polishing and Etching of Metals), Moscow: Mashgiz, 1947.
2. Shchigolev, P.V., *Elektroliticheskoe i khimicheskoe polirovanie metallov* (Electrolytic and Chemical Polishing of Metals), Moscow: Akad. Nauk SSSR, 1959.
3. Garber, M.I., *Dekorativnoe shlifovanie i polirovanie* (Decorative Grinding and Polishing), Moscow: Mashinostroenie, 1964.
4. Jacquet, P.A., *Electrolytic and Chemical Polishing, Metallurgical Reviews*, London: The Institute of Metals, 1956.
5. Grilikhes, S.Ya., *Elektrokhimicheskoe i khimicheskoe polirovanie: Teoriya i praktika* (Electrochemical and Chemical Polishing: Theory and Practice), Leningrad: Mashinostroenie, 1987.
6. Nikulin, V.N. and Tsypin, M.Z., *Zh. Prikl. Khim.*, 1960, vol. 39, no. 2, pp. 469–471.
7. Yuzikis, L.A., Yankauskas, T.Yu., and Buchinskas, D.A., *Zh. Prikl. Khim.*, 1979, vol. 52, no. 7, pp. 1659–1661.
8. Galanin, S.I., Chekotin, A.V., Lebedeva, T.V., and Galeev, A.R., *Vestn. Kostr. Gos. Tekhnol. Univ.*, Kostroma, 1999, issue 1, pp. 7–11.
9. Galanin, S.I. and Shorokhov, S.A., *Sbornik nauchnykh trudov 3-i regional'noi nauchno-tekhnicheskoi konferentsii "Sovremennaya elektrotekhnologiya v promyshlennosti tsentra Rossii"* (Proc. 3rd Regional Sci.-Technol. Conf. "Modern Electrotechnics in the Industry of Central Russia"), Tula: Tul. Gos. Univ., 2000, pp. 38–44.
10. Galanin, S.I. and Shorokhov, S.A., *Izv. Vyssh. Uchebn. Zaved., Khim. Khim. Tekhnol.*, 2000, vol. 43, no. 6, pp. 59–64.
11. Rybalko, A.V., Galanin, S.I., Paramonov, A.M., and Groza, I.A., *Elektron. Obrab. Mater.*, 1983, no. 5, pp. 89–90.

Russian Journal of Applied Chemistry, Vol. 74, No. 10, 2001, pp. 1686–1692. Translated from Zhurnal Prikladnoi Khimii, Vol. 74, No. 10, 2001, pp. 1636–1642.

CATALYSIS

Catalytic Properties of Platinum(II, III) Oxide in Ammonia Oxidation

N. I. Zakharchenko

Zhukovskii National Aerospace University, Kharkov, Ukraine

Received April 16, 2001

Abstract—Catalytic properties of Pt_3O_4 platinum oxide were studied in the high-temperature range. The optimal parameters of ammonia oxidation on the oxide catalyst and kinetic characteristics of the reaction were determined.

Catalytic oxidation of ammonia to nitrogen(II) oxide is the basis of the industrial method for production of nitric acid [1]. Industrial catalysts (Pt, Rh, and Pd alloys) undergo physicochemical transformations in the course of technological processes, with the surface structure and chemical composition changed [1–5]. A set of such transformations of platinoid catalysts results in the loss of difficult-to-obtain and expensive platinum metals. The mechanism of platinum metal loss remains debatable [1, 4–7]; the conversion products widely differ according to data of different authors [1, 4–8]. The catalytic properties of platinum compounds in ammonia oxidation have not been determined (except for PtO_2 [8]), which hinders the understanding of how ammonia is oxidized on platinoid catalysts and platinoids lost at elevated temperatures.

The present study is concerned with the catalytic and physicochemical properties of platinum(II, III) oxide Pt_3O_4 as a catalyst for ammonia oxidation, which has not been studied in the given process [1–8].

The catalyst was obtained by thermal treatment of ground hydrated platinum dioxide $PtO_2 \cdot nH_2O$ of chemically pure grade in inert medium (nitrogen) at 933 K. The reaction product was purified to remove the remaining platinum and PtO_2 in, respectively, boiling aqua regia and 48% HBr solution at 293 K [9] (with Pt_3O_4 not dissolved). The compound obtained was identified on a Siemens D-500 powder diffractometer in diffracted beam configuration, with Cu_{K_α} radiation and graphite monochromator. The phases observed in the obtained diffraction patterns were identified using the JCPDS file contained in the software package of the diffractometer. In parallel, the compound was subjected to chemical analysis [5, 9].

The content of oxygen in the oxide was determined from the mass loss in decomposition of samples in inert medium (nitrogen) in quartz ampules at 1173 K [10].

IR absorption spectra were measured on a Perkin–Elmer spectrophotometer in the spectral range 200–2000 cm^{-1} with KBr pellets as matrices.

The selectivity of the catalysts with respect to NO was determined on a flow-through setup with quartz reactor 2×10^{-2} m in diameter [11]. The bed of catalyst grains of size $(2 \times 3) \times 10^{-3}$ m was $(4–12) \times 10^{-2}$ m high; the time of contact was 6.50×10^{-2} s under standard conditions, i.e., the optimal according to previously obtained data [12]; and the pressure was 0.101 MPa. The temperature was varied within 813–1273 K, depending on the purposes of studies.

The composition of the products formed in ammonia oxidation and thermal decomposition of nitrogen(II) on the catalysts was determined chromatographically by means of the known technique [13] by analyzing the gas mixture for the content of NH_3, O_2, N_2, NO, and N_2O before and after the catalysts. The sensitivity of the employed analytical procedure was (vol %): 3.0×10^{-3} for NH_3; 3.5×10^{-3} for NO; and 5.0×10^{-3} for O_2, N_2, and N_2O.

The limiting load A of the catalysts with respect to NH_3 was determined by the procedure consisting in that the catalyst load was raised to a critical "decay" state, i.e., the state in which the thermal balance of a catalyst was disturbed when the reaction passed from the diffusion region into the kinetic one [14].

The catalyst particle size was determined on a JEM-7Y electron microscope [15]. A suspension of catalyst samples was prepared by ultrasonic disper-

1070-4272/01/7410-1686 $25.00 © 2001 MAIK "Nauka/Interperiodica"

sion of weighed portions of the substance in distilled water in a UZDV-2 device. As substrates were used carbon films obtained by thermal evaporation of graphite.

The specific surface area of the catalyst was determined from the low-temperature adsorption of nitrogen and calculated by the BET equation, using the standard procedure [16].

The synthesized catalyst (main lines in the X-ray diffraction pattern with interplanar spacings of 0.397, 0.253, 0.231, 0.1630, 0.1567, 0.1413, 0.1236, 0.1053, 0.0845 nm) corresponded to a cubic structure of Pt_3O_4 platinum oxide [17].

The IR spectrum of the compound contains absorption bands at 706, 590, 367, and 230 cm^{-1}, characteristic of platinum(II, III) oxide [18].

Chemical analysis was applied to determine the atomic ratio O/Pt = 1.31, which is in good agreement with the stoichiometry of the Pt_3O_4 compound.

The cubic structure of Pt_3O_4 is composed of square oxygen prisms filled with Pt atoms and perpendicular to one another (Fig. 1). Oxygen ions are arranged at cube corners. The Pt atoms center each oxygen square of these prisms. The cubic voids formed by the intersection of the prisms are empty. Such a structure corresponds to the ideal composition $PtO_{1.33}$ [17]. Deviations from the ideal composition can be attributed to formation of interstitial solid solutions. The excess, compared with the $PtO_{1.33}$ composition, platinum atoms can occupy (together with impurity ions Na^+, K^+, Ca^{2+}, Mg^{2+}, etc.) the cubic voids to form stable nonstoichiometric interstitial compounds of the type $Na_xPt_3O_4$ [9, 19].

The temperature dependence of the catalyst selectivity is shown in Fig. 2. The maximum selectivity of platinum(II, III) oxide (96.1%) is shifted to lower temperatures (953 K) as compared with most of other oxide catalysts [1, 12]. According to X-ray phase and chemical analyses, the catalyst starts to dissociate at 963–973 K with the formation of platinum, which corresponds to the following overall equation of the process [10, 20]

$$Pt_3O_4 = 3Pt + 2O_2. \quad (1)$$

According to X-ray phase analysis, the components of the system form no solid solutions under the given experimental conditions, being present as a mixture of two compounds. The formation of an interstitial solid solution in the system Pt_3O_4–Pt to give a stable structure of platinum oxide $Na_xPt_3O_4$ is slow [9, 17, 19]. The catalytic properties of the system Pt_3O_4–Pt at $T \geq 963$ K are determined by the physicochemical characteristics of the individual components and their relative amounts.

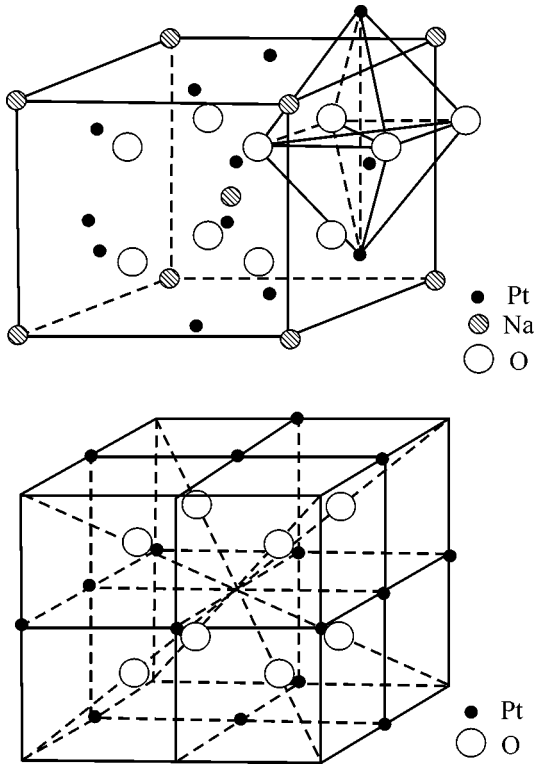

Fig. 1. Structure of Pt_3O_4 and $Na_xPt_3O_4$ by Muller [17].

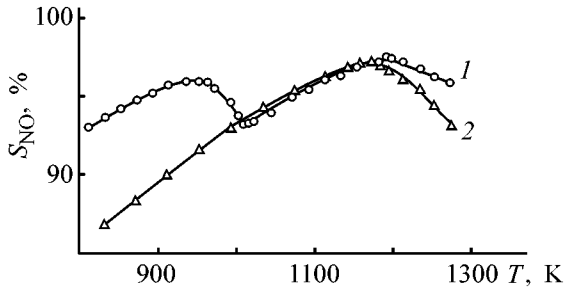

Fig. 2. Catalyst selectivity S_{NO} vs. process temperature T. Linear velocity of ammonia–air mixture 0.77 m s^{-1} (w.c.). (*1*) Pt_3O_4 (3 h of operation) and (*2*) catalyst after 170 h of operation.

Phase transformations of the catalyst at T ≥ 963 K make its selectivity lower, since a component (platinum) is formed whose selectivity at 963–973 K is not higher than 90.0–91.0% [1]. The catalyst selectivity was commonly determined after 2–3 h of operation at a given temperature. According to X-ray phase and chemical analyses, the catalyst partly dissociates at 1063–1073 K during this time, i.e., becomes a two-phase system Pt_3O_4–Pt. However, already after 7 h of

Characteristics of platinum(II, III) oxide catalyst

Catalyst	Phase composition	S_{sp}, $m^2\ g^{-1}$	S_{NO}^{max}, %	$A \times 10^{-3}$, $m^3\ h^{-1}\ m^{-2}$ (953 K)
Initial*	Pt_3O_4	12.5	96.1 (953 K)	13.80
After 170 h of operation	$M_xPt_3O_4 + Pt$	8.7	97.2 (1173 K)	9.58

* Body-centered cubic crystal structure, $Na_xPt_3O_4$ type, a = 0.5633.

tests at 1063–1073 K the catalyst completely decomposes into the components, with only one condensed phase (platinum) found in the system. In the range 1113–1273 K, the curve describing the temperature dependence of the catalyst selectivity (Fig. 2) coincides with a similar curve for Pt [1], i.e., after 2–3 h of tests the catalyst completely decomposes into simple substances at the given temperature. Consequently, the catalyst is only stable as an individual compound at $T \le 963$ K. The main characteristics of the catalyst are presented in the table.

Only two nitrogen compounds, NO and N_2, were found in the products of ammonia oxidation on the given catalyst: no "breakthrough" of ammonia was observed under the conditions that are far from critical. The total conversion of the starting substance is

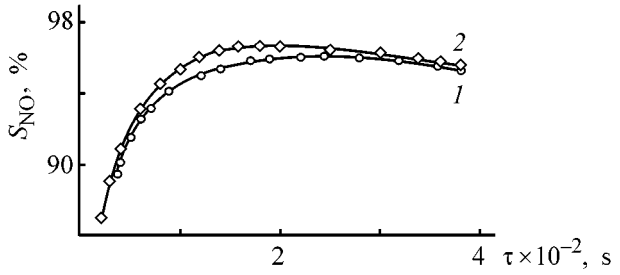

Fig. 3. Catalyst selectivity S_{NO} vs. contact time τ (w.c.). Linear velocity of ammonia–air mixture (m s^{-1}, w.c.): (*1*) 0.77 and (*2*) 1.19.

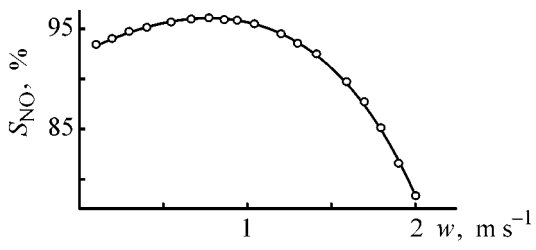

Fig. 4. Selectivity S_{NO} of platinum oxide vs. linear velocity of the ammonia–air mixture, w. Time of contact $\tau = 6.50 \times 10^{-2}$ s; T = 953 K.

100.0%, with only the ratio between the amounts of nitrogen(II) oxide and molecular nitrogen varying in the catalytic process, i.e., the catalyst selectivity with respect to NO (or nitrogen) changes. Thermal dissociation of NO makes lower the apparent selectivity of the catalyst with respect to nitrogen(II) oxide

$$2NO = N_2 + O_2. \quad (2)$$

According to experimental data, the degree of thermal dissociation of nitrogen(II) oxide on platinum oxide is 1.2% at 953 K and the optimal contact time $\tau = 6.50 \times 10^{-2}$ s. Thus, thermal dissociation of NO leads to a decrease in selectivity of platinum(II, III) oxide with respect to nitrogen(II) oxide by 1.1%. With increasing linear velocity of the components, i.e., the time of contact decreasing to 1.1×10^{-3} s (critical conditions of catalyst "decay"), no thermal dissociation of nitrogen(II) oxide is observed, in agreement with data for other oxide catalysts for ammonia oxidation [1, 21].

The fact that the catalyst selectivity depends on the contact time (Fig. 3) points to a kinetically complex mechanism of ammonia oxidation on platinum oxide [1, 12, 21].

The steep decrease in the catalyst selectivity at contact time $\tau < 8.0 \times 10^{-3}$ s (working conditions) is due to the occurrence of a side reaction of nitrogen defixation by the equation [1, 22]

$$4NH_3 + 6NO = 5N_2 + 6H_2O. \quad (3)$$

The gradual decrease in selectivity at contact time $\tau > (2.8–2.9) \times 10^{-2}$ s is mainly due to NO dissociation by scheme (2) [1]. The optimal contact time for platinum oxide is 2.46×10^{-2} and 1.58×10^{-2} s (w.c.) at linear velocities of the ammonia–air mixture of 0.77 and 1.19 m s^{-1} (w.c.), respectively.

The influence of the linear velocity of the reactants on the catalyst selectivity (Fig. 4) points to the outer-diffusion mechanism of the process [1, 12, 14, 21], in which the reaction rate is limited by diffusion of ammonia from the flow core to the platinum oxide surface.

The optimal linear velocity of the ammonia–air mixture for platinum oxide is 0.77 m s^{-1} (w.c.) at contact time $\tau = 6.50 \times 10^{-2}$ s (s.c.). With increasing linear velocity of the reactants, the "hot zone" shifts to the end of the catalyst bed, i.e., the temperature of its "frontal" layer becomes lower (Fig. 5). For example, at w = 1.80 m s^{-1} the temperature of the front layer of the catalyst falls to 803 K, which favors the occurrence of side reactions; in particular, the rate of nitrogen defixation by Eq. (3) is the highest at 673–873 K

[1, 22]. In addition, the low temperature of the front layer favors a parallel process

$$4NH_3 + 3O_2 = 2N_2 + 6H_2O, \quad (4)$$

which makes lower the selectivity of platinum oxide with respect to NO [1]. Low linear velocities of the ammonia–air mixture favor [1] the occurrence of a side reaction of NO dissociation, which leads to a gradual decrease in the catalyst selectivity with respect to nitrogen(II) oxide, since the rate of NO decomposition at 953 K is not high [1, 23]. Raising the linear velocity of the reactants to critical values ($\tau = 1.1 \times 10^{-3}$ s) leads to catalyst decay, i.e., to disturbance of the heat balance of the process because of a dramatic rise in heat losses. The heat losses can be compensated for by an increase in the amount of heat of the chemical processes occurring on platinum oxide in accordance with the heat balance equation [24]

$$Q_1 k C_S^n = \alpha(T_S - T_0) + Q_2, \quad (5)$$

where Q_1 is the heat effect of the reaction; k the reaction rate constant; C_S the ammonia concentration at the catalyst surface; n the reaction order; α the heat-transfer coefficient; T_s and T_0 the temperatures of, respectively, the catalyst surface and gas flow; and Q_2 the heat loss.

The increase in the heat effect of chemical processes occurring on the catalyst is ensured by faster rate (higher rate constant) of the reaction on the platinum oxide surface, with the grain surface temperature becoming higher. As follows from Eq. (5), the efficiency of the catalyst at constant temperature in the bed of platinum oxide grains strongly depends on the hydrodynamic characteristics of the ammonia–air mixture, and primarily on the linear velocity of the flow of reactants. The optimal linear velocities of the ammonia–air mixture lie within a limited range (Fig. 4).

The influence exerted by the ammonia concentration in the ammonia–air mixture on the selectivity of platinum(II, III) oxide is illustrated in Fig. 6 (w = const, h = const). At $[O_2]/[NH_3] > 1.6$–1.7 the catalyst surface is entirely covered with oxygen, and, consequently, mass transfer of NH_3 molecules to the platinum oxide surface is the rate-determining stage of the reaction [1, 14]. The ammonia oxidation rate r_{NH_3} per unit catalyst volume is equal to the rate of ammonia diffusion from the flow core to the platinum oxide surface [1, 14, 24].

$$r_{NH_3} = \beta S(C_0 - C_S), \quad (6)$$

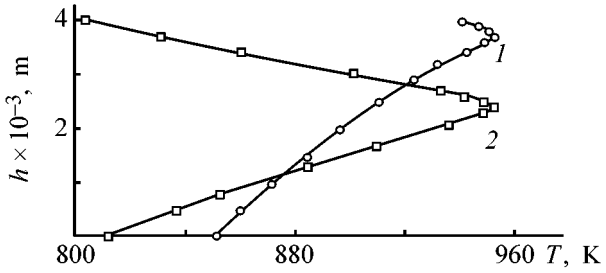

Fig. 5. Distribution of temperature T along the catalyst bed height h at the testing temperature of 953 K. Linear velocity of ammonia–air mixture (m s^{-1}; w.c.): (*1*) 0.77 and (*2*) 1.80.

Fig. 6. Selectivity of platinum(II, III) oxide with respect to NO, S_{NO}, vs. ammonia concentration C_{NH_3} in the ammonia–air mixture. Linear velocity of ammonia–air mixture w = 0.77 m s^{-1} (w.c.), T = 953 K; the same for Fig. 7.

where β is the mass-transfer coefficient; S the surface area of unit catalyst volume; and C_0 and C_S the ammonia concentrations in the flow core and at the catalyst surface, respectively.

Denoting $\beta_S = k$ and assuming that $C_0 >> C_S$ (deep-diffusion region of the process), we obtain

$$r_{NH_3} = KC_0. \quad (7)$$

At $[O_2]/[NH_3] < 1.5$ (C_{NH_3} = 12.3 vol %) the catalyst surface is insufficiently covered with oxygen and a possibility appears of a direct interaction between ammonia and the platinum oxide surface, which leads to reaction (4) with the formation of molecular nitrogen [1, 14].

In this case, the catalyst selectivity with respect to NO falls dramatically (Fig. 6).

The kinetic characteristics of the reaction were determined using the temperatures of "ignition" and "decay," i.e., the temperatures at the critical points, of an oxide catalyst pellet. The reaction rates were calculated using the method for determining the temperature limits of the outer-diffusion region with the use of the effect of catalyst pellet decay at lowered temperature of the ammonia–air mixture

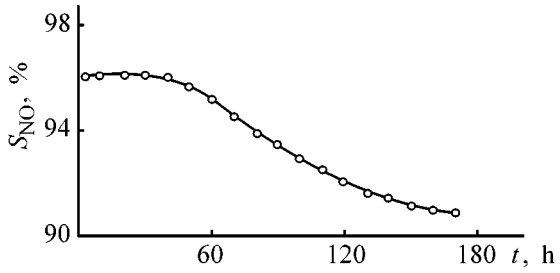

Fig. 7. Selectivity of Pt_3O_4 catalyst, S_{NO}, vs. operation time t.

[25]. The catalyst surface temperature was measured with a Chromel–Alumel thermocouple pressed in the pellet on the front surface of the pellet (with respect to the ammonia–air mixture flow direction). To prevent heat losses, a layer of platinum oxide grains $(2.0–3.0) \times 10^{-3}$ m was placed between the pellet and the reactor walls. The kinetic parameters of the process were calculated using the equation proposed by Buben [26] and solved for two reaction rates at constant concentration of oxygen. The Buben equation has the form

$$(1 + a)^2\left[1 + (m - 1)\frac{a}{b}\right] - \frac{a}{\varepsilon}\left(1 - \frac{a}{b}\right) = 0, \quad (8)$$

$$a = \frac{T}{T_0} - 1, \; b = \frac{Q\beta C_0}{\alpha T_0}, \; \varepsilon = \frac{RT_0}{E},$$

where m is the reaction order with respect to ammonia; T the catalyst surface temperature at the critical point (K); T_0 the temperature of the ammonia–air mixture; C_0 the concentration of ammonia in the flow; α and β the coefficients of, respectively, heat and mass transfer; Q the heat effect of the reaction; and E the activation energy of the reaction.

The coefficients α and β were calculated using the known equations [27].

The kinetic parameters of ammonia oxidation on platinum oxide are as follows:

Temperature of catalyst ignition	500
Ammonia concentration in the ammonia–air mixture, vol %	10.0
Activation energy E of the reaction, kJ mol^{-1} NH_3	9.06
Reaction order with respect to ammonia	0.17

A study of how the catalyst selectivity depends on the time of operation at the optimal temperature (953 K) demonstrated (Fig. 7) that the catalyst is stable during 40 h of operation and then undergoes deactivation. After 170 h of operation, the catalyst selectivity decreases by 5.2%. To reveal the causes of the deactivation, the chemical and phase composition of the catalyst and its structure (especially that of the surface layer of the catalyst, in view of the heterogeneous-catalytic nature of the reaction) were studied. According to X-ray phase and chemical analyses and X-ray photoelectron spectroscopy (XPS), the surface layer of a deactivated catalyst contains platinum and a nonstoichiometric compound $M_xPt_3O_4$ ($M = Na^+$, K^+, Ca^{2+}, Mg^{2+}, Fe^{3+}) of the $Na_xPt_3O_4$ structural type [9, 17, 19]. Compounds of such metals are present in the catalyst in the form of impurities and, in part, arrive with the ammonia–air mixture as contaminants, despite the purification of the reactants to remove them [1, 6]. According to XPS, the surface layers of catalyst grains are enriched (to a depth of 10–20 nm) in the above metal ions, compared with deeper lying layers. The appearance of platinum can be accounted for by the redox mechanism of the reaction occurring at the surface [1, 28], and by interaction of a strong reducing agent—ammonia, directly with parts of the catalyst surface that are characterized by low catalyst–oxygen binding energies [1, 28, 29]. Also, the temperature at which the catalyst was tested was close to the temperature of its dissociation. Partial dissociation of the catalyst is possible in the reaction medium at places of local catalyst surface temperature rise [9, 17, 20]

$$Pt_3O_4 = 2PtO_2 + Pt. \quad (9)$$

The forming platinum dioxide readily decomposes into simple substances (T_{dis} = 853–873 K) by the reaction [20]

$$PtO_2 = Pt + O_2. \quad (10)$$

Part of platinum dioxide sublimates and is carried away by the gas flow of the reaction medium [1, 6–8, 20].

Conditions are created for introduction of platinum atoms into the voids of the cubic structure of platinum(II, III) oxide to form a stable compound of the $Na_xPt_3O_4$ structural type. In this case, the atomic ratio O/Pt of the compound (170 h of operation) falls to 1.17 according to chemical analysis data. The crystal lattice constant of stabilized platinum oxide grows from 0.5633 to 0.5644 nm. The x value in a compound of the structural type $Na_xPt_3O_4$ may vary between 0 and 1 in the formation of stable interstitial structures [9, 19, 20]. The rate of formation of the variable-composition compound $Na_xPt_3O_4$ (in particular, upon introduction of platinum into platinum oxide) is low [9, 17]. For example, $Na_{0.1}Pt_3O_4$ is formed after 130–150 h of synthesis from sodium carbonate and α-PtO_2 [5, 9], and $CaPt_3O_4$, after 300–340 h of synthesis from calcium nitrate and α-PtO_2 [17, 30].

Probably, the concentration of platinum in the surface layer of the catalyst much exceeds the amount that can react with Pt_3O_4 under a given process conditions, i.e., part of platinum remains in the form of a separate phase. Both the interstitial solid solution ($M_xPt_3O_4$) and part of unreacted platinum are present in the surface layer of the catalyst as separate phases. The properties of the catalytic system at the chosen test parameters are determined by the composition and physicochemical characteristics of separate components and by the nature of their interaction. The selectivity of platinum at 953–973 K does not exceed 90–91% [1], i.e., the appearance of this phase in the surface layer makes the catalyst selectivity lower. The composition of the $M_xPt_3O_4$ compound varies with nature and concentration of interstitial ions in the structure and with the time of catalyst operation (at constant process parameters).

Under the action of elevated temperature the catalyst recrystallizes, with its specific surface area decreasing (see table). The rms size of particles of platinum oxide grows upon its conversion into a nonstoichiometric interstitial compound $M_xPt_3O_4$ from 170 to 230 nm (after 170 h of catalyst operation). Electron-microscopic studies of the surface of a catalyst that operated for a certain time demonstrated that the two-phase system $M_xPt_3O_4 + Pt$ contains both fine $M_xPt_3O_4$ particles and large, strongly recrystallized particles of platinum uniformly distributed over the surface. The $M_xPt_3O_4$ compound only slightly recrystallizes at the given temperature. The specific surface area of the catalytic system decreases in the course of operation from 12.5 to 8.7 $m^2 g^{-1}$ (mainly because of the recrystallization of platinum particles). Since the reaction proceeds under far-from-critical conditions, i.e., is limited by the diffusion of ammonia to the outer surface of the catalyst, the specific surface area exerts no decisive influence on the selectivity of platinum oxide with respect to NO [1, 12, 14, 21, 29]. This means that the decrease in the selectivity of the catalyst in the course of its operation at 953 K is mainly due to phase and chemical transformations of the catalyst. Under the critical conditions of the reaction (catalyst decay), the recrystallization and the decrease in the specific surface area of the catalyst decrease the limiting load on platinum oxide, i.e., diminish its activity [1, 14], from 13.8×10^3 to 9.58×10^3 $m^3 NH_3/(h\ m^2)$ 170 h of operation). The limiting load depends on the rate of the chemical reaction on the surface, which is, in turn, determined by the chemical composition of the catalyst. When the process is performed under the critical conditions ($\tau = 1.1 \times 10^{-3}$ s), no successive reaction of nitrogen(II) oxide decomposition by scheme (2) is observed, but part of unreacted ammonia is found after the catalyst, i.e., there occurs ammonia breakthrough.

The decrease in the specific surface area of the catalyst in the course of its operation is accompanied by an increase in ammonia breakthrough from 0.14 to 0.32%, which is due to the drop in the catalyst activity.

Thus, the whole set of chemical and phase transformations of the catalyst, leading to the formation of less active and less selective components ($M_xPt_3O_4$, Pt) with changed structure (recrystallization and decreasing specific surface area), is the reason for deactivation of platinum(II, III) oxide at 953 K.

A study of how the selectivity of a catalyst that undergoes phase and chemical transformations (170 h of operation) depends on temperature (Fig. 2) demonstrated that the peak selectivity of the catalyst (97.2%) is shifted to higher temperatures (1173 K), compared with platinum(II, III) oxide. The $M_xPt_3O_4 + Pt$ catalyst is thermally stable and does not undergo dissociation in the temperature range 953–1173 K. At $T > 1173$ K the compound $M_xPt_3O_4$ starts to decompose to give platinum and low-active oxides of the corresponding metals. At $T > 1173$ K the selectivity of the catalytic system decreases with increasing temperature.

The $M_xPt_3O_4$ phase can also be formed on the platinum surface in operation of the platinum catalyst in ammonia oxidation in view of the surface processes of high-temperature platinum oxidation and the presence of impurities of metal compounds in the ammonia–air mixture and the catalyst. In fact, the catalytic properties of platinum will be determined in this case by the composition and properties of the surface interstitial phase of platinum(II, III) oxide, i.e., $M_xPt_3O_4$. The assumptions that the key role in ammonia oxidation on platinum is played by PtO_2 [8] or PtO [31] are rather questionable, since both these compounds are unstable in the high-temperature region [5, 9, 17, 20].

The only possible candidate is the thermally stable modified platinum(II, III) oxide, i.e., $M_xPt_3O_4$. Studies of the catalytic properties of variable-composition compounds $M_xPt_3O_4$ (with account of the nature and concentration of the interstitial ions) give new insight into the mechanisms of high-temperature ammonia oxidation on platinum and deactivation and regeneration of the catalyst.

CONCLUSIONS

(1) The catalytic properties of platinum(II, III) oxide were studied in the temperature range 813–1273 K.

(2) The optimal parameters of the process of ammonia oxidation on oxide catalyst and the kinetic characteristics of the reaction were determined.

(3) It was established that at $T \geq 953$ K the catalyst undergoes structural (recrystallization, decreasing specific surface area), phase, and chemical transformations to give a nonstoichiometric compound $M_xPt_3O_4$ (Me = Na^+, K^+, Ca^{2+}, Mg^{2+}, Fe^{3+}, Pt^{2+}) and platinum. The reasons for the catalyst deactivation at $T \geq 953$ K are considered.

(4) Data on the catalytic properties of platinum(II, III) oxide can be used, in particular, in analyzing the mechanisms of high-temperature oxidation of ammonia on platinum and deactivation and regeneration of platinum catalysts.

REFERENCES

1. Karavaev, M.M., Zasorin, A.P., and Kleshchev, N.F., *Kataliticheskoe okislenie ammiaka* (Catalytic Oxidation of Ammonia), Moscow: Khimiya, 1983.
2. Phillips, W.Z., *Trans. ASM*, 1964, vol. 57, no. 1, pp. 33–37.
3. Shäfer, V.H. and Tebben, A.Z., *Z. anorg. allgem. Chem.*, 1960, vol. 304, nos. 3–4, pp. 317–321.
4. Karavaev, M.M., Mumgyan, E.G., Arutyunyan, V.A., *et al.*, *Azot. Prom–st.*, 1974, no. 5, pp. 26–29.
5. Holzmann, H., *Platinum Metals Rev.*, 1969, vol. 13, no. 1, pp. 2–8.
6. *Kataliticheskie i massoobmennye protsessy pod davleniem v tekhnologii neorganicheskikh veshchestv* (Catalytic and Mass-Exchange Processes under Pressure in Technology of Inorganic Substances), Loboiko, A.Ya., Ed., Kharkov: Osnova, 1993.
7. Arustamyan, E.S. and Chernyshev, A.K., *Sposoby ulavlivaniya platiny v promyshlennosti azotnoi kisloty: Obzor informatsii* (Methods for Recovery of Platinum in Nitric Acid Industry: Review), Moscow: NIITEKhIM, 1973.
8. Sikoza, H. and Blasiak, E., *Przem. Shem.*, 1967, vol. 46, no. 1, pp. 31–33.
9. Bergner, D. and Kohlhaas, R., *Z. anorg. allgem. Chem.*, 1973, vol. 401, no. 1, pp. 15–20.
10. Chaston, J.S., *Platinum Met. Rev.*, 1966, vol. 10, no. 1, pp. 91–96.
11. *Analiticheskii kontrol' proizvodstva v azotnoi promyshlennosti* (Analytical Production Control in Nitrogen Industry), Demin, L.A., Ed., issue 8, *Kontrol' proizvodstva v tsekhe slaboi azotnoi kisloty* (Production Control in Weak Nitric Acid Shop), Moscow: Goskhimizdat, 1958.
12. Zakharchenko, N.I. and Seredenko, V.V., *Zh. Prikl. Khim.*, 1999, vol. 72, no. 11, pp. 1921–1923.
13. Alkhazov, T.G., Gasan-zade, G.Z., Osmanov, M.O., and Sultanov, M.Yu., *Kinet. Kataliz*, 1975, vol. 16, no. 6, pp. 1230–1234.
14. Morozov, N.M., Luk'yanova, L.I., and Temkin, M.I., *Kinet. Kataliz*, 1966, vol. 7, no. 1, pp. 172–175.
15. Luk'yanovich, V.M., *Elektronnaya mikroskopiya v fizikokhimicheskikh issledovaniyakh: Metodika i primenenie* (Electron Microscopy in Physicochemical Studies: Procedure and Use), Moscow: Akad. Nauk SSSR, 1964.
16. Panichkina, V.V. and Uvarova, I.V., *Metody kontrolya dispersnosti i udel'noi poverkhnosti metallicheskikh poroshkov* (Methods for Monitoring of Dispersity and Specific Surface Area of Metal Powders), Kiev: Naukova Dumka, 1973.
17. Muller, O. and Roy, R., *J. Less-Common Metals*, 1968, vol. 16, no. 2, pp. 129–133.
18. Goncharenko, G.I., Lazarev, V.B., and Shaplygin, I.S., *Zh. Neorg. Khim.*, 1985, vol. 30, no. 12, pp. 3032–3037.
19. Collongues, R., *La Non-Stoechiometrie*, Paris: Masson et C , 1971.
20. Blagorodnye metally: *Spravochnik* (Noble Metals: Reference Book), Savitskii, E.M., Ed., Moscow: Metallurgiya, 1984.
21. Zakharchenko, N.I., *Zh. Prikl. Khim.*, 2000, vol. 73, no. 12, pp. 1960–1964.
22. Ganz, S.N. and Vashkevich, A.M., *Zh. Prikl. Khim.*, 1970, vol. 43, no. 1, pp. 13–18.
23. Zhidkov, B.A., Orlova, S.S., Bochenko, G.A., and Plygunov, A.S., *Khim. Tekhnol.*, 1979, no. 1, pp. 5–8.
24. Frank-Kamenetskii, D.A., *Diffuziya i teploperedacha v khimicheskoi kinetike* (Diffusion and Heat Transfer in Chemical Kinetics), Moscow: Nauka, 1967.
25. Beskov, V.S., Karavaev, M.M., Garov, D.V., and Arutyunyan, V.A., *React. Kinet. Catal. Lett.*, 1976, vol. 4, no. 3, pp. 351–357.
26. Buben, N.Ya., *Zh. Fiz. Khim.*, 1945, vol. 19, nos. 4–5, pp. 250–253.
27. Kasatkin, A.G., *Osnovnye protsessy i apparaty khimicheskoi tekhnologii* (Basic Processes and Apparatus of Chemical Technology), Moscow: Khimiya, 1973.
28. Golodets, G.I., *Geterogenno-kataliticheskie reaktsii s uchastiem molekulyarnogo kisloroda* (Heterogeneous-Catalytic Reactions Involving Molecular Oxygen), Kiev: Naukova Dumka, 1977.
29. Zakharchenko, N.I., *Zh. Fiz. Khim.*, 2001, vol. 75, no. 6, pp. 989–994.
30. USSR Inventor's Certificate, no. 1452793.
31. Chernyi, V.F., Kleshchev, N.F. and Bliznyuk, O.N., *Izv. Vyssh. Uchebn. Zaved., Khim. Khim. Tekhnol.*, 1997, vol. 40, no. 6, pp. 28–32.

Russian Journal of Applied Chemistry, Vol. 74, No. 10, 2001, pp. 1693–1697. Translated from Zhurnal Prikladnoi Khimii, Vol. 74, No. 10, 2001, pp. 1643–1647.

CATALYSIS

Effect of Sulfur Compounds and Higher Homologues of Methane on Hydrogen Cyanide Production by the Andrussow Method

N. V. Trusov

Kharkov State Polytechnic University, Kharkov, Ukraine

Received June 6, 2000; in final form, March 2001

Abstract—The influence of sulfur compounds and higher homologues of methane on the parameters of oxidative ammonolysis of methane was studied.

In [1, 2], the results obtained in technological calculations in terms of the empirical model of HCN production by the Andrussow method (the so-called oxidative ammonolysis of methane, OAM) were considered. The next step in a comprehensive study was to analyze the influence exerted by technological impurities present in natural gas on hydrogen cyanide formation.

The influence of sulfur compounds and higher homologues of methane—unavoidable components of natural gas—on the OAM parameters has been studied in sufficient detail [3–5]. A detailed analysis of patents and other published evidence was made in a monograph [6]. However, quite a number of questions, answers to which are exceedingly important from the standpoint of applications, remain unanswered. In particular, the effect of the time τ of contact with platinoid grids on the loss of catalytic activity upon prolonged action of technological impurities on a catalyst, has not been studied at all. A search of answer to this and other questions was the aim of the present study.

The author has collected during a long time data characterizing the operation of an industrial installation for HCN synthesis. The obtained body of evidence was used to compile a database, part of which is given in Table 1 (total number of measurements 116).

Table 1. Influence exerted by the concentration of sulfur compounds and higher homologues of methane in natural gas on the content of HCN in synthesis gas (selected data)

Starting mixture, vol %			Content in natural gas, mg m^{-3}		Flow rate of mixture, $m^3\ h^{-1}$	T, °C	τ, h	HCN content in synthesis gas, vol %
NH_3	CH_4	O_2	S	C_nH_{2n+2}				
11.00	11.66	15.26	1.06	0.24	7550	930	26	6.16
11.30	12.88	14.86	0.62	1.81	7660	945	94	7.05
10.79	12.55	15.42	0.58	1.54	9380	960	174	7.45
11.00	11.68	15.45	0.17	0.94	7500	930	240	7.31
11.24	12.52	15.71	0.72	0.69	7550	930	378	6.58
11.07	12.28	15.65	0.54	1.69	8700	925	455	7.17
11.39	11.48	15.11	0.61	1.17	7050	930	574	7.01
11.16	12.11	15.28	0.47	0.59	7550	910	656	7.98
10.73	11.29	15.51	0.51	0.02	7630	980	716	7.43
11.70	12.76	15.47	0.17	0.94	8700	945	833	7.57
11.47	12.10	15.74	0.51	0.67	8700	945	908	7.07
11.92	12.13	15.61	0.36	0.60	9640	960	1018	6.61
11.94	12.83	15.52	0.30	0.98	9610	945	1202	6.90
11.24	12.4	16.05	0.30	1.26	9720	970	1250	7.29

1070-4272/01/7410-1693 $25.00 © 2001 MAIK "Nauka/Interperiodica"

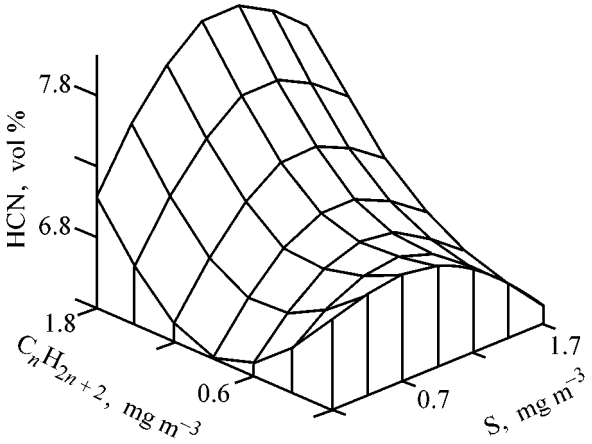

Fig. 1. Hydrogen cyanide concentration in the synthesis gas vs. content of sulfur compounds, S, and higher homologues of methane, C_nH_{n+2}, in natural gas.

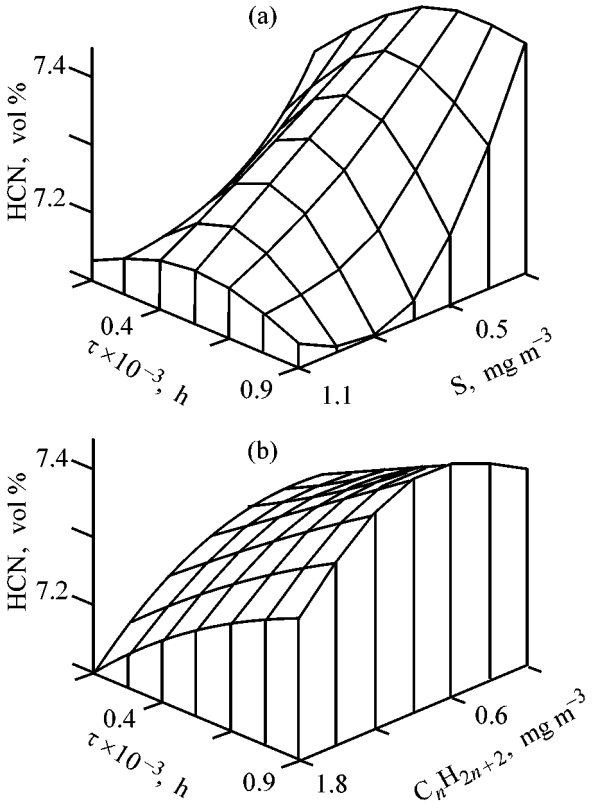

Fig. 2. Hydrogen cyanide concentration in the synthesis gas vs. (a) content of sulfur compounds, S, and (b) higher homologues of methane, C_nH_{n+2}, in natural gas at different times τ of contact with platinoid catalyst.

A preliminary processing of the entire body of information (representation in two-dimensional space) revealed a rather clearly pronounced correlation between the amount of sulfur compounds in natural gas and the volume concentration of hydrogen cyanide in the synthesis gas. There is no relationship between the content of HCN and the amount of C_nH_{n+2}. Therefore, it was suggested that the influence exerted by technological impurities present in natural gas has combined nature. This suggestion was confirmed by plotting the corresponding dependence in three-dimensional space (Fig. 1).

Noteworthy is the fact that the effect of sulfur compounds has extremal nature with a maximum at 1.0 mg m^{-3}: minor amounts block intermetallic compounds inevitably present in the alloy, thereby enhancing its selectivity; further increase in the content of sulfur in the gas leads to poisoning of platinum itself. The obtained results are in full agreement with the data of [7–9]. The influence of higher homologues of methane is on the whole positive in the investigated range of their concentrations, but, with this range expanded further, an abrupt drop in the output of hydrogen cyanide would be expected, as found experimentally by S.S. Bobkov [6]. A virtually similar conclusion is given in a patent [10].

Analysis of the data in Fig. 2 shows that the content of HCN exhibits extremal behavior with the time contact with the platinoid catalyst increasing at fixed content of sulfur compounds; at constant concentration of methane homologues the content of hydrogen cyanide grows with increasing time of passage.

The subsequent processing of the entire body of input data cast some doubts on the existence of a direct dependence of the volume content of HCN in the synthesis gas on the concentration of technological impurities in natural gas. A graphical interpretation of the averaged data of Table 1 (Fig. 3) indicates that this relationship cannot be considered in isolation from the changing flow rate of the starting mixture $Q \times 10^3$ (m^3 h^{-1}) and the spontaneously attained autothermic temperature T (°C) of the process. Anyway, none of the considered parameters (content of sulfur and C_nH_{n+2}, and also Q and T) correlates with the content of hydrogen cyanide in the reaction products.

In this regard, the following assumption seemed to be well justified. The problem in question can only be solved, with an empirical model adequate to the input data constructed, when the concentrations of technological impurities in a mixture supplied to conversion, rather than in natural gas (as it was done before [3–5, 7–10]), are used as control parameters.

A graphical presentation of the results of a representative sampling characterized by constant flow rate of the starting mixture (7550 m^3 h^{-1}) indicates

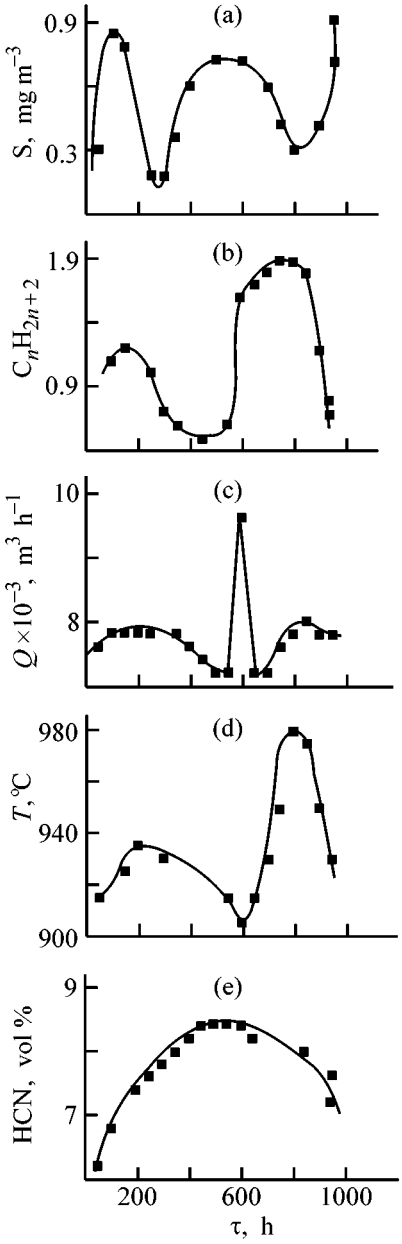

Fig. 3. Selected control parameters and response functions vs. time τ. (Q) Flow rate of the starting mixture and (T) temperature.

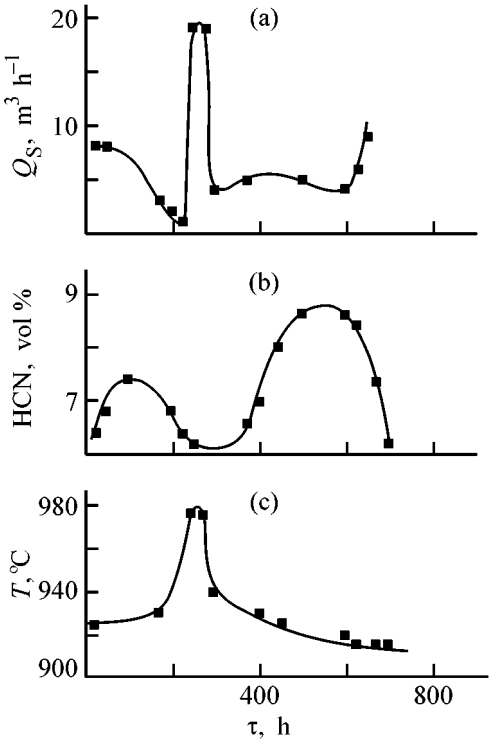

Fig. 4. Selected control parameters and response functions vs. time τ at constant flow rate of the starting mixture (7550 m^3 h^{-1}). (Q_S) Amount of sulfur and (T) temperature.

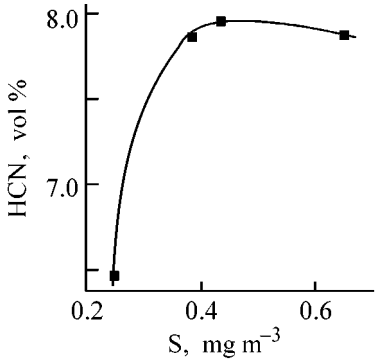

Fig. 5. Effect of the content S of sulfur compounds on the content of hydrogen cyanide in the synthesis gas. Load 7550 m^3 h^{-1}, temperature 915°C.

(Figs. 4a and 4b) that an abrupt increase in the amount of sulfur, Q_S (m^3 h^{-1}), fed into the reactor for HCN synthesis is accompanied by a virtually instantaneous, but not prolonged in any way, decrease in the content of hydrogen cyanide in the synthesis gas.

At the same time, the processing revealed a correlation between the content of sulfur compounds and the autothermic temperature of the process (Figs. 4a and 4c). For example, experiments with approximately constant temperature gave a dependence (Fig. 5) virtually coinciding with Warren's data, with the form of presentation of the content of sulfur compounds—as their concentration in natural gas or in the starting reaction mixture—being of no importance.

The entire body of the obtained data gave new insight into the problem of the influence exerted by technological impurities on the course of the OAM process. The revealed correlation between the content of sulfur compounds and the autothermic temperature suggested a similar relationship for higher homol-

Table 2. Database for determining the nature of the influence exerted by sulfur compounds on parameters of the OAM process.

Starting mixture, vol %			T, °C	τ, h	Natural gas		Amount of sulfur compounds, m^3		Content of HCN in synthesis gas, vol %
NH_3	CH_4	O_2			flow rate, $m^3\ h^{-1}$	content of sulfur compounds, vol %	running	integral	
10.93	11.76	15.17	925	73	1080	0.75	8.08	590	7.1
11.30	11.78	15.17	920	141	1100	0.67	7.35	1415	7.4
10.63	12.09	15.50	930	173	1070	0.61	6.52	2505	7.7
11.00	11.68	15.45	930	245	1095	0.17	1.87	3380	7.4
11.12	12.00	15.49	930	265	1100	0.16	1.76	3845	7.0
11.16	11.93	15.41	975	294	1090	1.74	18.98	6745	6.5
11.16	12.11	15.58	930	309	1095	0.36	3.95	10200	6.4
11.06	12.04	15.51	930	333	1115	0.50	5.56	11725	6.8
11.40	12.52	15.24	925	409	1130	0.40	4.53	13595	6.7
11.48	12.16	15.41	920	432	1135	0.51	5.80	15765	7.3
11.12	12.05	15.31	915	577	1105	0.27	2.99	17980	6.3
11.17	12.09	15.65	910	600	1135	0.37	4.20	20095	7.7
11.66	12.27	15.49	915	622	1140	0.72	8.19	23850	8.3
11.05	12.21	15.82	910	653	1120	0.47	5.25	28165	7.9
10.93	12.08	15.55	915	673	1110	0.51	5.65	31780	7.1

ogues of methane, too, the more so as the calorific value of these latter much exceeds the same characteristic for sulfur compounds [11].

Therefore, an assumption was made that the entire body of the previously obtained information reflects the accumulation of sulfur on the surface of a platinoid catalyst, rather than the prolonged nature of the influence of sulfur compounds. To verify (or reject) this hypothesis, a sample was formed (Table 2), characterized by constant flow rate of the starting mixture (7550 $m^3\ h^{-1}$). As an additional restrictive condition served the following: all the experiments belonged to the same run. The volume of sulfur compounds in a given period of the run is understood as the current amount of sulfur compounds passed through the reactor, and their progressive total volume, as the integral amount.

The graphical representation of the data of Table 2 indicates that there is no integral effect of sulfur on the course of the OAM process. No prolonged nature of this influence is observed either. Detailed analysis of the obtained data shows that sulfur compounds are to be regarded as catalytic poisons of instantaneous action.

Thus, it became apparent that it is only possible to construct an empirical model of the OAM process that would adequately describe not only the effect of the main technological parameters (as it was done in [6]), but also the influence exerted by sulfur compounds and higher homologues of methane if the following condition is satisfied. Deviations of calculated volume concentrations of methane from experimental values should be regarded as a direct consequence of the unaccounted-for effect of sulfur compounds and higher homologues of methane.

The subsequent statistical processing aimed at developing an empirical model (derived by the Brandon method in the form of a polynomial) took this factor into account and yielded a system of equations, including several submodels. These were the following: (a) calculation of the volume concentration of reagents in the starting mixture (ammonia, methane, oxygen), depending on its preparation conditions; (b) determination of the spontaneously attained process temperature; (c) finding the output parameters of the process (volume content of HCN in the synthesis gas, conversion of reagents into the target product, yield of the target product, etc.).

The results of a technological calculation performed using the derived system of empirical equations indicate (Fig. 6) that, with natural gas containing equal amounts of sulfur compounds and higher homologues of methane, an increase in the amount of impurities leads to a gradual rise in the process temperature, and this dependence passes through a maximum with increasing flow rate of the starting mixture.

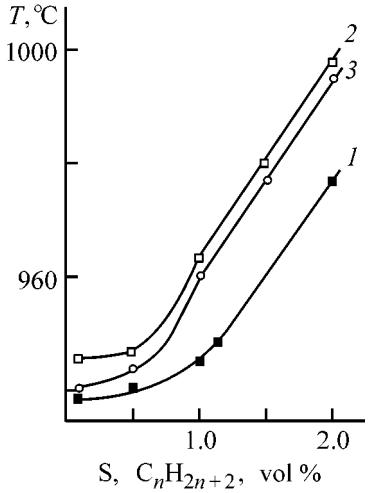

Fig. 6. Process temperature T vs. content of sulfur compounds, S, and higher homologues of methane, C_nH_{n+2}, in natural gas at their equal concentrations. Flow rate ($m^3\ h^{-1}$): (*1*) 7000, (*2*) 8000, and (*3*) 9000.

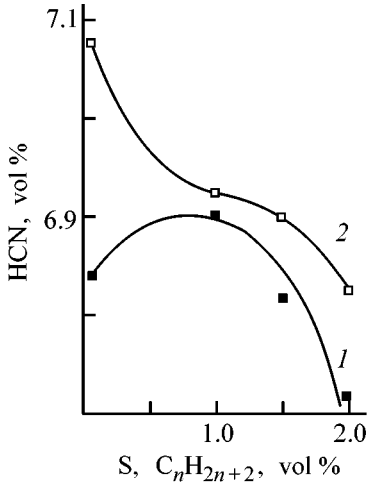

Fig. 7. Effect of the content of (*1*) sulfur compounds, S, and (*2*) higher homologues of methane, C_nH_{n+2}, on the concentration of hydrogen cyanide in the synthesis gas. Content (vol %): (*1*) C_nH_{n+2} 1.03 and (*2*) S 0.56.

An indisputable advantage of the proposed model is that it clearly demonstrates the effect of sulfur compounds and homologues of C_nH_{n+2} in "pure" form. The database in Table 1, characterized by exceedingly wide ranges of variation of all parameters of the OAM process, cannot do this by definition. It can be seen from Fig. 7 that the influence exerted by the content of sulfur compounds has extremal nature; the effect of higher homologues of methane on the content of hydrogen cyanide in the synthesis gas is negative (in calculations, the content of one of the natural gas components under consideration was fixed at the statistical-mean level).

It may be stated that only technological calculations based on the empirical model of the OAM process made it possible to avoid an erroneous conclusion that impurities contained in natural gas affect the HCN formation, drawn in the stage of preliminary processing of the initial database.

CONCLUSIONS

(1) Preliminary processing of experimental data was used to determine the nature of the influence exerted by technological impurities inevitably present in natural gas on parameters of oxidative ammonolysis of methane.

(2) Technological calculations performed using the constructed empirical model of oxidative ammonolysis of methane demonstrated an extremal influence of sulfur compounds and negative effects of higher homologues of methane on the content of hydrogen cyanide in the production gas.

(3) An increase in the time of contact with a platinoid catalyst in the case of presence of sulfur compounds and higher homologues of methane in natural gas exerts negative influence on the volume content of HCN in the synthesis gas.

REFERENCES

1. Grin', G.I. and Trusov, N.V., *Zh. Prikl. Khim.*, 1992, vol. 65, no. 10, pp. 2300–2305.
2. Grin', G.I., Trusov, N.V., and Dmitriev, N.V., *Zh. Prikl. Khim.*, 1993, vol. 66, no. 9, pp. 2025–2030.
3. Bobkov, S.S., *Khim. Nauka Prom–st.*, 1957, no. 2, pp. 34–45.
4. Andrussow, L., *Bull. Soc. chim. France*, 1951, no. 1–2, pp. 45–50.
5. Thomas, A., *Ann. chim.*, 1949, vol. 4, no. 3–4, pp. 258–285.
6. Trusov, N.V., Grin', G.I., Loboiko, A.Ya., and Koshovets, N.V., *Poluchenie sinil'noi kisloty po metodu Andrussova* (Preparation of Hydrocyanic Acid by the Andrussow Method), Kharkov: Osnova, 1999.
7. UK Patent 941 486.
8. US Patent 3 102 269.
9. FRG Patent 1 163 304.
10. US Patent 2 478 875.
11. Stull, D.R., Westrum, E.F., and Sinke, G.C., *The Chemical Thermodynamics of Organic Compounds*, New York: John Wiley & Sons, 1969.

Russian Journal of Applied Chemistry, Vol. 74, No. 10, 2001, pp. 1698–1701. Translated from Zhurnal Prikladnoi Khimii, Vol. 74, No. 10, 2001, pp. 1648–1650.

ENVIRONMENTAL PROBLEMS OF CHEMISTRY AND TECHNOLOGY

Deep Purification of Aqueous Solutions to Remove Chromium(III) with Industrial Carbonate-Containing Wastes

T. G. Lupeiko, M. O. Gorbunova, and E. M. Bayan

Rostov State University, Rostov-on-Don, Russia

Received November 17, 2000; in final form, April 2001

Abstract—The possibility of diminishing chromium(III) ion concentration in aqueous solutions to a MPC (maximum permissible concentration) level with the use of industrial carbonate-containing wastes was studied. The influence exerted by the chromium(III) ion concentration in a starting solution, duration of sorbent contact with the solution, anion composition of the solution, temperature, and other conditions on the degree of recovery of Cr(III) ions and on the sorbent consumption was investigated.

The problem of effective and inexpensive purification of wastewater of galvanic industry to remove heavy metals and, in particular, chromium(III) ions is of great importance for the national economy. Presently, the main technique for removal of chromium(III) ions from solutions is their neutralization and precipitation in the form of $Cr(OH)_3$. The afterpurification to an MPC level (0.5 mg l^{-1}) usually requires expensive synthetic cation exchangers [1]. It has been proposed to use inorganic carbonate-containing sorbents for recovery of heavy metals [2]. The use of industrial wastes as sorbents is of particular interest from the standpoint of cost efficiency and ecological safety.

The cumulative, embryotoxic, and mutagenic effects of chromium(III) ions have been well studied. The possibility of removing these ions from wastewater is the subject of the present study. We propose to use for this purpose an industrial waste containing calcium and magnesium carbonates as a readily accessible and inexpensive sorbent (for brevity, referred to as sorbent in what follows). The sorbent is a finely disperse white powder with creme tinge. According to the histogram in Fig. 1, the main fraction (49.2%) used in the study contains particles of size 0.25–0.5 mm.

The following elements were found in the sorbent (%): Ca 26.5 ± 0.1 (titrimetry), Mg 2.69 ± 0.05; Fe 2.00 ± 0.02; Al 1.10 ± 0.05 (spectrophotometry, KFK-2 apparatus), Si 2.4 ± 0.1 (gravimetry), Na 0.19 ± 0.01 (flame photometry, Flapho-4 photometer); Ni 0.0010 ± 0.0005, Pb 0.0013 ± 0.0005, Cu 0.0047 ± 0.0005 (spectral analysis, LMA-10 spectrograph).

Using an X-ray analysis (DRON-2 apparatus, Cu_{K_α} radiation), we found the following phases: $CaCO_3$ (calcite), $MgCO_3 \cdot 3H_2O$, β- and γ-$Fe_2O_3 \cdot H_2O$.

A water extract of the sorbent at dry substance to water ratio of 1 : 5 has pH 8.74 ± 0.05 (the pH values were measured with an I-120M ionometer).

Hydrolytic equilibria for chromium(III) ions were calculated for the 100 mg l^{-1} concentration, which corresponds to the average content of chromium ions in real wastewater [3]. As a result, the pH ranges

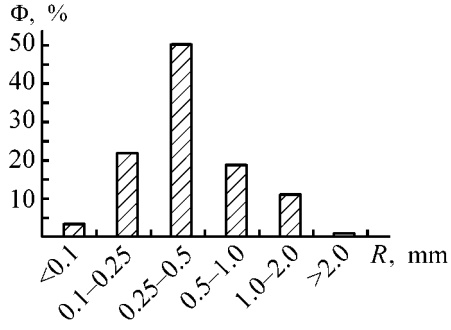

Fig. 1. Granulometric composition of the sorbent. (Φ) Content of a fraction in the sorbent and (*R*) particle size.

1070-4272/01/7410-1698 $25.00 © 2001 MAIK "Nauka/Interperiodica"

with the following predominant species were established: Cr^{3+} (pH < 4.0), $Cr(OH)^{2+}$ (4.0 < pH < 5.7), $Cr(OH)_2^+$ (5.7 < pH < 5.9), $Cr(OH)_3$ (5.9 < pH < 9.4), and $Cr(OH)_4^-$ (pH > 9.4). The range of maximal chromium(III) recovery at pH 6.5–10 was experimentally found by direct precipitation with sodium hydroxide solution. This pH range is in good agreement with the theoretically calculated range of $Cr(OH)_3$ predominance (Fig. 2a).

The calculated and experimental data, and also the fact that the solution above the sorbent has pH > 7, suggest that the industrial carbonate-containing waste can be used in purification of wastewater to remove chromium(III) ions.

The degree of chromium(III) recovery was monitored during the experiments by determining spectrophotometrically with diphenyl carbazide the concentration of chromium(III) ions in solution before and after contact with the sorbent [4]. The optical density was measured on a KFK-2 photometer with an error of no greater than 4%. Model solutions were prepared from analytically pure $CrCl_3 \cdot 6H_2O$. The sorption was carried out under static conditions with stirring.

We found experimentally for a model solution with chromium concentration of 100 mg l^{-1} and pH 3.41 (Fig. 2b, curve *3*) that purification to the MPC level is achieved at sorbent consumption of 10 g l^{-1} (pH 7.57). It is seen from how the pH value varies that the sorption is accompanied by neutralization of the initially acid solutions.

To optimize the sorbent consumption, we studied the effects of time, temperature, and other factors on the degree of chromium recovery. To assess the effect of contact duration, the sorbent (20 g l^{-1}) was placed in a solution to be purified (solution volume 100 ml) at 20°C. The obtained data (Fig. 2c) show that 20 min is sufficient for purification to the MPC level to be complete. In further experiments, the optimal duration of the sorbent–solution contact was 20 min.

The degree of chromium(III) recovery as a function of sorbent consumption at 20, 35, 50°C is shown in Fig. 2b. It can be seen that the sorbent consumption required for purification of aqueous solutions to the MPC level decreases dramatically with increasing temperature. For example, the sorbent consumption is about 10 g l^{-1} at 20°C and only 1 g l^{-1} at 50°C. Apparently, this is a consequence of the higher solubility of carbonates contained in the sorbent and increased degree of chromium(III) ion hydrolysis at elevated temperature.

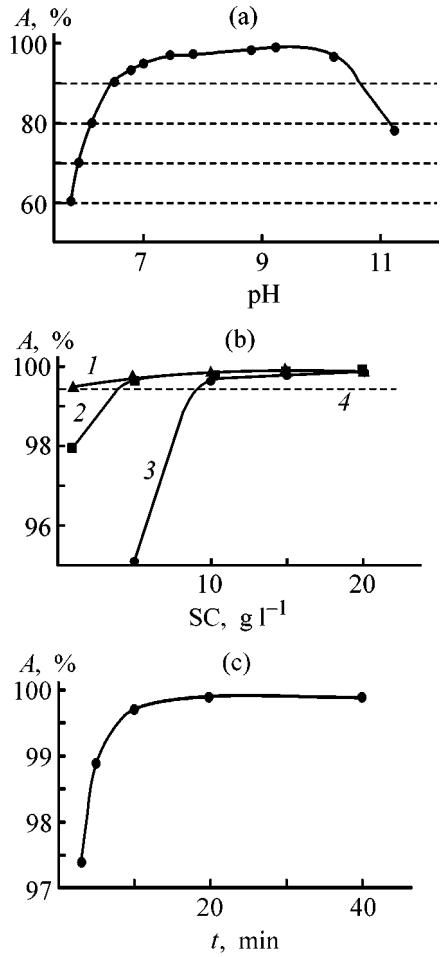

Fig. 2. Degree of Cr(III) recovery *A* vs. (a) pH value, (b) sorbent consumption SC, (c) time *t*. Temperature (°C): (*1*) 50, (*2*) 35, (*3*) 20; (*4*) MPC level.

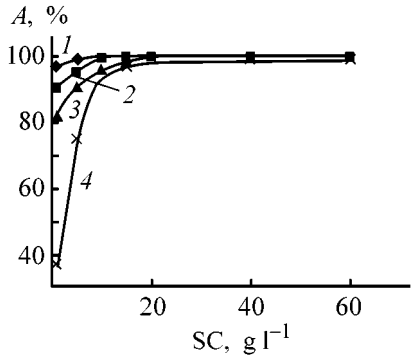

Fig. 3. Degree of Cr(III) recovery *A* vs. sorbent consumption SC at 20°C. Sorbent consumption RC (mg g^{-1} Cr): (*1*) 50, (*2*) 100, (*3*) 200, (*4*) 500.

To expand the possibilities of sorbent application, namely to purify spent electrolytes with chromium(III) content of up to 500 mg l^{-1}, we studied how the degree of chromium(III) recovery depends on the sorbent consumption at various initial concentrations of

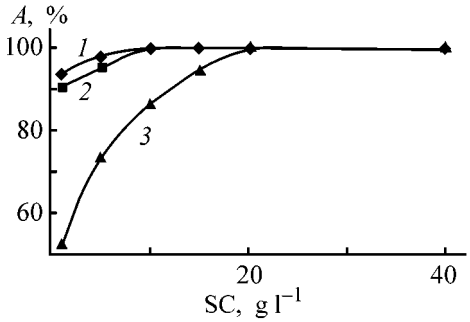

Fig. 4. Degree of Cr(III) recovery *A* vs. sorbent consumption SC for solutions of chromium (*1*) nitrate, (*2*) chloride, and (*3*) sulfate at 20°C.

chromium(III) in solutions (Fig. 3) and determined the sorbent consumption required to attain the MPC level in these cases. As expected, the sorbent consumption grows with increasing initial solution concentration and attains 60 g l^{-1} in the case of solutions with chromium(III) content of 500 mg l^{-1}.

Industrial chromium plating involves a stage of product pretreatment (mechanical cleaning, degreasing, etching, and rinsing) and direct electrolytic chromium deposition. Various acids can be used in etching. Thus, the galvanic sewage may have varying composition. Therefore, it is necessary to consider the effect of the anionic component of the solution on chromium sorption. For this purpose, we carried out additional experiments with chromium(III) nitrate and sulfate solutions (C_{Cr} = 100 mg l^{-1}). Comparison of thus obtained data (Fig. 4) and data on sorption from chloride solutions shows that the processes of sorption from chromium(III) chloride and nitrate solutions differ only slightly, although the degree of chromium(III) recovery from the nitrate solution is somewhat higher at the same sorbent consumption. The efficiency of chromium(III) recovery from the sulfate solution is essentially lower (Fig. 4). For example, when chromium(III) is removed from this solution, the MPC_{Cr} value is attained on adding 20 g l^{-1} of the sorbent. This can be accounted for by sorbent "gypsuming" in the course of chromium(III) sorption from sulfate solutions, i.e., a part of calcium ions of the sorbent becomes bound in the form of calcium sulfate. Moreover, a layer of difficulty soluble calcium sulfate appearing on the sorbent surface prevents diffusion of calcium ions into the solution and penetration of chromium(III) ions into the sorbent.

To verify the conclusions based on studying the sorption from model solutions, we carried out tests with real wastewater from electroplating shops of various plants. The wastewater compositions and analytical data are shown in the table. It follows from a comparison of the data for sample no. 1 and for the model solution with a similar concentration and the same sorbent consumption that the degree of chromium(III) recovery from sample no. 1 is much lower. This results from the presence of iron(III) and zinc(II), along with chromium(III), in the sorbent. The sorbent is presumably consumed for recovery of these ions. Moreover, in the case of sample no. 1, the pH value is much lower and part of the sorbent is consumed for neutralization of the acid medium. In fact, in the case of sample no. 4 with pH 3.34, the solution purification to remove chromium(III) to about the MPC level is attained on adding 20 g l^{-1} of the sorbent, whereas for sample no. 3 with pH 1.87 a similar result is obtained on addition of 60 g of the sorbent to 1 l of the solution. This conclusion is also well confirmed by the experimental data for samples nos. 5 and 6.

CONCLUSIONS

(1) A study of the chemical (elemental), phase, and granulometric composition of carbonate-containing industrial waste demonstrated the possibility of its use

Purification of real wastewater

Sample no.	Wastewater parameters			Sorbent consumption, g l^{-1}	C_{Cr}, residual, mg l^{-1}	Degree of Cr(III) recovery, %
	cations	pH	C_{Cr}, initial, mg l^{-1}			
1	Cr(III), Zn(II), Fe(III)	1.87	217.7	20	50.8	76.7
2	Cr(III), Zn(II), Fe(III)	1.87	217.7	40	11.6	94.7
3	Cr(III), Zn(II), Fe(III)	1.87	217.7	60	0.4	99.8
4	Cr(III), Zn(II), Fe(III)	3.34	217.7	20	0.7	99.7
5	Cr(III), Fe(III)	3.21	154.7	20	0.4	99.9
6	Cr(III), Zn(II), Fe(III)	3.51	275.2	20	0.4	99.9

as a sorbent in removal of chromium(III) ions from wastewater.

(2) Sorbent consumption decreases with increasing temperature and grows with increasing initial concentration of chromium(III) ions in the solution and also on passing from nitrate solutions to chloride, and especially to sulfate solutions.

(3) The results of the study were confirmed by tests with wastewater from electroplating shops of various plants. The efficiency and expediency of wastewater purification with the use of the carbonate-containing sorbent studied were demonstrated.

REFERENCES

1. *Galvanotekhnika* (Electroplating), Azhogin, F.F., Ed., Moscow: Metallurgiya, 1987.
2. Gudz', N.Ya. and Maksin, V.I., *Khim. Tekhnol. Vody*, 1991, vol. 13, no. 5, pp. 428–436.
3. Zhukov, A.I., Mongait, I.L., and Rodziller, I.D., *Kanalizatsiya promyshlennykh predpriyatii* (Sewerage of Industrial Enterprises), Moscow: Gosstroiizdat, 1962.
4. Lur'e, Yu.Yu., *Analiticheskaya khimiya promyshlennykh stochnykh vod* (Analytical Chemistry of Industrial Wastewater), Moscow: Khimiya, 1984.

Russian Journal of Applied Chemistry, Vol. 74, No. 10, 2001, pp. 1702–1705. Translated from Zhurnal Prikladnoi Khimii, Vol. 74, No. 10, 2001, pp. 1651–1654.

ENVIRONMENTAL PROBLEMS OF CHEMISTRY AND TECHNOLOGY

Ways to Develop Low-Waste Technology for Purification of Wastewater Containing Heavy Metal Compounds

N. E. Manvelova, I. V. Vol'f, and M. A. Sinyakova

Maikop State Technological Institute, Maikop, Russia

St. Petersburg State University of Plant Polymers, St. Petersburg, Russia

Received February 6, 2001

Abstract—A scheme is proposed for purification of wastewater of galvanic and printed circuit board shops. The scheme using reverse osmosis, ion exchange, and electrolysis techniques involves recycling of purified water and recovered metals.

Contamination of natural water with sewage water of galvanic industries is an ecological challenge. Discharge of this wastewater, containing highly toxic salts of heavy and non-ferrous metals, has a severe impact on the environment and leads to irretrievable loss of valuable metals in amounts of tens of thousands of tons.

The discharge of metals into water bodies of St. Petersburg was 3310.53 tons in 1999 [1]. The decline in galvanic manufacture in the succeeding years did not result in a proportional decrease in the environment contamination.

Most of domestic galvanic enterprises make use of outdated wastewater treatment facilities of 30–40-years-old conventional design. These bulky and cost-inefficient facilities fail to meet modern requirements to water recycling and heavy metal recovery. An essential drawback of such systems is the formation of a common wastewater flow including waste electrolytes, acidic and basic wastes, and rinsing water (see scheme). Mixing of wastes containing different ions in various concentrations hampers extraction of pollutants, and the mixed flow cannot be recycled even after reagent purification [2]. Purified wastewater is discharged into a sewer system or directly into a water body. Sediments formed in wastewater purification, i.e., sludges containing a combination of various heavy metal compounds, are transported to sludge stores, wherefrom these compounds are gradually washed out by ground waters and, all the same, find their way into the environment. Sludge processing is technologically complicated and economically inefficient.

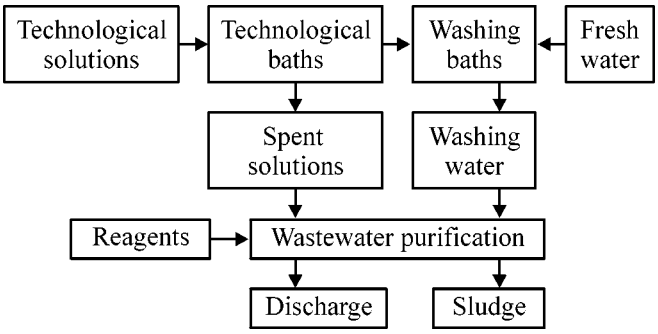

Scheme of water use in degreasing, etching, and electroplating.

Owing to the absence of water recycling, most of domestic galvanic plants consume fresh water in amounts of 2 m^3 and more per 1 m^2 of treated surface area, whereas in Sweden the same parameter is 0.05 $m^3\,m^{-2}$. A promising engineering solution of the problem under discussion consists in passing at galvanic shops to local purification systems recycling purified wastewater and recovering heavy metals. Local systems are intended for purification of wastewater with relatively invariable composition, produced by a certain technological line or separate installation, which allows use of compact purifying systems based on more effective and expensive purification techniques. The recoupment of such systems can be ensured by reduction of charges for the intake of pure water and disposal of wastewater and sludges. Moreover, wastewater produced by a particular technological line or separate installation usually contains ions of a single metal, rather than a mixture of metal ions, which significantly simplifies

1070-4272/01/7410-1702 $25.00 © 2001 MAIK "Nauka/Interperiodica"

its purification and creates new possibilities for further use of the recovered metals.

There are several efficient methods of purification, namely: adsorption and ion exchange [2–4], isolation of impurities by changing their aggregative state (distillation and freezing) [1, 2], and membrane techniques (electrodialysis, ultrafiltration, and reverse osmosis) [2, 5–9]. Comparative data [1] on capital investments and degree of nickel(II) removal from washing water are given in Table 1. The consumption of washing water was 0.2 $m^3 h^{-1}$, and the initial concentrations of Ni(II) and organic compounds, 32 and 54 mg l^{-1}, respectively. The cost of wastewater purification by ion exchange was conditionally taken to be unity.

Naturally, the relative costs and residual concentrations may vary with discharge parameters.

EXPERIMENTAL

The aim of this work was to study the possibility of, and conditions for creation of a low-waste technology for purification of wastewater produced by galvanic industry and printed circuit board manufacture.

The proposed purification scheme involves use of reverse osmosis for washing water purification, ion exchange for concentrating metal ion solutions, and electrochemical methods for metal recovery from concentrates of washing water and spent technological solutions.

The advantages of reverse osmosis consist in that no chemical reagents are required, the installations are compact, and water can be purified to remove impurities of varied nature.

Membranes used for reverse-osmosis purification retain any particles larger than 0.001 μm: inorganic ions, molecules of organic substances, and colloid particles. This leads to a high degree of purification and water becomes suitable for recycling.

Among disadvantages of reverse osmosis are the possibility of precipitate formation on membranes owing to the concentration polarization and the resulting necessity for periodic regeneration of the membranes.

We determined the most favorable conditions of reverse-osmosis purification of washing water of galvanic shop on a pilot installation comprising filters for rough and fine mechanical pre-purification and a reverse-osmosis apparatus with roll elements (see figure).

Table 1. Relative costs of purification of nickel-containing the washing waters by various methods and the attained degree of purification

Method	Relative cost	Residual concentration, mg l^{-1}	
		Ni(II)	organic substances
Ion exchange	1	0.008	–
Reverse osmosis	2–3	0.05	1.2
Electrolysis	3–4	0.3	–
Electrodialysis	5–10	0.55	6.7
Evaporation	8–12	0.1	4.1

Table 2. Reverse-osmosis purification of local washing water discharges

Source of washing water	Metal ion	$C_{M^{n+}}$, mg l^{-1}		Selectivity, %	pH
		initial solution	filtrate		
Acid etching line	Cu(II)	14.0	0.22	98.4	7.8
Nickel plating line	Ni(II)	10.2	0.44	95.7	7.05
Chromium plating line	Cr(VI)	18.0	1.6	91.1	5.6
Zinc plating line	Zn(II)	13.0	0.1	99.2	7.0

Comparative tests of the most widespread cellulose acetate membranes MGA-70, MGA-80, MGA-90, and MGA-100 demonstrated that MGA-100 membranes are the most effective under the test conditions, and these membranes were used in further studies. The possibility was established of purifiyng washing water containing various metal ions (Table 2). In all the experiments, the selectivity of a membrane, characterizing its separating ability, exceeded 90%, and the low residual content of metal ions in filtrates allowed their recycling as washing water.

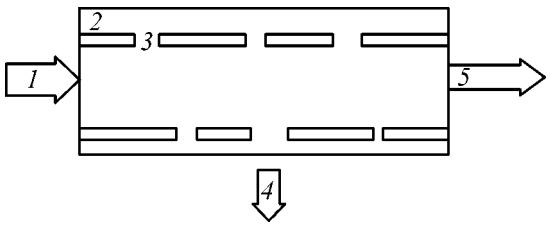

Schematic of a reverse-osmosis element: (*1*) wastewater input, (*2*) reverse-osmosis apparatus, (*3*) membrane, (*4*) purified filtrate, (*5*) concentrate.

The experiments demonstrated that the residual content of metal ion in the filtrate, $C_{M^{n+}}$, is in inverse relationship with the effluent concentrate fraction—the ratio of the concentrate volume to the volume of washing water to be purified. In most cases, this fraction was maintained at a level of 10–15%.

Our study of the efficiency and selectivity of membranes in relation to reverse-osmosis purification determined the following optimal parameters: pressure 2.0–2.5 MPa, velocity of purified water flow along membrane 0.8–1.2 m s^{-1}, water temperature 12–27°C. In this case the degree of purification to remove salts of heavy metals is no less than 90%, and the extent of recycling of purified water, no less than 90%.

Comparative tests of the efficiency of membrane regeneration with solutions of oxalic, citric, and malic acids allow us to recommend a 2% solution of oxalic acid for practical use. A complete restoration of the initial properties of membranes can be achieved if regeneration with this solution is carried out once a month.

In most cases, more effective isolation of metals from concentrates obtained in reverse-osmosis purification can be performed if the concentration of metal ions is no less than 4–10 g l^{-1}. In this case, concentration can be carried out in the second stage of a reverse-osmosis installation or on an ion-exchange installation.

Heavy metal ions can be recovered from primary concentrates using various types of ion-exchange resins. We have shown previously [10] that carboxylic cation-exchange resins in Na form are extremely selective in sorption of copper(II) and other metal ions forming sparingly soluble hydroxides in hydrolysis. If hydroxides or basic salts of the metals being extracted are poorly soluble in alkalis, they can be accumulated in a cationite phase in amounts exceeding severalfold the exchange capacity in a single sorption by treating a cationite alternately with primary concentrates containing ions of a metal to be extracted and with alkali solutions.

$$2R\text{–}COONa + Cu^{2+} = (R\text{–}COO)_2Cu + 2Na^+, \quad (1)$$

$$(R\text{–}COO)_2Cu + 2NaOH = 2R\text{–}COONa \cdot Cu(OH)_2, \quad (2)$$

$$2R\text{–}COONa \cdot Cu(OH)_2 + Cu^{2+} = (R\text{–}COO)_2Cu \cdot Cu(OH)_2 + 2Na^+, \quad (3)$$

$$(R\text{–}COO)_2Cu \cdot Cu(OH)_2 + 2NaOH = 2R\text{–}COONa \cdot 2Cu(OH)_2. \quad (4)$$

For example, a triple sorption of copper(II) ions on a KB-4P-2 cationite, following equations (1)–(4), allowed us to raise the copper(II) concentration in the cationite matrix to 10 mg-equiv g^{-1} or 320 mg g^{-1} (in terms of dry cationite) [10].

At a comparatively small (in terms of volume or weight) required of amount ionites, it may be expedient to use relatively expensive new-generation ion-exchange resins. These resins have high exchange capacity, good kinetic characteristics, and granules of uniform size; the last factor ensures low hydraulic resistance of an ionite layer in filtration.

To recover metal ions from concentrates formed in purification by reverse osmosis and ion-exchange and containing about 4–4.5 g l^{-1} of metal ions, we used direct electrolysis on installations equipped with metal cathodes and graphite anodes. Discharge of metal ions (Cu, Ni, Zn, or Cr) and deposition of a metal occurred on the metal cathode. The current efficiency by metal was determined by gravimetry.

The experiments demonstrated that use of cathodes with smooth surface at a cathode current density of 0.3–1.5 A dm^{-2} allows recovery of up to 80–85% of metals at current efficiency of 30–70%. In this case, the specific energy consumption for metal recovery is 4–8 kW h kg^{-1}.

With bulk flow-type complex-shape cathodes, the current density can be decreased to 0.02–0.5 A dm^{-2}, with the degree of metal recovery of 95–98% and current efficiency of 50–80%.

Metals deposited at the cathode had relatively high purity (up to 99.5%), and, therefore, could be used as soluble anodes in metal plating.

Spent etching solutions formed in printed circuit board manufacture can be recovered by direct electrolysis with cooled titanium cathodes and graphite anodes at 40–45°C, current density of 9.5–11 A dm^{-2}, and rate of spent solution supply of 5–10 l min^{-1}.

In this case, cathode deposition of copper and anode recovery of etching reagent occur simultaneously. The productivity of copper recovery was 3 kg h^{-1} at a current efficiency of 85%.

The results of the investigations performed allowed us to design an automated compact (required area of 95 m^2) installation for physicochemical purification of wastewater containing heavy metals.[1]

[1] The project will be implemented at the galvanic shop of Krasnoe znamya plant (Ryazan).

CONCLUSIONS

(1) Conditions were found for the effective joint use of reverse osmosis, ion exchange, and electrolysis for deep purification of wastewater containing heavy metal ions and for recovery of these metals.

(2) A low-waste technology for purification of wastewater of galvanic industry and printed circuit board manufacture, assuming recycling of purified water and recovered metals, was proposed for practical implementation.

REFERENCES

1. *Rekomendatzii po sokrascheniyu sbrosa metallov pri rabote gal'vanicheskikh predpriyatii* (Recommendations for Diminishing Metal Wastes at Galvanic Plants), Baev, A.S., Ed., St. Petersburg: Ekopolis i Kul'tura, 2000.
2. *Gibkie avtomatizirovannye linii* (Versatile Automated Lines), Zubchenko, V.L., Ed., Moscow: Mashinostroenie, 1989.
3. Sinyakova, M.A., Mikryukova, E.B., Vol'f, I.V., and Manvelova, N.E., *Zh. Prikl. Khim.*, 2000, vol. 73, no. 3, pp. 388–391.
4. Kazakov, E.V. and Pekarskii, L.D., *Promyshlennost' stroitel'nykh materialov: Ochistka stochnykh vod gal'vanicheskikh proizvodstv i regeneratsiya metallov iz nikh*, (Building Material Industry: Purification of Wastewaters of Galvanic Manufactures and Regeneration of Metals from them), Moscow: VNIINTI Ekonomiki Promyshl. Mater., 1988, ser. 10, no. 2.
5. Povarov, A.A., Kolomiitsev, A.G., Kuznetsov, M.S., *et al., Progress. Prirodookhran. Tekhnol., Akad. Nauk SSSR*, 1991, no. 9, ref. 95, pp. 131–135.
6. Naidenko, V.V., Bednova, L.I., Erekhinskii, A.V., *et al., Vodosnabzh. Santekhn.*, 1984, no. 6, pp. 3–6.
7. Manvelova, N.E., *Materialy konferentsii "Khozyaistvennopit'evye i stochnye vody, problemy ochistki i ispol'zovaniya"* (Proc. Conf. "Industrial, Drinking, and Waste Water: Problems of Purification and Use"), Penza, 2000, pp. 90–92.
8. Manvelova, N.E. and Vol'f, I.V., *Materialy mezhdunarodnoi konferentsii "Membrannye i sorbtsionnye protsessy"* (Proc. Int. Conf. "Membrane and Sorption Processes"), Krasnodar, 2000, pp. 18–19.
9. RF Patent 2 088 537.
10. Sinyakova, M.A. and Vol'f, I.V., *Ionn. Obmen Ionometr.*, 2000, no. 10, pp. 96–107.

Russian Journal of Applied Chemistry, Vol. 74, No. 10, 2001, pp. 1706–1714. Translated from Zhurnal Prikladnoi Khimii, Vol. 74, No. 10, 2001, pp. 1655–1663.

PROCESSES AND EQUIPMENT OF CHEMICAL INDUSTRY

Formation of Optimal Working Space in Adsorbers with Fixed and Moving Adsorbent Beds

N. A. Samoilov

Ufa State Technical University of Oil, Ufa, Bashkortostan, Russia

Received April 5, 2001

Abstract—The possibility of improving the adsorbent efficiency by means of transverse and longitudinal sectioning of adsorption apparatus is substantiated. Results of an experimental and calculation study of sectioned apparatus are presented. A number of designs of sectioned adsorbers with the optimal working space were developed.

Adsorption apparatus with fixed and moving adsorbent beds have rather widely varying designs [1–3]. For example, adsorbers with fixed adsorbent bed may have vertical, horizontal, multishelf, annular, or some other arrangement of the adsorbent bed in an adsorber [2, 3]. The bed shape is frequently defined by technology (e.g., annular adsorbent beds are used in the case of limitations on the loss of head in purification of a raw material), whereas the relative geometric dimensions of the bed receive much less attention. For example, the ratio of the bed height H to adsorbent bed diameter D in industrial vertical adsorbers varies rather widely—between 0.5 and 15, without any convincing substantiation of the adopted H/D values.

The aim of this study was to analyze the effect of the working space configuration of the adsorber on the working activity of the adsorbent and the purity of the obtained products.

Adsorption apparatus with fixed adsorbent bed. An important thing in improving the operation efficiency of an adsorption apparatus is to make higher the main performance parameter of the process—the breakthrough activity of the sorbent, a, reached by the instant of breakthrough of the component being extracted into the purified product, since it largely determines the adsorber size, adsorbent consumption, and energy expenditure for adsorbent regeneration.

In batch adsorption apparatus, a part of the adsorbent bed, which corresponds to the height of the mass-transfer zone, is saturated with the adsorbate to a lesser extent than the spent bed. This makes on the whole lower the integral activity of the adsorbent, regarded in experiments and calculations as real breakthrough activity. Let us introduce the coefficient of efficiency of adsorbent use under working conditions, K_e, characterizing the extent to which the sorbent is spent:

$$K_e = a_b/a_e,$$

where a_b is the dynamic activity of the adsorbent to conditional breakthrough (g of adsorbed substance per 1 g of adsorbent); and a_e is the total dynamic activity of the adsorbent under the conditions of equal adsorbate concentrations in the flow at the entrance into, and exit from the adsorbent bed, characterizing the potential adsorption activity of the sorbent (g of adsorbed substance per 1 g of adsorbent).

The K_e value strongly depends on the conditions under which the adsorption process is performed. For example, calculations show that, for apparatus with long absorption stage (e.g., 1 day) and the correspondingly large height of the adsorbent bed, the decrease in a_b relative to a_e is largely compensated for by the fact that the ratio of the bed height H_1 to the height L_0 of the mass-transfer zone is, as a rule, greater than 10 for apparatus of this kind. In these cases, the sorbent efficiency coefficient K_e is rather high and constitutes 0.95–0.99, depending on the symmetry factor f of the output curve of absorption dynamics. By contrast, for adsorbers used in short-cycle processes, the H_1 value exceeds L_0 only slightly. In these cases, the adsorbent activity under the working conditions is comparatively low and is much exceeded by the total dynamic activity, which reduces the efficiency coefficient K_e to 0.3–0.5.

1070-4272/01/7410-1706 $25.00 © 2001 MAIK "Nauka/Interperiodica"

Table 1. Comparison of characteristics of the conventional vertical adsorbers (I) with performance parameters of telescopic adsorbers (II) and adsorbers with vertical partitions (III)* (base adsorber—vertical with conventional values $H = 1$, $D = 1$, $W = 1$, $L_0 = 0.5$, total dynamic activity of the sorbent 15 wt %, $f = 0.5$)

Figure	n	Dimensions, m		W, m s^{-1}	H_s	L_0	H_s/L_0	a, wt %	K_e	Conventional steel intensity
		H	D		m					
Adsorber I										
1a, 2a, 3a	1	1	1	1	1	0.500	2.00	9.85	0.657	7.06
1b	2	2	0.705	2	2	0.705	2.84	11.18	0.743	7.55
1c	3	3	0.575	3	3	0.865	3.47	12.40	0.826	8.26
1d	4	4	0.500	4	4	1.000	4.00	12.88	0.858	9.00
Adsorber II										
2b	2	1	1	2	2	0.705	2.84	11.18	0.743	7.72
2c	3	1	1	3	3	0.865	3.47	12.40	0.826	8.36
2d	4	1	1	4	4	1.000	4.00	12.88	0.858	9.01
Adsorber III										
3b	2	1	1	2	2	0.705	2.84	11.18	0.743	7.34
3c	3	1	1	3	3	0.865	3.47	12.40	0.826	7.64
3d	4	1	1	4	4	1.000	4.00	12.88	0.858	7.92

* (n) Number of sections, (W) flow velocity, and (H_s) sorbent bed height.

Reducing the bed diameter n-fold at constant volume of the vertical adsorbent bed results in an increase by a factor of n^2 in the bed height and in the linear velocity of the flow being purified (Fig. 1), and by a factor of n in the mass-transfer zone length, which makes the efficiency coefficient K_e somewhat higher (Table 1). However, the adsorber dimensions change in this case to such an extent that the apparatus becomes less convenient in practice. For example, if the velocity of the flow being purified is raised 4-fold in an adsorber with bed diameter and height of, respectively, 2 and 10 m and mass-transfer zone length of 5 m, the apparatus will be 40 m high at bed diameter of 1 m and, although the mass-transfer zone length will increase to 10 m, the coefficient of adsorbent use efficiency, K_e, in the new design will, nevertheless, increase from 0.65 to 0.85. However, an adsorber with such a bed height is inconvenient since the low mechanical strength of the adsorbent will result in crushing of sorbent grains and loss of a part of ground sorbent with the flow of the product being purified. In addition, the hydraulic resistance of the sorbent bent increases dramatically. Such a high column is to be divided into several beds, which will make the apparatus more expensive and the operations of adsorbent charging and discharging more difficult.

One of variants of improving the working space of an adsorber is its design in the folded "telescopic" form, when a system of n shells inserted one into another leads to conditional longitudinal sectioning of the apparatus, with equal cross-sections of each of the annular zones and the central zone (Fig. 2). This ensures a constant flow velocity in each sections, which is $n + 1$ times that in the initial apparatus.

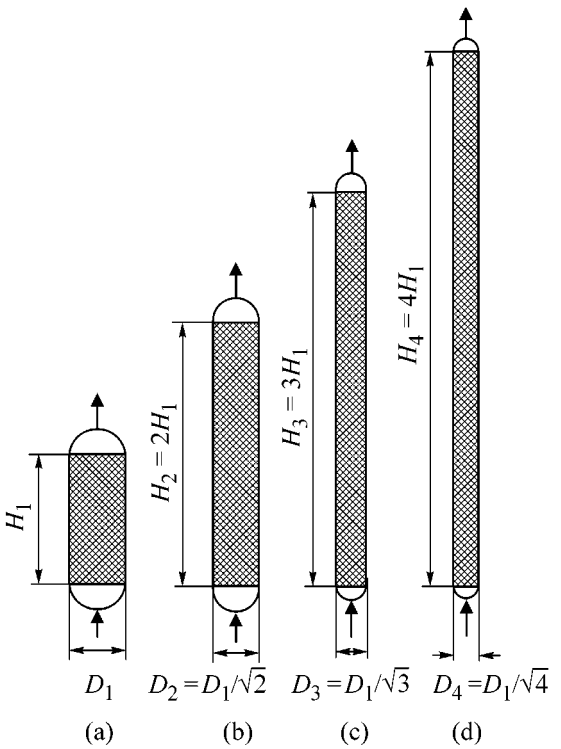

Fig. 1. Design variants of vertical adsorbers with the same charge of fixed adsorbent bed and varied height H and bed diameter D. H/D: (a) H_1/D_1, (b) $2.83H_1/D_1$, (c) $5.19H_1/D_1$, and (d) $8.0H_1/D_1$.

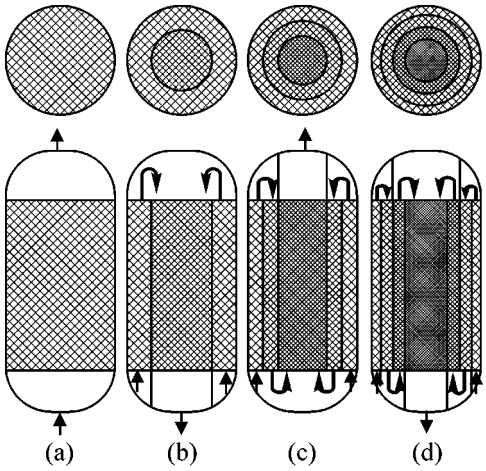

Fig. 2. Design variants of vertical sectioned adsorbers of telescopic type with the same charge of the fixed adsorbent bed. Adsorber: (a) of base type with bed height $H = H_1$, (b) with two sections with bed height $H = 2H_1$, (c) with three sections with bed height $H = 3H_1$, and (d) with four sections with bed height $H = 4H_1$.

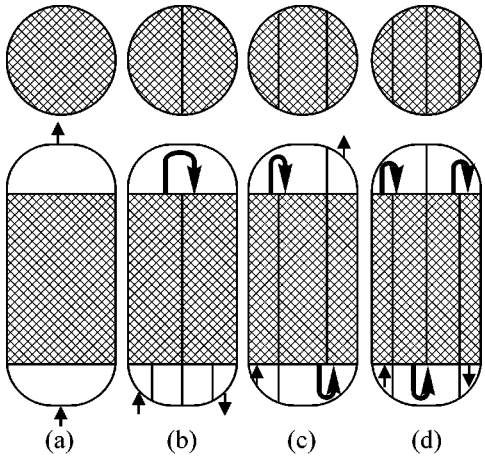

Fig. 3. Design variants of sectioned adsorbers with vertical partitions and the same charge of fixed adsorbent bed.

The telescopic design of the apparatus leads to a more perfect working space of the adsorber (Table 1), but has such disadvantages as high steel intensity and complicated systems for adsorbent charging and discharging.

This disadvantage is eliminated when the adsorbent bed is divided along the height by partitions parallel to the motion direction of the raw material being purified into several in-series connected sections (Fig. 3), which leads to an increase in the breakthrough activity of the sorbent [4–7]. This can be achieved because of the different effects of the section geometry on the flow velocity of a raw material being purified and on the mass-transfer zone length (Table 1).

Let us consider how the use of apparatus with adsorbent bed sectioned into n sections with $n + 1$ partitions parallel to the flow of a product being purified leads to intensification of short-cycle adsorption process.

With increasing number of sections, n, the path of a flow being purified along the apparatus becomes longer, i.e., the adsorbent height grows:

$$H_n = H_1 n, \tag{1}$$

where H_1 and H_n are, respectively, the path lengths of a flow in the adsorber through an adsorbent bed without sectioning and with n sections (m).

Simultaneously with the adsorbent bed height, grows the flow velocity

$$W_n = W_1 n, \tag{2}$$

where W_1 and W_n are, respectively, the velocities of adsorbate transport along apparatus without sectioning and with n sections (m s^{-1}).

The mass-transfer zone length L_0 depends on the flow velocity [8]:

$$L_0 = B\sqrt{W}, \tag{3}$$

which was also confirmed experimentally in [9, 10]. As applied to the operation conditions of a sectioned adsorber, relation (3) takes the form

$$L_{01}/L_{0n} = \sqrt{W_1/W_n}. \tag{4}$$

The mass-transfer zone length L_0 can be calculated using the equation [11]

$$L_0 = H_1 \frac{a_e - a_b}{a_e - (1 - f)a_b}, \tag{5}$$

where f is the symmetry factor of the output curve of the adsorption dynamics.

Writing Eq. (5) for the operation conditions of a conventional adsorber with bed height H_1 and n-sectioned adsorber with bed height H_n, we obtain an equation for calculating the efficiency coefficient

$$K_e = \frac{a_b}{a_e} = \frac{H_n - L_0\sqrt{W_n/W_1}}{H_n - L_0(1 - f)\sqrt{W_n/W_1}}. \tag{6}$$

Since the mass-transfer zone height is virtually independent of the adsorbent bed height and is proportional to $\sqrt{W}$, and W grows in sectioning in proportion to the height of the n-sectioned adsorber, this leads to

an increase in K_e, which intensifies the adsorption process because of the approach of a_b to a_e. The coefficient of adsorber operation efficiency depends on the number of sections in the apparatus, the symmetry factor of the output curve, and the H_n/L_0 ratio (Fig. 4); $K_e \to 1$ at $H_n/L_0 \to \infty$.

The effect of sectioning on the adsorbent efficiency was verified experimentally in separation of a 20% toluene–*n*-heptane mixture in liquid phase with NaX zeolites. A set of laboratory columns with adsorbent bed height of 0.27, 0.57, and 0.90 m allowed adjustment of the operation conditions of a sectioned adsorber by varying the total adsobent bed height in a set of in-series connected columns and the raw material flow rate equivalent to the necessary number of stages. The mass-transfer zone length was calculated by Eq. (5) and determined experimentally by sampling the product along the column height. The data presented in Fig. 5 and Table 2 confirm that sectioning makes it possible to raise the dynamic activity of the NaX zeolite with respect to toluene to a conditional breakthrough, and the efficiency coefficient K_e by 12–14 rel.%, with good qualitative and quantitative agreement between the experimental and the calculated values prognosticating the operation of a sectioned apparatus on the basis of experimental results obtained for the base unsectioned apparatus.

For concrete conditions of the adsorption process, the optimal number of sections forming the working space of an apparatus can be calculated; as a rule, the optimal number of sections is within 2–5 [12].

Adsorption apparatus with moving adsorbent bed. Adsorption apparatus with moving bed—hypersorbers, serve for separating multicomponent mixtures into fractions markedly enriched in one of components [2, 3, 13, 14]. In separating a multicomponent (e.g., four-component) mixture, the least readily sorbed component is discharged in the vapor phase from the upper zone of the adsorption section of the hypersorber, and the best sorbed component, as desorption product from the upper zone of the desorption section. Other components being separated are also discharged in vapor phase in succession along the height of the adsorption section operating in the chromatographic mode (Fig. 6a). The better a particular intermediate component is sorbed, the lower, along the adsorber height, lies the zone with the maximum concentration of the given component [14].

The indisputable advantages of the process with a moving adsorbent bed are as follows: lower adsorbent consumption (since the height of the adsorption section of the process exceeds only slightly the mass-transfer zone length and is several times smaller than the adsorbent bed height in apparatus with fixed sorbent bed), lower energy expenditure in the desorption stage, small size of the installation, and possibility of high-level automation of the process.

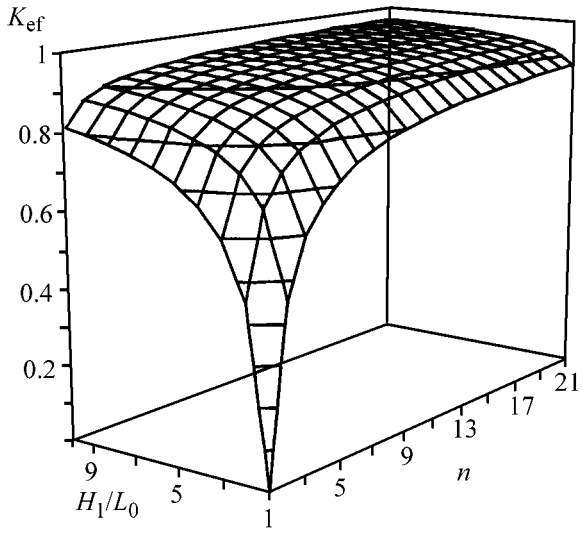

Fig. 4. Efficiency coefficient K_e vs. number of sections in adsorber, n, and ratio of adsorbent bed to mass-transfer zone height, H_1/L_0. Symmetry factor of the output curve $f = 0.5$.

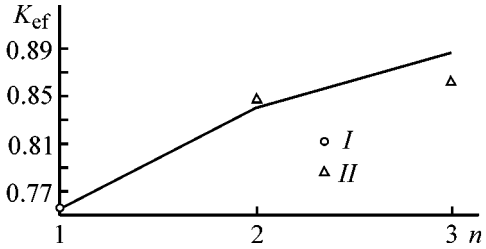

Fig. 5. Effect of the number of sections n on the efficiency coefficient K_e in liquid-phase separation of the toluene–*n*-heptane mixture with NaX zeolites. *Line*: calculation by Eq. (6); *points*: experiment [(*I*) base point for obtaining the calculated dependence and (*II*) control points].

Table 2. Dynamic activity of NaX zeolites with respect to toluene in liquid-phase separation of a toluene–*n*-heptane mixture

n	Dynamic activity, wt %	
	calculation	experiment
1	9.54	9.54
2	10.85	10.72
3	10.95	10.90

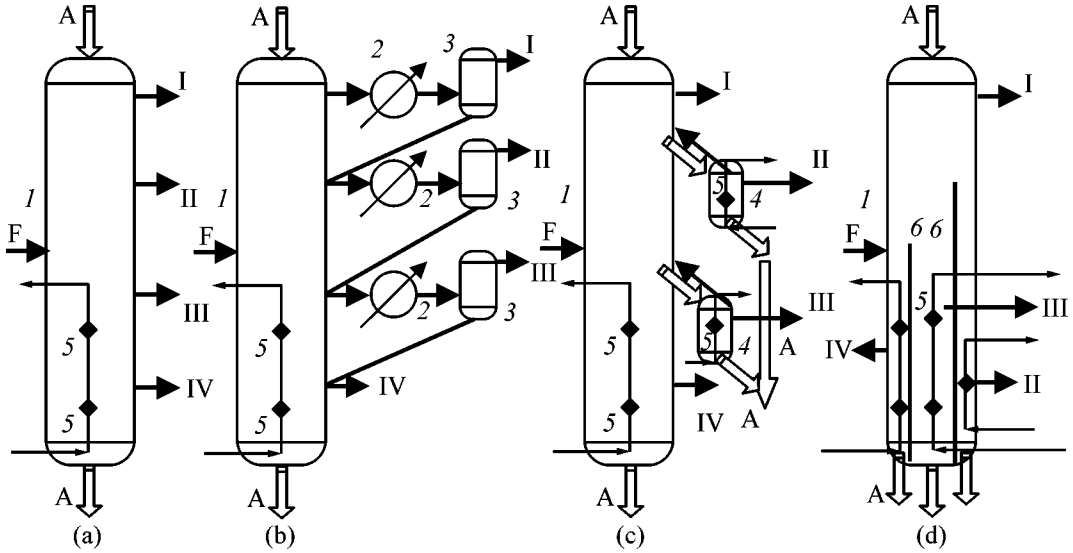

Fig. 6. Variants of separation of a four-component mixture in various designs of adsorbers with moving adsorbent bed. Hypersorber: (a) conventional; (b) supplemented with systems for cooling of discharged fractions with partial condensation of high-boiling components; (c) supplemented with system of stripping desorbers for removal of low-boiling components from the effluent fractions, with subsequent desorption of target fractions; and (d) with vertical sectioning partitions, equivalent to the system in variant (c). F, raw material; A, adsorbent; I–VI close-cut effluent fractions; (*1*) hypersorber, (*2*) condensers, (*3*) condensate collectors, (*4*) desorbers, (*5*) heat supply systems, and (*6*) sectioning partitions.

A disadvantage of the hypersorption process is the comparatively low purity of the intermediate components discharged at different heights along the adsorption section [13, 14], associated with the limitations on the column height. Improving the purity of products in side fractions requires a significant increase in the mass-transfer zone length and the resulting substantial increase in the number of theoretical plates with very low concentration gradient of a component being extracted in both the vapor and solid phases just at those parts of the bed where the efficiency of separation is markedly impaired [15]. As a consequence, the apparatus size, mass of circulating adsorbent, and energy expenditure for desorption grow dramatically.

Such an imperfection of the hypersorber operation can be eliminated, by analogy with the rectification process, by directing the products taken-off at different heights along the hypesorber in vapor phase to cooling with partial condensation of high-boiling components (Fig. 6b), which makes it possible to lower the concentration of these components in the discharged fractions and to increase the concentration of target products. In the limiting case, the system of single evaporation (condenser and evaporator vessel) can be replaced with an incomplete rectifying column, if the target component and impurities have markedly different volatilities. In some cases, it is necessary to remove low-boiling components from the effluent fraction and to increase thereby the concentration of the target components. Then the hypesorber can be equipped with a system of desorbers working as stripping columns (Fig. 6c) into which adsorbent saturated with the target product is delivered, since, according to the phase equilibrium laws, the concentration of the target component in the adsorbed phase is higher than that in the vapor phase. The admixture of a low-boiling component will be desorbed in the upper part of the "stripping" desorbers by the supplied heat and then returned into the hypersorber, and the target product will be discharged in their bottom part. Thus, in the two considered ways to solve the problem at hand, the intensification of the adsorption process with improvement of the quality of the discharged fractions is ensured by installing additional devices, and in the second of these by redistribution of the adsorbent mass and heat supply in the system. In this case, the velocity of adsorbent motion will decrease dramatically in the lower part of the base hypersorber, which will impair the operation of the already rather inefficient system of heat transfer from the heat transfer agent to the adsorbent in the desorption zone, or make necessary fabricating an apparatus with narrowed bottom part.

These shortcomings can be eliminated with the stripping desorbers placed directly in the adsorber with moving bed by mounting additional vertical sectioning partitions with lateral and bottom edges in contact

with the casing. The upper edges of the partitions must be higher than the feeding zone of the adsorption column. [16–19]. The number of partitions leading to parallel sectioning of the apparatus is equal to the number of discharged side fractions. Each section plays the part of a stripping desorber. In separating, e.g., a four-component mixture, mounting two additional partitions makes it possible to divide the adsorbent spent in the adsorption section into three flows delivered into chromatographic sections with individually optimal temperature modes. The component with the highest sorbability, absorbed by the adsorbent, is released into sections with higher desorption temperature, and that with intermediate adsorbability, into sections with lower temperature (Fig. 6d). Such a differentiated distribution of the adsorbent heating temperature over sections allows reduction of energy expenditure, compared with that in a conventional hypersorber, when the entire body of adsorbent is heated to the maximum temperature. The flow chart for a sectioned adsorber is shown in Fig. 7.

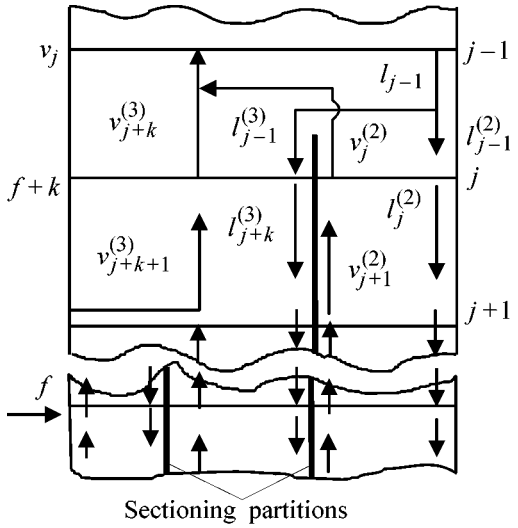

Fig. 7. Flows in a sectioned adsorber with moving adsorbent bed in separating a four-component mixture.

Previously [20, 21], the efficiency of a sectioned adsorber in extraction of two impurities from the base flow has been evaluated. The operation of a sectioned adsorbent column with moving adsorbent bed has been studied in detail and an analysis was made of the effect of sectioning on the quality of the extracted narrow-cut fractions—products of separation of a three-component mixture [22] As raw material was used a hypothetical three-component raw mixture fed into the column at component ratio of 30 : 40 : 30. The relative desorbabilities of the components, α_i (reciprocal of the relative adsorbability and equivalent of the relative volatility of components in rectification processes), were represented by the ratio $\alpha_1 : \alpha_2 : \alpha_3$ of 9 : 3 : 1, 16 : 4 : 1, or 25 : 5 : 1 and covered a rather wide range of variation of the sorbent adsorption properties and affinities of substances being separated for the sorbent. The discharge of the separation products was done with account of the balance relation of the main components: the first fraction had a yield fr_1 = 30; the second, fr_2 = 40; and the third, fr_3 = 30 kg per 100 kg of raw material.

A mathematical model of an adsorption column with moving adsorbent bed assumed a successive plate-by-plate calculation of the apparatus (from one stage of phase equilibrium to another) with account of the equilibrium and material balance equations at the contact device by means of the modified relaxation method which allowed a rather effective comparison of different variants of mass-exchange apparatus operation [23]. A specific feature of the model is that it relies in analyzing the phase equilibrium upon the notion of the relative desorbability of components of the mixture being separated, similar to relative volatility of components in calculating a rectification column.

The composition of the adsorbed mixture of components, which "flow down" together with a conditionally inert mass of adsorbent from j-th plate after contact on this plate of the countercurrent nonequilibrium flows of adsorbent from (j – 1)-th plate and vapor from (j + 1)-th plate and possible supply of raw material to j-th plate, can be determined from the material balance equation

$$x_{j,i} = \frac{l_{j-1}x_{j-1,i} + v_{j+1}y_{j+1,i} + f_j x_{f,j,i}}{l_{j-1} + v_{j+1} + f_j}, \quad (7)$$

where l_{j-1}, $x_{j-1,i}$ are the amount of flow descending from (j – 1)-th plate (flow absorbed by the adsorbent) and the content of i-th component in it; v_{j+1}, $y_{j+1,i}$ are the amount of vapor ascending from (j + 1)-th plate and the content of i-th component in it; f_j, $x_{f,j,i}$ are the amount of raw mixture and the content of i-th component in it. The composition of the vapor that is in equilibrium with the adsorbent being spent and ascends from j-th plate is found from the relation

$$y_{j,i} = \frac{\alpha_i x_{j,i}}{\Sigma\, \alpha_i x_{j,i}}, \quad (8)$$

where α_i is the relative desorbability of i-th component.

Table 3. Comparison of the quality of fractions discharged in operation of a hypersorber and sectioned adsorber in purification of a three-component mixture to remove admixtures of the second (2%) and third (3%) components

Composition of discharged fractions, %	Base hypersorber	Sectioned apparatus
Fraction 1 (95%):		
component 1	99.84	99.98
component 2	0.16	0.02
component 3	0.00	0.00
Fraction 2 (2%):		
component 1	0.10	1.34
component 2	90.81	98.37
component 3	9.08	0.29
Fraction 3 (3%):		
component 1	0.00	0.00
component 2	6.07	0.25
component 3	93.93	99.75

A calculation analysis of the operation of a three-section adsorber revealed the following main factors associated with the formation of the optimal working space in sectioned adsorbers with moving adsorbent bed with respect to flows and geometric parameters: distribution of adsorbent flow among sections, distribution of the cross-section areas of the sections, positions of upper edges of sectioning partitions in the adsorbent bed, place of raw material input into the adsorber, possibility of adjusting the working space characteristics upon a change in the flow rate or composition of the raw material.

Let us consider the operation of a sectioned adsorber in separation of a four-component mixture in the region of flow distribution between the first section, in which the second component is to be extracted (the first component is discharged at the top of the adsorber) and other sections. As follows from the flow chart of a sectioned adsorber (Fig. 7), part of sorbed substances, $l_{j-1}^{(3)}$, is diverted, together with the sorbent descending from a fixed (j – 1)-th plate, into the discharged zone of the third and fourth fractions by the sectioning partition. The remaining part of the sorbed flow, $l_{j-1}^{(2)}$, is moved to the discharge zone of the second ("intermediate") separation product, with $l_{j-1} = l_{j-1}^{(3)} + l_{j-1}^{(2)}$. The amount of sorbent discharged into this zone and, correspondingly, the flow $l_{j-1}^{(2)}$, and its composition were determined by the following two conditions: (1) the concentration of the third component in the flow $l_{j-1}^{(2)}$ should be as low as possible, and that of the fourth component should be virtually zero, which determines the purity of the second fraction with respect to the third component; and (2) the amount of adsorbed product in the flow $l_{j-1}^{(2)}$ descending into the second section (into the discharge zone of the second component) should be such that a balance amount of the second fraction is formed. In the case when the rate of the adsorbent flow arriving at the second section exceeds the balance value, the excess amount of the second component will ascend with the vapor flow into the first section and, as a result, the first fraction will be contaminated with the second component. In the case of the optimal formation of the working space of a sectioned adsorber, narrow-cut fractions are obtained in the apparatus, having much higher purity as compared with that achieved in the hypersorber (Table 3).

A mathematical modeling of the operation of the sectioned adsorber with a moving adsorbent bed demonstrated that the flow rate of spent adsorbent, G_i, arriving at an arbitrary stripping section, must ensure supply of the balance amount of the component discharged in this section and have the minimum content of the component next in order of increasing sorbability. The optimal positions of the sectioning vertical plates in the adsorber volume are governed by the relation

$$G_i/G_\Sigma = S_i/S, \quad (9)$$

where G_Σ is the total flow rate of separation products in all sections of the lower part of the adsorber, S_i is the cross-section area of the adsorber section between two adjacent sectioning partitions or between the extreme plates and the corresponding part of the shell, and S is the cross-section area of the adsorber.

The calculated position of the upper edge of the sectioning partition in the working space of the adsorber is found from the condition of minimizing the content of the component next in order of increasing sorbability, $x_{j,i+1}$, in the adsorbent flow arriving at the given section from j-th plate and is given by the relation

$$\frac{x_{j,i}}{x_{j,i+1}} = \frac{y_{\text{fin},i}}{(y_{\text{fin},i+1})_{\min}}, \quad (10)$$

where $x_{j,i}$ and $y_{\text{fin},i}$ are, respectively, the concentration of i-th component in the flow from j-th plate and its final concentration in the fraction discharged from the given section; and $(y_{\text{fin},i+1})_{\min}$ is the minimum admissible concentration of (i + 1)-th component in the fraction discharged from the given section.

The prescribed flow rates of the adsorbent, and, consequently, the flow rates of substances absorbed by the adsorbent (Fig. 7, e.g., $l_{j-1}^{(3)}$ and $l_{j-1}^{(2)}$) can be adjusted and maintained by varying the speeds of rotation of sector feeders mounted in lines discharging regenerated adsorbent from sections. In addition, an adsorber design with sliding partitions, allowing control over the volume of the adsorption space in each section separately, has been patented [18].

The raw material feed zone in the sectioned adsorption apparatus is somewhat shifted downwards along the column height, compared with the hypersorber, and, in optimizing the process, its position should be adjusted to achieve the maximum possible concentration of the target components in the discharged fractions (Fig. 8).

Calculations demonstrated that, as also in the case of any other mass-exchange processes, the purity of the fractions obtained in the sectioned apparatus depends on the flow rates of vapors being separated and adsorbent (Fig. 9). Results of mathematical modeling of hypersorbers and sectioned adsorbers indicate that mathematical processing of the information fields obtained in numerous kinds of apparatus calculations can be used to develop rather simple dependences relating the operation parameters of the sectioned adsorber and the base hypersorber [22]. The energy efficiency of the sectioned adsorber increases especially strongly when the content of the most difficultly desorbed component in the raw material is low. In these cases, the heat saving may be as high as 25–50%.

CONCLUSIONS

(1) It is shown that, with the working space of adsorbers divided by vertical partitions, it is possible to form in a single apparatus a conditional chain of in-series connected adsorbers with fixed adsorbent bed or parallel "stripping" zones in adsorbers with moving adsorbent bed.

(2) The possibility of optimizing the working space of adsorbers with fixed and moving adsorbent bed is substantiated theoretically.

(3) Optimization of the working space of an adsorber with fixed adsorbent bed makes it possible to find the optimal number of sections in the apparatus and raise the dynamic activity of the adsorbent.

(4) Optimization of the working space of an adsorber with moving adsorbent bed makes it possible to improve the quality of discharged fractions and reduce the energy expenditure for the process.

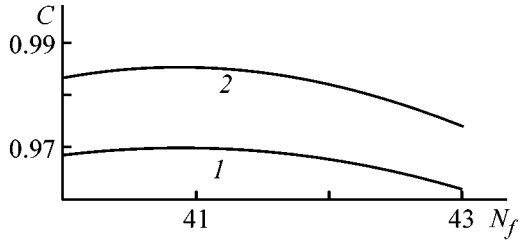

Fig. 8. Concentrations of extracted components, *C*, in the target fractions vs. number of raw material input plate, N_f, in separation of a three-component mixture with relative desorbabilities of the components $\alpha_1 : \alpha_2 : \alpha_3$ = 16 : 4 : 1. Component concentration: (*1*) second in the second fraction and (*2*) third in the third fraction.

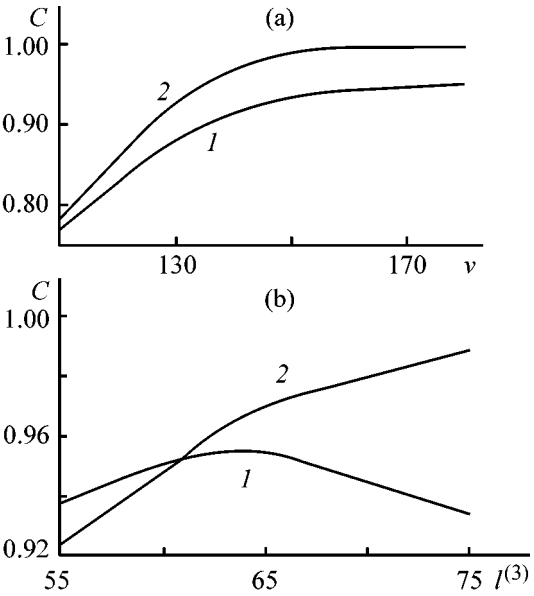

Fig. 9. Concentrations of the target components in the fractions, *C*, vs. (a) mass *v* of the vapor flow ascending into the discharge zone of the first component and (b) part of mass of the descending flow $l^{(3)}$ arriving from the discharge zone of the first component at that of the second component, in separation of a three-component mixture. Purity of fraction: (*1*) second and (*2*) third.

REFERENCES

1. Lukin, V.D. and Novosel'skii, A.V., *Tsiklicheskie adsorbtsionnye protsessy: Teoriya i raschet* (Cyclic Adsorption Processes: Theory and Calculation), Leningrad: Khimiya, 1989.
2. Kel'tsev, N.V., *Osnovy adsorbtsionnoi tekhniki* (Fundamentals of Adsorption Technology), Moscow: Khimiya, 1984, 2nd ed.
3. Serpionova, E.N., *Promyshlennaya adsorbtsiya gazov i parov* (Industrial Adsorption of Gases and Vapors), Moscow: Vysshaya Shkola, 1969, 2nd ed.
4. Samoilov, N.A. and Ibulaev, R.G., *Bash. Khim. Zh.*, 1998, vol. 5, no. 3, pp. 54–55.

5. Samoilov, N.A. and Ibulaev, R.G. *Sintez, modifitsirovanie i adsorbtsionnye svoistva tseolitov i tseolitopodobnykh molekulyarnykh sit: Materialy II seminara* (Synthesis, Modification, and Adsorption Properties of Zeolites and Zeolite-like Molecular Sieves: Proc. II Symp.), St. Petersburg, 1998, p. 58.
6. Samoilov, N.A., Abstracts of Papers, *Mezhdunarodnyi Seminar "Uglerodnye adsorbenty"* (Int. Symp. "Carbon Adsorbents"), Kemerovo, 1998, pp. 16–17.
7. Samoilov, N.A., *Zh. Prikl. Khim.*, 1998, vol. 71, no. 1, pp. 99–104.
8. Dubinin, M. and Yavich, S., *Zh. Prikl. Khim.*, 1936, vol. 9, no. 7, pp. 1191–1202.
9. Urban, G.V., Vinogradova, V.S., Komarova, V.N., and Kofman, L.S., *Tseolity, ikh sintez, svoistva i primenenie* (Zeolites, Their Synthesis, Properties, and Use), Moscow: Nauka, 1965, pp. 268–274.
10. Samoilov, N.A. and Fominykh, L.F., *Dokl. Neftekhim. Sektsii* (Reports of Petrochemical Section), Ufa: Bash. Resp. Pravlenie VKhO im. D.I.Mendeleeva, 1971, issue 7, pp. 221–227.
11. Samoilov, N.A. and Fominykh, L.F., *Tekhnologiya nefti i gaza: Voprosy fraktsionirovaniya* (Technology of Oil and Gas: Problems of Fractionation), Ufa: Bashknigoizdat, 1975, issue 3, pp. 255–258.
12. Samoilov, N.A. an Ibulaev, R.G., *Zh. Prikl. Khim.*, 2000, vol. 73, no. 9, pp. 1500–1505.
13. Romankov, P.G. and Lepilin, V.N., *Nepreryvnaya adsorbtsiya gazov i parov* (Continuous Adsorption of Gases and Vapors), Leningrad: Khimiya, 1968.
14. RF Patent 2 098 168.
15. Samoilov, N.A., *Zh. Prikl. Khim.*, 1986, vol. 59, no. 10, pp. 2326–2333.
16. Ustinov, E.A., *Zh. Prikl. Khim.*, 1995, no. 68, no. 5, pp. 774–780.
17. RF Patent 2 098 169.
18. RF Patent 2 144 417.
19. RF Patent 2 144 418.
20. Samoilov, N.A., *Aktual'nye problemy teorii adsorbtsii i sinteza sorbentov: Materialy 6-go Vserossiskogo simpoziuma s uchastiem inostrannykh uchenykh* (Topical Problems of the Theory of Adsorption and Sorbent Synthesis: Proc. 6th All-Russia Symp. with Participation of Foreign Scientists), Moscow–Klyaz'ma, 2000, p. 48.
21. Samoilov N.A., Ibulaev R.G. *Aktual'nye problemy teorii adsorbtsii i sinteza sorbentov: Materialy 6-go Vserossiskogo simpoziuma s uchastiem inostrannykh uchenykh* (Topical Problems of the Theory of Adsorption and Sorbent Synthesis: Proc. 6th All-Russia Symp. with Participation of Foreign Scientists), Moscow–Klyaz'ma, 2000, p. 46.
22. Ibulaev, R.G., Modeling of the Operatin of a Sectioned Adsorption Column, *Cand. Sci. Dissertation*, Ufa, 2000.
23. Kondrat'ev, A.A. and Samoilov, N.A., *Zh. Prikl. Khim.*, 1997, vol. 70, no. 9, pp. 1512–1517.

Russian Journal of Applied Chemistry, Vol. 74, No. 10, 2001, pp. 1715–1721. Translated from Zhurnal Prikladnoi Khimii, Vol. 74, No. 10, 2001, pp. 1664–1670.

ORGANIC SYNTHESIS AND INDUSTRIAL ORGANIC CHEMISTRY

Kinetics of Liquid-Phase Redox Reactions Involving Hydroxy- and Aminoalkanesulfinates

Yu. V. Polenov, V. V. Budanov, and E. V. Egorova

Ivanovo State Chemical Engineering University, Ivanovo, Russia

Received November 14, 2000; in final form, July 2001

Abstract—The mechanisms and kinetics of practically important redox reactions proceeding under the action of hydroxy- and aminoalkanesulfinates are analyzed. The general features allowing forecasting of the rates of reactions involving the above reducing agents are elucidated.

Hydroxy- and aminoalkanesulfinates are widely used as reducing agents in various branches of engineering and technology. The best known compounds, hydroxymethanesulfinate (HMS, technical name rongalite) and thiourea dioxide (TUDO, aminoiminomethanesulfinic acid), are used in textile industry, production of synthetic rubber, stabilizers for polymeric materials, uranium salts and salts of transuranium elements, electroless metal plating of polymeric materials, and other processes [1].

By now the experimental data on the kinetics and mechanisms of redox reactions involving the above compounds are quite extensive and, in our opinion, sufficient to generalize and elucidate the general features.

Based on an analysis of the concentration dependences of the reaction rates and the effect of various additives on the reaction rate, the reactions in hand can be divided into three groups. The reactions of the first group are characterized by the occurrence of an induction period, zero reaction order with respect to oxidizing agent for a long reaction time, first reaction order with respect to reducing agent, and abrupt decrease in the reaction rate, even to the point of complete inhibition, upon addition of formaldehyde. This group includes reduction of disodium 5,5'-indigotindisulfonate (indigocarmine) with sodium hydroxy- and aminoalkanesulfinates [2], 2-nitro-2'-hydroxy-5'-methylazobenzene (NAB) with HMS and TUDO [3, 4], Direct Red 2C azo dye with HMS and TUDO [5], uranyl acetate with TUDO [6], and iodine, bromine, and chlorite ions with HMS and TUDO [7]. Typical kinetic curves characteristic of this group of reactions are shown in Fig. 1.

The reactions of the second group have zero induction period, fractional reaction order with respect to the oxidizing agent, and first order with respect to the reducing agent. Addition of formaldehyde also inhibits the reaction, but to a lesser extent than for the reactions of the first group. The second group includes reduction of vat dye precursors with sodium hydroxy- and aminoalkanesulfinates [8], nickel and cobalt salts with HMS and TUDO [9], and ethylenediaminetetraacetatoferrate ($FeEDTA^-$) with TUDO [10].

The reactions in which formaldehyde exerts weak or practically no effect on the reduction rate belong to the third group. These reactions are first-order with respect to the oxidizing agent at moderately low temperatures, and a fractional reaction order is observed with increasing temperature; in all cases, the reaction order with respect to the reducing agent is 1. The ex-

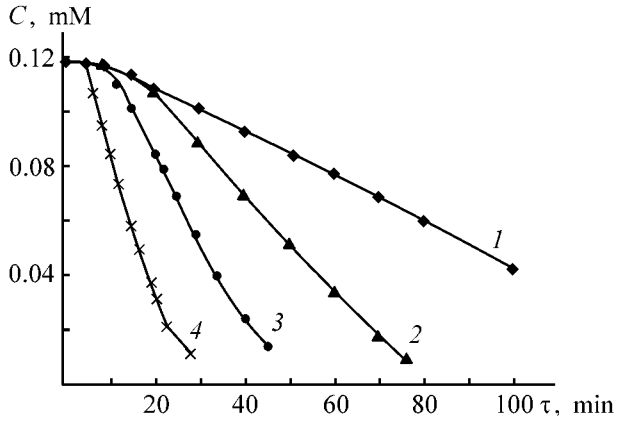

Fig. 1. Concentration of NAB C vs. time τ of its reduction with HMS. T = 298 K, C_{HMS} = 0.252 M. C_{NaOH} (M): (*1*) 0.78, (*2*) 1.74, (*3*) 2.43, and (*4*) 3.11.

1070-4272/01/7410-1715 $25.00 © 2001 MAIK "Nauka/Interperiodica"

amples of these reactions are reduction of $FeEDTA^-$ [11] and 4-nitrosodiphenylamine (4NDPA) [12] with rongalite and of *p*-benzoquinone with rongalite and TUDO [2].

Studies of decomposition of HMS and TUDO showed [13, 14] that the induction period is caused by the autocatalytic decomposition of molecules of the reducing agent, proceeding with rupture of the C–S bond (with HMS molecules as an example) in neutral

$$HOCH_2SO_2^- = HSO_2^- + CH_2O \quad (1)$$

or in alkaline medium:

$$HOCH_2SO_2^- + OH^- = SO_2^{2-} + CH_2(OH)_2. \quad (2)$$

To pass from the induction period to a steady state, it is necessary to accumulate a sufficient amount of decomposition catalysts ("active sulfur" and sulfide), which are by-products of processes (1) and (2). When the excess of the reducing agent is sufficiently high, the reactions of the first group proceed in quasi-steady-state mode to 90% and higher conversion of the oxidizing agent. The inhibiting effect of formadehyde is caused by a shift to the left of the equilibrium of reactions (1) and (2) and the resulting decrease in the quasi-steady-state concentration of the intermediates, anions of sulfoxylic acid (HSO_2^- and SO_2^{2-}) [1, 2].

The kinetic data suggest that the reduction with derivatives of aminoalkanesulfinic acids proceeds by two concurrent pathways: with preliminary cleavage of the C–S bond, accompanied by the formation of sulfur-oxygen intermediates by reactions (1) and (2), and by direct reaction between molecules of the oxidizing and reducing agents [i.e., with stages (1) and (2) by-passed]. The first pathway is arbitrarily named the dissociative pathway, and the second, the associative pathway [15].

Thus, as regards the nature of the reducing effect, the reactions of the first group can be classed with dissociative-autocatalytic reactions.

For the second group of reactions, the absence of the induction period in the kinetic curves suggests that the reduction rather easily proceeds by the dissociative pathway without accumulation of active sulfur able to catalyze stages (1) and (2).

For the third group of reactions, along with the reduction with HSO_2^- or SO_2^- anions, there occurs direct reaction of the oxidizing agent with molecules of the initial reducing agent (associative pathway).

The relative contribution of associative and dissociative pathways to the total process can be estimated from the corresponding reaction rates r_a and r_d determined in experiments with and without addition of formaldehyde. The rate r_a for the reactions proceeding by two pathways was determined under the condition $r_d = 0$, i.e., when an increase in the concentration of added formaldehyde did not affect the reaction rate. The rate r_d was evaluated on the basis of experimental data obtained in the absence of formadehyde addition, from the difference between the apparent reaction rate r and r_a. It should be noted that the ratio $r_a : r_d$, characterizing the contribution of the individual pathways, is governed by the following factors: (a) chemical nature of the oxidizing and reducing agents; (b) reaction conditions, primarily temperature and pH; and (c) process duration.

Let us consider the effect of each factor separately. Data on the kinetics and mechanisms of reactions involving HMS and TUDO are summarized in Tables 1 and 2.

According to the experimental data, associative mechanism is of the greatest importance in reduction of $FeEDTA^-$ with HMS (at a temperature below 303 K the reaction proceeds completely by the associative pathway).

In reduction of organic compounds, the dissociative pathway is dominant. For example, the ratio $r_a : r_d$ is 1 : 6 for 4NDPA (T = 308 K, C_{NaOH} = 1 M), and 1 : 380 for NAB (T = 308 K, C_{NaOH} = 1 M). Reduction of indigocarmine proceeds completely by the dissociative autocatalytic pathway.

The $r_a : r_d$ ratio depends on the nature of the reducing agent. In reduction with TUDO, reactions with an appreciable contribution of the associative pathway are less common than in reduction with HMS. This is apparently caused by the presence of sulfoxylates, which are more readily formed under conditions of reduction with TUDO, i.e., in alkaline media.

The temperature and acidity of the medium govern the degree and rate of cleavage of the reducing agent molecules and thus affect the ratio $r_a : r_d$. The temperature effect is particularly noticeable in reaction of $FeEDTA^-$ with HMS [16]. In this process the reaction proceeds below 303 K by the associative pathway ($r_d = 0$), and by both pathways above 303 K ($r_a : r_d$ = 1 : 2.5 at T = 308 K, $C_{HMS} = 6.5 \times 10^{-3}$ M, pH 10.8).

This fact is accounted for by stronger temperature dependence of the reaction rate in the case of dissociative mechanism (Table 1), which follows from a comparison of the activation energies E^I and E^{II}. There-

Table 1. Results of kinetic studies of the reactions involving sodium hydroxymethylsulfinate*

Oxidizing agent	Mechanism of the redox process	Evaluated kinetic parameters
NAB	$HOCH_2SO_2^- + OH^- \underset{k_{-1}}{\overset{k_1}{\rightleftarrows}} SO_2^{2-} + CH_2(OH)_2$ $NAB + SO_2^{2-} \xrightarrow{k_2} BTANO + SO_3^{2-}$	T = 308 K, C_{NaOH} = 0.1–4 M, $k_1 = (0.32 \pm 0.07) \times 10^{-6}$ M^{-1} s^{-1}, $k_{-1} = 8 \pm 5$ M^{-1} s^{-1}, $k_2 = (1.2 \pm 0.07) \times 10^{-2}$ M^{-1} s^{-1}, $E_{app} = 40 \pm 5$ kJ mol^{-1}
4NDPA	$HOCH_2SO_2^- + OH^- \underset{k_{-1}}{\overset{k_1}{\rightleftarrows}} SO_2^{2-} + CH_2(OH)_2$ $4NDPA + SO_2^{2-} \xrightarrow{k_2} Int + SO_3^{2-}$ $Int + SO_2^{2-} \xrightarrow{k_3} 4ADPA + SO_3^{2-}$ $4NDPA + HOCH_2SO_2^- \xrightarrow{k_4} Int + HOCH_2SO_3^-$ $Int + HOCH_2SO_2^- \xrightarrow{k_5} 4ADPA + HOCH_2SO_3^-$	T = 308 K, C_{NaOH} = 0.1–2 M, $k_1 = (0.47 \pm 0.08) \times 10^{-6}$ M^{-1} s^{-1}, $k_1 : k_2 = (13 \pm 4) \times 10^{4-}$, $E_{app} = 54 \pm 4$ kJ mol^{-1}
$FeEdta^-$	$HOCH_2SO_2^- \underset{k_{-1}}{\overset{k_1}{\rightleftarrows}} HSO_2^- + CH_2O$ $FeEdta^- + HSO_2^- \xrightarrow{k_2} FeEdta^{2-} + H\dot{S}O_2$ $FeEdta^- + H\dot{S}O_2 \xrightarrow{k_3} FeEdta^{2-} + SO_2 + H^+$ $FeEdta^- + HOCH_2SO_2^- \xrightarrow{k_4} FeEdta^{2-} + H\dot{S}O_2 + CH_2O$	T = 308 K, pH 10.8 (Robinson–Britton buffer solution), $k_1 = (0.14 \pm 0.01) \times 10^{-5}$ s^{-1}, $k_1 : k_2 = (0.7 \pm 0.1) \times 10^{-5}$, $k_4 = 0.55 \pm 0.07$ M^{-1} s^{-1}, $E^{I}_{app} = 21 \pm 4$ kJ mol^{-1}, $E^{II}_{app} = 109 \pm 8$ kJ mol^{-1}
$[IC(CO)_2]$	$HOCH_2SO_2^- \underset{k_{-1}}{\overset{k_1}{\rightleftarrows}} HSO_2^- + CH_2O$ $IC(CO)_2 + HSO_2^- \xrightarrow{k_2} ICCOCOH^- + SO_2$	T = 333 K, pH 10.5, $k_1 = 1.03 \times 10^{-5}$ s^{-1}, $k_1 : k_2 = 24 \times 10^{-3}$, $E_{app} = 114$ kJ mol^{-1}
$Ni^{2+}(NiCl_2)$	$HOCH_2SO_2^- \underset{k_{-1}}{\overset{k_1}{\rightleftarrows}} HSO_2^- + CH_2O$ $Ni^{2+} + HSO_2^- + H_2O \xrightarrow{k_2} Ni + HSO_3^- + 2H^+$ $2HSO_2^- \xrightarrow{k_3} HS^- + HSO_4^-$ $2HSO_2^- \xrightarrow{k_4} SO_3^{2-} + S + H_2O$ $Ni^{2+} + HS^- \xrightarrow{k_5} NiS + H^+$ – fast	T = 308 K, pH 4.0, $k_1 = 10^{-3}$ s^{-1}, $k_{-1} = 8.47 \times 10^2$ M^{-1} s^{-1}, $k_2 = 4.9 \times 10^{-2}$ M^{-1} s^{-1}, $k_3 = 27.6$ M^{-1} s^{-1}, $k_4 = 110.9$ M^{-1} s^{-1}, $E_{app} = 134 \pm 12$ kJ mol^{-1}

* (BTANO) Benzotriazole *N*-oxide; the reaction proceeds by the dissociative mechanism, contribution of the associative mechanism is insignificant; (Int) intermediate, (4ADPA) 4-aminodiphenylamine; (E^{I}_{app}) and (E^{II}_{app}) apparent activation energies for reactions proceeding by the associative and both pathways, respectively; (IC) indigocarmine; and (ICCOCOH) leuco form of indigocarmine.

fore, in all reducing reactions involving hydroxy- and aminoalkanesulfinates, the contribution of the associative pathway must grow with increasing temperature.

An increase in pH facilitates cleavage of TUDO molecules by the scheme

$$NHC(SO_2H)NH_2 + OH^- = HSO_2^- + (NH_2)_2CO. \quad (3)$$

Thereby, the contribution of the dissociative pathway to redox processes involving TUDO increases. The acidity of the medium affects the degree of dissociation of HMS and other derivatives of sodium alkanesulfinates in two ways. On the one hand, their dissociation becomes more pronounced with decreasing pH, owing to autocatalysis by the products of decomposition of the reducing agents [13, 14] and,

Table 2. Results of the kinetic studies of the reactions involving thiourea dioxide

Oxidizing agent	Mechanism of the redox process	Evaluated kinetic parameters
NAB	$NH_2CSO_2NH_2 \underset{k_{-1}}{\overset{k_1}{\rightleftarrows}} NHC(SO_2H)NH_2$ $NHC(SO_2H)NH_2 + OH^- \xrightarrow{k_2} HSO_2^- + (NH_2)_2CO$ $NAB + HSO_2^- \xrightarrow{k_3} BTANO + HSO_3^-$ $HSO_2^- \xrightarrow{k_4}$ Decomposition products in the presence of formaldehyde additive $CH_2O + HSO_2^- \underset{k_{-5}}{\overset{k_5}{\rightleftarrows}} HOCH_2SO_2^-$	T = 281 K, C_{NaOH} = 0.18 M, $k_5 : k_3 = (9.4 \pm 0.8) \times 10^{-3}$, $E_{app} = 60 \pm 5$ kJ mol^{-1}
$FeEdta^{-}$*	$NH_2CSO_2NH_2 \underset{k_{-1}}{\overset{k_1}{\rightleftarrows}} NHC(SO_2H)NH_2$ $NHC(SO_2H)NH_2 + OH^- \xrightarrow{k_2} HSO_2^- + (NH_2)_2CO$ $FeEdta^- + HSO_2^- \xrightarrow{k_3} FeEdta^{2-} + HSO_2^{\bullet}$ $FeEdta^- + HSO_2^{\bullet} \xrightarrow{k_4} FeEdta^{2-} + SO_2 + H^+$ $HSO_2^- \xrightarrow{k_5}$ Decomposition products	T = 301 K, pH 8.7, $k_5 : k_3 = (1.7 \pm 0.4) \times 10^{-4}$, $E_{app} = 110 \pm 10$ kJ mol^{-1}
Uranyl acetate**	$NH_2CSO_2NH_2 \underset{k_{-1}}{\overset{k_1}{\rightleftarrows}} NHC(SO_2H)NH_2$ $NHC(SO_2H)NH_2 + H_2O \xrightarrow{k_2} H_2SO_2 + (NH_2)_2CO$ $UO_2^{2+} + H_2SO_2 \xrightarrow{k_3} U^{4+} + SO_2 + 2OH^-$ $H_2SO_2 \xrightarrow{k_4}$ Decomposition products in the presence of formaldehyde additive $CH_2O + H_2SO_2 \underset{k_{-5}}{\overset{k_5}{\rightleftarrows}} HOCH_2SO_2H$	T = 323 K, C_{CH_3COOH} = 2.0 M, $k_5 : k_3 = 0.08$, $E_{app} = 39 \pm 5$ kJ mol^{-1}

* In the experiments with formaldehyde additive, the possibility of direct reaction of $FeEDTA^-$ with TUDO was found, but the contribution of the associative pathway is insignificant.

** $UO_2(CH_3COO)_2$.

on the other hand, a decrease in pH shifts the equilibrium of reaction (2) to the left, which decreases the contribution of the dissociative pathway when it is present. It is evident that the first factor plays a decisive role in this case. Previously, it has been shown [2] that in the reaction of *p*-benzoquinone with rongalite the reaction order changes from 1 to a fractional value with decreasing pH. It can be suggested that the contribution of the dissociative pathway of the reduction increases.

The following problems are very important for both elucidating the general features of the kinetics of the redox processes and solving the practical problems: (1) demonstration of the adequacy of the proposed reduction schemes, (2) goal-seeking control of the reduction rates, (3) forecasting of the rates and selectivity of the reduction depending on the nature of a reducing agent and an atom or a group of atoms to be reduced.

To prove the adequacy of the reduction schemes, we identified the intermediates of the redox reactions proceeding by the dissociative pathway, using polarography. It was found that the quasi-steady-state concentration of the intermediate active species ($S_2O_4^{2-}$, SO_2^{2-}, and SO^{2-}) varies in parallel with the reduction rate [17, 18]. As additional argument, we checked experimentally in a series of the reactions the kinetic equation obtained from the conditions of the quasi-

steady-state approximaton, which demonstrated a satisfactory agreement between the experimental and calculated reaction rates.

In the general form the reaction rates in the quasi-steady-state mode of many reactions involving HMS and its analogs can be described by the following equation (in alkaline medium):

$$\frac{dC_{Ox}}{d\tau} = \frac{k_1 k_2 C_{Red} C_{Ox} C_{OH^-}}{k_{-1} k_{CH_2O} + k_2 C_{Ox}} + k_3 C_{Red} C_{Ox}, \quad (4)$$

where k_1 is the constant of direct decomposition of the reducing agent (Red), k_{-1} is the constant of the reverse stage, k_2 is the rate constant of the reaction of the reducing agent with reduction intermediates, and k_3 is the rate constant of the associative pathway.

The first term in the right-hand side of Eq. (4) accounts for the reaction rate by the dissociative pathway, and the second, by the associative pathway.

For the reactions involving TUDO, the equations for the reaction rates have a more complicated form as a result of the presence of the stage of rearrangement and irreversible decomposition of the reducing agent molecules. However, in many cases, the experimental verification of the linear forms of the kinetic equations allows conclusion about the suitability of the quasi-steady-state approximation for reduction processes involving TUDO [4, 6, 10].

In the case of reduction of NAB, Ni^{2+},[1] and *N*,*N*' derivatives of binaphthylhexylcarboxylic acid diimide, we determined the kinetic parameters using the procedures of mathematic simulation with criterial selection of possible process schemes [19–21]. This approach makes it possible to determine the rate constants of individual stages or combination of these, estimate errors, and correlate the parameters with sufficient reliability.

The constants for NAB and Ni^{2+}, evaluated by the above procedures, are listed in Table 1.

It should be noted that the rate constants of the individual stages can be reliably determined only when the information content of the experimental data corresponds to the complexity of the system. When experimental data are scarce and the kinetic model is complex, a large number of parameter sets providing the same adequate description of the experimental data can be selected. Therefore, for some of reactions (Tables 1, 2) we determined not individual constants but their combinations.

Of some interest is to compare the rate constants of the same stages in different reduction reactions. It turns out that at 308 K the rate constant of the stage of HMS cleavage involving OH^- ions, k_1, determined from the kinetic data for reduction of NAB [$(0.32 \pm 0.07) \times 10^{-6}$ $M^{-1}\,s^{-1}$], is close to the k_1 value determined for reduction of 4NDPA [$(0.47 \pm 0.08) \times 10^{-6}$ $M^{-1}\,s^{-1}$]. The rate constants of the stages of HMS cleavage without OH^- ions involved in the reduction of $FeEDTA^-$ and indigocarmine are also comparable: $(0.14 \pm 0.01) \times 10^{-5}$ and $(0.17 \pm 0.03) \times 10^{-5}$ s^{-1}, respectively.

The k_1 values[2] for indigocarmine were recalculated from 333 to 308 K using the values E_{app} = 114 kJ mol^{-1} and $\ln p_{app}$ = 37. The kinetic parameters of the reaction of vat dye precursors of varied structures with HMS were evaluated in [22]. It was shown that for various hydroxyalkanesulfinates the rate constants of the stages of reaction of the same vat dye precursor with sulfoxylate anions [which corresponds to constant k_2 in Eq. (4)] agree within the order of magnitude. These facts additionally prove the adequacy of the proposed reaction schemes to experimental data.

The control of the reduction rate by addition of catalysts and formadehyde is only possible when the dissociative mechanism is dominant. For example, cobalt dioximines [23] and sodium sulfide [24] accelerate the process. It was found that cobalt dioximines exhibit high catalytic activity in reduction of azo dyes with rongalite and in reductive cyclization of nitroazobenzene to give light stabilizer of polymers, benzene P. The mechanism of the effect of dioximines consists in substitution of hydroxymethanesulfinate anion for one of the axial ligands, with its subsequent inner-sphere cleavage and release of sulfoxylate anions.

The effect of sodium sulfide is caused by an increase in the steady-state concentration of SO_2^{2-} owing to the inhibition of sodium hydroxyalkanesulfinate decomposition [13].

The selectivity of the reduction effect of alkanesulfinates of various structures is well seen in reductive cyclization of binaphthylhexacarboxylic acid der-

[1] The reduction of Ni^{2+} is arbitrarily considered homogeneous since it yields nickel in the solid state. However, owing to the irreversibility of the stage of solid nickel formation we can use the equations of homogeneous kinetics for mathematical description of the process.

[2] For reduction of Ni^{2+} ion, this rate constant is four orders of magnitude higher, which is caused by, first, the difference in pH and, second, different character of cleavage of reducing agent molecules, as mentioned above.

Table 3. Kinetic parameters of reduction of transition metal compounds

Oxidant + reductant	k_{app} (333 K), min^{-1}	E_{app}, kJ mol^{-1}	ln *p*	$\Delta_f H^0$ (298 K), kJ mol^{-1}
Co^{2+} + HMS	0.08×10^{-2}	74 ± 8	19 ± 1	–56.6
Ni^{2+} + HMS	0.11×10^{-2}	134 ± 12	42 ± 4	–53.1
$CuEdta^{2-}$ + HMS	13.3	189 ± 19	71 ± 6	1643.9
Co^{2+} + TUDO	0.52×10^{-2}	78 ± 7	22 ± 1	–56.6
Ni^{2+} + TUDO	12.5×10^{-2}	149 ± 15	51 ± 5	–53.1
$CuEdta^{2-}$ + TUDO	0.96	96 ± 10	35 ± 3	1643.9
UO_2^{2+} +TUDO	3.1×10^{-4}	39 ± 5	6 ± 2	–1024.9

ivatives. In this case, the final products of the reaction in solution are di- and tetraanions of perylenetetracarboxylic acid derivatives [25]. It was shown that the most probable process is concurrent formation of these derivatives from the corresponding initial compounds. For all of the studied derivatives of binaphthylhexacarboxylic acid, the relative yield of the product with four reduced carbonyl groups increases in the series of the reducing agents sodium dimethylaminomethanesulfinate < sodium diethylaminomethanesulfinate < sodium hydroxymethanesulfinate < sodium hydroxyethanesulfinate < sodium hydroxypropanesulfinate. It was shown [2] that the stabilities of the first three reducing agents are much the same, whereas introduction of alkyl substituent to α-carbon atom drastically decreases the stability of the reducing agent. The rise in the reducing power is due to an increase in the quasi-steady-state concentration of sulfoxylate anions, which, in turn, accelerates formation of products with four reduced groups.

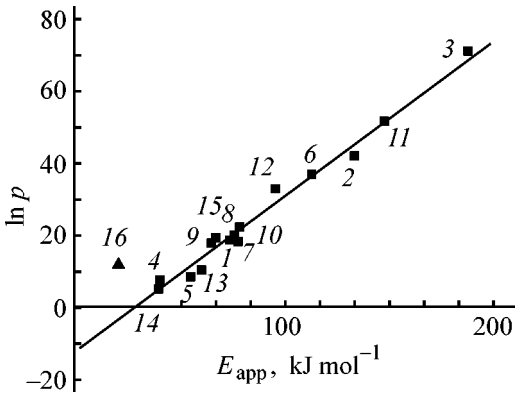

Fig. 2. Correlation between the Arrhenius parameters for reduction of various compounds with HMS and TUDO. (*p*) Pressure and (E_{app}) apparent activation energy. (*1*) Co^{2+} + HMS, (*2*) Ni^{2+} + HMS, (*3*) $CuEDTA^{2-}$ + HMS, (*4*) NAB + HMS, (*5*) 4NDPA + HMS, (*6*) $IC(CO)_2$ + HMS, (*7*) Direct Red 2C + HMS, (*8*) $CoEDTA^{2-}$ + HMS, (*9*) $NiEDTA^{2-}$ + HMS, (*10*) Co^{2+} + TUDO, (*11*) Ni^{2+} + TUDO, (*12*) $CuEDTA^{2-}$ + TUDO, (*13*) NAB + TUDO, (*14*) UO_2^{2+} + TUDO, (*15*) $IC(CO)_2$ + TUDO, and (*16*) $FeEDTA^-$ + HMS (by the associative pathway).

The correlations obtained on the basis of kinetic data for reduction of a wide variety of reducing agents may be useful for forecasting the rates of reduction of various compounds with rongalite and TUDO.

The kinetic parameters of reduction of transition metal ions and complex compounds with rongalite and TUDO are presented in Table 3. Comparison of the apparent rate constants and enthalpies of formation of oxidizing agents suggests that these parameters vary in parallel for both the reducing agents.

Figure 2 shows the compensation relation between the Arrhenius parameters, which is described by the equation

$$\ln p = 0.43E_{app} - 12.06 \quad (R = 0.987).$$

This dependence is observed for those reactions in which the dissociative mechanism of reduction is predominant. Therefore, the point with the coordinates E_{app} = 21 kJ mol^{-1} and ln *p* = 12, obtained for the reduction of $FeEDTA^-$ with rongalite proceeding at low temperatures by the associative pathway, falls out of this dependence. The observed compensation effect suggests the occurrence of the limiting stages of the reactions through transition states with similar configurations [26]. In the stages of decomposition of reducing agents, transition states are likely to form by protonation or deprotonation of hydrated molecules, as shown by quantum-chemical calculations for tautomeric conversion of TUDO as an example [2].

In conclusion, it should be noted that the data presented make it only possible to determine schemes of stoichiometric mechanisms of the processes. The existing experimental data are insufficient to come to reliable conclusions on the structure of transition states in particular stages.

REFERENCES

1. Budanov, V.V. and Makarov, S.V., *Khimiya serosoderzhashchikh vosstanovitelei* (Chemistry of Sulfur-Containing Reducing Agents), Moscow: Khimiya, 1994.
2. Makarov, S.V., Reactivity of Sulfur-Oxygen Reducing Agents with the C–S Bond, *Cand. Sci. Dissertation*, Ivanovo, 2000.
3. Sokolova, I.N., Budanov, V.V., Polenov, Yu.V., and Polyakova, I.R., *Izv. Vyssh. Uchebn. Zaved., Khim. Khim. Tekhnol.*, 1983, vol. 26, no. 7, pp. 822–825.
4. Polenov, Yu.V. and Budanov, V.V., *Izv. Vyssh. Uchebn. Zaved., Khim. Khim. Tekhnol.*, 1988, vol. 31, no. 8, pp. 66–70.
5. Budanov, V.V., Boleslavskaya, N.F., Muratova, T.P., *et al., Tr. Ivanov. Khim.-Tekhnol. Inst.*, 1975, no. 18, pp. 50–53.
6. Kolesnik, V.V., Makarov, S.V., Polenov, Yu.V., *et al.*, in *Khimiya Urana*, (Uranium Chemistry), Moscow: Nauka, 1989, pp. 296–299.
7. Makarov, S.V., Mundoma, C., Penn, J.H., *et al., J. Phys. Chem., Ser. A*, 1998, vol. 102, no. 17, pp. 2915–2920.
8. Kublashvili, G.D., Polenov, Yu.V., Budanov, V.V., *et al., Zh. Prikl. Khim.*, 1990, vol. 63, no. 7, pp. 1622–1625.
9. Egorova, E.V., Physicochemical Aspects of the Use of Reducing Agents, Derivatives of sulfoxylic Acid in Electroless Metal plating of Nitron Fiber, *Cand. Sci. Dissertation*, Ivanovo, 1991.
10. Polenov, Yu.V. and Budanov, V.V., *Izv. Vyssh. Uchebn. Zaved., Khim. Khim. Tekhnol.*, 1986, vol. 29, no. 5, pp. 53–56.
11. Polenov, Yu.V., Zalesova, T.S., Aleksandrova, A.N., and Budanov, V.V., *Izv. Vyssh. Uchebn. Zaved. Khim. Khim. Tekhnol.*, 1981, vol. 24, no. 5, pp. 577–581.
12. Polenov, Yu.V. and Budanov, V.V., *Izv. Vyssh. Uchebn. Zaved., Khim. Khim. Tekhnol.*, 1988, vol. 31, no. 4, pp. 40–43.
13. Makarov, S.V., Polenov, Yu.V., and Budanov, V.V., *Zh. Neorg. Khim.*, 1984, vol. 29, no. 10, pp. 2456–2460.
14. Polenov, Yu.V., Makarov, S.V., and Budanov, V.V., *Izv. Vyssh. Uchebn. Zaved., Khim. Khim. Tekhnol.*, 1986, vol. 29, no. 12, pp. 30–33.
15. Budanov, V.V., Abstracts of Papers, *Mezhdunarodnyi seminar "Sernistye soedineniya i okruzhayushchaya sreda"* (Int. Seminar "Sulfur-Containing Compounds and Environment"), Ivanovo: Ivanov. Gos. Khim.-Tekhnol. Akad., 1996, pp. 10–14.
16. Polenov, Yu.V., Budanov, V.V., and Kublashvili, G.D., *Izv. Vyssh. Uchebn. Zaved., Khim. Khim. Tekhnol.*, 1988, vol. 31, no. 3, pp. 58–61.
17. Budanov, V.V., Sokolova, I.N., and Mel'nikov, B.N., *Izv. Vyssh. Uchebn. Zaved., Khim. Khim. Tekhnol.*, 1974, vol. 17, no. 8, pp. 1155–1160.
18. Budanov, V.V., Sokolova, I.N., and Mel'nikov, B.N., *Izv. Vyssh. Uchebn. Zaved., Khim. Khim. Tekhnol.*, 1976, vol. 19, no. 2, pp. 240–244.
19. Polenov, Yu.V., Labutin, A.N., Tsareva, A.A., and Budanov, V.V., *Izv. Vyssh. Uchebn. Zaved., Khim. Khim. Tekhnol.*, 1987, vol. 30, no. 9, pp. 63–66.
20. Polenov, Yu.V., Labutin, A.N., Khalizov, R.L., *et al., Izv. Vyssh. Uchebn. Zaved., Khim. Khim. Tekhnol.*, 1999, vol. 42, no. 2, pp. 84–87.
21. Khalizov, R.L., Polenov, Yu.V., Labutin, A.N., and Budanov, V.V., *Izv. Vyssh. Uchebn. Zaved., Khim. Khim. Tekhnol.*, 1999, vol. 42, no. 2, pp. 79–83.
22. Polenov, Yu.V., Kublashvili, G.D., Labutin, A.N., and Budanov, V.V., *Izv. Vyssh. Uchebn. Zaved., Khim. Khim. Tekhnol.*, 1997, vol. 40, no. 1, pp. 52–55.
23. Budanov, V.V., Sokolova, I.N., and Mel'nikov, B.N., *Izv. Vyssh. Uchebn. Zaved., Khim. Khim. Tekhnol.*, 1975, vol. 18, no. 3, pp. 489–491.
24. Aleksandrova A.N., Polenov, Yu.V., Zvegintseva, G.B., *et al., Izv. Vyssh. Uchebn. Zaved., Khim. Khim. Tekhnol.*, 1983, vol. 26, no. 10, pp. 1188–1192.
25. Polenov, Yu.V., Kublashvili, G.D., Budanov, V.V., *et al., Zh. Prikl. Khim.*, 1992, vol. 65, no. 11, pp. 2570–2574.
26. Basolo, F. and Pearson, R.G., *Mechanisms of Inorganic Reactions. A Study of Metal Complexes in Solution*, New York: Wiley, 1967.

Russian Journal of Applied Chemistry, Vol. 74, No. 10, 2001, pp. 1722–1727. Translated from Zhurnal Prikladnoi Khimii, Vol. 74, No. 10, 2001, pp. 1671–1676.

ORGANIC SYNTHESIS AND INDUSTRIAL ORGANIC CHEMISTRY

Determination of Methylphosphonic Acid and Its Esters as Chemical Markers of Organophosphorus Chemical Warfare Agents

E. I. Savel'eva, A. S. Radilov, T. A. Kuznetsova, and N. F. Volynets

Research Institute of Hygiene, Professional Diseases, and Human Ecology, St. Petersburg, Russia

Received April 4, 2000; in final form, June 2000

Abstract—The feasibility of isolation and quantitative determination by gas chromatography of methylphosphonic acid and its mono- and dialkyl etsers, which originate from destruction of organophosphorus chemical warfare agents and have been detected in bitumen–salt compounds is examined.

Organophosphorus chemical warfare agents (OPCWAs), the most known of which are tabun, sarin, soman, and VX-group compounds, are extremely strong cholinergic antagonists.

By now, basic principles of OPCWA analysis have been developed and recommended for use in the practice of international examinations [1–3]. For practically all of the known OPCWAs, the physicochemical constants are known, and therefore their "confirming" identification involves no problems. However, the experience of chemical appraisals of the consequences of emergencies involving OPCWAs shows that, in most cases, the initial OPCWAs cannot be detected at sites of their application. Decomposition products of OPCWAs, formed in various media, cannot be predicted *a priori*, the more so as the type of the weapons used may be unknown. Therefore, it is very important to reveal long-lived "witness" compounds that would be always present among products of OPCWA decomposition and would retain information about the initial compound.

Such "witnesses," or markers, should also be revealed for setting up analytical and sanitation-chemical monitoring of processes used for destruction of chemical weapons. First, it is necessary to study the composition of degradation products of war gases and of intermediates released into the contact medium in the process. This stage involves identification of OPCWA conversion products and revealing of chemical markers. The next stage should involve examination of the emission of markers to various media and assessment of possible pathways of their further transformation. These results can serve as a basis for environmental monitoring of potentially hazardous sites.

At present, a two-stage flowsheet is being put into operation in Russia for destruction of OPCWAs, with chemical decomposition and subsequent bituminous grouting of the resulting solid wastes to obtain so-called bitumen–salt compounds (BSCs) [4, 5].

It has been shown previously that among the products of yperite decomposition, including its decomposition within BSCs, a versatile marker is 1,4-dithiane [6]. In this work, with the aim to reveal chemical markers, we studied by GC–MS the composition of BSCs containing the products of sarin, soman, and VX breakdown, and also that of gases released from, and aqueous extracts of BSCs. With respect to their origin, BSC components can be subdivided in three groups: products of OPCWA breakdown, deactivating agents, and bitumen components. The chemical markers should belong to the first group; in individual determinations, they should correspond to specific types of OPCWAs. They should also be stable in the matrix and selectively detectable against the background signals.

After disposal of BSCs, emergency seal failure of containers is possible, accompanied by washout of soluble BSC components by groundwater. To estimate the extent of marker emission into an aqueous-salt system simulating the chemical composition of groundwater at the site of a repository to be constructed, it was necessary to develop procedures for recovery of the markers from aqueous solutions and for their quantitative chemical analysis. For this purpose, we used gas chromatography (GC).

To reveal chemical markers, we initially identified components always present in gases released from,

1070-4272/01/7410-1722 $25.00 © 2001 MAIK "Nauka/Interperiodica"

Table 1. Procedures of sample preparation for analysis

Procedure	Analysis object	Analysis procedure
A	BSCs	Static head-space analysis
B	Aqueous extracts of BSCs	Extraction with dichloromethane (pH 7)
C	Aqueous extract after procedure B	Evaporation to dryness, redissolution in dichloromethane–acetonitrile (1 : 1), silylation
D	"	Saturation with NaCl, extraction with acetonitrile (pH 2), drying, redissolution, silylation

and aqueous extracts of, BSCs. The sample preparation procedures are summarized in Table 1. Such a fourstep scheme allowed us to expand to the maximum possible extent the group of BSC components determinable by GC analysis: from the most volatile (head-space analysis) to non-volatile (derivatives of aqueous extracts).

In the systems BSC–sarin and BSC–soman, the main decomposition products of sarin and soman are, respectively, isopropyl and pinacolyl alcohols, diisopropyl and dipinacolyl methylphosphonates, isopropyl and pinacolyl hydrogen methylphosphonates, and also methylphosphonic acid itself. The system BSC–VX is considerably more complex and includes several tens of volatile organic compounds; the major components are mono- and disulfides containing diethylaminoethyl group but lacking the phosphorus atom. The mass spectra of these compounds are difficultly discernible and in most cases contain only a single strong peak corresponding to the $(Et_2N{=}CH_2)^+$ ion. The major phosphorus-containing products are methylphosphonic acid and its mono- and dibutyl esters [by VX we mean *O*-isobutyl *S*-(2-diethylaminoethyl) methylphosphonothioate, whereas in the United States and some other countries its isomer, *O*-ethyl *S*-(2-diisopropylaminoethyl) methylphosphonothioate, is more widespread].

Thus, among products of sarin, soman, and VX decomposition by the two-stage process, we can distinguish homologous series of alkyl hydrogen and dialkyl methylphosphonates. Specifically these compounds, together with their hydrolysis product, methylphosphonic acid, seem to be the most suitable chemical markers for assessing the possible environmental pollution. Additional advantages of these compounds are the possibility of their selective detection and low probability of false positive results, because compounds with a P–C bond are very rare in nature.

Table 2 gives mass spectra of phosphorus-containing compounds that originate from the breakdown of OPCWAs and are present in BSCs. Among the compounds given in Table 2, only methylphosphonic acid diesters $MeP(O)(OR)_2$ can be determined by direct gas-chromatographic analysis. As compared with methylphosphonic acid and alkyl hydrogen methylphosphonates, dialkyl methylphosphonates are considerably more seldom mentioned in the literature as OPCWA decomposition products, although they are included in the lists of compounds to be monitored according to the Convention on the Prohibition of the Development, Production, Stockpiling, and Use of Chemical Weapons and on Their Destruction [7]. Under conditions of the existing process for OPCWA destruction, they can form by reaction of the monoester MeP(O)(OH)(OR) with the alcohol ROH (R = *i*-Pr, pinacolyl, or *i*-Bu for sarin, soman, and VX, respectively). Also, diesters of methylphosphonic acid can be present as impurities in the initial OPCWAs, especially after their prolonged storage. A scheme for classification of these compounds according to their mass spectra was proposed in [8]. Comparison of the intensity of the peak at m/z = 47, corresponding to the $[P{=}O]^+$ fragment, with the preset threshold is the first step of the algorithm. If the threshold is not exceeded, this fact is regarded, according to [8], as the absence of the compounds under consideration in a sample. However, according to our experience, the intensity of this signal in the mass spectra of alkyl methylphosphonates is so low that at their low concentrations (especially in such matrices as soil) it can hardly be detected.

Under the experimental conditions, the content of diisopropyl and diisobutyl methylphosphonates in BSCs was determined with sufficient reproducibility by static head-space analysis. Dipinacolyl methylphosphonate present in BSCs can be quantitatively determined only in extracts. Table 2 shows that the strongest peak in the mass spectra of all these three diesters is that at m/z = 97. Group analysis of dialkyl methylphosphonates in groundwater and soil by GC–MS is possible in the selective ion monitoring mode. Samples were prepared for analysis by procedure B. The sensitivity of the analysis is high: the de-

Table 2. Alkylphosphonates recovered from BSCs containing products of OPCWA destruction*

Compound	Mass spectrum, *m*/*z* (I_{rel}, %)	OPCWA being destroyed	Sample preparation procedure (Table 1)
Methylphosphonates:			
diisopropyl	165(4.1), 139(7.2), 137(3.1), 123(65.1), 121(9.0), 97(100.0), 80(7.2), 79(20.9), 65(3.6), 47(4.5), 45(7.3), 43(9.1)	Sarin	A, B**
diisobutyl	165(1.6), 153(4.5), 137(8.6), 135(3.1), 111(4.7), 110(8.7), 97(100.0), 80(7.8), 79(10.6), 57(11.1), 43(3.5)	VX	A, B**
dipinacolyl	208(4.0), 207(38.1), 181(1.7), 180(1.4), 165(11.5), 124(60.1), 123(99.5), 111(2.6), 97(100.0), 85(35.9), 80(12.4), 69(11.1), 57(15.6)	Soman	B
isopropyl hydrogen (converted to trimethylsilyl ester)	195(5.0), 169(14.9), 155(3.6), 154(8.3), 153(100.0), 152(5.1), 151(15.0), 137(4.4), 123(2.3), 121(4.4), 77(7.2), 75(22.7), 73(7.9), 45(8.6)	Sarin	C, D**
isobutyl hydrogen (converted to trimethylsilyl ester)	209(2.0), 170(2.5), 169(24.3), 167(3.9), 154(7.8), 75(20.2), 73(10.3), 153(100.0), 151(14.5), 137(3.0), 123(2.0), 77(6.7), 45(7.8)	VX	C, D**
pinacolyl hydrogen (converted to trimethylsilyl ester)	237(1.2), 196(14.7), 195(27.1), 179(3.7), 169(32.5), 153(100.0), 152(9.8), 151(25.5), 137(6.4), 121(10.5), 77(6.3), 75(19.8), 73(13.9), 45(6.7)	Soman	C, D**
Methylphosphonic acid [converted to bis(trimethylsilyl) ester]	240(7.6), 227(7.6), 226(17.8), 225(100.0), 209(3.8), 195(3.4), 153(7.2), 147(10.3), 135(7.3), 133(9.3), 105(7.7), 75(11.4), 73(18.5), 45(11.6)	Sarin, Soman, VX	C,** D

* Underlined are the *m*/*z* values for the strongest peaks.

** The best procedure for sample preparation.

tection limit in water is as low as 0.1 μg l^{-1}. At the same time, esters of dibasic carboxylic acids, alkenes, alkylthiophenes, and some other compounds often present in soils also give in mass spectra a strong peak at *m*/*z* = 97. Therefore, if the concentration level does not allow analysis of the total mass spectrum, identification of dialkyl methylphosphonates, especially in soil, requires additional confirmation. Dialkyl methylphosphonates fully meet the requirements to BSC chemical markers. Their main advantages are simple recovery from matrices and the possibility of direct selective gas-chromatographic determination. At the same time, it is known [9] that, in the presence of water, dialkyl methylphosphonates are hydrolyzed to give alkyl hydrogen methylphosphonates and then methylphosphonic acid. Thus, just alkyl hydrogen methylphosphonates and methylphosphonic acid, initially present in BSCs and formed by hydrolysis of dialkyl methylphosphonates, can be considered "long-lived" BSC markers. Alkyl hydrogen methylphosphonates in which the alkyl group is specific to a particular OPCWA can be regarded as individual chemical markers, and methylphosphonic acid, as group marker (Table 2):

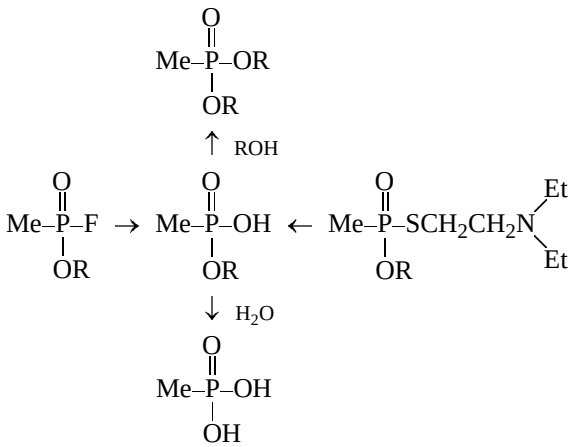

where R = *i*-Pr (sarin), pinacolyl (soman), or *i*-Bu (VX).

Methylphosphonic acid and alkyl hydrogen methylphosphonates are readily soluble in water; therefore,

Table 3. Comparative estimation of the efficiency and reproducibility of recovery of acidic methylphosphonates from aqueous solutions

Compound	Method of sample preparation	S_{av}	S_x	R
		%		
Hydrogen phosphonate:				
isopropyl	Calibration	0.920	–	–
	Evaporation	0.031	48.9	3.3
	Extraction*	0.074	17.1	80.0
isobutyl	Calibration	0.357	–	–
	Evaporation*	0.068	49.7	18.9
	Extraction	0.303	23.8	85.0
pinacolyl	Calibration	0.590	–	–
	Evaporation	0.094	67.0	15.8
	Extraction*	0.581	21.6	98.6
Methylphosphonic acid	Calibration	0.805	–	–
	Evaporation	0.610	23.6	75.8
	Extraction*	0.413	28.8	51.0

* The best procedure is marked with an asterisk.

they will migrate into groundwater in the case of a seal failure of BSC containers. At the same time, being polar and nonvolatile, these compounds are difficult objects for chemical analysis. However, they can be readily determined by HPLC. In this case, it is necessary to ensure efficient detection, which can be provided by introducing groups imparting UV absorption to a substance [10] or enhancing its electrical conductivity [11]. The feasibility of direct analysis of alkyl hydrogen alkylphosphonates by liquid chromatography, combined with mass spectrometry in the electrospray mode, was demonstrated in [12]. The main limitations of the procedures involving HPLC separation are problems with obtaining narrow peaks [10, 11] and the high cost of the equipment [12].

The majority of the methods developed for analysis of alkyl hydrogen alkylphosphonates are based on GC with various modification procedures for increasing the volatility of the compounds being analyzed. To prepare a sample for GC analysis, it is necessary to quantitatively recover it from aqueous solution and convert to a volatile form. These tasks are solved successively, since extractive alkylation procedures are inapplicable to these compounds. To recover alkyl hydrogen alkylphosphonates, Soderstrom *et al*. [9] evaporated aqueous solutions and biological fluids to dryness; Minami *et al*. proposed an alternative approach: extraction with acetonitrile [13].

In this study, we used both the procedures. To find the best conditions for recovery and modification of methylphosphonic acid and isopropyl, isobutyl, and pinacolyl hydrogen methylphosphonates, we used GC with a flame-ionization detector. The areas of the chromatographic peaks of the trimethylsilyl esters were measured, and their ratios to the area of the peak of tetradecane, used as internal reference, (relative peak areas) were determined.

The average relative peak areas S_{av} for each component in calibration solutions and in samples after evaporation and extraction are given in Table 3. The reproducibility of the analysis was characterized by the root-mean-square deviation S_x, and the efficiency of sample preparation, by the degree of recovery R. Data in Table 3 were obtained for the analyte concentration range 1–100 mg l^{-1}.

Table 3 shows that, in analysis of alkyl hydrogen methylphosphonates, satisfactory results are obtained only in extraction with acetonitrile (method D). We found that methylene chloride (method B) does not recover methylphosphonic acid and its acidic esters from both neutral and acidic (pH 1–6) aqueous solutions to a noticeable extent (R < 1%). Thus, there is practically no loss of methylphosphonic acid and its acidic esters in stage B of sample preparation (Table 1).

Methylphosphonic acid is recovered from aqueous solutions most difficultly. At the same time, with methylphosphonic acid, satisfactory analytical parameters are achieved by evaporation of the aqueous sample. Thus, the best procedures for analysis of methylphosphonic acid and its acidic esters are C and D, respectively (Table 1). However, in analysis of large

volumes of natural waters expected to contain methylphosphonic acid in low concentrations, procedure C is very power-consuming. In this case, procedure D becomes more appropriate, with correction made for the actual degree of recovery.

To choose a procedure for conversion of methylphosphonic acid and its acidic esters to volatile derivatives, we compared, using solutions of the corresponding reference samples in dichloromethane, the efficiencies of methylation (with diazomethane and methyl iodide) and silylation [with *N*,*O*-bis(trimethylsilyl)acetamide (BSA) and bis(trimethylsilyl)trifluoroacetamide (BSTFA)]. The highest relative yields, at a minimum of false positive results, were achieved with silylation (irrespective of the silylating agent used). The effect of trimethylchlorosilane (TMS) addition on the yield of silylation with BSTFA was studied in [13]; the highest yield was achieved at the ratio BSTFA : TMS = 1 : 9. Under our conditions, addition of TMS had no significant influence on the silylation efficiency and resulted only in sample contamination. As already noted, when choosing the optimal conditions for recovery from aqueous solutions and modification of alkyl hydrogen methylphosphonates, we used as recording device a gas chromatograph equipped with a flame-ionization detector, which was very convenient as applied to model, relatively concentrated (0.1–100 mg l^{-1}) solutions. However, for actual water samples, the sensitivity and selectivity of this procedure were insufficient. In this case, we used in GC analysis a thermoionic detector, with the same recovery and modification procedures. The detection limit of methylphosphonic acid and its esters was as low as 0.1–1 μg l^{-1}, approaching the sensitivity level of GC–MS with selective ion monitoring (m/z = 153 for alkyl hydrogen methylphosphonates and 225 for methylphosphonic acid).

EXPERIMENTAL

Head-space analysis (method A) was performed in the static mode: 1 g of a BSC sample was kept for 40 min in temperature-controlled 10-ml vessels with a Teflon membrane at 70°C, and 1-ml samples of the equilibrium vapor were taken for analysis.

Aqueous BSC samples were prepared as follows.[1] A bitumen–salt compound was poured into molds made of a chemically inert material and kept for 24 h, after which an aqueous-salt solution simulating the composition of natural waters at the site of intended BSC disposal was added, and the system was kept for 4 days at 25°C.

Neutral extracts from BSC aqueous extracts (method B) were prepared by treatment of 10 ml of an aqueous sample with methylene chloride (3 × 2 ml) at pH 7. The combined extract was dried, concentrated, and analyzed.

The aqueous residue was divided in two portions. An aliquot of the first portion was evaporated to dryness and dissolved in 10 μl of methylene chloride–acetonitrile (1 : 1), 20 μl of a methanolic solution of BSA or BSTFA was added, and the mixture was kept for 20 min at 60°C; after that it was diluted (if necessary) and analyzed (method C). The second portion was used for preparing acidic extracts from aqueous extracts. It was acidified to pH 1 with dilute sulfuric acid, saturated with sodium chloride, and extracted with acetonitrile (3 × 2 ml). The combined extract was dried, concentrated, again dried, and redissolved in 10 μl of methylene chloride–acetonitrile (1 : 1); 20 μl of a methanolic solution of BSA or BSTFA was added, and the mixture was kept for 20 min at 60°C (method D).

The solvents (methylene chloride and acetonitrile) were purified by standard procedures and distilled in a column; pure-grade anhydrous sodium sulfate was calcined in a muffle furnace at 400°C before use. BSA, BSTFA, and methyl iodide were purchased from Merck (Germany); diazomethane was prepared by decomposition of N-nitrosomethylurea.

The GC–MS analysis was performed on a Shimadzu device comprising a GC-17A gas chromatograph, a QP 5000 mass spectrometer equipped with a quadrupole analyzer, and a data processing system. The ionization was performed by electron impact at an ionizing electron energy of 70 eV. The ion source temperature was 280°C. The device was calibrated in the automated mode against perfluorotributylamine reference. A DB-5 25000 × 0.2-mm capillary column of fused quartz was used; the thickness of the stationary phase film was 0.33 μm. The flow rate of the carrier gas (He) was 1 ml min^{-1}. Liquid samples (0.5–1 μl) were injected in the splitless mode (0.3 min), and gas samples (1 ml), in the split mode. The injector temperature was 250°C. The column was heated from 40 to 270°C at a rate of 5 deg min^{-1} and kept at the final temperature for 15 min.

Compounds were separated on a Kristall-2000 gas chromatograph equipped with a flame-ionization de-

[1] The procedure was developed at the State Research Institute of Organic Chemistry and Technology (GosNIIOKhT); reference samples of methylphosphonic acid and its isopropyl, isobutyl, and pinacolyl esters were prepared and submitted by GosNIIOKhT staff members.

tector or a thermionic detector and a quartz capillary column (25 000 × 0.2 mm). The thickness of the stationary phase film (SE-54) was 0.2 μm. The flow rate of the carrier gas (nitrogen) was 1 ml min^{-1}; hydrogen and air were fed into the detector at rates of 15 and 250 ml min^{-1}, respectively. The temperature schedule was the same as in the GC–MS analysis.

Quantitative GLC analysis was performed with external reference.

CONCLUSIONS

(1) Methylphosphonic acid and its mono- and dialkyl esters present in bitumen–salt compounds as decomposition products of organophosphorus chemical warfare agents can be considered chemical markers.

(2) Dialkyl methylphosphonates can be quantitatively determined by gas chromatography. For determination of methylphosphonic acid and its acidic esters, they should be preliminarily extracted with acetonitrile from acidic solutions and silylated.

REFERENCES

1. *Second Official Inter-Laboratory Proficiency Test*, The Hague, OPCW, Helsinki: Technical Secretariat, 1997, vols. 1, 2.
2. *Third Official Inter-Laboratory Proficiency Test*, The Hague, OPCW, Helsinki: Technical Secretariat, 1997, vols. 1, 2.
3. *Fourth Official Inter-Laboratory Proficiency Test*, The Hague, OPCW, Helsinki: Technical Secretariat, 1998, vols. 1, 2.
4. Vasil'ev, I.A., Shvyryaev, B.V., Liberman, B.M., *et al.*, *Ross. Khim. Zh.*, 1995, vol. 39, no. 4, pp. 5–9.
5. Vasil'ev, I.A., Shvyryaev, B.V., Liberman, B.M., *et al.*, *Ross. Khim. Zh.*, 1995, vol. 39, no. 4, pp. 10–15.
6. Savel'eva, E.I., Radilov, A.S., Kuznetsova, T.A., and Apraksin, V.F., *Zh. Prikl. Khim.*, 1999, vol. 72, no. 9, pp. 1501–1506.
7. *Conference on Disarmament, The Convention on the Prohibition of the Development, Production, Stockpiling and Use of Chemical Weapons and on Their Destruction*, CD/1170, Geneva, August 1992, pp. 1–182.
8. Kireev, A.F., Rybal'chenko, I.V., Savchuk, V.I., *et al.*, *Zh. Anal. Khim.*, 2000, vol. 55, no. 9, pp. 933–941.
9. Soderstrom, M.T., Bjork, H., Hakkinen, V., *et al.*, *J. Chromatogr.*, 1996, vol. A742, pp. 191–203.
10. Bossle, P.C., Reutter, D.J., and Sarver, E.W., *J. Chromatogr.*, 1987, vol. 407, pp. 399–403.
11. Bossle, P.C., Martin, J.J., and Sarver, E.W., *J. Chromatogr.*, 1983, vol. 267, pp. 209–214.
12. D'Agostino, P.A., Hancock, J.R., and Provost, L.R., *J. Chromatogr.*, 1999, vol. A837, pp. 93–105.
13. Minami, M., Hui, D.-M., Katsumata, M., *et al.*, *J. Chromatogr.*, 1997, vol. B695, pp. 237–244.

Russian Journal of Applied Chemistry, Vol. 74, No. 10, 2001, pp. 1728–1734. Translated from Zhurnal Prikladnoi Khimii, Vol. 74, No. 10, 2001, pp. 1677–1683.

MACROMOLECULAR CHEMISTRY AND POLYMERIC MATERIALS

Monodisperse Microspheres Based on Acrolein Copolymers

A. Yu. Men'shikova, T. G. Evseeva, N. A. Chekina, Yu. O. Skurkis, and S. S. Ivanchev

Institute of Macromolecular Compounds, Russian Academy of Sciences, St. Petersburg, Russia

Received July 26, 2001

Abstract—Emulsifier-free emulsion copolymerization of acrolein with styrene and methyl methacrylate in the presence of potassium persulfate was developed to prepare microspheres with surface aldehyde groups. The kinetics of monomer copolymerization was studied and the conditions for preparing monodisperse microspheres 370–1000 nm in diameter were determined.

Monodisperse polymer microspheres are widely used in immunology as supports of biologically active compounds (BACs) [1]. These BACs are either simply sorbed on the support surface or bound to it by various chemical reactions with reactive groups on the microsphere surface. For example, surface aldehyde groups react with BAC amino groups yielding Schiff bases under mild conditions. As a rule, polymer microspheres with aldehyde groups are prepared by homopolymerization of unsaturated aldehydes (e.g., acrolein, formylstyrene) [1]. The monodisperse polyacrolein particles are often prepared by the anionic or radiation-induced radical polymerization in aqueous solutions [2–5]. However, these procedures give significant amounts of oligomeric products, which, in the course of storage of the latexes and preparations on their base, migrate to the particle surface, making its surface structure unstable. At the same time, only in few works, microspheres were prepared by radical copolymerization of acrolein and styrene [6–8], though such a procedure allows control over the fraction of acrolein units in the surface layer and, probably, over the degree of polymer cross-linking via aldehyde groups. Therefore, we studied in this work the copolymerization of acrolein with more hydrophobic monomers, such as styrene and methyl methacrylate (MMA), to prepare monodisperse microspheres containing surface aldehyde groups. Data on the synthesis of poly(styrene/acrolein) (PSAC) and poly(MMA/acrolein) (PMMAAC) latexes by emulsifier-free emulsion copolymerization are of particular interest for revealing the effect of water-soluble acrolein on the course and mechanism of particle formation.

EXPERIMENTAL

Preliminarily, styrene, MMA, acrolein, dimethylformamide (DMF), methyl ethyl ketone (MEK), and methylene chloride were purified by distillation according to standard procedures. Double-distilled water served as dispersion medium. Sodium chloride NaCl, sodium tertaborate $Na_4B_2O_7$, potassium dihydrogenphosphate NH_2PO_4, analytically pure hydroxylamine hydrochloride, and HCl and NaOH standard solutions were used without additional purification.

The emulsion radical emulsifier-free copolymerization of the monomer mixtures was carried out in the presence of potassium persulfate [9]. In order to obtain monodisperse microspheres of widely varying size, the molar ratio of the initial monomers, concentration of the monomer mixture in water, *w* (wt %), temperature, and concentrations of the initiating agent and buffer salt were varied (Table 1). The residual monomers were separated from the resulting latexes by distillation with steam. The monomer conversion was determined by gas chromatography with internal reference (butanol).

The measurement error was 5%. The particle size of the resulting latexes was measured with a JEM 100 S electron microscope (JEOL, Japan). Water-soluble admixtures were removed from the latex by three cycles of centrifugation and dispersion in double-distilled water. Then the surface concentration of the carboxy and aldehyde groups was determined by conductometric titration [8]. The aldehyde groups were analyzed after preliminary treatment of the latex with

1070-4272/01/7410-1728 $25.00 © 2001 MAIK "Nauka/Interperiodica"

hydroxylamine hydrochloride [9]. The content of the sol fraction in the copolymers was determined by fractional extraction with methylene chloride for 3 days. The IR spectra of the sol fraction solutions were registered in the 400–4000 cm^{-1} range. The thin-layer chromatograms of the sol fraction of the resulting polymers were studied on the silica support in comparison with the homopolymers: polystyrene (PS) and polymethyl methacrylate (PMMA). Polyacrolein is insoluble in the solvents used because of the strong intermolecular cross-linking [1] and thus cannot be used as reference. In the case of PS and PSAC, the mobile phase was toluene, whereas for PMMA and PMMAAC the mixture of toluene and MEK (5 : 7 volume ratio) was used. The chromatograms were developed using a mixture of sulfuric acid and potassium permanganate.

The procedure of the microsphere surface modification with protein is presented elsewhere [10]. As adsorbate protein we used the native bovine serum albumin (BSA); this protein is widely used in immunoassay as a carrier of small antigens and as a blocking agent, which fills the hydrophobic surface and thus hinders nonspecific interactions. The procedures for purification and analysis of serum albumin were given in [10].

The solutions of BSA before and after their interaction with the polymer particles were studied by both the traditional Lowry procedure and modern high-performance monolithic chromatography (HPMC) [11] on a CIM® Disk DEAE anion-exchange membrane (BIA Separations, Ljubljana, Slovenia). The gradient elution was performed using solution containing tris(hydroxymethyl)aminomethane hydrochloride (0.02 M) and sodium chloride (0.5 M), pH 8.0 at a rate of 3 ml min^{-1}. Albumin was detected at λ = 229 nm.

Monodisperse latexes with particle size of 370–670 nm were prepared by radical copolymerization of acrolein and styrene (Table 1). It was found that at equimolar monomer ratio the reaction proceeded most completely, whereas at a styrene : acrolein molar ratio of 2 : 1 the conversion was only 75 and 57% (Table 1, run nos. 2 and 11). These data agree with published results [8]. With the preparation temperature decreasing from 60 to 55°C, the diameter of the resulting monodisperse microspheres increases (Table 1, run nos. 1 and 3), which is due to the decrease in the decomposition rate of the initiating agent. However, upon additional decrease in the initiating agent concentration (Table 1, run no. 4), the size of the resulting microspheres did not increase further because of the significant decrease in the monomer conversion.

Table 1. Synthesis conditions, monomer conversion *K*, and diameter *D* of microspheres prepared by copolymerization of styrene and acrolein*

Run no.	Synthesis conditions			*K*, %	*D*, nm
	w, wt %	*T*, °C	$C_{salt} \times 10^{-2}$, M		
1	10	60	–	90	370
2	10	60	–	75	370
3	10	55	–	90	520
4	10	55	–	57	370
5	15	55	–	90	610
6	10	60	NaCl, 2	90	420
7	10	60	NaCl, 4	90	<700**
8	15	60	KH_2PO_4, 1	90	670
9	15	55	KH_2PO_4, 1	80	<700**
10	15	55	KH_2PO_4, 2	80	<800**
11	15	55	KH_2PO_4, 1	57	520

* Styrene : acrolein molar ratio 1 : 1, in run nos. 2 and 11 2 : 1; concentration of $K_2S_2O_8$ with respect to monomers was 1 wt %, and 0.5 wt % in run no. 4.

** The resulting latexes along with the main fraction of coarse particles contain finer particles.

In contrast, with increasing monomer concentration in the reaction mixture, their conversion reached 90%; in this case, coarser monodisperse microspheres 610 nm in diameter were formed (Table 1, run no. 5).

To make larger the resulting microspheres, we also raised the ionic strength of the reaction mixture. It was found, that with the NaCl concentration increasing to 0.02 M, the particle size grows somewhat (Table 1, run nos. 1 and 6), whereas in a more saline solution the resulting latex becomes polydisperse (run no. 7). It is well known that, during emulsion polymerization, the persulfate initiating agent reacts with water to form hydroxy radicals, and the reaction mixture becomes more acidic [12]. In our case, the pH of the resulting polymer dispersions was 2.5 after the reaction termination. The aggregation stability of the polymer–monomer particles (PMPs) in the dispersion medium with low pH and high ionic strength was insufficient owing to a decrease in the ionization of the surface sulfate and carboxy groups which can be formed during oxidation of the surface aldehyde groups in the acrolein units with persulfate.

To enhance the aggregation stability in the synthesis of coarse particles at high ionic strength of the dispersion phase, we used potassium dihydrophosphate buffer salt, which ensures a weakly acidic state of the reaction mixture. In the presence of this

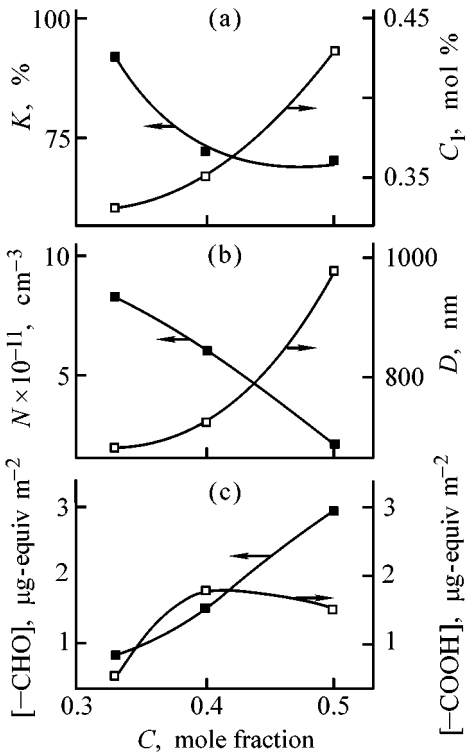

Fig. 1. (a) Acrolein conversion K and content of acrolein units in the latex C_1, (b) number of particles N and their diameter D, and (c) concentration of the surface aldehyde [–CHO] and carboxy [–COOH] groups vs. the acrolein mole fraction C in the mixture with MMA.

salt, a monodisperse latex with particle diameter of up to 670 nm was prepared (Table 1, run nos. 8 and 11). In this case, the size of the resulting microspheres also increased with decreasing temperature (Table 1, run nos. 9 and 10), but finer particles were detected along with a coarse fraction.

Table 2. Sol fraction in copolymers

Run no.	Content, mole fraction		Sol fraction in copolymer, %
	acrolein in the reaction mixture	number of acrolein units in copolymer	
Methyl methacrylate/acrolein			
12	0.33	0.33	100
13	0.40	0.35	72
14	0.50	0.43	50
Methyl methacrylate/styrene			
8	0.50	0.53	30

Copolymerization of acrolein with a less hydrophobic MMA was carried out under the conditions providing, in the case of acrolein and styrene, polymerization formation of coarse monodisperse particles and the most complete monomer conversion (Table 1, run no. 8). Since data on the emulsion copolymerization of acrolein with MMA are lacking, the effect of the monomer ratio on their conversion and the properties of the resulting latexes were studied in more detail. It was found that the acrolein conversion decreases with its increasing concentration in the reaction mixture (Fig. 1a), whereas the MMA conversion remains at a level of about 90%.

With increasing acrolein content in the initial mixture, the number of the polymer particles decreases and thus their size increases (Fig. 1b). With increasing acrolein content, the content of the surface aldehyde groups grows in parallel (Fig. 1c) with the number of acrolein units in the latex structure (Fig. 1a). However, there is no clear correlation between the concentration of the surface carboxy groups and the content of acrolein (Fig. 1c).

We found that the resulting microspheres are partially cross-linked systems and the content of the sol fraction increases with decreasing content of acrolein in the initial mixture (Table 2). These data confirm that the radical polymerization is accompanied by intermolecular cross-linking via the C=C and C=O groups of acrolein [1]. Thin-layer chromatograms (silica) of the sol fractions of the polymers prepared at equimolar MMA : acrolein or styrene : acrolein ratio show that these samples differ from, respectively, MMA and styrene homopolymers. For example, in the chromatograms with toluene eluent, PS moved in the front, whereas PSAC remained at the start. In the toluene/MEK mixture, PMMA advanced with the β-front and PMMAAC remained at the start. At the same time, in the case of MEK eluent, the PSAC and PMMAAC samples moved at the front. IR spectra of the PSAC and PMMAAC samples are shown in Fig. 2 in comparison with those of MMA and styrene homopolymers. The IR spectrum of the PSAC sample contains a strong absorption band at 1725 cm^{-1} (C=O vibrations) and a weak band at 2740 cm^{-1} (C–H asymmetric vibrations of the aldehyde group), which are absent in the IR spectrum of the PS sample. The IR spectrum of the PMMAAC sample contains a strong band at 1730 cm^{-1}, which can be attributed to vibrations of the carbonyl bond in both acrolein and MMA. A weak absorption at 2740 cm^{-1} confirms the presence of the aldehyde groups in this polymer. Hence, the PSAC and PMMAAC samples are copolymers of styrene or MMA with acrolein.

The copolymerization kinetics of acrolein with MMA and styrene at equimolar monomer mixtures is illustrated in Fig. 3. The kinetics of MMA conversion (Fig. 3a) shows that, at the start of polymerization, the contribution of this monomer is significantly smaller as compared with that of acrolein. Based on the slope of the conversion curves, the polymerization rates of MMA and acrolein during this induction period are 0.3×10^{-5} and 2.4×10^{-5} mol l^{-1} s^{-1}, respectively. The copolymerization constants for the MMA/acrolein system in dioxane are 10 and 0.2, respectively [13]. Thus, at equal concentrations of the required monomers in the reaction zone the rate of MMA polymerization must be significantly higher. The above result is probably due to the fact that the solubility of acrolein in water exceeds that of MMA: 3.7 and 0.15 M, respectively [14]. Gas chromatographic data show that, at the start of the process, nearly 70% of acrolein is in the aqueous solution. In the presence of water-soluble initiating agent, various oligomers and oligomeric radicals enriched with acrolein units are formed in solution; this provides their high solubility in water. Moreover, these compounds must possess low surface activity because of the low content of the MMA units and insignificant difference in polarity between the comonomer units. As a result, they form PMP later and their stabilization effect is smaller. Hence, we obtain coarser microspheres than in the case of acrolein copolymerization with more hydrophobic styrene (Fig. 4). Such a mechanism of PMP formation is confirmed by the fact that, at increased content of acrolein in the mixture with MMA, coarser particles are formed (Fig. 1b). In the second stage of polymerization, the rate of MMA consumption increases from 0.8×10^{-5} to 2.1×10^{-5} mol l^{-1} s^{-1}, whereas the rate of acrolein conversion remains constant. In this stage, polymerization proceeds predominantly on the PMP surface and thus the mole fraction of MMA in PMP may increase in the course of the experiment and acrolein consumption.

When the MMA conversion reaches nearly 35%, a gradual increase in the rate of MMA polymerization gives way to a pronounced gel effect: the rate of MMA consumption increases from 2.1×10^{-5} to 7.5×10^{-5} mol l^{-1} s^{-1}. Si-multaneously, the rate of acrolein consumption increases to 4.8×10^{-5} mol l^{-1} s^{-1}. This confirms the formation of a copolymer of acrolein and MMA in PMP. It should be noted that in this stage of polymerization the increase in the viscosity of the polymer-monomer mixture in the particles, which provides coexistence of several growing radicals and causes the gel effect, may be enhanced by cross-

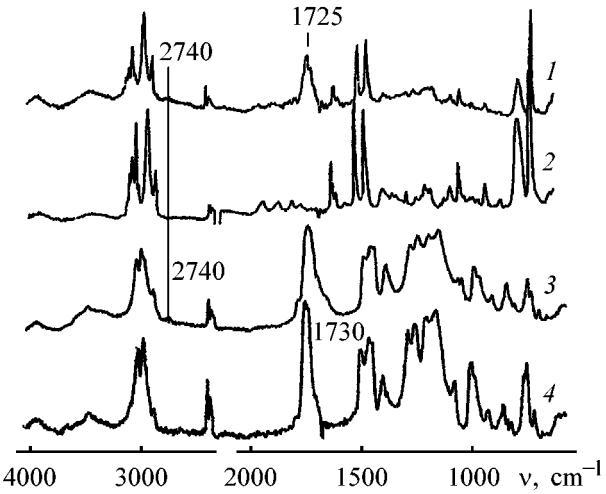

Fig. 2. IR spectra of sol fractions of (*1*) PS/AC and (*2*) PMMA/AC in comparison with IR spectra of (*3*) PS and (*4*) PMMA. (ν) Wave number.

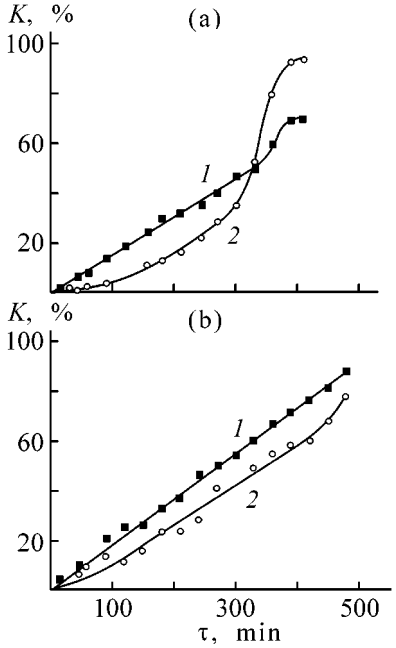

Fig. 3. Monomer conversion K vs. synthesis time τ in copolymerization of equimolar mixtures of (a) (*1*) acrolein with (*2*) MMA and (b) (*1*) acrolein with (*2*) styrene.

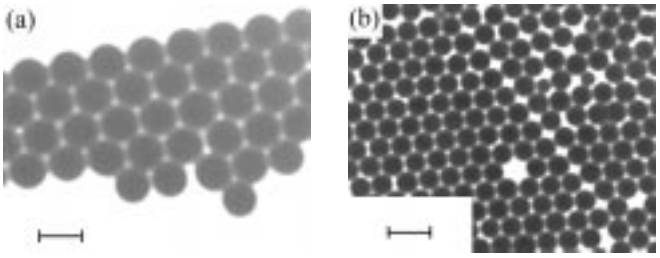

Fig. 4. Microspheres of (a) PMMA/AC and (b) PS/AC prepared by copolymerization of equimolar monomer mixtures.

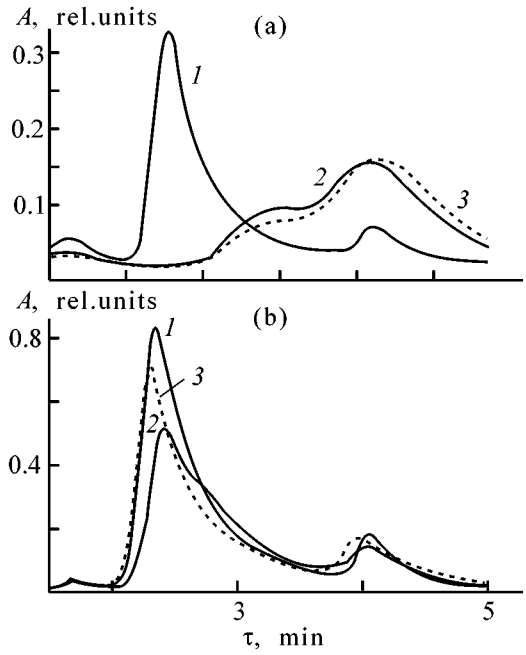

Fig. 5. HPMC curves of the albumin solutions in borate buffer (pH 9.2) (*1*) before and (*2*, *3*) after their interaction with microspheres of acrolein copolymers with (*2*) styrene and (*3*) MMA (a) without preliminary removal of oligomers and (b) after their separation. (*A*) Absorption and (τ) time. Albumin concentration, mg ml^{-1}: (a) 1 and (b) 1.5.

linking of macromolecules via acrolein units (Table 2). After the exhaustion of the monomers in PMPs, the copolymerization rate significantly decreases and plateaus are observed in the conversion curves. The acrolein conversion is incomplete, probably because its certain fraction is retained in water.

In the course of polymerization with styrene, acrolein is consumed at a constant rate of 2.7×10^{-5} mol l^{-1} s^{-1} (Fig. 3b), which is higher than the rate of its copolymerization with MMA before gelation (2.4×10^{-5} mol l^{-1} s^{-1}). This is due to the fact that copolymerization with styrene yields smaller particles, and, thus, the concentration of growing PMPs is higher. In this case, the induction period in the conversion curve of styrene is less pronounced than in the case of MMA copolymerization with acrolein. This suggests rapid formation of diphilic PMPs, which thus involve the surface-active oligomers and oligomeric radicals containing fragments of hydrophobic styrene (3.7×10^{-3} M solubility in water [14]) and hydrophilic acrolein. At moderate conversion of monomers, when copolymerization proceeds predominantly in PMPs, the rate of styrene consumption (2.6×10^{-2} mol l^{-1} s^{-1}) is close to that of acrolein. It was found [8] that, despite equal copolymerization constants of styrene and acrolein in dioxane (0.25 [13]), the number of acrolein fragments in the copolymer in the course of emulsion copolymerization grows only slightly with its increasing content in the reaction mixture and does not exceed 30% at styrene/acrolein molar ratio of 1 : 2. By contrast, we prepared in our case PSAC copolymer microspheres with acrolein content of 53 mol % even at the equimolar monomer ratio (Table 2). The similar reactivities of styrene and acrolein in this case can be accounted for by the presence of potassium dihydrogenphosphate in the reaction mixture, which decreases the acrolein solubility in water and shifts the polymerization predominantly into PMPs. As a result, the conversion of styrene in the course of copolymerization is slightly smaller than that of acrolein, which allows preparation of copolymer microspheres with high content of aldehyde groups.

To study the sorption of proteins by the surface of PSAC and PMMAAC copolymer microspheres, we performed binding of BSA with their surface aldehyde groups in alkaline medium. The residual concentration of BSA after chemisorption was determined by HPMC; the results suggested that, simultaneously with the formation of the Schiff bases on the particle surface, the polymeric chains enriched with carboxy and aldehyde groups can be washed out of the particles into solution, with their further binding with BSA in solution. As a result, broad peaks of BSA conjugates with the most soluble copolymer chains appear in the chromatograms in analysis of the residual BSA in the dispersion system after chemisorption (Fig. 5a). Their retention time is longer than that of the initial BSA, which is due to an increase in the number of anionic groups in this protein. This trend is the most pronounced under the chemisorption conditions at high concentration of the surface aldehyde groups and protein solution (pH > 9.0). This effect was eliminated when the microspheres were washed with borate buffer solution (pH 10.0) before chemisorption (Fig. 5b).

The data on the BSA chemisorption in several samples of copolymer microspheres with different copolymer compositions and surface concentrations of the functional groups are listed in Table 3. It was found that the BSA chemisorption on PSAC copolymer microspheres is somewhat stronger than that in the case of PMMAAC. This is probably due to higher surface hydrophobicity of the acrolein-styrene copolymer. The chemisorption efficiency depends on the pH of the dispersion medium. It was found that, with the pH of the albumin solution increasing in the course of chemisorption, the amount of BSA bound to the PMMAAC microspheres increases significantly,

Table 3. Conditions of albumin chemisorption

Sample no.	[–CHO]	[–COOH]	Buffer solution pH	Albumin concentration, mg ml^{-1}		Albumin chemisorption, mg m^{-2}
	μg-equiv m^{-2}			C_0	C_p	
Poly(styrene/acrolein)						
8	3.20	0.9	7.5	1.50	1.01	1.60
8	3.20	0.9	10.0	1.50	1.09	1.30
3	2.00	0.7	9.25	1.61	1.08	2.30*
3	2.00	0.7	10.2	1.64	1.10	2.08*
Poly(methacrylate/acrolein)						
14	2.96	1.7	10.0	1.50	1.23	1.27
13	1.53	1.8	7.5	1.00	0.93	0.35
13	1.53	1.8	8.2	1.00	0.90	0.65
13	1.53	1.8	9.20	1.50	1.29	0.72
13	1.53	1.8	10.0	1.00	0.79	1.10
12	0.81	0.5	8.2	0.50	0.46	0.35

* The concentrations of albumin and other polymers were determined by Lowry and HPMC procedures, respectively.

whereas in the case of PSAC microspheres the trend is reverse. It is obvious that certain fraction of BSA is physically sorbed on the surface of PSAC microspheres through the hydrophobic interactions. With increasing pH, the microsphere surface and albumin globules acquire a larger negative charge owing to ionization of their carboxy groups, and the albumin sorption must decrease because of the electrostatic repulsion and decreasing hydrophobic interaction [15]. The contribution of this mechanism to the BSA interaction with the surface of PSAC microspheres is confirmed by the fact that, with decreasing surface concentration of the carboxy groups, the albumin binding becomes more efficient (Table 3, sample nos. 3, 8); similar results were obtained in [16]. By contrast, the formation of the Schiff base becomes facilitated with increasing pH, which is observed in the course of BSA binding with the less hydrophobic surface of the PMMAAC microspheres. With increasing surface concentration of the aldehyde groups in the PMMAAC microspheres, the chemisorption efficiency also increases.

CONCLUSIONS

(1) Emulsifier-free emulsion copolymerization of acrolein with styrene and methyl methacrylate to prepare microspheres with surface aldehyde groups was developed. The copolymerization kinetics at the equimolar monomer ratios was studied. The results obtained allow control over the size of monodisperse microspheres (370–1000 nm), hydrophobicity of their surface, and content of the aldehyde groups providing the covalent binding of biologically active compounds.

(2) The albumin binding to the microsphere surface becomes stronger with increasing hydrophobicity of the polymer support, i.e., on passing from poly(methyl methacrylate/acrolein) to poly(styrene/acrolein). However, the contribution of chemisorption to the binding of the native bovine serum albumin is greater for poly(methyl metacrylate/acrolein) microspheres, because the efficiency of the albumin binding to the surface of this copolymer grows with increasing surface concentration of the aldehyde groups and the albumin solution pH.

ACKNOWLEDGMENTS

The work was financially supported by the Russian Foundation for Basic Research (project no. 01-03-32414).

REFERENCES

1. Prokopov, N.I., Gritskova, I.A., Cherkasova, V.R., and Chalykh, A.E., *Usp. Khim.*, 1996, vol. 65, no. 2, pp. 178–192.
2. Margel, S. and Wiesel, E., *J. Polym. Sci., Polym. Chem. Ed.*, 1984, vol. 22, no. 1, pp. 145–151.
3. Rembaum, A., Chang, M., and Richards, G., *J. Polym.*

Sci., Polym. Chem. Ed., 1984, vol. 22, no. 3, pp. 609–621.

4. Pavlova, I.S., Lukin, Yu.V., Kovalenko, V.A., *et al.*, *Bioorg. Khim.*, 1994, vol. 20, no. 7, pp. 731–739.
5. Zhorov, O.V., Preigerzon, V.A., Lukin, Yu.V., *et al.*, *Bioorg. Khim.*, 1995, vol. 21, no. 4, pp. 261–263.
6. LeDissez, C., Wong, P.C., Mitchell, A.R., and Brooks, D.E., *Macromolecules*, 1996, vol. 29, no. 3, pp. 953–959.
7. Kowalczuk, D., Marsault, J.-P., and Slomkowski, S., *Colloid Polym. Sci.*, 1996, vol. 274, no. 6, pp. 513–519.
8. Yan, C., Zanhg, X., and Sun, Z., *J. Appl. Polym. Sci.*, 1990, vol. 40, no. 1, pp. 89–98.
9. Lishanskii, I.S., Men'shikova, A.Yu., Evseeva, T.G., *et al., Vysokomol. Soedin.*, 1991, vol. 33, no. 6, pp. 413–416.
10. Men'shikova, A.Yu., Dmitrieva, I.B., Kuchuk, V.I., *et al., Kolloidn. Zh.*, 1999, vol. 61, no. 6, pp. 799–808.
11. Tennikova, T.B. and Freitag, R., *J. High Resol. Chromatogr.*, 2000, vol. 23, no. 1, pp. 27–38.
12. Eliseeva, V.I., *Polimernye dispersii* (Polymer Dispersions), Moscow: Khimiya, 1980.
13. *Copolymerization*, Ham, G.E., Ed., New York: Interscience, 1964.
14. Eliseeva, V.I. and Aslamazova, T.R., *Usp. Khim.*, 1991, vol. 60, no. 2, pp. 398–429.
15. Suzawa, T. and Shirahama, H., *Adv. Colloid Interface Sci.*, 1991, vol. 35, pp. 139–172.
16. Men'shikova, A.Yu., Skurkis, Yu.O., Kuchuk, V.I., *et al., Kolloidn. Zh.*, 2001, vol. 63, no. 5, pp. 678–686.

Russian Journal of Applied Chemistry, Vol. 74, No. 10, 2001, pp. 1735–1739. Translated from Zhurnal Prikladnoi Khimii, Vol. 74, No. 10, 2001, pp. 1684–1687.

MACROMOLECULAR CHEMISTRY AND POLYMERIC MATERIALS

Copolymerization of Magnesium and Calcium 2-Acrylamido-2-methylpropanesulfonates with *N*-Vinylpyrrolidone in Aqueous Solutions

V. F. Kurenkov, O. A. Zaitseva, and N. V. Isaeva

Kazan State Technological University, Kazan, Tatarstan, Russia

Received March 6, 2001

Abstract—The kinetics of radical copolymerization of magnesium and calcium 2-acrylamido-2-methylpropanesulfonates with *N*-vinylpyrrolidone in aqueous solutions at pH 9 and 50°C in the presence of an initiator, potassium peroxodisulfate, were studied dilatometrically, and the molecular characteristics of the resulting copolymers were determined.

The kinetics of radical (co)polymerization of unsaturated acid salts in ionizing media are largely affected by the nature of the cation, as demonstrated for polymerization of salts of acrylic, methacrylic [1, 2], *N*-vinylamidosuccinic [3], *p*-styrenesulfonic [4, 5], and 2-acrylamido-2-methylpropanesulfonic (H-AMS) [6, 7] acids and copolymerization of salts of acrylic acid [8, 9] and H-AMS with acrylamide [10, 11] and of lithium, sodium, and potassium salts of H-AMS with *N*-vinylpyrrolidone (*N*-VP) [12]. In this study, we examined the influence of the cation on the copolymerization of magnesium and calcium salts of H-AMS with *N*-VP. Such studies are stimulated not only by unusual, from the viewpoint of the classical theory, trends in copolymerization of ionic monomers, but also by practical significance of the copolymers, which are effective flocculants [13], antistatic agents, adhesives [14], etc.

EXPERIMENTAL

H-AMS was purchased from Lubrizol (UK); mp 185°C. H-AMS salts of alkaline-earth metals were prepared by neutralization of H-AMS in aqueous solutions to pH 9 with suspensions of $Mg(OH)_2$, CaO, and $Ba(OH)_2 \cdot 8H_2O$ with stirring and cooling with water; the insoluble residue was removed by filtration. *N*-Vinylpyrrolidone (Merck, Germany) was purified by double distillation in a vacuum in the presence of 0.1% KOH; n_D^{20} 1.5119. Potassium peroxosulfate (PP) was twice recrystallized from aqueous solutions; the content of main substance, determined by the redox procedure, was 97.8%. In all the experiments, we used distilled water. The other chemicals were of chemically pure grade.

The copolymerization kinetics was monitored dilatometrically at low conversions ($X < 3\%$). The procedures of copolymerization and dilatometric measurements and the techniques used were similar to those described in [15].

After copolymerization, the resulting copolymers were precipitated from aqueous solutions into acetone, washed with acetone, and vacuum-dried at 50°C to constant weight.

The yield of the copolymers was determined gravimetrically, and the content of ionic units, by elemental analysis for sulfur [16]. The molecular weight M of the copolymers was evaluated by the Mark–Houwink relationship $[\eta] \sim M$ from the intrinsic viscosity $[\eta]$, which was measured using a VPZh-3 capillary viscometer with d_c = 0.56 mm in 0.5 M NaCl at 30°C.

Degradation of Mg-AMS–*N*-VP copolymers was performed at 50°C under the action of PP in a glass vessel equipped with a temperature-contol jacket, a magnetic stirrer, and a VPZh-3 capillary viscometer, d_c = 0.56 mm. The viscometer was equipped with a jacket to keep the same temperature as in the reactor.

Copolymerization of H-AMS salts (M_1) with *N*-VP (M_2) was performed in water in the presence of PP initiator ($[PP] = 1.2 \times 10^{-3}$ M) at pH 9 and 50°C. At this pH, the hydrolysis of *N*-VP was prevented [17], and the initiation rate was insensitive to changes

1070-4272/01/7410-1735 $25.00

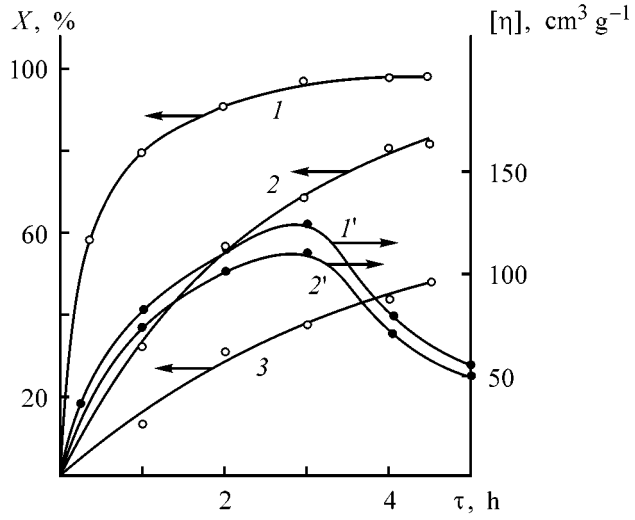

Fig. 1. Variation of (*1*–*3*) conversion *X* and (*1*', *2*') intrinsic viscosity [η] of the copolymers with time τ in the course of copolymerization of (*1*, *1*') Mg-AMS, (*2*, *2*') Ca-AMS, and (*3*) Ba-AMS with *N*-VP. $[M_1] + [M_2] = 14.7\%$; initial molar ratio $[M_1] : [M_2] = 7 : 3$.

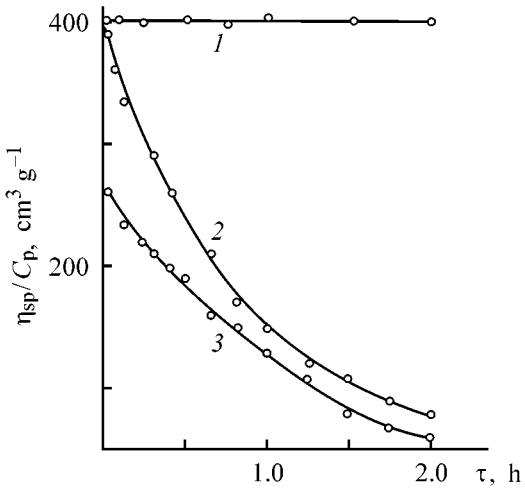

Fig. 2. Variation of the reduced viscosity η_{sp}/C_p of Mg-AMS–*N*-VP copolymers in water with time τ in the course of degradation at 50°C (*1*) in the absence and (*2*, *3*) in the presence of PP. $C_p = 0.1$, [PP] = 0.04%. Polymer samples: (*2*) C ([η] = 127 $cm^3 g^{-1}$, 49.5 mol % ionic units) and (*3*) D ([η] = 54 $cm^3 g^{-1}$, 42.0 mol % ionic units).

in the ionic strength [18] due to variation of the concentration of the ionic monomer in the course of copolymerization. Changes in the ionic strength had no effect on the reactivity of *N*-VP and the corresponding propagating radical [19]. Under the chosen conditions, no spontaneous copolymerization was observed in the absence of initiator.

Figure 1 shows the kinetic curves of copolymerization of H-AMS salts with *N*-VP, obtained with gravimetric monitoring of the reaction, and the intrinsic viscosities of the resulting copolymers. Copolymerization of Mg-AMS with *N*-VP and of Ca-AMS with *N*-VP occurred under homogeneous conditions to deep conversions, whereas copolymerization of Ba-AMS with *N*-VP was a heterogeneous process even at low conversions. Since phase separation considerably complicates copolymerization, our subsequent experiments were only concerned with homogeneous copolymerization of Mg-AMS and Ca-AMS with *N*-VP. Figure 1 shows that the initial rate of copolymerization with Mg-AMS is higher than that for Ca-AMS (curves *1*, *2*), and the molecular weight of the resulting copolymer with Mg-AMS is higher too (curves *1*', *2*'). Figure 1 also shows that, with increasing conversion, the intrinsic viscosities of the Mg-AMS–*N*-VP (curve *1*') and Ca-AMS–*N*-VP (curve *2*') copolymers pass through a maximum observed at a reaction time of 3 h. The increase in conversion had no noticeable effect on the composition of the Mg-AMS–*N*-VP copolymer: the content of the ionic units in the product was 50.8 mol %.

The decrease in [η] after the maximum of the function $[\eta] = f(\tau)$ (Fig. 1) may be due to occurrence under the experimental conditions of polymerization–degradation processes (under the action of radicals generated from PP), with the degradation becoming prevalent as the molecular weight grows. This suggestion is confirmed by monitoring of the variation in time of η_{sp}/C_p at C_p = const for Mg-AMS–*N*-VP copolymers in water under the action of PP at 50°C (Fig. 2). Figure 2 shows that η_{sp}/C_p does not change in the absence of PP (curve *1*) but decreases with time under the action of PP (curves *2*, *3*). These results are due to degradation of the macromolecules with cleavage of the C–C bonds in the backbone chain under the action of radicals generated from PP. Figure 2 also shows that the degradation of the macromolecules becomes more pronounced with increasing *M* (curves *2*, *3*).

The influence of the cation on the copolymerization of Mg-AMS and Ca-AMS with *N*-VP was examined in a wide range of compositions of the initial monomer mixture at $[M_1] + [M_2] = 14.7\%$ and fixed other parameters. The process kinetics was monitored dilatometrically. The inital sections of the kinetic curves were linear, and the initial copolymerization rate v_0 was determined from their slopes at low conversions ($X < 3\%$). The rate v_0 determined in these runs is plotted in Fig. 3 as a function of the content of ionic monomers M_1 in the initial mixture. For both systems

under consideration, $v_0 = f(M_1)$ passes through a maximum at the equimolar ratio of the monomers. The dependences plotted in Fig. 3 are well consistent with published data [12, 19] and suggest the donor–acceptor interaction between the H-AMS and *N*-VP salts. Figure 3 also shows that v_0 varies in the order $Mg^{2+} > Ca^{2+}$ (curves *1*, *2*) in a wide range of compositions of the initial monomer mixture. This sequence is consistent with the data in Fig. 1 (curves *1*, *2*).

Figure 4 shows how [η] and the conversion in copolymerization of Mg-AMS and Ca-AMS with *N*-VP depend on the mole fraction of the ionic monomer M_1 in the initial monomer mixture. It is seen that, in both systems, [η] and conversion drow with increasing M_1. Figure 4 also shows that, in a wide range of monomer ratios in the initial mixture, the intrinsic viscosity and conversion are higher for Mg-AMS, compared with Ca-AMS, which is well consistent with the data in Fig. 1 (curves *1*', *2*').

To explain the influence of the cation on v_0 in copolymerization of H-AMS salts with *N*-VP, let us consider the scheme of the equilibrium between the ionic groups in aqueous solutions

$$\underset{\mathbf{I}}{A^-X^+} \leftrightarrow \underset{\mathbf{II}}{A^-||X^+} \leftrightarrow \underset{\mathbf{III}}{A^- + X^+}, \qquad (1)$$

where A^- is the anion of the monomer and of the macroradical; X^+ is the cation; **I**, **II**, and **III** are, respectively, the contact and solvent-separated ion pairs and free ions.

It is known that the sulfonate groups in H-AMS salts and their units in copolymers of H-AMS salts with *N*-VP are totally ionized in aqueous solutions. However, with decreasing ionic strength of solutions (because of the varying concentration of the ionic monomers in the initial mixture and in the course of copolymerization) and with binding of cations with the polysulfonate anions, the ionization equilibrium (1) is shifted to the left. As a result, the intensity of intra- and intermolecular electrostatic interactions in the system decreases, and the reactivity of H-AMS salts and their macroradicals in copolymerization changes. Thus, the shift of the ionization equilibrium (1) results in that various ionic species of the monomers and radicals, differing in reactivity, are involved in the copolymerization. Because the reaction system is multicomponent and the conditions are not isoionic, the copolymerization "constants" $r_1 = k_{11}/k_{12}$ (for H-AMS salts) and $r_2 = k_{22}/k_{21}$ (for *N*-VP) change in the course of the process, which makes description of the reaction by classical equations [4] with fixed r_1 and r_2 impossible.

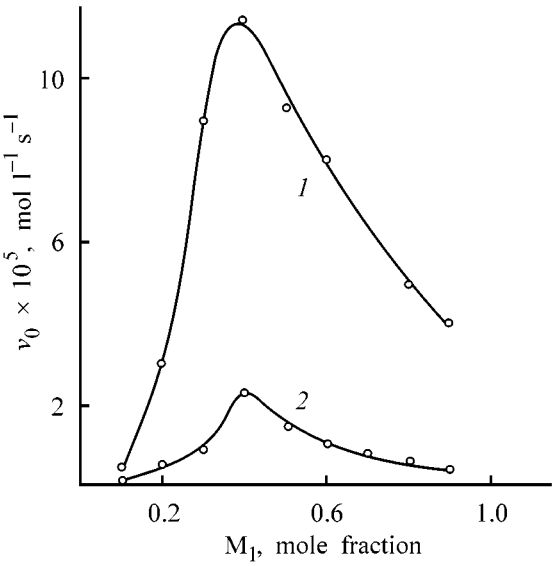

Fig. 3. Initial rate v_0 of copolymerization of (*1*) Mg-AMS and (*2*) Ca-AMS with *N*-VP in aqueous solution vs. the mole fraction of H-AMS salts in the initial monomer mixture M_1. $[M_1] + [M_2] = 14.7\%$; the same for Fig. 5.

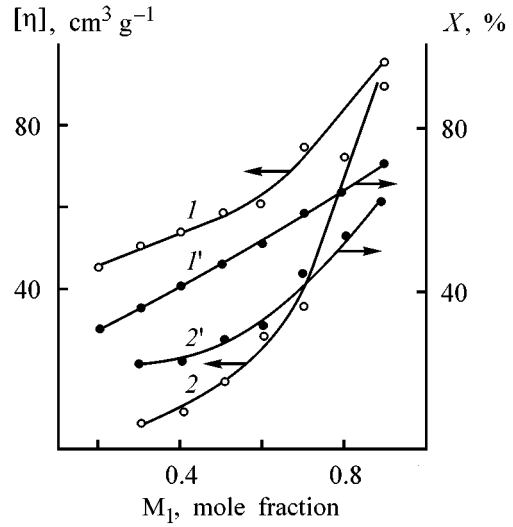

Fig. 4. (*1*, *2*) Intrinsic viscosity [η] at τ = 2h and (*1*', *2*') conversion *X* in copolymerization of (*1*, *1*') Mg-AMS and (*2*, *2*') Ca-AMS with *N*-VP vs. the mole fraction of H-AMS salts in the initial monomer mixture M_1. $[M_1] + [M_2] = 14.7\%$.

The degree of the cation binding with polysulfonate anions of the copolymers of H-AMS salts with *N*-VP decreases in the order $Mg^{2+} > Ca^{2+}$ [20]. The higher the degree of metal cation binding with sulfonate anions of the macroradical, the weaker the electrostatic repulsion between the similarly charged monomer and the macroradical with a terminal ionic

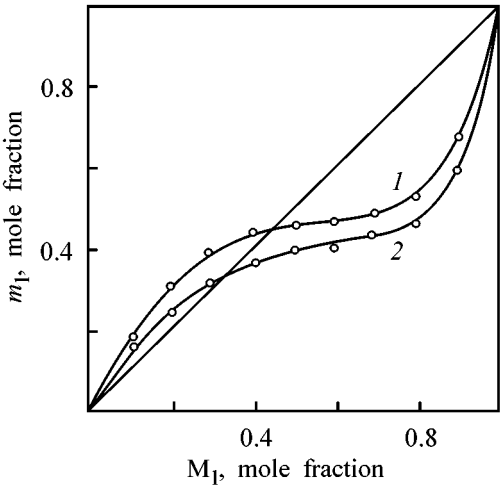

Fig. 5. Copolymer composition vs. the mole fraction of H-AMS salts in the initial monomer mixture M_1. Copolymerization of (*1*) Mg-AMS and (*2*) Ca-AMS with *N*-VP in aqueous solutions. (m_1) Mole fraction of ionic units in the copolymer.

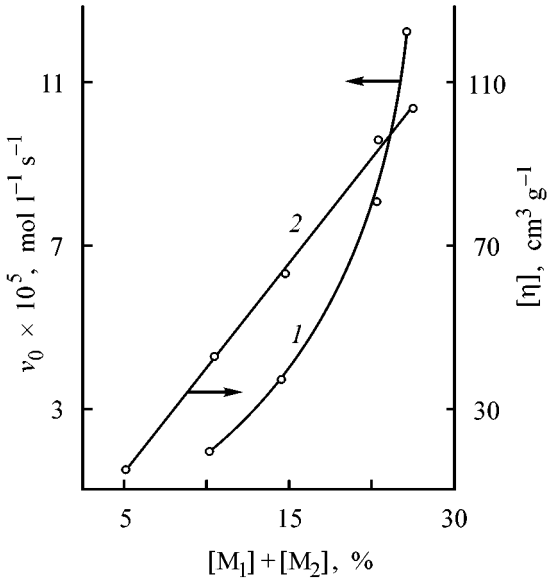

Fig. 6. (*1*) Initial copolymerization rate v_0 and (*2*) intrinsic viscosity [η] (reaction time 2 h) of Mg-AMS–*N*-VP copolymers in aqueous solutions as functions of the concentration of the initial monomer mixture $[M_1] + [M_2]$. Initial molar ratio $[M_1] : [M_2] = 1 : 1$.

unit, i.e., the higher the elementary propagation rate constant k_{11}. Therefore, v_0 (Fig. 3) and [η] (Fig. 4) decrease in the order $Mg^{2+} > Ca^{2+}$.

Figure 5 shows how the composition of the copolymers of Mg-AMS and Ca-AMS with *N*-VP depends on the composition of the initial monomer mixture at $[M_1] + [M_2] = \text{const}$. The dependences in Fig. 5 correspond to the relative activities of the monomers $r_1 < 1$ and $r_2 < 1$. We did not determine r_1 and r_2 for the systems in question, because r_1 and r_2 are apparent quantities for the copolymerization involving ionic monomers. Figure 5 shows that, in a wide range of compositions of the initial monomer mixture, the content of the ionic units in the copolymer increases in going from Ca-AMS to Mg-AMS (curves *1*, *2*). Obviously, the variation of the composition of the resulting copolymers is due to an increase in only one of four elementary propagation rate constants, k_{11}, describing the addition of the macroradical of H-AMS salts to the sulfonate anions of the monomer (H-AMS salt). This trend is due to a decrease in the degree of metal cation binding with the polysulfonate anions of the copolymers in the order $Mg^{2+} > Ca^{2+}$.

Also, we examined the effect on copolymerization of the concentration of the initial monomer mixture $[M_1] + [M_2]$ in the range 5–25%. Experiments were done at a fixed molar ratio $[M_1] : [M_2] = 1 : 1$ and invariable other conditions. The v_0 and [η] values obtained in this series of experiments are listed in Fig. 6. As seen from Fig 6, both v_0 and [η] grow with increasing concentration of the monomer mixture, which is consistent with fundamental aspects of radical copolymerization.

CONCLUSIONS

(1) The initial copolymerization rate v_0, conversion *X*, intrinsic viscosity [η] of copolymers, and the content of ionic units in them increase in the order $Ca^{2+} < Mg^{2+}$.

(2) The initial copolymerization rate v_0 grows with increasing concentration of the initial monomer mixture and, when considered as a function of the $[M_1] : [M_2]$ ratio, passes through a maximum at the equimolar monomer ratio.

(3) The intrinsic viscosity [η] drows with increasing concentration of the initial monomer mixture and content of the ionic monomer and passes through a maximum with increasing conversion.

ACKNOWLEDGMENTS

The study was financially supported by the Foundation for Basic Natural Science of the Ministry of Education of the Russian Federation (project no. 97-0-9.4-59) and the R&D Foundation of the Tatarstan Republic [project no. 19-03/2000 (F)].

REFERENCES

1. Hopkins, R.P., *Ind. Eng. Chem.*, 1995, vol. 47, pp. 2258–2262.
2. Morawetz, H. and Rubin, I.D., *J. Polym. Sci.*, 1962, vol. 57, no. 165, pp. 669–673.
3. Nikolaev, A.F. and Bondarenko, S.G., *Vysokomol. Soedin., Ser. A*, 1970, vol. 12, no. 4, pp. 885–889.
4. Kurenkov, V.F. and Myagchenkov, V.A., *Eur. Polym. J.*, 1979, vol. 15, no. 7, pp. 849–862.
5. Kurenkov, V.F., Vagapova, A.K., and Myagchenkov, V.A., *Eur. Polym. J.*, 1982, vol. 18, no. 9, pp. 763–767.
6. Kurenkov, V.F. and Safin, A.G., *Zh. Prikl. Khim.*, 1998, vol. 71, no. 1, pp. 136–140.
7. Kurenkov, V.F., Safin, A.G., and Almazova, E.I., *Zh. Prikl. Khim.*, 1998, vol. 71, no. 10, pp. 1704–1708.
8. Plochocka, K. and Wojnarowcky, T.I., *Eur. Polym. J.*, 1971, vol. 7, no. 7, pp. 797–804.
9. Plochocka, K. and Wojnarowcky, T.I., *Eur. Polym. J.*, 1972, vol. 7, no. 7, pp. 921–926.
10. Kurenkov, V.F. and Rodina, Yu.G., *Zh. Prikl. Khim.*, 1999, vol. 72, no. 10, pp. 1699–1704.
11. Kurenkov, V.F., Zaitseva, O.A., Vazeeva, D.G., and Solov'ev, D.A., *Zh. Prikl. Khim.*, 2001, vol. 74, no. 5, pp. 789–793.
12. Kurenkov, V.F., Zaitseva, O.A., and Karyagina, S.V., *Vestn. Kazan. Tekhnol. Univ.*, 2000, nos. 1–2, pp. 121–126.
13. Kurenkov, V.F., Sharapova, Z.F., and Khairullin, M.R., *Zh. Prikl. Khim.*, 1999, vol. 72, no. 8, pp. 1374–1378.
14. Shevtsova, S.A., Zaitseva, O.A., and Kurenkov, V.F., *Vestn. Kazan. Tekhnol. Univ.*, 2000, nos. 1–2, pp. 126–128.
15. Kurenkov, V.F., Sirotkin, R.O., Beryachkova, E.A., and Khairullin, M.R., *Zh. Prikl. Khim.*, 1998, vol. 71, no. 9, pp. 1533–1537.
16. Charlot, G., *Les methods de la chimie analytique. Analyse quantitative minerale*, Paris: Masson, 1961, 4th ed.
17. Breitenbach, Y., *J. Polym. Sci.*, 1957, vol. 23, no. 104, pp. 949–954.
18. Kolthoff, I.M. and Miller, I.K., *J. Am. Chem. Soc.*, 1951, vol. 73, no. 7, pp. 3055–3059.
19. Schulz, D.N., Kitano, K., Danic, J.A., and Kaladas, J.J., *Polym. Mater. Sci. End.*, 1987, vol. 57, pp. 149–153.
20. Kurenkov, V.F., Kolesnikova, I.Yu., and Solov'ev, D.A., *Zh. Prikl. Khim.*, 2001, vol. 74, no. 3, pp. 490–493.

Russian Journal of Applied Chemistry, Vol. 74, No. 10, 2001, pp. 1740–1743. Translated from Zhurnal Prikladnoi Khimii, Vol. 74, No. 10, 2001, pp. 1688–1695.

MACROMOLECULAR CHEMISTRY AND POLYMERIC MATERIALS

Cryoozonolysis of Some Perfluoroolefins and Use of Perfluoro Ozonides as Polymerization Initiators

D. P. Kiryukhin, I. M. Barkalov, and I. L. Ismoilov

Institute of Problems of Chemical Physics, Russian Academy of Sciences, Chernogolovka, Moscow oblast, Russia

Received May 7, 2001

Abstract—Low-temperature (77–280 K) ozonolysis of perfluoro-4-methyl-2-pentene and perfluoro-2,4-dimethyl-3-ethyl-2-pentene by direct contact with ozone in the absence of solvents and oxygen was studied. The resulting perfluoro ozonides can be used as initiators of low-temperature polymerization and copolymerization.

Low-temperature ozonolysis of tetrafluoroethylene (TFE) and hexafluoropropylene (HFP) by direct contact of the reactants in the absence of solvents and oxygen was studied in [1–3]. At equimolar ratio of ozone and perfluoroolefin, the corresponding ozonides are formed at low temperatures (140–230 K) in quantitative yield by addition of ozone across the double bond. The resulting perfluoro ozonides are stable up to 250–290 K and decompose at higher temperatures, with TFE ozonide being more stable than HFP ozonide. The decomposition products of TFE and HFP ozonides *in statu nascendi* initiate polymerization of TFE [1, 2] and some other monomers [3, 4].

In this work, we studied the mechanism of cryochemical ozonolysis of perfluoro-4-methyl-2-pentene (HFP dimer, DHFP) and perfluoro-2,4-dimethyl-3-ethyl-2-pentene (HFP trimer, THFP) and examined the possibility of using the resulting ozonides as polymerization initiators. Our experimental procedure, including sample preparation, excluded the uncontrollable explosion mode of the reaction and allowed ozonolysis of DHFP and THFP to be studied in the absence of solvents and oxygen at direct contact of ozone and perfluoroolefin.

EXPERIMENTAL

DHFP and THFP were purified by double distillation (bp 323.2 and 383 K, respectively). Ozone was generated by passing an oxygen stream through an electric-discharge glass ozonizer equipped with external and internal electrodes. The resulting ozone–oxygen mixture was condensed in a trap cooled with liquid nitrogen. Then, we removed oxygen from the solution of ozone in liquid oxygen by vacuum distillation at 77 K, and the remaining crystalline ozone was additionally purified by sublimation.

The phase state of the systems and the kinetics of low-temperature ozonolysis and polymerization were studied calorimetrically [5]. Known amounts of a fluoroolefin and ozone were condensed in a vacuum at 77 K in special glass calorimetric cells and sealed. The reaction was performed in a slowly warming-up calorimeter, and the reaction course was monitored by the heat release.

The IR spectra of the fluoroolefins and reaction products were taken on a Specord IR-75 spectrometer using standard cells.

On cooling to 77 K, DHFP passes into a glassy state. In the course of heating of such a sample, we observe in the calorimetric curve a characteristic change in the heat capacity due to a transition from the glassy state to a supercooled liquid (T_g 110 K), crystallization of the supercooled liquid (exothermic peak at 120–140 K), and melting at 160 K (Fig. 1, curve *1*). The heat of melting of DHFP, determined calorimetrically, is 11.8 ± 0.5 kJ mol^{-1}.

On heating a sample containing equimolar amounts of O_3 and DHFP, an exothermic reaction is observed starting from approximately 210 K (Fig. 1, curve *2*). The rate of cryoozonation (heat release) increases with temperature, reaching a maximum at 240–250 K. The total activation energy of the reaction in the range 210–240 K is 90 ± 5 kJ mol^{-1}. Upon further warming,

1070-4272/01/7410-1740 $25.00 © 2001 MAIK "Nauka/Interperiodica"

the ozonation rate decreases because of the exhaustion of the reactants. The thermal effect of DHFP ozonation, determined from a series of calorimetric runs, is 505 ± 5 kJ mol^{-1}.

In the IR spectrum of the ozonolysis products, compared with the initial DHFP, new bands appear at 1850 (R_f–FC=O bond [6]) and 1100 cm^{-1} (five-membered ring [7]).

These results suggest that, at low temperatures, ozonolysis of DHFP follows, similarly to that of TFE and HFP [1–3], the well-known three-stage Criegee mechanism [8], yielding the corresponding carbonyl compounds and DHFP ozonide. The primary reaction product is the so-called molozonide (**I**). It is unstable and rapidly decomposes to form a bipolar ion and a carbonyl compound. These intermediates couple again in another sequence, forming a more stable ozonide **II**:

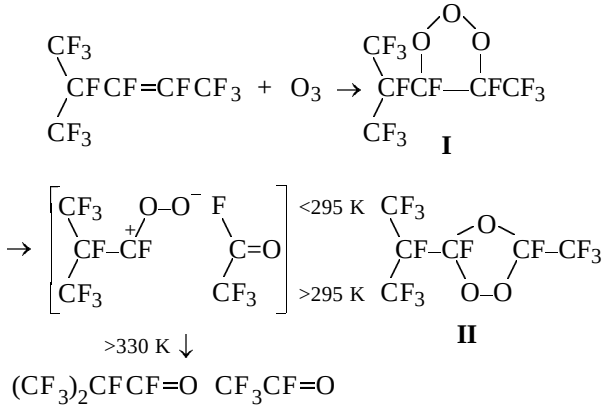

The theoretical calculation of the heat released in these three stages (kJ mol^{-1}) [9] gave 240 for the formation of molozonide, 32 for the formation of the bipolar ion and carbonyl compound, 214 for the formation of the final ozonide, and 486 for the overall reaction. The last value is nicely consistent with that determined calorimetrically, 505 ± 5 kJ mol^{-1}, which confirms the suggested mechanism of low-temperature ozonolysis of DHFP.

The resulting ozonide **II** is in dynamic equilibrium with the bipolar ion and carbonyl compound. At low temperatures (<300 K) the equilibrium is shifted toward formation of **II**, but at higher temperatures (325–335 K) this ozonide irreversibly decomposes into perfluoroacyl fluorides $(CF_3)_2CFCF=O$ and $CF_3CF=O$. This conclusion was confirmed in studies of polymerization effectively initiated by the obtained perfluoro ozonides.

DHFP ozonide initiates, similarly to TFE and HFP ozonides, polymerization of a number of monomers, e.g., TFE. As shown previously [1–4], polymerization

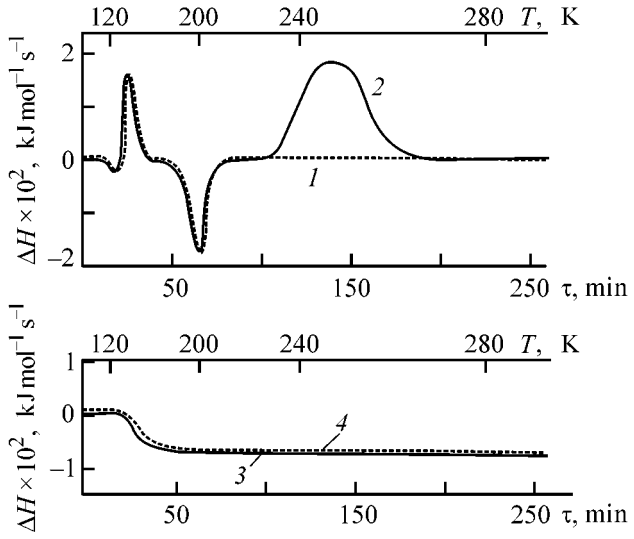

Fig. 1. Calorimetric heating curve: (ΔH) heat release, (τ) time, and (T) temperature; the same for Fig. 2. (*1*) DHFP, (*2*) system DHFP–O_3 (molar ratio 1 : 1), (*3*) THFP, and (*4*) system THFP–O_3 (molar ratio 1 : 1).

is initiated owing to the formation of a very reactive bipolar ion in the course of ozonide decomposition. Although ozonide **II** can be stored for a long time at room temperature, it initiates polymerization in the range 240– 300 K. If ozonide **II** formed by ozonolysis of DHFP is heated to 330 K, it irreversibly decomposes into perfluoroacyl fluorides, and these stable products do not initiate polymerization.

With increasing DHFP content in the initial samples (molar ratio DHFP : O_3 > 1 : 1), the thermal effect of ozonolysis in the temperature range 210–270 K remains unchanged (about 505 kJ mol^{-1}). This fact shows that, in the indicated temperature range, ozone molecules add across the double bond of DHFP in a 1 : 1 ratio only.

Also, we examined the possibility of cryoozonolysis of THFP. On cooling to 77 K, THFP fully turns into a glassy state. The calorimetric curve of heating of this compound shows only a characteristic change in the heat capacity due to transition from the glassy state to the liquid (T_g = 145 K; Fig. 1, curve *3*). No addition of ozone across the C=C bond is observed. No changes, compared with the case of pure THFP, are observed in the calorimetric curve recorded during warming of the system THFP–ozone (Fig. 1, curve *4*). Thus, THFP does not react with ozone in the range 77–300 K. Apparently, additional (compared with TFE, HFP, and DHFP) CF_3 groups in the THFP molecule shield the double bond and prevent access of ozone to this bond.

As already noted, ozonides of TFE, HFP, and DHFP initiate polymerization of many monomers.

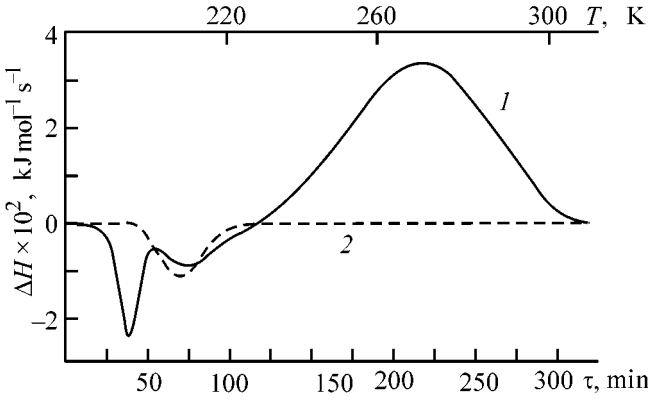

Fig. 2. Calorimetric heating curves. System ozonide **II**–TFE: (*1*) initial and (*2*) after TFE polymerization.

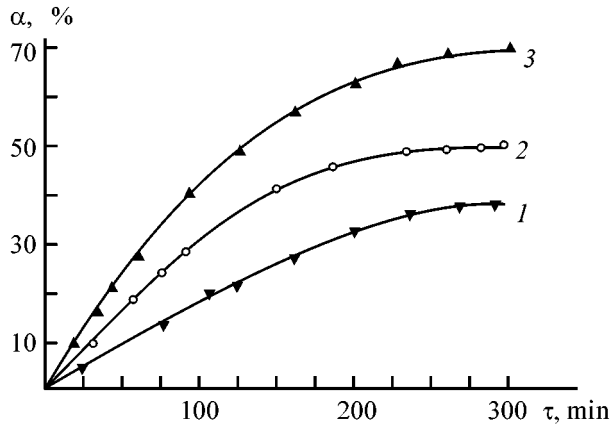

Fig. 3. Kinetic curves of TFE polymerization at different initial pressures of the monomer: (α) PTFE yield and (τ) time. *p*, mm Hg: (1) 250, (*2*) 500, and (*3*) 750 (295 K).

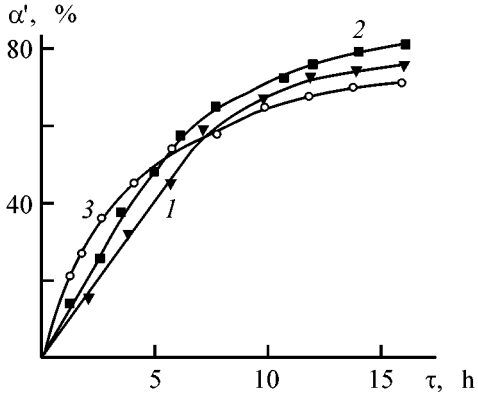

Fig. 4. Kinetic curves of MMA polymerization at different concentrations of the initiator (ozonide **II**): (α') polymer yield and (τ) time. *C*, mol %: (*1*) 2, (*2*) 2, and (*3*) 3 (295 K).

The polymerization initiated by fluoroolefin ozonides and the resulting products are of interest themselves; here, we only briefly discuss some features of the process.

As polymerization initiator, it is very convenient to use ozonide **II**, which is liquid at room temperature, is not dangerously explosive, and can be stored for a long time. Polymerization can be initiated in two ways: in slow cooling of the monomer and initiator in the range 77–300 K and in mixing of the monomer and initiator at constant temperature.

Figure 2 (curve *1*) shows a calorimetric curve of TFE heating in the presence of ozonide **II**. Ozonide **II** was prepared by warming the system DHFP–O_3 (molar ratio 2 : 1) from 77 K to room temperature. Actually, ozonide **II** was taken as a mixture with unchanged excess of DHFP. Then TFE was condensed into the calorimetric cell at 77 K, and the sample was slowly warmed. As seen from Fig. 2 (curve *1*), after thawing of TFE and a mixture of ozonide **II** with unchanged DHFP (endothermic peaks in the range 140–200 K in the calorimetric heating curve), heat release due to TFE polymerization is observed starting from approximately 230 K. The polymerization rate reaches a maximum at 275 K, and at 300 K the monomer is completely converted (yield of the polymer 100%).

Polymerization of TFE can also be initiated under similar conditions with ozonides of TFE and HFP [1–3] and occurs in the range 240–300 K. In the case when polymerization in the system TFE–HFP is initiated with HFP ozonide, a copolymer is formed, with the HFP content reaching 25 wt % [4].

Polymerization of TFE is initiated with ozonide **II** not only in the condensed phase on warming the system from 77 K to room temperature, but also in the gas phase at 295 K. Figure 3 shows kinetic curves of TFE polymerization at various initial pressures of the monomer. Experiments were performed in sealed ampules containing definite amounts of ozonide **II** and monomer. It is seen that, depending on the initial pressure of TFE, the conversion is 40–80% in 5 h.

It should be noted that perfluoro ozonides as polymerization initiators for fluoromonomers have fundamentally important advantages over the previously known initiators [10]. Ozonide **II** is not dangerously explosive and is safe in storage. The use of perfluoro ozonides allows polymerization of TFE under atmospheric pressure at room temperature with acceptable rate. Perfluoro ozonides enable, in principle, polymerization of fluoromonomers in the gas phase in the continuous mode. The use of gaseous TFE under normal pressure allows the process equipment to be significantly simplified, and abandoning the use of emulsions and water reduces the environmental impact of the process.

We also examined the possibility of initiating polymerization of monomers containing no fluorine. Ozonide **II** effectively initiates polymerization of liquid methyl methacrylate (MMA) and acrylonitrile (AN) at room temperature. Figure 4 shows kinetic curves of MMA polymerization at room temperature and various initial concentrations of ozonide **II**. The resulting polymer is insoluble in methyl ethyl ketone, which is untypical of polymethyl methacrylate. A chemical analysis showed incorporation of fluorine into the macromolecule in amounts significantly exceeding the content corresponding to addition of the initiator fragment in the initiation stage. Presumably, in the course of MMA polymerization, the decomposition products of the initiator or perfluoro-4-methyl-2-pentene are incorporated in the macromolecule. Preparation of polymethyl methacrylate containing perfluoro groups is also of practical interest.

Thus, ozonide **II** can be used as initiator for polymerization of various monomers; in contrast to usual initiators, it does not require use of elevated temperatures.

CONCLUSIONS

(1) Low-temperature ozonolysis of perfluoro-4-methyl-2-pentene involves addition of ozone across the double bond in equimolar ratio; cryoozonolysis of perfluoro-2,4-dimethyl-3-ethyl-2-pentene does not occur under these conditions.

(2) Perfluoro-4-methyl-2-pentene ozonide is stable at room temperature and can effectively initiate polymerization of commercial perfluoroolefins, methyl methacrylate, and acrylonitrile.

(3) Polymerization of methyl methacrylate initiated with ozonide yields a polymer containing perfluoro groups.

ACKNOWLEDGMENTS

The study was supported by the Russian Foundation for Basic Research, project no. 00-03-32212.

REFERENCES

1. Ismoilov, I.L., Atakulov, Sh.B., Muidinov, M.R., *et al.*, *Dokl. Akad. Nauk SSSR*, 1987, vol. 295, no. 5, pp. 1159–1163.
2. Ismoilov, I.L., Kiryukhin, D.P., Barkalov, I.M., *et al.*, *Khim. Fiz.*, 1989, vol. 8, no. 1, pp. 98–101.
3. Kiryukhin, D.P., Ismoilov, I.L., and Barkalov, I.M., Low-Temperature Ozonolysis of Fluoroolefins, *Preprint of the Division of the Institute of Chemical Physics, USSR Acad. Sci.*, 1988.
4. Kiryukhin, D.P., Barkalov, I.M., and Ismoilov, I.L., *Zh. Prikl. Khim.*, 2001, vol. 74, no. 4, pp. 682–683.
5. Barkalov, I.M. and Kiryukhin, D.P., *Int. Rev. Phys. Chim.*, 1994, vol. 13, no. 2, pp. 337–357.
6. Nielsen, A.A., Burke, T.G., Woltz, P.I., and Jones, E.A., *J. Chem. Phys.*, 1952, vol. 20, no. 3, pp. 596–604.
7. Razumovskii, S.D. and Zaikov, G.E., *Ozon i ego reaktsii s organicheskimi soedineniyami* (Ozone and Its Reactions with Organic Compounds), Moscow: Nauka, 1974.
8. Criegee, R., *Angew. Chem. Int. Ed.*, 1975, vol. 14, no. 21, pp. 596–604.
9. Cremer, D., *J. Am. Chem. Soc.*, 1981, vol. 103, no. 13, pp. 3633–3688.
10. Panshin, Yu.A., Malkevich, S.G., and Dunaevskaya, Ts.G., *Ftoroplasty* (Fluoroplastics), Leningrad: Khimiya, 1978.

Russian Journal of Applied Chemistry, Vol. 74, No. 10, 2001, pp. 1744–1747. Translated from Zhurnal Prikladnoi Khimii, Vol. 74, No. 10, 2001, pp. 1692–1695.

MACROMOLECULAR CHEMISTRY AND POLYMERIC MATERIALS

Epoxy Polymers Modified with Glycidyl Esters of Phosphorus Acids

L. M. Amirova and E. V. Sakhabieva

Tupolev State Technical University, Kazan, Tatarstan, Russia

Received April 16, 2001

Abstract—The softening point, heat and fire resistance, oxygen index, flammability, and smokiness of epoxy polymers modified with glycidyl esters of phosphorus acids were evaluated, and compression and bending tests of these materials were performed.

Epoxy polymers exhibit a set of valuable properties [1], but their major drawbacks are low fire and heat resistance and relatively low softening point. One of efficient ways to overcome these drawbacks, and also to make these polymers environmentally safer, is incorporation of phosphorus into their structure [2–5]. Among numerous organophosphorus compounds capable of incorporation into the structure of epoxy polymers, the most attractive are glycidyl esters of phosphorus acids (GEPs); their synthesis and properties are described elsewhere [6]. These compounds can be used as active diluents [7, 8]. However, studies of epoxy polymer compounds modified with GEPs are very limited and are reflected mainly in the patent literature [9].

In this work, we studied the properties of GEP-modified epoxy polymers.

EXPERIMENTAL

As investigation objects we chose epoxy–4,4'-isopropylidenediphenol oligomer ED-20 [GOST (State Standard) 10587–84); amine curing agent 4,4'-diaminodiphenylmethane [DADPM, TU (Technical Specifications) 6-14-415–70]; glycidyl esters of phosphorus acids of the general formula $RP(O)(OCH_2–\underset{\backslash O /}{CH}–CH_2)_2$, where R = $–OCH_2–\underset{\backslash O /}{CH}–CH_2$ (triglycidyl phosphate, **I**), $–OCH_3$ (diglycidyl methyl phosphate, **II**), and $–CH_3$ (diglycidyl methylphosphonate, **III**); and diglycidyl butanediol ether (**IV**).

The compounds were prepared as follows. ED-20 epoxy oligomer was mixed with various amounts of GEP, a stoichiometric amount of the curing agent was added, and the reaction was performed in a step mode. The completion of curing was judged from the attainment of a constant glass transition point T_g, from examination of the thermomechanical curves, and from the content of the gel and sol fractions. Thermomechanical curves were taken on a PTB-1 installation at a heating rate of 50 deg h^{-1}; a sample 8 mm in diameter and 11 mm high was compressed under a constant load in the range P = 9.8–39.2 N. The heat resistance of the compounds was evaluated with a Q-1500D MOM derivatograph (Hungary). The polymers were decomposed in air by heating at a rate of 5 deg min^{-1} to 350°C. The standard physicomechanical tests were performed on an FPZ tensile-testing machine following the prescriptions of GOST 4651–82 for compression tests and GOST 4648–71 for static bending tests.

To study the fireproofing power of the organophosphorus modifiers, we tested the polymeric materials for combustibility by evaluating the flammability according to GOST 21207–81 and determining the oxygen index (OI) according to GOST 12.1.044–89. The oxygen index is defined as the minimal content of oxygen in an oxygen–nitrogen flow moving at a velocity of 4 ± 1 cm s^{-1}, supporting the combustion of a sample for 180 ± 3 s or to a length of 50 mm, depending on what condition is fulfilled earlier.

To determine the smokiness in a wide range (2–70 units), we used a filtration procedure [10] based on deposition of the dispersed phase on the surface of filter paper, followed by photometry of the resulting carbon black spot. After passing a definite gas volume through a paper filter, we determined with an FM-56 photometer the reflection coefficient of the

1070-4272/01/7410-1744 $25.00 © 2001 MAIK "Nauka/Interperiodica"

carbon black spot on the filter R_S. Knowing the initial reflection coefficient of the clean paper filter R_W, we determined the smokiness number D:

$$D = \frac{R_W - R_S}{R_W}.$$

Figure 1 shows how the glass transition point of the compounds depends on the GEP content. It is seen that all the esters markedly raise the glass transition point of the epoxy–amine polymers. The modifier performance depends not only on the functional composition, but also on the chemical structure of GEP. For comparison, Fig. 1 (curve *4*) shows data for the ED-20–DADPM compound modified with **IV**.

Epoxy compounds modified with glycidyl esters of phosphorus acids were subjected to thermal oxidative degradation in air. Figure 2 shows the weight-loss curves for ED-20-based polymers cured with DADPM. Thermal degradation of the phosphorus-containing compounds (Fig. 2, curves *2–4*) occurs at higher temperatures as compared with the unmodified sample (curve *1*). For example, the temperature of 10% weight loss is 254°C for the unmodified compound and 281, 290, and 308°C for the compound modified with 15 wt % of **II**, **I**, and **III**, respectively. Introduction of the organophosphorus component somewhat inhibits degradation, especially with **III**; in order of increasing heat resistance the compounds can be arranged as follows: ED-20 < ED-20–**II** < ED-20–**I** < ED-20–**III**.

The modifier concentration also affects the resistance of epoxy compounds to thermal oxidative degradation. With increasing modifier content, the degradation temperature shifts to higher values, the process decelerates, and the coke yield increases.

Microscopic examination of the carbonized residues obtained in thermal oxidative degradation shows that the coke formed from the phosphorus-containing compounds exhibits higher crystallinity than the coke from the nonmodified compound. The coke residues from the compounds modified with the phosphates are looser and more foamed than those from the compounds modified with the phosphonate.

Thus, addition of GEPs enhances the heat resistance of epoxy compounds, and the effect depends on the concentration and structure of the modifier.

The combustibility of the epoxy compounds was evaluated by the combustion rate ϑ_c and oxygen index OI. The plots of ϑ_c and OI against the phosphorus content in the samples (Fig. 3) show that the oxygen index considerably increases on introduction of the organophosphorus component. The highest OI (up to 40%) is attained with the compounds modified with **III**. The compounds modified with **I** and **II** are somewhat more combustible, as indicated by lower OI.

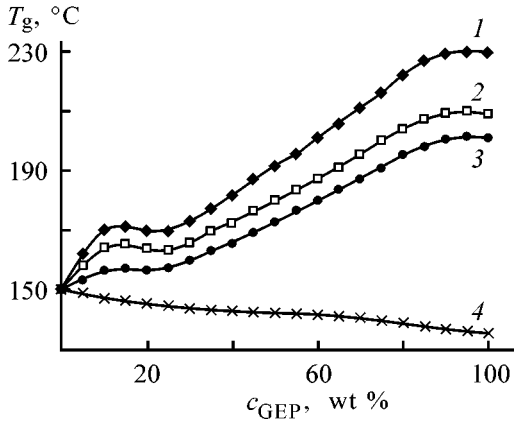

Fig. 1. Glass transition point T_g of ED-20–GEP–DADPM compounds vs. GEP concentration c_{GEP}. Modifier: (*1*) **I**, (*2*) **II**, (*3*) **III**, and (*4*) **IV**.

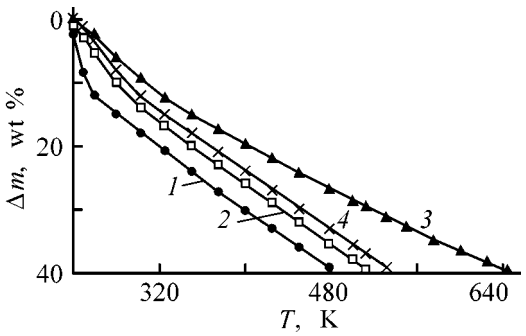

Fig. 2. Weight loss Δm on heating in air ED-20-based epoxy polymers cured with DADPM. (*T*) Temperature. Additive (15 wt %): (*1*) none, (*2*) **II**, (*3*) **I**, and (*4*) **III**.

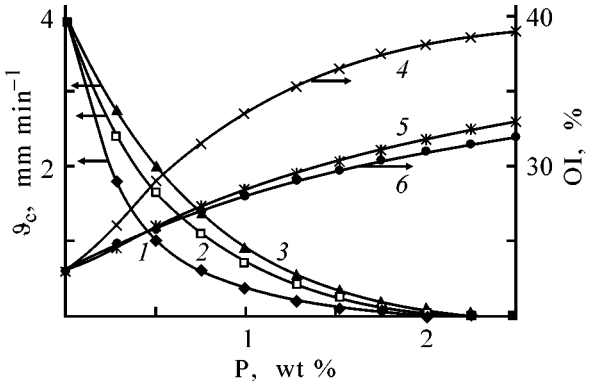

Fig. 3. (*1–3*) Combustion rate ϑ_c and (*4–6*) oxygen index OI of epoxy compounds cured with DADPM, vs. the content of the added GEPs in terms of phosphorus. Modifier: (*1*, *4*) **III**, (*2*, *5*) **I**, and (*3*, *6*) **II**; the same for Fig. 4.

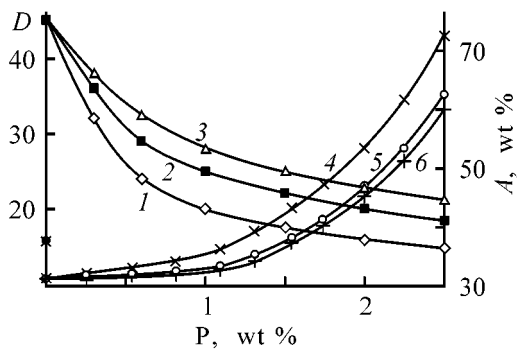

Fig. 4. (*1–3*) Smokiness number *D* and (*4–6*) coke yield *A* in combustion of epoxy compounds ED-20–GEP–DADPM vs. the phosphorus content P in the modified polymer.

Data on the combustion rate rather clearly correlate with the results of the OI tests. As seen from Fig. 3, phosphonate **III** is the most effective combustion inhibitor. Samples of compounds modified with phosphates show high ϑ_c. On the whole, experimental data allow the phosphorus-containing compositions to be classed with self-extinguishing compounds. The modified compounds burn to give a larger coke residue as compared with the initial formulation (Fig. 4); the higher the phosphorus content, the smaller the burnt-out fraction of the epoxy polymer. However, in this case, too, the coke yields for are different added phosphates and phosphonates at the same content of phosphorus in the compound. For example, at a 1.5% content of phosphorus the coke residue from samples modified with **III**, **I**, and **II** is 42, 38, and 37%, respectively (for the unmodified epoxy polymer it is 32%).

Table 1. Efficiency factors *a* of glycidyl esters of phosphorus acids, calculated by formula (1)*

GEP	*c*, wt %	ΔOI	*a*
I	2.16	8.8	3.2
II	1.80	8.0	3.3
III	1.74	12.0	5.1

* (*c*) Concentration of phosphorus in the modified epoxy polymer; $b_P = 0.62$.

Table 2. Breaking compression (σ_c) and bending (σ_b) stress of ED-20–DADPM–GEP compounds

c_m,* wt %	σ_b, MPa			σ_c, MPa		
	I	**II**	**III**	**I**	**II**	**III**
0	120	120	120	109	109	109
5	170	140	125	167	145	130
10	210	160	128	198	162	141
15	220	170	130	197	161	149
20	220	170	132	192	156	148
25	200	160	134	189	152	148
30	170	145	134	181	149	148

* (c_m) Modifier content.

When studying the fireproofing properties of GEPs, we noticed that addition of an organophosphorus component alters the character of the polymer combustion. The combustion of the unmodified samples is accompanied by the formation of carbon black, splashing of the polymer melt, and evolution of abundant smoke. By contrast, the phosphorus-containing polymers form a melt with a viscous surface layer, which is followed by carbonization. The combustion of phosphorus-containing epoxy polymers is accompanied by coke formation, with the coke yield and structure depending on the nature of GEP. The phosphate-modified compounds show strong foaming and intumescence. The phosphonate-modified compounds burn to give a large amount of dense coke, without intumescence. The coke yield grows with increasing phosphorus content.

Figure 4 shows that introduction of organophosphorus compounds considerably reduces the smokiness of epoxy compounds

The performance of fire retardants can be evaluated by the formula [11]

$$a = \Delta OI/(c + b), \quad (1)$$

where *a* is the coefficient of fire retardant performance; ΔOI is the change in the oxygen index; *c* is the concentration (wt %) of the element that diminishes the combustibility; and $b = 0.02A$ (*A* is the atomic weight of the element).

The coefficients *a* for the epoxy compounds studied are listed in Table 1; it is seen that phosphonate **III** exhibits the best performance.

Our results show that GEPs are effective fire retardants for epoxy polymers. Comparative analysis of the fireproofing powers of phosphonate and phosphates shows that, with the former, the oxygen index is higher and the combustion rate lower at the same content of phosphorus (Fig. 3).

The compression and bending tests of the modified polymers (Table 2) showed that the strength characteristics of the compound as functions of the modifier concentration pass through a maximum. The highest

values of σ_b and σ_c are observed at low GEP content, which is followed by a decrease in strength. The highest strength is shown by the compounds modified with trifunctional glycidyl phosphate; such compounds exhibit the highest crosslinking density and the highest glass transition point. Among the compounds modified with the bifunctional agent, those containing **II** are stronger. One of the major factors causing an increase in the strength of the GEP-modified epoxy polymers is, apparently, the lower content of structural defects, resulting from the lower viscosity of the initial formulation.

CONCLUSION

Our results showed that epoxy polymers modified with glycidyl esters of phosphorus acids exhibit, on the one hand, high levels of heat and fire resistance and high softening point and, on the other, increased strength and rigidity. A combination of such properties makes these compounds promising as versatile materials.

REFERENCES

1. Lee, H. and Nevill, K., *Handbook of Epoxy Resins*, New York: McGraw-Hill, 1967.
2. Lin, C.H. and Wang, C.S., *Polymer*, 2001, vol. 42, no. 5, pp. 1869–1878.
3. Wang, C.S. and Lin, C.H., *J. Appl. Polym. Sci.*, 2000, vol. 75, no. 3, pp. 429–436.
4. Telschow, J.E., *Phosphorus, Sulfur, Silicon Relat. Elem.*, 1999, vol. 146, pp. 33–36.
5. Cho, C.S., Fu, S.C., Chen, L.W., *et al.*, *Polym. Int.*, 1998, vol. 47, no. 2, pp. 203–209.
6. Rizpolozhenskii, N.I., Boiko, L.V., and Zvereva, M.A., *Dokl. Akad. Nauk SSSR*, 1964, vol. 155, no. 5, pp. 1137–1139.
7. Sakhabieva, E.V. and Amirova, L.M., in *Struktura i molekulyarnaya dinamika polimernykh sistem* (Structure and Molecular Dynamics of Polymer Systems), Ioshkar-Ola, 1995, part 2, pp. 178–180.
8. Amirova, L.M., Idiatullin, D.M., and Sakhabieva, E.V., in *Struktura i dinamika molekulyarnykh sistem* (Structure and Molecular Dynamics of Polymer Systems), Ioshkar-Ola, 1997, part 4, pp. 61–63.
9. USSR Inventor's Certificate, no. 794054.
10. Belov, R.A. and Doktor, I.Yu., *Determination of the Smokiness Level of Exhaust Gases of Aviation Gas-Turbine Engines by Filtration*, Tr. TsIAM, 1979, no. 849, p. 7.
11. Bulgakov, V.K., Kodolov, V.I., and Lipakov, A.M., *Modelirovanie goreniya polimernykh materialov* (Simulation of Combustion of Polymer Materials), Moscow: Khimiya, 1990.

Russian Journal of Applied Chemistry, Vol. 74, No. 10, 2001, pp. 1748–1752. Translated from Zhurnal Prikladnoi Khimii, Vol. 74, No. 10, 2001, pp. 1696–1700.

MACROMOLECULAR CHEMISTRY AND POLYMERIC MATERIALS

Effect of Oxidation Conditions in the System Dinitrogen tetroxide–Tetrachloromethane on Mechanical Characteristics of Viscose Threads

N. K. Yurkshtovich, A. K. Chekhovskii, N. V. Golub, and F. N. Kaputskii

Research Institute for Physicochemical Problems, Belarussian State University, Minsk, Belarus

Received May 24, 2001

Abstract—The relationship between the functional composition and mechanical characteristics of viscose cord threads with various linear densities, on the one hand, and oxidation conditions in the system N_2O_4–CCl_4 on the other, was studied. The effects of the oxidant composition and treatment time on the tensile strength of dry and wet threads, and those tied in a knot, and also on the stability in a phosphate buffer were analyzed. The optimal conditions for making threads with preset content of carboxy groups, having sufficient mechanical strength and stability in the phosphate buffer (pH 7.5) at 310 K, are determined.

Among cellulose derivatives, monocarboxycellulose (MCC), the product of cellulose oxidation with dinitrogen tetroxide, occupies a special place. Owing to its suitable biological and mechanical characteristics, MCC is widely used in medicine as a polymer carrier for drugs and also as a surgical suture material. However, large-scale employment of oxidized cellulose fibers in surgery has been limited till now by their insufficient mechanical strength and high biodegradation rate in living tissues.

It is known that the tensile strength of cellulose threads is controlled to a considerable extent by the preparation procedure, including chemical modification with dinitrogen tetroxide. It was demonstrated in [1, 2] that the loss of tensile strength on treatment with gaseous N_2O_4 of cellulose threads with a carboxy group content of 4.0–12.5% is 27.6–63.2%. In [2], effort was made to reduce the loss of tensile strength in cellulose threads by performing their oxidation in organic solvents (tetrachloromethane, trichlorofluoromethane, etc.) for a short time (15–30 min), with subsequent keeping at elevated temperature and pressure. In this case, the loss of strength in cotton and viscose threads with carboxy group content of 3.0–9.8% decreased to 19.9–28.9%. The threads thus treated lose their strength in living tissues in 5 ± 1 days. However, no detailed information is given in [2] on how the solution composition and oxidation time in each system affect the mechanical strength of the threads.

The purpose of this study was to optimize the process of oxidative treatment of viscose threads in the system N_2O_4–CCl_4 with respect to the mechanical strength and biodegradation rate in living tissues. Therefore, we studied the effects of the oxidant concentration, oxidation time, twisting of the threads, and the content of carboxy groups in them on the tensile strength of dry (P_d) and wet threads (P_w) and those tied in a knot (P_k), and also on the elongation $\Delta l/l$.

EXPERIMENTAL

In the study, we used twisted and untwisted viscose cord threads with linear density of 439 and 184 tex, respectively. The oxidative treatment was carried out in CCl_4 at 290 ± 1 K for 1–24 h with various concentrations of N_2O_4. Oxidation with gaseous N_2O_4 was performed at 318 ± 2 K and oxidant pressure of 2.5×10^5 Pa in the course of 15–30 min. After the oxidized samples were withdrawn from the reaction vessel, sorbed nitrogen oxides and CCl_4 were removed by passing an air stream for 30–45 min. Then the threads were thoroughly washed with distilled water to negative reaction for NO_2^- and NO_3^-. The carboxy group content in oxidized viscose threads was determined by the Ca-acetate method [3]. The tensile strength of dry (P_d) and wet (P_w) threads was measured on an RM-3-1 tensile-testing machine [4], and that of a thread tied in a knot (P_k), as for a dry thread. The thread was so arranged in clamps that the knot was at

1070-4272/01/7410-1748 $25.00

equal distances from the fixation points. The arithmetic mean of the results obtained and the coefficient of variation of the tensile strength of threads were estimated as in [4]. The relative tensile strength P_{rel} (cN tex^{-1}) was estimated to be

$$P_{rel} = P_a/T,$$

where P_a is the actual tensile strength (cN) and T is the linear density of the thread (tex).

The elongation was measured in parallel with determining the tensile strength on the elongation scale of the tensile-testing machine. The elongation of a thread is expressed in percent of its initial length.

Hydrolytic degradation of oxidized threads in living tissues was simulated using a phosphate buffer solution (pH 7.5) at 310 ± 1 K. After treatment for a fixed time, the threads were dried, and their tensile strength was measured.

Figure 1 demonstrates the effect of oxidation conditions in the system N_2O_4–CCl_4 on the content of carboxy groups in viscose threads. As seen, this parameter grows steadily with increasing oxidant concentration and oxidation time (within 12–16 h). For example, with the N_2O_4 concentration increasing from 5 to 30%, the carboxy group content in oxidized threads grows, depending on the oxidation time, from 0.3–6.3% [degree of substitution (DS) 1.1–23.0] to 1.6–15.5% (DS 5.9–58.5). In the oxidant concentration range 5–10%, the oxidation rate in the initial stage of the reaction is the most sensitive to the oxidant concentration. Use of N_2O_4 solutions with a concentration from this range allows fabrication of threads with $m_{COOH} \geq 3.0\%$, which well meets the medical and biological requirements to surgical suture materials. In this case, the dependence of m_{COOH} on t has a pronounced S-shaped form, suggesting that, in the initial stage of the reaction ($t < 5$ h), diffusion of dinitrogen tetroxide to the bulk of the fiber is hindered, and carboxy groups are accumulated preferentially in the surface layer. At a fixed N_2O_4 concentration in CCl_4 and fixed oxidation time, the carboxy group content in twisted and untwisted viscose threads is virtually the same, with the content of fixed nitrogen in all the samples not exceeding 0.1% of the initial weight of the threads.

Figure 2 demonstrates the influence exerted by the content of carboxy groups on the tensile strength of twisted and untwisted viscose threads oxidized in CCl_4 with various concentrations of N_2O_4. It should be pointed out that here we used experimental data corresponding to the initial stage of oxidation (rapid rise in the degree of oxidation) (Fig. 1). This is the optimal time interval for oxidation treatment, since,

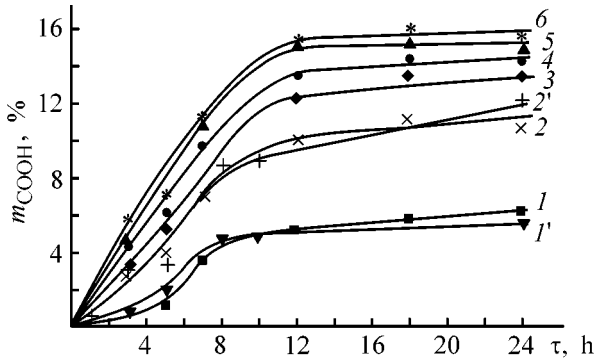

Fig. 1. Content of carboxy groups content, m_{COOH}, in viscose threads vs. the time t of oxidation with N_2O_4 in CCl_4. Linear density of threads (tex): (*1–6*) 184 and (*1'*, *2'*) 439. Dinitrogen tetroxide concentration (%): (*1*, *1'*) 5, (*2*, *2'*) 10, (*3*) 15, (*4*) 20, (*5*) 25, and (*6*) 30.

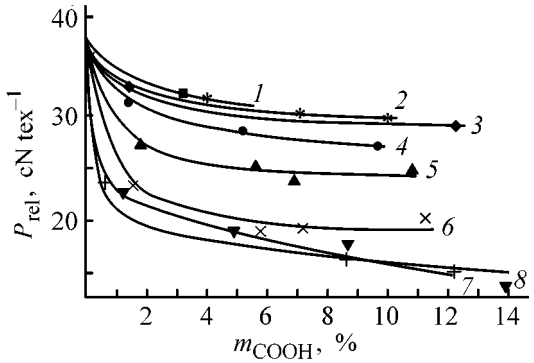

Fig. 2. Relative tensile strength of viscose threads, P_{rel}, vs. the content of carboxy groups, m_{COOH}. Linear density of threads (tex): (*1–6*) 184 and (*7*, *8*) 439. Dinitrogen tetroxide concentration (%): (*1*) 5, (*2*, *7*) 10, (*3*) 15, (*4*) 20, (*5*) 25, and (*6*, *8*) 30.

with t growing further, the content of carboxy groups no longer increases, and P_w of the resulting threads and their stability in phosphate buffer solutions decrease dramatically.

The results obtained show that the tensile strength of oxidized viscose threads depends not only on the content of carboxy groups and degree of twisting, but also on the oxidant concentration. The decrease in the tensile strength of oxidized threads is the most significant with the content of carboxy group increasing to 1.8–3.6%, which is attained in 1–7 h. Further increasing degree of oxidation has practically no effect on the tensile strength, being manifested essentially in the changing stability of the threads in the phosphate buffer (Table 1). Presumably, the maximum drop in the strength in the initial stage of oxidation is associated with the higher rate of variation of the degree of structural ordering and decrease in the degree of polymerization.

Table 1. Effect of the content of carboxy group and oxidation conditions on the stability of MCC threads in phosphate buffer

N_2O_4 concentration in CCl_4, %	m_{COOH}, %	P_d, cN tex^{-1}	Strength loss, %, after holding for indicated time *t*, day		
			3	7	10
Untwisted threads					
0	0	37.0 ± 1.4	–	8.0	9.4
5	0.4	33.4 ± 2.6	13.9	26.6	31.7
	1.7	32.6 ± 0.9	15.5	28.0	30.7
	2.4	32.3 ± 0.9	14.4	28.9	32.1
	3.1	32.6 ± 1.9	18.9	31.2	42.6
	3.3	32.5 ± 1.1	19.4	35.5	42.2
	5.1	31.9 ± 0.7	35.2	–	83.1
	6.1	30.6 ± 1.1	69.1	88.2	100
10	3.3	32.6 ± 1.2	29.7	44.7	62.6
	4.2	32.4 ± 2.4	54.2	100	100
	6.3	32.1 ± 1.3	100	–	–
Twisted threads					
5	2.8	21.8 ± 0.9	8.7	11.5	–

It follows from Fig. 2 that, with the N_2O_4 concentration increasing from 5 to 15%, the decrease in the tensile strength in untwisted threads with fixed content of carboxy groups is within the experimental error. At higher oxidant concentration the tensile strength decreases steadily with increasing N_2O_4 concentration. The supramolecular structure of the fibers degrades in parallel, as demonstrated by X-ray scattering data for the threads before and after treatment with N_2O_4 solutions (Fig. 3).

In the diffraction pattern of the initial viscose fiber, there is, instead of three distinct maxima typical of cellulose II, only one strong peak at $2\theta = 21–22°$, suggesting a relatively high degree of orientation in the initial fiber structure. With the oxidant concentration increasing from 5 to 10%, the extent of structural transformation in the oxidized threads with fixed m_{COOH} grows somewhat (peak intensity decreases). Therefore, the threads treated with a 10% N_2O_4 solution are characterized by a higher degree of disorientation and degradation of macromolecules, even despite the fact that the treatment time in this case is half as long as that for the 5% solution.

It can be seen from Fig. 4 that the increase in the elongation of oxidized threads with growing degree of oxidation, i.e., the effect of the oxidizing medium on the mechanical characteristics of viscose threads is similar to the effect of moisture. One may suggest that partial decomposition of the crystallites and disorientation of the macromolecules in amorphous regions in

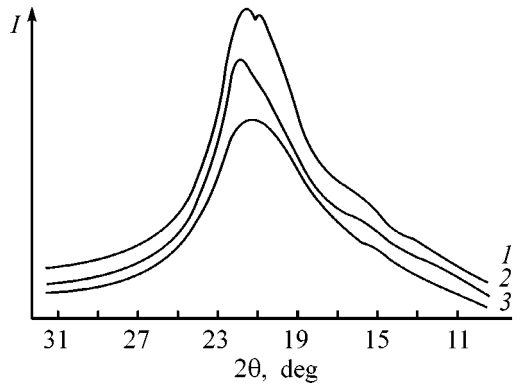

Fig. 3. X-ray diffraction patterns of (*1*) initial and (*2*, *3*) oxidized viscose cord threads (m_{COOH} = 3.3%). (*I*) X-ray scattering intensity and (θ) scattering angle. N_2O_4 concentration in CCl_4 (%): (*2*) 5 and (*3*) 10.

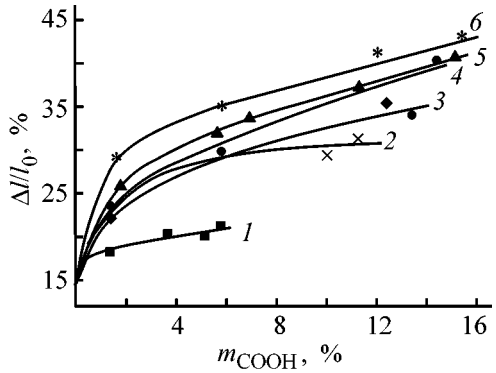

Fig. 4. Elongation $\Delta l/l_0$ of viscose threads (184 tex) vs. the content of carboxy group m_{COOH}. Oxidant concentration (%): (*1*) 5, (*2*) 10, (*3*) 15, (*4*) 20, (*5*) 25, and (*6*) 30.

Table 2. Effect of oxidation conditions on mechanical characteristics of MCC-based threads*

Parameter	N_2O_4 concentration in CCl_4, %			Treatment time in gas phase, min	
	0	5	10	30	45
Monothread with linear density of 184 tex (d = 0.67 ± 0.03 mm)					
m_{COOH}, %	0	3.5	7.1	6.3	7.7
P_d, cN tex	37.0 ± 1.4	32.9 ± 1.0	29.9 ± 1.0	23.2 ± 1.1	17.8 ± 5.0
P_w, cN tex	21.1 ± 1.5	20.9 ± 0.9	17.2 ± 1.3	15.8 ± 1.9	10.7 ± 0.9
P_k, cN tex	18.5 ± 1.2	16.9 ± 1.8	17.4 ± 1.5	17.7 ± 1.4	16.1 ± 1.3
ΔP, %		11.1	19.2	37.3	51.9
Twisted thread, 439 tex (d = 1.1 ± 0.1 mm)					
m_{COOH}, %	0	3.2	7.2	6.3	7.7
P_d, cN tex	29.6 ± 1.3	24.9 ± 0.9	18.2 ± 0.6	11.0 ± 0.7	12.4 ± 0.9
P_w, cN tex	21.4 ± 1.3	14.9 ± 0.6	12.8 ± 0.8		9.0 ± 1.2
P_k, cN tex	14.2 ± 1.4	13.1 ± 0.7	11.9 ± 1.1	7.4 ± 0.9	
ΔP, %		15.9	38.5	62.8	58.1

* Oxidation time in CCl_4 is 7 h. Conditions of oxidation in the gas phase: T = 318 K, p = 2.5 10^5 Pa. $\Delta P = P_d^0 - P_d^{ox})/P_d^0$.

the course of oxidation and washing are accompanied by a decrease in the intensity of interaction between cellulose macromolecules.

Under the same oxidation conditions, the maximum loss of strength was observed for twisted threads (Fig. 2). In this case, the effect of the N_2O_4 concentration on the tensile strength of oxidized twisted threads is less pronounced as compared with untwisted threads. Table 2 shows that at the optimal oxidation conditions in CCl_4 the loss of tensile strength ranges for twisted thread from 15.9 to 38.5%, depending on the content of carboxy groups, and for untwisted thread, from 11.1 to 19.2%. The most probable explanation of the observed effect is that, both in solids and in polymers, simultaneous action of a mechanical stress and an aggressive medium provides more significant changes in strength [5]. Therefore, to reduce the loss of tensile strength of a cellulose-based material as a result of oxidation, it is necessary to use threads with low twisting density.

Comparison of the mechanical characteristics of cellulose threads having close degrees of substitution, but obtained under different oxidation conditions, shows that the loss of strength is more pronounced when oxidation is performed in the gas phase (Table 2). In this case, the tensile strength decreases by 37–63%, which is consistent with published data.

According to the results of [2, 5], the rate of strength loss in a phosphate buffer solution (pH 7.5) at 310 ± 1 K quite adequately reproduces that in living tissues, where hydrolytic degradation proceeds at a higher rate. It was demonstrated in [2] that the stability of the threads in the phosphate buffer depends on the oxidation conditions. However, we found no information on the effect of the content of carboxy groups in oxidized cellulose on its stability.

The results obtained in studying the influence exerted by the content of carboxy groups on the loss of strength in oxidized viscose threads under the action of the phosphate buffer are given in Table 1. After oxidation of the threads in 5% N_2O_4 to a carboxy group content of 0.4%, i.e., after introduction of one carboxy group per 60–70 glucoside residues, their stability against the action of the phosphate buffer strongly decreases. The strength loss in these threads after a 10-day storage in the phosphate buffer was found to be 31.7%, and that for the initial (untreated) threads, 8.9%. The primary reason for the loss of strength in the oxidized threads in a buffer solution at pH 7.5 is the hydrolytic degradation of macromolecules [6, 7]. With the degree of oxidation increasing further (by a factor of 7–8) to a carboxy group content of 3.3%, the decrease in the stability of the threads in phosphate buffer becomes less pronounced, ranging from 5.5 to 10.5%, depending on the storage time. At a still higher content of carboxy groups (4.2% and more) the loss of strength progressively increases with time of storage in the buffer solution. Comparison of the stability of threads with the same carboxy group content, but treated in 5% or 10% N_2O_4 solutions, shows that the hydrolytic stability is lower in the latter case, while the tensile stress is virtually the same.

CONCLUSIONS

(1) The optimal mechanical characteristics are demonstrated by viscose threads oxidized with 5–15% dinitrogen tetroxide solutions; the loss of tensile strength of the threads with a carboxy group content of 3.0–9.9% is about 11–42%.

(2) The stability of the oxidized threads in a phosphate buffer (pH 7.5) largely depends on the carboxy group content and oxidation procedure. After oxidation of viscose threads with 5% N_2O_4 to a carboxy group content of 3.5%, the loss of strength was 42.2% after 10 days of storage in the buffer solution. The oxidation in more concentrated N_2O_4 solutions, as well as higher degree of oxidation strongly diminishes the stability of the threads in the phosphate buffer solution.

(3) Preparation of a surgical suture material by oxidative treatment of viscose threads in the system N_2O_4–CCl_4 is recommended to be performed at oxidant concentration of 5%, oxidation time 5–10 h, and temperature 290 ± 1 K.

REFERENCES

1. USSR Inventor's Certificate, no. 993951.
2. US Patent 4347057.
3. Kaputskii, V.E., Yurkshtovich, T.L., Balabaeva, M.D., *et al.*, *Vestn. Belorus. Gos. Univ., Ser. 2*, 1968, no. 1, p. 15.
4. *Trikotazhnye izdeliya* (Knitted Goods), USSR State Standards, Moscow: Izd. Standartov, 1975, vol. 1.
5. Perepelkin, K.E., Zarin, A.V., Andreev, A.S., and Zvegintseva, L.A., *Deistvie aktivnykh zhidkikh sred na khimicheskie volokna* (Effect of Aggressive Fluids on Chemical Fibers), Moscow: NIITEKhIM, 1982.
6. Kuz'mina, N.L., Biber, B.L., Abakumova, G.L., and Bershadskaya, E.N., *Problemy polucheniya i primeneniya khirurgicheskikh shovnykh nitei* (Problems of Making and Employment of Surgical Sutures), Moscow: NIITEKhIM, 1989.
7. Kaverzneva, E.D. and Kist', S.A., *Izv. Akad. Nauk SSSR, Otd. Khim. Nauk*, 1956, no. 5, pp. 604–614.

Russian Journal of Applied Chemistry, Vol. 74, No. 10, 2001, pp. 1753–1755. Translated from Zhurnal Prikladnoi Khimii, Vol. 74, No. 10, 2001, pp. 1701–1703.

BRIEF COMMUNICATIONS

Solubility of Lead Nitrate in Aqueous Solutions of Nitric Acid and Iron(III) Nitrate

S. V. Ostanova, S. V. Drozdov, G. L. Pashkov, A. G. Kholmogorov, V. V. Patrushev, V. G. Chumakov, and A. V. Chubarov

Institute of Chemistry and Technology, Siberian Division, Russian Academy of Sciences, Krasnoyarsk, Russia

Received February 5, 2001

Abstract—Solubility of lead(II) nitrate in the system H_2O–$Fe(NO_3)_3$–HNO_3 was studied using the simplex-lattice method of experiment design.

Use of solutions containing nitric acid and iron(III) for oxidation and dissolution of various materials has been studied in sufficient detail. However, the available data mainly refer to the characteristics necessary for industry [1]. Published data on the solubility of lead nitrate in nitric acid in the presence of iron(III) nitrate are lacking.

In this work, the solubility of lead nitrate in the system H_2O–$Fe(NO_3)_3$–HNO_3 was studied by means of the isothermal method.

EXPERIMENTAL

We used lead(II) nitrate, iron(III) nitrate, chemically pure grade nitric acid, and water. The equilibration time (40–42 h) was established experimentally. The tests were performed during 50 h at 25 ± 0.1 and 55 ± 0.1°C. After the tests were complete, the liquid phase was sampled and the content of lead(II) was determined by atomic absorption spectroscopy and titrimetry [2, 3], and the concentration of nitric acid, by titrimetry [3]. The solid phase was filtered off, washed with water and ethanol to remove mother liquor, dried at 50–60°C, and subjected to X-ray phase analysis.

The obtained results were processed by the simplex-lattice method of experiment design [4]. The vertices X_1, X_2, and X_3 of the concentration triangles represented the components H_2O (55.56 M), $Fe(NO_3)_3$ (1.8 M), and HNO_3 (3.2 M), respectively. As functions served lead nitrate concentrations in solution. The simplex-lattice plan for incomplete cubic model of the dependence of lead nitrate concentration on the above solution parameters is presented in the table.

The obtained results were used to estimate the coefficients of the polynomials of incomplete third order, having the following form:

$$Y_{25} = 1.50X_1 + 0.15X_2 + 0.28X_3 - 1.84X_1X_2 - 0.04X_2X_3 - 1.31X_1X_3 + 3.04X_1X_2X_3 \quad (25°C),$$

$$Y_{55} = 2.00X_1 + 0.25X_2 + 0.38X_3 - 2.30X_1X_2 - 0.06X_2X_3 - 0.95X_1X_3 - 0.17X_1X_2X_3 \quad (55°C).$$

The root-mean-square error in determining Y was 3%. Substitution of the data of tests nos. 8–10 in the equations showed that they adequately describe experimental data with 97% probability.

The obtained equations were used to plot isoconcentration curves for lead nitrate (see Figs. 1a and 1b).

$Pb(NO_3)_2$–HNO_3–H_2O system. Various methods for precipitation of lead nitrate by addition of nitric acid are known [5]. However, the fundamental aspects of this process and the $Pb(NO_3)_2$ solubility have not been determined previously. The solubility data show that, with increasing nitric acid concentration in the system studied, the solubility of lead nitrate markedly decreases to reach a minimum at the point with the highest concentration of nitric acid (under the experimental conditions). This is due to an increase in the concentration of NO_3^- ions, which leads to salting-out of lead nitrate.

$Pb(NO_3)_2$–$Fe(NO_3)_3$–H_2O system. To our knowledge, no data are available in the literature for the solubility of lead nitrate in iron(III) nitrate solutions. The obtained data indicate that, in the system studied, the concentration of lead nitrate is considerably lower

1070-4272/01/7410-1753 $25.00

The simplex–lattice plan for incomplete cubic model*

Test no.	X_1	X_2	X_3	Y_{e25}	Y_{c25}	Y_{e55}	Y_{c55}
1	1	–	–	1.500	1.500	2.000	2.000
2	–	1	–	0.152	0.150	0.251	0.250
3	–	–	1	0.280	0.280	0.380	0.380
4	0.5	0.5	–	0.370	0.370	0.551	0.550
5	–	0.5	0.5	0.200	0.200	0.300	0.300
6	0.5	–	0.5	0.562	0.560	0.951	0.950
7	0.33	0.33	0.33	0.401	0.400	0.500	0.500
8	0.15	0.15	0.7	0.303	0.300	0.440	0.440
9	0.15	0.7	0.15	0.200	0.200	0.260	0.260
10	0.7	0.15	0.15	0.841	0.840	1.152	1.150

* Y_{e25}, Y_{c25}, Y_{e55}, and Y_{c55} are experimental and calculated lead(II) sulfate concentrations in solution (M) at 25 and 55 °C.

than that in the case of its salting-out with nitric acid. The minimum concentration of lead nitrate is observed at the points 1.55 M $Fe(NO_3)$ at 25°C and 1.57 M at 55°C, with the lead salt concentration in solution reaching 0.12 and 0.22 M, respectively. An X-ray analysis of the deposits revealed no other compounds except lead nitrate.

$Pb(NO_3)_2$–$Fe(NO_3)_3$–HNO_3 system. A study of the $Pb(NO_3)_2$ solubility in the given system showed that the presence of iron(III) nitrate and nitric acid also decreases the concentration of lead nitrate in solution, and this effect becomes more pronounced with increasing iron(III) nitrate concentration.

$Pb(NO_3)_2$–H_2O–$Fe(NO_3)_3$–HNO_3 system. The calculated and experimental solubilities in the given quaternary system are presented in the isoconcentration triangles. When iron(III) nitrate and nitric acid are present in the solution simultaneously, the observed behavior is apparently the same as that in the ternary systems.

A comparison of the lead nitrate concentrations at 25 and 55°C showed that, with increasing temperature, the $Pb(NO_3)_2$ concentration grows and the general tendencies are preserved.

It should be noted that an X-ray analysis performed at all the points studied revealed only lead nitrate in the precipitate.

CONCLUSIONS

(1) A study of the lead nitrate solubility in the system H_2O–$Fe(NO_3)_3$–HNO_3 showed that the concentration of lead(II) ions decreases with increasing content of nitric acid and iron(III) nitrate in solution.

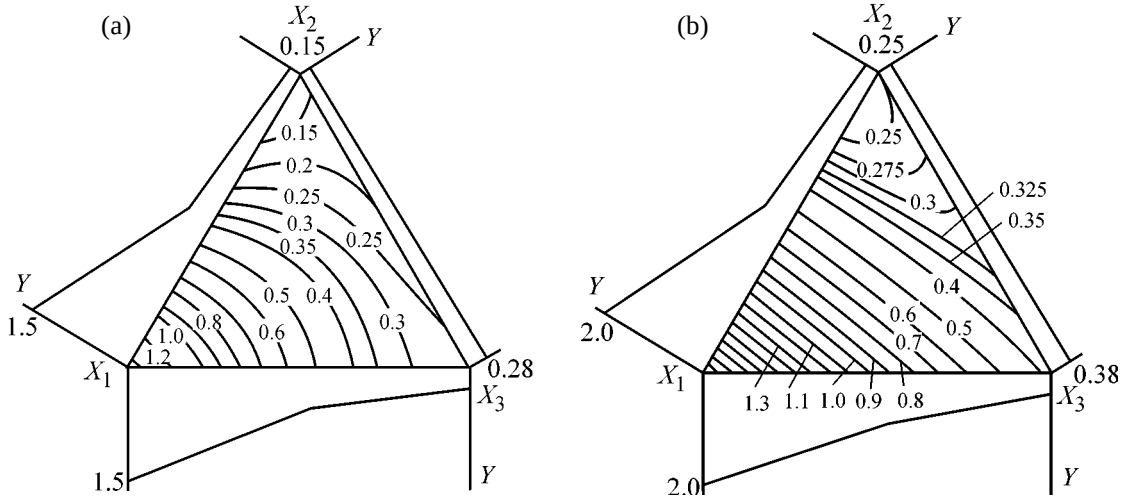

?Isoconcentration curve of lead(II) nitrate at (a) 25 and (b) 55°C. (X_1) distilled water, (X_2) 1.8M $Fe(NO_3)_3$, (X_3) 3.2 M HNO_3, and (Y) lead(II) nitrate concentration in solution (M).

(2) Only a single salt, lead nitrate, is precipitated in the system studied.

(3) Equations describing the lead nitrate solubility at 25–55°C were derived.

REFERENCES

1. Lochmann, J., and Pedlik, M., *Hydrometallurgy*, 1995, vol. 37, pp. 89–96.
2. Fainberg, S.Yu., and Filippova, R.A., *Analiz rud tsvetnykh metallov* (Analysis of Non-Ferrous Metal Ores), Moscow: Metallurgizdat, 1963.
3. Alekseev, V.I., *Kolichestvennyi analiz* (Quantitative Analysis), Moscow: Khimiya, 1972.
4. Akhnazarova, S.L., and Kafarov, V.V., *Optimizatsiya eksperimenta v khimii i khimicheskoi tekhnologii* (Optimization of Experiment in Chemistry and Technology), Moscow: Vysshaya Shkola, 1978.
5. Karyakin, Yu.V., and Angelov, I.I., *Chistye khimicheskie veshchestva* (Pure Chemicals), Moscow, 1974.

Russian Journal of Applied Chemistry, Vol. 74, No. 10, 2001, pp. 1756–1758. Translated from Zhurnal Prikladnoi Khimii, Vol. 74, No. 10, 2001, pp. 1703–1705.

BRIEF COMMUNICATIONS

Spark Dispersion of Aluminum and Its Subsequent Hydration

R. K. Bairamov, N. R. Vedernikova, and A. I. Ermakov

Novomoskovsk Institute of Mendeleev Russian University of Chemical Technology, Novomoskovsk, Russia
Olimpiya OOO, Novomoskovsk, Russia

Received March 1, 2001

Abstract—The influence exerted by components introduced into the working solution and by the temperature of sludge treatment on hydration of dispersed aluminum particles formed in the course of spark erosion was studied.

The behavior of dispersed metal particles formed in spark erosion has been insufficiently discussed in the literature. The products formed in this process frequently have composition different from that of the employed electrodes. For example, metal carbides are formed together with metal powder in spark erosion of niobium in organic solvents (heptane, kerosene, transformer oil), with niobium carbides with varied carbon content formed depending on the process mode [1, 2]. Spark-erosion dispersion of aluminum in water gives aluminum hydroxide [3, 4]. Depending on the conditions of the spark-erosion process, the forming dispersed metal particles may partially or completely react with the working solution. Therefore, studying the influence exerted by the conditions of spark erosion on the composition of its products is important.

This study is concerned with spark-erosion dispersion of aluminum and the influence exerted by additives introduced into the working solution (ammonium nitrate, carbonate, or acetate) and by the temperature of sludge treatment on the composition of spark-erosion products.

The experiments were done in a cylindrical reactor made of an insulating material (acrylic resin or polyvinyl chloride plastic) with aluminum electrodes symmetrically arranged at reactor edges. The reactor was charged with aluminum grains 5–8 mm in size to 2/3 of its height. As working solution pumped through the reactor was used distilled water. The grains between the electrodes were stirred by shaking with the help of a mechanical stirrer. Voltage pulses of amplitude 180 V and repetition frequency of 1000 Hz from a 1-kW generator were applied to the electrodes.

At points of grain-to-grain and grain-to-electrode contacts there occurred spark discharges in water, and aluminum was dispersed. The sludge (mixture of the working solution and erosion products) was fed into a tank to be subjected to thermal treatment there.

The sludge was filtered, the filtrate was recycled, and the obtained precipitate was dried at 100°C. The phase composition, specific surface area, and metallic aluminum content of the obtained product were determined. The phase composition of the precipitate was performed with a DRON-2 X-ray diffractometer.

Some of the obtained diffraction patterns are shown in Fig. 1. Interplanar spacings used to identify the products (interplanar spacing $d = 10^2$ pm: bayerite: 1.33, 1.39, 1.44, 1.55, 1.60, 1.72, 2.23, 2.47, 2.72, 3.23, 4.40, and 4.80; pseudoboehmite: 1.42, 1.85, 2.34, 3.20, and 6.30; aluminum: 1.99) are indicated at the lines. The specific surface area was determined by the method of thermal desorption of argon on a special installation with the use of Tsvet-200 instrument.

As an example, we present in more detail the results obtained in studying the effect of addition of ammonium nitrate to the working solution. Figure 1 shows X-ray diffraction patterns of aluminum spark-dispersion products obtained with working solutions without additive and with ammonium nitrate additive at different temperatures of sludge treatment. It can be seen that, with distilled water used as working solution and sludge treatment temperature of 25°C, the erosion products are mainly composed of bayerite-type aluminum hydroxide and a minor amount of powdered aluminum whose content was not higher than 3 wt % in all experiments (Fig. 1a). On elevating the treatment temperature to 90°C, pseudoboehmite appeared in the erosion products together with bayerite (Fig. 1b). A similar behavior was observed at lower temperature of about 25°C on introducing ammonium nitrate into the working solution (Fig. 1c). The forma-

1070-4272/01/7410-1756 $25.00 © 2001 MAIK "Nauka/Interperiodica"

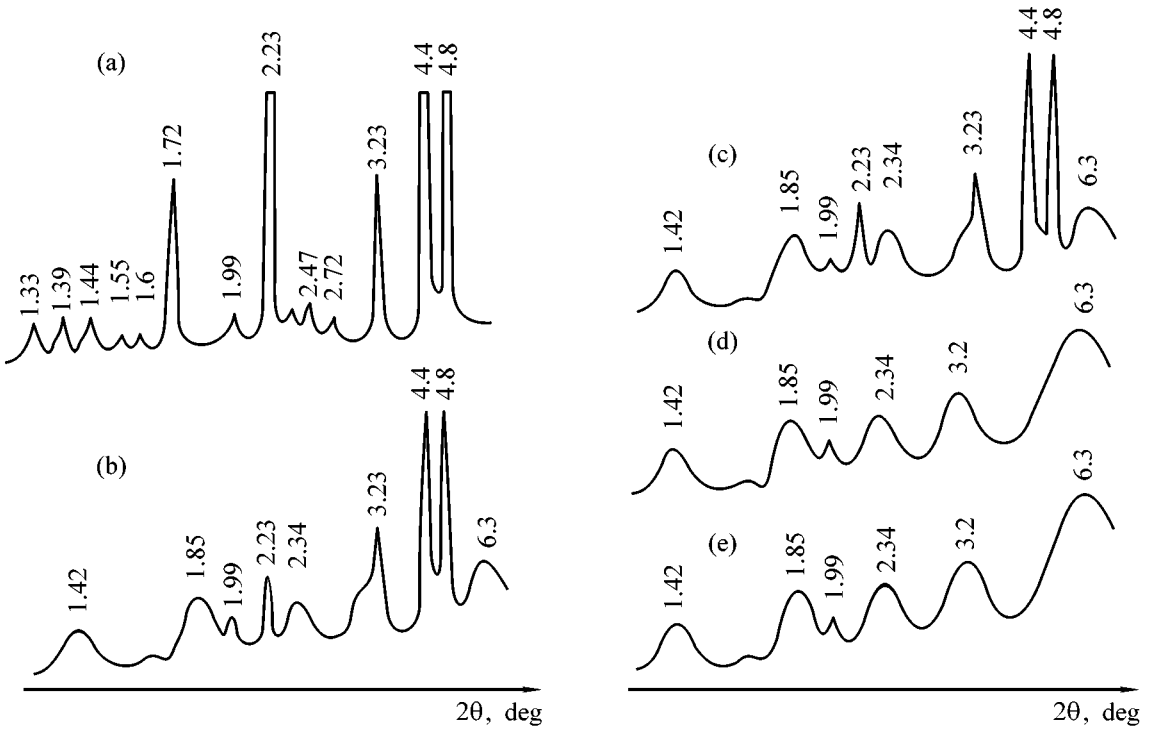

Fig. 1. X-ray patterns of products obtained in spark dispersion of aluminum in working solution (a), (b) without additive and (c)–(e) with addition of ammonium nitrate. (2θ) Bragg angle. Sludge treatment temperature (°C): (a), (c), (e) 25 and (b), (d) 90. Sludge treatment time (h): (a) 20, (b) 14, (c) 15, (d) 10, and (e) 6. NH_4NO_3 concentration (M): (c), (d) 0.017 and (e) 0.14.

tion of pseudoboehmite under these conditions is presumably not a consequence of bayerite dehydration, since the latter process onsets at 200°C [5]. On elevating the sludge treatment temperature to 90°C, dispersed metal is hydrated to give only pseudoboehmite (Fig. 1d). Raising the concentration of ammonium nitrate in the working solution also favors formation of boehmite, and, at concentrations exceeding 0.017M, pseudoboehmite is already formed at 25°C (Fig. 1e). Thus, a conclusion can be made that the hydration of dispersed aluminum is strongly affected by two factors: working solution composition and sludge treatment temperature.

The observed differences between the erosion products are presumably due to the fact that dispersed aluminum is hydrated to give both boehmite and bayerite. Figure 2 shows the effect of temperature on the specific surface area of aluminum oxides obtained from pseudoboehmite (curve *1*) and bayerite (curve *2*) formed in the course of spark erosion. The nature of the *S*–*T* curves is about the same for the given aluminum oxides and those obtained chemically from the corresponding aluminum hydroxide [5]. This also indicates that dispersed aluminum particles formed in spark erosion are hydrated to give bayerite and boehmite.

The following scheme of hydration of dispersed aluminum can be proposed on the basis of the obtained data:

$$Al + H_2O \rightarrow AlOH + 1/2H_2, \quad (1)$$

$$AlOH + H_2O \rightarrow Al(O)OH + H_2, \quad (2)$$

$$Al(O)OH + H_2O \rightleftarrows Al(OH)_3. \quad (3)$$

With distilled water as working solution and low treatment temperatures of sludge treatment, dispersed aluminum particles are hydrated to give bayerite,

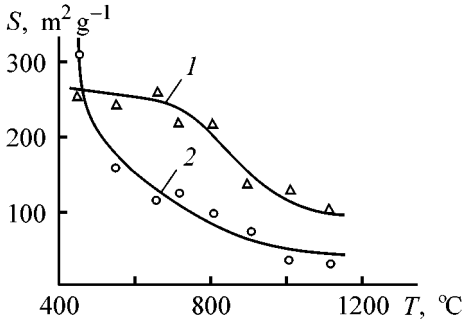

Fig. 2. Effect of temperature *T* on the specific surface area *S* of aluminum oxide obtained from (*1*) pseudoboehmite and (*2*) bayerite. Time of keeping at each temperature 6 h.

which is the final product of stage (3). Introducing certain additives into the working solution and elevating the sludge treatment temperature favor formation of boehmite.

CONCLUSIONS

(1) It is shown that, depending on the conditions under which the spark-erosion process is performed, the forming dispersed aluminum particles are hydrated to give bayerite or boehmite modification of aluminum hydroxide.

(2) Raising the temperature of sludge treatment and introducing ammonium nitrate, carbonate, or acetate into the working solution favor formation of boehmite-type aluminum hydroxide.

REFERENCES

1. Asanov, U.A. and Sakavov, I.E., *Izv. Akad. Nauk KirgSSR*, 1967, no. 4, pp. 71–75.
2. Asanov, U.A., Bazilova, S., and Sakavov, I.E., *Mekhanoemissiya i mekhanokhimiya tverdykh tel* (Mechanoemission and Mechanochemistry of Solids), Frunze: Ilim, 1974, pp. 174–175.
3. USSR Inventor's Certificate, no. 465078.
4. USSR Inventor's Certificate, no. 592753.
5. Vinnikova, T.S., Dzis'ko, V.A., and Kefeli, L.M., *Kinet. Kataliz*, 1968, vol. 9, no. 5, pp. 1331–1342.

Russian Journal of Applied Chemistry, Vol. 74, No. 10, 2001, pp. 1759–1761. Translated from Zhurnal Prikladnoi Khimii, Vol. 74, No. 10, 2001, pp. 1706–1708.

BRIEF COMMUNICATIONS

Formation of Metal Powder in Spark Dispersion of Aluminum

R. K. Bairamov, A. I. Ermakov, and N. R. Vedernikova

Novomoskovsk Institute of Mendeleev Russian University of Chemical Technology, Novomoskovsk, Russia

Olimpiya OOO, Novomoskovsk, Russia

Received March 13, 2001

Abstract—The effect of additives introduced into the working solution on the behavior of dispersed aluminum particles formed in spark erosion was studied. The conditions under which products of a given composition are formed were determined on the basis of thermodynamic and kinetic factors.

Depending on the conditions under which the spark-erosion process is performed, the obtained dispersed aluminum particles, interacting with the working solution, form a bayerite or boehmite modification of aluminum hydroxide [1]. Aluminum hydroxide is obtained in those cases when the forming dispersed aluminum is free of an oxide film and exhibits high reactivity. It is of interest to enlarge the body of data on the influence exerted by various spark-erosion process conditions on the composition of the products.

In this study, the influence of acids introduced into the working solution (distilled water) on the composition of the spark-erosion process was analyzed. The experiments were done on the installation, and using the technique, described in [1]. The content of metallic aluminum in the erosion products was determined volumetrically [2].

Figure 1a shows an X-ray pattern of products obtained in spark dispersion of aluminum, with nitric acid introduced into the working solution. For comparison, Figs. 1b and 1c present X-ray diffraction patterns of erosion products obtained in the working solution (distilled water) and a solution of ammonium nitrate. It can be seen that addition of nitric acid results in that aluminum powder is the main product of spark erosion. The content of aluminum in the erosion products is about 97 wt %. In other cases, boehmite and bayerite forms of aluminum hydroxide are produced, differing in the number of water molecules per aluminum oxide molecule [1]. The differences in the composition of the erosion products are presumably due to the fact that introduction of ammonium nitrate into the working solution hinders access of water

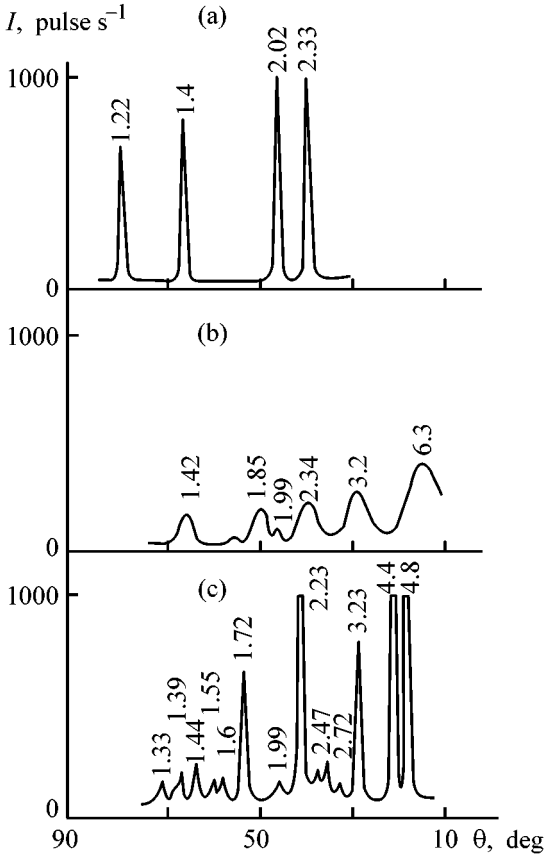

Fig. 1. X-ray patterns of products formed in spark dispersion of aluminum. Sludge treatment temperature 25°C. (*I*) Intensity and (θ) Bragg angle. Sludge treatment time (h): (a) 4, (b) 6, and (c) 20. Additive to working solution (M): (a) HNO_3 0.016, (b) NH_4NO_3 0.14, and (c) distilled water. Interplanar spacing $d \times 10^2$ (pm): aluminum: 1.22, 1.4, 1.99, 2.02, and 2.33; bayerite: 1.33, 1.39, 1.44, 1.55, 1.60, 1.72, 2.23, 2.47, 2.72, 3.23, 4.40, and 4.80; pseudoboehmite: 1.42, 1.85, 2.34, 3.20, and 6.30.

1070-4272/01/7410-1759 $25.00 © 2001 MAIK "Nauka/Interperiodica"

molecules to dispersed aluminum particles. As a result, dispersed aluminum is hydrated to give boehmite. On adding nitric acid to the working solution, no hydration occurs. This is possibly due to formation of a protective oxide film on the surface of dispersed aluminum particles under the action of nitric acid. It should be noted that, at nitric acid concentration in the working solution of less than 0.003 M, aluminum hydroxide is formed in large amounts together with powdered metal. Raising the acid concentration leads to an increase in the amount of forming powdered metal, and, at solution concentrations exceeding 0.008 M, powdered metal becomes the main erosion product. Formation of aluminum powder was also observed upon introduction of other acids into the working solution [3]. The limiting concentrations of these acids, necessary for only powdered metal to be formed as the main erosion product, depend on the type of acid.

On the basis of [1], the scheme of hydration of dispersed aluminum in a working solution with addition of nitric acid can be represented as follows:

$$Al + H_2O \rightarrow AlOH + 1/2H_2, \quad (1)$$

$$2Al + 6HNO_3 \xrightarrow{t} Al_2O_3 + 6NO_2 + 3H_2O, \quad (2)$$

$$AlOH + H_2O \rightarrow Al(O)OH + H_2, \quad (3)$$

$$Al(O)OH + H_2O \rightleftarrows Al(OH)_3. \quad (4)$$

It is known that strongly diluted or cold concentrated nitric acid does not dissolve aluminum because of the formation of an oxide film [4]. Under the conditions of an electric spark discharge, when the released energy is, in principle, sufficient for atomization of oxygen of oxygen-containing acid residues, it is also not improbable that aluminum oxidation may proceed in dilute acid solutions [reaction (2)]. For this reason, other acids (phosphoric, chromic) can passivate aluminum in the course of spark erosion to give mainly powdered metal as a product [3].

Thus, at low temperatures of sludge treatment in distilled water, dispersed metal particles formed in the course of erosion are hydrated to give bayerite, which is the final product of stage (4). Introduction of salts into the working solution and raising the sludge treatment temperature [1] favor formation of boehmite, which is the final product of stage (3) or of reverse reaction in stage (4).

The change in the standard Gibbs energy, ΔG, calculated using the data of [5] for reaction (4), is about –4 kJ. This points to a slim, but still existing thermodynamic possibility of occurrence of the process. Calculation of the enthalpy and entropy factors of the given process indicates that, for the given reaction, the dependence of the change in Gibbs energy on temperature T (K) has the form

$$\Delta G = -18.8 + 0.005T.$$

At 90°C, ΔG = –0.65 kJ. As a result, passing from 25 to 90°C results in only a slight shift of the equilibrium toward boehmite formation. However, at 90°C the equilibrium of the system (4) may shift to the left in accordance with the Le Chatelier principle, because of the removal of water from the reaction sphere.

At the same time, it is not improbable that there may exist different rates of boehmite formation and consumption by reactions (2) and (4), respectively. Experimental verification of this assumption is difficult under the conditions of the experiment. Therefore, the relative reaction rates were evaluated on the basis of theoretical considerations. Let us assume that complexes between the substrate [i.e., Al, AlOH, or Al(O)OH] and water molecule are preliminarily formed near the transient states of the reactions in question. Then, the higher the energy gain in such a complexation, the lower must be the activation energy of the reaction and the higher its rate. Results of quantum-chemical calculations of the structure of the complexes by the PM3 method are presented below:

Complex 1 Complex 2 Complex 3

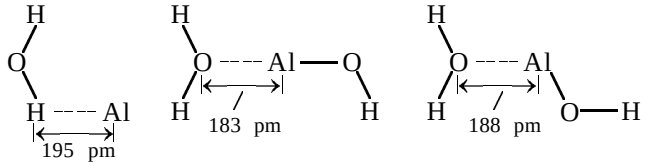

The complexation energy is (kJ mol^{-1}) 104 for complex no. 1, 185 for no. 2, and 96 for no. 3. The stabilization energy of complex no. 2 is the highest, which assumes fast conversion of aluminum monohydroxide into aluminum oxohydroxide [reaction (3)]. At the same time, aluminum oxohydroxide is the least stabilized in complexation with water, and, therefore, it is anticipated that its further hydration to give aluminum trihydroxide [reaction (4)] will proceed at lower rate than the rate of aluminum oxohydroxide formation. Consequently, it would be expected that boehmite is primarily accumulated in products via reactions (1) and (3), rather than as a result of bayerite

dehydration. This confirms the previous assumptions concerning the mechanism of boehmite formation [1].

Thus, the process can be directed toward formation a required product by varying the conditions of spark dispersion of aluminum.

CONCLUSION

Depending on the process conditions, different products can be obtained in spark erosion of aluminum; in particular, introduction of nitric acid into the working solution favors formation of metal powder. Changes in the composition of spark-erosion products with the process conditions may be governed both by thermodynamic and by kinetic factors of the process.

REFERENCES

1. Bairamov, R.K., Vedernikova, N.R., and Ermakov, A.I., *Zh. Prikl. Khim.*, 2001, vol. 74, no. 10, pp. 1703–1705.
2. Tolmachev, I.P., *Proizvodstvo alyuminievogo poroshka, alyuminievoi pudry i termita* (Manufacture of Aluminum Powder, Fine Aluminum Powder, and Thermite), Moscow: GONTI, 1938.
3. USSR Inventor's Certificate, no. 1 358 214.
4. Glinka, N.L., *Obshchaya khimiya* (General Chemisty), Ermakov, A.I., Ed., Moscow: Integral-Press, 2000.
5. Karapet'yants, M.Kh. and Karapet'yants, M.L., *Osnovnye termodinamicheskie konstanty organicheskikh i neorganicheskikh veshchestv* (Basic Thermodynamic Constants of Organic and Inorganic Substances), Moscow: Khimiya, 1968.

Russian Journal of Applied Chemistry, Vol. 74, No. 10, 2001, pp. 1762–1764. Translated from Zhurnal Prikladnoi Khimii, Vol. 74, No. 10, 2001, pp. 1708–1710.

BRIEF COMMUNICATIONS

Effect of Some Organic Compounds on Composition of Products of Spark Dispersion of Aluminum

R. K. Bairamov, A. I. Ermakov, and N. R. Vedernikova

Novomoskovsk Institute of Mendeleev Russian University of Chemical Technology, Novomoskovsk, Russia
Olimpiya OOO, Novomoskovsk, Russia

Received May 10, 2001

Abstract—The influence exerted by the nature of organic components of the working solution on the composition of products formed in spark dispersion of aluminum was studied.

In spark erosion of aluminum, the interaction of the forming dispersed metal particles with the working solution depends on the process conditions [1, 2]. The reaction products are bayerite, boehmite, and aluminum powder. The fact that mainly aluminum powder is obtained in the process is due to the formation of an oxide film on the surface of dispersed particles. The film formation may involve oxygen produced together with other elements in the decomposition of working solution components in the electric spark discharge zone. The possibility of occurrence of such a reaction is indicated by data obtained in studying the spark erosion of a metal in a working solution containing organic compounds (e.g., niobium in the presence of heptane etc.), in which metal carbides are formed together with the metal powder [3]. The carbides are products of the reaction of dispersed particles with carbon formed in destruction of organic compounds in the course of spark erosion.

This study is concerned with the influence exerted on spark erosion of aluminum by a number of organic compounds added to the working solution (distilled water). The experiments were carried out on an installation similar to that described in [1].

Figure 1 shows the results of a study of the effect of sludge treatment temperature (a) and concentration of introduced organic compounds (b) on the composition of the obtained products. It can be seen that the content of boehmite in erosion products obtained in the working solution and solutions containing organic components grows with increasing sludge treatment temperature. The thermal treatment of the sludge was carried out outside the spark-discharge zone (outside the reactor in the collector vessel) [1]. At the same time, approximately constant sludge temperature within the reactor (≤40°C) was ensured by controlling

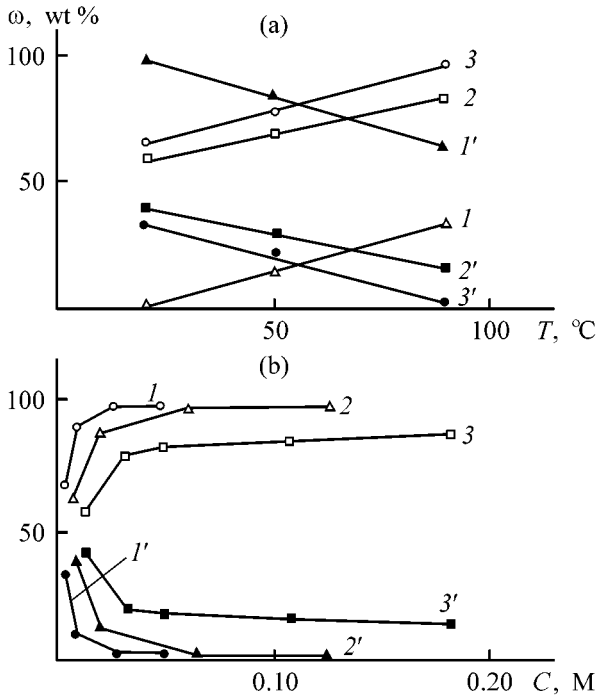

Fig. 1. Content ω of (*1–3*) boehmite and (*1′–3′*) bayerite in products of spark dispersion of aluminum vs. (a) temperature *T* of sludge treatment and (b) concentration *C* of organic substance in the working solution. (a) Additive concentration (M): (*1, 1′*) 0, (*2, 2′*) 0,05, and (*3, 3′*) 0,039. (b) Sludge treatment temperature 90°C. Additive: (a) (*2, 2′*) ethanol, (*3, 3′*) ammonium acetate; (b) (*1, 1′*) saccharose, (*2, 2′*) glycerol, and (*3, 3′*) ethanol. Sludge treatment time τ (h): (a) (*1, 1′*) 15, (*2, 2′*) 12, (*3, 3′*) 8; (b) (*1, 1′*) 15, (*2, 2′*) 9, and (*3, 3′*) 12.

1070-4272/01/7410-1762 $25.00 © 2001 MAIK "Nauka/Interperiodica"

Effect of working solution components on the composition of products formed in spark dispersion of aluminum*

Run no.	Working solution	Additive, M	τ, h	Product composition, wt %		
				boehmite	bayerite	Al powder
1	Distilled water	–	15	35	65	0
2	Ethanol	0.05	12	75	25	0
3	Ethyl acetate	0.07	20	70	30	0
4	Glycerol	0.055	9	100	0	0
5	Saccharose	0.036	8	100	0	0
6	Urea	0.12	9	100	0	0
7	Ammonium acetate	0.039	8	100	0	0
8	Acetic acid	0.15	4	100	0	0

* Sludge treatment temperature T (°C): (1–7) 90 and (8) 25.

the feed rate of the working solution. Since the thermal treatment mode affects the composition of spark-erosion products, the presented experimental data indicate the occurrence of "secondary" reactions in the sludge receiver. The difference in the compositions of products obtained upon thermal treatment of sludge at different temperatures are probably due to the varied, temperature-dependent extent of metal hydration. In particular, the extent of hydration of dispersed metal decreases with increasing temperature. This leads, in the end, to a higher amount of boehmite in spark-erosion products.

The fact that aluminum powder is obtained in the final product may be due to the formation in the spark-discharge zone of a uniform oxide film on the surface of dispersed particles (primary process) protecting the metal from further reaction with the working solution. Probably, partial formation of the oxide film on the surface of the dispersed metal may also occur in the spark-discharge zone in those cases when no metal powder is formed, e.g. with distilled water used as working solution. This film may play important role further, in secondary processes. The assumption made is most clearly confirmed when solutions containing various organic substances are used in the process (Fig. 1b). It can be seen that, with increasing concentration of organic substances used in the spark-erosion process, the content of boehmite in the product first grows steeply (portion *I*) and then gradually approaches the limiting value (portion *II*), which depends on the nature of the organic component of a working solution. The observed run of the ω–*C* curves suggests that the fraction of dispersed metal surface covered with oxide film grows in the spark discharge zone with increasing concentration of an organic substance in the working solution. This oxide film may be formed because of the appearance of atomic oxygen upon introduction of components into the working solution. In the spark-discharge zone, the temperature may be as high as several thousand degrees, which is sufficient for atomization of chemical elements. As a result, the fraction of aluminum surface occupied by oxygen grows with increasing concentration of an organic substance (portion *I*) and, as a consequence, the extent of hydration in the sludge receiver decreases. In the end, this leads to an increase in the fraction of the forming boehmite and a decrease in that of bayerite.

Thus, the differences in the compositions of spark-erosion products are associated with differences in the processes occurring in aluminum oxidation. It is known that oxidation of aluminum by water leads to hydrated forms of aluminum hydroxide. At the same time, no oxide phase is formed in this case. However, the influence exerted by the electric energy released in the spark discharge on the components of the medium leads to the appearance of atomic oxygen consumed for formation of the oxide phase of aluminum. As follows from the table, no metal powder is formed in electric spark dispersion in pure water. A quantum-mechanical calculation by the PM3 method [4] of the energy of formation of atomic oxygen from water

$$H_2O \rightarrow 2H + O, \quad \Delta E = 910 \text{ kJ mol}^{-1}; \qquad (1)$$

$$H_2O + e \rightarrow 2H + O^-, \quad \Delta E = 820 \text{ kJ mol}^{-1} \qquad (2)$$

points to a comparatively large energy expenditure, with reaction (2) involving electrons in the spark-discharge zone. However, in this case, too, the energy necessary for atomic oxygen to be formed from water remains high. Therefore, because of the deficiency of oxygen oxidizing aluminum, the main products of spark erosion in distilled water are various forms of aluminum hydroxide, with the predominance of the bayerite form.

To reveal the reasons for the increase in the fraction of boehmite in the reaction products formed in working solutions with organic substances, the possibility of their thermal decomposition to give atomic oxygen and organic radicals was considered on the basis of the results obtained in quantum-chemical calculations of the energy of formation of atomic oxygen from the additives introduced into the working solution. Account was only taken of the energy required to rupture bonds of a single oxygen atom with other atoms of a molecule. It was found that the energies of oxygen atomization from all of the used organic additives are less than that for atomization from water. For example, the energy of oxygen atomization from ethanol and ethyl acetate is 140–240 kJ mol^{-1} lower, and that from saccharose, urea, and ammonium acetate, 260–350 kJ mol^{-1} lower than that from water. A correlation between the fraction of boehmite in the reaction products and the energy of formation of atomic oxygen is observed. The easier the formation of atomic oxygen, the larger the fraction of boehmite. This may be a consequence of the appearance of a certain fraction of the oxide phase in metal dispersion, since boehmite can be regarded as an intermediate phase between aluminum oxide and the form hydrated to the maximum possible extent—bayerite. Thus, introduction of an organic additive into the working solution favors an increase in the fraction of oxygen consumed for aluminum oxidation to give boehmite.

The proposed scheme of hydration of dispersed aluminum [1] assumed that, only dispersed metal is formed in the spark-discharge zone and reacts with the working solution to give various forms of aluminum hydroxide. The analysis of experimental data, made in this study, suggests that dispersed metal with partly oxidized surface is also formed in the spark-discharge zone. This oxide film favors formation of boehmite in secondary processes occurring in solution. Thus, the hydration of dispersed aluminum can be represented as follows:

$$\left.\begin{aligned} &Al \rightarrow Al_d, \\ &Al \rightarrow Al_d[Al_xO_y], \end{aligned}\right\}\ \text{Processes occurring in the spark-discharge zone}$$

$$\left.\begin{aligned} &Al_d + H_2O \rightarrow AlOH + 0.5H_2, \\ &AlOH + H_2O \rightarrow Al(O)OH + H_2, \\ &Al_d[Al_xO_y] + H_2O \rightarrow Al(O)OH + H_2, \\ &Al(O)OH + H_2O \rightarrow Al(OH)_3 + H_2, \end{aligned}\right\}\ \text{Processes occurring in solution}$$

where Al is compact aluminum, Al_d dispersed aluminum, $Al_d[Al_xO_y]$ partly oxidized dispersed aluminum, Al(O)OH boehmite, and $Al(OH)_3$ bayerite.

CONCLUSION

Introduction of organic oxygen-containing additives into the working solution exerts strong influence on the spark erosion of aluminum. A plausible mechanism by which various forms of aluminum hydroxide are produced in spark dispersion of the metal is proposed.

REFERENCES

1. Bairamov, R.K., Vedernikova, N.R., and Ermakov, A.I., *Zh. Prikl. Khim.*, 2001, vol.74, no. 10, pp. 1703–1705.
2. Bairamov, R.K., Ermakov, A.I., and Vedernikova, N.R., *Zh. Prikl. Khim.*, 2001, vol. 74, no. 10, pp. 1706–1708.
3. Asanov, U.A., Bazilova, O., and Sakavov, I.K., *Mekhanoemissiya i mekhanokhimiya tverdykh tel* (Mechanoemission and Mechanochemistry of Solids), Frunze: Ilim, 1974, pp. 174–178.
4. Dewar, M.J.S. and Steward, J.J.P., *J. Comp. Chem.*, 1989, vol. 10, pp. 209, 221.

Russian Journal of Applied Chemistry, Vol. 74, No. 10, 2001, pp. 1765–1767. Translated from Zhurnal Prikladnoi Khimii, Vol. 74, No. 10, 2001, pp. 1711–1713.

BRIEF COMMUNICATIONS

Synthesis and Study of Carbon Sorbent Prepared from Polyethylene Terephthalate

N. T. Kartel', N. V. Gerasimenko, N. N. Tsyba, A. D. Nikolaichuk, and G. A. Kovtun

Institute of Sorption and Endoecological Problems, National Academy of Sciences of Ukraine, Kiev, Ukraine
Institute of Bioorganic and Petroleum Chemistry, National Academy of Sciences of Ukraine, Kiev, Ukraine

Received February 22, 2001

Abstract—The optimal conditions for preparing activated carbons from polyethylene terephthalate polymer wastes were determined. The pore structure and sorption properties of the resulting product were studied.

Nonutilizable synthetic macromolecular man-made pollutants give rise to serious environmental problems. The removal, disposal, or incineration of these products as ways to diminish their environmental impact are often ineffective. Various procedures of their partial utilization [1–3] predominantly involve production of consumer's goods or intermediates for other cheap products. An alternative procedure allowing preparation of novel products is treatment of these wastes to obtain relatively cheap carbon sorbents whose working properties are comparable with the properties of common activated carbons prepared from wood, lignin, and coal dust.

In this work, we studied the possibility of preparing activated carbon from polyethylene terephthalate (PETP) plastic containers; accumulation of these containers only in the Ukraine reaches several million tons a year.

The treatment of this polymeric material is based on the thermal carbonization–activation in the presence of dehydrating agents [4, 5] improving the yield of the carbonized product and leading to the development of a microporous and transport pore system in the resulting material. Further steam activation provides additional development of the microporous structure (i.e., increases the volume of sorption pores and the specific surface area) and thus significantly improves the sorption properties.

EXPERIMENTAL

In our study, we used the PETP crumb intended for production of plastic containers and the polymer crumb obtained in utilization of used containers.

As modifying agents we studied a 30% $ZnCl_2$ solution and also concentrated orthophosphoric and sulfuric acids.

The preparation of a carbon sorbent by pyrolysis of the polymer crumb involves several stages. First, the samples were kept in solutions of the above modifying agents for 24 h. After impregnation, the crumb was dried at 150°C for 2 h.

The carbonization and activation were performed in a quartz reactor placed in a horizontal furnace. One side of the reactor was sealed, so that the process occurred almost without access of air, which in the course of heating promotes autocatalytic burning-out of the carbon-containing material. As a result, the crumb was heated in our process in the atmosphere of pyrolysis products. The heating rate was 20 deg min^{-1}; the maximum activation temperature was 800°C. Then, the carbon samples were additionally activated with steam at the same temperature for 1 h.

To confirm the effect of chemical modification, we performed simultaneously a pyrolysis of a sample without impregnation with modifying agents.

In all the stages, the pore volume of the carbon product was determined with respect to benzene W_s and methanol W'_s [6]. The size distribution of the macro- and mesopores was studied by the mercury porosimetry on a Pore-Sizer 9300 device (Cultronix, France). The sorption properties of the carbon sorbents were determined by sorption of Methylene Blue (A) and iodine (A') [6, 7].

The physicochemical properties of activated carbons prepared by activation of PETP polymer crumb

1070-4272/01/7410-1765 $25.00

Table 1. Physicochemical properties of activated carbons prepared by carbonization of PETP crumb*

Modifying agent	R_w, %	R_v, %	Δ, g cm^{-3}	W_s, cm^3 g^{-1}	Aqueous extract pH	A, mg g^{-1}
$ZnCl_2$	18.9	51.4	0.35	0.22	5.1	97
H_3PO_4	15.8	41.3	0.35	0.07	4.3	4
H_2SO_4	14.8	57.4	0.15	0.48	5.0	199
–	15.5	29.6	0.49	0.11	5.4	62

* R_w is the weight yield, R_v the volume yield, and Δ the bulk density.

Table 2. Pore characteristics of activated carbons in relation to time of sample keeping in sulfuric acid τ and impregnation coefficient K

τ, h	K, %	W_s, cm^3 g^{-1}	S_{sp}, m^2 g^{-1}
1	28	0.12	142
5	28	0.22	258
18	28	0.31	362
24	28	0.36	420
48	28	0.37	427
24	23	0.27	318
24	33	0.36	424

Table 3. Pore characteristics of activated carbons prepared from polyethylene crumb by chemical and additional physical activation with steam

Activation	W_s, cm^3 g^{-1}	W'_s, cm^3 g^{-1}	A, mg g^{-1}	A', %	S_{sp} with respect to Ar, m^2 g^{-1}
Chemical	0.36	0.27	76	48	420
Chemical + steam	0.54	0.51	230	90	1230

in the presence of chemical modifying agents and without them are listed in Table 1. As seen, at a similar combustion loss the modifying agent strongly affects the sorption properties of the sorbents. The carbon sorbent modified with orthophosphoric acid exhibits the smallest sorption capacity with respect to Methylene Blue and benzene vapor; in this case, the sorption capacity is even smaller than that for sorbents obtained without use of modifying agents.

The highest sorption capacity is exhibited by activated carbons modified with concentrated sulfuric acid. The sorption capacity of such a sorbent with respect to benzene reaches 0.47 cm^3 g^{-1}, the sorption of Methylene Blue is 200 mg g^{-1}, which is comparable with AR, AG, BAU, and OU activated carbons, etc., widely used in industrial sorption processes.

In our further tests, we used concentrated sulfuric acid as a modifying agent.

The optimal conditions of PETP crumb pyrolysis were determined by varying the time of sample keeping in sulfuric acid and the impregnation coefficient K (%) calculated using the expression given in [4]:

$$K = (V_{imp}/V_{\Sigma}) \times 100,$$

where V_{imp} is the volume of the impregnation solution (sulfuric acid) (ml) and V_{Σ} is the total volume of the impregnated crumb and modifying agent (sulfuric acid) (ml).

The data characterizing the development of the pore structure of the resulting activated carbons, as influenced by variation of the above parameters, are listed in Table 2. As seen, the best pore characteristics are achieved at a time of keeping in sulfuric acid of 24 h and an impregnation coefficient of 28%.

The pore characteristics of the activated carbons prepared from utilized crumb by chemical and subsequent physical activation with steam are listed in Table 3. The results suggest that the additional activation with steam significantly improves the sorption properties of the resulting carbons: the parameters characterizing the pore structure (pore volume with respect to benzene and methanol, and specific surface area with respect to argon) increase appreciably.

The resulting carbon sorbent is a highly porous carbon material with a developed system of macro-, meso-, and micropores. For example, upon chemical activation the pore volumes with respect to benzene and methanol are 0.36 and 0.27 cm^3 g^{-1}, whereas in the case of additional steam activation they increase to 0.54 and 0.51 cm^3 g^{-1}, respectively. In this case, the specific pore surface area increases by a factor of 3, which suggests predominant formation of the microporous structure.

The integral and differential curves of the mesopore and micropore volume distribution with respect to radius, determined from the mercury porosimetry data, are shown in the figure. As seen, the resulting activated carbon has a significant fraction of meso-

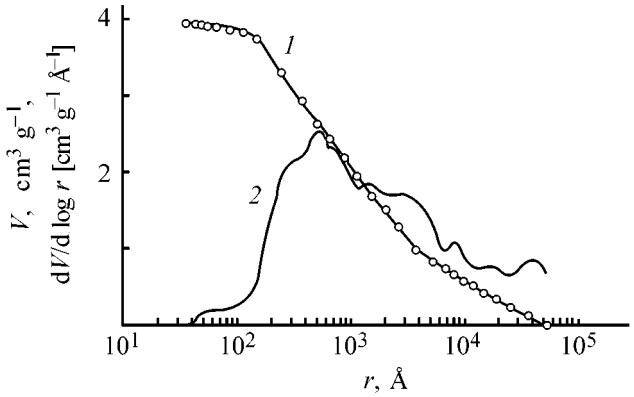

(*1*) Integral and (*2*) differential distribution curves of mesopore and macropore volume V with respect to effective pore radius r. (dV/d log r) Differential distribution of pore volume with respect to radius.

pores with effective radius of 500 Å. The total pore volume of activated carbons in question reaches 3.5 cm^3 g^{-1}.

CONCLUSIONS

(1) The optimal conditions for preparing activated carbons from polyethylene terephthalate polymer wastes were determined.

(2) Concentrated sulfuric acid is the most efficient chemical modifying agent for thermochemical carbonization–activation of polyethylene terephthalate wastes.

(3) The possibility was demonstrated of preparing activated carbons with developed structure, having pores of various types providing high sorption activity comparable with that of industrial activated carbons.

REFERENCES

1. Klushin, V.N., Rodionov, A.I., Kasel'man, I.L., *et al.*, *Uglerodnye sorbenty na osnove polimersoderzhashchikh otkhodov* (Carbon Sorbents Based on Polymer-Containing Wastes), Moscow: Biolarus, 1993.
2. Rodionov, A.I., Klushin, V.N., and Torocheshnikov, N.S., *Tekhnika zashchity okruzhayushchei sredy* (Environmental Protection Techniques), Moscow: Khimiya, 1989.
3. *Handbook of Solid Waste Management*, Vilson, D.G., Ed., Van Nostrand Renhold Co., 1977.
4. Mukhin, V.N., Tarasov, A.V., and Klushin, V.N., *Aktivnye ugli Rossii* (Russian Activated Carbons), Moscow: Metallurgiya, 2000.
5. Von Kinle, H. and Bader, E., *Antivkohle und ihre industrielle Anwendung*, Stutgart: Enke, 1980.
6. Kolyshkin, D.A. and Mikhailova, K.K., *Aktivnye ugli: Spravochnic* (Activated Carbons: Handbook), Leningrad: Khimiya, 1972.
7. Kel'tsev, N.K., *Osnovy adsorbtsionnoi tekhniki* (Fundamentals of Adsorption Engineering), Moscow: Khimiya, 1984.

Russian Journal of Applied Chemistry, Vol. 74, No. 10, 2001, pp. 1768–1770. Translated from Zhurnal Prikladnoi Khimii, Vol. 74, No. 10, 2001, pp. 1714–1716.

BRIEF COMMUNICATIONS

Effect of Sodium Chloride on Ultrafiltration of Aqueous Sulfonol Solutions

S. V. Kozlov

Karpov Physicochemical Research Institute, Moscow, Russia

Received November 23, 2000; in final form, June 2001

Abstract—Effect of NaCl on ultrafiltration of micellar aqueous Sulfonol solutions through a UFM-50 membrane is studied, including its effect on the permeate flux, retention factor, and hydrodynamic resistance of the membrane. Dependences of the hydrodynamic resistanse of dynamic membranes on the time of filtration are found.

Surfactants are widely used in everyday life and various branches of industry. Electrolytes improve surfactant performance characteristics, and, therefore, surfactants are often employed as mixtures with inorganic salts. Since ultrafiltration is an efficient method for surfactant concentration, it was of interest to study the effect of salts on this process. Previously, Yaroshenko *et al*. [1] have studied ultrafiltration separation of aqueous and aqueous-salt solutions of alkylpyridinium chloride on acetyl cellulose membranes. It was demonstrated that, at the same alkylpyridinium chloride concentration, the retention factor in 0.2 M NaCl is considerably higher as compared with that in a straight aqueous solution.

Recently, we have studied the ultrafiltration of aqueous Sulfonol solutions [2]. In the present study, we analyzed the effect of NaCl on the ultrafiltration of micellar Sulfonol solutions.

EXPERIMENTAL

The anionic surfactant Sulfonol is a mixture of sodium salts of alkylbenzenesulfonic acids $RC_6H_4SO_3Na$, where R = C_nH_{2n+1}, n = 12–18. In our experiments, the Sulfonol concentration C_1 was 10 g l^{-1}. The NaCl concentration C_2 was varied from 0.02 to 0.2 M. At these concentrations, the systems were homogeneous. The Sulfonol concentration was determined as the difference between the total weight of the solid residue and the amount of NaCl in it. In ultrafiltration experiments, we used several samples of a UFM-50 aromatic polyamide membrane with mean pore size of 30 nm.

The ultrafiltration was performed with a DKRI-021 nonflow-type module at 293 K without stirring. The pressure was set by compressed air. The working area of the membrane was 0.0117 m^2. The data scatter was 5%, and the within-sample variance, 0.6%.

For Sulfonol the critical micelle concentration (CMC) is 1.88 g l^{-1} [3], and, therefore the Sulfonol solution contained both micelles and surfactant molecules.

It is known that electrolytes make the CMC lower and the aggregation number and micelle weight higher [4], and also affect the adsorption of surfactants on the surface and in the pores of the membrane. Previously, it has been shown that the adsorption of cetylpyridinium chloride and sodium alkylbenzenesulfonate grows with increasing NaCl concentration [5]. Furthermore, electrolytes initiate compaction of the electric double layer around micelles [6]. All these factors can influence the ultrafiltration of surfactants.

In the course of ultrafiltration, Sulfonol molecules and micelles are accumulated and agglomerated on the ultrafilter surface, forming a dynamic membrane and making higher the hydrodynamic resistance to the permeate flow. The permeate flow velocity is given by the formula [7]

$$\frac{1}{J^2} = \frac{(R_m\eta)^2}{(\Delta P)^2} + \frac{2aC_s\eta R(1-K)}{\Delta P}t, \qquad (1)$$

where J is the permeate flow velocity, R_m is the hydrodynamic resistance of the ultrafilter, ΔP is the transmembrane pressure difference, η is the ultrafilter viscosity, a is the specific resistance to filtration, C_s is

1070-4272/01/7410-1768 $25.00 © 2001 MAIK "Nauka/Interperiodica"

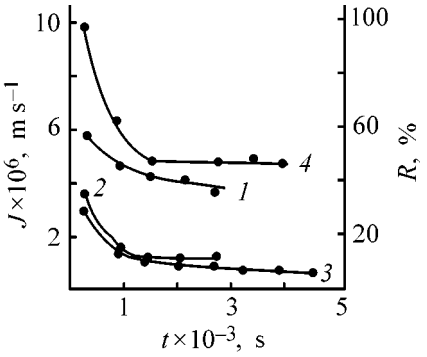

Fig. 1. (*1*, *3*) Permeate flow velocity J and (*2*, *4*) the retention factor R vs. time t on a UFM-50 membrane. Pressure 0.05 MPa, Sulfonol concentration 10 g l^{-1}; the same for Figs. 2 and 4. NaCl concentration (M): (*1*, *2*) 0.02 and (*3*, *4*) 0.2.

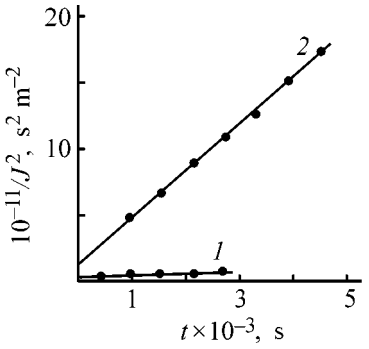

Fig. 2. Plot of $1/J^2$ vs. t for a UFM-50 membrane. NaCl concentration (M): (*1*) 0.02 and (*2*) 0.2; the same for Fig. 3.

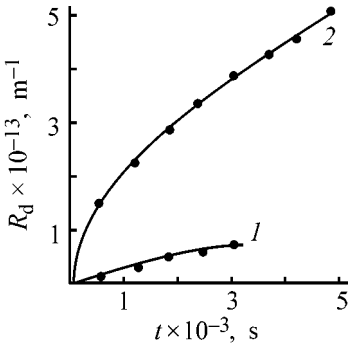

Fig. 3. Hydrodynamic resistance of dynamic membranes, R_d, vs. time t. Sulfonol concentration 10 g l^{-1}.

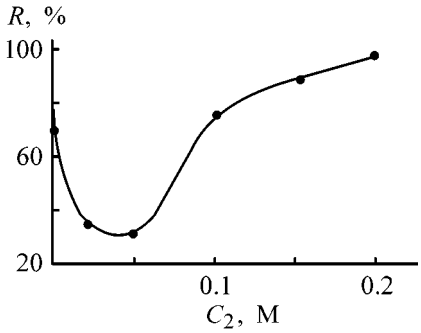

Fig. 4. Retention factor R vs. the NaCl concentration C_2 at a UFM-50 membrane.

the substance concentration in the solution, R is the retention factor, K is the fraction of the substance transferred from the membrane surface to the bulk of the solution by back diffusion, and t is time.

Let us introduce designation

$$q = \frac{2aC_s\eta R(1-K)}{\Delta P}. \quad (2)$$

The hydrodynamic resistance of a dynamic membrane is written as

$$R_d = \frac{aVC_sR(1-K)}{A}, \quad (3)$$

where V is the permeate volume and A is the membrane area.

From Eqs. (2) and (3) follows that

$$R_d = \frac{V\Delta P}{2A\eta}q. \quad (4)$$

Comparison of Eqs. (1) and (2) shows that the parameter q represents the slope of the time dependence of $1/J^2$. Since the retention factor decreases in the initial stage of filtration, it was averaged over the volume fractions in the filtrate. Sulfonol retained in filtration is found in the concentrate and, as a precipitate, on the ultrafilter. The coefficient K was determined as the ratio of the weight of Sulfonol in the concentrate to the total weight of retained Sulfonol. Knowing q, C_s, η, R, K, and ΔP, we could estimate the specific resistance a by means of Eq. (2). The hydrodynamic resistance of the dynamic membranes was estimated by Eq. (4) from data on q and the current permeate volume.

Figure 1 shows the time dependences of the permeate volume flux and retention factor of a UFM-50 membrane at an operating pressure of 0.05 MPa (Sulfonol concentration 10 g l^{-1}, NaCl concentration 0.02 and 0.2 M). The permeate flux is higher, and the retention factor, smaller at lower salt concentration. In the course of time, the permeate flux decreases, and the retention factor initially decreases and then remains unchanged.

Figure 2 shows the plots of $1/J^2$ vs. t. For 0.02 M NaCl, the specific resistance of the dynamic mem-

brane a was determined using Eq. (2) to be 3.44×10^{14} m kg^{-1} from the slope of curve *1* at $\eta = 1.005 \times 10^{-1}$ N s m^{-1}, $\Delta P = 5 \times 10^4$ N m^{-2}, $R = 0.179$, and $K = 0.17$. For 0.2 M NaCl (curve *2*, $R = 0.644$, $K = 0.33$), we estimated $a = 1.97 \times 10^{15}$ m kg^{-1}.

The time dependences of the hydrodynamic resistance of the dynamic membranes are presented in Fig. 3. The results show that R_d is much greater at high NaCl concentration.

Figure 4 demonstrates the effect of the NaCl concentration on the retention factor of Sulfonol (C_1 = 10 g l^{-1}, working pressure 0.05 MPa, t = 300 s). The retention factor initially decreases with increasing salt concentration, passes through a minimum at C_2 = 0.05 M, and then grows in the C_2 range 0.05–0.2 M. The increasing salt concentration initiates growth of micelles and simultaneous compaction of the electric double layer around Sulfonol particles [6]. The first circumstance makes the retention factor larger as a result of the screening effect. The second circumstance, conversely, causes a decrease in the retention factor by virtue of the decreasing electrostatic repulsion of the Sulfonol species from the membrane surface. Therefore, the shape of curve *2* in Fig. 4 is a result of the combined action of these two circumstance.

Let us examine the reliability of the results obtained. The membrane samples may have different permeabilities and selectivities. The hydrodynamic resistance of the dynamic membrane is proportional to the thickness of the Sulfonol layer on the ultrafilter. Therefore, somewhat different permeabilities of particular membrane samples are insignificant for determining the hydrodynamic resistance. The NaCl concentration has a strong effect on the Sulfonol retention factor, with changes in the retention factor under the action of sodium chloride much exceeding those caused by differences in the membrane selectivity.

The size of micelles is larger and their adsorption on the walls of pores of the ultrafilter is stronger at high salt concentrations. Therefore, the cross section of the membrane pores at an NaCl concentration of 0.2 M is lower than that at C_2 = 0.02 M. This circumstance accounts for the fact that the permeate volume flux at high NaCl concentrations is lower than that at low concentrations.

CONCLUSIONS

(1) Sodium chloride makes lower the Sulfonol retention factor on a UFM-50 membrane.

(2) With increasing salt concentration, the Sulfonol retention factor passes through a minimum.

(3) The specific resistance of dynamic membranes at a working pressure of 0.05 MPa, Sulfonol concentration of 10 g l^{-1}, and NaCl concentration of 0.02 and 0.2 M was found to be 3.44×10^{14} and 1.97×10^{15} m kg^{-1}, respectively.

ACKNOWLEDGMENTS

The author is grateful to S.F. Timashev for helpful discussions and to A.I. Bon for providing a membrane.

REFERENCES

1. Yaroshenko, N.A.,. Tsapyuk, E.A., Klimenko, N.A., and Bryk, M.T., *Kolloidn. Zh.*, 1989, vol. 51, no. 2, pp. 333–338.
2. Kozlov, S.V., *Zh. Prikl. Khim.*, 2000, vol. 73, no. 8, pp. 1391–1394.
3. *Poverkhnostno-aktivnye veshchestva: Spravochnik* (Surfactants: A Handbook), Abramzon, A.A. and Gaevoi, G.M., Eds., Leningrad: Khimiya, 1979.
4. Shinoda, K., Nakagawa, T., Tamamushi, B.-I., and Isemura, T., *Colloidal Surfactants. Some Physicochemical Properties*, New York: Academic, 1963.
5. Plakatina, T.P., Kim, V., and Kochergin, N.V., *Kolloidn. Zh.*, 1993, vol. 55, no. 6, pp. 79–84.
6. Voyutskii, S.S., *Kurs kolloidnoi khimii* (A Course of Colloid Chemistry), Moscow: Khimiya, 1976, 2nd ed.
7. Kozlov, S.V., *Kolloidn. Zh.*, 1996., vol. 58, no. 6, pp. 791–794.

Russian Journal of Applied Chemistry, Vol. 74, No. 10, 2001, pp. 1771–1773. Translated from Zhurnal Prikladnoi Khimii, Vol. 74, No. 10, 2001, pp. 1717–1719.

BRIEF COMMUNICATIONS

Mathematical Model of the Membrane-Chromatographic Process

N. N. Smirnov, E. B. Aronova, and V. A. Konstantinov

St. Petersburg State Technological Institute, St. Petersburg, Russia

Received April 27, 2001

Abstract—A mathematical description of the membrane-chromatographic process and its experimental verification are presented.

The membrane-chromatographic process is one of the new, advanced processes for separation of substances, in particular, proteins [1]. However, methods for simulation and engineering calculations of the separating modules have been insufficiently worked out, which hinders further development of this process in both theoretical and practical aspects.

Based on the physical concepts of the membrane-chromatographic process [2], we developed a mathematical model which, following the geometry and shape of the membrane element, includes the system of equations in cylindrical coordinates

$$\left.\begin{aligned} \frac{\partial C_1}{\partial \tau} + \frac{\partial (C_1 \overline{W} r_1)}{\partial r} &= D_1^* \left(\frac{\partial^2 C_1}{\partial r^2} + \frac{1}{r} \frac{\partial C_1}{\partial r} \right) - \frac{C_1 b W_{z_1}}{S} \\ \frac{\partial C_2}{\partial \tau} \left[1 + \frac{K}{(1 + KC_2)^2} \right] &+ W_{z_2} \frac{\partial C_2}{\partial z} = 0 \\ \frac{\partial C_3}{\partial \tau} + \frac{\partial (C_3 \overline{W} r_3)}{\partial r} &= D_2^* \left(\frac{\partial^2 C_3}{\partial r^2} + \frac{1}{r} \frac{\partial C_3}{\partial r} \right) - \frac{C_3 b W_{z_3}}{S} \end{aligned}\right\} \quad (1)$$

and the corresponding initial and boundary conditions:

$$C_1(0, r) = 0, \quad C_2(0, r) = 0, \quad C_3(0, r) = 0,$$

$$C_1(\tau, 0) = \delta(\tau), \quad C_2(z = S_1, \tau, r) = C_1(\tau, r), \quad (2)$$

$$C_3(\tau, r_0) = C_2, \quad \frac{\partial C_1}{\partial r}(\tau, r_0) = 0, \quad \frac{\partial C_3}{\partial r}(\tau, 0) = 0.$$

Here, index 1 refers to the pressure channel; 2, to the membrane; and 3, to the filtration channel; C is the concentration, mg ml^{-2}, W is the flow velocity, m s^{-1}, D^* is the effective coefficient of longitudinal diffusion, m^2 s^{-1}; τ is the time of the process, s; H_i is the channel height (i = 1, 3), m; z is the coordinate along the normal to the module surface; S is the flow cross section, m^2; and K is the Langmuir constant.

The first equation in the system (1) describes the concentration field in the pressure channel of the membrane-chromatographic element. The second equation describes the process of selective absorption of the substance in the membrane. This equation was derived with account of the fact that sorption in the chromatographic membrane is characterized by the Langmuir isotherm. The third equation in the system (1) describes the concentration field in the filtration channel. By $\overline{W}_{r_i}$ is understood the velocity averaged over the coordinate z.

To solve the mathematical model proposed, we need to know how the axial velocity varies with the element radius. To this end, we separately considered the patterns of velocity distributions in the pressure and filtration channels.

The flow continuity equation in the cylindrical coordinates

$$\frac{1}{r} \frac{\partial (W_r r)}{\partial r} + \frac{\partial W_z}{\partial z} = 0 \quad (3)$$

after averaging the velocity over z

$$\overline{W}_{r_1} = \frac{1}{H_1} \int_0^H W_r \, dz \quad (4)$$

acquires the form

$$\frac{1}{r} \frac{\partial (\overline{W}_{r_1} r)}{\partial r} + \frac{1}{H_1} W_{z_1} \Big|_0^{H_1} = 0, \quad (5)$$

where H_1 is the channel height, m.

1070-4272/01/7410-1771 $25.00 © 2001 MAIK "Nauka/Interperiodica"

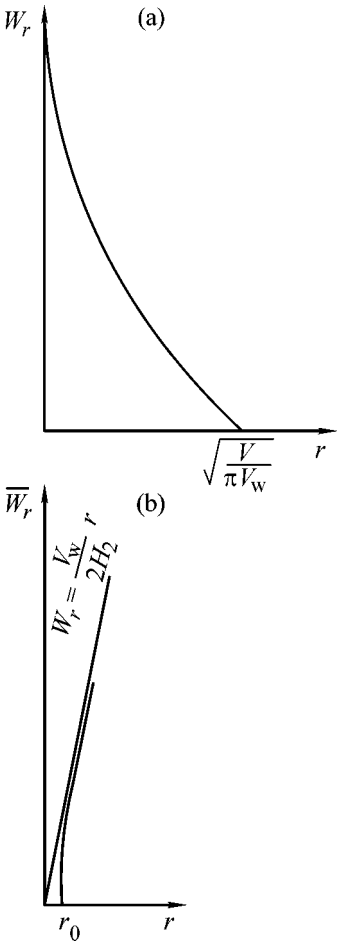

Fig. 1. Variation of the average radial velocity W_r along the radial coordinate r in (a) pressure and (b) filtration channels.

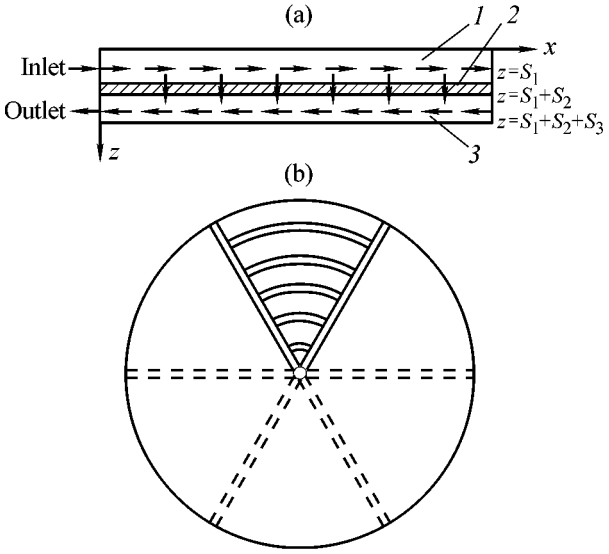

Fig. 2. Schematic of the flow movement in the membrane-chromatographic element: (a) Longitudinal cross section and (b) top view. (*1*) Pressure channel, (*2*) membrane, and (*3*) filtration channel.

Analytically, using the boundary conditions

$$z = 0,\ W_{z_1} = 0,$$
$$z = H_1,\ W_{z_1} = V_w, \quad (6)$$

where V_w is the filtration velocity, we obtained an ordinary linear inhomogeneous differential equation. The solution to this equation will be the dependence of velocity on radius, having the form

$$\overline{W}_{r_1} = -\frac{V_w}{2H_1} r + \frac{V}{2\pi H_1} \frac{1}{r}, \quad (7)$$

where V is the flow rate of the solution to be separated.

Similarly, we obtained the dependence for the filtration channel, by solving Eq. (8) with the boundary conditions (9):

$$\frac{1}{r} \frac{\partial(\overline{W}_{r_3} r)}{\partial r} + \frac{1}{H_3} \Big|_0^{H_3} = 0, \quad (8)$$

$$z = 0,\ W_{z_3} = V_w,$$
$$z = H_3,\ W_{z_3} = 0. \quad (9)$$

Here, H_3 is the filtration channel height, m.

As a result, we obtained the dependence

$$\overline{W}_{r_3} = \frac{V_w}{2H_3} r - \frac{V_w}{2H_3} r_0^2 \frac{1}{r}, \quad (10)$$

where r_0 is the module radius, m.

The obtained functions, describing the dependence of the axial velocity on radius were analyzed and graphically represented in Fig. 1. The plots in Fig. 1. suggest that the solution flow velocity in the pressure channel tends to vary monotonically along the channel from the initial value to zero and *vice versa* in the filtration channel. This will necessarily be manifested in nonuniformity of the velocity profile and a decrease in the substance separation efficiency owing to the blurring of the concentration field.

The system of Eqs. (1), (2), with account of the velocity distribution (7)–(10), describes the process of membrane-chromatographic separation.

The mathematical description developed in this study was tested experimentally for the case of protein separation in a cylindrical element (see flowsheet in Fig. 2 [3]). The flow distributors are represented by a series of concentric slits crossed by radial 1-mm-wide and 1-mm-deep slits in a metallic plate closely adjacent to the membrane. This design ensures

the most uniform and complete distribution of the substance being applied to the membrane surface.[1]

The proteins used in this work included lysozyme, ovalbumin, α-chymotrypsinogen, immunoglobulin, and hemoglobin; as components of the eluting systems served Na_2HPO_4, NaH_2PO_4, and NaCl (all of analytically pure grade, Russia). We used a JASCO (Japan) liquid chromatograph.

In this study, we developed on the basis of the physical model a mathematical description of the membrane-chromatographic process, including both the hydrodynamic and diffusion components. The theoretical and experimental data obtained by us show that the mathematical model makes it possible to calculate the concentration distribution in the separation module, estimate the separation efficiency, and determine the main geometric parameters of the module.

[1] Chromatographic membranes were manufactured by the Sorbopolimer Joint-Stock Company (Krasnodar); all the experiments were carried out at the Institute of Analytical Instrumentation, Russian Academy of Sciences.

REFERENCES

1. Tennikiva, T.B. and Svec, F., *J. Chromatogr.*, 1993, vol. 646, pp. 279–288.
2. Roper, D. and Lightfoot, E., *J. Chromatogr., Ser. A.*, 1995, vol. 702, pp. 3–26.
3. Aronova, E.B., Simulation of the Membrane-Chromatographic Process of Protein Separation, *Cand. Sci. Dissertation*, St. Petersburg, 1997.

Russian Journal of Applied Chemistry, Vol. 74, No. 10, 2001, pp. 1774–1776. Translated from Zhurnal Prikladnoi Khimii, Vol. 74, No. 10, 2001, pp. 1719–1721.

BRIEF COMMUNICATIONS

Nitrogen-Containing Organomineral Fertilizer Based on Wood Waste

M. V. Efanov, A. I. Galochkin, P. R. Schott, D. V. Dudkin, and A. G. Klepikov

Altai State University, Barnaul, Russia

Received December 7, 2000; in final form, May 2001

Abstract—A new nitrogen-containing fertilizer was obtained by oxidative ammonolyis from wood waste. The chemical composition of the fertilizer was studied by functional chemical analysis. The fertilizer was tested in field conditions.

Recently, researchers' attention has been focused on methods for preparing new types of inexpensive organic fertilizers. Among raw materials suitable for this purpose are industrial lignin [1, 2] and lingo-carbohydrate materials, including wood-waste-based composts [3, 4].

As known, slow microbiological degradation of lignin from plant residues yields organic products exerting a physiological effect on plants [5]. Kodina and Aleksandrova showed [5] that, when considering decay in soil of organic substances from wood, lignin can be regarded as a starting material for production of humic acids forming the base of soil humus.

Soil-microflora-induced humification of lignin involves oxidation (demethoxylation), which yields polyphenol compounds, followed by condensation and oxidation processes giving humic (biologically active) substances responsible for soil fertility [5].

However, the natural microbiological degradation of lignin, yielding physiologically active humic substances, is a rather protracted process taking several years. It can be accelerated by oxidative degradation of lignin to produce physiologically active groups in its structure. Such functional groups include, in the first place, those containing nitrogen in a bound, slowly assimilable form, produced in oxidative ammonolysis of lignin molecules.

The authors of [6–8] developed various procedures for preparing slowly assimilable nitrogen-containing fertilizers by oxidative ammonolysis of lignins under the action of oxygen in an ammonia medium in severe conditions (120–180°C, 5–50 atm). The main drawbacks of the oxoammonolysis methods proposed are low yields of products and the complexity and long duration of the technological process. Zakis *et al.* [9] proposed that, for oxidative fixation of nitrogen, lignin should be oxidized with an ammonia solution of ammonium peroxodisulfate at 20°C [9]. However, this method also has major disadvantages, namely, duration of over 100 h and large amount of nitrogen-containing reactants consumed.

The aim of this study was to prepare new nitrogen-containing fertilizers by oxidation of lingo-carbohydrate materials (LCM, aspen wood) with an ammonia solution of ammonium peroxodisulfate and to analyze their properties. With LCM as the starting material for preparing the fertilizers, it is possible to significantly expand the range of raw materials and to make the process less expensive [10].

EXPERIMENTAL

The LCM-based nitrogen-containing fertilizers were prepared as follows. Air-dry chips (1.0–1.5-cm fraction) with weight of 1.5 kg were treated with a solution of ammonium peroxodisulfate (0.1 kg per kg of wood) in a 25% aqueous ammonia solution (liquid-to-solid ratio 10) at 120–130°C for 1 h in an autoclave under pressure of 2.5 atm. The resulting product was washed with water until negative reaction for the sulfate ion and dried in air to constant weight.

The nitrogen content was determined by the Kjeldahl semimicromethod [11], and the amount of COOH groups, by conductometric titration [12]. Oxidation of LCM with oxygen (0.05 g per g of wood) for 1 h in the presence of NH_3 (10.0 g per g of wood) yielded an ammonized product containing 10.9% organical-

1070-4272/01/7410-1774 $25.00

Action of hydrolyzing agents on the product of oxidative ammonolysis of LCM (hydrolysis time 3 h, hydrolysis temperature 100°C)

Hydrolyzing agent, 1 g-equiv l^{-1}	Yield of solid residue	Nitrogen content in treated product	Nitrogen eliminated, % of initial content	Content of COOH groups	Increase in the content of COOH groups
	%			%	
–	–	10.9	–	8.92	–
NaOH	71.6	7.08	35.1	11.6	30.1
H_2SO_4	83.4	9.25	15.2	10.1	13.2

ly bound nitrogen, 8.92% carboxy groups, and 4.13% methoxy groups. The product was obtained in 81.5% yield.

To elucidate how strongly nitrogen is bound to lignin, a sample of oxidized wood was boiled with 1 N solutions of NaOH and H_2SO_4 for 3 h. In the resulting solid residue, we determined the content of nitrogen and COOH groups (see table).

The table shows that hydrolysis of the product of oxidative ammonolysis of LCM involves elimination of 15–35% of the bound nitrogen. This is accompanied by the corresponding increase in the content of COOH groups in the hydrolyzed samples.

Zakis *et al.* [9] showed that, under the actual conditions, hydrolysis of R-$COONH_4$ and R-$CONH_2$ yields free carboxylic acids (acid hydrolysis) or their salts (base hydrolysis) and free NH_3.

Therefore, if the ammonia liberation is due to the presence of the functional groups mentioned, the content of carboxy groups in the samples after hydrolysis must increase (see table).

Thus, the resulting nitrogen-containing derivative of LCM contains 15–35% (25% on the average) of readily eliminated nitrogen in the ammonium and amide forms, which are readily available for plants. The remaining nitrogen (75%) is strongly bound chemically to LCM and is slowly assimilable (see table).

This state of LCM facilitates its further degradation in soil to humic substances, and, as the ammonized wood degrades in soil, the chemically bound nitrogen turns to forms accessible for plants.

The previous vegetation experiments [13] demonstrated the ability of the products of oxidative ammonolysis of LCM to stimulate the growth of cereals and leguminous plants. The effect of the product of oxidative ammonolysis of wood on the wheat productivity was studied in the year of 2000 on a testing field [14].

The field experiment demonstrated the accessibility of nitrogen from ammonized LCM to plants. Introduction of a nitrogen-containing derivative of LCM into soil in amounts of 60–90 kg N/ha enhances the wheat growth by 5.3–8.5% and favors increase in the biomass of plants by 19–47% relative to the reference. Eventually, the cereal productivity increases by 4.8–7.0 centner per ha, or by 26–47% relative to the reference. Similar results were obtained with ammonium sulfate taken in appropriate amounts.

CONCLUSIONS

(1) Oxidation of aspen wood chips with ammonia solution of ammonium peroxodisulfate yields a high-molecular-weight product containing 10.9% organically bound nitrogen, 8.92% carboxy, and 4.13% methoxy groups.

(2) The resulting nitrogen-containing product contains 15–35% nitrogen which is readily eliminated by acid and base hydrolysis and is readily available for plants.

(3) The new nitrogen-containing derivative of wood is suitable as effective organomineral fertilizer for cereals, which increases their productivity by 26–47%.

REFERENCES

1. Chudakov, M.I., Mekler, N.A., Raskin, M.N., *et al.*, *Gidroliz. Lesokhim. Prom–st.*, 1971, no. 10, pp. 4–7.
2. USSR Inventor's Certificate, no. 333156.
3. Kononov, O.D. and Lagutina, T.B., *Khim. Sel'sk. Khiz.*, 1996, no. 6, pp. 14–17.
4. Geles, I.S., Fedorets, N.G., and Klemanskii, Yu.M., *Khim. Sel'sk. Khoz.*, 1997, no. 6, pp. 20–22.

5. Kodina, L.A. and Aleksandrova, G.V., *Usp. Mikrobiol.*, 1990, issue 24, pp. 156–189.
6. USSR Inventor's Certificate, no. 635 104.
7. USSR Inventor's Certiifcate, no. 535 264.
8. Mazhara, M.P. and Sapotnitskii, S.A., in *Produkty pererabotki drevesiny – sel'skomu khozyaistvu* (Wood Processing Products for Agriculture), Riga: Zinatne, 1973, vol. 2, pp. 147–154.
9. Zakis, G.F., Neiberte, B.Ya., and Sergeeva, V.N., *Khim. Drev.* (Riga), 1973, issue 13, pp. 85–92.
10. Pershina, L.A., Efanov, M.V., Zabelina, A.V., and Klepikov, A.G., *Khim. Rast. Syr'ya*, 2000, no. 4, pp. 65–71.
11. Klimova, V.A., *Osnovnye mikrometody analiza organicheskikh soedinenii* (Principal Methods for Microanalysis of Organic Compounds), Moscow: Khimiya, 1975.
12. Mozheiko, L.N., Sergeeva, V.N., and Yaunzems, V.R., *Khim. Drev.* (Riga), 1969, issue 3, pp. 139–141.
13. Efanov, M.V., Pershina, L.A., Zabelina, A.V., and Klepikov, A.G., Abstracts of Papers, *Mezhdunarodnaya nauchno-tekhnicheskaya konferentsiya "Malootkhodnye tekhnologii pererabotki drevesiny"* (Int. Scientific-Technical Conf. "Low-Waste Procedures of Wood Processing"), Moscow, September 6–7, 2000, p. 54.
14. *Praktikum po agrokhimii* (A Practical Guide on Agrochemistry), Mineev, V.G., Ed., Moscow: Agropromizdat, 1989.

Russian Journal of Applied Chemistry, Vol. 74, No. 10, 2001, pp. 1777–1779. Translated from Zhurnal Prikladnoi Khimii, Vol. 74, No. 10, 2001, pp. 1721–1723.

BRIEF COMMUNICATIONS

Use of Ozone for Preparing 4-Nitrobenzoic Acid in a Closed Process Cycle

A. G. Galstyan, N. F. Tyupalo, E. V. Patapenko, and P. Yu. Andreev

Rubezhnoe Branch, East Ukrainian National University, Rubezhnoe, Lugansk oblast, Ukraine

Received June 7, 2001

Abstract—The possibility of preparing 4-nitrobenzoic acid in a closed process cycle by oxidation of 4-nitrotoluene with an ozone–air mixture was examined. The optimal conditions of oxidation with multiple use of mother liquors were found, and the conditions for crystallization of 4-nitrobenzoic acid from the reaction mixture were determined. The effects of water, acetic anhydride, and catalyst on the oxidation performed in mother liquors after filtration of the target product were examined.

4-Nitrobenzoic acid is widely used in production of organic intermediates, dyes, and drugs [1]. In industry, it is produced by oxidation of 4-nitrotoluene with potassium dichromate in sulfuric acid [2], with dilute nitric acid [3], and with atmospheric oxygen in the presence of catalysts (metals of variable oxidation state and bromine compounds) [4]. Oxidation by mineral oxidants occurs under mild conditions but yields large amounts of toxic and difficult-to-utilize wastes. Oxidation by atmospheric oxygen occurs under rigorous conditions and, therefore, requires sophisticated equipment. In this context, low-temperature reaction of ozone with 4-nitrotoluene in acetic acid shows promise. In the presence of cobalt bromide catalyst, oxidation of 4-nitrotoluene by ozone–air mixture occurs under mild conditions (atmospheric pressure, 95°C), and the yield of 4-nitrobenzoic acid reaches 96% [5].

In this study, we developed a closed process cycle for production of 4-nitrobenzoic acid by oxidation of 4-nitrotoluene.

EXPERIMENTAL

Oxidation of 4-nitrotoluene was performed in a vertical cylindrical reactor equipped with a blade stirrer (7.5–13.3 rps) and a bubbler. The reactor was charged with 40 ml of glacial acetic acid, 4-nitrotoluene (0.5 M), cobalt(II) acetate (0.195 M), and potassium bromide (0.084 M). The stirring was switched on, and the mixture was heated to 95°C. After dissolution of the catalyst, an ozone–air mixture containing 4.7×10^{-4} M ozone was fed at a rate of 8.3×10^{-3} l s^{-1}. Oxidation was performed until complete exhaustion of 4-nitrotoluene and was monitored by GLC [6].

After oxidation, the reaction mixture was cooled to 13–14°C, and the precipitated carboxylic acid was filtered off, washed on the filter with hydrochloric acid, and recrystallized from water; yield 96%. The filtrate was returned to the oxidation stage. The wash

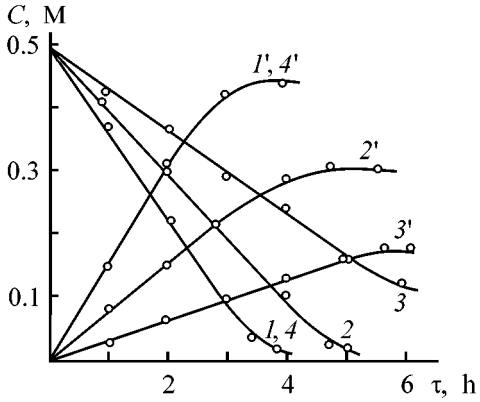

Fig. 1. Oxidation of 4-nitrotoluene by ozone–oxygen mixture in mother liquor. [ArH] = 0.5, $[O_3] = 4.7 \times 10^{-4}$, $[CoAc_2]$ = 0.0195, [KBr] = 0.084 M; T = 95°C; the same for Fig. 2. (C) Water concentration and (τ) time. Concentration of (*1*–*4*) 4-nitrotoluene and (*1'*–*4'*) 4-nitrobenzoic acid. Runs in the cycle: (*1*, *1'*) first; (*2*, *2'*) second with full catalyst loading; (*3*, *3'*) third with full catalyst loading; and (*4*, *4'*) second with addition of 0.495 M $(CH_3CO)_2O$, 0.01 M $CoAc_2$, and 0.063 M KBr.

1070-4272/01/7410-1777 $25.00 © 2001 MAIK "Nauka/Interperiodica"

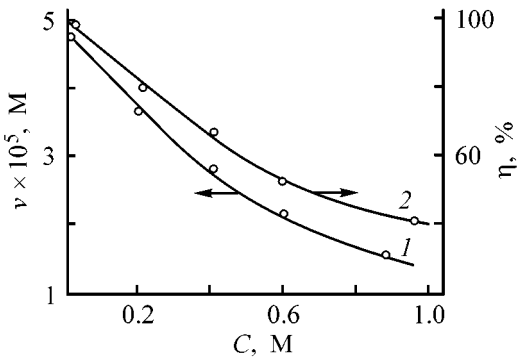

Fig. 2. Effect of water on (*1*) accumulation rate and (*2*) yield of 4-nitrobenzoic acid. (*v*) Accumulation rate, (η) yield, and (*C*) water concentration.

waters containing cobalt(II) chloride were evaporated, and the cobalt(II) salt was used as the reaction catalyst.

To optimize the crystallization conditions, we prepared standard mixtures consisting of 4-nitrobenzoic acid, cobalt(II) acetate, potassium bromide, and acetic acid taken in the same amounts as in the experiment on 4-nitrotoluene oxidation. The reaction solution obtained at 95°C was cooled with slow stirring. We found that the optimal conditions of quantitative isolation of 4-nitrobenzoic acid are cooling from 95 to 35°C at a rate of 1 deg min^{-1} and from 30 to 14°C at a rate of 0.5 deg min^{-1}. With this schedule, 30–60-μm crystals of the acid are formed.

Oxidation of 4-nitrotoluene by an ozone–oxygen mixture in a closed process cycle (95°C)*

Run no.	Degree of ozone utilization, %	4-Nitrobenzoic acid		
		yield, %	mp, °C	content, %
1	90.2	78.0	242.0	99.2
2	89.6	92.9	241.5	99.4
3	89.3	93.0	241.0	99.1
4	91.0	93.1	241.5	99.3
5	90.1	92.9	242.5	99.2
6	89.9	93.1	242.0	99.3
7	89.0	92.9	241.5	99.3
8	89.3	93.0	242.5	99.1
9	90.4	93.2	242.0	99.4
10	90.1	93.1	241.5	99.3

* Charged, M: 4-nitrotoluene 1.01, KBr 0.095 (in run no. 1, 0.126), Co(II) acetate or chloride 0.014 (in run no. 1, 0.023), acetic anhydride 3.7 (in run no. 1, 0); in run no. 1, CH_3COOH (40 ml); in run nos. 2–10, filtrate after filtering off 4-nitrobenzoic acid (36.3 ml) containing cobalt(II) and bromine compounds.

Then we studied the effect of the crystallization time at 14°C. Below are given the crystallization time (min) and acid yields (%): 0, 52; 3, 60; 6, 70; 10, 78; 15, 78; and 20, 78. Thus, it is appropriate to perform crystallization for 10 min.

After keeping for 10 min, 4-nitrobenzoic acid was washed with concentrated HCl to remove the absorbed cobalt(II) acetate. After fivefold use in the washing stage, hydrochloric acid was distilled off, and cobalt chloride was used in the oxidation stage without additional treatment.

When we used the filtrate from crystallization of the target product as the solvent, we noticed a progressing decrease in the accumulation rate and yield of the aromatic acid with increasing number of recycles (Fig. 1). This might be due to partial loss of the catalyst. However, even addition of a full portion of the catalyst in experiments with the filtrate had no noticeable effect on the oxidation results (Fig. 1, second and third runs of the cycle).

The oxidation deceleration may also be due to formation of oxidation inhibitors: phenols, nitrobenzene, and water. The effect of inhibitors on the oxidation was studied after compensating for the partial loss of the catalyst in the previous run. We found that the rate of 4-nitrotoluene oxidation in the presence of phenol and nitrobenzene does not change noticeably, whereas addition of water appreciably decreases the oxidation rate and the process selectivity (Fig. 2). Therefore, under conditions of multiple use of the filtrate, when the content of water formed by the reaction increases from run to run, the oxidation selectivity will decrease.

To bind the water formed by the reaction, we performed experiments with addition of acetic anhydride. We found that at a concentration of acetic anhydride in the primary filtrate of 0.495 M (provided that the catalyst loss is compensated for, see table), the oxidation rate becomes equal to the rate of 4-nitrotoluene oxidation in glacial acetic acid, and the yield of the aromatic acid reaches 93%. Further increase in the concentration of acetic anhydride decreases the oxidation rate and selectivity, because, when the water formed by the reaction is completely bound, excess acetic anhydride starts to react with intermediate 4-nitrobenzaldehyde to form 4-nitrobenzylidene diacetate, which is more resistant to ozone [7].

The amount of the catalyst lost in the cycle was determined in the presence of acetic anhydride (0.495 M). We found that, on adding potassium bromide (0.063 M, 75%) and cobalt diacetate (0.012 M, 61.5%) to the recycling filtrate, the selectivity of 4-ni-

trotoluene oxidation fluctuates about 93%, i.e., the amount of the added components corresponds to the catalyst loss.

To check the possibility of multiple use of mother liquors, we performed seven cycles, with ten runs in each, with addition of the catalyst, to compensate for its loss in the previous run, and acetic anhydride. The yield of 4-nitrobenzoic acid in oxidation of 4-nitrotoluene in the mother liquor was obtained at a level of 93% (see table).

CONCLUSION

It is feasible to prepare 4-nitrobenzoic acid by oxidation of 4-nitrotoluene in a closed process cycle with multiple use of mother liquors.

REFERENCES

1. Gray, T.C. and Geddes, I.C., *J. Pharmacy Pharmacol.*, 1954, vol. 6, no. 2, p. 89.
2. Lisitsyn, V.N., *Khimiya i tekhnologiya promezhutochnykh produktov* (Chemistry and Technology of Intermediates), Moscow: Khimiya, 1987.
3. USSR Inventor's Certificate, no. 421733.
4. JPN Patent 52-91837.
5. Galstyan, G.A., Matsegora, L.A., and Popova, I.A., *Zh. Prikl. Khim.*, 1982, vol. 49, no. 1, pp. 138–142.
6. Galstyan, G.A., Galstyan, T.M., and Sokolova, S.M., *Kinet. Katal.*, 1993, vol. 33, no. 4, pp. 779–787.
7. Potapenko, E.V. and Galstyan, G.A., *Zh. Prikl. Khim.*, 2000, vol. 73, no. 7, pp. 1218–1220.

Russian Journal of Applied Chemistry, Vol. 74, No. 10, 2001, p. 1780. Translated from Zhurnal Prikladnoi Khimii, Vol. 74, No. 10, 2001, p. 1724.

BOOK REVIEWS

Habashi, F., *Extractive Metallurgy Today: Progress and Problems*, Quebec City: Laval University, 2000, 312 pp.

Professor F. Habashi is a known Canadian scientist, a specialist in nonferrous metallurgy, and the author of a great number of books, part of which have been translated in Russia. His new review book makes an attempt to reflect, primarily for the example of Canada, the advance in metallurgy, made from 1960 till 2000, and to formulate the most currently pressing problems. During this period, new research centers concerned with various metallurgical processes appeared, the number of scientific conferences increased, and the dataware was improved. All these factors favored the development of energy-saving technologies, ensured a decrease in pollution, and promoted automation of both the technological processes themselves and methods for their control.

The book is excellently illustrated and contains numerous high-quality photographs and visual schemes. In the given case, this is an important constituent of the book, largely affecting the manner of presentation, since 21% of the entire book's volume is occupied by photographs, mainly colored, and further 14%, by various schemes. The information value of the book is even more increased by reference lists given at the end of each chapter.

The book comprises a brief introduction and 18 small chapters grouped into five parts. The first part, "General" (chapters 1, 2; pp. 3–14), contains most general evidence. In particular, the relationship between the most important sections of metallurgy—hydrometallurgy, pyrometallurgy, electrometallurgy—and their relations to other fields of science are discussed. The most important problems of metallurgy are indicated.

"Progress and Problems" (chapters 3–10; pp. 15–148) is the second, main part. The author considers a wide variety of issues, including processing of lean ores, recovery of metals from ores with complex composition (sulfide, oxide, oxide-sulfide), and manufacture of high-purity metals (modern analytical monitoring methods, electrolytic refining, chemical transport processes, physical methods). The entire material is illustrated by concrete examples. The same part of the book discusses the rise in production and consumption of a great number of metals during a long period from 1860 till 2000, the use of the metallurgical wastes and secondary raw materials, recovery of gaseous products and gas purification, and advances in application of new technologies.

The third part of the book, "Extractive Metallurgy at Laval University" (chapters 11–15; pp. 149–211) is concerned with investigations in metallurgy, performed at Laval University in Quebec (Canada). After a brief description of the history of the University and the Department of Mining and Metallurgy, the book considers the processes and systems studied there. As particular examples are discussed the reaction of chalcopyrite with hydrogen and chlorine and reduction of sulfates of a number of metals with hydrogen.

The fourth part of the book, "Industrial Minerals at Laval University" (chapters 16, 17; pp. 215–271), discusses the processing of phosphate ores containing compounds of rare earths and a number of silicate rocks.

The fifth part, "Literature Guide" (ch. 18; pp. 275–305), contains valuable evidence concerning the organizing and holding of metallurgical conferences of various levels and the relevant publications.

It should be noted once more that the book is excellently published, is written in a well-understandable manner, and contains a vast body of interesting and valuable information about processes of mainly nonferrous metallurgy.

A. G. Morachevskii and I. N. Beloglazov

1070-4272/01/7410-1780 $25.00 © 2001 MAIK "Nauka/Interperiodica"

Russian Journal of Applied Chemistry, Vol. 74, No. 11, 2001, pp. 1781–1785. Translated from Zhurnal Prikladnoi Khimii, Vol. 74, No. 11, 2001, pp. 1729–1733.

INORGANIC SYNTHESIS AND INDUSTRIAL INORGANIC CHEMISTRY

Specific Features of the Composition of Solid Phases in the $Na^+K^+Ca^{2+} \,||\, CO_3^{2-}OH^-–H_2O$ System

V. A. Lipin

Russian Aluminum and Magnesium Institute, St. Petersburg, Russia

Received March 14, 2001

Abstract—The composition of solid phases in the $Na^+K^+Ca^{2+} \,||\, CO_3^{2-}OH^-–H_2O$ system at 95°C was studied. Triple carbonates of alkali metals and calcium, different from the known synthetic and natural compounds, were found in the system.

Complex carbonates of alkali metals and calcium in the $Na^+K^+Ca^{2+} \,||\, CO_3^{2-}OH^-–H_2O$ system can be formed in several processes involving treatment of carbonate solutions or calcium-containing wastes and intermediate products and separation of metals. Compounds of the $M_2CO_3 \cdot CaCO_3 \cdot H_2O$ type (M is an alkali metal) are formed by reactions of calcium-containing materials with solutions of alkali metal carbonates if their concentration exceeds the equilibrium concentration with respect to the corresponding carbonates. This process can be schematically represented by the reaction

$$Ca(OH)_2 + 2M_2CO_3 + nH_2O = CaCO_3 \cdot M_2CO_3 \cdot nH_2O + 2MOH.$$

Gaylussite $M_2CO_3 \cdot CaCO_3 \cdot 5H_2O$ is the solid phase stable in the Na_2CO_3–$CaCO_3$–H_2O system at temperatures lower than 40°C, and at higher temperatures pirssonite $M_2CO_3 \cdot CaCO_3 \cdot 2H_2O$ is stable. Natrofairchildite $Na_2CO_3 \cdot CaCO_3$ and shortite $Na_2CO_3 \cdot 2CaCO_3$ are also known as natural minerals. In the K_2CO_3–$CaCO_3$–H_2O system buetschliite $K_2CO_3 \cdot CaCO_3$ can be obtained, which is converted by heating over 500°C to fairchildite differing from buetschliite by its crystal structure. In the Na_2CO_3–K_2CO_3–H_2O system the so-called "double salt" $Na_2CO_3 \cdot K_2CO_3 \cdot nH_2O$ (n = 0–6) is formed. Its isolation as an intermediate product is used in production of soda products by sintering of alkali aluminosilicate raw materials [1–4].

Relatively recent studies of plutonic and volcanic formations [5–7] revealed the presence in them of triple carbonates of calcium and alkali metals along with the double carbonates. To date at least three mineral kinds of triple carbonates of sodium, potassium, and calcium, named natrocarbonatites, have been found in the nature, namely, nyerereite, gregoryite, and zemkorite. Nyerereite $(Na,K)_2CO_3 \cdot CaCO_3$, close in its structure to natrofairchildite, and gregoryite $(Na_2,K_2,Ca)CO_3$ were first found in essentially sodium carbonate lavas and ashes of Oldoinyo Lengai active volcano [5, 6]. Specific features of this volcano, located not far from Kilimanjaro at the Kenya and Tanzania border, are the low temperature of lava eruption (540–593°C) and also the leading role of alkali and volatile components and complete absence of aluminum and silicon compounds in the eruption products. Zemkorite $(Na,K)_2CO_3 \cdot CaCO_3$, differing from nyerereite by its hexagonal crystal system, was found in Yakut kimberlites at a depth of 400–450 m [5]. Up to now, there is no general opinion on the mechanism of natrocarbonatite formation. Two versions are suggested: plutonic action of carbon dioxide on alkaline massifs of alkaline nature and secondary reactions of the eruption products with atmospheric factors.

The range of conditions for the formation of triple carbonates of alkali metals and calcium seems to be rather wide, which suggests the formation of these compounds during processing of various alkali mineral raw materials as a result of homogeneous and heterogeneous reactions. The elucidation of such a possibility is important for both the technology of separation of alkali metal salts and for the explanation of the mechanism of natrocarbonatite formation in the nature.

The aim of this work was to study the effect of the ratio of alkali metals on the composition of solid phases in the $Na^+K^+Ca^{2+} \,||\, CO_3^{2-}OH^-–H_2O$ system.

1070-4272/01/7411-1781$25.00

Table 1. Solubility in the $Na^+K^+Ca^{2+} \,||\, CO_3^{2-}OH^-–H_2O$ system at 95°C

Run no.	Liquid phase*				Solid phase	
	Na_2O	K_2O	$2OH^-$	Na_2O ($Na_2O + K_2O$), mol %	Na_2O ($Na_2O + K_2O$), mol %	main compounds**
	wt %					
1	–	25.22	1.59	0	0	$CaCO_3 + K_2CO_3 \cdot CaCO_3$
2	–	25.81	2.32	0	0	$K_2CO_3 \cdot CaCO_3 + CaCO_3$
3	–	27.52	2.97	0	0	″
4	–	36.97	2.97	0	0	″
5	0.74	31.31	6.16	3.5	12.3	Phase Y + $Ca(OH)_2$
6	1.15	24.46	2.85	6.7	12.1	Phase Y + $CaCO_3$
7	1.85	32.85	2.77	7.9	4.5	$K_2CO_3 \cdot CaCO_3$ + phase Y + $CaCO_3$
8	1.44	17.32	1.97	8.1	12.6	Phase Y + $CaCO_3$
9	1.54	17.61	2.86	11.8	15.4	$CaCO_3$ + phase Y
10	3.28	28.01	2.95	15.1	14.1	$K_2CO_3 \cdot CaCO_3 + CaCO_3$ + phase Y
11	3.05	25.46	2.95	15.4	37.4	$K_2CO_3 \cdot CaCO_3$ + phases Y and X + $CaCO_3$
12	2.32	18.82	3.31	15.8	12.8	$CaCO_3 + Ca(OH)_2$ + phases Y and X
13	3.52	23.40	2.30	18.6	29.1	$CaCO_3$ + phases X and Y + $K_2CO_3 \cdot CaCO_3$
14	3.72	24.31	2.92	18.9	32.4	Phases Y and X + $K_2CO_3 \cdot CaCO_3 + CaCO_3$
15	3.74	23.01	2.96	19.8	41.9	Phases X and Y + $CaCO_3$
16	5.66	31.45	2.06	21.5	17.7	$K_2CO_3 \cdot CaCO_3$ + phases X and Y
17	4.45	24.66	2.54	21.5	35.8	Phases X and Y + $CaCO_3$
18	4.46	24.33	2.24	21.8	30.2	Phases X and Y + $CaCO_3 + K_2CO_3 \cdot CaCO_3$
19	4.34	22.57	3.08	22.6	40.2	$CaCO_3$ + phases X and Y
20	4.30	22.43	3.69	22.7	45.0	$CaCO_3$ + phase X + $Ca(OH)_2$
21	7.23	34.94	1.97	23.9	41.1	$K_2CO_3 \cdot CaCO_3$ + phase X + $CaCO_3$
22	6.06	5.98	2.63	60.3	62.2	$CaCO_3 + Na_2CO_3 \cdot CaCO_3 \cdot 2H_2O$ + phase X
23	13.53	5.71	1.23	78.3	100	$Na_2CO_3 \cdot CaCO_3 \cdot 2H_2O + CaCO_3$
24	13.58	–	1.25	100	100	″

* CaO is contained in minute amounts in the liquid phase.
** By the data of IR spectral and X-ray analyses.

EXPERIMENTAL

The initial mixtures for setting equilibria in the system under study were prepared from solutions of alkali metal carbonates and calcium oxide. We used pure grade salts of the corresponding alkali metals to prepare carbonate solutions. Calcium oxide was prepared by calcination of calcium carbonate at 1150°C. In most experiments the amount of calcined calcium oxide for preparing the initial mixtures was limited by the $Ca(OH)_2$ solubility in the system under study. We varied the concentration of carbonates and the ratio between sodium and potassium ions in solution. To reach equilibria, the mixtures were vigorously stirred at 95°C for 330 h. The equilibrium solid phases were separated from the liquid by filtration, washed with alcohol, and analyzed by X-ray diffraction and IR spectroscopy. The X-ray patterns were taken on a Philips automatic powder diffractometer using CoK_α radiation and a graphite monochromator. The IR spectra were recorded in KBr pellets on a Perkin–Elmer spectrometer in the wave number range 400–3800 cm^{-1}. The differential thermal analysis (DTA) was carried out on a Q-1500D derivatograph (Hungary) by heating samples to 1000°C at a rate of 7.5 deg min^{-1}. The content of cations in the solid and liquid phases was determined by flame photometry. The content of OH^- ions in the equilibrium liquid phases was determined volumetrically after preliminary isolation of CO_3^{2-} as $BaCO_3$.

The data obtained are given in Tables 1 and 2 and in Fig. 1–3. They show that the presence of sodium carbonate in the liquid phase results in formation of compounds containing sodium ions in the solid phase. They appear at lower K_2CO_3 concentrations than it is necessary for buetschliite formation from solutions free from sodium ions. Furthermore, the presence of Na^+ ions in the solutions affects the ratio of equi-

librium concentrations of K_2CO_3 and buetschliite: buetschliite is formed at lower concentrations from a mixed solution. The formation of sodium-containing compounds from mixed sodium–potassium solutions is preferable compared to buetschliite.

The formation of new sodium-containing phases is proved by the X-ray and IR data.

The IR spectra of solid phases obtained in the reactions of calcium oxide with carbonate solutions (buetschliite, pirssonite, and a double salt) and also of the phase obtained in run no. 14 (Table 1) are shown in Fig. 1. It is seen that the IR spectrum of the solid phase obtained in run no. 14 differs from the spectra of all the double salts known to exist in the $Na^+K^+Ca^{2+}||CO_3^{2-}OH^-–H_2O$ system at temperatures below 100°C. The absence of the stretching bands of OH^- groups suggests that this phase is a mixture of complex carbonates. Apart from the characteristic stretching bands of calcite (880, 1430 cm^{-1}) and buetschliite (865, 1090 cm^{-1}, stretching bands at 670, 710, 870, 1008, 1050, 1075, 1400, 1465, 1760, and 3150 cm^{-1} are observed in the IR spectra of these solid phases. Splitting of the stretching band of the carbonate groups (1400 and 1465 cm^{-1}) and also occurrence of the so-called forbidden bands at 1050 and 1090 cm^{-1} indicate that the CO_3^{2-} group is distorted owing to the formation of a triple salt or of its mixture with another complex.

The X-ray diffraction patterns reveal two triple carbonates X and Y in the solid phase. The X-ray diffraction characteristics of the X and Y carbonates and also of the known natural triple carbonates of alkali metals and calcium are given in Table 2.

If the mole fraction of sodium oxide exceeds 3% of the sum of alkali metal oxides, the Y phase is formed in the solid phase (Table 1, run nos. 5–10). The X phase is in equilibrium with solutions in which the mole fraction of sodium oxide exceeds 15% of the sum of alkali metal oxides (run nos. 11–19). To obtain the X phase free from the Y phase, the fraction of sodium oxide must be greater than 23% (run nos. 20–22). If the mole fraction of sodium oxide exceeds 60%, pirssonite prevails in the solid phase (run nos. 23, 24). Calcite-free X and Y phases were not obtained under the experimental conditions. As the concentration of OH^- ions in the equilibrium liquid phase increases, the solubility of complex carbonates increases in the order X < Y < $K_2CO_3 \cdot CaCO_3$.

The IR spectrum of the solid phase in run no. 14 is indicative of a mixture of the X and Y phases

Table 2. Diffraction patterns of the phases formed in the system

d, Å	I/I_0, rel. units	d, Å	I/I_0, rel. units
Gregoryite $(Na_2,K_2,Ca)CO_3$ [4]		Phase X	
3.29	40	6.4	20
2.66	100	4.40	40
2.61	75	3.20	25
Zemkorite $(Na,K)_2,CaCO_3$ [7]		3.07	100
		2.54	90
6.36	90	2.20	20
4.36	100	2.08	55
4.13	40	1.94	20
3.95	10	1.815	15
3.80	30	1.805	15
3.59	30	Phase Y	
3.26	10	7.9	60
3.04	100	3.98	10
2.98	20	3.55	30
2.92	10	3.48	70
Nyerereite $(Na,K)_2,CaCO_3$ [4, 5]		3.01	60
		2.97	100
6.38	90	2.67	80
4.39	90	2.64	95
3.05	100	2.62	50
2.53		2.415	13
2.07		2.21	75
		2.01	10
		1.985	40
		1.955	5
		1.94	7
		1.84	8
		1.815	9

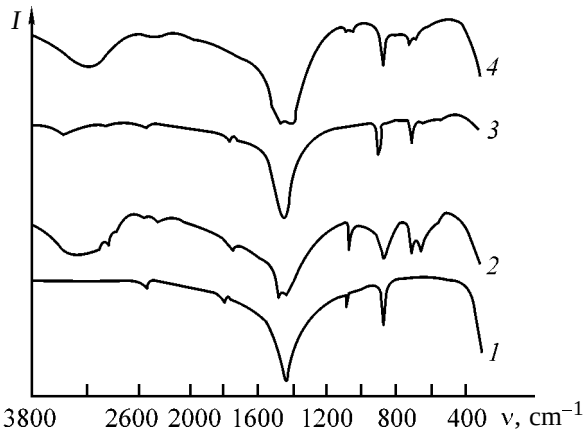

Fig. 1. IR spectra of (*1*–*3*) double carbonates of alkali metals and calcium formed at temperatures lower than 95°C and (*4*) of the phase obtained in the experiment. (*T*) transmission and (ν) wave number; the same for Fig. 2. Phase: (*1*) buetschliite $K_2CO_3 \cdot CaCO_3$, (*2*) pirssonite $Na_2CO_3 \cdot CaCO_3 \cdot 2H_2O$, (*3*) double salt $Na_2CO_3 \cdot K_2CO_3$, (*4*) solid phase from run no. 14.

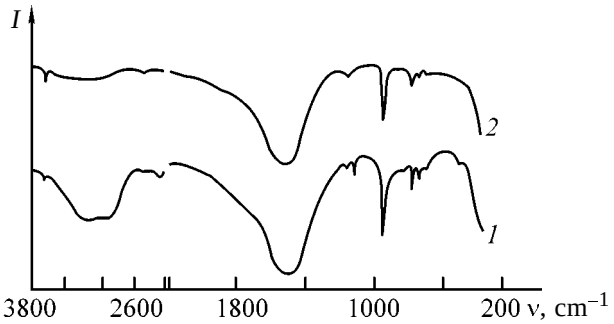

Fig. 2. IR spectra of $CaCO_3$ mixtures with phases Y (*1*) and X (*2*).

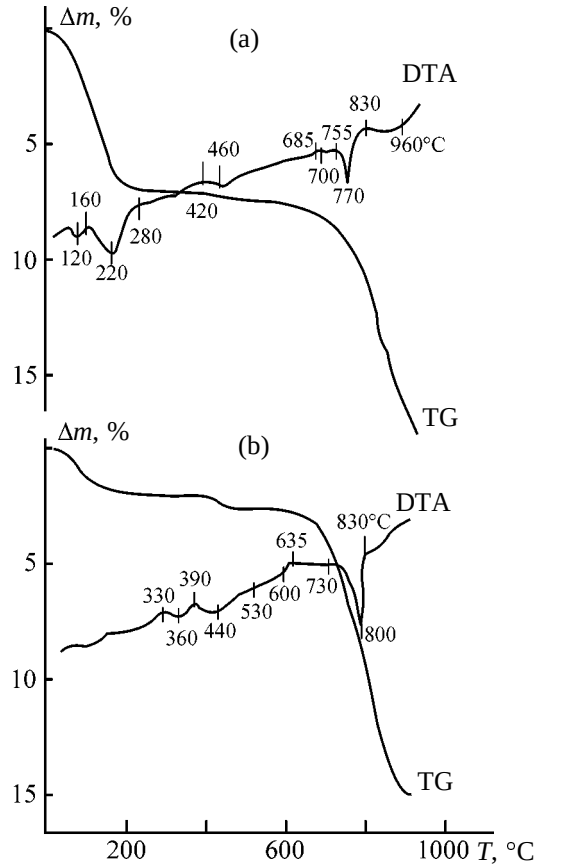

Fig. 3. Thermal characteristics of $CaCO_3$ mixtures with phases (a) Y and (b) X. (*m*) Weight loss and (*T*) temperature.

(Fig. 1). The solid phase in run no. 6 consists of the complex carbonate Y in a mixture with calcite without an impurity of the X phase. Its IR spectrum (Fig. 2) contains characteristic adsorption bands of the Y phase (630, 670, 710, 1080, 1460, 1500, 2950, and 3150 cm^{-1}). The presence of several bands of stretching vibrations of water molecules (2950 and 3150 cm^{-1}) suggests that these molecules enter the Y salt structure. It is most likely that the Y phase is a layered structure in which charged layers of CO_3^{2-} ions are kept together by alkali metal cations. Water molecules in this structure are inserted between the layers to form hydrogen bonds with oxygen atoms of the anion layer, the structure of the carbonate compound being not affected.

The solid phase from run no. 6 consists mainly of the Y phase, and its DTA curve (Fig. 3a) has a deep endothermic peak of dehydration in the range 160–220°C, weak endothermic peaks of a polymorphous transition at 420–460°C, and also peaks of the material melting above 685°C. The solid phase from run no. 20 consists of the complex carbonate X in a mixture with calcite without an impurity of the Y phase. Its IR spectrum (Fig. 2) has absorption bands at 700, 730, 840, 1075, 1450, and 3470 cm^{-1}. The DTA curve of the solid phase from run no. 20, in which the X phase prevails (Fig. 3b), differs from that of the solid phase from run no. 6. It involves a small thermal effect of removal of unbound water at about 160°C, a number of polymorphous transitions in the range from 330 to 730°C, an endothermic effect of the X phase dissociation to $Na_2CO_3 \cdot K_2CO_3$ and $CaCO_3$ in the range from 730 to 830°C, and an effect of the $CaCO_3$ dissociation to CaO and CO_2 above 1000°C. The retention of double sodium potassium carbonate in the product of the X phase calcination at 1000°C, confirmed by the IR spectra, suggests that the structure of this phase is close to the structure of dolomite $CaCO_3 \cdot MgCO_3$, which dissociates to $CaCO_3$, MgO, and CO_2 at 680–800°C.

Therefore, structures of the X and Y phases belong to different types, i.e., the mechanisms of their formation in the carbonate solutions are different. Correlation of the chemical analysis and DTA data suggests that the Y phase has a composition close to $Na_2CO_3 \cdot 7K_2CO_3 \cdot mCaCO_3 \cdot nH_2O$ ($m, n > 1$). The X phase is a triple carbonate of the composition $Na_2CO_3 \cdot K_2CO_3 \cdot pCaCO_3$ ($p > 1$). These phases have no known natural analogs and have been found in the system under study for the first time.

Processing of alkali aluminosilicate by sintering involves operations associated with the reactions of calcium-containing compounds with mixed solutions of alkali metal carbonates. These operations include the regeneration of the belite slime after leaching of the cake and of the white slime after desilication with a solution of Na_2CO_3 and K_2CO_3, and also the causticization of carbonate solutions [1].

Our experiments revealed the presence of a triple carbonate of sodium, potassium, and calcium in the solid phases after treating the white slime of alumina

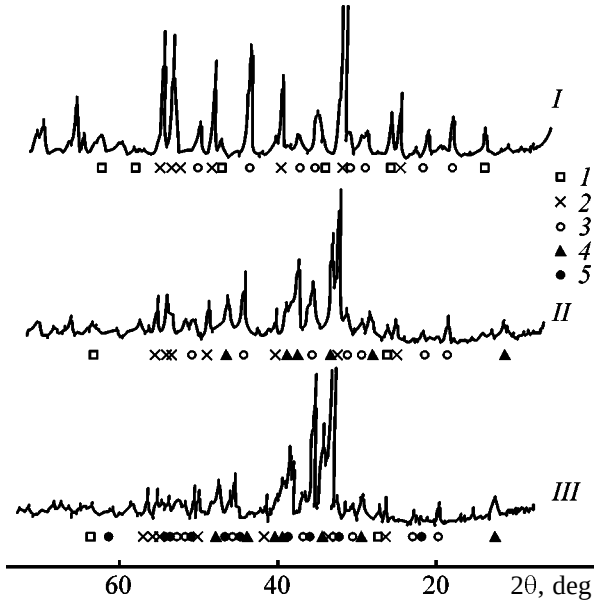

Fig. 4. X-ray patterns of (*I*) starting white slime of alumina production and the slime after treatment with K_2CO_3 solution at (*II*) 25 and (*III*) 90°C. (2θ) Bragg's angle. (*1*) Hydroaluminosilicates of alkali metals $Na_2O \cdot Al_2O_3 \cdot mSiO_2 \cdot nH_2O$ (m = 1.7–2.5, n = 1–3); (*2*) calcite $CaCO_3$; (*3*) calcium hydrogarnets $3CaCO_3 \cdot Al_2O_3 \cdot mSiO_2 \cdot (6–2m)H_2O$ (m = 0.1–0.8); (*4*) Y phase $Na_2CO_3 \cdot 7K_2CO_3 \cdot mCaCO_3 \cdot nH_2O$ (m,n > 1); and (*5*) buetschliite $K_2CO_3 \cdot CaCO_3$.

production with carbonate solutions. The slime of the composition (wt %) Na_2O 2.70, K_2O 1.20, CaO 40.66, Al_2O_3 12.49, and SiO_2 6.69 was treated with a carbonate solution containing (g dm^{-3}) Na_2O 19.6 and K_2O 570. The treatment was carried out for 2 h with stirring at 25–90°C. After separating the phases the solid phase was washed with ethanol and analyzed by X-ray diffraction.

The X-ray patterns of the starting and resulting solid phases (Fig. 4) point to the presence of the Y phase in the resulting products along with calcite, calcium hydrogarnets, and alkali metal hydroaluminosilicates. When the treatment temperature was increased from 25 to 90°C, buetschliite was also observed in the solid phase.

CONCLUSION

(1) Previously unknown triple carbonates of sodium, potassium, and calcium were found in the $Na^+K^+Ca^{2+} \,||\, CO_3^{2-}OH^- – H_2O$ system, and their main properties were described. The Y phase has a composition close to $Na_2CO_3 \cdot 7K_2CO_3 \cdot mCaCO_3 \cdot nH_2O$ (m,n > 1), and the X phase is the triple carbonate $Na_2CO_3 \cdot K_2CO_3 \cdot pCaCO_3$ (p > 1).

(2) The structure of the revealed compounds is different, which was confirmed by the IR spectral, X-ray phase, and thermal analyses.

(3) The possible formation of triple carbonates of sodium, potassium, and calcium in the intermediate products of processing mineral resources can significantly affect the distribution of alkali metal ions between the products. Therefore, the need in special process operations arises.

REFERENCES

1. Abramov, V.Ya., Alekseev, A.I., and Badal'yants, Kh.A., *Kompleksnaya pererabotka nefelino-apatitovogo syr'ya* (Complex Processing of Nepheline–Apatite Resources), Moscow: Metallurgiya, 1990.
2. *Spravochnik eksperimental'nykh dannykh po rastvorimosti mnogokomponentnykh vodno-solevykh sistem* (Handbook of Experimental Data on the Solubility in Multicomponent Water–Salt Systems), Pel'sh, A.D., Ed., Moscow: Khimiya, 1973–1975.
3. Fleisher, M., *Glossary of Mineral Species*, Tucson: The Mineralogical Record, 1987.
4. Robert, W.L., Campbell, T.J., and Rapp, G.R., *Encyclopedia of Minerals*, New York: Van Norstrand Reinhold, 1990, 2nd ed.
5. Kostov, I., *Mineralogy*, Edinburgh: Oliver and Boid, 1968.
6. *Carbonatite Volcanism: Oldoinyo Lengai and the Petrogenesis of Natrocarbonatites*, Bell, K. and Keller, J., Eds., Berlin: Springer, 1995.
7. Egorov, K.N., Ushchapovskaya, Z.F., Kashaev, A.A., *et al.*, *Dokl. Akad. Nauk SSSR*, 1988, vol. 301, no. 1, pp. 188–191.

Russian Journal of Applied Chemistry, Vol. 74, No. 11, 2001, pp. 1786–1788. Translated from Zhurnal Prikladnoi Khimii, Vol. 74, No. 11, 2001, pp. 1734–1736.

INORGANIC SYNTHESIS AND INDUSTRIAL INORGANIC CHEMISTRY

Composition of Solid Phases Isolated from Sulfuric Acid Solutions of Titanium(IV) by the Action of Phosphoric Acid

L. G. Gerasimova, M. V. Maslova, N. M. Zhdanova, and R. F. Okhrimenko

Tananaev Institute of Chemistry and Technology of Rare Elements and Mineral Raw Materials, Kola Scientific Center, Russian Academy of Sciences, Apatity, Murmansk oblast, Russia

Received January 30, 2001

Abstract—The composition of titanium phosphates precipitated in the course of the hydrothermal sulfuric acid decomposition of sphene concentrate in the presence of phosphoric acid was studied.

Titanium phosphate compounds, or, more exactly, titanium(IV) hydrophosphates, are known as effective inorganic ion exchangers (sorbents) removing from wastewater the ions of cobalt, nickel, cadmium, and radioactive elements [1, 2]. Production of such sorbents from solutions of titanium intermediate products and the influence of solution acidity [3, 4], temperature [5], and conditions of washing and heat treatment of hydrated synthesis products [3] on their properties were actively studied in Russia.

Titanium(IV) phosphates are also used as fillers of paper and rubber and in compositions of weatherproof paint-and-varnish materials [6–8]. In this case the requirements to titanium phosphate products are different from those for the sorbents. In particular, they should have pigmentary properties, and also high weather resistance [9].

The aim of this work was to synthesize such compounds and to study their composition and properties.

EXPERIMENTAL

Titanium(IV) solutions obtained upon the sulfuric acid decomposition of sphene $CaSiTiO_5$ were used as titanium intermediate products. Such solutions contain ($g\ l^{-1}$) TiO_2 80–120, H_2SO_4 400–500, and also impurities of iron, silicon, and calcium compounds. The filtrate obtained from the apatite decomposition with sulfuric acid (P_2O_5 content 30%) was used as a phosphorus-containing component.

Experimental technique consists in the following. Phosphoric acid was added into titanium(IV) sulfuric acid solution in the ratio $TiO_2 : P_2O_5 = 1 : (1–10)$. The process was carried out with stirring under hydrothermal conditions (~100°C) for 1.5–2 h, and the resulting suspension was kept without stirring for 10 h. Then the precipitate was separated from the liquid phase and washed with water at the solid : liquid ratio of 1 : 10. The precipitation conditions and precipitate compositions are given in Table 1.

The degree of titanium(IV) precipitation from solutions increases with increasing consumption of phosphoric acid; the filtration rate of the resulting suspension also increases, which is indicative of the formation of agglomerates with the surface low-active toward the liquid phase.

The freshly precipitated substances are X-ray amorphous. Their thermal treatment (~750°C) yields products consisting mainly of a single phase $(TiO)_2 \cdot P_2O_7$. The endothermic effects at 170–350°C are due to dehydration and to the loss of adsorbed water and water of crystallization. The exothermic effect at 730–750°C is not accompanied by a change in weight and is due to crystallization of the amorphous substance (Fig. 1).

We have studied in more detail the production of titanium phosphate precipitates from titanium(IV) sulfuric acid solutions, when phosphoric acid was taken not in excess but in the amount corresponding to the weight ratio $TiO_2 : P_2O_5 = 1 : 0.5$. The acid was added not before heating the initial titanium(IV) solution, but after boiling it for 2, 7, and 14 h. The initial sulfuric acid solution of titanium(IV) contained 110 $g\ l^{-1}$ of TiO_2 and 500 $g\ l^{-1}$ of H_2SO_4. Such "titanic" system is very stable, and without external actions (dilution with water and addition of seeds) the titanic phase is not formed, though the speciation of the dissolved titanium(IV) changes. Thus, whereas in

1070-4272/01/7411-1786$25.00

Table 1. Composition of titanium phosphate precipitates

$TiO_2 : P_2O_5$	Degree of titanium(IV) precipitation from solution, % TiO_2	Rate of suspension filtration, g m^{-2} h^{-1}	Calcination loss, %	Content in calcined product, %		Composition of air-dry titanium phosphate precipitates
				TiO_2	P_2O_5	
1 : 0.5	80.3	75	40.0	60.5	36.4	$3TiO_2 \cdot P_2O_5 \cdot 7H_2O$
1 : 1	95.0	100	31.6	52.2	42.4	$2TiO_2 \cdot P_2O_5 \cdot 8H_2O$
1 : 3	98.8	300	27.1	50.5	45.1	$2TiO_2 \cdot P_2O_5 \cdot 6H_2O$
1 : 5	99.0	400	26.2	51.8	46.5	$2TiO_2 \cdot P_2O_5 \cdot 5.5H_2O$
1 : 10	99.3	550	23.0	51.6	46.1	$2TiO_2 \cdot P_2O_5 \cdot 4H_2O$

the initial solution almost all titanium(IV) was in the reactive state, during heating the complexes form polymeric chains –Ti–O–, with the content of polymeric titanium(IV) increasing as the heating time increases. Such species seem to be a matrix for the formation of a solid phase under the action of external factors. In this case the system stability is disturbed owing to the addition of phosphoric acid to the solution. On the one hand, this addition gives rise to a decrease in acidity, and on the other hand, the presence of phosphate ions initiates the formation of an almost insoluble compound (titanium phosphate phase). It should be noted that the same amount of phosphoric acid added to the boiling suspension in different time after the start of boiling causes unequal decrease in the titanium(IV) concentration in solution. The longer the time of preliminary heating of the initial solution, the smaller the residual titanium(IV) content in the solution. This seems to be due to the fact that the mechanisms of the formation of titanium phosphate phases are different; therefore, the compositions of the resulting precipitates are also different. As fresh precipitates are X-ray amorphous, we determined their phase compositions after heat treatment at 750°C. The X-ray patterns of the precipitates under study are shown in Fig. 3. The most poorly crystallized is sample no. 3, in which the main phase is anatase and the impurity phase is oxotitanium diphosphate. The amount of anatase decreases, and sample nos. 1 and 2 consist mainly of titanium phosphate phases of the formulas $Ti_4P_6O_{23}$ and $(TiO)_2P_2O_7$. According to the chemical analysis of freshly precipitated samples, titanium phosphates precipitated under the above conditions correspond to the empirical formula (3–3.5)$TiO_2 \cdot P_2O_5 \cdot xH_2O$ (x = 1–5). The degree of hydration of the precipitates increases with increasing time of heat treatment of titanium(IV) sulfuric acid solutions before adding phosphoric acid.

We obtained white readily disaggregated products by thermal treatment of the precipitates under study

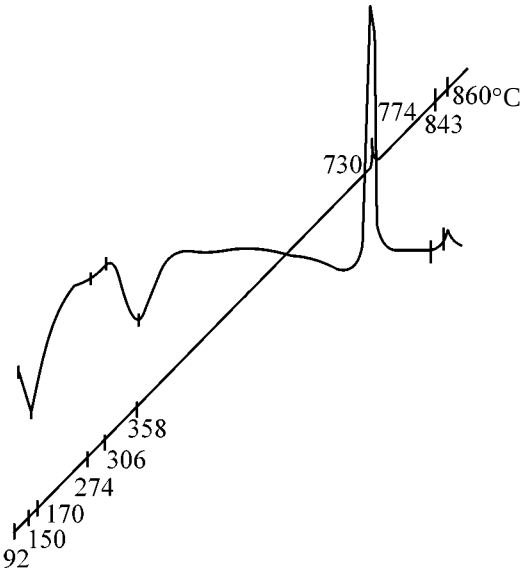

Fig. 1. Thermogram of a titanium phosphate precipitate isolated at the molar ratio $TiO_2 : P_2O_5$ = 1 : 5.

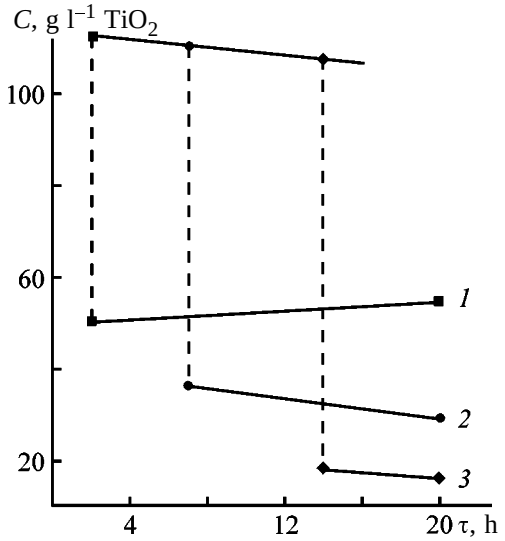

Fig. 2. Titanium(IV) content in a solution C as a function of the boiling time τ. H_3PO_4 was added to titanium(IV) sulfuric acid solution after boiling for (*1*) 2, (*2*) 7, and (*3*) 14 h; the same for Fig. 3.

Table 2. Pigmentary properties of titanium phosphate products

Sample no.	Refractive index	Whiteness, arb. units	Oil number, g/100 g of powder	Covering power, g m^{-2}	Contents of water-soluble salts, %
1*	2.50	96.0	30.0	42.5	1.0
2	2.08	96.5	42.8	69.3	0.8
3	2.12	96.4	41.4	60.4	0.7
4	2.42	96.0	39.4	51.3	0.75

* Pure titanium dioxide (anatase), A-1 grade pigment, GOST (State Standard) 9808–84.

(700–750°C) and determined their pigmentary properties (Table 2).

The results obtained were used to develop a process for the synthesis of a lightfast titanium phosphate pigmentary composition from sphene concentrate [10].

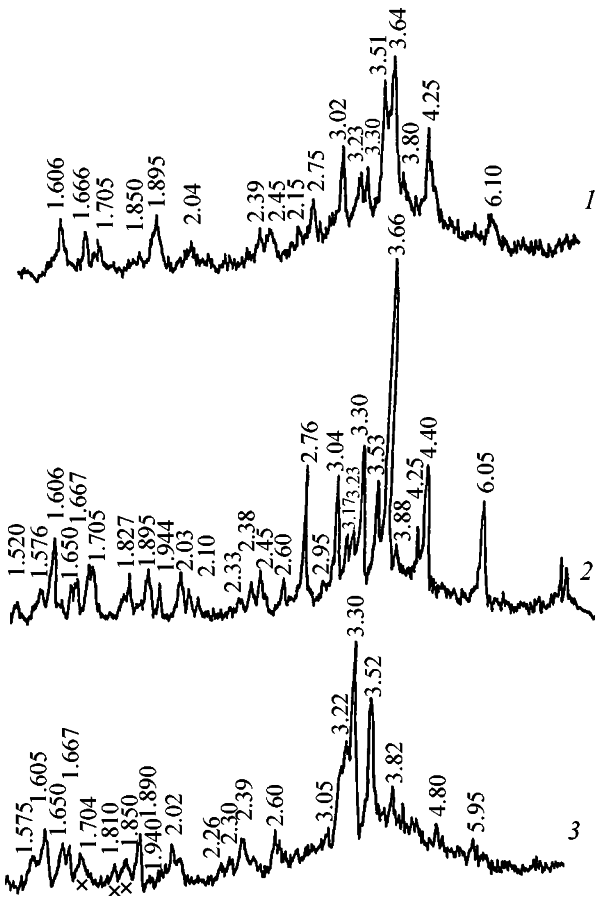

Fig. 3. X-ray diffraction patterns of titanium phosphate precipitates.

CONCLUSION

The titanium phosphate products synthesized have fairly good pigmentary quality and can be used for pigmenting filling of white paper, plastic, and rubbers. Taking into account high lightfastness of titanium phosphate, we can predict prolonged whiteness of materials filled with it.

REFERENCES

1. Yaroslavtsev, A.B., *Usp. Khim.*, 1998, vol. 66, no. 7, pp. 641–659.
2. Bortun, A.I., Malinovskii, G.A., Khainakov, S.A., *et al.*, *Ukr. Khim. Zh.*, 1990, vol. 56, no. 1, pp. 7–10.
3. Dolmatov, Yu.D. and Bulavina, Z.N., *Zh. Prikl. Khim.*, 1974, vol. 47, no. 7, pp. 1498–1503.
4. Tananaev, I.V., Rozanov, I.A., Avduevskaya, K.A., *et al.*, *Fosfaty chetyrekhvalentnykh elemetov* (Phosphates of Tetravalent Elements), Moscow: Nauka, 1972.
5. Spitsin, I.V. and Ippolitova, E.A., *Zh. Anal. Khim.*, 1951, vol. 4, no. 1, pp. 5–14.
6. Savostenko, E.S. and Titov, V.P., Abstracts of Papers, *Konferentsiya "Neorganicheskie pigmenty i napolniteli"* (Conf. "Inorganic Pigments and Fillers"), Cherkassy, 1984, p. 80.
7. Parkevich, I.P., Murashkevich, A.I., Kashuba, I.V., *et al.*, Abstracts of Papers, *Konferentsiya "Neorganicheskie pigmenty i napolniteli"* (Conf. "Inorganic Pigments and Fillers"), Cherkassy, 1984, pp. 76–77.
8. Titov, V.P., Starkova, L.M., and Kul'bitskaya, L.V., Abstracts of Papers, *Konferentsiya "Neorganicheskie pigmenty i napolniteli"* (Conf. "Inorganic Pigments and Fillers"), Cherkassy, 1984, pp. 78–79.
9. USSR Inventor's Certificate no. 1353788.
10. RF Patent 2150479.

Russian Journal of Applied Chemistry, Vol. 74, No. 11, 2001, pp. 1789–1792. Translated from Zhurnal Prikladnoi Khimii, Vol. 74, No. 11, 2001, pp. 1737–1740.

INORGANIC SYNTHESIS AND INDUSTRIAL INORGANIC CHEMISTRY

Phase Formation in the Synthesis of Special Clinkers from Industrial Waste Products

O. A. Miryuk and I. G. Luginina

Rudnyi Industrial Institute, Rudnyi, Kazakhstan
Belgorod State Technological Academy of Building Materials, Belgorod, Russia

Received March 13, 2001

Abstract—Phase formation on the calcination of sulfated clinkers with the use of ironstone concentration rejects and the effect of the raw mixture composition on the formation of magnesium calcium aluminosilicate were studied.

Cements based on sulfated clinkers are effective sort of special binders characterized by a power-saving production process, intense setting, expansiveness, and high construction parameters. Because of the shortage of natural raw materials, substandard rocks and industrial wastes characterized by diverse chemical and mineral compositions find growing use. The performance of a new raw material is determined by its effect on processes of the clinker formation and structure.

In this work we studied the sequence of phase formation in the synthesis of sulfated clinkers from industrial waste products, namely, from a mixture of limestone, lignite-bauxite, and ironstone concentration rejects. Substandard lignite-bauxite, which is enriched with carbonized wood residues, contains (%) Al_2O_3 31–50, SiO_2 10–17, and Fe_2O_3 2–5. Ironstone concentration rejects contain silicates and aluminosilicates of various structures (diopside, grossularite, epidote, scapolite, chlorites, and feldspars). Their dominating chemical components are (%) SiO_2 40–42, Al_2O_3 10–12, Fe_2O_3 15–17, CaO 12–13, and MgO 5–7. The presence of pyrite FeS_2 in the rejects predetermines a possibility for their use as a sulfur-containing component of a charge. The charge composition was taken to ensure the following composition of the clinker (%): SiO_2 16, Al_2O_3 20, Fe_2O_3 6, CaO 50, MgO 4, and SO_4 4.

Samples of the raw mixture were burnt at 800–1300°C and studied by X-ray diffraction. Examination of the diffraction patterns allowed us to suggest the following pattern of the phase formation in the mixture under study (Fig. 1). Burning at 800°C transforms all the raw components. The active character of the low-temperature transformations results from the catalytic effect of the products of pyrite and lignite oxidation formed at 450–600°C. The pyrite decomposition yields anhydrite $CaSO_4$. The acceleration of the reactions yielding aluminum-containing compounds is promoted by a high dispersity of aluminum-containing minerals of lignite-bauxite and a rather low temperature of their decomposition. The oxide Al_2O_3 arising from the dehydration of hydrargillite $Al(OH)_3$ reacts with $CaSO_4$ and CaO even at 700–800°C [1]. The first portions of belite Ca_2SiO_4 formed from the silicates of the rejects react with $CaSO_4$ to give cal-

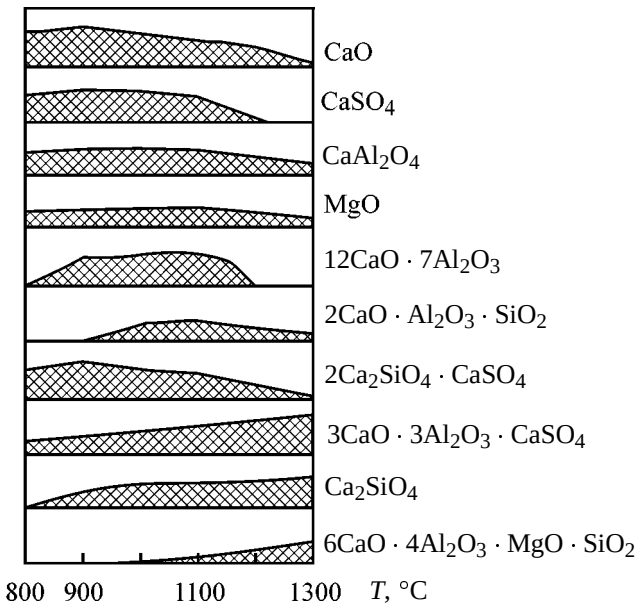

Fig. 1. Variation of the contents of phases during burning a sulfated mixture (by the intensity of diffraction reflections). (*T*) Temperature; the same for Fig. 4.

1070-4272/01/7411-1789$25.00

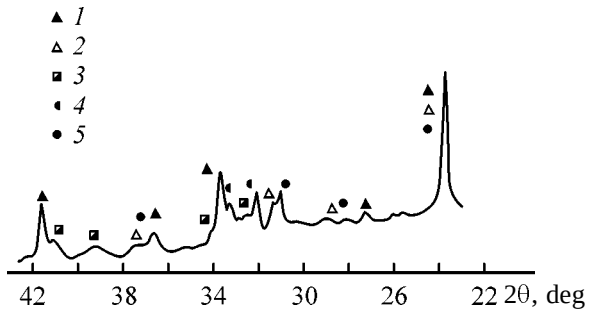

Fig. 2. Diffraction pattern of sulfated clinker. (θ) Bragg's angle; the same for Fig. 3. Phase: (*1*) $3CaO \cdot 3Al_2O_3 \cdot CaSO_4$, (*2*) $2CaO \cdot Al_2O_3 \cdot SiO_2$, (*3*) Ca_2SiO_4, (*4*) $4CaO \cdot Al_2O_3 \cdot Fe_2O_3$, and (*5*) $6CaO \cdot 4Al_2O_3 \cdot MgO \cdot SiO_2$.

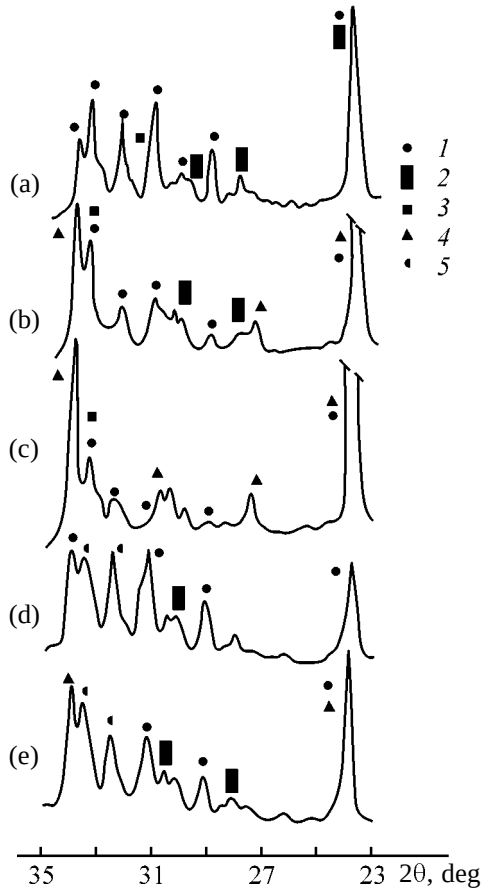

Fig. 3. Diffraction pattern of clinkers from alumina mixtures: (a) without additions and with additions of (b) 5% $CaSO_4$, (c) 10% $CaSO_4$, (d) 10% Fe_2O_3, (e) 5% $CaSO_4$, and (f) 10% Fe_2O_3. Phase: (*1*) $6CaO \cdot 4Al_2O_3 \cdot MgO \cdot SiO_2$, (*2*) $CaO \cdot Al_2O_3$, (*3*) $12CaO \cdot 7Al_2O_3$, (*4*) $3CaO \cdot 3Al_2O_3 \cdot CaSO_4$, and (*5*) $4CaO \cdot Al_2O_3 \cdot Fe_2O_3$.

cium sulfate silicate $2Ca_2SiO_4 \cdot CaSO_4$. This phase starts to decompose shortly after heating above 900°C to give the phases Ca_2SiO_4 and $CaSO_4$. The released $CaSO_4$ takes part in the formation of the main clinker phase calcium aluminate sulfate $3CaAl_2O_4 \cdot CaSO_4$.

Helenite $2CaO \cdot Al_2O_3 \cdot SiO_2$ is formed in the mixture under study from SiO_2, Al_2O_3, CaO, Ca_2SiO_4, and also from grossularite $3CaO \cdot Al_2O_3 \cdot 3SiO_2$, which is untroduced with ironstone concentration rejects according to the scheme

$$3CaO \cdot Al_2O_3 \cdot 3SiO_2 + 3CaO \rightarrow 2Ca_2SiO_4 + 2CaO \cdot Al_2O_3 \cdot SiO_2. \quad (1)$$

In the presence of $CaSO_4$ helenite is unstable [1]; its content decreases at temperatures higher than 1100°C. A smooth decrease in the amount of $2CaO \cdot Al_2O_3 \cdot SiO_2$ and its retention in the clinker are due to the restricted contents of CaO and $CaSO_4$ and the preferable reaction of $CaSO_4$ with $CaO \cdot Al_2O_3$ and $12CaO \cdot 7Al_2O_3$. The iron-containing part of the mixture forms calcium aluminate ferrites $4CaO \cdot Al_2O_3 \cdot Fe_2O_3$ in the clinker (Fig. 2).

The feature of the burnt mixture is the presence of magnesium calcium aluminosilicate $6CaO \cdot 4Al_2O_3 \cdot MgO \cdot SiO_2$, which is also known as magnesia pleochroite or phase Q [2]. Its appearance is preceded by various reactions [3] including (2) and (3).

$$2CaO \cdot Al_2O_3 \cdot SiO_2 + CaO \rightarrow Ca_2SiO_4 + CaO \cdot Al_2O_3, \quad (2)$$

$$4CaO \cdot Al_2O_3 + Ca_2SiO_4 + MgO \rightarrow 6CaO \cdot 4Al_2O_3 \cdot MgO \cdot SiO_2. \quad (3)$$

Magnesium oxide is formed in the burnt mixture by the decomposition of dolomite, which is introduced with chalkstone, and of magnesium silicates in ironstone concentration rejects.

Some authors [1, 2] consider the presence of $6CaO \cdot 4Al_2O_3 \cdot MgO \cdot SiO_2$ in cements as undesirable, referring to weak hydraulic properties of this phase. However, the data [3–5] on the formation and hydration of $6CaO \cdot 4Al_2O_3 \cdot MgO \cdot SiO_2$ point to its pronounced binding activity and high strength parameters of cements based on it. Therefore, it seems appropriate to convert inert helenite to a phase capable of active hydration [reactions (2) and (3)]. Furthermore, the origination of $6CaO \cdot 4Al_2O_3 \cdot MgO \cdot SiO_2$ is accompanied by a decrease in the fraction of free MgO, the content of which in cements is strictly regulated.

Sulfated clinkers are diverse in qualitative and quantitative composition [1]. It is necessary to elucidate whether the aluminate phase $6CaO \cdot 4Al_2O_3 \cdot MgO \cdot SiO_2$ can be formed in sulfate aluminate clinkers of various compositions. Such determinations in a multicomponent system are rather difficult. For

Composition of alumina mixtures and clinkers

Mixture composition, %				Calculated contents of oxides in clinker, %				
calcite	technical alumina	chlorite	diopside	SiO_2	Al_2O_3	Fe_2O_3	CaO	MgO
56	35	9	–	3.5	47.9	1.1	42.3	4.2
53	35	–	12	8.7	44.7	0.5	40.4	4.1

such a study we chose a mixture of dolomitized chalkstone and lignite-bauxite in amounts corresponding to formation of the aluminate clinker containing $6CaO \cdot 4Al_2O_3 \cdot MgO \cdot SiO_2$. Also we added $CaSO_4$ and Fe_2O_3, which are present in sulfated clinkers. The mixtures were burnt at 1200–1300°C to complete assimilation of calcium oxide. According to the diffraction patterns, the clinker made from the mixture without additions mainly contained $6CaO \cdot 4Al_2O_3 \cdot MgO \cdot SiO_2$, $12CaO \cdot 7Al_2O_3$, and $CaO \cdot Al_2O_3$ (Fig. 3). Stepwise addition of $CaSO_4$ results in a proportional reduction of the $6CaO \cdot 4Al_2O_3 \cdot MgO \cdot SiO_2$ content at the expense of the $3CaO \cdot 3Al_2O_3 \cdot CaSO_4$ formation. An addition of 10% Fe_2O_3 reduces the $6CaO \cdot 4Al_2O_3 \cdot MgO \cdot SiO_2$ content in the clinker and causes formation of calcium aluminate ferrites. This conclusion agrees with data of [3, 6].

When 5% of $CaSO_4$ and 10% of Fe_2O_3 are added into the mixture, the intensity of the diffraction peaks of $6CaO \cdot 4Al_2O_3 \cdot MgO \cdot SiO_2$ is higher than that for a clinker with the addition of only 5% of $CaSO_4$. It suggests that the presence of Fe_2O_3 in an aluminate sulfate clinker creates preferential conditions for the formation of $6CaO \cdot 4Al_2O_3 \cdot MgO \cdot SiO_2$, as compared to $3CaO \cdot 3Al_2O_3 \cdot CaSO_4$. Apparently, a decrease in the temperature of the appearance of a liquid phase in the iron-containing mixture accelerates the formation of $6CaO \cdot 4Al_2O_3 \cdot MgO \cdot SiO_2$.

The presence of MgO in the initial mixture favors the formation of $6CaO \cdot 4Al_2O_3 \cdot MgO \cdot SiO_2$. In industrial waste products magnesium silicates often serve as a source of MgO. Of magnesium-containing minerals, diopside $CaMg[Si_2O_6]$ and chlorite $Mg_5Al \cdot [AlSi_3O_{10}](OH)_8$ are present in ironstone concentration rejects. The formation of $6CaO \cdot 4Al_2O_3 \cdot MgO \cdot SiO_2$ with the participation of natural magnesium silicates deserves attention. It is rather difficult to monitor transformations in a polymineral mixture. Therefore, to obtain clinkers with equal content of magnesium and with calcium aluminates present, we prepared alumina mixtures with various mineral compositions (see table).

The X-ray diffraction analysis reveals the effect of magnesium minerals on the phase composition of burnt mixtures (Fig. 4). The thermal transformations in a chlorite-containing mixture start with the chlorite decomposition. The dissociation of the mineral is multistage [7]: the removal of chemically bound water at 550–800°C and the decomposition of the chlorite structure followed by the formation of forsterite Mg_2SiO_4 from amorphous decomposition products (MgO and SiO_2) at 820–840°C. The reaction of forsterite with calcite yields diopside $CaO \cdot MgO \cdot 2SiO_2$ and MgO [8]. The enhanced activity of the resulting $CaO \cdot MgO \cdot 2SiO_2$ provides its saturation with calcium oxide up to the formation of mervinite $3CaO \cdot MgO \cdot 2SiO_2$ (Fig. 4). The release of free CaO in decarbonation of calcite promotes formation of low-basic calcium aluminates. At higher calcination temperatures the number and content of aluminate phases

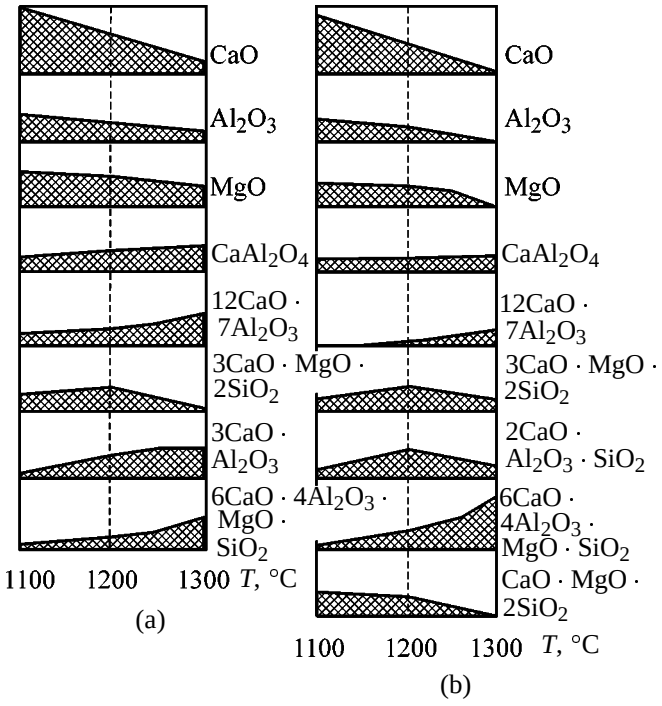

Fig. 4. Variation in the content of phases during calcination of mixtures: (a) chlorite-containing and (b) diopside-containing (by the intensity of diffraction reflections).

increase. The compound $6CaO \cdot 4Al_2O_3 \cdot MgO \cdot SiO_2$ is formed by the reaction

$$3CaO \cdot MgO \cdot 2SiO_2 + 4CaO \cdot Al_2O_3 + CaO \rightarrow 6CaO \cdot 4Al_2O_3 \cdot MgO \cdot SiO_2 + Ca_2SiO_4. \quad (4)$$

This reaction is followed by reaction (3). An increased basicity of the chlorite-containing mixture is responsible for the formation of calcium-rich aluminate $3CO \cdot Al_2O_3$ and the retention of free CaO in the clinker.

The mineral $CaO \cdot MgO \cdot 2SiO_2$ in a diopside-containing mixture is gradually saturated with CaO up to the formation of $3CaO \cdot MgO \cdot 2SiO_2$ (Fig. 4). The other transformations in many respects are similar to those described above. However, an increased fraction of silica in the diopside-containing mixture predetermines the appearance of $2CaO \cdot Al_2O_3 \cdot SiO_2$ and the formation of a greater, compared to a chlorite-containing mixture, amount of $6CaO \cdot 4Al_2O_3 \cdot MgO \cdot SiO_2$ completely binding MgO. The lack of free CaO is responsible for the stability of $2CaO \cdot Al_2O_3 \cdot SiO_2$ and $3CaO \cdot MgO \cdot 2SiO_2$ in the clinker.

Therefore, the presence of magnesium silicates in a raw material provides the formation of $6CaO \cdot 4Al_2O_3 \cdot MgO \cdot SiO_2$ in aluminate clinkers. The natural minerals diopside and chlorite supply non-carbonate CaO and the additional amount of Al_2O_3. As a result, the raw materials that are in a short supply are saved, and the power consumption for the clinker formation is decreased.

The data obtained suggest that the appearance of the phase $6CaO \cdot 4Al_2O_3 \cdot MgO \cdot SiO_2$ and its amount in clinkers depend on the chemical composition of the initial mixture. The appearance of $6CaO \cdot 4Al_2O_3 \cdot MgO \cdot SiO_2$ noticeably changes the ratio of phases in the clinker. However, the majority of known techniques for the calculation of the composition of charges do not take into account the presence of MgO in raw materials and the possibility of formation of $6CaO \cdot 4Al_2O_3 \cdot MgO \cdot SiO_2$. The calculation equations should be corrected to take into account complex compositions of clinkers and the variety of raw materials.

CONCLUSIONS

(1) The use of industrial waste products complicates the phase composition of sulfated clinkers at the expense of the formation of $6CaO \cdot 4Al_2O_3 \cdot MgO \cdot SiO_2$.

(2) The compound $4CaO \cdot 6Al_2O_3 \cdot MgO \cdot SiO_2$ can form in sulfated clinkers when the conditions for the formation of $3CaO \cdot 3Al_2O_3 \cdot CaSO_4$ are limited. The formation of $6CaO \cdot 4Al_2O_3 \cdot MgO \cdot SiO_2$ is preceded by transformations involving aluminosilicates and calcium and magnesium silicates.

(3) Appropriate choice of the chemical composition of the charge with the aim to obtain $6CaO \cdot 4Al_2O_3 \cdot MgO \cdot SiO_2$ will make it possible to convert undesirable $2CaO \cdot Al_2O_3 \cdot SiO_2$ and MgO phases to a hydraulically active compound.

REFERENCES

1. Kuznetsova, T.V., *Alyuminatnye i sul'foalyuminatnye tsementy* (Aluminate and Sulfoaluminate Cements), Moscow: Stroiizdat, 1986.
2. Berezhnoi, A.S., *Mnogokomponentnye shchelochnye oksidnye sistemy* (Multicomponent Alkaline Oxide Systems), Kiev: Naukova Dumka, 1988.
3. Luginina, I.G. and Miryuk, O.A., *Izv. Akad. Nauk SSSR, Neorg. Mater.*, 1991, vol. 27, no. 2, pp. 351–353.
4. Vasil'chenko, Yu.V. and Luginina, I.G., in *Energosberegayushchaya tekhnologiya stroitel'nykh materialov* (Power-Saving Technology of Building Materials), Belgorod: Belgorod. Tekhnol. Inst. Stroitel'nykh Materialov, 1988, pp. 8–12.
5. Luginina, I.G., Miryuk, O.A., and Akhmetov, I.S., Abstracts of Papers, *I Mezhdunarodnoe soveshchanie po khimii i tekhnologii tsementa* (I Int. Conf. on the Chemistry and Technology of Cement), Moscow, 1996, pp. 206–207.
6. Miryuk, O.A., *Zh. Prikl. Khim.*, 1993, vol. 66, no. 4, pp. 921–925.
7. Ivanova, V.P., Kasatov, B.K., Krasavina, T.N., and Rozanova, E.L., *Termicheskii analiz mineralov i gornykh porod* (Thermal Analysis of Minerals and Rocks), Leningrad: Nedra, 1974.
8. Vishnevskaya, I.I., Trusova, N.F., and Filatova, L.I., *Petrografiya tsentral'nogo Kazakhstana* (Petrography of Central Kazakhstan), Moscow: Nedra, 1967.

Russian Journal of Applied Chemistry, Vol. 74, No. 11, 2001, pp. 1793–1796. Translated from Zhurnal Prikladnoi Khimii, Vol. 74, No. 11, 2001, pp. 1741–1744.

PHYSICOCHEMICAL STUDIES OF SYSTEMS AND PROCESSES

Thermodynamic Analysis of Component Interaction in Liquid Alloys of the Potassium–Indium System

A. G. Morachevskii and M. A. Bykova

St. Petersburg State Technical University, St. Petersburg, Russia

Received July 10, 2001

Abstract— The thermodynamic properties of K–In liquid alloys were compared and discussed. The alternating positive and negative deviations from the ideal behavior were observed in the system.

Markedly different data are presented in the literature on the phase diagram of the potassium–indium system [1]. According to Thummel and Klemm [2], potassium and indium form the congruently melting compound K_5In_8 (mp 745 K) and incongruently melting compound KIn_4, with the peritectic horizontal lying at 698 K. In the composition range 50–90 mol % potassium the liquidus line is nearly horizontal, i.e., a tendency to separation is probable. According to Yatsenko *et al*. [3], the system has the phase separation region, and the compound K_5In_8 melts congruently at 753 K and has a very narrow homogeneity region. The composition KIn_3 was reported in that work for the incongruently melting compound. The presence of the homogeneity region in the system was confirmed by differential thermal [4] and magnetochemical [5] analyses and by electrical resistance measurements [6]. However, data on the upper critical temperature differ essentially. Bushmanov [4] reported 731 K, whereas Melekhov [5], 818 K. In Yatsenko's monograph [7], the immiscibility region is presented according to [5]. According to the later data [8, 9], the incongruently melting compound has the composition $K_{22}In_{39}$ (K_7In_{13}?), its melting point is 751 ± 6 K, and the upper critical temperature of separation does not exceed this value.

Thermodynamic properties of liquid K–In alloys were studied for the first time by the emf method using potassium glass (3.8 wt % K_2O) as solid cation-conducting electrolyte ($0.016 \le x_K \le 0.815$, 15 compositions, 720–810 K) [10]. It was found that the activity isotherm of potassium at 750 K has alternating deviations from the ideal behavior, and the corresponding curve for indium is located in the region of negative deviations from Raoult's law (Fig. 1). The integral molar excess Gibbs energy ΔG^{ex} is negative over the entire composition range (Fig. 2), with the curve extremum lying in the region of formation of intermetallic compounds.

More recently, Dergacheva *et al*. [11–14] studied, also by the emf method, the thermodynamic properties

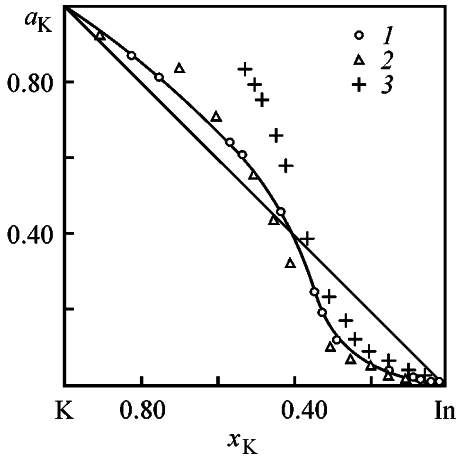

Fig. 1. Potassium activity a_K in K–In liquid alloys. (x_K) Potassium mole fraction; the same for Figs. 2–4. Reference, *T* (K): (*1*) [10], 750; (*2*) [11], 753; and (*3*) [15], 773; the same for Fig. 2.

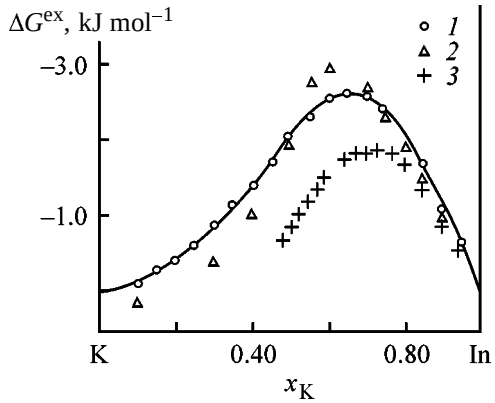

Fig. 2. Integral molar excess Gibbs energy ΔG^{ex} vs. composition in the K–In system.

1070-4272/01/7411-1793$25.00

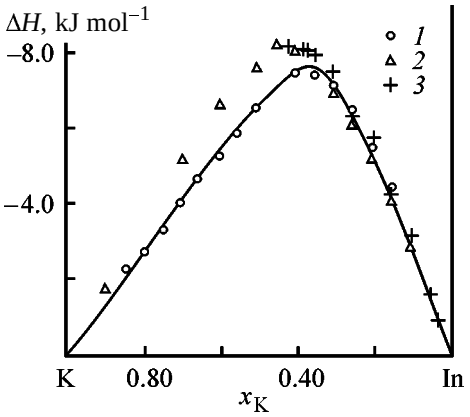

Fig. 3. Integral molar enthalpy of mixing ΔH vs. composition in the K–In system. Reference, T (K): (*1*) [16], 773; (*2*) [11], 753; and (*3*) [15], 773.

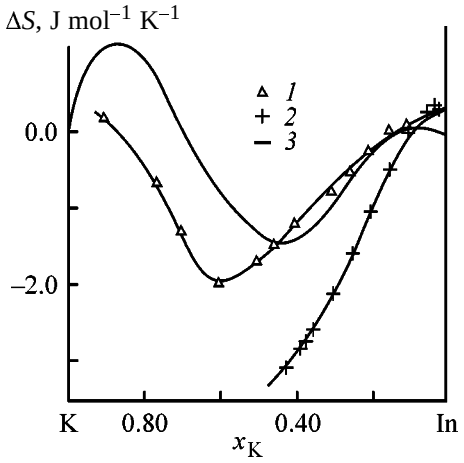

Fig. 4. Integral molar entropy of mixing ΔS vs. composition in the K–In system. Reference, T (K): (*1*) [11], 753; (*2*) [15], 773; and (*3*) the recommended values.

of the K–In liquid alloys ($0.10 \le x_K \le 0.90$, 11 compositions, 733–833 K). As seen from Fig. 1, the activity isotherms of potassium obtained in these studies reasonably agree with the data of [10]. The curves of the integral molar Gibbs energy are also close (Fig. 2). In these studies, the separation region at 750 K was not observed.

Takenaka *et al.* [15] used potassium β-alumina as solid electrolyte and the K–Bi alloy ($x_K = 0.08$) as reference in emf measurements. The alloy potential relative to pure potassium was known and was monitored at regular intervals in the course of the tests. The alloy composition was determined coulometrically with a potassium–lead liquid alloy ($x_K = 0.02$) as potassium source. The majority of tests were started with pure indium, and potassium was added in the course of the test. This made it possible to study the potassium-poor region of compositions (41 compositions, $0.030 \le x_K \le 0.520$, from the liquidus line to 823 K).

Takenaka *et al.* [15] noted that at very low potassium contents in the alloy ($x_K \le 0.001$) and at $x_K \ge 0.35$ the equilibrium is attained difficultly. As seen from Figs. 1 and 2, there are discrepancis between the data of [15] and the results of the previous studies. It is notable that the discrepancis are essential specifically at $x_K \ge 0.35$, i.e., in the composition range in which the equilibrium is attained difficultly.

The liquidus line of the K–In system ($x_K \le 0.42$), determined from the breaks in the $E = f(T)$ curves for the compositions studied [15], lies at somewhat higher temperatures than it was reported in [3, 6].

In [4, 16], a Calvet calorimeter was used to determine the enthalpy of mixing of liquid K–In alloys. The obtained values are in a reasonably good agreement with those calculated from the emf measurements [14, 15] (Fig. 3). At the same time, essentially different data were reported in [14, 15] on the integral molar entropies of mixing (Fig. 4).

Despite existing discrepancis, all the data on the thermodynamic properties of the K–In liquid alloys show that interaction between components is fairly strong. Even if a phase separation region does exist in the system, the upper critical temperature lies below 750 K.

The peak of the excess stability in the K–In system is close to $x_K = 0.35$ (55 kJ mol^{-1}) [15]. At the same time, the excess stability in the K–Pb and K–Bi systems at equiatomic compositions is 250 and 350 kJ mol^{-1}, respectively, [1], with the peak of the excess stability in the K–Bi system being even larger at the composition of the compound K_3Bi. The excess heat capacity was calculated from the emf measurements in [15], but the results are given without necessary clearness and are difficult to discuss.

Data on the electrical resistivity of liquid K–In alloys are available for the entire range of compositions at temperatures exceeding by 100 K the liquidus temperature of the system [6]. The resistivity reaches a maximum (480 ± 10 μΩ cm) at equimolar composition (723 K), with the temperature coefficient $d\rho/dT$ being minimal (–1.25 μΩ cm K^{-1}). The resistivity of liquid K–In alloys is considerably higher than that of the alloys with lithium or sodium, with the resistivity peak in the series Li–In, Na–In, and K–In shifting from the alkali-metal-rich region to the equimolar composition. In this case, the peak in the $\rho = f(x_K)$ curve should be ascribed to the corresponding groups

Thermodynamic properties of the potassium–indium liquid alloys at 750 K

x_K	a_K	γ_K	a_{In}	γ_{In}	ΔG	ΔG^{ex}	ΔH	ΔS, J mol^{-1} K^{-1}
					kJ mol^{-1}			
0.05	0.007	0.145	0.953	1.003	–1.82	–0.59	–1.7	0.17
0.10	0.016	0.160	0.895	0.994	–3.20	–1.17	–3.1	0.13
0.15	0.029	0.193	0.823	0.968	–4.35	–1.71	–4.4	–0.07
0.20	0.049	0.245	0.736	0.920	–5.29	–2.17	–5.4	–0.15
0.25	0.081	0.325	0.636	0.848	–6.03	–2.53	–6.3	–0.36
0.30	0.131	0.435	0.531	0.759	–6.57	–2.76	–7.1	–0.70
0.35	0.250	0.713	0.390	0.600	–6.85	–2.81	–7.7	–1.14
0.40	0.400	1.000	0.295	0.491	–6.84	–2.66	–7.9	–1.42
0.45	0.493	1.095	0.252	0.459	–6.71	–2.41	–7.8	–1.46
0.50	0.570	1.139	0.222	0.443	–6.46	–2.13	–7.4	–1.26
0.55	0.636	1.157	0.196	0.435	–6.13	–1.84	–6.8	–0.90
0.60	0.691	1.151	0.175	0.438	–5.73	–1.53	–6.2	–0.63
0.65	0.736	1.133	0.158	0.450	–5.28	–1.24	–5.5	–0.30
0.70	0.777	1.110	0.141	0.469	–4.77	–0.96	–4.6	0.22
0.75	0.814	1.085	0.125	0.499	–4.21	–0.70	–3.7	0.68
0.80	0.846	1.058	0.109	0.543	–3.60	–0.48	–2.8	1.07
0.85	0.881	1.037	0.090	0.598	–2.93	–0.29	–2.0	1.24
0.90	0.915	1.017	0.069	0.686	–2.17	–0.14	–1.3	1.16
0.95	0.954	1.004	0.040	0.797	–1.28	–0.05	–0.6	0.91

in potassium–indium liquid alloys. Their presence indirectly confirms the validity of the ideal associated solution model [17] for the given system.

The recommended values of the thermodynamic functions, obtained from treatment of the results of all studies on the liquid K–In alloys [10–16], are given in the table. In the potassium-rich part of the system our dependence of the entropy of mixing on the composition (Fig. 4) appreciably differs from the data of [11–14], but is similar to the analogous dependence for the Na–In system [1, 18]. Such a curve of the integral entropy of mixing is typical of systems with a fairly strong interaction between the components [19]. This result is confirmed by the thermodynamic characteristics [14, 20] of the solid phases formed in the K–In system: K_5In_8 (x_K = 0.385) and KIn_3 (x_K = 0.25). The saturated vapor pressure over K–In alloys in the solid state was measured by the molecular beam method. For the phase region K_5In_8 + KIn_3 the vapor pressure was measured in the temperature range 441–544 K, and for the phase region KIn_3 + In, in the 473–660 K range. For the phase region K + K_5In_8 the measured quantity is similar to the saturated vapor pressure of pure potassium. The integral thermodynamic characteristics of formation of the compounds from the pure liquid components at 540 K were estimated from the data obtained:

Compound	ΔG, kJ mol^{-1}	ΔH, kJ mol^{-1}	ΔS, J mol^{-1} K^{-1}
1/4 KIn_3	–(9.37 ± 0.55)	–(15.02 ± 1.76)	–(10.5 ± 2.9)
1/13 K_5In_8	–(11.18 ± 1.42)	–(18.41 ± 1.63)	–(13.4 ± 2.9)

Assuming that the difference between the heat capacities of the compounds and initial components ΔC_d is negligible, we calculated the standard thermodynamic characteristics of formation of the compounds from the solid components. For 1/4 KIn_3 ΔH^0_{298} = –(12.01 ± 2.76) kJ mol^{-1} and ΔS^0_{298} = –(2.85 ± 4.00) J mol^{-1} K^{-1}; for 1/13 K_5In_8 ΔH^0_{298} = –(15.48 ± 2.64) kJ mol^{-1} and ΔS^0_{298} = –(6.2 ± 4.2) J mol^{-1} K^{-1}. The difference between the ΔH values at 540 and 298 K is caused solely by the changed aggregation state of the pure initial components (potassium and indium).

As noted above, more recent studies of the K–In system revealed the compounds of somewhat different composition: $K_{22}In_{39}$ (x_K = 0.361) or K_7In_{13} (x_K = 0.350), and KIn_4 (x_K = 0.20). The correction of calculations taking into account the new boundaries of the phase regions does not alter significantly the integral thermodynamic characteristics, especially for the

congruently melting phase. It should be noted that the compounds are formed with considerable exothermic effects, and the entropies of their formation are negative. However, according to [15], in formation of potassium–indium liquid alloys from pure components, the change in the heat capacity ΔC_d is observed, reaching 12–14 J mol^{-1} in the composition range $0.35 \le x_K \le 0.42$ [15]. This suggests a deviation from the Neumann–Kopp rule for the solid phases, which affects the estimate of the standard parameters at 298 K.

Probably, the values obtained from calorimetric measurements in [21] for the enthalpy of formation of the potassium–indium compounds under the standard conditions are underestimated: $\Delta H^0_{298} = -(7.32 \pm 0.59)$ kJ mol^{-1} for 1/4 KIn_3 and $\Delta H^0_{298} = -(9.14 \pm 0.71)$ kJ mol^{-1} for 1/13 K_5In_8. In Yatsenko's monograph [7] the results of this study are given with no comments. The enthalpy of melting of 1/13 K_5In_8, determined calorimetrically, is 7.87 ± 0.54 kJ mol^{-1}. Presently available data on the thermodynamic properties of solid phases in the K–In system are insufficient for their optimization.

REFERENCES

1. Morachevskii, A.G., Beloglazov, I.N., and Kysymbekov, B.A., *Kalii: Svoistva, proizvodstvo, primenenie* (Potassium: Properties, Manufacture, and Application), Moscow: Ruda i Metally, 2000.
2. Thümmel, R., and Klemm, W., *Z. Anorg. Allg. Chem.*, 1970, vol. 376, no. 1, pp. 44–63.
3. Yatsenko, S.P., Chuntonov, K.A., Bushmanov, V.D., and Dieva, E.N., in *Struktura faz, fazovye prevrashcheniya i diagrammy sostoyaniya metallicheskikh sistem* (Phase Structure, Phase Transitions, and Phase Diagrams of Metal Systems), Moscow: Nauka, 1974, pp. 188–201.
4. Bushmanov, V.D., Interaction of Alkali Metals and Group III Elements, *Cand. Sci. Dissertation*, Sverdlovsk, 1980.
5. Melekhov, L.Z., Magnetic Properties and Interaction between Components in Alkali Metal Alloys with Indium, Tin, and Antimony, *Cand. Sci. Dissertation*, Sverdlovsk, 1983.
6. Meijer, J.A., Geerstma, W., and Lugt, W. van der, *J. Phys. F: Met. Phys.*, 1985, vol. 15, pp. 899–910.
7. Yatsenko, S.P., *Indii: Svoistva i primenenie* (Indium: Properties and Application), Moscow: Nauka, 1987.
8. *Diagrammy sostoyaniya dvoinykh metallicheskikh sistem: Spravochnik* (Phase Diagrams of Binary Metal Systems: Handbook), Lyakishev, N.P., Ed., Moscow: Mashinostroenie, 1999, vol. 3, book 1.
9. Pelton, A.D., and Larose, S., *Bull. Alloy Phase Diagr.*, 1990, vol. 11, no. 3, pp. 232–236.
10. Bykova, M.A., and Morachevskii, A.G., *Izv. Vyssh. Uchebn. Zaved., Tsvetn. Metall.*, 1973, no. 1, pp. 91–94.
11. Dergacheva, M.B., Kozin, L.F., and Khobdabergenova, G.R., *Izv. Akad. Nauk Kaz. SSR, Ser. Khim.*, 1978, no. 5, pp. 21–26.
12. Dergacheva, M.B., Kozin, L.F., and Khobdabergenova, G.R., in *Termodinamicheskie svoistva metallicheskikh rasplavov* (Thermodynamic Properties of Metal Melts), Alma-Ata: Nauka Kaz. SSR, 1979, part 2, pp. 30–35.
13. Kozin, L.F., Dergacheva, M.B., and Khobdabergenova, G.R., *Tr. Inst. Org. Katal. Elektrokhim. Akad. Nauk Kaz. SSR*, 1981, vol. 25, pp. 36–91.
14. Khobdabergenova, G.R., Thermodynamic Properties of Liquid Alloys Based on Alkali Metals, Indium, Thallium, and Mercury, *Cand. Sci. Dissertation*, Alma-Ata, 1984.
15. Takenaka, T., Petric, A., and Saboungi, M.-L., *J. Phys.: Condens. Matter*, 1991, vol. 3, pp. 1603–1612.
16. Bushmanov, V.D. and Yatsenko, S.P., *Zh. Fiz. Khim.*, 1981, vol. 55, no. 11, pp. 2951–2952.
17. Morachevskii, A.G., Mokrievich, A.G., and Maiorova, E.A., *Zh. Prikl. Khim.*, 1993, vol. 66, no. 7, pp. 1441–1447.
18. Morachevskii, A.G. and Bykova, M.A., *Zh. Prikl. Khim.*, 1999, vol. 72, no. 9, pp. 1549–1551.
19. Morachevskii, A.G. and Maiorova, E.A., *Tr. Leningr. Politekh. Inst.*, 1976, no. 348, pp. 3–12.
20. Dergacheva, M.B., Khobdabergenova, G.R., and Kozin, L.F., *Zh. Fiz. Khim.*, 1978, vol. 52, no. 11, pp. 2945–2946.
21. Yatsenko, S.P., Chuntonov, K.A., and Bushmanov, V.D., *Extended Abstracts of Papers, VI Vsesoyuznaya konferentsiya po kalorimetrii* (VI All-Union Conf. on Calorimetry), Tbilisi: Metsniereba, 1973, pp. 90–93.

Russian Journal of Applied Chemistry, Vol. 74, No. 11, 2001, pp. 1797–1800. Translated from Zhurnal Prikladnoi Khimii, Vol. 74, No. 11, 2001, pp. 1745–1748.

PHYSICOCHEMICAL STUDIES OF SYSTEMS AND PROCESSES

Interaction of Hafnium Chlorides with Magnesium, Aluminum, and Lead in Molten Alkali Metal Chlorides

N. A. Loginov and V. A. Oleinikova

Institute of High-Temperature Electrochemistry, Ural Division, Russian Academy of Sciences, Yekaterinburg, Russia

Received July 30, 2001

Abstract—The thermodynamic characteristics of the interaction of hafnium(II) and hafnium(IV) chlorides with magnesium, aluminum, and lead in molten alkali metal chlorides were calculated.

In electrolytic preparation and refining of hafnium, dilute solutions of its chlorides in molten alkali metal chlorides and their mixtures attract a great attention. In this context, it was interesting to examine the possibility of interaction of $HfCl_2$- and $HfCl_4$-containing solutions with magnesium, aluminum, and lead at temperatures above their melting points (T_m 650, 660.2, and 327.4°C, respectively) and to calculate the apparent equilibrium constants of some reactions in the 3LiCl–2KCl, NaCl–KCl, KCl, and CsCl melts in the range 950–1250 K.

In a chloride melt, metallic hafnium is in equilibrium with its double- and quadruple-charged ions [1–3]. Relatively volatile (T_{sub} = 315°C) hafnium tetrachloride is the intermediate product of preparation of metal itself and its compounds. Hafnium in an electrolyte is present in the form of complex ions ($HfCl_4^{2-}$, $HfCl_5^{3-}$, $HfCl_6^{2-}$, $HfCl_5^{-}$, etc.), differing in the configuration, energy of the Hf(II)–Cl^- and Hf(IV)–Cl^- bonds, and characteristic vibration frequencies.

The goal of the calculations was to show that, along with electrochemical recovery of metal from the electrolyte, magnesium-assisted thermal reduction of its chlorides can also occur, by analogy with production of metallic titanium. For this purpose, we used the data of [1–6] on the temperature dependences of the apparent standard electrode potentials and on the formal redox potentials for those concentration intervals in which the activity coefficient f^* is constant to within probable errors of the emf measurements (Table 1).

The equilibrium potentials of hafnium were determined by taking the isotherms and subsequently treating the results by a rather complex coulometric procedure [1–3], in which, however, direct analytical determination of the concentration is not necessary.

The calculation formulas and the obtained temperature dependences of the apparent equilibrium constants

Table 1. Equations for the temperature dependence of $E^*_{M^{n+}/M}$ and $E^*_{M^{n+}/M^{m+}}$ ($n > m$) in molten alkali metal chlorides vs. chlorine reference electrode

Salt system	$E^*_{M^{n+}/M}$ and $E^*_{M^{n+}/M^{m+}}$, V	References
	E^*Hf(II)/Hf	[1–3]
3LiCl–2KCl	$-2.60 + 7.0 \times 10^{-4}T \pm 0.01$	
NaCl–KCl	$-2.65 + 7.0 \times 10^{-4}T \pm 0.01$	
KCl	$-2.77 + 7.9 \times 10^{-4}T \pm 0.01$	
CsCl	$-2.84 + 8.0 \times 10^{-4}T \pm 0.01$	
	E^*Hf(IV)/Hf	[1–3]
3LiCl–2KCl	$-2.72 + 7.5 \times 10^{-4}T \pm 0.01$	
NaCl–KCl	$-2.80 + 7.8 \times 10^{-4}T \pm 0.02$	
KCl	$-2.90 + 8.1 \times 10^{-4}T \pm 0.02$	
CsCl	$-2.99 + 8.3 \times 10^{-4}T \pm 0.02$	
	E^*Hf(IV)/Hf(II)	[1–3]
3LiCl–2KCl	$-2.84 + 8.0 \times 10^{-4}T \pm 0.02$	
NaCl–KCl	$-2.94 + 8.5 \times 10^{-4}T \pm 0.02$	
KCl	$-3.04 + 8.3 \times 10^{-4}T \pm 0.02$	
CsCl	$-3.16 + 8.8 \times 10^{-4}T \pm 0.02$	
	E^*Mg(II)/Mg	[4]
3LiCl–2KCl	$-3.16 + 5.05 \times 10^{-4}T$	
NaCl–KCl	$-3.26 + 5.63 \times 10^{-4}T$	
KCl	$-3.32 + 5.7 \times 10^{-4}T$	
CsCl	$-3.412 + 6.07 \times 10^{-4}T$	
	E^*Al(III)/Al	[5]
NaCl	$-2.81 + 9.1 \times 10^{-4}T$	
KCl	$-2.92 + 9.1 \times 10^{-4}T$	
	E^*Pb(II)/Pb	[6]
NaCl–KCl	$-1.792 + 5.62 \times 10^{-4}T$	

1070-4272/01/7411-1797$25.00

Table 2. Equations for the temperature dependence of the apparent equilibrium constants $\log K_n^*$ for reactions (1)–(8) in molten alkali metal chlorides

Reaction	Salt medium; T, K	$\log K_n^*$
$HfCl_2(melt) + Mg(liq) = Hf(sol) + MgCl_2(melt)$ (1) $\log K_1^* = (2 \times 10^4/1.984T)(E^*Hf^{2+}/Hf - E^*Mg^{2+}/Mg)$	3LiCl–2KCl; 960–1120 NaCl–KCl; 1000–1200 KCl; 1100–1250 CsCl; 1000–1200	1.966 + 5645/T 1.381 + 6149/T 2.218 + 5544/T 1.946 + 5766/T
$HfCl_4(melt) + 2Mg(liq) = Hf(sol) + 2MgCl_2(melt)$ (2) $\log K_2^* = (4 \times 10^4/1.984T)(E^*Hf^{4+}/Hf - E^*Mg^{2+}/Mg)$	3LiCl–2KCl; 960–1120 NaCl–KCl; 1000–1200 KCl; 1100–1250 CsCl; 1000–1200	4.940 + 8871/T 4.375 + 9274/T 4.839 + 8468/T 4.496 + 8508/T
$HfCl_4(melt) + Mg(liq) = HfCl_2(melt) + MgCl_2(melt)$ (3) $\log K_3^* = (2 \times 10^4/1.984T)(E^*Hf^{4+}/Hf^{2+} - E^*Mg^{2+}/Mg)$	3LiCl–2KCl; 960–1120 NaCl–KCl; 1000–1200 KCl; 1100–1250 CsCl; 1000–1200	2.974 + 3226/T 2.893 + 3226/T 2.621 + 2823/T 2.752 + 2540/T
$3HfCl_2(melt) + 2Al(liq) = 3Hf(sol) + 2AlCl_3(melt)$ (4) $\log K_4^* = (6 \times 10^4/1.984T)(E^*Hf^{2+}/Hf - E^*Al^{3+}/Al)$	NaCl; 1100–1250 KCl; 1100–1250	–7.561 + 7863/T –3.629 + 4536/T
$3HfCl_4(melt) + 4Al(liq) = 3Hf(sol) + 4AlCl_3(melt)$ (5) $\log K_5^* = (12 \times 10^4/1.984T)(E^*Hf^{4+}/Hf - E^*Al^{3+}/Al)$	NaCl; 1100–1250 KCl; 1100–1250	–10.887 + 8468/T –6.048 + 1210/T
$HfCl_2(melt) + Pb(liq) = Hf(sol) + PbCl_2(melt)$ (6) $\log K_6^* = (2 \times 10^4/1.984T)(E^*Hf^{2+}/Hf - E^*Pb^{2+}/Pb)$	NaCl–KCl; 1000–1200	1.391 – 8649/T
$HfCl_4(melt) + 2Pb(liq) = Hf(sol) + 2PbCl_2(melt)$ (7) $\log K_7^* = (4 \times 10^4/1.984T)(E^*Hf^{4+}/Hf - E^*Pb^{2+}/Pb)$	NaCl–KCl; 1000–1200	4.395 – 20 323/T
$HfCl_2(melt) + PbCl_2(melt) = HfCl_4(melt) + Pb(liq)$ (8) $\log K_8^* = (2 \times 10^4/1.984T)(E^*Pb^{2+}/Pb - E^*Hf^{4+}/Hf^{2+})$	NaCl–KCl; 1000–1200	–2.903 + 11 573/T

of reactions (1)–(8) are given in Table 2. The most practically significant reactions are (1)–(3). The K_n^* values and the change in the Gibbs energy for these reactions as functions of temperature are presented in Table 3 ($\Delta G_r^* = -4.576 \times 4.184T \log K_n^*$, J mol^{-1}). The calculation error is 10–12%. Hafnium tetrachloride interacts with magnesium more actively than hafnium dichloride.

With growing temperature K_n^* somewhat decreases in each salt system. At a fixed temperature (1100 K), the apparent equilibrium constant, e.g., K_2^*, also decreases in the series (3LiCl–2KCl)–(NaCl–KCl)–KCl–CsCl [1.01×10^{13}, 6.40×10^{13}, 3.44×10^{12}, and 1.7×10^{12}, respectively (Table 3)].

According to the autocomplexation model of the structure of alkali metal chlorides, in chloride solutions the bond U of the alkali metal cation M with chloride anion Cl^- (M^+–Cl^-) decreases in going from a salt system with a smaller cation to a system with a larger cation. Introduction into the melt of complexing component, the quadruple-charged hafnium ion in our case, should increase the difference between the energies of the Hf^{4+}–Cl^- and M^+–Cl^- bonds. When such a replacement of the outer cationic surrounding takes place, a large number of M^+–Cl^- bonds will transform into stronger Hf^{4+}–Cl^- bonds. The latter bonds will become stronger in melts with alkali metal ions of larger radius. An example is the redox potential of the system Hf^{4+}/Hf^{2+}, given for different temperatures and different molten salts in Table 1. With the cationic radius of the electrolyte increasing at the constant temperature, the potential acquires the more negative values. This is due to a more pronounced increase in the stability of Hf^{4+} complexes compared to Hf^{2+} complexes. Thus, reduction of Hf(IV) to Hf(II) becomes more difficult in the series LiCl–CsCl. The same phenomenon (Table 3) was also observed for reaction (3). At 1100 K the apparent equilibrium constant K_3^* decreases from 8.07×10^5

Table 3. Reactions (1) and (2) in salt melts and reaction (3) in molten alkali metal chlorides

T, K	K_1^*	$-\Delta G_r^*$, kJ mol^{-1}	K_2^*	$-\Delta G_r^*$, kJ mol^{-1}	K_3^*	$-\Delta G_r^*$, kJ mol^{-1}
	reaction (1)		reaction (2)		reaction (3)	
			Eutectic mixture 3LiCl–2KCl			
960	7.02×10^7	144.2	1.52×10^{14}	260.6	2.16×10^6	116.4
1000	4.08×10^7	145.7	6.47×10^{13}	264.4	1.58×10^6	118.7
1050	2.20×10^7	147.6	2.45×10^{13}	269.15	1.11×10^6	121.6
1100	1.25×10^7	149.5	1.01×10^{13}	273.9	8.07×10^5	124.4
1120	1.01×10^7	150.2	7.25×10^{12}	275.8	7.15×10^5	125.5
			Equimolar mixture NaCl–KCl			
1000	3.39×10^7	144.17	4.46×10^{13}	261.3	1.32×10^6	117.2
1050	1.73×10^7	145.5	1.61×10^{13}	265.5	9.23×10^5	119.9
1100	9.35×10^6	146.8	6.40×10^{12}	269.7	6.69×10^5	122.7
1150	5.35×10^6	148.1	2.75×10^{12}	273.9	5.0×10^5	125.5
1200	3.20×10^6	149.5	1.27×10^{12}	278.1	3.81×10^5	128.2
			KCl			
1100	1.81×10^7	152.9	3.44×10^{12}	264.0	1.54×10^5	109.3
1150	1.09×10^7	155.0	1.60×10^{12}	268.7	1.19×10^5	111.8
1200	6.89×10^6	157.1	7.86×10^{11}	273.3	9.41×10^4	114.3
1250	4.50×10^6	159.2	4.11×10^{11}	278.0	7.58×10^4	116.8
			CsCl			
1000	5.15×10^7	147.65	1.01×10^{13}	249.0	1.96×10^5	101.3
1050	2.74×10^7	149.50	3.97×10^{12}	253.3	1.48×10^5	104.0
1100	1.54×10^7	151.4	1.70×10^{12}	257.6	1.15×10^5	106.6
1150	9.12×10^6	153.24	7.84×10^{11}	261.9	9.13×10^4	109.2
1200	5.64×10^6	155.1	3.85×10^{11}	266.2	7.39×10^4	111.9

to 1.15×10^5 in the series (3LiCl–2KCl)–CsCl. At the same time, K_2^* is higher by 6–7 orders of magnitude than K_1^* and K_3^*. This relationship is not valid for the decrease in K_1^* of reaction (1) in the 3LiCl–2KCl and NaCl–KCl melts at the same temperature (Table 3).

Reactions (4) and (5) with molten aluminum occur to a negligible extent; therefore, Al cannot be used as reductant for preparing the metal.

A great deal of attention was given in Russia to electrolytic refining of heavy nonferrous metals, among which metallurgy and reprocessing of lead and lead compounds [7–9] and electrochemical behavior in molten ionic electrolytes, e.g., in NaCl–KCl–$PbCl_2$ [7–12], occupy the prominent place. Therefore, it was of interest to calculate the reactions of hafnium di- and tetrachlorides with molten lead and $PbCl_2$ in equimolar NaCl–KCl mixture (Table 2).

Reactions (6) and (7) do not occur to a noticeable extent: K_6^* at 1100 K is 3.37×10^{-7} and K_7^*, 8.3×10^{-15}. Reaction (8) occurs practically quantitatively. The apparent equilibrium constant at 1100 K is equal to 4.15×10^7.

Compared to similar reactions of titanium tetrachloride in the NaCl–KCl melt [13], the reactions of $HfCl_4$ with magnesium occur less intensely. At 1100 K the constant K_2^* and K_3^* of the reaction of $TiCl_4$ with magnesium are 7.6×10^{17} and 9.6×10^{12}, respectively, and those for the reaction of $HfCl_4$ with Mg are 6.4×10^{12} and 6.69×10^5, i.e., they differ by 5–7 orders of magnitude.

CONCLUSIONS

(1) The temperature dependences of the apparent equilibrium constants are calculated for eight reactions of hafnium di- and tetrachloride with magnesium, aluminum, and lead in various molten salt solvents.

(2) Reactions (2) and (3) occur to a lesser extent than the analogous reactions of titanium tetrachloride with magnesium in the NaCl–KCl melt.

(3) The reaction of $HfCl_2$ and $HfCl_4$ with liquid aluminum and lead does not occur, and that with $PbCl_2$ is rather intense.

REFERENCES

1. Smirnov, M.V., *Elektrodnye potentsialy v rasplavlennykh khloridakh* (Electrode Potentials in Molten Chlorides), Moscow: Nauka, 1973.
2. Smirnov, M.V., Puzanova, T.A., and Loginov, N.A., *Elektrokhimiya*, 1971, vol. 7, no. 3, pp. 369–371.
3. Smirnov, M.V., Puzanova, T.A., and Loginov, N.A., Available from VINITI, 1969, Sverdlovsk, no. 900–69.
4. Lebedev, V.A., *Izbiratel'nost' zhidkometallicheskikh elektrodov v rasplavlennykh galogenidakh* (Selectivity of Liquid Metal Electrodes in Molten Halides), Chelyabinsk: Metallurgiya, 1993.
5. Smirnov, M.V., Kudyakov, V.Ya., Posokhin, Yu.V., *et al.*, *Tr. Inst. Elektrokhim. Ural. Nauchn. Tsentra Akad. Nauk SSSR*, 1978, issue 27, pp. 12–16.
6. Nichkov, I.F., Raspopin, S.P., and Karzhavin, S.P., *Izv. Vyssh. Uchebn. Zaved., Tsvetn. Metall.*, 1963, no. 6, pp. 83–86.
7. Delimarskii, Yu.K., Mikhailov, V.V., and Samodelov, A.P., *Elektrokhimichesloe rafinirovanie tyazhelykh i tsvetnykh metallov v rasplavlennykh solyakh* (Electrochemical Refining of Heavy and Nonferrous Metals in Molten Salts), Moscow: Tsvetmetinformatsiya, 1971, pp. 55–79.
8. Delimarskii, Yu.K., and Zarubitskii, O.G., *Elektroliticheskoe rafinirovanie tyazhelykh i tsvetnykh metallov v ionnykh rasplavakh* (Electrolytic Refining of Heavy and Nonferrous Metals in Ionic Melts), Moscow: Metallurgiya, 1975.
9. Smirnov, M.V., *Rafinirovanie svintsa i pererabotka poluproduktov* (Lead Refining and Reprocessing of Intermediates), Moscow: Metallurgiya, 1977.
10. Kozin, L.F., and Morachevskii, A.G., *Fizikokhimiya i metallurgiya vysokochistogo svintsa* (Physical Chemistry and Metallurgy of Ultrapure Lead), Moscow: Metallurgiya, 1991.
11. Morachevskii, A.G., Vaisgant, Z.I, and Demidov, A.I., *Pererabotka vtorichnogo svintsovogo syr'ya* (Reprocessing of Secondary Lead Resources), St. Petersburg: Khimiya, 1993.
12. Morachevskii, A.G., Vaisgant, Z.I, and Demidov, A.I., *Elektrokhimiya svintsa v ionnykh rasplavakh* (Electrochemistry of Lead in Ionic Melts), St. Petersburg: Khimiya, 1994.
13. Oleinikova, V.A., and Loginov, N.A., *Rasplavy*, 2001, no. 1, pp. 19–25.

Russian Journal of Applied Chemistry, Vol. 74, No. 11, 2001, pp. 1801–1805. Translated from Zhurnal Prikladnoi Khimii, Vol. 74, No. 11, 2001, pp. 1748–1752.

PHYSICOCHEMICAL STUDIES OF SYSTEMS AND PROCESSES

Physicochemical Properties of Methyl- and Ethylhalosilanes

I. B. Sladkov

St. Petersburg State Technical University, St. Petersburg, Russia

Received January 30, 2001

Abstract—Published data on the main physicochemical constants of methyl- and ethylhalosilanes were summarized. The lacking parameters were calculated by the methods whose reliability was checked by calculating parameters for which the experimental values are available.

Organometallic compounds find growing use in organic synthesis, preparation of metallic films and semiconducting materials, etc. [1, 2]. At the same time, physicochemical properties of organometallic compounds are studied insufficiently.

In this work, we summarized available data on the physicochemical constants of alkylhalosilanes and calculated the lacking parameters. The reliability of our calculations was confirmed by calculating parameters for which the experimental values are available.

We studied the compounds formed by substitution of the hydrogen atoms in the silane molecule by methyl and ethyl radicals and halogen atoms. Such substitution generates the homologous series of the SiR_4–SiR_3Hal–SiR_2Hal_2–$SiRHal_3$–$SiHal_4$ type, where R is methyl radical CH_3 or ethyl radical C_2H_5 and Hal is halogen (F, Cl, Br, I). Such molecules can also contain hydrogen atoms.

Methods for approximate calculation of the boiling point are few, applicable to a limited range of substances, and low-accurate [3]. We found that for the above compounds the boiling point can be fairly reliable estimated by Kinney's method [4]. In this method, a definite characteristic quantity n_b connected with the boiling point is assigned to atoms and atomic groups of the molecule. The characteristic of the molecule as a whole N_b is the sum of n_b parameters of atoms and groups with regard to the molecular stoichiometry.

The stoichiometric formula of a compound can be presented as

$$SiR_\alpha H_\beta Hal'_\gamma Hal''_\delta, \qquad \alpha + \beta + \gamma + \delta = 4, \qquad (1)$$

where R is an organic radical (CH_3 or C_2H_5), H is the hydrogen atom, and Hal is a halogen.

In terms of this concept,

$$N_b = n_b(Si) + \alpha n_b(R) + \beta n_b(H) + \gamma n_b(Hal') + \delta n_b(Hal'').$$

The boiling point is calculated by the equation

$$T_b = 230N_b^{1/3} - 270. \qquad (2)$$

In [5, 6], the n_b values are presented for Si (4.20), Cl (3.40), and Br (5.88). All these values are related to tetrahedral coordination. We determined n_b from the known boiling points of the above compounds for the following atoms and radicals: H 1.20, F 0.65, I 8.35, CH_3 3.65, and C_2H_5 6.80.

The average (in absolute value) error of the boiling point calculation by Eq. (2) with the above n_b values for 53 substances was 2.0% (Table 1).

The enthalpy of vaporization at the boiling point ΔH_b (J mol^{-1}) for our compounds can be estimated by Trouton's rule [9]

$$\Delta H_b = 88T_b. \qquad (3)$$

For 30 compounds with known ΔH_b [10–13], the average (in absolute value) error of the ΔH_b calculation by Eq. (3) was 3.0%.

To determine the critical temperature T_c, we used the two-stage iteration procedure [14]. Initially, using Guldberg's rule, we found the first approximation:

$$T_{c,0} = 1.5T_b. \qquad (4)$$

Then, the enthalpy of vaporization was calculated by Eq. (3) at the boiling point, and the refined value of the critical temperature was determined

$$T_c = T_b[1 + f\ln(10.255T_{c,0}/b)], \qquad (5)$$

1070-4272/01/7411-1801$25.00

Table 1. Error of calculation of the normal boiling point

Substance	T_b, K [7, 8]	Δ, %	Substance	T_b, K [7, 8]	Δ, %
$SiMe_3F$	290.0	5.9	$SiMeHCl_2$	314.7	–2.3
$SiMe_2F_2$	275.7	–2.8	$SiEt_2HCl$	372.7	1.5
$SiMeF_3$	243.2	–8.6	$SiEtH_2Cl$	316.0	0.9
$SiEt_3F$	383.2	5.7	$SiEtHCl_2$	348.7	–1.5
$SiEt_2F_2$	335.2	2.9	$SiMeH_2Br$	307.0	1.3
$SiEtF_3$	268.9	0.5	$SiEtHBr_2$	393.2	–0.1
$SiMe_3Cl$	333.2	1.7	$SiEt_2HBr$	394.5	1.8
$SiMe_2Cl_2$	343.5	–2.2	$SiMe_2HI$	365.2	–0.1
$SiMeCl_3$	338.8	–1.7	$SiMeH_2I$	345.0	–1.6
$SiEt_3Cl$	416.7	2.8	$SiMeHI_2$	432.2	–5.3
$SiEt_2Cl_2$	403.6	–1.2	$SiEt_2HI$	422.7	0.1
$SiEtCl_3$	371.4	–1.4	$SiMe_2ClF$	309.5	–1.8
$SiMe_3Br$	350.5	3.2	$SiMeCl_2F$	302.7	–0.6
$SiMe_2Br_2$	384.0	–0.8	$SiMeClF_2$	272.7	–3.1
$SiMeBr_3$	406.7	–1.9	$SiEtCl_2F$	335.4	0.6
$SiEt_3Br$	437.2	2.6	$SiEtClF_2$	298.2	1.1
$SiEt_2Br_2$	440.0	0.3	$SiMe_2BrCl$	363.2	–0.3
$SiEtBr_3$	433.4	0.1	$SiMeBr_2Cl$	380.7	0.9
$SiMe_3I$	380.7	2.1	$SiMeBrCl_2$	359.7	0.9
$SiEt_3I$	463.3	0.9	$SiEtBr_2Cl$	412.7	0.1
$SiEt_2I_2$	494.3	–3.1	$SiEtBrCl_2$	392.2	–0.5
$SiEtI_3$	524.0	–6.5	$SiMe_2ICl$	391.6	–1.2
$SiMe_2HF$	264.0	4.4	$SiMeI_2Cl$	446.2	–4.0
$SiMeHF_2$	237.5	–2.4	$SiMeICl_2$	389.6	–1.3
$SiMeH_2F$	229.2	4.7	$SiEt_2ICl$	449.6	–1.9
$SiMe_2HCl$	308.5	0.7	SiMeHClF	274.3	–0.6
$SiMeH_2Cl$	280.0	–0.2			

$$f = RT_{c,0}/\Delta H_b,$$

$$b = 1.27V_b - 6.$$

It was found that the critical volume well correlates with the parachor (the calculation of the latter for alkyl compounds is considered in detail in [6]). This correlation is linear (correlation coefficient 0.9961, root-mean-square error ±2.8%). As a result, the equation

$$V_c = 80\prod - 11 \quad (6)$$

can be used to calculate the critical volume.

The critical pressure can be found by the equation [10]

$$P_c = 1.039b/T_c. \quad (7)$$

Since experimental data on the critical parameters of halogen derivatives are very limited, we included in the data base the compounds that begin and complete each homologous series (SiR_4 and $SiHal_4$), and also alkyl compounds of the other Group IV elements (GeR_4, SnR_4, and PbR_4), whose thermodynamic similarity with the compounds discussed is doubtless. This improves the statistics and reliability of the calculation methods used. The errors of the calculation of the critical parameters are listed in Table 2.

Published data on the density of the compounds under consideration in the liquid state are extremely scarce. Experimental data on the temperature dependence of the density are available only for trichloromethylsilane [23]. For the other compounds, the density data are available only for separate temperatures (usually for room temperature). Initially, we consider prediction of the density (or molar volume) of a liquid at the boiling point.

When the density of a liquid is known at temperature T_1, its recalculation to the boiling point can be performed most precisely using the critical temperature of the substance by the equation [10]

$$\rho_b = \rho_1(2 - T_b/T)/(2 - T_1/T_c). \quad (8)$$

Table 2. Error Δ of calculation of the critical parameters*

Substance	T_c, K	V_c, cm^3 mol^{-1}	P_c, MPa	References	ΔT_c	ΔV_c	ΔP_c
					%		
$SiMe_4$	448.6	361.0	2.82	[16]	–0.2	1.1	–2.8
$SiMe_3Cl$	497.8	365.6	3.20	[17]	0.9	–2.5	–0.6
$SiMe_2Cl_2$	520.4	349.9	3.48	[17]	–0.1	–0.3	–2.0
$SiMeCl_3$	517.8	339.8	3.51	[18]	–0.8	0.3	1.5
$SiCl_4$	507.0	326	3.73	[19]	–1.3	2.1	–5.7
$SiEt_4$	603.7	585	2.60	[20]	4.0	0.1	–6.3
$SiEt_3Cl$	600.0	520	2.84	[20]	3.2	0.5	–3.0
$SiEt_2Cl_2$	595.8	455	3.06	[20]	1.7	1.1	2.4
$SiEtCl_3$	560.8	402.7	3.33	[17]	0.1	–1.7	–0.1
$GeMe_4$	476.0	380	2.81	[11]	–0.9	0.1	–0.3
$GeEt_4$	615.0	596.2	2.18	[11]	2.7	0.8	9.8
$SnMe_4$	521.8	400	2.98	[21]	0.4	0.4	0.2
$PbMe_4$	569.0	398.5	3.12	[22]	0.8	5.8	3.0

* The necessary data on T_b and V_b were taken from [15] and from Tables 1 and 3.

The critical parameters are known for only six alkylhalosilanes (Table 2). For these compounds, the volume properties at the boiling point can be calculated by Eq. (8). The densities and molar volumes of liquids at the boiling point, calculated by Eq. (8) from the density at T_1 = 293 K, are listed in Table 3. $Si(CH_3)Cl_3$, for which the experimental value is known [23], is the exception. For molecular inorganic compounds, the rms error of the calculation of ρ_b by Eq. (8) is ±0.7% [7]. Let us ascertain that for compounds considered this equation keeps the high accuracy. For this purpose, we should use the molar volume of a liquid at the boiling point for three substances that open and complete the homologous series: tetrachlorosilane, tetramethylsilane, and tetraethylsilane. The V_b values of these substances (cm^3 mol^{-1}) are equal to 121.1, 138.4, and 215.5, respectively [15, 19].

Using the listed set of nine substances, we can assess the reliability of data obtained by Eq. (8) by the method of comparative calculation. Variation of the molar volume of a liquid at the boiling point in the series of methyl- and ethylchlorosilanes is well described by the linear dependence (correlation coefficient 0.9993, rms error ±0.8%), which demonstrates high reliability of the data obtained. Thus, for substances with known critical parameters, recalculation of ρ at 293 K to T_b gives results close to the experimental data.

When the critical temperature of a substance is unknown, the recalculation of the density at a known temperature to that at the boiling point can be performed by the simpler equation [10]

$$\rho_b = \rho_1/[1 + 0.46(1 - T_1/T_b)]. \quad (9)$$

The high reliability of Eq. (9) as applied to alkyl compounds of Group II–VI elements was proved with a large data set [15]. Indeed, for the considered silicon compounds with known experimental ρ_b, such recalculation (from T = 293 to T_b) gives the error (%): +0.2 for $Si(CH_3)_4$, –0.1 for $Si(C_2H_5)_4$, –0.3 for $SiCl_4$, and +0.5 for $Si(CH_3)Cl_3$.

Thus, Eq. (9) also provides for recalculation of the density at arbitrary temperature T_1 to density at T_b with the error close to the experimental error. The results of calculation of the molar volume of a liquid at the boiling point by Eq. (9) for substances with known densities at room temperature are listed in Table 3.

When any data on densities of liquids are lacking, the molar volume at the boiling point $V_b = M/\rho_b$ can be calculated by two more methods. Earlier, we have found the following correlation for alkyl compounds of Group II–VI elements [6]:

$$V_b = 31\prod - 15. \quad (10)$$

In addition, it was found that the molar volume of liquid methyl- and ethylhalosilanes at the boiling point is well described by the additivity scheme. We determined the fractions of V_b for CH_3 and C_2H_5 radicals using the atomic fractions of V_b for silicon

Table 3. Volume properties of liquid methyl- and ethylhalosilanes

Substance	ρ_{293}, g cm^{-3} [8, 15, 23, 24]	T_b, K	V_b, cm^3 mol^{-1}
$SiMe_4$	0.646	300.1	138.4*
$SiMe_3Cl$	0.860	333.2	133.9**
$SiMe_2Cl_2$	1.070	343.5	129.4**
$SiMeCl_3$	1.282	338.8	125.3*
$SiMe_3Br$	1.189	350.5	138.5
$SiMe_2Br_2$	1.727	384.0	140.0
$SiMeBr_3$	2.253	406.7	141.7
$SiMeBr_2Cl$	1.892	380.7	139.4
$SiMeBrCl_2$	1.576	359.7	133.6
$SiMeH_2I$	1.768	345.0	104.0
$SiEt_4$	0.766	426.6	215.5*
$SiEt_3Cl$	0.925	416.7	188.6**
$SiEt_2Cl_2$	1.100	403.6	162.9**
$SiEtCl_3$	1.267	371.6	142.6**
$SiEt_3F$	0.838	383.2	177.6
$SiEt_2Br_2$	1.564	440.0	181.5
$SiEtBr_3$	2.079	433.4	164.1
$SiEtBr_2Cl$	1.777	412.7	161.0
$SiEtBrCl_2$	1.546	392.2	150.2
$SiEHCl_2$	1.089	348.7	127.3
$SiEtH_2Cl$	0.901	316.0	108.5
$SiEtHBr_2$	1.728	393.2	140.9

* Experimental values.
** Calculated by Eq.(8); the other values of V_b are calculated by Eq. (9).

Table 4. Atomic fractions V_b of CH_3 and C_2H_5 radicals

Compound	V_b, CH_3, cm^3 mol^{-1}	Compound	V_b, C_2H_5, cm^3 mol^{-1}
$SiMe_4$	25.7	$SiEt_4$	45.0
$SiMe_3Cl$	22.6	$SiEt_3Cl$	43.8
$SiMe_2Cl_2$	25.3	$SiEt_2Cl_2$	42.1
$SiMeCl_3$	25.0	$SiEtCl_3$	42.3
$SiMe_3Br$	25.3	$SiEt_2Br_2$	46.0
$SiMe_2Br_2$	25.2	$SiEtBr_3$	47.6
$SiMe_2Br_3$	25.2	$SiEtBr_2Cl$	49.9
$SiMeBr_2Cl$	28.3	$SiEtBrCl_2$	44.5
$SiMeBrCl_2$	27.9	$SiEtHCl_2$	45.8
$SiMeH_2I$	25.9	$SiEtH_2Cl$	45.8
		$SiEtHBr_2$	48.6
		$SiEt_3F$	44.2
Average	26.0		45.0

(35.5), hydrogen (2.8), fluorine (9.5), chlorine (21.6), bromine (27), and iodine (35) [10].

As seen from Table 4, the atomic fractions of V_b for CH_3 and C_2H_5 radicals found from data for various compounds vary within fairly narrow limits and amount to 26 and 45, respectively. This shows that the additive scheme can be used to calculate V_b of alkylhalosilanes:

$$V_b(SiR_\alpha Hal_\beta) = V_b(Si) + \alpha V_b(R) + \beta V_b(Hal). \quad (11)$$

The average (in absolute value) error of determining of V_b of halogen derivatives by Eqs. (1) and (11), calculated from data of Table 3, was 2.1 and 0.9%, respectively.

Another characteristic value of the density, especially important in applied chemistry, is the density at room temperature (293 K is considered as a standard temperature).

For alkyl compounds of Group II–VI elements, we proposed the equations [15]

$$\rho_{293} = [M/(31.5\prod - 15)](1.46 - 134.8/T_b), \quad (12)$$

$$\rho_{293} = M/(24.5\prod + 3.5). \quad (13)$$

To check the accuracy of Eqs. (12) and (13), we used data of Table 3 and found that the average (in absolute value) error is 2.1 and 3.0%, respectively.

CONCLUSION

Physicochemical properties of methyl- and ethylhalosilanes, not available from the literature, can be predicted fairly reliably by methods of approximate calculation.

REFERENCES

1. Razuvaev, G.A., Gribov, B.G., and Domrachev, G.A., *Metalloorganicheskie soedineniya v elektronike* (Organometallic Compounds in Electronics), Moscow: Nauka, 1972.
2. Efremov, A.A., Fedorov, V.A., and Grinberg, E.E., *Vysokochist. Veshch.*, 1988, no. 3, pp. 5–43.
3. Reid, R.G., Prausnitz, J.M., and Sherwood, T.K., *The Properties of Gases and Liquids*, New York: McGraw-Hill, 1977.
4. Kinney, C.R., *J. Am. Chem. Soc.*, 1938, vol. 60, no. 12, pp. 3032–3035.
5. Lewis, R.N. and Newkirk, A.T., *J. Am. Chem. Soc.*, 1947, vol. 69, no. 3, pp. 701–703.
6. Sladkov, I.B., *Zh. Prikl. Khim.*, 1999, vol. 72, no. 8, pp. 1266–1272.
7. Kaufman, H.C., *Handbook of Organometallic Compounds*, New York: IFL, 1961.

8. *Termicheskie konstanty veshchestv* (Thermal Constants of Substances), Glushko, V.P., Ed., Moscow: VINITI, 1970, issue 4.
9. Sladkov, I.B., *Zh. Prikl. Khim.*, 1998, vol. 71, no. 6, pp. 903–907.
10. Morachevskii, A.G. and Sladkov, I.B., *Fiziko-khimicheskie svoistva molekulyarnykh neorganicheskikh soedinenii* (Physicochemical Properties of Molecular Inorganic Compounds), Leningrad: Khimiya, 1996.
11. *Gmelins Handbuch der anorganischen Chemie Silicium*, Weinheim: Chemie, 1958, part 1C.
12. Kut'in, A.M., Zorin, A.D., and Kuznetsova, T.V., in *Vysokochistye veshchestva* (High-Purity Subatances), Nizhni Novgorod: Nizhegorod. Gos. Univ., 1990, pp. 3–8.
13. *Gmelins Handbuch der anorganischen Chemie. Germanium. Organogermanium Compounds*, Weinheim: Chemie, 1988, part 1.
14. Sladkov, I.B., *Zh. Prikl. Khim.*, 1993, vol. 66, no. 6, pp. 1206–1209.
15. Sladkov, I.B., *Zh. Prikl. Khim.*, 2000, vol. 73, no. 56, pp. 727–732.
16. McGlashan, M.L. and McKinnon, I.R., *J. Chem. Thermodyn.*, 1977, vol. 9, no. 12, pp. 1205–1212.
17. Stepanov, N.G. and Nozdrev, V.F., *Zh. Fiz. Khim.*, 1968, vol. 42, no. 10, pp. 2456–2461.
18. Stepanov, N.G., *Zh. Fiz. Khim.*, 1972, vol. 46, no. 3, pp. 801–802.
19. Lapidus, I.I. and Nisel'son, L.A., *Tetrakhlorsilan i trikhlorsilan* (Tetrachlorosilane and Trichlorosilane), Moscow: Khimiya, 1970.
20. Myers, K.H. and Danner, R.P., *J. Chem. Eng. Data*, 1993, vol. 38, no. 2, pp. 175–200.
21. Hugill, J.A., and McGlashan, M.L., *J. Chem. Thermodyn.*, 1978, vol. 10, no. 1, pp. 85–93.
22. *Gmelins Handbuch der anorganischen Chemie. Lead. Organolead Compounds*, Berlin: Springer, 1987, part 1C.
23. Sokolova, T.D., Prokof'ev, N.K., and Nisel'son, L.A., *Zh. Fiz. Khim.*, 1973, vol. 47, no. 1, pp. 268–269.
24. Rochow, E.G., Hurd, D.T., and Lewis, R.N., *The Chemistry of Organometallic Compounds*, New York: Wiley, 1957.

Russian Journal of Applied Chemistry, Vol. 74, No. 11, 2001, pp. 1806–1808. Translated from Zhurnal Prikladnoi Khimii, Vol. 74, No. 11, 2001, pp. 1753–1755.

SORPTION AND ION-EXCHANGE PROCESSES

Sorption of Water-Soluble Copper(II) Compounds on Clinoptilolite

Yu. N. Makurin, A. V. Yuminov, and V. G. Berezyuk

Ural State Engineering University, Yekaterinburg, Russia

Received August 9, 2000; in final form, June 2001

Abstract—Copper(II) sorption on clinoptilolite from aqueous solutions with different pH was studied. The results were analyzed using the calculated distribution of water-soluble copper(II) species at different pH. The best conditions of copper(II) sorption on clinoptilolite from aqueous solutions were determined.

Over a 3–4-thousand-year period copper is used for production of implements, dishware, decorations, and dyes. At present heat exchangers, vacuum apparatus, pipes, and electric wires are produced from copper. Copper alloys are applied as structural materials. Copper compounds are used in production of glass and enamels and in electroplating and ore enrichment. They are also used as wood preservatives, catalysts, etc.

The scale of application of copper and its compounds gives rise to environmental problems. Copper, like other heavy metals, plays a dual role in biochemistry of plants and animals. On the one hand, copper is involved in the metabolism, and on the other hand, it is a toxic metal. The biological functions of copper in cells are determined by its coordination properties, possibility of reaction with oxygen, and reversible reduction of copper compounds. Copper(II) in a cell exists in the form of complexes with biologically active compounds such as amino acids, nucleic acids, biogenic amines, and hormones. The average human consumption of copper with food is 2–5 mg daily. In the case of hard physical activity this value increases to 7 mg daily. When the consumption exceeds the daily demand, the organism is poisoned. The toxicity is due to coordination of the S–H groups of proteins and especially enzymes to copper(II) ions. Copper compounds increase the permeability of mitochondrial membranes. Acute intoxication with copper compounds is accompanied by hemolysis of erythrocytes and disorder of monoamine metabolism. As a rule, a human being is poisoned with copper under industrial conditions. However, poisoning with potable water containing 444 mg l^{-1} of copper(II) cations which are probably washed out from copper water pipes has been described [1].

When the copper concentration in natural water exceeds the productivity of the natural regeneration, its concentration in potable water should be reduced by special procedures. To decrease excess copper content in tap water, natural sorbents including clinoptilolite are used. Clinoptilolite is a cheap and readily available sorbent with a high capacity for copper [2].

We used clinoptilolite from the Kholin deposit (Buryatiya). Its average composition is described by the formula $(K_2Na_2Ca)_3Al_6Si_{30}O_{72} \cdot 22H_2O$. The silicon/aluminum ratio ranges from 4.2 to 5.2. The cross section of clinoptilolite openings is 0.40×0.55 nm; the free pore volume is 0.34. The soprtion capacity and stability of clinoptilolite in various media are described in [3].

To determine the best sorption conditions, we studied copper(II) sorption from aqueous solutions with different pH, since the distribution of water-soluble copper species exhibiting different sorption properties strongly depends on pH. Copper(II) cations are hydrolyzed in aqueous solution to form the following hydroxo complexes: $[Cu(OH)]^+$, $[Cu(OH)_2]$, $[Cu(OH)_3]^-$, and $[Cu(OH)_4]^{2-}$. The concentrations of these species are denoted as C_1, C_2, C_3, and C_4. Their instability constants are as follows [4, 5]:

$$pK_1 = 7.0,\ pK_{1-2} = 13.7,\ pK_{1-3} = 17.0,\ pK_{1-4} = 18.5.$$

The fractions of copper species being in equilibrium in an aqueous solution are related to the instability constant and pH by the following equations [6, 7]:

$$\alpha_0 = C_0/C_\Sigma = 1/\beta, \quad (1)$$

$$\alpha_1 = C_1/C_\Sigma = K_w/(K_1[H_3O^+]\beta), \quad (2)$$

1070-4272/01/7411-1806$25.00

Speciation of copper(II) in aqueous solution as influenced by pH

Parameter	pH				
	1.00	2.00	3.00	4.00	5.00
β	1.000	1.000	1.000	1.001	1.010
α_0	1.000	1.000	1.000	0.999	0.999
α_1	10^{-6}	10^{-5}	10^{-4}	10^{-3}	9.9×10^{-3}
α_2	5.0×10^{-13}	5.0×10^{-11}	5.0×10^{-9}	5.0×10^{-7}	5.0×10^{-5}
α_3	10^{-22}	10^{-19}	10^{-16}	10^{-13}	10^{-10}
α_4	3.0×10^{-34}	3.0×10^{-30}	3.0×10^{-26}	3.0×10^{-22}	3.0×10^{-18}
C_0, M	3.9×10^{-4}	3.9×10^{-4}	3.9×10^{-4}	3.9×10^{-4}	3.9×10^{-4}
C_Σ, M	3.9×10^{-4}	3.9×10^{-4}	3.9×10^{-4}	3.9×10^{-4}	3.94×10^{-4}
Parameter	pH				
	6.00	7.00	8.00	9.00	10.00
β	1.105	2.480	59.11	5.0×10^{3}	5.8×10^{5}
α_0	0.905	0.403	0.017	2.0×10^{-4}	2.0×10^{-6}
α_1	0.090	0.403	0.169	0.020	0.002
α_2	0.004	0.194	0.812	0.960	0.826
α_3	9.0×10^{-8}	4.0×10^{-5}	0.002	0.020	0.172
α_4	3.0×10^{-14}	10^{-10}	5.0×10^{-8}	6.0×10^{-6}	5.0×10^{-4}
C_0, M	3.5×10^{-4}	5.6×10^{-6}	5.6×10^{-8}	5.6×10^{-10}	5.6×10^{-12}
C_Σ, M	3.87×10^{-4}	1.4×10^{-5}	3.3×10^{-6}	2.85×10^{-6}	3.2×10^{-6}

$$\alpha_2 = C_2/C_\Sigma = K_w^2/(K_{1-2}[H_3O^+]^2\beta), \quad (3)$$

$$\alpha_3 = C_3/C_\Sigma = K_w^3/(K_{1-3}[H_3O^+]^3\beta), \quad (4)$$

$$\alpha_4 = C_4/C_\Sigma = K_w^4/(K_{1-4}[H_3O^+]^4\beta), \quad (5)$$

$$\beta = 1 + K_w/(K_1[H_3O^+]) + K_w^2/(K_{1-2}[H_3O^+]^2) + K_w^3/(K_{1-3}[H_3O^+]^3) + K_w^4/(K_{1-4}[H_3O^+]^4), \quad (6)$$

where K_w is the ionic product of water; C_Σ is the total concentration of water-soluble copper(II) species, $C_\Sigma = C_0 + C_1 + C_2 + C_3, C_4, C_0 = [Cu^{2+}]$.

The equilibrium compositions of aqueous copper(II) solutions with various pH, calculated by Eqs. (1)–(6), are presented in the table.

The stability of the copper(II) solution with respect to precipitation of copper hydroxide is of great practical interest, since this process can strongly decrease C_Σ. The equilibrium aqueous solution–$Cu(OH)_2$(s) is described by the equation:

$$[Cu^{2+}][OH^-]^2 = SP, \quad (7)$$

where SP is the solubility product of copper(II) hydroxide, equal to 5.6×10^{-20} [4].

Substitution of this value in Eq. (7) gives the following equation

$$pC_0^t = 2pH - 8.75, \quad (8)$$

where pC_0^t is the threshold concentration of C_0. At copper concentration higher than the threshold value $Cu(OH)_2$ starts to precipitate.

The diagram of stability of an aqueous Cu(II) solution with respect to $Cu(OH)_2$ precipitation is shown in Fig. 1. The dependence of the threshold concentration C_0^t described by Eq. (8) is represented by straight line *1*. Curve *2* determines the actual C_0 at $C_\Sigma = 3.9\times10^{-4}$ M. As seen from Fig. 1. copper hydroxide precipitates at pH > 6. These results will be used in interpretation of experimental data on copper(II) sorption form the tested solutions on clinoptilolite.

Copper(II) sorption on clinoptilolite from aqueous solutions with various pH was studied as follows. A weighed portion of clinoptilolite (10.0 ± 0.1 g) was placed in a round-bottomed flask. A buffer solution (10.0 ml) with pH ranging from 3 to 10 was added. Acidification to pH 1 and 2 was performed with 0.1 and 0.01 M hydrochloric acid solution prepared from standard samples. To adjust pH in the range 3–10, ammonia–acetate buffer was used [8].

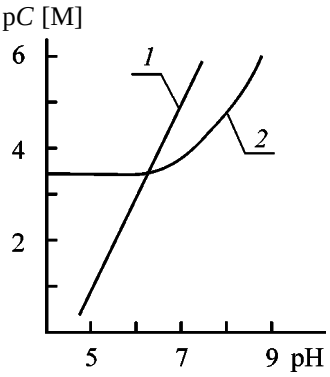

Fig. 1. Diagram of stability of a Cu(II) aqueous solution with respect to $Cu(OH)_2$ precipitation. (*C*) Copper(II) concentration. (*1*) pC_0^t and (*2*) pC_0.

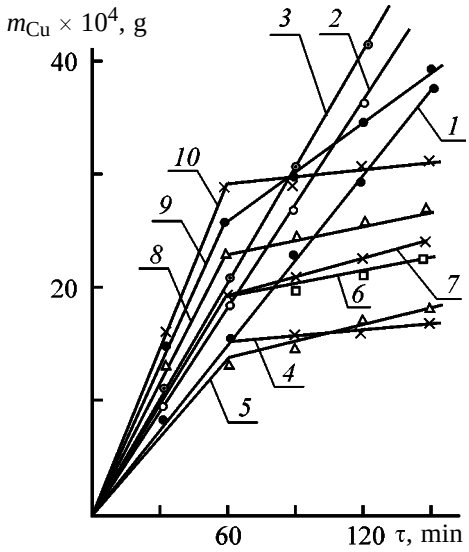

Fig. 2. Diagrams of Cu(II) accumulation on clinoptilolite m_{Cu} at pH (*1*) 1.10, (*2*) 1.85, (*3*) 3.0, (*4*) 4.05, (*5*) 5.0, (*6*) 6.0, (*7*) 7.10, (*8*) 8.0, (*9*) 9.06, and (*10*) 9.85. (τ) Time.

A 3.9×10^{-4} M standard copper(II) solution (10 ml) was added to the reaction mixture. The total volume of the system was 50 ml. The reaction mixture was shaken with a mechanical stirrer. Samples of the solution in contact with clinoptilolite were taken at 30-min intervals and analyzed for copper(II) by the procedure in [9]. The results are shown in Fig. 2. The copper(II) sorption was determined as the difference between the total copper(II) content and the copper(II) content in the solution.

As seen from the table, copper(II) in acidic solutions exists in the form of Cu^{2+} cations which can be rapidly sorbed both on the surface and in pores of clinoptilolite.

At higher pH copper(II) hydroxide precipitates. The copper(II) concentration in the solution sharply decreases (Fig. 1) and the sorption decelerates. In the first stages (t < 60 min) the sorption occurs by the globular mechanism and does not reach saturation (Fig. 2). As the sorption time increases (t > 60 min), zeolite pores are clogged with $Cu(OH)_2^s$ particles, internal diffusion is blocked, and the sorption sharply decreases. Globules of $Cu(OH)_2$ are weakly sorbed on the clinoptilolite surface and are readily washed off.

In alkaline solutions the soprtion is accelerated owing to intense nucleation of $Cu(OH)_2^s$ to form finely divided $Cu(OH)_2^s$ precipitate. The globular mechanism becomes more efficient.

CONCLUSIONS

(1) Speciation of water-soluble copper(II) forms at various pH was calculated. The stability of a Cu(II) solution with respect to precipitation of $Cu(OH)_2$ was analyzed.

(2) The kinetics of copper(II) sorption on clinoptilolite was studied as influenced by pH of the solution. The inflection point in the kinetic curves was assumed to be due to a change in the sorption mechanism depending on the copper(II) species present in the solution.

(3) At pH 1–3 copper(II) is efficiently sorbed by clinoptilolite for no less than 150 min. At pH 4–10 the sorption mechanism changes and the soprtion becomes efficient within the first 60 min.

REFERENCES

1. Khar'kovskaya, N.L., Lyashenko, L.F., and Rukhlina, I.S., *Khim. Shkole*, 1998, no. 4, pp. 9–13.
2. Barnashvili, L.N., in *Klinoptilolit* (Clinoptilolite), Tbilisi: Metsniereba, 1997, pp. 148–154.
3. Chelishchev, N.F., Berenshtein, B.G., and Volodin, V.F., *Tseolity – novyi tip mineral'nogo syr'ya* (Zeolites as a New Type of Mineral Raw Materials), Moscow: Nedra, 1987.
4. *Spravochnik khimika* (Chemist's Handbook), Nikol'skii, B.P., Ed., Moscow: Khimiya, 1954, vol. 5.
5. Gornovskii, I.T., Nazarenko, Yu.N., and Nekryach, E.F., *Kratkii spravochnik po khimii* (Brief Chemical Handbook), Kiev: Naukova Dumka, 1974.
6. Bulatov, M.N., *Raschety ravnovesii v analiticheskoi khimii* (Calculation of Equilibria in Analytical Chemistry), Leningrad: Khimiya, 1984.
7. Laitinen, G.A., *Khimicheskii analiz* (Chemical Analysis), Moscow: Khimiya, 1971.
8. Lur'e, Yu.Yu., *Spravochnik po analiticheskoi khimii* (Handbook on Analytical Chemistry), Moscow: Khimiya, 1971.
9. USSR Inventor's Certificate 825526.

Russian Journal of Applied Chemistry, Vol. 74, No. 11, 2001, pp. 1809–1812. Translated from Zhurnal Prikladnoi Khimii, Vol. 74, No. 11, 2001, pp. 1756–1759.

SORPTION AND ION-EXCHANGE PROCESSES

Adsorption of Oligomers from Dilute Solutions on the Surface of Ferromagnetic Fillers

I. S. Rodzivilova, N. L. Zaitseva, S. E. Artemenko, S. G. Kononenko, and T. G. Dmitrienko

Saratov State Technical University, Saratov, Russia
Engels Technological Institute, Engels, Saratov oblast, Russia

Received May 14, 2000; in final form, January 2001

Abstract—The adsorption of oligomers from their dilute solutions on the surfaces of dispersed barium and strontium oxide ferrites and of neodymium–iron–boron alloy was studied. The main thermodynamic functions of the system components were evaluated. The features of their variation were established.

The adsorption processes on the surface of fillers in solutions of oligomers and polymers govern the features of production of composite materials. The interaction of polymeric components of solutions with the filler surface is the initial event in formation of the interphase contact in composites based on these components [1]. Therefore, the study of adsorption of polymers and oligomers from dilute solutions is of theoretical and practical importance. These data give insight into the features of the adsorption equilibria of polymer and oligomer molecules with the surface of solids.

As a rule, the results of studying adsorption equilibria are presented in the form of dependences of the oligomer or polymer excess in the adsorption layer relative to its content in the equilibrium solution on the concentration of the polymer or oligomer in the solution (Gibbs adsorption isotherm) [2, 3]. In the range of moderate and high concentrations of polymer solutions, these dependences are complicated. Therefore, there is no common interpretation of the results [4]. As shown in a series of papers [5, 6], the study of adsorption of polymers from dilute solutions allows rather simple determination of the adsorption isotherm, which allows evaluation of the parameters of the adsorption equilibrium.

The aim of this work was to study the adsorption equilibria of phenol–formaldehyde oligomer (PFO) in its adsorption from dilute solution in alcohol–acetone mixture on the surface of magnetic fillers.

EXPERIMENTAL

We studied model systems including the following substances: barium and strontium oxide ferrites, $BaO \cdot 6Fe_2O_3$ and $SrO \cdot 6Fe_2O_3$, and also neodymium–iron–boron alloy Nd–Fe–B, used as sorbents; PFO used in rubber ferrites as a matrix; and oligooxypropylene glycol (OOPG), and epoxy-4,4'-isopropylidenediphenol resin (ED-20) used as modifiers for PFO. The physicochemical characteristics of the fillers are listed in Table 1.

Adsorption was carried out in hermetically sealed pycnometers at $25 \pm 1°C$ and the weight ratio of the liquid and solid phases of 10 : 1. The equilibrium solution of the oligomer was separated from the adsorbent by centrifuging; the concentrations of the equilibrium solutions were determined refractometrically. The adsorption Γ (mmol g^{-1}) according to Gibbs is an excess of the number of moles of the second component in the volume of adsorption layer over the number of moles in the same volume in the bulk of the equilibrium solution. The difference of concentrations of the second component in the initial solution C_0 and in the solution equilibrated with the adsorbent

Table 1. Physicochemical characteristics of the fillers

Sorbent	Composition, %	Specific surface area, $S \times 10^{-3}$, $m^2\ kg^{-1}$
Barium ferrite	BaO, 15, Fe_2O_3, 85	0.28
Strontium ferrite	SrO, 15, Fe_2O_3, 85	0.36
Neodymium–iron–boron alloy	Nd, 20–25, B, 1.0–1.6, Fe, 67.4–75.0	0.15

1070-4272/01/7411-1809$25.00

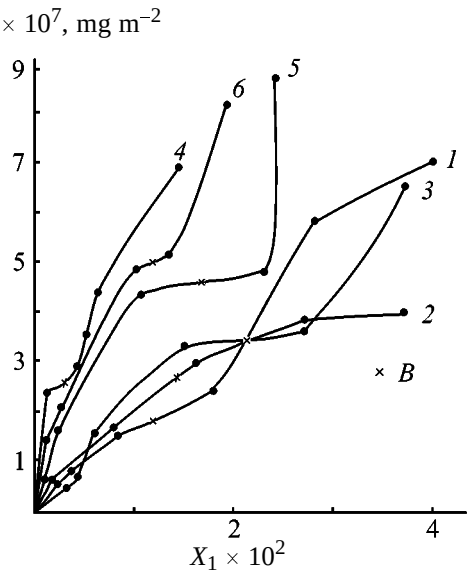

Fig. 1. Isotherm of PFO adsorption from its solutions in alcohol–acetone mixture on the surface of ferrite oxides and Nd–Fe–B alloy. (Γ_i) Excess adsorption and (X_1) PFO mole fraction in the mixture. PFO: (*1–3*) nonmodified and (*4–6*) modified with OOPG. (*1, 4*) Nd–Fe–B, (*2, 5*) barium ferrite, and (*3, 6*) strontium ferrite.

C_e is measured under static conditions. The excess adsorption was evaluated by the equation

$$\Gamma = \frac{(C_0 - C_e)V}{m},$$

where C_0 and C_e are the initial and equilibrium (after contact of the solution with the filler) concentrations of the oligomer (mM), respectively; m is the filler weight (g); and V is the solution volume (ml).

By recalculating on 1 m^2 of the sorbent surface, we obtain the absolute value of adsorption (mg m^{-2})

$$\Gamma = \frac{(C_0 - C_e)V}{mS},$$

where S is the specific surface area (m^2 kg^{-1}).

Table 2. Adsorption characteristics of the systems

System	$\Gamma_{max} \times 10^7$, mg m^{-2}	τ,* Å	K_e
PFO + solvent:			
Nd–Fe–B	1.5	1.1	2.18
$BaO \cdot 6Fe_2O_3$	2.5	1.9	2.00
$SrO \cdot 6Fe_2O_3$	3.1	2.3	2.14
+ OOPG:			
Nd–Fe–B	2.5	1.9	2.3
$BaO \cdot 6Fe_2O_3$	4.1	3.1	1.6
$SrO \cdot 6Fe_2O_3$	4.1	3.8	2.5
+ ED-20:			
$BaO \cdot 6Fe_2O_3$	3.9	2.9	2.1
$SrO \cdot 6Fe_2O_3$	4.2	3.2	3.6

* Thickness of the adsorption layer.

The experimental isotherms of the excess adsorption of PFO from its dilute alcohol–acetone solutions on the surface of various sorbents is presented in Fig. 1. This shape of the isotherms of adsorption from dilute solutions is characteristic of specific interaction of oligomer molecules with the sorbent surface. In adsorption of macromolecules from dilute solutions, when all components of the mixture are sorbed concurrently, determination of the limiting adsorption of the oligomer Γ_{max} presents some problems. Various approaches to determination of the limiting adsorption are considered in the literature, but they mainly concern adsorption of simple molecules [7, 8].

In adsorption from solutions of components that separate into layers in saturation, an S-shaped isotherm similar to isotherms of adsorption of vapors is obtained.

The limiting adsorption Γ_{max} was evaluated from the position of point *B* [8] in the isotherms of adsorption of the oligomer from dilute solution (Table 2). As seen, the highest Γ_{max} is observed with strontium ferrite, which is caused by its more developed surface and the charge effect of the double-charged strontium cation.

On adding OOPG into solution, the limiting adsorption increases by 60%, which is explained by improvement of solvent characteristics. The development of view on sorption from solutions is based on the concepts of excess and absolute adsorption (the total content). Based on these data, thermodynamic functions of adsorption solution can be evaluated using two procedures of thermodynamic consideration of adsorption systems: Gibbs method of excess quantities and the method of total content.

Isotherms of Gibbs adsorption do not carry information on the true parameters of adsorption layers formed on the filler surface. Adsorption of macromolecules from solutions is commonly accompanied by displacement of solvent molecules from the sorbent surface. Therefore, macromolecules of the oligomer always compete with the solvent for adsorption centers. It was shown [8] that, when the competition of solvent molecules is weak, adsorption can proceed to form an adsorption layer of oligomer macromolecules extended along the surface. Thermodynamic

parameters evaluated by the method of total content depend on the particular model of the adsorption solution (pore volume and limiting values of adsorption). These values reflect the real characteristics of the adsorption solution provided that the selected model is correct. As adsorption solution model, we can use a model considering sorption as mutual displacement of components, provided that

$$S = \Sigma n_i^S w_i,$$

where S is the specific surface area of the sorbent ($m^2 g^{-1}$), n_i^S is the number of moles of ith component in the surface layer, and w_i is the landing surface area of the adsorbent.

To check the reability of the selected parameters of the adsorption layer model (values of the limiting adsorption), we estimated variations of the Gibbs energy ΔG evaluated by the method of excess quantities and the method of total content ΔG_{mod} [9]. ΔG and ΔG_{mod} were evaluated by the equations

$$\Delta G = -\Delta\Phi + n^0 RT\Sigma X_{i0} \ln (X_i\gamma_i/X_{i0}\gamma_{i0}),$$

$$\Delta G_{mod} = -\Delta\Phi + n^0 RT\Sigma X_{i0} \ln (X_i/X_{i0}) + n^0[g^E(X) - g^E(X_0)] + n^S[g^{ES}(X^S) - g^E(X)],$$

$$g^E = RT\Sigma X_i \ln\gamma_i,$$

$$g^{ES} = RT\Sigma X_i^S \ln\gamma_i^S,$$

where $\Delta\Phi$ is variation in the chemical potential of the sorbent in its wetting with binary solution ($J g^{-1}$); g^E and g^{ES} are the excess energies of mixing of components in the solution and in the adsorption layer; γ_i and γ_i^S are activity coefficients of components in the solution and adsorption layer; and X_i and X_i^S are compositions of the solution and adsorption layer (mole fraction), respectively.

The activity coefficients of components in the solution were determined from the saturated vapor pressure. The activity coefficients of components in the adsorption layers were evaluated by the equation [9]

$$\ln\gamma_i^S = \ln (X_i/X_i^S) + \Delta\Phi/(\Gamma_{max} RT),$$

where Γ_{max} is the limiting adsorption ($mmol g^{-1}$).

Sufficiently good agreement between ΔG and ΔG_{mod} (Fig. 2) serves as a criterion of the validity of the selected model of adsorption layer and reliability of the proposed parameters of the adsorption phase.

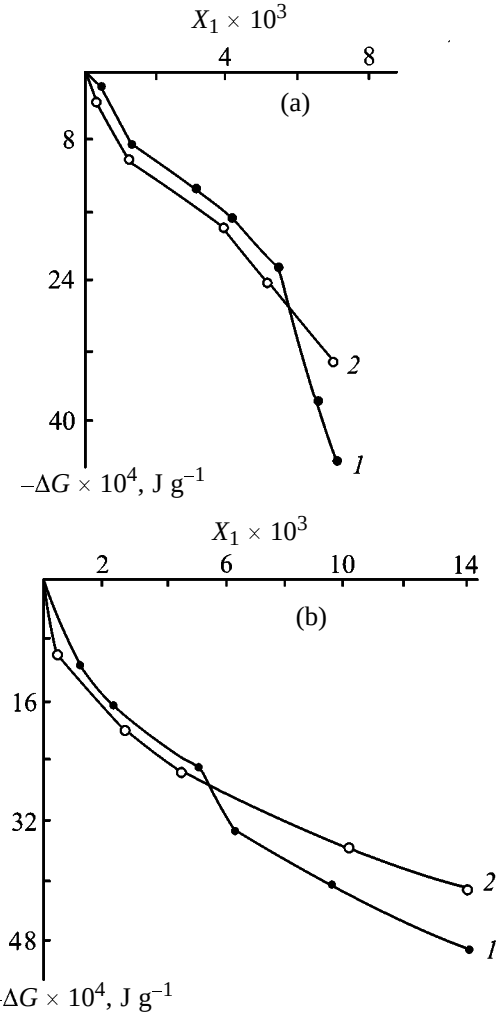

Fig. 2. Concentration dependences of variation of the system energy ΔG in adsorption of PFO modified with (a) ED-20 and (b) OOPG on the surface of Nd–Fe–B alloy, evaluated by the methods of (*1*) excess Gibbs parameters and (*2*) total content. (X_i) Mole fraction of PFO in the mixture.

The parameters of the adsorption phase Γ_{max} were used for evaluating the thickness of the adsorption layer and the equilibrium constant [10]. To estimate the thickness of the adsorption layer, we started from the assumption that the oligomer density in the adsorption state is identical to that in the samples. The thickness of the adsorption layer was evaluated by the equation

$$\tau = \overline{M}\Gamma_{max}/\rho,$$

where M is the reduced molecular weight of the oligomer, Γ_{max} is the limiting adsorption ($mg m^{-2}$), and ρ is the oligomer density ($g cm^{-3}$).

The thickness of the adsorption layer varied from 1

to 4 Å, which suggests parallel orientation of the adsorbed molecules extended along the surface.

In terms of the model of adsorption layer we evaluated the adsorption equilibrium constants (Table 2)

$$K_e = \frac{1}{1 - X_1^S},$$

were X_1^S is mole fraction of the component in the adsorption layer.

The resulting equilibrium constants suggest relatively weak interaction of oligomer macromolecules with the filler surface.

CONCLUSIONS

(1) Thermodynamic characteristics of adsorption systems were evaluated by the Gibbs method and the method of the total content. The features of their variation were established.

(2) The choice of the model of adsorption layer considering sorption as mutual displacement of components was substantiated.

REFERENCES

1. Lipatov, Yu.S., *Fiziko-khimicheskie osnovy napolnennykh polimerov* (Physicochemical Fundamentals of Filled Polymers), Moscow: Khimiya, 1991.
2. El'tekova, N.A., Kazanskii, A.S., and El'tekov, Yu.A., *Zh. Fiz. Khim.*, 1990, vol. 64, no. 8, pp. 2112–2116.
3. Stepin, S.N. and Bogatov, F.R., *Zh. Prikl. Khim.*, 1993, vol 66, no. 4, pp. 766–771.
4. Chuduk, N.A. and El'tekov, Yu.A., *Zh. Fiz. Khim.*, 1979, vol. 53, no. 4, pp. 1032–1037.
5. Kiselev, A.V., *Zh. Fiz. Khim.*, 1961, vol. 35, no. 2, pp. 233–242.
6. Larionov, O.G. and Kurbanbekov, E., in *Fizicheskaya adsorbtsiya iz mnogokomponentnykh faz* (Physical Adsorption from Multicomponent Phases), Moscow: Nauka, 1972, pp. 85–92.
7. Rakhlevskaya, M.N., Rodzivilova, I.S., and Okisheva, N.A., *Zh. Fiz. Khim.*, 1994, vol. 68, no. 9, pp. 1717–1719.
8. El'tekova, N.A. and El'tekova, Yu.A., *Ross. Khim. Zh.*, 1995, no. 6, pp. 33–42.
9. Larionov, O.G., in *Adsorbtsiya v mikroporakh* (Adsorption in Micropores), Moscow: Nauka, 1983, pp. 70–74.
10. El'tekov, Yu.A., in *Fizicheskaya adsorbtsiya iz mnogokomponentnykh faz* (Physical Adsorption from Multicomponent Phases), Moscow: Nauka, 1972, pp. 214–221.

Russian Journal of Applied Chemistry, Vol. 74, No. 11, 2001, pp. 1813–1816. Translated from Zhurnal Prikladnoi Khimii, Vol. 74, No. 11, 2001, pp. 1759–1762.

SORPTION AND ION-EXCHANGE PROCESSES

Quaternization of 1,1-Dimethylhydrazine with Chloromethylated Polystyrene and Properties of Thus Prepared Anion-Exchange Resins

L. M. Antonik, V. A. Lopyrev, M. P. Tiunov, and G. V. Dolgushin

Favorskii Institute of Chemistry, Siberian Division, Russian Academy of Sciences, Irkutsk, Russia
Novosibirsk Chemical Concentrates Plant, Joint-Stock Company, Novosibirsk, Russia

Received June 14, 2001

Abstract—Quaternization of 1,1-dimethylhydrazine with chloromethylated polystyrene is studied to optimize the procedure of preparation of new anion-exchange resins. Sorption characteristics of the resulting resins and their applicability to wastewater treatment to remove uranium are studied.

Cross-linked chloromethylated polystyrene (CMPS) is the basic intermediate for fabrication of anion-exchange resins. With primary and secondary amines, weakly basic anion exchangers are formed, and with tertiary amines, strongly basic anion exchangers [1]. 1,1-Dimethylhydrazine (DMH) shows promise as an aminating agent, since it can react with CMPS via both the primary and secondary amino groups to form anion-exchange resins with specific performance characteristics. Such resins are of particular interest in view of the fact that, being one of the basic components of propellants, DMH is accumulated in vast amounts in a number of countries. In context of the existing disarmament agreements this work is also of a social significance.

EXPERIMENTAL

Commercial CMPS (purchased from the OMIS Joint-Stock Company, Omsk) was washed with acetone and dried to constant weight. The chlorine content in the copolymer was found to be 16.1%. 1,1-Dimethylhydrazine was distilled at 63°C.

Quaternization of DMH with chloromethylated polystyrene was carried out as follows. The polymer (10 g) containing 0.43 mol of fixed chlorine was allowed to swell in 24 ml of dioxane for 15 or 60 min at room temperature. Then DMH in 50 ml of water was added. The amount of the aminating agent in the system is given in Table 1. The process was performed at 35–92°C. The resulting product was washed with distilled water and dried to constant weight.

The resulting resin was tested for the thermal and chemical resistance and anion-exchange performance according the standard procedures [2, 3]. The polymer samples in the H form (nitrogen content 8.4%) were placed in vials with distilled water and allowed to stand for 24 h at 80, 100, and 150°C. In studying the chemical resistance, 1 g of the air-dry resin was treated with 100 ml of 5 N NaOH, HNO_3, H_2SO_4, or 10% H_2O_2 at 20°C for 24 h or at 100°C for 1 to 90 h. Then the samples were washed, dried, and analyzed for the weight loss, nitrogen content, and exchange capacity. Sorption of the salts listed in Table 2 was studied with the resin in the corresponding salt and OH forms. A 1-g sample of the dry resin was stirred in 100 ml of 0.1 N salt solution until the equilibrium was reached (constant pH). The concentrations of Cu^{2+} and Mn^{2+} in the equilibrium solution were determined chelatometrically with Na_2EDTA and Murexide as an indicator, and that of Fe^{2+}, by titration with 0.1 N $KMnO_4$. The amount of absorbed metal was estimated from the difference between the metal concentration in the initial and equilibrium solutions. Sulfate was determined by titration with $Ba(NO_3)_2$ in the presence of the chelatometric indicator chlorophosphonazo III. The residual concentrations of MnO_4^-, $Cr_2O_7^{2-}$, $Fe(CN)_6^{3-}$, and AsO_3^- were determined by titration with 0.1 N $Na_2S_2O_3$ and $KMnO_4$. The amount of absorbed anions was determined from the difference between their concentrations in the initial and equilibrium solutions. The resin was tested as a sorbent for wastewater treatment to remove uranium. For comparison, several commercial sorbents were

1070-4272/01/7411-1813$25.00

Table 1. Modification of chloromethylated polystyrene with 1,1-dimethylhydrazine*

Run no.**	τ_s, min	τ, h	*T*, °C	N, %	α, %	SEC, mg-equiv g^{-1}
			Solvent H_2O			
1	–	1.0	92	1.56	12.2	1.0
2	–	2.5	92	4.61	36.0	2.1
3	–	1.0	92	2.02	15.8	1.2
4	–	2.5	92	7.45	58.1	3.0
			Solvent dioxane–H_2O			
5	15	1.0	92	7.36	57.4	2.5
6	15	2.5	92	8.55	66.7	3.0
7	15	1.0	92	8.47	66.1	2.3
8	15	2.5	92	7.90	61.6	3.1
9	15	2.5	55	4.99	38.8	2.3
10	15	4.0	55	9.04	70.5	3.2
11	60	2.5	55	7.63	59.5	3.1
12	60	4.0	55	9.13	71.2	3.4
13	60	4.0	35	None	0	–

* (τ_s, τ) Swelling and reaction times, respectively; (α) degree of amination; and (SEC) static exchange capacity.
** CMPS/DMH = 1 : 3 except for run nos. 1, 2, 5, and 6 (1 : 2).

Table 2. Sorption of salts on modified chloromethylated polystyrene

Salt	Sorption efficiency, %				Sorption, mg-equiv g^{-1}			
	resin in anionic form		resin in OH form		resin in anionic form		resin in OH form	
	cation	anion	cation	anion	cation	anion	cation	anion
$FeSO_4$	2.8	26.8	3.4	5.6	0.15	1.36	0.18	0.71
$CuSO_4$	1.9	45.0	4.0	12.1	0.08	2.01	0.25	0.82
$MnSO_4$	0.5	24.1	5.6	4.2	0.04	1.66	0.35	0.25
$KMnO_4$	–	98.8	–	97.6	–	2.85	–	3.20
$K_2Cr_2O_7$	–	99.2	–	95.6	–	5.46	–	4.60
$K_3[Fe(CN)_6]$	–	98.9	–	97.8	–	3.50	–	3.27
$NaAsO_3$	–	96.6	–	92.3	–	2.86	–	2.75

tested under the same conditions (Table 3).[1] The wastewater composition was as follows (mg l^{-1}): U 0.09, surfactants 3.72, sulfate <40, and phosphate 82.4 (pH 9.2). The sorption capacity was determined by the static method with intermittent stirring (sample weight 2.5 g, liquid phase volume 0.25 l, contact time 4 days). The sorption power was estimated from the distribution coefficient Γ (ml g^{-1}):

$$\Gamma = A \times 10^3/C,$$

where *A* is the equilibrium sorption capacity for U (mg g^{-1}) and *C* is the U concentration in the equilibrium solution (mg l^{-1}).

The reaction of CMPS with hydrazine and some of its derivatives, including DMH, was reported previously [4–6]. However, we found no data on properties of the resulting products. Therefore, we studied the reaction of CMPS with DMH and characteristics of the resulting polymeric anion exchangers. The reaction was carried out in water or 32% aqueous dioxane. We studied the effects of the temperature, reagent ratio, and swelling time of CMPS in dioxane. We found (Table 1) that the reaction between CMPS and DMH proceeds at a noticeable rate at a temperature above 35°C and is completed in 1–4 h, the degree of

[1] Tests were carried out at the Novosibirsk Chemical Concentrates Plant, Joint Stock Company, Novosibirsk, Russia.

amination being dependent on the reaction time and DMH concentration, maximally approaching 71%. The static exchange capacity of modified CMPS (MCMPS) in 0.1 N HCl ranges from 1 to 3.4 mg-equiv g^{-1} (Table 1), indicating that it is a strongly basic anion exchanger whose macromolecules bear ionic groups formed via quaternization of DMH with CMPS. With increasing temperature to 92°C or DMH concentration the reaction accelerates, and the degree of amination approaches 8.5% in an hour. However, as the reaction time is further increased to 2.5 h the nitrogen content decreases to 7.9%. In this case we visually observed the decomposition of the initial CMPS granules at elevated temperatures.

It should be noted that the heterogeneous reaction of DMH with CMPS depends to a considerable extent on the swellability of the initial polymer in the reaction mixture. For example, the reaction in water at 92°C initially (in the first hour) is rather slow; the degree of amination in this case is as low as 12%, while after CPMS was preliminarily swollen for 15 min in an aqueous dioxane solution, all other reaction conditions being equal, the degree of amination increased by a factor of 4.7, whereas with increasing reaction time to 2.5 h it increased by a factor of only 1.8.

To reduce the effect of side reactions on the composition and properties of the anion exchangers, quaternization of 1,1-dimethylhydrazine with CMPS was performed at 55°C. However, in this case the degree of amination of CMPS gained in 2.5 h (38.8%) appeared to be lower by a factor of 1.7 as compared to the high-temperature reaction. With increasing reaction time to 4 h it increased to 70–71%, regardless of the swelling time of the initial CMPS.

Therefore, the optimal conditions for quaternization of DMH with CMPS are as follows: preliminary swelling of the initial polymer, aqueous dioxane as a reaction medium, temperature of 50–55°C, and reaction time of up to 4 h. All the data given below are related to MCMPS obtained under the indicated conditions.

The thermal and chemical resistance of anion exchangers is among the most significant criteria of their practical use. The test results showed that treatment of MCMPS with water at 80°C for 24 h causes only a slight weight loss (0.4%), the exchange capacity remaining practically unchanged (SEC 2.9 mg-equiv g^{-1}). Furthermore, these parameters remain unchanged even after treatment of the polymers with concentrated acids, alkalis, and hydrogen peroxide for 24 h at 20–30°C. However, at higher treatment temperatures (150°C for water or 100°C for the corrosive medium, τ 6 h) the exchange capacity decreases by 20–47% (in this case the nitrogen content decreases to 4–5%).

Table 3. Characteristics of various sorbents in uranium sorption from wastewater

Sorbent	*C*,* mg l^{-1}	*P*,** mg g^{-1}	Γ, ml g^{-1}
MCMPS	0.0010	0.0089	8900.0
Amberjet 4400 Cl (strongly (basic anion exchanger)	0.0055	0.0084	1536.4
Purolite S 920 (chelating resin)	0.0025	0.0087	3500.0
AN-2F	0.0085	0.0081	958.8
AV-17-8	0.0023	0.0088	3813.0
AVZ-NT-3.0 (activated carbon)	0.0880	0.0002	2.3
K63-NT-3.0 (carbonized coal)	0.0700	0.0020	28.6

* (*C*) Concentration of U-containing pollutants in the solution.
** (*P*) Equilibrium concentration of U-containing pollutants in the sorbent phase.

A 90-h treatment of MCMPS with 5 N HNO_3 or NaOH provides a 20–46% weight loss, which is accompanied by total degradation of the polymer. Therefore, the operation temperature of the investigated anion exchanger should not exceed 80°C, and in the presence of strong acids or alkalis the temperature should be below 30°C.

The ion-exchange characteristics of the resin were studied by the static method. In the experiments we used the chloride and OH forms. The sorption was performed from metal sulfate solutions and also from solutions containing alkali metal salts with complex anions (Table 2). The results demonstrate that, depending on the metal, the sorption of sulfate with the resin in the chloride form is 24–45%, which is considerably higher than that with the OH form (4–12%) (Table 2). Simultaneously we observed that the resin sorbs cations from the metal sulfate solutions. The OH form sorbs more strongly the cations than the Cl form (by a factor of 2–10) (Table 2). It was demonstrated that the sorption of cations is pH-dependent to a considerable extent: the cations are not sorbed from strongly acidic sulfate solutions (pH 2–3).

In the case of alkali metal salts with complex anions it was demonstrated that the cations, being strongly hydrated, are less efficiently sorbed, whereas the anion-exchange efficiency reaches 97–99% (Table 2).

To conclude, ion exchange in the static mode with MCMPS appeared to be quite efficient method for concentration of metals contained in complex anions, since these anions are readily desorbed in regeneration.

This method, requiring no sophisticated equipment, proved efficient in U recovery and concentration from wastewater (Table 3). Comparative analysis of data obtained with various sorbents shows that MCMPS has the best sorption capacity for uranium (U distribution coefficient 8900 ml g^{-1}).

CONCLUSIONS

(1) A method for utilization of 1,1-dimethylhydrazine is proposed, based on its quaternization with cross-linked chloromethylated polystyrene. As a result, strongly basic anion exchangers are obtained. The static exchange capacity for chloride of the resulting resins, measured in 0.1 N HCl, is 1–3.4 mg-equiv g^{-1}.

(2) Results on the thermal and chemical resistance of the anion exchangers reveal that their operation temperature should be below 80°C, and in the presence of strong acids or alkalis, 20–30°C.

(3) Ion exchange in the static mode with MCMPS is a quite efficient method for recovery and concentration of metals, particularly, uranium.

REFERENCES

1. *Entsiklopediya polimerov* (Encyclopedia of Polymers), Moscow: Sov. Entsiklopediya, 1972, vol. 1, pp. 161–170.
2. *Khimicheski-aktivnye polimery i ikh primenenie* (Reactive Polymers and Their Applications), Saldadze, K.M., Ed., Leningrad: Khimiya, 1969.
3. Saldadze, K.M., Pashkov, A.B., and Titov, V.S., *Ionoobmennye vysokomolekulyarnye soedineniya* (Ion-Exchange Macromolecular Compounds), Leningrad: Goskhimizdat, 1960.
4. Ševšik, S., Wichterle, O., and Peška, J., *Coll. Czech. Chem. Commun*., 1964, vol. 29, no. 2, pp. 464–477.
5. Evans, R.F. and Jones, J.I., *Chem. Ind.*, 1958, p. 915.
6. Zupan, M., Krajnc, P., and Stavber, S., *J. Polym. Sci., Part A: Polym. Chem.*, 1996, vol. 34, no. 12, pp. 2325–2331.

Russian Journal of Applied Chemistry, Vol. 74, No. 11, 2001, pp. 1817–1820. Translated from Zhurnal Prikladnoi Khimii, Vol. 74, No. 11, 2001, pp. 1763–1766.

APPLIED ELECTROCHEMISTRY AND CORROSION PROTECTION OF METALS

Microdistribution in Electrodeposition of Tin–Antimony Alloy from Sulfate Electrolytes with Organic Additives

G. I. Medvedev, S. S. Kruglikov, and N. Yu. Fursova

Novomoskovsk Institute, Mendeleev Russian University of Chemical Engineering, Novomoskovsk, Tula oblast, Russia

Received April 12, 2001

Abstract—The process of microdistribution in deposition of a tin–antimony alloy from sulfate electrolytes with organic additives (Syntanol, formalin, butynediol, coumarin, and benzyl alcohol) was studied.

The electrodeposition of the Sn–Sb alloy from sulfate electrolytes with organic additives was studied in [1–5]. It was shown that lustrous alloy coatings are formed at current densities in the range 0.5–12 A dm^{-2} from electrolytes containing simultaneously Syntanol, formalin, and butynediol; or Syntanol, formalin, and coumarin; or Syntanol, formalin, and benzyl alcohol. The content of antimony in the alloy varies between 0.6 and 32.5 wt %, depending on the electrolyte composition. With increasing cathodic current density, the content of antimony in the alloy decreases. It was of interest to study the leveling power of the given electrolytes.

Sulfate electrolytes for electrodeposition of the tin–antimony alloy were prepared from $SnSO_4$ and H_2SO_4 (both of chemically pure grade). Antimony was introduced into the electrolyte as follows. Antimony was preliminarily ground to obtain a finely dispersed powder which was then dissolved in concentrated H_2SO_4 with heating. The obtained $Sb_2(SO_4)_3$ solution was added to the electrolyte. The following organic additives were used: Syntanol DS-10 [TU (Technical Specifications) 6-14-577–77], formalin [37% solution, GOST (State Standard) 1625–75], 1,4-butynediol 35% solution, TU 6-45-52–79), coumarin, and benzyl alcohol (the last two of chemically pure grade). The composition of the main electrolyte used in the study was as follows (g l^{-1}): $SnSO_4$, 10 and 30; $Sb_2(SO_4)_3$, 0.8; H_2SO_4, 100; Syntanol, 2; and also formalin, 6 ml l^{-1}. Additionally, the following organic agents were introduced into the electrolyte: butynediol, 40 ml l^{-1} (electrolyte no. 1); coumarin, 2 g l^{-1} (no. 2); and benzyl alcohol, 5 ml l^{-1} (no. 3). The study was carried out at 20–22°C. Polarization curves were measured on a rotating disk electrode with a P-5827 potentiostat in the potentiodynamic mode. Before measuring a polarization curve, a 10-μm-thick layer of the tin–antimony alloy was deposited onto the disk electrode surface. The leveling power (P) of the electrolytes was determined directly by profiling of the sample surface with a sinusoidal microprofile. P was calculated by the formula [6]

$$P = \frac{2.3a}{2\pi h_{av}} \log (H_0/H_\tau),$$

where a is the wavelength of the sinusoidal microprofile (μm); h_{av} is the average coating thickness (μm); and H_0 and H_τ are, respectively, the initial and final amplitudes of the sinusoidal microprofile (μm).

The electrodeposition was performed under stirring with a blade stirrer at a speed of rotation of 300 rpm. The deposit thickness was 10 μm.

To reveal the influence exerted by separate organic substances on the microdistribution process, the dependence P–i_c was studied in electrolytes with various organic substances. The presence of only Syntanol in the electrolyte leads to minor leveling (P = 0.25–0.15) only at i_c = 0.5–1.0 A dm^{-2}. With i_c increasing beyond these limits, antileveling is observed. Addition of formalin to an electrolyte with Syntanol enhances the antileveling at i_c = 0.5–4.0 A dm^{-2} (Fig. 1, curve *2*). With the current density increasing to 5–7 A dm^{-2}, the antileveling effect becomes weaker, and at i_c = 8 A dm^{-2} P = 0. In electrolyte nos. 1–3, surface leveling occurs (Fig. 1, curves *3*–*8*). Thus, the last three substances among the mentioned organic compounds (Syntanol, formalin, butynediol, coumarin, and benzyl alcohol) are leveling additives.

1070-4272/01/7411-1817$25.00

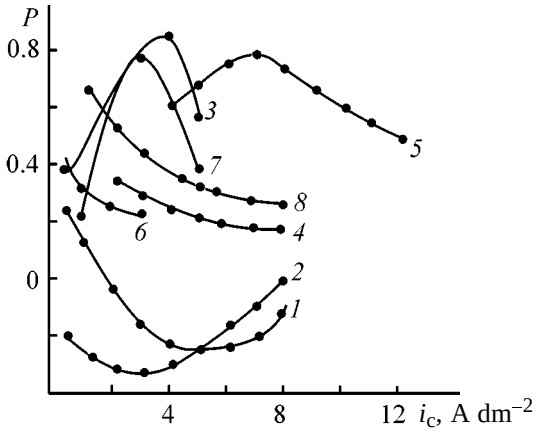

Fig. 1. Leveling power *P* of sulfate electrolytes in electrodeposition of Sn–Sb alloy vs. current density i_c. Electrolyte composition (g l^{-1}): $SnSO_4$ 30, $Sb_2(SO_4)_3$ 0.8, and H_2SO_4 100; the same for Fig. 2. (*1*) Electrolyte + Syntanol, 2 g l^{-1}; (*2*) *1* + formalin, 6 ml l^{-1}; (*3–5*) *2* + butynediol (40 ml l^{-1}), or coumarin (2 g l^{-1}), or benzyl alcohol (5 ml l^{-1}), respectively; (*6–8*) *3–5* with $SnSO_4$ (10 g l^{-1}).

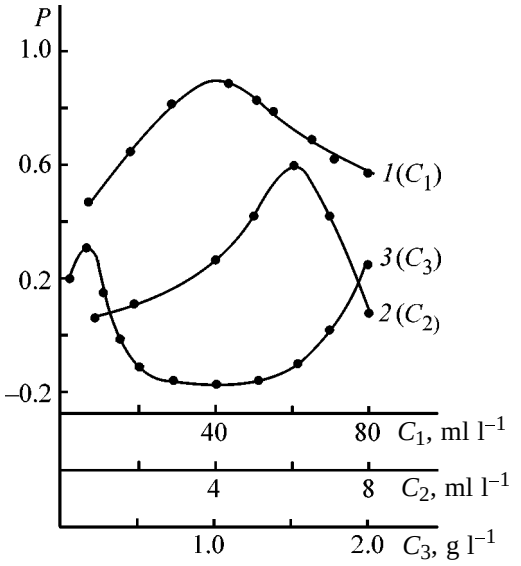

Fig. 2. Leveling power *P* of sulfate electrolytes for electrodeposition of Sn–Sb alloy vs. additive concentrations C_1, C_2, and C_3 at i_c = 4 A dm^{-2}. Additive: (*1*) butynediol, (*2*) benzyl alcohol, and (*3*) coumarin. Electrolyte + Syntanol (2 g l^{-1}) + formalin (6 ml l^{-1}); the same for Fig. 3.

Figure 1 shows that the dependence P–i_c is determined in electrolyte nos. 1–3 by the nature of a leveling additive and $SnSO_4$ concentration in the electrolyte. At $SnSO_4$ concentration of 30 g l^{-1} in electrolyte nos. 1 and 3 the dependence P–i_c passes through a maximum (curves *3*, *5*), and in electrolyte no. 2 *P* decreases with increasing i_c (curve *4*). In electrolyte nos. 1 and 3, containing 10 g l^{-1} of $SnSO_4$, the leveling power decreases with increasing i_c (curves *6*, *8*). In electrolyte no. 2, the dependence passes through a maximum, with the highest leveling power (P = 0.9) observed in the presence of butynediol (curve *3*).

The influence exerted by the concentrations of the leveling additives on *P* is illustrated in Fig. 2. It can be seen that, with increasing concentrations C_1 and C_2 of, respectively, butynediol (curve *1*) and benzyl alcohol (curve *2*), the *P* value passes through a maximum. For butynediol the highest leveling power (P = 0.9) is observed at concentration C_1 = 40, and for benzyl alcohol (P = 0.6), at C_2 = 6 ml l^{-1}. In electrolyte no. 2, the highest leveling power (P = 0.31) is achieved at C_3 = 0.1 g l^{-1} (curve *3*). Further increase in the coumarin concentration results in a dramatic decrease in *P*. At C_3 = 0.5–1.5 g l^{-1}, even antileveling of the surface is observed (P –0.1 to –0.18). At coumarin concentrations exceeding 1.5 g l^{-1} the degree of antileveling decreases, and at 2 g l^{-1} a weak leveling is again observed (Fig. 2, curve *3*).

Figure 3 presents cathodic polarization curves for alloy deposition from electrolytes with organic additives in relation to the speed of electrode rotation. It can be seen in Fig. 3a that raising the speed of rotation in electrolyte no. 3 to 200 rpm makes the cathodic polarization of the alloy deposition lower (curve *2*). However, with the speed of rotation increasing further, to 2000 rpm, the cathodic polarization grows somewhat (curve *3*). In electrolyte nos. 1 and 2 (Figs. 3b, 3c), a limiting-current plateau (I_{lim}) is observed in the cathodic polarization curves. With increasing speed of rotation, the i_{lim} value grows steeply and the cathodic polarization becomes lower (Figs. 3b, 3c, curves *1–6*). The i_{lim} value in these electrolytes is determined by adsorption of organic substances and formation on the electrode surface of polymolecular adsorption layers (Loshkarev effect) [7].

The mechanism of surface leveling is commonly explained in terms of the adsorption–diffusion theory [6] whose basic concepts are the following. All leveling additives inhibit electrodeposition of metals (alloys), with the extent of inhibition controlled by diffusion. Polarization curves measured with a rotating disk electrode at different speeds of rotation can qualitatively model the cathodic process at microprojections (high speeds of rotation) and in microdepressions (low speeds) [6]. The varied accessibility of the microprofile is the reason for nonuniform distribution of the rate of supply of organic substances to different parts of the microprofile. Since the inhibit-

ing influence exerted by leveling additives on metal (alloy) electrodeposition becomes stronger with increasing rate of diffusion of an additive toward the cathode (high speed of rotation), this influence is more pronounced at microprojections, and less so at microdepressions. This results in a nonuniform distribution of the metal electrodeposition rate. In view of the aforesaid, it was proposed to use for evaluating the influence of various additives the changes in cathodic polarization in going from one stirring mode to the other. If polarization grows with increasing speed of electrode rotation, then it would be expected that the additive should exert leveling influence under the given conditions.

Analysis of the polarization curves measured in electrolytes with organic additives shows that, in contrast to the cathodic polarization curves measured in electrolyte no. 3 (Fig. 3a), the polarization curves taken in electrolyte nos. 1 and 2 (Figs. 3b and 3c) in different stirring modes do not model the distribution of the alloy electrodeposition rate over the microprofile. The possible reason is that polymolecular adsorption layers are formed in this case. The hydrodynamic mode intensification affects the processes of formation and disintegration of such layers, with the rate of deposition of the alloy components changing in such a way that it outwardly looks like a manifestation of the antileveling effect. In view of this fact, the dependences P–i_c and P–C in electrolyte no. 3 can be accounted for as follows. With increasing i_c, first an increase in the leveling power is favored and then, at relatively high current densities, the high rate of surface renewal results in that the surface concentration of the additive and its inhibiting influence decrease even at microprojections, which must make the leveling effect weaker. At a too low content of an additive in the electrolyte, when the process of alloy electrodeposition is inhibited only slightly, it is unlikely that the leveling effect will be pronounced. At the same time, at too high additive concentrations the leveling power decreases, because the rate of supply of the additive and its inhibiting action are no longer diffusion-controlled.

It should be noted that the lower and upper limits of the concentration range with the maximum leveling power depend on (i) the electrolysis conditions (and current density, in particular) and (ii) the nature of leveling additives and presence of other organic substances in the electrolyte [6].

Electrodeposition from electrolytes in which polymolecular layers of organic substances are formed on the electrode surface has its specific features, e.g., the

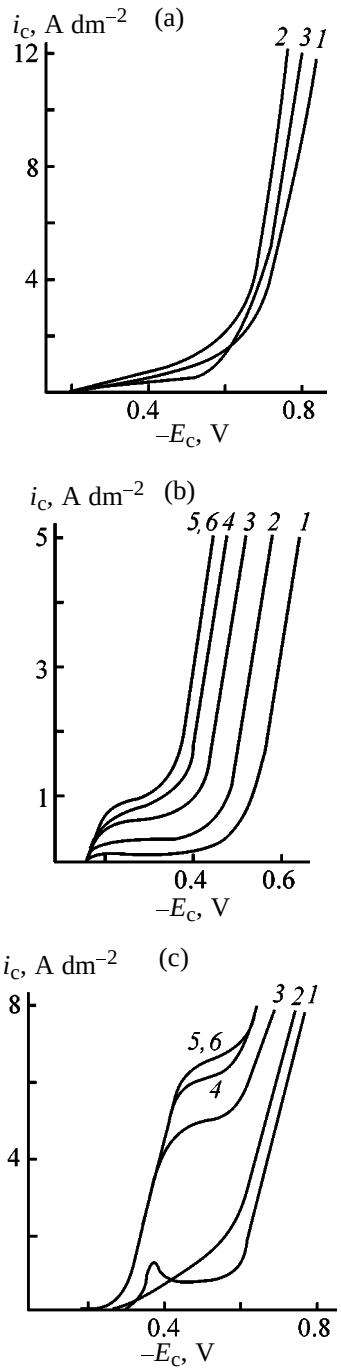

Fig. 3. Cathodic polarization curves of Sn–Sb alloy electrodeposition, measured in electrolyte nos. 1–3 at different speeds of electrode rotation. (i_c) Current density and (E) potential vs. standard hydrogen electrode. Electrolyte: (a) no. 3, (b) no. 1, and (c) no. 2. Speed of rotation (rpm): (*1*) 0, (*2*) 200, (*3*) 500, (*4*) 900, (*5*) 1500, and (*6*) 2000.

appearance of the adsorption-related limiting current. As seen from Fig. 3, this current markedly grows with increasing speed of rotation of the cathode. This is an indisputable proof of the influence exerted by the hy-

drodynamic mode on the properties of polymolecular layers. Their partial disintegration with increasing speed of rotation of the disk electrode leads to higher limiting current and lower cathodic polarization. At the same time, as indicated by direct measurements of the microdistribution of metal, the difference between the rates of supply of organic substances to microprojections and microdepressions, leading to the corresponding difference in their inhibiting influence, i.e., to positive leveling, is preserved at any particular hydrodynamic mode.

The change in the leveling powers of sulfate electrolytes with organic additives at $SnSO_4$ concentrations of 10 and 30 g l^{-1} (Fig. 1) shows that the adsorption–diffusion processes depend not only on the hydrodynamic conditions, but also on the metal ion concentration.

Thus, leveling of the surface microprofile is observed in electrodeposition of the Sn–Sb alloy from sulfate electrolytes with organic additives. Depending on the nature of organic substances, the cathodic polarization may either increase or decrease with increasing speed of rotation of the disk electrode. A decrease in the cathodic polarization with increasing speed of electrode rotation is observed in those cases when polymolecular adsorption layers are formed on the electrode surface. In systems of this kind, cathodic polarization curves obtained at different speeds of electrode rotation cannot model the distribution of the alloy electrodeposition rate over the microprofile because of the sensitivity of the adsorption layer, inhibiting the electrodeposition, to the hydrodynamic conditions. Apparently, measurements of cathodic polarization curves on a disk electrode at different speeds of rotation cannot be taken in this case as a basis for distinguishing between the leveling and nonleveling additives, as follows from the adsorption–diffusion theory of leveling [6].

CONCLUSIONS

(1) The microdistribution in electrodeposition of the tin–antimony alloy from sulfate electrolytes with organic additives (Syntanol, formalin, butynediol, coumarin, and benzyl alcohol) was studied. It is shown that, in electrolytes simultaneously containing Syntanol, formalin, and butynediol; or Syntanol, formalin, and coumarin; or Syntanol, formalin, and benzyl alcohol, the effect of leveling of the surface microprofile is observed.

(2) Depending on the nature of organic substances, the cathode polarization in alloy deposition may either increase or decrease with increasing speed of rotation of the disk electrode. The latter is observed in electrolytes in which polymolecular adsorption layers of organic substances are formed on the electrode surface.

(3) In the electrolytes in which polymolecular adsorption layers of organic substances are formed on the electrode surface, cathodic polarization curves obtained at different speeds of electrode rotation cannot model the distribution of the alloy electrodeposition rate over the microprofile and cannot serve as a basis for distinguishing between leveling and nonleveling additives.

REFERENCES

1. Medvedev, G.I., Zhuravlev, V.I., and Fursova, N.Yu., *Zh. Prikl. Khim.*, 1998, vol. 71, no. 7, pp. 1113–1120.
2. Medvedev, G.I. and Fursova, N.Yu., *Zh. Prikl. Khim.*, 2000, vol. 73, no. 3, pp. 403–406.
3. Medvedev, G.I., Zhuravlev, V.I., and Fursova, N.Yu., *Zh. Prikl. Khim.*, 2000, vol. 73, no. 4, pp. 673–676.
4. Medvedev, G.I. and Fursova, N.Yu., *Zashch. Met.*, 2000, vol. 36, no. 4, pp. 425–428.
5. Fursova, N.Yu., Erokhina, M.A., Medvedev, G.I., and Makrushin, N.A., *Progressivnaya tekhnologiya i voprosy ekologii v gal'vanotekhnike i proizvodstve pechatnykh plat: Materialy Rossiiskoi konferentsii* (Proc. Russian Conf. on Advanced Technologies and Environmental Problems in Electroplating and Printed-Circuit Board Production), Penza, 2000, pp. 20–22.
6. Kruglikov, S.S., A Study of Surface Microprofile Leveling in Electrodeposition of Metals, *Doctoral Dissertation*, Moscow, 1970.
7. Loshkarev, M.A. and Kryukova, A.A., *Zh. Fiz. Khim.*, 1949, vol. 23, no. 2, pp. 209–213.

Russian Journal of Applied Chemistry, Vol. 74, No. 11, 2001, pp. 1821–1828. Translated from Zhurnal Prikladnoi Khimii, Vol. 74, No. 11, 2001, pp. 1767–1774.

APPLIED ELECTROCHEMISTRY AND CORROSION PROTECTION OF METALS

Specific Features of Crystal Structure and Surface Topography of Copper Electrolytic Foils for Printed-Circuit Boards

B. N. Smirnov, V. N. Kozhanov, and V. N. Chuprakov

Ural Institute of Metals, State Scientific Center of the Russian Federation, Yekaterinburg, Russia
Institute of Metal Physics, Ural Division, Russian Academy of Sciences, Yekaterinburg, Russia
Uralelektromed' Joint-Stock Company, Verkhnyaya Pyshma, Sverdlovsk oblast, Russia

Received July 10, 2001

Abstract—Specific features of formation of a "pyramidal" surface relief and [110] texture in "raw" electrolytic copper foil obtained in industrial electrolyzers with rotating titanium drum cathode at varied current density and electrolyte composition and temperature were studied. The effect of how the drum cathode is treated prior to deposition on the crystal structure and surface topography of the raw foil was analyzed.

Presently, electrolytic copper foil (ECF) is most widely used for fabricating printed-circuit boards for radioelectronics. The foil is produced from "raw" ECF, thin (18–100 μm) solid electrolytic deposit of copper, commonly obtained in the form of a ribbon "continuously" coming out of an electrolyzer with rotating drum cathode. The deposition is performed at very high current densities and electrolyte circulation rates. It suffices to mention that deposition under the same current densities from unstirred electrolytes of the same composition must give powders [1–3].

Studies of thin solid electrolytic deposits of copper have been largely stimulated by the problem of obtaining raw ECF with a prescribed set of physical and technological properties, such as, e.g., roughness of the inner ("glossy") and outer ("rough") sides (relative to the cathode), continuity, plasticity, strength, etc. Nevertheless, published data on the structure, surface topography, and physical and technological properties of deposits formed on cathodes moving in a high-rate electrolyte flow are scarce [1, 2]. In this work we studied the structure and surface topography of copper deposits formed directly in industrial electrolyzers with rotating titanium drum cathode. The data are of interest not only from the technological standpoint, but also for revealing the specific features of copper electrocrystallization under such specific conditions.

EXPERIMENTAL

The foil was obtained in commercial KFE 1200/320 (henceforth KFE) and BEL-12M (BEL) electrolyzers and AIST 1600 M (AIST) pilot installation differing from BEL only in cathode diameter. The diameters of drum cathodes made of VT-1.0 forge titanium were, respectively, 320, 900, and 1600 mm. The foil width was 1200 mm. Detailed schematics of electrolyzers of this kind and their operation conditions were reported in [1, 2]. It is noteworthy that an additional insoluble anode made of an alloy of lead with silver was mounted at the bath exit of the KFE electrolyzer. In addition, prior to deposition, the surface of the drum cathode was subjected to mechanical polishing and anodizing in the case of KFE and only to mechanical polishing for BEL and AIST. The thickness of the raw foil was 32 ± 2.5 μm in all experiments, which was ensured by adjusting the speed of rotation of the drum cathode.

The electrodeposition conditions are presented in the table, with average "geometric" current densities D_c given. Figure 1b shows "local" current densities $D(L)$ in different parts of the drum cathode, situated near its section, circle, at a distance L from the entrance into the electrolyzer bath. For convenience of comparison, D and L are normalized to the maximum current density in the distribution, D_{max}, and the total length S of that part of the circumference of the drum cathode which is submerged in the electrolyte. These dependences are individual characteristics of electrolyzers, and their shape is close to that reported in [12]. The absolute $D(L)$ values can be readily found using the data in the table (D_c) and D_c/D_{max} values presented in Fig. 1b.

1070-4272/01/7411-1821$25.00

Preparation conditions and topographic and structural characteristics of raw ECF.* Content of chloride ions in the electrolyte 30 ± 5 mg l^{-1}; rate of electrolyte circulation, $m^3\ h^{-1}$: 100 for KEF and 25 for AIST and BEL

Sample no.	Electrodeposition conditions					Shape of projections on rough side of ECF	d, μm	$\Delta d/d$, %	P_{hkl}			
	$C_{C^{2+}}$, M	$C_{H_2SO_4}$, M	$C_{b.g.}$, mg l^{-1}	D_c, A dm^{-2}	T, °C				111	200	220	311
KFE apparatus												
1	1.1	0.9	1.0	46	40	Pyramid, hemisphere	7.3	25	0.1/0.7	0.1/0.8	3.4/1.5	0.4/1.0
2	0.8	1.0	1.0	49	40	Pyramid, hemisphere	4.1	37	0.6/0.8	0.3/1.0	2.4/1.2	0.7/1.0
3	0.8	0.9	1.0	39	40	Pyramid, hemisphere	5.5	29	0.2/0.6	0.2/0.8	3.2/1.3	0.5/1.2
4	0.8	0.9	2.5	39	40	Pyramid, hemisphere, globule	4.5	26	0.4/0.9	0.3/0.8	2.8/1.2	0.5/1.1
5	0.8	0.9	7.5	39	40	Pyramid, hemisphere, globule	2.0	37	1.0/1.1	0.8/0.9	1.2/1.1	1.0/0.9
AIST apparatus												
6	1.1	0.8	1.0	27	40	Pyramid	7.4	31	0.1/0.8	0.1/0.9	3.7/1.7	0.1/0.6
7	1.1	0.8	1.0	27	52	Pyramid, polyhedron	8.2	35	0.2/1.0	0.4/1.1	3.1/1.0	0.3/0.9
8	1.1	0.8	1.0	40	40	Pyramid	6.9	30	0.0/0.7	0.0/0.7	3.9/2.0	0.1/0.6
9	1.1	0.8	1.0	40	52	″	7.8	34	0.2/0.9	0.1/1.0	3.5/1.3	0.2/0.8
10	1.1	0.8	1.0	50	40	″	6.5	30	0.0/0.7	0.0/0.6	3.9/2.2	0.1/1.5
11	1.1	0.8	1.0	50	52	″	7.3	36	0.1/0.9	0.0/0.9	3.8/1.6	0.1/0.6
12	1.1	0.8	1.0	56	40	″	5.5	29	0.1/0.9	0.1/0.8	3.6/1.6	0.2/0.7
13	1.1	0.8	1.0	56	52	″	6.3	35	0.0/0.8	0.0/0.7	3.8/1.7	0.2/0.2
14	1.1	0.8	1.0	56	60	″	8.5	36	0.1/1.0	0.1/0.9	3.7/1.4	0.1/0.7
BEL apparatus												
15	1.1	0.8	1.0	47	52	Pyramid	6.1	26	0.1/0.7	0.0/0.8	3.8/1.6	0.1/0.8

* $C_{Cu^{2+}}$, $C_{H_2SO_4}$, and $C_{b.g.}$ are the concentrations of copper(II) ions, sulfuric acid, and bone glue, respectively, in the electrolyte; D_c is the ratio of the current load to the surface area of the cathode through which current is passed; T is the averaged electrolyte temperature at its entrance into, and exit from the interelectrode space (±1.5°C); P_{hkl}: data for the rough and glossy sides of ECF are given in the numerator and denominator, respectively.

The surface topography was studied using YCXA-733 and REM-100 U scanning electron microscopes at inclinations of the sample plane with respect to the horizontal plane of the microscopes equal to 0 and 30°. Outlines of projections (at base) were clearly seen in SEM surface images of the rough side of the foil, obtained without sample tilt (Fig. 2b). The conventional metallographic method of determining the average length of a segment intersecting a contour [4] was used to evaluate the average size of projection bases in the focal plane, d, and the averaged relative deviation of this value, $\Delta d/d$ (see table). The images obtained with inclined samples (Fig. 1) suggest that the projection height must not exceed substantially half their transverse size at base.

The surface topography was also studied using carbon–chromium replicas on an EMMA-4 transmission electron microscope (TEM) with a considerably higher resolution (Fig. 3). The results obtained in studying the surface topography were compared with TEM images of microstructure, obtained on the same microscope. For this purpose, ECF samples were thinned on both sides with a 66% aqueous solution of orthophosphoric acid.

The microstructure of ECF cross sections was

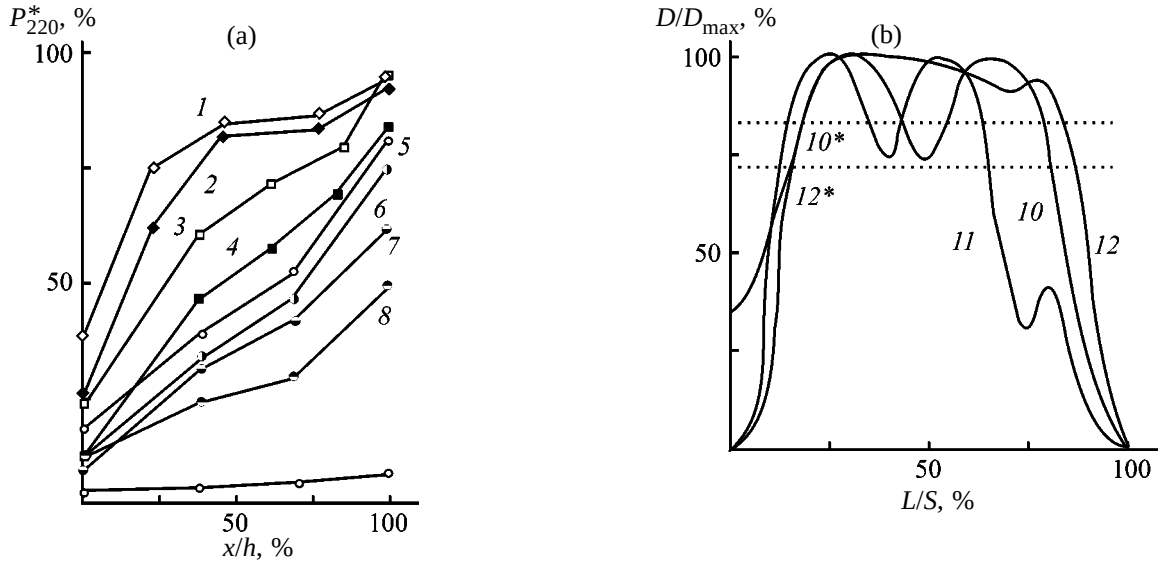

Fig. 1. (a) Variation of the texturing coefficient P^*_{220} with depth x/h and (b) current density D/D_{max} in different parts of the cross section of the drum cathode at a distance L/S from the entrance into the electrolyte. Sample no.: (*1*) 15, (*2*) 16, (*3*) 13, (*4*) 9, (*5*) 1, (*6*) 3, (*7*) 4, (*8*) 2, and (*9*) 5. Apparatus: (*10, 11*) KFE with and without additional anode, respectively; (*12*) BEL. (*10*, 12**) D_c/D_{max} (D_c values from table) for BEL and KFE, respectively.

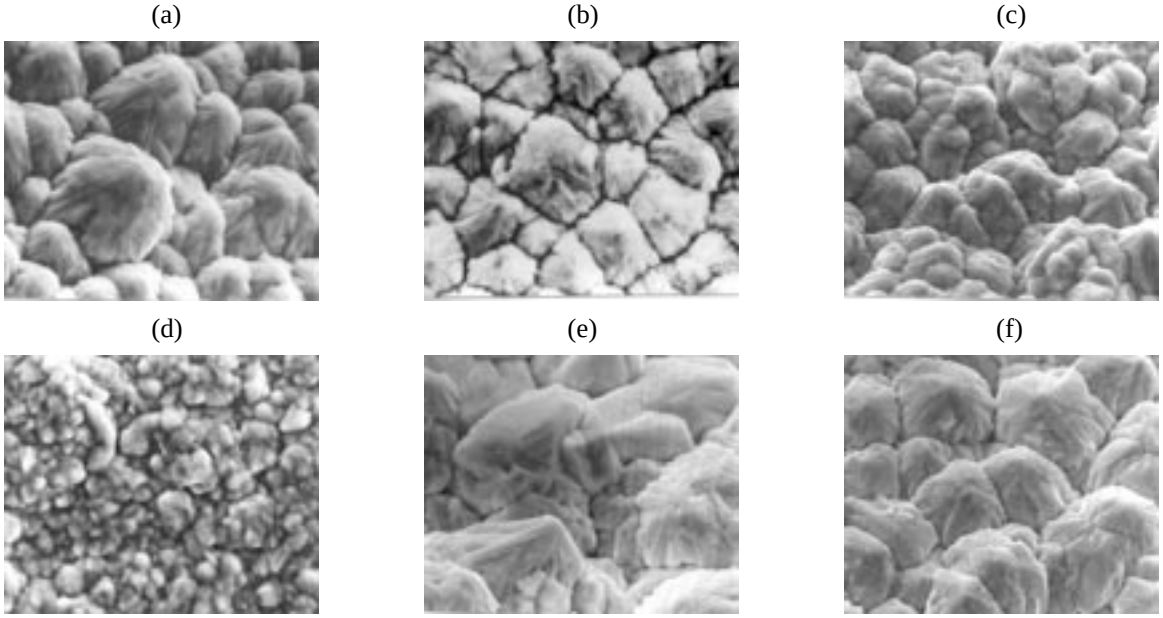

Fig. 2. SEM images of the ECF surface on the rough side. Sample no. and its inclination angle (deg) in the microscope, respectively: (a) 1, 30; (b) 3, 0; (c) 4, 30; (d) 5, 0; (e) 7, 30; and (f) 15, 30. Magnification: (a) 950, (b–d) 1300, (e) 1100, and (f) 700.

studied on an Ynavert optical microscope (Fig. 4). To reveal the microstructure, the cross sections were thoroughly polished and then etched for several seconds in a mixture of aqueous solutions of ammonia (25%, 50 ml) and hydrogen peroxide (3%, 50 ml). It is noteworthy that the finishing polishing was always done along the foil surface.

The texture was studied using a DRON-2.0 X-ray diffractometer with CoK_α radiation and iron filter. The texturing coefficient P_{hkl} was found in the experiment [3, 5]

$$P_{hkl} = n(I_{hkl}/I_{r,\,hkl})[\Sigma\,(I_{hkl}/I_{r,\,hkl})]^{-1}, \qquad (1)$$

where I_{hkl} and $I_{r,\,hkl}$ are the intensities of X-ray reflections in the sample being analyzed and texture-free

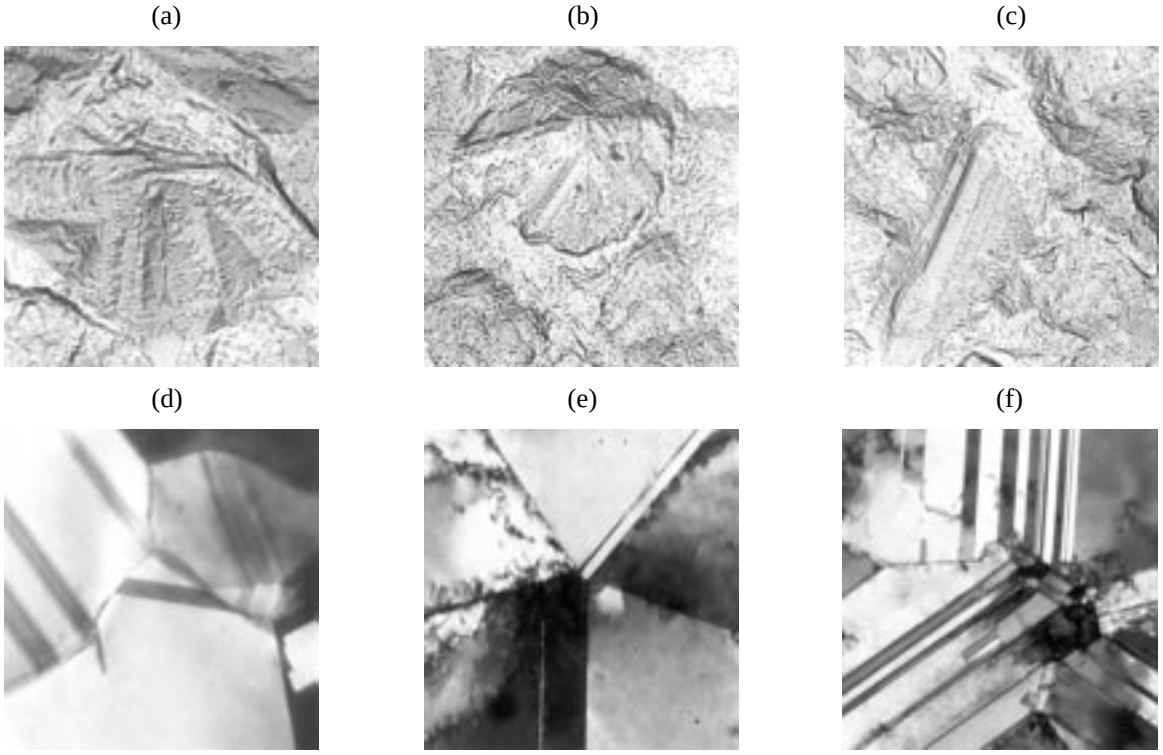

Fig. 3. TEM images of (a–c) surface and (d–f) microstructure of raw ECF (sample no. 2). Magnification: (a) 11 000, (b) 6500, (c) 5500, (d) 20 000, (e) 25 000, and (f) 15 000.

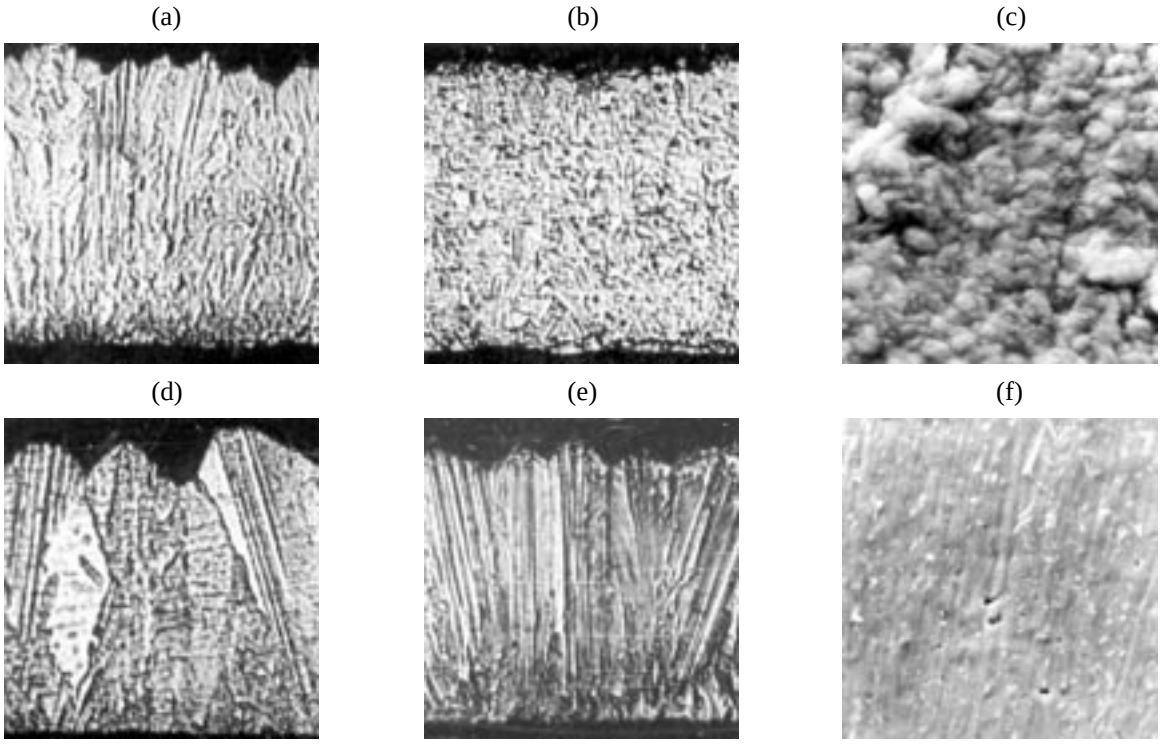

Fig. 4. (a, b, d, e) Optical images of cros sections and (c, f) SEM images of the glossy side. Sample no.: (a) 3, (b) 5, (c) 1–5, (d) 6, (e) 15, and (f) 6–16. Magnification: (a, b, d, e) 1100, (c) 2500, and (f) 1900.

(isotropic) sample, respectively; and n is the number of samples being analyzed.

For the texture-free sample, $P_{hkl} = 1$, whereas at full orientation of grains in a direction toward one of the (hkl) planes $P_{hkl} = n$. An analysis of P_{hkl} was made for the four strongest copper reflections (see table).

The thickness of the layer of 50–75% attenuation of the CoK_α X-ray radiation by copper in the considered range of Bragg reflection angles is 408 μm [6]. This makes it possible to trace changes in P_{hkl} across the foil thickness by successively removing from the foil surface layers 5–10 μm thick. To perform a layer-by-layer analysis, a foil sample was glued onto the surface of a diffractometer holder, and then polished mechanically on a Metapolan installation with controllable load on the ground section and time of polishing. The automated mode was used, ensuring chaotic motions of a sample in a suspension of GOI abrasive paste. The object thickness was determined with a micrometer with an accuracy of ±2.5 μm. For clarity, the reduced texturing coefficient was used (%) (Fig. 1a)

$$P^*_{220} = 100(P_{220} - 1)/3, \quad (2)$$

for the relative distance from the foil surface (depth) x/h, where h is the foil thickness. The value $x = 0$ corresponds to the glossy side.

It is known [5] that mechanical polishing of metals (including copper) gives rise to strains in the surface layer of thickness (0.5–1 μm) (Bilby layer), which lead to a profound change in its structure: grain becomes finer, deformation texture appears, etc. If the thickness of the object being analyzed is comparable with the Bilby layer thickness, the latter will make a noticeable contribution to the diffraction pattern, which is commonly the case in electron diffraction studies of mechanically polished samples. No noticeable broadening of X-ray reflections was observed in the present study on going from the initial glossy to a polished surface, which is the primary indication of the influence exerted by the fact that the grains become finer on the results of X-ray diffraction analysis. Even if the surface layer texturing does exist, the corresponding contribution to P_{hkl} at different analysis depth must be approximately the same in view of the identical polishing conditions.

For a foil from the KFE apparatus, the microprojections on the rough side have the form of pyramids or hemispheres (see table, Fig. 2). In more detail the structure of these surface units (growth forms) can be seen in TEM images of carbon–chromium replicas of the rough side of sample no. 2 (Fig. 3).

Two types of pyramids are clearly distinguished: pointed and truncated, with the former occurring more frequently than the latter (Figs. 3b and 3c). The pyramids have complex multifaceted relief of the lateral surface, characterized by the presence of a great number of reentering angles, which are presumably associated with the emergence of twinning planes to the lateral surface (Figs. 3a–3c). As a rule, the pyramids are much larger than hemispheres (Fig. 3b). Projections, represented by a single growth form, occur rarely. Elements of faceting are present on the lateral surface of the hemispheres (Fig. 3c). Presumably, with increasing size of separate projections, hemispheres turn into pyramids.

The size and relative content of projections of various shapes on the surface of ECF produced in the KFE apparatus strongly depend on the deposition conditions (see table). With decreasing current density or increasing volume content of copper ions in the electrolyte with prescribed content of additives, pyramids with rather close sizes and orientations relative to the normal to the surface occur as the main growth form on the surface (Figs. 2a, 2b, sample nos. 1, 3). Contrariwise, at higher current densities and low content of copper(II) in the electrolyte, the fraction of small hemispheres increases dramatically on the ECF surface, with larger pyramids also present (Fig. 3, sample no. 2). Correspondingly decreases the average size of projections and increases the averaged deviation $\Delta d/d$. It is noteworthy that increasing current density, decreasing concentration of discharging ions in the electrolyte bulk, and decreasing temperature of the electrolyte correspond to higher degree of concentration limitations on the course of the cathodic reaction (to a decrease down to zero of the concentration of ions discharging at the cathode surface) [7].

The texturing of the rough side of ECF strongly depends on its surface topography. The texturing coefficient P_{220} grows with increasing number of pyramids on the surface of the rough side, and falls with increasing number of hemispheres (see table). Lowering the content of bone glue in the electrolyte leads to a substantial decrease in projection sizes. The corresponding decrease in P_{220} may be due both to an increase in the fraction of hemispheres and to mutual misorientation of small pyramids, which make up large globular formations together with hemispheres (Figs. 2c, 2d).

According to [8], there exists a direct relationship

between the growth form on the surface and TEM images of the microstructure in the bulk of thin deposits of nickel, which is close to copper in crystal structure and electrochemical parameters. No clear-cut relationship of this kind was observed in the case of ECF. The electron-microscopic contrast in grains is a typical "twinning" contrast formed by a set of lines intersecting at multiple twinning sites or parallel to one another. It is only possible to distinguish elements of intragrain microstructure, corresponding to the established [8] twinned pentahedral pyramids with growth direction [110] (Fig. 3e). To the hemispheres presumably correspond microstructural elements shown in Fig. 3d. To truncated pyramids (with growth direction [211] [8]) must correspond grain microstructure with a set of equally spaced parallel twinning lines. Such elements can also be found in TEM images (Fig. 3f). Commonly, the intragrain structure is exceedingly complex and indicates the presence in a growing projection of several multiple-twinning axes (Fig. 3f). It is noteworthy that the TEM images of the microstructure of different ECF samples analyzed in this study are very similar. With increasing texturing of the rough side, only the number of twinning lines and nodes grows in the foil bulk.

The highly textured electrolytic deposits of copper must be characterized by "columnar" grain microstructure on cross sections [3]. It is of interest to correlate the data on the microstructure of cross sections of ECF obtained in the KFE apparatus (Figs. 4a, 4b) with changes in the texturing coefficient across the foil thickness (Fig. 1a). The pyramid growth presumably occurs only at a certain deposit height, nearer to the rough side of ECF. It is in this region that the columnar structural elements and the corresponding drastic increase in the texturing coefficient are most clearly observed (Figs. 4a, 1a, respectively). Sections of the texture-free sample no. 5 (Fig. 4b) show no elements of this kind. Fine randomly oriented pyramids (Fig. 2d) have no continuation in the bulk and, in all probability, are nuclei of this growth form on the surface of the rough ECF side.

ECF is formed in the KFE electrolyzer under the conditions when the spherulite and pyramidal growth forms coexist. It is known that, when concentration limitations are lifted, it is through the spherulites that the transition to solid textured copper deposits occurs [9, 10]. Spherulites [11] are three-dimensional (3D) nuclei developing in the radial direction. A solid deposit obtained under strong concentration limitations may be entirely composed of very fine spherulites [12].

The pyramid growth mainly occurs in the region where the foil exits the KFE electrolyzer bath. The appearance of the pyramidal growth form on the ECF surface as the main topographic element may be largely due to the presence of an additional anode at the KFE electrolyzer exit. Its presence makes longer the working path of the drum cathode with current flowing, thereby improving the electrolyzer efficiency, and, at the same time, ensures a delay in current density drop at the foil exit from the electrolyzer, as seen in Fig. 1. This presumably creates conditions for transition from the spherulite to the pyramidal growth form. Without an additional anode, the ECF has the same topographic characteristics as sample no. 4 (Fig. 2c). Concretions of fine pyramids and hemispheres are always present on its surface. The surface topography does not change significantly on varying the deposition conditions within the same limits.

The pyramids are the main structural element on the surface of the rough side of ECF obtained in BEL and AIST apparatus under any deposition conditions (see table). Lowering the current density (at fixed temperature) and elevating the electrolyte temperature (at fixed current density) equally lead to an increase in the pyramid size (see table, Figs. 2e, 2f). At the lowest current densities and elevated temperatures (sample no. 7), rather large polyhedra without clearly pronounced vertices appear together with the pyramids (Fig. 2e).

The optical cross-sectional images of foils produced in AIST and BEL apparatus clearly show "columnar" grains (Figs. 4d, 4e). Inside the grains, sets of parallel lines are present, intersecting the foil from both sides. Raising the current density and lowering the temperature leads to a more clearly pronounced microstructure of this kind over the entire section surface. It may be assumed that the formation of pyramids in the case of strongly textured foils produced on AIST and BEL apparatus begins in the immediate vicinity of the glossy side, and then the mechanism of their growth remains unchanged until the removal of the foil from the drum cathode. The observed intragrain microstructure may result from the presence within a pyramidal projection of several multiple twinning axes parallel to the direction of its growth and, correspondingly, from the intersection of the twinning surfaces with the section surface. The possible formation of such a kind of microstructure was mentioned in [8].

These results are in agreement with data on variation of the texturing coefficient across the ECF thickness (Fig. 1a). The most strongly textured foils are

characterized by a steep rise in P^*_{220} (x/h) already near the glossy side. The higher the current density and the lower the temperature, the higher the texturing coefficient at any distance from the surface (of those studied). Thus, in contrast to KFE, the deposition of foils with higher texturing coefficient in the BEL and AIST apparatus occurs under the conditions of enhanced concentration limitations on the cathodic reaction.

The variation tendencies displayed by the crystal structure and topography of ECF obtained in different apparatus under different deposition conditions are, on the whole, in agreement with the existing concepts of how various types of electrolytic copper deposits are formed [13, 14]. With increasing extent of concentration limitations, the structural types of solid electrolytic copper deposits must replace one another in the following order: BR $\rightarrow$ (Z $\rightarrow$ FT) $\rightarrow$ UD [14].

In experiments on AIST and BEL, the projection size grows, and even large polyhedra appear on the surface, with decreasing extent of concentration limitations. This presumably reflects a transition to layered deposits of the BR type, whose growth is commonly attributed to development of 2D nuclei.

Under virtually any deposition conditions, a foil is formed in AIST and BEL apparatus, whose cross-sectional microstructure is characteristic of deposits with twinning (Z) and fibrous (FT) types of texture. The growth of deposits of this kind may be related to development of "quasi-2D" layers whose growth rate in directions perpendicular to the cathode surface markedly exceeds the rate of their spreading along its surface [13].

The formation of solid fine-grained unoriented UD deposits is related to development of “3D” nuclei. In the case of the KFE apparatus, the UD structural type is the main constituent of the foil microstructure. With increasing extent of concentration limitations, the share of this component grows, whereas in the opposite case, with the concentration limitations becoming weaker, the fraction of the texture component grows. A transition to UD deposits must occur faster if the content of a surfactant in the electrolyte is raised [14]. This is well illustrated by the example of KFE foils obtained at different amounts of additives.

The shape of the pyramidal projections on the surface of deposits with [110] texture, studied in [3, 15–17], is in close agreement with that reported here. It should be emphasized that the problem of relationship between the shape of the pyramidal projection and the mechanism of its growth in the case of the [110] texture remains unsolved. Formation of pyramids with multifaceted relief of the lateral surface cannot be described in terms of a simple model of nucleation and growth of 2D layers [3, 14].

In the experiments, pyramids were formed under conditions close to (AIST, BEL), or exactly coinciding with (KFE) the conditions when the 2D nucleation is replaced by 3D nucleation. According to the obtained results, twinning may occur in the growth of a pyramidal projection not only on lateral (111) faces [3, 14, 18], but also with formation within the projection of multiple twinning axes in the direction of its vertical growth. It is the emergence of the twinning planes on the lateral face that possibly gives rise to its complex topography. In this study, the direction of preferred orientation was determined to be [110]. Nevertheless, a pyramidal projection may also be formed as a result of development of a multiply twinned quasi-2D nucleus of specific shape, e.g., with a [411]t twinning axis close to the [110] texture axis [15]. This issue invites further, more detailed investigation of the ECF texture by special diffraction techniques [5, 15].

The foil produced by the AIST and BEL apparatus markedly differs from that formed in KFE both in the surface topography of the rough side and in the microstructure and extent of its texturing, especially in the initial stages of growth. The difference between the growth mechanisms of deposits is clearly seen in SEM images of their glossy sides. The surfaces of the glossy sides of the AIST and BEL foils are identical (Fig. 4f), being an exact replica of the mechanically polished surface of the drum cathode. The presence of a minor amount of “nonlinkability” micropores indicates that atomic layers of the deposit spread over the cathode surface to the point of projection merging. The surface relief on the glossy side of the KFE ECF is much more pronounced. The obtained SEM images (Fig. 4c) indicate that a great number of 3D crystallites with faces of several micrometers in size grow in the immediate vicinity of the cathode. It should be emphasized that this difference between the topographies of the glossy sides of ECF was preserved under any deposition conditions, even in those cases when these conditions were close for all the three electrolyzers (sample nos. 1, 10, 15).

The observed difference in the ECF structure is possibly due to anodic oxidation of the drum cathode, which is an additional operation in surface treatment of the drum cathode of the KFE electrolyzer. Similar changes in the ECF surface topography and the texturing coefficient have already been observed previously

in studying the electrodeposition of copper onto stationary and submerged titanium cathodes with different types of surface treatment: mechanical polishing and anodic oxidation [16, 17, 19]. In the initial stage of deposit growth, anodizing the titanium cathode leads to greater number and smaller size of nuclei. Further effect of the layer formed in anodic oxidation is in all probability due to the increasing content of ions of titanium and its colloid particles, which are formed in cathodic reduction of an oxohydride titanium film [20].

CONCLUSIONS

(1) Electrolytic copper foil is obtained in electrolyzers with rotating titanium drum cathode under conditions close to, or exactly coinciding with the conditions of 3D deposit nucleation, which predetermines the texture and topography of the foil surface.

(2) The growth of a foil with [110] texture is accompanied by formation of pyramidal projections on its surface. The complex multifaceted relief of the lateral surface of these projections is presumably due not only to twinning at the crystallization front, but also to formation within a projection of [110] multiple twinning axes in the direction of the vertical growth of the projection.

(3) The deposition conditions under which the foil possesses the maximum extent of [110] texturing were determined. Anodizing the titanium drum cathode favors 3D nucleation and presumably accelerates the transition to electrolytic copper foil with unoriented microstructure and surface relief of fine hemispheres.

ACKNOWLEDGMENTS

The authors are grateful to A.D. Artem'ev, T.Yu. Karateeva, N.V. Andreeva, L.D. Naumova, V.V. Fedorenko, S.A. Simonyans, and N.I. Karimova for help in separate stages of the study.

REFERENCES

1. Kozlov, V.A., Naboichenko, S.S., and Smirnov, B.N., *Rafinirovanie medi* (Copper Refining), Moscow: Metallurgiya, 1992.
2. Orekhov, M.A., *Proizvodstvo mednoi elektroliticheskoi fol'gi* (Manufacture of Electrolytic Copper Foil), Moscow: Gintsvetmet (MP Fol'ga), 1992.
3. Kang, S., Yang, Y., and Lee, D., *Plat. Surface Finish.*, 1995, vol. 82, no. 10, pp. 67–70.
4. *Tools and Techniques in Physical Metallurgy*, Weinberg, F., Ed., New York: Springer, 1969.
5. Barrett, C.S. and Massalski, T.U., *Structure of Metals*, Oxford: Pergamon, 1980.
6. Mirkin, L.I., *Spravochnik po rentgenovskomu analizu polikristallov* (Handbook of X-ray Analysis of Polycrystals), Moscow: GIFMP, 1961.
7. Bagotskii, V.S., *Osnovy elektrokhimii* (Foundations of Electrochemistry), Moscow: Khimiya, 1988.
8. Epelboin, Y., Froment, M., and Maurin, G., *Plating*, 1969, vol. 28, no. 12, pp. 1356–1362.
9. Fukunaka, Y., Doi, H., and Kondo, Y., *J. Electrochem. Soc.*, 1990, vol. 137, no. 1, pp. 88–93.
10. Smirnov, B.N., Murashova, I.B., and Kozhanov, V.N., *Zh. Prikl. Khim.*, 1999, vol. 72, no. 9, pp. 1466–1475.
11. Mamontov, E.A., Kurbatova, L.A., and Volenko, A.P., *Elektrokhimiya*, 1987, vol. 23, no. 2, pp. 187–191.
12. Mamontov, E.A., Kurbatova, L.A., and Volenko, A.P., *Elektrokhimiya*, 1986, vol. 22, no. 5, pp. 629–633.
13. Fisher, H., *Plating*, 1969, vol. 56, no. 11, pp. 1229–1233.
14. Winand, R., *Trans. Inst. Min. Metall., Sect. C*, 1975, vol. 84, no. 823, pp. C67–C75.
15. Rashkow, S., Stoichev, D.S., and Tomov, I., *Electrochim. Acta*, 1972, vol. 17, pp. 1955–1964.
16. Samoilenko, V.N., Inozemtseva, O.A., Kozhanov, V.N., and Utrobina, I.F., *Gal'vanotekh. Obrab. Poverkhn.*, 1996, vol. 4, no. 3, pp. 5–11.
17. Samoilenko, V.N., Inozemtseva, O.A., Utrobina, I.F., and Kozhanov, V.N., *Zh. Prikl. Khim.*, 1998, vol. 71, no. 3, pp. 416–426.
19. Kucherov, A.A., Samoilenko, V.N., and Pomosov, A.V., *Elektrokhimiya*, 1989, vol. 25, no. 6, pp. 753–757.
20. Smirnova, E.N., Kozhanov, V.N., Samoilenko, V.N., and Merzlyakov, A.V., *Elektrokhimiya*, 1989, vol. 25, no. 5, pp. 659–662.

Russian Journal of Applied Chemistry, Vol. 74, No. 11, 2001, pp. 1829–1833. Translated from Zhurnal Prikladnoi Khimii, Vol. 74, No. 11, 2001, pp. 1775–1779.

APPLIED ELECTROCHEMISTRY AND CORROSION PROTECTION OF METALS

Anodic Dissolution of Titanium Alloys in Hydrofluoric-Sulfuric Acid Electrolytes with Additives

E. A. Fedorova

Nizhni Novgorod State Technical University, Nizhni Novgorod, Russia

Received July 2, 2001

Abstract—Anodic dissolution of VT1-0, VT6, and VT16 titanium alloys in hydrofluoric-sulfuric acid solutions with addition of alkali metal fluorides, glycerol, hexamethylenetetramine, and remantadine was studied in a wide range of potentials.

Commonly, the anodic behavior of "pure" metals, both in the range of limiting currents [1–3] and in the post-passive state [4], is accounted for in terms of diffusion mass-transfer [4, 5] and formation of a thin surface salt film on a metal [6]. The possibility that an anodic oxide film (AOF) is formed on the metal surface and is chemically dissolved in acid electrolytes for anodic treatment is not ruled out, either [1–4]. Specific features of anodic dissolution of alloys with varied extent of alloying are less understood. Of practical interest is anodic treatment of titanium alloys as a preliminary operation before depositing a titanium nitride layer on articles for aircraft, natural gas, and other industries [7–9]. As shown previously [8, 9], electrochemical treatment of the surface of VT1-0, VT6, and VT8 titanium alloys in the developed electrolytes made it possible to obtain the required functional characteristics of the surface of metalware: zero microstrain and relative leveling $K > 65\%$. Difficulties were encountered in anodic treatment of the VT16 alloy: the voltage across the electrolytic bath exceeded 10 V, samples were covered with a matte film, and the stressed-strained state of their surface was preserved [9].

In this work we analyzed the influence exerted by the extent of alloying of titanium alloys on their anodic behavior in electrochemical treatment in hydrofluoric-sulfuric acid solutions without additives and with addition of alkali metal fluorides, glycerol, hexamethylenetetramine, and remantadine at potentials E = 2–9 V (vs. s.h.e.), and the properties of the forming surface AOFs.

EXPERIMENTAL

The anodic treatment of VT1-0, VT-6, and VT16 titanium alloys containing various alloying components (Table 1) was done in hydrofluoric-sulfuric acid solutions of the following composition (M): H_2SO_4 11.2–11.7 and HF 11.5, without additives and with addition of potassium (or sodium) fluoride (0.5–0.52 M), glycerol (2 M), and hexamethyleneteramine and remantadine [$(2.0-4.0) \times 10^{-2}$ M] at 293 K. The solutions were prepared using double-distilled water from ultrapure and chemically pure grade chemicals.

Electrochemical measurements were carried out with a PI-50-1 potentiostat, an LKD-4 self-recorder, a three-electrode cell with separated electrode spaces,

Table 1. Content of alloying components and impurities in titanium alloys [according to GOST (State Standard) 19807–91]

Alloy brand	Alloying component, wt %			Impurities, no more than, wt %				
	Al	Mo	V	C	Fe	Si	H_2	O_2
VT1-0				0.05	0.2	0.08	0.015	0.1
VT6	4.3–6.2	–	3.8–4.3	0.1	0.1	0.1	0.1	0.1
VT16	3.8–6.3	4.5–5.5	4.0–5.5	0.1	0.25	0.15		0.15

1070-4272/01/7411-1829$25.00

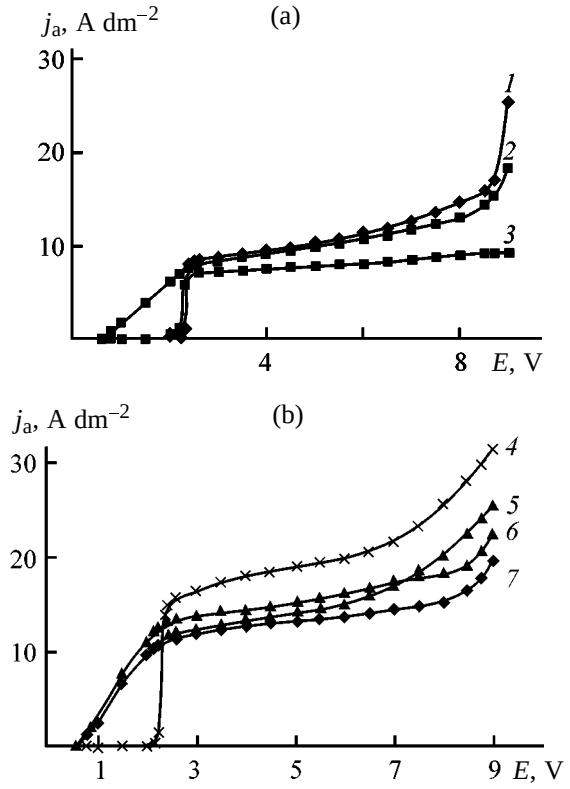

Fig. 1. Anodic potentiometric curves obtained on titanium alloys at 293 K. (j_a) Anodic current density and (E) potential; the same for Fig. 2. Titanium alloy: (*1*, *4*, *5*) VT1-0, (*2*) VT6, and (*3*, *6*, *7*) VT16. Solution (M): H_2SO_4 11.5, HF 11.5; the same for Fig. 2. (a) Solution with no additive; (b) additive, 0.52 M: (*4*, *7*) NaF and (*5*, *6*) KF.

and a saturated silver chloride reference electrode (with potential given relative to s.h.e.). The working electrodes, made of titanium alloys in the form of disks with reaction surface area of 1.256 cm^2, were mechanically cleaned and weighed prior to every experiment. Voltammograms were obtained at potential sweep rates V_s (V s^{-1}) of 0.01, 0.02, 0.05, 0.1, and 0.2.

Table 2. Current efficiency CE^{Ti} of anodic oxidation of VT titanium alloys in hydrofluoric-sulfuric acid solution and fraction of current, Q_{O_2}, consumed for evolution of gaseous O_2

j_a, A dm^{-2}	CE^{Ti}, %			Q_{O_2}, %		
	VT1-0	VT6	VT16	VT1-0	VT6	VT16
6.5	96.3	90.8	89.5	0	0	
7.5	88.9	88.2	85.6	3.7	5.2	2.8
9.5	86.7	85.7	79.6	5.9	7.6	4.6
10.5	78.0	77.5	75.2	11.6	12.8	9.3

The current efficiencies of alloy component ionization (methods for calculation of their electrochemical equivalents were described in [9]) were determined gravimetrically and by quantitative analysis of anolytes in an electrolyzer with separated electrode spaces. The content of ions of dissolving alloy components in the anolyte was determined quantitatively by atomic absorption analysis on an AAS-1 spectrophotometer with the detection limit of 0.05–0.1 mg l^{-1} [10] and by photocolorimetric analysis on a KFK-3 photoelectric photometer with the detection limit of 1.0 mg l^{-1} [11]. The fraction of current consumed for the partial process of oxygen evolution was estimated volumetrically.

The phase composition of anodically treated alloys was determined from X-ray diffraction patterns obtained on a DRON-3M diffractometer in CuK_α radiation. The elemental composition of the forming surface films was studied with a JXA-5A electronic X-ray fluorescence analyzer.

The anodic potentiostatic curves (Fig. 1a) obtained on VT1-0, VT6, and VT16 titanium electrodes in a hydrofluoric-sulfuric acid solutions exhibited, after a steep rise in current at $E \approx 2.0$ V, a deceleration of the anodic dissolution process in a wide range of potentials $2.0 < E < 8.5$ V. At $E > 8.5$ V, the VT1-0 and VT6 alloys passed into a transpassive state.

In the presence of alloying additions of aluminum and vanadium in the VT6 titanium alloy (Table 1), the run of the j_a–E curve was qualitatively about the same, but the currents in the oxide formation and transpassivation regions decreased as compared with technically pure titanium (Fig. 1a).

The presence of alloying additives (Al, V, and Mo) in the VT16 titanium alloy (Table 1) led to a significant change in the run of the potentiostatic curve (Fig. 1a): the current rise portion started much earlier, at $E = 0.6–0.65$ V, and did not reach the currents of anodic dissolution of "pure" titanium, and then the electrode passed into the passive state, up to potentials of 9.0–9.5 V. The appearance of a violet film was observed visually on the electrode surface.

The increase in the process overvoltage, exceeding 3–4-fold the overvoltage in, e.g., chromium steels [12], is due to the considerable ohmic resistance of the forming surface AOFs, which grows, as reported previously [9], with increasing extent of alloying of titanium alloys in the order VT1-0 < VT6 < VT16.

Experiments on determining the anodic current efficiencies demonstrated that, with the current density maintained constant, the current efficiency of

alloy component ionization decreases in the same order of alloys VT1-0 > VT6 > VT16 (Table 2). Thus, the film resistance presumably reflects in the given case mainly the ionic conduction, since only this mechanism assumes higher current efficiency of metal ionization.

In addition to ionic conduction, the surface AOF on titanium alloys exhibits electronic conduction, too, which is indicated by measurements of the photovoltaic effect on the surface of an anodically passivated VT1-0 electrode [9, 13, 14]. This enables oxygen evolution at the film–solution interface.

Monitoring of the evolution of oxygen formed on the surface of anodically polarized titanium electrodes (Table 2) suggests that the oxygen process involves two constituents: evolution of gaseous O_2 and consumption of oxygen for final oxidation of anodic products of alloy oxidation (subions migrating across the AOF at strong polarizations and recorded in anodic polishing of aluminum alloys [15]). The higher the ionic conductivity of a film (VT1-0 > VT6 > VT16), the larger fraction of oxygen must be consumed by the second constituent of the oxygen process. Part of ions in intermediate oxidation state do not have enough time to react with O_2, and they find their way into solution. For the VT16 alloy, the fraction of current consumed for evolution of gaseous oxygen is somewhat lower than that for the other alloys (Table 2).

Quantitative analysis of the anolyte in electrochemical dissolution of the VT1-0 alloy demonstrated approximately the same content of Ti^{3+} and Ti^{4+} ions in the supporting electrolyte, in agreement with the scheme of anodic dissolution of titanium in the presence of hydrofluoric acid acting as a catalyst of titanium ionization by the complexation mechanism [13].

Replacement of a part of hydrofluoric acid with equivalent amount of sodium or potassium fluoride, with the concentration of fluoride ions in the hydrofluoric-sulfuric acid solution maintained constant, led to significant changes in the run of the anodic curves j_a–E obtained on the VT1-0 and VT16 alloys (Fig. 1b). The Na^+ and K^+ ions present in the hydrofluoric-sulfuric acid solution in amount of 0.50–0.52 M accelerated anodic dissolution of titanium alloys. The most significant factors were the increase in the anodic dissolution currents, as compared to the electrolyte without added salts, and the appearance of a transpassive range of the process for the VT16 alloy (Fig. 1b).

The shape of the anodic voltammetric curves ob-

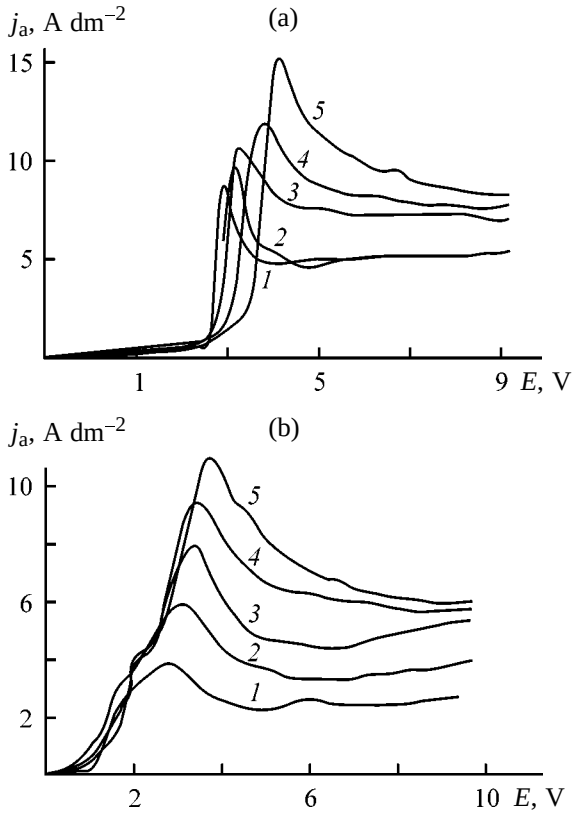

Fig. 2. Voltammetric curves of anodic oxidation of (a) VT1-0 and (b) VT16 titanium alloys at 293 K. Potential sweep rate (V s^{-1}): (*1*) 0.01, (*2*) 0.02, (*3*) 0.05, (*4*) 0.1, and (*5*) 0.2.

tained on the VT1-0 and VT16 titanium alloys (Fig. 2) was also largely determined by the presence of alloying additives, solution composition, and anodic polarization η_a.

The VT1-0 alloy in a hydrofluoric-sulfuric acid solution was characterized by a steep rise in current with increasing η_a up to the peak current j_p, whereas the VT16 alloy exhibited several successive current peaks (Fig. 2b. The appearance of these peaks in the anodic voltammetric curves is possible [16] in two cases: first, when there occurs step oxidation of reactants at the electrode, and, second, in the case of oxidation of several different substances.

Apparently, ionization of Ti in anodic dissolution of the VT16 alloy occurs in stages and is accompanied by preliminary anodic oxidation in stages of the alloying components contained in the alloy (Table 1) and possessing a more negative ionization potential, compared with the Ti base.

At potentials $E \geq 5.5$ V, corresponding to the electropolishing range, the voltammetric curves show characteristic inflections (Fig. 2) identified with peaks

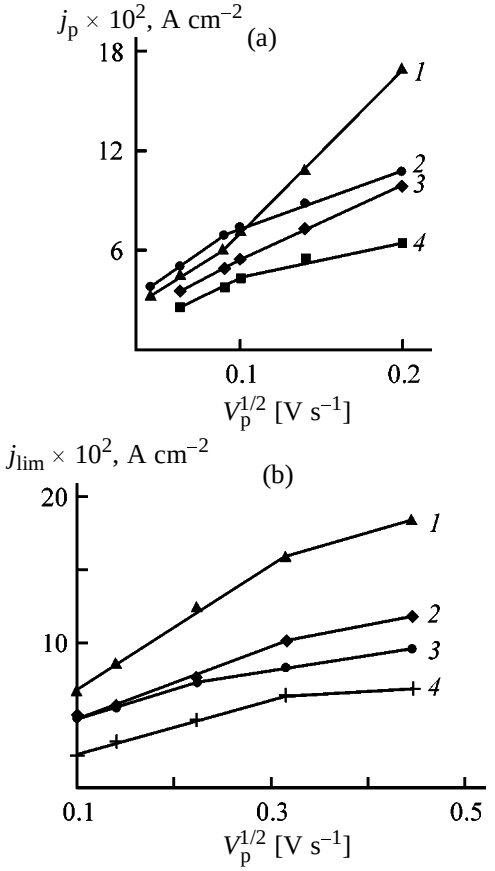

Fig. 3. Current densities (a) j_p and (b) j_{lim} vs. potential sweep rate V_s for titanium alloys (*1*, *3*) VT1-0 and (*2*, *4*) VT16. Solution (M): (*1*, *2*) H_2SO_4 11.5, HF 11.0, NaF 0.52; (*3*, *4*) H_2SO_4 11.5, HF 11.5.

of "limiting" current j_{lim} at anodic overvoltages of the process [17, 18]. Introduction of alkali metal cations into the hydrofluoric-sulfuric acid solution favored an increase in j_p and j_{lim} on titanium alloys, and especially on VT16.

At V_s = 0.01–0.05 V s^{-1} the currents j_p and j_{lim} linearly depend on the square root of the potential sweep rate (Fig. 3), which indicates diffusion control of the anodic dissolution of titanium alloys [16]. With the V_s values increasing further, to 0.1–0.2 V s^{-1}, the process of anodic dissolution of alloys passed first into the region of mixed diffusion–activation kinetics and then into that of purely activation control. Experimental studies demonstrated that solution agitation in measuring voltammetric dependences at V_s = 0.1–0.2 V s^{-1} has no effect on the curve shape, and, consequently, the ion diffusion must be limited to the solid-state oxide zone. Migration of ions of metals constituting the alloys, under the action of electric field in the surface oxide film, is the main driving force of the process.

Thus, the observed features of the anodic dissolution of titanium alloys—significant increase in overvoltage of transition of VT1-0 and VT6 titanium alloys into transpassive state as compared with, e.g., steels [13]; "deep" passivation of the VT16 alloy in the hydrofluoric-sulfuric acid solution; and also activation of anodic dissolution in the presence of alkali metal cations in the supporting electrolyte, especially pronounced for the VT16 alloy—cannot be related only to diffusion limitations on the process, but are also determined by properties of surface AOFs.

An analysis of the phase composition of a film formed on a VT16 titanium anode in the hydrofluoric-sulfuric acid electrolyte (Table 3) demonstrated the presence, in addition to TiO_2, of an amorphous phase containing MoO_3, δ-V_2O_5, and, in part, γ-Al_2O_3.

Partial substitution of Ti ions in the TiO_2 crystal lattice by Mo and V ions is possible if the atomic radii of the host and substituting metal ions differ by no more than 15%. This condition is satisfied for the VT16 alloy: Ti ion radius (r_{Ti} = 1.45 Å) is close the radii of the alloying components, Mo (r_{Mo} = 1.39 Å) and V (r_V = 1.34 Å) [19].

This suggests that Mo^{6+} and V^{5+} ions migrating through the oxide layer in anodic dissolution of the alloy substitute part of Ti^{3+} and Ti^{4+} in the crystal lattice of titanium oxide and thereby lead to lower rate of anodic dissolution of the VT16 alloy in the hydrofluoric-sulfuric solution and to surface passivation, with the thickness of the oxide film increasing; and this was, indeed, observed experimentally.

The observed acceleration of the anodic dissolution of titanium alloys on introducing alkali metal cations into the supporting electrolytes is apparently due to reduction of the diffusion resistance of the solid phase, caused by the possible introduction of Na^+ and K^+ ions into the film to form a substitutional solid solution. This process is possible if the atomic radii of the host and impurity ions are close, which is satisfied for Na^+ ions (r_{Na} = 1.90 Å). Introduction of Na^+ cations into aluminum oxide in cathodic activation and anodic dissolution of aluminum in chloride solutions was demonstrated in [20].

The atomic radius of K^+ ions (r_K = 2.35 Å) is 1.6 times that of Ti. An X-ray phase analysis of films formed on the VT16 alloy in a solution containing potassium fluoride revealed the presence of an amorphous phase of the type K_2O–MoO_3–V_2O_5 (Table 3). The fact that chemical compounds of elements contained in the electrolyte are present on the surface films formed on valve metals in the galvanostatic mode was demonstrated in [21].

Table 3. Elemental and phase composition of AOF on VT16 titanium alloy after electrochemical treatment at 5 A dm^{-2} for 5 min

Electrolyte, M	Elemental composition of film, wt %				Phase composition of film
	Ti	Al	Mo	V	
H_2SO_4, 11.5; HF, 11.5	86.2–87.0	2.8–3.0	5.2–5.4	3.7–3.9	TiO_2-rutile, amorphous phase MoO_3–δ-V_2O_5
H_2SO_4, 11.5; HF, 11.0; KF, 0.52	85.8–86.5	3.1–3.3	5.2–5.3	3.9–4.1	TiO_2-rutile, amorphous phase K_2O–MoO_3–δ-V_2O_5
H_2SO_4, 11.5; HF, 11.0; KF, 0.52; $C_3H_8O_3$, 2.0	86.5	3.3–3.5	5.0–5.2	3.9–4.0	TiO_2-rutile, amorphous phase K_2O–MoO_3–δ-V_2O_5–γ-Al_2O_3

The introduction of alkali metal cations into the hydrofluoric-sulfuric acid solution allowed intensification of the anodic dissolution of titanium alloys; however, the required leveling of VT16 alloy sample surface (K > 65%) and absence of surface microstrains could only be achieved on replacing water in the supporting electrolyte with another solvent, glycerol, taken in amount of up to 2 M, and additional introduction of hexamethylenetetramine additive [$(2.0–4.0) \times 10^{-2}$ M].

CONCLUSIONS

(1) Ionization of metals contained in titanium alloys subjected to anodic oxidation under strong polarization occurs in stages, with solid-phase limitations on the stage of ion migration through the forming anodic film.

(2) The surface semiconducting anodic oxide films may include components of dissolving titanium alloys and solutions for anodic treatment, which affect the process rate.

(3) It is recommended to use for electrochemical treatment of the VT16 titanium alloy a solution of the following composition (M): H_2SO_4 11.2–11.7, HF 11.0–11.5, KF (NaF) 0.50–0.52, $C_3H_8O_3$ 2.0, and $C_6H_{12}N_4$ $(2.0–4.0) \times 10^{-2}$.

REFERENCES

1. Mirzoev, R.A. and Davydov, A.D., *Elektrokhimiya*, 1995, vol. 31, no. 3, pp. 277–285.
2. Davydov, A.D., *Elektrokhimiya*, 1991, vol. 27, no. 9, pp. 947–952.
3. Grinberg, M.G., Shub, D.M., Kozlova, N.V., and Veselovskii, V.I., *Elektrokhimiya*, 1981, vol. 17, no. 11, pp. 1253–1256.
4. Mirzoev, R.A., Davydov, A.D., and Kabanov, B.N., *Elektrokhimiya*, 1983, vol. 19, no. 10, pp. 1415–1417.
5. Saushkin, B.P., Maslikov, S.V., and Maslov, A.V., *Izv. Vyssh. Uchebn. Zaved., Khim. Khim. Tekhnol.*, 1998, vol. 41, no. 5, pp. 72–75.
6. Landolt, D., *Elektrokhimiya*, 1995, vol. 31, no. 3, pp. 228–234.
7. Fedorova, E.A., Kuznetsova, T.A., and Flerov, V.N., *Zh. Prikl. Khim.*, 1998, vol. 71, no. 8, pp. 1311–1314.
8. Fedorova, E.A., Suchkov, A.I., Tsareva, I.N., and Flerov, V.N., *Fiz. Khim. Obrab. Mater.*, 2000, no. 1, pp. 63–67.
9. Fedorova, E.A., *Gal'vanotekh. Obrab. Poverkhn.*, 2001, vol. 9, no. 1, pp. 41–46.
10. Britske, M.E., *Atomno-absorbtsionnyi spektrokhimicheskii analiz* (Atomic-Absorption Spectrochemical Analysis), Moscow: Khimiya, 1982.
11. Sandell, E.B., *Colorimetric Determination of Traces of Metals*, New York: Interscience, 1959.
12. Fedorova, E.A., *Zh. Prikl. Khim.*, 2001, vol. 74, no. 4, pp. 598–602.
13. Tsygankova, L.E., Vigdorovich, V.I., Oshe, E.K., and Semerikova, I.A., *Elektrokhimiya*, 1987, vol. 23, no. 11, pp. 1498–1502.
14. Smirnova, E.N., Kozhanov, V.N., Samoilenko, V.N., and Merzlyakov, A.V., *Elektrokhimiya*, 1989, vol. 25, no. 5, pp. 659–662.
15. Karpova, I.G., Fedorova, E.A., and Flerov, V.N., *Izv. Vyssh. Uchebn. Zaved., Khim. Khim. Tekhnol.*, 1998, vol. 41, no. 6, pp. 72–75.
16. Galus, Zb., *Teoretyczne podstawy elektroanalisy chemicznej*, Warsaw: Naukowe, 1971.
17. Wieckowski, A., Ghah, E., and Huy Ha La, *J. Electrochem. Soc.*, 1984, vol. 131, no. 10, pp. 2024–2034.
18. Survila, A.A., *Elektrokhimiya*, 1986, vol. 22, no. 8, pp. 1045–1049.
19. Rabinovich, V.A. and Khavin, Z.Ya., *Kratkii khimicheskii spravochnik* (Concise Handbook of Chemistry), Moscow: Khimiya, 1977.
20. Tomashova, N.N., Chekavtsev, A.V., and Davydov, A.D., *Elektrokhimiya*, 1995, vol. 31, no. 3, pp. 313–315.
21. Yarovaya, T.P., Gordienko, P.S., Rudnev, V.S., and Nedozorov, P.M., *Elektrokhimiya*, 1994, vol. 30, no. 11, pp. 1395–1396.

Russian Journal of Applied Chemistry, Vol. 74, No. 11, 2001, pp. 1834–1837. Translated from Zhurnal Prikladnoi Khimii, Vol. 74, No. 11, 2001, pp. 1780–1783.

APPLIED ELECTROCHEMISTRY AND CORROSION PROTECTION OF METALS

Potentiometric Study of Oxidized Coals in Aqueous Solutions of Surface-Inactive Electrolytes

Yu. A. Tarasenko, S. A. Kopyl, V. F. Lapko, L. I. Zarubitskaya, and I. Tomizuka

Institute for Sorption and Endoecology Problems, National Academy of Sciences of Ukraine, Kiev, Ukraine

Received September 21, 2000; in final form, May 2001

Abstract—Stationary electrode potentials of oxidized synthetic coals of the SCN type are determined in aqueous solutions. The contributions of redox reactions with participation of the surface oxygen-containing functional groups and the potential of unoxidized areas of the coal surface to the total potential of oxidized coals in aerated solutions are studied. The potentials of oxidized carbons in deoxygenated solutions are also measured.

The potentials of activated carbon (AC) in aerated aqueous solutions were studied in [1–9]. It was demonstrated that formation of the stationary potential of AC is associated with oxygen reduction. Measurements of the potential of AC in deoxygenated solutions allowed estimation of the zero-charge potential (ZCP) [1]. At the same time, there is only limited data on the potentials of oxidized AC, and the available information is contradictory [4, 9]. Data on the potentials of oxidized AC in deoxygenated solutions are lacking at all.

In this work we determined the stationary potentials E_{st} of oxidized AC having various degrees of surface oxidation and studied the pH dependences of E_{st} in aerated and deoxygenated electrolyte solutions.

EXPERIMENTAL

In the work we used synthetic spherical granulated AC of the SCN type obtained by carbonization of a copolymer of vinylpyridine resin and divinylbenzene with subsequent activation with water vapor [10].

Oxidized SCN carbon (SCN_o) was prepared by treatment of SCN with concentrated nitric acid. The degree of oxidation was estimated from the static exchange capacity (SEC) of the carbons with respect to alkali, reflecting the amount of oxygen-containing surface functional groups [11]. We measured the potentials of the carbons with SEC of 0.31, 0.41, 0.54, 0.69, 0.86, 1.10, 1.25, 1.32, 1.63, 2.0, and 2.5 mg-equiv g^{-1}.

As the working solution we chose 0.1 N sodium sulfate, because the specific adsorption of Na^+ and SO_4^{2-} ions is low enough to have no effect on the measured potentials [12]. The solution pH was varied from 1 to 12 by adding sulfuric acid or NaOH and controlled with an EV-74 pH meter.

The cell for measurement of the potential was a 250-ml round-bottomed flask with sealed-in ground-glass joints. Through these joints to the cell were introduced a Pt microprobe, an AgCl reference electrode, a pH-metric glass electrode, and a dropping funnel for feeding the acid or alkali.

Measurements were performed with a suspended sample using a magnetic stirrer, which allowed suspended carbon particles to strike against the Pt microprobe. In so doing we were able to measure just the surface potential of the AC granules, but not the potential of the Pt microprobe in the electrolyte solution [13]. The potentials were measured with a V7-35 high-resistance voltmeter and recalculated against the standard hydrogen electrode. All experiments were conducted at $20 \pm 2°C$.

Preliminarily we measured the potential of the Pt microprobe in the working solution. This potential appeared to be considerably different from the potentials of AC (Fig. 1). While measuring the potentials of AC we introduced various concentrations of a mediator, $Fe_2(SO_4)_3$, in the solution. We found that its presence has no effect on the AC potentials, suggesting that the measurement procedure used is adequate.

Deoxygenation of the solution in the measuring cell was attained by a 24-h bubbling of Ar thoroughly purified to remove oxygen. It was demonstrated in special experiments that this time is sufficient for

1070-4272/01/7411-1834$25.00

deoxygenation. To remove adsorbed oxygen, the AC samples were heated at 120°C in an Ar flow for 2 h.

As an example, Fig. 1 demonstrates the kinetics of formation of the stationary potential of the oxidized carbons having SEC of 0.41, 2.0, and 2.5 mg-equiv g^{-1}, and, for comparison, of SCN activated carbon in acidic (pH 1) and basic (pH 12) aerated solutions. The time dependence of the AC potential is represented by a curve slowly approaching the stationary value (Figs. 1a, 1b, curves *1*), which is consistent with the published data [5, 6].

The stationary potentials of AC and oxidized AC are attained differently. For example, weakly oxidized AC (SEC 0.41 mg-equiv g^{-1}) is characterized by a considerable growth of the potential from the initial to the stationary value, which, however, is lower as compared to activated SCN (Figs. 1a, 1b, curves *2*). For SCN_o with a higher degree of oxidation (SEC 2.0 mg-equiv g^{-1}) the difference between the initial and stationary potentials is small, being within 50 mV (Figs. 1a, 1b, curves *3*). Finally, for strongly oxidized carbon (SEC 2.5 mg-equiv g^{-1}) the potential decreases with time, i.e., E_{st} of this carbon is lower than the initial potential (Figs. 1a, 1b, curves *4*), which is consistent with data of [9]. Carbons with intermediate degrees of oxidation show intermediate patterns.

The stationary potentials of oxidized carbons and the initial SCN are also different. The correlations of the stationary potentials of oxidized carbons with SEC at pH 1 and 12 are presented in Fig. 2 together with E_{st} of SCN. Although the potentials in both acidic and basic solutions vary in rather narrow ranges (695–775 and 220–305 mV, respectively), some trends are nevertheless seen. Thus, with increasing SEC from 0.31 to 1.25 mg-equiv g^{-1} the potential slightly decreases. With further increasing SEC from 1.25 to 2.0 mg-equiv g^{-1} the stationary potentials of the oxidized carbons drift toward more positive values, approaching the potential of the initial SCN. The reproducibility of E_{st} in our experiments was within 2 mV.

Figure 3 shows the pH dependences of E_{st} for oxidized carbons with SEC 0.41, 2.0, and 2.5 mg-equiv g^{-1} and also for the initial SCN in aerated solutions. Here the specific feature is that for strongly oxidized carbons (SEC 2.0, 2.5 mg-equiv g^{-1}) E_{st} is a linear function of pH over the entire pH range. For weakly oxidized carbon and the initial SCN the pH dependences are curves with two linear sections.

The pH dependences of E_{st} of SCN and oxidized SCN (SEC 2.0 mg-equiv g^{-1}) in deoxygenated sys-

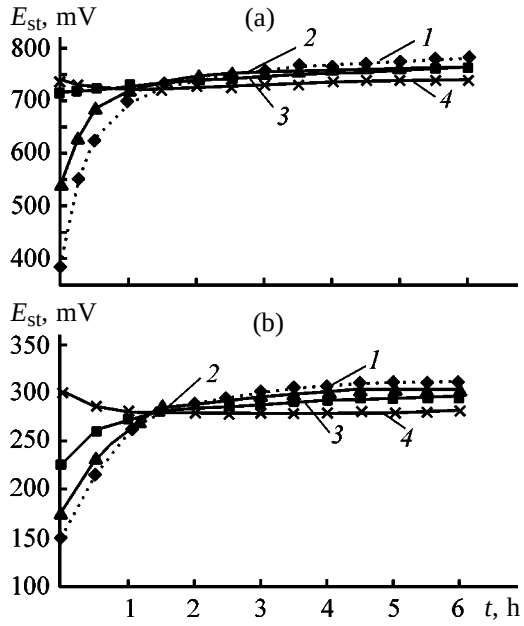

Fig. 1. Kinetics of establishment of the stationary potential of (*1*) activated SCN and (*2–4*) oxidized SCN_o in aerated 0.1 N $NaSO_4$. (E_{st}) Potential and (*t*) time. Static exchange capacity of SCN_o (mg-equiv g^{-1}): (*2*) 0.41, (*3*) 2.0, and (*4*) 2.5; the same for Fig. 3. pH: (a) 1 and (b) 12.

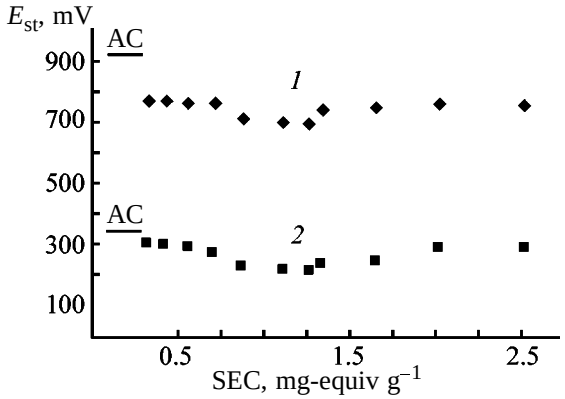

Fig. 2. Stationary potential E_{st} of oxidized carbons as a function of their static exchange capacity SEC. pH: (*1*) 1 and (*2*) 12.

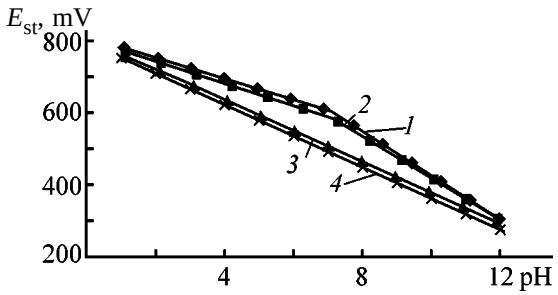

Fig. 3. Stationary potential E_{st} of (*1*) SCN and (*2–4*) SCN_o as a function of pH in aerated 0.1 N Na_2SO_4.

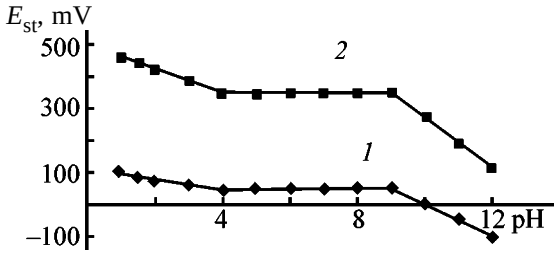

Fig. 4. Stationary potential E_{st} of (*1*) SCN and (*2*) SCN_o (SEC 2.0 mg-equiv g^{-1}) as a function of pH in deoxygenated solutions.

tems are given in Fig. 4. It is seen that the dependences are similar for the both types of carbons. Each of the curves has three linear sections; over the pH range from 4 to 9 the corresponding linear section represents a plateau. The plateau potentials of these samples are strongly different, being 350 and 50 mV for SCN_o and SCN, respectively. In the pH ranges below 4 and above 9 E_{st}, respectively, decreases and increases.

The observed considerable differences in the kinetic curves of the potential of SCN and SCN_o (Fig. 1) can be interpreted taking into account the chemical and energy heterogeneity of their surface [14]. The measured potentials are formed under the effect of several factors.

There are a wide spectrum of oxygen-containing functional groups (phenolic, alcoholic, carbonyl, carboxy, quinoid, lactone, etc.) on the surface of SCN_o, which are bound to the carbon matrix, as demonstrated by various physical (IR, NMR, ESR, etc.) and chemical methods used for identification of individual organic compounds [11, 15].

The surface of SCN_o has also unoxidized areas [8, 11] which can reduce chemisorbed oxygen.

Therefore, we can attribute the growth of the potentials of weakly oxidized carbons in aerated electrolyte solutions (Figs. 1a, 1b, curves *2*, *3*) to reduction of chemisorbed oxygen in unoxidized areas of the surface. The decrease in E_{st} of a strongly oxidized carbon (SEC 2.5 mg-equiv g^{-1}) relative to the initial SCN was assigned in [9] to dissociation of protonated oxygen-containing groups (their amount is higher in strongly oxidized carbons) and formation of a negative charge on the surface.

The effect of oxygen-containing groups on the stationary potentials of oxidized carbons is demonstrated in Fig. 2. The amount of these groups in weakly oxidized carbons is small, and in this case E_{st} is close to that of unoxidized SCN. The contribution of the redox potentials of these groups to E_{st} increases with increasing degree of oxidation of the carbons, being dependent not only on the amount of oxygen-containing groups, but also on their spectrum. According to the modern views [8, 16, 17], furan and phenol groups dominate on the surface of weakly oxidized carbons, which imparts a negative or weakly positive potential to the carbon surface [18]. With increasing degree of oxidation, in addition to the above-indicated groups, carboxy and lactone groups and branched chains with peripheral alcoholic groups are formed on the surface, which are characterized by high positive redox potentials [18, 19]. As a result, strongly oxidized carbons have higher potentials, which regularly increase with the degree of oxidation.

The pH dependences of E_{st} given in Fig. 3 for SCN and variously oxidized SCN_o confirm the common view that the electron-donor power of oxidized carbons is less pronounced. For SCN this dependence (Fig. 3, curve *1*) has two linear sections with the slopes of –29 and –58 mV per pH unit, which correspond to oxygen reduction on the surface, respectively, to hydrogen peroxide and to hydroxide ion in acidic and alkaline solutions by Eqs. (1) and (2).

$$O_2 + 2H^+ + 2e = H_2O_2, \quad (1)$$

$$O_2 + 2H_2O + 4e = 4OH^-. \quad (2)$$

For oxidized carbons with SEC of 2.0 and 2.5 mg-equiv g^{-1} the pH dependences of E_{st} are straight lines having a slope of –42 and –40 mV per pH unit, which can be regarded as a resultant of the processes of oxygen reduction on unoxidized areas of the surface by Eqs. (1) and (2) and redox reactions with participation of oxygen-containing functional groups.

The pH dependence of E_{st} of SCN_o (SEC 2.0 mg-equiv g^{-1}) in a deoxygenated solution (Fig. 4, curve *2*), given as an example, is similar to that for SCN (curve *1*). With the lack of oxygen the potential is unchanged over the pH range from 4 to 9 (plateaus in Fig. 4). However, the plateau potential of SCN_o is above that of SCN by 300 mV, which is due to a lower electron-donor power of the former [11]. The observed growth of E_{st} of SCN at pH <4 can be attributed to adsorption of hydrogen ions on the carbon surface and also to partial charge transfer from the carbon matrix, i.e., its oxidation, as was demonstrated in [1]. In this case the surface acquires a positive charge. The decrease in the potential at pH >9 is due to adsorption of hydroxide ions [8].

For SCN_o the observed pH dependence of E_{st} at pH <4 is evidently associated also with protonation of the surface acidic groups, and at pH >9, with their ionization with formation of negatively charged moieties [20].

One may say that the plateau potential of SCN_o (+350 mV) is an averaged (compromise) redox potential of oxygen-containing functional groups on its surface, which are lacking on the SCN surface. This potential is controlled by Eq. (3)

$$C + H_2O \rightarrow C(O) + 2H^+ + 2e, \quad (3)$$

where C(O) designates an oxidized state of carbon.

The plateau potential corresponds to E_{st} in the absence of electrochemically active gases.

CONCLUSIONS

(1) Stationary potentials of oxidized coals correspond to the averaged potentials of oxygen-containing functional groups chemically bound to the coal surface and of unoxidized areas. As the degree of oxidation of the coals increases, the potential grows, which is due to the transition from the furan and phenol groups, having negative or slightly positive redox potentials, to the carboxy and lactone groups with higher redox potentials.

(2) It follows from the pH dependence of the stationary potential that oxidized coals demonstrate less pronounced electron-donor power as compared to the activated coals. In deoxygenated solutions the pH dependences for both oxidized and activated coals have plateaus at pH 4–9. The plateau potential of the oxidized coal (SEC 2.0 mg-equiv g^{-1}) is +350 mV, which corresponds to the potential of the coal surface in the absence of electrochemically active gases in the solution, i.e., without specific adsorption.

REFERENCES

1. Klimenko, L.A., Strelko, V.V., Kazdobin, K.A., and Kartel', N.T., *Ukr. Khim. Zh.*, 1989, vol. 55, no. 2, pp. 167–171.
2. Frumkin, A.N., Ponomarenko, E.A., and Burshtein, R.Kh., *Dokl. Akad. Nauk SSSR*, 1963, vol. 149, no. 5, pp. 1123–1126.
3. Frumkin, A.N., Korobanov, A.A., Vilinskaya, V.S., and Burshtein, R.Kh., *Dokl. Akad. Nauk SSSR*, 1976, vol. 229, no. 1, pp. 153–156.
4. Strelko, V.V., Kartel', N.T., Klimenko, L.A., and Kazdobin, K.A., *Zh. Prikl. Khim.*, 1987, vol. 60, no. 6, pp. 1257–1260.
5. Tarasenko, Yu.A., Reznik, G.V., Bagreev, A.A., and Lysenko, A.A., *Zh. Fiz. Khim.*, 1993, vol. 67, no. 11, pp. 2333–2335.
6. Kinoshita, K., *Carbon: Electrochemical and Physicochemical Properties*, New York: Wiley, 1988.
7. Tarasenko, Yu.A., Reznik, G.V., Bagreev, A.A., and Strelko, V.V., *Proc. Int. Symp. "Hydrometallurgy'94,"* Cambridge (England), 1994, pp. 515–526.
8. Tarasevich, M.R., *Elektrokhimiya uglerodnykh materialov* (Electrochemistry of Carbonaceous Materials), Moscow: Nauka, 1984.
9. Dudarenko, V.V. and Kazdobin, K.A., *Ukr. Khim. Zh.*, 1987, vol. 53, no. 1, pp. 42–47.
10. USSR Inventor's Certificate no. 820 160.
11. Tarkovskaya, I.A., *Okislennyi ugol'* (Oxidized Coal), Kiev: Naukova Dumka, 1981.
12. Frumkin, A.N., *Potentsialy nulevogo zaryada* (Zero-Charge Potentials), Moscow: Nauka, 1979.
13. Losev, A.V. and Petrii, O.A., *Itogi Nauki Tekh., Ser.: Elektrokhim.*, 1979, vol. 14, pp. 120–167.
14. Goba, V.E., Tarkovskaya, I.A., and Zav'yalov, V.N., *Adsorb. Adsorb.*, 1980, no. 8, pp. 55–58.
15. Donnet, J.B., *Carbon*, 1968, vol. 6, no. 2, pp. 161–185.
16. Strelko, V.V., Stavitskaya, S.S., Strelko, V.V., Jr., and Street, M., *Teor. Eksp. Khim.*, 1998, vol. 34, no. 1, pp. 27–31.
17. Menendez, J.A., Bo Xia, Phillips, J., and Radovic, L.R., *Langmuir*, 1997, no. 13, pp. 3414–3421.
18. Ksenzhek, O.S. and Petrova, S.A., *Elektrokhimicheskie svoistva obratimykh biologicheskikh redoks-sistem* (Electrochemical Properties of Reversible Biological Redox Systems), Moscow: Nauka, 1986.
19. *Spravochnik po elektrokhimii* (A Handbook of Electrochemistry), Sukhotin, A.M., Ed., Leningrad: Khimiya, 1981.
20. Kazdobin, K.A., Lavrinenko-Ometsinskaya, E.D., and Klimenko, L.A., *Ukr. Khim. Zh.*, 1995, vol. 61, no. 4, pp. 47–51.

Russian Journal of Applied Chemistry, Vol. 74, No. 11, 2001, pp. 1838–1841. Translated from Zhurnal Prikladnoi Khimii, Vol. 74, No. 11, 2001, pp. 1784–1787.

APPLIED ELECTROCHEMISTRY AND CORROSION PROTECTION OF METALS

Electrodeposition of the Cr–Co Alloy from Acid Sulfate Electrolytes

A. I. Falicheva and B. A. Spiridonov

Voronezh State Technical University, Voronezh, Russia

Received July 4, 2001

Abstract—The kinetics of electrodeposition of Cr–Co alloys from sulfate electrolytes with monoethanolamine was studied. The influence of the dc and pulsed current modes on the composition and physicochemical properties of the Cr–Co coatings with cobalt content of 5–10% was examined.

Chromium coatings electrodeposited from electrolytes containing triple-charged chromium ions and iron-group metals have appreciably improved physicochemical properties: increased heat and oxidation resistance [1], lower fracturing [2, 3], and enhanced corrosion resistance. Sulfate [2–4] and chloride [1–5] electrolytes have been recommended for preparing electrolytic Cr–Co alloy. The previous studies have shown that Cr–Co coatings can be prepared from sulfate electrolytes with monoethanolamine (MEA) or hexamethylenetetramine in both static [3, 4] and pulsed [6] current modes. In this work, we continued the study of the electrodeposition of Cr–Co alloy from sulfate electrolytes.

EXPERIMENTAL

The electrolyte contained (M) 0.5 "modified" green chromium(III) sulfate (spectral characteristics: λ_1 = 415–416 nm and λ_2 = 582–583 nm; $\varepsilon_1 \approx \varepsilon_2 = 37$) [7, 8], 0.5 sodium sulfate, and 0.032 MEA. To the electrolyte, from 1 to 5 g l^{-1} of cobalt sulfate was added. For comparative studies on cobalt deposition we prepared electrolyte containing 2 g l^{-1} $CoSO_4$ and MEA.

The pulsed electrolysis was performed using a transistor generator of rectangular pulses. The pulse repetition frequency was varied from 0.1 to 10 Hz and the pulse length, from 0.1 to 50 s. Copper cathodes and platinum anodes were used.

The current efficiency (CE) by the alloy was determined gravimetrically using a copper coulometer with account taken of the alloy composition. The cobalt content of the alloy was determined spectrophotometrically with nitroso-R salt and the chromium content, by the persulfate–silver method. The cathodic polarization was studied galvanodynamically (6 mA min^{-1}) on a P-5827 M potentiostat with a KSP recording potentiometer. All the potentials are given vs. silver chloride reference electrode which served as reference; platinum was used as an auxiliary electrode. The partial polarization curves were obtained by resolution of the overall curves on the basis of data on the current efficiencies by hydrogen, chromium, and cobalt. The quality of the deposits was judged from outward appearance of the coatings; their reflectivity was studied with an FM-58 M photometer and the morphology, with an MIM-7 microscope. The phase analysis was done on the alloy films 500–1000 Å thick (separated from copper substrate) at a 100 kV voltage. The lattice period was determined according to [9]. The hydrogen content in the cathode deposits was determined by vacuum extraction [10].

Analysis of the partial polarization curves derived from the overall curve of Cr–Co deposition from sulfate electrolyte with MEA (Fig. 1) shows that chromium(III) is reduced to chromium(II) ($E^0_{Cr^{3+}/Cr^{2+}}$ = –0.41 V) simultaneously with the formation of hydrogen ($E^0_{H^+/H^0}$ = 0 V), cobalt ($E^0_{Co^{2+}/Co^0}$ = –0.277 V), and chromium ($E^0_{Cr^{3+}/Cr^0}$ = –0.71 V). The previous data show that, apart from hydrogen evolution, the formation of cobalt is the most probable from the thermodynamical standpoint. However, owing to the increase in the chromium(II) ion concentration and the shift of the $E_{Cr^{3+}/Cr^{2+}}$ potential toward negative region, chromium (curve *1c*) is deposited simultaneously with cobalt (curve *1d*), as revealed by analysis of the cathode deposits and partial curves. Reduction of chromium(III) ions during the alloy deposition occurs with lower polarization than deposition of pure

1070-4272/01/7411-1838$25.00

chromium (curve *2c*). From an electrolyte containing no cobalt(II) ions, chromium is electrodeposited at D_c = 25 A dm^{-2} (pH 0.75). At simultaneous deposition with cobalt, the necessary current density decreases to 15 A dm^{-2}, because the free energy decreases owing to formtion of the crystal lattice of the cathodic chromium–cobalt solid solution.

Electron-microscopic study of the chromium–cobalt deposits containing 10% cobalt showed that the simultaneous deposition of chromium and cobalt results in the formation of a solid solution with a lattice period of 2.87 Å. According to the phase diagram, the β-phase with a centered cubic lattice, which is a solid solution of cobalt in chromium [11], is formed in the chromium–cobalt system at cobalt content of up to 10%. The lattice period of chromium deposited from chromium-plating sulfate electrolyte with MEA under the similar conditions is a = 2.89 Å. Apparently, a slight decrease in the lattice period of Cr–Co alloy compared to chromium is explained by the decreased hydrogenation. For example, with the cobalt content of the alloy increased from 2.3 to 8.6%, the hydrogen content is decreased approximately 2.7-fold (Fig. 2). The decrease in the alloy hydrogenation with increasing cobalt content of the alloy can be explained by the decrease in the current efficiency by hydrogen in chromium-plating sulfate electrolyte with added $CoSO_4$. For example, with cobalt sulfate concentration increased from 1.0 to 5 g l^{-1}, the cobalt content of the alloy is increased from 1.8 to 12% and the CE by the alloy, from 6.2 to 10.3% (D_c = 20 A dm^{-2}, pH 0.75). Under these conditions the rate of hydrogen formation decreases simultaneously (see table), whereas that of cobalt formation increases approximately 4-fold.

The self-discharge of cobalt(II) ions occurs at a considerably higher rate (Fig. 1, curve *3*) than at simultaneous electroplating with chromium (curve *1d*). One of the reasons responsible for overpolarization of Co^{2+} discharge is the adsorption of colloidal surface-active $Cr(OH)_3$ on active sites of the cathode. As a result, the cobalt formation is hindered. This phenomenon is characteristic of codeposition of chromium with iron-group metals, for example, nickel [8] from sulfate electrolytes.

The alloy deposits containing up to 10–12% cobalt are lustrous and acquire a shadow typical of cobalt coatings at higher cobalt concentrations. With cobalt sulfate concentration increased from to 5 g l^{-1}, the D_c interval corresponding to deposition of lustrous coatings is broadened essentially (to 80 A dm^{-2}, pH 0.5).

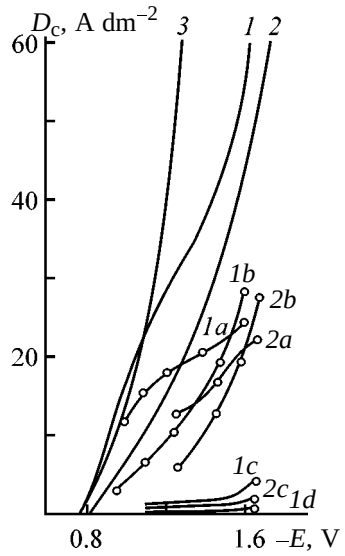

Fig. 1. Cathodic polarization curves of deposition of (*1*) Cr–Co alloy, (*2*) chromium, and (*3*) cobalt from sulfate electrolytes with MEA. (D_c) Current density and (E) potential. Partial curves of formation of (*1a*, *2a*) H_2, (*1b*, *2b*) Cr^{2+}, (*1c*, *2c*) Cr^0, and (*1d*) Co^0.

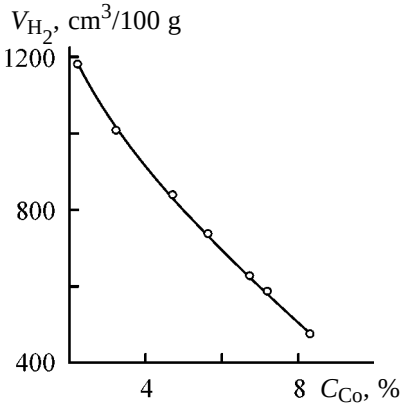

Fig. 2. Hydrogenation V_{H_2} of Cr–Co cathode deposits vs. cobalt content C_{Co} of the alloy. D_c = 30 A dm^{-2}, thickness 5 μm, pH 0.75, and T = 25°C.

With increasing electrolyte pH the rate of the alloy deposition increases. For example, with pH varied from 0.5 to 1.0, the hydrogen discharge current is decreased nearly twofold (from 19 to 10 A dm^{-2}) and the partial rate of the alloy deposition is increased approximately 9.50-fold (E = –1.4 V). Such a change in the electrolyte pH increases the current efficiency by the alloy (from 5 to 26% at D_c = 30 A dm^{-2}). Comparison of the partial current densities of the chromium(III) and cobalt(II) ion formation shows that with pH increasing in the given range the partial current density of the cobalt separation decreases from 6.2 to 1.8% (at D_c = 30 A dm^{-2}), and the alloy is

Partial current densities of hydrogen, chromium(II), cobalt, and chromium formation at 25°C

D_c, A dm^{-2}	i_{H_2}		$i_{Cr^{2+}}$		i_{Co^0}		i_{Cr^0}	
	A dm^{-2}, at indicated concentration of $CoSO_4$ in electrolyte, g l^{-1}							
	2	5	2	5	2	5	2	5
20	14.00	13.44	5.24	5.33	0.15	0.39	0.61	0.84
30	18.46	16.38	10.43	12.00	0.10	0.26	1.01	1.36
40	21.83	18.65	16.62	18.87	0.09	0.20	1.46	2.28

enriched with chromium. It should be noted that with decreasing electrolyte acidity the reflectivity of the coatings decreases, and at pH > 1.5 they become dull.

Increasing cathodic current density decreases cobalt content of the alloy. For example, as D_c is decreased from 10 to 60 A dm^{-2}, the cobalt content is decreased from 6 to 0.5%. One of the reasons of the appreciable dependence of alloy composition on D_c is the stronger polarization accompanying cobalt deposition into the alloy (Fig. 1, curve *1d*), which is ascribed to the increased pH_s and prevention of the Co^{2+} discharge by facilitated adsorption of $Cr(OH)_3$ on the cathode. To stabilize electrodeposition and make the dependence of alloy composition on D_c less appreciable, we studied the influence of the transient electrolysis mode using a rectangular pulsed current. It is seen from Fig. 3 that with the pulse to dead time ratio Q ($Q = \tau_p + \tau_d/\tau_p$, where τ_p is electrolysis time and τ_d is dead time) increased from 1.03 to 1.5, the cobalt content in the alloy is increased from 0.5 to 1.2% at D_c = 60 A dm^{-2}. This suggests that at high D_c the formation of chromium hydroxide film is hindered with increasing Q, thus creating the more favorable conditions for the Co^{2+} discharge compared to steady-state regime. At low D_c, the pH_s increase is slower, the chromium(III) ion concentration in the near-cathode space increases relative to cobalt(II) concentration, and the alloy is enriched with chromium. For example, at D_c = 10 A dm^{-2} the cobalt content in the alloy decreases from 4.6% (curve *2*) to 2% (curve *5*). The effect of the pulse repetition frequency on the alloy component ratio is less marked than that of the pulse to dead time ratio. For example, if f = 0.3 Hz, then at D_c = 10 A dm^{-2} the cobalt content in the alloy is lower by 0.8% (curve *5*) than at D_c = 60 A dm^{-2}. With f increasing to 0.35 Hz the cobalt content in the alloy decreases by 0.5% (curve *5'*). At f > 0.35 Hz and $Q \geq 2$ the current efficiency by the alloy is considerably lower (by ~ 12%), which can be explained by the cathode passivation at higher pulse repetition frequences typical of electrodeposition from sulfate electrolytes [12].

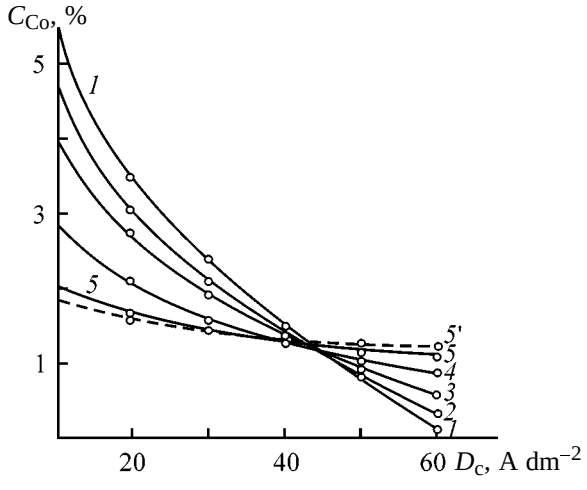

Fig. 3. Influence of the cathodic current density d_c on the cobalt content of the alloy C_{Co}. Electrolysis: (*1*) steady-state and (*2*–*5*) pulsed. Pulse to dead time ratio Q: (*2*) 1.03, (*3*) 1.1, (*4*) 1.2, and (*5*, *5'*) 1.5. Pulse repetition frequency f (Hz): (*2*–*5*) 0.3 and (*5'*) 0.35.

CONCLUSIONS

(1) Chromium and cobalt can be codeposited from electrolytes containing cobalt and chromium sulfates [the latter in the form of modified green chromium(III) sulfate] and luster-producing monoethanolamine.

(2) The method of partial curves has revealed that the electrodeposition of Cr–Co alloys occurs with depolarization, and that of cobalt, with enhanced polarization.

(3) The sulfate electrolyte with momoethanolamine is developed, allowing preparation of mirror-lustrous Cr–Co coatings (up to 10% Co) at D_c = 10–60 A dm^{-2}, T = 25°C, and pH 0.5–1.0. The current efficiency by the alloy is 15–25%.

(4) For the stabilization of the alloy composition, we recommend to perform electrolysis in the pulsed

current mode using rectangular pulses with a 0.3–0.35 Hz repetition frequency and the pulse to dead time ratio $Q = 1.5$.

REFERENCES

1. Vyacheslavov, P.M., *Elektroliticheskoe osazhdenie splavov* (ELectrolytic Deposition of Alloys), Leningrad: Mashinostroenie, 1980.
2. Potapov, I.I., and Kudryavtsev, N.T., *Zashch. Met.*, 1971, vol. 7, no. 1, pp. 55–57.
3. Falicheva, A.I., Spiridonov, B.A., Shalimov, Yu.N., and Zhernokleeva, S.V., *Zashch. Met.*, 1975, vol. 11, no. 5, pp. 622–623.
4. Spiridonov, B.A., *Tekh. Mashinostr.*, 1998, no. 3, pp. 41–42.
5. Harini, D., Clyde, R., and Dwain, C.H., *J. Electrochem. Soc.*, 1994, vol. 141, no. 7, pp. 1773–1779.
6. RF Patent 2130091.
7. Falicheva, A.I., *Elektrokhimiya*, 1968, vol. 4, no. 7, pp. 856–858.
8. Spiridonov, B.A. and Falicheva A.I., *Zh. Prikl. Khim.*, 2001, vol. 74, no. 2, pp. 210–215.
9. Gorelik, S.S., Rastorguev, L.N., and Skakov, Yu.A., *Rentgenograficheskii and elektronograficheskii analiz metallov* (X-ray and Electron Diffraction Analyses of Metals), Moscow: Metallurgiya, 1963.
10. Gulyaev, A.A., Study on Hydrogenation of Chromium Deposits Prepared from Electrolytes Containing Chromium(III) Compounds, *Cand. Sci. Dissertation*, Voronezh, 1973.
11. Hansen, M., and Anderko, K., *Constitution of Binary Alloys*, New York: McGraw-Hill, 1958.
12. Shalimov, Yu.N., Falicheva, A.I, and Spiridonov, B.A., *Zashch. Met.*, 1977, vol. 13, no. 5, pp. 623–625.

Russian Journal of Applied Chemistry, Vol. 74, No. 11, 2001, pp. 1842–1845. Translated from Zhurnal Prikladnoi Khimii, Vol. 74, No. 11, 2001, pp. 1787–1790.

APPLIED ELECTROCHEMISTRY AND CORROSION PROTECTION OF METALS

Electrodeposition of Tin from Sulfate Electrolyte with Organic Additives

G. I. Medvedev and N. A. Makrushin

Novomoskovsk Institute, Mendeleev Russian University of Chemical Engineering, Novomoskovsk, Tula oblast, Russia

Received June 7, 2001

Abstract—Electrodeposition of tin from sulfate electrolytes containing $SnSO_4$, H_2SO_4, Synthanol, formalin, and benzyl alcohol was studied.

It was shown in [1, 2] that dihydric alcohols (1,4-butynediol, 1,4-butenediol, and 1,4-butanediol), present in sulfate tin-plating electrolyte simultaneously with Synthanol and formalin, favor formation of lustrous tin coatings. Proceeding with these studies, we considered in this work electrodeposition of tin from a sulfate electrolyte in the presence of Synthanol, formalin, and benzyl alcohol.

The study was carried out in the electrolyte of the following composition (g l^{-1}); $SnSO_4$ 5–50, H_2SO_4 90–100. The organic substances were introduced in the following amounts: Synthanol DS-10 1–4 g l^{-1}; formalin (37% solution) 1–10 and benzyl alcohol 1–10 ml l^{-1}.

Tin coatings 6–24 μm thick were deposited onto copper samples. Polarization curves were obtained potentiodynamically with a P-5878 potentiostat. The leveling power of the electrolyte was measured on a flat sinusoidal microprofile. The leveling power P was calculated using the equation [3]

$$P = \log[(H_0 \times 2.3a)/(H_\tau \times 2\pi h_{av})],$$

where H_0 and H_τ are, respectively, the microprofile amplitudes before and after deposition of tin; a is the sinusoid wavelength, and h_{av} is the coating thickness (10 μm).

The coating luster was measured with an FB-2 photoelectric luster meter.

Our experiments showed that matte coatings with coarsely crystalline structure are formed in tin-plating electrolyte ($SnSO_4$ 30 and H_2SO_4 100 g l^{-1}) containing 1–4 g l^{-1} of Synthanol. In the presence of formalin and benzyl alcohol (in amount of 1–10 ml l^{-1} each), matte coatings with unsatisfactory quality are obtained. Addition of benzyl alcohol to an electrolyte with Synthanol does not lead to any significant change in the coating quality. In an electrolyte with Synthanol and formalin, silvery coatings are formed. The outward appearance of the coatings is much improved if benzyl alcohol (6–8 ml l^{-1}) is added to an electrolyte with Synthanol (2–3 g l^{-1}) and formalin (6–8 ml l^{-1}). In this case, lustrous tin coatings are obtained in the current density range i_c = 4–12 A dm^{-2}. When the concentrations of formalin and benzyl alcohol are beyond the above limits, semilustrous or silvery coatings are obtained, depending on i_c. At Synthanol concentrations lower than 2 g l^{-1}, the working range of current densities at which lustrous coatings are obtained becomes much narrower. At Synthanol concentrations exceeding 3 g l^{-1}, the interval of current densities in which lustrous coatings are obtained remains unchanged, but electrolyte foaming is much enhanced, which hinders the electrodeposition process. It should be noted that lustrous coatings can only be obtained with electrolyte stirring. We have examined the influence of the $SnSO_4$ concentration on the range of working current densities for preparing lustrous coatings. We found that raising the $SnSO_4$ concentration from 5 to 50 g l^{-1} in an electrolyte containing H_2SO_4 (90–100 g l^{-1}), Synthanol (2–3 g l^{-1}), formalin (6–8 ml l^{-1}, and benzyl alcohol (6–8 ml l^{-1}) makes higher the current density necessary for obtaining lustrous coatings. For example, lustrous coatings are formed in the following ranges of current densities (A dm^{-2}) at indicated $SnSO_4$ concentrations in the electrolyte: 1–7, 5 g l^{-1}; 1–8, 10–20 g l^{-1}; and 4–12, 30–50 g l^{-1}.

Data on current efficiency (CE) in tin-plating electrolyte with additives are presented in Fig. 1. It can be seen that CE grows with increasing $SnSO_4$ concentration in the electrolyte and decreases when i_c becomes

1070-4272/01/7411-1842$25.00

higher. The highest CE is observed in an electrolyte containing 50 g l^{-1} of $SnSO_4$. Lustrous tin coatings have finely crystalline structure and firmly adhere to the base metal.

To reveal the influence of organic substances on electrodeposition of tin, cathodic polarization curves were measured with immobile and rotating disk electrodes (Fig. 2). It can be seen that organic additives (curves *1* and *2*) make the deposition of tin slower and the cathodic polarization stronger. With increasing speed of electrode rotation, the overvoltage of tin deposition also grows (curves *2–4*).

The inhibiting action of organic substances in a tin-plating electrolyte is presumably due to their adsorption onto the electrode surface. This assumption is confirmed by measurements of the electrical double layer capacitance *C*. As seen from Fig. 2 (curves *5*, *6*), introduction of organic substances into the electrolyte leads to a decrease in the double layer capacitance in the potential range from –0.3 to –0.4 V from 32 to 8 μF cm^{-2}. At higher potentials, organic substances are desorbed from the electrode surface, which leads to higher capacitance of the double layer.

To reveal the effect of organic substances on the microdistribution of electrodeposited tin, we studied the dependence of the leveling power *P* of the electrolyte on the cathode current density upon addition of organic substance to the electrolyte. As seen from Fig. 3 (curve *1*), introduction of Synthanol into the tin-plating electrolyte leads to a certain leveling of the surface ($P = 0.1$) only at $i_c = 1$ A dm^{-2}. With the current density increasing further, surface antileveling is observed. On addition of formalin to an electrolyte with Synthanol (curve *2*), the leveling ($P = 0.14$–0.05) occurs at $i_c = 1$–10 A dm^{-2}. Introduction of benzyl alcohol into the electrolyte leads to more pronounced surface leveling (curve *3*). The leveling power of the mixture reaches its maximum value $P = 0.83$ at $i_c = 7$ A dm^{-2}.

Thus, the leveling additives in a mixture of organic substances are formalin and benzyl alcohol, with the latter ensuring the strongest surface leveling. A study of the influence exerted by the concentration of benzyl alcohol on the extent of leveling demonstrated that, with increasing concentration of benzyl alcohol (Fig. 3, curve *4*), the *P* value grows to reach a maximum of 0.69 at $C = 6$ ml l^{-1}. According to the adsorption–diffusion theory of surface leveling [3], the leveling additives inhibit electrodeposition of metals, with the extent of inhibition controlled by diffusion of an additive in the course of electrodeposition. The polarization curves measured on a rotating disk electrode at

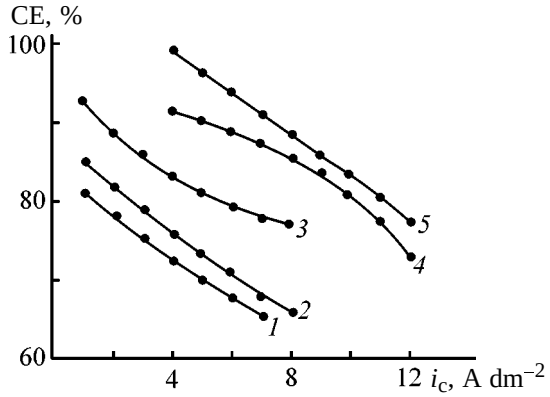

Fig. 1. Current efficiency CE vs. current density i_c at different $SnSO_4$ concentrations in the electrolyte. Mechanical stirring; the same for Fig. 2. Electrolyte composition: H_2SO_4 100, Synthanol 2 g l^{-1}; formalin 6, benzyl alcohol 6 ml l^{-1}. Electrolyte + $SnSO_4$ (g l^{-1}): (*1*) 5, (*2*) 10, (*3*) 20, (*4*) 30, and (*5*) 50.

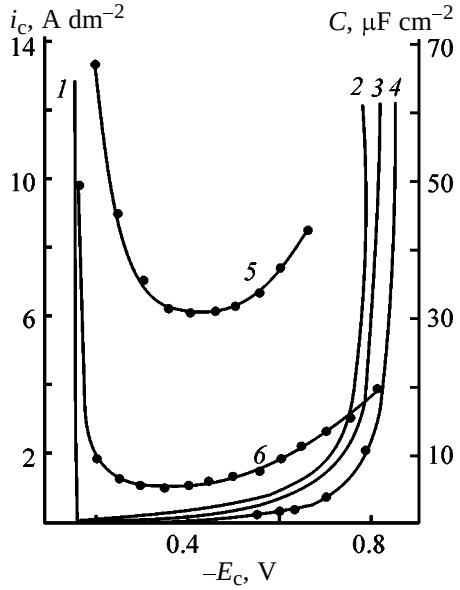

Fig. 2. (*1–4*) Cathodic polarization curves and (*5*, *6*) dependences of the capacitance of the electrical double layer, *C*, on the electrode potential E_c (vs. s.h.e), obtained in tin-plating electrolyte. Electrolyte composition (g l^{-1}): $SnSO_4$ 30, H_2SO_4 100; the same for Fig. 3. (i_c) Current density. (*1*, *5*) Electrolyte; (*2–4*, *6*) *1* + Synthanol, 2 g l^{-1}; formalin, 6 ml l^{-1}; and benzyl alcohol, 6 ml l^{-1}. Speed of electrode rotation (rpm): (*3*) 200 and (*4*) 2000.

different speeds of rotation can qualitatively model the cathodic process at microprojections (high speeds of electrode rotation) and at microdepressions (low speeds) [3]. The uneven accessibility of the microprofile is the reason for the nonuniform distribution of the rates at which additive is delivered to different parts of the microprofile. Since the inhibiting effect exerted by the leveling additives on electrodeposition

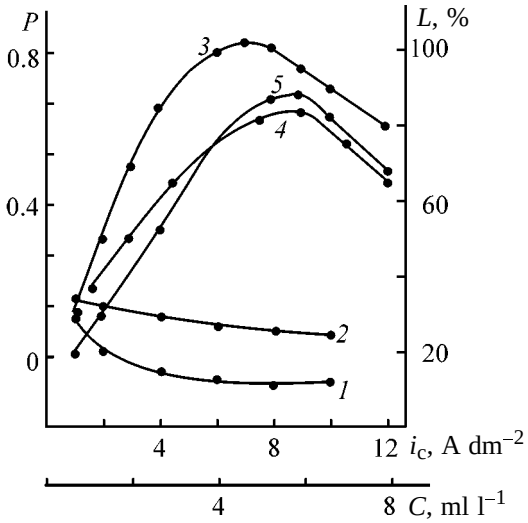

Fig. 3. Leveling power P vs. (*1–3*) current density i_c and (*4*) benzyl alcohol concentration C, and (*5*) coating luster L vs. current density for tin-plating electrolyte. (*1*) Electrolyte + Synthanol, 2 g l^{-1}; (*2*) *1* + formalin, 6 ml l^{-1}; (*3*, *5*) *2* + benzyl alcohol, 6 ml l^{-1}.

of metals becomes stronger with increasing rate of additive diffusion toward the cathode (high speed of rotation), this effect is more pronounced at microprojections, and less so at microdepressions, which leads to nonequilibrium distribution of the electrodeposition rates.

Analysis of the polarization curves measured in electrolytes with organic additives (Fig. 2, curves *2–4*) shows that the cathodic polarization curves measured at different speeds of rotation qualitatively model the distribution of the tin electrodeposition rate over the surface microprofile [3]. With increasing i_c, the leveling power first grows and then, at comparatively high current densities, the surface concentration of the additive and its inhibiting action decrease even at microprojections, which makes the leveling effect weaker. At too low content of additive in the electrolyte, when there occurs weak inhibition of tin electrodeposition, one cannot expect a pronounced leveling effect. At the same time, at too high concentrations of additive, the leveling power decreases because of the termination of the diffusion control over the rate of consumption of the additive and its inhibiting action. The phenomenon of leveling is related to the luster of electroplated coatings, since luster formation is also governed by leveling of submicrometer surface irregularities. According to [4], large microirregularities, from 0.2 to 100 μm and more in size, are eliminated in leveling, and very fine submicroirregularities of about 0.15 μm and less, in luster formation. Comparison of samples differing in luster and extent of leveling (Fig. 3, curves *3*, *5*) shows that these parameters are correlated: the higher the extent of leveling, the stronger the luster. Thus, leveling of submicro- and microirregularites on the cathode surface occurs in the course of electrolysis in a tin-plating electrolyte containing Synthanol, formalin, and benzyl alcohol.

On the basis of the performed investigations, a sulfate electrolyte of the following composition was developed for obtaining lustrous tin coatings (g l^{-1}): $SnSO_4$ 5–50, H_2SO_4 90–100, Synthanol DS-10 2–3; formalin 37% solution 6–8, benzyl alcohol 6–8 ml l^{-1}; deposition mode: i_c = 1–12 A dm^{-2}, CE = 65–98%. The process is carried out with mechanical stirring of the electrolyte. To obtain high-quality lustrous coatings, it is necessary to use anode made of pure tin. In order to prevent electrolyte contamination with sludge, the anodes are to be placed in sheaths made of polypropylene, before being submerged in the electrolyte. The electrolyte temperature is 20–25°C. At higher temperatures, the electrolyte rapidly turns turbid, and a large amount of precipitate is formed at the bath bottom, which impairs the coating quality. Long-term tests with the electrolyte demonstrated its high stability in operation. However, it should be noted that, during prolonged operation, a light yellow precipitate impairing the coating quality is formed on the bath bottom. The precipitate should be filtered off at regular intervals. The adjustment of the $SnSO_4$, H_2SO_4, and formalin content relies upon the results of chemical analysis [5]. The adjustment of the Synthanol content of the electrolyte should be done after passing 100 A h l^{-1} of electricity, by introducing 1 g l^{-1} of the additive into the bath. Since there is no technique for determining the concentration of benzyl alcohol in a tin-plating electrolyte, a spectrophotometric method was developed for this purpose. A 50-ml sample of a tin-plating electrolyte containing Synthanol, formalin, and benzyl alcohol was extracted with octanol (50 ml) under vigorous stirring in the course of 10 min. During this time, complete extraction was achieved. Part of the obtained organic phase was placed in a cell 10 mm thick, and spectra were recorded in the optical density–wavelength coordinates with an SF-26 spectrophotometer in the range 220–310 nm. As blank sample was used a solution obtained by extraction with octanol of a tin-plating electrolyte containing no benzyl alcohol. It was found that for all of the solutions studied the peak of the absorption band is observed at 252 nm, with the peak growing in height with increasing concentration of benzyl alcohol. It should be noted that the absorption is zero or very low in the employed wavelength range for all other components.

The obtained spectra were used to plot the calibration curve describing the dependence of the concentration of benzyl alcohol on the optical density at the maximum at 252 nm. This calibration curve can be used to monitor the concentration of benzyl alcohol in a tin-plating electrolyte. The scatter of measurement results in separate series does not exceed 5%.

CONCLUSIONS

(1) A study of tin electrodeposition from a sulfate electrolyte in the presence of organic substances demonstrated that high-quality lustrous deposits of tin are obtained in an electrolyte containing Synthanol, formalin, benzyl alcohol, $SnSO_4$, and H_2SO_4.

(2) A sulfate electrolyte and a deposition mode were developed for obtaining lustrous tin coatings with leveled surface.

REFERENCES

1. Medvedev, G.I. and Gorbunova, I.M., *Zh. Prikl. Khim*., 1990, vol. 63, no. 4, pp. 807–812.
2. Medvedev, G.I. and Mashutina, G.G., *Zh. Prikl. Khim*., 1992, vol. 65, no. 4, pp. 789–795.
3. Kruglikov, S.S., *Itogi Nauki Tekh., Ser.: Elektrokhim*., 1969, pp. 117–151.
4. Gnusin, N.P. and Kovarskii, N.Ya., *Sherokhovatost' elektroosazhdennykh pokrytii* (Roughness of Electrodeposited Coatings), Novosibirsk: Nauka, 1970.
5. Vyacheslavov, P.M. and Shmeleva, I.M., *Kontrol' elektrolitov i pokrytii* (Control of Electrolytes and Coatings), Leningrad: Mashinostroenie, 1965.

Russian Journal of Applied Chemistry, Vol. 74, No. 11, 2001, pp. 1846–1849. Translated from Zhurnal Prikladnoi Khimii, Vol. 74, No. 11, 2001, pp. 1791–1794.

CATALYSIS

Effect of High-Temperature Treatment of Pentasils on Their Acid and Catalytic Properties in Conversion of Straight-Run Naphthas

V. I. Erofeev, L. V. Adyaeva, and O. A. Kukharenko

Department of Scientific and Engineering Development, Tomsk Petrochemical Combine, Joint-Stock Company, Tomsk, Russia
Institute of Petroleum Chemistry, Siberian Division, Russian Academy of Sciences, Tomsk, Russia

Received May 7, 2001

Abstract—The acid and catalytic properties of Pentasil-type high-silica zeolites were studied as influenced by conditions of high-temperature treatment in the course of conversion of straight-run naphthas.

Zeolite-containing catalysts based on Pentasils are widely used in oil refining and petroleum chemistry. It was found [1–4] that the activity and selectivity of Pentasil-type high-silica zeolites (HSZs) in conversion of various hydrocarbons are determined by their not only acid, but also molecular-sieve properties. The efficiency of given catalytic process in conversion of hydrocarbon raw materials is determined by the optimal concentration ratio of the Brønsted and Lewis acid centers in the zeolite-containing catalysts. Along with modification using various additives, preliminary high-temperature treatment allows control of the catalytic and molecular-sieve properties of zeolite-containing catalysts.

In this work we studied the effect of high-temperature treatment on the acid and catalytic properties of Pentasil-type HSZs in the course of conversion of straight-run naphthas into lower olefins and arenes.

EXPERIMENTAL

High-silica zeolites of ZMS-5 type (silica ratio 30) were prepared from aluminosilicates by a hydrothermal procedure [5]. To convert Na-HSZs into the H form the samples were treated with 25% aqueous NH_4Cl at 90°C for 2 h, dried at 110°C, and calcined at 550°C for 8 h (Na_2O content ≤0.1%). The resulting HSZs were analyzed by IR spectroscopy and X-ray diffraction (XRD) (Mo anode, Ni filter). The effect of high-temperature treatment on the zeolite crystallinity was monitored by the comparing the interplanar spacings d (Å) and reflection intensities I (%) in the XRD patterns of the zeolite in question and reference compound.

The acid properties of HSZs were studied by thermal desorption of ammonia [6], and their catalytic properties were analyzed in the course of conversion of straight-run naphthas (from Surgut Gas Processing Plant) on a flow-type setup [7].

Data on the effect of high-temperature treatment on the activity and selectivity of HSZs in conversion of straight-run naphthas are listed in Table 1. With the initial NaHSZ (0.6 wt % Na^+), at 550–700°C and feed space velocity of 3 h^{-1}, the naphtha conversion increases from 85 to 88%. With increasing temperature the yield of gaseous hydrocarbons increases from 44.3 to 63.4%, the yield of C_2–C_4 olefins also increases from 19.8 to 39.1%, whereas the yield of aromatic hydrocarbons decreases from 47.9 to 31.1%.

After high-temperature treatment of an Na-HSZ sample at 800°C for 15 min its catalytic activity remains almost constant, and the yield of gaseous hydrocarbons and lower olefins increases in the temperature range studied. For example, at 650°C the yield of olefins (based on passed feed) increases from 29.3 to 39.0% and the yield of arenes decreases from 36.9 to 29.9% (Table 1). With the time of thermal treatment at 800°C increased to 30 min, high yield of C_2–C_4 olefins is retained. After treatment of an Na-HSZ sample at 900°C for 15 min, the yield of olefins at 550–600°C increases, but the catalytic activity decreases by 5% as compared to the initial sample. The selectivity of arene formation increases from 34.3 to 37.5 with increasing temperature.

Thus, our experimental data show that with increasing temperature of the catalyst thermal treatment from 750 to 900°C the yield of C_2–C_4 olefins increases; the

1070-4272/01/7411-1846$25.00

Table 1. Yield of conversion products of straight-run naphthas as influenced by the temperature of thermal treatment of HSZ catalysts

T, °C	Conversion, wt %	Yield based on passed feed, wt %						Content, wt %	
		gas	C_2–C_4 alkanes	C_2–C_4 alkenes	ethylene	propylene	arenes	C_2–C_4 alkenes in gas	arenes in catalyzate
Initial sample, min									
550	85	44.3	24.4	19.8	8.5	7.7	47.9	44.7	85.9
600	87	56.3	33.3	22.9	10.9	9.0	38.7	40.7	88.6
650	88	58.4	28.7	29.3	15.2	11.2	36.9	50.2	88.7
700	88	63.4	24.3	39.1	18.2	15.7	31.3	61.7	85.7
800°C, 5 min									
550	84	53.2	32.6	20.4	7.6	9.4	37.0	38.3	79.1
600	87	62.0	31.9	29.9	14.3	11.8	30.4	48.2	80.0
650	88	62.4	26.0	36.2	16.9	14.3	29.9	58.0	79.5
700	86	62.1	22.0	39.9	18.0	16.5	30.6	64.3	80.1
800°C, 15 min									
550	86	54.9	26.1	28.6	12.7	11.8	37.0	52.1	82.0
600	87	55.7	21.8	33.8	15.9	13.7	36.7	60.7	82.8
650	87	60.1	20.9	39.0	18.5	16.5	33.4	64.9	83.7
700	87	60.2	21.3	38.0	21.8	9.9	32.3	63.1	81.2
800°C, 30 min									
550	79	53.9	28.7	25.1	10.0	10.6	30.9	46.6	67.0
600	83	54.4	24.2	30.1	14.0	11.8	34.1	55.3	74.8
650	83	54.1	20.1	33.7	15.3	13.9	35.3	62.3	76.9
700	85	54.1	18.1	35.5	15.4	15.3	36.9	65.6	80.4
900°C, 15 min									
550	56	54.7	21.0	33.4	12.9	14.2	30.3	61.1	66.9
600	67	57.5	19.1	38.3	16.1	16.5	30.9	66.6	72.7
650	72	58.4	18.7	39.5	17.8	17.0	32.5	67.6	76.3
700	78	57.9	16.2	41.1	25.5	11.6	35.1	70.9	83.4

Table 2. Acid properties of HSZ heat-treated at various temperatures

Catalyst	T_{max}, °C		Concentration of acid centers, μmol g^{-1}	
	form I	form II	form I	form II
H-HSZ	194	406	623	526
Na-HSZ	198	Shoulder	927	0
Na-HSZ, 800°C	189	–	880	0
Na-HSZ, 900°C	174	–	836	0

optimal time of thermal treatment is 15 min. The effect of thermal treatment on the catalyst performance is the most pronounced at the temperature of the straight-run naphtha conversion of 550 – 600°C; with increasing conversion temperature the effect of the catalyst thermal pretreatment on the selectivity of formation of lower olefins and arenes decreases.

These trends in the conversion and selectivity of formation of lower olefins and arenes are probably due to variations in the acidity of the HSZ samples. It is known that the Brønsted acid centers are zeolite hydroxy groups, and their interaction with ammonia yields NH_4^+ ions [8]. In the case of zeolite containing residual Na^+ cations, ammonia sorption involves

Table 3. XRD patterns of Na-HSZ sample treated at various temperatures

d, Å	I_{rel}, %	*d*, Å	I_{rel}, %	*d*, Å	I_{rel}, %	*d*, Å	I_{rel}, %	*d*, Å	I_{rel}, %
initial sample		800°C, 5 min		900°C, 5 min		800°C, 30 min		900°C, 30 min	
11.13	48	11.13	40	11.13	44	11.13	21	11.16	25
10.04	39	10.04	34	10.04	34	10.04	19	10.06	23
6.65	5	6.35	7	6.35	8	–	–	6.35	7
6.35	14	5.98	13	5.98	15	6.03	10	5.94	10
5.55	15	5.69	12	5.60	12	5.68	10	5.64	13
4.99	10	5.02	10	4.98	8	5.01	7	5.06	10
4.27	18	4.25	19	4.27	20	4.3	16	4.27	22
3.82	100	3.81	100	3.83	100	3.84	100	3.84	100
3.75	72	3.71	71	3.72	73	–	78	3.75	61
3.47	32	3.44	32	3.53	33	–	–	–	–
3.36	35	3.35	35	3.37	33	3.37	36	3.36	38
3.01	24	3.02	26	3.04	25	3.02	20	3.07	22
–	–	2.98	27	2.99	26	–	–	2.98	20
2.56	10	–	–	–	–	2.59	10	2.6	11
2.49	11	2.49	10	2.50	12	2.51	10	2.51	9
2.41	8	2.42	10	2.41	9	2.42	6	2.42	7
–	–	2.22	5	–	–	2.22	3	2.16	4
–	–	2.08	6	–	–	2.11	5	2.11	4
1.99	16	1.99	16	2.00	16	2.00	12	2.00	13
–	–	1.92	7	–	–	1.83	4	1.87	6
1.66	6	1.67	7	1.67	6	1.67	3	1.67	5
1.45	7	1.45	–	1.45	7	–	–	–	–

formation of the coordination bond between the lone electron pair of nitrogen and sodium cations [9].

Data on the acid properties of the HSZ samples subjected to high-temperature treatment are shown in the figure and listed in Table 2. The curve of temperature-programmed NH_3 desorption from the initial Na-HSZ contains two peaks: low-temperature peak (T_{max} 198°C) and high-temperature shoulder (T_{max} 380°C), which suggests the presence of acid centers of two types. This is confirmed by the ammonia desorption curve registered for the H-HSZ catalyst (figure, curve *1*).

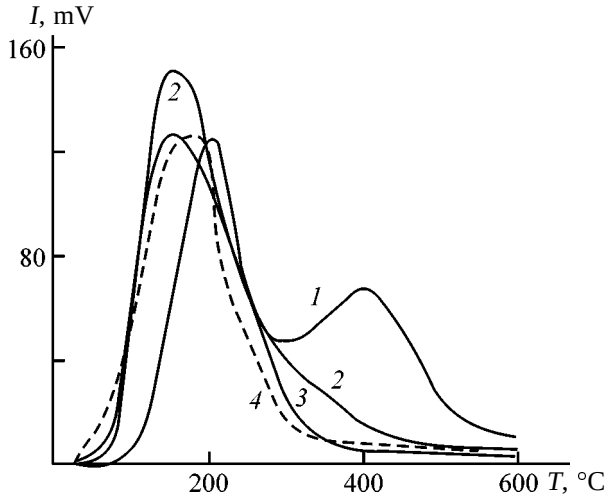

Curves of temperature-programmed ammonia desorption from HSZs. (*I*) intensity and (*T*) temperature. Sample: (*1*) H-HSZ, (*2*) Na-HSZ, (*3*) Na-HSZ (800°C), and (*4*) Na-HSZ (900°C).

High-temperature treatment of Na-HSZ at temperatures of up to 750°C does not affect its acid properties (Table 2). On further heating to 800°C and higher temperatures the strong acid centers almost completely disappear, and the content of more thermally stable weak acid centers slightly decreases. Moreover, on treatment at temperatures ≥900°C T_{max} of the low-temperature peak of ammonia desorption (form I) shifts to lower temperatures, i.e., the strength of the acid centers decreases. With increasing temperature of HSZ treatment the high-temperature form of ammonia desorption gradually disappears.

The XRD data on the initial HSZ and zeolite subjected to high-temperature treatment are listed in Table 3. The XRD patterns of the samples exhibit a set of Pentasil reflections typical for ZSM-5 [10]. Our

study of the thermal stability showed no changes in the HSZ structure at annealing of the zeolite samples for 15 min at 800 and 900°C. At more prolonged treatment (30 min) the reflection intensities slightly decrease.

Our experimental data on the acid and catalytic properties of HSZs allow evaluation of the role of the weak and strong acid centers in formation of C_2–C_4 olefins and arenes from straight-run naphtha. The activity of the zeolite catalyst is determined by the presence of both strong and weak acid centers. At high-temperature treatment the zeolite undergoes dehydroxylation. First of all at 750°C the content of strong acid centers sharply decreases, and at higher temperatures these acid centers completely disappear. Based on the IR data, it was supposed [1, 2] that high-temperature treatment of the zeolites (≥900°C) strongly decreases the content of the Brønsted acid centers (B-centers). At the same time, the Lewis centers (L-centers) are more thermally stable and start to degrade at higher temperatures. For example, in the case of Zn-Pentasils their L-centers are retained even after annealing at 1000°C. The L-centers of dehydrated zeolite [2] belong to two types: those of type I are three-coordinate Al^{3+} cations in the zeolite lattice with stronger acid properties, and those of type II are exchangeable Na^+ cations, coordination-unsaturated Al^{3+} ions outside the zeolite skeleton [8, 11], or three-coordinate Si^{4+}. The quantum-chemical calculations performed in [3] suggested the following scheme of zeolite dehydroxylation:

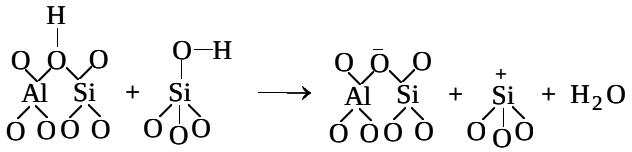

Thus, our experimental data show that, with the temperature of thermal treatment increased to 900°C, the strong acid centers completely disappear, the strength and concentration of the weak Lewis acid centers decrease, and the selectivity of formation of lower olefins from straight-run naphthas increases.

CONCLUSION

High-temperature treatment (up to 900°C) of high-silica zeolites of Pentasil type changes the ratio of the strong and weak acid centers in the catalyst. As a result, the weak Lewis acid centers become predominant, which increases the selectivity of formation of lower olefins from straight-run naphthas.

REFERENCES

1. Minachev, Kh.M., Kharson, M.S., Dergachev, A.A., *et al*., *Dokl. Akad. Nauk SSSR*, 1991, vol. 317, no. 2, pp. 378–381.
2. Spiridonov, S.E., Khadzhiev, S.N., Yaralov, N.G., and Limova, T.V., *Kinet. Katal*., 1986, vol. 27, no. 1, pp. 201–204.
3. Senchenya, I.N., Chuvylkin, N.D., and Kazanskii, V.B., *Kinet. Katal*., 1986, vol. 27, no. 1, pp. 87–92.
4. Vosmerikov, A.V. and Erofeev, V.I., *Zh. Prikl. Khim*., 1994, vol. 67, no. 7, pp. 1152–1156.
5. RF Patent 1527154.
6. Vosmerikov, A.V. and Erofeev, V.I., *Zh. Fiz. Khim*., 1995, vol. 69, no. 5, pp. 787–790.
7. Erofeev, V.I., Adyaeva, L.V., and Ryabov, Yu.V., *Zh. Prikl. Khim*., 2001, vol. 74, no. 2, pp. 231–234.
8. *Zeolite Chemistry and Catalysis*, Rabo, J.A., Ed., Washington: Am. Chem. Soc., 1976. Translated under the title *Khimiya tseolitov i kataliz na tseolitakh*, Moscow: Mir, 1980, pp. 147–346.
9. Rukhadze, A.D., Kapustin, G.I., Brueva, T.R., *et al*., *Kinet. Katal*., 1981, vol. 22, no. 2, pp. 134–138.
10. Limova, K.G., *Khim. Tekhnol. Topl. Masel*, 1992, no. 2, pp. 10–13.
11. Ione, K.G., Paukshtis, E.P., Mastikhin, V.M., *et al*., *Izv. Akad. Nauk SSSR, Ser. Khim*., 1981, no. 8, pp. 1717–1721.

Russian Journal of Applied Chemistry, Vol. 74, No. 11, 2001, pp. 1850–1853. Translated from Zhurnal Prikladnoi Khimii, Vol. 74, No. 11, 2001, pp. 1795–1798.

CATALYSIS

Direct Acid-Catalyzed Hydration of Camphene as a Route to Isoborneol

A. B. Radbil', B. A. Zolin, B. A. Radbil', T. V. Ryazanova, and T. V. Klimanskaya

Lesma Research and Promotion Firm, Limited Liabilty Company, Nizhni Novgorod, Russia
Lesosibirsk Rosin and Extraction Plant, Joint-Stock Company, Lesosibirsk, Krasnoyarsk krai, Russia

Received June 18, 2001

Abstract—Heterogeneous homophase hydration of camphene in the presence of $H_4SiW_{12}O_{40}$, $H_3PW_{12}O_{40}$, or $HClO_4$ was studied as a selective procedure for production of isoborneol.

Isoborneol, a bicyclic terpene alcohol, is widely used as initial substance in syntheses of biologically active substances for medicine, perfumery, cosmetics, and other fields. In particular, isoborneol is an intermediate in industrial synthesis of camphor, one of the main wood-chemical products.

The isomerization procedure used previously for producing camphor in Russia was multistage and involved catalytic isomerization of α- and β-pinene (turpentine) to camphene, esterification of camphene, saponification of the esters to isoborneol, and dehydrogenation of isoborneol to camphor [1]. The process was resource-, labor-, and power-consuming and gave rise to environmental problems; the quality of the target product was relatively poor. As a result, in the early 1990s the camphor production in Russia was fully stopped.

At the same time, it is known that China succeeded in improvement of the isomerization procedure and expanded the camphor production, so that at present it is practically the only producer and supplier of synthetic camphor to the world's market. Available publications suggest that the improved procedure for camphor production is based on the direct acid-catalyzed hydration of camphene to isoborneol, which allows not only reduction of the number of process stages but also improvement of the camphor quality. In the process, ion-exchange resins [2–4] or synthetic zeolites [5, 6] are used as catalysts.

Previous studies of homogeneous acid-catalyzed hydration of camphene in aqueous-organic media showed that effective catalysts are $H_4SiW_{12}O_{40}$ and $H_3PW_{12}O_{40}$ [7], and also $HClO_4$ [8]. Taking into account these results, we examined the behavior of these catalysts under conditions of heterogeneous homophase hydration.

Camphene hydration was performed in the presence of organic solvents immiscible with water (toluene or hexane), and also in the presence of dioxane and methyl ethyl ketone (MEK) added in amounts at which dissolution of the initial reactants was incomplete. In some cases, an emulsifier was used to improve the phase contact. In these experiments the organic phase was camphene or a solution of camphene in an organic solvent, and the aqueous phase was a solution of a catalyst in water.

The results of heterogeneous acid-catalyzed hydration of camphene in the absence of organic solvent are listed in Table 1. It is seen that the catalyst and reaction conditions strongly affect the composition and yield of the products.

With concentrated aqueous $HClO_4$ (40–60 wt %) as catalyst, the reaction yields exclusively camphene polymers (mainly a mixture of dimers). As the $HClO_4$ concentration is increased from 40 to 60%, the yield of the polymeric products at 65°C increases from 50 to 98%. As the reaction temperature is decreased to 50°C, with 40% $HClO_4$, the yield of the polymeric products appreciably decreases, becoming as low as 12%. No isoborneol or other alcohol is formed. Addition of ZnO to the catalyst (40% aqueous $HClO_4$, run no. 4) significantly increases the yield of the polymeric products, which reaches the level of 98% obtained with 60% $HClO_4$.

With less concentrated aqueous $HClO_4$ solutions, the camphene conversion considerably decreases, but isoborneol is detected in reaction products. As the $HClO_4$ concentration is decreased, the yield of the polymeric products regularly decreases, becoming zero with <11.6% $HClO_4$, whereas the content of isoborneol in the products remains constant down to

1070-4272/01/7411-1850$25.00

Table 1. Composition of reaction mixtures in heterogeneous homophase acid-catalyzed hydration of camphene in the absence of organic solvent*

Run no.	Catalyst	c_c, wt %	T, °C	Emlusifier	τ, h	$V_{cam} : V_{aq.s}$	Mixture composition, wt %		
							camphene	isoborneol	polymers
1	$HClO_4$	59.4	65	–	6	1 : 1	2.0		98.0
2	$HClO_4$	40.0	65	–	6	1 : 1	50.0		50.0
3	$HClO_4$	40.0	50	–	6	1 : 1	88.0		12.0
4	$HClO_4$ + ZnO	40.0	65	–	6	1 : 1	2.0		98.0
5	$HClO_4$	26.4	65	–	12	1 : 1	81.7	6.3	12.0
6	$HClO_4$	20.4	65	–	12	1 : 1	88.3	9.7	2.0
7	$HClO_4$	20.4	65	+	12	1 : 1	87.0	9.0	4.0
8	$HClO_4$	14.2	65	–	12	1 : 1	90.0	9.0	1.0
9	$HClO_4$	14.2	80	–	12	1 : 1	89.0	8.5	2.5
10	$HClO_4$	11.6	65	–	12	1 : 1	92.0	8.0	
11	$HClO_4$	6.3	65	+	12	1 : 3	92.3	7.7	
12	$HClO_4$	4.2	65	+	12	1 : 3	91.6	8.4	
13	$HClO_4$	2.1	65	+	12	1 : 3	96.2	3.8	
14**	$H_4SiW_{12}O_{40}$	16.7	65	–	6	1 : 3	93.3	6.3	
15**	$H_3PW_{12}O_{40}$	23.1	65	+	12	1 : 1	92.3	7.0	

* (c_c) Catalyst concentration in H_2O; (V_{cam}, $V_{aq.s}$) volumes of camphor and aqueous solution, respectively.
** Other alcohols, wt %: run no. 14, 0.4; run no. 15, 0.7.

the $HClO_4$ concentration of 4.2%. The increase in the reaction temperature to 80°C, variation of the volume ratio of camphor to aqueous acid solution, and addition of an emulsifier have no significant effect on the reaction selectivity and product composition.

With $H_3PW_{12}O_{40}$ and $H_4SiW_{12}O_{40}$ as catalysts of heterogeneous homophase hydration of camphene, we obtained the same results as with dilute aqueous solutions of perchloric acid: the yield of isoborneol, which was virtually the only reaction product, did not exceed 6–7% (Table 1).

The results of heterogeneous acid-catalyzed hydration of camphene in the presence of various solvents are given in Table 2. It is seen that addition of solvents immiscible with water (toluene or hexane) increases the content of undesirable impurities in the reaction products: camphene hydrate, pseudoborneol, and minor amounts of fenchol and isofenchol (all products were identified by GLC using reference compounds). The yield of isoborneol, with both heteropoly acids and perchloric acid as catalysts, does not change as compared to the process performed without a solvent.

The yield of the target product and the process selectivity appeared to be considerably higher when the process was performed with dioxane or methyl ethyl ketone (MEK) as solvent. These solvents were added in amounts that were insufficient to fully dissolve the initial compounds; therefore, the reaction conditions were also heterogeneous homophase.

Table 2 shows that even at a water : dioxane ratio of 2 : 1 (by volume; run no. 14) the yield of isoborneol increases to 15.6%. At the content of dioxane or MEK increased further, the content of isoborneol in the reaction mixture increases, reaching 25–28 wt % at the reaction selectivity of 98–99%. The nature of the catalyst has practically no effect on the yield of isoborneol and the process selectivity.

The perchloric acid concentration (3.4 wt %) ensuring the same yield of isoborneol is by a factor of almost 7 lower than the required concentration of heteropoly acids (23%), which is very important, taking into account high cost of heteropoly acids.

The heterogeneous hydration of camphene in MEK in the presence of perchloric acid was chosen as a procedure for preparative synthesis of isoborneol. The reaction product, isolated in 25% yield, after recrystallization from ethanol had mp 210.8°C (the reference value [9] for pure isoborneol is 212°C) and a 98.5% purity (GLC data). Such a product fully meets the requirements imposed upon isoborneol to be used for commercial production of synthetic camphor [1].

Table 2. Composition of reaction mixtures in heterogeneous homophase acid-catalyzed hydration of camphene in the presence of organic solvents*

Run no.	Solvent	$V_{cam} : V_{aq.s}$	$V_{H_2O} : V_o$	$V_{cam} : V_{aq\text{-}o}$	c_c, wt %	τ, h	Mixture composition, wt %		
							camphene	isoborneol	other alcohols
				Catalyst $H_4SiW_{12}O_{40}$					
1	Toluene	1 : 3	1.5 : 1	–	33.3	22	86.2	10.5	3.3
2	″	1 : 3	1.5 : 1	–	33.3	9	88.0	10.0	2.0
3	Toluene**	1 : 3	1.5 : 1	–	33.3	9	84.3	10.7	5.8
4	Dioxane	1.5 : 1	1 : 4	1 : 4	23.0	9	74.0	25.0	1.0
				Catalyst $HClO_4$					
5	Hexane	1 : 2	3 : 1	–	11.6	9	91.0	7.5	1.5
6	Toluene	1 : 2	3 : 1	–	14.2	9	90.0	8.8	1.2
7	Toluene**	1 : 2	3 : 1	–	14.2	9	80.1	10.9	9.0
8	Toluene	1 : 3	6 : 1	–	14.2	9	85.1	11.6	3.3
9	MEK	1 : 1	1 : 2	1 : 3	1.7	9	77.6	20.9	1.5
10	″	1 : 1	1 : 2	1 : 3	3.4	9	72.6	25.4	2.0
11	Dioxane	1 : 1	1 : 2	1 : 3	6.7	9	69.6	28.4	2.0
12	″	1 : 1	1 : 4	1 : 4	4	9	73.5	24.5	2.0
13	″	1 : 2	2 : 1	1 : 3	3.4	9	76.0	22.0	2.0
14	″	1 : 1	2 : 1	1 : 1.5	6.7	9	83.4	15.6	1.0

* (V_o, $V_{aq\text{-}o}$) Volumes of the organic and aqueous-organic solvents, respectively.
** An emulsifier was used.

The spent perchloric acid can be used repeatedly; neither the yield of isoborneol, nor the selectivity of hydration are deteriorated.

EXPERIMENTAL

Hydration of camphene was performed in a temperature-controlled reactor equipped with a heated jacket, a stirrer, and a reflux condenser. The reactor temperature was maintained to within ±0.5°C. The stirring rate was controlled with a tachometer. To improve the contact of aqueous and organic phases, Pektanoks emulsifier [OE-15 brand, TU (Technical Specifications) 2453-006-25588394–99] was added in some experiments. At certain time intervals after the start of the reaction, the mixture was quickly cooled, the reaction products were extracted with hexane, and the extract was neutralized with 10% aqueous Na_2CO_3, washed with water to pH 7, and dried over $MgSO_4$. After removing excess solvent, the reaction products were analyzed by GLC with a Chrom-5 chromatograph (flame-ionization detector, 3-m stainless steel column, stationary phase 15% PFMS-5 silicone oil on Chromaton N-AW-DMSC, 0.20–0.25 mm; column and vaporizer temperatures 110–180 and 250°C, respectively; carrier gas N_2, flow rate 60 ml min^{-1}). The content of the components was determined using tridecane as internal reference. The relative error of single analysis at a confidence level of 0.95 was within ±2%. The results of five parallel runs were averaged.

The melting point of isoborneol was determined in a capillary according to [10] with a PTP-2 device for melting point determination.

A solution of perchloric acid in aqueous MEK, after isolation of hydration products from the reaction mixture, was adjusted to the required concentration and reused.

REFERENCES

1. Rudakov, G.A., *Khimiya i tekhnologiya kamfary* (Chemistry and Technology of Camphor), Moscow: Lesnaya Prom–st., 1976.
2. Chinese Patent 1049842.
3. Cao Shuling, Cai Xiaojun, and Li Yunlong, *Linchan Huaxue Yu Gongye*, 1995, vol. 15, no. 3, pp. 25–30.

4. Lin Zhongxiang, Wang Afa, and Ju Zhaonian, *Linchan Huaxue Yu Gongye*, 1996, vol. 16, no. 2, pp. 29–32.
5. Nomura, M. and Fujihara, Y., *Res. Repts. Fac. Eng. Kinki Univ.*, 1985, vol. 19, no. 1, pp. 1–5.
6. Nomura, M. and Fujihara, Y., *J. Chem. Soc. Jpn.*, 1992, vol. 44, no. 1, pp. 63–65.
7. Radbil', A.B., Kulikov, M.V., Zolin, B.A., *et al.*, *Zh. Prikl. Khim.*, 2000, vol. 73, no. 2, pp. 241–245.
8. Radbil', A.B., Kulikov, M.V., Abstracts of Papers, *Pyataya nizhegorodskaya sessiya molodykh uchenykh* (Fifth Nizhni Novgorod Session of Young Scientists), Nizhni Novgorod, April 22–27, 2000, p. 142.
9. Glukhareva, M.I., Drozdov, N.P., Ermakova, L.A., *et al.*, *Spravochnik lesokhimika* (Handbook of Wood Chemist), Moscow: Lesnaya Prom–st., 1974.
10. Voskresenskii, P.I., *Tekhnika laboratornykh rabot* (Techniques of Laboratory Works), Moscow: Khimiya, 1972.

Russian Journal of Applied Chemistry, Vol. 74, No. 11, 2001, pp. 1854–1857. Translated from Zhurnal Prikladnoi Khimii, Vol. 74, No. 11, 2001, pp. 1799–1802.

PRODUCTION AND USE OF NEW MATERIALS

Factors Determining the Charge Transfer Rate in Polymers Based on Fe(II), Ru(II), and Os(II) Complexes with 5-Chloro-1,10-Phenanthroline

A. N. Borisov and G. A. Shagisultanova

St. Petersburg State University of Low-Temperature and Food Technologies, St. Petersburg, Russia
Herzen Russian State Educational University, St. Petersburg, Russia

Received June 29, 2001

Abstract—The effect of ionic diffusion on parameters of redox electrical conductivity in poly-$[M(5\text{-Cl-phen})_3]^{2+}$ (M = Fe, Ru, Os) was studied.

Supramolecular chemistry studying ordered associations of coordination-saturated species is an urgent branch of the modern basic science showing promise for high technologies [1–3]. Electroconducting supramolecular structures that are formed from polymers based on organometallic and coordination compounds of transition metals are of special interest. As a rule, these are intensely colored substances with a series of practically important properties such as redox electrical conductivity of polymeric complexes, photosensitivity, photo- and electroactivity, electrocatalytic and electrochromic properties.

From the viewpont of the practical use, polymeric structures with a high rate of charge transfer in the bulk of the solid phase, stable to action of chemical and physical factors, are of the most interest. Such complexes can be promising materials for production of sensors, chemotronic, photo- and electrocatalytic devices, and solid converters of the light energy [1].

In this work, we studied the electrochemical properties of polymers based on Fe(II), Ru(II), and Os(II) complexes with 5-chloro-1,10-phenanthroline with the aim to reveal factors determining the rate of charge transfer in the polymer bulk.

EXPERIMENTAL

Complexes $[M(5\text{-Cl-phen})_3](ClO_4)_2$ (M = Fe, Ru, Os; 5-Cl-phen = 5-chloro-1,10-phenanthroline) were synthesized by methods described in [4] and indentified by elemental analysis and electronic absorption spectra [5, 6].

(4,7-Diphenyl-1,10-phenanthroline)bis(5-chloro-1,10-phenanthroline)iron(II) perchlorate $[Fe(4,7\text{-ph}_2\text{-phen})(5\text{-Cl-phen})_2](ClO_4)_2$ was prepared by successively mixing the initial reagents 5-Cl-phen (0.466 mmol), $FeSO_4 \cdot 7H_2O$ (0.233 mmol), and 4,7-ph_2-phen (0.233 mmol) in 50 ml of hot ethanol. The resulting dark red solution was vigorously agitated at moderate heating for 2 h. The claret-colored complex (perchlorate form) was filtered off, washed with water, hot benzene, and diethyl ether, and dried in a vacuum over phosphorus(V) oxide. Yield 85%. Analytical data:

Found (%): C 61.89, H 2.74, N 7.45.
Calculated (%): C 62.06, H 2.58, N 7.24.

The electrochemical synthesis of polymeric $[M(5\text{-Cl-phen})_3]^{2+}$ was performed in the potentiostatic mode. The optimal conditions of growth of polymeric layers were as follows [7]: polarization potential of the working electrode in 2×10^3 M acetonitrile solutions of monomeric complexes E_p = –1.6 V, polarization time 7 min.

The electrochemical properties of the polymeric complexes were studied by cyclic voltammetry. A PI-50-1 pulse potentiostat with incorporated *IR*-compensation system set the potential of the working electrode. The potential of the working electrode was scanned in the cyclic mode at a rate of 10, 20, 50, 100, 200, and 500 mV s^{-1}. Voltammograms were recorded on a 307 two-coordinate potentiometric recorder.

Voltammetric measurements were performed in a hermetically sealed three-electrode Pyrex cell with separated compartments of the working, auxiliary, and reference electrodes.

1070-4272/01/7411-1854$25.00 © 2001 MAIK "Nauka/Interperiodica"

A 1-mm platinum wire (99.99% Pt) with the 0.21 cm^2 surface area sealed into Pyrex glass was the working electrode, and a platinum gauze with the 2.5 cm^2 surface area was the auxiliary electrode. All potentials are given vs. Ag–AgCl reference electrode filled with saturated aqueous NaCl solution.

The low-temperature electrochemical experiments were performed in a special three-electrode glass cell placed into a small thermostat with the temperature control of the supporting solution within the 243–293 K range.

A 0.1 M Bu_4NClO_4 solution in acetonitrile (the solvent was purified according to [8]), aerated with argon, was used as the supporting electrolyte. 1 M solutions of Bu_4NBF_4, Bu_4NPF_6, and CF_3COOBu_4N in acetonitrile were used to study the effect of supporting electrolyte on the charge diffusion coefficient D_{ct} in the bulk of the polymeric phase. The values of D_{ct} were obtained with an error of $\pm 0.5 \times 10^{-10}$ $cm^2 s^{-1}$.

During the electrochemical reduction of the Fe(II), Ru(II), and Os(II) complexes with 5-chloro-1,10-phenanthroline, red, orange, and olive green films, respectively, are formed on the surface of the platinum electrode. The possible mechanism of film formation involves reduction of the ligand into a radical anion followed by chloride ion elimination. Recombination of the resulting radicals generates polymeric chains and initiates growth of poly-$[M(5\text{-Cl-phen})_3]^{2+}$ polymers [4].

The polymeric complexes are electrochemically active within the potential range of metal-centered M(III)/M(II) transition. The potentials of the poly-$[M(5\text{-Cl-phen})_3]^{3+}/[M(5\text{-Cl-phen})_3]^{2+}$ couples were calculated as the mean values of the potentials of the cathodic and anodic maxima. They amounted to +1.12 (Fe), +1.36 (Ru), and +0.92 V (Os) [9].

Transition of the redox polymers from the reduced to oxidized state and back involves the electron transfer to the electrode–polymer phase boundary, the electron self-exchange between chain fragments (redox centers), and diffusion of the supporting electrolyte ions into the polymer bulk (and back) to keep macroelectroneutrality [10].

The rate of the charge transfer in the polymeric phase is mainly determined by the nature of the initial monomeric complex, supporting electrolyte, and morphology of the resulting polymer. It can be quantitatively characterized by D_{ct}.

Depending on the nature of the limiting stage, this quantity characterizes the electron self-exchange between heterocharged fragments or diffusion of supporting electrolyte ions in the polymeric phase.

Published data on the electron self-exchange with participation of octahedral low-spin Fe(III, II), Ru(III, II), and Os(III, II) complexes with polypyridyl ligands (bipy, phen, and their derivatives) show that it is not the limiting process. The electron transfer within the outer coordination sphere between the redox centers is accompanied by small variation of the metal–ligand bond length, because the transferred electron is located on the energetically favorable $d\pi$ orbitals of the metal ion: $d_\pi^5 + e = d_\pi^6$ [11]. This causes the high rate of the electron exchange in the above systems. For instance, in aqueous solutions the self-exchange constants reach the diffusion limit of 10^9 mol^{-1} s^{-1} [12].

The cyclic voltammograms of the redox processes with participation of poly-$[Os(5\text{-Cl-phen})_3]^{2+}$ recorded at various rates of scanning of the electrode potential V_p are shown in Fig. 1a, and in Fig. 1b are presented the currents of anodic maxima of voltammograms I_p^a as functions of V_p. The linear dependence between the above parameters at $V_p \le mV$ s^{-1} is observed, which indicates complete oxidation and reduction of the polymeric complexes in each cycle of potential scanning. This is characteristic for compounds adsorbed on the electrode surface. At the rates of potential scanning exceeding 50 mVs^{-1}, both oxidation and reduction of the polymeric complex in each scanning cycle is incomplete. In this case, the linear dependence $I_p^a = F(V_p^{1/2})$ is observed, i.e., the redox processes proceed in the mode equivalent to the semi-infinite diffusion of the electroactive substance directed to the electrode surface. The D_{ct} values calculated by the Randles–Shevchik equation [13] were about 2.0×10^{-10} cm^2 s^{-1} for all polymers studied and were independent of the polymer thickness.

The charge transfer in the bulk of the polymeric phase is a thermally activated process. The typical dependence $\ln D_{ct} = F(T^{-1})$ for poly-$[M(5\text{-Cl-phen})_3]^{2+}$ is shown in Fig. 2. The low-temperature voltammetric measurements showed that the activation barriers of the charge transfer are independent of the metal center nature and amount to about 25 kJ mol^{-1} for all the polymeric complexes studied. The lack of correlation between the degree of π-dative metal–ligand interaction increasing in the Fe–Ru–Os series and the height of the activation barrier to charge transfer indicate that the D_{ct} values found characterize the mobility of counterions in the polymeric phase.

To confirm the crucial importance of ionic diffu-

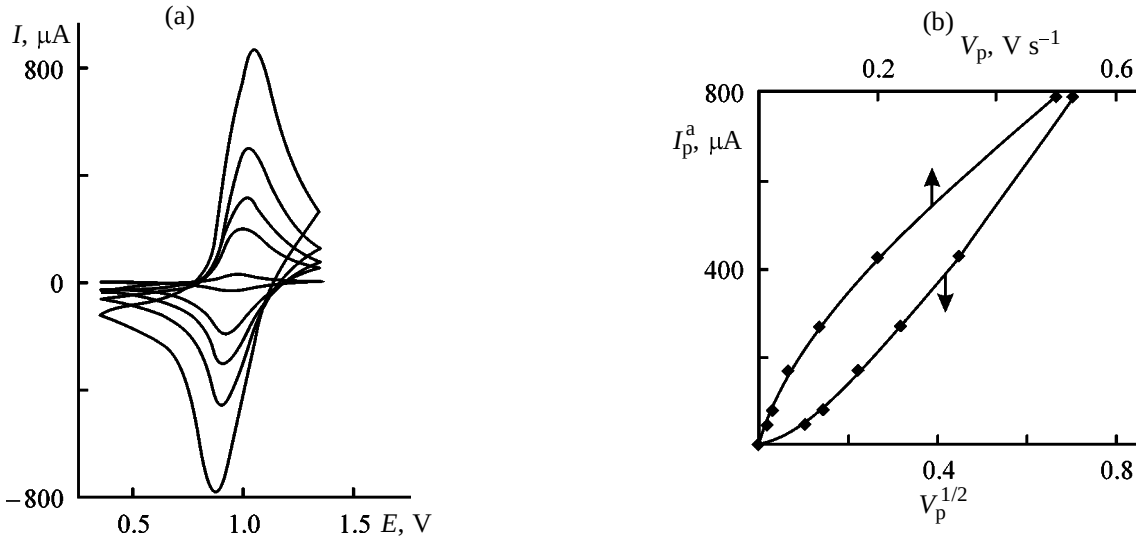

Fig. 1. (a) Chronoammograms of poly-$[Os(5\text{-Cl-phen})_3]^{2+}$ in the supporting electrolyte solution (0.1 M Bu_4NClO_4 in CH_3CN) and (b) dependence of the current of anodic maxima I_p^a in the chronovoltammograms on the rate of potential scanning V_p. (a) Rate of potential scanning (in the order of increase in chronovoltammogram current): 10, 20, 50, 100, and 500 mV s^{-1}. (*I*) Current and (*E*) potential; the same for Fig. 3.

sion in the charge transport in the poly-$[M(5\text{-Cl-phen})_3]^{2+}$ complexes, we examined the effect of the size and concentration of the supporting electrolyte ions on the charge diffusion coefficient. The diameters of ClO_4^-, BF_4^-, PF_6^-, and CF_3COO^- ions are 3.37, 3.70, 4.35, and 7.20 Å, respectively [14]. The experiment shows that the charge transfer activation energy regularly increases with increasing diameter of the counterion (to 37 and 46 kJ mol^{-1} for BF_4^- and PF_6^-, respectively). This can be explained as follows. The diffusion in the bulk of the polymer phase can be presented as a sequence of jumps occurring as a free volume is generated by segmentary motion near the moving particle [15]. The diffusion of bulkier particles involves larger energy consumption required to shift bulky polymeric fragments to form "holes" sufficient to accommodate the counterions.

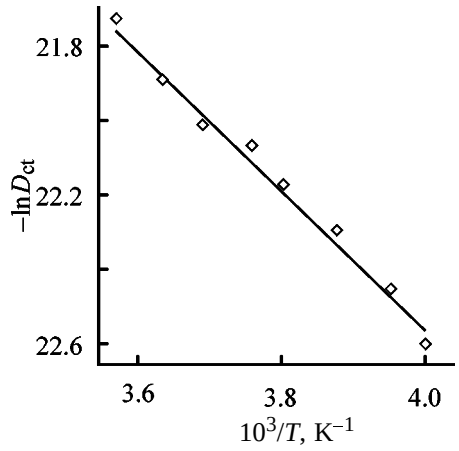

Fig. 2. Determination of the activation barrier of the charge transfer in poly-$[Ru(5\text{-Cl-phen})_3]^{2+}$. Supporting electrolyte 0.1 M Bu_4NClO_4 in CH_3CN. (D_{ct}) Charge diffusion coefficient and (*T*) temperature.

In the limiting case, mismatch of the sizes of the charge-compensating ions and holes of the polymer can cause polymer degradation. For instance, the use of 0.1 M CF_3COOBu_4N in CH_3CN as a supporting electrolyte leads to irreversible oxidation of the all polymers studied (Fig. 3, curve *2*) and practically complete loss of the electrical conductivity by these materials (Fig. 3, curve *3*) due to distortion of the π conjugation in the ligand system. This fact can be explained by impossibility of trifluoroacetate ions to penetrate deep into the polymer to compensate for the new charge state of the metal centers.

The rate of oxidation–reduction of poly-$[M(5\text{-Cl-phen})_3]^{2+}$ substantially depends not only on the nature of the supporting electrolyte but also on its concentration. The dependence of I_p^a on the Bu_4NClO_4 concentration C_S in acetonitrile for poly-$[Ru(5\text{-Cl-phen})_3]^{2+}$ is shown in Fig. 4. The dependence $I_p^a = F(C_S)$ is linear at $C_S \le 0.6$ M; within this concentration range D_{ct} increases by 25–30% owing to the growth of the gradient of the diffusing ion concentrations in the bulk of the polymer and in the supporting electrolyte solution. At $C_S > 0.6$ M, the linear character of the $I_p^a = F(C_S)$ dependence is broken, which reflects the transformations of the polymer morphology [16]. In concentrated solutions of the supporting electrolyte, the degree of shielding of the similarly charged centers of

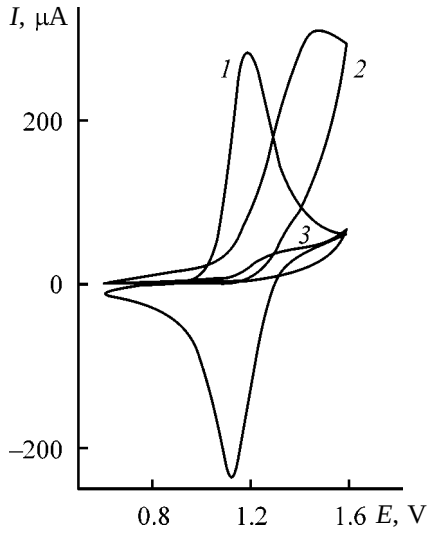

Fig. 3. Chronovoltammograms of poly-$[Fe(5\text{-Cl-phen})_3]^{2+}$ in supporting electrolyte solutions (*1*) 0.1 M Bu_4NClO_4 in CH_3CN and (*2*, *3*) 0.1 M CF_3COOBu_4N in CH_3CN. Rate of potential scanning 50 mV s^{-1}.

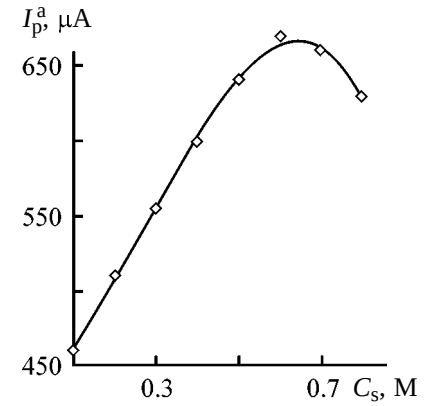

Fig. 4. Current of anodic maxima I_p^a for poly-$[Ru(5\text{-Cl-phen})_3]^{2+}$ as a function of Bu_4NClO_4 concentration in CH_3CN C_S. Rate of potential scanning 200 mV s^{-1}.

the polymeric complex increases, and therefore the macromolecule becomes more compact. As a result, the polymer free volume decreases, and ionic diffusion decelerates.

It should be noted that appropriate variation of the formation conditions and morphology of polymeric structures substantially increases the coefficient of the charge diffusion in the bulk of the polymer. For the polymer based on the heteroligand complex Fe(4,7-ph_2-phen)(5-Cl-phen)$_2$](ClO$_4$)$_2$, D_{ct} is equal to 4.7×10^{-10} cm^2 s^{-1}. Probably, bulky phenyl substituents in the inner sphere of the initial monomeric complex increase the polymer free volume and strengthen the mobility of counterions in the bulk of the polymer phase.

When a 0.1 M solution of CF_3COOBu_4N in CH_3CN is used as a supporting electrolyte in the synthesis of poly-$[M(5\text{-Cl-phen})_3]^{2+}$ with the subsequent transfer of the polymer into the 0.1 M solution of Bu_4NClO_4, D_{ct} increases to 7.5×10^{-10} cm^2 s^{-1}. Hence, these conditions of polymer formation provide the larger free volume of the polymer matrix.

CONCLUSION

The rate of charge transfer in polymers based on Fe(II), Ru(II), and Os(II) complexes with 5-chloro-1,10-phenanthroline is determined by the mobility of ions of the supporting electrolyte in the bulk pf the polymer phase.

REFERENCES

1. Balzani, V. and Scandola, F., *Supramolecular Photochemistry*, Chichester: Horwood, 1991.
2. Aleskovskii, V.B., *Khimiya nadmolekulyarnykh soedinenii* (Chemistry of Supramolecular Compounds), St. Petersburg: Sankt-Peterb. Gos. Univ., 1996.
3. Ward, G., *Chem. Soc. Rev.*, 1997, vol. 26, no. 3, pp. 365–375.
4. Fussa-Rudel, O., Zhang, H.-T., Zhang, J.T., *et al.*, *Inorg Chem.*, 1989, vol. 28, no. 8, pp. 1533–1537.
5. McWhinnie, W.R. and Miller, J.D., *Adv. Inorg. Chem. Radiochem.*, 1969, vol. 12, no. 4, pp. 135–139.
6. Lin, C.T., Botcher, W., Chon, M., *et al.*, *J. Am. Chem. Soc.*, 1976, vol. 98, no. 24, pp. 6536–6541.
7. Borisov, A.N., Timonov, A.M., Timofeev, V.A., and Shagisultanova, G.A., *Zh. Neorg. Khim.*, 1996, vol. 41, no. 3, pp. 468–473.
8. Coertzee, J.F., Cunningham, G.P., McGuire, D.K., and Padmanabhan, G.R., *Anal. Chem.*, 1962, vol. 34, no. 9, pp. 1139–1142.
9. Shagisultanova, G.A., Orlova, I.A., and Borisov, A.N., *J. Photochem. Photobiol. A: Chem.*, 1997, vol. 103, pp. 249–255.
10. Kaufmann, F.B., Shroeder, A.H., Engler, E.M., *et al.*, *J. Am. Chem. Soc.*, 1980, vol. 102, no. 2, pp. 483–488.
11. Kravtsov, V.I., *Ravnovesie i kinetika elektrodnykh reaktsii kompleksov metallov* (Equilibrium and Kinetics of Electrode Reactions of Metal Complexes), Leningrad: Khimiya, 1985.
12. Sutin, N. and Creutz, C., *J. Chem. Ed.*, 1983, vol. 60, no. 3, pp. 809–814.
13. Plambeck, J.A., *Electroanalytical Chemistry. Basic Principles and Applications*, New York: Wiley, 1982.
14. Leidner, C.R. and Murray, R.W., *J. Am. Chem. Soc.*, 1985, vol. 107, nos. 1–3, pp. 551–556.
15. Guillet, J., *Polymer Photophysics and Photochemistry. An Introduction to the Study of Photoprocesses in Macromolecules*, Cambridge: Cambridge Univ. Press, 1985.
16. Inzelt, G., *Electrochim. Acta*, 1989, vol. 34, no. 2, pp. 83–91.

Russian Journal of Applied Chemistry, Vol. 74, No. 11, 2001, pp. 1858–1863. Translated from Zhurnal Prikladnoi Khimii, Vol. 74, No. 11, 2001, pp. 1803–1808.

ENVIRONMENTAL PROBLEMS OF CHEMISTRY AND TECHNOLOGY

Selective Sorption Recovery of Metals from Wastewater of Electroplating Productions

V. B. Kargman, L. P. Sokolova, G. K. Saldadze, G. S. Beklemisheva, and A. K. Samsonov

Tsvetmetobrabotka Institute, Joint-Stock Company, Moscow, Russia
NIIPM and OMZP Joint-Stock Company, Moscow, Russia
Ekologiya Small-Scale Enterprise, Moscow, Russia

Received September 25, 2000; in the final form, April 2001

Abstract—The selectivity of S-930 chelating sorbent with respect to nonferrous metals present in the wastewater from electroplating productions was studied. This sorbent is advantageous as compared to KU-2 universal cation exchanger in recovery of microamounts of nonferrous metals from wastewter containing up to 2 g l^{-1} of alkaline-earth chlorides and sulfates.

A division for centralized reprocessing of the spent solutions from electroplating productions was set up at the Moscow Promotkhody plant. According to the flowsheet, spent solutions from electroplating productions are neutralized with sodium hydroxide aqueous solution to precipitate nonferrous metals and iron in the form of their hydroxides. After separation of these precipitates by filtration, the remaining solution contains up to 25.5 g l^{-1} of the sum of water-soluble salts, including minor amounts of nonferrous metals and iron.

On compacting the precipitate and washing the equipment and pipelines, the wastewater is formed containing up to 2 g l^{-1} of the sum of alkali and alkaline-earth metals and microamounts of nonferrous metals and iron. The metal content in the wastewater is given in Table 1.

Sulfates and chlorides of alkali and alkaline-earth metals (Na^+, Ca^{2+}, Mg^{2+}) are macrocomponents of the wastewater. Their content in wastewater discharged to a sewer system is not restricted; therefore, wastewater should be decontaminated only from impurities of nonferrous metals [Cr(III), Fe(II), Cu(II), Zn(II), and Ni(II)] to the levels lower than the maximum permissible concentrations (MPC) [1].

It is known that in decontamination of dilute wastewater (in particular, washing water) with the salt content not exceeding 2 g l^{-1}, the ion-exchange sorption is the most preferable. It is this technique that provides environmentally safe decontamination of industrial wastewater [2].

To ensure high efficiency of ion-exchange decontamination of wastewater, it is necessary to use the ion exchanger exhibiting the required sorption power, fast sorption kinetics, high granule strength, and also high chemical and osmotic stability [3].

In sorption removal of nonferrous metals and iron from multicomponent solutions containing large amounts of alkali and alkaline-earth metals, the sorbent should be sufficiently selective.

Chelating ion exchangers with amino acid functional groups fully meet these requirements [4]. These sorbents exhibit selectivity owing to their capability of forming metal complexes of various stabilities and structures in the resin phase. The highest selectivity is exhibited by chelating polyampholytes with the iminodiacetate complexing groups. Their selectivity decreases in the order Cu > Ni > Zn > Co > Ca >

Table 1. Metal ion content in wastewater

Metal ion	Concentration		MPC in discharging to sewer system, mg l^{-1}
	mg l^{-1}	mg-equiv l^{-1}	
Cr(III)	15	0.865	1.0
Fe(II)	50	1.8	3.0
Cu(II)	12	0.38	0.5
Ni(II)	15	0.51	0.5
Zn(II)	12	0.37	2.0
Ca(II)	156.3	7.8	Not restricted
Mg(II)	72.9	6.0	〃

1070-4272/01/7411-1858$25.00

Mg > Sr > Ba > Na, which correlates with the strength of complexes of these metals with the iminodiacetate functional groups in the resin phase [4].

At present, ANKB-35 and ANKB-50 sorbents with the iminodiacetate functional groups are not commercially produced in Russia. Their most available imported analog is S-390 produced by Purolite Corporation (The United States, the United Kingdom) [6].

Our experience of using S-930 sorbent for recovery of copper from multicomponent process salt solutions showed that this chelating sorbent surpasses in selectivity both ANKB-35 (Russian analog) and well-known MC-50 polyampholyte (Germany) [7].

It is known that the group concentration of the metal impurities can be performed on weakly acidic carboxylic cation exchangers exhibiting high sorption capacity and selectivity with respect to polyvalent metals [8]. However, these cation exchangers are efficient in weakly acidic media only (at pH about 3). Also, these sorbents do not meet the modern requirements to the osmotic stability and resin strength; therefore, their service life is limited.

Thus, carboxylic cation exchangers of KB type seem to be of little promise for solving the problems under consideration.

Selective sorption is a multifactor process depending not only on the ionic composition of solution but also on the ratio of the ions being recovered, pH, and the degree of protonation of the functional groups. Therefore, prior to the practical use, the sorbent with suitable characteristics should be experimentally chosen and conditions ensuring its highest performance should be found.

In this work the comparative study of sorption recovery of nonferrous metals [in particular, Cr(III)] and iron from wastewater from electroplating productions with both KU-2 × 8 strongly acidic sulfonic cation exchanger and S-930 selective chelating sorbent with the iminodiacetate functional groups was carried out to choose the sorbent ensuring the most efficient wastewater decontamination, suitable for industrial use.

EXPERIMENTAL

The sorption and desorption characteristics of KU-2 × 8 universal sorbent and S-930 selective sorbent were determined under dynamic conditions by passing appropriate solutions through columns packed with these ion exchangers.

S-930 sorbent is the monofunctional ion-exchange resin containing the iminodiacetate functional groups

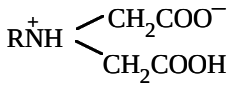

where R is the macroporous polymeric matrix based on styrene and divinylbenzene.

This sorbent consists of light yellow dull granules 0.4–1.0 mm in diameter exhibiting high levels of sorption capacity, chemical and thermal stability, mechanical strength, and osmotic stability.

The lack of standard recommendations for pretreatment of chelating polyampholytes hinders their use. The standard pretreatment is required to provide reproducibility of the sorption capacity and other characteristics of these sorbents.

In this work S-930 sorbent was converted to the neutral form by passing a 5% sodium hydroxide solution through the column packed with the commercial resin. Such treatment was continued until the sodium hydroxide concentrations at the inlet and outlet of the column became equal. Then, the column was washed with water to weakly alkaline reaction of the eluate (pH 8–9).

Treatment of the commercial sorbent with aqueous sodium hydroxide solution converts the sorbent to the dibasic cation-exchange iminodiacetate form:

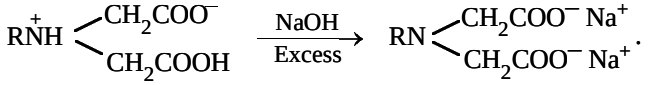

However, hydrolysis of this form of the sorbent makes the aqueous solution strongly alkaline, which is unacceptable for the practice.

To overcome this drawback, the cation exchanger in the Na form was washed with hot water to the weakly alkaline reaction of the eluate (pH 8–9). After such treatment the sorbent is converted to the stable neutral form:

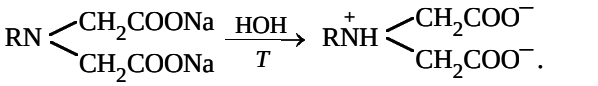

This coordination-active form of the sorbent is capable of binding the metal ions by coordination and ionic bonds:

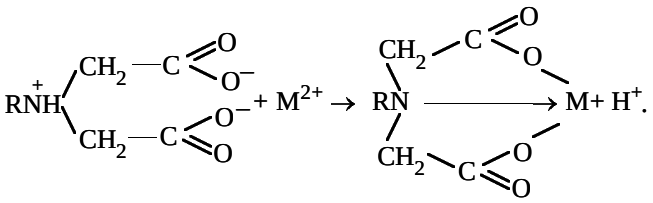

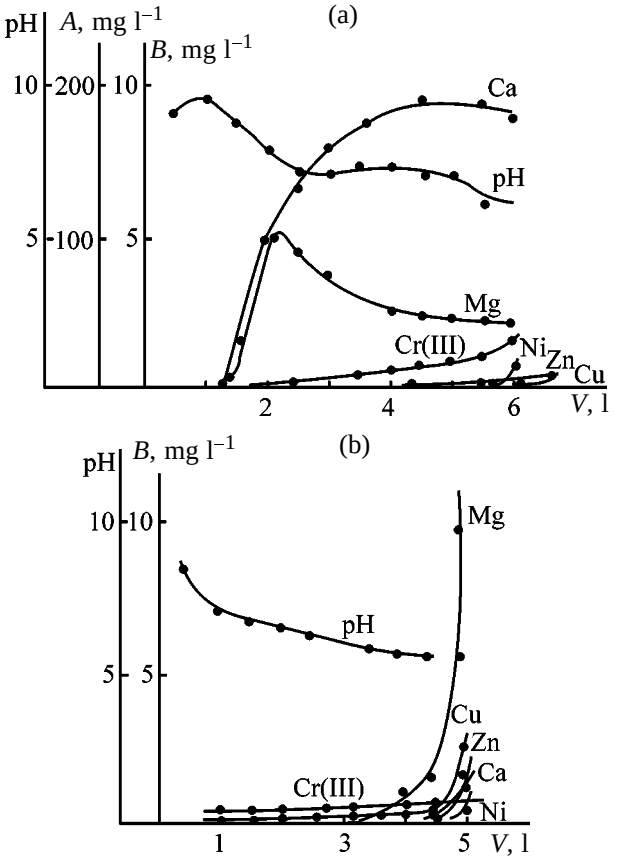

Fig. 1. Output curves of sorption of nonferrous metal [including (Cr(III)] cations on (a) S-930 selective sorbent and (b) KU-2 × 8 cation exchanger. (*A*) Ca and Mg content; (*B*) (a) nonferrous metal [including (Cr(III)] content and (b) metal content; (*V*) solution volume passed through column.

At the same time, this form of the ion exchanger does not sorb metals that do not form coordination bonds with the acetate functional groups or form weak complexes [9, 10]. Owing to these features, S-930 sorbent is selective to nonferrous metals and iron. To convert one volume of swollen polyampholyte to the Na form, six volumes of 5% NaOH are required. To wash one volume of this sorbent, four volumes of water are required.

KU-2 × 8 cation exchanger in the Na form was used as the reference sorbent.

Pretreatment of KU-2 × 8 cation exchanger and determination of its characteristics before testing were carried out in accordance with GOST (State Standard) [11, 12].

The sorbents were tested under dynamic conditions in standard glass columns 18 mm in diameter. The height of the swollen sorbent bed was 15 cm, and its volume, 40 cm^3.

In the tests, ten volumes of wastewater were passed through one sorbent volume per hour. The wastewater was passed through the column up to breakthrough of the least sorbable metals to concentration exceeding their maximum permissible concentration in water discharged to the municipal sewer system (Table 1). The initial and decontaminated wastewaters were analyzed for the metals by atomic-absorption technique on a Perkin–Elmer spectrophotometer [13].

The output curves of sorption of nonferrous metals [including Cr(III)] in the presence of macroamounts of Ca^{2+} and Mg^{2+} on S-930 and KU-2 × 8 cation exchangers are shown in Fig. 1.

As seen from Fig. 1, KU-2 × 8 cation exchanger absorbs the sum of the metals present in the wastewater, including Ca^{2+} and Mg^{2+}. In contrast to the sulfonic cation exchanger, S-930 sorbs alkaline-earth metal ions only at the beginning of the process. In further elution these metals are replaced by nonferrous metal [including Cr(III)] cations, and therefore their content in the eluate becomes equal to that in the feed. These results show that nonferrous metal [including (Cr(III)] cations are selectively sorbed on S-930 cation exchanger.

Table 2 shows that in sorption on KU-2 × 8 cation exchanger the nonferrous and alkaline-earth metals break through simultaneously. Thus, this sorbent exhibits no selectivity with respect to the metals concerned. In contrast to KU-2 × 8 cation exchanger, in sorption of these metals on S-930 cation exchanger chromium(III) and nickel break through first (among nonferrous metals), while zinc and copper cations are retained on the resin so that only traces of them are eluted. By breakthrough, as above, we mean the metal concentration in the eluate exceeding the maximum permissible concentration in wastewater discharged to a municipal sewer system (Table 1).

The fact that the volume of the wastewater decontaminated by one column volume of S-830 sorbent is twice that of KU-2 × 8 shows that the dynamic exchange capacity of S-930 is twice that of KU-2 × 8.

The averaged composition of wastewater passed through beds of S-930 and KU-2 × 8 resin, (water volumes are 6 and 5 l, respectively) are listed in Table 3.

The metals were desorbed from S-930 sorbent under dynamic conditions by passing 20% H_2SO_4 through the column at a filtration rate of 1–2 ml min^{-1}. Figure 2 shows that the eluate contains all nonferrous

Table 2. Number of column volumes of wastewater (*N*) passed through KU-2 × 8 and S-930 sorbents by the moment of breakthrough of the least sorbable metal ions

N	Metal concentration, mg l^{-1}						pH
	Cu	Zn	Ni	Cr	Ca	M	
KU-2 × 8 cation exchanger							
12.5	0.021	0.028	0.1	0.38	Not detected		8.3
25.0	0.05	0.025	0.1	0.41	″		7.0
37.5	0.1	0.03	0.1	0.44	″		6.8
50.0	0.07	0.031	0.1	0.42	″		6.5
62.5	0.06	0.02	0.1	0.45	″		6.2
75.0	0.09	0.01	0.1	0.51	″		6.0
87.5	0.11	0.06	0.1	0.56	″		5.7
100.0	0.24	0.16	0.1	0.63	0.05	1.0	5.6
112.6	0.37	0.25	0.1	0.65	0.45	1.5	5.9
125.0	2.48	2.56	0.7	0.69	1.4	10.0	5.5
S-930 sorbent							
13.0	0.13	0.1	0.1	0.1	1.0	1.0	9.16
26.0	0.04	0.1	0.1	0.1	1.0	1.0	9.60
39.0	0.05	0.1	0.1	0.1	32.1	34.0	8.9
52.0	0.04	0.1	0.1	0.1	104.2	106.9	7.9
65.0	0.05	0.1	0.1	0.14	136.0	87.5	7.1
91.0	0.07	0.1	0.1	0.17	160.0	77.8	7.2
117.0	0.05	0.1	0.1	0.29	152.0	85.0	7.35
143.0	0.08	0.1	0.1	0.39	170.0	58.3	7.4
169.0	0.09	0.1	0.1	0.80	196.0	56.0	7.2
195.0	0.03	0.1	0.1	0.89	194.0	53.5	7.2
221.0	0.02	0.1	0.1	0.76	192.0	53.5	6.2
247.0	0.03	0.1	0.85	1.5	180.0	65.5	6.5

Table 3. Averaged wastewater composition after decontamination with S-930 and KU-2 × 8 sorbents

Solution	pH	Metal concentration, mg l^{-1}					
		Cu	Zn	Ni	Cr(III)	Ca	Mg
Wastewater	5.1	29.5	8.2	7.95	13.7	156.3	72.9
After decontamination:							
on S-930	7.8	0.1	0.1	0.1	0.4	152.0	70.0
on KU-2 × 8	6.5	0.2	0.1	0.1	0.5	Not detected	Not detected

metals [including Cr(III)] present in the initial wastewater. Magnesium was not detected in the eluate. As for calcium, this cation is precipitated in the first fraction of the eluate (10% of the total eluate volume) as calcium sulfate. In the case of KU-2 cation exchanger, to prevent calcium sulfate precipitation within the sorbent bed, the metals were sequentially desorbed with 2 and 10% sulfuric acid at a filtration rate of 1–2 ml min^{-1}. In these experiments copper, zinc, nickel, calcium, and magnesium were eluted, whereas Cr(III) was desorbed poorly (Fig. 2). In all fractions of the eluate calcium sulfate was precipitated. To prevent calcium sulfate precipitation in regeneration of KU-2 cation exchanger and increase recovery of chromium(III), we recommend to use as eluent nitric or hydrochloric acid. However, with these reagents the sorbent regeneration is significantly complicated. Figure 2 shows that in regeneration of S-930 sorbent

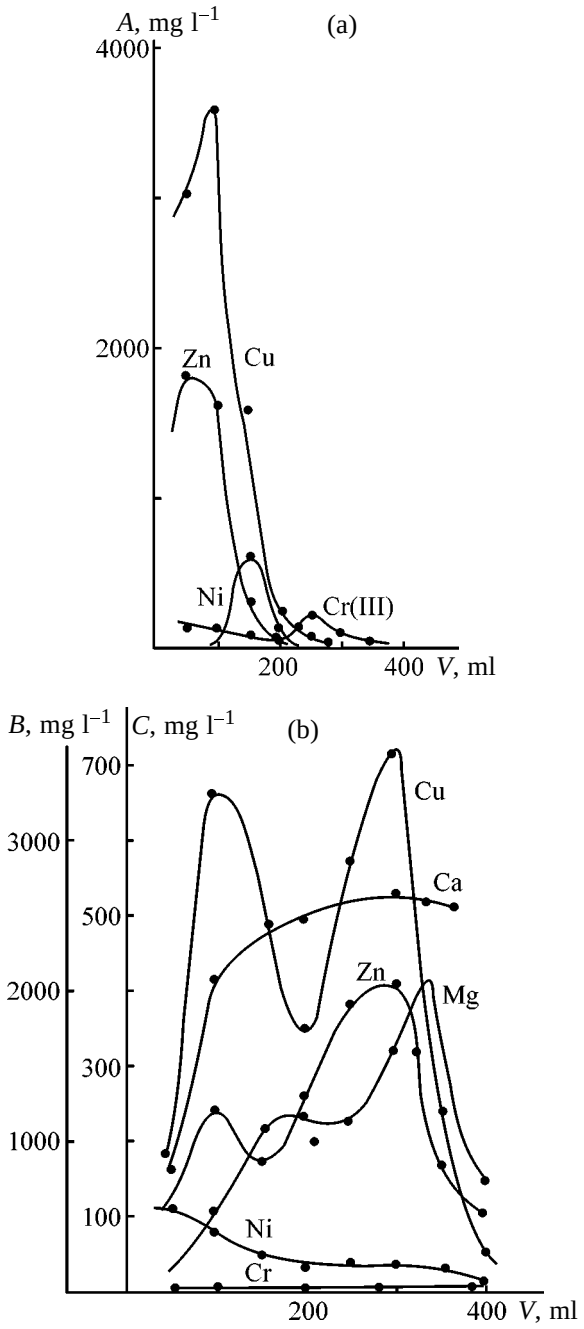

Fig. 2. Regeneration curves of (a) S-930 sorbent and (b) KU-2 × 8 cation exchanger. (*A*) Nonferrous metal [including Cr(III)] concentration, (*B*) Mg concentration, and (*C*) nonferrous metal [including Cr(III)] and calcium concentration; (*V*) eluate volume.

the main amount of nonferrous metals [including Cr(III)] is desorbed by the first portion of the eluent (40%). The remaining part of the eluate (60%) mainly contains chromium and traces of other nonferrous metals. This portion of the eluate is acidified with sulfuric acid to 20% concentration and reused in the first stage of S-930 regeneration after repeated sorption cycle. This procedure allows significant decrease of the sulfuric acid consumption.

All fractions of the eluate formed in the course of KU-2 × 8 regeneration contain calcium sulfate precipitate, which hinders their reuse for regeneration.

Comparison of S-930 selective sorbent and KU-2 × 8 universal cation exchanger in sorption of nonferrous metals [including Cr(III)] from wastewater and in regeneration of the spent sorbents shows advantage of the selective sorbent in both stages. Another advantage of S-930 is that it does not sorb the cations responsible for the solution hardness (Ca, Mg), which increases the filtration cycle and the sorption service life. With this sorbent it is possible to reuse the weakly concentrated eluate fractions (60% of the total eluate volume) after their adjustment with a small amount of sulfuric acid. This procedure decreases the consumption of sulfuric acid and the wastewater volume.

The technique developed by us for decontamination of the wastewater from electroplating productions by treatment with S-930 sorbent was put into operation at the Promotkhody plant.

CONCLUSIONS

(1) High selectivity of S-930 sorbent provides the required extent of decontamination of wastewater from electroplating productions and high degree of concentration of nonferrous metal impurities.

(2) The sorption capacity of S-930 in wastewater decontamination from microamounts of nonferrous metals is twice that of KU-2 × 8 cation exchanger.

(3) The use of S-930 sorbent for wastewater decontamination from nonferrous metals significantly decreases the reagent consumption in the regeneration stage.

(4) Testing of S-930 showed that this chelating sorbent can be recommended for decontamination of wastewater from electroplating productions. The use of this sorbent is promising from the viewpoint of both the process optimization and the environmental safety.

ACKNOWLEDGMENTS

The authors are grateful to staffmembers of the Promotkhody plant (Moscow) B.K. Medkov and E.G. Kozhinov for submitting objects for study, analytical support, and discussion of the results.

REFERENCES

1. *Pravila priema proizvodstvennykh stochnykh vod v Moskovskuyu gorodskuyu kanalizatsiyu* (Regulations for Discharge of Industrial Wastewater to the Moscow Municipal Sewer System), Moscow: Mosvodokanal, 1984.
2. Grebenyuk, V.D. and Mazo, A.A., *Obessolivanie vody ionitami* (Water Desalination with Ion Exchangers), Leningrad: Khimiya, 1989.
3. Senyavin, M.M., *Ionnyi obmen v analize neorganicheskikh veshchestv* (Ion Exchange in Analysis of Inorganic Compounds), Moscow: Khimiya, 1980.
4. Hering, R., *Chelatbildende Ionenaustauscher*, Berlin: Akademie, 1967.
5. Saldadze, K.M. and Kopylova, V.D., *Kompleksoobrazuyushchie ionity (kompleksity)* [Complexing Ion Exchangers (Complexites)], Moscow: Khimiya, 1980.
6. *Katalog ionitov* (Ion Exchanger Catalog), Purolite Int. Ltd., the Purolite Company, Moscow: NIIPM im. G.S. Petrova, 1994.
7. Saldadze, G.K., Kargman, V.B., Anufrieva, S.I., and Losev, Yu.N., *Zh. Fiz. Khim.*, 1999, vol. 73, no. 7, pp. 1294–1297.
8. Mekvabishvili, T.V., Klyueva, L.M., Kovaleva, M.P., *et al.*, *Sintez, svoistva i primenenie karboksil'nykh kationitov* (Synthesis, Properties, and Application of Carboxylic Cation Exchangers), Moscow: NIITE-KhIM, 1988, issue 11 (277).
9. Pirogov, V.S., Dmitrienko, L.V., Kipper, A.P., and Samsonov, G.V., *Zh. Prikl. Khim.*, 1972, vol. 99, no. 9, pp. 626–630.
10. Dzhumadilov, T.K., Bakaurova, Z.Kh., and Bekturov, E.A., *Tr. Inst. Khim. Nauk Akad. Nauk Kaz. SSR, Khim. Fiz. Khim. Polim.*, 1979, vol. 49, part 12, pp. 100–116.
11. *GOSTs* (State Standards) *from 10896–78 to 10898.5–84. Ion Exchangers. Preparation for Testing. Determination of the Specific Surface Area*.
12. *GOSTs* (State Standards) *20255.1–84 and 20255.2–89. Ion Exchangers. Technique for Determination of the Static Exchange Capacity. Ion Exchangers. Technique for Determination of the Dynamic Exchange Capacity*.
13. Price, W.J., *Analytical Atomic Absorption Spectrometry*, London: Heyden, 1974.

Russian Journal of Applied Chemistry, Vol. 74, No. 11, 2001, pp. 1864–1867. Translated from Zhurnal Prikladnoi Khimii, Vol. 74, No. 11, 2001, pp. 1808–1811.

ENVIRONMENTAL PROBLEMS OF CHEMISTRY AND TECHNOLOGY

Carbon Monoxide Semiconductor Sensors Based on SnO_2–Bi_2O_3

T. D. Malinovskaya, A. I. Aparnev, Yu. P. Egorov, and Yu. M. Yukhin

Siberian Physical and Engineering Institute, Tomsk, Russia
Institute of Chemistry of Solids and Mechanochemistry, Siberian Division, Russian Academy of Sciences, Novosibirsk, Russia

Received September 12, 2000; in final form, July 2001

Abstract—Gas-sensitive (sensory) properties of bismuth–tin oxide materials, including ceramic films with the $Bi_2Sn_2O_7$ composition and pyrochlore structure, were considered, as applied to the determination of H_2, CO, and CH_4 in an air mixture.

Carbon monoxide is known to be one of the main contaminants of the atmosphere. Its efficient monitoring requires development of highly sensitive selective chemical sensors. Doped tin dioxide is recognized as one of promising materials for manufacturing functional layers of such sensors [1–3]. Thin films based on tin dioxide with properly chosen dopants can selectively change electrical conductance when adsorbing various gases [4, 5].

The aim of this work was to study the possibility for the selective monitoring of carbon monoxide using bismuth-doped tin dioxide with a variable chemical composition.

EXPERIMENTAL

To study gas-sensitive properties of bismuth–tin oxide materials, we have manufactured adsorption-sensitive elements (ASEs). As an ASE substrate we used Polikor laminas of size $0.3 \times 0.3 \times 0.5$ mm. Comb-shaped measuring electrodes and zigzag-shaped heaters on the back side of substrates were formed by platinum magnetron sputtering with subsequent photoengraving. Sensitive ceramic layers of thickness 50 μm were made by covering measuring electrodes with a suspension of powdered bismuth stannates in an organic volatile binder and by subsequent sintering at 800°C in air for 1 h. The powders of bismuth stannates were synthesized by a hydrolytic procedure based on coprecipitation of bismuth(III) and tin(IV) from nitrate–chloride solutions by their neutralization with an alkali. The content of bismuth was varied from 5 to 90 at. %. The composition of the films was determined by X-ray and chemical methods [6, 7]:

Sn : Bi	Composition of thick films
20 : 1	$SnO_2 + Bi_2Sn_2O_7$
10 : 1	$SnO_2 + Bi_2Sn_2O_7$
5 : 1	$SnO_2 + Bi_2Sn_2O_7$
1 : 1	$Bi_2Sn_2O_7$
1 : 12	$Bi_2Sn_2O_7 + Bi_2O_3$

To study the temperature dependence of the adsorption response to gases (H_2, CO, and CH_4), ASEs were placed in a sealed quartz cell, through which filtered air with a constant humidity was passed using a PRB-2B gas flow booster. A sample containing a mixture of 100–1000 ppm of H_2, CO, and CH_4 with air (gas–air mixture) was fed to the measuring cell. The ratio R_a/R_g, where R_a is the film resistance in pure air and R_g is the film resistance in a gas–air mixture, was taken as a measure of the adsorption response to the gas action. The ASE resistance was measured with a VK-9 device accurate to within ±4% of the length of the working section of the ×10 Ω scale and to within ±2.5% on the other scales. The ASE temperature was varied by the corresponding variation of the heater power P_h from 0.1 to 4.0 W, which corresponded to the range from 100 to 500°C. The constant power of the heater was maintained during measurements with an accuracy of 5%.

The bismuth–tin oxide materials under study with tin–bismuth ratios from 5 to 1/12 have high resistance of the order of hundreds of MΩ, which decreased with increasing temperature, following an exponential law characteristic of semiconductors [8].

1070-4272/01/7411-1864$25.00

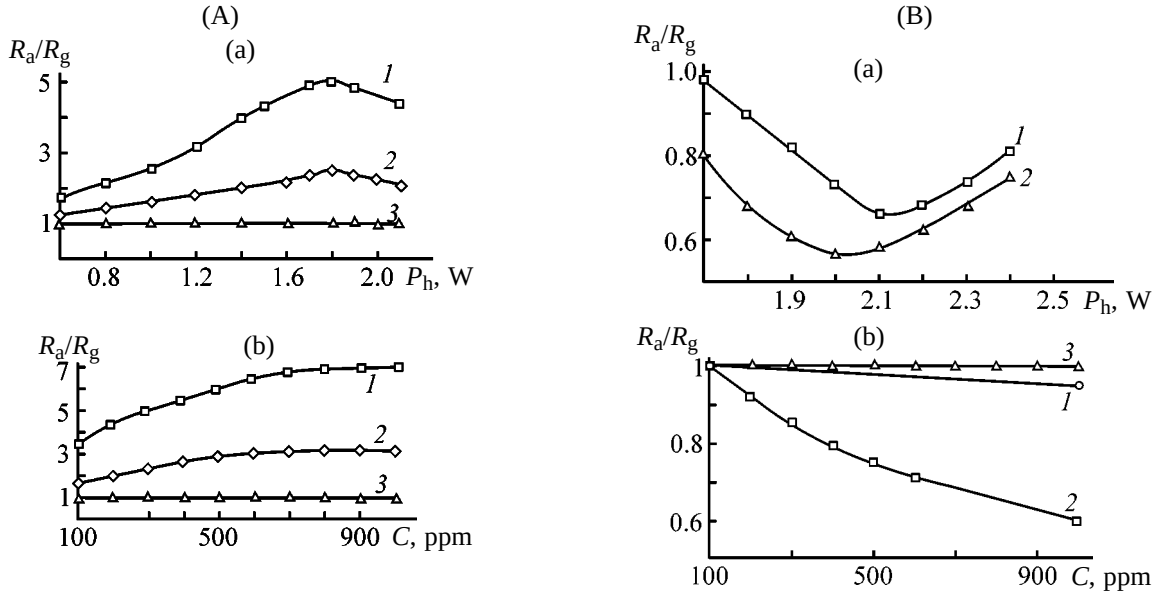

Fig. 1. Adsorption response R_a/R_g to the action of (*1*) H_2, (*2*) CO, and (*3*) CH_4 as a function of (a) heater power P_h and (b) gas concentration C. Composition of films: (A) SnO_2–$Bi_2Sn_2O_7$ (Sn : Bi = 20) and (B) $Bi_2Sn_2O_7$ (Sn : Bi = 1). (A, a; B, a) Concentration of gases 400 ppm; heater power P_h (A, b) 1.8 and (B, b) 2.0 W.

The adsorption-sensitive cells based on the bismuth–tin materials SnO_2–$Bi_2Sn_2O_7$, $Bi_2Sn_2O_7$, and $Bi_2Sn_2O_7$–Bi_2O_3 have an enhanced sensitivity to hydrogen and to carbon(II) monoxide and do not respond to methane up to 400°C. As follows from the concentration and temperature dependences (Fig. 1A), the ASEs under study based on thick films with the composition SnO_2–$Bi_2Sn_2O_7$ are sensitive to low concentrations of CO and H_2 (1.0×10^{-2} vol %). Their sensitivity to hydrogen is 1.5–2 times higher than to CO. At the atomic ratio Sn : Bi < 5 the sensitivity to H_2 and CO starts to drop, and at the Sn : Bi ratio of 1 and lower, the adsorption response is less than unity (Fig. 1B). In this case the concentration and temperature dependences of the adsorption response to the action of reducing gases are characteristic of the *p*-type semiconductor sensors. Hence, $Bi_2Sn_2O_7$, along with the known Bi_2O_3, are the *p*-type semiconductors.

These compounds are more sensitive to CO than to H_2. This difference is the most pronounced for the films with the composition $Bi_2Sn_2O_7$ below 380°C (which corresponds to $P_h \sim 2.0$ W). Thus, at such temperatures the $Bi_2Sn_2O_7$ films can be used in CO-selective sensors in a wide range of gas concentrations in the presence of H_2 and CH_4.

The adsorption response of ASEs passes through a maximum, which is reached at various temperatures depending on the chemical composition of the sensitive material and the nature of a gas under determination (P_h values; Figs. 1A, a and 1B, a). The temperature of the highest performance of sensors based on pure $Bi_2Sn_2O_7$ is maximal, being close to 380°C for CO and H_2. The value of T_m for $Bi_2Sn_2O_7$–Bi_2O_3 is much lower (~250°C). In the case of the SnO_2–$Bi_2Sn_2O_7$ ASEs with Sn : Bi from 5 to 20 T_m decreases with increasing content of the bismuth-containing component and reaches approximately 310°C at the Sn : Bi ratio equal to 5.

When detecting reducing gases, including CO and H_2 in air, gas molecules are oxidized on the surface of metal oxide semiconductors with adsorbed oxygen [3]. It is probable that gas-sensitive ASE characteristics essentially depend on the concentration of active oxygen, which is determined by the density of adsorption centers and also by the form of chemisorbed oxygen [9]. Our experimental data show that the adsorption response as a function of temperature passes through a maximum (when a reducing gas is introduced, the relative change in the electric conductance first grows with increasing temperature and then drops to zero at a fairly high temperature). Such a dependence, which is typical for a wide range of gas-sensitive cells, is presumably due to the formation of negatively charged adsorbed forms of oxygen. If the operation temperature of the sensor T_{op} is low, the reaction products (CO_2 in the case of CO and H_2O in the case of H_2) will not be desorbed, i.e., the regeneration of the oxygen adsorption centers will be impossible. If T_{op} is rather high, the adsorption of both oxygen and a reducing gas becomes impossible.

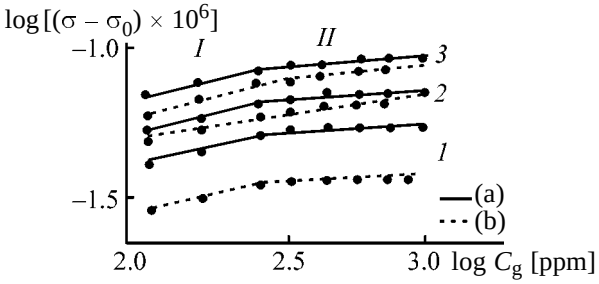

Fig. 2. Electrical conductance σ of SnO_2–$Bi_2Sn_2O_7$ films as a function of concentration C_g of (a) H_2 and (b) CO in air. (σ_0, σ) ASE conductance under normal conditions and specified temperatures, respectively. Atomic ratio Sn : Bi: (*1*) 5, (*2*) 10, and (*3*) 20. Heater power P_h, W: (*1*) 1.8 and (*2, 3*) 1.4.

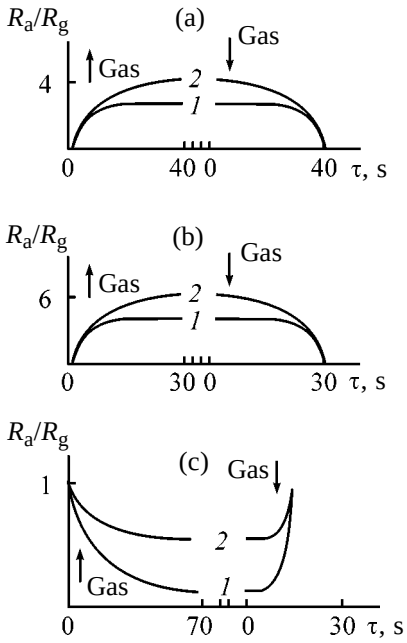

Fig. 3. Kinetic curves of adsorption response R_a/R_g for SnO_2–$Bi_2Sn_2O_7$ films (Sn : Bi = 10) in the presence of (a) CO and (b) H_2 in concentrations of (*1*) 100 and (*2*) 1000 ppm, and (c) for $Bi_2Sn_2O_7$ films in the presence of 1000 ppm of (*1*) CO and (*2*) H_2. (τ) Time. Heater power P_h, W: (a, b) 1.7 and (c) 2.0.

It is known that above 150°C O^- is the most stable oxygen species on the SnO_2 surface, and above 300°C the appearance of O^{2-} is probable [9]. As the temperature of the maximum response of ASEs under study is higher than 300°C, H_2 and CO can probably react with O^- and O^{2-}, except for the $Bi_2Sn_2O_7$–Bi_2O_3 film. The plots of the electric conductance of bismuth–tin oxide layers against concentrations of CO and H_2 in logarithmic coordinates are shown in Fig. 2. There are two clear linear segments *I* and *II* in the curves, which correspond to the power dependence $\sigma \sim P_g^m$ (P_g is the gas pressure) with different values of m (m_I and m_{II}). When H_2 and CO are detected, m_I and m_{II} values lie in the ranges 0.2–0.27 and 0.12–0.16, respectively, depending on the ratio Sn : Bi in the SnO_2–$Bi_2Sn_2O_7$ films. The parameter m changes at gas concentrations close to 400 ppm. A possible reason for low m values can be the lack of oxygen adsorption centers on the semiconductor surface [8]. At present the nature of these centers for bismuth–tin materials is unknown. It was found that Bi_2O_3 lowers the amount of adsorbed oxygen and supplies lattice oxygen for surface reactions [10]. Possibly $Bi_2Sn_2O_7$ also has such properties. It is the presence of $Bi_2Sn_2O_7$ in a mixture with SnO_2 that seems to considerably reduce the number of oxygen adsorption centers on the surface, which results in deceleration of the growth of adsorption response in the concentration curves (Fig. 1) as the H_2 and CO concentrations increase. We can assume that the high temperature of the maximum response (about 380°C) is caused by the dominating participation of lattice oxygen in surface reactions when "pure" $Bi_2Sn_2O_7$ is used for detecting CO and H_2. This assumption is also supported by the longer response time of the ASEs based on $Bi_2Sn_2O_7$ as compared to SnO_2–$Bi_2Sn_2O_7$ films (Fig. 3).

It is evident from Fig. 3 that increased concentration of a gas to be detected results in increased ASE response rate. It follows from the theory of semiconductors that the characteristics of a sensor depend on the value of the surface barrier U_s: the greater U_s, the lower the electron transfer rate and, hence, the response rate of the sensor. As the chemisorption of H_2 and CO reduces the surface barrier, the response rate increases with increasing CO and H_2 concentrations.

CONCLUSION

(1) Bismuth–tin compounds obtained by a hydrolytic procedure are promising materials for adsorption gas analyzers. At properly choosen compositions, they can be used in adsorption-sensitive cells of semiconductor sensors selective to carbon monoxide and hydrogen in the presence of methane, to hydrogen in the presence of carbon monoxide, and to carbon monoxide in the presence of hydrogen.

(2) $Bi_2Sn_2O_7$ in the composition of adsorption-sensitive cells is highly sensitive to low concentrations of CO and H_2 in air.

REFERENCES

1. Myasoedov, B.F. and Davydov, A.V., *Zh. Anal. Khim.*, 1990, vol. 45, no. 7, pp. 1259–1278.

2. Buturlin, A.I., Gabuzyan, T.A., and Golovanov, N.A., *Zarubezhn. Tekh.*, 1983, no. 10, pp. 3–40.
3. Myasnikov, I.A., Suzarev, V.Ya., Kupriyanov, L.Yu., and Zav'yalov, S.A., *Poluprovodnikovye sensory v fiziko-khimicheskikh issledovaniyakh* (Semiconductor Sensors in Physicochemical Research), Moscow: Nauka, 1991.
4. Gutman, E.I., *Zh. Fiz. Khim.*, 1984, vol. 7, no. 3, pp. 801–821.
5. Orlik, D.R., Ivanovskaya, M.I., and Gurlo, A.I., *Zh. Anal. Khim.*, 1997, vol. 52, no. 1, pp. 69–73.
6. Yukhin, Yu.M., Aparnev, A.I., Malinovskaya, T.D., and Afonina, L.I., *Zh. Prikl. Khim.*, 1999, vol. 72, no. 1, pp. 21–26.
7. Aparnev, A.I., Yukhin, Yu.M., Malinovskaya, T.D., and Smirnov, V.I., *Zh. Neorg. Khim.*, 1999, vol. 44, no. 3, pp. 367–371.
8. Vol'kenshtein, F.F., *Fizikokhimiya poverkhnosti poluprovodnikov* (Physical Chemistry of Semiconductor Surface), Moscow: Nauka, 1973.
9. McAller, J.F., Moseley, P.T., Norris, J.O.W., and Williams, D.E., *J. Chem. Soc., Faraday Trans. 1*, 1987, vol. 83, pp. 1323–1346.
10. Coles, G.S.V. and Gallagner, K.J., *Sens. Actuators*, 1985, no. 7, pp. 89–96.

Russian Journal of Applied Chemistry, Vol. 74, No. 11, 2001, pp. 1868–1871. Translated from Zhurnal Prikladnoi Khimii, Vol. 74, No. 11, 2001, pp. 1812–1814.

PROCESSES AND EQUIPMENT OF CHEMICAL INDUSTRY

Suspension Separation in a Centrifuge with Biconical Rotor

Yu. P. Volkov and S. A. Svetlov

Biisk Technological Institute, Altai State Technical University, Biisk, Altai krai, Russia

Received June 7, 2001

Abstract—Separation of cellulose nitrate suspensions in a centrifuge with biconical rotor was studied. An empirical equation was derived, enabling calculation of the efficiency of purification of process water and wastewater to remove the solid phase in centrifuges of this kind.

At present, sedimentation tanks (wastewater ponds) are used to purify wastewater to remove polydisperse solid impurities [1]. These installations have strong adverse effect on the environment and safety of humans; their maintenance requires gross expenditure. At the same time, use of other techniques intensifying the purification process and, in particular, centrifugal separation is difficult from both economical and technological standpoints. This is so because there exist no sufficiently simple to operate and comparatively low-cost centrifugal machines with mechanized sediment discharge and high degree of separation [2–5].

Centrifugal apparatus [6] and centrifuges are known [7] in which suspensions are separated in a rotor comprising two truncated conical cowlings mounted on a fast-rotating shaft. Preliminary calculations and experiments on a cylindrical sedimentation centrifuge demonstrated that the centrifuge with a biconical rotor must exhibit high efficiency of separation of finely dispersed and low-concentration suspensions at relatively high centrifugate output capacity.

The aim of this study was to analyze the influence of basic process parameters (speed of centrifuge rotor rotation, flow rate and initial concentration of the starting suspension) on the final concentration of solid particles in the centrifugate; and to derive empirical equations for calculating the relative concentration of the solid phase in the centrifugate, which allows prognostication of the quality of suspension separation in centrifuges of the given type.

EXPERIMENTAL

To perform experimental studies, we designed an installation comprising a centrifuge *1* and accessory equipment. A prepared suspension was fed into the centrifuge from a vessel *2* by means of a centrifugal pump *3*, with the flow rate monitored with rotameter *4*, and the speed of shaft rotation, with tachometer *5*. The centrifuge power drive allowed variation of the speed of rotor rotation in the range from 1000 to 6000 rpm.

The centrifuge rotor (Fig. 2) comprised two conical cowlings, upper *1* and lower *2*, and disk *3* pressed to the lower cowling with a bushing. Apertures through which the suspension is fed into the centrifuge rotor were made in the bushing *5*. The impermeability of the cowling junction was ensured by nut *6*.

An aqueous suspension of nitrocellulose with solid particles 1 to 280 μm in size was separated. The experiments were carried out as follows. A nitrocellulose suspension was poured into the vessel apparatus and continuously agitated there with blade stirrers, and a uniform concentration of the solid phase was maintained in the working volume of the apparatus. A variable power drive ensured rotor rotation at a required speed. Then the suspension was fed into the rotor, and purified liquid was sampled at the centri-

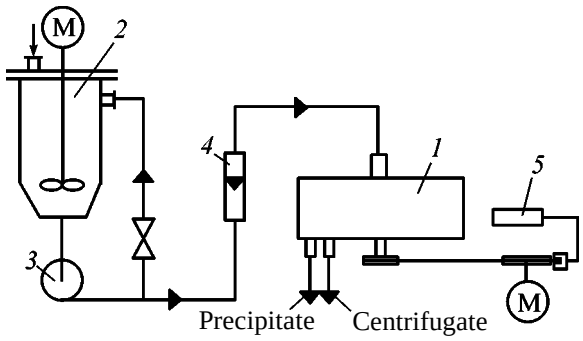

Fig. 1. Schematic of laboratory installation: (*1*) centrifuge, (*2*) apparatus with stirrer, (*3*) centrifugal pump, (*4*) rotameter, and (*5*) tachometer.

1070-4272/01/7411-1868$25.00 © 2001 MAIK "Nauka/Interperiodica"

fuge outlet. The samples were filtered and the concentration of solid impurities in the centrifugate was determined.

The study was carried out at speeds of rotor rotation, n, equal to 3000, 4000, 5000, and 6000 rpm, initial suspension concentration C_{in} = 13.28, 6.64, 3.32, and 1.66 g l^{-1}, and suspension flow rate varying between 9 and 100 l h^{-1}.

The obtained experimental data were presented in the form of a dependence of the concentration C_{out} of the solid phase in the centrifugate on the flow rate Q of the suspension at the centrifuge inlet.

Figure 3 shows such dependences for speeds of rotor rotation of 3000, 4000, and 5000 rpm and initial suspension concentration of 3.32 g l^{-1}.

As a parameter that characterizes the separation capacity of sedimentation centrifuges and facilitates simulation of their operation is commonly used the output capacity index

$$\Sigma = 2\pi RHF, \quad (1)$$

where H is the height of the cylindrical sedimentation surface of the rotor (m), and F is the separation factor at a radius R.

Using the known equation [2, 8] based on the Godin–Andreev formula [2, 3, 8], we derived a regression equation approximating the experimental data and determined the coefficients of this equation. Equation (2) allows a rather accurate prognostication (mean relative error of about 25%) of the relative concentration of the solid phase in the centrifugate in a wide range of speeds of rotor rotation and suspension concentrations and flow rates (for the investigated type of suspension):

$$C_{out}/C_{in} = 6.16 \times 10^5 (Q/\Sigma)^x, \quad (2)$$

where Σ is the throughput factor of the centrifuge (m^2).

The coefficient x in Eq. (2) is defined by the formula

$$x = \exp(a \ln C_{in} + b). \quad (3)$$

The coefficients appearing in Eq. (3) are given by

$$a = -3.75 \times 10^{-6} n + 0.038, \quad (4)$$

$$b = -2.52 \times 10^{-5} n + 0.526. \quad (5)$$

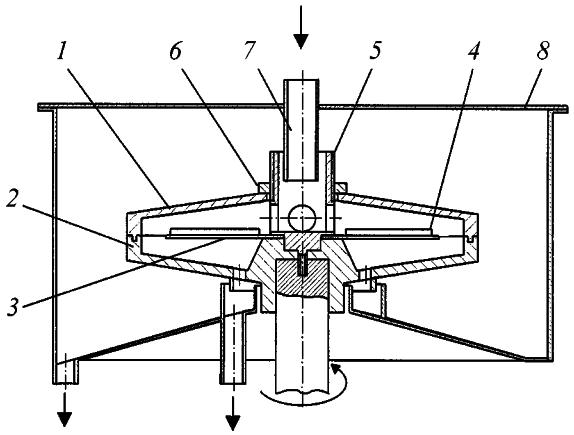

Fig. 2. Schematic of the centrifuge: (*1*) upper cowling, (*2*) lower cowling, (*3*) disk, (*4*) blades, (*5*) bushing, (*6*) nut, (*7*) pipe, and (*8*) case.

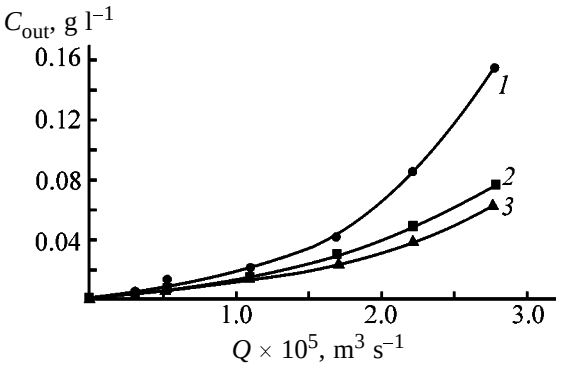

Fig. 3. Concentration of the solid phase in the centrifugate, C_{out}, vs. suspension flow rate Q. Initial concentration C_{in} = 3.32 g l^{-1}. Speed of rotor rotation n (rpm): (*1*) 3000, (*2*) 4000, and (*3*) 5000; the same for Fig. 4.

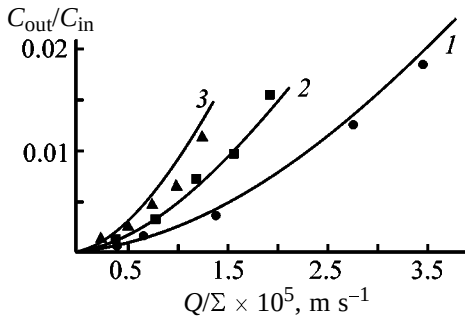

Fig. 4. Relative concentration C_{out}/C_{in} vs. parameter Q/Σ. Initial concentration C_{in} = 13.28 g l^{-1}.

Figure 4 shows by solid lines the calculated dependences of the relative concentration C_{out}/C_{in} on the parameter Q/Σ at different speeds of rotor rotation and initial suspension concentration of 13.28 g l^{-1}.

An analysis of the obtained experimental data

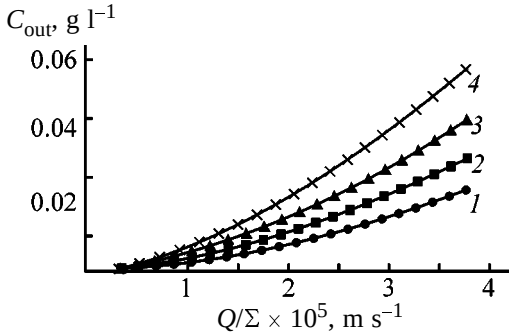

Fig. 5. Relative concentration C_{out}/C_{in} (calculated) vs. parameter Q/Σ. Number of rotor revolutions n = 3000 rpm. Initial concentration C_{in} (g l^{-1}): (*1*) 13.28, (*2*) 6.64, (*3*) 3.32, and (*4*) 1.66.

demonstrated that the separation efficiency grows with increasing concentration of the starting suspension (Fig. 5), in good agreement with the available published data [2]. At the same time, the separation efficiency falls with increasing speed of rotor rotation and decreasing concentration of the solid phase in the centrifugate (Fig. 4). This can be presumably accounted for by the presence of turbulence zones inside the centrifuge rotor, whose influence on the separation efficiency becomes more pronounced with increasing speed of rotor rotation [3], and also by the fact that the degree of destruction of solid phase particles and agglomerates of these grows with increasing angular speed of rotor rotation.

The following conditions should be satisfied in simulation of geometrically similar sedimentation centrifuges [4]: sedimentation of particles with close sizes in different centrifuges is ensured at the same separation factor; fluid flows are in the same automodel region. The equation for simulating geometrically similar centrifuges with the use of the output capacity index can be written as

$$Q/Q_m = \Sigma/\Sigma_m, \quad (6)$$

where Q_m is the output capacity of a centrifuge being simulated (m^3 s^{-1}), and Σ_m is the throughput factor of this centrifuge (m^2).

It may be considered that for suspensions with fibrous solid phase, in which the particle size changes significantly in the course of separation, the maximum ratio of centrifuge throughputs is equal to the ratio of cubed radii of rotor disks.

Based on the results obtained in processing the obtained experimental data and on methods of the similarity theory, an industrial variant of the centrifuge is designed. The centrifuge can be used for purification of process water and wastewater to remove solid impurities in manufacture of cellulose nitrates. Using the similarity theory [9–11], we calculated the basic geometrical parameters of the industrial centrifuge. The performance characteristics of the industrial centrifuge are as follows:

Throughput, m^3 h^{-1}	25
Number of rotor revolutions, rpm	5000
Rotor diameter, mm	600
Disk diameter, mm	500
Rotor height, mm	350

Use of centrifuges of this type makes it possible to improve, at low capital outlays, the efficiency of purification of industrial wastewater at the existing plants and ensure discharge to waste disposal plants of purified liquid with solid phase concentration corresponding to the maximum permissible concentration.

CONCLUSIONS

(1) The achieved degree of purification of low-concentration cellulose nitrate suspensions in a centrifuge with biconical rotor yields in certain separation modes a concentration of solid impurities in the centrifugate of no more than 20 mg l^{-1}.

(2) The derived empirical equation can be used to prognosticate with sufficient accuracy the relative concentration of the solid phase in the centrifugate in a wide rage of variation of the basic process parameters of the installation: initial concentration and flow rate of suspension and speed of rotor rotation.

(3) The obtained results demonstrate the possibility of using centrifuges of the given type in purification of industrial process water and wastewater to remove finely dispersed solid impurities.

REFERENCES

1. Epshtein, S.I., *Zh. Prikl. Khim.*, 1981, vol. 54, no. 8, pp. 1773–1776.
2. Sokolov, V.I., *Tsentrifugirovanie* (Centrifugation), Moscow: Khimiya, 1976.
3. Sokolov, V.I., *Sovremennye promyshlennye tsentrifugi* (Modern Industrial Centrifuges), Moscow: Mashinostroenie, 1967, 2nd ed.
4. Shkoropad, D.E. and Novikov, O.P., *Tsentrifugi i separatory dlya khimicheskikh proizvodstv* (Centri-

fuges and Separators for Chemical Industries), Moscow: Khimiya, 1987.

5. Luk'yanenko, V.M. and Taranets, A.V., *Tsentrifugi: Spravochnoe izdanie* (Centrifuges: Reference Book), Moscow: Khimiya, 1988.
6. USSR Inventor's Certificate no. 528120.
7. USSR Inventor's Certificate no. 129566.
8. Romankov, P.G. and Plyushkin, S.A., *Zhidkostnye separatory* (Liquid Separators), Leningrad: Mashinostroenie, 1976.
9. Semenov, E.V., Zhukov, V.G., and Shevel'kov, V.V., *Teor. Osn. Khim. Tekhnol.*, 1984, vol. 18, no. 6, pp. 797–800.
10. Bird, R.B., Stewart, W.E., and Lighfoot, E.N., *Transport Phenomena*, New York: Wiley, 1965.
11. Kogan, V.B., *Teoreticheskie osnovy tipovykh protsessov khimicheskoi tekhnologii* (Theoretical Foundations of Typical Processes of Chemical Technology), Leningrad: Khimiya, 1977.

Russian Journal of Applied Chemistry, Vol. 74, No. 11, 2001, pp. 1872–1876. Translated from Zhurnal Prikladnoi Khimii, Vol. 74, No. 11, 2001, pp. 1815–1819.

PROCESSES AND EQUIPMENT OF CHEMICAL INDUSTRY

Nitration of Chlorobenzene with Nitric Acid in a Continuous Installation

E. A. Veretennikov, B. A. Lebedev, and I. V. Tselinskii

St. Petersburg State Technological Institute, St. Petersburg, Russia

Received June 28, 2000

Abstract—The procedures of production of mononitrochlorobenzene by nitration with 75–97% nitric acid with the yield of the target product of 97.5% were developed. A procedure of precipitation of crystalline *p*-nitrochlorobenzene from the reaction mixture without additional purification was proposed.

Nitration of chlorobenzene with sulfuric acid–nitric acid mixtures is the main procedure of mononitrochlorobenzene (MNCB) production [1]. The drawback of this procedure is large amount of dilute spent sulfuric acid as waste. The present-day procedures of recovery of spent sulfuric acid do not eliminate its environmental impact. The growing importance of environmentally safe processes requires a search for new nitration procedures without using sulfuric acid.

One of such procedures can be nitration of chlorobenzene with nitric acid alone, which can be recovered on the industrial scale by environmentally safer procedures, compared to sulfuric acid [2]. As seen from published data, the major attention was focused on the use of 67–68% nitric acid for nitration. For example, it was proposed to carry out nitration of chlorobenzene with a 20–30-fold molar excess of nitric aicd in a tubular reactor or cascade of reactors at 90°C [3] or by adding chlorobenzene to an excess of boiling nitric acid with simultaneous removal of the reaction water [4]. Apparently, long reaction time, large amounts of acids to be recovered, and difficulties in temperature control of the process hinder industrial implementation of these procedures.

Kinetic studies of mononitration of chlorobenzene with aqueous nitric acid showed [5, 6] that, contrary to nitration in sulfuric acid medium, the reaction proceeds in a homogeneous medium with the rates of nitration close to or exceeding the rates of nitration of chlorobenzene with sulfuric–nitric acid mixtures; the significant (three orders of magnitude) difference in the rate constants of mono- and dinitration suggests that the use of nitric acid alone as a nitrating agent allows reduction or elimination of formation of the by-product, dinitrochlorobenzene (DNCB), during nitration.

Based on these data, we examined the possibility of using nitric acid alone for production of MNCB.

Nitration of chlorobenzene was carried out in a continuous installation (Fig. 1) including (*1*) main and (*2*) surge reactors and (*3*) dilution vessel, equipped with reflux condensers, blade stirrers, coil pipes, and jackets. The volume of the apparatus made from 1Cr18Ni10Ti steel was 60 ml. The components were dosed by piston pumps. Before start-up, the installation was filled with nitric acid with a composition close to that of spent acid. The steady state of the system was reached after passing a 5–6-fold volume of the reaction mixture through the apparatus. The temperature was maintaned with an accuracy of ±0.5°C using thermostats. After nitration completion, the reaction mixture was a solution of MNCB in spent acid. To recover the nitro product, the reaction mixture

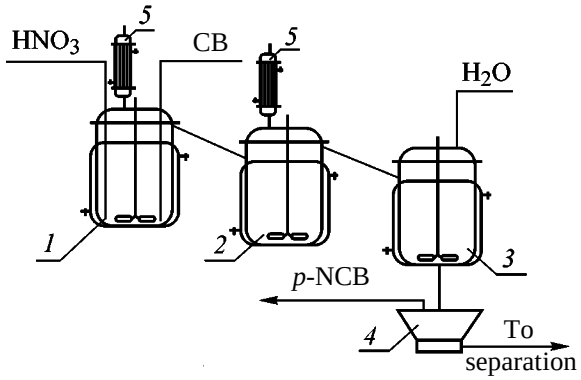

Fig. 1. Continious installation for nitration of chlorobenzene with nitric acid: (*1*) main reactor, (*2*) surge reactor, (*3*) dilution vessel, (*4*) vacuum funnel, and (*5*) reflux condensers.

1070-4272/01/7411-1872$25.00

Table 1. Nitration of chlorobenzene (CB) with 97% HNO_3

Run no.	HNO_3 : CB molar ratio	*T*, °C	τ, min	Yield of MNCB	Unreacted CB	Yield of DNCB
				%		
1	1.5	75	120	84.3	15.0	–
2	1.5	85	120	90.2	7.5	0.7
3	1.5	75/85*	120	89	8.0	0.8
4	2	65	180	87.0	10.0	2.5
5	2	75	60	87.0	10.0	2.0
6	2	75	120	90.0	7.0	3.0
7	2	75/65*	120	90.0	6.0	4.0
8	2.5	65	45	97.5	2.5	–
9	2.5	65	60	93.0	1.5	1.5
10	2.5	75	45	94.0	1.0	1.0
11	2.5	75	60	94.0	–	2.0
12	2.5	75	120	91.3	–	6.0
13	3	55	7.5	98.0	1.7	–
14	3	55	15	98.2	0.2	–
15	3	65	5	93.5	2.1	–
16	3	65	7.5	98.6	0.7	–
17	3	65	10	99.0	0.3	–
18	3	65	15	99.0	0.1	–
19	3	65	30	95.3	–	–
20	3	65	45	93.8	–	0.1
21	3	65	60	93.6	–	0.2
22	3	65	75	92.4	–	0.2
23	3	75	5	94.9	3.0	–
24	3	75	7.5	97.9	1.5	–
25	3	75	10	98.7	0.3	–
26	3	75	15	96.0	–	–
27	3	75	30	94.5	–	0.6
28	3	75	45	97.5	–	0.6
29	3	75	60	90.0	–	0.7
30	3	75	75	89.7	–	0.8

* Temperature in the surge reactor.

was diluted in apparatus *3* at 20°C with a calculated amount of water to the nitric acid concentration of 50.0%. The resulting nitro product, suspension of *p*-NCB crystals in the liquid mixture of isomers, was separated, washed with hot water, and dried. Dilute spent acid was extracted with chlorobenzene. The composition of the organic product was determined by gas–liquid chromatography. The concentration of nitric acid was determined by alkalimetric titration.

After reaching the steady state, the reaction mixture in the main reactor is heterogeneous and in the surge reactor, homogeneous. It is well known that in heterogeneous nitration of chlorobenzene with sulfuric acid–nitric acid mixtures the diffusion of the components into the reaction area affects substantially the nitration process, and stirring of the reaction mixture is one of the factors providing mass exchange in the reaction system, dispersity of phases, and, hence, the required residence time of components in the reaction zone [7]. Studying the effect of the strirring rate on nitration of chlorobenzene with nitric acid alone showed that in this reaction system variation in the stirring rate from 200 to 3000 rpm does not affect the reaction rate in the entire range of nitric acid concentrations studied. This fact suggests that the nitration occurs in the bulk of the acid phase and the rate-determining stage of the process is the reaction of chlorobenzene with nitric acid. Therefore, in the subsequent experiments the mixture was stirred at a rate of 400 rpm. The experimental results are listed in Table 1.

As seen from Table 1, the use of a 1.5–2-fold molar excess of nitric acid does not ensure complete

Table 2. Nitration of chlorobenzene with 90–68% HNO_3

Run no.	HNO_3, %	HNO_3 : CB molar ratio	*T*, °C	τ, min	Yield of MNCB	Unchanged CB
					%	
31	90	3	75	45	98.2	
32	90	3	75	60	98.2	
33	85	3	65	45	74.0	25.4
34	85	3	75	45	86.2	13.0
35	85	3	75	60	94.1	5.1
36	80	5	75	120	94.2	4.9
37	80	5	75	180	97.0	1.0
38	80	5	85	120	95.4	3.0
39	80	4	75	180	91.0	8.0
40	80	4	85	180	95.0	3.5
41	75	4	85	180	93.2	5.0
42	75	4	95	180	97.5	1.5
43	75	5	75	120	89.8	10.0
44	68	5	95	180	88.0	10.0
45	68	7	95	180	90.0	7.0
46	68	8	95	200	92	6

conversion of chlorobenzene to MNCB, and an attempt to increase the yield of the target product by increasing reaction temperature or time is accompanied by formation of 2–4% DNCB (run nos. 1–7). An increase in the amount of nitric acid to 2.5–3.0-fold molar excess results in practically complete conversion of chlorobenzene; in this case, the resulting nitration product contains no DNCB (run nos. 8, 13, 14, 16–18, and 24–26). It should be noted that at 55–75°C the reaction was complete in 7.5–10 min.

To elucidate the effect of the acid concentration on the yield of MNCB, we studied nitration of chlorobenzene with 90–68% nitric acid. The results are listed in Table 2.

The experiments showed that a decrease in the acid concentration below 85% is accompanied by noticeable increase in its molar excess, reaction temperature, and reaction time required to reach the maximum yield of MNCB. However, despite higher temperature and longer process time, DNCB was formed in none of the runs. For example, in nitration of chlorobenzene with 75% nitric acid at 95°C, fourfold molar excess of nitric acid, and the reaction time of 180 min, the yield of MNCB was 97.5% (run no. 39). A decrease in the nitric acid concentration to the composition of aqueous azeotrope (68% HNO_3) results in significant increase in the excess of nitric acid (more than eightfold by moles) and inhibition of the nitration process.

Thus, it was established that in a wide concentration range nitric acid can be used for producing MNCB in a nearly quantitative yield; the resulting product contains no DNCB impurity.

Based on this study, we developed two procedures for nitration of chlorobenzene with both concentrated and dilute nitric acid. With 90–97% nitric acid, the total amount of the nitrating agent required for attainment of the maximum conversion is lower, but the spent acid cannot be used for preparing nitrating mixture. On the contrary, with 75–85% nitric acid a part of spent acid can be used in production of MNCB.

We found that for nitration with 95% HNO_3 the optimum conditions are as follows: molar ratio HNO_3 : chlorobenzene 2.5, reaction temperature 65°C, and residence time in the main and surge reactors 45 min. The yield of MNCB was 97.5%.

The nitration process with partial acid circulation was tested with 75% HNO_3 as an example. The optimum conditions are as follows: molar ratio HNO_3 : chlorobenzene 4, reaction temperature 95°C, and residence time in the main and surge reactors 180 min. The acid mixture was prepared in the main reactor by dosing of 98% HNO_3 and spent 50% HNO_3. The yield of MNCB was 97.5%.

The MNCB formed by nitration has the following isomeric composition (%): *p*-NCB 68.0–70.0, *o*-NCB 29.5–31.9, and *m*-NCB 0.1–0.5. In nitration of chloro-

Table 3. Isolation of MNCB from the reaction mixture at various degrees of its dilution

Run no.	Concentration of spent acid, %	Temperature of dilution, °C	Product yield based on the total amount of MNCB,* %		
			crystalline phase (*p*-NCB)	liquid phase (mixture of *o*- and *p*-NCB)	residue extracted from spent acid
1	47	5	61.3	37.7	1.0[a]
2	47	25	54.4	45.3	0.4[b]
3	47	50	50.6	40.4[d]	9.0[c]
4	56	5	60.1	38.9	1.0
5	56	25	52.9	45.9	1.2
6	56	50	27.1	60.9	12.0
7	66	5	48.4	50.5	1.1
8	66	25	27.9	58.5	13.6
9	66	50	Crystalline phase is not precipitated		

* Isomeric composition, %: [a] *p*-NCB 46.4; *o*-NCB 14.6, *m*-NCB 39.0; [b] *p*-NCB 16.5, *o*-NCB 41.7, *m*-NCB 41.8; [c] *p*-NCB 18.9, *o*-NCB 35.5, *m*-NCB 45.6; [d] *p*-NCB 44.3, *o*-NCB 55.6, *m*-NCB 0.1.

benzene with sulfuric acid–nitric acid mixtures the amount of *m*-NCB reaches 2.0–2.5% [1].

We found that during dilution a significant part of *p*-NCB (up to 60% of the total amount in the mixture of isomers) precipitates from the reaction mixture in the crystalline form and can be separated by filtration. A high degree of purity of *p*-NCB isolated by this procedure (98.5–99.0%) allows this product to be used without additional purification, which undoubtedly facilitates the labor-consuming stage of isomer separation. The residual liquid mixture of isomers, containing on the average 20% *p*-NCB and 80% *o*-NCB, is separated from the spent acid and washed with water. Taking into account high solubility of MNCB in nitric acid, we studied the dependence of the yield of the nitro product on the temperature and degree of dilution of the reaction mixture with water.

We found that with increasing concentration of spent acid and temperature the solubility of MNCB in the spent acid noticeably increases, and the amount of the *para* isomer precipitated from the reaction mixture decreases (Table 3).

To substantiate the choice of the conditions for isolation of the nitro product, we studied the solubility of MNCB isomers in nitric acid of various concentration. As seen from Figs. 2a–2c, the solubilities of the isomers in 47–63% nitric acid in the range 0–80°C somewhat increase with increasing temperature and are comparable, but with increasing acid concentration to 74% the solubility of *p*- and especially *m*-NCB abruptly increases. Contrary to *para* and *meta* isomers, the solubility of *o*-NCB in 74% nitric acid decreases with increasing temperature.

The study of the interrelated effect of isomers on their solubility in nitric acid showed that in 47% HNO_3 the minimum solubility of all three isomers of MNCB is observed at 20°C; in this case, the concentration of both *ortho* and *meta* isomers in the solution

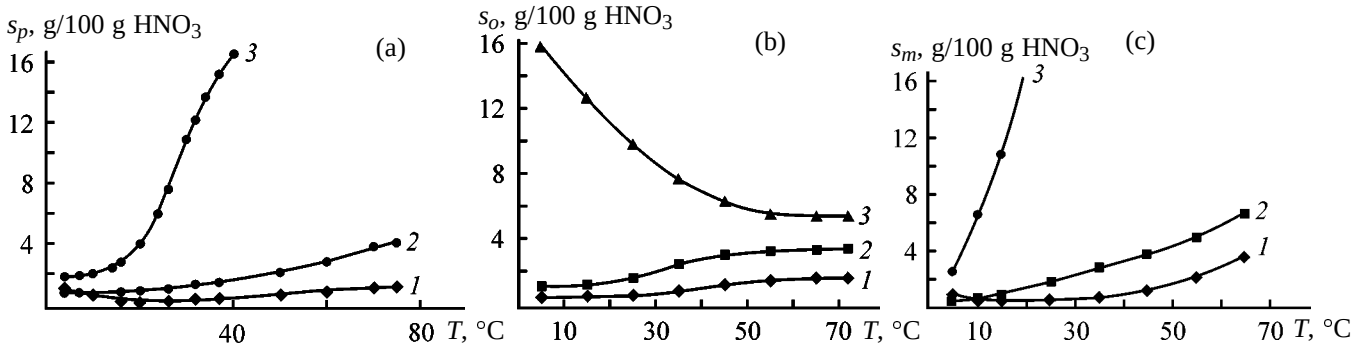

Fig. 2. Solubility of (a) *p*-NCB s_p, (b) *o*-NCB s_o, and (c) *m*-NCB s_m in nitric acid as a function of temperature T. Concentration of HNO_3 (wt %): (*1*) 47, (*2*) 63, and (*3*) 74.

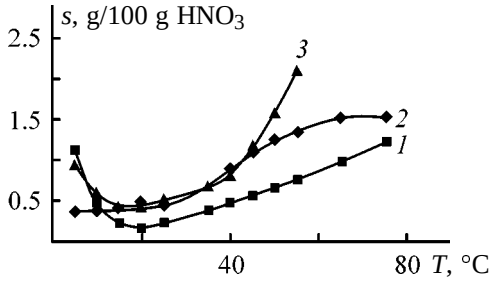

Fig. 3. Solubility *s* of MNCB isomers in 47% nitric acid as a function of temperature *T*. Isomers: (*1*) *para*, (*2*) *ortho*, and (*3*) *meta*.

is approximately two times greater than that of *p*-MNCB (Fig. 3). The mixture of isomers precipitated from nitric acid solution contains *o*- (40.5), *m*- (42.0), and *p*-NCB (17.5%), and its composition is close to that of the product isolated from the spent acid (Table 3, run no. 2). These data provide an explanation for the effect of temperature on the dilution process: an increase in the solubility of nitro compounds in spent acid with decreasing temperature (Table 3, run no. 1) and increase in the content of *ortho* and *meta* isomers of MNCB in spent acid with increasing temperature (Table 3, run no. 3).

Thus, the study of the solubility of MNCB isomers in nitric acid showed that, to increase the recovery of *p*-NCB from the mixture of isomers and to prevent the loss of the nitro product with the spent acid, the reaction mixture should be diluted at 18–22°C to a nitric acid concentration below 60%.

CONCLUSIONS

(1) Two methods were developed for production of mononitrochlorobenzene by nitration of chlorobenzene with 75–79% nitric acid, ensuring practically quantitative yield of the target product and the absence of dinitrochlorobenzene in the reaction products.

(2) Based on the study of the solubility of mononitrobenzene isomers in nitric acid, a procedure for isolation of *p*-mononitrobenzene from the reaction mixture in the crystalline form was proposed, which simplifies isomer separation.

REFERENCES

1. Orlova, E.Yu., *Khimiya i tekhnologiya brizantnykh vzryvchatykh veshchestv* (Chemistry and Technology of High Explosives), Leningrad, Khimiya, 1973, pp. 200–201.
2. Quakenbuh, A.B. and Pennington, B.T., *Am. Chem. Soc. Symp. Ser. 623*, Washington: Am. Chem. Soc., 1996, pp. 214–223.
3. FRG Patent no. 262313.
4. Belson, D.J.A., *Ind. Eng. Res*., 1990, vol. 29, pp. 1562–1569.
5. Veretennikov, E.A., Lebedev, B.A., and Tselinskii, I.V., *Zh. Org. Khim*., 2001, vol. 37, no. 7, pp. 1016–1020.
6. Veretennikov, E.A., Lebedev, B.A., and Tselinskii, I.V., *Zh. Org. Khim*., 2001, vol. 37, no. 10, pp. 1520–1523.
7. Cox, P.R. and Strachan, A.N., *Chem. Eng. Sci*., 1971, vol. 26, pp. 1013–1016.

Russian Journal of Applied Chemistry, Vol. 74, No. 11, 2001, pp. 1877–1879. Translated from Zhurnal Prikladnoi Khimii, Vol. 74, No. 11, 2001, pp. 1819–1821.

PROCESSES AND EQUIPMENT OF CHEMICAL INDUSTRY

A Calorimetric Study of the Kinetics of Chlorobenzene Mononitration with Nitric Acid

F. Yu. Sharikov, Yu. V. Sharikov, V. M. Belokhvostov, E. A. Veretennikov, B. A. Lebedev, and I. V. Tselinskii

Prikladnaya Khimiya Russian Scientific Center, St. Petersburg, Russia
St. Petersburg State Technological Institute, St. Petersburg, Russia

Received January 26, 2001

Abstract—The calorimetric method was applied to study the kinetics of chlorobenzene mononitration with 74.9 and 95.8% nitric acid and a kinetic model of the process was developed. A comparison of the thermodynamic parameters of nitration led to a conclusion concerning the limiting stage of the reaction.

The basic method for obtaining nitrochlorobenzene is nitration of chlorobenzene with a mixture of sulfuric and nitric acids. A specific feature of this technique is that it produces large amounts of dilute sulfuric acid whose regeneration cannot prevent at present its detrimental environmental effects.

To eliminate this shortcoming, it has been proposed to use for obtaining aromatic nitro compounds solely nitric acid as nitrating agent [1–3]. In [3], nitration of chlorobenzene with 68–97% nitric acid was studied and two versions of a procedure for producing nitrochlorobenzene with 75 and 95% nitric acid used for nitration were developed. These methods gave nitrochlorobenzene in nearly quantitative yield. The process was carried out in a cascade of two 60 cm^3 continuous reactors. To solve the problem of whether these results could be reproduced on industrial scale, it is necessary to develop a mathematical model of the process and study the possible choice of optimal and safe conditions under which the process can be performed in industrial nitration reactors.

The kinetics of the process was studied using the calorimetric method with a heat-flow calorimeter which makes it possible to obtain, together with data on the process kinetics, necessary information about the heat effect and thermal properties of the reaction mixture. As starting conditions were chosen those under which chlorobenzene is nitrated with 75 and 95% nitric acid [3].

EXPERIMENTAL

Chlorobenzene containing 99.0% main substance and 98% nitric acid were used in kinetic experiments. Prior to being used, nitric acid was distilled in a vacuum from a mixture with sulfuric acid and diluted at 0°C with distilled water to a prescribed concentration. The acid concentration was determined by alkalimetric titration. Deionized water was used to evaluate the thermal effects and relative rates of hydration.

The reaction kinetics were studied on a C-80 Setaram automated heat-flow calorimeter in special two-chamber chromium–nickel ampules. Nitric acid was placed in the bottom chamber and, after weighing, the necessary amount of chlorobenzene in the upper chamber was calculated. Prior to the reaction, the reactants were separated with a high-strength fluoroplastic film, which is stable against the action of corrosive media. A hermetically sealed ampule was placed in the sensitive zone of the calorimeter. At the beginning of an experiment the membrane was ruptured with a special-purpose rod stirrer and the components were subjected to primary agitation. Further agitation in the course of the experiment was provided by 180° rotation of the calorimetric unit together with the ampule fixed in it. After the experiment was complete, the reaction mass was diluted with water to nitric acid concentration of 35–40% and extracted with chloroform; the extract was washed with water and analyzed by gas–liquid chromatography. The yield and isomeric composition of the nitration product were in agreement with the data reported in [3]. The analytically obtained chlorobenzene conversions corresponded to the values found from the heat-release curve in each experimental series.

The C-80 calorimeter is automated with the use of an IBM-compatible computer and an appropriate interface. The experiments were carried out, experimental

1070-4272/01/7411-1877$25.00

Table 1. Conditions of kinetic experiments

Run no.	T, °C	HNO_3/CB molar ratio	Concentration, M		
			HNO_3	CB	H_2O
1	26.0	2.29	11.2337	4.9108	1.7238
2	25.5	2.23	11.0908	4.9779	1.7018
3	20.5	2.19	11.0445	5.0512	1.6947
4	25.4	21.14	20.3739	0.9638	3.1263
5	39.8	20.99	20.0071	0.9534	3.0700
6	40.8	2.39	11.2915	4.7251	1.7326
7	55.2	2.27	10.8331	4.7645	1.6623
8	63.5	2.32	10.8416	4.6668	1.6636
9	70.1	3.95	11.1847	2.8306	13.1324
10	95.1	3.93	10.8166	2.7490	12.7002
11	83.1	3.98	11.0250	2.7716	12.9449
12	60.2	3.98	11.3424	2.8519	13.3176

* Run nos. 1–8 were carried out at HNO_3 concentration of 95.8 wt %; run nos. 9–12, at 74.9 wt %; CB stands for chlorobenzene.

Table 2. Kinetic parameters of chlorobenzene mononitration with 74.9 and 95.8 wt % nitric acid

HNO_3, wt %	$\ln k_0$	E	ΔH	n_1	n_2
		kJ mol^{-1}			
95.8	–1.9519	8.003	154.12	1.0	2.0
74.9	12.2716	57.642	141.75	1.0	2.0

data collected, and the results of the experiments preprocessed using Eksperiment software (v4.3).[1] Preliminarily, the thermal characteristics and temperature calibration coefficients were determined for the given type of ampules.

The kinetic experiments were carried out in the isothermal temperature mode. In preparing data for kinetic analysis, true nonisothermal temperature modes were reconstructed for each experiment, with account taken of the overheating of the reaction mass, resulting from the considerable heat effect of the reaction and high rates of heat release. Such a temperature mode refinement is rather essential since the calculated overheating of an ampule with the reaction mass was several degrees relative to the temperature of the calorimetric unit. The experimental conditions are presented in Table 1.

The kinetic analysis was made with the use of MKF software.

[1] The Eksperiment and MKF software was developed at the Prikladnaya Khimiya Russian Scientific Center.

The obtained kinetic curves of heat release were described in terms of a reaction of nth order with respect to the reactants:

$$-\frac{dc_{CB}}{d\tau} = \exp\left(\ln k_0 - \frac{E}{RT}\right) c_{CB}^{n_1} c_{HNO_3}^{n_2},$$
$$\frac{dT}{d\tau} = \frac{\Delta H}{C_V}\left(-\frac{dc_{CB}}{d\tau}\right), \quad (1)$$

where k_0 is the pre-exponential factor of the reaction constant (l mol^{-1} min^{-1}); E is the activation energy (kJ mol^{-1}); n_1, n_2 are the reaction orders with respect to the components; ΔH is the heat effect of the reaction (kJ mol^{-1}); and C_V is the heat capacity of a unit volume of the reaction mixture (kJ l^{-1} K^{-1}).

The obtained kinetic parameters are listed in Table 2.

The obtained results indicate that the temperature dependences of nitration with 74.9 and 95.8% nitric acid differ so significantly that these reactions are to be regarded as two different processes in terms of a simple kinetic model. For example, the activation energy of chlorobenzene nitration with 74.9% nitric acid is 57.64 kJ mol^{-1}, which is close to values characteristic of reactions in which the rate of nitration of aromatic compounds is limited by the reaction of the nitrating agent with the substrate [4], whereas the activation energy of nitration with 95.5% nitric acid is 8.00 kJ mol^{-1}. Presumably, formation of a nitrating agent, nitronium cation, through self-protonation of nitric acid, rather than nitration proper, is the rate-determining stage under the given conditions. At the same time, there exists strict correlation between the chlorobenzene conversion and heat release in nitration with both 95.8 and 74.9% acid, and, thus, the rate of the chemical reaction can be expressed in terms of the experimentally measured rate of heat release.

It was impossible to take into account in terms of such a simple kinetic model the role played by the forming water and to generalize the description of experiments at different nitric acid concentrations, since the fundamentally different natures of these processes and temperature dependences of their rates suggest that the rate-determining stages are also different in these two cases. Therefore, the kinetic analysis was made separately for experiments with 74.9 and 95.8% nitric acid. The system of equations (1) with the determined values of the kinetic parameters, listed in Table 2, describes satisfactorily the obtained experimental data.

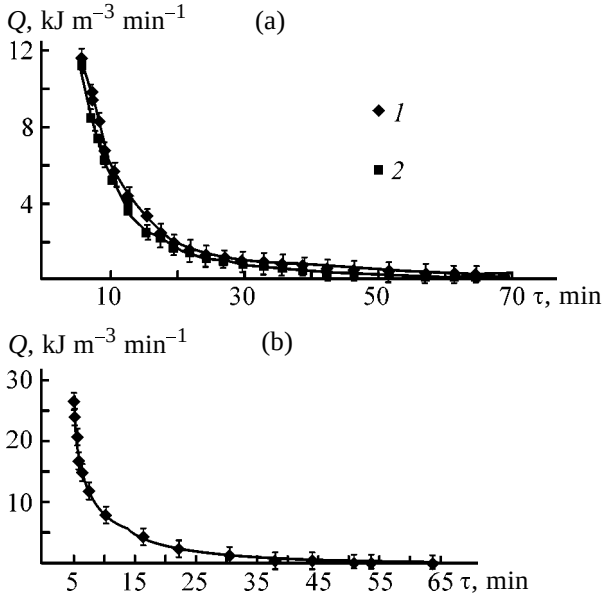

Fig. 1. Experimental and calculated curves describing heat release Q in chlorobenzene nitration in terms of a single-stage concentration model. (τ) Time. Nitrating agent: (a) 94.9% nitric acid, run nos. (*1*) 2 and (*2*) 7, joint kinetic description of runs nos. 1–8 (Table 1); (b) 74.9 nitric acid, run no. 10, joint kinetic description of run nos. 9–12 (Table 1).

Figures 1a and 1b present experimental and calculated data for kinetic experiments performed under the conditions given in Table 1.

Thus, the obtained kinetic equations can be used in developing a mathematical model of chlorobenzene nitration in a reactor in order to determine the safe process conditions.

CONCLUSIONS

(1) The kinetics of chlorobenzene nitration with nitric acid was studied on the basis of heat release rate. The obtained kinetic equations can be used in developing a mathematical model of chlorobenzene nitration in order to determine the safe process conditions.

(2) The presumed rate-determining stage in chlorobenzene nitration with 95.8% nitric acid is formation of the nitronium cation, which accounts for the low observed activation energy of the process, whereas in nitration with 74.9% nitric acid the rate of the process is determined by the rate of reaction between chlorobenzene and the nitrating agent.

REFERENCES

1. FRG Patent 262 313.
2. Belson, D.J.A., *Ind. Eng. Res*., 1990, vol. 29, pp. 1562–1569.
3. Veretennikov, E.A., Lebedev, B.A., and Tselinskii, I.V., *Zh. Prikl. Khim*., 2001, vol. 74, no. 11, pp. 1815–1819.
4. Belson, D.J. and Strachan, A.N., *J. Chem. Soc., Perkin Trans. 2*, 1989, no. 1, pp. 15–19.

Russian Journal of Applied Chemistry, Vol. 74, No. 11, 2001, pp. 1880–1883. Translated from Zhurnal Prikladnoi Khimii, Vol. 74, No. 11, 2001, pp. 1822–1825.

PROCESSES AND EQUIPMENT OF CHEMICAL INDUSTRY

Simulation of Chlorobenzene Mononitration with Nitric Acid in Flow-Through Vigorously Stirred Reactor

P. Yu. Smykalov, Yu. V. Sharikov, F. Yu. Sharikov, E. A. Veretennikov, B. A. Lebedev, and I. V. Tselinskii

Prikladnaya Khimiya Russian Scientific Center, St. Petersburg, Russia
St. Petersburg State Technological Institute, St. Petersburg, Russia

Received January 26, 2001

Abstract—A mathematical model of processes occurring in a continuous flow-through reactor was developed on the basis of data obtained in a calorimetric study of the kinetics of chlorobenzene nitration with 74.9 and 95.8% nitric acid. The parameters of safe nitration modes were found.

Conditions of chlorobenzene (CB) nitration to nitrochlorobenzene, determined on a laboratory flow-through installation with 75 and 95% nitric acid used as nitrating agents, were reported in [1]. However, industrial implementation of these processes requires that the possibility of their scaling should be determined as regards heat removal and maintenance a prescribed temperature mode, on the one hand, and process stability and safety, on the other. To solve this problem, it is necessary to develop a mathematical model of processes occurring in a continuous flow-through reactor commonly used for nitration under industrial conditions.

The mathematical model of the process was developed using the kinetic model of the nitration reaction, obtained on the basis of a calorimetric study of the nitration kinetics [2]. The following assumptions were made in developing the model: (i) the intensity of stirring is rather high and the reactor operates in the ideal mixing mode, (ii) the mixture densities at the reactor inlet and outlet are different, and (iii) the mixture density and the volume and mass of liquid in the reactor remain unchanged.

With account of the assumptions made, the mathematical model of nitration in the ideal mixing reactor has the form

$$\frac{dC_j}{dt} = G_t(C_i^f/\rho^f - C_i/\rho)V_r^{-1} + R_j(C), \quad (1)$$

$$c_p\frac{dT}{dt} = \sum_s(-\Delta H_s)r_s(C) + \frac{1}{V_r}\frac{G_t c_p^f(T^f - T)}{\rho^f} - h\frac{S(T - T^c)}{V_r},$$

where C_i are the component concentrations in the reactor (kmol m^{-3}), C_j^f are the component concentrations at the reactor inlet (kmol m^{-3}), c_p is the volume heat capacity of the mixture in the reactor (kJ m^{-3} K^{-1}), c_p^f is the volume heat capacity of the feed (kJ m^{-3} K^{-1}), G_t is the total mass flow (kg min^{-1}), h is the heat transfer coefficient (kJ m^{-2} min^{-1} K^{-1}), $-\Delta H_s$ is the heat effect of a stage (kJ kmol^{-1}), V_r is the reactor volume, T is the temperature in the reactor (K), T^f is the feed temperature (K), T^c is the coolant temperature (K), R_j are the reaction rates with respect to different components (kmol m^{-3} min^{-1}), r_s are the rates of different stages (kmol m^{-3} min^{-1}), S is the heat exchange surface area (m^2), t is time (min), ρ^f is the feed density (kg m^{-3}), and ρ is the mixture density in the reactor (kg m^{-3}).

The heat capacities of the feed and mixture in the reactor were found using the additivity rule from the heat capacities of the components and their mass fractions. The reaction rate was calculated using the equation [2]

$$r = K(T)C_{HNO_3}^{n(HNO_3)}C_{CB}^{n(CB)}, \quad (3)$$

where n is the kinetic coefficient (Table 1), and

Table 1. Kinetic parameters of chlorobenzene nitration with nitric acid

$[HNO_3]$, wt %	$\ln k_0$	E	ΔH	n_1	n_2
		kJ mol^{-1}			
95.8	–1.9519	8.003	154.12	1.0	2
74.9	12.2716	56.642	141.75	1.0	2

1070-4272/01/7411-1880$25.00

Table 2. Verification of the mathematical model of chlorobenzene nitration with nitric acid

Nitration conditions				Results of nitration								
$[HNO_3]$, wt %	T, °C	feeding rate, g h^{-1}		$[HNO_3]$, wt %			CB conversion, %			ρ, kg m^{-3}		
		CB	HNO_3	calcd.	expt.	Δ, %	calcd.	expt.	Δ, %	calcd.	expt.	Δ, %
95.8	65	39.16	70.59	83.16	82.86	0.36	0.939	0.975	3.69	1342.5	1367.5	1.8
74.9	95	7.26	21.67	65.33	65.92	0.9	0.967	0.975	0.82	1278.6	1326.1	3.58

C_{HNO_3} and C_{CB} are the concentrations of nitric acid and chlorobenzene, respectively.

The developed model was verified using the results of experiments on chlorobenzene nitration on a laboratory installation comprising a cascade of two flow-through reactors equipped with blade stirrer and heat-exchange jacket [1].

The reaction mixture densities at the outlet of each reactor, necessary for determining the residence time of the reaction mass in the apparatus and component concentrations in unit volume of the reaction mixture in relation to its composition and temperature, were calculated using equations based on the principle of additivity of the total density. The component densities at different temperatures were calculated on the basis of the properties of pure components: nitric acid, water, chlorobenzene, and nitrochlorobenzene, using the developed interpolation formulas. Verification of the obtained calculation formulas confirmed their precision, sufficient for studying the process.

The simulation was done with the use of the MKF software package[1] for processes in reactors of different types. Table 2 compares the results of calculation in terms of the mathematical model with experimental data.

It is seen that the error in calculating the chlorobenzene conversion is less than 4% and can be regarded as integrated characteristic of the simulation precision. A conclusion can be made that the kinetic model obtained on the basis of experiments in a heat-flow calorimeter is adequate and can describe satisfactorily the nitration process in a flow-through reactor with vigorous stirring. As shown in [1], chlorobenzene nitration with nitric acid does proceed under homogeneous conditions and a heat-flow calorimeter can be used to obtain an equation describing both the conversion rate and rate of heat release in this reaction.

The mathematical model developed for describing the nitration on a laboratory installation was used to construct a mathematical model of nitration in a flow-through reactor used in the industry for nitration of aromatic compounds. Commonly, vertical cylindrical resctors with spherical bottom, equipped with a stirrer, heat-exchange jacket, and coils, are used for these purposes. To describe chlorobenzene nitration in an apparatus of this kind, it is necessary to supplement the system of equations (1) with a heat balance equation that takes into account the heat removal through the heat-exchange jacket and coils and with equations for calculating the coefficients of heat transfer across the surfaces of the coil and heat-exchange jacket [3].

In simulation, the possible output capacity of a 2 m^3 reactor was determined together with the necessary intensity of heat exchange and parameters of the heat-exchange agent. As shown by simulation of nitration in a cascade of two reactors of the specified volume, the key factor is the operation mode of the first reactor, in which the chlorobenzene conversion is as high as 83–84%. Calculations demonstrated that, in nitration with 95.8% nitric acid, the output capacity of the reactor in terms of chlorobenzene may be as high as 100 kg min^{-1}, whereas with 74.9% nitric acid the maximum output capacity is 48 kg min^{-1}.

Thus, the developed model of the reactor makes it possible to either determine the reactor volume necessary for achieving a prescribed output capacity (in designing a new process) or find the maximum possible output capacity of a reactor (in developing a process in an existing shop). Of importance in solving both these problems is the safety of the newly revealed working modes, which is particularly important for the process in question, whose heat effect is about 150 kJ mol^{-1}. To find the safe mode parameters, the

[1] Developed at Prikladnaya Khimiya Russian Scientific Center.

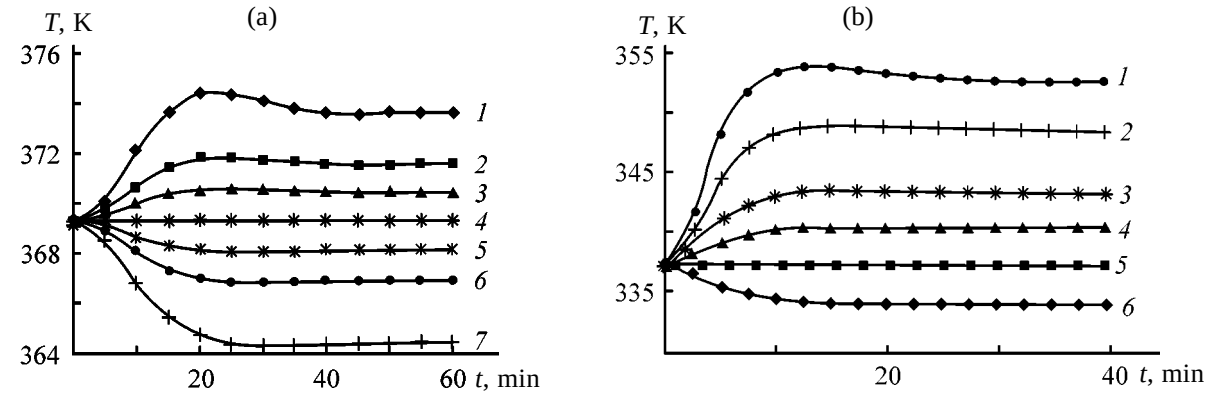

Fig. 1. Effect of changes in chlorobenzene flow rate on the temperature T in the reactor. HNO_3 concentration (wt %): (a) 74.9 and (b) 95.8; the same for Fig. 2. (t) Duration of the reaction; the same for Fig. 2. Factor by which increases (decreases) the mass flow rate of chlorobenzene at the reactor inlet at constant flow rate of nitric acid: (a) (*1*) 1.4, (*2*) 1.2, (*3*) 1.1, (*4*) 1.0, (*5*) 0.9, (*6*) 0.8, and (*7*) 0.6; (b) (*1*) 1.6, (*2*) 1.4, (*3*) 1.2, (*4*) 1.1, (*5*) 1.0, and (*6*) 0.9.

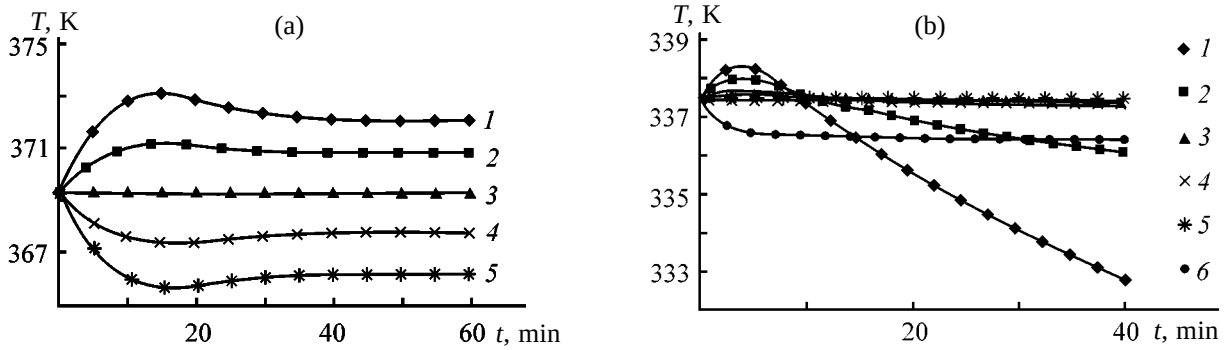

Fig. 2. Effect of changes in nitric acid flow rate on the temperature T in the reactor. Factor by which increases (decreases) the mass flow rate of nitric acid at the reactor inlet at constant flow rate of chlorobenzene: (a) (*1*) 0.6, (*2*) 0.8, (*3*) 1.0, (*4*) 1.2, and (*5*) 1.4; (b) (*1*) 0.4, (*2*) 0.6, (*3*) 0.8, (*4*) 1.0, (*5*) 1.2, and (*6*) 1.4.

sensitivity of the obtained modes to deviations from the optimal process parameters was studied.

Figures 1 and 2 show the parametric sensitivity of the given process to deviations of the parameters from the nominal values listed in Table 2.

As seen from Fig. 1, a decrease in the mass flow of chlorobenzene leads to a slight lowering of temperature in the reactor, whereas on raising the mass flow the temperature increases temporarily and then falls and tends to a new stationary level. These changes in temperature are more pronounced (up to 20°C) in nitration with 95.8% nitric acid.

Calculations also demonstrated that a decrease in the mass flow of nitric acid is accompanied by a short-time insignificant rise in the reactor temperature, which is more pronounced in nitration with 74.9% acid, and its subsequent fall. By contrast, raising the acid flow rate makes the reaction mass temperature lower.

Thus, the data obtained in studying the parametric sensitivity demonstrate that the process of chlorobenzene nitration with both 95.8 and 74.9% nitric acid is rather stable, with a transition to a new steady state occurring without any heat explosion upon steplike perturbations of the main parameters. This can be accounted for by the fact that, despite having high heat effect, the process is characterized by rather low activation energy (especially in nitration with 95.8% nitric acid). Therefore, the process passes to a new steady state rather gradually upon parameter perturbation.

Thus, the simulation results demonstrate that the process can be scaled and is rather stable.

CONCLUSIONS

(1) A mathematical model of nitration in a flow-through reactor with vigorous stirring was developed.

(2) The kinetic model developed in a calorimetric study of the nitration can be used to describe the process in a flow-through reactor.

(3) A study of the parametric sensitivity demonstrated that the process is stable at widely varying reactant concentrations.

(4) The simulation results can be used to determine the conditions for safe operation of the reactor.

REFERENCES

1. Veretennikov, E.A., Lebedev, B.A., and Tselinskii, I.V., *Zh. Prikl. Khim.*, 2001, vol. 74, no. 11, pp. 1815–1819.
2. Sharikov, F.Yu., Sharikov, Yu.V., Belokhvostov, V.M., *et al.*, *Zh. Prikl. Khim.*, 2001, vol. 74, no. 11, pp. 1819–1821.
3. Braginskii, L.N., Begachev, V.I., and Barabash, V.M., *Peremeshivanie v zhidkikh sredakh* (Stirring in Liquid Media), Leningrad: Khimiya, 1984.

Russian Journal of Applied Chemistry, Vol. 74, No. 11, 2001, pp. 1884–1887. Translated from Zhurnal Prikladnoi Khimii, Vol. 74, No. 11, 2001, pp. 1825–1828.

PROCESSES AND EQUIPMENT OF CHEMICAL INDUSTRY

On the Possibility of Using SPARK-1M Portable X-ray Spectrometer for Studying the Chemical Bond

B. D. Kalinin, R. I. Plotnikov, and Yu. P. Kostikov

NPP Burevestnik, St. Petersburg, Russia
St. Petersburg State University, St. Petersburg, Russia

Received July 10, 2001

Abstract—The possibility of using SPARK-1M spectrometer for studying the shift of emission lines belonging to the *K* series of X-ray spectra of transition metals (chemical shift of the lines) was studied. The possibility of using the spectrometer for measuring the chemical shift and evaluating the relative amounts of transition metals in different oxidation states is analyzed.

In studying the composition and properties of various materials, a necessity occasionally arises for analyzing the electronic structure of constituent atoms. To problems of this kind belongs, e.g., determination of the structure of various, and in the first place complex, compounds and refinement of the oxidation state of the constituent atoms. Another set of relevant problems includes quantitative determination of the relative contents of compounds containing some element in different oxidation states (e.g., the relative content of sulfate and sulfide sulfur in coal; Fe^{2+} and Fe^{3+} in kimberlite clays, micas, and other minerals; UO_2^{2+} and U^{4+} in process materials of nuclear power industry, etc.). One of the most promising methods for solving problems of this kind is to analyze the fine structure of emission X-ray spectra and to measure the shift of X-ray spectral lines (chemical shift). As a rule, the chemical shift of spectral lines does not exceed 0.1–1 eV and its measurement involves some difficulties.

The chemical shift of lines in X-ray emission spectra is commonly studied using special-purpose precision X-ray spectrometers characterized by high spectral resolution on the order of 1 eV and better (e.g., double-crystal spectrometers [1, 2]) or focusing spectrometers with large focal circle radius [3]. Nevertheless, numerous studies have employed conventional industrial scanning spectrometers with the Soller geometry, intended for analysis of the elemental composition of materials [3–5], or microanalyzers [6].

Despite the low spectral resolution of these devices (angular resolution is, as a rule, no better than 10–15′, to which corresponds, e.g., energy resolution of about 40–60 eV in the first order spectrum of iron in the *K* range), their high aperture ratio, combined with good reproducibility of angular settings, allows recording of spectral line shifts associated with the valence state of oxidation of the emitting atoms by hundredths of an electron volt.

Also, attempts have been made to study the chemical shift with a spectrometer based on a semiconductor detector with resolution of about 150 eV [7].

The present communication is concerned with the possibility of studying the chemical shift of lines belonging to the *K* series of transition metals with SPARK-1M portable X-ray spectrometer, which has been successfully used to analyze alloys and environmental objects [8, 9] and is distinguished by small size and low cost.

The SPARK-1M instrument is an automated short-wavelength scanning X-ray spectrometer with the Johansson geometry and focal circle radius R = 300 mm. X-ray spectra of chemical elements constituting a sample were excited using a BKh-7 X-ray tube with anode voltage of up to 45 kV, power of up to 10 W, and anode coating of (as a rule) Ag, deposited directly onto the beryllium window. This tube design makes it possible to bring a sample under study as close as 3–5 mm to the focus spot, which ensures high counting rates which are only 5–10 times less than those in conventional instruments with X-ray tubes having power of about 3 kW.

The scanning mechanism driven by a stepping motor ensures synchronous rotation of the crystal-

1070-4272/01/7411-1884$25.00

analyzer and detector (proportional xenon detector) at angles 2θ 24–88°. With the commonly used LiF |200| crystal, to this angular range corresponds wavelength interval 0.83–2.8 Å in which lie the *K* series of elements with *Z* 21(Sc)–51(Sb) (with the first and second reflection orders used) and *L* series of elements with *Z* 56(Ba) and more. The kinematic scheme of the spectrometer ensures the minimum scanning step of 0.125 mÅ in the entire wavelength range.

The angular resolution of the spectrometer with standard slits (input slit 0.2 mm wide, output slit 0.4 mm) is 6–8′ (15 eV for the CrK_β line) in the range of the *K* series of transition metals, which is at least twice better than the resolution of Soller-geometry spectrometers.

It should be noted that the angular resolution of the Johansson-geometry spectrometer can be substantially improved by making the slits narrower. For example, with 0.1-mm-wide input and output slits, it is possible to achieve, at the expense of a 2–3-fold decrease in intensity, a resolution of 1–2′, which ensures in the wavelength range 1.6–2.8 Å an energy resolution of 3–8 eV, comparable with the intrinsic width of the lines (~3 eV).

According to the technical documentation, the main instrumental error of the spectrometer does not exceed 0.5 rel. %; however, with the number of pulses exceeding 10^6, the actual reproducibility of measurement results is 0.1–0.15%.

The reproducibility of goniometer settings, evaluated by the reproducibility of intensity measurements at the wing of the FeK_α line under conditions of repeated setting of a prescribed wavelength, was about 0.0001° (0.015 eV).

To illustrate the possibilities of the spectrometer, Figs. 1a and 1b compare the spectra of iron oxide Fe_2O_3 and iron oxalate FeC_2O_4 (Fig. 1a) and chromium oxide Cr_2O_3 and potassium dichromate $K_2Cr_2O_7$ (Fig. 1b) for K_β lines of iron and chromium. In the measurements, the anode voltage was 35 kV, and the anode current, 0.2 mA. The counting rates at maximum were about 20000 pulse s^{-1} for iron and about 6000 and 2000 for chromium in, respectively, oxide and dichromate. The spectral scanning was done with a step of 0.0005 Å, with 10-s exposure at a point. Three sets of measurements were done for each preparation, with the obtained results averaged. After normalization (for each spectrum all ordinates were divided by a sum of ordinates), differences of counting rates $J_1 - J_2$ were determined and plotted against wavelength together with the profiles of the corresponding lines. For clarity, the differences for chromium and iron were multiplied by 5 and 50, respectively.

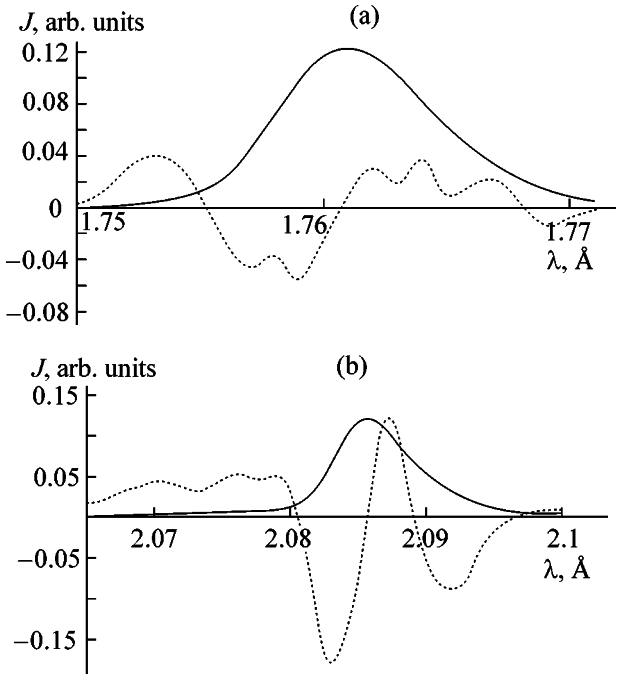

Fig. 1. Comparison of X-ray spectra of (a) Fe_2O_3 and FeC_2O_4 and (b) Cr_2O_3 and $K_2Cr_2O_7$. (*J*) Counting rate and (λ) wavelength. Dashed line: differential spectrum (×50).

As seen from Fig. 1a, the dependence of the difference $J_{Fe^{3+}} - J_{Fe^{2+}}$ (dashed line) on the wavelength is complicated. The S-shaped curve indicates the observed shift of the main Fe$K_{\beta_{1,3}}$ peak.

The peak at 1.753 Å and additional peaks superimposed on the main curve in the interval 1.755–1.76 Å are associated with the presence of the Fe$K_{\beta_{2,5}}$ line whose intensity and position depend on the oxidation state of iron. A similar structure in the long-wavelength part of the spectrum (1.76–1.77 Å) is due to the presence in the spectra of preparations of an Fe $K_{\beta'}$ line whose position and intensity strongly depend on the oxidation state of the metal (on the number of unpaired electrons).

Of similar nature is the differential curve $J_{Cr^{3+}} - J_{Cr^{6+}}$ (Fig. 1b). In this case, owing to the absence of the Cr $K_{\beta'}$ line in the spectrum of potassium dichromate, the long-wavelength part of the curve shows a single peak corresponding to the presence of this line in the spectrum of chromium(III) oxide.

The shift can be evaluated by comparing the abscissa of the point of intersection of the differential

Evaluation of the error in determining compounds with different oxidation states of metals in relation to counting rate in two spectral regions

Metal	Compound	Wavelength, Å		$R = J_1/J_2$	σ_R		σ_c, %
		λ_1	λ_2		calculation	statistical values	
Fe	Fe_2O_3	1.758	1.762	0.07107	0.00005	0.00003	2.8
	FeC_2O_4	1.758	1.762	0.06310	0.00002	0.00002	2.8
Cr	$K_2Cr_2O_7$	2.088	2.092	4.235	0.039	0.02	4.3
	Cr_2O_3	2.088	2.092	3.290	0.014	0.02	4.3

curve and the X axis with the position of the $K_{\beta_{1,3}}$ peak or, more precisely, by the amplitude of peaks in this curve. For example, in the case of approximation of the line shape with a Gaussian curve and small, compared with the peak half-width $H_{1/2}$, shift Δ, the shift can be determined using the approximate formula obtained in approximation of the line shape with a normalized Gaussian function:

$$\Delta = 0.35(A_d/A)H_{1/2}, \quad (1)$$

where A_d/A is the ratio of the difference of peak amplitudes in the S-shaped differential curve to the amplitude of the main peak.

Calculation by formula (1) for the examples presented in Figs. 1a and 1b demonstrated that the shift is 0.25 eV in passing from Fe_2O_3 to FeC_2O_4 and 0.53 eV, in reasonable agreement with the known data, in going from Cr_2O_3 to $K_2Cr_2O_7$.

The curves in Figs. 1a and 1b can be used not only in studying X-ray emission spectra of transition metal compounds, but also for determining quantitatively the relative contents of compounds with different metal oxidation states. Such an evaluation can be made, e.g., on the basis of position or height of peaks in the differential curves. The ratio of concentrations of compounds with different metal oxidation states, contained in a sample, can be evaluated more accurately by the ratio of the counting rates in two parts of the spectrum (after subtraction of the background). It is advisable to use points at the peak of the $K_{\beta_{1,3}}$ line and near the maximum or minimum in the differential curve.

As an example, table presents such ratios for the spectra of iron and chromium, shown in Figs. 1a and 1b, and evaluates the anticipated analysis error. In each case, six measurements with 10-s exposure were done with independent wavelength setting. Further, average values R and their rms deviations σ_R were calculated. The table also lists statistical errors of the ratios.

The anticipated error in determining the metal content, σ_c (%), was calculated using the expression

$$\sigma_c = (\sigma_{R_1} + \sigma_{R_2})^{1/2}/(R_1 - R_2) \times 100.$$

As follows from the data presented in the table, at a total measurement time on the order of $2 \times 6 \times 10$ s = 2 min and high metal contents, the error in determining metal forms in varied oxidation state on a SPARK-1M spectrometer is 3–4%, which corresponds to the results obtained in determining the iron oxidation state from the shift of lines belonging to the L series on a CAMEBAX microanalyzer [6].

The presented results suggest that the commercial SPARK instrument allows reliable measurements of the chemical shifts of X-ray emission lines. The information about the chemical shift of lines is important in solving chemical-analytical, geochemical, and environmental problems.

The dependence of the wavelengths (energies) of X-ray lines on the chemical state of an element being determined may also affect the results of quantitative analyses in the cases when the chemical states of an element being determined in a sample being analyzed and in the reference are different. For example, the error in determining titanium in titanium-containing oxide materials may be as high as 0.3–0.4% with metallic titanium used as reference. Therefore, in our opinion, any precise analytical studies should be started with evaluation of the chemical shift of analytical lines in a material under study with respect to references, with subsequent introduction, when necessary, of appropriate corrections.

CONCLUSION

The high reproducibility of angular settings of the SPARK-1M spectrometer allows this instrument to be

used in studying the chemical shift of spectral lines. Comparison of *K*-line spectra of transition metals, obtained using the instrument, makes it possible to study their oxidation state. If compounds of transition metal in different oxidation states are present in a sample being analyzed, the contents can be evaluated on the basis of the ratios of counting rates at wings of the K_β peak with an error not higher than 3–5 rel. %. The possibility that the chemical shift may affect the results of analysis should be taken into account in precise quantitative measurements.

REFERENCES

1. Brytov, I.A., Obolenskii, E.A., Gol'denberg, M.S., *et al.*, in *Apparatura i metody rentgenovskogo analiza* (Apparatus and Methods of X-ray Analysis), Leningrad: Mashinostroenie, 1983, issue 29, pp. 14–18.
2. Blokhin, M.A. and Nikiforov, I.Ya., in *Apparatura i metody rentgenovskogo analiza* (Apparatus and Methods of X-ray Analysis), Leningrad: Mashinostroenie, 1972, issue 10, pp. 89–94.
3. Li, Z., Ruqin, Y., Shi, L., and Wang, Q., *Anal. Chim. Acta*, 1991, vol. 248, no. 1, pp. 257–261.
4. Terada, S., Shikamori, Y., Fukushima, S., *et al.*, *J. Trace Microprobe Tech.*, 1989, vol. 7, nos. 1–2, pp. 31–45.
5. Pinkerton, A., Norrish, K., and Randall, P.J., *X-ray Spectrom.*, 1990, vol. 19, no. 2, pp. 63–65.
6. Hoffer, H.E., Brey, G.P., Schulz-Dobrick, B., and Oberhansli, R., *Eur J. Mineral.*, 1994, vol. 6, pp. 407–418.
7. Jshima, M., *Anal. Sci.*, 1998, vol. 14, no. 6, pp. 1139–1144.
8. Kalinin, B.D. and Plotnikov, R.I., *Zavod. Lab.*, 1998, vol. 64, no. 9, pp. 29–32.
9. Kalinin, B.D., Karamyshev, N.I., Plotnikov, R.I., *et al.*, *Zavod. Lab.*, 1998, vol. 64, no. 2, pp. 15–19.

Russian Journal of Applied Chemistry, Vol. 74, No. 11, 2001, pp. 1888–1891. Translated from Zhurnal Prikladnoi Khimii, Vol. 74, No. 11, 2001, pp. 1829–1832.

ORGANIC SYNTHESIS AND INDUSTRIAL ORGANIC CHEMISTRY

Synthesis and Perfume Characteristics of Acetals Containing an Aromatic Ring

O. G. Vyglazov, V. A. Chuiko, L. V. Izotova, Zh. V. Vintarskaya, and R. Ya. Yudenko

Institute of Physical Organic Chemistry, National Academy of Sciences of Belarus, Minsk, Belarus
Tereza-Inter Limited Liability Company, Moscow, Russia

Received March 15, 2001

Abstract—Aromatic acetals were prepared by condensation of 2-methyl-3-(4-R-phenyl)propanals (R = Me, *i*-Pr, *i*-Bu) with ethanol, methanol, ethylene glycol, 1,2-propanediol, methyl Cellosolve, and Cellosolve. The perfume characteristics of the acetals were studied.

Thanks to active development of synthetic organic chemistry, the set of available synthetic perfumes is rapidly extended, with new classes of compounds being involved. The use of new synthetic perfumes is characterized by two features: (1) as a rule, substances with interesting scent are discovered empirically; (2) the perfume characteristics are studied for as many structurally related compounds as possible, with the aim to apply the developed processes to synthesis of a wide set of perfumes.

Such an approach inevitably sets a task of revealing the structure–scent relationship for perfumes, with the aim to make a search for new perfumes purposeful. At the same time, to find such a relationship, it is necessary to prepare as many structural analogs as possible.

Such studies were performed previously [1] but became more active in the past years. For example, the structure–scent relationship was studied for the series of 7-oxanorbornanes [2], monoterpene lactones [3], and bicyclo[2.2.*n*]oximes [4].

In this work, starting from aldehydes in which the carbonyl group is located in a side chain of an aromatic ring, we prepared aromatic acetals and studied their perfume characteristics. The initial compounds were the aldehydes widely used in perfumery: jasmorange [2-methyl-3-(4-methylphenyl)propanal, **I**], cyclamenaldehyde [2-methyl-3-(4-isopropylphenyl)propanal, **II**], and lilial [2-methyl-3-(4-*tert*-butylphenyl)propanal, **III**]:

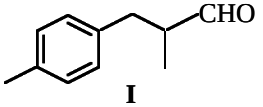

I

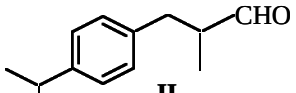

II

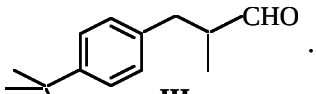

III

Acetals are widely used are synthetic perfumes. This mostly concernes diethyl, dimethyl, and ethylene acetals, although derivatives of some other alcohols (geraniol, isoamyl alcohol, 2-phenylethanol) are also used [5]. To systematically study the structure–scent relationship in the series of acetals derived from **I**–**III**, we prepared the acetals with methanol, ethanol, ethylene glycol, 1,2-propanediol, and also with methyl Cellosolve and Cellosolve (the two latter compounds were not used previously for these purposes).

The reaction is usually performed in the presence of an acid catalyst; from the viewpoint of process simplicity, it is convenient to use cation-exchange resins, e.g., granulated KU-2 cation exchanger. The reaction was performed in benzene in the presence of FIBAN K-1 fibrous sulfonic cation exchanger as catalyst. This resin was prepared by radiation-induced grafting ot styrene (98%)–1,4-divinylbenzene (2%) copolymer to a polypropylene thread, followed by sulfonation with sulfuric acid.

With this catalyst, owing to its developed surface [6], the reaction time was reduced by a factor of 1.5–2 as compared to KU-2. Furthermore, the fibrous ion exchanger did not noticeably lose its activity in repeated use, as demonstrated by the example of the reaction of aldehydes **I**–**III** with Cellosolve (Table 1).

The reaction progress was monitored by GLC. The structure of the acetals was confirmed spectroscopically. In the ^{1}H NMR spectra, a characteristic doublet

1070-4272/01/7411-1888$25.00

at 4.3–4.8 ppm (J 5–8 Hz) corresponds to the $HC(OR)_2$ proton. The IR spectra exhibit a characteristic acetal pattern consisting of five bands in the range 1185–1030 cm^{-1}.

The synthesis conditions and yields of the target products are given in Table 2, and the perfume characteristics of the acetals,[1] in Table 3.

Certain similarity of the scents of the initial aldehydes **I**–**III** is undoubtedly due to their similar molecular structure, not only topological but also steric. It was suggested [7] that all these molecules have a "rolled-up" conformation of the side chain (**A**, **B**), which is stabilized owing to conjugation of the π orbitals of the aromatic ring and carbonyl group. This factor is also responsible for the similar scent of these aldehydes and of 7-hydroxy-3,7-dimethyloctanal (hydroxycitronellal, **IV**). As suggested in [7], the molecule of **IV** in the vapor phase can take the rolled-up conformation **C** owing to hydrogen bonding:

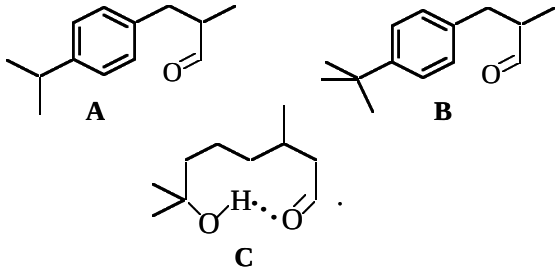

A **B**

C

However, optimization of the molecular geometry of **I**–**III** in the MM-2 approximation [8] shows that for each aldehyde the energies of the molecule in all the possible conformations differ by no more than ± 0.8 kJ mol^{-1}. Thus, the rolled-up conformation affords no additional stabilization of the aldehyde molecule. Furthermore, calculation shows that the angle between the planes of the aromatic ring and CHO group in **I**–**III** in the rolled-up conformation is 41.3°, 43.2°, and 44.5°, respectively. Such orientation excludes any overlap "through space" of the orbitals of the two nonbonded molecular fragments. It should be noted also that in conformation **C** of **IV** the distance between the hydroxyl hydrogen and carbonyl oxygen is 4.87 Å, which is too long for hydrogen bonding, especially in the gas phase when the molecule acquires additional energy.

[1] The perfume characteristics of acetals, tested as 10% solutions in purified 96% ethanol, were evaluated by the Tasting Council (eight experts) at the Accredited Control and Analytical Laboratory of Perfumes and Cosmetics, Tereza-Inter Limited Liability Company (Accreditation Certificate of the State Committee for Standards of the Russian Federation no. ROSS RU.0001.512.312, July 6, 2000).

Table 1. Yield of acetals in reactions of aldehydes **I**–**III** with Cellosolve, as influenced by catalysis conditions

Aldehyde	Catalyst	τ, min	Aldehyde conversion, %	
			first run	second run
I	FIBAN K-1	130	95	93
	KU-2	180	90	65
II	FIBAN K-1	150	95	91
	KU-2	220	92	58
III	FIBAN K-1	190	90	88
	KU-2	230	90	50

Table 2. Reaction time and yield of acetals from aldehydes **I**–**III**

Aldehyde	Alcohol used	τ, min	Conversion	Yield
			%	
I	Methanol	45	100	94
	Ethanol	55	100	95
	Ethylene glycol	70	93	88
	Propylene glycol	90	92	85
	Methyl Cellosolve	120	95	91
	Cellosolve	130	95	87
II	Methanol	55	100	95
	Ethanol	60	100	95
	Ethylene glycol	80	92	90
	Propylene glycol	90	90	87
	Methyl Cellosolve	150	95	92
	Cellosolve	150	95	90
III	Methanol	60	100	94
	Ethanol	75	100	93
	Ethylene glycol	100	93	88
	Propylene glycol	120	90	85
	Methyl Cellosolve	180	93	86
	Cellosolve	190	90	82

These data cast doubt on the "conformational" approach to scent analysis. The obtained set of acetals allows us to correlate variations of the scent with variations of, e.g., the number of alkyl substituents, with the conformation of the molecular core being preserved.

When considering the relationship between the scent of the initial aldehydes and their molecular structure, it should be noted that, in going from the methyl to isopropyl and then *tert*-butyl substituent, the scent changes from fresh fruit to fresh flower. In the series of the corresponding dimethyl acetals, the

Table 3. Scent characteristics of the synthesized acetals

Compound	Scent
2-Methyl-3-(4-methylphenyl)propanal dimethyl acetal	Green, flower, with a bittery tint
2-Methyl-3-(4-isopropylphenyl)propanal dimethyl acetal	Green, of cyclamen, with a bitter grassy note
2-Methyl-3-(4-*tert*-butylphenyl)propanal dimethyl acetal	Strong, flower, with a cold note of cyclamen and lily of the valley, light ozone
2-Methyl-3-(4-methylphenyl)propanal diethyl acetal	Green, fresh watermelon, with a note of spice herbs
2-Methyl-3-(4-isopropylphenyl)propanal diethyl acetal	Flower, of cyclamen, with a wood note
2-Methyl-3-(4-*tert*-butylphenyl)propanal diethyl acetal	Flower, of cyclamen and lily of the valley, with a wood note
2-Methyl-3-(4-methylphenyl)propanal di(2-methoxyethyl) acetal	Fresh, flower, of peony with a bright watermelon note
2-Methyl-3-(4-isopropylphenyl)propanal di(2-methoxyethyl) acetal	Fresh, of cyclamen, with a watermelon–ozone note
2-Methyl-3-(4-*tert*-butylphenyl)propanal di(2-methoxyethyl) acetal	Flower, with notes of cyclamen, lily of the valley, and sweet lime blossom
2-Methyl-3-(4-methylphenyl)propanal di(2-ethoxyethyl) acetal	Flower, grassy, with a fresh note of watermelon and heady anise and wood tint
2-Methyl-3-(4-isopropylphenyl)propanal di(2-ethoxyethyl) acetal	Flower, of cyclamen, with an anise–ozone note
2-Methyl-3-(4-*tert*-butylphenyl)propanal di(2-ethoxyethyl) acetal	Flower, fresh, with a beewax and honey tint, with a light bittery note
2-Methyl-3-(4-methylphenyl)propanal ethylene acetal	Flower-grassy with a tint of parsley, celery, and anise
2-Methyl-3-(4-isopropylphenyl)propanal ethylene acetal	Flower, of cyclamen, with a fresh watermelon note
2-Methyl-3-(4-*tert*-butylphenyl)propanal ethylene acetal	Flower, of cyclamen, with a sweet anise note
2-Methyl-3-(4-methylphenyl)propanal propylene acetal	Grassy, heady, wood, with seaweed note
2-Methyl-3-(4-isopropylphenyl)propanal propylene acetal	Fresh, flower, sweet, with a beewax tint
2-Methyl-3-(4-*tert*-butylphenyl)propanal propylene acetal	Flower, of cyclamen, sweet, powdery

scent changes from green fruit–watermelon through flower-grassy with a bittery note to fresh flower with an ozone note. With diethyl acetals, very gentle heady and wood notes appear. With methoxy and ethoxy groups introduced into the ethyl acetal moiety, the scent changes more significantly: the fresh fruit–watermelon note is enhanced, ozone freshness components disappear, and a sweet wood or honey note appears. These trends are observed with derivatives of all the three aldehydes. Smooth variation of the scent of the initial aldehydes corresponds to smooth variation of the scent in the series of similar acetals with linear alkyl or alkoxy groups.

With compounds containing a cyclic acetal groups (ethylene or propylene acetals), the trend is reverse. In the series of ethylene acetals, the scent varies very sharply with increasing size of the substituent in the phenyl moiety: first a fairly pronounced sweet flower note appears, then it is enhanced, and a fresh watermelon note is added. In the series of propylene acetals, a wood scent gives way to a fresh flower scent subsequently acquiring a warm powdery tint.

The acetals obtained show promise as components of fragrant and perfume formulations, because they produce a fairly wide range of scents of various tints and, in contrast to the initial aldehydes, are stable to oxidation in ready perfumes and cosmetics.

EXPERIMENTAL

The ^{1}H NMR spectra were taken with a Tesla BS-567A spectrometer ($CDCl_3$, internal reference HMDS). The IR spectra were recorded on a Specord 75-IR spectrometer (thin films). The GLC analysis of reaction mixtures was performed with a Chrom-5 chromatograph [flame-ionization detector, 2000 × 3-mm column, Chromaton N-AW-DMCS support (0.125–

0.160 mm), Reoplex-400 stationary phase, programmed heating from 100 to 180°C (4 deg min^{-1}), nitrogen carrier gas].

To prepare acetals, the catalyst (2 wt % relative to aldehyde) was added to a solution of 0.10 mol of aldehyde **I**–**III** and 0.11 mol of dihydric alcohol in 70 ml of benzene. The mixture was refluxed until the release of water ceased and the reaction was complete (monitored by GLC). The catalyst was separated by decanting, washed with benzene (2 × 5 ml), and reused; the wash solutions were combined with the reaction solutions. The solvent was distilled off. When necessary (if the acetal purity was less than 98%), the product was purified by chromatography (alumina, eluent hexane–diethyl ether with gradually increasing content of ether).

Monohydric alcohols were taken in a double amount. With dimethyl acetals, the released water was bound with a stoichiometric amount of triethyl orthoformate.

CONCLUSIONS

(1) A series of 2-methyl-3-(4-R-phenyl)propanal (R = Me, *i*-Pr, *t*-Bu) acetals was prepared; these compounds have pleasant scent and can be used as perfumes.

(2) In the series of acetals with the same monohydric alcohols, the scent changes smoothly depending on the substituent in the phenyl ring. In the series of diols, the scent changes more sharply.

ACKNOWLEDGMENTS

The authors are grateful to A.A. Shunkevich for submitting samples of FIBAN K-1 sulfonic cation exchanger.

REFERENCES

1. Ohloff, G., *Helv. Chim. Acta*, 1992, vol. 75, no. 7, pp. 2041–2108.
2. Weyerstahl, P. and Brendel, J., *Lieb. Ann.*, 1990, no. 10, pp. 1029–1036.
3. Tadeba, H. and Mihara, S. *Agr. Biol. Chem.*, 1990, vol. 54, no. 9, pp. 2271–2276.
4. Buchbauer, G., Spreitzer, H., and Kotlan, U., *Z. Naturforsch. (b)*, 1991, vol. 46, no. 9, pp. 1272–1274.
5. Voitkevich, S.A., *865 dushistykh veshchestv dlya parfyumerii i bytovoi khimii* (865 Fragrants for Perfumery and Domestic Chemicals), Moscow: Pishchevaya Prom–st., 1994.
6. Polyanskii, N.G., *Kataliz ionitami* (Catalysis with Ion Exchangers), Moscow: Khimiya, 1973.
7. Voitkevich, S.A. and Kheifets, A.A., *Ot drevnikh blagovonii k sovremennym parfyumerii i kosmetike* (From Ancient Fragrances to Modern Perfumes and Cosmetics), Moscow: Pishchevaya Prom–st., 1997.
8. Burkert, U. and Allinger, N.L., *Molecular Mechanics*, Washington, DC: Am. Chem. Soc., 1982.

Russian Journal of Applied Chemistry, Vol. 74, No. 11, 2001, pp. 1892–1898. Translated from Zhurnal Prikladnoi Khimii, Vol. 74, No. 11, 2001, pp. 1833–1839.

ORGANIC SYNTHESIS AND INDUSTRIAL ORGANIC CHEMISTRY

Synthesis of Surfactants Derived from Adamantane

E. V. Vashkevich, N. Ya. Yurashevich, N. G. Kozlov, V. I. Potkin, and T. N. Potkina

Institute of Physical Organic Chemistry, National Academy of Sciences of Belarus, Minsk, Belarus
Institute of General and Inorganic Chemistry, National Academy of Sciences of Belarus, Minsk, Belarus

Received July 5, 2000; in final form, July 2001

Abstract—Quaternary [1-(1-adamantyl)ethyl]- and (1-adamantyl)trimethylammonium, and also 3-(1-adamantyl)-3-chloro-2-propenylammonium salts were prepared, and their surface activity was studied.

Quaternary ammonium salts, owing to their specific features as cationic surfactants and to colloid-chemical properties, are widely used in various branches of industry as effective antistatics [1], as reagents imparting hydrophobicity to clay impurities in their flotation separation from potassium ores [2], in production of modified starch for multilayered and crimped cardboard [3], and in preparation of bitumen emulsions.

Major researchers' attention is given to adamantane derivatives as compounds with a high biological activity [4, 5]. Amines of the adamantane series—midantane (1-adamantylamine hydrochloride), remantadine {[1-(1-adamantyl)ethyl]amine hydrochloride}, and urotropin (1,3,5,7-tetraazaadamantane)—are effective antiviral agents [6]. 1-Adamantylammonium carboxylates (acetate, salicylate, propionate, etc.) show a high therapeutic activity and are used for treating influenza [7]. However, there are no data on adamantane derivatives containing [1-(1-adamantyl)ethyl]trimethylammonium, (1-adamantyl)trimethylammonium, or 3-(1-adamantyl)-3-chloro-2-propenylammonium cation in combination with an anion of an organic or inorganic acid.

The goal of this work was to prepare new quaternary [1-(1-adamantyl)ethyl]- and (1-adamantyl)trimethylammonium salts and also 3-(1-adamantyl)-3-chloro-2-propenylamine hydrochloride and to study their surface activity and flotation properties. As starting compounds we used (1-adamantylethyl)amine **I** prepared by hydroamination of 1-acetyladamantane **II** and 1-adamantylamine **III** prepared by treatment of aqueous solution of amine **IV** with NaOH (Schemes 1, 2).

By reactions of amines **I** and **III** with formaldehyde [8] in the presence of formic acid (reductant), we prepared (1-adamantylethyl)dimethylamine **V** and (1-adamantyl)dimethylamine **VI**. In the optimal procedure, the reagents are added over a period of 4.5–5 h at 50°C, after which the mixture is heated to 80°C to bring the reaction to completion. The ratio of the amine, formic acid, and formalin is 1 : 5 : 4. The reaction is complete in 21–22 h; the product yield is as high as 94–95%.

Quaternizzation of amines **V** and **VI** with methyl iodide [9] gave [1-(1-adamantyl)ethyl]trimethylammonium iodide **VII** and (1-adamantyl)trimethylammonium iodide **VIII**. Iodides **VII** and **VIII**, when treated with strongly basic AV-17 anion exchanger in the OH^- form [10], give (1-adamantylethyl)trimethylammonium hydroxide **IX** and (1-adamantyl)trimethylammonium hydroxide **X**. When the reaction was performed at 50–55°C and the equivalent ratio iodide : anion exchanger = 1 : 3, with addition of the resin in two portions, the reaction was complete in 18 h, with the yield of **IX** and **X** being as high as 98–99%.

(1-Adamantylethyl)trimethylammonium (**XI**) and (1-adamantyl)trimethylammonium (**XII**) salts were prepared by neutralization of solutions of hydroxides **IX** and **X** with a solution of isocamphanone-3-*exo*-sulfonic acid [11, 12]. Previous studies showed that the ammonium salt of this acid shows surface activity and is effective collector of potassium chloride in flotation of sylvinite ores [11]. Therefore, it was appropriate to study the surface activity of quaternary ammonium salts with the anion of isocamphanonesulfonic acid.

The structure of the compounds was proved by ^1H NMR and IR spectroscopy, and also by mass spectrometry. The ^1H NMR spectra of **VII**, **VIII**, **XI**, and **XII** contain signals at δ 1.6, 1.9, and 2.0 ppm, corresponding to 15 protons of the adamantane core. The signal at δ 3.2 ppm belongs to the $N(CH_3)_3$ moiety. The IR spectra of **XI** and **XII** contain absorption

1070-4272/01/7411-1892$25.00

Scheme 1.

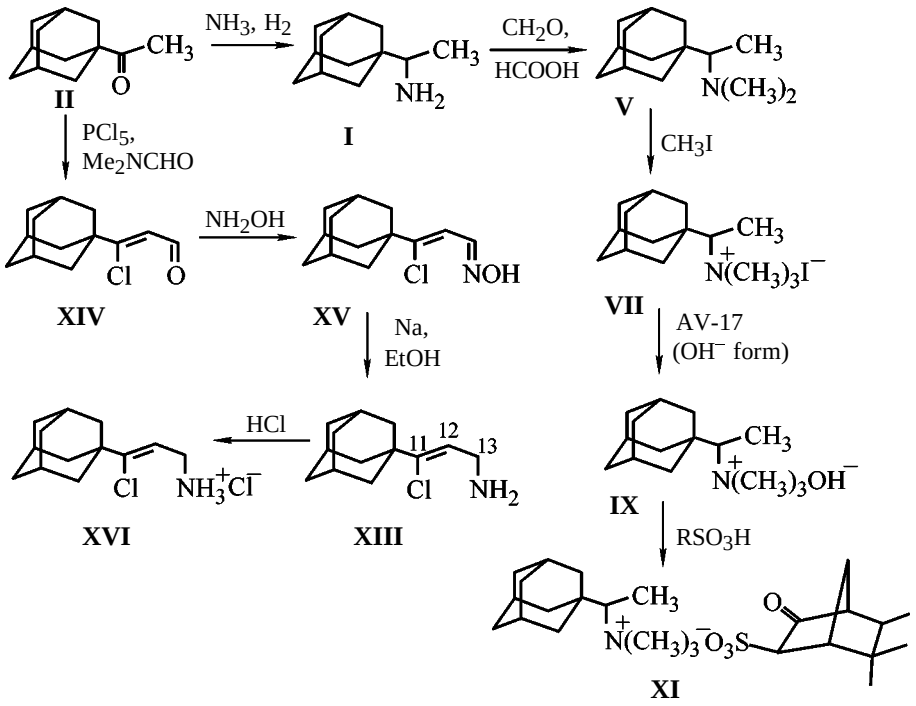

Scheme 2.

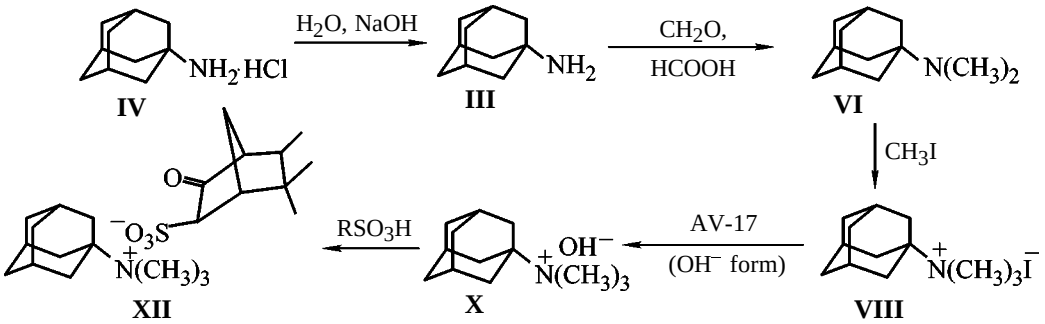

bands at 1740 [ν(C=O)], 1180 [ν(SO_2)], and 1070–1040 cm^{-1} [ν(C–O–S)]. In the mass spectra of **VII**, **VIII**, **XI**, and **XII** we identified the molecular peaks of the cation (without acid anion), with the relative intensity of 15%; the base peak was that at *m/z* 135, $[Ad]^+$.

Aliphatic amine salts are used in flotation of sylvinite ores. The flotation properties of amines containing the adamantane cores were not studied previously. To examine the behavior of such substances in flotation of potassium ores, we prepared 3-(1-adamantyl)-3-chloro-2-propenylamine (**XIII**) hydrochloride. The synthesis was performed as follows. First, by reaction of ketone **II** with PCl_5 and dimethylformamide (Vilsmeier–Haack complex [13]), we prepared in 60% yield *s-cis*-3-(adamantyl)-3-chloro-2-propenal **XIV**. In its ^1H NMR spectrum, the adamantane core protons give three broadened singlets at δ 1.8 (6H), 1.9 (6H), and 2.1 ppm (3H). The protons at C^{12} and C^{13} give doublets (δ 6.1 and 10.1 ppm, respectively), with the coupling constant ^3J 6 Hz, which corresponds to the *s-cis* arrangement [14]. The IR spectrum of **XIV** contains bands at 1680 [ν(C=O)], 1610 [ν(C=C)], and 875 cm^{-1} [ν(C–Cl)], and in the mass spectrum there are peaks of the molecular ion at *m/z* 224 and 226; their intensity ratio (100 : 33) corresponds to the presence of one chlorine atom. Treatment of **XIV** with hydroxylamine have *s-cis*-3-(adamantyl)-3-chloro-2-propenal oxime **XV** [15] in a quantitative yield. In its ^1H NMR spectrum, we identified characteristic signals of the tricyclic core in the form of three broadened singlets at δ 1.8 (6H), 1.9 (6H), and 2.1 ppm (3H), and also doublets of the C^{12} and C^{13} protons at δ 6.2 and 8.2 ppm, respectively (^3J 6 Hz). The absorption

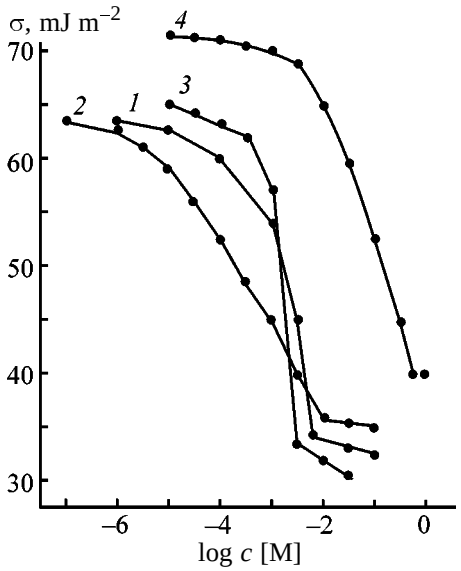

Surface tension isotherms of aqueous solutions of (*1*) **XI**, (*2*) **XVI**, (*3*) **XVII**, and (*4*) $RSO_3^-NH_4^+$. (σ) Surface tension and (*c*) concentration.

bands of the C=C, C=N, and C–Cl bonds are observed in the IR spectrum at 1610, 1640, and 850 cm^{-1}, respectively. The mass spectrum of oxime **XV** contains the peak of the molecular ion (I = 43%) and the fragment peaks corresponding to the loss of H_2O (100%), chlorine atom (86%), and adamantane core (31%).

Reduction of oxime **XV** with sodium in absolute ethanol gives 3-(1-adamantyl)-3-chloro-2-propenylamine **XIII** in 40% yield; by treatment with dry HCl it was converted to hydrochloride **XVI** in 90% yield.

Taking into account an important role of surfactants in various industrial processes, in particular, in flotation concentration of ores, we studied the surface activity and flotation properties of **XI**, **XII**, and **XVI**. The collector presently used for recovery of potassium chloride is octadecylamine hydrochloride. Until recently, it was believed that flotation separation of soluble salts occurs only under the action of aliphatic compounds with a hydrophilic group at a primary carbon atom. The longer the hydrocarbon chain of the collector, the higher the energy of dispersion interactions and hence the higher the stability and density of the adsorption layer on the KCl surface and the stronger the hydrophobization effect. Surfactants with radicals containing double bonds or with branched radicals show weaker collecting power. Secondary, tertiary, and quaternary ammonium salts are practically incapable of KCl flotation.

The synthesized compounds differ from sodium alkyl sulfates and aliphatic amines in that the hydrophilic groups in their molecules are linked not to a simple alkyl radical but to a bulky tricyclic fragment with a complex steric structrue. Compounds **XI** and **XII** and the ammonium salt $RSO_3^-NH_4^+$ contain a common surface-active anion with a polar sulfo group. However, in contrast to the ammonium salt, in **XI** and **XII** the cation is also surface-active. This fact can give rise to differences in the surface and volume properties and in the hydrophobizing effect of these surfactants.

The degree of adsorption of surfactants on the phase boundary, characterizing interchange of the molecules on the surface and in the bulk, is determined by the length of the hydrocarbon radical, the nature of polar groups (for straight-chain surfactants with the vertical orientation of the molecules in the surface layer), and by the surfactant solubility.

According to the surface tension isotherms (see figure), the compounds prepared behave in solution as typical lyophilic surfactants, markedly decreasing the surface tension of aqueous solutions (to 30–40 mJ m^{-2}) and showing clearly defined ranges of micelle formation. It should be noted that compounds **XI** and **XII** are less soluble in water (1.1×10^{-1} and 1.2×10^{-1} M, respectively) than the ammonium salt $RSO_3^-NH_4^+$ (0.68 M); therefore, the surface tension of their solutions decreases to a greater extent. As the solubility is decreased, the tendency of surfactant molecules to pass from the bulk of solution to the phase boundary becomes more pronounced. The minimal values of the surface tension give only a qualitative characteristic of the effect of the substance structure on the surface properties. To reveal a correlation between the surface and volume properties, we calculated from the experimental isotherms the parameters of the surface activity of the synthesized surfactants (Table 1). As compared to the ammonium salt $RSO_3^-NH_4^+$, the synthesized compounds show higher activity at the solution–air interface. As seen from Table 1, the surface activiy of **XI** and **XII** considerably exceeds that of $RSO_3^-NH_4^+$.

Thus, the presence in a molecule of a complex organic counterion capable of adsorption, together with a surface-active ion, on the liquid–gas interface and of association in the bulk to form micelles determines certain specific features of such compounds as **XI** and **XII**. Solutions of such surfactants exhibit a pronounced synergism manifested in high surface

Table 1. Colloid-chemical characteristics of surfactant solutions*

Compound	c_m, M	$A_{max} \times 10^{-6}$, mol m^{-2}	σ_{min}, mJ m^{-2}	CMC, M	G, mJ mmol^{-1}
XI	0.003	7.1	34	0.006	6.2
XII	0.001	7.8	30	0.004	10.5
XVI	0.0001	1.6	35	0.01	3.7
$RSO_3^-NH_4^+$	0.18	3.1	40	0.56	0.057

* (c_m) Saturation concentration of adsorption layer, determined as the point in which the σ–ln c plot starts to deviate from the straight line; (A_{max}) maximal adsorption calculated according to Gibbs; (σ_{min}) minimal surface tension; (CMC) critical micelle concentration determined from the break point in the σ–ln c isotherm; (G) surface activity determined from CMC according to Rebinder.

activity and low critical micelle concentration, as compared to salts of the surface-active ions with simple counterions. A close-packed adsorption layer is formed on the interface, which considerably decreases the surface tension on the liquid–gas interface (to 30 mJ m^{-2}), and association in solution starts at lower concentrations (10^{-3} M). Such a behavior of the surfactants under consideration is due to enhancement of hydrophobic interactions owing to formation (both on the surface and in the bulk) of electrically neutral complexes as a result of specific (electrostatic) interactions with charge compensation.

We have studied the flotation properties of the compounds. We found that adamantane derivatives **XI**, **XII**, and **XVI** can be used as collectors of KCl in flotation concentration of sylvinite ores. As seen from Table 2, agent **XII** ensures 93% recovery of KCl with the KCl content in the concentrate as high as 86%.

The surfactants synthesized are nontoxic, readily degradable biologically, and well compatible with the traditional surfactants, which makes them promising for industrial use.

EXPERIMENTAL

The ^{1}H NMR spectra were recorded with a Tesla BS-567A spectrometer (100 MHz, $CDCl_3$, internal reference TMS). The IR spectra were taken with a Protege-460 Fourier spectrometer, and the mass spectra, with an MKh-1320 mass spectrometer (electron impact, 50 eV).

The surface tension of the synthesized compounds in aqueous solutions was determined by the ring detachment method allowing measurement of the equilibrium surface tension [16]. The method is based on measuring the force required for detachment of a wire ring from a horizontal liquid surface. The detachment force was measured with a torsion balance calibrated using a reference liquid (hexane) with a known surface tension.

The flotation activity of the new compounds was studied with a laboratory machine (chamber volume 150 cm^3) using natural sylvinite ore of the Starobinskoe deposit (KCl content 27.4%, insoluble residue 3.4%). As the liquid phase we used a saturated solution of KCl and NaCl (d 1.235 g cm^{-3}), and as the agent depressing clay and carbonate impurities, sodium salt of carboxymethyl cellulose (Na-CMC). The agents were introduced in the following order: Na-CMC, stirring for 3 min; collector, stirring for 1 min; flotation. The solid flotation products were separated from the liquid phase on a Büchner funnel, dried, weighed, and analyzed for the KCl content. Flotation tails were analyzed by flame photometry, and concentrates, by precipitation of perchlorate or tetraphenylborate [17].

1-Adamantylamine III. A solution of 20 g of **IV** in 50 ml of water was heated to 45°C, and 4.25 g of solid NaOH was added in small portions with stirring over a period of 5 h. Then the mixture was heated to 60–65°C and kept at this temperature for 6 h. After cooling to room temperature, the precipitate of **III** was filtered off, washed with water (2 × 50 ml), and dried; yield 96%, colorless crystalline substance, mp 210–212°C.

[1-(1-Adamantyl)ethyl]dimethylamine V. A solution of 17.9 g of **I** in 100 ml of isopropyl alcohol was

Table 2. Parameters of flotation of sylvinite ore with **XI**, **XII**, and **XVI***

Q, g g^{-1}	β, %	ε, %	β, %	ε, %	β, %	ε, %
	XI		**XII**		**XVI**	
50	87.0	72.3	87.7	71.9	91.1	73.5
100	91.4	89.8	91.0	88.1	88.2	86.4
200	85.0	91.0	86.1	93.1	86.6	87.1

* (Q) Collector consumption, (β) content of KCl in the concentrate, and (ε) recovery of KCl into the concentrate.

heated with stirring to 50–53°C, and 27 g of 85% aqueous formic acid was added over a period of 40 min. In the process, the mixture warmed up to 60°C. After cooling to 50°C, 40 g of 30% formalin was added dropwise with vigorous stirring over a period of 4.5 h. Then the mixture was heated to 80°C and kept at this temperature for 21 h. After cooling, the mixture was alkalized (with phenolphthalein indicator) with 25% aqueous NaOH. The mixture was transferred into a dropping funnel, and the upper layer was separated, washed with water, and dried over $MgSO_4$. The solvent was distilled off, and the residue was vacuum-distilled. Compound **V** was obtained, yield 94%, bp 88–90°C (3 mm Hg), n_D^{20} 1.5064. IR spectrum, ν, cm^{-1}: 2950, 2860, 2780, 1460, 1170, 1090, 1050. ^1H NMR spectrum, δ, ppm: 1.47 d (3H, CH_3), 1.80 br.s (6H, $3CH_2$), 1.95 br.s (6H, $3CH_2$), 2.05 br.s (3H, 3CH), 3.22 s (6H, $2CH_3$), 3.30 q (1H, CH). Mass spectrum, *m*/*z*: 207 (M^+, 21%), 192, 163, 135 (100%).

Found, %: C 80.97, H 12.18, N 6.89.
$C_{14}H_{25}N$.
Calculated, %: C 81.15, H 12.07, N 6.76.

(1-Adamantyl)dimethylamine VI was prepared similarly from amine **III**; yield 90%, bp 83–85°C (3 mm Hg), n_D^{20} 1.5157. IR spectrum, ν, cm^{-1}: 3000, 2920, 2850, 1460, 1180. ^1H NMR spectrum, δ, ppm: 1.70 br.s (6H, $3CH_2$), 2.10 br.s (6H, $3CH_2$), 2.35 br.s (3H, 3CH), 3.30 s (6H, $2CH_3$). Mass spectrum, *m*/*z*: 179 (M^+, 19%), 164, 149, 135 (100%).

Found, %: C 80.32, H 11.80, N 7.75.
$C_{12}H_{21}N$.
Calculated, %: C 80.44, H 11.73, N 7.82.

[1-(1-Adamantyl)ethyl]trimethylammonium iodide VII. A solution of 20.7 g of amine **V** in 115 ml of isopropyl alcohol was heated to 45°C, and 14.2 g of methyl iodide was added with stirring at 45–55°C over a period of 50 min. Then the mixture was heated to 70–75°C and stirred at this temperature for 9–10 h. After cooling, the solvent was distilled off, and the residue was recrystallized from acetone. Iodide **VII** was obtained, yield 90%; colorless crystalline substance, mp 216–217°C. IR spectrum, ν, cm^{-1}: 3000, 2900, 2850, 1440, 840. ^1H NMR spectrum, δ, ppm: 1.47 d (3H, CH_3), 1.80 br.s (6H, $3CH_2$), 1.95 br.s (6H, $3CH_2$), 2.05 br.s (3H, 3CH), 3.22 s (9H, $3CH_3$), 3.30 q (1H, CH). Mass spectrum, *m*/*z*: 222 (M^+ – I, 23%), 207, 192, 163, 135 (100%), 127.

Found, %: C 51.53, H 7.91, N 4.07.
$C_{15}H_{28}IN$.
Calculated, %: C 51.57, H 8.02, N 4.01.

(1-Adamantyl)trimethylammonium iodide VIII was prepared similarly from amine **VI**; yield 90%, colorless crystalline substance, mp 334–335°C. IR spectrum, ν, cm^{-1}: 3040, 2920, 2850, 1460, 850. ^1H NMR spectrum, δ, ppm: 1.70 br.s (6H, $3CH_2$), 2.10 br.s (6H, $3CH_2$), 2.35 br.s (3H, 3CH), 3.30 s (9H, $3CH_3$). Mass spectrum, *m*/*z*: 194 (M^+ – I, 11%), 179, 164, 149, 135 (100%), 127, 123, 93, 85.

Found, %: C 48.63, H 7.43, N 4.31.
$C_{13}H_{24}IN$.
Calculated, %: C 48.59, H 7.47, N 4.36.

[1-(1-Adamantyl)ethyl]trimethylammonium hydroxide IX. To a solution of 13.96 g of **VII** in 170 ml of isopropyl alcohol, we added 15.4 g (dry weight; 0.06 mol) of AV-17 anion exchanger in the OH^- form and stirred at 55°C for 5 h. Then an additional 15.4-g portion of the resin was added, and the mixture was stirred at 55°C for an additional 5 h. After cooling to room temperature, the resin was filtered off. A 6.45% aqueous-alcoholic solution of hydroxide **IX** was obtained; pH 10, yield 99% (the concentration of hydroxide depends on the moisture content of the anion exchanger).

(1-Adamantyl)trimethylammonium hydroxide X was prepared similarly from salt **VIII**; yield 98%.

[1-(1-Adamantyl)ethyl]trimethylammonium isocamphanone-3-*exo*-sulfonate XI. An equivalent amount of aqueous-alcoholic solution of isocamphanone-3-*exo*-sulfonic acid was added to an aqueous-alcoholic solution of hydroxide **IX** with vigorous stirring. The solvents were removed, and the product was recrystallized from ethanol and vacuum-dried to constant weight; yield 85%, colorless powder, mp 229–230°C. IR spectrum, ν, cm^{-1}: 2910, 2850, 1740, 1176, 1060. ^1H NMR spectrum, δ, ppm: 0.90 d (3H, CH_3), 1.05 s (6H, $2CH_3$), 1.45 d (3H, CH_3), 1.7 br.s (6H, $3CH_2$), 1.80 br.s (6H, $3CH_2$), 2.05 br.s (3H, 3CH), 2.10–2.80 m (5H), 3.30 s (9H, $3CH_3$), 3.40 q (1H, CH), 3.70 d (1H, $HCSO_3$). Mass spectrum, *m*/*z*: 230 (M^+ – $C_{15}H_{28}N$, 12%), 214, 177, 163, 135 (100%), 119.

Found, %: C 66.12, H 9.15, N 2.99, S 7.01.
$C_{25}H_{42}NO_4S$.
Calculated, %: C 66.37, H 9.29, N 3.09, S 7.08.

(1-Adamantyl)trimethylammonium isocamphanone-3-*exo*-sulfonate XII was prepared similarly, by

neutralization of hydroxide **X**; yield 70%, colorless powder, mp 255–256°C. IR spectrum, ν, cm^{-1}: 3050, 2960, 2910, 2850, 1710, 1180, 1040. ^1H NMR spectrum, δ, ppm: 0.90 d (3H, CH_3), 1.00 s (6H, $2CH_3$), 1.50 m (1H, CH), 1.70 br.s (6H, $3CH_2$), 1.90 m (2H, 2CH), 2.00 br.s (6H, $3CH_2$), 2.10 m (1H, CH), 2.30 br.s (3H, 3CH), 2.60 m (1H, CH), 3.10 s (9H, $3CH_3$), 3.70 d (1H, CH). Mass spectrum, *m*/*z*: 328 ($M^+ - SO_4$, 10%), 253, 215, 179, 152, 136, 135 (100%), 122, 108, 93.

Found, %: C 65.03, H 8.90, N 3.25, S 7.60.
$C_{23}H_{38}NO_4S$.
Calculated, %: C 65.09, H 8.96, N 3.30, S 7.54.

3-(1-Adamantyl)-3-chloro-2-propenylamine XIII. Sodium (10 g) was added with stirring to 4 g of oxime **XV** in 185 ml of absolute ethanol. After complete dissolution of sodium, the mixture was refluxed for 35 min, poured onto ice, and acidified with 15% HCl. The alcohol was distilled off, and the aqueous solution was washed with diethyl ether and alkalized by adding anhydrous KOH with stirring and cooling. Then the mixture was extracted with diethyl ether, and the extract was dried over KOH. After removal of the solvent, 1.5 g of amine **XIII** was obtained; yield 40%. IR spectrum, ν, cm^{-1}: 2920, 2855, 1630, 1580, 1320, 870. ^1H NMR spectrum, δ, ppm: 1.8 br.s (6H, $3CH_2$); 1.9 br.s (6H, $3CH_2$); 2.1 br.s (3H, 3CH); 6.2 d, ^3J 6 Hz (1H, $C^{12}H$); 8.2 d (1H, $C^{13}H$).

Found, %: C 69.22, H 9.04, Cl 15.55, N 6.34. M^+ 225 (15%).
$C_{13}H_{20}N$.
Calculated, %: C 69.16, H 8.93, Cl 15.70, N 6.20. *M* 225.8.

3-(1-Adamantyl)-3-chloro-2-propenal XIV. To 134 ml of dimethylformamide at 25–30°C, 50.2 g of PCl_5 was added in portions over a period of 30 min. The mixture was stirred at 20–25°C for 3 h and then kept at this temperature for 12 h. To the resulting suspension of the Vilsmeier–Haack complex, a solution of 33 g of ketone **II** in 82.5 ml of dimethylformamide was added at 25–30°C over a period of 30 min. The mixture was stirred at 35–55°C for 67 h, after which 200 ml of water was added with cooling, and the mixture was allowed to stand at 20–25°C for a day. The crystalline precipitate of **XIV** was filtered off, washed with water, and vacuum-dried. Yield 24 g (60%), mp 57–59°C (from methanol). IR spectrum, ν, cm^{-1}: 2930, 2855, 1620, 1680, 1460, 1360, 875. ^1H NMR spectrum, δ, ppm: 1.8 br.s (6H, $3CH_2$); 1.9 br.s (6H, $3CH_2$); 2.1 br.s (3H, 3CH); 6.1 d, ^3J 6 Hz (1H, $C^{12}H$); 10.1 d (1H, $C^{13}H$).

Found, %: C 70.04, H 7.96, Cl 15.65. M^+ 224 (100%).
$C_{13}H_{17}ClO$.
Calculated, %: C 69.48, H 7.62, Cl 15.78. *M* 224.7.

3-(1-Adamantyl)-3-chloro-2-propenal oxime XV. A solution of 12 g of sodium acetate in 60 ml of water was added at room temperature with stirring to a mixture of 8 g of aldehyde **XIV** in 30 ml of ethanol and 10 g of hydroxylamine hydrochloride in 10 ml of water. The mixture was made homogeneous by adding 60 ml of ethanol and stirred for 10 h at 55–60°C. Then the mixture was diluted with water, and the precipitate of oxime **XV** was filtered off, washed with water, and vacuum-dried. Yield 6.5 g (76%), mp 158–160°C (from 2-propanol). IR spectrum, ν, cm^{-1}: 2925, 2850, 1640, 1610, 1320, 930, 850. ^1H NMR spectrum, δ, ppm: 1.8 br.s (6H, $3CH_2$); 1.9 br.s (6H, $3CH_2$); 2.1 br.s (3H, 3CH); 6.2 d, ^3J 6 Hz (1H, $C^{12}H$); 8.2 d (1H, $C^{13}H$).

Found, %: C 65.34, H 7.66, Cl 14.51, N 5.73. M^+ 239 (43%).
$C_{13}H_{18}ClN$.
Calculated, %: C 65.13, H 7.57, Cl 14.78, N 5.84. *M* 239.0.

3-Chloro-3-(1-adamantyl)-2-propenylamine hydrochloride XVI. A stream of dry HCl was passed for 2 h through an ether solution of 1.5 g of amine **XIII**. The precipitate of hydrochloride **XVI** was filtered off, washed with diethyl ether, and vacuum-dried. Yield 1.56 g (90%); mp 245°C. IR spectrum, ν, cm^{-1}: 2930, 2860, 1630, 1480, 1450, 1325, 980. ^1H NMR spectrum, δ, ppm: 1.7 br.s (6H, $3CH_2$); 1.8 br.s (6H, $3CH_2$); 2.1 br.s (3H, 3CH); 6.2 d, ^3J 6 Hz (1H, $C^{12}H$); 8.2 d (1H, $C^{13}H$).

Found, %: C 59.28, H 8.15, Cl 26.99, N 5.35. M^+ 262 (40%).
$C_{13}H_{21}Cl_2N$.
Calculated, %: C 59.54, H 8.07, Cl 27.04, N 5.34. *M* 262.2.

CONCLUSIONS

(1) Adamantane derivatives containing (1-adamantyl)trimethylammonium or [1-(1-adamantyl)ethyl]trimethylammonium cation in combination with an organic or inorganic acid anion were prepared.

(2) (1-Adamantyl)trimethylammonium isocamphanone-3-*exo*-sulfonate exhibits a high surface activity, and 3-(1-adamantyl)-3-chloro-2-propenylamine hydro-

chloride actively collects KCl in flotation concentration of sylvinite ores.

REFERENCES

1. Vasilenok, Yu.I., Konoplev, B.A., Lagunova, V.N., *et al.*, *Vestsi Akad. Navuk Bel. SSR, Ser. Khim. Navuk*, 1974, no. 1, pp. 42–45.
2. Yanovskaya, A.P., Shadskikh, G.S., Timoshenko, S.D., *et al.*, *Vestsi Akad. Navuk Bel. SSR, Ser. Khim. Navuk*, 1978, no. 5, pp. 55–58.
3. Swedish Patent 415679.
4. Germane, K.S., Polis, Ya.Yu., and Karine, L.Ya., *Khim.-Farm. Zh.*, 1977, no. 3, pp. 66–70.
5. Kovtun, Yu.Yu. and Plakhotnik, V.M., *Khim.-Farm. Zh.*, 1987, no. 3, pp. 931–940.
6. Mashkovskii, M.D., *Lekarstvennye sredstva* (Drugs), Moscow: Meditsina, 1993, vols. 1, 2.
7. US Patent 5157151.
8. Faingol'd, S.I., *Sinteticheskie moyushchie sredstva iz neftyanogo i slantsevogo syr'ya* (Synthetic Detergents from Petroleum and Shale Raw Materials), Leningrad: Nedra, 1964.
9. Vasilenok, Yu.I., Konoplev, B.A., Lagunova, V.N., *et al.*, *Vestsi Akad. Nauk Bel. SSR, Ser. Khim. Navuk*, 1975, no. 1, pp. 61–65.
10. RF Inventor's Certificate no. 1747462.
11. Korshuk, E.F., Potkina, T.N., Kozlov, N.G., *et al.*, *Vestsi Akad. Nauk Bel. SSR, Ser. Khim. Navuk*, 1989, no. 1, pp. 94–97.
12. Kozlov, N.G., Popova, L.A., Biba, V.I., *et al.*, *Zh. Obshch. Khim.*, 1988, vol. 58, no. 11, pp. 2593–2600.
13. Kozhich, D.T., Vasilevskii, V.I., Mironov, A.F., *et al.*, *Zh. Org. Khim.*, 1980, vol. 16, no. 4, pp. 849–855.
14. Kozlov, N.G., Korotyshova, G.P., and Zalesskaya, E.G., *Zh. Obshch. Khim.*, 1995, vol. 65, no. 8, pp. 1367–1369.
15. Ordubadi, M.D., Pekhk, T.I., and Belikova, N.A., *Zh. Org. Khim.*, 1984, vol. 20, no. 4, pp. 747–753.
16. *Poverkhnostnye yavleniya i poverkhnostno-aktivnye veshchestva: Spravochnik* (Surface Phenomena and Surfactants), Abramzon, A.A. and Shchukin, E.D., Eds., Leningrad: Khimiya, 1984.
17. *Analiz mineral'nogo syr'ya* (Analysis of Mineral Raw Materials), Knipovich, Yu.N. and Morachevskii, Yu.V., Eds., Leningrad: Goskhimizdat, 1956.

Russian Journal of Applied Chemistry, Vol. 74, No. 11, 2001, pp. 1899–1902. Translated from Zhurnal Prikladnoi Khimii, Vol. 74, No. 11, 2001, pp. 1839–1842.

ORGANIC SYNTHESIS AND INDUSTRIAL ORGANIC CHEMISTRY

Synthesis and Antioxidative Properties of New Sulfur-Containing Derivatives of Sterically Hindered Phenols

A. E. Prosenko, E. I. Terakh, N. V. Kandalintseva, P. I. Pinko, E. A. Gorokh, and G. A. Tolstikov

Novosibirsk State Pedagogical University, Novosibirsk, Russia
Vorozhtsov Institute of Organic Chemistry, Siberian Division, Russian Academy of Sciences, Novosibirsk, Russia

Received April 18, 2001

Abstract—3-(3,5-Di-*tert*-butyl-4-hydroxyphenyl)-1-chloropropane was converted into derivatives containing S(II) in various functional groups. The inhibiting power of the compounds with respect to thermal autooxidation of animal fat was evaluated.

Among inhibitors of free-radical oxidation of hydrocarbon substrates, a particular place is occupied by sulfur-containing derivatives of sterically hindered phenols, whose high antioxidative activity is due to the bifunctional mechanism of the antioxidative effect [1] and to internal synergism [2, 3]. Among such antioxidants is bis[3-(3,5-di-*tert*-butyl-4-hydroxyphenyl)-propyl] sulfide (SO-3), which shows a high performance as thermal stabilizer of polymer compounds based on polyethylene and polypropylene [4, 5]. As SO-3 is nontoxic, it can be used in production of household goods [6, 7]; also, the possibility was examined of its use as an antioxidant for fat-containing foodstuffs and fat-soluble drugs [8–10]. With the aim of searching for new high-performance inhibitors, we prepared in this work a series of structural analogs of SO-3 containing S(II) atoms in various functional groups and compared the antioxidative properties of these compounds with respect to thermal autooxidation of animal fat.

From 3-(3,5-di-*tert*-butyl-4-hydroxyphenyl)-1-chloropropane **I**, we prepared sulfur-containing derivatives **II**–**IX** by the following scheme:

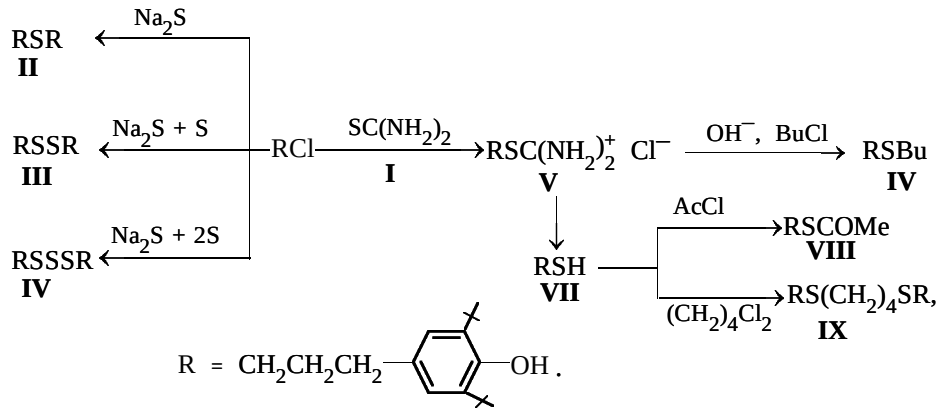

The compositions and structures of **II**–**IX** were proved by elemental analysis and spectroscopy.

The antioxidative properties of **II**–**IX** were studied with respect to thermal autooxidation of animal fat. The reference compound was 2,6-di-*tert*-butyl-4-methylphenol (Ionol), a commercial product used in food industry as an antioxidant for fat-containing foodstuffs [11]. As oxidation substrate we used lard; its oxidation was monitored by accumulation of hydroperoxides. The concentration of peroxides in a sample was

1070-4272/01/7411-1899$25.00

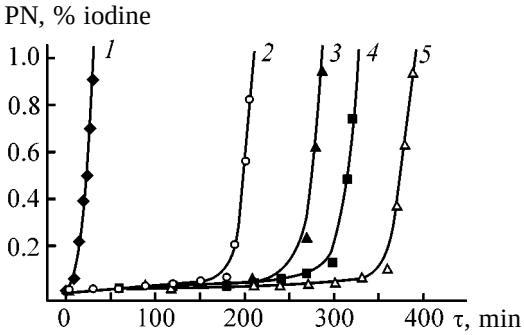

Fig. 1. Kinetic curves of lard oxidation in the presence of phenolic antioxidants. Antioxidant: (*1*) none, (*2*) Ionol, (*3*) **III**, (*4*) SO-3, and (*5*) **IX**. (PN) Peroxide number and (τ) time.

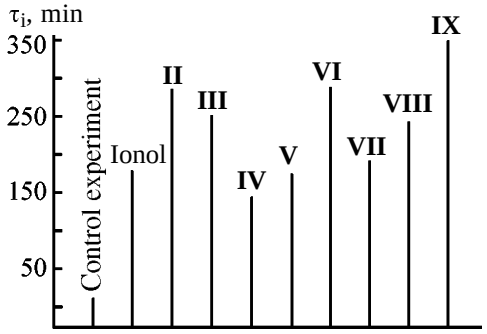

Fig. 2. Diagram of induction periods τ_i of lard oxidation inhibited with phenolic antioxidants (2.5 μmol g^{-1} fat, 130°C).

determined by Zinov'ev's version of the iodometric procedure [12]. The kinetic curves were plotted; they had similar shape for oxidation of the straight fat and the fat containing inhibitors (Fig. 1). The antioxidative activity (AOA) of inhibitors was judged from the duration of the induction period, defined as the time in which the peroxide number reaches 0.1 (the initial peroxide number was 0.003). The results are shown in Fig. 2.

Our results show that compounds **II**–**IX** exhibit pronounced AOA: the induction period of lard oxidation increases by a factor of 12–30. All the compounds except trisulfide **IV** and isothiuronium chloride **V** surpass Ionol in performance, which suggests their bifunctional activity. The AOA decreases in the order **II** (SO-3) > **III** > **IV**, which may be due to thermal oxidative cleavage of the S–S bonds with generation of thiyl radicals [13], which can participate not only in chain termination, but also in chain propagation [14]:

$$RSSR \rightarrow 2RS^{\bullet},$$

$$RS^{\bullet} + {}^{\bullet}OH \rightarrow RSOH,$$

$$RS^{\bullet} + XH \rightarrow RSH + X^{\bullet}.$$

Apparently, the possible formation of thiyl radicals is responsible for the relatively low inhibiting power of thiol **VII**:

$$RSH + {}^{\bullet}OH \rightarrow RS^{\bullet} + H_2O,$$

$$RSH + X^{\bullet} \rightarrow RS^{\bullet} + XH.$$

Among the new compounds, the most effective antioxidants are sulfide analogs of SO-3: unsymmetrical sulfide **VI** and bissulfide **IX**, with the latter appreciably surpassing SO-3 in the antioxidative effect under the experimental conditions. Our results show that compounds **II**, **III**, **VI**, **VIII**, and **IX** deserve further study as antioxidants for fat-containing foodstuffs.

EXPERIMENTAL

The ^1H NMR spectra were recorded with a Bruker spectrometer (500 MHz, external reference TMS). The IR spectra were taken with a Vektor-22 Fourier spectrometer (CCl_4 solutions or KBr pellets, 150 : 1). The melting points were determined with a PTP device.

Bis[3-(3,5-di-*tert*-butyl-4-hydroxyphenyl)propyl] sulfide **II** and bis[3-(3,5-di-*tert*-butyl-4-hydroxyphenyl)propyl disulfide **III** were prepared according to [15, 16].

Bis[3-(3,5-di-*tert*-butyl-4-hydroxyphenyl)propyl] trisulfide IV. A mixture of 3.51 g (45 mmol) of sodium sulfide, 2.88 g (90 mmol) of sulfur, and 80 ml of 2-propanol was refluxed for 2 h. After cooling to 50–60°C, 20 g (69 mmol) of **I** was added, and the mixture was refluxed for 4 h. The reaction mass was cooled and treated with toluene (80 ml). The extract was washed with water and dried over Na_2SO_4; the solvent was distilled off. The reaction product was purified by chromatography on silica gel, eluent hexane–diethyl ether (5 : 1). Yield of **IV** 17.3 g (84%); resinous yellow substance. ^1H NMR spectrum ($CDCl_3$), δ, ppm: 1.430 s (36H, *t*-Bu), 1.970–2.000 m (4H, $ArCH_2CH_2$), 2.612–2.642 t (4H, $ArCH_2$), 2.715–2.742 t (4H, CH_2S), 5.034 s (2H, OH), 6.971 s (4H, H_{arom}). IR spectrum (CCl_4), ν, cm^{-1}: 3640 (OH). UV spectrum (EtOH), λ_{max}, nm (log ε): 220 (4.20), 278 (3.57).

Found, %: C 69.11, H 9.13, S 17.44.
$C_{34}H_{54}O_2S_3$.
Calculated, %: C 69.09, H 9.21, S 16.27.

***S*-[3-(3,5-di-*tert*-butyl-4-hydroxyphenyl)propyl]-thiuronium chloride V.** A mixture of 4.24 g (15 mmol) of **I**, 0.95 g (12.5 mmol) of thiourea, and

30 ml of 1-butanol was refluxed for 5 h, after which the solvent was distilled off, and the product was washed with warm pentane, filtered off, and dried. Yield of **V** 4.13 g (92%); colorless crystalline substance, mp 165°C. ^{1}H NMR spectrum ($CDCl_3$), δ, ppm: 1.430 s (18H, *t*-Bu), 2.048 m (2H, $ArCH_2CH_2$), 2.726 t (2H, $ArCH_2$), 3.123 t (2H, CH_2S), 7.146 s (2H, H_{arom}). IR spectrum (KBr), ν, cm^{-1}: 3644 (OH), 3263 and 3062 (NH_2^+), 1650 (NH_2^+). UV spectrum (EtOH), λ_{max}, nm (log ε): 209 (1.84), 276 (0.16).

Found, %: C 59.89, H 8.92, Cl 9.74, N 7.52, S 8.71.
$C_{18}H_{31}ClN_2OS$.
Calculated, %: C 60.22, H 8.70, Cl 9.88, N 7.80, S 8.93.

Butyl 3-(3,5-di-*tert*-butyl-4-hydroxyphenyl)propyl sulfide VI. A mixture of 7 g (19.5 mmol) of isothiuronium chloride **V**, 1.72 g (43 mmol) of NaOH, 3.04 ml (29.3 mmol) of 1-chlorobutane, and 20 ml of ethanol was stirred for 1 h at 20°C under argon and then heated at 50–60°C for 2 h. The mixture was treated with toluene. The extract was washed with water and dried over Na_2SO_4, the solvent was distilled off, and the product was vacuum-distilled. Yield of **VI** 4.59 g (70%); bp 165°C (1 mm Hg). ^{1}H NMR spectrum ($CDCl_3$), δ, ppm: 0.892–0.921 t (3H, CH_2Me), 1.380–1.416 m (2H, CH_2Me), 1.430 s (18H, *t*-Bu), 1.532–1.591 m (2H, CH_2Et), 1.862–1.908 m (2H, $ArCH_2CH_2$), 2.498–2.524 t (2H, SCH_2Pr), 2.528–2.553 t (2H, CH_2SBu), 2.610–2.641 t (2H, $ArCH_2$), 5.030 s (1H, OH), 6.977 s (2H, H_{arom}). IR spectrum (CCl_4), ν, cm^{-1}: 3646 (OH). UV spectrum (EtOH), λ_{max}, nm (log ε): 208 (1.56), 277 (0.19).

Found, %: C 75.13, H 10.62, S 9.50.
$C_{21}H_{36}OS$.
Calculated, %: C 74.94, H 10.78, S 9.53.

3-(3,5-Di-*tert*-butyl-4-hydroxyphenyl)-1-propanethiol VII. A mixture of 30 g (106 mmol) of **I**, 9.7 g (127 mmol) of thiourea, and 100 ml of DMF was heated at 130°C for 2 h. After cooling to 50°C, a solution of 0.92 g (23 mmol) of NaOH in 3 ml of water was added, and the mixture was stirred for 2 h at 50°C, acidified with HCl, and treated with toluene. The extract was washed with water and dried over Na_2SO_4, the solvent was distilled off, and the reaction product was vacuum-distilled. Yield of **VII** 25.3 g (85%); mp 48, bp 138–145°C (1–2 mm Hg). ^{1}H NMR spectrum ($CDCl_3$), δ, ppm: 1.132 s (1H, SH), 1.430 s (18H, *t*-Bu), 1.912 m (2H, $ArCH_2CH_2$); 2.257–2.756 m (4H, $ArCH_2$, CH_2S), 4.852 s (1H, OH), 6.871 s (2H, H_{arom}). IR spectrum (KBr), ν, cm^{-1}: 3650 (OH). UV spectrum (EtOH), λ_{max}, nm (log ε): 207 (3.88), 278 (3.28).

Found, %: C 73.09, H 10.13, S 11.20.
$C_{17}H_{28}OS$.
Calculated, %: C 72.80, H 10.06, S 11.43.

***S*-[3-(3,5-Di-*tert*-butyl-4-hydroxyphenyl)propyl] ethanethioate VIII.** To a mixture of 5 g (17.8 mmol) of **I**, 5 ml (35.6 mmol) of triethylamine, and 20 ml of benzene, we added dropwise 1.3 ml (18.2 mmol) of acetyl chloride. The mixture was refluxed for 2 h, cooled, and treated with toluene. The extract was washed with water and dried over Na_2SO_4, the solvent was distilled off, and the reaction product was recrystallized from ethanol. Yield of **VIII** 5.12 g (89%), mp 57–58°C. ^{1}H NMR spectrum ($CDCl_3$), δ, ppm: 1.428–1.446 s (18H, *t*-Bu), 1.851–1.881 m (2H, $ArCH_2CH_2$), 2.328 s (3H, COMe), 2.580–2.611 t (2H, $ArCH_2$), 2.893–2.921 t (2H, CH_2S), 5.040 s (1H, OH), 6.952 s (2H, H_{arom}). IR spectrum (CCl_4), ν, cm^{-1}: 3647 (OH), 1695 (C=O). UV spectrum (EtOH), λ_{max}, nm (log ε): 206 (2.18), 229 (0.94), 221 (0.92), 277 (0.18).

Found, %: C 70.82, H 9.36, S 9.77.
$C_{19}H_{30}O_2S$.
Calculated, %: C 70.76, H 9.38, S 9.94.

1,4-Bis[3-(3,5-di-*tert*-butyl-4-hydroxyphenyl) propylthio]butane IX. A mixture of 5.05 g (18 mmol) od **I** and 1.3 g (19.7 mmol) of KOH was dissolved in 30 ml of ethanol, and 1.14 g (9 mmol) of 1,4-dichlorobutane was added. The mixture was refluxed for 2.5 h, cooled, and treated with toluene. The extract was washed with water and dried over Na_2SO_4, the solvent was distilled off, and the product was recrystallized from ethanol. Yield of **IX** 4.0 g (72%), mp 64–65°C. ^{1}H NMR spectrum ($CDCl_3$), δ, ppm: 1.430 s (36H, *t*-Bu), 1.691 m [4H, $SCH_2(CH_2)_2CH_2S$], 1.871 m (4H, $ArCH_2CH_2$), 2.526–2.556 m (8H, SCH_2), 2.603–2.635 t (4H, $ArCH_2$), 5.030 s (2H, OH), 6.970 s (4H, H_{arom}). IR spectrum (KBr), ν, cm^{-1}: 3643 (OH). UV spectrum (EtOH), λ_{max}, nm (log ε): 210 (1.84), 277 (0.36).

Found, %: C 74.47, H 10.31, S 10.65.
$C_{38}H_{62}O_2S_2$.
Calculated, %: C 74.21, H 10.16, S 10.43.

Oxidation of lard (50 g, Novosibirsk Meat Packing and Canning Plant) was performed at 130°C in an oxygen flow in an oxidation cell similar to that described in [17]. In the course of oxidation, 1-g sam-

ples were taken. The concentration of antioxidants (main substance content no less than 98–99%) was 2.5 μmol g^{-1} fat.

CONCLUSIONS

(1) The synthesized derivatives of 3-(3,5-di-*tert*-butyl-4-hydroxyphenyl)-1-chloropropane containing sulfur atoms in various functional groups (sulfide, disulfide, thiol, thio ester) are effective inhibitors of animal fat oxidation.

(2) Symmetrical and unsymmetrical 3-(3,5-di-*tert*-butyl-4-hydroxyphenyl)propyl sulfides considerably surpass in the antioxidative properties the commercial antioxidant Ionol used in food industry and deserve further study as promising antioxidants for fat-containing foodstuffs.

REFERENCES

1. Emanuel', N.M. and Lyasovskaya, Yu.N., *Tormozhenie protsessov okisleniya zhirov* (Inhibition of Fat Oxidation), Moscow: Pishchepromizdat, 1961.
2. Farsaliev, V.M., Fernando, W.S., and Scott, G., *Eur. Polym J.*, 1978, vol. 14, no. 10, pp. 785–788.
3. Scott, G. and Tusoff, M., *Eur. Polym. J.*, 1980, vol. 16, no. 6, pp. 497–501.
4. RF Patent 1 072 420.
5. RF Patent 1 007 405.
6. Sorokina, I.V., Lapik, A.S., Dolgikh, M.P., and Popova, L.P., *Izv. Sib. Otd. Akad. Nauk SSSR, Ser. Biol. Nauk*, 1987, no. 1, pp. 123–128.
7. Sheftel', V.O., *Vrednye veshchestva v plastmassakh: Spravochnoe izdanie* (Noxious Substances in Plastics: Handbook), Moscow: Khimiya, 1991.
8. Rezvukhin, A.I., Krysin, A.P., and Shalaurova, I.Yu., *Vopr. Med. Khim.*, 1995, vol. 41, no. 3, pp. 37–39.
9. Voevoda, T.V., Tolstikova, T.G., Sorokina, I.V., *et al.*, *Eksp. Klin. Farmakol.*, 2000, vol. 63, no. 4, pp. 57–60.
10. Orlova, T.N., Tolstikova, T.G., Sorokina, I.V., *et al.*, *Khim.-Farm. Zh.*, 2000, vol. 34, no. 9, pp. 9–11.
11. Shmulovich, V.G., *Vopr. Pitan.*, 1994, nos. 1–2, pp. 42–44.
12. Zinov'ev, A.A., *Khimiya zhirov* (Fat Chemistry), Moscow: Pishchepromizdat, 1952.
13. *Comprehensive Organic Chemistry. The Synthesis and Reactions of Organic Compounds*, Barton, D. and Ollis, W.D., Eds., vol. 3: *Sulphur Compounds*, Jones, D.N., Ed., Oxford: Pergamon, 1979. Translated under the title *Obshchaya organicheskaya khimiya*, Moscow: Khimiya, 1983, vol. 5, pp. 458–459.
14. Kadochnikova, G.D., Perevozkina, M.G., Ushkalova, V.N., and Moskvichev, Yu.A., in *Svobodnoradikal'noe okislenie lipidov v eksperimente i klinike* (Free-Radical Oxidation of Lipids: Experimental and Clinical Studies), Tyumen: Tyumen. Gos. Univ., 1997, part 2, pp. 113–119.
15. RF Patent 1 658 601.
16. RF Patent 1 642 708.
17. Shishkina, L.N., in *Issledovanie sinteticheskikh i prirodnykh antioksidantov in vivo i in vitro* (*In vivo* and *in vitro* Studies of Synthetic and Natural Antioxidants), Moscow: Nauka, 1992, pp. 26–30.

Russian Journal of Applied Chemistry, Vol. 74, No. 11, 2001, pp. 1903–1906. Translated from Zhurnal Prikladnoi Khimii, Vol. 74, No. 11, 2001, pp. 1843–1846.

ORGANIC SYNTHESIS AND INDUSTRIAL ORGANIC CHEMISTRY

Synthesis and Antioxidative Activity of Thio Esters Derived from ω-(3,5-Di-*tert*-butyl-4-hydroxyphenyl)alkanethiols

P. I. Pinko, E. I. Terakh, A. E. Prosenko, and I. A. Grigor'ev

Novosibirsk State Pedagogical University, Novosibirsk, Russia
Vorozhtsov Institute of Organic Chemistry, Siberian Division, Russian Academy of Sciences, Novosibirsk, Russia

Received July 11, 2001

Abstract—ω-(3,5-Di-*tert*-butyl-4-hydroxyphenyl)alkanethiols were converted into thio esters by reactions with aliphatic and aromatic carboxylic acid chlorides. The antioxidative activity of these compounds, evaluated with respect to thermal autooxidation of lard, was studied in relation to their structure.

Polyfunctional phenolic antioxidants (PPAOs) exhibiting simultaneously antiradical and antiperoxide activity and showing internal synergism are known as effective inhibitors of free-radical oxidation of organic and bioorganic substrates. For example, bis[3-(3,5-di-*tert*-butyl-4-hydroxyphenyl)propyl sulfide (SO-3 stabilizer) is used to stabilize polymer compounds based on polyethylene and polypropylene [1, 2] and also fat-containing foodstuffs [3–5]. Synthesis of related sulfur-, phosphorus-, and nitrogen-containing derivatives and screening of their antioxidative activity in relation to the structure is a promising line in searching for PPAOs of a new generation.

Thio esters derived from ω-(3,5-di-*tert*-butyl-4-hydroxyphenyl)alkanethiols show a high inhibiting activity with respect to polyethylene and acrylonitrile–butadiene–styrene copolymers [6, 7]. In this work we prepared thio esters derived from ω-(3,5-di-*tert*-butyl-4-hydroxyphenyl)alkanethiols **I** and studied how their antioxidative properties with respect to thermal oxidation of animal fat correlate with their structure.

Reactions of thiols **I** with aliphatic and aromatic carboxylic acid chlorides yielded the corresponding thio esters **II**:

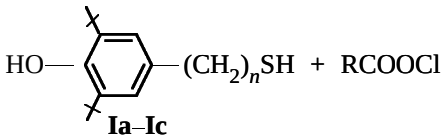

Ia–**Ic**

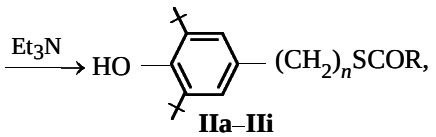

IIa–**IIi**

where n = 2 (**Ia**), 3 (**Ib**), 4 (**Ic**); n = 2, R = Me (**IIa**); n = 3, R = Me (**IIb**); n = 4, R = Me (**IIc**); n = 3, R = Bu (**IId**), C_5H_{11} (**IIe**), $C_{15}H_{31}$ (**IIf**),

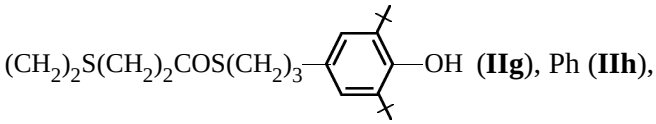

(**IIg**), Ph (**IIh**),

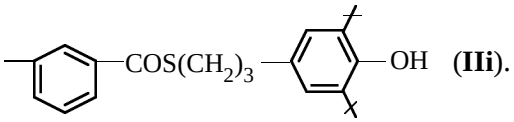

(**IIi**).

Syntheses were performed in benzene in the presence of triethylamine (to bind the released HCl) at approximately stoichiometric molar ratio of the reactants. The yields of the target thio esters were 75–89%. The composition and structure of the synthesized compounds were confirmed by elemental analysis and spectral characteristics.

Using thermal autooxidation of lard as model reaction, we studied the antioxidative activity (AOA) of **IIa**–**IIi** in relation to their structure and compared it with that of the known stabilizers: 2,6-di-*tert*-butyl-4-methylphenol (Ionol) and SO-3 stabilizer. The lard oxidation rate was monitored by accumulation of the primary oxidation products, hydroperoxides; the AOA was evaluated by the duration of the induction period τ, defined as the time in which the peroxide number of 0.1 is attained. The results are listed in the table.

Our results show that all the compounds studied exhibit a pronounced antioxidative activity and increase the induction period of lard oxidation by a factor of 5–8. Thio esters **IIa**–**IIi** surpass in AOA

1070-4272/01/7411-1903$25.00

Induction periods τ of lard oxidation inhibited by phenolic antioxidants ([PhOH] = 1 μmol g^{-1} fat, 130°C)

Antioxidant*	τ, min
$R(CH_2)_2SCOCH_3$ (**IIa**)	200
$R(CH_2)_3SCOCH_3$ (**IIb**)	253
$R(CH_2)_4SCOCH_3$ (**IIc**)	275
$R(CH_2)_3SCOC_4H_9$ (**IId**)	269
$R(CH_2)_3SCOC_5H_{11}$ (**IIe**)	264
$R(CH_2)_3SCOC_{15}H_{31}$ (**IIf**)	265
$R(CH_2)_3SCO(CH_2)_2S(CH_2)_2COS(CH_2)_3R$ (**IIg**)	265
$R(CH_2)_3SCOC_6H_5$ (**IIh**)	258
$R(CH_2)_3SCOC_6H_4COS(CH_2)_3R$ (**IIi**)	259
$R(CH_2)_3SH$ (**Ib**)	170
RCH_3 (Ionol)	169
$R(CH_2)_3S(CH_2)_3R$ (SO-3)	290
$RCH_3 + C_{12}H_{25}SCOCH_3$ (molar ratio 2 : 1)	184
$RCH_3 + C_{12}H_{25}SC_{12}H_{25}$ (molar ratio 2 : 1)	184
$C_{12}H_{25}SCOCH_3$	34
$C_{12}H_{25}SC_{12}H_{25}$	34

* R = 3,5-di-*tert*-butyl-4-hydroxyphenyl; in the control experiment (no antioxidant added), the induction period was 34 min.

Ionol and its synergistic mixture with dodecyl ethanethioate, which suggests the bifunctional mechanism of their antioxidative effect and internal synergism. We found that under the experimental conditions the AOA is significantly influenced by the length of the hydrocarbon chain between the phenol and thio ester moieties. For example, the inhibiting activity grows in the order **IIa** < **IIb** < **IIc**, as the distance between the sulfur atom and phenol ring increases. The substituent at the carbonyl carbon atom affects AOA to a lesser extent: the inhibiting activity of aliphatic and aromatic thio esters **IIb** and **IId**–**IIi** is similar.

The synergistic mixtures of Ionol with dodecyl sulfide and dodecyl ethanethioate showed a similar inhibiting activity, whereas SO-3 surpassed in the inhibiting effect its thio ester analogs, including thiodipropionic acid derivative **IIg**. The latter fact suggests that the internal synergism is the decisive factor responsible for the high performance of sulfur-containing derivatives of the ω-(3,5-di-*tert*-butyl-4-hydroxyphenyl)alkyl series; the extent of internal synergism depends on the nature of the sulfur-containing fragment and its localization in the *p*-alkyl substituent. In SO-3 the internal synergism is more pronounced than in the corresponding thio esters. The sulfide fragment in thiodipropionic acid derivative **IIg** is remote from the phenol ring; it is not involved in synergistic interactions and therefore does not affect the antioxidative activity.

Among the tested sulfur-containing derivatives of sterically hindered phenols, thiol **Ib** shows the lowest AOA. The weak inhibiting activity of this compound is probably due to the possibility of formation of thiyl radicals $RS^{\bullet}$, which can particilate in both chain termination and chain propagation [8]:

$$RSH + {}^{\bullet}OH \rightarrow RS^{\bullet} + H_2O,$$

$$RSH + R'^{\bullet} \rightarrow RS^{\bullet} + R'H,$$

$$RS^{\bullet} + {}^{\bullet}OH \rightarrow RSOH,$$

$$RS^{\bullet} + XH \rightarrow RSH + X^{\bullet}.$$

On the whole, thio esters **IIa**–**IIi** can be regarded as effective polyfunctional antioxidants.

EXPERIMENTAL

The ^1H NMR spectra were recorded on a Bruker spectrometer (500 MHz, $CDCl_3$, internal reference TMS). The IR spectra were taken on a Vektor 22 Fourier spectrometer from neat samples, CCl_4 solutions, or KBr pellets (150 : 1). The melting points were determined with a PTP device.

The initial thiols **I** were prepared according to [9].

***S*-[2-(3,5-Di-*tert*-butyl-4-hydroxyphenyl)ethyl] ethanethioate IIa**. To a mixture of 5.0 g (18.7 mmol) of thiol **Ia**, 5 ml (25.6 mmol) of triethylamine, and 20 ml of benzene, we added dropwise 1.35 ml (18.9 mmol) of acetyl chloride. The mixture was refluxed for 2 h, cooled, and treated with toluene. The extract was washed with water and dried over Na_2SO_4, the solvent was distilled off, and the residue was crystallized from ethanol. Yield of **IIa** 4.68 g (81%), mp 108°C. ^1H NMR spectrum, δ, ppm: 1.430 s (18H, *t*-Bu), 2.334 s (3H, $COCH_3$), 2.755–2.796 t (2H, $ArCH_2$), 3.070–3.150 t (2H, CH_2S), 5.098 s (1H, OH), 7.000 s (2H, H_{arom}). IR spectrum (KBr), ν_{max}, cm^{-1}: 3587 (OH), 1678 (C=O). UV spectrum [EtOH, λ_{max}, nm (log ε)]: 207 (2.24), 230 (1.10), 276 (0.19).

Found, %: C 70.34, H 9.27, S 10.61.
$C_{18}H_{28}O_2S$.
Calculated, %: C 70.08, H 9.15, S 10.39.

Thio esters **IIb**–**IIi** were prepared similarly.

***S*-[3-(3,5-Di-*tert*-butyl-4-hydroxyphenyl)propyl] ethanethioate IIb.** Yield 89%, mp 57–58°C. ^1H NMR spectrum, δ, ppm: 1.428–1.446 s (18H, *t*-Bu),

1.851–1.881 m (2H, $ArCH_2CH_2$), 2.328 s (3H, $COCH_3$), 2.580–2.611 t (2H, $ArCH_2$), 2.893–2.921 t (2H, CH_2S), 5.040 s (1H, OH), 6.952 s (2H, H_{arom}). IR spectrum (CCl_4), ν_{max}, cm^{-1}: 3647 (PhOH), 1695 (C=O). UV spectrum [EtOH, λ_{max}, nm ($\log\varepsilon$)]: 206 (2.18), 229 (0.94), 221 (0.92), 277 (0.18).

Found, %: C 70.82, H 9.36, S 9.77.
$C_{19}H_{30}O_2S$.
Calculated, %: C 70.76, H 9.38, S 9.94.

***S*-[4-(3,5-Di-*tert*-butyl-4-hydroxyphenyl)butyl] ethanethioate IIc.** Yield 78%, mp 65–66°C. ^1H NMR spectrum, δ, ppm: 1.431 s (18H, *t*-Bu), 1.638–1.652 m (4H, $ArCH_2CH_2CH_2$), 2.317 s (3H, $COCH_3$), 2.526 t (2H, $ArCH_2$), 2.903 t (2H, CH_2S), 5.020 s (1H, OH), 6.952 s (2H, H_{arom}). IR spectrum (KBr), ν_{max}, cm^{-1}: 3581 (OH), 1681 (C=O). UV spectrum [EtOH, λ_{max}, nm ($\log\varepsilon$)]: 206 (2.02), 228 (0.90), 277 (0.16).

Found, %: C 71.57, H 9.73, S 9.79.
$C_{20}H_{32}O_2S$.
Calculated, %: C 71.38, H 9.58, S 9.52.

***S*-[3-(3,5-Di-*tert*-butyl-4-hydroxyphenyl)propyl] pentanethioate IId.** Yield 75%, bp 190–192°C (1–2 mm Hg). ^1H NMR spectrum, δ, ppm: 0.894–0.923 t [3H, $(CH_2)_3CH_3$], 1.331–1.376 m (2H, $CH_2 \cdot CH_3$), 1.428 s (18H, *t*-Bu), 1.633–1.664 m (2H, $CH_2C_2H_5$), 1.835–1.896 m (2H, $ArCH_2CH_2$), 2.532–2.562 t (2H, $COCH_2$), 2.580–2.611 t (2H, $ArCH_2$), 2.889–2.918 t (2H, CH_2S), 5.052 s (1H, OH), 6.955 s (2H, H_{arom}). IR spectrum, ν_{max}, cm^{-1}: 3644 (OH), 1690 (C=O). UV spectrum [EtOH, λ_{max}, nm ($\log\varepsilon$)]: 206 (2.02), 221 (0.88), 229 (0.90), 277 (0.19).

Found, %: C 72.61, H 10.07, S 9.01.
$C_{22}H_{36}O_2S$.
Calculated, %: C 72.48, H 9.95, S 8.79.

***S*-[3-(3,5-Di-*tert*-butyl-4-hydroxyphenyl)propyl] hexanethioate IIe.** Yield 68%, bp 200–201°C (1–2 mm Hg). ^1H NMR spectrum, δ, ppm: 0.876–0.902 t (3H, $(CH_2)_4CH_3$), 1.297–1.323 m (4H, $CH_2CH_2CH_2$), 1.428 s (18H, *t*-Bu), 1.668 m (2H, $CH_2C_3H_7$), 1.867–1.882 m (2H, $ArCH_2CH_2$), 2.523–2.553 t (2H, $COCH_2$), 2.582–2.613 t (2H, $ArCH_2$), 2.889–2.918 t (2H, CH_2S), 5.055 s (1H, OH), 6.957 s (2H, H_{arom}). IR spectrum, ν_{max}, cm^{-1}: 3645 (OH), 1691 (C=O). UV spectrum [EtOH, λ_{max}, nm ($\log\varepsilon$)]: 208 (2.33), 221 (1.46), 229 (1.49), 277 (0.29).

Found, %: C 73.14, H 10.27, S 8.66.
$C_{23}H_{38}O_2S$.
Calculated, %: C 72.96, H 10.12, S 8.47.

***S*-[3-(3,5-Di-*tert*-butyl-4-hydroxyphenyl)propyl] hexadecanethioate IIf.** Yield 82%, mp 50–51°C. ^1H NMR spectrum, δ, ppm: 0.865–0.892 t (3H, $[(CH_2)_{14} \cdot CH_3]$), 1.257–1.299 s (24H, $[CH_2)_{12}CH_3]$), 1.428 s (18H, *t*-Bu), 1.660 m (2H, $CH_2C_{13}H_{27}$), 1.862 m (2H, $ArCH_2CH_2$), 2.527–2.557 t (2H, $COCH_2$), 2.578–2.610 t (2H, $ArCH_2$), 2.889–2.918 t (2H, CH_2S), 5.033 s (1H, OH), 6.952 s (2H, H_{arom}). IR spectrum (KBr), ν_{max}, cm^{-1}: 3642 (OH), 1691 (C=O). UV spectrum [EtOH, λ_{max}, nm ($\log\varepsilon$)]: 206 (2.14), 221 (0.91), 229 (0.94), 277 (0.18).

Found, %: C 76.45, H 11.39, S 6.33.
$C_{33}H_{58}O_2S$.
Calculated, %: C 76.38, H 11.26, S 6.18.

Bis-*S*-[3-(3,5-di-*tert*-butyl-4-hydroxyphenyl)-propyl] β,β′-thiodipropanethioate IIg was prepared as described in [6].

***S*-[3-(3,5-Di-*tert*-butyl-4-hydroxyphenyl)propyl] benzothioate IIh.** Yield 78%, mp 64–65°C. ^1H NMR spectrum, δ, ppm: 1.434 s (18H, *t*-Bu), 1.980–1.995 m (2H, $ArCH_2CH_2$), 2.658–2.689 t (2H, $ArCH_2$), 3.104–3.133 t (2H, CH_2S), 5.053 s (1H, OH), 6.990 s (2H, H_{arom}), 7.424–7.455 t (2H, *m*-H in C_6H_5), 7.554 t (1H, *p*-H in C_6H_5), 7.970–7.989 d (2H, *o*-H in C_6H_5). IR spectrum (KBr), ν_{max}, cm^{-1}: 3593 (OH), 1655 (C=O). UV spectrum [EtOH, λ_{max}, nm ($\log\varepsilon$)]: 208 (2.43), 233 (1.38), 273 (0.93).

Found, %: C 75.12, H 8.51, S 8.54.
$C_{24}H_{32}O_2S$.
Calculated, %: C 74.95, H 8.39, S 8.34.

Bis-*S*-[3-(3,5-di-*tert*-butyl-4-hydroxyphenyl)-propyl] *m*-phthalthioate IIi. Yield 78%, mp 78–80°C. ^1H NMR spectrum, δ, ppm: 1.433 s (36H, *t*-Bu), 1.976–2.006 m (4H, $ArCH_2CH_2$), 2.660–2.691 t (4H, $ArCH_2$), 3.130–3.159 t (4H, CH_2S), 5.045 s (2H, OH), 6.985 s (4H, H_{arom}), 7.544 t (1H, C_6H_4), 8.140–8.159 d (2H, C_6H_4), 8.561 s (1H, C_6H_4). IR spectrum (KBr), ν_{max}, cm^{-1}: 3640 (OH), 1651 (C=O). UV spectrum [EtOH, λ_{max}, nm ($\log\varepsilon$)]: 205 (2.84), 220 (1.97), 275 (0.69).

Found, %: C 73.15, H 8.57, S 9.47.
$C_{42}H_{58}O_4S_2$.
Calculated, %: C 72.99, H 8.46, S 9.28.

Oxidation of lard (Novosibirsk Meat Packing and Canning Plant) was performed in an oxidation cell described in [10], by oxygen bubbling at 130°C. The amount of lard in each experiment was 50 g, and the

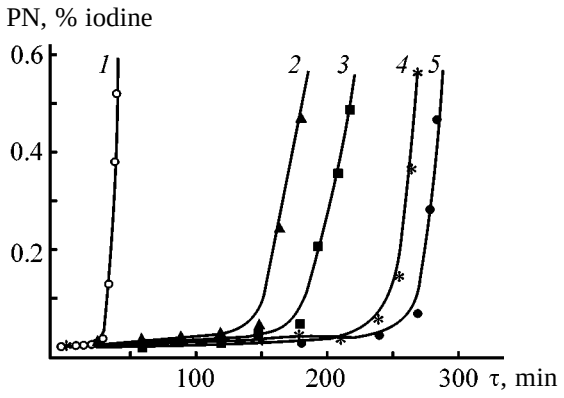

Kinetic curves of lard oxidation in the presence of inhibitors. Inhibitor: (*1*) none, (*2*) Ionol, (*3*) **IIa**, (*4*) **IIb**, and (*5*) **IIc**. (PN) Peroxide number and (τ) time.

concentration of antioxidants, 1 μmol g^{-1} fat. The progress of lard oxidation was monitored by accumulation of peroxy compounds. Their concentration was determined iodometrically [11] and expressed in peroxide numbers. The initial peroxide number was 0.002% I. The kinetic curves were plotted (see figure), and the induction periods were determined graphically.

CONCLUSIONS

(1) Thio esters derived from ω-(3,5-di-*tert*-butyl-4-hydroxyphenyl)alkanethiols show high inhibiting activity due to the bifunctional mechanism of the antioxidative effect and to internal synergism.

(2) Under the experimental conditions, the antioxidative activity of thio esters is largely influenced by the length of the hydrocarbon chain between the phenolic and thio ester moieties; substituents at the carbonyl carbon atoms affect the antioxidative activity to a lesser extent.

(3) Thio esters derived from ω-(3,5-di-*tert*-butyl-4-hydroxyphenyl)alkanethiols show promise as antioxidants preventing oxidation of fats.

REFERENCES

1. RF Patent 1072420.
2. RF Patent 1007405.
3. Rezvukhin, A.I., Krysin, A.P., and Shalaurova, I.Yu., *Vopr. Med. Khim.*, 1995, no. 3, p. 37.
4. Voevoda, T.V., Tolstikova, T.G., Sorokina, I.V., *et al.*, *Eksp. Klin. Farmakol.*, 2000, vol. 63, no. 4, pp. 57–60.
5. Orlova, T.N., Tolstikova, T.G., Sorokina, I.V., *et al.*, *Khim.-Farm. Zh.*, 2000, vol. 34, no. 9, pp. 9–11.
6. USSR Inventor's Certificate no. 1131869.
7. USSR Inventor's Certificate no. 1118654.
8. Kadochnikova, G.D., Perevozkina, M.G., Ushkalova, V.N., and Moskvichev, Yu.A., in *Svobodnoradikal'noe okislenie lipidov v eksperimente i klinike* (Experimental and Clinical Study of Free-Radical Oxidation of Lipids), Tyumen: Tyumen. Gos. Univ., 1997, part 2, pp. 113–119.
9. USSR Inventor's Certificate no. 1074865.
10. Shishkina, L.N., in *Issledovanie sinteticheskikh i prirodnykh antioksidantov in vivo i in vitro* (*In vivo* and *in vitro* Study of Synthetic and Natural Antioxidants), Moscow: Nauka, 1992, pp. 26–30.
11. Zinov'ev, A.A., *Khimiya zhirov* (Fat Chemistry), Moscow: Pishchepromizdat, 1952.

Russian Journal of Applied Chemistry, Vol. 74, No. 11, 2001, pp. 1907–1909. Translated from Zhurnal Prikladnoi Khimii, Vol. 74, No. 11, 2001, pp. 1847–1849.

ORGANIC SYNTHESIS AND INDUSTRIAL ORGANIC CHEMISTRY

New Monomer Derived from Monoethanolamine Vinyl Ether and 2,3-Dichloro-5,6-dicyano-1,4-benzoquinone, and Redox Resin Thereof

E. E. Ergozhin, B. A. Mukhitdinova, S. A. Shoinbekova, and A. I. Nikitina

Bekturov Institute of Chemical Sciences, Ministry of Education and Science of the Kazakhstan Republic, Almaty, Kazakhstan

Received April 25, 2001

Abstract—A procedure was developed for synthesis of a new monomer from monoethanolamine vinyl ether and 2,3-dichloro-5,6-dicyano-1,4-benzoquinone. The kinetics of its radical polymerization was studied polarographically. The optimal polymerization conditions and properties of the resulting redox resin were studied.

It is known that quinones are capable of reversible reduction–oxidation [1]. Their use in synthesis of macromolecular compounds allows preparation of resins exhibiting redox properties, which are widely used in various branches of science and engineering as reductants, oxidants, enterosorbents, hemosorbents, etc. [2–5]. However, available redox resins do not always exhibit the necessary properties; therefore, search for new available and cheap monomers and development of selective ion-exchange and redox resins thereof remains an urgent problem.

To extend the range of redox resins and simplify their preparation, we have developed a single-stage procedure for synthesis of a new unsaturated monomer exhibiting redox properties. The starting compound, monoethanolamine vinyl ether **I**, is readily available and cheap; therefore, the cost of the resulting redox polymers can be reduced. Furthermore, the possibility of repeatedly using and regenerating the redox resins will help to pay off them faster.

Previously reported procedures for preparing the required monomers include 5–7 stages, with the yields of the target compounds being relatively low [2, 3].

In this work we prepared a new monomer from ether **I** and 2,3-dichloro-5,6-dicyano-1,4-benzoquinone **II**. The kinetics of its radical polymerization was studied polarographically, the optimal polymerization conditions were determined, and some properties of the resulting redox resin were studied.

EXPERIMENTAL

Monoethanolamine vinyl ether was dried over freshly calcined K_2CO_3 and distilled from calcium hydride; bp 114°C, n_D^{20} 1.4382. 2,3-Dichloro-5,6-dicyano-1,4-benzoquinone (Aldrich) was used without preliminary purification; mp 213–216°C. Azobis(isobutyronitrile) **III** was recrystallized from absolute methanol, mp 102–103°C. The solvents were purified by known procedures [6].

2-(2-Vinyloxy)ethyl]amino-3-chloro-5,6-dicyano-1,4-benzoquinone IV. Amine **I** was added slowly with continuous stirring to a solution of quinone **II** in 3 ml of dimethylformamide (DMF) at room temperature, until the molar ratio of amine to quinone of 4 : 1 was reached. After 15 min, distilled water was added. The precipitate was filtered off, repeatedly washed with water, and dried, first in air and then in a vacuum oven at 25°C to constant weight. Compound **IV** was obtained in 90% yield; bright cherry-colored powder, mp 136°C.

Found, %: C 52.25, H 2.93, Cl 12.33, N 14.80. $C_{12}H_8ClN_3O_3$.
Calculated, %: C 51.90, H 2.91, Cl 12.77, N 15.13.

Polymer V. The monomer was placed in an ampule, and the solvent (DMF, to a concentration C 0–250 g l^{-1}) and initiator (**III**, 1–8 wt % relative to **IV**) were added. The ampule was sealed, thoroughly shaken, and placed in a thermostat preheated to 55–72°C. After reaction completion, the ampule was opened, and polymer **V** was precipitated with diethyl ether. The precipitate was filtered off and dried, first in air at 20–25°C and then in a vacuum at 40–50°C. Yield of the polymer 45–62%. Under the optimal conditions (DMF, 4 wt % **III**, 360 min), the yield of the polymer is 62%, $[\eta] = 0.25$.

Kinetic runs were performed similarly except that

1070-4272/01/7411-1907$25.00

a set of ampules was prepared, and after prescribed periods the ampules were successively withdrawn, quickly cooled with water and ice, and opened; samples for polarographic analysis were taken and diluted with ethanol to stop the reaction.

Polarographic measurements were performed in the following supporting electrolytes: phosphate buffer solution (pH 7.4) in 50% ethanol (reduction of C=O groups) and 0.2 M LiCl solution in 50% ethanol (reduction of the C=C bond).

The polarograms were taken in a temperature-controlled cell at 25±0.5°C with a PU-1 polarograph, using a mercury dropping electrode with the open-circuit characteristic of the capillary $m^{2/3}t^{1/6}$ = 4.38 $min^{2/3}\,s^{-1/2}$ and a saturated calomel reference electrode. Prior to polarographic measurements, the solutions were deoxygenated by argon bubbling for 5 min.

The IR spectra were recorded on a Specord M-80 spectrometer using KBr pellets. The ^1H NMR spectra were taken on a Varian Mercury-300 spectrometer (300 MHz, $CDCl_3$, internal reference HMDS), and the mass spectra, and a Hewlett–Packard HPGC-5890 device equipped with an HP MSD 5972 mass-selective detector.

The melting points were determined with a PTP unit.

The structure of **IV** was proved by mass spectrometry and IR and ^1H NMR spectroscopy.

Found M^+ 277 (by mass spectrometry).
$C_{12}H_8ClN_3O_3$.
Calculated M 277.

The IR spectrum of **IV** contains bands characteristic of C=O groups in quinones (about 1660 cm^{-1}), stretching (3228 cm^{-1}) and bending (1576 cm^{-1}) vibration bands of amino groups, and also =C–N (1340 cm^{-1}), =C–O–C (1196 cm^{-1}), C–Cl (756 cm^{-1}), and C≡N (2216 cm^{-1}) absorption bands.

In the ^1H NMR spectrum of **IV**, the signals of vinyl protons (*gem*, *cis*, and *trans*; δ 3.86, 4.18, and 6.48 ppm in $CDCl_3$) are essentially similar to those in the spectrum of **I**. The same is true for the CH_2O protons (δ 3.96 ppm). The signals of the NH_2 protons which are in direct contact with the electron-withdrawing substituent in quinone **II** are shifted downfield (δ 1.47 and 2.19 ppm), and the proton signals of the methylene group adjacent to NH_2, upfield (δ 2.94 and 2.20 ppm).

One of sensitive, quick, adequate, and reliable methods for studying and analyzing macromolecular compounds is polarography. This method is often used in kinetic studies of vinyl polymerizations [7–10]. The main criterion of the monomer reactivity is the polymerization rate constant; however, it was determined polarographically only in a few papers [10–15]. In some studies, a correlation was revealed between the rate constants of radical polymerization of monomers and their half-wave reduction potentials on a mercury dropping electrode [10]. We studied polarographically the polymerization kinetics of **IV**. The conversion was judged from the amount of unchanged monomer **IV**. We found that the height of the polarographic wave is a linear function of the concentration of **IV** in solution. The monomer content was determined from the calibration plot.

To calculate the overall polymerization rate constants, we determined the reaction order. The linear dependence of $\log c_{\mathbf{IV}}$ on the reaction time shows that under these conditions the reaction is first-order with respect to **IV**.

The rate constants of polymerization of **IV** calculated by the first-order kinetic equation [16, 17] are given below:

$k \times 10^4$, min^{-1}	T, K
12.70	335
18.74	341
24.34	345

The activation energy E_a is 47.34 kJ mol^{-1}.

In contrast to ether **I** which does not form homopolymers in the presence of radical initiators [18–20], monomer **IV** is capable of polymerization. Its activity is close to that of *N*-substituted methacrylamides [10]. The decisive factor affecting the homopolymerization rate is, apparently, the reactivity of the arising radical. The higher the electron density on the double bond, the higher the reactivity of the monomer [10]. Polarographic characterisrtics are also determined by the electron density on the double bond: The higher the density, the more negative is the half-wave reduction potential. That is, the more negative the reduction potential, the more readily the monomer polymerizes. This relationship is confirmed by our polarographic data: The half-wave reduction potential of the C=C bond is –1.80 V in the initial ether **I** and –1.85 V in **IV** (supporting electrolyte 0.2 M LiCl in 50% ethanol).

In the IR spectrum of **V**, the quinoid ring bands are broadened, which is typical of polymeric quinones

[21], and shifted to higher frequencies (1680 cm^{-1}, compared to 1660 cm^{-1} in **IV**).

The polymers show a high oxidative power, as evaluated by the yield of naphthalene in dehydrogenation of tetralin. The redox capacity of the samples, determined by potentiometric titration with 0.1 N $Fe_2(SO_4)_3$, is 2.6–4.8 mg-equiv g^{-1}.

CONCLUSIONS

(1) A single-stage procedure was developed for preparing a new redox monomer, 2-[2-(vinyloxy)ethyl]amino-3-chloro-5,6-dicyano-1,4-benzoquinone, from monoethanolamine vinyl ether and 2,3-dichloro-5,6-dicyano-1,4-benzoquinone. The monomer is fairly reactive in radical homopolymerization, with the polymer preserving the redox function.

(2) Radical polymerization of the synthesized monomer in solution was studied, and optimal conditions for preparing the polymeric redox resin were determined. The polymer shows a high oxidative power with respect to organic compounds and can be used as a dehydrogenating agent.

REFERENCES

1. Neiland, V.Ya., *Organicheskaya khimiya* (Organic Chemistry), Moscow: Vysshaya Shkola, 1988.
2. Cassidy, H.G. and Kun, K.A., *Oxidation–Reduction Polymers (Redox Polymers)*, Interscience, 1965.
3. Ergozhin, E.E. and Mukhitdinova, B.A., *Redoksionity* (Redox Ion Exchangers), Alma-Ata: Nauka, 1983.
4. Ergozhin, E.E., Mukhitdinova, B.A., Bakirova, R.Kh., *et al.*, *React. Polym.*, 1991/1992, vol. 16, no. 2, pp. 321–334.
5. Ergozhin, E.E. and Mukhitdinova, B.A., *Okislitel'no-vosstanovitel'nye ionoobmenniki* (Redox Ion Exchangers), Almaty: Redaktsionno-Izd. Otdel, Vysshaya Attestatsionnaya Komissiya Resp. Kazakhstan, 2000.
6. *Organic Solvents. Physical Properties and Methods of Purification*, Weissberger, A., Proskauer, E.S., Riddick, J.A., and Toops, E.E., Eds., New York: Interscience, 1955.
7. Mairanovskii, S.G., Stradyn', Ya.P., and Bezuglyi, V.D., *Polyarografiya v organicheskoi khimii* (Polarography in Organic Chemistry), Leningrad: Khimiya, 1975.
8. Heyrovsky, J. and Kuta, J., *Zaklady polarografie*, Prague: Ceskoslov. Acad. Ved, 1962.
9. Lingane, I., *Ind. Eng. Chem. An. ED*, 1943, vol. 15, no. 4, pp. 583–586.
10. Bezuglyi, V.D., *Polyarografiya v khimii i tekhnologii polimerov* (Polarogaphy in Polymer Chemistry and Technology), Moscow: Khimiya, 1968.
11. Bezuglyi, V.D. and Dmitrieva, V.N., *Zh. Prikl. Khim.*, 1957, vol. 30, no. 5, pp. 744–750.
12. Bobrova, M.I. and Matveeva, A.N., *Zh. Obshch. Khim.*, 1956, vol. 26, no. 7, pp. 1857–1860.
13. Alekseeva, A.T., Bezuglyi, V.D., Dmitrieva, V.N., and Zubkova, V.S., *Vysokomol. Soedin.*, 1963, vol. 5, no. 9, pp. 1382–1387.
14. Bezuglyi, V.D. and Alekseeva, T.A., *Vysokomol. Soedin., Ser. A*, 1967, vol. 9, no. 5, pp. 1185–1189.
15. Shur, A.M., Filimonov, B.F., and Filimonova, M.M., *Vysokomol. Soedin.*, 1961, vol. 3, no. 11, pp. 1661–1663.
16. Panchenkov, G.M. and Lebedev, V.P., *Khimicheskaya kinetika i kataliz* (Chemical Kinetics and Catalysis), Moscow: Mosk. Gos. Univ., 1961.
17. Emanuel', N.M. and Knorre, D.G., *Kurs khimicheskoi kinetiki* (Course of Chemical Kinetics), Moscow: Khimiya, 1974.
18. Shostakovskii, M.F. and Chekulaeva, I.A., *Izv. Akad. Nauk SSSR, Otd. Khim. Nauk*, 1953, no. 2, pp. 368–373.
19. Nurkeeva, Z.S. and Seitov, A.Z., in *Radiatsionnye effekty v geterogennykh sistemakh* (Radiation Effects in Heterogeneous Systems), Alma-Ata: Kaz. Gos. Univ., 1983, pp. 63–68.
20. Ergozhin, E.E., Nurkeeva, Z.S., Seitov, A.Z., and Shaikhutdinov, E.M., *Novoe o polimerakh i ikh primenenii* (New Data on Polymers and Their Use), Alma-Ata: Mektep, 1988.
21. Bellamy, L.J., *The Infra-Red Spectra of Complex Molecules*, New York: Wiley, 1957.

Russian Journal of Applied Chemistry, Vol. 74, No. 11, 2001, pp. 1910–1912. Translated from Zhurnal Prikladnoi Khimii, Vol. 74, No. 11, 2001, pp. 1850–1852.

ORGANIC SYNTHESIS AND INDUSTRIAL ORGANIC CHEMISTRY

Kinetic Features of the Synthesis of an Acid Corrosion Inhibitor, 5-Methyl-1,2,3,3a,4,8b-hexahydrocyclopent[*b*]indole

R. R. Gataullin, E. V. Khaziev, R. N. Khusnutdinov, I. M. Borisov, and I. B. Abdrakhmanov

Institute of Organic Chemistry, Ufa Scientific Center, Russian Academy of Sciences, Ufa, Bashkortostan, Russia
Bashkir State University, Ufa, Bashkortostan, Russia
Bashkir State Agricultural University, Ufa, Bashkortostan, Russia

Received April 16, 2001

Abstract—Kinetic features of thermal cyclization of 2-methyl-6-(cyclopent-2-enyl)aniline hydrochloride at 200–220°C were studied. The cyclization product shows a high performance as acid corrosion inhibitor.

Indoline compounds inhibit oxidation processes and acid corrosion [1, 2]; the highest performance is shown by 2-alkyl- and 2,2-dialkyl-substituted indolines [3]. With the aim of searching for new effective acid corrosion inhibitors, we studied in [4] formation of perhydrocyclopent[*b*]indolines by heterocyclization of hydrochlorides of *o*-(cyclopent-2-enyl)anilines [5] and their *N*-precursors which can be readily prepared from commercially available dicyclopentadiene. Heterocycles of this series, which are potential inhibitors of acid corrosion, are well known, but the kinetic features of their synthesis and the effect of reaction conditions on the product yield are studied insufficiently. In this work we studied some kinetic features of cyclization of 2-methyl-6-(cyclopent-2-enyl)aniline hydrochloride **I** (MCPA) and the inhibiting activity of the reaction product, 5-methyl-1,2,3,3a,4,8b-hexahydrocyclopent[*b*]indole **II**.

EXPERIMENTAL

Tests for protection of structural steels with inhibitor **II** were performed under laboratory conditions in 15% HCl and 20% H_2SO_4. Samples of St.3 steel [GOST (State Standard) 380–87], pretreated for corrosion tests, were placed in a corrosive medium for a prescribed time τ at 20°C. After that, the samples were worked up by an appropriate procedure and weighed with an accuracy of 0.0002 g. The corrosion rate ρ and degree z (%) of metal corrosion protection with the given inhibitor were determined by the formulas

$$\rho = (\Delta m)/S\tau,$$

$$z = (\rho_1 - \rho_2)/\rho_1 \times 100,$$

where Δm is the weight loss (g), S is the sample surface area (m^2), τ is the test time (h), ρ_1 is the corrosion rate without inhibitor (g m^{-2} h^{-1}), and ρ_2 is the corrosion rate in the presence of inhibitor (g m^{-2} h^{-1}).

The kinetic features of intramolecular cyclization of aniline **I** to indoline **II** were studied by the one experiment–one point procedure. The mixture was heated in sealed ampules in a thermostat at a definite temperature for a definite time. The concentrations of reaction products were determined by gas chromatography.

Data on the inhibiting activity of **II** are listed in Table 1. Thus, compound **II** can be regarded as a new inhibitor of acid corrosion of carbon steels.

When developing a synthesis process, it is necessary to elucidate how the reaction conditions (temperature, component ratio, reaction time, etc.) affect the yield of the target product. It was shown previously

Table 1. Performance of indoline **II** as inhibitor of acid corrosion of steel

Inhibitor, wt %	Acid, wt %	ρ, g m^{-2} h^{-1}	z, %
–	HCl, 15	5.0	–
0.4	HCl, 15	0.225	95.5
0.2	HCl, 15	0.585	88.3
0.1	HCl, 15	1.685	66.3
–	H_2SO_4, 20	21.0	–
0.4	H_2SO_4, 20	3.318	84.2
0.2	H_2SO_4, 20	6.279	70.1

1070-4272/01/7411-1910$25.00

[4] that heating of hydrochloride **I** at 200–220°C in excess *o*-toluidine yields indoline **II** and minor (up to 10%) amounts of 2-methyl-4-(cyclopent-2-enyl)aniline **III**:

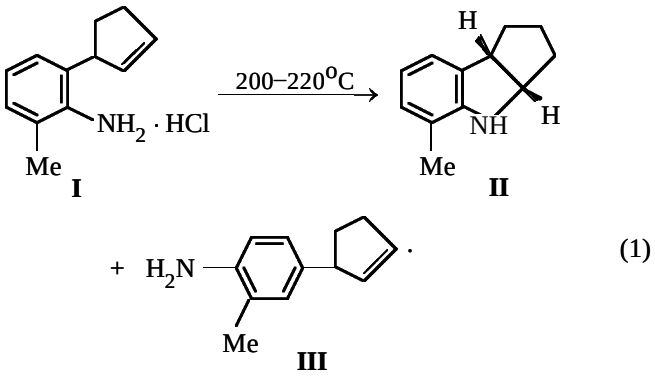

(1)

To find how the yield of the target product depends on the initial conditions and heating time, we studied the kinetic features of MCPA **I** consumption and indoline **II** accumulation. As seen from the kinetic curves shown in Fig. 1, the rate of MCPA consumption is the highest in the initial stages, and at 90% MCPA conversion the indoline concentration reaches a certain limit, C_i^∞. The yield of the target product was determined as the ratio of the limiting concentration of indoline **II** to the initial concentration C^0_{MCPA} (Table 2).

The kinetic curves of MCPA consumption are linear in the coordinates of the first-order reaction equation (Fig. 2):

$$\ln C_{MCPA} = \ln C^0_{MCPA} - kt, \qquad (2)$$

where C^0_{MCPA} and C_{MCPA} are the initial and current concentrations of MCPA, respectively; k is the apparent rate constant of consumption of **I**.

From the semilog kinetic plots, we determined the rate constants at various temperatures (Table 2) and obtained the Arrhenius equation

$$\ln k = -(20.1 \pm 5.2) - (98.1 \pm 2.2) \times 10^3/RT,$$

where $R = 8.31$ J mol^{-1} K^{-1}.

The activation energy of MCPA transformation, $E_a = 98.1 \pm 2.2$ kJ mol^{-1}, is consistent with published data. It should be noted that this is an apparent quantity, describing transformation of MCPA not only by scheme (1), but also into by-products.

For example, in the experiment performed at 200°C (Table 2) the yield of the target product was low. This may be due to the fact that the runs at 200°C

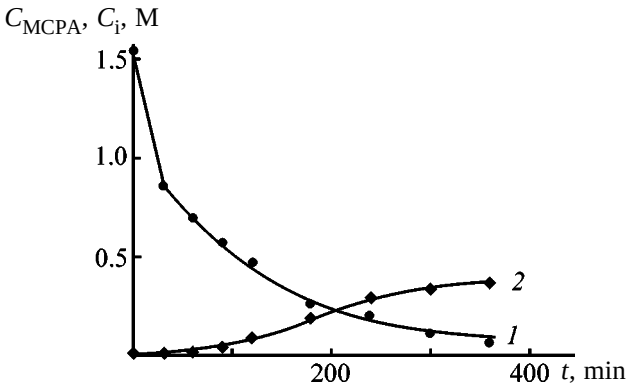

Fig. 1. Kinetic curves of (*1*) MCPA consumption and (*2*) indoline accumulation in intramolecular cyclization of 2-methyl-6-(cyclopent-2-enyl)aniline at 200°C. (C_{MCPA}, C_i) Concentrations of MCPA and indoline, respectively; (τ) time; the same for Fig. 2.

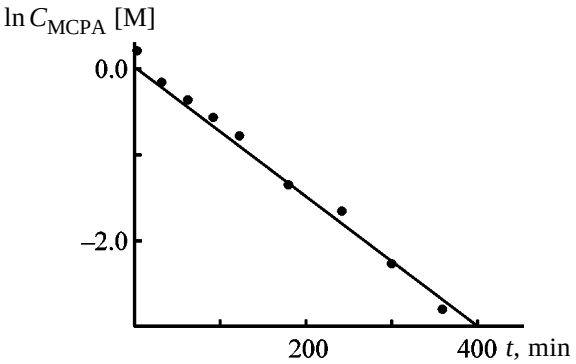

Fig. 2. Kinetic curve of MCPA consumption at 200°C, plotted in semilog coordinates.

were performed with an MCPA sample that had been stored for a month and had taken up moisture. At relatively high temperatures, traces of moisture could initiate the following side reactions:

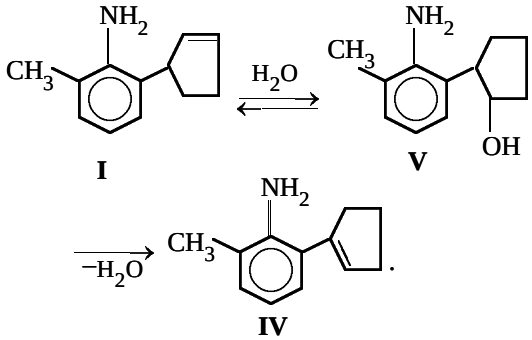

It was found previously [6] that, indeed, MCPA can transform into 2-methyl-6-(cyclopent-1-enyl)aniline **IV** in both alkaline and acid solutions. At high temperatures in the presence of HCl, this compound undergoes extensive tarring. An intermolecular reaction of 2-(2-hydroxycyclopentyl)aniline with MCPA, decreasing the yield of the target product, cannot be

Table 2. Yield of indoline **II** and apparent rate constant k as influenced by reaction temperature T (C^0_{MCPA} = 1.53 M)

T, °C	C_i^∞, M	C_i^∞/C^0_{MCPA}	$k \times 10^2$, min^{-1}
190	1.16	0.75	0.84
200	0.36	0.24	0.90
210	0.85	0.55	1.38
220	0.77	0.50	2.18
230	0.69	0.45	3.95

Table 3. Apparent rate constant and yield of indoline in isomerization of aniline **I** at 200°C, as influenced by the initial concentration of **I**

C^0_{MCPA}, M	$k \times 10^2$, min^{-1}	C_i^∞, M	C_i^∞/C^0_{MCPA}
1.53	0.9	0.36	0.24
1.15	0.6	0.18	0.16
0.76	0.8	0.05	0.07

ruled out either. Under the experimental conditions (sealed ampules), moisture is not evaporated; therefore, this pathway of MCPA transformation strongly affects the yield of the target product as a function of temperature (Table 2) and initial MCPA concentration (Table 3).

As seen from Table 3, the yield of **II** drastically decreases as the initial MCPA concentration is decreased.

CONCLUSIONS

(1) 5-Methyl-1,2,3,3a,4,8b-hexahydrocyclopent[*b*]-indole inhibits acid corrosion of carbon steels.

(2) The kinetic features of intramolecular cyclization of 2-methyl-6-(cyclopent-2-enyl)aniline were studied. The yield of the target product, indoline, decreases with decreasing initial concentration of the starting compound.

(3) Increase in temperature in the range 190–230°C is accompanied by a decrease in the yield of indoline.

REFERENCES

1. Shapiro, A.B., Medzhidov, A.A., and Rozantsev, E.G., *Zh. Obshch. Khim.*, 1966, vol. 36, no. 2, pp. 1873–1877.
2. Abdrakhmanov, I.B., Mustafin, A.G., and Tolstikov, G.A., *Izv. Akad. Nauk SSSR, Ser. Khim.*, 1983, no. 9, pp. 2171–2172.
3. Abdrakhmanov, I.B., Mustafin, A.G., Sharafutdinov, V.M., *et al.*, *Izv. Akad. Nauk SSSR, Ser. Khim.*, 1985, no. 9, pp. 839–842.
4. Gataullin, R.R., Kazhanova, T.V., Il'yasova, L.T., *et al.*, *Izv. Ross. Akad. Nauk, Ser. Khim.*, 1999, no. 5, pp. 975–978.
5. Abdrakhmanov, I.B., Sharafutdinov, V.M., and Tolstikov, G.A., *Izv. Akad. Nauk SSSR, Ser. Khim.*, 1982, no. 9, pp. 2160–2162.
6. Gataullin, R.R., Kazhanova, T.V., Fatykhov, A.A., *et al.*, *Izv. Ross. Akad. Nauk, Ser. Khim.*, 2000, no. 1, pp. 171–173.

Russian Journal of Applied Chemistry, Vol. 74, No. 11, 2001, pp. 1913–1919. Translated from Zhurnal Prikladnoi Khimii, Vol. 74, No. 11, 2001, pp. 1853–1858.

MACROMOLECULAR CHEMISTRY AND POLYMERIC MATERIALS

Polymerization/Depolymerization Mechanism for "Living" Sodium Poly-α-Methylstyryl and Sodium Polystyryl

K. K. Kalnin'sh

Institute of Macromolecular Compounds, Russian Academy of Sciences, St. Petersburg, Russia

Received June 29, 2001

Abstract—The equilibrium polymerization of sodium poly-α-methylstyryl in tetrahydrofuran was studied in the temperature range from –60 to 15°C. For the first time, the reversible process of formation/cleavage of the chemical bond was theoretically analyzed in terms of the electronic excitation views. On this basis, a new mechanism of the "living" polymer depolymerization was proposed. The geometry and electronic structure of the model fragments of "living" polymers comprised of two units were calculated *ab initio* by the 6-31G* method. The energies of the triplet excited states belonging to the complex of the reactants, on the one hand, and to the reaction product, on the other, proved to be close. The theoretical activation energies for depolymerization of sodium poly-α-methylstyryl reasonably agree with the experiment.

As known [1, 2], living sodium poly-α-methylstyryl (NaPMS) undergoes reversible polymerization/depolymerization in accordance with the equation

$$M_i^* + M \underset{K_{-1}}{\overset{K_1}{\rightarrow}} M_{i+1}^*, \quad (1)$$

Here, M_i^* and M_{i+1}^* denote the living polymer chains, and K_1 and K_{-1} are the growth and depolymerization rate constants, respectively [1, 2].

The thermodynamic and kinetic characteristics of depolymerization are given in [1–3], but published data on the elementary stages are lacking. Studies of reaction (1) were focused, for the most part, on determining the equilibrium constants K_{eq}, heats of polymerization, and equilibrium concentrations of the monomer M_{eq} [1, 4–8].

The depolymerziation (degradation) mechanisms for "dead" and living polymer chains, obviously, differ significantly. In the former case, free monomer is yielded by a chain radical process [9, 10] with a high activation energy (~209.0 kJ mol^{-1} [11]). Depolymerization of the living chains is a reversible process, yielding the monomer, which suggests that the structure of the active end of the living polymer is not deteriorated by the process.

The most extensively studied was the living polymer + α-methylstyrene (α-MST) system in tetrahydrofuran (THF) [1, 4–6] with a high equilibrium concentration of the monomer M_{eq}, for which holds

$$K_{eq} = K_1/K_{-1} \rightarrow 1/M_{eq} \quad (2)$$

at $M_0/M_i^* > 10$, where M_0 is the initial monomer concentration [1].

For this system, the growth activation energy was estimated at 20.9–29.3 kJ mol^{-1} [1], and the heat of polymerization and the entropy change, at $-\Delta H$ = 29.3 kJ mol^{-1} and $-\Delta S$ = 103.7 J mol^{-1} deg^{-1}, respectively [1, 3].

By contrast to α-methylstyrene, the equilibrium concentration of styrene in living sodium polystyryl NaPS is negligible (10^{-7} M at 0°C [7]), which points to the stability of this polymer under ordinary conditions. Polymerization/depolymerization of other living polymers was studied much less extensively.

In [12–14], we analyzed addition of styrene to the anionic end of the living polymer in terms of electronic excitation (transfer), with the reaction complex treated as the ion pair separated by the monomer. The back process of monomer detachment in the elementary stage is, evidently, similar to the forward, addition, process and can be treated in terms of the general concept of thermal electronic excitation in chemical reactions [14]. In [15], we analyzed the monomolecular thermochromic reactions in terms of electronic excitation, taking spiropyrans as an example. We showed that the calculated (by PM3 method) triplet energies of spiropyrans are close to the experimental activation energies of the six-membered pyran ring opening.

In this work, we attempted to explain the difference in the depolymerization character for NaPMS and

1070-4272/01/7411-1913$25.00

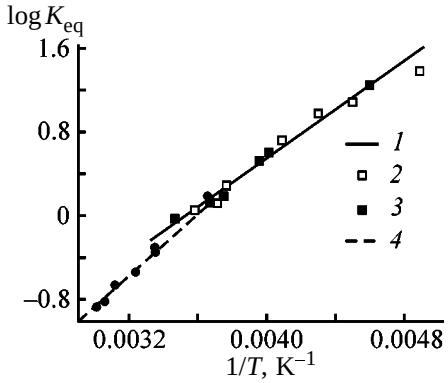

Fig. 1. Variation of the equilibrium constant K_{eq} with the temperature T. (*1*) Data of this work (NaPMS + α-MST, THF; M_0 = 1.1 M); (*2*) polymerization; (*3*) depolymerization; and (*4*) data from [5] (NaNaphth + α-MST, THF, M^0 = 0.75–7.5 M).

NaPS based on the views on thermal electronic excitation in chemical reactions. To this end, we performed quantum-chemical *ab initio* calculations for the NaPMS and NaPS fragments and their anionic forms comprised of two monomer units. The forward (polymerization) and back (depolymerization) reactions were studied theoretically, with the complexes formed by styrene and the end units of living polymers as an example. Also, we studied experimentally the equilibrium polymerization of NaPMS.

EXPERIMENTAL

Polymerization of α-MST was carried out in an IR cell with 0.15-cm-thick NaCl windows under conditions preventing the access of impurities able of deactivating the living polymer. The cell was cooled with liquid nitrogen vapor; the temperature was controlled accurately to within 2°C and varied at a rate of 1 deg min^{-1}. The α-MST concentration was determined from the absorption band at 1652 cm^{-1}. The methods of preparation and purification of the reactants were taken from [16].

Quantum-chemical calculations were carried out with PC GAMESS program, version 5.4, in the 6-31G* basis. The chosen molecular modules required significant PC resources, namely, over 3 Gb of disk memory and a no less than 1 GHz processor. Semiempirical calculations were carried out with HyperChem program, issue 6.0. The molecular geometry optimized by AM1 method served as initial approximation for *ab initio* calculations. The energies of the triplet states were calculated in the spin-unrestricted Hartree–Fock approximation as the differences between the total energies (*ab initio*) or heats of formation (semiempirical methods) of molecules in the triplet and singlet configurations. Because there is no parametrization for the Na atom in the semiempirical AM1 method, instead of sodium derivatives of living polymers we took the corresponding lithium analogs.

Polymerization/depolymerization. Equilibrium polymerization of α-MST was studied over a wide temperature range (from –60 to 15°C) in the NaPMS + α-MST system in THF. Figure 1 shows that the measured K_{eq} values reasonably agree with the published data [1, 4]. Also close are the heats of polymerization calculated with the use of these dependences and those from [4], namely, 23.4 against 29.3 kJ mol^{-1}. Our results and published data suggest that the equilibrium constants and thermodynamic characteristics of the NaPMS + α-MST + THF system do not depend significantly on the initial monomer concentration.

Semiempirical calculations. There exist two configurations of the calculated dimer model, namely, those with aromatic rings in *trans* and in *cis* positions. The *trans* structure is stable in the form of the anion (heat of formation H^{trans} 69.8, H^{cis} 88.2 kJ mol^{-1}), and *cis* structure is stable in the form of the ion pair (H^{cis} 209.8, H^{trans} 214.4 kJ mol^{-1}). For both structures we performed semiempirical calculations of the geometry and electronic states. Also, we considered oligomers $M_n^-Li^+$ and M_n^- with a chain comprised of 2–5 units (M is the monomer).

As known, the chemical activity is exhibited by intra- and intermolecular electronic states with charge transfer. Thus, our task consisted in taking the models chosen as an example and in finding such states with a low energy that can be thermally populated under ordinary conditions. Semiempirical calculations showed that there exist two centers of Li^+ cation localization, at the α-carbon atom in the anionic moiety carrying the maximal negative charge (structure I) and that above the neighboring noncharged aromatic ring (structure II). These two centers are separated by 5 Å in the case of the *trans* configuration of the dimer dim-α^{trans}, but they virtually coincide for the *cis* structure dim-α^{cis}–Li^+.

Structure I which is usually depicted for the ion pair of living polystyrene exhibits the highest stability in the ground electronic state. It is also stable chemically and is characterized by a small dipole moment of 5.7 D (AM1 method) in the case of the dim-α^{cis}–Li^+ model. The polar excited triplet state (μ = 8.5 D) is essentially a state with charge transfer from the anionic unit to the neighboring noncharged ring, but because of high energy (150.5 kJ mol^{-1}) it cannot be

populated at ordinary temperature and thus is chemically inactive.

Optimization of dim-α^{cis}–Lu^+ in the triplet excited state showed that the Li^+ cation occupies position II, above the center of the neighboring noncharged aromatic ring, to which the entire negative charge is transferred. The triplet energies $E(T_1) - E(S_0)$ for the model molecules of dim-α^{cis}–Li^+ and dim^{cis}–Li^+ were estimated at 8.4 and 73.6 kJ mol^{-1}, respectively. These values are, evidently, somewhat underestimated in the case of semiempirical AM1 calculations.

Thus, semiempirical quantum-chemical calculations showed that the lowest electronic transition in anionic systems $M_n^-Li^+$ or M_n^- involves, essentially, a charge (electron) transfer between the last (charged) and last but one (neutral) monomer units. In the case of trimer M_3^-, electronic excitation leads to electron transfer to the last but one monomer unit. By contrast to dimer and trimer, the triplet excitation for free anions of tetramer M_4^- and pentamer M_5^- are localized on the terminal unit. For free M_n^- anions, the lowest triplet state can be of two types: excitation in the terminal unit and charge-transfer excitation. Chemical activity with respect to depolymerization is exhibited by the latter excitation type, but its energy is fairly large for free anions. For example, the optimized (AM1) values of the energy gap $E(T_1) - E(S_0)$ for the dim-α^{trans}– model molecule is equal to 77.7 kJ mol^{-1}. This suggests a low chemical activity of free anions in the dark.

***Ab initio* calculations and structure of triplet states.** *Ab initio* calculations of dim-α^{cis}–Na^+, dim^{cis}–Na^+, and the corresponding anionic forms with full geometry optimization confirmed, on the whole, the relationships established by semiempirical AM1 calculations. For example, a lower energy and, hence, a greater stability of dim-α^{trans}– relative to dim-α^{cis}– [$\Delta(H^{trans} - H^{cis}) = -18.4$ kJ mol^{-1}], as determined by the AM1 method, is confirmed by the 6-31G* *ab initio* calculation: $\Delta(E^{trans} - E^{cis}) = -30.1$ kJ mol^{-1}. The 6-31G* basis satisfactorily describes the major features of the excited triplet states of the molecular models considered, that is, transfer of a negative charge and of the cation between the terminal and penultimate monomer units. Figure 2 illustrates the charge transfer in the triplet state T_1 from the negatively charged terminal unit to the last but one noncharged aromatic ring.

In the case of vertical (without geometry modification) transition, electron transfer to the neighboring monomer unit causes the dipole moment of the molecule to increase relative to the ground state (see table), as the cation retains its position. By contrast, in the equilibrium, optimized triplet state, where the Na^+ cation follows the electron in the transfer to the neighboring monomer unit, the dipole moment even tends to slightly decrease (see table), evidently, owing to closer arrangement of the charged particles.

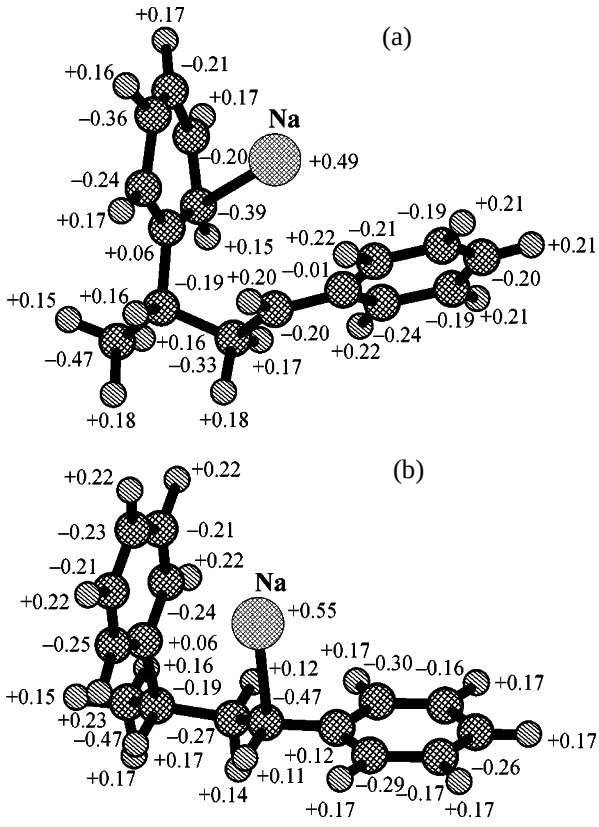

Fig. 2. Charge distribution on dim^{cis}–Na^+ atoms in the (a) ground singlet and (b) excited triplet states.

The energies of the vertical electronic transitions $T_1 \leftarrow S_0$ for the *cis* configuration of the dimer (see table) calculated as the $E(T_1) - E(S_0)$ differences are of the same order of magnitude as the triplet energy (189.8 kJ mol^{-1}), which is to be expected for the experimentally observed lowest singlet–singlet transition in the absorption spectrum of NaPMS at 29400 cm^{-1} (352.4 kJ mol^{-1}). The corresponding triplet energies for the *trans* configuration have higher energies (>334.4 kJ mol^{-1}). The table compares the energies of the vertical electronic transitions with those of "indirect", thermal transitions $T_1 \leftarrow\sim\sim S_0$ between the relaxed (optimized) states.

As already mentioned, the two living polymers, NaPMS and NaPS, which are close in chemical composition, differ significantly in thermodynamic charac-

Energies and dipole moments of the electronic states according to *ab initio* 6-31G* calculations (Figs. 3a–3c)

Molecule	$\Delta E(S_0)^*_{compl}$	$E(T_1)_{dim} - E(T_1)_{compl}$	Molecule	$E(T_1) - E(S_0)$, kJ mol^{-1}		μ, D		
	kJ mol^{-1}			E**	E***	S_0	T_1**	T_1***
α-mst + mon-α$^-$Na$^+$	61.0	19.6	dim-α^{cis-}Na$^+$	198.1	29.7	7.5	9.3	6.1
st + mon$^-$Na$^+$	39.7	11.3	dim^{cis-}Na$^+$	200.2	61.4	7.9	10.0	5.8
st + mon$^-$	23.0	15.0	dim-α^{trans-}Na$^+$	152.6	112.9			
			dim^{trans-}Na$^+$	149.2	112.4			

* Complexation energy in the ground S_0 state.
** One-point calculations (vertical transitions).
*** Optimization of singlet and triplet states.

teristics. The structural differences, evidently, should be manifested in the heats of reactions which determine equilibrium (1), as well as in the energies of the triplet states characterizing the reaction activation energy.

Let us consider the reversible model polymerization/depolymerization reactions:

$$\text{α-mst + mon-α}^-\text{Na}^+ \rightleftarrows {}^3(\text{charge-transfer complex}) \rightleftarrows {}^3(\text{dim-α}^{cis-}\text{Na}^+) \rightleftarrows {}^1(\text{dim-α}^{cis-}\text{Na}^+), \quad (3)$$

$$\text{st + mon}^-\text{Na}^+ \rightleftarrows {}^3(\text{charge-transfer complex}) \rightleftarrows {}^3(\text{dim}^{cis-}\text{Na}^+) \rightleftarrows {}^1(\text{dim}^{cis-}\text{Na}^+), \quad (4)$$

$$\text{st + mon}^- \rightleftarrows {}^3(\text{charge-transfer complex}) \rightleftarrows {}^3(\text{dim}^{trans-}) \rightleftarrows {}^1(\text{dim}^{trans-}), \quad (5)$$

where mon-α$^-$Na$^+$ is the monomer unit of sodium poly(α-methylstyryl), ^{3}(dim-α^{cis}Na$^+$) and ^{1}(dim-α^{cis}Na$^+$) are the triplet excited and singlet ground states of NaPMS dimer, respectively, st is styrene, and mon$^-$ is poly(styryl anion) monomer.

The results of 6-31D* *ab initio* calculations for all the stages of reactions (3)–(5) are shown schematically in Figs. 3a–3c.

The *cis* configuration of the dimer is of special importance for understanding the depolymerization mechanism. This configuration was experimentally confirmed by ^{1}H and ^{13}C NMR studies [17] of isomerization of living polymers during chain growth.

An essential result of *ab initio* calculations is the low energy of the optimized triplet state of the model dim-α^{cis-}Na$^+$ molecule (Fig. 3a), namely, 29.7 kJ mol^{-1}. High population of this state under ordinary conditions should afford rapid depolymerization, which is actually observed experimentally. The steric structure of the triplet differs from that of the singlet by a minor (~0.5 Å) shift of the Na$^+$ cation towards the neighboring unit. Also, two aromatic rings, which are located virtually perpendicularly in the singlet state, markedly approach each other during triplet optimization (Fig. 3b). The electronic singlet–triplet transitions of this kind are indirect transitions involving both electron transfer and heavy particle shift.

The number of methyl groups in the model molecule of dim^{cis-}Na$^+$ is by 2 less than in dim-α^{cis-}Na$^+$ (Figs. 3a, 3b), and no significant effect of structural features on the electronic characteristics could be expected. However, *ab initio* calculations show that the triplet energy markedly increases: $E(T_1) - E(S_0)$ = 61.4 kJ mol^{-1}. Tentative estimates show that the population of the triplet level of the dim^{cis-}Na$^+$ molecule should decrease relative to that of dim-α^{cis-}Na$^+$ by 5 orders of magnitude, with a similar difference in in the depolymerization rates [14].

A sharp difference in the chemical behavior of the two structurally related polymers, PMSNa and PSNa, is, evidently, due to the nature of the excited states. According to *ab initio* calculations, specific low-lying excited states are formed in the terminal units of living polymers through interaction of the last and the last but one aromatic rings via the common Na atom. This interaction, which is similar to chemical conjugation, is most strongly manifested in the dim-α^{cis-}Na$^+$ molecule with the maximally close rings (Fig. 3a). In the dim-α^{cis-}Na$^+$ molecule simulating poly(sodium styryl) the conjugation is manifested to a significantly smaller extent because of the large distance separating the aromatic rings (Figs. 3a, 3b). In our opinion, this is specifically responsible for the large difference in the energies of the lowest triplet states of the dim-α^{cis-}Na$^+$ and dim^{cis-}Na$^+$ molecules. It should be

noted that such interactions are not characteristic of the triplet states of dim-α^{cis-} and dim^{cis-} or dim-α^{trans-} and dim^{trans-} anions which do not contain a Na^+ cation.

The highest triplet energies were found for dim-α^{trans-} and dim^{trans-} anions, namely, 112.9 and 112.4 kJ mol^{-1}, respectively (Fig. 3c). Evidently, in these cases high activation barriers fully retard depolymerization. This is consistent with the results of semiempirical AM1 calculations predicting low chemical activity of free anions. Forward addition (polymerization) reactions characterized by low triplet energies of the complexes between the molecules of the reactants (Figs. 3a–3c) should have high rates in all the cases. It should be expected that the rate of forward reactions decreases in the series dim-$\alpha^{cis-}Na^+$ > $dim^{cis-}Na^+$ ≫ dim^{trans-}.

Based on the principle of reversibility of chemical processes, it can be qualitatively concluded that the electronic state responsible for cleavage of the chemical bond in depolymerization should be similar to that participating in bonding during polymerization. This, not evident, statement can be verified by comparing two stages in each of Eqs. (3)–(5): (1) conversion of the complex of the reactants (styrene + living polymer comprised of one unit) to the end product and (2) the back conversion of the dimer as the stable product to the initial reactants. The calculations revealed the following essential feature of the systems described by Eqs. (3)–(5): the energy of the triplet excited state of the end product is close to that of the triplet complex of the reactants (Figs. 3a–3c). This theoretical result was obtained for the first time; it is consistent with the general concept [14] stating that the forward (polymerization) and back (depolymerization) reactions proceed via the same electronically excited triplet state.

The chemical activity of the triplet states T_1 with respect to depolymerization events is determined by their biradical nature. The radical centers are localized on the last and last but one monomer units, as evidenced by the spin-density distribution pattern (Fig. 4). Similar pattern is characteristic of the vertical transition, when the cation is localized at the α-carbon atom of the terminal unit. This suggests the identity of the electronic states in these two cases differing in the cation position. Both states, vertical and relaxed (optimized), are able of dissociation of the bond linking the last and last but one monomer units. However, the vertical state is inactive in the depolymerization reaction because of high energy.

The $E(T_1) - E(S_0)$ parameters characterize the thermal degradation activation energy E_a^{depol} and, as follows from Table 1, differ significantly for the two cases of interest, dim-$\alpha^{cis-}Na^+$ and $dim^{cis-}Na^+$. The experimental value of E_a^{depol} for NaPMS can

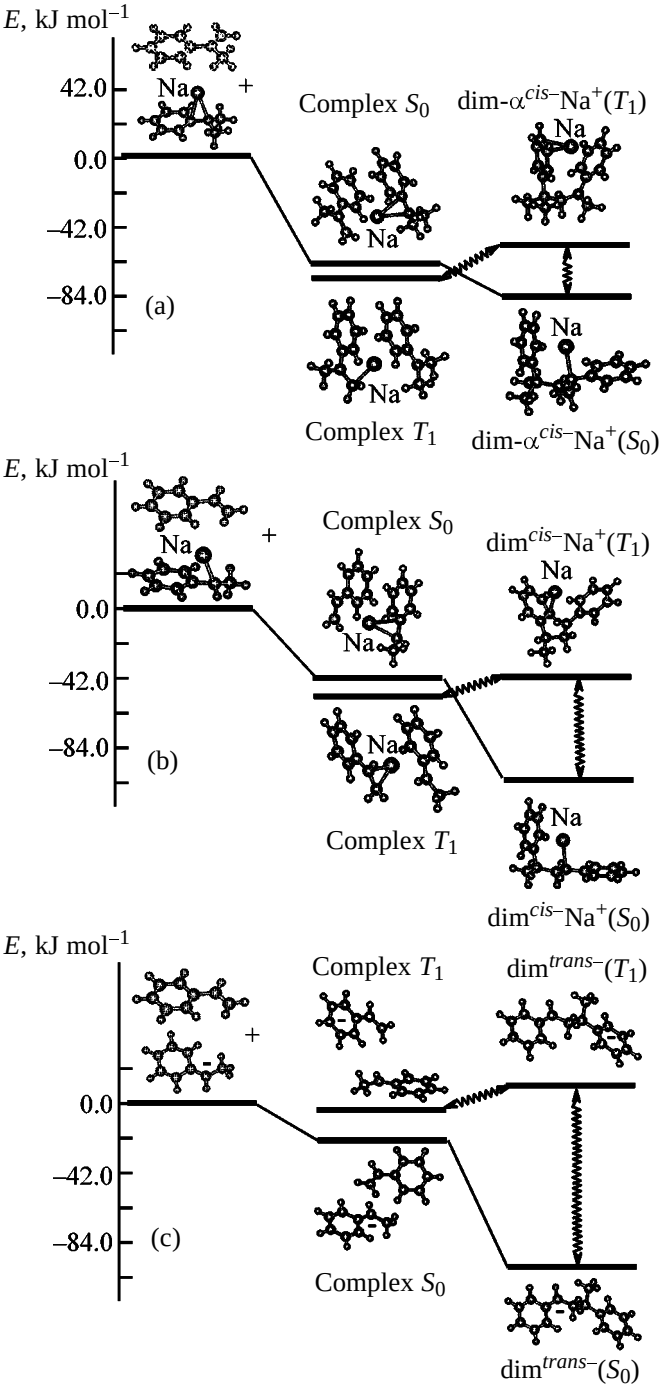

Fig. 3. Electronic state diagram for the polymerization/depolymerization reaction of (a) poly(sodium α-methylstyryl), (b) poly(sodium styryl), and (c) poly(styryl anion). 6-31G* *ab initio* optimization of the model system: (a) dim-$\alpha^{cis-}Na^+$, (b) $dim^{cis-}Na^+$, and (c) dim^{trans-}. (*E*) Energy.

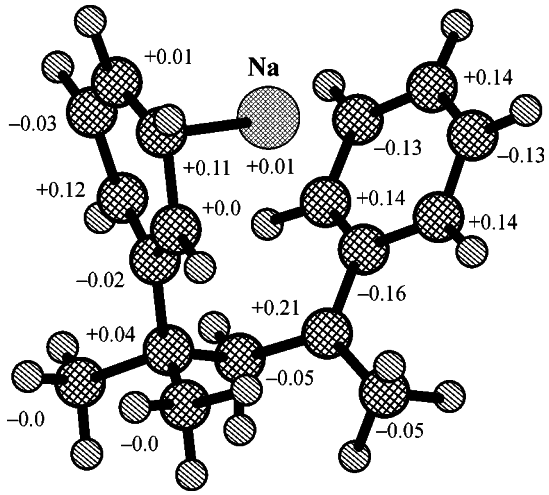

Fig. 4. Spin density distribution for heavy atoms of dim-α^{cis}–Na^+ in the triplet state.

be tentatively estimated as the sum of the growth activation energies E_a^{pol} (20.5 kJ mol^{-1}) and the heat of reaction $-\Delta H_r$ (23.4 kJ mol^{-1}): $E_a^{depol} = E_a^{pol} + |\Delta H_r| = 43.9$ kJ mol^{-1}. The same parameter was estimated theoretically by 6-31G* *ab initio* method at 29.7 kJ mol^{-1}, and the activation energy is taken equal to the triplet energy. For NaPS one can expect greater E_a^{depol} because of high polymerization heat: $-\Delta H_r = 72.7$ kJ mol^{-1} [1]. The calculated triplet energy for the model system dim$^-Na^+$ is also much greater than that for dim-α^-Na^+ of 61.4 kJ mol^{-1}.

Depolymerization of "dead" polymers. A well-known example of radical-chain depolymerization is thermal degradation of poly-α-methylstyrene (PMS) [9, 10] during which radical species are recorded. The latter are generated by heating the polymer to a high temperature (~250°C), and this is followed by rapid depolymerization releasing free monomer. Significant thermal activation is required for the initial cleavage of the C–C bond between the monomer units, which is, evidently, followed by fairly facile detachment of further monomer molecules.

The experimental activation energy of PMS thermal degradation is equal to 209.0 kJ mol^{-1} [11]. AM1 optimization of the "dead" PMS fragment comprised of three units yields $E(T_1) = 197.7$ kJ mol^{-1} for the triplet state, which is in satisfactory agreement with the experimental E_a value. The spin density in this state is concentrated on the central moiety of the "dead" trimer and the neighboring C–C bonds. In the elementary process, the chemical bond is cleaved in the low-lying electronically excited triplet state of the molecule [14].

CONCLUSION

Theoretical analysis of the depolymerization reaction of living polymers, by contrast to "dead" polymers, showed that the electronic state responsible for cleavage of the C–C bond between the terminal and the penultimate monomeric units is the triplet excited state of the terminal moiety of the polymer. First, this state is generated by electron transfer from the terminal unit to the neighboring aromatic ring. Second, simultaneously with electron transfer the cation is shifted in the same direction, yielding a biradical structure active in chemical bond cleavage events. Third, such states are characterized by low energy, which affords high reaction rate. Finally, after detachment of the monomer the initial ground state of the end of living polymer is regenerated, which is able of either chain growth or further depolymerization. Forward depolymerization reactions proceed via low-energy triplet states of the reactants. The 6-31G* *ab initio* calculations provided satisfactory explanation to the experimental kinetics of depolymerization reaction.

ACKNOWLEDGMENTS

The author is grateful to A.F. Podol'skii for assistance in experiments and for fruitful discussions.

REFERENCES

1. Szwarc, M., *Carbanions, Living Polymers, and Electron Transfer Processes*, New York: Interscience, 1968.
2. Szwarc, M. and Van Beylen, M., *Ionic Polymerization and Living Polymers*, New York: Chapman and Hall, 1993.
3. Dainton, F.S. and Ivin, K.J., *Quart. Rev.*, 1958, vol. 12, no. 1, p. 61.
4. McCormic, H.W., *J. Polym. Sci.*, 1957, vol. 25, no. 111, pp. 488–490.
5. Worsfold, D.J. and Bywater, S., *J. Polym. Sci.*, 1957, vol. 26, no. 114, pp. 299–304.
6. Vrancken, A., Smid, J., and Szwarc, M., *Trans. Faraday Soc.*, 1962, vol. 58, no. 478, pp. 2036–2045.
7. Bywater, S. and Worsfold, D.J., *J. Polym. Sci.*, 1962, vol. 58, no. 166, pp. 571–579.
8. Lee, C.L., Smid, J., and Szwarc, M., *J. Am. Chem. Soc.*, 1963, vol. 85, no. 7, pp. 912–914.
9. Guaita, M. and Chaintore, O., *Polym. Degrad. Stab.*, 1985, vol. 11, no. 2, pp. 167–180.

10. McNell, I.C., in *Comprehensive Polymer Science*, New York, Pergamon, 1989, vol. 6, pp. 466–470.
11. Amelin, A.V., Glagoleva, Yu.A., Podol'skii, A.F., *et al*., *Fiz. Tverd. Tela*, 1971, vol. 13, no. 9, pp. 2726–2735.
12. Kalnin'sh, K.K., Podol'skii, A.F., Kutsenko, A.D., *et al*., *Vysokomol. Soedin., Ser. A*, 1990, vol. 32, no. 2, pp. 316–321.
13. Kalnin'sh, K.K. and Podol'skii, A.F., *Vysokomol. Soedin., Ser. A*, 1991, vol. 33, no. 10, pp. 2215–2224.
14. Kalnin'sh, K.K., *Elektronnoe vozbuzhdenie v khimii* (Electronic Excitation in Chemistry), St. Petersburg: Univ. Tekhnologii i Dizaina, 1998.
15. Kalnin'sh, K.K., *Zh. Strukt. Khim.*, 1998, vol. 39, no. 5, pp. 787–797.
16. Podolsky, A.F. and Taran, A.A., *J. Polym. Sci., Polym. Chem. Ed.*, 1974, vol. 12, no. 11, pp. 2187–2195.
17. Wicker, R. and Elgert, K.F., *Makromol. Chem.*, 1977, vol. 178, no. 11, pp. 3063–3073.

Russian Journal of Applied Chemistry, Vol. 74, No. 11, 2001, pp. 1920–1923. Translated from Zhurnal Prikladnoi Khimii, Vol. 74, No. 11, 2001, pp. 1859–1862.

MACROMOLECULAR CHEMISTRY AND POLYMERIC MATERIALS

Acid–Base Interactions at the Modified Polyethylene–Metal Interface

I. A. Starostina, R. R. Khasbiullin, O. V. Stoyanov, and A. E. Chalykh

Kazan State Technological University, Kazan, Tatarstan, Russia
Institute of Physical Chemistry, Russian Academy of Sciences, Moscow, Russia

Received April 18, 2000; in final form, March 2001

Abstract—The acidity parameters of metal and polymeric surfaces were determined as influenced by the extent of surface oxidation of metals and by the modifier content in the polymer.

Acid–base interphase bonds, including hydrogen bonds, are considered at present as factors largely responsible for adhesion [1].

To evaluate the interaction of solids with a wetting liquid and of polymer layers with supports, data on the acidity and basicity of compounds involved are required. In this connection, procedures for measuring surface properties by gas chromatography, flow microcalorimetry, ellipsometry, and NMR and IR spectroscopy are actively developed [1–3].

Berger [4] proposed a simple and convenient procedure for determining the surface acidity of polymers and metals by measuring the contact angle between the surface and reference liquids.

Estimation of the adhesive properties of a material from its surface acidity is of special interest. The correlation between the strength of adhesion joints and the acid–base properties of adhesives and adherents was observed in many works [5].

Correct determination of the acidity of any smooth solid surfaces, increase in adhesion of a polymer to the metal surface by variation of this parameter, and prediction of the interface interactions in actual systems are urgent problems.

The aim of this work was to study the nature of interface interactions in corrosion-protective coatings of various polyethylenes (PEs) modified with various additives and to determine the main relationships of the acid–base interactions occurring in modified PEs during formation of their coatings.

EXPERIMENTAL

In this work we used the following materials: powdered (particle diameter less than 315 μm) nonstabilized high-density polyethylene (HDPE) prepared by the gas-phase procedure [for pipe production, GOST (State Standard) 16338–85]; powdered (particle diameter less than 315 μm) nonstabilized low-density polyethylene (LDPE) of 16803–070 trade mark [GOST (State Standard) 16337–77]; primary aromatic amines (PAAs) [4,4'-diamino-3,3'-dichlorodiphenylmethane (DC), polyamine T, and *o*-phenylenediamine (*o*-PDA)] and phenols [diphenylolpropane (DPP) and pyrocatechol] as modifiers; *N*,*N*'-*m*-phenylendimaleinimide (PDMI) and dithiodiphenylenedimaleinimide (TPDMI) as cross-linking agents. The supports were made of steels of various types, copper, aluminum, titanium, zinc, brass, etc.

The procedure for preparing PE–modifier composites and PE coatings on metal supports are described in our previous works [6–8].

The surface acidity was estimated by the Berger's procedure [4]. Cosines of the contact angles of six reference liquids with the tested surface were determined with a KM-8 cathetometer. The thermodynamic work of adhesion for each liquid W_a was calculated by the equation

$$W_a = \gamma_{lv}(1 + \cos\theta),$$

where γ_{lv} is the total free surface energy of the reference liquid.

The values of γ_{lv} are presented in Table 1. W_a was calculated from the measured cosines of angles between the reference liquids and the surface. The geometric mean of the total free surface energy of the support γ_s was determined by graphic solution of the Owens–Wendt equation

$$\gamma_{lv}(1 + \cos\theta)/2 = (\gamma_{lv}^d \gamma_s^d)^{1/2} + (\gamma_s^p \gamma_{lv}^p)^{1/2}$$

1070-4272/01/7411-1920$25.00

(γ_s^p and γ_s^d are polar and dispersion components of the free energy of the solid surface, $\gamma_s = \gamma_s^p + \gamma_s^d$), which can be transformed as follows:

$$W_a/2(\gamma_{lv}^d)^{1/2} = (\gamma_s^d)^{1/2} + (\gamma_s^p\gamma_{lv}^p)^{1/2}(\gamma_{lv}^d)^{-1/2}.$$

To determine γ_s, a straight line in the $W_a/2(\gamma_{lv}^d)^{1/2}$ (ordinate) and $(\gamma_{lv}^p/\gamma_{lv}^d)^{1/2}$ (abscissa) coordinates was plotted. This line intersects the ordinate at point $(\gamma_s^d)^{1/2}$ and angle $(\gamma_s^p)^{1/2}$. The dispersion and polar components of the free surface energy were calculated by raising $(\gamma_s^d)^{1/2}$ and $(\gamma_s^p)^{1/2}$ to the second power. The geometric mean total surface energy of the tested material is the sum of the resulting parameters.

The dispersion component of W_a for each of two Lewis acids and two Lewis bases was calculated as $W_a^d = 2(\gamma_{lv}^d\gamma_s^d)^{1/2}$ from γ_s^d. Then the acid–base component of W_a, W_a^{ab}, for the same liquids was calculated as $W_a^{ab} = W_a - W_a^d$.

Division of each W_a^{ab} by $(\gamma_{lv}^p)^{1/2}$ gives $W_a^{ab} \times (\gamma_{lv}^p)^{-1/2} = 2(\gamma_s^p)^{1/2}$. The surface acidity was quantitatively estimated from the equation

$$D = 2\{[\gamma_s^p(\text{aniline})]^{1/2} + [\gamma_s^p(\text{formamide})]^{1/2}\} - 2\{[\gamma_s^p(\text{phenol})]^{1/2} + [\gamma_s^p(\text{glycerol})]^{1/2}\}.$$

The free surface energy and its components were calculated from the experimental results for 10 drops of each liquid on each support. The determination error was 5%.

The surface acidity D was calculated from the base and height of the reference liquid drops by the specially developed program.

The adhesion of the coatings was estimated from their resistance to cathodic exfoliation by the procedure in [6]. The tested coating with a 3-mm initial defect was kept for 8 h in 0.1 N sodium chloride at the potential of 6 V and room temperature. The resistance to the cathodic exfoliation was estimated from the diameter of the defect (exfoliated coating) after experiment completion.

Correct assignment of the acid–base properties, i.e., whether compound is acidic, basic, neutral, or amphoteric, is important problem. We measured the acidity D of a series of smooth solid polymeric and metallic surfaces. The results are summarized in Table 2.

As seen from Table 2, the modifiers containing primary amino group decrease D of the polyethylene coatings to the negative values, i.e., the coatings modified with PAA exhibit pronounced basic properties. This is the reasonable conclusion since primary amines are Lewis bases.

Modification of PE with phenols, which are acids, increases the acidity of PE coatings. It should be noted that D slightly increases with increasing temperature and time of coating formation, which is due to oxidation of PE.

Relative acidity $\Delta D = D(\text{coating}) - D(\text{support})$ is used to estimate the adhesion of the coatings and to adequately evaluate the acidity of the coatings and supports. As ΔD increases, the difference in the acid–

Table 1. Free surface energy γ_{lv} of the reference liquids and its polar γ_{lv}^p and dispersion γ_{lv}^d components

Reference liquid	γ_{lv}^d	γ_{lv}^p	γ_{lv}
	mJ m^{-2}		
Water	22.0	50.2	72.2
Dimethylformamide	32.4	4.9	37.3
Glycerol	33.9	29.8	63.7
Formamide	31.8	25.7	57.5
Aniline	41.2	2.0	43.2
Phenol	37.8	2.6	40.4

Table 2. Acidity of modified polyethylene coatings

Surface	D, (mJ m^{-2})$^{1/2}$
HDPE:	
weakly oxidized	2.35
strongly oxidized	3.59
HDPE + additive, %	
o-PDA, 0.5	–0.50
PC, 0.5	7.05
DPP, 2.0	7.61
DC, 0.5	2.21
DC, 1.0	1.98
DC, 1.5	2.08
DC, 2.0	0.62
DC, 5.0	–1.28
LDPE	4.05
LDPE + PDMI, %:	
0.25	6.55
0.5	6.45
1.0	7.96
1.5	6.52
2.0	6.10
4.0	7.08

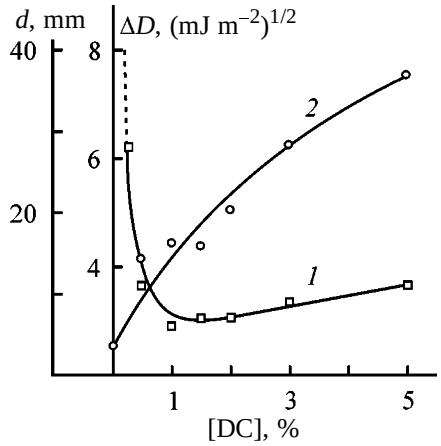

Fig. 1. (*1*) Defect diameter *d* at the cathodic exfoliation and (*2*) relative acidity Δ*D* of HDPE coating on ChZh-1 sheet iron as functions of [DC].

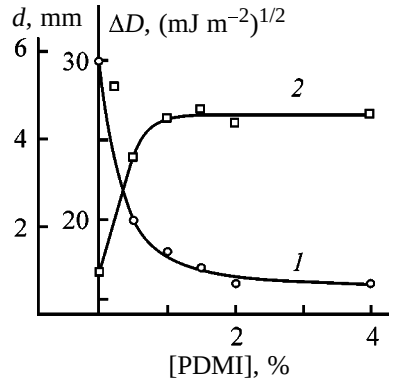

Fig. 2. (*1*) Defect diameter *d* at the cathodic exfoliation and (*2*) relative acidity Δ*D* of HDPE coating on ChZh-1 sheet iron as functions of [PDMI].

base properties of the polymer and support increases, and the interphase interaction should become stronger.

The concentration depedences of Δ*D* of modified PE coatings (Figs. 1, 2) show that the acidity strongly depends on the modifier concentration. The relative acidity of coatings of HDPE modified with DC and of LDPE modified with PDMI correlates with their resistance to cathodic exfoliation and hence with their adhesion. These results confirm the correlation of the acid–base properties of adhesives and adherents with the strength of the adhesive joints. Certain decrease in the resistance of the coatings of HDPE modified with DC to the cathodic exfoliation with increase in Δ*D* is due to concentration of unreacted DC at the interface with formation of weakly bonded intermediate layer [6, 7].

Table 3. Effect of the heat treatment on the acidity of metal supports

Metal	*D*, $(mJ\ m^{-2})^{1/2}$	
	initial	after heat treatment
Titanium	4.30	1.31
Brass	8.44	7.82
G-65 steel	4.54	4.21
St.20 steel	4.70	3.31
ChZh-1 sheet iron	6.45	5.50
Copper	3.25	4.95
Aluminum	–1.93	3.95
Zinc-plated sheet iron	5.05	8.50
Duralumin	–2.15	1.24

Heat treatment of a series of metal supports has ambiguous effect on their surface acidity. The acidity of copper, aluminum, and zinc-plated sheet iron increases after their heating at 150°C for 10–15 min, whereas *D* of titanium, brass, and steel decreases after this treatment.

This is probably caused by the different properties of the oxides formed during the heat treatment of the metal surface, which, in their turn, depend on the chemical state of the surface.

Previously we found [7] that the adhesion of DC-modified HDPE coating correlates with the acidity of their supports (Fig. 3). This experiment was performed as follows. An HDPE + 2% DC composition was applied to various metal supports under identical conditions. Then the resistance of these coatings to cathodic exfoliation was studied. It was found that, the higher *D* of the metal support, the smaller is the minimal diameter of the defect of this coating.

To confirm the theoretical correlation between the adhesion and acidity of adhesives and adherents, we examined the adhesive joints prepared from the components maximally differing in the acidity. Coatings with high adhesion (the diameter of the initial mechanical defect did not change after cathodic exfoliation) were prepared under appropriate conditions in the following systems: heat-treated titanium–LDPE + 1% PDMI, heat-treated titanium–HDPE + 2% DPP, brass–HDPE + 2% DC, and ChZh-1–HDPE + 2% DC.

Thus, adhesion of polyethylene to a metal support can be appreciably increased by varying the acid–base properties of these materials.

CONCLUSION

The acidity of a series of smooth solid metal and polymeric surfaces were measured. The dependence of these parameters on the extent of metal surface oxi-

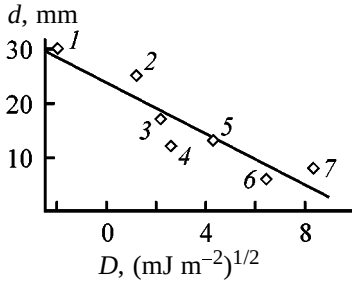

Fig. 3. Diameter of defect *d* formed at cathodic exfoliation of HDPE + 2% DC coating as a function of the acidity *D* of the metal support. Support: (*1*) aluminum, (*2*) duralumin, (*3*) St.3 steel, (*4*) St.20 steel, (*5*) G-65 steel, (*6*) ChZh-1 sheet iron, and (*7*) brass.

dation and on the modifier content in polyethylene was determined. A correlation was revealed between the acidity of these surfaces and the adhesion of the polyethylene coating to the metal support.

REFERENCES

1. Fowkes, F.M., *J. Adhes. Sci. Technol*., 1990, vol. 4, no. 8, p. 669.
2. Papirer, E. and Ballard, H., *J. Adhes. Sci. Technol*., 1990, vol. 4, no. 5, p. 357.
3. Finlayson, M.F. and Shan, B.A., *J. Adhes. Sci. Technol*., 1990, vol. 4, no. 5, p. 431.
4. Berger, E.J., *J. Adhes. Sci. Technol*., 1990, vol. 4, no. 5, p. 373.
5. Shreiber, H.J., *J. Adhes. Sci. Technol*., 1990, vol. 4, no. 4, p. 319.
6. Starostina, I.A., Role of Primary Aromatic Amines in Strengthening of Adhesion of Modified Polyethylene to Steel, *Cand. Sci. Dissertation*, Kazan, 1996.
7. Starostina, I.A., Stoyanov, O.V., Deberdeev, R.Ya., *et al*., *Polym. Polym. Composites*, 1998, vol. 5, no. 8, p. 52.
8. Stoyanov, O.V., Deberdeev, R.Ya., Privalko, V.P., and Zaikov, G.E., *Plast. Massy*, 1999, no. 7, pp. 7–12.

Russian Journal of Applied Chemistry, Vol. 74, No. 11, 2001, pp. 1924–1927. Translated from Zhurnal Prikladnoi Khimii, Vol. 74, No. 11, 2001, pp. 1863–1866.

MACROMOLECULAR CHEMISTRY AND POLYMERIC MATERIALS

Properties of Flax Cellulose Solutions in Tertiary Amine *N*-Oxides and of Films Thereof

N. S. Trofimova, N. M. Zabivalova, A. M. Bochek, and N. P. Novoselov

St. Petersburg State University of Technology and Design, St. Petersburg, Russia
Institute of Macromolecular Compounds, Russian Academy of Sciences, St. Petersburg, Russia

Received April 25, 2001

Abstract—The solubility of flax fibers differing in the degree of purity in triethylamine *N*-oxide monohydrate was studied. The size and amount of the associates in equiconcentrated solutions were estimated from the turbidity spectra. Rheological properties of solutions of cotton and flax cellulose were compared. Hydrated cellulose films were obtained from solutions, and their physicomechanical properties were studied. The films were characterized by IR spectroscopy.

In recent years production of flax-fiber-based textile materials increased. Simultaneously increased the amount of flax waste, namely, shive (flax stalks) and short fibers. The latter can be utilized in production of hydrated cellulose fibers. Modern processes utilize *N*-methylmorphopline *N*-oxide as cellulose solvent [1, 2].

It is of interest to study the dissolution of flax cellulose fibers, differing in the degrees of purity, in a mixture of triethylamine *N*-oxide monohydrate (mTEAO) with dimethyl sulfoxide (DMSO) as diluent. Utilization of short fibers in preparing cellulose solutions will extend the application field for flax fibers. In this work, we compared the properties of dilute and moderately concentrated solutions of flax cellulose in the mTEAO–DMSO system and showed their suitability for obtaining hydrated cellulose films.

EXPERIMENTAL

We utilized cotton cellulose with PD_η = 1500 and flax cellulose with PD_η = 1000 (PD_η is the polymerization degree determined viscometrically from the viscosity of cellulose in cadoxene). We used mTEAO as solvent. The water content of the latter was determined by Fischer titration [3]. Flax fibers were treated to remove fats, waxes, and pectins to various degrees of purity [4].

We studied the solubility in the mTEAO–DMSO system of flax fibers against cotton linter. Fiber samples were dissolved at T = 338 K for 60 min. Dilute solutions of flax cellulose and cotton linter samples (c = 0.5 wt %) were studied by the turbidity spectrum method [5, 6]. We calculated the average radius of the associates r, nm, and their amount in a unit volume N (number of associates per cm^3) by the equations

$$r = \alpha\lambda_{mid}/(2\pi n_D^{20}), \quad (1)$$

$$N = 1.26 \times 10^{17}\tau/[\lambda^2 k(\alpha, m)\alpha^2], \quad (2)$$

$$\lambda' = \lambda_{mid}/n_D^{20},$$

where r is the average radius of the associates, nm; α is the relative particle size; λ_{mid} is the wavelength corresponding to the middle of the range measured; n_D^{20} is the refractive index of the solvent at 293 K; τ is the turbidity of solvents, cm^{-1}; λ' is the light wavelength in the medium studied, nm; and $K(\alpha, m)$ is the scattering function tabulated for specific α and m [5].

The optical density and the turbidity were measured on a KFK-2 photoelectric colorimeter in a temperature-controlled cell in the wavelength range 490–750 nm. Moderately concentrated solutions were studied on a Rheotest 2.1 rheoviscometer. To this end we prepared 3% solutions of flax cellulose treated with benzene, hydrochloric acid, and a surfactant solution and those of cotton linter. The samples were dissolved on an oil bath with stirring for 2 h. The resulting solutions were filtered under pressure through 5 layers of glass fabric, and then kept for 1 h at room temperature to remove air bubbles (deaeration).

Hydrated cellulose films were cast onto Teflon plates through a laboratory spinneret with a controlled

1070-4272/01/7411-1924$25.00

Table 1. Viscosity, size, and amount of associates in cotton linter and flax cellulose solutions (0.5 wt %) in the mTEAO–DMSO system

Experiment no.	Initial material and treatment conditions	$\eta \times 10^3$, Ps s	r, nm	N, associates per cm^3
1	Cotton linter	9.1	92.1	2.62×10^{12}
2	Raw flax	9.3	184.2	3.53×10^{11}
	Flax treated with:			
3	benzene	8.2	65.8	5.32×10^{13}
4	cold water	9.1	78.9	1.39×10^{13}
5	benzene and cold water	10.0	240.1	5.01×10^{14}
6	aqueous surfactant solution	16.1	993.1	2.63×10^{11}
7	benzene and HCl	18.3	1144.9	9.21×10^{7}
8	benzene, HCl, and surfactant	12.7	960.6	7.41×10^{7}

slit. The solutions were applied to the plates, kept for 30 s in air, and immersed in a precipitation bath filled with distilled water. The resulting films were separated from the plates, kept for 1 h in the precipitation bath, and washed with several portions of distilled water for 4 h. Then films were fixed in rectangular frames and dried at room temperature for 12 h. This afforded 15–20-μm-thick hydrated cellulose films.

The mechanical characteristics of the films were determined in the uniaxial stretching mode on a UTS 10 setup at the stretching rate of 30 mm min^{-1}. The results were averaged over 5 measurements. The scatter was within 10%.

The IR spectra of the samples were measured on a Specord M80 spectrometer (KBr).

As known, dissolution of cellulose in tertiary amine *N*-oxides involves degradation of its macromolecules. This is explained by the stepwise dissolution of cellulose (swelling, degradation into individual crystallites or stacks of macromolecules, involving degradation of tie macrochains and their dissolution to molecular dispersion) and by oxidative degradation caused by oxygen that is released from amine oxide at elevated temperatures, yielding the initial amine [6, 7]. The solubility of the polymer is affected by concomitant substances. Flax fibers include lignin, fatty acids, waxy substances, pectins, pentosans, and dyes [8]. These substances modify the surface tension of fiber solutions [8], thereby affecting the flax cellulose solubility and self-association of solvated macromolecules in solution. We began our work with studying the solubility of cellulose from flax bast fibers differing in the degree of purity. Treatment of flax fibers with benzene removes, above all, fats and waxes, and then dilute solution of hydrochloric acid removes pectins, as well as pentosans (partially) [4]. Therefore, by dissolving in mTEAO flax fiber samples differing in the degree of purity it is possible to elucidate how the concomitant impurities affect the solubility of fibers in the mTEAO–DMSO system.

The initial fiber samples contain, along with cellulose, 10–15 wt % of other substances, while bleached cotton linter which served as the reference contains 99.8 wt % cellulose. Therefore, for cotton and flax fiber solutions with identical weight concentrations in nonaqueous mixed solvent the content of flax cellulose is lower than that of cotton cellulose. Flax fiber solutions can contain dissolved cellulose and other concomitant components. Fatty acids and waxes decrease the surface tension of fiber solutions and modify the conditions of sample dissolution. The greatest surface tension forces are exhibited by solutions of refined cellulose [8]. The concomitant substances passing into solution modify the properties of polymer solutions as well.

It should be noted that fats and pectins are removed at elevated temperatures (treatment with benzene, hydrochloric acid solution, boiling with a surfactant), which results in additional degradation of cellulose and modifies the solution viscosity. Therefore, comparison of the viscosity of solutions of cotton linter with those of flax fibers differing in the degree of purity reveals a combined effect of the molecular weight of cellulose proper and of various amounts of the impurities on the viscosity of solutions of a certain concentration.

Table 1 shows that the viscosities of solutions of cotton linter and raw flax fiber are comparable. Removal of fats and pectins (experiment nos. 6–8) causes the viscosity to increase. This can be explained by increase in the cellulose concentration and self-association of its solvated macromolecules. The sizes of the associates and their content per unit volume were estimated from the turbidity spectra [5]. In view

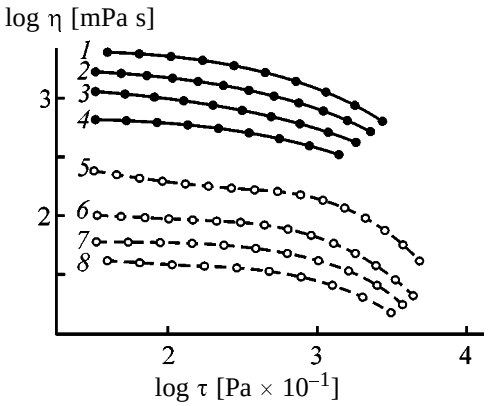

Fig. 1. Flow curves for 3% solutions of (*1–4*) cotton linter and (*5–8*) flax cellulose in the mTEAO–DMSO system. (η) Viscosity and (τ) shear stress. Temperature, °C: (*1, 5*) 20, (*2, 6*) 30, (*3, 7*) 40, and (*4, 8*) 50.

of the fact that the solutions were prepared under identical conditions and filtered through glass filters with identical pore sizes, we can make conclusions on the size of fluctuation associates that appear in solutions owing to intermolecular interactions of solvated macromolecules.

Our results show that removal of waxes and pectins causes the associates to grow in size (Table 1, experiment nos. 5–8). This can be explained by increase in the fraction of cellulose and by changes in the hydrogen bond system in solutions. It should be noted that flax fiber solutions in the mTEAO–DMSO system also contain hemicelluloses (pentosans, hexosans, mannan, etc.) whose removal from the initial material requires more severe conditions of flax fiber purification [4], which is beyond the scope of this work. Treatment with aqueous surfactant solution causes the viscosity of the solution and the size of the associates to grow (Table 1, experiment no. 6). Thus, comparative analysis of the viscosity and turbidity spectra of 0.5% solutions of flax and cotton linter fibers shows that mTEAO can dissolve flax fibers of various degrees of purity.

The rheological properties of the solutions were studied for a sample treated with benzene (removal of fats and waxes), hydrochloric acid (removal of pectins), and a surfactant solution. This choice was governed by the need in minimizing the influence of the impurities on the properties of moderately concentrated flax cellulose solutions. It is assumed that after the treatment runs listed above, the flax fiber contains the residual lignin, hemicellulose, and a mineral component. Figure 1 presents the flow curves of 3% solutions of cotton linter and refined flax cellulose. The solutions exhibit non-Newtonian flow patterns. The viscosity sharply decreases in the shear stress range $\log\tau = 2.6–2.8$. Substantial difference in the solution viscosity can be explained by the fact that flax fiber refining yields flax cellulose with DP_η 1000, whereas DP_η of cotton linter is 1500.

Table 2. Physicomechanical properties of hydrated cellulose films

Solution	*E*, GPa	σ_f, MPa	σ_t, MPa	ε_b, %
Cotton linter	8.7 ± 0.30	101 ± 2	112 ± 2	3.5 ± 0.2
Flax cellulose	7.9 ± 0.31	95 ± 2	109 ± 2	4.0 ± 1.0

* *E* is the elasticity modulus, σ_f is the forced elasticity limit, σ_t is strength, and ε_b is the elongation at break.

Using the temperature dependences, we calculated the viscous flow activation heats E_a which proved to be 43.4 and 38.2 kJ mol^{-1} for solutions of cotton linter in the mTEAO–DMSO system and flax cellulose solutions, respectively. The difference in these parameters may be due to different molecular weights of cotton linter cellulose and flax cellulose, as well as to the occurrence in the flax cellulose solution of hemicelluloses which can also affect structurization of solutions.

Thus, studies of the rheological properties of moderately concentrated solutions of cotton and flax cellulose show that these are non-Newtonian liquids with similarly shaped flow curves and similar viscous flow activation heats. This allows hydrated cellulose films to be prepared from the systems studied under identical conditions.

The composition of the precipitation bath affects the structure and the morphology of hydrated cellulose films. Therefore, by choosing appropriate composition of the precipitation bath it is possible to obtain films suitable as membranes [9, 10]. We formed hydrated cellulose films from two solutions by room-temperature precipitation of the polymer. The physicomechanical properties of these films are presented in Table 2. The resulting hydrated cellulose films differ in their physicomechanical properties insignificantly.

The composition of the films was studied by IR spectroscopy (Fig. 2). In the case of raw flax fibers the spectra contain absorption bands characteristic for lignin and pectins. The absorption bands characteristic for lignin are those at 1600, 1500, and 850 cm^{-1} [10]. The IR spectra of pectins contain the bands at 1740, 1615, and 1410 cm^{-1} [10, 11]. The absorption band at 1740 cm^{-1} belongs to free COOH groups of pectins.

The bands at 1615 and 1410 cm^{-1} are assigned to

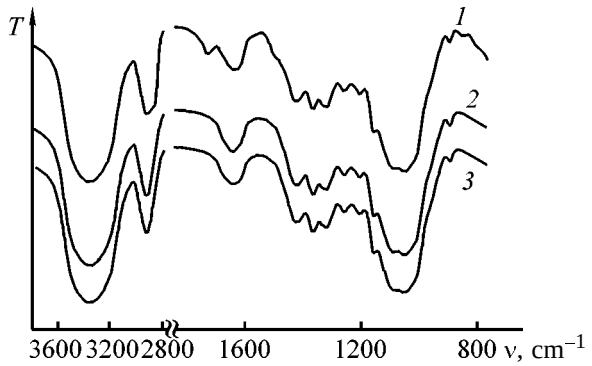

Fig. 2. IR spectra of (*1*) raw flax fibers and (*2*, *3*) hydrated cellulose films obtained from cotton linter and flax cellulose, respectively, in the mTEAO–DMSO system. (*T*) Transmission and (ν) wave number.

asymmetric and symmetric vibrations of ionized COO^- groups of pectins. A band characteristic of cellulose was observed at 2900 cm^{-1}; it is assigned to symmetric and asymmetric vibrations of CH_2 and CH groups of the polymer. The spectrum of pectin exhibits two absorption bands in the 2890–2925 cm^{-1} range [11]. The shoulder near 2900 cm^{-1} and the bands at 1740 cm^{-1} in the IR spectrum of raw flax cellulose suggest the presence of pectin. The presence of lignin is indicated by broadening of the band at 1650 cm^{-1} towards 1600 cm^{-1}, as well as by the appearance of a shoulder at 1500 and a band at 850 cm^{-1} [10].

The lack of characteristic absorption bands of lignin and pectin in the IR spectrum of hydrated cellulose film obtained from solution of refined flax cellulose in the system mTEAO–DMSO suggests that treatment of flax fibers followed by their dissolution and filtration of solutions removes lignins and pectins. The differences in the physicomechanical properties of hydrated cellulose films based on flax cellulose and cotton linter are due to different molecular characteristics of the polymer and to the presence of hemicelluloses in the films obtained from flax cellulose solutions.

CONCLUSIONS

(1) Comparative analysis of the solubility of flax fibers, differing in the degree of purity, in mixtures of triethylamine *N*-oxide monohydrate with dimethyl sulfoxide shows that the impurities in fibers modify the viscosity properties and the association structure of solutions. Removal of fats and pectins results in degradation of cellulose macromolecules.

(2) The size and amount of associates in solutions of identical concentrations depend on the degree of purity of the flax fibers. Moderately concentrated solutions of cotton linter and flax cellulose do not markedly differ in the mechanisms of their viscous flow.

(3) Physicomechanical properties and structural organization of the films obtained from cotton linter and flax fiber solutions differ insignificantly.

REFERENCES

1. Petropavlovskii, G.A., Bochek, A.M., and Shek, V.M., *Khim. Drev*., 1987, no. 2, pp. 3–21.
2. Maia, E. and Perez, S., *Nouv. J. Chim.*, 1983, vol. 7, no. 2, pp. 89–100.
3. Suslennikova, V.N. and Kiseleva, E.K., *Rukovodstvo po prigotovleniyu titrovannykh rastvorov* (Manual on Preparation of Titrated Solutions), Leningrad: Khimiya, 1973.
4. *Spravochnik po khimicheskoi tekhnologii obrabotki l'nyanykh tkanei* (Reference Book on Chemical Processes of Flax Fiber Treatment), Fridlyand, G.I., Ed., Moscow: Legkaya Industriya, 1973.
5. Klenin, V.I., Shchegolev, S.Yu., and Lavrushin, V.I., *Kharakteristicheskie funktsii svetorasseyaniya dispersnykh sistem* (Characteristic Functions of Light Scattering in Disperse Systems), Saratov: Saratov. Gos. Univ., 1977.
6. Belousov, Yu.Ya., Vasil'eva, N.V. Platonov, V.A., *et al*., *Khim. Volokna*, 1983, no. 1, pp. 32–33.
7. Chanzy, H. and Chaunis, S., Abstracts of *TAPPI Conf. Papers, 5th Int. Conf. on Dissolving Pulp*, Wien, 1980, pp. 105–108.
8. *Cellulose and Cellulose Derivatives: Physico-Chemical Aspects and Applications*, Kennedy, J.F., Phillips, G.O., Williams, P.O., *et al*., Eds., Cambridge: Woodhead, 1995.
9. Bochek, A.M., Petropavlovskii, G.A., Sidorovich, A.V., and Kallistov, O.V., *Khim. Drev*., 1991, no. 3, pp. 53–60.
10. Zhbankov, R.G., *Infrakrasnye spektry tsellyulozy i ee proizvodnykh* (IR Spectra of Cellulose and Its Derivatives), Minsk: Nauka i Tekhnika, 1964.
11. Aimukhammedova, G.B., Alieva, D.E., and Shelukhina, N.P., *Svoistva i primenenie pektinovykh sorbentov* (Properties and Application of Pectin-Based Sorbents), Frunze: Ilim, 1984.

Russian Journal of Applied Chemistry, Vol. 74, No. 11, 2001, pp. 1928–1932. Translated from Zhurnal Prikladnoi Khimii, Vol. 74, No. 11, 2001, pp. 1867–1871.

MACROMOLECULAR CHEMISTRY AND POLYMERIC MATERIALS

Graphitization of Polyacetylenes Prepared by Phase-Transfer Dehydrochlorination of Polyvinyl Chloride

V. N. Salimgareeva, Yu. A. Lebedev, N. S. Sannikova, S. V. Kolesov, and A. N. Chuvyrov

Institute of Organic Chemistry, Ufa Scientific Center, Russian Academy of Sciences, Ufa, Bashkortostan, Russia

Institute of Physics of Molecules and Crystals, Ufa Scientific Center, Russian Academy of Sciences, Ufa, Bashkortostan, Russia

Received April 4, 2001

Abstract—To develop procedures for producing graphite from polyacetylene, the effect of crystalline regions in the structure of homo- and copolymers of acetylene with vinyl chloride on the structure and properties of the products of their profound carbonization was studied.

Due to unique properties of graphitic carbon materials (high chemical, electrochemical, and thermal stability and significant thermal and electrical conductivity), they are widely used in various branches of industry.

These materials are mainly prepared from petroleum, pitch, and shale cokes by heat treatment at 2300–3000°C [1]. Graphitic carbon can also be produced by high-temperature (2000–3000°C) pyrolysis of macromolecular compounds, e.g., polyvinyl chloride (PVC) [2] and polyacrylonitrile [3], but their graphitization is low even at high temperatures.

With the aim of finding new precursors of graphitic carbon materials, it was of particular interest to study high-temperature pyrolysis of the simplest carbon-chain polymer with a system of conjugated double carbon–carbon bonds, polyacetylene (PAc), and copolymers of acetylene with vinyl chloride prepared by phase-transfer PVC dehydrochlorination.

EXPERIMENTAL

In our work we used polyacetylene prepared by complete dehydrochlorination of PVC and copolymers of acetylene with vinyl chloride, which are the products of incomplete conversion of PVC into PAc. For this purpose S-65 polyvinyl chloride (degree of polymerization 1950) was dehydrochlorinated with potassium hydroxide in the presence of tertiary ammonium salts [4]. The conversion was controlled by varying the concentration of the dehydrochlorinating agent in the reaction mixture.

The polymer was heated in the 100–1200°C range in a quartz ampule in a vacuum (10^{-3} mm Hg); at temperatures above 1200°C, a ceramic ampule was used. The heating rate was 1.5 deg min^{-1}; then the samples were kept at chosen temperature for 6 h. At the polymer graphitization the heating rate was 2.5 deg min^{-1}, the product was kept at 1100–1200°C and higher temperatures for 24 h. All manipulations were performed in an inert atmosphere (argon). The degrees of dehydrochlorination α and dehydrogenation C/H were determined by elemental analysis.

The TGA was performed on a Perkin–Elmer du Pont 900 thermal analyzer at a 3 deg min^{-1} heating rate in a helium flow (40 ml min^{-1}).

The concentration of paramagnetic species in the polymer was evaluated with an RE-1306 radiospectrometer.

The structure and morphology of the carbonized products were studied with an REM-100 scanning electron microscope and an EMMA-4 transmitting electron microscope. The reflections in the electron diffraction pattern were indexed with standard natural graphite references. The content of graphite C_{gr} in the pyrolysis products was determined using a DRON-2 diffractometer according to the procedure given elsewhere [5].

The specific electrical resistivity ρ of the pelletized samples (300 μm thick) was registered by the four-probe method using cells equipped with stainless steel electrodes and an E-7-8 ac bridge potentiometer (1 kHz).

1070-4272/01/7411-1928$25.00

The common feature of polymers with conjugated bonds is their high thermal stability, which is due to the decrease in the internal energy at polyconjugation. In study of the PAc thermal stability we found that the thermal degradation of this polymer begins at 300–320°C and is accompanied by significant weight loss and formation of volatile (predominantly benzene) and oily aromatic products. At higher temperatures formation of benzene is terminated. The polymers break down stepwise with maximal rates at 300–320 and 440–450°C, and the process is terminated at 600–650°C with formation of the coke residue (25–40% yield).

The mechanism of thermal degradation of PAc prepared by phase-transfer dehydrochlorination of PVC probably involves cleavage of the chain caused by the electron–proton exchange and in some cases by the ring closure [6]. The intermolecular electron migration and ring closure result in formation of benzene and other aromatic hydrocarbons.

The supramolecular structure affects the degradation processes in the polymer. In the case of crystalline PAc the degradation rate of macromolecules is lower and the yield of the carbonized residue is higher than in the amorphous sample: weight loss curve *1*' lies higher than curve *2*' (Fig. 1). The rigid crystal structure of PAc hinders elimination of macromolecular fragments, but facilitates carbonization of the polymer at heat treatment. Dehydrogenation of this polymer begins at 250–300°C and via several intermediate structures yields completely carbonized samples at 1100–1200°C. As seen from the dependences of the C/H ratio characterizing the hydrogen loss (Fig. 1), the dehydrogenation rate of crystalline PAc is higher compared to the amorphous polymer. The amorphous polymer is carbonized completely only at 2000°C. At certain temperature the dehydrogenation–hydrogenation equilibrium is attained, which is confirmed by appearance of the saturation plateau on the kinetic curve of hydrogen loss at fixed temperature (Fig. 2). This equilibrium is shifted toward dehydrogenation with increasing temperature.

These experimental results can be explained by features of macromolecular packing in the crystalline polymer. Electron diffraction and structural studies show that the distance between the macromolecules is 3.40 Å. This is significantly smaller than the sum of the van der Waals radii, which suggests interchain interaction. The distance between the hydrogen atoms in the neighboring macrochains of 1.40 Å was evaluated using model structures. This is probably responsible for facile hydrogen elimination with formation of two radical centers in the neighboring macromolecules.

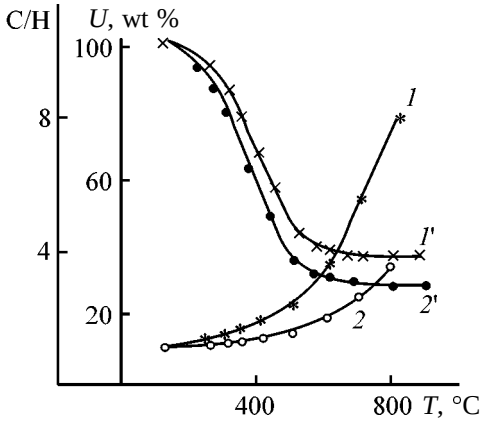

Fig. 1. (*1*, *2*) C/H ratio and (*1*', *2*') weight loss *U* in the (*1*, *1*') crystalline and (*2*, *2*') amorphous PAc polymers as functions of annealing temperature *T*.

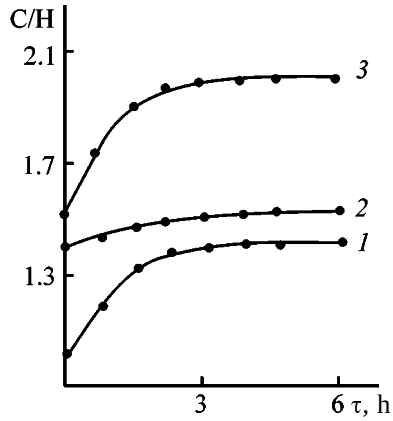

Fig. 2. Kinetic curves of thermolysis of crystalline PAc at (*1*) 300, (*2*) 350, and (*3*) 400°C. (C/H) Atomic ratio and (τ) time. Samples were preliminarily annealed at (*1*) 100, (*2*) 300, and (*3*) 350°C.

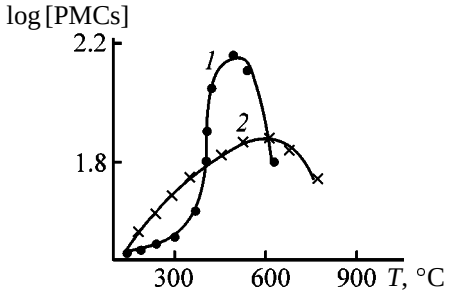

Fig. 3. Concentration of PMCs as a function of the temperature of thermal treatment *T* of (*1*) crystalline and (*2*) amorphous PAc polymers.

Dehydrogenation is accompanied by variation of the number of paramagnetic centers (PMCs) in the samples. The curves of PMC accumulation pass through maxima (Fig. 3) at 400–500 (crystalline polymer) and 500–600°C (amorphous polymer), when

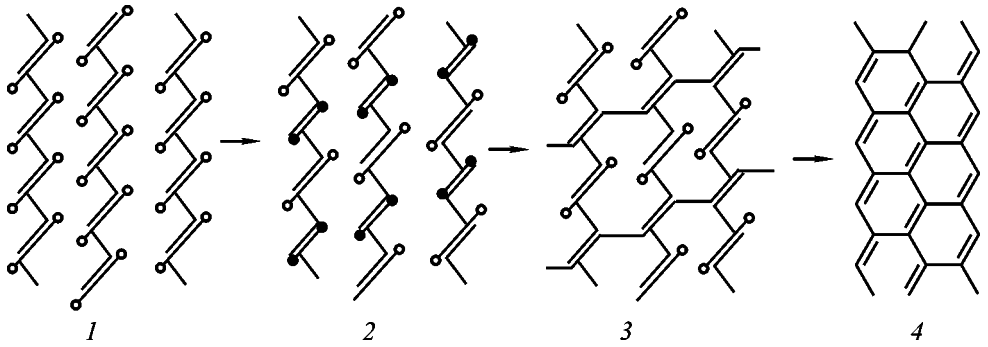

Fig. 4. Transformations of crystalline PAc in the course of thermal treatment in a vacuum: (*1*) initial PAc, (*2*, *3*) $-(C_2H)_n-$ product, and (*4*) condensed aromatics.

the $-(C_2H)_n-$ products are formed. These products are rather stable systems containing up to 10^{22} PMCs (i.e., one paramagnetic center per two carbon atoms). Enrichment with paramagnetic centers affects the magnetic and electrophysical properties of these products, which differ from those of the less and more carbonized products. As shown in [7, 8], the $-(C_2H)_n-$ products exhibit high paramagnetism and high tension sensitivity. The structure of the $-(C_2H)_n$ products can be presented by pattern *2* (Fig. 4). The rigid crystal structure hinders cross-linking and formation of the –C≡C– bonds, as these processes involve the contraction of the chains or their straightening, respectively. Further temperature rise increases the chain flexibility and promotes cross-linking, which decreases the number of PMCs. In this case the IR spectra exhibit the absorption bands at 1330 and 740 cm^{-1}, lacking in the spectrum of the initial polymer and characterizing the in-plane and out-of-plane bending vibrations of the =C–H group in the *cis* configuration.

The IR spectra of PAc prepared by phase-transfer dehydrochlorination of PVC contain bands belonging to the in-plane and out-of-plane bending vibrations of the =C–H group in the *trans* configuration: 1292 and 1015 cm^{-1}, respectively. The fact that the IR spectrum of the carbonized polymer contains the bands belonging to the *cis* structure with simultaneous decrease in the intensity of the bands of the =C–H group in the *trans* configuration can be explained by formation of structure *3* (Fig. 4) by cross-linking.

Further carbonization of the sample results in formation of compact planar layers of six-membered carbon rings (Fig. 4, structure *4*). These layers can be considered as a macromolecule consisting of condensed aromatic rings.

The products of incomplete carbonization of PAc polymer are intermediate between the linear polymers with a system of conjugated double bonds and the products of complete carbonization (carbon, graphite) involving two- and three-dimensionally ordered networks of six-membered rings. In nongraphitic carbon the layers are arranged in small stacks without mutual (azimuthal) ordering between the planes. In graphite there is a three-dimensional order of the carbon networks due to weak van der Waals attraction.

The thermal treatment at 1100–1200°C of both amorphous and crystalline PAc polymer yields nongraphitic carbon (Table 1). As known [1], mutually parallel orientation of the crystallites and the absence of strong cross-links between the aromatic layers at the crystallite edges are necessary conditions for good graphitization of cokes. In the case of PAc this condition is not met. The amorphous polymer contains no crystallites, whereas in the crystalline polymer interchain cross-links hinder graphitization.

Thermolysis of the products of incomplete dehydrochlorination of PVC (block copolymer of acetylene and vinyl chloride) is a gross process involving successive reactions of thermal dehydrochlorination and thermal dehydrogenation. The elimination of HCl is complete at about 300°C, and elimination of hydrogen from the macromolecule starts simultaneously. In this case the structure of the final products is determined by the conditions of the polymer synthesis, namely, the concentration of potassium hydroxide used as dehydroclorinating agent. As seen from Table 1, pyrolysis of copolymers prepared at high concentrations of KOH both in the initial solution and reaction mixture yields products with a disordered structure. With decreasing KOH concentrations in solution or in the reaction mixture the copolymer of vinyl chloride and acetylene is formed, whose thermolysis yields the product with an ordered structure, polycrystalline graphite, i.e., graphitic material with cross-linked small crystalline areas.

As shown previously [4], the concentration of

Table 1. Structure of the pyrolysis products (1100–1200°C) as influenced by the preparation conditions of PAc and copolymers of polyacetylene and polyvinyl chloride

Preparation conditions		Initial compound			Structure of pyrolysis products
[KOH],* wt %	[KOH],** g ml^{-1}	Cl, %	α, %	acetylene : vinyl chloride molar ratio	
50	0.42	0	100	–	Nongraphitic carbon
50	0.42	3.6	94	36 : 1	″
50	0.42	21.6	62	3 : 2	″
50	0.25	0	100	–	″
50	0.05	35.0	39	2 : 3	Graphitic + quasi-two-dimensional products
20	0.42	21.0	63	3 : 2	″

* Concentration of KOH in solution.

** Amount of KOH in the reaction mixture, gram of dry compound per milliliter of the organic phase (solution of PVC in nitrobenzene).

KOH solutions affects the density of the samples obtained by complete dehydrochlorination of the polymer. At a low concentration of potassium hydroxide the crystal packing is denser (d 1.35 g cm^{-3}) than at high hydroxide concentrations (1.25 g cm^{-3}). Obviously, the presence of compact crystallites in the products of incomplete dehydrochlorination of PVC is a prerequisite for high ordering in the pyrolysis products. The PAc crystallites in the copolymer of vinyl chloride and acetylene exhibit a three-dimensional ordering. The carbon networks formed during pyrolysis of this copolymer are ordered in all three dimensions, i.e., graphite crystals are formed. The topochemical transformations of the products of incomplete conversion of PVC proceed at relatively low temperatures of about 1200°C.

Three-dimensional ordering of the carbon networks (graphitization) starts at 900–1000°C. The samples studied involve both crystalline and amorphous fractions. The XRD patterns of the samples obtained in these stages of graphitization exhibit the reflections at 3.40 (crystalline PAc) and 3.35 Å (graphite), and a broad reflection at 3.60–3.80 Å (amorphous product). With increasing temperature the graphite structure is progressively formed (Table 2). At pyrolysis of this copolymer at 1100–1200°C the interlayer spacing sharply decreases from 3.40 to 3.35–3.38 Å, typical of graphite [9]. The electron diffraction patterns of PAc and polycrystalline graphite are shown in Figs. 5a and 5b, respectively. The crystallite size in graphite is 10^4–10^5 Å, whereas the size of two-dimensional island structures appearing in carbonization of amorphous polymer (Fig. 5d) does not exceed 50–60 Å.

The density and electrical conductivity of commercial synthetic graphite depend on the properties of the raw material (coke) and vary within 1.4–2.2 g cm^{-3} and 7–30 Ω cm [9], respectively. The pycnometric density and specific electrical conductivity of graphite prepared by pyrolysis of acetylene–vinyl chloride copolymer are 2.03–2.06 g cm^{-3} and 10 Ω cm, respectively.

Thus, the properties of graphite prepared by pyrolysis of acetylene–vinyl chloride copolymer are similar to those of graphite produced by coke pyrolysis. This product belongs to the class of filled graphites used, for example, in the diamond synthesis.

Along with polycrystalline graphite, in the course of pyrolysis at 1100–1200°C, a bright compact film

Table 2. Properties of pyrolysis products of acetylene–vinyl chloride copolymer*

τ, h	C_{gr}, wt %	ρ, Ω cm	C_{gr}, wt %	ρ, Ω cm
	1000°C		2000°C	
0	0	1×10^9	0	1×10^9
3	0	1×10^9	11	3×10^7
5	2	1×10^9	20	4×10^6
7	5	7×10^8	30	2×10^5
9	9	8×10^7	64	1×10^4
11	18	5×10^6	75	7×10^2
15	49	2×10^4	80	1×10^2
20	66	4×10^3	95	10
24	75	7×10^2	95	10

* Acetylene : vinyl chloride molar ratio 2 : 3.

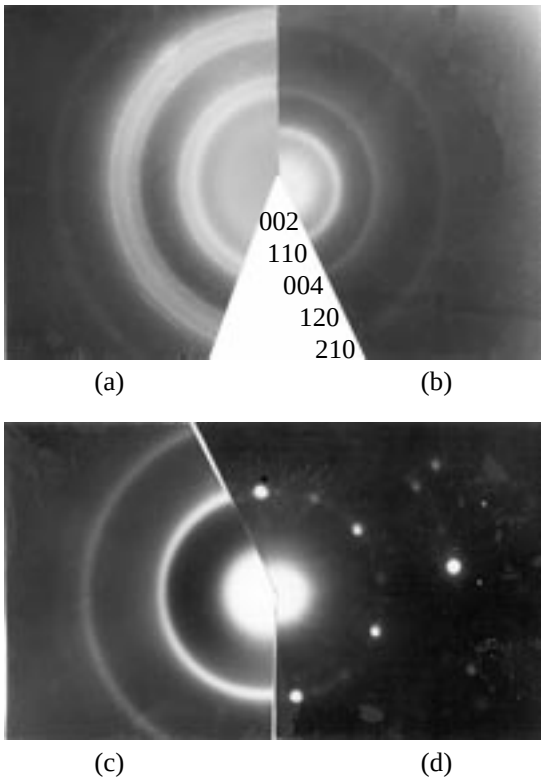

Fig. 5. Electron diffraction patterns of (a) PAc, (b) graphite prepared by pyrolysis of incompletely dehydrochlorinated PVC, (c) natural graphite, and (d) graphite island structures in pyrolyzed amorphous PAc.

of pyrolytic carbon (20–100 μm thick) is formed at the boundary between the polymer and reaction vessel wall. This film consists of azimuth-disordered graphite-like layers packed in parallel to each other with the interlayer spacing d_{002} 3.49 Å and can be identified as quasi-two-dimensional graphite. Heating of the film to temperatures higher than 2000°C improves the structure and packing of the graphite-like areas; the interlayer spacing decreases and at 2200°C it reaches 3.43 Å. This two-dimensional graphite with a high anisotropy of electrical and optical properties was described in [10].

Carbonization of acetylene–vinyl chloride copolymer in the presence of quartz and ceramic plates results in coating of their surface with pyrolytic carbon and formation of graphite. In the case of stainless steel supports, products with a random structure are formed.

CONCLUSIONS

(1) Crystalline amorphous polyacetylene prepared by phase-transfer dehydrochlorination of polyvinyl chloride to complete polymer conversion is not graphitized at heating to 1100–1200°C.

(2) The products of incomplete conversion of polyvinyl chloride, which are the block copolymers of acetylene and vinyl chloride involving crystalline regions, are converted into graphite at 1100–1200°C.

REFERENCES

1. Smirnov, B.N., Tyan, L.S., Fialkov, A.S., *et al.*, *Usp. Khim.*, 1976, vol. 45, no. 10, pp. 1731–1756.
2. Fialkov, A.S., *Uglegrafitovye materialy* (Graphitic Carbon Materials), Moscow: Energiya, 1979.
3. Renschler, C.L. and Sylwester, A.P., *Appl. Phys. Lett.*, 1987, vol. 50, no. 20, pp. 1420–1422.
4. Leplyanin, G.V. and Salimgareeva, V.N., *Izv. Ross. Akad. Nauk., Ser. Khim.*, 1995, no. 10, pp. 1886–1893.
5. Lipson, H. and Cochran, W., *The Determination of Crystal Structure*, vol. 3 of *The Crystalline State*, Bragg, L., Ed., London: Bell, 1953.
6. Chien, C.W., Uden, P.C., and Fun, Ju-Li, *J. Polym. Chem. Ed.*, 1982, vol. 20, no. 8, pp. 2159–2167.
7. Salimgareeva, V.N., Prochukhan, Yu.A., Korepanova, O.E., *et al.*, *Zh. Prikl. Khim.*, 1999, vol. 72, no. 5, pp. 831–836.
8. Salimgareeva, V.N., Prochukhan, Yu.A., Sannikova, N.S., *et al.*, *Vysokomol. Soedin., Ser. A.*, 1999, vol. 41, no. 4, pp. 667–672.
9. Vyatkin, S.E., Deev, A.N., Nagornyi, V.G., *et al.*, *Yadernyi grafit* (Nuclear Graphite), Moscow: Atomizdat, 1967.
10. Chuvyrov, A.N., Lebedev, Yu.A., Kornilov, V.M., *et al.*, *Synth. Met.*, 1991, vol. 42, nos. 1–2, pp. 1443–1446.

Russian Journal of Applied Chemistry, Vol. 74, No. 11, 2001, pp. 1933–1936. Translated from Zhurnal Prikladnoi Khimii, Vol. 74, No. 11, 2001, pp. 1872–1875.

MACROMOLECULAR CHEMISTRY AND POLYMERIC MATERIALS

Reactions of Polysaccharide Aldehydes with Aromatic Hydroxy Compounds

O. B. Suvorova, A. A. Iozep, and B. V. Passet

St. Petersburg State Academy of Pharmaceutical Chemistry, St. Petersburg, Russia

Received October 16, 2000; in final form, May, 2001

Abstract—Reaction of dextran polyaldehyde with phenol or its derivatives was suggested as a way to modify polysaccharides with aromatic hydroxy compounds.

Phenols readily enter into electrophilic substitution, even with such weak electrophiles as aldehydes. Reaction of polysaccharide aldehyde (PA) with phenols was not studied previously; therefore, it was appropriate to study this reaction with the aim to develop a new procedure for modifying polysaccharides.

Chemical modification of PA was performed as follows:

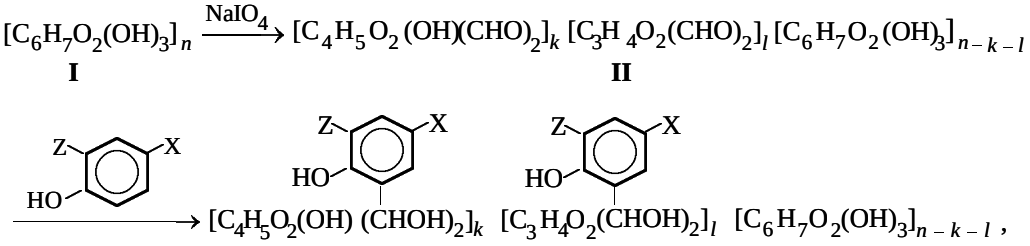

IIIa–**IIIf**

where Z, X = H (**IIIa**); X = CH_3, Z = H (**IIIb**); X = NO_2, X = H (**IIIc**); X = Cl, Z = H (**IIId**); X = COOH, Z = H (**IIIe**); X = H, Z = COOH (**IIIf**).

In our study we used extracellular microbial polysaccharides: aubasidan (branched β-1,3-β-1,6-α-1,4-glucan produced by yeast-like fungus *Aureobasidium pullulans*), rhodexman (β-1,3-β-1,4-mannan produced by *Rhodotorula rudra*), rhonasan (sulfated rhodexman), and also dextran commercially produced in Russia.

Polysaccharides **I** were activated by periodate oxidation [1] in acetate buffer solution (pH 4.1). The consumption of sodium periodate was checked spectrophotometrically at 222.5 nm [1]; the amount of the released formic acid was determined by volumetric titration. To prepare water-soluble polyaldehydes **II** derived from dextran (DPA), rhodexman, and rhonasan, the low-molecular substances were removed by dialysis, the solutions were concentrated in a vacuum at 60°C, and the polyaldehydes were precipitated with ethanol. Water-insoluble aubasidan polyaldehyde was filtered off and washed successively with distilled water, alcohol, and ether.

To determine the optimal conditions for reactions of aromatic hydroxy compounds with PA, we studied the reaction of DPA with phenol.

The reaction was performed in water at 20–90°C for 2–10 h. To prepare monohydroxyalkylation products, 1–5 mol of phenol was added per mole of aldehyde groups in the polysaccharide. After reaction completion, the product was precipitated with alcohol and reprecipitated from water to remove excess phenol. The absence of free phenol in the target product was checked by thin-layer chromatography.

The synthesized phenol–polysaccharide compounds are light yellow amorphous powders readily soluble in water and aqueous alkali but insoluble in alcohol, ether, and the majority of other organic solvents.

1070-4272/01/7411-1933$25.00

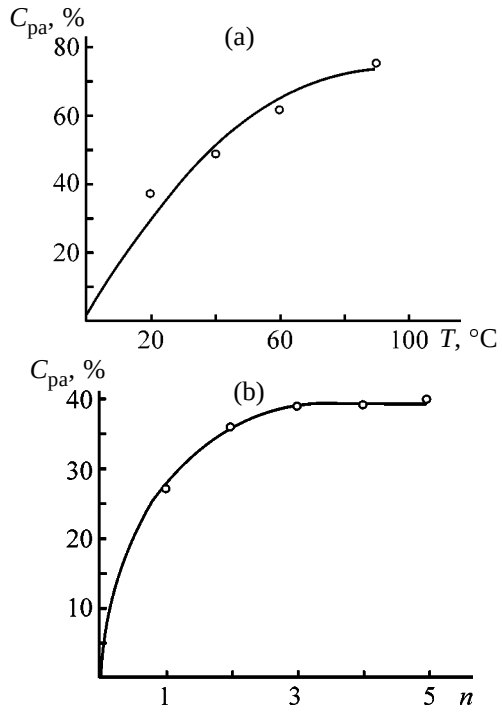

Fig. 1. Conversion of aldehyde groups C_{pa} in reaction of DPA with phenol as a function of (a) reaction temperature T and (b) molar ratio of the reactants n. Reaction time 2 h, pH 10; (a) 2 mol of phenol per mole of aldehyde groups; (b) 20°C.

The products of reaction of PA with phenols were studied by UV and IR spectroscopy, conductometric titration, and viscometry and characterized by the degree of substitution C_{sp} (number of phenolic fragments per polysaccharide monomeric unit) and degree of conversion $C_{ca} = (C_{sp}/C_{sa}) \times 100\%$, where C_{sa} is the content of aldehyde groups in the polymer.

The IR spectra of the products contain bands at 1500 cm^{-1}, assignable to the stretching vibrations of the C=C bonds in aromatic compounds, and at 695 and 770 cm^{-1}, corresponding to the out-of-plane bending vibrations of the C–H bond in 1,2-disubstituted benzene derivatives. The absorption band of 1,4-substituted benzene derivatives at 800–830 cm^{-1} is lacking, which suggests that under experimental conditions the electrophilic substitution in the benzene ring mainly occurs at the *o*-position relative to phenolic hydroxyl, yielding the 1,2 derivative as the major product.

The position of the UV absorption maxima of aqueous solutions of phenol–polysaccharide samples depends on pH (275 nm at pH < 7 and 290 nm at pH > 7) and differs from that characteristic of free phenol under similar conditions (λ_{max} 265 nm). Polysaccharides exhibit no absorption in this range.

Reactions of aldehydes with phenols can yield polymerization products by reaction of one phenolic fragment with several aldehyde groups. This should result in cross-linking of the polysaccharide chains, with a considerable increase in the molecular weight of the polymer and hence in the relative viscosity of polysaccharide solutions. However, the relative viscosity of aqueous solutions of the polyaldehyde does not increase after reaction with phenol. This fact suggests that phenols react with aldehyde groups of only one polymer chain, with no cross-linking.

It is known that polyaldehydes are unstable in alkaline solutions and are readily oxidized with atmospheric oxygen to carboxylic acids [2]. We found that in the presence of phenols under the synthesis conditions (20°C, pH 10, 2 mol of phenol per mole of aldehyde groups) PA is not oxidized. Carboxy groups were not detected in the samples.

To prove the absence of quinoid structures, PA–phenol samples were treated with hydroxylamine after reduction of aldehyde groups with sodium borohydride. The elemental analysis and IR spectra of the resulting samples showed the absence of nitrogen atoms and of absorption bands at 1640 cm^{-1} typical of oximes. Hence, the polysaccharide samples contain no quinoid structures. Therefore, the content of the residual aldehyde groups in phenol–polysaccharide samples was determined by the oxime method. It was found that approximately 2 mol of aldehyde groups are converted per mole of phenol.

The molecular-mechanics (MM+) simulation of the reaction products showed that structures obtained by reaction of phenol with two aldehyde groups of the same PA fragment (**III**) are the least stable. Quinoid structures **IV** are also poorly stable.

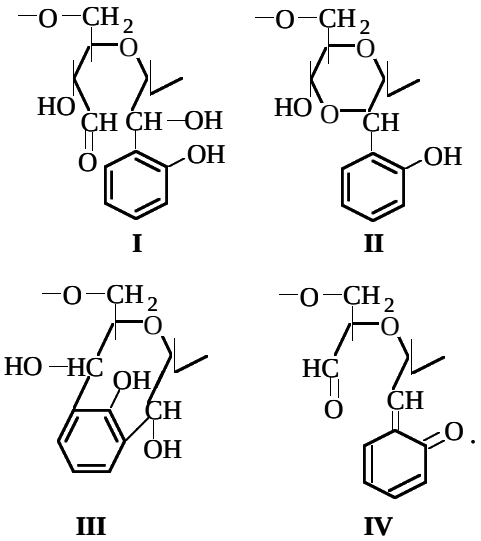

Our results suggest that the samples have lactol structures **II**. Such structures are fairly stable in neutral and alkaline solutions.

Thus, the most probable pathway of reaction of PA with phenol is monohydroxylation of phenol followed by closure of a six-membered lactol ring.

To find the conditions allowing incorporation of a preset amount of phenol into a polysaccharide, we studied how C_{sp} is influenced by temperature, time, reactant ratio, and pH, using as example the reaction of DPA with phenol (Figs. 1a, 1b).

We found that DPA readily reacts with phenol even at 15–20°C, with conversion of approximately 40% of aldehyde groups. Therefore, subsequent experiments were performed at room temperature.

At increased content of phenols in the reaction mixture, the content of phenolic fragments in the polysaccharide samples decreases. However, at the phenol-to-aldehyde ratio higher than 3 : 1, C_{sp} does not increase further.

To attain the desired conversion of DPA aldehyde groups in reaction with phenol at room temperature, we varied the reaction time and found that C_{pa} does not further increase after the 4-h reaction.

Finally, as seen from Table 1, the highest conversion is attained in alkaline solutions. When the reaction is performed at pH ≤ 7, C_{pa} drastically decreases.

Having determined, by the example of DPA, the optimal conditions for the reaction of PA with phenol, we studied the reactivity of the other polyaldehydes under the conditions allowing incorporation of the maximal amount of phenolic fragments.

Table 1. Conversion of aldehyde groups C_{pa} of the polymer in reaction of DPA with phenol as influenced by pH. 20°C, 4 h, 2 mol of phenol per mole of aldehyde groups, C_{sa} 1.32

pH	C_{sp}	C_{pa}, %
5	0.31	24
6	0.36	27
7	0.33	25
9.3 (0.25)*	0.44	41
9.85 (0.5)	0.8	74
10.2 (0.75)	0.91	84
10.65 (1.0)	0.92	85

* In parentheses is the amount of NaOH (moles per mole of phenol).

As expected, the structural features of polyaldehydes affect the reaction course and the product quality (Table 2).

The least active in the reaction with phenols is water-insoluble aubasidan polyaldehyde. Somewhat lower reactivity of rhodexman and rhonasan is probably due to the prevalence in their molecules of 2,3-oxidized fragments capable of forming three types of structures: dialdehyde **II**, is hemiacetal forms **IIa** and **IIb**, and hemiacetal–hydrate forms **IIc** and **IId** occurring in equilibrium [3]. In alkaline solutions, the equilibrium is shifted toward less reactive hemiacetal–hydrate structures:

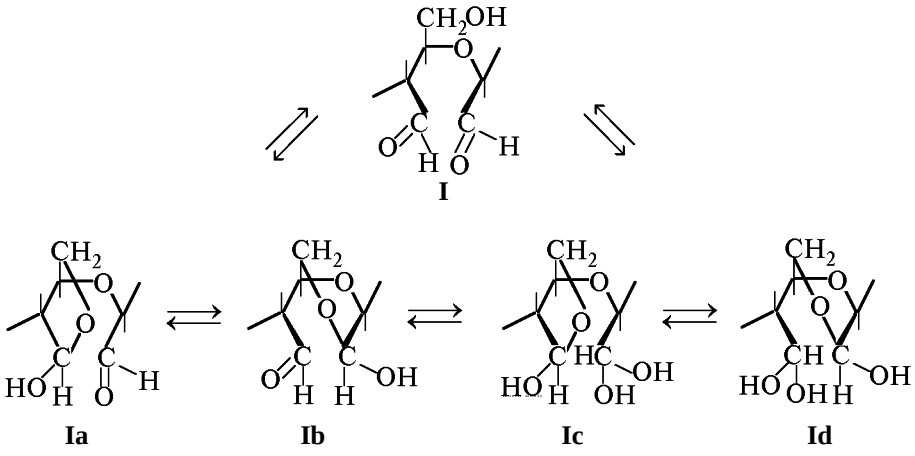

I

Ia **Ib** **Ic** **Id**

Table 2. Results of the reaction of PAs with phenol. 90°C, 4 h, 3 mol of phenol per mole of aldehyde groups, 0.5 mol of NaOH per mole of phenol

Compound	C_{sa}	C_{sp}	C_{pa}, %
Polyaldehyde of:			
dextran	1.09	0.8	74
aubasidan	0.62	0.36	58
rhodexman	0.78	0.51	65
rhonasan	0.5	0.32	64

As expected, electron-withdrawing substituents in the benzene ring appreciably hinder the reaction of DPA with phenolic compounds. On the contrary, introduction of an electron-donating substituent increases C_{pa}. The substituent effect on the reactivity of a compound can be quantitatively evaluated using the Hammett equation. In this contextm it was interesting to find a correlation between C_{pa} and the σ constants of substituents. We obtained a linear correlation: $C_{pa} = -46.032\sigma_p + 43.234$, $r = 0.9984$.

CONCLUSION

Reaction of polysaccharide aldehydes with phenol is a convenient route of polysaccharide modification. It is performed in aqueous solution at 20–40°C for 4 h at the molar ratio of phenol to aldehyde groups of 2–3. Up to 0.6–0.9 mol of phenolic fragments is introduced per mole of the monosaccharide unit. The highest conversion of aldehyde groups in attained in alkaline solutions (0.75–1.0 mol of alkali per mole of phenol). The reaction is not accompanied by oxidation of aldehyde groups with atmospheric oxygen or by gelation due to cross-linking.

REFERENCES

1. *Methods in Carbohydrate Chemistry,* Whistler, R.L. and Wolfrom, M.L., Eds., New York: Academic, 1962–1965.
2. Golova, O.P. and Nosova, N.I., *Usp. Khim.,* 1973, vol. 62, no. 4, pp. 743–767.
3. Drobchenko, S.N., Isaeva-Ivanova, L.S., Grachev, S.A., and Bondarev, S.N., *Vysokomol. Soedin., Ser. B,* 1990, vol. 32, no. 4, pp. 254–258.

Russian Journal of Applied Chemistry, Vol. 74, No. 11, 2001, pp. 1937–1942. Translated from Zhurnal Prikladnoi Khimii, Vol. 74, No. 11, 2001, pp. 1875–1880.

MACROMOLECULAR CHEMISTRY AND POLYMERIC MATERIALS

Physicochemical Modification of Siloxane Compounds for Electrical Engineering in the Course of Mixing

D. N. Lazarev, V. P. Britov, and V. V. Bogdanov

St. Petersburg State Technological Institute, St. Petersburg, Russia

Received December 20, 2000

Abstract—The effect of silica fillers, used separately or in combination, on the rheological properties of siloxane compounds based on low- and high-molecular-weight rubbers was studied. A model was suggested for formation of the structure of filled compounds during mixing under conditions of shear stresses, and a procedure was proposed for preparing compounds for shells of high-voltage insulators produced by pressure casting.

Wide use of polymeric insulators in contact wiring systems and high-voltage installations is due to their advantages over porcelain and glass insulators, such as high electrical parameters (low dielectric permittivity, high breakdown voltage, etc.), good service properties (high hydrophobicity, resulting in self-cleaning, so that it becomes unnecessary to wash insulators; resistance to vandalism), and also very favorable characteristics from the viewpoint of transportation and mounting (no damage at transportation because of the lack of friability; lower, by a factor of 2, weight as compared to the porcelain articles) [1].

At present, three classes of polymeric materials are used as protective coatings for insulators: epoxy resins highly filled with ground quartz or aluminum hydroxide, ethylene–vinyl acetate copolymers (with the same fillers), and silicone elastomers [2]. The latter compounds are the most promising materials. This is due to their high weather resistance, capability for long operation in a wide temperature range (from –60 to 60°C), and elasticity. In contrast to the majority of insulating materials, silicone elastomers are capable to preserve a low surface energy, which prevents formation of a continuous water film on the insulator surface and appearance of leakage arcs. Furthermore, silicone polymers are environmentally clean.

Development of procedures for fabrication of polymeric insulators is based on attempts to pass from successive coating with separate components to continuous pressure casting of protective shells of various shapes and sizes. The developed procedures for fabrication of insulator shells by casting mainly utilize thermoplastic materials or some types of thermosetting plastics (epoxy compounds) [3].

Protective siloxane shells for insulators can be made of compounds based on low- and high-molecular-weight rubbers. The advantages of one or anoter class of materials are not fully understood, despite a clear trend toward the use of liquid rubbers with the aim to perform casting efficiently. Certain drawbacks are inherent in compounds based on both high- (high viscosity) and low-molecular-weight (low strength, problems with introduction of reinforcing fillers) rubbers. The common drawback of both high- and low-molecular-weight siloxane compounds is the long vulcanization time, which significantly complicates casting.

To develop a casting process for preparing protective coatings for insulators, it is necessary to modify some properties of siloxane compounds (ensure high flowability, shorten vulcanization time); it seems more expedient to perform physicochemical modification in the course of compounding, rather than to adjust the formulation.

The goal of this study was to find procedures for physicomechanical modification of polysiloxane compounds for electrical engineering with the aim to develop an efficient process for pressure casting of protective insulator shells.

As the major investigation objects we chose compounds based on SKTV-1-NT high-molecular-weight siloxane rubber (hereinafter, SKTV), differing in the

1070-4272/01/7411-1937$25.00

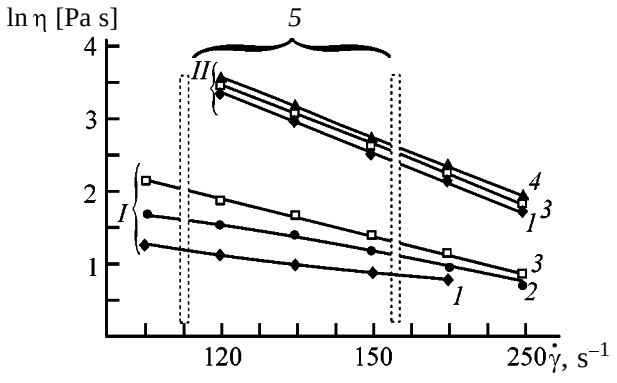

Fig. 1. Viscosity η of siloxane compounds as a function of the shear rate $\dot{\gamma}$. Compound based on (*I*) SKTN-A and (*II*) SKTV-1. Degree of filling with BS-50 white black (wt %): (*1*) 10, (*2*) 15, (*3*) 20, and (*4*) 30; (*5*) range of shear rates actually realized in commercial equipment.

content of Aerosil A-175, BS-50 white black, titanium dioxide, and aluminum hydroxide. To evaluate the physicomechanical and service properties, the compounds modified in the course of mixing were compared with traditional materials for electrical engineering based on SKTV-1 rubber (Lebedev Research Institute of Synthetic Rubber, St. Petersburg) and with the compounds produced by Wakker. In view of the existing predictions that low-molecular-weight rubbers will find growing use in production of siloxane articles, we also studied the behavior of compounds based on materials that are commercially produced in Russia (SKTN-A) and Germany (Bayer).

The compounds were prepared on different apparatus: laboratory rollers, a laboratory mixer with Z-shaped blades, and a closed rotary measuring mixer, with the aim to evaluate how apparatus features affect the compounding process.

Evaluation of the process characteristics of siloxane compounds and description of their behavior were based on the results of rheological tests performed by capillary and rotary viscometry.

Determination of the service properties of compounds (frost resistance coefficient, resistance to thermal aging, specific volume electrical resistivity, tangent of the dielectric loss angle, electrical strength, dielectric permittivity, tracking erosion resistance, arc resistance) were performed according to GOST (State Standard).

In the first stage of our studies, we performed a comparative analysis of the rheological behavior of model compounds based on high- and low-molecular-weight rubbers with the same degree of filling with white black. The viscosities of these compounds differ by a factor of 10 and more, and such a difference is preserved in the entire range of the actual shear rates used in the process equipment (Fig. 1). At the same time, by varying the processing conditions, it is possible to decrease the viscosity of high-molecular-weight compounds to the level characteristic of low-molecular-weight compounds [the viscosity of low-molecular-weight compounds at a shear rate of 10 s^{-1} corresponds to that of high-molecular-weight compounds at a shear rate of $(1–1.5) \times 10^2$ s^{-1}], which allows their processing by pressure casting.

The most important feature of the actual organosilicon compositions used for protective coatings of electrical insulators, from the viewpoint of their process behavior, is the presence of various fillers: aluminum hydroxide, titanium dioxide, and silica (Aerosil). Their total effect increases the viscosity of the system and does not allow production of articles by high-performance pressure casting.

The typical formulations of the compounds are as follows (wt parts): SKTV high-molecular-weight rubber 100, Aerosil A-175 20–30, anti-cross-linking additive 9–10, aluminum hydroxide 90–130, and titanium dioxide 5–7.

Among the ways to control the rheological behavior of the compounds (variation of the formulation, proper order of adding components, use of special methods of strain action), only the latter approach appeared to be feasible.

We have studied the effect of fillers, used separately or in combination, on the rheological behavior of the system. With both active (Aerosil) and inert (aluminum hydroxide) fillers, irrespective of the degree of filling, the viscosity decreased considerably in the range of shear rates 30–120 s^{-1}; at the shear rates of 180–240 s^{-1} the structures formed by the fillers degrade, and the compounds acquire flowability similar to that of Newtonian liquids. We suggested that this effect would be preserved in a compound filled with both types of fillers simultaneously, although the range of shear rates corresponding to the transition to the Newtonian flow would naturally be shifted to higher values. The experimental results (Fig. 2) confirm this suggestion.

The curves in Fig. 2 show that on introducing both types of fillers the increase in the viscosity is not additive. This fact can be accounted for as follows.

An inert filler prevents formation of a thixotropic skeleton formed of Aerosil elements (with the rubber adsorbed on the surface); the higher the content of an inert filler, the larger the deviation from the additivity.

When considering the mechanism of formation of the structure and properties of the compounds, we see that the strain action plays a decisive role. The behavior of a filled compound can be clearly demonstrated by a three-dimensional pattern characterizing the dependence of the viscosity on two parameters: degree of filling and shear rate (Fig. 3). Each section of this pattern can be described analytically by

$$\eta = \eta_0 \exp\left(\frac{\Phi}{1 - \Phi/\Phi_m} \frac{K}{\dot\gamma^x}\right), \quad (1)$$

where K is the form factor characteristic of a given type of filler; $\dot\gamma$ is the shear rate (s^{-1}); Φ is the true volume filling; Φ_m is the volume fraction of the filler at the closest packing of its particles (for randomly packed spheres, 0.61); and x is the coefficient accounting for physicochemical interactions in the system.

The second term inside the exponent characterizes the form factor, which is a function of the shear rate and is related to the strength of the reversible three-dimensional structures polymer–filler.

The calculations show that, e.g., for Aerosil A-175 $K = 50$, $x = 0.07$. The viscosities calculated by the suggested relationship are nicely consistent with the experimental data in a wide range of filler concentrations and shear rates.

It should be noted that, as the shear rate is increased and the degree of filling is decreased, $K/\dot\gamma^x$ tends to 2.5, i.e., the classical Einshtein equation is a particular case of the equation suggested by us.

Equation (1) sufficiently reliably describes the dependence of the viscosity on the degree of filling and shear rate. With several fillers, it can be represented as

$$\eta = \eta_0 \exp\left(\frac{\Phi_1}{1 - \Phi_1/\Phi_m} \frac{K_1}{\dot\gamma^{x_1}} + \frac{\Phi_2}{1 - \Phi_2/\Phi_m} \frac{K_2}{\dot\gamma^{x_2}} + \ldots + \frac{\Phi_n}{1 - \Phi_n/\Phi_m} \frac{K_n}{\dot\gamma^{x_n}}\right). \quad (2)$$

At the same time, in analysis of the effect of external actions on the physicomechanical and service

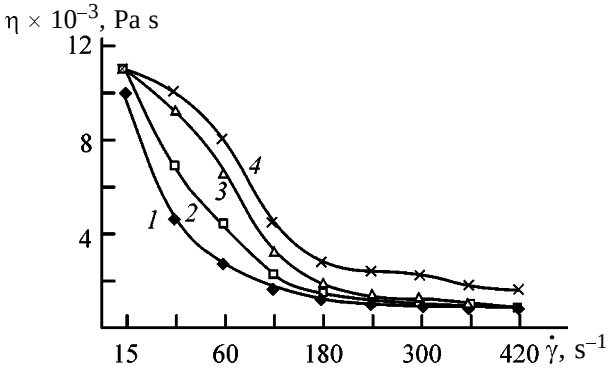

Fig. 2. Viscosity η of compounds with different fillers as a function of the shear rate $\dot\gamma$. Filler (wt parts): (*1*) Aerosil A-175, 30; (*2*) aluminum hydroxide, 130; (*3*) Aerosil A-175, 30 + $Al(OH)_3$, 130; and (*4*) theoretical viscosity of a compound with a complex filler.

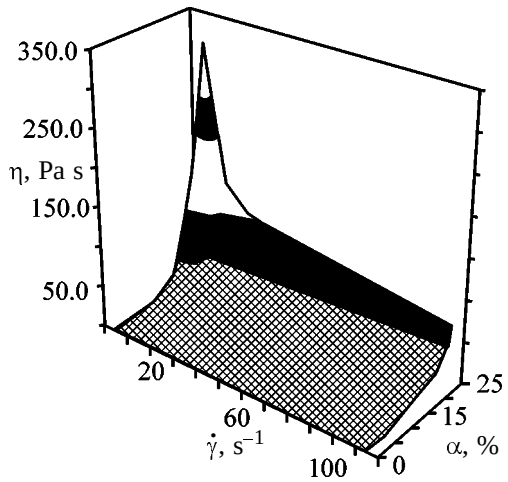

Fig. 3. Combined effect of the degree of filling α and shear rate $\dot\gamma$ on the viscosity η of compounds based on SKTN-A rubber and BS-50 white black.

characteristics of the compounds and process calculations, it is appropriate to use not the shear rate, shear strain, or its dispersion, but a generalized criterion whose physical sense is the strain energy density τΓ [where τ is the shear stress (Pa), and Γ is the shear strain].

The experimental dependences obtained by us allowed us to suggest a generalized model for structure formation in compounds based on both high- and low-molecular-weight rubbers and filled with various fillers. The model suggests the only possible order of introducing the components: first Aerosil with anti-cross-linking additive and then aluminum hydroxide.

Initially, at the instant of introducing the filler, the system is practically unmixed and consists of

Aerosil agglomerates and rubber matrix. Bulk interaction of the active filler with the rubber in this stage is insignificant, because it is aggregated, and the surface of the filler contacting with the polymeric matrix is shielded by the occluded air.

In the course of strain, aggregates and agglomerates of the filler are gradually broken down, and the polymer is adsorbed on the filler surface. The initial stage of adsorption involves "unrolling" of the polymer molecule on the filler surface. This process occurs in time, with its rate depending on the relaxation time of the polymer, and enhances the adsorption. With high-molecular-weight rubbers, the relaxation time is considerably longer, and in this case compounding should involve intermediate keeping as a special operation. When the filler content is sufficiently high, its particles link with each other directly or via adsorbed polymer to form chains and ultimately a three-dimensional network, i.e., a rigid skeleton. As a result, the compound becomes thixotropic (if the shear does not exceed a definite level). The shear stress in the course of compounding can increase even without changing the processing conditions. This is due to the fact that in the course of mixing the system becomes more homogeneous, the surface area of the boundary between the components increases, and hence the interactions in the system as a whole are enhanced. In the second stage of compounding, aluminum hydroxide is added. Its effect on the rheological properties of the system are dual. On the one hand, it increases the viscosity of the compound owing to intrinsic hydrodynamic resistance; on the other hand, it increases the shear stress in mixing and promotes further dispersion of Aerosil. When the required shear stress is attained, Aerosil chains are broken down, and separate particles are isolated from each other with the adsorbed polymer. In the limiting case, each particle can be enclosed in an envelope of the adsorbed polymer. Such a structure exhibits the properties of a Newtonian liquid and is suitable for processing by pressure casting.

It is well known that siloxane compounds, when allowed to stand, acquire thioxotropic properties. This case differs from the case of compounds subjected to strain in that the thioxotropic structure is restored by the other mechanism. After lifting the shear stress, the polymer layer on the surface of an active filler will grow owing to adsorption forces, increasing the apparent volume filling. As a result, the viscosity will increase, and at a certain degree of filling and keeping time the compound can lose flowability and become thixotropic. However, such a thixotropic structure is mainly formed via polymer layers, and it will be broken down reversibly, with the compound becoming fluid.

The results of testing the compounds showed that the vulcanization time largely depends on the strain treatment, which is due to the following facts.

(1) In the absence of strain, the silicone molecule as a constituent of a thioxotropic film on the surface of an active filler is largely unrolled in the adsorption field of the Aerosil particle. In this case it is highly probably that the terminal group is accessible for interaction with the cross-linking agent.

(2) The subsequent strain disturbs the adsorption equilibrium, with the molecule partially rolling up to form a globule; as a result, the number of freely interacting radical groups decreases, and hence the vulcanization time increases.

(3) Further increase in the strain results in significant unrolling of the molecule; as a result, the radical groups get free and become readily accessible for the peroxide, and the vulcanization time considerably decreases.

The combined consideration of the effect of strain on the viscosity, vulcanization time of compounds, and physicomechanical properties of the vulcanized products allows evaluation of appropriate conditions for strain treatment of the material. Figures 4a and 4b show that, as the criterion $\tau\Gamma$ is increased, the strength of the compound first increases and then slightly decreases. The hardness monotonically decreases with time, and the elasticity increases.

Thus, there are three different parameters affected by strain treatment of a material: (1) rheological characteristics (improving the processability of a compound); (2) vulcanization time (shortening the article fabrication time); and (3) physicomechanical characteristics (operation suitability). Simultaneous optimization of these parameters, which are all dependent on $\tau\Gamma$, will give the range of favorable values of $\tau\Gamma$ and allow the choice of the processing procedure, equipment, and process conditions.

Silicone compounds exhibiting required physicomechanical characteristics and ensuring the high service properties of insulators, as a rule, are highly viscous and do not pass to the viscous-flow state at elevated temperatures; therefore, their processing by casting is difficult.

The previously used procedures were unsuitable for efficiently fabricating articles from filled organosilicon rubbers by pressure casting, because of the high viscosity of the compound. At the same time, studies showed that such systems exhibit pronounced thixotropic properties, and their structure can be formed so that strain treatment will make the system fluid.

It was suggested to additionally subject the compounds to shear strain, ensuring $\tau\Gamma$ in the range $(8–16) \times 10^5$ kJ m^{-3} [4].

The procedure can be performed as follows. A standard compound is subjected to strain treatment in a mixer of any type (rotary, roller, screw), so as to ensure $\tau\Gamma$ in the range $(8–16) \times 10^5$.

The quantity Γ for a given mixer type is known (or can be calculated). The procedures for calculating Γ for different types of mixers are comprehensively described in the literature. The viscosity of a compound at a given shear rate is determined from rheological tests.

Based on our studies, a process was developed and put into operation[1] for fabricating polymeric insulators by pressure casting (Fig. 5). The main operations in fabrication of insulators from siloxane compounds are preparation of reinforcement (cutting of rod ends; drying and pressing of end tips); dosing of rubber stock ingredients; mixing of main ingredients; additional treatment of the compound, mixing with a curing agent, sheeting, molding of the article, and first stage of vulcanization; removal of the article from the mold and second stage of vulcanization in an oven; checkout and packaging.

By the developed process, batch production of trolley bus insulators [tension rod polymeric insulator NSK 36/800-7, TU (Technical Specifications) 3494-001-7 825 684 185–98] has been mastered. The article was certified. Also, a pilot batch of linear hanging rod insulators for a 20 kV voltage was produced.

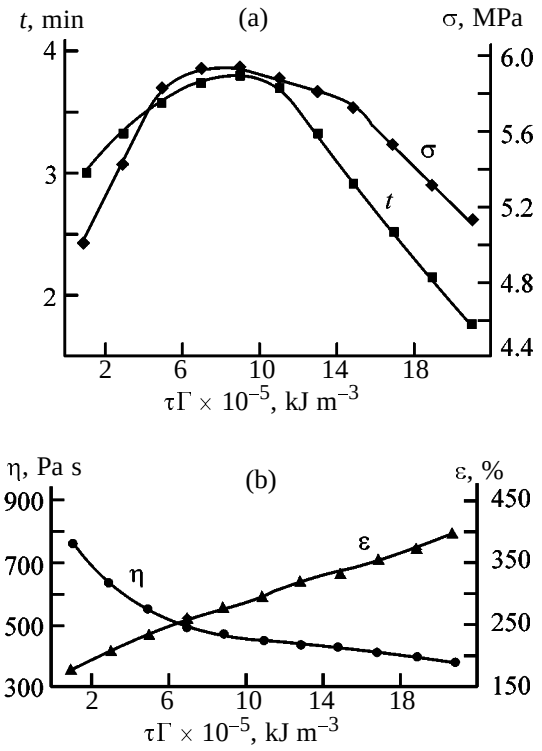

Fig. 4. Effect of strain action $\tau\Gamma$ on the rheological, vulcanometric, and physicomechanical properties of the compound: (*t*) vulcanization time, (σ) strength, (η) viscosity, and (ε) relative elongation.

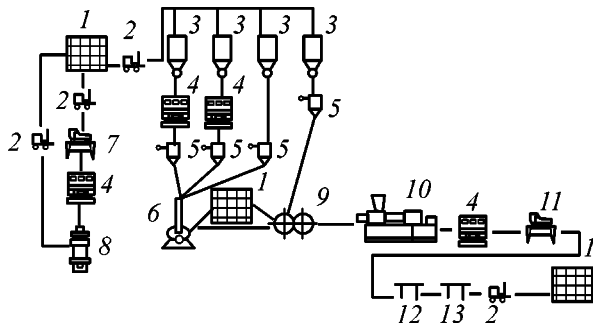

Fig. 5. Flowsheet of fabrication of polymeric insulators by pressure casting: (*1*) storehouse, (*2*) small truck, (*3*) bin, (*4*) oven, (*5*) dosing unit, (*6*) rotary mixer, (*7*) rod machining rig, (*8*) press, (*9*) rollers, (*10*) casting machine, (*11*) insulator machining rig, (*12*) checkout, and (*13*) packaging.

CONCLUSIONS

(1) The viscosity of compounds based on low- and high-molecular-weight rubbers with a complex filler is not an additive function of the content of the fillers; the higher the content of an inert filler, the larger the deviation from the additivity. These systems can also be converted to a fluid state for subsequent pressure casting.

(2) To characterize the external strain action

[1] Izolyator Research and Production Association, St. Petersburg.

on the system, it is appropriate to use a generalized criterion, the strain energy density in the physical sense, rather than traditional concepts of the shear strain.

(3) For the compounds under consideration, the optimal ranges of the strain action values ensuring the required flowability, minimal vulcanization time, and the required physicomechanical properties of insulator shells prepared by pressure casting are in are in the range $(8–16) \times 10^5$ kJ m^{-3}.

REFERENCES

1. Aleksandrov, G.N., Bogoyavlenskii, K.N., Goryachko, V.N., *et al.*, *Energ. Stroit.*, 1996, no. 8, pp. 2–6.
2. Bogdanov, V.V., Britov, V.P., Koryakin, I.N., *et al.*, *Materialy dlya polimernykh izolyatorov* (Materials for Polymeric Insulators), St. Petersburg, 1999, Available from VINITI, March 31, 1999, no. 981-V99.
3. Britov, V.P., Lazarev, D.N., Rebnitskii, S.V., and Bogdanov, V.V., *Kauzh. Rezina*, 1999, no. 6, pp. 18–20.
4. RF Patent 2 143 147.

Russian Journal of Applied Chemistry, Vol. 74, No. 11, 2001, pp. 1943–1946. Translated from Zhurnal Prikladnoi Khimii, Vol. 74, No. 11, 2001, pp. 1881–1884.

MACROMOLECULAR CHEMISTRY AND POLYMERIC MATERIALS

Modification of Epoxy Binders for Glass- and Basalt-Reinforced Plastics

L. M. Amirova, R. Kh. Saifutdinov, A. F. Magsumova, and R. R. Amirov

Tupolev Kazan State Technical University, Kazan, Tatarstan, Russia
Kazan State University, Kazan, Tatarstan, Russia

Received, May 22, 2001

Abstract—The process parameters of production of epoxy binders modified with glycidyl esters of phosphorus acids were studied, and the performance characteristics of glass- and basalt-reinforced plastics on their basis were determined.

Composites based on epoxy oligomers (EOs) and various fibers often have defective structure because of the low ability of the binder to impregnate the filler. This is due to the high viscosity and low wetting power of the binder. As a result, the strength properties of the fiber and matrix are not realized in full measure. Most often the viscosity of binders, in particular epoxy compounds, is decreased by adding appropriate solvents [1]. However, evaporation of the solvent during molding causes large shrinkage, significant internal stresses, and formation of defects, and thus the strength of the resulting composite decreases. All these disadvantages are not typical for active diluents [2, 3] containing one and more epoxy groups, which are incorporated into the polymer network. In this case the most preferable are various glycidyl esters of phosphorus acids (GEPs), whose preparation and properties were described previously in [4]. Epoxy polymers modified with GEP exhibit high levels of strength [5] and heat and fire resistance [6]. In this work we studied the preparation of glass- and basalt-reinforced plastics using binders based on epoxy resins modified with GEPs.

EXPERIMENTAL

In our work we used ED-20 epoxy-4,4'-isopropylidenediphenol oligomer [GOST (State Standard) 10587–84], 4,4'-diaminodiphenylmethane hardener (DADPM), glycidyl esters of phosphorus acids **I**–**III**, and butandiol diglycidyl ether **IV**:

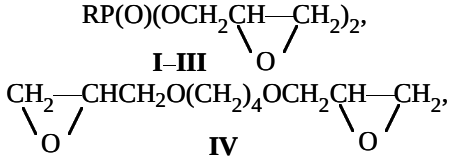

I–III

IV

where R = $OCH_2CH(O)CH_2$ (**I**), OCH_3 (**II**), CH_3 (**III**).

The matrices for the glass- and basalt-reinforced plastics were the T-11 glass fabric (GOST 19170–73) and BT-8 basalt fabric [TU (Technical Specifications) 5952-031-002004949–95].

The viscosity of the mixture of epoxy oligomers and GEPs was determined according to the GOST 10587–84 by the discharge time of the corresponding volume of the mixture through the capillary of a VPZh-1 viscometer (the capillary diameter varied from 0.54 to 5.1 mm). The angle of wetting θ of the surface of various materials by epoxy compounds was measured directly from the drop profile using a microscope equipped with a goniometer. The surface tension of the liquids at the liquid–air interface γ_{lg} was measured by the ring detachment method and by the method of a drop on a low-energy surface (Teflon). The impregnation rate v was determined on a KM-6 cathetometer using the dependence of the lifting height of the binder h in the fabric. In each time t for modified (m) and unmodified (um) binders we measured $(h_m)_t$ and $(h_{um})_t$ and calculated v_m and v_{um}, respectively. The effect of the modifying agent on the impregnating power of the binder was characterized by the relative rate of impregnation (v_m/v_{um}) and the ratio of the ultimate lifting heights of the binder in the fabric h_m/h_{um}.

The standard mechanical tests were performed on an FPZ tensile-testing machine: the tensile strength, according to GOST 25601–80, the bending strength, according to GOST 25604–82, the plane shear stress, according to GOST 24778–81, and the interlaminar

1070-4272/01/7411-1943$25.00

Table 1. Relative impregnation rate v_m/v_{um} of glass and basalt fabrics with phosphorus-containing binders and adhesion A of epoxy polymer modified with GEP to the glass and basalt fiber

GEP, wt %	v_m/v_{um}						A, MPa					
	glass fabric			basalt fabric			glass fiber			basalt fiber		
	I	**II**	**III**	**I**	**II**	**III**	**I**	**II**	**III**	**I**	**II**	**III**
0	1	1	1	1	1	1	33.5	33.5	33.5	36.1	36.1	36.1
5	1.5	1.4	1.3	1.5	1.4	1.3	42.0	41.8	41.5	45.6	44.3	44.0
10	2.2	2.0	1.6	2.2	2.0	1.6	46.3	45.5	44.5	49.4	48.0	47.2
15	2.4	2.2	1.9	2.5	2.3	2.0	54.1	48.2	45.1	57.0	52.1	50.8
20	2.5	2.3	2.0	2.6	2.4	2.1	51.5	47.2	46.3	55.4	50.3	48.2
25	2.5	2.3	2.0	2.6	2.4	2.1	49.8	45.9	45.5	53.8	48.6	47.1
30	2.4	2.2	1.9	2.5	2.3	2.0	47.6	44.1	43.8	52.2	47.4	46.6

shear stress, by tension of a strip with a transverse notch [7].

The adhesion of the fiber to the matrix was studied by the procedure presented elsewhere [8]. The porosity and volume content of the binder and filler in the plastics were evaluated microscopically. The thermal and moisture aging were studied by the procedure presented in [9].

As seen from Fig. 1, the effect of the modifying agents studied on the viscosity of the epoxy binder is most pronounced at their concentration of up to 15 wt %. All glycidyl esters and ethers, with respect to their effect on the decrease of the binder viscosity, can be ranked in the following order: **I** > **II** > **III** > **IV**. As seen, the effect of widely used active diluent **IV** is the weakest. Thus, our data suggest high impregnating power of the binder compositions based on GEPs.

Data on the impregnation of glass and basalt fabrics with epoxy binders with various GEP content are listed in Table 1. These data show that with addition of GEP into the binder the impregnation rate considerably increases and reaches constant values at the content of modifying agents ≥20 wt %. Further increase in the GEP content decreases the impregnation rate, but it remains higher than that for the unmodified binder. The accelerating effect of GEPs on impregnation of the glass and basalt fabrics varies in the order **I** > **II** > **III**, which agrees with the above data on the effect of GEPs on the EO viscosity. As seen, in the case of basalt fabrics the relative rate of impregnation with all GEPs is greater than that in the fiber glass fabrics. This is probably due to higher wettability of the basalt fiber surface as compared to glass fibers. The angles of wetting of the glass and basalt fibers with the epoxy oligomer modified with ester **I** are given in Table 2.

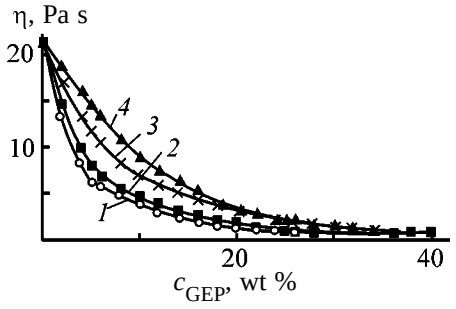

Fig. 1. Viscosity η of modified EP-20 epoxy oligomer as a function of the content c of the active diluent. Diluent: (*1*) **I**, (*2*) **II**, (*3*) **III**, and (*4*) **IV**.

Table 2 shows that with the same fabric the relative lifting height h_m/h_{um} of the binder in the fabric increases by factor of nearly two even at low content of GEP in the binder. At a further increase in the GEP content to 30 wt %, only slightly pronounced maximum in the h_m/h_{um} ratio is observed at a 15–20 wt % content of the modifying agent.

Impregnation of a fabric can be considered as the height of the binder lifting in a capillary (e.g., in the interfiber space). According to the Young–Laplace equation, the lifting height is directly proportional to the surface tension γ_{lg} and cosine of the wetting angle θ and inversely proportional to the liquid density ρ and capillary radius r.

For the same filler, i.e., at constant r, we calculated the relative lifting heights of the binders, which agree with the experimental h_m/h_{um} values (Table 2). These data show that, with respect to the decrease in the viscosity and increase in the relative lifting height and impregnation rate of the glass and basalt fabrics, the

Table 2. Wetting angles θ of glass and basalt fabrics, relative lifting height h_m/h_{um} in their impregnation with ED-20-I mixtures, surface tension γ_{lg}, density ρ, plane shear stress τ_{xy}, and interlaminar shear stress τ_{xz} of plastics modified with ester **I**

Content of **I**, wt %	γ_{lg}, mN m^{-1}	ρ, g cm^{-3}	θ, deg		h_m/h_{um}				τ, MPa			
			glass fiber	basalt fiber	glass fabric		basalt fabric		glass-reinforced plastic		basalt-reinforced plastic	
					expt.	calcd.	expt.	calcd.	τ_{xy}	τ_{xz}	τ_{xy}	τ_{xz}
0	49.0	1.175	65	64	1.00	1.000	1.00	1.000	48.2	34.0	50.1	36.1
5	49.3	1.170	36	33	1.93	1.934	1.93	1.933	51.4	39.6	53.4	41.6
10	49.6	1.170	34	31	1.99	1.994	1.99	1.988	53.8	44.2	55.7	46.7.
15	50.0	1.175	33	29	2.03	2.025	2.04	2.036	56.1	49.6	58.2	52.6
20	50.3	1.185	32	28	2.04	2.043	2.05	2.050	55.4	48.1	57.5	51.4
25	50.6	1.200	32	28	2.03	2.029	2.04	2.037	53.6	47.6	56.2	49.9
30	51.0	1.225	32	28	2.00	2.003	2.01	2.011	52.5	47.1	55.4	48.3

Table 3. Ultimate tensile strength σ_t and bending strength σ_b of glass- and basalt-reinforced plastics based on ED-20 epoxy oligomer modified with esters **I** and **III**

GEP, wt %	σ_t, MPa				σ_b, MPa			
	glass-reinforced plastic		basalt-reinforced plastic		glass-reinforced plastic		basalt-reinforced plastic	
	I	**III**	**I**	**III**	**I**	**III**	**I**	**III**
0	371	371	387	387	370	370	371	371
5	415	390	431	403	386	376	397	382
10	450	404	465	417	399	381	423	393
15	460	409	476	424	403	382	430	398
20	458	407	473	421	400	381	427	396
25	455	404	470	417	397	379	424	394
30	450	401	466	413	393	377	420	391

optimal GEP content in the binder is about 15 wt %. Based on the experimental data, the low-viscosity binders for reinforced plastics were developed and patented [10].

The strength properties of the composites prepared using the above binders were also studied. The experimental strength parameters for plastics (70 wt % filler content) modified with esters **I** and **III** (for **II** the intermediate values were obtained) are listed in Table 3. At equal strength (1.9 GPa) of the glass and basalt fibers the higher strength of the basalt-reinforced plastics is probably due to better wettability and impregnability of the basalt fabrics. As seen from Table 3, even insignificant amounts of GEPs improve the strength properties of epoxy composites. The highest strength of the plastics modified with ester **I** may be due to smaller number of defects thanks to its lower viscosity and higher wetting and impregnating power, to higher strength of the polymer matrix in the presence of **I** [5], and to stronger adhesion to the fiber. Data on the adhesion of modified matrices to the glass and basalt fibers are given in Table 1.

The increase of the adhesion strength with modification of the binder can be illustrated by the data on the plane shear stress τ_{xy} and interlaminar shear stress τ_{xz} of the plastics modified with ester **I** (Table 2). Modification of the binder with glycidyl esters of phosphorus acids does not noticeably affect the thermal and moisture aging of the resulting glass- and basalt-reinforced plastics (Fig. 2).

CONCLUSIONS

Modification of epoxy binders for reinforced plastics with glycidyl esters of phosphorus acids improves

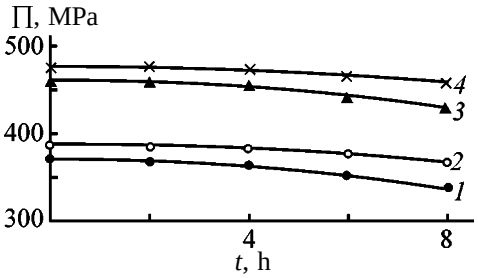

Fig. 2. Residual tensile strength ∏ of the (*1*, *3*) glass- and (*2*, *4*) basalt-reinforced plastics based on (*1*, *2*) unmodified epoxy resin and (*3*, *4*) binders modified with ester **I**, as a function of time *t*.

the wettability and impregnability of the binders. The resulting glass- and basalt-reinforced plastics exhibit high strength properties.

REFERENCES

1. Lee, H. and Nevill, K., *Handbook of Epoxy Resins*, New York: McGraw-Hill, 1967.
2. Dzhavadyan, E.A., Ivanova-Mumzhieva, V.G., Gorbatkina, Yu.A., *et al.*, *Vysokomol. Soedin., Ser. A.*, 1994, vol. 36, no. 8, pp. 1349–1352.
3. Fomicheva, T.N., Spitsyna, O.V., and Shode, L.G., *Plast. Massy*, 1991, no. 11, pp. 30–32.
4. Rizpolozhenskii, N.I., Boiko, L.V., and Zvereva, M.A., *Dokl. Akad. Nauk SSSR*, 1964, vol. 155, no. 5, pp. 1137–1139.
5. Sakhabieva, E.V., and Amirova, L.M., in *Struktura i molekulyarnaya dinamika sistem* (Structure and Molecular Dynamics of Systems), Ioshkar-Ola: Marisk. Gos. Tekh. Univ., 1995, part 2, pp. 178–180.
6. Amirova, L.M., Stroganov, V.F., and Sakhabieva, E.V., *Int. J. Polym. Mater.*, 2000, vol. 47, no. 1, pp. 43–60.
7. Ternopol'skii, Yu.M. and Kintsis, T.Ya., *Metody staticheskikh ispytanii armirovannykh plastikov* (Methods of Static Tests of Reinforced Plastics), Moscow: Khimiya, 1981.
8. Gorbatkina, Yu.G., *Adgezionnaya prochnost' v sistemakh polimer–volokno* (Adhesion Strength in Polymer–Fiber Systems), Moscow: Khimiya, 1987.
9. *Handbook of Composites*, Lubin, G., Ed., New York: Van Nostrand Reinhold, 1982.
10. RF Patent 2 141 493.

Russian Journal of Applied Chemistry, Vol. 74, No. 11, 2001, pp. 1947–1949. Translated from Zhurnal Prikladnoi Khimii, Vol. 74, No. 11, 2001, pp. 1884–1887.

MACROMOLECULAR CHEMISTRY AND POLYMERIC MATERIALS

Photoetching of Copper Surface with Photosensitive Polymeric Coatings

V. A. Anfinogenov, E. E. Sirotkina, N. G. Domina, and A. I. Khlebnikov

Polzunov State Engineering University, Barnaul, Russia
Institute of Petrochemistry, Siberian Division, Russian Academy of Sciences, Tomsk, Russia

Received November 14, 2000; in final form, August 2001

Abstract—Solid-phase photoetching of copper surface with photosensitive polyvinyl chloride compositions was studied. The depth of the relief was determined as influenced by the nature of photosensitizers present in the composition and by the exposure time of the photosensitive layer.

The main principles of photoetching were proposed in 1967 [1]. Preparation of a relief image consists of three steps: (1) application of a polymeric film containing photosensitive C–Hlg bonds on the metal surface (2) activating irradiation through a phototemplate, and (3) dissolution of the polymeric film.

The advantages of this procedure over, e.g., the photoresist process is smaller number of steps owing to etching of the surface during its irradiation and the absence of aggressive media.

The photoetching mechanism involves formation of active products in the polymeric matrix during photolysis of polyhalogenated organic compounds and reaction of these products with the metal surface [2].

The feasibility of etching is determined by the ability of the metal to form stable halides upon irradiation [3].

The necessary conditions for all photosensitive systems are photolysis of the etching agent with a high quantum yield, high thermal stability under these conditions, and compatibility of the components.

Solid-phase photoetching of the copper surface finished to the 14th grade was studied with the aim of producing reflecting diffraction grating with the line depth no less than 0.1 μm. Photosensitive compositions containing polyvinyl chloride resin and various photosensitizing agents were developed. The samples thermostated at 25±2°C were irradiated with a DRSh-250 lamp through a quartz phototemplate. The line depth on the copper surface was measured with an MII-4 microinterferometer after removal of the polymeric film and photoetching products.

Solid-phase etching strongly depends on the thickness of the polymeric film. The thicker the film, the faster the process but worse the resolution. Therefore, we studied how the polyvinyl chloride concentration in the casting solution C_{PVC} affects the thickness of photosensitive films l:

C, g ml^{-1}	l, μm
0.10	18.5
0.09	15.0
0.08	12.0
0.07	9.0
0.06	7.5
0.05	6.5
0.04	5.5

The films with the optimal thickness (8–15 μm), allowing formation of a sharp image without side etching, were prepared at the polymer concentration ranging from 0.07 to 0.09 g ml^{-1}.

Most of photosensitive polymers contain C–C, C–O, C–N, and C–Hlg bonds whose energy does not exceed 420 kJ mol^{-1} [4]. Since the energy of UV quanta is enough for homolytic rupture of these bonds, photolysis of these polymers almost always involves generation of radicals. Various organic and inorganic halogen-containing compounds used as photosensitive components are presented un Table 1. Inorganic additives have virtually no effect on the solid phase photoetching, probably because of poor compatibility with the polymeric matrix of the photosensitive layer. Bromoform, tetrachloro-9-octylcarbazole (TCOC) [5], and phenothiazine with *p*-toluenesulfonyl chloride are the most effective organic additives.

Etching of the inorganic surface depends also on the nature of solvent used for photosensitive film cast-

1070-4272/01/7411-1947$25.00

Table 1. Depth *h* of the relief produced on the copper surface after etching with various photosensitive compositions

Sample	PVC, g	Solvent, ml	Seinsitizer, g; weighed portion, g	τ,* min	*h*, μm
I	1.8	Dioxane, 20	*N*-Allylphenothiazine, 0.024; *p*-toluenesulfonyl chloride, 0.01	120	<0.05
II	1.8	Dioxane, 20	*N*-Allylphenothiazine, 0.024; *p*-toluenesulfonyl chloride 0.01	240	0.07
III	0.9	Bromoform, 10	TCOC, 0.025	120	0.08
IV	0.9	Bromoform, 10	TCOC, 0.025	240	0.10
V	0.9	Dioxane, 10	*N*-Allylphenothiazine, 0.12	120	<0.05
VI	0.9	Dioxane, 10	*N*-Allylphenothiazine, 0.12	240	0.06
VII	0.45	TCE, 5	*N*-Allylphenothiazine, 0.12	120	0.07
VIII	0.45	TCE, 5	*N*-Allylphenothiazine, 0.12	240	0.10
IX	0.9	Dioxane, 10	Bromoform, 0.2; TCOC, 0.02	120	<0.05
X	0.9	Dioxane, 10	Bromoform, 0.2; TCOC, 0.02	240	0.05
XI	0.9	TCE, 10	Bromoform, 0.2; TCOC, 0.02	120	0.07
XII	0.9	TCE, 10	Bromoform, 0.2; TCOC, 0.02	240	0.10
XIII	1.8	Dioxane, 20	PVC, 0.2; NaI, 0.001	240	0.05
XIV	0.9	Dioxane, 10	*N*-Allylphenoxazine, 0.024; *p*-toluenesulfonyl chloride, 0.01	120	<0.05
XV	0.9	Dioxane, 10	*N*-Allylphenoxazine, 0.024; *p*-toluenesulfonyl chloride, 0.01	240	0.05
XVI	0.9	TCE, 10	*N*-Allylphenoxazine, 0.024; *p*-toluenesulfonyl chloride, 0.01	120	0.08
XVII	0.9	TCE, 10	*N*-Allylphenoxazine, 0.024; *p*-toluenesulfonyl chloride, 0.01	240	0.12
XVIII	0.45	Dioxane, 5	Bromoform, 0.2; TCOC, 0.02	120	<0.05
XIX	0.45	Dioxane, 5	Bromoform, 0.2; TCOC, 0.02	240	0.07
XX	0.45	TCE, 5	Bromoform, 0.2; TCOC, 0.02	120	0.10
XXI	0.45	TCE, 5	Bromoform, 0.2; TCOC, 0.02	240	0.13
XXII	0.45	TCE, 5	Bromoform, 0.2	240	0.08
XXIII	0.45	TCE, 5	TCOC, 0.02	240	0.05
XXIV	0.9	TCE, 10	Phenothiazine, 0.05; *p*-toluenesulfonyl chloride, 0.02	120	0.08
XXV	0.9	TCE, 10	Phenothiazine, 0.05; *p*-toluenesulfonyl chloride, 0.02	240	0.10
XXVI	0.9	Dioxane, 10	$FeCl_3$, 0.002	240	<0.05
XXVII	0.9	Dioxane, 10	$ZnCl_2$, 0.004	240	<0.05
XXVIII	0.9	TCE, 10	–	120	0.05
XXIX	0.9	TCE, 10	–	240	0.07
XXX	0.9	Dioxane, 10	NaI, 0.007	240	<0.05

* (τ) Etching time.

ing. We found that 1,1,2,2-tetrachloroethane (TCE) and bromoform increase the line depth during photoetching, whereas dioxane and toluene have no effect on it (Table 1, 2). This fact can be explained as follows. A small amount of the solvent is retained in the polymeric film dried at 70±2°C for 4 h. The C–Hlg bonds in 1,1,2,2-tetrachloroethane and bromoform are cleaved on exposure to UV radiation with generation of free radicals. Reactions of these radicals with each other or with the photolysis products of polyvinyl chloride yield Hlg_2 and HHlg which, in their turn, react with the copper surface:

$$\text{—CH}_2\text{—CH(Cl)—CH}_2\text{—CH(Cl)—} \xrightarrow{h\nu} \text{—CH}_2\text{—}\dot{\text{C}}\text{(Cl)—CH}_2\text{—CH(Cl)—} + \text{H}^\bullet,$$

$$C_2H_2Cl_4 \xrightarrow{h\nu} Cl^\bullet + C_2H_2Cl_3^\bullet,$$

$$Cl^\bullet + Cl^\bullet \rightarrow Cl_2,$$

$$H^\bullet + Cl^\bullet \rightarrow HCl,$$

Table 2. Solvent effect on the line depth on the copper surface*

Solvent	PVC, g	Line depth, μm
TCE	0.9	0.07
	0.7	0.06
Dioxane	0.9	0.05
	0.7	0.05
Toluene	0.9	0.05
	0.7	0.05
Bromoform	0.9	0.08
	0.7	0.06

* Exposure time 240 min, irradiation with a DRSh-250 lamp, solvent volume 10 ml.

$$Cu + HCl \rightarrow CuCl + 1/2H_2,$$

$$Cu + Cl_2 \rightarrow CuCl_2.$$

The line depth on the copper surface depends on the exposure time. This dependence for samples **XVII**, **XXI**, and **XXIX** (Table 1) is shown in the figure. The exposure time should be no shorter than 240 min irrespective of the composition of the photosensitive mask. On longer irradiation the line depth does not increase owing to degradation of the polymeric film and decrease in the concentration of the etching agent on the copper surface.

The products of copper photoetching were removed from the copper surface with a mixture of *N*,*N*-dimethylacetamide and acetoacetic ester (1 : 1 volume ratio) and analyzed by reactions with diethyldithiocarbamate and potassium hexacyanoferrate [6]. We found that the main products of copper photoetching are copper(I) chloride and copper(II) chloride. This is confirmed by the fact that the absorption bands of these products appear in the range (780–800 nm) similar to that in the spectra of a mixture of copper(I) and copper(II) chloride in these solvents (800–820 nm).

Thus, we propose the following scheme for solid-phase photoetching of the copper surface with photosensitive polymer coatings.

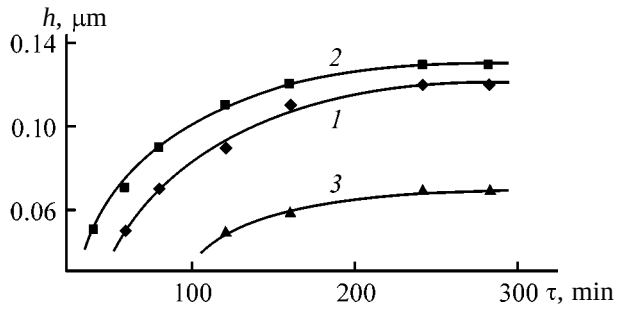

Line depth on the copper surface *h* as a function of the exposure time τ: (*1*) **XVII**, (*1*) **XXI**, and (*3*) **XXIX** (for compositions, see Table 1).

$$D \xrightarrow{h\nu} D^*,$$

$$D^* + PVC \rightarrow PVC^* + D,$$

$$PVC^* \rightarrow Cl^\bullet + PVC,$$

$$PVC + Cl^\bullet \rightarrow HCl + PVC,$$

$$Cu + HCl \rightarrow CuCl + 1/2H_2,$$

$$Cl^\bullet + Cl^\bullet \rightarrow Cl_2,$$

$$Cu + Cl_2 \rightarrow CuCl_2,$$

where D and PVC denote photosensitizer and polyvinyl chloride, respectively.

CONCLUSIONS

(1) Solid-phase photoetching of copper surface with photosensitive compositions based on polyvinyl chloride was studied. Solvents for polyvinyl chloride were found that, being partially retained in the polymeric matrix after evaporation, increase the etching depth owing to an increase in the concentration of etching agents on the copper surface.

(2) The dependence of the etching depth of the copper surface on the time of irradiation of the photosensitive layer was revealed.

(3) Photosensitizing additives to the polyvinyl chloride matrix, allowing photoetching of the copper surface at a depth of no less than 0.1 μm, were chosen.

(4) The composition of photoetching products was determined. The mechanism of photoetching of the copper surface with photosensitive polymeric coatings was proposed.

REFERENCES

1. US Patent 3346384.
2. Sirotkina, E.E. and Skorokhodova, T.S., in *Khimiki TGU na poroge tret'ego tysyacheletiya* (Chemists of Tomsk State University on the Eve of the Third Millenium), Tomsk: Tomsk. Gos. Univ., 1998, pp. 179–190.
3. US Patent 4252891.
4. Ranby, B.J. and Rabek, J.F., *Photodegradation, Photo-Oxidation, and Photostabilization of Polymers*, London: Wiley, 1975.
5. USSR Inventor's Certificate no. 1460936.
6. Charlot, G., *Les methods de la chimie analytique. Analyse quantitative minerale*, Paris: Masson, 1961, 4th ed.

Russian Journal of Applied Chemistry, Vol. 74, No. 11, 2001, pp. 1950–1954. Translated from Zhurnal Prikladnoi Khimii, Vol. 74, No. 11, 2001, pp. 1888–1892.

CHEMISTRY OF FOSSIL FUEL

Molecular Oxygen and Oxygen- and Nitrogen-Containing Compounds in Diesel Fractions of West-Siberian Oil

O. Yu. Begak and A. M. Syroezhko

Mendeleev Russian Research Institute of Metrology, State Unitary Enterprise, St. Petersburg, Russia
St. Petersburg State Technological Institute, St. Petersburg, Russia

Received July 30, 2001

Abstract—Heteroatomic compounds in middle-cut (200–360°C) distillates of West-Siberian oil were identified by gas chromatography–mass spectrometry.

The composition of diesel frtactions boiling in the range from 160–200 to 360°C is complex, and the existing analytical procedures do not allow complete identification of the components, especially of heteroorganic (N-, S-, and O-containing) compounds. The most studied components of diesel fractions are alkanes, isoalkanes, isoprenoids, and naphthene and aromatic hydrocarbons [1].

In this work we showed that in fractions boiling at higher temperatures than benzine the content of methane hydrocarbons (oils of grades A and B) decreases, the content of branched hydrocarbons increases, and isoprenoids appear in significant amounts. As for naphthenic hydrocarbons, their structure becomes more complex in going from benzine to diesel fractions; in particular, the number of rings in the molecule increases to 2–3.

Aromatic hydrocarbons of the diesel fraction consist of homologs of benzene, naphthalene, and, in part, phenanthrene and anthracene. Also, hybrid compounds are present, containing, along with one or two aromatic rings, also one or several naphthene rings. Primarily these are indane and tetralin derivatives. In going from the benzine to diesel fractions, the number and length of alkyl substituents in aromatic compounds increase, as well as the number of rings in the molecule; in particular, tricyclic condensed aromatic hydrocarbons (phenanthrene derivatives) appear.

Heteroorganic compounds of the diesel fraction are oxygen-, sulfur-, and nitrogen-containing derivatives of the above-mentioned hydrocarbons.

The oxygen-containing compounds are mainly mono- and dibasic petroleum acids and phenols (dimethyl-, trimethyl-, and methylethylphenols) [2].

Sulfur-containing compounds of the diesel fraction are sulfides (thiacyclanes) and thiophene derivatives. The content of thiols and disulfides in the diesel fractions is low.

Nitrogen-containing compounds of the diesel fraction are mainly derivatives of pyridine, quinoline, and, to a lesser extent, aniline. Very small amounts of porphyrins can be present. On the whole, it is desirable to obtain more detailed information on the composition of oxygen- and nitrogen-containing compounds of the diesel fraction in various stages of commercial refining of a mixture of West-Siberian crude oils at the Kirishinefteorgsintez Production Association, Limited Liability Company.

EXPERIMENTAL

Molecular oxygen dissolved in diesel fractions (sample nos. 1–5[1]) was determined chromatographically.

Hydroperoxide in diesel fractions were determined iodometrically [3].

Heteroorganic compounds were concentrated with a Diapak silica gel cartridge (BiokhimMak, Moscow).

[1] Diesel fractions (five samples) were taken March 28, 2001, from L-24/6 and L-24/2000 installations of the Kirishinefteorgsintez Production Association. Sample nos. 1–3 were supplied from the Parex installation (200–300°C fraction) to the L-24/6 installation and were taken from the 225 reservoir in the feed pumping line (sample no. 1), at the outlet of the TsN-2 feed pump (sample no. 2), and at the outlet of the TsN-4 feed pump (sample no. 3). Sample nos. 4 and 5 (200–360°C fraction) were taken from the L-24/2000 installation at the inlet of the N-201 feed pump (sample no. 4) and at the line of pumping into reservoir 261 (sample no. 5).

1070-4272/01/7411-1950$25.00

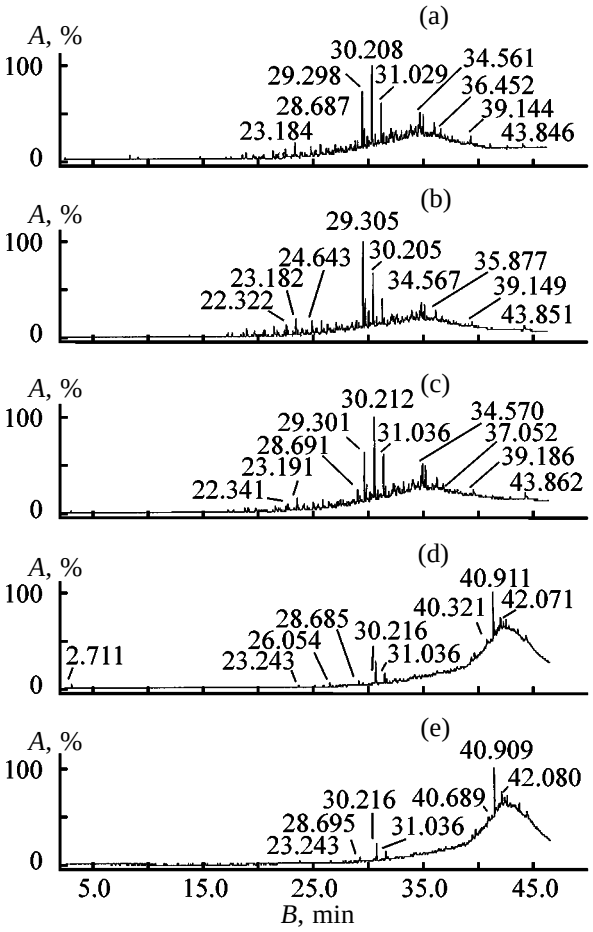

Fig. 1. Chromatograms of extracts of diesel fractions. (*A*) peak intensity and (*B*) retention time; the same for Fig. 2. Sample no.: (a) 1, (b) 2, (c) 3, (d) 4, and (e) 5.

The cartridge was washed with *n*-hexane, and 100 ml of a diesel fraction sample was passed. Then the cartridge was repeatedly washed with *n*-hexane and dried in a nitrogen flow. The extracted O- and N-containing compounds were eluted from the cartridge with 5 ml of methanol. The methanol extract was evaporated in a nitrogen flow to 1 ml and analyzed by GC–MS.

Mass-spectrometric analysis of diesel fuel extracts was performed with an MD 800 device (Fisons, the United States). The components of the diesel fuel extracts (five samples) that gave separate or partially overlapping chromatographic peaks were identified using MassLab and AMDIS software with an electronic library of the mass spectra. The programs provided for calculation of the direct and inverse similarity parameters of the experimental and reference mass spectra. When identifying individual compounds, we took into account the general parameters characterizing the similarity between the mass spectra of the discovered compounds and reference mass spectra from the library, the identity of the molecular ions in the mass spectra being compared, the similarity between the relative intensities of the major peaks in the mass spectra being compared (difference by no more than 20–30%), and the results obtained by running the expert block of the AMDIS program. These criteria allow identification of individual compounds or group identification.

The content of dissolved molecular oxygen in the analyzed samples varied from 0.7×10^{-3} to 1.8×10^{-3} M, namely: sample no. 1, 1.8×10^{-3}; no. 2, 1.1×10^{-3}; no. 3, 1.4×10^{-3}; no. 4, 0.76×10^{-3}; and no. 5, 0.72×10^{-3} M). Samples are not saturated with oxygen; the oxygen solubility in them is 2×10^{-3} M.

The concentration of hydroperoxides is low: sample nos. 1 and 2, below detection limit (5×10^{-5} M); no. 3, 1.3×10^{-4}; and nos. 4 and 5, 7×10^{-5} M. That is, the diesel fractions are not appreciably oxidized. The extent of oxidation increases in the course of storage and use of the diesel fuel.

The chromatograms of the extracts of the heteroatomic compounds from the diesel fractions (sample nos. 1–5) are shown in Fig. 1.

The identified heteroorganic compounds corresponding to the major peaks in the chromatograms are listed in the table. The corresponding peak numbers are indicated in the chromatograms (Fig. 2).

Thus, in diesel fractions we detected diverse oxygen- and nitrogen-containing organic compounds C_6–C_{18}: alcohols and ketones of the paraffin and naphthenic series, alkylphenols, pyridines, quinolines, and possibly other nitrogen-containing heterocyclic compounds.

In the mass spectra we detected no peaks, even on the trace level, characteristic of carboxylic acids; these compounds, apparently, appear in diesel fuel on storage, at higher extents of oxidation.

The total content of oxygen-containing compounds in various samples of diesel fuels, as estimated from data in the table and peak areas in the chromatograms of the extracts, is very low: $(0.5–6.1) \times 10^{-4}$%. This value is considerably lower than their content in gasolines in the course of production (0.002–0.004%) [3–5] and in A-76 gasoline "in the initial state before storage" (an equivalent parameter, content of acetone-soluble resins, is 1.9 mg ml^{-1}, or 0.003% [6]). Thus, data on the quantitative content of oxygen-containing organic compounds and on their qualitative composi-

Content of oxygen- and nitrogen-containing compounds in samples of diesel fuels

Peak no.	Compound	Empirical formula and/or molecular weight	Content $C \times 10^5$, wt %, in indicated sample				
			no. 1	no. 2	no. 3	no. 4	no. 5
1	Cyclohexyl-2-propanone	$C_9H_{16}O$	0.19	0.56	0.18	0.00	0.00
2	2-Ethylidenecyclohexanone	$C_8H_{12}O$	0.06	0.28	0.13	0.00	0.00
3	2-Nonanol	$C_9H_{20}O$, 144	0.59	0.55	0.96	0.11	0.17
4	3,5-Dimethylphenol	$C_8H_{10}O$	1.2	2.3	1.5	0.22	0.04
5	2,4-Dimethylphenol	$C_8H_{10}O$	0.69	1.6	0.75	0.00	0.02
6	4-*n*-Propylphenol	$C_9H_{12}O$	0.50	1.2	0.31	0.03	0.00
7	2-*n*-Propylphenol	$C_9H_{12}O$	0.83	1.7	1.2	0.00	0.00
8	3-*n*-Propylphenol	$C_9H_{12}O$	0.43	0.90	0.67	0.00	0.00
9	2-Isopropylphenol	$C_9H_{12}O$	0.26	0.49	0.30	0.00	0.00
10	3-Isopropylphenol	$C_9H_{12}O$	0.83	1.7	1.4	0.33	0.42
11	4-Isopropylphenol	$C_9H_{12}O$	0.87	1.8	1.3	0.15	0.36
12	2,6-Diethylphenol	$C_{10}H_{14}O$	1.4	2.3	2.3	0.66	0.22
13	4-*n*-Butylphenol	$C_{10}H_{14}O$	0.80	1.1	1.7	0.20	0.38
14	2-*n*-Butylphenol	$C_{10}H_{14}O$	0.79	1.6	0.96	0.14	0.36
15	3-*n*-Butylphenol	$C_{10}H_{14}O$	0.43	0.76	0.71	0.24	0.04
16	4-*n*-Amylphenol	$C_{11}H_{12}O$	1.2	2.6	1.7	0.28	0.34
17	3-*n*-Amylphenol	$C_{11}H_{12}O$	0.51	0.95	1.09	0.04	0.57
18	2-*n*-Amylphenol	$C_{11}H_{12}O$	0.87	1.7	1.6	0.19	1.01
19	2-Methyl-4-*tert*-butylphenol	$C_{11}H_{12}O$	1.4	2.4	2.3	0.48	0.16
20	2-Methyl-6-*tert*-butylphenol	$C_{11}H_{12}O$	0.56	1.4	1.6	0.81	0.36
21	3-Methyl-6-*sec*-butylphenol	$C_{11}H_{12}O$	0.33	0.67	0.55	0.38	0.60
22	2-Methyl-6-*n*-butylphenol	$C_{11}H_{12}O$	0.38	0.73	0.67	0.31	0.51
23	2-Methyl-6-isobutylphenol	$C_{11}H_{12}O$	0.72	1.4	1.3	0.48	0.27
24	2-Methyl-6-*sec*-butylphenol	$C_{11}H_{12}O$	0.22	0.47	0.32	0.03	0.33
25	One of dimethylquinolines	$C_{11}H_{11}N$	0.43	0.56	1.1	0.27	0.68
26	2-Ethyl-4-*n*-amylpyridine	$C_{12}H_{19}N$	0.72	1.5	1.2	0.08	0.20
27	Nitrogen-containing heterocyclic compound	$C_{10}H_{14}N$	0.24	0.54	0.51	0.39	0.32
28	2-Ethyl-4-butylphenol	$C_{12}H_{18}O$	0.48	0.92	0.87	0.15	0.49
29	2-Ethyl-6-*tert*-butylphenol	$C_{12}H_{18}O$	0.79	1.1	1.2	0.00	0.30
30	3-Propyl-4-*sec*-amylpyridine	$C_{12}H_{19}N$	0.62	1.4	1.2	0.18	0.27
31	Nitrogen-containing heterocyclic compound	217	1.0	1.8	2.0	0.81	1.78
32	One of trimethylquinolines	$C_{12}H_{13}N$	0.66	0.87	1.0	0.12	0.25
33	Cyclohexylidenecyclohexanone	$C_{12}H_{18}O$	5.2	14.0	8.3	0.00	0.00
34	Naphthenic ketone	$C_{12}H_{20}O$	1.8	4.7	2.9	0.00	0.00
35	Nitrogen-containing heterocyclic compound	231	7.2	9.4	14.3	8.2	8.3
36	Nitrogen-containing heterocyclic compound	229	3.1	4.1	6.8	3.5	3.6
37	Naphthenic compound containing two oxygen atoms	$C_{13}H_{22}O_2$, 211	1.3	3.8	4.5	0.00	0.00
38	Naphthenic diketone	$C_{12}H_{18}O_2$	1.8	5.1	4.2	0.00	0.00
39	Nitrogen-containing heterocyclic compound	$C_{14}H_{16}N_2$	0.71	2.8	1.1	0.00	0.00
40	Nitrogen- and oxygen-containing heterocyclic compound	$C_{14}H_{15}ON$	0.92	1.9	1.5	0.00	0.00
41	Nitrogen-containing heterocyclic compound	227	0.58	0.79	0.74	0.00	0.00
42	Nitrogen-containing heterocyclic compound	$C_{17}H_{23}N$, 241	0.30	0.27	0.67	13.6	13.1
43	Nitrogen-containing heterocyclic compound	$C_{18}H_{25}N$	0.00	0.00	0.00	4.8	7.5
	Total content of oxygen-containing compounds, $C \times 10^5$, %		27.4	60.8	47.5	5.2	6.9
	Total content of nitrogen-containing compounds, $C \times 10^5$, %		15.5	24	30.6	32	36

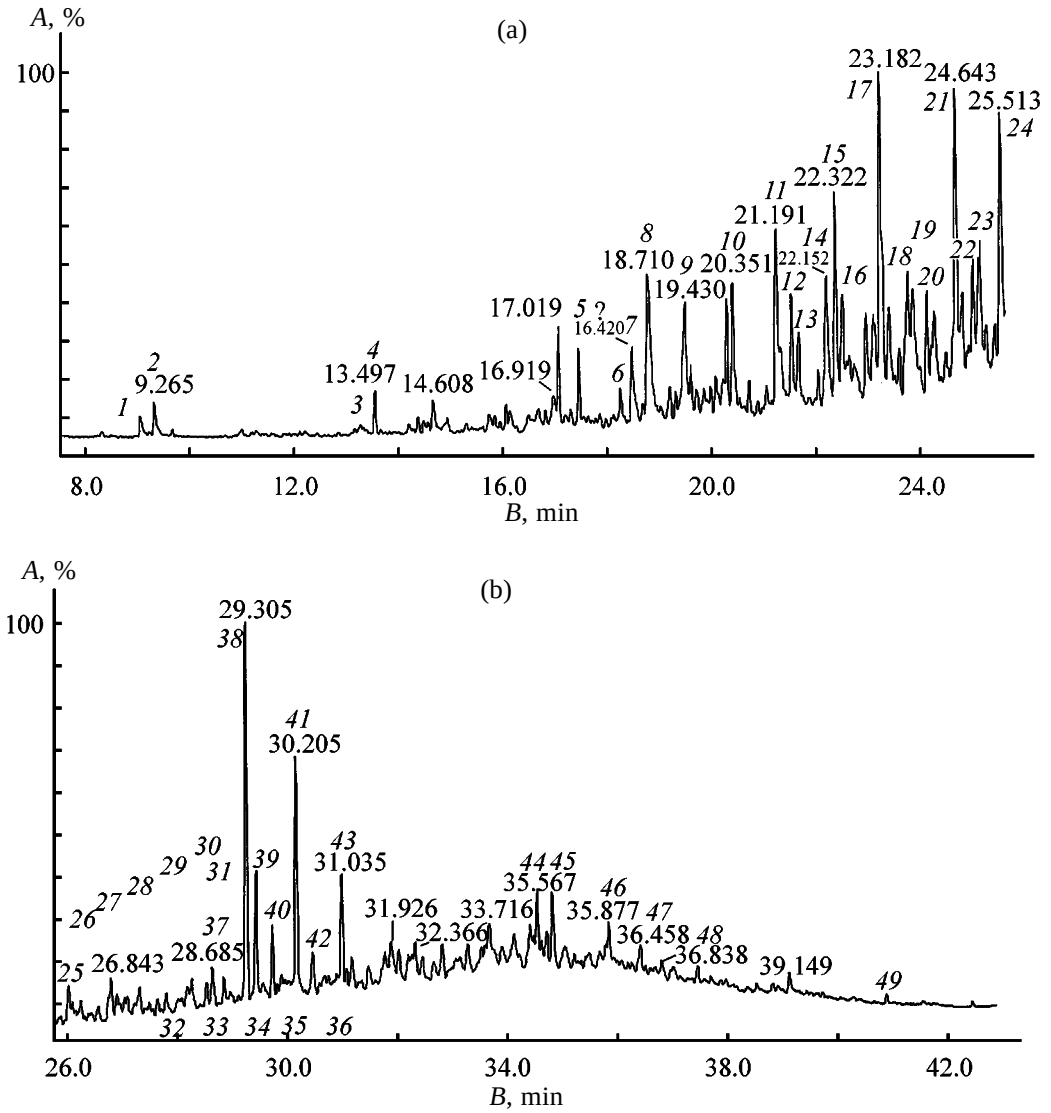

Fig. 2. (a) Initial and (b) final sections of the chromatogram of the diesel fraction extract (sample no. 2). For peak identification, see table.

tion (lack of acids), in combination with the results of determination of molecular oxygen and hydroperoxides, correspond to a certain, very low ("natural") extent of oxidation of hydrocarbon components of oil. It is notable that in diesel fuels the content of phenols relative to nonaromatic oxygen compounds is higher than in gasolines, which can considered as a stabilizing factor.

Diesel fuel sample nos. 1–3 are similar in composition and contain practically all the oxygen compounds mentioned in the table. Sample nos. 4 and 5 are wider-cut fractions, the total weight fraction of oxygen compounds in them is lower by a factor of 4–12; in these samples, the lowest-boiling compounds of those mentioned in the table are absent. Also, these samples contain no cyclohexylidenecyclohexanone (or isomeric naphthenic ketone), which is the major component in sample nos. 1–3 and is presumably formed by condensation of cyclohexanone.

At the same time, the identified nitrogen-containing compounds are present in all the samples in approximately equal amounts [$(1.5–3.6) \times 10^{-4}$% in total], comparable wtih the content of oxygen compounds in sample nos. 1–3 (see table). The composition of nitrogen-containing compounds in sample nos. 1–3 somewhat differs from that in sample nos. 4 in 5. In the first three samples the major components are those with the molecular weight of approximately

230, most probably, pyridine and/or quinoline derivatives (see table and Figs. 2a, 2b, peaks *41*, *43*; the compound corresponding to peak *41* may also contain oxygen). These two compounds are present in approximately the same amounts in the wider-cut fractions (sample nos. 4, 5), but in this case the major component is that corresponding to peak *49* (see table and Fig. 2b), most probably C_8-alkylquinoline (molecular weight 241).

It should be noted that the presence of pyridine and quinoline derivatives in the samples agrees with published data on the composition of middle-cut oil distillates.

CONCLUSIONS

(1) Diesel fuel samples from installations L-24/8 and L-24/2000 of the Kirishinefteorgsintez Production Association in the course of their processing are not saturated with molecular oxygen. Their oxygen content is lower than that of samples of the main gasoline components (reformer naphthas) and in commercial gasoline.

(2) A total of 43 heteroatomic compounds (O- and N-containing) present in diesel fractions of a commercial mixture of West-Siberian crude oil were identified. These are paraffinic and cycloparaffinic alcohols and ketones, alkylphenols with one or two alkyl (C_1–C_5) substituents, pyridine and quinoline derivatives, and probably some other nitrogen-containing heterocyclic compounds.

(3) The total content of oxygen-containing compounds in the examined diesel fuel samples is lower than in commercial gasoline.

REFERENCES

1. *Khimiya nefti i gaza: Uchebnoe posobie* (Oil and Gas Chemistry), Proskuryakov, V.A., Ed., St. Petersburg: Khimiya, 1995.
2. Kam'yanov, V.F. *et al.*, *Geteroatomnye komponenty neftei* (Heteroatomic Components of Crude Oils), Novosibirsk: Nauka, 1983.
3. Becker, H., Berger, W., Domschke, G., *et al.*, *Organikum. Organisch-chemisches Grundpraktikum*, Berlin: Wissenschaften, 1976. Translated under the title *Organikum*, Moscow: Mir, 1979, vol. 2, p. 98.
4. *Khimicheskaya entsiklopediya* (Chemical Encyclopedia), Moscow: Bol'shaya Ross. Entsiklopediya, 1992, vol. 3, p. 493.
5. Begak, O.Yu., Varshavskii, O.M., Zalishchevskii, G.D., *et al.*, *Sbornik nauchnykh trudov OOO PO "Kinef" za 1998–2000 gg.* (Coll. of Scientific Works of the Kinef Production Association, Limited Liability Company, of 1998–2000), Moscow: TsNIITEneftekhim, 2001, pp. 25–39.
6. Golubeva, I.A., Klinaeva, E.V., Kelarev, V.I., *et al.*, *Khim. Tekhnol. Topl. Masel*, 1997, no. 5, pp. 38–40.

Russian Journal of Applied Chemistry, Vol. 74, No. 11, 2001, pp. 1955–1957. Translated from Zhurnal Prikladnoi Khimii, Vol. 74, No. 11, 2001, pp. 1893–1895.

BRIEF COMMUNICATIONS

Study of Co–Mn–O- and Li–Co–Mn–O-Containing Layers Synthesized by Successive Ionic Layer Deposition on Silica Surface

L. B. Gulina, V. P. Tolstoi, and I. V. Murin

St. Petersburg State University, St. Petersburg, Russia

Received December 7, 2000; in final form, March 2001

Abstract—The possibility for preparing $Co_3MnO_x \cdot nH_2O$ and $LiCo_3MnO_x \cdot nH_2O$ nanolayers by successive ionic layer deposition was examined. The resulting layers were studied by X-ray photoelectron spectroscopy, UV–Vis diffuse reflection spectroscopy, Fourier transmission IR spectroscopy, atomic absorption spectroscopy, ellipsometry, and X-ray powder diffraction.

The aim of this work was to synthesize nanolayers of double cobalt and manganese oxide, doped with Li^+ ions, by successive ionic layer deposition. This compound is known to be used in lithium batteries as cathode material [1].

EXPERIMENTAL

The synthesis was carried out by the ionic layer deposition described in [2] using cobalt and manganese salts. The Li^+ ions were introduced by impregnation from 0.1 M $LiNO_3$ solutions in alcohol. An excess of the lithium salt was washed out with the solvent from the surface. The supports were silica gel (Merck-60, specific surface area 360 $m^2\ g^{-1}$) and wafers of single-crystal silicon ⟨100⟩. Before the synthesis all the supports were subjected to the standard treatment [3].

The resulting layers were studied by X-ray photoelectron spectroscopy, UV-Vis diffuse reflectance spectroscopy, Fourier transmission IR spectroscopy, and powder X-ray diffraction. The X-ray photoelectron spectra were obtained on a Perkin–Elmer-5400 spectrometer using MgK_α exciting radiation. The quantitative content of each element in a layer was evaluated by the standard technique [4] accurate to within 10%. The diffuse reflectance spectra were recorded on a Perkin–Elmer Lambda-9 spectrophotometer at a scanning rate of 50 nm min^{-1} and a 2 nm slit program. The Fourier transmission IR spectra were recorded on a Perkin–Elmer-1760 IR spectrometer by means of 50 scans at 4 cm^{-1} resolution. The lithium and manganese content in a layer synthesized was determined by atomic absorption spectroscopy. For this purpose a weighed sample of silica gel with the layer synthesized was treated with concentrated sulfuric acid and thoroughly washed with distilled water. Proportions of elements in the filtrate were determined by atomic absorption technique on an AAS-1 spectrometer in propane–air flame. A hollow cathode lamp (wavelength 279.48 nm) was used to determine manganese contents. Lithium was determined in the emission mode at a wavelength of 640.78 nm. The error of these determinations did not exceed 5%. The layer thickness was measured on an ellipsometer with an incidence angle of 45° and light wavelength of 632.8 nm. The X-ray patterns of silica gel samples with the layers synthesized were obtained on a DRON-3.0 diffractometer using CuK_α radiation (recorder tape velocity 2400 cm h^{-1}, rate of sample rotation 2 rpm, current 18 mA, and voltage 36 kV).

The diffuse reflection spectra of Co–Mn–O-containing nanolayers formed on the silica surface by the layer deposition reactions are given in Fig. 1, which shows that the intensity of the absorption band in the range of 300–700 nm, and hence the layer thickness, increases as the number of deposition cycles is increased.

The thickness of synthesized layers on the surface of single-crystal silicon was monitored by ellipsometry. The layer thickness was found to increase linearly with the number of successive ionic layer deposition cycles, a layer with a thickness of 0.49 nm being formed in each successive cycle.

The X-ray photoelectron spectrum of the layer syn-

1070-4272/01/7411-1955$25.00

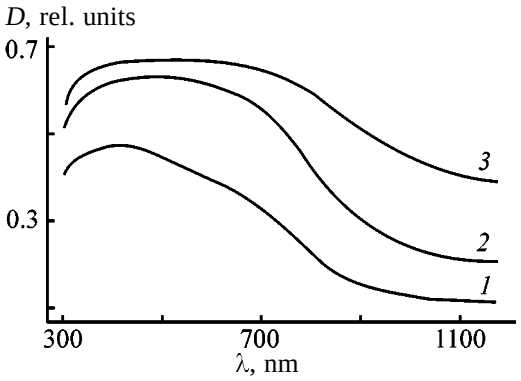

Fig. 1. Differential (against the initial silica gel) UV–Vis diffuse reflection spectra of Co–Mn–O-containing layers synthesized on the silica gel surface. (*D*) Optical density and (λ) wavelength. Number of successive ionic layer deposition cycles: (*1*) 1, (*2*) 3, and (*3*) 5.

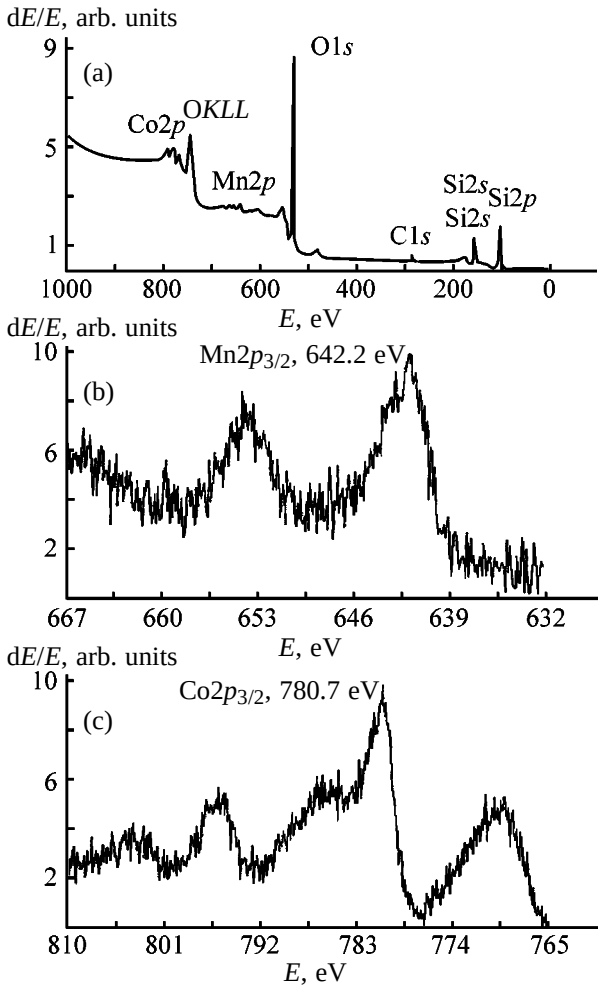

Fig. 2. X-ray photoelectron spectrum of a Co–Mn–O-containing layer synthesized on the silicon surface by 30 successive ionic layer deposition cycles: (a) total spectrum, (b) cobalt range, and (c) manganese range. (d*E*/*E*) Peak intensity and (*E*) binding energy.

thesized on the silica gel surface by 30 successive ionic layer deposition cycles (Fig. 2) contains bands with the maximal binding energies of 780.7 and 642.2 eV related to 2*p* electrons of Co and Mn, respectively [4]. According to the X-ray photoelectron spectra, the oxidation state of manganese in the compound is +4. As for the oxidation state of cobalt, examination of the relevant reference data shows that the band maxima of Co^{2+} and Co^{3+} ions are close to each other. However, the ratio of the intensities in the X-ray photoelectron spectrum indicates that the Co : Mn ratio in the layer is 3 : 1. This is an indirect evidence for the existence of Co^{3+} ions, as, according to the synthesis procedure [2], the layer is formed as a result of a redox reaction in the layer of Mn^{7+} and Co^{2+} ions adsorbed on the surface. In this case manganese is reduced from the oxidation state +7 to the state +4, which means that three electrons from three Co^{2+} ions participate in the reduction.

By the data of X-ray powder analysis, the layer synthesized was amorphous; however, its X-ray pattern contains a weak peak at $2\theta = 22.56°$ corresponding to CoOOH [5].

The data of X-ray photoelectron spectroscopy and X-ray powder analysis are in good agreement with the data of Fourier transmission IR spectroscopy (Fig. 3). Thus, in the range 1500–1400 cm^{-1} of the spectrum there are absorption bands of the bending vibrations of O–H bonds in a metal hydroxide, most likely in CoOOH, and the band with a maximum at 605 cm^{-1} corresponding to β-MnO_2 [6]. The spectrum also contains a broad band in the range 4000–3000 cm^{-1} (not shown in Fig. 3), corresponding to the O–H stretching vibrations in OH groups and water molecules transferred from solution into the layer.

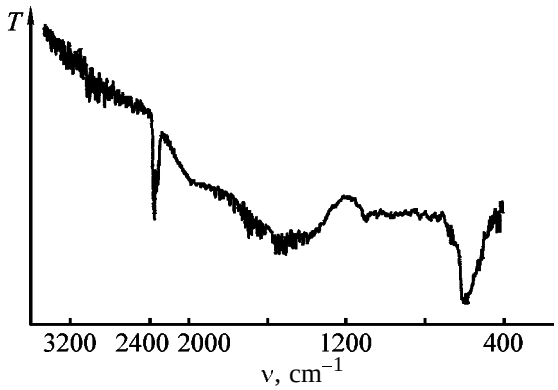

Fig. 3. Fourier transmission IR spectrum of a Co–Mn–O-containing layer synthesized on the surface of single-crystal silicon by 30 successive ionic layer deposition cycles. (*T*) Transmission and (ν) wave number.

Analysis of the synthesized layer containing hydrated manganese oxide $MnO_2 \cdot nH_2O$ and cobalt hydroxide CoOOH reveals incorporation of Li^+ ions [7]. The lithium content was determined by atomic absorption spectroscopy, which showed that the Li : Mn ratios after one, five, or ten cycles are the same (1 : 1). According to the X-ray powder analysis, the resulting layer is amorphous.

CONCLUSION

The composition of Co–Mn–O- and Li–Co–Mn–O-containing nanolayers can be described as $Co_3MnO_x \cdot nH_2O$ and $LiCo_3MnO_x \cdot nH_2O$, respectively, and the thickness of the layers can be precisely specified by the number of layer deposition cycles.

ACKNOWLEDGMENTS

The work was financially supported by the Universities of Russia—Fundamental Research program and NWO (Holland).

REFERENCES

1. Hosoya, M., Ikuta, H., and Wakihara, M., *Solid State Ionics*, 1998, vol. 111, no. 1/2, pp. 153–157.
2. Tolstoy, V.P., *Russ. Chem. Rev.*, 1993, vol. 62, no. 3, pp. 260–265.
3. Tolstobrov, E.B. and Tolstoy, V.P., *Zh. Obshch. Khim.*, 1999, vol. 69, no. 6, pp. 890–895.
4. Nefedov, V.I., *Rentgenoelektronnaya spektroskopiya khimicheskikh soedinenii: Spravochnik* (X-ray Photoelectron Spectroscopy of Chemical Compounds: Handbook), Moscow: Khimiya, 1984.
5. *Index to Cristallographic Data Compilation*, ASTM, no. 26-480.
6. *Gmelin Handbook of Inorganic Chemistry, Mn*, Chemie, 1973.
7. Kanasaku, T., Amezawa, K., and Yamamoto, N., *Solid State Ionics*, 2000, vol. 133, no. 1, pp. 51–56.

Russian Journal of Applied Chemistry, Vol. 74, No. 11, 2001, pp. 1958–1959. Translated from Zhurnal Prikladnoi Khimii, Vol. 74, No. 11, 2001, pp. 1895–1897.

BRIEF COMMUNICATIONS

Electrodeposition of Palladium–Zinc Alloy from the Ammonium Chloride–Na_2EDTA Electrolyte

S. V. Kabanov and Yu. P. Perelygin

Penza State University, Penza, Russia

Received April 26, 2001

Abstract—The influence of the electrolysis regime and electrolyte composition on the cathodic current efficiency by the palladium–zinc alloy and on the alloy composition was studied.

Coatings with alloys of palladium and a number of metals have found application owing to lower consumption of noble metal and enhanced physicomechanical and chemical properties [1]. A metallurgical palladium–zinc alloy is a complex system consisting of a solid solution at a zinc content of up to 6% and of a few chemical compounds at higher zinc contents [2]. In this work wee examined electrodeposition of the palladium–zinc alloy, which was not studied previously.

Electrodeposition was performed from the ammonium chloride–Na_2EDTA solution in a 100-ml glassy rectangular bath using permanent graphite anodes. Zinc in the alloy was determined by complexometric titration after separating palladium in the form of palladium dimethylglyoximate [3].

The influence of the electrolysis conditions and electrolyte composition on the cathodic current efficiency (CE) by the alloy and the alloy composition were studied in a solution containing (g l^{-1}) palladium chloride 20 (in terms of metal), zinc oxide 5 (in terms of metal), ammonium chloride 20, and Na_2EDTA 40. The temperature was 20°C, current density, 0.5 A dm^{-2}, and pH 9.

As the zinc concentration in the electrolyte is increased, its content in the coating increases and the CE by the alloy decreases.

Zn concentration in solution, g l^{-1}	2	3	4	5
Zn content of the alloy, %	2.7	4.1	5.5	7.8
Cathodic CE by the alloy, %	98	98	98	96

The dependence of the relative content of the alloy metals on the relative concentration of their ions in the electrolyte is described by the equation [4]

$$\log\frac{[Pd]}{[Zn]} = 0.4 + 1.16\log\frac{[Pd^{2+}]}{[Zn^{2+}]}.$$

The correlation coefficient of the equation is 0.993.

At the zinc concentration in the electrolyte increased to 10 g l^{-1}, the CE by the alloy decreases from 96 to 33% and the zinc content in the alloy increases from 7.8 to 31%. Decreasing palladium concentration in the electrolyte under the similar conditions results in the deterioration of the deposit quality.

The influence of the current density, temperature, and pH was studied in an electrolyte with a zinc concentration of 5 g l^{-1}. At the current density increased from 0.25 to 1.25 A dm^{-2}, the CE by the alloy decreases from 96 to 83% and the zinc content in the alloy, from 18 to 4.5% (Fig. 1, curves *1* and *2*, respectively). At higher current densities the coating quality gets worse. As the temperature is increased from 10 to 40°C, the CE by the alloy grows from 74 to 98%

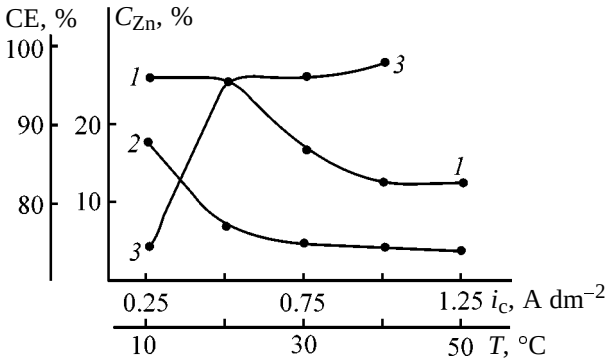

Fig. 1. (*1, 3*) Current efficiency CE by the alloy and (*2*) zinc content of the alloy C_{Zn} vs. (*1, 2*) cathodic current density i_c and (*3*) temperature T.

1070-4272/01/7411-1958$25.00

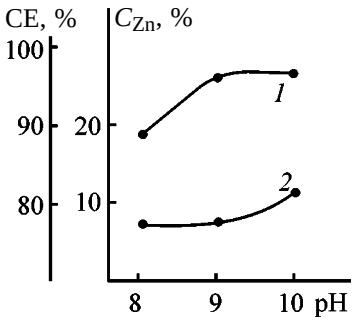

Fig. 2. (*1*) Current efficiency CE by the alloy and (*2*) zinc content of the alloy C_{Zn} vs. pH.

(curve *3*), with the alloy composition virtually unaffected and the coating quality improved. With solution pH varied from 8 to 10 the CE increases from 88 to 96% (Fig. 2, curve *1*) and the zinc content in the alloy, from 7.5 to 11% (curve *2*). In this case, the deposit quality is unaffected.

Stirring of the electrolyte with a magnetic stirrer decreases the CE by the alloy from 96 to 88%, with the zinc content in the alloy slightly increased (from 7.8 to 8.5%).

Increasing the ammonium chloride concentration in the electrolyte from 20 to 80 g l^{-1} does not affect the alloy composition. The increase in the Na_2EDTA concentration from 30 to 40 g l^{-1} inconsiderably increases the cathodic CE by the alloy (from 92 to 96%) and does not affect the alloy composition. At lower Na_2EDTA concentrations the deposit quality gets worse.

Thus, for the deposition of semilustrous alloy coatings with the zinc content from 3 to 8%, we can recommend an electrolyte containing (g l^{-1}) palladium oxide 20 (in terms of metal), zinc oxide 2–5 (in terms of metal), ammonium chloride 20, and Na_2EDTA 30–40, with pH 9. The optimal conditions of deposition are 20°C and the current density, 0.5 A dm^{-2}. Under these conditions the CE by the alloy is 92–96%. In the course of the process, to compensate for exhaustion of the components, the electrolyte composition should be adjusted with palladium chloride and zinc oxide and its pH, with an ammonia solution.

The study by method [5] of the transient electrical resistance of the alloy coatings with a zinc content of 7.8% showed that, with the load on the contact increased from 0.5 to 3 N, the transient resistance decreases from 0.044 to 0.026 Ω. Apparently, this is due to the depression of a passivation film and increase in the contact area. At a 1 N contact load the transient electrical resistance surpasses that of pure palladium coating (0.028 and 0.015 Ω, respectively). This result is ascribed to the growth of the alloy electrical resistance and to a greater tendency to passivation of the alloy-coated surface.

As the coating thickness is increased from 10 to 20 μm, the microhardness of the alloy coating containing 7.8% zinc increases from 258 to 321 kg m^{-2}, i.e., to a value exceeding 1.2–1.5 times that for pure palladium coating.

REFERENCES

1. Vinogradov, S.N., *Elektroosazhdenie splavov palladiya* (Electrodeposition of Palladium-Base Alloys), Saratov: Saratov. Univ., 1978.
2. Savitskii, E.M., Polyakova, V.P., and Tylkina, M.A., *Splavy palladiya* (Palladium-Base Alloys), Moscow: Nauka, 1967.
3. Budyak, N.F., and Ekimenkova, T.A., *Analiz kontaktnykh i provodnikovykh splavov* (Analysis of Contact and Conductor Alloys), Moscow: Metallurgiya, 1975.
4. Akhumov, E.I., and Rozen, B.Ya., *Dokl. Akad. Nauk SSSR*, 1956, vol. 109, no. 6, pp. 1149–1151.
5. Perelygin, Yu.P., *Gal'vanotekh. Obrab. Poverkh.*, 1993, vol. 2, no. 4, p. 65.

Russian Journal of Applied Chemistry, Vol. 74, No. 11, 2001, pp. 1960–1961. Translated from Zhurnal Prikladnoi Khimii, Vol. 74, No. 11, 2001, pp. 1897–1898.

BRIEF COMMUNICATIONS

Effect of Methods Used to Fabricate the Combined Matrix of Air Electrode on Its Electrical Characteristics

M. O. Danilov and N. V. V'yunova

Vernadsky Institute of General and Inorganic Chemistry, National Academy of Sciences of Ukraine, Kiev, Ukraine

Received July 3, 2001

Abstract—Electrochemical characteristics of electrodes based on a combined matrix obtained in two ways: by successive electrochemical deposition of polyaniline and electrolytic manganese dioxide and by mechanical mixing of these components, were studied.

Electrically conducting polymer polyaniline (PAN), obtained by electrochemical synthesis from aniline, is used as cathode material for chemical power cells with salt electrolyte [1–4]. Its synthesis and electrochemical properties were described in [1, 5]. Previously, it has been shown that the working voltage can be raised by addition of electrochemical manganese dioxide (EMD) to the combined matrix of the air electrode [6].

The aim of the present study was to analyze the effect of methods of EMD introduction into a comined PAN-based matrix on the electrochemical characeristics of air electrodes in prototype zinc–air chemical power cells.

The air electrode comprised a hydrophobic and an active layer. The active layer is a combined matrix based on PAN, EMD, and carbon fiber. Two ways to introduce EMD were studied: mechanical mixing and electrochemical deposition of manganese dioxide onto a finished electrode, with or without preliminary deposition of PAN. The electrochemical deposition of EMD was done using a standard solution based on manganese(II) sulfate and sulfuric acid. PAN was deposited from sulfuric acid solutions of aniline. The current used in anodic synthesis of manganese dioxide and PAN was 5 mA cm^{-2} per apparent surface area of the electrode. The electrolysis duration was chosen depending on the amount of substance to be deposited. When the EMD layer was electrochemically deposited onto a preliminarily formed PAN layer, the deposit was uniform and homogeneous. If first EMD and then PAN were deposited, the obtained PAN coating was nonuniform and contained groups of clusters. The clusters were removed and ground after washing and drying. If the mass of PAN was insufficient after this procedure, then the ground powder was pressed onto the electrode. The amount of deposited substance was determined gravimetrically after washing and drying at 110°C before and after substance deposition.

Electrodes were fabricated by pressing in the form of pellets 3 cm in diameter. The hydrophobic layer of mass 0.4 g was the same in all electrodes. It was composed of 75% acetylene black and 25% FD-4D fluoroplastic emulsion in terms of dry substance. The active layer compositions are presented in the table. The compositions differ in the methods by which EMD and PAN are introduced into the combined matrix and in the order in which their layers are deposited in the case of electrochemical introduction

Compositions of the active layer of the combined matrix in the air electrode

Composition no.	Component	Mass, g	Method of EMD and PAN introduction
1	PAN	0.46	Mechanical mixture
	CF*	0.14	
2	PAN	0.32	
	EMD	0.14	
	CF	0.14	
3	PAN	0.32	Electrochemical deposition
	EMD	0.14	of EMD on a layer of PAN
	CF	0.14	on CF
4	PAN	0.32	Electrochemical deposition
	EMD	0.14	of PAN on a layer of EMD
	CF	0.14	on CF

* CF is carbon fiber.

1070-4272/01/7411-1960$25.00

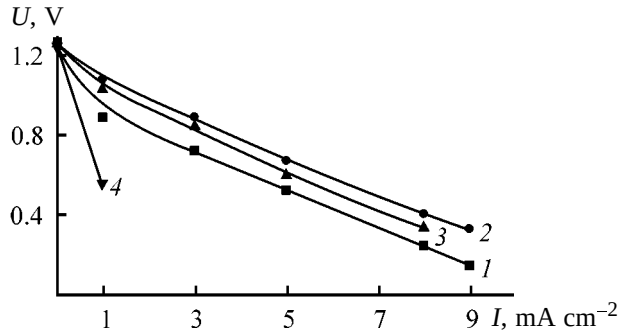

Current–voltage characteristics of air electrodes based on combined matrices obtained by (*1*) depositing PAN onto carbon fiber, (*2*) mechanical mixing of components, (*3*) depositing EMD onto PAN layer on carbon fiber, and (*4*) depositing PAN onto EMD layer on carbon fiber. (*U*) Voltage and (*I*) current density. Digits at curves correspond to matrix composition numbers in the table.

of the components. The procedure used for electrochemical tests was described in [6].

The figure shows dependences of the voltage on the working current density for air electrodes in a prototype chemical power cell based on their combined matrices. The compositions of these matrices are presented in the table. Analysis of the obtained characteristics shows that the highest current densities can be achieved with a combined matrix obtained by mechanical mixing of PAN deposited onto carbon fiber with EMD (see figure, curve *2*). The electrode matrix obtained by depositing EMD on a PAN layer on carbon fiber gives better characteristics (curve *3*) than that prepared by depositing PAN onto an EMD layer preliminarily deposited on the carbon fiber (curve *4*). This difference in characteristics is due to the fact that the coating obtained by depositing PAN onto EMD is nonuniform and cluster-like because of the low electrical conductivity of the EMD layer. In depositing EMD onto a PAN layer, the electrical conductivity of the latter is high and uniform over the surface, with the result that the coating quality is high in this case. The electrical characteristics of such an air electrode are better than those of an electrode fabricated by depositing PAN onto EMD, but worse than the characteristics of an electrode formed by mechanical mixing of the components. This is presumably due to PAN surface blocking by EMD in deposition of EMD onto PAN, resulting in that not all EMD and PAN particles interact with one another. Mechanical mixing of the components results in more uniform intermixing of EMD and PAN particles, with nearly all particles interacting with one another and the electrical characteristics improved.

Thus, it is shown that the electrical characteristics can be improved through interaction between PAN and EMD only by creating a homogeneous matrix of PAN and EMD with uniform particle distribution. Electrochemical deposition of PAN and EMD layers fails to ensure their uniform distribution at any succession of the layers. This goal can be obtained by mechanical mixing.

REFERENCES

1. Mengoli, G., Musiani, M.M., Pletcher, D., and Valcher, S., *J. Appl. Electrochem.*, 1987, vol. 17, no. 3, pp. 515–524.
2. Mengoli, G., Musiani, M.M., Pletcher, D., and Valcher, S., *J. Appl. Electrochem.*, 1987, vol. 17, no. 3, pp. 525–531.
3. Mu, S., Ye, G., and Wang, Y., *J. Power Sources*, 1993, vol. 45, no. 2, pp. 153–159.
4. Koni, U. and Schultze, J.W., *J. Electroanal. Chem.*, 1988, vol. 242, no. 1, pp. 243–254.
5. Danilov, M.O. and V'yunova, N.V., *Zh. Prikl. Khim.*, 2000, vol. 73, no. 3, pp. 418–420.
6. Danilov, M.O. and V'yunova, N.V., *Zh. Prikl. Khim.*, 2001, vol. 74, no. 2, pp. 335–337.

Russian Journal of Applied Chemistry, Vol. 74, No. 11, 2001, pp. 1962–1964. Translated from Zhurnal Prikladnoi Khimii, Vol. 74, No. 11, 2001, pp. 1899–1901.

BRIEF COMMUNICATIONS

Electrochemical Regeneration of Polishing Electrolytes of Chromium-Containing Steels

V. V. Bakaev, E. A. Fedorov, and V. N. Flerov

Nizhni Novgorod State Technical University, Nizhni Novgorod, Russia

Received August 2, 2001

Abstract—A diaphragm-separated electrolysis method was used for regeneration of spent phosphoric–sulfuric acid solutions for electropolishing of chromium-containing steels (12Cr18Ni10Ti, 40Cr13, and others). The process regime and the cathode materials were optimized.

In a number of processes [1, 2], electrochemical polishing (ECP) is an irreplaceable method for treatment of the surface of metallic parts, but its applicability is impeded by the lack of practically acceptable methods for regeneration of spent ECP solutions. The previous sorption method [3] using activated carbons for regeneration of spent polishing electrolytes is relatively cheap and simple, but sometimes it is accompanied by considerable loss of concentrated solutions (from 20 to 40 vol %).

In the course of ECP of chromium-containing steels there occurs anodic dissolution of their components. The strongest negative effect on the polishing properties of phosphoric–sulfuric acid (PS) electrolyte of ECP is produced by the iron(III) ions [3]. When more than 25 g l^{-1} of these ions is present, the degree of polishing decreases by 20%, and at Fe^{tot} > 70–72 g l^{-1} (Fe^{tot} is the total concentration of Fe ions), the solution performance is lost completely [3]. The Cr(III) and Cr(VI) ions present in ECP electrolyte did not deteriorate the polishing quality.

In this work, we studied electrochemical regeneration of spent ECP electrolytes of chromium-containing steels including cathodic reduction of Fe^{3+} ions followed by removal of iron compounds from the catholyte by freezing the latter in the form of iron(II) sulfate monohydrate sparingly soluble in the PS electrolyte [4].

EXPERIMENTAL

Spent PS electrolyte for ECP of chomium-containing steels (12Cr18Ni10Ti and 40Cr13) was regenerated electrochemically in an organic glass electrolyzer with its anode and cathode spaces separated by an acid-resistant microporous plastic diaphragm of lead batteries. The ratio of anolyte to catholyte volumes was maintained at 1 : 5 [5]. The anode was made of lead, and the cathode, of lead [5] or (and) fibrous carbon material (FCM) with a specific surface area of up to 500 – 600 cm^2 cm^{-3} and a ratio of anode to cathode areas $S_a : S_c = 1 : 10$ [6]. Regenerated (or model) solution fed into the cathode space of the electrolyzer had the folloring initial composition: H_3PO_4 10 M, H_2SO_4 4 M, Fe^{tot} 50 g l^{-1}, $Fe^{3+} : Fe^{2+} = 4 : 1$, and Cr^{tot} 7–9 g l^{-1}. Into the anode space, a 20% solution of H_2SO_4 was fed.

The cathodic current density (per geometric surface) was varied within 1–10 A dm^{-2}. At each current density the similar quantity of electricity (22 A h per 1 l catholyte) was passed through the solution. After purification, the solution was analyzed photocolorimetrically for the content of Fe^{2+} and Fe^{3+} ions [7]. The degree of metal ion extraction from the electrolyte (%) was determined by the formula

$$\eta = (C^i_{init} - C^i_{fin})/C^i_{init} \times 100,$$

where C^i_{init} and C^i_{fin} are concentrations of the ith metal ion in the solution before and after regeneration, respectively.

The current efficiency (CE, %) of the cathodic reduction of Fe^{3+} to Fe^{2+} and the specific power consumption W (W h) were calculated by the equations

$$CE = (C^{Fe}_{init} - C^{Fe}_{fin})V_{cath}/Q q^{Fe} \times 100,$$

$$W = QU_{av}/(C^{Fe}_{init} - C^{Fe}_{fin})V_{cath},$$

where Q is the passed quantity of electricity (A h), q^{Fe} is the electrochemical equivalent of Fe^{3+} ion re-

1070-4272/01/7411-1962$25.00

duction (g A^{-1} h^{-1}), C_{init}^{Fe} and C_{fin}^{Fe} are the Fe^{3+} ion concentrations in the solution before and after regeneration, respectively, and V_{cath} is the catholyte volume (l).

During electrochemical regeneration of solutions for ECP of chromium-containing steels, the following reactions can occur on the cathode:

$$Fe^{3+} + e \rightarrow Fe^{2+}, \quad E_0 = 0.771 \text{ V}, \qquad (1)$$

$$Cr_2O_7^{2-} + 14H^+ + 6e \rightarrow 2Cr^{3+} + 7H_2O, \quad E_0 = 1.36 \text{ V}, \qquad (2)$$

$$2H^+ + 2e \rightarrow H_2. \qquad (3)$$

In the solution bulk (mainly in the near-cathode space), the Cr^{6+} ions are reduced to Cr^{3+}:

$$Cr_2O_7^{2-} + 6Fe^{2+} + 14H^+ \rightarrow 2Cr^{3+} + 6Fe^{3+} + 7H_2O, \qquad (4)$$

Reactions (2)–(4) lead to undesirable power consumption for the conversion of Fe^{3+} ions in the catholyte.

Reactions (2) and (3) are electrocatalytic, with their rate dependent on the cathode material, electrolyte composition, and electrolysis conditions (the observed trends can strongly vary in such concentrated solutions as polishing electrolytes). At the same time, reactions (1) and (4) are mainly diffusion-controlled. When two redox systems (Cr^{6+}/Cr^{3+} and Fe^{3+}/Fe^{2+}) are present in a solution, their redox potentials become closer. This may be due to the differently controlled processes and to reaction (4) occurring in the near-cathode space of the solution.

It was unreasonable from the economical standpoint to use monolithic lead cathodes because of prolonged regeneration. If the operation time of the chromium-plating solutions is 280–300 A h l^{-1}, then at bulk and cathodic current densities of 1.1 A l^{-1} and 0.5 A dm^{-2}, respectively, the time of cyclic operation of a regeneration bath with monolithic Pb cathodes reaches 14 h, i.e., a 124 A h l^{-1} charge must be passed to decrease by 32% the Fe^{tot} concentration in a solution.

A considerable intensification of the electrochemical regeneration was attained using FCM cathode instead of monolithic lead cathode. A strong increase in the actual working surface area of such cathodes allowed the bulk regeneration current density to be increased considerably without marked decrease in the cathodic current efficiency by the Fe^{3+} reaction.

The dependences of the regeneration parameters

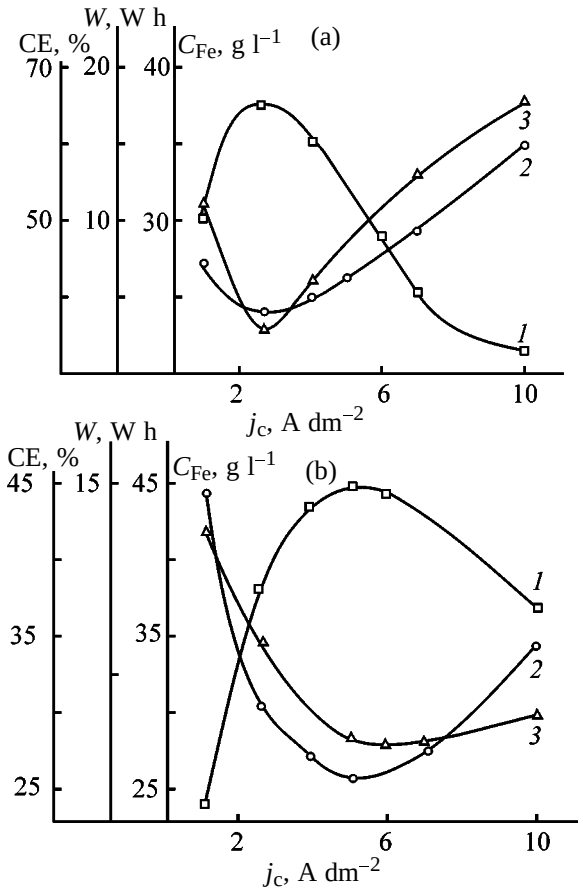

Fig. 1. (*1*) Current efficiency CE, (*2*) power consumption *W*, and (*3*) iron concentration C_{Fe} vs. cathodic current density j_c. Initial solution: H_3PO_4 10 M, H_2SO_4 4 M; Fe^{tot} 50 g l^{-1}, and Cr^{tot} 7–9 g l^{-1}. Steel: (a) 40Cr13 and (b) 12Cr18Ni10Ti.

were taken for actual spent PS solutions of ECP of 40Cr13 and 12Cr18Ni10Ti steels with the initial concentration of Fe^{tot} ions of 50 g l^{-1} (Fig. 1). For steels of the first brand, the final concentration of Fe^{tot} ions decreases with increasing cathodic regeneration current to j_c = 2–3 A dm^{-2}, when the current efficiency by the target reaction is maximal (Fig. 1a). A more marked effect with CFM cathodes was observed in regeneration of spent solutions of ECP of 12Cr18Ni10Ti steels. In this case, the optimal regeneration current density was about 5 A dm^{-2} (Fig. 1b). The effect was higher by approximately one order of magnitude than with monolithic Pb cathodes at virtually the similar specific power consumption.

The measured dependences of the total iron concentration on the quantity of electricity per liter of electrolyte at optimal regeneration cathodic current densities of ECP of 40Cr13 and 12Cr18Ni10Ti steels (Fig. 1) showed that at the low quantity of the passed electricity (up to 10–20 A h l^{-1}) the efficiency of

current utilization for exhaustive purification of ECP solution to remove noxious impurities (iron salts) is determined by the amount of the $FeSO_4 \cdot H_2O$ solid phase separated from the solution in a crystallizer cooled to 277–270 K. Crystallization of the solid iron(II) salt was accelerated by dosed addition into the solution of 0.05–0.25 M of finely crystalline potassium sulfate (seed). The degree of Fe^{tot} recovery from the solution with FCM cathodes was 45–54% at a power consumption of 5.2–7.5 W h per gram of extracted iron(II) salt. After separation, iron(II) salt can be used for technical purposes.

In the course of regeneration, the anolyte composition of the regenerator varied slightly owing to the high acidity of the solutions (large transport numbers of H^+ cations) and slow anion migration, which did not noticeably affect the overall regeneration process during a few cycles. After regeneration, the ECP solution added with a new portion of adamantane (1 g l^{-1}) [3] acquired additional polishing power corresponding to the passage of 240–260 A h l^{-1} of electricity.

CONCLUSIONS

(1) Solutions for ECP of chromium-containing steels can be regenerated electrochemically by cathodic reduction of noxious impurity [iron(III) salts] in a diaphragm-separated regenerator. As a cathode, we recommend to use fibrous carbon material, allowing regeneration of the solutions to be accelerated 5–10-fold.

(2) The contributions of the main reaction of cathodic reduction of Fe^{3+} ions and the side reactions of Cr(VI) reduction and H_2 evolution were studied. The stage of freezing of the $FeSO_4 \cdot H_2O$ solid phase from the catholyte of the regenerator was considered.

REFERENCES

1. Vinogradov, S.S., *Ekologicheski bezopasnoe gal'vanicheskoe proizvodstvo* (Environmentally Clean Electroplating Manufacture), Moscow: Globus, 1998.
2. Fedorova, E.A., *Ekol. Prom–st. Ross.*, 1999, no. 1, pp. 12–16.
3. Fedorova, E.A., Kurnoskin, G.A., and Flerov, V.N., *Zh. Prikl. Khim.*, 1990, vol. 63, no. 7, pp. 1586–1588.
4. RF Inventor's Certificate no. 14735.
5. Kochergin, V.P., Artemova, V.A., and Samoilova, L.I., *Tr. Voronezh. Univ.*, 1968, no. 2, pp. 55–57.
6. *Gibkie avtomatizirovannye gal'vanicheskie linii* (Adaptable Automated Electroplating Lines), Zubchenko, V.L., Ed., Moscow: Mashinostroenie, 1989.
7. Sandell, E.B., *Colorimetric Determination of Traces of Metals*, London: Interscience, 1959.

Russian Journal of Applied Chemistry, Vol. 74, No. 11, 2001, pp. 1965–1967. Translated from Zhurnal Prikladnoi Khimii, Vol. 74, No. 11, 2001, pp. 1901–1903.

BRIEF COMMUNICATIONS

On the Possibility of Recovery of Heavy Metals from Excess Activated Sludge at 6–37°C

I. V. Zykova, E. A. Alekseeva, and V. P. Panov

Novgorod State University, Velikii Novgorod, Russia
St. Petersburg State University of Technology and Design, St. Petersburg, Russia

Received January 15, 2001

Abstract—A method for recovery of heavy metals (Fe, Zn, Cu, Cr, Ni, Pb, Co) from excess activated sludge is proposed, based on substitution of heavy metals in the cells of microorganisms by calcium after introducing poorly soluble calcium salts into the system at 6–37°C.

Industrial wastewater generally contains high concentration of heavy metals. Occasionally, this concentration approaches tens milligrams per liter. In biological treatment of such wastewater or its mixtures with residential wastewater at a treatment plant heavy metals are accumulated by microorganisms of activated sludge [1].

Utilization of excess activated sludge, contaminated with heavy metals, as an organic fertilizer for farming or raw material for biosynthesis of various useful products becomes impractical. Disposal by incineration is rather expensive, requiring thorough cleaning of waste gases. By virtue of these factors excess activated sludge is often simply stored in sludge sites. With time the amount of excess sludge increases, which requires steadily growing areas for its storage. Correspondingly increases the heavy-metal contamination hazard for the environment. According to the estimates of some German companies, the cost needed for utilization of excess activated sludge by drying with subsequent disposal approaches 450–800 DM per ton dry substance; by warehousing, 600 DM; and by incineration, 800–1200 DM. If the utilization method provides the use of excess sludge in farming, the cost may be reduced to 250–300 DM per ton dry substance. Therefore, the problem of treatment of excess sludge to remove heavy metals is an issue of the day.

According to the existing regulations, the maximal permissible concentrations of heavy metals in excess sludge for use as a fertilizer in farming are as follows (mg kg^{-1} dry substance): Ni 100, Pb 100, Cr 300, Cu 600, and Zn 1500 [2]. In excess activated sludge of a municipal treatment plant before filter presses (moisture content 96%), i.e., before sludge thickening to a 91% moisture content, the concentrations of heavy metals were as follows (mg kg^{-1} dry substance): Co 57, Pb 95, Ni 120, Cr 250, Cu 810, and Zn 1710 (data obtained in 1997). The metal concentrations in the aqueous phase (mg dm^{-3}) are as follows: Co 0.6, Pb 1.7, Ni 3.5, Cr 3.3, Cu 5.4, and Zn 1.8. After the filter presses the heavy metal concentrations in excess activated sludge increased to the following values (mg kg^{-1} dry substance): Co 66, Pb 160, Ni 220, Cr 320, Cu 1010, and Zn 2300; the concentrations in the aqueous phase increased also. Unconditionally, such a sludge is unsuitable as a fertilizer. The existing methods for recovery of heavy metals from sludge [3, 4] find no wide application, and by now the utilization of excess activated sludge is at a level of about 1.5% of the total all over the world.

We developed a method for recovery of heavy metals from excess activated sludge, based on substitution of heavy metals in the cells of microorganisms by calcium after introducing poorly soluble calcium material in the system at 6–37°C. Activated sludge was dried at 106°C to constant weight and analyzed for heavy metals on a Saturn atomic absorption spectrophotometer and a Perkin–Elmer spectrophotometer. Excess activated sludge before thickening (moisture content 96%) or after thickening (moisture content 90–92%) was mechanically mixed with poorly soluble calcium salts, $CaCO_3$ and $CaSO_4 \cdot 2H_2O$ (both of chemically pure grade), in the proportion 15 parts per 100 parts of sludge in open vessels for 3–6 h. The pH 6–8 of the aqueous phase remained unchanged throughout the experiment. The results obtained with various ratios of salt to sludge a and mixing times τ are given in the table.

The results show that heavy metals can be effec-

1070-4272/01/7411-1965$25.00

Heavy metal concentrations in sludge after treatment at 293 K

Experimental conditions			Metal concentration, mg kg^{-1} dry substance						
salt	*a*	τ, h	Fe	Zn	Cu	Ni	Cr	Pb	Co
Initial sludge before thickening									
–	–	–	6060	1710	810	120	250	90	57
$CaSO_4 \cdot 2H_2O$	5 : 100	4.5	2900	960	580	47	116	0	7
	5 : 100	6	2900	870	540	42	120	0	4
	10 : 100	6	1600	480	400	30	110	0	1
	15 : 100	6	900	320	350	16	95	1	1
	10 : 100	3	2000	750	460	40	135	0	6
	10 : 100	4.5	1700	580	420	31	105	1	4
Initial sludge after thickening									
–	–	–	8100	2300	1010	220	320	160	66
$CaCO_3$	5 : 100	6	2050	560	510	49	140	1	4
	10 : 100	6	1820	510	460	24	110	0	0
	15 : 100	6	1420	460	370	17	85	0	0
	10 : 100	3	2100	780	560	62	146	2	2
	10 : 100	4.5	1840	710	510	36	124	0	0
$CaSO_4 \cdot 2H_2O$	10 : 100	4.5	1700	580	400	31	100	1	6

tively recovered from activated sludge using poorly soluble Ca salts (Figs. 1, 2). In some experiments the degree of recovery of Pb, Co, and Ni was over 90%.

The possible mechanism of recovery of heavy metals from sludge is as follows. The introduced poorly soluble calcium salts serve as a mineral support for immobilization of cells of the microorganisms and of enzymes produced by them, which activates and stabilizes all processes with participation of the enzymes, including biodegradation of the sludge organic matter, particularly that complexing heavy metals. Metals transferred to the aqueous phase, for example, in the form of hydroxo compounds, can be sorbed on the porous surface of the support. Calcium salts provide an increased concentration of Ca ions in the extracellular space, resulting in opening of the potential-dependent Ca^{2+} channels. Calcium ions penetrate into the intracellular space by these channels and also with the help of carrier proteins; the Ca concentration increases there, initiating opening of Ca-dependent K^+ and Na^+ channels, by which heavy metals can be discharged from the cells [6]. Furthermore, heavy metals can be replaced by calcium by ion exchange on the cell surface.

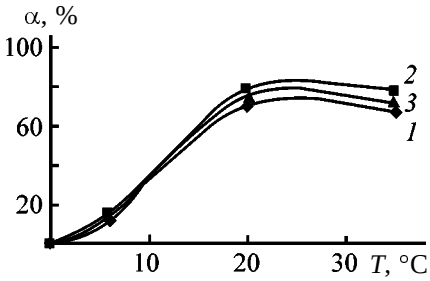

Fig. 1. Degree of recovery α of heavy metals from activated sludge before thickening with $CaSO_4 \cdot 2H_2O$ as a function of the temperature *T*: (*1*) Zn, (*2*) Cu, and (*3*) Ni; the same for Fig. 2.

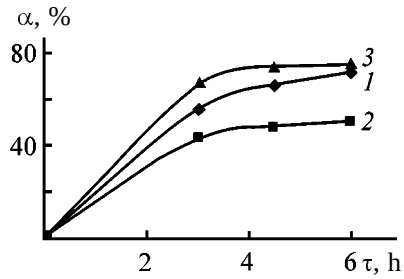

Fig. 2. Degree of recovery α of heavy metals from activated sludge before thickening with $CaSO_4 \cdot 2H_2O$ as a function of the process time τ.

One part of heavy metals, recovered from activated sludge in the form of sols, is sorbed on the solid material surface and the other part passes to the aqueous phase in soluble and colloidal forms. After phase separation by settling sludge goes to further processing into an organomineral fertilizer, as now meeting the requirements on the heavy metal concentrations. The calcium material can be recycled after washing with water or even without washing. Heavy metals,

concentrated in the aqueous phase to tens or even hundreds milligrams per liter, can be recovered by precipitation or sorption.

CONCLUSIONS

(1) Treatment of excess activated sludge to remove heavy metals is proved to be a pressing problem in the context of utilization of sludge as a fertilizer for farming needs.

(2) A method for recovery of heavy metals from excess activated sludge is proposed, based on substitution of heavy metals in the cells of microorganisms by calcium after introducing a poorly soluble calcium salt in the system.

(3) The results obtained demonstrate that heavy metals can be sufficiently effectively recovered from activated sludge using poorly soluble Ca salts. The resulting sludge meets the requirements on the residual heavy metal content for sludge suitable for use as a fertilizer for farming.

REFERENCES

1. Ilyaletdinov, A.A., *Mikrobiologicheskoe prevrashchenie metallov* (Microbiological Conversion of Metals), Alma-Ata: Nauka, 1975.
2. *Course of Waste Treatment Technologies*, Suonio, T., Ed., Helsinki: Management of Water Resources and Environment, 1992.
3. Turovskii, I.S., *Obrabotka osadkov stochnykh vod* (Treatment of Sewage Sludge), Moscow: Stroiizdat, 1992, 3rd ed.
4. *Khimiya promyshlennykh stochnykh vod* (Chemistry of Industrial Wastewater), Rubin, A., Ed., Moscow: Khimiya, 1983.
5. RF Patent no. 2133231.
6. Kotyk, A. and Janaček, K., *Membrane Transport: An Interdisciplinary Approach*, New York: Plenum, 1977.

Russian Journal of Applied Chemistry, Vol. 74, No. 11, 2001, pp. 1968–1969. Translated from Zhurnal Prikladnoi Khimii, Vol. 74, No. 11, 2001, pp. 1904–1905.

BRIEF COMMUNICATIONS

Synthesis and Antimicrobial Activity of Surface-Active Alkoxycarbonylmethyldimethyl(4-penten-2-ynyl)ammonium Chlorides

A. V. Babakhanyan, A. Kh. Gyul'nazaryan, T. A. Saakyan, S. A. Ovakimyan, Zh. R. Babayan, and R. S. Arutyunyan

Institute of Organic Chemistry, National Academy of Sciences of Armenia, Yerevan, Armenia
Abovyan Armenian State Teacher's Training University, Yerevan, Armenia
Yerevan State University, Yerevan, Armenia

Received May 21, 2001

Abstract—Quaternary ammonium salts containing a 4-penten-2-ynyl group in addition to the alkoxycarbonylmethyl group are synthesized. The surface activity and antimicrobial action of the resulting compounds are studied.

The practical significance of surface-active quaternary ammonium salts (QASs) is caused by the possibility of their use as emulsion stabilizers [1–3] and antimicrobial agents [4, 5]. Quaternary ammonium salts containing acryloyl, acetylene, diene, and vynyl groups as polymerizable fragments are of interest as monomers for preparation of the corresponding polyelectrolytes [6].

Previously we synthesized micelle-forming QAS surfactants containing 5-methyl-2,4-hexadienyl group in addition to a hydrophobic radical [7] and demonstrated the antimicrobial activity of these compounds with respect to Gram-positive and Gram-negative microorganisms [8].

In this work we synthesized new surface-active ionic complex monomers and characterized their antimicrobial activity. Quaternary ammonium salts **I**–**IV** containing 4-penten-2-ynyl group (see table) were synthesized by the reaction

$$(CH_3)_2NCH_2C{\equiv}CCH{=}CH_2 + ROCOCH_2Cl \longrightarrow ROCOCH_2N(CH_3)_2CH_2C{\equiv}CCH{=}CH_2]^+Cl^-,$$

I–**IV**

where R = C_7H_{15} (**I**), C_8H_{17} (**II**), $C_{10}H_{21}$ (**III**), and $C_{12}H_{25}$ (**IV**).

The critical micelle concentration (CMC) of compounds **I**–**IV** was determined from the surface tension isotherms [9]. The foaming power was estimated from data on the foam stability *h* in aqueous QAS solutions as the ratio of the height of the foam column 5 min after its formation to the initial height [10]. It follows from the table that CMC and σ_{CMC} decrease and the foam stability increases with increasing length of the alkyl radical in the QAS molecules.

The antimicrobial activity of compounds **I**–**IV** was studied by the method of disinfection of cambric test objects [11] seeded with standard strains of *Staphylococcus aurous* (strain 906) and *Escherichia coli* (strain 1257). Cambric test objects were infected with a suspension of the indicated microorganisms, containing 2 billions cells per ml. The exposure was 5–30 min at 20°C.

The results obtained show that compounds **I**–**IV** possess the bactericidal action (see table), which depends on the length of the alkyl radical R. The maximal bactericidal action is shown by compound **IV**. A 0.2% aqueous solution of this compound kills *Escherichia coli* and *Staphylococcus aurous* in 5 min.

EXPERIMENTAL

Infrared spectra were registered on UR-20 and Specord 75-IR spectrometers in liquid paraffin or KBr, and the ^1H NMR spectra, on a Mercury-300 Varian spectrometer (300 MHz) in CD_3OD or $(CD_3)_2SO$ using TMS an internal reference.

Ammonium salts **I**–**IV** were synthesized as follows. An equimolar mixture of dimethyl(4-penten-2-ynyl)amine and the corresponding alkyl chloroace-

1070-4272/01/7411-1968$25.00

Physicochemical and antimicrobial characteristics of quaternary ammonium bases **I**–**IV**

QAS	Yield, %	Found, %		Formula	Calculated, %		σ_{CMC}, dyne cm^{-1}	CMC × 10^3	*h*	*c*, %	τ,* min	
		N	Cl^-		N	Cl^-					strain 906**	strain 1257***
I	80	4.76	11.53	$C_{16}H_{28}ClNO_2$	4.64	11.75	32	70.2	0.2	1	25	30
II	85	4.25	11.00	$C_{17}H_{30}ClNO_2$	4.43	11.22	30	31.7	0.3	2	5	5
										1	5	5
										0.5	30	30
III	75	4.18	10.65	$C_{19}H_{34}ClNO_2$	4.07	10.31	29	10.2	0.4	0.5	5	5
										0.3	25	30
										0.2	>30	>30
IV	90	4.00	9.70	$C_{21}H_{38}ClNO_2$	3.77	9.53	28	5.4	0.5	0.2	5	5
										0.1	15	25
										0.05	25	30

* Life time of the microorganisms. ** *Staphylococcus aurous.* *** *Escherichia coli.*

tate was allowed to stand for 5–6 days at room temperature. Th resulting waxy mass was washed several times with absolute diethyl ether and dried; mp of salt **IV** 33–34°C.

Along with complex multiplets typical of the alkyl groups of an ester, in the ^1H NMR spectra of compounds **I**–**IV** we found the following signals, δ (ppm): 3.41 s (6H, NCH_3), 3.90–4.10 s (2H, CH_2COO), 4.30–4.45 s (2H, $CH_2C{\equiv}$), and 5.93–6.00 m (3H, $CH{=}CH_2$).

The infrared spectra of compounds **I**–**IV** show the adsorption bands typical of the pentenyne and ester groups at 1645 ($CH{=}CH_2$), 2260 (C≡C), 1180, and 1740 cm^{-1} (COO).

CONCLUSIONS

(1) Surface-active ammonium salts containing a 4-penten-2-ynyl group in addition to the alkoxycarbonylmethyl group are synthesized. With increasing length of the alkyl radical the critical micelle concentration and σ_{CMC} decrease and the foam stability increases.

(2) The ammonium compounds obtained demonstrate a bactericidal action; their bactericidal activity depends on the length of the alkyl radical R in the ester group. The maximal bactericidal activity is shown by dodecylcarbonylmethyldimethyl(4-penten-2-ynyl)ammonium chloride.

REFERENCES

1. Arutyunyan, R.S., Kausas, Kh., Grigoryan, Dzh.D., *et al.*, *Khim. Zh. Arm.*, 1996, vol. 49, nos. 1–3, p. 158–160.
2. Arutyunyan, R.S., Grigoryan, Dzh.D., Babakhanyan, A.V., and Beileryan, N.M., *Kolloidn. Zh.*, 1999, vol. 61, no. 5, pp. 605–609.
3. Haroutyunian, R., Babakhanian, A., and Beylerian, N., *J. Surf. Sci. Technol.*, 1998, vol. 14, nos. 1–4, pp. 55–59.
4. Babakhanyan, A.V. and Babayan, Zh.R., *Biol. Zh. Arm.*, 1995, vol. 48, no. 3, p. 26–27.
5. Babayan, Zh.R., Margaryan, A.V., Aleksanyan, Yu.T., *et al.*, *Zh. Mikrobiol. Epidemiol. Immunobiol.*, 1996, no. 6, pp. 63–64.
6. Egorov, V.V. and Zubov, V.P., *Usp. Khim.*, 1987, vol. 56, no. 12, pp. 2076–2097.
7. Babakhanyan, A.V., Arutyunyan, R.S.,, and Sargasyan, A.B., *Arm. Khim. Zh.*, 1991, vol. 44, no. 1, pp. 54–57.
8. Babakhanyan, A.V., Grigoryan, L.G, Babayan, Zh.R., and Akopyan, G.S., *Biol. Zh. Arm.*, 1990, vol. 43, no. 2, pp. 148–150.
9. *Praktikum po kolloidnoi khimii* (Practical Course of Colloid Chemistry), Neiman, R.E., Ed., Moscow: Vysshaya Shkola, 1972, pp. 126, 136.
10. *Poverkhnostno-aktivnye veshchestva: Spravochnik* (Surfactants: A Handbook), Abramzon, A.A. and Gaevoi, G.M., Eds., Leningrad: Khimiya, 1979.
11. Lavrskii, P.P. and Sokolova, N.F., in *Problemy dezinfektsii i sterilizatsii: Sbornik nauchnykh trudov VNII dezinfektsii i sterilizatsii* (Problems of disinfection and Sterilization: Coll. of scientific Works of the All-Union Research Institute of Disinfection and Sterilization), Moscow, 1971, issue 21, vol. 2, pp. 186–199.

Russian Journal of Applied Chemistry, Vol. 74, No. 11, 2001, pp. 1970–1971. Translated from Zhurnal Prikladnoi Khimii, Vol. 74, No. 11, 2001, pp. 1906–1907.

BRIEF COMMUNICATIONS

Phosphorylation of 4-Oxo-2-thioxo-1,3-thiazolidine with $POCl_3$ in the Solid Phase

E. B. Aronova and A. I. Ginak

St. Petersburg State Technological Institute, St. Petersburg, Russia

Received October 2, 2000; in final form, July 2001

Abstract—Lithium salt of 4-oxo-2-thioxo-1,3-thiazolidine was phosphorylated with $POCl_3$.

Phosphorylation of heterocyclic compounds is of great interest as a route to valuable substances: curing agents, vulcanization rate regulators [1], herbicides, plant and microorganism growth regulators [2]. However, in most cases heterocyclic compounds are ambifunctional and in reactions with phosphorylating agents (phosphoric chlorides, $POCl_3$, phosphoramidic chlorides) yield difficultly separable isomer mixtures [3, 4], often contaminated with side alkylation products [5]:

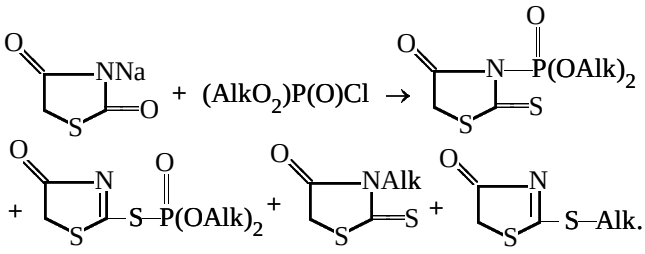

Synthesis of phosphorylated heterocycles by cyclization of phosphorylated fragments also yields complex reaction mixtures from which the pure product can be isolated difficultly and with a low yield [6].

By varying the factors that affect the reaction pathways of ambident compounds (solvent, counterion, nature of substrate and reagent) [7], it is possible to increase somewhat the yield of the target product, but the impurities remain the same. At the same time, it is known [8] that nucleophilic substitution reactions of crystalline ambident substrates with gaseous electrophiles occur more selectively, often yielding only one of the isomers. We attempted phosphorylation of ambident thiazolidones in the system gas–solid. As substrate we took crystalline lithium salt of 4-oxo-2-thioxo-1,3-thiazolidine, and as phosphorylating agent, $POCl_3$. The reaction was performed in an electrically heated tubular reactor (1 cm diameter, 10 cm height) in which the temperature could be adjusted in the range 25–250°C. A mixture of $POCl_3$ vapor with an inert gas (nitrogen, argon) was passed through a fixed bed of the substrate. The reaction progress was monitored by thin-layer chromatography (TLC). After reaction completion, excess $POCl_3$ was blown off, and ethanol or diethylamine vapor was fed to replace the chlorine atom and obtain, respectively, diethyl 4-oxo-2-thioxo-1,3-thiazolidine-3-phosphonate **I** and tetraethyl 4-oxo-2-thioxo-1,3-thiazolidine-3-phosphonic diamide **II**:

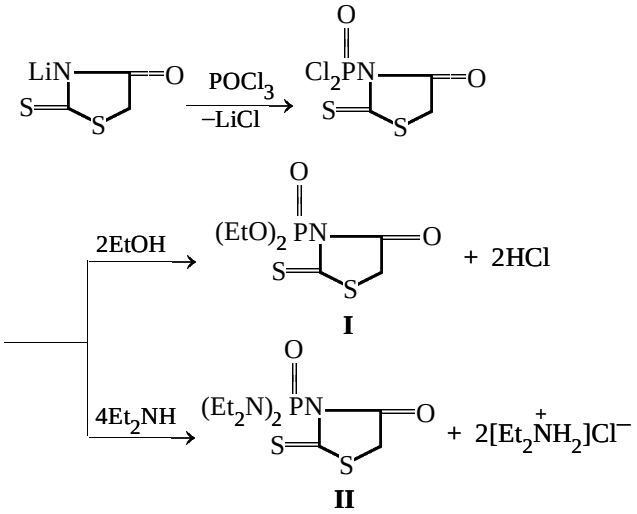

The phosphorylation pathway was judged by the hydrolysis products of **I** and **II**. Phosphorylation of the nitrogen atom of the heteroring is confirmed by formation of 4-oxo-2-thioxo-1,3-thiazolidine. Hydrolysis of the hypothetical product formed by phosphorylation of the exocyclic sulfur atom would yield 1,3-thiazolidine-2,4-dione, but it was not detected.

4-Oxo-2-thioxo-1,3-thiazolidine was identified by TLC (Silufol UV-254, eluent acetone–hexane–acetic acid, 1 : 2 : 0.01) [7] and by comparison of its IR

1070-4272/01/7411-1970$25.00

spectrum with that of an authentic sample [8] [ν(C=O) 1760, ν(C=S) 1100 cm^{-1}].

Diethyl 4-oxo-2-thioxo-1,3-thiazolidine-3-phosphonate I. Yield 97%, mp 29°C, R_f 0.54, λ_{max} 294 nm ($\log\varepsilon$ 4.01).

***N,N,N,N*-Tetraethyl-4-oxo-2-thioxo-1,3-thiazolidine-3-phosphonic diamide II.** Yield 94%, mp 72°C, R_f 0.15, λ_{max} 294 nm ($\log\varepsilon$ 4.01).

REFERENCES

1. Shenina, G.M., Ratnikova, T.V., and Ginak, A.I., *Kauch. Rezina*, 1978, no. 5, pp. 16–18.
2. Mel'nikov, N.N., Volkov, A.I., and Korotkova, O.A., *Pestitsidy i okruzhayushchaya sreda* (Pesticides and the Environment), Leningrad: Khimiya, 1977.
3. Ginak, A.I., V'yunov, K.A., and Sochilin, E.G., *Zh. Obshch. Khim.*, 1970, vol. 40, no. 4, pp. 1423–1424.
4. Ginak, A.I., V'yunov, K.A., and Sochilin, E.G., *Sb. Tr. Leningr. Tekhnol. Inst. im. Lensoveta*, 1975, no. 5, pp. 3–7.
5. Ginak, A.I., V'yunov, K.A., and Sochilin, E.G., *Zh. Obshch. Khim.*, 1969, vol. 39, no. 3, pp. 1180–1181.
6. Ginak, A.I., V'yunov, K.A., and Sochilin, E.G., *Sb. Tr. Leningr. Tekhnol. Inst. im. Lensoveta*, 1975, no. 6, pp. 6–9.
7. V'yunov, K.A., Ginak, A.I., and Ramsh, S.M., *Zh. Org. Khim.*, 1983, vol. 19, no. 1, pp. 212–215.
8. Ginak, A.I., V'yunov, K.A., Volkova, A.A., *et al.*, *Zh. Prikl. Khim.*, 1971, vol. 44, no. 6, pp. 2123–2124.

Russian Journal of Applied Chemistry, Vol. 74, No. 11, 2001, pp. 1972–1974. Translated from Zhurnal Prikladnoi Khimii, Vol. 74, No. 11, 2001, pp. 1908–1910.

ANNIVERSARIES

Andrei Georgievich Morachevskii (to 75th Birthday Anniversary)

On October 1, 2001, Andrei Georgievich Morachevskii, a known scientist working in the field of physical chemistry of metals and alloys and high-temperature electrochemistry, doctor of technical science, professor, honored scientist and technologist of the Russian Federation, head of Chair of Physical Chemistry at St. Petersburg Technical University, and deputy Editor-in-Chief of *Zhurnal Prikladnoi Khimii* was 75. He also accomplished 50 years of engineering, scientific, and pedagogical activities.

In 1950, A.G. Morachevskii graduated from Lensovet Technological Institute in Leningrad as a specialist in physical chemistry. In 1951–1953, he worked at enterprises of the Ministry of Interior. At the Krasnoyarsk plant of nonferrous metals he took direct part, under supervision of profs. Ya.I. Bashilov and R.L. Myller, in the development of a technology for electrolytic manufacture of rhodium.

He became a postgraduate student at Kalinin Polytechnic Institute in Leningrad (now St. Petersburg State Technical University) in December 1953; an assistant at the chair of physical chemistry at the same institute, in 1956; a docent at the same chair, in 1961; a professor, in 1970; and headed the chair of physical chemistry in 1973. He backed his candidate dissertation in 1957 and doctoral dissertation in 1969.

Andrei Georgievich has performed extensive investigations of thermodynamic and other properties of binary, ternary, and more complex metal systems in liquid and solid states. He studied in detail the thermodynamic properties of liquid alloys with strong interatomic interaction and revealed characteristic features of the concentration dependence of thermodynamic functions in these alloys. Morachevskii and co-workers were the first to study the thermodynamic properties of dilute solutions of alkali and alkaline-earth metals in various liquid–metal solvents and gave detailed recommendations on how to calculate the thermodynamic properties of ternary and more complex metal systems from data on binary subsystems. Morachevskii paid much attention in his works to computer simulation of thermodynamic properties of liquid metal systems with varied nature of component interaction and gave recommendations on compiling an appropriate database.

Morachevskii and co-workers studied the thermodynamic properties of a great number of chalcogenides and metal–chalcogen systems, developed new investigation techniques, studied equilibria between the chalcogenide and salt phases, and analyzed the interaction of sulfur and sulfides with molten salts. The thermodynamics and kinetics of alloying on liquid and solid electrodes and processes of joint discharge of impurities at liquid cathodes were studied in detail on various objects.

In cooperation with a number of institutions, Morachevskii took part in large-scale investigations in the field of manufacture of high-purity metals, production of alkali metals and their alloys, and development of new chemical power sources for various purposes. In recent years, the scientist has been paying much attention to creating an environmentally safe technology for processing of secondary lead and to new methods for refining of black lead.

In 1986, Morachevskii was awarded, as a member of a group of researchers, a State Prize of the Ukraine in science and technology for the study *"Physicochemical Foundations, Technology, and Industrial*

Implementation of Manufacture of Ultra-High-Purity Metals (Mercury, Cadmium, Zinc, Lead, Bismuth, Gallium, Indium, Thallium, Tellurium)."

The results of his studies have been reported in quite a number of monographs, including: *Elektrody sravneniya dlya rasplavlennykh solei* (Reference Electrodes for Molten Salts, Moscow: Metallurgiya, 1965, translated in the United States); *Zhidkie katody* (Liquid Cathodes, Tbilisi, 1978); *Fizikokhimiya i metallurgiya vysokochistogo svintsa* (Physical Chemistry and Metallurgy of High-Purity Lead, Moscow: Metallurgiya, 1991); *Natrii: Svoistva, proizvodstvo, primenenie* (Sodium: Properties, Manufacture, and Use, St. Petersburg: Khimiya, 1992); *Pererabotka vtorichnogo svintsovogo syr'ya* (Processing of Secondary Lead, St. Petersburg: Khimiya, 1993); *Elektrokhimiya svintsa v ionnykh rasplavakh* (Electrochemistry of Lead in Ionic Melts, St. Petersburg: Khimiya, 1994); and *Kalii: Svoistva, proizvodstvo, primenenie* (Potassium: Properties, Manufacture, and Use, Moscow: Ruda i Metally, 2000). Morachevskii wrote a large number of spacious reviews.

Together with staff member of his chair and specialists from other institutions, Morachevskii received more than 60 Inventor's Certificates; he was awarded a breastplate "Inventor of the USSR."

During his entire scientific career, professor Morachevskii has been paying much attention to preparation and publication of reference literature and to problems of scientific information. Under his editorship and with his supplements were published in translation three volumes of the Reference Book of Molten Salts (Leningrad: Khimiya, 1971, 1974). Also published were (together with I.B. Sladkov) reference books *Termodinamicheskie raschety v metallurgii* (Thermodynamic Calculations in Metallurgy, Moscow, 1985; supplemented edition 1993), *Fiziko-khimicheskie svoistva molekulyarnykh neorganicheskikh soedinenii* (Physicochemical Properties of Molecular Inorganic Compounds, Leningrad: Khimiya, 1987; translated into Japanese; supplemented edition 1996). Morachevskii took part in compilation of *Spravochnik po elektrokhimii* (Handbook of Electrochemistry, Leningrad: Khimiya, 1981, translated into Japanese). In 1957–1967 Morachevskii annually published reviews on electrochemistry of molten salts, which attracted much interest of specialists in russia and other countries. Morachevskii published in scientific journals more than 100 reviews of monographs, reference books, and textbooks of domestic and foreign authors.

During the years of his pedagogical activities, Andrei Georgievich wrote a great number of tutorials and developed a number of special courses. The book *Termodinamika rasplavlennykh metallicheskikh i solevykh sistem* (Thermodynamics of Molten Metal and Salt Systems, Moscow: Metallurgiya, 1987; translated into Polish) was highly appreciated by specialists and recommended for students specializing in physicochemical investigations of metallurgical processes. For students of the same specialty were written tutorials *Fizikokhimicheskie svoistva zhidkikh metallov i splavov* (Physicochemical Properties of Liquid Metals and Alloys, Leningrad: Leningr. Politekh. Inst., 1986), *Vysokotemperaturnaya elektrokhimiya* (High-Temperature Electrochemistry, Leningrad: Leningr. Politekh. Inst., 1986), etc.

Under Morachevskii's supervision, 47 candidate dissertations have been prepared and successfully backed, and this work is being continued now. Graduates from higher school institutions from all over the country were Morachevskii's postgraduate students, and they are teaching now in Vologda and Cherepovets, Volgograd and Vladikavkaz, Krasnoyarsk, Irkutsk, Ulan-Ude. Four lecturers of the chair backed their doctoral dissertation. Specialists from Poland, Germany, Czechoslovakia, Italy, and China have been trained at the chair. Morachevskii is a scientifically broad-minded person possessing deep knowledge in physical chemistry of metallurgical systems and processes, inorganic materials science, and applied electrochemistry. For a long time he was a member of specialized councils entitled to award the doctor-of-science degree at Leningrad State University and Mining Institute. More than 30 times he was an official opponent at presentations of doctoral dissertations in Moscow and St. Petersburg, Kiev and Sverdlovsk, Tbilisi and Alma-Ata.

Morachevskii carries out extensive scientific-organization work. Since 1980 he has been a member of the Editorial Board of *Zhurnal Prikladnoi Khimii* (deputy Editor-in-Chief since 1986) and a member of the Editorial Board of *Rasplavy* (Melts) journal. During many years he was a member of the editorial boards of *Izvestiya Vysshikh Uchebnykh Zavedenii: Tsvetnaya Metallurgiya* (Bulletin of Higher School Institutions: Nonferrous Metallurgy) journal and *Fiziko-khimicheskie issledovaniya metallurgicheskikh protsessov* (Physicochemical Studies of Metallurgical Processes) intercollegiate collection. Morachevskii took active part in the work of the Scientific Council of the Academy of Sciences of the USSR for physical chemistry of ionic melts and solid electrolytes, and headed a section of the Council. Also, he was a member of Scientific Councils of the Academy of Sciences of the USSR for chemical thermodynamics and ther-

mochemistry and for electrochemistry and corrosion. Morachevskii took part, as a member of the Organizing Committee, in preparing and holding All-Union Symposia on physical chemistry of ionic melts and solid electrolytes and on thermodynamics of metal systems; he is one of organizers of the regularly held Kola symposia on electrochemistry of less-common metals.

In recent years, Morachevskii has been paying much attention to the history of chemistry and chemical technology and published quite a number of works concerned with this subject matter.

Andrei Georgievich originates from a St. Petersburg professor's family, he is distinguished by high working capacity, sense of duty, and readiness to help colleagues, postgraduate students, and students.

The Editorial Board and Editorial Staff of *Zhurnal Prikladnoi Khimii* congratulate Andrei Georgievich Morachevskii on the jubilee and wish him sound health and further creative success.

Editorial Board and Editorial Staff
of *Zhurnal Prikladnoi Khimii*

Russian Journal of Applied Chemistry, Vol. 74, No. 11, 2001, pp. 1975–1976. Translated from Zhurnal Prikladnoi Khimii, Vol. 74, No. 11, 2001, pp. 1911–1912.

HISTORY OF CHEMISTRY AND CHEMICAL TECHNOLOGY

Andrei Egorovich Pereverzev (to Centennial Birthday Anniversary)

In November 2001, Andrei Egorovich Pereverzev, a prominent scientist, excellent pedagogue, talented organizer and top manager, doctor of technical science, professor, honored scientist and technologist of the Russian Soviet Federative Republic and Tartar Autonomous Soviet Socialist Republic, founder and head of the chair of ammunition charging (1939–1972), and rector of the Technological Institute (1945–1946), would be 100.

Andrei Egorovich Pereverzev was born on November 29, 1901, into a poor peasant family. In 1918, when being 17, he joined Red Army as a volunteer.

Pereverzev created a scientific school that predetermined the development in the field of ammunition charging for many years and developed safe methods of formation and use of charges of various-purpose explosives. Many leading specialists and top industry managers were, and still are, his pupils.

In his work, Andrei Egorovich always strove for close relation of scientific research to the practical needs of the industry. He was a prominent scientist possessing a creative mind of researcher and combined pedagogic talent with organization abilities.

In the severe years of the World War II, Andrei Egorovich was appointed director of the Kazan Institute of Chemical Engineering (KKhTI) and simultaneously supervised important scientific research of great military value. By Andrei Egorovich's initiative, large workshop for charging of varied-purpose ammunition was organized.

After the war, Pereverzev, then director of LTI im. Lensoveta (Leningrad Technological Institute), much contributed to the reconstruction and consolidation of the Institute as a scientific and pedagogical center of Leningrad. Simultaneously, Andrei Egorovich continued his scientific activities. In 1947, he successfully backed his doctoral dissertation.

In 1926, Andrei Egorovich entered Leningrad Technological Institute and graduated as engineer in 1934. Then he worked as deputy director of the Institute, was a post-graduate student, backed his candidate dissertation, and, finally, organized in 1939 a chair of

technology of ammunition charging and headed it for 32 years. During this time, the chair became one of the leading chairs of LTI im. Lensoveta. The scientific interests of Andrei Egorovich started to take shape under the influence of Semen Petrovich Vukolov, professor of the Technological Institute and D.I. Mendeleev's pupil.

Under Pereversev's supervision, blend formulations based on high-power explosives and thermoplastic (thermoreactive) polymers were developed and introduced into practice. The formulations were used to create charges with controllable energy and performance characteristics. In particular, charges of unique design and power, formed by casting under pressure, were used for explosive pumping of chemical lasers. The same formulations were used to create thin-walled spherical charges and cumulative charges of various purposes.

Andrei Egorovich possessed unique creative intuition and was one of the first in the country to appreciate the potentialities of computers, which were widely used at his chair for calculating processes of article fabrication and thermodynamic processes occurring in explosion of explosive charges.

A particular place in this group of works is oc-

1070-4272/01/7411-1975$25.00

cupied by investigations aimed at the development of a continuous process for pressing of elongated charges from elastic and plastic explosives.

A prominent contribution to the technology of ammunition charging was made by Pereverzev's works concerned with the development of vibrational and pneumatic methods for mixing of explosives and blended solid propellants. These works laid foundations of the theory and gave methods for calculation of component mixing processes and demonstrated advantages of the vibrational and pneumatic methods for manufacture of explosive mixtures and solid propellants.

Being one of the leading scientists in the field of ammunition charging technology, Andrei Egorovich developed theoretical foundations of a number of processes and reported on this issue in his lectures and in the manual *Tekhnologiya snaryazheniya boepripasov* (Technology of Ammunition Charging).

Preverzev was the author of numerous scientific papers and recipient of Inventor's Certificates and patents in chemical technology. Under Andrei Egorovich's supervision, more than 70 candidate and several doctoral dissertations were prepared and backed. Andrei Egorovich trained numerous cadre of engineers, specialists in ammunition charging technology.

In 1999, St. Petersburg Technical Institute celebrated 60th anniversary of the foundation by professor Pereverzev of the chair of chemical power engineering. The main results of the research and pedagogical activities of the chair during this period of time were generalized. Particular emphasis was placed on the outstanding role played by Pereverzev in the creation of a scientific school.

During the time of its existence, the chair trained 1700 specialists, of whom 10 became doctors of technical science, and 175, candidates of science.

The history of the chair includes periods of varied significance; but its staff members always honestly and skillfully performed its main task: trained students, carried out research, and preserved and developed traditions of the institute, faculty, and chair, founded by Pereverzev.

Andrei Egorovich Pereverzev did everything in his power and gave all his knowledge for the welfare of the domestic science in order to improve the defensive capacity of the Motherland and train specialists in ammunition charging.

B. V. Gidaspov and O. A. Ryzhukhin

Russian Journal of Applied Chemistry, Vol. 74, No. 11, 2001, pp. 1977–1979. Translated from Zhurnal Prikladnoi Khimii, Vol. 74, No. 11, 2001, pp. 1913–1915.

HISTORY OF CHEMISTRY AND CHEMICAL TECHNOLOGY

Scientific, Pedagogical, and Public Activities of Professor N.N. Sokolov (to 175th Birthday Anniversary)

One of honorable places in the history of the domestic chemical science of the XIX century belongs to Nikolai Nikolaevich Sokolov, a talented scientist and pedagogue, organizer of scientific investigations, founder of the first Russian chemical journal.

N.N. Sokolov was born on December 13, 1826, in Yaroslavl province into a merchant's family. Having entered, when being very young, St. Petersburg University, he graduated from the then existing cameral department of the faculty of law, and later, in 1847, from the natural department with a candidate degree. At that time, chemistry was taught at the University by a known scientist and excellent pedagogue, A.A. Voskresenskii (1809–1880), who graduated in 1836 from the Central Pedagogical Institute in St. Petersburg and worked in 1836–1837 at the laboratory of J. Liebig (1803–1873) at Giessen University (Germany).

In 1848, to complete his education, Sokolov went abroad and, at first, also worked at Liebig's laboratory and carried out quite a number of investigations there. He, in particular, studied the behavior of creatinine in products of vital activity of herbivorous animals and birds. Together with A. Strecker (1822–1871), Liebig's co-worker, he synthesized hippuric acid, converted it into benzoglycolic acid, and for the first time obtained glycolic acid by its hydrolysis (*Ann. Chim.*, 1851). At the same place, at Giessen University, Sokolov studied crystallography and mineralogy under supervision of Prof. H.F. Kopp (1817–1892). Sokolov retained interest in crystals and minerals for his whole life. In 1852, Nikolai Nikolaevich moved to Paris and began investigations at the laboratory of Prof. C.-F. Gerhardt (1816–1856) who in his time (1836–1837) was taught by J. Liebig in Giessen. Charles Gerhardt and another French chemist, Auguste Laurent (1807–1853), made an outstanding contribution to the development of the atomic-molecular theory. In his book Introduction to Study of Chemistry by the Unitary System (1848), Gerhardt substantiated a novel concept of the molecule as an indivisible integrated system of atoms, "unitary system," and

clearly distinguished the concepts of atom, molecule, and equivalent. He established that radicals do not exist independently, being rather groups of atoms, whose combination forms molecules. Sokolov completely adopted these and other new, by that time, concepts of French scientists and, owing to him, chemistry was taught in Russia in the framework of the new scheme already in the late 1850s, earlier than in other countries, including France [1].

In Paris, Sokolov also worked at the chemical laboratory of Henri Regnault (1810–1878), an organic chemist, also a representative of Liebig's school, and a foreign corresponding member of the St. Petersburg Academy of Sciences (since 1848).

In 1854, Sokolov returned to Russia and started to work at the Mining School (Mining Institute since 1866; founded in 1773) in St. Petersburg as teacher of mineralogy and curator of the mineralogical museum. In 1855, on the instructions of the Mining Department he traveled across the Urals and exhibited much interest in minerals formed in metallurgical processes.

1070-4272/01/7411-1977$25.00


1631

ХИМИЧЕСКІЙ ЖУРНАЛЪ

Н. СОКОЛОВА и А. ЭНГЕЛЬГАРДТА.

Augustin Thierry.

ТОМЪ I.

САНКТПЕТЕРБУРГЪ.

1859.

In 1857, he defended master of chemistry's dissertation in this field.

In 1857, Sokolov organized, together with A.N. Engel'gardt (1832–1893), the Russia's first private public chemical laboratory, at which all comers could perform investigations for a relatively small fee. Engel'gardt graduated from Mikhail Artillery College; in 1853–1865, he headed the chemical and foundry laboratories of the St. Petersburg Arsenal; in 1866–1870, he was a professor of chemistry at the St. Petersburg Agricultural Institute (transformed into Forestry Institute in 1877; later, Forestry Academy).

Sokolov and Engel'gardt's chemical laboratory existed for three years and was closed in 1860; the laboratory equipment was passed, without compensation, to St. Petersburg University, where Sokolov himself started to work, too.

In May 1859, Nikolai Nikolaevich successfully backed at St. Petersburg University his doctoral (Chem.) dissertation "Treatise of Hydrogen in Organic Compounds." The dissertation contained a vast experimental material and was a major contribution to the development of organic chemistry of fatty compounds. The author described for the first time synthesis of glyceric acid by glycerol oxidation, considered alcohol oxidation processes in general, and pointed to different functional features of hydrogen in organic compounds. As mentioned in memoirs of N.A. Menshutkin (1842–1907) [2], the concept of difference between hydrogen atoms is especially important. It was shown for the example of four acids: glycolic, β-hydroxypriopionic, lactic, and glyceric, that part of hydrogen atoms in hydroxy acids has acidic, and another part, alcoholic nature, with the relative amounts of these parts in the mentioned acids correctly determined.

In 1859, Sokolov and Engel'gardt started to publish Russia's first periodical in the field of chemistry: *Khimicheskii zhurnal N.N. Sokolova i A.N. Engel'gardta* (Chemical Journal by N.N. Sokolov and A.N. Engel'gardt). During the two years of its existence, 4 volumes containing 6 issues each were published. The journal published both original articles and abstracts in Russian of the most interesting works of foreign authors, reports on dissertation presentations, and other information of value for chemists. The journal, in particular, published Sokolov's extensive fundamental paper "On Modern Directions in Chemistry," the full text of his doctoral dissertation, experimental works of the leading Russian chemists D.I. Mendeleev (1834–1907), N.N. Beketov (1827–1911), A.M. Butlerov (1828–1886), and N.N. Zinin (1812–1880). To the first Russian journal was devoted Yu.S. Musabekov's work [3].

In September 1860, as a member of the Russian delegation together with Mendeleev, Zinin, A.P. Borodin (1833–1887), and other scientists, Sokolov took part in the First International Chemical Congress in Karlsruhe (Germany). The Congress clearly distinguished the fundamental notions of chemistry (those of molecule, atom, equivalent, and valence). Sokolov and Engel'gardt were members of the initiative group which organized the Congress.

In view of Mendeleev's going to a business trip abroad in 1860, Nikolai Nikolaevich was invited to St. Petersburg University as privatdocent, and then extraordinary professor, to deliver lectures in organic chemistry. Warm recollections of these lectures were written by Menshutkin [2], who studied at the university at that time. Sokolov managed to do much to expand the experimental facilities of the chemical laboratory at the university, but, unfortunately, because of deteriorated health, he had to go to southern Europe for treatment already in 1862.

The scientist continued his pedagogical and scientific activities at the end of 1864 in Odessa, where

Novorossiya University was opened at the beginning of 1865. In May of the same year, a chair of chemistry was organized at the university, and Sokolov was invited there as its first professor [4–6]. The chair conducted courses in inorganic, organic, and analytical chemistry. During his relatively short stay in Odessa (1864–1871), Sokolov, with gusto characteristic of him, created and provided with equipment the chemical laboratory at the university, making it the best in Russia, so that a new center of domestic chemical science emerged in Russia. The closest Sokolov's associate was A.A. Verigo (1837–1905), who became a docent in 1866, extraordinary professor in 1871, and head of the chemical laboratory at Novorossiya University in 1873. A known chemical school formed in Odessa, to which belonged, in particular, V.M. Petriashvili (1845–1908), S.M. Tanatar (1849–1917), P.G. Melikishvili (1850–1927), N.D. Zelinskii (1861–1953), and P.I. Petrenko-Kritchenko (1866–1944).

In Odessa, Sokolov performed a number of experimental studies. In particular, he continued studies of lactic acid, commenced in St. Petersburg. In 1871, Nikolai Nikolaevich left the chair of chemistry at Novorossiya University and returned, on completing his treatment, to St. Petersburg, where he started teaching at the Agricultural Institute in 1872, having replaced Engel'gardt at the chair of chemistry. This period of scientist's life was described in recollections of his closest associates P.A. Lachinov (1837–1891) and M.G. Kucherov (1850–1911) [7, 8].

Nikolai Nikolaevich Sokolov died on July 13, 1877, at the age of 51. The Russian Physicochemical Society, whose member Sokolov was from the time of its foundation, set up in 1880 the N.N Sokolov Prize to be awarded to Russian scientists for outstanding works in the field of chemistry. The prizes wee awarded till 1888. The first of these was awarded in 1882 to Menshutkin for his work in the field of chemical kinetics: "Effect of Isomerization of Alcohols and Acids on Formation of Esters." In 1883, the Sokolov Prize was awarded to G.G. Gustavson (1843–1908), professor of Peter's Agricultural and Forestry Academy in Moscow for studies of reactions involving organic compounds in the presence of aluminum halides. In 1885, the prize was awarded to M.G. Kucherov for the discovery and investigation of reactions between acetylene hydrocarbons and mercury compounds. In 1888, the prize was awarded for the last time to A.E. Favorskii (1860–1945) for the discovery and investigation of isomerization of acetylene hydrocarbons.

Detailed evidence concerning Sokolov's life and activities can be found in works by Musabekov [3, 9] and N.S. Kozlov [10]. His role in the development of domestic chemistry was discussed in a monograph by Yu.I. Solov'ev [11].

In a paper devoted to the history of the chair of chemistry at Leningrad University (1819–1939) [12], Academician V.E. Tishchenko (1861–1941) named Sokolov "one of the most talented Russian chemists, with his pupils having the warmest recollections of him." Sokolov's activities were highly appreciated by K.A. Timiryazev (1843–1920): "Hardly any other teacher... has been equipped with such a full knowledge of modern science, had such broad views, and demonstrated such exuberant versatile activities as N.N. Sokolov. Brilliant, ingenious, with a somewhat skeptical mind and implacable logic, he was a professor in the finest sense of the word" [10]. Nikolai Nikolaevich Sokolov can be rightfully regarded as one of the most prominent chemists of the second half of the XIX century.

REFERENCES

1. Arbuzov, A.E., *Izbrannye raboty po istorii khimii* (Selected Works on the History of Chemistry), Moscow: Nauka, 1975.
2. Menshutkin, N.A., *Zh. Ross. Fiz.-Khim. O–va.*, 1878, vol. 10, no. 1, pp. 8–15.
3. Musabekov, Yu.S., *Materialy po istorii otechestvennoi khimii* (Materials on the History of Domestic Chemistry), Moscow: Akad. Nauk SSSR, 1953, pp. 288–302.
4. Markevich, A.O., *Dvadtsatipyatiletie imper. Novorossiiskogo universiteta* (Twenty-Fifth Foundation Anniversary of Imperial Novorossiya University), Odessa, 1890.
5. Turchenko, Ya.I., *Osnovnye puti razvitiya obshchei, neorganicheskoi i fizicheskoi khimii na Ukraine* (Main Directions of Development of General, Inorganic, and Physical Chemistry in the Ukraine), Kiev: Kiev. Gos. Univ., 1957.
6. *Razvitie neorganicheskoi khimii na Ukraine* (Development of Inorganic Chemistry in the Ukraine), Gorodyskii, A.V., Ed., Kiev: Naukova Dumka, 1987.
7. Lachinov, P.A., *Zh. Ross. Fiz.-Khim. O–va.*, 1878, vol. 10, no. 1, pp. 15–21.
8. Kucherov, M.G., *Zh. Ross. Fiz.-Khim. O–va.*, 1892, vol. 24, no. 8, pp. 567–614.
9. Musabekov, Yu.S., *Zh. Prikl. Khim.*, 1949, vol. 22, no. 11, pp. 1133–1142.
10. Kozlov, N.S., *Usp. Khim.*, 1953, vol. 22, no. 1, pp. 119–128.
11. Solov'ev, Yu.I., *Istoriya khimii v Rossii* (History of Chemistry in Russia), Moscow: Nauka, 1985.
12. Tishchenko, V.E., *Priroda*, 1939, no. 7, pp. 102–106.

A. G. Morachevskii

Russian Journal of Applied Chemistry, Vol. 74, No. 11, 2001, p. 1980. Translated from Zhurnal Prikladnoi Khimii, Vol. 74, No. 11, 2001, p. 1916.

BOOK REVIEWS

Utkin, N.I., *Proizvodstvo tsvetnykh metallov* (Manufacture of Nonferrous Metals),

Moscow: Intermet Inzhiniring, 2000, 442 pp.

The book published in the framework of the Federal Special-Purpose Program of book publishing in Russia is intended for specialists of widely varied professional skills, working at nonferrous metallurgical plants. The author covered a wide variety of problems concerning the theory and technology of manufacture of the most important nonferrous metals. The presented material is grouped into five sections. The first of these (pp. 9–112) contains general evidence, including description of the main methods and operations for dressing of ores of nonferrous metals, characterization of products and intermediates of metallurgical plants, preparation of raw materials for metallurgical processing, and problems of environment protection.

The second section (pp. 112–294) is devoted to metallurgy of heavy nonferrous metals: copper, nickel, lead, zinc, and gold. The third section (pp. 294–382) discusses processes used in manufacture of aluminum, magnesium, and titanium. The fourth section (pp. 382–417) presents evidence concerning the metallurgy of two less-common metals: tungsten and molybdenum. A small concluding fifth section (pp. 417–441) gives notion of the manufacture of a number of nonferrous metals (copper, aluminum, lead, and tin) and their alloys from secondary raw materials. The recommended bibliographic list (p. 442) includes the most important domestic publications in the field of nonferrous metallurgy, which have mainly appeared in the last 15–20 years.

With the publication assessed, on the whole, positively and account taken of the fact that this book is far from being the first concerned with manufacture of nonferrous metals, it seems appropriate to express some wishes. The presented material could be markedly enlivened by data on the scale of production of various nonferrous metals in Russia as a whole and at separate largest plants. In contrast to the recent times, such evidence is accessible now, being regularly published in our country and abroad. The book gives virtually no data of economical nature. Some materials presented by the author are markedly out-of-date and fail to reflect the present state of affairs. As a characteristic example can be mentioned data on lead consumption. In our opinion, the book contains insufficient amount of specific data concerning the largest plants of different branches of nonferrous metallurgy, such as, e.g., Norilsk combine or Bratsk aluminum plant.

Of noble metals, the author considered only gold, making absolutely no mention of platinum metals whose manufacture is most closely associated with processing of copper–nickel ores of the Norilsk deposit. The presented characteristics of the domestic ore raw materials are insufficient.

Admittedly, the quality of much of the illustrative material presented in the book is not too high. The book of such a level needs clear schemes not burdened with abundant minor details. Instead of, e.g., a general scheme illustrating the operation principle of the shaft furnace, the book presents its design with all details and dimensions (Fig. 98). The same refers to many other figures. It is hardly appropriate to use in material presentation such out-of-date terms as “vapor tension” or “dissociation tension.” The remarks made are, naturally, debatable and do not cast doubt upon the usefulness and high scientific level of the publication.

A. G. Morachevskii

1070-4272/01/7411-1980$25.00 © 2001 MAIK “Nauka/Interperiodica”

Russian Journal of Applied Chemistry, Vol. 74, No. 12, 2001, pp. 1981–1984. Translated from Zhurnal Prikladnoi Khimii, Vol. 74, No. 12, 2001, pp. 1921–1924.

INORGANIC SYNTHESIS AND INDUSTRIAL INORGANIC CHEMISTRY

A Study of Calcium Nitrate Purification

A. A. Fakeev and A. I. Sukhanovskaya

State Research Institute of Chemical Reagents and Ultrapure Chemical Substances, Moscow, Russia

Received September 25, 2000; in final form, March 2001

Abstract—Two methods of calcium nitrate purification were studied: crystallization from aqueous solutions and joint precipitation of impurities from aqueous solutions onto inorganic collectors (calcium hydroxide or carbonate and hydrated aluminum or zirconium oxides). The efficiency of purification of calcium nitrate solutions was studied and the purification coefficients were calculated for hydrated aluminum or zirconium oxides as collectors.

Calcium nitrate is widely used in metallurgical, chemical, and food industries, glass manufacture, agriculture, etc. [1].

In chemical industry, calcium nitrate is a key compound for preparing the most practically significant calcium products (carbonate, hydroxide, phosphate, chromate, oxalate, etc.) [2, 3].

In recent years, ultrapure calcium compounds (carbonate, phosphate, and fluoride) have found application in fabrication of optical fibers, optical glass, single crystals, and phosphors. This required the development of a method for deep purification of calcium nitrate, which is the most accessible raw material [2]. The great number of publications devoted to calcium nitrate purification stems from the necessity for preparing pure and ultrapure calcium salts.

The efficiency of crystallization purification of calcium nitrate can be estimated from data on phase equilibria in water–salt systems. Analysis of the solubility diagrams in the systems $Ca(NO_3)_2$–$M^{n+}(NO_3)_n$–H_2O, where M^{n+} is Sr, Ba [4], Be [5], Ni [6, 7], Ag [8], Cu(II) [9], Fe(III) [10], Co [11, 12], or Mn(II) [12], at 25°C indicates the lack of isomorphism (i.e., the systems are of simple eutonic type), and the apparent possibility of separating calcium nitrate and nitrates of the above metals. However, joint crystallization of nonisomorphous impurities is a much more complex process, since the quantitative characteristics of the component distribution at low concentrations of one of the components cannot be, as a rule, predicted solely on the basis of solubility diagrams [13]. It is this fact that made necessary prolonged and rather complex experimental studies.

Crystallization from aqueous solutions as a method for purification of calcium nitrate was proposed in [3, 14]. It was shown that double crystallization results in the removal of iron salts and makes the lead concentration 15–20 times lower.

The impurity distribution upon crystallization of calcium nitrate from nitric acid solutions has not been studied. However, by analogy with strontium and barium nitrates, this process seems to be efficient for calcium nitrate purification, with, however, the solubility of the compound being rather high (29.8 wt % in 40% HNO_3 at 25°C [4]). This necessitates treatment of large volumes of mother liquors and makes the technology more complex.

A way to purify 20% calcium nitrate solutions by precipitation of sparingly soluble metal sulfides at pH 4.5–5.0, addition of H_2O_2 at pH 7.6, and subsequent adsorption of impurities onto glass wool has been described [15]. The thus obtained product contains 5×10^{-6}–5×10^{-5} iron ions and 1×10^{-5} wt % manganese and heavy metal ions each.

Use of complexing reagents (sodium diethyldithiocarbamate [16], sodium salt EDTA [17], lumogallion IREA, and rubeanic acid [18]), with subsequent adsorption of the formed complexes, excess amount of complexing reagents, and products of their partial decomposition onto ion-exchange resins or activated carbon, is an efficient method for purification of calcium nitrate solutions. However, the described methods involve introduction of complexing agents, which makes necessary their thorough removal from the purified solutions and special pretreatment of sorbents (resin, carbon).

1070-4272/01/7412-1981 $25.00 © 2001 MAIK "Nauka/Interperiodica"

Table 1. Impurity fractionation in crystallization of calcium nitrate from aqueous solutions at 25°C

Impurity, wt %	α	K^*_{pur}
Fe(III):		
5×10^{-4}	0.35	10.0 ± 1.0
1×10^{-3}	0.35	9.6 ± 1.0
5×10^{-4}	0.55	11.0 ± 1.3
1×10^{-3}	0.55	10.0 ± 1.2
Co(II):		
5×10^{-5}	0.35	8.5 ± 1.2
1×10^{-4}	0.35	10.0 ± 1.0
5×10^{-5}	0.55	9.0 ± 1.0
1×10^{-4}	0.55	11.0 ± 1.2

* K_{pur} is the purification factor for $Ca(NO_3)_2 \cdot 4H_2O$ crystals.

The high efficiency, especially at low component concentrations, and the feasibility of simultaneous removal of a great number of impurities make joint precipitation onto collectors a rather promising method for salt purification [19]. The joint precipitation of impurities from solutions of calcium nitrate has been studied with $CaCO_3$ [15, 16, 18, 20], $CaHPO_4$ [18], hydrated titanium dioxide [21], and other collectors. However, the technological aspect of these processes has been studied insufficiently, and data on the impurity distribution are lacking.

Extraction of 8-oxyquinolinate of heavy metals with chloroform [22] or with its mixture with isoamyl alcohol [23] from calcium nitrate solutions is an efficient method. However, this technique is complex and encounters considerable difficulties in removal of the residual amounts of organic substances from a purified solution.

Barium, strontium, iron, copper, and manganese ions can be removed from $Ca(NO_3)_2 \cdot 4H_2O$ by zone smelting (at ~42°C) [24].

The analysis of the presented data on calcium nitrate purification shows that the crystallization from aqueous solutions and joint precipitation of impurities onto inorganic collectors are the most promising methods.

The aim of the present study was to analyze the process of calcium nitrate purification.

EXPERIMENTAL

We studied two methods of calcium nitrate purification: crystallization from aqueous solutions and joint precipitation of impurities onto inorganic collectors.

The distribution of iron and cobalt (typical triply and doubly charged ion impurities) upon crystallization of calcium nitrate from aqueous solutions was studied using radioactive tracers. Into 75 ml of 40% aqueous solution of calcium nitrate [chemically pure grade, GOST (State Standard) 4142–77] was introduced ^{59}Fe iron or ^{60}Co cobalt isotope, and the mixture was thoroughly stirred for 2–3 h. The solution was evaporated on a water bath to obtain solid phase in varied yield and cooled under continuous agitation. The precipitated $Ca(NO_3)_2 \cdot 4H_2O$ crystals were carefully squeezed between two sheets of filtering paper to remove mother liquor. The specific activities were determined for the initial solution and squeezed crystals (upon dissolution in water).

The gamma radiation was recorded using a BDIS-3-05 sensor with a detector (thallium-activated sodium iodide) and a PS-2 counter unit. The accuracy of the radiometric measurements of activity was 2–3 rel.%. The purification factors for the crystals (the ratio of the crystal activities before and after crystallization) and the degree α of precipitation of the main substance into the solid phase during crystallization were calculated from the results of radiometric analysis [19].

Analysis of the obtained results shows that, with the yield of the $Ca(NO_3)_2 \cdot 4H_2O$ crystals increasing from 0.35 to 0.55, the purification factors for iron and cobalt impurity ions remain virtually unchanged (Table 1). Unfortunately, experiments on crystal washing could not be carried out owing to the considerable solubility of the salt in water and nitric acid [4]. The use of saturated aqueous calcium hydrate solution or organic solvents miscible with water used as washing liquid led to changes in the crystal mass even upon minor temperature fluctuations.

Apparently, the low degree of purification of $Ca(NO_3)_2 \cdot 4H_2O$ crystals to remove iron and cobalt impurities (Table 1) is due to occlusion of the mother liquor by crystals [14], which is confirmed by published data [10, 11].

The results obtained (Table 1) are accounted for by the high stability of the metastable supersaturated solutions, characteristic of calcium nitrate, and by changes in the crystal habitus, depending on the cooling rate [25]. This leads to changes in the crystal growth mechanism, facilitates formation of closed cavities and capillaries, and causes surface damage, which results in pronounced entrapment of mother liquor (purification factors are about the same at 55–60% yield).

Presently, the efficiency of solution purification onto collectors cannot be calculated theoretically. Therefore, the purification of calcium nitrate solutions

was studied experimentally. As inorganic collectors served calcium hydroxide, calcium carbonate, and hydrated oxides of aluminum or zirconium, which were precipitated in a solution being purified by addition of calculated amounts of aqueous solutions of sodium hydroxide, ammonia, or ammonium carbonate. The study was performed with use of radioactive tracers for the example of iron and cobalt impurities (^{59}Fe and ^{60}Co). To 50 ml of a 20% solution of calcium nitrate (chemically pure grade) were added solutions containing radioactive isotopes of the elements studied, the mixture was stirred, and a sample was taken for the radiometric measurements. Then, calculated amounts of a 20% aluminum nitrate solution (17-3 special-purity grade, [TU (Technical Specification) 6-09-3657–74] or a 20% solution of oxodichlorozirconium (chemically pure grade, TU 6-09-3677–74) were introduced into the solution to precipitate, respectively, hydrated oxide of aluminum or zirconium, and the solution pH, monitored by a pH262 pH-meter, was adjusted to 7–8 by gradual addition of 25% aqueous ammonia (17-4 special-purity grade, TU 6-09-3282–7) under agitation, and the mixture was stirred for 0.5–1.0 h. Calcium hydroxide and calcium carbonate were precipitated from the initial calcium nitrate solution by calculated amounts of 25% solution of NaOH [18-3 ultrapure grade; OST (All-Union Standard) 6-01-302–74] or 20% solution of ammonium carbonate (chemically pure grade, GOST 3770–75). The precipitated collectors were separated on a TsLN-2 centrifuge, and the purified solution was sampled for radiometric analysis. The methods for measuring the activity before and after purification and the procedures for calculating the purification factors are described above.

The preliminary estimates of the efficiency of inorganic collectors for purification of calcium nitrate solutions for the example of iron(III) and cobalt(II) impurities show (Table 2) that hydrated oxides of aluminum and zirconium are the most promising materials. Calcium carbonate is efficient as collector solely for purification to remove iron(III) impurity, in satisfactory agreement with published data [15, 16, 18, 20].

Comparison of the obtained results (Table 2) and published data, with account taken of accessibility and cost of collector-forming materials, shows the practicability of using aluminum hydroxide as collector for deep purification of aqueous calcium nitrate solution.

The obtained results show that heteronuclear hydroxo complexes of complex composition are formed in the nitrate systems Al(III)–M^{n+}–NO_3^-–H_2O [M^{n+} = Fe(III), Cr(III), Co(II), Ni(II), or Cu(II)] [26–28]. ESR spectroscopy revealed formation of three paramagnetic complexes in the system Al(III)–Fe(III)–NO_3^-–H_2O at low iron(III) concentrations and pH 7–10 [29]. Apparently, the forming heteronuclear hydroxo complexes of iron(III) and aluminum(III) of complex composition have a chain-like structure [28–30].

The processes of coprecipitation of impurities onto aluminum hydroxide as a result of heteronuclear complexation are of great practical importance and require further investigation.

Larger-scale experiments on calcium nitrate purification by crystallization from aqueous solutions

Table 2. Impurity distribution in purification of $Ca(NO_3)_2$ solution on inorganic collectors

Collector, %	Impurity	Specific activity of solution, pulse min^{-1} g^{-1}		$K_{pur} = A_1/A_2$
		before purification A_1	after purification A_2	
$Ca(OH)_2$:				
9	Fe(III)	92000	70000	1.3 ± 0.2
18		84000	52200	1.6 ± 0.2
8	Co(II)	115000	95900	1.2 ± 0.2
18		121000	70010	1.7 ± 0.2
$CaCO_3$, 8	Fe(III)	172000	600	300 ± 30
	Co(II)	300840	230410	1.3 ± 0.2
$Al_2O_3 \cdot nH_2O$,	Fe(III)	129410	432	300 ± 35
1.0, pH 7–8	Co(II)	92830	1862	50 ± 5
$ZrO_2 \cdot nH_2O$,	Fe(III)	62400	780	80 ± 10
2.0, pH 7–8	Co(II)	22750	650	35 ± 4

* Concentration (wt %): solution 20, impurities (1–5) × 10^{-4}; time of contact between solution and collector 0.5 h; temperature 25 ± 1°C.

Table 3. Quality of initial and purified calcium nitrate samples and the best foreign products (according to catalogues)

Sample	Content, $C \times 10^6$, wt %					
	Fe	Mn	Cu	Cr	Ni	Co
Laboratory:						
initial	200	50	70	50	20	5
purified	30	<5	6	4	<1	<1
Chemically pure grade, GOST 4142–77, Russia	100					
Aldrich, USA	40		10			
RPE, C. Erba, Italy	300		200			
Suprapur, E. Merck, Germany	5	1	1		1	1

were performed in laboratory. The conditions of the experiment are described above. The quality of the obtained samples was analyzed chemically and spectroscopically [31].

Comparison of the quality of the initial calcium nitrate samples and those purified by crystallization from aqueous solutions (Table 3) confirmed that this method is promising for preparing rather pure samples of the product.

CONCLUSIONS

(1) Purification of calcium nitrate by crystallization from aqueous solutions was studied using radioactive tracers. The purification factors were calculated. It was shown for the example of iron(III) and cobalt(II) impurity ions that the moderate values of the purification factors are due to occlusion of the mother liquor.

(2) The purification of aqueous calcium nitrate solutions by the coprecipitation of impurities onto inorganic collectors (calcium hydroxide, calcium carbonate, and hydrated oxides of aluminum or zirconium) was studied by the method of radioisotope tracers. The high efficiency of hydrated oxides of aluminum and zirconium was demonstrated.

REFERENCES

1. Pozin, M.E., *Tekhnologiya mineral'nykh solei* (Technology of Mineral Salts), Leningrad: Khimiya, 1974.
2. Fakeev, A.A., *Vysokochist. Veshchestva*, 1987, no. 4, pp. 26–35.
3. Karyakin, Yu.V., and Angelov, I.I., *Chistye chimicheskie veshchestva* (Pure Chemical Substances), Moscow: Khimiya, 1974.
4. Protsenko, P.I., Razumovskaya, O.N., and Brykova, N.A., *Spravochnik po rastvorimosti nitritnykh i nitratnykh sistem* (Reference Book of Solubilities of Nitrite and Nitrate Systems), Leningrad: Khimiya, 1971.
5. Balashova, E.F., and Protsenko, P.I., *Geterogennye nitritno–nitratnye sistemy* (Heterogeneous Nitrite–Nitrate Systems), Elista: Znanie, 1970, pp. 50–54.
6. Andreeva, T.A., Pozharskaya, S.S., and Golovanova, T.G., *Zh. Neorg. Khim.*, 1973, vol. 18, no. 11, pp. 3078–3082.
7. Deich, A.Ya., and Karpukhina, A.A., *Izv. Akad. Nauk Latv. SSR, Ser. Khim.*, 1975, no. 5, pp. 630–631.
8. Khutsistova, F.M., Protsenko, P.I., and Berdyukova, V.A., *Zh. Neorg. Khim.*, 1979, vol. 24, no. 10, pp. 2815–2818.
9. Rodimtseva, I.Yu., Savel'eva, L.V., and Fakeev, A.A., *Zh. Neorg. Khim.*, 1977, vol. 22, no. 1, pp. 261–263.
10. Novikova, A.N., Savel'eva, L.V., Rodimtseva, I.Yu., *et al., Zh. Neorg. Khim.*, 1977, vol. 22, no. 7, pp. 2017–2018.
11. Rodimtseva, I.Yu., Savel'eva, L.V., and Fakeev, A.A., *Zh. Neorg. Khim.*, 1978, vol. 23, no. 2, pp. 562–563.
12. Balarew, C., *Z. Kristallogr.*, 1987, vol. 181, no. 1, pp. 35–82.
13. Glazov, V.M., and Novikov, I.I., *Zh. Fiz. Khim.*, 1974, vol. 48, no. 5, pp. 1134–1136.
14. Ryabukha, A.A., Sytnik, N.A., Gordienko, E.M., and Abakumova, I.N., *Khim. Prom–st.*, 1986, no. 1, pp. 33–34.
15. Angelov, I.I., and Khainson, S.I., *Raboty laboratorii instituta: Trudy IREA* (Investigations of the Laboratories of the Institute: Coll. of Works of the Institute of Chemical Reagents and Ultrapure Chemical Substances), Moscow: Goskhimizdat, 1956, no. 21, pp. 93–95.
16. Papageorgrios, P., and Lobacz, B., *Chemia Stosowan.*, 1973, vol. 17, no. 1, pp. 3–9.
17. Nakhodnova, A.A., Krivobok, V.I., and Artyushenko, A.I., *Zh. Prikl. Khim.*, 1966, vol. 39, no. 3, pp. 498–501.
18. Volkov, V.I., Dubinina, M.P., Bezrukov, V.I., *et al., Zh. Neorg. Khim.*, 1979, vol. 52, no. 6, pp. 1215–1219.
19. Stepin, B.D, Gorshtein, I.G, Blyum, G.Z., *et al., Metody polucheniya osobo chistykh veshchestv* (Methods for Preparation of Ultrapure Substances), Leningrad: Khimiya, 1969.
20. Ryabukha, A.A., Sytnik, N.A., Gordienko, E.M., and Abakumova, I.N., *Zh. Prikl. Khim.*, 1985, vol. 58, no. 3, pp. 647–650.
21. Koryukova, V.P., Koval'chuk, L.I., Shabanov, E.V., and Smirnova, L.V., *Zh. Prikl. Khim.*, 1980, vol. 53, no. 3, pp. 495–498.
22. Lepiku, T.A., Allsalu, M.-L., and Engel', Kh., *Uchen. Zap. Tartus. Univers* (Transactions of Tartu University), 1968, vol. 219, pp. 174–177.
23. Smolik, M., and Ogiolda, K., *Zesz. Nauk. Psl.*, 1979, no. 596, pp. 53–62.
24. Mokhosoev, M.V., Got'manova, T.T., and Kokot, I.F., *Zh. Neorg. Khim.*, 1964, vol. 9, no. 11, pp. 2518–2525.
25. Pacak, P., and Oesterreicherova, H., *Cryst. Res. Technol.*, 1981, vol. 16, no. 10, pp. 1117–1121.
26. Kopylovich, M.N., Radion, E.V., and Baev, A.K., *Koord. Khim.*, 1995, vol. 21, no. 6, pp. 458–460.
27. Kopylovich, M.N., and Baev, A.K., *Koord. Khim.*, 1996, vol. 22, no. 2, pp. 114–118.
28. Kopylovich, M.N., and Baev, A.K., *Koord. Khim.*, 1996. vol. 22, no. 6, pp. 443–446.
29. Kurmanguzhina, L.K., Marov, I.N, Evtikova, G.A., *et al., Zh. Neorg. Khim.*, 1982, vol. 27, no. 6, pp. 1490–1493.
30. Pykhteev, O.Yu., Efimov, A.A., and Moskvin, L.N., *Zh. Prikl. Khim.*, 1999, vol. 72, no. 1, pp. 11–21.
31. Chupakhin, M.S., Sukhanovskaya, A.I., Krasil'shchik, V.Z., *et al., Metody analiza chistykh khimicheskikh reaktivov* (Methods for Analysis of Pure Chemical Reagents), Khimiya, 1984.

Russian Journal of Applied Chemistry, Vol. 74, No. 12, 2001, pp. 1985–1989. Translated from Zhurnal Prikladnoi Khimii, Vol. 74, No. 12, 2001, pp. 1925–1929.

INORGANIC SYNTHESIS AND INDUSTRIAL INORGANIC CHEMISTRY

New Colloid Silicate Solutions for Restoration and Conservation of Stone Facades

V. I. Tarasov

Institute of Silicate Chemistry, Russian Academy of Sciences, St. Petersburg, Russia

Received March 12, 2001

Abstract—The kinetics of water absorption by samples taken from facades of buildings (marbled footing limestone, bricks, plaster), both in initial state and those treated with solutions of classical water repellents and new hydrophilic and hydrophobic colloid silicates, was studied, and the state of the initial material was assessed. Recommendations on how to stabilize stone and protect it from the destructive influence of the humid atmosphere are given.

The mechanism of disintegration of stone materials is well known [1–3]. Hydrophilic pores of the stone surface take up excess atmospheric moisture, favorable for life activity of bacteria promoting the dissolution of minerals constituting stone. The dissolved components may migrate and be deposited in pores as new formations when water evaporates or freezes as a result of atmospheric changes in the environment. The presence of alkaline or acid components in the liquid phase on the porous surface accelerates dissolution of minerals and structural disintegration of stone. For example, limestone building materials are carbonized in the course of time under the action of carbon dioxide contained in air. In addition, the carbonate-containing surface of stone used to build city monuments of architecture is continuously subject to the action of sulfur dioxide; the stone destruction is especially intensive in the presence of nitrogen oxides contained in industrial and exhaust gases [4].

An effective way to protect stone materials from the aggressive action of the atmosphere is to treat their surface with solutions of water-repellent organosilicon liquids [5, 6]. Silicone molecules penetrating into pores interact with minerals constituting the surface, imparting to it water-repellent (hydrophobic) properties. Water can penetrate into such pores only under pressure. The excess moisture is easily removed from stone pores. As a result, the frost resistance of the stone is improved, its heat conductivity decreases, and life activities of bacteria are terminated.

In the 1950s, a technique was developed [7] for modifying the facade surface of the Marble Palace and other historical monuments of St. Petersburg by treatment with a nonaqueous solution of trimethylchlorosilane:

$$2CaCO_3 + 2(CH_3)_3SiCl \rightarrow Ca[OSi(CH_3)_3]_2 + CaCl_2 + 2CO_2. \quad (1)$$

The treated facades have retained up to now fresher appearance (natural color) as compared with other, untreated objects. However, organochlorosilane solutions have limited applicability because of their being toxic. Sodium alkyl siliconates (SAS), which are well soluble in water and low-toxic, are used for hydrophobization of building materials (including calcareous, silicate, carbonate, and sulfate materials) [6, 8]. The reaction of carbonate surface modification with SAS solution occurs to give sodium carbonate in solution:

$$CaCO_3 + 2NaOSi(OH)_2(C_2H_5) \rightarrow Ca[OSi(OH)_2(C_2H_5)]_2 + Na_2CO_3. \quad (2)$$

The longevity of the hydrophobic effect of such a surface layer does not exceed 2–4 years [9], since the alkali metal cation makes higher the solubility of components and favors their transport, which leads to development of a porous structure in the stone and its disintegration [10]. Poly(ethoxyhydrosiloxane) (PEHS) is used in the form of aqueous emulsions or nonaqueous solutions [5] for hydrophobization of concrete, roofing slate, and lime-sand and ceramic brick:

1070-4272/01/7412-1985 $25.00 © 2001 MAIK "Nauka/Interperiodica"

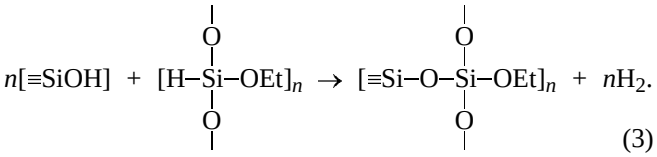

$$n[\equiv SiOH] + [H-Si(O)(O)-OEt]_n \rightarrow [\equiv Si-O-Si(O)(O)-OEt]_n + nH_2. \quad (3)$$

For calcium carbonates (marble, limestone), and especially for calcium sulfate (gypsum), PEHS solutions are inefficient as water repellents for the surface layer, compared with SAS solutions [6].

These circumstances stimulate a search for more effective silicate solutions for obtaining protective coatings on stone materials [11, 12].

The aim of the present study was to perform comparison tests of classical (SAS, PEHS) and new colloid silicate solutions in desulfurization and hydrophobization of stone materials in some buildings of the historical center of St. Petersburg.

EXPERIMENTAL

Experiments were done with typical stone material samples (footing materials, red brick and its binder, plaster), taken from facades of buildings in St. Petersburg along the Nevsky Avenue and Fontanka River embankment. These buildings had been in use under St. Petersburg conditions for more than 100 years and were not heated for several recent years in expectation of reconstruction. Samples of stone material were taken in the form of pieces with weight ranging from 20 to 100 g into plastic sachets, weighed in laboratory, and left to dry indoors (commonly for 3 days at 20°C and 50% relative humidity) to constant weight. A sample of each representative of a stone facade material included no less than 4–5 pieces for tests, treatment, and characterization. The phase composition of facade samples (and presence of calcium sulfate dihydrate) was determined by comparing X-ray patterns obtained on a DRON-2 instrument and reference data from the ASTM file.

To treat the stone material, the following solutions were prepared: (1) aqueous solution of 10 wt % SAS (GKZh-10; Khimprom AO, Novocherkassk); (2) isopropanol solution of 5 wt % PEHS (GKZh-136-41; Silan ZAO, Dankov); (3) aqueous colloid solution of 10 wt % sodium polysilicate $Na_2O \cdot 4SiO_2$ (Goltar OOO, St. Petersburg); and (4) aqueous-alcoholic sol of hydrophobic silica (10 wt %), prepared by the sol–gel technology [13, 14]. Dried samples were treated with solutions nos. 1 and 2 by full submersion for 15–20 min at 20°C. The samples were weighed before and after submersion. Drying of the samples was done under room conditions (20°C, 50% relative humidity) to constant weight. Samples were treated with sols nos. 3 and 4 as follows. The samples were submerged in an aqueous weakly alkaline silicate sol no. 3 for 15–20 min and then dried under room conditions for 1 day, submerged in water for 15–20 min, again dried under room temperature conditions for 1 day, and submerged in water for 15–20 min. Then the samples were again dried for 3 days and submerged in water for 15–20 min. After that the samples were dried under room temperature conditions for 7 days and impregnated with aqueous–alcoholic sol of hydrophobic silica (no. 4), dried under room temperature conditions for 1 day, and placed on an atmospheric stand. After 7 days and 3 and 12 months, the kinetics of water absorption by samples (preliminarily kept under room temperature conditions for 1 day) was determined.

The samples were weighed in air and in water (at a depth of 15 mm at 20°C). The difference of weights of dry sample in air, m_1, and that saturated with water (having density ρ of 1 g cm^{-3}), m_2, allows evaluation of the sample volume V and calculation of its density m_1/V: $m_1 = m_2 - V\rho$. The technique enables recording of the course of sample saturation with water. At the initial instant of complete submersion in water a sample has mass m_0 and contains a certain volume of pores, V_0, filled with air (and giving rise to buoyancy force). This volume is filled, during a certain period of time, with water, and the mass of the submerged sample increases to m_2. The pore volume is equal to the difference between masses of submerged samples in the initial and final stages of the process of saturation with water, divided by the density of water: $V_0 = (m_2 - m_0)/\rho$. The ratio of water volume absorbed by a sample to its dry mass is shown as a function of time elapsed upon sample submersion into water in Fig. 1. The total time of sample submersion was no less than 1 day. The increase in the mass of absorbed water with time can also be followed by weighing a sample in air and its periodic submersion for a certain time.

Table 1 presents the results of determining the moisture content in initial samples, those saturated with water, and those treated with various solutions. The content of moisture in the initial samples of footing limestone from different parts of a building was in the range 0.6–1.8 wt %, and increased, 5 min after full submersion in water, to 1.5–4.5 wt % and then remained virtually unchanged for 24 h. The sample density was 2.8 g cm^{-3}. The phase composition of the samples is mainly represented by calcite, wollastonite, and admixture of quartz and gypsum. The

Table 1. Moisture content in various samples of facade materials

Sample	Moisture content (wt %) in indicated samples										
	initial		hydrophobized								
			GKZh-10, 10%			GKZh-136-41, 5%			silicate sols		
	F	I	$W_{0.2}$	W_3	W_{12}	$W_{0.2}$	W_3	W_{12}	$W_{0.2}$	W_3	W_{12}
Limestone	1.9	4.5	2.5	2.7	3.5	2.1	2.2	2.2	1.6	1.7	1.8
Brick	5.1	15	8.9	9.0	12	6.4	7.2	8.4	4.6	4.5	4.5
Binder	9.9	20	12	13	16	17	17	18	5.8	5.7	5.8
Plaster	2.7	18	6	8	16	12.5	14	16	5.0	5.1	5.2

* (F) Samples from a building facade and (W_n) samples submerged in water for 24 h after *n* months of additional keeping under atmospheric conditions.

density and the phase composition of the samples indicate that the footing material is composed of partly marbled limestone (sedimentary limestone subjected to high temperature and pressure). The difference between the saturating amounts of water for samples taken from different parts of a building presumably indicates different conditions of stone weathering. Red brick samples were humid (12–17 wt %) and porous (saturating amount of moisture 17–20 wt % upon 24 h of full submersion in water) near building drains. In moisture-protected parts of the building, samples were less humid (3–7 wt % water), stronger, and less porous (saturating amount of water 13–16 wt %). The mineral phase composition of brick mainly included quartz and kaolin. Brickwork binder samples contained 8–10 wt % moisture in the initial state and up to 17 wt % upon saturation. The phase composition of the binder mainly includes

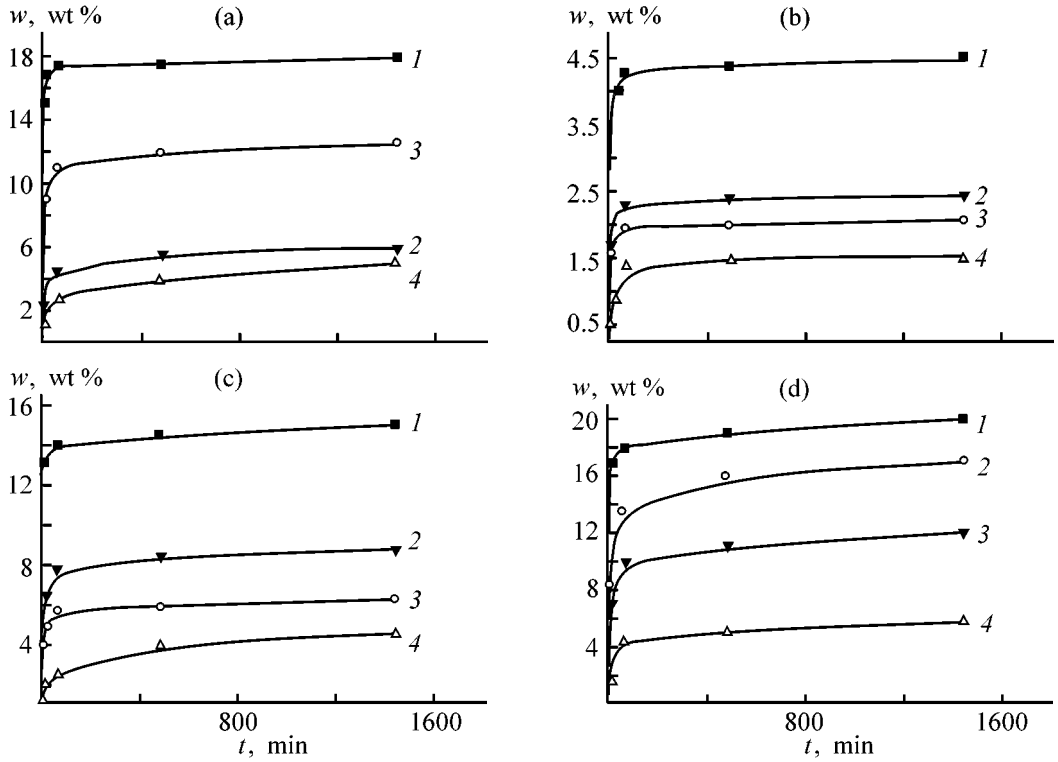

Fig. 1. Water absorption *w* by (*1*) initial and (*2–4*) hydrophobized samples of facade material vs. time *t*. Sample: (a) plaster, (b) limestone, (c) brick, and (d) binder. Water repellent (wt %): (*2*) GKZh-10, 10; (*3*) GKZh-136-41, 5; and (*4*) Goltar silicate sols, 10.

Table 2. X-ray diffraction pattern of facade plaster and reference samples

d, Å	*I*, %	*d*, Å	*I*, %	*d*, Å	*I*, %
7.5413	31.4	2.7772	4	2.1220	28.37
7.61[1]	45[1]	2.788[1]	20[1]	2.0809	8.59
4.2378	77	2.7330	2.3	2.087[1]	14[1]
4.28[2]	90[2]	2.7190	2.6	2.09[2]	27[2]
4.26[3]	22[3]	2.486[1]	20[1]	2.0708	7.05
3.8408	3.3	2.6745	12	2.073[1]	20[1]
3.7797	7.5	2.684[1]	50[1]	2.0421	2.4
3.85[2]	29[2]	2.5879	2.7	1.9883	2.7
3.5564	3	2.4879	8.5	1.9747	3.6
3.3306	100	2.4504	16.2	1.9094	3.6
3.34[3]	100[3]	2.46[3]	8[3]	1.91[2]	17[2]
3.2282	23	2.3953	2	1.8952	5.25
3.1736	16	2.2764	16	1.8752	7.04
3.0527	33	2.28[2]	18[2]	1.87[2]	34[2]
3.07[1]	30[1]	2.28[3]	8[3]	1.8551	4.24
3.03[2]	100[2]	2.2301	5.7	1.8149	13.79
3.0276	26.72	2.2129	5.8	1.82[3]	14[3]
2.8631	18	2.1878	1.6	1.7927	3
2.871[1]	100[1]				

Note: Superscripts: (1) gypsum, (2) calcite, and (3) quartz.

quartz and calcite. Samples of facade plaster contained 1.5–8 wt % moisture in the initial state and up to 13–18 wt % upon saturation. The phase composition of the plaster mainly includes quartz, calcite, and gypsum (Table 2).

Figure 1 shows the kinetics of water absorption by selected samples of limestone, brick, binder, and plaster on their submersion in water. Pores in the initial samples are virtually completely filled with water during the first 5 min. The amount of moisture absorbed by samples upon submersion in water both during the first 5 min and in 24 h can be reduced by treating the initial samples of the stone material both with conventional solutions nos. 1 and 2 and with new sols nos. 3 and 4 (see Fig. 1, Table 1). A comparison of how treatment with the conventional solutions affects the moisture-protective properties of samples demonstrated that solution no. 1 has advantage for the binder and plaster, and solution no. 2 for marbled limestone and, especially, brick. The amount of absorbed moisture is reduced to the maximum extent for all samples after their technological treatment with silicate sols nos. 3 and 4. The reason for such a difference in efficiency between the hydrophobizing solutions is that the plaster and binder contain calcium carbonates and sulfates. These minerals react with SAS in solution no. 1 by reaction (2), whereas PEHS in solution no. 2 mainly reacts with surface hydroxy groups [reaction (3)] of minerals, e.g., kaolin, quartz (brick), and wollastonite (limestone). Impregnation of sulfated samples with an aqueous sol of sodium silicate $Na_2O \cdot 4SiO_2 \cdot nH_2O$ leads to an exchange reaction between the sulfate on the stone surface and hydroxylated silicate of the aqueous-alkaline liquid phase of sol in the stone pores:

$$CaSO_4 \cdot 2H_2O + 2Na^+ + SiO_2(OH)_2^{2-} + 3SiO_2 \rightarrow CaSiO_2(OH)_2 \cdot 3SiO_2 \cdot 2H_2O + 2Na^+ + SO_4^{2-}. \quad (4)$$

Subsequent washing of the surface with water removes sodium sulfate from the poorly soluble gel of calcium hydrosilicate and silica formed in the stone pores. Pores in the surface layer of the stone decrease in size, but remain hydrophilic, i.e., covered with hydroxy groups. To hydrophobize the surface, the pores in the surface layer were dried and impregnated with active sol no. 4 of hydrophobic silica [13]. This procedure leads to reaction of the hydroxy groups in the surface layer with active radicals of hydrophobic particles of sol in colloid solution no. 4

$$\equiv SiOH + C_2H_5OSi(O)_3[SiO_2]_nO_3SiC_2H_5 \rightarrow \equiv SiOSiO_3[SiO_2]_nO_3SiC_2H_5 + C_2H_5OH, \quad (5)$$

pore filling with hydrophobic silica, and the corresponding decrease in pore radius. In this case, in accordance with the Jurene formula [15], a much higher pressure is necessary for water to penetrate into hydrophobic pores of smaller diameter.

The durability of moisture-protective properties of the surface layer of various samples can be illustrated by the data in Table 1. The moisture-protective properties of the surface layer of samples treated with solution no. 1 deteriorate by 40–50% after 1 year of keeping under atmospheric conditions. Apparently, introduction of the alkali metal cation into the surface layer of stone with solution no. 1 makes higher the solubility of its components and favors their transport, development of a porous structure in the stone, and stone decomposition. For example, calcium silicate decomposes under the action of sodium hydrocarbonate solution to give calcite and soluble sodium silicate:

$$2CaO \cdot SiO_2 + 2NaHCO_3 \rightarrow 2CaCO_3 + Na_2[SiO_2(OH)_2]. \quad (6)$$

The presence of an alkaline component favors origination and development of cracks and disintegration of concrete constructions [10].

The moisture-protective properties of the surface layer of samples treated with colloid solutions nos. 3 and 4 remained unchanged after a year of keeping under atmospheric conditions.

It should be noted that, under the atmospheric conditions, the stone surface is continuously subjected to abrasive action of specks of dust and grains of sand driven by wind, which impairs the hydrophobic effect of the surface. Moreover, mutual diffusion of the components of the surface layer will also impair its moisture-protective properties in the course of time. Therefore, treatment of the surface layer of stone should be repeated every 10–20 years.

CONCLUSIONS

(1) It was found, with the historical center of St. Petersburg serving as an example, that plaster over brickwork and binder in brick walls of buildings are subject to deep sulfation and fail to accomplish their moisture-protective functions. In spring, pores in brick walls of buildings are filled with moisture to no less than 50%.

(2) It is recommended that, prior to impregnation with a sol of hydrophobic silicate, the sulfated and carbonized surface layer of stone materials should be treated with a weakly alkaline aqueous silicate sol and dried under atmospheric conditions in summer.

REFERENCES

1. Winkler, E.M., *Eng. Geol.*, 1966, vol. 1, no. 5, pp. 381–400.
2. Aleksandrov, V.G. and Zak, G.A., *Mikrobiologiya*, 1950, vol. 19, no. 2, pp. 97–104.
3. Fobe, B.O., Vleugels, G.J., Roekens, E.J., *et al.*, *Environ. Sci. Technol.*, 1995, vol. 29, no. 1, pp. 1691–1698.
4. Johansson, L.-G., Lindqvist, O., and Mangio, R.E., *Durability of Building Materials*, 1988, no. 5, pp. 439–446.
5. Sobolevskii, M.V., Skorokhodov, I.I., Grinevich, K.P., *et al.*, *Oligoorganosiloksany: Svoistva, poluchenie, primenenie* (Oligoorganosiloxanes: Properties, Manufacture, and Use), Moscow: Khimiya, 1985.
6. Pashchenko, A.A., Voronkov, M.G., Mikhailenko, L.A., *et al.*, *Gidrofobizatsiya* (Hydrophobization), Kiev: Naukova Dumka, 1973.
7. Voronkov, M.G. and Dolgov, B.N., *Priroda*, 1954, no. 5, pp. 145–147.
8. Pouchol, J.-M. and Chauffriat, H., *Eur. Coating J.*, 1990, no. 11, pp. 633–635.
9. Putterill, K.E. and Oberholster, R.E., *Investigation of Different Variables of Concrete Caused by Alkaliaggregate Reaction under Natural Environmental Conditions*, Pretoria: Nat. Build. Inst., 1985.
10. Nielson, A., *Cement Concrete Research*, 1994, vol. 24, no. 1, pp. 83–88.
11. Kharitonov, N.P., Ivanov, Yu.I., and Glushkova, N.E., *Kremniiorganicheskie soedineniya i materialy dlya povysheniya dolgovechnosti betona* (Organosilicon Compounds and Materials for Improving Durability of Concrete, Leningrad: Nauka, 1982.
12. Sidorov, V.I. and Malyavskii, N.I., *Prom. Grazhd. Str–vo*, 1997, no. 8, pp. 52–54.
13. Tarasov, V.I., *12 Ibasil. Weimar*, 1994, vol. 2, pp. 286–289.
14. Prabakar, S. and Assink, R.A., *J. Non-Cryst. Solids*, 1997, vol. 211, no. 1, pp. 39–43.
15. Lord, D.L., Demond, A.H., Salenzadeh, A., and Hayes, K.F., *Environ. Sci. Technol.*, 1997, vol. 31, no. 2, pp. 2052–2058.

Russian Journal of Applied Chemistry, Vol. 74, No. 12, 2001, pp. 1990–1993. Translated from Zhurnal Prikladnoi Khimii, Vol. 74, No. 12, 2001, pp. 1930–1933.

INORGANIC SYNTHESIS AND INDUSTRIAL INORGANIC CHEMISTRY

Specific Features of Preparation of Liquid Glass-Based Colloid Solutions for Synthesis of Glass Coatings

Ya. I. Vakhula, I. N. Yashchishin, V. A. Vasiichuk, A. S, Romaniv, and O. R. Semchuk

L'vovskaya Politekhnika State University, Lviv, Ukraine

Received March 28, 2000; in final form, June, 2001

Abstract—Conditions for obtaining stable colloid solutions for synthesis of alkali-silicate glass coatings based on lithium, sodium, and potassium liquid glass were studied. The influence of the solution pH and the nature and concentration of liquid glass on the gel formation was established.

The sol-gel method is one of the most promising and universal among a number methods for obtaining glass coatings. In many cases, sols [1, 2], colloid solutions [3, 4], gels, or their dried powders [5, 6] are used. The choice of a specific solution state or solution-based products for the formation of glass coatings depends on a support material and its final destination. In each case, the technological process starts from solution preparation. The preparation of a highly homogeneous and stable solution with required composition and concentration is an important and complicated task.

The main problem in obtaining homogeneous colloid solutions based on liquid glass arises from the fact that addition of even insignificant amounts of solutions of IIA and IIIA group elements to silicate solutions breaks the homogeneity of the corresponding systems due to the formation of difficulty soluble silicates of most of metals. Obviously, addition of boron-containing compounds gives rise to precipitation of amorphous silicic acid.

It is known [1, 7] that the ability of colloid solutions to be in fluid state for a long time determines their stability and depends on a number of factors, in particular, on their composition, concentration, pH, and the order of component mixing. Therefore, the conditions of solution preparation are of paramount significance.

The aim of this work was to find optimal component concentrations and technological parameters for obtaining high-quality colloid solutions for synthesis of coatings of various technical destinations.

EXPERIMENTAL

Boron aluminosilicate glasses and, in some cases, silicophosphate glasses form the base of the majority of glass coatings. Thus, the main problem is to obtain a colloid solution containing liquid glass, aluminum salts, and also salts of boric and phosphoric acids.

A specific character of silicates of alkali metals requires use of an unconventional approach to the choice of aluminum-, boron-, and phosphorus-containing compounds for obtaining stable colloid solutions. These compounds must satisfy a number of requirements: 1) absence of reactions with alkali metal silicates resulting in the formation of heterogeneous systems; 2) high water-solubility and low decomposition or melting point; 3) high content of a required oxide (Al_2O_3, B_2O_3, P_2O_5, etc.) in solution.

A glass formed in the system $Na_2O(K_2O)$–Al_2O_3–B_2O_3–SiO_2 is used for obtaining protective corrosion-resistant coatings. Sodium and potassium liquid glasses with a modulus of M = 2–4 were used as bases for preparation of colloid solutions. The concentration of alkali metal silicates was 5.5–10 wt %.

Hydroxoaluminates are appropriate for use as aluminum-containing compounds. It is the hydroxo complex $R[Al(OH)_4(H_2O)_2]$ or similar compounds that are alkali metal aluminates obtained in solutions. Therefore, we further use the general formula $R_n[Al(OH)_m]$ for alkali metal aluminates. The composition of a resulting compound depends on pH and the concentration of reacting solutions.

As shown in [8], among boron-containing reagents, only boric acid meets the above-mentioned requirements.

1070-4272/01/7412-1990 $25.00 © 2001 MAIK "Nauka/Interperiodica"

Presently, it is agreed that monoborate ions and polymeric forms of boric acid are present in its solutions with concentrations greater than 0.1–0.2 M. Therefore, silicic acids are very likely to precipitate upon pouring together liquid glass and H_3BO_3 solutions under the action of both H_3BO_3 and polyboric acids.

To obtain high-concentrated (5–12 wt %) colloid solutions, we used a sodium aluminate solution with concentrations of aluminum ions and boric acid of 0.6 and 0.1 M, respectively. Depending on a modulus, the pH of liquid glass solution was 12.0–13.4, and the pH of sodium aluminate solution was fixed at 13.1.

Addition of an even insignificant amount of an aluminate solution (0.5–1.0 ml) to 10 ml of liquid glass results in the formation of a gelatinous substance at the boundary between these liquids, whereas dropwise introduction of this solution does not give rise to this phenomenon. Taking this fact into account, we prepared colloid solutions by adding small portions of the sodium aluminate solution under vigorous stirring to liquid glass. However, it is worth noting that the solution homogeneity was retained only up to a certain critical aluminate concentration, which, in turn, depends on the nature of an alkali metal cation and on the liquid glass modulus. For the same modulus (M = 3), gelatination is observed upon addition of 10.6 and 8.0 ml of the aluminate solution to potassium and sodium liquid glass solutions, respectively. The liquid glass modulus has the most pronounced effect on this process: an increase in the modulus to four leads to gel formation on addition of only 3.2 ml of the aluminate solution.

Thus we have determined the critical content of alkali metal aluminate in terms of Al_2O_3 which can be introduced in the liquid glass composition before gelatination occurs:

x in $Na_2O \cdot xSiO_2$	3	3.5	4
Al_2O_3(critical), wt %	8.0	6.3	3.2
x in $K_2O \cdot xSiO_2$	2	2.5	3
Al_2O_3(critical), wt %	14.1	12.3	10.6

The resulting critical content of Al_2O_3 is sufficient for obtaining glass coatings with high service characteristics [9].

As already mentioned, the system $K_2O \cdot nSiO_2$–$Na_n[Al(OH)_m]$ is more stable toward gelatination than the system $Na_2O \cdot nSiO_2$–$Na_n[Al(OH)_m]$. At the same modulus (M = 3) and concentration, the critical content of Al_2O_3 in the potassium system is significantly higher. This trend is likely to be first of all related to the nature of cation and to the structure of solutions of alkali metal silicates. It should be noted that the difference in coagulation action of various single-charged ions was observed also in [10]. An increase in stability of systems based on liquid glass with low modulus results from a decrease in the amount of high-polymeric SiO_2 forms.

The oxide B_2O_3 was introduced into the system in the form of boric acid solution. A white jelly-like precipitate was formed upon addition of H_3BO_3 as a result of the pH decrease from 12–13.4 to 10.

An examination of the data obtained suggests that the addition of aluminate to alkali metal silicates gives rise to an interaction between the system components in solution. Along with an increase in size of SiO_2 colloid particles in such a solution, a three-dimensional gel skeleton is formed from these particles, $Si(OH)_4$ groups, and negatively charged $Al(OH)_4^-$ particles. Addition of an H_3BO_3 solution to the system results in the formation of a precipitate owing to decreasing pH of the $R_2O \cdot nSiO_2$–$Na_n[Al(OH)_m]$–H_3BO_3 system. It is evident that $Al(OH)_3$ is first precipitated due to decreasing aluminate stability at low pH values. It is necessary to note that the "coagulation threshold" (pH value at which a precipitate starts to form) for potassium systems is 11.6, whereas for sodium it is 12. This fact once more confirms the greater stability of the system based on potassium liquid glass.

The stability of such solutions strongly depends on the order in which the components are poured together when preparing colloid solutions. It is necessary to note that we added to the solutions soluble salts that do not react with solution components in order to obtain coatings with specified technological parameters (low melting point, adhesion, and color). The optimal order of pouring together component of the colloid solutions, as found experimentally, is: $Na_2O \cdot 2SiO_2$ + $Na_nK[Al(OH)_m]$ + H_3BO_3 + adhesion promoters + pigments.

The system Li_2O–K_2O–BaO–Al_2O_3–B_2O_3–SiO_2 is of great importance for the production of electrically insulating glass materials. Aluminum oxide was introduced into the solution in the form of potassium aluminate. In addition, we studied the behavior of aluminum and barium nitrates.

A mixture of lithium (M = 10) and potassium (M = 3.5) liquid glasses was prepared in a preliminary stage. The total mixture concentration was 13 wt % and pH was 11.8. It should be noted that suspended particles were present in lithium liquid glass. Mixing these components does not break the solution homogeneity, and no precipitate is formed. However, an additional

pouring of both the aluminate and aluminum or barium nitrate (c = 0.3 M) results in the immediate formation of a precipitate, and a little later the entire solution is transformed to a gel. An increase in pH to 11.6 does not improve its stability.

One of effective means for stabilization of colloid solutions is variation of their concentration [11]; therefore, the prepared lithium-potassium liquid glass was gradually diluted with water to a concentration of 6.5 wt %. In this case, further addition of required components (aluminum and barium salts) does not give rise to gel formation. In so doing an insignificant precipitate is formed, which dissolves in the course of time.

Our experiments have proved that the probability of gelatination grows with increasing concentrations of silicate ions SiO_3^{2-} and also of SiO_2 colloid particles. In order to avoid formation of precipitates in the colloid solutions, liquid glass must contain no more than 6.5 wt % of salts.

The general sequence of component pouring together and solution preparation is the following: $K_2O \cdot 3.5SiO_2 + Li_2O \cdot 10SiO_2 + LiOH + Al(NO_3)_2 + H_3BO_3 + Ba(NO_3)_2$.

Using X-ray diffraction analysis, we found that the powder obtained on drying the solution contains aluminum and barium nitrates. Thus, the data obtained prove the absence of chemical reactions between the solution components.

A glass of the system K_2O–Al_2O_3–B_2O_3–SiO_2–P_2O_5 is used in production of low-melting decorative coatings. To prepare the solutions, we used potassium liquid glass (M = 3.5, c = 14.47 wt %) and the following solutions (M): KOH 9, $(NH_4)_2HPO_4$ 1.5, and H_3BO_3 0.7. The total concentration of the colloid solution was 17.7 wt %, pH 9.1.

Solutions of this system show strong tendency toward gelatinization. This tendency is rather sensitive to the concentration of hydrogen ions. We found experimentally that a drastic change in the solution behavior takes place at pH close to 10. Therefore, it was of importance to find conditions for obtaining solutions of this system at various pH values. We established specific features of preparation of each particular solution. For the case of solution with pH < 10, the order of pouring together components is as follows: $(NH_4)_2HPO_4 + H_3BO_3 + KOH + K_2O \cdot 3.5SiO_2 + K_n[Al(OH)_m]$.

When liquid glass is added in the course of solution preparation, a gel of orthosilicic acid H_4SiO_4 is precipitated, and, upon addition of an aluminate solution, $Al(OH)_3$ flakes also appear.

We found by X-ray diffraction analysis that a crystalline phase of $0.73NH_4H_2PO_4 \cdot 0.27KH_2PO_4$ composition is formed during drying of the gel at 50°C [12].

The time during which the solution is in the fluid state depends on concentration and may be as long as 20 days.

To obtain a colloid solution of the system under study with pH > 10, we added aqueous ammonia solution to the $(NH_4)_2HPO_4 + H_3BO_3$ mixture, which resulted in the formation of a precipitate. Therefore, we changed the order of pouring together the components and found the following appropriate sequence: $K_n[Al(OH)_m] + KOH + K_2O \cdot 3.5SiO_2 + [H_3BO_3 + (NH_4)_2HPO_4]$.

With increasing pH, the lifetime of the solutions grows up to 40 days.

CONCLUSIONS

(1) The procedure for obtaining glass coatings includes high-temperature treatment of finely dispersed raw powder mixtures. Mostly the quality of the coatings depends on the homogeneity of colloid solutions.

(2) The preparation of colloid homogeneous solutions based on liquid glass differs fundamentally from the preparation involving tetraethoxysilane. As the solution composition becomes more complex, the probability of formation of an insoluble precipitate or of instantaneous gelatination appears. The stability of the solutions depends on their composition, concentration, and pH. This problem should be specifically solved in each particular case. The order of pouring together the components depends on their composition and pH value.

(3) To avoid precipitate formation, it is necessary to add aluminum ions to solution in an anionic form. If aluminum and barium ions are added in the form of nitrates, the resulting solution must be diluted as much as possible. Solutions based on liquid potassium glass are more stable than sodium-based solutions. Their stability increases with decreasing silicate modulus.

REFERENCES

1. Borisenko, A.I. and Nikolaeva, L.V., *Tonkosloinye stekloemalevye i steklokristallicheskie pokrytiya*

(Thin-layer Glass-enamel Covers), Leningrad: Nauka, 1980.

2. Shevchenko, V.V., *Fiz. Khim. Stekla*, 1990, vol. 16, no. 4, pp. 577–581.
3. Atkarskaya, A.B., *Steklo Keram.*, 1998, no. 3, pp. 14–18.
4. Yashchyshyn, I.M., Vakhula, Ya.I., and Vasijchuk, V.O., *Proc. Int. Conf. "Fundamentals of Glass Science and Technology,"* Vaxjo, 1997, pp. 181–186.
5. Clasen, R., *Proc. Int. Conf. "Fundamentals of Glass Science and Technology,"* Vaxjo, 1997. pp. 166–173.
6. Pavlushkina, T.K. and Gladushko, O.A., *Steklo Keram.*, 1991, no. 4, pp. 20–24.
7. Yashchishin, I.N., Vakhula, Ya.I., Romaniv, A.S., and Vasiichuk, V.A., *Zh. Prikl. Khim.*, 1999, vol. 72, no. 12, pp. 187–191.
8. Brinker, C.J. and George, W.S., *Sol–Gel Science: the Physics and Chemistry of Sol–Gel Processing*, San-Diego: Academic, 1990.
9. Petzold, A. and Poeschmann, H., *Email und Emailliertechnik*, Leipzig: VEB Deutscher Verlag fuer Grundstoffindustrie, 1986.
10. Watillon, A.J., *Colloid Interfase Sci.*, 1970, vol. 33, no. 6. pp. 430–434.
11. Iler, R.K., *The Chemistry of Silica*, New York: Wiley–Interscience, 1979.
12. *Set of X-ray Diffraction Data Cards*, Philadelphia, Pa: Joint Committee on Chemical Analysis by X-ray Diffraction Methods, 1967.

Russian Journal of Applied Chemistry, Vol. 74, No. 12, 2001, pp. 1994–1996. Translated from Zhurnal Prikladnoi Khimii, Vol. 74, No. 12, 2001, pp. 1934–1936.

PHYSICOCHEMICAL STUDIES OF SYSTEMS AND PROCESSES

Thermodynamic Analysis of Component Interaction in the System Lithium–Sulfur

A. G. Morachevskii

St. Petersburg State Technical University, St. Petersburg, Russia

Received September 11, 2001

Abstract—Data on the thermodynamic properties of liquid and solid phases in the system lithium–sulfur are compared and discussed.

Only one congruently melting compound Li_2S is formed in the system lithium–sulfur. The sulfur-rich part of the system has a stratification region. Several, virtually simultaneous studies [1, 2] of the phase diagram of this system gave rather close results. The phase diagram of the system, taken from Janz and Tomkins' handbook [3], is presented in Fig. 1. The melting point of the compound Li_2S lies in the range from 1367 to 1382°C, and the monotectic horizontal, at 362 ± 3°C. At this temperature, the liquid phase, containing 34.5 mol % Li, is in equilibrium with a phase of virtually pure sulfur (containing less than 0.035 mol % Li). The upper critical temperature of separation is estimated to be within 838–860°C. No lithium polysulfides were found in the system. No essential differences in the main parameters of the phase diagram of the Li–S system have been found in later studies [4, 5].

The emf value of a Li–S cell in the separation region ($0.026 \le x_{Li} \le 0.346$, 11 compositions, 400–445°C, x_{Li} is the molar fraction of lithium in the system) was determined using a solid glassy electrolyte with lithium-ion conductivity [6, 7]. The average emf at 420°C is 2.215 ± 0.007 V. Correspondingly, the lithium activity in this region of compositions is $(7.95 \pm 0.97) \times 10^{-17}$. The partial molar Gibbs energy of lithium ΔG_{Li} is -213.7 ± 0.7 kJ mol^{-1}.

In [8], the cathode potential of a sulfur electrode in the $LiNO_3$–$LiNO_2$–LiOH melt was determined by measuring polarization curves in pulsed galvanostatic mode. At 150°C, below the monotectic horizontal, the potential of the sulfur electrode relative to lithium reference is constant (2.216 ± 0.002 V at a confidence probability of 0.95) over the entire polarization range. In this case, the electrochemical reaction reduces to the formation of lithium sulfide from pure components:

$$2Li(s) + S(l) = Li_2S(s). \quad (1)$$

The change in the Gibbs energy, corresponding to reaction (1), is -427.6 ± 0.6 kJ, and that corresponding to the formation of one mole of $Li_{0.667}S_{0.333}$ equals -142.5 ± 0.2 kJ (423 K). Only a single potential plateau (2.215 ± 0.003 V relative to lithium reference electrode) is clearly observed in the switch-off curves recorded upon cathodic polarization of the electrode in the above electrolyte (at 150°C).

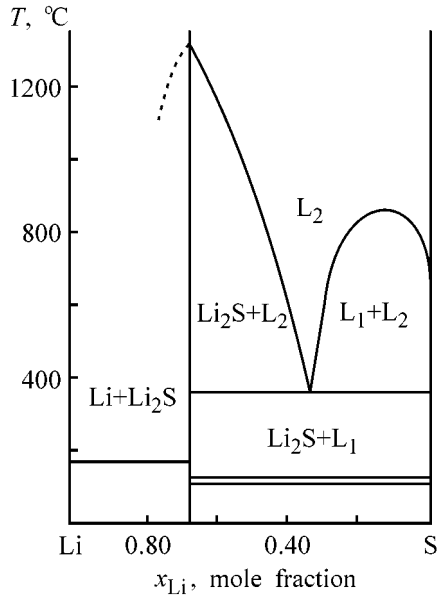

Fig. 1. Phase diagram of the lithium–sulfur system. (T) temperature, (x_{Li}) lithium content in the system, and (L_1 and L_2) liquid phases.

1070-4272/01/7412-1994 $25.00 © 2001 MAIK "Nauka/Interperiodica"

At higher temperatures (377°C, above the monotectic horizontal) the polarization curve of the halide melt LiF–LiCl–LiI also shows a potential plateau (2.195 ± 0.009 V relative to lithium reference). In the given case, the potential is associated with the occurrence of the reaction:

$$2Li(l) + S(l) = Li_2S(s), \quad (2)$$

with a change in the Gibbs energy of -423.6 ± 1.7 kJ (650 K). Correspondingly, for one mole of $Li_{0.667}S_{0.333}$, $\Delta G = -141.2 \pm 0.6$ kJ.

A reference book [9] contains evidence concerning the thermodynamic properties of the compound Li_2S. The authors are mainly based on the results of calorimetric measurements of the enthalpy of formation of the compound [10] and on estimates of the standard entropy and heat capacity of Li_2S in terms of different models [11]. As noted in [9], the presented data need refinement.

In [10], the enthalpy of formation of the compound Li_2S was determined by means of dissolution calorimetry to be ($\Delta H^0_{298} = -445.6$ kJ mol^{-1}). The enthalpy of formation of not only Li_2S, but also a hypothetical compound Li_2S_2 was determined by dissolution calorimetry in a later study [12]. The following results were obtained: $\Delta H^0_{298} = -427.4 \pm 4.6$ kJ mol^{-1} for Li_2S and $\Delta H^0_{298} = -432.6 \pm 5.4$ kJ mol^{-1} for Li_2S_2.

The thermodynamic properties of lithium sulfide have been analyzed in detail by Khachkuruzov [13]. The author used experimental data and approximate methods to determine the thermodynamic functions of Li_2S in crystalline and liquid state in the range 298–3000 K with a step of 200 K. The following values were obtained for Li_2S under the standard conditions:

$$H^0_{298} - H^0_0 = 10.1 \pm 0.2 \text{ kJ mol}^{-1},$$

$$S^0_{298} = 62 \pm 2 \text{ J mol}^{-1} \text{ K}^{-1},$$

$$C^0_{p,298} = 61 \pm 3 \text{ J mol}^{-1} \text{ K}^{-1}.$$

The above value of the standard entropy is in good agreement with $S^0_{298} = 60.67$ J mol^{-1} K^{-1} from reference book [9]. However, according to [13], the heat capacity of crystalline Li_2S varies with increasing temperature more strongly than it is accepted in [9]. In the temperature range 298–1450 K, the $C_p = f(T)$ dependence is expressed by the equation (J mol^{-1} K^{-1}) [13]:

$$C_p(T) = 24.48 + 0.1157T + 2.269 \times 10^{-5}T^2.$$

Thermodynamic functions for lithium sulfide Li_2S

Function	Data of [9]		Data of [13]	
	400 K	600 K	400 K	600 K
H, kJ mol^{-1}	–438.96	–423.68	–440.41	–422.79
S, J mol^{-1} K^{-1}	82.21	113.13	81.785	117.119
G, kJ mol^{-1}	–471.85	–491.56	–473.12	–493.06
ΔG^0_T, kJ mol^{-1}	–434.56	–424.60	–435.83	–426.10

At the relatively low temperatures of interest (up to 700°C) the data of [13] give the following heat capacities (J mol^{-1} K^{-1}): 74.39 (400 K), 88.00 (500 K), 102.07 (600 K), and 116.59 (700 K). In reference book [9], the following C_p values are given: 74.38 (400 K), 76.40 (500 K), 78.48 (600 K), 80.43 J mol^{-1} K^{-1} (700 K).

The difference in heat capacities tells upon the standard entropies of crystalline Li_2S. According to [13], S^0_T (J mol^{-1} K^{-1}) is 81.785 (at 400 K), 117.119 (600 K), and 150.478 (800 K). At the same time, the following values were reported in [9]: 82.21 (at 400 K), 113.13 (600 K), and 136.24 J mol^{-1} K^{-1} (800 K).

The reference book [14] gives the following thermodynamic characteristics for Li_2S in the standard state: $\Delta H^0_{298} = -447.3 \pm 1.3$ kJ mol^{-1}, $S^0_{298} = 62.8 \pm 8.4$ J mol^{-1} K^{-1}, and $\Delta G^0_{298} = -439.1 \pm 2.8$ kJ mol^{-1}. The melting point of Li_2S is reported to be 1370 ± 10°C.

Taking into account the scarcity of data on the temperature dependence of the lithium sulfide thermodynamic properties and the fact that the thermodynamic functions reported in [9, 13] are to a certain extent based on different approaches, let us consider in more detail the feasibility of using data [9, 13] for estimating the standard Gibbs energy of Li_2S formation from pure components. The H, S, and G functions for chemical compounds and individual substances at various temperatures with a step of 100°K are presented in the tabulated form in a reference book [9].

$$H = \Delta H^0_{298} + (H_T - H_{298}),$$

$$S = S^0_T, \; G = H - TS.$$

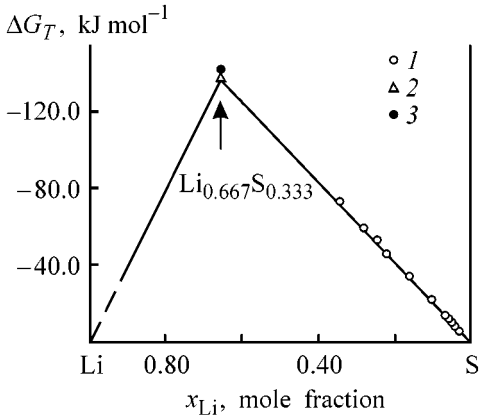

Fig 2. Integral molar Gibbs energy ΔG_T vs. composition. (*1*) Data of [6], 420°C; (*2*) calculated from data of [9], 420°C; (*3*) data of [8], 377°C.

The ΔG_T^0 value for reactions (1) or (2) is obtained by algebraic summation of the functions *G* for Li_2S and pure components (lithium and sulfur) in the corresponding aggregate state. The *H*, *S*, and *G* functions at 400 and 600 K [9, 13] are given in the table. The discrepancy between the ΔG_T^0 values is very small.

Calculation of ΔG_{423}^0 for reaction (1) from the data of [9] yields −433.66 kJ, i.e., the deviation from the experimental value (−427.6 kJ) [8] does not exceed 1.4%. Correspondingly, the calculated ΔG_{650}^0 for reaction (2) is −421.75 kJ, i.e., the deviation from the experimental value (−423.6 kJ) [8] is less than 0.5%. Thus, determining the standard Gibbs energy of Li_2S formation from pure components by means of polarization measurements gives reasonably reliable results. Also, these measurements indirectly confirm the absence of an intermediate phase (Li_2S_2) at the experimental temperatures (423–650 K).

The activity of sulfur in the system Li–S was determined in [5] by the emf method with solid electrolyte for a number of compositions both in the homogeneity region, which is very narrow at 400°C, and in the separation region. Unfortunately, no numerical data were given, but, as follows from the presented plots, the activity of sulfur in the separation region is 0.90. Since pure sulfur is taken as the standard state, and one of equilibrium phases is virtually pure sulfur, the above value of its activity is probably somewhat underestimated. According to [6], the activity of sulfur in the separation region at 420°C is 0.947 ± 0.011.

At 420°C the plot of the molar Gibbs energy of the Li–S system against composition shows no homogeneity region (Fig. 2).

The emf of the cell (–) Li | Li^+ | Li, S (+), observed in the separation region (2.215 V at 420°C), differs only slightly from the emf established at the corresponding temperature in the two-phase region Li_2S(s) + liquid. The results of the performed thermodynamic analysis of the Li–S system are not in quite good agreement with the emf of a lithium–sulfur circuit, reported in [5].

REFERENCES

1. Sharma, R.A., *J. Electrochem. Soc.*, 1972, vol. 119, no. 11, pp. 1439–1443.
2. Cunningham, P.T., Johnson, S.A., and Cairns, E.J., *J. Electrochem. Soc.*, 1972, vol. 119, no. 11, pp. 1448–1450.
3. Janz, G.J., Tomkins, R.P.T., *Physical Properties Data Compilations Relevant to Energy Storage. IV. Molten Salts*, Washington: NSRDS–NBS, 1981.
4. Cleaver, B., and Upton, S.M., *Electrochim. Acta*, 1991, vol. 36, no. 3–4, pp. 673–677.
5. Cleaver, B., and Upton, S.M., *Electrochim. Acta*, 1991, vol. 36, no. 3–4, pp. 679–681.
6. Morachevskii, A.G., Chekoev, N.G., and Demidov, A.I., *Zh. Prikl. Khim.*, 1978, vol. 51, no. 6, pp. 1259–1262.
7. Chekoev, N.G., and Morachevskii, A.G., *Izv. Vyssh. Uchebn. Zaved.*, Tsvetn. Metall., 1987, no. 6, pp. 124–126.
8. Demidov, A.I., Dukhanin, G.P., Simikov, I.A., and Morachevskii, A.G., *Elektrokhimiya*, 1985, vol. 21, no. 6, pp. 853–854.
9. Barin, I., Knacke, O., and Kubaschewski, O., *Thermochemical Properties of Inorganic Substances: Supplement*, Berlin: Stahleisen m.B.H Dusseldorf, 1977.
10. Juza, R., and Uphoff, W., *Z. anorg. allgem. Chem.*, 1956, vol. 287, no. 3, pp. 113–119.
11. Mills, K.C., *Thermodynamic Data for Inorganic Sulphides, Selenides and Tellurides*, London: Butterworths, 1974.
12. Letoffe, J.-M., Thourey, J., Perachon, G., and Bousquet, J., *Bull. soc. chim. France*, 1976, no. 3–4, pp. 424–426.
13. Khachkuruzov, G.A., *Termodinamika i kinetika khimicheskikh protsessov* (Thermodynamics and Kinetics of Chemical Processes), Leningrad: Gos. Inst. Prikl. Khim., 1985, pp. 3–9.
14. *Termicheskie konstanty veshchestv* (Thermal Constants of Substances), Moscow: VINITI Acad. Nauk SSSR, 1981, no. 10.

Russian Journal of Applied Chemistry, Vol. 74, No. 12, 2001, pp. 1997–2001. Translated from Zhurnal Prikladnoi Khimii, Vol. 74, No. 12, 2001, pp. 1937–1941.

PHYSICOCHEMICAL STUDIES OF SYSTEMS AND PROCESSES

Liquid–Liquid and Liquid–Vapor Phase Equilibria in Stratifying Binary System *n*-Hexane–Water

A. R. Rasulov and S. M. Rasulov

Institute of Physics, Daghestan Scientific Center, Russian Academy of Sciences, Makhachkala, Daghestan, Russia

Received October 5, 2000; in final form, April 2001

Abstract—Thermal properties of a binary system *n*-hexane–water were studied by the constant-volume-piezometer method for seven concentrations of water on the basis of isochores at temperatures of 372.75–620.55 K, homogeneous phase densities in the range 66.87–834.30 kg m^{-3}, and pressures of up to 65 MPa.

Studying the thermal properties on *n*-alkane–water mixtures is of not only theoretical, but also practical interest, since natural hydrocarbon mixtures are, as a rule, in contact with water. In addition, stratifying water–hydrocarbon systems are widely used in chemical technology, petroleum and petrochemical industries, and power engineering.

The properties (*PVT*) of the *n*-hexane–water binary system, which can be considered a simple model of a stratal mixture, were studied in a number of works [1–7]. However, data on phase liquid–liquid and liquid–vapor equilibria are scarce.

In this work, thermal properties of the *n*-hexane–water binary system was studied by the constant-volume piezometer method at temperatures of 372.75–620.55 K, homogeneous phase densities ρ of 66.87–834.30 kg m^{-3}, and pressures of up to 65.34 MPa for seven concentrations *x* of water (mol fraction): 0.166, 0.257, 0.347, 0.615, 0.827, 0.935, and 0.964. The measurements cover a parameter range between the liquid–liquid and liquid–vapor phase equilibria.

The temperature of the system was maintained automatically within ±0.01 K by means of three heat controllers. The pressure was controlled using a membrane transducer with sensitivity of 0.005 MPa and measured with standard pressure-gage at pressures below 1 MPa and MP-600 deadweight gage with accuracy of 0.05% at pressures exceeding 1 MPa. The piezometer volume (21.160 ± 0.025 cm^3) was determined by calibration against water. The piezometer was filled under vacuum through a valve at the piezometer edge. Mixtures were prepared using degassed twice-distilled water and *n*-hexane of 99.94% purity. The mixture components were weighed on analytical balance with an error not exceeding 0.5 mg. The error in density measurements was 0.12–0.15%. The setup was described in detail in [8].

The measurements were made using isochores. For each composition, 7–9 isochores were obtained, which covered a wide range of densities. The dependences of pressure *P* on temperature *T* along the isochores exhibit inflections corresponding to liquid–liquid and liquid–vapor phase transitions. A typical *P*–*T* dependence along different isochores for a composition with $x = 0.935$ is given in Fig. 1. Lines connecting the inflection points are phase equilibrium

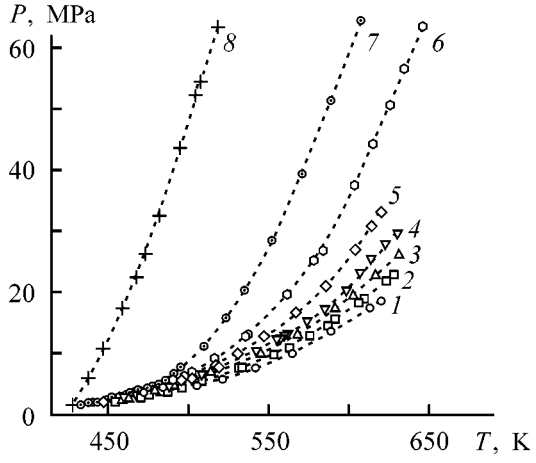

Fig. 1. Dependence of *P* on temperature *T* for *n*-hexane–water binary system of composition $x = 0.935$ along isochores. ρ (kg m^{-3}): (*1*) 205.1, (*2*) 273.4, (*3*) 341.7, (*4*) 410.1, (*5*) 478.4, (*6*) 546.8, (*7*) 615.1, and (*8*) 649.3.

1070-4272/01/7412-1997 $25.00 © 2001 MAIK "Nauka/Interperiodica"

Table 1. Temperature and pressure corresponding to liquid–liquid and liquid–vapor phase transitions in the *n*-hexane–water binary system

x, mole fraction of H_2O	ρ, kg m^{-3}	T_{ll}, K	P_{ll}, MPa	T_{lg}, K	P_{lg}, MPa	*x*, mole fraction of H_2O	ρ, kg m^{-3}	T_{ll}, K	P_{ll}, MPa	T_{lg}, K	P_{lg}, MPa
0.166	66.9	420.01	0.994	469.25	1.853	0.615	546.8	456.35	2.576		
	133.7	440.51	1.307	484.04	2.669		615.1	415.02	1.623		
	200.6	456.01	1.760	488.45	3.043		649.3	385.55	0.459		
	267.5*	458.90*	1.974*	500.45*	3.627*		702.4	327.05	0.098		
	334.3	457.60	2.251	499.46	3.782		720.8	305.95	0.034		
	401.2	453.90	2.169	462.95	2.528	0.827	159.0	454.40	2.196	566.95	10.41
	468.1	446.00	1.942	450.25	2.004		238.0	474.45	3.682	603.85	19.67
	534.9	427.75	1.315	427.75	1.315		317.7	493.41	5.241	610.15	23.22
	601.8	372.75	0.401	372.75	0.401		397.2*	494.76*	5.724*	617.25	31.71
0.257	135.0	455.05	2.125	579.75	7.201		476.6	481.06	4.870	621.65	42.10
	202.5	482.65	3.574	518.55	5.355		556.1	462.65	3.425	625.65	60.23
	270.0	493.85	4.933	497.65	5.071		635.5	447.27	2.632		
	286.8*	494.55*	5.010*	494.55*	5.010*		714.9	395.65	0.817		
	337.5	490.55	4.776	499.55	5.483	0.935	176.9	433.75	1.392	620.55	18.53
	405.0	477.75	4.062	533.05	8.902		265.4	454.62	2.189	629.15	22.94
	435.7	468.65	3.646				353.9*	464.76*	2.583*	631.65*	25.86*
	472.5	456.15	2.884				442.4	461.25	2.687	630.65	29.61
	540.0	425.95	1.672				530.9	454.19	2.403	621.15	33.04
	607.5	382.35	0.596				619.3	443.51	1.951	646.65	63.55
0.347	137.5	465.45	2.835	507.35	5.000		707.8	433.15	1.430		
	204.8	487.15	4.463	519.30	6.280		796.3	428.41	1.351		
	273.1*	494.55*	5.281*	522.15	7.340	0.964	92.7	418.16	0.834	581.45	9.826
	341.4	489.52	4.830	533.15	10.82		185.4	442.15	1.803	607.25	14.72
	409.7	477.65	4.034	550.25	17.82		298.1	455.15	2.470	634.55	21.53
	477.9	462.95	2.984	570.15	33.21		370.8*	455.30*	2.554*	632.15*	23.71*
	546.2	428.45	1.400	581.25	59.15		463.5	455.25	2.603	627.95	25.83
0.615	205.1	452.90	1.974	562.45	11.39		556.2	455.15	2.575	626.15	32.70
	273.4	472.85	3.089	575.15	15.53		648.9	452.05	2.517	628.15	37.80
	341.7	492.30	5.153	594.65	23.50		741.6	447.65	2.336		
	410.1*	494.62*	5.611*	611.65	33.25		834.3	425.95	1.390		
	478.4	486.63	4.836	625.15	47.75						

* Critical parameters.

Table 2. Critical parameter β, amplitudes B_0, B_1, B_2, B_3 and region of approximation with Eq. (1) for liquid–liquid coexistence curves in the *n*-hexane–water mixture

x, mole fraction H_2O	β	B_0	B_1	B_2	B_3	Approximation region
0.166 (r)*	0.320 ± 0.021	2.217 ± 0.143	0.507 ± 0.047	–	–	8×10^{-2}–6×10^{-5}
0.166 (l)	0.370 ± 0.044	1.493 ± 0.122	0.954 ± 0.092	–	–	8×10^{-2}–6×10^{-5}
0.257 (r)	0.344 ± 0.018	1.676 ± 0.102	0.575 ± 0.061	–	–	7×10^{-2}–6×10^{-5}
0.257 (l)	0.382 ± 0.050	1.198 ± 0.088	0.434 ± 0.048	–	–	7×10^{-2}–6×10^{-5}
0.347 (r)	0.341 ± 0.016	0.925 ± 0.076	0.590 ± 0.059	4.166 ± 1.234	–0.750 ± 0.302	6×10^{-2}–1×10^{-4}
0.347 (l)	0.357 ± 0.029	1.217 ± 0.133	0.361 ± 0.042	–	–	6×10^{-2}–1×10^{-4}
0.615 (r)	0.352 ± 0.030	0.647 ± 0.051	0.261 ± 0.033	1.398 ± 0.409	–1.234 ± 0.511	6×10^{-2}–4×10^{-5}
0.615 (l)	0.301 ± 0.027	0.753 ± 0.079	0.334 ± 0.037	1.309 ± 0.441	–1.479 ± 0.672	6×10^{-2}–4×10^{-5}
0.827 (r)	0.430 ± 0.082	0.613 ± 0.054	0.567 ± 0.064	2.410 ± 0.700	–1.032 ± 0.503	6×10^{-2}–8×10^{-5}
0.827 (l)	0.349 ± 0.044	1.189 ± 0.102	0.643 ± 0.071	1.213 ± 0.389	–1.245 ± 0.576	6×10^{-2}–8×10^{-5}
0.935 (r)	0.422 ± 0.056	1.728 ± 0.158	0.741 ± 0.089	4.876 ± 1.284	–1.991 ± 0.809	6×10^{-2}–9×10^{-5}
0.935 (l)	0.437 ± 0.062	1.333 ± 0.124	0.578 ± 0.074	1.098 ± 0.255	–1.731 ± 0.774	6×10^{-2}–9×10^{-5}
0.964 (r)	0.291 ± 0.033	3.088 ± 0.311	0.796 ± 0.091	5.193 ± 1.998	–10.67 ± 4.23	7×10^{-2}–2×10^{-5}
0.964 (l)	0.291 ± 0.035	1.422 ± 0.152	0.643 ± 0.077	2.000 ± 0.366	–1.901 ± 0.794	7×10^{-2}–2×10^{-5}

* Indices "r" and "l" refer to, respectively, right and left branches of the liquid–liquid coexistence curve.

lines separating the triple-phase region from the double-phase region, and the latter from the single-phase one. An isochore without inflection passes through the point of maximum temperature—cricondentherm of the phase equilibrium line. The thus obtained temperatures and pressures, corresponding to liquid–liquid (T_{ll}, P_{ll}) and liquid–vapor (T_{lg}, P_{lg}) phase transitions along different isochores for all of the measured compositions of the *n*-hexane–water binary system, are given in Table 1.

Figure 2 presents critical point lines in the *T*–*x* coordinates for the *n*-hexane–water binary mixture. According to van Koninenburg and Scott's classification [9], the phase diagram of the *n*-hexane–water binary system belongs to type III. This means that the liquid–vapor critical state does not exist in the concentration range 0.257–0.882 mol fraction of water. The lower locus of the liquid–vapor critical line *1* begins at the critical point of *n*-hexane CP1 and ends in the upper terminal critical point (UTCP) corresponding to $x = 0.257$ mol fraction of water. The upper part begins at the critical point of water, CP2, passes through the double critical point (DCP; $x = 0.935$), and, with decreasing concentration of water, goes to the region of higher values. The dashed line represents the line of discontinuity of liquid–vapor critical points. This line is so designated because the *P*–*T* line shows an inflection despite the absence of a critical state. The same is indicated by investigations of the caloric properties [6] in which an abrupt change in isochoric heat capacity is observed in intersecting line *3*.

The curve of liquid–liquid phase equilibrium was approximated by the expression [10, 11]

$$\frac{\rho - \rho_c}{\rho_c} = \pm B_0 |t|^{\beta} \pm B_1 |t|^{\beta + \Delta} + B_2 |t|^{1-\alpha} + B_3 t, \quad (1)$$

where β, Δ, and α are the critical indices, with Δ and α fixed [9] (Δ = 0.50, α = 0.11); B_0, B_1, B_2, and B_3 are the critical amplitudes; $t \equiv (T_c - T)/T_c$ is the reduced temperature; ρ_c and T_c are, respectively, the critical density and temperature; the signs plus and minus refer to, respectively, the right- and left-hand branches of the liquid–liquid coexistence curve (Fig. 3).

Table 2 presents calculated values of the critical index β, critical amplitudes B_0, B_1, B_2, and B_3, and the region of approximation by Eq. (1) for the liquid–liquid equilibrium curves for the *n*-hexane–water mixture of various compositions. The results of calculations indicate that for the liquid–liquid phase transition the critical indices β are close (within calculation error) to 0.325. This confirms the validity of the conclusion that, near the liquid–liquid phase transition point, the liquids belong to universal three-dimensional Ising systems.

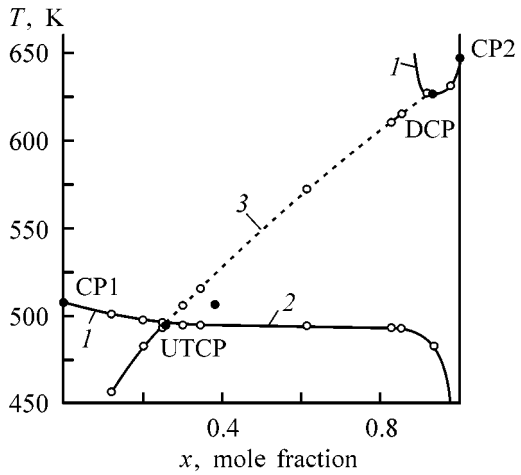

Fig. 2. Lines of critical points in the *n*-hexane–water binary system. (*T*) Temperature and (*x*) water content. (*1*) Liquid–vapor, (*2*) liquid–liquid, (*3*) "pseudocritical" curve; CP1 and CP2 are the critical points of, respectively, straight *n*-hexane and water; UTCP is the upper terminal critical point, and DCP is the double critical point.

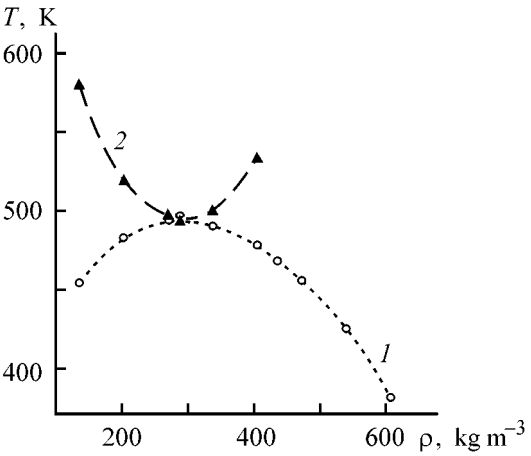

Fig. 3. Phase diagram *T*–ρ of the *n*-hexane–water binary mixture of composition $x = 0.257$. (*1*) Liquid–liquid and (*2*) liquid–vapor.

The liquid–vapor coexistence curve was described in accordance with the equation [10, 12]

$$\frac{\rho_l - \rho_g}{2\rho_c} = B |t|^{\beta}, \quad (2)$$

where ρ_1 and ρ_2 are, respectively, the liquid and vapor phase densities; and *B* is the critical amplitude.

The results of calculations for four compositions (for which the liquid–vapor critical point exists) of

Table 3. Calculated values of the critical index β, amplitude *B*, and the region of approximation with respect to *t* by Eq. (2) for the liquid–vapor coexistence curve for the *n*-hexane–water binary mixture

x, mole fraction H_2O	β	*B*	Approximation region
0.166	0.478 ± 0.012	2.638 ± 0.024	1×10^{-2}–9×10^{-4}
0.257	0.317 ± 0.030	0.620 ± 0.030	1×10^{-2}–1×10^{-3}
0.935	0.556 ± 0.083	5.421 ± 0.346	8×10^{-3}–8×10^{-4}
0.964	0.331 ± 0.047	1.060 ± 0.045	5×10^{-3}–8×10^{-4}

the *n*-hexane–water binary mixture are presented in Table 3. It can be seen that the critical index β obtained for compositions with $x = 0.257$ and 0.964 is close to 0.325, a value characteristic of three-dimensional Ising systems. The value $\beta = 0.556$ for $x = 0.964$ corresponds (within calculation error) to the assumption of [13] that critical indices are doubled in the double critical point.

The thermodynamic properties of the *n*-hexane–water binary system near the liquid–vapor critical line were described using the crossover equation of state [14, 15]. This method consists in obtaining crossover functions transforming the six-term Landau expansion into Wegner expansion for the Helmholtz free energy of liquid in the near-critical region.

The specific Helmholtz energy $A(\tau, \rho, \zeta)$ is written as [14]

$$A(\tau, \rho, \zeta) = \frac{P_c(\zeta)}{RT_c(\zeta)}[\Delta A(\tau, \rho, \zeta) + A_0(\tau, \zeta) + \rho h_0(\tau, \zeta)], \quad (3)$$

where ζ is the field variable corresponding to the concentration *x*, *R* the molar gas constant, P_c the critical pressure, $\tau = [T - T_c(\zeta)]/T$, $\Delta A(\tau, \rho, \zeta)$ the singular part of the free Helmholtz energy, $h_0(\tau, \zeta)$ and $A(\tau, \zeta)$ regular functions represented as truncated Taylor series.

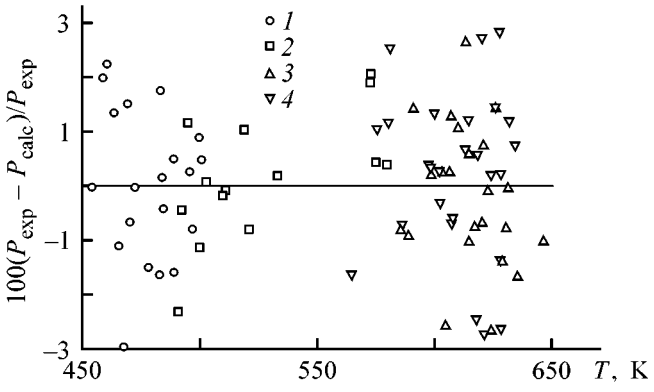

Fig. 4. Deviation of the calculated pressures P_{calc} from the experimental values P_{exp} for the *n*-hexane–water binary mixture. *x* (mole fraction): (*1*) 0.166, (*2*) 0.257, (*3*) 0.935, and (*4*) 0.964.

The quantity $\Delta A(\tau, \rho, \zeta)$ depends on the so-called crossover function *Y*; according to the value of this function, the singular part of the Helmholtz free energy transforms into a Wegner expansion (in close vicinity of the critical point) or into classical Landau series (far from the critical point). To identify the dependences of the critical parameters on the variable ζ as dependences on *x*, a condition that $x = \zeta$ along the critical line is imposed.

The asymmetry of the real liquid is taken into account on passing from model to physical variables. Nonuniversal constants of substance, characterizing the individual properties of the system, were calculated on the basis of published data and authors' *PVTx* experimental investigations [16].

The critical parameters for *n*-hexane were taken from [17]: $T_c = 507.20$ K, $P_c = 3.025$ MPa, $\rho_c = 233.5$ kg m^{-3}; and for water, from [18]: $T_c = 647.047$ K, $P_c = 22.046$ MPa, $\rho_c = 322.788$ kg m^{-3}. The concentration dependences of the critical parameters, necessary for calculations, were approximated by polynomials and splines.

Figure 4 shows deviations of the calculated pressures P_{calc} from the experimental values P_{exp}. The crossover equation of state makes it possible to describe the pressure of the *n*-hexane–water binary mixture with an error not exceeding 3% for densities in the range $0.50\rho_c \le \rho \le 1.7\rho_c$ (at $T = T_c$) and temperatures in the range $0.95T_c \le T \le 1.7T_c$ (at $\rho = \rho_c$).

ACKNOWLEDGMENTS

The study was financially supported by the Russian Foundation for Basic Research (grant no. 00-02-17 320).

REFERENCES

1. Brunner, E., *J. Chem. Thermodyn.*, 1990, vol. 22, pp. 335–353.
2. De Loos, Th.W., Penders, W.G., and Lichtenthaler, R.N., *J. Chem. Thermodyn.*, 1982, vol. 14, pp. 83–91.
3. Reber,t Ch.J. and Hayworth, K.E., *Am. Inst. Chem. Eng. J.*, 1967, vol.13, no. 1, pp. 118–121.
4. Tsonopoulos, C. and Wilson, G.M., *Am. Inst. Chem. Eng. J.*, 1983, vol.29, no. 6, pp. 990–999.
5. Victorov, A.I., Fredensland, Ad., and Smirnova, N.A., *Fluid Phase Equilibria*, 1991, vol. 66, pp. 187–210.

6. Kamilov, I.K., Stepanov, G.V., Malysheva, L.V., *et al.*, *High Temp.-High Press.*, 1997, vol. 29, pp. 491–495.
7. Abdulagatov, I.M., Bazaev, A.R., and Ramazanova, A.E., *Teplofiz. Vys. Temp.*, 1992, vol. 30, no. 5, pp. 897–907.
8. Rasulov, S.M. and Khamidov, M.M., *Prib. Tekh. Eksp.*, 1999, no. 1, pp. 148–150.
9. Van Konynenburg, P.H. and Scott, R.L., *Phil. Trans. Roy.*, London, 1980, vol. 298, no. A1442, pp. 495–540.
10. Anisimov, M.A., *Kriticheskie yavleniya v zhidkostyakh i zhidkikh kristallakh* (Critical Phenomena in Liquids and Liquid Crystals), Moscow: Nauka, 1987.
11. Aizpiri, A.G., Correa, J.A., and Pena, M.D., *J. Chem. Phys.*, 1988, vol. 88, no. 3, pp. 1934–1943.
12. Aizpiri, A.G., Correa, J.A., Rubio, R.G., and Pena, M.D., *Phys. Rev. B*, 1990, vol. 41, no. 13, pp. 9003–9012.
13. Anisimov, M.A., Gorodetskii, E.E., Kulikov, V.D., and Sengers, J.V., *Phys. Rev. E*, 1995, vol. 51, no. 2, pp. 1199–1215.
14. Jin, G.X., Tang, S., and Sengers, J.V., *Phys. Rev. E*, 1993, vol. 47, no. 1, pp. 388–402.
15. Kiselev, S.B. and Povodyrev, A.A., *Teplofiz. Vys. Temp.*, 1996, vol. 34, no. 4, pp. 626–646.
16. Rasulov, S.M. and Rasulov, A.R., *Teplofiz. Vys. Temp.*, 2000, vol. 38, no. 3, pp. 412–417.
17. Gerasimov, A.A. and Grigor'ev, B.A., *Teplofiz. Vys. Temp.*, 1993, vol. 31, no. 2, pp. 197–206.
18. Tang, S. and Sengers, J.V., *J. Supercrit. Fluids*, 1991, vol. 4, no. 4, pp. 209–214.

Russian Journal of Applied Chemistry, Vol. 74, No. 12, 2001, pp. 2002–2004. Translated from Zhurnal Prikladnoi Khimii, Vol. 74, No. 12, 2001, pp. 1942–1944.

PHYSICOCHEMICAL STUDIES OF SYSTEMS AND PROCESSES

Determination of Internal Rotation Barrier

V. M. Yanborisov, M. Yu. Zaitsev, and Yu. B. Monakov

Bashkortostan State University, Ufa, Bashkortostan, Russia

Received June 14, 2001

Abstract—The interrelation between the experimental heights of the potential barrier to internal rotation about the C–C bond and those calculated by the semiempirical and nonempirical quantum-chemical methods for 25 compounds was studied. The height of the potential barrier to internal rotation about the C–C bond can be determined by the AM1 semiempirical method with correction introduced according to the correlation dependence established.

Studies of thermomechanical characteristics and deformation of polymers have long been utilizing the rotamer theory [1]. To determine the statistical weights of rotamers, it is necessary to know the difference in the free energies ΔG for these conformers. In the case that the entropy difference for the rotamers is negligible, it is possible to use for rotamers the energy difference ΔE instead of ΔG. The internal rotation barrier U for polymers is typically determined from the ΔG or ΔE values for low-molecular-weight analogs, found experimentally or by quantum-chemical calculations. However, in the latter case the results obtained by semiempirical methods strongly differ from experimental data, and nonempirical calculations require elucidating how the basis affects the results, which consumes much computer time.

In this work, we propose a technique for promptly calculating the parameter U. This technique is based on the correlation between U_{exp} and U_{calc}, established for 25 low-molecular-weight compounds (see figure and Tables 1, 2).

The figure presents the correlation dependences

$$U_{calc} = cU_{exp} + d. \quad (1)$$

Here, c and d are coefficients yielded by calculations for low-molecular-weight compounds listed in Table 2 by various quantum-chemical methods: semiempirical methods AM1, MNDO, and PM3 and nonempirical methods in the 3-21G* basis which affords adequate results for the problem and the class of compounds under consideration [12, 13].

For a compound for which the experimental value U_{exp} is unknown, we propose to determine the height of internal rotation barrier by the inverse relationship

$$U = aU_{calc} + b. \quad (2)$$

The coefficients a and b are listed in Table 3. In expressions (1) and (2) for semiempirical methods AM1, MNDO, and PM3, we used the relation

$$U_{calc} = \Delta_f H^0_{max} - \Delta_f H^0_{min}.$$

Here, $\Delta_f H^0_{min}$ is the enthalpy of formation calculated from the optimal geometry of the molecule, $\Delta_f H^0_{max}$ is the enthalpy of formation calculated for the maximum in the dependence of the enthalpy on the internal rotation angle $\Delta_f H^0(\varphi)$.

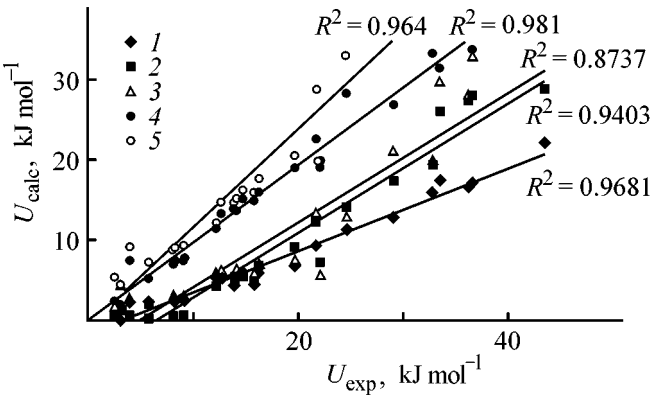

Correlation between the experimental (U_{exp}) and calculated, by various quantum-chemical methods, (U_{calc}) heights of potential barrier to internal rotation about the C–C bond in molecules (Table 2). (*1*) AM1, (*2*) MNDO, (*3*) PM3, (*4*) 3-21G* (*E*), and (*5*) 3-21G* (*G*).

1070-4272/01/7412-2002 $25.00 © 2001 MAIK "Nauka/Interperiodica"

Table 1. Height of internal rotation barrier in ethane

$\Delta G^{\#}$, kJ mol^{-1}	Measurement method*	References	$\Delta G^{\#}$, kJ mol^{-1}	Measurement method*	References
12.029	T, VS	[2]	12.058	MW	[5]
12.13	MW	[3]	12.26	VS	[6]
12.68	VS	[4]			

* VS vibrational spectroscopy, MW microwave spectroscopy, and T thermodynamic methods.

Table 2. Experimental and calculated heights of the potential barrier to internal rotation about the C–C bond

Compound	U_{calc}, kJ mol^{-1}					U_{exp}, kJ mol^{-1}		
	AM1	MNDO	PM3	3-21G*		U	measurement method	references
				U_1^*	U_2^{**}			
CH_3CH_3	5.23	4.24	5.98	11.51	12.30	12.23	U_{av}^{***}	[2–5]
CH_3CH_2CN	5.56	5.49	6.29	13.30	14.74	12.7	VS	[2]
CH_3CH_2F	4.46	4.79	5.84	13.93	14.79	13.93	MW	[3]
CH_3CH_2Cl	5.98	5.62	6.00	15.28	16.45	14.76	MW	[4]
CH_3CH_2OH	4.61	4.99	5.67	14.94	16.12	15.9	MW	[5]
$CH_3CH_2CH_3$	5.54	5.19	6.46	13.64	15.27	14.2	MW	[6]
$CH_3CH(CH_3)_2$	6.02	6.64	6.87	16.12	17.81	16.3	MW	[3]
$CH_3C(CH_3)_3$	6.71	9.18	7.27	19.04	20.66	19.7	T	[3]
CH_3CHCl_2	7.11	7.30	5.67	19.26	20.11	22.18	VS	[7]
$CH_3CH_2C(CH_3)_3$	9.36	12.38	13.54	22.68	28.95	21.8	NMR	[8]
$ClCH_2C(CH_3)_3$	11.53	14.17	13.08	28.52	33.23	24.7	NMR	[8]
$C(CH_3)_2CNC(CH_3)_3$	16.81	27.57	28.33	36.97	48.29	36.4	NMR	[9]
$C(CH_3)_2ClC(CH_3)_3$	22.26	29.17	29.40	41.58	53.37	43.64	NMR	[10]
$C(CH_3)_2FC(CH_3)_3$	17.72	26.25	30.01	31.70	41.82	33.64	NMR	[9]
$CH(CH_3)ClC(CH_3)_3$	16.05	19.55	20.10	33.49	41.31	32.93	NMR	[10]
$CH(CH_3)_2C(CH_3)_3$	12.95	17.52	21.28	27.08	38.98	29.16	NMR	[10]
$C(CH_3)_3C(CH_3)_3$	17.35	28.20	33.24	34.00	40.07	36.8	NMR	[8]
trans-$CH_3CH{=}CHCl$	2.41	0.79	2.82	7.51	9.20	9.08	MW	[3]
cis-$CH_3CH{=}CHCl$	0.59	0.85	1.82	2.33	5.49	2.59	MW	[3]
trans-$CH_3CH{=}CHCH_3$	2.22	0.62	2.67	7.49	9.15	3.97	MW	[3]
cis-$CH_3CH{=}CHCH_3$	0.19	1.21	4.44	2.04	4.41	3.12	MW	[11]
trans-$CH_3CH{=}CHCN$	2.31	0.68	2.90	7.05	8.89	8.12	MW	[11]
cis-$CH_3CH{=}CHCN$	2.27	0.26	2.28	5.23	7.38	5.86	MW	[3]
trans-$CH_3CH{=}CHF$	2.41	0.67	2.98	7.80	9.38	9.20	MW	[3]
$CH_3CH{=}CH_2$	2.31	0.73	2.82	7.41	9.00	8.28	MW	[11]

* Calculated by formula (3), ** calculated by formula (4), *** the average value according to data in Table 1.

Table 3. Parameters of the correlation dependence $aU_{calc} + b$ in calculation of U_{calc}

Calc. method	$a \pm \Delta a$	$b \pm \Delta b$, kJ mol^{-1}	R^2	ΔU,* kJ mol^{-1}	Calc. method	$a \pm \Delta a$	$b \pm \Delta b$, kJ mol^{-1}	R^2	ΔU,* kJ mol^{-1}
AM1	1.85 ± 0.07	3.97 ± 0.68	0.9719	0.83	3-12G**	1.01 ± 0.03	0.26 ± 0.61	0.9810	0.98
MNDO	1.16 ± 0.06	7.17 ± 0.82	0.9403	0.86	3-12G***	0.78 ± 0.03	1.26 ± 0.82	0.9639	1.02
PM3	1.09 ± 0.09	6.43 ± 1.30	0.8737	1.41					

* ΔU calculated by formula (5) for ethane, ** U_{calc} calculated by formula (3), *** U_{calc} calculated by formula (4).

In the case of nonempirical calculation in the 3-21G* basis, the barrier height was determined either as difference of total energies

$$U_{calc} = E_{total}^{max} - E_{total}^{min}, \quad (3)$$

or that of free energies

$$U_{calc} = G_{max} - G_{min}. \quad (4)$$

The criterion of the transition state was the occurrence of a single negative value of the force constant of the chemical bond. The parameters of dependence (2) for the quantum-chemical methods utilized are given in Table 3.

The choice of quantum-chemical method for calculating U_{calc} is dictated by the following criteria (Table 3): correlation factor R^2, coefficients a and b (ideally, $a = 1$, $b = 0$), inaccuracy ΔU, and the computer time spent.

As regards the first criterion, namely, the correlation factor, the most suitable are AM1 method among semiempirical methods and, certainly, nonempirical method in the 3-21G* basis. It should be noted that from the viewpoint of all the criteria, calculation of the height of the internal rotation barrier as difference of total energies yields better results than calculation as difference of free energies (Table 3). The reason can be that in certain experimental works, especially those utilizing NMR method, specifically the height of the potential barrier was determined rather than the difference free of energies for conformers.

As regards the second criterion, namely, the coeffiicents a and b, the first place is, naturally, occupied by the nonempiirical method ($a = 1.01$, $b = 0.26$).

As to the third criterion, namely, inaccuracy in U, we calculated the standard inaccuracy ΔU by the formula

$$\Delta U = \sqrt{U_{calc}^2 \Delta a^2 + \Delta b^2}. \quad (5)$$

Hence, ΔU depends not only on the inaccuracies Δa and Δb, which are close for all the quantum-chemical methods applied (Table 3), but also on the calculated U_{calc} parameter, which is at a minimum for the AM1 method. The drawback of the AM1 method, namely, major underestimation of U_{calc}, compared with the experimental values, turns to advantage in the given case, as the accuracy in determining U increases.

Lastly, nonempirical calculations consume an order of magnitude longer computer time than semiempirical calculations.

CONCLUSION

The height of the potential barrier to internal rotation about the C–C bond can be calculated by semiempirical (AM1, MNDO, and PM3) or nonempirical methods with correction introduced according to the correlation dependences established. Among the methods considered the most suitable from the viewpoint of both accuracy and required computer time is AM1. This technique determines the height of the internal rotation barreir to within 1 kJ mol^{-1}, which is comparable with the accuracy of experimental methods.

REFERENCES

1. Vol'kenshtein, M.V., *Molekuly i zhizn'* (Molecules and the Life), Moscow: Nauka, 1965.
2. Lowe, J.P., *Progr. Phys. Org. Chem.*, 1968, vol. 6, no. 1, pp. 1–80.
3. Dashevskii, V.G., *Konformatsii organicheskikh molekul* (Conformations of Organic Molecules), Moscow: Khimiya, 1974.
4. Hirota, E., Saito, S., and Endo, Y., *J. Chem. Phys.*, 1979, vol. 71, no. 2, pp. 1183–1187.
5. Hirota, E., Endo, Y., and Saito, S., *J. Mol. Spectrosc.*, 1981, vol. 89, no. 2, pp. 285–295.
6. *Internal Rotation in Molecules*, Orville-Thomas, W.J., Ed., London: John Wiley and Sons, 1974.
7. Heise, H.M., Winter, F., and Lutz, H., *J. Mol. Spectrosc.*, 1981. vol. 90, no. 2, pp. 531–571.
8. Stahl, W., Dreizler, H., and Hayashi, M., *Z. Naturforsch., A*, 1983, vol. 38, no. 9, pp. 1010–1014.
9. Kakar, R.K. and Quade, C.R., *J. Chem. Phys.*, 1980, vol. 72, no. 8, pp. 4300–4307.
10. Zefirov, N.S., *Zh. Vsesoyuzn. Khim. O–va im. D.I. Mendeleeva*, 1977, vol. 22, no. 3, pp. 261–273.
11. Krishnaji-Srivastava, S.L., Narain, N.K., and Johri, G.K., *J. Sci. Ind. Res.*, 1979, vol. 38, no. 3, pp. 112–132.
12. Hehre, W.H., Radom, L., Schleger, P.U.R., and Pople, J.A., *Ab initio Molecular-Orbital Theory*, New York: Wiley, 1985.
13. Di Cesare, N., Belletete, M., and Leclerc, M., *Synth. Met.*, 1998, vol. 94, pp. 291–298.

Russian Journal of Applied Chemistry, Vol. 74, No. 12, 2001, pp. 2005–2008. Translated from Zhurnal Prikladnoi Khimii, Vol. 74, No. 12, 2001, pp. 1945–1948.

PHYSICOCHEMICAL STUDIES OF SYSTEMS AND PROCESSES

Steady-State Concentration of Trace Amounts of Aromatic Hydrocarbons from Gas–Vapor Mixtures on Sorbent Surface

A. N. Marinichev, E. D. Makarov, and B. V. Stolyarov

St. Petersburg State University, St. Petersburg, Russia

Received July 12, 2001

Abstract—Features of sorption–desorption in solid-phase microextraction of aromatic hydrocarbons are considered in terms of the model with two consecutive steps. The data processing method proposed is based on determination of the steady-state microextraction parameters from experimental data obtained in the initial stage of the process.

Sorbent trapping of ecotoxicants from the atmosphere or air of production areas finds a wide practical use. It is realized with either total absorption of analytes on a sorbing material or establishment of steady-state mode of the gas flow as a result of sorption–desorption [1]. Finding out this mode may require full calibration of the peak area of a sorbed component against the gas–vapor mixture volume contacted with the sorbent. Competition between individual components for sorption sites may result in appearance of maxima in the calibration curves [2]. It is evident also that determination of the steady-state mode of sorption becomes complicated with increasing number of analytes.

In this study, we analyzed the possibility of predicting the solid-phase microextraction on the basis of experimental data obtained only in the initial stages of the process in terms of the second-order autoregressive model. Previously, this model has been successfully used in studying slow chemical and mass-exchange processes by interrupted or flow perturbation GC [3, 4].

EXPERIMENTAL

Gas-vapor mixtures of aromatic hydrocarbons C_6–C_8 (benzene, toluene, ethylbenzene, and *p*-xylene) in high-purity nitrogen with concentrations of 40–50 and 4–5 mg m^{-3} were prepared using a certified vapor generator (Monitoring Research and Production Association) or the original laboratory setup operating on the principle of phase distribution of volatiles between the coexisting gas and condensed phases [5, 6]. As a sorbing material we used domestically produced sorbent PDF-1 [poly(diphenylphthalide), S_{sp} ~250 m^2 g^{-1}, grain size 0.20–0.25 mm, sorbent bed 1 cm)] packed in a steel capillary (internal diameter about 0.5 mm).

Solid-phase microextraction of aromatic hydrocarbons was performed by passing the gas–vapor mixture through the sorbent bed at a rate of 5 to 20 ml min^{-1}. The flow rate was monitored and kept constant with an IRG-10 electronic flow meter/controller (Tsvet Public Corporation). The sorption time was measured with a stopwatch.

The amounts of individual hydrocarbons in the sorbent phase were estimated from data on their exhaustive desorption in a vaporizer of a gas chromatograph (nitrogen carrier gas, temperature 300°C). The response of the flame-ionization detector was measured with a Multichrom automatic chromatographic system. To separate the analytes, we used a quartz capillary column (20 m × 0.2 mm) with DB-1 stationary phase (analog of SE-30). The column temperature was 65°C, and the carrier gas (high-purity nitrogen) flow rate, 0.9 ml min^{-1}. The readings were taken at equal 100-ml intervals of the gas–vapor mixture passed through the sorbent. The calibration curve represented the dependence of the volume of the gas–vapor mixture passed through the sorbent on the peak area in the strippant chromatogram.

The table presents the results as a set of equidistant chromatographic peak areas A (equispaced by ΔV_g, where V_g is the volume of the gas–vapor mixture). Such data files are often treated in the frame-

1070-4272/01/7412-2005 $25.00 © 2001 MAIK "Nauka/Interperiodica"

work of the second-order autoregressive model (AR-2) correlating any three neighboring readings $A(V_g + 2\Delta V_g)$, $A(V_g + \Delta V_g)$, and $A(V_g)$:

$$A(V_g) + 2\Delta V_g) = pA(V_g + \Delta V_g) + qA(V_g) + r, \quad (1)$$

where p and q are the so-called slopes and r is the absolute term of the AR-2 model.

The difference equation (1) has a general solution

$$A(V_g) = A(0) + C_1\exp(-k_1V_g) + C_2\exp(-k_2V_g), \quad (2)$$

if the roots of the characteristic equation

$$z^2 + pz + q = 0 \quad (3)$$

are real numbers (z_1 and z_2). Modeling of sampled data as a linear combination of exponentials is known in the literature as Prony's method [7]. Note that in the chemical kinetics [8, 9], when considering consecutive two-step reactions of the type ($B_1 \xrightarrow{k_1} B_2 \xrightarrow{k_2} B_3$), the current concentration of compound B_3 [B_3] as a function of time t is described by a similar expression:

$$[B_3](t) = b_0[1 - \frac{k_2}{k_2 - k_1}\exp(-k_1t) + \frac{k_1}{k_2 - k_1}\exp(-k_2t)], \quad (4)$$

where b_0 is the initial concentration of B_1 ($t = 0$) and k_1 and k_2 are the rate constants of the corresponding stages.

The similarity of Eqs. (2) and (4) is evident, which will be used in the subsequent analysis of experimental data. In the case of complex roots ($z_{1,2} = m \pm n\sqrt{-1}$), the difference equation (2) has a general solution (5).

$$A(V_g) = A(0) + \exp(-kV_g)[C_1\cos(\varphi V_g) + C_2\sin(\varphi V_g)]. \quad (5)$$

The constants k_1 and k_2 in Eq. (2) are estimated as

$$k_i = -\frac{\ln z_i}{\Delta V_g} \quad (i = 1, 2).$$

The constants in Eq. (5) can be expressed as

$$k = -\frac{\ln(\sqrt{m^2 + n^2})}{\Delta V_g}, \quad \varphi = \frac{\arctan(n/m)}{\Delta V_g}.$$

The linear coefficients $A(0)$, C_1, and C_2 in Eqs. (1) and (2) can be easily estimated by the least-squares method {$A(0)$ can be also estimated as $A(0) = r/(1 + p + q)$ [10]}.

It should be noted that, just in processing equidistant data with AR-2 model, it becomes possible to obtain unique solutions for all target values (of course, if the model is adequate, i.e., has high coefficients of variation or determination), despite that Eqs. (2) and (5) are nonlinear in some of them.

Below are given equations similar to Eqs. (2) or (5), obtained by processing the $\bar{A}(V_g)$ data taken from the table according to the proposed procedure. In the parentheses are presented the mean (σ) and standard deviations (S) of the absolute values of the differences between the experimental [$\bar{A}(V_g)$] and estimated values [$\hat{A}(V_g)$].

For gas–vapor mixture I (see table) the expressions are as follows (coefficients of determination >0.95): for benzene (σ 0.2, S 0.2)

$$\hat{A}(V_g) = 31.5 + \exp(-0.0014V_g)[-13.1\cos(0.0090V_g) + 14.0\sin(0.0090V_g)],$$

for toluene (σ 1.1, S 1.5)

$$\hat{A}(V_g) = 171.3 + \exp(-0.0086V_g)[105.7\cos(0.011V_g) - 341.4\sin(0.011V_g)],$$

for *p*-xylene (σ 9, S 6)

$$\hat{A}(V_g) = 1458 - 1477\exp(-0.0006V_g) + 20\exp(-0.005V_g),$$

and for ethylbenzene (σ 6, S 6)

$$\hat{A}(V_g) = 727 - 751\exp(-0.00088V_g) + 28\exp(-0.0058V_g).$$

For mixture II (see table) the expressions are as follows: for benzene (σ 0.6, S 0.8)

$$\hat{A}(V_g) = 51.9 + \exp(-0.015V_g)[-247.1\cos(0.0088V_g) + 836.6\sin(0.0088V_g)],$$

for toluene (σ 1.3, S 1.4)

$$\hat{A}(V_g) = 391.4 + \exp(-0.0092V_g)[-1657\cos(0.0086V_g) + 1405\sin(0.0086V_g)],$$

and for *p*-xylene (σ 16, S 14)

$$\hat{A}(V_g) = 1892 - 4331\exp(-0.0084V_g) + 3858\exp(-0.020V_g).$$

The results demonstrate a satisfactory agreement of the theoretical $\hat{A}(V_g)$ and experimental peak areas $\bar{A}(V_g)$ (see table). Note also that for *p*-xylene and eth-

Analysis of gas–vapor mixtures of hydrocarbons* [mixture composition (mg m^{-3}): (I) benzene 5.8, toluene 4.6, ethylbenzene 4.5, and *p*-xylene 4.1 and (II) benzene 49, toluene 42, and *p*-xylene 51]

Component	V_g, ml	Peak area $A(V_g)$, μV s					
		run no. 1	run no. 2	run no. 3	run no. 4	mean $\overline{A}(V_g)$	theoretical $\hat{A}(V_g)$
				Mixture I			
Benzene	100	33.7	35.5	32.7	33.9	34.0	34.0
Toluene	100	62.8	61.5	59.4	61.9	61.4	61.2
Ethylbenzene	100	57.9	57.7	52.9	55.8	56.0	55.0
p-Xylene	100	76.0	74.7	71.7	79.3	75.4	75.0
Benzene	200	43.0	44.0	45.1	43.3	43.9	44.0
Toluene	200	111.6	114.5	108.8	113.7	112.1	112.1
Ethylbenzene	200	98.6	109.5	100.5	104.5	103.0	106.0
p-Xylene	200	143.9	142.8	138.7	143.4	142	148.0
Benzene	300	44.3	43.2	43.8	42.8	43.5	43.0
Toluene	300	176.7	164.3	165.6	170.4	169.2	169.2
Ethylbenzene	300	182.6	158.5	161.7	171.4	169.0	155.0
p-Xylene	300	243.7	214.5	240.8	241.9	235.0	218.0
Benzene	400	31.6	31.5	35.4	37.6	34.0	34.5
Toluene	400	184.8	172.3	183.3	179.5	180.0	181.1
Ethylbenzene	400	208.0	211.4	201.1	199.5	205.0	202.0
p-Xylene	400	287.0	281.0	259.1	269.3	274.0	286.0
Benzene	500	25.4	24.4	28.7	26.8	26.3	26.0
Toluene	500	188.9	160.3	178.5	188.9	179.1	175.3
Ethylbenzene	500	267.3	235.3	236.0	255.2	248.0	245.0
p-Xylene	500	381.8	326.3	306.5	346.2	340.0	350.0
Benzene	600	21.3	24.1	24.0	24.3	23.4	23.3
Toluene	600	164.3	170.9	169.2	172.8	169.3	171.1
Ethylbenzene	600	304.3	298.1	304.8	286.9	298.0	285.0
p-Xylene	600	442.4	446.5	402.1	391.4	421.0	411.0
				Mixture II			
Benzene	100	194.0	177.3	163.5	148.9	157.9	155.9
Toluene	100	399.7	409.0	389.6	381.8	387.0	386.6
p-Xylene	100	552.2	580.9	545.4	563.7	557.0	553.0
Benzene	200	188.2	92.7	92.8	90.0	93.3	92.1
Toluene	200	389.5	641.6	632.4	665.6	651.5	651.5
p-Xylene	200	530.3	1099.3	1133.3	1139.4	1128.0	1153.0
Benzene	300	61.8	58.8	59.4	53.7	58.4	58.2
Toluene	300	511.5	517.1	553.0	527.9	527.4	527.0
p-Xylene	300	1567.8	1588.9	1600.3	1593.6	1588.0	1550.0
Benzene	400	56.7	53.5	50.4	46.7	51.8	51.7
Toluene	400	416.9	414.4	417.1	425.1	418.4	420.4
p-Xylene	400	1787.2	1742.2	1767.0	1734.1	1758.0	1741.0
Benzene	500	55.4	53.4	49.6	46.6	51.3	51.5
Toluene	500	388.2	393.4	386.8	386.8	388.8	384.9
p-Xylene	500	1812.4	1859.1	1822.1	1825.8	1830	1826.0
Benzene	600	53.5	54.9	51.4	47.7	51.9	51.8
Toluene	600	377.4	384.4	386.9	380.8	382.4	383.4
p-Xylene	600	1819.5	1891.1	1888.3	1877.6	1869.0	1864.0

* Sorbent bed about 1 cm; gas–vapor mixture feed rate 20 ml min^{-1}.

ylbenzene the dependences of the peak area on V_g are described by expressions like Eq. (2) and for benzene and toluene, by expressions like Eq. (4).

Let us consider the features of sorption of *p*-xylene and ethylbenzene. A process described by the AR-2 model may be stationary or nonstationary [11]. Mathematically, the stationary condition is that roots of the characteristic equation should be within a unit disk, i.e., $|z_i| < 1$. Starting from certain V_g^*, $\hat{A}(V_g \geq V_g^*)$ remains practically constant and equal to the absolute term of the regression equation (in other words, steady-state mode is established). Just such a mode is realized for both *p*-xylene and ethylbenzene. Drawing an analogy with a consecutive two-step process, one may accept that these steps are sorption of a hydrocarbon on, and its desorption from the sorbent, and the instrumental signal $A(V_g)$ reflects here the concentration of the hydrocarbon that participated in sorption–desorption in the carrier gas that passed through the sorbent bed. Assuming that the sorption stage is reflected in the equations as the exponential term with the minus sign, one can recognize that the exponential indices (sorption rate constants) in the equations for *p*-xylene and ethylbenzene are different, whereas those in the terms with the plus sign appear to be close for these components (they can be regarded as the characteristics of desorption).

By virtue of complex roots of the characteristic equations, the regression equations obtained for benzene and toluene describe an oscillating (occasionally called pseudoperiodic) process [11].

To conclude, the model with two consecutive steps for sorption–desorption processes allows thorough characterization of the sorption behavior of each analyte of a complex gas–vapor mixture, making it possible to determine what volume of the gas–vapor mixture should be passed through the sorbent bed for the process to become stationary.

REFERENCES

1. Beyermann, K., *Organic Trace Analysis*, Chalmers, R.A., Ed., New York: Wiley, 1984.
2. Shojania, S., Oleschuk, R.D., McComb, M.E., *et al.*, *Talanta*, 1999, no. 50, pp. 193–205.
3. Katsanos, N.A., *Flow Perturbation Gas Chromatography*, New York: Dekker, 1988.
4. Marinichev, A.N. and Stolyarov, B.V., *Zh. Obshch. Khim.*, 1994, vol. 64, no. 1, pp. 101–106.
5. Vittenberg, A.G. and Kostkina, M.I., *Vestn. Leningr. Gos. Univ.*, 1980, no. 4, pp. 110–117.
6. Ioffe, B.V., Kostkina, M.I., and Vittenberg, A.G., *Anal. Chem.*, 1984, vol. 56, pp. 2500–2503.
7. Marple, S.L., Jr., *Digital Spectral Analysis with Applications*, New Jersey: Prentice-Hall, 1987.
8. Panchenkov, T.M. and Lebedev, V.P., *Khimicheskaya kinetika i kataliz* (Chemical Kinetics and Catalysis), Moscow: Khimiya, 1974.
9. Rodigin, N.M. and Rodigina, E.N., *Posledovatel'nye khimicheskie reaktsii: Matematicheskii analiz i raschet* (Consecutive Chemical Reactions: Mathematical Analysis and Calculations), Moscow: Akad. Nauk SSSR, 1960.
10. Marinichev, A.N. and Bureiko, A.S., *Zh. Prikl. Khim.*, 1991, vol. 64, no. 3, pp. 569–573.
11. Karmalita, V.A., *Tsifrovaya obrabotka sluchainykh kolebanii* (Numerical Treatment of Stochastic Fluctuations), Moscow: Mashinostroenie, 1986.

Russian Journal of Applied Chemistry, Vol. 74, No. 12, 2001, pp. 2009–2012. Translated from Zhurnal Prikladnoi Khimii, Vol. 74, No. 12, 2001, pp. 1949–1952.

PHYSICOCHEMICAL STUDIES OF SYSTEMS AND PROCESSES

Kinetics of Water Desorption from Wheat Cereals

B. L. Korsunskii, N. V. Chukanov, V. P. Tarasov, and O. V. Anan'ina

Institute for Problems of Chemical Physics, Russian Academy of Sciences, Chernogolovka, Moscow oblast, Russia

Received February 15, 2001

Abstract—Water desorption from wheat cereals was studied by thermogravimetry, IR spectroscopy, and NMR relaxation in the temperature range 94–220°C. The process kinetics were described in terms of polychromic reactions. The kinetic parameters of the process were determined.

Sorption of water vapor by wheat cereals and other plant products and reverse desorption are of scientific and practical importance. The most commonly used method for determining the moisture content of cereals is based on measurements of water desorption and involves measurement of weight loss under thermostatic control (in the case of wheat cereals) at 130°C for 40 min [GOST (State Standard) 13586.5–93]. Moisture is desorbed in the course of drying of cereals. Water contained in cereals is actively involved in various physiological processes, and the features of sorption and desorption are closely related to these processes. From the purely chemical standpoint, sorption and desorption of water in cereals is a special case of hydration and dehydration of solids. These reactions are extremely widespread (in particular, for crystal hydrates [1]); in the case of cereals, the specific feature of hydration and dehydration consists in that these processes occur in essentially heterogeneous solids.

Here we report the kinetic features of water desorption from wheat[1] that was not subjected to premilling.

EXPERIMENTAL

The main characteristics of wheat were as follows: type IV, subtype 4, class 5, nature 760, passing through a sieve 1.7 × 20, the gluten amount corresponds to the second group; content of impurities (%): weedy, 0.8 and cereal, 1.2.

The drying kinetic were monitored by the variation of the wheat weight, using ATV-13R automatic thermal balance designed and manufactured at the Institute for Problems of Chemical Physics. The experiments were carried out in the temperature range 94–220°C. At a temperature of 110°C and above, the typical weighed portion of wheat was 40–50 mg, i.e., a single wheat cereal was studied. At lower temperatures, when the reaction proceeds extremely slowly, larger weighed portions, up to 1 g, were used.

When the samples were heated to high temperature, irreversible chemical transformations occurred in wheat in addition to water desorption. The composition of gaseous products formed in these transformations was determined by IR spectroscopy. For this purpose, the gaseous products were condensed in a glass trap cooled to –196°C. After defrosting, the products were extracted with ether, the ether solution was applied on a KBr window, and ether was allowed to evaporate. Then, the window was placed in a Specord M82 spectrometer and a spectrum was recorded.

The NMR spectra were recorded on an RI-23-03 pulse spectrometer operating at 60 MHz for protons. The spin–spin relaxation time T_2 was measured. The pulse length was 1.5–2 ms. The time interval of signal strobbing was 1 μs. The measurements were carried out in the temperature range from –150 to 150°C.

The typical kinetic curves of water desorption from wheat are shown in Fig. 1. It is seen that the process includes two clearly pronounced macroscopic stages: the first stage is very fast and then the process substantially self-decelerates. For example, at 110°C (curve *1*) the desorption rate at a 67% degree of desorption is a factor of 32 lower than the initial rate.

The kinetic curve of desorption is complicated and cannot be described by a simple kinetic equation (e.g.,

[1] Wheat from Tula oblast (harvest 1998, Mironovskii-88 sort) was used.

1070-4272/01/7412-2009 $25.00 © 2001 MAIK "Nauka/Interperiodica"

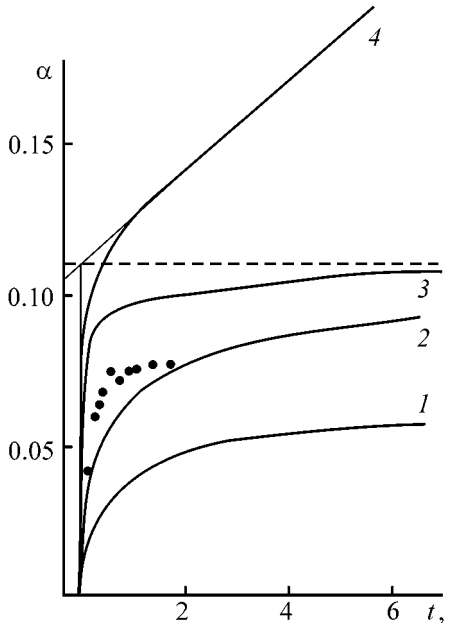

Fig. 1. Gravimetric kinetic curves of dehydration of wheat cereals: [$\alpha = (m_0 - m)/m_0$] degree of conversion, (m_0) initial weighed portion, (m) sample weight, and (t) time. Temperature (°C): (*1*) 110, (*2*) 130, (*3*) 160, and (*4*) 220. (*Dashed line*) total moisture content in cereals; (*points*) data on desorption kinetics obtained by the NMR relaxation.

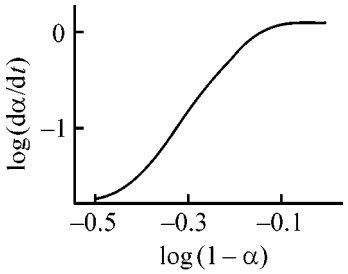

Fig. 2. Rate of water desorption from wheat cereals vs. the current water content in cereals. Temperature 130°C.

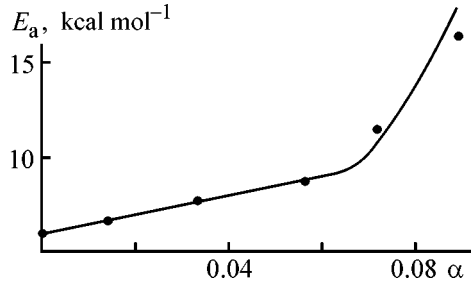

Fig. 3. Apparent activation energy E_a of water desorption from wheat cereals with initial moisture content of 11.25% vs. the amount of the released moisture.

equation of an *n*th-order reaction). Actually, when the reaction is described by an *n*th-order kinetic equation

$$\log(1 - \alpha) = f[\log(d\alpha/dt)], \quad (1)$$

where $\alpha = (m_0 - m)/m_0$ is the degree of conversion, m_0 is the initial weighed portion of the substance, and m is the current weight of the sample, a straight line with a slope equal to n should be obtained. It is seen from Fig. 2 that the actual plot is essentially nonlinear. That is, the reaction order n determined as the slope in the coordinates of Eq. (1) is not constant but varies in the course of the reaction. In the initial stage, n is close to 0, and then it passes through a maximum ($n_{max} \approx 7$) and tends to 1 at high degrees of dehydration.

This complicated kinetic behavior of the system does not allow determination of the activation energies with the standard procedures. Therefore, the activation energy of the process was found as follows. At a given temperature T_1 and degree of desorption α (corresponding to the reaction rate w_1) the system was heated to a higher temperature T_2, and the process rate w_2 was measured. Since the system was heated up rapidly (in approximately 3 min), we assumed that w_1 and w_2 values correspond to the same value of α. Then, the activation energy was determined from the expression

$$(E_a/R)[(1/T_1) - (1/T_2)] = \ln(w_2/w_1). \quad (2)$$

This method was detailed and substantiated in [2].

It was found that the apparent activation energy of desorption is not constant but varies during the process. For example, for wheat cereals with moisture content of 8.45% (determined from the weight loss at 130°C in 40 min), the activation energy increases from 5.9 in the initial stage of the process to 9.4 kcal mol^{-1} at a degree of dehydration of 80.5% (Fig. 3). At higher α, attempts to measure the activation energy failed, since under these conditions the reaction is extremely slow. In this case, an increase in temperature (which can noticeably accelerate dehydration at these values of α) is impossible, since this requires a heating that results in irreversible chemical transformations. In the special series of experiments, we studied the dependence of the activation energy at given α on temperature at which this α value was reached. For this purpose, the reaction was brought to $\alpha = 0.04$ at 91, 110, and 130°C and then the temperature was abruptly raised by 20°C. It was found that the activation energy was practically constant within the limits of experimental error; at the above temperatures it was 8.2, 7.9, and 7.1 kcal mol^{-1}.

As seen from Fig. 1, water is completely removed from wheat cereals within several hours only at approximately 160°C. At a higher temperature the reaction also proceeds in two stages (Fig. 1, curve *4*). However, in this case, the second slower stage of the reaction involves not dehydration but irreversible

chemical transformations. Actually, in this run the cereals were carbonized and various organic compounds were present in gaseous reaction products. In the IR spectrum of these products, absorption bands at 3620 (weak hydrogen bonds), 3300–3400 (water and alcohols), 3220 (OH or NH), 2930 (methyl groups), 2860 (methylene and methyl groups), 2500 (carboxy groups), and 1710 cm^{-1} (C=O stretching modes) were found. It should be noted that, according to IR data, dehydration of cereals at 160°C for 1 h is accompanied by transition of only water to the gas phase. The stage corresponding to chemical transformations in cereals has higher activation energy, which is close to 25 kcal mol^{-1} for the temperature range 180–220°C.

The results of NMR relaxation studies of wheat cereals are presented in Fig. 4. Curve *1* was obtained for the initial cereals, and curve *2*, for cereals subjected to heating at 130°C for 100 min. In both curves, there are two portions corresponding to fast and slow proton relaxation (*A* is fraction of oriented spins). The fast decay corresponds to the low-mobile protons of starch, and slow decay, to mobile protons of water molecules. Computer simulation showed that the slow decay in curve *2* is exponential and the decay in curve *1* is two-exponential. A computer extrapolation of the two-exponential portion to the initial instant of time showed that the amount of water protons in the initial cereals is about 30% of the total amount of protons in cereals. At the same time, for curve *2* (i.e., after heat treatment) this fraction decreases to 8–10%. The kinetic curve describing the decrease in the amount of mobile protons β (%) during heating of wheat cereals at 130°C is presented in Fig. 5.

The kinetic curve of water desorption from wheat cereals at 130°C, obtained from NMR data, is shown in Fig. 1 in the form of experimental points. Comparison of this curve with curve *2* (Fig. 1) shows that the results of gravimetric and NMR measurements are in reasonable agreement.

In discussing the results obtained, it is appropriate to consider only the processes related to water desorption and not to irreversible chemical transformations accompanied by formation of various organic products. The above data suggest that in wheat cereals there are at least two types of water molecules, relatively weakly and relatively strongly bonded. As seen from Fig. 3, the boundary between these two types corresponds to $\alpha = 6.6\%$ and activation energy of 9.4 kcal mol^{-1}. It is interesting that the latter value is close to the heat of water vaporization, 9.7 kcal mol^{-1} [3]. In the initial stages of dehydration, the apparent activation energy is noticeably lower than the heat of

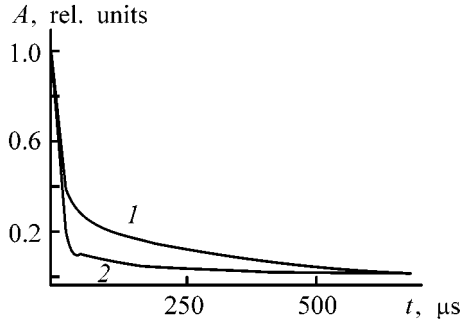

Fig. 4. Free induction decay *A* of (*1*) the initial wheat cereals and (*2*) cereals preliminarily heated at 130°C for 100 min. (*t*) Time.

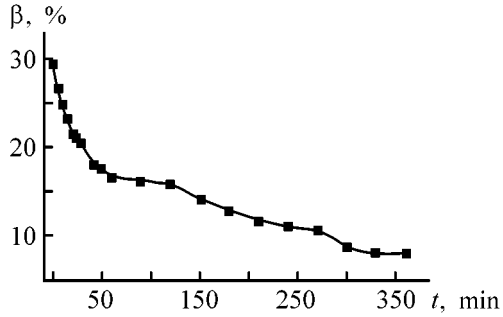

Fig. 5. Fraction of mobile protons in wheat cereals β vs. time *t* at 130°C.

water vaporization. Hence, water desorption from wheat is controlled in these stages not by vaporization (i.e., rupture of several hydrogen bonds is not limiting stage), but, evidently, by diffusion. By contrast, when $\alpha > 6.6\%$, the activation energy is higher than the heat of water vaporization, i.e., in this case, dehydration is controlled not only by water diffusion but also involves overcoming of the difficulties produced by the material of wheat cereals.

Thus, it is reasonable to speak about distribution of water molecules with respect to their reactivity during dehydration of wheat. Similar phenomena, namely, different reactivities of molecules of the same substance in different sites of the reaction mixture, are common in chemistry of solids and are termed "polychromic processes" [4]. The kinetic curves presented in Fig. 1 are typical of such reactions [5].

As already mentioned, the right branch of curve *4* (Fig. 1) corresponds to chemical degradation of cereals, rather than to water desorption. Therefore, extrapolation of this curve to zero time must correspond to weight loss due to dehydration only. In Fig. 1, the corresponding weight loss is shown by dashed line; it characterizes the true moisture content of cereals, equal to 11.25% for this specific case. It is of interest that the same line is the asymptote for kinetic curve *3* obtained at 160°C. In other words,

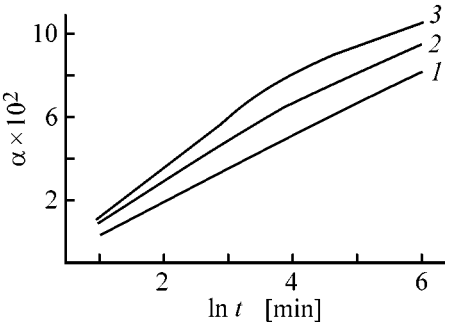

Fig. 6. Kinetic curves of water desorption from wheat cereals in the coordinates of the Elovich equation. (*t*) Time. Temperature (°C): (*1*) 110, (*2*) 130, and (*3*) 150.

this curve describes only dehydration (without chemical destruction); in this case, virtually complete removal of water is attained within several hours. Thus, the kinetic approach to water desorption from wheat cereals allows determination of the total content of water in cereals with high accuracy without grinding required by GOST 13586.5–93.

It was already noted that there is a qualitative agreement between the gravimetric and NMR relaxation data. However, there is no close similarity. As seen from Fig. 1, the process described by the NMR relaxation is somewhat faster and is finished earlier than it follows from gravimetric measurements. In addition, this process is very complex: at high degrees of desorption the process becomes multistage (Fig. 5). This disagreement with data of gravimetric measurements suggests that during heating water molecules not only leave cereals but are also subjected to transformations involving, in particular, the loss of their mobility.

Considering two types of water molecules in wheat cereals (weakly and strongly bonded), we somewhat simplified the situation. The point is that water molecules differ in activation energy even within each type (Fig. 3). In the simplest case, polychromic kinetics can be described by the Elovich equation [6], in which it is assumed that the activation energy depends linearly on the degree of conversion. In the case in hand, it would be expected that two straight portions corresponding to one or another type of water molecules can be obtained in the coordinates of this equation. The data obtained in the temperature range 110–150°C are presented in Fig. 6. As seen, the linear dependence is actually obeyed up to $\alpha \approx 7\%$, i.e., practically to the degree of conversion corresponding, according to Fig. 3, to the boundary between different types of water molecules. It should be noted that this degree of conversion, up to which the Elovich equation is obeyed, is temperature-independent within experimental error. Then, there is a bend in the curve, and, after short transition portion, the Elovich equation is obeyed again, but with another slope corresponding to the other type of water molecules (strongly bound water).

CONCLUSIONS

(1) Water desorption from wheat cereals not subjected to grinding was studied by gravimetry, IR spectroscopy, and NMR relaxation in the temperature range 94–220°C. At temperatures below 160°C and heating time of about several hours, water desorption from wheat cereals is the only process; at higher temperatures, along with water desorption, irreversible chemical transformations occur, accompanied by release of various organic substances.

(2) The kinetic data suggest that water is present in wheat cereals in two forms: weakly and strongly bound. The kinetics of desorption of both weakly and strongly bound water were described in terms of the model of polychromic reactions, according to which the activation energy is a function of the degree of desorption. The kinetic parameters of the process were determined.

(3) Kinetic data on water desorption can be effectively used for determination of the moisture content of wheat cereals.

ACKNOWLEDGMENTS

The study was financially supported by the International Science and Technology Center (project no. 355).

REFERENCES

1. Lyakhov, N.Z. and Boldyrev, V.V., *Usp. Khim.*, 1972, vol. 41, no. 11, pp. 1960–1977.
2. Satoh, M. and Hirota, M., *Bull. Chem. Soc. Jpn*, 1996, vol. 69, no. 7, pp. 2031–2038.
3. *Spravochnik khimika* (Chemisit's Handbook), Nikol'skii, B.P., Ed., Leningrad: Gos. Nauchno-Tekh. Izd. Khim. Lit., 1963.
4. Emanuel', N.M. and Buchachenko, A.L., *Khimicheskaya fizika stareniya i stabilizatsii polimerov* (Chemical Physics of Aging and Stabilization of Polymers), Moscow: Nauka, 1982.
5. Karpukhin, O.N., *Usp. Khim.*, 1978, vol. 47, no. 6, pp. 1119–1143.
6. Elovich, S.Yu. and Kharakhorin, F.F., in *Problemy kinetiki i kataliza. III. Adsorbtsiya gazov i parov tverdymi telami* (Problems of Kinetics and Catalysis. III. Adsorption of Gases and Vapors with Solids), Leningrad: Khimteoret, 1937, pp. 222–250.

Russian Journal of Applied Chemistry, Vol. 74, No. 12, 2001, pp. 2013–2016. Translated from Zhurnal Prikladnoi Khimii, Vol. 74, No. 12, 2001, pp. 1953–1956.

SORPTION AND ION-EXCHANGE PROCESSES

Sorption Removal of Heavy Metal from Solutions of Their Complexes with a Sorbent Prepared from Shells of *Musca Domestica* Larvas

O. Gyliene and A. Pigaga

Institute of Chemistry, Vilnius, Lithuania

Received November 23, 2000; in final form, March 2001

Abstract—Sorption of Cu(II) and Ni(II) complexes with ammonia, aminoacetic acid, and EDTA and sorption of chromium(VI) by shells of *Musca Domestica* larvas was studied.

Metal complexes are widely used in various branches of industry (electroplating, textile industry, production of dyes and drugs, radioelectronics, etc.). The presence of ligands forming strong complexes with these metals prevents precipitation of the metals from solutions. In this case, to remove metal ions from solutions, these ligands are decomposed. In solutions containing carboxylate anions, coprecipitation of metal hydroxides and carboxylates provides almost complete removal of the metal from solutions [1]. To precipitate bivalent metal ions in the form of oxalates from solutions of their amino complexes, the solutions are acidified to pH 0–1. The degree of removal of metals from these solutions is 95–98% [2]. Removal of metals from solutions by their reduction or electrodeposition is also incomplete. In this case, additional purification is required after removal of the major portion.

Natural sorbents or industrial wastes, such as peat and wood sawdust, are widely used to remove heavy metals from dilute solutions [3, 4]. Among these sorbents is the material of Shells of *Musca Domestica* larvas (SMDL) which is produced by biological treatment of protein raw materials.[1] These shells contain 40% of natural polysaccharide [(1→4)-2-acetamido-2-deoxy-β-*D*-glucan] exhibiting good sorption properties with respect to heavy metal ions [5–7]. It should be noted that sorption of metal complexes on both synthetic and natural sorbents has been poorly studied. Previously, we have studied [8] the sorption properties of chitin prepared by conventional treatment of SMDL with HCl and NaOH solutions [8]. It was found that this chitin sorbs only free heavy metal cations, whereas degreased SMDL do not sorb free ions of most of heavy metals at all [9]. Relatively good sorption of metal complexes form solutions on SMDL was surprising.

In this work, sorption of metal complexes from solutions on SMDL was studied in detail.

EXPERIMENTAL

To make SMDL wettable, they were degreased by treatment with a 40 g l^{-1} NaOH solution at room temperature for 24 h. During this treatment, proteins partially dissolved, as indicated by a decrease in the nitrogen content from 7.8 to 6.2 wt %. The study of the sorption kinetics showed that, with stirring, the equilibrium between the solid and liquid phases was attained within 2–3 h, although an insignificant decrease in metal concentration was observed throughout the experiment (up to 20 days). A metal complex solution containing washed and dried shells was stirred at room temperature for 4 h. When sorption isotherms were studied, the shells were additionally kept in the solution for 5 days with intermittent stirring to attain the true equilibrium. The pH was adjusted with NaOH or H_2SO_4 solutions. The sorption of metal ions and glycine was estimated from the difference of their concentrations before and after the experiment, which, in their turn, were determined by complexometric titration and, at trace level, by colorimetry.

Since the metal sorption is almost independent of the degree of SMDL grinding, we used partially ground shells in the form of 0.5–2.0 mm^2 flakes, which are

[1] About 20 kg of SMDL is formed daily during processing of food wastes with *Musca Domestica* at Chitinas Joint Stock Company (Vilnius).

1070-4272/01/7412-2013 $25.00 © 2001 MAIK "Nauka/Interperiodica"

Table 1. Metal sorption on SMDL*

Metal ion	Ligand, mM	pH	Metal ion concentration, mg l^{-1}		SC,** mmol g^{-1}
			initial	residual	
Cu(II)	–	4.0	635	635	0
	NH_3:				
	30	4.0	635	457	0.7
	1000	4.0	635	463	0.7
	30	4.0	635	0.3	
	Glycine:				
	60	5.5	128	76.5	0.2
	60	5.0	128	0.2	0.6
	6	5.5	12.7	< 0.1	
	Tartrate:				
	10	6.7	130	0.4	0.6
	5	9.0	7.5	< 0.1	
Ni(II)	Citrate:				
	20	4.5	840	670	0.7
	2	9.0	8.4	< 0.05	
	Glycine:				
	1	9.0	6.6	< 0.05	
	30	5.2	590	510	0.3
	3	5.2	59	35	0.1
Cr(VI)	–	3.3	162	162	0
	–	3.3	50	< 0.1 Cr(VI) 7.5 Cr(III)	
	–	7.8	50	36 Cr(VI) < 0.1 Cr(III)	

* Shell content 4 g l^{-1}.

** SC denotes sorption capacity.

Table 2. Sorption capacity of SMDL at pH 3.2 in solutions containing Ni(II) and glycine*

Initial concentration		Residual Ni(II) concentration, mg l^{-1}	SC, mmol g^{-1}	Initial concentration		Residual Ni(II) concentration, mg l^{-1}	SC, mmol g^{-1}
Ni(II), mg l^{-1}	glycine, mM			Ni(II), mg l^{-1}	glycine, mM		
125	4	0.7	0.4	2500	40	1650	2.8
250	4	68	0.6	610	400	150	1.5
250	40	3.4	0.8	2500	400	1920	2.0
610	40	35	1.9				

* Shell content 10 g l^{-1}.

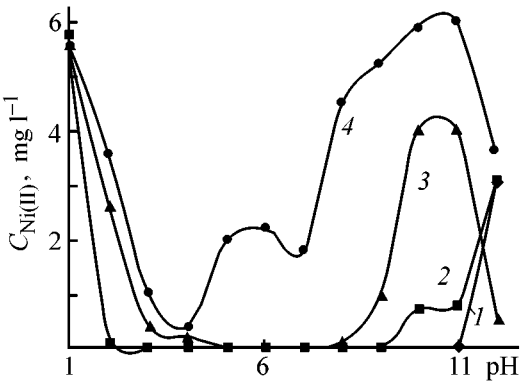

Fig. 1. Residual concentration of nickel ions after sorption $C_{Ni(II)}$ vs. solution pH. Amount of SMDL 10 g l^{-1}, initial Ni(II) concentration 0.1 mM Glycine concentration (mM): (*1*) 0.4, (*2*) 4.0, (*3*) 40, and (*4*) 400.

readily stirrable, filterable and washable. The shells were repeatedly used after regenration with 3–6 M acetic acid. After this treatment, their sorption capacity even slightly increased.

We studied sorption of metal complexes widely used in electroplating and production of printed-circuit boats. The results presented in Table 1 show that SMDL, to a greater or lesser extent, sorb metal complexes from solutions. The metal sorption depends on both pH and the ligand concentration in the solution. In acidic solutions, the shells probably reduce Cr(VI) to Cr(III), which is not the case at higher pH.

A study of the sorption of Ni(II) glycine (aminoacetate) complexes widely used in nickel plating showed a rather complex dependence of the residual

N(II) concentration on the solution pH. The sorption is maximal at pH 3–6 and ~12 (Fig. 1). This may be due to the pH dependence of the composition of Ni glycinate complexes [10]. In acidic solutions, $[Ni(gly)]^+$ is formed. At higher pH, $[Ni(gly)_2]$ exists in solution. At pH > 10, $[Ni(gly)_3]^-$ is detected. The ligand concentration also affects the metal sorption (Fig. 1, Table 2). The sorption of nickel ions decreases with increasing ligand concentration in the solution. Strong effect of glycine on the sorption properties of SMDL suggests cosorption of nickel ions with the ligand. Determination of the glycine content in the solutions showed that the sorption of glycine on SMDL is even higher than that of nickel ions (Fig. 2).

Sorption on SMDL of Cu(II)–EDTA complexes used for electroless copper plating of perforations in printed-circuit boards differs somewhat (Fig. 3, 4). When the EDTA concentration in the solution is lower than the Cu(II) concentration, SMDL sorb copper ions only from alkaline solutions (pH ≈ 12). In this case, $[Cu(EDTA)(OH)]^{3-}$, rather than $[Cu(EDTA)]^{2-}$, is probably sorbed [11].

As the EDTA-to-Cu(II) ratio increases, the copper sorption grows. When this ratio is in the range 100–1000, copper is readily sorbed at pH 3–12. In more acidic solutions (pH 0–2), EDTA exists in the form of difficulty soluble acid H_4EDTA, which decreases the copper sorption.

Since EDTA enhances copper sorption, SMDL can be used for additional removal of copper ions from electroless copper plating solutions. These solutions contain, after preliminary copper removal by precipitation with oxalate or reduction on active CuO, 10–250 and 0.1–0.5 mM ligand and copper, respectively.

Our previous experimental results [9] suggest that metal complexes are not sorbed by chitin, which is the main component of the shells. The sorption involves formation of complexes with other compounds present in the shell, such as keratins, melanins, inorganic compounds, etc. [6]. This agrees with the fact that sorption of heavy metals on Khizit (waste of processing of crab armors) is about 8 times higher [4] than on chitin.

CONCLUSIONS

(1) Shells of *Musca Domestica* larvas sorb ammonia, citrate, tartrate, glycinate, and EDTA complexes of nickel and copper, which are difficultly removed from solutions.

(2) The sorption capacity and degree of metal removal depend in the complex manner on the ligand concentration in the solution and on pH. An increase in the ligand fraction suppresses nickel sorption from glycine solutions and enhances copper sorption from EDTA solutions.

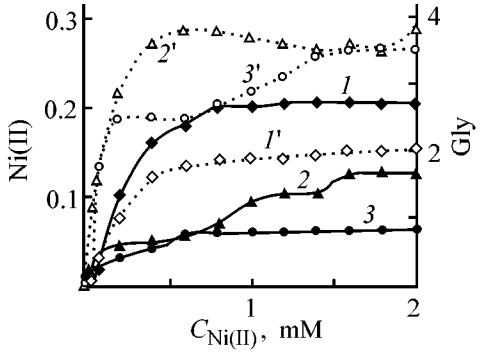

Fig. 2. Sorption isotherms of (*1*–*3*) nickel and (*1*'–*3*') glycine at nickel(II)-to-glycine molar ratio of (*1*, *1*') 4 : 1, (*2*, *2*') 40 : 1, and (*3*, *3*') 200 : 1. Amount of SMDL 10 g l^{-1}, pH 3.6.

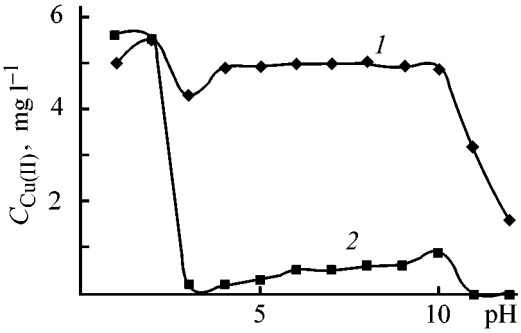

Fig. 3. Residual copper concentration $C_{Cu(II)}$ after sorption vs. the solution pH. Amount of SMDL 10 g l^{-1}, initial Cu(II) concentration 0.1 mM. EDTA concentration (mM): (*1*) 0.2 and (*2*) 200.

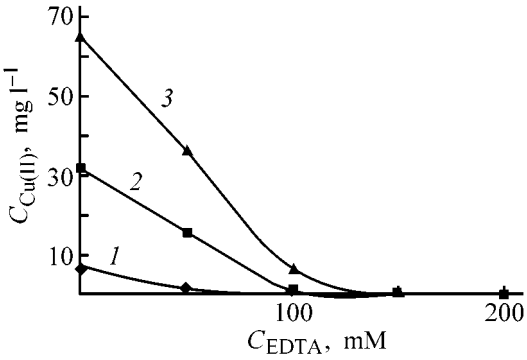

Fig. 4. Residual Cu(II) concentration $C_{Cu(II)}$ (mg l^{-1}) after sorption vs. EDTA concentration C_{EDTA} in the solution. Amount of SMDL 10 g l^{-1}, pH 12.4. Initial Cu(II) concentration (mM): (*1*) 0.1, (*2*) 0.5, and (*3*) 1.

ACKNOWLEGMENTS

We are grateful to S. Taratsyavichyus (principal manager of Chitinas Joint-Stock Company, Vilnius) for assistance in this study.

REFERENCES

1. Gyliene, O., Šalkauskas, M., and Juskenas, R., *J. Chem. Technol. Biotechnol.*, 1997, vol. 70, no. 1, pp. 11–115.
2. Gyliene, O. and Šalkauskas, M., *Plat. Surface Finish.*, 1995, no. 10, pp. 61–63.
3. Bailey, S.E., Alin, T.J., Bricka, R.M., and Adrian, D.D., *Water Res.*, 1999, vol. 33, no. 11, pp. 2469–2479.
4. Selivestrov, A.F., Emel'yanova, A.Yu., and Ershov, B.G., *Zh. Prikl. Khim.*, 1993, vol. 66, no. 10, pp. 2331–2336.
5. Muzzarelli, R.A.A. and Tubertini, O., *Talanta*, 1969, vol. 16, no. 12, pp. 1571–1577.
6. Feofilova, E.P., Nemtsev, D.V., Tereshina, V.N., and Kozlov, V.P., *Prikl. Biokhim. Mikrobiol.*, 1996, vol. 32, no. 5, pp. 483–492.
7. *Novye perspektivyv issledovanii khitina i khitozana: Materialy V konferentsii* (New Outlook for the Study of Chitin and Chitosan: Proc. of V Conf.), Moscow: VNIRO, 1999.
8. Onsoyen, E. and Skaugrud, O., *J. Chem. Technol. Biotechnol.*, 1990, vol. 49, pp. 395–404.
9. Gyliene, O. and Pigaga, A., *Global Symp. on Recycling, Waste Treatment and Clean Technology*, Gabalah, I., Hager, J., and Solozabal, R., Eds., Sen Sebatian: Inasmet, 1999, pp. 2243–2247.
10. Lunyatskas, A. and Lyankaitene, Yu., *Tr. Akad. Nauk Lit. SSR, Ser. B*, 1985, Vol. 1(145), pp. 23–30.
11. Norkus, E., Vaškelis, A., and Žakaite, I., *Talanta*, 1996, vol. 43, pp. 465–470.

Russian Journal of Applied Chemistry, Vol. 74, No. 12, 2001, pp. 2017–2020. Translated from Zhurnal Prikladnoi Khimii, Vol. 74, No. 12, 2001, pp. 1957–1961.

SORPTION AND ION-EXCHANGE PROCESSES

Sorption Modification of Fine Silica with Polyvinylpyrrolidone

N. V. Guzenko, E. M. Pakhlov, N. A. Lipkovskaya, and E. F. Voronin

Institute of Surface Chemistry, National Academy of Sciences of Ukraine, Kiev, Ukraine

Received July 19, 2000; in final form, December 2000

Abstract—The interaction of fine silica with polyvinylpyrrolidone in aqueous medium was studied by IR spectroscopy.

Due to its specific properties, fine amorphous silica is widely used in biotechnology, agriculture, medicine, and pharmaceutics [1, 2]. Silica sorbents with required properties can be prepared by their chemical modification. Modification involves substitution of the initial functional surface groups of silica by other groups or coating of the surface by a monomolecular layer of the corresponding polymer. Modification of the surface of fine silica with polyvinylpyrrolidone (PVP) allows preparation of silica sorbents with new properties [3].

Polyvinylpyrrolidone is used in medicine, pharmacy, and cosmetics. This hydrophilic polymer is soluble in water and other solvents and can participate in complex formation. Such PVP properties as stabilization of emulsions and suspensions, prolongation of the effect of some drugs, and nontoxicity [2] are important in the pharmaceutical industry.

In our study, we used A-300 brand Aerosil with specific surface area of 287 $m^2 g^{-1}$, containing spherical primary particles (9–10 nm in diameter). The surface of these particle contains isolated hydroxy groups ≡Si–OH (silanol groups), hydroxy groups linked by hydrogen bonds in various combinations, and molecular water in various forms, from coordination-bound to physically sorbed. The concentration of silanol groups, which are the main sorption centers, on the surface of the silica studied was 0.65 mmol g^{-1}, and the total water content, 4–5 wt %. Owing to hydrogen bonds, these primary Aerosil particles form secondary particles or aggregates 200–500 nm in diameter [1, 4].

As modifying agent we used a 5% aqueous solution of pharmacopeia grade PVP (molecular weight about 12000). Since PVP is rather hygroscopic, PVP solutions are more convenient for experimental work than powders. Aqueous PVP solutions are stable for a long time after their sterilization for 15–20 min.

In this work, we studied the interaction of fine silica with PVP and the effect of sorption modification of the surface on some sorbent properties.

EXPERIMENTAL

The PVP sorption was performed under static conditions at room temperature. Solutions of PVP (initial concentration 0.1–0.6 wt %) were mixed with a 5% silica suspension so that the solution : sorbent ratio was constant, 10 ml : 100 mg. After 1-h contact the mixture was centrifuged for 30 min at 8000 rpm. The amount of sorbed PVP was determined photocolorimetrically with iodine [5] from the difference in the PVP concentrations in solution before and after interaction with silica.

The curve of PVP sorption on the fine silica surface is described by the Langmuir isotherm (Fig. 1). In the C_e/A–C_e coordinates, where C_e is the equilib-

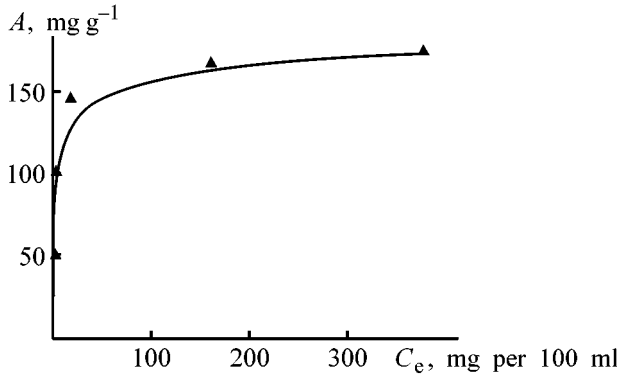

Fig. 1. Isotherm of PVP sorption on the fine silica surface (A) PVP sorption and (C_e) equilibrium PVP concentration.

1070-4272/01/7412-2017 $25.00 © 2001 MAIK "Nauka/Interperiodica"

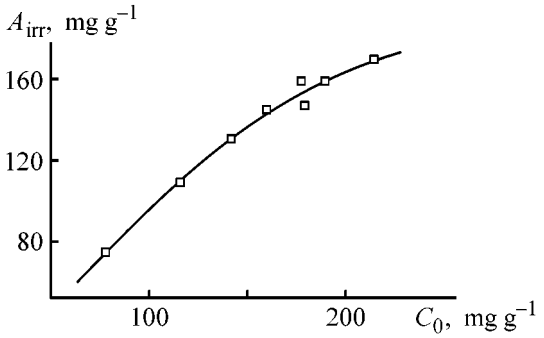

Fig. 2. Amount of irreversibly sorbed PVP on the silica surface vs. initial content of the polymer on the silica surface C_0. (A_{irr}) Irreversible PVP sorption.

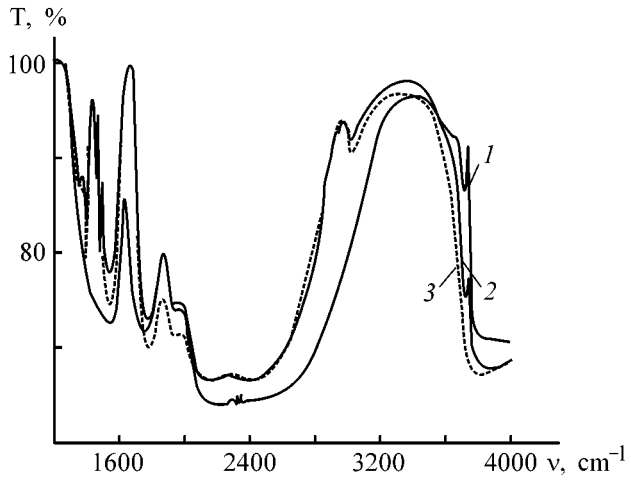

Fig. 3. IR spectra of silica samples after contact with (*1*) water and (*2*, *3*) PVP solutions and drying in air at 20°C. (T) Transmission and (ν) wave number. Initial concentration of the PVP solution: (*2*) 100 and (*3*) 200.

rium concentration of a dissolved compound and A is the PVP sorption, this isotherm is a straight line. This allows evaluation of the maximal sorption of the PVP polymer A_{max} [6], equal to 200 mg g^{-1}. According to the Langmuir theory, A_{max} corresponds to the monolayer capacity.

In amounts of up to 100 mg g^{-1}, PVP is irreversibly sorbed on the Aerosil surface and is not removed from the sample upon contact with pure water. At higher PVP content the polymer is partially desorbed. It was found that, with increasing initial PVP content, the degree of its desorption increases, simultaneously the absolute amount of the irreversibly sorbed polymer increases also (Fig. 2). Since the stability of composition and properties of sorbents in the course of their operation is an important requirement [7], we should distinguish, for more correct characterization of the sorbents in question, two parameters. These are the PVP sorption A_{PVP} (total content of polymer in the surface layer) and the degree of surface modification θ_{mod}, namely, the ratio of the amount of irreversibly sorbed PVP to a value of 100 mg g^{-1}, which, taking into account the above data (Figs. 1, 2), can be considered 100% modification (θ_{mod} = 100%).

To analyze the structure of the adsorption layers and conformation of macromolecules in them, we must know the fraction of fragments of the polymeric chains directly interacting with the silica surface, because, in contrast to the sorption of low-molecular-weight compounds, simultaneous interaction of all the fragments of macromolecular chain with the sorbent surface is impossible. In this case, the parameter p is used, namely, the ratio of the number of fragments directly interacting with the sorbent surface to the total number of fragments in the polymer sorbed.

The number of fragments in the macromolecular chains directly interacting with silica surface can be effectively determined by IR spectroscopy [6]. As seen from Fig. 3, the intensity of the absorption band at 3750 cm^{-1}, belonging to free silanol groups ≡Si–OH, decreases with increasing coverage of the silica surface with PVP, and a new absorption band appears at 3350 cm^{-1}, which belongs to the silanol groups linked by hydrogen bonds. The absorption bands at 1350–1550 and 2800–3000 cm^{-1} belong, respectively, to the bending and stretching vibrations of the C–H bonds in the polymer, whereas the absorption in the 1600–1750 cm^{-1} range is typical of the C=O carbonyl groups [8].

The degree of participation of the surface OH groups in the interaction with PVP can be determined from the ratio of the optical densities of the band at 3750 cm^{-1} before and after sorption (D_0 and D, respectively) using the following expression:

$$\theta = 1 - D/D_0.$$

Analysis of the structures of the silica surface and PVP molecule and the experimental IR data suggest that the polymer adsorption proceeds predominantly through formation of hydrogen bonds between the oxygen atom of the carbonyl group in the PVP molecule and hydrogen of the silanol group:

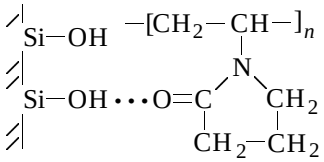

It is often assumed that strong sorption of PVP on silica is also due to the formation of an additional hy-

drogen bond between the hydrogen atom of the silanol surface group and nitrogen atom of the pyrrolidone ring ≡Si–OH···N(PVP) [9]. However, we found no characteristic absorption bands in the IR spectra attributable to the interaction of the PVP nitrogen atom with the silica surface (Fig. 3). Analysis of the chemical properties of lactams (such as PVP) suggests that nitrogen atom in the pyrrolidone ring loses its electron-donor power and thus cannot form hydrogen bonds [10].

To determine the quantitative ratio between the sorbent and sorbate, we regard the polymer macromolecule as a sum of vinylpyrrolidone (VP) units. Then, using the data on the PVP sorption A_{PVP} for each sample, we can determine the total concentration of the carbonyl groups α_{CO} in the polymer layer, which is obviously equal to the content of VP units on the surface:

$$\alpha_{CO} = \alpha_{VP} = A_{PVP}/M_{VP},$$

where α_{CO} is the total content of the carbonyl groups (mmol g^{-1}), α_{VP} the content of the VP fragments (mmol g^{-1}), A_{PVP} the PVP sorption (mg g^{-1}), and M_{VP} the molecular weight of the VP unit (111 mg $mmol^{-1}$).

Since a single VP unit forms bond with a single silanol group on the silica surface, the number of the carbonyl groups, α'_{CO}, participating in the linking is equal to the number of the hydroxy groups, α'_{OH}, and can be determined from the following equation:

$$\alpha'_{CO} = \alpha'_{OH} = \alpha_{OH}\theta,$$

where α'_{CO} is the concentration of the carbonyl groups interacting with the silica surface (mmol g^{-1}), α'_{OH} the concentration of the excited silanol groups (mmol g^{-1}), α_{OH} the initial concentration of the surface silanol groups (0.65 mmol g^{-1}), and θ the degree of involvement of the silanol groups in hydrogen bonding with VP units.

Thus, the criterion p describing the conformation of the adsorbed macromolecules can be calculated by the following expression:

$$p = \alpha'_{CO}/\alpha_{CO} = \alpha_{OH}\theta/(A_{PVP}/M_{VP})$$
$$0.65\theta/(A_{PVP}/111) = 72.15\theta/A_{PVP}.$$

As seen from our calculations (Fig. 4), p depends on the PVP content at the silica surface. At low polymer sorption, p = 0.8, which corresponds to a highly compact sorption layer [6]. At higher degrees of coverage, p decreases, which suggests formation of looser structure of the adsorption layer with saturation of the sorbent surface. At higher coverage of the surface the sorption layer undergoes certain rearrangement.

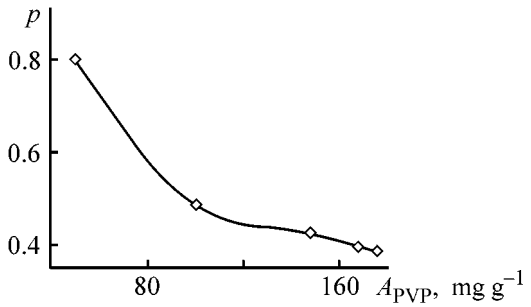

Fig. 4. Fraction of bound carbonyl groups p vs. PVP sorption A_{PVP}.

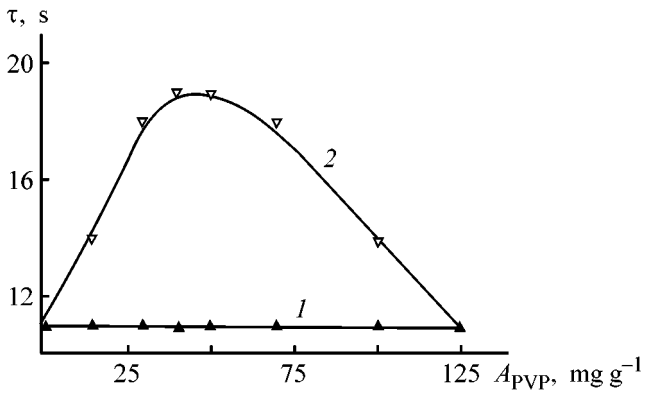

Fig. 5. Efflux time of 5% suspension τ vs. PVP sorption A_{PVP}. Solvent: (*1*) distilled water and (*2*) 0.9% NaCl solution.

The appearance of free carbonyl groups on the surface would obviously cause certain changes in the sorption and other properties of the modified silica sorbents.

We studied the rheological properties of the silica suspensions in relation to the degree of their surface modification. The viscosity of suspensions was determined using a VZ-4 viscometer designed as a 100-ml plastic beaker in which the conical bottom had a calibrated 4-mm outlet.

The measurements were performed as follows. The viscometer was filled with a suspension and the efflux time, which is inversely proportional to the viscosity of the sample, was determined at 20°C. It was found that the viscosity of our suspensions is almost independent of the PVP content and is only slightly higher than that of water. However, when the suspensions were prepared using normal saline (0.9% NaCl solution), the dependence of the suspension viscosity on the degree of modification passes through a maximum (Fig. 5). With increasing degree of Aerosil modifica-

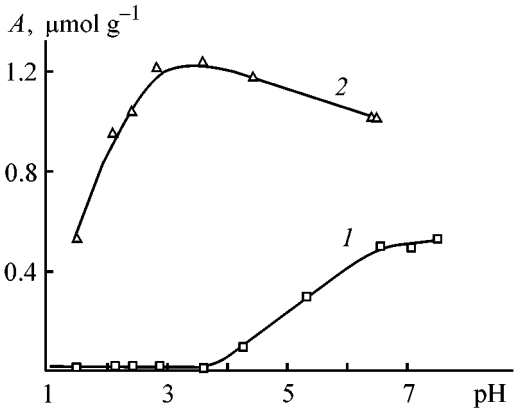

Fig. 6. Sorption of quercetin *A* on the (*1*) initial and (*2*) PVP-modified (θ_{mod} = 100%) sorbents vs. the suspension pH.

tion with PVP, the suspension viscosity first increases, reaching a maximum at θ_{mod} = 50%, and then gradually decreases. We assume that such a dependence is due to the interaction of free carbonyl groups appearing at the surface of a silanol particle with the silanol groups still preserved on the surface of another silica particle. Apparently, the strongest interaction is observed when the number of the silanol and carbonyl groups on the silica particles is close. At complete filling of the sorbent surface with PVP the interaction between the Aerosil particles would rather be similar to contacts between polymer macromolecules.

A question arises as to why such a significant increase in the interparticle interaction is observed only in the presence of NaCl. We assume that the effective interaction between partially modified Aerosil aggregates is hindered by certain, most probably steric factors. However, according to [1], cations occurring in silica colloids or suspensions can act as linking agents forming bridges between particles. Hence, appearance of hydrated sodium cations in the suspensions in question promotes linking of the particles and leads to formation of three-dimensional networks, which, in turn, increases the suspension viscosity.

Since PVP easily forms complexes with various (including aromatic) compounds, we suggested that modification of the silica surface with PVP would affect the sorption properties of modified sorbents with respect to phenols, which are not noticeably sorbed on the initial silica. We studied sorption of natural polyphenol quercetin from aqueous alcohol on Aerosil containing 100 mg g^{-1} of PVP (θ_{mod} = 100%).

The sorption was performed under static conditions: the solution : sorbent ratio was 10 ml : 100 mg, the initial quercetin concentration was $C_0 = 3.2 \times 10^{-5}$ M, the suspension pH was adjusted using HNO_3 and NaOH. After 1-h contact the mixture was centrifuged for 30 min at 8000 rpm. The sorption capacity was evaluated from the difference of the quercetin concentrations in solution before and after interaction with silica by spectrophotometry (λ = 367 nm [11]).

The isotherms of the quercetin sorption (Fig. 6) show that modification of the silica surface with PVP strongly affects its sorption properties, especially in weakly acidic solutions. No quercetin is sorbed on the initial silica at pH < 4, whereas in the case of the modified sorbent the highest sorption capacity is observed at pH 3–4.

CONCLUSION

Our experimental results show that sorption modification with polyvinylpyrrolidone allows control of the properties of fine silica and composites based on it.

REFERENCES

1. Iler, R.K., *The Chemistry of Silica*, New York: Wiley, 1979.
2. *Polimery v farmatsii* (Polymers in Pharmacy), Tentsova, A.I. and Alyushina, M.T., Eds., Moscow: Meditsina, 1985.
3. Ivanov, A.E., Saburov, V.V., and Zubov, V.I., *Zh. Vses. Khim. O-va im. D.I. Mendeleeva*, 1989, vol. 34, no. 3, pp. 368–376.
4. Chuiko, A.A. and Gorlov, Yu.I., *Khimiya poverkhnosti kremnezema: stroenie poverkhnosti, aktivnye tsentry, mekhanizmy sorbtsii* (Chemistry of Silica Surface: Surface Structure, Active Centers, and Sorption Mechanisms), Kiev: Naukova Dumka, 1992.
5. Pohloudek-Fabini, R. and Beyrich, Th., *Organische Analyse*, Leipzig: Academische Verlagsgesellschaft, 1975.
6. Lipatov, Yu.S. and Sergeeva, L.M., *Adsorbtsiya polimerov* (Adsorption of Polymers), Kiev: Naukova Dumka, 1972.
7. *Modifitsirovannye kremneszemy v sorbtsii, katalize i khromatografii* (Modified Silicas in Sorption, Catalysis, and Chromatography), Lisichkin, G.V., Ed., Moscow: Khimiya, 1986.
8. Gordon, A.J. and Ford, R.A., *The Chemist's Companion. A Handbook of Practical Data, Techniques and References*, New York: Wiley, 1972.
9. Eremenko, B.V., Baranchuk, N.D., and Malysheva, M.L., *Kolloidn. Zh.*, 1985, vol. 47, no. 4, pp. 678–684.
10. Reid, K.F., *Properties and Reactions of Bonds in Organic Molecules*, London: Longmans, 1968.
11. Georgievskii, V.P., Komissarenko, N.F., and Dmitruk, S.E., *Biologicheski aktivnye veshchestva lekarstvennykh rastenii* (Biologically Active Compounds in Herbs), Novosibirsk: Nauka, 1990.

Russian Journal of Applied Chemistry, Vol. 74, No. 12, 2001, pp. 2021–2026. Translated from Zhurnal Prikladnoi Khimii, Vol. 74, No. 12, 2001, pp. 1962–1967.

CATALYSIS

Oxidation of *D*-Glucose to *D*-Gluconic and *D*-Glucaric Acids Catalyzed by Sodium Nitrite

I. A. Grigor'eva, S. S. Chernaya, and S. R. Trusov

Riga Technical University, Riga, Latvia

Received January 30, 2001

Abstract—Kinetics of catalytic oxidation of *D*-glucose in the $HClO_4$–H_2O–sulfolane system containing $NaNO_2$ was studied. Kinetic equations of the process were derived. A scheme for oxidation of *D*-glucose with oxygen in the presence of $NaNO_2$ was proposed.

Conventional oxidation of organic compounds with oxygen in the presence of metal complexes is not always selective. Recently, alternative catalytic procedures have been proposed, involving, in particular, oxygen-containing nitrogen compounds [1, 2].

Previously, we showed that alcohols are selectively oxidized by oxygen in stronly acidic solutions containing catalytic amounts of $NaNO_2$ [3]. The reaction rate and yield of the products increase in the presence of organic sulfones [4].

In this study, we used this procedure for oxidation of monosaccharides, with *D*-glucose as an example, since the products of its selective oxidation are widely used in pharmaceutics.

EXPERIMENTAL

The kinetics of the process was studied by the gasometric procedure described in [5]. The concentrations of *D*-glucose, *D*-gluconic acid, $NaNO_2$, and $HClO_4$ were varied in the following ranges (M): 0.5–1.5, 0.5–1.5, 0.01–0.25, and 4.0–6.0, respectively. The partial oxygen pressure in the gas phase, p_{O_2}, was varied from 0.2×10^5 to 1.0×10^5 Pa, and temperature, from 313 to 343 K. A mixture of $HClO_4$, water, and sulfolane was used as solvent. The total pressure in the system was kept constant at 1×10^5 Pa. The volume of the liquid V_l and gas phase V_g was 5 and 80 ml, respectively. The fact that the rate of oxygen uptake is independent of the hydrodynamic parameters (reactor volume, shape of its walls, frequency and amplitude of rocking) indicates that the rate-determining step of the process in the chemical reaction.

The quantitative and qualitative composition of the oxidation products was determined by GLC [6]. The structure of the products was confirmed by elemental analysis, ^{1}H NMR, and chromato-mass spectrometry. The total equilibrium concentration of N(III) compounds in the liquid phase {[N(III)], M} was determined by spectrophotometry [7] and chromato-mass spectrometry.

We found that oxidation of *D*-glucose under these conditions is described by the equation

$$\underset{D\text{-glucose}}{RCHO} + \frac{1}{2}O_2 \xrightarrow[H^+]{NaNO_2} \underset{\substack{D\text{-gluconic}\\ \text{acid}}}{RCOOH} + O_2 \xrightarrow[H^+]{NaNO_2} \underset{\substack{D\text{-glucaric}\\ \text{acid}}}{R_1(COOH)_2} + H_2O. \quad (I)$$

The results of GLC and gasometry showed that the volume of oxygen taken up and the concentration of the oxidation products correspond to the stoichiometry of Eq. (I). Therefore, in further studies, the volume of oxygen taken up was recalculated to the concentration of the reactants by Eq. (I).

In the absence of sodium nitrite, all other conditions being the same, *D*-glucose is not noticeably oxidized. At $NaNO_2$ concentration from 0.075 to 0.25 M, *D*-glucose is almost quantitatively converted within 2 min into *D*-gluconic acid, which is slowly oxidized to *D*-glucaric acid (Fig. 1a). This makes impossible a kinetic study of oxidation of *D*-glucose to *D*-gluconic acid (the first step) under these conditions. At catalyst concentration of 0.01–0.05 M, reaction (I) is appreciably slower (Fig. 1b), with the rate of the second step (oxidation of *D*-gluconic acid to *D*-glucaric acid) being negligible as compared with that of the first step up to 60% conversion of *D*-glucose. This allowed kinetic study of the first step of reaction (I) at the initial $NaNO_2$ concentration from 0.01 to 0.05 M.

1070-4272/01/7412-2021 $25.00 © 2001 MAIK "Nauka/Interperiodica"

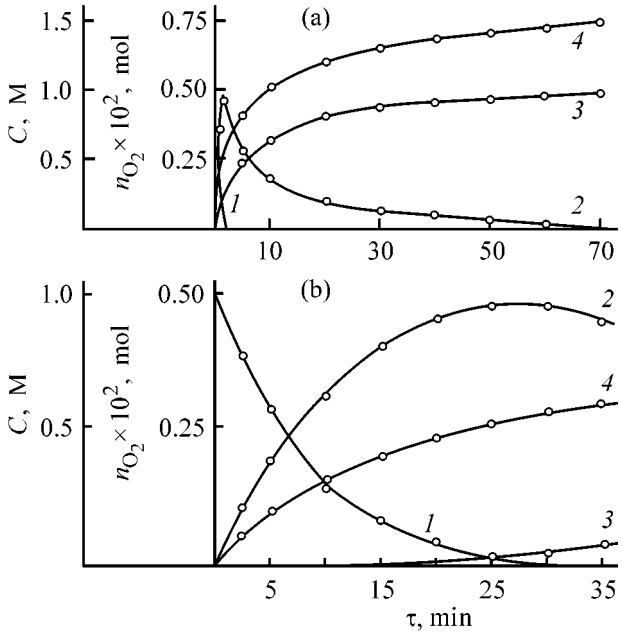

Fig. 1. Kinetic curves of *D*-glucose oxidation by oxygen at (a) high (2.5×10^{-1} M) and (b) low (2×10^{-2} M) $NaNO_2$ concentration. Initial concentrations of RCHO, $HClO_4$, and sulfolane 1.0, 6.0, and 2.6 M, respectively; $T = 333.2$ K; the same for Figs. 2–4. $p_{O_2} = 1 \times 10^5$ Pa; the same for Fig. 3. (*C*) Current concentration of (*1*) RCHO, (*2*) RCOOH, and (*3*) $R_1(COOH)_2$; (*4*) amount of oxygen up-take, n_{O_2}; (τ) time.

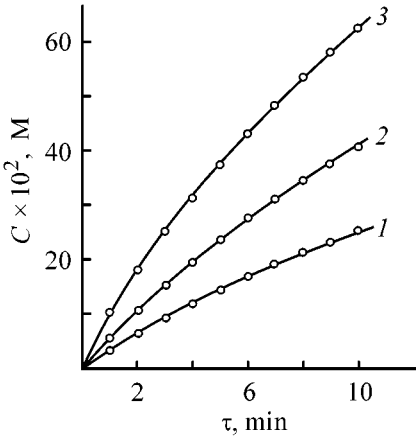

Fig. 2. Kinetic curves of *D*-glucose oxidation at partial oxygen pressure p_{O_2} of (*1*) 0.21×10^5, (*2*) $0.38\ 10^5$, and (*3*) 1.0×10^5 Pa. $NaNO_2$ concentration 2×10^{-2} M; the same for Fig. 4. (*C*) Current concentration of gluconic acid, (τ) time; the same for Fig. 3.

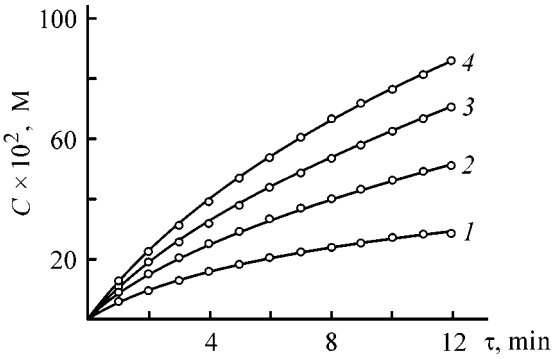

Fig. 3. Kinetic curves of *D*-glucose oxidation at $NaNO_2$ concentration C_{cat} of (*1*) 1.0×10^{-2}, (*2*) 1.5×10^{-2}, (*3*) 2.0×10^{-2}, and (*4*) 2.5×10^{-2} M; the same for Fig. 6.

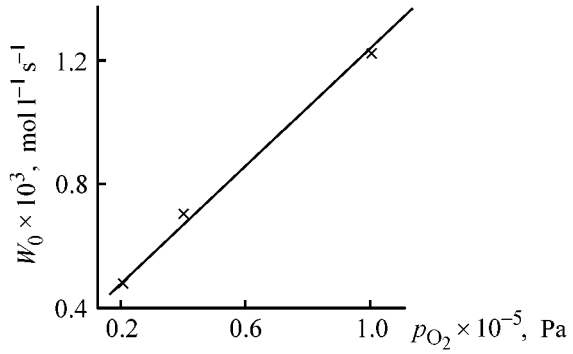

Fig. 4. Initial rate of *D*-glucose oxidation W_0 vs. the partial oxygen pressure p_{O_2}.

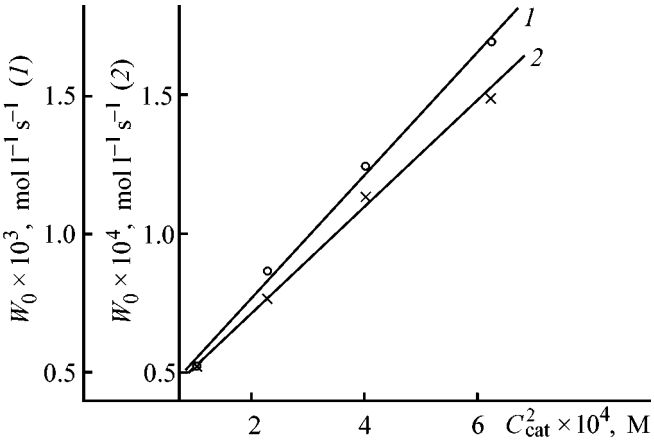

Fig. 5. Initial rate of oxidation W_0 of (*1*) *D*-glucose and (*2*) *D*-gluconic acid as a function of the $NaNO_2$ concentration C_{cat}. Initial concentration of (*1*) RCHO, (*2*) RCOOH, $HClO_4$, and sulfolane 1.0, 1.0, 6, and 2.6 M, respectively. $T = 333.2$ K, $p_{O_2} = 1 \times 10^5$ Pa; the same for Fig. 6.

The experimental kinetic curves of *D*-glucose oxidation to *D*-gluconic acid are shown in Figs. 2, 3. The following dependences of the initial rate of *D*-glucose oxidation W_0 (mol l^{-1} s^{-1}) on the reaction conditions was derived by mathematical processing of these results:

$$\frac{\partial W_0}{\partial C_g} = 0,\ \frac{\partial W_0}{\partial T} = 0,\ \frac{\partial W_0}{\partial C_a} = 0,\ \frac{\partial W_0}{\partial C_{cat}} > 0,\ \frac{\partial W_0}{\partial p_{O_2}} > 0, \quad (1)$$

where C_g, C_a, and C_{cat} are the initial concentrations (M) of glucose, perchloric acid, and sodium nitrite, respectively.

Processing of the data presented in Figs. 4, 5 gives

$$W_0 = k_{exp} C_{cat}^2 p_{O_2}, \quad (2)$$

where $k_{exp} = (0.42 \pm 0.08) \times 10^{-4}$ mol^{-1} l s^{-1} Pa^{-1}.

To explain these kinetic dependences, let us consider the composition of the catalytic sustem and possible reactions of its compounds. Chemical transformations of sodium nitrite in 4–9 M aqueous solutions of perchloric acid can be described by the following scheme [8]:

$$NO_2^- + H^+ \rightleftarrows HNO_2, \quad (II)$$

$$HNO_2 + H^+ \overset{K_{NO^+}}{\rightleftarrows} NO^+ + H_2O, \quad (III)$$

$$NO_2^- + NO^+ \rightleftarrows NO + NO_2. \quad (IV)$$

Bayliss and Watts found [8] that equilibrium (III) is almost completely shifted to the right. Thus, we suggest that, in the liquid phase of the catalytic system, the catalyst occurs partially in the form of HNO_2 and NO^+. The gas phase probably contains nitrogen oxides NO and NO_2. Since the system is closed, the mass balance must be fulfilled:

$$n(NaNO_2) = n(HNO_2) + n(NO^+) + n(NO) + n(NO_2), \quad (3)$$

where $n(NaNO_2)$ is the initial amount of sodium nitrite (mole); $n(HNO_2)$, $n(NO^+)$, $n(NO)$, and $n(NO_2)$ are the amounts (mole) of the respective components of the catalytic system in the course of oxidation.

Then

$$C_{cat} = [HNO_2] + [NO^+] + \frac{V_g(p_{NO} + p_{NO_2})}{V_l \times 10^3 RT}, \quad (4)$$

$$[N(III)] = [HNO_2] + [NO^+], \quad (5)$$

where p_{NO} and p_{NO_2} are the partial vapor pressures (Pa) of the nitrogen oxides, and $[HNO_2]$ and $[NO^+]$ are the equilibrium concentrations (M) of nitrous acid and nitrosonium cation, respectively.

It is known [3, 4, 8–13] that, in aqueous solutions of nitric and nitrous acids, the nitrosonium cation NO^+ is an oxidizing agent with respect to a wide range of organic compounds. Based on analysis of published data and kinetic relationships obtained in this work, we propose the following scheme of catalytic oxidation of *D*-glucose by oxygen in the presence of sodium nitrite in a strongly acidic solution: reactions (II)–(IV), then

Table 1. Rate of *D*-glucose oxidation to *D*-gluconic acid at different $NaNO_2$ amounts

V_l, ml	$C_{cat} \times 10^2$, M	$n(NaNO_2) \times 10^4$ mol	W_{O_2}, ml min^{-1}
5	2	1	1.4
10	2	2	2.7
15	2	3	4.0
10	1	1	1.3
20	0.5	1	1.4

* Initial concentration of RCHO and $HClO_4$ 1.0 and 6.0 M, respectively; T = 333 K; $P = 1 \times 10^5$ Pa; τ = 20 min.

$$RCHO + NO^+ \xrightarrow{k_2} [^-R–HC^+–O–N=O] \rightarrow NO + [R–CHO]^{+\cdot}, \quad (V)$$

$$NO_{(l)} \rightleftarrows NO_{(g)}, \quad (VI)$$

$$2NO_{(g)} + O_2 \xrightarrow{k_1} 2NO_{2(g)}, \quad (VII)$$

$$NO_{2(g)} \rightleftarrows NO_{2(l)}, \quad (VIII)$$

$$[RCHO]^{+\cdot} + NO_2 \xrightarrow{k_3} HNO_2 + [R–C=O]^+, \quad (IX)$$

$$[R–C=O]^+ + H_2O \xrightarrow{k_4} RCOOH + H^+. \quad (X)$$

The experimental dependence (2) obtained at a constant volume of the liquid phase in the system, V_l = 5 ml, and unusual dependence of the oxygen uptake rate W_{O_2} on the volume of the liquid phase at constant initial concentration of $NaNO_2$ (Table 1) indicate that the rate-determining step of the process is gas–phase reaction (VII). As seen from Table 1, at a constant volume of the liquid phase, W_{O_2} depends on the initial $NaNO_2$ concentration, which, in its turn, determines $n(NaNO_2)$ and the partial vapor pressures of the gaseous components (e.g., p_{NO}). Variation of V_l at constant initial concentration of $NaNO_2$ also affects $n(NaNO_2)$ and p_{NO} in the system, with W_{O_2} changing significantly. At simultaneous variation of V_l and the initial $NaNO_2$ concentration, it was possible to keep $n(NaNO_2)$ constant. In this case W_{O_2} did not change noticeably. Thus, W_{O_2} is determined by the absolute amount of sodium nitrite introduced into the reactor, rather than by its initial concentration. The experiments with different V_l were performed with V_g varying by no more than 19%, which had virtually no effect on the partial pressure of the gaseous components. The p_{NO} depends mainly on $n(NaNO_2)$.

Table 2. Initial rate of *D*-glucose oxidation (τ = 2–3 min) under various conditions*

C_{cat}	[N(III)] × 10^3	$p_{O_2} \times 10^{-5}$, Pa	*T*, K	$W_{0\,exp} \times 10^3$	$W_{0\,calc} \times 10^3$
M				mol l^{-1} s^{-1}	
0.025	8.1	1.0	333.2	1.70	1.75
0.020	6.2	1.0	333.2	1.25	1.63
0.015	3.0	1.0	333.2	0.88	0.82
0.010	1.8	1.0	333.2	0.52	0.41
0.02	4.5	0.4	333.2	0.71	0.59
0.02	1.6	0.2	333.2	0.48	0.42
0.02	7.0	1.0	323.2	1.18	1.11
0.02	7.5	1.0	313.2	1.21	1.09

* Initial concentration of RCHO and $HClO_4$ 1.0 and 6.0 M, respectively; V_l = 5, V_g = 80 ml.

These data suggest that the rate–determining step of *D*-glucose oxidation under the examined conditions is step (VII). The kinetic equation of gas-phase reaction (VII) is as follows [14]:

$$W_{O_2} = k_1 p_{O_2} p_{NO}^2 \ (\text{Pa s}^{-1}), \qquad (6)$$

where $k_1 = 2.62 \times 10^{-10}\exp(644/T)$ $(\text{Pa}^{-2}\,\text{s}^{-1})$.

It is known [13] that reactions of NO_2 with organic radical cations are considerably faster than reaction (VII). We assume that

$$\partial p_{NO_2}/\partial\tau = 0, \text{ hence, } p_{NO} \gg p_{NO_2}. \qquad (7)$$

Taking into account Eqs. (4), (5), and (7)

$$p_{NO} = \frac{10^3 V_l RT}{V_g}(C_{cat} - [\text{N(III)}]). \qquad (8)$$

Recalculation of the oxygen uptake rate W_{O_2} [Eq. (6)] to the rate of *D*-glucose oxidation in the liquid phase, *W* (mol l^{-1} s^{-1}), gives

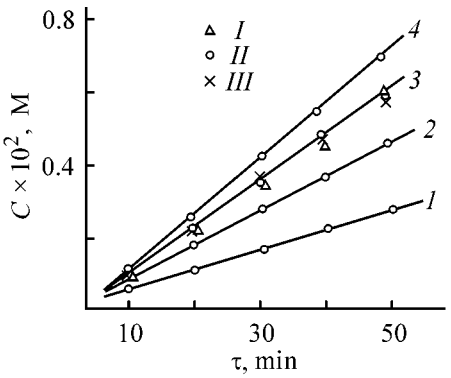

Fig. 6. Kinetic curves of *D*-gluconic acid oxidation at (*1–4*) different $NaNO_2$ concentrations. Initial concentration of *D*-gluconic acid, M: (*3*) (*I*) 1.2, (*II*) 1.0, and (*III*) 0.5 M; (*1, 2, 4*) 1.0. (*C*) Concentration of glucaric acid; (τ) time. Initial concentrations of $HClO_4$ and sulfolane 6.0 and 2.6 M, respectively.

$$W = 2k_1 p_{O_2}(C_{cat} - [\text{N(III)}])^2 \frac{10^3 V_l RT}{V_g}. \qquad (9)$$

The initial rate of glucose oxidation W_0 was calculated by Eq. (9) from the N(III) concentration in the liquid phase, determined spectrophotometrically. The N(III) concentrations in the first oxidation steps (τ = 2–3 min) are presented in Table 2. The initial rates of *D*-glucose oxidation, calculated by Eq. (9) at various initial $NaNO_2$ concentrations, p_{O_2}, and *T*, are close to the experimental values (Table 2). This confirms our conclusion about the rate-determining step and assumption (7). According to [14], reaction (VII) decelerates with increasing temperature. However, as seen from Eq. (1), W_0 is almost independent of temperature. This discrepancy is due to the fact that the solubility of N(III) in the liquid phase decreases with temperature (Table 2), and hence p_{NO} increases. The decrease in k_1 is compensated for by an increase in p_{NO}.

The nonlinearity of the kinetic curves (Fig. 2, 3) of the first step of reaction (I) suggests that the oxidation product, *D*-gluconic acid, reacts with the catalyst and removes it from the catalytic cycle. In addition, oxidation of *D*-gluconic acid to *D*-glucaric acid (second step of *D*-glucose oxidation) can also affect the shape of the kinetic curves. To understand these phenomena, we studied the kinetics of oxidation of *D*-gluconic acid to *D*-glucaric acid under conditions similar to those of oxidation of *D*-glucose to *D*-gluconic acid.

The kinetic curves of *D*-gluconic acid oxidation are shown in Fig. 6. In all cases, the oxidation rate is independent of the *D*-gluconic acid concentration and coincides, all reaction conditions being the same, with that of the second step or reaction (I), when *D*-glucose is completely spent and the *D*-gluconic acid accumulated is oxidized (Fig. 1b). Thus, reaction (I) involves consecutive oxidation of *D*-glucose to *D*-gluconic acid and of *D*-gluconic acid to *D*-glucaric

Table 3. Kinetic parameters of *D*-gluconic acid oxidation with oxygen under different reaction conditions*

C_{ga}^{**}	C_{cat}	$p_{O_2} \times 10^{-5}$,	$W_{exp} \times 10^4$,	$[N(III)]_{sp} \times 10^3$	$[N(III)]_{exp} \times 10^3$	$[N(III)]_{calc} \times 10^3$
M		Pa	mol l^{-1} s^{-1}	M		
1.0	0.025	1.0	1.45	11.2	20.7	20.1
1.0	0.020	1.0	1.18	8.0	14.0	15.6
1.0	0.015	1.0	0.78	5.9	10.4	11.4
1.0	0.010	1.0	0.52	5.1	8.1	7.4
0.5	0.020	0.2	0.61	7.9	13.9	16.8
0.5	0.020	0.4	0.82	8.5	14.5	16.4
0.5	0.020	1.0	1.10	8.6	14.6	15.8
1.5	0.020	1.0	1.23	7.2	13.2	15.5

* Initial concentration of $HClO_4$ 6.0 M; T = 333.2 K; V_l = 5, V_g = 80 ml.

** C_{ga} is the initial concentration of *D*-gluconic acid.

acid. The dependence of the initial rate of *D*-gluconic acid oxidation W_0 on the initial concentration of the catalyst is shown in Fig. 5 (curve *2*).

The rate of *D*-gluconic acid oxidation is also described by Eqs. (1) and (2); however, $k_{exp} = (0.25 \pm 0.05) \times 10^{-5}$ mol^{-1} l s^{-1} Pa^{-1}, i.e., k_{exp} is lower by an order of magnitude than that of *D*-glucose oxidation to *D*-gluconic acid.

A nitrite derivative of *D*-gluconic acid was detected among the oxidation products by chromato-mass specmetry. Since its amount is approximately 0.5% of the initial content of *D*-gluconic acid, about 30 ± 8% of the catalysts is converted into the nitrite derivative of *D*-gluconic acid, i.e., is removed from the catalytic cycle by the reaction

$$R_2CH_2OH + NO^+ \rightleftarrows R_2CH_2ONO + H^+, \quad (XI)$$

where R_2CH_2OH is *D*-gluconic acid, RCOOH and

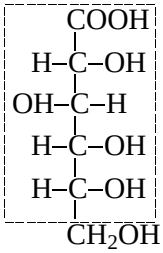

The kinetics of *D*-gluconic acid oxidation can be described by the scheme proposed for *D*-glucose oxidation [reactions (II)–(X)] with additional step (XI). Taking into account the stoichiometry of reaction (I) and assumption (7), the rate of *D*-gluconic acid oxidation in the liquid phase (mol l^{-1} s^{-1}) is described by the equation

$$W = k_1 p_{O_2} (C_{cat} - [N(III)])^2 \frac{10^3 V_g RT}{V_l}, \quad (10)$$

$$[N(III)] = [HNO_2] + [NO^+] + [R_2CH_2ONO]. \quad (11)$$

The total concentration [N(III)] in the liquid phase was calculated by Eq. (10), using the kinetic data obtained (Table 3). This concentration was also measured over the course of the whole process of *D*-gluconic acid oxidation. The concentrations $[N(III)]_{sp} = [HNO_2] + [NO^+]$ and $[R_2CH_2ONO]$ were determined by spectrophotometry and chromato-mass spectrometry, respectively. The concentration $[N(III)]_{exp}$ remains constant up to ~60% conversion of *D*-gluconic acid. As seen from Table 3, the $[N(III)]_{calc}$ values are close to $[N(III)]_{exp}$. In addition, the N(III) concentration in the case of *D*-gluconic acid oxidation is considerably higher than that in the initial steps of *D*-glucose oxidation (Table 2, 3), p_{O_2}, and T, being the same. Hence, p_{NO} is higher in the course of *D*-glucose oxidation than that in the course of *D*-gluconic acid oxidation [Eq. (8)]. In the course of *D*-glucose oxidation, the N(III) concentration increases owing to accumulation of the nitrite derivative of *D*-gluconic acid, and p_{NO} decreases, thus decelerating the rate-determining step (VII). The decrease in p_{NO} may be due to the fact that the rate constant of reaction (V) is higher than that of the reaction

$$\underset{\text{acid}}{\underset{D\text{-gluconic}}{R_2CH_2OH}} + NO^+ \xrightarrow{k_2'} [R_2CH_2OH]^+ + NO. \quad (XII)$$

Hence, the initial rate of *D*-glucose oxidation is higher than that of *D*-gluconic acid oxidation to *D*-glucaric acid, with the rate-determining step being the same. The nonlinearity of the kinetic curves

of the first step of reaction (I) is due to a decrease in p_{NO} and *D*-glucose concentration.

CONCLUSION

Sodium nitrite catalyzes oxidation of *D*-glucose by oxygen in strongly acidic $HClO_4$–H_2O–sulfolane solution. Under these conditions, *D*-glucose is successively oxidized to *D*-gluconic and then to *D*-glucaric acid. The rate-determining step of the process is oxidation of nitrogen monoxide to nitrogen dioxide in the gas phase. A scheme of catalytic oxidation was proposed. The kinetic equation of the process was derived.

REFERENCES

1. Bosch, E., Rathore, R., and Kochi, J.K., *J. Org. Chem.*, 1994, vol. 59, no. 9, pp. 2529–2535.
2. Semmelhack, M.F., Schmid, C.R., Cortes, D.A., and Chon, C.S., *J. Am. Chem. Soc.*, 1984, vol. 106, no. 11, pp. 3374–3376.
3. Levina, A.B., Chernaya, S.S., Trusov, S.R., and Stel'makh, T.V., *Kinet. Katal.*, 1991, vol. 32, no. 6, pp. 1336–1342.
4. Levina, A.B. and Trusov, S.R., *Kinet. Katal.*, 1991, vol. 32, no. 6, pp. 1343–1348.
5. Grigor'eva, I.A., Stel'makh, T.V., Trusov, S.R., and Chernaya, S.S., *Latv. Kim. Ž.*, 1993, no. 6, pp. 707–713.
6. Fel'dman, D.P., Voitenko, M.Yu., Shimanskaya, M.V., and Lidak, M.Yu., *Khim.-Farm. Zh.*, 1984, vol. 18, no. 11, pp. 1356–1360.
7. Babko, A.K. and Pilipenko, A.G., *Fotometricheskii analiz* (Photometric Analysis), Moscow: Khimiya, 1974.
8. Bayliss, N. and Watts, D., *Aust. J. Chem.*, 1963, vol. 16, pp. 927–931.
9. Eberson, L. and Radner, F., *Acc. Chem. Res.*, 1987, vol. 20, no. 2, pp. 53–59.
10. Olah, G.A. and Ho, T.-L., *Synthesis*, 1976, no. 9, pp. 609–610.
11. Ross, D.S., Gu, C.-L., Hum., G.P., and Malhotra, R., *Int. J. Chem. Kinet.*, 1986, vol. 18, no. 11, pp. 1277–1288.
12. Moodie, R. and Richards, S., *J. Chem. Soc.*, Perkin Trans., 1996, no. 11, pp. 1833–1837.
13. Morkovnik, A.S., *Usp. Khim.*, 1988, vol. 57, no. 2, pp. 254–261.
14. Atroshchenko, V.I. and Kargin, S.I., *Tekhnologiya azotnoi kisloty* (Production of Nitric Acid), Moscow: Khimiya, 1970.

Russian Journal of Applied Chemistry, Vol. 74, No. 12, 2001, pp. 2027–2034. Translated from Zhurnal Prikladnoi Khimii, Vol. 74, No. 12, 2001, pp. 1968–1974.

APPLIED ELECTROCHEMISTRY AND CORROSION PROTECTION OF METALS

Mathematical Modeling of Corrosive Alloy Cracking on the Basis of Generalized Dimensionless Electrochemical Factor

V. V. Maslov, N. V. Adamova, and N. V. Makarova

St. Petersburg State Technical University, St. Petersburg, Russia

Received April 17, 2001

Abstract—A new generalized dimensionless electrochemical factor of corrosive alloy cracking was developed and a quantitative theory of corrosive-mechanical destruction was constructed on its base. The existence of a threshold value of the proposed factor, above which there is no corrosion cracking, was revealed.

One of the most dangerous and frequently occurring kinds of corrosion, leading to severe emergency damage to machine and metalwork parts, is corrosion cracking (CC) [1–4]. In view of the complexity of physicochemical phenomena associated with CC (local anodic dissolution, hydrogen embrittlement, adsorption-induced deterioration of the surface strength) [5–8] and specificity of the process (not all materials are subject to CC, not at any tensile stresses, and not in any media [9]), no unified theoretical concept of CC has been constructed and the main cause of CC has not been revealed. As a result, there is no satisfactory mathematical description of corrosive-mechanical destruction, despite numerous theoretical and experimental investigations.

The aim of the present study was to develop a generalized dimensionless electrochemical factor of CC of metallic materials and construct on its base a mathematical model of CC. For this purpose, account was taken of the recommendations of [10–13] concerning the most important role of the electrochemical aspects of CC. In particular, the conditions of, and processes occurring in CC are closely associated with the conditions of, and processes in other kinds of local corrosion: crevice, pitting, etc. Therefore, in developing the mechanism of local anodic dissolution (LAD) of materials on the basis of the known mechanisms [13–15], we assume that the main cause of CC is the nonuniform electric field distribution over the surface of metal, affecting not only the rate of LAD, but also the amount of surfactant adsorption and the rate of possible hydrogen pickup. The development and experimental verification of the generalized electrochemical factor of CC were done with the use of the basic electrochemical characteristic of a material—its anodic polarization curve.

It was shown in [15] that the electrochemical length X (cm), corresponding to nonuniformity of electric field distribution in crevice corrosion, depends on metal nature [slope of the anodic polarization curve, k (A cm^{-2} V^{-1}), near the steady-state potential], nature of electrolyte [conductivity æ (Ohm^{-1} cm^{-1})], and geometric size of the system [crevice width a (cm)] and is defined by

$$X = [æa/(4k)]^{1/2}. \quad (1)$$

It is known [16] that the most important geometric factor of CC of metallic materials is the ratio of the cross-section area to the perimeter, S/Per (cm). Replacing in (1) the quantity a with the ratio S/Per, characterizing geometric changes in the system in the case of CC, we obtain an expression for the current electrochemical length γ (cm) corresponding to nonuniformity of the electric field distribution in CC at an arbitrary instant of time:

$$\gamma = [æ(S/\mathrm{per})/(4k)]^{1/2}, \quad (2)$$

where æ and k are current values of the electrochemical characteristics of the system.

Beginning with the instant of time when strained metal is brought in contact with a medium, not only k and æ, but also the geometric size of the system, S/Per, may change as a result of, e.g., formation of protective films on the surface and their possible local

1070-4272/01/7412-2027 $25.00

destruction under the action of tensile stresses under conditions of CC. Therefore, let us consider now the initial period of the process and take kinetic features into account later. Denoting the fraction of the surface area covered with a protective film by θ and introducing notions of the base system (θ = 0) and that under study (0 < θ ≤ 1), we obtain respective expressions for the electrochemical lengths corresponding to nonuniformity of electric field distribution under the conditions of CC at the initial instant of time:

$$\gamma_0 = [æ_0(S/\mathrm{Per})_0/(4k_0)]^{1/2}, \quad (3)$$

$$\gamma'_0 = [æ'_0(S/\mathrm{Per})_0(1 - \theta)/(4k'_0)]^{1/2}, \quad (4)$$

where $æ_0$, k_0, $(S/\mathrm{Per})_0$, $æ'_0$, k'_0, and $(S/\mathrm{Per})'_0(1 - \theta)$ are the initial values of the electrochemical characteristics and geometric sizes of the base system and that under study, respectively; $(1 - \theta)$ is the fraction of the surface not occupied by the protective film.

Under the general corrosion conditions, the fraction of the surface area not occupied by the protective film can be described by [17]

$$1 - \theta = j'_{a,0}/j_{a,0}, \quad (5)$$

where $j_{a,0}$ and $j'_{a,0}$ are the anode current densities at the steady-state potential E_s without and with an inhibitor present in the medium, respectively.

With account taken of the possible changes in potential, ΔE, in the case of local kinds of corrosion [18], including that by 0.2 V in corrosion cracking [19], it seems appropriate to replace the ratio of current densities in (5) with the ratio of areas under anodic polarization curves, N'_0/N_0, at potentials in the range 0–0.2 V, i.e.,

$$1 - \theta = N'_0/N_0, \quad (6)$$

where N_0 and N'_0 are the areas under the anodic polarization curve at potentials of 0–0.2 V without and with inhibitor.

Substituting (6) into Eq. (4), we obtain an expression for the initial electrochemical length in any system studied:

$$\gamma'_0 = \{[æ'_0(S/\mathrm{Per})_0(N'_0/N_0)]/(4k'_0)\}^{1/2}. \quad (7)$$

Let us assume that the ratio of left-hand sides of expressions (7) and (3) can be used to describe the corrosion-mechanical behavior of any system studied not only at the initial stage of the process, but also at any arbitrary instant of time. Let us denote by z this quantity, which is a generalized dimensionless electrochemical factor simultaneously taking into account the nature of metal, corrosive medium, and, in part, the role played by tensile stresses (via changes in the geometric size of the system). For the initial instant of time, we can write

$$z = \gamma'_0/\gamma_0 = (\bar{æ}\bar{N}/\bar{k})^{1/2}, \quad 0 < z \le 1, \quad (8)$$

$$æ = \bar{æ}'_0/æ_0, \quad (9)$$

$$\bar{k} = k'_0/k_0, \quad \bar{k} \in \bar{k}(\Delta E = 25\text{–}75 \text{ mV}), \quad (10)$$

$$\bar{N} = N'_0/N_0, \quad \bar{N} \in \bar{N}(\Delta E = 0\text{–}200 \text{ mV}). \quad (11)$$

It can be seen from formulas (8)–(11) that the numerical values of the dimensionless factor corresponding to condition (8) can be found from a set of three dimensionless electrochemical characteristics calculated using expressions (9)–(11).

To verify experimentally the above assumptions, we carried out a set of corrosion-mechanical and electrochemical measurements under the conditions of natural aeration of solutions at room temperature. We passed from one system to another by changing the composition of a medium by introducing into the base solution various CC-inhibiting additives (see table, systems nos. 4–10, 12, 13) or by diluting the base solution with distilled water (systems nos. 2, 3, 11). As material was used St.70 high-strength carbon steel [GOST (State Standard) 9389–60]. The choice of the base system was governed by the high sensitivity of St.70 to CC in acid sulfide-containing media [20].

The electrical conductivity æ of the solutions was measured with R5058 high-frequency ac bridge and an Arrhenius vessel with platinum-plated electrodes under conditions of thermostating at 25°C [21]. The obtained æ values are presented in the table.

Polarization measurements were done with a P-5827M potentiostat with separated cathode and anode spaces in the potentiodynamic mode with potential sweep rate of 2 mV s^{-1}. The inoperative surfaces of the unstrained electrodes under study were insulated with a 1 : 1 mixture of wax and rosin. Platinum was used as auxiliary electrode, and silver chloride electrode, as reference. The potentials are given relative to a standard hydrogen electrode. Prior to measuring anodic polarization curves, samples were subjected to cathodic activation at E = –1.2 V for 10 min. The anodic polarization curves obtained on St.70 in the media under study are presented in Fig. 1, and the table lists the results of their processing (values of k and N) and, in descending order, the

Effect of the systems studied and their characteristics on CC of St.70 steel

System no.	System*	æ, $Ohm^{-1}\ cm^{-1}$	k, $A\ cm^{-2}\ V^{-1}$	$N \times 10^4$, $A\ V\ cm^{-2}$	τ, h	z	α
1	B	0.0844	0.1172	20.0	(0.13 ± 0.09)**	1.0	–
2	B : H_2O:						
	1 : 1	0.0487	0.0306	5.9	0.45	0.807	3.5
3	1 : 3	0.0267	0.0239	7.0	1.32	0.737	10.1
4	B + urotropine, 1 g l^{-1}	0.0513	0.0680	9.3	1.33	0.698	10.2
5	B + 25% solution NH_4OH, 40 ml l^{-1}	0.0374	0.0397	7.23	1.50	0.688	11.5
6	B + MEA, 20 ml l^{-1}	0.0281	0.0176	3.79	(2.9 ± 0.6)***	0.648	22.3
7	B + benzotriazole, 5 g l^{-1}	0.068	0.0188	1.2	19	0.549	146
	B + 25% solution NH_4OH, ml l^{-1}:						
8	80	0.0343	0.0213	1.5	(505 ± 130)***	0.422	3885
9	160	0.0311	0.1183	9.4	(648 ± 128)***	0.414	4985
10	320	0.0250	0.0050	0.48	(1088 ± 400)***	0.408	8369
11	B : H_2O = 1 : 10 B + MEA, ml l^{-1}:	0.0123	0.0274	5.3	7000****	0.406	>53846
12	160	0.0165	0.0341	4.5	7000****	0.389	>53846
13	320	0.0085	0.0340	7.9	7000****	0.370	>53846

* B is the base solution of composition (M): H_2SO_4 0.25, Na_2S 6×10^{-4}; MEA is monoethanolamine.

** Average of 12 runs.

*** Average of 13 runs.

**** No sample destruction occurs.

numerical values of the factor z, calculated using formulas (8)–(11) for the systems studied.

The corrosion-mechanical tests of St.70 wire samples 0.09 cm in diameter were carried out under constant strain conditions [20, 22] without polarization and with a waterline at stresses exceeding the elastic limit and corresponding to approximately 74% of the ultimate strength. For this purpose, a sample 110 mm long without stress concentrator was bent, after standard pretreatment, in its middle part, fixed in apertures of the support plank, thoroughly degreased, and submerged in a solution under study (50 ml), and the time to cracking, τ (h), was determined at the chosen test duration of 7000 h, exceeding the average τ in the base system St.70–H_2SO_4 (0.25 M)–Na_2S (6×10^{-4} M (see table, E_s = –0.32 V, z = 1) more than 5×10^4-fold. Cells with samples were covered with a special glass case to prevent changes in solution composition in the course of the tests. The distance between the apertures of the support plank, h, and the sample curvature radius R_w were, respectively, 32 and 16 mm, which ensured a tensile stress in the lower, U-shaped, part of a sample in solution, corresponding to metal deformation in the case of metal corrosion under strain. The occurrence of plastic de-

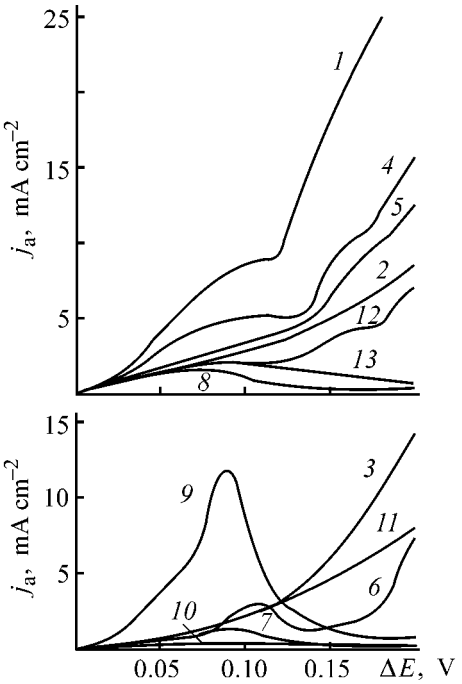

Fig. 1. Anode current density j_a vs. potential shift ΔE reckoned from the steady-state value E_s for St.70 in solutions of various compositions. *Digits at curves* correspond to system numbers in the table.

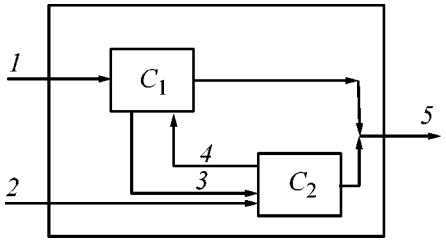

Fig. 2. Schematic of the process of corrosion cracking as a complex system. C_1 and C_2, elements of the system: C_1 electrochemical process; C_2, mechanical process; (*1*, *2*) external couplings of the system: (*1*) *z*, (*2*) σ; (*3*, *4*) internal couplings between the elements of the system; (*5*) output (result of functioning) of the system (τ_{in}, $\tau_{c.g.}$, τ, α).

formation was confirmed in a blank run: on removing the sample from the support plank it retained a U-bent shape ($R > R_w$). The numerical value of the tensile stress under the conditions of constant strain (~$0.74\sigma_u$) was found on performing an additional set of experiments (under conditions of constant, as measured with dynamometer, axial tension in the base system, $z = 1$) ensuring close values of the time to cracking, τ. The effect α of protection against CC upon introduction of an inhibiting additive into the base solution was calculated using the formula

$$\alpha = \tau/\tau_0, \qquad (12)$$

where τ_0 and τ are the times to cracking of, respectively, the base system ($z = 1$) and that under study ($0 < z < 1$).

The results of corrosion-mechanical tests are presented in the table. It can be seen that a correlation is clearly traced between the generalized factor *z* and susceptibility of St.70 to CC: with decreasing *z*, the time τ to cracking becomes longer. It should be noted that no other separately taken characteristic of the system (æ, *k*, *N*) exerts such an influence. Also, the factor *z* has a threshold value z_{th}, which accounts for the specific course of the CC process: at $z \le z_{th}$ (systems nos. 11–13) there is no cracking and the material can be assessed under these conditions (at the same level of tensile stress) as stable against CC. For example, high susceptibility of St.70 to CC in acid sulfide-containing media (system no. 1) is completely suppressed by introduction of MEA into solutions, in concentrations ensuring a generalized factor value $z < z_{th}$ (systems nos. 12, 13). Low concentration of MEA (system no. 6), not ensuring a threshold value of the factor *z*, fails to rule out CC, even though producing a substantial protective inhibiting effect (see table). It should be emphasized that the error of experimental determination of z_{th} does not exceed 0.5% since the z_{th} value corresponds to a rather narrow interval $0.406 \le z < 0.408$.

To develop a quantitative theory of the CC process, based on the nonuniformity of electric field distribution over the surface of strained metal in a corrosive medium and on the general principles of systems analysis [23–25], we proceed from the assumption that the total time to destruction is a sum of two times [5]:

$$\tau = \tau_{in} + \tau_{c.g}, \qquad (13)$$

where τ_{in} is the incubation time in which a stress concentrator of the type of a crack is formed under conditions of a corrosive-mechanical process, and $\tau_{c.g}$ is the time of crack growth in strained metal to a critical value corresponding to its destruction in a corrosive medium.

The corrosion-mechanical process will be regarded as a complex deterministic dynamic system with distributed parameters (factors), comprising an electrochemical and a mechanical processes (Fig. 2) with inequiprobable couplings in different stages of CC. In the stage of crack formation, the electrochemical process exerts strong influence on the mechanical process, whereas the reverse influence is less significant and can be neglected. By contrast, in the crack growth stage, only the mechanical process affects the CC substantially. Let us assume that the dimensionless factors of these elementary processes are, respectively, the mean dimensionless electrochemical length corresponding to nonuniformity of the electric field distribution in the system ($z = \gamma'/\gamma_0$, where $0 < z \le 1$), and the mean dimensionless externally applied (or internal residual) tensile stress ($\sigma = \sigma/\sigma_u$, where σ_u is the ultimate strength of the metal). Applying the systems principle of kinetic hierarchy [24, 25] to CC, we reduce the problem of a kinetic description of the system to a study of the behavior of the slowest stage. We assume, with account of the data of [26], that under the CC conditions

$$\tau_{in} >> \tau_{c.g}, \qquad (14)$$

i.e., the rate *V* of the corrosive-mechanical process is determined by the stage of stress concentrator formation, V_{in}. Then, taking as a measure of the rate of stress concentrator formation under the CC conditions the rate of change (increase) in the dimensionless electrochemical length, V_{in}, we obtain the following kinetic equation for the incubation period of CC:

$$\pm\partial z/\partial\tau = (1/T)f(z, \bar{\sigma}), \qquad (15)$$

where $1/T$ is a positive variable factor accounting for the possible low CC rates ($0 < 1/T << 1$), and $\pm$ is the sign of the partial derivative $\partial z/\partial\tau$, depending on the chosen initial condition [(+) if $z(0) = z_{min}$, and (–) if $z(0) = z_{max} = 1$].

Applying another systems principle—decomposition [24], and the known Fourier method, we can represent the rate of the incubation period of CC as a product of three functions, two of which are mutually independent, and the third, $F(z, \bar{\sigma})$, accounts for the interaction of elementary processes:

$$-\partial z/\partial\tau = F(z, \bar{\sigma})f(z)f(\bar{\sigma}), \quad (16)$$

$$z \in \varphi(z), \quad \varphi(z) = z - z_{th} > 0, \quad (17)$$

$$\bar{\sigma} \in \Psi(\bar{\sigma}), \quad \Psi(\bar{\sigma}) = \bar{\sigma} - \bar{\sigma}_{th} > 0, \quad (18)$$

$$z(0) = z_{max} = 1, \quad (19)$$

where $f(z)$ is the nonstationarity function of the z field; $f(\bar{\sigma})$ is the nonstationarity function of the $\bar{\sigma}$ field [$f(\bar{\sigma}) = f(z, \bar{\sigma})/f(z)$]; $F(z, (\bar{\sigma}))$ is the nonuniformity function of the z and σ fields [$F(z, (\bar{\sigma})) = 1/T$]; and z_{th} and $\bar{\sigma}_{th}$ are the mean threshold values of dimensionless factors, beginning with which there is no CC.

Assuming a relationship between the electrochemical and mechanical processes in the form

$$z_{th} = F(\bar{\sigma}), \quad (20)$$

$$\bar{\sigma}_{th} = \Psi(z, z_{th}), \quad (21)$$

we have

$$F(z, \bar{\sigma}) = F(z, z_{th}). \quad (22)$$

If we take that the nonuniformity function $F(z, z_{th})$ contains graddiv z (or grad z), the mathematical construction (16)–(19) can be solved for a system with distributed parameters only numerically, on a computer. To obtain an analytical solution to (16)–(19), we assume [with account of the experimentally revealed strong influence of z on the rate of CC (see table)] that the mathematical expectation of the distribution function of the dimensionless factors with respect to their mean values (22) is described by the exponential Poisson distribution, which is widely used in practice [28]:

$$F(z, z_{th}) = [F(z_{th})/z]\exp\{-[F(z_{th})/z]\}, \quad (23)$$

where $F(z_{th})/z$ is the parameter of the distribution, assuming at any particular instant of time a unique value, with $F(z_{th})/z >> 1$; $F(z_{th})$ is a dimensionless function accounting for tensile stresses.

Combination of conditions (20) and (23) makes it possible to replace $f(\sigma)$ in (16) with a new function $\Psi(z_{th})$ taking into account tensile stresses:

$$\Psi(z_{th}) = f(\bar{\sigma})F(z_{th}). \quad (24)$$

Further, taking $f(z) = z^3$, i.e., assuming that the effect of z on the CC rate is similar, with account of (23), to the effect of temperature on the rate of chemical processes [29] and passing from a partial to total derivative with the use of the initial condition (19), we obtain a kinetic equation of CC

$$-dz/d\tau = \Psi(z_{th})z^2\exp\{-[F(z_{th})/z]\}, \quad (25)$$

whose boundary and initial conditions are, respectively, expressions (17) and (19).

Provided that the tensile stresses are constant (or strain is constant, which is the case in the experimental part of this study), the functions $\Psi(z_{th})$ and $F(z_{th})$ in expression (25) remain invariable. Denoting these functions by the constants

$$c = \Psi(z_{th}) = \varphi(\bar{\sigma}), \quad (26)$$

$$B = F(z_{th}) = \Phi(\bar{\sigma}), \quad (27)$$

we pass to a particular case of a kinetic equation describing the incubation period of CC

$$-dz/d\tau = cz^2\exp(-B/z), \quad (28)$$

where c has the meaning of the rate constant of the incubation period (h^{-1}).

Separating the variables, we obtain

$$(-1/z^2)\exp(B/z)dz = cd\tau, \quad (29)$$

$$\exp(B/z)d(1/z) = cd\tau. \quad (30)$$

Upon integration with the initial condition (19) we have the following expression for the duration of the incubation period of CC:

$$\tau_{in} = [1/(cB)]\exp(B/z) - [1/(cB)]\exp B, \quad (31)$$

where $z_{th} < z < 1$.

Introducing the following designation

$$A = 1/(cB) = \gamma(z_{th}) = \beta(\bar{\sigma}) \quad (32)$$

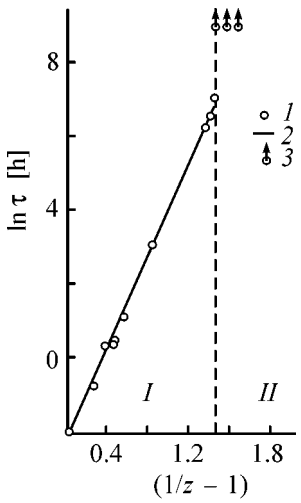

Fig. 3. Dependence of the time to cracking, τ, on the generalized parameter (1/*z* – 1) for the systems studied. (*1*) Experiment, (*2*) calculations using model (33), and (*3*) no sample destruction during the chosen testing time. (*I*, *II*) Regions of model applicability and absence of CC, respectively.

and comparing (31) and (13), we find expressions for calculating the time of crack growth and the total time to destruction under CC conditions:

$$\tau_{c.g} = A\exp B, \quad (33)$$

$$\tau = A\exp(B/z), \quad (34)$$

where $z_{th} < z \leq 1$.

The data obtained in our corrosion-mechanical investigations (see table) made it possible to find particular values of the applicability threshold of model (34) and its parameters:

$$z_{th}(\bar{\sigma} = 0.74) = 0.407, \quad (35)$$

$$B(\bar{\sigma} = 0.74) = 6.036, \quad (36)$$

$$A(\bar{\sigma} = 0.74) = 3.11 \times 10^{-4} \text{ h}, \quad (37)$$

and then establish general expressions for functions (27) and (32), describing the relationship between the model parameters and the threshold value of the proposed factor:

$$B = 1/z_{th}^2, \quad (38)$$

$$A = \tau_0/\exp B = \tau_0/\exp(1/z_{th}^2), \quad (39)$$

where τ_0 is the total time to metal destruction in the base system with $z_{max} = 1$ [see table, $\tau_0(\bar{\sigma} = 0.74) = 0.13$ h].

In this connection, the mathematical model (34) describing the total time to destruction under the conditions of plastic deformation of a metal in a corrosive medium ($\bar{\sigma}$ = const) assumes, on substitution of expression (39), with account of the clear physical meaning of the pre-exponential factor τ_0, a more convenient form

$$\tau = \tau_0\exp[B(1/z - 1)], \quad (40)$$

where z is the proposed generalized factor ($z_{th} < z \leq 1$); B and τ_0 are the obtained parameters of the model.

The results of a calculation relying upon the linearized model (40) (Fig. 3) are in satisfactory agreement with the obtained experimental data. A verification by means of Fisher's test [23–25] demonstrated the adequacy of the constructed model [$F^{calc}(9, 10) = 0.19$], with mean calculation error not exceeding 17% at average experimental error in determining the time to destruction equal to 34%. Therefore, the obtained mathematical model (40) of the CC process and its variety (34) can be used to prognosticate CC, provided that all the conditions specified in the study are satisfied.

The adequacy of the model described by expression (40) for evaluating the durability of a metallic material under the CC conditions also makes it possible to analyze a number of dependences and parameters obtained in its derivation. For example, it follows from a comparison of (33) and (39) that the duration of the crack growth period in a metal at arbitrary value of the factor z ($z_{th} < z < 1$) can be evaluated using the total time to metal destruction under the conditions corresponding to $z_{max} = 1$ and the same fixed tensile stress $\bar{\sigma}$. The exponential in (40) is the factor by which the total time to destruction exceeds the crack growth time at a given stress $\bar{\sigma}$. Another meaning of the exponential follows from a comparison of expressions (12) and (40). It reflects the protective (CC-inhibiting) effect, α, and can be used to evaluate this characteristic:

$$\alpha = \exp[B(1/z - 1)] = \exp[(1/z_{th}^2)(1/z - 1)]. \quad (41)$$

In addition, comparison of dependences (32), (38), and (39) gives a general expression for the function (26) describing the rate constant of CC:

$$c = 1/(\tau_0 B)\exp B = (z_{th}^2/\tau_0)\exp(1/z_{th}^2). \quad (42)$$

It should be noted that the adequacy of the mathematical model described by expression (40) apparent-

ly confirms the validity of the hypotheses put forward and assumptions made in this study for developing not only the generalized electrochemical factor of CC, z, but also a quantitative theory of CC in metallic materials in electrolyte solutions in general. The last circumstance requires additional experimental verification, which, in particular, refers to the quantitative condition (2).

CONCLUSIONS

(1) A new generalized dimensionless electrochemical factor of corrosion cracking, which takes into account the metal nature and the type of corrosive medium simultaneously, was developed and experimentally verified under conditions of constant plastic strain and test duration of 7000 h.

(2) A correlation between the generalized factor and the susceptibility of a material to corrosion cracking and the existence of the threshold value of this factor, above which there is no cracking, were established.

(3) A quantitative theory of corrosion cracking of alloys in electrolyte solutions was proposed, and mathematical models for evaluating the durability of a metallic material and the effect of inhibition of the corrosion cracking, adequately describing experimental data, were developed on its base.

REFERENCES

1. Logan, H.L., *The Stress Corrosion of Metals*, New York: Wiley, 1966.
2. Karpenko, G.V. and Vasilenko, I.I., *Korrozionnoe rastreskivanie stalei* (Corrosion Cracking of Steels), Kiev: Tekhnika, 1971.
3. Azhogin, F.F., *Korrozionnoe rastreskivanie i zashchita vysokoprochnykh stalei* (Corrosion Cracking and Protection of High-Strength Steels), Moscow: Metallurgiya, 1974.
4. Melekhov, R.K., *Korrozionnoe rastreskivanie titanovykh i alyuminievykh splavov* (Corrosion Cracking of Titanium and Aluminum Alloys), Kiev: Tekhnika, 1979.
5. Marichev, V.A. and Rozenfel'd, I.L., *Itogi nauki i tekhniki: Korroziya i zashchita ot korrozii* (Advances of Science and Technology: Corrosion and Corrosion Protection), Moscow: VINITI, 1978, vol. 7, pp. 5–41.
6. Ryabchenkov, A.V., Gerasimov, V.I., and Sidorov, V.P., *Itogi nauki i tekhniki: Korroziya i zashchita ot korrozii* (Advances of Science and Technology: Corrosion and Corrosion Protection), Moscow: VINITI, 1976, vol. 5, pp. 48–106.
7. *Zashchita ot korrozii, stareniya i biopovrezhdenii mashin, oborudovaniya i sooruzhenii: Spravochnik* (Protection from Corrosion, Aging, and Biodamage to Machines, Equipment, and Buildings), Gerasimenko, A.A., Ed., Moscow: Mashinostroenie, 1987, vol. 1.
8. Marichev, V.A., *Fiz.-Khim. Mekh. Mater.*, 1974, vol. 10, no. 3, pp. 3–7.
9. Speidel, M.O., *VGB Kraftwerkstechnik*, 1981, vol. 61, no. 5, pp. 417–427.
10. Kolotyrkin, Ya.M. and Novakovskii, V.M., Abstracts of Papers, *12-i Mendeleevskii s''ezd po obshchei i prikladnoi khimii* (12th Mendeleev Congress on General and Applied Chemistry), Moscow, 1981, no. 3, pp. 276–277.
11. Ryabchenkov, A.V. and Sidorov, V.P., *Zashch. Met.*, 1969, vol. 5, no. 4, pp. 376–381.
12. Petrov, L.N., *Fiz.-Khim. Mekh. Mater.*, 1981, vol. 17, no. 2, pp. 21–25.
13. Maslov, V.V., Sukhotin, A.M., and Reingeverts, M.D., *Zashch. Met.*, 1984, no. 1, pp. 120–124.
14. Sukhotin, A.M. and Reingeverts, M.D., *Extended Abstr. 2nd USSR–Japan Corrosion Seminar*, Tokyo, October 23–26, 1979, Tokyo, 1979, pp. 143–149.
15. Reingeverts, M.D. and Sukhotin, A.M., *Elektrokhimiya*, 1980, vol. 16, no. 1, pp. 46–49.
16. Skorchelletti, V.V., *Korroziya i zashchita metallov* (Corrosion and Metal Protection), Leningrad: Len. Politekhn. Inst., 1970.
17. Rozenfel'd, I.L., *Ingibitory korrozii* (Corrosion Inhibitors), Moscow: Khimiya, 1977.
18. Pickering, H.W. and Frankenthal, R.P., *J. Electrochem. Soc.*, 1972, vol. 119, no. 10, pp. 1287–1304.
19. Ryabchenkov, A.V. and Nikiforova, V.M., *Metalloved. Obrab. Met.*, 1956, no. 8, p. 2.
20. Zaitsev, V.A. and Leont'eva, N.A., *Zh. Prikl. Khim.*, 1996, vol. 69, no. 11, pp. 1885–1889.
21. Valueva, T.V., Baturova, L.P., and Skorchelletti, V.V., *Elektroprovodnost' rastvorov elektrolitov: Metodicheskie ukazaniya k laboratornym rabotam* (Electrical Conductivity of Electrolyte Solutions: Laboratory Manual), Leningrad: Len. Politekhn. Inst., 1976.
22. Borshchevskii A.M., Zaitsev V.A., Baturova L.P. *Korroziya i zashchita metallov: Metodicheskie ukazaniya k laboratornym rabotam* (Corrosion and Metal Protection: Laboratory Manual), St. Petersburg: SPb. Gos. Tekhn. Univ., 1993.
23. Sovetov, B.Ya. and Yakovlev, S.A., *Modelirovanie*

sistem (Modeling of Systems), Moscow: Vysshaya Shkola, 1985.

24. Aleksandrov, S.E., Golod, V.M., Lunev, V.A., and Fedotov, B.V., *Matematicheskoe modelirovanie metallurgicheskikh protsessov: Uchebnoe posobie* (Mathematical Modeling of Metallurgical Processes: Manual), Leningrad: Len. Politekhn. Inst., 1988.
25. Zakgeim, A.Yu., *Vvedenie v modelirovanie khimikotekhnologicheskikh protsessov* (Introduction into Modeling of Chemical-Technological Processes), Moscow: Khimiya, 1982.
26. Marichev, V.A., *Zashch. Met.*, 1973, vol. 9, no. 6, pp. 650–665.
27. Bukhbinder, A.I., *Teoriya potokov* (Theory of Flows), Leningrad: Len. Politekhn. Inst., 1973.
28. Maksimov, Yu.D., *Matematika. Vypusk 7. Teoriya veroyatnostei: Opornyi konspekt* (Mathematics, Issue 7, Probability Theory: Synopsis), St. Petersburg: SPb. Gos. Tekhn. Univ., 2000.
29. Patrov, B.V. and Sladkov, I.B., *Khimicheskaya kinetika: Uchebnoe posobie* (Chemical Kinetics: Manual), St. Petersburg: SPb. Gos. Tekhn. Univ., 1999.

Russian Journal of Applied Chemistry, Vol. 74, No. 12, 2001, pp. 2035–2039. Translated from Zhurnal Prikladnoi Khimii, Vol. 74, No. 12, 2001, pp. 1975–1979.

APPLIED ELECTROCHEMISTRY AND CORROSION PROTECTION OF METALS

Composite Copper-Based Coatings with Ultradispersed Phase

T. V. Rezchikova, E. N. Kurkin, V. N. Troitskii, L. S. Kiryukhina, A. V. Ivanov

Institute for Problems of Chemical Physics, Russian Academy of Sciences, Chernogolovka, Russia

Received April 10, 2001

Abstract—The electrolytic deposition of composite copper-based coatings with an ultradispersed phase (TiN or Al_2O_3) was studied. Conditions for obtaining coatings with the maximum microhardness were determined.

To improve the chemical and mechanical properties of electrolytic coatings, composite deposition of metallic layers with powdered high-melting compounds (nitrides, carbides, oxides, etc.) is commonly used [1–6]. However, with commercial coarse-grained (1–30 μm) powders, formation of composite electrolytic coatings with particles uniformly distributed on the microscopic level over the surface and across the thickness cannot be achieved, and the mechanical and chemical resistance of the coatings is improved only slightly.

It is known that formation of composite electrolytic coatings is essentially affected by particle size [1]. With crystalline ultradispersed powders (UDPs) having particle size in the range from tens to hundreds of nanometers, composite materials and coatings with improved physicochemical and mechanical properties can be obtained.

Ultradispersed powders are characterized by physicochemical properties different from those of macropowders (high surface energy, enhanced energy excitation of the crystal lattice, etc.). Studies are known, in which composite electrolytic coatings were obtained on the basis of nickel and chromium with the use of using UDPs. Analysis of published data shows that that the use of UDPs of niobium or titanium nitride [7, 8], tantalum nitride [9, 10], silicon carbide [11], or silicon nitride [12] as components of a composite electrolyte gives coatings with uniform finely grained structure and improved corrosion and mechanical properties (wear resistance, hardness, etc.).

In the present study, we analyzed the effect of UDP on the microhardness of copper coatings and pressed powder crystalline precipitates obtained from electrolytes widely used in industry.

Ultradispersed powders of titanium nitride and aluminum oxide with particle size of about 60 and 80 nm, respectively, were used in the study. Titanium nitride was obtained by decomposition of TiH_2 in arc-discharge nitrogen plasma, and Al_2O_3, by oxidation of ASD-4 aluminum powder in arc-discharge air plasma [13, 14].

EXPERIMENTAL

The coatings were deposited from simple copper-plating acid electrolytes containing (g l^{-1}): $Cu(BF_4)_2$ 400 ± 50, HBF_4 30, H_3BO_3 15 [fluoroborate electrolyte (I)]; $CuSO_4 \cdot 5H_2O$ 220, H_2SO_4 60, ethanol 8 [sulfate electrolyte (II)].

An ultradispersed powder was poured in an electrolyte prepared with distilled water, and the mixture was stirred. The electrolysis was carried out at room temperature with constant stirring of the electrolyte in a 2-l electrolytic bath (Fig. 1). Anodes were made of copper, as a cathode served a copper plate $15 \times 15 \times 1$ mm in size, on which a coating was

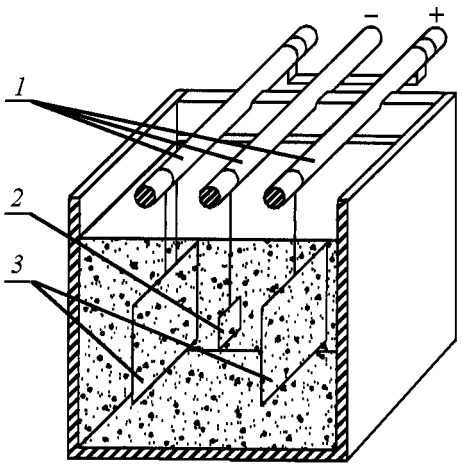

Fig. 1. Electrolytic bath. (*1*) Copper rods, (*2*) sample (copper plate), and (*3*) anodes.

1070-4272/01/7412-2035 $25.00 © 2001 MAIK "Nauka/Interperiodica"

Table 1. Effect of the TiN content in electrolyte on Ti content C_{Ti} in a coating and on microhardness H_μ

Electrolyte	C_{Ti}, mg g^{-1} / H_μ, HPa, at TiN content in electrolyte, g l^{-1}								i, A dm^{-2}
	0	0.2	0.4	1.0	2.0	2.5	10	100	
(I)	–/0.93	0.09/–	–/–	0.61/1.11	0.67/1.10	1.10/1.11	–/–	–/–	7.4
	–/1.08	–/–	–/1.18	–/1.23	–/1.24	–/1.27	–/–	–/–	11.0
(II)	–/0.74	–/–	–/–	–/–	–/0.77	–/–	0.76/0.74	1.48/0.86	7.4
	–/0.74	–/–	–/–	–/–	0.11/0.87	0.22/–	0.77/0.90	7.60/1.06	11.0

deposited. Prior to electrolysis, the copper plates were treated as described in [15] to remove an oxide layer and various impurities. The treatment involved: (1) etching in a 10% solution of H_2SO_4 at 60–70°C to remove oxides, (2) etching at room temperature in a mixture of equal volumes of concentrated HNO_3 and H_2SO_4 with addition of 5–10 g l^{-1} of NaCl to obtain a glossy, to the point of being lustrous, surface. Before etching, the copper plates were ground to luster with a micropowder.

The microhardness of the coatings was determined by the method of static indentation of a diamond pyramid under a load of 50 g on a Neophot device with measured diagonal values averaged over 10–12 indentations for each sample. The coating thickness was 100–200 μm.

The elemental compositions of the electrolyte and coatings were determined by means of chemical analysis. The high reactivity of UDPs and, in particular, TiN could result in their reaction with the electrolyte, and, therefore, we determined the content of dissolved titanium species in the composite electrolyte. The content of titanium and aluminum was determined in coatings and crystalline deposits. The content of the dispersed phase in composite coatings was calculated from the chemical analysis data. It is known that coarse powder of titanium nitride is sparingly soluble in acids. In particular, the solubility of TiN in dilute and concentrated sulfuric acid is 2%. To estimate the electrolyte stability, we determined the solubility of TiN UDPs in electrolyte (II) at varied content of the nitride:

TiN content in the electrolyte, g l^{-1}	2	10	100
Concentration of Ti(IV) ions in the electrolyte, mg ml^{-1}	0.27	0.43	1.13

The enhanced UDP solubility, compared with that of coarse-grained powders, seems to be associated with the large specific surface area of UDPs, with dissolution involving the oxidized surface layer covering the particles. It should be noted that the oxidation proceeds slowly and has a continuous nature, which was confirmed by X-ray phase analysis. X-ray diffraction patterns of the deposits taken from the bottom of the electrolytic bath within several months show that the deposits consist of TiN. Within three years, TiN in the deposit is almost completely converted into TiO_2 (all TiO_2 reflections and a single, the highest-intensity TiN reflection with *hkl* [200] were present in the diffraction pattern). This circumstance should be taken into consideration when working with the electrolyte.

Table 1 presents data on the content of titanium (mg per 1 g of coating) in coatings obtained in both electrolytes in relation to powder content in an electrolyte. The content of titanium is greater in the coatings, although the deposition rate in electrolyte (I) exceeds that in electrolyte (II). For the coatings obtained in electrolyte (I) at TiN content of 2.5 g l^{-1}, the content of the second phase in terms of TiN is 0.15 wt %, which is the highest value, since, according to X-ray phase analysis, a coating contains inclusions of the Cu_2O phase at greater TiN content in the electrolyte.

Despite the considerable increase in Ti content (0.19–0.98 wt % of TiN) in coatings obtained in electrolyte (II) at powder content of 100 g l^{-1}, this mode was not used further, as outgrowths are formed in large quantities on the edges of coatings. These outgrowths are easily chopped off, and the coating flakes away in places.

We optimized the current density for each electrolyte in obtaining composite electrolytic coatings. For this purpose, we determined the current density ranges, in which the titanium content in coatings is the highest and high-quality coatings are formed. In the range 7.4–11.0 A dm^{-2}, the average content of titanium nitride in coating (I) is 0.23 wt %. Beyond this range, the content of the second phase decreases, and, in addition, coatings with a rough crystalline surface are formed at current densities exceeding 11 A dm^{-2}.

In the same range of current densities, the titanium nitride content of 0.10–0.11 wt % in coatings remains unchanged in the case of electrolyte (II) with titanium nitride content of 10 g l^{-1}.

The microhardness of coatings H_μ was measured at various concentrations of titanium nitride in electrolytes and at current densities of 7.4 and 11.0 A dm^{-2} (Table 1). The microhardness of coatings obtained in electrolyte (I) varies between 0.93 (simple electrolyte) and 1.11 (i = 7.4 A dm^{-2}) and between 1.08 and 1.27 HPa (i = 11.0 A dm^{-2}), i.e., it is 1.3–1.5 times that of pure copper (0.85 HPa).

The microhardness of coatings obtained in electrolyte (II) has a maximum value of 1.06 HPa at TiN content of 100 g l^{-1}, which is 1.2 times the microhardness of pure copper. However, poorquality coatings were obtained in this case.

Coatings with Al_2O_3 UDPs were obtained in electrolyte (II) at powder content of 12.5 g l^{-1} and current densities of 7.4, 11.0, and 14.8 A dm^{-2}. The maximum current density was determined by the outward appearance of coatings (finely crystalline surface). Above the indicated current density, a rough surface and, according to X-ray diffraction patterns, the Cu_2O phase are formed. According to chemical analysis, the aluminum content in the coating is 0.22 wt % (or 0.41 wt % in terms of Al_2O_3; Table 2), irrespective of the current density. However, in contrast to coatings containing titanium nitride, the microhardness increases twofold, compared with that in pure copper (Table 2), being equal to 1.77 HPa at i = 14.8 A dm^{-2}.

Apart from deposition of strengthened coatings, it was of interest to obtain three-dimensional samples modified with an ultradispersed phase. For this purpose, we obtained powder crystalline precipitates, pressed to obtain compact samples.

Composite copper plating was carried out on six copper wire electrodes of diameter 0.18 mm and length 10 mm in electrolyte (II) containing 12.5 g l^{-1} of the Al_2O_3 UDP. The current strength was varied between 1 and 4 A, which provided the formation of easily removed deposits.

The resulting crystals were washed with distilled water and dried. To measure the microhardness, the crystals were pressed in a mold (cold pressing) under a pressure of 1.7 HPa. The fillets obtained were 8 mm in diameter, 3 mm in height and had porosity of 1.8%.

With the current strength raised from 1 to 4 A, the content of aluminum in crystalline copper precipitates increases from 0.21 to 0.84 wt % (or from 0.41 to 1.6 wt % in terms of Al_2O_3; Fig. 2, curve *1*). Correspondingly, the microhardness of pressed crystals grows from 1.37 to 1.75 HPa (Fig. 3, curve *1*).

Table 2. Effect of current density on the composition and microhardness of coatings

i, A dm^{-2}	Content in a coating, %		H_μ, HPa
	Al	Al_2O_3	
7.4	0.22	0.41	1.31
11.0	0.17	0.32	1.68
14.8	0.21	0.40	1.77

Thus, the microhardness of coatings and compact (pressed) finely crystalline precipitates containing Al_2O_3 UDP as the second phase increases twofold as compared with the microhardness of pure copper.

To reveal the possibility to vary the microhardness of cast copper by its modification with Al_2O_3 UDP, a sample was subjected to vacuum melting (1100°C). The sample was pressed from crystalline precipitates obtained at current strength of 1 A. Measurements of the microhardness of pressed and cast samples demonstrated that the microhardness of a cast sample is lower by 40%. The microhardness of the cold-pressed sample is 1.42, and that of the cast sample, 0.85 HPa,

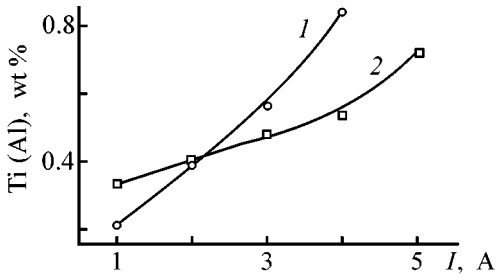

Fig. 2. Effect of current strength I on the Ti (Al) content in crystalline powder precipitates obtained in electrolyte (II). Content of UDP in electrolyte (g l^{-1}): Al_2O_3 12.5, TiN 10. Metal: (*1*) Al, (*2*) Ti; the same for Fig. 3.

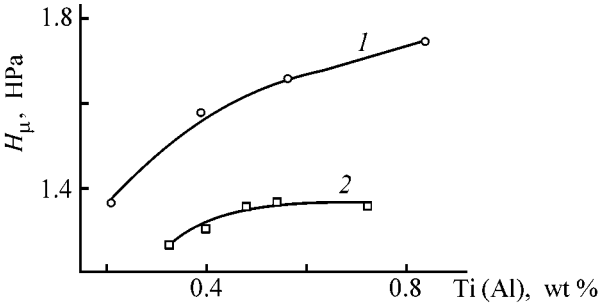

Fig. 3. Microhardness H_μ of pressed crystalline precipitates vs. the Ti (Al) content.

Table 3. Calculated contents of particles of the second phase in a unit volume of coating

Condition	Phase	d, μm	$V_p \times 10^{12}$, cm^3	N_c		$N_c / V_c \times 10^{-10}$
				wt %	vol %	
1	TiN	0.06	1.1×10^{-4}	0.15	0.88	10^4
	Al_2O_3	0.08	2.4×10^{-4}	0.41	1.6	10^4
2	TiN	1–5	0.52–65.4	0.15	0.88	$2–10^{-2}$
	Al_2O_3	1–5	0.52–65.4	0.41	1.6	$3–12 \times 10^{-2}$
3	TiN	1–5	0.52–65.4	10	63	$1.2 \times 10^2–1$
	Al_2O_3	1–5	0.52–65.4	10	40	$0.8 \times 10^2–0.6$

which corresponds to the microhardness of pure copper.

After vacuum melting, a gray powder in amount of 0.47 wt % relative to the weight of the initial sample was present in an ampule alongside with the sample. According to chemical analysis, the content of aluminum in crystals obtained as a result of electrolytic copper plating at a current strength of 1 A was 0.21 wt % (0.41 wt % in terms of Al_2O_3). Thus, the decrease in the microhardness of the cast sample is related to the removal of Al_2O_3 from it. Upon melting, Al_2O_3 was isolated from the bulk sample owing to the low wettability of Al_2O_3.

The titanium content of crystalline deposits obtained from electrolyte (II) with 10 g l^{-1} of TiN grows from 0.33 to 0.70 wt % (from 0.42 to 0.93 wt % in terms of TiN) with the current strength increasing in the range 1–5 A (Fig. 2, curve *2*). In this case, the microhardness of pressed compacts increases from 1.26 to 1.37 HPa (Fig. 3, curve *2*), i.e., by a factor of 1.6 as compared with the microhardness of pure copper, being somewhat greater than that in coatings.

It is known that the content of Al_2O_3 in coatings obtained from a sulfate composite electrolyte with coarse powders is 0.2–0.5 wt % at powder concentrations in the electrolyte of 50–200 g l^{-1} [1]. In practice, the microhardness of Cu–Al_2O_3 coatings obtained from a sulfate composite electrolyte can be raised to 2.4–2.9 HPa by introducing special additives into the electrolyte [1], with the Al_2O_3 content increasing up to 5.5–7.3 wt %.

To find the content of the second phase in the coating, we calculated the content N_c of particles in the formulation bulk at a known percentage X_p and average particle volume V_p [3]:

$$N_c = V_c X_p / 100 \times V_p.$$

The calculation was performed under the following conditions: (1) size of TiN particles 0.06 μm, that of Al_2O_3 particles – 0.08 μm; content of TiN and Al_2O_3 0.15 and 0.41 wt %, respectively (experimental data); (2) content of the second phase the same, but with particle size assumed to be 1–5 μm; (3) particle size 1–5 μm, content of the second phase 10 wt % (assumption).

The calculation demonstrated (Table 3) that the use of UDPs without special additives at small content of the second phase (0.15–0.41 wt %) gives the content of particles in a coating of about 10^{14}, whereas the content of 1–5-μm particles is 10^{10}–10^8, i.e., the content of ultradisperse particles is greater by 4–6 orders of magnitude. When the content of the second phase is 10 wt %, the content of 1–5-μm particles is 10^{10}–10^{12}, i.e., under the same conditions the content of ultradisperse particles is greater by 2–4 orders of magnitude. In this case, the microhardness is 1.5–2 times higher.

The mechanism of strengthening of the electroplated metal by dispersed particles was considered in [3]. The dispersed particles, being incorporated in a metal being deposited, distort its crystal structure and form defects (dislocations), which results in coating strengthening, since the action of force on the metal causes a shear deformation of the crystal, which propagates along the least distorted directions of the crystal lattice. The dispersed particles incorporated into coatings take up the shear stress and also hinder displacement of microlayers. The presence in the electrolyte of particles in direct contact with the cathode also results in coating strengthening, since at the instance of impact a particle screens the cathode, thereby disrupting the original sequence of atomic layers.

The use of UDPs at low content of the second phase in coatings and deposits gives rise to a signif-

icant number of dislocations hindering the propagation of the shear deformation and making the electrolytic deposits stronger, which results in higher microhardness of coatings and powder crystalline deposits. We can assume that the electrical conductivity of copper coatings remains unchanged at the indicated content of the second phase in the coatings.

CONCLUSIONS

(1) Introduction of ultradispersed powder of titanium nitride and aluminum oxide with particle size of 0.06–0.08 μm in a composite electrolyte, instead of the commonly used coarse powders (1–5 μm), allows the microhardness of copper coatings and precipitates to be raised by a factor of 1.5 (with TiN) and 2 (with Al_2O_3), compared with pure copper coatings.

(2) The increase in microhardness was achieved: (a) at lower content of the ultradispersed phase in electrolytes (TiN 2.5 and Al_2O_3 12.5 g l^{-1}), compared with the content of coarse powders (50–200 g l^{-1}); and (b) at lower content of the second phase in coatings and deposits (0.15–1.6 wt %), compared with the case of coarse powders (2–10 wt %). This makes it possible to largely retain in a coating the properties inherent in the copper substrates.

(3) The calculation demonstrated that the number of ultradispersed particles in unit coating volume is 4–6 orders of magnitude greater than that of particles 1–5 μm in size. As a consequence, a significant amount of dislocations is formed, which hinders propagation of shear deformation and makes electrolytic deposits stronger.

REFERENCES

1. Saifullin, R.S., *Neorganicheskie kompositsionnye materialy* (Inorganic Composite Materials), Moscow: Khimiya, 1983.
2. Saifullin, R.S., *Kombinirovannye elektrokhimicheskie pokrytiya i materialy* (Combined Electrochemical Coatings and Materials), Moscow: Khimiya, 1972.
3. Antropov, L.I. and Lebedinskii, Yu.N., *Kompositsionnye elektrokhimicheskie pokrytiya i materialy* (Composite Electrochemical Coatings and Materials), Kiev: Tekhnika, 1986.
4. Borodin, I.N., *Poroshkovaya gal'vanotekhnika* (Powder Electroplating), Moscow: Mashinostroenie, 1990.
5. Lukashev, E.A., *Elektrokhim.*, 1994, vol. 30, no. 1, pp. 93–97.
6. Shatov, Yu.S., Kozyr™, I.G., Korobeinikov, S.N., and Bairikov, Yu.K., *Izv. Vyssh. Uchebn. Zaved., Chern. Metall.*, 1998, no. 7, pp. 55–56.
7. Khaldeev, G.V., Yagodkina, L.M., Popova, N.A., and Grebtsova, O.M., *plazmokhimicheskie protsessy v technologii nitridov: Sbornik nauchnykh trudov* (Plasmochemical Processes in the Technology of Nitrides: Coll. of Sci. Works), Zhavoronkov, N.V., Ed., Chernogolovka, 1984, pp. 71–77.
8. Yagodkina, L.M., Khaldeev, G.V., Andryushechkin, V.I., and Berestenko, V.I., *Plazmokhimicheskie protsessy v technologii nitridov: Sbornik nauchnykh trudov* (Plasmochemical Processes in the Technology of Nitrides: Coll. of Sci. Works), Zhavoronkov, N.V., Ed., Chernogolovka, 1984, pp. 77–82.
9. Ageenko, N.S., Kornilov, A.A., Gavrilko, V.P., and Gusev, A.A., *Primenenie nizkotemperaturnoi plazmy v technologii neorganicheeskikh veshchestv i poroshkovoi metallurgii: Sbornik nauchnykh trudov* (Application of a Low-temperature Plasma in the Technology of Inorganic Substances and Powder Metallurgy: Coll. of Sci. Works), Miller, T.N., Ed., Riga: Zinatne, 1985, vol. 2, pp. 149–153.
10. Ageenko, N.S. and Gavrilko, V.P., *Zh. Prikl. Khim.*, 1984, vol. 57, no. 10, pp. 2269–2272.
11. Ageenko, N.S., Galevskii, G.V., Gordina, L.D., and Baranova, L.N., *Plazmennye protsessy v khimicheskoi promyshlennosti: Sbornik nauchnykh trudov* (Plasma Processes in Chemical Industry: Coll. of Sci. Works), Polak, L.S. , Ed., Chernogolovka, 1987, pp. 46–54.
12. Zharostoikie neorganicheskie pokrytiya (Temperature-Resistant Inorganic Coatings), Borisenko, A.I., Ed., Leningrad: Nauka, 1990.
13. Alekseev, N.V., Samokhin, A.V., Troitskaya, E.V., and Balikhin, I.L., Absracts of Papers, *Mezdunarodnyi simpozium po teoreticheskoi i prikladnoi plazmokhimii* (Int. Symposium on Theoretic and Applied Plasmochemistry), Riga, 1991. Riga, 1991, pp. 21–25.
14. Alekseev, N.V., Balikhin, I.L., Kurkin, E.N., *et al.*, *Fiz. Khim. Obrab. Mater.*, 1994, no. 4–5, pp. 72–78.
15. Lainer, V.I., *Zashchitnye pokrytiya metallov* (Protective Coatings of Metals), Moscow: Metallurgiya, 1974.

Russian Journal of Applied Chemistry, Vol. 74, No. 12, 2001, pp. 2040–2044. Translated from Zhurnal Prikladnoi Khimii, Vol. 74, No. 12, 2001, pp. 1980–1984.

APPLIED ELECTROCHEMISTRY AND CORROSION PROTECTION OF METALS

A Study of Charge Preservation with Coulometer Based on Solid Copper-Ion-Conducting Electrolyte

I. E. Shpak and A. M. Mikhailova

Saratov State Technical University, Saratov, Russia

Received February 2, 2001

Abstract—The influence of the material of an inert electrode on the coulometric reversibility of electrodeposition and dissolution of copper in a cell with $Rb_4Cu_{16}C_{13}I_7$ solid electrolyte was studied. The reasons for time instability of the electrolyte and coulometric reversibility were analyzed.

Compared with analogous liquid-phase systems, solid-electrolyte (SE) electrochemical cells have a number of advantages: they are manufactured by simpler technology, are more suitable for miniaturization, have high resistance to mechanical action, can operate in a wide temperature range (–60–200°C), possess long service and storage life (up to 10 years), and can be manufactured in a single run with fabrication of an electronic unit. As a rule, the known coulometers are based on silver systems [1]. A study of copper-conducting electrochemical systems is necessitated by their possible application to exclude use of precious metals. In this case, the ability of a coulometer to preserve coulometric reversibility in the course of time is a key issue.

EXPERIMENTAL

Coulometer samples were prepared in a box in dry argon. The copper electrode was a mixture of powdered copper and copper-ion-conducting electrolyte of composition $Rb_4Cu_{16}Cl_{13}I_7$ (mass ratio 1 : 1). As inert electrodes were used platinum, carbon black–graphite mixture with polyacrylonitrile (PAN) binder, and glassy carbon. As current lead served titanium wire. The internal ac resistance of the samples was within 8–12 Ω.

The nonequivalence of the quantities of electricity passed during the cathodic and anodic processes for all the three inert electrodes is illustrated in the table. The presented data show that, except in the case of

Nonequivalence of the quantities of electricity passed in deposition and dissolution of copper on various electrodes at 25°C

Current, μA	Nonequivalence of the quantity of electricity, %, in indicated cycle									
	1st	2nd	3rd	4th	5th	6th	7th	8th	9th	10th
Graphite electrode										
50	31.2	29.7	28.2	27.5	27.2	26.7	24.4	23.6	23.1	22.2
100	12.5	10.7	8.8	8.2	7.8	7.0	6.6	6.2	5.4	5.3
500	10.9	11.5	12.5	13.5	14.2	14.4	14.0	15.0	15.1	15.1
Glassy carbon electrode										
50	14.3	13.7	13.4	13.0	13.4	12.4	12.4	12.0	11.9	11.8
100	10.5	10.7	10.8	11.0	11.0	11.0	11.0	10.9	10.9	10.7
500	–	–	3.0	2.7	2.5	2.2	2.2	2.0	2.0	2.0
1000	4.5	3.5	3.0	2.4	2.0	1.6	1.5	1.1	1.3	1.1
Platinum electrode										
50	37.0	36.0	35.3	35.0	34.7	34.0	33.7	33.3	33.0	32.0
100	18.2	17.0	18.1	15.7	15.4	15.3	15.2	14.8	14.7	14.5
500	10.7	10.0	9.0	8.5	8.1	7.5	7.1	6.9	6.6	6.4
1000	6.9	3.7	3.4	3.2	3.0	2.9	2.8	2.3	2.1	2.0

1070-4272/01/7412-2040 $25.00 © 2001 MAIK "Nauka/Interperiodica"

the graphite electrode, the nonequivalence is high during several first cycles and decreases approximately linearly with cycling and increasing current density. The best reversibility of cathodic and anodic processes is characteristic of the inert glassy carbon electrode.

If copper is deposited onto a mixture of graphite with PAN binder and the deposit is anodically dissolved after 1 h, then the nonequivalence of the cathodic and anodic quantities of electricity will be 35%. This value decreases somewhat in further cycling of the electrode. When copper deposit is dissolved 2 h after its preparation, the coulometric nonequivalence becomes as high as 50%. The same was observed on the platinum electrode. For a deposit stored for 1 day after preparation, the nonequivalence increases to 80% and remains large till the 10th cycle.

The cells cycled continuously for a long time (~1 month) degraded, which was manifested in an increase in their internal resistance and impossibility to pass high current densities through the cells.

The stationary potentials of the inert electrodes were 0.545–0.550, 0.53–0.538, and 0.519–0.525 V for graphite, platinum, and glassy carbon, respectively. The closeness of these potentials to the potential of the iodine electrode suggests that the solid electrolyte decomposes at the interface with inert electrodes or, at least, the concentration of free iodine in the near-electrode layer of the electrolyte is noticeable. This assumption is corroborated by the fact that, when the potential of the inert electrode of an assembled cell is shifted from the stationary value toward positive potentials, high currents are observed in the current–voltage characteristic (Fig. 1). The polarization resistances, calculated using the initial parts of the curves, were 640, 1660, and 133 $\Omega\,cm^2$, on the average, for graphite, platinum, and glassy carbon electrodes, respectively, at 25°C.

The cyclic polarization curves of solid electrolyte oxidation and reduction of electrolyte oxidation products at the interface between the solid electrolyte and the platinum electrode are presented in Fig. 2. The character of these curves reflects the stage-by-stage nature of oxidation–reduction processes in the solid electrolyte.

The observed dependence of the oxidation and reduction current peak potentials on the potential sweep rate indicates the irreversibility of these processes.

The whole set of the presented data shows that the electrolyte decomposes at some rate even at potentials close to 0.5 V. This instability of the electrolyte was also manifested in that, despite the termination of

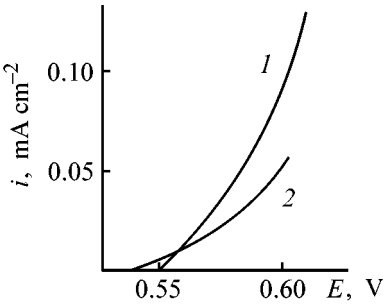

Fig. 1. Initial portions of cyclic potentiodynamic curves in the first cycle for various inert electrodes. Electrode: (*1*) Carbon black–graphite + PAN and (*2*) Pt.

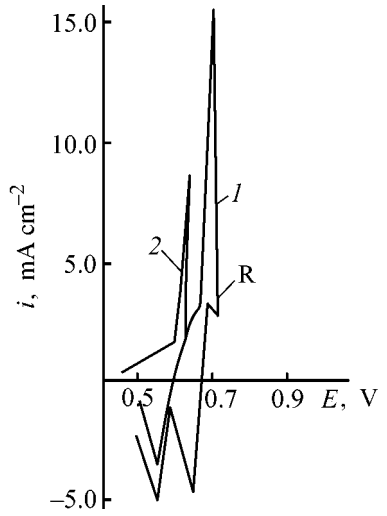

Fig. 2. Cyclic potentiodynamic curves of the $SE(Cu^+)\,|\,Pt$ interface at different potentials of potential sweep direction switching, E_R. $V_s = 8 \times 10^{-4}$ V s^{-1}, T = 25°C; the same for Fig. 3. E_R (V): (*1*) 0.72 and (*2*) 0.65.

cell cycling each time after the cathodic semi-cycle, ensuring reduction of the oxidation products, and even after deposition and subsequent dissolution of copper on an inert electrode, prolonged storage of the cell (~1 month) led to complete degradation of the solid electrolyte. This is manifested, in the first place, in a drastic decrease in currents in electrode polarization. The change in the phase composition of SE was confirmed by X-ray phase analysis.

Noteworthy is the presence near E = 0.6 V of a weakly pronounced peak of current of electrolyte oxidation on the platinum electrode in the initial portion of curve *2*, possibly associated with copper dissolution occurring independently of electrolyte oxidation. With account taken of the small capacity (5–6 mC cm^{-2}) under the peak, it may be suggested that this current peak corresponds to dissolution of a copper microphase layer from the surface of platinum

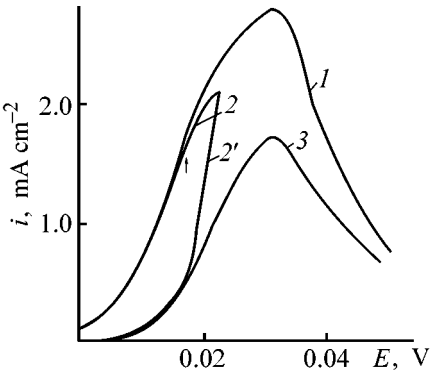

Fig. 3. Potentiodynamic curves of copper deposit dissolution from glassy carbon. Curve numbers: (*1*) taken to a potential of 0.055 V; (*2*, *2*′) anodic semi-cycle to 0.022 V; and (*3*) obtained immediately after measuring curve *2*.

(adsorption layer). The difference ΔE_d of the peak potentials of macro- and microphase dissolution is linearly related to the difference of the electron work functions, $\Delta\Phi$, of deposited metal and material of the inert electrode by the equation [2]

$$\Delta E_d = \alpha\Delta\Phi, \quad (1)$$

where $\alpha = 0.5$ V eV^{-1}.

Estimation of ΔE_d by means of Eq. (1) at $\Delta\Phi$ = 0.85 eV gives 0.425 V, a value rather close to the experimental ΔE_d = 0.576 V.

The coulometric reversibility of copper deposition onto, and dissolution from an inert glassy carbon electrode was studied by chronovoltammetry at copper amounts deposited onto electrode, ensuring the microphase formation. In this case, the amount of the deposit, expressed in charge units, varied between 37.5 and 750 mC cm^{-2}. The minimum thickness of the layer formed by the reaction

$$Cu^+ + e = Cu^0,$$

was 200–300 monolayers. It was found that copper dissolution from the glassy carbon surface occurs in two stages, which is indicated by the presence of two current peaks in the potentiodynamic curves of copper dissolution (Fig. 3). These two processes occur in parallel to a +0.022 V potential. The transfer coefficients β, calculated from the dependences $\ln\{-i/\exp(-nF\eta/RT) - 1\}-\eta$ plotted for the initial portions of curves *1* and *2* at n = 1 and 2, are considerably higher than unity (1.22–3.87). Such large coefficients, and also the nonlinearity of the dependences at low overvoltages, can be accounted for by the control exerted over the process by the rate of dissolution of two-dimensional nuclei. In the overvoltage range in question, this mechanism of control is not replaced yet by the charge-transfer-controlled mechanism. Analysis of the dependences of the dissolution current peak potentials on ln V_s allowed calculation of the number of electrons involved in the reaction, which was found to be approximately 2, i.e., two electrons are transferred in the second, reversible stage of copper dissolution.

Storage of an electrode with copper deposit for several days leads to a decrease in the intensity of the current peaks and to a nonlinear dependence of the peak potential on the logarithm of the potential sweep rate, which may be due to electrolyte degradation.

Owing to the large amount of deposit on the inert electrode, it is difficult to account for the presence of two peaks in the potentiodynamic curves of copper dissolution by the existence of two energy states of copper on the glassy carbon surface. It is reasonable to assume that the second peak corresponds to the reaction

$$Cu^0 - 2e = Cu^{2+}. \quad (2)$$

The assumption that the first peak is attributable to the reaction

$$Cu^0 - e = Cu^+, \quad (3)$$

is at variance with the data of Fig. 3. Since only a minor portion of the deposit dissolves during the anodic semi-cycle at potentials of up to 0.022 V, the activity of the copper electrode and the phase composition at the metall–electrolyte interface do not alter. Then, two peaks should have also been observed in subsequent anodic semi-cycle, which is not the case in the experiment. Apparently, it is more reasonable to assume that the first peak corresponds to oxidation of Cu^+ to Cu^{2+}.

The proposed interpretation of the potentiodynamic curves of copper dissolution in a solid electrolyte with conduction by copper cations is in agreement with the mechanism of the well-known instability of copper-conducting solid electrolytes [3]. This mechanism is based on the possibility of electrochemical or chemical oxidation of the conducting ions of the solid electrolyte from Cu^+ to Cu^{2+}. The concomitant increase in the hole concentration makes higher the hole conductivity of SE. As a result, copper cations can be reduced not only at the electrode surface, but also in the near-electrode layer of ES. This results in the formation of a thin electrolyte layer with high electron-hole conductivity. The copper atoms in this layer are uniformly distributed in the bulk. Evidently,

the current peaks in copper dissolution in such a layer will be dependent on the amount of preliminarily deposited copper.

Apparently, the patterns of anodic dissolution from such a layer must be similar to those observed in dissolution of metals from thin films of their amalgams, characterized by a proportional dependence of the peak current on V_s^{λ}, where λ may assume, depending on film thickness, values ranging from 0.5 to 1.0 (for thick and thin films, respectively). In accordance with this assumption, the dependence of $\ln i_d$ on $\ln V_s$ must be linear with a slope equal to λ. The constructed plots are well described by a linear dependence (Fig. 4). A calculation of λ by the least-squares method yielded a value of 0.83 ± 0.03, 0.95 for Q_0 = 75 mC cm^{-2} and 0.712 ± 0.025, 0.95 for Q_0 = 150 mC cm^{-2} at correlation coefficients of 0.9988 and 0.9996, respectively. The presented data show that λ increases with decreasing Q_0, and, therefore, with decreasing layer thickness, in line with the behavior of amalgam films.

It follows from the proposed model that, if the anodic dissolution of copper yields Cu^{2+} ions and the main conducting ions of ES are oxidized (from Cu^+ to Cu^{2+}), degradation of the solid electrolyte (i.e., a decrease in its ionic conductivity and increase in hole conductivity) is inevitable. This degradation is inherent, to some extent, to all solid electrolytes with conduction by Cu^+ ions. It may be assumed that, owing to the weak binding of Cu^+ cations to the SE anion sublattice, the rates of these processes will depend only slightly on the composition of the sublattice.

It is difficult to account for the comparatively high peak current densities of copper dissolution by the large diffusion coefficient of doubly charged cations in SE. More likely, they can be accounted for by the high hole diffusion rate in the electrolyte, with hole motion accompanied by transfer of unit charge from Cu^{2+} to a neighboring Cu^+ cation. Macroscopically, this is perceived as diffusion of doubly charged cations.

If the electrolyte were free from Cu^{2+} cations, then, owing to the conversion of a copper atom into a doubly charged cation, capacities markedly larger than Q_0 would be observed during anodic semicycles in deposit dissolution from the surface of the inert electrode. At the same time, the experimental coulometric reversibility was usually less than, and close to unity. This suggests that either a high concentration (comparable with that of Cu^+) of doubly charged copper cations discharging in deposition is present in the electrolyte, or the $Cu^+ \rightarrow Cu^{2+}$ and $Cu \rightarrow Cu^{2+}$

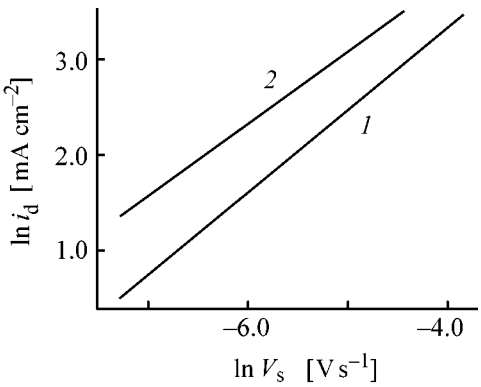

Fig. 4. Current density i_d at peaks of the potentiodynamic polarization curves of copper dissolution from the surface of glassy carbon vs. potential sweep rate V_s. Deposition current density 2.5 mA cm^{-2}, T = 25°C. Q_0 (mC cm^{-2}): (*1*) 75 and (*2*) 150.

transitions make small (as regards the current and capacity) contribution to the potentiodynamic curves of deposit dissolution, and the peak shape is mainly determined by the $Cu \rightarrow Cu^+$ process. As shown by the presented data, the last process is irreversible, i.e., is controlled by charge transfer, and $\beta n \approx 0.5$, which gives $\beta = 0.5$ at $n = 1$.

The presence of an amalgam-like layer inevitably leads to the loss of capacity in dissolution, which occurs, at least, owing to deterioration of the electrical contact between the grains of the layer and between grains and electrode, or owing to a decrease in the copper concentration in the layer in the course of dissolution, which makes lower its electronic conductivity. This fact can account for, in particular, the existence of noticeable currents in the potentiodynamic curves at potentials much exceeding the current peak potentials, just at which the residual copper in the layer is oxidized. This range of potentials is directly responsible for the abrupt change in potential in galvanostatic curves of copper dissolution from the surface of the inert electrode.

Evidently, such a layer will undergo recrystallization when in storage. As a result, the electrical contact between copper in the layer and the electrode may be deteriorated, and the area of contact between copper in the layer and the solid electrolyte, may decrease.

The given near-electrode layer of electrolyte may be formed not only by the above mechanism, but also as a result of the difference in energies of binding between metal and inert electrode and between atoms of deposited metal [4].

Probably, a similar electrochemical behavior will be also observed in other copper-conducting solid electrolytes, which impairs the feasibility of preparing

systems with high coulometric reversibility on their basis.

CONCLUSION

The model of anodic oxidation and cathodic reduction of copper on the surface of an inert electrode was proposed. The model is based on the assumption that redox processes may occur not only on the electrode surface but also in the near-electrode layer of solid electrolyte owing to its comparatively high hole conductivity. This assumption furnishes a qualitative explanation for specific features of processes occurring at the interface between the inert electrode and copper-conducting solid electrolyte.

REFERENCES

1. Karamov, F.A., Elements of Functional Electronics Based on Superionic Conductors, *Doctoral Dissertation*, Kazan, 1997.
2. Brainina, Kh.Z. and Neuman, E.Ya., *Tverdofaznye reaktsii v elektroanaliticheskoi khimii* (Solid-Phase Reactions in Electroanalytical Chemistry), Moscow: Khimiya, 1982.
3. Raleigh, D.O., *J. Electrochem. Soc.*, 1976, vol. 123, no. 7, pp. 1063–1065.
4. Vydra, F., Stulik, K., and Julakova, E., *Rozpousteci polarografie a voltammetrie* (Inversion Voltammetry), Praha, 1980.

Russian Journal of Applied Chemistry, Vol. 74, No. 12, 2001, pp. 2045–2050. Translated from Zhurnal Prikladnoi Khimii, Vol. 74, No. 12, 2001, pp. 1985–1990.

ENVIRONMENTAL PROBLEMS OF CHEMISTRY AND TECHNOLOGY

Optimization of Natural Water Purification to Remove Nickel and Copper Ions with Carbonate Flour

V. N. Makarov, S. I. Mazukhina, T. N. Vasil'eva, I. P. Kremenetskaya, and O. P. Korytnaya

Tananaev Institute of Chemistry and Technology of Rare Elements and Mineral Raw Materials, Kola Scientific Center, Russian Academy of Sciences, Apatity, Russia

Institute for Problems of Industrial Ecology of the North, Kola Scientific Center, Russian Academy of Sciences, Apatity, Russia

Received March 19, 2001

Abstract—The reaction of nickel(II) and copper(II) sulfate solutions with carbonate flour prepared from carbonatite was simulated thermodynamically and studied experimentally. The conditions under which open systems and those isolated from the atmosphere attain stationary state (carbonatite consumption and grain size, pH of the medium) were determined. The ionic and mineral composition of new formations and the theoretically possible degree of purification were found.

In the affected zones by mining-and-smelting plants in natural basins, a substantial increase in the content of acid oxides and ions of a number of heavy metals exerting negative influence on living organisms is observed in some cases [1]. These contaminants may adversely affect the human health if such water basins are sources of drinking water.

The contamination is caused by acid rains and uncontrollable discharges from tailing dumps and waste piles, containing sulfides of nonferrous metals and iron.

A liter of acid rain with pH in the range from 3.6 to 4.7 contains from 0.002 to 1.15 mg l^{-1} of nickel(II), 0.003 to 2.36 mg l^{-1} of copper(II), and a number of other ions of toxic metals, and also 2.1 to 52.7 mg l^{-1} of the sulfate ion. In winter, the contaminants are accumulated in the snow cover and are discharged to water basins during snow thawing. During this period of time, the content of acid oxides and heavy metal ions in water much exceeds the maximum permissible concentration (MPC) [1, 2].

During storage of mining wastes, the constituent sulfides are oxidized and nonferrous metals pass into readily soluble sulfates. This process is particularly intensive in the case of alternating moistening and drying [3–5]. The MPC may be exceeded 18-fold for cobalt(II) ions, 180-fold for copper(II), and 880-fold for nickel(II) [6].

Water basins can be decontaminated to remove metal ions and inorganic acids with the use of carbonate flour prepared from carbonatite [7]. Use of more active reagents, e.g., suspended $Ca(OH)_2$ is inadmissible for open water basins because of the impossibility of stirring, with the result that the local concentration of the reagent may exceed the MPC and, therefore, adversely affect the ecosystem of a water basin. The optimal acidity (for fish) is within $6.5 < pH < 8.5$, with relatively safe conditions achieved at $5.5 < pH < 9.0$ [8].

It has also been found that the carbonate flour can be used to remove such contaminants as ions of some heavy metals and nickel(II) and copper(II), in particular. However, the purification methods are somewhat different in this case.

In the case of near-surface water contamination with only sulfur oxides (SO_2, SO_3), it is recommended to use for purification a finely dispersed carbonate flour having large specific surface area [4–6, 9]. This ensures a high rate of the reaction and the minimum consumption of the reagent. The use of finely dispersed reagents for purification to remove nickel(II) and copper(II) ions leads to formation of even more finely dispersed secondary products, which stay suspended for a long time. Therefore, it is appropriate to use a reagent with coarser grain and raise its expenditure, to achieve incomplete dissolution of carbonate particles and their settling out together with hydroxides

1070-4272/01/7412-2045 $25.00 © 2001 MAIK "Nauka/Interperiodica"

Table 1. Variation of residual concentrations, pH value, and content of solid phases in reaction of nickel(II) ions with calcite (initial Ni(II) concentration 2.9 mg l^{-1}, T = 25°C, P = 1 atm)

Calcite consumption, mg l^{-1}	Content of solid phase, mg l^{-1}			Residual concentration in solution, mg l^{-1}			pH value
	$CaCO_3$	$Ni(OH)_2$	NiS	Ni^{2+}	$Ni(OH)^+$	NiO	
Open system							
0.01	–	–	–	3.00	9.53×10^{-6}	1.48×10^{-10}	5.67
0.0136	–	–	–	2.99	1.1×10^{-5}	2.97×10^{-10}	5.74
0.100	–	–	–	2.99	1.5×10^{-5}	3.89×10^{-10}	5.88
0.316	–	–	–	2.99	3.1×10^{-5}	5.85×10^{-9}	6.20
1.00	–	–	–	2.99	9.1×10^{-5}	5.02×10^{-8}	6.63
3.16	–	–	–	2.99	1.64×10^{-4}	4.73×10^{-7}	7.14
10.0	–	–	–	2.99	8.80×10^{-4}	4.50×10^{-6}	7.64
31.6	–	1.03×10^{-4}	–	2.99	2.74×10^{-3}	4.6×10^{-5}	8.14
56.3	7.51	1.30	–	2.18	2.94×10^{-3}	7.3×10^{-5}	8.32
Closed system							
0.01	–	–	0.0366	2.96	1.4×10^{-5}	1.54×10^{-9}	5.98
0.0316	–	–	–	2.95	4.6×10^{-5}	1.80×10^{-8}	6.658
0.100	–	–	0.0132	2.94	8.47×10^{-4}	3.2×10^{-6}	7.63
0.316	–	0.0601	–	2.89	3.20×10^{-3}	6.6×10^{-5}	8.25
1.00	–	0.362	–	2.70	3.80×10^{-3}	8.6×10^{-5}	8.25
3.16	–	1.39	–	2.08	2.93×10^{-3}	7.4×10^{-5}	8.32
10.0	–	4.26	–	0.263	1.04×10^{-3}	7.4×10^{-5}	8.77
31.6	14.8	4.63	–	0.00597	1.57×10^{-4}	7.4×10^{-5}	9.59

and basic sulfates and carbonates of heavy metals, formed on their surface. A certain excess of carbonates will hinder reverse reactions in both settled and stirred sludge.

To optimize the purification of natural and wastewater to remove nickel and copper ions, computer simulation of the reaction of dilute solutions with carbonate flour prepared from carbonatite, whose active component is calcite $CaCO_3$, was performed and a set of laboratory experiments was carried out. The computer simulation was done with Selektor PC [10]. The method of physicochemical simulation of natural mineral formation processes is based on finding the minimum Gibbs energy. The reaction of the solid phase with a solution may give a new secondary product compatible with the solution. In this case, despite the established equilibrium between the secondary products and the solution, the primary rock continues to react with the liquid phase and the process goes on [11]. The process of irreversible dissolution can be represented as a sequence of elementary stages, which yields eventually the chronological or spatial succession of changes occurring in the system on its way to equilibrium. The thermodynamic data were taken from [12–15].

The computer simulation was used to study the nature of the reaction of nickel-containing solutions with calcite in open and closed (isolated from the atmosphere) systems at different salt concentrations. The conditions of nickel(II) precipitation from solutions with varied concentration of nickel(II) sulfate were modeled by the thermodynamic system N–C–Ca–Ni–S–O–H–e, containing 32 components in the aqueous phase, including Ni^{2+}, $Ni(OH)^+$, NiO, $HNiO_2^-$; 10 components in the gas phase; and 14 solid phases. The system included nickel and calcium carbonates, oxides, sulfides, and sulfates, and nickel hydroxide $Ni(OH)_2$. According to the results of calculation, precipitation of nickel hydroxide starts in an open system at an initial $NiSO_4$ concentration of 5×10^{-5} M (2.9 mg l^{-1} Ni^{2+}) at pH 8.14 (Table 1), with pH tending to 8.3, and the degree of purification is 24%. Raising the reagent concentration in the system leads to its precipitation, with neither the amount of $Ni(OH)_2$, nor residual concentrations of nickel ions in solution changed. A study of this system in isolation from the atmosphere at the same concentration of nickel(II) ions in solution demonstrated that nickel hydroxide is formed at lower reagent expenditure of 1.78×10^{-4} g l^{-1} at pH 8.059.

Raising the calcite content in the system further leads to a rise in pH, increase in the $Ni(OH)_2$ concentration, decrease in the residual concentration of nickel ions in solution, and transition of the system to a steady state.

In a solution with initial Ni(II) concentration of 1×10^{-5}, no $Ni(OH)_2$ precipitation occurs. The theoretically possible minimum nickel(II) concentration in an open system is 3.8×10^{-5} M (2.23 mg l^{-1}), which corresponds to pH 8.32 of a solution saturated with $CaCO_3$.

In a closed system (Table 1), the maximum pH value in $CaCO_3$-containing solutions (9.85) is higher than that in the open system. The nickel ion concentration in the pH range 8–9.5 is 1–2 orders of magnitude lower than that in the open system, and virtually the entire amount of nickel passes into the solid phase at pH 9.75 and 9.58, and initial nickel concentrations of 1×10^{-5} and 5×10^{-5} M (0.6 and 2.9 mg l^{-1}), respectively. Water purification to remove nickel with calcium carbonate in a closed system is much more efficient as compared with that in the open system. The maximum degree of purification of a $NiSO_4$ solution with initial concentration of 5×10^{-5} M is 25 and 99.8% in open and closed systems, respectively. At an initial Ni(II) concentration of 1×10^{-5} M, no nickel precipitation occurs in the open system, with the degree of purification being as high as 99.7% in the closed system.

The kinetics of reagent reaction with solutions was studied experimentally under laboratory conditions. To avoid reverse reactions, the reagent with products should be precipitated as soon as possible. At the same time, the residence of each grain in the bulk of water being purified must be long enough for the forward reaction to occur. Figure 1 presents a kinetic curve of carbonatite dissolution in distilled water (consumption 0.5 g l^{-1}, fraction 0.4 mm), and Fig. 2, that of carbonatite reaction with a nickel sulfate solution [Ni(II) concentration 2.91 mg l^{-1}]. It can be seen from Fig. 2 that the reaction is virtually complete in 20 min, when the maximum degree of solution purification to remove nickel ions is reached. This approximately corresponds to the time of attainment of the maximum pH value in carbonatite dissolution. Further reaction of the solution with calcium carbonate leads to a slight increase in Ni(II) concentration, which is possibly due to partial dissolution of the newly formed phase.

The number of newly formed phases is small, since the reagent is taken in gross excess. Their precise identification is impossible, since they are characterized by high dispersity and low ordering of the crystal lattice. However, comprehensive studies, including optical and X-ray determinations, revealed that the newly formed phases are close to zaratite $Ni_3[(OH)_4CO_3] \cdot 4H_2O$.

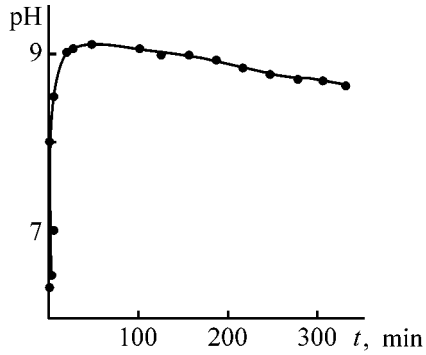

Fig. 1. Variation of pH in the course of carbonate flour dissolution. Grain size 0.4 mm, consumption 0.5 g l^{-1}. (*t*) Time.

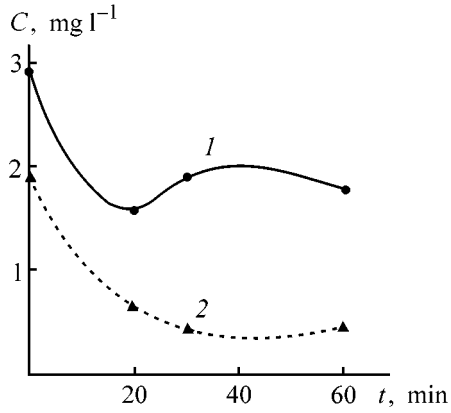

Fig. 2. Kinetic curves describing the reaction of (*1*) nickel sulfate and (*2*) copper sulfate solutions with carbonate flour. (*C*) Metal ion concentration and (*t*) time.

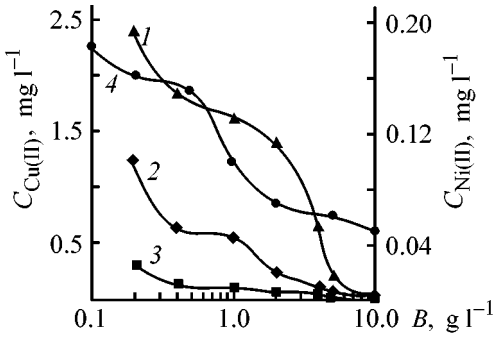

Fig. 3. Residual metal ion concentration *C* in solution vs. carbonate flour consumption *B*. Initial concentration (mg l^{-1}): Cu(II): (*1*) 5.10, (*2*) 3.22, and (*3*) 1.42; Ni(II): (*4*) 0.3; the same for Fig. 4.

Table 2. Change in residual concentrations, pH values, and concentrations of solid phases in reaction of copper(II) ions with calcite (initial Cu(II) concentration 5.1 mg l^{-1}, T = 25°C, P = 1 atm)

Calcite consumption, mg l^{-1}	Content of solid phase, mg l^{-1}		Residual concentration in solution, mg l^{-1}				pH value
	$CaCO_3$	brochantite	Cu^{2+}	Cu^{+}	$CuOH^{+}$	$Cu(CO_3)_2^{2-}$	
Open system							
0.001	–	–	5.222	–	0.0337	3.46×10^{-10}	5.65
0.032	–	–	5.18	–	0.0368	4.84×10^{-10}	5.69
0.1	–	–	5.17	–	0.0490	6.87×10^{-10}	5.81
0.32	–	0.00016	5.06	–	0.0694	6.48×10^{-9}	6.00
1.00	–	0.00117	4.48	–	0.0674	8.04×10^{-9}	6.02
3.16	–	0.00426	2.71	–	0.0582	2.01×10^{-8}	6.16
10.0	–	0.00905	0.0674	–	0.0174	0.000011	7.25
31.6	–	0.00905	0.00433	–	0.00696	0.00114	8.05
100	0.0485	0.00905	0.00187	–	0.00528	0.00480	8.30
Closed system							
0.001	–	–	4.97	0.135	0.028	–	5.59
0.032	–	–	4.79	0.378	0.013	–	5.20
0.1	–	–	4.91	0.238	0.021	–	5.46
0.32	–	0.00025	4.90	0.00284	0.068	–	5.99
1.00	–	0.00075	4.61	0.016	0.069	–	6.00
3.16	–	0.00239	3.71	3.52×10^{-12}	0.065	–	6.07
10.0	–	0.00769	0.842	1.72×10^{-12}	0.04	–	6.52
31.6	0.0136	0.00905	2.7×10^{-5}	0	0.00128	–	9.52

As seen in Figs. 3 and 4, at initial Ni(II) concentrations of 0.3 mg l^{-1}, corresponding to contamination in the immediate vicinity of a source, adding even a minor amount of carbonate flour leads to a dramatic decrease in the content of nickel(II). The degree of purification at reagent consumption of 2 g l^{-1} is 76.67%. With the reagent expenditure raised to 10 g l^{-1}, the degree of purification can be made as high as 83.3%. However, further increase in reagent expenditure is inefficient. The MPC values adopted for fishing basins (0.01 mg l^{-1}) could not be achieved even at reagent consumption of 20 g l^{-1}. Presumably, the residual concentration of nickel(II) ions in water being purified is comparable in this case with the solubility limit of the newly formed phases.

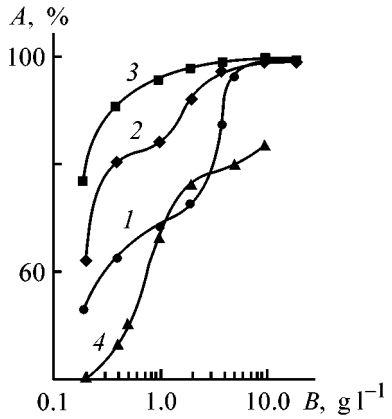

Fig. 4. Degree of solution purification, A, vs. carbonate flour consumption B at different initial metal ion concentrations.

A comparison of the experimental data with results of computer simulation demonstrated that equilibrium is not attained in the system as a whole in reaction of nickel(II) with calcite in real solutions. Local equilibria are created near the surface of grains, simulating conditions that are intermediate between those for the open and closed systems. As a result, the measured residual concentrations of nickel(II) were found to be lower than the calculated values for the corresponding pH values in the open system.

The conditions of copper(II) precipitation from sulfate solutions were found on studying the thermodynamic system N–C–Ca–Cu–S–O–H–e, containing 34 components in the aqueous phase, including Cu^{2+}, Cu^{+}, $Cu(OH)^{+}$, $HCuO_2^{-}$, CuO_2^{2-}, and $Cu(CO_3)_2^{2-}$; 10 components in the gas phase; and 18 solid phases. As also in the case of nickel sulfate solutions, the nature of reaction of copper sulfate solutions with calcite in open and closed systems at Cu(II) concentrations of 1.4 and 5.1 mg l^{-1} was studied by means of computer simulation. At initial Cu(II) concentra-

tion of 5.1 mg l^{-1} in a system open to the action of atmosphere, brochantite $Cu_4SO_4(OH)_6$ is formed at 5.97 < pH < 7.24 (Table 2). Raising the calcite content in the system further does not change the amount of brochantite, with the pH of the system becoming 8.3. Under the conditions when a system is isolated from the atmosphere, brochantite is formed at the same calcite consumption (Table 2). Its concentration grows gradually with increasing reagent consumption and tends to a constant value. The residual concentrations of copper-containing ions are much lower than in the case of an open system. At initial salt concentration of 1.4 mg l^{-1} in an open system, brochantite is formed at pH 6.47 and calcite consumption of 0.001 g l^{-1}, and, additionally, malachite $Cu_2(OH)_2CO_3$, at pH 8.1 and calcite consumption of approximately 0.03 g l^{-1}. The concentrations of copper-containing ions decrease by 2–3 orders of magnitude.

Figure 2 presents a kinetic curve of calcium carbonate reaction with copper sulfate solution [Cu(II) concentration 1.90 mg l^{-1}]. It can be seen that the reaction is virtually complete in 30 min. In contrast to the similar curve for nickel sulfate, no rise in the Cu(II) concentration with increasing reaction time is observed.

As in the preceding case, the number of newly formed phases is small, and their structure is exceedingly imperfect. As a result, they could not be identified precisely. However, comprehensive studies, including optical and X-ray determinations, established that the newly formed phases are close to the natural pozdnyakite and langite [16, 17], with composition $Cu_4SO_4(OH)_6 \cdot H_2O$. The newly formed phase has finely crystalline structure, and, therefore, only averaged refractive index could be evaluated, which gave no way of performing a more precise identification. The X-ray pattern shows only the strongest lines, having close positions in both minerals. Interestingly, pozdnyakite and langite are insoluble in water in contrast to copper sulfates. At the same time, artificial analogs of pozdnyakite or langite could not be synthesized in the system $CuO–SO_3–H_2O$ [18]. Presumably, minerals of this kind can only be formed in strongly diluted solutions.

As it can be seen from Figs. 3 and 4, at initial Cu(II) concentrations of 1.4–5.1 mg l^{-1}, addition of even minor amounts of carbonate flour leads to a dramatic decrease in the content of copper ions. The degree of purification at reagent consumption of 2 g l^{-1} is 75–95%. With the reagent expenditure raised to 10 g l^{-1}, the degree of purification can be made as high as 95–99%. However, at lower contaminant concentrations, the efficiency of the reagent decreases drastically. The MPC values adopted for fishing basins (0.001 mg l^{-1}) could be achieved even at reagent consumption of 20 g l^{-1}. Presumably, the residual concentration of copper ions in water being purified is comparable in this case with the solubility limit of the newly formed phases. As shown by investigations on natural objects, the solubility of basic copper sulfates depends on the pH value: the sulfates are virtually insoluble at pH > 7, but their solubility increases dramatically at lower pH values.

CONCLUSIONS

(1) A comparison of the results of a thermodynamic simulation with experimental data on the reaction of dilute nickel and copper sulfate solutions with carbonate flour demonstrated that the nature of the process is determined by kinetic factors and local equilibria between solution and newly formed phases on the surface of carbonate grains, and between these phases and carbonates, which are established 20–30 min after the beginning of the reaction. In this case, the maximum degree of purification is achieved. The grain size of the carbonate flour must ensure settling out, during this time, of the excess amount of the reagent together with newly formed phases.

(2) The thermodynamic computer simulation was used to find the conditions (carbonatite consumption, pH of the medium) for transition of an open or isolated (from the atmosphere) system to a steady state, establish the ionic and newly formed mineral composition, and determine the theoretically possible degree of purification. The obtained theoretical and experimental data are compared. It is shown that, even though local pH values may be as high as 9.6, the value of this parameter in the water basin bulk does not exceed 8.3, which is safe for living organisms.

REFERENCES

1. Moiseenko, T.I., *Teoreticheskie osnovy normirovaniya antropogennykh nagruzok na vodoemy Subarktiki* (Theoretical Foundations of Regulation of Antropogenic Load on Water Basins of Subarctics), Apatity: Kola Nauchn. Tsentr Ross. Akad. Nauk, 1997.
2. Moiseenko, T.I., *Vodn. Resursy*, 1998, vol. 25, no. 1, pp. 16–23.
3. Kalinnikov, V.T., Makarov, V.N., and Kremenetskaya, I.P., *Khim. Interes. Ustoich. Razv.*, 1997, vol. 5, no. 3, pp. 169–178.
4. Makarov, V.N., *Ekologicheskie problemy khraneniya i utilizatsii gornopromyshlennykh otkhodov* (Ecolog-

ical Problems of Storage and Utilization of Mining Waste), Apatity: Kola Nauchn. Tsentr Ross. Akad. Nauk, 1998, parts 1 and 2.

5. Makarov, V.N., Masloboev, V.A., and Kremenetskaya, I.P., *Waste Solidification – Stabilisation Processes*, Nancy, France, 1997, pp. 515–518.
6. Vasil'eva, T.N., Electrochemical Oxidation of Sulfides in Stored Mining Waste and Its Impact on the Environment and Quality of Technological Deposits, *Cand. Sci. Dissertation*, Apatity, 1999.
7. Makarov, V.N., Zinov'ev, Yu.Z., and Kremenetskaya, I.P., *Tekhnologiya i svoistva stroitel'nykh i tekhnicheskikh materialov na osnove syr'ya Kol'skogo poluostrova* (Technology and Properties of Building and Technological Materials Produced from Raw Materials of Kola Peninsula), Apatity: Kola Nauchn. Tsentr Ross. Akad. Nauk, 1996, pp. 81–86.
8. Izrael', Yu.A., Nazarov, I.M., Pressman, A.Ya., *et al.*, *Kislotnye dozhdi* (Acid Rains), Leningrad: Gidrometeoizdat, 1983.
9. Joung, Th.C., De Pinto, J.V., Rhea, J.R., and Scheffe, R.D., *Canad. J. Fish. Aquat. Sci.*, 1989, vol. 46, no. 2, pp. 315–322.
10. Karpov, I.K., *Fiziko-khimicheskoe modelirovanie na EVM v geokhimii* (Computerized Physicochemical Modeling in Geochemistry), Novosibirsk: Nauka, 1981.
11. Kashik, S.A. and Karpov, I.K., *Fiziko-khimicheskie modeli v geokhimii* (Physicochemical Models in Geochemistry), Novosibirsk: Nauka, 1988, pp. 160–177.
12. Garrels, R.M. and Christ, Ch.L., *Christ, Solutions, Minerals, and Equilibria*, New York: Harper and Row, 1965.
13. Naumov, G.V., Ryzhenko, B.N., and Khodakovskii, I.L., *Spravochnik termodinamicheskikh velichin (dlya geologov)* [Reference Book of Thermodynamic Quantities (for Geologists)], Moscow: Atomizdat, 1971.
14. Robie, R.A. and Hemingway, B.S., *U. S. Geological Survey Bulletin*, 2131, U. S. Government Printing Office, Washington, 1995.
15. Shock, E.L., Oelkers, E.H., Johnson, J.W., *et al.*, *J. Chem. Soc.*, London, Faraday Trans., 1992, vol. 88, pp. 803–826.
16. Komkov, A.I. and Nefedov, E.I., *Zap. VMO*, 1967, part 96, issue 1, pp. 58–62.
17. Komkov, A.I. and Nefedov, E.I. *Byull. VSEGEI*, 1958, vol. 1.
18. Alekseev, L.S., *Khim. Tekhnol. Vody*, 1989, vol. 11, no. 11, pp. 1014–1018.

Russian Journal of Applied Chemistry, Vol. 74, No. 12, 2001, pp. 2051–2053. Translated from Zhurnal Prikladnoi Khimii, Vol. 74, No. 12, 2001, pp. 1991–1993.

ENVIRONMENTAL PROBLEMS OF CHEMISTRY AND TECHNOLOGY

Effect of Some Ion Impurities on Accuracy of Fluorometric Determination of Aluminum(III) Concentration in Natural Water

V. L. Krasikov and V. P. Belokurov

St. Petersburg University of Electrical Engineering, St. Petersburg, Russia

Received December 29, 2000

Abstract—The possibility of determining the aluminum(III) concentration in aqueous solutions in the form of a complex compound with lumogallion by means of fluorometry with a portable analyzer and the effect of impurities on the accuracy of determining this concentration were studied.

The fluorometric analytical technique, based on measuring the intensity of fluorescence of a complex compound of aluminum with lumogallion [1] under the action of short-wavelength visible or UV light, is widely used to find the content of aluminum(III) in various media. Owing to its high sensitivity and selectivity, this method is frequently employed to analyze water, eatables, various biological media, etc. [2–8].

Devices for fluorometric analysis frequently use as light sources gas-discharge lamps, halogen incandescent lamps, or lasers [9], with the result that these devices are bulky, power-consuming, and electric mains–dependent. However, it is desirable in many cases to have a precise portable instrument with low power consumption, weight, and size. Such a device could be designed owing to the fact that the fluorescence peak of the aluminum(III) complex with lumogallion is observed at 576 nm, and the wavelength of exciting light must be 450–500 nm [1]. This allowed use of a blue LED with emission peak at 473 nm and brightness of 1 cd at nominal current of 20 mA, instead of power-consuming sources of excitation light. The device is based on a double-beam scheme with the illuminance of a glass measuring cell monitored and maintained constant and account taken of the fluorescence decay with increasing temperature and the possibility of working under scattered daylight.

The aim of this study was to determine the intensity of fluorescence in relation to the aluminum concentration in solution and also to analyze the effect of impurities present in natural water on the accuracy of determining the aluminum concentration.

In view of the high sensitivity of the fluorometric analytical technique, particular attention was given to the purity of laboratory vessels and reagents. State standard aluminum(III) samples of precisely known concentration, reagents of special-purity and chemically pure grades, and lumogallion of pure grade were used.

Working solutions were prepared by pouring approximately 10 ml of distilled water in a clean 50-ml flask and adding by means of a calibrated pipette a calculated amount of a solution containing an aluminum compound. Further, a second pipette was used to introduce 6 ml of a solution containing lumogallion and acetate buffer, with a prescribed amount of a solution of impurity compound introduced when necessary, and the volume of the solution in flask was brought to the mark with distilled water.

Measuring vessels with the solutions were heated. For this purpose, they were placed in a vessel with boiling water for 5 min and then cooled in cold water to room temperature. This procedure was necessary since the fluorescent complex compound is formed at room temperature in several hours (and, correspondingly, the intensity of fluorescence gradually grows during this time), but this process is markedly accelerated at elevated temperatures. Heating for 5 min was sufficient for converting all forms of aluminum(III) into an analytical form.

The main components of the auxiliary solution were as follows (M): lumogallion (0.00012, acetic acid 1.1, and sodium acetate 0.167. Prior to measurements, glass cuvettes were thrice rinsed, with all

1070-4272/01/7412-2051 $25.00 © 2001 MAIK "Nauka/Interperiodica"

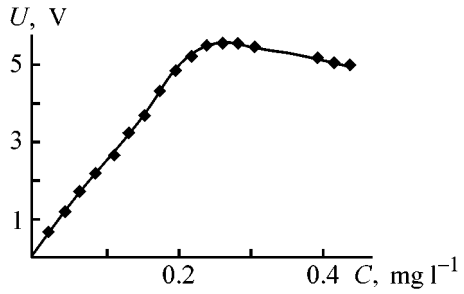

Fig. 1. Output signal of fluorescence, *U*, vs. aluminum(III) concentration *C* in solution.

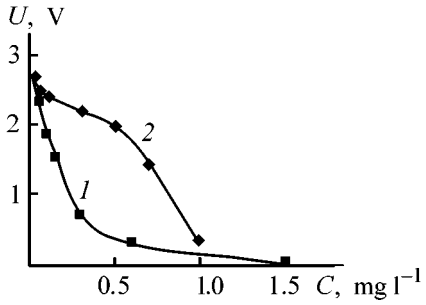

Fig. 2. Output signal of fluorescence, *U*, vs. concentration *C* of (*1*) fluoride ins and (*2*) iron(III) in solution at constant aluminum(III) concentration of 0.11 mg l^{-1}.

necessary precautions, with a solution to be analyzed and then charged with this same solution, by always pouring-in one and the same volume of 5 ml with a pipette. The total volume of the measuring cuvette was about 7 ml. The cuvette with a solution to be analyzed was inserted into the optical compartment of the measuring cell and the intensity of fluorescence was measured. To assess more precisely the reproducibility of the results, three vessels with solution of the same composition were prepared and each solution was analyzed two or three times. On the whole, the experimental procedure had no fundamental differences from that described in [1].

EXPERIMENTAL

In order to use the device for measuring the aluminum(III) concentration, it was necessary to find the dependence of the fluorescence intensity on the concentration of aluminum(III) in a solution being analyzed and determine the concentration range in which this dependence is linear, i.e., to plot the calibration curve. For this purpose, a set of solutions with varied aluminum(III) concentration and the same constant concentration of lumogallion were prepared and then the dependence of the output signal (in volts) on the aluminum(III) concentration in solution was plotted. The data obtained are presented in Fig. 1.

It can be seen that a linear rise in fluorescence signal is observed at aluminum(III) concentrations in the range 0–0.22 mg l^{-1}. At higher concentrations of aluminum(III) this dependence exhibits deviation from linear behavior, and then the fluorescence intensity starts to decrease gradually. In a blank sample without aluminum(III) in solution, the output signal intensity was as low as 0.06 ± 0.02 V, on the average, which may be due to the presence of trace amounts of aluminum(III) in the sample and also to luminescence of glass in the measuring cuvettes etc.

In the linear portion of the calibration curve (Fig. 1), the dependence of the fluorescence signal on the concentration of aluminum(III) in solution is expressed by a straight line with a slope of 23.32 V mg^{-1} aluminum(III) per liter. The scatter of the results of parallel runs did not exceed ±(0.03–0.04) V, i.e., the accuracy of determining the aluminum(III) concentration in the upper linear portion of the calibration curve was ±0.6%. The detection limit of aluminum(III) was about 0.004 mg l^{-1}.

It is known that fluoride ions hinder photometric determination of the aluminum(II) concentration with aluminon [10]. As shown by preliminary experiments, the presence of fluoride ions in solution also leads to a pronounced distortion of results obtained in fluorometric determination of aluminum(III) concentration, and, therefore, the effect of fluoride ions was studied in more detail. For this purpose, solutions were prepared containing 0.11 mg l^{-1} of aluminum(III), which corresponds to the middle of the linear portion of the calibration curve (Fig. 1), with addition of 0.05, 0.1, 0.15, 0.3, 0.6, and 1.5 mg l^{-1} of fluoride ions.

The results obtained in determining the aluminum(III) concentration in the presence of fluoride ions are presented in Fig. 2. As seen from the figure, curve *1*, the measured aluminum(III) concentrations become significantly underestimated with increasing content of fluoride ions. In particular, at a fluoride concentration of fluorides of 1.5 mg l^{-1} in a sample being analyzed (which corresponds to maximum permissible concentration in drinking water [11]) the actual concentration of aluminum(III) is underestimated approximately 60-fold. This is probably due to decomposition of the colored fluorescent complex compound of aluminum with lumogallion to give more stable colorless nonluminescing fluoride complex compound of aluminum $[AlF_6]^{3-}$. Therefore, if a solution being analyzed contains fluoride ions, the results of aluminum(III) concentration measurements may be distorted.

In a similar way was studied the influence of other anions that are frequently present in natural water. It was found that the accuracy of aluminum(III) determination in water is not affected by the following ions in the concentration ranges (mg l^{-1}): chloride ions 0–500, sulfate ions up to 2000, phosphate ions up to 10, hydrocarbonate ions up to 1000, and nitrate ions up to 100 (in the form of sodium salts).

The accuracy of aluminum(III) determination in water is not affected, either, by the following cations in the concentration ranges (mg l^{-1}): sodium 0–1000, potassium up to 500, calcium up to 1000, ammonium up to 500, and magnesium up to 500 (in the form of acetates or sulfates). However, a strong influence is exerted by the presence in water of ions of iron—one of the most widely occurring impurities.

To study the effect of iron(III) concentration, solutions containing 0.11 mg l^{-1} of aluminum(III) and 0.01, 0.02, 0.06, 0.1, 0.3, 0.5, 0.7, and 1.0 mg l^{-1} of iron(III) were prepared. The results of determining the concentration of aluminum(III) in the presence of iron(III) ions are presented in Fig. 2, curve *2*.

It can be seen that the output signal decreases with increasing concentration of iron(III); however, the nature of the influence exerted by iron(III) on the accuracy of aluminum(III) determination is fundamentally different from that of fluoride ions. In a solution being analyzed at pH 8, iron(III) is present mainly in colloid form as brown hydroxide $Fe(OH)_3$, which absorbs the exciting blue light, thereby leading to an underestimated measured concentration of aluminum(III).

Thus, fluorometric analysis for the content of aluminum(III) in natural water is not hindered by phosphate, chloride, sulfate, hydrocarbonate, and nitrate ions in concentrations as high as their maximum permissible concentrations in drinking water, and by high water hardness caused by presence of calcium and magnesium compounds.

At the same time, presence of fluoride ions or iron(III) leads to underestimated measurement results, which requires that appropriate methods to mask the hindering ions should be used.

The use of a miniature LED as light source allowed the development of a portable and sufficiently accurate instrument for fluorometric analysis of solutions in field conditions.

REFERENCES

1. Tikhonov, V.N., *Analiticheskaya khimiya alyuminiya* (Analytical Chemistry of Aluminum), Moscow: Nauka, 1971.
2. Hoch, R.L., *Analyst*, 1999, vol. 124, no. 5, pp. 793–796.
3. Uchiumi, A., Takatsu, A., and Teraki, Y., *Analyst*, 1998, vol. 123, no. 4, pp. 759–762.
4. Lee, B.L., Chua, L.H., Ong, H.Y., *et al.*, *Chin. Chem.*, 1996, vol. 42, no. 9, pp. 1405–1411.
5. He, H.-B., Lee, H.-K., Li, S.F.Y., *et al.*, *J. Chromatogr. Sci.*, 1997, vol. 35, no. 7, pp. 333–336.
6. Teraki, Y., Uchiumi, A., and Takatsu, A., *Acta Anat. Nippon*, 1998, vol. 73, no. 4, pp. 317–328.
7. Takatsu, A., Eyama, S., and Uchiumi, A., Chromatographia, 1995, vol. 40, no. 3/4, pp. 125–128.
8. Uchiumi, A., Takatsu, A., and Teraki, Y., *Biomed. Res. Trace Elements*, 1996, vol. 7, no. 3, pp. 17–18.
9. Golovina, A.P. and Levshin, L.V., *Khimicheskii lyuminestsentnyi analiz neorganicheskikh veshchestv* (Chemical Fluorescence Analysis of Inorganic Substances), Moscow: Khimiya, 1978.
10. *GOST* (State Standard) *18165–81: Potable Water. Method for Determining the Mass Concentration of Aluminum.*
11. *GOST* (State Standard) *2878–82, Potable Water. Hygienic Requirements and Quality Control*.

Russian Journal of Applied Chemistry, Vol. 74, No. 12, 2001, pp. 2054–2060. Translated from Zhurnal Prikladnoi Khimii, Vol. 74, No. 12, 2001, pp. 1994–2000.

PROCESSES AND EQUIPMENT OF CHEMICAL INDUSTRY

Effect of Polydisperse Drop Composition on Hydrodynamics of Gas-Fluid Jet

O. I. Protod'yakonova, S. V. Aniskin, and Yu. I. Kadashevich

St. Petersburg State Technical University of Plant Polymers, St. Petersburg, Russia

Received July 12, 2001

Abstract—A model is constructed describing the hydrodynamics of a polydisperse gas-fluid jet outflowing from a single-plume atomizer in a spray scrubber. Results of a calculation of hydrodynamic characteristics of a polydisperse plume, obtained using the proposed model, are presented and assessed.

Description of flowing gas-fluid jets in spray mass-exchange apparatus is an essential component of models of adsorption processes carried out in these apparatus. In a number of studies [1, 2], models of such jets were constructed, assuming that drops in the gas-fluid jet are monodisperse. However, it is known that the amount of a component sorbed by absorber drop strongly depends on the size of a drop and time of its contact with the gas flow. Therefore, a model of a mass-exchange process in the gas-fluid jet must take into account the polydisperse drop-size composition. Correspondingly, a model of a flowing gas-fluid jet, which is an important component of the model of a mass-exchange process, must take account of the effect of the polydisperse drop composition on specific features of the flow of a gas-fluid jet.

The aim of this study was to construct a model of a flowing gas-fluid jet that would take into account the effect of the polydisperse drop composition on the jet dynamics. To solve this problem, we use as a basis the previously developed hydrodynamic model of a free plume of atomized fluid [2] whose main advantages over the known models consist in that there is no necessity for determining preliminarily the gas jet boundaries in calculating the flow and in the possibility of taking into account the nonuniform gas velocity distribution in the jet.

In this study, the model taking into account the drop polidispersity is constructed for that region of the gas-fluid jet in which the process of fluid flow breakup into drops may be considered complete. In constructing the model, we make the following assumptions. There is no drop breakup or coagulation. The jet flow is stationary. The distribution of all parameters of the gas-fluid jet is axially symmetric. There is no heat exchange in the dispersed system. The stress in the gas jet developing within the plume of dispersed fluid is negligible as compared with the stresses created in this jet by the drop flow. The drops are polydisperse and have spherical shape. The gas-fluid jet is directed vertically downwards.

Equations describing the flow of a polydisperse gas-fluid jet are derived using the following considerations. We assume that the jet plume can be represented as a certain combination of m interpenetrating plumes, each constituted by drops of the same size. Let us introduce in the space a cylindrical system of coordinates φ, Y, Z. In accordance with the assumption that the plume is axially symmetric, we consider in what follows that all flow parameters are independent of the angle φ.

Let us divide each of the above m plumes into n cone jets in such a way that the fluid flow rate G_{kj} within each of these jets is constant. We also assume that the fluid is uniformly distributed over the cross-section of each so-defined jet. Thus, the following conditions are satisfied:

$$G_{kj} = \text{const}, \quad k = 1, 2, \ldots, n; \quad j = 1, 2, \ldots, m; \quad (1)$$

$$\frac{dG}{dS} = \text{const}, \text{ if } dG \in G_{kj},$$

where indices k and j are, respectively, the number of fluid jet in spatial partitioning of the plume and the number of fraction of drops with certain size; S is the cross-sectional area of the jet.

The total number of jet in such partitioning of the gas-fluid plume is given by the product mn. Appar-

1070-4272/01/7412-2054 $25.00 © 2001 MAIK "Nauka/Interperiodica"

ently, the trajectories of drops of different sizes are dissimilar, which gives rise to a shift of jets composed of drops of one size with respect to jets constituted by drops of other sizes. We assume that such a shift begins at a distance L from the atomizer nozzle exit, where breakup of the fluid flow into drops is complete.

Figure 1 shows a cross-section of a polydisperse plume with a plane passing through the Z axis. The scheme shown in Fig. 1 illustrates the above-described partitioning of a polydisperse axially symmetric plume of a gas-fluid flow by monodisperse jets and their relative shift. The scheme shows streamlines delimiting jets with constant flow rate. The index belonging to jet is assigned to a streamline delimiting the corresponding jet from its outer side. Let us derive the equation of momentum conservation in a gas-fluid jet for the coordinates z and y. For this purpose, let us single out at an arbitrary distance z from the jet cross-section L (Fig. 1) an elementary layer of height dz. Let us consider a part of this layer, delimited by lateral surfaces ac and bd, chosen in such a way that they coincide with the streamlines delimiting the jet k,m. In what follows, we name the volume $abcd$ the ith part of the distinguished layer of height Δz (Fig. 1).

Let us determine the flow rate Q_i of fluid passing through the cross-section of the elementary volume $abcd$. We represent this flow rate as a sum of components defined by fluid jets passing through ab either entirely (as, e.g., jet k,m composed of drops of the largest size, forming the fraction denoted by m) or partially (as, e.g., jet k,j and jet $k+1,j$ composed of drops belonging to the fraction denoted by j).

With account of of the previously made assumption that the distribution of spraying density is uniform within each jet k,j, it may be considered that the flow rate of fluid in jet k,j through section ab is given by

$$G_{ikj} = G_{kj}\frac{(b')^2 - a^2}{(b')^2 - (a')^2}, \qquad (2)$$

where G_{ikj} is part of fluid in jet k,j passing through section ab.

For convenience of further transformation, we replace the quantities, a, b, a', b' by the corresponding values of the radial coordinate y. The relation (2) takes the form

$$G_{ikj} = G_{kj}\frac{y_{kj}^2 - y_{k-1,m}^2}{y_{km}^2 - y_{k-1,m}^2}. \qquad (3)$$

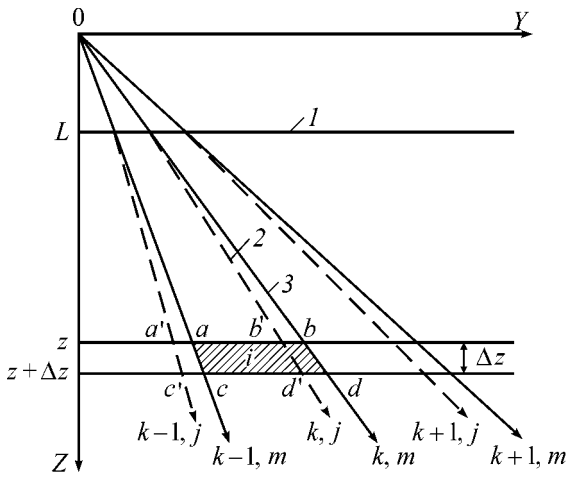

Fig. 1. Scheme of partitioning of a polydisperse plume of a gas-fluid flow into monodisperse jets. (*1*) Line drawn at a distance L from the atomizer nozzle exit—that boundary of the gas-fluid jet flow, at which the fluid flow breakup into drops is considered to be complete; (*2*) streamline of fluid jet k,j, where k = 1, 2, ..., n, j = 1, 2, ..., m are indices denoting, respectively, the number of fluid jet and that of some drop fraction; m is the index denoting the fraction number of drops having the maximum size; (*3*) streamline of fluid jet at $j = m$, distinguishing i-th element of the plume space in a layer.

In a similar way can be written an expression for that part of the fluid flow rate which belongs to jet $k+1,j$ and passes through section ab

$$G_{i,k+1,j} = G_{k+1,j}\frac{y_{km}^2 - y_{kj}^2}{y_{k+1,j}^2 - y_{k,j}^2}. \qquad (4)$$

Let us introduce coefficient θ_{ij} defined by

$$\theta_{ijk} = G_{ijk}/G_{kj}. \qquad (5)$$

This coefficient defines that part of the flow rate of fluid in jet k,j which passed through ith part of the plume layer. Then the total flow rate G_i of fluid passing through section ab can be written as

$$G_i = \sum_{k=1}^{n}\sum_{j=1}^{m}\theta_{ikj}G_{kj}. \qquad (6)$$

Apparently, the coefficient θ_{ikj}, defined as the ratio of flow rates G_{ikj} and G_{kj}, generally depends on the y value. In this case, four ways to calculate the θ_{ikj} are possible, chosen depending on how a particular jet passes through ith layer of the plume, e.g., with its left- or right-hand side coinciding with, or passing within, or by-passing this layer. To these cases correspond the following formulas for calculating θ_{ikj}:

$$y_i > y_{ki} > y_{i-1} \text{ and } y_{k-1,j} \le y_{i-1},$$

$$\theta_{ikj} = \frac{y_{kj}^2 - y_{i-1}^2}{y_{kj}^2 - y_{k-1,j}^2}; \quad (7)$$

$$y_i \ge y_{kj} > y_{i-1} \text{ and } y_{k-1,j} \ge y_{i-1},$$

$$\theta_{ikj} = 1; \quad (8)$$

$$y_i > y_{k-1,j} \ge y_{i-1} \text{ and } y_{kj} > y_i,$$

$$\theta_{ikj} = \frac{y_i^2 - y_{k-1,j}^2}{y_{kj}^2 - y_{k-1,j}^2}; \quad (9)$$

$$y_{kj} \le y_{i-1} \text{ or } y_{k-1,j} \ge y_i,$$

$$\theta_{ikj} = 0. \quad (10)$$

We assume that the variation of the coefficient θ across the layer Δz is negligible. Then the change in the fluid momentum W_i in ith part of the elementary layer of the plume will depend only on a change in fluid velocity, du_{kj}, which occurs as a result of drop deceleration in the gas-fluid jet and can be described as follows:

$$\frac{d}{dz} W_{zi} \sum_{k=1}^{n} \sum_{j=1}^{m} \theta_{ikj} G_{kj} \frac{du_{zkj}}{dz}, \quad (11)$$

$$\frac{d}{dz} W_{yi} \sum_{k=1}^{n} \sum_{j=1}^{m} \theta_{ikj} G_{kj} \frac{du_{ykj}}{dz}, \quad (12)$$

It should be noted that the components u_{zkj} and u_{ykj} of the fluid velocity u_{kj} in jet k, j, appearing in expressions (11) and (12), are defined as quantities averaged over the entire section z of the elementary layer in jet k, j. These can be found from the expressions

$$\frac{du_{zkj}}{dz} = \sum_{i=1}^{n} \theta_{ikj} \frac{du_{zikj}}{dz}, \quad (13)$$

$$\frac{du_{ykj}}{dz} = \sum_{i=1}^{n} \theta_{ikj} \frac{du_{yikj}}{dz}, \quad (14)$$

where du_{zikj} and du_{yikj} are the components of changes in the velocity u_{kj} of jet k, j in elementary layer i in the directions of the Z and Y axes, respectively.

The sought-for equations for describing the changes in momentum in a layer dz of the gas-fluid jet in the case of a polydisperse drop composition, written for the coordinates z and y, will differ from similar equations derived in [2] for monodisperse drops only in the term W_i expressing the momentum flux of ith fluid jet. Therefore, they can be written as

$$\frac{d}{dz} \sum_{i=1}^{i} (\rho_g Q_{gi} v_{zi}) - \rho_g v_{z\,i+1} \sum_{i=1}^{i} \frac{d}{dz} Q_g + \sum_{i=1}^{i} \frac{d}{dz} W_{zi} + \sum_{i=1}^{i} S_i \frac{dP_i}{dz} = 0, \quad (15)$$

$$2\pi(P_{i+1} - P_i) y_i + \frac{d}{dz} W_{yi} = 0, \quad (16)$$

where ρ_g is the gas density (kg m^{-3}), Q_{gi} the volumetric flow rate of gas (m^3 s^{-1}), v_i the gas velocity (m s^{-1}), P_i pressure (kg m^{-2}), and S_i the cross-sectional area of ith layer (m^2).

In developing a model of gas-fluid jet flow, which would take into account the polydisperse drop composition, Eqs. (13) and (14) must be supplemented with gas flow continuity equations, equations describing fluid drop motion, and fluid streamline equations, and also with closing relations derived in [2]. Let us write these additional equations and closing relations with the use of indexation introduced in the present study.

The gas flow continuity equation has the form

$$\sum_{i=1}^{i} \frac{d}{dz} Q_{gi} = -2\pi y_{i+1} v_{y,\,i+1}. \quad (17)$$

Equation describing the fluid drop motion

$$\frac{du_{zikj}}{dz} = -\xi_{ikj} \frac{3\rho_g (u_{ikj}^{rel})^2}{4 d_{kj} u_{zkj} \rho_l} \cos\alpha_{ikj} + \frac{g}{u_{zkj}}, \quad (18)$$

$$\frac{du_{yikj}}{dz} = -\xi_{ikj} \frac{3\rho_g (u_{ikj}^{rel})^2}{4 d_{kj} u_{zkj} \rho_l} \cos\alpha_{ikj}, \quad (19)$$

where ξ_{ikj} is the coefficient of resistance to drop motion in the gas medium, α_{ikj} the angle between the z axis and the direction of the resistance force, and u_{ikj}^{rel} the relative velocity of motion of drops belonging to jet k, j in the gas flow of layer i.

The equations of fluid streamlines coinciding with the trajectories of drop motion have the form

$$\frac{dy_{kj}}{dz} = \frac{u_{ykj}}{u_{zkj}} \quad (20)$$

The obtained system of equations, describing the hydrodynamics of a polydisperse gas-fluid jet, can be supplemented with closing relations

$$Q_{gi} = S_i v_{zi}, \quad (21)$$

$$S_i = \pi(y_i^2 - y_{i-1}^2), \quad (22)$$

$$v_{ikj}^{\text{rel}} = \sqrt{(u_{ykj} - v_{yj})^2 + (u_{zkj} - v_{zi})^2}, \quad (23)$$

$$\alpha_{ikj} = \text{arctg}\left(\frac{u_{ykj} - v_{yi}}{u_{zkj} - v_{zi}}\right), \quad (24)$$

$$\xi_{ikj} = \frac{24}{\text{Re}_{ikj}}(1 + 0.125\text{Re}_{ikj}^{0.72}). \quad (25)$$

Relation (25) is valid for the region $0.1 < \text{Re} < 1000$. The boundary conditions for the closed system of equations of the model, obtained here, have the form

$$\text{at } z = L,\ G_{kj} = G_{kj}^{(L)},\ u_{zkj} = u_{zkj}^{(L)},\ u_{ykj} = u_{ykj}^{(L)},$$
$$v_{zi} = v_{zi}^{(L)},\ v_{yi} = v_{yi}^{(L)},\ y_i = y_i^{(L)} \quad y_{kj} = y_i^{(L)},$$
$$d_j = d_j^{(L)},\ k = i; \quad (26)$$

$$\text{at } y = 0\ v_{yi} = 0. \quad (27)$$

At the outer boundary of the jet, at $y = y_{n+1}$

$$v_{z,\,n+1} = 0, \quad P_{n+1} = P_a, \quad (28)$$

where P_a is the atmospheric pressure (Pa).

To calculate the quantities appearing in relations (26), it is necessary to use the distribution functions of spraying density and disperse composition. The experimentally observed spraying density distributions over the cross-section of a gas-fluid jet outflowing from a single-plume atomizer can be described using the distribution function

$$I = \frac{a_0}{1 + b_0 r^{h_0}} - \frac{c_0}{1 + d_0 r^{h_0}} \quad (29)$$

(I is the dimensionless spraying density; r the dimensionless radius; a_0, b_0, c_0, d_0, and h_0 constants),

$$I = J/\bar{J},\ r = y/y_R,\ \bar{J} = 0.95G_n/(\pi y_R^2), \quad (30)$$

where J is the spraying density (m s^{-1}), $\bar{J}$ the average spraying density in a cross-section of a plume with radius y_R, and y_R the radius of a plume within which passes 95% of fluid, G_n, outflowing in unit time from the nozzle.

Using function (29), we obtain an expression for determining the fluid flow rate in ith jet at a distance L from the atomizer nozzle exit:

$$G_i = \sum_{j=1}^{m} G_{kj} = 1.9\, G_n \int_{r_{i-1}}^{r_i} I r dr, \quad (31)$$

where r_i are the initial values of the dimensionless radius.

These values make it possible to find the initial coordinates y_{kj} of the jets distinguished, using the formula

$$y_{kj} = y_i = r_i Y_R. \quad (32)$$

the y_R value is determined from the maximum spraying density $I_{\max}$ in accordance with the relation

$$y_R = R_n \sqrt{T_{\max}/\beta}, \quad (33)$$

where R_n is the atomizer nozzle radius and β is the volume content of fluid, taken to be 0.02.

The L value can be found, with account of (33), using the formula

$$L = \frac{y_R - R_n}{\text{tg}\,\alpha}, \quad (34)$$

which enables calculation of the initial values of the gas and fluid velocities. The angle α determines the boundary of that part of the gas-fluid jet, which contains 95% of the fluid.

If we neglect the deceleration of fluid in the first zone, the velocity distribution can be set as follows

$$v_{zi} = u_{zkj} = \frac{Lu}{\sqrt{L^2 + y_i^2}}, \quad (35)$$

$$v_{yi} = u_{ykj} = \frac{y_i u}{\sqrt{L^2 + y_i^2}}, \quad (36)$$

where u is the velocity of fluid outflow from the atomizer nozzle, determined using the Bernoulli formula

$$u = \mu\sqrt{2P_f/\rho_f}, \quad (37)$$

where P_f is the fluid pressure before the atomizer, and μ is the coefficient of fluid outflow velocity.

The initial values of the fluid flow rate G_{kj} can be conveniently found using the integral drop volume distribution S with respect to drop size. It is known that the best fit to the real distribution in fluid spraying by atomizers is given by the Rosin–Rammler distribution

$$S^{\text{RR}} = 1 - e^{-(d/a)^l}, \quad (38)$$

where a and l are the characteristic constants of the given distribution.

Formula (38) can be used to determine the part of fluid volume, S_j, constituted by drops having diameter less than d_j.

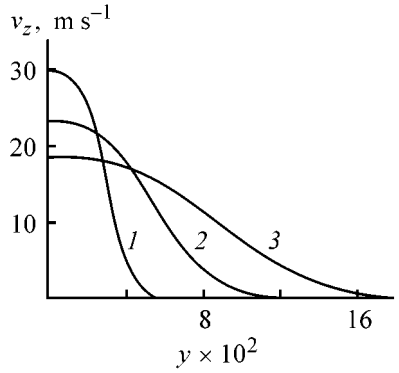

Fig. 2. Distribution of gas velocities v_z across the plume. Distance z (m) from section L: (*1*) 0.2, (*2*) 0.5, and (*3*) 1.0.

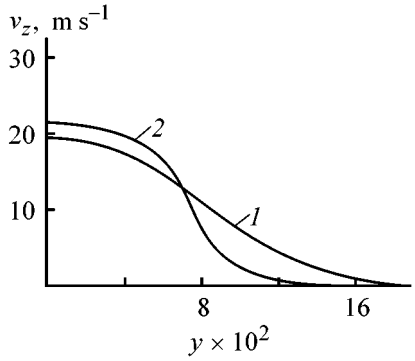

Fig. 3. Comparison of distributions of gas velocity v_z for (*1*) polydisperse and (*2*) monodisperse gas-fluid flows at $z = 1$ m.

With account of (38), the flow rate G_{kj} of fluid in jet kj can be expressed as

$$G_{kj} = G_i(S_j - S_{j-1}). \quad (39)$$

The constant a in the formula describing the Rosin–Rammler distribution (38) is found from the average volume-surface diameter (Sauter diameter)

$$a = 1.3542 d_{32}. \quad (40)$$

If the sprayed fluid is water, then the d_{32} value can be found by the formula [3]

$$d_{32} = 0.154 P_l^{-0.44} (2R_n)^{0.23}, \quad (41)$$

where the quantities d_{32} and R_n are expressed in millimeters, and P_l, in megapascals.

We define the quantities $d_j^{(L)}$ as average volume-surface diameters of drops of each fraction, necessary for calculating the hydrodynamic parameters:

$$d_j^{(L)} = \frac{S_j - S_{j-1}}{\int_{x_{j-1}}^{x_j} \frac{dS}{dx} \frac{1}{x} dx}, \quad (42)$$

where d_j is the Sauter diameter for drops of jth fraction, x the drop diameter, and x_j the boundary value of the diameter of drops belonging to jth fraction.

The constructed closed system of Eqs. (1), (6)–(29) with boundary conditions (26), describing the hydrodynamics of a polydisperse plume of the gas-fluid jet, can be solved only numerically. To find the solution, this system of first-order differential equations was preliminarily reduced to the canonical form and then solved by the Adams–Bashfort method. The solution was obtained for the following values of the parameters determining the fluid spraying mode: P_l = 0.6 MPa, R_n = 1.5 mm, $\alpha = 12.5°$, $a_\perp = 3.0$, $b = 49.0$, $c = 1.06$, $d = 32\,544$, $h = 6.4$, $I_{max} = 2.87$, $\mu = 0.96$, $l = 3$, $\rho_g = 1.2$ kg m^{-3}, $\nu_g = 1.51 \times 10^{-5}$ m^2 s^{-1}, where ν_g is the kinematic viscosity of air, necessary for determining the Reynolds number Re.

The curves plotted using the result of numerical solution of the equations of the model are presented in Figs. 2–5. Figure 2 shows gas velocity distribution across the plume. It is similar to the known distribution of this parameter across the gas jet. A distribution of the same kind was obtained in an experimental study of a gas-fluid jet [4]. This means that the theoretical results obtained in the present study are sound. The calculation results presented in Fig. 2 confirm the possibility of finding gas velocity fields without setting boundaries of the gas jet inside the fluid flow.

Figures 3–5 present calculated dependences which reveal the influence of taking the flow polydispersity into account on the results obtained in calculating the hydrodynamic parameters. Figure 3 shows gas velocity distribution curves obtained for a polydisperse flow of drops, and also those for a monodisperse flow. These latter were calculated at a volume-surface Sauter diameter d_{32} = 0.248 mm. Comparison of these curves suggests that taking the polydisperse nature of the drop flow into account markedly affects the results obtained in calculating the gas velocity. For example, in the near-axis region of the flow, the gas velocity calculated using the model taking into account the polydispersity of the drop flow is higher than that calculated in terms of the model based on the assumption that this flow is monodisperse.

In the region close to plume boundaries, the calculated gas velocity in a monodisperse flow is lower than that in a polydisperse flow. The differences in

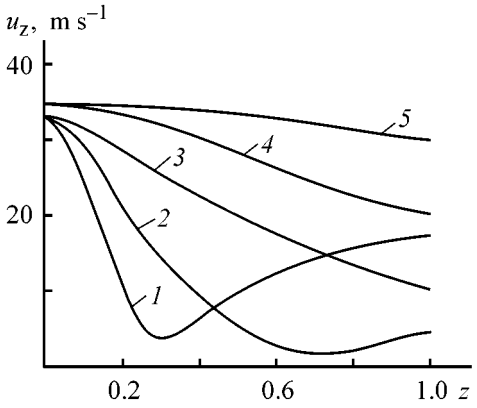

Fig. 4. Variation of drop velocity u_z along the plume length. Drop motion: (*1–3*) along the plume boundary and (*4, 5*) along the plume axis. Drop diameter d_j (mm): (*1, 4*) 0.117, (*2*) 0.202, and (*3, 5*) 0.453.

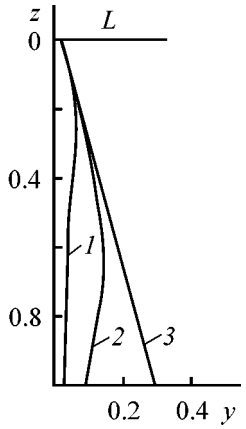

Fig. 5. Trajectory of drops starting their motion at the plume boundary. Drop diameter d_j (mm): (*1*) 0.117, (*2*) 0.202, and (*3*) 0.453.

the nature of curves presented in Fig. 3 indicate that the calculated width of the gas jet is smaller for the monodisperse plume, compared with the polydisperse one.

Figure 4 presents calculated curves characterizing changes in the velocity of drops with different diameters, which started their motion in the second zone from two different points in the section L of the plume. One of these points lies on the plume axis, and the other, on its boundary.

According to formula (35) the velocity u_z at points lying on the plume axis is higher than that at points on its boundary. This boundary was found from the condition that the amount of fluid flowing in unit time within the region delimited by this boundary constitutes 99% of the total rate of fluid outflow from the atomizer.

The specificity of drop motion in a polydisperse plume consists, as follows from Fig. 4, in that, irrespective of how the above points in the section L are chosen, the motion velocities of drops having different sizes rapidly become markedly different in the initial stage of the deceleration process. Fine drops are decelerated in their motion faster than large drops. In the case illustrated by Fig. 4, this feature is characteristic of all particles in the zone delimited by distance z = 0.3 m along the Z axis.

Another hydrodynamic feature of the polydisperse plume, which is illustrated in Fig. 4, consists in that fine drops beginning their motion at points lying on plume boundaries start to increase their velocity at $z > 0.3$ m (Fig. 4, curves *1* and *2*). This phenomenon occurs because of the displacement of fine drops in their motion toward the middle of the plume, where the gas velocity is higher, which leads to acceleration of just fine drops.

The calculated trajectories of drops whose motion is characterized by curves *1–3* in Fig. 4 are presented in Fig. 5. It can be seen that trajectories of fine drops do show a significant displacement toward the plume axis at distances $z > 0.3$ from section L. In the process, the drops shift from the near-boundary region with low gas velocities to a flow region with higher gas velocity. It is this circumstance that is the reason why fine drops starting to move from the near-boundary region of the plume exhibit the above specific feature of motion.

The results obtained in this study suggest that, compared with the model of monodisperse gas-fluid jet, the model constructed here yields significantly different calculated values of such highly important hydrodynamic characteristics of the system in question as the relative velocity and time of drop motion, and their spatial coordinates in relation to their initial position in the plume cross-section, drop size, and initial velocity of drop motion. Thus, taking into account the polydisperse nature of the drop flow in constructing a hydrodynamic model of the dispersed system in question exerts strong influence on the quantitative description of mass-exchange process occurring in systems of this kind and, in particular, absorption process.

For example, in the case when the absorption rate is limited by resistance in the fluid phase, the calculation of this velocity is strongly affected by the results of calculation of the drop motion time and coordinates. The time of drop motion is determined

by the time of absorption, and drop coordinates yield information about the filed of concentration of a component being absorbed around a drop. In those cases when the absorption rate is limited by resistance in the gas phase, the procedure for calculation of the absorption process is, in addition, markedly affected by the result of calculation of the relative velocity of phase motion. The last hydrodynamic characteristic determines, through the Reynolds number entering into the Sherwood number, the calculated intensity of mass transfer.

CONCLUSIONS

(1) The results of the study enable calculation of hydrodynamic characteristics of both poly- and monodisperse gas-fluid jets, without a preliminary setting of the gas jet boundaries, on the basis of the real shape of the spraying density distribution across the plume.

(2) The size distribution of drops strongly affects the results of calculation of the most important hydrodynamic characteristics of a gas-fluid jet outflowing from a single-plume atomizer.

REFERENCES

1. Galustov, V.S. and Pazhi, D.G., *Osnovy tekhniki raspylivaniya zhidkostei* (Fundamentals of Fluid Spraying Technology), Moscow: Khimiya, 1984.
2. Aniskin, S.V. and Protod'yakonova, O.I., *Zh. Prikl. Khim.*, 2001, vol. 74, no. 3, pp. 445–451.
3. Galustov, V.S., *Pryamotochnye raspylitel'nye apparaty v teploenergetike* (Direct-Flow Spraying Apparatus in Heat-and-Power Engineering), Moscow: Energoatomizdat, 1969.
4. Katalov, V.I., Gushchin, Yu.I., and Basargin, B.N., *Massoobmennye i teploobmennye protsessy khimicheskoi tekhnologii* (Mass- and Heat-Exchange Processes in Chemical Technology), Yaroslavl: Yarosl. Politekhn. Inst., 1965, pp. 13–16.

Russian Journal of Applied Chemistry, Vol. 74, No. 12, 2001, pp. 2061–2065. Translated from Zhurnal Prikladnoi Khimii, Vol. 74, No. 12, 2001, pp. 2001–2005.

PROCESSES AND EQUIPMENT OF CHEMICAL INDUSTRY

Breakup Mechanism of Drops of Viscous Fluid in Spraying Apparatus

Yu. G. Chesnokov

St. Petersburg State Technological Institute, St. Petersburg, Russia

Received April 25, 2001

Abstract—Wave development on the drop surface in the course of fluid dispersion in a spray apparatus is analyzed theoretically. The equation derived allows calculation of the process of drop breakup in relation to wavelength.

Solution drying frequently poses the problem of obtaining grains uniform in size, which can be solved if drops of solution outflowing from atomizer have approximately equal sizes. The problem of creating a flow of drops having the same size in dispersion of a fluid in apparatus of chemical technology invites a theoretical analysis of drop breakup in a gas flow under the action of surface tension forces. In performing the analysis, account should be taken of the fact that a solution drop moving in a gas flow can be deformed by this same flow, with waves of different lengths and amplitudes formed on its surface. Breakup of a drop is associated with the appearance on its surface of waves having length at which the rate of wave amplitude rise will be the highest. Hence the necessity for employing in calculations of the hydrodynamic modes of the apparatus in question of an equation relating the mentioned wavelength to the amplitude of the wave, Reynolds number, and Weber number. Deriving an equation of this kind by means of a theoretical analysis of wave development on the drop surface is the aim of this study.

It is assumed that a fluid drop acquires an initial, nonuniform along its length, velocity distribution and is deformed under the action of inertia forces. As a result of elongation, the drop loses stability with respect to capillary forces, so that secondary drop breakup can be observed. This process can be described using a theory based on investigations of capillary waves on the surface of a cylindrical fluid jet [1]. The problem of stability of a viscous fluid jet subjected to uniaxial tension and flowing into another viscous fluid, immiscible with the former, was first considered by Tomotika [2]. In [3], the problem of the stability of an elongate cylindrical drop in an external shear flow was considered. In both these studies [2, 3], it was assumed that inertia forces are negligible as compared with viscous friction and surface tension forces, so that the fluid flow, both inside and outside the jet, can be described using linear Stokes equations. Another important case of flows of this kind, when the inertia and surface tension forces are the most important and viscous friction forces can be neglected, was considered in [1, 4].

In the case when both inertia and surface tension forces and viscous friction forces are to be taken into account, the problem of perturbation development on the surface of a fluid jet is more complicated. Even when the perturbation amplitude is small and linearized equations can be used, it is difficult to construct an analytical solution to the problem. Therefore, of particular importance is the question as to whether or not it is possible to construct such an approximate solution that would describe the most essential features of the phenomenon under study.

As shown in [1], the behavior of a sinusoidal perturbation of the surface of a cylindrical jet of ideal fluid depends on the initial perturbation wave-length. Long-wavelength perturbations, whose wave-length exceeds the circumference of the jet cross-section at the initial instant of time, start to build-up immediately; however the rate of their build-up is relatively low because of the comparatively strong influence of fluid inertia on the development of perturbations. If a perturbation is short-wavelength, the jet surface executes oscillatory motion during

1070-4272/01/7412-2061 $25.00 © 2001 MAIK "Nauka/Interperiodica"

the initial period of time, with the amplitude of oscillations changing only slightly and their period increasing.

The aim of this study was to analyze long-wavelength perturbations on the surface of a cylindrical viscous fluid jet. In the course of time the radius of the cylindrical jet decreases, and the perturbation wavelength, contrariwise, increases. Therefore, whatever the initial perturbation wavelength, any perturbation can be considered longwavelength after a certain interval of time. Consequently, the results obtained in this study are valid not only for perturbations with large initial wavelength, but also for any other perturbations. However, the results become applicable to short-wavelength perturbations only after the current wavelength exceeds the current jet radius.

Long-wavelength perturbations can be described in terms of an approximate theory based on application of approximate one-dimensional (1D) equations of jet dynamics. These 1D equations are derived on the assumption that the transverse scale of variation of hydromechanical quantities is small as compared with the scale of variation along the jet axis. Approximate 1D equations of this kind have been considered in numerous studies. For example, approximate 1D equations describing the dynamics of a capillary jet of ideal fluid were proposed in [5, 6]. More exact 1D equations (so-called Kosser equations) were used in [7–9] to describe capillary waves on the surface of a semi-bounded jet. In [10], equations were constructed in a next approximation in small parameter for ideal fluid jet. One-dimensional equations were also used to describe the development of perturbations in viscous fluid jets. For example, such equations were used in [11] to numerically simulate the dynamics of a capillary jet. In [12], 1D equations were applied to study nonlinear development of capillary waves in a viscous fluid jet by expanding the solution to the problem in a small parameter (perturbation amplitude). Various kinds of approximate 1D equations were compared in [13]. A method for constructing approximate equations, which can, in principle, be used to obtain approximate equations in any approximation in small parameter (transverse to longitudinal flow scale ratio), was developed in [14].

Let us assume that the fluid jet has cylindrical shape, with the shape preserved in the course of time and the jet radius possibly changing. The surface area of the jet decreases as a result of development of axially symmetric perturbations on its surface. Therefore, jet breakup into drops may occur as a result of evolution of just these perturbations, and the present study is concerned with perturbations of this kind. In the case when the fluid velocity in the jet is sufficiently high, the effect of the gravity force on the process of jet breakup into drops can be neglected. This condition will be considered satisfied. Let us introduce dimensionless variables. We denote the jet radius at the initial instant of time by r_0, time by t, and the derivative of the jet radius with respect to time at the initial instant of time by $r_t(0)$. The quantity r_0 can be used as characteristic linear scale of the problem, and $t_0 = -r_0[2r_t(0)]$, as time scale. The quantity r_0/t_0 can be used as velocity scale, and the quantity $p_0 = \sigma/r_0$, where σ is the surface tension at the interface between the jet and its environment (gas), as the pressure scale. Let us introduce a cylindrical system of coordinates (r, ϑ, z) whose z axis coincides with the jet axis. Let us denote the axial and radial components of the fluid velocity vector by, respectively, u and v; and pressure by p. Then equations describing fluid motion in a jet, which are the continuity equation and projections of the Navier–Stokes equation onto the axes z and r of the cylindrical system of coordinates, can be written as

$$v_r + \frac{v}{r} + u_z = 0,$$

$$u_t + vu_r + uu_z = -\frac{1}{\mathrm{We}} p_z + \frac{1}{\mathrm{Re}}\left[\frac{1}{r}(ru_r)_r + u_{zz}\right],$$

$$v_t + vv_r + uv_z = -\frac{1}{\mathrm{We}} p_r + \frac{1}{\mathrm{Re}}\left[\frac{1}{r}(rv_r)_r - \frac{v}{r^2} + v_{zz}\right].$$

In writing the equations, the symbol subscripts of the variables denote differentiation with respect to the corresponding variable, e.g., $u_t = \partial u/\partial t$ etc. The Reynolds and Weber numbers Re and We in these equations are introduced as follows

$$\mathrm{Re} = \frac{\rho h_0^2}{\mu t_0^2}, \quad \mathrm{We} = \frac{\rho h_0^3}{\sigma t_0^2},$$

where μ is fluid viscosity.

The jet surface can be defined by the following relation

$$r = \eta(z, t).$$

Three boundary conditions are to be set on this surface. The kinematic boundary condition is as follows:

$$\eta_t + u\eta_z = v \text{ at } r = \eta.$$

The existence of surface tension forces results in that the normal stresses at the jet surface on the sides of liquid and gas differ by $\sigma(1/R_1 + 1/R_2)$, where R_1 and R_2 are the principal radii of surface curvature in the longitudinal and transverse directions. Therefore,

one of the boundary conditions on the jet surface has the form

$$p - \frac{We}{Re}[2v_r - (u_r + v_z)\eta_z] = p_e + \frac{1}{R_1} + \frac{1}{R_2},$$

where p_e is the environment pressure.

This quantity is assumed to be constant. In the cylindrical system of coordinates, the principal radii of curvature are calculated as follows:

$$\frac{1}{R_1} = \frac{1}{\eta(1+\eta_z^2)^{1/2}}, \quad \frac{1}{R_2} = -\frac{\eta_{zz}}{\eta(1+\eta_z^2)^{3/2}}.$$

The third boundary condition means that the tangential (to the jet surface) component of the viscous strain vanishes on this surface:

$$2v_r\eta_z + (u_r + v_z)(1 - \eta_z^2) - 2u_z\eta_z = 0 \text{ at } r = \eta.$$

Let us assume that the jet radius changes, but the jet retains its cylindrical shape, i.e., $\eta_z = 0$ at any t. The above-formulated problem has a solution of the following kind

$$u = u^{(0)} = \frac{z}{\tau}, \quad v = v^{(0)} = -\frac{r}{2\tau}, \quad \eta = \eta^{(0)} = \tau^{-1/2},$$

$$p = p^0 = p_e + \tau^{1/2} + \frac{3We}{8\tau^3}(1 - \tau r^2) - \frac{We}{Re\,\tau},$$

where $\tau = 1 + t$.

This solution describes the uniaxial tension of the jet. The solution differs from that considered in [1] only in the additional term in the expression for pressure.

The development of small perturbations in the given flow can be described using linearized equations and boundary conditions. However, in the case of a viscous fluid, solutions to these equations are difficult to obtain. The present study is concerned with long-wavelength perturbations. Such perturbations can be described using approximate 1D equations. Here, we use the following equations [13]:

$$\eta_t + w\eta_z = -\frac{1}{2}\eta w_z, \tag{1}$$

$$w_t + ww_z - \frac{1}{8\eta^2}\left[\eta^4\left(w_{zt} + ww_{zz} - \frac{1}{2}w_z\right)\right]_z = \frac{1}{We}\left(\frac{\eta_z}{\eta^2} + \frac{\eta_z\eta_{zz}}{\eta} - \frac{\eta_z^3}{2\eta^2} + \eta_{zzz}\right) + \frac{1}{Re\,\eta^2}\left[3\eta^2 w_z + \frac{3}{4}\eta^3\eta_{zz}w_z - \frac{9}{4}\eta^2\eta_z^2 w_z\right]_z, \tag{2}$$

where w is the cross-section-averaged axial component of the fluid velocity.

The written equations have a solution describing the uniaxial tension of the jet

$$\eta^{(0)} = \tau^{1/2}, \quad w^{(0)} = z/\tau.$$

Let us assume that at the initial instant of time there exists a small-amplitude perturbation of the mentioned flow. Solution to Eqs. (1) and (2) will be sought in the form

$$\eta = \eta^{(0)} + \delta\eta, \quad w = w^{(0)} + \delta w. \tag{3}$$

The quantities $\delta\eta$ and δw are assumed to be small. Substituting (3) into Eqs. (1) and (2) and neglecting products of small quantities, we obtain equations for small perturbations of the main flow

$$\delta\eta_t + \frac{z}{\tau}\delta\eta_z + \frac{1}{2}\tau^{-1/2}\delta w_z + \frac{1}{2}\tau^{-1}\delta\eta = 0, \tag{4}$$

$$\delta w_t + \frac{z}{\tau}\delta w_z - \frac{1}{8}\left[\frac{1}{\tau}\left(\delta w_{tz} + \frac{z}{\tau}\delta w_{zz} - \frac{1}{\tau}\delta w_z\right) - \frac{6}{\tau^{5/2}}\delta\eta\right]_z = \frac{1}{We}\left(\tau\delta\eta_z + \delta\eta_{zzz}\right) + \frac{3}{Re}\left[\delta w_z + \frac{2}{\tau^{1/2}}\delta\eta + \frac{1}{4}\tau^{-3/2}\delta\eta_{zz}\right]_z. \tag{5}$$

Let us consider a sinusoidal perturbation. A solution to equations for small perturbations will be sought in the form

$$\delta\eta = \tau^{-1/2}h(\tau)\exp(ikz), \quad \delta w = \tau^{-1}s(\tau)\exp(ikz), \tag{6}$$

where $k(\tau)$ is the wave number, i is imaginary unit, and multipliers $\tau^{-1/2}$ and τ^{-1} are introduced for convenience. The variable z is eliminated from the equations if the wave number varies with time following the law

$$k = k_0/\tau,$$

where k_0 is the initial wave number.

Substituting (6) into Eqs. (4) and (5), we obtain two ordinary differential equations for $h(\tau)$ and $s(\tau)$:

$$h_t = -\frac{iks}{2\tau}, \tag{7}$$

$$s_t + \frac{k^2}{8}\left(\frac{s_t}{\tau} - \frac{2s}{\tau^2}\right) + \frac{3ikh}{4\tau^2} = \frac{ik\tau^{3/2}h}{We}\left(1 - \frac{k^2}{\tau}\right) + \frac{3}{Re}\left(-k^2 s + 2ikh - \frac{ik^3 h}{4\tau}\right). \tag{8}$$

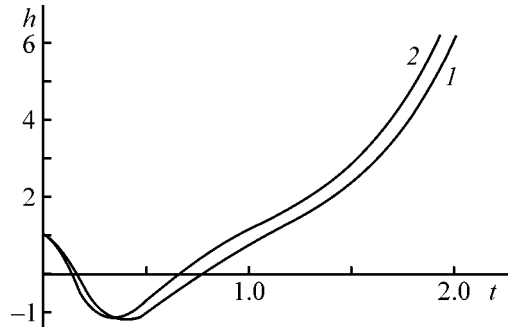

Fig. 1. Development of perturbations on the surface of ideal fluid jet, calculated using (*1*) exact and (*2*) approximate theories. Weber number 0.1, initial wave number 2.7. (*h*) Amplitude of jet radius perturbation and (*t*) time; the same for Fig. 2.

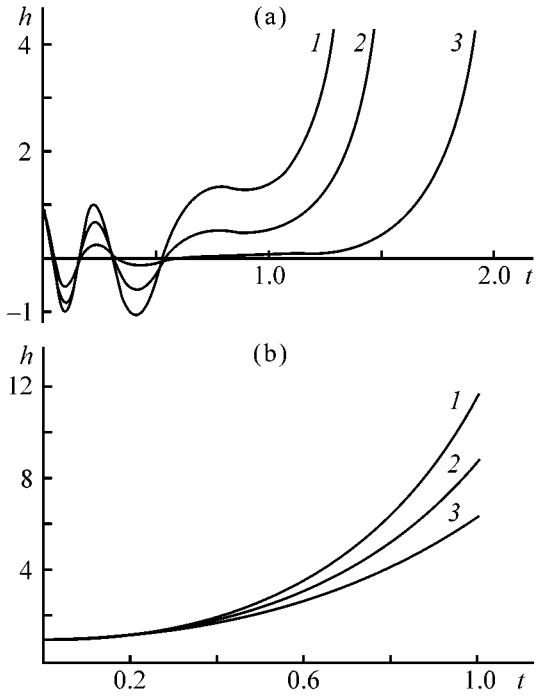

Fig. 2. Effect of Reynolds number on the rate of build-up of the amplitude of jet radius perturbation at small Weber number (We = 0.01) and comparatively (a) large and (b) small initial wave number k_0. Wave number k_0: (a) 2.5 and (b) 0.8. Reynolds number: (a): (*1*) 20, (*2*) 3, and (*3*) 1; (b): (*1*) 20, (*2*) 0.5, and (*3*) 0.2.

Eliminating the variable $s(\tau)$ from Eq. (8) with the use of Eq. (7), we obtain a second-order ordinary differential equation for $h(\tau)$

$$\left(1 + \frac{k^2}{8\tau}\right)h_{tt} + \left(\frac{2}{\tau} + \frac{3k^2}{\mathrm{Re}}\right)h_t + \left[\frac{3k^2}{8\tau^2} - \frac{3k^2}{\mathrm{Re}\,\tau}\left(1 - \frac{k^2}{8\tau}\right) - \frac{k^2\tau^{1/2}}{2\mathrm{We}}\left(1 - \frac{k^2}{\tau}\right)\right]h = 0. \quad (9)$$

Equation (9) is applicable to describing the evolution of jet radius perturbations for which the initial wave number is sufficiently small. For an ideal fluid, a comparison can be made with the exact solution obtained in [1]. As it can be seen from Fig. 1, the exact and approximate solutions are in good agreement even at comparatively large k_0. The solution was constructed using the following initial conditions:

$$h = 1,\ h_t = 0 \text{ at } t = 0.$$

In the case when the initial wave number is not small, the obtained equation for the amplitude of jet radius perturbation remains applicable, but only beginning with that instant of time when the current wavelength becomes larger than the current jet radius.

The type of solution is determined by values of the following three parameters: Weber and Reynolds numbers and initial wave number. The effect of viscosity forces on the development of perturbations is manifested in different ways, depending on the Weber number. If the Weber number is small, i.e., surface tension forces are important, the following pattern is observed. At relatively large initial wave numbers in the initial period of time, the solution has oscillatory nature (Fig. 2a). In the course of time, the current perturbation wavelength increases (in inverse proportion to τ). Simultaneously, the current jet radius decreases in proportion to $\tau^{-1/2}$. Therefore, after a certain time elapses, the fluid flow in the jet loses stability and the amplitude of the jet radius perturbation starts to grow fast. The effect of viscosity is manifested in that, in the initial period of time, the oscillation amplitude decreases in the course of time with decreasing Reynolds number. Simultaneously, with decreasing Reynolds number, the instant of time when the perturbation amplitude starts to grow steadily comes later. At small Weber numbers and relatively small wave numbers, the amplitude of jet radius perturbation starts to grow immediately (Fig. 2b). Here too, the effect of viscosity is manifested in that the development of perturbations is slower at smaller Reynolds numbers. However, the situation changes with increasing Weber number. Initially, the amplitude of jet radius perturbation is larger for those perturbations, which are characterized by smaller Reynolds numbers (Fig. 3a). In the course of time, the amplitude of those perturbations for which the Reynolds number is larger starts to grow faster and their amplitude becomes higher than that of perturbations characterized by smaller Reynolds numbers (Fig. 3b). Thus, at comparatively small Weber numbers, the viscosity exerts stabilizing influence on the development of perturba-

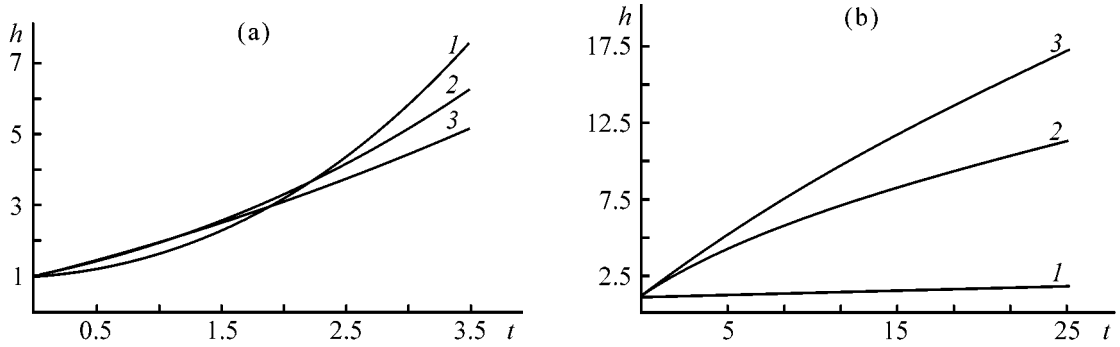

Fig. 3. Amplitude of jet radius perturbation, h, vs. time t at $k_0 = 0.8$. Weber number: (a) 0.08 and (b) 2.0. Reynolds number: (*1*) 50, (*2*) 0.1, and (*3*) 0.03.

tions. However, with increasing Weber number, the presence of viscous strain in a jet leads to its instability.

It should be noted that the derived equation describing the mechanism of fluid jet breakup in a spray apparatus can be used not only for describing the disintegration of this jet in the case of long-wavelength perturbations of the jet radius, but also for perturbations with arbitrary initial wave number.

CONCLUSIONS

(1) An equation is derived on the basis of a theoretical analysis of how a drop disintegrates as an element of a dispersed system in a spray apparatus. This equation relates the amplitude of the fluid jet radius perturbation, wave number, and Weber and Reynolds numbers.

(2) The equation obtained allows calculation of the time necessary for a fluid jet to breakup into drops in a spray apparatus.

REFERENCES

1. Razumovskii, N.A. and Chesnokov, Yu.G., *Izv. Ross. Akad. Nauk, Mekh. Zhidk. Gaza*, 1999, no. 6, pp. 97–104.
2. Tomotika, S., *Proc. Roy. Soc. London., Ser. A*, 1936, vol. 153, no. 879, pp. 302–318.
3. Khakhar, D.V. and Ottino, J.M., *Int. J. Multiphase Flow*, 1987, vol. 13, no. 1, pp. 71–86.
4. Andreev, V.K., *Prikl. Mekh. Tekh. Fiz.*, 1972, no. 4, pp. 80–84.
5. Markova, M.P. and Shkadov, V.Ya., *Izv. Akad. Nauk SSSR, Mekh. Zhidk. Gaza*, 1972, no. 3, pp. 30–37.
6. Lee, H.C., *IBM J. Res. Dev.*, 1974, vol. 18, no. 4, pp. 364–369.
7. Bogy, D.B., *Phys. Fluids*, 1978, vol. 21, no. 2, pp. 190–197.
8. Bogy, D.B., *Trans. ASME, J. Appl. Mech.*, 1978, vol. 45, no. 3, pp. 469–474.
9. Bogy, D.B., *Phys. Fluids*, 1979, vol. 22, no. 2, pp. 224–230.
10. Chesnokov, Yu.G., *Zh. Prikl. Khim.*, 2000, vol. 73, no. 3, pp. 448–452.
11. Eggers, J. and Dupont, T.F., *J. Fluid Mech.*, 1994, vol. 262, pp. 205–221.
12. Chesnokov, Yu.G., *Zh. Teor. Fiz.*, 2000, vol. 70, no. 8, pp. 31–38.
13. Garsia, F.J. and Castellanos, A., *Phys. Fluids*, 1994, vol. 6, no. 8, pp. 2676–2689.
14. Bechtel, S.E., Karlson, C.D., and Forest, M.G., *Phys. Fluids*, 1995, vol. 7, no. 12, pp. 2956–2971.

Russian Journal of Applied Chemistry, Vol. 74, No. 12, 2001, pp. 2066–2072. Translated from Zhurnal Prikladnoi Khimii, Vol. 74, No. 12, 2001, pp. 2006–2012.

PROCESSES AND EQUIPMENT OF CHEMICAL INDUSTRY

A Study of Convective Mass Exchange between Dispersed Flows in a Valve-Pulsatory Apparatus with Permeable Partition

R. Z. Aliev, M. R. Aliev, and A. R. Aliev

Daghestan Research Institute of Viticulture and Products of Vine Processing, Mamedkala, Daghestan, Russia
Institute of Physics, Daghestan Scientific Center, Russian Academy of Sciences, Makhachkala, Daghestan, Russia

Received April 5, 2000; in final form, April 2001

Abstract—A mathematical model of convective mass exchange between dispersed flows in a valve-pulsatory apparatus with permeable partition for carrying out processes with finely dispersed solid phase is proposed. The mass exchange between flows of aqueous Na_2CO_3 solution and distilled water, or pearlite suspension in water and aqueous solution of NaCl was studied on a pilot apparatus.

Interaction of different phases in technological apparatus commonly yields hydro- or aerodispersed heterogeneous systems composed of a continuous and a dispersed phases. The output capacity of a unit volume of the reaction space depends on parameters of the intercomponent interaction, interfacial contact area per unit volume, and rates of transfer within phases and exchange between phases. The interfacial area per unit volume is determined by the concentration and dispersity of phases; and the rates of transfer within phases and between phases are governed by, among other things, the particle size in the dispersed phase and hydrodynamics of the flow of the continuous phase about the particles. All other conditions being the same, the smaller the particle size and the higher the velocity of the flow about them, the higher the intensity of a process. However, the known scheme of technological processes—counterflow of the dispersed and continuous phases—has limitations imposed by the laws of particle motion in a medium. The maximum achievable velocity of flow about particles in counterflow of phases depends on the particle size, difference in density between the particles and the medium, and viscosity of the medium, being small for fine particles of the dispersed phase. At high flow rate of the continuous phase the dispersed phase is carried away from the reaction space and the counterflow of phases is disrupted. This is the reason why, e.g., washing or extraction of a component from a finely dispersed solid phase is commonly carried out by mixing it with an extracting agent and subsequent multistage counterflow mixing–separation of solid and liquid phases in apparatus comprising several mixers, decanters, pumps, and transporters.

The essence of the previously proposed methods for carrying out extraction in the solid–liquid system [1], chemical reactions yielding a dispersed solid phase [2], sorption and ion exchange in the solid–liquid system [3], and heat exchange between media [4] consists in the use of convective mass and heat exchange between dispersed flows separated by a permeable partition (permeable to continuous, and impermeable to dispersed phases in the flows). In the course of extraction, convective mass exchange occurs between the flow of a suspended dispersed solid material and that of an extracting agent; in carrying out chemical reactions, between the flow of a sediment suspension, catalyst, or reagent and the flow of a medium to be treated; and in performing sorption or ion exchange, between the flow of suspended sorbent or ion exchanger and that of a medium to be treated. In the proposed technique, convective heat exchange is carried out between dispersed flows through a permeable partition without mixing of their dispersed phases. The above-mentioned convective mass exchange is also carried out with a combination of extraction and sorption, when suspended sorbent or ion exchanger is used as extracting agent, in performing chemical reactions, sorption, or ion exchange, with hydro- or aerodispersed media.

For example, it is proposed to carry out extraction as follows (Fig. 1). The solid phase containing a soluble component is mixed in reactor R with a part of

1070-4272/01/7412-2066 $25.00 © 2001 MAIK "Nauka/Interperiodica"

extracting agent to form a suspension. During the time of suspension residence in reactor R, the component is extracted from dispersed particles into the liquid phase. Further, continuous counterflow convective mass exchange between the flows of this suspension and the main part of the extracting agent is carried out through a permeable partition in a valve-pulsatory mass-exchange apparatus (VPMEA). By the convective mass exchange between flows through a permeable partition is meant, in the given case, exchange of components dissolved in liquid phases without mixing of the dispersed phases of the flows. This process replaces several stages of phase mixing–separation. Component-depleted washed suspension is obtained at the output of channel *2* of VPMEA, and component-enriched extract, at the output of channel *1*. Compared with multiple mixing–separation of phases, the proposed process has technological advantages: possibility of working with finely dispersed kinetically favorable phases at high counterflow velocities, smaller number of technological procedures and employed equipment units, compactness, and high specific volume output capacity [1–4].

The outcome of the process is defined by the achieved degree of component extraction from particles of the solid phase into the liquid continuous phase of suspension in reactor R and also by the degree of convective transfer of the component from the suspension flow in channel *2* into the flow of a liquid extracting agent in channel *1* of VPMEA. The processes of phase interaction in stirred displacement reactor have been studied in sufficient detail.

The task to be accomplished consists in establishing the fundamental aspects of convective mass exchange between dispersed flows, in developing calculation procedures, and in designing efficient VPMEAs. Previously, a procedure for calculating the mass-transfer coefficient and a mathematical model of mass-transfer in a shell-and-tube extractor of the "tube-in-tube" type with permeable inner tube and piston pulsator have been reported [5, 6]. The present communication is concerned with the case when the exchange between flows separated by a permeable partition in VPMEA is achieved by creating sign-alternating pressure differential between the flows with the use of more advanced, computer-controlled valve-pulsatory system.

The operation of VPMEA (Fig. 1) consists in alternating stages defined by positions of valves *4–7*. The duration of each stage is t_s. In the first stage, valves *4* and *7* are open, and valves *5* and *6*, closed. In this case, the first suspension (the general case of convective mass exchange between flows of two suspensions is considered) with initial concentration

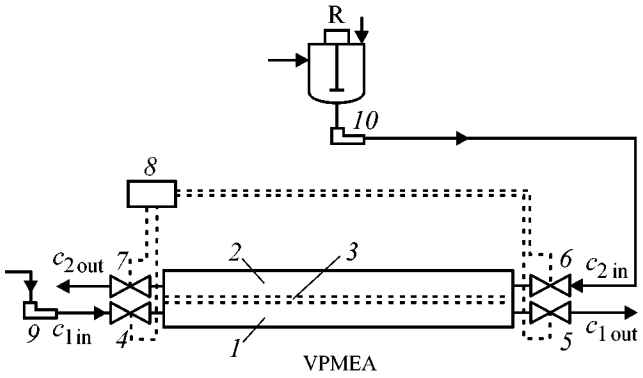

Fig. 1. Schematic of the unit. R is reactor; VPMEA, valvepulsatory mass-exchange apparatus; (*1*, *2*) VPMEA channels; (*3*) permeable partition; (*4–7*) valves; (*8*) valve control unit; and (*9*, *10*) pumps.

of the component $c_{1\,in} = c_1(0, t)$ is delivered by pump *9* through valve *4* into channel *1* and filtered through permeable partition *3*, creating a flow in channel *2*, discharged with concentration $c_{2\,out} = c_2(0, t)$ through valve *7*. In the second stage, valves *4* and *7* are closed, and valves *5* and *6*, opened. In this case, the second suspension with initial concentration $c_{2\,in} = c_2(l, t)$ is delivered from the reactor through valve *6* into channel *2* and filtered through partition *3*, creating a flow in channel *1*, discharged with outlet concentration $c_{1\,out} = c_1(l, t)$ through valve *5*. Here, c is the mass of the component in unit volume of the liquid phase, l is the channel length, and t is time. Thus, sign-alternating pressure differentials between the channels are created. In the course of such a pulsatory motion, the first and second suspensions repeatedly exchange portions of liquid phases, without mixing of their dispersed phases. As a result of this counterflow (Π scheme of flow) convective mass exchange, the concentration $c_{2\,out}$ is close to $c_{1\,in}$, and $c_{1\,out}$, to $c_{2\,in}$.

The aim of the present study was to study convective mass exchange between flows of suspension and liquid (both Newtonian) in the VPMEA. In doing so, mass-transfer or any other interaction between the solid and liquid phases within VPMEA was disregarded. Let us write a system of equations of convective mass exchange in the form

$$\oiint_s w\,ds = 0, \quad \oiint_s \rho w(w\,ds) + \oiint_s p\,ds - \oiint_s \sigma\,ds = 0,$$
$$\iiint_\omega \frac{\partial \varepsilon}{\partial t}\,d\omega + \oiint_s \varepsilon w\,ds = 0, \qquad (1)$$
$$\iiint_\omega \frac{\partial (\varepsilon c)}{\partial t}\,d\omega + \oiint_s \varepsilon c w\,ds = 0,$$

where w, ρ, and ε are the velocity, density, and porosity of the suspension; ω and s are an arbitrary vol-

ume and closed surface delimiting it; σ is the friction stress tensor, and p is pressure.

It is assumed that the density ρ_l and viscosity μ_l of the liquid phase are independent of concentration c, and the volume of the dissolved component can be neglected, compared with the volume of the liquid phase. We also neglect the time of hydrodynamic relaxation in passing from one stage to another, compared with the stage duration t_s.

Let us apply system (1) to a suspension flow along a permeable channel [7]. We direct the x axis along the channel and choose a closed surface s formed by two sections f of the channel and part of lateral surface between the sections. We then perform integration in system (1) and find projections onto the x axis, divide the equations by the distance dx between the section, and make dx approach zero. The layer of deposit formed on the partition will be considered thin as compared with the equivalent channel diameter d_{equiv}. Therefore, the section f is considered constant along the entire channel. Let us assume that the longitudinal velocity w_x is zero at channel walls [8, 9]. Let, also, the pressure p be constant over the section f [10]. We assume that the concentration c and porosity ε are also constant over the section f. This assumption is, in part, justified by the fact that transverse sign-alternating flows are created in VPMEA. Using the coefficients of friction, ξ, and momentum flux, β [11–13], we write

$$\begin{gathered}\frac{du}{dx} + \frac{\pi_v}{f}v = 0,\\ \frac{dp}{dx} + \rho\frac{d}{dx}(\beta u^2) + e_u\frac{\pi_f}{f}\frac{\xi}{8}\rho u^2 = 0,\\ \frac{\partial\varepsilon}{\partial t} + \frac{\partial}{\partial x}(\varepsilon u) + \frac{\pi_v}{f}v = 0,\\ \frac{\partial}{\partial t}(\varepsilon c) + \frac{\partial}{\partial x}(\varepsilon c u) + \frac{\pi_v}{f}c_\delta v = 0,\end{gathered} \tag{2}$$

where π_f and π_v are the perimeter of the channel cross-section and its permeable part, u is the cross-section-average longitudinal velocity, and v is the filtration rate averaged over the permeable part of the perimeter, $e_u = u/|u|$.

The c_δ value depends on the sign of the filtration rate v. At $v > 0$ (filtration from the channel) $c_\delta = c$, at $v < 0$ (filtration into the channel) c_δ is equal to the component concentration in the liquid phase in the partition pores at the boundary of the channel under consideration. If the partition thickness can be neglected, then, at $v < 0$, c_δ is equal to the component concentration in the liquid phase outside the channel and, in particular, in an adjacent channel.

The pressure in the channel can be related to the filtration rate by the Darcy law:

$$v(x) = \frac{p(x) - p_0}{\mu_l r_{ef}}, \quad r_{ef} = r_p\delta_p + r_d\delta_d, \tag{3}$$

where p_0 is the pressure outside the channel, e.g., in an adjacent channel; r_{ef} is the filtration resistance (m^{-1}); r_p, r_d, δ_p, and δ_d are the resistances (m^{-2}) and thicknesses (m) of the partition and deposit. The expression for r_{ef} in (3) is valid for the case of a planar wall. Passing to dimensionless variables in Eqs. (2), we obtain

$$\begin{gathered}\frac{dU}{dX} + \frac{l}{d_{equiv}}\frac{Re_0}{R_{ef}}Eu = 0,\\ \frac{dEu}{dX} + \rho_{rel}\frac{d}{dX}(\beta U^2) + e_u\frac{l}{d_{equiv}}\frac{\xi}{2}\rho_{rel}U^2 = 0,\\ \frac{\partial\varepsilon}{\partial Ho} + U\frac{\partial\varepsilon}{\partial X} - \frac{dU}{dX}(1-\varepsilon) = 0,\\ \frac{\partial C}{\partial Ho} + U\frac{\partial C}{\partial X} - \frac{1}{\varepsilon}\frac{dU}{dX}(C_\delta - C) = 0,\end{gathered} \tag{4}$$

where $X = x/l$, $U = u/u_0$, $V = v/u_0$, $C(X, Ho) = [c(x, t) - c']/(c'' - c')$, c' and c'' are arbitrary constants, $Ho = tu_0/l$ is the homochronicity number, $Eu(X) = [p(x) - p_0]/(\rho_l u_0^2)$ is the Euler number, $\rho_{rel} = \rho/\rho_l$, $u_0 = u(0)$, $R_{ef} = fr_{ef}/\pi_v$, and $C_\delta = (c - c')/(c'' - c')$.

Let us consider two adjacent channels separated by a permeable wall. For each channel we write Eqs. (4) and take into account that the liquid cross-flow occurs because of the pressure difference between the channels. Then we have

$$\begin{gathered}\frac{dU_1}{dX} + \frac{f_2}{f_1}\frac{dU_2}{dX} = 0, \quad \frac{dU_1}{dX} + \frac{l}{d_{equiv\,1}}\frac{Re_{01}}{R_{ef\,1}}Eu_v = 0,\\ \frac{dEu_v}{dX} + \frac{d}{dX}(\rho_{rel\,1}\beta_1 U_1^2 - \rho_{rel\,2}\beta_2 U_2^2)\\ + \frac{e_{u1}l}{2d_{equiv1}}\rho_{rel\,1}\xi_1 U_1^2 - \frac{e_{u2}l}{2d_{equiv2}}\rho_{rel\,2}\xi_2 U_2^2 = 0,\\ \frac{\partial\varepsilon_1}{\partial Ho} + U_1\frac{\partial\varepsilon_1}{\partial X} - \frac{dU_1}{dX}(1-\varepsilon_1) = 0,\\ \frac{\partial C_1}{\partial Ho} + U_1\frac{\partial C_1}{\partial X} - \frac{1}{\varepsilon_1}\frac{dU_1}{dX}(C_{\delta1} - C_1) = 0,\\ \frac{\partial\varepsilon_2}{\partial Ho} + U_2\frac{\partial\varepsilon_2}{\partial X} - \frac{dU_2}{dX}(1-\varepsilon_2) = 0,\\ \frac{\partial C_2}{\partial Ho} + U_2\frac{\partial C_1}{\partial X} - \frac{1}{\varepsilon_2}\frac{dU_2}{dX}(C_{\delta2} - C_2) = 0,\end{gathered} \tag{5}$$

where index denotes the channel number, and $Eu_v(X) = [p_1(x) - p_2(x)]/(\rho_l u_0^2)$.

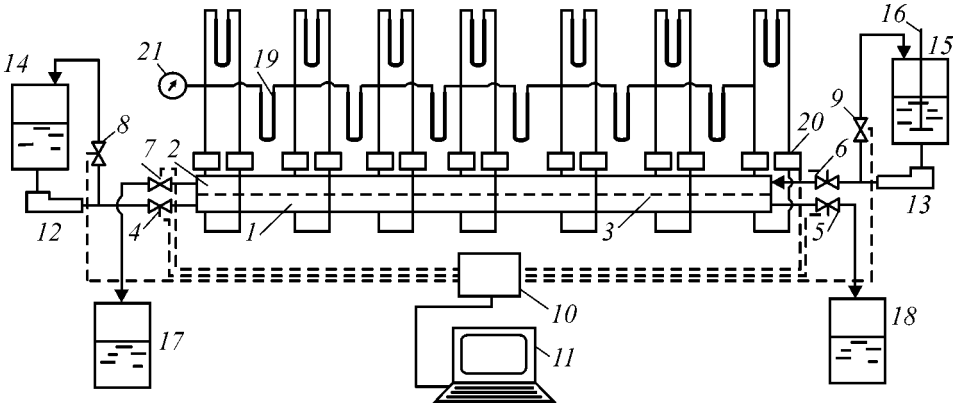

Fig. 2. Schematic of experimental setup for studying convective mass exchange in VPMEA: (*1, 2*) first and second channels of VPMEA, (*3*) permeable partition, (*4–9*) controlled valves, (*10*) computer interface, (*11*) microcomputer, (*12, 13*) pumps, (*14, 15, 17, 18*) vessels, (*16*) stirrer, (*19*) differential pressure gages, (*20*) expansion vessels, and (*21*) standard pressure gage.

So, we obtained the system of equations (5) for $U_1(X)$, $U_2(X)$, $\mathrm{Eu}_v(X)$, $C_1(X, \mathrm{Ho})$, $C_2(X, \mathrm{Ho})$, $\varepsilon_1(X, \mathrm{Ho})$, $\varepsilon_2(X, \mathrm{Ho})$. Setting the boundary $[U_1(0), U_2(0), U_1(1), \mathrm{U}_2(1), C_1(0, \mathrm{Ho}), C_2(1, \mathrm{Ho}), \varepsilon_1(0, \mathrm{Ho}), \varepsilon_2(1, \mathrm{Ho})]$ and initial $[C_1(X, 0), C_2(X, 0), \varepsilon_1(X, 0), \varepsilon_2(X, 0)]$ conditions defines the boundary-value problem for mass exchange between the flows.

The given model can be used, with the assumptions made, also for describing heat exchange between flows with temperature-inactive particles.

In practice, $c_1(0, t) = c_{1\,\mathrm{in}} = \mathrm{const}$ during the first stage and $c_2(l, t) = c_{2\,\mathrm{in}} = \mathrm{const}$ during the second stage. In this case, the maximum concentration in the VPMEA will be, e.g., $c_{1\,\mathrm{in}}$, and the minimum concentration $c_{2\,\mathrm{in}}$. Let us choose $c' = c_{2\,\mathrm{in}}$, $c'' = c_{1\,\mathrm{in}}$. Then the dimensionless concentration $C(X, \mathrm{Ho}) = [c(x, t) - c_{2\,\mathrm{in}}]/(c_{1\,\mathrm{in}} - c_{2\,\mathrm{in}})$, and the boundary conditions become universal: in the first stage $C_1(0, \mathrm{Ho}) = C_{1\,\mathrm{in}} = 1$, and in the second, $C_2(1, \mathrm{Ho}) = C_{2\,\mathrm{in}} = 0$. This means that the dimensionless output concentrations $C_1(1, \mathrm{Ho}) = C_{1\,\mathrm{out}}(\mathrm{Ho})$ and $C_2(1, \mathrm{Ho}) = C_{2\,\mathrm{out}}(\mathrm{Ho})$ are independent of the input concentrations $c_{1\,\mathrm{in}}$ and $c_{2\,\mathrm{in}}$, being universal in this sense. Therefore, the degree of mass exchange [14]

$$E = \lim_{\mathrm{Ho}\to\infty} C_{2\,\mathrm{out}}(\mathrm{Ho}) = \lim_{t\to\infty} \frac{c_{2\,\mathrm{out}}(t) - c_{2\,\mathrm{in}}}{c_{1\,\mathrm{in}} - c_{2\,\mathrm{out}}} \qquad (6)$$

is a characteristic of VPMEA. It is independent of input concentrations and characterizes component transfer between the flows.

For experimental studies, we fabricated a planar model of VPMEA (Fig. 2). The model is made of two organic glass plates with 7.5-m-long grooves with 6×6 mm square cross-section. The permeable partition—capron filter fabric is placed in stretched state between the plates, after which the latter are firmly pressed to one another by means of bolted clamps. In doing so, the plates are in such a position that their grooves are opposite one another. This gives adjacent channels *1* and *2* separated by permeable partition *3*. The flows are fed-in and discharged by means of pipes. The programmed control of electromagnetic sphincter valves *4–9* is done by a microcomputer *11* with interface *10*. Hose-type pumps *12* and *13* are operated by the same drive, HShR-15M, to make equal their volumetric flow rates.

Liquid is fed from vessel *14* into channel *1* by pump *12* through valve *4* and discharged through valve *5* into vessel *18*. The suspension is fed by pump *13* in the counterflow mode from vessel *15* with stirrer *16* into channel *2* through valve 6 and discharged from the channel through valve *7* into vessel *17*. Valves *4–7* are program-controlled by a microcomputer *11*. To prevent blocking by valves *4* and *6* of flows delivered by pumps *12* and *13*, the pumps are equipped with bypass lines with valves *8* and *9*. Valve *8* is opened when valve *4* is closed, and valve *9* is opened when valve *6* is closed. The pressure distributions in the channels are measured with differential pressure gages *19* with expansion vessels *20*. Prior to experiments, air bubbles were removed from the VPMEA by switching-on pumps *12* and *13* with open valves *4–7* and closed valves *8* and *9*.

An experimental study of the convective mass exchange between flows of two liquids—distilled water and Na_2CO_3 solution was performed as follows. A solution was prepared in vessel *15*, and vessel *14* was filled with water. To remove air and ensure specified initial conditions, the solution from vessel *15* was fed into both channels at open valves *4–7*, with the solution from the channel outlets directed into the

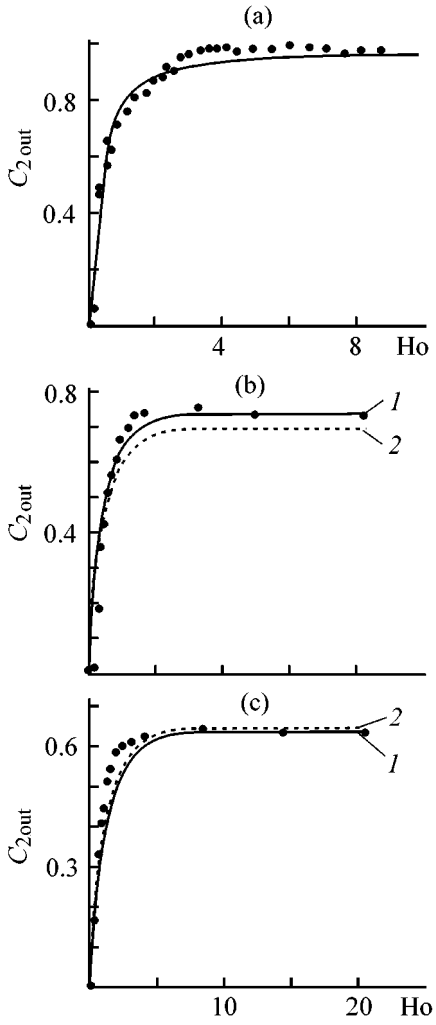

Fig. 3. Time dependence of $C_{2\,out}$(Ho). (a) Re_0 = 1892, l/d_{equiv} = 1250, ε_{in} = 1.0, Sr = 0.137, $R_{ef} = 1.4 \times 10^6$, Δ_p = 0.03; (b) Re_0 = 2754, l/d_{equiv} = 1250, ε_{in} = 0.99, Sr = 0.11; Δ_p = 0.025; R_{ef} = (*1*) 8.8×10^6, (*2*) 11.4×10^6; (c) Re_0 = 2754, l/d_{equiv} = 1250, ε_{in} = 0.97, Sr = 0.11, Δ_p = 0.025; R_{ef} = (*1*) 18.8×10^6, (*2*) 17.6×10^6. *Curves*, calculation; *points*, experiment; the same for Fig. 4.

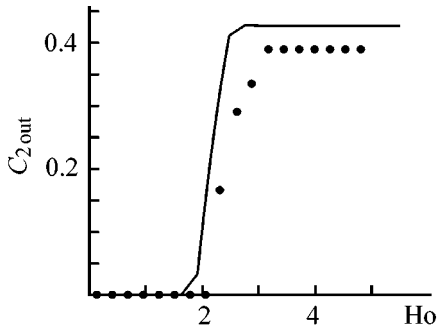

Fig. 4. Time dependence of $C_{2\,out}$(Ho) = C_2(1, Ho) at direct-flow delivery of flows. Re_0 = 1892, l/d_{equiv} = 1250, ε_{in} = 1.0, Sr = 0.137, $R_{ef} = 1.4 \times 10^6$, Δ_p = 0.03.

same vessel *15*. After that the lines of solution feed and discharge were put in the state corresponding to Fig. 2, the program controlling the valves was initiated, and pumps *12*, *13* switched on. Simultaneously, sampling was commenced at the outlet of channel *2*. In the steady state, samples were taken at the outlets of both channels. The Na_2CO_3 concentration in the samples was determined by means of refractometry. The experiments were carried out repeatedly. The results obtained are presented in Fig. 3a.

A set of experiments was carried out on studying the convective mass exchange between liquid and suspension flows. An aqueous solution of NaCl was taken as liquid, and suspension of ground pearlite in distilled water, as model suspension. The choice of pearlite as model dispersed material was governed by its inertness toward the transported component—NaCl. The inertness of pearlite was judged from the results of refractometric measurements of the NaCl solution concentration before and after introducing a weighed portion of pearlite into the solution. The pearlite fraction with particle size in the range 10–100 μm was selected by sieving. The apparent density of pearlite was 300 kg m^{-3} [15]. The porosity of pearlite was determined pycnometrically to be 0.75.

The experimental study was carried out as follows. First, suspension was fed into channel *1* of the VPMEA, and distilled water, into channel *2*, at open valves *4–7*. After the channels were filled and air removed from them, the program of valve control was started and the input line of the liquid delivery pump *12* was connected to the vessel with solution. Simultaneously, sampling was commenced at the outlet of channel *1*. The experiments were conducted at ε = 0.97 and ε = 0.99 for two partitions with different R_{ef} values an suspension–liquid counterflow velocity of 0.5 m s^{-1} (Figs. 3b and 3c).

Also, the convective mass exchange between flows of distilled water and Na_2CO_3 solution was studied with a *Z*-scheme of flow delivery. In this case, flows are delivered in the direct-flow mode into channel *1* through valve *4* and into channel *2* through valve *7* (Fig. 2). In the first stage, valves *4* and *6* are open, and valves *5* and *7*, closed. In the second stage, the situation is the opposite. The experiments were carried out in the following sequence. First, the channels were filled with the solution through open valves *4–7*. Then water was delivered to channel *2* and samples were taken at the outlet of channel *1*. The results obtained are shown in Fig. 4.

As seen from Fig. 4, the residence time of the liquid in the VPMEA is $2l/u_0$ (Ho = 2). Virtually sta-

tionary concentrations are attained at the apparatus outlets at homochronicity number Ho ≈ 3. For the counterflow Π scheme, the degree of mass exchange between the flows reaches values of 0.64–0.99 at Ho = 3 (Figs. 3a–3c). This indicates the possibility of creating a high-efficiency VPMEA for dispersed flows on the basis of the proposed principle.

Figures 3 and 4 show, in addition to experimental points, curves calculated for the experimental conditions with $l/d_{\text{equiv}1} = l/d_{\text{equiv}2} = l/d_{\text{equiv}}$, $f_1 = f_2$. The rates of flow delivery into the first and second channels are the same. The flow characteristics are as follows: $\varepsilon_1 = 1$, $\rho_1 = \rho_l$, $\mu_{\text{rel}1} = 1$, $\mu_1 = \mu_l$, $\varepsilon_2 = \varepsilon$, $\rho_2 = \varepsilon\rho_l + (1 - \varepsilon)\rho_s$, $\rho_{\text{rel}2} = \rho_{\text{rel}}$, $\mu_2 = 0.59\ \mu_l(\varepsilon - 0.23)^{-2}$ [16], where ρ_s is the density of the solid phase, μ_1 and μ_2 are the viscosities of the first and second suspensions, and $\text{Sr} = t_s u_0/l$ is the Struchal number. It was assumed in the calculations that R_{ef} is constant along the longitudinal coordinate X.

The coefficients ξ and β were determined for the given channel in relation to the Reynolds number in this channel [14, 17].

For the Π scheme, we have the following boundary and initial conditions:

$$U_1(0) = 1,\ U_2(0) = -1,\ U_1(1) = 0,\ U_2(1) = 0,$$
$$C_1(0,\ \text{Ho}) = 1, \qquad (7)$$

$$U_1(0) = 0,\ U_2(0) = 0,\ U_1(1) = 1,\ U_2(1) = -1,$$
$$C_2(1,\ \text{Ho}) = 0,\ \varepsilon(1,\ \text{Ho}) = \varepsilon_{\text{in}}, \qquad (8)$$

$$C_1(X,\ 0) = 1,\ C_2(X,\ 0) = 0,\ \varepsilon(X,\ 0) = \varepsilon_{\text{in}}. \qquad (9)$$

For the Z scheme, the boundary and initial conditions have the form

$$U_1(0) = 1,\ U_2(0) = 0,\ U_1(1) = 0,\ U_2(1) = 1,$$
$$C_1(0,\ \text{Ho}) = 1, \qquad (10)$$

$$U_1(0) = 0,\ U_2(0) = 1,\ U_1(1) = 1,\ U_2(1) = 0,$$
$$C_2(0,\ \text{Ho}) = 0,\ \varepsilon(1,\ \text{Ho}) = 1, \qquad (11)$$

$$C_1(X,\ 0) = 1,\ C_2(X,\ 0) = 1,\ \varepsilon(X,\ 0) = 1, \qquad (12)$$

where (7), (10) and (8), (11) are the boundary conditions for the first and second stages, respectively; (9) and (12) are the initial conditions.

With account of the boundary conditions (7), (8) for the Π scheme or (10), (11) for the Z scheme, the hydrodynamic part of system (5) was solved by the method of iterations with respect to U_1, U_2, and Eu_v. Each iteration was calculated by the method of orthogonal matrix run [18]. The obtained functions $U_1(X)$, $U_2(X)$, and $\text{Eu}_v(X)$ were used to calculate concentrations and porosities by means of equations of system (5).

In the course of calculations, account was taken of the change in the position of the interface between liquids with concentrations $C_1(X, \text{Ho})$ and $C_2(X, \text{Ho})$ inside the permeable partition for any point of the apparatus. The displacement of the interface in a time ΔHo related to the partition thickness δ_p is equal to $V\Delta\text{Ho}/(\Delta_p D_{\text{equiv}})$, where $\Delta_p = \delta_p/d_{\text{equiv}}$.

The calculation was started using the equations for the first stage with initial conditions (9) and (12). Then the calculation was continued using the equations of the second stage. For the initial distribution of concentrations and porosities for each subsequent stage was taken the final distribution for the preceding stage.

All parameters of the model, except for the dimensionless resistance R_{ef}, can be determined exactly. To find the real R_{ef} values of permeable partitions, we performed an experiment on measuring the pressure difference $\text{Eu}_v(X)$ between the channel with distilled water flowing in accordance with the Π scheme [17]. The experimental data were processed using the second equation of system (5). Let us integrate this equation over X from 0 to 1 with account of condition (7):

$$R_{\text{ef}} = \frac{l}{d_{\text{equiv}}}\,\text{Re}_0 \int_0^1 \text{Eu}_v(X)\,dX. \qquad (13)$$

The experimentally found $\text{Eu}_v(X)$ were integrated using the method of trapezoids. In processing the results of hydraulic experiments [17], the filtration resistance of the partition was found to be $r_{\text{ef}} = (9.3 \pm 2.1) \times 10^6$. The r_{ef} measurement error was 22%. Therefore, the dimensionless resistance R_{ef} was chosen as the model identification parameter.

The values of this parameter were selected so as to achieve the best fit of calculation to the experiment. In the experiment on mass exchange between flows of two liquids (Fig. 3a), the selected R_{ef} value and that measured by the technique described above coincided (1.4×10^6). In experiments on mass exchange between liquid and suspension flows at $\varepsilon_{\text{in}} = 0.99$ (Fig. 3b) the selected (solid line) and measured (dashed line) R_{ef} values are 8.8×10^6 and 11.4×10^6, respectively; for $\varepsilon_{\text{in}} = 0.97$ (Fig. 3c), the respective values are 18.8×10^6 and 17.6×10^6.

In the modes studied, the average resistance of deposit accumulated during a stage is small, compared with the partition resistance. Estimation of the average dimensionless resistance of the deposit at specific resistance of pearlite $r_d = 10^{12}$ m^{-2} [19] and suspension porosity of 0.97 gives a value of 5.4×10^4, which is two orders of magnitude less than the R_{ef} of the partition. Therefore, we used in calculations for the first and second stages the R_{ef} value for the partition. This circumstance also justifies the assumption that R_{ef} is independent of X, made in calculations.

The maximum deviation of the degrees of mass exchange, calculated for the selected values of the parameter R_{ef}, from those calculated for the measured R_{ef} is 6.2%. Therefore, R_{ef} can be regarded with satisfactory accuracy in calculating VPMEA as a real dimensionless resistance, rather than the identification parameter of the mathematical model. In filtration from the liquid channel, the parameter R_{ef} can be considered equal to the dimensionless resistance of the partition, found from experiment or from the literature. In filtration from the suspension channel, the parameter R_{ef} is defined as a sum of dimensionless resistances of the partition and the deposit layer.

The operation principle of the mass-exchange apparatus VPMEA, the mathematical model, the developed software for design calculations, and the obtained experimental results may serve as a basis of effective apparatus and technological schemes for carrying out combined and involving a small number of operations processes with finely dispersed solid phase: extraction, sorption, ion exchange, chemical reactions, and heat exchange.

CONCLUSIONS

(1) A mathematical model of convective mass exchange between dispersed flows in a two-channel apparatus with permeable partition and controlled valve-pulsatory system is proposed.

(2) The results of an experimental study demonstrate that numerical solutions obtained using the model are in satisfactory agreement with the measured dependences of concentration variation at the flow outlets on the homochronicity number and that the model is adequate to the experiment at the following parameters: Re_0 = 1892–2754, l/d_{equiv} = 1250, Sr = 0.11–0.137, ε_{in} = 0.97–1.0, $R_{ef} = (1.4–18.8) \times 10^6$, Δ_p = 0.025–0.03.

(3) The stationary concentrations at the apparatus outlet are attained at homochronicity number Ho $\approx$ 3.

(4) The possibility is established of creating apparatus with degree of mass exchange between flows of up to 0.9, and software is developed for their design calculations to achieve a prescribed degree of mass exchange.

REFERENCES

1. USSR Inventor's Certificate, no. 548290.
2. RF Patent 1337133.
3. RF Patent 1182722.
4. RF Patent 1091018.
5. Aliev, A.Z., Aliev, R.Z., and Kurochkina, M.I., *Zh. Prikl. Khim.*, 1981, vol. 54, no. 2, pp. 459–462.
6. Aliev, A.Z., Aliev, R.Z., and Konstantinov, E.N., *Izv. Vyssh. Uchebn. Zaved., Pishch. Tekhnol.*, 1985, no. 4, pp. 119.
7. Aliev, M.R. and Aliev, R.Z., *Teor. Osn. Khim. Tekhnol.*, 1997, vol. 31, no. 1, pp. 102–104.
8. Sergeev, S.P., Dil'man, V.V., and Genkin, V.S., *Inzh.-Fiz. Zh.*, 1974, vol. 27, no. 4, pp. 588–595.
9. Kochenov, I.S. and Novosel'skii, O.Yu., *At. Energ.*, 1967, vol. 23, no. 2, pp. 113–120.
10. Babenko, V.A., *Inzh.-Fiz. Zh.*, 1986, vol. 51, no. 3, pp. 375–383.
11. Bystrov, P.I. and Mikhailov, V.S., *Gidrodinamika kollektornykh teploobmennykh apparatov* (Hydrodynamics of Collector Heat-Exchange Apparatus), Moscow: Energoizdat, 1982.
12. Eroshenko, V.M. and Zaichik, L.I., *Gidrodinamika i teplomassoobmen na pronitsaemykh poverkhnostyakh* (Hydrodynamics and Heat-and-Mass Exchange on Permeable Surfaces), Moscow: Nauka, 1984.
13. Meerovich, I.G. and Muchnik, G.F., *Gidrodinamika kollektornykh sistem* (Hydrodynamics of Collector Systems), Moscow: Nauka, 1986.
14. Aliev, M.R., Aliev, R.Z., and Aliev, A.R., *Mat. Model.*, 1998, vol. 10, no. 7, pp. 48–60.
15. Lur'e, A.A., *Sorbenty i khromatograficheskie nositeli* (Sorbents and Chromatographic Supports), Moscow: Khimiya, 1972.
16. Pavlov, K.F., Romankov, P.G., and Noskov, A.A., *Primery i zadachi po kursu protsessov i apparatov khimicheskoi tekhnologii* (Exercises and Problems for the Course of Processes and Apparatus of Chemical Technology), Leningrad: Khimiya, 1976.
17. Aliev, M.R., Aliev, R.Z., and Aliev, A.R., *Teor. Osn. Khim. Tekhnol.*, 1999, vol. 33, no. 1, pp. 23–29.
18. Samarskii, A.A. and Nikolaev, E.S., *Metody resheniya setochnykh uravnenii* (Methods for Solving Finite-Difference Equations), Moscow: Nauka, 1978.
19. Zhuzhikov, V.A., *Fil'trovanie* (Filtration), Moscow: Khimiya, 1971.

Russian Journal of Applied Chemistry, Vol. 74, No. 12, 2001, pp. 2073–2078. Translated from Zhurnal Prikladnoi Khimii, Vol. 74, No. 12, 2001, pp. 2013–2018.

PROCESSES AND EQUIPMENT OF CHEMICAL INDUSTRY

Combined Processes of Polymerization and Drying of Prepolymer Grains in Double-Section Apparatus with Fluidized Bed

A. G. Lipin, S. V. Fedosov, and A. A. Shubin

Ivanovo State University of Chemical Technology, Ivanovo, Russia
Ivanovo State Architectural Academy, Ivanovo, Russia

Received March 23, 2001

Abstract—The possibility of combining polymerization and drying in obtaining polymers from derivatives of methacrylic acid was revealed experimentally. A mathematical model of combined polymerization and solvent removal under conditions of a fluidized bed of the material was developed.

Water-soluble polymers based on derivatives of acrylic and methacrylic acids are used in various fields of technology as flocculants, thickeners, water-retaining agents, and substances reducing the hydraulic resistance [1].

Highly promising for manufacture of water-soluble acrylic polymers are continuous methods in which the process is carried out in a set of apparatus, e.g., reactor–extruder–granulator–drying chamber, combined in a single installation.

One of the possible ways to make the technological cycle shorter consists in combining the process of polymerization with high conversion and solvent removal from the reaction mass [2]. In addition, this reduces the power consumption, since moisture is partly evaporated by the heat of the chemical reaction. In synthesizing water-soluble polymers, water is the reaction medium. Therefore, the process of drying must not occur in advance of the polymerization. Otherwise, the reaction terminates at low conversions [3].

To reveal the possibility of combining the processes of polymerization and drying, special-purpose experiments were carried out. The initial stage of synthesis was performed in concentrated aqueous solutions. For example, in copolymerization of sodium methacrylate (SMA) with methacrylamide (MAA), the concentration of the solution of the starting monomers was 66 wt %. The copolymerization was done in the course of 1200 s at 65°C. During this time, the conversion was as high as 67%. Further, the prepolymer was ground and dried.

Selected results of the experiments are presented in Fig. 1 as dependences of the conversion and the humidity of the product on the process time. During the first 1800 s of drying, the conversion became as high as 93, 96, and 98%, and the humidity as low as 25, 23, and 20%, at temperatures of, respectively, 70, 90, and 105°C. Further drying during 13 500 s raises the conversion only slightly. In all experiments, the conversion was 99.5%. The product humidity decreased to 10, 4, and 1%.

The results of the experiments demonstrated that, in the course of prepolymer drying, the rate of the chemical process much exceeds that of solvent (water) removal. Under these conditions, the polymerization

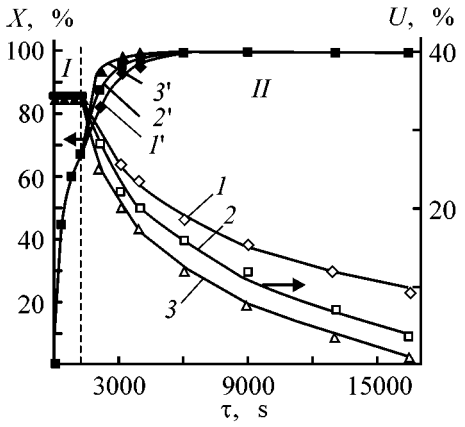

Fig. 1. Variation of the conversion X and humidity U with time τ. Drying temperature (°C): (*1*, *1'*) 70, (*2*, *2'*) 90, and (*3*, *3'*) 105. (*I*) Polymerization and (*II*) drying + polymerization.

1070-4272/01/7412-2073 $25.00 © 2001 MAIK "Nauka/Interperiodica"

process goes till virtually complete exhaustion of the starting monomers. Rather effective is performing combined processes in apparatus with fluidized bed.

The performed investigations of the process of copolymerization of SMA with MAA in its final stage allowed development of a mathematical description of drying and additional polymerization of the granulated prepolymer. The description includes units related to chemical kinetics, kinetics of heat-and-mass exchange for isolated particle, and material and heat balances for the apparatus as a whole.

In developing a mathematical model of processes occurring in an isolated inclusion of the dispersed phase, the following assumptions were made: stirring of the material in the fluidized bed is intensive, heat-transfer coefficients are high, small particle size leads to absence of temperature fields, each grain is a microreactor operating in the quasistationary mode. The particles are spherical.

In describing the kinetics of SMA copolymerization with MAA, account is taken of the reactions of chain initiation, growth, and termination. The system of kinetic equations for the concentrations of the initiator and monomers and initial moments of the molecular weight distribution has the form [4]

$$dI/d\tau = -k_d I, \quad (1)$$

$$dC_A/d\tau = -k_{pAA}R_A C_A - k_{pBA}R_B C_A, \quad (2)$$

$$dC_B/d\tau = -k_{pAB}R_A C_B - k_{pBB}R_B C_B, \quad (3)$$

$$dR_A/d\tau = fk_d I + k_{pBA}R_B C_A - k_{pAB}R_A C_B - k_{tAA}R_A^2 - k_{tAB}R_A R_B, \quad (4)$$

$$dR_B/d\tau = fk_d I + k_{pAB}R_A C_B - k_{pBA}R_B C_A - k_{tBB}R_B^2 - k_{tBA}R_B R_A, \quad (5)$$

$$dP/d\tau = k_{tAA}R_A^2 + k_{tAB}R_A R_B + k_{tBA}R_B R_A + k_{tBB}R_B^2, \quad (6)$$

where I, C_A, C_B, R_A, R_B, and P are the concentrations of initiator, SMA, MAA, growing radicals with SMA and MAA end units, and inactive chains (M); τ time (s); f the efficiency of initiation; k_d the rate constant of initiator decomposition (s^{-1}); k_p, k_t the rate constants of chain growth and termination ($M^{-1}\ s^{-1}$).

The efficiency of initiation and the rate constants of elementary reactions, which vary in the course of the process, are calculated using the formulas reported in [4]. The grain temperature is found from the heat balance equation

$$\rho_m(c_m + \bar{U}c_w)\frac{dT}{d\tau} = 6\frac{\alpha}{d_{equiv}}(T_g - T) - \left(\frac{dC_A}{d\tau} + \frac{dC_B}{d\tau}\right)\Delta H + \frac{d\bar{U}}{d\tau}r^*\rho_m, \quad (7)$$

where d_{equiv} is the equivalent particle diameter (m); ρ_m the material density ($kg\ m^{-3}$); α the heat-transfer coefficient ($W\ m^{-2}\ K^{-1}$); ΔH the heat effect of polymerization ($J\ mol^{-1}$); T the particle temperature (°C); T_g the temperature of the drying agent (°C); r^* the latent heat of vaporization ($J\ kg^{-1}$); $\bar{U}$ the absolute humidity of the material ($kg\ kg^{-1}$); c_m, c_w the specific heats of dry material and water, respectively ($J\ kg^{-1}\ K^{-1}$).

The last term in the right-hand side of Eq. (7) accounts for the relationship between heat and moisture transfer processes. The mathematical description is supplemented with an equation characterizing the kinetics of variation of the moisture content of a prepolymer grain. As is known, in drying of materials with high diffusion resistance to moisture transfer, to which also belongs the copolymer of SMA with MAA, the equilibrium humidity is virtually instantaneously attained on the body surface [5]. In this case, the variation of the moisture-content field in a material being dried is described by a differential mass-transfer equation with a boundary condition of the first kind with variable coefficient of moisture transfer. For a spherical particle we have

$$\frac{\partial U(r,\tau)}{\partial \tau} = k_m(\bar{U}, T)\left[\frac{1}{r}\frac{\partial^2 (rU)}{\partial r^2}\right], \quad 0 \le r \le R,\ \tau > 0, \quad (8)$$

$$\frac{\partial U(0,\tau)}{\partial r} = 0, \quad U(0,\tau) \ne \infty, \quad (9)$$

$$U(R,\tau) = U_p, \quad (10)$$

$$U(r,0) = U_{in}. \quad (11)$$

The moisture-transfer coefficient $k_m(\bar{U}, T)$ is a complex function of the moisture content and temperature of a particle. Exact analytical solution of the problem (8)–(11) is impossible. An approximate solution to this problem will be sought for in the classical form [5] at finite number of expansion elements:

$$U(x,\tau) = U_p + (U_0 - U_p)\frac{R}{r}\sum_{j=1}^{n} A_j(\tau)\sin\left(j\pi\frac{r}{R}\right). \quad (12)$$

Let us use the Petrov–Galerkin method [6]. We substitute a trial solution (12) into Eq. (8) and require

that the residual should be orthogonal to the calibration functions of the type

$$\Psi_k(r) = \frac{r}{R}\sin\left(k\pi\frac{r}{R}\right), \quad (13)$$

$$\sum_{j=1}^{n}\frac{\partial A_j(\tau)}{\partial\tau}\int_0^R (U_0 - U_\mathrm{p})\frac{R}{r}\sin\left(j\pi\frac{r}{R}\right)\frac{r}{R}\sin\left(k\pi\frac{r}{R}\right)$$

$$= k_\mathrm{m}(\bar{U}, \tau)\sum_{j=1}^{n}A_j(\tau)\int_0^R \frac{1}{r}\frac{\partial^2}{\partial r^2}\left\{r\left[U_\mathrm{p} + \left(U_0 - U_\mathrm{p}\right)\frac{R}{r}\sin\left(j\pi\frac{r}{R}\right)\right]\right\}$$

$$\times \frac{r}{R}\sin\left(k\pi\frac{r}{R}\right), \quad k = 1, ..., n. \quad (14)$$

We come to a system of explicit ordinary differential equations in unknown coefficients $A_j(\tau)$:

$$\frac{\mathrm{d}A_j(\tau)}{\mathrm{d}\tau} = -\frac{k_\mathrm{m}(\bar{U}, \tau)}{R^2}(j\pi)^2 A_j(\tau), \quad j = 1, ..., n. \quad (15)$$

We find the coefficients A_j at $\tau = 0$, applying the Petrov–Galerkin method to the initial condition (11):

$$\int_0^R [U_\mathrm{p} + (U_0 - U_\mathrm{p})\frac{R}{r}\sum_{j=1}^{n}A_j^0\sin\left(j\pi\frac{r}{R}\right) - U_0]\frac{r}{R}\sin\left(k\pi\frac{r}{R}\right)\mathrm{d}r = 0,$$
$$k = 1, ..., n, \quad (16)$$

$$A_j^0 = 2(-1)^{j+1}/(j\pi), \quad j = 1, ..., n. \quad (17)$$

Now, we determine the average moisture content of a particle:

$$\bar{U} = \frac{3}{R^3}\int_0^R r^2 U(r, \tau)\,\mathrm{d}r$$

$$= U_\mathrm{p} + (U_0 - U_\mathrm{p})\frac{3}{\pi}\sum_{j=1}^{n}A_j(\tau)(-1)^{j-1}/j. \quad (18)$$

Differentiating expression (18), we obtain a relation for the rate of drying $\mathrm{d}\bar{U}/\mathrm{d}\tau$, appearing in formula (7):

$$\frac{\mathrm{d}\bar{U}}{\mathrm{d}\tau} = (U_0 - U_\mathrm{p})\frac{3}{\pi}\sum_{j=1}^{n}\frac{(-1)^{j-1}}{j}\frac{\mathrm{d}A_j(\tau)}{\mathrm{d}\tau}. \quad (19)$$

The system of equations (1)–(7), (15), (18), and (19) gives a mathematical description of combined polymerization and drying for an isolated particle. The coefficient k_m, appearing in Eq. (8), was found using the Rudobashta method [7]. For this purpose, special experiments were carried out on drying and additional polymerization of granulated prepolymer with initial humidity of 0.42 kg moisture/kg absolutely dry material and monomer conversion of 75–80%. The prepolymer was obtained by copolymerization of SMA with MAA in aqueous medium

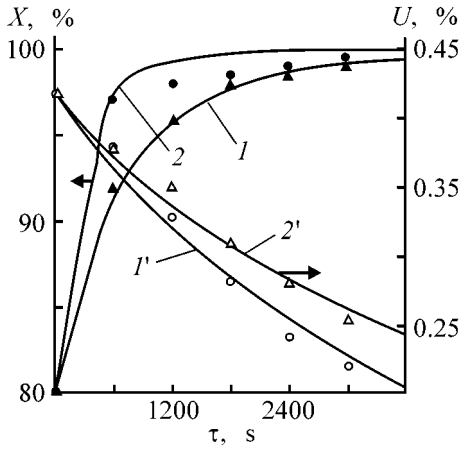

Fig. 2. Variation of the conversion X and humidity U in the course of additional polymerization and drying in an apparatus with fluidized bed. Equivalent particle diameter d_equiv = 0.004 m, air flow velocity 2.5 m s^{-1}. Bed temperature (°C): (*1*, *1*') 70 and (*2*, *2*') 90.

at total concentration of monomers of 6.75 M and monomer ratio of 1 : 1 (mol : mol). The kinetics of drying was studied in the temperature range 60–105°C under conditions ruling out any outer-diffusion resistance. Experimental data processing yielded the following relation for calculating the mass-conductivity coefficient for humidities in the range $0.03 < U < 0.42$:

$$k_\mathrm{m} = 10^{-10}[1.854 + 7.35\times10^{-5}\exp(0.086T)]/(1 + 15.1\bar{U}^2). \quad (20)$$

To confirm the adequacy of the mathematical model of the process of drying and additional polymerization, experiments were carried out in batch mode in an apparatus with gas-distributing grate area of 0.013 m^2. Prepolymer grains poured in the apparatus were there in fluidized state. Samples were taken at regular intervals. The results of analysis of these samples are given in Fig. 2. The solid lines in the figure represent the results of calculations in terms of the mathematical model, the points show the results of analysis. Comparison of the data in Fig. 2 shows that discrepancy of the experimental and calculated values does not exceed 5% for conversion and 10% for material humidity. This allows the given mathematical description to be used for practical purposes.

In the case of a continuous process of manufacture of a water-soluble polymer, the combined installation employs a double-section fluidized-bed dryer with vertical arrangement of sections [2]. The diagram of material flows in the dryer is presented in Fig. 3. The apparatus operates on the counterflow principle.

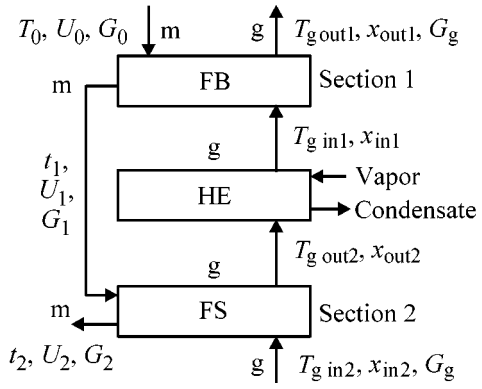

Fig. 3. Diagram of material flows in a double-section dryer. BB, fluidized bed; FB, filter section; HE, heat exchanger; g, gas; and m, material.

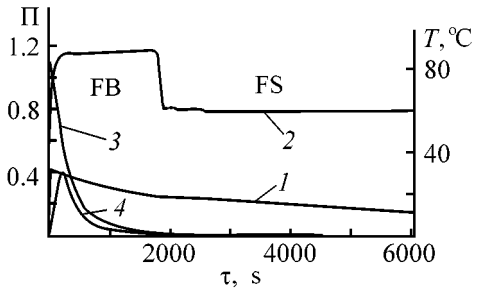

Fig. 4. Basic parameters Π of the combined processes vs. residence time τ in a fluidized bed. (*1*) Polymer humidity, (*2*) grain temperature *T*, (*3*) monomer concentration, and (*4*) Q_p/Q_c ratio.

Grained prepolymer is fed into the top section (FB) where the main part of moisture is removed. The fluidization number K_w = 2–3. From the first section, the material comes through a downpipe to the bottom section and is additionally dried there under the filter section conditions (K_w = 1.2–1.3). The drying agent (air) passes successively the bottom and top sections, with its heat potential increasing, in going from the filter section to the fluidized bed, in the heat exchanger mounted between the sections.

The continuous process of drying of prepolymer grains is considered on the assumption of complete displacement for the drying agent flow. The parameters of the drying agent at the inlet and outlet of each section are found from the system of heat (21) and material balance (22) equations and additional relations

$$G_g(c_g + c_v x_{in\,i})(T_{g\,in\,i} - T_{g\,out\,i}) + G_{ad}(c_m + c_w U_{i-1})T_{i-1} + Q_{pi} = G_{ad}(r^* + c_v T_{g\,out\,i})(U_{i-1} - U_i) + G_{ad}(c_m + c_w U_i)T_i, \quad (21)$$

$$x_{out\,i} = x_{in\,i} + G_{ad}(U_{i-1} - U_i)/G_g, \quad (22)$$

$$\frac{T_{g\,in\,i} - T_{g\,out\,i}}{T_{g\,in\,i} - T_{gi}} = [1 - \exp(-B_i H_i)]\left[1 - \frac{1 - \exp(-B_i H_i)}{-B_i H_i}\right], \quad (23)$$

$$B_i = 6\alpha_i(1 - \varepsilon_i)S_i/(c_g G_g d), \quad (24)$$

$$Q_{pi} = G_{ad}(1 + U_{i-1})C_m^0(X_i - X_{i-1})\Delta H/\rho_f, \quad (25)$$

$$G_g(c_g + c_v x_{out\,2})(T_{g\,in\,1} - T_{g\,out\,2}) = \frac{K_t F_t(T_{g\,in\,1} - T_{g\,out\,2})}{\ln[(T_{gv} - T_{g\,in\,1})/(T_{gv} - T_{g\,out\,2})]}, \quad i = 1, 2, \quad (26)$$

where G_g, G_{ad} are mass flow rates of gas and absolutely dry material (kg s^{-1}); c_g, c_v, c_m, c_w the specific heats of gas, water vapor, dry material, and water, respectively (J kg^{-1} K^{-1}); *T* the material temperature (°C); *i* the section number; $T_{g\,in}$, $T_{g\,out}$ the gas temperatures at the inlet and outlet of *i*th section (°C); Q_{ri} the heat flow released as a result of the polymerization reaction (W); ε_i, H_i the porosity and height of fluidized bed in *i*th section (%, m); S_i the cross-sectional area of *i*th section (m^2); X_i monomer conversion at the outlet of *i*th section (fraction units); ρ_{pp} prepolymer density (kg m^{-3}); C_m^0 the initial total concentration of monomers (mol m^{-3}); K_t the heat-transfer coefficient (W m^{-2}); F_t the heat-exchange surface area (m^2); and T_{hs} the temperature of heating steam (°C).

Expression (22) relates the average $\overline{T}_{gi}$ and final T_{gfi} temperatures of the drying agent in the fluidized bed [8]. The relationship between the temperature of the drying agent at the outlet of the second section and after the heat exchanger is defined by formula (26).

The system of Eqs. (1)–(7), (12), (15), and (17)–(26) is a mathematical description of the processes of additional polymerization and drying of prepolymer grains in a double-section apparatus with material fluidization in terms of the adopted simplifying assumptions.

Calculation of a double-section dryer, through which continuously passes a flow of prepolymer grains, consists in a search for such a combination of process parameters to be determined that would ensure prescribed characteristics of the technological process and, in particular, the moisture content of the material and conversion of starting monomers.

The above organization of the process in the apparatus leads to certain specific features of the kinetics and dynamics of drying. The combined processes of additional polymerization and drying in a prepolymer grain were simulated using the proposed mathematical model.

Figure 4 shows the temperature, grain humidity, total concentration of monomers, and ratio of the polymerization heat to heat supplied by convection as functions of the residence time of the material in the double-section dryer.

In the fluidized bed (top section), a prepolymer particle with equivalent diameter of 4 mm is heated from 50 to 90°C in about 200 s. The increase in temperature leads to weaker diffusion limitations on the reactions of chain initiation and growth, which makes higher the polymerization rate. By the end of the heating period the rate of the chemical process reaches its maximum value. A characteristic peak appears in the plot characterizing the ratio of the reaction heat to the heat delivered by convection. Further, the rate of polymerization decreases. Nevertheless, under the created conditions (temperature of about 90°C, sufficient content of water in the prepolymer), the process goes during the residence time of the material in the top section of the apparatus to virtually complete exhaustion of the monomers.

Figure 5a illustrates the variation of the moisture-content field in a prepolymer grain in relation to its residence time in the fluidized bed. The moisture distribution within the grain is highly nonuniform. After 1800 s, the content of water in the surface layer of thickness 0.07*R* (20% of the grain weight) is less than 0.1 kg moisture/kg absolutely dry material. The moisture content at the grain center remains virtually equal to the initial content.

It was established experimentally that the product with humidity less than 0.1 kg moisture/kg absolutely dry material poorly dissolves in water. This undesirable phenomenon can be eliminated by changing the drying mode in the bottom section of the apparatus. The air flow velocity in this section is 1.25 m s^{-1}, and the average air temperature, 60°C.

The process in the filter bed occurs in two stages. In the first stage, the moisture content of a particle remains unchanged. Arriving in the second section, the particle is cooled (Fig. 4) and the moisture is redistributed in the material. The moisture content decreases at the particle center and increases on the surface from the equilibrium humidity $U_{eq1} = 0.048$ in the first section to $U_{eq2} = 0.123$ in the second, which is illustrated in Fig. 5b. To describe this stage, the mathematical model was supplemented. By differentiating the expression

$$\overline{U} = U_s + (U_0 - U_s)\frac{3}{\pi}\sum_{j=1}^{n} A_j(\tau)(-1)^{j-1}/j = \text{const}, \quad (27)$$

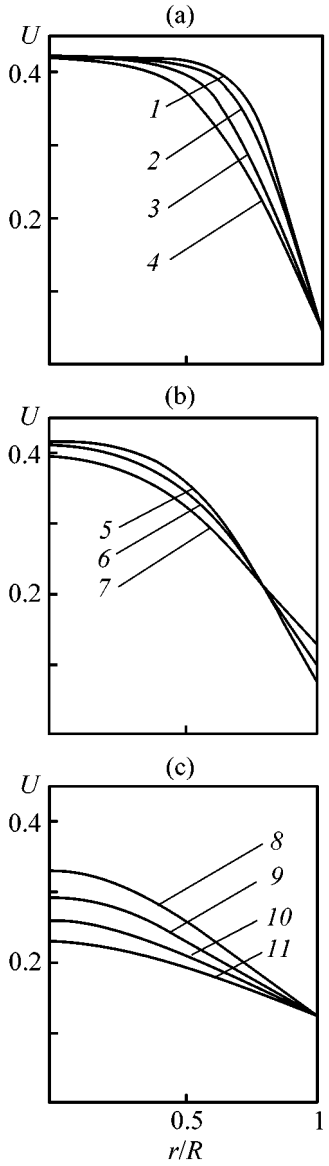

Fig. 5. Distribution of moisture content *U* along the grain radius. Time (s): (*1*) 792, (*2*) 1080, (*3*) 1440, (*4*) 1800, (*5*) 1932, (*6*) 2130, (*7*) 2440, (*8*) 3880, (*9*) 4600, (*10*) 5320, and (*11*) 6040.

which defines the average moisture content in a particle, an equation was derived for calculating the humidity at the grain surface

$$\frac{dU_s}{d\tau} = \frac{(U_s - U_0)\frac{3}{\pi}\sum_{j=1}^{n}\frac{dA_j(\tau)}{d\tau}(-1)^{j-1}/j}{1 - \frac{3}{\pi}\sum_{j=1}^{n}\frac{dA_j(\tau)}{d\tau}(-1)^{j-1}/j}. \quad (28)$$

The moisture content profile is calculated by

$$U(r, \tau) = U_s + (U_0 - U_s)\frac{R}{r}\sum_{j=1}^{n} A_j(\tau)\sin\left(j\pi\frac{r}{R}\right). \quad (29)$$

The second stage of the process in the filter section is characterized by constant particle temperature and particle humidity. The moisture content at the grain center and moisture content gradients decrease gradually, as seen from Fig. 5c.

CONCLUSIONS

(1) The possibility of combining the processes of polymerization and drying in the final stage of synthesis of water-soluble acrylic polymers was established experimentally. Thermal treatment of the prepolymer leads to weakening of the diffusion limitations on the reactions of initiation and growth of the polymeric chain, which favors reaction till virtually complete exhaustion of the monomer and makes it possible to combine the final polymerization with moisture removal from the obtained product.

(2) The moisture-transfer coefficient was determined experimentally for the prepolymer, and a functional dependence of this coefficient on temperature and moisture content was obtained.

(3) A mathematical description of combined processes of polymerization and drying in an isolated particle and a mathematical model of a double-section dryer were developed.

(4) It was shown that, for obtaining a water-soluble polymer with required quality characteristics and preventing the undesirable phenomenon of crust formation, the prepolymer should be dried in a double-section apparatus with fluidized bed under conditions of variable thermal and hydrodynamic modes.

REFERENCES

1. Nikolaev, A.F. and Okhrimenko, G.I., *Vodorastvorimye polimery* (Water-Soluble Polymers), Moscow: Khimiya, 1979.
2. Shubin, A.A., Kisel'nikov, V.N., and Vyalkov, V.V., Abstracts of Papers, *II Vsesoyuznoe Nauchno-Tekhnicheskoe Soveshchanie "Sozdanie i vnedrenie sovremennykh apparatov s aktivnymi gidrodinamicheskimi rezhimami dlya tekstil'noi promyshlennosti i proizvodstva khimicheskikh volokon", Moskva, 18–20 noyabrya 1981 g.* (II All-Union Sci.-Technol. Symp. "Development and Implementation of Modern Apparatus with Active Hydrodynamic Modes for Textile Industry and Manufacture of Chemical Fibers," Moscow, November 18–20, 1981), Moscow, 1981, p. 85.
3. Kisel'nikov, V.N., Vyalkov, V.V., Kruglov, V.A., *et al.*, *Izv. Vyssh. Uchebn. Zaved., Khim. Khim. Tekhnol.*, 1976, vol. 19, no. 8, pp. 1272–1275.
4. Lipin, A.G., Bubnov, V.B., Shubin, A.A., and Lebedev, V.Ya., *Izv. Vyssh. Uchebn. Zaved., Khim. Khim. Tekhnol.*, 1999, vol. 42, no. 4, pp. 71–73.
5. Lykov, A.V., *Teoriya sushki* (Theory of Drying), Moscow: Energiya, 1968.
6. Fletcher, C.A.J., *Computational Galerkin Methods* (Springer Ser. In Computational Physics), New York: Springer, 1984.
7. Rudobashta, S.P., *Massoperenos v sistemakh s tverdoi fazoi* (Mass Transfer in Systems with Solid Phase), Moscow: Khimiya, 1980.
8. Frolov, V.F., *Modelirovanie sushki dispersnykh materialov* (Simulation of Drying of Dispersed Materials), Leningrad: Khimiya, 1987.

Russian Journal of Applied Chemistry, Vol. 74, No. 12, 2001, pp. 2079–2082. Translated from Zhurnal Prikladnoi Khimii, Vol. 74, No. 12, 2001, pp. 2019–2022

ORGANIC SYNTHESIS AND INDUSTRIAL ORGANIC CHEMISTRY

Oxidizing Alkoxylation of Phosphine in Alcoholic Solutions of Iodine

G. S. Polimbetova and A. K. Borangazieva

Sokol'skii Institute of Organic Catalysis and Electrochemistry, Ministry of Education and Science of Kazakhstan Republic, Almaty, Kazakhstan

Received May 23, 2000; in final form, July 2001

Abstract—Oxidizing alkoxylation of PH_3 to trialkyl phosphates was performed in pyridine-alcoholic solutions of iodine. The optimal conditions of the reaction were found.

The reaction of PH_3 with I_2 was studied in detail in [1, 2]. Iodine solutions are widely used for gas treatment to remove PH_3 [3] and for phosphine analysis [4]. Hypophosphorous, phosphorous, or phosphoric acids are formed depending on I_2/PH_3 ratio [1–3].

Reaction of PH_3 with I_2 in alcohols has not been studied [5]. We found that alcoholic solutions of I_2 rapidly oxidize PH_3 at 25–70°C into phosphoric acid:

$$4I_2 + PH_3 + 4ROH \rightarrow (HO)_3PO + 4RI + 4HI, \quad (1)$$

where R is Me, Et, Bu, Am, and Oct.

In pyridine-alcoholic solutions, I_2 oxidizes PH_3 into trialkyl phosphate:

$$4I_2 + PH_3 + 4ROH + 7PyH \rightarrow (RO)_3PO + RI + 7PyH \cdot HI \quad (2)$$

with the formation of a white precipitate of pyridine hydroiodide. Reaction (2) quantitatively yields trialkyl phosphates, which are widely used in extraction of rare earth elements and preparation of polymers [6]. Due to the high rate and high selectivity, the new reaction (2) can be used for utilization of PH_3 contained in exhaust gases from phosphorus plants [3]. In this work, we studied reactions (1) and (2) by IR and ^{31}P and ^{13}C NMR spectroscopy, gas chromatography, potentiometry, and the differential kinetic method.

EXPERIMENTAL

Oxidizing alkoxylation of PH_3 in alcoholic solutions of iodine was studied in a flow-type installation equipped with a vigorously shaken isothermal reactor, a unit for redox potential measurement, and supply and sampling of gaseous, solid and liquid reagents and products, a gasometer with an Ar–PH_3 mixture, and a rheometer for measuring the gas flow rate. The reactor volume was 150 ml, and that of supplied liquid, 10 ml. The relative error of measurements of the uptake rate and the volume of the converted PH_3 was within 8–10%. The reactor was charged with alcohol (or alcohol–pyridine mixture) and iodine, purged with Ar, the shaker was switched on, the redox potential measurement was started, and then the Ar–PH_3 gas mixture was supplied into the reactor. The rate of the gas mixture supply was controlled so as to obtain the constant PH_3 concentration at the outlet (~1 Pa). During the experiment, the redox potential, the rate of PH_3 uptake w (mol l^{-1} min^{-1}), and the amount of PH_3 taken up Q (M) were continuously measured, and the compositions of the liquid and gas phases were analyzed at regular intervals. The experiment was continued until the PH_3 uptake ceased. The rate of oxidizing alkoxylation of phosphine (2) was determined from the consumption of PH_3 and alcohol and the accumulation of trialkyl phosphate and alkyl iodide. The concentrations of the reaction components were varied depending on particular alcohol as follows (M): 0.4–1.2 (I_2), 0.0–22.2 (ROH), 0.0–12.4 (PyH), and p_{PH_3} (1.6–4.0) $\times 10^{-3}$ Pa. The temperature T was 25–70°C.

Phosphine was prepared by acid decomposition of Zn_3P_2. Gases (PH_3 and Ar) were dried over granulated NaOH. Alcohols were purified by distillation from CaO, and pyridine by distillation from Na metal. Analytically pure iodine was used without additional purification. The I_2 concentration was determined titrimetrically [8].

1070-4272/01/7412-2079 $25.00 © 2001 MAIK "Nauka/Interperiodica"

Redox alkoxylation of phosphine in alcoholic solutions of iodine

Solution composition, M			$p_{PH_3} \times 10^{-3}$, Pa	T,°C	Q_{PH_3}, M	I_2/PH_3	$(RO)_3PO$, M	Yield of $(RO)_3PO$, %
I_2	PyH	RON						
				BuOH				
0.8	12.4	–	2.3	25	0.3	3	–	–
0.8	12.4	–	1.4	70	0.3	3	–	–
0.4	–	10.9	1.1	25	0.1	4	0.002	1.0
0.8	–	10.9	0.7	70	0.2	4	0.002	1.0
0.8	1.2	9.8	2.3	25	0.2	4	0.2	100.0
0.8	1.2	9.8	1.4	70	0.2	4	0.2	100.0
0.8	2.5	8.7	1.4	70	0.2	4	0.2	100.0
0.8	5.0	6.5	1.4	70	0.2	4	0.2	100.0
0.8	7.4	4.3	1.4	70	0.2	4	0.2	100.0
0.8	9.9	2.2	1.4	70	0.2	4	0.1	64.0
0.8	11.2	1.1	1.4	70	0.2	4	0.2	82.0
0.4	1.2	9.8	2.0	50	0.1	4	0.1	100.0
0.8	2.5	8.7	2.0	50	0.2	4	0.2	100.0
1.2	5.0	6.5	2.0	50	0.3	4	0.3	100.0
				OctOH				
0.4	1.2	5.7	2.3	50	0.1	4	0.1	100.0
0.8	2.5	5.0	2.3	50	0.2	4	0.2	100.0
				AmOH				
0.4	1.2	8.3	2.0	50	0.1	4	0.1	100.0
				EtOH				
0.4	1.2	15.4	2.0	50	0.1	4	0.1	100.0
				MeOH				
0.4	1.2	22.2	2.0	50	0.1	4	0.1	100.0

The chromatographic analysis of PH_3 in the initial gas mixture was performed on an LKhM-8 MD chromatograph equipped with a heat conductivity detector and a steel column packed with Porapak *Q* at 100°C at a helium flow rate of 12 ml min^{-1}. Unreacted phosphine was determined colorimetrically [9]. The stationary redox potential of alcoholic solutions of I_2 was continuously measured with a pH-121 millivoltmeter, using calomel and platinum electrodes, with a ground-glass stopper wetted with KCl solution as an electrolytic junction [10].

The chromatographic analysis of alcohols, pyridine, alkyl iodides, and organic products was performed on a 3700 chromatograph with a flame-ionization detector and a 3.0 m × 3.0 mm steel column packed with Chromaton-N-AW-DMCS impregnated with PEG-20M (10%). The column temperature was programmed from 100 to 200°C at a carrier gas (argon) flow rate of 30 ml min^{-1}.

Inorganic phosphates were determined colorimetrically in the form of vanadomolybdophosphate on an FEK-56 PM in 4-cm cells relative to water at 370 nm [8].

Trialkyl phosphates were recovered by vacuum distillation at 1–10 mm Hg after separation of the PyH · HI precipitate by decanting. The products obtained were identified by the boiling point, refractive index, and IR and ^{31}P and ^{13}C NMR spectra.

The IR spectra in the 400–4000 cm^{-1} range were recorded on a Specord IR-75 spectrometer with KBr windows. The ^{31}P and ^{13}C NMR spectra were registered on a Bruker WP-80 spectrometer [31.44 MHz (^{31}P) and 20.55 MHz (^{13}C)]. The main physicochemical constants of the isolated products agreed well with reference data [11]. In the ^{31}P NMR spectra, the signal at δ from –0.3 to –0.9 ppm relative to 85% H_3PO_4 corresponds to the chemical shift of trialkyl phos-

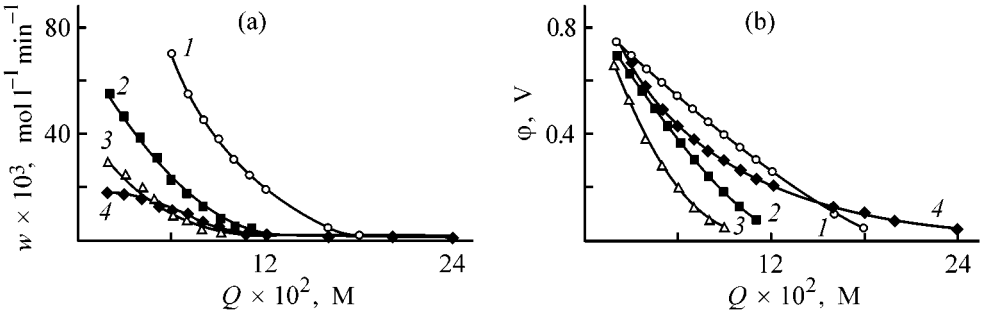

Fig. 1. (a) Conversion and (b) potentiometric curves of phosphine uptake by iodine solution. (*w*) Rate of phosphine uptake, (φ) potential, and (*Q*) amount of phosphine taken up. c_{I_2} (M): (*1*, *4*) 0.8; and (*2*, *3*) 0.4. c_{Py} (M): (*1*) 0, (*2*, *3*) 1.2, and (*4*) 12.4. c_{BuOH} (M): (*1*) 10.9, and (*2*) 9.8; (*3*) c_{OctOH} 5.7; (*4*) No alcohol. $p_{PH_3} \times 10^{-3}$ (Pa): (*1*) 1.6, (*2*, *4*) 3.3, and (*3*) 4.0. *T* (°C): (*1*) 70, (*2*, *3*) 50, and (*4*) 25.

phates [12]. The IR spectra of the trialkyl phosphates obtained coincided with those of the reference samples and contained characteristic bands of P=O (ν = 1260–1285 cm^{-1}) and P–O–C (ν = 1020–1045 cm^{-1}) groups [13]. The ^{13}C NMR spectra of the products contained signals with chemical shifts $\delta(CH_3) = 19.5 \pm 0.5$, $\delta(CH) = 29.5 \pm 0.5$, and $\delta(CH_2) = 73.6 \pm 0.5$ ppm, characteristic of trialkyl phosphates.

The PH_3–I_2–ROH system. The alcoholic solution of I_2 is fairly stable at 20–70°C. The I_2/I^- redox potential was constant for a long time (30 min). The I_2 concentration did not change, and no products of alcohol oxidation with iodine were detected [14]. Introduction of PH_3 into this solution is accompanied by a cathodic shift of the redox potential φ from 0.8 to 0.1 V because of the decrease in the I_2 concentration due to reaction (1). In the course of PH_3 uptake by iodine alcoholic solution, I_2 is reduced to RI and HI, and PH_3 is oxidized to phosphoric acid by Eq. (1). The yield of organic phosphates is 1–2% (see the table). The *W*–*Q* conversion and φ–*Q* potentiometric curves are descending (Figs 1a, 1b, curves *1*). The alcoholic solution of iodine eliminates from Ar–PH_3 mixtures even trace amounts of PH_3 (< 10 Pa). The PH_3 uptake stops only when I_2 is completely reduced and, correspondingly, the reddish brown alcoholic solution of I_2 is decolorized.

The PH_3–I_2–ROH–PyH system. The pyridine-alcoholic solution of I_2 is fairly stable at 20–70°C. The redox potential of the I_2/I^- couple remains constant for 30–40 min. During this time, the I_2 concentration is also unchanged, and products of alcohol and pyridine oxidation by iodine do not appear. Introduction of PH_3 into the pyridine-alcoholic solution of I_2 is accompanied by uptake of PH_3, decrease in the I_2 concentration, and cathodic shift of the redox potential from 0.7 to 0.05 V (Fig. 1). During the experiment, the initial reddish brown solution of I_2 is decolorized, and a white precipitate of PyH · HI is formed. The uptake of PH_3 by the pyridine-alcoholic solution is accompanied by the oxidizing alkoxylation of PH_3 (2) with the formation of trialkyl phosphates in high yields (see table). The table illustrates the effect of the temperature and concentration of iodine, phosphine, pyridine, and alcohol on the trialkyl phosphate yield. Under the optimal conditions, the yield is 100%. The increase in PyH concentration in the alcoholic solution of I_2 from 1.2 to 7.4 M does not affect the tributyl phosphate (TBP) yield. At the pyridine concentration of 9.9 M, the TBP yield decreases to 64%. The pyridine solution of I_2 takes up PH_3, and a yellow precipitate of, probably, P_2I_4 is formed [15], with no organophosphorus compounds detected in the solution. The effect of alcohol on reaction (2) was studied at the optimal $[PyH]/[I_2]$ ratio close to the stoichiometric ratio. The character of conversion and potentiometric curves of PH_3 uptake by pyridine-alcoholic solutions of I_2 are similar to those for alcoholic solutions of I_2. The rate of reaction (2) grows with increasing concentration of I_2 and PH_3, temperature, and alcohol acidity and decreases with accumulation of PyH · HI (Fig. 1).

CONCLUSION

At 20–70°C, pyridine-alcoholic solutions of I_2 rapidly take up PH_3 from gas mixtures with selective formation of trialkyl phosphates. The optimal conditions of this reaction are *T* = 25–50°C, p_{PH_3} = $(1.4–2.3) \times 10^{-3}$ Pa, and $c_{I_2} = c_{PyH}$ = 10–30 wt% (the remainder is ROH).

REFERENCES

1. Dorfman Ya.A., Yukht, I.M., Levina, L.V., *et al.*, *Usp. Khim.*, 1991, vol. 60, no. 6, pp. 1190–1228.

2. Dorfman, Ya.A., Zakharov, V.I., Kel'man, I.V., and Karinskaya, A.S., *Zh. Neorg. Khim.*, 1991, vol. 36, no. 10, pp. 2699–2703.
3. Koverya, V.M., Monin, V.Ya., and Belyakov, V.P., *Sposoby ochistki pechnogo gaza ot fosfora i fosfina* (Methods of Furnace Gas Treatment to Remove Phosphorus and Phosphine), Moscow: NIITEKhIM, 1986.
4. Strizhevskii, I.I., *Tekhnika bezopasnosti pri proizvodstve atsetilena* (Accident Prevention in Production of Acetylene), Moscow: Khimiya, 1978.
5. Erastov, O.A. and Nikonov, G.E., *Funktsional'nozameshchennye fosfiny i ikh proizvodnye* (Functionally Substituted Phosphines and Their Derivatives), Moscow: Nauka, 1986.
6. Corbridge, D.E., *Phosphorus. An Outline of its Chemistry, Biochemistry and Technology*, Amsterdam–Oxford–New York: Elsevier, 1980.
7. Gordon, A.J. and Ford, R.A., *The Chemist's Companion. A Handbook of Practical Data, Techniques and References*, New York: Wiley Interscience, 1972.
8. Williams, W.J., *Handbook of Anion Determination*, London: Butterworths, 1979.
9. Peregud, E.A., Bykhovskaya, M.S., and Gernet, E.V., *Bystrye metody opredeleniya vrednykh veshchestv v vozdukhe* (Quick Methods of Determination of Noxious Substances in Air), Moscow: Khimiya, 1970.
10. Vetter, K.J., *Electrochemische Kinetik*, Berlin: Springer, 1961.
11. Nifant'ev, E.E., *Khimiya fosfororganicheskikh soedinenii* (Chemistry of Organophosphorus Compounds), Moscow: Mosk. Gos. Univ., 1971.
12. Nifant'ev, E.E. and Vasyanina, L.K., *Spektroskopiya YaMR ^{31}P* (^{31}P NMR Spectroscopy), Moscow: Mosk. Gos. Pedag. Inst., 1986.
13. Shagidullin, R.R., Chernova, A.V., Vinogradova, V.S., and Mukhametov, F.S., *Atlas IK spektrov fosfororganicheskikh soedinenii (interpretirovannye spectrogrammy)* [Atlas of IR Spectra of Organophosphorus Compounds (Interpreted Patterns)], Moscow: Nauka, 1984.
14. Becker, H., Berge, W., Domschke, G. *et al., Organicum. Organisch-chemisches Grundpractikum*, Prof. Schwentlick, K., Dr., Ed., Berlin: VEB Deutscher Verlag der Wissenschaften, 1976.
15. Kudryavtseva, L.I., *Zh. Obshch. Khim.*, 1987, vol. 57, no. 5, pp. 1081–1086.

Russian Journal of Applied Chemistry, Vol. 74, No. 12, 2001, pp. 2083–2086. Translated from Zhurnal Prikladnoi Khimii, Vol. 74, No. 12, 2001, pp. 2023–2026.

ORGANIC SYNTHESIS AND INDUSTRIAL ORGANIC CHEMISTRY

Mechanism of the Antioxidative Effect of Bis(4-hydroxy-3,5-di-*tert*-butylphenyl) Sulfide and Polysulfides in Cumene Oxidation

V. M. Farzaliev, M. A. Allakhverdiev, R. I. Sattar-zade, and I. A. Rzaeva

Institute of the Chemistry of Additives, Academy of Sciences of Azerbaijan, Baku, Azerbaijan
Baku State University, Baku, Azerbaijan

Received May 15, 2001

Abstract—Bis(4-hydroxy-3,5-di-*tert*-butylphenyl) sulfide and polysulfides were prepared, and their inhibiting power was studied in relation to the number of sulfur atoms.

Studies concerned with synthesis of oxidation inhibitors and the mechanism of their antioxidative effect showed that hydroxyaryl sulfides and polysulfides [1, 2] containing simultaneously a phenolic moiety and sulfur atom(s) are oxidation inhibitors with a complex effect.

Proceeding with studies in this field [3–10], we prepared new compounds of this group and examined their inhibiting effect on cumene oxidation in relation to the number of sulfur atoms.

As the initial compound we chose commercially available 2,6-di-*tert*-butylphenol (**I**).

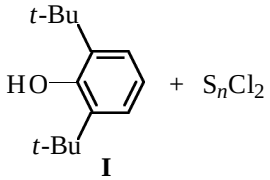

I

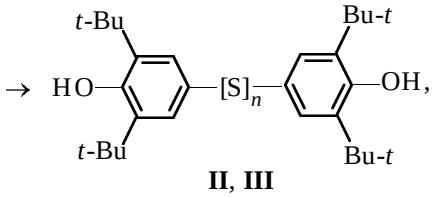

II, **III**

where n = 1 (**II**), 2 (**III**).

Reduction of bis(4-hydroxy-3,5-di-*tert*-butylphenyl) disulfide (**III**) with hydrogen yielded 4-hydroxy-3,5-di-*tert*-butylthiophenol (**IV**), which is a precursor of the corresponding trisulfide (**V**) and tetrasulfide (**VI**).

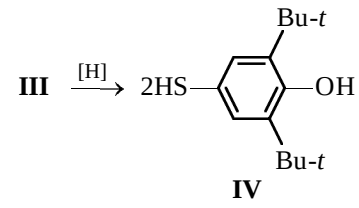

IV

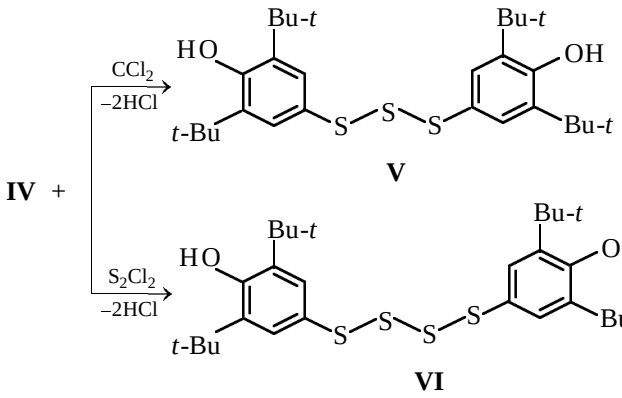

V

VI

To evaluate the antioxidative power of **II**–**VI** in elementary stages of cumene oxidation, we studied the reactions of these compounds with cumylperoxy radicals and cumyl hydroperoxide (CHP). The capability of mono- and polysulfides **II**–**VI** to terminate oxidation chains by reaction with peroxy radicals was studied for the example of cumene oxidation at 60°C, intiated with azobis(isobutyronitrile) (AIBN). As seen from Fig. 1, sulfides **II**–**VI** suppress initiated oxidation of cumene.

From the duration of the induction period τ we calculated the stoichiometric coefficient of inhibition f, equal to the number of oxidation chains terminated on

1070-4272/01/7412-2083 $25.00 © 2001 MAIK "Nauka/Interperiodica"

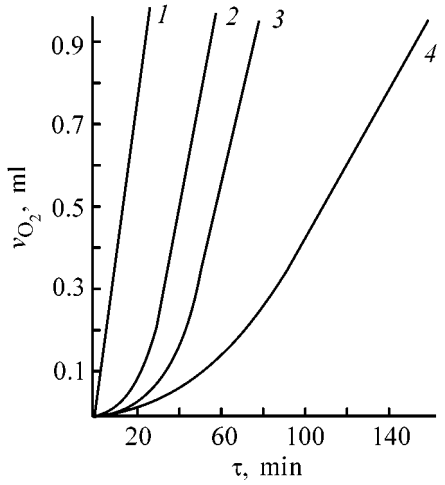

Fig. 1. Initiated oxidation of cumene in the presence of **IV**. (V_{O_2}) Oxygen volume and (τ) time; the same for Fig. 2. $c_{\mathbf{IV}}$, M: (*1*) 0, (*2*) 3×10^{-4}, (*3*) 4×10^{-4}, and (*4*) 5×10^{-4}.

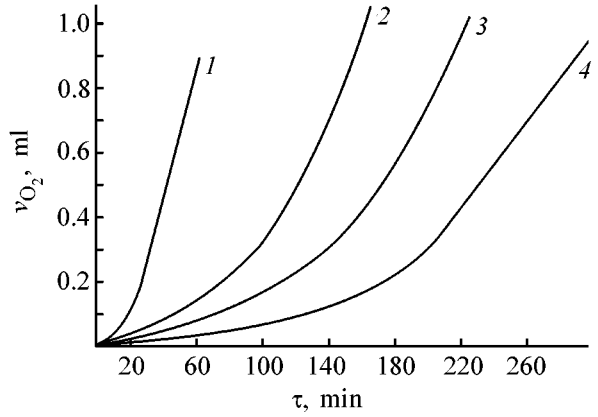

Fig. 2. Autooxidation of cumene in the presence of **III**–**V** at 60°C. Inhibitor (10^{-5} M): (*1*) none, (*2*) **III**, (*3*) **IV**, and (*4*) **V**.

one molecule of the inhibitor and its transformation products:

$$f = \tau v_i / [\mathrm{InH}]_0,$$

where τ is the induction period (s), v_i is the initiation rate (under our conditions, $v_i = 2 \times 10^{-7}$ mol l^{-1} s^{-1}), and $[\mathrm{InH}]_0$ is the initial inhibitor concentration.

Table 1. Kinetic parameters of reactions of sulfides **II**–**VI** with cumylperoxy radicals

Compound	f	k_7, l mol^{-1} s^{-1}
II	1.96	2.69
III	1.08	2.24
IV	2.80	4.18
V	2.30	5.82
VI	2.80	6.43

Note: 60°C, [AIBN] = 2×10^{-2} M, $v_i = 2 \times 10^{-7}$ mol l^{-1} s^{-1}.

From the kinetics of oxygen uptake, we calculated the rate constants of the reactions of **II**–**VI** with peroxy radicals k_7 [11, 12]. To do this, we plotted the oxygen uptake curves in the coordinates $[O_2]^{-1}$–τ^{-1} and determined k_7 from the slope of the straight line [11]:

$$\tan\alpha = \frac{fk_7[\mathrm{InH}]_0}{k_2[\mathrm{RH}]_{v_i}},$$

$$k_7 = \frac{\tan\alpha\, k_2 [\mathrm{RH}]_{v_i}}{f[\mathrm{InH}]_0},$$

where $k_2 = 1.51$ l mol^{-1} s^{-1} is the rate constant of chain initiation [11, 12]; [RH] = 6.9 M.

The high antioxidative activity of **II**–**VI** is also manifested in autooxidation of cumene at 110°C (Fig. 2).

The kinetic parameters of the reactions of **II**–**VI** with cumylperoxy radicals are listed in Table 1. It is seen that the stoichiometric coefficient f for **II**–**VI** varies from 1.08 to 2.80. The inhibition rate constant k_7 varies from 2.24×10^{-4} to 6.4×10^{-4} l mol^{-1} s^{-1}. Inhibitors with $f \le 1$ usually terminate a single oxidation change. Since the molecules under consideration contain two functional groups, sulfide and hydroxy, the coefficient f is somewhat higher than unity. The products formed in reactions of **II**–**VI** with cumylperoxy radicals also show certain inhibiting power: The oxidation rate after the induction period is somewhat lower than in the case of noninhibited oxidation.

In initiated oxidation of cumene in the presence of sulfides **II**–**VI**, in which the sulfur atom is directly bonded to the benzene ring, the stoichiometric coefficient of inhibition f is close to unity (Table 1). In compounds in which the sulfur atom is linked to the benzene ring via methylene bridge, $f = 2$ [13].

It is known that for alkylphenols $f = 2$ [12, 14], i.e., they terminate two oxidation chains:

$$\mathrm{InH} \xrightarrow{\mathrm{RO_2^{\cdot}}} \mathrm{In}^{\cdot} \xrightarrow{\mathrm{RO_2^{\cdot}}} \text{Inactive products.}$$

Presumably, termination of only one oxidation chain by monosulfides in which the sulfur atom is directly bonded to the benzene ring is due to stabilization of the arising phenoxy radical by resonance with electron delocalization involving the unpaired electron of oxygen and the vacant 3*d* orbital of sulfur. In hydroxyaryl sulfides containing a methylene group between the benzene ring and sulfur atom, the πp–$d\pi$ conjugation is impossible, and the arising phenoxy radical is capable of reacting with the second peroxy radical.

In the case of disulfides, thiyl radicals [7] formed by homolysis of the S–S bond can participate along with OH groups in reaction with peroxy radicals. This fact probably accounts for the high inhibiting power of disulfides.

Our studies showed that all the compounds **II**–**VI** actively decompose CHP. The kinetic curve of CHP decomposition in the presence of the examined compounds has a shape typical of autocatalytic reactions (Fig. 3). The autocatalytic character of the kinetic curves shows that CHP decomposition is effected by products formed in the first, slow stage of the reaction, rather than by inhibitors **II**–**VI** proper.

To determine the reaction order, we studied how the initial rate of catalytic decomposition of CHP depends on the reactant concentrations. We found that the reaction is first-order with respect to both inhibitor (InH) and CHP:

$$v = k[\mathrm{InH}][\mathrm{CHP}].$$

To determine the reaction stoichiometry, CHP was taken in excess. The stoichiometric coefficient γ was calculated by the formula

$$\gamma = \frac{[\mathrm{ROOH}]_0 - [\mathrm{ROOH}]_\infty}{[\mathrm{InH}]_0},$$

where $[\mathrm{ROOH}]_0$ and $[\mathrm{ROOH}]_\infty$ are, respectively, the initial and final concentrations of CHP and $[\mathrm{InH}]_0$ is the initial concentration of the inhibitor.

Our data show that transformation products of a single inhibitor molecule decompose from several hundreds to several tens of thousands of CHP molecules.

The kinetic parameters of catalytic decomposition of CHP under the action of **II**–**VI** are listed in Table 2. Similarly to the reaction with cumylperoxy radicals, the catalytic activity of **II**–**VI** in decomposition of CHP depends on the number of sulfur atoms. The greater the number of sulfur atoms in the molecule, the higher *k*, and tetrasulfide **VI** is the most active.

EXPERIMENTAL

The IR spectra were recorded on a Specord IR-75 spectrophotometer (mulls in mineral oil), and the ^{1}H NMR spectra, on Varian-60 and Tesla (80 MHz) spectrometers; the chemical shifts δ (ppm) are given relative to TMS as internal reference.

Thin-layer chromatography was performed on Silufol UV-254 plates, with ethanol–hexane (1 : 5) as eluent.

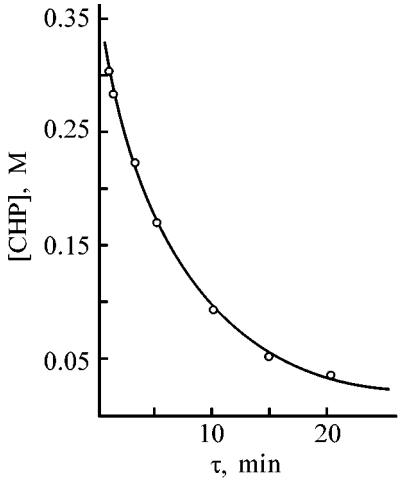

Fig. 3. Catalytic decomposition of CHP under the action of **V** (4×10^{-5} M) at 110°C. [CHP] CHP concentration and (τ) time.

Cumyl hydroperoxide was purified according to [15] with subsequent distillation; chlorobenzene and cumene were purified by a conventional procedure based on sulfonation of impurities with concentrated sulfuric acid [16, 17]. The CHP concentration was determined by iodometric titration [15] of samples taken at regular intervals. Experiments on decomposition of CHP were performed in chlorobenzene at 110°C in a glass bubbler in an inert atmosphere; the CHP concentration was varied within 0.16–0.64 M, and the concentration of the inhibitors, from 10^{-4} to 5×10^{-4} M.

Experiments on initiated oxidation of cumene were performed on a manometric installation [17]. The initiator was AIBN; at 60°C, its initiation rate constant is 10^{-6} s^{-1} [18]. The initiator concentration was 2×10^{-2} M in all the experiments, and the concentration of the inhibitors, 10^{-5} M.

Bis(4-hydroxy-3,5-di-*tert*-butylphenyl) sulfide II, mp 139°C, was prepared by reaction of SCl_2 with phenol **I** in acetonitrile at a temperature from –15 to –30°C.

Table 2. Kinetic parameters of catalytic decomposition of CHP under the action of **II**–**VI** at 110°C

Compound	k, l mol^{-1} s^{-1}	γ
II	9.5	6900
III	18.6	12500
IV	29.8	32600
V	42.7	58500
VI	46.0	60800

Bis(4-hydroxy-3,5-di-*tert*-butylphenyl) disulfide III was prepared similarly by reaction of S_2Cl_2 with phenol **I**; mp 145–146°C [19, 20].

4-Hydroxy-2,5-di-*tert*-butylthiophenol was prepared according to [21].

Bis(4-hydroxy-3,5-di-*tert*-butylphenyl) trisulfide V. A mixture of 12 g of thiophenol **IV** and 50 ml of acetonitrile was cooled to a temperature from –15 to –30°C, and a solution of 2.5 g of SCl_2 in 20 ml of acetonitrile was added. The mixture was stirred at the same temperature for 1 h, washed with water, and treated with diethyl ether. After distillation of the solvent, the product was recrystallized from hexane. Yield of **V** 10.7 g (85%), mp 129–130°C, R_f 0.52. ^{1}H NMR spectrum, δ, ppm: 1.45 s (36H), 4.75 s (2H), 6.85 s (2H). IR spectrum, ν, cm^{-1}: 3625, 1805, 685, 465.

Found, %: C 66.51, H 8.51, S 18.31.
$C_{28}H_{42}O_2S_3$.
Calculated, %: C 66.35, H 8.35, S 18.98.

Bis(4-hydroxy-3,5-di-*tert*-butylphenyl) tetrasulfide VI was prepared similarly from 12 g of thiophenol **IV** and 3.4 g of S_2Cl_2; yield 12 g (90%), R_f 0.46. ^{1}H NMR spectrum, δ, ppm: 1.41 s (36H), 4.83 s (2H), 6.73 s (2H). IR spectrum, ν, cm^{-1}: 3620, 1810, 690, 475.

Found, %: C 64.62, H 8.01, S 23.17.
$C_{28}H_{42}O_2S_4$.
Calculated, %: C 62.41, H 7.86, S 23.80.

CONCLUSIONS

(1) Bis(4-hydroxy-3,5-di-*tert*-butylphenyl) sulfide and polysulfides were prepared and characterized.

(2) These compounds effectively reduce the rate of cumene oxidation by catalyzing decomposition of the hydroperoxide and terminating the oxidation chains via reaction with peroxy radicals generated from cumene. The inhibiting activity of the compounds grows with the increasing number of sulfur atoms in the molecule.

REFERENCES

1. Kuliev, F.A., Farzaliev, V.M., Denisov, E.T., *et al.*, Neftekhimiya, 1981, vol. 21, no. 6, pp. 898–905.
2. Aliev, A.S., Farzaliev, V.M., Abdullaeva, F.A., and Denisov, E.T., *Neftekhimiya*, 1975, vol. 15, no. 6, pp. 890–895.
3. Kuliev, F.A., Allakhverdiev, M.A., Farzaliev, V.M., and Voronkov, M.G., *Zh. Org. Khim.*, 1981, vol. 17, no. 8, pp. 1699–1703.
4. Kuliev, A.M., Farzaliev, V.M., Mamedov, Ch.I., *et al.*, *Zh. Obshch. Khim.*, 1982, vol. 52, no. 9, pp. 2122–2126.
5. Medzhidov, A.A., Kasumov, V.T., Farzaliev, V.M., *et al.*, *Zh. Obshch. Khim.*, 1982, vol. 52, no. 1, pp. 101–106.
6. Gasanov, B.R., Farzaliev, V.M., Allakhverdiev, M.A., *et al.*, *Zh. Obshch. Khim.*, 1988, vol. 58, no. 1, pp. 120–128.
7. Magerramov, A.M., Sattar-zade, R.I., Farzaliev, V.M., *et al.*, *Vestn. Bakinsk. Gos. Univ., Estestv. Nauki*, 2000, no. 3, pp. 26–31.
8. Magerramov, A.M., Sattar-zade, R.I., Farzaliev, V.M., *et al.*, *Vestn. Bakinsk. Gos. Univ., Estestv. Nauki*, 2000, no. 4, p. 5.
9. Kuliev, A.M., Farzaliev, V.M., Allakhverdiev, M.A., *et al.*, Abstracts of Papers, *XVI Nauchnaya sessiya po khimii i tekhnologii organicheskikh soedinenii sery i sernistykh soedinenii* (XVI Scientific Session on Chemistry and Technology of Organic Sulfur Compounds and Sulfur-Containing Compounds), Riga, 1984, p. 98.
10. Farzaliev, V.M., Allakhverdiev, M.A., Rzaeva, I.A., *et al.*, *Zh. Prikl. Khim.*, 1994, vol. 67, no. 6, pp. 1025–1028.
11. Emanuel', N.M., Denisov, E.T., and Maizus, Z.K., *Tsepnye reaktsii okisleniya uglevodorodov v zhidkoi faze* (Chain Oxidation of Hydrocarbons in the Liquid Phase), Moscow: Nauka, 1965.
12. Emanuel', N.M. and Denisov, E.T., *Neftekhimiya*, 1976, vol. 16, no. 13, pp. 366–368.
13. Denisov, E.T. and Kovalov, G.I., *Okislenie i stabilizatsiya reaktivnykh topliv* (Oxidation and Stabilization of Jet Fuels), Moscow: Khimiya, 1983, p. 178.
14. Denisov, E.T., *Usp. Khim.*, 1973, vol. 42, no. 3, pp. 361–390.
15. Karnojitzki, V., *Les peroxides organiques*, Paris: Hermann, 1958.
16. *Organic Solvents. Physical Properties and Methods of Purification*, Weissberger, A., Proskauer, E.S., Riddick, J.A. and Toops, E.E., Eds., New York: Interscience, 1955.
17. Emanuel', N.M., Gladyshev, G.P., Denisov, E.T., *et al.*, Order of Testing Chemical Compounds as Stabilizers of Polymeric Materials, *Preprint of the Inst. of Chemical Physics, USSR Acad. Sci.*, Chernogolovka, 1976.
18. Denisov, E.T., *Konstanty skorosti gomoliticheskikh zhidkofaznykh reaktsii* (Rate Constants of Homolytic Liquid-Phase Reactions), Moscow: Nauka, 1971.
19. US Patent 3211794.
20. US Patent 3250712.
21. Muller, E., Stegmann, H., and Scheffer, R., *Lieb. Ann.*, 1961, vol. 645, no. 1, p. 79.

Russian Journal of Applied Chemistry, Vol. 74, No. 12, 2001, pp. 2087–2090. Translated from Zhurnal Prikladnoi Khimii, Vol. 74, No. 12, 2001, pp. 2027–2030.

ORGANIC SYNTHESIS AND INDUSTRIAL ORGANIC CHEMISTRY

Hydrolytic Polycondensation of Ethyl Silicate with Copper Salts of Mineral and Organic Acids in Sol-Gel Process

V. A. Sviderskii, M. G. Voronkov, S. V. Klimenko, and D. N. Bystrov

Kiev Polytechnic Institute, Ukrainian National Technical University, Kiev, Ukraine

Favorskii Institute of Chemistry, Siberian Division, Russian Academy of Sciences, Irkutsk, Russia

Received May 15, 2001

Abstract—The structure and composition of polyheterosiloxanes formed in hydrolytic polycondensation of ethyl silicate in the presence of copper salts under the conditions of base catalysis (NH_4OH) were studied as influenced by the nature of acid anion (SO_4^{2-}, Cl^-, NO_3^-, CH_3COO^-).

Sol-gel process is widely used to prepare high-tech materials for modern engineering thanks to the high versatility of sol-gel methods, their low power consumption, and large assortment of the resulting three-dimensional macromolecular structures. The possibility of controlling the topological features of amorphous and crystalline polyheterosiloxane fractal structures of the products of sol-gel synthesis using metal ions [1] is of particular importance.

The most important mode of the sol-gel synthesis of polyheterosiloxane is based on hydrolysis and polycondensation of tetraalkoxysilanes in nonaqueous solutions in the presence of metal salts [2]. Rather difficult control of these reactions complicates obtaining the reaction products with reproducible composition, structure, and properties.

EXPERIMENTAL

In our study, we used commercial ethyl silicate-40 (partially hydrolyzed tetraethoxysilane), 2-propanol (solvent), and copper salts [$CuCl_2 \cdot 2H_2O$, $Cu(NO_3)_2 \cdot 3H_2O$, $CuSO_4 \cdot 5H_2O$, and $Cu(CH_3COO)_2 \cdot 2H_2O$]. These salts were chosen taking into account their ability to form hydrate and ammine complexes playing an important role in sol-gel synthesis of polyheterosiloxane [3]. The ethyl silicate : water : 2-propanol molar ratio was 1 : 8 : 4; the temperature and time of synthesis were 25, 35, and 45°C and 1, 3, and 5 h, respectively. After that, gelation was induced by adding 25% aqueous ammonia to pH 11.0.

The products of hydrolytic polycondensation were thoroughly washed by decantation and dried to xerogel for 16 h at 120 ± 0.5°C. Then the reaction products were studied by thermography in air (MOM derivatograph, heating rate 10 deg min^{-1}) and IR spectroscopy (Specord IR-75 device, KBr pellets).

Polycondensation of ethyl silicate with copper salts under the conditions of basic catalysis yields polymeric structures containing Si–O–Cu–O fragments and residual ethoxy and isopropoxy groups formed in the course of ester interchange. This is confirmed by a shift of the characteristic absorption band ν(Si–O) in the IR spectra of copper-containing polyalkoxysiloxane xerogels as compared with silica xerogels [ν(Si–O) = 1093 cm^{-1}]. This shift is determined by the nature of the anion in the initial copper salt (Table 1). As seen, for copper-containing polyalkoxysi-

Table 1. Shift of the absorption band ν(Si–O) in the IR spectra of copper-containing polyalkoxysiloxane xerogels with respect to silica xerogel [ν(Si–O) = 1093 cm^{-1}]

Preparation conditions		ν, cm^{-1}			
T, °C	τ, h	$Cu(NO_3)_2$	$CuSO_4$	$CuCl_2$	$Cu(OCOCH_3)_2$
25	1	–13	–7	–3	–15
	3	0	–14	+13	–12
	5	+13	–14	+17	–10
35	1	0	–13	+17	–17
	3	–12	–6	0	–10
	5	–4	–33	–3	–
45	1	–27	–7	–5	–26
	3	+7	–20	–13	–
	5	+9	–9	–	–

1070-4272/01/7412-2087 $25.00 © 2001 MAIK "Nauka/Interperiodica"

Table 2. Half-width $\Delta\nu_{1/2}$ of the absorption band ν(Si–O) in the IR spectra of copper-containing polyalkoxysiloxane xerogels

Preparation conditions		$\Delta\nu_{1/2}$,* cm^{-1}			
T, °C	τ, h	$Cu(NO_3)_2$	$CuSO_4$	$CuCl_2$	$Cu(OCOCH_3)_2$
25	1	293	293	273	313
	3	240	300	266	259
	5	320	300	266	253
35	1	306	320	266	286
	3	286	260	253	260
	5	273	333	346	–
45	1	253	233	346	340
	3	233	352	280	–
	5	99	266	–	–

* In the IR spectrum of silica xerogel, $\Delta\nu_{1/2}$ = 186 cm^{-1}.

Table 3. Weight loss of copper-containing polyalkoxysiloxane xerogels in the course of heating in the 200–450°C range

Preparation conditions		Weight loss,* wt %			
T, °C	τ, h	$Cu(NO_3)_2$	$CuSO_4$	$CuCl_2$	$Cu(OCOCH_3)_2$
25	1	3.25	3.04	6.50	2.50
	3	3.00	3.00	2.50	2.50
	5	2.75	2.75	2.50	2.65
35	1	3.25	2.66	2.10	2.50
	3	3.25	2.66	1.90	3.25
	5	2.75	2.33	1.75	–
45	1	3.00	3.12	1.75	3.5
	3	2.50	2.25	4.0	–
	5	2.50	2.00	–	–

* Weight loss for silica xerogel is 1.50 wt %.

loxanes prepared using $CuSO_4$ the ν(Si–O) band is shifted by 6–33 cm^{-1} toward lower frequencies, whereas in the case of $Cu(NO_3)_2$ this band moves toward both lower and higher frequencies by 0–27 and 0–13 cm^{-1}, respectively. We found no regular trends in the value and direction of the band shift. Similar phenomenon was observed in the case of $CuCl_2$.

The IR data show that inorganic copper salts promote formation of thermodynamically unstable structures characterized by random redistribution of the mobile fragments in the siloxane matrix. This is typical of copper-containing siloxanes prepared using copper salts of inorganic acids and is inevitable in common procedures of their drying [4].

In the case of $Cu(CH_3COO)_2$, a different pattern is observed. In the IR spectra of copper-containing polyalkoxysiloxanes prepared using copper acetate, the ν(Si–O) band is shifted to lower frequencies by 10–26 cm^{-1}. This shift decreases steadily with increasing process time at a given temperature. A similar trend was found for the half-width of this band, characterizing the number of siloxane and metal–siloxane bonds, i.e., the degree of three-dimensional cross-linking (Table 2).

It should be noted that copper acetate sharply decreases the gel time and the process is complete at 35 and 45°C in, respectively, 2.5 and 1 h. This is probably due to the fact that, compared with copper chloride, nitrate, and sulfate, copper acetate is more reactive in heterofunctional polycondensation proceeding by the following reaction:

$$CuX_2 + 2ROSi{\equiv} \rightarrow {\equiv}Si–O–Cu–O–Si{\equiv} + 2RX, \quad (1)$$

where R is H or alkyl and X is the acid anion (CH_3COO^-) [4].

Using copper acetate, more thermodynamically stable copper-containing polyalkoxysiloxane structures are prepared. Moreover, in contrast to $CuCl_2$, $CuSO_4$ and $Cu(NO_3)_2$, the gel obtained in the case of $Cu(CH_3COO)_2$ contains no residual metal salt or its ammine complexes. In thermal formation of xerogel, the former salts cause cleavage and redistribution of the siloxane groups according to the scheme given in [4]:

$$CuX_2 + 2{\equiv}Si–O–Si{\equiv} \rightarrow {\equiv}Si–O–Cu–O–Si{\equiv} + 2XSi{\equiv}, \quad (2)$$

$$\equiv SiX + ROSi{\equiv} \rightarrow {\equiv}Si–O–Si{\equiv} + RX, \quad (3)$$

where X = Cl, NO_3, $0.5SO_4$ and R–H, alkyl.

The insignificant amount of the organic component in the resulting products is confirmed by the weight loss in the range of thermal degradation of the ethoxy groups (Table 3, 200–450°C).

Depending on the anion in the initial copper salt, the exothermic peaks in the DTA curves of copper-containing polyalkoxysiloxane xerogels have different intensities and widths, with maxima in the 295–350°C range. The shift of the exothermic maximum toward higher temperatures as compared with silica xerogel (250°C) is due to the shielding of the ethoxy groups by new Si–O–Cu–O–Si fragments (Table 4).

The results of thermal analysis also confirm the effect of the copper salt anion on the product nature. In copper-containing polyalkoxysiloxanes prepared

using copper salts of strong mineral acids, the content of alkoxy groups decreases with the synthesis time increasing from 1 to 5 h, which is confirmed by the DTA and DTG data. This fact can be accounted for by further hydrolysis and heterofunctional condensation (1). At synthesis time of 3 h at 45°C, the relative weight loss is 25, 38, and 23 wt % for copper-containing polyalkoxysiloxanes prepared using copper sulfate, chloride, and nitrate, respectively.

The resulting heteropolyalkoxysiloxanes retain 1.50–2.25 wt % water and hydroxy groups upon heating even to 1000°C. As seen from the DTA and DTG data, the composition and structure of the resulting copper-containing polyalkoxysiloxanes depends on the copper salt anion and on the time and temperature of synthesis. On the whole, the yield of the product of hydrolytic polycondensation grows with increasing temperature, whereas the relative content of copper-containing siloxane slightly decreases owing to the significant amount of sorbed water.

In the case of copper sulfate and temperatures of 35 and 45°C, the increase in the synthesis time does not affect noticeably the composition and structure of the resulting heterosiloxane; in the 200–450°C range, the weight loss only slightly decreases, whereas the temperature maximum remains almost constant. In the presence of copper nitrate at 45°C, the temperature of the maximal weight loss sharply grows (from 270 to 340°C) with the synthesis time increasing from 1 to 5 h, T_{max} in the DTA curve grows by 15°C, and the range of the exothermic peak extends from 260 to 390°C. This is probably due to the side reactions of nitration and oxidation of the alkoxy groups by copper nitrate, which causes formation of a more random structure of the heterosiloxane.

In the presence of copper acetate, the structure and composition of the resulting heterosiloxanes strongly depend on the preparation conditions. The yield of heterosiloxane decreases with increasing synthesis temperature; this is typical of 25 and 35°C. In contrast to copper sulfate, nitrate, and chloride, in the case of copper acetate, the content of sorbed water, organic fraction, and hydroxy groups grow by 67.5 and 25 wt %, respectively with increasing synthesis time. As the synthesis time increases to 2.5 h at 35°C, the content of sorbed water and organic component in the resulting copper-containing polyalkoxysiloxane grows by 15 and 30 wt %, whereas the content of hydroxy groups remains almost constant. This process is accompanied by a sharp increase in the intensity and by a certain change in the shape of the exothermic peak in the DTA curves (see Fig. 1). All these data suggest that more uniform but less condensed heterosiloxanes are formed with increasing temperature and time of the synthesis in the case of copper acetate.

Table 4. Temperature of the exothermic peak T_{max} of copper-containing polyalkoxysiloxane xerogels

Preparation conditions		T_{max}, °C			
T, °C	τ, h	$Cu(NO_3)_2$	$CuSO_4$	$CuCl_2$	$Cu(OCOCH_3)_2$
25	1	320* 320**	340 225	330 390	340 270
	3	320 270	340 200	330 270	340 270
	5	310 260	340 200	330 260	300 270
35	1	340 280	340 200	350 160	300 270
	3	340 260	340 200	350 120	300 270
	5	340 250	340 180	350 120	–
45	1	325 260	340 220	350 150	295 240
	3	340 300	340 200	350 150	–
	5	340 390	340 190	–	–

* Exothermic peak is given in the numerator.

** Exothermic effect range is given in the denominator.

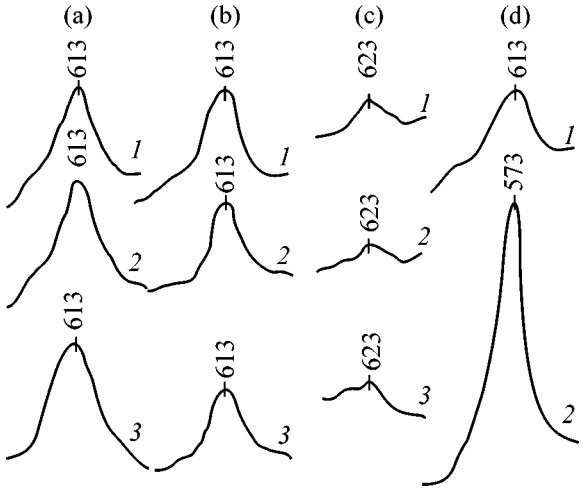

Fig. 1. DTA curves of copper-containing polyalkoxysiloxane xerogels based on (a) $CuSO_4$, (b) $Cu(NO_3)_2$, (c) $CuCl_2$, and (d) $Cu(CH_3COO)_2$ at 35°C. Synthesis time, h: (*1*) 1, (*2*) 3, and (*3*) 5.

On the whole, the sol–gel synthesis from ethyl silicate and copper salts in 2-propanol solutions under the conditions of base catalysis (NH_4OH) yields highly uniform cross-linked copper-containing polyalkoxysiloxanes.

The conditions of copper salt hydrolysis are also of particular importance. Due to hydrolysis, solutions of copper sulfate, chloride, and nitrate are weakly acidic (pH 4). As a result, they decrease the total basicity of the reaction mixture, decelerating the hydrolytic polycondensation. Moreover, these salts form strong ammine complexes. As a result, when the amount of ammonia in the reaction mixture is insufficient, the time of hydrolytic polycondensation increases to 3–5 h. In the case of copper acetate solution (pH 7), the process is complete in 2.5 h at 35°C and in 1 h at 45°C.

Thus, the rate and yield of hydrolytic polycondensation and the structure and properties of copper-containing polyalkoxysiloxanes and the resulting copper-containing siloxane xerogels (copper polysilicates) strongly depend on the anion.

The anion of the copper salts studied also affects the water sorption capacity of the copper-containing polyalkoxysiloxanes (wt %): 39.8 for $CuCl_2$, 15.6 for $Cu(NO_3)_2$, 16.3 for $CuSO_4$, and 37.5 wt % for $Cu(CH_3COO)_2$.

CONCLUSIONS

(1) The anion in copper salts [$CuCl_2$, $Cu(NO_3)_2$, $CuSO_4$, $Cu(CH_3COO)_2$] affects the rate and yield of their hydrolytic polycondensation with ethyl silicate, and also the composition, structure, and properties of the resulting copper-containing polyalkoxysiloxanes.

(2) In the case of copper salts of mineral acids, thermally unstable copper-containing polyalkoxysiloxanes with random distribution of the mobile fragments in the siloxane matrix are formed, whereas in the presence of copper acetate, the resulting structure is thermodynamically stable and has predictable properties.

REFERENCES

1. Hench, L.L. and West, J. K., *Chem. Rev.*, 1990, vol. 90, no. 1, pp. 33–72.
2. Sviderskii, V.A., Voronkov, M.G., Klimenko, V.S., and Klimenko, S.V., *Zh. Prikl. Khim.*, 1996, vol. 69, no. 6, pp. 951–957.
3. Sviderskii, V.A., Voronkov, M.G., Klimenko, V.S., and Klimenko, S.V., *Zh. Prikl. Khim.*, 1997, vol. 70, no. 10, pp. 1698–1703.
4. Voronkov, M.G., Maletina, E.A., and Roman, V.K., *Geterosiloksany* (Heterosiloxanes), Novosibirsk: Nauka, 1984.

Russian Journal of Applied Chemistry, Vol. 74, No. 12, 2001, pp. 2091–2094. Translated from Zhurnal Prikladnoi Khimii, Vol. 74, No. 12, 2001, pp. 2031–2034.

ORGANIC SYNTHESIS AND INDUSTRIAL ORGANIC CHEMISTRY

Recovery of Trimethylchlorosilane from Its Azeotropic Mixture with $SiCl_4$

M. G. Voronkov, V. P. Baryshok, and G. A. Kuznetsova

Favorskii Institute of Chemistry, Siberian Division, Russian Academy of Sciences, Irkutsk, Russia

Received July 30, 2001

Abstract—Reaction of tetraethoxysilane with the azeotropic mixture Me_3SiCl–$SiCl_4$ in the presence of certain cyclic (tetrahydrofuran, dioxane) and acyclic (diethyl ether) ethers, ethanol, or dimethylformamide was studied with the aim of $SiMe_3Cl$ recovery.

Trimethylchlorosilane is one of the most important organosilicon monomers. It is used to incorporate inert terminal groups into oligoorganosiloxanes to be applied as heat- and frost-resistant oils, lubricants, liquid dielectrics, heat carriers, hydrophobizing components, lacquers, and enamels; also, it is widely used as trimethylsilylating agent in organic and organometallic chemistry [1].

Direct synthesis of methylchlorosilane by reaction of CH_3Cl with the Si–Cu contact mass yields up to 10% of the azeotropic mixture Me_3SiCl–$SiCl_4$ [2]. The majority of methods proposed for its separation [azeotropic distillation with acetonitrile; partial hydrolysis or alcoholysis; chemical binding of $SiCl_4$ in the form of solid complexes with tertiary aliphatic and aromatic amines, formamide, and dimethylformamide (DMF), insoluble in the reaction medium; fluorination in aqueous solution] have a number of drawbacks: low yield of Me_3SiCl, strongly corrosive medium, gelation, and formation of abundant by-products whose utilization requires sophisticated procedures [3–5].

Simple procedures for Me_3SiCl recovery from the azeotropic mixture Me_3SiCl–$SiCl_4$ have been developed only recently. They are based on binding of $SiCl_4$ with organylalkoxysilanes, ethyl silicate, and bottoms from its synthesis in the presence of alcohols, traces of moisture, metal salts, and acid catalysts [6, 7].

The reaction between alkoxy- and chlorosilanes occurs either as exchange of an alkoxy group for a halogen atom [scheme (1), *a*] or as heterofunctional condensation [scheme (1), *b*] [1]:

$$X{-}Si^{*} + RO{-}Si{-} \overset{a}{\rightleftarrows} {-}Si{-}X + {-}Si^{*}{-}OR \xrightarrow{b} RX + {-}Si{-}O{-}Si^{*}{-}. \quad (1)$$

Both pathways, *a* and *b*, are accelerated in the presence of HCl. As a rule, the contribution of pathway *b* becomes appreciable at elevated temperatures.

Reaction of $SiCl_4$ with $Si(OEt)_4$ at 150–160°C yields a mixture of OEt–Cl exchange products [8–10]. In the presence of 0.24 wt % ethanol, this reaction is 76–97% complete in 20–70 h at molar ratio $SiCl_4$: $Si(OEt)_4$ = 1 : 3 and 20–22°C [11].

A procedure has been developed for separation of a technical azeotropic mixture Me_3SiCl–$SiCl_4$ containing $MeSiHCl_2$ and $HSiCl_3$ impurities by binding $SiCl_4$ with tetraethoxysilane to form ethoxychlorosilanes in a selective reaction in the presence of initiators, with subsequent fractionation of the reaction mixture [12, 13].

To this end, a technical azeotropic mixture was brought into reaction with $Si(OEt)_4$ in the presence of 0.2–10 wt % DMF, tetrahydrofuran (THF), dioxane, diethyl ether, or ethanol. The reaction was performed at 20–25°C or at refluxing (60–65°C) for 2–72 h until conversion of $SiCl_4$ into ethoxychlorosilanes and -siloxanes was complete:

$$SiCl_4 + (EtO)_4Si \rightarrow Cl_{4-n}Si(OEt)_n + [Cl_mSi(OEt)_{3-m}O]_kSiCl_p(OEt)_{3-k-p}, \quad (2)$$

where n, m, k, p = 1–3.

With the above initiators, it was possible to recover 6–88% of Me_3SiCl from the reaction mixture. In the presence of DMF, the mixture undergoes partial tarring due to low thermal stability of DMF–$SiCl_4$ complexes [14].

1070-4272/01/7412-2091 $25.00 © 2001 MAIK "Nauka/Interperiodica"

Conditions and isolated products of the reaction of $Si(OEt)_4$ with $SiCl_4$ in an industrial azeotropic mixture with Me_3SiCl

Reaction conditions					Yield of indicated exchange product, g					Yield of 99% Me_3SiCl, %
initiator, wt %	*T*, °C	τ, h	azeotrope, g	$(EtO)_4Si$, g	$EtOSiCl_3$	$(EtO)_2SiCl_2$	$(EtO)_3SiCl$	$(EtO)_4Si$	ethoxychloro-polysiloxanes	
THF:										
1.0	60–65	10	10.15	15.6	3.4	4.7	8.9	5.1	0.6	66
1.0	60–65	15	10.15	15.6	–	4.5	15.6	1.8	0.6	70
1.0	25	72	10.15	15.6	1.1	1.8	14.9	3.6	0.6	80
2.0	60–65	5	5.08	7.8	0.5	3.9	4.6	1.5	0.5	80
2.0	25	72	5.08	7.8	2.0	3.1	3.6	1.8	0.2	88
Dioxane:										
1.0	60–65	15	10.15	15.6	2.2	6.2	6.3	6.8	0.6	78
1.0	25	72	10.15	15.6	1.0	6.3	11.7	2.4	1.2	68
2.0	60–65	5	5.08	7.8	1.5	1.4	3.9	3.6	0.3	84
2.0	25	72	5.08	7.8	1.0	2.3	5.0	2.6	0.2	72
Ethanol:										
0.2	60–65	10	10.15	15.6	1.0	4.2	12.8	3.1	1.2	68
0.2	60–65	15	10.15	15.6	0.75	3.95	13.8	1.5	2.25	71
DMF:										
5.0	60–65	18	25.00	11.5	0.9	1.6	4.4	2.9	3.5	72

Reaction (2) performed in the presence of 0.2 wt % ethanol, 1 wt % THF or dioxane, or 2 wt % diethyl ether mainly yields triethoxychlorosilanes, with relatively low content of siloxanes originating from heterofunctional condensation (see table). Raising the concentration of THF or dioxane to 2 wt % noticeably decreases the yield of ethoxychlorosilanes and favors formation of oligosiloxanes even at 20–25°C (see table). At THF content as high as 10 wt %, Me_3SiCl is also involved in the heterofunctional condensation.

Initiation of exchange between alkoxy groups and chlorine atoms in reactions of chlorosilanes with alkoxysilanes under the action of HCl (usually present in chlorosilanes because of their partial hydrolysis by atmospheric moisture) is believed to occur in two stages [1]:

$$-\overset{|}{\underset{|}{Si}}-OEt + HCl \rightleftarrows -\overset{|}{\underset{|}{Si}}-Cl + HOEt, \quad (3a)$$

$$-\overset{|}{\underset{|}{Si^*}}-Cl + HOEt \rightleftarrows -\overset{|}{\underset{|}{Si^*}}-OEt + HCl. \quad (3b)$$

The initial rate of the reaction between trimethylmethoxysilane and $SiCl_4$ in the presence of HCl or hydroxyl-containing compounds ROH (R = H, MeO, PhCO, Et_3Si) releasing HCl in the reaction with $SiCl_4$, is proportional to squared HCl concentration [15]. In this connection, formation of intermediate associates like $Me_3SiOMe \cdot 2HCl$, decomposing with cleavage of the Si–O bond, was suggested:

$$Me_3SiOMe \cdot 2HCl \rightleftarrows Me_3SiCl + HOMe + HCl. \quad (4)$$

In a solvent forming associates with HCl, the equilibrium of reaction (4) is significantly shifted to the left. This fact is nicely consistent with the previously found [13] catalytic activity of ethanol in reaction (3). However, addition of acyclic (Et_2O) and cyclic (THF, dioxane) ethers, capable of forming oxonium complexes with HCl [16], must enhance the catalytic effect of HCl. In the case of THF, the oxonium complex can transform into 4-chloro-1-butanol whose capability for etherification of type (3b) is considerably lower than that of ethanol. This fact could decrease the content of HCl in the reaction mixture and hinder reaction (3). However, when THF is added in an amount as large as 10 wt %, the reaction is not inhibited; moreover, more inert Me_3SiCl is involved in the process.

Nucleophilic substitution at the silicon atom is accelerated in the presence of strong nucleophiles (DMF, HMPA, F^-, $RCOO^-$, Cl^-) and is a first-order reaction with respect to the initial silane, alcohol, and activating nucleophile [17, 18]. The suggested reaction mechanism involves formation of an intermediate

with a five-coordinate Si atom and its subsequent attack by a nucleophile (Nu):

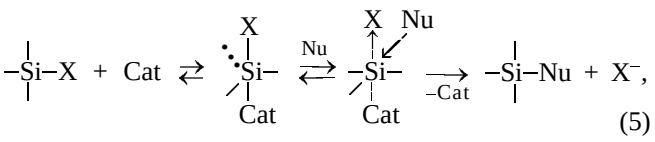

(5)

where X = H, OR, NR_2, Cl.

Presumably, DMF in reaction (2), forming a complex with $SiCl_4$, enhances the nucleophilicity of the Cl atoms. However, THF, dioxane, and diethyl ether are quite inert relative to $SiCl_4$ and $Si(OEt)_4$ [19, 20]. A common property of ethers (and alcohols) is their capability to form oxonium complexes with hydrogen halides. In such complexes, the nucleophilicity of chloride ions is enhanced, and their exchange with ethoxy groups is activated. Presumably, reaction (2) involves formation of a six-membered cyclic transition state in which cleavage of the Si–O bond (i) yields exchange products, and cleavage of the $O–CH_2Me$ bond (ii), heterofunctional cyclization products:

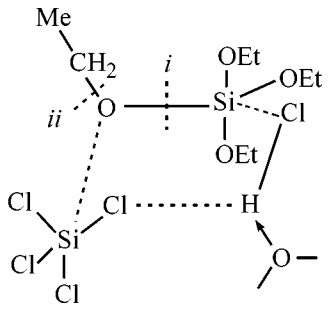

EXPERIMENTAL

The azeotropic mixture $SiCl_4$–Me_3SiCl obtained from synthesis of chlorosilanes[1] contained 49.07% Me_3SiCl, 37.05% $SiCl_4$, 12.00% $MeSiHCl_2$, 0.77% SiH_2Cl_2, 0.74% $SiHCl_3$, and 0.21% $Me_3SiOSiMe_3$.

Chromatographic analysis was performed with a Hewlett–Packard HP 5890 device (EI, 70 eV, HP 5971 A mass-selective detector, 50-m Ultra-2 column coated with polymethylsilicone containing 5% phenyl groups, vaporizer temperature 250°C, column temperature 50–280°C).

Reaction of $Si(OEt)_4$ with $SiCl_4$ in azeotropic mixture with Me_3SiCl in the presence of initiator. (a) A mixture of 10.15 g of $Me_3SiCl–SiCl_4$ azeotrope, 15.6 g of $Si(OEt)_4$, and 1.0 wt % THF was heated for 10 h at 60–65°C and fractionated. Yield of Me_3SiCl 3.3 g (66%), purity 99%.

(b) A mixture of 25.0 g of $Me_3SiCl–SiCl_4$ azeotrope, 11.5 g of $Si(OEt)_4$, and 1.83 g (5.0 wt %) of DMF was heated to reflux for 18 h and cooled to room temperature; the liquid phase was separated by decanting and fractionated.

(c) A mixture of 17.9 g of $Me_3SiCl–SiCl_4$ azeotrope, 10.7 g of $Si(OEt)_4$, and 6.0 g of the complex $SiCl_4 \cdot 2H(O)CNMe_2$ was heated to reflux for 4 h. After cooling to room temperature, the liquid phase was separated from the precipitate (4.9 g) by decanting and distilled to give 5.9 g (67%) of Me_3SiCl, bp 55–56°C; 4.9 g of $(EtO)SiCl_3$, bp 102–105°C; 3.7 g of $(EtO)_2SiCl_2$, bp 137–139°C; and 5.8 g of $(EtO)_3 \cdot SiCl$, bp 156–158°C.

At other reaction times and temperatures and with other amounts of catalysts, the mixtures were worked up similarly. The experimental conditions and reaction products are listed in the table.

Reaction of $Me_3SiCl–SiCl_4$ azeotrope with $Si(OEt)_4$ in the presence of 10 wt % THF. A mixture of 5.08 g of $Me_3SiCl–SiCl_4$ azeotrope, 7.8 g of $Si(OEt)_4$, and 10 wt % THF was heated at 60–65°C for 10 h. The resulting mixture was analyzed by GC–MS. Component content, wt %: Me_3SiCl 7.7, THF 8.5, $(EtO)_2SiCl_2$ 5.5, $(EtO)_3SiCl$ 58.5, $Si(OEt)_4$ 15.0, $(EtO)_3SiOMe_3$ 3.2, $(EtO)_2Si(OSiMe_3)_2$ 1.5, and $EtOSi(OSiMe_3)_3$ and unidentified products <0.5.

Reaction of $SiCl_4$ with $Si(OEt)_4$ in the presence of Et_2O. (a) A mixture of 4.25 g of $SiCl_4$, 5.2 g of $Si(OEt)_4$, and 2 wt % Et_2O was heated at 60–65°C for 10 h and then analyzed by GC–MS. Component content, wt %: Et_2O 0.2, $EtOSiCl_3$ 1.1, $(EtO)_2SiCl_2$ 14.9, $(EtO)_3SiCl$ 76.7, $Si(OEt)_4$ 5.1, and ethoxychloropolysiloxanes 2.0.

(b) A mixture of 1.7 g of $SiCl_4$, 6.24 g of $Si(OEt)_4$, and 2 wt % Et_2O was heated at 60–65°C for 10 h and then analyzed by GC–MS. Component content, wt %: Et_2O 1.6, $EtOSiCl_3$ 22.4, $(EtO)_2SiCl_2$ 2.5, $Si(OEt)_4$ 69.0, $Cl_3SiOSi(OEt)_3$ 2.7, and unidentified compounds 1.8.

CONCLUSION

Treatment of the azeotropic mixture $Me_3SiCl–SiCl_4$ with $Si(OEt)_4$ at 25–65°C in the presence of 0.2–10 wt % cyclic (THF, dioxane) or acyclic (diethyl ether) ethers, ethanol, or dimethylformamide allows isolation of 99% pure trimethylchlorosilane in up to 88% yield.

[1] Sibirskii Silikon Joint-Stock Company (Usol'e-Sibirskoe, Irkutsk oblast).

REFERENCES

1. Voronkov, M.G., Mileshkevich, V.P., and Yuzhelevskii, Yu.A., *Siloksanovaya svyaz'* (Siloxane Bond), Novosibirsk: Nauka, 1976.
2. Andrianov, K.A., *Metody elementoorganicheskoi khimii* (Methods of Organometallic Chemistry), Moscow: Nauka, 1968.
3. Molokanov, Yu.K., Korablina, T.P., Kleinovskaya, M.A., and Shchelkunova, M.A., *Razdelenie smesei kremniiorganicheskikh soedinenii* (Separation of Mixtures of Organosilicon Compounds), Moscow: Khimiya, 1974.
4. Kleinovskaya, M.A., Andrianov, K.A., and Golubtsov, S.A., *Plast. Massy*, 1959, no. 2, pp. 41–45.
5. Muller, R. and Dathe, Chr., *Z. Anorg. Allg. Chem.*, 1963, vol. 325, nos. 3–4, pp. 149–155.
6. RF Patent 2119490.
7. RF Patent 2119491.
8. Friedel, C. and Ladenburg, A., *Ber.*, 1870, vol. 3, pp. 15–20.
9. Kumada, M. and Tarama, K., *J. Chem. Soc. Jpn., Ind. Chem. Sect.*, 1952, vol. 55, pp. 371–373.
10. Kumada, M., *J. Inst. Polytech. Osaka City Univ., Ser. C*, 1952, vol. 2, pp. 139–146.
11. Chernyshev, E.A., Lebedev, E.N., Kleshchevnikova, S.I., *et al.*, *Zh. Obshch. Khim.*, 1995, vol. 65, no. 7, pp. 1142–1144.
12. RF Patent 2166507.
13. RF Patent 2166977.
14. Piper, T.S. and Rochow, E.G., *J. Am. Chem. Soc.*, 1954, vol. 76, no. 17, pp. 4318–4320.
15. Yastrebov, V.V. and Chernyshev, A.N., *Zh. Obshch. Khim.*, 1971, vol. 41, no. 3, pp. 713–714.
16. *Vodorodnaya svyaz'* (Hydrogen Bond), Sokolov, N.D., Ed., Moscow: Nauka, 1981.
17. Corriu, R.J.P., Dabosi, G., and Martineau, M., *J. Organomet. Chem.*, 1978, vol. 150, pp. 27–38.
18. Corriu, R.J.P., Dabosi, G., and Martineau, M., *J. Organomet. Chem.*, 1980, vol. 186, pp. 25–37.
19. Alpatova, N.M. and Kessler, Yu.M., *Zh. Strukt. Khim.*, 1964, vol. 5, no. 2, pp. 332–353.
20. Voronkov, M.G. and Deich, A.Ya., *Izv. Akad. Nauk Latv. SSR, Ser. Khim.*, 1963, no. 4, pp. 417–430.

Russian Journal of Applied Chemistry, Vol. 74, No. 12, 2001, pp. 2095–2097. Translated from Zhurnal Prikladnoi Khimii, Vol. 74, No. 12, 2001, pp. 2035–2037.

ORGANIC SYNTHESIS AND INDUSTRIAL ORGANIC CHEMISTRY

Spectrophotometric Study of Interaction in the System Sodium Dodecyl Sulfate–Cetylpyridinium Chloride–Methylene Blue

T. V. Vladimirova and E. E. Morgunova

Institute of Solution Chemistry, Russian Academy of Sciences, Ivanovo, Russia

Received May 7, 2001

Abstract—Complexation of a cationic dye (Methylene Blue) with anionic and cationic surfactants (sodium dodecyl sulfate and cetylpyridinium chloride) was studied spectrophotometrically. The formation constants of complexes formed in the system were estimated. Dispersion of the investigated system was studied as a function of time and cetylpyridinium chloride concentration.

The presence of surfactants in wastewater overburdens the treatment by commonly accepted methods. By virtue of the fact that surfactants are physically and chemically reactive compounds, it is significant to know which components of waste they can interact with and what degree of their decomposition is reached as a result.

Multicomponent systems containing two or more different surfactants are of considerable theoretical interest and practical significance. For example, systems containing a surfactant and a dye are widely used in textile manufacture, making it topical to study interaction between compounds of various classes in solutions.

Previously, we studied the interaction in systems cationic dye–anionic surfactant and cationic dye–anionic surfactant–nonionic surfactant [1].

It is known [2] that cationic surfactants may exist in the presence of anionic surfactants in three forms: (1) monomers (unassociated molecules), (2) mixed micelles (after reaching CMC), and (3) precipitated solid (at concentration above the product solubility).

It has been demonstrated previously [1] that Methylene Blue (MB) and sodium dodecyl sulfate (SDS) form an ionic associate in solution.

EXPERIMENTAL

The concentrations of MB (cationic dye), DDS (anionic surfactant), and cetylpyridinium chloride (CPC) (cationic surfactant) in the system investigated were 10^{-3}, 10^{-2}, and 10^{-3} M, respectively. The quality of SDS and CPC was determined as in [3]. The optical density of the solutions was measured on an SF-46 spectrophotometer over the range 200–700 nm at $l = 1$ cm. The residual concentration of SDS and CPC was determined photometrically after extraction with chloroform [4].

To estimate the scattering factor F_r, we measured the absorption spectra over the range 500–700 nm and then determined the slope of the linear portion of the $\ln A$–$\ln \lambda$ plot. The size of colloid aggregates was determined turbidimetrically [5]. The solution turbidity was estimated as $\tau = 2.3A/l$, where A is the optical density measured at $\lambda = 400$ nm and l is the layer thickness.

We measured absorption spectra of MB over a wide concentration range in the presence of SDS and CPC. In the visible range, we found formation of no associates other than the ionic associate SDS–MB. In the UV range, we observed changes in the shapes and positions of absorption bands in the systems MB–CPC and MB–SDS–CPC as compared with the spectra of the individual compounds (Fig. 1). These evolutions reflect the interaction occurring in the investigated systems, suggesting the formation of new compounds [6]. From the optical density data obtained in solutions with various concentrations of the components, the logarithms of the association constants ($\log K$) for MB–SDS, MB–CPC, and MB–CPC–SDS were estimated by the procedure described in [7] to be 2.50 ± 0.09, 4.66 ± 0.33, and 8.42 ± 0.55, respectively.

Presumably, formation of MB–CPC–SDS is caused by both coulombic and hydrophobic interactions [6].

1070-4272/01/7412-2095 $25.00 © 2001 MAIK "Nauka/Interperiodica"

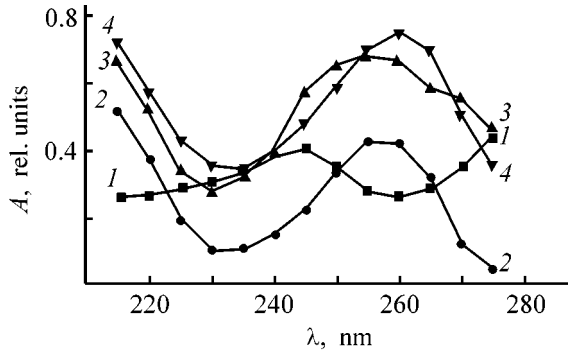

Fig. 1. Absorption spectra of solutions: (*1*) MG, (*2*) CPC (*3*), MB + CPC, and (*4*) MB + SDS + CPC. Concentration (M): MG 2×10^{-5}, SDS 2×10^{-3}, and CPC 1×10^{-4}. (*A*) Optical density and (λ) wavelength.

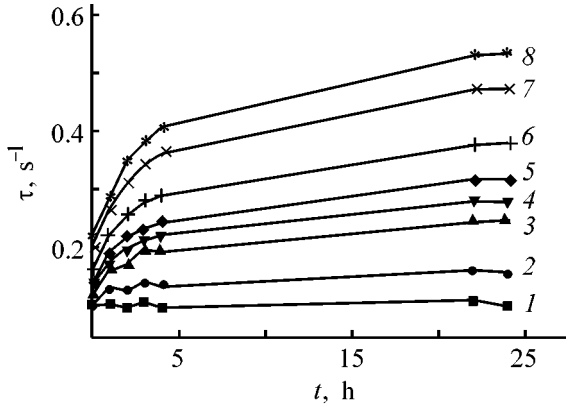

Fig. 3. Solution turbidity τ in the system MG–SDS–CPC vs. time *t*. CPC concentration $C \times 10^4$ (M): (*1*) 0, (*2*) 0.4, (*3*) 1.0, (*4*) 1.2, (*5*) 1.4, (*6*) 1.8, (*7*) 2.4, and (*8*) 2.8.

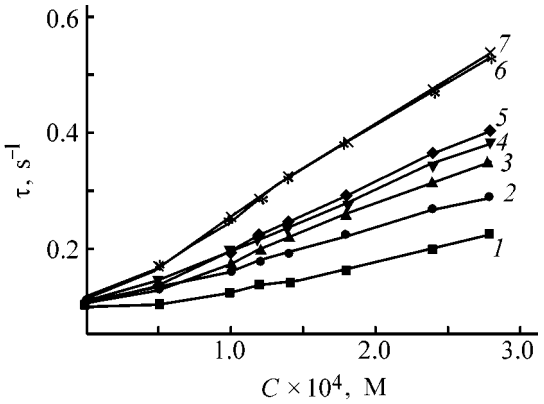

Fig. 2. Solution turbidity τ in the system MG–SDS–CPC vs. the CPC concentration *C*. Time elapsed after solution preparation (h): (*1*) 0, (*2*) 1, (*3*) 2, (*4*) 3, (*5*) 4, (*6*) 22, and (*7*) 24.

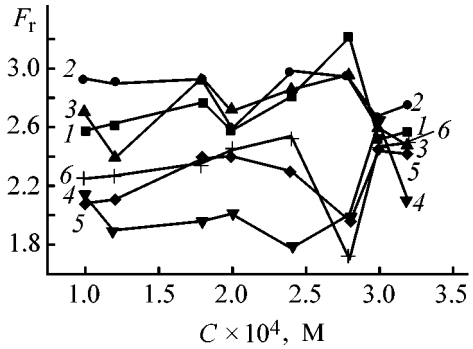

Fig. 4. Effect of the CPC concentration *C* on the scattering factor F_r in the systems (*1–3*) SDS–CPC and (*4–6*) MG–SDS–CPC. Time elapsed after system preparation (h): (*1*, *4*) 0, (*2*, *5*) 1, and (*3*, *6*) 2.

Interaction of the cationic dye, MB, having a delocalized positive charge [8], with the cationic surfactant, CPC, probably proceeds by the mechanism similar to micelle formation. Such interactions have been observed, for example, for merocyanine dyes with surfactants and chrome dyes with lignosulfonic acid [10].

In our experiments, as the CPC concentration in the system increases, the MB and SDS concentrations being unchanged, the initially clear, homogenous solution becomes opalescent. Similar changes (appearance of opalescence) were also observed in aging of initially homogeneous MB–SDS–CPC solutions, suggesting that this system is thermodynamically unstable.

The solution turbidity grows with increasing CPC concentration (Fig. 2) and time (Fig. 3). The turbidity increases more rapidly in the first 4 h after decanting, but continues even a month later.

The size of colloid aggregates of the associates MB–SDS–CPC and SDS–CPC was estimated from the scattering data. It is seen from Fig. 4 that both the associates are aggregatively stable over a broad concentration range and may be classified with colloids by their size ($F_r < 4$). Over the CPC concentration range $(1–2.8) \times 10^{-4}$ M, the colloid aggregates MB–SDS–CPC have larger radius, and their solutions, lower F_r than those of SDS–CPC aggregates. At a CPC concentration above 3×10^{-4} M the threecomponent system becomes more stable with time: during the first 1 h after solution preparation, the size of colloid aggregates MB–SDS–CPC increases and then remains practically unchanged. The system SDS–CPC is more aggregatively stable in time.

We also performed experiments on removal of the dye, SDS, and CPC from the solution by sorption on freshly precipitated aluminum hydroxide, using the procedure described in [1]. The results are given in

Degree of removal of MB, SDS, and CPC at various CPC initial concentrations C^*

$C \times 10^4$, M	Degree of removal, %		
	dye	SDS	CPC
2.0	99	89.2	99.9
2.8	99	88.2	98.8
3.2	99	89.1	99.5

* pH 4.5; $Al_2(SO_4)_3$ concentration 1.9 g l^{-1}; the initial dye concentration 10^{-5}; and SDS concentration 2×10^{-3} M.

the table. As seen, the sorption allows efficient clarification of the solution and removal of up to 90% of the anionic surfactant and up to 99% of the cationic surfactant.

CONCLUSIONS

(1) The logarithms of the formation constants of associates formed in the investigated system are determined to be 2.50 ± 0.09, 4.66 ± 0.33, and 8.42 ± 0.55 for Methylene Blue–sodium dodecyl sulfate, Methylene Blue–cetylpyridinium chloride, and Methylene Blue–cetylpyridinium chloride–sodium dodecyl sulfate, respectively.

(2) The associates Methylene Blue–sodium dodecyl sulfate–cetylpyridinium chloride are aggregatively stable over the CPC concentration range $(1–3.2) \times 10^{-4}$ M and may be classified with colloids by their size ($F_r < 4$).

(3) The possibility of simultaneous recovery of the cationic dye and anionic and cationic surfactants from solutions by coagulation with aluminum hydroxide is demonstrated.

REFERENCES

1. Vladimirova, T.V., Tikhomirova, M.V., and Grishina, E.P., *Zh. Prikl. Khim.*, 1999, vol. 72, no. 1, pp. 133–136.
2. Kevin, L.S., Joel, C.A., and John, F.S., *J. Colloid. Interface Sci.*, 1988, vol. 132, no. 1, pp. 186–201.
3. Abramzon, A.A., Zaichenko, L.P., and Faingol'd, S.I., *Poverkhnostno-aktivnye veshchestva* (Surfactants), Leningrad: Khimiya, 1988.
4. Lur'e, Yu.Yu., *Analiticheskaya khimiya promyshlennykh stochnykh vod* (Analytical Chemistry of Industrial Wastewater), Moscow: Khimiya, 1984.
5. Kulichenko, S.A., Maksimyuk, E.G., and Sukhan, V.V., *Khim. Tekhnol. Vody*, 1995, vol. 17, no. 1, pp. 34–38.
6. Savvin, S.B., Chernova, R.K., and Shtykov, S.R., *Poverkhnostno-aktivnye veshchestva* (Surfactants), Moscow: Nauka, 1991.
7. Vasil'ev, V.P., Borodin, V.A., and Kozlovskii, E.V., *Primenenie EVM in khimiko-analiticheskikh raschetakh* (Use of Computers in Analytical Chemistry), Moscow: Vysshaya Shkola, 1993.
8. Stepanov, B.I., *Vvedenie v khimiyu i tekhnologiyu organicheskikh krasitelei* (Introduction to the Chemistry and Technology of Organic Dyes), Moscow: Khimiya, 1964.
9. Smirnova, S.V., Ledneva, I.A., Mel'nikov, B.N., *et al.*, *Tekstil. Khim.*, 1998, no. 1, pp. 28–31.
10. Minch, M.J. and Sadiq Shah, S., *J. Org. Chem.*, 1979, vol. 44, no. 18, pp. 3252–3260.

Russian Journal of Applied Chemistry, Vol. 74, No. 12, 2001, pp. 2098–2102. Translated from Zhurnal Prikladnoi Khimii, Vol. 74, No. 12, 2001, pp. 2038–2042.

ORGANIC SYNTHESIS AND INDUSTRIAL ORGANIC CHEMISTRY

In memory of distinguished physical chemist and outstanding person Professor Ariel' Abramovich Abramzon

Optimization of the Component Concentrations in Solutions of Synthetic Detergents

A. A. Kotomin, M. B. Petel'skii, A. A. Abramzon,† A. E. Punin, and O. D. Yakimchuk

St. Petersburg State Technological Institute, St. Petersburg, Russia

Received April 25, 2001

Abstract—The detergency of formulations composed of organic and inorganic components that form the basis of synthetic detergents was studied. Mathematical design of experiment—method of orthogonal Latin rectangles, was applied to determine the component concentrations corresponding to the maximal detergency. Thus obtained concentrations of the detergent components in aqueous solutions can be used for optimization of the detergent formulation.

Detergency is of great practical importance both in household and in industrial sectors, but its mechanism is far from comprehensive understanding now. In our previous work [1], we discussed the detergency of individual components of synthetic detergents. In this work, we studied detergency of a formulation as a whole as influenced by its formula. This approach is essential for development and application of detergents.

At the present, detergent formulations are composed empirically, because physicochemical mechanisms of elementary events in detergency have been studied inadequately. Modern methods of mathematical designing of experiments can yield a mathematical model of a chemical process even when its mechanism is unknown. Also, mathematical designing of experiments significantly reduces the number of experiments and minimizes the costs involved [2].

In this work, we determined the optimal concentrations of the components of complex detergent mixtures by the method of orthogonal Latin rectangles. The method consists in assessing the variation of the output parameter (in our case, detergency) by varying to a certain extent the influencing factors, namely, the concentrations of the components. These concentrations were varied at four levels. According to the scheme of orthogonal design, the number of experiments was in the formulation, and $i = 4$ is the number of the concentration variation levels (Table 1). In this scheme, each concentration of one of the eight components is combined with each concentration of any other component the same number of times (two in our case) [3].

$n \times i = 32$, where $n = 8$ is the number of components

More than 50-year practice of using detergents showed what components endow the composition with high efficiency and desired consumer's properties [4–8].

Modern detergents have surfactants (typically, anionic and nonionic ones) as the major components [9]. By combining these two types of surfactants, as well as high-molecular-weight surfactants stabilizing contaminants in solutions and preventing their resorption onto the surface to be cleaned and substances binding the hardness salts, it is possible to gain the optimal effect. The most widely used components are sodium tripolyphosphate; sodium carbonate which imparts alkalinity to solution; silicates, in particular, sodium metasilicate, which are protecting colloidal systems; substances that chemically and biologically degrade contaminants; oxidizing and bleaching agents (e.g., peroxy salts), as well as enzymes; and optical bleaching agents, that is, substances "painting over" contaminants.

Also used are components that virtually do not contribute to removal of contaminants: sodium sulfate (provides friability of the detergent formulation), hydrotrops (facilitate dissolution of organic compounds

† Deceased.

1070-4272/01/7412-2098 $25.00 © 2001 MAIK "Nauka/Interperiodica"

Table 1. Experiment designing matrix for low-concentration range (1–10 g l^{-1}) of solution*

Experiment no.	Concentration of detergent formulation components c, g l^{-1}								Σc, g l^{-1}	$\overline{M}$
	SABS	DS-10	Na_2CO_3	STPP	SHDS	Na_2SO_4	$Na_2C_2O_6$	NaCMC		
1	0.050	0.150	0.500	0.500	0.250	0.500	0.500	0.025	2.475	0.93
2	0.050	0.350	0.500	1.200	1.250	1.500	0.750	0.100	5.700	1.00
3	0.050	0.550	0.850	0.500	0.950	1.500	1.250	0.050	5.700	0.99
4	0.050	0.750	0.850	1.200	0.600	0.500	1.000	0.150	5.100	1.07
5	0.050	0.150	1.200	1.500	1.250	0.850	1.000	0.050	6.050	1.05
6	0.050	0.350	1.200	0.850	0.250	1.200	1.250	0.150	5.300	1.11
7	0.050	0.550	1.500	1.500	0.600	1.200	0.750	0.025	6.175	1.14
8	0.050	0.750	1.500	0.850	0.950	0.850	0.500	0.100	5.550	1.01
9	0.500	0.350	0.850	0.850	0.600	0.850	0.750	0.050	4.800	0.97
10	0.500	0.150	0.850	1.500	0.950	1.200	0.500	0.150	5.800	1.09
11	0.500	0.750	0.500	0.850	1.250	1.200	1.000	0.025	6.075	0.84
12	0.500	0.550	0.500	1.500	0.250	0.850	1.250	0.100	5.500	1.10
13	0.500	0.350	1.500	1.200	0.950	0.500	1.250	0.025	6.275	1.10
14	0.500	0.150	1.500	0.500	0.600	1.500	1.000	0.100	5.850	1.08
15	0.500	0.750	1.200	1.200	0.250	1.500	0.500	0.050	5.950	1.05
16	0.500	0.550	1.200	0.500	1.250	0.500	0.750	0.150	5.400	1.03
17	1.000	0.550	1.200	1.200	0.950	1.200	1.000	0.100	7.200	1.12
18	1.000	0.750	1.200	0.500	0.600	0.850	1.250	0.025	6.175	0.90
19	1.000	0.150	1.500	1.200	0.250	0.850	0.750	0.150	5.850	1.08
20	1.000	0.350	1.500	0.500	1.250	1.200	0.500	0.050	6.350	1.18
21	1.000	0.550	0.500	0.850	0.600	1.500	0.500	0.150	5.650	0.91
22	1.000	0.750	0.500	1.500	0.950	0.500	0.750	0.050	6.000	1.12
23	1.000	0.150	0.850	0.850	1.250	0.500	1.250	0.100	5.950	1.08
24	1.000	0.350	0.850	1.500	0.250	1.500	1.000	0.025	6.475	0.91
25	1.500	0.750	1.500	1.500	1.250	1.500	1.250	0.150	9.400	1.06
26	1.500	0.550	1.500	0.850	0.250	0.500	1.000	0.050	6.200	1.17
27	1.500	0.350	1.200	1.500	0.600	0.500	0.500	0.100	6.250	1.00
28	1.500	0.150	1.200	0.850	0.950	1.500	0.750	0.025	6.925	1.13
29	1.500	0.750	0.850	0.500	0.250	1.200	0.750	0.100	5.900	1.04
30	1.500	0.550	0.850	1.200	1.250	0.850	0.500	0.025	6.725	1.13
31	1.500	0.350	0.500	0.500	0.950	0.850	1.000	0.150	5.800	1.09
32	1.500	0.150	0.500	1.200	0.600	1.200	1.250	0.050	6.450	0.99

* SABS is linear sodium alkylbenzenesulfonate, STPP is sodium tripolyphosphate, SHDS is sodium hydrosilicate, and NaCMC is sodium salt of carboxymethyl cellulose.

in water), and enzyme stabilizers. Fragrances and dyes make the formulation aesthetically attractive.

In this work, we studied substances that facilitate surface decontamination: linear sodium alkylbenzenesulfonate C_{10-14}–$(C_6H_4)SO_3Na$, Synthanol DS-10 C_{10-18}–$O(C_2H_4O)_{10}H$, anhydrous sodium carbonate Na_2CO_3, sodium tripolyphosphate $Na_5P_3O_{10}$, sodium hydrosilicate $2SiO_2 \cdot Na_2O \cdot 2H_2O$, sodium sulfate Na_2SO_4, sodium percarbonate $Na_2C_2O_6$ and sodium perborate $NaBO_3 \cdot 4H_2O$, and sodium salt of carboxymethyl cellulose $[C_6H_7O_2(OH)_{3-x}$–$(OCH_2COONa)_x]_n$.

Detergency involves a number of successive events ensuring separation of contaminants and their emulsification in aqueous solutions [8]: (1) surface wetting and displacement of contaminants; (2) dispersion of contaminants; (3) stabilization of contaminants in aqueous solution; (4) solid surface protection; (5) solubilization; (6) chemical and biological degradation of contaminants; and (7) foaming.

These elementary events are qualitatively clear, but there is no equation to describe them. Numerous attempts to develop the detergency theory on the basis of a thermodynamic approach have been unsuccessful. In our opinion, the most practically promising way is to establish experimentally a correlation between the detergency, on the one hand, and the detergent formulation and process conditions, on the other. In the first stage, we obtained systematized experimental data concerning the detergency of individual components of detergents depending on their concen-

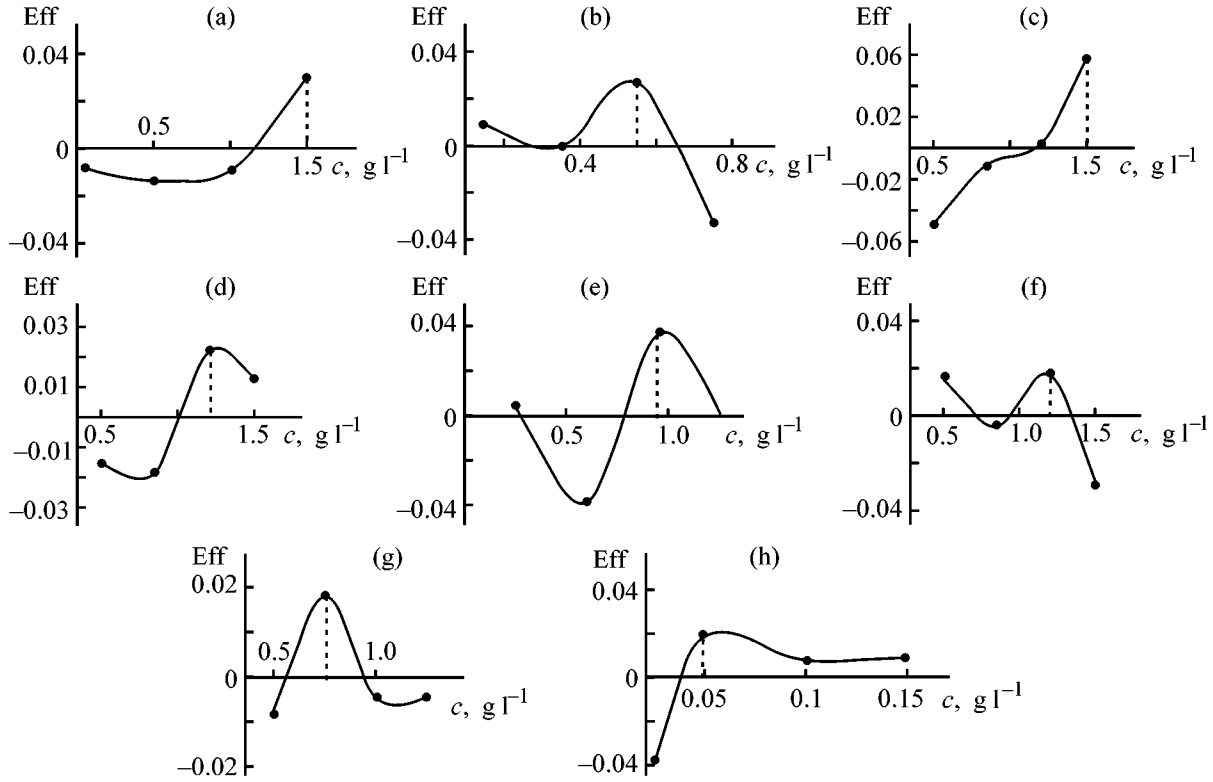

Fig. 1. Component effect Eff vs. component concentration *c*, in solutions. Solution: (a) SABS, (b) Synthanol DS-10, (c) Na_2CO_3, (d) STPP, (e) SHDS, (f) Na_2SO_4, (g) $Na_2C_2O_6$, and (h) NaCMC.

tration in aqueous solutions [1]. In this work, we studied more complex objects—detergent formulations.

We studied aqueous solutions of detergent formulations in two practically important concentration ranges: 1–10 and 15–40 g l^{-1}, characteristic of detergents intended for household and technical application, respectively. A separate study of these two concentration ranges affords a better sensitivity in solving the optimization problems. The variation ranges for concentrations of each component of a detergent formulation were suggested by published data [6–9] and the authors' experience.

Detergency was estimated from variation of the whiteness of a cotton fabric during washing out of the contaminants from the detergent solution under study [1]. The detergencies obtained were compared for all the solutions studied with that of a standard solution M_{st} determined under identical conditions. The standard solution corresponded to OST (Branch Standard) 6-15-1574–87 and contained SABS (1 g l^{-1}) and STPP (2 g l^{-1}). The results obtained were analyzed using the relative detergency of a substance $\overline{M} = M/M_{st.}$

Table 1 presents for the concentration range 1–10 g l^{-1} the experimental $\overline{M}$ values for each of the detergent formulations made up by the orthogonal Latin rectangle scheme.

For all the components at each concentration c_i we estimated the effect of the component on the formulation detergency:

$$\mathrm{Eff}_{c_i} = \frac{\sum_{c_i}\overline{M}}{8} - M_{av}. \quad (1)$$

Here, $\sum_{c_i} \overline{M}/8$ is the average $\overline{M}$ value for all the cases when the component concentration c_i was at the *i*th level, and $\overline{M}_{av}$ is the average relative detergency for the whole experimental series.

For each component we plotted the component effect Eff vs. concentration in solutions *c* (Fig. 1). This made it possible to determine the optimal concentrations of the components corresponding to maximal effects. The plots show that the maximal detergency of solutions should be afforded by the following concentrations of the components, g l^{-1}: SABS 1.5, Synthanol 0.55, Na_2CO_3 1.5, STPP 1.2, SHDS 0.95, Na_2SO_4 1.2, $Na_2C_2O_6$ 0.75, and NaCMC 0.05. The total concentration of components in solution amounts to 7.7 g l^{-1}. It should be noted that none of the 32

experiments involved such concentration ratio for the components.

Next, using the optimal concentrations of the components in solutions, we formulated the corresponding composition OK-1 and studied its detergency in the concentration range 0.5–10 g l^{-1}. The resulting plot of $\overline{M}$ vs. concentration of this formulation in solution is shown in Fig. 2. Combined analysis of the data in Fig. 2 and Table 1 shows that the maximal detergency of the formulation is observed not only at the total concentration of the components of 7.7 g l^{-1}, as yielded by optimization, but also throughout the concentration range covered (0.5–10 g l^{-1}). Thus, the ratio of the chosen components should be considered the optimal for the low-concentration range.

We have shown previously [1] that the relative detergency and the concentrations of individual components, as well as the parameters $1/\overline{M}$ and $1/c$, are related by linear dependences. For the optimal formulation OK-1 prepared by us, the plot of $1/\overline{M}$ vs. $1/c$ is close to a straight line (Fig. 3, straight line *1*), with correlation factor of 0.994. This confirms the validity of the detergency equation derived by us in [1]:

$$\overline{M} = \frac{\overline{M}_{\max} c}{\alpha + c}. \qquad (2)$$

Here, $\overline{M}_{\max}$ is the maximal relative detergency, and α is the coefficient having the dimensionality of the concentration and depending on the energy parameters of the process.

Based on the data presented in Fig. 3, we estimated for the formulation OK-1 the $\overline{M}_{\max}$ and α values to be 1.49 and 1.22, respectively.

Similarly, we optimized the concentrations of the components for the concentration range 15–40 g l^{-1}. The formulations had the same qualitative composition as that at low concentrations, except for the bleaching agent. In this case, sodium perborate $NaBO_3 \cdot 4H_2O$ served as bleaching agent. The optimal concentrations of the components were estimated as follows, g l^{-1}: SABS 1.0, Synthanol 2.0, STPP 4.0, Na_2CO_3 4.0, SHDS 2.5, NaCMC 0.7, sodium perborate 6.0, and Na_2SO_4 1.0. The total concentration of the components in solution was 21.2 g l^{-1}.

The plot of the relative detergency vs. concentration for the optimal component ratio (formulation OK-2) looks similar to that obtained for low concentrations. The detergency is also at a maximum not only for the total component concentration yielded by optimization, 21.2 g l^{-1}, but also throughout the 15–40 g l^{-1} range. In this concentration range, the solutions are saturated, and an extensive factor, i.e., the total concentration of the components, is of less importance, whereas the mutual influence of the components (closeness of their ratio to the optimum) is of greater importance. The plot of inverse relative detergency vs. inverse concentration for the OK-2 formulation, $1/\overline{M}$–$1/c$, is also described by a straight line with correlation factor of 0.992 (Fig. 3, curve *2*). The maximal detergency $\overline{M}_{\max}$ and parameter α were estimated for this optimal formulation to be 1.56 and 1.52.

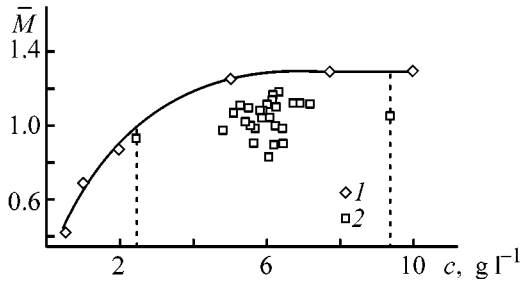

Fig. 2. (*1*) Relative detergency $\overline{M}$ of the optimal formulation OK-1 vs. the concentration c, in aqueous solutions and (*2*) experimental $\overline{M}$ values for formulations derived from the experimental design matrix (Table 1).

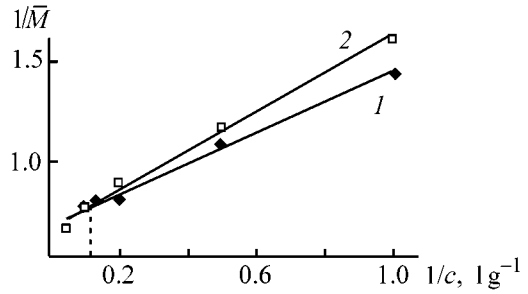

Fig. 3. Inverse relative detergency $\overline{M}$ vs. inverse concentration $1/c$, for the optimal formulations in the range of (*1*) low and (*2*) high concentrations.

The numerical values of the parameters $\overline{M}_{\max}$ and α can serve as convenient characteristics of the detergency of solution. The maximal relative detergency characterizes the maximum attainable detergency at the detergent concentration in solution tending to infinity, and α is related to the rate of the $\overline{M}$ growth with increasing concentration. The greater $\overline{M}_{\max}$ and the smaller α, the more effective is the detergent solution. The parameter α plays especially significant role in the low-concentration range of detergent solutions.

The parameter α has the dimensionality of concentration, and formula (2) shows that it must be numerically equal to the concentration corresponding to the detergency of $1/2\overline{M}_{\max}$. Table 2 compares the experimental c values obtained at $\overline{M} = 1/2\overline{M}_{\max}$ and the α values calculated as the slope of the

Table 2. Experimental values of the concentration c for $\overline{M} = 1/2\overline{M}_{max}$ and of the parameter α

Substance and formulation	$1/2\overline{M}_{max}$	c, g l^{-1}	α	Substance and formulation	$1/2\overline{M}_{max}$	c, g l^{-1}	α
SABS	0.405	1.69	1.59	Sodium hydrosilicate	0.435	0.99	0.95
Synthanol DS-10	0.380	0.29	0.25	NaCMC	0.225	1.95	1.81
Neonol AF_{9-12}*	0.380	0.25	0.20	Household soap**	0.490	1.19	1.13
Sodium carbonate	0.435	0.52	0.56	OK-1***	0.745	1.23	1.22
Sodium perborate	0.445	1.11	1.09	OK-2***	0.780	1.50	1.52

* C_{9-12}–(C_6H_4)–$O(C_2H_4O)_{12}H$.

** C_{10-18}–COONa.

*** OK-1 and OK-2 are the optimal detergent formulations for low- and high-concentration ranges of solutions, respectively.

$1/\overline{M}$–$1/c$ dependence multiplied by $\overline{M}_{max}$ for individual components of detergents [1] and the formulations prepared in this work. Table 2 shows that the calculated and experimental values of α and concentrations agree reasonably at $\overline{M} = 1/2\overline{M}_{max}$.

Figure 3 compares the plots of inverse detergency vs. inverse concentration for the optimal formulations in the range of (1) low and (2) high concentrations. The resulting straight lines actually intersect, and the intersection point corresponds to the concentration of 8.4 g l^{-1}, below which a greater detergency is achieved at the component ratio obtained for the low concentration range (OK-1 formulation) and above which the formulation optimized for high concentrations is more effective (OK-2 formulation).

The method of mathematical designing of experiment allows optimization of detergent formulations not only with respect to one output parameter, detergency (as in this work), but also with respect to several paramaters. As optimization criteria can serve prime cost and environmental, technological, and consumer's attractiveness of a detergent formulation. Other influencing factors are, along with concentration, temperature, time, hydrodynamic parameters of detergents process, etc.

CONCLUSIONS

(1) The synthetic detergent formulations can be optimized by mathematical designing of the experiment, using the orthogonal Latin rectangles method. An experimental-statistical model of detergency was developed; the optimal concentrations of the main organic and inorganic components in solutions of synthetic detergents, affording the maximal detergency, were determined.

(2) The equation derived, which relates the detergency to the concentration in aqueous solutions, is valid for both individual components and complex detergent formulations. The physical meaning of the parameters $\overline{M}_{max}$ and α in the detergency equation was disclosed. These parameters were proposed as quantitative characteristics of detergency of synthetic detergent formulations.

ACKNOWLEDGMENTS

The authors are grateful to N. P. Shirokov and I.P. Podreshetnikov for assistance in conducting the experiments.

REFERENCES

1. Abramzon, A.A. and Kotomin, A.A., *Zh. Prikl. Khim.*, 2000, vol. 73, no. 11, pp. 1902–1904.
2. Sautin, S.N. and Punin, A.E., *Mir komp'yuterov i khimicheskaya tekhnologiya* (Computer World and Chemical Technology), Leningrad: Khimiya, 1991.
3. Sautin, S.N., Punin, A.E., and Stoyanov, S., *Primenenie EVM dlya planirovaniya eksperimenta: uchebnoe posobie* (Use of Computers in Experiment Designing: Textbook), Leningrad: Leningr. Tekhnol. Inst., 1988.
4. Linder. K., *Tenside-Textilhilfmittel-Waschrostoffe*, Stuttgart: Wissenschaftliche, 1964–1971.
5. *Detergency*, Culter, W.A., and Dasis, R., Eds., New York: Dekker, 1964–1988, vols. 1–4.
6. Bukhshtab, Z.I., Mel'nik, A.P., and Kovalev, V.M., *Tekhnologiya sinteticheskikh moyushchikh sredstv* (Technology of Synthetic Detergents), Moscow: Legkaya Prom–st., 1988.
7. Kovalev, V.M. and Petrenko, D.S., *Tekhnologiya proizvodstva sinteticheskikh moyushchikh sredstv* (Technology of Producing Synthetic Detergents), Moscow: Khimiya, 1992.
8. Abramzon, A.A., *Chto nuzhno znat' o moyushchikh sredstvakh* (What One Needs To Know about Detergents), St. Petersburg: Khimizdat, 1999.
9. *Poverkhnostno-aktivnye veshchestva i moyushchie sredstva: Spravochnik* (Surfactants and Detergents: Reference Book), Abramzon, A.A., Ed., Moscow: Giperoks, 1993.

Russian Journal of Applied Chemistry, Vol. 74, No. 12, 2001, pp. 2103–2105. Translated from Zhurnal Prikladnoi Khimii, Vol. 74, No. 12, 2001, pp. 2043–2045.

MACROMOLECULAR CHEMISTRY AND POLYMERIC MATERIALS

High-Molecular-Weight Compounds and Related Materials Cross-Linking of Macrochains in Thermal Degradation of Poly(Vinyl Chloride)

V. M. Yanborisov, K. S. Minsker, and G. E. Zaikov

Bashkortostan State University, Ufa, Bashkortostan, Russia

Emanuel Institute of Biochemical Physics, Russian Academy of Sciences, Moscow, Russia

Received June 26, 2001

Abstract—Macrochain cross-linking in thermal degradation of PVC was studied. The onset time of gelation was determined as a function of the content of oxoallyl groups in the polymer.

Macrochain cross-linking is thought to be among the reactions leading to breakdown of the conjugated chain in polyene sequences formed in degradation of poly(vinyl chloride) (PVC). In the absence of agents promoting cross-linking by the radical mechanism, this reaction proceeds via the Diels–Alder mechanism [1–3]. This conclusion is supported by the following experimental results: (1) in the presence of reactive dienophiles (maleic anhydride, maleic acid esters or metal salts) reacting with polyene blocks via the Diels–Alder mechanism, the onset time of gelation in degraded PVC increases [1]; (2) in treatment of the cross-linked polymer with maleic anhydride, the gel phase is degraded by virtue of diene recondensation of polyenes with the stronger dienophile [2], suggesting also that the macrochain cross-linking in PVC is a reversible reaction; (3) the closeness of the kinetic parameters of PVC macrochain cross-linking in thermal degradation ($E_a = 50 \pm 8$ kJ mol^{-1}, $\log A = 6.3 \pm 0.5$ [3]) to those of the Diels–Alder reaction (E_a = 40–80 kJ mol^{-1}, $\log A$ = 5–7 [4]); and (4) modification of PVC with conjugated dienes increases the onset time of gelation in thermal degradation as compared with the initial polymer as a result of competition of the cross-linking and the reaction of conjugated dienes with polyenes [5].

It was suggested in [3, 6] that the cross-linking proceeds with participation of polyene sequences (ketopolyenes), such as ~C(O)–(–CH=CH–)$_n$~. In this case, each block of conjugated C=C bonds can serve as both a diene and a dienophile.

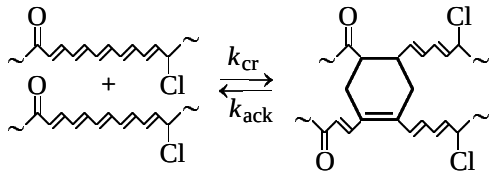

If PVC macrochain cross-linking involves polyene sequences whose formation is initiated by the oxoallyl (OA) groups ~C(O)–CH=CH~, as the gel fraction is formed, the sol fraction must be depleted in polyene sequences of the type ~C(O)–(–CH=CH–)$_n$~. The amount γ_0 of such ketopolyenes can be easily determined by the hydrolytic cleavage method as the change in the intrinsic viscosity of the sol fraction after alkaline hydrolysis of PVC [7]:

$$\gamma_0 = \frac{62.5 \times 1.86}{\overline{M}_v^0}\left\{\left(\frac{\eta_0}{\eta}\right)^{1.38} - 1\right\}, \qquad (1)$$

where η_0 and η are the intrinsic viscosities before and after macrochain degradation and $\overline{M}_v^0$ is the initial viscosity-average molecular weight.

Indeed, the experimental results show (Fig. 1) that the amount of ketopolyenes in the sol fraction gradually decreases with increasing PVC degradation time. Therefore, one may suggest that the macrochain cross-linking in PVC degradation directly involves polyene sequences whose formation is promoted by OA groups.

1070-4272/01/7412-2103 $25.00 © 2001 MAIK "Nauka/Interperiodica"

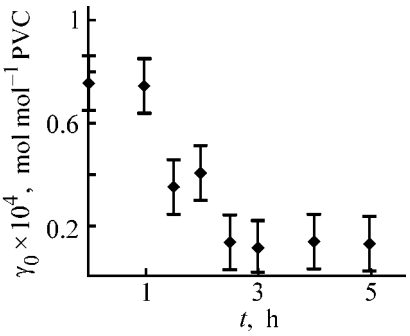

Fig. 1. OA group content γ_0 in the sol fraction of degraded PVC vs. degradation time *t*. Polyvinyl chloride S-70 ($\overline{M}_v$ 110 000).

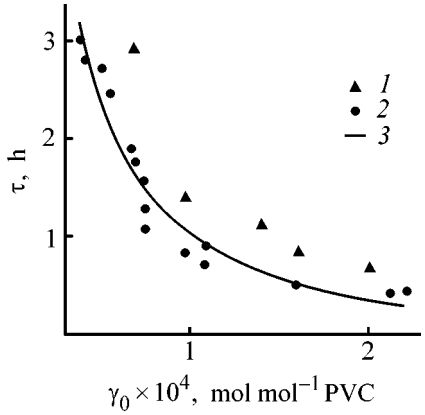

Fig. 2. Gelation time τ vs. the OA group content in PVC. Temperature 448 K; pressure 1×10^{-2} Pa. (*1*) Continuous removal of HCl [6], (*2*) barium stearate added, and (*3*) estimated by Eq. (3) at $n = 1.26$.

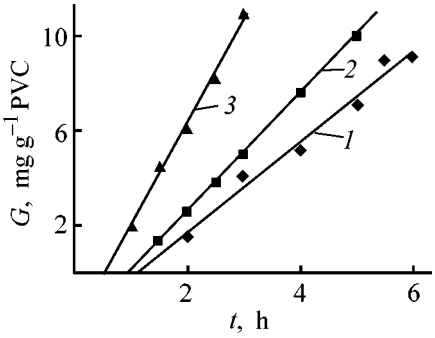

Fig. 3. Amount of gel *G* formed in thermal degradation of PVC. Pressure 1×10^{-2} Pa; $BaSt_2$. (*t*) Time. OA group content $\gamma_0 \times 10^{-4}$: (*1*) 0.76, (*2*) 0.098, and (*3*) 1.60.

However, cross-linking of only ketopolyene sequences cannot produce the observed yield of the gel phase at a degradation time much over the onset time of gelation τ [6, 8], since the fraction of the OA-containing PVC molecules is small (8–10%). Therefore, diene recondensation may occur at later stages of PVC degradation, with polyene blocks formed as a result of activation by β-chloroallyl groups originating from HCl elimination in ordinary VC units and tertiary chloride groups [3]. In performing PVC degradation in the presence of barium stearate, an effective acceptor for HCl, the reverse reaction of HCl addition to polyene sequences is suppressed [9]. In this case, the most probable secondary reactions are macrochain cross-linking [1–5] and polyene cyclization [10]. It has been demonstrated previously [6] that the onset time of gelation depends on the OA group content (Fig. 2, curve *1*). In the study cited, thermal degradation of PVC was performed with continuous removal of HCl from the reaction zone by freezing.

To obtain the best suited equation for τ as a function of γ_0, it is necessary to study experimentally this dependence over a wide range of γ_0. At the same time, γ_0 of the ordinary commercial and laboratory samples of PVC varies within a narrow range $(0.8–1.4) \times 10^{-4}$ mol mol^{-1} PVC. That is why samples with low OA group content were specially prepared in the present study by modification of PVC with maleic anhydride [11]. This reaction provides irreversible decrease in the OA group content in PVC. As a result, the rate of its dehydrochlorination decreases by virtue of decreasing amount of polyene sequences formed. The characteristics of thus modified PVC are given in the table. At low OA group content in PVC the error of γ_0 determination from viscometric data by Eq. (1) is high. Therefore, this parameter for modified PVC (γ_0^m) was occasionally estimated more exactly by Eq. (2).

$$\gamma_0 = (V_{HCl} - V_c)/k_p, \quad (2)$$

where V_{HCl} is the experimental rate of rough dehydrochlorination (see the table), $V_c = 0.8 \times 10^{-7}$ mol mol^{-1} PVC s^{-1} is the rate of HCl elimination from ordinary PVC units, and $k_p = 0.75 \times 10^{-2}$ s^{-1} is the constant of HCl elimination from polyene sequences [3].

Typically, the dependence of the amount of the gel phase formed on the PVC degradation time is linear; the onset time of gelation was determined by linear extrapolation of the plot to the abscissa (Fig. 3).

Performing the reaction in the presence of barium stearate inhibits readdition of HCl to polyenes to a greater extent, as demonstrated by the decrease in the gelation time as compared with the preceding case (Fig. 2, curve *2*).

Generally, the dependence τ–γ_0 can be fitted to Eq. (3).

$$\tau = C\gamma_0^{-n}, \quad (3)$$

where *n* is the order of macrochain cross-linking by the conjugated bond blocks.

Characteristics of PVC modified with maleic anhydride (MA)*

$\bar{M}_v^0$	$\gamma_0^{in} \times 10^4$	[MA] × 10^2	T_m, K	τ_m, s	$[\eta]_0$	$[\eta]$	$\gamma_0^m \times 10^4$	$V_{HCl} \times 10^3$ (448 K)	τ, s (448 K)
	mol mol^{-1} PVC				dl g^{-1}		mol mol^{-1} PVC		
110000	0.76	1	373	2400	1.09	1.04	0.70	0.61	6300
110000	0.76	1	373	3600	1.09	–	0.68**	0.59	6800
105000	0.80	1	383	4800	1.07	–	0.75**	0.64	5600
110000	0.76	1	373	12000	1.09	1.05	0.57	0.51	8800
110000	0.76	4	373	10800	1.09	–	0.52**	0.47	9700
110000	0.76	4	398	7200	1.09	–	0.42**	0.40	10100

* (τ_m) Modification time.

** Estimated by Eq. (3).

Processing of the logarithmic form of Eq. (3) by the least-squares method gives $n = 1.26 \pm 0.17$ (r 0.979) at a 0.95 confidence level.

Thus, the reaction order with respect to ketopolyenes is close to unity. Therefore, it appears more probable that macrochain cross-linking in thermal degradation of PVC is caused not only by interaction of the polyene blocks, as suggested previously [6], but also, and to a greater extent, by the reaction of the polyenes with other unsaturated groups in PVC macrochains. Among such groups can be unsaturated terminal groups whose content in PVC is about 10^{-3} mol mol^{-1} PVC [2], and backbone β-chloroallyl moieties formed in PVC thermal degradation via random elimination of HCl from both the tertiary chloride and ordinary units of the macrochain.

EXPERIMENTAL

PVC was modified according to the procedure described in [11]. Degradation of PVC was performed at 448 K in sealed ampules evacuated to a residual pressure of 10^{-2} Pa. The liberated HCl was absorbed with barium stearate and then determined mercurometrically. The gel fraction of degraded PVC was washed and then separated by centrifugation with fresh portions of cyclohexane in the same ampules. To remove unreacted $BaSt_2$, the precipitate was triply washed with decyl alcohol at 373 K. The resulting gel was triply washed with ether to remove the residual solvent and dried to constant weight at 348 K. The error of determination of the gel amount G was within 10%. The gelation time was determined by linear extrapolation of the G-vs.-t plot to the abscissa axis. Alkaline hydrolysis of PVC and measurement of the intrinsic viscosity to determine the oxoallylgroup content were performed as in [7].

The sol fraction of degraded PVC was prepared by centrifugation for 1 h at 5000 rpm.

CONCLUSION

It was confirmed experimentally that cross-linking of macrochains in thermal degradation of PVC to proceeds by the Diels–Alder mechanism, which involves conjugated bond blocks formed in activation with oxoallyl moieties serving as dienes and with unsaturated terminal and inner β-chloroallyl moieties as dienophiles.

REFERENCES

1. Razuvaev, G.A., Troitskaya, L.S., and Troitskii, B.B., *J. Polym. Sci., part A-1*, 1971, vol. 9, no. 9, pp. 2673–2688.
2. Kelen, T., Ivan, B., Nagy, T., Nurcsanyi, B., and Kennedy, J.P., *Polym. Bull.*, 1978, vol. 1, no. 2, pp. 79–84.
3. Minsker, K.S., *Chemistry of Chlorine-Containing Polymers: Synthesis, Degradation, Stabilization*, New York: Nova, 2000.
4. Ingold, C.K., *Structure and Mechanism in Organic Chemistry*, Ithaca: Cornell Univ., 1969.
5. Minsker, K.S., Kolesov, S.V., and Petrov, V.V., *Vysokomol. Soedin., Ser. A*, 1983, vol. 25, no. 4, pp. 732–737.
6. Berlin, Al.Al., Minsker, K.S., Kolesov, S.V., and Balandina, N.A., *Vysokomol. Soedin., Ser. B*, 1977, vol. 19, no. 2, pp. 132–134.
7. Lisitskii, V.V., Kolesov, S.V., Gataullin, R.F., and Minsker, K.S., *Zh. Anal. Khim.*, 1978, vol. 33., no. 11, pp. 2202–2207.
8. Kelen, T.J., *Macromol. Sci., Ser. A*, 1978, vol. 12, no. 3, pp. 349–360.
9. Oleinik, E.P., Vasileiskaya, N.S., and Razuvaev, G.A., *Izv. Akad. Nauk SSSR, Ser. Khim.*, 1968, no. 3, pp. 482–486.
10. Troitskii, B.B. and Troitskaya, L.S., *Int. J. Polym. Mater.*, 1998, vol. 41, pp. 285–324.
11. Minsker, K.S., Kolesov, S.V., and Petrov, V.V., *Dokl. Akad. Nauk SSSR*, 1983, vol. 268, no. 3, pp. 632–635.

Russian Journal of Applied Chemistry, Vol. 74, No. 12, 2001, pp. 2106–2110. Translated from Zhurnal Prikladnoi Khimii, Vol. 74, No. 12, 2001, pp. 2046–2050.

MACROMOLECULAR CHEMISTRY AND POLYMERIC MATERIALS

Kinetics of Starch Oxidation in the System Nitrogen(IV) Oxide–Tetrachloromethane

S. M. Butrim, T. D. Bil'dyukevich, and T. L. Yurkshtovich

Research Institute for Physicochemical Problems, Belarussian State University, Minsk, Belarus

Received January 30, 2001

Abstract—Kinetics of potato starch oxidation by dinitrogen tetroxide in CCl_4 was studied as influenced by the oxidant concentration, temperature, and starch to N_2O_4 ratio. The starch oxidation products were analyzed by IR spectroscopy.

Starch is a mixture of polysaccharides, amylopectin and amylose, differing in their degree of polymerization, macromolecular packing, and nature of bonding between the α-*D*-anhydroglucopyranose units. Starch is widely used in textile, food, paper, and other branches of industry. In pharmacology, starch and some of its derivatives (carboxymethyl starch, hydroxyethyl starch, etc.), having low toxicity and good assimilability in the organism, serve exclusively as aids in manufacture of pills, pastes, and suspensions.

At the same time, high reactivity of the polysaccharide components of starch allows purposeful synthesis of starch derivatives and introduction of functionalities, imparting required medicobiological properties to the product, on the basis of modern concepts of processes occurring in living bodies. In this case, it is possible to obtain both substances of bioactive compounds and derivatives suitable for immobilization of various drug preparations with the purpose of their durable action on the basis of starch or its polysaccharides.

Starch oxidation products containing carboxy groups show promise for these purposes. Data are available on oxidation of starch with various oxidizing agents ($KMnO_4$, Br_2, NaClO, etc.) aimed at preparation of starch derivatives capable of forming pasters of a preset viscosity [1–3]. However, the abovementioned oxidants are not selective, and the resulting oxidation products are structurally nonuniform. The most selective oxidants for polysaccharides are periodic acid and dinitrogen tetroxide. The former oxidizes primarily the hydroxy groups at the positions C_2 and C_3 of the elementary unit to aldehyde groups, and the latter, the hydroxy groups at the position C_6 to carboxy groups. The product of oxidation with periodic acid, starch dialdehyde, is used in medicine as a sorbent for ammonia and urea in peroral treatment of patient with uremia [4], and Li and Na salts of starch oxidized with dinitrogen tetroxide demonstrate analgesic, antipyretic, and antidysrhythmic effects [5, 6]. However, oxidation of starch and its polysaccharides by dinitrogen tetroxide is not virtually understood yet [7, 8], which hampers targeted synthesis of carboxy derivatives with fixed degree of oxidation and desired physicochemical and medicobiological properties. Therefore, we studied in this work the effects of various factors on the kinetics of starch oxidation by dinitrogen tetroxide in tetrachloromethane. The starch oxidation products were characterized by IR spectra.

EXPERIMENTAL

As starting materials we used potato starch (amylose content 23.8 wt %, degree of polymerization (DP) 1760, ash content 0.31%, moisture content 12.5%, and acid number 15.5 [9]); CCl_4 (analytically pure grade), and N_2O_4 containing <2 wt % of foreign compounds (recalculated to nitric acid).

Starch was oxidized at 0–18°C in CCl_4 with 5, 10, 20, and 60 wt % N_2O_4 at various starch : N_2O_4 molar ratios. A dispersed weighed portion of starch in a fixed volume of the reaction mixture was allowed to stand at a prescribed temperature for a fixed time. Then oxidized starch was separated from the solution on

1070-4272/01/7412-2106 $25.00 © 2001 MAIK "Nauka/Interperiodica"

a glass filter no. 1, washed with a water/isopropanol mixture (1 : 1 by volume) to neutral reaction, and air-dried at room temperature. The oxidation kinetics was monitored by increase in the carboxy group content, using the Ba acetate method [10]. The selectivity of oxidation was monitored by means of IR spectra recorded in the range 400 – 4000 cm^{-1} in KBr pellets (Specord IR-75 spectrometer). The carbonyl group content was determined by the modified hydroxylamine method [11]. The degree of substitution (DS) with respect to COOH groups was estimated as

$$DS_{COOH} = \frac{162.15C_{COOH}}{4500 - 14C_{COOH}},$$

where 162.15 is the molecular weight of an anhydroglucopyranose unit and C_{COOH} is the carboxy group content (wt %).

Starch oxidation by dinitrogen tetroxide proceeds essentially by the following scheme:

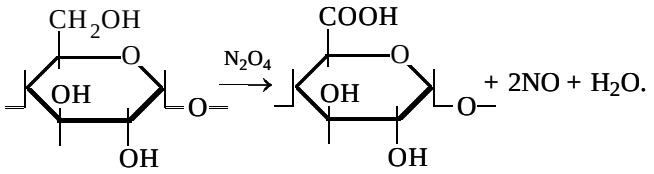

Depending on the reaction conditions, side reactions may occur, which results in insignificant accumulation of carbonyl and nitro ester groups in the polysaccharide macromolecules. The yield of oxidized starch in all cases approaches 100%, i.e., no soluble low-molecular-weight products are formed.

The effect of the starch : N_2O_4 molar ratio at constant oxidant concentration on the starch oxidation rate is demonstrated in Fig. 1a. Raising the amount of the oxidant, all other conditions being equal, provides an increase in both the carboxylation rate and degree of oxidation over the experimental time interval. Raising the amount of the oxidant further, to above 10 mol per mole starch units, provides no additional gain in the indicated parameters. Therefore, all the subsequent kinetic experiments were carried out at a 10-fold excess of N_2O_4 against the stoichiometric amount needed for total oxidation of the primary hydroxy groups to carboxy groups.

With the N_2O_4 concentration increasing from 5 to 20 wt % at constant reactant ratio (1 : 10), the degree of oxidation and the reaction rate constant k grow (Fig. 1b, Table 1), which can be attributed to the activating effect of the oxidant polar molecules initiating rupture of the intermolecular hydrogen bonds.

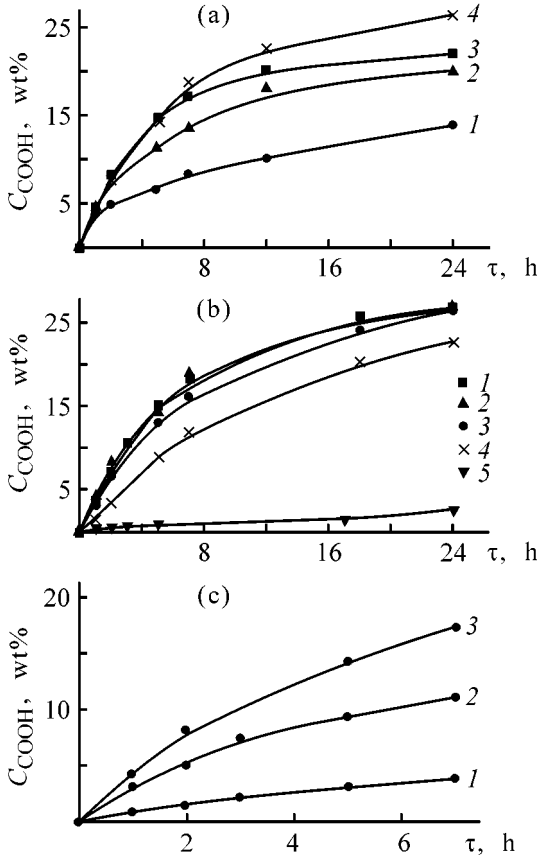

Fig. 1. Carboxy group content C_{COOH} vs. the time τ of starch oxidation by N_2O_4 in CCl_4. (a) N_2O_4 concentration 20 wt %, temperature 18°C. Starch : N_2O_4 molar ratio: (*1*) 1 : 1, (*2*) 1 : 2.5, (*3*) 1 : 5, and (*4*) 1 : 10; (b) Starch : N_2O_4 = 1 : 10, temperature 18°C. CCl_4 concentration (wt %): (*1*) 60, (*2, 5*) 20 (in experiment no. 5 starch was dried to constant weight before oxidation), (*3*) 10, and (*4*) 5; and (c) N_2O_4 concentration 20 wt %, starch : N_2O_4 = 1 : 10. Temperature (°C): (*1*) 0, (*2*) 10, and (*3*) 18.

Penetrating into the starch grains, N_2O_4 promotes diffusion processes so that the reaction becomes quasi-homogeneous. The structural features of starch, responsible for the inaccessibility of a part of the hy-

Table 1. Conditions and kinetic parameters of starch oxidation*

$C_{N_2O_4}$, wt %	T, °C	K, h^{-1}	k, h^{-1}	n
5	18	0.0478	0.142	1.35
10	18	0.129	0.162	1.08
60	18	0.175	0.190	1.03
20**	18	0.170	0.189	1.04
20**	10	0.0891	0.0540	0.87
20**	0	0.0297	0.0144	0.86

* Starch : N_2O_4 molar ratio 1 : 10.

** E_a = 88.2 kJ mol^{-1} is estimated by the Arrhenius equation $k = A\exp(-E_a/RT)$.

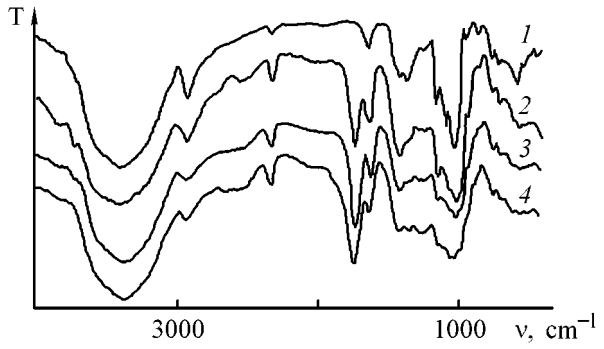

Fig. 2. Infrared spectra of (*1*) native starch and (*2*–*4*) products of oxidation of starch having various carboxy group contents with dinitrogen tetroxide in CCl_4. (T) Transmittance and (ν) wave number. C_{COOH} (wt %): (*2*) 8.4, (*3*) 14.80, and (*4*) 22.13.

droxymethyl groups for the oxidant, have only a slight effect on the reaction, since only the linear polysaccharide of starch, amylose, shows pronounced tendency to crystallize, while the content of the highly branched amorphous amylopectin in starch approaches 80 wt %. As a result, starch grains absorb the oxidizing mixture quite rapidly, which produces their strong swelling, increasing with the N_2O_4 concentration in CCl_4. With the oxidant concentration increasing further, to 60 wt %, the reaction rate constant no longer changes (Table 1), so that the kinetic curves *1* and *2* virtually coincide, and one can say that, under the experimental conditions used, 20 wt % N_2O_4 in CCl_4 provides the maximal rate of reagent diffusion to the active centers.

Note that the moisture content in the initial starch is an important factor influencing the oxidation rate and the maximal content of the COOH groups in 5-carboxy starch (Fig. 1b). The results show that even after a 17-h oxidation of starch dried to constant weight with N_2O_4 in CCl_4, the COOH content is as low as 1.35 wt % (DS_{COOH} = 0.049). Probably, this is due to the fact that hydration water immediately participates in the initial or intermediate oxidation stages and also promotes reagent penetration to active centers of the macromolecules and rapid swelling of the polysaccharide. It is also known [12] that hydration water influences the chain conformation so that even an insignificant decrease in the moisture content initiates a polymorphic transformation of starch B into starch A, in which the linear chains take the place of hydration water stacks, also decreasing the accessibility of the hydroxymethyl groups to the reagent. It was demonstrated in our experiments that dry starch does not swell in the reaction mixture throughout the process, and the observed insignificant formation of carboxy groups is probably due to surface oxidation of the starch grains.

The experimental data (Table 1) were processed using the Erofeev–Kolmogorov topokinetic equation [13].

$$\alpha = 1 - \exp(-K\tau^n),$$

where α is the degree of conversion of starch by a time τ, K is a constant, and n is the kinetic factor.

The reaction order n was determined from the slope of the anamorphoses. The results suggest that the reaction is chemically controlled in most cases (condition $n \geq 1$). Also, the estimated effective activation energy E_a is too high for the diffusion-controlled kinetics to be the case [14].

To obtain the apparent rate constants of starch oxidation, we used the equation proposed by Sakovich [15]:

$$\log k = \frac{1}{n}\log K + \log n,$$

where K and n are the parameters of the Erofeev–Kolmogorov equation, and k is the oxidation rate constant.

Raising the temperature of the reaction mixture from 0 to 18°C results in an abrupt growth in the reaction rate in the correspondence with van't Hoff's law. The estimated n values suggest that, with temperature increasing in the experimental temperature range, the reaction passes from the diffusion to kinetic control. This may be associated to some extent with increasing degree of dissociation of N_2O_4 with the formation of more reactive NO_2.

Formation of carboxy groups can be monitored by the strong band at 1743 cm^{-1} due to C=O stretching vibrations in the IR spectrum of oxidized starch (Fig. 2). Oxidation of the primary hydroxy groups in the position C_6 of the α-*D*-anhydroglucopyranose unit is reflected in decreasing intensity of the band at 1420 cm^{-1} due to CH_2 bending vibrations and also of the band at 928 cm^{-1} due to vibrations of the COH groups at C_6 [16, 17]. Analyzing IR spectra of oxidized cellulose, Ermolenko noted [18] that oxidation is reflected in increasing absorption at 2700–2400 cm^{-1} assigned to stretching vibrations of OH groups of carboxyls strongly associated through hydrogen bonding. Increased absorption in this range is observed in oxidized starch too. The considerable low-frequency shift of this band relative to the band due to vibrations of the hydroxy groups of the anhy-

Table 2. Variations in the carbonyl and carboxy group contents in oxidation of starch with N_2O_4 in CCl_4*

τ, h	Content, wt %		$C3_{COOH}$	C=O/COOH, %	τ, h	Content, wt %		$C3_{COOH}$	C=O/COOH, %
	C=O	COOH				C=O	COOH		
5 wt % N_2O_4 in CCl_4					20 wt % N_2O_4 in CCl_4				
1	0.21	1.31	0.047	16.0	1	0.23	4.28	0.16	5.40
3	0.57	3.47	0.13	16.1	3	0.84	8.16	0.30	10.3
5	0.86	8.85	0.33	9.72	5	1.46	14.18	0.53	10.3
7	1.27	11.83	0.44	10.7	7	1.95	18.87	0.72	10.3
24	2.16	22.69	0.88	9.52	24	3.10	26.48	1.04	11.7

* Starch : N_2O_4 = 1 : 10; T = 18°C.

droglucopyranose ring suggests that the carboxylic hydroxy groups form starch in 5-carboxy new strong hydrogen bonds.

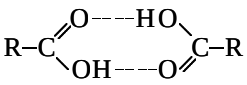

It is not inconceivable that fairly strong intramolecular hydrogen bonds formed by the carboxy and hydroxy groups of the same unit also contribute significantly to the absorption in this range. It should be pointed out that the IR spectra of oxidized starch clearly demonstrate the structure of the complex absorption band at 1200–990 cm^{-1}, including stretching vibrations of C–O and C–C groups and cyclic structures and COH bending vibrations [19]. In the IR spectra of oxidized samples, the intensity of the absorption bands at 1200–1350 cm^{-1} is higher, and that of the bands at 1015 and 1156 cm^{-1}, lower, compared with native starch. With increasing degree of starch oxidation, these differences become more pronounced. It is not improbable that some of the absorption bands in the investigated range can be assigned to vibrations of the secondary and primary hydroxy groups. However, at present thorough interpretation of the spectrum is problematic. One may suggest that the observed evolutions of the spectra can be caused by the fact that, along with the main reaction path (oxidation of primary hydroxy groups at C_6 to carboxy groups), the side reaction also takes place, producing carbonyl and carboxy groups at C_2 and C_3 of the α-*D*-anhydroglucopyranose unit, which is supported by the chemical analysis data (Table 2). In highly oxidized samples, the COOH content was demonstrated to be even higher than the theoretical value of 25.57 wt % corresponding to the case when all the hydroxymethyl groups are oxidized, and the carbonyl group content grows steadily with increasing oxidation time and oxidant concentration.

CONCLUSIONS

(1) It follows from the estimated kinetic factor n and activation energy E_a that the oxidation rate of potato starch in the system N_2O_4–CCl_4 is limited by the chemical stage.

(2) A 20 wt % solution of dinitrogen tetroxide in CCl_4 ensures the maximal rate of starch oxidation, all other conditions being equal. The presence of moisture in starch is the necessary condition for efficient oxidation.

(3) The IR spectra show that the OH groups of the α-*D*-anhydroglucopyranose unit of starch are preferentially oxidized to carboxy groups.

REFERENCES

1. Agoshkova, T.G., Zhushman, A.I., and Luk'yanov, A.B., *Sakh. Prom–st.*, 1984, no. 9, pp. 45–47.
2. Boruch, V.M., *Stärke*, 1985, vol. 37, no. 3, pp. 91–98.
3. Zusman, A.J., *Nahrung*, 1985, vol. 29, no. 9, pp. 905–910.
4. Mehltretter, C.Z., *Stärke*, 1985, vol. 37, no. 9, pp. 294–297.
5. USSR Inventor's Certificate, no. 1 829 373.
6. RF Patent no. 2 045 264.
7. Kaputskii, F.N., Yurkshtovich, T.L., Dranitsa, V.V., *et al., Vestsi Akad. Navuk Belarusi, Ser. Khim. Navuk*, 1996, no. 2, pp. 33–36.
8. Kaputskii, V.E. and Mikhailovskii, Yu.K., *Izv. Vyssh. Uchebn. Zaved., Khim. Khim. Tekhnol.*, 1996, vol. 39, nos. 4–5, pp. 112–16.
9. Richter, M., Augustat, S., and Schierbaum, F., *Ausgewahlte Methoden der Starkechemie*, Leipzig: Fachbuchverlag, 1968.

10. Kaputskii, V.E., Yurkshtovich, T.L., and Balabaeva, M.D., *Vestn. Belorus. Gos. Univ.*, 1978, Ser. II, no. 1, pp. 15–18.
11. Kaverzneva, E.D. and Salova, A.S., *Zh. Anal. Khim.*, 1953, vol. 8, no. 6, pp. 365–368.
12. *Water in Polymers*, Rowland, S.P., Ed., Washington, DC: Am. Chem. Soc., 1980.
13. Bytenskii, B.Ya., Kuznetsova, E.P., and Klenkova, N.I., *Zh. Prikl. Khim.*, 1966, vol. 39, no. 1, pp. 185–193.
14. Panchenko, G.M. and Lebedev, V.P., *Khimicheskaya kinetika i kataliz* (Chemical Kinetics and Catalysis), Moscow: Khimiya, 1985.
15. Sakovich, G.V., *Uchen. Zap. Tomsk. Univ.: Khim.*, 1955, vol. 26, pp. 103–110.
16. Cael, J.J., Koenig, J.L., and Blackwell, J., *Biopolymers*, 1975, vol. 14, pp. 1885–1903.
17. Cael, J.J., Gardner, K.H., Koenig, J.L., and Blackwell, J., *J. Chem. Phys.*, 1975, vol. 62, no. 3, pp. 1145–1153.
18. Ermolenko, I.N., *Spektroskopiya v khimii okislennykh tsellyuloz* (Spectroscopy in Oxidized Cellulose Chemistry), Minsk: Nauka i Tekhnika, 1959.
19. Zhbankov, R.G., *Infrakrasnye spektry i struktura uglevodov* (Infrared Spectra and Structure of Carbohydrates), Minsk: Nauka i Tekhnika, 1972.

Russian Journal of Applied Chemistry, Vol. 74, No. 12, 2001, pp. 2111–2114. Translated from Zhurnal Prikladnoi Khimii, Vol. 74, No. 12, 2001, pp. 2051–2054.

MACROMOLECULAR CHEMISTRY AND POLYMERIC MATERIALS

Degradation Treatment of Butadiene–Styrene Copolymer Wastes

S. S. Nikulin and Yu. A. Sergeev

Voronezh State Forestry Engineering Academy, Voronezh, Russia

Received April 16, 2001

Abstract—Degradation of butadiene–styrene rubber production wastes, coagulums, using a catalytic system based on hydroperoxide, variable-valence metal salt, and alcohol was studied.

Industrial progress inevitably involves formation of growing amounts of wastes and by-products, with a hazard of environmental pollution [1–3]. Therefore, development and commercial implementation of new processes should be primarily based on using environmentally safe systems, with utilization of secondary raw materials, rejects, and production wastes.

One of promising procedures for processing rejected and spent polymeric products and polymeric deposits formed on equipment surfaces in the course of polymer synthesis is degradation treatment. Oxidative degradation of polymers yields lower-molecular-weight products containing functional groups: carbonyl, carboxy, and hydroxy. Classical oxidative degradation of polymers is performed by heating in an organic solvent in the presence of air, organic derivatives of variable-valence metals, and/or compounds generating free radicals [4–7].

Degradation processes are very important and promising as ways of treating polymeric wastes from synthetic rubber industry and of cleaning process equipment to remove polymeric deposits (coagulums). Cleaning the equipment to remove polymeric deposits is a difficult and labor-consuming process, often requiring manual labor and much time. Furthermore, mechanical cleaning does not ensure complete removal of polymeric deposits from the surfaces of reactors and other process equipment and, on the other hand, a problem arises of processing the removed wastes.

In this work, we studied degradation of butadiene–styrene rubbers in the presence of a catalytic system consisting of a radical initiator and a variable-valence metal compound.

We chose peroxides widely used in synthetic rubber industry: isopropylbenzene hydroperoxide and cyclohexylisopropylbenzene hydroperoxide as substances decomposing by the radical mechanism, and iron, cobalt, and nickel chlorides as variable-valence metal compounds.

Degradation experiments were performed with samples of polymeric deposits (coagulums) taken from reactor walls and stirrers and from the surfaces of other equipment used in commercial production of emulsion butadiene–styrene rubbers. These coagulums were virtually insoluble or sparingly soluble in hydrocarbon solvents.

Degradation of polymeric deposits was performed as follows. A vessel was charged with 10 g of coagulum and 130 g of a hydrocarbon solvent, stirring was switched on, and 7.0 g of a 4.0% solution of a variable-valence metal salt in 1-butanol and a hydroperoxide were added in succession. The reaction was performed in contact with atmospheric oxygen at a prescribed temperature for a prescribed time. The degradation progress was monitored gravimetrically (by the weight loss of the solid residue in the hydrocarbon phase), by variation of the intrinsic viscosity $[\eta]$, and visually.

In the first stage of our study, we examined the influence of the hydroperoxide concentration on degradation treatment of coagulum of SKS-30 ARK rubber. As seen from Table 1, the optimal concentration of isopropylbenzene hydroperoxide is 0.6–6.0 wt % based on coagulum. At higher hydroperoxide concentrations, the intrinsic viscosity grows, suggesting the occurrence of secondary cross-linking, although dissolution of the coagulum is complete under these conditions too.

The influence of temperature on degradation of SKS-30 ARK rubber in the presence of the chosen catalytic system is illustrated in Fig. 1a. It is seen that the optimal temperature is 50–100°C. At 40°C,

1070-4272/01/7412-2111 $25.00 © 2001 MAIK "Nauka/Interperiodica"

Table 1. Influence of isopropylbenzene hydroperoxide concentration *C* on degradation of the coagulum of SKS-30 ARK rubber*

C, wt %	Dissolution, %	[η], dl g^{-1}
0.1	59.5–62.4	1.91–1.99
0.2	72.2–77.8	1.18–1.23
0.6	100	0.52–0.57
2.0	100	0.43–0.48
6.0	100	0.41–0.45
12.0	100	0.42–0.47
15.0	100	0.49–0.54

* The process was performed in toluene at 60°C for 3 h in the presence of $FeCl_3$.

the degradation rate and the degree of coagulum dissolution decrease. Temperatures above 100°C are also unsuitable, because of the occurrence of secondary cross-linking, decreasing the solubility of the coagulum and increasing the viscosity of the solutions. The intrinsic viscosity is the lowest when the degradation is performed in the range 50–80°C, and this range should be considered the optimal.

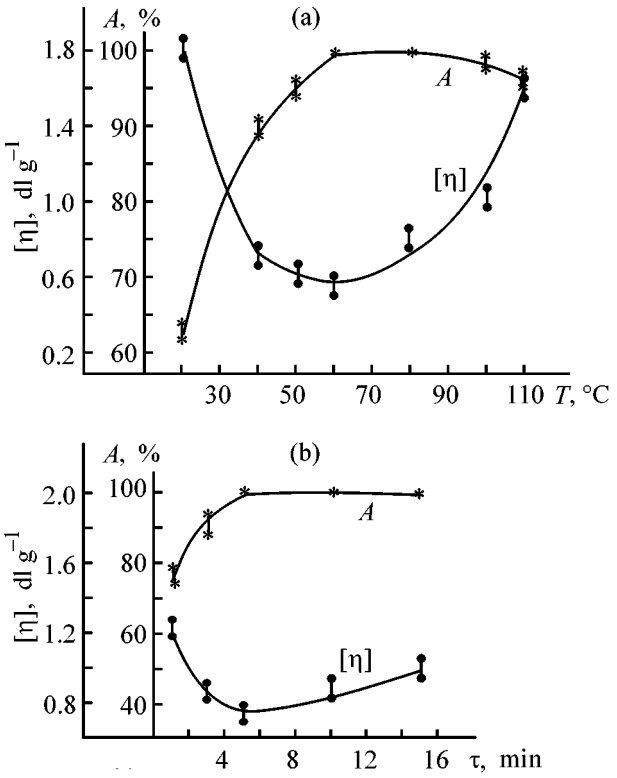

Fig. 1. Effects of (a) temperature *T* and (b) time τ of degradation on the instrinsic viscosity [η] and degree of dissolution *A* of the coagulum of SKS-30 ARK rubber. Solvent toluene; 2.0 wt % isopropylbenzene hydroperoxide based on coagulum; $FeCl_3$; (a) 5 h; (b) 80°C.

One of the most important parameters of degradation is the process time. As seen from Fig. 1b, the optimal time is 5 h. Longer treatment results in higher intrinsic viscosity, which may be due to secondary cross-linking. The viscosity of the resulting polymer solutions is a very important process parameter, because high viscosity prevents transport of the solutions through pipelines after equipment cleaning.

The process of oxidative degradation of polymeric chains can be represented as follows.

Preliminarily dissolution in butanol of a variable-valence metal salt, followed by addition of this solution to the system under treatment, ensures fine dispersion of the salt in the bulk of the system. The first stage of the reaction is, most probably, reduction of Fe(III) ions to Fe(II). The possible reductants are mercaptans, phenol and its derivatives, and also polybutadiene units [4] present in the coagulum of the rubber produced by emulsion (co)polymerization:

$$\sim CH_2{-}CH{=}CH{-}CH_2\sim + Fe^{3+}$$
$$\rightarrow \sim\dot{C}H{-}CH{=}CH{-}CH_2\sim + Fe^{2+}.$$

Oxidative degradation of butadiene–styrene rubber may occur by several pathways, namely, with participation of the redox system in which the variable-valence metal (Fe, Co, Ni, etc.) promotes, on the one hand, oxidative degradation of the polymers in the presence of oxygen and, on the other, decomposition of the hydroperoxide:

$$R{-}OOH + Fe^{2+} \rightarrow RO^{\cdot} + HO^{-} + Fe^{3+}.$$

Oxidative degradation of the polymeric chains of the butadiene–styrene coagulum can be represented as oxidative degradation of butadiene blocks:

$$\sim CH_2{-}CH{=}CH{-}CH_2{-}CH_2{-}CH{=}CH{-}CH_2\sim + RO^{\cdot}$$
$$\rightarrow \sim CH_2{-}CH{=}CH{-}\dot{C}H{-}CH_2{-}CH{=}CH{-}CH_2\sim + ROH,$$

$$\sim CH_2{-}CH{=}CH{-}\dot{C}H{-}CH_2{-}CH{=}CH{-}CH_2\sim + O_2 + RH$$
$$\rightarrow \sim CH_2{-}CH{=}CH{-}\underset{\displaystyle OOH}{\underset{|}{CH}}{-}CH_2{-}CH{=}CH{-}CH_2\sim,$$

$$\sim CH_2{-}CH{=}CH{-}\underset{\displaystyle OOH}{\underset{|}{CH}}{-}CH_2{-}CH{=}CH{-}CH_2\sim$$
$$\rightarrow \sim CH_2{-}CH{=}CH{-}CHO + \underset{\displaystyle OH}{\underset{|}{CH_2}}{-}CH{=}CH{-}CH_2\sim.$$

Secondary cross-linking of the resulting low-molecular-weight polymeric chains can occur as follows:

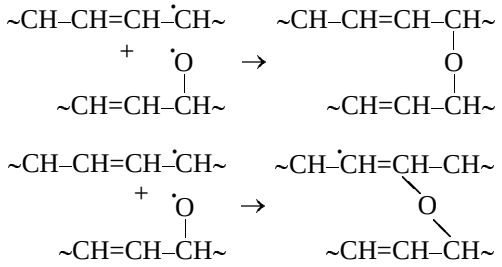

Degradation of the coagulum from production of BS-65 (A) butadiene–styrene latex was studied with catalytic systems containing Fe(III), Co(II) and Ni(II) chlorides (in 1-butanol) as variable-valence metal salts. The influence of the kind of the catalytic system and reaction time on degradation of the BS-65 (A) coagulum is illustrated in Fig. 2. It is seen that a combination of isopropylbenzene hydroperoxide with a butanol solution of iron, cobalt, and nickel chlorides facilitates degradation of coagulums with high content of styrene units. With these catalytic systems, dissolution of the coagulum is virtually complete in 35 h.

Similar results were obtained with other radical initiators, e.g., cyclohexylisopropylbenzene hydroperoxide, and with other solvents [xylene, Nefras S-4-150/200 (petroleum solvent based on butylbenzene), white spirit]. As solvents for variable-valence metal salts, some other alcohols (e.g., ethanol, propanol) can be used along with 1-butanol. However, low-boiling alcohols are removed from the system at elevated temperatures, which results in agglomeration of the metal salts and negatively affects the degradation process.

Thermal oxidative degradation is accompanied by breakdown of gel structures and decrease in the molecular weight of the polymers, so that solutions of low-molecular-weight polymers can be obtained. Such solutions prepared from solid rubber production wastes can be used for modification of bitumens, production of film-forming substances, mastics, and sealants, protective treatment of wood items, etc.

For example, low-molecular-weight copolymers can be used in production of composite drying oil. Its optimal composition is as follows (wt %): polydiene-M (copolymer based on styrene and unsaturated compounds of toluene distillation bottoms from production of butadiene rubber; for synthesis description, see [8–11]; the product is commercially available) 44.0, degraded butadiene–styrene rubber 5.0, siccative 6.0, and solvent (Nefras S-4-150/200) 45. Coatings obtained from this composite drying oil exhibit satisfactory properties (Table 2), and this material can be used in production of paint-and-varnish materials.

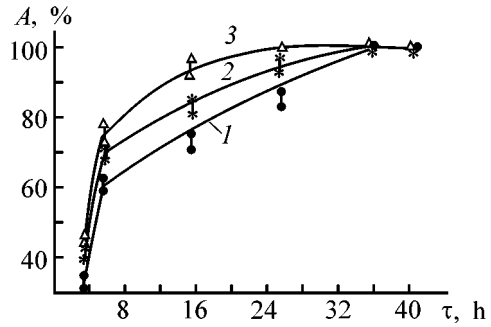

Fig. 2. Degree of dissolution *A* of BS-65 (A) coagulum vs. degradation time τ. 90°C, solvent toluene, 2.0 wt % isopropylbenzene hydroperoxide based on coagulum. (*1*) $FeCl_3$, (*2*) $NiCl_2$, and (*3*) $CoCl_2$.

The hydrocarbon solution of degraded SKS-30 ARK rubber can be used for preparing a cold-curable two-component sealant which shows promise for industry and civil engineering, and also for sealing airport pavement seams. To prepare the first component, low-molecular-weight polyethylene and indene–coumarone resin are dissolved at 95–100°C with continuous stirring in a toluene solution of degraded SKS-30 ARK rubber, which is followed by distillation of the solvent to 60–70 wt % content of the nonvolatile fraction and addition of the antioxidant.

As the cross-linking component we used polyisocyanates (3.0–5.0 wt %).

The major advantage of this sealant is the absence of shrinkage, which is due to the chemical reaction of the isocyanate groups with the hydroxy and carbonyl groups:

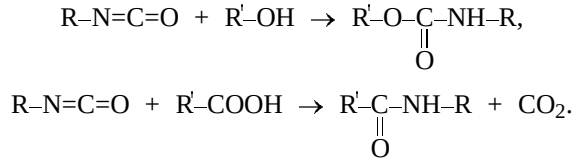

Carbon dioxide released in the reaction imparts high porosity to the sealant, eliminating any shrinkage.

Table 2. Properties of coatings based on composite drying oil

Parameter	Testing results
Color on iodometric scale (IMS units)	700–800
Viscosity by VZ-246 viscometer, s	25–28
Bending strength, mm	1
Hardness by ME-3	0.1
Time of drying to degree of dryness 3, h	24

The performance characteristics of the sealant are as follows:

Working life after component mixing, h	1.5
Curing time, h	24
Cohesion strength, MPa	0.6–0.7
Relative elongation at cohesion break, %	250–270
Adhesion to concrete, MPa	0.5
Brittle point, °C	–60

CONCLUSIONS

(1) The optimal concentration of the hydroperoxide is 0.6–6.0 wt % based on coagulum, and the optimal temperature, 50–100°C.

(2) The degradation rate depends on the styrene content in the coagulum. The higher the styrene content, the longer the process.

(3) It is appropriate to perform degradation of high-styrene coagulums on catalytic systems containing Co(II) or Ni(II) salts; in this case, the degradation time is shorter.

(4) The resulting hydrocarbon solutions of low-molecular-weight copolymers can find wide use in production of paint-and-varnish materials, mastics, sealants, and also as components of polymeric-concrete and asphalt formulations.

REFERENCES

1. Nikulin, S.S., Shein, V.S., Zlotskii, S.S., *et al.*, *Otkhody i pobochnye produkty neftekhimicheskikh proizvodstv – syr'e dlya organicheskogo sinteza* (Petrochemical Wastes and By-Products as a Raw Material for Organic Synthesis), Moscow: Khimiya, 1989.
2. Ravich, B.M., Okladnikov, V.A., Lygach, V.N., and Menkovskii, M.A., *Kompleksnoe ispol'zovanie syr'ya i otkhodov* (Integrated Utilization of Raw Materials and Wastes), Moscow: Khimiya, 1988.
3. Shein, V.S., Ermakov, V.I., and Norkhin, Yu.G., *Obezvrezhivanie i utilizatsiya vybrosov i otkhodov pri proizvodstve i pererabotke elastomerov* (Rendering Harmless and Utilization of Rejects and Wastes in Production and Processing of Elastomers), Moscow: Khimiya, 1987.
4. Lemaev, N.V. and Zaboristov, V.N., *Destruktivnye metody pererabotki otkhodov elastomerov* (Degradation Processing of Elastomer Wastes), Moscow: TsNIITEneftekhim, 1985.
5. Sirazetdinova, R.D., Bazhenov, Yu.P., Pronyaev, V.N., and Vasil'ev, V.A., *Proizv. Ispol'z. Elastom.*, 1999, no. 1, pp. 10–11.
6. Pchelintsev, V.V., *Termookislitel'naya destruktsiya dienovykh kauchukov* (Thermal Oxidative Degradation of Diene Rubbers), Moscow: TsNIITEneftekhim, 1986.
7. Grassie, N. and Scott, G., *Polymer Degradation and Stabilisation*, Cambridge: Cambridge Univ., 1985.
8. Nikulin, S.S., Filimonova, O.N., Sergeev, Yu.A., *et al.*, *Proizv. Ispol'z. Elastom.*, 2000, no. 1, pp. 10–14.
9. Nikulin, S.S., Dmitrenkov, A.I., Sakhokiya, I.A., and Sergeev, Yu.A., *Proizv. Ispol'z. Elastom.*, 2000, no. 2, pp. 7–12.
10. Nikulin, S.S. and Filimonova, O.N., *Zh. Prikl. Khim.*, 2000, vol. 73, no. 1, pp. 148–152.
11. Nikulin, S.S., Filimonova, O.N., Dmitrenkov, A.I., and Sakhokiya, I.A., *Zh. Prikl. Khim.*, 2000, vol. 73, no. 9, pp. 1565–1567.

Russian Journal of Applied Chemistry, Vol. 74, No. 12, 2001, pp. 2115–2118. Translated from Zhurnal Prikladnoi Khimii, Vol. 74, No. 12, 2001, pp. 2055–2058.

CHEMISTRY OF FOSSIL FUEL

Molecular Oxygen and Oxygen-Containing Compounds in Kerosene Fractions of West-Siberian Oils

O. Yu. Begak and A. M. Syroezhko

Mendeleev Russian Research Institute of Metrology, State Unitary Enterprise, St. Petersburg, Russia
St. Petersburg State Technological Institute, St. Petersburg, Russia

Received April 28, 2001

Abstract—Oxygen-containing compounds that are present in straight-run kerosenes produced by the Kinef, Ltd. were identified by chromato-mass spectrometry.

The presence of olefins and of oxygen-containing and other heteroatomic compounds in gasolines, kerosenes, and diesel fuels, as a rule, deteriorates their stability in storage and use. At the same time, some oxygen-containing compounds (e.g., phenols) play a positive role, behaving as antioxidants. Some sulfur- and nitrogen-containing compounds present in these fuels (especially in kerosenes and diesel fuels) also play a positive role as polyfunctional additives (antiwear, antiscuff, dispersing, etc.).

By now, no qualitative and quantitative data are available on the content of molecular oxygen and composition of oxygen-containing compounds in jet fuels (kerosenes). Obtaining such data was the goal of this work.

EXPERIMENTAL

Straight-run kerosene (TS-1) samples (nos. 1, 2) were used.[1] Molecular oxygen dissolved in these fractions of TS-1 fuel (sample nos. 1, 2) was determined chromatographically [1]. Hydroperoxides in kerosene fractions were determined by iodometric titration [2, 3]. Oxygen-containing compounds were concentrated with a Diapak silica gel cartridge (BiokhimMak, Moscow).

The cartridge was washed with *n*-hexane, and 100 ml of a kerosene fraction to be analyzed was passed. Then the cartridge was repeatedly washed with *n*-hexane and dried in a nitrogen flow. The extracted oxygen-containing compounds were eluted from the cartridge with 5 ml of methanol. The methanol extract was evaporated in a nitrogen flow to a volume of 1 ml and analyzed by chromato-mass spectrometry.

A mass-spectrometric analysis of the extracts of TS-1 kerosene fractions was performed with an MD 800 device (Fisons, USA). To indetify compounds present in these extracts and giving resolved or partially overlapping peaks in the chromatograms, we used the MassLab and AMDIS software, with the electronic libraries of the mass spectra. The programs provide for calculation of the direct and inverse parameters of similarity of the experimental and reference mass specrta. When identifying individual compounds, we took into account the general similarity parameters of the mass spectra of the detected compounds and the reference mass spectra, the identity of the molecular peaks in the spectra being compared, and the similarity of the relative intensities of the major peaks in the mass spectra being compared (difference of no more than 20–30% was admissible), and also the results of running the expert modulus of the AMDIS program. These criteria allow identification of individual compounds or group identification.

The content of dissolved molecular oxygen was 1.7×10^{-3} M in sample no. 1 and 1.9×10^{-3} M in

[1] Straight-run samples of kerosene (TS-1) produced by the Kirishinefteorgsintez, Ltd. from a commercial mixture of West-Siberian crude oils were taken May 24, 2001, from the AT-6 unit. Sample no. 1 was the process feed before the storage tank of the AT-6 unit, and sample no. 2, the process feed after this tank, at the inlet of the feed pump.

1070-4272/01/7412-2115 $25.00 © 2001 MAIK "Nauka/Interperiodica"

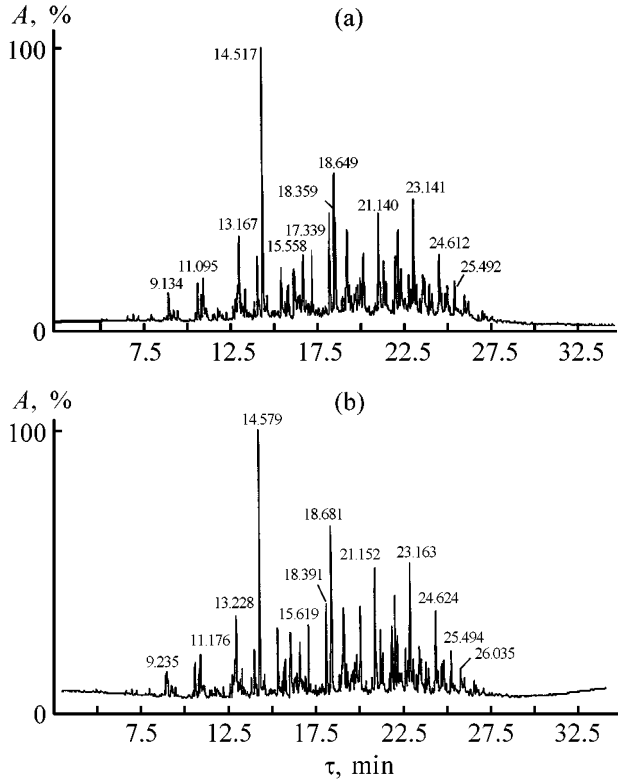

Fig. 1. Comparison of chromatograms of kerosene extracts. Sample nos. (a) 1 and (b) 2. (*A*) Signal intensity and (τ) retention time; the same for Fig. 2.

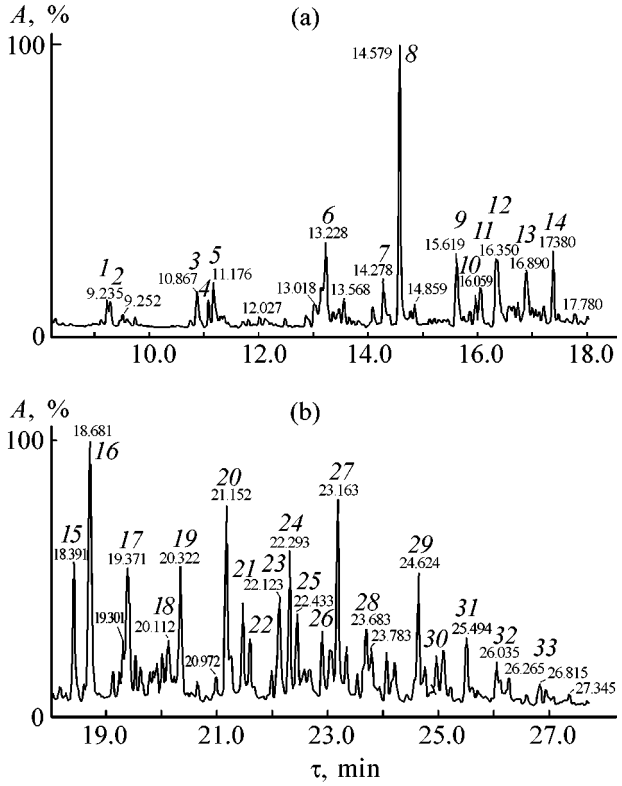

Fig. 2. (a) Initial and (b) final sections of a chromatogram of the kerosene extract. For peak identification, see Table 1.

sample no. 2. This value is well consistent with the volume fraction of oxygen in components of gasolines produced by Kinef (2.3–4.6% [4]) and are somewhat higher than the corresponding values for the diesel fuel (1.6–4.1%). As shown by special experiments, the solubility of oxygen in the samples under consideration was 5.1% (2.3×10^{-3} M) in the case of their saturation with air. Thus, in the course of oil refining on AT-6, the kerosine fractions are not saturated with oxygen. We found that the limiting solubility of molecular oxygen increases in the order diesel fuel (4.4%) < kerosene (5.1%) < benzine (6.5%).

The concentration of hydroperoxides in sample nos. 1 and 2 was as low as 1.3×10^{-4} and 5×10^{-5} M, respectively, i.e., the extent of hydrocarbon oxidation in the examined kerosene fractions is very low.

The total chromatograms of the kerosene extracts are shown in Fig. 1, and the initial and final sections of a chromatogram of the extracts of oxygen-containing and other heteroatomic compounds, in Figs. 2a and 2b.

The identified heteroorganic (mainly oxygen-containing) compounds corresponding to the major peaks in the chromatograms of the extracts of sample nos. 1 and 2 are shown in Fig. 1. It is seen that the kerosene contains a wide variety of organic compounds C_7–C_{12}: paraffinic and naphthenic alcohols and ketones, aromatic alcohols (alkylphenols), and one of dialkylpyridines. Identification of individual compounds is not always possible because of the close similarity of the mass spectra of structurally similar compounds (isomers). Therefore, many peaks are assigned in Table 1 not to a definite compound, but to unknown representative(s) of a certain group of isomers.

It should be noted that carboxylic acids were not detected in noticeable amounts. On the whole, the content of various groups of oxygen-containing compounds in kerosene decreases in the order aromatic > aliphatic > naphthenic compounds.

This relation differs from that observed in benzines and diesel fuels. The content of oxygen-containing derivatives of aliphatic and aromatic hydrocarbons in kerosenes is intermediate between those in benzines and diesel fuels (Table 2).

The total content of oxygen-containing compounds in kerosenes (Table 1) is low and varies within relatively narrow concentration limits: 0.0015–0.003%. This parameter is approximately an order of mag-

Table 1. Content of heteroorganic compounds in kerosenes

Peak no. in the chromatogram	Compound*	Empirical formula	Content $c \times 10^5$, wt %, in indicated sample	
			no. 1	no. 2
1	Methylcyclohexanol	$C_7H_{14}O$	1.6	2.7
2	2-Heptanone	$C_7H_{14}O$	1.5	3.0
3	2-Methyl-2-heptanol or 2,5-dimethylhexanol	$C_8H_{18}O$	2.7	4.9
4	Naphthenic alcohol or aliphatic ketone	$C_8H_{16}O$	1.4	2.7
5	2-Methyl-2-heptanone	$C_8H_{16}O$	3.5	6.9
6	Naphthenic alcohol	$C_8H_{16}O$	6.1	13
7	Methylethylpyridine	$C_8H_{11}N$	4.6	6.2
8	2-Ethyl-1-hexanol	$C_8H_{18}O$	18	34
9	*o*-Cresol	C_7H_8O	4.2	10
10	Naphthenic ketone	$C_9H_{16}O$	1.4	2.8
11	Naphthenic alcohol or aliphatic ketone	$C_9H_{18}O$	2.6	5.2
12	*m*- or *p*-Cresol	C_7H_8O	7.0	16
13	Aliphatic alcohol	$C_9H_{20}O$	4.2	5.2
14	Cyclohexylpropanone	$C_9H_{16}O$	3.8	8.4
15	Aliphatic alcohol	$C_9H_{20}O$	7.5	12
16	Xylenol**	$C_8H_{10}O$	14	33
17	Xylenol**	$C_8H_{10}O$	4.4	7.5
18	Xylenol**	$C_8H_{10}O$	2.1	5.1
19	C_3-Alkylphenol***	$C_9H_{12}O$	5.9	14
20	C_3-Alkylphenol***	$C_9H_{12}O$	7.6	17
21	C_3-Alkylphenol***	$C_9H_{12}O$	3.7	7.1
22	C_3-Alkylphenol***	$C_9H_{12}O$	2.2	3.8
23	C_3-Alkylphenol***	$C_9H_{12}O$	5.9	13
24	C_3-Alkylphenol***	$C_9H_{12}O$	5.5	12
25	C_3-Alkylphenol***	$C_9H_{12}O$	2.9	6.4
26	C_4-Alkylphenol****	$C_{10}H_{14}O$	2.5	5.7
27	C_3-Alkylphenol***	$C_9H_{12}O$	8.3	16
28	C_4-Alkylphenol****	$C_{10}H_{14}O$	4.07	9.56
29	C_5-Alkylphenol*****	$C_{11}H_{16}O$	5.6	12
30	C_5-Alkylphenol*****	$C_{11}H_{16}O$	3.1	5.8
31	C_5-Alkylphenol*****	$C_{11}H_{16}O$	2.8	6.5
32	C_6-Alkylphenol******	$C_{12}H_{18}O$	1.3	3.6
33	C_5-Alkylphenol*****	$C_{11}H_{16}O$	0.93	2.2

* By C_n-phenols are meant phenols containing alkyl substituents with n carbon atoms (in total).

** One of isomeric dimethylphenols.

*** One of isomeric trimethyl-, methylethyl-, propyl-, and isopropylphenols.

**** One of isomeric tetramethyl-, dimethylethyl-, methylpropyl-, etc., phenols.

***** One of isomeric pentamethyl-, trimethylethyl-, dimethylpropyl-, etc., phenols.

****** One of isomeric tetramethylethyl-, trimethylpropyl-, etc., phenols.

Table 2. Content of oxygen-containing compounds of various groups in petroleum products

Group composition	Relative content, wt %			Group composition	Relative content, wt %		
	benzine [1–3]	diesel fuel [4]	kerosene		benzine [1–3]	diesel fuel [4]	kerosene
Aliphatic	50–58	1–3	21–24	Aromatic	28–35	50–98	61–66
Naphthenic	15	0–48	11	Sum	100	100	100

nitude higher than that observed for diesel fuels [$(0.05–6.5) \times 10^{-4}$%] but similar to that observed in gasoline components in the course of their production {$(2–4) \times 10^{-3}$% [4]} and in A-76 gasoline "in the initial state before storage" (the equivalent parameter, content of "acetone-soluble resins," is 1.9 mg ml^{-1}, or 0.003% [5]).

Thus, data on the quantitative content of identified oxygen-containing organic compounds and on their qualitative composition (absence of acids), combined with the results obtained in determining molecular oxygen and peroxides, correspond to certain low ("natural") extent of oxidation of petroleum hydrocarbon components.

CONCLUSIONS

(1) A total of 33 organic oxygen-containing compounds C_7–C_{12} were identified in kerosene by GC–MS, including paraffinic and cycloparaffinic alcohols and ketones, alkylphenols with several alkyl substituents (up to C_6 in total), and one of dialkylpyridines. No carboxylic acids were detected.

(2) The content of oxygen-containing compounds in kerosenes under consideration decreases in the order aromatic > aliphatic > cycloaliphatic (naphthenic) compounds. The total content of these compounds does not exceed 10^{-3}%.

REFERENCES

1. Petsev, N. and Kotsev, N., *Nar"chnik po gazova khromatografiya* (Handbook on Gas Chromatography), Sofia: Nauka i Izkustvo, 1984.
2. Becker, H., Berge, W., Domschke, G., *et al.*, *Organikum. Organisch-chemisches Grundpraktikum*, Berlin: Wissenschaften, 1976.
3. *Khimichskaya entsiklopediya* (Chemical Encyclopedia), Knunyants, I.L., Ed., Moscow: Bol'shaya Ross. Entsiklopediya, 1992, vol. 3, p. 493.
4. Begak, O.Yu., Varshavskii, O.M., Zalishchevskii, G.D., *et al.*, *Sbornik nauchnykh trudov OOO PO "Kinef" za 1998–2000 gg.* (Coll. of Scientific Works of Kinef Production Association, Limited Liability Company, Performed in 1998–2000), Moscow: TsNIITEneftekhim, 2001, pp. 25–39.
5. Golubeva, I.A., Klinaeva, E.V., Kelarev, V.I., *et al.*, *Khim. Tekhnol. Topl. Masel*, 1997, no. 5, pp. 38–40.

Russian Journal of Applied Chemistry, Vol. 74, No. 12, 2001, pp. 2119–2121. Translated from Zhurnal Prikladnoi Khimii, Vol. 74, No. 12, 2001, pp. 2059–2061.

BRIEF COMMUNICATIONS

Kinetics of Reaction of Aluminum Hydroxide with Dimethyl Hydrogen Phosphite in Nitrobenzene

S. N. Bondarenko, T. V. Khokhlova, O. I. Tuzhikov, M. P. Lyabin, and S. M. Moskvichev

Volgograd State Technical University, Volgograd, Russia

Received May 22, 2001

Abstract—The kinetics of the reaction of aluminum hydroxide with dimethyl hydrogen phosphite in nitrobenzene was studied.

Polymeric composite materials based on epoxy oligomers are widely used in electric devices, TV and radio equipment, building, mechanical engineering, and auto repair. Their substantial disadvantage is high combustibility. It can be decreased by introducing a fireproofing compound, aluminum hydroxide. Its use is preferable, because it forms no toxic products at high temperatures, decreases the toxicity of the products of the polymer thermal decomposition, and reduces smoke formation.

However, introduction of aluminum hydroxide deteriorates physicomechanical characteristics of polymers. We showed in [1] that this disadvantage can be diminished by modification of aluminum hydroxide (**I**) with dimethyl hydrogen phosphite (**II**). Furthermore, the fire-extinguishing properties of the novel fireproofing compound are thus enhanced:

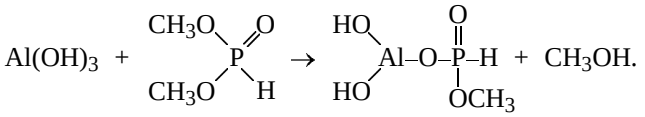

I **II**

In this study the kinetics of this reaction was examined.

EXPERIMENTAL

The reaction was performed in nitrobenzene at temperatures in the range 126–146°C, maintained to within ±0.2°C with UTU-2 ultrathermostat. The mixture was continuously stirred with removal of the methanol formed. The reaction course was monitored potentiometrically by the change of the phosphite concentration. The reaction was stopped by cooling to 2–5°C.

Under experimental conditions, when compound **I** occurs mainly in the solid phase, its concentration in solution is constant and equal to the solubility. Therefore, the actual order of the reaction with respect to **I** cannot be determined. The apparent reaction order with respect to **I** is zero. In the experiments in

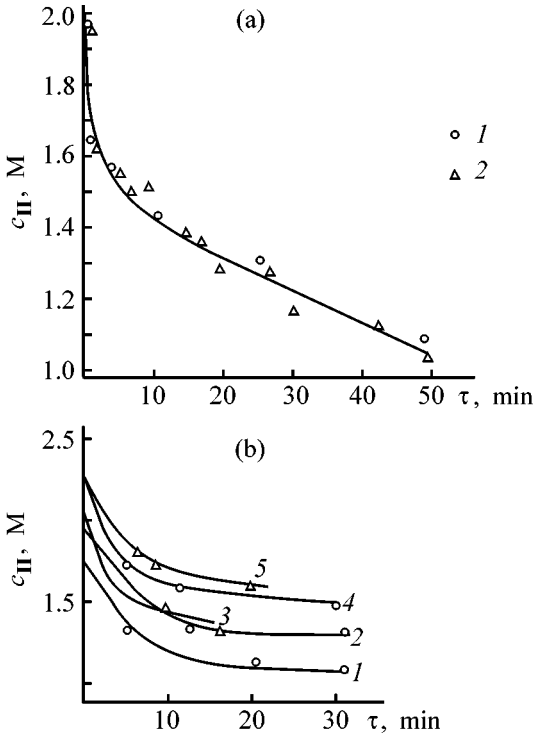

Fig. 1. Concentration of dimetyl hydrogen phosphite **II** c_{II} vs. time τ in the reaction with aluminum hydroxide **I** in nitrobenzene. (a) $c_I^0 = c_{II}^0$; (b) c_{II}^0 (M): (*1*) 1.717, (*2*) 1.972, (*3*) 1.991, (*4*) 2.245, and (*5*) 2.310. $v_I : v_{II}$: (a) (*1*) 1.0 and (*2*) 2.0; (b) (*1*) 1.125, (*2*) 1.0, (*3*) 0.717, (*4*) 0.883, and (*5*) 0.853.

1070-4272/01/7412-2119 $25.00 © 2001 MAIK "Nauka/Interperiodica"

Kinetic parameters of the reaction of aluminum hydroxide **I** with dimethylphosphite **II** in nitrobenzene*

Amounts of reagent, mol		Molar ratio **I** : **II**	$c^0_{\mathbf{II}}$, M	T, °C	$V_0 \times 10^{-3}$, mol l^{-1} s^{-1}	k_{ap}, s^{-1}
I	**II**					
Determination of the reaction order with respect to Dimethyl hydrogen phosphite						
0.099	0.088	1.125	1.717	146	0.001415	7.8126×10^{-4}
0.100	0.100	1.000	1.972	146	0.001527	
0.099	0.112	0.883	2.245	146	0.001810	
0.099	0.116	0.853	2.310	146	0.001948	
0.071	0.099	0.717	1.991	146	0.001691	
Determination of the total reaction order						
0.100	0.100	1.000	1.9724	146	0.001527	7.9305×10^{-4}
0.070	0.070	1.000	1.4265	146	0.001295	
0.050	0.050	1.000	0.9880	146	0.007421	
Confirmation of the total reaction order						
0.100	0.100	1.000	1.9800	136	0.00871	4.5543×10^{-4}
0.100	0.100	1.000	1.9970	126	0.006125	2.7695×10^{-4}

* All calculations were performed by the least-squares method; $c^0_{\mathbf{II}}$ is the initial concentration of **II**, V_0 the initial reaction rate, and k_{ap} the apparent reaction rate constant.

which the initial concentrations of **II** and the amount of the diluent were constant and the amount of **I** was varied, the kinetic dependences were virtually the same (deviations were within the experimental error) (Fig. 1a). This confirms the apparent zero order with respect to **I** and shows that the reaction proceeds in the solution bulk, rather than on the surface of aluminum hydroxide. Otherwise, larger amounts of **I** in the reaction mixture and hence the increased contact surface area would accelerate the reaction.

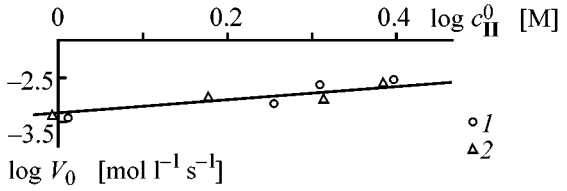

Fig. 2. Dependence $\log V_0$–$\log c^0_{\mathbf{II}}$ plot for the reaction between aluminum hydroxide **I** and dimethyl hydrogen phosphite **II**: (*1*) determination of the reaction order with respect to **II** and (*2*) determination of the total reaction order.

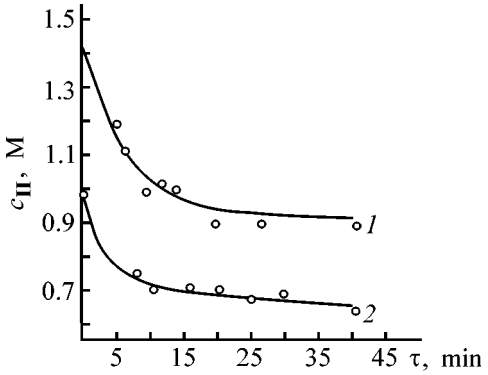

Fig. 3. Variation with time τ of dimethyl hydrogen phosphite **II** concentration $c_{\mathbf{II}}$ in the reaction with aluminum hydroxide **I** in nitrobenzene at the equimolar ratio of reactants (146°C). $c^0_{\mathbf{II}}$ (M): (*1*) 1.4265 and (*2*) 0.988.

To determine the reaction order with respect to **II**, we measured the initial reaction rates at the same amounts of **I** and the initial concentrations of **II** varied in the 1.717–2.31 M range (see table and Fig. 1b).

The partial reaction order with respect to **II** was determined from the $\log V_0 = f(\log c^0_{\mathbf{II}})$ plot (Fig. 2). As seen from Fig. 2, the slope of the straight line is equal to 1, i.e., the reaction is first-order with respect to **II**. Taking into account the pseudo-zero order with respect to **I**, the total reaction order is also close to unity. The linear equation

$$\log V_0 = \log k + n_1 \log c_{\mathbf{I}} + n_2 \log c^0_{\mathbf{II}}$$

[here k is the reaction rate constant and n_1 and n_2 are the orders with respect to **I** and **II**, respectively (under the experimental conditions $n_1 \log c_{\mathbf{I}} = \text{const}$)] takes the form

$$\log V_0 = (-3.1072 \pm 0.03898) + (1.083 \pm 0.124) \log c^0_{\mathbf{II}}.$$

It follows from this equation that more precise value of the apparent reaction order with respect to **II** n_2 is 1.08 ± 0.12.

To confirm the obtained value of the total reaction order, we performed experiments in which the initial concentration of **II** was varied, keeping the equimolar ratio of reactants in the reaction mixture constant (see table and Fig. 3).

For the set of the initial concentrations of **II**, we obtain the dependence

$$\log V_0 = \log k_{ap} + n\log c^0_{\mathbf{II}}$$
$$= (-3.1007 \pm 0.055) + (1.053 \pm 0.28)\log c^0_{\mathbf{II}}$$

characteristic of first-order reactions. From this dependence, the reaction rate constant (which is probably a function of the concentration of **I** in the liquid phase) was determined. The reaction rate is described by the Arrhenius equation: the dependence $\log k_{ap} = f(1/T)$ is linear

$$\log k_{ap} = \log A + \log \alpha \times 10^3 \times 1/T$$
$$= (5.277 \pm 0.878) + (-3.525 \pm 0.561) \times 10^3 \times 1/T.$$

The activation energy E_a found from this equation in the Arrhenius coordinates is 67.7 kJ mol^{-1}. The activation entropy calculated by Eyring's equation $\Delta S^{\neq}$ is –154.6 J mol^{-1}deg^{-1}, the activation free energy $\Delta G^{\neq}$ is 127.2 kJ mol^{-1}, and the enthalpy $\Delta H^{\neq}$ is 64.2 kJ mol^{-1}. The relatively small E_a and $\Delta H^{\neq}$ suggest that the reaction between **I** and **II** involves formation of a highly structurized intermediate.

CONCLUSIONS

(1) The reaction of aluminum hydroxide with dimethyl hydrogen phosphite in nitrobenzene is first-order with respect to dimethyl hydrogen phosphite, and the total reaction order is close to unity.

(2) The reaction proceeds in solution, rather than on the aluminum hydroxide surface.

(3) The calculated activation parameters of the reaction suggest the formation of a highly structurized intermediate.

REFERENCES

1. Tuzhkov, O.I., Bondarenko, S.N., Khokhlova, T.V., *et al.*, in *Sbornik Nauchnykh Trudov* (Collection of Science Papers), Volgograd: Volgograd. Gos. Tekh. Univ., 1993, pp. 86–90.
2. Emanuel', N.M. and Knorre, D.G., *Kurs khimicheskoi kinetiki* (Course of Chemical Kinetics) Moscow: Vyshchaya Shkola, 1974.

Russian Journal of Applied Chemistry, Vol. 74, No. 12, 2001, pp. 2122–2124. Translated from Zhurnal Prikladnoi Khimii, Vol. 74, No. 12, 2001, pp. 2062–2064.

BRIEF COMMUNICATIONS

Preparation of an Ion-Exchange Fiber by Polymer-Analogous Transformations in Polycaproamide–Polyglycidyl Methacrylate Grafted Chains

I. V. Lavnikova and V. F. Zheltobryukhov

Volgograd State Technical University, Volgograd, Russia

Received November 13, 2000; in final form, April 2001

Abstract—The possibility of preparing an ion-exchange fiber based on polycaproamide–polyglycidyl methacrylate graft copolymers was examined. Specific features of phosphorylation of epoxy groups in grafted polycaproamide–polyglycidyl methacrylate chains were revealed.

Natural and synthetic sorbents are widely used in scientific research and engineering, in particular, for treatment of exhaust gases and wastewater, with recovery of valuable substances. Chemisorbents are especially effective for these purposes [1]. Among the procedures developed for preparing ion-exchange fibers, graft polymerization followed by polymer-analogous transformations is one of the most promising [2, 3]. Preparation of ion exchangers by chemical transformations involves certain problems: the processes are multistage; toxic compounds are used; macromolecules of the initial polymers undergo partial degradation; and the chemical transformation is incomplete [4]. However, despite these drawbacks, it is possible to introduce into the side chains new functional groups by using polymer-analogous transformations and thus to prepare new polymeric materials with valuable properties.

Among a wide variety of monomers used in graft polymerization, mention should be made of glycidyl methacrylate (GMA). Glycidyl methacrylate contains reactive epoxy groups allowing subsequent polymer-analogous transformations in grafted polycaproamide–polyglycidyl methacrylate (PCA–PGMA) chains with the aim to incorporate new functional groups into the side chain of the copolymer [5].

In this study, we developed a procedure for preparing a complexing sorbent containing P–OH groups from the graft copolymer by phosphorylation of grafted PGMA chains.

As phosphorylating agent we used 1-hydroxyethylidenediphosphonic acid (HEDP) $C_2H_3(OH)[PO(OH)_2]_2$, a white crystalline powder, mp 198–199°C, readily soluble in water and organic solvents. Owing to a combination in the HEDP molecule of two phosphonic acid groups capable of complexation in strongly acidic solutions and hydroxyethyl group OH–C–CH_3, HEDP is a versatile complexing agent exhibiting complexing power in a wide pH range [6].

To develop an efficient procedure for preparing an ion-exchange fiber, we studied how the kinetic features of polymer-analogous transformations of PGMA affect the phosphorus content in the graft copolymer, the degree of transformation of epoxy rings, and the static exchange capacity (SEC).

Phosphorylation presumably follows the scheme

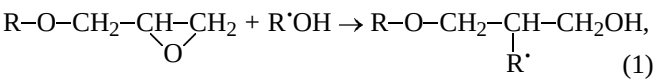

(1)

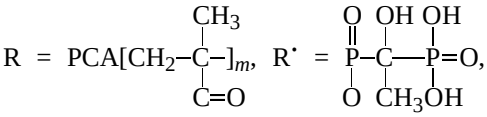

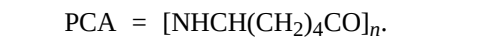

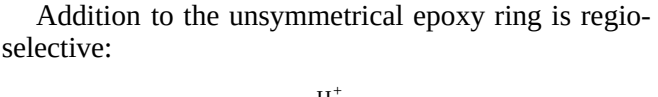

(2)

1070-4272/01/7412-2122 $25.00 © 2001 MAIK "Nauka/Interperiodica"

The RO group stabilizes the positive charge on the β-carbon atom; as a result, normal addition occurs with the formation of β-derivatives [8].

The heterophase reaction of the PCA–PGMA fiber with an aqueous solution of HEDP is influenced by such factors as HEDP concentration in solution, temperature and time of phosphorylation, and use of catalyst; the effect of each factor was studied separately.

The influence of HEDP concentration on the phosphorus content in the graft polycaproamide copolymer (GPC) and conversion of epoxy groups is illustrated by Table 1. As the HEDP concentration is increased from 0.81 to 4.04 M, the phosphorus content in the graft PGMA copolymer grows substantially. Further increase in the HEDP concentration is not appropriate, because the reaction decelerates. Furthermore, at HEDP concentrations higher than 4.86 M the fiber undergoes partial degradation.

The kinetic parameters of phosphorylation are listed in Table 2. These data show that the initial rate of phosphorylation is high in the examined range of HEDP concentrations. For example, the reaction rate is 0.28×10^{-4} mol l^{-1} s^{-1} at [HEDP] = 0.81 M, and 0.83×10^{-4} mol l^{-1} s^{-1} at [HEDP] = 4.04 M, with simultaneous increase in the phosphorus content in GPC to 2.7%. From the data obtained for the HEDP concentration range 0.81–4.04 M, we calculated using the procedure described in [7] the reaction order: $n = 1.92$.

Data on the effect of phosphorylation temperature on the content of phosphorus in graft PGMA copolymer are listed in Table 3. These data show that phosphorylation occurs at a high rate. It should be noted that, as the temperature is raised by 20°C, the reaction rate increases by a factor of 1.8. From the temperature dependence of the reaction rate constant, determined from the kinetic curves, we calculated the activation energy of the process: $E_a = 51.74$ kJ mol^{-1}. This value is nicely consistent with published data [8].

The amount of incorporated phosphorus strongly depends on the reaction time. The phosphorus content in GPC increases during 300 min, after which the process decelerates and fully stops in 350 min. Acid–base catalysts can accelerate phosphorylation of grafted PGMA chains. However, reactions of organophosphorus acids with epoxy compounds can also occur in the absence of catalyst [8]. Pyridine tested as catalyst had no appreciable effect on the phosphorus content in GPC. The phosphorus content was 2.9% at a pyridine content of 1 wt % relative to the polymer weight and 2.4% without pyridine; therefore, phosphorylation was performed without a catalyst.

Table 1. Influence of HEDP concentration on the amount of phosphorus in GPC C_P and on the conversion of epoxy groups*

[HEDP], M	C_P, %	Conversion, %
0.81	0.70	46.5
1.62	0.87	49.8
2.43	1.2	54.5
3.24	2.0	63.7
4.04	2.9	67.9
4.86	2.93	78.5

* PGMA concentration 43%, τ = 300 min, bath ratio 30, 90°C.

Table 2. Kinetic parameters of phosphorylation*

[HEDP], M	C_P, %	$V_{in} \times 10^4$	$V_{max} \times 10^4$
		mol l^{-1} s^{-1}	
0.81	1.4	0.28	0.4
1.62	1.9	0.5	1.0
4.04	2.7	0.83	1.6

* Reaction order $n = 1.92$.

Table 3. Effect of phosphorylation temperature T_P on the phosphorus content in GPC*

T_P, °C	C_P, %, at indicated reaction time, min						$V_{max} \times 10^4$, mol l^{-1} s^{-1}
	50	100	150	200	250	300	
70	0.8	0.9	1.0	1.3	1.5	1.5	1.4
80	1.25	1.6	1.9	2.0	2.3	2.5	2.0
90	1.5	1.7	2.0	2.3	2.5	2.98	2.6

* HEDP concentration 4.04 M.

Modification of PCA by graft polymerization was performed in an emulsion of HMA monomer (2.35 M) at 70°C for 60 min. The content of PGMA in the graft copolymer was 43–50 wt %. Subsequent polymer-analogous transformations of grafted PGMA chains allowed preparation of an ion-exchange fiber with the following characteristics: SEC 3.96 mg-equiv g^{-1}, relative breaking tensile load 24.3 cN tex^{-1}, breaking elongation 34.8%. The proposed procedure for chemical modification of PCA–PGMA allows preparation of new polymeric materials based on PCA.

EXPERIMENTAL

Modification of GPC was performed by its treatment with a 0.84–4.86 M HEDP solution at 70–90°C for 50–300 min in a flask equipped with a reflux con-

denser. After phosphorylation completion, the resulting copolymer was thoroughly washed with distilled water and dried to constant weight. The phosphorus content in the fiber was determined according to [9]. The total activation energy was calculated from the temperature dependence of K.

CONCLUSION

Incorporation of the P–OH group into the side chain of a macromolecule allows preparation of a fibrous sorbent capable of ion exchange and complexation.

REFERENCES

1. Zverev, M.P., *Khemosorbtsionnye volokna* (Chemisorption Fibers), Moscow: Khimiya, 1981.
2. Druzhinina, T.V., Tvorogova, M.M., and Mosina, N.Yu., *Khim. Volokna*, 1997, no. 3, pp. 13–16.
3. Druzhinina, T.V. and Nazar'ina, N.A., *Khim. Volokna*, 1997, no. 2, pp. 11–14.
4. Zubankov, L.V., Tevlina, A.S., and Davankov, A.V., *Sinteticheskie ionoobmennye materialy* (Synthetic Ion-Exchange Fibers), Moscow: Khimiya, 1978.
5. RF Patent 2 118 963.
6. Dyatlova, R.M., Telekina, V.Ya., and Panov, K.I., *Kompleksony i kompleksonaty metallov* (Complexones and Metal Complexonates), Moscow: Khimiya, 1988.
7. Emanuel', N.M. and Knorre, D.G., *Kinetika khimicheskikh protsessov: Uchebnoe posobie dlya khimiko-tekhnologicheskikh vuzov* (Kinetics of Chemical Processes: Textbook for Chemical and Technological Higher Schools), Moscow: Vysshaya Shkola, 1969, 2nd ed.
8. Shur, A.M., *Vysokomolekulyarnye soedineniya: Uchebnik dlya universitetov* (Macromolecular Compounds: Textbook for Universities), Moscow: Vysshaya Shkola, 1981, 3rd ed.
9. *Praktikum po khimii i fizike polimerov: Uchebnoe izdanie* (Practical Course of Polymer Chemistry and Physics: Textbook), Kurenkov, V.F., Ed., Moscow: Khimiya, 1990.

Russian Journal of Applied Chemistry, Vol. 74, No. 12, 2001, pp. 2125–2127. Translated from Zhurnal Prikladnoi Khimii, Vol. 74, No. 12, 2001, pp. 2065–2067.

BRIEF COMMUNICATIONS

Binary Oxide Systems in Catalytic Synthesis of 2-Methylpyrazine from 1,2-Propylene Glycol and Ethylenediamine

D. S. Balpanov, L. A. Krichevskii, and A. D. Kagarlitskii

Institute of Phytochemistry, Ministry of Education and Science of the Kazakhstan Republic, Karaganda, Kazakhstan
Buketov State University, Karaganda, Kazakhstan

Received August 16, 2001

Abstract—A series of binary catalysts based on oxides of zinc and variable-valence metals were tested in synthesis of 2-methylpyrazine by catalytic dehydrocyclization of 1,2-propylene glycol with ethylenediamine.

The growing incidence of tubercular diseases calls for improving the synthesis processes and increasing the production of tuberculostatic means. One of the most important antitubercular preparations is Pyrazinamide. Its active agent, which is also the starting compound for preparing low-toxic bacteriostatics [1], is pyrazine-2-carboxamide, prepared by oxidative ammonolysis of 2-methylpyrazine (MP) [2].

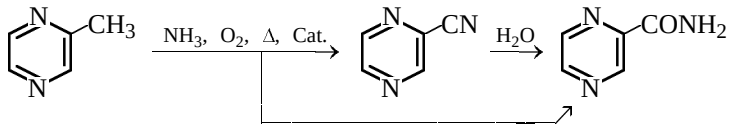

By now, fairly selective catalysts have been developed for oxidative ammonolysis of MP, allowing preparation, depending on reaction conditions, of either 2-cyanopyrazine [3] or 2-pyrazinamide [4] in yields of 80% and higher; however, there are no commercially acceptable procedures for synthesis of the starting compound.

The existing routes to MP, involving synthesis and subsequent dehydrogenation of 2-methylpiperazine [5] or reaction of propylene oxide with ethylenediamine at elevated pressure [6], are of no promise for commercial production of MP.

One of efficient routes to MP can be catalytic dehydrocyclization of ethylenediamine with 1,2-propylene glycol.

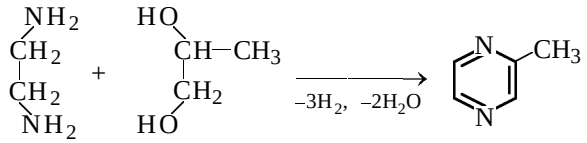

At present, the most frequently used cyclizing and dehydrogenating catalysts for this reaction are those based on oxides of Zn [7–9], Cu, or Cr(III) [10]; in their presence, the yield of MP reaches 60–70%. The best results are obtained with catalysts prepared by mixing the components to a pasty state, with subsequent extrusion and drying [8].

In this study, we tested MoO_3-modified zinc oxide catalysts prepared by such a procedure. The dependence of the MP yield on the catalyst composition and reaction temperature is illustrated by Fig. 1. We found that the catalyst containing ZnO and MoO_3 in 1 : 0.3 molar ratio ensures a yield of the target product as high as 75–80% in the temperature range 420–460°C.

However, we found that the catalysts prepared by extrusion are rapidly coked and require frequent regeneration, which results in the loss of mechanical strength and, finally, in decreased yield of the target product. The service life of such catalysts does not exceed 10 h.

To prolong the service life of the zinc–molybdenum catalysts and enhance their mechanical strength, the catalysts were prepared by pelletizing with sub-

1070-4272/01/7412-2125 $25.00 © 2001 MAIK "Nauka/Interperiodica"

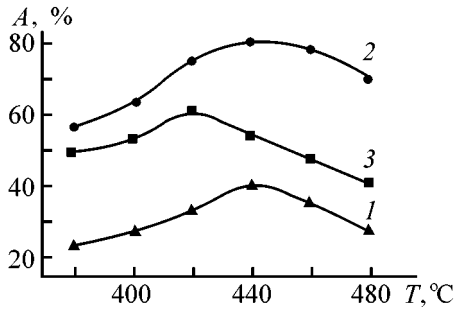

Fig. 1. MP yield *A* vs. temperature *T*. Catalyst $ZnO–MoO_3$ prepared by extrusion; $ZnO : MoO_3$ ratio: (*1*) 1 : 0.2, (*2*) 1 : 0.3, and (*3*) 1 : 0.4.

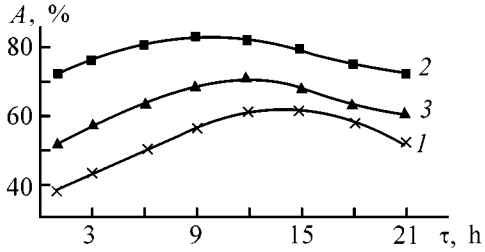

Fig. 2. Effect of the granulometric composition of the 1 : 0.3 $ZnO–MoO_3$ catalyst on the MP yield *A* at 460°C. (τ) Time of catalyst operation. Grain size, mm: (*1*) 0–1, (*2*) 1–2, and (*3*) 2–3.

sequent calcination. The results obtained with pelletized catalysts were similar to those obtained with the catalysts prepared by extrusion (see table). Although the mechanical strength increased considerably, the service life between regenerations decreased to 6 h, probably owing to a decrease in the specific surface area in the course of pelletizing.

MP yield at various compositions of binary catalysts. Feed space velocity 120 h^{-1}

Catalyst*	MP yield, %, at indicated temperature, °C					
	380	400	420	440	460	480
$ZnO : MoO_3$:						
1 : 0.2	23	27	34	42	37	30
1 : 0.3	58	63	74	82	79	67
1 : 0.4	53	57	62	55	50	44
$ZnO : V_2O_5$:						
1 : 0.2	22	31	40	45	37	31
1 : 0.3	30	46	58	50	43	35
1 : 0.4	27	39	49	47	38	34
$ZnO : WO_3$:						
1 : 0.1	29	38	42	51	55	50
1 : 0.2	27	33	38	43	52	50

* Molar ratio of the components is given.

Data in the table also show that we failed to improve the properties of zinc oxide catalysts by their modification with vanadium and tungsten oxides.

The results obtained in dehydrocyclization of 1,2-propylene glycol with ethylenediamine in the presence of $ZnO–MoO_3$ catalyst of the composition $ZnO : MoO_3$ = 1.0 : 0.3, prepared by granulation, deserve attention. The service life of this catalyst between regenerations, 20 h, is twice that of the catalyst prepared by extrusion. It should be noted that the optimal selectivity of this catalyst noticeably depends on the grain size (Fig. 2).

EXPERIMENTAL

Extrudates were prepared according to [11]. To obtain catalysts as pellets, the oxides were thoroughly mixed to uniform state and pressed at 100 atm (catalyst with WO_3, at 500 atm) in plunger dies with cell size of 4 × 4 mm. Pellets were dried at 105°C for 2 h, promoted with 1% $MnSO_4$ and 3% H_3PO_4 solutions [11], and again dried under the same conditions, with subsequent calcination in a muffle furnace at 650°C for 1 h.

For granulation, we used ZnO and MoO_3 with particle size of 10–40 and 40–60 μm, respectively. The oxides were mixed to uniform state and pelletized in a cup granulator by spraying a 5% NaOH solution in amount of 5–20% of the mixture weight. The resulting pellets were dried successively at 50–80 (2 h) and 100–150°C (2 h). The dried grains were sieved to obtain 0–1-, 1–2-, and 2–3-mm fractions and promoted similarly to the pellets prepared by pressing. Then the grains were dried for 2 h at 250°C.

The catalyst (extrudates, pellets, or grains) was charged in an amount of 150 cm^3 into a straight-flow reactor with a stainless steel tube (400 mm long, 20 mm i.d.), into which an equimolar mixture of ethylenediamine and 1,2-propylene glycol, diluted with 40 vol % water and preheated in a steam heater to 280–300°C, was fed at a space velocity of 120 h^{-1}. The reaction temperature was adjusted within 420–470°C; the reaction products were cooled in the trapping system.

MP was isolated from the reaction mixture as an azeotrope with water {bp 97°C (737 mm Hg), MP content 45% [12]}, from which the target product was recovered by extraction with chloroform or diethyl ether.

The reaction course was monitored by GLC (Chrom-5 chromatograph, flame-ionization detector, 2500 × 3-mm glass column, stationary phase 5% SE-30 on Chromaton N-AW-HMDS, column temperature 100°C, vaporizer temperature 180°C, detector temperature 190°C, carrier gas argon, flow rate 20 ml min^{-1}).

The constants of the isolated MP after distillation (bp 135°C, n_D^{20} 1.4967, d_4^{20} 1.030) were consistent with published data [13].

The mass spectrum of MP, taken on an MKh-1300 spectrometer (*m*/*z* 94, 67, 26, 39, 40, 53, 38, 42, 28, 41) confirms the structure of the synthesized MP [14].

CONCLUSIONS

(1) New zinc oxide catalysts modified with Mo, V, and W oxides were developed and tested in synthesis of 2-methylpyrazine from 1,2-propylene glycol and ethylenediamine.

(2) The selectivity of the mixed oxide catalyst $ZnO–MoO_3$ (molar ratio 1 : 0.3) with respect to 2-methylpyrazine is as high as 75–82% under the optimal conditions (420–460°C).

(3) The Zn–Mo–O catalyst produced by granulation has a considerably longer service life between regenerations than the catalysts prepared by pelletizing and extrusion.

REFERENCES

1. Vontor, T., Palat, K., and Odlerova, Z., *Cs. Farm.*, 1987, vol. 36, no. 6, pp. 277–280.
2. Krichevskii, L.A. and Kagarlitskii, A.D., Abstracts of Papers, *Konferentsiya "Prikladnye aspekty sovershenstvovaniya khimicheskikh tekhnologii i materialov"* (Conf. "Applied Aspects of Improvement of Chemical Technologies and Materials"), Biisk, 1998, part 1, pp. 27–31.
3. FRG Patent Appl. 3107756.
4. Kagarlitskii, A.D. and Krichevskii, L.A., in *Novosti organicheskoi khimii i uglekhimii Tsentral'nogo Kazakhstana* (News of Organic Chemistry and Coal Chemistry of Central Kazakhstan), Karaganda, 1983, pp. 115–117.
5. Isagulyants, G.V., Gitis, K.M., and Myasnikov, V.A., *Izv. Akad. Nauk SSSR, Ser. Khim.*, 1990, no. 7, pp. 1483–1486.
6. US Patent 4097478.
7. Kushner, S., *J. Am. Chem. Soc.*, 1952, vol. 74, no. 4, pp. 3617–3622.
8. Forni, L., *J. Catal.*, 1988, vol. 111, no. 1, pp. 199–209.
9. Gazaliev, A.M., Sim, E.P., Matveev, Yu.A., *et al.*, *Izv. Akad. Nauk Kaz. SSR, Ser. Khim.*, 1984, no. 5, pp. 78–80.
10. Shimizu, Sh., *J. Catal. Soc. Jpn.*, 1993, vol. 35, no. 1, pp. 21–29.
11. JPN Patent Appl. 54-132588.
12. Ogorodnikov, S.K., Lestova, T.M., and Kagan, V.B., *Azeotropnye smesi: Spravochnik* (Azeotropic Mixtures: Handbook), Leningrad: Khimiya, 1971, p. 72.
13. Kitchen, L.J. and Hanson, E.S., *J. Am. Chem. Soc.*, 1951, vol. 73, no. 2, p. 1838.
14. *Katalog sokrashchennykh mass-spektrov* (Catalog of Concise Mass Spectra), Novosibirsk: Nauka, 1981, p. 31.

Russian Journal of Applied Chemistry, Vol. 74, No. 12, 2001, pp. 2128–2129. Translated from Zhurnal Prikladnoi Khimii, Vol. 74, No. 12, 2001, pp. 2068–2069.

ANNIVERSARIES

Mikhail Grigor'evich Voronkov (To the 80th of his anniversary birthday)

On December 6, 2001, Academician Mikhail Grigor'evich Voronkov was 80. In the same year of 2001, 50 years elapsed since his first paper appeared in *Zhurnal Prikladnoi Khimii* (Russian Journal of Applied Chemistry) (*Zh. Prikl. Khim.*, 1951, vol. 24, no. 1, p. 93). During the last 50 years he has published in this journal exactly 100 papers.

Mikhail Grigor'evich Voronkov is a well-known scientist, a specialist in chemistry of organoelement compounds, organic, and physical organic chemistry.

From 1970 till 1994, Voronkov headed the Irkutsk Institute of Organic Chemistry, Siberian Division, Russian Academy of Sciences. Since 1995, he has been an advisor of the Russian Academy of Sciences and headed the Laboratory of organoelement compounds of the same institute.

Voronkov's scientific life has been very successful. A disciple of three prominent chemical schools headed by academicians A.E. Favorsky, N.D. Zelinsky, and V.N. Ipatyev, Mikhail Grigor'evich has carried out fundamental investigations in the field of chemistry of organosilicon and other organoelement compounds, organic derivatives of sulfur (one of reactions involving these compounds is named after him), and unsaturated and heteroatomic organic compounds. He has created a new field of the chemistry of silicon—bioorganic chemistry.

Voronkov's basic research in the field of chemistry, physical chemistry, biology and pharmacology of silatranes, and other compounds of hypervalent silicon has received particularly wide recognition in the USSR and abroad. Silatranes proved to be a new class of physiologically active substances and have already found wide use in agriculture and medicine. In 1997, Voronkov was awarded the State Prize of the Russian Federation for the creation and development of the chemistry of pentacoordinated silicon.

Voronkov was the first in the USSR to commence extensive studies of hydrophobization of various materials with organosilicon monomers and oligomers. In 1952–1958, he developed methods for hydrophobization of building materials, metals, glass, paper, woven fabrics, leather, and Circulite. In 1952, as a result of these investigations, the facade of the Marble Palace, the sculptural frieze of the Russian Museum, and a number of other sculptures and architectural decorations, and, later, facades of many other buildings in Leningrad, were treated with water-proofing agents. This was the beginning of water-proofing organosilicon coatings in building practice.

Voronkov developed methods for paper sizing with organosilicon compounds (Goznak factory, Leningrad, 1957); proposed an original organosilicon water-repellent agent and developed effective water-proofing agents MN and EN, which were manufactured at the pilot plant of the Institute of Organic Synthesis, Academy of Sciences of the Latvian SSR. He studied the stability of water-proofing organosilicon coatings against aggressive media, hydrothermal treatment, and thermal-oxidative breakdown.

In 1981, Voronkov was awarded State Prize of the USSR for the development and introduction of polymolecular organosilicon coatings.

Voronkov and his co-workers were the first to create dirt-repellent organosilicon coatings.

Organosilicon sorbents and ion-exchange resins were for the first time synthesized on the basis of carbofunctional organosilicon monomers of the $R(CH_2)_nSi(OR)_3$ type. Some of these sorbents are used to recover from strongly diluted solutions and

1070-4272/01/7412-2128 $25.00 © 2001 MAIK "Nauka/Interperiodica"

separate mercury, silver, gold, platinum metals and rare-earth elements. Plasmochemical methods for depositing doped films of silicon dioxide or silicon nitride onto the surface of semiconductor materials and circuits have been developed. Other ways have been found for using organosilicon monomers and oligomers in microelectronics. For these developments, Voronkov was awarded the Prize of the Council of Ministers of the USSR in 1991.

Voronkov developed and introduced a number of sulfide break-in, antiwear, and antiseizure lubricant oil and motor fuel additives.

A versatile aqueous quenching medium, which replaced the previously used mineral oils, was put in practice at the largest plants of the country.

Voronkov's original designs were introduced into practice in industry, agriculture, and medicine (biostimulants, adaptogens, catalysts for microbiological synthesis, water-repellent and bioprotective organosilicon coatings, sorbents and ion-exchangers, special materials for microelectronics. Versatile aqueous quenching medium, lubricant oil additives, hydrodynamic resistance–reducing polymers, materials for special technologies, etc.). A number of original medical products having no analogues world medicine (feracryl, argacryl, acizole, trecrezan, silakist, silimine, dibutyrine, cobasole, sibusole, etc.) have been created under his supervision.

In 1983, Voronkov was given the rank of "Honorary Chemist of the USSR" and his name was put into the Book of Honor of the Ministry of Chemical Industry of the USSR.

The results of sixty years of Voronkov's investigations are reflected in more than 2000 scientific papers, of which 200 have been published abroad, in 45 monographs (of which 15 have been published in the US, UK, Japan, GDR, Poland, Romania), and also in 60 reviews published in national and foreign editions and in wide variety of popular-science articles. He received about 500 USSR Inventor's Certificates and more than 50 foreign patents.

Voronkov combined his intensive scientific work with extensive scientific-organizational and public activities. In 1970–1994, he headed the Institute of Organic Chemistry, Siberian Division, Russian Academy of Sciences; from 1973 till 1984, he was deputy chairman of the Presidium of the Eastern-Siberian Branch (later, Irkutsk Scientific Center, Siberian Division, Academy of Sciences of the USSR); in 1982–1989, he was director general of Khimiya research-and-production association. In 1965, he became deputy chairman, and in 1986, chairman of the Scientific Council for "Chemistry and Technology of Organic Compounds of Sulfur" of the State Committee for Science and Technology of the USSR (later, Ministry of Industry, Science, and Technology of the Russian Federation). He is also an expert for science and technology of this ministry. Voronkov was elected a corresponding member of the Academy of Sciences of Latvian SSR in 1966, a corresponding member of the Academy of Sciences of the USSR in 1970, and full member of the Academy of Sciences of the USSR in 1990. He is a member of the editorial boards of *Zhurnal Obshchei Khimii* (Russian Journal of General Chemistry) and a number of international journals.

The international recognition of Voronkov's scientific merits was manifested in that he was elected a foreign member of the Latvian Academy of Sciences (1992), corresponding member of Braunschweig scientific society (FRG, 1976), *honoris causa* doctor (Poland, 1975), member of the international society for environmental research and health protection SIRES (France), honorary member of Florida Institute of Heterocyclic Chemistry (USA, 1998), and member of the chemical societies of Japan and Latvia. He was awarded a medal of the Academy of Sciences of the Mongolian People's Republic, Polar Star Order and Friendship medal (Mongolia).

Mikhail Grigor'evich is a veteran of the Great Patriotic War, participant of the defense of Leningrad; he was awarded Orders of Great Patriotic War, Red Banner of Labor, Peoples' Friendship, For Services to Motherland, and 18 medals.

Voronkov still demonstrates high capacity for work, wide variety of original scientific ideas, broad scope of scientific interests, great erudition, benevolent attitude toward colleagues, and inexhaustible humor. Voronkov continues his scientific activities at Irkutsk Institute of Chemistry, Siberian Division, Russian Academy of Sciences. He is advisor of the Russian Academy of Sciences and consultant of a number of chemical plants, scientific centers, and institutes in Russia, Ukraine, China, and Mongolia. Only during the year of 1997, he reported on his most recent investigations at three international conferences, and in 1998 and 2001, at two conferences each year.

The Editorial Board and Editorial staff of *Zhurnal Prikladnoi Khimii* heartily congratulate Mikhail Grigor'evich Voronkov, Doctor of chemical sciences, professor, and academician, on his eightieth birthday and wish him sound health, happiness, and further success.

Editorial Board and Editorial staff
of *Zhurnal Prikladnoi Khimii*

Russian Journal of Applied Chemistry, Vol. 74, No. 12, 2001, pp. 2130–2133. Translated from Zhurnal Prikladnoi Khimii, Vol. 74, No. 12, 2001, pp. 2070–2073.

INFORMATION

IV Scientific Conference "Development of Russia's Rare-Earth Industry on the Basis of Loparite"

IV Scientific Conference "Development of Russia's Rare-Earth Industry on the Basis of Loparite" with more than 110 participants from Russia, Ukraine, Kazakhstan, Estonia, and Austria was held in St. Petersburg on May, 22–24, 2001. This event was initiated by the Institute of Chemistry, Kola Scientific Center, Russian Academy of Sciences; Rosredmet AO (St. Petersburg), and Administration of Murmansk Oblast on whose territory lies a unique deposit of loparite ores. The main effort in organizing the conference was made by Rosredmet AO, a company that expressed most earnest intention to create a plant for manufacturing of tantalum, niobium, titanium, and rare-earth products on the basis of this deposit.

The preceding "loparite" conference was held more than ten years ago, when the USSR was one of the largest world's manufacturers of rare-earths, and the Lovozero deposit of loparite stably provided its raw materials to satisfy country's demand for tantalum, niobium, rare-earths and, in part, titanium. Cooperation of the Lovozero ore mining and processing combine, Solikamsk magnesium plant, Slantsekhimicheskii plant (Estonia), Ul'binsk metallurgical and Irtysh chemical-metallurgical plants (Kazakhstan) enabled manufacture of a wide assortment of products for electronics and electrical engineering, ferrous and nonferrous metallurgy, nuclear power engineering, petrochemistry, optics, and many other industries.

After 1991, stable connections between the plants were disrupted, part of the plants is out of action, and loparite manufacturer—Sevredmet AO is going bankrupt. Here, the largest Russia's tantalum reserve is concentrated: the Karnasurt mine is to serve during 30 years, and the Umbozero mine is provided with resources for 50 years. The loparite concentrate from Lovozero has been and still is the main source of niobium in the country. It contains 25% of the total Russia's reserve of rare earths. The titanium component of the loparite concentrate is also of vital importance.

Possessing the necessary raw material resources and substantial scientific potential, we virtually do not produce tantalum, and, as regards such a fundamentally important parameter as niobium consumption per ton of steel, Russia is exceeded by a factor of 6 by the European Community, 9-fold by the US, and by a factor of 11 by Japan. Rare-earths are virtually not produced at all. All this leads to a pronounced dependence of the country from foreign markets and, undoubtedly, could serve to exert pressure on the country in a complicated situation.

The conference program included 40 oral and 17 poster presentations. Three reports concerned with the basic problems considered at the conference were delivered at plenary sessions.

V.E. Kalinnikov's report (Apatity), opening the scientific part of the conference, made a brief historical review of the chemical technology of loparite. It emphasized that the complex nature of the raw material containing more than 80% valuable components required a combined approach to its processing and was a real challenge to chemists-technologists and specialists in closely related fields. Solving this problem required many years' effort of scientists headed by Ya.G. Goroshchenko, who laid foundation of acid methods for loparite concentrate processing. Then, during decades, technological schemes have been under development, which employed a wide variety of mineral acids, depending on plant location, economic situation, and necessity for manufacture of one or another product. The report compared the advantages and disadvantages of these schemes and the constituent operations and mentioned important scientific advances made in their development. The author formulated basic principles of construction of the optimal schemes for processing of complex titanium–rare-earth raw materials, having emphasized that the schemes must be combined to ensure the necessary and readily reshaped assortment, product quality, and environmental safety.

As the most efficient way to exploit the mineral resources of the Kola peninsula, the report considered the possibility of creating a regional ore mining and processing combine intended for maximum intensification of processing of conventional and new types of rare-earth raw materials.

A.V. Elutin (Moscow) considered in his report the state and prospects of the market of processed loparite

1070-4272/01/7412-2130 $25.00 © 2001 MAIK "Nauka/Interperiodica"

concentrate and the economy of their manufacture by various technological schemes. He noted that the ores of the Lovozero loparite deposit have been and still remain the main source of niobium, tantalum, and rare-earth products in the country, but only Lovozero mining company (LGK) and Solikamsk magnesium plant (SMZ), processing loparite by the chlorine method, remained in the chain from the previously existing, well-developed system of plant cooperation. A study of prospects for development of the market of finished products of the technology indicates an unlimited demand on the foreign markets for the tantalum and niobium components, excess of demand for rare-earths over their supply, and the expected increase in the domestic demand for tantalum, niobium, and rare earths by 2005.

The report proposed a scheme for meeting the demand with account of the capacity of reserves of these metals. The scheme is based on raising the manufacture of loparite, use of the production capacity of Silmet AO (Estonia), and creation of a new plant for concentrate processing in Russia. According to the author's estimates, the nitric acid–chloride technology seems to be the most promising in this regard. The report presented the results of economic calculations confirming the efficiency of the future enterprise.

The problem of the present state of the analytical facilities of the rare-metal industry and, in particular, of the analytical monitoring of the quality of the loparite concentrate and products of its processing were considered in the report presented by Yu.A. Karpov (Moscow). Analyzing the general trends in the development of analytical chemistry—transition from labor-consuming and slow classical chemical methods to high-performance instrumental techniques, he noted that the leading research institute of the industry and a number of plants participating in loparite processing were equipped with modern precision analytical instruments. In the author's opinion, the simultaneous presence in loparite of a wide variety of elements imposes quite a number of stringent and specific requirements on the analytical monitoring and makes more important atomic emission, atomic absorption, and X-ray fluorescence techniques. A prominent place is occupied by the atomic emission analysis with inductively coupled plasma, determining separately simultaneously present rare-earth elements by means of modern software. Analysis of high-purity objects, whose share in products obtained by processing rare-earth-metal raw materials is growing all over the world, is made by mass-spectrometric techniques. A specific feature of plasma mass-spectrometry is its versatility enabling quantitative analysis for a wide variety of elements with large to ultrasmall content and determining the isotopic composition of samples. A separate problem mentioned by the author is fabrication of reference composition samples, updating of the regulating documents, and accreditation of laboratories.

T.Yu. Usova (Moscow) analyzed the state of the world market of tantalum, niobium, and rare-earth elements of the cerium group and considered the reasons for a dramatic increase in prices of tantalum-containing ores and final products. Of particular interest was the report by L.Z. Bykhovskii (Moscow), concerned with the importance of loparite ores in the mineral resources and manufacture of rare metals.

Undoubtedly, manufacturers of tantalum and niobium products are working at improving their quality in order to reduce their cost and use them in new fields of technology. The influence exerted by the market of final products on the technology of tantalum and niobium was revealed in a report by E.G. Polyakov (St. Petersburg). M.A. Polyakova (Moscow) considered in her communication new fields of use of rare-earth metals of the cerium group. One of, undoubtedly, the most important issues concerning the technological and economic prerequisites for efficient work of a plant for loparite concentrate processing was discussed in a report by Z.D. Gritsai (St. Petersburg).

An objective assessment of investments in the development of mineral resources of the Lovozero deposit for obtaining titanium, tantalum, niobium, and rare-earth products is impossible without analyzing the state of the mining facilities for manufacture of the loparite concentrate. The problems and prospects of the mining facilities of the Lovozero deposit were considered in a detailed report by I.I. Bessonov (Apatity). The report of A.I. Rakaev (Apatity) was concerned with pretreatment of loparite ores before gravitational dressing, aimed at the maximum possible recovery of valuable components at their minimum possible disintegration.

New trends in creation of promising technological materials on the basis of chemical compounds of tantalum and niobium were the subject of the report by A.A. Titov (Moscow). The development of high-capacity tantalum capacitor powders, conditions of sodium-reduction of potassium heptafluorotantalate, effect of subsequent treatment on the physical, physicomechanical, and electrical characteristics of powders and sintered capacitor anodes were considered in a report by V.M. Orlov (Apatity).

Various methods for loparite concentrate decomposition were reflected in a considerable number of reports and gave rise to lively discussion. The main ways of development, unused possibilities, and prospects of the sulfuric acid technology of loparite and its chemical and technological foundations were discussed in their reports by L.I. Sklokin and D.L. Molotov (Apatity); nitric acid decomposition of the loparite concentrate, by A.N. Sviridov (Moscow); nitric acid–hydrofluoride processing of loparite, by S.V. Shestakov (St. Petersburg); nitric acid–hydrochloride technology, by V.A. Krokhin; chlorine technology, by A.V. Chub (Soikamsk); hydrochloride technology, by A.I. Nikolaev (Apatity); hydrofluoride technology, by L.I. Sklokin (Apatity); combined processing of loparite, including nitric acid decomposition, chlorine technology (fractionation and condensation) or hydrofluoride processing of the hydrated cake, by S.A. Pirkovskii (Moscow); and autoclave method of recovery with unconventional chlorine-containing agents, by Yu.L. Garmazov (Irkutsk).

Despite the wide variety of the presented technological schemes for decomposition of the loparite concentrate, each having its own advantages and disadvantages, the nitric acid scheme is, not counting the sulfuric acid and chlorine techniques, the best-developed and well-tried on the industrial scale. One of its indisputable advantages is the reliable separation of the rare-earth and rare-metal parts of the concentrate. This, together with the high recovery of valuable components, is a prerequisite for setting-up a plant for processing of industrial products formed upon decomposition to well-marketable commercial compounds of tantalum, niobium, titanium, and rare-earth elements, satisfying the requirements of the present-day market.

The conference participants paid close attention to the report by F.H. Bayerhold, a representative of Andritz AG Ruthner (Wien, Austria), "Pyrohydrolysis: Basic Principles and Use in Non-Ferrous and ferrous Metallurgy since the approaches used in his technique are applicable to a HNO_3/HF mixture and to fluoride media formed in selective leaching of Nb, Ti, and Ta. The report presented new developments of the company, intended for regeneration of a mixture of acids (PYROMARS) or HCl.

Five interesting reports concerned with extraction technology were presented by Institute of Rare Element and Mineral Chemistry and Technology, Kola Research Center, Russian Academy of Sciences (IKhTREMS KNTs RAN), (Apatity). The extraction recovery of tantalum and niobium compounds in hydrated cake processing in the technology of loparite and joint tests of the proposed extraction technology by Rosredmet AO and IKhTREMS KNTs RAN on a pilot installation created by Rosredmwet AO at Sevredmet AO (Revda settl., Murmansk Province) were discussed in two reports by A.I. Nikolaev; extraction purification of fluorotitanium solutions for loparite concentrate processing, by V.A. Tyuremnov; fundamental aspects of extraction of niobium, tantalum, and titanium extraction with octanol, by I.V. Baklanova; and extraction recovery of metals from solutions for hydrochloric acid leaching of the loparite concentrate, by N.I. Kasikova. The extraction technology of processing of rare-earth metal solutions obtained from the loparite concentrate was considered by E.B. Mikhlin (FGUP Giredmet, Moscow).

Among poster reports, mention should be made of a study of the crystal structure of loparite from the Lovozero alkaline deposit (A.V. Arakcheeva, Moscow) and the development of schemes for monitoring analytically the processing of loparite concentrate and the quality of final products (T.G. Kashulina, Apatity).

The reports on "Manufacture and Use of Nonsiliceous Ligatures in Industry" were delivered in a special section. M.M. Verklov (Moscow), A. A. Kosilov (St. Petersburg), and M.D. Lyubalin (St. Petersburg) considered in their reports the state and problems of manufacture of various alloys containing rare-earth metals for creating new brands of construction steels. Examples of successful use of products obtained in loparite concentrate processing in manufacture of nickel- and iron-based rare-earth ligatures were given in a report by B.M. Freidin (Apatity). The prospects for use of industrial products and wastes of the Severonikel' combine in manufacture of complex rare-earth ligatures were covered by A.G. Kasikov (Apatity). Much attention was attracted by the report by A.A. Vasil'ev (St. Petersburg) on the resumption of manufacture of nonsiliceous complex ligatures on nickel base and analysis of the state of their market in Russia and CIS countries. The author demonstrated that nonsiliceous complex ligatures, including rare-earth metals, titanium, and niobium obtained from loparite, ensure deep deoxidation and modification of steel. As a result, the strength characteristics, impact elasticity, wear resistance, cold-resistance of steel are enhanced, its grain size becomes smaller, and casting properties are improved.

During the conference, a round-table discussion was organized, including more than 20 representatives of industrial enterprises; it was recommended to expand the assortment of ligatures with account of customers' demand, pay attention to the quality of the

starting raw materials, search ways to make lower the ligature cost, analyze and generalize the comments of plants using ligatures. The participants of the section considered the first experience of discussion and opinion exchange, involving specialists from the industry, a success and proposed to use this form of conference work in the future.

The discussion of the delivered reports on the final day of the conference took, in fact, the shape of a general discussion of the state of affairs in Russia as regards the self-sufficiency of the country with respect to such strategically important metals as tantalum, niobium, titanium, and rare-earth metals. The speakers noted that the recent decade resulted in substantial changes in the market of rare metals—it increasingly belongs to high-tech products with wide variety of stringent and markedly different requirements to the chemical and physical characteristics of materials on rare metals. The participants spoke with anxiety about the disruption of customary connections between those who produce raw materials, process them, and manufacture final products, such as tantalum capacitor powders, and emphasized the necessity for coordination among them and activation of scientific research in this direction.

The resolution of the conference proposes that the Kola Scientific Center, Russian Academy of Sciences, and a number of other institutions should initiate setting a State program of interbranch research into the problem of loparite mining and processing, and efficient use of tantalum, niobium, and rare earths in high-tech fields of industry. To assess the proposed technological schemes of loparite processing, it is advisable to use the services of a specialized designing institute. The conference participants consider it necessary to ensure state and financial support of research and design work aimed to create a rare-metal plant working on loparite from the Lovozero deposit.

A decision was made to request the Ministry of Economic Development and the Ministry Industry and Science of the Russian Federation to support the efforts of plants that mine and process loparite at the Lovozero deposit, which is presently the main source of tantalum, niobium, and rare-earth metals in the country, including Solikamskii magnievyi zavod AO, Rossiiskie redkie metally AO, and Sevredmet AO.

E. G. Polyakov and L. P. Polyakova